
**Springer Handbook
of Atmospheric
Measurements**

Springer Handbooks provide a concise compilation of approved key information on methods of research, general principles, and functional relationships in physical and applied sciences. The world's leading experts in the fields of physics and engineering will be assigned by one or several renowned editors to write the chapters comprising each volume. The content is selected by these experts from Springer sources (books, journals, online content) and other systematic and approved recent publications of scientific and technical information.

The volumes are designed to be useful as readable desk book to give a fast and comprehensive overview and easy retrieval of essential reliable key information, including tables, graphs, and bibliographies. References to extensive sources are provided.

Springer Handbook of Atmospheric Measurements

Thomas Foken (Ed.)

With 752 Figures and 526 Tables



 Springer

Editor
Thomas Foken
University of Bayreuth
Bayreuth, Germany

ISBN 978-3-030-52170-7 e-ISBN 978-3-030-52171-4
<https://doi.org/10.1007/978-3-030-52171-4>

© Springer Nature Switzerland AG 2021

This work is subject to copyright. All rights are reserved by the Publisher, whether the whole or part of the material is concerned, specifically the rights of translation, reprinting, reuse of illustrations, recitation, broadcasting, reproduction on microfilms or in any other physical way, and transmission or information storage and retrieval, electronic adaptation, computer software, or by similar or dissimilar methodology now known or hereafter developed.

The use of general descriptive names, registered names, trademarks, service marks, etc. in this publication does not imply, even in the absence of a specific statement, that such names are exempt from the relevant protective laws and regulations and therefore free for general use.

The publisher, the authors and the editors are safe to assume that the advice and information in this book are believed to be true and accurate at the date of publication. Neither the publisher nor the authors or the editors give a warranty, express or implied, with respect to the material contained herein or for any errors or omissions that may have been made. The publisher remains neutral with regard to jurisdictional claims in published maps and institutional affiliations.

This Springer imprint is published by the registered company Springer Nature Switzerland AG.
The registered company address is: Gewerbestrasse 11, 6330 Cham, Switzerland

Foreword

Taking measurements in the atmosphere means to work in a “non-periodic”, chaotic environment. Consequently, it is impossible to repeat any measurements under same conditions, because every state of the atmosphere is unique and will never occur again. Another consequence is the basic impossibility to find a representative location for a measurement because of the non-linear scale interaction in the atmosphere. Processes on any scale interacts with those on all other scales. The basic requirement of reproducibility, any laboratory experiment has to meet, can, therefore, never be fulfilled by measurements in the atmosphere.

To address this dilemma atmospheric scientists have learned to think in spatial and time scales and to select such information from measurements which is relevant for the scale of interest. This is achieved by selecting suitable designs of the field experiments, station networks, instrumentation, and data processing. Therefore, the requirements on observation systems and the applied observation technologies are progressing continuously with the state of science and technology.

The World Meteorological Organization (WMO) has established under the “WMO Integrated Global Observing System” (WIGOS) a process to monitor these “rolling” requirements and to document them with the web-based “Observing Systems Capability Analysis and Review Tool” (OSCAR). OSCAR provides a structure along scales, applications, and variables and is an open tool to which everybody can contribute.

Systematic meteorological observations were established when scientists began to develop classifications (taxonomies) of natural phenomena. Up to day, we still use a cloud classification scheme inspired by the British pharmacist *Luke Howard*, who developed its basic version at the beginning of the nineteenth century. Meanwhile we have learned to describe and predict the state of the atmosphere with quantitative methods based on physical principles formulated with mathematical equations. Consequently, we are not able today to use phenomenological descriptions anymore. Today we need information on physically well-defined variables. From my perspective, this is the challenge for the further development of observing systems and the required measurement techniques. It is also an opportunity to improve and extend our knowledge about the atmosphere.

This book supplements the guidance provided by the intergovernmental Technical Commission for Observation, Infrastructure and Information Systems (COIIS) of the World Meteorological Organization (WMO), which is tasked as a specialized UN organization “to promote standardization of meteorological and related observations. . .” (Article 2 of WMO Convention).

Prof. Dr. Gerhard Adrian
President German Meteorological Service (DWD)
and World Meteorological Organization (WMO)



Gerhard Adrian
President DWD and WMO
(photo: © Bildkraftwerk-
Bela/DWD)

Preface

The *Springer Handbook of Atmospheric Measurements* is the result of many rounds of discussion with renowned scientists and the publisher, with the intention of developing a reference work that comprehensively covers all aspects of measurements in the atmosphere and at its interface with plants, soil, and water, including some general aspects of metrology. I was happy to bring to this project my nearly 50 years of experience in atmospheric measurements, with a strong focus on micrometeorology, and my more than 25 years of experience working in the standardization of meteorological measurements for VDI (The Association of German Engineers) and DIN (the German Institute of Standardization).

Several developments have made this handbook necessary and timely. Most of the classical in-situ instruments have been replaced by electrical measuring devices. Not only has the toxicity of mercury led to international agreements preventing its use in barometers and thermometers, but the reduction in visual weather observations has resulted in a requirement for low-maintenance electrical sensors and automatic stations. Besides the use of discrete sensors for the various meteorological elements at classical weather and climate stations, more compact sensors are now available. These incorporate all of the sensors into a small weather station with dimensions of 10–30 cm. Furthermore, so-called smart sensors with wireless connectivity and satellite positioning data enable anyone to measure meteorological parameters. The issue of quality control is then shifted from the single sensor to the network, and the crowdsourcing approach necessitates intelligent software to separate biased from accurate data.

Remote sensing instruments were the exclusive domain of meteorological services or scientific institutions, but more recently they have—with the exception of some very complicated instruments and instruments that are in development—passed into more general use. Besides weather radar, ceilometers and radar wind profilers have recently become standard instrumentation in meteorological networks. The fast development of the wind power industry has supported the development of Doppler wind lidars, and these instruments have become much smaller and even relatively inexpensive.

Similarly, throughout their long history, meteorological observations have been the task of meteorologists alone—until recently. Nowadays, agencies that carry out environmental monitoring use meteorological data and have their own networks, as does industry.

With the ability to measure fluxes, ecologists have become an important group that apply atmospheric measurements. The handbook therefore also includes specific measurements at the interface between the atmosphere and the biosphere and pedosphere.

As already mentioned, quality control and standardization are important procedures for ensuring that highly accurate meteorological information with high spatial resolution is made available. This is not only a task for calibration laboratories. It is important that the developers and implementers of software tools understand the complicated structure of the atmosphere in terms of the vertical and horizontal fields of meteorological elements, particularly in heterogeneous areas such as cities and their surroundings.

This handbook is divided into five parts. Part A is an introduction to the handbook, with chapters covering the structure of the atmosphere, the basics of measurements, the fundamentals of quality control, and the standardization of measurements. Furthermore, quantities that are necessary for measurements in the atmosphere and the soil are provided in abundant tables. Some of those tables are also available online. All quantities are given in accordance with the International Temperature Scale (ITS-90).

Part B includes all in-situ measurement methods, and starts with an overview of ground-based platforms. Besides classical measurements such as temperature, humidity, wind, pressure, radiation, precipitation, and visibility, sensors for electricity, trace gases, aerosols, stable isotopes, and radioactivity are also described. Only basic information is provided for the latter category because other monographs are available for trace gas and aerosol measurements. A final chapter covers the relatively new technique of optical-fiber-based measurements in addition to classical odor and visual observations.

Parts C and D are devoted to remote sensing techniques, which are separated into ground-based and aircraft/satellite-based techniques. An introduction to airborne platforms is included. The discussion of ground-based measurements (Part C) includes sodar, RASS, different types of lidar, radar, scintillometers, spectrometric methods that use light of different wavelengths and microwaves. Furthermore, tomographic methods that use sound waves, and electromagnetic waves of satellite navigation systems, are chapters of the handbook. Because aircraft- and satellite-based methods have become more and more important for an-

alyzing a very large number of meteorological elements and properties of the Earth's surface, they are considered separately in Part D, in spite of some overlap with earlier discussions of lidar, radar, and methods based on microwaves, visible light, or infrared light.

Part E is largely atypical for a book concerning atmospheric measurements. It describes the combination of different sensors for specific applications and measurements at the interface between the atmosphere and the underlying surface. First, horizontally distributed observations—including classical weather stations, crowdsourcing, and mesometeorological networks—are considered, followed by vertical measurement systems such as aerological measurements and composite profiling. Here, horizontally moving systems are aircraft, unmanned aircraft systems, and ground-based moving systems. Subsequent chapters focus on special applications such as measurements of different types of renewable energy and urban measurements, and then on measurement techniques for and applications of fluxes: fog deposition, dry deposition, the eddy-covariance technique and similar measurements, lysimeter and evapotranspiration measurements and calculations, and chamber measurements at plants and the soil surface. Finally, short chapters describe measurements in soil and water.

Part F—the final part of this handbook—discusses networks, which play important roles in rendering measurements comparable and achieving a high standard of measurement quality. The two chapters in Part F give an overview of networks of atmospheric and ecological measurements.

Given the timeframe of the present edition of this handbook, it was not possible to provide complete coverage of all instruments used for atmospheric measurements. However, the editor and Springer are hopeful that, in a future edition, the minor gaps in coverage will be filled by recruiting authors who are able to take on the time-consuming task of providing new chapters on instruments not discussed here.

Some comments on the organization of this handbook may be helpful. Most of the chapters are struc-

ured in the same way for easier orientation of the reader, although the subject matter of some chapters meant that they could only broadly follow this schema. Section 1 of each chapter gives a short overview of the measured variables and their dimensions as well as the main measurement principles. Section 2 is a historical part, which we included not only because this is quite interesting but also because many techniques have not been in use for the last 10–50 years. For currently used measurement methods, Section 3 presents the theory and Section 4 the applicable devices. In most of the chapters, the advantages and disadvantages of the various relevant sensors or methods are also listed at the end of Section 4. In the majority of the chapters, Section 5, on specifications, allows the reader to rapidly review the measurement ranges, accuracies, or response times of the devices and methods in tabulated form. Quality control, calibration, and reference standards are discussed in Section 6, and Section 7 gives an overview of necessary maintenance actions along with the appropriate time intervals. Some selected examples of applications of the devices and methods are shown in Section 8, and further developments are discussed in Section 9. Monographs, overview papers, and standards are available for many of the techniques, and these are listed in the Further Reading section. Every chapter ends with a long list of references.

I want to thank the 140 authors and, in particular, the corresponding authors for their significant contributions to this handbook, as well as the more than 60 reviewers for their helpful reviews of all chapters. Many thanks are due to Dr. Judith Hinterberg for developing the concept of the handbook, and to Ursula Barth, both from Springer Nature Heidelberg, for the intensive communication with me and the authors and Jeannette Krause (le-tex, Leipzig) for the preparation of the final manuscript. Last but not least, I thank my wife and our family for their sympathy and support of this project over the last four years.

Bayreuth, Germany
August 2021

Thomas Foken

About the Editor

Thomas Foken is retired Professor of Micrometeorology at the University of Bayreuth (Bayreuth Center of Ecology and Environmental Research), Germany. He obtained his doctoral degree (Dr rer nat) from Leipzig University in 1978 and his second doctoral degree (Dr sc nat) from the Humboldt University of Berlin in 1990. He headed the Laboratories of Boundary Layer Research and Land Surface Processes of the Meteorological Service of the GDR and the German Meteorological Service (DWD) at the Observatories at Potsdam (1981–1994) and Lindenberg (1994–1997). In 1997, Thomas Foken was appointed Professor of Micrometeorology at the University of Bayreuth. He has taught courses on micrometeorology in Berlin, Potsdam, and Bayreuth. His main research areas are related to the interaction between the Earth's surface and the atmosphere, and the measurement and modeling of energy and matter fluxes, with a strong focus on measurement devices. He has organized and participated in experiments at the international level, e.g. in Russia, USA, Tibet, and Antarctica. He has published in peer-reviewed journals as well as textbooks and has made significant advancements in the application of the eddy-covariance method. These scientific contributions have been recognized through various awards, including the Dionyz Stur Medal in Silver of the Slovak Academy of Science, the Award for Outstanding Achievements in Biometeorology of the American Meteorological Society, the Honor Badge of the Association of German Engineers (VDI), and Honorary Membership of the Hungarian Meteorological Society. In recent years, he has been consultant for Arctic and forest fire projects, and lecturer at the Eötvös Loránd University Budapest. In Germany, Thomas Foken is responsible for the standardization of atmospheric in-situ measurement techniques (VDI/DIN, ISO). As a specialist for climate and climate change in Northern Bavaria, he is regularly invited to give lectures for school students at events organized by the Fridays for Future movement.



Thomas Foken
(photo: U. Krzywinski)

About the Authors

Bianca Adler

NOAA/Physical Sciences Laboratory
CIRES, University of Colorado Boulder
Boulder, CO, USA
bianca.adler@noaa.gov

Richard Allen

Soil and Water Systems
University of Idaho
Kimberly, USA
rallen@uidaho.edu

Christof Ammann

Climate and Agriculture
Agroscope Research Institute
Zürich, Switzerland
christof.ammann@agroscope.admin.ch

Marc Aubinet

TERRA Teaching and Research Centre
University of Liege
Gembloux, Belgium
marc.aubinet@uliege.be

Jens Bange

Centre for Applied Geo-Science
University of Tübingen
Tübingen, Germany
jens.bange@uni-tuebingen.de

Karsten Baumann

Environmental Sciences and Engineering
University of North Carolina at Chapel Hill
Chapel Hill, USA
kbaumann@unc.edu

Andreas Behrendt

Institute of Physics and Meteorology
University of Hohenheim
Stuttgart, Germany
andreas.behrendt@uni-hohenheim.de

Klaus Behrens

Nuthetal, Germany
klaus.behrens@mailbox.org

Michael Bender

FE12 Datenassimilation
German Meteorological Service (DWD)
Offenbach, Germany
michael.bender@dwd.de

Alec Bennett

Biral
Portishead, UK
alec.bennett@biral.com

Frank Beyrich

Meteorologisches Observatorium Lindenberg –
Richard-Aßmann-Observatorium
Lindenberg, Germany
frank.beyrich@dwd.de

Jacqueline Bieringer

Atmospheric Radioactivity and Trace Analysis
Federal Office for Radiation Protection
Freiburg, Germany
jbieringer@bfs.de

Christina Bogner

Institute of Geography
University of Cologne
Cologne, Germany
christina.bogner@uni-koeln.de

Annette Borowiak

Air and Climate Unit
Joint Research Centre
Ispra, Italy
annette.borowiak@ec.europa.eu

Jerald A. Brotzge

New York State Mesonet
University at Albany
Albany, USA
jbrotzge@albany.edu

Steven S. Brown

NOAA Chemical Sciences Laboratory
Boulder, USA
steven.s.brown@noaa.gov

William Brown

Earth Observing Laboratory
National Center for Atmospheric Research
Boulder, USA
wbrown@ucar.edu

Henk A.R. Bruin

Bilthoven, The Netherlands
hardb@xs4all.nl

Matthias Budde

Institute of Telematics, TECO / Chair for Pervasive Computing Systems
Karlsruhe Institute of Technology (KIT)
Karlsruhe, Germany
and
Disy Informationssysteme GmbH
Karlsruhe, Germany
matthias.budde@disy.net

Arianna Cauteruccio

DICCA – Dep. Civil, Chemical and Environmental Engineering
University of Genova
Genova, Italy
arianna.cauteruccio@edu.unige.it

Jan Cermak

Institute of Meteorology and Climate Research and Institute of Photogrammetry and Remote Sensing
Karlsruhe Institute of Technology (KIT)
Karlsruhe, Germany
jan.cermak@kit.edu

Shih-Chieh Chang

Department of Natural Resources and Environmental Studies, Center for Interdisciplinary Research on Ecology and Sustainability
National Dong Hwa University
Hualien, Taiwan
scchang@gms.ndhu.edu.tw

Matteo Colli

DICCA – Dep. Civil, Chemical and Environmental Engineering
University of Genova
Genova, Italy
matteo.colli@unige.it

Heinz Coners

Plant Ecology and Ecosystems Research
University of Göttingen
Göttingen, Germany
hconers@uni-goettingen.de

Susanne Crewell

Institute for Geophysics and Meteorology
University of Cologne
Köln, Germany
susanne.crewell@uni-koeln.de

Matthias Cuntz

UMR Silva
Université de Lorraine, AgroParisTech, INRAE
Nancy, France
matthias.cuntz@inrae.fr

Axel Delan

IFU GmbH Privates Institut für Analytik
Frankenberg, Germany
axel.delan@ifu-analytik.de

Julien Delanoë

LATMOS/IPSL, UVSQ Université Paris-Saclay, Sorbonne Université, CNRS
Guyancourt, France
julien.delanoë@latmos.ipsl.fr

Raymond L. Desjardins

Science and Technology Branch
Agriculture and Agri-Food Canada
Ottawa, Canada
ray.desjardins@canada.ca

Galina Dick

GFZ German Research Centre for Geosciences, Department 1: Geodesy
Helmholtz Centre Potsdam
Potsdam, Germany
galina.dick@gfz-potsdam.de

Anna Dzvankovskaya

Helzel Messtechnik GmbH
Kaltenkirchen, Germany
dzvankovskaya@gmail.com

André Ehrlich

Leipzig Institute for Meteorology (LIM)
University of Leipzig
Leipzig, Germany
a.ehrlich@uni-leipzig.de

Scott Ellis

Research Applications Laboratory
National Center for Atmospheric Research
Boulder, USA
sellis@ucar.edu

Stefan Emeis

Institute of Meteorology and Climate Research
Karlsruhe Institute of Technology (KIT)
Garmisch-Partenkirchen, Germany
stefan.emeis@kit.edu

Florian Ewald

Institut für Physik der Atmosphäre
Deutsches Zentrum für Luft- und Raumfahrt e. V.
(DLR)
Weßling, Germany
florian.ewald@dlr.de

Christopher A. Fiebrich

Oklahoma Mesonet/Oklahoma Climatological
Survey
University of Oklahoma
Norman, USA
fiebrich@ou.edu

Anita Flohr

Ocean and Earth Science
University of Southampton
Southampton, UK
a.flohr@southampton.ac.uk

Thomas Foken

University of Bayreuth
Bayreuth, Germany
thomas.foken@uni-bayreuth.de

Wolfgang Foken

Automotive Engineering
University of Applied Sciences in Zwickau
Zwickau, Germany
wolfgang.foken@online.de

Jeffrey French

Department of Atmospheric Science
University of Wyoming
Laramie, USA
jfrench@uwyo.edu

Julia Fuchs

Institute of Meteorology and Climate Research
and Institute of Photogrammetry and Remote
Sensing
Karlsruhe Institute of Technology (KIT)
Karlsruhe, Germany
julia.fuchs@kit.edu

Masatomo Fujiwara

Faculty of Environmental Earth Science
Hokkaido University
Sapporo, Japan
fuji@ees.hokudai.ac.jp

Ulrich Görndorf

Meteorologisches Observatorium Lindenberg –
Richard Aßmann Observatorium
German Meteorological Service (DWD)
Lindenberg, Germany
ulrich.goersdorf@dwd.de

Sue Grimmond

Department of Meteorology
University of Reading
Reading, UK
c.s.grimmond@reading.ac.uk

Martin Hagen

Institut für Physik der Atmosphäre
Deutsches Zentrum für Luft- und Raumfahrt e. V.
(DLR)
Weßling, Germany
martin.hagen@dlr.de

Samuel Haimov

Atmospheric Science Department
University of Wyoming
Laramie, USA
haimov@uwyo.edu

R. Michael Hardesty

Cooperative Institute for Research in
Environmental Sciences
University of Colorado Boulder
Boulder, USA
r.michael.hardesty@colorado.edu

Giles Harrison

Department of Meteorology
University of Reading
Reading, UK
r.g.harrison@reading.ac.uk

Oscar K. Hartogensis

Environmental Sciences – Meteorology and Air
Quality
Wageningen University
Wageningen, The Netherlands
oscar.hartogensis@wur.nl

Matthew Hayman

Earth Observing Laboratory
National Center for Atmospheric Research
Boulder, USA
mhayman@ucar.edu

Dwayne Heard

School of Chemistry
University of Leeds
Leeds, UK
d.e.heard@leeds.ac.uk

Andreas Held

Environmental Chemistry and Air Research
Technische Universität Berlin
Berlin, Germany
held@tu-berlin.de

Olaf Hellmuth

Modeling Department
TROPOS Leibniz Institute for Tropospheric Research
Leipzig, Germany
olaf.hellmuth@tropos.de

Gerald Heymsfield

Mesoscale Atmospheric Processes Laboratory
Goddard Space Flight Center
Greenbelt, USA
gerald.heymsfield@nasa.gov

Klaus Heyn

Sensing Technologies
Vaisala GmbH
Hamburg, Germany
klaus.heyn@vaisala.com

Jochen Horstmann

Ocean Surface Dynamics
Institute of Coastal Ocean Dynamics of the
Helmholtz-Zentrum hereon, Germany
Geesthacht, Germany
jochen.horstmann@hereon.de

Bernd Huwe

Soil Physics
University of Bayreuth
Bayreuth, Germany
bernd.huwe@uni-bayreuth.de

Andreas Ibrom

Environmental Engineering
Technical University of Denmark (DTU)
Lyngby, Denmark
anib@env.dtu.dk

Simon Jäckel

VDI e.V. – The Association of German Engineers
Düsseldorf, Germany
jaeckel@vdi.de

Jürgen Junk

Environmental Research and Innovation (ERIN)
Luxembourg Institute of Science and Technology
(LIST)
Belvaux, Luxembourg
juergen.junk@list.lu

Norbert Kalthoff

Institute of Meteorology and Climate Research,
Department Troposphere
Karlsruhe Institute of Technology (KIT)
Karlsruhe, Germany
no.kalthoff@web.de

Ayse Kilic

School of Natural Resources and Dept. Civil
Engineering
University of Nebraska–Lincoln
Lincoln, USA
akilic@unl.edu

Bruce Kindel

Laboratory for Atmospheric and Space Physics
University of Colorado at Boulder
Boulder, USA
bruce.kindel@lasp.colorado.edu

Olaf E. E. Kolle

Field Experiments and Instrumentation
Max-Planck-Institute for Biogeochemistry
Jena, Germany
olaf.kolle@bgc-jena.mpg.de

Christoph Kottmeier

Institute of Meteorology and Climate Research,
Department Troposphere
Karlsruhe Institute of Technology (KIT)
Karlsruhe, Germany
christoph.kottmeier@kit.edu

Lars Kutzbach

Institute of Soil Science
Universität Hamburg
Hamburg, Germany
lars.kutzbach@uni-hamburg.de

Gerhard Lammel

Multiphase Chemistry Department
Max Planck Institute for Chemistry
Mainz, Germany
g.lammel@mpic.de

Luca G. Lanza

DICCA – Dep. Civil, Chemical and Environmental Engineering
University of Genova
Genova, Italy
luca.lanza@unige.it

Volker Lehmann

Meteorologisches Observatorium Lindenberg
German Meteorological Service (DWD)
Lindenberg, Germany
volker.lehmann@dwd.de

Ingeborg Levin

Institut für Umweltphysik
Heidelberg University
Heidelberg, Germany
ingeborg.levin@iup.uni-heidelberg.de

Martin Löffler-Mang

School of Engineering
htw saar, University of Applied Sciences
Saarbrücken, Germany
loeffler-mang@htwsaar.de

Ulrich Löhnert

Institute for Geophysics and Meteorology
University of Cologne
Köln, Germany
ulrich.loehnert@uni-koeln.de

Ian MacPherson

National Research Council of Canada
Ottawa, Canada
ian.macpherson@rogers.com

Alexander Mangold

Scientific Service Observations
Royal Meteorological Institute of Belgium
Brussels, Belgium
alexander.mangold@meteo.be

Matthias Mauder

Institute of Hydrology and Meteorology
Technische Universität Dresden
Dresden, Germany
matthias.mauder@tu-dresden.de

Mario Mech

Institute for Geophysics and Meteorology
University of Cologne
Köln, Germany
mario.mech@uni-koeln.de

Stefan Metzger

National Ecological Observatory Network (NEON);
Battelle
Boulder, USA
smetzger@battelleecology.org

Volker Mohrholz

Physical Oceanography and Instrumentation
Leibniz-Institute for Baltic Sea Research
Warnemünde
Rostock, Germany
volker.mohrholz@io-warnemuende.de

J. William Munger

John A. Paulson School of Engineering and Applied Sciences
Harvard University
Cambridge, USA
jwmunger@seas.harvard.edu

Christoph Münkel

Vaisala GmbH
Hamburg, Germany
cmuenkel@web.de

Axel Murk

Institute of Applied Physics
University of Bern
Bern, Switzerland
axel.murk@iap.unibe.ch

Sascha Nehr

European University of Applied Sciences
Brühl, Germany
s.nehr@eufh.de

Reinhard Nolz

Institute for Soil Physics and Rural Water Management
University of Natural Resources and Life Sciences,
Vienna
Wien, Austria
reinhard.nolz@boku.ac.at

Samuel Ortega-Farías

Research and Extension Center for Irrigation and Agroclimatology (CITRA)
Universidad de Talca
Talca, Chile
sortega@utalca.cl

Eberhard Parlow

Department of Environmental Sciences
Atmospheric Sciences
University Basel
Basel, Switzerland
eberhard.parlow@unibas.ch

Elizabeth Pattey

Science and Technology Branch
Agriculture and Agri-Food Canada
Ottawa, Ontario, Canada
elizabeth.pattey@canada.ca

Kyaw Tha Paw U

Land, Air and Water Resources
University of California
Davis, CA, USA
ktpawu@ucdavis.edu

Andrew L. Pazmany

ProSensing Inc.
Amherst, USA
pazmany@prosensing.com

Oscar Perez-Priego

Biological Science
Macquarie University
Sydney, NSW, Australia
oscarperezpriego@gmail.com

Gerhard Peters

Metek, Meteorologische Messtechnik GmbH
Elmshorn, Germany
peters@metek.de

Ralf Petrich

IFU GmbH Privates Institut für Analytik
Frankenberg, Germany
ralf.petrich@ifu-analytik.de

Rolf Philipona

Federal Office of Meteorology and Climatology
MeteoSwiss
Davos Dorf, Switzerland
rolf.philipona@gmail.com

Peter Pilewskie

Laboratory for Atmospheric and Space Physics and
Department of Atmospheric and Oceanic Sciences
University of Colorado Boulder
Boulder, USA
peter.pilewskie@lasp.colorado.edu

Andreas Platis

Centre for Applied Geo-Science
University of Tübingen
Tübingen, Germany
andreas.platis@uni-tuebingen.de

Christopher Pöhlker

Multiphase Chemistry Department
Max Planck Institute for Chemistry
Mainz, Germany
c.pohlker@mpic.de

Catherine Prigent

LERMA
CNRS, Observatoire de Paris
Paris, France
catherine.prigent@obspm.fr

Armin Raabe

Leipzig Institute for Meteorology (LIM)
University of Leipzig
Leipzig, Germany
raabe@uni-leipzig.de

Corinna Rebmann

Department Computational Hydrosystems
Helmholtz Centre for Environmental Research
Leipzig, Germany
corinna.rebmann@ufz.de

Oliver Reitebuch

Institut für Physik der Atmosphäre
Deutsches Zentrum für Luft- und Raumfahrt e. V.
(DLR)
Weßling, Germany
oliver.reitebuch@dlr.de

Sascha Reth

UGT GmbH
Hallbergmoos, Germany
sascha.reth@ugt-online.de

Joachim Reuder

Geophysical Institute, and Bjerknes Centre for
Climate Research
University of Bergen
Bergen, Norway
joachim.reuder@gfi.uib.no

Janne Rinne

Department of Physical Geography and Ecosystem
Science
Lund University
Lund, Sweden
janne.rinne@nateko.lu.se

David Risk

Earth Sciences
St. Francis Xavier University
Antigonish, Canada
drisk@stfx.ca

Christoph Ritter

Physics of the Atmosphere
Alfred-Wegener-Institute
Potsdam, Germany
christoph.ritter@awi.de

Raymond Rülke

Langendorf, Germany

Klaus Schäfer

Atmospheric Physics Consultant
Garmisch-Partenkirchen, Germany
schaefer@atmosphericphysics.de

Robert S. Schemenauer

FogQuest: sustainable water solutions
Kamloops, Canada
fogquest@shaw.ca

Hans Peter Schmid

Institute of Meteorology and Climate Research –
Atmospheric Environmental Research
Karlsruhe Institute of Technology (KIT)
Garmisch-Partenkirchen, Germany
hape.schmid@kit.edu

K. Sebastian Schmidt

Laboratory for Atmospheric and Space Physics
University of Colorado at Boulder
Boulder, USA
sebastian.schmidt@lasp.colorado.edu

John Selker

Oregon State University
Corvallis, USA
john.selker@oregonstate.edu

Jörg E.E. Seltmann

Hohenpeissenberg Observatory
German Meteorological Service (DWD)
Hohenpeissenberg, Germany
joerg.seltmann@yandex.com

Dietrich Sonntag

Berlin, Germany

Scott M. Spuler

Earth Observing Laboratory
National Center for Atmospheric Research
Boulder, USA
spuler@ucar.edu

Brian Stacey

Ricardo Energy and Environment
Didcot, UK
brian.stacey@ricardo.com

Mattia Stagnaro

DICCA – Dep. Civil, Chemical and Environmental
Engineering
University of Genova
Genova, Italy
mattia.stagnaro@unige.it

Manuela Starke

Chair of Meteorology
Technische Universität Dresden
Tharandt, Germany
manuela.starke@tu-dresden.de

Thomas Steinkopff

Surveillance of Radioactivity
German Meteorological Service (DWD)
Offenbach, Germany
tommy_theater@t-online.de

Ulrich Stöhlker

IMIS measurement tasks
Federal Office for Radiation Protection
Freiburg, Germany
ustoehlker@bfs.de

Cove Sturtevant

National Ecological Observatory Network (NEON);
Battelle
Boulder, USA
csturtevant@battelleecology.org

Jens-Arne Subke

Biological and Environmental Sciences
University of Stirling
Stirling, UK
jens-arne.subke@stir.ac.uk

Christoph K. Thomas

Micrometeorology
University of Bayreuth
Bayreuth, Germany
christoph.thomas@uni-bayreuth.de

Anni Torri

Vaisala Oyj
Vantaa, Finland
anni.torri@vaisala.com

Ivonne Trebs

Environmental Research and Innovation (ERIN)
Luxembourg Institute of Science and Technology (LIST)
Belvaux, Luxembourg
ivonne.trebs@list.lu

Ricardo Trezza

California Irrigation Management Information System (CIMIS)
California Department of Water Resources
Sacramento, USA
ricardo.trezza@water.ca.gov

Isabel F. Trigo

Portuguese Institute for the Sea and the Atmosphere (IPMA)
Lisboa, Portugal
isabel.trigo@ipma.pt

Holger Vömel

Earth Observing Laboratory
National Center for Atmospheric Research
Boulder, USA
voemel@ucar.edu

Emanuele Vuerich

Italian Air Force
Rome, Italy
emanuele.vuerich@aeronautica.difesa.it

Helen C. Ward

Department of Atmospheric and Cryospheric Sciences
University of Innsbruck
Innsbruck, Austria
helen.ward@uibk.ac.at

Konradin Weber

Laboratory for Environmental Measurement Techniques
Duesseldorf University of Applied Sciences
Duesseldorf, Germany
konradin.weber@hs-duesseldorf.de

Tammy M. Weckwerth

Earth Observing Laboratory
National Center for Atmospheric Research
Boulder, USA
tammy@ucar.edu

Manfred Wendisch

Physics and Earth Sciences
University of Leipzig
Leipzig, Germany
m.wendisch@uni-leipzig.de

Mark Wenig

Department of Physics, Meteorological Institute Munich
Ludwig-Maximilians-University Munich
Munich, Germany
mark.wenig@lmu.de

Lisa K. Whalley

School of Chemistry
National Centre for Atmospheric Science,
University of Leeds
Leeds, UK
l.k.whalley@leeds.ac.uk

Bodo Wichura

Climate and Environment Consultancy, Regional Office Potsdam
German Meteorological Service (DWD)
Potsdam, Germany
bodo.wichura@dwd.de

Stefan Wilbert

Institut für Solarforschung
Deutsches Zentrum für Luft- und Raumfahrt e. V. (DLR)
Almeria, Spain
stefan.wilbert@dlr.de

Martin Wirth

Institut für Physik der Atmosphäre
Deutsches Zentrum für Luft- und Raumfahrt e. V. (DLR)
Weßling, Germany
martin.wirth@dlr.de

Devon E. Worth

Science and Technology Branch
Agriculture and Agri-Food Canada
Ottawa, Canada
devon.worth@canada.ca

Volker Wulfmeyer

Institute of Physics and Meteorology
University of Hohenheim
Stuttgart, Germany
volker.wulfmeyer@uni-hohenheim.de

Astrid A. Ziemann

Chair of Meteorology
Technische Universität Dresden
Tharandt, Germany
astrid.ziemann@tu-dresden.de

Mark A. Zondlo

Civil and Environmental Engineering
Princeton University
Princeton, USA
mzondlo@princeton.edu

Contents

List of Abbreviations	XLI
List of Symbols	LV
Part A Basics of Atmospheric Measurement Techniques	
1 Introduction to Atmospheric Measurements	
<i>Thomas Foken, Frank Beyrich, Volker Wulfmeyer</i>	3
1.1 Measuring Meteorological Elements	4
1.2 History	7
1.3 The Structure of the Atmosphere	9
1.4 Devices, Systems, and Typical Specifications	23
1.5 Applications	26
1.6 Future Developments	27
1.7 Further Reading	28
References	28
2 Principles of Measurements	
<i>Wolfgang Foken</i>	33
2.1 Basics of Measurements	34
2.2 History	34
2.3 Errors in Measurement	34
2.4 Regression Analysis	38
2.5 Time Domain and Frequency Domain for Signals and Systems	39
2.6 Dynamics of Measuring Systems	40
2.7 Analog and Digital Signal Processing	44
2.8 Hardware for Digital Measurement Systems	46
2.9 Further Reading	47
References	47
3 Quality Assurance and Control	
<i>Cove Sturtevant, Stefan Metzger, Sascha Nehr, Thomas Foken</i>	49
3.1 Principles and Definition	50
3.2 History	51
3.3 Elements of Quality Management	52
3.4 Application	77
3.5 Future Developments	84
3.6 Further Reading	85
References	85
4 Standardization in Atmospheric Measurements	
<i>Simon Jäckel, Annette Borowiak, Brian Stacey</i>	93
4.1 Background and Definitions	93
4.2 History	94
4.3 Principles and Procedures	96
4.4 Standardization in the Field of Atmospheric Measurements	98

4.5	Future Developments	103
4.6	Further Reading	104
	References	104
5	Physical Quantities	
	<i>Thomas Foken, Olaf Hellmuth, Bernd Huwe, Dietrich Sonntag</i>	107
5.1	Selection of Parameters	108
5.2	History and Thermodynamic Standards	108
5.3	Units and Constants	111
5.4	Parameters of Air, Water Vapor, Water, and Ice	115
5.5	Parameterization of Optical Properties of Clouds	130
5.6	Absorption Coefficients for Water Vapor, Ozone, and Carbon Dioxide	141
5.7	Parameters of Soil	142
5.8	Time and Astronomical Quantities	146
5.9	Tables in Other Chapters	147
5.10	Future Developments	148
5.11	Further Reading	148
	References	148
Part B In situ Measurement Techniques		
6	Ground-Based Platforms	
	<i>Olaf Kolle, Norbert Kalthoff, Christoph Kottmeier, J. William Munger</i>	155
6.1	Principles of Platforms	156
6.2	History	157
6.3	Theory	158
6.4	Platforms and Sensor Installations	160
6.5	Specification	174
6.6	Quality Control and Safety	175
6.7	Maintenance	175
6.8	Applications	176
6.9	Future Developments	178
6.10	Further Readings	179
	References	180
7	Temperature Sensors	
	<i>Thomas Foken, Jens Bange</i>	183
7.1	Measurement Principles and Parameters	184
7.2	History	187
7.3	Theory	190
7.4	Devices and Systems	196
7.5	Specifications	201
7.6	Quality Control	202
7.7	Maintenance	203
7.8	Applications	204
7.9	Future Developments	205
7.10	Further Reading	206
	References	206

8 Humidity Sensors	
<i>Dietrich Sonntag, Thomas Foken, Holger Vömel, Olaf Hellmuth</i>	209
8.1 Measurement Principles and Parameters	210
8.2 History	212
8.3 Theory	217
8.4 Devices and Systems	222
8.5 Specifications	233
8.6 Quality Control	234
8.7 Maintenance	236
8.8 Application	237
8.9 Future Developments	238
8.10 Further Readings	238
References	238
9 Wind Sensors	
<i>Thomas Foken, Jens Bange</i>	243
9.1 Measurement Principles and Parameters	244
9.2 History	245
9.3 Theory	249
9.4 Devices and Systems	257
9.5 Specifications	262
9.6 Quality Control	263
9.7 Maintenance	266
9.8 Application	267
9.9 Future Developments	269
9.10 Further Reading	270
References	270
10 Pressure Sensors	
<i>Anni Torri, Thomas Foken, Jens Bange</i>	273
10.1 Measurement Principles and Parameters	274
10.2 History	275
10.3 Theory	278
10.4 Devices and Systems	283
10.5 Specifications	290
10.6 Quality Control	291
10.7 Maintenance	292
10.8 Application	292
10.9 Future Developments	293
10.10 Further Reading	294
References	294
11 Radiation Sensors	
<i>Klaus Behrens</i>	297
11.1 Measurement Principles and Parameters	298
11.2 History	303
11.3 Theory	315
11.4 Devices and Systems	320
11.5 Specifications	339
11.6 Quality Control	341
11.7 Maintenance	348

11.8 Applications.....	349
11.9 Future Developments	352
11.10 Further Reading	353
References	353
12 In-situ Precipitation Measurements	
<i>Arianna Cauteruccio, Matteo Colli, Mattia Stagnaro, Luca G. Lanza, Emanuele Vuerich</i>	359
12.1 Measurement Principles and Parameters.....	360
12.2 History.....	362
12.3 Theory	367
12.4 Devices and Systems	370
12.5 Specifications	375
12.6 Quality Control, Uncertainty, and Calibration	376
12.7 Maintenance.....	392
12.8 Application.....	394
12.9 Future Developments	396
12.10 Further Reading	397
References	397
13 Visibility Sensors	
<i>Martin Löffler-Mang, Klaus Heyn</i>	401
13.1 Measurement Principles and Parameters.....	402
13.2 History.....	403
13.3 Theory	405
13.4 Devices and Systems	414
13.5 Specifications	417
13.6 Quality Control.....	418
13.7 Maintenance.....	421
13.8 Application.....	423
13.9 Future Developments	426
13.10 Further Reading	427
References	428
14 Electricity Measurements	
<i>Giles Harrison, Alec Bennett</i>	431
14.1 Measurement Principles and Parameters.....	432
14.2 History.....	432
14.3 Theory	434
14.4 Devices and Systems	441
14.5 Specifications	448
14.6 Quality Control.....	448
14.7 Maintenance.....	450
14.8 Applications.....	452
14.9 Future Developments	453
14.10 Further Reading	453
References	453

15 Radioactivity Sensors	
<i>Jacqueline Bieringer, Thomas Steinkopff, Ulrich Stöhlker</i>	457
15.1 Measurement Principles and Parameters.....	458
15.2 History.....	459
15.3 Theory.....	460
15.4 Devices and Systems.....	463
15.5 Specifications.....	467
15.6 Quality Control.....	468
15.7 Maintenance.....	469
15.8 Application.....	469
15.9 Future Developments.....	470
15.10 Further Reading.....	471
References	471
16 Gas Analysers and Laser Techniques	
<i>Dwayne Heard, Lisa K. Whalley, Steven S. Brown</i>	475
16.1 Measurement Principles and Parameters.....	476
16.2 History.....	478
16.3 Theory.....	480
16.4 Devices and Systems.....	486
16.5 Specifications.....	494
16.6 Quality Control.....	495
16.7 Maintenance.....	496
16.8 Applications.....	498
16.9 Future Developments.....	502
16.10 Further Reading.....	502
References	502
17 Measurement of Stable Isotopes in Carbon Dioxide, Methane, and Water Vapor	
<i>Ingeborg Levin, Matthias Cuntz</i>	509
17.1 Measurement Principles and Parameters.....	510
17.2 History of Stable Isotope Measurements in Atmospheric CO ₂ , CH ₄ and H ₂ O.....	512
17.3 Theory.....	513
17.4 Devices and Systems.....	516
17.5 Specifications.....	523
17.6 Quality Control.....	524
17.7 Maintenance.....	525
17.8 Application.....	525
17.9 Future Developments.....	527
17.10 Further Readings.....	527
References	527
18 Measurement of Fundamental Aerosol Physical Properties	
<i>Andreas Held, Alexander Mangold</i>	533
18.1 Measurement Principles and Parameters.....	534
18.2 History.....	537
18.3 Theory.....	537
18.4 Devices and Systems.....	542
18.5 Specifications.....	552

18.6	Quality Control	553
18.7	Maintenance	555
18.8	Application	556
18.9	Future Developments	558
18.10	Further Reading	558
	References	559
19	Methods of Sampling Trace Substances in Air	
	<i>Christopher Pöhlker, Karsten Baumann, Gerhard Lammel</i>	565
19.1	Measurement Principles and Parameters	566
19.2	History	568
19.3	Theory	570
19.4	Devices and Systems	576
19.5	Specifications	589
19.6	Quality Control	590
19.7	Maintenance	592
19.8	Application	593
19.9	Future Developments	596
19.10	Further Reading	596
	References	596
20	Optical Fiber-Based Distributed Sensing Methods	
	<i>Christoph K. Thomas, John Selker</i>	609
20.1	Measurement Principles and Parameters	610
20.2	History	613
20.3	Theory	614
20.4	Devices	619
20.5	Specifications	623
20.6	Quality Control	624
20.7	Maintenance	625
20.8	Applications	626
20.9	Future Developments	629
20.10	Further Reading	629
	References	629
21	Odor Measurements	
	<i>Ralf Petrich, Axel Delan</i>	633
21.1	Measurement Principles and Parameters	634
21.2	History	635
21.3	Theory	635
21.4	Devices and Systems	638
21.5	Specifications	639
21.6	Quality Control	640
21.7	Maintenance	641
21.8	Application	641
21.9	Future Developments	642
21.10	Further Readings	642
	References	642

22 Visual Observations	
<i>Thomas Foken, Raymond Rülke</i>	645
22.1 Principles of Visual Observations	645
22.2 History	646
22.3 Theory	647
22.4 Observed Parameters	647
22.5 Quality Control	655
22.6 Application	655
22.7 Future Developments	655
22.8 Further Readings	656
References	656
Part C Remote-Sensing Techniques (Ground-Based)	
23 Sodar and RASS	
<i>Stefan Emeis</i>	661
23.1 Measurement Principles and Parameters	662
23.2 History	665
23.3 Theory	666
23.4 Devices and Systems	670
23.5 Specifications	674
23.6 Quality Control	675
23.7 Maintenance	677
23.8 Applications	677
23.9 Future Developments	679
23.10 Further Reading	680
References	680
24 Backscatter Lidar for Aerosol and Cloud Profiling	
<i>Christoph Ritter, Christoph Münkel</i>	683
24.1 Measurement Prinziples and Parameters	684
24.2 History	686
24.3 Theory	687
24.4 Devices and Systems	700
24.5 Specifications	706
24.6 Quality Control	707
24.7 Maintenance	709
24.8 Applications	710
24.9 Further Reading	714
References	714
25 Raman Lidar for Water-Vapor and Temperature Profiling	
<i>Volker Wulfmeyer, Andreas Behrendt</i>	719
25.1 Measurement Principles and Parameters	720
25.2 History	721
25.3 Theory	722
25.4 Devices and Systems	725
25.5 Specifications	728
25.6 Quality Control	729

25.7	Maintenance.....	731
25.8	Applications.....	731
25.9	Future Developments	733
25.10	Further Reading	733
	References	734
26	Water Vapor Differential Absorption Lidar	
	<i>Scott M. Spuler, Matthew Hayman, Tammy M. Weckwerth</i>	741
26.1	Measurement Principles and Parameters.....	742
26.2	History.....	743
26.3	Theory	744
26.4	Devices and Systems	749
26.5	Specifications	751
26.6	Quality Control	751
26.7	Maintenance.....	752
26.8	Applications.....	752
26.9	Future Developments	753
26.10	Further Readings	754
	References	754
27	Doppler Wind Lidar	
	<i>Oliver Reitebuch, R. Michael Hardesty</i>	759
27.1	Measurement Principles and Parameters.....	760
27.2	History.....	762
27.3	Theory	765
27.4	Devices and Systems	773
27.5	Specifications	782
27.6	Quality Control	783
27.7	Maintenance.....	784
27.8	Applications.....	785
27.9	Future Developments	790
27.10	Further Readings	791
	References	791
28	Spectrometers	
	<i>Klaus Schäfer, Mark Wenig, Mark A. Zondlo, Axel Murk, Konradin Weber</i> ..	799
28.1	Measurement Principles and Parameters.....	800
28.2	History.....	801
28.3	Theory	803
28.4	Devices and Systems	805
28.5	Specifications	809
28.6	Quality Control	810
28.7	Maintenance.....	811
28.8	Applications.....	812
28.9	Future Developments	813
28.10	Further Readings	813
	References	814

29 Passive Solar and Microwave Spectral Radiometers	
<i>Susanne Crewell, Manfred Wendisch, Ulrich Löhnert</i>	821
29.1 Measurement Principles and Parameters	822
29.2 History	825
29.3 Theory	826
29.4 Devices and Systems	830
29.5 Specifications	832
29.6 Quality Control	833
29.7 Maintenance	834
29.8 Application	835
29.9 Future Developments	837
29.10 Further Readings	837
References	838
30 Weather Radar	
<i>Jörg E.E. Seltmann</i>	841
30.1 Measurement Principles and Parameters	842
30.2 History	843
30.3 Theory	845
30.4 Radar Systems	858
30.5 Specifications	869
30.6 Quality Control	871
30.7 Maintenance	882
30.8 Applications	883
30.9 Future Developments	895
30.10 Further Reading	896
References	896
31 Radar Wind Profiler	
<i>Volker Lehmann, William Brown</i>	901
31.1 Measurement Principles and Parameters	902
31.2 History	903
31.3 Theory	904
31.4 Systems	916
31.5 Specifications	920
31.6 Quality Control	923
31.7 Maintenance	924
31.8 Applications	925
31.9 Future Developments	926
31.10 Further Reading	926
References	927
32 Radar in the mm-Range	
<i>Gerhard Peters</i>	935
32.1 Measurement Principles and Parameters	935
32.2 History	938
32.3 Theory	938
32.4 Devices and Systems	946
32.5 Specifications	946
32.6 Quality Control	947
32.7 Maintenance	947

32.8	Application.....	948
32.9	Future Developments	948
32.10	Further Reading	948
	References	949
33	High Frequency Radar	
	<i>Jochen Horstmann, Anna Dzvonkovskaya</i>	953
33.1	Measurement Principles and Parameters.....	953
33.2	History.....	954
33.3	Theory	955
33.4	Devices and Systems	956
33.5	Specifications	959
33.6	Quality Control.....	961
33.7	Maintenance.....	961
33.8	Applications.....	962
33.9	Future Developments	965
33.10	Further Reading	965
	References	965
34	Scintillometers	
	<i>Frank Beyrich, Oscar K. Hartogensis, Henk A.R. de Bruin, Helen C. Ward</i> ...	969
34.1	Measurement Principles and Parameters.....	970
34.2	History.....	971
34.3	Theory	972
34.4	Devices and Systems	979
34.5	Specifications	984
34.6	Quality Control.....	985
34.7	Maintenance.....	987
34.8	Applications.....	989
34.9	Future Developments	991
34.10	Further Readings	992
	References	992
35	Acoustic Tomography	
	<i>Armin Raabe, Manuela Starke, Astrid A. Ziemann</i>	999
35.1	Measurement Principles and Parameters.....	1000
35.2	History.....	1001
35.3	Theory	1001
35.4	Devices and Systems	1012
35.5	Specifications	1015
35.6	Quality Control.....	1015
35.7	Maintenance.....	1017
35.8	Application.....	1017
35.9	Future Developments	1020
35.10	Further Readings	1021
	References	1021

36 GNSS Water Vapor Tomography	
<i>Michael Bender, Galina Dick</i>	1025
36.1 Measurement Principles and Parameters	1026
36.2 History	1028
36.3 Theory	1028
36.4 Devices and Systems	1033
36.5 Specifications	1039
36.6 Quality Control	1040
36.7 Maintenance	1041
36.8 Application	1042
36.9 Future Developments	1045
36.10 Further Reading	1046
References	1046
Part D Remote Sensing Techniques (Space- and Aircraft-Based)	
37 Satellite and Aircraft Remote Sensing Platforms	
<i>Manfred Wendisch, André Ehrlich, Peter Pilewskie</i>	1053
37.1 Principles of Platforms	1054
37.2 History	1054
37.3 Issues and Instrumental Requirements	1056
37.4 Available Platforms for Active and Passive Remote Sensing	1056
37.5 Future Development	1057
37.6 Further Reading	1065
References	1065
38 Airborne Lidar	
<i>Martin Wirth</i>	1067
38.1 Measurement Principles and Parameters	1067
38.2 History	1071
38.3 Theory	1072
38.4 Devices and Systems	1084
38.5 Specifications	1089
38.6 Quality Control	1089
38.7 Maintenance	1089
38.8 Applications	1090
38.9 Future Developments	1090
38.10 Further Reading	1091
References	1091
39 Airborne Radar	
<i>Martin Hagen, Julien Delanoë, Scott Ellis, Florian Ewald, Jeffrey French, Samuel Haimov, Gerald Heymsfield, Andrew L. Pazmany</i> ..	1097
39.1 Measurement Parameters and Principles	1098
39.2 History	1100
39.3 Theory	1102
39.4 Devices and Systems	1108
39.5 Specifications	1114
39.6 Calibration and Quality Control	1114

39.7	Maintenance.....	1117
39.8	Applications.....	1117
39.9	Future Developments	1123
39.10	Further Reading	1124
	References	1125
40	Airborne Solar Radiation Sensors	
	<i>K. Sebastian Schmidt, Manfred Wendisch, Bruce Kindel</i>	1131
40.1	Measurement Principles and Parameters.....	1132
40.2	History.....	1132
40.3	Theory	1134
40.4	Devices and Subsystems	1135
40.5	Specifications	1138
40.6	Calibration and Quality Control	1139
40.7	Maintenance.....	1141
40.8	Applications.....	1141
40.9	Future Developments	1146
40.10	Further Readings	1146
	References	1147
41	Spaceborne Microwave Radiometry	
	<i>Susanne Crewell, Catherine Prigent, Mario Mech</i>	1151
41.1	Measurement Principles and Parameters.....	1152
41.2	History.....	1155
41.3	Theory	1156
41.4	Devices and Systems	1159
41.5	Specifications	1162
41.6	Quality Control.....	1163
41.7	Maintenance.....	1163
41.8	Application.....	1164
41.9	Future Developments	1167
41.10	Further Readings	1167
	References	1167
42	Imaging Techniques	
	<i>Jan Cermak, Isabel F. Trigo, Julia Fuchs</i>	1171
42.1	Measurement Principles and Parameters.....	1171
42.2	History.....	1172
42.3	Theory	1175
42.4	Devices and Systems	1177
42.5	Specifications	1179
42.6	Quality Control.....	1180
42.7	Maintenance.....	1180
42.8	Applications.....	1180
42.9	Future Developments	1180
42.10	Further Reading	1182
	References	1182

Part E Complex Measurement Systems – Methods and Applications

43 Atmospheric Measurements for Different Purposes	
<i>Bodo Wichura, Thomas Foken</i>	1187
43.1 Principles of Atmospheric Measurement Station Classification	1188
43.2 History.....	1190
43.3 Theory	1190
43.4 Devices and Systems	1192
43.5 Specifications	1195
43.6 Quality Control.....	1195
43.7 Maintenance.....	1195
43.8 Applications.....	1196
43.9 Future Developments	1196
43.10 Further Reading	1197
References	1197
44 Crowdsourcing	
<i>Matthias Budde</i>	1199
44.1 Measurement Principles and Parameters.....	1200
44.2 History.....	1201
44.3 Theory	1202
44.4 Devices and Systems	1207
44.5 Specifications	1212
44.6 Quality Control.....	1213
44.7 Maintenance.....	1217
44.8 Applications.....	1218
44.9 Future Developments	1227
References	1227
45 Mesometeorological Networks	
<i>Jerald A. Brotzge, Christopher A. Fiebrich</i>	1233
45.1 Measurement Principles and Parameters.....	1234
45.2 History.....	1235
45.3 Theory	1235
45.4 Devices and Systems	1237
45.5 Specifications	1239
45.6 Quality Control.....	1240
45.7 Maintenance.....	1240
45.8 Applications.....	1242
45.9 Future Development	1243
45.10 Further Readings	1244
References	1244
46 Aerological Measurements	
<i>Holger Vömel, Masatomo Fujiwara</i>	1247
46.1 Measurement Principles and Parameters.....	1248
46.2 History.....	1250
46.3 Theory	1254
46.4 Devices and Systems	1260
46.5 Specifications	1268

46.6	Quality Control	1270
46.7	Maintenance	1272
46.8	Application	1272
46.9	Further Development	1275
46.10	Further Readings	1276
	References	1276
47	Composite Atmospheric Profiling	
	<i>Christoph Kottmeier, Bianca Adler, Norbert Kalthoff, Ulrich Löhnert, Ulrich Görtsdorf</i>	1281
47.1	The Relevance of Composite Atmospheric Measurements	1282
47.2	History	1285
47.3	Theory	1287
47.4	Observation Platforms	1291
47.5	Specifications	1294
47.6	Quality Control	1294
47.7	Maintenance	1295
47.8	Applications	1295
47.9	Future Developments	1299
47.10	Further Reading	1299
	References	1300
48	Aircraft-Based Flux Density Measurements	
	<i>Raymond L. Desjardins, Devon E. Worth, Ian MacPherson, Matthias Mauder, Jens Bange</i>	1305
48.1	Measurement Principles and Parameters	1306
48.2	History	1307
48.3	Theory	1308
48.4	Devices and Systems	1310
48.5	Specifications of Sensors for Flux Density Measurements	1313
48.6	Quality Control	1314
48.7	Maintenance	1315
48.8	Applications	1315
48.9	Future Developments	1320
48.10	Further Reading	1321
48.A	Appendix	1321
	References	1325
49	Unmanned Aircraft Systems	
	<i>Jens Bange, Joachim Reuder, Andreas Platis</i>	1331
49.1	Measurement Principles and Parameters	1332
49.2	History	1332
49.3	Theory	1333
49.4	Devices and Systems	1334
49.5	Specifications	1339
49.6	Quality Control	1339
49.7	Maintenance	1340
49.8	Applications	1341
49.9	Future Developments	1344
49.10	Further Readings	1344
	References	1344

50 Ground-based Mobile Measurement Systems	
<i>Eberhard Parlow, Thomas Foken</i>	1351
50.1 Measurement Principles and Parameters	1352
50.2 History	1353
50.3 Theory	1354
50.4 Devices and Systems	1358
50.5 Specifications	1361
50.6 Quality Control	1361
50.7 Maintenance	1362
50.8 Application	1362
50.9 Future Developments	1365
50.10 Further Readings	1365
References	1366
51 Measurement Systems for Wind, Solar and Hydro Power Applications	
<i>Stefan Emeis, Stefan Wilbert</i>	1369
51.1 Measured Parameters	1370
51.2 History	1371
51.3 Theory	1373
51.4 Devices and Systems	1377
51.5 Specifications	1382
51.6 Quality Control	1383
51.7 Maintenance	1383
51.8 Application	1384
51.9 Future Developments	1386
51.10 Further Readings	1386
References	1387
52 Urban Measurements and Their Interpretation	
<i>Sue Grimmond, Helen C. Ward</i>	1391
52.1 Measurement Principles and Variables	1392
52.2 History	1394
52.3 Theory	1396
52.4 Devices and Systems	1400
52.5 Specifications	1407
52.6 Quality Control	1408
52.7 Maintenance	1409
52.8 Applications	1409
52.9 Future Developments	1412
52.10 Further Reading	1413
References	1413
53 Fog Deposition	
<i>Shih-Chieh Chang, Robert S. Schemenauer</i>	1425
53.1 Measurement Principles and Parameters	1426
53.2 History	1430
53.3 Theory	1432
53.4 Devices and Systems	1436
53.5 Specifications	1438
53.6 Quality Control	1439

53.7	Maintenance.....	1440
53.8	Applications.....	1441
53.9	Further Developments	1441
53.10	Further Reading	1442
	References	1442
54	Immission and Dry Deposition	
	<i>Ivonne Trebs, Christof Ammann, Jürgen Junk</i>	1445
54.1	Measurement Principles and Parameters.....	1446
54.2	History	1448
54.3	Theory	1449
54.4	Devices and Systems	1454
54.5	Specifications	1458
54.6	Quality Control	1459
54.7	Maintenance.....	1460
54.8	Application.....	1460
54.9	Future Developments	1462
54.10	Further Reading	1463
	References	1463
55	Eddy-Covariance Measurements	
	<i>Matthias Mauder, Thomas Foken, Marc Aubinet, Andreas Ibrom</i>	1473
55.1	Measurement Principles and Variables	1474
55.2	History	1477
55.3	Theory	1478
55.4	Devices and Systems	1486
55.5	Specifications	1489
55.6	Quality Control	1489
55.7	Maintenance.....	1494
55.8	Application.....	1494
55.9	Future Developments	1495
55.10	Further Readings	1496
	References	1496
56	Alternative Turbulent Trace Gas Flux Measurement Methods	
	<i>Janne Rinne, Christof Ammann, Elizabeth Pattey, Kyaw Tha Paw U, Raymond L. Desjardins</i>	1505
56.1	Measurement Principles and Parameters.....	1506
56.2	History.....	1507
56.3	Theory	1509
56.4	Devices and Measuring Systems.....	1516
56.5	Specifications	1522
56.6	Quality Control	1523
56.7	Maintenance.....	1523
56.8	Application.....	1524
56.9	Future Developments	1525
56.10	Further Readings	1525
	References	1525

57 Evapotranspiration Measurements and Calculations	
<i>Richard Allen, Thomas Foken, Ayse Kilic, Ricardo Trezza, Samuel Ortega-Farias</i>	1531
57.1 Principles of Evapotranspiration Determination	1532
57.2 History.....	1532
57.3 Theory	1535
57.4 Devices and Methods	1555
57.5 Specifications	1556
57.6 Quality Control.....	1556
57.7 Maintenance.....	1559
57.8 Application.....	1560
57.9 Future Developments	1561
57.10 Further Reading	1561
References	1562
58 Lysimeter	
<i>Sascha Reth, Oscar Perez-Priego, Heinz Coners, Reinhard Nolz</i>	1569
58.1 Principles and Parameters.....	1570
58.2 History.....	1571
58.3 Theory	1572
58.4 Devices and Systems	1574
58.5 Specifications	1578
58.6 Quality Control.....	1578
58.7 Maintenance.....	1579
58.8 Applications.....	1579
58.9 Future Developments	1581
58.10 Further Reading	1581
References	1582
59 Plant Chamber Measurements	
<i>Oscar Perez-Priego</i>	1585
59.1 Measurement Principles and Parameters.....	1586
59.2 History of Chamber Measurements	1587
59.3 Theory	1587
59.4 Devices and Systems	1591
59.5 Specifications	1593
59.6 Quality Control.....	1593
59.7 Maintenance.....	1594
59.8 Application.....	1594
59.9 Future Developments	1597
59.10 Further Readings	1598
References	1598
60 Soil Chamber Measurements	
<i>Jens-Arne Subke, Lars Kutzbach, David Risk</i>	1603
60.1 Measurement Approaches, Principles, and Parameters	1604
60.2 History of Soil Chamber Measurements.....	1606
60.3 Theory	1608
60.4 Devices and Systems	1612
60.5 Specifications	1616
60.6 Quality Control.....	1616

60.7	Maintenance.....	1619
60.8	Application.....	1619
60.9	Future Developments	1621
60.10	Further Readings	1621
	References	1621
61	Soil Measurements	
	<i>Bernd Huwe, Christina Bogner, Thomas Foken</i>	1625
61.1	Measurement Principles and Parameters.....	1626
61.2	History.....	1630
61.3	Theory	1631
61.4	Devices, Systems, and Analyses	1634
61.5	Specifications	1646
61.6	Quality Control	1647
61.7	Maintenance.....	1647
61.8	Applications.....	1648
61.9	Further Developments	1650
61.10	Further Reading	1651
	References	1651
62	Water Measurements	
	<i>Volker Mohrholz, Anita Flohr</i>	1657
62.1	Measurement Principles and Parameters.....	1658
62.2	History.....	1660
62.3	Theory	1662
62.4	Devices and Systems	1667
62.5	Specifications	1673
62.6	Quality Control.....	1674
62.7	Maintenance.....	1675
62.8	Application.....	1676
62.9	Future Developments	1678
62.10	Further Reading	1678
	References	1678
 Part F Measurement Networks		
63	Networks of Atmospheric Measuring Techniques	
	<i>Rolf Philipona</i>	1687
63.1	Relevance and Parameters of Networks	1688
63.2	History.....	1691
63.3	Network Structure	1693
63.4	Other Important Networks.....	1699
63.5	Quality Control.....	1708
63.6	Maintenance.....	1709
63.7	Application.....	1709
63.8	Future Developments	1710
63.9	Further Reading	1710
	References	1710

64 Integration of Meteorological and Ecological Measurements	
<i>Hans Peter Schmid, Corinna Rebmann</i>	1713
64.1 Relevance and Parameters of Networks	1714
64.2 History	1716
64.3 Structures of Notable Networks	1717
64.4 Temporal and Spatial Scales	1720
64.5 Quality Control of Ecological Measurement Networks	1720
64.6 Maintenance	1721
64.7 Applications	1721
64.8 Further Developments	1721
64.9 Further Reading	1722
References	1722
Subject Index	1727

List of Abbreviations

1-D	one-dimensional	AHSRL	Arctic High-Spectral Resolution Lidar
2-D	two-dimensional	AI	artificial intelligence
3-D	three-dimensional	AIRMoN	Atmospheric Integrated Research Monitoring Network
3DVar	3-D variational	AIRS	Atmospheric Infrared Sounder
4-D	four-dimensional	AIS	Air Ion Spectrometer
4DVar	4-D variational	ALADIN	Atmospheric Laser Doppler Instrument
		ALADINA	Application of Light-weight Aircraft for Detecting In Situ Aerosol
A			
A-TOM	acoustic travel-time tomography	ALC	Automatic Lidar and Ceilometers
A-Train	afternoon train	ALINE	America Lidar Network
A/D	analog/digital	ALISSA	L'Atmosphère Par Lidar Sur Saliout
A2D	Aladin Airborne Demonstrator	ALOMAR	Arctic Lidar Observatory
AATSR	Advanced Along Track Scanning Radiometer	AMDAR	Aircraft Meteorological Data Relay
		AMF	ARM mobile facility
ABI	advanced baseline imager	AMF	air mass factor
ABL	atmospheric boundary layer	AMMA	African Monsoon Multidisciplinary Analysis
AC	alternating current		
AC	air capacity	AMNet	Atmospheric Mercury Network
ACARS	Aircraft Communications Addressing and Reporting System	AMoN	Ammonia Monitoring Network
		AMR	antenna-mounted receiver
ACCC	Aluminum Conductor Composite Core	AMS	aerosol mass spectrometer
ACE	Aerosol–Cloud–Ecosystem	AMSR	Advanced Microwave Scanning Radiometer
ACMS	Aircraft Condition Monitoring System		
ACONS	Aircraft-Fixed Orthonormal System	AMSU	Advanced Microwave Sounding Unit
ACP	Absolute Cavity Pyrgeometer	AOD	aerosol optical depth
ACS	auto-correlation spectrometers	AOM	acousto-optic modulator
ACTRIS	Aerosols, Clouds and Trace Gases Research Infrastructure	AOS	acousto-optical spectrometers
		AOT	aerosol optical thickness
AD2CP	Acoustic Doppler Dual Current Profiler	APAR	airborne phased array radar
ADC	analog digital converter	APD	avalanche photodiode
ADCP	acoustic Doppler current profiler	API	application programming interface
ADD	aircraft-derived data	APi-TOF	Atmospheric Pressure Interface Time-of-flight
ADER	Ambient Dose Equivalent Rate		
ADONS	aerodynamic coordinate system	APRS	Automated Packet Reporting System
ADP	acoustic Doppler profiler	APS	aerodynamic particle sizer
ADR	amplitude domain reflectometry	aqSOA	aqueous secondary organic aerosol
ADS	automatic dependent surveillance	ARE	acoustic received echo
ADV	acoustic Doppler velocimeter	ARISE	Arctic Radiation IceBridge Sea and Ice Experiment
AERI	Atmospheric Emitted Radiance Interferometer		
		ARM	Atmospheric Radiation Measurement
AERONET	Aerosol Robotic Network	ART	Algebraic Reconstruction Technique
AESA	active electronically scanned array	ARTS	Atmospheric Radiative Transfer Simulator
AFC	automatic frequency control		
aFC	available field capacity	ASAP	Automated Shipboard Aerological Program
AFIB	aerodynamic fluxes using iterative energy balance	ASCAT	Advanced Scatterometer
		ASCENDS	Active Sensing of CO ₂ Emissions over Nights, Days and Seasons
AFTIR	Airborne FTIR		
AGAGE	Advanced Global Atmospheric Gases Experiment	ASCII	American Standard Code for Information Exchange
AGC	automatic gain control	ASL	above sea level
AGL	above ground level	ASL	atmospheric surface layer
AGM	aerodynamic gradient method	ASOS	Automated Surface Observing System
AHI	Advanced Himawari Imager		

ASR	Absolute Sky-scanning Radiometer	BR	Bowen ratio
ASR	Arctic System Reanalysis	BRDF	bidirectional reflectance distribution function
ASTAR	Arctic Study of Tropospheric Aerosol and Radiation	BREB	Bowen ratio energy balance
ASTER	Advanced Spaceborne Thermal Emission and Reflection Radiometer	BREEAM	building research establishment environmental assessment method
ASTEX	Atlantic Stratocumulus Transition Experiment	BRF	body reference frame
ASY	asymmetry parameter	BS	biosensor
AT	acoustic tomography	BSRN	Baseline Surface Radiation Network
ATC	air traffic control	BSU	beam steering unit
ATD	arrival time difference	BT	Bluetooth
ATLID	Atmospheric Lidar	BT	brightness temperature
ATMS	Advanced Technology Microwave Sounder	BUFR	binary universal form for the representation of meteorological data
ATOVS	Advanced TIROS Operational Vertical Sounder	BWT	beam widening telescope
ATS	Applications Technology Satellite		
ATS	Applications Technology System	C	
AUV	Autonomous Underwater Vehicle	CAENEX	Complete Atmospheric Energetics Experiment
AVAPS	Airborne Vertical Atmospheric Profiling System	CAL	calibration factor
AVHRR	Advanced Very High Resolution Radiometer	CAL/VAL	calibration and validation
AVIRIS	Airborne Visible/Infrared Imaging Spectrometer	CAL/VAL	Cloud–Aerosol Lidar with Orthogonal Polarization
AVIRIS-NG	Next-Generation Airborne Visible/Infrared Imaging Spectrometer	CALIPSO	Cloud–Aerosol Lidar and Infrared Pathfinder Satellite Observation
AVV	Allgemeine Verwaltungsvorschrift	CAMS	Copernicus Atmosphere Monitoring Service
AW	available water	CAPE	convective available potential energy
AWS	Automatic Weather Station	CAPMoN	Canadian Air and Precipitation Monitoring Network
		CAPS	Cavity-attenuated Phase-shift Spectroscopy
B		CARIBIC	Civil Aircraft for the Regular Investigation of the Atmosphere Based on an Instrument Container
BADM	Biological, Ancillary, Disturbance, and Metadata	CASIE	Characterization of Arctic Sea Ice Experiment
BAPMoN	Background Air Pollution Monitoring Network	CASTNET	Clean Air Status and Trends Network
BB	broadband	CAT	clear-air turbulence
BBCES	Broadband Cavity-enhanced Spectrometer	CATS	cloud–aerosol transport system
BBR	Broad Band Radiometer	CBD	central business district
BBS	bulletin board systems	CBL	convective boundary layer
BC	black carbon	CC	cloud-to-cloud
BCE	Before the Common Era	CCA	constant-current anemometer
BD	beam dump	CCD	charge-coupled device
BDC	Brewer–Dobson circulation	CCN	cloud condensation nucleus
BDS	BeiDou Navigation Satellite System	CCOR	clutter correlation
BE	beam expander	CDD	cooling degree days
BEARPEX	Biosphere Effects on Aerosol and Photochemistry Experiment	CDR	climate data record
BITE	built-in test equipment	CDR	circular depolarization ratio
BL	boundary laser	CDT	Central Daylight Time
BLE	Bluetooth low energy	CE	Common Era
BLS	boundary-layer scintillometer	CERES	Clouds and the Earth’s Radiant Energy System
BOMEX	Barbados Oceanographic and Meteorological Experiment	CES	cavity-enhanced spectroscopy
BOREAS	Boreal Ecosystem–Atmosphere Study	CESAR	Cabauw Experimental Site for Atmospheric Research
BPLO	backpropagated local oscillator	CET	Central European Time

CF	Climate and Forecasting	CT	computer-assisted tomography
CF	fractional cloud cover	CT	cloud type
CFC	chlorofluorocarbon	CTA	constant-temperature anemometer
CFD	computational fluid dynamics	CTBT	Comprehensive Nuclear-Test-Ban Treaty
CFH	cryogenic frostpoint hygrometer	CTD	conductivity-temperature-depth
CFHC	carbon-fiber heated cable technology	CTH	cloud top height
CFL	constant flux layer	CTM	chemical transport modeling
CFSR	Climate Forecast System Reanalysis	CTS	chirp transform spectrometers
CG	cloud to ground	CubeRRRT	CubeSat Radiometer Radio Frequency Interference Technology Validation
CHAM	chamber method	CVA	constant-voltage anemometer
CHIOTTO	continuous high-precision tall tower observations of greenhouse gases	CW	continuous wave
CIMR	Copernicus Imaging Microwave Radiometer	CWC	condensed water content
CIMS	chemical ionization mass spectrometry	CWOP	Citizen Weather Observer Program
CIN	convective inhibition		
CLARREO	Climate Absolute Radiance and Refractivity Observatory	D	
CLD	chemiluminescence detector	DA	data assimilation
ClearLo	Clean Air for London	DAPPLE	Dispersion of Air Pollution and its Penetration into the Local Environment
CLRTAP	Convention on Long-Range Transboundary Air Pollution	DARE	direct aerosol radiative effect
CNC	Condensation Nucleus Counter	DART	discrete anisotropic radiative transfer
CNR	carrier-to-noise ratio	DAS	Direct Absorption Spectroscopy
COBALD	Compact Optical Backscatter and Aerosol Detector	DASE	differential absorption of scattered energy
COD	cloud optical depth	DBH	diameter at breast height
CODAR	Coastal Ocean Dynamics Applications Radar	DBLS	double-beam laser scintillometer
CODE	California Ozone Deposition Experiment	DBS	Doppler beam swinging
COHO	highly coherent oscillator	DC	direct current
CONRAD	Convection Development in Operational Radar Products	DCM	4-(dicyanomethylene)-2-methyl-6-(4-dimethylaminostyryl)-4h-pyran
COOP	Cooperative Observer Program	DD	double difference
COPS	Convective and Orographically-induced Precipitation Study	DDA	discrete dipole approximation
COR	coherent on receive	DDIM	dry deposition inferential method
COST	European Cooperation in Science and Technology	DDPIR	double direction precision infrared radiometer
COT	cloud optical thickness	DDS	direct digital waveform synthesis
CPC	condensation particle counter	DE	detection efficiency
CPL	Cloud Physics Lidar	DEA	Disjunct Eddy Accumulation
CPR	Cloud Profiling Radar	DEBITS	Deposition of Biogeochemically Important Trace Species
CPU	Central Processing Unit	DEC	Disjunct Eddy Covariance
CR	catch ratio	DELTA	Denuder for Long-Term Atmospheric Sampling
CR	color ratio	DER	cloud droplet effective radius
CR	capillary rise	DFG	Difference Frequency Generation laser spectroscopy
CRDS	Cavity Ring-down Spectroscopy	DFIR	double fence intercomparison reference
CRLB	Cramer Rao lower bound	DFR	differential frequency ratio
CRN	clutter ratio narrow	DFS	dynamic frequency selection
CRNS	cosmic-ray neutron sensor	DFT	discrete Fourier transform
CRS	cloud radar system	DHI	diffuse horizontal irradiance
CRT	cathode ray tube	DIAL	differential-absorption lidar
CRTM	Community Radiative Transfer Model	DIC	dissolved inorganic carbon
CS	citizen science	DIF	Directory Interchange Format
CSAR	cryogenic solar absolute radiometer	DIN	Deutsche Industrienorm
CSC	concentrating solar technologies	DIW	deionized water
CSET	Cloud System Evolution in the Trades	DIY	do-it-yourself
CSIP	Convective Storms Initiation Project	DMA	differential mobility analyzer
CSP	concentrating solar power		

DMPS	differential mobility particle sizer	EMEP	European Monitoring and Evaluation Programme
DNI	direct normal irradiance	EMF	electromotive force
DNS	direct numerical simulation	EMI	electromagnetic interference
DOAS	differential optical absorption spectroscopy	EN	European standard
DOF	degrees of freedom	ENTA	Environmental and Networking Technologies and Applications
DOI	digital object identifier	EO	Earth observation
DORIS	Doppler Orbitography and Radiopositioning Integrated by Satellite	EOL	Earth Observing Laboratory
DOY	day of the year	EOS	Earth Observing System
DP	depth of percolation	EPC	electronic pressure controller
DPR	dual-frequency precipitation radar	EPOS	Earth Parameter and Orbit System
DQO	data quality objective	EPS	EUMETSAT Polar System
DSD	drop-size distribution	EPS-SG	EUMETSAT Polar System—Second Generation
DSM	digital surface model	ERF	Environmental Response Function
DSP	digital signal processor	ERP	Earth rotation parameter
DSY	design summer year	ESAS	Earth Science and Applications from Space
DTS	distributed temperature sensing	ESM	electric supplementary material
DWL	Doppler Wind Lidar	ESM	mobile experience sampling
DWR	dual-wavelength ratio	ESTAR	Electronically Scanned Thinned Array Radiometer
DYN	dynamic range	ET	evapotranspiration

E

EA	eddy accumulation	ETM+	Enhanced Thematic Mapper Plus
EAA	electrical aerosol analyzer	EUMETNET	European Meteorological Network
EAUNET	Acid Deposition Monitoring Network in East Asia	EUPHORE	European Photoreactor
EARLINET	European Aerosol Research Lidar Network	EURDEP	European Radiological Data Exchange Platform
EBCM	extended boundary condition method	EUV	Extreme Ultraviolet
EBEX	Energy Balance Experiment	EVA-GRIPS	Evaporation at Grid-Pixel Scale
EC	eddy covariance	EVI	Enhanced Vegetation Index
EC	Executive Committee	EXCO	extinction coefficient
ECC	electrochemical concentration cell	EXRAD	ER-2 X-Band Radar
ECD	electron capture detector		
ECMWF	European Centre for Medium-Range Weather Forecasts		
ECV	essential climate variable		
EDFA	erbium-doped fiber amplifier		
EDOP	ER-2 Doppler Radar		
EEFlux	Earth Engine Flux		
EEPS	Engine Exhaust Particle Sizer		
EESS	Earth Exploration Satellite Service		
EFEDA	European Field Experiment in a Desertification-Threatened Area		
EG-CLIMET	European Ground-Based Observations of Essential Variables for Climate and Operational Meteorology		
EIA	extended-interaction amplifier		
EIK	extended-interaction klystron		
EIKA	extended-interaction klystron amplifier		
ELDORA	Electra Doppler Radar		
ELF	extremely low frequency		
ELPI	electrical low-pressure impactor		
ELVOC	extremely low-volatility organic compound		
EM	electromagnetic		
eMAS	Enhanced MODIS Airborne Simulator		

F

FA	fractional absorption
FAGE	Fluorescence Assay by Gas Expansion
FAPAR	Fraction of Absorbed Photosynthetically Active Radiation
FAR	false alarm rate
FASTEM	fast microwave emissivity model
FBG	fiber Bragg grating
FC	field capacity
FCA	full correlation analysis
FCDR	fundamental climate data records
FD	forced diffusion
FDI	frequency-domain interferometry
FDL	flux detection limit
FDMS	filter dynamic measurement system
FDR	frequency domain reflectometry
FET	field-effect transistors
FFT	Fast Fourier Transform
FFTS	Fast Fourier Transform Spectrometer
FGGE	First GARP Global Experiment
FHP	five-hole probe
FIA	flow injection analysis
FIFE	First ISLSCP Field Experiment

FIR	finite impulse response	GF (s.c.)	glass fiber filter coated with s.c.
FIR	fog interception rate	GHG	greenhouse gas
FLEX	FLuorescence EXplorer	GHI	global horizontal irradiance
FLEX	Fluorescence Explorer	GHOST	Global Horizontal Sounding Technique
FLUXNET	Network of FLUX Measurement Sites	GIS	Geographic Information System
FM	flow meter	GLAS	Geoscience Laser Altimeter System
FMCW	frequency-modulated continuous wave	GLONASS	Global Navigation Satellite System
FMCW radar	frequency-modulated continuous-wave radar	GLORIA	Gimballed Limb Observer for Radiance Imaging in the Atmosphere
FMICW	frequency-modulated interrupted continuous wave	GM	Geiger–Müller
FMPS	fast mobility particle sizer	GM	gradient method
FMS	frequency modulation	GMD	geometric mean diameter
FNBW	first null beam width	GMI	GPM Microwave Imager
FO	fiber-optic	GMS	Geostationary Meteorological Satellite
FOM	figure of merit	GMT	Greenwich Mean Time
FORTRAN	Formula Translation	GNSS	Global Navigation Satellite System
FOV	field of view	GO3OS	Global Ozone Observing System
FPGA	field-programmable gate array	GOCE	Gravity Field and Steady-State Ocean Circulation Explorer
FPH	frostpoint hygrometer	GOES	Geostationary Operational Environmental Satellite
FRAND	fair, reasonable, nondiscriminatory	GOEME	Global Ozone Monitoring Experiment
FRP	fire radiative power	GOMS	Geostationary Operational Meteorological Satellite
FSOI	forecast sensitivity to observation index	GORN	Liaison Group on Radar Networking
FSS	forward scatter signal	GOS	Global Observing System
FT	free troposphere	GOSAT	Greenhouse Gases Observing Satellite
FTIR	Fourier-transform Infrared Spectroscopy	GPM	Global Precipitation Measurement
FTIR	Fourier-Transform Infrared Spectroscopy	GPS	Global Positioning System
FTP	file transfer protocol	GPSRO	GPS Radio Occultation
FTS	Fourier-transform Spectrometer	GRACE-II	Gravity Recovery and Climate Experiment II
FVFD	fractional vertical flux divergence	GRAS	GNSS Receiver for Atmospheric Sounding
FWHM	full width at half maximum	GRP	glass-fiber reinforced plastic

G

GAARS	Global Atmospheric Aerosol and Radiation Study	GRUAN	GCOS Reference Upper-Air Network
GaAsP	gallium arsenide phosphide	GSO	geosynchronous orbit
GACM	Global Atmospheric Composition Mission	GTI	global tilted irradiance
GARP	Global Atmospheric Research Program	GTS	Global Telecommunication System
GAW	Global Atmosphere Watch	GUAN	GCOS Upper-Air Network
GAW-PFR	Global Atmosphere Watch–Precision Filter Radiometer	GUM	Guide to the Expression of Uncertainty in Measurement
GAWSIS	GAW Station Information System	GURME	GAW Urban Research Meteorology and Environment Project
GC	gas chromatography	GV	Gulfstream V
GCM	Global Climate Model	GW	ground water
GCOS	Global Climate Observing System		
GCRF	Geocentric Celestial Reference Frame		
GDACCS	Geometrical Displacement and Conduction Current Sensor		
GDP	Global Drifter Program		
GEO-CAPE	Geostationary Coastal and Air Pollution Event		
GEOSS	Global Earth Observing System of Systems		
GERB	Geostationary Earth Radiation Budget Experiment		
GEWEX	Global Energy and Water Exchanges		

H

HADCP	horizontal ADCP
HALO	High Altitude and Long Range Research Aircraft
HAMP	HALO Microwave Package
HAPEX	Hydrologic Atmospheric Pilot Experiment
HAR	High-Altitude Radar
HATPRO	Humidity and Temperature Profiler
HATS	Halocarbons and other Atmospheric Trace Species

HCI	human–computer interaction	ICL	Interband Cascade Laser
HCP	height corrected pressure	ICM	Implementation and Coordination Meeting
HCR	HIAPER Cloud Radar		
HD	hazard distance	ICON-LEM	Icosahedral Nonhydrostatic Large Eddy Model
HD	high dose		
HDD	heating degree days	ICOS	Integrated Carbon Observation System
HDF	Hierarchical Data Format	ICOS	Integrated Cavity Output Spectroscopy
HDF5	Hierarchical Data Format, version 5	IE	intercomparison exercise
HDPE	high-density polyethylene	IF	intermediate frequency
HDSS	High-Definition Sounding System	IF	interference filter
HEPA	high-efficiency particulate air	IFC	intensive field campaign
HF	high frequency	IFD	intermediate frequency digitizer
HFC	hydrofluorocarbon	IFS	integrated forecast system
HIAPER	High-Performance Instrumented Airborne Platform for Environmental Research	IGACO	Integrated Global Atmospheric Chemistry Observation
HIRDLS	High-Resolution Dynamics Limb Sounder	IGBT	insulated gate bipolar transistor
		IGRA	infrared absorption gas analyzer
HIRS/4	High-Resolution Infrared Radiation Sounder	IGY	International Geophysical Year
		IHOP	International Water Vapor Project
HITRAN	High-Resolution Transmission Molecular Absorption Database	IIR	infinite impulse response
		IIR	Imaging Infrared Radiometer
HIWRAP	High-Altitude Imaging Wind and Rain Airborne Profiler	IL	interception loss
		ILS	instrumental line shape
HMMS	Horizontal Mobile Measurement System	IMIS	Integrated Measuring and Information System for the Surveillance of Environmental Radioactivity
HOM	highly oxidized multifunctional molecule		
		IMPROVE	Interagency Monitoring of Protected Visual Environments
HOPE	HD(CP) ² Observational Prototype Experiment		
		IMS	International Monitoring System
HPBW	half-power beam width	IMS	ion-mobility spectroscopy
HPLC	high-performance liquid chromatography	IMU	inertial measurement unit
		IN	ice nucleus
HRDL	High Resolution Doppler Lidar	INDAAF	International Network to Study Deposition and Atmospheric Chemistry in Africa
HREA	Hyperbolic Relaxed Eddy Accumulation		
HS	heterogeneous sensor	INS	inertial navigation system
HSB	Humidity Sounder for Brazil	IOMS	instrument odor measurement system
HSR	high spectral resolution	IoT	internet of things
HSRL	High Spectral Resolution Lidar	IP	internet protocol
HTDMA	Hygroscopic Tandem Differential Mobility Analyzer	IPAB	International Programme for Antarctic Buoys
HWS	horizontal wind speed	IPC	International Pyrheliometer Comparison
HYMEX	Hydrological Cycle in the Mediterranean Experiment	IPDA	integrated path differential absorption
		IPgC	International Pyrgeometer Comparison
		IPM	inflection point method
		IPS	International Pyrheliometric Scale
		IPT	integrated profiling technique
		IR	infrared
IABP	International Arctic Buoy Program	IRGA	infrared gas analyzer
IAGC	instantaneous automatic gain control	IRIS	Infrared Integrating Sphere Radiometer
IAGOS	In-service Aircraft for Global Observing System	IRMS	Isotope Ratio Mass Spectrometry
		IRS	Inertial Reference System
IASI	Infrared Atmospheric Sounding Interferometer	IRSR	interim reference sunshine recorder
		IRT	infrared thermometer
IC	ion chromatograph	ISA	ICAO standard atmosphere
IC	ion chromatography	ISD	ice crystal size distribution
IC	intracloud	ISL	inertial sublayer
IC	interception capacity	ISLSCP	International Satellite Land Surface Climatology Project
ICESat-II	Ice, Cloud, and Land Elevation Satellite II		
ICI	Ice Cloud Imager		

ISR	intermediate storage reservoir	LF	low frequency
ITC	integral turbulence characteristics	LGB	Lehmann–Groß–Bahn
ITOS	Improved TIROS Operational System	LHC	lefthanded circular
ITRF	international terrestrial reference frame	LHN	latent heat nudging
ITS	International Temperature Scale	LI	lifted index
ITS-90	International Temperature Scale 90	lidar	light detection and ranging
IWC	ice water content	LIF	laser-induced fluorescence
IWP	ice water path	LIN	linear channel
IWV	integrated water vapor	LIP	laser-induced phosphorescence
I&Q	In-phase & Quadrature	LIPGLOS	laser-induced phosphorescence of (methyl)glyoxal spectrometry
<hr/>			
J			
JPSS	Joint Polar Satellite System	LIST	Lidar Surface Topography
JRAS	Jena Reference Air Set	LITE	Lidar In-space Technology Experiment
<hr/>			
K			
KENDA	kilometer-scale ensemble data assimilation	LITFASS	Lindenberg Inhomogeneous Terrain—Fluxes Between Atmosphere and Surface: a Long-Term Study
KO	konvektiv-index	LM	laser mirror
KPR	Ka-Band Precipitation Radar	LMS	localized multifunction sensor
KU	kurtosis	LNA	low-noise amplifier
<hr/>			
L			
L	lens	LNG	lidar aerosols nouvelle génération
LACROS	Leipzig Aerosol and Cloud Remote Observations System	LN ₂	liquid nitrogen
LADCP	Lowered Acoustic Doppler Current Profiler	LO	local oscillator
LAFE	Land–Atmosphere Feedback Experiment	LO	local reference frame
LAI	Leaf-area Index	LoA	letter of agreement
LALINET	Latin America Lidar Network	LOD	limit of detection
LAN	Local Area Network	LOG	logarithmic channel
LAPSE-RATE	Lower Atmospheric Process Studies at Elevation—a Remotely Piloted Team Experiment	LOPAP	Long-Path Absorption Photometer
LAS	large-aperture scintillometer	LOS	line of sight
LASE	Lidar Atmospheric Sensing Experiment	LPI	low-pressure impactor
LASS	Location-aware Sensing System	LR	lidar ratio
LBA	Large-Scale Biosphere–Atmosphere	LRU	line replaceable units
LBLRTM	Line-By-Line Radiative Transfer Model	LSA	land surface analysis
LCZ	local climate zone	LSB	least significant bit
LD	low dose	LSC	liquid scintillation spectroscopy
LDA	laser Doppler anemometer	LSE	least squares estimation
LDM	local data manager	LSQ	least squares
LDR	linear depolarization ratio	LSSF	large-scale single function
LE	latent heat	LST	land surface temperature
LEANDRE	lidar pour l'étude des interactions aérosols nuages dynamique rayonnement et du cycle de l'eau	LT	local time
LED	light-emitting diode	LTERR	Long-Term Ecological Research
LEED	leadership in energy and environmental design	LTI	linear time-invariant
LER	least expensive radar	LTST	local true solar time
LES	Large Eddy Simulation	LU	lower-upper (matrix decomposition)
LETKF	Local Ensemble Transform Kalman Filter	LWC	liquid water content
		LWIM	Low-power Wireless Integrated Microsensors
		LWP	liquid water path
<hr/>			
M			
M-GGA	Microportable Greenhouse Gas Analyzer		
M2AV	Meteorological Mini Aerial Vehicle		
MAAP	Multi-angle Absorption Photometer		
MAD	absolute deviation from the median		
MAGS	Mackenzie GEWEX Study		
MaNiP	manipulation nitrogen and phosphorous		
MART	multiplicative algebraic reconstruction technique		
MASC	Multi-purpose Airborne Sensor Carrier		

MASTER	MODIS/ASTER Airborne Simulator	MOST	Monin–Obukhov similarity theory
MAV	micro air vehicle	MOUDI	Micro-orifice Uniform Deposit Impactor
MBR	modified Bowen ratio method	MOZAIC	Measurement of Ozone and Water Vapour on Airbus In-service Aircraft
MC	Monte Carlo	MPD	MicroPulse DIAL
MCM	master chemical mechanism	MPL	Micro-Pulse Lidar
MCP	microchannel plate	MPLNET	Micro-Pulse Lidar Network
MCS	mobile crowdsourcing	MPM	microwave propagation model
MCSE	minimum chi square estimation	MPSS	Mobility Particle Size Spectrometer
MDN	Mercury Deposition Network	MR	measurement result
MDS	minimum detectable signal	MRA	Mutual Recognition Arrangement
MELTEX	Impact of Melt Ponds on Energy and Momentum Fluxes between Atmosphere and Sea Ice	MRT	Magnetic Resonance Tomography
		MRU	Motion Reference Unit
MEMS	microelectromechanical system	MS	mesosphere
MESH	maximum estimated size of hail	MS	mass spectrometer
METEOSAT	Meteorological satellite	MSG	METEOSAT Second Generation
MetOp	Meteorological Operational Satellite	MSI	Multispectral Imager
MetOp-SG	Meteorological Operation Satellite, Second Generation	MSI	Multispectral Instrument
METRIC	Mapping Evapotranspiration at High Resolution Using Internalized Calibration	MSL	mean sea level
		MSP	Mie spectrometer
METROMEX	Metropolitan Meteorological Experiment	MSS	Multispectral Scanner
		MST	mesosphere-stratosphere-troposphere
MFC	mass flow controller	MST	Mountain Standard Time
MFP	multihole flow probe	MSU	Microwave Sounding Unit
MFRSR	multifilter rotating shadowband radiometer	MTBF	Mean Time Between Failures
		MTG	METEOSAT Third Generation
MG	measurement guideline	MTI	Moving Target Indicator
MH	mixing height	MTP	Microwave Temperature Profiler
MHS	Microwave Humidity Sounder	MUSIC	MULTiple Signal Classification
MIMIC	Microwave and Millimeter-wave Integrated Circuit	MVIRI	METEOSAT Visible and Infrared Imager
		MW	microwave
MIMO	Multiple-input Multiple-output	MWI	Microwave Imager
MIR	mid-infrared	MWR	microwave radiometry
MISR	Multi-angle Imaging SpectroRadiometer	MWR	microwave radiometer
MITRA	monitor to measure the integral transmittance	MWS	microwave sounder
		MWS	microwave scintillometer
ML	mixed layer	MZI	Mach–Zehnder Interferometer
MLE	maximum likelihood estimation		
MLH	mixed-layer height	N	
MLS	maximum length sequence		
MLS	Microwave Limb Sounder	NADP	National Atmospheric Deposition Program
MLT	mean local time	NAIS	Neutral Cluster and Air Ion Spectrometer
MM	multimode	NARVAL	Next-Generation Aircraft Remote Sensing for Validation
MMIC	Monolithic Microwave-integrated Circuit	NAST-I	NPOESS Airborne Sounder Testbed Interferometer
MODE-S EHS	Mode-Selective Enhanced Surveillance Data	NAWDEX	North Atlantic Waveguide and Downstream Impact Experiment
MODIS	Moderate Resolution Imaging Spectroradiometer	NBL-K	nocturnal boundary-layer Keeling plot
MODTRAN	MODerate resolution atmospheric TRANsmission	NDACC	Network for the Detection of Atmospheric Composition Change
MONS	Meteorological Orthonormal Coordinate System	NDDN	National Dry Deposition Network
MOPA	master oscillator power amplifier	NDSC	Network for the Detection of Stratospheric Change
MOPITT	Measurements of Pollution in the Troposphere	NDVI	Normalized Difference Vegetation Index
MOR	meteorological optical range	NEDT	noise equivalent differential temperature

NEE	Net Ecosystem Exchange
NEON	National Ecological Observatory Network
NetCDF	network common data form
NEWA	Network for Environmental and Weather Application
NEXRAD	Next-generation Radar
NF	noise figure
NH	northern hemisphere
NIM	Nuclear Instrumentation Module
NIP	Normal Incidence Pyrheliometer
NIR	near-infrared
NMC	National Meteorological Center
NMHC	non-methane hydrocarbons
NOHD	Nominal Ocular Hazard Distance
NPOESS	National Polar-orbiting Operational Environmental Satellite System
NRC	National Radiation Center
NRCS	normalized radar cross-section
NRWI	non-rain water input
NSBL	nocturnal stable boundary layer
NTC	negative temperature coefficient
NTN	National Trends Network
NWC SAF	Nowcasting SAF
NWM	Numerical Weather Model
NWP	Numerical Weather Prediction

O

OA-ICOS	off-axis integrated cavity output spectroscopy
OD	optical depth
ODIM	OPERA Data Information Model
OFDS	Optical-fiber-based Distributed Sensing
OLCI	Ocean and Land Colour Instrument
OLI	Operational Land Imager
OMI	Ozone Monitoring Instrument
OMPS	Ozone Mapping and Profiler Suite
OMS	optical-microwave scintillometer
OMT	orthomode transducer
OPC	optical particle counter
OPD	optical path difference
OPERA	Operational Programme for the Exchange of Weather Radar Information
OPO	optical parametric oscillator
OPS	optical particle spectrometer
ORACLES	Observations of Aerosols above Clouds and Their Interactions
OSCAR	Observing Systems Capability Analysis and Review Tool
OSCR	ocean surface current radar
OSI SAF	Ocean and Sea Ice SAF
OU	odor unit
OVOC	oxygenated VOC
OWS	ocean wind speed

P

P(p.a.)	p.a.-coated paper filter
PAH	polyaromatic hydrocarbon
PAN	peroxyacetyl nitrate
PAR	Photosynthetically Active Radiation
PARASOL	Polarization and Anisotropy of Reflectances for Atmospheric Science coupled with Observations from a Lidar
PASS	Photoacoustic Soot Spectrometer
PATH	Precipitation and All-Weather Temperature and Humidity
PAX	Photoacoustic Extinctionmeter
PBDE	polybrominated diphenyl ether
PBL	planetary boundary layer
PBP	Pellin–Broca prism
PBS	polarizing beam splitter
PC	personal computer
PCB	polychlorinated biphenyl
PCDD	polychlorinated dibenzodioxin
PCDF	polychlorinated dibenzofuran
PD	public domain
PDCA	plan–do–check–act
PDE	partial differential equation
PDF	portable digital format
PDT	Pacific Daylight Time
PE	polyethylene
PE	permutation entropy
PE-HD	polyethylen high density
PECAN	Plains Elevated Convection at Night
PERCA	peroxy radical amplifier
PF	photo-fragmentation
PFA	perfluoroalkoxy
PFB	polyphase filter-bank
PFN	pulse forming network
PG	potential gradient
PIA	path-integrated attenuation
PIMS	programmable ion mobility spectrometer
PIR	Precision Infrared Pyrometer
PLS	polystyrene latex sphere
PM	Penman–Monteith
PM	particulate matter
PMM	probability matching method
PMS	Particle Measuring Systems
PMT	photomultiplier tube
PNNL	Pacific Northwest National Laboratory
POFD	probability of false detection
POLDER	Polarization and Directionality of the Earth's Reflectances
POP	persistent organic pollutant
POSH	Probability of Severe Hail
PP	polypropylene
PPFD	Photosynthetic Photon Flux Density
PPGIS	Public Participatory Geographic Information Systems
PPI	plan position indicator
PPLN	periodically poled lithium niobate
PPP	precise point positioning
PPP	public–private partnerships

PPP	pulse-pair processing
PRF	pulse repetition frequency
PRT	pulse repetition time
PS	participatory sensing
PS	Primary Standard
PSAP	Particle Soot Absorption Photometer
PSD	particle-size distribution
PSP	precision spectral pyranometer
PTC	positive temperature coefficient
PTFE	polytetrafluoroethylene
PTR	proton transfer reaction
PUF	polyurethane foam
PV	photovoltaic
PVC	polyvinyl chloride
PW	precipitable water
PW	pulse width
PWD	present weather detector
PWS	personal weather station
PWV	precipitable water vapor
PZT	lead zirconate titanate

Q

QA	quality assessment
QA	quality assurance
QBO	quasi-biennial oscillation
QC	quality control
QCL	quantum cascade laser
QCLAS	quantum cascade laser absorption spectroscopy
QE	quantum efficiency
QMS	quadrupole mass spectrometer
QNH	atmospheric pressure adjusted to sea level
QPC	quadratic phase coding

R

RA	regional association
radar	radio direction and ranging
RAF	Research Aviation Facility
RANS	Reynolds-averaged Navier–Stokes
RASS	Radio-Acoustic Sounding System
RASS	Radio-acoustic Sounding System
RASTA	Radar System Airborne
RAWS	remote automatic weather station
RC	resistor-capacitor
RCC	Regional Calibration Centre
RDF	radio direction finder
RE	radiative effect
REA	Relaxed Eddy Accumulation
REPARTEE	Regents Park and Tower Environmental Experiment
REV	representative elementary volume
REW	readily evaporable water
REWS	rotor-equivalent wind speed
RF	radio frequency
RFI	radio-frequency interference

RG	rain gauge
RHC	righthanded circular
RHI	range-height indicator
RIM	range imaging
RMS	root mean square
RMSE	root-mean-square error
RODOS	Realtime Online Decision Support System
ROE	receiver-over-elevation (gear)
RP	receiver protectors
RPA	remotely piloted aircraft
RPAS	remotely piloted aircraft system
RPM	revolutions per minute
RPT	resonant pressure transducer
RR	rotational Raman
RRC	regional radiation center
RS	radiosonde
RS	remote sensing
RSI	rotating shadowband irradiometer
RSL	roughness sublayer
RSP	Research Scanning Polarimeter
RSP	Rayleigh spectrometer
RSP	rotating shadowband pyranometer
RSR	rotating shadowband radiometer
RT	radiative transfer
RTE	radiative transfer equation
RTTOV	radiative transfer for ATOVS
RTTOV-gb	ground-based radiative transfer for TIROS operational vertical sounder
RUC	rapid update cycle
RV	research vessel
RVH	recirculating ventilation and heating
RVR	runway visual range
RWIS	roadway weather information system
RWP	radar wind profiler

S

SA	spaced antenna
SAF	Satellite Application Facility
SAFIRE	Service des Avions Francais Instrumentés pour la Recherche en Environnement
SAI	surface area index
SAMUM	Saharan Mineral Dust Experiment
SAPHIR	Simulation of Atmospheric Photochemistry in a large Reaction Chamber
SAR	Synthetic Aperture Radar
SASBE	site atmospheric state best estimate
SBL	stable stratified boundary layer
SbS	side by side
SBS	stimulated Brillouin scattering
Scale-X	Scale-crossing Land-surface and Boundary Layer Processes
SCD	slant column density

SCIAMACHY	Scanning Imaging Absorption Spectrometer for Atmospheric Cartography	SORA	Specific Operations Risk Assessment
SCLP	Snow and Cold Land Process	SOWER	Sounding of Ozone and Water in the Equatorial Region
SCMS	Small Cumulus Microphysics Study	SPN	sunshine pyranometer
SCU	scatter meter calibration units	SPOT	Satellite Pour l'Observation de la Terre
SDS-WAS	Sand and Dust Storms Warning Advisory and Assessment System	SQI	signal quality index
SEBAL	Surface Energy Balance Algorithms for Land	SR	surface renewal
SEVIRI	Spinning Enhanced Visible and Infrared Imager	SRAL	Synthetic Aperture Radar Altimeter
SF	stemflow	SS	single scattering
SFC	Standard Fog Collector	SSA	single-scattering albedo
SGP	Southern Great Plains	SSM	solid-state modulator
SH	southern hemisphere	SSM/I	Special Sensor Microwave/Imager
SHADOZ	Southern Hemisphere Additional Ozonesondes	SSMIS	Special Sensor Microwave Imager/Sounder
SHD	slant hydrostatic delay	SSPA	solid-state power amplifier
SI	International System of Units (Système international d'unités)	SSS	sea surface salinity
SIA	sea-ice-air	SST	sea surface temperature
SIC	sea ice concentration	SSW	sudden stratospheric warming
SIP	sorbent-impregnated PUF	ST	stratosphere
SIRT	simultaneous iterative reconstruction technique	STALO	Stable Local Oscillator
SIS	shortwave incoming surface radiation	STAR	simultaneous transmit and receive
SIWV	slant-integrated water vapor	STD	slant total delay
SJAC	Steam-jet Aerosol Collector	STINHO	Structure of Turbulent Processes Under Inhomogeneous Surface Conditions
SK	skewness	sUAS	small unmanned aircraft system
SL	surface layer	SUI	Solar Ultraviolet Imager
SLS	surface-layer scintillometer	SUMO	Small Unmanned Meteorological Observer
SLSTR	Sea and Land Surface Temperature Radiometer	Suomi-NPP	National Polar-orbiting Partnership
SM	single mode	SUV	sport utility vehicle
SM-DTS	soil moisture distributed temperature sensing	SVD	singular value decomposition
SMA	social media analytic	SVF	sky-view factor
SMACEX	Soil Moisture Atmosphere Coupling Experiment	SVN	Apache Subversion
SMAP	Soil Moisture Active-Passive	SVOC	semivolatile organic compound
SML	surface mixed layer	SVP	Surface Velocity Program
SMMR	scanning multichannel microwave radiometer	SVPB	surface velocity program barometer
SMOS	Soil Moisture and Ocean Salinity	SWAT	Soil and Water Assessment Tool
SMPS	Scanning Mobility Particle Spectrometer	SWC	water content of soil
SMR	submillimeter radiometer	SWD	slant wet delay
SND	Schotanus-Nieuwstadt-DeBruin	SWE	snow water equivalent
SNODAR	Surface Layer Non-Doppler Acoustic Radar	SWOT	Surface Water and Ocean Topography
SNR	signal-to-noise ratio	SWR	standing wave ratio
SO	observatory service	SYNOP	Surface Synoptic Observations
SOA	secondary organic aerosol	SYRSOC	synergistic remote sensing of cloud
SOC	system on chip	SZA	solar zenith angle
sodar	sonic detection and ranging	S&H	sample and hold
SONAR	sound navigation and ranging		
SONET	Sun/sky-radiometer Observation Network		
SOP	standard operating procedure		
		T	
		T(IC)	Teflon filter for ion chromatographic analysis
		T(XRF)	Teflon filter for x-ray fluorescence analysis
		TAC	traditional alphanumeric code
		TBG	tipping-bucket gauge
		TBR	tipping-bucket rain gauge
		TCCON	Total Carbon Column Observing Network

TCDR	thematic CDR		Intensity with a Constellation of Smallsats
TC ⁴	Tropical Composition, Cloud and Climate Coupling	TROPOMI	TROPOspheric Monitoring Instrument
TDCF	table-driven code form	TRY	test reference year
TDDR	Total Direct and Diffuse Radiometer	TS	total scattering
TDL	tunable diode laser	TSEB	two source energy balance
TDLAS	Tunable Diode Laser Absorption Spectroscopy	TSG	test signal generator
TDLIF	thermal desorption laser-induced fluorescence	TSG	thermosalinograph
TDLS	tunable diode laser spectroscopy	TSI	total solar irradiance
TDR	time-domain reflectometry	TSP	total suspended matter
TDSI	time-dependent stochastic inversion	TSP	total suspended particles
TEA	Technology for Enabling Awareness	TTS	thermodynamic temperature scale
TEA	transverse-excited, atmospheric pressure	TV	television
TELSEM ²	Tool to Estimate the Land Surface Emissivity from the Microwaves to the Millimeter Waves	TVS	tornado vortex signature
TEM	transmission electron microscope	TWT	traveling-wave tube
TEOM	tapered element oscillating microbalance	TWTA	travelling-wave tube amplifier
TEOS-10	International Thermodynamic Equation of Seawater – 2010	TX	transmitter
TERENO	Terrestrial Environmental Observatories		
TES	Tropospheric Emission Spectrometer	U	
TESSEM ²	Tool to Estimate Sea Surface Emissivity from Microwave to Submillimeter Waves	UA	unmanned aircraft
TEW	total amount of water that can be evaporated	UA	unmanned autonomous
TFT	thin-film transistor	UARS	Upper Atmospheric Research Satellite
TGA	trace gas analyzer	UAS	unmanned aircraft system
TIR	thermal infrared	UAV	unmanned aerial vehicle
TIROS	Television Infrared Observation Satellite	UBL	urban boundary layer
TIRS	thermal infrared sensor	UCL	urban canopy layer
TKE	turbulent kinetic energy	UFP	ultrafine particle
TLE	transient luminous event	UHF	ultra-high frequency
TLSE	total least squares estimation	UHI	urban heat island
TLT	true local time	ULF	ultra low frequency
TM	Thematic Mapper	UNEP	United Nations Environment Programme
TMI	TRMM Microwave Imager	UPS	uninterruptible power supply
TMY	typical meteorological year	URL	uniform resource locator
TOA	top of the atmosphere	USB	Universal Serial Bus
TOPAZ	Tunable Optical Profiler for Aerosol and Ozone	UT	universal time
TOPROF	Towards Operational Ground Based Profiling With Ceilometers, Doppler Lidars and Microwave Radiometers for Improving Weather Forecasts	UTC	Coordinated Universal Time
TOS	TIROS Operational System	UTCI	universal thermal climate index
TRAM	Transect Measurement	UTLS	upper troposphere lower stratosphere
TREX	trace gas extractor	UV	ultraviolet
TRF	TSI radiometer facility	UW	uniform wind
TRIPEx	Triple-frequency and Polarimetric Radar Experiment	V	
TRL	temperature rotational Raman lidar	VAD	velocity azimuth display
TRL	temperature Raman lidar	VCD	vertical columns density
TRMM	Tropical Rainfall Measuring Mission	VCP	volume coverage pattern
TROPICS	Time-Resolved Observations of Precipitation structure and storm	VCPC	Variable Conditions Pyrheliometer Comparison
		VCSEL	vertical cavity surface emitting laser
		VGI	volunteered geographic information
		VGM	van Genuchten–Mualem
		VHF	very high frequency
		VI	vegetation index
		VII	vertically integrated ice
		VIIRS	Visible Infrared Imaging Radiometer Suite
		VIL	vertically integrated liquid

VILD	vertically integrated liquid density	WOUDC	World Ozone and Ultraviolet Radiation Data Centre
VIS	visual range	WOW	Weather Observation Website
VLF	very low frequency	WP	wilting point
VLOS	visual line of sight	WPDN	Wind Profiler Demonstration Network
VOC	volatile organic compound	WPE	weighted permutation entropy
VPD	vapor pressure deficit	WPL	Webb–Pearman–Leuning
VPDB	Vienna Pee Dee Belemnite	WPMM	Window Probability Matching Method
VPR	video plankton recorder	WRC	water retention curve
VRP	vertical reflectivity profile	WRF	weather research and forecasting
VSMOW	Vienna Standard Mean Ocean Water	WRR	World Radiometric Reference
VSWR	voltage standing wave ratio	WSN	wireless sensor networks
VTDMA	volatility tandem differential mobility analyzer	WSOC	water-soluble organic carbon
VTOL	vertical takeoff and landing	WSOG	water-soluble organic gas
VWV	vertical wind variance	WTR	wind-temperature radar
W		WUE	water use efficiency
WAD	wet annular denuder	WVDIAL	water-vapor differential absorption lidar
WALES	Water Vapour Lidar Experiment in Space	WVR	water vapor radiometer
WARMs	Wyoming Air Resource Monitoring System	WVRL	water-vapor Raman lidar
WCC	World Calibration Centre	WVTRL	water-vapor and temperature Raman lidar
WCRP	World Climate Research Programme	WWC	wilting point water capacity
WERA	Wellen Radar	WWRP	World Weather Research Programme
WFC	Wide Field Camera	X	
WG	weighing gauge	XDD	Expendable Digital Dropsonde
WG	working group	XLAS	extra large-aperture scintillometer
WIGOS	WMO Integrated Global Observing System	XML	Extensible Markup Language
WINS	wireless integrated network sensors	XOVWM	Extended Ocean Vector Winds Mission
WIS/WIGOS	WMO Integrated Global Observation System	Y	
WLAN	Wireless Local Area Network	YAG	yttrium aluminum garnet
WLSE	weighted least squares estimation	Z	
WMO	World Meteorological Organization	ZHD	zenith hydrostatic delay
WMO–SPICE	World Meteorological Organization Solid Precipitation Intercomparison Experiment	ZTD	zenith total delay
WMS	wavelength modulation	ZWD	zenith wet delay
WOCE	World Ocean Circulation Experiment		

List of Symbols

All symbols used in each chapter are explained within that chapter itself, allowing each chapter to be read independently of this list of symbols. However, some basic symbols are identical in most of the chapters and are listed below. Because of the different scientific communities that have contributed to this handbook, some of the parameters may be represented by different symbols in some chapters.

Latin symbols

a	absolute humidity	kg m^{-3}
a_G	molecular heat conductance coefficient in soil	$\text{W m}^{-1} \text{K}^{-1}$
a_T	molecular heat conductance coefficient in air	$\text{W m}^{-1} \text{K}^{-1}$
Bo	Bowen ratio	
c	sound speed	m s^{-1}
c	speed of light in vacuum	m s^{-1}
c	concentration (general)	*
c_p	specific heat at constant pressure	$\text{J kg}^{-1} \text{K}^{-1}$
c_v	specific heat at constant volume	$\text{J kg}^{-1} \text{K}^{-1}$
C_G	volumetric heat capacity	$\text{W s m}^{-3} \text{K}^{-1}$
C_H	Stanton number	
C_{nn}	structure parameter of refraction	$\text{m}^{-2/3}$
C_{TT}	structure parameter of temperature	$\text{K m}^{-2/3}$
d	displacement height	m
d	measuring path	m
DOY	day of the year: Jan. 1 = 1	
e	base of the natural logarithm	
e	water vapour pressure	hPa
E	water vapour pressure at saturation	hPa
E	electric field	V m^{-1}
E	Irradiance, direct solar radiation	W m^{-2}
ET	Evapotranspiration	W m^2 or mm
E_d	diffuse solar radiation	W m^{-2}
E_g	global radiation	W m^{-2}
F	sensor surface area	m^2
F	force	kg m s^{-2}
F	flux (general)	*
F_c	dry deposition	$\text{kg m}^{-2} \text{s}^{-1}$
f	function (general)	*
f	frequency	s^{-1} or Hz
f	Coriolis parameter	s^{-1}
f	enhancement factor	
f_g	cut frequency	s^{-1} or Hz
f_s	sampling (Nyquist) frequency	s^{-1} or Hz
g	acceleration due to gravity	m s^{-2}
H	wave height	m
h	Planck's constant	Js
I	Intensity	*
J	Photolysis frequency	s^{-1}
k	absorption coefficient	m^{-1}
k	Boltzmann constant	J K^{-1}

k	thermal conductivity	$\text{W m}^{-2} \text{K}^{-1}$
L	Obukhov length	m
L	characteristic length scale	m
m	mixing ratio, mass fraction	kg kg^{-1}
M_a, m_d	molar mass of dry air	kg mol^{-1}
M_w, m_w	molar mass of water vapor	kg mol^{-1}
m_s	molar mass of a scalar	kg mol^{-1}
MOR	meteorological optical range	m
n	index of refraction	
N	particle number	m^{-3}
Nu	Nusselt number	
N_A	Avogadro constant	mol^{-1}
P	Particle scattering phase function	
p	air pressure	hPa
p_s	static air pressure	hPa
Pr	Prandtl number	
Pr_t	turbulent Prandtl number	
q	specific humidity	kg kg^{-1}
Q_E	latent heat flux	W m^{-2}
Q_E	latent heat flux expressed as a water column	mm
Q_G	ground heat flux	W m^{-2}
Q_H	sensible heat flux	W m^{-2}
r_a	turbulent atmospheric resistance	s m^{-1}
r_b	molecular-turbulent resistance	s m^{-1}
r_c	canopy resistance	s m^{-1}
r_s	stomatal resistance	s m^{-1}
R	resistance	Ω
R	radius	m
R, RH	relative humidity	%
R, R^*	universal gas constant	$\text{mol kg}^{-1} \text{K}^{-1}$
R_d	gas constant of dry air	$\text{J kg}^{-1} \text{K}^{-1}$
R_w	gas constant of water vapour	$\text{J kg}^{-1} \text{K}^{-1}$
Re	Reynolds number	
RF	Relative fugacity	
s_c	temperature dependence of specific humidity at saturation	$\text{kg kg}^{-1} \text{K}^{-1}$
S	solar constant	W m^{-2}
t	time	s
t	temperature	$^{\circ}\text{C}$
t_d	dewpoint temperature	$^{\circ}\text{C}$
t_w	wet-bulb temperature	$^{\circ}\text{C}$
T	absolute temperature, temperature difference	K
T_s	sonic (acoustic) temperature	K
T_v	virtual temperature	K
U	Voltage	V
U	Magnitude of the wind (module)	m s^{-1}
u	wind speed (general)	m s^{-1}
u	longitudinal/zonal component of the wind velocity	m s^{-1}
u_h	horizontal wind velocity	m s^{-1}
u_*	friction velocity	m s^{-1}
v	lateral/meridional component of the wind velocity	m s^{-1}
v_g	lateral component of the geostrophic wind	m s^{-1}
v_D	deposition velocity	m s^{-1}

V	Volume	m^3
V	characteristic velocity	m s^{-1}
V_N	standard visual range	m
w	vertical component of the wind velocity	m s^{-1}
x	measurement value	*
x	horizontal direction (length, fetch)	m
y	horizontal direction (length, perpendicular to x)	m
Z	geopotential height	gpm
Z	equation of time	min
z	height (general, geometric)	m
z_i	mixed-layer height	m
z_0	roughness parameter, roughness height	m

Greek symbols

α, ρ	albedo	
α	cubic thermal expansion coefficient	K^{-1}
β	backscatter coefficient	$\text{m}^{-1} \text{sr}^{-1}$
δ	Height of the internal boundary layer	m
ε	energy dissipation	$\text{m}^2 \text{s}^{-3}$
ε	emissivity	
θ	potential temperature	K
θ_v	virtual potential temperature	K
κ	von-Kármán constant	
κ	wave number	
λ	wavelength	m
λ	latent heat of evaporation for water	J kg^{-1}
λ	geographical longitude	°
μ	dynamic viscosity	$\text{kg m}^{-1} \text{s}^{-1}$
ν	kinematic (molecular) viscosity	$\text{m}^2 \text{s}^{-1}$
ρ	mass density	kg m^{-3}
σ_{SB}	Stefan-Boltzmann constant	$\text{W m}^{-2} \text{K}^{-4}$
σ_x^2	variance of the random variable x	*
τ	momentum flux	$\text{kg m}^{-1} \text{s}^{-2}$
τ	time constant	s
τ	optical thickness	m
φ	geographical latitude	°
φ_m	universal function for momentum	
φ_H	universal function for heat	
Φ	geopotential	$\text{m}^2 \text{s}^{-2}$
χ	mole fraction, mixing ratio	
Ω	Earth angular velocity	s^{-1}

Indices

a	air
d	dry
i	ice, sublimation
v	water vapor
w	water (also wet bulb)
0	standard values in meteorology, surface value

Other symbols

$\bar{\theta}$	time average of random variable θ
$\langle \theta \rangle$	ensemble average of random variable θ
$\theta' = \theta - \langle \theta \rangle$	zero-mean fluctuation of random variable θ
\vec{u}	vector of the variable u

Remark

* dimension according to the use of the parameter

Basics of Part A

Part A Basics of Atmospheric Measurement Techniques

1 Introduction to Atmospheric Measurements

Thomas Foken, Bayreuth, Germany
Frank Beyrich, Lindenberg, Germany
Volker Wulfmeyer, Stuttgart, Germany

2 Principles of Measurements

Wolfgang Foken, Zwickau, Germany

3 Quality Assurance and Control

Cove Sturtevant, Boulder, USA
Stefan Metzger, Boulder, USA
Sascha Nehr, Brühl, Germany
Thomas Foken, Bayreuth, Germany

4 Standardization in Atmospheric Measurements

Simon Jäckel, Düsseldorf, Germany
Annette Borowiak, Ispra, Italy
Brian Stacey, Didcot, UK

5 Physical Quantities

Thomas Foken, Bayreuth, Germany
Olaf Hellmuth, Leipzig, Germany
Bernd Huwe, Bayreuth, Germany
Dietrich Sonntag

1. Introduction to Atmospheric Measurements

Thomas Foken , Frank Beyrich, Volker Wulfmeyer 

Measurements in the atmosphere differ from measurements in other media because of the thermodynamic and radiative properties of air (e.g., low density, low heat capacity, and transparency to a large part of the electromagnetic spectrum) and the fact that the air is almost always in (often turbulent) motion. The vertical and horizontal distributions of meteorological elements and the spatial and temporal scales of processes strongly influence the selection of appropriate measurement methods and devices. This chapter gives a brief overview of the different ways of classifying atmospheric measurements, the relevant states and processes that influence measurements in the atmosphere, and basic measurement techniques (including some fundamental aspects of the performance and interpretation of these techniques). It focuses in particular on the so-called atmospheric boundary layer, since most measurements are performed in this region and most human activities take place there.

1.1	Measuring Meteorological Elements	4
1.2	History	7
1.2.1	Historical Measurements	7
1.2.2	First Measurement Networks	8

1.2.3	The Establishment of Global Meteorological Organizations	8
1.2.4	Historical Textbooks on Meteorological Measurements	9
1.3	The Structure of the Atmosphere	9
1.3.1	Vertical Distribution of Meteorological Elements	10
1.3.2	Horizontal Distribution of Meteorological Elements	15
1.3.3	Temporal Variability of Meteorological Elements	18
1.3.4	Scale Representativeness of Atmospheric Measurements	20
1.3.5	Scale Requirements for Data Assimilation	22
1.4	Devices, Systems, and Typical Specifications	23
1.5	Applications	26
1.5.1	Meteorological Measurement Databases and Visualization	26
1.5.2	Networks and Experiments	26
1.5.3	Applied Meteorology and Other Disciplines	27
1.6	Future Developments	27
1.7	Further Reading	28
	References	28

The weather and the climate crucially influence human life, ecosystems, and the environment. Agriculture, water management, energy production and transmission, traffic, health services, tourism, and other sectors of modern human society require high-quality meteorological services. Useful meteorological data and services are obtained by performing measurements and observations. These provide the basis for understanding Earth-system processes and for the development, operation, and verification of various types of models, ranging from complex global and regional numerical weather prediction and climate models to relatively simple parametric models used in engineering appli-

cations. Therefore, atmospheric data are collected not only by meteorological services but also by many other institutions, companies, and private users. Scientists need atmospheric data in different fields of research beyond meteorology and climatology; examples include remote sensing, biogeoscience, hydrology, and soil science. Many relevant applications require high-quality data and the use of the best measuring methods. Furthermore, climatological studies require data that can accurately be compared over long time periods (many decades)—it is important to ensure that climatological trends are not influenced by changes in instrumentation.

Because air is almost always in motion, measurements performed at a certain point in the atmosphere are always influenced by processes occurring not only at or close to this point but also over a larger domain, the size of which depends on the type and position of the measurement (especially the height above the surface). Therefore, when it is necessary to perform atmospheric measurements over land (i.e., to select appropriate sen-

sors and methods, sites, and measurement heights as well as the appropriate time resolution and averaging), it is important to consider the distributions and variability of meteorological elements in space and time over a wide range of scales above a mostly heterogeneous underlying surface, as far as measurements over land are concerned.

1.1 Measuring Meteorological Elements

The atmosphere can be described as a multiphase physicochemical system consisting of molecular nitrogen and oxygen, water in its three phases as well as a variety of trace gases, aerosol particles, and hydrometeors. *Meteorological elements* (or variables) are physical and chemical properties of air that characterize its thermodynamic state (e.g., pressure and temperature) and dynamics (wind), the composition of the atmosphere (trace gas concentrations, including humidity), and the processes that occur in it (e.g., fluxes of energy, momentum, and matter, as well as cloud physics). Measurements are usually performed to quantify these variables or to determine integral and macroscopic properties of the atmosphere (e.g., the cloud base height and type, and the visibility). Measurements are also performed to quantify processes at the interface between the atmosphere and the underlying surface (i.e., at the surfaces of water, rocks, soil, vegetation, snow, and ice). A variety of instruments and observation methods are available to determine these variables (chapters in Part E of this book). For many applications, multiple instruments are organized into sensor clusters, measurement systems, and networks (chapters in Part F of this book).

When performing measurements in the atmosphere, the basic principles of metrology (Chap. 2) and quality assurance and control (Chap. 3) are applied, and standardization may also be necessary (Chap. 4). These topics, together with tables of physical constants and atmospheric properties (Chap. 5), comprise the content of Part A of this book.

The measurements discussed in this book can be categorized into those performed with in-situ sensors and those obtained with remote sensing techniques. When measurements are carried out in-situ, the sensor is situated within the atmospheric volume that is being probed. The sensor may be fixed at a particular location or it may be moving along a measuring path. Such measurements require a sensor platform, which is typically a ground-based mast, tower, tripod, bar, or buoy (Chap. 6). Alternatively, in-situ sensors can be

carried by tethered or free-flying balloons, kites, and airborne platforms such as unmanned aerial systems, helicopters, and aircraft (Chaps. 37 and 49).

Remote sensing systems perform measurements in regions of the atmosphere that are located away from the sensor. They typically make use of the known propagation characteristics of light, radio, or sound waves in air to derive the values of atmospheric variables. These systems may be located at the Earth's surface (ground-based systems; Part C of this book) or on airborne or spaceborne platforms, such as satellites or space stations (Part D of this book). Remote sensing techniques can be further categorized into active and passive systems depending on whether they actively transmit the radiation used to derive the atmospheric properties or they simply detect radiation emitted from the atmosphere or from other sources (e.g., from the Sun or other stars).

Table 1.1 provides a basic overview of the methods used to derive the values of meteorological state and process variables from instrumental measurements, along with references to the different chapters of this book that discuss the techniques in detail. Besides instrumental measurements, visual observations and manual measurements are still performed to characterize the weather, visibility, cloud type and cover, snow depth and cover, etc. However, these visual observations are in the process of being replaced with more reproducible instrument-based techniques (Chap. 22). Different sensors can be combined in weather stations and profiling systems (Part E of this book), and these stations can be arranged in networks for a variety of applications (Part F of this book).

Figure 1.1 illustrates the variety of measuring methods and platforms used in the Global Observation System (GOS, Chap. 63). Similar diagrams could be presented for networks or experiments focusing on the so-called *mesoscale* (about 100–10 000 km²; see Sect. 1.3.3) or for measurements at the soil–vegetation–atmosphere interface for ecosystem studies.

Table 1.1 Overview of in-situ and remote sensing techniques used to measure variables in the atmosphere and at the interface between the atmosphere and the underlying surface (DIAL: differential absorption lidar; GNSS: Global Navigation Satellite System; HF: high frequency; IR: infrared; RASS: radio-acoustic sounding system; TDR: time-domain reflectometry)

Meteorological variable	In-situ sensor or technique (combination of sensors)	Chapters in this handbook	Remote sensing method	Chapters in this handbook
Thermodynamic and dynamic variables				
Temperature (and acoustic/virtual temperature)	Thermometer	Chap. 7	RASS	Chaps. 23, 31
	Sonic anemometer	Chap. 9	Raman lidar	Chap. 25
	Glass fiber technique	Chap. 20	(Acoustic) tomography	Chap. 35
	Simple sensors	Chap. 44		
Humidity	Hygrometer, gas analyzers	Chap. 8	Raman lidar	Chaps. 25, 38
	Glass fiber technique	Chap. 20	Spectrometer	Chap. 28
	Simple sensors	Chap. 44	DIAL	Chap. 26
			(Ground-based) GNSS	Chap. 36
Microwave radiometer	Chaps. 29, 41			
Sun photometer	Chap. 29			
Wind vector (wind speed and direction)	Anemometer/wind vane	Chap. 9	Doppler sodar	Chap. 23
	Glass fiber technique	Chap. 20	Doppler lidar	Chaps. 27, 38
	Simple sensors	Chap. 44	Weather radar	Chap. 30
	Pitot tube	Chaps. 48, 49	Doppler radar	Chaps. 31, 39
			HF radar	Chap. 33
			Scintillometer	Chap. 34
			(Acoustic) tomography	Chap. 35
Pressure	Barometer	Chap. 10		
	Simple sensors	Chap. 44		
Radiation	Pyranometer, pyrgeometer, net radiometer, etc.	Chap. 11	Radiometer	Chap. 29
	Glass fiber technique	Chap. 20	Sun photometer	Chap. 29
	Simple sensors	Chap. 44	Solar radiation sensor	Chap. 40
Sunshine duration	Radiation sensor	Chap. 11		
Precipitation	Precipitation gauge, disdrometer	Chap. 12	Weather radar	Chap. 30
	Simple sensors	Chap. 44	Radar in mm range	Chap. 32
Other variables				
Visibility	Transmissometer, scattered light sensor	Chap. 13	Backscatter lidar	Chap. 24
Atmospheric electricity	Potential probe	Chap. 14		
	Lightning detector			
Radioactivity	Radioactivity sensors	Chap. 15		
Trace gas concentrations	Gas analyzer, tunable diode laser	Chap. 16	Raman lidar	Chaps. 25, 38
			DIAL	Chap. 26
	Simple sensors	Chap. 44	Spectrometer	Chap. 28
			Radiometer	Chaps. 29, 41
Stable isotope concentrations	Gas analyzer, tunable diode laser	Chap. 17		
Aerosols, gases, and particles	Aerosol-measuring sensors Sampler	Chap. 18 Chap. 19	Backscatter lidar	Chap. 24
			Spectrometer	Chap. 28
			Sun photometer	Chap. 29
Cloud height and type			Backscatter lidar	Chap. 24
			Weather radar	Chap. 30
			Airborne radar	Chap. 39
Odor	Odor testing, measurements	Chap. 21		

Table 1.1 (Continued)

Meteorological variable	In-situ sensor or technique (combination of sensors)	Chapters in this handbook	Remote sensing method	Chapters in this handbook
Turbulent fluxes				
Momentum flux ^{a,b}	Eddy-covariance technique	Chaps. 48, 49, 55	Scintillometer	Chap. 34
Turbulent kinetic energy (TKE) and dissipation	Eddy-covariance technique	Chaps. 49, 55	Doppler wind lidar	Chap. 27
Sensible heat flux ^{a,c}	Eddy-covariance technique	Chaps. 48, 49, 55	Scintillometer	Chap. 34
Evapotranspiration ^{a,c}	Eddy-covariance technique	Chaps. 48, 49, 55	Scintillometer	Chap. 34
	Calculation techniques	Chap. 57		
	Lysimeter	Chap. 58		
Trace gas flux ^{a,c} (dry deposition)	Eddy-covariance technique	Chap. 55		
	Accumulation methods	Chap. 56		
	Calculation techniques	Chap. 54		
	Plant chambers	Chap. 59		
	Soil chambers	Chap. 60		
Fog deposition	Fog sampler	Chap. 53		
Variables at the interface between the atmosphere and the underlying surface				
Soil and canopy temperature	Thermometer	Chaps. 7, 61	IR remote sensing	Chap. 42
			Microwave remote sensing	Chap. 41
Soil and canopy moisture	TDR sensor	Chap. 61	Microwave remote sensing	Chap. 41
	Tensiometer	Chap. 61		
	Gravimetry	Chap. 61		
Soil heat flux	Heat flux plate	Chap. 61		
	Temperature profile	Chaps. 7, 61		
Gas flux at the soil–atmosphere interface	Soil chamber	Chap. 60		
Gas flux at the plant–atmosphere interface	Canopy chamber	Chap. 59		
Vegetation indices			Visible and IR remote sensing	Chap. 42
Water temperature	Thermometer	Chaps. 7, 62		
Water salinity, etc.	Different sensors	Chap. 62		
Gas flux at the water–atmosphere interface	Gradient measurements	Chap. 62		
Wave height	Wave sensor	Chap. 62	HF radar	Chap. 33

^a Turbulent fluxes can also be determined from profile measurements of wind, temperature, humidity, and trace gases. The method used is described in detail in Chap. 54 and briefly in Sect. 1.3.1.

^b Momentum flux is also relevant in the nonturbulent atmosphere (gravity waves)

^c Flux measurements can be performed with combinations of different remote sensing techniques; see the relevant chapters

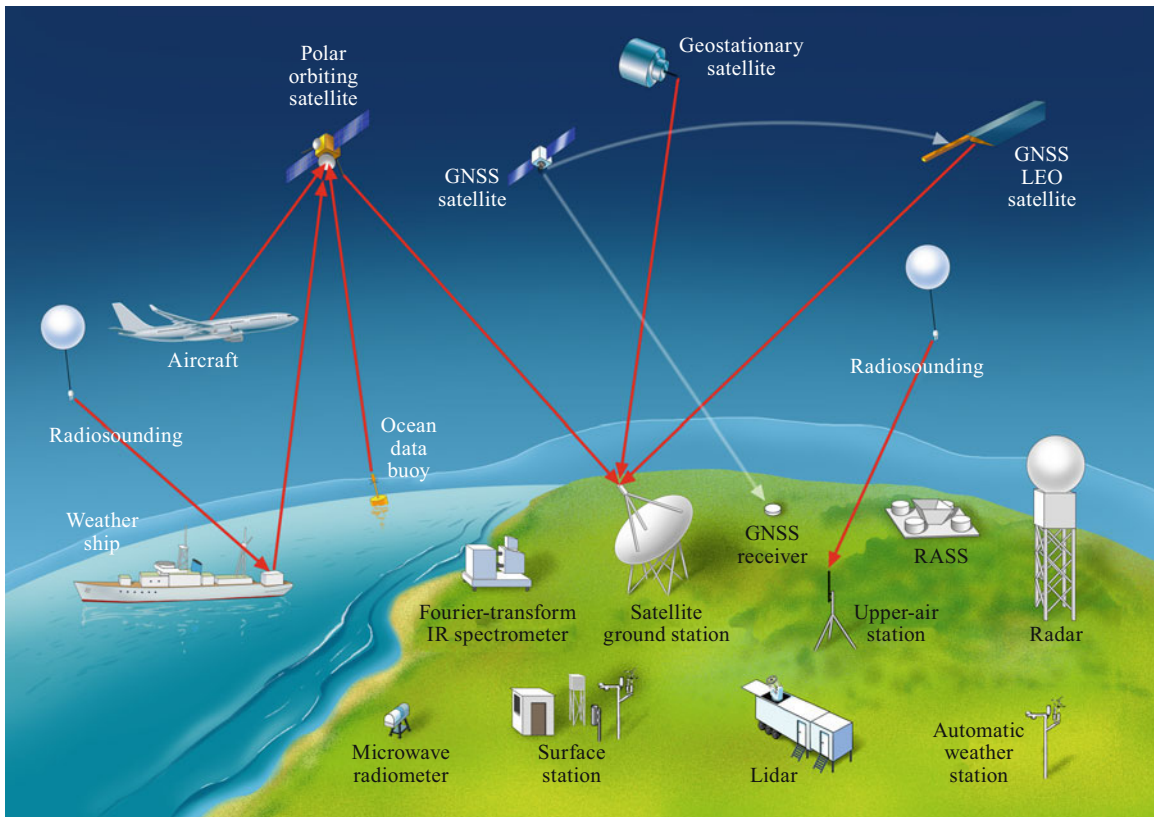


Fig. 1.1 Scheme of the Global Observing System (GOS) of the World Meteorological Organization (WMO) that illustrates how the most important in-situ systems and passive and active remote-sensing systems are used synergistically (after [1.1], reproduced with permission from John Wiley & Sons, Inc.)

1.2 History

The history of meteorology and measurements in the atmosphere has been described in many publications [1.2, 3]. A comprehensive timeline up to the middle of the last century is provided in [1.4]. Many of the measurement techniques and methods used early in the history of meteorology are not used anymore, but they are still important for understanding the atmospheric measurements performed today. Therefore, each chapter of this book has a small history section. Only a few aspects of general interest, mostly based on European history, are discussed below.

1.2.1 Historical Measurements

The first meteorological observations to be described and documented occurred in ancient times (e.g., in the *Meteorologica* written by *Aristotle* [1.5]). The first hygrometers were likely developed in the Western Han dynasty of ancient China between 200 BCE and

10 CE [1.6]. During the Renaissance period, great advances were made in the natural sciences, and some of the first instruments were constructed and built by *Leonardo da Vinci* (1452–1512) and *Galileo Galilei* (1564–1642). These instruments were thermometers, barometers, hygrometers, and wind vanes (see the chapters on temperature, pressure, humidity, and wind). By the middle of the seventeenth century, the academy at Florence had accumulated a collection of various instruments [1.7].

In a meteorological context, the thermometers made by *Gabriel Daniel Fahrenheit* (1686–1736), *René-Antoine Ferchault de Réaumur* (1683–1757), and *Anders Celsius* (1704–1744) are particularly well known. After first attempting to create water barometers, *Evangelista Torricelli* (1608–1647), a student of Galilei, developed the mercury barometer. In Europe, the first hair hygrometer was invented by *Benedict de Saussure* (1740–1799), and the first applicable psychrometer was

developed by *Ernst Ferdinand August* (1795–1870). Rain gauges have been employed since ancient times in India and China, but the first cylindrical gauges were used by *Benedetto Castelli* (1577–1644) in Perugia. The first wind vanes were constructed by *Egnato Danti* (1537–1586) in Bologna, and the rotation anemometer was developed by *Michael Lomonosow* (1711–1765). *Robert Hooke* (1635–1703) developed a combination of different instruments known as the weather clock. By the end of the eighteenth century, a combination of instruments for measuring several meteorological elements simultaneously was available, and it was used during scientific expeditions such as that performed by *Alexander von Humboldt* (1769–1859) to South America. The first systematic weather observations were also carried out during this period [1.8, 9].

From the seventeenth to the nineteenth centuries, meteorological variables were measured in various units that depended on the time period and location in which the measurements were performed. The most important of these units are described in the historical parts of the relevant chapters.

1.2.2 First Measurement Networks

Around 1660, *Robert Hooke* (1635–1703) provided the first instructions for weather observations. In addition to the date and time of the observation, he recommended recording the temperature, humidity, pressure, and coverage (amount) and genera (types) of clouds, as well as special observations. One of the oldest records of weather observations covering several years were made by an abbot, *Mauritius Knauer* (1613 or 1614–1664), from the Langheim monastery in Germany. The records were for the period 1652–1658, and were published in 1700 as the so-called Hundred-Year Calendar. Unfortunately, this erroneous and misleading expression is still in use today. This calendar was based on the incorrect assumption that the weather is governed by the Sun, the Moon, and the five planets known at that time (Mercury, Venus, Mars, Jupiter, and Saturn), implying that weather patterns repeat every seven years.

In 1723, the English physicist *James Jurin* (1684–1750) published an invitation for meteorological observations. The Royal Society in London and the academies of science in Berlin and St. Petersburg responded to this invitation. In 1771, *Johann Heinrich Lambert* (1728–1777) at the Berlin Academy of Sciences proposed the creation of a worldwide meteorological network.

One of the first meteorological networks was organized by *Karl Theodor*, Elector of Bavaria (1724–1799), who initially founded a scientific academy at Mannheim in 1763 before establishing the first meteo-

rological society, the *Societas Meteorologica Palatina*, in 1780 [1.8, 10]. *Johann Jakob Hemmer* (1733–1790) developed this network with 36 stations in Europe, two in North America, and one in Greenland. This network had a significant influence on, for example, the standardization of the times of the day at which climatological observations are performed (07:00 LT, 14:00 LT, and 21:00 LT; with LT being the local time). Data from that network were published for the period 1781–1792. Indeed, the temperature measurements that have been carried out at the Hohenpeißenberg in Germany (at 989 m ASL) since 1781, which represent the longest time series of temperature measurements at a mountain site worldwide, were influenced by the work of the *Societas Meteorologica Palatina*. Further mountain stations were established almost a century after the Hohenpeißenberg; e.g., in 1881 at Hochobir, in 1876 at Puy de Dôme, and in 1886 at Sonnblick [1.8]. Since the second half of the eighteenth century, continuous time series of meteorological observations have been available, such those from Basel (1761), Prague (1775), and Vienna (1775) [1.11].

Smaller networks have operated over short periods, such as that initiated by *Johann Wolfgang von Goethe* (1749–1832) in Duchy of Saxe-Weimar-Eisenach in 1821–1832. That network included the weather station at Jena, which started operating in 1813 and is still in operation today. Another network, founded in Saxony by *Karl Christian Bruhns* (1830–1881), comprised 22 stations and operated from 1863 to 1876. In 1826, *Heinrich Wilhelm Brandes* (1777–1834) constructed the first weather map based on weather observations made across Europe at 18 h on December 24, 1821 [1.12].

Following the development of hot-air balloons, *Gay-Lussac* (1787–1850) performed the first balloon cruises for scientific purposes in 1804. *James Glaisher* (1809–1903) went up to a height of 8839 m in 1862. At the end of the nineteenth century, a network of aerological stations using balloons and kites as sensor platforms was established, and the era of radiosoundings began around the year 1930 (Chap. 46).

1.2.3 The Establishment of Global Meteorological Organizations

The founding of the *Accademia del Cimento* in Florence in 1654 and the *Societas Meteorologica Palatina* in 1780 provided the impetus for international cooperation in the field of meteorological measurements. By the mid-nineteenth century, meteorological services existed in most of the developed nations. Another initial step on the path to organized international cooperation in this field was a conference on marine meteorology held in Belgium in 1853.

The year 1872, when *K.C. Bruhns* (Leipzig), *C. Jelinek* (Vienna), and *H. Wild* (St. Petersburg) invited meteorologists to Leipzig, marked the start of the era of regular international meteorological conferences. Participants agreed on a Permanent Meteorological Committee, which was established during the 1873 International Meteorological Congress in Vienna, and *C.H.B. Buys-Ballot* (Utrecht) was elected as the first president of the International Meteorological Conference (later renamed the *International Meteorological Organization*, IMO). The second conference was held 1879 in Rome. At that time, it was not possible that countries officially invited to a next conference. Therefore, *Wild* and *Scott* (England) organized the next congress in Munich in 1891. A series of conferences of the heads of meteorological services were then held until 1935. The founding of a permanent secretariat was declared in Vienna in 1926, and a general secretary was established in 1929. The secretariat was initially located in De Bilt, but was moved to Lausanne in 1939. The outcome of the 12th Conference of Directors of the nongovernmental IMO in Washington, DC in 1947 was a document proposing the creation of a new intergovernmental organization. With the foundation of the *World Meteorological Organization* (WMO) in 1951, the secretariat moved to Geneva (for further details, see e.g., [1.13–16]). In 1947, the IMO initiated the preparation of a guide to international meteorological instrument and observing practices, several editions of which have since been published [1.17]. This guide is an important reference work on the standard meteorological measurement and observation practices. In 1951, at the First Congress of the WMO, the Commission for Instruments and Methods of Observation

(CIMO) was founded. This provided another example of the strong focus on international coordination and standardization in the field of atmospheric measurements that started with the conference at Leipzig almost 80 years earlier.

1.2.4 Historical Textbooks on Meteorological Measurements

Measurement practices and devices have been discussed in most meteorological textbooks since the sixteenth century [1.4]. Probably the first modern textbook on sensors for atmospheric measurements was edited by *E. Kleinschmidt* in 1935 [1.18], and included contributions from *F. Albrecht*, *P. Duckert*, *W. Grundmann*, *M. Robitzsch*, and *R. Süring*. More than 30 years later, a similar textbook with many historical contributions was written by *W.E.K. Middleton* [1.9]. Furthermore, the *Meteorological Handbook*, edited by *F. Linke* and *F. Baur* [1.19], has a large instrumental part written by *W. Grundmann* and *F. Woelfle*. The first book about remote sensing techniques was edited by *D. Lenschow* in 1986 [1.20], and is still a standard textbook for these techniques. Another very interesting textbook is the one edited in 1980 by *F. Dobson*, *L. Hasse*, and *R. Davis* [1.21], in which the authors linked the different measuring techniques with air–sea interaction processes. Over the last 20 years, several textbooks on atmospheric measurements have been published [1.22–27], each with a very specific focus on particular methods and devices. The present book aims to provide a more general and comprehensive overview of the status and application of meteorological measurements in a uniform format of all chapters.

1.3 The Structure of the Atmosphere

The vertical and horizontal structure of the atmosphere and the typical timescales of atmospheric phenomena influence the design and performance of atmospheric measurement techniques. These properties must be taken into account to ensure that measurement techniques provide high-quality data that can be used for different purposes. For instance, the locations of different atmospheric layers and the vertical gradients of thermodynamic variables must be considered when deciding on the measurement range, measurement levels, and the vertical spacing of profile measurements. The timescales of atmospheric processes determine the measurement frequencies, averaging times, and appropriate response times of sensors.

The uncertainty of a meteorological measurement is due to the error of the sensor as well as the spatiotemporal variability in the meteorological element being measured. Some typical situations and examples together with their theoretical foundations are discussed in the following sections. More details are provided in relevant textbooks [1.28–32].

Each meteorological process has typical spatial and temporal scales. The reason for this is the underlying physics and the spectral organization of atmospheric turbulence and wavelike processes, where relevant wavelengths (spatial extents) relate to distinct durations (frequencies). The principle of scale classification was formulated by *Isidoro Orlanski* [1.33]. There

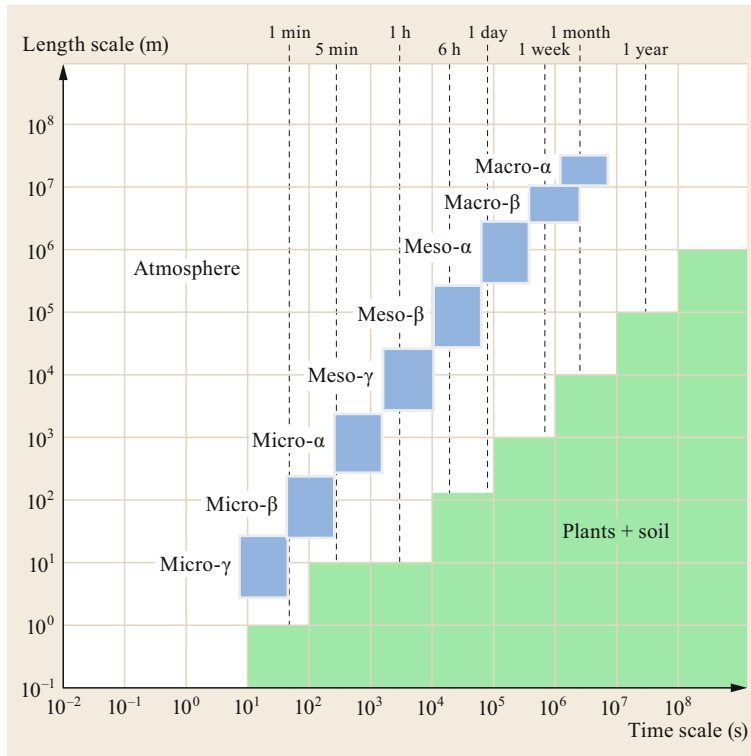


Fig. 1.2 Temporal and spatial scales of atmospheric, biospheric, and soil processes. *Blue boxes* indicate atmospheric scales [1.33], each with a range of one order of magnitude (micro- γ to macro- α scales are shown). The scales of plant and soil processes involved in exchanges of energy and matter with the atmosphere [1.34] are shown as the *green area* [1.35, 36] (after [1.37] with permission of © Author(s) CC Attribution 3.0 License)

is typically a close link between atmospheric processes and their characteristic spatial and temporal scales: large phenomena typically have long durations whereas local processes occur on short timescales. This contrasts with other compartments of the Earth system; for instance, hydrological processes in soils (Chaps. 58, 60, and 61) and plant ecosystems (Chap. 59) may occur over large timescales but at rather small spatial scales (Fig. 1.2). Therefore, it is an experimental challenge to combine measurements of the soil–vegetation system with measurements of the atmosphere. Examples of relevant scale-dependent processes are presented in Table 1.2. Some processes may occur at different scales depending on the specific situation. For instance, the extent of the circulation of a sea breeze depends on the sizes of the water and land bodies involved, thermal differences, and the background wind regime.

1.3.1 Vertical Distribution of Meteorological Elements

The typical vertical structure of the atmosphere is shown in Fig. 1.3. Except for the thermosphere, which begins at a height of around 80 km, the air in the atmosphere is not ionized and can be considered a homogeneous gas mixture. The vertical air column is subdivided into several characteristic layers based on

the typical mean vertical temperature profile [1.29, 31]. In the lowest layer, the troposphere, the temperature changes with altitude at an average rate of -6.5 K km^{-1} . The temperature remains nearly constant (about 220 K) with height in the lowest part of the stratosphere. It then increases to about 270 K in the upper stratosphere before decreasing with height in the mesosphere to below 200 K. The temperature finally increases with height in the thermosphere. The interfacial zones between these layers are called the tropopause, stratopause, and mesopause, respectively. Pressure and density decrease almost logarithmically with height.

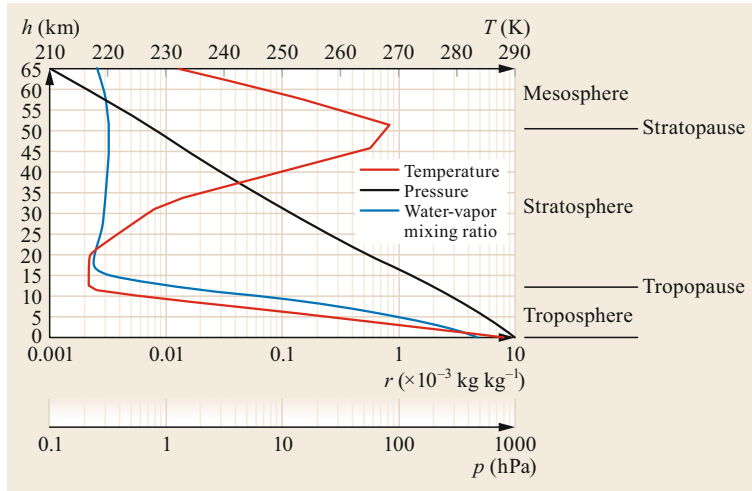
Structure of the Stratosphere and Mesosphere

The stratosphere is a stably stratified layer between the tropopause and the stratopause at a height of approximately 50 km. Its temperature increases with height from about 220 K to nearly 270 K. This increase in temperature with altitude is due to the absorption of solar ultraviolet radiation by the ozone layer. About 20% of the mass of the atmosphere is contained in the stratosphere.

The temperatures in the stratosphere vary with an annual cycle due to the absorption of solar radiation in combination with meridional exchange processes. The largest variation in temperature takes place over the poles in the lower stratosphere; variations at lower and

Table 1.2 Scales of atmospheric processes and phenomena (after [1.33])

Scale	Time	Space	Process
Macro- α	> 10–30 d	> 10 000 km	Standing waves
Macro- β	3 to 10–30 d	2000–10 000 km	Rosby waves, tidal waves, large high-pressure systems
Meso- α	12–72 h	200–2000 km	Low-pressure systems, fronts, hurricanes
Meso- β	3–12 h	20–200 km	Low-level jets, squall lines, inertial waves, cloud clusters, vorticity banners
Meso- γ	30–180 min	2–20 km	Thunderstorms, deep convection, urban effects, clear air turbulence, thermally driven flows (valley winds, sea breezes)
Micro- α	5–30 min	200–2000 m	Gravity waves, tornadoes
Micro- β	1–5 min	20–200 m	Wakes, coherent structures, dust devils, boundary-layer turbulence
Micro- γ	< 1 min	< 20 m	Roughness, surface-layer turbulence

**Fig. 1.3** Vertical distributions of the mean temperature (T), pressure (p), and water vapor mixing ratio (r) in the lowest 65 km of the atmosphere, based on the US Standard Atmosphere [1.38, 39] (Table 5.9)

higher altitudes are smaller. The wind system is mainly driven by quasi-biennial changes in wind direction from west to east, the zonal quasi-biennial oscillation (QBO) [1.40], and the meridional Brewer–Dobson circulation (BDC) [1.41].

The mesosphere is the layer above the stratopause. In the mesosphere, the temperature decreases with altitude. This effect is due to a gradual reduction in solar heating and increasing cooling through radiative emission by CO_2 . The top of the mesosphere, called the mesopause, is the coldest part of Earth’s atmosphere. Temperatures at the mesopause can fall to as low as 170 K, depending on the latitude and season. The exact upper and lower boundaries of the mesosphere also vary with latitude and season, but it usually ends at a height of around 100 km except in mid- and high latitudes during summer, when it descends to a height of about 85 km.

Structure of the Troposphere

The atmospheric measurements discussed in this book relate mainly to the troposphere, which ranges in thickness between about 5 km in the polar regions and approximately 16 km in the tropics. Most weather phe-

nomena occur within this layer. The upper part of the troposphere is called the free troposphere (free atmosphere), and is stably stratified except in regions with strong, deep convection. The wind in the free troposphere is generated by the pressure gradient in this layer and Coriolis forces (geostrophic wind).

The lowest part of the troposphere (near to the ground) is called the atmospheric boundary layer (ABL). It is “[...] directly influenced by the Earth’s surface and responds to surface forcings at timescales of about an hour or less” [1.32]. The ABL has a typical thickness of about 1–2 km during the daytime over land and about 0.7 km over the oceans. In the daytime ABL, the potential temperature and specific humidity are nearly constant with height due to strong vertical mixing of the air by turbulence. The ABL is usually capped by a statically stable layer or temperature inversion. Strong temperature, humidity, and wind gradients often occur across a relatively shallow interfacial layer separating the ABL from the free troposphere. This layer is part of the entrainment zone, where air from the free troposphere mixes into the ABL [1.42]. The thickness of the entrainment zone is typically approximately 10% of the depth of the ABL, but it can be much

larger under certain conditions. Entrainment processes have been shown to propagate down to the surface layer. The nighttime stable ABL over land has a typical depth of 100–200 m, but for very stable stratification, it can be just 10 m thick (or even less). The structure and temporal evolution of the ABL are most strongly influenced by turbulence.

In the ABL, the wind speed decreases from its geostrophic value in the free troposphere to zero at the surface, and the wind turns counterclockwise (in the Northern Hemisphere) by about 15° – 60° (depending on the atmospheric stability). Thermal interaction with the surface also influences the structure of the ABL. The temperature may therefore decrease by 1–5 K within the lowest 100 m over strongly heated surfaces (strongly unstable stratification); on the other hand, it may increase by 10 K or more within the lowest 100 m when there is strong surface cooling [1.32].

The lowest part (approximately the lowest 10%) of the ABL is called the surface layer (SL). Historically, this layer has also been called the constant-flux layer or Prandtl layer because the turbulent flux was assumed to remain approximately constant with height within the SL. This makes it possible to estimate surface turbulent fluxes from gradient or profile measurements of mean variables within this layer. The SL is highly turbulent, and molecular exchange processes only dominate within a few millimeters of the surface. Above tall vegetation or buildings, the constant flux layer assumption becomes invalid due to high friction, so the surface layer must be subdivided (Fig. 1.4). Turbulent mixing is increased in the roughness sublayer (also called the mixing layer), which extends from immediately above the canopy up to roughly twice the canopy height [1.43]. If the vegetation is not too high, a surface layer may develop above the mixing layer, but with a reduced thickness.

Scaling in the Atmospheric Boundary Layer

In order to derive the requirements for measurements in the lower troposphere, it is important to characterize the typical variability of atmospheric variables in the ABL and its sublayers with time and height. Due to solar heating during the daytime over land, the SL is characterized by unstable conditions that result in a decrease in temperature with height, whereas the SL is almost always stably stratified during the night due to radiative cooling at the surface, which often results in an increase in temperature with height. In the SL, the typical variability in temperature and moisture with height can be described using so-called surface scaling variables, namely the dynamic temperature and dynamic

Magnitude of height (m)	Layer of the troposphere	
10 000	Free troposphere	
1000	Capping inversion	Entrainment zone
	Upper layer	
10–100	Turbulent layer	Surface layer
	Roughness sublayer	
0.01	Viscous sublayer	
0.001	Laminar boundary layer	

Fig. 1.4 Structure of the troposphere and the ABL (after [1.28, 44]). The shaded area is the relatively thin capping inversion (interfacial layer) between the free troposphere and the upper layer. The roughness sublayer does not develop over short vegetation

moisture scales

$$\theta_*^{\text{SL}} = -\frac{(\overline{w'\theta'})_s}{u_*} \quad (1.1)$$

$$q_*^{\text{SL}} = -\frac{(\overline{w'q'})_s}{u_*}, \quad (1.2)$$

where θ is the potential temperature (the temperature corrected for the effect of the variation in pressure with height, see below), q is the specific humidity, u_* is the friction velocity, and $(\overline{w'\theta'})_s$ and $(\overline{w'q'})_s$ are the turbulent fluxes of temperature and humidity at the surface, respectively.

Typically, during nighttime, $u_* \approx 0.1 \text{ m s}^{-1}$ and the sensible and latent heat fluxes are $\pm 20 \text{ W m}^{-2}$, so $\theta_*^{\text{SL}} \approx 0.15 \text{ K}$ and $q_*^{\text{SL}} \approx 0.08 \times 10^{-3} \text{ kg kg}^{-1}$. These are very small fluctuations that need to be resolved. During the daytime, the variability is somewhat larger. Using typical values over vegetated surfaces of $u_* \approx 0.3 \text{ m s}^{-1}$, 100 W m^{-2} for the sensible heat flux, and 300 W m^{-2} for the latent heat flux for the climatic conditions in the temperate zone, $\theta_*^{\text{SL}} \approx 0.3 \text{ K}$ and $q_*^{\text{SL}} \approx 0.4 \times 10^{-3} \text{ kg kg}^{-1}$, which provide important requirements for the temporal and spatial resolutions of measurement devices. The size of the eddies to be resolved scales with the height above the surface, and measurement lengths of at least one magnitude smaller than the measurement height are required in the lowest few meters to capture the full spectrum of fluctuations.

In the mixed layer (ML), a suitable scaling variable for velocity is Deardorff's convective velocity scale w_* [1.45], which can be used to derive scaling variables

for temperature and moisture according to

$$w_* = \left[\frac{gz_i}{\theta_v} \left(\overline{w'\theta'_v} \right)_s \right]^{1/3}, \quad (1.3)$$

$$\theta_*^{\text{ML}} = - \frac{\left(\overline{w'\theta'} \right)_s}{w_*}, \quad (1.4)$$

$$q_*^{\text{ML}} = - \frac{\left(\overline{w'q'} \right)_s}{w_*}, \quad (1.5)$$

where θ_v is the virtual potential temperature, g is the acceleration due to gravity, z_i is the mixed layer height, and $\left(\overline{w'\theta'_v} \right)_s$ is the buoyancy flux at the surface.

For instance, for a CBL (convective boundary layer) with a depth of 1000 m, a surface heat flux of 100 W m^{-2} , and a mean virtual potential temperature of 300 K, $w_* \approx 1.4 \text{ m s}^{-1}$, meaning that the temperature and moisture fluctuations are generally smaller than those in the unstable SL (see above), which in turn yields $\theta_*^{\text{ML}} \approx 0.06 \text{ K}$ and $q_*^{\text{ML}} \approx 0.1 \times 10^{-3} \text{ kg kg}^{-1}$. These values set stringent requirements on the accuracy of instruments; however, the spatial and temporal resolutions of the measurement devices are relaxed because the size of the energy-carrying eddies scales with the height above the ground.

For many applications, it is very important to obtain information on the strength of the inversion at the top of the CBL and to estimate scaling functions in the entrainment zone. The vertical extent of an inversion is typically a few 100 m, and the inversion strength is between 0.001 and 0.1 K m^{-1} . Therefore, inversion detection requires measurements with a high vertical resolution of a few decameters and a high relative accuracy of the derived temperature, particularly for weak inversions. The scaling of wind, temperature, and moisture fluctuations is still an active area of research and is of great interest when studying entrainment fluxes. It is expected that velocity fluctuations scale with w_* and the wind shear strength. Furthermore, moisture and temperature fluctuations scale not only with w_* and wind shear but also with the temperature and moisture gradients across the entrainment zone [1.46]. Due to these gradient relationships, the moisture and temperature fluctuation profiles reach their maxima at the top of the CBL. Recent measurements of well-developed CBLs suggest that the atmospheric standard deviations of temperature and moisture in the entrainment zone are $0.5\text{--}1.0 \times 10^{-3} \text{ kg kg}^{-1}$ [1.46, 47] and $0.5\text{--}1.0 \text{ K}$, respectively [1.46, 48].

Vertical Profiles in the Surface Layer

A brief description of typical vertical profiles in the surface (Prandtl) layer is presented below. For more details, please refer to relevant textbooks [1.28, 30, 32, 44].

These vertical profiles are shaped by the turbulent exchange of momentum, heat, and trace gases. The wind gradient near the surface in the case of neutral stratification is

$$\frac{\partial u}{\partial z} = \frac{u_*}{\kappa z}, \quad (1.6)$$

where u is the wind speed, z is the height, u_* is the friction velocity, and the von Kármán constant is $\kappa = 0.4$. The height dependence of the wind speed gradient implies that the wind speed is proportional to the logarithm of the height, i.e.,

$$\frac{\partial u}{\partial \ln z} = \frac{u_*}{\kappa}. \quad (1.7)$$

There is a similar relationship for the temperature gradient,

$$\frac{\partial T}{\partial \ln z} = \text{Pr}_t \frac{\overline{w'T'}}{\kappa u_*}, \quad (1.8)$$

where T is the temperature, the turbulent Prandtl number $\text{Pr}_t \approx 0.8\text{--}0.95$, and the sensible heat flux in kinematic units (m K s^{-1}) is expressed as the covariance $\overline{w'T'}$ of the turbulent fluctuations of the vertical wind speed w' and the temperature T' ; compare with (1.1). Similar equations hold for water vapor and other trace gases. Integrating (1.7) and (1.8) between two levels gives

$$u(z_1) - u(z_2) = \frac{u_*}{\kappa} \ln \frac{z_1}{z_2} \quad (1.9)$$

and

$$T(z_1) - T(z_2) = \text{Pr}_t \frac{\overline{w'T'}}{\kappa u_*} \ln \frac{z_1}{z_2}. \quad (1.10)$$

Above closed canopies or built-up areas, the reference level for these profile formulae is the upper part of the vegetation or building structures. For instance, for measurements above a canopy (or buildings), all geometric heights must be reduced by the so-called zero-plane displacement height, which is assumed to be two-thirds of the canopy height.

Upon extrapolating the logarithmic wind profile to the surface, the wind speed will be zero at z_0 , which is called the roughness length ($u(z_0) = 0$)

$$u(z) = \frac{u_*}{\kappa} \ln \frac{z}{z_0}. \quad (1.11)$$

The roughness length is a function of the characteristics of the underlying surface and is on the order of 10^{-4} – 10^{-3} m for water, 10^{-2} m for short grass, 10^{-1} m for cropland, and 1 m for forest [1.28]. An estimate of z_0 is required when selecting measurement heights in the (lower) surface layer. For the temperature profile, a fictional roughness length can be defined that corresponds to the length at which the temperature approaches the value at the surface. This length is at least one order of magnitude smaller than the roughness length for the wind profile.

The equations above are only valid for near-neutral stratification. Applying the so-called universal functions of momentum $\varphi_m(\zeta)$ and $\varphi_H(\zeta)$ of Monin–Obukhov similarity theory [1.49] as well as sensible heat exchange to profile equations (1.3) and (1.4), we obtain

$$\frac{\partial u}{\partial \ln z} = \frac{u_* \varphi_m(\zeta)}{\kappa} \quad (1.12)$$

and

$$\frac{\partial T}{\partial \ln z} = \text{Pr}_t \frac{\overline{w'T'} \varphi_H(\zeta)}{\kappa u_*}, \quad (1.13)$$

where $\zeta = z/L$ is the Obukhov stability parameter with the Obukhov length

$$L = -\frac{u_*^3}{\kappa \frac{g}{T} \overline{w'T'}}. \quad (1.14)$$

Today, universal functions that were first proposed by Businger and subsequently modified by Höögström [1.50] are widely used. For further details on this topic, including the integration of (1.12) and (1.13) and necessary modifications for the roughness sublayer, please refer to relevant textbooks [1.28, 29, 32].

Figures 1.5 and 1.6 show typical vertical wind and temperature profiles near the surface for stable, neutral, and unstable stratification as well as typical differences in wind speed and temperature at different levels with respect to the meteorological standard measuring levels at 10 m for wind and 2 m for temperature [1.17]. Some implications for the performance of atmospheric measurements can be derived from these profiles. For example, for neutral stratification over grass, the wind speed at a height of 2 m is only 77% of the wind speed at the reference height of 10 m. The typical measuring error for temperature of 0.1 K includes a tolerance for the standard measurement height (2 m) of about ± 0.2 m.

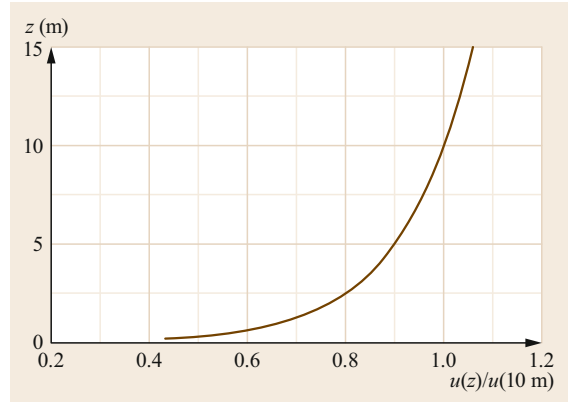


Fig. 1.5 Wind speed profile normalized to the value at 10 m for neutral stratification over short grass ($z_0 = 1$ cm). The profiles are similar for slightly stable and unstable stratification

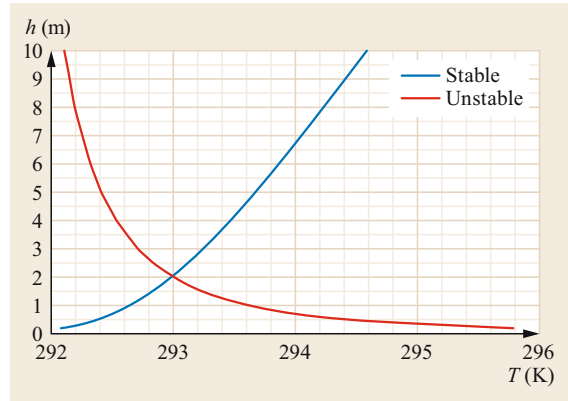


Fig. 1.6 Typical temperature profiles for stable ($u_* = 0.15 \text{ m s}^{-1}$, $Q_H = -20 \text{ W m}^{-2}$, $z/L = 0.13$ at 2 m height) and unstable ($u_* = 0.20 \text{ m s}^{-1}$, $Q_H = 200 \text{ W m}^{-2}$, $z/L = -0.56$ at 2 m height) stratification (Q_H is the sensible heat flux)

Generalized Temperature and Pressure Variables

Due to compression or expansion, the temperature of a vertically displaced air parcel is higher near the surface and lower in the upper layer of the boundary layer or the upper layer of the troposphere. In order to compare temperatures or to determine the stratification of the atmosphere, it is important to correct the temperature for the effect of pressure variations with height. This can be done by transforming the absolute temperature into the potential temperature θ via *Poisson's* equation [1.29, 31, 51]

$$\theta = T \left(\frac{p_0}{p} \right)^{\frac{R_d}{\varphi}}, \quad (1.15)$$

where R_d is the gas constant for dry air, c_p is the specific heat at constant pressure, and $p_0 = 1000$ hPa. For some applications it can be useful to replace p_0 with the surface pressure, which gives $T = \theta$ at the surface. At a height of 10 m, the difference between the temperature and the potential temperature is about 0.1 K. Therefore, when analyzing the stability of the atmosphere, temperature measurements performed above 10 m should be transformed into potential temperatures. Typical examples include measurements carried out at the tops of tall towers and radiosonde measurements (Chap. 46).

Because the acceleration due to gravity depends on the latitude and height above sea level, it is often replaced with the mean constant gravitational acceleration at sea level $g_0 = 9.81 \text{ m s}^{-2}$ [1.52]. Based on this, a generalized height scale, the so-called geopotential height Z [1.51], can be defined as the geopotential

$$\Phi(z) = \int_0^z g(z') dz', \quad (1.16)$$

normalized by the constant gravitational acceleration $g_0 = 9.81 \text{ m s}^{-2}$, i.e.,

$$Z = \frac{\Phi}{g_0}. \quad (1.17)$$

The pressure at a particular height Z can be approximately calculated from the pressure at sea level $p_0 = p(Z=0)$ using the mean virtual temperature T_v (Chap. 7) between sea level and Z and the barometric equation

$$p(Z) = p(Z=0) e^{-\frac{g_0}{R_d T_v} Z}. \quad (1.18)$$

In the lower troposphere, the geopotential height differs only slightly from the geometric height. In addition, depending on the required accuracy, the virtual temperature can be replaced with the actual temperature (Chap. 10).

1.3.2 Horizontal Distribution of Meteorological Elements

The horizontal distribution of meteorological elements depends on the synoptic situation but mainly on the topography and the land cover. This dependence is particularly pronounced close to the surface. By definition, effects of the surface on the structure of the atmosphere are confined to the ABL. Inside the ABL, the effects of different surface types usually decrease with height and can become very small or undetectable; they are blended above a certain level known as the *blending*

height [1.53]. This blending height is assumed to occur between a few decameters and about 100 m above a surface of low vegetation. Its precise value depends on the size of patches of vegetation with uniform surface characteristics, on the magnitude of the difference in surface properties between different surface patches, and on the wind speed. In the case of strong convection under weak wind conditions, surface signatures can be observed across the whole boundary layer (for more details on this topic, see [1.54, 55]). Below the blending height, obstacles and changes in surface characteristics that induce the formation of internal boundary layers strongly influence meteorological variables and must be considered when performing meteorological measurements.

Influence of Obstacles near the Surface

Obstacles have a remarkable influence on meteorological measurements. Their ability to disturb the fields of meteorological variables is most pronounced on the downwind side but can also be detected on the windward side. Therefore, in general, measurements that are presumed to be representative of a large area with undisturbed flow conditions should be performed far from large obstacles. However, this is often impossible in forests, mountainous regions, and urban environments. For classical meteorological measurements, especially flux measurements, any direct influence of obstacles should be suppressed as much as possible.

Rough approximations and recommendations for distances from the sensor to the nearest obstacle have been developed for wind measurements based on German standards [1.56] and on the European Wind Atlas [1.57]. They are presented in Chap. 9. For measurements of energy fluxes, the recommended distances should be increased by a factor of 2–5. It should be noted that the sensor platform itself (tower, balloon, or aircraft) often acts as an obstacle that can influence the measurements (Chaps. 6 and 37).

Internal Boundary Layers

Land surfaces are often heterogeneous: surface characteristics differ markedly between neighboring patches with different land uses. Different patches have other thermal and dynamic properties, meaning that those patches also differ appreciably in their heat and momentum fluxes. This can result in significant local variations in near-surface wind and temperature profiles over a patchy landscape. Due to the horizontal mean wind, these different profiles are shifted downstream, forming a layer of discontinuity called an internal boundary layer. Several sharp changes in surface properties over short distances may result in a complex lower ABL structure, as illustrated in Fig. 1.7.

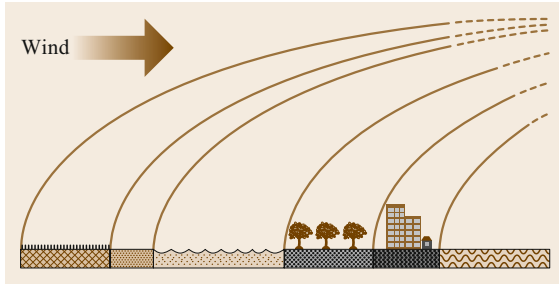


Fig. 1.7 Generation of internal boundary layers above an inhomogeneous surface (after [1.32])

The formation of internal boundary layers leads to discontinuities in the vertical profiles of atmospheric state variables. Close to the ground, conditions are in equilibrium with the local surface. Above the discontinuity zone, the profiles are influenced by the surfaces upwind of the site. The development of mechanical internal boundary layers is influenced by the roughness lengths over neighboring surfaces. The height of a mechanical internal boundary layer depends on the fetch (the distance to the roughness change; for more on this, see [1.28, 32, 58, 59]). According to internal boundary layer theory, the height depends on the roughness lengths and the friction velocities on both sides of the change in surface roughness [1.60]. For many practical applications, the depth of the new equilibrium layer δ can be predicted by the empirical relation [1.61]

$$\delta = 0.3 \text{ m}^{0.5} \sqrt{x}, \quad (1.19)$$

where δ and the fetch x are in meters.

Just as a mechanical internal boundary layer is caused by a step change in surface roughness, a thermal internal boundary layer develops downstream of a step change in surface temperature. Such changes may be triggered by differences in land-use characteristics, soil moisture content, or turbulent exchange conditions. However, these layers are not as significant as the mechanical internal boundary layers, except when the thermal properties change dramatically when moving from surface to surface, such as from cold water to heated land.

Thermal inhomogeneities in the vertical temperature profile that are not associated with advection develop in the late afternoon, when the temperature of the first few meters above the surface decreases and a shallow surface-based inversion develops. The height of the inflection point between stable stratification near the surface and unstable stratification in the upper layer grows over time. In this flat inversion layer, the sensible heat flux is directed downwards, whereas it is still upwards above the inversion [1.62]. This is the iner-

tial process for the development of a nocturnal stable boundary layer. In the early morning, a similar effect occurs when a shallow unstable layer develops close to the ground due to radiative heating of the surface while there is still a stable nocturnal boundary layer above. The unstable layer typically lasts for a much shorter time than the stable layer in the evening, which has a duration of many hours. This phenomenon is relevant to the measurement and modeling of gradients near to the surface and in the lower part of the ABL.

Clear signatures from a specific surface are often only detectable above for a certain distance downwind of the change in surface characteristics. At larger horizontal distances, they merge at the blending height (see above). Experimentally, internal boundary layers can be identified as discontinuities in the vertical profiles of wind speed and temperature. The presence of internal boundary layers must be carefully considered when planning measurements of the conditions above a given surface (e.g., when measuring the turbulent fluxes of momentum, heat, and trace gases).

Spatial Representativeness of Meteorological Measurements near the Surface and in the Atmospheric Boundary Layer

Measurements at a given site can be considered to be spatially representative if the measured variable does not vary significantly over a certain distance around the site. The typical spatial variability varies significantly for different elements [1.28] and may also depend on the meteorological and site conditions. For instance, global and diffuse radiation show very little spatial variability in the absence of clouds and over flat terrain, but greater variability can occur in mountainous regions [1.63], and very high variability can be observed under heterogeneous cloud cover. Net radiation is strongly dependent on the albedo of the underlying surface as well as its temperature and moisture. Considerable spatial variability may occur even if the downward short-wave and downward long-wave radiative fluxes appear to be horizontally homogeneous.

The wind field is mainly determined by the large-scale pressure distribution, but it is modified close to the surface by the topography, surface roughness, and obstacles, all of which can lead to significant small-scale differences. The air temperature and moisture in a uniform air mass at a particular height show very little horizontal variation except close to the surface. Such temperature and moisture variability close to the surface is particularly strong during high insolation and during nights with significant radiative cooling. Thus, the nocturnal temperature minima near the ground can show remarkable variation, even over small distances.

Table 1.3 Aspects of micro- and meso- γ scale horizontal variability of meteorological elements near to surfaces away from forests and urban areas (after [1.28])

Meteorological element	Range and reason for variability	Conditions for low variability
Global and diffuse radiation	Generally small	Free horizon, no clouds
Net radiation	Partly significant due to differences in albedo and surface temperature, especially in mountainous regions	Unlimited horizon and uniform underlying surface
Wind velocity and wind direction	Partly significant in complex terrain, over strongly varying roughness, and in the presence of obstacles	Large fetch over uniform surfaces, no obstacles
Temperature and air humidity	Often small	Open landscape
Minimum temperature, temperature near the surface, temperature of the upper soil layers	Partly significant, especially in valleys and hollows (and at very small scales); mainly for stable stratification	Open landscape
Precipitation	Often significant, but for stratiform clouds mostly in the range of the measurement error	Open landscape

The horizontal variability of precipitation strongly depends on the synoptic situation. Steady rain ahead of a warm front often results in a relatively homogeneous horizontal distribution of the measured precipitation, while very strong small-scale differences can occur in connection with showers or thunderstorms. Precipitation patterns are also strongly influenced by the orography and land surface heterogeneity.

The main reasons for potentially significant spatial variability of meteorological elements close to the surface are summarized in Table 1.3.

At a certain height (about 50–100 m) that is above the blending height [1.53], measurements are assumed to be representative of a larger area than just that represented by the local underlying surface. This is relevant to profile measurements performed at tall towers or the use of ground-based remote-sensing techniques, as well as to measurements performed along horizontal paths with aircraft or using scintillometers.

Footprint Concept for the Surface Layer. Measurements performed at a particular position in the SL probe the surface properties upwind of the sensor rather than those immediately below it. The effective area of influence is called the *footprint* [1.64]. While the footprint phenomenon has been known of for a long time, the term itself is only about 30 yr old. The footprint function f , which relates the source area Q_η of a measured signal η (scalar, flux) to its spatial extent and its intensity distribution (as illustrated in Fig. 1.8), is given by

$$\eta(x_m, y_m, z_m) = \iint_{-\infty}^{\infty} Q_\eta(x', y', z' = z_0) \times f(x_m - x', y_m - y', z_m - z_0) dx' dy'. \quad (1.20)$$

Footprint models can be classified based on their dimensions and theoretical basis. Dimensions are given

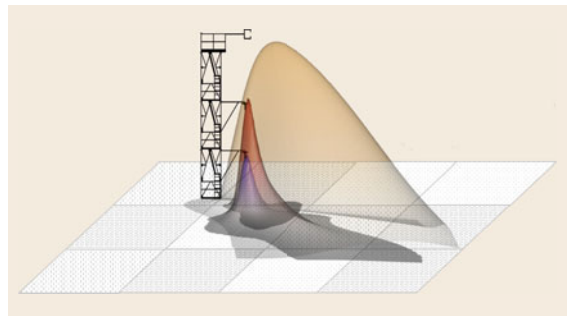


Fig. 1.8 Footprint areas of measurements obtained in the direction upwind of the measuring position. The measurements were performed at three different heights at a tower. The grid elements relate to the land-use distribution (after [1.65], reproduced with permission from Elsevier)

for the source and the footprint. The first (and simplest) one-dimensional models used a line source and determined the footprint along a horizontal axis upwind of the sensor. They integrated the footprint along the cross-wind component. However, more sophisticated models that are applicable to heterogeneous surfaces and various heights have recently been developed.

Two easy-to-use models are recommended for practical applications. Basic estimates can be obtained using the simple analytical model proposed by *Kormann and Meixner* [1.66, 67]. A more sophisticated *Lagrangian* model with backward trajectories has been developed by *Kljun et al.* [1.68]; a parameterized version of this model was recently updated [1.69].

One important application of footprint models is to obtain the footprint climatology for a selected measurement site. Therefore over a long time period footprint datasets, each covering a 30–60 min period, are required to calculate the footprint climatology. It then becomes possible to identify the land-use types in the area that contribute to the measured fluxes. In a similar way, footprint models can be linked with the data qual-

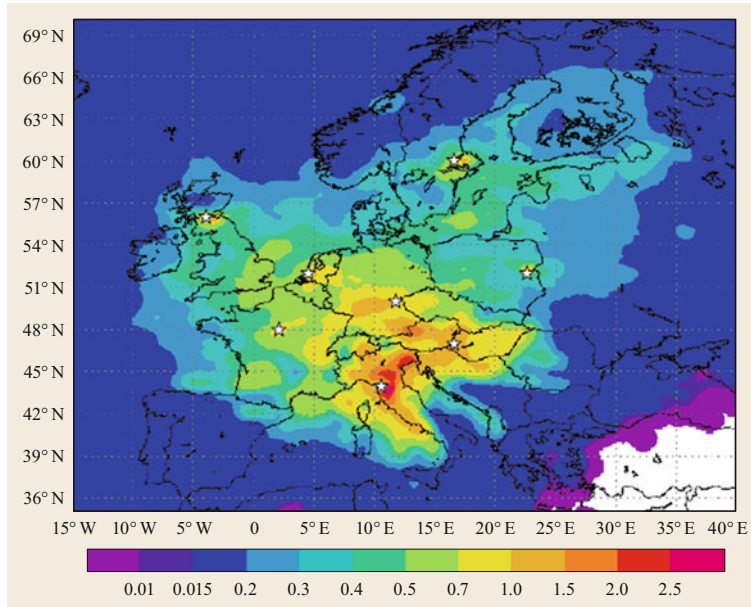


Fig. 1.9 Tall tower measurement stations and their footprint in the European tall tower network (from the project “Continuous high-precision tall tower observations of greenhouse gases”, called CHIOTTO). The color of each pixel indicates the footprint function and its contribution as a percentage of the largest value detected. Pixels with > 0.2 – 0.3% of the maximum contribute significantly. The towers included in CHIOTTO are located in Orleans (France), Ochsenkopf (Germany), Hegyhatsal (Hungary), Florence (Italy), Cabauw (the Netherlands), Bialystok (Poland), Norunda (Sweden), and Griffin (UK) (after [1.70], reproduced with permission from Dr. Vermeulen)

ity to identify possible areas with low data accuracy, which is often used for flux measurements (Chap. 55). Footprint models are especially helpful when planning experiments that are to be performed in complex terrain [1.64].

Footprint Concept for the Boundary Layer. Tall tower networks have been established at continental scales in various land regions around the world to facilitate the global monitoring of atmospheric greenhouse gas concentrations. A footprint modeling framework was established to interpret the resulting data. Inverse Lagrangian footprint modeling strategies allow to affiliate the contributions of emissions from agricultural, forest, and urban regions to a particular concentration measurement [1.71]. For the European tall tower project “Continuous high-precision tall tower observations of greenhouse gases”, called CHIOTTO, the source distribution was calculated using a Lagrangian trajectory model at the European scale (Fig. 1.9; [1.72]). Similar approaches can be applied for measurements performed along a path, such as those carried out using aircraft [1.73] (for an overview of this topic, see [1.64]).

Spatial Representativeness of Meteorological Measurements Above the Atmospheric Boundary Layer. Above the ABL, the horizontal variability of atmospheric variables is significantly reduced due to the vanishing influence of the highly variable (land) surface as a lower boundary. The variability is essentially determined by atmospheric processes at the meso- γ and

larger scales. Except for fronts and cells or deep convection systems, and away from larger mountain ranges, measurements of basic atmospheric variables in the free atmosphere can often be considered to be spatially representative at scales of 10^2 – 10^3 km.

The variability of atmospheric variables at these scales is mainly driven by the large-scale heterogeneity of landmasses, land–sea contrasts, orography, and by the presence of deep convection and synoptic-scale structures. Consequently, mesoscale variability is observed, as defined in Fig. 1.2, starting at the meso- γ scale.

Another way to assess horizontal variability in the atmosphere is through high-resolution reanalysis based on atmospheric models, though the quality of these simulations is limited by the performance of sub-grid-scale parameterizations. Consequently, the study of the mesoscale variability of atmospheric variables in the free troposphere is still an important research area in the atmospheric sciences. A safe approach concerning the accuracy and resolution of meteorological measurements is to apply the same requirements as for measurements in the ABL, given due to the higher temporal and spatial variability of ABL processes.

1.3.3 Temporal Variability of Meteorological Elements

Most atmospheric variables show considerable variability over a wide range of timescales, ranging from changes in the climate at the Earth’s surface (10^2 – 10^6 years) to turbulent fluctuations with charac-

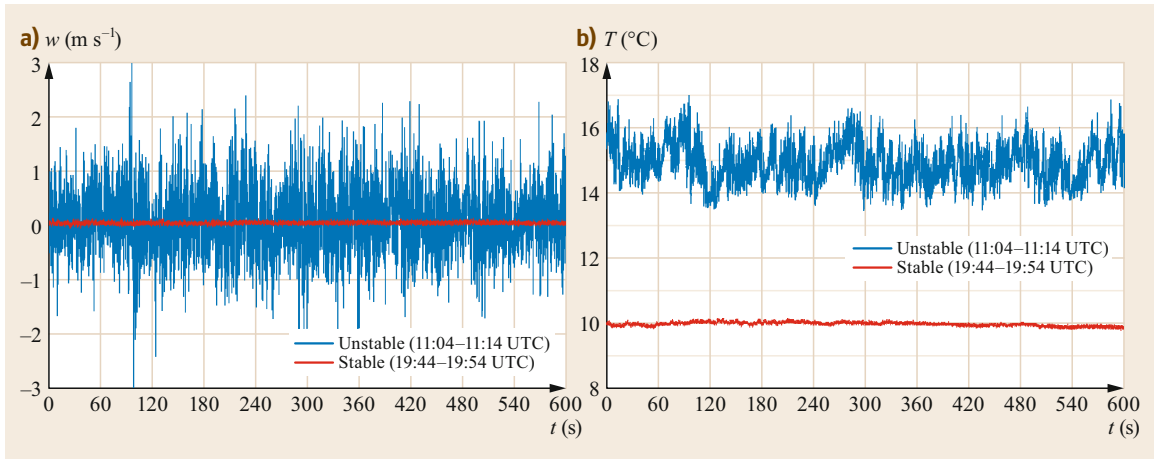


Fig. 1.10a,b Time series of the vertical wind vector component (a) and air temperature (b) at 2.4 m AGL for unstable and stable stratification over a 10-min time period at 20 Hz resolution on 01.05.2018 in Falkenberg (data from the German Meteorological Service at the Lindenberg Meteorological Observatory – Richard-Aßmann-Observatory)

teristic timescales of 10^{-1} – 10^2 s. Changes over periods of more than 10^1 – 10^2 years are beyond the scope of this book as such a timescale exceeds the lifetime of any meteorological instrument used thus far. Analyzing changes over timescales that are beyond the period for which instrumental measurements are available is the task of paleoclimatology. On the other hand, it is possible to assess climate change and climate variability over the last 100–150 years based on instrumental measurements. Such studies require accurate and well-documented reproducible measurements. In climate analysis, the statistics for atmospheric variables over a period of at least 30 years are considered. The period 1961–1990 is generally used as the official reference period. Climate statistics—in particular extreme values—are important considerations when designing measurement programs, as they influence the required measurement ranges of meteorological sensors.

Factors that determine the temporal variability of any atmospheric variable on intermediate timescales include the geographical coordinates (latitude and height) of a location and its position in relation to larger water bodies and mountain ranges. These factors strongly determine the magnitudes of annual and diurnal cycles and the variability due to the predominant weather systems in the area.

Processes that occur on timescales of about an hour or less are often related to atmospheric turbulence [1.74], which is a specific feature of atmospheric flows with air parcels (turbulent elements or turbulent eddies that are much larger than molecules), the characteristics of which vary irregularly and randomly around a mean state. Studies of turbulence require sensors or measurement systems with (very) high spatial and tem-

poral resolutions as well as high resolution with respect to the measured variable.

Turbulent elements can be seen, for example, in high temporal resolution plots of wind and temperature time series (Fig. 1.10). The intensity of the fluctuations depends strongly on the stratification. The fluctuations are much more pronounced under unstable conditions, when phenomena with different timescales are present. Short-period fluctuations are typically about $\pm(1-2)$ K around the mean temperature and about $\pm(10-20)\%$ around the mean horizontal wind speed (or larger in weak wind conditions). A comprehensive description of turbulent processes in the atmosphere is given in [1.75].

Of special importance is the inertial subrange, which is characterized by isotropic turbulence and a steady decrease in the energy density with increasing frequency. Between about 0.01 and 5 Hz, there is no dominant direction of motion for turbulent elements. In the inertial subrange, the turbulent kinetic energy is redistributed from larger to smaller eddies in a well-defined way according to *Kolmogorov's* $-5/3$ law [1.76]. The existence of the inertial subrange and its characteristics is crucial to the principles of several remote sensing techniques (see Parts C and D of this book).

To characterize the turbulence, each measured value x is represented as the sum of a mean part \bar{x} and a randomly fluctuating part x' ; in other words,

$$x = \bar{x} + x' . \quad (1.21)$$

This equation is called Reynolds' decomposition. Meteorological measurements are typically aggregated into average values over 10, 30, or 60 min. If this average represents the mean atmospheric conditions, \bar{x}

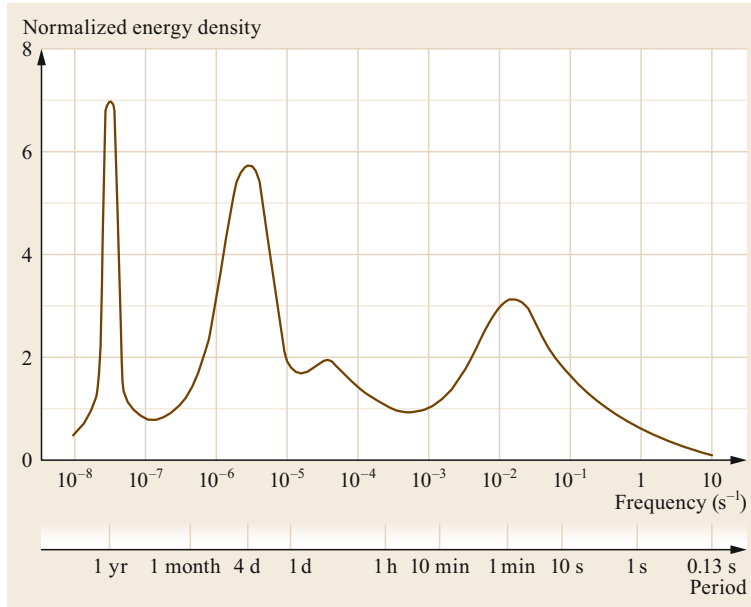


Fig. 1.11 Schematic plot of an energy spectrum of atmospheric motions (after [1.77]). Frequencies $> 10^{-3}$ Hz correspond to turbulent energy exchange. The other maxima correspond to an annual cycle, the typical cycles of circulation in the mid-latitudes, and the diurnal cycle

must be zero. In order to measure the turbulence and determine the turbulent fluxes of momentum, energy, and trace gases, the statistics of x' must be analyzed. This requires sampling rates of between about 1 Hz and several kHz depending on the technique applied and the measurement height above the ground.

An energy spectrum for a time series of wind measurements is shown in Fig. 1.11 (based on [1.78]). It exhibits four pronounced maxima due to an annual cycle, changes in high- and low-pressure systems over timescales of 3–6 d in the mid-latitudes, the diurnal cycle, and the turbulent transport of energy, momentum, and trace gases at frequencies ranging from 0.0001 to 10 Hz.

One of the most obvious examples of temporal variability in atmospheric phenomena is the diurnal cycle exhibited by many meteorological variables over land, which is largely caused by the regular diurnal variation of incoming short-wave radiation and the transformation of radiative energy at the Earth's surface. It is thus most pronounced in the surface layer under a clear sky and in the presence of weak-to-moderate wind conditions. Close to the surface, the temperature can easily vary by 20 K or more within 24 h, and the relative humidity can change from $< 50\%$ to saturation. Surface winds at night may be light or even calm, while those during the daytime may be highly variable with substantial gustiness. The opposite diurnal behavior of the wind speed is often observed several hectometers above the ground, with moderate winds occurring during the daytime but increased winds (between 10 and 20 m s^{-1}) at night due to inertial oscillations. Convection during

the daytime may result in the generation of cumulus clouds, which can form extended stratocumulus layers below the capping inversion in the afternoon, thereby reducing insolation. These layers often dissolve in the (late) afternoon due to subsidence.

This diversity of processes that occur at different heights and over different timescales and their effect on the structure of the ABL is illustrated in Fig. 1.12, which includes turbulence, waves, and large-scale subsidence. Therefore, aside from adequate time averaging, appropriate sensor localization and spatial averaging are often necessary.

1.3.4 Scale Representativeness of Atmospheric Measurements

Scaling principles are fundamental to measurements of atmospheric processes and the use of measured data. The measurement frequency and the spatial coverage and resolution of the measurements must be related to the changes in the meteorological elements over time and to the spatial representativeness. This applies at all scales, and the sampling theorem (Chap. 2) implies that phenomena can only be observed if measurements are performed over spatial and temporal scales that are smaller than those represented by the phenomenon itself.

It is important to know the spatial and temporal representativeness of any atmospheric measurement performed using in-situ and remote sensing measurement techniques (Table 1.4). Spatial representativeness is important in all applications. For in-situ and remote sensing techniques, the sensor platform determines the

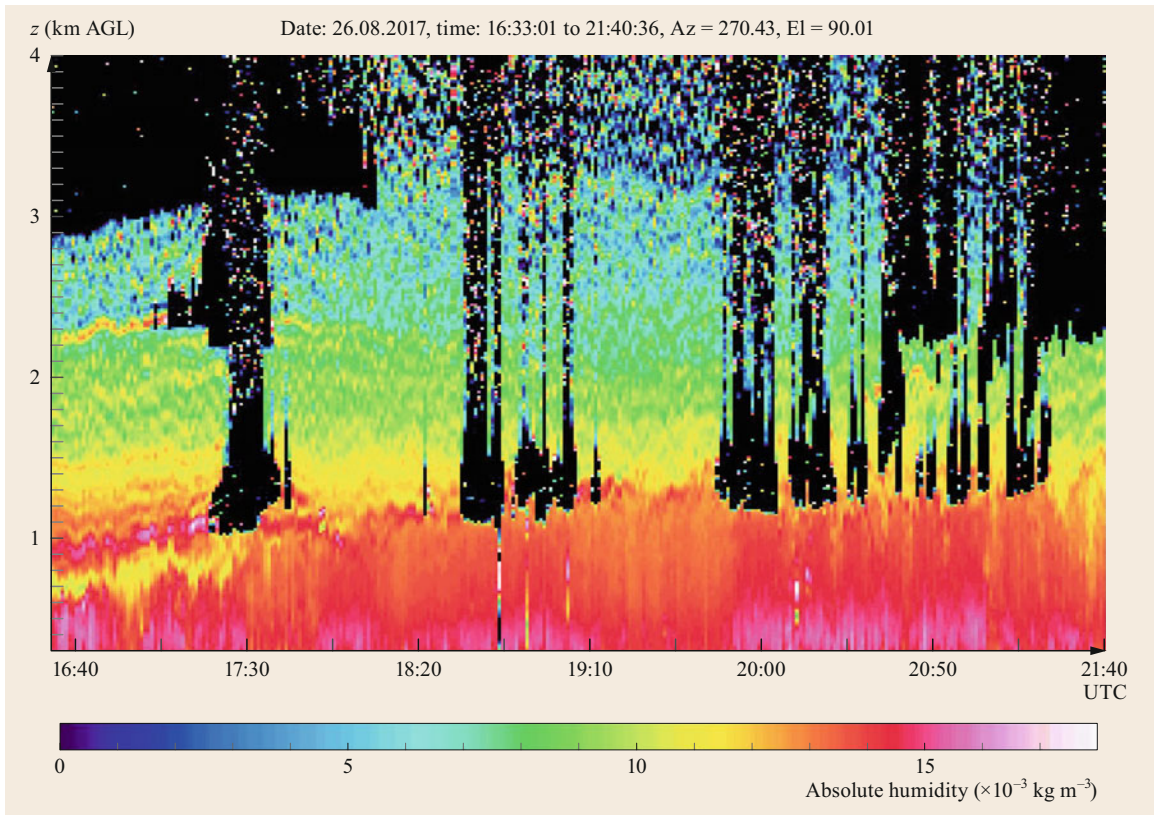


Fig. 1.12 Highly variable structure of the absolute humidity in the atmospheric boundary layer and the lower troposphere as measured with a differential absorption lidar on 26.08.2017, in Oklahoma, USA. *Black and white areas* correspond to detector overload caused by strong backscattering from clouds. The local time is UTC -5 h. The temporal resolution of the measurements is 10 s and the height resolution is 60 m. The figure shows the evolution of the CBL in the late morning including entrainment of residual layers from the previous day up to 6 pm UTC. Turbulent eddies are resolved often resulting in the formation of clouds as well as entrainment of dry air between the clouds. During daytime, a CBL depth of approx. 1.4 km is reached (reproduced with permission from F. Späth, Institute of Physics and Meteorology, University of Hohenheim, Germany)

Table 1.4 Scale representativeness of different in-situ and remote sensing systems; the *gray shading* shows the degree of scale assignment (after [1.28])

Sensor system	Macro- β scale	Meso- α scale	Meso- β scale	Meso- γ scale	Micro- α scale	Micro- β scale	Micro- γ scale
Radiosonde	Gray						
Boundary layer sonde			Gray				
Tower > 100 m			Gray	Gray			
Mast < 50 m				Gray	Gray	Gray	
Turbulence sensors (near surface)						Gray	Gray
Satellite	Gray						
Radar wind profiler		Gray	Gray	Gray			
Sodar				Gray	Gray		
RASS			Gray		Gray		
Lidar			Gray		Gray	Gray	

scale (see Chaps. 6 and 37), whereas the footprint determines the scale near the ground. Furthermore, most ground-based remote-sensing techniques have insufficient resolution near the surface. The scale representativeness of the measurement system is very important if its data are to be used as input variables for atmospheric models. The smaller the scales resolved by a model, the more important it is for the data to have sufficiently high vertical, horizontal, and temporal resolution to force and to evaluate the model.

In practice, the spatial density of a measurement network is always a compromise between the desire to resolve the variability and cover phenomena across all scales of interest and the practical limitations on doing so (resulting from logistic, instrumental, and economic factors). As an example, the spatial density of the global aerological network of radiosondes (Chap. 46) over land can provide the input data needed to drive macro- and meso- α scale numerical weather prediction (NWP) models of the Northern Hemisphere, but the data obtained by this network over the oceans and over most regions of the Southern Hemisphere is insufficient to initialize such models. Moreover, the temporal separation between consecutive soundings (typically 12 h) does not allow the diurnal cycle of the ABL to be properly characterized. However, it is adequate to describe temporal changes in the free troposphere (except for fronts). Data from radar wind profilers (Chap. 31) can be used to explore the temporal variability of the wind, but such networks only exist in certain regions of Europe, the US, and East Asia. Measuring techniques for the ABL and processes occurring at micro scales and at the meso- γ scale require a high spatial density of observations, which can be provided by some mesoscale networks (Chap. 45). Airborne measurements performed with commercial aircraft are a valuable supplement to the classical aerological network, as they provide relatively dense data coverage, both spatially and temporally, along standard traffic routes and close to some major airports (Chap. 43). However, most of the major airports are situated in the Northern Hemisphere, so these airborne measurements cannot fill the gap in upper air data for the Southern Hemisphere. Aircraft measurements realized with research aircraft are able to cover a range of scales, depending on the type of aircraft—small unmanned aircraft systems (UAS) are usually operated inside the ABL at the meso- γ scale and below, and special aircraft have been built and equipped for long-range, high-altitude flights to explore the meso- α to macro- β scales. However, an aircraft cannot provide vertical profile data for most of its flight unless it is equipped with remote sensing systems. Research aircraft are generally employed for process studies and do not provide continuous data series over

long time periods. These few examples illustrate the importance of considering the scale representativeness of each measurement technique when planning, performing, and analyzing atmospheric measurements.

1.3.5 Scale Requirements for Data Assimilation

Because weather phenomena are classified according to their spatial and temporal scales, the scales of climate and weather prediction models must be classified in a similar way. This means that the horizontal and vertical grid resolutions must be related to the time steps for the various models. The real horizontal resolution of a model is typically on the order of $6\Delta x$ where Δx is its horizontal grid increment [1.79]. There are similar relationships for global spectral models [1.80]. In order to resolve the relevant wavenumbers on the grid, a time step of seconds must typically be employed, which is a factor of 100 smaller than the grid increment in meters [1.81]. Therefore, it is possible to estimate the ability of a spectral or grid-based model system to resolve weather phenomena, as shown in Table 1.2. For example, large-scale circulation models are assigned to the macro- β range. Classical weather forecasts corresponded to the meso- α scale, but with the development of high-resolution models such as the Icosahedral Non-hydrostatic Large Eddy Model (ICON-LEM) of the German Meteorological Service (DWD) [1.82], they have been assigned to the meso- β and meso- γ scales. Quasi-operational modes of forecast models such as ICON-LEM are progressing to the micro- α scale.

The successful assimilation of measurement data depends on the consistency of the temporal and spatial scales between the model grid boxes affected by the observation as well as the representativeness and accuracy of the measurements (for more details, see [1.83]). The time interval between consecutively measured data and the spatial resolution and coverage of the data should correspond to the temporal and spatial evolutions of the model variables in the data assimilation interval as well as to the levels used in the vertical model. Observations (and error estimates) are usually interpolated to the model grid [1.84]. Representativeness errors are difficult to assess, and are easier to estimate if the observing system has high temporal and spatial resolution or even a scanning capability. For instance, for lidar measurements, the representativeness error can be estimated from the atmospheric variance observed during an averaging time set to the grid box size divided by the horizontal wind speed. Furthermore, depending on the complexity of the sensors, an error covariance matrix of the measurement must be provided. This is easier for in-situ sensors and active remote-sensing systems because

of their direct derivation of the variable of interest and the negligible sensitivity to other parameters.

The required density of observations depends mainly on the resolution and coverage of the model. Unfortunately, considering the typical resolution of the mesoscale models discussed above, there is currently no observing system network that can fulfill the needs of mesoscale data assimilation. The accuracy of the

observations must exceed the accuracy of the model background error covariance matrix. If this is a high-quality matrix with a reasonable flow-dependent update (e.g., achieved with a local ensemble transform Kalman filter), it is sufficient to operate a network of temperature and moisture profiles separated by a few hundred km to achieve a positive impact on weather forecasts on the meso- γ scale [1.85].

1.4 Devices, Systems, and Typical Specifications

This section provides a brief and general overview of in-situ sensors and remote sensing systems and their basic characteristics. For more on this topic, and discussions of sensors not mentioned here, please refer to the relevant chapters in this book. Further specifications and maintenance requirements are also outlined in those chapters. General remarks about quality assurance and quality control are provided in Chap. 3.

In-situ measurements (Part B of this book) are typically performed relatively close to the surface or on towers up to a few hundred meters in height. They are also performed on airborne platforms such as aircraft and balloons. Standard measuring heights have been recommended for many meteorological elements [1.17], so that measurements are comparable. The most important sensors and their basic characteristics are listed in Table 1.5.

Several process variables such as some turbulent fluxes cannot be measured with a single instrument. These are determined either from synchronous measurements performed with different sensors, from parameterizations that rely on mean values measured with

slow-response sensors, or using specially constructed devices (e.g., lysimeters). These methods are presented in detail in Part E; a brief overview is given in Table 1.6.

Active remote-sensing techniques are increasingly being applied in meteorology. These techniques make use of the scattering and extinction of sound waves and electromagnetic waves (in different spectral regions, from ultraviolet, visible and infrared light, to micro waves and radio waves) that propagate in the atmosphere. They are usually operated in a monostatic configuration (i.e., the transmitter and receiver are either identical or collocated). The signal originates from backscattering at an angle of 180° . Sound and electromagnetic waves can be scattered by molecules (a very important component of the lidar signal), hydrometeors and particles (clouds and raindrops, aerosols, dust, and insects), or density inhomogeneities in the air. Scattering elements normally move with the mean wind, causing the frequency of the sound or electromagnetic signal to shift due to the Doppler effect. The basic variables analyzed for sodar, lidar, and radar measurements are the intensity and the frequency of the backscattered

Table 1.5 Selected in-situ measurements and recommended characteristics for performing standard measurements (for more details, see the relevant chapters)

Parameter	Most relevant sensor type	WMO recommended height for standard measurements [1.17]	Uncertainty	Response time (time constant)
Temperature	Pt resistance with radiation screen	2.0 m	1 K	1 min
	Pt resistance, ventilated with radiation screen	2.0 m	0.1 K	10 s
Relative humidity	Capacitive sensor, ventilated with radiation screen	2.0 m	1%	30 s
Wind speed and direction	Cup anemometer with wind vane	10.0 m	0.2 m s^{-1} , 3°	10 s^a
	Sonic anemometer	10.0 m	0.1 m s^{-1} , 2°	$< 0.1 \text{ s}$
Pressure	Electric sensor	Exact height above sea level must be known	0.1 hPa	10 s
Precipitation	Precipitation gauge	1.0 m	0.1 mm, resolution of about 10%	1 min
Global radiation	Pyranometer	about 2.0 m	10 W m^{-2}	10 s

^a dependent on wind speed, see Sect. 9.3.1

Table 1.6 Surface fluxes determined from measurements obtained with multiple sensor types, and the typical characteristics of those sensors when they are used near to the surface

Parameter	Typical sensors used	Typical accuracy (%)	Typical sampling rate	Typical aggregation time
Evapotraspiration/ latent heat flux	Sonic anemometer, fast-response humidity sensor	10–15	0.05–0.1 s	10–30 min
	Net radiometer, and profile measurements with anemometers and psychrometers	10–20	1–10 s	10–30 min
	Net radiometer, anemometer and psychrometer (parameterization)	20–50	10–60 min	1 h to 1 month ^a
	Lysimeter	5–10	≥ 1 h	1 d
Sensible heat flux	Sonic anemometer	5–10	0.05–0.1 s	10–30 min
	Net radiometer and profile measurements with anemometers and ventilated thermometers	10–20	1–10 s	10–30 min
Trace gas fluxes/ dry deposition	Sonic anemometer, gas analyzer	10–15	0.05–0.1 s	10–30 min
	Gas analyzer (parameterization)	20–50	10–60 min	1 h to 1 month ^a
Wet deposition	Wet-only sampler	10–20	≥ 1 h	≥ 1 h

^a dependent on the method

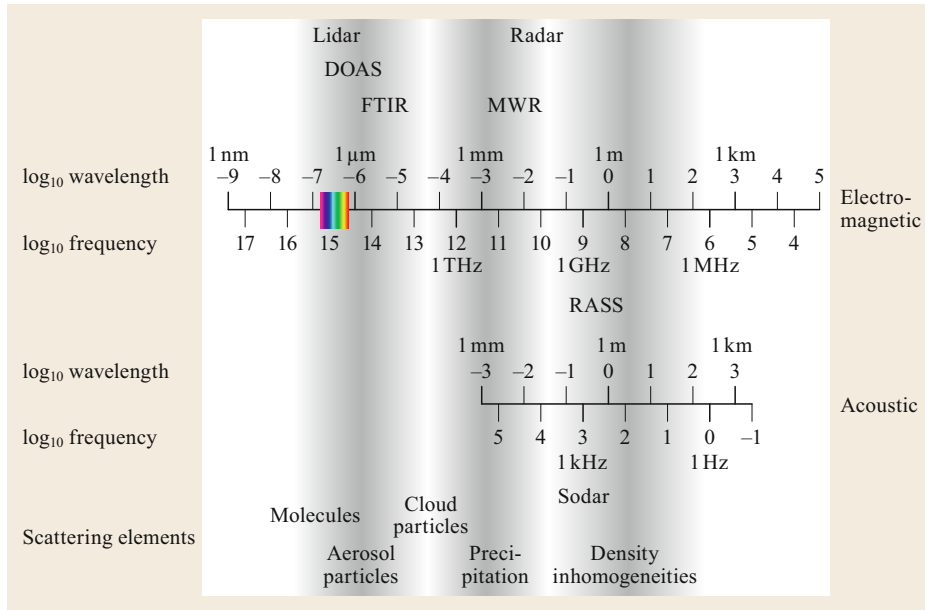


Fig. 1.13 Regions of the electromagnetic spectrum and acoustic spectrum used by active and passive remote-sensing techniques; spectral ranges monitored by specific techniques are shaded (diagram designed by S. Emeis (after [1.24] with permission from Prof. Dr. S. Emeis))

signal. Additional variables can be derived for some systems, such as the spectral shape and width and the polarization. Recently, some active remote-sensing instruments have begun to provide reliable data at heights of less than 10–50 m AGL due to extended scanning capabilities. When such instruments are unavailable, in-situ measurements are necessary to perform measurements at low altitudes.

In contrast to active remote-sensing techniques, passive techniques use natural sources of radiation such as the Sun, Moon, stars, and even the atmosphere. Monitoring the absorption lines of different gases in the electromagnetic spectrum makes it possible to deter-

mine integrated gas concentrations in the column above the sensor and across the whole atmosphere.

Figure 1.13 shows the electromagnetic and acoustic frequency ranges in which different remote-sensing methods typically operate. Remote-sensing measurements are performed from the ground (Part C of this book) or by using airborne platforms (aircraft and satellites; Part D of this book). Most remote-sensing techniques are able to measure different meteorological elements. A brief overview of these techniques is given in Table 1.7. For more details, please refer to the relevant chapters of parts C and D of this book. Overviews of this subject are also given in [1.24, 25, 86].

Table 1.7 Selected ground-based remote sensing techniques for measuring basic dynamic and thermodynamic atmospheric variables and some of their typical specifications (with information from [1.1, 25, 86], for more details see the relevant specific chapters, zenith angle < 30°)

Remote sensing system	Variables derived/uncertainty			Height range		Height resolution	Averaging time ^b
	Horizontal wind vector	Temperature	Humidity	Lower limit	Upper limit ^a		
Active systems							
Sodar (with RASS)							
• Minisodar (3–4.5 kHz)	0.05–0.3 m s ⁻¹			10–30 m	200–300 m	5–10 m	5–30 min
• Classical sodar (1.0–3.0 kHz)	0.3–0.5 m s ⁻¹			30–60 m	800–1000 m	20–50 m	10–30 min
• Sodar/RASS		0.5–1 K		30–60 m	400–600 m	20–50 m	10–30 min
Radar (with RASS)							
• 50 MHz	1–3 m s ⁻¹			0.2–3 km	15–20 km	150–1000 m	10–60 min
• 400 MHz	0.2–1.3 m s ⁻¹			300–600 m	10–15 km	150–500 m	10–60 min
– with RASS		0.5–1 K		300–600 m	2–4 km	150–500 m	10–60 min
• 1000 MHz	0.2–0.8 m s ⁻¹			100–200 m	3–6 km	50–200 m	10–30 min
– with RASS		0.5–1 K		100–300 m	1–2 km	50–200 m	10–30 min
Lidar							
• Direct detection Doppler wind lidar	0.5–3 m s ⁻¹			0.1–10 km	10–80 km	100–2000 m	10–30 min
• Coherent Doppler wind lidar, continuous wave	0.1–1 m s ⁻¹			10–20 m	100–200 m	0.1–20 m	1–10 min
• Coherent Doppler wind lidar, pulsed wave	0.1–1 m s ⁻¹			20–100 m	2–10 km	20–100 m	1–10 min
• Raman lidar		0.5–1 K	2–20%	50–500 m	8–15 km	7.5–600 m	10 s–30 min
• DIAL			2–10%	50–150 m	4–10 km	30–600 m	10 s–30 min
Passive systems							
Infrared spectrometer/interferometer							
Microwave radiometer		1–2 K	5–30%	c	3–4 km	50–1000 m	1–10 min
Sun/star/lunar photometer		0.5–2 K	0.2–1.5 g m ⁻³	c	3–5 km	10–3000 m	1–10 min
GNSS			≈ 1 kg m ⁻²	c			
			2–5 kg m ⁻²	c	2–30 km	100–1000 m	30 min–24 h

^a The numbers indicate the technical height range, the actual range strongly depends on the atmospheric conditions and may be considerably lower

^b The temporal resolution of the individual measurements is sometimes significantly higher. The averaging interval specified here is necessary to obtain data with the uncertainty given e.g. for the wind vector

^c Basically, provide column-integrated values, smooth profiles may be obtained from multifrequency or scanning systems

1.5 Applications

This section discusses *classical* applications of meteorological measurements in fields such as weather forecasting, climate monitoring, aviation, and agriculture. However, applications of meteorological measurements aimed at exploiting solar, wind, and water energy are becoming increasingly prominent; these are the subject of Chap. 51. One major challenge in this field is to combine meteorological measurements with performance data from power stations.

1.5.1 Meteorological Measurement Databases and Visualization

Databases are an important tool for organizing meteorological data and making that data readily available to a broad user community. They have widely replaced diaries and printed media over the last 20–30 years. Such databases are often available online. Databases can be used to retrieve a meteorological measurement or observation made at a specific time and specific location (characterized by its geographic coordinates: latitude, longitude, height of the site above sea level, height of the measurement above ground). Further information relevant to the analysis and interpretation of meteorological data is also stored in databases, including site characteristics (e.g., land cover, vegetation height, and conditions in the surroundings), sensor characteristics (e.g., sensor type and calibration), measurement errors and uncertainties, and maintenance activities (e.g., cleaning and alignment). This additional information is called metadata and should be always linked in the database to the measured values. Only well-documented datasets can be applied for a multitude of purposes.

For some applications, and in some areas of research, optimal visualization of the data is crucial. For instance, besides typical weather maps, horizontal distributions of meteorological parameters with listed numbers or isolines are used. Illustrations of more than one element are typically created when analyzing the vertical profile (Chaps. 46 and 47). In climatology, line graphs are typically generated for continuously measured parameters (such as temperature) and bar charts are drawn for parameters measured as accumulated values (such as precipitation). In geography, the climate diagram proposed by *Walter and Lieth* [1.87]—where the graphs for temperature and precipitation are organized to facilitate the classification of months or climates into dry and wet—is very popular.

The so-called *Hovmöller* diagram is increasingly being used to present fluxes and meteorological data in ecology because it affords a quick overview of relevant temporal and spatial scales [1.88]. The diagram was orig-

inally devised as a means to illustrate the evolution of meteorological parameters over time as a function of latitude, longitude, or height [1.89]. A more sophisticated but very instructive way to study spatial-frequency relationships is the Wheeler–Kiladis diagram [1.90].

1.5.2 Networks and Experiments

In order to achieve the spatial coverage and resolution required by a particular application, sensors and measurement systems are often organized into networks. The dimensions of such networks range from the meso- γ to the macro- α scale, and the number of sensors or stations included in such networks typically range between 10^1 and 10^3 . Prominent examples are urban air quality and climate-monitoring networks (Chap. 52), regional-scale networks (Chap. 45), continental-scale networks (e.g., the Atmospheric Radiation Measurement (ARM) [1.91] Climate Research Facility and the European Wind Profiler Radar Network), and global networks (e.g., synoptic weather stations across the globe, the Baseline Surface Radiation Network (BSRN), and the Global Climate Observing System (GCOS) including the Reference Upper-Air Network (GRUAN); Chap. 63). However, there is still a strong need to develop networks for observing water vapor, temperatures, and wind profiles at the meso- γ and meso- β scales.

In many cases, comprehensive information on the structure of the atmosphere and on atmospheric processes can only be derived from measurements performed by a combination of sensors or measurement systems. Examples range from automatic weather stations that integrate sensors for a variety of standard meteorological variables (e.g., temperature, humidity, wind, pressure, and precipitation) to integrated vertical profiling stations (e.g., the CloudNet approach see Chap. 63, or the ARM Mobile Facility [1.91]).

Detailed studies of specific atmospheric processes are often not possible using operational meteorological measurement systems due to the high spatial resolution required, the need to measure nonstandard variables, and the application of techniques that require human operators (e.g., tethered balloon and aircraft measurements). Such studies have been performed for decades as field experiments.

The first large field experiments, performed in the middle of the last century, were mostly limited to surface and boundary layer studies over flat and uniform terrain. However, over the last 30 years, many meteorological field experiments have been conducted over heterogeneous landscapes, and have often included boundary layer and chemical measurements (see [1.28,

Table 1.8 Routine measurements performed by meteorological networks for typical applications (further specifications are given in Chap. 43). ✓ indicates that the data are only used for verification purposes (based on documentation from the German Meteorological Service, DWD)

Variable	Application						
	Weather briefing	Numerical weather prediction	Climate monitoring	Climate modeling	Aviation	Agriculture	Hydrology
Temperature	✗	✗	✗	✗	✗	✗	✗
Soil temperature	✗	✗	✗	✗	✗	✗	✗
Humidity	✗	✗	✗	✓	✗	✗	✗
Wind speed	✗	✗	✗	✗	✗	✗	✗
Wind direction	✗	✗	✗	✗	✗	✗	✗
Pressure	✗	✗	✗	✗	✗	✗	✗
Amount of precipitation	✗	✗	✗	✗	✗	✗	✗
Precipitation type	✗	✗	✗		✗	✗	✗
Global radiation	✗	✓	✗	✓	✗	✗	✗
Sunshine duration	✗		✗			✗	✗
Visibility	✗	✗			✗		
Cloud cover (amount)	✗		✗		✗	✗	
Cloud type (genera)	✗				✗		
Cloud base height					✗		
Snow height	✗	✗	✗	✗	✗	✗	✗
Snow-water equivalent	✗	✗			✗	✗	✗
Weather phenomena	✗		✗		✗	✗	

92] for an overview of these experiments). Recently, many experiments have been conducted in cities or urban agglomerations to investigate heat islands or air pollution [1.93]. The availability of ground-based and airborne remote-sensing techniques and aircraft measurements has led to a new class of experiments focusing on cloud microphysics and air chemistry in the troposphere and stratosphere. Special experiments (frequently organized by the WMO) are also performed to characterize and compare different sensors and measurement systems (Chaps. 11 and 12).

1.5.3 Applied Meteorology and Other Disciplines

Besides weather prediction and climate monitoring, there is a broad need for meteorological data in many

areas of society, ranging from classical agro- and hydrometeorology to air quality and water management, energy production and transmission, traffic, tourism, and the insurance sector, as illustrated by Table 1.8. This table also shows the data required for model assimilation and verification in weather prediction and for climate services.

Ecological studies are a fast-growing area of application of meteorological measurements. Therefore, this book also includes chapters on measurements at the interface between the ecosystem and the atmosphere. Unfortunately, there is a large gap between scales in the atmosphere and those in the canopy and the soil (Sect. 1.3 and Fig. 1.2). It is therefore still a major challenge to combine atmospheric measurements with soil and plant measurements (for more on this topic, see [1.28, 30, 94, 95]).

1.6 Future Developments

The number and variety of practically applied techniques for measuring meteorological elements are decreasing. Only the most stable and easy-to-handle systems are widely used. Indeed, many of the measurement principles that were popular in the past are only mentioned in the history sections of the chapters of this book.

Many remote sensing techniques are now commercially available for a reasonable price. They have replaced in-situ techniques (mainly on towers) and offer new possibilities for a variety of applications, such as renewable energy technologies. Besides classical precipitation radar, other techniques such as wind profiling

radar and lidar techniques for the measurement of wind, temperature, and humidity profiles have been incorporated into operational networks.

Meteorological services use automation extensively in their observational networks, and classical visual observations are being replaced by alternative approaches.

Before replacing older sensor techniques with new measuring principles and sensors, it is important to carry out detailed comparison experiments. This is particularly important for measurements of meteorological elements that are used to characterize the climate and to detect signals of climate change (Tables 1.1 and 1.3). Such comparisons are required to ensure that long time series of climate observations are homogeneous and free of trends or breaks due to sensor changes.

It is becoming increasingly popular to use compact sensors or sensor systems for many practical applications in the medium-cost sector. These sensors measure many elements in a small volume—often even wind and precipitation, which are normally separated from other

measurements (Chaps. 9, 12). Manufacturers offer different measurement techniques for the same element. Both of these factors have suppressed the implementation of such sensors in larger networks, which remains an issue to be solved.

Besides these general tendencies, sensor-specific problems and perspectives are discussed in the relevant chapters of this book from the measurement of meteorological elements up to complex networks.

Atmospheric measurements are a fast-growing sector of the applications of measuring techniques. Sensors for meteorological variables are included in many everyday products such as cellphones and cars, as well as in many technical applications such as control systems in buildings. Measurements for these applications normally do not follow the recommendations for measurements in the atmosphere, but there is the potential to make these data available for meteorological applications through the use of sophisticated mathematical-statistical models. This approach is known as *crowdsourcing* (Chap. 44).

1.7 Further Reading

- X. Lee: *Fundamentals of Boundary-Layer Meteorology* (Springer, Cham 2018)
- D.H. Lenschow (Ed.): *Probing the Atmospheric Boundary Layer* (American Meteorological Society, Boston 1986)
- M.L. Salby: *Physics of the Atmosphere and Climate* (Cambridge University Press, Cambridge 2012)
- R.B. Stull: *An Introduction to Boundary Layer Meteorology* (Springer, Dordrecht, 1988)

References

- 1.1 V. Wulfmeyer, R.M. Hardesty, D.D. Turner, A. Behrendt, M.P. Cadet, P. Di Girolamo, P. Schlüssel, J. Van Baelen, F. Zus: A review of the remote sensing of lower tropospheric thermodynamic profiles and its indispensable role for the understanding and the simulation of water and energy cycles, *Rev. Geophys.* **53**, 2014RG000476 (2015)
- 1.2 Sir K.C.B.N. Johnson: Milestones in a century of meteorology, *Weather* **5**, 87–90 (1950)
- 1.3 N.R. Dalezios, P.T. Nastos: Milestones of the diachronic evolution of meteorology, *Int. J. Glob. Environ. Issues* **15**, 49–69 (2016)
- 1.4 K. Schneider-Carius: Geschichtlicher Überblick über die Entwicklung der Meteorologie. In: *Meteorologisches Taschenbuch, Neue Ausgabe*, 2nd edn., Vol. 1, ed. by F. Linke, F. Baur (Akademische Verlagsges. Geest & Portig K.-G., Leipzig 1962) pp. 662–708
- 1.5 Aristotle: *Meteorology* (Clarendon Press, Oxford 350 BCE (1908, 2017))
- 1.6 P.K. Wang, D. Zhang: An introduction to some historical governmental weather records of China, *Bull. Am. Meteorol. Soc.* **69**, 753–758 (1988)
- 1.7 Accademia del Cimento: Saggi di naturali esperienze fatte nell' (1666). In: *Neudrucke von Schriften und Karten über Meteorologie und Erdmagnetismus*, Vol. 7, ed. by G. Hellmann (Berlin 1893–1904) p. 278 (Nachdruck Hansebooks, Norderstedt 2017)
- 1.8 H.-G. Körber: *Vom Wetteraberglauben zur Wetterforschung* (Edition Leipzig, Leipzig 1987)
- 1.9 W.E.K. Middleton: *Invention of the Meteorological Instruments* (Johns Hopkins Press, Baltimore 1969)
- 1.10 Societas Meteorologica Palatina: *Ephemerides Societatis Meteorologicae Palatinae. Observationes Anni 1789* (Societas Meteorologica Palatina, Mannheim 1793)
- 1.11 F. Linke, F. Baur (Eds.): *Meteorologisches Taschenbuch, Neue Ausgabe*, Vol. 1, 2nd edn. (Akademische Verlagsgesellschaft Geest & Portig K.-G., Leipzig 1962)
- 1.12 M. Börngen: *Heinrich Wilhelm Brandes (1777–1834)* (Edition am Gutenbergplatz, Leipzig 2017)
- 1.13 K. Keil: Die internationalen Verbindungen auf dem Gebiet der Meteorologie. In: *Meteorologisches Taschenbuch, Neue Ausgabe*, 2nd edn., Vol. 1, ed. by

- F. Linke, F. Baur (Akad. Verlagsges. Geest & Portig, Leipzig 1962) pp. 621–635
- 1.14 M. Schlegel: World Meteorological Organization (WMO). In: *Landolt-Börnstein – Group V Geophysics 4a*, ed. by G. Fischer (Springer, Berlin, Heidelberg 1987) pp. 460–466
- 1.15 WMO: *WMO, 50 Years of Service, WMO-No. 912* (World Meteorological Organization, Geneva 2000)
- 1.16 O.M. Ashford, S. Gupta, P.J. Meade, H. Taba, G. Weiss (Eds.): *Forty Years of Progress and Achievement, WMO-No. 721* (World Meteorological Organization, Geneva 1990)
- 1.17 WMO: *Guide to Instruments and Methods of Observation, WMO-No. 8, Volume I, Measurement of Meteorological Variables* (World Meteorological Organization, Geneva 2018)
- 1.18 E. Kleinschmidt (Ed.): *Handbuch der meteorologischen Instrumente und ihrer Auswertung* (Springer, Berlin 1935)
- 1.19 F. Baur (Ed.): *Linkes Meteorologisches Taschenbuch, Neue Ausgabe, Band III* (Akademische Verlagsges. Geest & Portig K.-G., Leipzig 1957)
- 1.20 D.H. Lenschow (Ed.): *Probing the Atmospheric Boundary Layer* (American Meteorological Society, Boston 1986)
- 1.21 F. Dobson, L. Hasse, R. Davis (Eds.): *Air–Sea Interaction, Instruments and Methods* (Plenum Press, New York 1980)
- 1.22 F.V. Brock, S.J. Richardson: *Meteorological Measurement Systems* (Oxford Univ. Press, New York 2001)
- 1.23 T.P. DeFelice: *An Introduction to Meteorological Instrumentation and Measurement* (Prentice Hall, Upper Saddle River 1998)
- 1.24 S. Emeis: *Measurement Methods in Atmospheric Sciences* (Borntaege Science Publishers, Stuttgart 2010)
- 1.25 S. Emeis: *Surface-Based Remote Sensing of the Atmospheric Boundary Layer* (Springer, Dordrecht, Heidelberg, London, New York 2011)
- 1.26 G.R. Harrison: *Meteorological Measurements and Instrumentation* (John Wiley & Sons, Chichester 2015)
- 1.27 I. Strangeways: *Measuring the Natural Environment*, 2nd edn. (Cambridge Univ. Press, Cambridge 2003)
- 1.28 T. Foken: *Micrometeorology*, 2nd edn. (Springer, Berlin, Heidelberg 2017)
- 1.29 N. Mölders, G. Kramm: *Lectures in Meteorology* (Springer, Cham 2014)
- 1.30 J.L. Monteith, M.H. Unsworth: *Principles of Environmental Physics*, 3rd edn. (Elsevier, Academic Press, Amsterdam, Boston 2008)
- 1.31 M.L. Salby: *Physics of the Atmosphere and Climate* (Cambridge Univ. Press, Cambridge 2012)
- 1.32 R.B. Stull: *An Introduction to Boundary Layer Meteorology* (Springer, Dordrecht 1988)
- 1.33 I. Orlanski: A rational subdivision of scales for atmospheric processes, *Bull. Am. Meteorol. Soc.* **56**, 527–530 (1975)
- 1.34 P.K. Schoonmaker: Paleocological perspectives on ecological scales. In: *Ecological Scale*, ed. by D.L. Peterson, V.T. Parker (Columbia Univ. Press, New York 1998) pp. 79–103
- 1.35 G. Blöschl, M. Sivapalan: Scale issues in hydrological modelling – A review, *Hydrol. Process.* **9**, 251–290 (1995)
- 1.36 H.-J. Vogel, K. Roth: Moving through scales of flow and transport in soil, *J. Hydrol.* **272**, 95–106 (2003)
- 1.37 T. Foken, F.X. Meixner, E. Falge, C. Zetzsch, A. Serafimovich, A. Bargsten, T. Behrendt, T. Biermann, C. Breuninger, S. Dix, T. Gerken, M. Hunner, L. Lehmann-Pape, K. Hens, G. Jocher, J. Kesselmeier, J. Lüers, J.C. Mayer, A. Moravek, D. Plake, M. Riederer, F. Rütz, M. Scheibe, L. Siebicke, M. Sörgel, K. Staudt, I. Trebs, A. Tsokankunku, M. Welling, V. Wolff, Z. Zhu: Coupling processes and exchange of energy and reactive and non-reactive trace gases at a forest site – Results of the Eger Experiment, *Atmos. Chem. Phys.* **12**, 1923–1950 (2012)
- 1.38 NOAA: *U.S. Standard Atmosphere, 1976* (National Oceanic and Atmospheric Administration, Washington 1976)
- 1.39 ESA: *WALES – Water Vapour Lidar Experiment in Space* (ESA Publications Division, Noordwijk 2004)
- 1.40 S. Fueglistaler, P.H. Haynes: Control of interannual and longer-term variability of stratospheric water vapor, *J. Geophys. Res. Atmos.* **110**, D24108 (2005)
- 1.41 S. Dhomse, M. Weber, J. Burrows: The relationship between tropospheric wave forcing and tropical lower stratospheric water vapor, *Atmos. Chem. Phys.* **8**, 471–480 (2008)
- 1.42 J.W. Deardorff: The counter-gradient heat flux in the lower atmosphere and in the laboratory, *J. Atmos. Sci.* **23**, 503–506 (1966)
- 1.43 J.R. Garratt: Flux profile relations above tall vegetation, *Q. J. R. Meteorol. Soc.* **104**, 199–211 (1978)
- 1.44 X. Lee: *Fundamentals of Boundary-Layer Meteorology* (Springer, Cham 2018)
- 1.45 J.W. Deardorff: Convective velocity and temperature scales for the unstable planetary boundary layer and for Rayleigh convection, *J. Atmos. Sci.* **27**, 1211–1213 (1970)
- 1.46 V. Wulfmeyer, S.K. Muppa, A. Behrendt, E. Hammann, F. Späth, Z. Sorbjan, D.D. Turner, R.M. Hardy: Determination of convective boundary layer entrainment fluxes, dissipation rates, and the molecular destruction of variances: Theoretical description and a strategy for its confirmation with a novel lidar system synergy, *J. Atmos. Sci.* **73**, 667–692 (2016)
- 1.47 D.D. Turner, V. Wulfmeyer, L.K. Berg, J.H. Schween: Water vapor turbulence profiles in stationary continental convective mixed layers, *J. Geophys. Res. Atmos.* **119**, 11151–11165 (2014)
- 1.48 A. Behrendt, V. Wulfmeyer, E. Hammann, S.K. Muppa, S. Pal: Profiles of second- to fourth-order moments of turbulent temperature fluctuations in the convective boundary layer: First measurements with rotational Raman lidar, *Atmos. Chem. Phys.* **15**, 5485–5500 (2015)
- 1.49 A.S. Monin, A.M. Obukhov: Osnovnye zakonomernosti turbulentnogo peremesivanija v prizemnom sloe atmosfery (Basic laws of turbulent mixing in the atmosphere near the ground), *Tr. Geofiz. Inst. AN SSSR* **24**(151), 163–187 (1954)

- 1.50 U. Högström: Non-dimensional wind and temperature profiles in the atmospheric surface layer: A re-evaluation, *Bound.-Layer Meteorol.* **42**, 55–78 (1988)
- 1.51 R. Stull: *Practical Meteorology: An Algebra-Based Survey of Atmospheric Science* (© Author, CC Attribution 4.0 License, Vancouver 2015)
- 1.52 M. Hantel: *Einführung Theoretische Meteorologie* (Springer Spektrum, Berlin, Heidelberg 2013)
- 1.53 P.J. Mason: The formation of areally-averaged roughness length, *Q. J. R. Meteorol. Soc.* **114**, 399–420 (1988)
- 1.54 M. Claussen: Flux aggregation at large scales: On the limits of validity of the concept of blending height, *J. Hydrol.* **166**, 371–382 (1995)
- 1.55 J.R. Philip: Blending and internal boundary-layer heights, and shear stress, *Bound.-Layer Meteorol.* **84**, 85–89 (1997)
- 1.56 VDI: *Umweltmeteorologie, Meteorologische Messungen, Wind (Environmental Meteorology, Meteorological Measurements, Wind)*, VDI 3786, Blatt (Part) 2 (Beuth Verlag, Berlin 2018)
- 1.57 I. Troen, E. Lundtang Petersen: *European Wind Atlas* (Risø National Laboratory, Roskilde 1989)
- 1.58 S.A. Savelyev, P.A. Taylor: Notes on an internal boundary-layer height formula, *Bound.-Layer Meteorol.* **101**, 293–301 (2001)
- 1.59 S.A. Savelyev, P.A. Taylor: Internal boundary layers: I. Height formulae for neutral and diabatic flow, *Bound.-Layer Meteorol.* **115**, 1–25 (2005)
- 1.60 W.P. Elliott: The growth of the atmospheric internal boundary layer, *Trans. Am. Geophys. Union* **39**, 1048–1054 (1958)
- 1.61 A. Raabe: On the relation between the drag coefficient and fetch above the sea in the case of offshore wind in the near shore zone, *Z. Meteorol.* **33**, 363–367 (1983)
- 1.62 J. Zelený, T. Foken: Ausgewählte Ergebnisse des Grenzschichtexperimentes in Bohunice 1989, *Z. Meteorol.* **41**, 439–445 (1991)
- 1.63 N. Matzinger, M. Andretta, E.V. Gorsel, R. Vogt, A. Ohmura, M.W. Rotach: Surface radiation budget in an Alpine valley, *Q. J. R. Meteorol. Soc.* **129**, 877–895 (2006)
- 1.64 M.Y. Leclerc, T. Foken: *Footprints in Micrometeorology and Ecology* (Springer, Heidelberg, New York, Dordrecht, London 2014)
- 1.65 S. Metzger: Surface-atmosphere exchange in a box: Making the control volume a suitable representation for in-situ observations, *Agric. For. Meteorol.* **255**, 68–80 (2018)
- 1.66 R. Kormann, F.X. Meixner: An analytical footprint model for non-neutral stratification, *Bound.-Layer Meteorol.* **99**, 207–224 (2001)
- 1.67 C. Spirig, C. Ammann, A. Neffel: Art footprint tool, Zenodo (2017), <https://doi.org/10.5281/zenodo.816236>
- 1.68 N. Kljun, M.W. Rotach, H.P. Schmid: A three-dimensional backward Lagrangian footprint model for a wide range of boundary layer stratification, *Bound.-Layer Meteorol.* **103**, 205–226 (2002)
- 1.69 N. Kljun, P. Calanca, M.W. Rotach, H.P. Schmid: A simple two-dimensional parameterisation for flux footprint prediction (FFP), *Geosci. Model Dev.* **8**, 3695–3713 (2015)
- 1.70 A.T. Vermeulen: *CHIOTTO – Final Report* (Energy Research Centre of the Netherlands, Petten 2007)
- 1.71 M. Gloor, P. Bakwin, D. Hurst, L. Lock, R. Draxler, P. Tans: What is the concentration footprint of a tall tower?, *J. Geophys. Res.* **106**(D16), 17831–17840 (2001)
- 1.72 A.T. Vermeulen, M. van Loon, P.J.H. Buitjes, J.W. Erisman: Inverse transport modelling of non-CO₂ greenhouse gas emissions of Europe. In: *Air Pollution Modeling and Its Applications XIV*, ed. by G. Schiermeier (Kluwer, New York 2001) pp. 631–640
- 1.73 R.W.A. Hutjes, O.S. Vellinga, B. Gioli, F. Miglietta: Disaggregation of airborne flux measurements using footprint analysis, *Agric. For. Meteorol.* **150**, 966–983 (2010)
- 1.74 M. Beniston: *From Turbulence to Climate* (Springer, Berlin, Heidelberg 1998)
- 1.75 J.C. Wyngaard: *Turbulence in the Atmosphere* (Cambridge Univ. Press, Cambridge 2010)
- 1.76 A.N. Kolmogorov: Rassejanie energii pri lokalno-isotropoi turbulentnosti (Dissipation of energy in locally isotropic turbulence), *Dokl. AN SSSR* **32**, 22–24 (1941)
- 1.77 W. Roedel, T. Wagner: *Physik unserer Umwelt: Die Atmosphäre* (Springer, Berlin, Heidelberg 2011)
- 1.78 I. Van der Hoven: Power spectrum of horizontal wind speed in the frequency range from 0.0007 to 900 cycles per hour, *J. Meteorol.* **14**, 160–164 (1957)
- 1.79 W.C. Skamarock: Evaluating mesoscale NWP models using kinetic energy spectra, *Mon. Weather Rev.* **132**, 3019–3032 (2004)
- 1.80 P.N. Wedi: Increasing horizontal resolution in numerical weather prediction and climate simulations: Illusion or panacea?, *Philos. Trans. R. Soc. A* **372**, 20130289 (2014)
- 1.81 W.C. Skamarock, J.B. Klemp: A time-split nonhydrostatic atmospheric model for weather research and forecasting applications, *J. Comput. Phys.* **227**, 3465–3485 (2008)
- 1.82 R. Heinze, A. Dipankar, C.C. Henken, C. Moseley, O. Sourdeval, S. Trömel, X. Xie, P. Adamidis, F. Ament, H. Baars, C. Barthlott, A. Behrendt, U. Blahak, S. Bley, S. Brdar, M. Brueck, S. Crewell, H. Deneke, P. Di Girolamo, R. Evaristo, J. Fischer, C. Frank, P. Friederichs, T. Göcke, K. Gorges, L. Hande, M. Hanke, A. Hansen, H.C. Hege, C. Hoose, T. Jahns, N. Kalthoff, D. Klocke, S. Kneifel, P. Knippertz, A. Kuhn, T. van Laar, A. Macke, V. Maurer, B. Mayer, I.C. Meyer, K. Muppa Shrivani, A.J. Neggers Roeland, E. Orlandi, F. Pantillon, B. Pospichal, N. Röber, L. Scheck, A. Seifert, P. Seifert, F. Senf, P. Siligam, C. Simmer, S. Steinke, B. Stevens, K. Wapler, M. Weniger, V. Wulfmeyer, G. Zängl, D. Zhang, J. Quaas: Large-eddy simulations over Germany using ICON: A comprehensive evaluation, *Q. J. R. Meteorol. Soc.* **143**, 69–100 (2017)
- 1.83 E. Kalnay: *Atmospheric Modeling, Data Assimilation and Predictability* (Cambridge Univ. Press, Cambridge 2012)
- 1.84 S. Adam, A. Behrendt, T. Schwitalla, E. Hammann, V. Wulfmeyer: First assimilation of temperature lidar data into an NWP model: Impact on the simulation

- of the temperature field, inversion strength and PBL depth, Q. J. R. Meteorol. Soc. **142**, 2882–2896 (2016)
- 1.85 D. Leuenberger, A. Haefele: Assimilation of temperature and humidity profiles from a Raman lidar. In: *6th Int. Symp. Data Assim.* (ISDA, Munich 2018)
- 1.86 R.L. Schwiesow: A comparative overview of active remote-sensing techniques. In: *Probing the Atmospheric Boundary Layer*, ed. by D.H. Lenschow (American Meteorological Society, Boston 1986) pp. 129–138
- 1.87 H. Walter, H. Lieth: *Klimadiagramm Weltatlas* (VEB Gustav Fischer Verlag, Jena 1960–67)
- 1.88 A. Persson: The story of the Hovmöller diagram: An (almost) eyewitness account, Bull. Am. Meteorol. Soc. **98**, 949–957 (2016)
- 1.89 E. Hovmöller: The trough-and-ridge diagram, Tellus **1**, 62–66 (1949)
- 1.90 M.C. Wheeler, G.N. Kiladis: Convectively-coupled equatorial waves: Analysis of clouds and temperature in the wave-number-frequency domain, J. Atmos. Sci. **56**, 374–399 (1999)
- 1.91 M.A. Miller, K. Nitschke, T.P. Ackerman, W.R. Ferrell, N. Hickmon, M. Ivey: The ARM mobile facilities, Meteorol. Monogr. **57**, 9.1–9.15 (2016)
- 1.92 V. Wulfmeyer, D.D. Turner, B. Baker, R. Banta, A. Behrendt, T. Bonin, W.A. Brewer, M. Buban, A. Choukulkar, E. Dumas, R.M. Hardesty, T. Heus, J. Ingwersen, D. Lange, T.R. Lee, S. Metzendorf, S.K. Muppa, T. Meyers, R. Newsom, M. Osman, S. Raasch, J. Santanello, C. Senff, F. Späth, T. Wagner, T. Weckwerth: A new research approach for observing and characterizing land-atmosphere feedback, Bull. Am. Meteorol. Soc. **99**, 1639–1667 (2018)
- 1.93 T.R. Oke, G. Mills, A. Christen, J.A. Voogt: *Urban Climates* (Cambridge Univ. Press, Cambridge 2017)
- 1.94 A.F. Moene, J.C. van Dam: *Transport in the Atmosphere-Vegetation-Soil Continuum* (Cambridge Univ. Press, Cambridge 2014)
- 1.95 R. Monson, D. Baldocchi: *Terrestrial Biosphere-Atmosphere Fluxes* (Cambridge Univ. Press, New York 2014)

Thomas Foken

University of Bayreuth
Bayreuth, Germany
thomas.foken@uni-bayreuth.de



Thomas Foken is a retired Professor of Micrometeorology at the University of Bayreuth. He was the head of Laboratories at the meteorological observatories at Potsdam (1981–1994) and Lindenberg (1994–1997). His research interests include the interaction between the Earth's surface and the atmosphere and the measurement and modeling of energy and matter fluxes, with a strong focus on experimental meteorology. His scientific contributions have been recognized through various international awards.

Frank Beyrich

Meteorologisches Observatorium
Lindenberg –
Richard-Aßmann-Observatorium
Lindenberg, Germany
frank.beyrich@dwd.de



Frank Beyrich has been Head of the Boundary Layer Processes Group at the Meteorological Observatory Lindenberg of the German Meteorological Service (DWD) since 1997. He organized the LITFASS field experiments in 1998, 2003, and 2009 that focused on the area-averaging of energy fluxes over a heterogeneous land surface. He has been performing atmospheric research with scintillometers since 1994, when he received his PhD at Freie Universität Berlin.

Volker Wulfmeyer

Institute of Physics and Meteorology
University of Hohenheim
Stuttgart, Germany
volker.wulfmeyer@uni-hohenheim.de



Volker Wulfmeyer is Professor and Chair of Physics and Meteorology at the University of Hohenheim. The research goals of his team include: high-resolution, seamless weather and seasonal forecasting as well as climate projections; understanding of land-atmosphere feedback and turbulent transport processes in the planetary boundary layer; and the development and application of 3D scanning active remote sensing systems for water-vapor, temperature, and wind measurements.

Principles of

2. Principles of Measurements

Wolfgang Foken 

Modern metrology involves three aspects: practical techniques for measuring physical data, international conventions for scale units, and the theoretical background for measurements and signal processing. This chapter covers the most important themes of the third aspect as well as some notes on international conventions. After a short historical overview, the general theoretical principles of measurements are described. This includes the concept of uncertainty as well as the influence of signal dynamics on the result of a measurement or the possibilities of regression analyses. Furthermore, this chapter deals with the transmission behavior of measuring systems. From this point of view, the properties of a measuring system are described in both the time and frequency domains. Because of the general use of digital data processing systems, the influence of sampling and discretization on the measured analog signal is also presented.

2.1	Basics of Measurements	34
2.2	History	34
2.3	Errors in Measurement	34
2.3.1	Systematic Errors.....	35
2.3.2	Random Errors.....	36
2.3.3	Statement of a Final Result.....	38
2.4	Regression Analysis	38
2.5	Time Domain and Frequency Domain for Signals and Systems	39
2.6	Dynamics of Measuring Systems	40
2.6.1	Test Functions	40
2.6.2	Response to Test Function for a First-Order System.....	41
2.6.3	Step Response of Second-Order Systems	42
2.6.4	Frequency Response for a First-Order System.....	42
2.6.5	Frequency Response for a Second-Order System	42
2.7	Analog and Digital Signal Processing	44
2.7.1	Analog Measurement Chain	44
2.7.2	Digital Measurement Chain	44
2.8	Hardware for Digital Measurement Systems	46
2.9	Further Reading	47
	References	47

Modern metrology is an interdisciplinary technology that is essential to natural science and engineering as a form of quality assurance.

Metrology involves three important aspects:

- *Practical metrology* covers all the application-oriented aspects, e.g., how to measure physical data like temperature, flow, humidity, and pressure.
- *Statutory metrology* deals with regulations, standardizations, and international conventions (Chap. 4).
- The *theory of measurements* includes the questions of dynamics, signal analysis, and the theory of uncertainty.

This chapter focuses on the last aspect.

In a broader sense, metrology is a special category of testing methods – more precisely, it is dimensional testing. This might be done by means of counting or comparing. The measuring process is characterized by capturing physical data. These data are eventually represented by a combination of the measured value and a scale unit that should be in agreement with international conventions. Therefore, this procedure is always a comparison of the measured value with a standard unit.

2.1 Basics of Measurements

Evidently, the measurement of physical quantities seems to be a distinct practical process. But our common sense tells us that each measurement is not precise. Therefore, theoretical considerations help evaluate the results of measurements. In this context, the theory of errors and the dynamics of measuring systems are of great significance. To solve these problems, mathematical statistics and probability theory are necessary.

The dynamic behavior of the measured quantity and measurement system both require a description of the measuring process in the time domain as well as in

the frequency domain. In this context, signal analytical methods such as the Fourier transformation expand the significance of the measurement results. Digital signal and data processing make it very easy to transform time domain signals into frequency domain signals using the fast-Fourier-transformation (FFT). Unfortunately, the digitalization process of the analog signals creates special errors both in time and amplitude. Therefore, it is necessary to have a closer look at the digital measuring chain.

2.2 History

Measurements for the purpose of determining distances, counting, or weighing were well known in all ancient advanced civilizations. There was a strong interrelation between measurement and cultural development. Distances and weights were important in everyday life. Often, the human body provided the units. Examples are the cubit and the yard, which refers to the distance from the nose of Henry I, King of England in the 12th century, to his thumb. Even 100° on the Fahrenheit temperature scale refers to the normal temperature of the human body (37.7°C). Often, weather and astronomical phenomena were observed and recorded by the leaders of the respective religion and later by scientists.

In ancient Greece, philosophy and natural science were not separated. This is illustrated by the rough translation of the paraphrase ascribed to the ancient Greek philosopher *Platon* (427–347 BCE):

Objective observation combined with logical thinking is the source of every finding in natural science. The best tool against misperceptions is to measure, count, or weight. That is a thing of the spirit and the ability of thinking [2.1].

Temperature recordings became more precise when it became possible to make glass capillaries. It is known that 17th century scientists used these capillaries. For instance, the Italian professor of medicine *Santorio Santorio* (1561–1636) measured body temperature [2.2] and the German scientist *Otto von Guericke* (1602–1686) used a gas thermometer for weather observations using a seven-section temperature scale (very cold, cold, cool, medium, lukewarm, warm, and very warm) [2.3].

Measurement technology is not a standalone science. Nowadays, measurement technology provides a considerable contribution to the further development of the natural sciences and engineering. Within nearly every part of science and technology, measurement develops into pure electrical data processing. Nonelectrical quantities are transformed into electrical signals. Sensors are the link between physical quantities and electrical data processing. The most important benefit of electrical signals is the fact that it is possible to measure the two quantities *frequency* and *time* with very high precision.

2.3 Errors in Measurement

Generally, measurements are more or less accurate. The error can be defined as the deviation Δx of the measured value x from the fictive true value x_w .

Figure 2.1 shows a scheme of the multiple influences on a measuring system symbolized as a black box.

Different types of errors influence the result of a measuring process. Therefore, the results should not

be accepted without an appropriate error analysis. The errors in measurement can be divided in different categories (unless they are gross errors or mistakes):

- *Representation errors*

If there exists a deterministic correlation only within certain limits between the measured quantity and the measured value, but the quantity runs

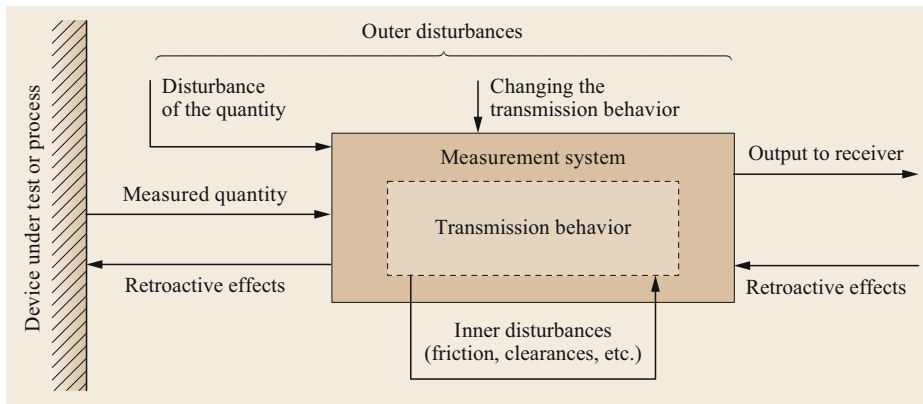


Fig. 2.1 The measuring system is influenced by disturbances

out of these limits, then this type of errors arises. For example, some measuring systems for flow show correct values only within fixed limits of the Reynolds number.

- **Static and dynamic errors**

Provided that the measuring system delivers a constant value for a time-constant quantity, the deviation between the nominal value and the measured value is defined as the static error.

If the measured quantity varies in time, the relation between a measured quantity and measured value is characterized by a differential equation. As a consequence, a dynamic error results.

- **Errors from digital data processing**

The discretization of amplitude and time results in two special errors: the quantization error and the aliasing effect. These will be discussed in detail in Sect. 2.3.

- **Systematic error and random error**

For analog practical metrology, these two categories of errors are of particular importance. Generally, systematic errors are attributed to the measuring system. Random errors are caused by randomized variations of multiple independent influencing factors.

- **Guaranteed error limits**

Manufacturers of measuring instruments specify the accuracy by means of these guaranteed error limits. The error limit is given by a percentage from the upper limit of the range of a measuring device.

2.3.1 Systematic Errors

Multiple repetitions of a measurement under constant conditions always result in an equal deviation from the true value x_w . Intentionally changing the measuring conditions leads to predictable change to the deviation

Δx . If it is possible to identify these systematic errors, the true value can be calculated by a correction of the measured value x

$$x_w = x - \Delta x \quad \text{resp.} \quad x_w = x \left(1 - \frac{\Delta x}{x} \right). \quad (2.1)$$

Δx and $\Delta x/x$ are the absolute systematic error and the relative systematic error, respectively.

Causes of Systematic Errors

- Nonstochastic environmental influences: imperfect stability of the measuring conditions, retroactive effects from the measuring system to the process, etc.
- Imperfectness of the measuring device: nonlinearity, hysteresis error, inaccurate zero balance, etc.
- Unsatisfactorily skilled experimenter: insufficient theoretical knowledge, prepossession (measuring the values one wishes to measure), etc.

Avoidance of Systematic Errors

- Precise review of the theoretical correlation concerning the measuring process
- Targeted changes to the conditions that should not influence the measured value
- Use of a totally different principle to measure the quantity

Error Propagation for Systematic Errors

Often a quantity y can't be measured, but there exists a unique functional dependency on several measured quantities x_i containing systematic errors

$$y = f(x_1, x_2, \dots, x_n) \quad \text{with} \quad x_i = x_{i,w} - \Delta x_i, \quad (2.2)$$

$$\begin{aligned} \Delta y &= y - y_w \\ &= f(x_{1,w} + \Delta x_1, x_{2,w} + \Delta x_2, \dots, x_{n,w} - \Delta x_n) \\ &\quad - f(x_{1,w}, x_{2,w}, \dots, x_{n,w}). \end{aligned} \quad (2.3)$$

To determine the systematic error of y it is necessary to use so-called error propagation. Usually the error is very small. Therefore, it is possible to expand y in a Taylor series truncated after the first element

$$\Delta y = \frac{\partial f}{\partial x_1} \Delta x_1 + \frac{\partial f}{\partial x_2} \Delta x_2 + \dots + \frac{\partial f}{\partial x_n} \Delta x_n. \quad (2.4)$$

For simple unique functional dependencies, such as a linear combination or a product of x_i , we find the following rules for error propagation

$$\begin{aligned} \text{If } & y = a_1 x_1 + a_2 x_2 + \dots + a_n x_n, \\ \text{then } & \Delta y = a_1 \Delta x_1 + a_2 \Delta x_2 + \dots + a_n \Delta x_n, \\ \text{or if } & y = a_1 x_1^{\alpha_1} a_2 x_2^{\alpha_2} \dots a_n x_n^{\alpha_n}, \\ \text{then } & \frac{\Delta y}{y} = \alpha_1 \frac{\Delta x_1}{x_1} + \alpha_2 \frac{\Delta x_2}{x_2} + \dots + \alpha_n \frac{\Delta x_n}{x_n}. \end{aligned} \quad (2.5)$$

2.3.2 Random Errors

We know from experience that measurements are not exactly reproducible even under constant conditions. Through multiple repetitions of a measurement, the results fall within a certain range of variation. It is possible to formulate three general reasons for this variation:

- The measured quantity is a stochastic quantity itself (e.g., the statistical interpretation of the gas pressure in a closed volume due to impacts of the gas molecules on the walls).
- A number of physical, chemical, or biological systems show a specific chaotic behavior. Small deviations of the outer conditions induce large orderless fluctuations (e.g., double pendulums under large deflections). This effect is described as deterministic chaos.
- If there are a variety of factors influencing the measuring process, then the measurements are not reproducible. These factors should be independent of each other and unascertainable. In this case we are talking about random errors. These errors are described using statistical principles.

Density Function and Probability Distribution Function

Usually, the measured x_i are collected in cohorts of size Δx_k . This procedure yields a histogram. Due to normalization to the respective class size of the columns in the histogram, the areas of these columns are proportional to the number of values within the respective class.

The relative frequency h_k is defined as the quotient of the measured value n_k in the cohort k to the total number of measurements n normalized to the class size Δx_k . If passing n to infinity and Δx_k to zero, the relative frequency is converted to the continuous density function $h(x)$. Integration of the density function yields a probability distribution function $H(x)$. The definition of the density function is closely connected to stochastic theory, in particular to the question concerning the probability of finding an arbitrary measured value within specified limits.

Compare the following formulas

$$h_k = \frac{n_k}{\Delta x_k n}, \quad \lim_{\substack{n \rightarrow \infty \\ \Delta x_k \rightarrow 0}} h_k = h(x)$$

$$\text{and } H(x_1 < x \leq x_2) = \int_{x_1}^{x_2} h(x) dx, \quad (2.6)$$

$$H(x) = H(x \leq x_1) = \int_{-\infty}^{x_1} h(x) dx$$

$$\text{with } H(-\infty < x \leq \infty) = \int_{-\infty}^{\infty} h(x) dx = 1. \quad (2.7)$$

Statistical Universe and Sample

In the field of metrology, any possible measurement of a quantity is termed the statistical universe. Any finite number of these measurements is termed a sample.

The statistical postulates for the mean \bar{x} and the mean variation S , calculated from samples, can be interpreted as estimations of the expectation value μ and the standard deviation σ , respectively.

From the sample data it is possible to calculate a density function and distribution function. Based on these data, a distribution model hypothesis for the statistical universe can be formulated. The most important distribution model, especially for continuous measurement values, is the normal, or Gaussian, distribution.

After measuring the values of a sample, it is necessary to clarify which is the best estimate for the characteristic parameters of the distribution model. To solve this question, the following postulates are helpful [2.4]:

- Assuming an infinite number of values within the sample, the estimates should be equal to the values of the universe.
- The estimate with the least mean variation should be the best one.

Mean and Deviation of the Normal (Gaussian) Distribution

According to the two postulates above, the mean \bar{x} is the estimate of the expectation value μ

$$\bar{x} = \frac{1}{n} \sum_{i=1}^n x_i \quad \text{and} \quad \mu = \lim_{n \rightarrow \infty} \bar{x}. \quad (2.8)$$

In the same way, the mean variation S of the sample can be considered the estimate of the standard deviation σ . The square of σ is known as variance

$$S^2 = \frac{1}{n-1} \sum_{i=1}^n (x_i - \bar{x})^2$$

$$\text{and } \sigma^2 = \lim_{n \rightarrow \infty} \frac{1}{n} \sum_{i=1}^n (x_i - \mu)^2. \quad (2.9)$$

S and \bar{x} are parameters of the sample, while σ and μ are parameters of the statistical universe.

Density Function and Probability Distribution Function of the Normal Distribution

With the help of the estimates for σ and μ , the density function and the distribution function of the normal distribution are predictable

$$h(x) = \frac{1}{S\sqrt{2\pi}} e^{-\frac{(x-\bar{x})^2}{2S^2}}$$

$$\text{and } H(x) = \frac{1}{S\sqrt{2\pi}} \int_{-\infty}^{x_1} e^{-\frac{1}{2}\left(\frac{x-\bar{x}}{S}\right)^2} dx. \quad (2.10)$$

Because the mean and the mean variation are specific parameters for each measuring task, it is useful

to find a universal normalization. The substitution $t = (x - \bar{x})/S$ fulfills this purpose and yields a normalized density function $h(t)$ and the distribution function $H(t)$. The integral $H(t)$ is not solvable but tabulated [2.5]

$$H(t) = \frac{1}{\sqrt{2\pi}} \int_{-\infty}^{x_1} e^{-\frac{t^2}{2}} dx. \quad (2.11)$$

Figure 2.2 shows these normalized functions. The abscissa is divided in multiples of S . The mean is converted to zero and the maximum of the density function is converted to 0.398

$$h(t)_{\max} = S h(x)_{\max} \frac{1}{\sqrt{2\pi}} = 0.398. \quad (2.12)$$

Error Propagation of Random Errors

The calculation of error propagation for random errors is the same as for systematic errors. The quantity y can't be measured directly, but there exists a unique functional dependency on several measurable quantities x_i with random errors. Mean and mean variation are the result of

$$\bar{y} = f(\bar{x}_1, \bar{x}_2, \dots, \bar{x}_n)$$

$$\text{and } S_y = \sqrt{\sum_{i=1}^n \left(\frac{\partial y}{\partial x_i} S_{x_i} \right)^2}. \quad (2.13)$$

Mean Variation of the Mean

With the help of the following calculations it is possible to quantify the reliability of the estimate for the expectation value. After calculating the mean variation of the single measurements S_x , it is necessary to determine the

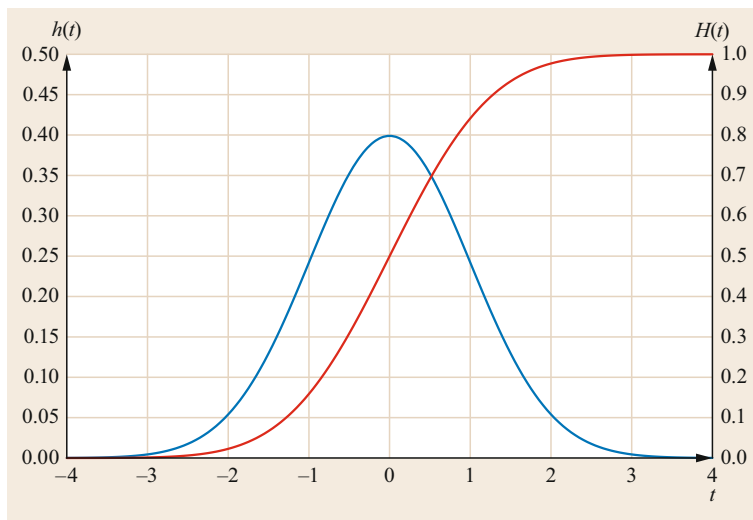


Fig. 2.2 Normalized density function (blue) and distribution function (red) of the normal distribution $t = (x - \bar{x})/S$

Table 2.1 *t*-Factors for common confidence ranges and selected sample sizes

<i>n</i>	Confidence range		
	68.3%	95.5%	99.7%
5	1.15	2.88	6.62
10	1.06	2.33	4.09
50	1.01	2.06	3.16
100	1.00	2.03	3.08
200	1.00	2.02	3.04

mean error of the mean, i.e., the mean variation $S_{\bar{x}}$. The statistical correlation between $S_{\bar{x}}$ and S_x is the result of

$$S_{\bar{x}} = t \frac{S_x}{\sqrt{n}}, \quad (2.14)$$

where n is the number of measurements. With the help of the Student's distribution it is possible to determine the *t*-factor depending on the number of measurements and the selected confidence range. For a huge number of degrees of freedom (the number of measurements in a sample), the Student's distribution turns into the normal distribution. Generally speaking, $S_{\bar{x}}$ defines the range in which to find the true value with the selected statistical certainty (confidence range).

Table 2.1 shows selected values of the Student's distribution for the most common confidence ranges and several sample sizes [2.5].

2.4 Regression Analysis

The regression analysis is closely connected to the theory of random errors. At this point, the discussion is limited to the linear dependency between two variables x and y . The starting point is the linear relation $y = mx + n$.

Drawing the pairs of variates (x_i, y_i) on an xy plot results in a cluster of points. This cluster shows a more or less linear dependency.

The aim is now to find the best linear equation to describe the dependency between x and y by minimizing the so-called error squares. There are two possible ways to determine the best linear dependency.

Assuming that the values x_i are nearly free from errors, an error equation follows that has to be minimized

$$\begin{aligned} \varepsilon_i &= y(x_i) - y_i \quad \text{and} \\ \sum_{i=1}^n \varepsilon_i^2 &= \sum_{i=1}^n (mx_i + n - y_i)^2 \implies \text{MINIMUM}. \end{aligned} \quad (2.16)$$

2.3.3 Statement of a Final Result

Frequently a quantity y has to be calculated from several quantities x_i . Some of these quantities x_i are affected by random errors (type A), while others are affected by errors that can't be calculated with the help of statistical methods (type B). Uncertainties of type B might be obtained from former measurements, a calibration process, or manufacturer specifications. Based on the *ISO Guide to the Expression of Uncertainty in Measurement*, it is possible to formulate a final result [2.6]

$$\begin{aligned} y &= f(\bar{x}_i) \pm u_C \\ &\text{with combined standard uncertainty} \\ u_C &= \sqrt{u_A^2 + u_B^2}, \end{aligned} \quad (2.15)$$

where u_A and u_B are the uncertainties of type A or type B, respectively.

Finally, it is possible to apply an extended standard uncertainty u instead of u_C for a fixed confidence range ($u = ku_C$). The factor $k = 1$ represents a confidence range of 68.3%, which is appropriate for the natural and engineering sciences. For the reliability of systems, a confidence range of 95% ($k = 2$) or even 99% ($k = 3$) is often used.

This procedure results in two equations for m and n to determine the best linear correlation

$$\begin{aligned} m &= \frac{\sum x_i \sum y_i - n \sum x_i y_i}{(\sum x_i)^2 - n \sum x_i^2} \quad \text{and} \\ n &= \frac{\sum x_i \sum x_i y_i - \sum y_i \sum x_i^2}{(\sum x_i)^2 - n \sum x_i^2}. \end{aligned} \quad (2.17)$$

Otherwise, if it is possible to determine the values y_i with a higher accuracy, we find the following error equation

$$\varepsilon_i = x(y_i) - x_i = \frac{y_i - n}{m} - x_i. \quad (2.18)$$

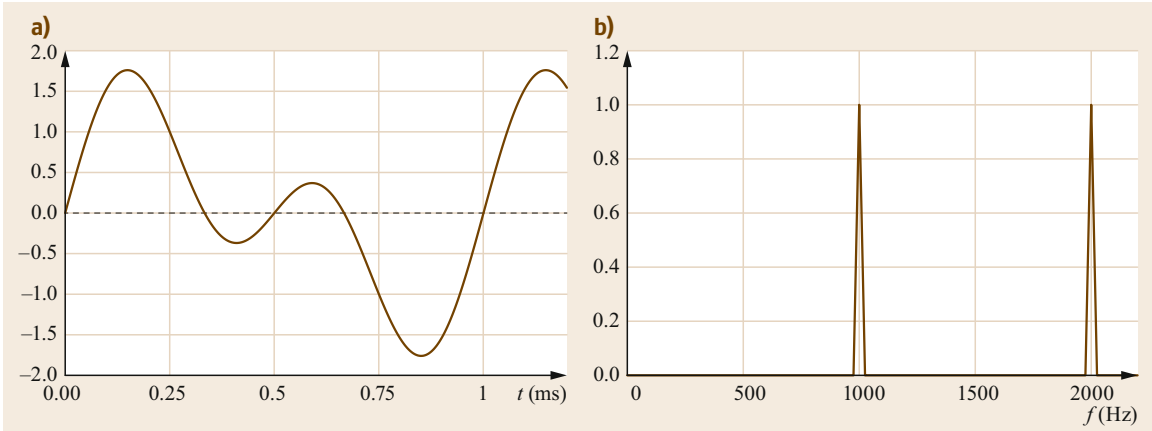


Fig. 2.3a,b Idealized time function (a) and spectrum (b) of the signal $A = A_1 \sin(\omega t) + A_2 \sin(2\omega t)$ with $\omega = 2\pi f$; $f = 1000$ Hz and $A_{1,2} = 1$

2.5 Time Domain and Frequency Domain for Signals and Systems

Typically, measured quantities are nonstatic values, especially for vibrations but even for pressure measurements or temperature fluctuations. For such dynamic signals, the pure time function isn't sufficient to describe the dynamic behavior of the measuring process symbolized in Fig. 2.2. Therefore, the time functions are transformed from the time domain to the frequency domain. This process (Fourier transformation) yields a frequency spectrum.

Generally, periodic signals show a line spectrum. Otherwise, nonperiodic signals (stochastic signals, transient signals) show continuous spectra. Fortunately, many signals are periodical or contain at least periodical components. From the mathematics, we know that periodical signals can be expanded into a Fourier series as a sum of harmonic functions (sine and cosine functions). If we know the behavior of the measuring systems for harmonic functions, the result is applicable to all periodic signals.

Figure 2.3 shows the time function and spectrum of a simple (idealized) periodical signal, while the Fourier series consists only of two harmonic components with equal amplitudes.

Generalized measuring systems may be regarded as a special signal processing system. The measured physical quantity, e.g., the corresponding measured signal, is the input of the measuring system. According to the transmission behavior of the measuring system, an output signal arises that may be used for a display as well as for automatic control purposes. Usually, input and output signals are already electrical signals.

A simplified system may be regarded as a so-called *linear time-invariant (LTI) system*. For this reason, there exists a mathematical correlation between the input signal $x_c(t)$ and output signal $x_a(t)$ in the time domain and between the input spectrum $X_E(\omega)$ and the output spectrum $X_A(\omega)$ in the frequency domain. The transfer behavior of the system is described by the pulse response $g(t)$ in the time domain and the frequency response $G(\omega)$ in the frequency domain. The link between the time and frequency domain is always given by the Fourier transformation $F(\omega)$ or its own inverse function $F^{-1}(\omega)$. Figure 2.4 shows this principle. The mathematical operation convolution is marked with a $*$.

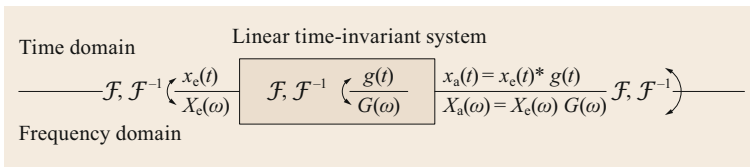


Fig. 2.4 Linear time-invariant system in the time and frequency domains

2.6 Dynamics of Measuring Systems

There are different possibilities for defining the dynamic of a measuring system. The definition of the transfer function as a differential equation is the most general one

$$e_0 x_e(t) + e_1 \frac{dx_e(t)}{dt} + \dots + e_m \frac{d^m x_e(t)}{dt^m} = a_0 x_a(t) + a_1 \frac{dx_a(t)}{dt} + \dots + a_n \frac{d^n x_a(t)}{dt^n} \quad (2.19)$$

For LTI systems, the coefficients e_i and a_i are constants. The left-hand side of the equation describes the input signal of the measuring system and the right-hand side describes the output signal.

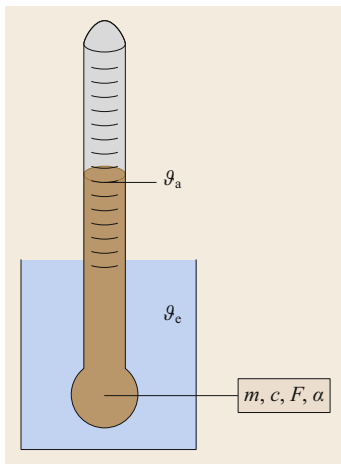


Fig. 2.5 Principle of temperature measurements with contact to the test medium (m = mass of the sensor, c = specific heat capacity, F = surface area of the sensor inside the medium, α = heat transfer coefficient (medium–sensor), ϑ_c = temperature of the medium under test, ϑ_a = displayed temperature)

For simple systems it is possible to determine the transfer function analytically with the help of fundamental physical relations such as heat balances or equations of motion. Figure 2.5 shows the principle of a temperature measurement with contact to the medium under test. This principle is applicable to nearly all temperature sensors except, for instance, radiation pyrometers.

The example in Fig. 2.5 may be solved using the heat balance of the applied heat and the stored heat (the discharged heat is neglected)

$$\alpha F (\vartheta_c - \vartheta_a) = 0 + mc \frac{d\vartheta_a}{dt}$$

resp. $\vartheta_c = \vartheta_a + \tau \frac{d\vartheta_a}{dt}$

with $\tau = \frac{mc}{\alpha F}$. (2.20)

This equation represents a transfer function according to (2.19); however, most of the coefficients are zero. The value τ is known as a time constant. The highest order of the differential (2.20) is equal to 1. Therefore, those systems are characterized as first-order systems. For more complex systems, it becomes nearly impossible to set up the transfer function analytically.

2.6.1 Test Functions

Assuming they are LTI systems, it is appropriate to use simple test functions to identify the behavior of measuring systems. For nearly all measurement quantities, these functions are at least approximately simple to create. Table 2.2 shows the most common test functions.

The pulse function and the related response function (pulse response) are of particular importance. The normalized pulse function is known as the ideal Dirac

Table 2.2 Test functions

Pulse function $\rho(t)$	Step function $\varepsilon(t)$	Ramp function $\delta(t)$

Table 2.3 Response functions

Formula of the response function	Graphic representation
Step response $x_a(t) = kx_e(t) \left(1 - e^{-\frac{t}{\tau}}\right)$, with $x_{e,\text{step}}(t) = x_0 = 1$; $x_{a,\text{step}}(t) = k \left(1 - e^{-\frac{t}{\tau}}\right)$	
Pulse response $x_{a,\text{pulse}}(t) = \frac{d}{dt} \left[k \left(1 - e^{-\frac{t}{\tau}}\right) \right] = \frac{k}{\tau} e^{-\frac{t}{\tau}}$	
Ramp response $x_{a,\text{ramp}}(t) = \int_0^t \left[k \left(1 - e^{-\frac{t}{\tau}}\right) \right] dt = kt - k\tau \left(e^{-\frac{t}{\tau}} - 1\right)$	

pulse. The Dirac pulse can be created from a rectangular pulse with a pulse width Δt and a height $1/\Delta t$ by applying $\Delta t \rightarrow 0$.

Starting from the pulse function, the step function and the ramp function are obtained by integration. In the opposite direction, the ramp functions can be transformed into the others by differentiation. For LTI systems, the same rules are applicable to the corresponding response functions of the measuring system.

2.6.2 Response to Test Function for a First-Order System

Because the step function is easy to obtain, it is best to start with this function. That means we have to solve the first-order transfer function according to (2.19). Pulse response and ramp response can be obtained by differentiation or integration of the step response, respectively. The analytical solutions and the corresponding graphs are summarized in Table 2.3.

2.6.3 Step Responseprotect of Second-Order Systems

As a general rule, mechanical systems with movable masses may be described according to (2.19) as second-order systems (oscillatory system) with the spring rate k , the damping coefficient c , and the mass m

$$x_e(t) = kx_a(t) + c\dot{x}_a(t) + m\ddot{x}_a(t). \quad (2.21)$$

Figure 2.6 shows the step response (unit step) for different damping (two different damping coefficients and aperiodic oscillations). For higher damping, the system runs into the borderline case. One example of the oscillating behavior is a wind vane, but the same relations are valid for mechanical chart recorders or galvanometers.

2.6.4 Frequency Response for a First-Order System

By applying a measuring system (LTI system) with a sinusoidal signal of any frequency and constant amplitude, the output is also a sinusoidal signal of the same frequency, but the amplitude and the phase shift depend on the frequency.

For further discussion it is useful to shift to a complex description of the input and output signal of the measuring system

$$\begin{aligned} x_e(t) &= \hat{x}_e e^{j\omega t} \equiv X_e(j\omega), \\ x_a(t) &= \hat{x}_a e^{j(\omega t + \varphi)} \equiv X_a(j\omega). \end{aligned} \quad (2.22)$$

$X_e(j\omega)$ und $X_a(j\omega)$ are the spectra of the signals. The complex frequency response $G(j\omega)$ is defined as the ratio of output spectrum to input spectrum, where the

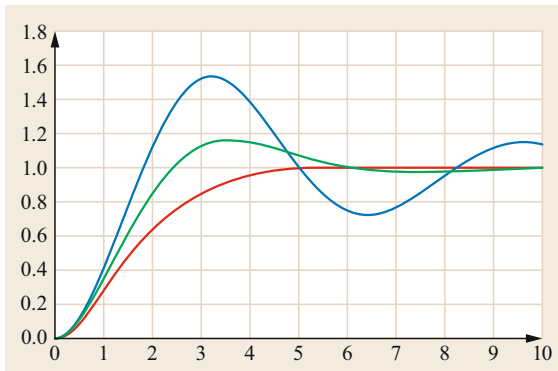


Fig. 2.6 Step response for a second-order system with different damping coefficients in terms of unit time and unit amplitude

amount of $G(j\omega)$ is termed amplitude response and the phase relation is termed phase response

$$\begin{aligned} G(j\omega) &= \frac{X_a(j\omega)}{X_e(j\omega)} = \frac{\hat{x}_a e^{j(\omega t + \varphi)}}{\hat{x}_e e^{j\omega t}} = \frac{\hat{x}_a}{\hat{x}_e} e^{j\varphi} \\ &= |G(j\omega)| e^{j\varphi}. \end{aligned} \quad (2.23)$$

To determine the frequency response of a first-order system we use the general transfer function according to (2.19) and the complex descriptions from (2.22)

$$\begin{aligned} kx_e(t) &= x_a(t) + \tau\dot{x}_a, \\ \hat{x}_a e^{j(\omega t + \varphi)} + j\omega\tau\hat{x}_a e^{j(\omega t + \varphi)} &= k\hat{x}_e e^{j\omega t} \quad \text{leads to} \\ \hat{x}_a(1 + j\omega\tau) e^{j\varphi} &= k\hat{x}_e. \end{aligned} \quad (2.24)$$

According to (2.23), the amplitude response and the phase response are calculable

$$\begin{aligned} G(j\omega) &= \frac{k}{1 + j\omega/\omega_g}, \\ |G(j\omega)| &= \frac{k}{\sqrt{1 + (\omega/\omega_g)^2}}, \\ \tan \varphi(\omega) &= -\frac{\omega}{\omega_g} \quad \text{with} \quad \omega_g = \frac{1}{\tau}. \end{aligned} \quad (2.25)$$

To obtain the graphs of the amplitude and the phase response in Fig. 2.7, it is useful to apply the following boundary conditions

$$\begin{aligned} \omega \ll \omega_g &\rightarrow |G| = k, \\ \omega = \omega_g &\rightarrow |G| = k \frac{1}{\sqrt{2}}, \\ \omega \gg \omega_g &\rightarrow |G| \approx \frac{1}{\omega}. \end{aligned}$$

2.6.5 Frequency Response for a Second-Order System

In principle it is possible to calculate the frequency response of a second-order system in the same way as for a first-order system. A second-order system may be considered as a simple mass oscillator with a harmonic force exciting the mass. Therefore, the equation of motion for the first-order system becomes

$$kx_a + c\dot{x}_a + m\ddot{x}_a = \hat{F} e^{j\omega t}. \quad (2.26)$$

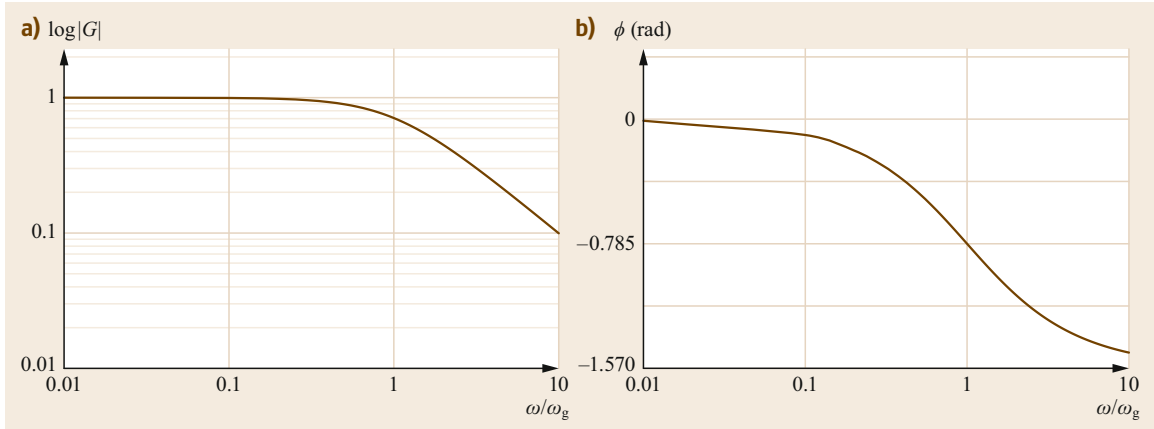


Fig. 2.7a,b Generalized amplitude (a) and phase response (b) of a first-order system (with $k = 1$)

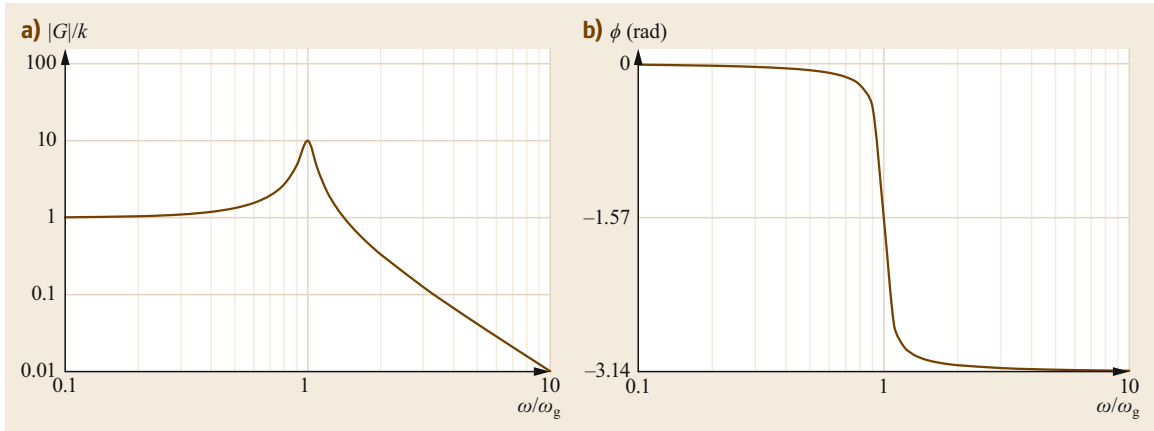


Fig. 2.8a,b Generalized amplitude (a) and phase response (b) of a second-order system (with $k = 1$)

With the assumptions from (2.23), the amplitude response and the phase response are calculable

$$G(j\omega) = \frac{X_a(j\omega)}{F(j\omega)} = \frac{\hat{x}_a}{\hat{F}} e^{j\varphi} = \frac{1}{(k - \omega^2 m) + j\omega c} \quad \text{and}$$

$$|G(j\omega)| = \frac{1}{\sqrt{(k - \omega^2 m)^2 + (\omega c)^2}},$$

$$\varphi = \arctan \left[\frac{-\omega c}{k - \omega^2 m} \right]. \quad (2.27)$$

To obtain the graphs of the amplitude and the phase response in Fig. 2.8, it is useful to apply the following boundary conditions

$$\omega \rightarrow 0: \quad |G| \rightarrow \frac{1}{k},$$

$$\omega = \omega_0: \quad |G| = \text{maximally}, \quad \left[\omega_0 = \sqrt{\frac{k}{m}} \right],$$

$$\omega \rightarrow \infty: \quad |G| \approx \frac{1}{\omega^2 m} \quad \text{because of} \\ (\omega^2 m)^2 \gg (\omega c)^2.$$

2.7 Analog and Digital Signal Processing

The world around us is an analog one, at least for our observational skills. Usually, measured signals from sensors are analog values. In most cases sensors provide electrical voltages or currents depending on any physical quantity. Nevertheless, in most areas, digital technology has been established, including measurement technology. There are objective reasons for this development. Besides real technical reasons, the economic benefits of digital technology are important.

Table 2.4 compares analog and digital technology.

2.7.1 Analog Measurement Chain

In most cases, the sensing elements or transducers provide analog electrical signals. In other words, the electrical properties of the transducers vary as a function of physical values like temperature, humidity, or displacement.

Simplified, the analog measurement chain consists of the four principle elements shown in Fig. 2.9.

The transducer converts the physical value into an electrical signal. Often it is necessary to use filters to reduce noise or to select a special frequency range. Depending on the sensor output, it is useful to convert an electrical current, an electrical charge, or an ohmic resistance into a voltage signal. Usually these electrical

voltage signals are very small. Therefore, it is necessary to use electrical amplifiers. At the end of the measuring chain the signal value is displayed or used to control actuators.

2.7.2 Digital Measurement Chain

Figure 2.10 shows a typical measurement processing chain in the digital world.

The central element is the interface between the analog signal and the corresponding digital word. The state of the art is a digital word length of 16 bit. The step from the analog signal to the digital word needs time (analog/digital (A/D) converter). Therefore, the sample and hold (S&H) unit keeps the analog signal fixed during this time-consuming procedure.

In order to handle signals in the digital world, a quantization of time as well as amplitude is necessary. In other words, the continuous time function of the measured signal is mapped to a finite set of digital words of different digital word length stored in the memory of the digital measuring system. Obviously, this approach induces a loss of information. This might be interpreted as a special form of error to be discussed later.

Quantization Error

Figure 2.11 illustrates an example of the development of quantization error during the analog-to-digital procedure for a 2-bit and 3-bit A/D converter. The two rows on the right side of Fig. 2.11 are the binary codes of the analog signal represented by numerical values.

Obviously, the given amplitude range is divided into three possible steps for the 2-bit A/D converter and into seven steps for the 3-bit A/D converter. According to Fig. 2.11, the number of possible steps is equal to $(2^N - 1)$, where N is equal to the number of bits for the digital word. Simplified, in Fig. 2.11, the step always takes place at the analog values that represent half of the step width.

As a result, without loss of generality, the quantization error always varies between plus and minus of the half-step width represented by the least significant bit (LSB). Therefore, the quantization error q is defined by

$$-\frac{\text{LSB}}{2} \leq q < \frac{\text{LSB}}{2} \tag{2.28}$$

Table 2.4 Analog and digital technology comparison

Analog technology	Digital technology
Theoretical infinitely high resolution for the amplitude	Possibly high precision of the digital display (limited by the number of decimal places/length of the digital word)
Processing and calculating speed are practically in real time (limited by the signal propagation delay)	Processing and calculating speed are <i>not</i> in real time (controlled by the clock frequency)
Uncomplicated signal conversion	Signal transmission largely interference-free
Signal transformations only conditionally obtainable (connected with high effort)	Simple obtainment of rather complex signal transformations
Complex technology for the electrical connection (electrical connection partly not obtainable as an integrated circuit)	Cost-effective solutions for the electrical-connection technology and programmable microcomputer technology

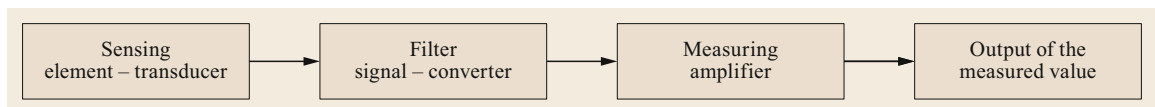


Fig. 2.9 Simplified analog measurement chain

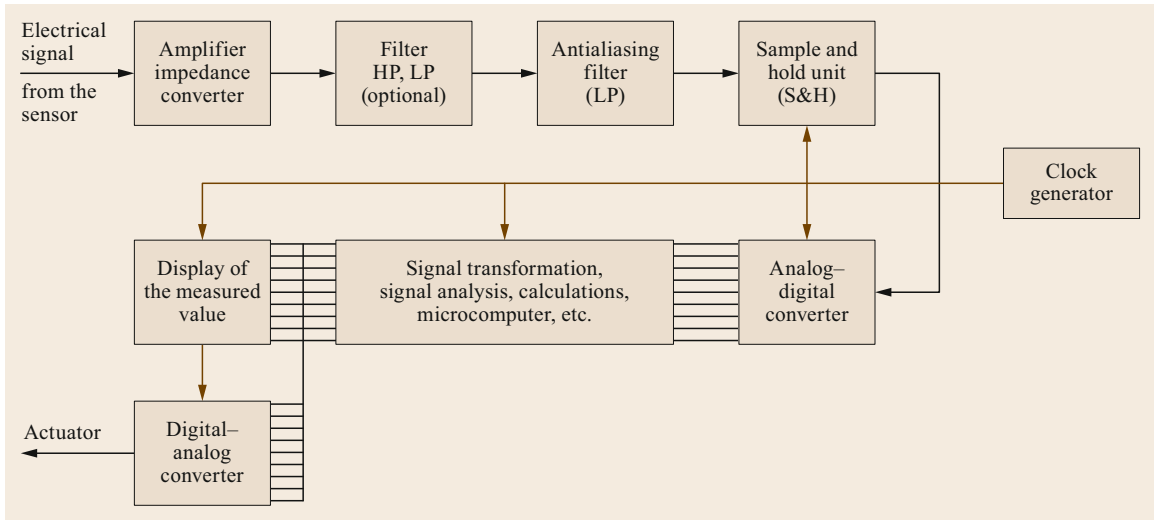


Fig. 2.10 Typical digital measurement processing chain (HP: high-pass filter, LP: low-pass filter, S&H: sample and hold)

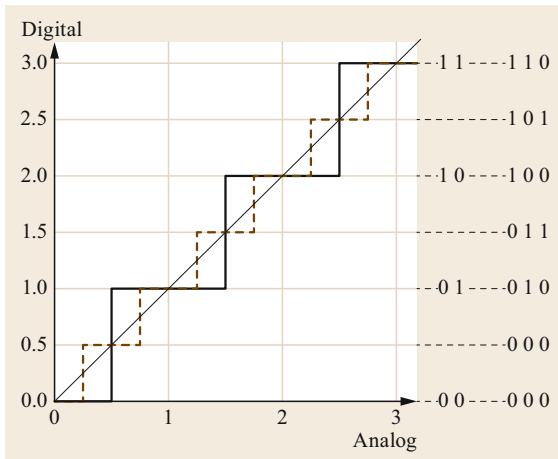


Fig. 2.11 Principle of A/D converting for 2-bit and 3-bit converters

The LSB in Fig. 2.11 has a significance of $2^0 = 1$ (2-bit A/D converter) or $2^{-1} = 0.5$ (3-bit A/D converter).

The quantization error is mapped to the range of the analog value, for instance, to the voltage range U_M of the A/D converter. Finally, the relative and absolute quantization errors can be determined

$$F_q = \frac{U_M}{2^N - 1}, \quad F_{q,\text{rel}} = \frac{1}{2^N - 1},$$

$$\text{for high numbers of } N \quad F_{q,\text{rel}} \approx \frac{1}{2^N}. \quad (2.29)$$

Digital word lengths of 8, 10, or 16 bit are typical for common A/D converters. This results in quantization errors of 0.4%, 0.1%, and 0.015%, respectively.

These are the theoretical minima of the quantization error because in reality it is impossible to adjust the analog value (voltage value) to the full voltage range of the A/D converter. In other words, the quantization error rises inverse to the *used* length of the digital word.

Aliasing Effects

As well as the discretization of the amplitude, the discretization of time generates a specific error. This error is called the aliasing error. To understand this problem, it is necessary to have a closer look at the sampling of the analog value in the time and frequency domains. Figure 2.12 illustrates these two processes.

A prerequisite is that the analog signal is band-limited. In other words, the signal spectrum contains no higher frequencies than a fixed upper cut-off frequency f_g .

The sampling process may be considered a multiplication of the signal with a so-called sampling function (equidistant sequence of delta functions/Dirac pulses). This leads to the sampled signal, which exists only at the points of time where the sampling function is unequal to zero.

The transition into the frequency range (Fourier transformation) provides the spectra of the measured signal and the sampling function, respectively. For practical reasons we only use the positive part of the Fourier integral.

Usually, measured signals are not periodic. We know from the mathematics that the spectra of those functions are continuous. However, the sampling function is in fact a periodic function with discrete lines at the integral multiples of the sampling frequency.

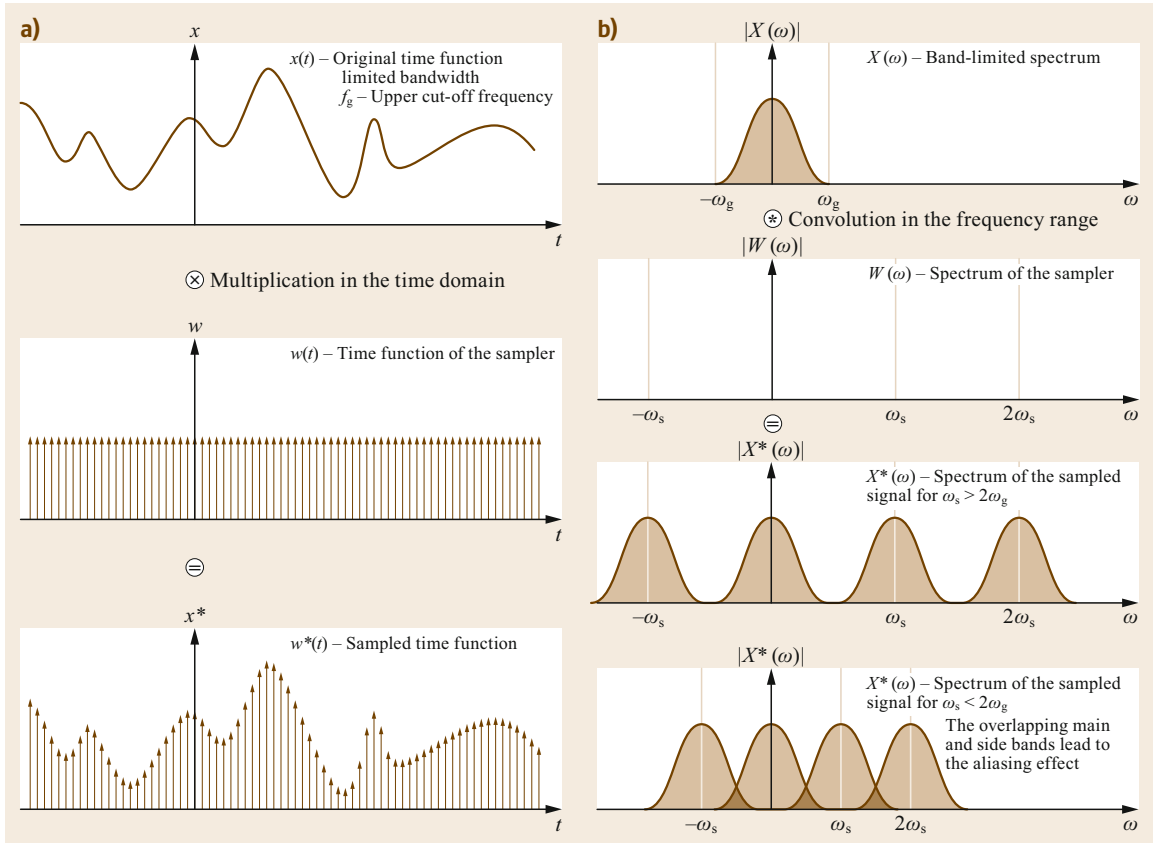


Fig. 2.12a,b Sampling procedure in the time (a) and frequency (b) domains

In the time domain, the signal function is multiplied by the sampling function. In the frequency domain the equivalent mathematical operation is the convolution (*). Simplified, it is possible to say that the convolution combines the properties of the two functions. The envelope of the spectra of the sampled function has the same shape as the continuous spectrum of the original signal, but the shape of the signal is echoed at the discrete lines of the spectrum of the sampler. Figure 2.12b highlights two possible versions of this process. Depending on the frequency of the sampler, we consider the periodic shapes of the signal spectrum as overlapping or not overlapping. Obviously, if the sampling frequency f_s is higher than twice the cut-off frequency f_g , no overlapping occurs. This boundary condition is known as *sam-*

pling theorem (Nyquist–Shannon sampling theorem)

$$f_s \geq 2f_g \tag{2.30}$$

The sampling frequency f_s is also known as the Nyquist frequency.

The overlapping of the periodic shapes of the spectrum is called aliasing. The aliasing effect results in an overestimation near the cut-off frequency of the signal. This effect is also considered an error, the so-called aliasing error.

For digital measuring systems, the sampling frequency is often defined as $f_s = 2.56f_g$.

To prevent these errors, it is necessary to use a low-pass filter according to the sampling theorem. This is the antialiasing filter within the measuring chain of Fig. 2.10.

2.8 Hardware for Digital Measurement Systems

Sensors for typical quantities, e.g., temperature, pressure, or humidity, usually deliver an analog voltage. A voltage-to-current converter transmits the sen-

sor signal over larger distances to any display unit or analyzing unit based on the 4–20 mA standard [2.7].

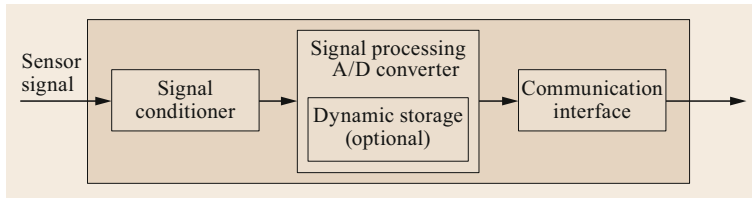


Fig. 2.13 Principle structure of smart sensors

Moreover, the digital technology provides the opportunity to integrate signal conditioning, A/D converting, and a standardized interface within the sensor housing. Often this new type of sensor is named a *smart sensor* [2.8] (Chap. 44). Sometimes these sensors are combined with internal data storage, e.g., these sensors have their own data logger system. An advanced block diagram is shown in Fig. 2.13.

For the communication interface, a lot of possible opportunities are found. The most common interfaces are USB or WLAN [2.9]. For standalone solutions it is also possible to store the measured data on an internal SSD card to analyze them later on an external analyzing system.

For more complex tasks with many, different sensors, standalone data loggers are usually the best solution. Often these loggers have an integrated *real-time clock* providing all data with a time stamp. Data loggers have a large number of different possibilities to connect sensors, for instance, voltage inputs, either grounded or differential, inputs for various thermocouples, capacitive sensors, and resistance sensors.

To communicate with a supervising computer system, various bus systems are available. The Ethernet interface is very common to construct distributed systems for network technology. With the help of cloud services, the measured data may be available worldwide.

2.9 Further Reading

- W. H. Gränicher: *Messung beendet – was nun?* (vdf Hochschulverlag, Zürich 2010)
- I. G. Hughes, T. P. A. Hase: *Measurements and their Uncertainties* (Oxford University Press, Oxford 2010)

References

- 2.1 A. Becker: *Platons "Politeia". Ein systematischer Kommentar* (Reclam, Stuttgart 2017)
- 2.2 D. Schäfer: Santorio Santorio. In: *Enzyklopädie Medizingeschichte*, ed. by W.E. Gerabek, B. Haage, G. Keil, W. Wegner (De Gruyter, Berlin, New York 2005)
- 2.3 A. Kistner: *Geschichte der Physik I – Die Physik bis Newton* (G. J. Göschensche Verlagsbuchhandlung, Leipzig 1906)
- 2.4 W.H. Gränicher: *Messung beendet – was nun?* (vdf Hochschulverlag, Zürich 2010)
- 2.5 J.A. Greenwood, H.O. Hartley: *Guide to Tables in Mathematical Statistics* (Princeton Univ. Press, Princeton 2017)
- 2.6 ISO/IEC GUIDE 98-3:2008: *Uncertainty of Measurement – Part 3: Guide to the Expression of Uncertainty in Measurement (GUM:1995)* (VDE, Berlin 2008)
- 2.7 IEC 60381-1:1982: *Analogue Signals for Process Control Systems. Part 1: Direct Current Signals* (VDE, Berlin 1982)
- 2.8 J. Sauerer: Smart Sensors. In: *Sensorik für erneuerbare Energien und Energieeffizienz, Workshop* (ForschungsVerbund Erneuerbare Energien, AMA Fachverband für Sensorik, Berlin 2013) pp. 18–24
- 2.9 F. Wittgruber: *Digitale Schnittstellen und Bussysteme*, 2nd edn. (Springer, Berlin, Heidelberg 2002)

Wolfgang Foken

Automotive Engineering
University of Applied Sciences in Zwickau
Zwickau, Germany
wolfgang.foken@online.de



Wolfgang Foken is a retired Professor of Measurement Technology at the Faculty of Automotive Engineering at the University of Applied Sciences in Zwickau, Germany. He received his Diploma in Physics from Leipzig University (1979). His research interests are the problems of noise and vibrations of vehicles, including their psychoacoustic effects. He is a member of the Acoustical Society of Germany and led the working group of Automotive Acoustics for several years.

Quality Assurance

3. Quality Assurance and Control

Cove Sturtevant , Stefan Metzger , Sascha Nehr , Thomas Foken 

Quality assurance and control is fundamental to ensuring the scientific usefulness of atmospheric measurements. Quality is relevant to all stages of data generation, from site selection and system design to all physical components of a measurement system (including their calibration, operation, and maintenance) as well as data handling and processing. This chapter describes useful practices and techniques for a comprehensive quality management program that is designed to minimize problems and quantify quality along the entire data generation chain. Widely applicable methods of post-field data quality control for instrumented (in-situ), visual, and remotely sensed observations are presented. The chapter concludes with example applications of QA/QC in measurement networks, and a discussion of common data problems. Finally, future developments in quality assurance and quality control are presented.

3.1	Principles and Definition	50	3.2	History	51
3.1.1	Defining Quality	50	3.3	Elements of Quality Management	52
3.1.2	Principles of Quality Management	50	3.3.1	Quality Planning	53
			3.3.2	Site and Instrument Selection and Configuration	56
			3.3.3	Calibration and Testing	59
			3.3.4	Inspection and Maintenance	64
			3.3.5	Data Processing and Management	68
			3.3.6	Post-field Data Quality Control	71
			3.3.7	Performance Monitoring	74
			3.3.8	Audits	76
			3.4	Application	77
			3.4.1	QA/QC Systems of Meteorological Measurement Networks	77
			3.4.2	Common Data Problems	79
			3.5	Future Developments	84
			3.5.1	Machine Learning	84
			3.5.2	The Oracle Problem in Scientific Software Testing	84
			3.6	Further Reading	85
			References		85

Atmospheric data are collected by many different entities and exchanged locally or worldwide for use in a wide range of applications. Examples include basic research, agricultural operations, fire danger forecasting, numerical weather prediction, air pollutant dispersion, and global climate models, to name but a few. Assuring and characterizing data quality and adhering to international or community standards where applicable is imperative for reliable analysis and interpretation. The quality of atmospheric data can be adversely affected at nearly every point in the data generation chain. For instance, poor data quality may result from a bad choice of site, poor instrument selection and config-

uration, inadequate maintenance, sensor malfunctions, environmental fouling, data processing errors, or unsatisfactory delivery to users. A quality management system is needed to determine and assure the quality of atmospheric measurements. However, such a system can and should be based on a scaled approach that considers the project goals, intended data use, and resources available. The policies and procedures implemented to assure and control quality can almost always be improved. The specific details of a quality management system should be tailored to fit the priorities and requirements of the project or application.

3.1 Principles and Definition

Quality assurance (QA) and quality control (QC) are important topics in technology and science (see also Chap. 4). Therefore, general principles have been developed that are applicable in almost all fields. This section introduces the basics of QA and QC with specific relevance to the field of atmospheric measurements.

3.1.1 Defining Quality

Several terms relating to quality that are used in this chapter and throughout this handbook are defined below.

Quality

This is the degree to which a set of inherent characteristics fulfills requirements [3.1].

Inherent characteristics are defined as aspects of an atmospheric measurement system for which requirements exist, such as the performance characteristics and operating conditions of the sensors, details of the measurement location and configuration, how the sensors are maintained, and how data are collected, stored, processed, and provided to users.

Data Quality

This is the degree to which data are fit for use by data consumers [3.2].

The end product or service of an atmospheric measurement system is most often data. For this reason, the term *quality* in this context typically refers to the data. Because different applications have different requirements for data coverage, uncertainty, etc., it is the data consumer who decides what is fit for use. Thus, the assignment of data quality is specific to the use case. High-quality data is “intrinsically good, contextually appropriate for the task, clearly represented, and accessible to the data consumer” [3.2].

Quality Management

This is the process of specifying and performing the methods required to achieve the necessary quality [3.3].

Quality management focuses on achieving consistently high quality of atmospheric data and services by specifying and performing the methods used to achieve, maintain, and improve the required quality. Thus, quality management includes quality planning, quality assurance, quality control, and quality improvement.

Quality Planning

This is the process of identifying quality requirements and how to fulfill them.

Quality planning includes defining the objective(s) of the atmospheric measurements, generating requirements to ensure the objective will be met, and specifying the resources and procedures that will be used to meet the requirements and test that they are met.

Quality Assurance

This is the process of checking for compliance with all planned and systematic activities implemented within the quality management system (and demonstrated as needed) in order to provide adequate confidence that an establishment meets the quality requirements [3.1].

Compliance in this context means purposefully controlling all factors that have a direct impact on the quality of the end product or service.

Quality Control

The operational techniques and activities that are used to fulfill the quality requirements [3.1].

Quality control of data is the best-known aspect of QA/QC (quality assurance/quality control) in atmospheric measurements, and involves examining the data to verify it meets the quality requirements. When the quality requirements are not met, quality control options include flagging data as suspect, correcting the data, or deleting it. However, quality control is not limited to the final data. It involves controlling the quality of all processes and products in the data generation chain by monitoring their performance and taking action when needed to meet quality requirements.

Quality Improvement

This is the process of purposefully changing methods and/or procedures in order to improve quality and its consistency.

Improvements in the quality of atmospheric measurements are made possible by monitoring the quality or performance of all aspects of the data generation chain that have a direct impact on the quality of the end product or service.

3.1.2 Principles of Quality Management

The goal of any quality management system is to ensure that end products and services are of consistently high quality by identifying objectives, determining the resources and methods required to meet them, and linking policies and procedures implemented throughout the organization. The International Organization for Standardization (ISO) provides a set of international standards and guidelines for quality management in the ISO 9000 series [3.4] (see Chap. 4). An organization may certify to

ISO 9001 [3.5]—which specifies the requirements for an effective quality management system—by demonstrating that the required elements are in use. Seven quality management principles [3.4] form the foundation for any quality management system, and the requirements of ISO 9001 are based upon them. These principles are not ordered steps but rather characteristics to incorporate throughout all aspects of a project or organization in order to promote and improve quality. How the principles are prioritized will depend on the specific goals at hand. The seven principles are:

Customer Focus

Deliver data and services that meet or exceed user needs and expectations. This creates confidence in the data and the organization.

Leadership

Unify goals and strategies across the organization and create an environment that facilitates the attainment of quality objectives. This includes providing adequate resources and establishing a culture that values quality.

Engagement of People

Recognize, involve, and empower everyone's role in managing quality.

Process Approach

There are no isolated aspects of quality. Recognize and utilize the connectedness of processes and their impact on quality.

Improvement

Look ahead to upcoming needs. Identify, plan, and act upon processes and products that need improvement.

Evidence-Based Decision Making

Collect and analyze data and information to assess and improve quality.

Relationship Management

Identify dependencies and communicate with stakeholders about quality. Collaborate with them to improve quality.

3.2 History

The earliest efforts to control the quality of atmospheric measurements involved standardizing weather observations, which began with the establishment of the first meteorological networks in the eighteenth century [3.6]. For example, James Jurin of the Royal Society developed a scheme for standardized weather reports for locations in England, Europe, North America, and India in 1723, and the first meteorological society, *Societas Meteorologica Palatina* (Meteorological Society of Mannheim, formed in 1780), set local times for weather observation. Standardized instruments and weather observations expanded during the nineteenth century to include measurements of precipitation, dry and wet bulb air temperatures, cloud cover and movement, wind speed and direction, and barometric pressure [3.7]. By the mid-nineteenth century, meteorology had become an exacting science with standardized, calibrated instrumentation and regulated observers. Precision, accurate record-keeping, and rigorous numerical analysis were strongly promoted by the British Meteorological Society (formed in 1850). Regular international conferences among meteorologists were initiated in 1872 at Leipzig to facilitate the development and communication of standardized methods, and the Permanent Meteorological Committee, later called the International Meteorological Organization

(IMO), was established during the 1873 Vienna International Meteorological Congress (see also Chap. 1).

In the twentieth century, general progress in quality paradigms facilitated international standardization for many industries, including meteorology. Working at Bell Laboratories in the mid-1920s, Walter Shewhart expanded the concept of quality to processes involved in manufacturing [3.8]. He was also the first to apply statistical methods to quality control [3.9, 10]. Simultaneously, international trade was growing, and 25 countries met in 1946 to discuss the unification of industrial standards. This resulted in the establishment of the International Organization for Standardization in 1947. That same year, the IMO began preparing the Guide to International Meteorological Instrument and Observing Practices, which focused on standardized measurements. 1950 saw the formation of the World Meteorological Organization (WMO), and the First Congress of the WMO formed the Commission for Instruments and Methods of Observation (CIMO) in 1951 to provide technical standards for meteorological instrumentation as well as guidelines to ensure that data are quality controlled and comparable. The result was the 1954 release of the first edition of the Guide to Meteorological Instruments and Methods of Observation (WMO-No. 8). The latest edition of this guide

was published in 2014, and the most recent update was released in 2017 [3.11].

Another major contribution of the WMO to quality in atmospheric measurements was the establishment of reference standards, which can be traced to the CIMO conference of 1977 in Hamburg [3.12]. Probably the first initiative originated in 1985 from the Radiation Commission. *Fritz Kasten* [3.13] proposed a system of standards with different quality levels: primary standards, secondary standards, and finally traveling standards. Such an initiative was highly important because the burgeoning discussion of climate change necessitated more accurate radiation instruments. Therefore, the Baseline Surface Radiation Network (BSRN) was founded in 1994 to establish standards for radiation instruments [3.14]. The initiation of this network helped to significantly increase the data quality and accuracy of radiation measurements [3.15] (see Chaps. 11 and 63), and provided an example of how to classify instruments and standards for other devices within the WMO and in other areas such as flux measurements [3.16] (see Chaps. 64 and 55).

The advent of automated weather stations—which expanded data gathering substantially—resulted in a need to control the quality of the collected data. Operational development of automated weather stations in the USA began in 1939 [3.17]. Transmitting data via telegraph and radio Morse code, these stations collected measurements of air pressure, temperature, relative humidity, wind speed and direction, and rainfall. The development of meteorological character codes (pub-

lished in the WMO Manual on Codes [3.18]) facilitated the timely, standardized transmission and international exchange of meteorological observations. Until the late twentieth century, the focus of data QC was the statistical identification of outliers [3.19]. An evolution towards complex data quality assurance began in the 1980s, involving several tests and a decision tree for data flagging [3.20–24]. Today, advanced methods such as machine learning are being developed to identify outliers and errors in data with little human input [3.25].

Work aimed at improving the quality of atmospheric measurements continues today through the expansion of highly standardized, cross-disciplinary environmental networks such as Integrated Carbon Observation System (ICOS) and National Ecological Observatory Network (NEON), whereby network stations employ standardized infrastructure, instrumentation, measurement protocols, and processing methods. This coordination among stations makes it possible to answer grand questions in environmental science that span numerous disciplines and spatial and temporal scales [3.26, 27]. The antecedents of these highly standardized networks began—and continue today—as data sharing efforts among independent stations. For example, the FLUXNET network [3.28], which began as a means of sharing data on land–atmosphere fluxes of heat, water vapor, and carbon dioxide, helped to advance the standardization of measurement variables, computational algorithms, and data formats. The resultant comparability of data among stations revealed that, globally, photosynthesis is more sensitive than respiration to drought [3.29].

3.3 Elements of Quality Management

Quality management begins well before the first measurement is made, and is maintained throughout the data generation chain (Fig. 3.1). The first step is to define the objectives of the project, which are used to generate the requirements. Measurements to ensure that the requirements are met are then planned. Planning the measurements is often the hardest yet most important part, as ensuring the quality of the final data requires advanced planning of the site, instruments, and their configuration, the measurement details, and how instruments will be calibrated and maintained. In addition, planning should include how data will be processed, managed, and delivered to users, and how the project will be monitored to ensure the requirements are met and that high-quality data are obtained. There are often tradeoffs in costs and human resources that should be reconciled during the planning process, and tests are performed to verify that the measurement plan will

work. Once planning is complete, the site can be set up and configured, and operations can begin. Since most measurements are now automated, the effort required to operate a project has largely shifted to maintenance and to monitoring and controlling the quality of data. The expertise and effort required to perform these tasks should not be underestimated.

It is easy to see how the seven principles of quality management (see Sect. 3.1.2) are incorporated in this workflow. The goals of the data user inform the requirements of the measurement system and how data are delivered (*customer focus*). Quality becomes central to the project through planning and quality-focused operation (*leadership*). All personnel, from project planners to maintenance staff, have roles to play in ensuring quality (*engagement of people*). Performance monitoring allows continuous improvement of quality (*improvement; evidence-based decision making*). Audits facili-

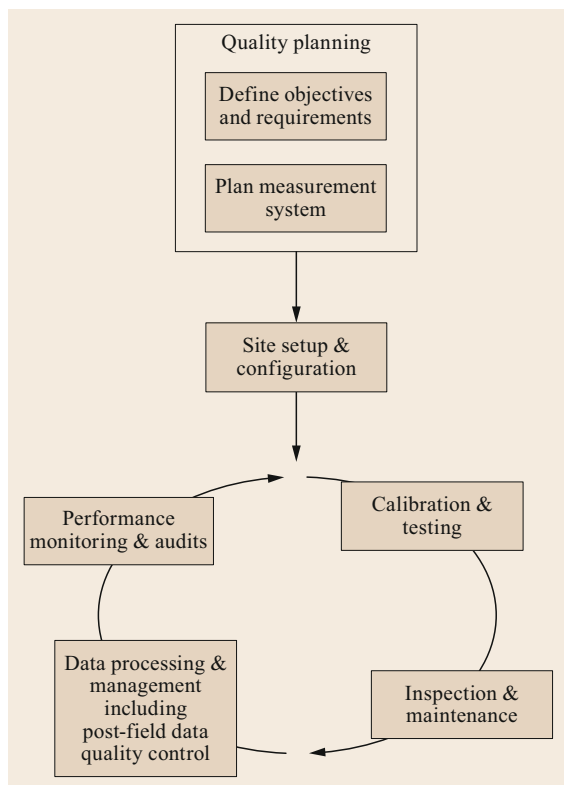


Fig. 3.1 Workflow for quality management

tate communication with and quality improvement in internal and external dependencies (*relationship management*). Finally, the interconnectedness of the system is explicit (*process approach*). The elements of this workflow are described detail in the following sections.

3.3.1 Quality Planning

Atmospheric measurements focus on answering selected questions that lead to a better understanding of the state and temporal evolution of the continuously changing atmosphere (see Chap. 1). Thus, it is of the utmost importance to first precisely define the objective of the atmospheric measurements, because it is the basis for deriving the minimum requirements for the data characteristics, which are then used to determine the measurement system requirements. These challenging tasks are accomplished by means of quality planning in accordance with the seven principles of quality management.

This section provides an overview of the major steps involved in quality planning, while the remaining sections go into greater detail about the quality considerations involved in the individual aspects of a measurement program.

Define Objective

Quality planning is primarily determined by the measurement objective. In general terms, atmospheric measurements are performed for basic research, the development or application of technology, or to check compliance with (legally) binding limit values. This differentiation is important, as the reason for performing atmospheric measurements influences the options available to meet the objective and the performance criteria of the applied measurement techniques.

Strict measurement standards are not prescribed for basic research studies. However, the research questions dictate how strict the measurement requirements must be, considering the statistical power required to evaluate hypotheses and make robust conclusions. Centuries of scientific study have yielded rigorous state-of-the-art atmospheric measurement methods that are employed in long-term monitoring programs (Global Atmosphere Watch of the WMO [3.30]), regional programs (European Monitoring and Evaluation Program [3.31]), and national networks (see Chap. 63). Even if the research conducted does not belong to these programs, state-of-the-art methods should be followed to maximize the quality and comparability of the data and the resulting robustness of analyses. Many of these monitoring programs and measurement networks have their own QA/QC guidelines (as outlined in Sect. 3.4.1). The objectives and constraints of basic research studies or monitoring programs may even contribute to the development of new measurement technologies. For example, a new measurement technology may be deployed as research instrumentation with hardly any knowledge of its performance characteristics. Results from comprehensive instrument intercomparisons (see Sect. 3.3.3) within a monitoring program can demonstrate equivalence or superiority to an established measurement technique. Accordingly, the development of a new technology can also be the primary objective of atmospheric measurements.

In order to demonstrate compliance, the frequency with which pollutant concentrations exceed safe limits for ecosystems and human health (determined via legally binding air quality standards) is reported. This concept facilitates law enforcement. However, developing ambient air quality standards requires more than adopting a set of limit values for airborne pollutants. First and foremost, it is important to characterize the physical state of the atmosphere, since the air, water vapor, and numerous organic and inorganic atmospheric trace constituents (gaseous, liquid, and solid) are always in motion (see Chap. 1). In addition to being physically transported, these trace constituents undergo chemical transformations. Thus, it is mandatory to link the ambient air quality standards with measurement meth-

ods, sampling site locations and frequency of sampling, quality control measures, and statistical data analysis. This link is established by prescribing official measurement method standards that are enforced by (for example) national laws or ordinances.

When defining the objective of atmospheric measurements, it is helpful to develop scientific or technical use cases for the data. Use cases are concrete examples of the objective that help to guide the development of requirements relating to the following building blocks: (i) site(s); (ii) hardware and firmware; (iii) software; (iv) measurement and evaluation strategy; and (v) people-to-people interactions. Good planning involves the integrative/iterative design of (i)–(v) to maximize the quality of the data and return on investment. Use cases include predicting atmospheric quantities or events, answering a specific scientific question, or using the data to accomplish a task. Creating a use case involves (i) giving it a name and briefly describing its scope, (ii) identifying the actors involved, (iii) specifying any preconditions, (iv) defining the basic and any alternate workflows for the steps taken to accomplish the use case goal, (v) identifying any exceptions that will prevent the goal from being accomplished, and (vi) specifying the conditions that indicate a successful outcome [3.32].

Develop Requirements

In all of the measurement objectives outlined above (basic/applied research, technology development, and checking compliance with legally binding limit values), the aim (from a data quality perspective) is to achieve predefined data quality attributes. These data quality attributes are defined in relation to the data user's needs. Accordingly, data are of sufficient quality if they satisfy the stated and implied needs (i.e., meet the objective). A proper quality management program ensures that data requirements for the intended application are met. Good data are not necessarily excellent, but it is essential that their quality is known and demonstrable. Table 3.1 gives an overview of the core data quality attributes.

One aim of atmospheric measurements is to attain results that are spatially and temporally representative according to the objective. In this context, the measurement results must reflect the actual conditions in the spatiotemporal domain of interest [3.41]. A further example is the representativeness with respect to legally binding limit values/guide values (see the discussion of spatial and temporal representativeness in Chap. 1).

However, quality planning goes far beyond specifying representativeness or the other core data quality attributes listed in Table 3.1. Section 3.3.2 outlines how data quality attributes are further addressed in site selection and configuration.

Table 3.1 Core data quality attributes

Data requirement	Description
Internal consistency	Theoretical compatibility of the estimated value with other parameter values derived from the same observations
Validity	Extent to which an assessment achieves its aims by measuring what it is supposed to measure and producing results which can be used for their intended purpose [3.33]
Spatial/temporal representativeness	Ability of a series of observations to provide an unbiased estimate of a parameter of a specified statistical population [3.34]
Completeness	Extent to which the information provided enables the data user to draw conclusions in accordance with the goal and scope definition [3.35]
Coverage	Spatial and/or temporal distribution of measurement locations in the area under investigation [3.36]
Availability	Property of being accessible and usable upon demand by an authorized entity [3.37]
Traceability	Ability to relate the result of a measurement to appropriate measurement standards—generally international or national standards—through an unbroken chain of comparisons [3.38]
Timeliness	Undelayed and frequent availability of data for the intended use to support information needs and quality management decisions [3.39]
Reliability	Degree to which data are provided in an agreed or expected manner during a defined time period under specified conditions [3.40]

Hitherto, the concept of quality has related to the explicit and implicit needs of the data user for a specific use (*user perspective*). At this point, it is important to distinguish between data quality and measurement uncertainty, and to understand how these concepts are related. In terms of scientific measurement, the uncertainty quantifies how much is unknown about the measurements. In contrast, quality is subjective and defined according to the desired data use. The requirements relate uncertainty to quality by defining the maximum uncertainty that the data can exhibit while meeting the objective.

Unless required by law or a governing body, requirements should focus on the characteristics of the measurements and not the specific methods of achieving them. For example, rather than specifying the exact measurement method or sensor to be used, the perfor-

Table 3.2 Overview of instrument characteristics that are applied to characterize and quantify the performance of a measurement system based on the concept of uncertainty (see also Chap. 2)

Instrument characteristic	Description
Accuracy	Proximity of the result of a measurement to the true value of the measurand [3.42]. This expresses the systematic uncertainty of measurement [3.43]
Precision	Level of agreement among a set of results of the same measurand [3.42]. This expresses the random uncertainty of measurement [3.43]
Sensitivity	Quotient of the change in the response of a measuring system to the corresponding change in the value of the quantity being measured [3.44]
Linearity	Straight-line relationship between the (mean) result of the measurement (the signal) and the quantity to be determined [3.45]
Reproducibility	Level of agreement between the results of measurements of the same measurand carried out under changed measurement conditions (see [3.46])
Repeatability	Level of agreement between the results of successive measurements of the same measurand carried out under the same measurement conditions (see [3.46]). Often used to assess the precision
Temporal resolution	Equipment-related variable describing the shortest time interval from which independent signal information can be obtained [3.47]
Threshold	Minimum input signal value below which no change in the output signal can be detected [3.48]
Drift	Change over time of a characteristic (generally an output quantity) of the measuring system [3.49]
Stability	Ability of a measurement system to retain its performance throughout its specified operating time [3.48]
Range or span	The particular values of a quantity that a measurement system is designed to measure [3.48]
Speed of response	Rapidity of the response of a measurement system to changes in the measured quantity [3.48]
Measuring lag	Retardation of or time delay in the response of a measurement system to changes in the measured quantity [3.48]
Dynamic error	Difference between the true value of a time-varying quantity and the value indicated by the measurement system if no static error (accuracy) is assumed [3.48]

mance characteristics (such as accuracy and precision) of the measurements that are needed to meet the objective should be defined. This provides extra flexibility when planning the measurement system—tradeoffs can be made among cost, required maintenance, and site access and arrangement while still meeting the project objective. Without this flexibility, it may not be possible to conduct the measurements at all.

Table 3.2 gives an overview of instrument characteristics that are applied to characterize and quantify the performance of a measurement system based on the concept of uncertainty (*technical realization perspective*).

The data requirements and instrument characteristics strongly influence the choice of the measurement technique and the specifics of its implementation. Other chapters of this handbook show that there are several options for classifying atmospheric measurement techniques:

- In-situ measurement (part B of this handbook) versus remote sensing (parts C and D)
- Mobile measurement platforms (Chaps. 37, 39, 48, 49, and 50) versus stationary measurement platforms (Chap. 6)
- Discontinuous versus continuous measurement
- Measurement of an individual quantity versus measurement of a sum quantity

- Measurement in the field versus measurement in the laboratory versus measurement in a simulation chamber (e.g., the European Photoreactor EUPHORE versus the SAPHIR (Simulation of Atmospheric PHotochemistry in a large Reaction Chamber) atmosphere simulation chamber; see [3.50, 51]).

Specific QA/QC considerations for the abovementioned categories are addressed in the corresponding chapters. It is assumed that the theory applied to transfer these signals into meteorological quantities is valid.

Plan the Measurement System

The final step in quality planning is to select the details of the measurement system according to the predefined requirements (both data requirements and instrument characteristics). To assure the quality of the final data, the entire data generation chain should be planned, all the way from measurement site selection to how the data are processed and provided to users.

Defining the spatial arrangement involves specifying the location of an individual measurement site or the density of multiple measurements sites within a given area. Defining the temporal measurement pattern involves designating the measurement time, duration, and frequency in a given investigation area. During the course of quality planning, the measurement

Table 3.3 Quality planning checklist for atmospheric measurements

Category	Examples	Further reading
<i>Define objective</i>		
Basic/applied research	<ul style="list-style-type: none"> • Meteorology/atmospheric physics • Atmospheric chemistry • Biogeosciences 	[3.11, 52, 53]
Technology development	<ul style="list-style-type: none"> • Development/improvement of new measurement technology • Development/improvement of numerical models for atmospheric forecasting 	[3.54, 55]
Check compliance with legally binding values/guide values	<ul style="list-style-type: none"> • Emissions (stationary/fugitive) • Immissions (protection of human health, environmental protection, protection of inanimate objects/cultural heritage) 	[3.56, 57]; Chap. 54
<i>Develop requirements</i>		
Data requirements	<ul style="list-style-type: none"> • The concept of quality is applied to satisfy the predefined objective for a specific use case of the data (<i>user perspective</i>; see Table 3.1). 	[3.33–40]
Instrument characteristics	<ul style="list-style-type: none"> • The concept of uncertainty is applied to characterize and quantify the performance of a measurement system (<i>technical realization perspective</i>; see Table 3.2). 	[3.42–48]
<i>Plan measurement system</i>		
Spatial arrangement of the measurement site	<ul style="list-style-type: none"> • Location of a measurement site • Density of multiple measurement sites 	[3.58]; Chap. 1; Sect. 3.3.2
Temporal arrangement of the measurement	<ul style="list-style-type: none"> • Measurement time • Measurement duration • Measurement frequency 	[3.58]; Chap. 1
Instrument configuration	<ul style="list-style-type: none"> • Variables to measure • Instrument settings • Instrument installation 	Sect. 3.3.2
Personnel requirements	<ul style="list-style-type: none"> • Setup • Operation • Maintenance • Data evaluation 	[3.11]
Data handling	<ul style="list-style-type: none"> • Data recording • Data storage • Data processing 	Sect. 3.3.5
Documentation	<ul style="list-style-type: none"> • Measurement protocol • Maintenance plan 	[3.11]
Quality monitoring	<ul style="list-style-type: none"> • Method used to evaluate adherence to data quality requirements • Method used to quantify measurement uncertainty 	Sect. 3.3.6; Sect. 3.3.7

variables (measurands) must be determined. Measurement protocols are used to document the instruments deployed as well as the settings and installation (e.g., orientation) of the instrument. Maintenance schedules and tasks must be planned and personnel requirements for setting up, operating, and maintaining the sensor must be determined. How should the data be recorded, stored, and processed? Finally, it is also necessary to decide how the data should be evaluated and how the system will be monitored to check that it conforms to the requirements. This involves specifying the method used to evaluate adherence to data quality requirements as well as the method employed to quantify the measurement uncertainty.

A brief checklist for quality planning is given in Table 3.3. More details of the quality considerations involved in these selections are provided in subsequent sections.

3.3.2 Site and Instrument Selection and Configuration

Measurement planning can commence once the data product requirements have been defined for a given measurement objective (Sect. 3.3.1). Site and instrument selection and configuration are important components of the planning stage. This section addresses quality and practical considerations involved in those selections, and summarizes best practices.

Measurements are strongly influenced by the characteristics of the measurement site. It is therefore important to investigate whether a site is representative considering the measurement objective and data product requirements, i.e., the extent to which it reflects the actual conditions in the spatiotemporal domain of interest [3.41]. This is particularly important for highly derived data products that comprise multiple data streams

Table 3.4 Best practices for defining site selection requirements. This example of general recommendations (after [3.3, 11]) applies to a range of common measurement objectives from baseline meteorological observations to anchor forecasting. It may be necessary to adjust and consider the resulting uncertainty for specialized and new measurement objectives, such as the investigation of new measurement conditions

Characteristic	Description
Administration	<ul style="list-style-type: none"> Any necessary approvals and permits (e.g., from the building authority or the regulatory agency) should be available Planning for maintenance, care, repair, and exchange should consider vehicle access, access on foot, necessary aids Skilled staff should be available for monitoring, maintenance, care, repair, and exchange as well as for the inspection, storage, and further processing of data
Surface	<ul style="list-style-type: none"> The ground surface should be representative of the locality There should be no steep slopes in the vicinity, and the site should not be situated in a hollow or on a mound^a The site should be well away from obstructions such as tall vegetation, buildings, and walls^a
Exposure	<ul style="list-style-type: none"> Instruments should be exposed according to their operating requirements, preferably in close collocation to each other Tradeoffs should be evaluated per data product requirement, e.g., among open sites with unobstructed views of the horizon for radiation and cloud measurements, and sheltered sites suitable for precipitation measurements Night observations of cloud and visibility should be made from a site unaffected by extraneous lighting
Sustainability and provenance	<ul style="list-style-type: none"> The site should be surrounded by open fencing or palings to exclude unauthorized persons, and the open fencing or palings should be sufficiently far from the instruments that they do not disturb the measurements themselves Sites should be chosen to minimize the effects of changing characteristics over time, such as the growth of trees or the erection of buildings in the vicinity^a

^a Assuming that this is not the subject of the research or that it is not a relevant characteristic of the targeted locality.

that possibly originate from a range of instruments and measurement principles.

In Chap. 1, Sects. 1.3.2 and 1.3.3 provide a general discussion of spatial and temporal variability and representativeness. Here, we specifically address aspects of siting and exposure that should be addressed to avoid quality issues related to site selection. Possible influencing factors are large vertical or horizontal gradients of the investigated variables at the measurement site (e.g., they may be affected by heterogeneous surroundings, obstacles, etc.). It is therefore important during site selection to consider and document whether the physical effects of the surroundings permit joint analysis of the measured variables in support of the data product requirements [3.59].

A commonly made assumption is that variables measured at the same site represent a common *target area* or environment. While this remains a weak assumption in uniform settings, the individual source area and spatial representativeness of each variable should be considered in heterogeneous environments [3.60]. For example, measurements of the atmospheric state, thermodynamics, and composition are subject to dispersion: they represent a large ($\approx 10^4 \text{ m}^2$) upwind area that changes over time with diel and synoptic wind patterns, the local flow field and disturbances (obstructions), and

topography. Quantifying this variable area is the subject of footprint analysis (see Chap. 1; [3.61]). On the other hand, measurements of, say, surface optical properties typically represent a smaller ($\approx 10^2 \text{ m}^2$) area that is stationary. In addition, optical measurements are directly affected by the aspect, slope, and shading from obstructions. Measurements performed in the soil have an even smaller source area (on the order of 10^{-2} m^2), and often only represent their immediate surroundings. Hence, covering a spatial scale comparable to atmospheric or optical measurements can necessitate a multitude of distributed soil measurements.

Moreover, the observer effect (the effect of measurements on each other and their surroundings) must be taken into account. This introduces two contradictory requirements: that the measurements should be representative of the same target area while minimally impacting each other and their environment. Defining zones of mutual representativeness and exclusion can help to quantitatively optimize this collocation [3.62]: the zone of mutual representativeness identifies the joint target areas of the measurements, while placing each sensor outside the exclusion zones of the other sensors ensures that reciprocal and environmental impacts remain below the required threshold. Alternatively, it is possible to apply post-field corrections for environmental effects [3.3].

Table 3.5 Best practices for defining instrument requirements (after [3.3, 11])

Characteristic	Description
Instrument performance	<ul style="list-style-type: none"> • Uncertainty, including accuracy, precision, resolution, detection limit, range, speed of response, and cross-sensitivity • Reliability and long-term stability
Cost, durability, convenience of operation and maintenance	<ul style="list-style-type: none"> • Acceptable cost of instrument, consumables, and spare parts • Energy consumption and possibility of off-grid power supply • Robustness with respect to environmental conditions • Simplicity of design and maintainability
Safety	<ul style="list-style-type: none"> • Safe for staff and the environment

Table 3.6 Best practices for defining installation and configuration requirements (after [3.3, 11])

Scope	Description
Installation	<ul style="list-style-type: none"> • The quantity to be measured should not be falsified significantly by the instrument itself or by its structural parts, or by a cover to protect it • Support structures such as towers and boom arms should be designed with static requirements to withstand loads from (for example) thunderstorms and other site-specific phenomena • Additional devices that are required to operate the system (power supply, anti-theft device, lightning protection) should be available
Configuration	<ul style="list-style-type: none"> • The devices required for data acquisition should be implemented (data transport, transmission lines, operational requirements for acquisition systems)

Best practices for defining site selection requirements are provided in [3.3, 11] and are summarized in Table 3.4. In addition, [3.63] provides a detailed study of siting and exposure, and [3.64] provides a recent review of the topic in relation to setting up ICOS member sites. However, the measurement objective and requirements can necessitate deliberate deviations from these best practices. In this case, the usefulness of the measured variables remains specific to the measurement objective, and deviations from best practices should be thoroughly documented in the metadata.

All atmospheric variables change spatially and temporally under the influence of the characteristics of the measurement site. Consequently, the instrument response and sampling characteristics (see Table 3.2 and Chap. 2) must be able to resolve the spatial and temporal scales of the relevant atmospheric processes or the data quality may be significantly reduced. (For more on the scales of atmospheric processes and the relevant instrumentation, see Chap. 1.) Defining the instrument requirements provides a quantitative framework for acceptance testing and instrument selection and configuration in accordance with the measurement objective, data product requirements, and selected site. Inverting or numerically solving relevant equations permits instrument requirements to be derived from data product requirements. Such sensitivity analysis and uncertainty attribution is particularly useful for ensuring the quality of highly derived data products that encompass multiple data streams. Table 3.5 provides an overview of best practices for defining instrument requirements. Instrument selection should be based on the

degree to which these requirements are fulfilled, and the measurement objective should be considered when weighing the importance of individual requirements. For example, instrument stability is indispensable for long-term observations. However, it may be less important for short-term intensive measurement campaigns, where attaining spatial resolution through a batch of less expensive sensors may better address the objective. Where possible, instrument selection can be optimized through integrative design, i.e., interfacing the measurement objective and data product requirements not only with site and instrument requirements but also software developments. One example of this is provided by the adaptive calibration models that are used to improve instrument performance [3.65].

Once the instrument has been selected, it is important to ensure that its installation and the end-to-end data acquisition chain support the measurement objective and data product requirements. This can be accomplished by specifying installation and configuration requirements. Table 3.6 provides an overview of best practices. First and foremost, the sensor installation and configuration should permit the spatial and temporal scales of the relevant atmospheric processes to be resolved (see instrument requirements). Important considerations include measurement height above the ground and time of the day for optical measurements. Formal systems integration and verification should include installation and test plans and lead to an initial operations capability review. In addition to instrument deployment, considerations include digital versus analog signal processing, data logger versus

traditional computer versus single-board computer for data acquisition, polling, on-site (in-wire) application of calibration coefficients (traceability), and timestamping (Global Positioning System, the Network Time Protocol, the Precision Time Protocol, and quartz, e.g., in an offline personal computer). Particular attention should be paid to ring storage, where the oldest data are overwritten once capacity is reached, and to checking hashes during data transfer operations.

Documenting the site, instrument, installation, and configuration is paramount to ensuring the usefulness of the resulting data products. In the systems integration and verification process, machine-readable documentation for sensor configuration, the location hierarchy, and as-built drawings are used for this purpose. The geolocation should be recorded (e.g., geodetic system and model, height above mean sea level of the ground on which the supporting structure is erected, the locations of individual instruments relative to the reference point in a local coordinate system, consideration of true north versus magnetic north and declination). Any deviations from the above best practices should be recorded in the metadata, and the documentation for the site geography and its exposure should be regularly updated. When an instrument needs to be replaced, observations from the new instrument should be compared to those from the old instrument over an extended interval (at least one year; [3.66]) before the latter is taken out of service.

3.3.3 Calibration and Testing

Sensor calibration establishes the relationship between the values of quantities indicated by the sensor and the corresponding values realized by standards [3.67]. QA/QC should comprise initial calibration prior to a measurement series, final calibration after the completion of the measurement series, and regular assessment of the measurement data, so that failures are identified immediately. A long-term measurement campaign may require several measurement series so that calibrations are performed at designated intervals recommended by the manufacturer or as necessary to maintain the required measurement characteristics (e.g., accuracy and precision).

Typically, a sensor is calibrated in a sequence of operations under predefined measurement conditions by providing a known physical input to the instrument and recording the output. Thus, the purpose of calibration experiments is to determine the analytic function of a measurement method for a specified state variable [3.68]. Prior to determining the analytic function, it is necessary to specify the measurement range, the measurement conditions, the mathematical shape of the analytic function, and the number and distribu-

tion of reference states. The measurement conditions of the calibration experiment should correspond as far as possible to the conditions that may arise in the measurement task considered, and should be completely documented. The definitions used in this handbook are summarized in Table 3.7.

Calibration Practices

A calibration includes a calibration experiment and a mathematical evaluation of the experimental results. In the calibration experiment, the measured signal is measured at reference states. Subsequently, the observed relationship between the reference state and the measured signal is mathematically described by the analytic function for the corresponding range of values. The contribution of uncertainty to calibration is determined by statistically evaluating the results of the calibration experiment.

The characteristics of the measured signal as well as the characteristics of the corresponding reference values affect the choice of the calibration procedure (see Table 3.8) as well as the choice of the statistical evaluation method that is used to estimate the parameters of the analytic function (see Table 3.9). It is generally recommended that the calibration instructions provided by the sensor manufacturer should be consulted prior to defining the calibration conditions and the corresponding calibration strategy.

The input data for the estimation methods shown in Table 3.9 are the coordinates of the calibration points determined in the experiment (the reference value of the state variable and the corresponding value of the measured signal) as well as the uncertainties in one or both coordinates. The calculation is based on regression analysis, which takes the stated uncertainties into account. The results of the regression analysis are the parameters of the analytic function (see also Chap. 2).

The reference states should be chosen in accordance with the selected shape of the analytic function such that the reference values of the state variable appropriately represent the specified range of measured values. The reference states are generated with calibration devices. A good calibration device should always be combined with a proper measurement standard. Examples include feeding a certified test gas of known composition to gas sensors or operating a liquid bath temperature calibration chamber equipped with certified thermometers. The uncertainties in the reference values should be presented as standard deviations. Possible data sources include the uncertainty of the standard reference method and the uncertainty of the calibration device. Multiple independent replicate measurements should be taken at each reference state [3.68]. The average and the standard deviation should be calculated

Table 3.7 Terms and definitions used in the context of calibration (afetr [3.70])

Term	Definition	Remarks
Calibration function	Mathematical presentation of the measured signal as a function of the state variable for a specified range of values	Calibration function and analytic function are the inverse of each other.
Analytic function	Mathematical presentation of the state variable as a function of the measured signal for a specified range of values	The shape of the function is specified on the basis of preliminary information on the response of the measurement system
Reference state	State of the measuring object, where the value of the state variable is known with specified uncertainty	The generation of reference states is performed with calibration devices such as a reference material or a standard reference measurement method. The number of reference states required depends on the shape of the function. The minimum number is [3.68]: <ul style="list-style-type: none"> • Three reference states for a linear function • Five reference states for a second-order polynomial • Seven reference states for a third-order polynomial • Five reference states for a potential function • Five reference states for an exponential function (see Chap. 2)
Reference value	Value of the state variable in a reference state	Wherever possible, reference values and their uncertainties should be traceable to corresponding international or national standards
Measured signal	Quantity with values that are provided by the measurement system	The measured signal is the quantity that is generated by the measurement system as an image of the measurement object.
State variable	Quantitative characteristic describing the state of a system [3.69]	If the measured signal and the state variable are continuous quantities, then both functions increase or decrease monotonically across the range of values considered
Measurement range	Range of values of the state variable for the measurement task considered	See also Sect. 3.3.1
Measurement uncertainty	Parameter that is associated with the result of a measurement and characterizes the accuracy and precision of the values that could reasonably be attributed to the measurand	In this handbook, the measurand is the state variable, which is the objective of the measurement

Table 3.8 Selection of the calibration procedure according to the characteristics of the measured signal and the corresponding reference value

Characteristics of the measured signal	Characteristics of the corresponding reference value	Calibration procedure
Defective	Subject to a comparatively small stated uncertainty	Direct calibration [3.71, 72]
Uncertainty of the measured signal is smaller than the uncertainty of the reference value	Defective (comparatively large stated uncertainty)	Indirect calibration [3.71, 72]
Defective	Defective	Orthogonal calibration [3.71, 73, 74]

from the multiple replicate values for each reference state. These average values should be used as the values of the measured signal. The standard deviations of the averages are used as the corresponding uncertainties.

Finally, calibration is required to define the bias (or the average deviation from the standard), the random errors, the measurement thresholds, and the nonlinear response regions. Hysteresis should be identified by cycling the sensor across its operating range during cal-

ibration. Drift is identified by periodically performing calibrations over a longer time period.

In long-term measurement programs, it is especially important to quantify (and possibly correct for) instrument drift between calibrations and/or sensor changes to maintain quality and consistency in the data and associated uncertainty estimation. When a sensor is exchanged for a new one of the same type due to damage or wear or to perform calibration, it is vital to perform

Table 3.9 Overview of established estimation methods for the parameters of the analytic function (after [3.76, 77])

Method used to estimate the parameters of the analytic function	Description	Applications	Limitations
Least squares estimation (LSE)	The parameters of the analytic function are calculated by minimizing the sum of squares of the distances (along the dependent variable axis) between the measured values and the analytic function	The advantage of the LSE is that there is no need to assume a distribution type, only the relationship between the expected value and the unknown parameter. Thus, this estimation method is applicable to a wide range of problems. LSE is used when the uncertainties in the independent variable are insignificant	As LSE only uses information about the expected value but not information about the distribution (in contrast to the MLE method), the resulting estimators are not as good as those provided by MLE. If the expected value is not linearly related to the parameter, numerical approximation methods are generally employed to determine the minimum in LSE. Only residuals for dependent variables are considered
Total least squares estimation (TLSE)	The parameters of the analytic function are calculated by minimizing the sum of squares of the orthogonal distances between the measured values and the analytic function	TLSE accounts for observational errors in both the measurement signal and the reference value. It is a generalization of orthogonal regression, and can be applied to both linear and nonlinear models	Difficulties arise if the dependent and independent variables are not measured in the same units
Weighted least squares estimation (WLSE)	WLSE attaches nonnegative constants (weights) to the data points	It is particularly applicable to data of varying quality	WLSE requires that the weights are known. Weight estimation can have unpredictable results, especially when dealing with small samples. Therefore, the technique should only be used when the weight estimates are fairly precise
Minimum chi square estimation (MCSE)	MCSE is similar to LSE, but it is assumed that the random variables take discrete values (including categorized data)	MCSE is only applied to frequencies (such as the frequency of observations per class; e.g., photon counting). Observations are randomly sampled	It is difficult to find the minimum of the sum of squared errors because the minimization algorithm must take discontinuities into account
Maximum likelihood estimation (MLE)	In contrast to LSE, MLE requires that the type of distribution of the sample variable is known. The parameters of the distribution depend on the parameter sought. The estimated value of the parameter is the value that would most likely produce the observed sample	The advantage of MLE is the nature of the estimator: it is often consistent (i.e., increasing the number of observations improves the accuracy of the estimated value) and asymptotically efficient, and it is possible to formulate general significance tests for model comparisons	A major disadvantage of MLE is that the type of distribution of the sample variable must be known; choosing an inappropriate distribution type results in poor accuracy of the estimated value. Furthermore, in order to find the parameter, it is usually necessary to perform numerical maximization, which may end up in a local rather than a global maximum. However, if the precisions of the measured signals and the references are recorded, MLE will still provide superior performance [3.75]

pre- and post-deployment calibration of both sensors in order to account and/or correct for differences in readings that are simply due to the sensor change. So long as both sensors meet the measurement requirements (which should have been verified initially and throughout the program; see Sects. 3.3.2 and 3.3.7), changing the instrumentation should not diminish the ability of the measurement program to achieve the objective.

Nonetheless, such a change should be thoroughly documented to aid data interpretation (see Sects. 3.3.4 and 3.4.2). When a sensor is replaced with another of a different type (due to improvements in technology or because the model of the original sensor has been discontinued), it is necessary to perform and document a thorough instrument intercomparison (see below) that characterizes and accounts for differences in the in-

Table 3.10 Standards used for different meteorological parameters (after [3.11]) (for more details see Chaps. 7, 8, 9, and 10)

Level of standard	Description	Temperature	Humidity	Wind ^a	Pressure
Primary standard	Highest metrological quality; value accepted without reference to other standards	High-grade platinum resistance at an accredited calibration laboratory ^b	Gravimetric method, humidity generator at national standard laboratories	Wind tunnel according to ISO guidelines [3.78, 79]	Piston gauge with loaded piston
Secondary standard	Value assigned by comparison with a primary standard		Chilled mirror hygrometer ^c or WMO reference psychrometer [3.80]		Electric barometers, such as silicon diaphragm barometers with long-term stability
Reference standard	A standard that is generally of the highest metrological quality and is used in a given location or by a given organization to calibrate measurements	Well-calibrated reference thermometers or WMO reference psychrometer [3.80] ^d	Chilled mirror hygrometer ^c or WMO reference psychrometer [3.80]		Electric barometers, such as silicon diaphragm barometers with long-term stability
Working standard	Standard used to routinely calibrate or check measurement systems	Well-calibrated reference thermometers or WMO reference psychrometer [3.80] ^d	Chilled mirror hygrometer or Assmann psychrometer	Inspections	High-precision electric barometers
Traveling standard	A standard that is intended to be transported between different locations (and is therefore sometimes specially constructed to facilitate this)				High-precision digital barometer

^aThe WMO has not defined any standards
^bTermed a laboratory standard
^cHighly accurate instruments such as the Thygan (see Chap. 8) are recommended for use as secondary standards
^dTermed a field standard

struments across the range of expected measurement conditions.

Measurement Traceability

Sensor calibration is usually performed by comparing the output of the sensor to one or more measurement standards. These standards are classified according to their metrological quality [3.11]. Examples for the most important atmospheric parameters are summarized in Table 3.10. Unfortunately, the same levels of standards are not used for all meteorological parameters.

The primary standard is usually only available at a single institution (such as the World Radiation Center, Davos, Switzerland) or at authorized laboratories. Secondary standards are distributed to the regional centers of the WMO or even national centers. Reference standards should be available in all regions. Depending on the physical parameter considered or the instruments available, all of the sensors in a particular region should be calibrated against the appropriate reference standard for that region via working or traveling standards or traveling devices.

In addition to the list given in Table 3.10, there are also international standards that are authorized by inter-

national agreements for use in assigning values to other standards. Similarly, national standards for a particular country are authorized for use in assigning values to other standards in that country.

All equipment used for tests and/or calibrations—including equipment used for subsidiary measurements (e.g., of environmental conditions) that have a significant effect on the accuracy or validity of the test result, calibration, or sampling—should be calibrated before being put into service. The laboratory should have an established program and procedure for calibrating its equipment [3.81].

The equipment calibration program used in a calibration laboratory should be designed and operated so as to ensure that calibrations and measurements made by the laboratory are traceable to the International System of Units (SI) and recommended scales such as the International Temperature Scale (ITS-90; see Chap. 5). The measurement standards and sensors used by the calibration laboratory should be traceable to the SI through an unbroken chain of calibrations or comparisons linking them to the relevant primary standards for the SI units of measurement. This link to SI units may be achieved through reference to national measurement

standards. National measurement standards may be primary standards, which are primary realizations of the SI units or agreed representations of SI units based on fundamental physical constants, or they may be secondary standards, which are standards calibrated by another national metrology institute. When using external calibration services, measurement traceability should be assured through the use of calibration services from laboratories that can demonstrate competence, measuring ability, and traceability (see Sect. 3.3.8).

Instrument Intercomparison

Instrument intercomparisons complement the calibration process and can be performed in the laboratory (e.g., interlaboratory round robins), in the field (e.g., side-by-side field tests), or in environmental or emission test chambers (see [3.82–85]). Moreover, intercomparisons can be performed among different measurement platforms, techniques, and at the international, national, regional, multilateral, or bilateral level. In particular, intercomparisons should be performed before introducing new measurements and observation technologies.

Laboratory tests are essential for sensor calibration and for obtaining baseline information on the quality characteristics of the data from sensors. By extension, interlaboratory tests provide complementary information on the sensors and the laboratories involved. Those tests are temporally and spatially limited measurement comparisons that are used to demonstrate the competence and performance of the laboratories or to validate a measurement method (see [3.86]). The design of the interlaboratory test is intended to demonstrate how and the degree to which each measurement step affects the quality of the measurement result [3.87]. Interlaboratory testing schemes can be used to evaluate the performance of a laboratory when it carries out specific tests or measurements and to continuously monitor laboratory performance. Thus, interlaboratory tests allow the detection of problems with measurements performed by a particular laboratory, which should prompt corrective action. They can also be used to highlight interlaboratory differences. Overall, they reassure laboratory customers that the measurement methods used by that laboratory are effective and comparable. Furthermore, the outcomes of interlaboratory tests can be used by the participating laboratories to improve their own practices. Interlaboratory tests are also important for assigning values to reference materials and assessing their suitability for use in specific measurement procedures. Accordingly, claims regarding measurement uncertainty and the equivalence of measurements from national metrology institutes can be validated [3.88].

Aside from laboratory calibration and characterization, the atmospheric conditions (e.g., radiation and turbulence) can substantially alter the data quality properties of a sensor. For example, laboratory and field intercomparison tests can be performed to characterize measurement repeatability and reproducibility under controlled and varying environmental conditions, respectively. Field intercomparison tests are essential for determining the uncertainty bounds for sensor-based measurements that are substantially less reproducible than they are repeatable. Table 3.11 summarizes the complementarity of laboratory and field tests for some typical measurands.

Field intercomparisons must fulfill several requirements that go far beyond investigating sensor characteristics under laboratory conditions [3.92]. In general, field intercomparisons should be performed under measurement conditions that are reproducible and as close to ideal as possible. If the measurement conditions for a specific use case differ substantially from the ideal conditions, the instruments should be compared under the target conditions. First and foremost, a high-quality instrument—an *etalon*—should be applied for the comparison. This could be a primary- or secondary-standard sensor that shows long-term stability in laboratory calibrations and is probably less influenced than other instruments by radiation or flow distortion in the wind field. In general, the local topography of the measuring field can cause difficulties in field intercomparisons. For instance, the topography perturbs land–atmosphere interactions (including radiation), the air temperature, wind, and turbulence. Therefore, it is recommended that a horizontal and uniform measuring field with prevailing turbulence and negligible flow convergence and divergence should be selected. In addition, the measuring field should be free of obstacles in all wind directions. A measuring field in which the wind field does not change direction very often (e.g., in large valleys) may be useful. The mean radiation and mean wind speed should be identical in all parts of the measuring field, as should the turbulence statistics (standard deviations and normalized standard deviations; see Chap. 55). In addition, the measuring height should be identical for all sensors, and it should be high enough to ensure that the typically large gradients that occur near the surface do not influence the sensors (see Chap. 1). The distance between the sensors to be compared must be large enough that they do not influence each other or generate flow distortions; otherwise, the positions of the sensors should be changed several times during the intercomparison.

A notable variant of field intercomparisons utilizes traveling standards such as individual sensors or entire integrated measurement and data acquisition systems as *etalons*. This variant is commonly used in meteoro-

Table 3.11 Overview of intercomparisons performed in the laboratory or in the field

Measurand	Laboratory test	Field test
Temperature	<i>Thermometers</i> are calibrated with a very high degree of accuracy in thermostats with water or oil. However, they are used in temperature screens in which there is a significantly higher uncertainty attributed to heating of the sensors by shortwave radiation (see Chap. 7)	<i>Temperature screen</i> intercomparisons must be performed for different solar angles, wind velocities, and wind directions. The sensors should be rotated in a homogeneous wind field. One etalon that can be used in this context is the WMO reference psychrometer [3.80], and a possible experiment is described in [3.89] (see Chap. 7). Similar conditions are needed when comparing humidity sensors (see Chap. 8)
Wind speed	<i>Anemometers</i> are calibrated in a wind tunnel against an accurate hot-wire, <i>Prandtl</i> (pitot) tube, or laser anemometer. However, a wind tunnel has almost laminar flow and so the accuracy or flow distortion may differ from that associated with turbulent flow in the atmosphere	<i>Rotation anemometer and sonic anemometer</i> intercomparisons should be performed in a wind field with a dominant wind direction so that the anemometer installation does not have to be adjusted according to the wind direction to reduce flow distortion effects. It is important to know and restrict how turbulence parameters change across the measuring field. The distance between the sensors should be large enough to reduce flow distortion effects. Etalons for such comparisons are unavailable. A sensor type that is less affected by flow distortion and has undergone long-term calibration stability in a wind tunnel should be chosen as the etalon. One example of such a field experiment is given in [3.90] (see Chap. 9)
Precipitation	<i>Precipitation gauges</i> can be calibrated with simulated water inflows of different intensities. In the real atmosphere, the wind field, flow structures around the gauges, or evaporation can significantly reduce the accuracy	<i>Precipitation gauges</i> should be compared under changing wind (speed and direction) and evaporation conditions. To reduce any possible flow distortion effects, the positions of the sensors should be switched between the edge and the center of the sensor array. One possible etalon is a precipitation gauge which has the upper part at ground level and a small evaporating surface and shows stable calibration. A possible experiment is described in [3.91] (see Chap. 12)

logical measurement networks (Sect. 3.4.1) to ensure reproducibility across sites and time. One example is the AmeriFlux portable eddy covariance system, which consists not only of sensors but also mounting hardware, data acquisition, power options, software, and several optional components. The complete system can be requested by network member sites, where it is used to conduct side-by-side field intercomparisons of eddy-covariance, meteorological, and radiation measurements (see <http://ameriflux.lbl.gov/tech/pecs/>).

Intercomparisons can be performed among different measurement platforms—for example between remote sensing instruments (sodar, lidar, radar) and towers or radiosondes. Reports of such studies are available [3.93–95], but these studies have the disadvantage of comparing volume-averaged remote sensing data with point measurements, and the datasets that are compared probably utilize different time averaging [3.96]. Therefore, it is standard to apply post-field data quality control to the remote sensing data (see Sect. 3.3.6).

Satellite remote sensing is possible for levels ranging from the troposphere to the upper mesosphere. Relevant in-situ methods such as dropsondes launched with rockets are only rarely available. However, long-term stability is problematic below the upper stratosphere due to the difficulty of maintaining a stable instrumental spectral baseline. Thus, intercomparisons between satellite and ground-based instruments facilitate a com-

parison of their biases. Furthermore, the datasets can be used to assess the stability of the instruments (both satellite and ground-based) and the long-term trends in the variation of the measurand.

3.3.4 Inspection and Maintenance

Data quality issues are often irreversible, meaning they cannot be corrected after the fact. Therefore, the importance of regular inspection and maintenance cannot be overstated, as they can minimize or eliminate such issues entirely. Diligent inspection and maintenance of the site infrastructure and sensors will lead to higher data quality and fewer costly and time-consuming corrective maintenance bouts. Table 3.12 lists essential inspection and maintenance tasks that should be included in any long-term measurement program. Similar tables for measurement-specific maintenance frequencies are also provided in other chapters in this handbook.

The simplest yet most important routine task is frequent data inspection. This allows problems to be caught early, minimizing sensor downtime and improving overall quality. The frequency of data inspection and the method used to perform the inspection will depend on the scale of the project and the availability of remote communications. Meteorological services are increasingly using automatic unmanned systems that rely on remote data transmission and automated

Table 3.12 Essential inspection and preventative maintenance tasks. Note that the example frequencies given in the table would need to be adjusted to the site and sensor conditions and/or to manufacturers' recommendations

Activity	Example of frequency
Remote/on-site inspection of sensor readings	Daily or as frequently as possible
Document sensor status and environmental conditions, preferably including photographs	Every maintenance bout
Physical inspection of sensors, their configuration, and the measurement environment	Biweekly
Sensor cleaning	Biweekly or as needed
Vegetation, snow, and animal management (if applicable)	Biweekly or as needed during active season
Ensure site security	Biweekly
Physical inspection of infrastructure, including rust management	Monthly
Tighten nuts, bolts, and terminal connections	Quarterly
Service infrastructure and power systems; look for corrosion and solar degradation of physical components	Quarterly or as needed
Replace filters and/or desiccant packs, lubricate moving parts (sensors and infrastructure)	Semiannually or per manufacturers' recommendations
Field calibration/validation	Semiannually or per manufacturers' recommendations

checks [3.97]. Alerts are generated automatically for common problems (e.g., low battery, sensor error, out-of-range values) and sent via an email or text message to maintenance personnel. In the absence of automated checks, daily manual data inspection is relatively easy to accomplish if the project is small and data are communicated remotely in real time (or, more commonly, near real time). Otherwise, data inspection may have to wait until site visits are performed, but it should be done as frequently as possible. In addition to remote or on-site data inspection, routine physical inspection of sensors and infrastructure is vital to maintaining the safety of sensors and personnel and ensuring that the sensors are operating properly and measuring the intended environment. Many quality problems are difficult to detect from the data alone but are obvious upon physical inspection. For example, radiation sensors are often deployed on booms extending from a tower high above the ground. These are attractive perches for birds that consequently foul the sensors (Fig. 3.2). In such a scenario, sensor readings will likely remain within the expected range, but a routine site visit will quickly identify the problem. Without inspection, the data quality cannot be determined. Of course, it is also good practice to cross-compare data among replicate and related sensors in order to detect problems. However, replicate or related sensors are not always available, and routine physical inspection remains one of the best ways to assure data quality.

Regular preventative maintenance is required to keep infrastructure and sensors in good working order and ensure adequate measurement conditions. Dust, debris, and fouling must be removed; filters and desiccant packs must be changed; the appropriate sensor orientation and any specific operating conditions must



Fig. 3.2 Bird fouling on a radiation sensor at the NEON Lyndon B. Johnson National Grasslands site in Texas, USA (photo © Gary Henson, National Ecological Observatory Network, USA)

be maintained. Many atmospheric measurements are conducted in the natural environment, requiring regular animal and vegetation management to maintain measurement integrity. Frequent preventative maintenance allows many quality issues to be mitigated before they affect the data. For example, nuts, bolts, and terminal connections tend to unscrew or loosen over time due

to repeated (daily) thermal contraction and expansion cycles. Regularly tightening connections avoids data loss.

Maintenance bouts should periodically include instrument tests that can be performed on-site and may be a subset or modified versions of laboratory-based calibration and testing procedures (see Sect. 3.3.3). For example, tipping bucket rain gauges can be tested to ensure that the correct number of tips occur when a known amount of water is poured into the collector, and they can even be calibrated directly in the field. Tests may also include a roving reference to ensure calibration integrity between calibration intervals or to troubleshoot problematic readings. Field validation establishes a time point at which the readings were definitely valid (or invalid). Standardized thresholds for the maximum acceptable difference between the roving reference and the field-based sensor should be defined beforehand. In all cases, detailed records should be made of field-based testing and calibration, including pre- and post-calibration errors, to ensure that the information is correctly applied and evaluated during data processing.

Planning for Inspection and Maintenance

Every measurement program has unique maintenance needs that depend on the sensors or methods used and the environment in which the measurements are collected. It is important to identify the likeliest and greatest threats to quality and to then adjust maintenance schedules and activities to prioritize their mitigation. Thus, the frequency of preventative maintenance and the tasks involved will be program, environment, and sensor specific. For example, sensors deployed in a dusty environment will require more frequent cleaning and filter changes than those in a cold environment, where more important maintenance tasks may include clearing snow and ensuring that instrument heaters are operational. Table 3.13 provides a planning checklist for routine inspection and maintenance. The steps in this checklist should be periodically revisited as the measurement program progresses and experience and knowledge are gained.

Often, the desire for high preventative maintenance frequency must be balanced against the inherent limitations on the funds and personnel available. For example, preventative maintenance at the Oklahoma Mesonet (see Chap. 45) is limited to three site visits per year due to the costs incurred from salaries, travel, and vehicle use [3.98]. All of the materials required should be assembled and visits should be planned so that maintenance time and resources can be spent efficiently. Maintenance bouts should be evaluated afterward to clarify the amount of maintenance that can actually be

Table 3.13 Inspection and maintenance planning checklist

Activity	Notes
Create a maintenance schedule	Balance the desire for high maintenance frequency with available resources
Develop task lists and standard operating procedures (SOPs)	Prioritize the mitigation of common problems; develop SOPs for preventative and corrective maintenance
Create record templates/checklists	Preferably in electronic format
Assemble the materials required	Prepare a handy maintenance kit with commonly needed materials

accomplished in one visit. Standard operating procedures (SOPs) that provide step-by-step instructions for conducting routine preventative maintenance as well as common corrective maintenance tasks should be developed. Standardizing maintenance procedures through the application of SOPs helps to ensure that a consistent level of quality is achieved regardless of the time at which it was performed or the technician involved, and it increases efficiency because the workflow tasks are ingrained in the technician's memory. Where available, manufacturers' guidelines should be followed when creating SOPs. A training program should be developed for new technicians and procedures, and a mechanism permitting feedback on and adjustments to the SOPs based on practical experience should be incorporated.

It is also important to develop easy-to-use record templates or checklists (Fig. 3.3) that can serve as maintenance logs. Detailed logs of maintenance, measurement conditions, and other activities related to data collection are a valuable source of metadata, which can be used within the organization and can be provided to users to help them to interpret the corresponding data. Even if the same person sets up the measurement program, collects the data, maintains the sensors, and analyzes the data, it is very unlikely that they will remember all of the important details about the actions they performed and the conditions present on a particular day. This is particularly important given that the time delay between data collection and data analysis can be months or even years. Preferably electronic and machine-readable standardized logs that indicate the action performed and other relevant details facilitate data interpretation and analysis as well as improvements in long-term and system-wide patterns of sensor performance and data quality. Level shifts or other abrupt changes in data patterns are often associated with maintenance bouts in which a sensor was replaced with a freshly calibrated one or other maintenance (e.g., cleaning) was performed [3.99]. Maintenance logs tie

D14, SRER, 2018-01-17	
NEON Site	Domain 14, SRER
domainID	D14
siteID	SRER
Date	2018-01-17
Technician 1	
Technician 2	
Day 1 Arrival Time	08:28
Day 1 Departure Time	15:49
Tower Infrastructure Inspection	
Tower COM/Power/Breaker Boxes	OK
Ascension Line	OK
Safety Clipping Points	OK
Tower Electrical Grounding	OK
Signal/Power Cables	OK
Tower Access Gate/Top Hatch	OK
Boom Inspection	
Roller Boxes	OK
Guy Wires	OK
Winches	OK
Routine Sensor Maintenance	
Triple Aspirated Air Temperature	OK/Cleaned
PAR	OK/Cleaned
Primary Pyranometer (if applicable)	OK/Cleaned
Sunshine Pyranometer (Direct and Diffuse)	OK/Cleaned
Net Radiometer	OK/Cleaned
Cimel Sun Photometer (if applicable)	
Cimel Maintenance Start Time	23:33
Cables & Connectors	OK
Check all Connections at White Connector Panel	OK
Check Foam Spacer on Box Door	OK
Sensor Head Strap & Buckle	OK
Is Sensor Head Flush with the Mounting Claw?	Yes/OK
Was Sensor Head Adjusted to be Flush with Mounting Claw?	No
Check System Date and Time	Problem
Check Battery Voltage	OK
Check the Wet Sensor	OK/Cleaned
Verify Full Range of Motion	Problem
CIMEL Notes	Time is way off. Read at 18:33 when time was 11:33. CIMEL not responsive to any commands beyond setting it to manual mode.
Cimel Maintenance End Time	23:45
Total Cimel Maintenance Time (min)	12

Fig. 3.3 Excerpt from an electronic meteorological tower maintenance log at the National Ecological Observatory Network, USA (© National Ecological Observatory Network, Battelle)

Table 3.14 Checks to complete during remote or on-site data inspection

Check	Notes and examples
Are data being recorded?	Check that all data streams are present and that the frequencies are correct
Are the sensor diagnostic codes reporting that the sensor is operating correctly?	Sensor manuals describe diagnostic codes and provide troubleshooting hints
Are the values plausible?	Also check ancillary data streams that are indicators of correct operation, such as flow rates for pump systems, the internal temperature and pressure of a sensor, the battery charge of a solar power system, etc.
Are values consistent between related sensors?	Identify sensors that should show correlated readings and ensure that they are consistent with each other

the change in the data to the (probable) cause. This knowledge can then be used to correct the data, exclude or flag erroneous data to prevent faulty interpretations, and/or make adjustments to the maintenance and calibration frequency and/or procedures in order to avoid subsequent data shifts. All of these actions improve quality. Even when the instruments are found to be in good order and are simply cleaned during a maintenance bout, the records containing this information verify that the maintenance frequency is adequate. Maintenance records indicating problem-free site and sensor conditions can be used to identify efficiencies, especially if the logs are standardized and digitized to facilitate analysis. Standardized logs can be implemented with simple spreadsheets or (mobile) applications that control the units and language used to describe activities, conditions, and problems. Fields for the date/time and technician should be included, and the serial numbers of the sensors should be recorded or verified, especially during sensor swaps. As measurement programs increase in size, complexity, and duration, it is becoming increasingly important for the metadata linked to inspection to be recorded in a digital, machine-readable format and hosted in a centrally accessible repository in near real time. This allows project operations to be efficiently coordinated and for quality-related metadata to remain organized and accessible to all project personnel, automated analyses, and ultimately to end users.

For large measurement programs, additional valuable tools include issue management and asset management systems. An issue management system is used to report, track, and record the resolution of problems. It facilitates communication and collaboration between the different roles in an organization and serves as a knowledge base for solving future problems (reducing downtime). Asset management systems track the locations and status of sensors and equipment, and are highly recommended for measurement programs with many sensors. The databases behind asset management systems can be leveraged during data processing to automatically apply the correct calibration coefficients or other required metadata for the date range and location of interest.

Performing Inspection and Maintenance

Prior to performing any maintenance, a remote or on-site inspection of data streams and sensor health should be carried out (Table 3.14). Remote data inspection prior to arriving on-site is highly preferable (especially if the travel time is significant), as it can be used to ensure that any materials needed for troubleshooting or repair are gathered ahead of time. This minimizes sensor downtime and reduces the need for follow-up visits. The automated generation of real-time graphs and statistics can speed up this task significantly, as can automated scripts that check important values and issue alerts for suspect data streams.

While performing any maintenance that may impact observations, it is important to either disconnect data collection, remove the data collected during the maintenance bout, or raise a quality control flag for the data that warns of potential measurement interference. Readings should be checked and recorded before and after cleaning/maintenance to quantify any change. The resulting data can be used to analyze the impact of cleaning/maintenance frequency on data quality, and potentially for data correction.

Digital photographs should be taken of the sensors, infrastructure, surroundings, and any identified concerns. Photos provide valuable context when interpreting measurements and quickly documenting the status of the sensors and measurement environment, especially across changes in personnel. A standardized, machine-readable file-naming system should be implemented to distinguish important characteristics such as location, date, time, and orientation or target view.

3.3.5 Data Processing and Management

Assuring the quality of atmospheric measurements does not stop at data collection. How the data are processed, stored, and made accessible to users are just as important as data collection. A data management plan specifies these details in advance to ensure that project resources are adequate to ensure data integrity, reproducibility, and access. In fact, most funding agencies (e.g., the US National Science Foundation since Jan-

Table 3.15 Characteristics of data standards

Type	Description	Examples
Variable notation	Reserved letters, words, or symbols that unambiguously denote measured quantities	<ul style="list-style-type: none"> • P = precipitation • Journal policies on notation (e.g., [3.100])
Naming convention	A set of rules for the character sequence that forms or combines identifiers	<ul style="list-style-type: none"> • ISO date format (YYYY-MM-DD) [3.101] • Filenames • Additional identifiers (e.g., position) appended to variable names
Unit of measurement	A definite magnitude of a quantity	<ul style="list-style-type: none"> • SI units • Imperial (English) units
File format	A standard way of encoding information for storage in digital media	<ul style="list-style-type: none"> • ASCII text, delimited (e.g., .csv, .txt) • Binary • XML • NetCDF, HDF
Coding systems	Shorthand descriptors of data values that are used to reduce data storage requirements	<ul style="list-style-type: none"> • Station names • Weather phenomena • Missing data designators • See the <i>WMO Manual on Codes</i> [3.18]

uary 2011 [3.102]) now require the inclusion of a data management plan in any research proposal. Regardless of whether it is required by a funding agency, a data management plan should be crafted during the planning process, and it should specify:

- The type(s) of data to be collected
- Products generated by the measurement program
- Standards to use for the format and content of the data and metadata
- How the data will be stored, processed, archived, and made accessible
- Policies for data reuse and redistribution.

The remainder of this section provides discussions of data and algorithm standards, metadata, processing considerations, and data archival from the perspective of data quality.

Data and Algorithm Standards

Data standards are the rules that must be followed when describing and recording data [3.103]. Standardizing the format and meaning of data ensures that the data will be interpreted consistently by users around the world. Table 3.15 provides common characteristics specified in data standards. There are organizations that devote considerable energy to crafting and promoting data standards, such as the WMO Information System [3.104] and DataOne [3.105].

Algorithm standards are accepted sequences of procedures that are implemented to statistically reduce data and derive data products from measured quantities. They also apply to the parameters and physical constants used within algorithms (see Chap. 5). Community standards for algorithms evolve as scientific

knowledge improves and new sensors that can measure the target quantity in different ways are developed. Many algorithms or portions of algorithms are well established, such as the basic sequence of mathematical operations that is applied to compute turbulent fluxes of mass and energy using eddy covariance instrumentation [3.106] (see Chap. 55). Others remain under active investigation, such as the use of particular corrections to account for instrument or computational bias. There are often multiple equally acceptable algorithms—all based on different theoretical approaches, applications, assumptions, or instrumentation—for a particular task. Each chapter in this handbook describes algorithm standards and areas of active investigation that are applicable to each measurement type. In all cases, it is important to justify and document algorithmic choices and to follow algorithm standards where available/applicable.

Metadata

Metadata is descriptive information about the collected data, including the origins of the data, the conditions and settings in which measurements were made, and any operations performed on the data. This information is invaluable, because data are practically useless without context. Scientific advances are made when studies are validated and repeated by others. This requires knowledge of the provenance of the data—a historical record of the data and their origins. The provenance of the data is provided as metadata. Metadata should provide traceability from the point of collection to the point of dissemination, and the information provided should be sufficiently detailed to enable the measurements to be reproduced or reprocessed. At a minimum, the metadata should describe:

Table 3.16 Metadata schemas

Name	Application	Description
ISO 19115	Geographic data	International standard for describing geographic information and services
ISO/IEC 11179	Data semantics and representation	International standard for describing data of any kind to promote a common understanding of data across organizations
DIF	Scientific datasets	Directory interchange format: a standard format for creating directory entries that describe scientific datasets
DOI	Resources on digital networks	Digital object identifier: a standard for registering and using persistent interoperable identifiers for resources (such as datasets) on digital networks

- Measurement methods, including sensor models and manufacturers
- Instrument settings and details of data logging
- Measurement location(s) and date ranges
- Calibration dates and methods
- Maintenance intervals and activities
- Significant events (and their dates) that may impact the data or its quality
- Processing steps and algorithm details
- The data format
- The version of the data and any software used to produce it.

Several schemas are available that can standardize metadata for specific applications so that the metadata can be easily shared and interpreted. These schemas specify the format and syntax of the metadata as well as the elements included and a controlled vocabulary for populating element values. Table 3.16 lists several metadata schemas that are relevant to atmospheric data.

Versioning and Testing

Scientific results are increasingly being obtained through the use of custom software tools created by scientists, even though scientists typically have no formal training in software engineering [3.107]. Software development practices are primarily learned by scientists from their peers or through self-study. As a result, scientific software and the results they yield vary greatly in quality [3.108, 109]. Two critical aspects of assuring the quality of scientific software and derived data products are versioning and testing. Implementing these methods can be a daunting task. Thankfully, several organizations provide resources that can help scientists to improve the quality of their scientific software. Examples include the Software Sustainability Institute [3.110], Software Carpentry [3.111], and the Kepler Project [3.112]. Furthermore, software can be made publicly available on, for instance, the Zenodo server [3.113] in order to make the application of the software clear to users.

Although the original data collected should never be modified, changes to derived data products and processing software are commonplace and must be

documented. This is accomplished through versioning. Versioning designates a unique identifier to progressive changes in data or processing code. An example of a versioning specification used for publically available scientific software is semantic versioning [3.114], which provides a set of rules for how version numbers should be assigned and incremented. Version numbers have the format

MAJOR . MINOR . PATCH,

where a MAJOR version makes non-backwards-compatible application programming interface (API) changes, a MINOR version adds functionality that is backwards compatible, and a PATCH makes backwards-compatible bug fixes. One of the main benefits of this specification is the automatic management of software dependencies. The version number explicitly identifies whether software that depends on another software package or is used by another software package will continue to work with subsequent versions. Versions of data and software should be annotated with *release notes* that provide a natural language summary of changes between the previous version and the current version. Both the version number and the release notes are important metadata and provide traceability between the data product and the software used to produce it.

Version control software facilitates the implementation of software versioning as well as collaboration in joint software development. Git and Apache Subversion (SVN) are two prominent open-source version control systems that are free, although there are many others. These systems regulate and track changes to code, documents, and other information so that a complete history is retained along with attribution. Learning about such systems is not a trivial task, but the benefits are well worth the investment.

A program of software testing should be implemented to routinely test code during development and upon progressive changes. Software testing verifies that the processing code and algorithms are fit for use, which typically involves finding errors and bugs during software execution. Testing assures the quality and integrity

Table 3.17 Testing methods commonly used in scientific software development

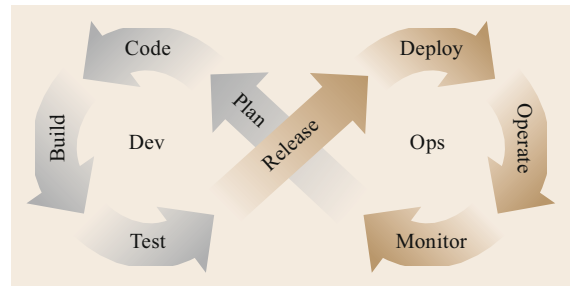
Testing method	Description	Examples of scientific applications
Unit testing	Verifies the functionality of a specific section or module of code tested independently of the rest of the software	[3.115–120]
System testing	Tests the entire integrated software system for the expected functionality and performance	[3.115, 117]
Regression testing	Compares previous output to new output to find unintended errors and bugs in existing software components after changes or additions have been made	[3.117, 119]

of the processing algorithms and derived data products, and minimizes the number of data and code versions that result from errors discovered after release. Table 3.17 lists three testing methods that are commonly used for scientific software [3.108].

Scientific software applications continue to increase in complexity and involve many developers and integrated computation modules. In response, software engineering philosophies that are developed specifically to address these complexities and improve software quality [3.121–123] are gaining traction in science. Two of the main philosophies are Agile development and DevOps. Agile software development [3.124] advocates continuous planning with short delivery cycles in which work is broken into small, demonstrable increments. Cross-functional teams work in close collaboration through daily communication, and working software is reviewed at the end of each short cycle (1–4 weeks). The advantages of this philosophy include adaptation to changing requirements and circumstances, minimizing risks through early and frequent feedback, and continuous improvement. DevOps is a related philosophy that builds off the Agile framework and focuses on collaboration between software developers and operators through the use of tools to continuously iterate the development, building, testing, packaging, and release of software and achieve a rapid turnaround [3.125, 126] (Fig. 3.4). DevOps promotes the recipe- or script-based generation of the computational environment, which then serves as explicit documentation of the dependencies and software components. This improves the accessibility, extensibility, and reproducibility of scientific software [3.122, 127]. The philosophies of Agile and DevOps rely on automated tools for continuous testing, integration, and versioning. Many of the example applications listed in Table 3.17 employ such tools within an Agile or DevOps framework.

Data Archival

Data archival is the preservation of data for future use. Most research funding agencies now require the inclusion of data archival in a proposal before they will award funding. Sufficient metadata must be included

**Fig. 3.4** The DevOps workflow

to ensure that the data are fully understood and can be used regardless of who produced the data [3.128]. The World Data Center (WDC) system is an international collective of data archive centers, each of which hosts data specific to a particular scientific discipline. Table 3.18 provides information on the WDCs that host atmospheric data products covered in this handbook. The International Science Council (ISC) World Data System [3.129] established in 2009 aims to transition from these existing standalone services to a common globally interoperable distributed data system that incorporates emerging technologies and new scientific data activities. Several of the WDCs mentioned in Table 3.18 are already members of the ISC World Data System.

3.3.6 Post-field Data Quality Control

The most important part of quality assurance is quality control (QC)—the use of operational techniques and activities to evaluate whether the quality requirements have been fulfilled. Applying these techniques leads to the quality-controlled dataset and corrective actions. Hence, QC should be performed in near real time, as this will minimize data loss by reducing the time taken to detect and solve problems [3.130]. This section provides an overview of post-field data QC approaches. Other aspects of QC are performed in-situ by the observer (Sect. 3.3.4) and as part of problem tracking and resolution (Sect. 3.4.1).

Data QC can be performed manually or automatically. Manual QC provides the foundations for data

Table 3.18 World Data Center archives of atmospheric measurements

Data archive	Summary of holdings	Web address, Accessed 10 Oct. 2021
PANGAEA	Georeferenced data from Earth-system research	https://www.pangaea.de/
WDC for Aerosols	Microphysical, optical, and chemical properties of atmospheric aerosols	https://www.gaw-wdca.org/
WDC for Climate	Climate model simulation data	http://www.wdc-climate.de/
WDC for Greenhouse Gases	Observations of greenhouse gases (CO ₂ , CH ₄ , CFCs, N ₂ O, etc.) and related gases (e.g., CO) in the atmosphere and oceans	https://gaw.kishou.go.jp/
WDC for Meteorology, Asheville	Surface meteorology, historical climatology, radiosonde, global synoptic observations	https://www.ncdc.noaa.gov/wdcmet
WDC for Meteorology, Beijing	Surface meteorology, synoptic meteorology, atmospheric chemistry, satellite, special observation platforms, dendroclimatology	https://data.cma.cn/en
WDC for Meteorology, Obninsk	Surface meteorology, marine meteorology, aerology, radiosonde	http://meteo.ru/
WDC for Remote Sensing of the Atmosphere	Remotely sensed atmospheric trace gases, aerosols, dynamics, radiation, cloud physical parameters, and ancillary data on surface parameters	http://wdc.dlr.de/
World Ozone and Ultraviolet Radiation Data Centre	Total column ozone and vertical profile data from lidar measurements, ozonesonde flights, and the Umkehr technique; ultraviolet (UV) radiation, including broadband, multiband, and high-resolution spectral data types	https://woudc.org
World Radiation Data Centre	Global radiometric observations, including global, diffuse, and direct solar radiation, downward atmospheric radiation, net total and terrestrial surface radiation, spectral radiation components, and sunshine duration	http://wrdc.mgo.rssi.ru/

QC [3.3, 130, 131]. For example, violations of requirements such as measurement obstructions or changes in the environment are often first identified by observers in the field. Similarly, atypical and suspicious data patterns are initially detected through post-field visual inspection by experts and data users. All QC procedures can be applied manually in principle, but the time required to do so is typically prohibitive. Additionally, while manual QC benefits from expert knowledge and human pattern recognition, it can suffer from human bias, operator-to-operator differences, and operator fatigue. Automated QC attempts to standardize the work done in manual QC and perform much of it programmatically. Parametric tests are generally used in automated QC, although adaptive tests based on machine learning are becoming increasingly popular [3.25]. The main advantages of automated QC are objectivity and repeatability, uniformity, practically unlimited test specifications, and efficient application to large datasets [3.1]. For this reason, automated QC has become the de facto standard for station networks (Sect. 3.4.1). Nevertheless, not all tests can be automated (examples of such tests include field observations and transfer standards); nor are automated tests infallible—they do not account for causation and multicollinearity, for instance. This underscores the importance of human supervision of automated QC procedures for ensuring that such procedures are effective at identifying suspicious data [3.130, 131].

In the following, QC tests for sample and observer data, time series data, and spatial data are summarized, followed by strategies for determining test thresholds. Sample and observer data collections are typically less uniform than instrument readings. For this reason, observer training is a particularly important element of any integrated quality management system [3.4]. QC of sample and observer data involves regular cross-validation, round robins, and blind tests, and focuses in particular on referential integrity, process quality, and data plausibility [3.132, 133]. Referential integrity refers to the absence of duplicate, orphaned, and/or *childless* records from datasets. Process quality corresponds to how much of the expected data and/or how many of the intended samples are obtained within a well-defined time interval. Data plausibility statements provide a qualitative assessment of whether data are *reasonable* or not. Standard operating procedures to examine the plausibility of the data should include a check that accepted abbreviations are used, an investigation of the consistency between variable statistics, pictorial representations, and diagrams, and simplified mathematical checks [3.1].

Table 3.19 provides an overview of characteristic tests of time series data as well as examples of their application. Initially, plausibility tests should be applied to constrain the data to electronically and atmospherically feasible values. Examples of such tests include those that examine the range of the recorded values,

Table 3.19 Overview of characteristic tests for time series data and examples of their application

Test	Purpose	Examples
Plausibility tests	Ensure only electronically and atmospherically feasible values are retained	Range test, sigma test, delta test, step test, null test, gap test [3.134]
Spike test	Outlier removal	Windowed tests [3.135, 136], filter-based tests [3.137, 138]
Higher-order moments of statistical distribution	Check the statistical plausibility of the values	Skewness, kurtosis [3.139, 140]
Application-specific tests	Check application-specific assumptions	Stationarity and mixing [3.141, 142], location bias [3.143]
Comparison with collocated/independent data	Check data consistency	Climatological and temporal checks [3.11], spatial consistency [3.131]

their variance structure, and step changes in those values [3.131, 134]. Once the data have been precleaned, spike tests can be used to remove any remaining outliers [3.135, 137]. It is important to note that several plausibility and spike tests require the time series to be equidistant, which can be achieved through regularization during preprocessing. The statistical plausibility of the values should then be evaluated further through the use of higher-level moments [3.139]. After that, application-specific tests should be performed to ensure that the methodological assumptions are fulfilled. Examples of such tests for eddy covariance measurements are stationarity and mixing tests [3.141, 142] as well as tests for location bias [3.143]. Lastly, the consistency of the data should be evaluated through comparison with collocated/independent data for instance. The *WMO Guide to Instruments and Methods of Observation* [3.11] provides detailed guidelines for climatological and temporal tests.

In principle, spatial data QC can utilize many of the time series tests listed in Table 3.19, some of which may require reduced dimensionality. Additional checks can also be made of the spatial coverage and correlation [3.144], cloud cover for optical measurements [3.145], and comparison of results among up/downscaled spatial resolutions and spatial aggregates [3.146].

Data quality control for remote sensing techniques such as radar and lidar is done as a post-field comparison with the results of weather prediction models. Two methods are applied. First, the vertical profile of the difference between the measured and modeled data and the root mean square (RMS) is determined. Such data can be averaged over periods of up to a month, and the resulting data products are available from several meteorological services. Bias and shifts in remote sensing data are clearly visible. Second, the forecast sensitivity to observation index (FSOI) [3.147]—a measure of how important the data are to the final model—is determined. If the data have little or even a negative influence on the model, the remote sensing systems should be checked.

All data QC relies on the use of thresholds—if a test result exceeds a predefined value, the corresponding observation is marked as suspicious. The challenge is then to determine suitable thresholds, because universal, absolute values do not necessarily apply across environments. One solution is to formulate either the test itself or the threshold value as a relationship that applies across a range of environmental conditions. Such an approach provides the consistency and uniformity gained from using a single relationship across a station network for example, and it also permits the necessary adaptivity to facilitate measurements across a variety of environments. One example of an adaptive test formulation with a universal, absolute threshold is that for integral turbulence characteristics (see Chap. 55; [3.141]). An example of an absolute test formulation with adaptive threshold values is the detection of the friction velocity change point in [3.142]. Alternatively, site-specific thresholds can be determined and tabulated automatically from sampling distributions of historic test results [3.134]. Gaussian statistics or robust statistics can be used for this purpose, as can a guided, semimanual approach combining sampling distributions with expert knowledge [3.148].

Post-field data QC aggregates over a test sequence, yielding a quality-controlled dataset and leading to corrective actions (Fig. 3.5). (i) Planning tests should be performed to determine whether site requirements are met. In addition, for sensor-based measurements, calibration, installation, and data acquisition requirements should be tested. For sample and observer data, the standard operating procedure should specify collection requirements. (ii) Next, in-situ tests should include sensor diagnostics and sample and observer data quality reports. (iii) During post-field tests, electronically and atmospherically feasible values, outliers, the statistical plausibility of the values, application-specific assumptions, and data consistency should be evaluated (Table 3.19). (iv) Both flat and hierarchical schemes can be used for quality aggregation. Flat schemes are often rank-based and provide a concise

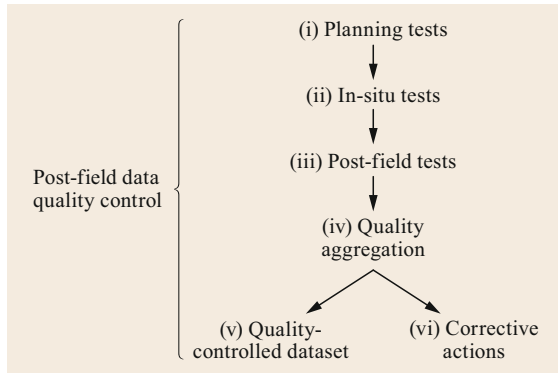


Fig. 3.5 Schematic of post-field data quality control: aggregating over a test sequence yields a quality-controlled dataset and leads to corrective actions (detailed explanations of items (i)–(vi) are given in Sect. 3.3.6)

depiction of overall data quality [3.149]. Because of their specificity to individual use cases, their extensibility (e.g., to different types of measurements and to sample and observer data) is typically limited. On the other hand, hierarchical aggregation schemes are by definition modularly extensible and permit the incorporation of visual data quality information for many data types [3.150]. They are most suitable for station networks because they allow quality information to be traced throughout the data generation chain. (v) Steps (i)–(iv) yield the quality-controlled dataset through the removal of suspect data points and/or by providing quality indications (*flags*) that should be documented as part of the metadata. (vi) If suspect quality conditions are identified, not only should the corresponding data points be marked but corrective actions should also be triggered. Two such corrective actions are issue management for tracking problems and how they are resolved (see Sects. 3.3.4 and 3.3.7) and data product adjustments for systematic deviations. Issue management informs the overall quality assurance workflow (Sect. 3.3) with the findings from post-field data quality control, and should include a formal communication process. Data product adjustments for systematic deviations are often use-case specific. For this reason, it is important to carefully evaluate (and document in the metadata) whether adjustments should be performed on the original data product or whether a subproduct should be created for this purpose. Examples include the conversion from station pressure to sea level pressure and from the measured wind speed to a reference height above ground, or the correction of measured precipitation for environmental effects [3.3].

3.3.7 Performance Monitoring

Performance monitoring facilitates continual improvement and evidence-based decision-making. Performance data should be collected and analyzed at every step in the data generation chain where this is possible/practical, as well as during other important processes carried out within the organization, to ensure that system requirements and quality objectives are being met. It is at this stage that we see the advantages of defining testable requirements during the planning stage and integrating monitoring into system design. The type of monitoring and the monitoring interval employed will depend on the requirement. Some monitored elements must be checked manually, while others can be evaluated continuously using automated methods.

It is also useful to periodically evaluate the requirements themselves. Because the planning stage is laborious, and requirements are sometimes constructed using incomplete information, some requirements may be found to be too lenient or too stringent to facilitate the objectives of the program. Continual improvement involves periodically evaluating the impact of the requirements on the final product or service and making adjustments where warranted to improve efficiency while maintaining quality. This allows valuable resources to be redirected toward areas in which quality is suffering.

Where possible, automated scripts and procedures should be used to monitor performance efficiently. Monitoring systems can be constructed in-house or using off-the-shelf analytics software. Reports should be generated, automatically if possible. These reports should be reviewed and used to identify and justify necessary improvements, and the reports and summaries should be distributed throughout the organization and the user community to improve awareness. A communication pathway to notify, track, and resolve problems identified by performance monitoring is required. A formal communication pathway is often included in off-the-shelf issue management systems.

Table 3.20 provides an overview of the performance monitoring that should be conducted for the various aspects of data generation. Monitoring site and instrument performance is a relatively straightforward task, as most of the requirements in this category are testable using the collected data. For visual observations and manual measurements, managers or dedicated staff should periodically audit sampling bouts to verify that measurement protocols are followed and performed consistently by different personnel.

Table 3.20 Performance monitoring conducted for various aspects of data generation

Performance category	Monitored elements	Examples of evaluations	Corrective actions
Site and instrument performance	<ul style="list-style-type: none"> • Measurement specifications • Instrument settings • Operational performance characteristics 	<ul style="list-style-type: none"> • Data frequency, resolution, coverage meets expectations • Appropriate instrument flow rates, internal temperature, etc. • Adequate power supply and system uptime (especially for remote installations) 	<ul style="list-style-type: none"> • Selection of a different sensor or manufacturer • Additional training • Addition or adjustment of resources
Calibration and testing performance	<ul style="list-style-type: none"> • Calibration frequency • Sensor accuracy and precision 	<ul style="list-style-type: none"> • Planned versus actual calibration frequency • Sensor degradation and lifetime • Calibration interval is adequate to keep the drift within the required range 	<ul style="list-style-type: none"> • Calibration interval adjustment • Sensor replacement • Additional training
Inspection and maintenance	<ul style="list-style-type: none"> • Maintenance frequency • Sensor and infrastructure conditions • Diagnostic data 	<ul style="list-style-type: none"> • Planned versus actual maintenance frequency • Maintenance interval is adequate to maintain proper operational status • Incident and failure analysis 	<ul style="list-style-type: none"> • Adjustment of maintenance frequency • Adjustment of maintenance tasks or equipment to reduce workload, increase efficiency, and prevent failure • Additional training
Data processing and management	<ul style="list-style-type: none"> • System resource load (memory, CPU, disk space) • Latency between raw data collection and end-user availability • Data products (including metadata) 	<ul style="list-style-type: none"> • Adequacy of system resources • Data product availability and completeness meet requirements 	<ul style="list-style-type: none"> • Addition or adjustment of system resources • Implementation of automated workflow and workload managers
Post-field data quality	<ul style="list-style-type: none"> • Quality flags • User satisfaction surveys 	<ul style="list-style-type: none"> • Proportion of data marked as suspect • Manual/expert evaluation of test thresholds [3.148, 151] • User satisfaction 	<ul style="list-style-type: none"> • Adjustment of data products (Sect. 3.3.6) • Adjustment of quality test thresholds • Addition or modification of quality tests • Adjustment of sensors and/or maintenance protocols

Calibration records and field testing data provide periodic status reports for sensor accuracy and precision, including calibration drift. Analyzing these statistics over time facilitates evidence-based adjustment of calibration intervals to improve efficiency and minimize the need to correct for calibration drift after it has occurred. Analyzing calibration records also helps to identify sensors that are degrading or do not meet expected performance requirements, and leads to a better understanding of sensor lifetimes.

Maintenance performance monitoring relies on accurate logs, and is aided in particular by the use of standardized and machine-readable language in maintenance records. Maintenance intervals should be adjusted according to the sensor conditions noted during inspection. If a sensor is found to be dirty or misaligned every maintenance bout, the return interval may need to be shortened or the infrastructure may need adjusting.

Alternatively, if sensors are found to be operating optimally over multiple maintenance bouts, a less frequent return interval could be justified, as this could free up resources for other areas in need of attention. Incident and failure analysis should be implemented by associating maintenance and calibration activities and other sensor diagnostic data with incident and failure statistics in order to find the root causes, which can then be corrected.

It is also relatively straightforward to monitor processing systems provided that system load data are retained. Workflow and workload managers are especially helpful for coordinating recurring processing tasks and computational system resources, respectively.

Real-time or near-real-time monitoring of data quality metrics should be performed to trigger corrective action when quality drops below acceptable levels. Issues identified at this stage can result from problems at

any point in the data generation chain, making traceability paramount. It is important to know not only that a data point was flagged but also why it was flagged, and to be able to trace the data point through all previous interactions to the point of origin. Finally, the user community should be leveraged to evaluate whether overall quality and usability goals are being met (customer focus). This should include sending out surveys and implementing mechanisms for user feedback.

3.3.8 Audits

An audit is a systematic, independent, and documented process for obtaining audit evidence (verifiable records or statements of fact) and evaluating it objectively to determine the extent to which the audit criteria (a set of policies, procedures, or requirements) are fulfilled [3.152]. An audit is therefore not an examination situation. It is a process in which the audited entity can expect great benefit in the sense of real added value—at least when the laboratory and the auditor actively support this idea. Typically, audits are distinguished according to the status of the auditor (the person with the competence to conduct an audit).

The procedures referred to as *first-party audits* are usually carried out by an internal auditor, who is usually (but not necessarily) a trained laboratory member. In this case, only one party—the laboratory itself—is involved. Nevertheless, internal audits can also be carried out by external auditors, but only on the condition that another certifier is utilized for a possible certification audit. *Second-party audits* are procedures involving two parties. Here, one organization is auditing another with which it has (or is going to have) a contract or agreement to supply goods or services. In this case, the auditor is often the quality management representative of a laboratory. Finally, *third-party audits* can only be carried out by external auditors (independent third parties) who are approved for the underlying regulatory framework. This is the scenario for certification audits. Certification is the procedure by which a third party gives written assurance that a product, process, or service conforms to specified requirements.

An audit that takes place in the course of certification according to an ISO standard is subject to the ISO audit criteria. The requirements for bodies that provide auditing and certification of management systems are laid down by ISO/IEC 17021 [3.153], and the guidelines for auditing management systems are given in ISO 19011 [3.154]. Detailed information on the requirements for bodies that certify products, processes, and services is provided by ISO/IEC 17065 [3.155]. Finally, the process of accreditation is also based on an international standard: ISO 17011 [3.156].

Certification and Accreditation

The difference between accreditation and certification is that accreditation is the validation and recognition of professional competence for certain tasks, while certification confirms that certain requirements are being met.

Accreditation is the independent evaluation of a conformity assessment body against recognized standards for carrying out specific activities [3.157, 158]. Such an evaluation is performed to ensure the impartiality and competence of the body. Applying national and international standards increases the confidence of governments, procurers, and consumers in the calibration and test results, inspection reports, and certifications provided. Accreditation bodies are established in many countries, and their main role is to ensure that conformity assessment bodies are subject to oversight by an authoritative body. Once they have been peer evaluated as competent, accreditation bodies sign regional and international arrangements to demonstrate their competence. These accreditation bodies then assess and accredit conformity assessment bodies to the relevant standards.

The Competence of Testing and Calibration Laboratories

The general requirements for the competence of testing and calibration laboratories include the establishment of a management system [3.81]. A management system is a set of interrelated or interacting elements of an organization that establish policies and objectives as well as processes to achieve those objectives [3.159]. A quality management system for a testing and calibration laboratory specifies procedures (e.g., standard operating procedures for instrument maintenance and calibration, the corresponding documentation, and training of personnel) to assure the quality of the test and/or the calibration results. Furthermore, the laboratory should periodically, and in accordance with a predetermined schedule and procedure, conduct internal audits of its activities to verify that its operations continue to comply with the requirements of the management system. The internal audit program should address all elements of the management system, including the testing and/or calibration activities. Such audits should be carried out by trained and qualified personnel who are independent of the activity to be audited. The laboratory should continually improve the effectiveness of its management system through auditing and by implementing corrective as well as preventive actions. The cycle for internal auditing, which is commonly known as the plan–do–check–act (PDCA) cycle, should normally be completed in one year.

ISO/IEC 17025 provides detailed technical requirements for assessing the correctness and reliability of testing and/or calibration laboratories. Table 3.21 gives an overview of factors used in such assessments.

Table 3.21 Factors for assessing the correctness and reliability of tests and/or calibrations performed by a laboratory according to ISO/IEC 17025

Assessment factor	Key criteria
Human factor	<ul style="list-style-type: none"> • Competence of personnel • Education, training, experience of personnel • Supervision of personnel
Accommodation and environmental conditions	<ul style="list-style-type: none"> • Energy sources • Lighting • Environmental conditions
Test and calibration methods and method validation	<ul style="list-style-type: none"> • Appropriate methods and procedures for the sampling, handling, transport, storage, and preparation of items to be tested and/or calibrated • Appropriate methods and procedures for estimating the measurement uncertainty as well as statistical techniques for analyzing test and/or calibration data • SOPs for the equipment • Up-to-date instructions, standards, manuals, and reference data • Deviations from test and calibration methods must be documented, technically justified, authorized, and accepted by the data user
Equipment	<ul style="list-style-type: none"> • Equipment and software used for testing, calibration, and sampling should be capable of achieving the required accuracy and should comply with relevant specifications • Calibration programs should be established for key quantities
Measurement traceability	<ul style="list-style-type: none"> • Equipment calibration should be designed and performed such that the traceability of calibrations and measurements to SI is ensured
Sampling	<ul style="list-style-type: none"> • A sampling plan and procedures for sampling should be established
Handling of test and calibration items	<ul style="list-style-type: none"> • Procedures for transportation, receipt, handling protection, and storage should be established • Quality control procedures for monitoring the validity of tests and calibrations

3.4 Application

This section presents real-world applications of QA/QC in atmospheric measurements. First, Sect. 3.4.1 gives an overview of QA/QC approaches for meteorological measurement networks. After that, Sect. 3.4.2 discusses common data problems, including their origins and mitigation.

3.4.1 QA/QC Systems of Meteorological Measurement Networks

QA/QC systems are commonplace in meteorological measurement networks ranging from regional to federal to global scales. Basic commonalities include the implementation of both manual and automated tests as well as the utilization of both in-situ testing and post-field testing at central data centers. QA/QC systems mainly differ in cross-site standardization and the connectivity of quality planning and in-situ tests, as well as in the method employed for a particular test.

In general, bottom-up network management structures allow for increased flexibility and optimization of QA/QC procedures at the site level. The quality program is implemented and managed individually by each site, allowing procedures to be tailored to site-specific concerns. However, this approach can mean

that communicating detailed quality information along the entire data generation chain becomes a challenge. Examples of such networks are the Aerosol Robotic Network (AERONET) [3.160], AmeriFlux [3.131, 161], FLUXNET [3.162], ICOS [3.26], the Cooperative Observer Program (COOP) of the National Weather Service (NWS) [3.163], and the WMO Global Observing System [3.1]. Conversely, top-down network management—as employed at the ARM [3.164], NEON [3.27], NOAA [3.165], NRCS [3.166], and USGS [3.167] station networks—enables end-to-end standardization across locations with a unified quality program (see Chaps. 63 and 64). Table 3.22 summarizes the unique characteristics of bottom-up and top-down quality management approaches.

As an example of a bottom-up management structure, AmeriFlux manages the network-level standardization, QA/QC, and distribution of data collected and submitted by network members (Fig. 3.6). AmeriFlux provides QA/QC resources to the network; however, training, preventative maintenance, sensor calibration, sensor health monitoring, data aggregation and site-level QC are performed by the network members according to their individual requirements. Problem tracking and resolution transcends the member level;

Table 3.22 Unique characteristics of bottom-up and top-down quality management approaches

Characteristic	Bottom-up quality management	Top-down quality management
Standardization	<ul style="list-style-type: none"> • Flexibility and optimization of QA/QC procedures at the site level • Site-specific choice of method for a particular test 	<ul style="list-style-type: none"> • End-to-end standardization across sites within a unified quality program • Adaption to site level through functional relationships
Quality planning and implementation	<ul style="list-style-type: none"> • Network provides QA/QC resources • Network members manage and implement individual quality programs 	<ul style="list-style-type: none"> • End-to-end science operations management framework • Standardized quality program across sites
Problem tracking and resolution	<ul style="list-style-type: none"> • Semiautomated reporting of quality information along the data generation chain • Iterative data quality assessment between network level and network members 	<ul style="list-style-type: none"> • Electronic sensor health reporting by field personnel and automated software • Direct integration with supervised alert, issue management, and data flagging systems

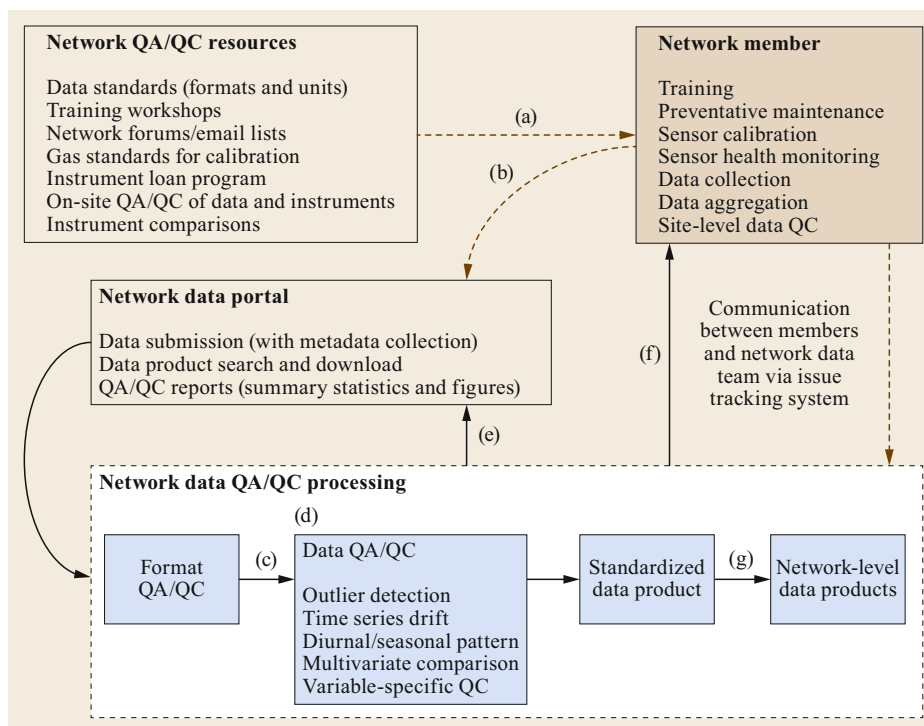


Fig. 3.6 Within the AmeriFlux data QA/QC framework, network members (a) voluntarily access network QA/QC resources and (b) upload data to the network in AmeriFlux standard data format. In the AmeriFlux data QA/QC processing pipeline, (c) automated format corrections are applied if necessary before (d) data QA/QC is applied to the entire data record. Results of QA/QC assessments are communicated to network members through (e) online summaries and reports as well as (f) via emails prompted by an issue tracking system. (g) Network-level data products are produced by applying standardized methods and QA/QC (e.g., data filtering and gap filling). Figure © Danielle Svehla Christianson, Lawrence Berkeley National Laboratory, with the support of the Office of Science, Office of Biological and Environmental Research of the US Department of Energy under contract no. DE-AC02-05CH11231 as part of the AmeriFlux Management Project

this requires semiautomated data processing at the network level that accommodates iterative solutions. Upon data submission, online results from data format checks are immediately available for network member review and correction. The data format assessment also in-

cludes an automated attempt to fix minor format errors. Next, automated network-level QA/QC is implemented to identify potentially erroneous data and communicate them online to members via easy-to-interpret graphics. Lastly, an issue-tracking system facilitates a problem

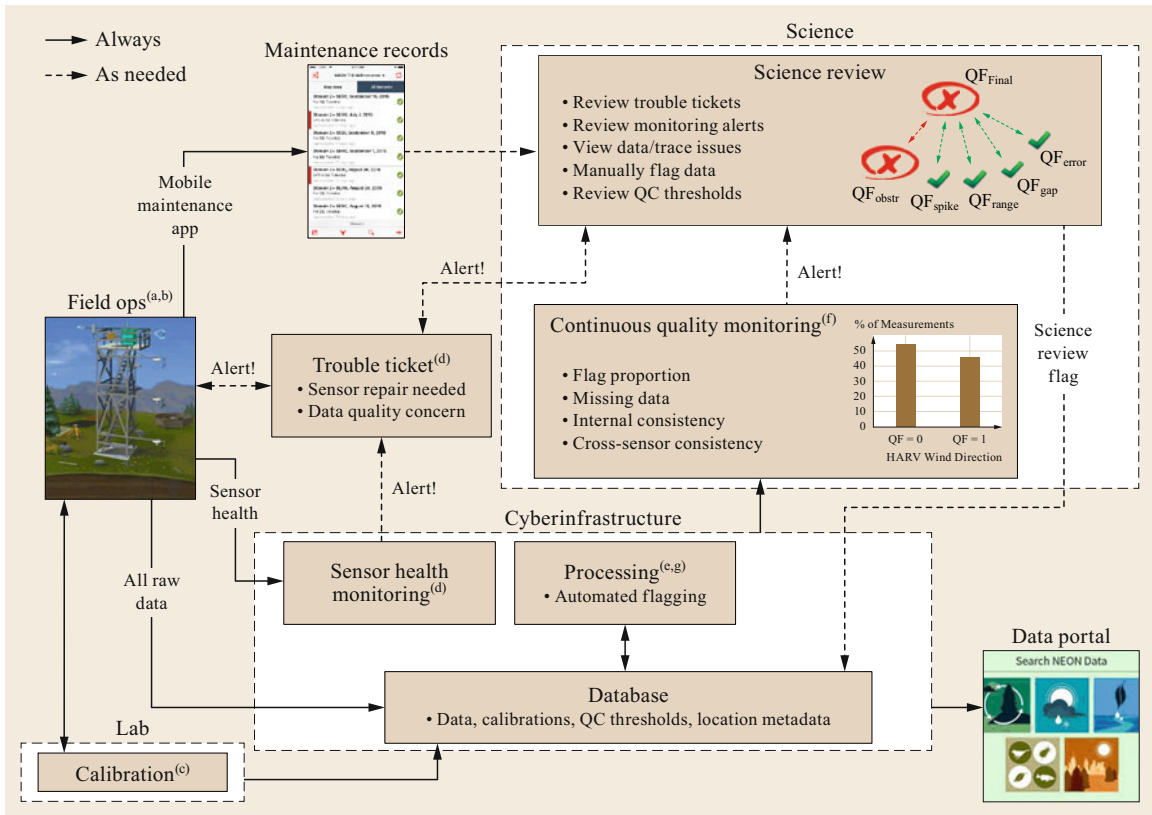


Fig. 3.7 The NEON science operations management framework for terrestrial instrument system quality assurance and quality control. The major components include (a) training, (b) preventive maintenance of sensors, (c) sensor calibration, (d) sensor health status monitoring, incident tracking and resolution, (e) data processing, (f) continuous data quality monitoring, and (g) data revising. Figure © National Ecological Observatory Network, Battelle

tracking and resolution process between the network-level data processing team and its individual members [3.168].

As an example of a top-down management structure, NEON's tight design integration and standardization enables an integrated, end-to-end science operations management framework for the QA/QC of terrestrial instrument systems (Fig. 3.7). This begins with sensor maintenance training, which is provided via curriculum lesson plans and hands-on demonstrations by qualified NEON staff. Preventative maintenance is then performed biweekly according to procedures developed by the NEON science and engineering departments; maintenance findings are recorded electronically on a mobile application. Most sensors are rotated out of the field at specified intervals and passed to the NEON Calibration and Validation Laboratory, where calibration is performed to traceable national and international standards (e.g., ITS-90 for temperature measurements). Sensor health is monitored by field personnel as well as re-

motely through software that interfaces directly with the data acquisition system at each site. An automated alert system monitors sensor health in near-real-time and issues are tracked in NEON's issue management system upon actual or impending sensor malfunction. Automated quality tests are applied during processing and are used to remove and/or flag suspect values. Continuous quality monitoring identifies potentially erroneous data patterns. Trouble tickets and data marked as suspect undergo scientific review for problem tracking and resolution and to ultimately accept or reject the data.

3.4.2 Common Data Problems

This section presents visual examples of common data problems, along with their causes and methods of avoiding or correcting them. In all cases, detecting these problems requires routine inspection of data and sensors, performance monitoring, and post-field quality control tests.

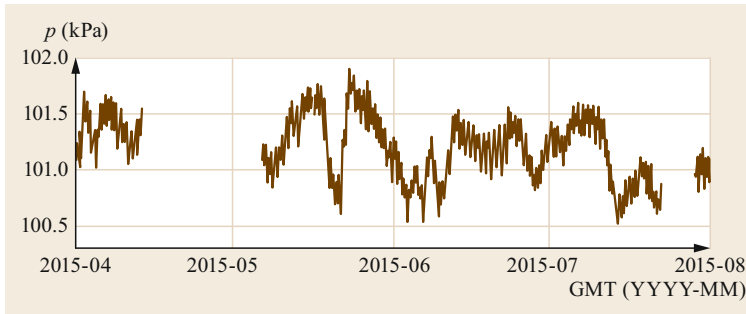


Fig. 3.8 Gaps in barometric pressure measurement due to datalogger failures (after [3.169])

Data Dropouts

Data dropouts (periods of missing data) are pervasive in atmospheric measurements since there are numerous potential causes of measurement failure, including a sensor malfunction, power failure, or the failure of a critical system component. Figure 3.8 presents an example of data loss due to datalogger failures. Data dropouts can also manifest as periods of constant sensor output, also known as a *stuck sensor*, which can be detected during postprocessing by testing for unusually low variation in data values [3.22].

Although it is difficult to completely eliminate data gaps, they can be minimized by performing near-real-time monitoring of data streams and regular preventative maintenance of sensors and infrastructure, as well as by planning for redundancy (of the power supply, instrumentation, and other critical system components). Correcting for data dropouts involves filling the data gap with suitable alternative measurements, such as those from a nearby or redundant sensor or values imputed from a statistical model. Thankfully, there are many general and measurement-specific gap-filling methods that can be applied to address this problem [3.171–175]. Any gap-filled values in the final dataset must be clearly marked.

Quantification Error

One type of error that is relevant to older instruments, mainly those in which the signal is measured in only a small part of the measuring range, is the quantification or digitization error [3.176]. Older instruments digitized the measuring range to only 12 bit, leading to $2^{12} = 4096$ possible values, whereas newer instruments digitize the measuring range to at least 16 bit ($2^{16} = 65\,536$). The use of 12 bit digitization can be problematic for temperature measurements and gas analyzers, where the measuring range is large and the range of the measured signal is small [3.139, 170], as demonstrated by the example shown in Fig. 3.9.

The deviation of the digitized data from the original data may be significant if the signal variation is small. Simulation tests should be made with an instrument with better resolution, to determine the impact of digitization on the intended data use and under which conditions the error may be significant. This is generally only an issue with some older datasets. Old instruments or data acquisition systems should therefore be replaced or the measurement range of the instrument should be reduced to the possible range of the signal.

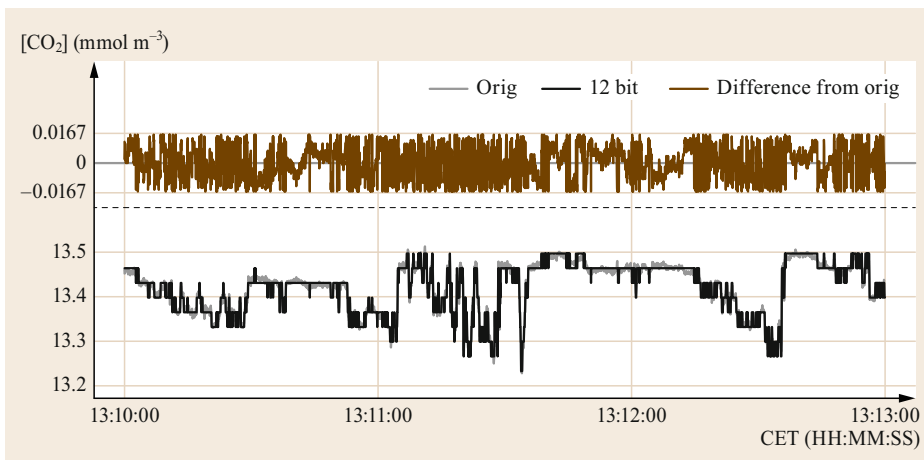


Fig. 3.9 Carbon dioxide concentration data obtained with a LI-COR 7500 instrument (orig) and then reduced to 12 bit resolution (after [3.170], © the authors)

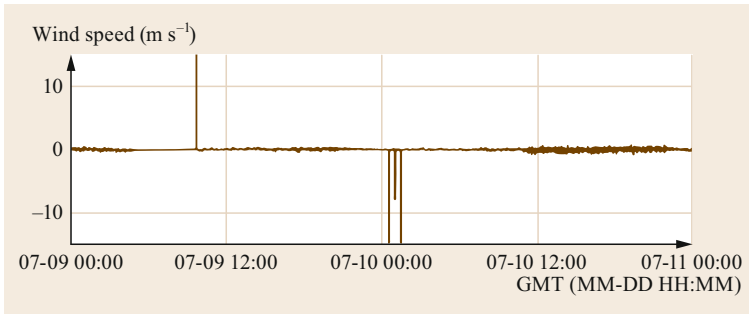


Fig. 3.10 Spikes of no known cause recorded in 1 Hz measurements of wind speed (v -vector component) by a Gill Wind Observer II 2-D sonic anemometer. The raw sensor data were obtained from the National Ecological Observatory Network

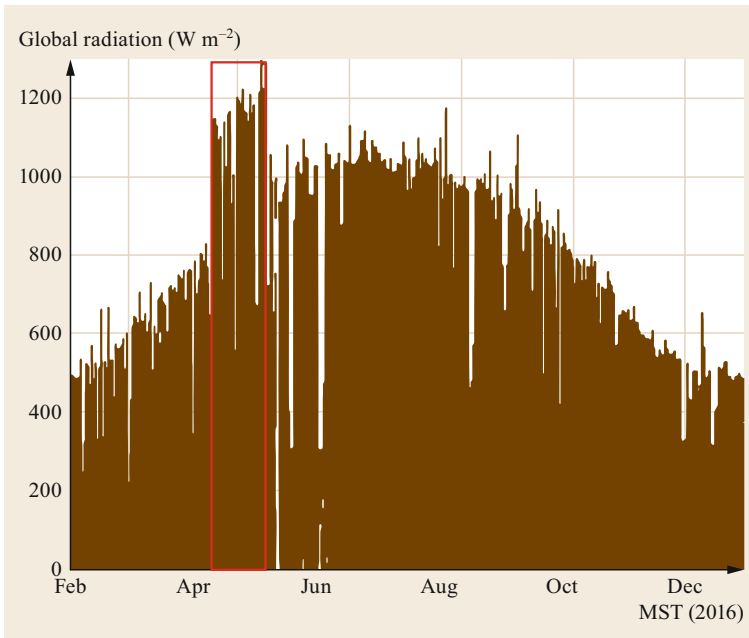


Fig. 3.11 Level shift in global radiation measurements (outlined in red) caused by changes in sensor calibration (after [3.169])

Spikes

Spikes are sudden and excessive changes in data value. An example is shown in Fig. 3.10. Spikes can seem to occur at random with no known cause, although a poor electrical connection or momentary measurement interference from the environment is often to blame. Regular preventative maintenance and inspection of sensors and infrastructure can reduce the likelihood of spikes, as can implementing methods to deter known sources of interference from the environment, such as birds or insects. If deterrents are used, it is important to evaluate their impact on the measurements to ensure that measurement integrity is not compromised. Even so, spikes are hard to avoid, so they are commonly removed during postprocessing using despiking algorithms or other QC tests (see Sect. 3.3.6).

Data Shifts

One problem commonly encountered in long-term measurement programs is an abrupt change in the data value level. An example of this is provided in Fig. 3.11. Data shifts are usually due to changes in calibration or instrumentation that occur when sensors are recalibrated or replaced due to damage or wear. Data shifts can also arise from an unplanned sensor movement leading to measurements of a different target, or after the sensor has been cleaned following a long interval of missed maintenance when the sensor was fouled. Data shifts can also occur more gradually over time rather than abruptly, as in the case of calibration drift. This common problem highlights the benefits of regular preventative maintenance and cleaning of sensors as well as adhering to a calibration frequency that minimizes drift.

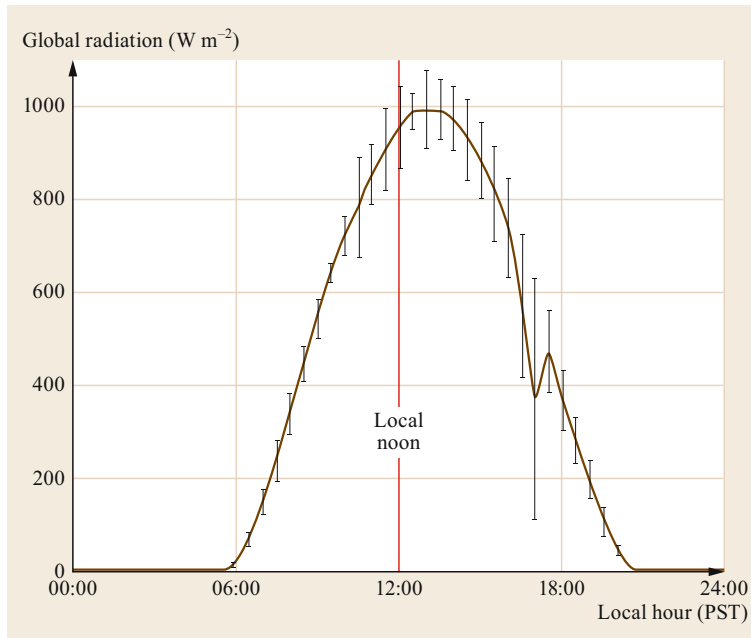


Fig. 3.12 Approximately one month of diel average global radiation measurements at Twitchell Island, CA, showing improper time zone application as well as shadowing of the sensor by site infrastructure in the afternoon. Error bars indicate standard deviations

Data shifts can be corrected for using statistical methods such as the pairwise comparison approach [3.99], by back-correcting for calibration drift [3.177], or by developing a regression based on a period of overlapping measurements for planned changes in instrumentation. In all cases, it is important to ascertain the reason for the data shift, as some may result from true changes in the measured quantity, such as the impact of a change in surface albedo on net radiation measurements [3.131]. For this reason, it is imperative to collect complete, accurate, and accessible records of sensor maintenance and calibration.

Time Shifts

An error that is common but easily corrected for in atmospheric measurements is a time shift, where data patterns are shifted in time with respect to theoretical expectations. It is easy to visualize this error by plotting radiation measurements according to time of day in local standard time, as in Fig. 3.12, where the long-term diel average should show a peak near noon. This error results from the incorrect application of a time zone offset during processing or incorrect time settings in internal instrument computers or dataloggers. However, it is more difficult to detect this error in measurements that do not have an expected temporal pattern. In this case, real-time checks of measurement timestamps should be performed during data collection. To correct for this error, the offset between the actual and the intended time zone of measurement must be determined and applied. Avoiding this error is a simple matter of

ensuring that the time settings of instrumentation and processing algorithms are correct.

Infrastructure Interference

Infrastructure interference is a pernicious error in atmospheric measurements; avoidance of this error requires careful site planning and configuration, and detection requires close scrutiny of the data. It is crucial to avoid this error as it is often impossible to correct for afterwards. Figure 3.12 shows an example of infrastructure interference with global radiation measurements in which the sensor was shadowed by infrastructure in the afternoon. This type of error can only be corrected for if the magnitude, pattern, and timing of the effect can be determined. Otherwise, the affected data must be removed or flagged as suspect. Better yet, proper site planning and configuration (see Sect. 3.3.2) should involve performing data collection tests before the experiment to ensure that measurements will not be significantly impacted by the measurement platform itself.

Internal/Theoretical Inconsistency

Data processing code and algorithms are often written specifically for the measurement program at hand and by the scientists who are also busy running the project. As such, errors in algorithms are common but can be identified and corrected through a program of software testing (see Sect. 3.3.5) that includes checks for violations of internal (including unit) consistency and mathematical and atmospheric theory. An example of this type of error is shown in Fig. 3.13, where a coding error

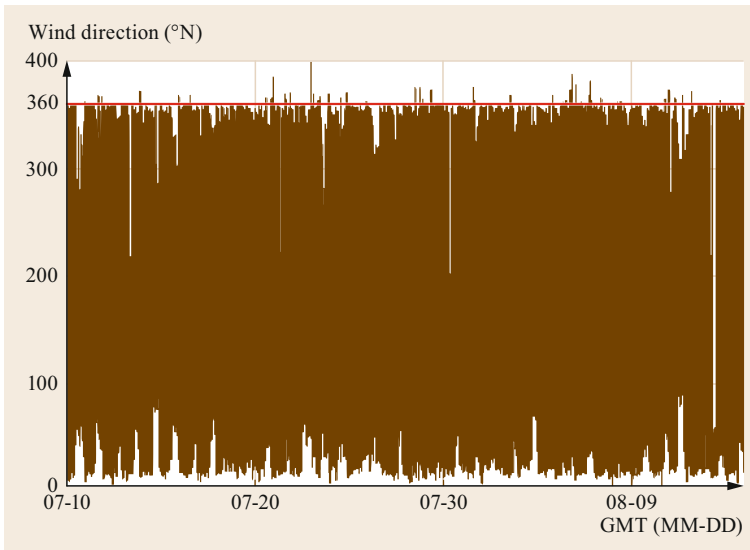


Fig. 3.13 Erroneously calculated wind direction data based on measured vector components of a 2-D sonic anemometer; note that some of the data values are beyond the theoretical limit of 360° N (after [3.169])

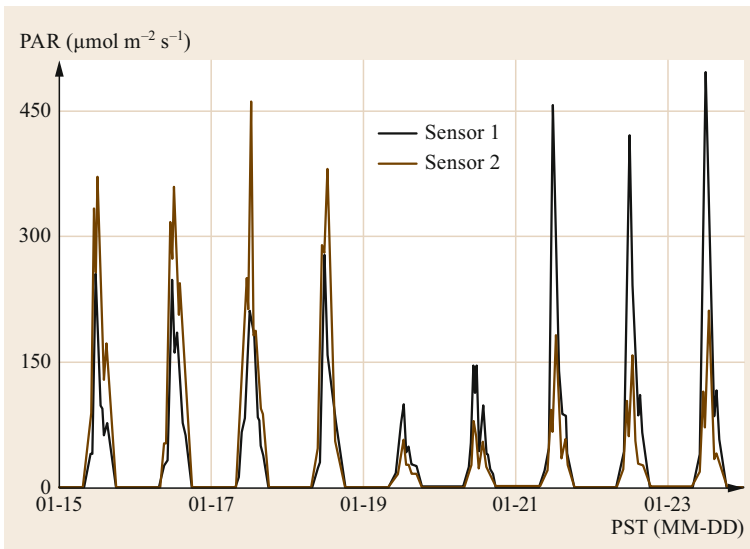


Fig. 3.14 Change in the relationship between two ground-based PAR sensors after sensor 2 was covered in dirt by fire-prevention activities on 18 January (after [3.169])

led to calculated wind directions outside the expected range of 0–360° N. Thankfully, processing errors can be mitigated by correcting the algorithm and reprocessing the data. The versions of the code and data should be incremented if the errors are discovered after release. Because computational errors of this nature are quite common, it is vitally important to retain the raw data in a form that is as close as possible to the original sensor readings.

Field Interference

Field interference includes a broad array of data problems resulting from the random interference of the natural environment or human factors with a measure-

ment. An example of this type of error is shown in Fig. 3.14, where fire prevention activities covered an understory photosynthetically active radiation (PAR) sensor with dirt, causing attenuation of the measurements. Such errors can be caused by any number of factors, are difficult to avoid, and are often difficult to detect with automated quality tests, making it imperative to frequently and diligently inspect the measurement conditions, as this can reduce the amount of data affected by field interference. Thorough maintenance records and photographs of the conditions at the site can help to narrow the time interval that must be considered when determining the data to remove or flag as suspect.

3.5 Future Developments

Some likely future developments in the area of QA/QC for atmospheric measurements include progress through the introduction of new technologies as well as the resolution of theoretical challenges associated with scientific software testing.

3.5.1 Machine Learning

The potential widespread use of machine learning techniques such as neural networks, Bayesian networks, random forests, and support vector machines in QA/QC of atmospheric and environmental sensor measurements shows considerable promise. These techniques are powerful because they require very little prior knowledge of sensor measurement theoretical basis and characteristics, and they do not require assumptions about functional relationships. Instead, they empirically identify patterns and dependencies based on the data alone. Examples of machine learning approaches in QA/QC include the quality control of sensor data, error analysis, and calibration. These are briefly described below.

Two main machine learning approaches have been used for the automated detection of outliers and/or the assignment of quality flags in environmental sensor data. The first approach constructs a model for the expected output and defines measurements that fall outside prediction bounds to be errors [3.178, 179]. The second approach directly classifies trustworthy or suspect data [3.180]. However, both approaches involve some challenges during application. Attention must be paid to the settings of the algorithm to avoid overfitting and thus maintain sufficient generalization for the algorithm to work well with new, previously unobserved data. In addition, data must be split into training and testing sets. For the latter approach (direct classification), this requires prior knowledge (and enough examples) of data anomalies to be successful. Though it is already recognized to be a powerful tool for quality control, addressing these issues would likely expand the use of machine learning in data QC.

Another area where machine learning is improving the quality of atmospheric measurements is in the quantification of systematic errors. Even when machine learning is not used, post-field corrections are commonly performed for some systematic effects, such as a height correction for measured wind speeds or a correction for wind-induced errors in data from precipitation gauges [3.3]. Treatments of other systematic observation effects are often more limited, such as linking measurements that represent different source areas with each other (Sect. 3.3.2) or with models [3.181].

Therefore, as an example, eddy-covariance flux observations are subject to transient location bias [3.41, 182] on the order of tens of percent—an order of magnitude larger than typical sensor errors. Here, machine learning concepts can improve our understanding of measurement techniques and environmental processes by extracting new information from joining observations. For example, through explicit point-to-area projections over heterogeneous surfaces, the environmental response function (ERF [3.60]) technique can combine the spatial coverages of different measurements into a joint target area. At the technical level, ERF complements existing mathematical descriptions of better-understood processes such as sensor functioning and atmospheric dispersion with observations from towers, aircraft, and satellites about less-understood phenomena. It then mines the joint information content, yielding the most complete solution possible based on the processes and observations provided.

Finally, one published example has shown the power of machine learning to resolve difficult calibration situations. The use of random forests has improved calibration models for low-cost air quality monitoring instrumentation, which was previously difficult to achieve using traditional laboratory procedures [3.65].

3.5.2 The Oracle Problem in Scientific Software Testing

A challenge specific to scientific software development is the lack of an *oracle* for testing. An oracle is an expected result that is used to verify the output of the software. Determining an oracle for scientific software is often difficult or impossible in applications in which (i) the software is developed in order to find as-yet unknown answers, (ii) the software tests a scientific theory and involves complex computations, (iii) uncertainty in the model prevents it from yielding a single answer for a specific set of inputs, (iv) the software is exploratory in nature, or (v) complex floating point operations are involved, making it difficult to select oracle tolerances [3.108]. As reviewed in [3.108], several studies have proposed methods to address this challenge, including the development of a *pseudo oracle*, which is independently developed software that produces the same output. Other techniques include comparing the output with analytically derived or experimental results, the use of simplified data, and the application of expert knowledge. However, more research is needed to thoroughly evaluate the efficacies of these and other emerging methods at detecting software errors without an oracle [3.108].

3.6 Further Reading

For a reference guide to quality management tools that are generally applicable in many fields and industries, see:

- N.R. Tague: *Quality Toolbox*, 2nd edition (ASQ Quality Press, Milwaukee 2005)

The following resources provide further details on quality assurance and quality control of atmospheric measurements:

- WMO: *Guide to Instruments and Methods of Observation*, WMO-No. 8, Volume I - Measurement of Meteorological Variables. (World Meteorological Organization, Geneva, 2018)
- VDI: *Umweltmeteorologie, Meteorologische Messungen, Grundlagen* (Environmental Meteorology, Meteorological Measurements, Fundamentals, in German and English), VDI 3786 Blatt (Part) 1 (Beuth, Berlin 2013)

References

- 3.1 WMO: *Guide to the Global Observing System*, WMO-No. 488 (World Meteorological Organization, Geneva 2010)
- 3.2 R.Y. Wang, D.M. Strong: Beyond accuracy: What data quality means to data consumers, *J. Manag. Inf. Syst.* **12**, 5–33 (1996)
- 3.3 VDI: *Environmental Meteorology – Meteorological Measurements – Fundamentals*, VDI 3786 Part 1 (Beuth, Berlin 2013)
- 3.4 ISO: *Quality Management Systems – Fundamentals and Vocabulary*, ISO 9000 (International Organization for Standardization, Geneva 2015)
- 3.5 ISO: *Quality Management Systems – Requirements*, ISO 9001 (International Organization for Standardization, Geneva 2015)
- 3.6 J.A. Kington: The Societas Meteorologica Palatina: An eighteenth-century meteorological society, *Weather* **29**, 416–426 (1974)
- 3.7 N. Westcott: *Quality Control of 19th Century Weather Data* (Midwestern Regional Climate Center, Champaign 2011)
- 3.8 WMO: *Guide to the Implementation of a Quality Management System for National Meteorological and Hydrological Services*, WMO-No. 1100 (World Meteorological Organization, Geneva 2013)
- 3.9 NIST/Sematech: *e-Handbook of Statistical Methods* (2013). <http://www.itl.nist.gov/div898/handbook/>, Accessed 06 July 2021
- 3.10 W.A. Shewhart: Finding causes of quality variations, *Manuf. Ind.* **11**, 125–128 (1926)
- 3.11 WMO: *Guide to Instruments and Methods of Observation*, WMO-No. 8, Volume I – Measurement of Meteorological Variables (World Meteorological Organization, Geneva 2018)
- 3.12 WMO: *Commission for Instruments and Methods of Observation (CI MO) – Abridged Final Report of the Seventh Session*, WMO-No. 490 (World Meteorological Organization, Geneva 1977)
- 3.13 F. Kasten: Maintenance, calibration and comparison, *Instrum. Obs. Methods Rep.* **23**(WMO/TD 51), 65–84 (1985)
- 3.14 H. Gilgen, C.H. Whitlock, F. Koch, G. Müller, A. Ohmura, D. Steiger, R. Wheeler: *Technical Plan for BSRN Data Management, World Radiation Monitoring Centre (WRMC)*, Technical Report 1, 1994) p. 56
- 3.15 A. Ohmura, E.G. Dutton, B. Forgan, C. Fröhlich, H. Gilgen, H. Hegner, A. Heimo, G. König-Langlo, B. McArthur, G. Müller, R. Philipona, R. Pinker, C.H. Whitlock, K. Dehne, M. Wild: Baseline surface radiation network (BSRN/WCRP): new precision radiometry for climate research, *Bull. Am. Meteorol. Soc.* **79**, 2115–2136 (1998)
- 3.16 T. Foken, S.P. Oncley: Results of the workshop 'Instrumental and Methodical Problems of Land Surface Flux Measurements', *Bull. Am. Meteorol. Soc.* **76**, 1191–1193 (1995)
- 3.17 L.E. Wood: Automatic weather stations, *J. Meteor.* **3**, 115–121 (1946)
- 3.18 WMO: *Manual on Codes*, WMO-No. 306 (World Meteorological Organization, Geneva 2011)
- 3.19 R.S. Leavenworth, E.L. Grant: *Statistical Quality Control* (Tata McGraw-Hill Education, Boston 2000)
- 3.20 D.Y. Graybeal, A.T. DeGaetano, K.L. Eggleston: Improved quality assurance for historical hourly temperature and humidity: development and application to environmental analysis, *J. Appl. Meteorol. Climatol.* **43**, 1722–1735 (2004)
- 3.21 D.W. Meek, J.L. Hatfield: Data quality checking for single station meteorological databases, *Agric. For. Meteorol.* **69**, 85–109 (1994)
- 3.22 K.G. Hubbard, S. Goddard, W.D. Sorensen, N. Wells, T.T. Osugi: Performance of quality assurance procedures for an applied climate information system, *J. Atmos. Ocean. Technol.* **22**, 105–112 (2005)
- 3.23 L.S. Gandin: Complex quality control of meteorological observations, *Mon. Weather Rev.* **116**, 1137–1156 (1988)
- 3.24 R.E. Eskridge, O.A. Alduchov, I.V. Chernykh, Z. Pan-mao, A.C. Polansky, S.R. Doty: A comprehensive aerological reference data set (CARDS): Rough and systematic errors, *Bull. Am. Meteorol. Soc.* **76**, 1759–1776 (1995)
- 3.25 J.L. Campbell, L.E. Rustad, J.H. Porter, J.R. Taylor, E.W. Dereszynski, J.B. Shanley, C. Gries, D.L. Henshaw, M.E. Martin, W.M. Sheldon, E.R. Boose: Quantity is nothing without quality: Automated QA/QC for streaming sensor networks, *BioScience* **63**(7), 574–585 (2013)
- 3.26 D. Franz, M. Acosta, N. Altimir, N. Arriga, D. Arrouays, M. Aubinet, M. Aurela, E. Ayres, A. López-

- Ballesteros, M. Barbaste, D. Berveiller, S. Biraud, H. Boukir, T. Brown, C. Brümmer, N. Buchmann, G. Burba, A. Carrara, A. Cescaati, E. Ceschia, R. Clement, E. Cremonese, P. Crill, E. Darenova, S. Dengel, P. D'Odorico, G. Filippa, S. Fleck, G. Fratini, R. Fuß, B. Gielen, S. Gogo, J. Grace, A. Graf, A. Grelle, P. Gross, T. Grünwald, S. Haapanala, M. Hehn, B. Heinesch, J. Heiskanen, M. Herbst, C. Herschlein, L. Hörtnagl, K. Hufkens, A. Ibrom, C. Jolivet, L. Joly, M. Jones, R. Kiese, L. Klemedtsson, N. Kljun, K. Klumpp, P. Kolari, O. Kolle, A. Kowalski, W. Kutsch, T. Laurila, A. de Ligne, S. Linder, A. Lindroth, A. Lohila, B. Longdoz, I. Mammarella, T. Manise, S.M. Jiménez, G. Matteucci, M. Mauder, P. Meier, L. Merbold, S. Mereu, S. Metzger, M. Migliavacca, M. Mölder, L. Montagnani, C. Moureaux, D. Nelson, E. Nemitz, G. Nicolini, M.B. Nilsson, M.O. de Beeck, B. Osborne, M.O. Löfvenius, M. Pavelka, M. Peichl, O. Peltola, M. Pihlatie, A. Pitacco, R. Pokorný, J. Pumpanen, C. Ratié, C. Rebmann, M. Roland, S. Sabbatini, N.P.A. Saby, M. Saunders, H.P. Schmid, M. Schrumpf, P. Sedláč, P.S. Ortiz, L. Siebicke, L. Šigut, H. Silvennoinen, G. Simioni, U. Skiba, O. Sonnentag, K. Soudani, P. Soulé, R. Steinbrecher, T. Tallec, A. Thimonier, E.–S. Tuittila, J.–P. Tuovinen, P. Vestin, G. Vincent, C. Vincke, D. Vitale, P. Waldner, P. Weslien, L. Wingate, G. Wohlfahrt, M. Zahniser, T. Vesala: Towards long-term standardised carbon and greenhouse gas observations for monitoring Europe's terrestrial ecosystems: A review, *Int. Agrophys.* **32**, 439–455 (2018)
- 3.27 S. Metzger, E. Ayres, D. Durden, C. Florian, R. Lee, C. Lunch, H. Luo, N. Pingintha–Durden, J.A. Roberti, M. SanClements, C. Sturtevant, K. Xu, R. Zulueta: From NEON field sites to data portal: A community resource for surface–atmosphere research comes online, *Bull. Am. Meteorol. Soc.* **100**(11), 2305–2325 (2019)
- 3.28 D. Baldocchi, E. Falge, L.H. Gu, R. Olson, D. Hollinger, S. Running, P. Anthony, C. Bernhofer, K. Davis, R. Evans, J. Fuentes, A. Goldstein, G. Katul, B. Law, X.H. Lee, Y. Malhi, T. Meyers, W. Munger, W. Oechel, K.T. Paw U, K. Pilegaard, H.P. Schmid, R. Valentini, S. Verma, T. Vesala, K. Wilson, S. Wofsy: FLUXNET: A new tool to study the temporal and spatial variability of ecosystem-scale carbon dioxide, water vapor, and energy flux densities, *Bull. Am. Meteorol. Soc.* **82**, 2415–2434 (2001)
- 3.29 C.R. Schwalm, C.A. Williams, K. Schaefer, A. Arneeth, D. Bonal, N. Buchmann, J. Chen, B. Law, A. Lindroth, S. Luyssaert, M. Reichstein, A.D. Richardson: Assimilation exceeds respiration sensitivity to drought: A FLUXNET synthesis, *Glob. Chang. Biol.* **16**, 657–670 (2010)
- 3.30 WMO: *WMO Global Atmosphere Watch (GAW) Implementation Plan: 2016–2023*, GAW Report–No. 228 (World Meteorological Organization, Geneva 2017)
- 3.31 A.S.H. Prevot, D. Simpson, M. Sutton, H.C. Hansson, M.E. Beekmann: *EMEP – An Integrated System of Models and Observations in Support of European Air Quality and Policy*, Atmospheric Chemistry and Physics Special Issue (Copernicus, Göttingen 2009)
- 3.32 Bridging the Gap: *How to Write a Use Case* (2018). <http://www.bridging-the-gap.com/what-is-a-use-case/>, Accessed 03 July 2021
- 3.33 ISO: *Information Technology – A Code of Practice for the Use of Information Technology (IT) in the Delivery of Assessments*, ISO/IEC 23988:2007 (International Organization for Standardization, Geneva 2007)
- 3.34 ISO: *Air Quality – Guidelines for Estimating Measurement Uncertainty*, ISO 20988:2007 (International Organization for Standardization, Geneva 2007)
- 3.35 ISO: *Environmental Management – Life Cycle Assessment – Requirements and Guidelines*, ISO 14044:2006 (International Organization for Standardization, Geneva 2006)
- 3.36 H. Wan, X. Zhang, W. Zwiars Francis, H. Shioyama: Effect of data coverage on the estimation of mean and variability of precipitation at global and regional scales, *J. Geophys. Res. Atmos.* **118**, 534–546 (2013)
- 3.37 ISO: *Health Informatics – Privilege Management and Access Control – Part 1: Overview and Policy Management*, ISO 22600–1:2014 (International Organization for Standardization, Geneva 2014)
- 3.38 ISO: *Soil Quality – Vocabulary*, ISO 11074:2015 (International Organization for Standardization, Geneva 2015)
- 3.39 Three Rivers District Council: *Three Rivers District Council Data Quality Strategy* (Three Rivers District Council, Rickmansworth 2008)
- 3.40 ISO: *Information Technology – Systems and Software Engineering – Application Management*, ISO/IEC 16350:2015 (International Organization for Standardization, Geneva 2015)
- 3.41 C.J. Nappo, J.Y. Caneill, R.W. Furman, F.A. Gifford, J.C. Kaimal, M.L. Kramer, T.J. Lockhart, M.M. Pendergast, R.A. Pielke, D. Randerson, J.H. Shreffler, J.C. Wyngaard: The workshop on the representativeness of meteorological observations, June 1981, Boulder, Colorado, *Bull. Am. Meteorol. Soc.* **63**, 761–764 (1982)
- 3.42 ISO: *Accuracy (Trueness and Precision) of Measurement Methods and Results – Part 1: General Principles and Definitions*, ISO 5725–1:1994 (International Organization for Standardization, Geneva 1994)
- 3.43 J.R. Taylor, E.R. Cohen: An introduction to error analysis: The study of uncertainties in physical measurements, *Meas. Sci. Technol.* **9**, 1015 (1998)
- 3.44 ISO: *Workplace Air – Terminology*, ISO 18158:2016 (International Organization for Standardization, Geneva 2016)
- 3.45 ISO: *Water Quality – Determination of Selected Elements by Inductively Coupled Plasma Optical Emission Spectrometry (ICP–OES)*, ISO 11885:2007 (International Organization for Standardization, Geneva 2007)
- 3.46 JGCM: *Evaluation of Measurement Data – Guide to the Expression of Uncertainty in Measurement*,

- JCGM 100:2008 (Joint Committee for Guides in Metrology, Sèvres 2008)
- 3.47 ISO: *Air Quality – Environmental Meteorology – Part 1: Ground-Based Remote Sensing of Visual Range by lidar*, ISO 28902-1:2012 (International Organization for Standardization, Geneva 2012)
- 3.48 J.G. Webster: *The Measurement, Instrumentation and Sensors Handbook* (CRC Press, Boca Raton 1998)
- 3.49 ISO: *Air Quality – Definition and Determination of Performance Characteristics of an Automatic Measuring System*, ISO 9169:2006 (International Organization for Standardization, Geneva 2006)
- 3.50 K.J. Brockmann, V. Kriesche, T. Etzkom, R. Volkamer, K. Wirtz: The European photoreactor EUPHORE: A technical description. In: *Proc. EUROTRAC Symp.* (1996) pp. 457–461
- 3.51 F. Rohrer, B. Bohn, T. Brauers, D. Brüning, F.J. Johnen, A. Wahner, J. Kleffmann: Characterisation of the photolytic HONO-source in the atmosphere simulation chamber SAPHIR, *Atmos. Chem. Phys.* **5**, 2189–2201 (2005)
- 3.52 D. Heard: *Analytical Techniques for Atmospheric Measurement* (Wiley-Blackwell, Oxford 2009)
- 3.53 B.J. Finlayson-Pitts, J.N. Pitts Jr.: *Chemistry of the Upper and Lower Atmosphere: Theory, Experiments, and Applications* (Academic Press, San Diego 1999)
- 3.54 C.C. Hoerger, A. Claude, C. Plass-Duelmer, S. Reimann, E. Eckart, R. Steinbrecher, J. Aalto, J. Arduini, N. Bonnaire, J.N. Cape, A. Colomb, R. Connolly, J. Diskova, P. Dumitrean, C. Ehlers, V. Gros, H. Hakola, M. Hill, J.R. Hopkins, J. Jäger, R. Junek, M.K. Kajos, D. Klemp, M. Leuchner, A.C. Lewis, N. Locoge, M. Malone, D. Martin, K. Michl, E. Nemitz, S. O’Doherty, P.P. Ballesta, T.M. Ruuskanen, S. Sauvage, N. Schmidbauer, T.G. Spain, E. Straube, M. Vana, M.K. Vollmer, R. Wegener, A. Wenger: ACTRIS non-methane hydrocarbon intercomparison experiment in Europe to support WMO GAW and EMEP observation networks, *Atmos. Meas. Tech.* **8**, 2715–2736 (2015)
- 3.55 S. Janssen, C. Guerreiro, P. Viaene, E. Georgieva, P. Thunis: *Guidance Document on Modelling Quality Objectives and Benchmarking, Version 2.1* (Fairmode, Ispra 2017)
- 3.56 European Union: Directive 2008/50/EC of the European Parliament and of the Council of 21 May 2008 on ambient air quality and cleaner air for Europe, *Off. J. Eur. Union* **152**, 1–44 (2008)
- 3.57 WHO: *WHO Air Quality Guidelines for Particulate Matter, Ozone, Nitrogen Dioxide and Sulphur Dioxide. Global Update 2005. Summary of Risk Assessment* (World Health Organization, Geneva 2005)
- 3.58 VDI: *Environmental Meteorology – Quality Assurance of Meteorological Data for Dispersion Modelling According to TA Luft and GIRL*, VDI 3783 Part 21 (Beuth, Berlin 2017)
- 3.59 M. Saunders, S. Dengel, P. Kolari, C. Moureaux, L. Montagnani, E. Ceschia, N. Altimir, A. López-Ballesteros, S. Marañón-Jimenez, M. Acosta, K. Klumpp, B. Gielen, M.O. de Beeck, L. Hörtnagl, L. Merbold, B. Osborne, T. Grünwald, D. Arrouays, H. Boukir, N. Saby, G. Nicolini, D. Papale, M. Jones: Importance of reporting ancillary site characteristics, and management and disturbance information at ICOS stations, *Int. Agrophys.* **32**, 457–469 (2018)
- 3.60 S. Metzger: Surface–atmosphere exchange in a box: Making the control volume a suitable representation for in-situ observations, *Agric. For. Meteorol.* **255**, 68–80 (2018)
- 3.61 M.Y. Leclerc, T. Foken: *Footprints in Micrometeorology and Ecology* (Springer, Berlin, Heidelberg 2014)
- 3.62 G.T. Bromley, D. Durden, E. Ayres, D. Barnett, R. Krauss, H. Luo, C.L. Meier, S. Metzger: Optimizing collocation of instrument measurements and field sampling activities, *AGU Fall Meet. Abstr.* **33**, B33A-0628 (2015)
- 3.63 WMO: *Guide on the Global Data-Processing System (GDPS)*, WMO-No. 305 (World Meteorological Organization, Geneva 1993)
- 3.64 C. Rebmann, M. Aubinet, H. Schmid, N. Arriga, M. Aurela, G. Burba, R. Clement, A. De Ligne, G. Fratini, B. Gielen, J. Grace, A. Graf, P. Gross, S. Haapanala, M. Herbst, L. Hörtnagl, A. Ibrom, L. Joly, N. Kljun, O. Kolle, A. Kowalski, A. Lindroth, D. Loustau, I. Mammarella, M. Mauder, L. Merbold, S. Metzger, M. Mölder, L. Montagnani, D. Papale, M. Pavelka, M. Peichl, M. Roland, P. Serrano-Ortiz, L. Siebicke, R. Steinbrecher, J.-P. Tuovinen, T. Vesala, G. Wohlfahrt, D. Franz: ICOS eddy covariance flux-station site setup: A review, *Int. Agrophys.* **32**, 471–494 (2018)
- 3.65 N. Zimmerman, A.A. Presto, S.P.N. Kumar, J. Gu, A. Haurlyliuk, E.S. Robinson, A.L. Robinson, R. Subramanian: A machine learning calibration model using random forests to improve sensor performance for lower-cost air quality monitoring, *Atmos. Meas. Tech.* **11**, 291–313 (2018)
- 3.66 WMO: *Guide to Climatological Practices*, WMO-No. 100 (World Meteorological Organization, Geneva 2011)
- 3.67 ISO: *Graphic Technology – Spectral Measurement and Colorimetric Computation for Graphic Arts Images*, ISO 13655:2017 (International Organization for Standardization, Geneva 2017)
- 3.68 VDI: *Measurement Methods Test Criteria – General Method For The Determination Of The Uncertainty Of Calibratable Measurement Methods*, VDI 2449 Part 3 (Beuth, Berlin 2001)
- 3.69 ISO: *Statistics – Vocabulary and Symbols – Part 2: Applied Statistics*, ISO 3534-2:2006 (International Organization for Standardization, Geneva 2006)
- 3.70 BIPM, IEC, IFCC, ISO, IUPAC, IUPAP, OIML: *International Vocabulary of Basic and General Terms in Metrology* (International Organization for Standardization, Geneva 1993)
- 3.71 K. Danzer: *Analytical Chemistry: Theoretical and Metrological Fundamentals* (Springer, Berlin, Heidelberg 2007)
- 3.72 J. Tellinghuisen: Inverse vs. classical calibration for small data sets, *Fresenius J. Anal. Chem.* **368**, 585–588 (2000)

- 3.73 K. Danzer, M. Wagner, C. Fischbacher: Calibration by orthogonal and common least squares – theoretical and practical aspects, *Fresenius J. Anal. Chem.* **352**, 407–412 (1995)
- 3.74 J.W. Einax, W. Bremser, B. Machelett: Inverse-variance weighted regression with uncertainty in both variables for the quantitative description of traffic-emitted lead transfer into plants, *Fresenius J. Anal. Chem.* **364**, 673–677 (1999)
- 3.75 B.D. Ripley, M. Thompson: Regression techniques for the detection of analytical bias, *Analyst* **112**, 377–383 (1987)
- 3.76 W.H. Press: *Numerical Recipes 3rd Edition: The Art of Scientific Computing* (Cambridge Univ. Press, New York 2007)
- 3.77 G.D. Dunn: *Statistical Evaluation of Measurement Errors: Design and Analysis of Reliability Studies* (Wiley, Chichester 2009)
- 3.78 ISO: *Meteorology – Sonic Anemometer/Thermometer – Acceptance Test Method for Mean Wind Measurements*, ISO 16622 (International Organization for Standardization, Geneva 2002)
- 3.79 ISO: *Meteorology – Wind Measurements – Part 1: Wind Tunnel Test Methods for Rotating Anemometer Performance*, ISO 17713-1 (Beuth, Berlin 2007)
- 3.80 R.G. Wylie, T. Lalas: *Measurement of Temperature and Humidity*, WMO Technical Note 194 (World Meteorological Organization, Geneva 1992) p. 77
- 3.81 ISO: *General Requirements for the Competence of Testing and Calibration Laboratories*, ISO/IEC 17025 (International Organization for Standardization, Geneva 2017)
- 3.82 H. Fuchs, H.P. Dorn, M. Bachner, B. Bohn, T. Brauers, S. Gomm, A. Hofzumahaus, F. Holland, S. Nehr, F. Rohrer, R. Tillmann, A. Wahner: Comparison of OH concentration measurements by DOAS and LIF during SAPHIR chamber experiments at high OH reactivity and low NO concentration, *Atmos. Meas. Tech.* **5**, 1611–1626 (2012)
- 3.83 L. Onel, A. Brennan, M. Gianella, G. Ronnie, A. Lawry Aguila, G. Hancock, L. Whalley, P.W. Seakins, G.A.D. Ritchie, D.E. Heard: An inter-comparison of HO₂ measurements by fluorescence assay by gas expansion and cavity ring-down spectroscopy within HIRAC (highly instrumented reactor for atmospheric chemistry), *Atmos. Meas. Tech.* **10**, 4877–4894 (2017)
- 3.84 J. Cordes, B. Stoffels, D. Wildanger: Geruchsringversuche an der Emissionssimulationsanlage. In: *Jahresbericht 2015 des Hessischen Landesamtes für Umwelt und Geologie* (Hessisches Landesamt für Umwelt und Geologie, Wiesbaden 2016)
- 3.85 M. Dal Maso, L. Liao, J. Wildt, A. Kiendler-Scharr, E. Kleist, R. Tillmann, M. Sipilä, J. Hakala, K. Lehtipalo, M. Ehn, V.M. Kerminen, M. Kulmala, D. Worsnop, T. Mentel: A chamber study of the influence of boreal BVOC emissions and sulfuric acid on nanoparticle formation rates at ambient concentrations, *Atmos. Chem. Phys.* **16**, 1955–1970 (2016)
- 3.86 T. Umezawa, C.A.M. Brenninkmeijer, T. Röckmann, C. van der Veen, S.C. Tyler, R. Fujita, S. Morimoto, S. Aoki, T. Sowers, J. Schmitt, M. Bock, J. Beck, H. Fischer, S.E. Michel, B.H. Vaughn, J.B. Miller, J.W.C. White, G. Brailsford, H. Schaefer, P. Sperlich, W.A. Brand, M. Rothe, T. Blunier, D. Lowry, R.E. Fisher, E.G. Nisbet, A.L. Rice, P. Bergamaschi, C. Veidt, I. Levin: Interlaboratory comparison of $\delta^{13}\text{C}$ and δD measurements of atmospheric CH₄ for combined use of data sets from different laboratories, *Atmos. Meas. Tech.* **11**, 1207–1231 (2018)
- 3.87 VDI: *Quality Assurance – Requirements for Interlaboratory Tests in Immission Control – Requirements for Providers of Interlaboratory Tests*, VDI 4221 Part 1 (Beuth, Berlin 2015)
- 3.88 ISO: *Conformity Assessment – General Requirements for Proficiency Testing*, ISO/IEC 17043 (International Organization for Standardization, Geneva 2010)
- 3.89 EURAMET: *Publishable JRP Summary Report for ENV58 MeteoMet2, Metrology for Essential Climate Variable* (JRP, Torino 2017)
- 3.90 M. Mauder, S.P. Oncley, R. Vogt, T. Weidinger, L. Ribeiro, C. Bernhofer, T. Foken, W. Kohsiek, H.A.R. DeBruin, H. Liu: The energy balance experiment EBEX-2000. Part II: Intercomparison of eddy covariance sensors and post-field data processing methods, *Boundary-Layer Meteorol.* **123**, 29–54 (2007)
- 3.91 E. Vuerich, C. Monesi, L.G. Lanza, L. Stagi, E. Lanzinger: WMO field intercomparison of rainfall intensity gauges, *Instrum. Obs. Methods Rep.* **99**, 1–290 (2009)
- 3.92 T. Foken: *Micrometeorology*, 2nd edn. (Springer, Berlin, Heidelberg 2017)
- 3.93 P.L. Finkelstein, J.C. Kaimal, J.E. Gaynor, M.E. Graves, T.J. Lockhart: Comparison of wind monitoring systems. Part II: Doppler sodars, *J. Atmos. Ocean. Technol.* **3**, 594–604 (1986)
- 3.94 J. Keder, T. Foken, W. Gerstmann, V. Schindler: Measurement of wind parameters and heat flux with the sensiron Doppler sodar, *Boundary Layer Meteorol.* **46**, 195–204 (1989)
- 3.95 J. Gottschall, M.S. Courtney, R. Wagner, H.E. Jørgensen, I. Antoniou: LiDAR profilers in the context of wind energy – A verification procedure for traceable measurements, *Wind Energy* **15**, 147–159 (2011)
- 3.96 V. Lehmann: *Traceability for Surface-Based Remote Sensing Methods – Radar Wind Profilers*, CIMO_ET-ORST_CBS_ET-SB01/Doc.3.3(4), Technical Report (World Meteorological Organization, Geneva 2015)
- 3.97 M.A. Shafer, C.A. Fiebrich, D.S. Arndt, S.E. Fredrickson, T.W. Hughes: Quality assurance procedures in the Oklahoma Mesonet, *J. Atmos. Ocean. Technol.* **17**, 474–494 (2000)
- 3.98 C.A. Fiebrich, D.L. Grimsley, R.A. McPherson, K.A. Kesler, G.R. Essenberg: The value of routine site visits in managing and maintaining quality data from the Oklahoma Mesonet, *J. Atmos. Ocean. Technol.* **23**, 406–416 (2006)
- 3.99 M.J. Menne, C.N. Williams: Homogenization of temperature series via pairwise comparisons, *J. Clim.* **22**, 1700–1717 (2009)

- 3.100 W.E. Reifsnnyder, K.G. McNaughton, J.R. Milford: Symbols, units, notation. A statement of journal policy, *Agric. For. Meteorol.* **54**, 389–397 (1991)
- 3.101 ISO: *Data Elements and Interchange Formats – Information Interchange – Representation of Dates and Times*, ISO 8601 (International Organization for Standardization, Geneva 2004)
- 3.102 National Science Foundation: *Dissemination and Sharing of Research Results* (2018). <https://www.nsf.gov/bfa/dias/policy/dmp.jsp>, Accessed 03 July 2021
- 3.103 USGS Data Management: *Data Standards* (2018). <https://www.usgs.gov/products/data-and-tools/data-management/data-standards>, Accessed 03 July 2021
- 3.104 WMO: *Technical Regulations, Volume I: General Meteorological Standards and Recommended Practices*, WMO–No. 49 (World Meteorological Organization, Geneva 2015)
- 3.105 DataONE: *Homepage* (2018). <https://www.dataone.org/>, Accessed 03 July 2021
- 3.106 M. Aubinet, T. Vesala, D. Papale: *Eddy Covariance: A Practical Guide to Measurement and Data Analysis* (Springer, Dordrecht 2012)
- 3.107 J.E. Hannay, C. MacLeod, J. Singer, H.P. Langtangen, D. Pfahl, G. Wilson: How do scientists develop and use scientific software? In: *2009 ICSE Workshop on Softw. Eng. Comput. Sci. Eng., Vancouver, BC* (2009) pp. 1–8, <https://doi.org/10.1109/secse.2009.5069155>
- 3.108 U. Kanewala, J.M. Bieman: Testing scientific software: A systematic literature review, *Inf. Softw. Technol.* **56**, 1219–1232 (2014)
- 3.109 S.M. Easterbrook: Climate change: A grand software challenge. In: *Proc. FSE/SDP Workshop Future Softw. Eng. Res.* (ACM, Santa Fe 2010) pp. 99–104, <https://doi.org/10.1145/1882362.1882383>
- 3.110 The Software Sustainability Institute: *Homepage* (2018). <https://www.software.ac.uk/>, Accessed 03 July 2021
- 3.111 Software Carpentry: *Homepage* (2018). <https://software-carpentry.org/>, Accessed 03 July 2021
- 3.112 The Kepler Project: *Homepage* (2018). <https://kepler-project.org/>, Accessed 03 July 2021
- 3.113 Zenodo: *Homepage* (2018). <https://zenodo.org/>, Accessed 03 July 2021
- 3.114 T. Preston–Werner: *Semantic Versioning 2.0.0* (2018). <https://semver.org/>, Accessed 24.01.2021
- 3.115 T. Clune, R. Rood: Software testing and verification in climate model development, *IEEE Software* **28**, 49–55 (2011)
- 3.116 S.L. Eddins: Automated software testing for Matlab, *Comput. Sci. Eng.* **11**, 48–55 (2009)
- 3.117 P.E. Farrell, M.D. Piggott, G.J. Gorman, D.A. Ham, C.R. Wilson, T.M. Bond: Automated continuous verification for numerical simulation, *Geosci. Model Dev.* **4**, 435–449 (2011)
- 3.118 D. Kelly, S. Thorsteinson, D. Hook: Scientific software testing: Analysis with four dimensions, *IEEE Software* **28**, 84–90 (2011)
- 3.119 J.B. Drake, P.W. Jones, G.R. Carr Jr.: Overview of the software design of the community climate system model, *Int. J. High Perform. Comput. Appl.* **19**, 177–186 (2005)
- 3.120 P.C.R. Lane, F. Gobet: A theory-driven testing methodology for developing scientific software, *J. Exp. Theor. Artif. Intell.* **24**, 421–456 (2012)
- 3.121 D.W. Kane, M.M. Hohman, E.G. Cerami, M.W. McCormick, K.F. Kuhlman, J.A. Byrd: Agile methods in biomedical software development: A multi-site experience report, *BMC Bioinformatics* **7**, 273 (2006)
- 3.122 C. Boettiger: An introduction to Docker for reproducible research, *SIGOPS Op. Syst. Rev.* **49**, 71–79 (2015)
- 3.123 S. Metzger, D. Durden, C. Sturtevant, H. Luo, N. Pingintha–Durden, T. Sachs, A. Serafimovich, J. Hartmann, J. Li, K. Xu, A.R. Desai: eddy4R 0.2.0: A DevOps model for community-extensible processing and analysis of eddy-covariance data based on R, Git, Docker, and HDF5, *Geosci. Model Dev.* **10**, 3189–3206 (2017)
- 3.124 Agile Alliance: *Homepage* (2018). <https://www.agilealliance.org/>, Accessed 03 July 2021
- 3.125 F. Erich, C.A. Amrit, M. Daneva: A mapping study on cooperation between information system development and operations. In: *Proc. 15th Int. Conf. Prod.–Focus. Softw. Proc. Improv. (PRO-FES)* (Springer, Cham 2014), https://doi.org/10.1007/978-3-319-13835-0_21
- 3.126 M. Loukides: *What is DevOps? – O’Reilly Radar* (2012). <http://radar.oreilly.com/2012/06/what-is-devops.html>, Accessed 03 July 2021
- 3.127 D. Clark, A. Culich, B. Hamlin, R. Lovett: BCE: Berkeley’s common scientific compute environment for research and education. In: *Proc. 13th Python Sci. Conf.*, ed. by S. van der Walt, J. Bergstra (2014) pp. 4–12
- 3.128 National Centers for Environmental Information (NCEI) formerly known as National Climatic Data Center (NCDC): *Archiving your Data* (2018). <https://www.ncdc.noaa.gov/customer-support/archiving-your-data>, Accessed 03 July 2021
- 3.129 The ICSU World Data System: *Homepage* (2018). <https://www.worlddatasystem.org/>, Accessed 03 July 2021
- 3.130 T. Foken, M. Gockede, M. Mauder, L. Mahrt, B. Amiro, W. Munger: Post-field data quality control. In: *Handbook of Micrometeorology: A Guide for Surface Flux Measurement and Analysis*, ed. by X. Lee, W.J. Massman, B.E. Law (Kluwer Academic, Dordrecht 2004) pp. 181–208
- 3.131 G. Pastorello, D. Agarwal, T. Samak, C. Poindexter, B. Faybishenko, D. Gunter, R. Hollowgrass, D. Papale, C. Trotta, A. Ribeca, E. Canfora: Observational data patterns for time series data quality assessment. In: *Proc. 2014 IEEE 10th Int. Conf. e-Sci., Sao Paolo* (2014) pp. 271–278, <https://doi.org/10.1109/eScience.2014.45>
- 3.132 L. Sebastian–Coleman: *Measuring Data Quality for Ongoing Improvement: A Data Quality Assessment Framework*, 1st edn. (Morgan Kaufmann, San Francisco 2013)
- 3.133 C. Flagg, J. Spencer, K. Thibault, S.C. Elmendorf, N. Schroeter: *AOS/TOS Protocol and Procedure: Man-*

- ual Data Transcription, NEON.DOC.001271 (National Ecological Observatory Network, Boulder 2016)
- 3.134 J.R. Taylor, H.L. Loescher: Automated quality control methods for sensor data: A novel observatory approach, *Biogeosciences* **10**, 4957–4971 (2013)
- 3.135 J. Hojstrup: A statistical data screening procedure, *Meas. Sci. Technol.* **4**, 153 (1993)
- 3.136 S. Metzger, W. Junkermann, M. Mauder, F. Beyrich, K. Butterbach-Bahl, H.P. Schmid, T. Foken: Eddy-covariance flux measurements with a weight-shift microlight aircraft, *Atmos. Meas. Tech.* **5**, 1699–1717 (2012)
- 3.137 F.V. Brock: A nonlinear filter to remove impulse noise from meteorological data, *J. Atmos. Ocean. Technol.* **3**, 51–58 (1986)
- 3.138 D. Starkenburg, S. Metzger, G.J. Fochesatto, J.G. Alfieri, R. Gens, A. Prakash, J. Cristóbal: Assessment of despiking methods for turbulence data in micrometeorology, *J. Atmos. Ocean. Technol.* **33**, 2001–2013 (2016)
- 3.139 D. Vickers, L. Mahrt: Quality control and flux sampling problems for tower and aircraft data, *J. Atmos. Ocean. Technol.* **14**, 512–526 (1997)
- 3.140 P.L. Finkelstein, P.F. Sims: Sampling error in eddy correlation flux measurements, *J. Geophys. Res. Atmos.* **106**, 3503–3509 (2001)
- 3.141 T. Foken, B. Wichura: Tools for quality assessment of surface-based flux measurements, *Agric. For. Meteorol.* **78**, 83–105 (1996)
- 3.142 A.G. Barr, A.D. Richardson, D.Y. Hollinger, D. Papale, M.A. Arain, T.A. Black, G. Bohrer, D. Dragoni, M.L. Fischer, L. Gu, B.E. Law, H.A. Margolis, J.H. McCaughey, J.W. Munger, W. Oechel, K. Schaeffer: Use of change-point detection for friction-velocity threshold evaluation in eddy-covariance studies, *Agric. For. Meteorol.* **171–172**, 31–45 (2013)
- 3.143 B. Chen, N.C. Coops, D. Fu, H.A. Margolis, B.D. Amiro, A.G. Barr, T.A. Black, M.A. Arain, C.P.A. Bourque, L.B. Flanagan, P.M. Lafleur, J.H. McCaughey, S.C. Wofsy: Assessing eddy-covariance flux tower location bias across the Fluxnet-Canada research network based on remote sensing and footprint modelling, *Agric. For. Meteorol.* **151**, 87–100 (2011)
- 3.144 H. Veregin: Data quality parameters. In: *Geographical Information Systems*, 2nd edn., ed. by P. Longley, M.F. Goodchild, D.J. Maguire, D.W. Rhind (Wiley, Hoboken 2005) pp. 177–189
- 3.145 NASA: *MODIS Land Products Quality Assurance Tutorial: Part-1, How to Find, Understand, and use the Quality Assurance Information for MODIS Land Products* (LP DAAC, Sioux Falls 2016)
- 3.146 K. Kohnert, B. Juhls, S. Muster, S. Antonova, A. Serafimovich, S. Metzger, J. Hartmann, T. Sachs: Toward understanding the contribution of waterbodies to the methane emissions of a permafrost landscape on a regional scale—A case study from the Mackenzie Delta, Canada, *Glob. Chang. Biol.* **24**(9), 3976–3989 (2018), <https://doi.org/10.1111/gcb.14289>
- 3.147 R.H. Langland, N.L. Baker: Estimation of observation impact using the NRL atmospheric variational data assimilation adjoint system, *Tellus A* **56**, 189–201 (2004)
- 3.148 I. Durre, M.J. Menne, R.S. Vose: Strategies for evaluating quality assurance procedures, *J. Appl. Meteorol. Climatol.* **47**, 1785–1791 (2008)
- 3.149 M. Mauder, M. Cuntz, C. Drüe, A. Graf, C. Rebmann, H.P. Schmid, M. Schmidt, R. Steinbrecher: A strategy for quality and uncertainty assessment of long-term eddy-covariance measurements, *Agric. For. Meteorol.* **169**, 122–135 (2013)
- 3.150 D.E. Smith, S. Metzger, J.R. Taylor: A transparent and transferable framework for tracking quality information in large datasets, *PLoS One* **9**, e112249 (2014)
- 3.151 I. Durre, M.J. Menne, B.E. Gleason, T.G. Houston, R.S. Vose: Comprehensive automated quality assurance of daily surface observations, *J. Appl. Meteorol. Climatol.* **49**, 1615–1633 (2010)
- 3.152 ISO: *Environmental Management – Vocabulary*, ISO 14050:2009 (International Organization for Standardization, Geneva 2009)
- 3.153 ISO: *Conformity Assessment – Requirements for Bodies Providing Audit and Certification of Management Systems*, ISO/IEC 17021:2011 (International Organization for Standardization, Geneva 2011)
- 3.154 ISO: *Guidelines for Auditing Management Systems*, ISO 19011:2011 (International Organization for Standardization, Geneva 2011)
- 3.155 ISO: *Conformity Assessment – Requirements for Bodies Certifying Products, Processes and Services*, ISO/IEC 17065:2012 (International Organization for Standardization, Geneva 2012)
- 3.156 ISO: *Conformity Assessment – Requirements for Accreditation Bodies Accrediting Conformity Assessment Bodies*, ISO 17011:2017 (International Organization for Standardization, Geneva 2017)
- 3.157 International Laboratory Accreditation Cooperation: *Homepage* (2018). <https://ilac.org/>, Accessed 24.01.2021
- 3.158 International Accreditation Forum: *Homepage* (2018). <https://www.iaf.nu/>, Accessed 24.01.2021
- 3.159 ISO: *Environmental Management Systems – Requirements with Guidance for Use*, ISO 14001:2015 (International Organization for Standardization, Geneva 2015)
- 3.160 Aerosol Robotic Network: *Homepage* (2018). <https://aeronet.gsfc.nasa.gov/>, Accessed 24.01.2021
- 3.161 AmeriFlux: *Homepage* (2018). <http://ameriflux.lbl.gov/>, Accessed 24.01.2021
- 3.162 Fluxdata: *The Data Portal Serving the FLUXNET Community* (2018). <https://fluxnet.org/data/>, Accessed 24.01.2021
- 3.163 National Weather Service: *Cooperative Observer Program (COOP)* (2018). <https://www.weather.gov/coop/overview>, Accessed 24.01.2021
- 3.164 ARM Climate Research Facility: *Homepage* (2018). <https://www.arm.gov/>, Accessed 24.01.2021
- 3.165 National Oceanic and Atmospheric Administration: *Homepage* (2018). <http://www.noaa.gov/>, Accessed 24.01.2021

- 3.166 Natural Resources Conservation Service: *Homepage* (2018). <https://www.nrcs.usda.gov/wps/portal/nrcs/site/national/home/>, Accessed 24.01.2021
- 3.167 U.S. Geological Survey: *Homepage* (2018). <https://www.usgs.gov/>, Accessed 24.01.2021
- 3.168 D.S. Christianson, N. Beekwilder, S. Chan, Y.W. Cheah, H. Chu, S. Dengel, F. O'Brien, G. Pastorello, M. Sandesh, M.S. Torn, D. Agarwal: AmeriFlux data processing: Integrating automated and manual data management across software technologies and an international network to generate timely data products. In: *Proc. 50th AGU Annu. Fall Meet.* (2017)
- 3.169 NEON (National Ecological Observatory Network): *2D wind speed and direction (DPI.00001.001), Barometric pressure (DPI.00004.001), Short-wave and longwave radiation (net radiometer) (DPI.00023.001), Photosynthetically active radiation (quantum line) (DPI.00066.001)*. Provisional dataset: <http://data.neonscience.org>, Accessed 03 July 2021
- 3.170 T. Foken, W. Babel, C. Thomas: Possible errors in flux measurements due to limited digitalization, *Atmos. Meas. Tech.* **12**, 971–976 (2019)
- 3.171 N. Vuichard, D. Papale: Filling the gaps in meteorological continuous data measured at FLUXNET sites with ERA-interim reanalysis, *Earth Syst. Sci. Data* **7**, 157–171 (2015)
- 3.172 A.M. Moffat, D. Papale, M. Reichstein, D.Y. Hollinger, A.D. Richardson, A.G. Barr, C. Beckstein, B.H. Braswell, G. Churkina, A.R. Desai, E. Falge, J.H. Gove, M. Heimann, D.F. Hui, A.J. Jarvis, J. Kattge, A. Noormets, V.J. Stauch: Comprehensive comparison of gap-filling techniques for eddy covariance net carbon fluxes, *Agric. For. Meteorol.* **147**, 209–232 (2007)
- 3.173 T. Schneider: Analysis of incomplete climate data: Estimation of mean values and covariance matrices and imputation of missing values, *J. Clim.* **14**, 853–871 (2001)
- 3.174 E. Nkiaka, N.R. Nawaz, J.C. Lovett: Using self-organizing maps to infill missing data in hydro-meteorological time series from the Logone catchment, Lake Chad basin, *Environ. Monit. Assess.* **188**, 400 (2016)
- 3.175 C. Yozgatligil, S. Aslan, C. Iyigun, I. Batmaz: Comparison of missing value imputation methods in time series: The case of Turkish meteorological data, *Theor. Appl. Climatol.* **112**, 143–167 (2013)
- 3.176 E.C. Ifeachor, B.W. Jervis: *Digital Signal Processing – A Practical Approach* (Addison-Wesley, Wokingham 2002)
- 3.177 K.M. Talluru, V. Kulandaivelu, N. Hutchins, I. Marusic: A calibration technique to correct sensor drift issues in hot-wire anemometry, *Meas. Sci. Technol.* **25**, 105304 (2014)
- 3.178 D.J. Hill, B.S. Minsker: Automated fault detection for in-situ environmental sensors. In: *Proc. 7th Int. Conf. Hydroinform.* (2006)
- 3.179 E.W. Dereszynski, T.G. Dietterich: Spatiotemporal models for data-anomaly detection in dynamic environmental monitoring campaigns, *ACM Trans. Sen. Netw.* **8**, 3:1–3:36 (2011)
- 3.180 A. Rahman, D.V. Smith, G. Timms: A novel machine learning approach toward quality assessment of sensor data, *IEEE Sens. J.* **14**, 1035–1047 (2014)
- 3.181 A.R. Desai, B.R. Helliker, P.R. Moorcroft, A.E. Andrews, J.A. Berry: Climatic controls of interannual variability in regional carbon fluxes from top-down and bottom-up perspectives, *J. Geophys. Res. Biogeosci.* **115**, G02011 (2010)
- 3.182 H.P. Schmid, C.R. Lloyd: Spatial representativeness and the location bias of flux footprints over inhomogeneous areas, *Agric. For. Meteorol.* **93**, 195–209 (1999)

Cove Sturtevant

National Ecological Observatory Network (NEON); Battelle
Boulder, USA
csturtevant@battelleecology.org



Cove Sturtevant is a biometeorologist and data scientist at the National Ecological Observatory Network. His research activities focus on understanding the biophysical controls of greenhouse gas exchange between ecosystems and the atmosphere in relation to environmental change and land management. He holds a Master's degree in aerospace engineering from the University of Colorado and a PhD in ecology from San Diego State University.

Stefan Metzger

National Ecological Observatory Network (NEON); Battelle
Boulder, USA
smetzger@battelleecology.org



Stefan Metzger is a micrometeorologist and the Surface-Atmosphere Exchange Science Lead at the National Ecological Observatory Network, the largest single-provider flux tower network globally. His research activities include novel measurement techniques, community-extensible data processing, and data-mining approaches that reduce observational bias in boundary layer meteorology. He holds a Master's degree in geocology and a PhD in micrometeorology from the University of Bayreuth, Germany.

**Sascha Nehr**

European University of Applied Sciences
Brühl, Germany
s.nehr@eufh.de

Sascha Nehr is a chemical engineer and environmental management expert. His fields of expertise include process hazard analyses and quantitative risk assessment in the chemical industry as well as dispersion modelling of airborne pollutants. He holds a diploma in chemical engineering from the Niederrhein University of Applied Sciences and a PhD in physical chemistry from the University of Wuppertal. Since 2019, he is professor for management and engineering at the European University of Applied Sciences.

**Thomas Foken**

University of Bayreuth
Bayreuth, Germany
thomas.foken@uni-bayreuth.de

Thomas Foken is a retired Professor of Micrometeorology at the University of Bayreuth. He was the head of Laboratories at the meteorological observatories at Potsdam (1981–1994) and Lindenberg (1994–1997). His research interests include the interaction between the Earth's surface and the atmosphere and the measurement and modeling of energy and matter fluxes, with a strong focus on experimental meteorology. His scientific contributions have been recognized through various international awards.

4. Standardization in Atmospheric Measurements

Simon Jäckel, Annette Borowiak, Brian Stacey

Standardization is a means to establish order. Standards are a collection of practical knowledge. They allow an action to be repeated, are a prerequisite for the application of uniform criteria, and prevent distortion of competition. Standards also facilitate trade and provide governments with technical support. Standards developing organizations provide a forum for cooperation and consensus utilizing expert knowledge. This chapter first broadly considers the principles, procedures, and products of standardization and then focuses on standardization in the field of atmospheric measurements including its benefits and possible shortcomings.

4.1	Background and Definitions	93
4.2	History	94
4.3	Principles and Procedures	96
4.3.1	Common Principles	96
4.3.2	The Role of the Standards Developing Organization (SDO)	96
4.3.3	Levels of Standardization	96
4.4	Standardization in the Field of Atmospheric Measurements	98
4.4.1	General	98
4.4.2	Measurement of Atmospheric Pollutants	99
4.4.3	Meteorological Measurements	101
4.4.4	Benefits and Shortcomings of Standardization in Atmospheric Measurements	102
4.5	Future Developments	103
4.6	Further Reading	104
	References	104

Standardization is a regulatory instrument of the technical world. It is an integral part of the existing economic, social, and legal system. Standards are an easily accessible source of information about the state of the art.

They represent an important tool in worldwide technology transfer and fulfill a number of protective functions, such as in environmental protection.

4.1 Background and Definitions

The need for standardization is undisputed. A smooth exchange of goods and knowledge presupposes uniformity of basic standards. Standardization usually produces significant positive economic effects [4.1]. Refer to, for example, [4.2–11] for details on the positive impact on the economy and other key drivers behind standards development.

The term standardization has a broad definition. It ranges from government regulatory activities (legal standards) and public standardization to industry standardization (from consortia and alliances to standardization within enterprises). Figure 4.1 depicts the different kinds of standards developed worldwide on

a company, industry, national, or international scale. This chapter deals exclusively with public standardization and its products, namely voluntary consensus standards and specifications, which are the results of work performed by standards development organizations (SDOs). Due to their negligible importance to standardization in atmospheric measurements, this chapter does not address company or de facto standards. State regulations, like parliamentary legitimated laws, are also not discussed.

As there is some confusion regarding the definitions of many of the terms used in this chapter, the following basic definitions are provided [4.12]:

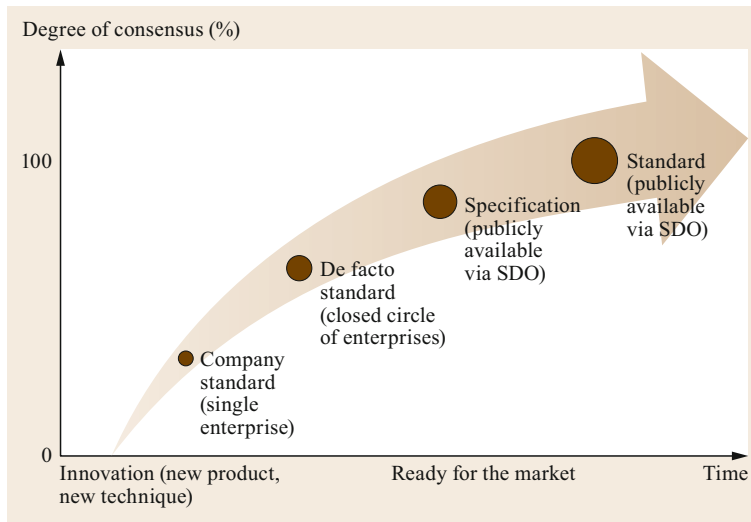


Fig. 4.1 Different kinds of standards shown with their respective degree of consensus and elaboration time

- *Standardization* is the activity of establishing, with regard to actual or potential problems, provisions for common and repeated use, aimed at the achievement of the optimum degree of order in a given context. In particular, the activity consists of the processes of formulating, issuing, and implementing standards.
 - *International standardization* is standardization in which involvement is open to relevant bodies from all countries.
 - *Regional standardization* is standardization in which involvement is open to relevant bodies from countries from only one geographical, political, or economic area of the world.
 - *National standardization* is standardization that takes place at the level of one specific country.
 - A *standard* is a document, established by consensus and approved by a recognized body, that provides, for common and repeated use, rules, guidelines or characteristics for activities or their results, aimed at the achievement of the optimum degree of order in a given context.
 - *Consensus* is a general agreement, characterized by the absence of sustained opposition to substantial issues by any important part of the concerned inter-
- ests and by a process that involves seeking to take into account the views of all parties concerned and to reconcile any conflicting arguments.
- *State of the art* is a developed stage of technical capability at a given time as regards products, processes, and services, based on the relevant consolidated findings of science, technology, and experience.

Standards are accessible to everyone. Whoever uses standards must ensure correct application in their individual case. Standards are not the one source of knowledge for technically correct behavior. They cannot cover all possible individual cases where further or restrictive measures may be required. Nevertheless, they are a benchmark for perfect technical performance. It should also be kept in mind that standards can only take account of the state of the art prevailing at the time of the respective publication. By applying standards, no one can escape responsibility for their own actions. The use of standards is generally voluntary. It is only when standards become the content of contracts or when the legislator refers to and requires compliance with them that standards become binding. SDOs do not have a mandate to require compliance.

4.2 History

The development of standards began in parallel with the need to measure [4.13]. Honest weighing became a factor in trade around 3000 BCE. At the same time, standardized building blocks made the construction of

the Egyptian pyramids possible [4.2]. As early as 2650 BCE, a closed system of measurement was established by *Shulgi*, King of Ur. Around 2000 BCE this system of measurement became the global standard. When in-

dustrialization began about 200 years ago, the need to unify the newly created objects was growing intensely. Several notable standards that were agreed upon by the nineteenth century were the metric system in Europe and the railway track gauge and screw threads in the English-speaking parts of the world [4.13]. Although a technical object can perform its task flawlessly in many variations, its industrial production is only meaningful if it can be used interchangeably in a particular design at different locations. The invention of the interchangeable system of manufacture by *Eli Whitney* (1765–1825) laid the foundation for mass production and higher productivity by means of simplification, modularization, and unification and made him the father of well-organized in-company standardization in the USA [4.14].

With the advent of a widespread division of labor and of industrial technology, the need to organize became more intense by the beginning of the twentieth century. It became more and more commanding to create special bodies, the national standards committees, which brought together the entire standardization work in their country. The organizational structure of standardization as we know it today started in 1901 with the founding of the British Standardization Institute (BSI), the first national standardization organization in the world [4.14, 15]. The initiative was copied by many countries in subsequent years and most followed the centralized UK model [4.15]. More information on the national standards bodies founded roughly in the first quarter of the twentieth century can be found in [4.14, 16].

The first international standardization organization was the International Electrotechnical Commission (IEC), which was founded in 1906 and focused on electronic and electrical engineering [4.14]. Another cooperation of the national standards committees led to the foundation of the International Federation of the National Standardization Associations (ISA) in 1928, which laid the foundation for international cooperation with a focus on mechanical engineering [4.14]. Participation in the ISA's activities was mainly limited to continental European countries [4.17]. The ISA distributed the detailed work to its members. In the technical committees, the management was transferred to the standards committee of a country. As a result, the general secretariat was able to limit itself to general matters, the preparation of meetings, and the monitoring of work in progress. The ISA did not publish international standards, but only recommendations in the form of ISA bulletins, which the individual national standards committees could use to shape their national standards. Whether members took these recommen-

dations into account or not was therefore completely voluntary. A total of 32 bulletins were issued and their content has been reflected in many national standards. Some have been introduced so extensively that they can rightfully be called world standards. These include, for example, the reference temperature of 20 °C and the standards for motion pictures (standard film 35 mm and substandard film 16 mm) [4.14]. In 1939, with the beginning of the Second World War, the work of the ISA came to a standstill, and the intergovernmental work remained restricted to direct trade between individual countries.

In 1944 the United Nations Standards Coordinating Committee (UNSCC) was set up with a time-limited statute [4.14, 17]. In 1946, after the end of the Second World War, the UNSCC, together with ISA representatives, met in London and decided to join forces and set up a new organization for international standardization [4.14, 17]. In 1947 the International Organization for Standardization (ISO) was launched, which was open to all countries of the world that wished to collaborate; each had equal duties and equal rights [4.17]. The ISO adopted most of the statutes and rules of procedure from the ISA, including the distribution of work to its members, and produced a list of the first 67 technical committees, roughly two thirds of which were previous ISA committees [4.17]. Thus, it is not surprising that a focus of the first years of the ISO's work was mechanical engineering. The initial strategy of the ISO was to evolve international standards from those already evolved nationally, and then to reimplement them nationally [4.17]. The IEC affiliated with ISO in 1947 and separated again in 1976 [4.14].

The impossibility of finding successful outcomes in certain technical areas mixed with many issues being relevant only to certain regions in the world and the urgent need for the elimination of trade barriers led to the foundation of regional standardization organizations, the first being the European Committee for Standardization (CEN) in 1961. Many others followed in the 1960s to 1990s, representing all major regions in the world (see Tab. 4.1).

On a national level, standardization in the field of atmospheric measurements started quite early, for example, in Germany with the foundation of the VDI (Association of German Engineers) Commission on Air Pollution Prevention in 1957, but on the international level it took almost 40 years longer before the first committee on standardization of atmospheric measurements – ISO/TC 146 Air quality – was founded in 1994. Standardization of meteorological measurements followed in 1994 with the foundation of ISO/TC 146/SC 5 Meteorology.

4.3 Principles and Procedures

This section states the common principles most SDOs share, shows how standards are developed, and defines the role of SDOs at the different levels (national/regional/international) of standardization.

4.3.1 Common Principles

Most SDOs share several features, regardless of their national, regional, or international level. The key features are clearly defined by a set of rules of procedure, which commonly include:

- Every stakeholder is allowed to submit a new work item proposal for the development of a standard and/or to have fair, reasonable, nondiscriminatory (FRAND), voluntary, and open access to contribute and share their expertise. Broad participation and transparency ensure acceptance of the resulting standard both in the public and in the market due to resulting social equity and fairness to all parties involved. The responsibility for the outcome of the standardization process lies with the world at large as it is assumed that everyone's interests have been taken into account when the standard was set [4.10].
- The solutions recorded in standards are not based on majority, but based on mutual consent, making the standard the outcome of a negotiation process between different interests. What is technically possible and economically feasible is negotiated.

In addition to the rules of procedure, some more general requirements are considered:

- Standardization works within the framework that scientific knowledge dictates and thus reflects the state of the art.
- The benefit of the general public stands above the advantage of individuals. Therefore, standards have to include societal goals.
- The aim of standardization is a world free of trade barriers. Therefore, the standardization work of international and regional SDOs takes precedence over purely national standardization.
- Standardization is not static but rather dynamic. Standards must be checked on a regular basis to see if they are still state of the art and thus have a typical review cycle of five years.

4.3.2 The Role of the Standards Developing Organization (SDO)

SDOs are usually nonprofit organizations [4.14] representing a formal and structured way of achieving consensus on things that impact millions of people around the globe and are service providers for standardization. Under their project lead, business experts, researchers, public authorities and consumers work together to develop standards. The SDOs ensure a smooth development process, to which the working group experts contribute their knowledge. Project managers plan and document meetings and ensure that the directives are followed. The resulting standards are published by the SDOs. In addition to that, SDOs:

- Coordinate national, regional, and international projects and ensure that all regulations are adhered to, which assures the acceptance of standards
- Provide the information as a public good and usually cover their administrative costs through membership fees and publication sales
- Inform the public about all standardization activities, starting with new work items and ending with the published standards
- Promote the application of standards

The SDOs usually use backwards planning to make sure that projects are published on time. The publication date of the finished standard, which is fixed at the very beginning of any project, is seen as the project end date. The time needed to reach each milestone along the path to a successfully published standard, for example, developing the content of the standard, consensus building, and public inquiry, is then calculated.

4.3.3 Levels of Standardization

This section defines the different levels of standardization, using the most important SDOs as examples.

National

The reason national standards differ between nations often lies in different ideas about what needs to be standardized. Unique national standards are most frequently prepared in conjunction with unique national legislation [4.18].

The majority of countries followed the BSI and decided to have a centralized approach on standardization [4.15]. In contrast, several countries followed a decentralized and thus sector-specific approach. The most diverse standardization system in the world is found in the USA [4.14], where at least 600 nongovernmental SDOs [4.19, 20] exist. Germany, with around 150 nongovernmental SDOs [4.21], is somewhere between diverse and centralized. More information on the different models can be found in [4.22].

Regional

There are several regional SDOs distributed all over the world (Table 4.1). Most of them deal with matters other than atmospheric measurements, such as promoting trade by the harmonization of standards in the given region.

One regional SDO – the European Committee for Standardization (CEN) – is engaged in air quality and atmospheric measurements. The CEN was founded in 1961 and is a nonprofit organization under Belgian law. Members of the CEN are the EU and European Free Trade Association (EFTA) countries. The main goal of European standardization can be defined as the unification of all standards that apply within Europe, which means harmonization of national standards. This results in the elaboration and subsequent adoption of European standards by all national SDOs that are members of CEN. In the CEN, each country is represented by one national SDO and the voting process is based on population of the countries of the CEN members, giving each member a specific weight in the voting process (cf. the ISO, where 1 nation = 1 vote).

Table 4.1 Examples of regional SDOs (after [4.14])

Region	Name
Association of Southeast Asian Nations (ASEAN)	ASEAN Consultative Committee on Standards and Quality (ACCSQ)
Arabian Peninsula and North Africa	Arab Industrial Development & Mining Organization (AIDMO)
Africa	African Organization for Standardization (ARSO)
Europe	European Committee for Standardization (CEN)
Europe	European Committee for Electrotechnical Standardization (CENELEC)
America	Pan American Standards Commission (COPANT)
Asia, Europe	Euro-Asian Council for Standardization, Metrology and Certification (EASC)
Europe	European Telecommunications Standards Institute (ETSI)
Pacific Rim	Pacific Area Standards Congress (PASC)

There are two specialties in the European standardization system worth mentioning. One is the process of *forced harmonization*, which means that every European standard must be adopted unchanged and by all members while at the same time withdrawing all conflicting national standards. The CEN standards are mandatory for EU member states. This is because of the strong political commitment to unification [4.20] and according to [4.23] is an effective harmonization tool in the case of markets with a stable variety, but at the same time is the more expensive solution because of, for example, the necessity of passing legislative procedures, the requirement of enforcement activities for sanctions, and distribution cost. The second specialty in the European standardization system is the use of standards as *policy tools*. The legal framework as set out in [4.24] allows the European Commission to request the CEN to draft a European standard by means of a standardization mandate leading to a so-called harmonized standard for the application of EU legislation. By using standardization as a policy tool [4.24], EU directives only need to determine the politically desired level of, for example, air quality. These basic requirements are then substantiated by harmonized European standards. This process is called the new approach [4.25] and has existed since 1985 [4.26]. Standards become regulatory when referenced in EU directives and they then cease to be voluntary. If additional scientific research is needed to be able to elaborate a harmonized European standard, the European Commission is willing to fund, for example, validation campaigns of measurement devices.

The technical work is performed in technical committees (CEN/TCs), consisting of representatives of the national SDOs. TCs usually build up several working groups to work on the different topics at hand. The CEN is comprised of more than 300 TCs with around 1500 working groups. Full-time secretaries who are paid by the individual national SDOs supervise all committees and working groups. The administrative work is therefore handled by the CEN member organizations. The national SDOs usually set up national mirror committees, which are open to all stakeholders on the national level. These national mirror committees build a national position on the standardization topic, which will then be represented on the international level.

When talking about atmospheric measurements, only CEN/TC 264 Air quality seems to be of relevance. Created in October 1990 as proposed by the VDI Commission on Air Pollution Prevention, CEN/TC 264 is responsible for elaborating standards of methods for air quality characterization of emissions, ambient air, indoor air, gases in and from the ground, and deposition, in particular measurement methods for air pollutants [4.27].

International

The International Organization for Standardization (ISO) is an independent, nongovernmental organization and a global network of national standards bodies from 162 countries. The ISO has published more than 22 000 ISO standards covering almost all aspects of technology and business; it is the world's largest developer and publisher of international standards.

The main goal of international standardization can be defined as the facilitation of the global exchange of goods and services and the promotion of international cooperation in technical, economic, scientific, and intellectual fields. The ISO standardizes topics of global relevance, which means that the international standard can be used as broadly as possible by affected industries and other stakeholders in markets around the world.

The ISO sets voluntary standards (cf. the CEN). According to [4.23], voluntary standards do not necessarily implement harmonization. Difficulties in the necessary harmonization may arise if the existing variety is stable and not everyone is willing to accept the voluntary standard. Following this assumption, voluntary standards are best suited for markets with unstable variety.

The technical work is performed in the same way as the CEN. There is a difference in the voting procedure; at the ISO level, each country has one vote.

In 1971, the ISO created its first technical committee in the environmental field: ISO/TC 146 Air quality. The objectives of standardization are related to tools for air quality characterization of emissions, workspace air, ambient air, and indoor air, in particular measurement methods for air pollutants (particles, gases, odors, and micro-organisms), meteorological parameters, measurement planning, procedures for quality assurance/quality control (QA/QC), and methods for

the evaluation of results including the determination of uncertainty [4.28].

The ISO committee ISO/TC 146/SC 5 Meteorology is responsible for the elaboration of meteorological ISO standards. The working group members of ISO/TC 146/SC 5 develop, build, sell, and use equipment covered by the standard practices, guides, and testing methods. Everybody involved in meteorological measurements should be aware of these ISO standards and consider using them as reference tools when procuring equipment and operating measurement programs. The focus of ISO/TC 146/SC 5 Meteorology lies on remote sensing techniques, such as lidar and radar, that are applied around the globe.

The World Meteorological Organization (WMO) has been accepted by the ISO as an international standardizing body. The WMO and the ISO also agreed on the development of common ISO–WMO standards. Thus, many standardization projects in the interest of WMO are developed in close cooperation, for example, through the WMO's Technical Commission on Instruments and Methods of Observation (CIMO). The CIMO's mission is to give advice on good practices for meteorological measurements and observations and to provide best practices, procedures, and basic capabilities of instruments and systems. The CIMO assists national meteorological and hydrological services, as well as other operators of observing systems, in the preparation of their manuals and procedures for meeting their specific measurement and observation needs by giving recommendations on the general features most common to various configurations of a given instrument or measurement system, thus enabling wide areas for further development [4.29]. More information on the WMO can be found in Chap. 1 Atmospheric Measurements, Sect. 1.2.3 Establishment of the World's Meteorological Organizations.

4.4 Standardization in the Field of Atmospheric Measurements

This section provides an in-depth overview of several atmospheric measurement topics, gives exemplary success stories clearly showing the effect standardization can have, and lists benefits and possible shortcomings.

4.4.1 General

Atmospheric measurements must be performed in a uniform way to make them comparable. Standards in this field produce methods for identifying instruments that facilitate comparable measurements, support users

both in planning and in execution of measurements, and are needed by manufacturers to communicate the performance characteristics of their equipment. Standards in atmospheric measurements usually provide:

- Terms and definitions
- Necessary basics
- Descriptions and/or definitions of the measurement targets (e.g., PM_{10})
- Specifications for measurements and measurement planning

- Methods of determining equipment characteristics and proper application of measuring equipment including:
 - Calibration
 - Monitoring
 - Maintenance
- Requirements for the selection and preparation of a measurement site
- Requirements on data collection, processing, and evaluation

Some standards go beyond that, specifying competencies and staff training, and discussing life-cycle management (ISO 19926-1 [4.30]).

Standards in atmospheric measurements are developed by those who apply them later. They give clear guidance to all stakeholders performing measurements and help prevent information asymmetry by providing all necessary information and sets of minimum admissible attributes, for example, for the measurement devices themselves. Standards even facilitate fair competition between vendors responding to calls for tender.

There are several different political, regulatory, and administrative approaches in the different countries of the world that tackle environmental problems and measurement tasks at various levels, such as local, regional, and national [4.31]. Standards provide a basis and a framework for consistent decision making at any level.

4.4.2 Measurement of Atmospheric Pollutants

The measurement of atmospheric pollutants is a major part of technical air pollution control and an important instrument for monitoring compliance with mandated values. Ambient air quality limit or target values set by administrations are used to report the frequency with which pollutant concentrations exceed harmful levels. It is advisable to link these values with measurement methods, sampling site locations, and the frequency of sampling, quality control measures, and statistical data analysis as defined by voluntary consensus standards [4.32]. Area-wide measurements according to measurement standards enable administrations to monitor the success of actions and abatement strategies.

Particulate matter has been monitored for a long time, mainly with filter-based techniques. The optical properties of particulate matter, such as black smoke, have also been monitored since the early 1960s. National legislation to protect human health has been in place since the London and Ruhr area smog episodes. As air pollution is a transboundary problem that does not respect national borders, European countries put

a directive in place with limit values and requirements to monitor suspended particulates in air in 1980. Driven mainly by health impact assessments, European legislation has been revised and reviewed on many occasions since 1980. Comparable air quality data and results from harmonized measurement methods are of major importance for the implementation and evaluation of legislation. Standard measurement methods are referred to in EU legislation to guarantee comparable assessments of air quality based on common criteria and the required accuracy of monitoring techniques. The development of European standards by the CEN goes hand in hand with advancing EU legislation.

For example, the air quality within the European Union has to be assessed by common methods within defined data quality objectives. Institutes and networks performing measurements need to employ standard measurement techniques and procedures. The CEN develops these harmonized methodologies, allowing for comparable assessment of air quality.

Exemplary Success Story: Gaseous Air Pollution

The measurement of NO_x, CO, O₃, and SO₂ in ambient air is important for monitoring air pollution levels, finding connections to health effects, and understanding the success or failure of emission abatement strategies. The measurement of these gases has been undertaken since the 1950s using a variety of different techniques, ranging from wet chemistry and diffusive samplers through to automatic point source analyzers and optical spectroscopic techniques.

Measurement of Gaseous Air Pollution. Up until 2005, the measurement of gases in the European Union followed a series of ISO standard methods, for example:

- ISO 7996 Nitrogen Dioxide [4.33]
- ISO 10498 Sulphur Dioxide [4.34]
- ISO 13964 Ozone [4.35]

In 2005, the CEN published a series of standard methods for gases:

- EN 14211 Oxides of Nitrogen [4.36]
- EN 14212 Sulphur Dioxide [4.37]
- EN 14625 Ozone [4.38]
- EN 14626 Carbon Monoxide [4.39]
- EN 14662 Parts 1–5 Benzene [4.40–44]

For the first time, these standards set out procedures for type testing in laboratory and field tests, ongoing quality control, and calculating measurement uncertainties at prescribed limit values. Like any standard, they are subject to review every five years and are updated to re-

flect improvements in test protocols and understanding of key components of the measurement processes.

The current EC Directive on Air Quality and Cleaner Air for Europe (2008/50/EC) [4.45] and its subsequent amendment (EU/2015/1480) [4.46] specify that measurements and associated measurement uncertainties shall be reported in accordance with procedures set out in the standard methods described above, using analyzers that have been tested using the standard methods. The data produced by the analyzers must conform to data quality objectives set out in 2008/50/EC; users are provided with all the details necessary to perform these assessments themselves.

Estimating the Benefits from Standardization of this Success Story. In 1992, the European Commission, led by the European Reference Laboratory for Air Pollution (ERLAP), initiated a campaign to evaluate the level of harmonization of air pollution measurements throughout Europe. It brought together national reference laboratories (NRLs) from many member states to demonstrate that they could measure standard test gas mixtures accurately, precisely, and comparably to each other. The benefit of such a test was manifold. It allowed testing under controlled conditions at a range of different concentrations for a large number of laboratories simultaneously. Each NRL was required to measure the test mixtures and report the concentration and measurement uncertainties, thus allowing for a comparison.

The ERLAP devised a series of test criteria to determine the performance of each NRL for the concentrations measured. These first tests, termed inter-comparison exercises (IEs), were conducted in Essen in May 1992 (under a WHO collaboration) and in Ispra in April 1993, and showed that 66.7% of the measurements reported by NRLs fell within the definition of *good* results (defined as a Z-score within ± 2).

These results identified that measurements across Europe in 1992/1993 were lacking in accuracy and harmonization. The ERLAP, working with the NRLs, began a campaign to promote best practice and develop standard procedures across all member states. Their work began by comparing calibration standards and certified reference materials and then moved to devising operating protocols for the calibration and testing of gas analyzers. The ERLAP and the WHO continued to develop and improve the testing program, which has continued since 1992 and has been arranged annually since at least 2007.

The activities of the key NRLs and ERLAP participants led to the formation of the Air Quality National Reference Laboratory Network (AQUILA) and participation in CEN working groups to develop formal standard methods for each of the pollutants. After many

years of preparation, this culminated in the publication of NO_x, CO, SO₂, and O₃ standard methods in 2005. These standards were adopted into the 2008/50/EC directive, and provided, for the first time, a legislative framework to evaluate analyzer performance and fitness for purpose. Users were able to specify that analyzers met a minimum performance standard, which ensured they fulfilled the required data quality objectives.

These tests, coupled with detailed procedures for operation, calibration, and ongoing quality assurance and quality control has had a dramatic effect on the performance of NRLs in subsequent IEs. Since 2005, over 95% of measurements in IEs have been *good*. In fact, with the exception of one exercise, 98% of IE measurements have been *good* since 2011.

This demonstrates that the work done since 1992 to devise and implement standard methods has had an overwhelmingly beneficial effect on the quality of measurements made by NRLs throughout Europe.

Exemplary Success Story: Measurement of Particulate Air Pollution

Particles can be characterized by a variety of parameters, such as mass concentration, number concentration, size, size distribution, surface area, radiation absorption, light reflection, or chemical analysis of compounds. The most common methods also reflected in the field of standardization are related to mass concentration measurement, particle size, and the chemical analysis of organic and metallic compounds of particulate matter. Several national SDOs, like the American Society for Testing and Materials (ASTM International), but also the international and regional SDOs ISO and CEN, have published standard methods to characterize air quality.

Whereas for gaseous pollutants several standard methods describe the preparation of standard atmospheres for calibration purposes (ISO 6141 through ISO 6145 on preparation of gas mixtures [4.47–51]), there is no such international equivalent for the preparation of particulate atmospheres. Most methods to characterize particulate air pollution are so-called methods by convention, but not necessarily traceable to SI units.

Physical Characterization. The most commonly used method to determine particulate pollution is a filter-based method, where ambient air enters a size-selective sampling head and further flows through a filter, where particles are deposited. A commonly used setup is described, for example, in the European standard EN 12341 [4.52], which is at the same time considered as the reference method for sampling and determination of the particulate matter (PM) size fractions PM_{2.5} and PM₁₀ with regard to EU air policy.

There are certain limitations to this reference method and it might not be the method with the highest metrological quality. This type of set up has been used for many years throughout the EU and the method has proven its suitability for practical use in air pollution monitoring.

Another important standard method developed by the CEN is EN 16450 [4.53], which describes performance requirements and procedures for automated PM measuring systems. Following this standard method, continuously working monitors are considered, for instance the oscillating microbalance mass sensor method, the beta-ray attenuation method, or optical methods such as light scattering.

While the traditional filter-(mass-)based ambient particle measurement biases the metric towards the measurement of large particles, the measurement of particle numbers shifts this emphasis to ultrafine particles (or nanoparticles). The European technical specification CEN/TS 16976 [4.54] describes the use and requirements for condensation particle counters. The ISO has published standards on the measurement of, for example, black smoke, asbestos fibers, and tire and road wear.

Chemical Characterization. The chemical characterization of particulate matter focuses on the content of ions, metals, polycyclic aromatic hydrocarbons, and elemental carbon/organic carbon in the PM matrix. There have been four EN standard methods developed by the CEN (EN 16913 [4.55], EN 16909 [4.56], EN 15549 [4.57], and EN 14902 [4.58]) to satisfy the measurement needs required by EU air policy. Further EN standard methods deal with the deposition of metals and polycyclic aromatic hydrocarbons. At the ISO level, standards exist to determine lead (ISO 9855 [4.59]) and polycyclic hydrocarbons (ISO 16362 [4.60]) in the particulate phase.

Estimating the Benefits from Standardization of this Success Story. At the European level, two international interlaboratory comparisons of standard reference methods were carried out between 2004 and 2006 [4.61] and then with a different setup in 2015 [4.62]. During the early exercises, a mobile laboratory visited monitoring stations and NRLs in 18 member states. The measurement results that did not match the data quality objectives of the EU directive [4.45] were 7.1% for PM₁₀ and 23.8% for PM_{2.5}. During the 2015 exercise, where 22 national samplers for each PM fraction were sampling at the same location, only 1.3% of the results did not match the data quality objective for PM₁₀ and 0.4% for PM_{2.5}. This strong improvement in performance can be partially explained by the different exercise setups, but certainly

the progress and wide acceptance of standard methods for PM_{2.5} and PM₁₀ have led to better quality and more harmonization in measurements as well.

4.4.3 Meteorological Measurements

Meteorological measurements are performed for a variety of reasons. They are used, for example, for the preparation of weather analyses, forecasts, severe weather warnings, the study of climate, local weather-dependent operations such as aerodrome flying operations, hydrology and agricultural meteorology, and for research in meteorology and climatology [4.29]. Usually the following meteorological parameters are measured and are thus the subject matter of standards [4.63]:

- Wind speed and direction
- Air temperature
- Air humidity
- Atmospheric pressure
- Precipitation
- Solar and terrestrial radiation
- Atmospheric turbidity

Meteorological measurements of these parameters are needed for measurement tasks such as [4.63]:

- General weather forecast and climatological applications
- Hydrological applications (e.g., flood warning, evaporation, water balance, and structural measurements)
- Wind and solar energy
- Source identification of air pollutants (e.g., depicting pollutant roses)
- Assessment of ambient air quality measurements (e.g., trend analyses, comparisons with other investigation areas, planning of industrial plants, and urban and regional planning)
- Input data for model calculations concerning the dispersion and transport of air pollutants (e.g., impact forecast, clean-air and precautionary plans, and smog situations) as well as for radiation protection, major accidents, disaster prevention, and environmental impact assessment
- Determination and assessment of the local climate and of its effects on humans, animals, plants, and materials (e.g., urban development planning, traffic planning, plant location planning, water management planning, urban climate, and climate of health resorts)
- Agrometeorological and forest meteorological assessment of plant populations and soils (e.g., vegetation management, pest control, and yield predictions)

Exemplary Success Story: Lidar Systems and the Definition of Conventional Range

Lidar systems have become commercially available instruments from many different vendors around the globe with applications like wind energy site assessment, wind turbine verification and control, operational meteorology, airport hazard detection, and air quality monitoring [4.64]. An ever-increasing number of commercial lidar systems is available and applied in lidar networks [4.65]. Accurate metrology is key to valuable measurements and every vendor promises, of course, that their respective lidar system shows good traceability of parameters and optimal performance. The international standards series ISO 28902 [4.66, 67], available since 2012 and with occasional additions, reduces the user's uncertainty about lidar characteristics and is thus increasing demand and confidence in the technology in the market. The series of standards is a good example of how standards eliminate information asymmetry between users and manufacturers, for example, by sharing scientific basics, methods that could be applied, and typical system characteristics.

Before standards were developed, lidar system owners simply had to trust the vendors and their research or had to perform their own research programs, for example, to compare different systems. Some vendors tended to report the maximum range of their lidar systems rather than the range that can be applied in practice. The maximum range varies significantly in different atmospheric conditions, such as precipitation, visibility, turbulence, aerosol types, and content [4.64]. The selection of the winning bid from a call for tender, for example, was quite difficult prior to standardization. One major step towards solving the issue of comparing different lidar systems is the so-called conventional range. Every vendor is asked to report this range, which is calculated for certain atmospheric characteristics, thus ensuring a uniform communication of this very important lidar characteristic. In addition, the standards series ISO 28902 gives companies a strategic tool to differentiate their products, creating market segmentation and a softening of competition.

4.4.4 Benefits and Shortcomings of Standardization in Atmospheric Measurements

The key benefits of standards in atmospheric measurements are:

- Prevention of information asymmetry: Standards reduce the degree of information asymmetry between the producer and consumer [4.68]. One group of stakeholders – public agencies – is particularly interested in the outcome of the standardization process,

as they are in need of the firm establishment of agreed-upon methods and the guidance to implement them. Public agencies have the most power to affect the future but at the same time have the least information about what would be the best choice. [4.69] therefore calls government agencies *blind giants*.

- Fair competition between vendors: Standards ensure better compliance with the rules of competition, by uncovering competitors who fail to comply.
- Reduction of transaction costs: Costs between producers and consumers can be reduced by reducing the amount of time consumers spend searching for the proper measurement device they want to buy, which generally also avoids customer dissatisfaction [4.10].
- Division of labor between administration and SDO: The job of public agencies is to set targets and timetables as well as to ensure the necessary implementation. The detailed technical work is performed by the SDOs. This way, administrations admit they cannot claim the required competence in this significant area of technical civilization. Administrations and SDOs are not in competition with each other, but there is a reciprocal relationship. The SDO provides the administration with expertise and a balance of interests, while the administration may offer the application of the law and other resources.
- Ensuring comparable data on air quality: The standardization of measurement and calibration methods combined with quality assurance programs, systems, and procedures has led to the availability of robust and comparable data on air quality in Europe, which are an important basis for impact assessments. By establishing international measurement standards, a worldwide comparability of air quality data will be reached.
- Boost economic growth: Standardization connects scientific developments with industry and regulations and is therefore an important boost to economic growth. The application of standard methods leads to confidence in measurements and a wide acceptance of results and data.
- Simplification of technical transfer: From the viewpoint of a developing country, international standards provide the transfer of technology from technological leaders to the developing country and thus lessen the dependence on imports [4.4, 70].

There are also several possible shortcomings:

- Amount of time for the development of a standard: Although SDOs are working on speeding up the standardization process, it takes an average of five

years to publish a standard [4.4, 71]. Although this is faster than it was in the 1970s and 1980s, when the average time to produce an international standard was seven years [4.17, 71], and in the 1990s when the average elapsed time was six years [4.71], it is still a frequent criticism of SDOs developing standards in sectors where technological advance is rapid [4.3]. The number of products with short product life cycles is growing, so there is an increasing need for standardization to be fast, although this may conflict with the wish to involve all interested parties in the process and to have consensus-based decision making [4.72]. To meet the demands of enterprises wanting faster results and sped up standardization processes in general, SDOs have launched faster standardization services like speci-

fications or reports for which participation and full consensus of all stakeholders are not necessarily required [4.71]. In addition, improved project management has proven to be successful at reducing delays.

- Underrepresentation of SME: Two groups of stakeholders, namely users and experts coming from small- and medium-sized enterprises, are often underrepresented due to their unwillingness or inability to spend substantial time and travel money for developing a standard. This is a known shortcoming not only in the field of atmospheric measurements [4.6]. Smaller enterprises usually get involved at the inquiry stage, where they can contribute by commenting on the draft standard.

4.5 Future Developments

Looking at standardization in general, we are still at a point in history where numerous countries are developing national standards at considerable cost. Then begins international standardization, which tries to use the knowledge of national standards and integrate it into a common international standard. As discussed earlier, standardization has the objective of harmonizing national standards to, for example, reduce trade barriers. If successful, the standards have to be changed in many countries. Industry, administration, users, etc., are faced with the need for conversion. The authors regard it as nonsensical to set national standards apart from each other at the national level, and then, when finished and introduced, laboriously coordinate them. It must therefore be achieved that international standardization starts as early as possible. It is a question of workload and efficiency. Why do the same work a dozen times in different countries when it can be done internationally for everyone? Cost also plays a role. Large countries can carry out extensive standardization work with numerous expert committees, whereas small or developing countries mostly cannot. This is because the sales of standard sheets do not cover the printing costs, and therefore cannot finance the standardization work.

Looking at standardization in the field of atmospheric measurements, numerous future challenges await us, including the following:

- Numerous studies have shown that air pollution is hazardous to human health (e.g., [4.21, 73, 74]) and was responsible for approximately seven million premature deaths worldwide in 2012 [4.75]. To tackle this problem, an important step would be the worldwide adoption of the WHO air quality guide-

lines into national air quality policies together with the prompt involvement of governments in monitoring their success [4.76, 77]. This is where standardization of atmospheric measurements comes into play. As of 2017, ISO/TC 146 Air quality offers a catalogue of 167 published and 34 international standards under preparation ranging from emission reduction and measurement of air pollutants to meteorological measurements [4.28]. The WHO guideline values and international standards are ready to be implemented and possibly updated, as the needs of developing countries may not yet be fully incorporated. The potential for the future is immense. It was shown that 27% of all countries in the world do not have any air quality policy and that there is no information available from an additional 12%, meaning that the implementation of air quality policy is pending in up to 39% of all countries in the world [4.77].

- In the case of changed preferences, or when new technologies become available inducing new questions, standards are introduced to find suitable solutions [4.78]. Recently, it has become more demanding to standardize atmospheric dispersion modeling approaches because citizens are interested in knowing the current air quality at their place of residence, which could be far away from a measurement station. Atmospheric dispersion modelling is used to establish a relationship between pollutant emissions and air quality in a given area [4.31]. Measurement data is needed to validate the model's output. In several regions of the world, for example in Europe, dispersion modelling is used as a tool to support air quality assessment, planning, and forecasting.

4.6 Further Reading

- Spivak, S.M. and Brenner, F.C.: *Standardization Essentials – Principles and Practice* (Marcel Dekker, New York, 2001)

References

- 4.1 European Commission: Guidelines on the applicability of Article 101 of the Treaty on the Functioning of the European Union to horizontal co-operation agreements. Notices from European Union institutions, bodies, offices and agencies, Off. J. Eur. Union C 11, 01 (2011), 14.01.2011
- 4.2 I. Mårtson: The essence of standardization and a way of calculating its benefits. In: *EURAS Yearbook of Standardization (EYS)*, Vol. 2, ed. by M.J. Holler (Accedo, München 1999) pp. 401–415
- 4.3 Department of Trade and Industry: *The Empirical Economics of Standards*, DTI Economics Paper, Vol. 12 (Department of Trade and Industry, London 2005)
- 4.4 Deutsches Institut für Normung e. V.: *Economic Benefits of Standardization – Summary of Results – Final Results and Practical Examples* (Beuth, Berlin 2000)
- 4.5 U. Blum: How standards make the world flat, *Homo Oecon.* 23(3/4), 347–377 (2006)
- 4.6 G.M.P. Swann: *The Economics of Standardization. Final Report for Standards and Technical Regulations Directorate – Department of Trade and Industry* (Manchester Business School, Manchester 2000)
- 4.7 Deutsches Institut für Normung e. V.: *The Economic Benefits of Standardization* (Beuth, Berlin 2011), An update of the study carried out by DIN in 2000
- 4.8 Standards Council of Canada: *Economic Value of Standardization* (Conference Board of Canada, Ottawa 2007)
- 4.9 Standards Australia: *Standards, Innovation and the Australian Economy* (Standards Australia, Canberra and Sydney 2006)
- 4.10 BERL economics: *The Economic Benefits of Standards to New Zealand* (The Standards Council of New Zealand and the Building Research Association of New Zealand, Wellington 2011)
- 4.11 Association Française de Normalisation: *The Economic Impact of Standardization – Technological Change, Standards and Long-Term Growth in France* (Association Française de Normalisation, Paris 2009)
- 4.12 ISO/IEC: *ISO/IEC Guide 2: Standardization and Related Activities – General Vocabulary* (ISO, Geneva 2004)
- 4.13 S.M. Spivak: Through the ages with standards. In: *Standardization Essentials – Principles and Practice*, ed. by S.M. Spivak, F.C. Brenner (Marcel Dekker, New York 2001) pp. 7–14
- 4.14 W. Ping: *A Brief History of Standards and Standardization Organizations: A Chinese Perspective*, East-West Center Working Paper No. 117 (East-West Center, Honolulu 2011)
- 4.15 R.C. McWilliam: Business standards and government: the roles taken by the British government in the formation of British standards. In: *EURAS Yearbook of Standardization (EYS)*, Vol. 3, ed. by M.J. Holler (Accedo, München 2000) pp. 323–344
- 4.16 N.F. Harriman: *Standards and Standardization* (McGraw-Hill, New York 1928)
- 4.17 ISO: *Friendship Among Equals – Recollections from ISO's First Fifty Years* (ISO Central Secretariat, Geneva 1997)
- 4.18 S.P. Oksala: National versus international standards: products and processes. In: *Standardization Essentials – Principles and Practice*, ed. by S.M. Spivak, F.C. Brenner (Marcel Dekker, New York 2001) pp. 91–100
- 4.19 R.B. Toth: The U.S. standardization system: a new perspective. In: *Standardization Essentials – Principles and Practice*, ed. by S.M. Spivak, F.C. Brenner (Marcel Dekker, New York 2001) pp. 131–147–159
- 4.20 E. Auriol, M. Benaim: Standardization in decentralized economies, *Am. Econ. Rev.* 90(3), 550–570 (2000)
- 4.21 M.E. Héroux, H. Ross Anderson, R. Atkinson, B. Brunekreef, A. Cohen, F. Forastiere, F. Hurley, K. Katsouyanni, D. Krewski, M. Krzyzanowski, N. Künzli, I. Mills, X. Querol, B. Ostro, H. Walton: Quantifying the health impacts of ambient air pollutants: recommendations of a WHO/Europe project, *Int. J. Public Health* 60, 619–627 (2015)
- 4.22 S.M. Spivak: National and international standardization. In: *Standardization Essentials – Principles and Practice*, ed. by S.M. Spivak, F.C. Brenner (Marcel Dekker, New York 2001) pp. 67–75
- 4.23 V. Simmering: *The Evolution of Standards*, Gabler Edition Wissenschaft (Deutscher Universitätsverlag, Wiesbaden 2003)
- 4.24 European Parliament, European Council: Regulation (EU) No 1025/2012 of the European Parliament and of the Council of 25 October 2012 on European standardization, Off. J. Eur. Union L 316, 12 (2012)
- 4.25 European Committee for Standardization: New approach and other directives, <https://www.cen.eu/work/supportLegislation/Directives/Pages/default.aspx>, Accessed 03 July 2021
- 4.26 Council Resolution of 7 May 1985 on a new approach to technical harmonization and standards (85/C 136/01), [http://eur-lex.europa.eu/legal-content/EN/TXT/?uri=celex:31985Y0604\(01\)](http://eur-lex.europa.eu/legal-content/EN/TXT/?uri=celex:31985Y0604(01)), Accessed 03 July 2021
- 4.27 European Committee for Standardization: CEN/TC 264 – Air quality, https://standards.cen.eu/dyn/www/f?p=204:7:0:::FSP_ORG_ID:6245&cs=178094E67E1897102F190938A48C7A285, Accessed 03 July 2021
- 4.28 International Organization for Standardization: ISO/TC 146 Air quality, <https://www.iso.org/committee/52702.html>, Accessed 03 July 2021

- 4.29 WMO: *Guide to Instruments and Methods of Observation, WMO-No. 8, Volume I – Measurement of Meteorological Variables* (WMO, Geneva 2018)
- 4.30 ISO 19926-1: *Meteorology – Weather Radar – Part 1: System Performance and Operation* (ISO, Geneva 2018)
- 4.31 World Health Organization Regional Office for Europe: *Air Quality Guidelines for Europe*, WHO Regional Publications, European Series, Vol. 91, 2nd edn. (WHO, Copenhagen 2000)
- 4.32 S. Nehr, I. Franzen-Reuter, C. Kucejko: New directions: future approaches to the standardized assessment of airborne pollutants affecting environmental quality, *Atmos. Environ.* **166**, 570–572 (2017)
- 4.33 ISO 7996: *Ambient Air – Determination of the Mass Concentration of Nitrogen Oxides – Chemiluminescence Method* (ISO, Geneva 1985)
- 4.34 ISO 10498: *Ambient Air – Determination of Sulphur Dioxide – Ultraviolet Fluorescence Method* (ISO, Geneva 2004)
- 4.35 ISO 13964: *Air Quality – Determination of Ozone in Ambient Air – Ultraviolet Photometric Method* (ISO, Geneva 1998)
- 4.36 EN 14211: *Ambient Air – Standard Method for the Measurement of the Concentration of Nitrogen Dioxide and Nitrogen Monoxide by Chemiluminescence* (CEN, Brussels 2012)
- 4.37 EN 14212: *Ambient Air – Standard Method for the Measurement of the Concentration of Sulphur Dioxide by Ultraviolet Fluorescence* (CEN, Brussels 2012)
- 4.38 EN 14625: *Ambient Air – Standard Method for the Measurement of the Concentration of Ozone by Ultraviolet Photometry* (CEN, Brussels 2012)
- 4.39 EN 14626: *Ambient Air – Standard Method for the Measurement of the Concentration of Carbon Monoxide by Non-dispersive Infrared Spectroscopy* (CEN, Brussels 2012)
- 4.40 EN 14662-1: *Ambient Air Quality – Standard Method for Measurement of Benzene Concentrations – Part 1: Pumped Sampling Followed by Thermal Desorption and Gas Chromatography* (CEN, Brussels 2005)
- 4.41 EN 14662-2: *Ambient Air Quality – Standard Method for Measurement of Benzene Concentrations – Part 2: Pumped Sampling Followed by Solvent Desorption and Gas Chromatography* (CEN, Brussels 2005)
- 4.42 EN 14662-3: *Ambient Air – Standard Method for the Measurement of Benzene Concentrations – Part 3: Automated Pumped Sampling with in Situ Gas Chromatography* (CEN, Brussels 2016)
- 4.43 EN 14662-4: *Ambient Air Quality – Standard Method for Measurement of Benzene Concentrations – Part 4: Diffusive Sampling Followed by Thermal Desorption and Gas Chromatography* (CEN, Brussels 2005)
- 4.44 EN 14662-5: *Ambient Air Quality – Standard Method for Measurement of Benzene Concentrations – Part 5: Diffusive Sampling Followed by Solvent Desorption and Gas Chromatography* (CEN, Brussels 2005)
- 4.45 European Parliament, European Council: Directive 2008/50/EC of the European Parliament and of the Council of 21 May 2008 on ambient air quality and cleaner air for Europe, *Off. J. Eur. Union* **L 152**, 1 (2008), 11.6.2008
- 4.46 European Parliament, European Council: Commission Directive (EU) 2015/1480 of 28 August 2015 amending several annexes to Directives 2004/107/EC and 2008/50/EC of the European Parliament and of the Council laying down the rules concerning reference methods, data validation and location of sampling points for the assessment of ambient air quality, *Off. J. Eur. Union* **L 226**, 4 (2015), 29.8.2015
- 4.47 ISO 6141: *Gas Analysis – Contents of Certificates for Calibration Gas Mixtures* (ISO, Geneva 2015)
- 4.48 ISO 6142: *Gas Analysis – Preparation of Calibration Gas Mixtures – Part 1: Gravimetric Method for Class I Mixtures* (ISO, Geneva 2015)
- 4.49 ISO 6143: *Gas Analysis – Comparison Methods for Determining and Checking the Composition of Calibration Gas Mixtures* (ISO, Geneva 2001)
- 4.50 ISO 6144: *Gas Analysis – Preparation of Calibration Gas Mixtures – Static Volumetric Method* (ISO, Geneva 2003)
- 4.51 ISO 6145: *Gas Analysis – Preparation of Calibration Gas Mixtures Using Dynamic Methods – Part 6: Critical Flow Orifices* (ISO, Geneva 2017)
- 4.52 EN 12341: *Ambient Air – Standard Gravimetric Measurement Method for the Determination of the pm10 or pm2,5 Mass Concentration of Suspended Particulate Matter* (CEN, Brussels 2014)
- 4.53 EN 16450: *Ambient Air – Automated Measuring Systems for the Measurement of the Concentration of Particulate Matter (pm10; pm2,5)* (CEN, Brussels 2017)
- 4.54 CEN/TS 16976: *Ambient Air – Determination of the Particle Number Concentration of Atmospheric Aerosol* (CEN, Brussels 2016)
- 4.55 EN 16913: *Ambient Air – Standard Method for Measurement of NO₃⁻, SO₄²⁻, Cl⁻, NH₄⁺, Na⁺, K⁺, Mg²⁺, Ca²⁺ in PM_{2,5} as Deposited on Filters* (CEN, Brussels 2017)
- 4.56 EN 16909: *Ambient Air – Measurement of Elemental Carbon (EC) and Organic Carbon (OC) Collected on Filters* (CEN, Brussels 2017)
- 4.57 EN 15549: *Air Quality – Standard Method for the Measurement of the Concentration of Benzo[a]Pyrene in Ambient Air* (CEN, Brussels 2008)
- 4.58 EN 14902: *Ambient Air Quality – Standard Method for the Measurement of Pb, Cd, As and Ni in the pm10 Fraction of Suspended Particulate Matter* (CEN, Brussels 2005)
- 4.59 ISO 9855: *Ambient Air – Determination of the Particulate Lead Content of Aerosols Collected on Filters – Atomic Absorption Spectrometric Method* (ISO, Geneva 1993)
- 4.60 ISO 16362: *Ambient Air – Determination of Particle-Phase Polycyclic Aromatic Hydrocarbons by High Performance Liquid Chromatography* (ISO, Geneva 2005)
- 4.61 F. Lagler, C. Belis, A. Borowiak: *A Quality Assurance and Control Program for PM_{2.5} and PM₁₀ measurements in European Air Quality Monitoring Networks*, EUR 24851 EN (Publications Office of the European Union, Luxembourg 2011)
- 4.62 F. Lagler, M. Barbieri, A. Borowiak, J. Putaud: *Evaluation of the Field Comparison Exercise for PM₁₀ and PM_{2.5} Ispra, February 13th April 9th, 2015*, EUR 28107 EN (Publications Office of the European Union, Luxembourg 2016)
- 4.63 Verein Deutscher Ingenieure: *VDI 3786 Part 1: Environmental meteorology – Meteorological measurements – Fundamentals* (Beuth, Berlin 2013)
- 4.64 J.-P. Cariou, L. Thobois, R. Parmentier, M. Boquet, S. Loaec: *Assessing the metrological capabilities*

- of Wind Doppler Lidars, http://www.tsc.upc.edu/clrc/wp-content/uploads/Manuscripts/clrc2013_submission_18.pdf, Accessed 03 July 2021
- 4.65 D. Althausen, S. Emeis, H. Flentje, J. Guttenberger, S. Jäckel, V. Lehmann, I. Mattis, C. Münkel, G. Peters, C. Ritter, M. Wiegner, H. Wille: Standards – an important step for the (public) use of lidars. In: *27th Int. Laser Radar Conf. (ILRC 27)*, EPJ Web of Conferences, Vol. 119 (2016)
- 4.66 ISO 28902-1: *Air Quality – Environmental Meteorology – Part 1: Ground-Based Remote Sensing of Visual Range by Lidar* (ISO, Geneva 2012)
- 4.67 ISO 28902-2: *Air Quality – Environmental Meteorology – Part 2: Ground-Based Remote Sensing of Wind by Heterodyne Pulsed Doppler Lidar* (ISO, Geneva 2017)
- 4.68 P. Jones, J. Hudson: The gains of standardization from reduced search costs. In: *EURAS Yearbook of Standardization (EYS)*, Vol. 1, ed. by M.J. Holler (Accedo, München 1997) pp. 331–346
- 4.69 P.A. David: Some new standards for the economics of standardisation in the information age. In: *Economic Policy and Technological Performance*, ed. by P. Dasgupta, P. Stoneman (Cambridge University Press, Cambridge 1987)
- 4.70 B. Bhagowalia: Standardization and quality assurance in developing countries. In: *Standardization Essentials – Principles and Practice*, ed. by S.M. Spivak, F.C. Brenner (Marcel Dekker, New York 2001) pp. 237–247
- 4.71 J. Farrell: *Choosing the Rules for Formal Standardization* (University of California, Berkeley 1996)
- 4.72 H.J. de Vries: *Standardization: A Business Approach to the Role of National Standardization Organizations* (Springer, Berlin 1999)
- 4.73 R.D. Brook, S. Rajagopalan, C.A. Pope: Particulate matter air pollution and cardiovascular disease: an update to the scientific statement from the American Heart Association, *Circulation* **68**, 224–230 (2010)
- 4.74 M. Adam, T. Schikowski, A.E. Carsin, Y. Cai, B. Jacquemin, M. Sanchez, A. Vierkötter, A. Marcon, D. Keidel, D. Sugiri, Z. Al Kanani, R. Nadif, V. Siroux, R. Hardy, D. Kuh, T. Rochat, P.-O. Bridevaux, M. Eeftens, M.-Y. Tsai, S. Villani, H. Chandra Phuleria, M. Birk, J. Cyrus, M. Cirach, A. de Nazelle, M.J. Nieuwenhuijsen, B. Forsberg, K. de Hoogh, C. Declerq, R. Bono, P. Piccioni, U. Quass, J. Heinrich, D. Jarvis, I. Pin, R. Beelen, G. Hoek, B. Brunekreef, C. Schindler, J. Sunyer, U. Krämer, F. Kauffmann, A.L. Hansell, N. Künzli, N. Probst-Hensch: Adult lung function and long-term air pollution exposure. ESCAPE: a multicentre cohort study and meta-analysis, *Eur. Respir. J.* **45**, 38–50 (2015)
- 4.75 WHO: *7 Million Premature Deaths Annually Linked to Air Pollution* (WHO, Geneva 2014)
- 4.76 M. Kutlar Joss, M. Eeftens, E. Gintowt, R. Kappeler, N. Künzli: Time to harmonize national ambient air quality standards, *Int. J. Public Health* **62**(4), 453–462 (2017)
- 4.77 B. Brunekreef, N. Künzli, J. Pekkanen, I. Annesi-Maesan, B. Forsberg, T. Sigsgaard, M. Keuken, F. Forastiere, M. Barry, X. Querol, R.M. Harrison: Clean air in Europe: beyond the horizon?, *Eur. Respir. J.* **45**, 7–10 (2015)
- 4.78 T. Vandemoortele: *Political and Economic Theory of Standards*, Faculteit Economie en Bedrijfswetenschappen No. 361 (Katholieke Universiteit, Leuven 2011), Doctoral Dissertation

Simon Jäckel

VDI e.V. – The Association of German Engineers
Düsseldorf, Germany
jaeckel@vdi.de



Simon Jäckel is a DIN-certified standardization expert and project manager at the VDI Society on Automotive and Traffic Systems Technology and secretary of the VDI Society Technologies of Life Sciences. After his study of applied geosciences at Darmstadt University of Technology, he worked for several years at the VDI/DIN Commission on Air Pollution Prevention in the fields of meteorology and environmental measurements.

Annette Borowiak

Air and Climate Unit
Joint Research Centre
Ispra, Italy
annette.borowiak@ec.europa.eu



Annette Borowiak is a project leader at the European Commission's Joint Research Centre in Ispra, Italy. She has a chemical engineering background and has worked on ambient air monitoring for more than 25 years. Her areas of interest include the development, validation, and standardization of measurement techniques for gaseous and particulate air pollutants, the organization of quality assurance programs, and supporting the implementation and development of European air quality legislation.



Brian Stacey

Ricardo Energy and Environment
Didcot, UK
brian.stacey@ricardo.com

With 30 years' experience, Brian Stacey is Ricardo's air quality monitoring knowledge leader. He oversees ISO 17025 accredited quality assurance and quality control for UK air pollution measurements. He participates in collaborative programs on air quality monitoring techniques in the UK and Europe. As one half of the certification committee, Brian reviews and assesses the demonstration of equivalence tests under the UK government "MCERTS for PM in the UK" scheme.

Physical Quantities

5. Physical Quantities

Thomas Foken , Olaf Hellmuth , Bernd Huwe , Dietrich Sonntag

This chapter follows the tradition of classical textbooks on meteorology and presents relevant parameters for meteorology, including measurements in dry and moist air, water, and soil, as well as cloud physical quantities. Tables present the pressure, temperature, and humidity dependency of these parameters. Furthermore, soil physical quantities and calculation procedures are presented to calculate parameters of the solar and Earth system and of the time system.

5.1	Selection of Parameters	108	5.4.2	Water Vapor, Dry Air, and Humid Air	116
5.2	History and Thermodynamic Standards	108	5.4.3	Water, Seawater, and Ice	129
5.2.1	ITS-90	109	5.5	Parameterization of Optical Properties of Clouds	130
5.2.2	TEOS-10.....	109	5.5.1	Warm Clouds.....	130
5.3	Units and Constants	111	5.5.2	Ice Clouds (Cold Clouds).....	137
5.4	Parameters of Air, Water Vapor, Water, and Ice	115	5.6	Absorption Coefficients for Water Vapor, Ozone, and Carbon Dioxide	141
5.4.1	Calculation of Data According to TEOS-10.....	115	5.6.1	Effective Mass Absorption Coefficient for Water Vapor and Ozone.....	141
			5.6.2	Effective Molar Absorption Coefficient for Carbon Dioxide.....	142
			5.7	Parameters of Soil	142
			5.8	Time and Astronomical Quantities	146
			5.8.1	Time Definitions	146
			5.8.2	Calculation of Astronomical Quantities	146
			5.9	Tables in Other Chapters	147
			5.10	Future Developments	148
			5.11	Further Reading	148
			References		148

Physical quantities and their dependencies on temperature, pressure, or humidity are essential for atmospheric measurements. Even when the accuracy of several measurements is much lower than the possible accuracy of physical quantities, in the following, the quantities are given in the highest possible accuracy on the basis of the newest scales, like the International Temperature Scale of 1990 (ITS-90). For several quantities of

metrological interest, their dependencies on temperature, pressure, and humidity are given in the typical meteorological range of application. The corresponding tables are presented here, even if the quantities can be easily calculated from the given equations, because the visual inspection of the quantities and its sensitivity to other influencing factors is very instructive for atmospheric measurements.

Electronic Supplementary Material The online version contains supplementary material available at https://doi.org/10.1007/978-3-030-52171-4_5.

5.1 Selection of Parameters

The basis for the measurement of all parameters is the International System of Units (SI). Only a few parameters are also given in other units, which are mainly used in some Anglo-American countries. The parameters were selected according to recent textbooks on meteorology or updated versions of former books with tables of atmospheric parameters. If possible, all data are given for the new temperature scale ITS-90.

The tables in this chapter provide the most relevant physical units and constants (Sect. 5.3), thermodynamic parameters of air, water vapor, water, and ice (Sect. 5.4), optical parameters of clouds (Sect. 5.5), absorption coefficients of selected absorber gases (Sect. 5.6), physical parameters of soil (Sect. 5.7), and the time and astronomical quantities required for many meteorological measurements (Sect. 5.8).

This chapter does not aim at a complete documentation of the relevant atmospheric parameters necessary for the execution and evaluation of atmospheric measurements. Instead, it is intended to facilitate the exploitation of this book in daily measurement practice. Already for some time now, books have lost their exclusive status as the primary media to transfer and communicate such data. Owing to their flexibility, storage capacity, and network capabilities, nowadays databases and/or software tools and even apps occupy the traditional place of book tables. In any case, a meaningful documentation and comprehensive references to the basic sources of the data are indispensable. Table 5.1 gives a list of such databases without claiming completeness.

5.2 History and Thermodynamic Standards

Tables or lists of properties of the dry and wet atmosphere are part of many textbooks of the nineteenth and early twentieth century. A complete list of these books is given by *Karl Schneider-Carius* (1896–1959) [5.3]. The first book of meteorological tables was published in 1852 by *Arnold Henry Guyot* (1807–1884) [5.4], a reprint of which was recently (2012) published. The first edition of the International Meteorological Tables was published in 1890 on the basis of a conclusion of the International Meteorological Congress held in Rome in 1879 (Chap. 1).

Franz Linke (1878–1944) edited a Handbook of Meteorology (*Meteorologisches Taschenbuch*) with five volumes [5.5], where volumes 1 and 2, published in 1931

and 1933, are the first edition, and volumes 3–5 from 1939 are the second edition. The book was edited after the Second World War by *Franz Baur* (1887–1977) and issued in three volumes [5.6–8], where volume II has a large part with tables with relevant parameters.

The World Meteorological Organization (WMO) decided in Toronto in 1953 to update the International Meteorological Tables from 1890. After the work of a panel of experts, S. Letestu edited the new tables in 1966, which were updated up to 1973 [5.9]. This material was the main reference for the tables in Landolt–Börnstein [5.1], see below.

A general handbook of parameters and tables from physics, chemistry, and materials science was published

Table 5.1 List of some relevant databases of atmospheric and other parameters

Name	Parameter	URL, Accessed 03 July 2021
Springer Materials (identical to [5.1])	Physical and chemical properties of the atmosphere	http://materials.springer.com
The Max-Planck-Institute-Mainz UV/VIS Spectral Atlas of Gaseous Molecules of Atmospheric Interest	Spectroscopic data	http://satellite.mpic.de/spectral_atlas
Thermodynamic Equation Of Seawater – 2010 (TEOS-10)	International thermodynamic standard of water, ice, seawater, and humid air and their mutual equilibria for oceanological and atmospheric applications	http://www.teos-10.org/
International Association for the Properties of Water and Steam (IAPWS)	Thermophysical properties of water and steam for industrial and scientific applications	http://www.iapws.org/
National Institute of Standards and Technology (NIST)	NIST ITS-90 Thermocouple Database NIST Standard Reference Database 60, Version 2.0	https://srdata.nist.gov/its90/main/its90_main_page.html
SPECTRA [5.2]	System Spectroscopy of Atmospheric Gases	http://spectra.iao.ru/home

Table 5.2 Tables of relevant atmospheric parameters in Landolt–Börnstein, Meteorology, Part 4A [5.1] and similar tables in Linke’s Meteorologisches Taschenbuch [5.7], and comparable tables in this chapter

Table of parameters	Landolt–Börnstein [5.1]	Linke [5.7]	Comparable table in this chapter
Specific heat capacity	Tables 9, 10	Tables 53, 54	Tables 5.34, 5.35, 5.40
Specific latent heat	Table 11	Tables 53, 54	Table 5.40
Virtual temperature increment of saturated humid air	Table 13	–	Tables 5.19, 5.20
Compressibility of dry and humid air	Table 15	–	–
Mass density of dry and humid air	Tables 14, 15	Table 45	Tables 5.17, 5.18, 5.22, 5.23
Mass density of water vapor at saturation with respect to liquid water and ice	Tables 16–19	Table 50	Tables 5.15, 5.16
Water vapor pressure at saturation with respect to water and ice	Table 22	Table 46	Tables 5.10, 5.11
Potential temperature (and inverse Exner function)	Tables 20, 21	–	see Chap. 1
Dewpoint temperature	Table 23	–	Tables 5.26, 5.27
Frostpoint temperature	Table 24	–	Tables 5.28, 5.29
Mixing ratio as function of dry and wet-bulb and ice-bulb temperature	Table 25, 26	–	see Chap. 8
Conversion of geometrical in geopotential height	Table 27	Table 39	Table 5.9
ICAO (International Civil Aviation Organization) standard atmosphere	Table 34	Table 33	Table 5.9

in 1883 by *Hans Heinrich Landolt* (1831–1910) and *Richard Börnstein* (1852–1913) in one volume. Since then this book has been a standard work of natural science. The 6th edition (1951–1976) already comprised 15 volumes. Meteorology was first considered in this edition of the Landolt–Börnstein and published in 1952 [5.10]. In 1980, this series was finished with the title *Landolt–Börnstein: Zahlenwerte und Funktionen aus Physik, Chemie, Astronomie, Geophysik und Technik* (Numerical Data and Functional Relationships in Physics, Chemistry, Astronomy, Geophysics, and Techniques), and a new series started with the title *Landolt–Börnstein: Numerical Data and Functional Relationships in Science and Technology – New Series*. Up to the end of 2017 about 560 volumes were published. References should be made to the single chapters but not to volumes. The Landolt–Börnstein is now part of the online Springer Materials (<http://materials.springer.com/>). Meteorology is part of Group V *Geophysics and Space Research*; Volume 4 *Meteorology* edited by *G. Fischer* [5.1] was published in 1987 and is still part of Springer Materials. Of meteorological relevance are the volumes 4A *Meteorology · Thermodynamical and Dynamical Structures of the Global Atmosphere* and 4B *Meteorology · Physical and Chemical Properties of the Air*. This chapter is mainly based on volume 4A, while 4B with cloud physical parameters and radiation is more relevant for the remote sensing chapters (see Parts C and D). The tables can still be used, but they are based on the temperature scale IPTS-68 and not on the recently valid scale ITS-90, which is not relevant within

the accuracy of many applications. The most relevant tables for the present book are listed in Table 5.2.

5.2.1 ITS-90

The Committee on Data for Science and Technology (CODATA) of the International Council of Scientific Unions (ICSU) published a table of physical constants [5.11] in 1973. On this basis the International Temperature Scale 1968 (IPTS-68) was developed [5.12]. This temperature scale differs from the Thermodynamic Temperature Scale (TTS) from +0.013 to –0.026 K [5.13]. Following the new recommendations by CODATA for physical constants in 1986 [5.14, 15], overcoming shortcomings of IPTS-68, and realizing a recommendation of the Committee on Thermometry (CCT), the International Committee on Weight and Measures (CIPM) adapted the new temperature scale ITS-90 [5.16], which is identical with TTS [5.13]. Differences between IPTS-68 and ITS-90 are shown in Table 5.3.

5.2.2 TEOS-10

The emergence of highly accurate mathematical formulations of thermodynamic potentials for fluid water, air, ice, and seawater in the first decade of the new millennium stimulated the development of a new seawater standard by the Scientific Committee on Oceanic Research (SCOR) and the International Association for Physical Science of the Ocean (IAPSO) Working Group

Table 5.3 Differences of the temperature scales IPTS-68 (index 68) and ITS-90 (index 90) for temperature (T) and water vapor pressure of saturation with respect to water (E_w) and ice (E_i) [5.13, 16]

Temperature ITS-90 t_{90} (°C)	Water vapor pressure of saturation $E_w(t_{90})$ (hPa)	$E_w(t_{90}) - E_w(t_{68})$ (hPa)	$t_{90} - t_{68}$ (K)
40	73.8530	0.0403	-0.010
30	42.4703	0.0183	-0.007
20	23.3925	0.0071	-0.005
10	12.2813	0.0019	-0.002
0.01	6.11657	0.0000	0.000
0	6.11213	0.0000	0.000
-10	2.8652	-0.050	0.002
-20	1.2559	-0.040	0.004
-30	0.51032	-0.028	0.006

Temperature ITS-90 t_{90} (°C)	Water vapor pressure of satu- ration $E_i(t_{90})$ (hPa)	$E_i(t_{90}) - E_i(t_{68})$ (hPa)
0.01	6.11657	0.000
0	6.11154	0.000
-10	2.59893	-0.047
-20	1.03239	-0.040
-30	0.379994	-0.023
-40	0.128370	-0.011

127 (WG 127). This new standard is based on the realization of a very general algorithm to describe thermodynamic systems:

1. Formulation of the fundamental thermodynamic relation of the system of interest.
2. Determination of a suitable thermodynamic potential (containing by definition all information about the system) from experimental data or on the basis of microscopic theories within the framework of statistical thermodynamics.
3. Calculation of the thermodynamic properties, the thermic and caloric equations of state, and all other state variables of interest from the thermodynamic potential.

The joint efforts of WG 127 to realize this concept resulted in a new seawater standard for oceanological and meteorological applications, called the International Thermodynamic Equation Of Seawater 2010 (TEOS-10), which was adopted in June 2009 by the International Oceanographic Commission of the United Nations Educational, Scientific, and Cultural Organization (UNESCO/IOC) on its 25th General Assembly in Paris. To support the application of this standard, WG 127 developed a comprehensive source code library for

the thermodynamic properties of liquid water, water vapor, ice, seawater, and humid air, referred to as the sea-ice-air (SIA) library. The background information and equations (including references for the primary data sources) required for the determination of the properties of single phases and components, as well as of phase transitions and composite systems as implemented in the library, were presented in two key papers [5.17, 18], the TEOS-10 Manual [5.19], and the introductory and guidance papers [5.20, 21]. TEOS-10 is based on four independent thermodynamic functions defined in terms of the independent observables temperature, pressure, density, and salinity: a Helmholtz function of fluid water [5.22, 23], a Gibbs function of ice [5.24, 25], a Gibbs function of sea salt dissolved in water [5.26–28], and a Helmholtz function for dry air [5.29]. In combination with air-water cross-virial coefficients [5.30–32] this set of thermodynamic potentials is used as the primary standard for pure water (liquid, vapor, and solid), seawater, and humid air from which all other properties are derived by mathematical operations, i.e., without the need for additional empirical functions.

The IAPWS-95 fluid water formulation, which is of key importance for the description of atmospheric water within the framework of TEOS-10, is based on ITS-90 and on the evaluation of a comprehensive and consistent data set, which was assembled from a total of about 20 000 experimental data of water. The authors took into account all available information given in the scientific articles describing the data collection and critically reexamined the available data sets with respect to their internal consistency and their basic applicability for the development of a new equation of state for water [5.22, 23]. Only those data were incorporated into the final nonlinear fitting procedure that were judged to be of high quality. These selected data sets took into account experimental data that were available by the middle of the year 1994 [5.22]. A compilation of the experimental data used to develop IAPWS-95 can be downloaded from the official IAPWS website (see the reference in Table 5.1).

The availability of reliable experimental data on subcooled liquid water (i.e., metastable with respect to the solid) was restricted to a few data sets for several properties only along the isobar $p = 1013.25$ hPa, which set the lower limit of the temperature range of IAPWS-95 (and so of TEOS-10) to $T = 236$ K ($t = -37.15$ °C) [5.22]. This temperature is called the temperature of homogeneous ice nucleation (or homogeneous freezing temperature), T_H , which represents the lower limit below which it is very difficult to subcool water. Therefore, the TEOS-10 table values presented in Sect. 5.4 are restricted to temperatures $t \geq -37.15$ °C. The assessment of the accuracy of the IAPWS (Inter-

national Association for the Properties of Water and Steam) guideline IAPWS-95 in the temperature range of subcooled water ([5.22, Section 7.3.2]) revealed that TEOS-10 fully satisfies the meteorological needs with respect to accuracy down to this temperature.

Classical thermodynamic tables usually also contain data of subcooled water, which were extrapolated to temperatures below the homogeneous freezing temperature. While such low temperatures can occur in the upper troposphere, stratosphere, and mesosphere, the properties of liquid water in this range are not accessible by experiments, because even tiny water droplets will homogeneously freeze to ice. Upon hyperquenching of liquid water at extremely high cooling rates, water will be transformed at $T_{\text{VITR}} = 155 \text{ K}$ into an amorphous (vitreous) form, called amorphous ice [5.33]. While information on subcooled water in the temperature interval between T_{VITR} and T_{H} are experimentally not accessible (i.e., direct experimental proofs of the existence of water in that range are not available), different theories on the behavior of sub-

cooled water in this temperature range exist [5.33, 34]. Assuming the thermodynamic continuity between liquid water and amorphous ice at atmospheric pressure, the authors of [5.33] used experimental data on amorphous ice to constrain the thermodynamic functions of water at intermediate temperatures $T_{\text{VITR}} \leq T \leq T_{\text{H}}$. Employing experimental data on subcooled water and amorphous ice, those authors derived a user-friendly parameterization of the saturation water vapor pressure with respect to subcooled water in the extended temperature range of $123 \text{ K} \leq T \leq 332 \text{ K}$ [5.33, Eq. 10], which is recommended for application at atmospheric temperatures below the homogeneous freezing temperature. A list with typographical errors in the literature on vapor pressures for atmospheric applications (inclusive documents of WMO) is given in [5.33], which are highly relevant for any application of the incriminated expressions and table values and which were commented by those authors with the sentence “*no doubt there are additional errors awaiting discovery*”.

5.3 Units and Constants

In the present book, SI units are used (Table 5.4) for most of the quantities. However, in some Anglo-American countries non-SI units are still in use (Table 5.5). According to the recent definition of SI units, seven constants are chosen in such a way that any unit of the SI can be written either through a defining constant itself or through products or quotients of defining constants [5.35]: the unperturbed ground-state hyperfine transition frequency of the caesium 133 atom, the speed of light in vacuum, the Planck constant, the elementary charge, the Boltzmann constant, the Avogadro constant, and the luminous efficacy of monochromatic radiation of frequency $540 \times 10^{12} \text{ Hz}$ (Table 5.6).

Even though the accuracy of meteorological measurements is at most only three to five significant digits,

the following physical constants in Table 5.6 are given with errors expressed in ppm, because sometimes in the literature different values are reported. Temperature-dependent parameters are listed in Table 5.7.

In meteorology several standard parameters are given to simplify calculations or make calculations comparable (Table 5.8). They base partly on the ICAO-Standard Atmosphere [5.43], which gives a distribution of temperature, pressure, and density with height for air navigation (Table 5.9). This model atmosphere uses standard parameters at sea level (1013.25 hPa, 15.0 °C) and a lapse rates of -0.0065 K m^{-1} up to a height of 11 000 m, isothermal conditions up to 20 000 m and an increase of the temperature of 0.0010 K m^{-1} up to 32 000 m.

Table 5.4 SI-units used in physics and meteorology, the basic units are **bold** highlighted [5.35, 36]

Name	SI-unit	Symbol	Calculation
Length	meter	m	
Plane angle	radian	rad	1 rad = 1 m m ⁻¹
Solid angle	steradian	sr	1 sr = 1 m ² m ⁻²
Time	second	s	
Velocity		m s ⁻¹	1 km h ⁻¹ = (1/3.6) m s ⁻¹
Acceleration		m s ⁻²	
Frequency	hertz	Hz	1 Hz = 1 s ⁻¹
Mass	kilogram	kg	
Density		kg m ⁻³	
Impulse		kg m s ⁻¹	1 kg m s ⁻¹ = 1 N s
Force	newton	N	1 N = 1 kg m s ⁻²
Pressure, stress	pascal	Pa	1 Pa = 1 N m ⁻² 1 Pa = 1 kg m ⁻¹ s ⁻²
Air pressure	hectopascal	hPa	1 hPa = 100 Pa = 0.1 kPa
Work, energy, amount of heat	joule	J	1 J = 1 N m = 1 W s 1 J = 1 kg m ² s ⁻²
Power, radiant flux	watt	W	1 W = 1 J s ⁻¹ = 1 N m s ⁻¹ 1 W = 1 kg m ² s ⁻³
Energy flux density		W m ⁻²	1 W m ⁻² = 1 kg s ⁻³
Thermodynamic temperature	kelvin	K	
Celsius temperature	degree Celsius	°C	0 °C = 273.15 K
Temperature difference	kelvin, degree Celsius	K, °C	
Amount of substance	mole	mol	
Electric current	ampere	A	
Voltage, electric potential difference	volt	V	1 V = 1 W A ⁻¹ = 1 kg m ² s ⁻³ A ⁻¹
Electric charge	coulomb	C	1 C = 1 s A
Capacitance	farad	F	1 F = 1 C V ⁻¹ = 1 kg ⁻¹ m ⁻² s ⁴ A ²
Electrical resistance	ohm	Ω	1 Ω = 1 V A ⁻¹ = 1 kg m ² s ⁻³ A ⁻²
Electrical conductance	siemens	S	1 S = 1 A V ⁻¹ = 1 kg ⁻¹ m ⁻² s ³ A ²
Magnetic flux	weber	Wb	1 Wb = 1 V s = 1 kg m ² s ⁻² A ⁻¹
Magnetic flux density	tesla	T	1 T = 1 Wb m ⁻² = kg s ⁻² A ⁻¹
Inductance	henry	H	1 H = 1 Wb A ⁻¹ = kg m ² s ⁻² A ⁻²
Luminous intensity	candela	cd	
Luminous flux	lumen	lm	1 lm = 1 cd sr
Illuminance	lux	lx	1 lx = 1 lm m ⁻²
Activity referred to a radionuclide, radioactivity	becquerel	Bq	1 Bq = 1 (decay) s ⁻¹
Absorbed dose, kerma	gray	Gy	1 Gy = 1 J kg ⁻¹ = 1 m ² s ⁻²
Dose equivalent	sievert ^a	Sv	1 Sv = 1 J kg ⁻¹ = 1 m ² s ⁻²
Catalytic activity	katal	kat	1 kat = 1 mol s ⁻¹

^a 1 Sv = Q × 1 Gy, with the dimensionless factor Q [5.37]**Table 5.5** Non-SI units used in meteorology in some Anglo-American countries [5.38]

Name	Non-SI-unit	Symbol	Calculation
Length	feet	ft	1 ft = 0.305 m
Length	inch	in	1 in = 0.0254 m
Mass	pound	lb	1 lb = 0.45359237 kg ≈ 0.454 kg
Temperature	degree Fahrenheit	°F	t(°F) = 1.8 t(°C) + 32 t(°F) = 1.8 T(K) - 459.67
Speed	km per hour	km h ⁻¹	1 km h ⁻¹ = (1/3.6) m s ⁻¹
	miles per hour	mph	1 mph = 0.447 m s ⁻¹
	knot	kn	1 kn = 0.515 m s ⁻¹

Table 5.6 Physical constants according to the international temperature scale ITS-90 [5.13, 15] and recent SI definitions for general constants [5.35]

Constant	Symbol	Value	Error Reference
General constants			
Speed of the light in vacuum	c	$299\,792\,458\text{ m s}^{-1}$	exact
Planck's constant	h	$6.62607015 \times 10^{-34}\text{ J s}$	exact
Avogadro constant	N_A	$6.02214076 \times 10^{23}\text{ mol}^{-1}$	exact
Boltzmann constant	k	$1.380649 \times 10^{-23}\text{ J K}^{-1}$	exact
Elementary charge	e	$1.602176634 \times 10^{-19}\text{ C}$	exact
Unperturbed ground state hyperfine transition frequency of the caesium 133 atom	$\Delta\nu_{\text{Cs}}$	$9\,192\,631\,770\text{ Hz}$	exact
Luminous efficacy of monochromatic radiation of frequency $540 \times 10^{12}\text{ Hz}$	K_{cd}	683 lm W^{-1}	exact
Physical-chemical constants			
Atom mass $^{12}\text{C}/12$	m_{u}	$1.6605402(10) \times 10^{-27}\text{ kg}$	0.59
Universal gas constant	R	$8.314510(70)\text{ J mol}^{-1}\text{ K}^{-1}$	8.4
Molar volume (ideal gas)	RT_0/p_0	$22.41410(19)\text{ l mol}^{-1}$	8.4
Stefan–Boltzmann constant	σ_{SB}	$5.67051(19) \times 10^{-8}\text{ W m}^{-2}\text{ K}^{-4}$	34
Wien's constant	$\lambda_{\text{max}}T$	$2.897756(24) \times 10^{-3}\text{ m K}$	8.4
Thermodynamical constants			
Molar mass of dry air	M_{a}	$0.0289645(5)\text{ kg mol}^{-1}$	17
Molar mass of water vapor	M_{w}	$0.01801528(50)\text{ kg mol}^{-1}$	27
Ratio $M_{\text{w}}/M_{\text{a}}$	ε	$0.62198(2)$	33
Gas constant of dry air	R_{d}	$287.0586(55)\text{ J kg}^{-1}\text{ K}^{-1}$	19
Gas constant of water vapor	R_{w}	$461.525(13)\text{ J kg}^{-1}\text{ K}^{-1}$	29
Other constants and quantities			
Psychrometric constant (water)		$6.53 \times 10^{-4}(1 + 0.000944t_{\text{w}})p\text{ K}^{-1}$ ^a	[5.13]
Psychrometric constant (ice)		$5.75 \times 10^{-4}p\text{ K}^{-1}$	[5.13]
Temperature of the triple point of water		273.16 K	
Earth angular velocity	Ω	$7.292115 \times 10^{-5}\text{ rad s}^{-1}$	[5.39, 40]
Coriolis parameter	f	$1.458423 \times 10^{-4}\text{ sin } \varphi\text{ s}^{-1}$	[5.39, 40]
Solar constant	S	Energy units: 1361 W m^{-2} Kinematic units: 1.119 K m s^{-1}	[5.41]
^a t_{w} wet-bulb temperature in $^{\circ}\text{C}$			

Table 5.7 Temperature and pressure-dependent physical parameters given for atmospheric standard conditions (1013.25 hPa and 288.15K, see Table 5.8)

Quantity	Symbol	Value	Remark
Air			
Specific heat capacity of dry air at constant pressure	$(c_p)_d$	1006.0 J kg ⁻¹ K ⁻¹	Table 5.34, [5.17, 18]
Specific heat capacity of dry air at constant volume	$(c_v)_d$	717.5 J kg ⁻¹ K ⁻¹	Table 5.35, [5.17, 18]
Ratio of the specific heat capacities for dry air	$(c_p/c_v)_d$	1.4	
Ratio of the gas constant and the specific heat capacities for dry air	R_d/c_{pd}	0.285	
Mass density of dry air	ρ_d	1.225 kg m ⁻³	Tables 5.17, 5.18, [5.17, 18]
Dynamic molecular viscosity	$\mu = \rho_d \nu$	1.797 × 10 ⁻⁵ kg m ⁻¹ s ⁻¹	Table 5.37 [5.42]
Thermal conductivity	k	2.52 × 10 ⁻² W m ⁻¹ K ⁻¹	Table 5.37 [5.42]
Molecular mass diffusivity (kinematic viscosity)	$\nu_m = \mu/\rho$	1.466 × 10 ⁻⁵ m ² s ⁻¹	Table 5.37 [5.42]
Molecular thermal diffusivity	$\nu_{th} = k/(c_p \rho)$	2.043 × 10 ⁻⁵ m ² s ⁻¹	Table 5.37 [5.42]
Molecular Prandtl number	$Pr = \nu_m/\nu_{th}$	0.718	Table 5.37 [5.42]
Water vapor			
Specific isobaric heat capacity of saturated water vapor	$(c_p)_v$	1900.2 J kg ⁻¹ K ⁻¹	Table 5.34, [5.17, 18]
Specific isochoric heat capacity of saturated water vapor	$(c_v)_v$	1431.4 J kg ⁻¹ K ⁻¹	Table 5.35, [5.17, 18]
Ratio of the isobaric specific heat capacities	$(c_p/c_v)_v$	1.328	
Ratio of the water vapor gas constant and the isobaric specific heat capacity	R_w/c_{pv}	0.243	
Mass density of saturated water vapor	ρ_v	1.284 × 10 ⁻² kg m ⁻³	Tables 5.15, 5.16, [5.17, 18]
Water			
Specific isobaric heat capacity	$(c_p)_w$	4188.46 J kg ⁻¹ K ⁻¹	Table 5.40, [5.17, 18]
Specific isochoric heat capacity	$(c_v)_w$	4174.42 J kg ⁻¹ K ⁻¹	Table 5.40, [5.17, 18]
Mass density	ρ_w	999.1 kg m ⁻³	Table 5.38, [5.17, 18]
Latent heat of vaporization	λ	2.4654 × 10 ⁶ J kg ⁻¹	Table 5.40, [5.17, 18]

Table 5.8 Standard values used in meteorology

Constant	Symbol	Value	Reference
Standard air pressure	p_0	1013.25 hPa	[5.43, 44]
Standard temperature	T_0	288.15 K = 15.0 °C	[5.43, 44]
Freezing point of water		273.15 K = 0.0 °C	[5.16]
Standard air density	ρ_0	1.2250 kg m ⁻³	[5.43]
Standard acceleration due to gravity at latitude 45°	g^a	9.80665 m s ⁻²	[5.44]
Constant gravity acceleration	g_0	9.81 m s ⁻²	[5.45]

^a $g^{45^\circ} = 9.806199203 \text{ m s}^{-2}$ according to Geodetic Reference System 1980 [5.40]

Table 5.9 ICAO Standard Atmosphere [5.43, 46]

Geopotential height (gpm)	Geometric height (m)	p (hPa)	T (°C)	ρ_{air} (kg m ⁻³)
-1000	-1000	1139.29	21.5	1.3470
0	0	1013.25	15.0	1.2250
1000	1000	898.75	8.5	1.1116
2000	2001	794.95	2.0	1.0065
3000	3001	701.09	-4.5	0.9091
5000	5004	540.20	-17.5	0.7361
7000	7008	410.61	-30.5	0.5895
9000	9013	307.42	-43.5	0.4663
11 000	11 019	226.32	-56.5	0.3692
20 000	20 063	54.75	-56.5	0.08803
32 000	32 162	8.68	-44.5	0.01332
47 000	47 350	1.11	-2.5	0.001497
51 000	51 413	0.670	-2.5	0.0009069
71 000	71 802	0.040	-58.5	0.00006421
80 000	81 020	0.0089	-76.5	0.00001570

5.4 Parameters of Air, Water Vapor, Water, and Ice

All tables in this section were calculated on the basis of equations and software sources according to TEOS-10 [5.17, 18] and have not been published before.

5.4.1 Calculation of Data According to TEOS-10

Owing to its rigorous foundation on phenomenological and statistical thermodynamics, the employment of carefully selected experimental data and IAPWS guidelines, its quality assurance according to IAPWS certified protocols and procedures, and its adoption as an international seawater standard for oceanography by UNESCO/IOC, TEOS-10 provides the hitherto most advanced standard for the calculation of thermodynamic properties for meteorological applications. The disposability of the TEOS-10 SIA library in the program languages FORTRAN and Visual Basic allows a user-specific determination of any thermodynamic parameter from the generating thermodynamic potentials, which is defined within the framework of classical thermodynamics. However, for quick-look purposes, selected lookup tables of the atmospherically most important parameters and their dependence on temperature, pressure, humidity, etc., are presented here with a parameter resolution specified as a compromise between the table size and user needs.

In TEOS-10 the mass density of humid air, $\rho_a(m_d, T, p)$ is determined as a function of three independent observables: the mass fraction of dry air m_d , the temperature T , and the pressure p . The mass fraction of dry air is related to the specific humidity q and mole fraction of water vapor in humid air χ_w by

$$m_d = 1 - q = \frac{1 - \chi_w}{1 - (1 - \varepsilon)\chi_w}, \quad (5.1)$$

where

$$\varepsilon = \frac{M_w}{M_a} = 0.622 \quad (5.2)$$

denotes the ratio of the molar mass of water to that of dry air. Using the meteorological notion of virtual temperature T_v , the number of independent variables in a lookup-table of the humid air mass density can be reduced from three variables (m_d , T , p) to two variables (T_v , p). The virtual temperature is by definition the temperature at which dry air would have the same mass density as humid air at the given water vapor mole fraction, temperature, and pressure (Chap. 8). This definition of the virtual temperature allows the approximate determination of the mass density of humid air

ρ_a from lookup tables for the virtual temperature excess of saturated humid air and for the mass density of dry air only, both of which are well-defined thermodynamic functions of temperature and pressure. To ensure consistency with the TEOS-10 based formulation of ρ_a as a function of the mass fraction of dry air, temperature, and pressure, the expression for ρ_a was linearized with respect to temperature and humidity [5.47]. By this linearization the number of lookup tables for the calculation of ρ_a could be reduced to two, resulting in a user-friendly and sufficiently accurate form similar to Tables 13–15 already published in [5.1].

According to *William Henry* (1774–1836) [5.48], the amount of dissolved gas in an aqueous phase is proportional to the partial pressure of the dissolved species in the gas phase. This rule is known as Henry's law, and the proportionality factor is called Henry's constant. Henry's law is reconcilable with *Henry Louis Le Chatelier's* (1850–1936) principle, according to which a perturbation of a thermodynamic system at equilibrium by changing the concentration, temperature, volume, or pressure, will cause a readjustment of the system to a new equilibrium state to counteract the effect of the applied changes. Depending on the metrics used for the definition of the aqueous and gas phase concentrations of the dissolved species, there are different formulations of Henry's law, for example [5.49, Eqs. (4), (15)]

$$H_i = \frac{\chi_{aq,i}}{p_i|_{sat,h}} = \frac{1}{K_{H,i}}. \quad (5.3)$$

Here, H_i denotes the Henry's law solubility constant of species i (in Pa^{-1}), $K_{H,i}$ the corresponding volatility constant (in Pa), $p_i|_{sat,h}$ the partial vapor pressure of species i in humid air at saturation with respect to liquid water, and $\chi_{aq,i}$ is the molar mixing ratio of the dissolved species i in the aqueous phase at equilibrium vapor pressure $p_i|_{sat,h}$. In the present chapter, the volatility constant of dry air (composed of N_2 , O_2 , and Ar) is presented in Table 5.36.

The irreversible exchange of a substance between two different thermodynamic macrophases of a nonequilibrium system is described by the so-called Onsager force (*Lars Onsager*, 1903–1976), which represents the entropic driving force toward the thermodynamic equilibrium [5.50]. Subsaturated air in contact with liquid water or seawater is such a nonequilibrium system, in which the evaporation of liquid water into subsaturated air is an irreversible process [5.50, p. 116]. Owing to its pivotal role for the quantification of the hydrological cycle and the energy budget of the globe [5.51], in [5.52] a calculus for the determination of the evaporation flux of water from a seawater reser-

voir to a reservoir of humid air was proposed, which is based on a generalized definition of relative humidity in terms of relative activity and relative fugacity. The relative humidity according to the WMO definition [5.53] can be recovered from this generalized definition as the ideal-gas limit. The enhancement factor of water vapor in humid air is a humidity metric to describe real-gas effects of humid air. This factor is defined as the ratio of the partial water vapor pressure in saturated humid air to the saturation pressure of pure water vapor [5.54, 55]. More details can be found in Chap. 8.

According to the experimental data base underlying TEOS-10, all thermodynamic single-phase and equilibrium properties involving liquid water are restricted to temperatures above the homogeneous freezing temperature.

5.4.2 Water Vapor, Dry Air, and Humid Air

The Tables 5.10 to 5.35 presented in this section contain parameters of water vapor, dry air, and humid air according to TEOS-10 [5.17, 18].

Table 5.10 Saturation water vapor pressure above liquid water (in hPa) as a function of temperature calculated according to TEOS-10 [5.17, 18]. This table with an enhanced resolution of the temperature of 0.1 K between 40 °C and −30 °C is available as electric supplementary material (ESM) at https://doi.org/10.1007/978-3-030-52171-4_5

Temperature (°C)	Temperature increment (K)									
	0	1	2	3	4	5	6	7	8	9
100	1014.18	1050.9	1088.74	1127.68	1167.77	1209.031	1251.485	1295.2	1340.1	1386.29
90	701.818	728.9	756.843	785.675	815.415	846.085	877.707	910.30	943.90	978.517
80	474.145	493.67	513.871	534.758	556.351	578.670	601.733	625.56	650.17	675.581
70	312.009	325.75	340.003	354.777	370.089	385.954	402.388	419.41	437.03	455.270
60	199.464	208.88	218.670	228.848	239.426	250.416	261.831	273.69	285.99	298.760
50	123.519	129.78	136.312	143.123	150.222	157.621	165.329	173.36	181.71	190.413
40	73.849	77.878	82.096	86.508	91.124	95.950	100.994	106.27	111.77	117.519
30	42.470	44.969	47.596	50.354	53.251	56.290	59.479	62.823	66.328	70.002
20	23.393	24.882	26.453	28.111	29.858	31.699	33.639	35.681	37.831	40.092
10	12.282	13.130	14.028	14.981	15.990	17.058	18.188	19.384	20.647	21.983
0	6.112	6.571	7.060	7.581	8.135	8.726	9.354	10.021	10.730	11.483
−0	6.112	5.682	5.279	4.901	4.548	4.218	3.909	3.620	3.350	3.099
−10	2.864	2.646	2.442	2.253	2.077	1.913	1.761	1.619	1.488	1.367
−20	1.255	1.150	1.054	0.965	0.883	0.807	0.737	0.673	0.614	0.559
−30	0.509	0.463	0.420	0.382	0.346	0.314	0.284	0.257	0.232	0.209

Table 5.11 Saturation water vapor pressure above ice (sublimation pressure) (in hPa) as a function of temperature calculated according to TEOS-10 [5.17, 18]. This table with an enhanced resolution of the temperature of 0.1 K between 0 °C and −30 °C is available as ESM at https://doi.org/10.1007/978-3-030-52171-4_5

Temperature (°C)	Temperature increment (K)									
	0	1	2	3	4	5	6	7	8	9
−0	6.1115	5.6266	5.1770	4.7604	4.3745	4.0174	3.6870	3.3817	3.0995	2.8391
−10	2.5988	2.3772	2.1730	1.9849	1.8119	1.6528	1.5065	1.3722	1.2490	1.1360
−20	1.0324	0.9376	0.8508	0.7715	0.6990	0.6328	0.5724	0.5173	0.4672	0.4216
−30	0.3801	0.3424	0.3081	0.2771	0.2490	0.2235	0.2004	0.1796	0.1607	0.1437
−40	0.1284	0.1146	0.1022	0.0911	0.0810	0.0720	0.0640	0.0568	0.0503	0.0445
−50	0.0394	0.0348	0.0307	0.0271	0.0240	0.0209	0.0184	0.0161	0.0141	0.0124
−60	0.0108	0.0094	0.0082	0.0072	0.0060	0.0054	0.0047	0.0041	0.0035	0.0030
−70	0.0026	0.0023	0.0019	0.0017	0.0010	0.0012	0.0010	0.0009	0.0008	0.0006
−80	0.0005	0.0005	0.0004	0.0003	0.0003	0.0002	0.0002	0.0002	0.0001	0.0001
−90	0.0001	0.0001	0.0001	0.0001	0.0000	0.0000	0.0000	0.0000	0.0000	0.0000
−100	0.0000	0.0000	0.0000	0.0000	0.0000	0.0000	0.0000	0.0000	0.0000	0.0000

Table 5.12 Water vapor pressure in equilibrium with seawater (in hPa) as a function of temperature and salinity calculated according to TEOS-10 [5.17, 18]. This table with an enhanced resolution of the temperature of 1 K is available as ESM at https://doi.org/10.1007/978-3-030-52171-4_5

Temperature (°C)	Salinity ($\times 10^{-3}$ kg kg $^{-1}$)							
	0.0	5.0	10.0	15.0	20.0	25.0	30.0	35.0
35	56.290	56.142	55.997	55.850	55.701	55.550	55.396	55.240
30	42.470	42.358	42.248	42.137	42.025	41.911	41.795	41.678
25	31.699	31.616	31.534	31.451	31.368	31.283	31.196	31.109
20	23.393	23.332	23.271	23.210	23.149	23.086	23.022	22.958
15	17.058	17.013	16.969	16.925	16.880	16.834	16.788	16.741
10	12.282	12.250	12.218	12.186	12.154	12.121	12.088	12.054
5	8.726	8.703	8.680	8.658	8.635	8.612	8.588	8.565
0	6.112	6.096	6.080	6.064	6.049	6.032	6.016	6.000
-3	4.901	4.889	4.876	4.863	4.851	4.838	4.825	4.811

Table 5.13 Ratio of the saturated water vapor pressure over ice to that over water as a function of temperature calculated according to TEOS-10 [5.17, 18]

Temperature (°C)	Temperature increment (K)									
	0	1	2	3	4	5	6	7	8	9
0	1.000	0.990	0.981	0.971	0.962	0.953	0.943	0.934	0.925	0.916
-10	0.907	0.898	0.890	0.881	0.873	0.864	0.856	0.847	0.839	0.831
-20	0.823	0.815	0.807	0.799	0.792	0.784	0.776	0.769	0.761	0.754
-30	0.747	0.740	0.733	0.726	0.719	0.712	0.706	0.699	0.693	0.686

Table 5.14 Difference between the saturated water vapor pressure over water and over ice (in hPa) as a function of temperature calculated according to TEOS-10 [5.17, 18]

Temperature (°C)	Temperature increment (K)									
	0	1	2	3	4	5	6	7	8	9
0	0.001	0.055	0.102	0.141	0.174	0.200	0.222	0.238	0.251	0.260
-10	0.266	0.269	0.269	0.268	0.265	0.260	0.254	0.247	0.239	0.231
-20	0.222	0.213	0.203	0.194	0.184	0.174	0.165	0.156	0.146	0.137
-30	0.129	0.120	0.112	0.105	0.097	0.090	0.084	0.077	0.071	0.066

Table 5.15 Mass density of water vapor at saturation with respect to liquid water (in 10^{-3} kg m $^{-3}$) as a function of temperature calculated according to TEOS-10 [5.17, 18]

Temperature (°C)	Temperature increment (K)									
	0	1	2	3	4	5	6	7	8	9
50	83.147	87.103	91.217	95.494	99.938	104.556	109.351	114.330	119.499	124.862
40	51.242	53.871	56.614	59.474	62.457	65.565	68.803	72.176	75.688	79.343
30	30.415	32.102	33.868	35.717	37.651	39.674	41.790	44.001	46.311	48.723
20	17.314	18.354	19.448	20.598	21.806	23.075	24.406	25.804	27.269	28.805
10	9.407	10.021	10.670	11.355	12.078	12.841	13.645	14.493	15.385	16.325
0	4.851	5.196	5.563	5.952	6.365	6.802	7.266	7.757	8.276	8.826
-0	4.851	4.526	4.221	3.933	3.663	3.410	3.172	2.948	2.739	2.543
-10	2.359	2.188	2.027	1.877	1.737	1.606	1.484	1.370	1.264	1.166
-20	1.074	0.989	0.910	0.836	0.768	0.705	0.646	0.592	0.542	0.496
-30	0.453	0.414	0.378	0.344	0.314	0.285	0.259	0.236	0.214	0.194

Table 5.16 Mass density of water vapor at saturation with respect to ice (in $10^{-3} \text{ kg m}^{-3}$) as a function of temperature calculated according to TEOS-10 [5.17, 18]

Temperature (°C)	Temperature increment (K)									
	0	1	2	3	4	5	6	7	8	9
0	4.8508	4.4822	4.1391	3.8200	3.5233	3.2476	2.9917	2.7541	2.5338	2.3296
−10	2.1405	1.9654	1.8034	1.6537	1.5153	1.3876	1.2697	1.1610	1.0609	0.9687
−20	0.8838	0.8058	0.7341	0.6683	0.6079	0.5526	0.5019	0.4554	0.4130	0.3742
−30	0.3387	0.3064	0.2769	0.2500	0.2256	0.2033	0.1831	0.1648	0.1481	0.1330
−40	0.1194	0.1070	0.0958	0.0857	0.0766	0.0684	0.0610	0.0544	0.0484	0.0430
−50	0.0382	0.0339	0.0301	0.0266	0.0235	0.0208	0.0184	0.0162	0.0142	0.0125

Table 5.17 Mass density of dry air (in kg m^{-3}) as a function of temperature and pressure (in the pressure range 1100–650 hPa) as calculated according to TEOS-10 [5.17, 18]. The mass density of humid air is approximately obtained by evaluating the mass density of dry air at the virtual temperature $T_v \approx T + RH\Delta T_{v,\text{sat}}$, where RH denotes the relative humidity according to the WMO definition (Chap. 8), and $\Delta T_{v,\text{sat}}(T, p)$ the virtual temperature increment of saturated humid air (Table 5.19) [5.47]. This table with an enhanced resolution of the temperature of 1 K is available as ESM at https://doi.org/10.1007/978-3-030-52171-4_5

Temperature (°C)	Pressure (hPa)									
	1100	1050	1000	950	900	850	800	750	700	650
−40	1.6460	1.5710	1.4961	1.4212	1.3464	1.2715	1.1966	1.1217	1.0469	0.9720
−35	1.6112	1.5379	1.4646	1.3913	1.3179	1.2447	1.1714	1.0981	1.0248	0.9516
−30	1.5779	1.5061	1.4343	1.3625	1.2907	1.2190	1.1472	1.0754	1.0037	0.9319
−25	1.5459	1.4756	1.4053	1.3349	1.2646	1.1943	1.1240	1.0537	0.9834	0.9131
−20	1.5153	1.4463	1.3774	1.3085	1.2395	1.1706	1.1017	1.0328	0.9639	0.8950
−15	1.4858	1.4182	1.3506	1.2830	1.2154	1.1479	1.0803	1.0127	0.9452	0.8776
−10	1.4574	1.3911	1.3248	1.2585	1.1923	1.1260	1.0597	0.9934	0.9272	0.8609
−5	1.4301	1.3651	1.3000	1.2350	1.1699	1.1049	1.0399	0.9749	0.9098	0.8448
0	1.4038	1.3400	1.2761	1.2123	1.1485	1.0846	1.0208	0.9570	0.8931	0.8293
5	1.3785	1.3158	1.2531	1.1904	1.1278	1.0651	1.0024	0.9397	0.8771	0.8144
10	1.3541	1.2925	1.2309	1.1694	1.1078	1.0462	0.9847	0.9231	0.8615	0.8000
15	1.3305	1.2700	1.2095	1.1490	1.0885	1.0280	0.9675	0.9070	0.8465	0.7861
20	1.3077	1.2483	1.1888	1.1294	1.0699	1.0104	0.9510	0.8915	0.8321	0.7726
25	1.2858	1.2273	1.1688	1.1104	1.0519	0.9935	0.9350	0.8765	0.8181	0.7597
30	1.2645	1.2070	1.1495	1.0920	1.0345	0.9770	0.9195	0.8621	0.8046	0.7471
35	1.2439	1.1874	1.1308	1.0742	1.0177	0.9611	0.9046	0.8481	0.7915	0.7350
40	1.2240	1.1684	1.1127	1.0571	1.0014	0.9458	0.8901	0.8345	0.7788	0.7232
45	1.2047	1.1499	1.0952	1.0404	0.9856	0.9309	0.8761	0.8213	0.7666	0.7118
50	1.1860	1.1321	1.0782	1.0243	0.9704	0.9164	0.8625	0.8086	0.7547	0.7008

Table 5.18 As in Table 5.17 but for the pressure range 650–200 hPa with $T_{v,\text{sat}}(T, p)$ from Table 5.20. This table with an enhanced resolution of the temperature of 1 K is available as ESM at https://doi.org/10.1007/978-3-030-52171-4_5

Temperature (°C)	Pressure (hPa)									
	650	600	550	500	450	400	350	300	250	200
–40	0.9720	0.8972	0.8224	0.7476	0.6728	0.5980	0.5232	0.4484	0.3737	0.2989
–35	0.9516	0.8783	0.8051	0.7318	0.6586	0.5854	0.5122	0.4390	0.3658	0.2926
–30	0.9319	0.8602	0.7885	0.7168	0.6450	0.5733	0.5017	0.4300	0.3583	0.2866
–25	0.9131	0.8428	0.7726	0.7023	0.6320	0.5618	0.4915	0.4213	0.3511	0.2808
–20	0.8950	0.8261	0.7573	0.6884	0.6195	0.5507	0.4818	0.4130	0.3441	0.2753
–15	0.8776	0.8101	0.7426	0.6750	0.6075	0.5400	0.4725	0.4049	0.3374	0.2699
–10	0.8609	0.7947	0.7284	0.6622	0.5959	0.5297	0.4635	0.3972	0.3310	0.2648
–5	0.8448	0.7798	0.7148	0.6498	0.5848	0.5198	0.4548	0.3898	0.3248	0.2599
0	0.8293	0.7655	0.7017	0.6379	0.5741	0.5103	0.4465	0.3827	0.3189	0.2551
5	0.8144	0.7517	0.6891	0.6264	0.5637	0.5011	0.4384	0.3758	0.3132	0.2505
10	0.8000	0.7384	0.6769	0.6153	0.5538	0.4922	0.4307	0.3692	0.3076	0.2461
15	0.7861	0.7256	0.6651	0.6046	0.5442	0.4837	0.4232	0.3627	0.3023	0.2418
20	0.7726	0.7132	0.6537	0.5943	0.5349	0.4754	0.4160	0.3566	0.2971	0.2377
25	0.7597	0.7012	0.6428	0.5843	0.5259	0.4674	0.4090	0.3506	0.2921	0.2337
30	0.7471	0.6896	0.6321	0.5747	0.5172	0.4597	0.4023	0.3448	0.2873	0.2298
35	0.7350	0.6784	0.6219	0.5653	0.5088	0.4523	0.3957	0.3392	0.2826	0.2261
40	0.7232	0.6676	0.6119	0.5563	0.5007	0.4450	0.3894	0.3338	0.2781	0.2225
45	0.7118	0.6571	0.6023	0.5475	0.4928	0.4380	0.3833	0.3285	0.2738	0.2190
50	0.7008	0.6469	0.5930	0.5391	0.4852	0.4312	0.3773	0.3234	0.2695	0.2156

Table 5.19 Virtual temperature excess of saturated humid air $\Delta T_{v,\text{sat}}(T, p)$ (in K) as a function of temperature and pressure (in the pressure range 1100–650 hPa), calculated by linearization of the TEOS-10-based expression of the mass density of humid air [5.17, 18] as a function of temperature, pressure, and mass fraction of dry air. The virtual temperature is given as a function of temperature, pressure, and relative humidity as $T_v \approx T + RH\Delta T_{v,\text{sat}}$, where RH denotes the relative humidity according to the WMO definition (Chap. 8) [5.47]. This table with an enhanced resolution of the temperature of 1 K is available as ESM at https://doi.org/10.1007/978-3-030-52171-4_5

Temperature (°C)	Pressure (hPa)									
	1100	1050	1000	950	900	850	800	750	700	650
–35	0.025	0.027	0.028	0.030	0.031	0.033	0.035	0.037	0.040	0.043
–30	0.042	0.044	0.046	0.049	0.052	0.055	0.058	0.062	0.066	0.072
–25	0.068	0.072	0.075	0.079	0.084	0.089	0.094	0.100	0.108	0.116
–20	0.108	0.114	0.119	0.126	0.133	0.140	0.149	0.159	0.171	0.184
–15	0.168	0.177	0.185	0.195	0.206	0.218	0.232	0.248	0.265	0.286
–10	0.257	0.269	0.283	0.298	0.315	0.333	0.354	0.378	0.405	0.436
–5	0.386	0.404	0.425	0.447	0.472	0.500	0.532	0.567	0.608	0.655
0	0.570	0.597	0.627	0.660	0.697	0.738	0.785	0.837	0.897	0.967
5	0.828	0.868	0.911	0.960	1.013	1.073	1.141	1.217	1.304	1.405
10	1.187	1.243	1.306	1.375	1.452	1.538	1.634	1.744	1.869	2.013
15	1.677	1.757	1.846	1.943	2.052	2.173	2.309	2.464	2.641	2.844
20	2.339	2.451	2.574	2.711	2.862	3.031	3.221	3.437	3.683	3.967
25	3.223	3.377	3.547	3.735	3.943	4.176	4.438	4.735	5.074	5.466
30	4.389	4.599	4.830	5.086	5.369	5.686	6.043	6.447	6.910	7.443
35	5.911	6.194	6.505	6.849	7.231	7.658	8.138	8.682	9.304	10.022
40	7.876	8.253	8.667	9.125	9.634	10.203	10.843	11.568	12.397	13.354
45	10.390	10.887	11.433	12.038	12.709	13.459	14.303	15.260	16.353	17.614
50	13.575	14.224	14.938	15.727	16.604	17.584	18.687	19.936	21.365	23.012

Table 5.20 As in Table 5.19 but for the pressure range 650–200 hPa. This table with an enhanced resolution of the temperature of 1 K is available as ESM at https://doi.org/10.1007/978-3-030-52171-4_5

Temperature (°C)	Pressure (hPa)									
	650	600	550	500	450	400	350	300	250	200
–35	0.043	0.047	0.051	0.056	0.063	0.070	0.081	0.094	0.113	0.141
–30	0.072	0.078	0.085	0.093	0.104	0.117	0.133	0.156	0.187	0.234
–25	0.116	0.126	0.137	0.151	0.168	0.189	0.216	0.252	0.302	0.378
–20	0.184	0.199	0.217	0.239	0.266	0.299	0.342	0.399	0.479	0.599
–15	0.286	0.310	0.338	0.372	0.413	0.465	0.532	0.621	0.745	0.932
–10	0.436	0.473	0.516	0.568	0.631	0.710	0.812	0.948	1.137	1.422
–5	0.655	0.710	0.774	0.852	0.947	1.066	1.218	1.422	1.706	2.134
0	0.967	1.047	1.143	1.258	1.398	1.573	1.798	2.098	2.519	3.149
5	1.405	1.522	1.661	1.828	2.032	2.286	2.613	3.050	3.661	4.577
10	2.013	2.181	2.380	2.619	2.910	3.275	3.744	4.369	5.244	6.557
15	2.844	3.082	3.363	3.700	4.113	4.628	5.290	6.174	7.410	9.265
20	3.967	4.299	4.691	5.161	5.736	6.455	7.379	8.610	10.335	12.922
25	5.466	5.923	6.463	7.111	7.902	8.892	10.165	11.862	14.238	17.801
30	7.443	8.065	8.800	9.682	10.760	12.108	13.841	16.151	19.385	24.237
35	10.022	10.860	11.850	13.037	14.489	16.304	18.637	21.747	26.102	32.635
40	13.354	14.470	15.788	17.371	19.305	21.722	24.831	28.975	34.777	43.480
45	17.614	19.086	20.825	22.912	25.463	28.652	32.751	38.218	45.870	57.349
50	23.012	24.935	27.207	29.933	33.266	37.431	42.787	49.927	59.924	74.920

Table 5.21 Examples of the relative deviation (in percent) of the approximated mass density of humid air (Tables 5.17, 5.18, 5.19, and 5.20) from the exact TEOS-10-based expression [5.17, 18] of the mass density of humid air at selected temperatures, pressures, and humidities

Temperature (°C)	Relative humidity (%)					
	0	20	40	60	80	100
1000 hPa						
–20	0.0000	0.0000	0.0000	0.0000	0.0000	0.0000
0	0.0000	0.0001	0.0002	0.0003	0.0004	0.0005
20	0.0000	0.0008	0.0020	0.0036	0.0055	0.0078
40	0.0000	0.0062	0.0170	0.0325	0.0526	0.0772
800 hPa						
–20	0.0000	0.0000	0.0000	0.0000	0.0000	0.0000
0	0.0000	0.0001	0.0002	0.0004	0.0006	0.0008
20	0.0000	0.0011	0.0029	0.0053	0.0084	0.0122
40	0.0000	0.0086	0.0251	0.0492	0.0811	0.1207
600 hPa						
–20	0.0000	0.0000	0.0000	0.0000	0.0000	0.0001
0	0.0000	0.0002	0.0004	0.0007	0.0010	0.0015
20	0.0000	0.0017	0.0047	0.0090	0.0147	0.0216
40	0.0000	0.0136	0.0419	0.0849	0.1425	0.2148
400 hPa						
–20	0.0000	0.0000	0.0000	0.0001	0.0001	0.0001
0	0.0000	0.0003	0.0007	0.0014	0.0023	0.0033
20	0.0000	0.0031	0.0096	0.0193	0.0324	0.0487
40	0.0000	0.0266	0.0883	0.1851	0.3172	0.4848
200 hPa						
–20	0.0000	0.0000	0.0001	0.0002	0.0004	0.0006
0	0.0000	0.0008	0.0025	0.0052	0.0088	0.0133
20	0.0000	0.0101	0.0347	0.0737	0.1271	0.1950
40	0.0000	0.0907	0.3301	0.7202	1.2646	1.9684

Table 5.22 Mass density of saturated humid air (in kg m^{-3}) as a function of temperature and pressure (in the pressure range 1100–650 hPa) calculated according to TEOS-10 [5.17, 18]. This table with an enhanced resolution of the temperature of 1 K is available as ESM at https://doi.org/10.1007/978-3-030-52171-4_5

Temperature (°C)	Pressure (hPa)									
	1100	1050	1000	950	900	850	800	750	700	650
–35	1.6110	1.5377	1.4644	1.3911	1.3178	1.2445	1.1712	1.0979	1.0247	0.9514
–30	1.5776	1.5058	1.4340	1.3622	1.2905	1.2187	1.1469	1.0752	1.0034	0.9317
–25	1.5455	1.4752	1.4048	1.3345	1.2642	1.1939	1.1236	1.0533	0.9830	0.9127
–20	1.5146	1.4457	1.3767	1.3078	1.2389	1.1700	1.1011	1.0322	0.9633	0.8944
–15	1.4848	1.4172	1.3496	1.2820	1.2145	1.1469	1.0793	1.0118	0.9442	0.8767
–10	1.4560	1.3897	1.3234	1.2571	1.1908	1.1245	1.0583	0.9920	0.9257	0.8595
–5	1.4281	1.3630	1.2980	1.2329	1.1679	1.1028	1.0378	0.9728	0.9078	0.8428
0	1.4009	1.3371	1.2732	1.2094	1.1455	1.0817	1.0179	0.9540	0.8902	0.8264
5	1.3744	1.3117	1.2490	1.1863	1.1236	1.0610	0.9983	0.9356	0.8729	0.8103
10	1.3484	1.2868	1.2252	1.1637	1.1021	1.0405	0.9790	0.9174	0.8558	0.7943
15	1.3227	1.2622	1.2017	1.1412	1.0807	1.0202	0.9598	0.8993	0.8388	0.7783
20	1.2973	1.2378	1.1783	1.1189	1.0594	1.0000	0.9405	0.8811	0.8216	0.7622
25	1.2718	1.2133	1.1549	1.0964	1.0380	0.9795	0.9211	0.8626	0.8041	0.7457
30	1.2461	1.1886	1.1311	1.0736	1.0162	0.9587	0.9012	0.8437	0.7862	0.7287
35	1.2200	1.1634	1.1069	1.0503	0.9938	0.9372	0.8807	0.8241	0.7676	0.7110
40	1.1931	1.1375	1.0818	1.0262	0.9705	0.9149	0.8592	0.8036	0.7480	0.6923
45	1.1653	1.1105	1.0557	1.0010	0.9462	0.8914	0.8367	0.7819	0.7271	0.6724
50	1.1361	1.0822	1.0283	0.9743	0.9204	0.8665	0.8126	0.7587	0.7047	0.6508

Table 5.23 As in Table 5.22 but for the pressure range 650–200 hPa. This table with an enhanced resolution of the temperature of 1 K is available as ESM at https://doi.org/10.1007/978-3-030-52171-4_5

Temperature (°C)	Pressure (hPa)									
	650	600	550	500	450	400	350	300	250	200
–35	0.9514	0.8781	0.8049	0.7317	0.6585	0.5852	0.5120	0.4388	0.3656	0.2925
–30	0.9317	0.8599	0.7882	0.7165	0.6448	0.5731	0.5014	0.4297	0.3580	0.2863
–25	0.9127	0.8424	0.7721	0.7019	0.6316	0.5613	0.4911	0.4209	0.3506	0.2804
–20	0.8944	0.8255	0.7566	0.6877	0.6189	0.5500	0.4812	0.4123	0.3435	0.2746
–15	0.8767	0.8091	0.7416	0.6740	0.6065	0.5390	0.4715	0.4040	0.3365	0.2690
–10	0.8595	0.7932	0.7270	0.6607	0.5945	0.5283	0.4620	0.3958	0.3296	0.2634
–5	0.8428	0.7777	0.7127	0.6477	0.5827	0.5177	0.4527	0.3878	0.3228	0.2578
0	0.8264	0.7626	0.6988	0.6349	0.5711	0.5073	0.4435	0.3797	0.3160	0.2522
5	0.8103	0.7476	0.6849	0.6223	0.5596	0.4970	0.4343	0.3717	0.3090	0.2464
10	0.7943	0.7327	0.6712	0.6096	0.5481	0.4865	0.4250	0.3635	0.3019	0.2404
15	0.7783	0.7178	0.6573	0.5969	0.5364	0.4759	0.4154	0.3550	0.2945	0.2340
20	0.7622	0.7027	0.6433	0.5838	0.5244	0.4649	0.4055	0.3461	0.2866	0.2272
25	0.7457	0.6873	0.6288	0.5704	0.5119	0.4535	0.3950	0.3366	0.2782	0.2197
30	0.7287	0.6712	0.6138	0.5563	0.4988	0.4413	0.3839	0.3264	0.2689	0.2115
35	0.7110	0.6545	0.5979	0.5414	0.4848	0.4283	0.3718	0.3152	0.2587	0.2022
40	0.6923	0.6367	0.5810	0.5254	0.4698	0.4141	0.3585	0.3029	0.2472	0.1916
45	0.6724	0.6176	0.5628	0.5081	0.4533	0.3985	0.3438	0.2890	0.2343	0.1795
50	0.6508	0.5969	0.5430	0.4891	0.4352	0.3813	0.3273	0.2734	0.2195	0.1656

Table 5.24 Water-vapor mole fraction of saturated humid air (in %) as a function of temperature and pressure (in the pressure range 1100–650 hPa), calculated according to TEOS-10 [5.17, 18]. This table with an enhanced resolution on of the temperature of 1 K is available as ESM at https://doi.org/10.1007/978-3-030-52171-4_5

Temperature (°C)	Pressure (hPa)									
	1100	1050	1000	950	900	850	800	750	700	650
–35	0.287	0.300	0.315	0.332	0.350	0.371	0.394	0.420	0.450	0.484
–30	0.465	0.487	0.511	0.538	0.568	0.601	0.639	0.681	0.729	0.785
–25	0.738	0.773	0.811	0.854	0.901	0.954	1.013	1.080	1.157	1.246
–20	1.146	1.201	1.260	1.326	1.400	1.482	1.574	1.679	1.798	1.936
–15	1.747	1.830	1.921	2.022	2.134	2.259	2.400	2.559	2.741	2.952
–10	2.616	2.740	2.877	3.028	3.195	3.382	3.593	3.832	4.105	4.420
–5	3.852	4.034	4.235	4.457	4.704	4.980	5.290	5.642	6.044	6.507
0	5.581	5.846	6.137	6.459	6.817	7.217	7.666	8.176	8.758	9.430
5	7.968	8.346	8.761	9.221	9.732	10.302	10.944	11.672	12.504	13.463
10	11.215	11.747	12.332	12.979	13.698	14.501	15.405	16.430	17.600	18.951
15	15.576	16.315	17.128	18.027	19.026	20.142	21.397	22.820	24.446	26.322
20	21.362	22.376	23.492	24.724	26.094	27.625	29.347	31.298	33.529	36.103
25	28.950	30.325	31.836	33.507	35.363	37.438	39.772	42.417	45.440	48.928
30	38.792	40.634	42.659	44.898	47.386	50.166	53.294	56.838	60.890	65.564
35	51.425	53.866	56.552	59.520	62.818	66.504	70.650	75.349	80.720	86.916
40	67.480	70.684	74.208	78.103	82.431	87.268	92.709	98.875	105.922	114.053
45	87.696	91.860	96.439	101.501	107.125	113.410	120.481	128.494	137.651	148.217
50	112.923	118.284	124.181	130.698	137.939	146.031	155.135	165.451	177.240	190.842

Table 5.25 As in Table 5.24 but for the pressure range 650–200 hPa. This table with an enhanced resolution of the temperature of 1 K is available as ESM at https://doi.org/10.1007/978-3-030-52171-4_5

Temperature (°C)	Pressure (hPa)									
	650	600	550	500	450	400	350	300	250	200
–35	0.484	0.525	0.572	0.629	0.699	0.786	0.898	1.047	1.257	1.570
–30	0.785	0.851	0.928	1.020	1.133	1.275	1.456	1.699	2.038	2.547
–25	1.246	1.349	1.472	1.618	1.798	2.022	2.310	2.695	3.233	4.041
–20	1.936	2.097	2.287	2.515	2.794	3.143	3.591	4.188	5.025	6.280
–15	2.952	3.197	3.487	3.835	4.260	4.791	5.475	6.386	7.661	9.575
–10	4.420	4.787	5.221	5.742	6.379	7.175	8.198	9.563	11.473	14.338
–5	6.507	7.048	7.688	8.455	9.392	10.564	12.071	14.081	16.894	21.113
0	9.430	10.214	11.141	12.253	13.612	15.310	17.494	20.407	24.483	30.599
5	13.463	14.583	15.905	17.493	19.433	21.859	24.977	29.135	34.956	43.687
10	18.951	20.527	22.389	24.624	27.356	30.770	35.160	41.013	49.207	61.498
15	26.322	28.511	31.098	34.203	37.997	42.740	48.838	56.968	68.350	85.423
20	36.103	39.105	42.654	46.912	52.116	58.621	66.985	78.136	93.748	117.164
25	48.928	52.998	57.807	63.578	70.631	79.448	90.783	105.896	127.052	158.785
30	65.564	71.017	77.461	85.195	94.646	106.460	121.648	141.898	170.245	212.759
35	86.916	94.145	102.688	112.940	125.468	141.128	161.261	188.101	225.673	282.018
40	114.053	123.538	134.748	148.199	164.637	185.183	211.596	246.807	296.091	369.993
45	148.217	160.542	175.107	192.584	213.941	240.634	274.947	320.685	384.697	480.666
50	190.842	206.709	225.458	247.954	275.443	309.797	353.954	412.807	495.158	618.589

Table 5.26 Dewpoint temperature (in °C) as a function of the water-vapor mole fraction in humid air (in ‰) and pressure (in the pressure range 1100–650 hPa), calculated according to TEOS-10 [5.17, 18]. This table with an enhanced resolution of the water vapor mole fraction of 0.4‰ is available as ESM at https://doi.org/10.1007/978-3-030-52171-4_5

Mole fraction (‰)	Pressure (hPa)									
	1100	1050	1000	950	900	850	800	750	700	650
0.0										
2.0	−13.35	−13.92	−14.51	−15.13	−15.78	−16.47	−17.19	−17.95	−18.76	−19.62
4.0	−4.50	−5.11	−5.75	−6.42	−7.12	−7.86	−8.63	−9.46	−10.33	−11.26
6.0	1.00	0.36	−0.31	−1.01	−1.74	−2.51	−3.33	−4.19	−5.10	−6.07
8.0	5.06	4.40	3.70	2.98	2.22	1.43	0.59	−0.30	−1.24	−2.24
10.0	8.30	7.62	6.91	6.17	5.39	4.57	3.71	2.80	1.84	0.81
12.0	11.01	10.32	9.59	8.84	8.04	7.21	6.33	5.40	4.41	3.36
14.0	13.36	12.65	11.91	11.14	10.33	9.48	8.58	7.64	6.63	5.56
16.0	15.42	14.70	13.95	13.16	12.34	11.48	10.57	9.61	8.59	7.50
18.0	17.27	16.54	15.77	14.98	14.14	13.27	12.34	11.37	10.34	9.23
20.0	18.94	18.20	17.43	16.62	15.78	14.89	13.96	12.97	11.92	10.81
22.0	20.48	19.73	18.95	18.13	17.28	16.38	15.43	14.43	13.37	12.25
24.0	21.89	21.14	20.35	19.52	18.66	17.75	16.79	15.79	14.71	13.57
26.0	23.21	22.45	21.65	20.81	19.94	19.03	18.06	17.04	15.96	14.81
28.0	24.44	23.67	22.87	22.02	21.14	20.22	19.24	18.22	17.12	15.96
30.0	25.60	24.82	24.01	23.16	22.27	21.34	20.36	19.32	18.22	17.05
32.0	26.69	25.91	25.09	24.23	23.34	22.40	21.40	20.36	19.25	18.07
34.0	27.72	26.93	26.11	25.25	24.34	23.40	22.40	21.34	20.23	19.04
36.0	28.71	27.91	27.08	26.21	25.30	24.35	23.34	22.28	21.15	19.95
38.0	29.64	28.84	28.00	27.13	26.21	25.25	24.24	23.17	22.04	20.83
40.0	30.54	29.73	28.88	28.00	27.08	26.12	25.10	24.02	22.88	21.67

Table 5.27 As in Table 5.26 but for the pressure range 650–200 hPa. This table with an enhanced resolution of the water-vapor mole fraction of 0.4‰ is available as ESM at https://doi.org/10.1007/978-3-030-52171-4_5

Mole fraction (‰)	Pressure (hPa)									
	650	600	550	500	450	400	350	300	250	200
0.0										
2.0	−19.62	−20.55	−21.55	−22.63	−23.81	−25.12	−26.59	−28.26	−30.20	−32.53
4.0	−11.26	−12.25	−13.32	−14.49	−15.76	−17.17	−18.74	−20.53	−22.62	−25.11
6.0	−6.07	−7.11	−8.23	−9.44	−10.77	−12.24	−13.88	−15.75	−17.92	−20.53
8.0	−2.24	−3.32	−4.47	−5.73	−7.10	−8.61	−10.31	−12.24	−14.48	−17.16
10.0	0.81	−0.29	−1.48	−2.76	−4.17	−5.72	−7.46	−9.43	−11.73	−14.47
12.0	3.36	2.24	1.03	−0.29	−1.72	−3.31	−5.08	−7.09	−9.43	−12.23
14.0	5.56	4.42	3.18	1.85	0.39	−1.23	−3.03	−5.08	−7.45	−10.30
16.0	7.50	6.34	5.09	3.73	2.25	0.61	−1.22	−3.30	−5.72	−8.61
18.0	9.23	8.06	6.79	5.41	3.91	2.25	0.39	−1.71	−4.16	−7.09
20.0	10.81	9.61	8.33	6.94	5.41	3.73	1.86	−0.28	−2.75	−5.71
22.0	12.25	11.04	9.74	8.33	6.79	5.09	3.19	1.04	−1.46	−4.46
24.0	13.57	12.35	11.04	9.62	8.06	6.35	4.43	2.25	−0.27	−3.30
26.0	24.80	14.08	12.25	10.81	9.24	7.51	5.58	3.38	0.83	−2.22
28.0	15.96	14.72	13.38	11.93	10.35	8.60	6.65	4.43	1.86	−1.22
30.0	17.05	15.79	14.44	12.98	11.38	9.62	7.65	5.42	2.83	−0.27
32.0	18.07	16.80	15.44	13.97	12.36	10.59	8.60	6.35	3.74	0.62
34.0	19.04	17.76	16.39	14.91	13.29	11.50	9.50	7.23	4.60	1.46
36.0	19.95	18.67	17.29	15.80	14.17	12.36	10.35	8.07	5.42	2.26
38.0	20.83	19.54	18.15	16.64	15.00	13.19	11.16	8.87	6.20	3.02
40.0	21.67	20.37	18.97	17.45	15.80	13.98	11.94	9.63	6.95	3.74

Table 5.28 Frostpoint temperature (in °C) as a function of the water-vapor mole fraction in humid air (in ‰) and pressure (in the pressure range 1100–650 hPa), calculated according to TEOS-10 [5.17, 18]. This table with an enhanced resolution of the water vapor mole fraction of 0.2‰ is available as ESM at https://doi.org/10.1007/978-3-030-52171-4_5

Mole fraction (‰)	Pressure (hPa)									
	1100	1050	1000	950	900	850	800	750	700	650
0.0										
0.4	−28.64	−29.09	−29.56	−30.05	−30.56	−31.11	−31.68	−32.29	−32.94	−33.63
0.8	−21.71	−22.18	−22.68	−23.20	−23.74	−24.32	−24.93	−25.57	−26.25	−26.98
1.2	−17.47	−17.96	−18.47	−19.01	−19.57	−20.17	−20.79	−21.46	−22.17	−22.92
1.6	−14.37	−14.87	−15.40	−15.95	−16.53	−17.14	−17.78	−18.46	−19.18	−19.96
2.0	−11.92	−12.43	−12.97	−13.53	−14.12	−14.74	−15.39	−16.08	−16.82	−17.61
2.4	−9.88	−10.40	−10.94	−11.51	−12.11	−12.74	−13.41	−14.11	−14.86	−15.66
2.8	−8.13	−8.65	−9.21	−9.78	−10.39	−11.03	−11.70	−12.42	−13.17	−13.98
3.2	−6.59	−7.13	−7.68	−8.27	−8.88	−9.53	−10.21	−10.93	−11.70	−12.52
3.6	−5.22	−5.76	−6.33	−6.92	−7.54	−8.19	−8.88	−9.61	−10.38	−11.21
4.0	−3.99	−4.53	−5.10	−5.70	−6.32	−6.98	−7.68	−8.41	−9.19	−10.03
4.4	−2.86	−3.41	−3.98	−4.58	−5.21	−5.88	−6.58	−7.32	−8.11	−8.95
4.8	−1.82	−2.37	−2.95	−3.56	−4.19	−4.86	−5.57	−6.32	−7.11	−7.96
5.2	−0.86	−1.41	−2.00	−2.61	−3.25	−3.92	−4.63	−5.39	−6.19	−7.04
5.6		−0.52	−1.11	−1.72	−2.37	−3.04	−3.76	−4.52	−5.32	−6.18
6.0			−0.27	−0.89	−1.54	−2.22	−2.94	−3.71	−4.52	−5.38
6.8					−0.03	−0.72	−1.45	−2.22	−3.04	−3.91
7.6							−0.11	−0.88	−1.71	−2.59
8.4									−0.51	−1.40
9.2										−0.30

Table 5.29 As in Table 5.28 but for the pressure range 650–200 hPa. This table with an enhanced resolution of the water-vapor mole fraction of 0.2‰ is available as ESM at https://doi.org/10.1007/978-3-030-52171-4_5

Mole fraction (‰)	Pressure (hPa)									
	650	600	550	500	450	400	350	300	250	200
0.0										
0.4	−33.63	−34.37	−35.17	−36.04	−37.00	−38.06	−39.25	−40.61	−42.20	−44.12
0.8	−26.98	−27.77	−28.61	−29.53	−30.54	−31.66	−32.92	−34.36	−36.03	−38.05
1.2	−22.92	−23.73	−24.60	−25.56	−26.60	−27.76	−29.05	−30.54	−32.27	−34.35
1.6	−19.96	−20.79	−21.68	−22.66	−23.72	−24.91	−26.24	−27.75	−29.52	−31.65
2.0	−17.61	−18.45	−19.37	−20.36	−21.45	−22.65	−24.00	−25.55	−27.35	−29.52
2.4	−15.66	−16.52	−17.44	−18.45	−19.55	−20.78	−22.15	−23.72	−25.54	−27.75
2.8	−13.98	−14.85	−15.79	−16.81	−17.93	−19.17	−20.56	−22.15	−24.00	−26.23
3.2	−12.52	−13.40	−14.35	−15.38	−16.51	−17.76	−19.17	−20.77	−22.64	−24.90
3.6	−11.21	−12.10	−13.06	−14.10	−15.24	−16.51	−17.93	−19.55	−21.44	−23.71
4.0	−10.03	−10.92	−11.89	−12.94	−14.10	−15.37	−16.80	−18.44	−20.35	−22.64
4.4	−8.95	−9.85	−10.83	−11.89	−13.05	−14.34	−15.78	−17.43	−19.35	−21.66
4.8	−7.96	−8.87	−9.85	−10.92	−12.09	−13.39	−14.84	−16.50	−18.44	−20.77
5.2	−7.04	−7.96	−8.95	−10.02	−11.20	−12.51	−13.97	−15.64	−17.59	−19.94
5.6	−6.18	−7.11	−8.10	−9.18	−10.37	−11.68	−13.16	−14.84	−16.80	−19.16
6.0	−5.38	−6.31	−7.31	−8.40	−9.59	−10.91	−12.40	−14.09	−16.06	−18.43
6.8	−3.91	−4.85	−5.86	−6.96	−8.17	−9.51	−11.01	−12.72	−14.71	−17.11
7.6	−2.59	−3.54	−4.57	−5.68	−6.90	−8.24	−9.76	−11.48	−13.50	−15.92
8.4	−1.40	−2.35	−3.39	−4.51	−5.74	−7.10	−8.62	−10.36	−12.39	−14.83
9.2	−0.30	−1.26	−2.30	−3.43	−4.67	−6.05	−7.58	−9.34	−11.38	−13.84

Table 5.29 (Continued)

Mole fraction (%)	Pressure (hPa)									
	650	600	550	500	450	400	350	300	250	200
10.0		-0.26	-1.31	-2.44	-3.69	-5.07	-6.62	-8.39	-10.45	-12.93
12.0				-0.25	-1.52	-2.93	-4.50	-6.30	-8.39	-10.91
14.0						-1.08	-2.68	-4.50	-6.62	-9.17
16.0							-1.08	-2.92	-5.07	-7.65
18.0								-1.51	-3.68	-6.29
20.0								-0.24	-2.43	-5.06
22.0									-1.29	-3.95
24.0									-0.24	-2.92
26.0										-1.96
28.0										-1.07
30.0										-0.24

Table 5.30 Water-vapor enhancement factor with respect to liquid water as a function of temperature and pressure (in the pressure range 1100–650 hPa), calculated according to TEOS-10 [5.17, 18]. This table with an enhanced resolution of the temperature of 1 K is available as ESM at https://doi.org/10.1007/978-3-030-52171-4_5

Temperature (°C)	Pressure (hPa)									
	1100	1050	1000	950	900	850	800	750	700	650
-35	1.00575	1.00549	1.00524	1.00498	1.00472	1.00446	1.00420	1.00395	1.00369	1.00343
-30	1.00547	1.00523	1.00498	1.00474	1.00450	1.00425	1.00401	1.00377	1.00352	1.00328
-25	1.00522	1.00499	1.00476	1.00453	1.00430	1.00407	1.00384	1.00361	1.00338	1.00315
-20	1.00501	1.00479	1.00457	1.00436	1.00414	1.00392	1.00370	1.00348	1.00326	1.00305
-15	1.00483	1.00462	1.00442	1.00421	1.00400	1.00379	1.00359	1.00338	1.00317	1.00296
-10	1.00468	1.00448	1.00429	1.00409	1.00389	1.00370	1.00350	1.00330	1.00310	1.00291
-5	1.00457	1.00438	1.00419	1.00400	1.00381	1.00363	1.00344	1.00325	1.00306	1.00287
0	1.00448	1.00430	1.00412	1.00395	1.00377	1.00359	1.00341	1.00323	1.00305	1.00287
5	1.00443	1.00426	1.00409	1.00392	1.00375	1.00358	1.00341	1.00324	1.00306	1.00289
10	1.00442	1.00426	1.00409	1.00393	1.00377	1.00360	1.00344	1.00327	1.00311	1.00295
15	1.00445	1.00429	1.00413	1.00397	1.00382	1.00366	1.00350	1.00334	1.00319	1.00303
20	1.00451	1.00436	1.00421	1.00405	1.00390	1.00375	1.00360	1.00345	1.00329	1.00314
25	1.00461	1.00446	1.00432	1.00417	1.00402	1.00388	1.00373	1.00358	1.00343	1.00328
30	1.00475	1.00461	1.00446	1.00432	1.00418	1.00404	1.00389	1.00375	1.00360	1.00345
35	1.00492	1.00479	1.00465	1.00451	1.00437	1.00423	1.00408	1.00394	1.00380	1.00365
40	1.00513	1.00500	1.00486	1.00472	1.00458	1.00444	1.00430	1.00416	1.00401	1.00386
45	1.00537	1.00524	1.00510	1.00496	1.00482	1.00468	1.00453	1.00438	1.00423	1.00407
50	1.00563	1.00549	1.00535	1.00521	1.00506	1.00491	1.00476	1.00460	1.00444	1.00427

Table 5.31 As in Table 5.30 but for the pressure range 650–200 hPa. This table with an enhanced resolution of the temperature of 1 K is available as ESM at https://doi.org/10.1007/978-3-030-52171-4_5

Temperature (°C)	Pressure (hPa)									
	650	600	550	500	450	400	350	300	250	200
–35	1.00343	1.00318	1.00292	1.00266	1.00240	1.00215	1.00189	1.00163	1.00138	1.00112
–30	1.00328	1.00304	1.00279	1.00255	1.00231	1.00207	1.00182	1.00158	1.00134	1.00110
–25	1.00315	1.00292	1.00269	1.00246	1.00223	1.00200	1.00177	1.00154	1.00131	1.00108
–20	1.00305	1.00283	1.00261	1.00239	1.00217	1.00196	1.00174	1.00152	1.00130	1.00108
–15	1.00296	1.00276	1.00255	1.00234	1.00214	1.00193	1.00172	1.00151	1.00131	1.00110
–10	1.00291	1.00271	1.00251	1.00232	1.00212	1.00192	1.00172	1.00153	1.00133	1.00113
–5	1.00287	1.00269	1.00250	1.00231	1.00212	1.00194	1.00175	1.00156	1.00137	1.00118
0	1.00287	1.00269	1.00251	1.00233	1.00215	1.00197	1.00179	1.00161	1.00143	1.00125
5	1.00289	1.00272	1.00255	1.00238	1.00221	1.00203	1.00186	1.00169	1.00151	1.00134
10	1.00295	1.00278	1.00262	1.00245	1.00229	1.00212	1.00195	1.00179	1.00161	1.00144
15	1.00303	1.00287	1.00271	1.00255	1.00239	1.00223	1.00207	1.00190	1.00173	1.00156
20	1.00314	1.00299	1.00283	1.00268	1.00252	1.00236	1.00220	1.00204	1.00187	1.00169
25	1.00328	1.00313	1.00298	1.00283	1.00268	1.00252	1.00236	1.00219	1.00201	1.00182
30	1.00345	1.00331	1.00316	1.00300	1.00285	1.00269	1.00252	1.00235	1.00215	1.00193
35	1.00365	1.00350	1.00335	1.00319	1.00303	1.00286	1.00269	1.00249	1.00227	1.00201
40	1.00386	1.00371	1.00355	1.00338	1.00321	1.00303	1.00283	1.00261	1.00235	1.00202
45	1.00407	1.00391	1.00374	1.00356	1.00337	1.00316	1.00293	1.00266	1.00234	1.00191
50	1.00427	1.00409	1.00391	1.00370	1.00348	1.00323	1.00295	1.00261	1.00219	1.00161

Table 5.32 Sound speed of humid air (in m s^{-1}) as a function of temperature, pressure, and relative humidity at isobars 1000, 850, and 700 hPa, and isohumes 0%, 20%, and 40% relative humidity, calculated according to TEOS-10 [5, 17, 18]. This table with an enhanced resolution of the temperature of 1 K is available as ESM at https://doi.org/10.1007/978-3-030-52171-4_5

Temperature (°C)	Pressure (hPa)								
	1000	850	700	1000	850	700	1000	850	700
	Relative humidity (%)								
	0	0	0	20	20	20	40	40	40
–30	312.68	312.69	312.69	312.69	312.69	312.70	312.69	312.70	312.70
–25	315.89	315.89	315.89	315.90	315.90	315.90	315.91	315.91	315.91
–20	319.06	319.06	319.06	319.08	319.08	319.08	319.09	319.09	319.10
–15	322.21	322.20	322.20	322.23	322.22	322.23	322.24	322.25	322.25
–10	325.31	325.31	325.30	325.34	325.34	325.35	325.37	325.38	325.39
–5	328.39	328.39	328.38	328.44	328.44	328.44	328.48	328.49	328.50
0	331.44	331.43	331.42	331.50	331.51	331.51	331.57	331.58	331.61
5	334.46	334.45	334.44	334.55	334.56	334.57	334.64	334.66	334.70
10	337.45	337.44	337.42	337.58	337.59	337.61	337.71	337.74	337.80
15	340.41	340.40	340.38	340.59	340.61	340.64	340.77	340.83	340.91
20	343.34	343.33	343.31	343.60	343.63	343.68	343.85	343.92	344.04
25	346.25	346.23	346.22	346.60	346.64	346.71	346.94	347.05	347.21
30	349.13	349.11	349.10	349.60	349.66	349.77	350.06	350.21	350.44
35	351.99	351.97	351.95	352.61	352.70	352.84	353.23	353.44	353.74
40	354.82	354.80	354.78	355.64	355.77	355.96	356.47	356.75	357.15

Table 5.33 As in Table 5.32 but for isohumes 60%, 80%, and 100% relative humidity. This table with an enhanced resolution of the temperature of 1 K is available as ESM at https://doi.org/10.1007/978-3-030-52171-4_5

Temperature (°C)	Pressure (hPa)								
	1000	850	700	1000	850	700	1000	850	700
	Relative humidity (%)								
	60	60	60	80	80	80	100	100	100
-30	312.70	312.70	312.71	312.70	312.71	312.72	312.71	312.71	312.72
-25	315.91	315.92	315.93	315.92	315.93	315.94	315.93	315.94	315.95
-20	319.10	319.11	319.12	319.11	319.12	319.13	319.13	319.14	319.15
-15	322.26	322.27	322.28	322.28	322.29	322.31	322.30	322.32	322.34
-10	325.40	325.41	325.43	325.43	325.45	325.47	325.46	325.48	325.51
-5	328.52	328.54	328.57	328.57	328.59	328.63	328.61	328.64	328.69
0	331.63	331.66	331.70	331.69	331.73	331.79	331.76	331.80	331.88
5	334.73	334.77	334.83	334.82	334.88	334.96	334.91	334.98	335.09
10	337.84	337.90	337.98	337.97	338.05	338.17	338.09	338.20	338.35
15	340.96	341.04	341.17	341.14	341.25	341.43	341.31	341.46	341.68
20	344.10	344.22	344.40	344.35	344.51	344.76	344.59	344.80	345.11
25	347.28	347.45	347.70	347.63	347.86	348.19	347.96	348.25	348.68
30	350.53	350.76	351.11	350.99	351.31	351.77	351.45	351.85	352.43
35	353.86	354.18	354.64	354.48	354.91	355.54	355.09	355.63	356.43
40	357.30	357.73	358.35	358.12	358.70	359.55	358.94	359.67	360.74

Table 5.34 Specific isobaric heat capacity of humid air (in $10^3 \text{ J kg}^{-1} \text{ K}^{-1}$) as a function of temperature and specific humidity at 1000 hPa and at relative humidities $\leq 100\%$ and of saturated water vapor (in $10^3 \text{ J kg}^{-1} \text{ K}^{-1}$) calculated according to TEOS-10 [5.17, 18]

Temperature (°C)	Humid air					Saturated water vapor
	Specific humidity ($\times 10^{-3} \text{ kg kg}^{-1}$)					
	0.0	5.0	10.0	15.0	20.0	
-60	1.0062					
-40	1.0057					
-20	1.0055					1.8672
0	1.0057					1.8843
20	1.0061	1.0105	1.0150			1.9059
40	1.0069	1.0113	1.0157	1.0201	1.0247	1.9314
60	1.0080	1.0124	1.0168	1.0212	1.0257	1.9648
80	1.0094	1.0138	1.0182	1.0227	1.0271	

Table 5.35 Specific isochoric heat capacity of humid air (in $10^3 \text{ J kg}^{-1} \text{ K}^{-1}$) as a function of temperature and specific humidity at 1000 hPa and at relative humidities $\leq 100\%$ and of saturated water vapor (in $10^3 \text{ J kg}^{-1} \text{ K}^{-1}$) calculated according to TEOS-10 [5.17, 18]

Temperature (°C)	Humid air					Saturated water vapor
	Specific humidity ($\times 10^{-3} \text{ kg kg}^{-1}$)					
	0.0	5.0	10.0	15.0	20.0	
-60	0.7161					
-40	0.7162					
-20	0.7165					1.4038
0	0.7169					1.4184
20	0.7177	0.7211	0.7247			1.4359
40	0.7186	0.7221	0.7256	0.7292	0.7327	1.4552
60	0.7199	0.7234	0.7269	0.7304	0.7340	1.4789
80	0.7215	0.7250	0.7285	0.7320	0.7356	

Table 5.36 Henry’s volatility constant of dry air (N₂, O₂, and Ar) dissolved in liquid water (in GPa), $K_H = H^{-1}$ (where H denotes Henry’s solubility constant), as a function of temperature according to [5.56, 57], based on [5.30]

Temperature (°C)	Temperature increment (K)									
	0	1	2	3	4	5	6	7	8	9
50	9.194	9.258	9.321	9.381	9.440	9.497	9.552	9.606	9.657	9.707
40	8.453	8.535	8.615	8.693	8.770	8.845	8.918	8.990	9.059	9.127
30	7.557	7.653	7.747	7.840	7.932	8.023	8.112	8.200	8.286	8.370
20	6.542	6.648	6.752	6.856	6.959	7.062	7.163	7.263	7.362	7.460
10	5.459	5.569	5.678	5.788	5.897	6.005	6.114	6.222	6.329	6.436
0	4.367	4.475	4.583	4.692	4.801	4.910	5.020	5.129	5.239	5.349

In Table 5.37, the dynamic viscosity of dry air is calculated after [5.42, Eq. (38)]; superscript LJ2004 refers to [5.58],

$$\frac{\mu}{10^{-6} \text{ kg m}^{-1} \text{ s}^{-1}} = -9.8601 \times 10^{-1} + 9.080125 \times 10^{-2} T / \text{K} - 1.17635575 \times 10^{-4} T^2 / \text{K}^2 + 1.2349703 \times 10^{-7} T^3 / \text{K}^3 - 5.7971299 \times 10^{-11} T^4 / \text{K}^4, \quad 250 \text{ K} \leq T \leq 600 \text{ K}, \quad (5.4)$$

$|\mu - \mu^{\text{LJ2004}}| / \mu^{\text{LJ2004}} \leq 0.191\%$, in the subrange $250.15 \text{ K} \leq T \leq 335.15 \text{ K}$ at $p = 1013.25 \text{ hPa}$, and the thermal conductivity of dry air is calculated after [5.42, Eq. (39)]

$$\frac{k}{\text{W m}^{-1} \text{ K}^{-1}} = -2.276501 \times 10^{-3} + 1.2598485 \times 10^{-4} T / \text{K} - 1.4815235 \times 10^{-7} T^2 / \text{K}^2$$

$$+ 1.73550646 \times 10^{-10} T^3 / \text{K}^3 - 1.066657 \times 10^{-13} T^4 / \text{K}^4 + 2.47663035 \times 10^{-17} T^5 / \text{K}^5, \quad 250 \text{ K} \leq T \leq 1050 \text{ K}, \quad (5.5)$$

$|k - k^{\text{LJ2004}}| / k^{\text{LJ2004}} \leq 1.252\%$, in the subrange $250.15 \text{ K} \leq T \leq 335.15 \text{ K}$ at $p = 1013.25 \text{ hPa}$.

Unfortunately, there is an error in the original paper [5.42, p. 1103, left column above Eq. (39)]. The dimension of k on the left-hand side of the tailored Eq. (39) must be $\text{W m}^{-1} \text{ K}^{-1}$. Compare with [5.42, Fig. 3 therein] for correct order of magnitude. As the reference for the accuracy assessment of μ and k the highly accurate equations of state for viscosity and thermal conductivity as functions of temperature and air density proposed in [5.58] were used.

The other quantities were calculated accordingly. The kinematic viscosity (momentum diffusivity) in units $\text{m}^2 \text{ s}^{-1}$

$$\nu_m = \frac{\mu}{\rho}, \quad (5.6)$$

Table 5.37 Transport properties of dry air for 1000 hPa [5.42]

Temperature (°C)	Dynamic viscosity ($\times 10^{-6} \text{ kg m}^{-1} \text{ s}^{-1}$)	Thermal conductivity ($\times \text{W m}^{-1} \text{ K}^{-1}$)	Kinematic viscosity ($\times 10^{-5} \text{ m}^2 \text{ s}^{-1}$)	Thermal diffusivity ($\times 10^{-5} \text{ m}^2 \text{ s}^{-1}$)	Prandtl number (–)
–20	16.23	0.02253	1.1781	1.6264	0.7244
–15	16.48	0.02291	1.2204	1.6873	0.7233
–10	16.73	0.02330	1.2632	1.7490	0.7222
–5	16.99	0.02368	1.3065	1.8116	0.7212
0	17.23	0.02406	1.3504	1.8750	0.7202
5	17.48	0.02444	1.3949	1.9393	0.7193
10	17.72	0.02482	1.4399	2.0044	0.7184
15	17.97	0.02519	1.4854	2.0704	0.7175
20	18.21	0.02556	1.5315	2.1371	0.7166
25	18.44	0.02593	1.5780	2.2047	0.7158
30	18.68	0.02630	1.6251	2.2731	0.7149
35	18.92	0.02666	1.6727	2.3422	0.7141
40	19.15	0.02703	1.7208	2.4122	0.7134
45	19.38	0.02739	1.7694	2.4829	0.7126
50	19.61	0.02775	1.8185	2.5544	0.7119
55	19.83	0.02810	1.8682	2.6266	0.7112
60	20.06	0.02846	1.9183	2.6995	0.7106

Table 5.38 Mass density of stable liquid water and seawater (in kg m^{-3}) as a function of temperature and salinity at 1000 hPa, calculated according to TEOS-10 [5.17, 18]

Temperature (°C)	Pure water	Salinity ($\times 10^{-3} \text{ kg kg}^{-1}$)						
		5.0	10.0	15.0	20.0	30.0	35.0	40.0
60	983.2							
55	985.7							
50	988.0							
45	990.2							
40	992.2	995.9	999.5	1003.2	1006.8	1010.5	1014.2	1017.8
35	994.0	997.7	1001.4	1005.1	1008.7	1012.4	1016.1	1019.8
30	995.6	999.4	1003.1	1006.8	1010.5	1014.2	1017.9	1021.6
25	997.0	1000.8	1004.5	1008.2	1012.0	1015.7	1019.5	1023.2
20	998.2	1002.0	1005.8	1009.5	1013.3	1017.1	1020.9	1024.6
15	999.1	1002.9	1006.7	1010.6	1014.4	1018.2	1022.0	1025.8
10	999.7	1003.6	1007.5	1011.3	1015.2	1019.1	1022.9	1026.8
5	1000.0	1003.9	1007.9	1011.8	1015.7	1019.7	1023.6	1027.5
0	999.8	1003.9	1007.9	1011.9	1015.9	1019.9	1024.0	1028.0
-3	999.6	1003.7	1007.8	1011.8	1015.9	1020.0	1024.0	1028.1

the thermal diffusivity in units $\text{m}^2 \text{s}^{-1}$

$$\nu_{\text{th}} = \frac{k}{\rho c_p}, \quad (5.7)$$

and the molecular Prandtl number

$$\text{Pr} = \frac{\nu_m}{\nu_{\text{th}}}, \quad (5.8)$$

5.4.3 Water, Seawater, and Ice

The tables presented in this section contain parameters of water, seawater, and ice according to TEOS-10 [5.17, 18]. The mass density of seawater and the boiling temperature of water are given in Tables 5.38 and 5.39.

For Table 5.40, the following approximations (derived by O. Hellmuth on the basis of [5.17, 18]) are valid for the vaporization enthalpy

$$\begin{aligned} \frac{\lambda_v}{\text{J kg}^{-1}} &= 0.7166 \times 10^7 - 0.6970 \times 10^4 \frac{T}{\text{K}} \\ &\quad - \frac{0.1166 \times 10^{10}}{T/\text{K}} + \frac{0.1126 \times 10^{12}}{(T/\text{K})^2} \end{aligned}$$

with $235 \text{ K} \leq T \leq 333 \text{ K}$:

$$\frac{|\lambda - \lambda^{\text{TEOS-10}}|}{\lambda^{\text{TEOS-10}}} \leq 1.3\%, \quad (5.9)$$

for the fusion (melting) enthalpy

$$\begin{aligned} \frac{\lambda_m}{\text{J kg}^{-1}} &= 0.23536 \times 10^8 - 0.27193 \times 10^6 \frac{T}{\text{K}} \\ &\quad + 1049.07 \left(\frac{T}{\text{K}}\right)^2 - 1.3345 \left(\frac{T}{\text{K}}\right)^3 \end{aligned}$$

with $234 \text{ K} \leq T \leq 273.15 \text{ K}$:

$$\frac{|\lambda_m - \lambda_m^{\text{TEOS-10}}|}{\lambda_m^{\text{TEOS-10}}} \leq 1.6\%, \quad (5.10)$$

Table 5.39 Boiling temperature of pure water as a function of pressure calculated according to TEOS-10 [5.17, 18]

Air pressure (hPa)	Boiling temperature (°C)
1100	102.292
1050	100.976
1000	99.606
950	98.178
900	96.687
850	95.125
800	93.486
750	91.758
700	89.932
650	87.993
600	85.926
550	83.709
500	81.317
450	78.715
400	75.857
350	72.681
300	69.095
250	64.963
200	60.058

and for the sublimation enthalpy

$$\begin{aligned} \frac{\lambda_s}{\text{J kg}^{-1}} &= 0.263 \times 10^7 + 0.174 \times 10^4 \frac{T}{\text{K}} - 3.63 \left(\frac{T}{\text{K}}\right)^2 \end{aligned}$$

with $173 \text{ K} \leq T \leq 273.15 \text{ K}$:

$$\frac{|\lambda_s - \lambda_s^{\text{TEOS-10}}|}{\lambda_s^{\text{TEOS-10}}} \leq 0.3\%. \quad (5.11)$$

Table 5.40 Specific isobaric and isochoric heat capacity and enthalpy of the phase transition (latent heat) of water and ice calculated according to TEOS-10 [5.17, 18]

Temperature (°C)	Specific heat capacity ($\times 10^3 \text{ J kg}^{-1} \text{ K}^{-1}$)			Enthalpy of phase transition ($\times 10^6 \text{ J kg}^{-1}$)		
	Water, isobaric	Water, isochoric	Ice, isobaric	Vaporization	Fusion (melting)	Sublimation
60	4.1850	3.9765		2.3577		
50	4.1813	4.0262		2.3819		
40	4.1794	4.0734		2.4060		
35	4.1793	4.0958		2.4179		
30	4.1798	4.1172		2.4298		
25	4.1813	4.1376		2.4417		
20	4.1841	4.1567		2.4535		
15	4.1885	4.1744		2.4654		
10	4.1952	4.1906		2.4772		
5	4.2050	4.2049		2.4890		
0	4.2195	4.2170	2.0967	2.5009	0.3334	2.8344
−5	4.2405	4.2263	2.0599	2.5129	0.3200	2.8356
−10	4.2721	4.2321	2.0231	2.5250	0.3054	2.8366
−15	4.3210	4.2333	1.9864	2.5373	0.2907	2.8374
−20	4.4012	4.2288	1.9498	2.5498	0.2769	2.8381
−25	4.5418	4.2173	1.9133	2.5629	0.2646	2.8385
−30	4.8009	4.1966	1.8769	2.5770	0.2551	2.8387
−35	5.2957	4.1573	1.8407	2.5929	0.2494	2.8388
−40			1.8045		0.2494	2.8386
−45			1.7685		0.2572	2.8383
−50			1.7326		0.2762	2.8378
−60			1.6612			
−70			1.5905			
−80			1.5205			
−90			1.4512			
−100			1.3827			

5.5 Parameterization of Optical Properties of Clouds

Clouds can affect the atmospheric energy balance considerably through scattering and absorption of electromagnetic radiation at solar and infrared wavelengths. The ability of clouds to affect the radiative balance depends on their microphysical and optical properties. A key optical metric of a cloud with cloud base z_B and cloud top z_T is the dimensionless optical thickness τ

$$\tau = \int_{z_B}^{z_T} \beta_e(z) dz. \quad (5.12)$$

Here, $\beta_e(z)$ (in units of m^{-1}) denotes the height-dependent volumetric extinction coefficient of the cloud. This quantity depends essentially on cloud microphysical parameters, such as the cloud droplet size distribution and the geometrical shape of the cloud's constituent hydrometeors. Knowledge of the geometrical shape of an elementary *cloud particle* allows us to determine its optical parameters within the framework

of Mie theory (*Gustav Adolf Feodor Wilhelm Ludwig Mie*, 1868–1957) [5.59]. However, the latter is known to be computationally very expensive and to not be practicable for real-time applications such as cloud modeling and remote-sensing inversion. To overcome this difficulty, precalculated lookup tables are available for the most relevant optical parameters (extinction coefficient, single-scattering albedo, asymmetry factor of the phase function), on the basis of which user-friendly parameterizations in terms of easily accessible observables (and/or derivables) have been derived. In the following, the corresponding parameterizations of optical properties for warm and cold clouds that allow a quick calculation with a sufficiently high accuracy for most applications will be presented.

5.5.1 Warm Clouds

The total number concentration of a population of cloud particles, N (in m^{-3}), with radii in the interval $R_{\min} \leq$

$R \leq R_{\max}$ reads [5.60, Eq. (5.2.114)]

$$N = \int_{R_{\min}}^{R_{\max}} \frac{dN(R)}{dR} dR. \quad (5.13)$$

Here, $n(R) = dN(R)/dR$ denotes the particle size distribution (PSD) (in m^{-4}). The volumetric extinction and scattering coefficients of the cloud droplet population, β_e and β_s (in units of m^{-1}), are defined as follows [5.60, Eqs. (5.2.115) and (5.2.116)]

$$\beta_e = \int_{R_{\min}}^{R_{\max}} \sigma_e(R) n(R) dR, \quad (5.14)$$

$$\beta_s = \int_{R_{\min}}^{R_{\max}} \sigma_s(R) n(R) dR. \quad (5.15)$$

Here, $\sigma_e(R)$ and $\sigma_s(R)$ are the extinction and scattering cross sections (in units of m^2) [5.60, Eqs. (5.2.94) and (5.2.98)]

$$\sigma_e(R) = \pi R^2 Q_e(R), \quad (5.16)$$

$$\sigma_s(R) = \pi R^2 Q_s(R). \quad (5.17)$$

The quantities $Q_e(R)$ and $Q_s(R)$ are the dimensionless extinction and scattering efficiencies, respectively, which can be calculated within the framework of Mie theory as a function of the size parameter $x = 2\pi R/\lambda$, where λ denotes the wavelength [5.59]. The dimensionless single-scattering albedo, ω_s , and the dimensionless asymmetry factor, g , of an ensemble of cloud droplets are defined as follows [5.60, Eqs. (5.2.117) and (6.5.9a)]

$$\omega_s = \frac{\beta_s}{\beta_e}, \quad (5.18)$$

$$g = \frac{1}{2} \int_{-1}^1 P(\cos \Theta) \cos \Theta d \cos \Theta = \langle \cos \Theta \rangle. \quad (5.19)$$

In (5.19), $P(\cos \Theta)$ is the dimensionless phase function (or scattering indicatrix) as a function of the scattering angle Θ , as defined in [5.60, Fig. 6.1]. The asymmetry factor is the mean value of the cosine of the scattering angle, $\langle \cos \Theta \rangle$.

For a given PSD $n(R)$, the equivalent (or effective) radius R_e is defined as the ratio of the third to the second

moments of the PSD [5.61, Eq. (5)]

$$R_e = \frac{\int_0^{\infty} R^3 n(R) dR}{\int_0^{\infty} R^2 n(R) dR}. \quad (5.20)$$

For shortwave radiation, the droplet radius is large compared to the wavelength, $x \gg 1$, and the extinction efficiency asymptotically approaches the limit $Q_e = 2$. Therefore, and by virtue of (5.14) and (5.16), the volumetric extinction coefficients β_e reads

$$\beta_e \approx 2\pi \int_0^{\infty} R^2 n(R) dR. \quad (5.21)$$

The liquid water content (LWC) of a cloud, defined as the mass of condensed water per volume of air (in units of kg m^{-3}), is given by the following relation

$$\begin{aligned} \text{LWC} &= \rho_w \int_0^{\infty} V_w(R) n(R) dR \\ &= \frac{4}{3} \pi \rho_w \int_0^{\infty} R^3 n(R) dR. \end{aligned} \quad (5.22)$$

Here, ρ_w denotes the mass density of liquid water and $V_w(R) = 4\pi R^3/3$ the geometric volume of a single droplet. Inserting (5.21) and (5.22) into (5.20) yields an approximate expression for β_e in terms of LWC and R_e [5.61, Eq. (6), given therein in cgs units]

$$\beta_e \approx \frac{3 \text{LWC}/\rho_w}{2 R_e}. \quad (5.23)$$

Equation (5.23) provides the basis for the parameterization of cloud optical properties in terms of the effective radius and the liquid water content, which circumvents time-consuming Mie calculations. In [5.61, Eq. (7)], the corresponding lookup-tables were calculated using a generalized gamma distribution to represent the PSD

$$n(R) = \frac{N_0}{\Gamma(\gamma) R_m} \left(\frac{R}{R_m} \right)^{\gamma-1} \exp \left(-\frac{R}{R_m} \right). \quad (5.24)$$

Here, N_0 is the total number concentration of cloud droplets (in units of m^{-3}), and $\Gamma(\gamma)$ is the gamma function with γ denoting the dimensionless shape parameter determining the skewness of the PSD (large values correspond to broad distribution). The quantity R_m is a characteristic length scale, defined as the inverse of the frequently employed rate parameter of the

PSD. A bimodal gamma size distribution can be described as a superposition of two gamma distributions with the weighting factor $0 \leq c \leq 1$ [5.61, p. 729],

$$n(R) = (1 - c)n_1(R) + cn_2(R). \tag{5.25}$$

The following relation between the equivalent radius R_e and the characteristic radius R_m was derived from the insertion of $n(R)$ into (5.20) [5.61, Eq. (8a)]

$$R_e = \frac{\left[(1 - c)(\gamma_1 + 2)(\gamma_1 + 1)\gamma_1 R_{m,1}^3 + c(\gamma_2 + 2)(\gamma_2 + 1)\gamma_2 R_{m,2}^3 \right]}{\left[(1 - c)(\gamma_1 + 1)\gamma_1 R_{m,1}^2 + c(\gamma_2 + 1)\gamma_2 R_{m,2}^2 \right]} \tag{5.26}$$

For a single mode ($c = 0$ or $c = 1$), (5.26) reduces to [5.61, Eq. (8b)]

$$R_e = (\gamma + 2)R_m. \tag{5.27}$$

In [5.61, Eqs. (13)–(15)], a general functional dependence on the equivalent radius was adopted for the parameterization on the extinction coefficient β_e , the single-scattering co-albedo $1 - \omega_s$, and the asymmetry factor g for both solar and terrestrial wavelengths in the form of the following numerical value equations

$$\frac{\beta_e}{\text{m}^{-1}} = \frac{\text{LWC}}{10^{-3} \text{ kg m}^{-3}} \left[a_1 \left(\frac{R_e}{\mu\text{m}} \right)^{b_1} + c_1 \right], \tag{5.28}$$

$$1 - \omega_s = a_2 \left(\frac{R_e}{\mu\text{m}} \right)^{b_2} + c_2, \tag{5.29}$$

$$g = a_3 \left(\frac{R_e}{\mu\text{m}} \right)^{b_3} + c_3. \tag{5.30}$$

The parameter triples (a_i, b_i, c_i) for $i = 1, 2, 3$ are given in Tables 5.41–5.46.

Table 5.41 Fitting parameters a_1 , b_1 , and c_1 in the numerical value equation (5.28) for the volumetric extinction coefficient β_e as a function of equivalent radius $R_e = 2.5\text{--}60 \mu\text{m}$ (for small, medium, and large sizes) and electromagnetic wavelength λ (solar radiation $\lambda = 0.290\text{--}3.690 \mu\text{m}$) [5.61, Table 1]

λ (μm)	2.5–12.5 μm			12.5–30 μm			30–60 μm		
	a_1	b_1	c_1	a_1	b_1	c_1	a_1	b_1	c_1
0.290	1.63E+03	-1.03E+00	7.66E-01	1.63E+03	-1.03E+00	9.90E-01	9.40E+02	-8.06E-01	-1.01E+01
0.314	1.67E+03	-1.04E+00	3.83E+00	1.61E+03	-1.02E+00	5.44E-01	9.41E+02	-8.06E-01	-1.01E+01
0.344	1.67E+03	-1.04E+00	3.49E+00	1.62E+03	-1.02E+00	6.34E-01	9.42E+02	-8.06E-01	-1.02E+01
0.379	1.68E+03	-1.05E+00	4.26E+00	1.64E+03	-1.03E+00	8.33E-01	9.48E+02	-8.08E-01	-1.01E+01
0.419	1.70E+03	-1.05E+00	4.49E+00	1.64E+03	-1.02E+00	6.44E-01	9.54E+02	-8.10E-01	-9.99E+00
0.459	1.72E+03	-1.06E+00	4.99E+00	1.65E+03	-1.03E+00	7.23E-01	9.55E+02	-8.10E-01	-1.00E+01
0.499	1.73E+03	-1.06E+00	5.13E+00	1.66E+03	-1.03E+00	8.13E-01	9.62E+02	-8.12E-01	-9.95E+00
0.544	1.75E+03	-1.07E+00	5.95E+00	1.67E+03	-1.03E+00	8.73E-01	9.63E+02	-8.12E-01	-9.98E+00
0.603	1.76E+03	-1.06E+00	5.01E+00	1.68E+03	-1.03E+00	9.28E-01	9.70E+02	-8.14E-01	-9.91E+00
0.664	1.79E+03	-1.07E+00	5.98E+00	1.69E+03	-1.03E+00	9.89E-01	9.76E+02	-8.16E-01	-9.84E+00
0.719	1.81E+03	-1.08E+00	6.85E+00	1.70E+03	-1.04E+00	1.04E+00	9.78E+02	-8.16E-01	-9.89E+00
0.766	1.84E+03	-1.09E+00	8.81E+00	1.71E+03	-1.04E+00	1.01E+00	9.84E+02	-8.18E-01	-9.79E+00
0.821	1.86E+03	-1.09E+00	8.61E+00	1.73E+03	-1.04E+00	1.16E+00	9.91E+02	-8.20E-01	-9.74E+00
0.929	1.87E+03	-1.09E+00	8.41E+00	1.74E+03	-1.04E+00	1.19E+00	9.99E+02	-8.22E-01	-9.69E+00
1.046	1.91E+03	-1.10E+00	7.51E+00	1.77E+03	-1.05E+00	1.46E+00	1.01E+03	-8.24E-01	-9.65E+00
1.142	1.94E+03	-1.11E+00	1.01E+01	1.78E+03	-1.05E+00	1.32E+00	1.01E+03	-8.26E-01	-9.61E+00
1.232	1.96E+03	-1.11E+00	9.29E+00	1.80E+03	-1.05E+00	1.50E+00	1.03E+03	-8.30E-01	-9.44E+00
1.393	1.98E+03	-1.11E+00	7.61E+00	1.83E+03	-1.06E+00	1.63E+00	1.04E+03	-8.32E-01	-9.40E+00
1.587	2.01E+03	-1.11E+00	8.80E+00	1.87E+03	-1.06E+00	1.93E+00	1.05E+03	-8.36E-01	-9.31E+00
1.855	2.15E+03	-1.15E+00	1.42E+01	1.91E+03	-1.07E+00	1.96E+00	1.07E+03	-8.40E-01	-9.22E+00
2.247	3.26E+03	-1.46E+00	5.42E+01	1.99E+03	-1.08E+00	2.54E+00	1.09E+03	-8.46E-01	-9.08E+00
2.618	4.56E+03	-1.61E+00	5.74E+01	2.05E+03	-1.09E+00	2.66E+00	1.12E+03	-8.52E-01	-8.94E+00
3.145	2.71E+03	-1.27E+00	2.35E+01	2.02E+03	-1.08E+00	2.24E+00	1.12E+03	-8.52E-01	-8.99E+00
3.690	5.29E+03	-1.73E+00	7.34E+01	2.17E+03	-1.10E+00	3.01E+00	1.17E+03	-8.64E-01	-8.67E+00

Table 5.42 Fitting parameters a_1 , b_1 , and c_1 in the numerical value equation (5.28) for the volumetric extinction coefficient β_e as a function of equivalent radius $R_e = 2.5\text{--}60\ \mu\text{m}$ (for small, medium, and large sizes) and electromagnetic wavelength λ (terrestrial radiation $\lambda = 3.900\text{--}150.000\ \mu\text{m}$) [5.61, Table 4]

λ (μm)	2.5–12.5 μm			12.5–30 μm			30–60 μm		
	a_1	b_1	c_1	a_1	b_1	c_1	a_1	b_1	c_1
3.9	6.40E+03	-1.79E+00	7.03E+01	2.24E+03	-1.11E+00	3.32E+00	1.20E+03	-8.70E-01	-8.51E+00
4.1	5.42E+03	-1.63E+00	4.78E+01	2.26E+03	-1.12E+00	3.29E+00	1.22E+03	-8.74E-01	-8.38E+00
4.3	4.30E+03	-1.42E+00	1.52E+01	2.28E+03	-1.12E+00	3.16E+00	1.23E+03	-8.76E-01	-8.35E+00
4.5	3.32E+03	-1.19E+00	-3.31E+01	2.28E+03	-1.11E+00	2.91E+00	1.24E+03	-8.78E-01	-8.32E+00
4.7	2.69E+03	-9.84E-01	-9.66E+01	2.28E+03	-1.11E+00	2.66E+00	1.26E+03	-8.82E-01	-8.19E+00
4.9	2.29E+03	-7.86E-01	-1.89E+02	2.28E+03	-1.11E+00	2.42E+00	1.27E+03	-8.84E-01	-8.16E+00
5.1	2.03E+03	-5.46E-01	-3.88E+02	2.28E+03	-1.11E+00	2.19E+00	1.28E+03	-8.88E-01	-8.03E+00
5.3	2.52E+03	-2.26E-01	-1.30E+03	2.30E+03	-1.11E+00	2.25E+00	1.30E+03	-8.92E-01	-7.90E+00
5.4	-4.31E+04	8.00E-03	4.41E+04	2.34E+03	-1.12E+00	2.60E+00	1.31E+03	-8.94E-01	-7.86E+00
5.5	-1.10E+03	2.04E-01	1.96E+03	2.41E+03	-1.13E+00	3.47E+00	1.31E+03	-8.94E-01	-7.90E+00
5.7	-2.61E+02	4.58E-01	9.55E+02	2.76E+03	-1.19E+00	6.82E+00	1.32E+03	-8.96E-01	-7.82E+00
5.9	-1.84E+02	5.00E-01	7.83E+02	3.12E+03	-1.24E+00	9.51E+00	1.30E+03	-8.92E-01	-7.94E+00
6.0	-4.93E+02	2.70E-01	1.11E+03	2.92E+03	-1.22E+00	8.24E+00	1.27E+03	-8.84E-01	-8.20E+00
6.1	-3.15E+04	8.00E-03	3.23E+04	2.74E+03	-1.19E+00	6.86E+00	1.28E+03	-8.86E-01	-8.14E+00
6.2	1.95E+03	-2.50E-01	-9.02E+02	2.61E+03	-1.16E+00	5.49E+00	1.30E+03	-8.90E-01	-8.04E+00
6.3	2.41E+03	-1.86E-01	-1.38E+03	2.62E+03	-1.16E+00	5.36E+00	1.32E+03	-8.94E-01	-7.92E+00
6.5	-1.14E+03	1.86E-01	1.95E+03	2.76E+03	-1.18E+00	6.34E+00	1.35E+03	-9.00E-01	-7.76E+00
6.7	-1.87E+02	5.32E-01	8.45E+02	3.03E+03	-1.22E+00	8.35E+00	1.37E+03	-9.04E-01	-7.66E+00
7.0	-4.36E+01	9.24E-01	5.82E+02	3.56E+03	-1.29E+00	1.16E+01	1.39E+03	-9.08E-01	-7.56E+00
7.1	-1.76E+01	1.20E+00	4.99E+02	4.06E+03	-1.34E+00	1.40E+01	1.40E+03	-9.10E-01	-7.52E+00
7.3	-7.13E+00	1.49E+00	4.43E+02	4.74E+03	-1.40E+00	1.65E+01	1.41E+03	-9.12E-01	-7.48E+00
7.6	-1.97E+00	1.91E+00	3.87E+02	5.98E+03	-1.49E+00	1.96E+01	1.42E+03	-9.14E-01	-7.47E+00
8.0	-2.89E-01	2.57E+00	3.35E+02	8.00E+03	-1.60E+00	2.25E+01	1.44E+03	-9.16E-01	-7.48E+00
8.6	-1.29E-02	3.65E+00	2.84E+02	9.63E+03	-1.66E+00	2.26E+01	1.46E+03	-9.20E-01	-7.42E+00
9.0	-2.60E-04	5.06E+00	2.48E+02	8.53E+03	-1.59E+00	1.83E+01	1.50E+03	-9.28E-01	-7.15E+00
9.6	-7.62E-02	3.00E+00	3.02E+02	7.52E+03	-1.55E+00	1.91E+01	1.52E+03	-9.30E-01	-7.13E+00
10.0	-9.91E-06	6.00E+00	1.95E+02	2.37E+03	-1.02E+00	-1.69E+01	1.96E+03	-1.02E+00	-3.73E+00
10.5	-5.91E+04	-6.00E+00	1.55E+02	8.17E+02	-4.24E-01	-1.35E+02	2.45E+03	-1.09E+00	-1.57E+00
11.0	-3.88E-05	5.24E+00	1.40E+02	7.94E+02	-1.48E-01	-4.23E+02	1.68E+03	-9.66E-01	-5.84E+00
11.5	-1.79E+00	1.36E+00	1.66E+02	5.38E+02	-2.88E-01	-1.48E+02	9.77E+02	-7.88E-01	-1.28E+01
12.5	-8.34E+01	4.12E-01	3.51E+02	7.11E+02	-6.06E-01	-3.72E+01	8.92E+02	-7.62E-01	-1.35E+01
13.5	-4.90E+02	1.66E-01	8.69E+02	1.07E+03	-7.94E-01	-1.73E+01	1.03E+03	-8.08E-01	-1.15E+01
14.0	-7.78E+02	1.28E-01	1.20E+03	1.28E+03	-8.62E-01	-1.27E+01	1.13E+03	-8.36E-01	-1.05E+01
14.5	-7.47E+02	1.38E-01	1.19E+03	1.40E+03	-8.94E-01	-1.08E+01	1.19E+03	-8.50E-01	-1.01E+01
15.0	-6.18E+02	1.64E-01	1.07E+03	1.50E+03	-9.18E-01	-9.58E+00	1.24E+03	-8.62E-01	-9.66E+00
15.5	-4.56E+02	2.08E-01	9.07E+02	1.59E+03	-9.38E-01	-8.61E+00	1.28E+03	-8.72E-01	-9.37E+00
16.5	-2.83E+02	2.90E-01	7.28E+02	1.73E+03	-9.66E-01	-7.26E+00	1.35E+03	-8.86E-01	-8.97E+00
17.0	-1.82E+02	3.78E-01	6.15E+02	1.82E+03	-9.82E-01	-6.67E+00	1.40E+03	-8.96E-01	-8.67E+00
17.5	-1.23E+02	4.66E-01	5.41E+02	1.89E+03	-9.94E-01	-6.18E+00	1.44E+03	-9.04E-01	-8.42E+00
18.0	-7.98E+01	5.70E-01	4.81E+02	1.95E+03	-1.00E+00	-6.07E+00	1.47E+03	-9.10E-01	-8.28E+00
19.0	-3.52E+01	7.86E-01	4.02E+02	2.02E+03	-1.01E+00	-6.14E+00	1.53E+03	-9.20E-01	-8.01E+00
20.0	-9.86E+00	1.16E+00	3.30E+02	2.03E+03	-1.00E+00	-7.63E+00	1.61E+03	-9.34E-01	-7.58E+00
25.0	-1.22E-01	2.61E+00	2.37E+02	1.69E+03	-8.92E-01	-2.02E+01	1.81E+03	-9.66E-01	-6.71E+00
32.0	-7.27E-06	6.00E+00	1.76E+02	9.38E+02	-5.44E-01	-8.44E+01	2.13E+03	-1.01E+00	-5.72E+00
40.0	-2.93E+04	-5.18E+00	1.44E+02	1.19E+03	-9.20E-02	-8.08E+02	1.86E+03	-9.52E-01	-8.68E+00
50.0	-3.93E+03	-3.69E+00	1.35E+02	-7.38E+02	8.00E-02	1.03E+03	1.52E+03	-8.72E-01	-1.30E+01
60.0	-4.00E-02	-1.60E+00	1.39E+02	-9.44E+01	3.06E-01	3.34E+02	1.54E+03	-8.62E-01	-1.45E+01
80.0	8.63E+01	2.92E-01	-6.76E+01	-4.07E-01	1.48E+00	1.32E+02	1.36E+03	-7.90E-01	-2.17E+01
100.0	1.71E+00	1.36E+00	2.87E+01	-1.90E-07	5.41E+00	8.89E+01	6.85E+02	-4.68E-01	-6.75E+01
150.0	3.93E-02	2.35E+00	1.90E+01	-4.49E+03	-1.84E+00	7.12E+01	-2.26E-01	1.29E+00	8.10E+01

Table 5.43 Fitting parameters a_2 , b_2 , and c_2 in the numerical value equation (5.29) for the single-scattering co-albedo ($1 - \omega_s$) as a function of equivalent radius $R_e = 2.5\text{--}60\ \mu\text{m}$ (for small, medium, and large sizes) and electromagnetic wavelength λ (solar radiation $\lambda = 0.290\text{--}3.690\ \mu\text{m}$) [5.61, Table 2]

λ (μm)	2.5–12.5 μm			12.5–30 μm			30–60 μm		
	a_2	b_2	c_2	a_2	b_2	c_2	a_2	b_2	c_2
0.290	1.42E-06	7.66E-01	-1.02E-06	9.00E-07	9.42E-01	-9.60E-07	3.14E-06	6.88E-01	-1.16E-05
0.314	-2.33E-05	-2.32E-01	1.95E-05	5.08E-07	9.88E-01	5.97E-07	2.18E-06	6.90E-01	-7.64E-06
0.344	-2.03E-05	-1.52E+00	4.01E-06	3.68E-07	9.22E-01	-4.01E-08	7.50E-07	7.82E-01	-2.36E-06
0.379	1.43E-07	9.52E-01	-2.31E-08	3.94E-07	7.06E-01	-7.93E-07	3.42E-07	7.64E-01	-1.07E-06
0.419	2.57E-08	1.21E+00	1.01E-07	1.67E-07	7.12E-01	-3.65E-07	1.35E-07	7.78E-01	-3.94E-07
0.459	2.10E-08	1.13E+00	5.59E-08	2.75E-07	5.16E-01	-6.04E-07	6.85E-08	8.22E-01	-1.44E-07
0.499	3.72E-09	1.60E+00	1.07E-07	2.77E-08	9.74E-01	-1.07E-08	2.25E-07	5.48E-01	-7.05E-07
0.544	1.82E-08	1.21E+00	6.89E-08	3.23E-08	1.01E+00	4.62E-08	9.12E-08	7.94E-01	-3.12E-07
0.603	2.70E-07	7.34E-01	-2.43E-07	1.19E-07	9.76E-01	6.76E-08	3.32E-07	7.62E-01	-1.09E-06
0.664	5.47E-07	8.14E-01	-1.41E-07	5.91E-07	8.46E-01	-9.34E-07	8.34E-07	7.78E-01	-2.25E-06
0.719	9.95E-07	8.56E-01	-4.37E-07	1.88E-07	1.32E+00	3.08E-06	2.03E-05	3.32E-01	-4.32E-05
0.766	5.93E-07	1.26E+00	1.69E-06	4.52E-06	6.72E-01	-8.03E-06	6.16E-06	6.52E-01	-2.04E-05
0.821	8.03E-07	1.44E+00	5.04E-06	3.79E-05	3.82E-01	-6.22E-05	6.09E-06	7.88E-01	-1.23E-05
0.929	7.42E-06	1.05E+00	5.08E-06	1.58E-05	8.30E-01	-1.64E-05	3.08E-05	7.12E-01	-9.82E-05
1.046	2.36E-04	4.10E-01	-2.69E-04	2.82E-05	1.00E+00	4.65E-05	1.50E-04	6.60E-01	-5.20E-04
1.142	1.59E-04	7.86E-01	-1.33E-04	8.54E-05	9.62E-01	5.50E-05	3.58E-04	6.70E-01	-1.21E-03
1.232	3.11E-04	8.20E-01	-2.17E-04	2.27E-04	9.14E-01	-3.57E-05	7.03E-04	6.90E-01	-2.34E-03
1.393	1.01E-03	7.16E-01	-9.84E-04	4.62E-04	9.44E-01	1.57E-04	1.97E-03	6.50E-01	-6.45E-03
1.587	1.38E-03	7.90E-01	-1.29E-03	7.25E-04	9.58E-01	7.05E-04	3.65E-03	6.28E-01	-1.15E-02
1.855	4.00E-03	6.88E-01	-4.48E-03	2.10E-03	8.66E-01	-4.43E-04	1.32E-02	5.06E-01	-3.44E-02
2.247	1.25E-02	6.02E-01	-1.62E-02	5.81E-03	8.08E-01	-3.69E-03	4.81E-02	4.08E-01	-1.06E-01
2.618	2.00E+00	4.60E-02	-2.06E+00	5.92E-01	1.06E-01	-5.89E-01	-1.13E+00	-1.34E-01	9.75E-01
3.145	-1.22E+00	-1.90E+00	4.93E-01	-9.00E-05	1.40E+00	4.85E-01	2.17E-01	-7.48E-01	4.57E-01
3.690	-5.94E-01	-5.24E-01	4.22E-01	-2.76E+00	-4.00E-02	2.76E+00	-1.17E+00	-5.40E-01	5.37E-01

Table 5.44 Fitting parameters a_2 , b_2 , and c_2 in the numerical value equation (5.29) for the single-scattering co-albedo ($1 - \omega_s$) as a function of equivalent radius $R_e = 2.5\text{--}60\ \mu\text{m}$ (for small, medium, and large sizes) and electromagnetic wavelength λ (terrestrial radiation $\lambda = 3.900\text{--}150.000\ \mu\text{m}$) [5.61, Table 5]

λ (μm)	2.5–12.5 μm			12.5–30 μm			30–60 μm		
	a_2	b_2	c_2	a_2	b_2	c_2	a_2	b_2	c_2
3.9	1.69E-01	2.84E-01	-2.17E-01	6.57E-02	4.66E-01	-8.47E-02	-1.68E+00	-1.64E-01	1.20E+00
4.1	1.40E-01	3.60E-01	-1.90E-01	1.44E-01	3.40E-01	-1.86E-01	-1.55E+00	-3.58E-01	7.30E-01
4.3	1.50E-01	4.04E-01	-2.07E-01	1.29E+00	8.80E-02	-1.41E+00	-2.84E+00	-7.66E-01	5.42E-01
4.5	1.40E-01	4.70E-01	-1.93E-01	-1.27E+00	-2.24E-01	9.81E-01	-8.65E+00	-1.29E+00	4.93E-01
4.7	7.89E-02	6.28E-01	-1.08E-01	-1.19E+00	-2.94E-01	8.33E-01	-1.15E+01	-1.41E+00	4.90E-01
4.9	3.83E-02	8.28E-01	-4.42E-02	-1.27E+00	-2.34E-01	9.60E-01	-8.50E+00	-1.28E+00	4.96E-01
5.1	1.77E-02	1.06E+00	-3.46E-03	-1.39E+00	-1.92E-01	1.10E+00	-6.49E+00	-1.16E+00	5.03E-01
5.3	6.96E-03	1.36E+00	2.61E-02	-1.48E+00	-1.74E-01	1.19E+00	-5.09E+00	-1.04E+00	5.13E-01
5.4	3.68E-03	1.57E+00	3.91E-02	-1.50E+00	-1.74E-01	1.19E+00	-4.41E+00	-9.76E-01	5.20E-01
5.5	2.29E-03	1.73E+00	4.96E-02	-1.35E+00	-2.30E-01	9.83E-01	-4.50E+00	-9.88E-01	5.19E-01
5.7	1.92E-03	1.87E+00	1.16E-01	-3.34E+00	-1.14E+00	5.09E-01	-4.19E+01	-2.02E+00	4.82E-01
5.9	9.32E-04	2.07E+00	2.70E-01	-1.59E+03	-3.99E+00	4.93E-01	-1.15E-04	1.15E+00	4.97E-01
6.0	1.32E-04	2.61E+00	3.96E-01	-6.31E+04	-6.00E+00	5.02E-01	3.19E-01	-6.20E-01	4.59E-01
6.1	2.13E-03	1.62E+00	3.72E-01	-1.05E-11	6.00E+00	5.02E-01	4.34E-01	-7.44E-01	4.61E-01
6.2	3.83E-02	7.74E-01	2.31E-01	-6.06E-10	4.87E+00	5.00E-01	4.03E-01	-7.22E-01	4.57E-01
6.3	3.56E-02	8.60E-01	1.74E-01	-6.27E+04	-6.00E+00	4.93E-01	1.82E-01	-3.40E-01	4.33E-01
6.5	7.68E-03	1.41E+00	1.63E-01	-9.39E+01	-2.84E+00	4.87E-01	-1.93E-12	5.20E+00	4.82E-01
6.7	2.28E-03	1.83E+00	1.59E-01	-2.36E+01	-2.12E+00	4.90E-01	-6.01E+06	-6.00E+00	4.80E-01
7.0	6.59E-04	2.26E+00	1.67E-01	-1.95E+01	-1.96E+00	4.91E-01	-2.54E+04	-4.21E+00	4.80E-01

Table 5.44 (continued)

λ (μm)	2.5–12.5 μm			12.5–30 μm			30–60 μm		
	a_2	b_2	c_2	a_2	b_2	c_2	a_2	b_2	c_2
7.1	2.80E-04	2.56E+00	1.69E-01	-1.79E+01	-1.87E+00	4.92E-01	-2.77E+03	-3.47E+00	4.81E-01
7.3	1.13E-04	2.87E+00	1.72E-01	-1.78E+01	-1.83E+00	4.93E-01	-9.06E+02	-3.09E+00	4.82E-01
7.6	2.67E-05	3.38E+00	1.82E-01	-2.00E+01	-1.84E+00	4.95E-01	-5.94E+02	-2.93E+00	4.83E-01
8.0	1.96E-06	4.33E+00	1.96E-01	-1.97E+01	-1.79E+00	5.01E-01	-5.23E+02	-2.87E+00	4.85E-01
8.6	1.91E-08	6.00E+00	2.21E-01	-1.40E+01	-1.59E+00	5.23E-01	-1.45E+03	-3.18E+00	4.87E-01
9.0	1.35E+02	-6.00E+00	2.47E-01	-6.68E+00	-1.23E+00	5.66E-01	-5.13E+03	-3.55E+00	4.89E-01
9.6	2.69E-08	5.93E+00	2.38E-01	-1.55E+01	-1.69E+00	5.19E-01	-4.70E+04	-4.33E+00	4.85E-01
10.0	7.67E+00	-3.08E+00	2.96E-01	-1.68E+00	-2.14E-01	1.28E+00	-1.79E+05	-4.55E+00	4.96E-01
10.5	1.70E+00	-1.50E+00	3.23E-01	8.00E-03	9.36E-01	2.74E-01	-6.31E+04	-4.19E+00	5.03E-01
11.0	1.07E+00	-8.10E-01	3.27E-01	3.01E-08	4.04E+00	4.57E-01	-1.82E+04	-3.99E+00	5.05E-01
11.5	9.80E-01	-4.36E-01	2.31E-01	4.73E+01	-2.67E+00	5.07E-01	-3.52E-04	9.38E-01	5.21E-01
12.5	9.43E-01	-3.90E-01	2.32E-01	1.96E+00	-1.16E+00	4.82E-01	8.68E-01	-8.10E-01	4.64E-01
13.5	8.57E-01	-5.22E-01	3.42E-01	1.09E+00	-8.90E-01	4.58E-01	1.05E+00	-8.48E-01	4.52E-01
14.0	8.38E-01	-6.18E-01	3.88E-01	8.47E-01	-7.82E-01	4.47E-01	9.69E-01	-8.14E-01	4.45E-01
14.5	8.36E-01	-6.76E-01	4.08E-01	7.25E-01	-7.08E-01	4.39E-01	9.26E-01	-7.92E-01	4.42E-01
15.0	8.41E-01	-7.32E-01	4.25E-01	6.30E-01	-6.34E-01	4.31E-01	8.83E-01	-7.68E-01	4.39E-01
15.5	8.53E-01	-7.86E-01	4.38E-01	5.55E-01	-5.60E-01	4.21E-01	8.43E-01	-7.44E-01	4.36E-01
16.5	8.82E-01	-8.72E-01	4.55E-01	4.70E-01	-4.34E-01	3.95E-01	7.97E-01	-7.12E-01	4.32E-01
17.0	9.18E-01	-9.46E-01	4.66E-01	4.34E-01	-3.24E-01	3.59E-01	7.58E-01	-6.84E-01	4.29E-01
17.5	9.54E-01	-1.01E+00	4.73E-01	4.48E-01	-2.24E-01	2.94E-01	7.25E-01	-6.60E-01	4.27E-01
18.0	1.00E+00	-1.07E+00	4.80E-01	6.34E-01	-1.06E-01	6.19E-02	6.95E-01	-6.36E-01	4.24E-01
19.0	1.10E+00	-1.17E+00	4.86E-01	-2.97E-01	1.08E-01	9.35E-01	6.35E-01	-5.86E-01	4.19E-01
20.0	1.22E+00	-1.25E+00	4.88E-01	-2.33E-02	4.34E-01	6.10E-01	5.41E-01	-4.94E-01	4.08E-01
25.0	1.39E+00	-1.23E+00	4.71E-01	-8.04E-04	1.05E+00	5.44E-01	5.33E-01	-1.28E-01	1.71E-01
32.0	1.38E+00	-9.68E-01	4.13E-01	6.00E+04	-6.00E+00	5.21E-01	-1.42E-03	8.88E-01	5.51E-01
40.0	1.27E+00	-5.24E-01	2.35E-01	1.18E+02	-3.02E+00	5.23E-01	-2.62E-04	1.22E+00	5.44E-01
50.0	1.92E+00	-1.90E-01	-5.67E-01	9.23E+00	-1.75E+00	5.15E-01	-9.94E-02	2.04E-01	7.38E-01
60.0	-1.05E+01	2.40E-02	1.18E+01	9.92E+00	-1.74E+00	5.15E-01	-1.26E-01	1.86E-01	7.78E-01
80.0	-3.03E-01	4.12E-01	1.49E+00	4.12E+01	-2.28E+00	5.18E-01	-4.56E-04	1.09E+00	5.54E-01
100.0	-3.95E-02	9.70E-01	1.12E+00	3.91E+01	-2.12E+00	5.02E-01	1.16E-01	-3.16E-01	4.91E-01
150.0	-1.37E-03	2.03E+00	1.01E+00	1.06E+01	-1.31E+00	4.12E-01	1.62E+07	-6.00E+00	5.13E-01

Table 5.45 Fitting parameters a_3 , b_3 , and c_3 in the numerical value equation (5.30) for the asymmetry factor g as a function of equivalent radius $R_e = 2.5\text{--}60\ \mu\text{m}$ (for small, medium, and large sizes) and electromagnetic wavelength λ (solar radiation $\lambda = 0.290\text{--}3.690\ \mu\text{m}$) [5.61, Table 3]

λ (μm)	2.5–12.5 μm			12.5–30 μm			30–60 μm		
	a_3	b_3	c_3	a_3	b_3	c_3	a_3	b_3	c_3
0.290	1.11E-01	9.40E-02	7.30E-01	-3.15E-01	-1.47E+00	8.78E-01	-9.92E-02	-9.08E-01	8.80E-01
0.314	-8.06E-02	-7.62E-01	8.83E-01	-8.43E-02	-8.06E-01	8.82E-01	-1.30E-01	-9.86E-01	8.81E-01
0.344	-8.29E-02	-6.88E-01	8.84E-01	-9.08E-02	-8.06E-01	8.81E-01	-1.50E-01	-1.01E+00	8.80E-01
0.379	-6.75E-02	-6.12E-01	8.82E-01	-1.63E-01	-1.02E+00	8.81E-01	-2.64E-01	-1.18E+00	8.80E-01
0.419	-9.98E-02	-8.00E-01	8.82E-01	-1.02E-01	-7.80E-01	8.83E-01	-1.77E-01	-1.01E+00	8.82E-01
0.459	-1.09E-01	-7.24E-01	8.86E-01	-1.11E-01	-7.88E-01	8.84E-01	-1.77E-01	-9.80E-01	8.83E-01
0.499	-1.15E-01	-7.56E-01	8.85E-01	-1.09E-01	-7.48E-01	8.85E-01	-1.84E-01	-9.66E-01	8.83E-01
0.544	-1.24E-01	-7.82E-01	8.85E-01	-1.20E-01	-7.48E-01	8.86E-01	-2.07E-01	-9.84E-01	8.84E-01
0.603	-1.24E-01	-6.02E-01	8.94E-01	-1.33E-01	-7.66E-01	8.86E-01	-2.05E-01	-9.52E-01	8.84E-01
0.664	-1.37E-01	-6.76E-01	8.90E-01	-1.55E-01	-8.16E-01	8.85E-01	-2.03E-01	-9.20E-01	8.84E-01
0.719	-1.41E-01	-6.94E-01	8.89E-01	-1.57E-01	-7.82E-01	8.86E-01	-2.14E-01	-9.16E-01	8.85E-01
0.766	-2.31E-01	-1.23E+00	8.75E-01	-1.15E-01	-6.28E-01	8.89E-01	-2.55E-01	-9.74E-01	8.84E-01
0.821	-1.71E-01	-8.26E-01	8.83E-01	-1.67E-01	-7.44E-01	8.88E-01	-2.58E-01	-9.36E-01	8.85E-01
0.929	-1.86E-01	-8.24E-01	8.84E-01	-1.74E-01	-7.24E-01	8.88E-01	-2.89E-01	-9.42E-01	8.85E-01
1.046	-2.13E-01	-8.00E-01	8.87E-01	-2.12E-01	-7.82E-01	8.88E-01	-2.74E-01	-8.86E-01	8.87E-01

Table 5.45 (continued)

λ (μm)	2.5–12.5 μm			12.5–30 μm			30–60 μm		
	a_3	b_3	c_3	a_3	b_3	c_3	a_3	b_3	c_3
1.142	-3.14E-01	-1.20E+00	8.71E-01	-2.08E-01	-7.10E-01	8.91E-01	-2.84E-01	-8.62E-01	8.88E-01
1.232	-3.74E-01	-1.25E+00	8.71E-01	-2.06E-01	-6.68E-01	8.94E-01	-2.84E-01	-8.16E-01	8.90E-01
1.393	-4.61E-01	-1.31E+00	8.71E-01	-2.19E-01	-6.34E-01	8.99E-01	-2.31E-01	-6.54E-01	8.98E-01
1.587	-5.82E-01	-1.39E+00	8.70E-01	-2.38E-01	-5.96E-01	9.06E-01	-2.20E-01	-5.34E-01	9.10E-01
1.855	-3.58E-01	-6.40E-01	9.25E-01	-2.51E-01	-5.02E-01	9.23E-01	-2.31E-01	-4.10E-01	9.35E-01
2.247	5.98E-03	1.10E+00	7.66E-01	-3.01E-01	-4.30E-01	9.58E-01	-2.94E-01	-2.68E-01	1.01E+00
2.618	4.06E-08	5.44E+00	8.61E-01	-6.56E-01	-8.78E-01	9.63E-01	-3.87E-01	-5.70E-01	9.86E-01
3.145	-2.85E-01	-6.56E-01	1.01E+00	-3.20E+00	-2.16E+00	9.65E-01	-1.65E+00	-1.94E+00	9.65E-01
3.690	1.80E-03	1.67E+00	7.56E-01	-6.08E-01	-6.50E-01	9.87E-01	-8.86E-01	-8.10E-01	8.76E-01

Table 5.46 Fitting parameters a_3 , b_3 , and c_3 in the numerical value equation (5.30) for the asymmetry factor g as a function of equivalent radius $R_e = 2.5\text{--}60\ \mu\text{m}$ (for small, medium, and large sizes) and electromagnetic wavelength λ (terrestrial radiation $\lambda = 3.900\text{--}150.000\ \mu\text{m}$) [5.61, Table 6]

λ (μm)	2.5–12.5 μm			12.5–30 μm			30–60 μm		
	a_3	b_3	c_3	a_3	b_3	c_3	a_3	b_3	c_3
3.9	3.90E-08	5.68E+00	7.74E-01	-6.01E-01	-4.78E-01	1.01E+00	-6.42E-01	-4.50E-01	1.03E+00
4.1	1.25E-08	6.00E+00	7.88E-01	-8.16E-01	-6.62E-01	9.86E-01	-8.09E-01	-5.84E-01	1.01E+00
4.3	9.54E-09	6.00E+00	8.04E-01	-1.23E+00	-8.54E-01	9.84E-01	-1.50E+00	-8.82E-01	9.91E-01
4.5	7.39E-09	6.00E+00	8.21E-01	-1.94E+00	-1.07E+00	9.84E-01	-3.76E+00	-1.28E+00	9.81E-01
4.7	1.75E+01	-4.88E+00	8.27E-01	-2.34E+00	-1.13E+00	9.84E-01	-4.67E+00	-1.36E+00	9.80E-01
4.9	1.72E+00	-3.05E+00	8.24E-01	-2.36E+00	-1.11E+00	9.84E-01	-3.80E+00	-1.27E+00	9.82E-01
5.1	2.80E-01	-1.51E+00	8.17E-01	-2.20E+00	-1.06E+00	9.88E-01	-3.20E+00	-1.19E+00	9.84E-01
5.3	-6.52E-01	4.00E-02	1.55E+00	-1.77E+00	-9.28E-01	1.00E+00	-2.82E+00	-1.13E+00	9.87E-01
5.4	-4.16E-03	9.86E-01	8.76E-01	-1.41E+00	-7.94E-01	1.02E+00	-2.68E+00	-1.10E+00	9.88E-01
5.5	-4.37E-04	1.76E+00	8.67E-01	-1.15E+00	-6.66E-01	1.05E+00	-2.99E+00	-1.14E+00	9.88E-01
5.7	-5.23E+01	-6.00E+00	8.75E-01	-1.14E+00	-7.46E-01	1.04E+00	-1.64E+01	-1.86E+00	9.78E-01
5.9	-9.70E-01	-2.10E+00	9.23E-01	-1.75E+00	-1.24E+00	9.93E-01	-7.22E+01	-2.64E+00	9.76E-01
6.0	-5.59E-01	-1.36E+00	9.59E-01	-2.36E+00	-1.63E+00	9.79E-01	-7.59E+00	-2.13E+00	9.75E-01
6.1	-4.23E-01	-1.04E+00	9.67E-01	-5.93E+00	-2.02E+00	9.73E-01	-3.65E+00	-1.92E+00	9.72E-01
6.2	-3.36E-01	-4.00E-01	1.05E+00	-1.78E+01	-2.39E+00	9.67E-01	-3.95E+00	-1.94E+00	9.68E-01
6.3	-3.84E-01	-2.18E-01	1.13E+00	-1.79E+01	-2.26E+00	9.69E-01	-1.63E+01	-2.30E+00	9.67E-01
6.5	-6.21E-01	-1.90E+00	8.83E-01	-5.65E+00	-1.59E+00	9.82E-01	-7.50E+01	-2.55E+00	9.69E-01
6.7	-1.88E+01	-4.55E+00	8.67E-01	-2.49E+00	-1.14E+00	1.00E+00	-8.29E+01	-2.46E+00	9.71E-01
7.0	-4.02E+01	-5.00E+00	8.69E-01	-1.15E+00	-7.08E-01	1.05E+00	-7.77E+01	-2.38E+00	9.72E-01
7.1	-4.01E+01	-4.93E+00	8.71E-01	-8.21E-01	-4.06E-01	1.15E+00	-7.41E+01	-2.33E+00	9.73E-01
7.3	-2.79E+01	-4.58E+00	8.74E-01	-1.43E+00	-8.80E-02	2.01E+00	-7.32E+01	-2.29E+00	9.74E-01
7.6	-1.34E+01	-3.92E+00	8.80E-01	9.07E-02	3.50E-01	6.46E-01	-8.13E+01	-2.30E+00	9.75E-01
8.0	-6.30E+00	-3.21E+00	8.89E-01	3.98E-03	9.94E-01	8.26E-01	-9.01E+01	-2.30E+00	9.76E-01
8.6	-3.17E+00	-2.50E+00	9.05E-01	1.09E-04	1.88E+00	8.78E-01	-9.10E+01	-2.28E+00	9.78E-01
9.0	-2.30E+00	-2.11E+00	9.20E-01	4.55E-06	2.68E+00	9.00E-01	-6.16E+01	-2.15E+00	9.81E-01
9.6	-3.24E+00	-2.44E+00	8.84E-01	8.45E-03	8.12E-01	8.04E-01	-1.01E+02	-2.33E+00	9.72E-01
10.0	-1.84E+00	-1.71E+00	8.47E-01	8.52E-05	1.74E+00	9.17E-01	-7.45E+00	-1.53E+00	9.88E-01
10.5	-1.76E+00	-1.55E+00	9.72E-01	-2.24E-01	-5.46E-01	9.94E-01	-7.39E-01	-8.40E-01	1.00E+00
11.0	-1.85E+00	-1.50E+00	9.82E-01	-1.16E+00	-1.33E+00	9.82E-01	-4.65E-01	-8.54E-01	9.94E-01
11.5	-2.02E+00	-1.50E+00	9.84E-01	-1.78E+00	-1.46E+00	9.83E-01	-1.27E+00	-1.31E+00	9.86E-01
12.5	-2.24E+00	-1.50E+00	9.75E-01	-2.12E+00	-1.48E+00	9.74E-01	-2.06E+00	-1.46E+00	9.75E-01
13.5	-2.40E+00	-1.48E+00	9.63E-01	-2.30E+00	-1.48E+00	9.61E-01	-2.32E+00	-1.47E+00	9.61E-01
14.0	-2.46E+00	-1.46E+00	9.57E-01	-2.41E+00	-1.47E+00	9.54E-01	-2.51E+00	-1.48E+00	9.54E-01
14.5	-2.51E+00	-1.44E+00	9.54E-01	-2.51E+00	-1.47E+00	9.50E-01	-2.69E+00	-1.48E+00	9.50E-01
15.0	-2.53E+00	-1.42E+00	9.52E-01	-2.62E+00	-1.46E+00	9.46E-01	-2.89E+00	-1.49E+00	9.46E-01
15.5	-2.56E+00	-1.40E+00	9.51E-01	-2.73E+00	-1.46E+00	9.43E-01	-3.10E+00	-1.50E+00	9.43E-01

Table 5.46 (continued)

λ (μm)	2.5–12.5 μm			12.5–30 μm			30–60 μm		
	a_3	b_3	c_3	a_3	b_3	c_3	a_3	b_3	c_3
16.5	-2.57E+00	-1.35E+00	9.51E-01	-2.92E+00	-1.46E+00	9.39E-01	-3.49E+00	-1.52E+00	9.39E-01
17.0	-2.58E+00	-1.32E+00	9.52E-01	-3.06E+00	-1.45E+00	9.37E-01	-3.84E+00	-1.53E+00	9.36E-01
17.5	-2.57E+00	-1.29E+00	9.53E-01	-3.16E+00	-1.44E+00	9.36E-01	-4.15E+00	-1.54E+00	9.34E-01
18.0	-2.56E+00	-1.26E+00	9.55E-01	-3.25E+00	-1.44E+00	9.35E-01	-4.53E+00	-1.56E+00	9.33E-01
19.0	-2.53E+00	-1.21E+00	9.61E-01	-3.36E+00	-1.42E+00	9.35E-01	-5.26E+00	-1.58E+00	9.32E-01
20.0	-2.51E+00	-1.15E+00	9.71E-01	-3.39E+00	-1.37E+00	9.37E-01	-6.63E+00	-1.62E+00	9.31E-01
25.0	-2.38E+00	-9.36E-01	1.03E+00	-3.29E+00	-1.24E+00	9.44E-01	-1.20E+01	-1.71E+00	9.30E-01
32.0	-2.27E+00	-5.48E-01	1.32E+00	-3.79E+00	-1.16E+00	9.49E-01	-1.57E+01	-1.67E+00	9.31E-01
40.0	-7.79E+01	-6.00E-03	7.75E+01	-6.69E+00	-1.29E+00	9.38E-01	-1.24E+01	-1.50E+00	9.32E-01
50.0	2.73E-01	5.40E-01	-4.70E-01	-8.99E+00	-1.29E+00	9.31E-01	-1.59E+01	-1.49E+00	9.17E-01
60.0	7.07E-02	8.84E-01	-1.65E-01	-7.52E+00	-1.10E+00	9.47E-01	-2.02E+01	-1.48E+00	9.00E-01
80.0	2.47E-02	1.15E+00	-7.20E-02	-4.07E+00	-6.80E-01	1.10E+00	-1.66E+01	-1.29E+00	9.02E-01
100.0	7.53E-03	1.48E+00	-2.62E-02	-3.12E+00	-2.98E-01	1.75E+00	-1.07E+01	-1.03E+00	9.32E-01
150.0	9.87E-04	1.99E+00	-6.72E-04	1.89E+01	1.80E-02	-1.97E+01	-4.38E+00	-5.46E-01	1.14E+00

5.5.2 Ice Clouds (Cold Clouds)

Ice crystals have a nonspherical shape, and ice crystal size distributions are usually expressed in terms of the maximum geometric dimension of crystals [5.62]. Analogously to the definition of the equivalent (or effective) radius of a population of warm cloud droplets, the mean effective size of a population of hexagonal ice crystals can be defined as follows [5.62, Eq. (2.1)]

$$D_e = \frac{\int_{L_{\min}}^{L_{\max}} [D(L)]^2 L n(L) dL}{\int_{L_{\min}}^{L_{\max}} D(L) L n(L) dL}. \quad (5.31)$$

Here, D denotes the width of an ice crystal and $n(L)$ denotes the ice crystal size distribution (ISD) (in m^{-4}) as the function of the length of the ice crystals, $L_{\min} \leq L \leq L_{\max}$, respectively. The geometric cross-sectional area for oriented hexagonal ice crystals generally deviates from the product DL . The ice water content (IWC) of an ice cloud is defined as the mass of frozen water per volume of air (in units of kg m^{-3}), given by the following relation [5.62, Eq. (2.2)]

$$\begin{aligned} \text{IWC} &= \rho_i \int_{L_{\min}}^{L_{\max}} V_i(L) n(L) dL \\ &= \frac{3\sqrt{3}}{8} \rho_i \int_{L_{\min}}^{L_{\max}} D^2 L n(L) dL. \end{aligned} \quad (5.32)$$

Here, ρ_i denotes the mass density of hexagonal ice, and $V_i = 3\sqrt{3}D^2L/8$ the volume of a hexagonal ice crystal. The volumetric extinction coefficient of a population of ice crystals reads [5.62, Eq. (2.3)]

$$\beta_e = \int_{L_{\min}}^{L_{\max}} \sigma_e(D, L) n(L) dL. \quad (5.33)$$

Here, $\sigma_e(L)$ is the extinction cross section (in units of m^2) [5.62, Eq. (2.4)]

$$\sigma_e(D, L) = \frac{3}{2} D \left(\frac{\sqrt{3}}{4} D + L \right). \quad (5.34)$$

Analogously, one can define the volumetric absorption coefficient

$$\beta_a = \int_{L_{\min}}^{L_{\max}} \sigma_a(D, L) n(L) dL. \quad (5.35)$$

Here, $\sigma_a(L)$ is the absorption cross section (in units of m^2), which is for small absorption proportional to the product of the imaginary part of the refractive index of ice and the ice crystal volume [5.62, Eq. (2.7)]

$$\sigma_a(D, L) \approx \frac{3\sqrt{3}\pi m_i(\lambda)}{2\lambda} D^2 L. \quad (5.36)$$

In (5.36), $m_i(\lambda)$ denotes the imaginary part of the refractive index of ice as function of wavelength λ . Inserting (5.34) into (5.33) and using the definition of D_e according to (5.31) and of IWC according to (5.32)

yields the following expression for β_e [5.62, Eqs. (2.5a) and (2.5b)]

$$\beta_e = \text{IWC} \left[\frac{1}{\rho_i} \frac{\int_{L_{\min}}^{L_{\max}} D^2 n(L) dL}{\int_{L_{\min}}^{L_{\max}} D^2 L n(L) dL} + \frac{4}{\sqrt{3} \rho_i} \frac{1}{D_c} \right] \approx \text{IWC} \left(a + \frac{b}{D_c} \right). \tag{5.37}$$

Here, a and b are physical constants. The approximate form of (5.37) is based on an analysis of the orders of magnitude of both summands in the brackets on the right-hand side of (5.37). By virtue of (5.33) and (5.35) and with consideration of $\beta_e = \beta_s + \beta_a$, the single-scattering co-albedo of a population of ice crystals, $1 - \omega_s$, is given by the following relation [5.62, Eq. (2.6)]

$$1 - \omega_s = \frac{\beta_e - \beta_s}{\beta_e} = \frac{\beta_a}{\beta_e} = \frac{\int_{L_{\min}}^{L_{\max}} \sigma_a(D, L) n(L) dL}{\int_{L_{\min}}^{L_{\max}} \sigma_e(D, L) n(L) dL} \approx c + d D_c. \tag{5.38}$$

Here, c and d are physical constants. With consideration of empirical findings from aircraft observations,

Table 5.48 Values of the regression coefficients a_n in (5.39) for the parameterization of the volumetric extinction coefficient β_e (in m^{-1}). The coefficients are determined for a reference ice mass density of $\rho_{i,0} = 916.7 \text{ kg m}^{-3}$ [5.62, Table 3]

Band i	a_0	a_1	a_2
1–6	– 6.656E-03	3.686	0.00
7	– 7.770E-03	3.734	11.85
8	– 8.088E-03	3.717	17.17
9	– 8.441E-03	3.715	19.48
10	– 9.061E-03	3.741	26.48
11	– 9.609E-03	3.768	34.11
12	– 1.153E-02	4.109	17.32
13	– 8.294E-03	3.925	1.315
14	– 1.026E-02	4.105	16.36
15	– 1.151E-02	4.182	31.13
16	– 1.704E-02	4.830	16.27
17	– 1.741E-02	5.541	– 58.42
18	– 7.752E-03	4.624	– 42.01

in [5.62, Eqs. (2.9) and (2.10)], the following generalized parameterizations for $\beta_e(\text{IWC}, D_c)$ and $\omega(D_c)$ were postulated

$$\frac{\beta_e}{\text{m}^{-1}} = \frac{\text{IWC}}{10^{-3} \text{ kg m}^{-3}} \sum_{n=0}^N a_n \left(\frac{D_c}{\mu\text{m}} \right)^{-n}, \tag{5.39}$$

$$1 - \omega_s = \sum_{n=0}^N b_n \left(\frac{D_c}{\mu\text{m}} \right)^n. \tag{5.40}$$

The spectral division used in the parameterization and the regression coefficients a_n and b_n are given in Tables 5.47–5.49, respectively. The coefficients a_n in Table 5.48 are determined for a reference ice mass density of $\rho_{i,0} = 916.7 \text{ kg m}^{-3}$ yielding the reference volumetric extinction coefficient $\beta_{e,0}$. By virtue of (5.37) the volumetric extinction coefficient at the actual ice mass

Table 5.47 Spectral division used in the parameterization [5.62, Table 2]

Solar spectrum			Infrared spectrum		
Band i	Central wavelength (μm)	Band limits (μm)	Band i	Central wavelength (μm)	Band limits (cm^{-1})
1	0.55	0.2–0.7	7	4.9	2200–1900
2	1.0	0.7–1.3	8	5.6	1900–1700
3	1.6	1.3–1.9	9	6.5	1700–1400
4	2.2	1.9–2.5	10	7.6	1400–1250
5	3.0	2.5–3.5	11	8.5	1250–1100
6	3.7	3.5–4.0	12	9.6	1100–980
			13	11.3	980–800
			14	13.7	800–670
			15	16.6	670–540
			16	21.5	540–400
			17	30.0	400–280
			18	70.0	280–1

Table 5.49 Values of the regression coefficients b_n in (5.40) for the parameterization of the single-scattering co-albedo $1 - \omega_s$ [5.62, Table 4]

Band i	b_0	b_1	b_2	b_3
1	1.0998E-06	-2.6101E-08	1.0896E-09	-4.7387E-12
2	2.0208E-05	9.6483E-06	8.3009E-08	-3.2217E-10
3	1.3590E-04	7.3453E-04	2.8281E-06	-1.8272E-08
4	-1.6598E-03	2.0933E-03	-1.3977E-06	-1.8703E-08
5	4.6180E-01	2.4471E-04	-2.7839E-06	1.0379E-08
6	4.2362E-02	8.6425E-03	-7.5519E-05	2.4056E-07
7	1.9960E-01	3.7800E-03	-1.4910E-05	0.0000E+00
8	3.0140E-01	2.6390E-03	-1.1160E-05	0.0000E+00
9	3.9080E-01	1.2720E-03	-5.5640E-06	0.0000E+00
10	3.1050E-01	2.6030E-03	-1.1390E-05	0.0000E+00
11	2.0370E-01	4.2470E-03	-1.8100E-05	0.0000E+00
12	2.3070E-01	3.8300E-03	-1.6160E-05	0.0000E+00
13	5.6310E-01	-1.4340E-03	6.2980E-06	0.0000E+00
14	5.2070E-01	-9.7780E-04	3.7250E-06	0.0000E+00
15	3.2540E-01	3.4340E-03	-3.0810E-05	9.1430E-08
16	1.0280E-01	5.0190E-03	-2.0240E-05	0.0000E+00
17	3.9640E-01	-3.1550E-03	6.4170E-05	-2.9790E-07
18	8.0790E-01	-7.0040E-03	5.2090E-05	-1.4250E-07

density ρ_i reads

$$\beta_c = \left(\frac{\rho_{i,0}}{\rho_i} \right) \beta_{c,0}. \quad (5.41)$$

In [5.62], it was found that $N = 2$ is sufficient for the extinction coefficient expression to achieve an accuracy within 1%, and $N = 3$ for the single-scattering albedo.

For the representation of the phase function $P(\cos \Theta)$ and the asymmetry factor g of the ISD in the solar wavelengths in [5.62, Eqs. (2.11)–(2.13)], the following parameterizations were proposed

$$P(\cos \Theta) = \sum_{l=0}^M \tilde{\omega}_l P_l(\cos \Theta), \quad (5.42)$$

$$g = \frac{\tilde{\omega}_1}{3}, \quad (5.43)$$

$$\tilde{\omega}_0 = 1,$$

$$\tilde{\omega}_l = (1 - f_\delta) \tilde{\omega}_l^* + f_\delta (2l + 1), \quad (5.44)$$

$$l = 1, 2, 3, \dots,$$

$$\tilde{\omega}_l^* = \sum_{n=0}^N c_{n,l} \left(\frac{D_c}{\mu\text{m}} \right)^n, \quad (5.45)$$

$$f_\delta = \sum_{n=0}^N d_n \left(\frac{D_c}{\mu\text{m}} \right)^n. \quad (5.46)$$

Here, $P_l(\cos \Theta)$ denotes the Legendre polynomials (polynomial solutions to Legendre's differential equation), $\tilde{\omega}_l$ are the expansion coefficients of the four-stream approximation of the phase function, $\tilde{\omega}_l^*$ represents the expansion coefficient for the phase function in which the forward δ -function peak has been removed, and f_δ is the contribution from the forward δ -function peak. The quantity g is the asymmetry factor. The regression coefficients $c_{n,l}$ and d_n for the solar wavelengths are given in Tables 5.50 and 5.51. It was found in [5.62] that $N = 3$ is sufficient for the series expansions of $\tilde{\omega}_l$ and f_δ to achieve an accuracy within 1%.

For the parameterization of $\tilde{\omega}_l$ and g in the thermal infrared wavelengths, in [5.62, Eqs. (2.14) and (2.15)], the following expressions were proposed

$$\tilde{\omega}_l = (2l + 1)g^l, \quad (5.47)$$

$$g(\text{IR}) = \sum_{n=0}^N c'_n \left(\frac{D_c}{\mu\text{m}} \right)^n. \quad (5.48)$$

The regression coefficients c'_n for the infrared wavelengths are given in Table 5.52. In [5.62], it was found that $N = 3$ is sufficient for the series expansions of $\tilde{\omega}_l$ in the infrared region to achieve an accuracy within 1%.

Table 5.50 Values of the regression coefficients $c_{n,l}$ in (5.45) for the parameterization of the expansion coefficients for the phase function in the solar wavelengths [5.62, Table 5a]

Band i	l	$c_{0,l}$	$c_{1,l}$	$c_{2,l}$	$c_{3,l}$
1	1	2.2110E+00	-1.0398E-03	6.5199E-05	-3.4498E-07
	2	3.2201E+00	9.4227E-04	8.0947E-05	-4.7428E-07
	3	4.1610E+00	7.4396E-04	8.2690E-05	-4.5251E-07
	4	5.1379E+00	5.1545E-03	1.1881E-05	-1.5556E-07
2	1	2.2151E+00	-7.7982E-04	6.3750E-05	-3.4466E-07
	2	3.1727E+00	1.5597E-03	8.2021E-05	-4.9665E-07
	3	4.0672E+00	2.5800E-03	7.1550E-05	-4.3051E-07
	4	4.9882E+00	8.6489E-03	-1.8318E-05	-5.9275E-08
3	1	2.2376E+00	1.0293E-03	5.0842E-05	-3.0135E-07
	2	3.1549E+00	4.7115E-03	7.0684E-05	-4.7622E-07
	3	3.9917E+00	8.2830E-03	5.3927E-05	-4.1778E-07
	4	4.8496E+00	1.5998E-02	-3.9320E-05	-4.3862E-08
4	1	2.3012E+00	3.3854E-03	2.3528E-05	-2.0068E-07
	2	3.1730E+00	9.3439E-03	3.6367E-05	-3.8390E-07
	3	3.9298E+00	1.6424E-02	1.0502E-05	-3.5086E-07
	4	4.7226E+00	2.5872E-02	-7.7542E-05	-2.1999E-08
5	1	2.7975E+00	2.9741E-03	-3.2344E-05	1.1636E-07
	2	4.3532E+00	1.1234E-02	-1.2081E-04	4.3435E-07
	3	5.6835E+00	2.4681E-02	-2.6480E-04	9.5314E-07
	4	6.8271E+00	4.2788E-02	-4.5615E-04	1.6368E-06
6	1	1.9655E+00	2.0094E-02	-1.7067E-04	5.0806E-07
	2	2.8803E+00	3.6091E-02	-2.8365E-04	7.9656E-07
	3	3.4613E+00	5.8525E-02	-4.6455E-04	1.3444E-06
	4	3.9568E+00	8.1480E-02	-6.4777E-04	1.9022E-06

Table 5.51 Values of the regression coefficients d_n in (5.46) for the parameterization of the expansion coefficients for the phase function in the solar wavelengths [5.62, Table 5a]

Band i	d_0	d_1	d_2	d_3
1	1.2495E-01	-4.3582E-04	1.4092E-05	-6.9565E-08
2	1.2363E-01	-4.4419E-04	1.4038E-05	-6.8851E-08
3	1.2117E-01	-4.8474E-04	1.2495E-05	-6.2411E-08
4	1.1581E-01	-5.5031E-04	9.8776E-06	-5.0193E-08
5	-1.5968E-04	1.0115E-05	-1.2472E-07	4.8667E-10
6	1.3830E-01	-1.8921E-03	1.2030E-05	-3.1698E-08

Table 5.52 Values of the regression coefficients c'_n in (5.48) for the parameterization of the asymmetry factor [5.62, Table 5b]

Band i	c'_0	c'_1	c'_2	c'_3
7	7.9550E-01	2.524E-03	-1.022E-05	0.000E+00
8	8.6010E-01	1.599E-03	-6.465E-06	0.000E+00
9	8.9150E-01	1.060E-03	-4.171E-06	0.000E+00
10	8.7650E-01	1.198E-03	-4.485E-06	0.000E+00
11	8.8150E-01	9.858E-04	-3.116E-06	0.000E+00
12	9.1670E-01	5.499E-04	-1.507E-06	0.000E+00
13	9.0920E-01	9.295E-04	-3.877E-06	0.000E+00
14	8.4540E-01	1.429E-03	-5.859E-06	0.000E+00
15	7.6780E-01	2.571E-03	-1.041E-05	0.000E+00
16	7.2900E-01	2.132E-03	-5.584E-06	0.000E+00
17	7.0240E-01	4.581E-03	-3.054E-05	6.684E-08
18	2.2920E-01	1.724E-02	-1.573E-04	4.995E-07

5.6 Absorption Coefficients for Water Vapor, Ozone, and Carbon Dioxide

The incoming longwave atmospheric radiation flux (atmospheric back-radiation flux) impinging on the Earth's surface is a key quantity for climate monitoring and is largely controlled by the absorption of radiation due to different atmospheric gases in dependence on the atmospheric temperature and humidity distribution. Band-model calculations of the back-radiation flux require absorption data for different absorber gases in a large number of spectral lines. In the literature, different methods have been developed for the approximative calculation of this radiation flux on the basis of the radiative transfer equation (RTE), e.g., [5.63].

5.6.1 Effective Mass Absorption Coefficient for Water Vapor and Ozone

The effective mass absorption coefficients $\tilde{\kappa}_{\Delta\lambda}$ of water vapor (in the wavelength interval $5\ \mu\text{m} < \lambda < 44\ \mu\text{m}$) and ozone (in the wavelength interval $9\ \mu\text{m} < \lambda < 10\ \mu\text{m}$) are presented in Tables 5.53 and 5.54. In the wavelength interval $13\ \mu\text{m} < \lambda < 17\ \mu\text{m}$, the absorption of longwave radiation is significantly affected by carbon dioxide (absorption centered at $\lambda \approx 15\ \mu\text{m}$). The absorption effect of carbon dioxide is considered by appropriate adjustment of the effective mass absorp-

Table 5.53 Effective mass absorption coefficient for water vapor, $\tilde{\kappa}_{\Delta\lambda}$ (in $\text{m}^2\ \text{kg}^{-1}$) [5.63, Table 1a]

λ (μm)	$\Delta\lambda$ (μm)	$\tilde{\kappa}_{\Delta\lambda}$ ($\text{m}^2\ \text{kg}^{-1}$)	λ (μm)	$\Delta\lambda$ (μm)	$\tilde{\kappa}_{\Delta\lambda}$ ($\text{m}^2\ \text{kg}^{-1}$)	λ (μm)	$\Delta\lambda$ (μm)	$\tilde{\kappa}_{\Delta\lambda}$ ($\text{m}^2\ \text{kg}^{-1}$)
5.25	0.5	4.0	13.31	0.16	0.15	24.47	0.12	0.05
6.00	1.0	20.0	13.47	0.16	0.40	24.59	0.12	0.10
6.75	0.5	15.0	13.67	0.25	0.80	24.71	0.12	0.20
7.06	0.13	0.75	13.90	0.20	0.90	24.83	0.12	0.30
7.14	0.025	1.00	14.50	1.00	20.0	25.45	1.12	2.50
7.22	0.13	0.55	15.50	1.00	20.0	26.28	0.52	0.50
7.36	0.15	0.30	16.17	0.34	0.80	26.79	0.52	0.80
7.56	0.255	0.50	16.50	0.33	0.90	27.18	0.27	2.50
7.80	0.21	0.40	17.17	1.00	0.40	27.52	0.40	0.30
7.95	0.10	0.08	17.71	0.09	0.30	27.86	0.28	2.50
8.08	0.16	0.015	17.80	0.09	0.15	28.50	1.00	11.0
8.22	0.13	0.01	17.93	0.17	0.10	29.50	1.00	12.0
8.46	0.35	0.015	18.06	0.09	0.15	30.50	1.00	15.0
8.70	0.13	0.008	18.29	0.36	0.30	31.50	1.00	15.0
8.92	0.30	0.007	18.56	0.18	0.15	32.50	1.00	15.0
9.17	0.19	0.006	18.79	0.28	0.10	33.50	1.00	16.0
9.29	0.06	0.006	18.97	0.08	0.15	34.50	1.00	9.0
9.36	0.08	0.006	19.06	0.10	0.20	35.50	1.00	20.0
9.44	0.08	0.006	19.47	0.72	0.30	36.50	1.00	20.0
9.54	0.13	0.006	19.90	0.14	0.40	37.50	1.00	20.0
9.68	0.13	0.006	20.02	0.10	0.30	38.02	0.10	0.90
9.80	0.12	0.006	20.07	0.20	0.25	38.20	0.19	0.50
9.90	0.09	0.006	20.32	0.10	0.15	38.48	0.38	0.30
10.00	0.09	0.006	20.42	0.10	0.15	38.86	0.38	0.50
10.09	0.09	0.006	20.62	0.30	0.25	39.15	0.20	1.00
10.24	0.22	0.006	20.92	0.30	0.15	39.38	0.25	20.0
10.49	0.28	0.006	21.44	0.73	0.65	40.00	1.00	20.0
10.74	0.22	0.005	22.00	0.40	1.20	40.85	0.71	20.0
11.05	0.40	0.005	22.30	0.20	0.30	41.31	0.20	1.10
11.44	0.38	0.006	22.70	0.60	0.65	41.51	0.20	0.60
11.95	0.65	0.015	23.30	0.60	0.30	41.72	0.21	0.35
12.37	0.18	0.030	23.83	0.46	2.50	42.00	0.41	0.10
12.55	0.18	0.065	24.11	0.11	0.80	42.34	0.21	0.15
12.84	0.39	0.050	24.23	0.12	0.20	42.54	0.21	0.50
13.13	0.20	0.080	24.35	0.12	0.10	42.83	0.35	0.90

Table 5.54 Effective mass absorption coefficient for ozone, $\tilde{\kappa}_{\Delta\lambda}$ (in $\text{m}^2 \text{kg}^{-1}$) [5.63, Table 1b]

λ (μm)	$\Delta\lambda$ (μm)	$\tilde{\kappa}_{\Delta\lambda}$ ($\text{m}^2 \text{kg}^{-1}$)	λ (μm)	$\Delta\lambda$ (μm)	$\tilde{\kappa}_{\Delta\lambda}$ ($\text{m}^2 \text{kg}^{-1}$)
9.17	0.19	35	9.68	0.13	330
9.29	0.06	120	9.80	0.12	200
9.36	0.08	260	9.90	0.09	110
9.44	0.08	420	10.00	0.09	40
9.54	0.13	400	10.09	0.09	7

tion coefficients of water vapor in Table 5.53. Other atmospheric constituents, such as N_2O , CO , etc., have negligible effects on the absorption of longwave radiation [5.63].

5.6.2 Effective Molar Absorption Coefficient for Carbon Dioxide

The molecular absorption coefficients of carbon dioxide, K_a (in units of $\text{cm}^2 \text{molecule}^{-1}$), in the $15 \mu\text{m}$ absorption band (corresponding to the wavenumber interval $\nu = 582\text{--}752 \text{cm}^{-1}$) are presented in Table 5.55. The table values were calculated using the Information System Spectroscopy of Atmospheric Gases (SPECTRA, <http://spectra.iao.ru/home>) [5.2, 64]. The online databank SPECTRA enables user-friendly access to many spectroscopic parameters for a large variety of atmospheric gases. Depending on the application of interest the user is free in the specification of the gas isotopes, spectral range, spectral resolution, temperature, pressure, etc., considered.

Table 5.55 Molecular absorption coefficient of CO_2 , K_a in units of $\text{cm}^2 \text{molecule}^{-1}$, in the $15 \mu\text{m}$ absorption band as function of wavenumber ν ($\nu = 582\text{--}752 \text{cm}^{-1}$, $\Delta\nu = 1 \text{cm}^{-1}$, $T = 296 \text{K}$, $p = 1000 \text{hPa}$). The data are taken from the Information System Spectroscopy of Atmospheric Gases (SPECTRA, <http://spectra.iao.ru/home>) [5.2]. This table with an enhanced resolution of the wave number of 1cm^{-1} is available as ESM at https://doi.org/10.1007/978-3-030-52171-4_5 ►

The mass absorption coefficient of CO_2 κ_a (in $\text{m}^2 \text{kg}^{-1}$), is given by the following relation

$$\kappa_a = \frac{K_a N_A}{M_{\text{CO}_2}} \tag{5.49}$$

Here, N_A denotes the Avogadro number (Table 5.6) and $M_{\text{CO}_2} = 44.01 \text{g mol}^{-1}$ the molar mass of CO_2 .

ν (cm^{-1})	K_a ($\text{cm}^2 \text{molecule}^{-1}$)
582	7.0639E-23
587	2.0953E-22
592	2.2289E-21
597	3.0192E-21
602	5.2842E-22
607	4.3098E-22
612	6.9304E-22
617	1.7436E-20
622	1.2453E-21
627	3.4878E-21
632	1.0925E-20
637	2.2836E-20
642	7.8329E-21
647	2.8744E-20
652	2.8165E-19
657	3.2502E-20
662	1.7572E-20
667	3.0673E-19
672	2.8237E-20
677	2.7711E-20
682	5.1890E-20
687	1.3928E-19
692	3.0359E-19
697	3.7331E-20
702	9.0945E-21
707	3.8941E-21
712	3.4580E-21
717	3.0707E-21
722	1.3779E-21
727	5.3740E-21
732	9.1882E-22
737	5.4612E-22
742	1.0969E-21
747	1.1692E-21
752	1.0132E-22

5.7 Parameters of Soil

Soil temperature has a measurable impact on water properties relevant for heat storage, heat transport, water binding, and water transport. There is evidence from Table 5.56 that this influence is moderate for most parameters over a range of -5 to 50°C , except for dynamic viscosity, which has a direct impact on soil water

conductivity. For water density and specific heat, see Tables 5.38 and 5.39, respectively.

The bulk density, porosity, and void ratio in natural soil are given in Table 5.57. Loam soils have the highest compaction potential, while clay soils come up with the highest porosity (due to the *cardhouse* structure of the

Table 5.56 Temperature dependence of selected soil water properties [5.65]

Temperature (°C)	Surface tension ($\times 10^{-2} \text{ kg s}^{-2}$)	Thermal conductivity ($\text{J m}^{-1} \text{ s}^{-1} \text{ K}^{-1}$)	Dynamic viscosity ($\times 10^{-2} \text{ kg m}^{-1} \text{ s}^{-1}$)
-5	7.64	–	–
0	7.56	0.561	0.179
4	7.50	0.570	0.157
10	7.42	0.587	0.131
20	7.27	0.603	0.100
30	7.11	0.620	0.080
40	6.95	0.633	0.065
50	6.79	0.645	0.055

Table 5.57 Variation of bulk density, porosity, and void ratio in natural soil [5.66, modified]

	Bulk density (10^3 kg m^{-3})	Porosity (%)	Void ratio
Sand	1.16–1.70	56–36	1.27–0.56
Silt	1.17–1.63	56–38	1.27–0.62
Loam	1.20–2.00	55–30	1.22–0.43
Clay	0.93–1.72	65–35	1.85–0.54

Table 5.58 Average water retention curves for typical soil texture classes [5.67, simplified]; for more detailed tables see [5.67]

Soil texture (for symbols, see Fig. 5.1d)	Volumetric water content (%)					
	$-\infty$	0.5	1.8	2.5	3.5	4.2
Ss	42	41	19	12	6	4
St3	42	41	29	24	18	15
Su4	42	41	31	23	12	9
Ls2	42	42	34	25	19	18
Lt3	43	43	38	34	28	26
Lu	42	41	35	29	20	18
Uu	43	42	37	32	19	12
Us	42	41	35	29	16	10
Ut3	42	41	37	32	19	13
Tt	44	43	41	39	34	28
Tu4	42	42	37	33	27	20
Ts4	41	40	32	30	25	19

Table 5.59 Relation of soil moisture parameters and pore size; the potential values characterize the specific binding energy and are clearly related to pore size by the capillary rise equation (assuming the applicability of a capillary bundle model) [5.67, simplified]. Air capacity corresponds to coarse pores, plant available field capacity to middle pores, and wilting point water capacity to fine pores

Water retention interval	Total pore space		
	Air capacity	Field capacity	Plant available field capacity
Matric potential 10^{-2} m ($\approx \text{hPa}$)	> -60	-60 to -15 000	< -15 000
Water tension 10^{-2} m ($\approx \text{hPa}$)	< 60	60 to 15000	> 15 000
pF-value ($\log_{10}(\psi)$, ψ in 10^{-2} m)	< 1.8	1.8 to 4.2	> 4.2
Equivalent pore size (μm)	> 50	50 to 0.2	< 0.2

Table 5.60 Hydraulic conductivities (m d^{-1}) in saturated soil for three bulk density groups and typical soil texture classes [5.67, simplified]; for more detailed tables, see [5.67]. Please note that typically hydraulic conductivities exhibit a pronounced variability due to structural impacts (cracks, macropores, aggregation, see Fig. 61.17 in Chap. 61)

Soil texture ^a	Bulk density ($\times 10^3 \text{ kg m}^{-3}$)		
	>1.2–1.4	1.4–1.6	1.6–<1.8
Ss	0.375	0.340	0.230
St3	0.114	0.042	0.024
Su4	0.058	0.038	0.017
Ls2	0.053	0.023	0.010
Lt3	0.020	0.007	0.003
Lu	0.045	0.016	0.006
Uu	0.032	0.013	0.002
Us	0.037	0.022	0.005
Ut3	0.041	0.012	0.003
Tt	0.004	0.003	0.002
Tu4	0.033	0.012	0.003
Ts4	0.051	0.038	0.008

^a symbols see Fig. 5.1d

primary platy clay minerals). However, water in clay pores is—to a high percentage—strongly bound in very fine pores and cannot be extracted by plant roots.

Particle size distribution is typically aggregated to soil texture classes, which are mostly represented in triangular diagrams as functions of clay, silt, and sand contents. Unfortunately, most nations have their own size classification and triangle diagrams. Figure 5.1 shows exemplary soil texture classes according to FAO/HYPRES (Food and Agriculture Organization of the United Nations, European Soil Bureau working group *Hydraulic Properties of European Soils*), USDA (United States Department of Agriculture), GEPPRA (Groupe d'Etude des Problèmes de Pédologie Appliquée, France), and the Soil Science Society of Germany (SSSG). According to SSSG particle size classes are defined by: clay (T): < 2 μm , silt (U): 2 μm to 63 μm ,

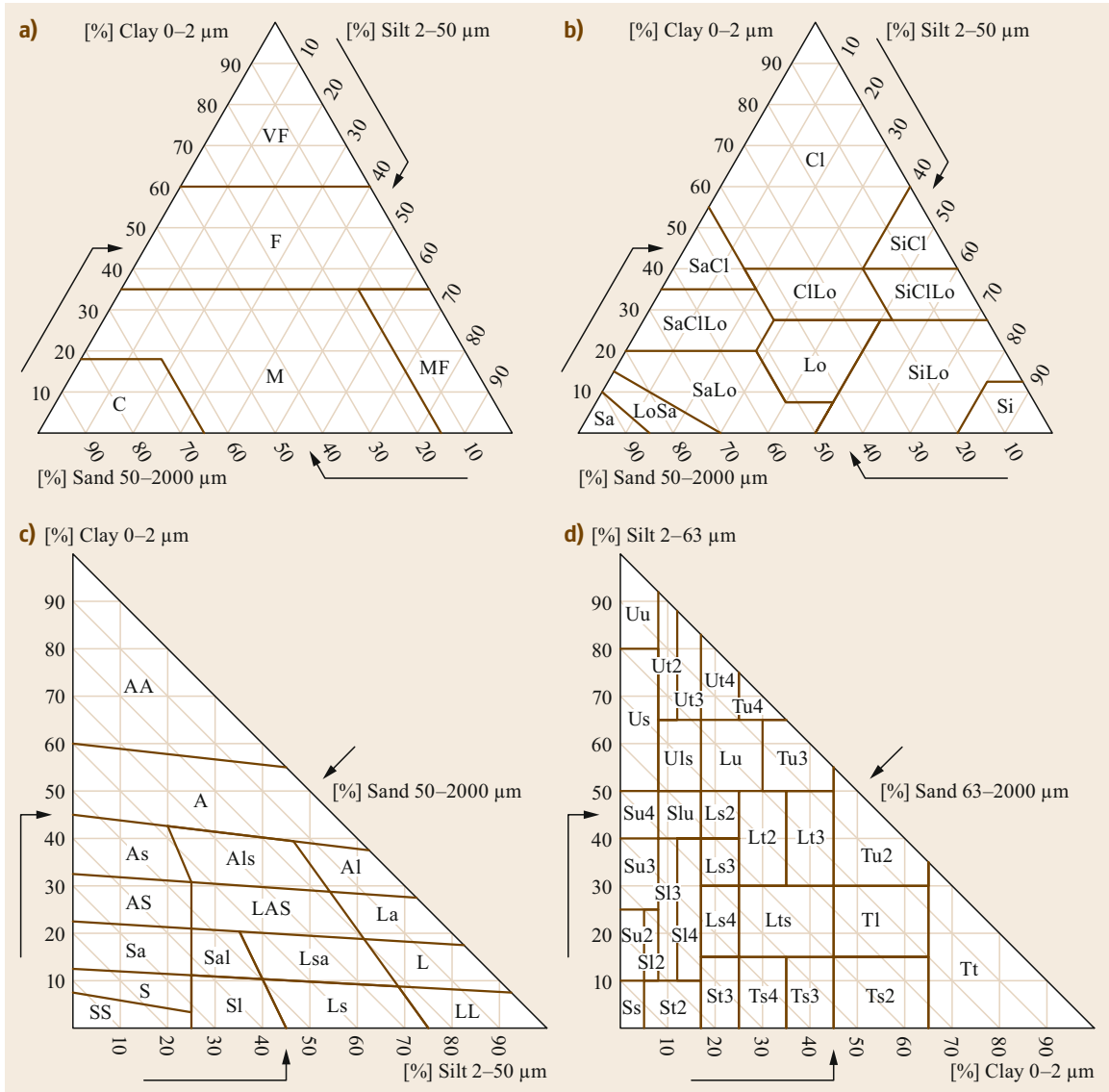


Fig. 5.1a–d Soil texture triangle according to (a) the Food and Agriculture Organization of the United Nations, the European Soil Bureau working group *Hydraulic Properties of European Soils*, (b) the United States Department of Agriculture, (c) the Groupe d’Etude des Problèmes de Pédologie Appliquée, France, and (d) the Soil Science Society of Germany, generated based on (after [5.68–70])

sand (S): 63 to 2000 μm (the same as FAO; the USDA classification differs only slightly, [5.65, 66]).

Soil texture is the aggregated equivalent particle size distribution of soil and conveys basic information about every soil (please note that texture is not the same as soil type, which means the entire soil body with its characteristic horizon pattern). The following tables relate soil texture, bulk density, porosity, and water content to important soil hydrological and

physical (thermal) properties. They provide rough estimates of water retention curves and derived ecological parameters (Tables 5.58–5.61), hydraulic conductivities (Table 5.60), thermal properties (Table 5.62), and parameters of a widely used parameterization of water retention curves and hydraulic conductivity curves [5.71]. However, in most cases, these tables give a first impression but cannot replace detailed measurements.

Table 5.61 Ecological characterization of pore space (%) with an average bulk density ($1.4 \times 10^3 \text{ kg m}^{-3}$ to $1.6 \times 10^3 \text{ kg m}^{-3}$) for different soil textural classes [5.67, simplified]; for more detailed tables see [5.67]

Soil texture (for symbols, see Fig. 5.1d)	Air capacity $pF < 1.8$	Plant available field capacity $1.8 \leq pF < 4.2$	Field capacity $pF \geq 1.8$	Wilting point water capacity $pF \geq 4.2$
Ss	32	7	11	4
St3	14	15	30	15
Su4	11	23	32	9
Ls2	9	16	34	18
Lt3	5	12	39	27
Lu	7	17	36	19
Uu	7	26	38	12
Us	9	25	35	10
Ut3	6	25	37	12
Tt	3	13	43	30
Tu4	6	17	37	20
Ts4	10	14	32	18

Table 5.62 Typical thermal properties of various soil materials and soils [5.76, slightly modified] for a temperature range of $10\text{--}20^\circ\text{C}$ (resulting from different sources)

Material or soil moisture (%)	Density ($\times 10^3 \text{ kg m}^{-3}$)	Specific heat capacity ($\times 10^3 \text{ J kg}^{-1} \text{ K}^{-1}$)	Volumetric heat capacity ($\times 10^6 \text{ J m}^{-3} \text{ K}^{-1}$)	Thermal conductivity ($\text{W m}^{-1} \text{ K}^{-1}$)	Thermal diffusivity ($\times 10^{-6} \text{ m}^2 \text{ s}^{-1}$)	Diurnal damping depth (m)
Soil components [5.72]						
Quartz	2.66	0.80	2.13	8.8	4.2	
Clay mineral	2.65	0.90	2.39	2.9	1.2	
Organic Matter	1.3	1.9	2.47	0.25	0.10	
Water ^a	1.0	4.18	4.18	0.57	0.14	
Air ^a	0.0012	1.004	0.00012	0.025	21	
Sandy soil, loosely packed (pore fraction 0.4) [5.72, 73]						
0%	1.60	0.80	1.28	0.24	0.19	0.080
20%	1.80	1.18	2.12	2.1	0.99	0.152
40%	2.00	1.48	2.96	2.5	0.85	0.143
Sandy soil, tightly packed (pore fraction 0.33) [5.72, 73]						
0%	1.78	0.80	1.42	0.29	0.20	
15%	1.93	1.06	2.05	2.5	1.2	
33%	2.11	1.33	2.81	2.9	1.0	
Clay soil (pore fraction 0.4) [5.72]						
0%	1.59	0.90	1.43	0.15	0.10	0.074
20%	1.79	1.27	2.27	0.9	0.40	0.124
40%	1.99	1.56	3.10	1.4	0.45	0.122
Peat soil (pore fraction 0.9) [5.72, 74]						
0%	0.13	1.90	0.25	0.04	0.16	
45%	0.58	3.67	2.13	0.27	0.13	
90%	1.03	3.89	4.01	0.50	0.12	
Other materials [5.75]						
Rock	2.7	0.75	2.03	2.9	1.4	
Ice	0.9	2.09	1.88	2.5	1.3	
Fresh snow	0.2	2.09	0.42	0.1	0.3	
Old snow	0.8	2.09	1.67	1.7	1.0	

^a for values with temperature dependence see Table 5.34, 5.35, and 5.38

Table 5.63 Parameters for the van Genuchten–Mualem (VGM) model [5.77] presented in Chap. 61; θ_r : residual volumetric water content, θ_s : saturated volumetric water content, α , n : empirical coefficients in the VGM model, K_s : saturated hydraulic conductivity, K_o : field-saturated hydraulic conductivity, L : dimensionless tortuosity parameter; for texture classes, see Fig. 5.1b

Texture class	θ_r ($\text{m}^3 \text{m}^{-3}$)	θ_s ($\text{m}^3 \text{m}^{-3}$)	$\log(\alpha)$ $\log(1/10^{-2} \text{m})$	$\log_{10}(n)$	K_s $\log_{10}(10^{-2} \text{m d}^{-1})$	K_o $\log_{10}(10^{-2} \text{m d}^{-1})$	L
Clay	0.098	0.459	−1.825	0.098	1.169	0.472	−1.561
C loam	0.079	0.442	−1.801	0.151	0.913	0.699	−0.763
Loam	0.061	0.399	−1.954	0.168	1.081	0.568	−0.371
L sand	0.049	0.390	−1.459	0.242	2.022	1.386	−0.874
Sand	0.053	0.375	−1.453	0.502	2.808	1.389	−0.930
S clay	0.117	0.385	−1.476	0.082	1.055	0.637	−3.665
S C L	0.063	0.384	−1.676	0.124	1.120	0.841	−1.280
S loam	0.039	0.387	−1.574	0.161	1.583	1.190	−0.861
Silt	0.050	0.489	−2.182	0.225	1.641	0.524	0.624
Si clay	0.111	0.481	−1.790	0.121	0.983	0.501	−1.287
Si C L	0.090	0.482	−2.076	0.182	1.046	0.349	−0.156
Si loam	0.065	0.439	−2.296	0.221	1.261	0.243	0.365

5.8 Time and Astronomical Quantities

The exact definition of time and several astronomical parameters are essential for the documentation of measurements in the atmosphere. For more details, see textbooks on astronomy, like [5.78].

5.8.1 Time Definitions

For time determination, the following definitions are used [5.79]:

Universal Time (UT) is the time scale of the mean solar time, which is related to the zero meridian (Greenwich Meridian), using the mean solar day as a base unit.

Universal Time coordinated (UTC) is the time scale—based on *International Atomic Time*—which, by definition of the zero point of the seconds count, is tied to Universal Time. This time is used in most countries as a basis for civil and scientific time.

Mean Local Time (MLT) is the same time (civil time)—based on the meridian of the place of observation—for all places at the same geographical longitude. It is the solar time measured from the time of the lower culmination of the mean sun by adding of 4 min to the universal time (UT) per degree of longitude in eastern direction.

Official Time is MLT mostly in steps of the 15th degree of longitude. For example, Central European Time (CET) corresponds to the mean local time of the 15th degree east of longitude and is UTC +1 hour.

Daylight Time is that time of the year when the clock is advanced by 1 h in relation to the official time observed to the rest of the year. In most of the countries that use daylight time, summer time begins at 1 a.m.

UTC on the last Sunday in March and ends at 1 a.m. on the last Sunday in October.

Time Equation indicates the periodically changing difference between the real time and the mean solar time due to Kepler’s laws. The time equation is positive if the real solar time culminates earlier than the mean solar time (day of sun). It varies between about −14 min 24 s (about mid-February) and 16 min 21 s (around the beginning of November), see [5.53]

True Local Time (TLT) is the same time (civil time) based on the meridian of the place of observation for all places at the same geographical longitude. The true local time is determined daily by the culmination of the sun. Therefore it varies with the variation of the time equation.

5.8.2 Calculation of Astronomical Quantities

In some applications, it is often necessary to determine the solar inclination angle as a function of time. The following approximations for some of these calculations must be applied in several steps [5.80]:

To determine the declination of the sun, δ , the latitude of the sun, φ_s , must first be calculated [5.81, 82]

$$\begin{aligned}\varphi_s &= x - 77.51^\circ + 1.92^\circ \sin x \\ x &= 0.9856^\circ \text{DOY} - 2.72^\circ, \end{aligned} \quad (5.50)$$

where DOY is the day of the year where the 1st of January has the number 1. Tables for DOY are available, e.g., [5.83].

The declination is given by

$$\sin \delta = 0.3978 \sin \varphi_S . \quad (5.51)$$

To determine the position of the sun, the hour angle ω

$$\omega = (LTST - 12 \text{ h}) \times 15^\circ \text{ in } ^\circ \quad (5.52)$$

must be calculated, which gives the angular difference between δ and the zenith of the sun [5.84]; thereby $LTST$ is the local true solar time. It is necessary to apply the equation of time Z [5.85], which gives the difference between the local true and the mean solar time (x , see (5.50))

$$\begin{aligned} Z = & -7.66 \sin x \\ & -9.87 \sin (2x + 24.99^\circ + 3.83^\circ \sin x) \text{ in min.} \end{aligned} \quad (5.53)$$

The time distance to culmination of the sun, t_H , (for Central European Time $\lambda = 15^\circ$) is given by

$$t_H = \left\{ t - \left[12 + Z + \frac{(15 - \lambda)4}{60} \right] \right\} 3600 , \quad (5.54)$$

where t is time in hours, and λ is longitude.

With the latitude φ in radians of a location, the angle of inclination of the sun can be determined for any time

$$\sin \gamma = \sin \delta \sin \varphi + \cos \delta \cos \varphi \cos \omega . \quad (5.55)$$

Table 5.64 Coefficients of (5.57) [5.86]

n	a_n	b_n
0	1.000110	
1	0.034221	0.001280
2	0.000719	0.000077

To determine the incoming extraterrestrial radiation at the upper border of the atmosphere from the solar constant S (Table 5.6) the variability of the distance between the sun and the Earth must be taken into account

$$K \downarrow_{\text{extraterr.}} = S \left(\frac{r_0}{r} \right)^2 \sin \varphi , \quad (5.56)$$

where r_0 is the mean distance of the Earth from the Sun (149 597 870.66 km) and r is the actual distance. The ratio of both can be determined as a Fourier series [5.86]

$$\left(\frac{r_0}{r} \right)^2 = \sum_{n=0}^2 a_n \cos(n\theta_d) + b_n \sin(n\theta_d) , \quad (5.57)$$

with

$$\theta_d = \frac{2\pi \text{DOY}}{365} , \quad (5.58)$$

where in the case of a leap year, the denominator is 366. The coefficients for (5.57) are given in Table 5.64.

5.9 Tables in Other Chapters

More specific tables are available in other chapters. These are listed in Table 5.65.

Table 5.65 Tables of parameters in other chapters

Table number	Content of the table
7.7	Resistance of thin platinum wires
7.9	Thermocouple output voltage for reference temperature 0 °C
8.7	Contraction of normal and rolled hair for hair hygrometers
8.10	Pressure dependence of the psychrometric coefficient
8.15	Saturated salt solution at 25 °C and their characteristic relative humidity
10.5	Correction factor for pressure on sea level

5.10 Future Developments

After the application of the new temperature scale ITS-90 many atmospheric parameters have an extremely high accuracy, which is not necessary for many practical issues. Therefore, it can be assumed that in the near future, no update of the tables given above will be necessary for atmospheric applications.

Recently, a number of metrological challenges for the measurement of the relative humidity was identified as a key climatological observable [5.52, 87, 88]. The corresponding studies deal, among others, with a generalized definition of relative humidity in terms of fundamental thermodynamic notions like *fugacity* and *activity*, which contain the *de-facto* standard relative humidity definitions as limiting cases. Of special in-

terest for atmospheric applications is the definition of relative humidity by the relative fugacity, which can be directly determined from the TEOS-10/SIA library or from analytical expressions as functions of water vapor mole fraction (or any other humidity measure), temperature, and pressure. The aim is to support the establishment of a SI-compatible standard for the definition of relative humidity for general use (see also Chap. 8).

Changes in the ITS-90 and TEOS-10, which will originate from the application of the new SI definition, are expected to remain safely within the confidence interval of atmospheric measurements of the table values presented here.

5.11 Further Reading

- G. Fischer (ed): *Landolt–Börnstein: Numerical Data and Functional Relationships in Science and Technology, Group V: Geophysics and Space Research, Volume 4: Meteorology* (Springer, Berlin, Heidelberg 1988)
 - IOC, SCOR and IAPSO: *The international thermodynamic equation of seawater – 2010: Calculation and use of thermodynamic properties: Intergovernmental Oceanographic Commission, Manuals and Guides No. 56*, UNESCO (English) 2010, 196 pp. http://www.teos-10.org/pubs/TEOS-10_Manual.pdf, Accessed 06 July 2021
 - *Le Système International D'unités (The International System of Units), 9th Edition* (Bureau International des Poids et Mesures, Sèvres 2019)
- Acknowledgments.** The authors acknowledge Dr. Rainer Feistel for helpful discussions and his support in the application of the TEOS-10 SIA library.

References

- | | | | |
|-----|---|------|---|
| 5.1 | G. Fischer (Ed.): <i>Landolt–Börnstein: Numerical Data and Functional Relationships in Science and Technology, Group V: Geophysics and Space Research, Volume 4: Meteorology</i> (Springer, Berlin, Heidelberg 1988) | 5.5 | F. Linke (Ed.): <i>Meteorologisches Taschenbuch</i> , Vol. 1–5 (Akademische Verlagsanstalt m. b. H., Leipzig 1939), 1931–1939 |
| 5.2 | S.N. Mikhailenko, Y.L. Babikov, V.F. Golovko: Information-calculating system spectroscopy of atmospheric gases. The structure and main functions, <i>Atmos. Ocean. Opt.</i> 18 , 685–695 (2005) | 5.6 | F. Linke, F. Baur (Eds.): <i>Meteorologisches Taschenbuch</i> , Vol. I, 2nd edn. (Akademische Verlagsgesellschaft Geest and Portig K.-G., Leipzig 1962) |
| 5.3 | K. Schneider-Carius: Geschichtlicher Überblick über die Entwicklung der Meteorologie. In: <i>Meteorologisches Taschenbuch</i> , 2nd edn., Vol. 1, ed. by F. Linke, F. Baur (Akademische Verlagsges. Geest and Portig K.-G., Leipzig 1962) pp. 662–708 | 5.7 | F. Linke, F. Baur (Eds.): <i>Meteorologisches Taschenbuch</i> , Vol. II, 2nd edn. (Akademische Verlagsgesellschaft Geest and Portig K.-G., Leipzig 1970) |
| 5.4 | A. Guyot: <i>A Collection of Meteorological Tables: With Other Tables Useful in Practical Meteorology</i> (Smithsonian Institution, Washington 1852), (Reprint 2012 by Forgotten Books) | 5.8 | F. Linke, F. Baur (Eds.): <i>Linkes meteorologisches Taschenbuch</i> , Vol. III (Akademische Verlagsgesellschaft Geest and Portig K.-G., Leipzig 1957) |
| | | 5.9 | S. Letestu (Ed.): <i>International Meteorological Tables, WMO No. 188, Tp 94, Updated 1973</i> (World Meteorological Organization, Geneva 1966) |
| | | 5.10 | J. Bartels, P. ten Bruggencate (Eds.): <i>Landolt–Börnstein: Numerical Data and Functional Relationships in Science and Technology</i> , Astronomy and Geophysics (Springer, Berlin, Heidelberg 1952) |

- 5.11 CODATA: *Recommended Consistent Values of the Fundamental Physical Constants*, CODATA Bulletin, Vol. 11 (Council of Scientific Unions—Committee on Data for Science and Technology, Paris 1973)
- 5.12 Comité International des Poids et Mesures: The International Practical Temperature Scale of 1968, *Metrologia* **5**, 35 (1969)
- 5.13 D. Sonntag: Important new values of the physical constants of 1986, vapour pressure formulations based on the ITS-90, and psychrometer formulae, *Z. Meteorol.* **40**, 340–344 (1990)
- 5.14 CODATA: *The 1986 Adjustment of the Fundamental Physical Constants (Report of the Codata Task Group on Fundamental Constants)*, CODATA Bulletin, Vol. 63 (Council of Scientific Unions—Committee on Data for Science and Technology, Paris 1986)
- 5.15 E.R. Cohen, B.N. Taylor: *The 1986 Adjustment of the Fundamental Physical Constants*, CODATA-Bull., Vol. 63 (International Council of Scientific Unions (ICSU), Committee on Data for Science and Technology (CODATA), Paris 1986) p. 36
- 5.16 H. Preston-Thomas: The International Temperature Scale of 1990 (ITS-90), *Metrologia* **27**, 3–10 (1990)
- 5.17 R. Feistel, D.G. Wright, D.R. Jackett, K. Miyagawa, J.H. Reissmann, W. Wagner, U. Overhoff, C. Guder, A. Feistel, G.M. Marion: Numerical implementation and oceanographic application of the thermodynamic potentials of liquid water, water vapour, ice, seawater and humid air – part 1: background and equations, *Ocean Sci.* **6**, 633–677 (2010)
- 5.18 D.G. Wright, R. Feistel, J.H. Reissmann, K. Miyagawa, D.R. Jackett, W. Wagner, U. Overhoff, C. Guder, A. Feistel, G.M. Marion: Numerical implementation and oceanographic application of the thermodynamic potentials of liquid water, water vapour, ice, seawater and humid air – part 2: the library routines, *Ocean Sci.* **6**, 695–718 (2010)
- 5.19 IOC, SCOR, IAPSO: *The International Thermodynamic Equation of Seawater – 2010: Calculation and Use of Thermodynamic Properties*, Manuals and Guides, Vol. 56 (UNESCO, 2010)
- 5.20 R. Feistel: TEOS-10: a new international oceanographic standard for seawater, ice, fluid water, and humid air, *Int. J. Thermophys.* **33**, 1335–1351 (2012)
- 5.21 R. Feistel: Thermodynamic properties of seawater, ice and humid air: TEOS-10, before and beyond, *Ocean Sci.* **14**, 471–502 (2018)
- 5.22 W. Wagner, A. Pruß: The IAPWS formulation 1995 for the thermodynamic properties of ordinary water substance for general and scientific use, *J. Phys. Chem. Ref. Data* **31**, 387–535 (2002)
- 5.23 IAPWS R6-95: *Revised Release on the IAPWS Formulation 1995 for the Thermodynamic Properties of Ordinary Water Substance for General and Scientific Use* (International Association for the Properties of Water and Steam, Dresden 2016)
- 5.24 R. Feistel, W. Wagner: A new equation of state for H₂O ice Ih, *J. Phys. Chem. Ref. Data* **35**, 1021–1047 (2006)
- 5.25 IAPWS R10-06: *Revised Release on the Equation of State 2006 for H₂O Ice Ih* (International Association for the Properties of Water and Steam, Doorwerth 2009)
- 5.26 R. Feistel: A new extended Gibbs thermodynamic potential of seawater, *Prog. Oceanogr.* **58**, 43–114 (2003)
- 5.27 R. Feistel: A Gibbs function for seawater thermodynamics for –6 to 80 °C and salinity up to 120 g kg⁻¹, *Deep Sea Res. I: Oceanogr. Res. Pap.* **55**, 1639–1671 (2008)
- 5.28 IAPWS R13-08: *Release on the IAPWS Formulation 2008 for the Thermodynamic Properties of Seawater* (International Association for the Properties of Water and Steam, Berlin 2008)
- 5.29 E.W. Lemmon, R.T. Jacobsen, S.G. Penoncello, D.G. Friend: Thermodynamic properties of air and mixtures of nitrogen, argon, and oxygen from 60 to 2000 K at pressures to 2000 MPa, *J. Phys. Chem. Ref. Data* **29**, 331–385 (2000)
- 5.30 R.W. Hyland, A. Wexler: Formulations for the thermodynamic properties of the saturated phases of H₂O from 173.15 K to 473.15 K, *ASHRAE Transactions* **89**, 500–519 (1983)
- 5.31 A.H. Harvey, P.H. Huang: First-principles calculation of the air–water second virial coefficient, *Int. J. Thermophys.* **28**, 556–565 (2007)
- 5.32 R. Feistel, D.G. Wright, H.J. Kretzschmar, E. Hagen, S. Herrmann, R. Span: Thermodynamic properties of sea air, *Ocean Sci.* **6**, 91–141 (2010)
- 5.33 D.M. Murphy, T. Koop: Review of the vapour pressures of ice and supercooled water for atmospheric applications, *Quart. J. Roy. Meteorol. Soc.* **131**, 1539–1565 (2005)
- 5.34 V. Holten, J.V. Sengers, M.A. Anisimov: Equation of state for supercooled water at pressures up to 400 MPa, *J. Phys. Chem. Ref. Data* **43**, 043101 (2014)
- 5.35 SI: *Le Système International D’unités (the International System of Units)*, 9th edn. (Bureau International des Poids et Mesures, Sèvres 2019)
- 5.36 B.N. Taylor, A. Thompson (Eds.): *The International System of Units (SI)*, NIST Special Publication, Vol. 330, 2008th edn. (National Institute of Standards and Technology, Gaithersburg 2008)
- 5.37 P.J. Allisy-Roberts: Radiation quantities and units—understanding the Sievert, *J. Radiol. Prot.* **25**, 97 (2005)
- 5.38 M.L. Salby: *Physics of the Atmosphere and Climate* (Cambridge University Press, Cambridge 2012)
- 5.39 D.W. Moore: Dynamical meteorology I Coriolis force. In: *Encyclopedia of Atmospheric Sciences*, 2nd edn., ed. by G.R. North, J. Pyle, F. Zhang (Academic Press, Oxford 2015) pp. 313–316
- 5.40 H. Moritz: *Geodetic Reference System 1980*, Paper presented at XVII General Assembly of the IUGG, (IUGG, Canberra 1980)
- 5.41 G. Kopp, J.L. Lean: A new, lower value of total solar irradiance: evidence and climate significance, *Geophys. Res. Letters* **38**, L01706 (2011)
- 5.42 P.T. Tsilingiris: Thermophysical and transport properties of humid air at temperature range between 0 and 100 °C, *Energy Convers. Manag.* **49**, 1098–1110 (2008)
- 5.43 ICAO: *Manual of the ICAO Standard Atmosphere: Extended to 80 Kilometres (262500 Feet)*, ICAO Doc 7488,

- 3rd edn. (International Civil Aviation Organization, Montréal 1993)
- 5.44 T.S. Glickman (Ed.): *Glossary of Meteorology*, 2nd edn. (Am. Meteorol. Soc., Boston, MA 2000)
- 5.45 M. Hantel: *Einführung Theoretische Meteorologie* (Springer Spektrum, Berlin, Heidelberg 2013)
- 5.46 NOAA: *U.S. Standard Atmosphere, 1976* (National Oceanic and Atmospheric Administration, Washington D.C. 1976)
- 5.47 O. Hellmuth, R. Feistel, T. Foken: Intercomparison of different state-of-the-art formulations of the mass density of humid air, *Bull. Atmos. Sci. Technol.* **3**, in press (2022), <https://doi.org/10.1007/s42865-021-00036-7>
- 5.48 W. Henry: Experiments on the quantity of gases absorbed by water, at different temperatures, and under different pressures, *Phil. Trans. R. Soc. London* **93**, 29–276 (1803)
- 5.49 R. Sander: Compilation of Henry's law constants (version 4.0) for water as solvent, *Atmos. Chem. Phys.* **15**, 4399–4981 (2015)
- 5.50 R. Feistel, W. Ebeling: *Physics of Self-Organization and Evolution* (Wiley-VCH, Weinheim 2011)
- 5.51 R. Feistel, O. Hellmuth: Zur Rolle des Wassers in der Energiebilanz des Klimasystems (On the role of water in the energy balance of the climate system), *Sitzungsberichte der Leibniz-Sozietät der Wissenschaften zu Berlin*, **144**, 51–130 (2020)
- 5.52 R. Feistel, J.W. Lovell-Smith: Defining relative humidity in terms of water activity. Part 1: definition, *Metrologia* **54**, 566 (2017)
- 5.53 WMO: *Guide to Instruments and Methods of Observation*, WMO-No. 8, Volume I – Measurement of Meteorological Variables (World Meteorological Organization, Geneva 2018)
- 5.54 R. Feistel, J.W. Lovell-Smith, O. Hellmuth: Virial approximation of the TEOS-10 equation for the fugacity of water in humid air, *Int. J. Thermophys.* **36**, 44–68 (2015)
- 5.55 J.M. Prausnitz, R.N. Lichtenthaler, E.G. de Azevedo: *Molecular Thermodynamics of Fluid-Phase Equilibria*, 3rd edn. (Prentice Hall, Upper Saddle River 1999)
- 5.56 IAPWS G7-04: *Guideline on the Henry's Constant and Vapour-Liquid Distribution Constant for Gases in H₂O and D₂O at High Temperatures* (International Association for the Properties of Water and Steam, Kyoto 2004)
- 5.57 S. Herrmann, H.-J. Kretzschmar, D.P. Gatley: Thermodynamic properties of real moist air, dry air, steam, water, and ice (RP 1485), *HVAC and R Research* **15**, 961–986 (2009)
- 5.58 E.W. Lemmon, R.T. Jacobsen: Viscosity and thermal conductivity equations for nitrogen, oxygen, argon, and air, *Int. J. Thermophys.* **25**, 21–69 (2004)
- 5.59 G. Mie: Beiträge zur Optik trüber Medien, speziell kolloidaler Metallösungen, *Ann. Phys.* **25**(4), 377–445 (1908)
- 5.60 K.N. Liou: *An Introduction to Atmospheric Radiation* (Academic Press, Amsterdam, Boston, London 2002)
- 5.61 Y.X. Hu, K. Stamnes: An accurate parameterization of the radiative properties of water clouds suitable for use in climate models, *J. Climate* **6**, 728–742 (1993)
- 5.62 Q. Fu, K.N. Liou: Parameterization of radiative properties of cirrus clouds, *J. Atmos. Sci.* **50**, 2008–2025 (1993)
- 5.63 J.W. Ramsey, H.D. Chiang, R.J. Goldstein: A study of the incoming longwave atmospheric radiation from a clear sky, *J. Appl. Meteorol.* **21**, 566–578 (1982)
- 5.64 L.S. Rothman, I.E. Gordon, Y. Babikov, A. Barbe, D.C. Benner, P.F. Bernath, M. Birk, L. Bizzocchi, V. Boudon, L.R. Brown, A. Campargue, K. Chance, E.A. Cohen, L.H. Coudert, V.M. Devi, B.J. Drouin, A. Fayt, J.M. Flaud, R.R. Gamache, J.J. Harrison, J.M. Hartmann, C. Hill, J.T. Hodges, D. Jacquemart, A. Jolly, J. Lamouroux, R.J. Le Roy, G. Li, D.A. Long, O.M. Lyulin, C.J. Mackie, S.T. Massie, S. Mikhailenko, H.S.P. Müller, O.V. Naumenko, A.V. Nikitin, J. Orphal, V. Perevalov, A. Perrin, E.R. Polovtseva, C. Richard, M.A.H. Smith, E. Starikova, K. Sung, S. Tashkun, J. Tennyson, G.C. Toon, V.G. Tyuterev, G. Wagner: The HITRAN2012 molecular spectroscopic database, *J. Quantit. Spectrosc. Radiat. Transf.* **130**, 4–50 (2013)
- 5.65 D. Hillel: *Environmental Soil Physics* (Academic Press, New York 1998)
- 5.66 H.-P. Blume, G.W. Brümmer, H. Fleige, R. Horn, E. Kandeler, I. Kögel-Knabner, R. Kretzschmar, K. Stahr, B.-M. Wilke: *Scheffer/Schachtschabel Soil Science* (Springer, Berlin, Heidelberg 2016)
- 5.67 W. Eckelmann, H. Sponagel, W. Grotenthaler, K.-J. Hartmann, R. Hartwich, P. Janetzko, H. Joisten, D. Kühn, K.J. Sabel, R. Traidl: *Bodenkundliche Kartieranleitung*, 5th edn. (Ad-hoc AG Boden, Bundesanstalt für Geowissenschaften und Rohstoffe und Niedersächsisches Landesamt für Bodenforschung, in Kommission. E. Schweizerbart, Stuttgart 2005)
- 5.68 R Core Team: *R: A Language and Environment for Statistical Computing* (R Foundation for Statistical Computing, Vienna 2016)
- 5.69 J. Moeys: *The Soil Texture Wizard: R Functions for Plotting, Classifying, Transforming and Exploring Soil Texture Data*, online tutorial in [5.65] 2015)
- 5.70 J. Moeys, W. Shangquan, R. Petzold, B. Minasny, B. Rosca, N. Jelinski, W. Zelazny, R. Marcondes Silva Souza Safanelli Caten, J.L. Safanelli, A. ten Caten: *Soiltexture-Package – for Soil Texture Plot, Classification and Transformation*, online tutorial in [5.65] 2018)
- 5.71 M.T. van Genuchten: A closed-form equation for predicting the hydraulic conductivity of unsaturated soils, *Soil Sci. Soc. Am. J.* **44**, 892–898 (1980)
- 5.72 D.A. de Vries: Thermal properties of soils. In: *Physics of the Plant Environment*, ed. by W.R. van Wijk (North-Holland Publ. Co, Amsterdam 1963) pp. 210–235
- 5.73 K.M. Smits, T. Sakaki, A. Limsuwat, T.H. Illan-gasekare: Thermal conductivity of sands under varying moisture and porosity in drainage-wetting cycles, *Vadose Zone J.* **9**, 172–180 (2010)
- 5.74 J.A. O'Donnell, V.E. Romanovsky, J.W. Harden, A.D. McGuire: The effect of moisture content on the thermal conductivity of moss and organic soil hori-

- zons from black spruce ecosystems in interior alaska, *Soil Sci.* **174**, 646–651 (2009)
- 5.75 R. Lee: *Forest Microclimatology* (Columbia Univ. Press, New York 1978)
- 5.76 A.F. Moene, J.C. van Dam: *Transport in the Atmosphere-Vegetation-Soil Continuum* (Cambridge Univ. Press, Cambridge 2014)
- 5.77 M.G. Schaap, F.J. Leij, M.T. van Genuchten: Neural network analysis for hierarchical prediction of soil hydraulic properties, *Soil Sci. Soc. Am. J.* **62**, 847–855 (1998)
- 5.78 H. Karttunen, P. Kröger, H. Oja, M. Poutanen, K.J. Donner (Eds.): *Fundamental Astronomy* (Springer, Berlin, Heidelberg 2017)
- 5.79 VDI: *Umweltmeteorologie – Meteorologische Messungen – Grundlagen (Environmental Meteorology – Meteorological Measurements – Basics)*, VDI 3786, Blatt (Part) 1 (Beuth-Verlag, Berlin 2013)
- 5.80 T. Foken: *Micrometeorology*, 2nd edn. (Springer, Berlin, Heidelberg 2017)
- 5.81 D. Sonntag: Formeln verschiedenen Genauigkeitsgrades zur Berechnung der Sonnenkoordinaten, *Abh. Meteorol. Dienstes DDR* **143**, 104 (1989)
- 5.82 VDI: *Umweltmeteorologie – Wechselwirkungen zwischen Atmosphäre und Oberflächen-Berechnung der spektralen kurz- und der langwelligen Strahlung*, VDI 3789 (Beuth-Verlag, Berlin 2018)
- 5.83 NOAA Earth System Reserch Laboratory (ESRL): *Day-Of-Year Calender*, <https://www.esrl.noaa.gov/gmd/grad/neubrew/Calendar.jsp>, Accessed 06 July 2021
- 5.84 K.N. Liou: *Radiation and Cloud Processes in the Atmosphere* (Oxford University Press, Oxford 1992)
- 5.85 D.W. Hughes, B.D. Yallop, C.Y. Hohenkerk: The equation of time, *Monthly Notices Roy. Astron. Soc.* **238**, 1529–1535 (1989)
- 5.86 D.L. Hartmann: *Global Physical Climatology* (Academic Press, San Diego, New York 1994)
- 5.87 R. Feistel, R. Wielgosz, S.A. Bell, M.F. Camoes, J.R. Cooper, P. Dexter, A.G. Dickson, P. Fisi-caro, A.H. Harvey, M. Heinonen, O. Hellmuth, H.J. Kretzschmar, J.W. Lovell-Smith, T.J. McDougall, R. Pawlowicz, P. Ridout, S. Seitz, P. Spitzer, D. Stoica, H. Wolf: Metrological challenges for measurements of key climatological observables: oceanic salinity and pH, and atmospheric humidity. Part 1: overview, *Metrologia* **53**, R1–R11 (2016)
- 5.88 J.W. Lovell-Smith, R. Feistel, A.H. Harvey, O. Hellmuth, S.A. Bell, M. Heinonen, J.R. Cooper: Metrological challenges for measurements of key climatological observables. Part 4: Atmospheric relative humidity, *Metrologia* **53**, R40–R59 (2016)

Thomas Foken

University of Bayreuth
Bayreuth, Germany
thomas.foken@uni-bayreuth.de



Thomas Foken is a retired Professor of Micrometeorology at the University of Bayreuth. He was the head of Laboratories at the meteorological observatories at Potsdam (1981–1994) and Lindenberg (1994–1997). His research interests include the interaction between the Earth's surface and the atmosphere and the measurement and modeling of energy and matter fluxes, with a strong focus on experimental meteorology. His scientific contributions have been recognized through various international awards.

Olaf Hellmuth

Modeling Department
TROPOS Leibniz Institute for Tropospheric Research
Leipzig, Germany
olaf.hellmuth@tropos.de



Olaf Hellmuth is Senior Scientist in the Modeling Department of the TROPOS Leibniz Institute for Tropospheric Research Leipzig. In 1985, he received a diploma in meteorology and in 1988, he was awarded a Dr. rer. nat. His research activities comprise atmospheric sol formation, cloud microphysics with focus on hygroscopic growth and freezing processes, and theoretical aspects of hygrometry. He is member of the Leibniz Sozietät Berlin.

Bernd Huwe



Soil Physics
University of Bayreuth
Bayreuth, Germany
bernd.huwe@uni-bayreuth.de

Bernd Huwe received his Habilitation degree in 1991 in Soil Physics. From 1992 to 2017, he was Professor of Soil Physics at the University of Bayreuth. His research addressed theoretical and practical questions of water, heat, and nutrient and pollutant transport in soils. In this context, soil landscape modeling, regionalization of soil processes, effective modeling, and risk and parameter uncertainty analysis were important tools of his research group.

Dietrich Sonntag (deceased)



Dietrich Sonntag received his doctoral degree from the University of Leipzig in Meteorology in 1951 and his Habilitation degree from the Humboldt University Berlin in 1965. He developed several meteorological sensors mainly for humidity and radiation measurements. In 1988, he was one of the first scientists to be awarded the Professor Dr Vilho Väisälä Award of the WMO. He retired in 1992 and passed away in 2018.

In situ **Part B** M

Part B In situ Measurement Techniques

- 6 Ground-Based Platforms**
Olaf Kolle, Jena, Germany
Norbert Kalthoff, Karlsruhe, Germany
Christoph Kottmeier, Karlsruhe, Germany
J. William Munger, Cambridge, USA
- 7 Temperature Sensors**
Thomas Foken, Bayreuth, Germany
Jens Bange, Tübingen, Germany
- 8 Humidity Sensors**
Dietrich Sonntag
Thomas Foken, Bayreuth, Germany
Holger Vömel, Boulder, USA
Olaf Hellmuth, Leipzig, Germany
- 9 Wind Sensors**
Thomas Foken, Bayreuth, Germany
Jens Bange, Tübingen, Germany
- 10 Pressure Sensors**
Anni Torri, Vantaa, Finland
Thomas Foken, Bayreuth, Germany
Jens Bange, Tübingen, Germany
- 11 Radiation Sensors**
Klaus Behrens, Nuthetal, Germany
- 12 In-situ Precipitation Measurements**
Arianna Cauteruccio, Genova, Italy
Matteo Colli, Genova, Italy
Mattia Stagnaro, Genova, Italy
Luca G. Lanza, Genova, Italy
Emanuele Vuerich, Rome, Italy
- 13 Visibility Sensors**
Martin Löffler-Mang, Saarbrücken, Germany
Klaus Heyn, Hamburg, Germany
- 14 Electricity Measurements**
Giles Harrison, Reading, UK
Alec Bennett, Portishead, UK
- 15 Radioactivity Sensors**
Jacqueline Bieringer, Freiburg, Germany
Thomas Steinkopff, Offenbach, Germany
Ulrich Stöhlker, Freiburg, Germany
- 16 Gas Analysers and Laser Techniques**
Dwayne Heard, Leeds, UK
Lisa K. Whalley, Leeds, UK
Steven S. Brown, Boulder, USA
- 17 Measurement of Stable Isotopes in Carbon Dioxide, Methane, and Water Vapor**
Ingeborg Levin, Heidelberg, Germany
Matthias Cuntz, Nancy, France
- 18 Measurement of Fundamental Aerosol Physical Properties**
Andreas Held, Berlin, Germany
Alexander Mangold, Brussels, Belgium
- 19 Methods of Sampling Trace Substances in Air**
Christopher Pöhlker, Mainz, Germany
Karsten Baumann, Chapel Hill, USA
Gerhard Lammel, Mainz, Germany
- 20 Optical Fiber-Based Distributed Sensing Methods**
Christoph K. Thomas, Bayreuth, Germany
John Selker, Corvallis, USA
- 21 Odor Measurements**
Ralf Petrich, Frankenberg, Germany
Axel Delan, Frankenberg, Germany
- 22 Visual Observations**
Thomas Foken, Bayreuth, Germany
Raymond Rülke, Langendorf, Germany

Ground-Based

6. Ground-Based Platforms

Olaf Kolle , Norbert Kalthoff , Christoph Kottmeier , J. William Munger 

Ground-based platforms for atmospheric measurements are carriers for instruments, devices, or systems with the purpose of measuring meteorological variables, atmospheric composition, or more broadly the properties of the land or ocean surface. These platforms can be masts or towers with a wide range of heights and shapes; they can also be buoys and ships.

Starting in the nineteenth century, ground-based atmospheric measurement platforms were needed by national weather services while implementing networks of weather stations. Later, measurement masts and towers became an important tool for fundamental meteorological research. For example, wind data from tall towers in the vicinity of nuclear power plants can be used to help predict the direction of a radioactive plume after a hazardous incident. Tall towers are also built to address climate change questions. Furthermore, dense networks of weather stations are needed to improve weather forecasting and find suitable areas for wind farms. Each measurement platform must be planned and designed with regard to the specific measurement type, purpose, and desired instrumentation. Every platform impacts the measurements themselves and problems such as flow distortion or light reflections must be accounted for during the planning phase. Data from moving platforms like some buoys need to undergo special processing to eliminate artifacts as a result of movement. Most measurement platforms must comply with national and/or international rules and specifications, both structurally and in terms

of safety and regular maintenance. The chapter concludes with examples that illustrate the diverse applications of ground-based platforms for atmospheric measurements.

6.1	Principles of Platforms	156
6.2	History	157
6.3	Theory	158
6.3.1	Flow Distortion	158
6.3.2	Impact on Other Measured Variables ...	159
6.4	Platforms and Sensor Installations	160
6.4.1	Small Towers	160
6.4.2	Tall Towers	164
6.4.3	Buoys and Floats	168
6.4.4	Infrastructure	171
6.4.5	Relevant Sensors for Different Platform Types	173
6.5	Specification	174
6.6	Quality Control and Safety	175
6.7	Maintenance	175
6.8	Applications	176
6.8.1	Vehicle-Induced Turbulence	176
6.8.2	Internal Boundary Layer	176
6.8.3	Large-Scale Manipulation Experiment ..	176
6.8.4	Tall-Tower Observatories	178
6.9	Future Developments	178
6.10	Further Readings	179
	References	180

With most ground-based platforms, atmospheric measurements only take place within the atmospheric boundary layer (ABL, see Chap. 1). Energy conversion and circulation processes in this layer of the lower troposphere strongly influence the biosphere, weather patterns, the climate, and consequently the living conditions for all

plants and animals, in particular for us humans. For these reasons we want to understand all of the processes and feedback at the surface as well as within the atmospheric near-surface layer by trying to measure all relevant environmental variables. The following are advantages of ground-based measurement platforms:

- Simplest way to obtain atmospheric measurements and in many cases easy to install.
- Normally, a high spatial resolution of measurements can be obtained.
- Long-term measurements even at high temporal resolutions are possible (see Chap. 43).
- Various power supply systems can be deployed.
- Flexibility in power consumption and thus suitable for remote places.
- With tall towers, radio transmission masts, and other high buildings, heights of up to several hundred meters (currently more than 800 m) can be reached.

On land, ground-based measurement platforms are usually rigid, stable, and easy to implement. The higher

such structures become, the more complex they will be in terms of stability, safety, and regulations. Moreover, it is always necessary to find a compromise between the stability of a structure and the negative influence of the structure itself on the measurements.

On water, measurement platforms such as ships, floats, or buoys can either actively change their position, move with water currents, or be anchored. Besides horizontal movement, such platforms are exposed to irregular vertical movements and tilting effects due to waves. Therefore, some atmospheric measurements, for instance monitoring wind speed and direction, become more complex and additional postprocessing of the data is needed to correct for the effects of the unstable measurement platform.

6.1 Principles of Platforms

Ground-based measurement platforms are the oldest installations for carrying atmospheric measurement instruments. It is crucial to provide a structure that can carry instruments, sensors, or air inlets exposed to an undisturbed environment, where the meteorological conditions and atmospheric properties are representative for the vicinity. However, the influence of the local conditions on the measurements decreases while moving the sensor vertically upwards, and, at the same time, the area which contributes to the measured values (footprint) increases in size and in distance from the platform. This footprint area must be considered when choosing the position for an observation platform (see annotation in text). The corresponding footprint area can be quite large for tall towers (e.g., [6.1]).

Stationary ground-based measurement platforms must be stable and safe, including for the instrumen-

tion. It must also be technically feasible to attach, maintain, and exchange sensors and instruments without too much effort. Masts and towers can be made of different materials (such as steel, aluminum, or wood), the construction can be open or closed, the structures can be self-supporting or guyed, and they can be of fixed or adjustable height. As the kind of the construction has an effect on the measurements (flow distortion, shadowing, see Sect. 6.3.1) this must be considered in the planning of the observation platform.

Buoys drifting on the water surface or sea ice, or anchored at a fixed location, are made of buoyant bodies of stainless steel or plastic. Their diameters and lengths vary widely and are adapted for the load to be carried. They contain and carry sensors, cabling, electronics, and batteries. Buoys on sea ice need very solid hull material to withstand ice pressure and are shaped to

Table 6.1 Types of platforms

Type	Setup location	Purpose	Remark
Poles and tripods	Land	All types of meteorological and flux measurements	Heights up to 3 m
Small towers	Land	All types of meteorological, air pollution, and flux measurements	Heights up to 80 m or variable heights
Tall towers	Land		Heights up to 350 m
Radio transmission masts and high buildings	Land	Selected meteorological measurements	Heights up to 800 m
Moving platforms	Land	Selected meteorological and air pollution measurements	See Chaps. 37 and 50
Floats	Lakes (low wave height)	Selected meteorological, air pollution, and flux measurements	Additional measurements in the water or on ice
Buoys	Lakes, ocean, sea ice	Selected meteorological and air pollution measurements	
Ships	Rivers, lakes, ocean	Selected meteorological and air pollution measurements	

keep them at the surface. They are deployed either from ships via cranes or smaller systems can be mounted using helicopter transport or by parachute dropping from fixed-wing aircraft.

6.2 History

Weather vanes (or wind vanes) were the earliest sensors used for indicating the actual weather situation and making simple weather predictions. In the early first century BCE, the 13-m-high *Tower of Winds* (see Fig. 6.1) was built in Athens by the Greek architect *Andronikos of Kyrrhos* [6.2]. On top of this tower a weather vane shaped like a *Triton*, a daemon of the ocean, and made of bronze was spinning [6.3].

Such ancient weather vanes made of textile or metal arose and have been used where it was important to be able to predict the weather by reading wind direction

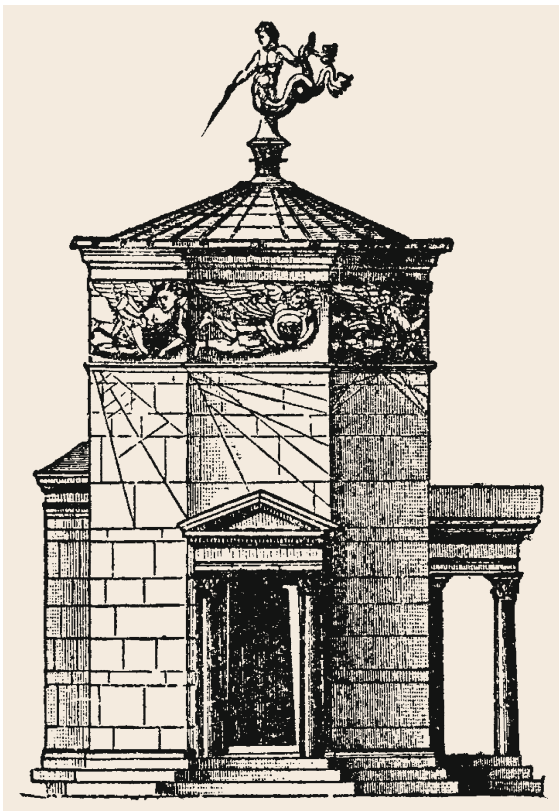


Fig. 6.1 An illustration of the *Tower of Winds*, which was built between 100 and 50 BCE in Athens, Greece. It is considered the world's first meteorological station (after [6.4], clipart courtesy FCIT)

Table 6.1 summarizes the major types of ground-based platforms. Airborne platforms and moving platforms are described in detail in Chaps. 37 and 50, respectively.

and wind velocity from the direction and rotary motion of the weather vane. The ground-based platforms for these early sensors were usually simple metal poles on high buildings such as steeples or lighthouses, on roof ridges, or on ship masts.

In 1780, the *Societas Meteorologica Palatina*, the Meteorological Society of Mannheim, Germany, was founded. This was the first society that organized transnational meteorological observations carried out at fixed reading times. Later, in the middle of the nineteenth century, the need for specific sensor platforms arose with the rise of continuously recording instruments. Early versions of recording instruments had paper charts and mechanical apparatus to record on the paper. This, and the need to measure from a standard height above ground, gave rise to the standardized louvered box that was typically deployed at weather stations. The installation had a roof overhead to protect the instruments from weather and shield them from direct sunlight, but had well-ventilated sides so the temperature inside the box would be the same as the outside air temperature away from the structure. To measure wind velocity and wind direction at the standard height of 10 m above ground, the wind instruments were mounted on the top of a self-supporting or guyed mast.

Nuclear fission research and the beginning of peaceful uses of nuclear energy with the world's first nuclear power plant in Obninsk in the former Soviet Union, which began delivering electrical energy on 26 June 1954, forced the erection of meteorological masts in the vicinity of such nuclear plants. In Obninsk, a 315-m-high cable-stayed steel-tube mast was constructed in 1958 with several measurement platforms carrying instruments to measure radioactivity and meteorological variables. The first nuclear research reactor in Germany was established in 1957 at Garching and in 1959 a 50-m-high measurement mast was completed and then replaced by the 62-m-high Oskar-von-Miller Tower in 2010. The building permit for any nuclear plant usually requires the erection of a measurement mast. In the case of a major plant failure with radioactive leakage, it is essential to have access to current meteorological data to be able to forecast the propagation of the radioactive plume.

When researchers started to experimentally investigate atmospheric turbulence, fluxes of momentum, and sensible and latent heat in the early 1960s, they used smaller masts and towers with heights of up to 16 or 32 m. During the first experiments (e.g., [6.5]), profiles of wind velocity, air temperature, and humidity were measured at several heights to utilize the data for analysis of the turbulent transfer processes for heat and water vapor. In 1968 and 1973, the well-known Kansas and Minnesota boundary-layer experiments were conducted and, besides profile measurements, eddy-covariance instrumentation was also deployed on the measurement masts [6.6].

During the first decade of the twentieth century, an international cooperation was initiated to establish a weather monitoring network based on merchant and postal ships as moving platforms, making use of radio transmission techniques to communicate the observations and data to the national weather services in real time. Starting in 1941, the allies established a network of eleven stationary weather ships in the North Atlantic, which was active for 30 years. Beginning in the 1960s, the weather ships were increasingly pushed aside as weather satellites, long range aircraft, and weather buoys became more and more common. The last weather ship, the *Polarfront*, was suspended from service by the Norwegian government in 2009. During the Second World War, the German Navy distributed approximately 15 weather buoys using radio transmis-

sion (WFS buoys) in the North Atlantic. In regular intervals, these buoys were able to automatically surface from their underwater standby position to take measurements and transmit data to the navy weather service.

With this progress in meteorology and atmospheric sciences, a huge development in atmospheric measurement techniques and instrumentation followed. Measurements ought to expand in space and should at the same time increase their spatial and temporal resolution. This leads to an enormous demand for a variety of measurement platforms carrying all kinds of instruments. Ground-based measurement platforms can be categorized as follows:

- Weather stations: Instrument shelter 2 m above ground and masts up to 10 m high
- Stations to measure meteorological variables and turbulent fluxes at a single height or as profiles: Tripods, small poles, and masts for bare soil and low vegetation; tall masts and towers up to 100 m above ground for high vegetation
- Stations to deliver data for modeling (back) trajectories above the boundary layer and to measure trace gas and aerosol concentrations in and above the boundary layer: Tall towers 200–400 m above ground
- Stations to measure meteorological variables, turbulent fluxes, trace gases, and aerosols above water (lakes and open sea): Buoys and ships

6.3 Theory

A number of partly obvious difficulties and problems that can occur when using ground-based measurement platforms must be addressed to avoid artifacts in the results of the measurements by misinterpretation of the collected data. Masts and towers can influence the variables that in fact ought to be unaffectedly measured by the instruments attached to the structure. The first subsection will address such problems and present some guidelines and recommendations on appropriate measurement setups. When using buoys or ships to perform atmospheric measurements it is particularly necessary to correct the wind data for the movement of the platform itself. All ground-based platforms may be affected by oscillations, vibrations, and resonance phenomena triggered by wind or motion of the sea, which must be accounted for, especially in case of turbulence measurements. Wind-induced oscillations, on the other hand, can endanger the structure itself and may result in the collapse of the mast or tower [6.7].

6.3.1 Flow Distortion

The support structure for meteorological instrumentation inevitably distorts the microclimate and wind field nearby. The goal when establishing a measurement site is to reach an optimal solution that minimizes measurement biases while still providing a safe and reliable platform. Extensive theory and observations made in wind tunnels and in the field provide ample guidance on the magnitude and extent of flow distortion and modification of microclimates around structures.

Wind flow is impacted on all sides of a structure [6.8,9]. Based on field observations and wind-tunnel experiments with a scale model, a substantial downwind tower shadow effect with up to 40% interference within two structure diameters was reported [6.10]. In this case, the tower was an open structure triangular radio-type tower and not a solid structure. Some results suggest that the magnitude and

size of structure wake effects depend on wind speed. Increased turbulence at higher wind speed may limit the persistence of downwind wake [6.11–13]. A stagnation point forms on the upwind side of a structure where wind is blocked and flow streamlines diverge around the obstacle. Field observations and wind-tunnel models find wind speed reductions of up to 30% extending out to one structure diameter upwind of the platform [6.10, 12, 13]. Mass conservation causes wind flow to accelerate as it passes around an obstacle [6.14]. Observed wind speed increases in the range of 10–20% extending out to two structure diameters are reported for towers in the field and wind-tunnel models [6.10, 12, 13]. Wind flow is distorted above a structure as well as to the side. Some of the diverted flow goes up and over the structure rather than around the side [6.12, 13, 15]. As much as 40% acceleration of wind in the vertical axis at the upwind face of a large box-like structure was reported [6.12, 13]. Where there is flow distortion or wake turbulence, wind direction will be influenced as well, contributing both mean offsets and increased variability. Apart from the reduction of the mean wind speed, the spectra and cospectra exhibit a strong anisotropy for such cases. The results from [6.16] demonstrate the significant influence of a tower on turbulence spectra in the wake region of a meteorological tower. A major source of wind measurement uncertainty is due to complex wind flow distortion caused by the lattice geometries of masts. In [6.17], computational fluid dynamics and wind-tunnel experiments were used to study those effects to quantify this uncertainty and suggest guidelines for mounting instruments. The *European Wind Atlas* [6.18] also formulates clear selection criteria for high-quality wind observation sites and claims to avoid selecting stations where flow distortion or sheltering by nearby obstacles is suspected at the anemometer location.

6.3.2 Impact on Other Measured Variables

Platform structures can affect other meteorological parameters as well. Shadows and reflections alter light measurements. Similarly, differences in heating or cooling of the platform structure compared to the surroundings can influence long-wave radiation measurements. Anomalous heating and cooling of the platform structure will alter the temperature of air close to or passing through the platform structure. Shifts in temperature cause shifts in relative humidity. Furthermore, temperature and wind can directly interact with each other. Temperature differences near the structure will induce convective flows that introduce a vertical component

to wind measurement as well as distorting the vertical wind profile. The vertical components of wind that are induced by diversion around the structure will distort the vertical temperature profile.

On account of physical affects from platform structures that bias meteorological parameters, the best advice is to make the structure as small and open as possible. Available evidence suggests that sensors should be placed a minimum distance of two structure diameters away from the platform face. Being outside the region of flow disturbance should be sufficient to ensure unbiased temperature measurements. For smaller, lighter structures the two-diameter limit will be easier to achieve without imposing serious engineering challenges. Horizontal booms oriented into the prevailing wind direction are usually sufficient. Alternatively, anemometers could be installed at two opposing sides of a tower to allow selecting the data from the windward exposed anemometer only [6.1] (see Fig. 6.1). Note that because structures may induce vertical flows (also referred to as the chimney effect), vertical posts extending directly above a structure are not an ideal solution. On the other hand, the top of the structure is an ideal location for measuring downwelling radiation because there is nothing above to cast shadows. Sensors for measuring upwelling radiation will need to be positioned as far from a structure as possible in order to minimize the area of structure that is in the sensor field of view. Many radiation sensors combine the upward and downward components. They should be placed on the equatorward side of structure so the sun stays in front of the sensor and the structure is behind.

Oscillation and vibration platforms, outriggers, and booms can directly have a negative influence on the performance or operation of specific instruments due to resonance phenomena. Some gas analyzers have built-in rotating chopper disks that might resonate with platform vibrations and provoke malfunction of the instrument [6.19]. Thermocouples with very fine wires are susceptible to vibrations and can be damaged at specific amplitudes and oscillation frequencies [6.20]. The same applies to the filament of the infrared source of some gas analyzers. If tipping bucket rain gauges are not installed stiff enough on a tower, tipping might be triggered by strong or gusty winds. Turbulence measurements with fast sonic anemometers or sphere anemometers can be distorted by oscillations or vibrations of the instrument's carrier [6.21]. Generally, sensors mounted on towers will be subjected to wind-induced vibration, so it is important to make sure that locking nuts are used to secure the equipment [6.22].

6.4 Platforms and Sensor Installations

In the following subsections, various ground-based measurement platforms and their application areas will be described in detail.

6.4.1 Small Towers

To be able to obtain worldwide comparable meteorological data that can be used for a synoptic overview and as input for weather forecast models, it is essential to measure and collect the data as similarly as possible at all observation stations. For this reason the World Meteorological Organization (WMO) developed regulations and guidelines for the setup of weather stations [6.23] (see Chap. 43). These guidelines were adapted by the national weather services and implemented whenever the networks for manual and automated weather stations were established and extended.

A commonly accepted weather station consists of at least three ground-based platforms:

- An instrument shelter housing sensors for air temperature and humidity that protects the instruments from rain and solar radiation (see Fig. 6.2)
- A short pole carrying the rain gauge so that the receiving surface is 1 m above ground level (AGL) (AGL))
- A mast on top with a height between 10 and 12 m carrying sensors for wind velocity and wind direction

Today we have tens of thousands official and private weather stations worldwide, most of them long-term or permanent installations. In addition, a large variety of small masts and towers (< 100 m high) are deployed for atmospheric measurements ranging from short-term experiments to long-term observations.

Small towers are normally used to measure profiles of meteorological and air chemical parameters in the surface layer. This is done over bare soil or over low vegetation as well as in and above forests. Additionally, small towers are used to determine the different components of the energy balance equation of the underlying Earth's surface. For this, profiles of either temperature, humidity, and wind speed are captured (profile method, e.g., [6.24]), the Bowen ratio (e.g., [6.25–27]) is applied (see Chap. 57), or the eddy-covariance method (e.g., [6.28]) is utilized (see Chap. 55). Typically such masts and towers are also used as platforms for various spectrographic measurements, for carrying cameras to follow the phenological development of the vegetation, or to support laser scanners investigating the structure of forests.



Fig. 6.2 Instrument shelter and mast for wind measurements at the Hohenpeißenberg Meteorological Observatory (photo (enlarged detail) © Christoph Radtke)

Masts and towers have a wide spectrum of structural shapes, geometries, and materials used for their construction.

Poles and Tripods

The simplest ground-based measurement platforms are short vertical poles with or without supporting guys



Fig. 6.3 A temporary weather station on a tripod with instruments for wind velocity, wind direction, air temperature, and humidity as well as a precipitation gauge on a simple pole (photo © Olaf Kolle, MPI-BGC)

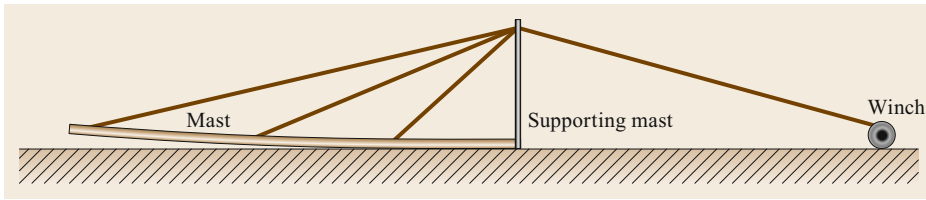


Fig. 6.4 Erecting short (and flexible) masts by folding up with a winch

or tripods to carry single instruments, Bowen-ratio systems, subcanopy eddy-covariance measurements or small weather stations as shown in Fig. 6.3.

Flexible Tube-Type Masts

Short masts up to approximately 16 m can be constructed of tubing made of steel, aluminum, or glass-fiber reinforced plastic (GRP) material as a single piece or as pluggable segments; a single wooden pole is also conceivable. The great benefit of the metal and GRP types is their small diameter so that any disturbance by the structure itself is minimized. As a function of height, diameter, material, wall thickness, load, and tolerable oscillation, such masts can be self-supporting or guyed. A common method to erect such short masts is shown in Fig. 6.4. Using a supporting mast and a swivel joint at the structure base, the mast is lifted up from the horizontal ground position to the vertical position by a manual or electric winch.

The thin tube-type masts shown in Fig. 6.5 cannot be climbed, so the instrumentation must be mounted to the mast in the horizontal position before erecting the structure. In this case, the attachment, the correct orientation, and the fault-free functioning of the instruments must be examined accurately beforehand. At a later stage, the devices attached to the mast can only be accessed after folding down the mast again.

Masts and Towers of Special Material

More solid and higher masts and towers are fabricated from steel, aluminum, or in some special cases from wood. To avoid corrosion, steel structures are commonly galvanized or coated with anticorrosion paint; stainless steel can also be used (see Fig. 6.6).

Metal structures that are located close to a coastline are exposed to salt aerosols and salty sea spray, which usually results in near-term damage such that a mast or tower may become unstable and inoperable. An appropriate alternative for such environmental conditions is a mast constructed from timber. Figure 6.7 shows a 30-m-high tower close to the shore of the island São Vicente (Cape Verde Islands) as an atmospheric measurement platform for the *Cabo Verde observatorio atmosférico Humberto Duarte Fonseca*. Initially, a metal tower (galvanized scaffolding material) was built, but unfortunately the corrosion was so intense that safety



Fig. 6.5 A line of thin tube-type masts during the LOTREX 10E (Longitudinal Land-Surface Traverse Experiment 10 E)–HIBE 88 (Hildesheimer Börde Experiment 1988) experiment (see also Sect. 6.8.2) (photo © Olaf Kolle, MPI-BGC)

could not be guaranteed after only two years of operation. Subsequently a walk-up tower made of timber with connecting and clamping elements of stainless steel was erected, which has been a long-lasting solution.

The shape of masts and towers is usually rectangular (Figs. 6.6–6.9), triangular (Fig. 6.10), or round (less frequent). Self-supporting structures must have a tapered shape in the vertical direction so that the bending moments can be absorbed adequately and the forces can be transferred into the concrete foundation. For guyed masts, a ballast bed of at least 0.5 m depth is sufficient.



Fig. 6.6 The 10-m-high, stainless-steel, and self-supporting mast on the roof of the Max Planck Institute for Biogeochemistry in Jena, Germany (photo © Olaf Kolle, MPI-BGC)



Fig. 6.8 A 15-m walk-up tower near Majadas (Spain) with eddy-covariance system and instruments for radiation and standard meteorological measurements (photo © Martin Hertel, MPI-BGC)



Fig. 6.7 A 30-m guyed-timber mast on the coast of São Vicente (Cape Verde Islands) (photo © Reimo Leppert, MPI-BGC)



Fig. 6.9 Installation of a 45-m walk-up tower in a beech forest in Thuringia, Germany (photo © Martin Hertel, MPI-BGC)

The adjustable legs of the mast should stand on wooden planks, concrete slabs, or special aluminum frames. The shape and dimensions of guyed masts are predominantly identical over the entire height of the structure. Rectangular masts are anchored in four directions and triangular ones in three directions. The anchoring

heights along the tower, the angles and tension of the guy wires, and the type and dimensions of the anchors may be prescribed by the manufacturer of the tower material or must be calculated by a structural engineer. The angles of the guy wires with respect to the horizontal should range between 30 and 60°. Strong soil pegs or special bolts for soil, rocks, or big blocks of concrete



Fig. 6.10 A 36-m triangular mast near Tanguro, Brazil, during the installation of isolated lightning protection wire (photo © Martin Hertel, MPI-BGC)

can be used as anchors. For a short-term installation, masts in forests may also be guyed to the base of trees.

Walk-Up Towers

Among the climbable masts and towers, we distinguish between so-called walk-up towers (Figs. 6.7–6.9), which have an integrated staircase, and structures that can be accessed only by a vertical ladder or by using the structural elements themselves for climbing (Figs. 6.6, 6.10). Walk-up towers consist either of identical segments that are stacked one upon the other or they are assembled by many individual pieces of scaffolding material. The base area of such towers is approximately $2.0\text{ m} \times 1.5\text{ m}$ and the individual aluminum segments are between 1.8 and 2.0 m high. For transport, the connecting bars are released and the segments are folded flat. This kind of tower can reach maximum heights of approximately 80 m.

A group of technically skilled and physically trained people is able to erect a 50-m-high segmented walk-up tower within three days. The segments are lifted with a crane that is gradually raised so that it is always on the top segment. If the tower is built in a forest, a crossbow with a fishing line attached to the arrow



Fig. 6.11 A 10-m tower of box-type aluminum profile on a wooden platform in a swampy area in Central Siberia close to the Zotino Tall Tower Observatory (ZOTTO) (photo © Martin Hertel, MPI-BGC)

can be used to find the path for the guy wires through the crowns of the trees (see Fig. 6.9).

Masts for Vertical Climb

Masts for vertical climb have a smaller base area with an edge length between 30 and 60 cm. In most cases, these masts are of triangular or rectangular shape and consist of segments 3–6 m in length. The typical triangular mast material shown in Fig. 6.10 is normally used to carry antennas for the mobile network.

The rectangular box-type aluminum profile of the tower shown in Fig. 6.11 is assembled from many identical aluminum sheets of $1.2\text{ m} \times 0.3\text{ m}$, which are bent by 45° along both long sides so that the sheets can be bolted together. The sheets are vertically shifted, which gives more stability to the whole structure. This type of tower is very well suited for remote areas because all parts can be transported in easy-to-handle boxes that are no longer than 1.25 m. Some disadvantages are the higher wind resistance compared to an open mast,



Fig. 6.12 A telescopic mast on an agricultural field near Gebesee, Germany (photo © Martin Hertel, MPI-BGC)

the more pronounced wind field distortion, and the influence on radiation fluxes, which can be reduced to some extent by coloring the surface. Furthermore, special mounting material is needed to attach outriggers and sensors.

To make the vertical climb more convenient and safe, it is strongly recommended to equip such masts and towers with a combination of rungs and safety rails as shown in Figs. 6.10 and 6.11.

Special-Purpose Masts

For special purposes, mobile towers and telescopic masts are available. The telescopic mast shown in Fig. 6.12 was used to be able to adjust the measurement height of the eddy-covariance system to maintain the flux source area independent of the height of the vegetation. Following a simple model, the measurement height can be increased while the plant cover is growing.

Mobile masts as shown in Fig. 6.13 can easily be moved between different deployment locations and are operational within a few hours. These devices are also usually telescopic masts mounted on a trailer. The masts



Fig. 6.13 A mobile mast with a maximum height of 25 m in the Spanish Dehesa (photo © Olaf Kolle, MPI-BGC)



Fig. 6.14 A 10-m mast with rotatable arm on top (photo © Olaf Kolle, MPI-BGC)

are lifted up either by a winch and a complex steel cable system inside the box profiles of the segments or by a hydraulic system. On telescopic masts, it is not possible to attach outriggers or instruments at any freely selectable height.

Figure 6.14 shows a special mast installation with a rotatable arm at a height of 10 m that carries a net radiometer and sensors for radiation measurements in narrow spectral bands with a small field of view. By rotating the arm in regular intervals the radiative properties of the tree and the surrounding grassland can be compared using the same set of instruments. An antenna rotator is used to turn the horizontal arm to any desired direction.

6.4.2 Tall Towers

Tall towers, which reach 200–325 m AGL, are predestined for investigation of the nocturnal stable boundary layer (NSBL) because they cover the corresponding layer. For studies of the convective boundary layer, a combination with additional systems is necessary (e.g., see Chap. 47). Furthermore, tall towers are very well suited to investigate issues related to wind energy (as most tall towers cover the hub height of the wind turbines) and the environment of forests. Finally, the

Table 6.2 Selection of tall towers for meteorological observations

Name of tower	City/Region	Country	Height (m AGL)	Year built	Research field
Amazon Tall Tower Observatory (ATTO)	Vila de Balbina	Brazil	325	2015	Climate studies and exploration of the rainforest biosphere
Zotino Tall Tower Observatory (ZOTTO)	Zotino	Russia	302	2006	For measurements of meteorological variables and of concentration of greenhouse gases and aerosols
Ochsenkopf TV Tower	Ochsenkopf	Germany	188	1958; measurements since 2003	For meteorological and trace gas measurements, ICOS Atmospheric Measurement Network
Jaslovské Bohunice Meteorological Tower	Jaslovské Bohunice	Slovakia	212	1986	Nuclear power plant
IAP (Institute of Atmospheric Physics, Chinese Academy of Sciences) Meteorological Tower	Beijing	China	325	1979	For meteorological measurements, studies of air pollution, and studies of the atmospheric boundary layer
Boulder Atmospheric Observatory (BAO)	Boulder	United States	300	1977 (out of service since 2016)	Planetary boundary layer studies and testing and calibrating atmospheric sensors
Cabauw Tower (KNMI)	Cabauw	Netherlands	213	1972	For meteorological research
Karlsruhe Institute for Technology Integrated Atmospheric Observation System (KITcube)	Karlsruhe	Germany	200	1972	For meteorological and climatological research
Obninsk Meteorological Tower	Obninsk	Russia	310	1958	For meteorological and radioactivity measurements

towers are often used to test novel remote-sensing systems. Table 6.2 summarizes some of the tallest towers and their fields of research. Some of them are discussed in more detail below.

Amazon Tall Tower Observatory

The Amazon Tall Tower Observatory (ATTO) is a scientific research facility located in the Amazon rainforest of Brazil that has a 325-m-high lattice structure shown in Fig. 6.15 [6.29]. Also part of the research site are two smaller 80-m towers, one of which is a rectangular scaffolding walk-up tower and the other a triangular mast [6.30]. The official start of the project was in 2009, the foundation stone ceremony for the tall tower was in August 2014, and the structure was completed in August 2015. The ATTO tower, currently the highest structure in South America, it is located 150 km northeast of Manaus at 2.1458694° S, 59.0055889° W, and 80 m above main sea level (ASL). The major research goals of this observatory are:

- To collect data that improves our knowledge of the influence of the huge rainforest area on the climate (atmosphere–biosphere model validation)
- To locate and understand sources and sinks of greenhouse gases such as CO₂, CH₄, and N₂O
- To investigate aerosol formation, which is important for cloud formation

- To investigate transport processes of air masses over large distances of several hundred kilometers (atmospheric chemistry monitoring)
- To investigate smaller-scale transport processes within the turbulent boundary layer

The rectangular tall tower, with an edge length of 3 m, is guyed in four directions at six levels. Twelve measurement levels, each with a narrow balcony and a 4.5-m-long folding outrigger, are distributed along the tower at heights of 42, 81, 99, 126, 150, 171, 195, 222, 246, 273, 297, and 321 m AGL. The outriggers point in the northeast direction because this is the prevailing wind direction and in 80% of all cases the wind is coming from the sector ± 90 degrees relative to the outrigger direction. To also be able to catch the remaining 20% of weather situations, there is one additional measurement level at 192 m where the outrigger points in the opposite direction towards the southwest.

At all levels, temperature-humidity sensors and 3-D sonic anemometers are installed. Additional flux measurement systems for CO₂ and H₂O are available at 83 m AGL and on both outriggers at around 195 m AGL, where two net radiometers with short- and long-wave incoming and outgoing radiation components as well as sensors for photosynthetically active radiation are installed. Air inlets for instruments sitting inside containers at the tower base for measurements of aerosols (two



Fig. 6.15 The ATTO tall tower near Manaus, Brazil (photo © Martin Hertel, MPI-BGC)

lines), greenhouse gases (six lines), and reactive gases (three lines) are distributed along the tower at different levels. Due to the gap in the forest at the tower base it makes no sense to continue the profile measurements below the 44 m level. Therefore, more densely staggered profile recordings of meteorological variables, trace gas concentrations, and fluxes are continued on the 80-m scaffolding tower close by because there is virtually no disturbance of the forest structure. In the center of the tower, there is a lift shaft for a freight elevator that can carry up to 250 kg. A novel battery-powered personnel lift for operational work (HighStep Systems) can bring an individual to the top of the tower within 13 min.

Zotino Tall Tower Observatory

The Zotino Tall Tower Observatory (ZOTTO) is a climate research facility located in the Siberian Taiga close to the village Zotino, which is situated at the shore of the Jenissei river approximately 600 km north of Krasnojarsk [6.31]. The research station has been operational since October 2006. The coordinates of the facility are 60.7983920° N, 89.3535260° E and the



Fig. 6.16 The ZOTTO tall tower near Zotino, Central Siberia (photo © Michael Hielscher, MPI-BGC)

tower base is at 120 m ASL. The tall tower is a triangular guyed structure consisting of discrete segments, each 6.5-m long, with a total height of 301 m AGL (see Fig. 6.16). The edge length is 3 m, the segments are made of welded steel tubes, and they are connected to each other by bolted flanges. Vertical ladders lead to the top and every 13 m on a small platform the ladder segments are horizontally displaced; there is no elevator.

The major research goals of this observatory are similar to those of ATTO (see above), but in a very different climate zone and above a different ecosystem. Measurement platforms with a balcony are located at 4, 52, 92, 158, 227, and 301 m AGL. At these levels, continuous high-precision gas concentration measurements of CO_2 and CH_4 , as well as meteorological measurements (air temperature and humidity, 3-D turbulent wind field, and partly air pressure), are implemented. Air inlets for aerosol and CO measurements are installed at 301 and 52 m AGL, but only at 30 m for ozone and NO_x .

Ochsenkopf (Integrated Carbon Observation System Atmospheric Measurement Network)

The Ochsenkopf TV Tower shown in Fig. 6.17 is a reinforced concrete structure built in 1958 on top of the Ochsenkopf Mountain in the Fichtelgebirge at an elevation of 1024 m ASL and at 50.029888° N, 11.808337° E. The tower is 188 m high and in 2003 the Max Planck Institute for Biogeochemistry equipped it with instruments as part of the Tall Tower Atmospheric Gas Measurements framework.

Gas analyzers for continuous trace gas measurements and a flask-filling facility have been installed in a container at the tower base. Meteorological variables are measured continuously at a height of 163 m AGL. After a measurement technology upgrade, the site was integrated into the Integrated Carbon Observation System (ICOS) project (see Chap. 64).



Fig. 6.17 The Ochsenkopf TV Tower, where the German Meteorological Service (DWD) operates an ICOS atmospheric measurement facility (photo © Falk Hänsel, MPI-BGC)

Boulder Atmospheric Observatory

The 300-m-high Boulder Atmospheric Observatory (BAO) tower—an open lattice structure built in 1977—

was located on gently rolling terrain 25 km east of the foothills of the Colorado Rockies 1584 m ASL at 40.0500279° N, 105.0038355° W [6.32] (see Fig. 6.18). It was installed to serve as a research facility for studying the ABL and calibrating and testing meteorological sensors (e.g., [6.33]). It served the needs of a broad range of users. The tower was decommissioned in July 2016. On the tower, the instrumentation for measurements of mean and turbulent parameters was distributed at 10, 22, 50, 100, 150, 200, 250, and 300 m AGL [6.34]. Due to the tower's height, its top almost always extended above the nocturnal ABL, thus enabling observations of turbulence structure in stable layers [6.35]. Another research topic, also related to stable stratification, was the investigations of gravity waves and turbulence [6.36] and gravity wave climatology [6.37]. As the top of the tower nearly extended above 25% of the daytime convective boundary layer (CBL) [6.34], convective properties could be investigated as well like the diurnal behavior of boundary-layer winds [6.38]. A summary of the most important experiments conducted at BAO appears in [6.39].

Karlsruhe Institute for Technology Integrated Atmospheric Observation System (KITcube)

The Karlsruhe Institute for Technology (KIT) meteorological tower (see Fig. 6.19) was built in 1972 and is part of the KITcube observation system [6.40], which consists of a transportable [6.41] and fixed part. The measurements started in December 1972 and have been running to this day without any long breaks. With a height of 200 m AGL, this observation platform is among the largest meteorological towers in Europe. The

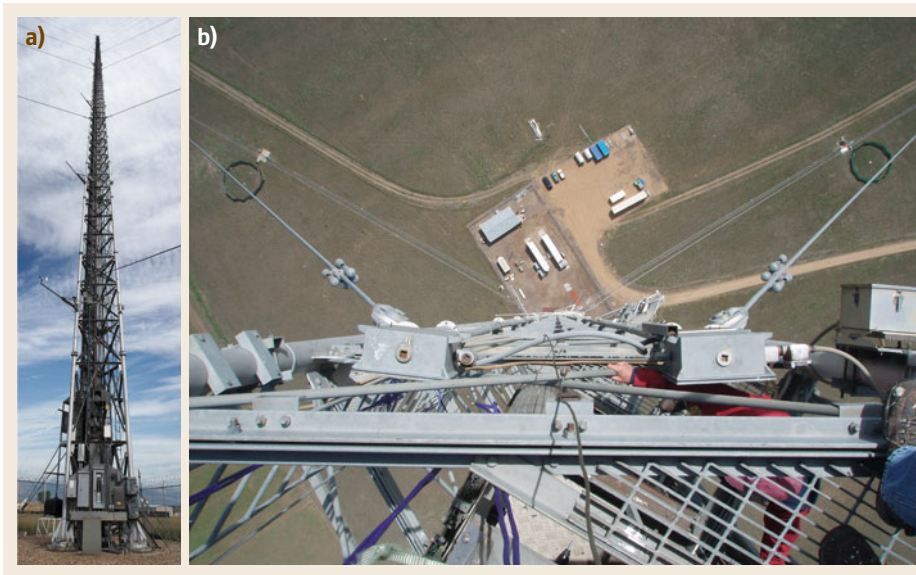


Fig. 6.18 (a) The Boulder Atmospheric Observatory with a 300-m triangular-segmented tower (photo © Shelby Frisch, NOAA Earth System Research Laboratory); (b) View from tower top to ground facilities (photo © Jon Kofler, NOAA/ESRL Global Monitoring Division)



Fig. 6.19 The Karlsruhe KITcube tower, where anemometers are installed at the two prevailing wind directions to minimize the effect of wind distortion on the measurements (photo © Stephan Kraut, KIT)

lattice tower is situated at 49.0925° N, 8.4258333° E, and 110.4 m ASL in the upper Rhine Valley in the southwestern part of Germany [6.1, 42]. The tower is equipped with sensors to monitor profiles of temperature, humidity, wind speed, and wind direction. Booms for the sensors are at 20, 30, 40, 50, 60, 80, 100, 130, 160, and 200 m AGL. Sonic anemometers at three heights (40, 100, and 200 m AGL) provide turbulence information. Additionally, air pressure, short- and long-wave radiation components, and precipitation are measured on a meadow close by. To avoid wind measurement disturbances due to the structure of the tower, the wind measurements at each level, except for those at the lowest and uppermost levels, are carried out on two different booms, one oriented to the west, the other to the east. Depending on the mean wind direction, the measurement from the respective windward direction is taken to calculate the mean wind speed.

The tower is used for climate studies [6.1], investigation of phenomena in the boundary layer, like counter currents in broad valleys [6.42], and for validation of remote-sensing instruments like sodar (sonic detection and ranging) or Doppler lidar (light detection and ranging) systems [6.43].

Koninklijk Nederlands Meteorologisch Instituut (KNMI) Cabauw Tower

The Cabauw Tower is part of the experimental site for atmospheric research (CESAR [6.44]) observatory, which is located in the western part of the Netherlands. The coordinates of the tower are 51.9711111° N, 4.9266667° E, and the foot of the tower is at 0.5 m below mean sea level. The surroundings are flat with surface elevation changes of at most a few meters within a radius of 20 km consisting of meadows and ditches, with scattered villages, orchards, and lines of trees. The tower was built in 1972 and was first described in [6.45]. Booms for temperature, humidity, or wind are at 0, 0.6, 2, 10, 20, 40, 60, 80, 140, 180, and 200 m AGL. Short-wave radiation is measured at the tower's top (214 m AGL). Additional information about the facilities can be found in [6.46]. Close to the tower, micrometeorological measurements of the energy balance components, including soil temperatures and various radiation measurements, complement the tower observations. The tower is operated to study relationships between land–surface properties, the state of the ABL, and general weather conditions. For example, in [6.47] the tower data were used for the validation of a model determining the growth of the ABL height. A comparison of resistance laws with observations for the height of the stationary boundary layer during stable lapse rate conditions from the Cabauw tower has been described in [6.48]. The tower also serves as a reference for the comparison of ABL diffusion schemes and air pollution models [6.49, 50]. Figure 1.9 shows the footprints of tall towers in Europe.

6.4.3 Buoys and Floats

A buoy is a buoyant floating device that can have many purposes. Buoys can be moored or they can drift on the ocean surface, sea ice floes, or icebergs. Drifting and moored data buoys are now generally accepted and getting widespread application as a very cost-effective means for obtaining meteorological and oceanographic data from remote ocean areas. Data buoys measure and transmit data automatically in near real time via satellite telecommunication systems such as Argos, ORBCOMM[®] (International company for Asset Tracking, Monitoring and Control), and Iridium. Observations with data buoys make significant contributions to our ability to understand, describe, model, and predict global weather, as well as to monitor surface weather and climate on all time and space scales. The data collected are used to validate data from other platforms, such as from ships or weather satellites. By transmitting data via the Global Telecommunications System (GTS), automatic buoys are used for data assimilation in forecast models.

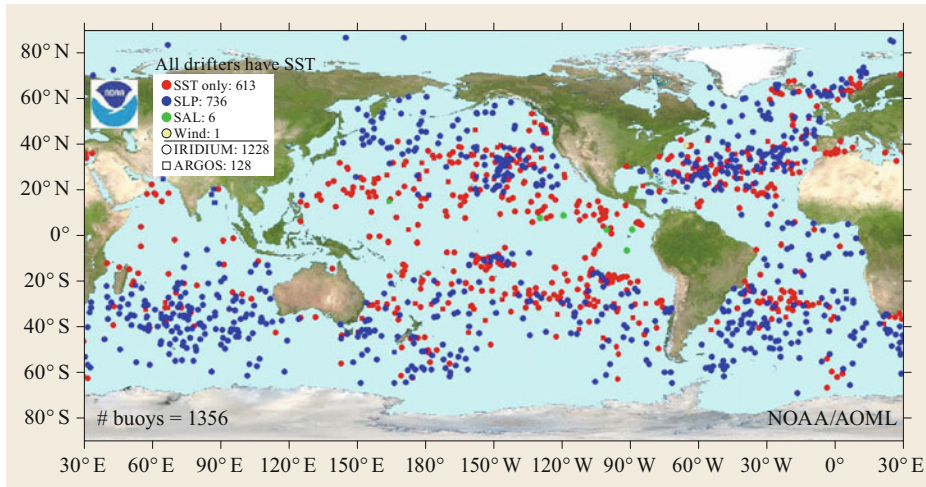


Fig. 6.20 A global composite of drifting buoy locations on an arbitrary day (13 May 2019). It covers the subset of drifters with meteorological sensors and documents the large international efforts in maintaining a global observation network with major gaps only in the polar regions and certain tropical parts of the oceans (adapted with permission from NOAA/AOML)

Many different types of drifting buoys and moored buoys (see Table 6.5) have been deployed and national activities are coordinated by various international organizations and working groups, such as the Data Buoy Cooperation Panel (DBCP), the International Arctic Buoy Program (IABP) and International Programme for Antarctic Buoys (IPAB) of the World Climate Research Programme (WCRP), the Global Drifter Program (GDP), and associated data centers. Figure 6.20 shows a typical example of the global composite of drifting buoy locations.

Drifting Buoys

Drifting buoys on the open ocean measure ocean surface and atmospheric conditions. Drogues or subsurface sails are attached to them to get a drift representative of the upper ocean current at a depth of about 10 m. Buoys that track surface currents are called Lagrangian drifters. They can be deployed easily, are cost-efficient, and easy to operate for an average lifetime of 18 months [6.51]. Buoys that track surface currents in this way track ocean currents at the depth corresponding to the length of their drogue while collecting surface and subsurface measurements. They have been used for a long time in oceanography and marine meteorology. There have also been many types of drifting buoys used for meteorological purposes since the First GARP (Global Atmospheric Research Program) Global Experiment (FGGE) in the 1970s. Lagrangian drifters were first designed and deployed in the world oceans in the context of the Surface Velocity Program (SVP) of the World Ocean Circulation Experiment (WOCE), which

became the GDP. The Data Buoy Cooperation (formerly Data Buoy Cooperation Panel DBCP) [6.51] was established decades ago to design standardized drifting buoys to fulfill observational requirements for meteorological and oceanographic applications. The SVP drifters were standardized in 1991, with small spherical hulls and floats, and a large drogue centered at 15 m below the surface. In 1993, drifters with barometer ports, called surface velocity program barometer (SVPB) drifters were tested in the high seas and proven reliable. The Lagrangian barometer drifter, designed by the GDP, is now commercially available at low cost and meets both oceanographic requirements (research: measurements of sea surface currents and sea temperature) and meteorological requirements (operational: sea surface temperature and air pressure).

Ice Buoys

Ice buoys, as shown in Fig. 6.21, have been used to some extent in Arctic and Antarctic regions to track sea ice or iceberg movement and are available commercially for deployment by ships or aircraft. Such buoys are equipped with low temperature electronics and lithium batteries that can operate at temperatures down to -50°C . In addition to the original locations from the Argos satellite system (accuracy ≈ 350 m), modern ice buoys are equipped with receivers for satellite navigation systems, which can compute the positions more accurately (better than 50 m). Buoy positions are determined from Doppler shifts of transmitter signals observed from different satellite positions (see Fig. 6.22). The accuracy of the position depends on transmitter sta-



Fig. 6.21 An antarctic sea ice buoy deployed during the 1989 Winter Weddell Gyre Study by Alfred Wegener Institute Bremerhaven/Univ. Hannover. It takes meteorological observations with a propeller/wind vane anemometer on a 3-m tripod, air pressure, air temperature, and ocean mixed-layer temperatures with a 200-m-long thermistor chain beneath the 2-m-thick ice flow, and sea ice temperature profiles with a thermistor rod (photo © D. Engelbart)

bility and satellite constellation geometry. Buoy data logging systems collect and average the sensor data, usually over 10 min, and transmit them to polar-orbiting satellites every 60 or 90 s. Depending on latitude and area of coverage during the satellite overpass, 16 to 22 independent data transmissions are available for each platform per day. Only the data set with the largest number of identical transmissions within a satellite pass is saved in preprocessing the data [6.53].

Atmospheric pressure is measured with various buoy devices, including aneroid cells, beam balance quartz crystal transducers, and piezoresistive transducers. The inlet or pressure port allows the ambient pressure to be transmitted freely into the sensing element. The error or pressure change is related to the shape and configuration of the inlet. In most cases, the pressure error is related to the square of the wind velocity. Atmospheric pressure measurements from a small drifting buoy in the open ocean are difficult to obtain due to natural atmospheric pressure variation, wind interaction with the sensor, sensor error, sensor calibration, long-term drift, telemetry bit errors, and other factors.

Air temperature measurements are typically conducted with a thermistor contained within a radiation-shielded housing about 1 m above the ocean surface. Thermistors also measure sea surface temperature. A source of error is the heating effect produced when solar and infrared radiation strike the air temperature transducer. This error can be significant during direct insolation and low winds, but can be reduced by improving radiation shields or, when battery capacity allows for it, by using forced ventilation during sunshine.

Moored Buoys and Wave Buoys

In contrast to drifting buoys, moored buoys are anchored at fixed locations and collect a larger variety of atmospheric and oceanographic variables (Fig. 6.23). Their data are used for data assimilation in numerical weather prediction and for maritime safety needs. Be-

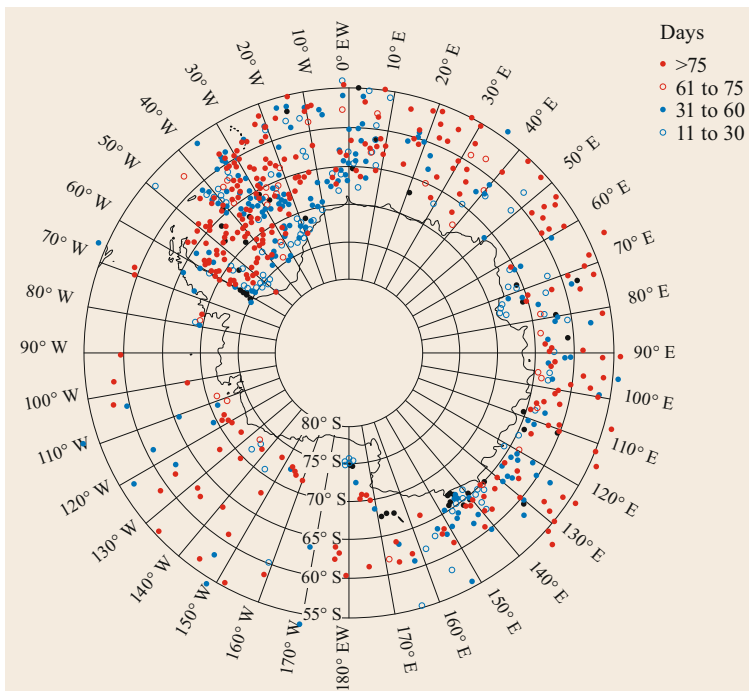


Fig. 6.22 Locations of buoys drifting on Antarctic sea ice at quarter-year resolution, from 1986 to 2001. Symbols give the numbers of days a buoy was active within the three months (after [6.52])

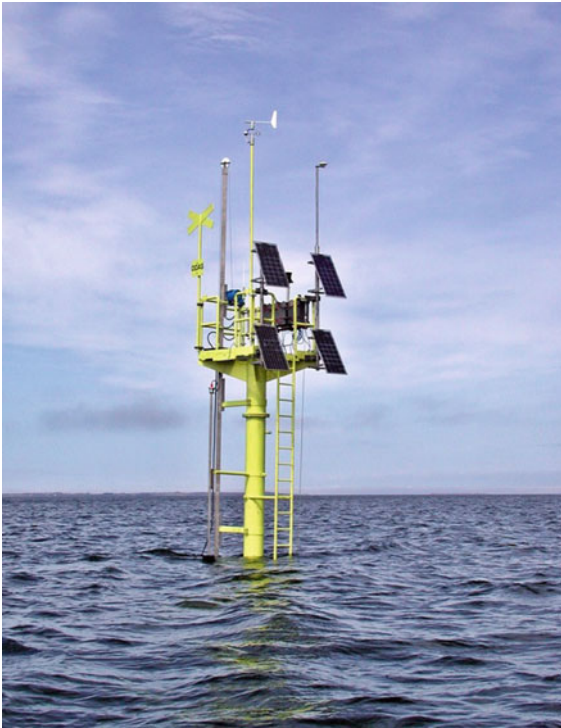


Fig. 6.23 The meteorological/oceanographic station anchored offshore Hörnum/Sylt in the North Sea. Powered by a solar panel, it takes wind, temperature, radiation, turbidity, and salinity observations (photo © H. Garbe, Helmholtz-Center Geesthacht)

cause of their size and instrumentation, moored buoys are large and expensive. Their size can vary from a few meters in height and width, to over 12 m [6.51]. Variables being measured are surface variables (wind speed and direction, air and sea surface temperature, salinity, and air pressure), as well as subsurface temperatures down to a depth of suspended cables of up to several hundred meters. Data are usually collected through one of the Argos, Iridium, polar orbiting (ORBCOMM[®]), or geostationary satellites, transmitted in real time and shared on the GTS of the World Meteorological Organization (WMO). They have a typical maintenance interval of one year and their construction, in particular the tether line keeping the buoys at a constant location, must be very robust to withstand storms or high seas. Many different designs exist for moored buoys depending on the ocean application purposes and the environmental influences on operations.

Because of limited data transmission, the fixed buoys often store more data on board than they send in real time. When a moored buoy is recovered, the data are processed offline by the operators. A major part of the DBCP's moored buoy network is the Tropical Moored Buoy Implementation Panel array, which con-



Fig. 6.24 A Technical University of Dresden measurement float with eddy-covariance sensors on a reservoir during the project Greenhouse gas emissions from reservoirs (TREGATA) (photo © Dr. Uwe Spank)

sists of arrays of moorings in each ocean basin and is used to monitor large-scale phenomena such as El Niño and the Southern Oscillation, showing the importance in the annual variability of global climate [6.51].

Many types of wave buoys exist to capture and model information about ocean dynamics on the surface. These buoys measure the frequency and size of wave energy (known as the spectra) from which significant wave height, dominant wave period, and average wave period are derived. Even the direction of wave propagation is measured on many moored buoys. This information can be used to greatly improve the predictions of and warnings for dangerous storms.

Platforms and Floats

For measurements on shallow lakes with short fetches, platforms and floats (also called pontoons) are often deployed. The short fetch is necessary to reduce the wave height; however, the footprint of the measurements should be within the fetch. Platforms are fixed at the bottom of the lakes. Floats are airtight hollow structures assembled to rectangular or triangular structures (Fig. 6.24). The floats are fixed in the ground with at least one anchor. The movement of the floats due to waves and wind must be controlled and the measurements must be corrected if required. In the past, floats were often used for evaporation pans; more recently, they have been equipped with several instruments for measurements in air and water including eddy-covariance measurements. An overview of experiments with floats is given in [6.54].

6.4.4 Infrastructure

Before any ground-based measurement platform is installed, all relevant national and local regulations must be taken into consideration and all required approvals must be obtained from the competent authorities or any other relevant parties such as property owners. For masts and

towers, a building permit might be needed depending on the height of the structure and the planned duration of the installation. Tall towers and buoys must be equipped with appropriate beaconing following international and national regulations for aviation or shipping.

It is now necessary to define the power supply system(s) for an installation, which should be selected based on the availability of power sources and the energy demands of the measurement systems including all accompanying infrastructural elements. If line power is not directly available nearby but the power demand is high (> 1 kW), the cost–benefit ratio, environmental protection and aspects of sustainability should be arguments for the decision between a connection to the closest line power distribution or a self-sufficient power supply system. Installing an underground power line over a distance of four to five kilometers can cost up to 100 000 €; an overhead line would be cheaper but is more prone to damage. The following power supply systems are commonly used as energy sources for ground-based measurement platforms:

- Line power from public electricity supplier: from conventional power plants or renewable energy; up to many kW; maintenance-free.
- Local power generator based on petrol, diesel, or propane/butane engine: up to several kW; emission of exhaust gases might be an issue for the measurements; noise emissions; intensive care and maintenance required; regular costs for spare parts or complete replacement. In large installations, two or even three identical systems are needed to avoid power interruption.
- Solar energy based on photovoltaic modules: up to a few kW (increasing space requirements); shading should be avoided; strong gradient in yield rate from high latitudes to low latitudes; no emissions; maintenance-friendly (cleaning; replacement of broken/damaged modules); long lifetime. Batteries of sufficient capacity are needed to store surplus energy that will bridge the nights and cloudy phases.
- Fuel cells: preferably operated with methanol as liquid fuel, which is easy to handle and can be shipped worldwide inside approved canisters; up to 500 W; emission of CO_2 can potentially bias the measurements. Batteries of sufficient capacity continuously power the measurement system and are recharged by the fuel cell every time the batteries are discharged to a certain extent. Cell lifetime is limited to a few years.
- Small wind energy systems: up to 1 kW; only useful in areas with reliable wind and mostly used as additional support for other systems.
- Batteries only: must be manually replaced in regular intervals; recommended only for systems with very low power consumption (< 1 W) and where regular and easy access to the site is ensured.

Often it is necessary to combine different types of power supply systems to guarantee an energy supply as reliable as possible. It is common to combine a solar energy system (third bullet point in the left column of this page) with a power generator (second item) that automatically starts operation every time the batteries are discharged to a certain extent and no solar energy is available. Also, a system comprised of solar energy modules (third item) and a fuel cell (fourth item) is very efficient and reliable (see Fig. 6.13). To avoid measurement system shutdowns in the case of short power interruptions, uninterruptible power supply (UPS) systems are recommended, at least for the most sensitive instruments and to automatically and orderly power down computers. It is recommended to set up the measurement system in a way that all instruments, computers, and data acquisition restart properly without taking action manually.

To have full access to the instruments and data acquisition systems (computers or data loggers) the site must be connected to the Internet. This can be obtained by landline connection, mobile network, or satellite, which can be cost intensive if large data volumes must be transmitted. In very remote places, including the oceans, it might be appropriate to only set up a one-way connection to transmit the collected data to a base station following a fixed schedule. Besides the satellite systems already mentioned in Sect. 6.4.3, the geostationary satellites of the British Inmarsat communication company provide worldwide Internet access except in the very high latitudes; the US provider HugesNet offers high-speed Internet access covering the Americas.

To avoid damage to the instrumentation, data acquisition systems, and communication systems by thunderstorms, it is essential to install an appropriate lightning protection system. Such systems can be a simpler design with less protection or more complex, which requires the following levels and elements of protection:

- External lightning protection:
 - Lightning rods on top of the structure and potentially on outriggers to capture the lightning
 - Lightning conductor that can be the metal tower itself or an isolated conductor at some distance (≈ 1 m) from the structure
 - Proper grounding via deep earther, ring earther, or foundation earther depending on specific application
- Internal lightning protection (inside the building or inside the electrical cabinet):
 - Sufficient distance between conductors
 - Proper shielding and earthing of cables and electronic devices

- Surge protection for all wires that enter from outside

Any lightning protection always acts only as a reduction of the risk of severe damage; protection will never reach 100%.

All instruments and electronic devices are limited to an operational temperature range and the environmental temperature should not exceed this range to ensure proper functioning of the equipment. In many cases, it is sufficient to use fans and small heating or cooling devices for this purpose. High-precision gas analyzers or other temperature sensitive instruments may require highly stable ambient conditions that can only be achieved by using self-regulating air conditioning systems and adequate insulation. Underground installations of laboratory containers and the use of heat-exchanger tubes deep below the surface can significantly contribute to stabilizing the laboratory temperature and reducing the energy required to operate air conditioning systems.

For all towers that can be climbed, proper and correct safety measures for the personnel working on the structure must be implemented. The safety devices must at least meet the national safety regulations, but it is reasonable to deploy a safety setup that is compliant with the requirements of all nations from which people are accessing the mast or tower. Towers that are climbed vertically by a ladder should be equipped with a safety rail or safety rope with fall arresters. If not present, personal protective equipment with a Y-type shock absorber must be used while climbing the mast. Signs must indicate potential risks and point to basic procedural rules.

To protect the installations from damage by bigger animals such as cows, sheep, and elephants, it is very important to use fences that are strong enough or even electrified to prevent animals from entering the vulnerable area. A fence is also recommended to safeguard the installations against vandalism and to avoid self-endangerment of curious people. Any electrical or other control cabinets should be secured against smaller animals such as mice, termites, wasps, snakes, and spiders because they may damage cables and electronic devices and pose a potential risk for people accessing the cabinets due to toxicity.

At larger tall-tower installations in remote areas, it is necessary to establish facilities such as accommodation, laboratories, office containers, a kitchen, toilets, and showers. Internal communication devices between the tower and the camp or along the tower are needed as well as an external means of communication such as satellite telephones, especially to organize help in emergency situations. A rescue concept must be established as complete chains, e.g., starting from rescuing a person in trouble from the tower, followed by an ini-

tial treatment by trained personnel, and ending with the evacuation of the person if necessary.

6.4.5 Relevant Sensors for Different Platform Types

The selection of sensors for any ground-based measurement platform is, besides many other criteria, dependent on weather, climate, the environment in general, and thus on the location of the platform itself. The sensor specifications must meet the environmental conditions especially with regard to temperature and humidity ranges for operation of the sensor. In most cases, in particular for continuous long-term measurements, sensors must be optimized for outdoor use (complies with protection class IP65 (dust-tight and protected against water jets) or better [6.55]). Sensors and connectors must be waterproof against heavy rain and the instruments should provide valid measurements even in rainy conditions (important for sonic anemometers). If the weather conditions regularly stimulate the accretion of ice on the structure and sensors, then instruments with integrated heating should be chosen. It may also be an option to equip a sensor with homemade heating. In situations with ice formation, sensors and sensor mounts must be robust enough to take the additional loads [6.56]. Sensors and cables should be resistant to UV radiation, especially if the site is located in the tropics or subtropics. Sensors and connectors used on platforms close to the shoreline or on ships and buoys in seawater must be highly resistant to corrosion; often only custom-built sensors or special versions meet such requirements.

On masts and towers, not only in areas with a high thunderstorm frequency, it is recommended to mount the sensors isolated against the structure and connect the instrument body with a thick grounding cable to a common earthing point. Instruments and sensors with high-grade integrated surge protection are preferred over ones with less or no overvoltage protection.

At some sites, birds use the mast or tower and the sensors in particular to rest or look out. Sensors for downwelling radiation can't be protected against birds



Fig. 6.25 An automatic bird scarer for radiation instruments (photo © Nadine Hempel, MPI-BGC)

with fixed metal spikes because of shadowing effects. A useful installation is a thin metal stick attached to an enclosed electric wiper motor (see Fig. 6.25) that swings forth and back approximately 120° every minute during the daytime.

Small-sized vertically movable platforms automatically travelling up and down a tall tower, drifting buoys,

or any other moving platforms must be equipped with instruments and sensors with small time constants to ensure a measurement signal that represents the true conditions along the motion path as much as possible. Longer time constants lead to delayed signals and smoothed data series, which can numerically be traced back to the true signal only to a certain extent (see also Chap. 50).

6.5 Specification

Table 6.3 summarizes the most common types of small masts and towers, their approximate maximum heights, and further specific information. The first five types of masts, which are all cable-stayed, do not necessarily require a concrete foundation, but measures must be taken to ensure the stability of the mast or tower basis and to avoid subsidence effects. Any self-supporting structures will require a concrete foundation. For almost all masts

and towers, the use of personal protective equipment to prevent falls is mandatory while climbing, except for larger structures where an inside staircase exists. Nevertheless, the use of protective equipment is also strongly recommended in this case.

In Table 6.4 the most relevant types of tall towers including examples and further specifications are listed. Tall towers are sometimes equipped with an el-

Table 6.3 Small towers for meteorological and eddy-covariance measurements

Type of tower	Maximum height (m)	Guyed	Climbable	Secured climbing	Instrument installation
Pole and tripod	≈ 3	Yes/No	No	NA	At ground
Thin tube round closed	≈ 20	Yes	No	NA	At ground
Telescopic rectangular/round closed	≈ 30	Yes	No	NA	At ground
Segmented, small triangular/rectangular open	≈ 80	Yes	Ladder or structure	Yes	On mast
Segmented or single elements, small rectangular/round closed	≈ 50	Yes	Ladder	Yes	On mast
Segmented, large rectangular open	≈ 80	Yes	Stairs	No	On mast
Lattice structure or in one piece conical shape open	≈ 30	No	Ladder or structure	Yes	On mast

Table 6.4 Tall towers for meteorological, eddy-covariance, and trace gas measurements

Type of tower	Typical height (m)	Guyed	Climbable	Secured climbing
Segmented (e.g., ZOTTO) triangular/rectangular open	150–350	Yes	Ladder or stairs	Yes/No
Lattice structure (e.g., ATTO, KIT) triangular/rectangular open	150–350	Yes	Ladder or stairs	Yes/No
Tube type (e.g., Obninsk) round closed	150–350	Yes	Ladder	Yes
Concrete (e.g., Ochsenkopf) conical shape closed	150–350	No	Ladder	Yes

Table 6.5 Characteristics of different buoy types. In general there exists a wide range of different specifications and sensors

Type of buoy	Robustness needed against	Material	Typical dimensions (m)	Lifetime (y)	Maintenance visits (y ⁻¹)	Climbable
Drifting ocean buoys	Wave motion, sea spray	Steel	W: 1–2, H: 1–5	1–3	Not accessible	No
Drifting ice buoys	Ice pressure, low temperatures	Steel, plastic	W: 1, H: 1–3	0.5–3	Not accessible	No
Moored buoys	Waves and sea spray	Steel	W: 3–8, H: 1–10	5	1–2	Yes
Wave buoys	Waves and sea spray	Steel	W: 1–3, H: 1–3	5	1–2	Yes/No
Floats	Waves and sea spray	Steel, plastic, wood	W: 3–5, H: 1–3	10	Can be frequent	Yes/No

evator, which might only be a freight elevator or also suitable for transporting people; special lifts for transporting a single person also exist (see Sect. 6.4.2).

Table 6.5 summarizes the most common buoy types, which in many cases are deployed in harsh environ-

mental conditions. The buoy housings and instrument materials must be robust, especially against sea spray, but also against cold conditions. If accessible, regular and accurate maintenance can help extend the limited lifetime of this kind of measurement platform.

6.6 Quality Control and Safety

All relevant national and, in special cases, international safety regulations and quality requirements for setting up the particular structure must be met. During the planning phase for a mast or a tower, structural calculations may be needed to determine the overall stability of the construction and the admissible additional loads due to wind and weight. This defines the area and weight of instruments, devices, cables, tubing, etc., that can be installed on and attached to the mast or tower. The environmental conditions at the site where the structure will be built must also be considered. It might be necessary to select specific or special material and selective combinations of materials for the structure and various extensions because of high corrosion potential (for locations close to coastlines) or large differences between the possible temperature extremes such that diverging expansion coefficients of different materials would cause problems. Special measures must be taken if the site is located:

- In an area with high earthquake potential
- In a region where extremely high wind velocities may occur (tornadoes, hurricanes)
- Where the potential for inundations is high or where recurring flooding occurs
- In a region with high thunderstorm frequency (see Sects. 6.4.4 and 6.4.5)
- In a region with cold climatic conditions where severe ice buildup may occur [6.56]
- Where strong electromagnetic radiation may result in technical faults of the measurements, e.g., when instruments are installed on a transmission mast or close to other sources of electromagnetic fields [6.57]

6.7 Maintenance

All ground-based platforms must be maintained in regular intervals. Depending on the dimensions of the structure, the environmental conditions the platform is exposed to, the complexity of the installations, and the potential risk to life but also to valuable objects, maintenance ranges from a simple visual inspection to a time-consuming prescribed service procedure by ex-

A concept for a highly reliable power supply with almost 100% availability is, as part of the infrastructure (see Sect. 6.4.4), essential for the quality assurance of ground-based measurement platforms. All elements, devices, instruments, and other items that are attached to the tower must be thoroughly secured against falling to minimize the risk of serious injury to persons working on the ground or on the tower.

For the overall quality of a ground-based platform, a key criterion is also the scientific usability of the measurements obtained using the particular structure. The selection of the terrain, the climate zone, and the ecosystem, together with the footprint area [6.1] for the measurements, are the most important site factors. On one hand, these are determined by scientific issues, but on the other hand they determine the long-term perspective and usability of an installation.

When a tower or mast is in standard operation, retroactively installed extensions must exceed the admissible additional wind and/or weight loads. After natural events like storms, lightning strikes, or inundation, a thorough examination of the structure and all installations must be carried out for safety reasons. This must happen even if a standard maintenance and examination procedure has recently been conducted. In winter, subfreezing air temperatures associated with gale-force winds can cause severe ice accretion on the structures. When these get too heavy or as temperatures increase, blocks of ice can fall and cause damage and endanger life. Protection measures and a timely closure of the tower vicinity are part of the essential duties of the operator in such situations.

ternal experts from qualified authorities or companies. For small towers without any moving parts, visually inspecting the structure and testing all clamps and other mechanical connections for instruments, outriggers, and other attachment parts is sufficient. If the structure consists of hollow sections and ambient temperatures are around or below 0°C, freezing water inside hol-

low spaces may crack even metal tubes, which require particular attention during inspection. In the case of a guyed mast, all parts of the anchoring (clamps, guy-wires, anchors, etc.) must be checked and the tension of the guy ropes must be measured and adjusted if required. This procedure should be performed every four to six weeks. Falling trees in close vicinity of a tower can cause severe damage to the installation and may tear down masts of lower steadiness especially when hitting the guy wires. It is recommended to regularly check the health and stability of surrounding trees and to cut down the ones that pose a risk to the installations.

For tall towers, a typical test procedure that should be carried out in one- or two-year intervals consists of:

- Checking the vertical alignment of the structure and adjusting, if required
- Checking the tower foundation and guy wire anchor points
- Inspecting the status of the mast construction and outriggers by checking for:
 - Loose, missing, or fallen mechanical connections
 - Bent, twisted, or buckled parts
 - A defective tower base
 - Defective joints
- Controlling the guy ropes:
 - Check the tension and adjust, if required
 - Visual inspection of the wires (also by binoculars) and the connection points at the tower and anchor foundation
- Controlling stairs, ladders, and tread areas

- Checking for corrosion and controlling the status of protective coating
- Checking for ease of operation of any moving parts (e.g., outriggers) and greasing if required
- Inspecting and testing the aircraft warning light system

At intervals of several years, it is necessary to inspect the steel cables holding tall towers for inspection and maintenance (coating or greasing). In general, guy wires must be replaced as soon as they no longer meet the quality and safety requirements.

A detailed examination of any means of transport such as lifts or elevators either for freight or for passengers must be conducted one or two times per year. Also, all electrical components must be checked in regular intervals:

- Ground fault circuit interrupter every six months
- Portable electrical devices that can be connected to line voltage every two years
- Permanently installed electrical devices connected to line voltage every four years

Every personal protective equipment component must be annually reviewed and any defective or outdated parts must be taken out of service.

All inspections must only be conducted by qualified and/or authorized persons. Any identified shortcomings must be rectified as soon as possible. If danger to life is determined, permission to operate must be temporarily withdrawn.

6.8 Applications

The following subsections briefly describe some applications where the combination of different ground-based measurement platforms support diverse measurement strategies and enable the investigation of complex atmospheric processes and interactions between ecosystems and the atmosphere.

6.8.1 Vehicle-Induced Turbulence

In order to investigate the intensity and range of vehicle-induced turbulence in comparison to the natural atmospheric turbulence, a combination of small observation platforms (4–48 m high) has been installed adjacent to a motorway (see Fig. 6.26) [6.58]. The instrumental setup allowed for the measurement of the mean and turbulent wind field as well as the stratification. Most of the towers were installed on the downwind side of the

motorway to cover the spatial range of the turbulence anomaly.

6.8.2 Internal Boundary Layer

To investigate the growth of an internal boundary layer, a set of small towers (4.5–18 m high) was deployed over two adjacent fields with different vegetation (see Fig. 6.27) [6.59]. Two energy-balance stations provided information about the stratification.

6.8.3 Large-Scale Manipulation Experiment

MaNiP (Manipulation Nitrogen and Phosphorous) is a long-term experimental project that aims to help us understand the responses to different eddy-covariance sites from nutrient loading (primarily N and P) and wa-

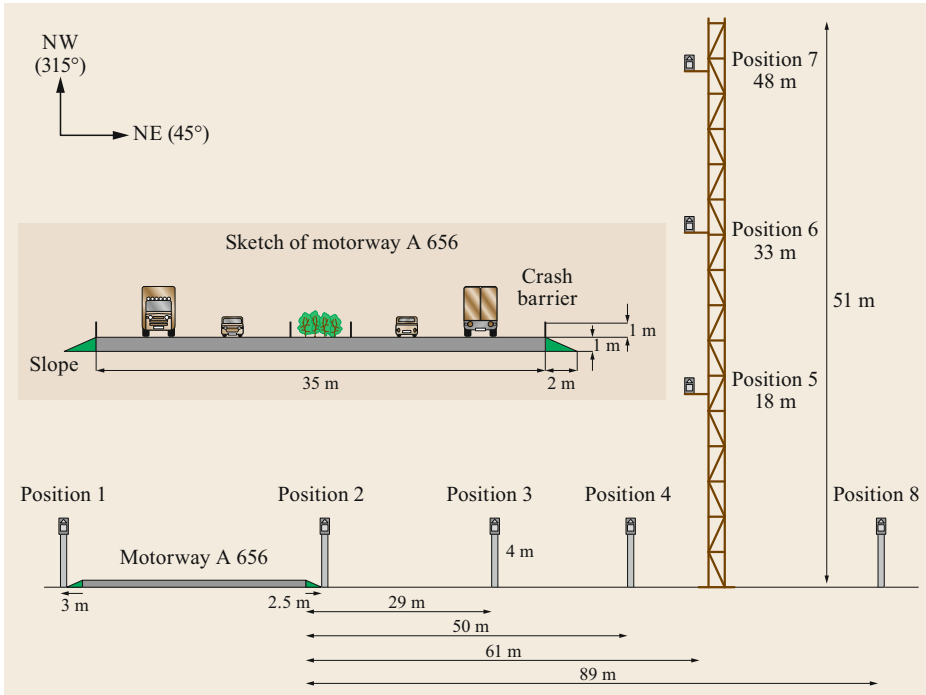


Fig. 6.26 A schematic representation of a motorway with the positions of the eight turbulence measurement sites (after [6.58] with permission from Elsevier)

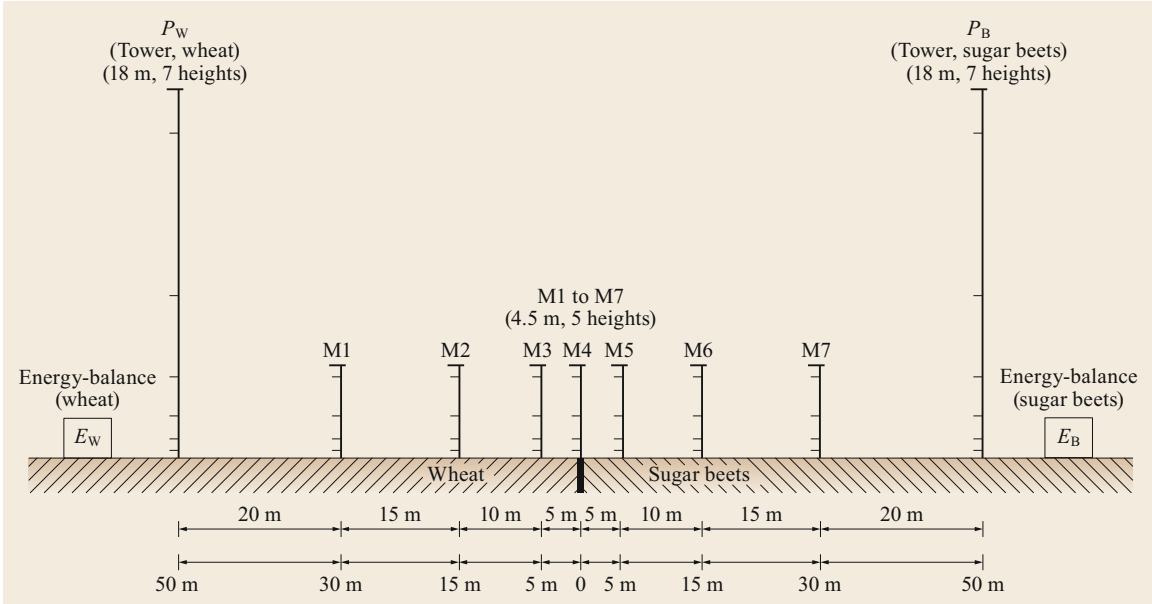


Fig. 6.27 The installation of a combination of small towers to investigate the modification of turbulent fluxes and temperature fields in the surface layer of two adjacent agriculturally used areas (after [6.59] with permission from Gauthier-Villars)



Fig. 6.28 A measurement setup near Majadas, Spain with a subcanopy eddy-covariance system on tripod (*left*), a 15-m walk-up tower with eddy-covariance system and meteorological measurements (*center*), and a 10-m triangular mast with rotatable arm for spectral radiative measurements (*right*) (photo © Tiana Hammer, MPI-BGC)

ter availability on ecosystem-level carbon, water fluxes, and their interannual variability [6.60].

The two study areas in a Mediterranean savanna ecosystem are located in the Extremadura region in the southwest of Spain. The installations are in both cases situated in a *dehesa*, a multifunctional, agrosilvopastoral system. The distance between the sites is 165 km and the more southern site receives significantly less precipitation. Figures 6.28, 6.13 and 6.14 show the deployment of various platforms for a wide range of measurement methods and instrumentation: walk-up towers and a telescopic mast for eddy flux and profile measurements above the canopy, tripods for eddy flux measurements below the tree canopy, and masts with a rotatable arm for radiative measurements above different surfaces. Dendrometers, sap flow sensors, chambers for respiration, and photosynthesis measurements as well as lysimeters, soil moisture, and soil temperature profile probes are utilized.

6.8.4 Tall-Tower Observatories

The two tall-tower observatories ATTO and ZOTTO are both examples of multiplatform installations each consisting of three towers or masts. Besides the tall tower, one walk-up tower and one thin triangular mast, both 80 m high, are also part of ATTO (see Fig. 6.29). The walk-up tower is similarly equipped with instruments as the tall tower (see Sect. 6.4.2) and continues the flux and profile measurements into the undisturbed canopy and down to the trunk space. The triangular mast is used to carry a number of air inlets for trace gas concentration



Fig. 6.29 Two 80-m masts in proximity to the ATTO tall tower (photo © Martin Hertel, MPI-BGC)

measurements with gas analyzers located inside a container at the mast base. This mast needs to be climbed only occasionally. This setup is well suited to investigate, for instance, the flux gradient or the variance method to estimate fluxes over tall forests [6.61].

At ZOTTO, two small towers for eddy-covariance flux measurements are utilized in two different ecosystems (forest and bog) in addition to the tall tower (see Sect. 6.4.2). The combination of measurements of trace gas and aerosol concentrations, solar radiation, and CO_2 exchange allows investigating the effect of aerosol loading on solar radiation and the subsequent effect on photosynthesis as a relevant question for estimating climate feedback mechanisms [6.62]. High aerosol concentrations regularly result from smoke from wildfires.

6.9 Future Developments

An article in *Windpower Monthly* has the provocative title “Do we still need met masts?” [6.63], which in this case is related to weather monitoring within the scope of onshore and offshore wind farms. Met masts can in many cases be replaced by remote-sensing (RS) devices

like lidar [6.64] and sodar (light/sonic detection and ranging). Both traditional met masts and RS devices, which can be ground-based or mounted on the nacelle, have their strengths and weaknesses and are summarized in Table 6.6.

Table 6.6 Comparison of met masts and remote-sensing devices

Met masts	Remote-sensing devices
Strengths	
Measurements technically well understood	Are portable and relatively easy to deploy
Broad industry acceptance	Ideal for prospecting potential sites
Traceability back to a standard	Lower installation costs
Weaknesses	
Siting permits required	RS devices can get buried in deep snow
Mechanical failure and lightning strikes	Struggle in certain atmospheric conditions
Highly visible to competitors and opponents	Can't measure hub-height, temperature, pressure, or humidity
Measurements impacted by tower shadow	
Instruments may stop working in severe ice	More vulnerable to theft

All of this is, of course, mostly applicable to investigations and the infrastructure related to wind energy technologies. For weather services and science, masts and towers will remain of fundamental importance, but

remote-sensing technologies and devices will gain in importance, which holds true for ground-based instruments as well as for airborne and space-based systems. On the other hand, the enormous increase in the number of wind turbines in many countries results in an enhanced availability of meteorological data on the upper border of the surface layer because most windmills carry some sensors for atmospheric measurements on top of their nacelle.

Unmanned aircraft systems (UAS) like multicopters are becoming more and more common in many fields of science (see Chap. 49). With the miniaturization of sensors, instruments, computers, and other devices, UASs can be used for a large number of applications. Atmospheric measurements on masts and towers can be extended vertically and horizontally so that 2-D or 3-D datasets can be gained by deploying such platforms.

The unique HighStep system [6.65] is an innovative development to facilitate reaching elevated working positions, in particular on high masts or towers. Climbing and walking up is replaced with a technical climbing device driven by electric engines running on a vertical rail. Instruments with a total weight of up to 150 kg are able to fully automatically move up and down a tower in regular intervals.

6.10 Further Readings

- M. Aubinet, T. Vesala, D. Papale (eds.): Eddy Covariance. A particle guide to measurement and data analysis. Springer Atmospheric Sciencis, Springer Dordrecht (2012)
- F. Brock, S. J. Richardson: Meteorological measurement systems. Oxford University Press, New York (2001)
- J. Scheer: Versagen von Bauwerken: Hochbauten und Sonderbauwerke. Ernst & Sohn Verlag für Architektur und technische Wissenschaften GmbH, Berlin (2001)
- Wind measurements tower—guidance and siting, Tech. Doc: 1.0, Date: 28.01.2011, <http://www.powered-ipa.it/wp-content/uploads/2012/05/WIND-MEASUREMENTS-TOWER-GUIDANCE-AND-SITING.pdf>, Accessed 04 July 2021
- Wind farms construction home page: <http://www.windfarmbop.com/category/met-mast/>, Accessed 04 July 2021
- T. Leiding, I. Bastigkeit, F. Bégué, L. Gates, K. Herklotz, S. Müller, T. Neumann, P. Schwenk, R. Sedlatschek, C. Senet, B. Tinz and F. Wilts: Standardization of Marine Meteorological Data from FINO Offshore Platforms. 10. Deutsche Klimatagung 21.–24. September 2015 Hamburg https://izw.baw.de/e-medien/dkt10-klimatagung/pdf/klimawandel/DKT10-71_Leiding_et_al-Poster.pdf, Accessed 04 July 2021
- National Oceanic and Atmospheric Administration: Ocean Climate Stations. <https://www.pmel.noaa.gov/ocs/>, Accessed 04 July 2021

References

- 6.1 M. Kohler, J. Metzger, N. Kalthoff: Trends in temperature and wind speed from 40 years of observations at a 200-m high meteorological tower in Southwest Germany, *Int. J. Climatol.* **38**, 23–34 (2018)
- 6.2 Wikipedia, The Free Encyclopedia: Tower of the Winds, https://en.wikipedia.org/w/index.php?title=Tower_of_the_Winds&oldid=882731086, Accessed 05 July 2021
- 6.3 Ancient Origins: <https://www.ancient-origins.net/ancient-technology/ingenious-invention-tower-winds-001902>, Accessed 20 Mai 2019
- 6.4 Florida Center for Instructional Technology: ClipArt ETC, License confirmation number SC1200081137, https://etc.usf.edu/clipart/58000/58069/58069_tower-wind.htm, Accessed 05 July 2021
- 6.5 W.C. Swinbank, A.J. Dyer: An experimental study in micro-meteorology, *Q. J. R. Meteorol. Soc.* **93**(398), 494–500 (1967)
- 6.6 J.C. Kaimal, J.C. Wyngaard: The Kansas and Minnesota experiments, *Bound.-Layer Meteorol.* **50**, 31 (1990)
- 6.7 Wikipedia, The Free Encyclopedia: Radio masts and towers, https://en.wikipedia.org/w/index.php?title=Radio_masts_and_towers&oldid=892449253, Accessed 05 July 2021
- 6.8 W.F. Dabberdt: Wind disturbance by a vertical cylinder in atmospheric surface layer, *Bull. Am. Meteorol. Soc.* **49**(7), 767–771 (1968)
- 6.9 J. Wucknitz: Flow distortion by supporting structures. In: *Air–Sea Interaction*, ed. by F. Dobson, L. Hasse, R. Davis (Springer, Boston 1980)
- 6.10 J.E. Cermak, J.D. Horn: Tower shadow effect, *J. Geophys. Res.* **73**(6), 1869–1876 (1968)
- 6.11 H. Moses, H.G.D. Daubek: Errors in wind measurements on the towers associated with tower-mounted anemometers, *Bull. Am. Meteorol. Soc.* **42**, 190–194 (1961)
- 6.12 C.W. Thornthwaite, W.J. Superior, R.T. Field: Evaluation of an ocean tower for measurement of climatic fluxes, *Publ. Climatol. Lab. Climatol.* **15**(3), 289–351 (1962)
- 6.13 C.W. Thornthwaite, W.J. Superior, R.T. Field: Disturbance of airflow around Argus island tower near Bermuda, *J. Geophys. Res.* **70**(24), 6047–6052 (1965)
- 6.14 B.R. Munson, D.F. Young, T.H. Okiishi: *Fundamentals of Fluid Mechanics*, 3rd edn. (Wiley, New York 1998)
- 6.15 M. Sanuki, N. Tsuda: What are we measuring on the top of a tower?, *Pap. Meteorol. Geophys.* **8**(1), 98–101 (1957)
- 6.16 C. Barthlott, F. Fiedler: Turbulence structure in the wake region of a meteorological tower, *Bound.-Layer Meteorol.* **108**, 175–190 (2003)
- 6.17 M.F. Lotfi: *Atmospheric Wind Flow Distortion Effects of Meteorological Masts*, Master Thesis (Master of Computational Mechanics), Faculdade de Engenharia da Universidade do Porto, (2015), <https://doi.org/10.13140/RG.2.2.14794.62409>
- 6.18 I. Troen, E. Lundtang Peterson: *European Wind Atlas* (Risø National Laboratory, Roskilde 1989)
- 6.19 G. Burba: *Eddy Covariance Method for Scientific, Industrial, Agricultural and Regulatory Applications* (LI-COR® Biosciences, Lincoln 2013)
- 6.20 K. Yamanoi, R. Hirata, K. Kitamura, T. Maeda, S. Matsuura, T. Miyama, Y. Mizoguchi, S. Murayama, Y. Nakai, Y. Ohtani, K. Ono, Y. Takahashi, K. Tamai, Y. Yasuda, Y. Mizoguchi, S. Yuta: *Practical Handbook of Tower Flux Observation* (FFPRI, Tsukuba 2011)
- 6.21 H. Heißelmann: *The Sphere Anemometer—Optimization for Atmospheric Wind Measurements*, Dissertation (Carl von Ossietzky University, Oldenburg 2017)
- 6.22 The International Renewable Energy Agency (IRENA): Wind resource measurement: guidelines for islands, https://www.irena.org/-/media/Files/IRENA/Agency/Publication/2015/IRENA_Island_Wind_Measurement_2015.pdf (2015), Accessed 14 July 2021
- 6.23 WMO: *Guide to Instruments and Methods of Observation*, WMO–No. 8, Volume I – Measurement of Meteorological Variables (World Meteorological Organization, Geneva 2018)
- 6.24 J. Vilà-Guerau de Arellano, C.C. van Heerwaarden, B.J.H. van Stratum, K. van den Dries: *Atmospheric Boundary Layer. Integrating Air Chemistry and Land Interactions* (Cambridge University Press, New York 2015)
- 6.25 T.R. Oke: *Boundary Layer Climates*, 2nd edn. (Methuen, London, New York 1987)
- 6.26 R.B. Stull: *An Introduction to Boundary Layer Meteorology* (Kluwer, Dordrecht 1988)
- 6.27 N. Kalthoff, M. Fiebig-Wittmaack, C. Meißner, M. Kohler, M. Uriarte, I. Bischoff-Gauß, E. Gonzales: The energy balance, evapo-transpiration and nocturnal dew position of an arid valley in the Andes, *J. Arid Environ.* **65**, 420–443 (2006)
- 6.28 M. Aubinet, T. Vesala, D. Papale (Eds.): *Eddy Covariance. A Particle Guide to Measurement and Data Analysis*, Atmospheric Sciences (Springer, Dordrecht 2012)
- 6.29 Max Planck Institute for Chemistry: ATTO – Amazonian Tall Tower Observatory, <https://www.attoproject.org/>, Accessed 14 July 2021
- 6.30 M.O. Andreae, O.C. Acevedo, A. Araùjo, P. Artaxo, C.G.G. Barbosa, H.M.J. Barbosa, J. Brito, S. Carbone, X. Chi, B.B.L. Cintra, N.F. da Silva, N.L. Dias, C.Q. Dias-Júnior, F. Ditas, R. Ditz, A.F.L. Godoi, R.H.M. Godoi, M. Heimann, T. Hoffmann, J. Kesselmeier, T. Köneemann, M.L. Krüger, J.V. Lavric, A.O. Manzi, A.P. Lopes, D.L. Martins, E.F. Mikhailov, D. Moran-Zuloaga, B.W. Nelson, A.C. Nölscher, D. Santos Nogueira, M.T.F. Piedade, C. Pöhlker, U. Pöschl, C.A. Quesada, L.V. Rizzo, C.–U. Ro, N. Ruckteschler, L.D.A. Sá, M. de Oliveira Sá, C.B. Sales, R.M.N. dos Santos, J. Saturno, J. Schöngart, M. Sörgel, C.M. de Souza, R.A.F. de Souza, H. Su, N. Targhetta, J. Tóta, I. Trebs, S. Trumbore, A. van Eijck, D. Walter, Z. Wang, B. Weber, J. Williams, J. Winderlich, F. Wittmann, S. Wolff, A.M. Yáñez-Serrano: The Amazon Tall Tower Observatory (ATTO): overview of pilot measurements on ecosystem ecology, meteorology, trace gases, and

- aerosols, *Atmos. Chem. Phys.* **15**(18), 10723–10776 (2019)
- 6.31 Zotino Tall Tower Observatory (ZOTTO), <http://www.zottoproject.org/index.php/Main/Home>, Accessed 05 July 2021
- 6.32 F.F. Hall: The Boulder Atmospheric Observatory, *Opt. News* **3**, 14–18 (1977)
- 6.33 M.J. Post, R.L. Schwiesow, R.E. Cupp, D.A. Haugen, J.T. Newman: A comparison of anemometer- and lidar-sensed wind velocity data, *J. Appl. Meteorol.* **17**, 1179–1181 (1978)
- 6.34 J.C. Kaimal, J.E. Gaynor: The Boulder Atmospheric Observatory, *J. Appl. Meteorol.* **22**, 863–880 (1983)
- 6.35 J.C.R. Hunt, J.C. Kaimal, J.E. Gaynor: Some observations of turbulence structure in stable layers, *Q. J. R. Meteorol. Soc.* **111**, 793–815 (1985)
- 6.36 J.J. Finnigan, F. Einaudi: The interaction between an internal gravity wave and the planetary boundary layer. Part II: Effect of the wave on the turbulence structure, *Q. J. R. Meteorol. Soc.* **107**, 807–832 (1981)
- 6.37 F. Einaudi, A.J. Bedard, J.J. Finnigan: A climatology of gravity waves and other coherent disturbances at the Boulder Atmospheric Observatory during March–April 1984, *J. Atmos. Sci.* **46**, 303–329 (1989)
- 6.38 C.J. Hahn: A study of the diurnal behavior of boundary-layer winds at the Boulder Atmospheric Observatory, *Bound.-Layer Meteorol.* **21**, 231–245 (1981)
- 6.39 D. Wolfe, R. Lataitis: Boulder Atmospheric Observatory 1977–2016: the end of an era and lessons learned, *Bull. Am. Meteorol. Soc.* **99**(7), 1345–1358 (2018)
- 6.40 Karlsruhe Institute of Technology, Institute of Meteorology and Climate Research: KITcube, <http://www.imk-tro.kit.edu/4635.php>, Accessed 05 July 2021
- 6.41 N. Kalthoff, B. Adler, A. Wiese, M. Kohler, K. Träumner, J. Handwerker, U. Corsmeier, S. Khodayar, D. Lambert, A. Kopmann, N. Kunka, G. Dick, M. Ramatschi, J. Wickert, C. Kottmeier: KITcube—a mobile observation platform for convection studies deployed during HyMeX, *Meteorol. Z.* **22**, 633–647 (2013)
- 6.42 N. Kalthoff, B. Vogel: Counter-current and channeling effect under stable stratification in the area of Karlsruhe, *Theor. Appl. Climatol.* **45**, 113–126 (1992)
- 6.43 R. Calhoun, A. Wieser, M. Princevac, C. Kottmeier: Comparison of LIDAR data with tower, profiler, radiosonde, and tethered data. In: *European Geosciences Union General Assembly 2005, Vienna, Austria, 24–29 April* (2005)
- 6.44 A. Apituley, H. Russchenberg, H. van der Marel, F. Bosveld, R. Boers, H. ten Brink, G. de Leeuw, R. Uijlenhoet, B. Arbresser-Rastburg, T. Röckmann: Overview of research and networking with ground based remote sensing for atmospheric profiling at the Cabauw Experimental Site for Atmospheric Research (CESAR)—The Netherlands. IGARSS 2008 – 2008 IEEE International Geoscience and Remote Sensing Symposium, 2008, pp. III – 903–III – 906 (2008)
- 6.45 A.G.M. Driedonks, H. van Dop, W.H. Kohsiek: Meteorological Observations on the 213 m mast at Cabauw, in the Netherlands. In: *Proc. Fourth Symp. Meteorol. Observ. Instr., Denver* (Am. Meteorol. Soc., Boston 1978) pp. 41–46
- 6.46 W.A.A. Monna, J.G. van der Vliet: *Facilities for research and weather observations on the 213 m tower at Cabauw and remote locations*, KNMI Scientific reports WR-nr87-5, 2nd edn. 1987)
- 6.47 A.G.M. Driedonks: Models and observations of the growth of the atmospheric boundary layer, *Bound.-Layer Meteorol.* **23**, 283–306 (1982)
- 6.48 F.T.M. Nieuwstadt: The steady-state height and resistance laws of the nocturnal boundary layer: theory compared with Cabauw observations, *Bound.-Layer Meteorol.* **20**, 3–17 (1981)
- 6.49 A.A.M. Holtslag, E. van Meijgaard, W.C. de Rooy: A comparison of boundary layer diffusion schemes in unstable conditions over land, *Bound.-Layer Meteorol.* **76**, 69–95 (1995)
- 6.50 P. Hurley, A. Luhar: Modelling the meteorology at the Cabauw tower for 2005, *Bound.-Layer Meteorol.* **132**, 43–57 (2009)
- 6.51 Data Buoy Cooperation Panel: Data buoy types, <http://dbcp.jcommops.org/platforms/types.html>, Accessed 05 July 2021
- 6.52 C. Schmitt, C. Kottmeier, S. Wassermann, M. Drinkwater: Atlas of antarctic sea ice drift, <https://data.meereisportal.de/gallery/eisatlas.php> (2004), Accessed 12 July 2021
- 6.53 C. Kottmeier, L. Sellmann: *Buoy-Based Observations of Mixed-Layer Variability in the Weddell Sea. Report of the First Session of the WCRP International Programme for Antarctic Buoys (IPAB)*, WCRP Informal Report No. 13/1997, 1997) p. 9, Appendix I, Annex 3
- 6.54 A. Nordbo, S. Launiainen, I. Mammarella, M. Lepäranta, J. Huotari, A. Ojala, T. Vesala: Long-term energy flux measurements and energy balance over a small boreal lake using eddy covariance technique, *J. Geophys. Res.* **116**, D02119 (2011)
- 6.55 DSM&T: Ingreso protection (IP) rating chart, <http://www.dsmt.com/resources/ip-rating-chart/>, Accessed 05 July 2021
- 6.56 C. Arbeza, K. Tetea, A. Amossea, J.-B. Boucher, H. Ibrahimac: Met mast configuration and choice of sensors in cold climate conditions, *Measurement* **95**, 156–165 (2017)
- 6.57 C. Barthlott, N. Kalthoff, F. Fiedler: Influence of high-frequency radiation on turbulence measurements on a 200 m tower, *Meteorol. Z.* **12**, 67–71 (2003)
- 6.58 N. Kalthoff, D. Bäumer, U. Corsmeier, M. Kohler, B. Vogel: Vehicle-induced turbulence near a motorway, *Atmos. Environ.* **39**, 5737–5749 (2005)
- 6.59 N. Kalthoff, U. Corsmeier, F. Fiedler: Modification of turbulent fluxes and temperature fields in the atmospheric surface layer over two adjacent agricultural areas: a case study, *Ann. Geophys.* **9**, 521–533 (1991)
- 6.60 T.S. El-Madany, M. Reichstein, O. Pérez-Priego, A. Carrara, G. Moreno, M.P. Martín, J. Pacheco-Labrador, G. Wohlfahrt, H. Nieto, U. Weber, O. Kolle, L. Yunpeng, N. Carvalhais, M. Migliavacca: Drivers of spatio-temporal variability of carbon dioxide and energy fluxes in a Mediterranean savanna ecosystem, *Agric. Forest Meteorol.* **262**, 258–278 (2018)
- 6.61 T.L. Chor, N.L. Dias, A. Araújo, S. Wolff, E. Zahn, A. Manzi, I. Trebs, M.O. Sá, P.R. Teixeira, M. Sörgel:

- Flux-variance and flux-gradient relationships in the roughness sublayer over the Amazon forest, *Agric. Forest Meteorol.* **239**, 213–222 (2017)
- 6.62 E. Ezhova, I. Ylivinkka, J. Kuusk, K. Komsaare, M. Vana, A. Krasnova, S. Noe, M. Arshinov, B. Belan, S.-B. Park, J.V. Lavrič, M. Heimann, T. Petäjä, T. Vesala, I. Mammarella, P. Kolari, J. Bäck, Ü. Rannik, V.-M. Kerminen, M. Kulmala: Direct effect of aerosols on solar radiation and gross primary production in boreal and hemiboreal forests, *Atmos. Chem. Phys.* **18**, 17863–17881 (2018)
- 6.63 J. Dodd: Do we still need met masts? *Wind-power Monthly*, <https://www.windpowermonthly.com/article/1458018/need-met-masts> (March 2018), Accessed 02 May 2019
- 6.64 C. Stawiarski, K. Träumner, C. Knigge, R. Calhoun: Scopes and challenges of dual-doppler lidar wind measurements—an error analysis, *J. Atmos. Ocean. Technol.* **30**, 2044–2062 (2013)
- 6.65 HighStep Systems home page, <https://highstepsystems.com/en>, Accessed 05 July 2021

Olaf E. E. Kolle

Field Experiments and Instrumentation
Max-Planck-Institute for Biogeochemistry
Jena, Germany
olaf.kolle@bgc-jena.mpg.de



Olaf Kolle, who received a meteorology diploma in 1986 from the University of Karlsruhe, heads the Service Facility for Field Experiments and Instrumentation at the Max Planck Institute for Biogeochemistry in Jena, Germany. He and his team provide service for experimental research and build, deploy, and maintain instruments, measurement systems, and field installations worldwide. His main interests are eddy-covariance measurements, software development, and data acquisition and process control systems.

Norbert Kalthoff

Institute of Meteorology and Climate
Research, Department Troposphere
Karlsruhe Institute of Technology (KIT)
Karlsruhe, Germany
no.kalthoff@web.de



Norbert Kalthoff leads the Land Surface and Boundary Layer research group at the Institute of Meteorology and Climate Research (Department Troposphere) at the Karlsruhe Institute of Technology in Germany until 2010. He received his PhD in meteorology in 1986 from the University of Bonn, Germany. His team contributes to field campaigns worldwide, investigating the impact of land-surface processes on the atmospheric boundary layer and the initiation of moist convection.

Christoph Kottmeier



Institute of Meteorology and Climate
Research, Department Troposphere
Karlsruhe Institute of Technology (KIT)
Karlsruhe, Germany
christoph.kottmeier@kit.edu

Christoph Kottmeier is professor of meteorology and headed the Institute of Meteorology and Climate Research (Department Troposphere) at the KIT until 2020. His team conducts tropospheric research by applying advanced observation techniques (aircraft, automatic buoys, lidar, and radar) as well as numerical modelling with COSMO and ICON model systems. He initiated the construction of the KITcube facility for integrated observation.

J. William Munger



John A. Paulson School of Engineering
and Applied Sciences
Harvard University
Cambridge, USA
jwmunger@seas.harvard.edu

J. William Munger is a senior research fellow in atmospheric chemistry at the Harvard School of Engineering and Applied Sciences. He received an MS in ecology in 1981 from the University of Minnesota and a PhD in environmental engineering science from the California Institute of Technology in 1988. His research uses field observations to quantify biosphere-atmosphere exchange of carbon and air pollutants.

Temperature

7. Temperature Sensors

Thomas Foken , Jens Bange 

Techniques that are used to measure the temperature of the atmosphere include liquid-in-glass thermometers, electrical thermometers, bimetallic thermometers, and the most commonly used instruments: resistance thermometers. Radiation shields and ventilation are important for minimizing erroneous results. Fine-wire thermometers and sonic temperature measurement are important techniques for turbulence measurements. In addition to providing technical data, this chapter describes maintenance requirements and quality control and calibration methods for temperature sensors.

7.1	Measurement Principles and Parameters	184	7.3.5	Semiconductors	193
7.1.1	Measured Parameters	184	7.3.6	Thermocouple	193
7.1.2	Principles of Temperature Measurement	186	7.3.7	Sonic Anemometers	193
7.1.3	Site Considerations	186	7.3.8	Radiation Error	194
7.2	History	187	7.3.9	Radiation Screens	195
7.2.1	History of Temperature Measurements	187	7.3.10	Influence of the Surrounding Area on Temperature Measurements	196
7.2.2	Temperature Scales	189	7.4	Devices and Systems	196
7.3	Theory	190	7.4.1	Liquid-in-Glass Thermometers	196
7.3.1	Liquid-in-Glass Thermometers	190	7.4.2	Bimetallic Thermometers	198
7.3.2	Bimetallic Thermometers	190	7.4.3	Resistance Thermometers	198
7.3.3	Metal Resistance Thermometers	190	7.4.4	Radiation Screens	199
7.3.4	Thermistors	192	7.4.5	Sensor Comparison	201
			7.5	Specifications	201
			7.6	Quality Control	202
			7.6.1	Reference Standards	202
			7.6.2	Temperature Calibration	203
			7.6.3	Specific Quality Control Methods	203
			7.7	Maintenance	203
			7.8	Applications	204
			7.8.1	Temperature Measurements for Meteorology and Climatology	204
			7.8.2	Further Applications	205
			7.9	Future Developments	205
			7.10	Further Reading	206
			References		206

Air temperature is the most important atmospheric parameter in daily life. It provides a subjective measure of the weather and is used for climate classification and more recently to evaluate climate change. Temperature measurements have a long tradition but they still present a challenge when high accuracy is required. In particular, radiation and insufficient ventilation can significantly increase the temperatures of in-situ sensors. While the technical possibilities in this field are now greater than ever, errors in measurement are often significantly underestimated, as addressed by *Fritz Albrecht* (1896–1965) [7.1] nearly 100 years ago. These errors can be minimized by using special radiation shields and ventilation systems with temperature sensors. The main prin-

ciple of classical temperature measurement is the expansion of a liquid or solid material. The temperature dependence of resistance is the dominant measuring principle in currently available sensors. To overcome problems with radiation error, remote-sensing techniques (e.g., sonic anemometers; see also Chap. 9) are applied to measure the temperature (mainly for turbulence measurements). As well as the air temperature at a given time, extreme values such as the daily or annual minimum and maximum temperature are often of interest, with these values ranging from about +60 °C to below –90 °C near the Earth's surface. For more on the spatiotemporal distribution of temperature, see relevant meteorology and climatology textbooks [7.2, 3] and Chap. 1.

7.1 Measurement Principles and Parameters

This section reviews temperature measurement scales and principles and highlights the typical temperature measurements performed in meteorology.

7.1.1 Measured Parameters

Temperature is defined as the thermodynamic temperature, symbol T , and is measured in kelvin (symbol K), which is $1/273.16$ of the thermodynamic temperature of the triple point of water [7.4]. The zero point of this absolute thermodynamic scale is absolute zero (-273.15°C). Precise definitions of various temperature scales have been formulated, with the most recently accepted scale being the International Temperature Scale of 1990 (ITS-90), which was adopted by the International Committee of Weights and Measures at its meeting in 1989; for more on the history of temperature scales, see Chap. 5. Earlier temperature scales were defined based on the ice and boiling points of water under standard pressure conditions: 273.15 and 373.15 K, respectively. The thermodynamic temperature expressed in this way is known as the Celsius temperature, symbol t , with units of degrees Celsius (symbol $^\circ\text{C}$). It is calculated via

$$t [^\circ\text{C}] = T [\text{K}] - 273.15. \quad (7.1)$$

A difference in temperature is given in kelvin or degrees Celsius, although it is more common to refer to the difference in kelvin.

The International Temperature Scale of 1990 (ITS-90) defines both the International Kelvin Temperature (symbol: T_{90} , unit: kelvin) and the International Celsius Temperature (symbol: t_{90} , unit: degree Celsius). The relation between these is given by

$$t_{90} [^\circ\text{C}] = T_{90} [\text{K}] - 273.15. \quad (7.2)$$

The ITS-90 is constructed in such a way that the numerical value of T_{90} is a close approximation to the numerical value of T for any given temperature. This was achieved through a series expansion, with the relevant fixed points in the meteorological temperature range being the triple point of mercury (234.3156 K), the triple point of water (273.16 K), and the melting point of gallium (302.9146 K). For further details, see [7.4, 5] and Table 7.1; for more on the differences between this and other scales, see Chap. 5.

Besides the air temperature at a given time, extreme temperature values are also of interest in meteorology, climatology, and applied sciences, so special sensors to measure these parameters have been developed. An overview of temperatures of interest is given in Table 7.2.

Furthermore, special temperatures are calculated in atmospheric science to overcome physical effects that are related to the temperature, as outlined below.

The air density depends not only on the temperature but also on the humidity. A special temperature is used

Table 7.1 Recommended temperature scales (for other scales, such as those that were more popular in the past, see Sect. 7.2)

Scale	Lower fixed point	Upper fixed point	Difference
Kelvin scale	Absolute zero (-273.15°C)	Triple point of water (0.01°C)	$1 \text{ K} = 1^\circ\text{C}$
Celsius scale	Melting point of ice (0°C) at 1013.25 hPa	Boiling point of water (100°C) at 1013.25 hPa	$1^\circ\text{C} = 1/100$ of the difference between both fixed points

Table 7.2 Parameters measured by temperature sensors (LT: local time)

Parameter	Description	Unit	Symbol
Absolute temperature	Temperature with the absolute zero point as a reference	K	T
Celsius temperature	Temperature with the melting point of ice and boiling point of water as references (see Table 7.1); usually measured at 2 m height	$^\circ\text{C}$	t
Temperature difference	Difference between two temperature values	K ($^\circ\text{C}$)	$T_1 - T_2$ ($t_1 - t_2$)
Water temperature	Temperature measured at a certain depth in a water body (lake, ocean, etc.)	$^\circ\text{C}$	t_w
Soil temperature	Temperature measured at a certain depth in the soil (typically up to 1 m deep)—usually 5, 10, 20, 50, or 100 cm deep	$^\circ\text{C}$	t_s
Minimum temperature	Minimum temperature within a given time interval (typically 18:00 to 6:00 LT)	$^\circ\text{C}$	t_{\min}
Maximum temperature	Maximum temperature within a given time interval (typically 6:00 to 18:00 LT)	$^\circ\text{C}$	t_{\max}
Minimum temperature at 5 cm height	Minimum temperature at 5 cm height during the night	$^\circ\text{C}$	$t_{\min-5 \text{ cm}}$

only with the gas constant of dry air R_d and is applied in the law of ideal gases, where the pressure is the sum of the individual pressures of dry air and water vapor,

$$\begin{aligned} p &= T \sum_i \rho_i R_i = T(\rho_d R_d + \rho_w R_w) \\ &= TR_d \left[(\rho - \rho_w) + \rho_w \frac{R_w}{R_d} \right]. \end{aligned} \quad (7.3)$$

The parameters in this equation are the air pressure p , the density of moist air ρ , the density of dry air ρ_d , the density of water vapor ρ_w , and the gas constant of water vapor R_w . This equation for moist air can be transformed into an equation for the specific humidity using the gas equation for moist air

$$p = \rho R_d T_v, \quad (7.4)$$

where T_v is the *virtual temperature* (see [7.2, 6] and Chap. 8), given by

$$T_v = T \left(1 + q \frac{R_w - R_d}{R_d} \right) = T(1 + 0.608q). \quad (7.5)$$

Here, q is an approximation for the specific humidity that is calculated via

$$\begin{aligned} q &= \frac{M_w}{M_w + M_d} = \frac{M_w}{M_d} \frac{e}{p - \left(1 - \frac{M_w}{M_d}\right) e} \\ &= 0.622 \frac{e}{p - 0.378e} \approx 0.622 \frac{e}{p} \end{aligned} \quad (7.6)$$

(M_w : molecular weight of water, M_d : molecular weight of dry air, and e : water vapor pressure). Also, note that

$$T_v \approx T \left(1 + 0.38 \frac{e}{p} \right). \quad (7.7)$$

The temperature increases under compression and decreases under expansion. To compare temperatures obtained at different atmospheric pressures, the *potential temperature* is calculated for a pressure of 1000 hPa using the *Poisson* equation (see [7.2, 6] and Chap. 46) as

$$\theta = T \left(\frac{1000 \text{ hPa}}{p} \right)^{\frac{R_d}{c_p}} = T \left(\frac{1000 \text{ hPa}}{p} \right)^{\frac{2}{7}}, \quad (7.8)$$

where c_p is the specific heat at constant pressure and $2/7 \approx 0.286$. For some applications it is useful to replace 1000 hPa with the pressure at the ground (Chap. 1).

The potential temperature is a state variable for an adiabatic process in unsaturated air. A similar state variable is defined for saturated air: the *equivalent potential temperature* θ_e of a pseudo-adiabatic process, which is calculated via the thermodynamic law for saturated air [7.2] as

$$\theta_e = \theta \exp \left(\frac{\lambda r_c}{c_p T} \right), \quad (7.9)$$

where r_c is the saturation mixing ratio and λ is the latent heat of evaporation (Chap. 5). It is assumed that an air parcel is raised to $z = \infty$ and the temperature is increased by the latent heat of condensation as the condensate is removed. After the maximum temperature has been reached, the air parcel is moved dry adiabatically to the surface and adopts the equivalent potential temperature.

The dependence of the speed of sound c on the temperature and moisture can also be applied to measure the temperature via the *Laplace* equation

$$c = \sqrt{\gamma \frac{p}{\rho}} \quad [\text{m s}^{-1}]. \quad (7.10)$$

The coefficient γ for dry air is

$$\gamma_d = \frac{c_{pd}}{c_{vd}} = \frac{7}{5} = 1.4, \quad (7.11)$$

where c_{pd} and c_{vd} are the specific heats of dry air at constant pressure and constant volume. The coefficient of the specific heats of water vapor at 1013.25 hPa and 15 °C,

$$\gamma_v = \frac{c_{pv}}{c_{vv}} = \frac{4}{3} = 1.328, \quad (7.12)$$

differs from the coefficient for dry air. Both of these γ coefficients must be applied to determine the speed of sound in moist air via (7.10). The ratio p/ρ for moist air in this equation can be calculated in a similar way to (7.3). Like the gas constant, the coefficient γ must be split into values for dry air and water vapor. Consequently, with the application of $q = \rho_w/\rho$, we get

$$\begin{aligned} c &= \sqrt{TR_d \gamma_d \left[\left(1 - \frac{\rho_w}{\rho}\right) + \frac{\rho_w}{\rho} \frac{R_w}{R_d} \frac{\gamma_v}{\gamma_d} \right]} \\ &= \sqrt{TR_d \gamma_d \left(1 + q \frac{R_w \gamma_v - R_d \gamma_d}{R_d \gamma_d} \right)}. \end{aligned} \quad (7.13)$$

Table 7.3 Definitions of selected temperatures that are considered in the atmospheric sciences

Special Temperature	Definition	Unit	Symbol
Virtual temperature	Temperature of dry air if it had the same density as moist air	K	T_v
Potential temperature	Temperature of air compressed/expanded to 1000 hPa	K	θ
Virtual potential temperature	Temperature of dry air if it had the same density as moist air at 1000 hPa	K	θ_v
Equivalent potential temperature	Temperature of air compressed/expanded to 1000 hPa and increased/decreased by the temperature equivalent of the latent heat due to the condensation of water vapor in the column up to $z = \infty$	K	θ_e
Sonic temperature	Temperature relating to the speed of sound (nearly identical to the virtual temperature)	K	T_s
Wind-chill index	Effect of the wind speed on cold sensation and cooling	°C	$t_{\text{wind-chill}}$

Table 7.4 Temperature measurement principles and their applications [7.7]

Measuring device	Method			Application	
	Thermodynamic	Electric	Sound	Mean	Turbulence
Bimetallic thermometer	✓			✓	
Liquid-in-glass thermometer	✓			✓	
Electric resistance thermometer		✓		✓	✓
Thermistor		✓		✓	
Semiconductor thermometer		✓		✓	
Thermocouple		✓		✓	✓
Sonic thermometer			✓	(✓)	✓

Using the appropriate numerical values and the approximation for the specific humidity given in (7.6), we obtain

$$c = \sqrt{401.88T(1 + 0.531q)} \approx \sqrt{401.88T \left(1 + 0.33 \frac{e}{p} \right)}. \quad (7.14)$$

This equation can be used to define a *sonic temperature* [7.8, 9],

$$T_s = T(1 + 0.531q) \approx T \left(1 + 0.33 \frac{e}{p} \right), \quad (7.15)$$

where the numerical value 0.33 differs because of the application of ITS-90 (formerly 0.32).

Comparing (7.7) and (7.15), the difference between both temperatures is less than 1‰ under typical atmospheric conditions, so the sonic temperature can be replaced with the virtual temperature.

There are several temperatures that are used to describe the influence of weather and climate on people. The latest is the universal thermal climate index (UTCI) [7.10]. A parameter that is well established in daily life and weather forecasts is the *wind-chill temperature* or *index*, which reflects the sensation of the air feeling cooler than it actually is due to the wind. After several modifications over the years, the current equa-

tion for this temperature is [7.11]

$$t_{\text{wind-chill}} [^\circ\text{C}] = 13.12 + 0.621t - 11.37u^{0.16} + 0.3965tu^{0.16}, \quad (7.16)$$

where the temperature t is in °C and the wind speed u is in km h^{-1} and is measured at 10 m above ground level.

Table 7.3 defines various special temperatures that are considered in the atmospheric sciences.

7.1.2 Principles of Temperature Measurement

The measurement principle of temperature sensors is—in most cases directly—based on the temperature dependence of a particular property, such as the volume of a liquid or solid material, the resistance of a metallic or other material, or the speed of sound. Recently used thermometers and their measuring principles are listed in Table 7.4, together with their utilization for slow measurements (i.e., mean values for time intervals of seconds to many minutes), including measurements of extreme values, and turbulence (5–100 Hz).

7.1.3 Site Considerations

Temperature sensors are often used together with humidity sensors (Chap. 8), but in such a scenario the

sensors should not influence each other. If the temperature measurements are used for the correction or transformation of humidity measurements, both sensors should measure the same small air volume and should be as close as possible to each other (at most 1 m apart). Radiation protection is important, and ventilation is necessary. The sensors should therefore be installed within meteorological shelters (Sect. 7.4.5 and Chap. 42). The standard installation height above

the ground is 2 m. Strong vertical temperature gradients (Chap. 1 and Sect. 7.3.10) mean that accurate leveling is essential. Temperature sensors should be protected against rain and moisture because moist sensors measure the wet temperature (Chap. 8), which can be several degrees lower than the actual temperature. Temperature sensors may be installed in different arrangements for specific purposes as long as the sensors are properly exposed (Chap. 6).

7.2 History

An excellent account of the history of thermometers in meteorology, written by *William Edgar Knowles Middleton* (1902–1998) [7.12], has provided the basis for many other historical studies [7.13, 13, 14]. The history of thermometers and temperature measurements is closely connected with the history of temperature scales. Here is a brief overview.

7.2.1 History of Temperature Measurements

The phenomenon of the expansion of air with increasing heat and the opposite phenomenon in cold conditions have been known since ancient times. *Philon of Byzantium* (about 250 BCE) and *Heron of Alexandria* (about 62 BCE) constructed thermoscopes. A description of a thermoscope as a heated or cooled globe connected by a tube to a bottle of water was published in 1575 in Italy, in Latin. But the first use of a thermoscope to measure the air temperature is attributed to *Galileo Galilei* (1564–1642), who used an air thermoscope that is thought to have been similar to that in Fig. 7.1a in his lessons during 1592–1593 at the University of Padua. Another instrument is often linked to Galileo: the Galileo thermometer, which was available in Florence at the beginning of the seventeenth century. In this sensor, several glass balls of different densities drift in a water-filled glass vessel. Depending on the temperature, the balls rise or drop (Fig. 7.1b). Decorative forms of this thermometer are still available.

There is no doubt that by the year 1613 Galileo had claimed to be the inventor of the air thermometer, this is evident from series of letters written to him ... [7.15]

Initial publications on the use of thermoscopes originate from *Santorio Santorio* (1561–1636), a professor of medicine at Padua, who used the device in 1612 to measure the body temperature in the mouth, and from *Giuseppe Biancani* or *Blancanus* (in 1617).

Giovafrancesco Sagredo (1561–1620) was the first to use snow as a fixed point, according to a letter to Galileo. North of the Alps, the Welsh musician *Robert*



Fig. 7.1 (a) Reconstruction of Galileo's thermoscope (photo © Deutsches Thermometermuseum Geraberg, Germany; the original is on display at the Museo Galileo in Florence). (b) Galileo thermometer (photo courtesy of TFA Dostmann, Wertheim, Germany)

Fludd and *Cornelius Drebbel* from the Netherlands constructed similar thermoscopes. *Otto von Guericke* (1602–1686) built an instrument that was combined with a barometer and had a scale showing the coldest and warmest days of the year. Around 1640, he found that the height of the air column of the thermoscope is a function of not only the temperature but also the pressure (Chap. 10).

The liquid-in-glass thermometer solved the problem of the pressure dependence of the temperature. Its development was supported by the Grand Duke of Tuscany, *Ferdinando II de' Medici* (1610–1670) and the *Accademia des Cimento* [7.16], and was probably available from 1641. Several instruments were constructed with 50- and 100-degree scales (among other scales), using alcohol as the liquid (Fig. 7.2). The resulting instrument with a scale was termed a *thermometer*. Thermometers were sent to many monasteries in Italy and north of the Alps to facilitate the first meteorological observations (Chap. 1). In 1828 in Florence, a comparison experiment was performed, and those involved were astonished to find that the 50-degree thermometers were extremely stable. Their zero point of the Florence small °Gk scale corresponded to -18.75°C and their 50-degree point to 55°C . At the Royal Society, *Robert Hooke* (1635–1703) built a similar thermometer as well as other instruments, and for the first time used the freezing point of water as a fixed point. He also had a calibration instrument that remained forgotten until the following century, when it was developed separately by Réaumur. Many thermometers dating from the end of the seventeenth century and the eighteenth century are shown in [7.14].

With the beginning of the eighteenth century, serious attempts were made to produce accurate thermometers with well-defined fixed points. The first, by *Daniel Gabriel Fahrenheit* (1686–1736), was probably significantly influenced by earlier works of the Danish astronomer *Ole Rømer* (1644–1710), with whom he was in contact. The lower fixed point on his scale was the freezing point of a mixture of water and sea salt ($0^{\circ}\text{F} \approx -20^{\circ}\text{C}$), which was not very accurate. It is also reported that this was the coldest temperature experienced in a winter in Gdansk. The upper fixed point was the body temperature of humans ($96^{\circ}\text{F} \approx 37^{\circ}\text{C}$). Until recently, the ice point of water was defined as 32°F and its boiling point as 212°F . Around the year 1716, Fahrenheit also used mercury as a liquid.

René-Antoine Ferchault de Réaumur (1690–1757) followed Hooke's idea of using just one fixed point: the freezing point of water. He made a special effort to use salt-free water, because he found that the freezing point depended on the salinity. Therefore, 0°R is 0°C . But

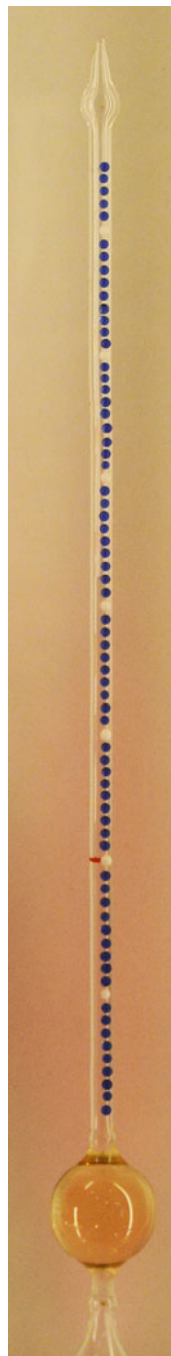


Fig. 7.2 Reconstruction of a liquid-in-glass thermometer of the *Accademia des Cimento* (photo © Deutsches Thermometermuseum Geraberg, Germany; original is on display at the Museo Galileo at Florence)

the other point, 80°R , corresponded to the boiling point of a specific dilution of alcohol. After 1730, 80°R was taken to be the boiling point of water, 100°C . A similar scale was devised by *Joseph Nicolas Delisle* (1688–1768), a French astronomer working in St. Petersburg.

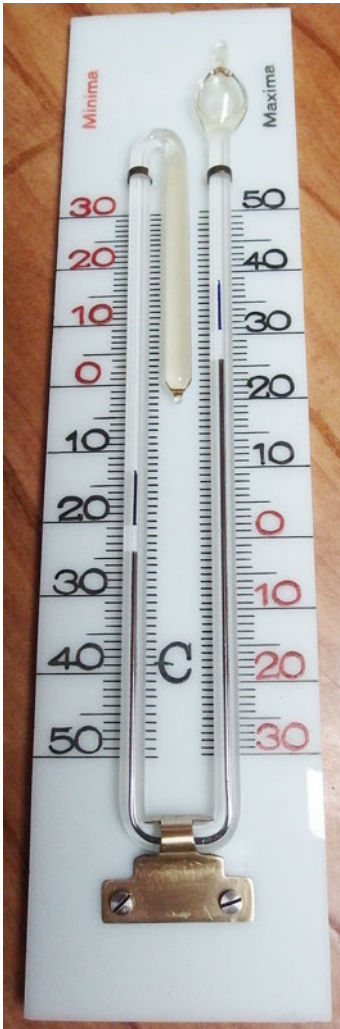


Fig. 7.3 Six's thermometer (photo © Daniel Kobrle, Mělník, Czech Republic, <http://danyk.cz>)

On his scale, 0°D was the boiling point of water, and the other fixed point was the near-constant temperature of the water of the Neva River below the ice (149.5°D), so the freezing point of water was set to 150°D .

In Uppsala, the Swedish astronomer *Anders Celsius* (1701–1744) performed experiments with the thermometers devised by Réaumur and Delisle. In 1741, he created a scale for a mercury thermometer in which the boiling point of water was 0°C and the freezing point was 100°C . In 1750, after his death, the successor to his professorship, *Mårten Strömer* (1707–1770), inverted his scale, yielding the Celsius scale that is still in use today.

Of special interest was the measurement of maximum and minimum temperatures. Overflow thermometers were first described by both *Daniel Bernoulli* (1700–1782) and (mainly) *Lord Charles Cavendish* (1704–1783) in 1754. The minimum–maximum thermometer devised by *James Six* (1731–1793) is still in use (Fig. 7.3), but it is not in meteorological service due to its low accuracy. The fluid used in this thermometer is alcohol (in the bulb on the minimum side), and mercury is only used for indication.

In 1790, *Daniel Rutherford* (1749–1819) described the construction of independent maximum and minimum thermometers; his minimum thermometer design is still used by meteorological services today (Sect. 7.4.1).

The beginning of the eighteenth century saw the creation of deformation thermometers. An example is the metallic thermometer constructed by *Samuel Frothingham* in 1748. In this, a brass bar was screwed to an iron bar. The first published report of a bimetallic thermometer, originated by *Johann Heinrich Lambert* (1728–1777), dates from 1779.

7.2.2 Temperature Scales

As already discussed in Sect. 7.2.1, the development of thermometers was closely connected to the development of temperature scales. The scales of Réaumur and Delisle were used for a period in France or Russia. Many other scales were not used for extended periods or were only employed in a particular small region. The 50-degree scale of the Accademia des Cimento has special historical relevance, as it is associated with the first regular meteorological measurements.

In 1848, *William Thomson* (1824–1907; *Lord Kelvin of Largs* from 1892) pinpointed the lowest possible temperature, the temperature at which the molecules in a material have zero energy. He proposed an absolute temperature scale with $0\text{ K} = -273.15^{\circ}\text{C}$ and where an increment of 1 K was equal to an increment of one degree on the Celsius scale.

Besides the Kelvin and Celsius scales that are now defined by the ITC-90, the Fahrenheit scale is still in use in some Anglo-American countries. These scales are linked such that

$$T_{\text{F}} [^{\circ}\text{F}] = 1.8t [^{\circ}\text{C}] + 32 = 1.8T [\text{K}] - 459.67 [\text{K}]. \quad (7.17)$$

Transformations between the different scales mentioned in this section are defined in Table 7.5.

Table 7.5 Transforming between temperature scales [7.14]

Unit	Kelvin K	Celsius °C	Fahrenheit °F	Réaumur °R	Delisle °D	Florence small °Gk
K	1	$K - 273.15$	$1.8 \times K - 495.7$	$0.8 \times K - 218.52$	$\frac{K}{-0.667} + 559.73$	$0.68143 K - 172.6$
°C	$°C + 273.15$	1	$1.8 \times °C + 32$	$0.8 \times °C$	$\frac{°C}{-0.667} + 150$	$0.68143 \times °C + 13.5$
°F	$0.556 \times °F + 255.4$	$0.556 \times °F - 17.78$	1	$0.444 \times °F - 14.22$	$\frac{°F}{-1.2} + 176.67$	$0.37857 \times °F + 1.39$
°R	$1.25 \times °R + 273.15$	$1.25 \times °R$	$2.25 \times °R$			
°D	$\frac{°D}{-1.5} + 373.15$	$\frac{°D}{-1.5} + 100$	$\frac{°D}{-0.83} + 212$			
Florence small °Gk	$1.4675 \times °Gk + 253$	$1.4675 \times °Gk - 19.8$	$2.6415 \times °Gk - 3.66$			

7.3 Theory

This section describes the theory behind three physical principles of temperature measurement: those based on thermal expansion, changes in electrical resistance, and variations in the speed of sound. It also discusses typical errors in temperature measurements and thermometer screens.

7.3.1 Liquid-in-Glass Thermometers

Liquid-in-glass thermometers are widely used for general temperature measurements. They make use of the cubic (volumetric) thermal expansion of a liquid in a glass bore with a constant circular cross-section (Fig. 7.4). The volumetric expansion of the liquid due to a change in the temperature T (which is close to neither the boiling nor the freezing point of the liquid) is given by [7.17, 18]

$$\Delta V = \alpha V_0(T - T_0), \quad (7.18)$$

where ΔV is the change in liquid volume due to the change in temperature, α is the cubic thermal expansion coefficient, and V_0 is the volume of the liquid at temperature T_0 . The change in the length of the liquid column Δh in the cylindrical glass bore of radius r upon a change in temperature ΔT is calculated via

$$\Delta h = \frac{\alpha V_0(T - T_0)}{\pi r^2}. \quad (7.19)$$

Typically, ethanol, with a cubic thermal expansion coefficient of $\alpha = 109 \times 10^{-5} \text{ K}^{-1}$, is the liquid used in modern liquid-in-glass thermometers. Historically, mercury ($\alpha = 18 \times 10^{-5} \text{ K}^{-1}$) was commonly employed, but applications of this toxic liquid are now restricted due to the regulation of toxic substances [7.19, 20].

Besides the expansion of the liquid, the expansion of the glass and the scale must also be taken into account (Chap. 10), but both are small, so they are included in the measurement error (Sect. 7.4.1).

7.3.2 Bimetallic Thermometers

A bimetallic thermometer consists of a strip of one metal bonded to a strip of another metal with a different metallic expansion coefficient. The bimetallic strip is fixed at one end. When the temperature changes, the strip bends in a circular arc (Fig. 7.5). The reference temperature is taken to be the temperature when the strip is planar. The passive part of the strip typically has an expansion coefficient of $< 5 \times 10^{-6} \text{ K}^{-1}$; e.g., the nickel-iron alloy Invar (FeNi36) has a very low expansion coefficient of $1.2 \times 10^{-6} \text{ K}^{-1}$. The active component typically has a thermal expansion coefficient of $15 \times 10^{-6} \text{ K}^{-1}$ and is made from an alloy of iron, nickel, manganese, and chrome. For small temperature changes, the deflection of the free end of the strip is given by [7.17]

$$y = \frac{K \Delta T L^2}{D}, \quad (7.20)$$

where K is a constant that depends on the material, L is the length of the strip, and D is the thickness of the strip.

7.3.3 Metal Resistance Thermometers

Platinum wires have come to dominate temperature measurement because of their stable temperature–

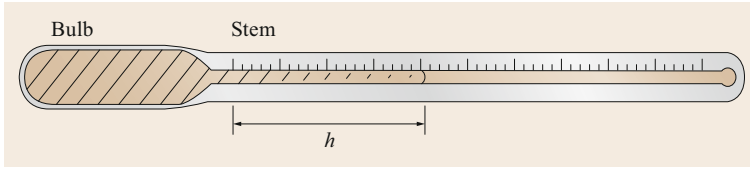


Fig. 7.4 Liquid-in-glass thermometer (after [7.17], with the permission of Oxford University Press)

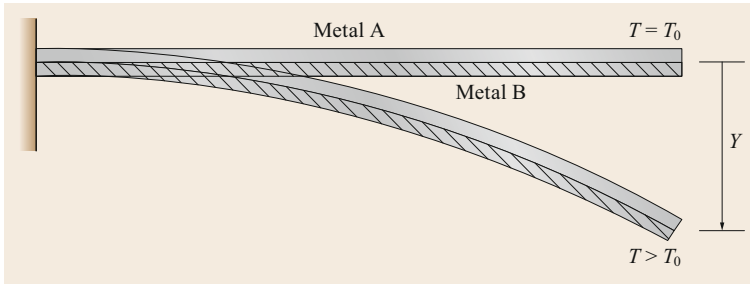


Fig. 7.5 Schematic of a bimetallic thermometer (after [7.17], with the permission of Oxford University Press)

resistance relationship. The temperature dependence of the resistance R is given by the equation [7.5, 17, 18]

$$R(T) = R_0[1 + \alpha(T - T_0)], \quad (7.21)$$

or, with $T_0 = 273.15$ K,

$$R(t) = R(0^\circ\text{C})[1 + \alpha t], \quad (7.22)$$

where α is the temperature coefficient of resistance in the vicinity of T_0 , which ranges from 0.00385 to 0.00392 K^{-1} depending on the purity of the platinum. By adding iridium, the brittleness of the wire can be reduced, which typically leads to lower temperature coefficients than for pure platinum. In the meteorological measurement range of -50 to 50°C , an almost linear temperature dependence is obtained. For larger temperature ranges, a modified version of (7.21),

$$R(T) = R_0[1 + \alpha(T - T_0) + \beta(T - T_0)^2], \quad (7.23)$$

where β is about $-5.85 \times 10^{-7}\text{ K}^{-2}$, is more accurate. Typical platinum thermometers have a resistance $R(0^\circ\text{C}) = 100\ \Omega$ ($1000\ \Omega$ is also available) and are standardized [7.21, 22]. $100\ \Omega$ platinum resistance thermometers (Pt100) are categorized into accuracy classes

(Table 7.6) according to the linear approximation (7.22). Class AA is the most common Pt100 class used in atmospheric measurements. Even more accurate are those that comply with Standard 1/10 DIN class B (DIN: Deutsches Institut für Normung; the German Institute for Standardization).

Thin-Wire Thermometers

Very thin wires with diameters of $< 20\ \mu\text{m}$ are used for turbulence measurements. The diameters of these wires are on the order of the wavelength of an electron in a platinum wire with contaminated surface [7.23] (about $\lambda = 1.62\ \mu\text{m}$). Therefore, the specific resistance ρ_d is greater than that of an infinitely thick wire ($\rho_\infty = 9.8 \times 10^{-8}\ \Omega\ \text{m}$) and can be approximated by the equation [7.23]

$$\rho_d = \rho_\infty \left(1 + \alpha \frac{\lambda}{d} \right), \quad (7.24)$$

where d is the thickness of the wire and the coefficient $\alpha = 3/8$ [7.24]. Specific resistances of wires with various diameters are given in Table 7.7. The time constant of a $20\ \mu\text{m}$ thick platinum wire is about $0.01\ \text{s}$ [7.25, 26]. The maximum currents without self-heating for 2, 5, and $25\ \mu\text{m}$ thick platinum wires are 2, 5, and $50\ \text{mA}$, respectively [7.27].

Table 7.6 Maximal tolerance for $100\ \Omega$ platinum resistance thermometers [7.21, 22]

Temperature °C	Maximal tolerance		Class B		Class AA ^a	
	Class A K	Ω	K	Ω	K	Ω
-100	±0.35	±0.14	±0.8	±0.32	±0.27	±0.11
0	±0.15	±0.06	±0.3	±0.12	±0.10	±0.04
100	±0.35	±0.13	±0.8	±0.30	±0.27	±0.11

^a Formerly 1/3 DIN class B.

Table 7.7 Specific resistances of very thin platinum wires [7.27]

Diameter of the wire (μm)	Specific resistance ($\times 10^{-8} \Omega \text{ m}$)	Resistance of 1 m length of the wire ($\Omega \text{ m}^{-1}$)
1	15.8	201 200
2	12.8	50 300
5	11.0	5600
10	10.4	1320
15	10.2	577
20	10.1	321
30	10.0	141
50	9.9	50

Electronic Circuits for Resistance Thermometers

A bridge circuit is used to perform electrical measurements in a resistance thermometer. The classical *Wheatstone* bridge is seldom used with two- and three-wire circuits because of nonlinearity and poor compensation for wire resistances. For the circuits given in Fig. 7.6a, with a temperature-sensitive resistance $R_1 + \Delta R$ and a reference resistance R_2 , it follows that if $R_1 + \Delta R \neq R_2$, the output voltage (source voltage of the bridge U) is [7.28]

$$U_{\text{out}} = U \frac{\Delta R R_4}{(R_1 + \Delta R + R_2)(R_3 + R_4)}. \quad (7.25)$$

The error in the output voltage is only lower than 1% if ΔR refers to a temperature difference of less than 5 K. Therefore, different linearization methods have been developed [7.28]. A second problem arises from the cables between the sensor and the bridge, because all metallic cables exhibit temperature sensitivity. The two-wire circuit (Fig. 7.6a) was replaced with a three-wire circuit in which two cables were attached to one side of $R_1 + \Delta R$, with one of the cables connected to R_2 and the other linked to the galvanometer. More effective is the Thomson bridge with four cables. In recent

years, most of these bridges have been replaced with constant-current circuits in which the temperature sensor is connected to four cables. These circuits are linear and unaffected by the temperature sensitivity of the cables (Fig. 7.6b).

7.3.4 Thermistors

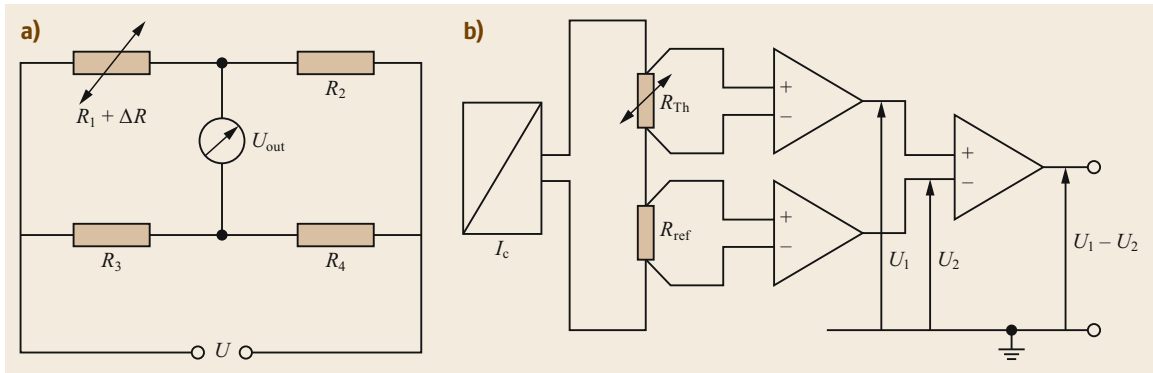
Thermistors are resistors with larger temperature coefficients than standard resistors. They are grouped into those with a positive temperature coefficient (PTC) and those with a negative temperature coefficient (NTC). Thermistors used in the atmospheric sciences are typically of the latter type, which are made from sintered metal oxides.

Resistance-measuring devices with integrated electronic circuits have largely replaced thermistors [7.29, 30] as measurement sensors, because even though thermistors have tenfold greater temperature sensitivity, they also exhibit nonlinear characteristics. Thermistors must undergo heat and cold aging before use, and frequent recalibrations are often necessary during operation. Modern thermistors are as stable as platinum wires [7.31]. The temperature dependence is given by the β equation

$$R(T) = R(0^\circ \text{C}) e^{\left(\frac{\alpha}{T} + \frac{\beta}{T^3}\right)}, \quad (7.26)$$

where, typically, $\alpha \approx 4500 \text{ K}$ and $\beta \approx -1.5 \times 10^7 \text{ K}^3$ [7.17]. The most important areas of application are in radiosondes and for measurements of body and dome temperatures in radiation sensors. Thermistors have been used in bridge circuits with a logarithmic approximation for possible linearization of the output signal [7.30]. Another approximation is the *Steinhart–Hart* equation [7.32]

$$T = \frac{1}{A + B \ln(R) + C [\ln(R)]^3}, \quad (7.27)$$


Fig. 7.6a,b Electronic circuits used in resistance thermometers: (a) classical Wheatstone bridge and (b) constant-current difference amplifier (I_c : constant current source)

which is often used for linearization in microcomputers.

Thermistors are more affected by self-heating than the platinum wires usually used in resistance thermometers. The highest input power to a thermistor is 0.06 mW, which guarantees self-heating of below 0.1 K [7.31].

7.3.5 Semiconductors

Semiconductor temperature sensors are not very common in atmospheric science. These sensors make use of the temperature dependence of the voltage across a semiconductor *pn* junction such as a diode. The simplest silicon diodes have a temperature sensitivity of about -2 mV K^{-1} [7.18]. The benefit of using a semiconductor is that it is simple to include the sensor in an electronic circuit.

7.3.6 Thermocouple

A thermocouple consists of two junctions of dissimilar metals [7.17, 18] with different *Seebeck coefficients*. If the temperatures of the two junctions are different, the thermocouple produces a temperature-dependent voltage called the Seebeck or thermoelectric effect. If one junction is kept at a constant temperature (the reference temperature), the thermocouple voltage is a measure of the temperature difference between the two junctions. A vessel with a water–ice mixture (0°C) or a metallic block at a constant temperature as regulated using an

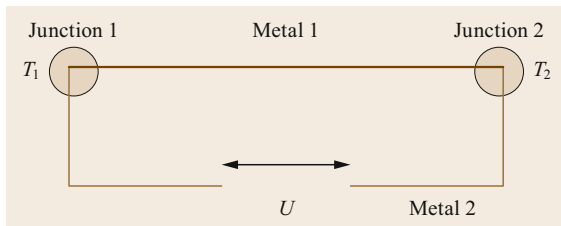


Fig. 7.7 Schematic of a thermocouple (after [7.18], with the permission of Wiley and Sons)

other temperature measurement can be used to obtain the reference temperature. A schematic of the electric circuit of a thermocouple is shown in Fig. 7.7.

The two metals (and thus the electrical properties of the metals) used in a thermocouple can vary. Thermocouples used for meteorological temperatures are listed in Table 7.8.

The characteristics of thermocouples are given by the equation [7.33, 34]

$$U [\mu\text{V}] = \sum_{i=0}^n c_i t^i, \quad (7.28)$$

where the temperature t is in $^\circ\text{C}$. The first four coefficients for the most common copper–constantan thermocouple according to ITS-90 are $c_0 = 0.0 \mu\text{V K}^{-1}$, $c_1 = 3.874811 \times 10^1 \mu\text{V K}^{-1}$, $c_2 = 4.419443 \times 10^{-2} \mu\text{V K}^{-2}$ (-270 to 0°C), $c_3 = 3.329223 \times 10^{-2} \mu\text{V K}^{-2}$ (0 to 400°C); for further coefficients see [7.33, 34]. It is obvious that only the coefficient c_1 (Table 7.8) is relevant given the typical accuracy of the measurements. Relevant thermoelectric voltages are given in Table 7.9.

7.3.7 Sonic Anemometers

Modern sonic anemometers (Chap. 9) use the travel time principle and direct time determination [7.35]. In this method, a sonic signal (about 100 kHz) is transmitted from each side of a measurement path and received at the opposite side. The wind velocity u causes one signal to be faster than the other. The exact travel times of the sonic signals from each side ($t_{1,2}$) are used to determine the wind velocity via

$$t_{1,2} = \frac{\sqrt{c^2 - u_n^2} \pm u_d}{c^2 - u^2} d, \quad (7.29)$$

where d is the path length, u_d is the wind component along the path, u_n is the normal component of the wind, and c is the speed of sound. The sum of the reciprocal

Table 7.8 Thermocouple type definitions [7.33, 34] along with values of the coefficient c_1 according to (7.17) ($c_0 = 0.0 \mu\text{V K}^{-1}$ if no other value is given)

Type	Composition	Temperature range ($^\circ\text{C}$)	Coefficient c_1 ($\mu\text{V K}^{-1}$)
E	Ni-Cr alloy versus Cu-Ni alloy (constantan)	-270 to 1000	5.866551×10^1
J	Fe versus Cu-Ni alloy (constantan)	-210 to 760	5.038119×10^1
K	Ni-Cr alloy versus Ni-Al alloy	-270 to 0	3.945013×10^1
		0 to 1372	3.892120×10^1 ($c_0 = -1.760041 \times 10^1$)
N	Ni-Cr-Si alloy versus Ni-Si-Mg alloy	-270 to 0	2.615911×10^1
		0 to 1300	2.592939×10^1
R	Pt-13% Rh versus Pt	-50 to 1064.18	5.289617
S	Pt-10% Rh versus Pt	-50 to 1064.18	5.403133
T	Cu versus Cu-Ni alloy (constantan)	-270 to 400	3.874811×10^1

Table 7.9 Thermocouple output voltages (in mV) from various types of thermocouples (see Table 7.8) according to ITC-90 when the reference temperature is 0 °C [7.33, 34] (complete data set at https://srdata.nist.gov/its90/main/its90_main_page.html, Accessed 04 July 2021)

Temperature (°C)	E	J	K	N	R	S	T
-50	-2.787	-2.431	-1.889	-1.269	-0.226	-0.236	-1.819
-40	-2.255	-1.961	-1.527	-1.023	-0.188	-0.194	-1.475
-30	-1.709	-1.482	-1.156	-0.772	-0.145	-0.150	-1.121
-20	-1.152	-0.995	-0.778	-0.518	-0.100	-0.103	-0.757
-10	-0.582	-0.501	-0.392	-0.260	-0.051	-0.053	-0.383
0	0.000	0.000	0.000	0.000	0.000	0.000	0.000
10	0.591	0.507	0.397	0.261	0.054	0.055	0.391
20	1.192	1.019	0.789	0.525	0.111	0.113	0.790
30	1.801	1.537	1.203	0.793	0.171	0.173	1.196
40	2.420	2.059	1.612	1.065	0.232	0.235	1.612
50	3.048	2.585	2.023	1.340	0.296	0.299	2.036

travel times gives the speed of sound through the equation

$$\frac{1}{t_1} + \frac{1}{t_2} = \frac{2}{d}c\sqrt{1 - \frac{u_n^2}{c^2}} \approx \frac{2}{d}c, \quad (7.30)$$

which is a function of the temperature and the moisture according to (7.15) (e : water vapor pressure, p : pressure), similar to the virtual temperature (Sect. 7.1.1),

$$T_s = \frac{d^2}{1607.52} \left(\frac{1}{t_1} + \frac{1}{t_2} \right)^2. \quad (7.31)$$

Recalculation of the true temperature is possible by applying the geometric parameters of the sonic anemometer (Chap. 55).

7.3.8 Radiation Error

The influence of radiation on temperature measurement is called the radiation error, which can be estimated as the additional heating caused by the absorption of radiation by the sensor. As well as the shortwave radiation and the properties of the sensor, the heating depends on three other parameters: the Prandtl number [7.7, 27],

$$\text{Pr} = \frac{\nu}{a_T}, \quad (7.32)$$

which is the ratio of the kinematic viscosity ν to the molecular thermal conductivity ($a_T = 0.71$ for air); the Reynolds number

$$\text{Re} = \frac{LV}{\nu}, \quad (7.33)$$

which is the ratio of inertial forces to frictional forces at the characteristic length scale L and the characteristic

velocity scale V ; and the Nusselt number

$$\text{Nu} = f(\text{Re}, \text{Pr}), \quad (7.34)$$

which is a function of the heat conductance and the flow characteristics. For forced convection ($0.01 < \text{Re} < 10000$) of air [7.36],

$$\text{Nu} = 0.39 + 0.51\sqrt{\text{Re}}. \quad (7.35)$$

The radiation error ΔT , the difference between the true and measured temperatures, is therefore a function of the radiation balance at the sensor surface Q_s , the sensor surface area F , and the heat transfer properties α , such that

$$\Delta T = \frac{Q_s}{\alpha F}, \quad (7.36)$$

where

$$\alpha = \text{Nu} \frac{\lambda}{d}, \quad (7.37)$$

$$Q_s = aK_{\downarrow}F_R. \quad (7.38)$$

Here, a is the absorption capacity of the surface, λ is the molecular heat transfer number, d is the sensor length, K_{\downarrow} is the downwelling shortwave radiation, and F_R is the area affected directly by the radiation.

On this basis, the radiation error of a cylindrical sensor with the dimensionless constant $c = 0.62$ can be calculated as [7.17, 18]

$$\Delta T = \frac{K_{\downarrow}(1-a)}{c\lambda} \sqrt{\frac{\nu d}{V}}. \quad (7.39)$$

Therefore, the radiation error is proportional to the shortwave radiation at the sensor surface and the square

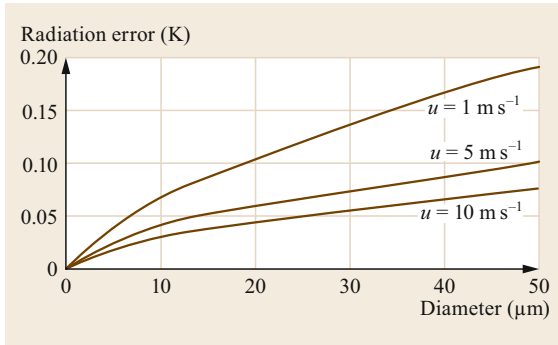


Fig. 7.8 Radiation errors for thin platinum wires with $K_{\downarrow} = 800 \text{ Wm}^{-2}$ and $a = 0.5$ in the presence of various wind velocities u (after [7.27] with permission from Wiley-VCH)

root of the sensor diameter and inversely proportional to the square root of the characteristic velocity.

Extensive investigations of the use of resistance wires for turbulence measurements have been performed [7.26, 27, 37]. Radiation errors for the absorption capacity of platinum ($a = 0.5$) are given in Fig. 7.8. Thus, radiation errors of $< 0.1 \text{ K}$ are only realized for wire diameters of $< 20 \mu\text{m}$.

Given the difficulties involved in measuring the temperature increase due to radiation error, the measurement accuracy outside of closed rooms is typically about 0.1 K (ventilated radiation shield; see Sect. 7.3.9), although the accuracy can reach 0.05 K for very well-maintained devices. Therefore, the radiation error is much greater than the errors of a well calibrated platinum wire sensor ($< 0.001 \text{ K}$).

7.3.9 Radiation Screens

To reduce the radiation error, *static (passive) radiation screens* have long been used in climate observations. A temperature shelter [7.18, 39] should protect the sensor from direct radiation, suppress any radiation-induced warming of the thermometer, prevent reflected radiation from the thermometer, exclude external sources of heat, allow air to flow freely around the thermometer, and protect it from precipitation. The utilization of various double-louvered screens (Venetian blinds) is well established in this context (Sect. 7.4.5). Several comparison experiments are available, but a theory that could inform guidelines for optimal construction is still missing. Multiple sensors can be housed in a shelter with Stevenson-type wooden screens, while a single sensor can be protected by a Gill multiplate shield, which is optimized to minimize errors [7.38]. Figure 7.9 shows the overall structure of such a shield (see also Fig. 7.15) along with a modeled flow distribution. Natural ventilation helps to reduce the error caused by housing the sensor in a confined space (the hut error) [7.40] to $1\text{--}2 \text{ K}$.

Besides the hut error, large static radiation screens have a lag time of up to 30 min in near-calm conditions [7.41]. This lag time is given by the approximation [7.42]

$$L = 2.5u^{-0.7} [\text{min}] . \quad (7.40)$$

To overcome the radiation error, the screen can be ventilated. Such a screen is known as an *active screen*. The hut error is reduced to below 1 K [7.31] when active screens are used, and can be even removed completely by adopting a system involving sufficient forced venti-

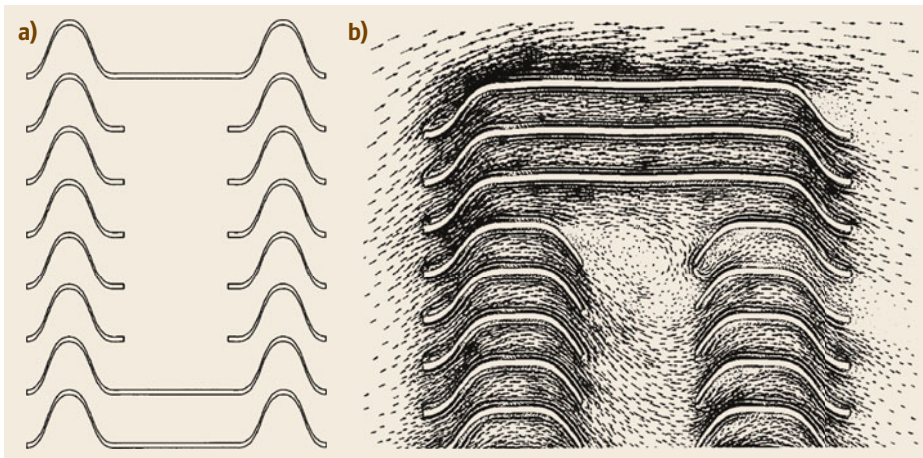


Fig. 7.9a,b The Gill multiplate shield. (a) Schematic showing a cross-section. (b) Velocity vectors calculated with a numerical model. Flow enters from the left at 1.0 m s^{-1} ; the speed is proportional to the length of the vector. The largest velocity, 1.6 m s^{-1} , occurs at the top leading edge of the shield (after [7.38] with permission from the American Meteorological Society)

Table 7.10 Classification of temperature and humidity measurement sites based on site characteristics [7.5]

Class	Terrain	Ground cover vegetation	No shadow when sun is higher than	Area covered with heat sources ^a within a large radius of	Area covered with heat sources ^a within a medium radius of	Area covered with heat sources ^a within a small radius of	Additional uncertainty
1	Flat horizontal land, slope < 19°	< 0.1 m, also in the region	> 5°	100 m: < 5%	30 m: < 5%	10 m: < 1%	–
2	Flat horizontal land, slope < 19°	< 0.1 m, also in the region	> 7°	30 m: < 10%	10 m: < 5%	5 m: < 1%	–
3		< 0.25 m, also in the region	> 7°		10 m: < 10%	5 m: < 5%	≤ 1 K
4					10 m: < 50%	3 m: < 30%	≤ 2 K
5	Site does not meet the requirements of class 4						≤ 5 K

^a Buildings, water (unless significant of the region), etc.

lation of double-tube radiation shields, similar to those of the *Assmann psychrometer* (Chap. 8).

7.3.10 Influence of the Surrounding Area on Temperature Measurements

The siting recommendation for temperature measurements is based on the structure of the temperature field near the surface and the vertical gradients (Chap. 1). The recommendation is also valid for humidity measurements (Chap. 8). Sensors should be installed inside a radiation screen at a height of between 1.25 and 2 m [7.5].

The main factors that influence temperature and humidity measurements are the presence of obstacles close to the screen (leading to a shadow effect and reduced nighttime cooling) and artificial surfaces, which may affect wind conditions, reflections, etc. Shadow effects due to the natural relief are not taken into account. The vegetation should be lower than the height of the screen. The World Meteorological Organization has developed a clear schema for the classification of temperature and humidity measurement sites based on site characteristics [7.5], as shown in Table 7.10 (see also Chap. 43).

7.4 Devices and Systems

Several previously popular measurement methods have either been supplanted in the last few decades or are now used only for special applications. These include thermocouples, semiconductors, and thermistors. Very fine thermocouples are still used for turbulence measurements (Chap. 55). Due to restrictions on the application of mercury (which is toxic) and the trend for automating measurements, liquid-in-glass sensors are also increasingly being sidelined. Therefore, this chapter only describes sensors that are still in use. For more on sonic thermometers, see the discussion of sonic anemometers in Chap. 9.

7.4.1 Liquid-in-Glass Thermometers

Liquid-in-glass thermometers are still commonly used for routine air temperature observations, including maximum, minimum, and wet-bulb temperatures [7.5]. In such a sensor, the expansion of the liquid as the temperature increases should be much larger than the expansion of the glass container. The stem is a fine bore of

constant circular cross-section that is only partly filled with the liquid and is connected to the main liquid-filled bulb. The inside surface of the bore should be coated to reduce adhesion forces. Thermal expansion of the liquid causes the length of the liquid column to change, allowing the change in temperature to be gauged. Usually the stem is sheathed and the temperature scale is engraved on the stem or on a glass strip attached to the stem. Nowadays, alcohol is generally used as the liquid rather than the previously popular mercury due to the toxicity of the latter material [7.19, 20]. A liquid with properties similar to mercury has recently become available. This eutectic alloy of gallium, indium, and tin, marketed as Gallistan® [7.43], has a melting point of -19°C and gives stable results above -2°C . This liquid is used in maximum thermometers intended for medical purposes. It could also be applied for meteorological observations in areas that are always above freezing. In this case, the bore is coated with gallium oxide to increase adhesion forces so that it is not necessary to narrow the bore in the maximum thermometer (Fig. 7.10c).

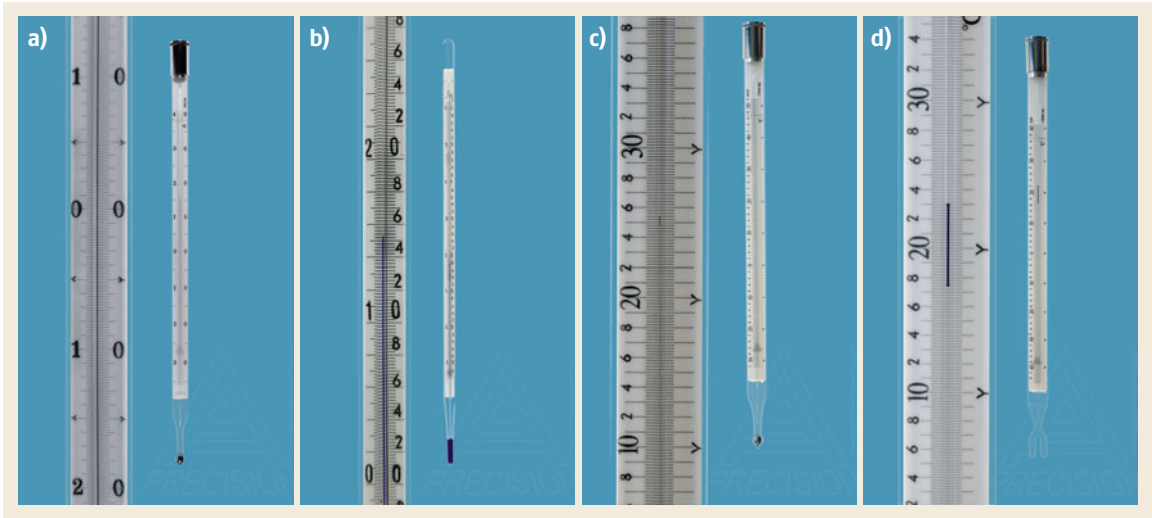


Fig. 7.10a–d Liquid-in-glass thermometers: (a) station thermometer (August psychrometer), (b) station thermometer (Assmann psychrometer), (c) maximum thermometer, (d) minimum thermometer (photos © Amarell GmbH & Co. KG, Kreuzwertheim, Germany)

Different types of liquid thermometers are available (Fig. 7.10) for meteorological applications according to the British standard [7.44] or German standards [7.45]. These thermometer types are only used in classical thermometer screens. The ordinary station thermometer has a scale increment of 0.2 K, or occasionally 0.5 K, and is available in a larger form for use in the August psychrometer (Chap. 8) or in a smaller form for use in the Assmann psychrometer (Chap. 8). Minimum and maximum thermometers are also available. The minimum thermometer has a dark glass index (Fig. 7.11), about 2 cm long, that is immersed in the spirit. This thermometer should be orientated in a near-horizontal position. The maximum thermometer is a mercury-in-glass thermometer with a reduced diameter and a constriction in the bore between the bulb and the beginning of the scale (Fig. 7.11). This constriction prevents the mercury column from receding with falling temperatures. The observer can reset the thermometer by holding it bulb end downwards and swinging their arm until the mercury column is reunited. The maximum thermometer should be mounted at an angle of about 2° from the horizontal position. Soil thermometers have an inclined stem that permits measurements down to a depth of 20 cm. To probe greater depths, an ordinary thermometer is mounted on a wooden or plastic tube and sunk into the ground to the required depth (Chap. 61). For a discussion of the application of liquid-in-glass thermometers to climatological observations, see Sect. 7.8.1.

Thermometers should be read as rapidly as possible in order to avoid changes in temperature caused by the

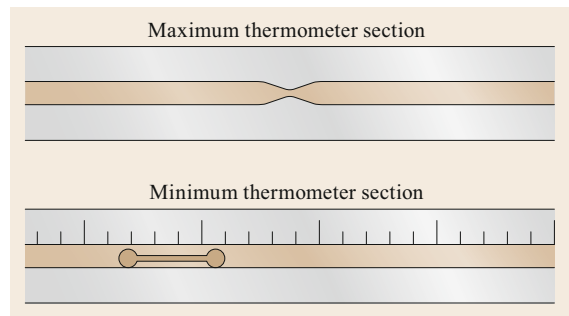


Fig. 7.11 Schematic showing cross-sections of maximum and minimum thermometers with a reduced bore and constriction and a dark index, respectively (after [7.17] with permission from Oxford University Press)

observer's presence [7.5]. The liquid meniscus (or index) and the thermometer scale should be in the same plane to avoid parallax errors. Readings should be made to tenths of a degree (important in psychrometry; see Chap. 8), even when the scale is divided into fifths or even halves of a degree. Corrections for scale errors that are given in the calibration certificate should be applied to the readings.

The following errors may be applicable to measurements made using liquid-in-glass thermometers [7.5]:

- The *reversible elastic error* is important when the thermometer is exposed to a large range of temperatures in a short time interval, and depends on the quality of the glass (it ranges from 0.03 to 1 K for a temperature range of 0 and 100°C). This type of

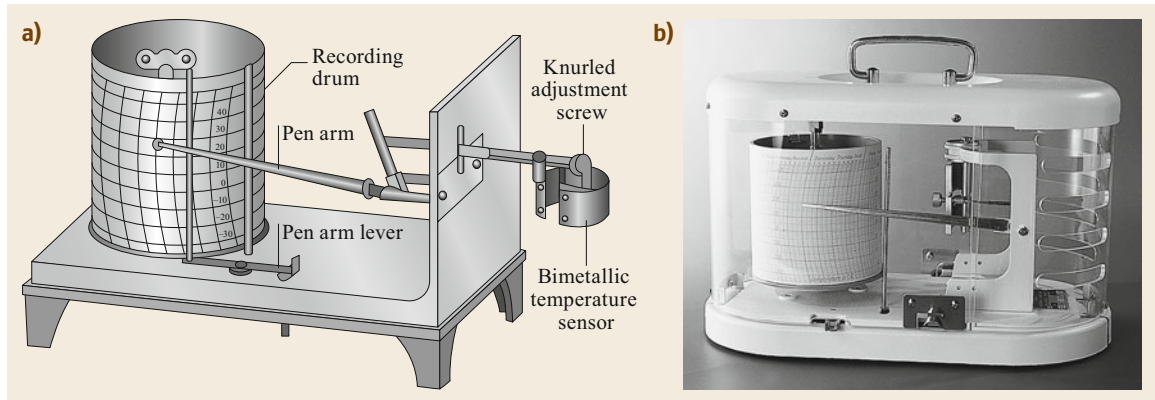


Fig. 7.12 (a) Schematic of a bimetallic thermograph (after [7.45] with permission of VDI e. V., Düsseldorf, Germany) and (b) a recently produced device (photo courtesy of Feingerätebau K. Fischer GmbH, Drebach, Germany, 2018)

error is relatively unimportant for most of meteorological measurements.

- *Irreversible elastic error* occurs when the bulb slowly contracts over a period of years. Even for high-quality glass, this error will be about 0.01 K during the first year of use.
- *Error due to an emergent stem* occurs if the thermometer is not completely surrounded by air at a uniform temperature. This error may be relevant during calibrations.
- *Parallax error* occurs if the viewing angle is not perpendicular to the stem of the thermometer.
- *The gross reading error* is usually 1°, 5°, or 10°. Therefore, the observer should read to the nearest tenth of a degree.
- *The error due to the different cubical expansion coefficients of the alcohol and the glass* necessitates careful calibration. This error is more relevant for mercury thermometers than alcohol thermometers, which have a much higher expansion coefficient.
- Thermometers with organic liquids have some special errors, such as *errors due to liquid adhesion to the glass or liquid polymerization with age*. The liquid column may be broken, mainly due to transport, or drops of liquid may form in the upper part of the thermometer stem due to evaporation and condensation (see also Sect. 7.7).

7.4.2 Bimetallic Thermometers

Bimetallic thermometers are mainly used in thermographs for atmospheric measurements. They are often employed in combined thermo-hygrographs (Chap. 8) but not as single temperature sensors. Furthermore, bimetallic thermometers are used for temperature compensation in hair hygrometers (Chap. 8) and in aneroid barometers (Chap. 10).

A bimetallic thermograph for measurements in large temperature screens or for indoor measurements is shown in Fig. 7.12 [7.5]. The movement of the recording pen is controlled by the change in curvature of the bimetallic strip, which has one fixed end. The arm with the pen should be adjustable so that the zero of the instrument can be changed if necessary. Instrument errors are related to the mechanics of the instrument, mainly the lever, the recording drum, and the strip chart, as well as possible corrosion of the bimetallic strip. Sometimes the strip is replaced with a *Bourdon tube* (a curved metal tube filled with alcohol), which has a faster response time but is less sensitive.

7.4.3 Resistance Thermometers

Resistance thermometers can only be used in thermometer screens or in specially constructed instruments. Typical resistances are 100 Ω (Pt100) or 1000 Ω (Pt1000). AA class resistance thermometers [7.21, 22] that utilize four-wire sensors (two cables on each side of the resistance; see Sect. 7.3.3) are mainly used for atmospheric measurements. A simple resistance thermometer construction is shown in Fig. 7.13. Often the sensor is combined with a capacitive humidity sensor,

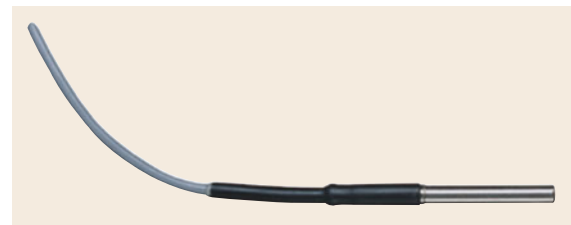


Fig. 7.13 A resistance thermometer (photo © Adolf Thies GmbH & Co. KG, Göttingen, Germany, 2018)

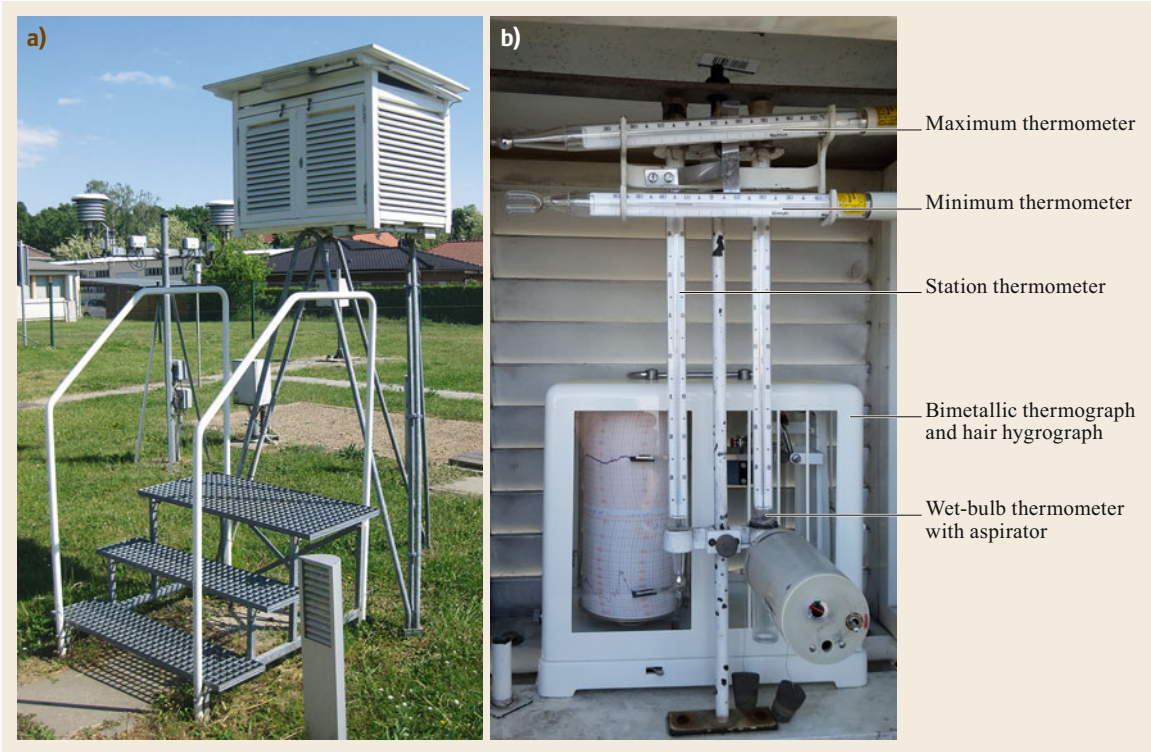


Fig. 7.14 (a) Stevenson temperature screen (photo © T. Foken). (b) View inside a temperature screen showing the classical instrumentation setup; the station thermometer and the wet-bulb thermometer together comprise an August psychrometer (see Fig. 9.17) (photo © T. Foken)

as shown in Fig. 8.17b, while the sensitive measuring element is shown in Fig. 8.17a.

Typical error sources for resistance thermometers include [7.5]:

- *Self-heating of the measurement element.* Depending on the diameter of the wire, the current should be less than 2 mA so that the self-heating is significantly lower than 0.1 K [7.46].
- *Inadequate compensation for the lead error.* A four-wire circuit is thus recommended.
- *Inadequate compensation for nonlinearities.* The sensor should be selected according to the possible range of temperatures that will be encountered (excessively large range should be avoided). The resulting error due to nonlinearities will depend on the resistance class (see Table 7.6).
- *Sudden changes in switch contact properties,* which can occur as the switch ages.

Fine-wire fast response thermometers are no longer commercially available. Some institutionally made sensors are described in the literature [7.27, 47]. Because fine wires are difficult to handle, *Wollaston wire*, which

is a very fine (< 0.01 mm diameter) platinum wire clad in silver, can be used. After fixing the wire in place, the silver can be eliminated using an electrolytic method in which potassium cyanide is used as the electrolyte [7.48].

7.4.4 Radiation Screens

Any radiation or temperature shield or screen should be designed such that it provides an enclosure with an internal temperature that is both uniform and the same as that of the outside air [7.5]. Temperature screens for meteorological and climatological sensors vary widely between countries [7.39]. The most common temperature screen is that of Stevenson (see Fig. 7.14a).

The rising popularity of automatic weather stations has led to a significant increase in the number of screen designs. The screen should completely surround the thermometer and exclude radiant heat, precipitation, and other phenomena that might influence the measurements. To ensure that the shelter (hut) effect is comparable between shelters, the comparison procedure as well as the main construction details are standardized [7.49]. To avoid biases due to differ-



Fig. 7.15a–e A selection of nonventilated (**a,b**) and ventilated (**c–e**) temperature screens: (**a**) screen developed by Gill (model 41003; photo © R. M. Young/GWU Umwelttechnik GmbH, Erfstadt, Germany); (**b**) naturally aspirated helical radiation screen (photo © baranidesign, Bratislava, Slovakia); (**c**) ventilated screen of the German Meteorological Service with four sensors (photo © Eigenbrodt GmbH & Co. KG, Königsmoor, Germany); (**d**) aspirated screen (photo © Apogee Instruments, Logan, UT, USA); (**e**) ventilated temperature screen (model 43502; photo © R. M. Young/GWU Umwelttechnik GmbH, Erfstadt, Germany)

ences between the microclimate inside the screen and properties of the surrounding air, screens with forced ventilation are often used. When artificial ventilation is used, the sensors should not be affected by water droplets, etc., and the ventilation motor should not heat up the air inside the screen. The shield material should be highly reflective and have low heat absorption. Naturally ventilated thermometer screens permit accurate air temperature measurements, to ± 0.1 K in most circumstances, but occasionally differ by more than 0.5 K in light winds or because of a slow response. Furthermore, during low wind conditions maximum temperatures are underestimated and minimum temperatures are overestimated [7.50]. Some comparison experiments of temperature shields have been reported,

but mainly only as internal reports of various meteorological services [7.5, 51].

Figure 7.15 shows a selection of small nonventilated and ventilated temperature screens. Only the classical screen developed by Gill (Fig. 7.15a) is well described [7.38]. The helical radiation screen provides natural aspiration [7.51] (Fig. 7.15b). Figure 7.15c shows the ventilated radiation screen design used by the German Meteorological Service. The ventilated radiation screen in Fig. 7.15d is a double tube filled with insulating material. The sensor can be mounted from the side. Figure 7.15e shows a ventilated double tube with the sensor in the middle. Comparison experiments show that the radiation error for nonventilated screens drops significantly with increasing wind speed, but for

Table 7.11 Advantages and disadvantages of different temperature sensors

Devices	Advantages	Disadvantages
Liquid-in-glass instrument	Easy to handle	Not suitable for registration, only for use in radiation screens
Bimetallic thermometer	Easy to use for mechanical registration systems	No electrical output signal, only for use inside radiation screens or for indoor measurements
Resistance thermometer with Pt100/Pt1000 sensor	Accurate and almost linear signal	Only for use inside radiation screens
Resistance thermometer with thin wire < 20 μm diameter	Temperature measurements (turbulence) with no radiation error	Very sensitive and difficult to handle
Thermistor	Tenfold higher temperature coefficient than resistance thermometers	Highly nonlinear characteristic, self-heating possible
Thermocouple	Very thin thermocouples can be used for turbulence measurements	Reference temperature required, not as accurate as resistance thermometers



Fig. 7.16 Assmann aspirated psychrometer with one sensor (a resistance thermometer), ventilation, and a double-tube radiation shield (photo © Theodor Friedrichs & Co., Schenefeld, Germany, 2018)

mann's guidelines for the dimensions of the double radiation shield are followed and the ventilation velocity is larger than 2.5 m s^{-1} [7.52] (Chap. 8, Fig. 8.20). A version of this instrument with just one temperature sensor (a resistance thermometer) is shown in Fig. 7.16.

Several small temperature screens are available for the combination of a resistance thermometer with a capacitive humidity sensor (see Fig. 8.17b), some of which are partly ventilated (Sect. 7.4.5).

7.4.5 Sensor Comparison

The number of methods used for atmospheric measurements has decreased over the last few decades because of the trend away from visual measurements with liquid-in-glass thermometers, the restrictions on mercury thermometers, and the increasing popularity of electronic sensors that can be used in automatic stations. Even the bimetallic thermograph has been largely replaced; nowadays, it is only applied for climatological and indoor measurements. The resistance thermometer has the most advantages of any electronic sensor, including high accuracy, the nearly linear output signal of a constant-current circuit, and easy handling. Because of the availability of good amplifiers, its relatively low temperature coefficient is no longer a restriction. Resistance thermometers can be made very small, leading to a fast response time. They have therefore even replaced thermistors in radiosondes (Chap. 46). An overview of the advantages and disadvantages of different temperature sensors is given in Table 7.11.

low wind speeds ($< 2 \text{ m s}^{-1}$) it is still several degrees (1–2 K), although it varies significantly depending on the type of screen used. The radiation error for ventilated screens is always below 1 K [7.31].

The requirements of a radiation screen—excellent radiation protection and sufficient ventilation—are best realized with an Assmann aspirated psychrometer (Chap. 8 and Fig. 8.19). This device consists of two thermometers that are ventilated at $> 2.5 \text{ m s}^{-1}$ and equipped with a double radiation shield. Liquid-in-glass thermometers are generally used (Fig. 7.11b), although electrical sensors are also relatively accurate if Ass-

7.5 Specifications

Typical uncertainties in the measurements obtained using various temperature sensors are given in Table 7.12, and typical response times are provided in Table 7.13.

For turbulence measurements, only sonic thermometers, fine-wire resistance thermometers, or thermocouples with a diameter of $< 20 \mu\text{m}$ can be used. When a

Table 7.12 Specifications of various temperature sensors [7.5, 45]

Method	Typical total uncertainty (K)	Typical temperature range (°C)	Remark
Liquid-in-glass	≤ 0.2	−40 to 50	Mercury should not be used below −38.9 °C
Liquid-in-glass (maximum and minimum thermometers)	≤ 0.5	−30 to 50, −40 to 40	
Bimetallic thermograph	≤ 1	−40 to 50	Flow rate ≥ 2.5 m s ^{−1}
Resistance thermometer	≤ 0.1	−40 to 50	
Thermistor	≤ 0.2	−40 to 50	
Thermocouple	≤ 0.5	−40 to 50	

Table 7.13 Time constants of temperature sensors

Measurement device	Time constant (s)
Sonic thermometer	< 0.01
Thin resistance wire (< 20 μm diameter)	< 0.01
Thermocouple	1–2, < 0.01 (< 20 μm diameter)
Thermistor	0.1–1
Liquid-in-glass and resistance thermometers (3–5 mm diameter)	10–30
Bimetallic thermograph	25 s (ventilation 5 m s ^{−1})
Required response time [7.5]	20 s

liquid-in-glass or resistance thermometer is used in a psychrometer (Chap. 8), the uncertainty should be 0.1 K

or less. Well-calibrated resistance thermometers can be used as a reference standard.

7.6 Quality Control

After calibrating a temperature sensor with a reference standard, corrections are required for at least each 10 K interval. The characteristics given in Table 7.14 should be fulfilled for these corrections.

7.6.1 Reference Standards

The World Meteorological Organization has developed some standards for data quality control [7.5], which are separated into laboratory standards and field standards.

Laboratory Standards

Primary-standard high-grade platinum resistance thermometers should be held and maintained at national standards laboratories, which may be national meteorological or other accredited calibration laboratories. Because the triple point of water is known precisely,

these thermometers should be checked periodically in a water triple-point cell with an uncertainty of 1×10^{-4} K.

Field Standards

Well-calibrated reference thermometers should be used for comparisons in the field. While the World Meteorological Organization recommends the WMO reference psychrometer [7.53], which is a free-standing instrument with radiation shield and ventilation (Sect. 8.4.4) and an uncertainty of 0.04 K, this instrument is only rarely available. However, the working standard of humidity measurements—the Assmann aspiration psychrometer—can also be used (Sect. 8.6.1).

Several calibration points can easily be generated in a Dewar flask, such as 0 °C (using a mixture of ice pieces and water) or −20 °C (with one part ice and three parts sodium chloride).

Table 7.14 Required thermometer characteristics for different types of thermometers [7.5]

Characteristic	Ordinary	Maximum	Minimum
Scale range (°C)	−30 to 45	−30 to 50	−40 to 40
Calibration range (°C)	−30 to 40	−25 to 40	−30 to 30
Maximum error (K)	< 0.2	0.3	0.2
Maximum difference between maximum and minimum corrections within the range (K)	0.2	0.5	0.3
Maximum variation in the correction within any 10 K interval (K)	0.1	0.1	0.1

Table 7.15 Typical test criteria for temperature measurements

Method	Error	Reason
All sensors	Temperature too low in comparison to other nearby temperature measurements Temperature too high (> 1–2 K) in comparison to other nearby temperature measurements Temperature is constant for more than 3–6 h	Sensor element is wet and provides a temperature close to the wet-bulb temperature Sensor is influenced by shortwave radiation; check the radiation shield and the ventilation Functionality of the sensor and/or the circuit is impaired; replacement required
Liquid-in-glass thermometer	Temperature too low in comparison to other temperature measurements Temperature too high in comparison to other temperature measurements	The liquid has partly evaporated and is seen in the upper part of the glass bore; maintenance or replacement required The liquid has partly evaporated and air is present in the middle of the liquid column in the glass bore; maintenance or replacement required
Electrical thermometer	Temperature out of the measurement range Temperature is a few degrees too high or low in comparison to other temperature measurements	Broken wire or defective measurement circuit; replacement required Contact problem; maintenance of all connectors required

7.6.2 Temperature Calibration

Temperature sensors should be calibrated against the reference sensor in a vessel of water. The calibration should be performed indoors to exclude the effects of radiation. The sensors should be separated by a distance of around 1 cm or less. For liquid-in-glass thermometers, the temperature difference between the water and the temperature of the room should be smaller than 5 K to ensure that the liquid and the glass have nearly the same temperature.

According to the ITS-90, resistance thermometers should be calibrated using the *Callendar–Van Dusen* equation [7.5, 22], which is the interpolation

$$R_t = R_0 [1 + A t + B t^2 + C (t - 100)t^3], \quad (7.41)$$

where R_0 is the resistance at 0 °C and A , B , and C are constants ($C = 0$ when $t > 0$ °C).

7.6.3 Specific Quality Control Methods

When performing quality control of temperature measurements, it is useful to compare the data with other temperature measurements obtained with temperature sensors in other devices such as net radiometers in the surrounding area or with sensors at other measurement heights. It should be taken into account that typical variations are also possible within the daily cycle (Chap. 1). For temperatures at different heights, a linear or (better) logarithmic approximation should be derived according to the profile equations (1.8) and (1.10). Sensors that do not follow this approximation during the daytime should be checked. Possible reasons for over- or underestimating the temperature are listed in Table 7.15.

7.7 Maintenance

The thermometer should be installed in a manner that guarantees that the measuring element is always dry, otherwise the (lower) wet-bulb temperature will be measured. Furthermore, visual checks of liquid-in-glass thermometers are very important because evaporation of the liquid in the glass bore will interrupt the liquid column, meaning that higher temperatures will be simulated.

Maintenance activities should be scheduled at regular intervals, as shown in Table 7.16. Inspections should include all electrical cables and their connections. The result of the inspections should be documented in the metadata.

Table 7.16 Maintenance of temperature measurement systems [7.45]

Maximum interval	Liquid-in-glass thermometer	Bimetallic thermograph	Resistance thermometer
1 week	Visual check and cleaning if necessary (dirt and cobwebs)		
	Comparison with a ventilated thermometer	Comparison with the station thermometer	
6 months		Compare measurements with a calibrated reference thermometer	
		Check mechanical functions	
2 years	Calibration of the sensor in the laboratory		
			Replace the fan

7.8 Applications

Temperature sensors are widely used in atmospheric measurements because a reference temperature is needed to perform corrections to various measurements or to carry out additional calculations, such as the determination of the air density (Chap. 5). The most prominent application of temperature sensors is, of course, to measure the temperatures used for weather prediction and climatology.

7.8.1 Temperature Measurements for Meteorology and Climatology

The most important measurements are listed in Table 7.2. Because of the horizontal heterogeneity of the temperature field and strong vertical gradients (Chap. 1), several requirements must be fulfilled to ensure that temperature measurements are comparable. For general meteorological work, the observed air temperature should be representative of the free-air conditions surrounding the station at a height of between 1.25 and 2 m above ground level and over an area as large as possible [7.5]. Liquid-in-glass or (more recently) resistance thermometers are used, all within a temperature screen, and ventilated if possible. Specific instructions for meteorological stations are given in Chap. 43. Besides the temperature at a particular time, the minimum (measured from 18:00 to 6:00 LT) and maximum (measured from 6:00 to 18:00 LT) temperatures should also be measured at the same height. The minimum at 5 cm above ground should be measured too. Because the sensor is used without a radiation screen, the measured value can only be used for the minimum, which occurs around sunrise. The soil temperature is usually measured at depths of 5, 10, 20, 50, and 100 cm (Chap. 61).

Calculation of Mean Values

Modern data acquisition technologies allow sampling rates of 0.1 to 10 s. The typical averaging interval for temperature is 10 min, but intervals of 30 or 60 min are also used. For standard meteorological measurements in Central Europe, the daily mean temperature is calculated from 24 temperatures t_i recorded at one-hour intervals between 23:50 UTC of the previous day and 22:50 UTC of the current day [7.45], i.e.,

$$\bar{t}_{\text{day}} = \frac{1}{24} \sum_{i=0}^{23} t_i. \quad (7.42)$$

For other time zones, the averaging times must be adjusted accordingly. The climatological daily mean is

calculated according to (7.42). If more than four successive hourly values are not available, the daily mean is calculated from the arithmetic mean of the measurements at 00:00, 06:00, 12:00, and 18:00. At climate reference stations, the daily mean is derived by averaging the temperatures measured at 6:30, 13:30, and 20:30 UTC [7.54], i.e.,

$$\bar{t}_{\text{day}} = \frac{t_{6:30} + t_{13:30} + 2 t_{20:30}}{4}. \quad (7.43)$$

Furthermore, days are assigned to climatological classes based on the minimum and/or maximum temperature during the day; see Table 7.17.

Effect of Changing the Sensor on Climatological Data

The temperature is an important indicator of climate change. The effect of changing the temperature scale on the bias of the measured temperature is small, as illustrated by Fig. 7.17. The bias is only significant for very low and very high temperatures before 1968, but even then it is still $< |0.05 \text{ K}|$ [7.46].

However, changes in instrumentation—mainly from liquid-in-glass thermometers housed in large thermometer screens to resistance thermometers protected by ventilated or nonventilated small thermometer screens—have had a much greater influence on the bias. That said, extensive investigations of this effect are still lacking. Based on data from an analysis by the German Meteorological Service [7.55], changing from using a liquid-in-glass thermometer to a resistance thermometer decreases the measured temperature by $-0.03 \pm 0.16 \text{ K}$. Also, changing the equation used to calculate the daily mean from (7.43) to (7.42) leads to a drop in temperature of $-0.08 \pm 0.52 \text{ K}$. Therefore, changes in the measurement sensors and calculation procedure used cannot explain the increase in atmospheric temperatures observed in recent decades, as together they would be expected to decrease measured temperatures by about -0.1 K .

Table 7.17 Climatological classification of days based on the minimum and/or maximum temperature

Type of day	Minimum temperature (°C)	Maximum temperature (°C)
Ice day		$t_{\text{max}} < 0$
Frost day	$t_{\text{min}} < 0$	$t_{\text{max}} > 0$
Ground frost day	$t_{\text{min}-5 \text{ cm}} < 0$	
Summer day		$t_{\text{max}} \geq 25$
Hot day		$t_{\text{max}} \geq 30$
Tropical day	$t_{\text{min}} \geq 20$	

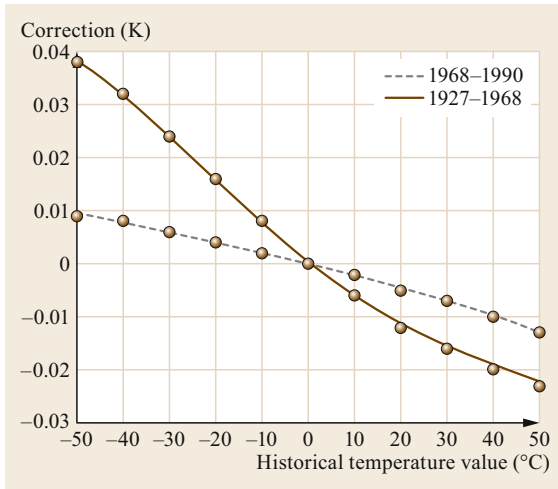


Fig. 7.17 Plot showing the correction that must be made to historical temperature data measured before the application of the ITS-90 in 1990 as a function of temperature (after [7.46] with permission from Wiley & Sons)

Climate Diagrams

Temperature data are an important part of climate diagrams, which are calculated for thirty-year climate periods. The reference period for these diagrams is generally 1961–1990, before the strong recent increase in atmospheric temperatures, although the period 1981–2010 is sometimes used. Climate diagrams are often combined with precipitation sum data for the same

7.9 Future Developments

Measuring principles that allow digital data recording and have a near-linear response characteristic dominate. These criteria are fulfilled in particular by resistance thermometers, as well as—for turbulence measurements—sonic thermometers and, on occasion, thin platinum wires. Liquid-in-glass or bimetallic sensors are still popular as visual display in private areas or for classical reference measurements. Because platinum sensors can be integrated into chips and miniaturized, they can have low response times, and have therefore replaced thermistors for aerological measurements. The number of measurement principles in use has significantly decreased in the last few decades, and this trend will continue. A eutectic alloy of gallium, indium, and tin that is marketed under the tradename Gallistan® [7.43] can be used as the liquid in maximum

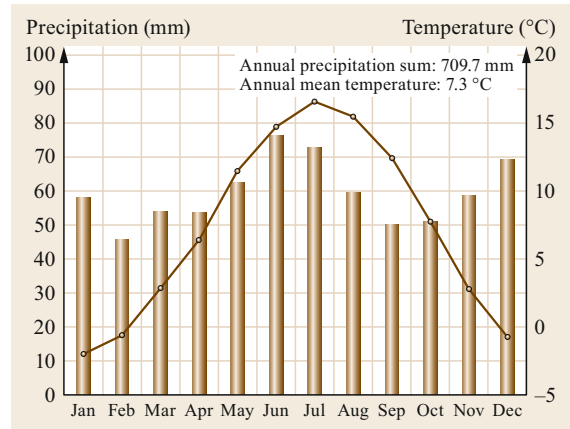


Fig. 7.18 Climate diagram for Bayreuth, Germany during 1961–1990, plotting both precipitation and temperature (after [7.56], © the authors)

period; an example is shown in Fig. 7.18. For other climatologically relevant illustrations, see Chap. 1.

7.8.2 Further Applications

Besides their application in meteorology, temperature measurements in the atmosphere are necessary for many technical processes. Radiation shields and ventilation are necessary for accurate measurements. The influence of shortwave radiation and heat sources can be excluded from indoor measurements.

thermometers for warm areas and in thermometers employed in Assmann psychrometers, because the accuracy of this psychrometer is too low below 0 °C.

Temperature sensors are included in many devices used in daily life, such as smartphones and cars. Because many sensors can now be accessed online, the number of temperature sensors in the atmosphere has increased dramatically. Of course, these sensors are not being applied in accordance with the recommendations given above, but the extremely large number of sensors available offers the possibility of filtering the data with mathematical models to make this information usable. This method is called crowdsourcing thermometry (Chap. 44). It can be assumed that a very detailed description of the horizontal temperature distribution will become available in the near future.

7.10 Further Reading

- VDI: *Umweltmeteorologie, Meteorologische Messungen, Temperatur (Environmental meteorology, meteorological measurements, temperature)*, VDI 3786 Blatt(Part) 4 (Beuth-Verlag, Berlin 2013)
- WMO: *Guide to Instruments and Methods of Observation*, WMO-No. 8, Volume I - Measurement of Meteorological Variables. (World Meteorological Organization, Geneva, 2018)
- G.R. Harrison: *Meteorological measurements and instrumentation* (John Wiley and Sons, Chichester 2015)
- F.V. Brock, S.J. Richardson: *Meteorological measurement systems* (Oxford University Press, New York 2001)
- J.M. Blonquist Jr. and B. Bugbee: Air temperature. In: J.L. Hatfield, M.V.K. Sivakumar, J.H. Prueger (eds.), *Agroclimatology: linking agriculture to climate*, Agronomy Monographs 60 (American Society of Agronomy, Madison 2020) pp. 51–72.

Acknowledgments. We acknowledge Mr. Kobrle, several companies, and the German Thermometer Museum for allowing us to use their photographs.

References

- 7.1 F. Albrecht: Thermometer zur Messung der wahren Temperatur, *Meteorol. Z.* **24**, 420–424 (1927)
- 7.2 M.L. Salby: *Physics of the Atmosphere and Climate* (Cambridge Univ. Press, Cambridge 2012)
- 7.3 D.L. Hartmann: *Global Physical Climatology*, 2nd edn. (Elsevier, Amsterdam 2016)
- 7.4 H. Preston-Thomas: The international temperature scale of 1990 (ITS-90), *Metrologia* **27**, 3–10 (1990)
- 7.5 WMO: *Guide to Meteorological Instruments and Methods of Observation*, WMO, Vol. 8 (World Meteorological Organization, Geneva 2014), update 2017
- 7.6 N. Mölders, G. Kramm: *Lectures in Meteorology* (Springer, Cham, Heidelberg, New York, Dordrecht, London 2014)
- 7.7 T. Foken: *Micrometeorology*, 2nd edn. (Springer, Berlin, Heidelberg 2017)
- 7.8 J.C. Kaimal, J.A. Businger: A continuous wave sonic anemometer-thermometer, *J. Clim. Appl. Meteorol.* **2**, 156–164 (1963)
- 7.9 J.C. Kaimal, J.E. Gaynor: Another look to sonic thermometry, *Bound.-Layer Meteorol.* **56**, 401–410 (1991)
- 7.10 G. Jendritzky, R. de Dear, G. Havenith: UTCI—why another thermal index?, *Int. J. Biometeorol.* **56**, 421–428 (2012)
- 7.11 R. Osczevski, M. Bluestein: The new wind chill equivalent temperature chart, *Bull. Am. Meteorol. Soc.* **86**, 1453–1458 (2005)
- 7.12 W.E.K. Middleton: *A History of the Thermometer and Its Use in Meteorology* (John Hopkins Press, Baltimore 1968)
- 7.13 H.-G. Körber: *Vom Wetteraberglauben zur Wetterforschung* (Edition Leipzig, Leipzig 1987)
- 7.14 R. Holland, G. Stöhr: *Thermometer, Skalen und deren Väter* (Freunde alter Wetterinstrumente, Riedlingen 2013)
- 7.15 W.E.K. Middleton: *Invention of the Meteorological Instruments* (Johns Hopkins Press, Baltimore 1969)
- 7.16 Accademia Del Cimento: Saggi Di Naturali Esperienze Fatte Nell' (1666). In: *Neudrucke von Schriften und Karten über Meteorologie und Erdmagnetismus*, Vol. 7, ed. by G. Hellmann (1904) p. 278, Berlin 1893–1904
- 7.17 F.V. Brock, S.J. Richardson: *Meteorological Measurement Systems* (Oxford Univ. Press, New York 2001)
- 7.18 G.R. Harrison: *Meteorological Measurements and Instrumentation* (John Wiley & Sons, Chichester 2015)
- 7.19 EU: Commission Regulation (EU) No 847/2012 of 19 September 2012 Amending Annex XVII to regulation (EC) No 1907/2006 of the European Parliament and of the Council on the Registration, Evaluation, Authorisation and Restriction of Chemicals (REACH) as regards mercury, *Off. J. Eur. Union* **L 253**, 1–4 (2012)
- 7.20 UNEP: *The Minamata Convention on Mercury* (2014)
- 7.21 DIN-EN: *Industrial Platinum Resistance Thermometers and Platinum Temperature Sensors [Industrielle Platin-Widerstandsthermometer und Platin Sensoren]* (Beuth, Berlin 2009), IEC 60751:2008, DIN-EN 60751
- 7.22 IEC: *Industrial Platinum Resistance Thermometer, Edition 2.0* (International Electrotechnical Commission, Geneva 2008), IEC 60751
- 7.23 H. Reuter: Bestimmung des spezifischen Widerstandes von Platin in Abhängigkeit von der Drahtdicke, als Beitrag zur Kenntnis der freien Weglänge der Leitungselektronen, *Ann. Phys.* **422**, 494–504 (1937)
- 7.24 R. Nossek: Der Einfluss der Grenzflächen auf die Eigenschaften der Metalle, Anomalien dünner Schichten. In: *Leitungsmechanismus und Energieumwandlung in Festkörpern*, ed. by E. Justi (Vandenhoeck & Ruprecht, Göttingen 1965) pp. 67–76
- 7.25 S.I. Kretschmer: Metodika izmerenija mikropulsacii skorosti vetra i temperatura v atmosferu [A method to measure the fluctuations of the wind velocity and the temperature], *Trudy Geofiz. Inst. AN SSSR* **24**(151), 43–111 (1954)
- 7.26 L.R. Tsvang: Izmerenija tschastotnyh spektrov temperaturnyh pulsacij v prizemnom sloe atmosfery [Measurement of the spectra of the temperature fluctuations in the near surface layer of the atmosphere], *Izv. AN SSSR Ser. Geofiz.* **10**, 1252–1262 (1960)
- 7.27 T. Foken: Temperaturmessung mit dünnen Platin-drähten, *Z. Meteorol.* **29**, 299–307 (1979)
- 7.28 A. Ziermann: Die richtige Bemessung der Widerstände einer zweckgebundenen Wheatstone'schen Brücke, Teil I–V, *Arch. Tech. Mess.* **Lfg 389–393**, 129–220 (1968)

- 7.29 J. Rink: Thermistore und ihre Anwendung in der Meteorologie, Abh. Meteorol. Hydrol. Dienstes DDR **63**, 58 (1961)
- 7.30 C.R. Droms: Thermistors for temperature measurements. In: *Temperature: Its Measurement and Control in Science and Industry*, Vol. 3, ed. by J.F. Schooley (Instrument Society of America, New York 1962) pp. 139–146, Part 2
- 7.31 J.M. Blonquist Jr., B. Bugbee: Air temperature. In: *Agroclimatology: Linking Agriculture to Climate*, Agronomy Monographs, Vol. 60, ed. by J.L. Hatfield, M.V.K. Sivakumar, J.H. Prueger (American Society of Agronomy, Madison 2018) pp. 51–72
- 7.32 J.S. Steinhart, S.R. Hart: Calibration curves for thermistors, Deep Sea Res. Oceanogr. Abstr. **15**, 497–503 (1968)
- 7.33 G.W. Burns, M.G. Scroger, G.F. Strouse, M.C. Croarkin, W.F. Guthrie: Temperature–electromotive force reference functions and tables for the letter-designated thermocouple types based on the ITS–90, Natl. Inst. Stand. Technol. Monogr. **175**, 630 (1993)
- 7.34 DIN-EN: *Temperature – Electromotive Force (EMF) Tables for Pure-Element Thermocouple Combinations (IEC 62460:2008) [Temperatur – Tabellen der Elektromotorischen Kraft (EMK) für Kombinationen von Reinelement-Thermoelementen, EN 62460:2008]* (Beuth, Berlin 2009)
- 7.35 T. Hanafusa, T. Fujitana, Y. Kobori, Y. Mitsuta: A new type sonic anemometer–thermometer for field operation, Pap. Meteorol. Geophys. **33**, 1–19 (1982)
- 7.36 B.G. van der Hegge Zijnen: Modified correlation formulae for heat transfer by natural and by forced convection from horizontal cylinders, Appl. Sci. Res. **A6**, 129–140 (1956)
- 7.37 A.F.G. Jacobs, K.G. McNaughton: The excess temperature of a rigid fast–response thermometer and its effects on measured heat fluxes, J. Atmos. Ocean. Technol. **11**, 680–686 (1994)
- 7.38 S.J. Richardson, F.V. Brock, S.R. Semmer, C. Jirak: Minimizing errors associated with multiplate radiation shields, J. Atmos. Ocean. Technol. **16**, 1862–1872 (1999)
- 7.39 W.R. Sparks: *The Effect of Thermometer Screen Design on the Observed Temperature*, WMO, Vol. 315 (World Meteorological Organization, Geneva 1972)
- 7.40 E. Erell, V. Leal, E. Maldonado: Measurement of air temperature in the presence of a large radiant flux: an assessment of passively ventilated thermometer screens, Bound.–Layer Meteorol. **114**, 205–231 (2005)
- 7.41 D. Bryant: An investigation into the response of thermometer screens – the effect of wind speed on the lag time, Meteorol. Mag. **97**(256), 183–186 (1968)
- 7.42 R.G. Harrison: Lag–time effects on a naturally ventilated large thermometer screen, Q.J.R. Meteorol. Soc. **137**, 402–408 (2011)
- 7.43 G. Speckbrock, S. Kamitz, M. Alt, H. Schmitt: Clinical Thermometer, Patent (1996)
- 7.44 BS: *Meteorological Thermometers*, British Standard, Vol. 692, 2nd edn. (British Standards Institution, London 1958), Revision
- 7.45 VDI: *Umweltmeteorologie, Meteorologische Messungen, Lufttemperatur [Environmental Meteorology, Meteorological Measurements, Air Temperature]* (Beuth, Berlin 2012), VDI 3786 Blatt 3 (Part 3)
- 7.46 A. Merlone, F. Sanna, G. Beges, S. Bell, G. Beltramino, J. Bojkovski, M. Brunet, D. del Campo, A. Castrillo, N. Chiodo, M. Colli, G. Coppa, R. Cucaro, M. Dobre, J. Drnovsek, V. Ebert, V. Fernicola, A. Garcia–Benadí, C. Garcia–Izquierdo, T. Gardiner, E. Georgin, A. Gonzalez, D. Groselj, M. Heinonen, S. Hernandez, R. Högström, D. Hudoklin, M. Kalemci, A. Kowal, L. Lanza, P. Miao, C. Musacchio, J. Nielsen, M. Nogueras–Cervera, S.O. Aytakin, P. Pavlasek, M. d. Podesta, M.K. Rasmussen, J. del-Río–Fernández, L. Rosso, H. Sairanen, J. Salminen, D. Sestan, L. Šindelářová, D. Smorgon, F. Sparasci, R. Strnad, R. Underwood, A. Uytun, M. Voldan: The Meteomet2 project—highlights and results, Meas. Sci. Technol. **29**, 025802 (2018)
- 7.47 R.G. Harrison, M.A. Pedder: Fine wire thermometer for air temperature measurement, Rev. Sci. Instrum. **72**, 1539–1541 (2001)
- 7.48 E. von Angerer, H. Ebert: *Technische Kunstgriffe der physikalischen Untersuchungen* (B. G. Teubner, Leipzig 1964)
- 7.49 ISO: *Meteorology—Air Temperature Measurements—Test Methods for Comparing the Performance of Thermometer Shields/Screens and Defining Important Characteristics* (International Organization for Standardization, Geneva 2007), ISO 17714:2007
- 7.50 R.G. Harrison, S.D. Burt: Quantifying uncertainties in climate data: measurement limitations of naturally ventilated thermometer screens. Environ. Res. Commun. **3**:1–10 (2021)
- 7.51 L.G. Sotelino, N. De Coster, P. Beirinckx, P. Peeters: Intercomparison of Shelters in the RMI AWS Network. (WMO–CIMO, P1_26, Geneva, 2018)
- 7.52 E. Frankenberger: Untersuchungen über den Vertikalaustausch in den unteren Dekametern der Atmosphäre, Ann. Meteorol. **4**, 358–374 (1951)
- 7.53 R.G. Wylie, T. Lalas: Measurement of Temperature and Humidity, WMO Techn. Note **194**, 77 (1992)
- 7.54 L.F. Kämtz: *Lehrbuch der Meteorologie* (Gebauersche Buchhandlung, Halle 1831)
- 7.55 F. Kaspar, L. Hannak: Zur Auswirkung der Automatisierung der Temperaturmessungen auf die Messreihen des Deutschen Wetterdienstes, Mitt. DMG **2**, 8–9 (2016)
- 7.56 T. Foken, J. Lüers, G. Aas, M. Lauerer: *Unser Klima – Im Garten, Im Wandel* (Ökologisch–Botanischer Garten der Universität Bayreuth, Bayreuth 2016)

Thomas Foken

University of Bayreuth
Bayreuth, Germany
thomas.foken@uni-bayreuth.de



Thomas Foken is a retired Professor of Micrometeorology at the University of Bayreuth. He was the head of Laboratories at the meteorological observatories at Potsdam (1981–1994) and Lindenberg (1994–1997). His research interests include the interaction between the Earth's surface and the atmosphere and the measurement and modeling of energy and matter fluxes, with a strong focus on experimental meteorology. His scientific contributions have been recognized through various international awards.

Jens Bange

Centre for Applied Geo-Science
University of Tübingen
Tübingen, Germany
jens.bange@uni-tuebingen.de



Jens Bange is a Professor for Environmental Physics at the University of Tübingen since 2010. He received a PhD in meteorology in 1998 and a diploma in physics in 1992 at the University of Hannover. His research interests include atmospheric turbulence, boundary-layer meteorology, wind-energy research, airborne meteorology, and environmental measurement technology. He is a founding member of the research networks ISARRA and WindForS.

Humidity Sensors

Dietrich Sonntag, Thomas Foken , Holger Vömel , Olaf Hellmuth 

For measurements of atmospheric humidity, a variety of different techniques has been used in the past, such as hair hygrometers, polymer sensors, optical instruments, and also those based on thermodynamic properties of moist air. Current sensor technology is mostly based on the psychrometric method, dewpoint measurements, and optical measurements, as well as capacitive sensors. Of special interest are the psychrometric theory and the theory of optical measurements. Technical specifications, exposure recommendations, necessary maintenance associated with different methods, as well as methods of quality control and calibration are presented.

8.1	Measurement Principles and Parameters	210	8.3.2	Hair Hygrometer	219
8.1.1	Measured Parameters	210	8.3.3	Lithium Chloride Heated Condensation Hygrometer (Dew Cell)	219
8.1.2	Principles of Measurements	211	8.3.4	Capacitive Hygrometer	219
8.1.3	Siting Considerations	212	8.3.5	Psychrometric Method	220
8.2	History	212	8.3.6	Dewpoint and Frostpoint Hygrometers	221
8.2.1	Hygrosopes	212	8.3.7	Optical Method	221
8.2.2	Hair Hygrometer	213	8.4	Devices and Systems	222
8.2.3	Other Absorption and Adsorption Hygrometers	214	8.4.1	Hair Hygrometer	222
8.2.4	Psychrometer	214	8.4.2	Lithium Chloride Heated Condensation Hygrometer (Dew Cell)	224
8.2.5	Dewpoint and Frostpoint Sensor	215	8.4.3	Capacitive Hygrometer	224
8.2.6	Fast Response Hygrometers – Optical Sensors	217	8.4.4	Psychrometer	225
8.3	Theory	217	8.4.5	Dewpoint and Frostpoint Hygrometers	229
8.3.1	Fundamental Equations of Relative Humidity	217	8.4.6	Optical Hygrometers	230
			8.4.7	Comparison of the Methods	232
			8.5	Specifications	233
			8.6	Quality Control	234
			8.6.1	Reference Standards	234
			8.6.2	Primary Standards	234
			8.6.3	Salt Solutions	235
			8.6.4	Quality Control Procedures	235
			8.6.5	Calibration of Optical Hygrometers	236
			8.6.6	Documentation and Metadata	236
			8.7	Maintenance	236
			8.8	Application	237
			8.8.1	Climatology of Humidity	237
			8.8.2	Daily and Annual Cycles	237
			8.9	Future Developments	238
			8.10	Further Readings	238
			References		238

Water occupies a special place among the constituents of air because it exists in the solid, liquid, or gaseous phase. Furthermore, it exhibits the strongest contribution to the natural greenhouse effect. Due to precipitation, evaporation, and long-range transport, the water-vapor content of air varies considerably throughout the atmosphere. Depending on the temperature, concentrations of wa-

ter vapor near the surface are on the order of $0.1\text{--}30 \times 10^{-3} \text{ kg m}^{-3}$. The water vapor is mostly concentrated in the lowest kilometer of the atmosphere (atmospheric boundary layer), whereas less than $0.3 \times 10^{-6} \text{ kg m}^{-3}$ of it is present in the stratosphere. Comprehensive descriptions of water vapor in the atmosphere are contained in textbooks of meteorology and climatology [8.1, 2].

8.1 Measurement Principles and Parameters

The humidity of air is measured as several parameters, such as the degree of saturation or the water-vapor pressure. Some of these parameters are measured but others must be calculated. The following section gives an overview of the different parameters and measurement principles.

8.1.1 Measured Parameters

Most humidity sensors measure relative humidity, which is the ratio of water-vapor pressure in the atmosphere in relation to the water-vapor pressure at saturation for a given temperature. Relative humidity is a temperature-sensitive parameter, which must be taken into account when calculating other humidity parameters. Therefore, a temperature measurement (Chap. 7) is essential. Some instruments measure absolute humidity or mixing ratio directly. Other measured parameters are dewpoint or frostpoint temperature and psychrometric difference – the temperature difference between a dry-bulb and wet-bulb thermometer – used for psychrometric methods. Table 8.1 gives an overview of parameters and their units measured by humidity sensors.

For many applications other humidity parameters are used. These are mainly water-vapor partial pressure, specific humidity, absolute humidity, or saturation vapor pressure that are given in Table 8.2 and possible calculations between humidity units are given in Table 8.3.

Of high importance is the maximum possible amount of water vapor in the air for a given temperature,

known as the water-vapor pressure of saturation. This relationship is given on the basis of the thermodynamic laws by the Clausius–Clapeyron equation [8.1, 2]

$$\frac{dE_w}{dT} = \frac{\lambda}{T\Delta v}, \quad (8.1)$$

where E_w is the saturation vapor pressure, T is the absolute temperature, λ is the specific heat of evaporation (λ_v) or sublimation (λ_i), and Δv is the difference between the specific volumes of water and water vapor. Assuming $\lambda = \text{const.}$, neglecting the volume of liquid water compared to that of water vapor, and adopting ideality of the gas mixture, it follows with the gas constant of water $R_w = 461.525 \text{ J kg}^{-1} \text{ K}^{-1}$

$$\frac{dE_w}{E_w} = \frac{\lambda}{R_w} \frac{dT}{T^2}. \quad (8.2)$$

After integration the saturation vapor pressure can be written as

$$E_w = E_{w0} \exp\left(\frac{\lambda}{R_w T_0} \frac{T - T_0}{T}\right) \quad (8.3)$$

with $E_{w0} = 6.112 \text{ hPa}$ and $T_0 = 273.15 \text{ K}$. From (8.3) it follows that with the specific latent heat of evaporation

$$\lambda = \lambda_v = 2.50 \times 10^6 \text{ J kg}^{-1},$$

the water-vapor pressure over water, and with the latent heat of sublimation

$$\lambda = \lambda_i = 2.83 \times 10^6 \text{ J kg}^{-1}$$

Table 8.1 Measured parameters of humidity sensors

Parameter	Description	Unit	Symbol
Relative humidity	Ratio of water-vapor pressure to saturation water-vapor pressure	%	RH
Absolute humidity	Mass of water vapor per volume of moist air	kg m^{-3}	a
Psychrometric difference	Difference between the dry-bulb and wet-bulb (or ice-bulb) temperature	K	$t - t_w$
Dewpoint	Temperature at which the saturation vapor pressure over water is reached	$^{\circ}\text{C}$	t_d
Frostpoint ^a	Temperature at which the saturation vapor pressure over ice is reached	$^{\circ}\text{C}$	t_f
Mixing ratio ^b	Mass of water vapor per mass of dry air	kg kg^{-1}	r

^a Below 0°C the dewpoint temperature is lower than the frostpoint temperature at a constant partial water-vapor pressure. Above 0°C the frostpoint temperature is not defined.

^b The mixing ratio can be replaced with sufficient accuracy by the specific humidity (see Table 8.2) or vice versa.

Table 8.2 Other relevant parameters for humidity measurements

Parameter	Description	Unit	Symbol
Vapor pressure	Partial pressure of water vapor in air	hPa	e
Specific humidity	Mass of water vapor per mass of moist air	kg kg^{-1}	q
Saturation vapor pressure over water	Vapor pressures in air in equilibrium with pure bulk water at a flat interface	hPa	E_w
Saturation vapor pressure over ice	Vapor pressures in air in equilibrium with pure bulk ice at a flat interface	hPa	E_i
Virtual temperature	Temperature of dry air if it had the same density as moist air at the same pressure	K	T_v

(both values for 0 °C, see Chap. 5) follows the water-vapor pressure over ice. This widely used analytical form is the Magnus equation, which is recommended [8.4] in the form given in Table 8.3. In some English speaking countries the Tetens equation is often used (Table 8.3).

In the ideal-gas approximation the density of moist air is a function of temperature, pressure, and specific humidity [8.1, 2]

$$\rho_a = \frac{p}{R_d T (1 + 0.608q)}, \quad (8.4)$$

with the gas constant of dry air

$$R_d = 287.0586 \text{ J kg}^{-1} \text{ K}^{-1},$$

the pressure p . Thereby,

$$T_v = T(1 + 0.608q) \quad (8.5)$$

is the virtual temperature (Table 8.3), which can be used in the gas equation together with the gas constant of dry

air instead of that for moist air. An approximation of the virtual temperature with the water-vapor pressure is given in Chap. 7. This parameter is also used as a parameter for humidity measurements.

The specific heat of evaporation and sublimation is a function of temperature (Chap. 5); for the heat of evaporation the following temperature dependence can be used

$$\lambda_v = 2500827 - 2360(T - 273.15\text{K}) [\text{J kg}^{-1}]. \quad (8.6)$$

The expressions for the dewpoint and frostpoint temperatures in Table 8.3 follow directly from the Magnus equation in the same table, neglecting the temperature dependency in $f(p, T)$ [8.4, 13] (see footnote in Table 8.3).

8.1.2 Principles of Measurements

Historically many physical and chemical principles have been used to measure atmospheric humidity. Dif-

Table 8.3 Relationship between water-vapor pressure and different humidity units (after [8.4–8]), based on the new ITS-90 temperature scale [8.5, 9]. For dimensions and symbols see Tables 8.1 and 8.2; p : air pressure in hPa, e : water-vapor pressure in hPa, T : absolute temperature in K, t : temperature in °C. Note: For the often used calculation according to *Wexler* [8.10–12] a transformation on the ITS-90 scale is recently available [8.9]

Humidity unit	Equation
Relative humidity	$RH = 100 \frac{e}{E_{w,i}}$
Water-vapor pressure for saturation with Tetens's equation over water [8.3], only of historical relevance	$E_w = 6.11 \exp\left(\frac{17.2694(T-273.16\text{K})}{T-35.86\text{K}}\right)$
Water-vapor pressure for saturation with Magnus's equation (−45 to +60 °C over water, pure phase) [8.4, 5] For moist air	$E_w(t) = 6.112 \exp\left(\frac{17.62t}{243.12+t}\right)$ $E'_w(t, p) = f_w(p)E_w(t)$ ^{a,b}
Water-vapor pressure for saturation with Magnus's equation (−65 to +0.01 °C over ice, pure phase) [8.4, 5] For moist air	$E_i(t) = 6.112 \exp\left(\frac{22.46t}{272.62+t}\right)$ $E'_i(t, p) = f_i(p)E_i(t)$ ^{a,b}
Dewpoint temperature for water (−45 to +60 °C)	$t_d = \frac{243.12 \ln\{e/[6.112f_w(p)]\}}{17.62 - \ln\{e/[6.112f_w(p)]\}}$ ^{a,c}
Frostpoint temperature for ice (−65 to +0.01 °C)	$t_f = \frac{272.62 \ln\{e/[6.112f_i(p)]\}}{22.46 - \ln\{e/[6.112f_i(p)]\}}$ ^{a,c}
Psychrometric formula for water	$e = E'_w(p, t_w) - 6.53 \times 10^{-4} p (1 + 9.44 \times 10^{-4} t_w) (t - t_w)$
Psychrometric formula for ice	$e = E'_i(p, t_i) - 5.75 \times 10^{-4} p (t - t_i)$
Absolute humidity	$a = \frac{0.21667e}{T}$ ^d
Specific humidity	$q = 0.62198 \frac{e}{p-0.378e}$ ^e
Mixing ratio	$r = 0.62198 \frac{e}{p-e}$ ^e
Virtual temperature	$T_v = T(1 + 0.608q)$

^a $f(p) = 1.0016 + 3.15 \times 10^{-6} p - 0.074 p^{-1}$, $f(p)$ is the enhancement factor (Sect. 8.3.1) and a function of both pressure and temperature, i.e., $f = f(p, t)$ [8.13]. In practice, the temperature dependency ($\pm 0.1\%$) is much weaker than the pressure dependency (0.0 to +0.6%). Therefore, the temperature dependency has been omitted in the formula above. This formula, however, should be used only for pressure around 1000 hPa (i.e., surface measurements) and not for upper-air measurements, for which Table 4.10 in [8.13] should be used.

^b For lower temperatures, see [8.8, 10].

^c For dewpoint and frostpoint temperatures outside this range, inversions should be used.

^d e in hPa and T in K.

^e e and p in hPa.

Table 8.4 Properties of humidity measurements and applications for mean values and turbulence measurements [8.6, updated]

Type of sensor	Properties			Application	
	Thermodynamic	Absorption of radiation	Material	Mean	Turbulent
Hair hygrometer			✓	✓	
Lithium chloride sensor			✓	✓	
Capacity hygrometer			✓	✓	
Psychrometer	✓			✓	
Dewpoint and frostpoint hygrometer	✓			✓	
Ultraviolet hygrometer		✓		(✓)	✓
Infrared hygrometer		✓		(✓)	✓

ferent sensor types and methods, listed in Table 8.4, are used for slow (mean values, seconds to many minutes) and fast response (turbulence measurements, 5–100 Hz) humidity measurements. This chapter concentrates on these methods, and only in Sect. 8.2 are historically relevant methods described.

8.1.3 Siting Considerations

Humidity measurements can be interpreted only in connection with temperature, and are generally measured together [8.4, 7]. The distance between the humidity and temperature sensor should be as short as possible (at most 1 m); however, the sensors should not

influence each other, yet measure the same small air volume. Depending on the sensor, radiation protection and ventilation may be necessary. The standard height above ground for humidity measurements is 2.0 m. Except in the case of UV hygrometers or IR hygrometers, sufficient radiation protection may be achieved by installing the sensor inside a meteorological shelter [8.4] (Chaps. 7 and 43). For specific purposes humidity instruments may also be installed in different arrangements as long as the sensor is properly exposed (Chap. 6). Moisture sensors should not be exposed to atmospheric contaminants, rain, or wind. Furthermore, the material of the housing should neither adsorb nor desorb water vapor.

8.2 History

Many methods are available for measuring atmospheric humidity. A comprehensive review of methods available up to the 1960s was given by *Sonntag* [8.14] and *Wexler* [8.15]. Only the most important methods and instruments, which are based on the principles still in use, are reviewed here.

8.2.1 Hygrosopes

Moisture in the air and its effect of increasing the weight of some materials, mainly wood, has been known since antiquity, e.g., in the Western Han dynasty in ancient China between 200 BCE and 10 CE [8.16] from East Asia. The first hygroscope, dated to about 1450, was developed by the German *Nicholas of Cusa* (*Nikolaus von Kues*, lat. *Cusanus*) (1401–1464) [8.17, 18], who used a weight scale and an unspecific hygroscopic material. A more accurate description is from the architect *Leon Battista Alberti* (1404–1472), who used a sponge and a scale to measure the “heaviness

and dryness of the wind and air” [8.18]. *Leonardo da Vinci* (1452–1519) made several drawings showing such a system, for instance a scale with a sponge [8.19] in a sketch made for his famous painting *The Last Supper*.

In the seventeenth and eighteenth century, several humidity-dependent materials from animals, plants (Table 8.5), and minerals were tested, but all instruments using these were still classified as hygrosopes because they were only indicators of the humidity. The hygrometer from *Johann Heinrich Lambert* (1728–1777), who used catgut string, dates from this time (Fig. 8.1). The torsion of the material was used to rotate a hand about 360° from low to high humidities [8.20]. At the end of the eighteenth century, the use of terms like saturation or relative amount of water (*Ludwig Achim von Arnim*, 1781–1831) marked the beginning of quantitative hygrometry. A further often-used instrument was built by *Jean-André de Luc* (1727–1817) in 1772 using ivory as a measuring element.

Table 8.5 Hygroscopic material used for hygrometers (after [8.18])

Source	Material	Hygroscopic properties
Animal and human	Catgut string	Torsion
	Amnion	Expansion
	Ivory	Expansion
	Whalebone	Expansion
	Horn	Expansion
	Leather	Expansion
	Human hair	Expansion
	Sponge	Weight
	Skin	Expansion
Herbal	Cotton	Expansion, weight
	Oat beard	Torsion, flexion
	Hemp, twisted	Torsion, expansion
	Paper	Expansion, weight

**Fig. 8.1** Lambert's hygrometer from about 1772 (after [8.18]), using the torsion of catgut string. Translation of the German engraving: two graduations are 3 degrees of humidity within a cubic foot of air (photo © Freunde alter Wetterinstrumente, Riedlingen, Germany)

8.2.2 Hair Hygrometer

The philosopher *Horace Bénédicte de Saussure* (1740–1799) experimented with human hair and found that untreated thin and soft hair from men and women – the latter was more usable because of its length – could be used after some preparation [8.18]. This was mainly degreasing by cooking, and treatment with cold water and soda solution. The tension on the hair and hand was exerted by a small weight. A hair hygrometer similar to the prototype of 1781 is shown in Fig. 8.2. From the beginning the scales of the hygrometers were linear, but the extension of the human hair was found to be nonlinear. *Wilhelm Klinkerfues* (1827–1884) devel-

**Fig. 8.2** Hair hygrometer according to the prototype of 1781 by Horace Bénédicte de Saussure [8.18] (photo © Freunde alter Wetterinstrumente, Riedlingen, Germany)

oped a system to linearize the scale in 1882. Some years earlier he had developed the bifilar hygrometer with a second nonhygroscopic hair to reset the hand. This instrument was produced at Göttingen in 1875 by *Wilhelm Lambrecht* (1834–1904). In 1880 Lambrecht developed the *Polymer*, which combined a hair hygrometer and a thermometer, both of which had two scales. The thermometer had an additional scale indicating the water-vapor pressure at saturation, and the hygrometer a scale for the calculation of the dewpoint, which is the difference between the temperature and its value at this scale. He also developed a thermo-hygroscope in 1881. The mechanical connection of a hygrometer with a bimetal-thermometer made it possible to determine the increase or decrease of the absolute humidity. The round form of the hygrometer similar to Lambert's hygrometer (Fig. 8.1) has been prevalent since approximately 1850, and not much has changed in this respect up to now.

The theory of the hair hygrometer is based on *Sresnevsky* 1895 [8.21], who assumed that a hair is a capillary tube. If the hair is immersed in water the hair is filled with water up to the capillary rise. The curvature of the meniscus in the pores of the hair determines the maximum water-vapor pressure in the pores. This was set proportional to the absolute value of the logarithm of the relative humidity. The largest extension of the hair occurs at 100% relative humidity and the largest

contraction was assumed for 7.8%, with no further contraction below this value. For the contraction δL (range 0.0–1.0) follows [8.14, 22]

$$1.104\delta L = -\log\left(\frac{RH}{100}\right). \quad (8.7)$$

The theory was updated by *Whipple* in 1921 [8.23]. He found that for very narrow capillaries the hydrostatic pressure is larger than the barometric pressure in the upper part of the capillary, where negative pressures of 0.012 hPa for 99% relative humidity and 2.1 hPa for 20% humidity occur. This still forms the basis of the recent theories presented in Sect. 8.3.2.

8.2.3 Other Absorption and Adsorption Hygrometers

The metal-paper coil hygrometers are based on early works with two strips, where one is humidity dependent. The first was made in 1867 by *Robert Wolf* with the bark of a fir tree [8.24]. Several constructions have been reported since that time. The method is still in use with a metallic spiral covered on one side with a hygroscopic material. The principle is similar to a bimetal thermometer.

The first proposals to use goldbeater's skin, a treated outer membrane of the intestine of an animal, which was normally used to produce gold leaf, was already reported by *Vincenzo Chiminello* (1741–1815) in 1783 [8.14] – the so-called goldbeater's skin hygrometer. Because of its faster response time for lower temperatures in comparison to human hair, it remained in use for a long time.

With the invention of radiosondes at the beginning of the 1930s, intensive research started to develop electric and faster sensors. Experiments were done with many chemical solutions and salts. The most successful salt was lithium chloride (LiCl). *Dunmore* [8.25] used copper wire electrodes wound around a glass tube. He found the best results with a 5% aqueous LiCl solution that had a time constant of about 4.5 s. The disadvantage of the sensor was the high resistance and a cross sensitivity to temperature. Tests were made with several materials [8.14, 15], and some progress was achieved by *Jones* in 1960 [8.26] using glass plates coated with a film of barium fluoride (BaF₂) over a metallic electrode. A minimized version of such a sensor (3.0 × 4.5 mm²) could reach time constants of down to 0.1 s [8.27].

A problem with these sensors is the temperature dependence and the low calibration stability, so that these sensors were mainly used for radio sounding or similar applications. At the end of the 1950s, the LiCl sensor was modified to a heated dewpoint sensor [8.28],

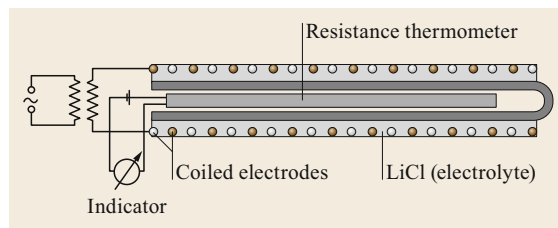


Fig. 8.3 A basic view of a heated lithium chloride sensor (after [8.29])

which is shown in Fig. 8.3. The method is based on the equilibrium between the water-vapor pressure of the heated aqueous LiCl solution and the water-vapor pressure in the air (Sect. 8.3.3). The temperature sensor measures the dewpoint. This type of sensor is still currently in use.

Another class of sensors uses solid materials. Since the 1930s it has been known that graphite changes its resistance with humidity. Mainly through industrial research, carbon humidity elements, also called carbon hygrometers, were constructed for radio soundings [8.14, 15]. Polymers were another material found in industrial research that adsorbed water at the surface, changing the resistance. These materials are used as a dielectric of a capacitor [8.30–32]. The benefit is a nearly linear response of capacitance to the change of humidity. The frequency output of a resonant circuit is transformed into a voltage or current. Today, these capacitive polymer sensors are widely used as humidity sensors [8.33, 34], for example the Humicap[®] technology developed by the company Vaisala Oyj (Sect. 8.3.4).

8.2.4 Psychrometer

Before 1792, *James Hutton* (1726–1797) in Edinburgh found a cooling effect on thermometers with a wet bulb, and *John Leslie* (1766–1832), who found that this resulted from the drying quality of the atmosphere, constructed a differential thermometer in 1790 – called the Leslie hygrometer – which was the prototype of a psychrometer [8.35] (Fig. 8.4). In 1802 *M.A.F. Lüdicke* proposed separation of the U-form of the differential thermometer into two discrete thermometers. In a comparison of the Leslie hygrometer with the devices by de Saussure and de Luc, *Böckmann* found in 1803 [8.36] that the measurements depended on temperature, pressure and, to a large extent, on wind. The first equation describing the behavior of a psychrometer was presented in 1822 by *Joseph Louis Gay-Lussac* (1778–1850).

The theory of the psychrometer [8.37] is based on *James Clerk Maxwell's* (1831–1879) diffusion theory of 1877 [8.38], the convection theory of *J. Ivory*

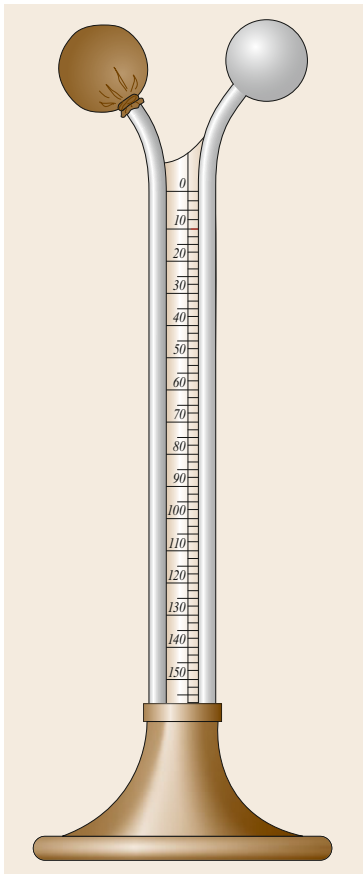


Fig. 8.4 Schematic view of the Leslie differential thermometer with a wet and dry bulb filled with sulfuric acid (with permission from Educational Technology Clearinghouse – University of South Florida)

1822 [8.35] and *Ernst Ferdinand August* (1795–1870) in 1825 [8.39, 40], and the theory of influence of the wind [8.41], which was for a long time the limiting factor in the application of the method. *Richard Assmann* (1845–1918) developed a psychrometer in the 1880s where both thermometers were ventilated in parallel [8.42, 43], while the earlier type by *August* [8.44] used a nonventilated thermometer (later the wet-bulb thermometer was ventilated), Fig. 8.5. The aspirated psychrometer of *Assmann*, finally described in 1892 [8.45], is still in use and one of the best instruments for measuring humidity (Sect. 8.4.4). *Assmann* also made the sling or whirling hygrometer more popular [8.46], which has two parallel thermometers – one with a wet bulb, one with a dry bulb, which the user whirls in open air. This instrument is still available.

About 50 years ago, when no fast response hygrometers were available, tests with thin cold wire thermometers, where one was covered with a thin cotton thread, were tested with partial success [8.47].

Because of the complexity of the calculation of psychrometric data, psychrometric charts were developed, the first in 1904 by *Willis H. Carrier*

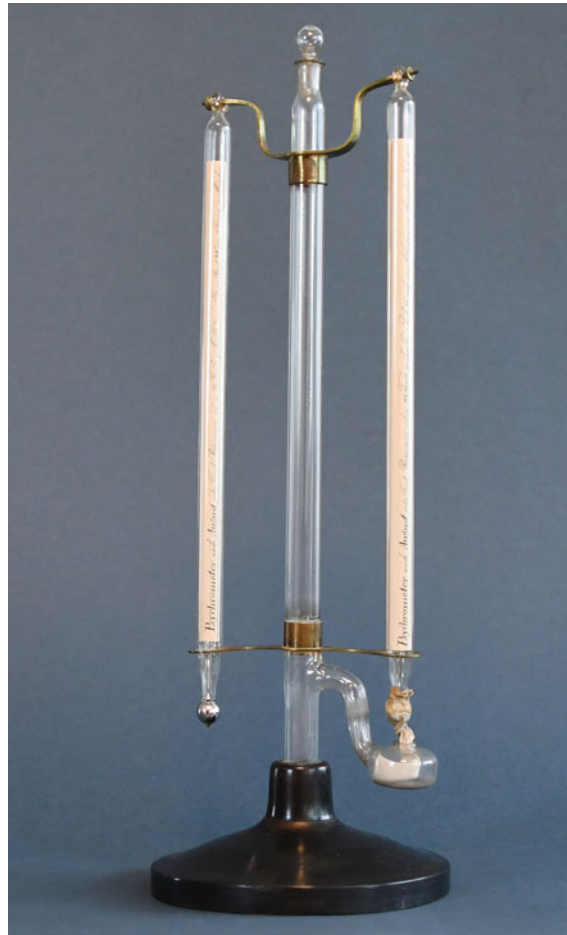


Fig. 8.5 Historical psychrometer according to August A. Greiner, Munich, 1850 (photo © Prof. Jürgen Baumüller)

(1876–1950) [8.48] (Fig. 8.6). Several such charts were developed in the previous century, and psychrometric slide rules were used as well. Nowadays smartphone apps are available, but unfortunately the user cannot be sure that the right equations are used.

8.2.5 Dewpoint and Frostpoint Sensor

The knowledge of obtaining moisture measurements using a cool material that becomes covered with dew if the temperature of the material is lower than the dewpoint has been well known since the Roman Empire. The effect has been applied since the beginning of the nineteenth century to construct several types of dewpoint hygrometers. One of the most impressive is the instrument by *John Frederic Daniell* (1790–1845) from 1820 [8.50, 51] (Fig. 8.7). He used two evacuated and connected glass balloons. The balloon with the thermometer was filled up to 2/3 of its volume with ether.

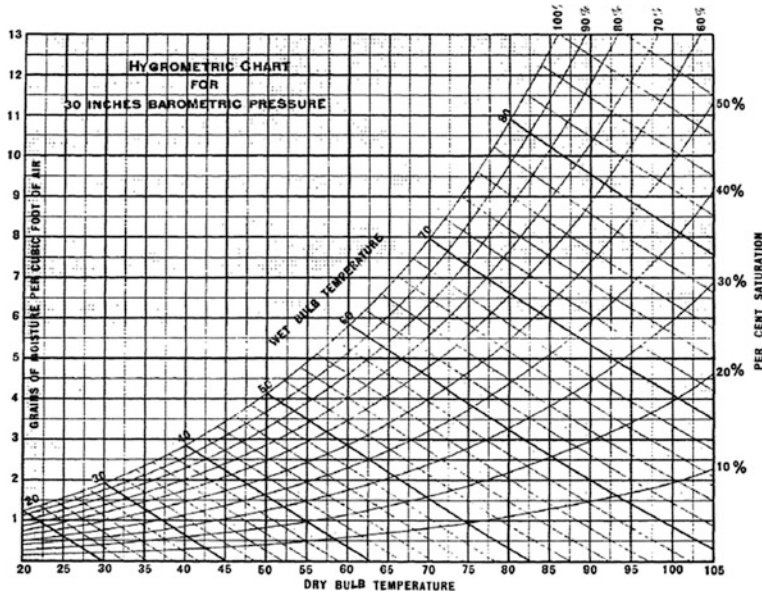


Fig. 8.6 Psychrometric chart according to Carrier 1904 (after [8.48]), temperatures in °F. *Left ordinate:* absolute humidity in grain per cubic foot ($\approx 1/4 \text{ g m}^{-3}$). *Right ordinate:* relative humidity, pressure 30 inch (approximately 1015.9 hPa) (after [8.48] with permission from the American Society of Heating, Refrigerating and Air-Conditioning Engineers, Inc., Atlanta GA, USA)



Fig. 8.7 Dewpoint hygrometer according to Daniell (photo © Prof. Jürgen Baumüller)

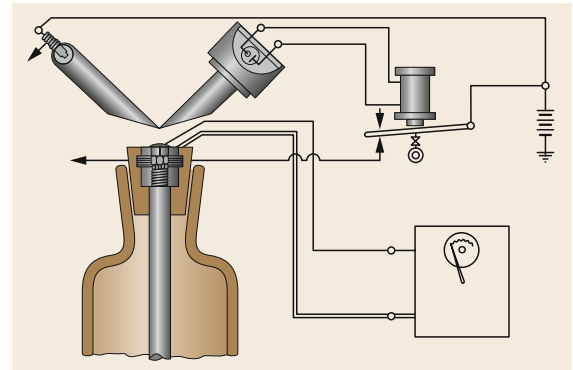


Fig. 8.8 Dewpoint hygrometer according to Thornthwaite (after [8.49] with permission from National Oceanic and Atmospheric Administration, Central Library)

The other balloon was covered with a gauze bandage and was wetted with ether that evaporated. Therefore it cooled down and the ether in the other balloon evaporated too and cooled the balloon. At the dewpoint in the air a dew film covered the balloon and the dewpoint temperature could be measured with the thermometer. This type of hygrometer – also called visual dewpoint hygrometer – was used up to the twentieth century.

The prototype of the currently used photoelectric chilled-mirror dewpoint hygrometers is the device by Charles Warren Thornthwaite (1899–1963) from 1939 [8.49] (Fig. 8.8). It is a photoelectric system with a mirror of chromium-plated copper. The mirror is con-

Table 8.6 First developments of fast response hygrometers (for an overview see [8.63])

Hygrometer type	Institution	Year, Reference
UV hygrometer, Lyman-alpha line	Institute of Oceanology, Moscow, Russia	1973 [8.52]
	Institute of Cosmos Research, Berlin, former GDR	1973 [8.53]
	National Center for Atmospheric Research, Boulder CO, USA	1973 [8.54]
	Royal Netherlands Meteorological Institute, De Bilt, The Netherlands	1986 [8.55]
UV hygrometer, Krypton line	Campbell Sci. Inc., Logan UT, USA	1985 [8.56]
IR hygrometer	Institute of Atmospheric Physics, Moscow, Russia	1962 [8.57]
	Flinders University, Adelaide, Australia	1978 [8.58]
	Okayama University, Okayama, Japan	1982 [8.59] ^a
	Main Meteorological Observatory, Potsdam, former GDR	1989 [8.60]
	University of Guelph, Canada	1989 [8.61] ^a
	Royal Netherlands Meteorological Institute, De Bilt, The Netherlands	1991 [8.62] ^a

^a Including measurement of carbon dioxide

ected by a copper rod with a cooling liquid and is heated. The dew on the mirror can be detected with a lamp and a photocell. Heater and photocell are parts of an electric circuit.

Besides visual and photoelectric dewpoint hygrometers, other electrical sensors, such as radiometric and crystal oscillator dewpoint hygrometers were constructed [8.14, 64].

8.2.6 Fast Response Hygrometers – Optical Sensors

Progress in the use of the eddy-covariance method (Chap. 55) at the beginning of the 1960s required the development of fast response sensors for water-vapor flux measurements (latent heat flux). The first versions of fast response psychrometers or adsorption hygrometers were not successful for general use [8.47]. Only the optical systems following Bouguer–Lambert–Beer’s law incorporated a change that allowed practical use of (8.21). The first infrared sensors were less practical due to the low sensitivity and long path lengths necessary [8.57]. At the end of the 1960s, sensors for measuring the UV light in the Lyman-alpha line of 121.56 nm were developed for satellite applications. Used together with a hydrogen

lamp, the Lyman-alpha hygrometer was developed at the beginning of the 1970s almost in parallel in the USA, the Soviet Union, and the former GDR [8.52–54], but only the American device was commercially produced for many years, by AIR Inc., Boulder, CO. About ten years later a second type of UV hygrometer was developed using a krypton lamp [8.56]. The benefits of this device were a longer lifetime and easier production. But the absorption band is not directly located in the Lyman-alpha band and has a cross sensitivity to oxygen. Fast response hygrometers are nowadays an important part of all measuring complexes for turbulent energy fluxes. There has been a significant change in measuring systems within the last 15–20 years. While sensors that were commercially available in the 1990s mainly used UV absorption lines, at present there is almost exclusive use of sensors working with the IR absorption lines. This is because the hydrogen lamp for hygrometers working at the Lyman-alpha line is not very stable, and the lamps were mainly handmade. Lyman-alpha hygrometers are only in use today for aircraft applications. At the same time, the sensitivity of IR sensors has been increased and these sensors have been the only commercially available sensors since the end of the 1990s. The pioneering work in the development of fast-response hygrometers is shown in Table 8.6.

8.3 Theory

This section gives a short introduction to the theory of the exact definition of relative humidity. Furthermore, the theories of the different measurement methods are briefly described.

8.3.1 Fundamental Equations of Relative Humidity

Relative humidity is a key observable quantity in atmospheric science, especially in climate monitoring,

the SI compatible definition and measurement of which poses a great metrological challenge. In the climate system, heat and matter fluxes of water are essentially controlled by the differences of chemical potentials of water between the ocean, sea ice, and humid air at their mutual interfaces. These chemical potential differences can be exactly expressed in terms of the relative fugacity of atmospheric water vapor [8.65]. The relative humidity according to the World Meteorological Organization (WMO) definition can be recovered from the

relative fugacity as its ideal-gas limit. Considering humid air to be a nonideal binary gaseous mixture of water vapor and dry air, relative humidity, in its most general and physically rigorous form, is defined by the relative fugacity RF [8.65–68]

$$RF(\chi_w^{(g)}, T, p) = \frac{f_w^{(g)}(\chi_w^{(g)}, T, p)}{f_w^{(g)}(\tilde{\chi}_w^{(g)}(T, p), T, p)},$$

$$f_w^{(g)}(\chi_w^{(g)}, T, p) = \chi_w^{(g)} p \varphi_w^{(g)}(\chi_w^{(g)}, T, p). \quad (8.8)$$

The relative fugacity is a function of three independent variables, namely the mole fraction of water (subscript w) in humid air (superscript (g) for the gas phase), $\chi_w^{(g)}$, the temperature T , and the pressure p . The functions $f_w^{(g)}(\chi_w^{(g)}, T, p)$ and $\varphi_w^{(g)}(\chi_w^{(g)}, T, p)$ denote the fugacity and the fugacity coefficient of water in humid air, where the latter is given in analytical form by its virial approximation [8.67]. The quantity $\tilde{\chi}_w^{(g)}(T, p)$ is the water-vapor mole fraction of saturated humid air (term with $\tilde{}$), i.e., of humid air in thermodynamic equilibrium with the condensed phase of water, which can either be pure or air-saturated water (i.e., an ideal mixture of water (solvent) and dry air (solute)) or pure hexagonal ice. The definition of relative humidity in terms of relative fugacity is motivated by the fact that the relative fugacity is the generating observable quantity for the thermodynamic driving force, the so-called Onsager force [8.66, 69], controlling the exchange of water between the vapor and condensed phases of humid air [8.66].

The standard WMO definition of relative humidity RH is obtained as the ideal-gas limit of the relative fugacity [8.70]

$$\lim_{p \rightarrow 0} \varphi_w^{(g)}(\chi_w^{(g)}, T, p) = 1$$

$$\rightarrow RH(\chi_w^{(g)}, T, p) = \lim_{p \rightarrow 0} RF(\chi_w^{(g)}, T, p) = \frac{\chi_w^{(g)}}{\tilde{\chi}_w^{(g)}}. \quad (8.9)$$

The fugacity coefficient,

$$\varphi_w^{(g)}(\chi_w^{(g)}, T, p) = \frac{f_w^{(g)}(\chi_w^{(g)}, T, p)}{\chi_w^{(g)} p}, \quad (8.10)$$

is closely related to the so-called enhancement factor (subscript E) of humid air [8.67, 71] with respect to the condensed water phase (c)

$$f_{E,w}^{(c)}(T, p) = \frac{\tilde{\chi}_w^{(g)}(T, p)p}{e_w^{(c)}(T)}$$

$$\approx \frac{\varphi_w^{(g)}(1, T, e_w^{(c)})}{\varphi_w^{(g)}(\tilde{\chi}_w^{(g)}, T, p)} \Pi^{(c)}(T, p) \geq 1. \quad (8.11)$$

The enhancement factor describes the effect of air on the saturated partial pressure of water vapor,

$$\tilde{p}_w = \tilde{\chi}_w^{(g)} p. \quad (8.12)$$

The approximation sign in (8.11) results from the neglect of the solubility of air in liquid water. The quantity $\Pi^{(c)}(T, p)$ denotes the dimensionless Poynting correction factor for liquid water [8.71]

$$\Pi^{(c)}(T, p) = \exp \left\{ \frac{1}{R_w T} \int_{e_w^{(c)}(T)}^p v_w^{(c)}(T, p') dp' \right\}$$

$$\approx \exp \left\{ \frac{[p - e_w^{(c)}(T)] v_w^{(c)}}{R_w T} \right\}. \quad (8.13)$$

Here, $e_w^{(c)}(T)$ is the saturation vapor pressure of pure water vapor with respect to the condensed water phase, which can be stable liquid water, supercooled liquid water, or hexagonal ice. The quantity $v_w^{(c)}(T, p)$ is the specific volume of the condensed phase, and R_w is the specific gas constant of water. The enhancement factor is fully determined by the thermodynamic functions $\tilde{\chi}_w^{(g)}(T, p)$, $e_w^{(c)}(T)$, and $v_w^{(c)}(T, p)$, which are provided by TEOS-10 (Thermodynamic Equation Of Seawater – 2010) [8.72] on the basis of the corresponding IAPWS (International Association for the Properties of Water and Steam) formulations for fluid water, supercooled water, and hexagonal ice (Chap. 5).

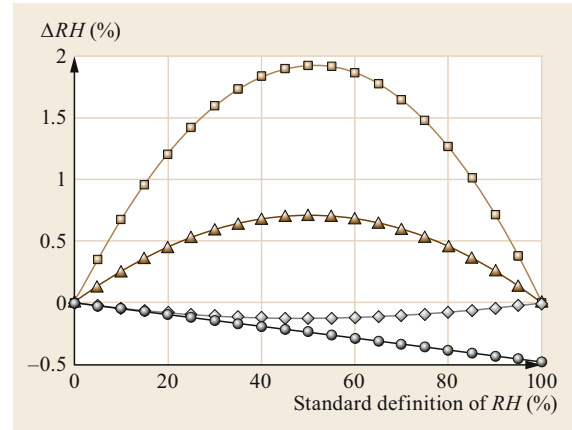


Fig. 8.9 Differences between the standard definition of relative humidity according to WMO (Table 8.3) and four nonstandard definitions at 40 °C and 1000 hPa. The nonstandard definitions are of the form where the relative humidity is quantified by the mixing ratio ($RF = (m/m_{\text{sat}}) \times 100\%$, squares), the specific humidity (triangles), the fugacity (diamonds), and the IUPAC (International Union of Pure and Applied Chemistry) definition (circles) (after [8.70] with permission from IOP Publishing)

Table 8.7 Contraction of normal and rolled hair on the basis of a simplified theory [8.73] and on the basis of validation measurements [8.14]

Relative humidity (%)	Normal hair		Rolled hair	
	$\bar{m}\%$	$\frac{\Delta L_0}{\Delta L_{0s}}$	$\bar{m}\%$	$\frac{\Delta L_0}{\Delta L_{0s}}$
100	100	1.000	100	1.000
90	75	0.939	72	0.927
80	65	0.877	62	0.854
70	57.5	0.813	55	0.782
60	51	0.746	49	0.709
50	45.5	0.676	43.5	0.636
40	40	0.604	38	0.564
30	35	0.514	33	0.477
20	29	0.392	27.5	0.357
10	20	0.218	20	0.210
5	13.5	0.120	13.5	0.115
1	5.3	0.025	5.3	0.025
0	0	0.000	0	0.000

The mole fraction of water vapor, $\chi_w^{(g)}$, can be easily transformed into any other meteorological humidity metrics such as the water-vapor mass-mixing ratio and the specific humidity [8.65, 70] (Fig. 8.9). The differences between the real-gas and ideal-gas formulations of relative humidity are quantified in [8.70].

8.3.2 Hair Hygrometer

The first steps toward a theory of hair hygrometers were already described in Sect. 8.2.2 [8.21–23], and these still form the basis for the recent theory. The contraction of the hair is given by [8.74]

$$\frac{\Delta L}{L} = \frac{\rho_v R^* T}{Y M_w} \ln \frac{100}{RH}, \quad (8.14)$$

with the mass density of water vapor ρ_v , the universal gas constant R^* , the modulus of elasticity of the hair Y (in units of Pa), the molecular weight of water M_w , and length of the saturated hair L .

In a simple model [8.73] it was assumed that between the cells of the hair are flexible chains of molecules that can absorb the moisture. The distance between the cells is L and the contraction in the moist state is ΔL_s , and in the dry state ΔL_0 with $\Delta L_{0s} = L_s - L_0$. From this theory follows a linear relationship between the logarithm of the scale of the hygrometer $(\Delta L_{0s}/\Delta L_0) - 1$ and the ratio $(m_s - m)/m$, with m the absorbed mass of water (index s in the case of saturation)

$$\log \xi + \zeta \log \frac{m_s - m}{m} = \log \left(\frac{\Delta L_{0s}}{\Delta L_0} - 1 \right). \quad (8.15)$$

The results of the theory [8.73] were validated for normal and rolled hair with the coefficients $\xi = 1.612$ and $\zeta = 0.3733$ [8.14]. The results are given in Table 8.7.

8.3.3 Lithium Chloride Heated Condensation Hygrometer (Dew Cell)

The basis of this method [8.4, 29, 75] is the physical circumstance (Raoult's law) that the equilibrium vapor pressure at the surface of a saturated salt solution is less than that for a similar surface of pure water at the same temperature, and that lithium chloride has a very low equilibrium vapor pressure (Sect. 8.2.3). If the aqueous salt solution is heated, the vapor equilibrates with the vapor pressure of the ambient air. At this point, the balance will shift from condensation to evaporation, and eventually, there will be a phase transition from the liquid solution to a solid hydrate (crystalline) form (efflorescence). The transition point may be detected through a characteristic decrease in the electrical conductivity of the solution as it crystallizes. The temperature of the solution at which the ambient vapor pressure is reached provides a measure of the ambient vapor pressure. Due to the underlying physical principle, the hygrometer does not work below 15% relative humidity at 0 °C [8.4]. The ambient dewpoint can be determined by empirical relationships.

8.3.4 Capacitive Hygrometer

In capacitive humidity sensors the dielectric material can either be a sandwiched structure with two electrode surfaces on each side or it can be placed between two interleaved comb electrodes. The ceramic aluminum oxide or, more recently, dielectric poly-

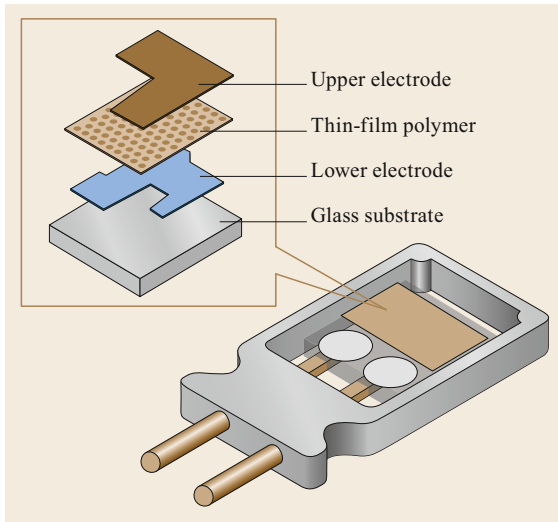


Fig. 8.10 Schematic configuration of the capacitive hygrometer (source: Vaisala Oyj, Finland)

mer film is positioned between these electrodes [8.32, 75], where atmospheric water-vapor molecules are deposited. A capacitive-type thin film humidity sensor called Humicap[®] was developed by Vaisala Oyj in Finland and is now widely used. The schematic of a polymer humidity sensor is shown in Fig. 8.10. It consists of two electrodes that are attached to a glass or ceramic highly insulating substrate. A thin film sensing layer of cellulose acetate is applied on top of one of the two bottom electrodes. Finally, a water-permeable layer of gold is deposited as the upper electrode on top of the polymer layer and electrically connected to other of the two bottom electrodes. The thickness of the gold layer is around 10–20 nm and porous enough to allow water-vapor transport through it. Due to the significant difference in the relative permittivity (dielectric constant) of $\epsilon_r = 80.1$ for water and $\epsilon_r = 1.00059$ for air at 18 °C and 50 Hz, the capacity changes dramatically, and the output signal is proportional to the relative humidity [8.8]. The sensor capacitance changes from 45 to about 70 pF for a relative humidity range of 0–100%, and it shows a rapid response time of approximately 1 s to reach 90% of the output value [8.32].

8.3.5 Psychrometric Method

The first theoretical derivation of the psychrometric method was proposed in 1822 by *Ivory* [8.35], later called convection or mixing theory [8.14]. It was assumed that the air in contact with the wet bulb is always saturated and the heat of evaporation originates from the same air. This method does not consider different ventilation velocities and applies for a well-

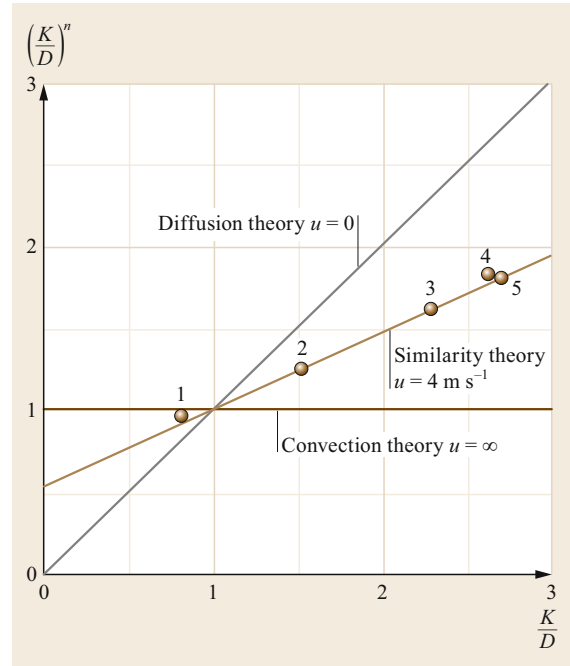


Fig. 8.11 Comparison of the factor $(K/D)^n$ for the three psychrometer theories for different liquids (1: water, 2: methyl alcohol, 3: propyl alcohol, 4: toluene, 5: ethyl propionate) (after [8.37])

ventilated psychrometer. The theory of nonventilated air is called diffusion theory [8.14] and was developed by Maxwell [8.38]. In both theories the heat transfer is not exactly determined, leading to a third theory – the similarity theory (following Reynolds similarity theory).

The basis of all theories is the psychrometric equation

$$e = E(t_w) - \frac{c_p p}{\gamma \lambda_v} \left(\frac{K}{D} \right)^n (t - t_w), \quad (8.16)$$

with the water-vapor pressure e , the dry-bulb temperature t in °C, the wet-bulb temperature t_w in °C, the water-vapor pressure for saturation E , the specific heat capacity for constant pressure c_p , the pressure p , the ratio of the molecular masses of water vapor and dry air $\gamma = 0.62198$, the specific heat of evaporation λ_v , the diffusion coefficient for heat K , the diffusion coefficient for water vapor D , and the exponent n , which is the ratio of the wind speed at the boundary layer u_h and the ventilation speed u . For the convection theory with $u = \infty$ follows $n = 0$ and for the diffusion theory $n = 1$. For the similarity theory, n is in the interval from 0 to 1 and depends on the construction of the psychrometer. The three theories are illustrated in Fig. 8.11.

It is obvious that water is the preferential liquid for psychrometers, because for all three theories K/D and $(K/D)^n$ are approximately 1, which reduces the parameters in (8.15), and the generally used psychrometer equation (Sect. 8.4.2) follows. Further theories were developed to investigate special effects of psychrometer construction like laminar flow, heat conduction, etc. [8.14].

8.3.6 Dewpoint and Frostpoint Hygrometers

The basic principle of most dewpoint and frostpoint hygrometers lies in the temperature of the liquid or solid condensate layer that is in equilibrium with the vapor phase in the air above. From the measured dewpoint or frostpoint [8.4]

$$t_d = \frac{243.12 \ln \{e / [6.112f_w(p)]\}}{17.62 - \ln \{e / [6.112f_w(p)]\}} \quad (8.17)$$

$$t_f = \frac{272.62 \ln \{e / [6.112f_i(p)]\}}{22.46 - \ln \{e / [6.112f_i(p)]\}}, \quad (8.18)$$

the water-vapor pressure for saturation can be calculated over water or ice using the enhancement factor (8.11) $f_{w,i}(p) = 1.0016 + 3.15 \times 10^{-6}p - 0.074p^{-1}$, which describes the deviation of the equilibrium vapor pressure in presence of another gas at higher pressure. The relative humidity can be calculated as

$$RH_w = 100 \frac{e}{E_w(t)} = 100 \frac{E_w(t_d)}{E_w(t)}, \quad (8.19)$$

$$RH_i = 100 \frac{e}{E_i(t)} = 100 \frac{E_i(t_f)}{E_i(t)}. \quad (8.20)$$

The definition of the dewpoint is related to a plane surface covered with a film of water. But water droplets have a curved surface over which the saturation vapor pressure is higher due to the Kelvin effect. Contaminants in the condensate layer may lower the dewpoint or frostpoint (Raoult effect), but can be minimized with careful maintenance of the hygrometer. Both effects can together raise or lower the dewpoint, but they are minimized if the critical droplet size is large, which reduces the curvature effect and lowers the concentration of the soluble contaminant [8.4].

8.3.7 Optical Method

All optical hygrometers make use of Bouguer–Lambert–Beer's law

$$I = I_0 \exp(-\rho_v kx), \quad (8.21)$$

where I is the light intensity at the detector, I_0 the light intensity of the lamp, ρ_v the absolute humidity, k the mass absorption coefficient, and x the path length between lamp and receiver. Emission and detection efficiencies as well as any absorption do not affect I_0 . For absolute humidity measurements, the lamp intensity must be known. For turbulence measurements only the relative fluctuations need to be determined. However, knowledge of k and x is required for proper scaling of fluctuations in ρ_v . The physical principle of optical instruments is shown in Fig. 8.12. Water-vapor concentrations can be measured at specific absorption lines in the ultraviolet and infrared band wavelengths.

The absorption coefficient for water vapor used in the UV range with a spectral resolution of 0.05 nm [8.76, 77] and for oxygen in the same spectral range with a spectral resolution of about 0.1 nm [8.77, 78] are shown in Fig. 8.13.

Of practical relevance are the wavelengths shown in Table 8.8. The advantage of the Lyman-alpha band is the negligible absorption by oxygen. Unfortunately, the emission of atomic hydrogen lamps is not very stable. Therefore krypton lamps are often used, which are more stable, but emit at two wavelengths, which are absorbed both by water vapor and oxygen. The absorption by ozone is negligible. Because of the oxygen cross sensitivity, the sensor can only be used under constant pressure conditions and is not well suited for absolute measurements.

In the IR range, different wavelengths are used, some with cross sensitivities between water vapor and carbon dioxide.

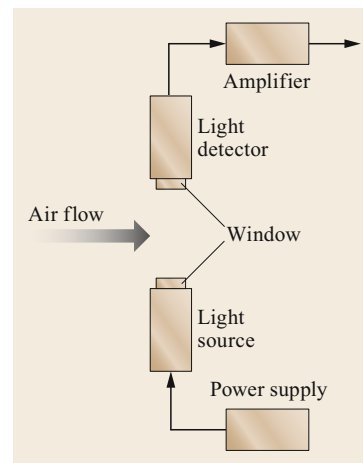
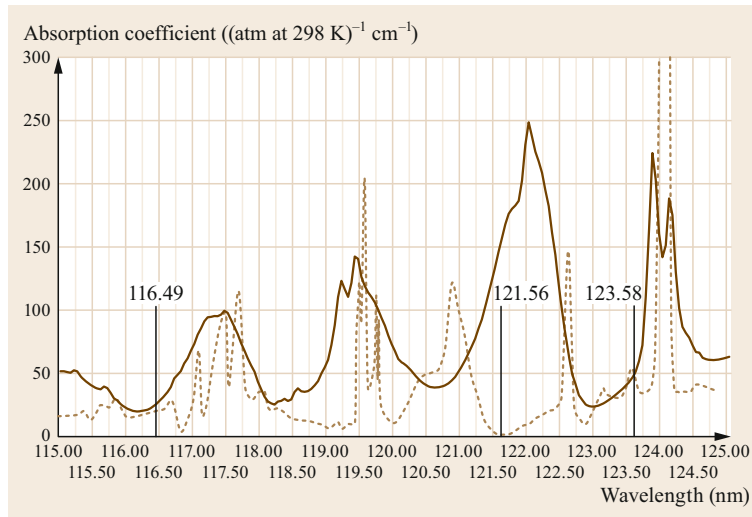


Fig. 8.12 Schematic representation of an absorption hygrometer (after [8.6])

Table 8.8 Selected spectral lines of the water-vapor absorption

Range	Wavelength (μm)	Radiation source	Measuring path	Absorber
UV	0.12156	Atomic hydrogen (Lyman-alpha)	(3–10) mm	H ₂ O
	0.12358 0.11647	Krypton	(5–15) mm	H ₂ O, (O ₂ , O ₃)
IR-A,B	Different wavelengths	Stable light bulbs	(0.125–1) m	H ₂ O, CO ₂

**Fig. 8.13** Volume absorption coefficient of water vapor between 115 nm and 125 nm (*solid line*) (after [8.76]) and for oxygen (*dotted line*) (after [8.78]), the data were transformed from base e (\ln) to base 10 (\log) (after [8.79, 80], © authors)

8.4 Devices and Systems

In addition to Sect. 8.2, this section describes humidity sensors that are still in use and can be applied for measurements with different accuracy and response characteristics.

8.4.1 Hair Hygrometer

Hair hygrometers [8.4, 7, 31] are still in widespread use as single instruments for room climate. These instruments appeal due to their simplicity, and for applications with relaxed requirements, they are often preferred over electronic sensors (Fig. 8.14).

The basic design of these instruments and the preparation of the hairs has not changed much since the original work of de Saussure. They typically use a bundle of specially prepared hair, which has been degreased and specially aged for durability. It is important that the hair has not been chemically treated. Often longer hairs of women are preferred. After being degreased, the hair must undergo a special aging procedure with low and high temperatures applied. Details are often a trade se-

cret of the producer. For low temperatures, hair treated by rolling is preferred. Besides hair, synthetic or textile fibers may also be used. Similar instruments are also available as metal-paper coil or bispiral hygrometers. One side of a metallic spiral is covered with a hygroscopic material. Such instruments, however, should not be used for very high or low humidities and are not as accurate as hair hygrometers, but they have a good long-term stability [8.81].

The change of the length of the hair with the humidity is a nonlinear function. At high humidity, the change in length is smaller than at low humidity, which can be compensated for by using linkages and levers to provide a nonlinear amplification. However, chemical treatments with barium or sodium sulfite may increase the linearity. Temperature effects can be compensated for by the insertion of a bimetallic strip into the sensor support. However, hair hygrometers have a hysteresis for increasing and decreasing humidity.

Hair hygrometers are rarely used for atmospheric measurements. But they do have certain advantages for

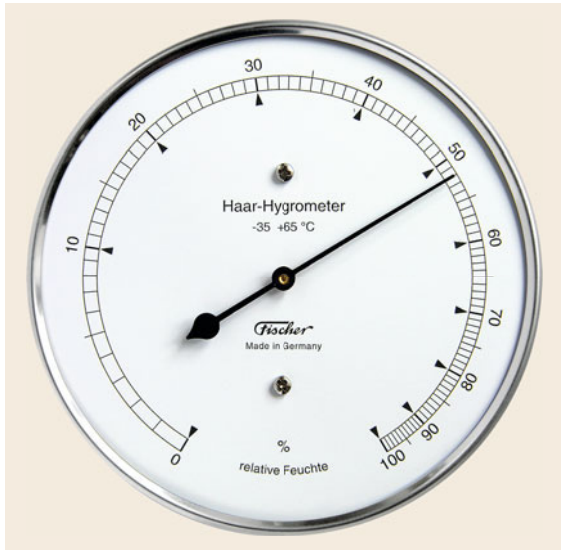


Fig. 8.14 Hair hygrometer (photo © Feingerätebau K. Fischer GmbH, Drebach, Germany)

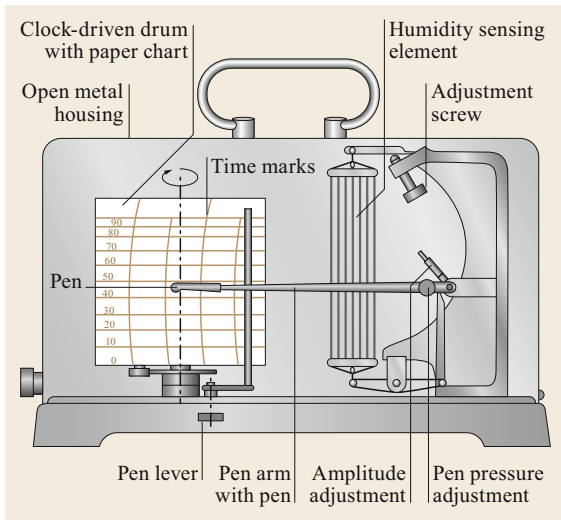


Fig. 8.15 Hair hygrograph (after [8.7] with permission of VDI e. V., Düsseldorf, Germany)

measurements at low temperatures, when psychrometers, for example, can no longer be used. Still in use for climatological measurements in meteorological screens (Chap. 7) is the drum recorder with a spring mechanism (hygrograph, Fig. 8.15). The change in length of the sensing hair can be converted into an analog electrical signal, e.g., by an inductive displacement transducer [8.82]. Figure 8.16 shows an electric hair hygrometer using a bimetal temperature compensation.

Hair hygrometers should be employed in moderate climates that are neither very dry nor very wet. Good

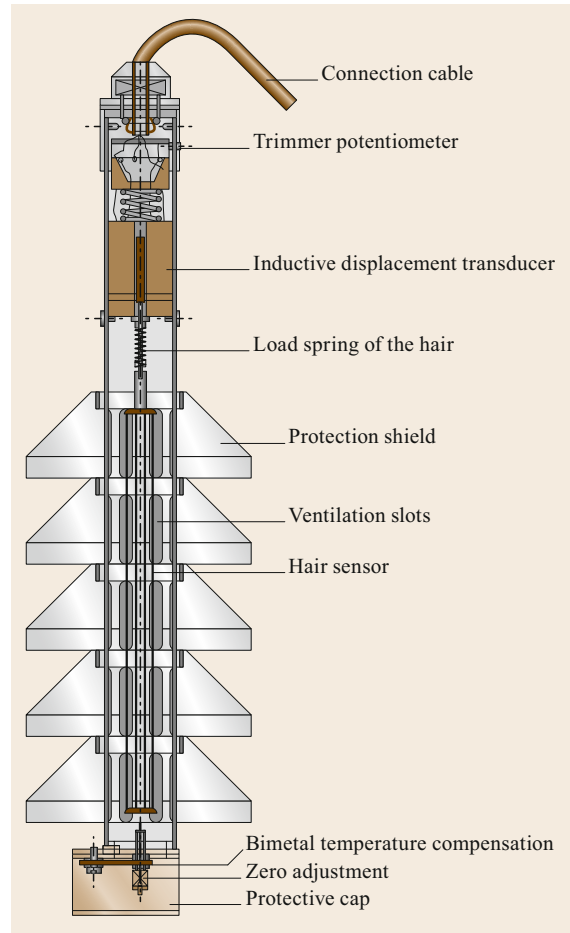


Fig. 8.16 Example of a hair hygrometer with analog voltage output (after [8.7, 82] with permission of VDI e. V., Düsseldorf, Germany)

instruments have an accuracy of $\pm 3\%$. The response time strongly depends on temperature, ranging from half a minute for high temperatures to several minutes for low temperatures. High humidities of nearly 100% relative humidity regenerate the hair. If this is not the case, such as in a dry climate or for indoor measurements, the regeneration should be made by covering the instrument with a sheet – wetted with warm water – for about 30 min. If a hygrometer is not regenerated, the indicated humidity increases for most of the instruments over a period of several years before it stays constant [8.81].

In polluted air, the hair should be cleaned by washing with water. In ammonia-polluted air hair hygrometers should not be used. Besides the regeneration, a zero-offset occurs due to changes of the tension of the hair. This can be corrected during regeneration by turning the adjustment screw. Regular comparison with an

Assmann aspiration hygrometer or another higher quality hygrometer are essential (Sect. 8.4.4).

Hysteresis in the hair sensing element is a short-term effect and not a cause for significant errors [8.4]; however, hysteresis in the mechanism may be significant, in particular if it is polluted. Therefore, the hygrometer should be tipped lightly to reduce any tension in the mechanical system before the measurement. It should be noted that the hair hygrometer measures the humidity above liquid water even at temperatures below 0 °C.

8.4.2 Lithium Chloride Heated Condensation Hygrometer (Dew Cell)

Because of the progress of the capacitive hygrometers and the effort required for maintenance, this sensor type is no longer produced.

8.4.3 Capacitive Hygrometer

Over a period of the last forty years capacitive sensors using thin polymer films as dielectric material have become the most widely used humidity sensors because of their small size, low maintenance, and nearly linear response [8.33]. These sensors were at first developed by Vaisala Oyj for radiosondes under the trademark Humicap®, but are now used for all types of humidity measurements from meteorological to industrial applications [8.34]. Due to the dependence of relative humidity on temperature, these sensors are often combined with temperature sensors in the same housing.

The basic design of the capacitive polymer humidity sensors consists of an upper electrode, a polymer film, and a lower electrode on a glass substrate as shown

in Fig. 8.10. For surface-based measurements, the sensor element and its electronics are typically mounted in a tube, sometimes combined with a Pt100 platinum thermometer. To minimize particulate contamination, the sensor is shielded by a filter cap. The filter cap is part of the sensor and technical parameters like response time need to consider the effect of the protective cap. The sensor shown in Fig. 8.17 is typical for most producers of meteorological instruments. Capacitive sensors are considered stable in arid conditions, but may experience nonnegligible drift at higher humidities [8.83].

To address problems, which may occur at high relative humidities, several manufacturers have introduced heated polymer humidity sensors. By heating the sensor, the immediate sensor environment is at lower relative humidity than the surrounding air. An integrated measurement of the humidity sensor temperature allows calculating the ambient relative humidity using

$$RH_{\text{ambient}} = RH_{\text{sensor}} \frac{E_w(t_{\text{sensor}})}{E_w(t_{\text{ambient}})}, \quad (8.22)$$

where RH_{ambient} is the relative humidity of the surrounding air, RH_{sensor} is the relative humidity by the heated sensor at its elevated temperature t_{sensor} , and t_{ambient} is the ambient air temperature, which must be measured nearby, but outside the air parcel impacted by the heated humidity sensor. This technique requires an additional measurement of the sensor temperature, which must be calibrated to the same level or better than the corresponding air temperature measurement.

Capacitive sensors for low absolute humidities used in radiosondes are described in Chap. 46.



Fig. 8.17a,b Capacitive humidity sensor: (a) sensor element (*lower*: view of the temperature sensor, *upper*: view of the humidity sensor); (b) housing of the sensor with filter screen and electronic tube (photos © Vaisala Oyj., Vantaa, Finland)

Table 8.9 Error in derived relative humidity resulting from errors in the psychrometer difference at 50% relative humidity [8.4] updated

Air temperature in °C	Error in relative humidity for an error of the psychrometer difference of	
	0.5 K (%)	0.1 K (%)
−30		12.1
−20	27.2	5.6
−10	13.9	2.8
0	8.4	1.7
10	5.3	1.1
20	3.7	0.7
30	2.7	0.5
40	2.2	0.4
50	1.8	0.3

8.4.4 Psychrometer

The psychrometer measures the psychrometric difference between a dry-bulb and wet-bulb thermometer while both thermometers are radiation shielded and ventilated with at least 3.5 m s^{-1} , because at lower ventilation rates, there is a sensitivity to the ventilation speed. Furthermore, the atmospheric pressure at the level of the station must be measured with sufficient accuracy. The wet bulb has a wick fitting closely around the sensing element (well-washed cotton, without synthetic fibers).

The formula currently used to calculate water-vapor partial pressure in hPa [8.8, 84] over water at standard atmospheric pressure of 1013.25 hPa is

$$e = E'_w(p, t_w) - 6.53 \times 10^{-4} \times p (1 + 9.44 \times 10^{-4} t_w) (t - t_w). \quad (8.23)$$

For temperatures above 30°C the following equation should be applied

$$e = E'_w(p, t_w) - 6.53 \times 10^{-4} (p - E_w(p, t_w)) \times (1 + 9.44 \times 10^{-4} t_w) (t - t_w). \quad (8.24)$$

The water-vapor partial pressure over ice (ice-covered wet-bulb thermometer, t_i) is

$$e = E'_i(p, t_i) - 5.75 \times 10^{-4} p (t - t_i). \quad (8.25)$$

The factors (numerical value and pressure and temperature-dependent parts) in the summand with the psychrometer difference is called the psychrometer coefficient with the dimension hPa K^{-1} – sometimes also called the psychrometer constant – and a function of temperature and pressure. These formulae are tabulated in more recent psychrometer charts [8.85] and can

be used for calculation, using the measured dry-bulb and wet-bulb temperatures as a basis. The uncertainty of the psychrometer coefficient per 0.1 K error of the wet-bulb temperature is $0.15 \times 10^{-4} p \text{ K}^{-1}$ [8.86] (Table 8.9). A pressure difference of 10 hPa in comparison to the standard air pressure causes an error of the psychrometer difference of about 1%. The resulting error of the relative humidity is temperature-dependent (Table 8.10). Therefore, near sea level the calculation can be made using the standard pressure if no extreme low pressure system passes the station. For stations above sea level the partial pressure of water vapor should be calculated with the local pressure. Because psychrometer charts and diagrams are often no longer in use, apps to calculate relative humidity from psychrometer readings should only be used if they are well documented and use pressure as an input parameter.

Below 0°C , the psychrometer difference is small and can cause large errors in relative humidity as shown in Table 8.9. The error in wet-bulb temperature under these conditions can be large, because the cotton wick must be fully covered by ice. This can be realized for single measurements but is a problem for continuously running electric psychrometers. In principle, water can be replaced by an ammonia solution, but only for psychrometers without metallic parts. Because of these problems, in winter psychrometers are replaced by hair hygrometers or, more recently, by capacitive hygrometers.

For all types of psychrometers, several requirements must be fulfilled [8.4]:

- At sea level the ventilation speed should not be lower than 2.5 m s^{-1} (better 3.5 m s^{-1}) and not larger than 10 m s^{-1} . At lower pressure the speed limits should be adjusted inversely proportional to the density of the atmosphere. Typically, a ventilation speed of 3.5 m s^{-1} is used, which does not need a correction for height above sea level.
- The ventilation speed should not be impacted by the wind field if the instrument is not in a meteorological screen, otherwise the ventilation speed has a dependency on the wind direction and speed. A vertical orientation of the flow around the thermometer is preferred.
- The wet bulb and dry bulb must be protected from radiation using a ventilated double shield, which should be polished, unpainted, and thermally isolated from other parts of the psychrometer.
- Both thermometers should be separately ventilated with an inflow of ambient air close to the thermometers.
- Great care should be taken to prevent transfer of heat from an aspirating motor or from the outer shields to the thermometers. Also recirculation of

Table 8.10 Psychrometer coefficient in hPa K^{-1} as a function of the pressure and the wet-bulb temperature (only for water) for water or ice on the cotton wick; difference to the standard values of 0.667 hPa K^{-1} (water) or 0.575 hPa K^{-1} (ice): bold ($< 1\%$) and bold-italic ($< 5\%$), for equations see Table 8.3

Pressure (hPa)	Water on cotton wick Wet-bulb temperature in $^{\circ}\text{C}$						Ice on cotton wick
	-10	0	10	20	30	40	
1030	0.666	0.673	0.679	0.685	0.692	0.698	0.592
1020	0.660	0.666	0.672	0.679	0.685	0.691	0.587
1010	0.653	0.660	0.666	0.672	0.678	0.684	0.581
1000	0.647	0.653	0.659	0.665	0.671	0.678	0.575
990	0.640	0.646	0.653	0.659	0.665	0.671	0.569
980	0.634	0.640	0.646	0.652	0.658	0.664	0.564
970	0.627	0.633	0.639	0.645	0.651	0.657	0.558
960	0.621	0.627	0.633	0.639	0.645	0.651	0.552
950	0.614	0.620	0.626	0.632	0.638	0.644	0.546
940	0.608	0.614	0.620	0.625	0.631	0.637	0.541
930	0.602	0.607	0.613	0.619	0.624	0.630	0.535
920	0.595	0.601	0.606	0.612	0.618	0.623	0.529
910	0.589	0.594	0.600	0.605	0.611	0.617	0.523
900	0.582	0.588	0.593	0.599	0.604	0.610	0.518
890	0.576	0.581	0.587	0.592	0.598	0.603	0.512
880	0.569	0.575	0.580	0.585	0.591	0.596	0.506
870	0.563	0.568	0.573	0.579	0.584	0.590	0.500
860	0.556	0.562	0.567	0.572	0.577	0.583	0.495
850	0.550	0.555	0.560	0.566	0.571	0.576	0.489

air must be prevented. This may be a problem inside screens or in low winds and stable stratification.

- The water reservoir and wick should be arranged such that the distilled water reaches the wet-bulb thermometer, but not affect the temperature of the dry bulb. Furthermore, the level in the water reservoir should be nearly constant.
- The cotton wick of the wet bulb should fit tightly around the sensing element and extend at least 2 cm up the stem of the thermometer. Before installation, it should be washed thoroughly in an aqueous solution of sodium bicarbonate at a dilution of 5 g per liter, and rinsed several times in distilled water. Alternatively, a solution of pure detergent in water may be used.
- The response time of both thermometers should be similar. For the same bulb dimension, the wet-bulb thermometer will be faster.

Several systematic errors may occur, which depend partly on the construction of the psychrometer [8.4]:

- The index error of the thermometers should be corrected. The effects of the index error and all other temperature errors are presented in Table 8.9.
- The space between the sensors and the radiation shield should not be bridged by water droplets or

ice, as this would enable heat conduction from the shield to the sensor.

- At temperatures below 0°C , it must be determined whether the bulb is covered with ice (completely) or with supercooled water.
- Errors due to contamination of the wet-bulb wick or to water impurities.
- Errors due to heat conduction from the thermometer stem to the wet-bulb system if the stem is insufficiently covered.

Common types of psychrometers are the August psychrometer for use in meteorological screens, the Assmann aspiration psychrometer, and electrical psychrometers based on the Assmann principle. Mercury thermometers, which are used in older instruments, have been replaced by alcohol liquid-in-glass thermometers. The Assmann aspiration psychrometer is considered a reference psychrometer for comparison experiments. There is a large number of electrical instruments available, most of which were developed at research institutions, with only a few being commercially available. Those based on the Assmann principle are the most common. In accordance to a proposal of the World Meteorological Organization, a WMO reference psychrometer was developed and is used as a WMO primary standard.

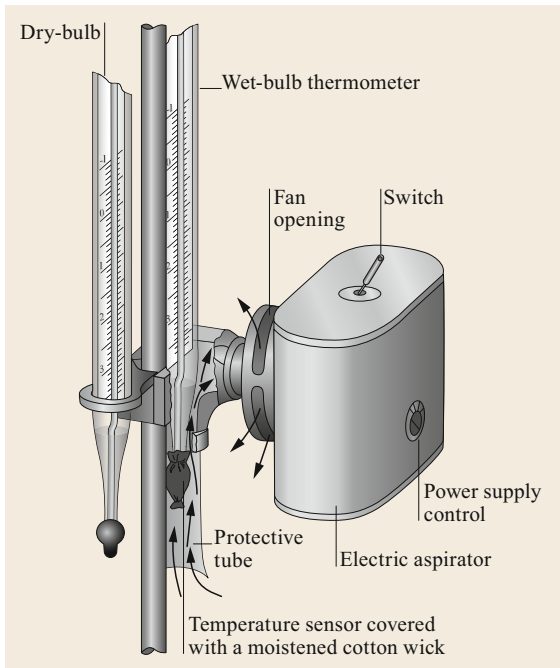


Fig. 8.18 Psychrometer according to August, with forced ventilation of the wet-bulb thermometer (after [8.7] with permission from VDI e. V., Düsseldorf, Germany)

Psychrometer According to August

The psychrometer according to August [8.39, 40] for measurements in meteorological screens (Figs. 8.5, 8.18) using liquid-in-glass thermometers is still in widespread use at climate stations (Chap. 43). These instruments have two vertically oriented thermometers, but only the wet-bulb thermometer is ventilated. The wetting of the bulb must be done by hand before each measurement. The aspirator is driven by a spring or, more recently, an electrical motor. Ventilation should be started approximately 5 min before the measurement.

Psychrometer According to Assmann

The Assmann aspirated psychrometer [8.4, 7, 14, 45] uses liquid-in-glass thermometers, originally filled with mercury and more recently with alcohol. This instrument is not suitable for continuous measurements, but rather the Assmann aspirated psychrometer is still among the most accurate humidity measuring instruments. Besides the original version, many similar constructions are currently in use. In 1987 the World Meteorological Organization compared a large number of these psychrometers against the WMO reference psychrometer. This study found that psychrometers with the original dimensions were the most accurate instruments [8.84].

The dry and wet thermometers are protected against radiation by a double radiation shield and are ventilated.

The distance between both bulbs and the radiation shield is large enough that water droplets or ice cannot bridge this gap, which would otherwise lead to heat conduction. Both thermometers are ventilated separately. The ventilation speed should be about 3.5 m s^{-1} so that it is not reduced significantly by the larger wet bulb. Normally a spring driven aspirator is used. The speed may be controlled by the number of rotations made by the casing box of the spring within a certain time interval. The spring may also be replaced by an electric motor. Details of the construction are illustrated in Fig. 8.19.

The measurements should be made following the standard operating procedures listed below. During the measurements, the instrument should be vertically oriented so that the influence of the wind speed is minimized. The instrument should not be oriented towards the sun and should be placed sufficiently far from the body of the observer. Installation on a separate boom is helpful. The typical height of measurement is 1.25–2.0 m. Before taking measurements the instrument should be in equilibrium with the air, which can be tested by taking several readings of the dry temperature. Outdoor psychrometric measurements should be repeated at least three times and averaged because of the fast changing air temperature. The order of the steps is [8.4]:

- Moisten the wet bulb.
- Wind the spring drive (or start the electric motor).
- Wait 2–3 min or until the wet bulb reading has stabilized.
- Read the dry-bulb thermometer.
- Read the wet-bulb thermometer.
- Check the reading of the dry-bulb thermometer again.

Electrical Psychrometer

Many types of electrical psychrometers, where the liquid in glass thermometers are replaced by Pt100 resistance thermometers (Chap. 7), are available, often built by research institutes. Of the commercially produced psychrometers, the types that best fulfill any given requirement are constructed similarly to the Assmann aspiration psychrometer. One such instrument is the psychrometer according to *Ernst Frankenberger* (1899–1985) [8.87], with resistance thermometers (Pt100) and a double screen radiation shield in the same dimension as the original instrument. Figure 8.20 shows this instrument, which is suitable for continuous measurements above 0°C .

A disadvantage of this instrument is the nonvertical orientation of the tubes of the thermometers, which can generate a slight dependence of the ventilation speed on the wind speed and direction. Furthermore, the length of the cotton wick between the sensor and the water

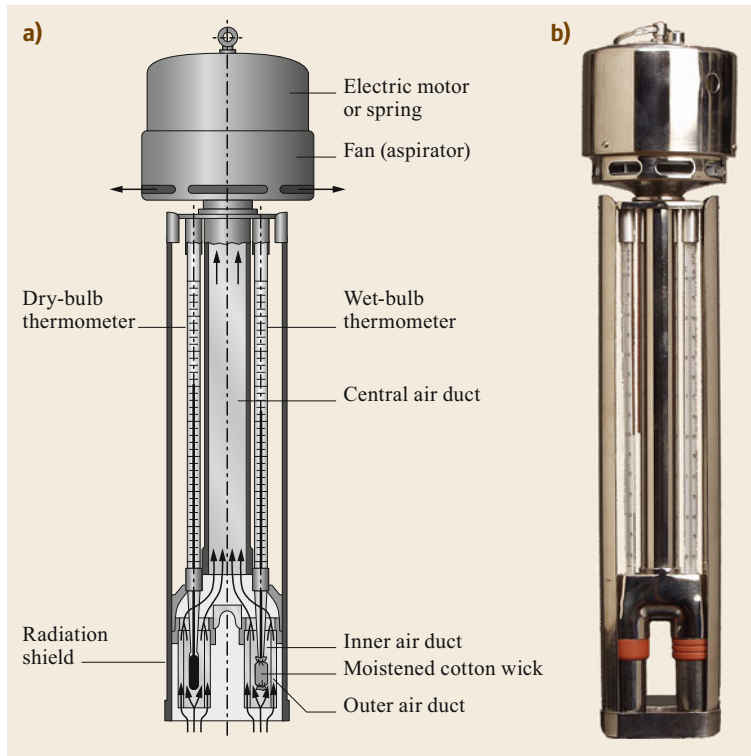


Fig. 8.19 (a) Schematic view of an Assmann aspirated psychrometer (after [8.7] with permission from VDI e. V., Düsseldorf, Germany). (b) A production model (photo © Theodor Friedrichs & Co., Schenefeld, Germany)

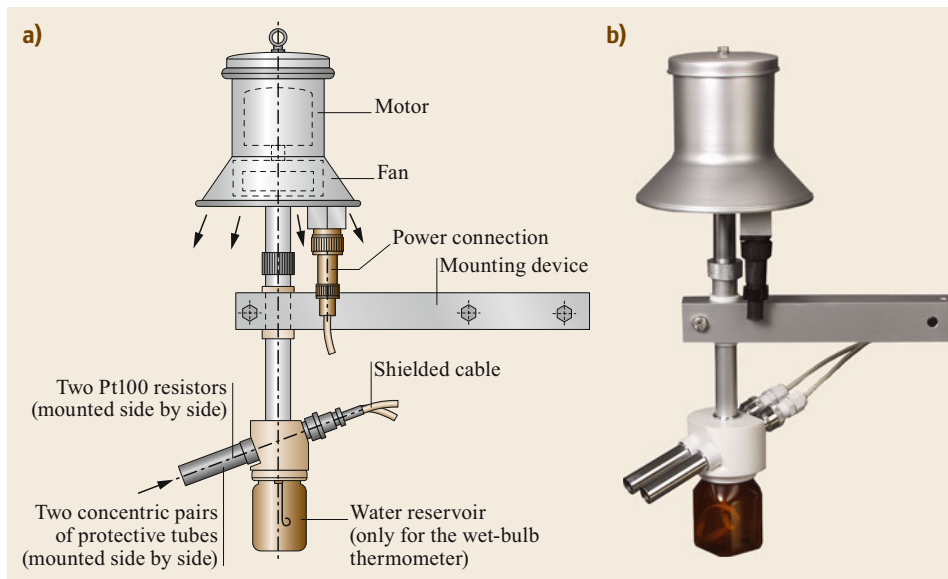


Fig. 8.20 (a) Schematic view of the psychrometer according to Frankenberger (after [8.7] with permission from VDI e. V., Düsseldorf, Germany), and (b) a recently produced type (photo © Theodor Friedrichs & Co., Schenefeld, Germany)

level can change, and the water flow can be interrupted at high evaporation or if the water level in the reservoir is allowed to drop too low. The water level should be checked every few days, especially during summer. To reduce possible re-circulation under conditions of weak winds or stable stratification, sensor and aspirator

should be separated, which can be easily realized. The tubes of the thermometers should be oriented towards north (northern hemisphere).

Below $0\text{ }^{\circ}\text{C}$, water in the wet-bulb wick may freeze, leading to measurement ambiguity. To avoid this problem and since the water-vapor pressure does not depend

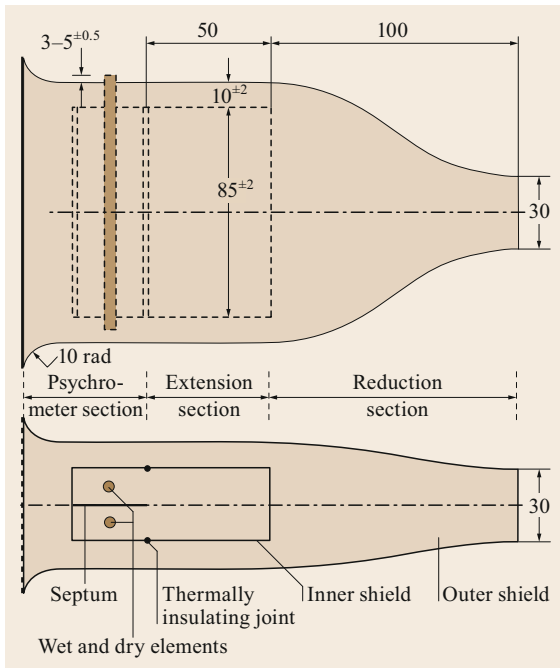


Fig. 8.21 Construction details of the proposal for a WMO reference psychrometer (after [8.88] with permission from World Meteorological Organization, Geneva, Switzerland). *Upper: top view. Lower: side view*

on temperature, a heated psychrometer was used. The heated psychrometer has a dry-bulb thermometer for ambient temperature and a heated and ventilated chamber ($\approx 10^\circ\text{C}$) with wet-bulb and dry-bulb thermometers according to the psychrometric principle [8.4]. The relative humidity at ambient temperature can then be calculated based on these measurements.

The WMO Reference Psychrometer

In 1957, the second session of the WMO Commission for Instruments and Methods of Observation (CI MO) at Paris recommended building a reference psychrometer, which was directed by the Working Group on Hygrometry (lead by *Russell G. Wylie*, Australia). A final report was given at the sixth session in Helsinki in 1973. First, four types were constructed in the USA, Australia, the UK, and Japan. The main recommendations were to achieve a psychrometer coefficient close to the theoretical value of $6.53 \times 10^{-1} \text{ hPa K}^{-1}$ at 20°C , 1000 hPa and 50% relative humidity. The construction sketch is shown in Fig. 8.21. In this design, evaporation at the wet-bulb thermometer should be very efficient, and an external heating or heat conduction from the mounting should be excluded. Both thermometers should be double shielded, well-ventilated, and horizontally oriented. The water level should be constant, which can be im-

plemented using an airtight reservoir above the sensors (not shown in Fig. 8.21), a downpipe, and a reservoir below the wet-bulb sensor having a constant water level.

According to these recommendations, finally two WMO reference psychrometers were constructed in Germany (former GDR) [8.89] and Australia [8.88]. The comparison of both reference psychrometers with the standard Assmann psychrometer showed good agreement within the given accuracy [8.84].

The WMO reference psychrometer is a primary standard for meteorology, because its performance is very predictable with few external influences only. This instrument can be used inside a screen together with other instruments. Special attention needs to be given to the aspiration and the cleanliness of the wet-bulb thermometer. Comparison experiments should be conducted by experienced personnel following WMO recommendations [8.88].

8.4.5 Dewpoint and Frostpoint Hygrometers

Dewpoint and frostpoint hygrometers are among the most stable and accurate instruments [8.8], since they measure dewpoint or frostpoint temperature directly. For that reason, they are often used as reference instruments [8.4]. Most dewpoint and frostpoint hygrometers are based on the chilled mirror principle [8.90]. In these instruments, a small mirror is cooled until water condenses on its surface, either as liquid water or ice. An electronic detector senses the reflectivity of this condensate and regulates the mirror temperature such that the measured reflectivity remains constant. Under this condition, the condensate is in equilibrium with the gas phase of water in the air above the mirror, and the temperature of the condensate is a direct measurement of the equilibrium temperature. This temperature represents the dewpoint temperature, if the condensate on the mirror is liquid, or the frostpoint temperature, if the condensate is ice.

Cooling of the mirror may be done using electronic Peltier coolers, through cryogenic cooling or a combination of both. Some research instruments have also used Stirling coolers. Some systems have an automatic mirror-cleaning heating cycle, in which volatile contaminants are evaporated, or use a mechanical wiper to clean the mirror.

A dewpoint or frostpoint hygrometer requires a minimum flow rate of approximately $0.25\text{--}1 \text{ L min}^{-1}$ to achieve an acceptable response time and stable operations [8.4]. For temperatures below 0°C the phase of the condensate on the mirror must be known to distinguish between supercooled water, i.e., the mirror

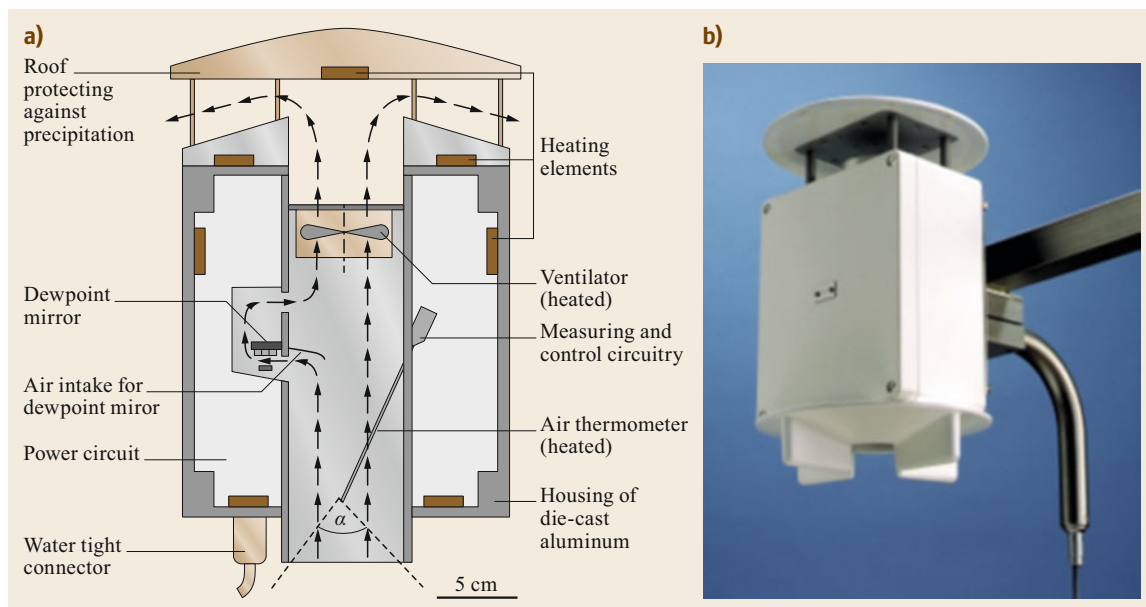


Fig. 8.22a,b Dewpoint hygrometer Thygan VTP6: (a) Schematic view (after [8.91] with permission from Meteolabor AG, Wetzikon, Switzerland); (b) sensor (photo © Meteolabor AG, Wetzikon, Switzerland)

temperature corresponds to dewpoint temperature, and ice, i.e., the mirror temperature corresponds to frost-point temperature.

One dewpoint hygrometer, used occasionally as reference instrument for atmospheric water-vapor concentrations, is made by Meteolabor AG [8.91,92] (Fig. 8.22). Less complicated but still highly accurate instruments are available from other manufacturers. But dewpoint hygrometers are seldom used as in-situ sensors because of possible contamination. They are the standard instrument in dewpoint generators for humidity calibration. Dewpoint hygrometers are also used in balloon borne and aircraft observations for measurements of upper air humidity (Chap. 46).

8.4.6 Optical Hygrometers

Optical instruments are the only instruments suitable for measuring humidity fluctuations at frequencies up to about 100 Hz. These instruments are mainly used for turbulence and flux measurements (Chap. 55), less frequently for measurements of humidity (absolute humidity, mixing ratio) due to possible drifts and long-term stability issues. IR hygrometers dominate the market despite their lower sensitivity and have almost completely replaced the more sensitive but less stable UV hygrometers. Infrared hygrometers are available as either an open-path instrument for measurements near the wind sensor, or as a closed-path instrument, where

an inlet near the anemometer is connected to the analyzer through a tube. Some trace-gas analyzers may also measure water vapor, usually based on the principles discussed here (Chap. 16).

UV Hygrometers

The Lyman-alpha hygrometer was the first instrument used for humidity flux measurements. Due to the high light absorption of water vapor in the Lyman-alpha band (Fig. 8.13), the instrument – composed of a hydrogen lamp and a detector – is very sensitive, even for path lengths as short as 10–20 mm and low absolute humidities. Because of the low stability of the lamp, this system is mainly used on aircrafts (Chaps. 48 and 49).

The more stable krypton hygrometer KH20 produced by Campbell Sci. Inc. (Fig. 8.23) uses a low-pressure krypton glow tube as a light source and is still in use. The krypton lamp emits a minor band at 116.49 nm (band 1) and a major band at 123.58 nm (band 2). Radiation at 123.58 nm is strongly attenuated by water vapor, whereas absorption by other gases is relatively weak (Fig. 8.13). Radiation at the shorter wavelength (116.49 nm) is attenuated by water vapor as well as oxygen molecules, but the intensity of the transmitted beam is considerably attenuated by magnesium fluoride windows used at the lamp and detector tubes [8.56]. The measured signal I (I_{01} and I_{02} are the intensities of the source at both wavelengths) depends

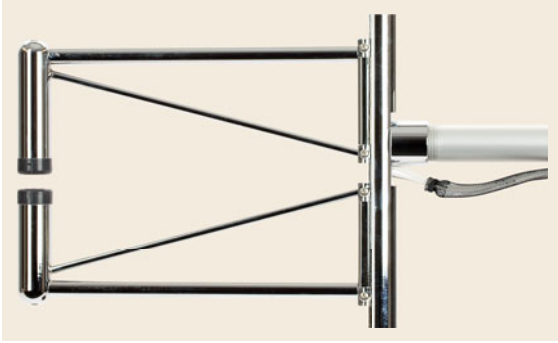


Fig. 8.23 Krypton hygrometers (image © Campbell Scientific, Inc., Logan UT, USA, 2017). The design of Lyman-alpha hygrometers was similar, but with a slightly larger lamp

on the path length x , the mass absorption coefficients k , and the densities ρ of both absorbers: water vapor (index w) and oxygen (index O) [8.56, 93]

$$I = I_{01} \exp[-x(k_{v1}\rho_v + k_{O1}\rho_O)] + I_{02} \exp[-x(k_{v2}\rho_v + k_{O2}\rho_O)], \quad (8.26)$$

where the indices 1 and 2 refer to the two wavelengths at 116.49 nm and 123.58 nm, respectively.

The absorption coefficient at the short wavelength is half of that at the longer wavelength [8.94]. Since only the signal of these two wavelengths is measured, it is possible to extract the water-vapor absorption signal from the combined measurement with a combined value k_v . The fraction of the oxygen absorption of band 1 is f and of band 2 is $(1 - f)$. The simplified (8.26) is

$$I = I_0 \exp(-xk_v\rho_v) \times [f \exp(-xk_{O1}\rho_O) + (1 - f) \exp(-xk_{O2}\rho_O)]. \quad (8.27)$$

For most applications, the additional oxygen absorption can be ignored and the basic equation for the calculation of krypton hygrometer KH20 is

$$\ln(V) = \ln(V0) - \rho_v x K_v, \quad (8.28)$$

with the intercept $\ln V0$ in $\ln(\text{mV})$, $\approx 8 - 10 \ln(\text{mV})$, the calibration coefficient (effective absorption coefficient for water vapor) K_v in $\ln(\text{mV}) \text{ m}^3 \text{ g}^{-1} \text{ cm}^{-1}$, the coefficient xK_v in $\ln(\text{mV}) \text{ m}^3 \text{ g}^{-1}$ for a given path length x in cm and the absolute humidity ρ_v in g m^{-3} . This simplification is possible because only fluctuations of absolute humidity are of interest (see Chap. 55) and the oxygen concentration is assumed not to change (for nearly constant air pressure, therefore no application on

aircrafts possible). Nevertheless, small corrections are recommended [8.95, 96].

Equation (8.26) can also be used for calibration: assuming a constant absolute humidity, the path length can be changed to determine the calibration coefficient. This method was already developed for Lyman-alpha hygrometers because of the low source stability but can also be applied for krypton hygrometers [8.97]. But here the calibration is against oxygen and assumes a similar contamination of the windows or the source for both gases – oxygen and water vapor [8.98].

IR Hygrometers

The absorption of infrared radiation by water vapor is not as strong as that of ultraviolet radiation. Therefore, the absorption is often measured at two nearby wavelengths, where one is strongly absorbed by water vapor, the other not. Alternatively, in closed-path systems, two measurements may be taken, where one measurement is that of the air sample, the other that of dry reference gas. From the difference of both signals the concentration can be calculated. The devices often measure not only water vapor but also carbon dioxide. Because the sensitivity is much lower than for UV devices, the path length of approximately 15 cm is about tenfold that of the UV devices. To increase the path length, mirror systems are designed that reflect the light beam multiple times. A chopper system measures the different spec-

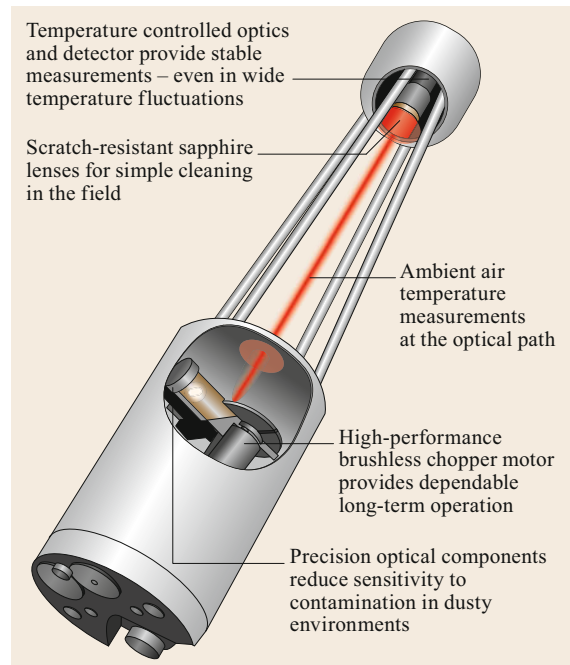


Fig. 8.24 Open-path $\text{H}_2\text{O-CO}_2$ -gas analyzer (LI-7500-DS) (image: ©, LI-COR, Inc., Lincoln NE, USA)

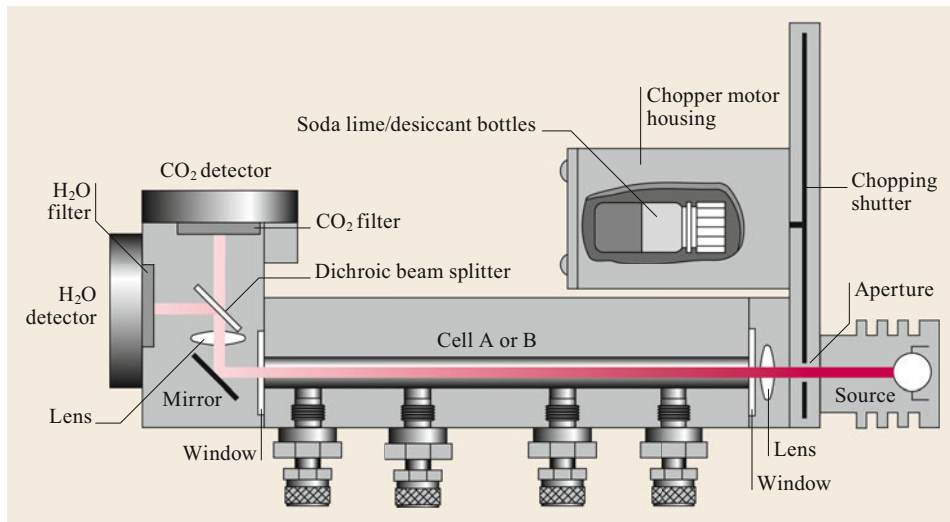


Fig. 8.25 Closed-path gas analyzer (LI-7000), for details see text (image: ©, LI-COR, Inc., Lincoln NE, USA). One cell measures the air sample, while the other measures the dry reference gas

tral lines separately. Due to the fast response time the systems can measure at a sampling rate up to 20 Hz. The frequency of measurement is currently limited by the sensitivity of the electronics and not by any physical principle.

IR-hygrometers are available as open-path (Fig. 8.24) and closed-path systems (Fig. 8.25). While open-path systems measure the air volume of interest directly, i.e., near the sonic anemometer for eddy-covariance measurements (Chap. 55), the closed-path instrument extract air from a volume of interest using a tube and measure the water-vapor concentration in a closed cell nearby. Both systems detect the concentration as mass density (mass unit per volume) with some differences [8.99]. In the open-path system the concentration is affected by ambient temperature, requiring a specific density correction for water vapor – the WPL-correction according to *Webb, Pearman, and Leuning* [8.100] –, which is only a few percent for water vapor but may be large for trace gases. The advantage of open-path systems is a good frequency response, which is only limited by the path length. In closed-path systems, the optical cell has a uniform temperature and pressure, so that the mass density can be easily converted into the mass-mixing ratio

$$r_{\text{wm}} = \frac{R^*T}{M_d(p-e)} \rho_v, \quad (8.29)$$

(where R^* is the universal gas constant and M_d the dry air molar mass, ρ_v the density of water vapor), or into the mol fraction

$$\chi_w = \frac{R^*T}{M_v(p-e)} \rho_v, \quad (8.30)$$

with M_v the molar mass of water vapor. For more details see Chap. 55 and Table 55.3. The frequency response of closed-path systems is significantly slower than open-path systems due to the extractive sampling and transport of the air sample to the optical cell through the sampling tube. For turbulent flows the Reynolds number in the tube should always be larger than the critical Reynolds number of about 2500.

Manufacturers have recently attempted to combine the benefits of both systems, building closed-path systems that have very short sampling lines (about 1 m), or open-path systems with high-frequency temperature and pressure measurements. The direct measurement of the mixing ratio does not require the WPL-correction (Chap. 55).

8.4.7 Comparison of the Methods

The number of sensor principles and sensor types has significantly decreased in the last 20 years. One reason is that the capacitive polymer sensor, which has a nearly linear output signal, has been significantly improved and is now considered sufficiently stable. In contrast, lithium chloride dew cells are nearly out of use. Similarly for fast hygrometers, UV hygrometers have been replaced by IR hygrometers, which are more stable and have recently expanded their sensitivity range to low absolute humidities. The classical hair hygrometer has been used for a long time and continues to be used, mainly for indoor measurements or for instruments with mechanical registration. Psychrometers and dewpoint hygrometers continue to be used as reference instruments and for special applications, mainly in research. A brief description of advantages and disadvantages of each method is given in Table 8.11.

Table 8.11 Advantages and disadvantages of the different methods

Devices	Advantages	Disadvantages
Hair hygrometer	Simple mechanical instrument	Long time drift, regeneration necessary
Lithium chloride hygrometer	First electrical sensor to replace hair hygrometers	Handling of lithium chloride solution difficult, rarely used anymore
Capacitive hygrometer	Simple and stable electrical sensor	Screen may be necessary
Assmann psychrometer	High accuracy, reference instrument	No electrical output, difficult measurements < 0 °C
Electrical psychrometer	Electrical instrument, accurate	Not suitable for temperatures < 0 °C
Dewpoint and frostpoint sensor	Often very accurate, reference instrument	High level of maintenance required for accurate measurements
UV hygrometer	Fast response hygrometer, very sensitive at low absolute humidities	Unstable light source, rarely used anymore
IR hygrometer	Fast response hygrometer, sensitive over a large range of humidities, open-path and closed-path instruments	Density and other corrections necessary, especially for flux applications

8.5 Specifications

Typical uncertainties of different humidity sensors are given in Table 8.12. Most of the available dewpoint and capacitive sensors may be considered WMO working standards or even as reference standards (Sect. 8.6.1 and Table 8.14). In many applications the limiting factor is the housing of the sensor, not the sensor itself, in particular in low-cost installations. Details of the possible

influences of sensor enclosures on the measurements are described in Chap. 7.

Typical response times are given in Table 8.13. For turbulence measurements, optical sensors are generally used; for moving platforms, such as balloons and aircrafts capacitive polymer sensors and dewpoint and frostpoint hygrometers may also be found (Chaps. 46, 48, and 49).

Table 8.12 Typical characteristics for humidity sensing methods [8.7]. Some high quality sensors may have better characteristics than listed here

Method	Typical total uncertainty	Temperature range	Humidity range
Hair hygrometer	± 5% RH	−10 to 50 °C	> 40% RH
Capacitive hygrometer	± 3% RH ± 5% RH	0 to 45 °C −10 to 0 °C	5–100% RH 5–95% RH
Psychrometer	± 2% RH	0 to 50 °C wet-bulb temperature	> 5% RH
Dewpoint and frostpoint hygrometer	± 0.2 K	−100 to 50 °C dewpoint or frostpoint temperature	
Optical hygrometer	± 5–10% of absolute humidity	−10 to 50 °C	

Table 8.13 Typical time constant (63%) in seconds at 85% relative humidity for humidity sensing methods [8.4, updated]

Method	20 °C	0 °C	−20 °C
Hair hygrometer			
Ordinary human hair	32	75	440
Rolled hair	10	10	12
Goldbeater's skin	10	16	140
Electrical capacitive hygrometer	1–10	1–10	1–10
Psychrometer	30–50	30–50	30–50
Dewpoint and frostpoint hygrometer	1–50	1–50	1–50
Optical hygrometer	< 0.01	< 0.01	< 0.01

8.6 Quality Control

The section dealing with quality control for humidity sensors includes the definition of standards, calibration procedures, and the detection of typical errors.

8.6.1 Reference Standards

The WMO has developed a system of standards and instruments for calibration [8.4]. The requirements for these standards are given in Table 8.14. The primary standards (Sect. 8.6.2) should be available at the national standards and calibration laboratories. Secondary standards are required for national or regional calibration laboratories of meteorological services, etc. These standards must be compared against a primary standard every year. Reference standards for indoor calibration have almost a similar accuracy as secondary standards. Chilled-mirror dewpoint hygrometers or the WMO reference psychrometer [8.88] may be used as secondary or reference standards. Outdoor comparisons of humidity measurements may be done against working standards. These standards are chilled-mirror dewpoint hygrometers or the Assmann aspiration psychrometer

and must be compared against a reference standard at least annually. For an easy verification of the calibration of an instrument, salt solutions (Sect. 8.6.3) may be used. Ultraviolet hygrometers may also be calibrated in-situ by changing the path length (Sect. 8.4.6).

8.6.2 Primary Standards

Primary standards are maintained at the national metrology laboratories, where three different methods are in use [8.4]. The gravimetric method is based on an exact determination of the mass-mixing ratio. This is obtained by removing the water vapor from an air sample with a drying agent like phosphorous pentoxide (P_2O_5) or magnesium perchlorate ($Mg(ClO_4)_2$). The mass of the agent is determined by weighing before and after absorption of the vapor. Therefore a complex apparatus is required to accurately control the measurement conditions to determine the density of the sample.

The dynamic two-temperature standard humidity generator saturates air at one temperature. The saturated

Table 8.14 Typical measurement range for humidity standard instruments [8.4]

Standard instruments	Dewpoint temperature		Relative humidity	
	Range (°C)	Uncertainty (K)	Range (%)	Uncertainty (%)
Primary standard				
Requirement	−60 to −15	0.3	5–100	0.2
	−15 to +40	0.1	5–100	0.2
Gravimetric humidity generators	−60 to −35	0.25		
	−35 to +35	0.03		
	+35 to +60	0.25		
Standard two-temperature humidity generator	−75 to −15	0.25		
	−15 to +30	0.1		
	+30 to +80	0.2		
Standard two-pressure humidity generator	−75 to +30	0.2		
Secondary standard				
Requirement	−80 to −15	0.75	5–100	0.5
	−15 to +40	0.25	5–100	0.5
Chilled-mirror hygrometer	−60 to +40	0.15		
WMO reference psychrometer			5–100	0.6
Reference standard				
Requirement	−80 to −15	1.0	5–100	1.5
	−15 to +40	0.3	5–100	1.5
Chilled-mirror hygrometer	−60 to +40	0.3		
WMO reference psychrometer			5–100	0.6
Working standard				
Requirement	−15 to +40	0.5	5–100	2
Chilled-mirror hygrometer	−10 to +30	0.5		
Assmann psychrometer	−10 to +25		40–90	1
Electrical capacitive hygrometer	−20 to +40		5–90	2
	+15 to +30		5–90	1

Table 8.15 Saturated salt solution at 25 °C and their characteristic relative humidity [8.4, 101, updated]

Salt	Chemical symbol	Relative humidity (%)	Solubility (g/100 mL)
Potassium sulfate	K ₂ SO ₄	97.3	23
Barium chloride	BaCl ₂	90.3	37
Potassium chloride	KCl	84.3	34
Sodium chloride	NaCl	75.3	36
Potassium iodide	KI	68.9	144
Sodium bromide	NaBr	57.6	91
Magnesium nitrate	Mg(NO ₃) ₂	52.9	71
Potassium carbonate	K ₂ CO ₃	43.2	112
Magnesium chloride	MgCl ₂	32.8	54
Calcium chloride	CaCl ₂	29.0	135
Potassium acetate	KCH ₃ COO	22.5	228
Lithium chloride	LiCl	11.3 [8.101]	83
Lithium bromide	LiBr	6.4	160

air is then heated up to a second temperature for which the relative humidity can be calculated on the basis of the water-vapor pressure for saturation at the first temperature.

The dynamic two-pressure standard humidity generator has two chambers, one filled with air saturated over liquid water at the pressure p_0 . The air is expanded isothermally into a second chamber at a lower pressure p . Both chambers must have the same temperature. The relative humidity in the second chamber is defined by the ratio of the pressures in each of the two chambers through Dalton's law [8.4, 14]

$$RH = 100 \frac{e}{E_w} = 100 \frac{p}{p_0} \quad \text{in } \% . \quad (8.31)$$

Relative humidity with respect to saturation over ice is defined analogously to the procedure given above if the air at high pressure has been saturated over ice.

Most humidity generators use dewpoint hygrometer as a reference instrument. Recently, well-calibrated capacitive hygrometers have also been used as a reference sensor.

8.6.3 Salt Solutions

Air above the surface of a saturated salt solution equilibrates at a characteristic value of relative humidity (Table 8.15), which may depend slightly on temperature. This effect can be used for the calibration of small humidity sensors. Great care needs to be taken that the salt solution is properly saturated and that the entire system is thermally well equilibrated when a sensor calibration or calibration check is performed. Using an array of different salt solutions allows calibration over a large range of relative humidities. This method is very practical for checks of individual small sensors,

but does not supersede the comparison with reference hygrometers [8.4].

8.6.4 Quality Control Procedures

The quality control of humidity measurements must be part of the quality control procedures of all sensors at a meteorological station (Chaps. 3 and 43). A typical range of relative humidity is between 10 and 100%, with maximal changes within 1 min (10 min, 1 h) of 10% (30%, 50%). Nearly constant values within 6 h are questionable and constant values within 12 h are to be considered erroneous [8.102]. The upper limit of humidity is 100%, corresponding to saturation water-vapor pressure over water at a given temperature. Small values of supersaturation over water may be possible for a short amount of time (minutes), while supersaturation over ice may last significantly longer (up to hours). Table 8.16 gives some sensor-specific criteria that may be applied in quality control procedures. If the cause for invalid data cannot be determined and rectified, then a specialist should check the sensor and measurement setup.

Humidity sensors should be installed in meteorological screens or in a ventilated double shield for protection against radiation and rain. For open installations such as for optical instruments, a radiation error correction may be necessary and the instrument may fail all together under rainy conditions. If the sensor does not provide internal error coding, parallel rain detection may be necessary. Significant air pollution may lead to contamination of dry-bulb and wet-bulb wicks, mirrors or sensor windows. Wind may affect the ventilation rate leading to a dependence of the measurements on the wind direction in many instruments. Ventilation rates greater than 2.5 m s⁻¹ should be guaranteed for all wind directions and wind speeds.

Table 8.16 Typical tests criteria for humidity measurements

Method	Error	Reason
All instruments	$RH < \text{minimum for climate zone}$	Humidity too low for the method, new calibration necessary
Hair hygrometer	$RH > 100\%$ for more than 1 h $RH = \text{const.}$ for more than 3–6 h	New calibration necessary Mechanics must be cleaned
Capacitive hygrometer	$RH > 100\%$ for more than 1 h Low sensitivity	New calibration necessary Filter cap may be contaminated
Psychrometer	$RH \geq 100\%$ for more than 1–3 h Unusually small differences between dry-bulb and wet-bulb temperature	Dry-bulb thermometer is wet or wet-bulb thermometer is dry No or low aspiration or contamination of the wick of the wet-bulb thermometer
Dewpoint and frostpoint hygrometer	Measured dewpoint temperature larger than ambient temperature for more than 1–3 h, or reduced sensitivity	Mirror contaminated or detector dirty; most instruments give an error code
Optical hygrometer	Measured absolute humidity larger than saturation absolute humidity for the ambient temperature for more than 1–3 h, or reduced sensitivity	Windows contaminated or reduced signal of the light source

8.6.5 Calibration of Optical Hygrometers

Optical hygrometers can be calibrated with gases with a given humidity. For this, a calibration tunnel is installed in the optical path and the calibration gas flows through at a controlled and not too large flow rate. The zero-point must first be calibrated normally with dry nitrogen gas. Next, for the span calibration, a certain water-vapor concentration can be generated with dewpoint generators. The dewpoint can be easily recalculated as absolute humidities. Optical systems for water vapor that are applied for other trace gases like carbon dioxide can be calibrated in a similar way with a zero-gas and one or more calibration gases with a given concentration (see also Chap. 55). In any case, the calibration instructions of the manufacturer should be carefully applied.

8.6.6 Documentation and Metadata

Sensors have significantly changed over the last 20–30 years. Sensors such as lithium chloride dew cell have been almost completely replaced by the capacitive polymer sensors in automatic weather stations. For the maintenance of atmospheric climate records as well as for operational observations it is vital that all sensor changes, updates, replacements, and other measures impacting the observations are meticulously documented [8.83]. This includes documentation of parallel observations with old and new sensors during periods of transition and overlap and other comparison experiments. However, calibration updates and comparisons with working or reference standards must be documented. These efforts are of utmost importance and constrain the impact that sensor changes may have on long-term climate records or input observations for short-term weather forecasting.

8.7 Maintenance

Some general rules for maintenance should be followed for all instruments [8.4]: Sensors and housings should be kept clean, as well as the meteorological screen if necessary. This is very important for radiation shields, but particularly for those of psychrometers. Some sensors, for example chilled-mirror, optical hygrometers, and hair hygrometers, may be regularly cleaned with distilled water. Where available, instructions by the manufacturer should be consulted.

Monthly comparisons with a working reference hygrometer, such as an Assmann aspiration psychrometer,

are essential. For sensors relying on air temperature measurements, such as psychrometers and dewpoint hygrometers, that temperature sensor should be checked as well, which may easily be done with the Assmann psychrometer. Calibration against a reference standard in the laboratory should be done at regular intervals, such as annual or biannual and should include checks of the electronic data acquisition system.

Table 8.17 gives an overview of required maintenance for the most commonly used sensor types. Further information is given in Sect. 8.4.

Table 8.17 Maintenance of humidity measurement systems [8.7, updated]

Maximum interval	Hair hygrometer	Capacitive hygrometer	Psychrometer	Dewpoint and frost-point hygrometer	Optical hygrometer
1 week	Regeneration of hair and readjustment, if necessary		Refill water	Clean mirror, if not done automatically	Clean window with methanol or ethanol
1 month	Function and plausibility check, comparison with working reference such as Assmann psychrometer				
3 month	Check the mechanical function	Check and replace the filter cap, if necessary	Replacement of the cotton wick; may be required more frequently in areas with high levels of air pollution; inspection of the aspirator		Calibration in a climate test chamber, for IR hygrometers after 6–12 months, if necessary
2 year	Calibration of the instrument				
If a check indicates a possible malfunction, an instrument is to be replaced					

8.8 Application

Humidity is a standard meteorological parameter measured at nearly all meteorological stations (Chaps. 43 and 45) and is an important parameter for determining evapotranspiration (Chap. 57) and latent heat flux (Chap. 55). Many physical and chemical processes in the atmosphere involve water vapor. Absolute humidity and water-vapor pressure are sufficient to characterize an air mass; however, but the relative humidity must always be recorded together with air temperature.

8.8.1 Climatology of Humidity

Modern data acquisition technologies allow sampling rates of 1–10 s. Typical averaging intervals for humidity are 10 min, but intervals of 30 min or 60 min are also used. For standard meteorological measurements in Central Europe the daily mean is calculated from 24 values a_i , which may be relative humidity, absolute humidity or water-vapor pressure, recorded at one-hour intervals between 23:50 UTC of the previous day and 23:50 UTC of the current day [8.7]

$$\overline{a_{\text{day}}} = \frac{1}{24} \sum_{i=0}^{23} a_i. \quad (8.32)$$

For other time zones the averaging times must be adjusted accordingly. The climatological daily mean is calculated according to (8.32). If more than four continuous hourly values are not available, the daily mean is calculated from the arithmetic mean measured at 00:00 UTC, 06:00 UTC, 12:00 UTC and 18:00 UTC. At climate reference stations, the mean of the humidity values obtained at 6:30 UTC, 13:30 UTC and 20:30 UTC is calculated from only these three readings.

8.8.2 Daily and Annual Cycles

Long-term averages of humidity carry only a limited significance. The frequency distributions of hourly averages are of higher significance. Instead of monthly means of relative humidity, the mean value at a fixed time, e.g., at 3 p.m., may be a better indicator for characterizing humidity at a station.

The daily cycle may be more instructive because high temperatures are related to low relative humidity and vice versa; for example, during a fine summer day the absolute humidity or the water-vapor pressure may not show significant changes or a daily cycle, whereas temperature and relative humidity do show a significant daily cycle (Fig. 8.26).

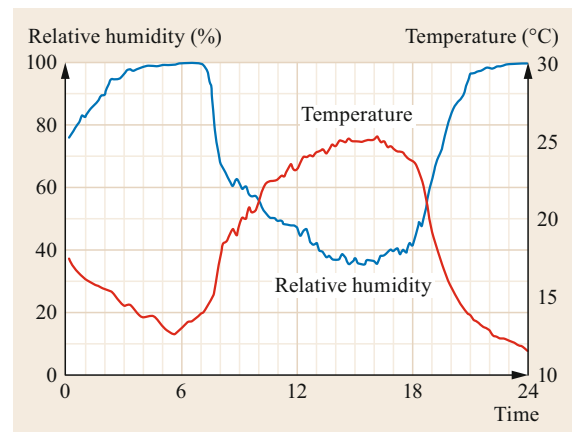


Fig. 8.26 Daily cycle of relative humidity and temperature during an arbitrary summer day (Bayreuth, Germany, Aug. 28, 2017)

8.9 Future Developments

The last review of hygrometry, including new developments in thermodynamics and devices, was made more than 20 years ago [8.8] and is a main reference in this field of research and measurements [8.4]. Since that time, the number of commercially used measurement principles has significantly decreased. Significant progress has been made to reduce drift in capacitive sensors particularly in humid environments. Dewpoint

hygrometers (except Thygan) are rarely used as in-situ instruments but they remain important laboratory reference instruments and essential instruments in humidity generators. The development of the capacitive polymer technology continues with an expanding use of heated polymer sensors. A significant extension of the use of well-calibrated capacitive polymer hygrometers seems likely in the near future.

8.10 Further Readings

A comprehensive review of the diverse sensors, applications and maintenance of hygrometry is given by:

- VDI: Umweltmeteorologie, Meteorologische Messungen, Luftfeuchte (Environmental Meteorology, Meteorological Measurements, Air Humidity, in German and English), VDI 3786 Blatt(Part) 4, (Beuth-Verlag, Berlin 2013)
- WMO: Guide to Instruments and Methods of Observation, WMO-No. 8, Volume I – Measurement of Meteorological Variables. (World Meteorological Organization, Geneva, 2018)
- J.M. Baker, T.J. Griffis: Atmospheric Humidity. In: Agroclimatology: Linking Agriculture to Climate, Agronomy Monographs, vol 60, ed. by J.L. Hatfield, M.V.K. Sivakumar, J.H. Prueger (American Society of Agronomy, Crop Science Society of America, and Soil Science Society of America, Inc., Madison, WI 2020)
- G. Korotcenkov: Handbook of Humidity Measurement, Volume 1: Spectroscopic Methods of Humidity (CRC Press, Boca Raton, London, New York 2018)
- G. Korotcenkov: Handbook of Humidity Measurement, Volume 2: Electronic and Electrical Humidity Sensors (CRC Press, Boca Raton, London, New York 2019)

Acknowledgments. We acknowledge several companies for using photographs.

References

- 8.1 N. Mölders, G. Kramm: *Lectures in Meteorology* (Springer, Cham, Heidelberg, New York, Dordrecht, London 2014)
- 8.2 M.L. Salby: *Physics of the Atmosphere and Climate* (Cambridge Univ. Press, Cambridge 2012)
- 8.3 R.B. Stull: *An Introduction to Boundary Layer Meteorology* (Kluwer, Dordrecht 1988)
- 8.4 WMO: *Guide to Instruments and Methods of Observation, WMO No. 8, Volume I, Measurement of Meteorological Variables* (World Meteorological Organization, Geneva 2018)
- 8.5 D. Sonntag: Important new values of the physical constants of 1986, vapour pressure formulations based on the ITS-90, and psychrometer formulae, *Z. Meteorol.* **40**, 340–344 (1990)
- 8.6 T. Foken: *Micrometeorology*, 2nd edn. (Springer, Berlin, Heidelberg 2017)
- 8.7 VDI: *Umweltmeteorologie, Meteorologische Messungen, Luftfeuchte (Environmental Meteorology, Meteorological Measurements, Air Humidity), VDI 3786 Blatt(Part) 4* (Beuth, Berlin 2013)
- 8.8 D. Sonntag: Advancements in the field of hygrometry, *Meteorol. Z.* **3**, 51–66 (1994)
- 8.9 B. Hardy: ITS-90 formulations for vapor pressure, frost point temperature, dew point temperature, and enhancement factors in the range –100 to +100 °C, National Physical Laboratory. In: *Proc. Pap. Abstr. Third Int. Symp. Humidity Moisture* (1998) pp. 214–222
- 8.10 R.W. Hyland, A. Wexler: Formulations for the thermodynamic properties of the saturated phases of H₂O from 173.15 K to 473.15 K, *ASHRAE Transactions* **89**, 500–519 (1983)
- 8.11 A. Wexler: Vapor pressure formulation for water in range 0 to 100°C. A revision, *J. Res. National Bureau Stand. A. Phys. Chem.* **80A**, 776–785 (1976)
- 8.12 A. Wexler: Vapor pressure formulation for ice, *J. Res. National Bureau Stand. A. Phys. Chem.* **81A**, 5–20 (1977)
- 8.13 S. Letestu (Ed.): *International Meteorological Tables, WMO No. 188, TP 94* (World Meteorological Organization, Geneva 1966), Updated 1973
- 8.14 D. Sonntag: *Hygrometrie* (Akademie-Verlag, Berlin 1966–1968)
- 8.15 A. Wexler, R.E. Ruskin (Eds.): *Humidity and Moisture: Principles and Methods of Measuring Humid-*

- ity in Gases, Vol. 1 (Reinhold Publishing, New York 1965)
- 8.16 P.K. Wang, D. Zhang: An introduction to some historical governmental weather records of China, *Bull. Amer. Meteorol. Soc.* **69**, 753–758 (1988)
- 8.17 L. Rezende: *Chronology of Science* (Checkmark Books, New York 2007)
- 8.18 R. Holland, G. Stöhr: *Geschichte der Hygrometer* (Freunde alter Wetterinstrumente, Riedlingen 2011)
- 8.19 P. Duham: *Études Sur Léonard De Vinci* (Librairie Scientifique A. Herrmann et Fils, Paris 1906)
- 8.20 J.H. Lambert: *Hygrometrie oder die Abhandlung von den Hygrometern (French Original: Essais D' Hygromètre, Ou Sur La Mesure D' Humidité)* (Klett, Augsburg 1774)
- 8.21 B. Sresnevsky: Theorie des Haarhygrometers, *Beibl. Ann. Phys. Chem.* **19**, 875 (1895)
- 8.22 J. Pircher: Über das Haarhygrometer, *Denkschr. math. nat. Kl. Königl. Akad. Wiss. Wien* **73**, 267–300 (1901)
- 8.23 F.J.W. Whipple: The Theory of the Hair Hygrometer. In: *Proc. Phys. Soc. Lond.*, Vol. 34 (1921) pp. i–v
- 8.24 R. Wolf: Das Asthygrometer, *Z. österreichische Ges. Meteorol.* **2**, 410 (1867)
- 8.25 F.W. Dunmore: An electric hygrometer and its application to radio meteorography, *J. Res. National Bureau Stand.* **20**, 723–744 (1938)
- 8.26 F.E. Jones, A. Wexler: A barium fluoride film hygrometer element, *J. Geophys. Res.* **65**, 2087–2095 (1960)
- 8.27 T. Foken, N. Hippmann, U. Lehmann, D. Sonntag: Feuchtigkeitsmessung mit Bariumfluorid-Meßfühlern, *Z. Meteorol.* **28**, 26–30 (1978)
- 8.28 W.F. Hickey: Humidity measurements by a new system, *Refriger. Eng.* **54**(388), 351–354 (1947)
- 8.29 M. Miess: Meßfehler bei der Taupunktmessung mit Lithiumchlorid-Feuchtefühlern, *Arch. Meteorol. Geophys. Bioklim. Ser. B* **16**, 151–163 (1968)
- 8.30 F.V. Brock, S.J. Richardson: *Meteorological Measurement Systems* (Oxford Univ. Press, New York 2001)
- 8.31 G.R. Harrison: *Meteorological Measurements and Instrumentations* (John Wiley & Sons, Chichester 2015)
- 8.32 H. Farahani, R. Wagiran, M.N. Hamidon: Humidity sensors principle, mechanism, and fabrication technologies: A comprehensive review, *Sensors* **14**, 7881–7939 (2014)
- 8.33 T.S. Suntola: Capacitive Humidity Transducer, Patent US4164868 (1979)
- 8.34 R.A. Davis, S.R. Foote, R. Foster, A.K.I.I. Richard: Relative Humidity Sensor with Integrated Signal Conditioning, Patent US4500940 (2004)
- 8.35 J. Ivory: On the hygrometer by evaporation, *Phil. Mag. J.* **60**, 81–88 (1822)
- 8.36 C.W. Böckmann: Gleichzeitige Beobachtungen der Hygrometer von Leslie, Saussure und De Luc, *Ann. Phys.* **15**, 355–376 (1803)
- 8.37 J.H. Arnold: The theory of the psychrometer. I. The mechanism of evaporation, *Physics* **4**, 255–262 (1933)
- 8.38 J.C. Maxwell: Theory of the wet bulb thermometer. In: *Encyclopedia Britannica*, 9th edn., Vol. 7, ed. by E. Smellie (Colin Macfarquhar and Andrew Bell, Edinburgh 1877) p. 218
- 8.39 E.F. August: Ueber die Verdunstungskälte und deren Anwendung auf Hygrometrie, *Ann. Phys.* **81**, 69–88 (1825)
- 8.40 E.F. August: Ueber die Verdunstungskälte und deren Anwendung auf Hygrometrie, *Ann. Phys.* **81**, 335–344 (1825)
- 8.41 J.H. Arnold: The theory of the psychrometer. II. The effect of velocity, *Physics* **4**, 334–340 (1933)
- 8.42 R. Assmann: Das Aspirationspsychrometer, ein neuer Apparat zur Ermittlung der wahren Temperatur und Feuchtigkeit der Luft, *Wetter* **4**, 245–286 (1887)
- 8.43 R. Assmann: Das Aspirationspsychrometer, ein neuer Apparat zur Ermittlung der wahren Temperatur und Feuchtigkeit der Luft, *Wetter* **5**, 1–22 (1888)
- 8.44 E.F. August: *Über die Fortschritte der Hygrometrie* (T. Trautwein, Berlin 1830)
- 8.45 R. Assmann: Das Aspirations-Psychrometer. Ein Apparat zur Bestimmung der wahren Temperatur und Feuchtigkeit der Luft, *Abh. Königlichen Preussischen Meteorol. Inst.* **1**, 1–270 (1892)
- 8.46 R. Assmann: Das Schleuderpsychrometer, *Z. österreichische Ges. Meteorol.* **19**, 154–162 (1884)
- 8.47 A.J. Dyer, F.J. Maher: Automatic eddy-flux measurement with the evapotron, *J. Appl. Meteorol.* **4**, 622–625 (1965)
- 8.48 D.P. Gatley: Psychrometric chart celebrates 100th anniversary, *ASHRAE Journal* **46**(11), 16–20 (2004)
- 8.49 C.W. Thornthwaite, J.C. Owen: A dew point recorder for measuring atmospheric moisture, *Monthly Weather Rev.* **68**, 315–318 (1940)
- 8.50 J.F. Daniell: *Observations on a New Hygrometer, Which Measures the Force and Weight of Aqueous Vapour in the Atmosphere, and the Corresponding Degree of Evaporation* (E.D. Cousins, London 1820)
- 8.51 H. Bongards: *Feuchtigkeitsmessung* (Oldenbourg, München, Berlin 1926), Reprint: De Gruyter, Berlin (2019)
- 8.52 S.I. Kretschmer, J.V. Karpovitsch: Maloinercionnyj ultrafioletovyy vlagometer (Sensitive ultraviolet hygrometer), *Izv. AN SSSR Fiz. Atmos. Okeana* **9**, 642–645 (1973)
- 8.53 L. Martini, B. Stark, G. Hunsalz: Elektronisches Lyman-Alpha-Feuchtigkeitsmessgerät, *Z. Meteorol.* **23**, 313–322 (1973)
- 8.54 A.L. Buck: Development of an improved Lyman-alpha hygrometer, *Atmos. Technol.* **2**, 213–240 (1973)
- 8.55 W. Kolsiek: The KNMI Lyman-alpha hygrometer, *KNMI Technical Report* 87, 12 (1986)
- 8.56 G.S. Campbell, B.D. Tanner: A krypton hygrometer for measurement of atmospheric water vapour concentrations. In: *Moisture and Humidity* (Instrument Society of America, Research Triangle Park 1985) pp. 609–614
- 8.57 L.G. Elagina: Optitscheskij pribor dlja izmerenija turbulentnych pulsacii vlasnosti (Optical sensor for the measurement of turbulent humidity fluctuations), *Izv. AN SSSR, ser. Geofiz.* **12**, 1100–1107 (1962)

- 8.58 M.R. Raupach: Infrared fluctuation hygrometer in the atmospheric surface layer, *Quart. J. Roy. Meteorol. Soc.* **104**, 309–322 (1978)
- 8.59 E. Ohtaki, T. Matsui: Infrared device for simultaneous measurement of fluctuations of atmospheric carbon dioxide and water vapor, *Bound.-Layer Meteorol.* **24**, 109–119 (1982)
- 8.60 G. Mückel: Turbulenzmesstechnik: Infrarot-Absorptionshygrometer zur Bestimmung turbulenter Feuchtefluktuationen, *Veröff. Meteorol. Dienst. DDR* **27**, 5–29 (1989)
- 8.61 M.J. Heikinheimo, G.W. Thurtell, G.E. Kidd: An open path, fast response IR spectrometer for simultaneous detection of CO₂ and water vapor fluctuations, *J. Atm. Ocean. Techn.* **6**, 624–636 (1989)
- 8.62 W. Kolsiek: Infrared H₂O/CO₂ Sensor with fiber optics. In: *Proc. 7th Symp. Meteorol. Obs. Instrum., American Meteorological Society* (1991)
- 8.63 T. Foken, R. Dlugi, G. Kramm: On the determination of dry deposition and emission of gaseous compounds at the biosphere-atmosphere interface, *Meteorol. Z.* **4**, 91–118 (1995)
- 8.64 E. Kleinschmidt (Ed.): *Handbuch der Meteorologischen Instrumente und ihrer Auswertung* (Springer, Berlin 1935)
- 8.65 R. Feistel, R. Wielgosz, S.A. Bell, M.F. Camoes, J.R. Cooper, P. Dexter, A.G. Dickson, P. Fisi-caro, A.H. Harvey, M. Heinonen, O. Hellmuth, H.J. Kretzschmar, J.W. Lovell-Smith, T.J. McDougall, R. Pawlowicz, P. Ridout, S. Seitz, P. Spitzer, D. Stoica, H. Wolf: Metrological challenges for measurements of key climatological observables: Oceanic salinity and pH, and atmospheric humidity. Part 1: Overview, *Metrologia* **53**, R1–R11 (2016)
- 8.66 R. Feistel, J.W. Lovell-Smith: Defining relative humidity in terms of water activity. Part 1: Definition, *Metrologia* **54**, 566 (2017)
- 8.67 R. Feistel, J.W. Lovell-Smith, O. Hellmuth: Virial approximation of the TEOS-10 equation for the fugacity of water in humid air, *Intern. J. Thermophys.* **36**, 44–68 (2015)
- 8.68 H.T. Davis: *Statistical Mechanics of Phases, Interfaces and Thin Films* (Wiley-VCH, Weinheim 1995)
- 8.69 R. Feistel, W. Ebeling: *Physics of Self-Organization and Evolution* (Wiley-VCH, Weinheim 2011)
- 8.70 J.W. Lovell-Smith, R. Feistel, A.H. Harvey, O. Hellmuth, S.A. Bell, M. Heinonen, J.R. Cooper: Metrological challenges for measurements of key climatological observables. Part 4: Atmospheric relative humidity, *Metrologia* **53**, R40–R59 (2016)
- 8.71 J.M. Prausnitz, R.N. Lichtenthaler, E.G. de Azevedo: *Molecular Thermodynamics of Fluid-Phase Equilibria*, 3rd edn. (Prentice Hall, Upper Saddle River 1999)
- 8.72 D.G. Wright, R. Feistel, J.H. Reissmann, K. Miyagawa, D.R. Jackett, W. Wagner, U. Overhoff, C. Guder, A. Feistel, G.M. Marion: Numerical implementation and oceanographic application of the thermodynamic potentials of liquid water, water vapour, ice, seawater and humid air – Part 2: The library routines, *Ocean Sci.* **6**, 695–718 (2010)
- 8.73 J. Kobayashi: Investigations on hygrometry, *Pap. Meteorol. Geophys.* **11**, 213–338 (1960)
- 8.74 H. Spencer-Gregory, E. Rourke: *Hygrometry* (Crosby Lockwood & Son, London 1957)
- 8.75 N. Yamazoe, Y. Shimizu: Humidity sensors: Principles and applications, *Sens. Actuators* **10**, 379–398 (1986)
- 8.76 R. Mota, R. Parafita, A. Giuliani, M.J. Hubin-Frankin, J.M.C. Lourenço, G. Garcia, S.V. Hoffmann, M.J. Mason, P.A. Ribeiro, M. Raposo, P. Limão-Vieira: Water VUV electronic state spectroscopy by synchrotron radiation, *Chem. Phys. Lett.* **416**, 152–159 (2005)
- 8.77 MPI: The MPI-Mainz UV/VIS Spectral Atlas of Gaseous Molecules of Atmospheric Interest, http://satellite.mpic.de/spectral_atlas. (2017)
- 8.78 S. Ogawa, M. Ogawa: Absorption cross sections of O₂(a¹Δ_g) and O₂(X³Σ_g⁻) in the region from 1087 to 1700 Å, *Can. J. Phys.* **53**, 1845–1852 (1975)
- 8.79 B.J. Finlayson-Pitts, J.N. Pitts: *Chemistry of the Upper and Lower Atmosphere* (Academic Press, San Diego 2000)
- 8.80 T. Foken, H. Falke: Technical note: calibration device for the krypton hygrometer KH20, *Atmos. Meas. Tech.* **5**, 1861–1867 (2012)
- 8.81 D. Sonntag: Vergleichsmessungen mit Hygrometern über einen Zeitraum bis zu 50 Jahren, *Mitt. DMG* **16**(3), 27–28 (2014)
- 8.82 A. Lang: Neue Wege der Entwicklung haarhygrometrischer Sensoren, *Meteorol. Rundsch.* **32**, 97–108 (1979)
- 8.83 B. Ingleby, D. Moore, C. Sloan, R. Dunn: Evolution and accuracy of surface humidity reports, *J. Atm. Ocean. Techn.* **30**, 2025–2043 (2013)
- 8.84 D. Sonntag: WMO Assmann aspiration psychrometer intercomparison, *WMO, Instruments Observ. Methods* **34**, 1–185 (1989)
- 8.85 Deutscher Wetterdienst: *Aspirations-Psychrometer-Tafeln* (Friedr. Vieweg & Sohn, Braunschweig, Wiesbaden 1997)
- 8.86 G. Scholz: Bestimmung des Psychrometerkoeffizienten für das Aspirationspsychrometer nach Assmann, *Z. Meteorol.* **37**, 229–230 (1987)
- 8.87 E. Frankenberger: Untersuchungen über den Vertikalaustausch in den unteren Dekametern der Atmosphäre, *Ann. Meteorol.* **4**, 358–374 (1951)
- 8.88 R.G. Wylie, T. Lalas: Measurement of temperature and humidity, *WMO, Techn. Note* **194**, 1–77 (1992)
- 8.89 R. Schädlich, D. Sonntag: Ein elektrisches Aspirationspsychrometer nach einem WMO-Vorschlag, *Z. Meteorol.* **25**, 236–247 (1975)
- 8.90 H. Vömel, P. Jeannot: Balloon-borne frostpoint-hygrometry. In: *Monitoring Atmospheric Water Vapour, Ground-Based Remote Sensing and in-situ Methods*, ISSI Scientific Report Series, Vol. 10, ed. by N. Kämpfer (Springer, New York, Dordrecht, Heidelberg, London 2013) pp. 39–53
- 8.91 H. Richner, P. Ruppert, B. Neininger: Performance characteristics of a miniaturized dew point mirror in air-born and surface applications. In: *Proc. 7th Symp. Meteorol. Observ. Instrum., Boston, American Meteorological Society* (1991) pp. 307–310

- 8.92 J. Skaar, K. Hegg, T. Moe, K. Smedstud: WMO international hygrometer intercomparison, WMO, Instrum. Obs. Methods **38**, 1–246 (1989)
- 8.93 A.L. Buck: The variable-path Lyman-alpha hygrometer and its operating characteristics, Bull. Am. Meteorol. Soc. **57**, 1113–1118 (1976)
- 8.94 J.E. Tillman: Water vapor density measurements utilizing the absorption of vacuum ultraviolet and infrared radiation. In: *Humidity and Moisture, Measurement and Control in Science and Industry, Principles and Methods of Measuring Humidity in Gases*, Vol. 1, ed. by R.E. Ruskin (Reinhold, New York 1965) pp. 428–433
- 8.95 B.D. Tanner, E. Swiatek, J.P. Greene: Density fluctuations and use of the krypton hygrometer in surface flux measurements. In: *Management of Irrigation and Drainage Systems: Integrated Perspectives*, ed. by R.G. Allen (American Society of Civil Engineers, New York 1993) pp. 945–952
- 8.96 A. van Dijk, W. Kohsiek, H.A.R. DeBruin: Oxygen sensitivity of krypton and Lyman-alpha hygrometers, J. Atm. Oceanic Techn. **20**, 143–151 (2003)
- 8.97 T. Foken, A.L. Buck, R.A. Nye, R.D. Horn: A Lyman-alpha hygrometer with variable path length, J. Atm. Oceanic Techn. **15**, 211–214 (1998)
- 8.98 T. Foken, H. Falke: Technical note: calibration instrument for the krypton hygrometer KH20, Atmos. Meas. Tech. **5**, 1861–1867 (2012)
- 8.99 A.S. Kowalski, P. Serrano-Ortiz: On the relationship between the eddy covariance, the turbulent flux, and surface exchange for a trace gas such as CO₂, Bound.-Layer Meteorol. **124**, 129–141 (2007)
- 8.100 E.K. Webb, G.I. Pearman, R. Leuning: Correction of the flux measurements for density effects due to heat and water vapour transfer, Quart. J. Roy. Meteorol. Soc. **106**, 85–100 (1980)
- 8.101 L. Greenspan: Humidity fixed points of binary saturated aqueous solutions, J. Res. National Bureau Stand. A. Phys. Chem. **81A**, 89–96 (1977)
- 8.102 VDI: *Umweltmeteorologie – Meteorologische Messungen – Grundlagen (Environmental Meteorology – Meteorological Measurements – Basics)*, VDI 3786, Band1 (Part 1) (Beuth, Berlin 2013)



Dietrich Sonntag (deceased)

Dietrich Sonntag received his doctoral degree from the University of Leipzig in Meteorology in 1951 and his Habilitation degree from the Humboldt University Berlin in 1965. He developed several meteorological sensors mainly for humidity and radiation measurements. In 1988, he was one of the first scientists to be awarded the Professor Dr Vilho Väisälä Award of the WMO. He retired in 1992 and passed away in 2018.

Thomas Foken

University of Bayreuth
Bayreuth, Germany
thomas.foken@uni-bayreuth.de



Thomas Foken is a retired Professor of Micrometeorology at the University of Bayreuth. He was the head of Laboratories at the meteorological observatories at Potsdam (1981–1994) and Lindenberg (1994–1997). His research interests include the interaction between the Earth's surface and the atmosphere and the measurement and modeling of energy and matter fluxes, with a strong focus on experimental meteorology. His scientific contributions have been recognized through various international awards.



Holger Vömel

Earth Observing Laboratory
National Center for Atmospheric Research
Boulder, USA
voemel@ucar.edu

Holger Vömel is a scientist at the National Center for Atmospheric Research at Boulder, CO, USA. He graduated in Physics from the University Heidelberg, Germany in 1990 and received a PhD in Chemical Physics from the University of Colorado at Boulder in 1996. His research interests focus around high-quality observations of atmospheric parameters such as water vapor, ozone, temperature, pressure, and winds, to provide reliable data for studies of climate change and atmospheric processes.



Olaf Hellmuth

Modeling Department
TROPOS Leibniz Institute for Tropospheric Research
Leipzig, Germany
olaf.hellmuth@tropos.de

Olaf Hellmuth is Senior Scientist in the Modeling Department of the TROPOS Leibniz Institute for Tropospheric Research Leipzig. In 1985, he received a diploma in meteorology and in 1988, he was awarded a Dr. rer. nat. His research activities comprise atmospheric sol formation, cloud microphysics with focus on hygroscopic growth and freezing processes, and theoretical aspects of hygrometry. He is member of the Leibniz Sozietät Berlin.

Wind Sensors

9. Wind Sensors

Thomas Foken , Jens Bange 

Various techniques are used to measure the wind speed in the atmosphere, including cup, propeller, and sonic anemometers; the latter can also be used to measure the wind vector. Wind direction measurements are also performed using wind vanes. Sonic anemometers are the devices most commonly used for turbulence measurements. Hot-wire anemometers are employed for special measurements, and Pitot tubes are utilized for aircraft-based measurements. It is also important to note that the conditions at the measuring site can strongly influence the accuracy of wind measurements.

This chapter discusses the variables measured by all of the above devices as well as the corresponding measurement principles and their theoretical foundations. The technical data that each technique provides is presented, the maintenance that must be carried out when using each technique is described, and relevant quality control and calibration methods are introduced. The history of the development of wind sensors is also briefly summarized, and some examples of the application of wind measurements are presented.

9.1	Measurement Principles and Parameters	244
9.1.1	Measured Parameters	244
9.1.2	Measurement Principles	244
9.1.3	Siting Considerations	245
9.2	History	245
9.2.1	Wind Vanes	245
9.2.2	Mechanical Anemometers	246
9.2.3	Sonic Anemometers	248
9.2.4	Pressure Tube Anemometers	249
9.3	Theory	249
9.3.1	Cup and Propeller Anemometers	249
9.3.2	Sonic Anemometers	251
9.3.3	Thermal Anemometers	252
9.3.4	Hot-Wire Anemometers	252
9.3.5	Laser Doppler Anemometers	252
9.3.6	Pitot-Static or Prandtl Tubes	253
9.3.7	Wind Vanes	253
9.3.8	Scalar and Vector Averaging	253
9.3.9	Influence of the Surrounding Area on Wind Measurements	254
9.4	Devices and Systems	257
9.4.1	Rotation Anemometers	257
9.4.2	Wind Vanes	257
9.4.3	Combinations of a Rotation Anemometer with a Wind Vane	258
9.4.4	Sonic Anemometers	258
9.4.5	Thermal Anemometers	261
9.4.6	Hot-Wire Anemometers	261
9.4.7	Laser Anemometers	261
9.4.8	Pitot-Static or Prandtl Tubes	262
9.4.9	Comparison of Different Methods	262
9.5	Specifications	262
9.6	Quality Control	263
9.6.1	Wind Tunnel Calibration	263
9.6.2	Zero-Wind Chamber Calibration of Sonic Anemometers	265
9.6.3	Specific Quality Control Methods	265
9.7	Maintenance	266
9.8	Application	267
9.8.1	Climatology of Wind Parameters	267
9.8.2	Geostrophic Wind: Daily and Annual Cycles	267
9.8.3	Gusts	269
9.9	Future Developments	269
9.10	Further Reading	270
	References	270

The airflow in the atmosphere—the wind field—is crucial to the transport of air masses caused by the pressure field. Wind measurements are therefore necessary at all levels of the atmosphere to support weather forecasting

and to improve our understanding of global circulation and climate systems (see Chap. 1). Furthermore, fluctuations in the wind velocity (mainly its vertical component) are responsible for fluxes of momentum, heat, and

matter. The wind essentially determines the dispersion, transport, residence times, and changes in the mixing and concentrations of gases and particles. The high vari-

ability and significant vertical gradients in the wind field as well as the effects of heterogeneous landscapes on this field make measuring the wind a challenging task.

9.1 Measurement Principles and Parameters

The wind velocity is a vector with three components. For nonturbulent problems, usually only the horizontal wind speed and the direction of the mean wind are relevant, which are measured with separate sensors. This increases the number of wind parameters measured and sensor principles employed.

9.1.1 Measured Parameters

For the wind vector \mathbf{u} , it is assumed that

$$\mathbf{u} = f(U, \alpha), \tag{9.1}$$

where U is the magnitude (modulus) of the wind vector and α is the direction of the wind vector from north via east. For the horizontal wind components u (east–west direction) and v (north–south direction), it follows that

$$u = U \sin \alpha \tag{9.2}$$

$$v = U \cos \alpha, \tag{9.3}$$

and the vertical wind component

$$w = U \sin \beta, \tag{9.4}$$

where β is the inclination of the wind field.

The fluctuations in the components

$$\begin{aligned} u &= \bar{u} + u' \\ v &= \bar{v} + v' \\ w &= \bar{w} + w' \end{aligned} \tag{9.5}$$

describe the turbulence (from Reynolds decomposition) [9.1]. Here, an overbar indicates an average and a prime symbol indicates a fluctuation. Typical averaging periods range from 10 to 30 min, with 10 min being a particularly common averaging period for operational wind observations. The sampling rate required to get an adequate description of the turbulent part is typically ≥ 10 Hz. The parameters that are measured are listed in Table 9.1. In the SI system (see Chap. 5), speeds are measured in meters per second (m s^{-1}). However, other units are also used for speed in some Anglo-American countries and in particular fields, for example in aviation and in nautical applications (Table 9.2).

9.1.2 Measurement Principles

Many of the various techniques used to measure wind speeds were devised centuries ago, but anemometers based on them are still available commercially today and have their own fields of application. However, one of the more recently invented devices, the sonic anemometer, is becoming increasingly dominant (see Sect. 9.9) due to its ability to measure not just the mean wind speed but the whole three-dimensional wind vector (and therefore the wind direction). It is also able to measure the wind velocity with high resolution at frequencies of several tenths of a Hz. Instruments that can also be applied for turbulence measurements, such as hot-wire or laser anemometers, are less useful for performing measurements in the atmosphere and are therefore used mainly for calibration purposes. An overview of the various wind measurement principles is given in Table 9.3.

Table 9.1 Parameters measured by wind sensors

Parameter	Description	Unit	Symbol
Windway	Distance that an air parcel covers within a certain time interval (older instruments)	m	
Wind speed	Horizontal wind velocity (mean value of both horizontal components)	m s^{-1}	u_h
Wind gust	A burst of high-velocity wind	m s^{-1}	g_u
Wind components, see (9.2)–(9.4)	Components of the wind vector in the Cartesian coordinate system: u, v are the horizontal components and w is the vertical component	m s^{-1}	u, v, w
Fluctuations in the wind components	Fluctuations in the components of the wind vector in the Cartesian coordinate system: u', v' are the horizontal components and w' is the vertical component	m s^{-1}	u', v', w'
Wind direction	Direction that the wind comes from	°	

Table 9.2 Units of wind speed

Unit	Transformation	Application
Beaufort	See Chap. 22	Nautical applications, partly in weather forecasting
Meter per second (m s^{-1})	$1 \text{ m s}^{-1} = 2.236 \text{ mph} = 3.6 \text{ km h}^{-1}$	Widely used in meteorology and science
Kilometer per hour (km h^{-1})	$1 \text{ km h}^{-1} = 0.62 \text{ mph} = 0.278 \text{ m s}^{-1}$	Traffic, partly in weather forecasting
Mile per hour (mph)	$1 \text{ mph} = 1.609334 \text{ km h}^{-1} = 0.44704 \text{ m s}^{-1}$	Meteorology (in some countries)
Knot (kn)	$1 \text{ kn} = 1.852 \text{ km h}^{-1} = 0.514 \text{ m s}^{-1}$	Nautical applications

Table 9.3 Wind measurement techniques and their applicability to mean wind speed or turbulence measurements according to (9.5) [9.2]

Measuring device	Properties used to measure the wind				Applicability	
	Mechanical	Thermodynamic	Sound	Other	Mean	Turbulence
Cup anemometer	x				x	
Propeller anemometer	x				x	(x)
Thermal anemometer		x			x	
Hot-wire anemometer		x			x	x
Sonic anemometer			x		x	x
Laser anemometer				x	x	x
Pitot tube				x	x	x

9.1.3 Siting Considerations

Wind measurements can be strongly influenced by the measurement site. To obtain a representative wind field for a large region, the surroundings of the measurement site should be flat and free of obstacles; if this is not the case, the influence of the obstacles must be taken into account (see Sect. 9.3.9). These requirements are very important for measurements of the vertical gradient of the wind speed near the ground (see Chap. 54). Furthermore, when instruments such as cup anemometers and wind vanes are positioned relatively close, they should not disturb each other (ideally, the cup anemometer should be positioned about 0.1 m above the vane, and

the two instruments should be separated by about 1 m horizontally [9.3]).

According to the international guidelines [9.4], the standard measuring height in obstacle-free terrain is 10 m above the ground. The distance to the nearest obstacle should be ten times the obstacle height. In any case, the instrument must be installed 6–10 m above the mean height of buildings or the height of the surrounding vegetation.

Lightning strikes and other electric discharges pose a risk to wind-measuring instruments, as they can interfere with the measurements or destroy the equipment. The presence of lightning conductors can only remedy this situation to a limited extent.

9.2 History

The wind has been observed since ancient times; indeed, both Homer and the Bible speak poetically of four winds [9.5]. It is also known that the *Tower of Winds* in Athens (50 BCE) had an eight-point wind rose. During the Greek and Roman periods and right up to the sixteenth century in Italy, the wind direction was categorized into twelve winds: four groups of three centered on the four principal directions. The initials N, NNE, NE, ... were first used on a compass card in 1536 [9.6]. In addition, the history of wind measurements goes back about 2000 years.

9.2.1 Wind Vanes

Wind vanes have been in use since ancient times; for instance, the Tower of Winds had a wind vane. Wind vanes in the shapes of animals (such as snakes and dragons) or flags of kings were often used. Vanes in the shape of a rooster have been used on Christian churches ever since *Pope Nicholas I* (pontificate: 858–867) decreed that all churches must display this bird as an emblem [9.8]. The history of scientific instruments for measuring the wind started when the wind vane was

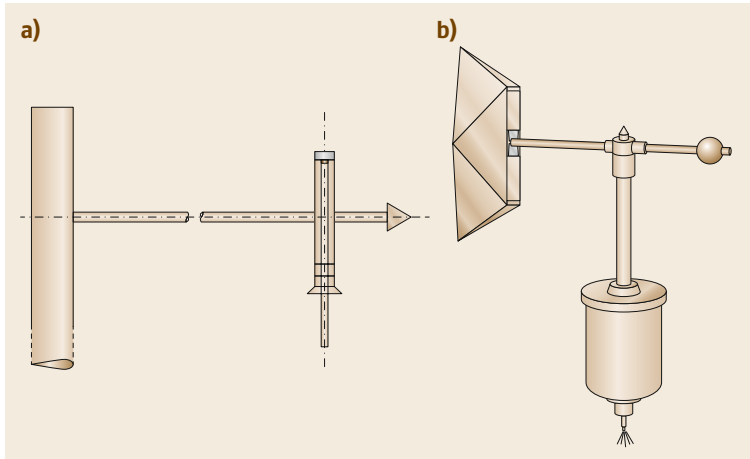


Fig. 9.1a,b Typical types of wind vanes: (a) the English R.A.E. pattern vane, (b) the German vane produced by Fuess (after [9.7], reproduced with permission from Springer, Berlin)

combined with a hand to show (and, later on, to register) the wind direction. In Florence in 1578, *Egnatio Danti* (1536–1586), a professor of mathematics at Bologna, built a wind vane with a single hand on a vertical dial, which was positioned on a 17 m high tower to ensure that wind measurements were not influenced by surrounding buildings [9.9]. A significant improvement in wind vane design was made by *Georges-Frédéric Parrot* (1767–1852) [9.6], the first rector of the Imperial University of Dorpat (now Tartu, Estonia). His design—a splayed vane—was a combination of two plates that diverged from the axis of the vane. His vane was relatively small; it was only about 19 cm in length and had a counterweight that was 11 cm long. This type of vane was used up to the twentieth century. However, in 1918, *Sir Geoffrey Ingram Taylor* (1886–1975) proposed a vane with an airfoil profile that became known in England as the *R.A.E. pattern vane* [9.10]. This vane precisely measures wind direction fluctuations with periods larger than 5 s [9.7]. In Germany, the wind vane produced by Fuess became popular (Fig. 9.1).

In 1788, *Franz Carl Achard* (1753–1821) developed an inclined wind vane to measure the vertical orientation of the wind field [9.6]. This system was used by micrometeorologists in combination with a propeller anemometer to measure the vertical wind velocity right up to the second half of the twentieth century, before sonic anemometers became available.

Weather vanes have long been employed to determine the wind direction; more recently, they have also been used in combination with anemometers [9.6]. Such vanes were included in the first meteographs (weather clocks, combinations of several instruments, including clocks), such as those constructed by *Robert Hooke* (1635–1703) in about 1678 and *Sir Christopher Wren* (1632–1723) in 1689. In 1789, the pastor *Christian Gotthold Herrmann* (1730–1792) of Cämmerswal-

de in Saxony constructed a machine with a twelve-point wind rose [9.11]. In this machine, a wheel was rotated by a wind vane carrying twelve radial compartments, and a hammer ejected a numbered cube from a magazine into the appropriate compartment of the relevant wind direction once every hour.

A professor of experimental physics in Milan, *Marsilio Landriani* (1751–1815), constructed a wind vane with eight pencils that marked the wind direction on a horizontal plate rotated by a clock. The professor of mathematics *James Henry Coffin* (1806–1873) at Easton (PA, USA) constructed a sand wind vane that used the same principle as Herrmann's instrument and distributed sand into 32 reservoirs. This instrument is currently being exhibited in the Museum of History and Technology in Washington, DC. In 1850, *Karl Kreil* (1789–1862), director of the observatory at Prague and the first director of the *Central Meteorological and Magnetic Bureau* at Vienna (from 1851), constructed another a wind vane using a pencil [9.12]. Several other instruments, including electrical recorders, have been constructed since then.

9.2.2 Mechanical Anemometers

Mechanical anemometers, which use the dynamic pressure of the wind field (see Chap. 12), can be grouped into swinging plate anemometers and rotation anemometers, while the latter can be further categorized into propeller and cup anemometers.

Swinging Plate Anemometers

Around 1450, the Italian humanist and scientist *Leon Battista Alberti* (1404–1472) constructed the first swinging plate anemometer, where a plate moves along a scale under the influence of dynamic pressure (Fig. 9.2). Later, *Leonardo da Vinci* (1452–1519)

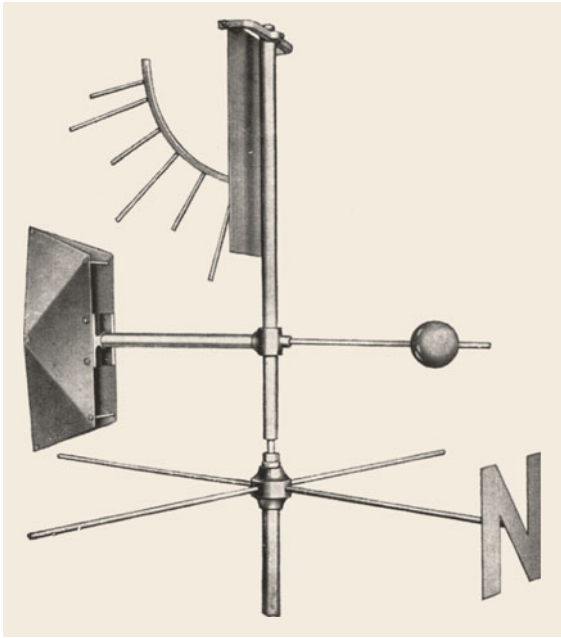


Fig. 9.2 Swinging plate anemometer (*upper part*) made by von Wild (reprinted with permission from Dr. Alfred Müller, Meteorologische Instrumente KG, R. Fuess, Königs Wusterhausen, Germany)

painted the design of an instrument that looked similar to the one made by *Robert Hooke* (1635–1703) in 1684. Hooke’s construction—which was used by the Swiss meteorologist *Heinrich von Wild* (1833–1902), who was also the director of the St. Petersburg Observatory—can still be found in some stations and is available commercially (Fig. 9.2). Several more constructions, some of which form parts of more complex meteographs, are illustrated in [9.6].

Rotation Anemometers

The principle of a rotation anemometer is similar to that used by windmills, which have been employed in Europe since the twelfth century. Around 1678, *Robert Hooke* used this system for his weather clock. This principle was also used by the famous Russian scientist *Mikhail Vasilyevich Lomonosov* (1711–1765) for his anemometer, but he replaced the windmill with an overshoot water wheel [9.6]. In the first half of the nineteenth century, it was discovered that the rotation speed of this type of anemometer is dependent on the wind direction. This problem was overcome by combining the propeller with a wind vane (see Sect. 9.4.3) or through the precise application of the cosine dependency (see Sect. 9.4.1) of a propeller in helicoidal form. The first helicoid anemometer was built by the British meteorologist *William Henry Dines* (1855–1927) [9.13].



Fig. 9.3 Robinson’s cup anemometer from 1846 [9.15] (courtesy of the NOAA Photo Library, National Oceanic and Atmospheric Administration, Department of Commerce)

The earliest known windmills with a vertical axis occurred in Persia in the seventh century CE; such windmills were not used in Europe, except in Poland. Those anemometers looked like present-day wind power generators with a vertical axis. The most famous vertical-axis windmill was built in 1734 by the postmaster of Louis XIV, *Louis-Léon Pajot, comte d’Ons-en-Bray* (1678–1754), and can be viewed in the exhibition of the Conservatoire National des Arts et Métiers in Paris. A similar device was built by the English scientist *William Whewell* (1794–1866) in 1838 [9.6].

Anemometers similar to the cup anemometer have probably been available since the end of the eighteenth century, as reported by the physician *Georg Wilhelm Munke* (1772–1747). The first cup anemometer dates back to 1846 and was constructed by the Irish astronomer *Thomas Romney Robinson* (1792–1882) [9.6, 14] (see Fig. 9.3), who modified Whewell’s anemometer and postulated a theory for the forces on the sensor. He got the idea for this novel design from the writer and engineer *Richard Lowell Edgeworth* (1744–1817), who constructed a windmill with a counter in 1793.

There is a long list of instruments that combine a wind vane with a rotation anemometer and a registration method [9.6, 7]. A modified version of one such instrument developed in the factory of R. Fuess in Berlin (*Heinrich Ludwig Rudolf Fuess*, 1838–1917) at the end

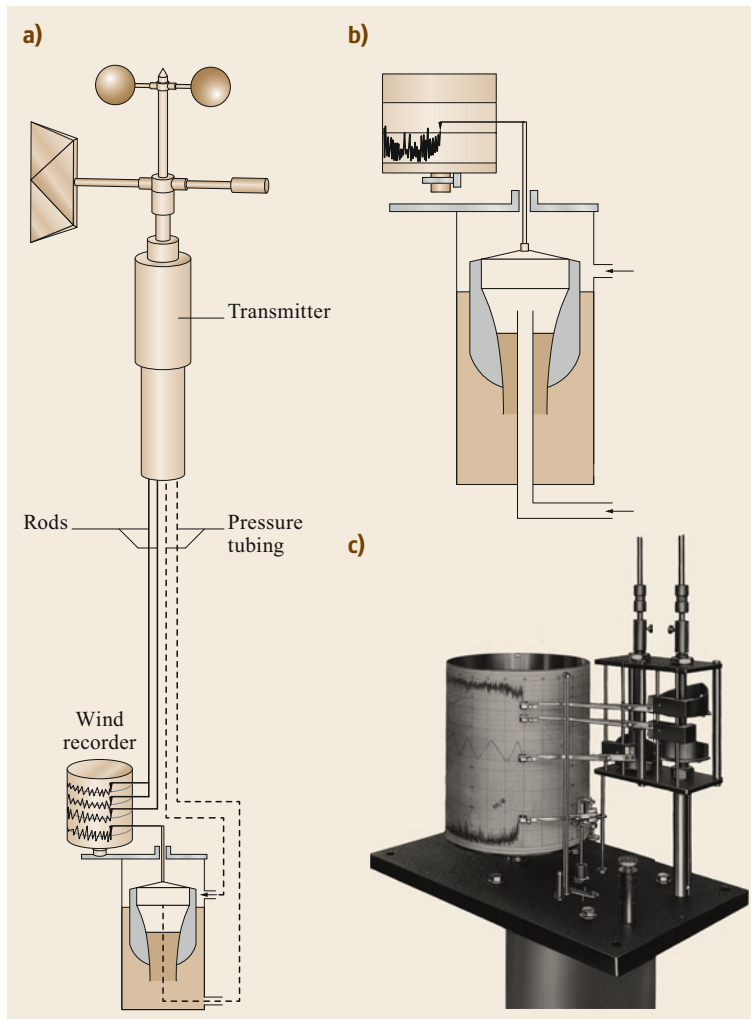


Fig. 9.4a–c Wind registration system invented by R. Fuess: **(a)** schematic view, **(b)** gust recorder, and **(c)** wind recorder unit (*upper part*: wind direction separated into N-E-S and S-W-N, *middle*: windway, *lower part*: gusts). Reprinted with permission from Dr. Alfred Müller, Meteorologische Instrumente KG, R. Fuess, Königs Wusterhausen, Germany

of the nineteenth century was used right up to the second half of the twentieth century, and is still commercially available. It combines a wind vane with a cup anemometer, measures the wind speed as the windway, and uses a Pitot tube (see Sect. 9.2.4) combined with a hydraulic system to measure gusts (this was termed a pressure-tube anemometer by *William Henry Dines* (1855–1927) in 1892 [9.6]; see Sect. 9.2.4 and Fig. 9.4).

9.2.3 Sonic Anemometers

The development of the eddy covariance method (see Chap. 55) required anemometers that responded rapidly. The basic equations for such anemometers were published in 1955 [9.16]. Following the development of the first sonic thermometer [9.17], a vertical sonic anemometer with a path length of 1 m was developed by *Verner Edward Suomi* (1915–1995) [9.18] and was used during the O’Neill experiment in 1953 [9.19]. Mod-

ern sonic anemometer designs are based on a system developed in 1960 by *Viktor Markovich Bovscheverov* (1905–1995) [9.20], which used the phase shift between sonic signals transmitted in different directions to calculate the wind vector. Subsequently, *Jagdish Chandran Kaimal* (1930–2021) and *Jost A. Businger* [9.21] (in 1963) and *Y. Mitsuta* [9.22] (in 1966) used the travel time of the sound in two directions to determine the velocity. The anemometer design used by the latter (Fig. 9.18a) is still employed today. Another sensor design that is still in use is the K-probe [9.23], so named because the sensor configuration is K-shaped.

However, the wind velocity measured using these instruments is temperature and humidity dependent. An approach that provided velocity measurements which were not subject to those influences was first realized in 1982 by *T. Hanafusa et al.* [9.27], who calculated the velocity components from the reciprocal travel times. This has become the dominant method in use

Table 9.4 Milestones in sonic anemometer development (for further details, see [9.30])

Type of sonic anemometer	Institution	Year and reference
Phase shift	Institute of Physics of the Atmosphere, Moscow, Russia	1960 [9.20], 1973 [9.24]
	School of Agriculture, University of Nottingham, Loughborough, UK	1979 [9.25]
Travel time	University of Washington, Seattle, WA, USA	1963 [9.21]
	Disaster Prevention Research Institute, Kyoto University, Kyoto, Japan	1966 [9.22]
	Commonwealth Scientific and Industrial Research Organisation (CSIRO), Canberra, Australia	1983 [9.26]
	National Oceanic and Atmospheric Administration, Earth System Research Laboratories (NOAA/ESRL) Wave Propagation Laboratory, Boulder, CO, USA	1990 [9.23]
Reciprocal travel time	Meteorological Research Institute, University of Kyoto, Kyoto, Japan	1982 [9.27]
	University of Washington, Seattle, WA, USA	1986 [9.28, 29]

today. To reduce flow distortion effects and increase the accuracy of the vertical wind component, *John C. Wyngaard* and coworkers [9.28, 29] developed the University of Washington anemometer design, which is now widely used (Fig. 9.18b) and forms the basis of all omnidirectional anemometers.

9.2.4 Pressure Tube Anemometers

In 1675, the Paris-based instrument maker *Hubin* was intrigued to hear that Hooke could measure the wind without seeing it. Therefore, developing an idea proposed by *Pierre Daniel Huet* (1630–1721), Bishop von Soissons, France, he built an instrument consisting of a mercury-

filled U-tube with one open limb that was oriented towards the wind. Under the influence of the wind, the mercury in the U-tube moved into the other limb; the distance moved by the mercury was dependent on the wind speed. Unfortunately, however, the measured signal was very small [9.6]. In 1732, this concept was used by the French engineer *Henri Pitot* (1695–1771) to measure water flow [9.31], and the instrument was modified into its present form—the so-called Pitot tube—by the French scientist *Henry Darcy* (1803–1858) [9.32] in the middle of the nineteenth century. In the 1890s, *William Henry Dines* (1855–1927) modified the instrument to measure gusts in a similar manner to the device built by R. Fuess in Berlin (see Sect. 9.2.2).

9.3 Theory

Mechanical anemometers and wind vanes are classic examples of first- and second-order dynamical systems. A general description of these systems is given in Chap. 2. In the following section, relevant characteristics of these instruments and other anemometers are listed together with factors that influence them and the theory behind these measurement principles.

9.3.1 Cup and Propeller Anemometers

Classical wind measuring devices such as cup and propeller anemometers (see Figs. 9.12 and 9.13) are based on a mechanical principle whereby the dynamic pressure of the airflow is transformed into rotational movement. The horizontal wind speed u can be calculated directly from the geometry of the cup anemometer when the drag coefficients C_D of the cups are known. According to Bernoulli's law (see Chap. 10), the force F on any fixed surface with an area A perpendicular to the wind is given by [9.33]

$$F = C_D A \frac{\rho}{2} u^2, \quad (9.6)$$

where ρ is the air density. Without any loss of generality, we can assume that the cup anemometer consists of only two cups. If there is no acceleration (i.e., assuming stationarity), the forces on both cups are the same. Now consider the instant that the lever arm connecting the cups is perpendicular to the flow. At this point, one cup exposes its convex (closed) side to the flow. This cup is moving towards the flow with a rotational speed u_{rot} . Its surface experiences a wind speed of $u + u_{\text{rot}}$. The other cup shows its concave (open) side to the flow and is moving away from it. The balance of forces is therefore

$$C_D^{\text{closed}} A \frac{\rho}{2} (u + u_{\text{rot}})^2 = C_D^{\text{open}} A \frac{\rho}{2} (u - u_{\text{rot}})^2. \quad (9.7)$$

This quadratic equation leads to two solutions, but only one is physically meaningful,

$$u = u_{\text{rot}} \frac{\sqrt{C_D^{\text{open}}} + \sqrt{C_D^{\text{closed}}}}{\sqrt{C_D^{\text{open}}} - \sqrt{C_D^{\text{closed}}}} > u_{\text{rot}}. \quad (9.8)$$

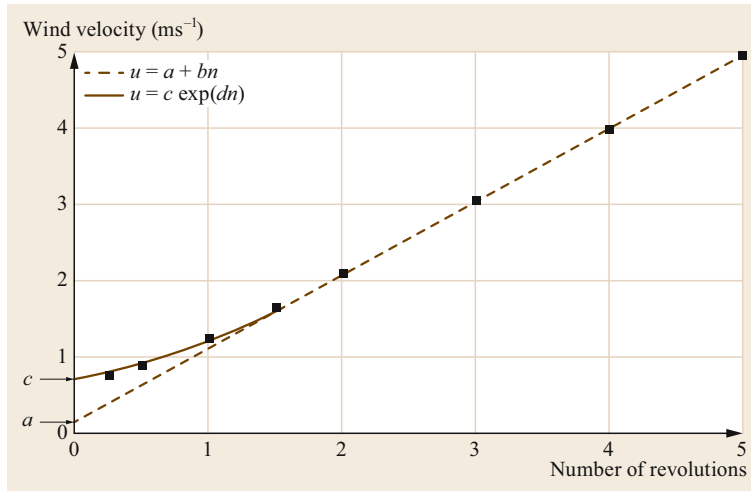


Fig. 9.5 Transfer function of a cup anemometer; n is the number of revolutions of the anemometer, u is the wind speed, and a , b , c , and d are constants (after [9.3], reproduced with permission from VDI e.V., Düsseldorf, Germany)

For spherical cups, $C_D^{\text{open}} \approx 1.33$ and $C_D^{\text{closed}} \approx 0.33$ are good approximations.

In order to calibrate mechanical anemometers, it is very important to know the transfer function between the speed in a wind tunnel and the speed measured with the anemometer. This is the linear relationship between the wind speed and the rotation speed of the anemometer within a defined working range, which must be determined in a wind tunnel [9.34–36]. It takes the form

$$u = a + bn, \quad (9.9)$$

where u is the wind speed, n is the number of rotations, a is the extrapolation of the transfer function to zero revolutions, and b is a constant: the sensitivity of the instrument. This relationship is linear over a wide range of speeds, but at low speeds ($< 2\text{--}4 \text{ m s}^{-1}$) it is necessary to use the exponential approximation

$$u = c \exp(dn) \quad (9.10)$$

because a rotating anemometer has a threshold speed c (about $0.1\text{--}0.3 \text{ m s}^{-1}$), which is the lowest wind speed that causes the rotating anemometer to move continuously (this should not be confused with a in the linear transfer function). This is illustrated in Fig. 9.5.

The time constant (see Chap. 2) of a rotation anemometer depends on the wind velocity. Therefore, the velocity-independent distance constant [9.34–36]

$$L = u_\infty \tau, \quad (9.11)$$

where u_∞ is the final velocity and τ is the time constant, is a measure of the inertia of the anemometer and gives the wind path (the passage of the air within a certain time interval or the exact product of wind

speed and time) required for an anemometer to register 63% of a wind speed difference. The distance constant is an important parameter of the inertia of mechanical anemometers; it is about 1 m for sensitive propeller anemometers, about 2–3 m for small cup anemometers, and about 5 m for larger anemometers. This constant should be used instead of the threshold speed to assess the measurement quality because the starting speed is generally below $0.5\text{--}1.0 \text{ m s}^{-1}$, and the turbulent wind field is not fully developed at these speeds. Low values for the response characteristics are required for gust measurements (see Sect. 9.8.3), where the usual averaging interval is 3 s and the sampling rate $\leq 4 \text{ Hz}$ [9.4].

As the distance constant increases, overestimation of the wind speed starts to occur due to torque on the cup rotor (overspeeding [9.36]). This overestimation of the measured wind speed relative to the true wind speed is induced by turbulence. Wind gusts will cause a mechanical anemometer to rapidly rotate due to a high torque. However, after the gust, the anemometer will require some time to adjust to the moderate wind speeds. There is no compensation for these additional rotations when the wind speed is low. Overspeeding can be as large as 10% of the wind velocity and is particularly large for low wind speeds and high distance constants. The overspeeding is proportional to $(\sigma_u/u)^2$, where σ_u is the standard deviation of the wind speed (u is the horizontal wind speed here). If overspeeding in measurements near the ground is not accounted for, wind gradients will be inaccurate.

A cosine response cannot be assumed for cup anemometers. If there is only a moderate inclination of the flow, the measured wind speed will always be roughly the same. This means that cup anemometers overestimate the wind speed for an inclined flow [9.35].

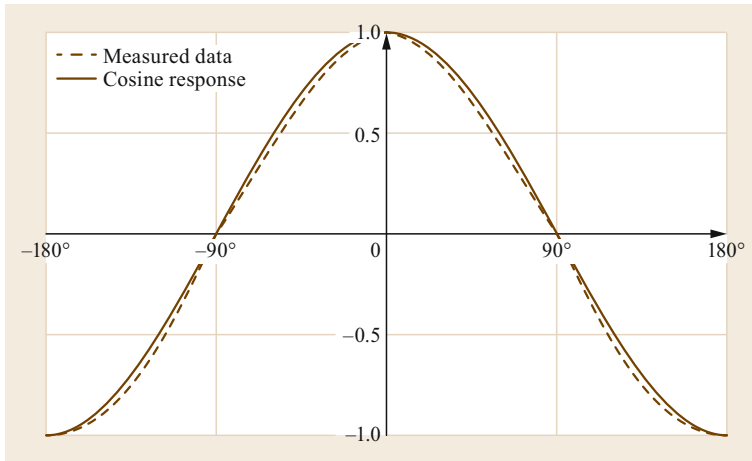


Fig. 9.6 Cosine response of a propeller anemometer (after [9.2])

For propeller anemometers (see Sect. 9.4.1), the cosine response is defined as the ratio of the measured wind speed for a certain angle of incidence α to the wind speed of the horizontal wind field $u(\alpha = 0)$ multiplied by the cosine of the angle, i.e.,

$$F(\alpha) = \frac{u(\alpha)}{u(0) \cos \alpha} \quad (9.12)$$

An ideal cosine response is $F(\alpha) = 1$. For propeller anemometers, deviations of up to 15% occur for incidence angles of about 45° (Fig. 9.6). For the light helicoidal propellers that tend to be used in three-dimensional propeller anemometers, these deviations can be relatively simply corrected using the relation

$$u_{\text{corr}}(\alpha) = u_{\text{meas}}(\alpha) [\cos \alpha - a \sin(2\alpha)], \quad (9.13)$$

where $a = 0.085$ [9.37] or $a = 0.140 - 0.009u$ [9.38]. For crosswinds ($\pm 90^\circ$, see Fig. 9.6), there is a dead zone of approximately $\pm 2^\circ$ where the propeller does not rotate. In measurements of the vertical wind, the dead zone is eliminated by employing two inclined sensors. It is recommended that a shank extension should be used for flow from the front [9.39] so that the dynamic conditions of the propeller are nearly identical for flow from the front and flow from behind.

9.3.2 Sonic Anemometers

Modern sonic anemometers use the travel time principle and direct time determination [9.27]. In this method, a sonic signal (about 100 kHz) is transmitted from both sides of the measurement path and received on the opposite sides (Fig. 9.7). Due to the wind velocity, one signal is faster than the other. The wind velocity is de-

termined from the exact travel times of the sonic signals

$$t_{1,2} = \frac{\sqrt{c^2 - u_n^2} \pm u_d}{c^2 - u^2} d, \quad (9.14)$$

where d is the path length, u_d is the wind component along the path, u_n is the normal component of the wind, and c is the speed of sound. This relation is based on the assumption that the flow in the sonic anemometer is slightly shifted by an angle γ from the measurement path, and the travel times are given by [9.35, 40]

$$t_{1,2} = \frac{d}{c \cos \gamma \pm u_d}. \quad (9.15)$$

The difference in reciprocal travel times gives the wind velocity along the measurement path, i.e.,

$$\frac{1}{t_1} - \frac{1}{t_2} = \frac{2}{d} u_d, \quad (9.16)$$

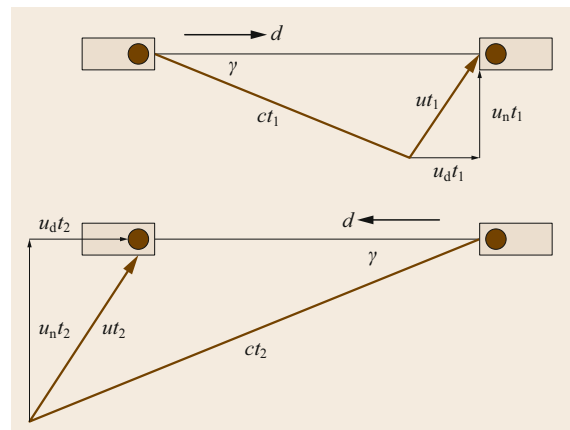


Fig. 9.7 Vector graph of the sound paths of a sonic anemometer (after [9.2])

and the sum of the reciprocal travel times eliminates the speed of sound, from which the so-called sonic temperature can be calculated (see Chap. 7). This equation also gives the computational detection limit for the wind speed based on the resolution of the runtime measurement $t_{1,2}$ and the error in the measuring path length. In practice, the detection limit is often given by the zero-point drift of the speed measurement, which can be verified in a null wind chamber [9.41] (see Sect. 9.6.2). The transducers and the mounting rods deform the wind field. These effects can be determined through wind tunnel calibrations. However, this shadow error is usually lower in the turbulent wind field. This is discussed in detail in Chap. 55.

9.3.3 Thermal Anemometers

Thermal anemometers use a protected cylinder at $\Delta T = 50\text{ K}$ higher than the air temperature T as a measuring element. Temperature sensors are arranged over the cylinder's surface. The heater voltage U to keep the temperature difference constant in time at $\Delta T = 50\text{ K}$ (using a loop control system) is used to measure the wind speed u via [9.3]

$$u = c_t \frac{T}{p} (U^2 - U_0^2)^2, \quad (9.17)$$

where c_t is a sensor-specific constant, p is the air pressure, and U_0 is the reference voltage at $u = 0\text{ m s}^{-1}$. The wind direction is obtained from the measured temperature distribution on the cylinder's surface using a compensating curve.

9.3.4 Hot-Wire Anemometers

Depending on the measurement electronics employed, a hot-wire anemometer can be utilized as a constant-voltage anemometer (CVA), constant-current anemometer (CCA), or constant-temperature anemometer (CTA). The latter requires a constant electrical resistance R and is a very common instrument in atmospheric physics. A number of variables determine the voltage that is required to keep the resistance $R(T)$ of the wire, and thus its temperature T , constant: the voltage U applied to the wire, the electrical current I through the wire, the Reynolds number Re of the flow across the wire (expressed by an exponent $n \approx 2$ for most atmospheric flows, see below), the temperature difference $T_{\text{wire}} - T_{\text{air}}$ between the wire and the ambient, the air density ρ , the heat capacity and conductivity of the wire (expressed by two material constants, c_1 and c_2), the heat H transferred from the wire to the ambient through convection, the heat radiated, by the wire and heat conducted from the wire to the mounting.

Above a certain wind speed u , the heat transfer H to the ambience is governed by forced convection, so radiation and heat conduction to the mounting can be neglected, implying that

$$H \approx [c_1 + c_2(\rho u)^{\frac{1}{n}}](T_{\text{wire}} - T_{\text{air}}). \quad (9.18)$$

This means that a CTA only works correctly for significant wind speed (typically above 0.2 m s^{-1}).

The heat Q stored in the wire changes over time t according to *King's law* of convective heat transfer,

$$\frac{dQ}{dt} = I^2 R - H = \frac{U^2}{R} - H, \quad (9.19)$$

after applying Ohm's law. In the quasi-stationary state $dQ/dt = 0$, the electrical heating equals the loss of H , and *King's law* becomes

$$U^2 = [c_1 + c_2(\rho u)^{\frac{1}{n}}](T_{\text{wire}} - T_{\text{air}})R(T_{\text{wire}}), \quad (9.20)$$

assuming the presence of a loop control circuit that keeps the wire temperature (and thus R) constant and allows the voltage U to be measured. Of course, the air temperature T_{air} must also be measured, preferably using a similar method (a cold thin-wire resistance thermometer, see Chap. 7) that delivers highly resolved turbulent temperature data. For further details on hot-wire (and hot-film) anemometers, see [9.42]; for more on air density, please refer to Chap. 5.

9.3.5 Laser Doppler Anemometers

Laser Doppler anemometers tend to be applied more commonly in laboratories and wind tunnels than in the atmosphere, with its fluctuating aerosol concentration. Such anemometers usually employ two monochromatic light beams that cross at a small angle ϕ . The beams generate a standing interference field, and the frequency of the fluctuations is equal to the Doppler shift between the incident and scattered light. The frequency f is proportional to the velocity component u_a parallel to the measurement axis [9.3] (see also Fig. 9.8) such that

$$f = \frac{|u_a|}{d_f}, \quad (9.21)$$

where d_f is the period of the interference field, which depends on the wavelength of the light and the angle ϕ .

The simplest geometry involves the reflection of a single light beam of wavelength λ (and frequency $f_{\text{laser}} = c/\lambda$, where c is the speed of light) by an air particle moving along the direction of light propagation with a velocity component u . Due to the Doppler shift,

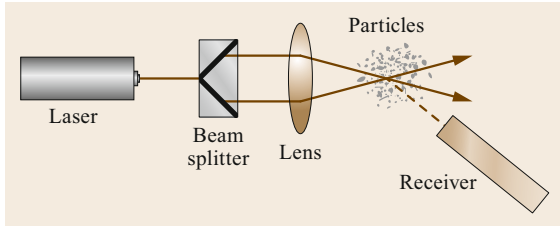


Fig. 9.8 Schematic of a dual-beam laser Doppler anemometer

the reflected light (along the direction of light propagation) is shifted in frequency (f_{scatter}) towards the blue when the particle is moving towards the photodetector and towards the red when the particle is moving away from the sensor. The velocity component u_a can be calculated using

$$u_a = \frac{\lambda}{2} (f_{\text{laser}} - f_{\text{scatter}}). \quad (9.22)$$

A two-beam geometry allows the measurement of the velocity component v perpendicular to the direction of propagation of the light. In this case, the laser beam is split into two beams with identical wavelengths that are focused at an angle ϕ . A photodetector on the opposite side of the focus detects the two beams with different frequencies f_1 and f_2 due to the movement perpendicular to the beam axis. The corresponding velocity component of the scattering particle is

$$v = \frac{\lambda (f_2 - f_1)}{2 \sin \frac{\phi}{2}}. \quad (9.23)$$

Further details on laser Doppler anemometers (LDAs) can be found in [9.42, 43].

9.3.6 Pitot-Static or Prandtl Tubes

In order to measure the wind velocity norm $u = |\mathbf{u}|$ using Bernoulli's equation (see Chap. 10) along with a Pitot-static tube (also known as a Prandtl tube) in combination with (for instance) a wind vane, it is necessary to measure the pressure p_{stag} at the stagnation point of the tube (i.e., the sum of the kinetic and potential energies of the flow) as well as the static air pressure p_s ; see Fig. 9.9. The wind velocity can then be calculated



Fig. 9.9a–c Schematics of various Pitot tube configurations: (a) simple Pitot tube (sum of the dynamic and static pressures), (b) static tube (static pressure only), and (c) Pitot-static tube (Prandtl tube)

using (10.9) (see Chap. 10) as the dynamic pressure enhancement, i.e.,

$$u = \sqrt{2 \frac{p_{\text{stag}} - p_s}{\rho}}. \quad (9.24)$$

9.3.7 Wind Vanes

The wind vane is the classical instrument for measuring the wind direction. It is a second-order dynamical system (see Chap. 2). A wind vane consists of a wind direction indicator that can rotate about a vertical axis. The wind produces a torque on the vane that is proportional to the square of the wind speed and turns the vane in the direction of the wind. Turbulence generates oscillations that over- and undershoot the true wind direction ϕ_f . Wind vanes are designed to achieve a sufficiently short response time and high resolution. The damped natural wavelength is given by [9.3]

$$\lambda_d = Pu, \quad (9.25)$$

where P is the period of the damped oscillation. The undamped natural wavelength is

$$\lambda_n = \lambda_d \sqrt{1 - D^2}, \quad (9.26)$$

where D is the damping ratio, which should be between 0.3 and 0.7 [9.4] to limit any overshooting [9.44] and achieve a reasonable response time [9.45], and which is also given by a distance constant d , often for 50% of the change in wind direction (see Fig. 9.10). The damping ratio can be obtained from [9.35, 44, 46, 47]

$$D = \frac{1}{\sqrt{1 + \left[\frac{\pi}{\ln(a_2/a_1)} \right]^2}}, \quad (9.27)$$

where a_1 is the deviation of the wind vane and a_2 is the amplitude of the first overshoot, as illustrated in Fig. 9.10.

9.3.8 Scalar and Vector Averaging

The typical averaging interval for wind data is 10 min, although an interval of 30 or 60 min is used in some applications. Due to the vectorial nature of the wind,

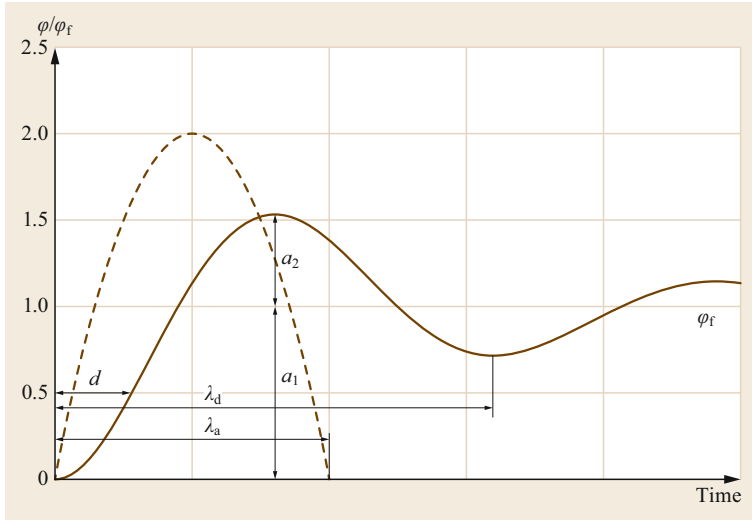


Fig. 9.10 Plot showing the parameters involved in the damping of a wind vane

the averaging of wind data at a much greater temporal resolution than 10 min (e.g., 10 s) necessitates special calculations [9.3].

Averaging with time intervals of more than an hour is not meaningful; when the time intervals are large, probability density functions are calculated instead (see Sect. 9.8.1).

Vector Averaging

Vector averaging is the most physically precise of these calculations, although it assumes that the vertical wind component is zero during the averaging period for a horizontal wind field.

Direct averaging of the wind direction leads to systematic mistakes (e.g. averaging northern wind directions 350° and 1° would lead to 180°). Thus for the direction of the mean horizontal wind vector, both horizontal components *u* (9.2) and *v* (9.3) have to be averaged separately. The mean wind components from *N* individual values are defined as

$$\bar{u} = \frac{1}{N} \sum_{i=1}^N u_i \tag{9.28}$$

and

$$\bar{v} = \frac{1}{N} \sum_{i=1}^N v_i \tag{9.29}$$

The mean horizontal wind speed can be calculated from both components as

$$\bar{u}_h = \sqrt{\bar{u}^2 + \bar{v}^2} \tag{9.30}$$

Table 9.5 Direction angle $\bar{\alpha}$ as a function of the signs of the components *u* and *v* of the wind vector [9.3]

\bar{u}	≥ 0	≥ 0	< 0	< 0
\bar{v}	> 0	< 0	< 0	> 0
$\bar{\alpha}$	$\bar{\alpha}'$	$180^\circ - \bar{\alpha}'$	$180^\circ + \bar{\alpha}'$	$360^\circ - \bar{\alpha}'$

and the initial mean wind direction is

$$\bar{\alpha}' = \arctan \left| \frac{\bar{u}}{\bar{v}} \right|, \text{ where } 0^\circ \leq \bar{\alpha}' \leq 90^\circ \tag{9.31}$$

Note that *v* = 0 is not allowed in this equation. In this case, $\bar{\alpha} = 90^\circ$ for *u* > 0 and $\bar{\alpha} = 270^\circ$ for *u* < 0. The true mean direction angle $\bar{\alpha}$ can be obtained from the signs of the components of the wind vector in accordance with Table 9.5.

Scalar Averaging

When the measurements obtained are scalar means (e.g., data from cup anemometers), the mean horizontal wind speed can be calculated as

$$\bar{u}_h = \frac{1}{N} \sum_{i=1}^N u_{hi} \tag{9.32}$$

Since the wind direction scale is discontinuous at north, if there are direction changes that take place via north, the scale must be extended beyond 360° when calculating the mean wind direction.

9.3.9 Influence of the Surrounding Area on Wind Measurements

Wind measurements are significantly influenced by buildings, trees, and other obstacles in the vicinity of

the measurement site. Several more or less phenomenological rules have been developed to aid the selection of measurement sites and the correction of measurements. Very expensive wind tunnel studies or large eddy simulations are needed to exactly determine the influences of nearby obstacles. The methods outlined below are recommended for standard wind measurements.

The World Meteorological Organization (WMO) has developed a clear schema for classifying and correcting wind measurements [9.4, 48]. The recommended height at which measurements should be performed is 10 m. Because not all sites have the ideal characteristics of being exactly flat and having low roughness and no obstacles, it is recommended that stations should be classified as shown in Table 9.6 (see also Chap. 43), and that terrains should be classified based on the roughness length (Table 9.7; see also Chap. 1).

It is generally difficult to correct wind measurements precisely. However, the following three methods can be used to correct wind measurements sufficiently to allow rough comparisons between data obtained at different locations. Note that the methods do not give precisely comparable results, and corrections should only be made if the site is not too rough ($z_0 \leq 0.5$ m).

WMO has proposed a correction method for the station classification mentioned above [9.4, 48] that depends on the roughness length, a flow distortion cor-

rection [9.28, 52], and a topographic correction [9.53, 54]. For the corrected wind speed, it follows that

$$u_{\text{corr}} = u_{\text{meas}} C_F C_T \frac{\ln(10 \text{ m}/z_{0u})}{\ln(z/z_{0u})} \times \frac{\ln(60 \text{ m}/z_{0u}) \ln(10 \text{ m}/z_0)}{\ln(10 \text{ m}/z_{0u}) \ln(60 \text{ m}/z_0)}, \quad (9.33)$$

where z_0 is the roughness length at the site, z_{0u} is the effective roughness length of the terrain upstream of the site, C_F is the flow distortion factor (which is 1 for a free-standing mast), and C_T is the topographic correction factor, which is the ratio of the regional average wind speed to the wind speed at the site (this ratio is 1 for flat terrain). The effective roughness length is a correction for roughness effects and obstacles up to 2 km upstream of the site. To determine the effective roughness length, the climatology (one year) of the standard deviation of the horizontal wind speed σ_{uh} and the standard deviation of the wind direction σ_d (in radians) for sectors of roughly 30° must be applied, i.e.,

$$\frac{\sigma_{uh}}{u} = c_u \kappa \left[\ln \left(\frac{z_0}{z_{0u}} \right) \right]^{-1} \quad (9.34)$$

or

$$\frac{\sigma_d}{u} = c_v \kappa \left[\ln \left(\frac{z_0}{z_{0u}} \right) \right]^{-1}, \quad (9.35)$$

Table 9.6 Recommended classification of wind measurement sites (modified from [9.4, 48])

Class	Minimum distance to obstacles		Angular width (degrees)	Remark	Roughness class (see Table 9.7)	Uncertainty (correction required) (%)
	Surrounding obstacles	Thin obstacles more than 8 m high (masts, thin trees)				
1	> 30 times the height of obstacles	> 15 times the height of thin obstacles	≤ 1.9	Obstacles < 4 m high should be ignored	2–4	–
2	> 10 times the height of obstacles	> 15 times the height of thin obstacles	≤ 5.7	Obstacles < 4 m high should be ignored	2–5	≤ 30
3	> 5 times the height of obstacles	> 10 times the height of thin obstacles	≤ 11.3	Obstacles < 5 m high should be ignored		≤ 50
4	> 2.5 times the height of obstacles; no obstacles with an angular width > 60° and a height > 10 m within 40 m		≤ 21.8	Obstacles < 5 m high should be ignored		> 50
5	Sites that do not meet the requirements of class 4 are not recommended for wind measurements					

Table 9.7 Recommended terrain classification based on the roughness length z_0 [9.4] (updated according to [9.2, 49, 50]); x is the fetch and H is the obstacle height

Class	Surface	Obstacles	Roughness length z_0 (m)
1	Open sea	$x \geq 5$ km	0.002
2	Flat bare soil, snow	No	0.005
3	Open flat terrain, grass	No	0.03
4	Low crops	Occasional obstacles $x/H > 20$	0.1
5	High crops	Scattered obstacles $15 < x/H < 20$	0.25
6	Parkland, bushes	Numerous obstacles $x/H \approx 10$	0.5
7	Suburb, forest	Regular large obstacles	1.0
8	City center	High- and low-rise buildings	2.0

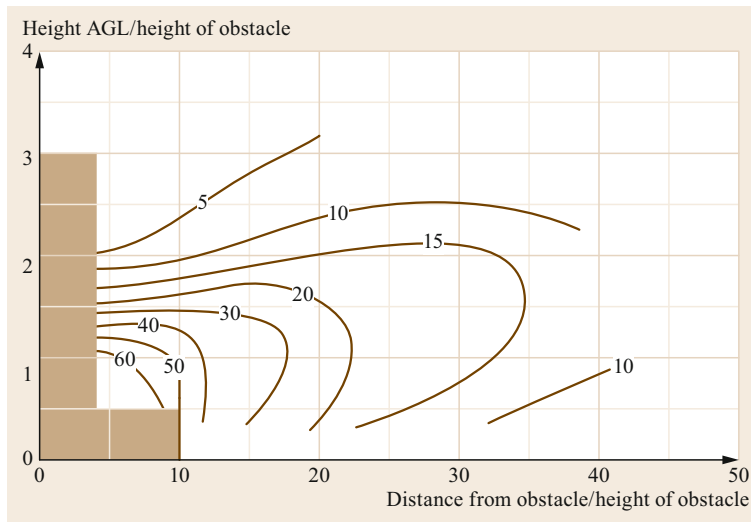


Fig. 9.11 Determination of the factor R_1 (after [9.51], reproduced with the permission of the Danish Technical University, Roskilde, Denmark)

where $c_u = 2.2$, $c_v = 1.9$ [9.2], and the *von Kármán* constant $\kappa = 0.4$.

A similar method was developed by the German Meteorological Service based on older versions of the WMO guidelines [9.4, 55]. This method is based on obstacle width (B) and height (H). For tall, narrow obstacles ($H \gg B$), the distance A between the measuring instrument and the obstacle is

$$\begin{aligned} A &\geq 0.5H + 10B && \text{for } B \ll H \leq 10B \\ A &\geq 15B && \text{for } H > 10B. \end{aligned} \quad (9.36)$$

For $H \approx B$, it follows that

$$A \geq 5(H + B), \quad (9.37)$$

and for flat, elongated obstacles ($H \ll B$),

$$\begin{aligned} A &\geq 0.5B + 10H && \text{for } H \ll B \leq 10H \\ A &\geq 15H && \text{for } B > 10H. \end{aligned} \quad (9.38)$$

When there are circular obstacles of radius r surrounding the installation site (e.g., the site is surrounded by houses or forest clearings), it follows that

$$\begin{aligned} A &\geq \pi r + 10H && \text{for } H \geq \frac{\pi}{5}r \\ A &\geq 15H && \text{for } H < \frac{\pi}{5}r. \end{aligned} \quad (9.39)$$

If the minimum distance A cannot be complied with (9.36)–(9.39), the wind speed will not be corrected, but the instrument's pole must be raised by h' , where

$$h' = \frac{H}{A} (A - A_D). \quad (9.40)$$

Here, A is the distance assessed using (9.38) to (9.41), and A_D is the distance between the obstacle and the actual measurement site.

The European Wind Atlas [9.51] applies a method based on [9.56] to determine the lee side of an obstacle. Accordingly, a corrected wind velocity can be calculated from the measured velocity and the porosity P of the obstacle (buildings: $P = 0.0$; trees: $P = 0.5$) as

$$u_{\text{corr}} = u_{\text{meas}} [1 - R_1 R_2 (1 - P)]. \quad (9.41)$$

The factor R_1 can be obtained from Fig. 9.11, and

$$R_2 = \begin{cases} \left(1 + 0.2 \frac{A}{B}\right)^{-1} & \text{for } \frac{B}{A} \geq 0.3 \\ 2 \frac{B}{A} & \text{for } \frac{B}{A} < 0.3. \end{cases} \quad (9.42)$$

For measurements of turbulent fluxes (see Chap. 55), the recommended distances should be enlarged by a factor of 5–10. The footprint (see Chap. 1) should also be taken into account. Similar conditions must be fulfilled for measurements of the vertical gradients of the horizontal wind speed, which are sometimes gauged to determine the stratification conditions in the atmosphere or energy and substance exchanges (see Chaps. 54 and 57), and are usually performed at small heights (< 10 m). For a discussion of the influence of the sensor installation (i.e., the tower), see Chap. 6. Special requirements may also call for the sensor to be installed at a greater or lower height than normal (e.g., at source height) or the measurement of locally relevant data (e.g., in street canyons).

9.4 Devices and Systems

Anemometers and wind vanes are available as individual instruments or they can be integrated into one system. Rotation anemometers and wind vanes are installed close together, while sonic and thermal anemometers that measure the wind speed and direction are usually integrated into one sensor. Hot-wire, laser, and Pitot anemometers are seldom applied in the atmosphere, but they are used for calibration in wind tunnels.

9.4.1 Rotation Anemometers

Until about 5–10 years ago, cup and propeller anemometers were the most common sensors used to measure wind speed. The cups used in anemometers have a round or preferably conical form, while the propellers have a helicoidal form that ensures a near-cosine response. Both systems consist of two parts: the rotor and the signal generator.

However, rotation anemometers are gradually being replaced by sonic anemometers, which can measure the wind vector with high accuracy and less maintenance than required for rotation anemometers. Classified cup anemometers are still used in the wind energy industry [9.57]. Cup anemometers positioned on high towers can perform measurements in the presence of inclination, acceleration, and vibration.

Handheld cup anemometers are also available. These have dynamo or mechanical counters; the lat-



Fig. 9.12 Cup anemometer (photo © Th. Friedrichs & Co., Schenefeld, Germany)

ter give the windway, which can be recalculated into a wind speed within a certain time interval. Impeller wheel cup anemometers can also be obtained. While cup anemometers (Fig. 9.12) have distance constants of 2–5 m, those of propeller anemometers are on the order of 1–2 m. The latter are also able to measure turbulent fluctuations of up to 1–5 Hz and are available as three-component systems that can determine the wind vector (Fig. 9.13). An overview of different signal generators is given in Table 9.8.

Cup anemometers intended for application in moist and cold ($< 0^{\circ}\text{C}$) weather conditions can be heated. The main components of the anemometer that are heated are the cups, the axis, and the bearings.

9.4.2 Wind Vanes

Wind vanes (Fig. 9.14) must be well balanced or they will adopt a preferred position at low wind speeds. When using mechanical anemometers, the wind direction can be determined using optical, electrical



Fig. 9.13 The Gill 27005T UVW three-component propeller anemometer (photo © R.M. Young Company/GWU-Umwelttechnik GmbH, Erfstadt, Germany)

Table 9.8 Overview of the signal generators used in cup and propeller anemometers [9.3]

Transducer	Outputs ^a	Power supply required?	Special features
Cup anemometer			
Current generator	AS (mA)	No	Manual anemometer
Contact transmitter with or without a counter	FS (Hz)	No	Selectable contact output sequence (manual anemometer)
Pulse generator (magnetic or inductive)	FS (Hz)	Yes	Not dependent on line resistances, linear output signal (standard signal)
Pulse generator (optoelectronic)	FS (Hz)	Yes	
Pulse generator with integrated signal converter	SS (mA, V)	Yes	
Propeller anemometer			
Optical pulse generator	FS (Hz)	Yes	Suitable for fluctuation measurements

^a FS frequency signal (in Hz); AS scaled but often not linearized analog signal (resistance, voltage, or current); SS linearized standard signal, e.g., 0–20 mA, 4–20 mA or 0–5 V, 0–10 V

**Fig. 9.14** Mechanical wind vane (photo © Adolf Thies GmbH & Co. KG, Göttingen, Germany)

(potentiometer), or coding methods, as shown in Table 9.9. Potentiometers either have a dead zone near 360° or are 540° multiturn potentiometers. Similar to cup anemometers, heated wind vanes can be obtained for moist and cold weather conditions.

9.4.3 Combinations of a Rotation Anemometer with a Wind Vane

Various designs of systems combining a rotation anemometer with a wind vane are available. The cup anemometer may be separated from the wind vane vertically or horizontally (Fig. 9.15). In the case of horizontal separation, a large distance of about 1.0 to 1.5 m may be used to minimize interactions. When they are separated vertically, the lower of the two sensors may be affected by the mounting brackets.

A widely used sensor is the combination of a wind vane and a propeller anemometer (skyvane, Fig. 9.16). When there are large fluctuations in the wind direction, the wind speed measurement may be reduced due to the cosine response (see Sect. 9.3.1). Furthermore, the wind speed and the wind direction can be calculated from propeller anemometers with 2-D or 3-D designs (Fig. 9.13). An overview of different signal generators is given in Table 9.10.

9.4.4 Sonic Anemometers

Early sonic anemometers had a three-dimensional design, and their measurement paths were predominantly Cartesian oriented [9.27]. They were mainly applied for flux measurements (see Chap. 55). Modern sonic anemometers have larger measurement path angles to reduce flow distortion. Technical progress in the last 10–20 years has reduced the cost of a sonic anemometer dramatically, and this measuring principle is now also available for two-dimensional sensors that measure wind speed and direction. These sensors—which have a relatively open or compact design (Fig. 9.17)—are replacing rotating anemometers and wind vanes,

Table 9.9 Overview of the signal generators used in mechanical wind vanes [9.3]

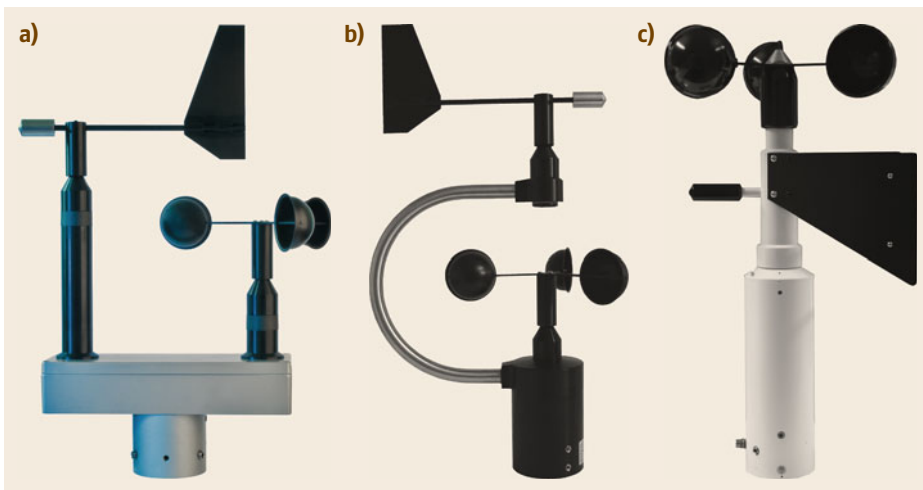
Transducer	Outputs ^a	Power supply required?	Special features
Potentiometer	AS (Ω)	Yes	Very suitable for simple recorders/displays
Absolute angle encoder	GC, DP (serial or parallel)	Yes	Usually very expensive, encoding depends on manufacturer
(Optoelectronic) encoder	GC, DP (serial)	Yes	Standard, Gray code depends on manufacturer
Encoder with integrated signal converter	SS (mA, V)	Yes	Linear output signal (standard signal)

^a AS scaled but often not linearized analog signal as resistance, voltage, or current signal; DP data protocols, e.g., via RS-232/485, SDI/MODBUS; GC Gray code: serial or parallel; SS linearized standard signal, e.g., 0–20 mA, 4–20 mA or 0–5 V, 0–10 V

Table 9.10 Overview of the signal generators used in combinations of a rotation anemometer with a mechanical wind vanexo [9.3]

Devices combined	Transducer	Outputs ^a	Power supply required?	Special features
Cup anemometer combined with wind vane: vertical arrangement (coaxial)	Electric; see Tables 9.8 and 9.9		Yes	Compact design
Cup anemometer combined with wind vane: horizontal arrangement	Electric; see Tables 9.8 and 9.9		Yes	Large separation between the sensing devices
Wind vane with integrated propeller anemometer	Electric	FS (Hz), GC	Yes	
2-D (3-D) orthogonal propeller anemometer	Optical pulse generator	FS (Hz)	Yes	Suitable for fluctuation measurements

^a FS frequency signal (in Hz); GC Gray code: serial or parallel

**Fig. 9.15a–c** Three combined system designs consisting of a cup anemometer and mechanical wind vane: (a) horizontally separated system (note: the distance between the sensors should be increased), (b) vertically separated system, (c) vertically separated system intended for application on ships (photo © Lambrecht Meteo GmbH, Göttingen, Germany)

even those used by meteorological services. They are available from many manufacturers and often included in complex weather sensors (see Chap. 43). Even one-dimensional sensors have become available; these

are used for measurements in a one-dimensional flow (Fig. 9.17c, industry) or in a combination of three sensors, such as in the wind turbine spinner [9.58] (see also Chap. 51).



Fig. 9.16 Combination of a propeller anemometer with a mechanical wind vane, also called a skyvane (photo © R.M. Young Company/GWU-Umwelttechnik GmbH, Erftstadt, Germany)

An increasing number of designs and signal processing methods are becoming available for eddy covariance measurements. Figure 9.18 illustrates four different sensor types that are widely used. The DA700 (Fig. 9.18a) is the most recent version of the Kaijo-Denki PAT and DAT series of sensors that were used from the 1970s to 1990s in many scientific papers and are described in [9.22, 27]. The CSAT3 (Fig. 9.18b) is based on a prototype constructed at the University of

Washington [9.29], and has been used since the 1990s for scientific measurements. Both of these types are applied to a selected wind direction sector. If there is no preferred wind direction, omnidirectional anemometers are employed; two such sensors are shown in Fig. 9.18c, d. Further details on these sensors are given in Chap. 55.

Due to various issues with eddy covariance measurements, efforts have been made to reduce flow distortion by, for example, using smaller transducers or including a vertically oriented path that permits better resolution of the vertical wind velocity, even in omnidirectional sensors. Similar results of the reduction of the flow distortion are possible analyzing the signals between all transducers and not only along one path and the non-disturbed signals can be selected for the analysis. These investigations are ongoing, because wind tunnel measurements cannot be easily transferred to the turbulent atmosphere above various rough surfaces. Numerical studies are also used to improve anemometer design [9.59].

It is possible to heat a sonic anemometer in moist and frosty weather conditions, but this may influence the data [9.60, 61]. Because of the energy used in the transducers, a thin rough-frost layer does not significantly affect the measurements.

The wind data obtained using a sonic anemometer do not depend on the air density, but the power of



Fig. 9.17 (a,b) Two-dimensional sonic anemometers with open path lengths; the latter has a compact construction (photos © Adolf Thies GmbH & Co. KG, Göttingen, Germany). (c) One-dimensional sonic anemometer (photo © METEK GmbH, Elmshorn, Germany)

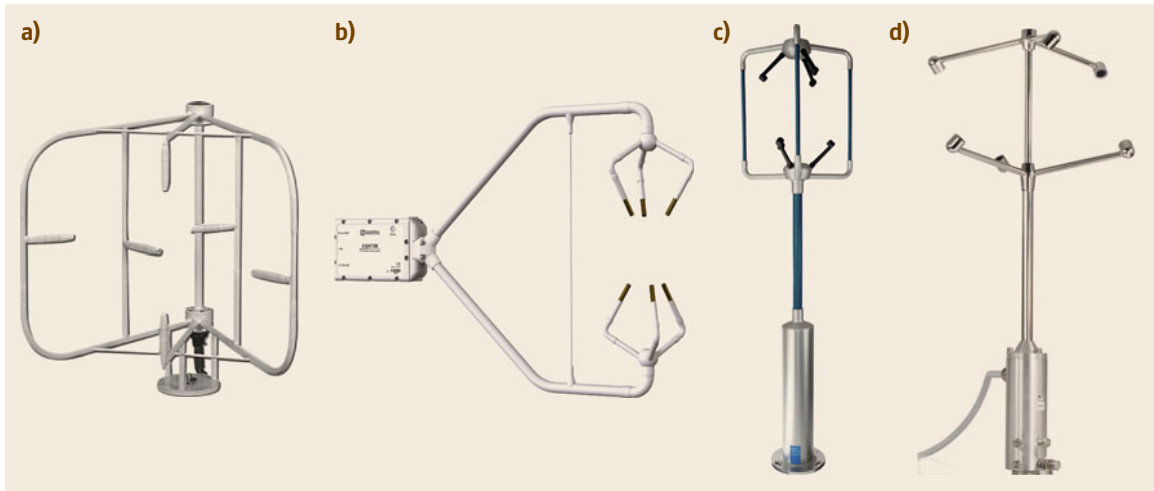


Fig. 9.18a–d Different types of three-dimensional sonic anemometers (the anemometers in (a) and (b) are orientated in one wind direction and those in (c) and (d) are omnidirectional types): (a) DA700 (photo © Sonic Corp., Tokyo, Japan), (b) CSAT3B (photo © Campbell Sci. Inc., Logan, UT, USA), (c) R3-50 (photo © Gill Instruments Ltd., Lymington, UK), and (d) uSonic-3 Scientific (formerly USA-1, photo © METEK GmbH, Elmshorn, Germany)

the sound transferred is density dependent. Most instruments have enough power to enable measurements to be performed at altitudes of up to about 5000 m, but the manufacturer should be consulted before performing such measurements.

9.4.5 Thermal Anemometers

Thermal anemometers are robust sensors that are often combined with other sensors (see Chap. 43). This type of sensor type can be used in rough conditions. An example is shown in Fig. 9.19. The signal is either analog or digital (serial output).

9.4.6 Hot-Wire Anemometers

Hot-wire anemometers use a thin metal wire (tungsten is common) or a quartz fiber (e.g., 70 μm) with a thin metal coating (e.g., 0.5 μm of nickel) a few millimeters in length that is mounted on two needle-shaped prongs. The application of a combination of three wires can allow 3-D wind-vector measurements (Fig. 9.20).

Hot-wire anemometers have extremely high frequency responses and fine spatial resolutions compared to other measurement methods. Since the wire is very thin and hot, it is very delicate, it can be contaminated by gases and particles, and it suffers from aging. These sensors are therefore mainly employed in detailed studies of turbulent flows, preferably in clean air (laboratories), or for short field campaigns. Hot-wire anemometers only work correctly when the wind velocity is significant (typically above 0.2 m s^{-1}), but they can be used at transsonic and sonic speeds.



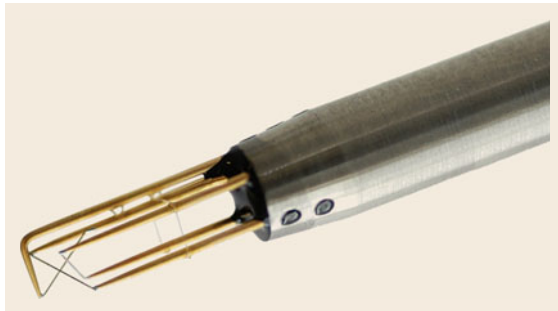
Fig. 9.19 Thermal anemometer (top part) combined with a temperature screen (photo © Lambrecht Meteo GmbH, Göttingen, Germany)

9.4.7 Laser Anemometers

The laser Doppler anemometer (LDA) has several advantages compared with most other techniques discussed in this chapter. First, due to their measurement principle, LDAs do not have to be calibrated! The observed Doppler shift is a linear function of the velocity component. However, the electronics needed to determine the Doppler shift is quite complex. Furthermore,

Table 9.11 Advantages and disadvantages of different wind-measuring methods

Method or device	Advantages	Disadvantages
Cup anemometer	Simple and inexpensive anemometer, choice of many signal formats	Mechanical system, slow response time (large distance constant)
Propeller anemometer	Fast response time (low distance constant), but not good enough for turbulent flux measurements	Mechanically sensitive
Wind vane	Simple and inexpensive wind vane, choice of many signal formats	Mechanical system, slow response time (large distance constant)
Sonic anemometer	Nonmechanical device for measuring wind velocity and wind direction; fast response time, turbulence measurements are possible	Relatively expensive, special data calculations are necessary
Thermal anemometer	Nonmechanical device for measuring wind speed and wind direction	Low accuracy
Hot-wire anemometer	Very high wind velocities, very high resolution	Only for laboratory measurements, very sensitive mechanically
Laser anemometer	Fast-response anemometer	Only for laboratory measurements; requires the presence of a certain aerosol concentration
Pitot anemometer	Very robust, high wind velocities, high resolution	Requires high wind velocities, no wind direction (see multihole probe); beware of icing

**Fig. 9.20** Three-dimensional hot-wire anemometer (photo © Dantec Dynamics, Skovlunde, Denmark)

the measurement setup must be realized with high precision, and the angle ϕ is almost linearly related to the wind component.

LDAs work very rapidly and offer very high temporal resolutions. Also, the measurement volume is extremely small—less than a millimeter in diameter. Since they have no moving parts, LDAs are low maintenance. They do not require contact with the medium and are unaffected by pressure, density, or temperature fluctuations in the flow.

9.5 Specifications

The general requirement for any wind-speed measuring device [9.4] is the ability to measure the wind speed up to 75 m s^{-1} . However, depending on the climate and measurement height (see Chap. 1), this range can be reduced for many sites. The required resolution and uncertainty depend on whether the application involves standard measurements or the measurement

of vertical gradients (which are commonly measured in research or for wind power studies). The typical requirements in both cases are given in Table 9.12. Requirements for standard wind direction measurements are given in Table 9.13. The specifications of the different types of wind sensors are given in Table 9.14.

9.4.8 Pitot-Static or Prandtl Tubes

This method is mainly used at high velocities (e.g., aboard aircraft). A further development of the Prandtl tube is commonly used aboard research aircraft: the so-called multihole probe, which delivers not only the wind vector norm but all three components of the wind vector (see Chaps. 48 and 49).

9.4.9 Comparison of Different Methods

The appropriate wind sensor to use is determined by the measurement task. The essential aspects are the detection limit, resolution, dynamic behavior, measurement range, and either mechanical components or ultrasound. A comparison of the advantages and disadvantages of the various wind sensors described above is shown in Table 9.11.

Table 9.12 Requirements for wind-speed sensing devices

Property	Standard use [9.3, 4]	Vertical gradients for flux calculations [9.3]
Range of wind speeds (m s^{-1})	0–75	Dependent on measurement height
Distance constant (m)	2–5	≤ 3
Response threshold/detection limit (m s^{-1})	≤ 0.5	≤ 0.3
Speed resolution (m s^{-1})	± 0.5	± 0.1
Uncertainty	$\pm 0.5 \text{ m s}^{-1}$ for wind speeds $\leq 5 \text{ m s}^{-1}$ 10% for wind speeds $> 5 \text{ m s}^{-1}$	$\pm 0.1 \text{ m s}^{-1}$

Table 9.13 Requirements for wind-direction sensing devices [9.3, 4]

Property	Wind vane	Ultrasound and thermal anemometers
Angular resolution (degrees)	5 for wind speeds $\geq 1 \text{ m s}^{-1}$	3 for wind speeds $\geq 1 \text{ m s}^{-1}$
Damping ratio	> 0.3	
Uncertainty (degrees)	± 5 at $u \geq 1 \text{ m s}^{-1}$	3 for wind speeds $\geq 1 \text{ m s}^{-1}$

Table 9.14 Specifications of different methods for measuring the wind velocity and direction (given the large number of sensors available, the manufacturer's information should be used to retrieve more specific information on a particular sensor)

Sensor type	Typical uncertainty	Temperature range ($^{\circ}\text{C}$)	Remark
Cup anemometer	$\pm 0.3 \text{ m s}^{-1}$	-40 to $+70^{\text{a}}$	
Propeller anemometer (sky vane)	$\pm 0.1 \text{ m s}^{-1}$	-40 to $+60^{\text{b}}$	$0-35 \text{ m s}^{-1}$
Sonic anemometer	$\pm 0.1 \text{ m s}^{-1}, \pm 2^{\circ}$	-40 to $+70^{\text{a}}$	Resolution 0.01 m s^{-1}
Thermal anemometer	$\pm 0.5 \text{ m s}^{-1}, \pm 3^{\circ}$	-40 to $+70^{\text{a}}$	
Hot-wire anemometer	$\pm 0.01 \text{ m s}^{-1}$	-20 to $+70$	
Laser anemometer			
Pitot anemometer	0.5–5%	-40 to $+70^{\text{a}}$	
Wind vane	$\pm 5^{\circ}$	-40 to $+70^{\text{a}}$	

^a When used at temperatures $< 0^{\circ}\text{C}$ and in moist conditions, the sensor should be heated

^b When used at temperatures $< 0^{\circ}\text{C}$ and in moist conditions, the combined sensor and wind vane should be heated; otherwise, this combined system should only be used at temperatures above zero and in a dry climate

9.6 Quality Control

In contrast to other meteorological elements, the WMO [9.4] has not categorized standards for wind measurements. The ISO standards for wind tunnel calibration are applied to rotation and sonic anemometers [9.34, 41] (see Chap. 4), whereas cup anemometers for the wind energy industry are categorized by the International Electrotechnical Commission (IEC) [9.57]; see Chap. 51. A very general classification is used for sonic anemometers that are employed for flux measurements [9.62, 63]; see Table 9.15 and Chap. 55.

Anemometers are typically calibrated in wind tunnels. Because the calibrations are relatively stable over long periods, long time intervals can be left between calibrations (see Sect. 9.7) if the sensors are not mechanically deformed or corroded. However, wind tunnels provide near-laminar flow, and the characteristics in the turbulent atmosphere may be different to this.

This particularly applies to the flow distortion effects of sonic anemometers, which are usually reduced. For flux measurements performed using sonic anemometers, it is usual to carry out intercomparisons of different sensors. It is recommended that the instruments should not generate flow distortion effects for other sensors, the wind field should have the same turbulence characteristics for all sensors, and an instrument (etalon) for which the characteristics are already known should be used for comparison. For further aspects of such comparisons, see Chaps. 3 and 55.

9.6.1 Wind Tunnel Calibration

Rotation anemometers [9.34] must be calibrated in a wind tunnel to determine the linear transfer function (9.9), the nonlinear transfer function (9.10) (if they are

Table 9.15 Classification of sonic anemometers based on the scheme given in [9.62, 63]

Anemometer class	Application	Sensor type
A	Flux measurements for basic research	3-D anemometer for flux measurements with an open sector of 120–300° when there are no significant flow distortion influences, e.g. Fig. 9.18a,b
B	General use for flux measurements	3-D anemometer for omnidirectional flux measurements (0–360°) when there are flow distortion influences due to the mounting structures, e.g. Fig. 9.18c,d
C	General use for wind measurements	2-D anemometer used only for the wind speed and direction, e.g. Fig. 9.17a,b

to be used to measure low wind speeds), the distance constant (9.11), and the cosine response (9.12); see Sect. 9.3.1 on rotation anemometers. With the exception of the distance constant and the nonlinear transfer function, the same characteristics of other types of anemometers (e.g., sonic anemometers) can also be measured in a wind tunnel.

Requirements for the Wind Tunnel

The wind tunnel should be large enough that the anemometer and of all the constructions required for the calibration cover less than 5% of the cross-sectional

area of a closed wind tunnel or less than 10% of the cross-sectional area of an open wind tunnel (Fig. 9.21). The cross-sectional profile of the anemometer and the constructions needed for calibration should remain the same during the process of calibration. If the diameter of the wind tunnel is too small for the anemometer, it is possible to calibrate the anemometer through comparison with another well-calibrated reference anemometer of the same type.

The wind speed of the tunnel should range from 0 m s^{-1} up to 50% of the maximum wind speed that the anemometer will encounter [9.34]. The speed should be kept constant to within $\pm 0.2 \text{ m s}^{-1}$. It is necessary to monitor the speed of the wind tunnel with well-calibrated (by a certificated institute), sensitive anemometers such as a hot-wire anemometer (Sect. 9.4.6), laser anemometer (Sect. 9.4.7), or Pitot tube (Sect. 9.4.8). The wind speed in the area of the anemometer should be uniform to within $\pm 1\%$. For wind speeds above 10 m s^{-1} , the turbulence intensity (the standard deviation of the mean wind speed divided by the mean wind speed) should be less than 2%. The turbulence intensity can be measured with a hot-wire or laser anemometer.

When determining the response threshold and the distance constant, the air density in the air stream should not vary by more than 3%, and for application of the Pitot anemometer, temperature and air density are necessary. Therefore, these parameters, together with the humidity, should be documented during the calibration.

Performing the Calibration

The lowest calibration point is approximately double the response threshold speed [9.34]. Other calibration points are 10, 20, 30, 40, and 50% of the maximum wind speed that the anemometer will encounter. Before calibration, the wind speed in the tunnel should be in a steady state. The averaging interval employed during calibration is 30–100 s, or even longer for anemometers with impulse output. The calibration should be repeated three times. The linear transfer function can be analyzed using regression analysis (see Chap. 2). If the

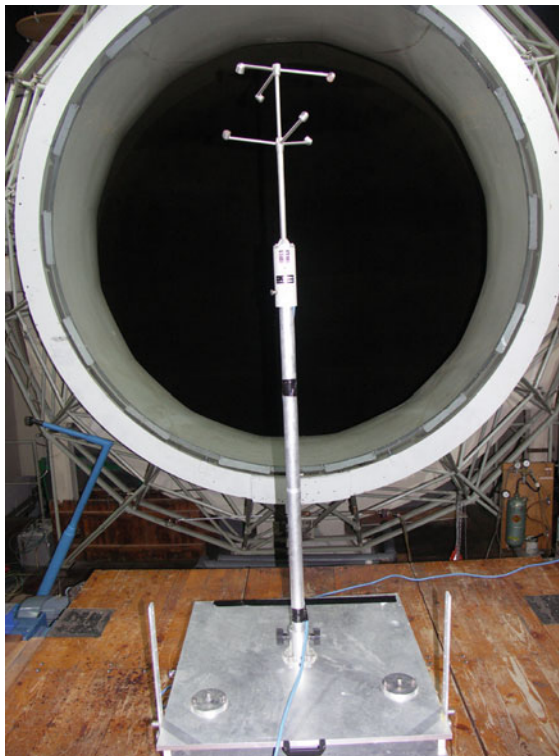


Fig. 9.21 Wind tunnel calibration of a sonic anemometer in the low wind speed tunnel of the Technical University Dresden, Germany (photo © L. Siebicke)

relationship between the tunnel speed and the number of rotations or speed of the anemometer is not linear at lower wind speeds (Fig. 9.1), these wind speeds must be excluded from the linear transfer function and analyzed with (9.9), probably with the aid of more calibration points.

The determination of the distance constant should be repeated ten times for tunnel speeds of 5 m s^{-1} and 10 m s^{-1} . First the anemometer should be locked. After unlocking the anemometer, about ten measurements separated by time intervals that depend on the distance constant should be performed. The response time (see Chap. 2) is the time taken for the anemometer to change from 30 to 74% of the steady-state wind tunnel speed [9.34]. The distance constant is the average of all the measurements calculated with (9.11).

The cosine response calculated via (9.12) should be tested (with ten repetitions) for tunnel speeds of 5 and 10 m s^{-1} . To achieve this, the anemometer should be inclined in 5° steps up to 30° using a special construction. The cosine response of a cup anemometer should be negligible up to $10\text{--}20^\circ$ [9.35]. Propeller and sonic anemometers should adhere closely to the cosine response; only small deviations are permissible for the propeller anemometer (Fig. 9.2). If necessary, the range of inclination can be extended to more than 30° .

9.6.2 Zero-Wind Chamber Calibration of Sonic Anemometers

The calibration of sonic anemometers is very stable for a long time. However, before the first use of the anemometer, a zero-point test should be carried out in a closed zero-wind chamber [9.41]. The size of the chamber required depends on the signal power of the anemometer and should be available from the manufacturer. Measurements of the wind components or wind speed in the chamber should be averaged over the same time interval as during the planned measurements. If the value is below the threshold of approximately $0.01\text{--}0.1 \text{ m s}^{-1}$, the test is complete. If not, there should be a check to see whether the test failed due to air flow in the chamber or signal reflection at the walls. If it did fail for either of these reasons, the position of the anemometer in the chamber should be changed. If the test fails again, the anemometer must be recalibrated by the manufacturer.

9.6.3 Specific Quality Control Methods

The following unrealistic values caused by a sensor malfunction or faulty data transmission during standard wind measurements should be identified through default testing and excluded [9.3, 64]:

- Negative values
- Wind speeds below the response threshold with a wind direction of 1° to 360°
- Wind speeds above the response threshold with a wind direction of 0°
- Wind speeds $> 60 \text{ m s}^{-1}$ at elevations $< 600 \text{ m}$ above mean sea level in Central Europe
- Wind speeds $> 80 \text{ m s}^{-1}$ at elevations $> 600 \text{ m}$ above mean sea level in Central Europe
- Wind direction $> 360^\circ$
- A constant wind speed and/or direction for at least six hours.

Meteorological measurements can be tested by comparisons with climatological values regarding the variability of the wind speed and wind direction between two readings, or comparisons with wind measurements of nearby meteorological stations if they are not affected by their surroundings. This allows jumps in the readings (e.g., due to increased friction in the bearings) to be identified. Furthermore, the persistence of constant readings can be checked in order to identify blockages in the sensing device or a failed connection between the sensing device and data processing. The limit values are usually determined based on the typical measurements at the site.

Wind measurements taken at several sites or several altitudes can be tested by comparison with other data. The usual method is to identify measurement errors from a numerical analysis of weather reports for an extended area. The measurement of vertical gradients in the atmosphere near the ground can be checked by applying the typical logarithmic profile and obtaining approximate exponential profiles from tower measurements (see Chap. 1).

The abovementioned test can be performed not only for rotation anemometers but analogously for sonic and thermal anemometers. However, the measurement of standard deviations of wind variables or turbulent fluxes requires more comprehensive testing (see Chap. 55).

9.7 Maintenance

There are some general maintenance rules that should be followed for all wind-measuring instruments [9.3, 4]. The installed measuring system must be included in all maintenance actions (see Chap. 6). This includes the safety standards for masts, attachments, the fitting of a lightning conductor (on the upwind side of the anemometer), and meteorological requirements for the site, such as an undisturbed inflow direction (see Sect. 9.3.9).

Because wind sensors—especially mechanical sensors—are highly affected by environmental conditions, the following issues should be addressed during the maintenance:

- Lubricant viscosity and bearing properties are affected by aging and changes in temperature. Friction increases at low temperatures, which leads to erroneous measurement data. The manufacturers' instructions regarding temperature-related behavior must be observed.
- All wind-measuring instruments are subject to corrosion, especially when they are used in regions with high levels of air pollution, in coastal regions, or at sea. Corrosion effects should be identified and repaired.
- Appropriate measures should be put in place to ensure that birds cannot settle on the measuring instruments. A slightly higher mast close to and downwind of the tower can be helpful.

- Rain and snow can affect the properties of the equipment. In particular rime, hoar frost, and ice formation can completely interrupt the proper functioning of the measuring instrument unless these effects can be minimized (e.g., by heating).

For some sites, special actions are necessary, or the interval between maintenance should be shortened.

The calibration, inspection, and audit intervals of the sensing device and the data transmission and processing systems should be defined based on the required and specified accuracy and temporal changes, as should the interval between calibrations of electrical modules (which may present drift). Additional audits are necessary when the weather conditions (e.g., storms or snowfall) could affect the measurement process and/or the results obtained. Table 9.16 lists the maximum intervals between audits for standard meteorological measurements.

If regular weekly audits (see Table 9.16) of the equipment and the results of quality control (Sect. 9.6) indicate that the measuring and recording equipment is malfunctioning, immediate and more extensive inspections are necessary, as described in the other rows of Table 9.16. If the cause cannot be identified and remedied, the sensor should be replaced.

Table 9.16 Maintenance of wind-measuring systems (updated from [9.3])

Maximum interval	Wind direction (wind vane)	Wind speed (rotation anemometer) ^a	Wind velocity and direction (sonic anemometer)
One week	Time control for digital recordings (time correction where required) Inspection of the data transmission Approximate review of the readings		
Six months	Inspection of the equipment carrier, including the sensing device and its mounting Inspection of the ambient conditions		
		Comparison of the measuring instrument with the reference instrument	
Two years	Inspection of the positioning Sensor calibration		Inspection of the zero-point drift [9.41]
If a check indicates that there is a possible malfunction, the instrument should be replaced			
^a Similar actions for thermal anemometers			

9.8 Application

Wind data are widely used in science, weather prediction, the economy, and technical applications. From an economic perspective, wind climatology is useful for mitigating the damage caused by storm events, and for providing specific forecasts for wind power stations (see Chap. 51). Several technical processes are controlled by wind measurements, such as indoor climate control. All of these examples require precise standard measurements by meteorological stations and/or specific measurements performed near the objects of interest. For many purposes like wind power, building, and construction industry, special recommendations from international and national organizations are available.

Part E of this handbook discusses several methods that require wind data as input. Table 9.17 provides an overview of these methods and the wind measurements they require.

9.8.1 Climatology of Wind Parameters

As mentioned above, mean values of wind speed and direction over climatological periods of weeks, months, and up to 30-year periods are often meaningless, especially for the wind direction. The mean wind speed and its deviation from the long-term average are used to classify the availability of wind energy for wind power applications (see Chap. 51) during a particular period. Probability graphs that show the frequency distributions of different wind speed and wind direction classes (as

shown in Fig. 9.22) are much more useful. Such a graph allows the frequency of a certain wind speed or wind direction class to be determined for a potential application or site description. A frequency distribution such as that shown in Fig. 9.22b is also often presented in polar coordinates (a plot known as a *wind rose*, see Fig. 9.23a). Indeed, the wind-speed frequency distributions for particular wind-direction classes may be plotted in a similar manner (Fig. 9.23b). Such graphs can aid the interpretation of wind data for all wind-dependent processes. They are drawn for climatological periods (30 years) but should not be used for periods of less than ten years when attempting to characterize a site. Homogeneity of instrumentation and site conditions is required. For other purposes, shorter periods are possible.

9.8.2 Geostrophic Wind: Daily and Annual Cycles

The wind field is generated by differences in the amount of solar heat received by different regions of the Earth with the consequence of high- and low-pressure areas in the atmosphere that are significantly modified near the ground and by the rotation of the Earth. Above the atmospheric boundary layer (see Chap. 1), the wind is unaffected by the Earth's surface. This wind is called the geostrophic wind, and its speed can be calculated from the pressure gradients. For a positive Coriolis pa-

Table 9.17 Wind data requirements for the measurement methods discussed in part E of this handbook (standard measurements are based on the WMO requirements [9.4])

Chapter no.	Chapter	Specific wind measurements
43	Weather Observation Stations for Different Purposes	Standard measurements
44	Crowdsourcing	All available measurements for crowdsourcing
45	Mesometeorological Networks	Standard and/or network-specific measurements
46	Aerological Measurements with Sondes	Standard measurements at the launch site
47	Vertical Composite Profiling	Standard measurements and vertical gradients at (high) towers
48	Aircraft-Based Measurements	Application of Pitot anemometers
49	Unmanned Aircraft System Measurements	Application of Pitot anemometers
50	Ground-Based Mobile Measurement Systems	Standard measurements and measurements on mobile platforms
51	Measurement Systems for Wind, Solar, and Hydro Power Applications	Standard measurements, vertical gradients at (high) towers, and measurements at wind power stations (spinners)
52	Urban Measurements and Interpretation	Standard measurements, vertical and horizontal gradients in complex terrain
54	Immision and Dry Deposition	Standard measurements, vertical gradients near the surface
55	Eddy-Covariance Measurements	Fluctuations of the wind vector and mean components
56	Alternative Surface Layer Flux Measurement Methods	Fluctuations of the wind vector and mean components
57	Evapotranspiration/Evaporation Measurements and Calculations	Standard measurements, vertical gradients near the surface, or fluctuations of the wind vector

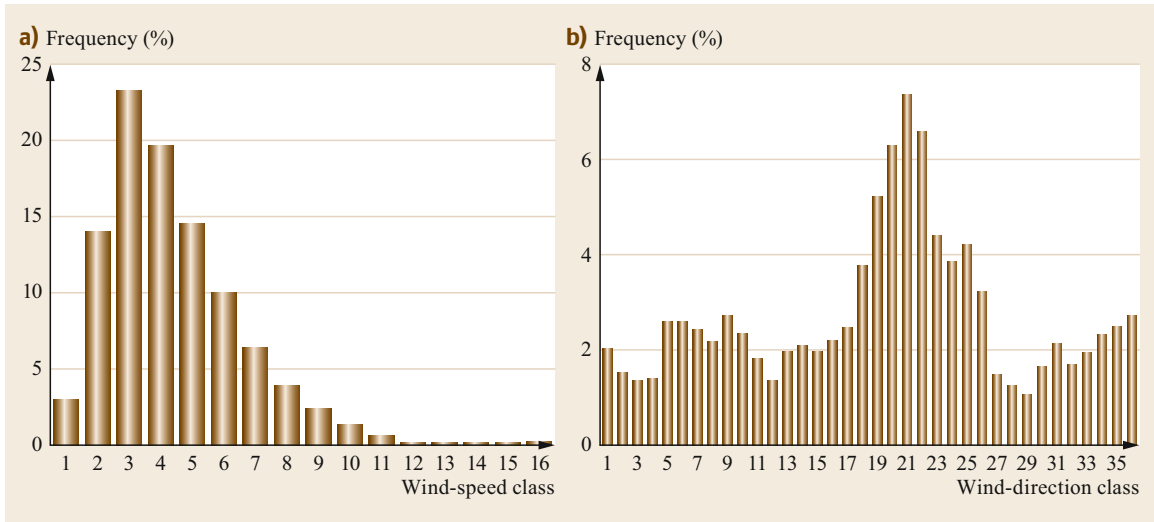


Fig. 9.22a,b Histograms showing typical frequency distributions for the wind speed (a) and the wind direction (b) (after [9.3] with permission from VDI e.V., Düsseldorf, Germany)

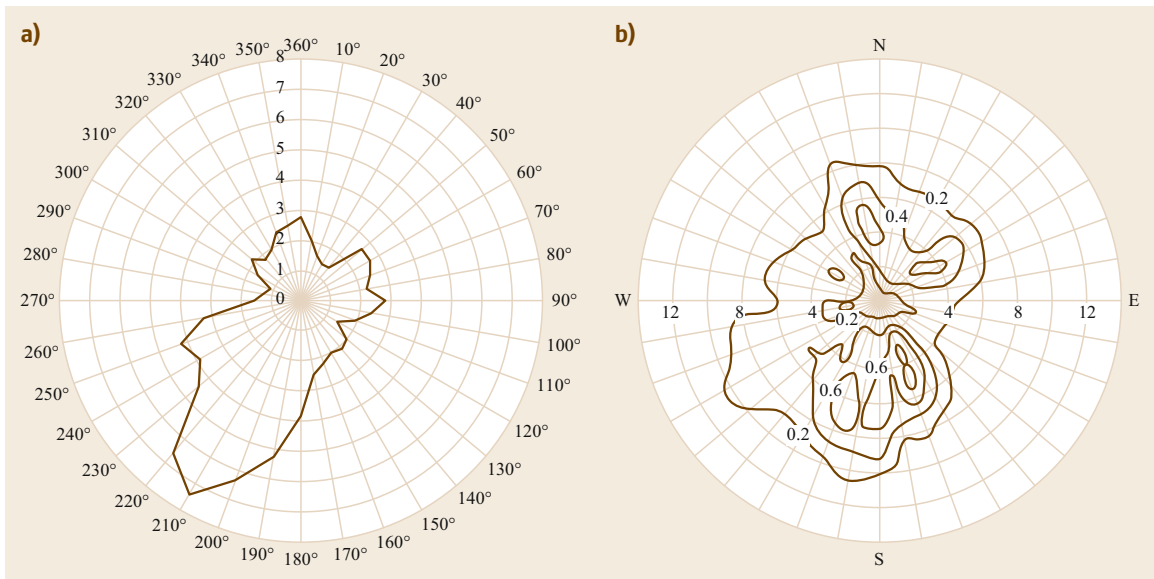


Fig. 9.23a,b Typical frequency distributions for the wind direction and wind speed plotted in polar coordinates (wind roses). Plot (a) shows the overall frequency distribution for the wind direction; the distance from the center of the plot is the relative frequency (in %) of the wind-direction class of interest. Plot (b) shows the frequency distribution (0.0–1.0) of the wind-speed as a function of the wind-direction class. Here, the distance from the center of the plot is the wind speed. In these plots, the wind direction and wind speed are split into classes 10° and 1 m s^{-1} wide, respectively (after [9.3] with permission from VDI e.V., Düsseldorf, Germany)

parameter f , the longitudinal component is

$$\overline{u}_g = -\frac{1}{\rho f} \frac{\partial p}{\partial y} \quad (9.43)$$

and the lateral component is

$$\overline{v}_g = \frac{1}{\rho f} \frac{\partial p}{\partial x}, \quad (9.44)$$

where ρ is the air density, p is the pressure, and

$$f = 2\Omega \sin \varphi, \quad (9.45)$$

in which Ω is the angular velocity of the rotation of the Earth and φ is the geographical latitude. Geostrophic wind data can also be derived from pressure observations by meteorological stations and are available in databases.

Within the atmospheric boundary layer and near the ground, the wind speed typically exhibits a daily cycle with low wind speeds at night (when there is stable stratification of the atmosphere) and high wind speeds during the day (when there are unstable and convective conditions). The opposite cycle can be observed on a mountain above the nighttime inversion (see Chap. 1): at this altitude, the wind speed is not affected by the roughness of the Earth's surface, but the wind is slowed during the daytime by thermal processes that occur near to the surface of the mountain. Both of these daily cycles are illustrated in Fig. 9.24.

The annual cycle of the wind speed depends on the climate zone considered. In the temperate zone, high wind speeds are typically seen during transition times (spring and autumn) when low-pressure areas dominate. In other climate zones, wind systems such as trade winds, the monsoon, or even the hurricane season influence the annual cycle.

9.8.3 Gusts

Gusts are sudden, brief increases in the wind speed [9.65] that are barely affected by the surface

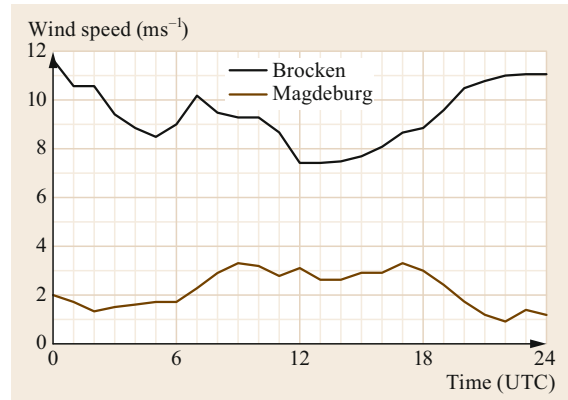


Fig. 9.24 Daily cycle of the wind speed on Brocken, an isolated mountain (1142 m ASL) in Northern Germany, and the corresponding cycle about 75 km east of Brocken in the lowlands (Magdeburg, 76 m ASL) on 5 May 2018 during a high-pressure period (data from the DWD—the German Meteorological Service)

roughness or obstacles. Gusts are reported when the peak wind speed is larger than 8 m s^{-1} , the difference between the peak and the lulls is larger than 4.5 m s^{-1} , and the duration of the peak is less than 20 s. Because gusts can potentially cause damage, it is important to record them with anemometers, which requires a measurement range that reaches up to 150 m s^{-1} and an output averaging time of 3 s [9.4]. The sampling frequency should be about 4 Hz [9.66]. The recommended accuracy is only 10% [9.4]. Gusts are the main type of wind that can affect barometric readings [9.67] (see Chap. 10). The gustiness or turbulence intensity can be calculated; for example, for the longitudinal wind component [9.65],

$$g_u = \frac{\sqrt{u'^2}}{U}, \quad (9.46)$$

where U is the magnitude (modulus) of the wind vector. The other wind components and the horizontal wind speed are defined analogously.

9.9 Future Developments

As also seen for other in-situ methods of obtaining atmospheric measurements, there has been a significant reduction in the variety of wind-measuring methods in recent decades. While hot-wire, laser, and Pitot anemometers are only applied for calibration purposes in laboratories, there has been an unmistakable shift from rotation anemometers to sonic anemome-

ters. The number of sonic anemometers available has increased significantly over the last two decades. Specially designed devices that can perform flux measurements and analyze trace gases are available (see Chap. 55), and most manufacturers of meteorological instruments offer 2-D sonic anemometers as individual devices or within compact combined instruments (see

Chap. 43). Thermal anemometers are not an alternative to sonic anemometers and are only used for a few special purposes. Even meteorological services have replaced their rotation anemometers and wind vanes with sonic anemometers, albeit only with 2-D instruments (3-D instruments would offer more possibilities, including the ability to examine the stratification of the atmosphere). Only the wind power industry still recommends the use of rotation anemometers [9.57], and it has directed effort into increasing the accuracy of these instruments (see Chap. 51). Propeller

anemometers are only used in combination with wind vanes.

We can assume that this trend will continue, meaning that sonic anemometers will be the dominant devices used to measure the wind in-situ. Improving flow distortion correction (mainly the transducer correction; see Chap. 55) and facilitating multiple data analysis of all possible measurement paths will increase data accuracy and availability. Furthermore, sensor heating is easier to achieve for sonic anemometers than for rotation anemometers.

9.10 Further Reading

- VDI: Umweltmeteorologie, Meteorologische Messungen, Wind (Environmental Meteorology, Meteorological Measurements, Wind, in German and English), VDI 3786 Blatt(Part) 2, (Beuth-Verlag, Berlin 2018)
- WMO: Guide to Instruments and Methods of Observation, WMO-No. 8, Volume I - Measurement of Meteorological Variables. (World Meteorological Organization, Geneva, 2018)
- G. R. Harrison: Meteorological Measurements and Instrumentations, (John Wiley and Sons, Chichester 2015)
- F. V. Brock, S. J. Richardson: Meteorological Measurement Systems, (Oxford University Press, New York 2001)

Acknowledgments. We acknowledge several companies for allowing the reproduction of the photographs included in this chapter.

References

- 9.1 J.C. Wyngaard: *Turbulence in the Atmosphere* (Cambridge Univ. Press, Cambridge 2010)
- 9.2 T. Foken: *Micrometeorology*, 2nd edn. (Springer, Berlin, Heidelberg 2017)
- 9.3 VDI: *Umweltmeteorologie, Meteorologische Messungen, Wind (Environmental Meteorology, Meteorological Measurements, Wind)*, VDI 3786, Blatt (Part) 2 (Beuth, Berlin 2018)
- 9.4 WMO: *Guide to Instruments and Methods of Observation*, WMO-No. 8, Volume I, Measurement of Meteorological Variables (WMO, Geneva 2018)
- 9.5 G. Hellmann: The dawn of meteorology, Q. J. R. Meteorol. Soc. **34**, 221–232 (1908)
- 9.6 W.E.K. Middleton: *Invention of the Meteorological Instruments* (The Johns Hopkins Press, Baltimore 1969)
- 9.7 E. Kleinschmidt (Ed.): *Handbuch der meteorologischen Instrumente und ihrer Auswertung* (Springer, Berlin 1935)
- 9.8 H.-G. Körber: *Vom Wetteraberglauben zur Wetterforschung* (Edition Leipzig, Leipzig 1987)
- 9.9 M. Centofanti: Egnazio Danti (1536–1586). In: *Distinguished Figures in Descriptive Geometry and Its Applications for Mechanism Science: From the Middle Ages to the 17th Century*, ed. by M. Cigola (Springer, Cham 2016) pp. 129–152
- 9.10 E. Gold: Wind in Britain: The Dines anemometer and some notable records during the last 40 years, Q. J. R. Meteorol. Soc. **62**, 167–206 (1936)
- 9.11 C.G. Herrmann: *Mechanisch verbesserter Wind-, Regen und Trockenheitsbeobachter* (Crazische Buchhandlung, Freyberg and Annaberg 1789)
- 9.12 K. Kreil: *Entwurf eines meteorologischen Beobachtungs-Systems für die österreichische Monarchie mit 15 Tafeln* (Kaiserlich-königliche Hof- und Staatsdruckerei, Wien 1850), nebst einem Anhang enthaltend die Beschreibung der an der K. K. Sternwarte zu Prag aufgestellten Autographen-Instrumente: Windfahne, Winddruckmesser, Regen- und Schneemesser
- 9.13 W.H. Dines: A new form of velocity anemometer, Q. J. R. Meteorol. Soc. **13**, 218–223 (1887)
- 9.14 T.R. Robinson: Description of an improved anemometer for registering the direction of the wind, and the space which it traverses in given intervals of time, Trans. R. Ir. Acad. **22**, 155–178 (1849)
- 9.15 C. Abbe: *The Aims and Methods of Meteorological Work*, Vol. I (Johns Hopkins Press, Baltimore 1899)
- 9.16 R.M. Schotland: The measurement of wind velocity by sonic waves, J. Meteorol. **12**, 386–390 (1955)
- 9.17 E.W. Barrett, V.E. Suomi: Preliminary report on temperature measurement by sonic means, J. Meteorol. **6**, 273–276 (1949)
- 9.18 V.E. Suomi: Sonic anemometer – University of Wisconsin. In: *Exploring the Atmosphere's First Mile*, Vol. 1, ed. by H.H. Lettau, B. Davidson (Pergamon, London, New York 1957) pp. 256–266

- 9.19 H.H. Lettau, B. Davidson (Eds.): *Exploring the Atmosphere's First Mile*, Vol. 1 (Pergamon, London, New York 1957)
- 9.20 V.M. Bovscheverov, V.P. Voronov: Akustitscheskii fljuzer (Acoustic rotor), *Izv. Akad. Nauk SSSR Geofiz.* **6**, 882–885 (1960)
- 9.21 J.C. Kaimal, J.A. Businger: A continuous wave sonic anemometer–thermometer, *J. Climate Appl. Meteorol.* **2**, 156–164 (1963)
- 9.22 Y. Mitsuta: Sonic anemometer–thermometer for general use, *J. Meteorol. Soc. Jpn.* **44**, 12–24 (1966)
- 9.23 J.C. Kaimal, J.E. Gaynor, H.A. Zimmerman, G.A. Zimmerman: Minimizing flow distortion errors in a sonic anemometer, *Bound.-Layer Meteorol.* **53**, 103–115 (1990)
- 9.24 V.M. Bovscheverov, B.M. Kaprov, M.I. Morduchovic: O trechkomponentnom akusticeskom anemometr (About a three-component acoustic anemometer), *Izv. Akad. Nauk SSSR Fiz. Atmos. Okeana* **9**, 434–437 (1972)
- 9.25 G.S. Campbell, M.H. Unsworth: An inexpensive sonic anemometer for eddy correlation, *J. Appl. Meteorol.* **18**, 1072–1077 (1979)
- 9.26 P.A. Coppin, K.J. Taylor: A three-component sonic anemometer/thermometer system for general micrometeorological research, *Bound.-Layer Meteorol.* **27**, 27–42 (1983)
- 9.27 T. Hanafusa, T. Fujitana, Y. Kobori, Y. Mitsuta: A new type sonic anemometer–thermometer for field operation, *Papers Meteorol. Geophys.* **33**, 1–19 (1982)
- 9.28 J.C. Wyngaard: The effects of probe-induced flow distortion on atmospheric turbulence measurements, *J. Appl. Meteorol.* **20**, 784–794 (1981)
- 9.29 S.F. Zhang, J.C. Wyngaard, J.A. Businger, S.P. Oncley: Response characteristics of the U.W. sonic anemometer, *J. Atmos. Ocean. Technol.* **2**, 548–558 (1986)
- 9.30 T. Foken, R. Dlugi, G. Kramm: On the determination of dry deposition and emission of gaseous compounds at the biosphere–atmosphere interface, *Meteorol. Z.* **4**, 91–118 (1995)
- 9.31 H. Pitot: Description d'une machine pour mesurer la vitesse des eaux courantes et le sillage des vaisseaux. In: *Histoire de l'Académie royale des sciences avec les mémoires de mathématique et de physique tirés des registres de cette Académie*, ed. by Académie des sciences (Imprimerie Royale, Paris 1732) pp. 363–376
- 9.32 H. Darcy: Note relative à quelques modifications à introduire dans le tube de Pitot, *Ann. Ponts Chaussées Ser. 3* **1**, 351–359 (1858)
- 9.33 H. Herwig: *Strömungsmechanik: Einführung in die Physik von technischen Strömungen* (Springer, Berlin, Heidelberg 2016)
- 9.34 ISO 17713-1: *Meteorology – Wind Measurements – Part 1: Wind Tunnel Test Methods for Rotating Anemometer Performance* (Beuth, Berlin 2007)
- 9.35 F.V. Brock, S.J. Richardson: *Meteorological Measurement Systems* (Oxford Univ. Press, New York 2001)
- 9.36 L. Kristensen: Cup anemometer behavior in turbulent environments, *J. Atmos. Ocean. Technol.* **15**, 5–17 (1998)
- 9.37 R. Drinkov: A solution to the paired gill–anemometer response function, *J. Climate Appl. Meteorol.* **11**, 76–80 (1972)
- 9.38 T. Foken, H. Kaiser, W. Rettig: *Propelleranemometer: Überblick und spezielle Entwicklungen am Meteorologischen Hauptobservatorium Potsdam*, Veröffentlichungen des Meteorologischen Dienstes der Deutschen Demokratischen Republik, Vol. 24 (Adademie-Verlag, Berlin 1983)
- 9.39 A.J. Bowen, H.W. Teunissen: Correction factors for the directional response of gill propeller anemometer, *Bound.-Layer Meteorol.* **37**, 407–413 (1986)
- 9.40 J.C. Kaimal, J.J. Finnigan: *Atmospheric Boundary Layer Flows: Their Structure and Measurement* (Oxford Univ. Press, New York 1994)
- 9.41 ISO 16622: *Meteorology – Sonic Anemometer/Thermometer – Acceptance Test Method for Mean Wind Measurements* (Beuth, Berlin 2002)
- 9.42 H. Eckelmann: *Einführung in die Strömungsmesstechnik* (Teubner, Stuttgart 1997)
- 9.43 A.-E. Albrecht, M. Borys, N. Damaschke, C. Tropea: *Laser Doppler and Phase Doppler Measurement Techniques* (Springer, Berlin, Heidelberg 2003)
- 9.44 P.B. MacCready, H.R. Jex: Response characteristics and meteorological utilization of propeller and vane wind sensors, *J. Appl. Meteorol.* **3**, 182–193 (1964)
- 9.45 J. Wieringa: Evaluation and design of wind vanes, *J. Appl. Meteorol.* **6**, 1114–1122 (1967)
- 9.46 T.P. DeFelice: *An Introduction to Meteorological Instrumentation and Measurement* (Prentice Hall, Upper Saddle River 1998)
- 9.47 P.L. Finkelstein: Measuring the dynamic performance of wind vanes, *J. Appl. Meteorol.* **20**, 588–594 (1981)
- 9.48 ISO 19289:2015: *Air Quality – Meteorology – Siting Classifications for Surface Observing Stations on Land* (WMO, Geneva 2015)
- 9.49 A.G. Davenport, C.S.B. Grimmond, T.R. Oke, J. Wieringa: Estimating the roughness of cities and sheltered country. In: *Proc. 12th Conf. App. Climatol* (American Meteorological Society, Boston, MA 2000) pp. 96–99
- 9.50 J. Wieringa: Updating the Davenport roughness classification, *J. Wind Eng. Ind. Aerodyn.* **41**, 357–368 (1992)
- 9.51 I. Troen, E. Lundtang Peterson: *European Wind Atlas* (Risø National Laboratory, Roskilde 1989)
- 9.52 E.L. Mollo-Christensen, J.R. Seesholtz: Wind tunnel measurements of the wind disturbance field of a model of the Buzzards Bay entrance light tower, *J. Geophys. Res.* **72**, 3549–3556 (2012)
- 9.53 P.A. Taylor, R.J. Lee: Simple guidelines for estimating wind speed variations due to small scale topographic features, *Climatol. Bull.* **18**, 3–22 (1984)
- 9.54 J.L. Walmsley, I. Troen, D.P. Lalas, P.J. Mason: Surface-layer flow in complex terrain: comparison of models and full-scale observations, *Bound.-Layer Meteorol.* **52**, 259–281 (1990)
- 9.55 WMO: *Meteorological Aspects of the Utilization of Wind as an Energy Source*, Techn. Note 175 (WMO, Geneva 1981)

- 9.56 M.D. Perera: Shelter behind two dimensional solit and porous fences, *J. Wind Eng. Ind. Aerodyn.* **8**, 93–104 (1981)
- 9.57 IEC 61400-12-1: *Wind Energy Generation Systems – Part 12-1: Power Performance Measurements of Electricity Producing Wind Turbines*, 2017-03, 2nd edn. (VDE, Berlin 2017)
- 9.58 F.P. Troels, N.N. Sørensen, L. Vita, P. Enevoldsen: *Optimization of Wind Turbine Operation by Use of Spinner Anemometer*, Risø-Report No. 1654, 2008) p. 45
- 9.59 S. Huq, F. De Roo, T. Foken, M. Mauder: Evaluation of probe-induced flow distortion of campbell Csat3 sonic anemometers by numerical simulation, *Bound.-Layer Meteorol.* **165**, 9–28 (2017)
- 9.60 F. Kittler, W. Eugster, T. Foken, M. Heimann, O. Kolle, M. Göckede: High-quality eddy-covariance CO₂ budgets under cold climate conditions, *J. Geophys. Res. Biogeosci.* **122**, 2064–2084 (2017)
- 9.61 J.P. Goodrich, W.C. Oechel, B. Gioli, V. Moreaux, P.C. Murphy, G. Burba, D. Zona: Impact of different eddy covariance sensors, site set-up, and maintenance on the annual balance of CO₂ and CH₄ in the harsh arctic environment, *Agric. Forest Meteorol.* **228/229**, 239–251 (2016)
- 9.62 T. Foken, S.P. Oncley: Results of the workshop instrumental and methodical problems of land surface flux measurements, *Bull. Am. Meteorol. Soc.* **76**, 1191–1193 (1995)
- 9.63 M. Mauder, C. Liebenthal, M. Göckede, J.-P. Leps, F. Beyrich, T. Foken: Processing and quality control of flux data during LITFASS-2003, *Bound.-Layer Meteorol.* **121**, 67–88 (2006)
- 9.64 A.T. DeGaetano: A quality-control routine for hourly wind observations, *J. Atmos. Ocean. Technol.* **14**, 308–317 (1997)
- 9.65 T.S. Glickman (Ed.): *Glossary of Meteorology*, 2nd edn. (Am. Meteorol. Soc., Boston, MA 2000)
- 9.66 J. Wieringa: Representativeness of wind observations at airports, *Bull. Am. Meteorol. Soc.* **61**, 962–971 (1980)
- 9.67 H. Liu, G.L. Darkow: Wind effect on measured atmospheric pressure, *J. Atmos. Ocean. Technol.* **6**, 5–12 (1989)

Thomas Foken

University of Bayreuth
Bayreuth, Germany
thomas.foken@uni-bayreuth.de



Thomas Foken is a retired Professor of Micrometeorology at the University of Bayreuth. He was the head of Laboratories at the meteorological observatories at Potsdam (1981–1994) and Lindenberg (1994–1997). His research interests include the interaction between the Earth's surface and the atmosphere and the measurement and modeling of energy and matter fluxes, with a strong focus on experimental meteorology. His scientific contributions have been recognized through various international awards.

Jens Bange

Centre for Applied Geo-Science
University of Tübingen
Tübingen, Germany
jens.bange@uni-tuebingen.de



Jens Bange is a Professor for Environmental Physics at the University of Tübingen since 2010. He received a PhD in meteorology in 1998 and a diploma in physics in 1992 at the University of Hannover. His research interests include atmospheric turbulence, boundary-layer meteorology, wind-energy research, airborne meteorology, and environmental measurement technology. He is a founding member of the research networks ISARRA and WindForS.

Pressure Sensors

10. Pressure Sensors

Anni Torri, Thomas Foken , Jens Bange 

For measurements of the pressure of the atmosphere, the different techniques in use include liquid barometers, aneroid barometers, and electronic barometers. The history and theory of all these methods is described. Electronic sensors, such as piezoresistive pressure sensors, capacitive pressure sensors, and resonant pressure sensors have recently become the most used devices. Some types are also applicable for turbulence measurements. Besides technical data, the necessary maintenance associated with different methods, as well as the methods of quality control and calibration, are presented.

10.1	Measurement Principles and Parameters	274	10.3.2	Corrections	279
10.1.1	Pressure Units and Quantities.....	274	10.3.3	Liquid Barometers.....	279
10.1.2	Principles of Measurements.....	274	10.3.4	Aneroid Barometers.....	280
10.1.3	Site Considerations.....	274	10.3.5	Hypsometer	281
10.2	History	275	10.3.6	Electronic Barometers	281
10.2.1	Liquid Barometers.....	275	10.4	Devices and Systems	283
10.2.2	Aneroid Barometer	275	10.4.1	Liquid Barometers.....	283
10.2.3	Hypsometer	277	10.4.2	Aneroid Barometers.....	285
10.2.4	Electronic Barometers.....	277	10.4.3	Hypsometer	286
10.2.5	Historically Relevant Pressure Units....	278	10.4.4	Electronic Barometers	286
10.3	Theory	278	10.4.5	Piston Gauge	289
10.3.1	Static and Dynamic Pressure.....	278	10.4.6	Comparison of the Methods	290
			10.5	Specifications	290
			10.6	Quality Control	291
			10.6.1	Reference Barometer	291
			10.6.2	Calibration.....	291
			10.6.3	Comparison with a Reference Barometer	291
			10.6.4	Specific Quality Control Methods	292
			10.7	Maintenance	292
			10.8	Application	292
			10.8.1	Meteorology and Climatology	292
			10.8.2	Pressure Measurements for Aircrafts ...	293
			10.9	Future Developments	293
			10.10	Further Reading	294
			References		294

Pressure is probably the most important meteorological variable because pressure information is necessary for weather prediction and the determination of mean circulation patterns in climatology. The beginning of meteorological measurements is also connected to the first barometer constructed in 1643 by *Torricelli*. However, pressure measurements are also necessary for a wide range of measurement instruments, because many phys-

ical parameters are pressure dependent. Besides the pressure at a certain time and place, the reduced pressure at sea level [10.1] (extrapolated to sea level) is important for regional comparisons. In recent times, classical instruments like liquid mercury barometers—because of regulations for the use of the toxic substance mercury—and aneroid barometers have been widely replaced by electronic instruments.

10.1 Measurement Principles and Parameters

While the hectopascal is the accepted unit for atmospheric pressure in the SI system, other units are still in use, and the number of measurement principles is quite large for this standard parameter in meteorology.

10.1.1 Pressure Units and Quantities

Pressure measurement instruments, in general, measure absolute, gauge, and differential pressure. In meteorology, atmospheric pressure is the most important pressure quantity. Atmospheric pressure is an absolute pressure: the weight of atmosphere per area at a certain time and place. The other pressure measure used in meteorology is pressure trend (Table 10.1). Pressure trend describes the amount of change in pressure over certain time period.

Atmospheric pressure is closely related to altitude in the atmosphere. There are pressure-related calculated parameters used in aviation to describe the height related to a reference level or sea level in pressure, such as HCP (height corrected pressure) or QNH (atmospheric pressure adjusted to sea level).

Independent from the principle of measurement, the pressure (symbol p) is recalculated in meteorology mainly in hectopascals. The International System of Units (SI) unit for pressure is pascal (Pa) or N m^{-2} (Chap. 5). In meteorology, the prefix *hecto* is accepted, with the pressure being given in hectopascals (1 hPa = 100 Pa). This is largely because one hectopascal equals one millibar (mbar), the formerly used unit [10.1]. In some Anglo-American countries, the kilopascal (1 kPa = 1000 Pa = 10 hPa) is also used. Older scales of barometers are graduated in millimeters or inches of mercury under standard conditions ($(\text{mm Hg})_n$ or $(\text{in Hg})_n$), often reduced to millimeter mercury or inch mercury. Standard conditions are 1013.250 hPa, 0.0 °C, and a gravitational acceleration of 9.80620 m s^{-2} [10.2], for which the column of mercury has a height of 760 $(\text{mm Hg})_n$. The units still in use are given in Table 10.2.

10.1.2 Principles of Measurements

There are many kinds of barometers, all of which measure the same quantity, namely atmospheric pressure, but in different ways. Most pressure sensors trans-

form mechanical input to a measure of pressure. This involves either a movement of a film or change in vibration or level of a liquid. The form of the output signal leads us to divide pressure sensors into several groups, as listed in Table 10.3.

10.1.3 Site Considerations

Pressure measurements are typically made indoors or in dry cabinets or enclosures. Influencing factors on the instruments, like radiation, temperature, wind, vibration, must be excluded according to the particular type of instrument. The exact height above sea level of the sensor must be determined.

Table 10.1 Measured parameters of pressure sensors

Parameter	Description	Unit	Symbol
Pressure	Atmospheric pressure on a given surface	hPa	p
Pressure trend or pressure difference	Pressure tendency of trend is the amount of atmospheric pressure change for a 3 h or other specified period ending at the time of observation	hPa per time unit	$\Delta p, p3h$

Table 10.2 Transformation of pressure units (only pascal is a valid SI unit) [10.1]

Unit	hPa	kPa	$(\text{mm Hg})_n$	$(\text{in Hg})_n$
hPa	1	10	1.333224	33.863867
kPa	0.1	1	0.1333224	3.3863867
$(\text{mm Hg})_n$	0.750062	7.50062	1	25.4
$(\text{in Hg})_n$	0.029530	0.29530	0.03937008	1

Table 10.3 Principles of pressure measurements and applications for pressure and pressure tendency

Measuring device	Method			Application	
	Mechanical	Thermal	Electrical	p	Δp
Mercury barometer	×			×	×
Hypsometer		×		×	(×)
Resonator	×			×	×
Aneroid	×			×	×
Electronic	×		×	×	×

10.2 History

The first instruments to measure the atmospheric pressure, dating back to the sixteenth century, were mainly liquid barometers. In the seventeenth century, aneroid barometers and pressure hypsometers followed, while electronic barometers are developments of the twentieth century.

10.2.1 Liquid Barometers

The principle of the liquid barometer has been known since ancient times even though the reason for different levels of a liquid in a cistern with two limbs, where one limb was closed, could not be explained. These instruments are known as weatherglasses or Goethe barometers (Fig. 10.1), and are still available as objects of art for decoration.

Systematic investigations with water and mercury began in the sixteenth century [10.3–5], but at that time problems arose because the existence of the vacuum and the weight of air were unknown. Under the influence of *Galileo Galilei* (1564–1642) at the beginning of the seventeenth century, *Gasparo Berti* (about 1600–1643) and *Raffaello Magiotti* (1597–1656), working in Rome, built a water barometer with a water cistern on the ground and a 10 m long vertical tube with taps at both ends. The tube was filled with water and the upper tap was closed. After opening of the tap near the cistern, the development of a vacuum in the upper part of the tube was observed. Successful experiments with mercury were carried out by *Evangelista Torricelli* (1608–1647), and in about 1643/1644, he developed the

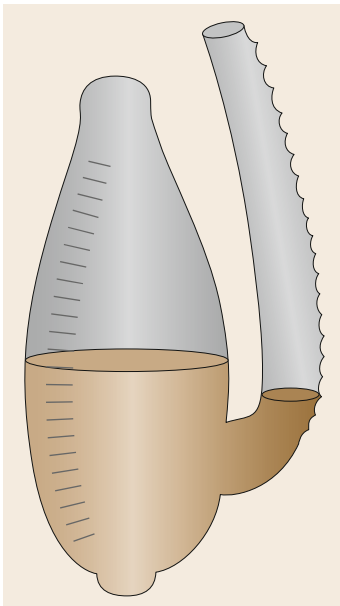


Fig. 10.1 The weatherglass or Goethe barometer. Above the liquid in the cistern of the instrument shown is a gas with a pressure lower than the ambient pressure

mercury barometer. *René Descartes* (1596–1650) and *Blaise Pascal* (1623–1662) assumed that the pressure decreases with increasing altitude. On September 19, 1648, *Florin Périer* (1605–1672) showed this on an ascent of the Puy de Dôme (1465 m). Later, *Robert Boyle* (1627–1691) and *Robert Hooke* (1635–1703) found that the air pressure change is associated with a change of weather phenomena.

Torricelli's experiments with different evacuated tubes at different inclinations showed that the height of the mercury column above the level in the cistern is independent of the form of the tube, which is called the hydrostatic paradox. Immediately after his experiments, different designs of barometers were built [10.5] aiming at a better resolution of the indication scale; *Samuel Morland* (1625–1695) built a barometer with an 88.5° inclined tube to attain a 2.75 m scale length. Hooke combined the open limb of the U-tube with a float and a pointer hand (Fig. 10.2a) in 1665. *Jean Hyacinthe de Magellan* (1723–1790), and possibly Morland some time earlier, made significant changes to a scale barograph (Fig. 10.2b), whereby the weight of the mercury in the tube above the level in the cistern was determined. In addition, two-liquid (e.g., Descartes) and three-liquid (e.g., Hooke) barometers were proposed. Both scientists used, instead of mercury, another less heavy liquid above the mercury level in the part of the tube at the scale. A special type with two liquids is the short tube barometer according to *Guillaume Amontons* (1663–1705) built in 1688 (Fig. 10.2c). An improvement of all barometer types was the so-called *Bunten's* tip (Fig. 10.3) developed in Paris in 1828, which is still in use. An air trap above the tip collects any air that has entered the barometer and prevents it from reducing the vacuum.

Two types of the mercury barometers with cisterns were in use until recent times. The so-called Kew-pattern barometer, designed about 1850 by *John Welsh* (1824–1859), has a fixed cistern, and the barometer scale is constructed so that it allows changes of the level of mercury in the cistern [10.6]. More popular is the Fortin barometer (*Jean Nicholas Fortin*, 1750–1831), where the level of the mercury in the cistern can be adjusted with an ivory pointer [10.4] (Sects. 10.3.3 and 10.4.1).

10.2.2 Aneroid Barometer

In a letter to *Johann Bernoulli* (1667–1748), in 1698, *Gottfried Wilhelm Leibniz* (1646–1716) discussed his idea of using an evacuated box to measure the pressure as a replacement for the not easy to use Torricelli barometer [10.4, 7]. After several unsuccessful developments, such as the marine barometer in 1763 by *Johann Ernst Zeiher* (1725–1784), it was not until

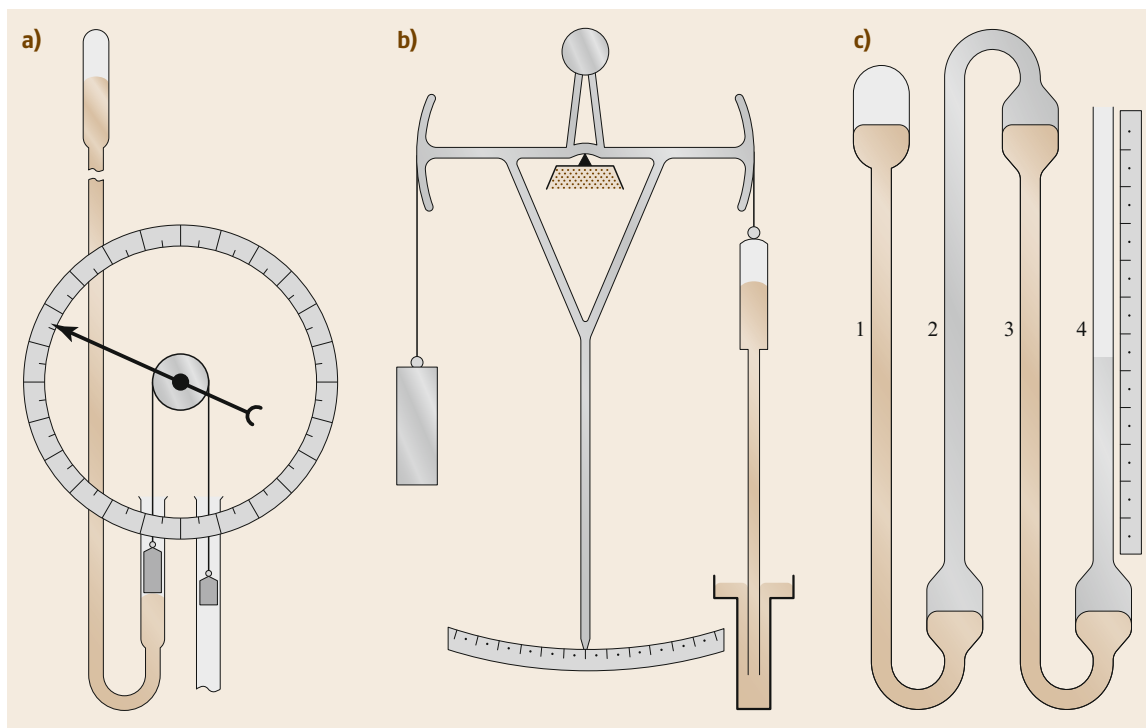


Fig. 10.2a–c Different functional principles of the mercury barometer (after [10.5] with permission from R. Holland): (a) barometer using a hand indicator (R. Hooke); (b) scale barometer (J.H. de Magellan); (c) two-liquid barometer with reduced tube length (G. Amontons); mercury is in tubes 1 and 3 and the lower parts of types 2 and 4; the other liquid has a much lower weight

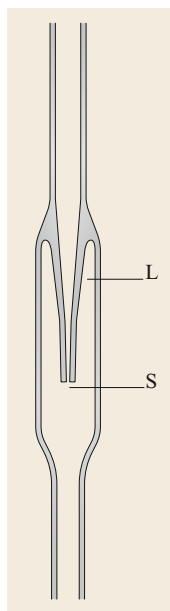


Fig. 10.3 Bunten's tip (after [10.5] with permission of R. Holland (L: air trap, S: tip))

1844 that *Lucien Vidie* (1805–1866) constructed the first aneroid barometer, which was patented in the same year in London and Paris. He used a strong evacuated brass chamber with a corrugated diaphragm. The force against the air pressure was achieved with 33 helical springs. In a later French patent (1845), he used an external spring; one of the first instruments is shown in Fig. 10.4. In a patent of 1858, he used a split C-form leaf spring. Both systems are still in use (Sect. 10.3.4).

At nearly the same time, *Eugène Bourdon* (1806–1884) used an evacuated curved type tube with an elliptical cross section, which was patented in France in 1849 and is called the Bourdon tube. The instrument is rarely used in meteorology except for balloon soundings and calibration, but it is still the basis for manometers. After a 10-year legal struggle, Vidie was finally accepted as the inventor of the aneroid barometer and could use the name for his instrument (1858). Both instruments were shown at the world exhibition of 1851 in London.

Two changes were made in the second half of the nineteenth century. First, the use of a spiral spring inside an evacuated brass box to provide a force against the atmospheric pressure was developed by *Antoine Redler* (1817–1892), who built the first instruments for

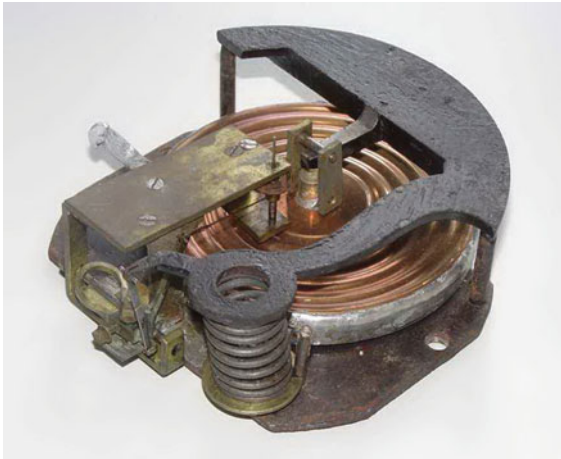


Fig. 10.4 View of the first Vidie barometer with external spring (1845) (photo © R. Holland)

Vidie, and second, a bimetal spring for temperature correction was introduced by *Otto Bohne* in 1863 in Berlin.

10.2.3 Hypsometer

The hypsometer was one of *Alexander Humboldt's* (1769–1859) instruments during his expedition to Latin America (1799–1804) [10.8] and uses the dependence of the boiling point of water on the pressure. Less is reported about this instrument in textbooks of the history of meteorology. A short history and full description was found in [10.9]. The first description of thermometers used for measurement of the boiling point of water and, therefore, the air pressure came from *Daniel Gabriel Fahrenheit* (1686–1736) in 1724 [10.11] and *Tiberius Cavallo* (1749–1809) in 1781 [10.12]. After the first theory of evaporation by *John Dalton* (1766–1844) in 1810, *Francis John Hyde Wollaston* (1762–1823) improved the instrument in 1817 [10.13]. The temperature measurement was no longer made in boiling water but in the water steam above it, and a reservoir was included in the thermometer capillary to enlarge the scale within

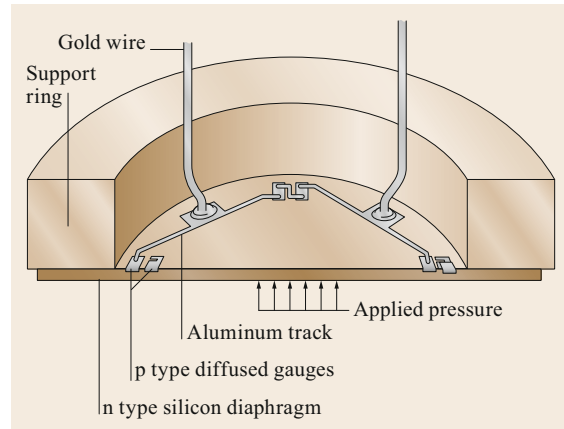


Fig. 10.5 A cross-sectional view of a silicon pressure sensor from the early 1970s (after [10.10] with permission from Emerald Publishing Limited). Note the planar (non-microengineered) diaphragm mounted on the support ring and the diffused rather than implanted *gauges* (piezoresistors)

the relevant temperature range. However, the theory behind the hypsometer was founded in 1834 by *Émile Clapeyron* (1799–1864). Hypsometers were used for pressure measurements during balloon expeditions and as pressure sensors in radiosondes [10.14] up to the end of the last century but are now no longer used [10.1].

10.2.4 Electronic Barometers

The transition from mercury barometers and aneroids to electronic barometers started with the combination of metal aneroids with an electronic measurement circuit. The reading of an indicator by the human eye or the print on a barograph were replaced by an electronic output connected to a computer or a digital display in the next step.

In the 1960s, silicon technology enabled the development of silicon pressure sensors. Earlier, the effect of piezoresistance in silicon was discovered in 1954 by

Table 10.4 Selected historical length scales for pressure measurements [10.5]

Country	Period of time in use	Name	Length (cm)	Scale divider	Name	Length (mm)	Scale divider
France	up to 1840	Pied de Roi	32.433940	12	Pouce	27.070	12
Great Britain		Foot	30.479726	12	Inch	25.400	10
Germany, e.g.,							
– Baden	1810–1871	Badischer Fuß	30.000000	10	Zoll	30.000	10
– Bavaria	1806–1871	Bayerischer Fuß	29.185920	12	Zoll	24.322	12
– Prussia	1772–1871	Rheinländ. Fuß	31.385346	12	Zoll	26.154	12
– Saxony	1772–1871	Sächsischer Fuß	28.265500	12	Zoll	23.555	12
The Netherlands	up to 1820	Voet	28.307692	11	Duimen	25.734	11
Austria	1814–1871	Wiener Fuß	31.608067	12	Zoll	26.340	12
Switzerland	up to 1877	Schweizer Fuß	30.000000	10	Zoll	30.000	10
Unit in astronomy		Pied	33.077810	12	Pouce	27.565	12

C.S. Smith [10.15]. This was the starting point of the development work to replace bulky electromechanical sensors with MEMS (microelectromechanical system) sensors [10.16, 17]. Figure 10.5 shows one of the first piezoresistive silicon MEMS sensors.

In the early days, thin silicon diaphragms were first manufactured by drilling and later—in the 1970s—by anisotropic etching of silicon [10.18]. Anisotropic etching enabled the development of silicon capacitive sensors in the late 1970s [10.19, 20].

10.3 Theory

After some basics about static and dynamic pressure and the pressure correction at sea level follows the theory of all relevant measurements methods.

10.3.1 Static and Dynamic Pressure

The basis for the understanding of the static and the dynamic pressure of a flow (e.g., the atmosphere) is the Euler momentum conservation equation [10.21–23] for an adiabatic and inviscid flow with velocity \mathbf{u} and the time t

$$\begin{aligned} \frac{d\mathbf{u}}{dt} &= \frac{\partial \mathbf{u}}{\partial t} + (\mathbf{u}\nabla)\mathbf{u} \\ &= -\text{grad } \Phi - \frac{1}{\rho} \text{grad } p = 0. \end{aligned} \quad (10.1)$$

In a length scale regime of in-situ measurements, the influence of the Earth's rotation can usually be neglected. This is why (10.1) does not contain the Coriolis force but only the air density ρ and gradients of pressure p and geopotential Φ . Since turbulence and any fast changes at any fixed location are excluded in the experimental setup, stationarity ($\partial \mathbf{u} / \partial t = 0$) can be assumed, leaving only the advection term on the left-hand side of (10.1)

$$(\mathbf{u}\nabla)\mathbf{u} = -\text{grad } \Phi - \frac{1}{\rho} \text{grad } p. \quad (10.2)$$

Applying the Weber transformation [10.24]

$$\text{grad } |\mathbf{u}|^2 = 2(\mathbf{u}\nabla)\mathbf{u} + 2\mathbf{u} \times (\text{rot } \mathbf{u}) \quad (10.3)$$

and assuming that the flow is not rotating ($\text{rot } \mathbf{u} = 0$) the Eulerian equation (10.1) transforms to

$$\begin{aligned} (\mathbf{u}\nabla)\mathbf{u} &= \frac{1}{2} \text{grad } |\mathbf{u}|^2 \\ &= -\text{grad } \Phi - \frac{1}{\rho} \text{grad } p. \end{aligned} \quad (10.4)$$

10.2.5 Historically Relevant Pressure Units

Because of different length scales in different countries, pressure measurements were not comparable before the metric system was applied in most countries in the nineteenth century. The inch is still in use in only some Anglo-American countries (Table 10.2). A selection of historically relevant length scales—which were used for barometer scales—is given in Table 10.4.

Finally, assuming a divergence-free, i.e., incompressible flow (sound waves are neglected), the nabla operator can be pulled out

$$\text{grad} \left(\frac{|\mathbf{u}|^2}{2} + \frac{p}{\rho} + \Phi \right) = 0. \quad (10.5)$$

Integration in space provides the commonly known Bernoulli equation [10.23]

$$\rho \frac{|\mathbf{u}|^2}{2} + p + \rho \Phi = \text{const}. \quad (10.6)$$

Bernoulli's equation (10.6) shows that kinetic (first term) and potential (second and third term) energy are in balance. That is, in an incompressible and non-rotating stationary flow, at each location (here locations 1 and 2) the sum of potential and kinetic energy must be the same

$$\rho \frac{|\mathbf{u}_1|^2}{2} + p_1 = \rho \frac{|\mathbf{u}_2|^2}{2} + p_2, \quad (10.7)$$

and if the measurement situation position 1 is not too far away from position 2, so that the geopotential Φ is the same at both locations and disappears in (10.7). A pitot tube (also known as a Prandtl tube [10.24], see Chap. 9), measures the total p_{stag} in a bore hole at the tip (stagnation point) of a tube pointing directly into the fluid flow with velocity \mathbf{u} . At the tip the velocity is, of course, zero. Thus, (10.7) becomes

$$p_{\text{stag}} = \rho \frac{|\mathbf{u}|^2}{2} + p_s. \quad (10.8)$$

i.e., the pressure p_{stag} at the stagnation point is the sum of both kinetic and potential energy, with the latter expressed by the static air pressure p_s .

Now, a pitot-static tube has an additional bore hole along the tube, where the flow is assumed to be undisturbed, and the static air pressure p_s can be expected.

The pressure difference between the tip and this static port is identical to the dynamic pressure enhancement

$$p_q = p_{\text{stag}} - p_s = \rho \frac{|\mathbf{u}|^2}{2} \quad (10.9)$$

and can be used to calculate the fluid velocity $|\mathbf{u}|$ for given air density ρ (Chaps. 9, 48, and 49).

However, any instrument assigned to measure the static air pressure only has to make sure that no dynamic pressure enhancement p_q disturbs the measurements. That is, at the position of any static-pressure sensor the component of the flow velocity \mathbf{u} perpendicular to the sensor has to be insignificant (see also the principle of a static head in Sect. 10.3.2).

10.3.2 Corrections

A comparison of pressure measurements from different locations with different altitudes requires that they are reduced to sea level. Furthermore, the possible influence of the wind velocity must be corrected or excluded.

Reduction of the Pressure to Sea Level

The air pressure is a function of the height and the temperature given by the hydrostatic equation [10.21, 22]

$$dp = -g\rho dz, \quad (10.10)$$

with the pressure p in Pa, the height z in m, the gravity acceleration g in m s^{-2} , and the air density ρ in kg m^{-3} . The latter is given by the gas equation

$$\rho = \frac{p}{R_d T_v}, \quad (10.11)$$

where R_d is the gas constant of dry air ($287.059 \text{ J kg}^{-1} \text{ K}^{-1}$) and T_v the virtual temperature in K (Chap. 7). Because of the dependence of the temperature and gravity acceleration on height, a standard gravity acceleration (Chap. 5; for pressure correction $g_0 = 9.80620 \text{ m s}^{-2}$ is recommended [10.1, 2]) and a mean virtual temperature are applied. Instead of the height in m, the geopotential height Z is used ((1.11); see Chaps. 1 and 5; below 1500 m the difference between the geometric height, and the geopotential height is $< 1 \text{ m}$ [10.25]). From the integration of (10.10), it follows that ((1.12))

$$p_0 = p_s \exp \frac{g_0 Z_s}{R_d T_{\text{mv}}}, \quad (10.12)$$

with the pressure at sea level p_0 in hPa, the pressure at the station level p_s in hPa, the height of the station above

sea level Z_s in gpm ($1 \text{ gpm} = 9.8 \text{ m}^2 \text{ s}^{-2}$), and the constant (in practice, the mean is used) virtual temperature of a column from the sea to the station level T_{mv} in K, which can be calculated as [10.1]

$$T_{\text{mv}} = T_s + \frac{aZ_s}{2} + cE_s, \quad (10.13)$$

with the temperature at the station T_s in K, the water vapor pressure of saturation at the station E_s in hPa, and the mean gradients $a = 0.0065 \text{ K gpm}^{-1}$ and $c = 0.12 \text{ K hPa}^{-1}$. A factor for the reduction of the pressure to sea level is given in Table 10.5.

For heights below 50 m, the pressure correction can be done with a constant value [10.1]

$$p_0 = p_s \left(1 + \frac{Z_s}{29.17 T_{\text{mv}}^*} \right), \quad (10.14)$$

where T_{mv}^* is the mean annual normal value of the virtual temperature at the station in K.

The pressure reduction according to the standard atmosphere [10.25] uses a temperature at sea level of 15°C .

Wind Correction

The air flow around buildings or the housing of the barometer can, according to the Bernoulli equation, generate pressure fluctuation [10.26, 27], e.g., 0.4 hPa for a wind velocity of 8 m s^{-1} [10.27] or 5 hPa for a wind velocity of 45 m s^{-1} [10.26] are reported in the literature. This can be corrected by sampling with a static head [10.28], shown in Fig. 10.6. Aneroid and electronic barometers can simply be connected to a static head, which should be located in an open environment not affected by buildings, etc. For measurement of the turbulent pressure fluctuations, static heads are required [10.29]. Static heads are commercially available, but comparisons are still an outstanding issue [10.1].

10.3.3 Liquid Barometers

The physical basis of liquid barometers is the hydrostatic equation (see, also (10.10))

$$\Delta p = \rho g \Delta h, \quad (10.15)$$

where h is the height of the liquid column. According to (10.11), the density is a function of the temperature, see Chap. 5. Therefore, temperature and gravity corrections are necessary. In order to obtain acceptable column heights (less than 1 m) for the pressure difference between vacuum and normal pressure at sea level, mercury was selected as a liquid due to its high density ($1.35951 \times 10^4 \text{ kg m}^{-3}$ at 0°C [10.1]). Instead

Table 10.5 Factor for the pressure reduction to sea level according to (10.12); the geopotential height is identical with the geometric height in m with an error lower 1 m

Geopotential height in gpm	Mean virtual temperature between sea level and geopotential height in °C								
	-30	-20	-10	0	10	20	30	40	50
0	1.0000	1.0000	1.0000	1.0000	1.0000	1.0000	1.0000	1.0000	1.0000
50	1.0070	1.0068	1.0065	1.0063	1.0061	1.0058	1.0057	1.0055	1.0053
100	1.0141	1.0136	1.0131	1.0126	1.0121	1.0117	1.0113	1.0110	1.0106
150	1.0213	1.0204	1.0197	1.0189	1.0183	1.0176	1.0170	1.0165	1.0160
200	1.0285	1.0274	1.0263	1.0253	1.0244	1.0236	1.0228	1.0221	1.0214
250	1.0357	1.0343	1.0330	1.0318	1.0306	1.0296	1.0286	1.0276	1.0268
300	1.0431	1.0413	1.0397	1.0382	1.0369	1.0356	1.0344	1.0333	1.0322
350	1.0504	1.0484	1.0465	1.0447	1.0431	1.0416	1.0402	1.0389	1.0377
400	1.0578	1.0555	1.0533	1.0513	1.0494	1.0477	1.0461	1.0446	1.0432
450	1.0653	1.0626	1.0602	1.0579	1.0558	1.0538	1.0520	1.0503	1.0487
500	1.0728	1.0698	1.0671	1.0645	1.0622	1.0600	1.0580	1.0561	1.0543
550	1.0803	1.0770	1.0740	1.0712	1.0686	1.0662	1.0639	1.0618	1.0599
600	1.0880	1.0843	1.0810	1.0779	1.0751	1.0724	1.0700	1.0676	1.0655
650	1.0956	1.0917	1.0880	1.0847	1.0816	1.0787	1.0760	1.0735	1.0711
700	1.1033	1.0991	1.0951	1.0915	1.0881	1.0850	1.0821	1.0794	1.0768
750	1.1111	1.1065	1.1023	1.0983	1.0947	1.0913	1.0882	1.0853	1.0825
800	1.1190	1.1140	1.1094	1.1052	1.1013	1.0977	1.0943	1.0912	1.0883
850	1.1268	1.1215	1.1167	1.1122	1.1080	1.1041	1.1005	1.0972	1.0940
900	1.1348	1.1291	1.1239	1.1191	1.1147	1.1106	1.1067	1.1032	1.0998
950	1.1428	1.1368	1.1313	1.1262	1.1214	1.1171	1.1130	1.1092	1.1056
1000	1.1508	1.1445	1.1386	1.1332	1.1282	1.1236	1.1193	1.1153	1.1115
1050	1.1590	1.1522	1.1460	1.1403	1.1351	1.1302	1.1256	1.1214	1.1174
1100	1.1671	1.1600	1.1535	1.1475	1.1419	1.1368	1.1320	1.1275	1.1233
1150	1.1754	1.1679	1.1610	1.1547	1.1488	1.1434	1.1384	1.1337	1.1293
1200	1.1836	1.1758	1.1686	1.1619	1.1558	1.1501	1.1448	1.1399	1.1353
1250	1.1920	1.1837	1.1762	1.1692	1.1628	1.1568	1.1513	1.1461	1.1413
1300	1.2004	1.1918	1.1838	1.1766	1.1698	1.1636	1.1578	1.1524	1.1473
1350	1.2089	1.1998	1.1916	1.1839	1.1769	1.1704	1.1643	1.1587	1.1534
1400	1.2174	1.2080	1.1993	1.1914	1.1840	1.1772	1.1709	1.1650	1.1595
1450	1.2260	1.2161	1.2071	1.1988	1.1912	1.1841	1.1775	1.1714	1.1657
1500	1.2346	1.2244	1.2150	1.2064	1.1984	1.1910	1.1842	1.1778	1.1718

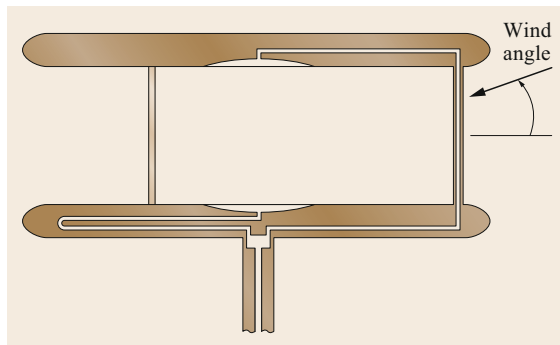


Fig. 10.6 Schema of a static pressure probe (static head) (after [10.28] with permission of the American Meteorological Organization)

of U-tubes, systems with a large cistern for the liquid under ambient pressure and a thin tube with vacuum are applied (Fig. 10.7a). The air pressure balances the

weight of mercury in the tube, which is equal to the weight of the air column. The expansion or contraction of tubes and mercury due to temperature changes and gravity must be corrected (Sect. 10.4.1).

Because the pressure is proportional to the height of the mercury in the tube between the upper level in the tube and in the cistern, a fixed scale is not practicable. Therefore, barometers with a movable scale of the Kew-pattern barometer type and with a fixed scale and an index of the Fortin barometer type are in use (Fig. 10.7b). The latter has an adjusting screw that moves a membrane so that the upper level of the mercury in the cistern is always at the same height.

10.3.4 Aneroid Barometers

The aneroid barometer has remained nearly unchanged since the middle of the nineteenth century, except for the use of new material and small modifications.

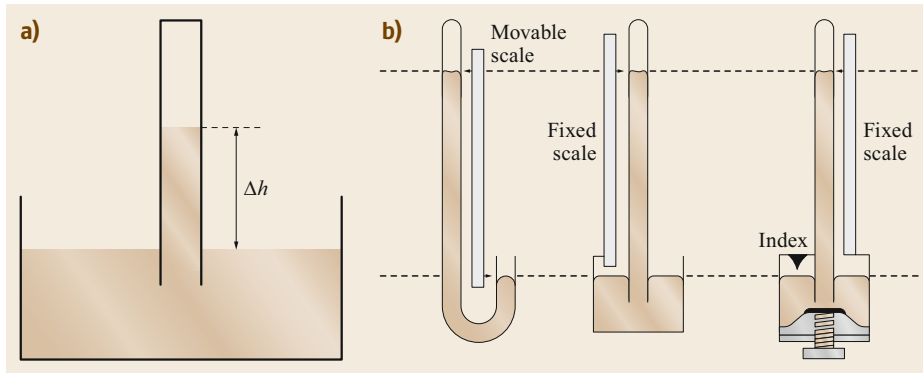


Fig. 10.7a,b Principle of a liquid barometer (a) and barometer scales (b) (after [10.30] with permission from VDI e. V. Düsseldorf, Germany)

A theoretical equation for the calibration of an aneroid barometer is [10.31, 32]

$$p = \frac{16Et^4}{3R^4(1-\nu^2)} \left[\frac{y}{t} + 0.488 \left(\frac{y}{t} \right)^3 \right], \quad (10.16)$$

with the pressure p in Pa, the modulus of elasticity E in N m^{-2} , the deflection of the diaphragm center y in m, the diaphragm thickness t in m, the diaphragm radius R in m, and Poisson's ratio ν , which for metals is $1/3$. The deflection ratio y/t of the diaphragm is a linear function of the pressure in the case of a coated diaphragm, or a curved line for a flat-plane diaphragm.

Mainly two mechanical systems are employed [10.33], which are shown in Fig. 10.8: first the system with the external spring (Vidie, 1845) and secondly an instrument with a split C-form leaf spring (Vidie, 1858). The screw is necessary to reduce the pressure to sea level and for calibration.

10.3.5 Hypsometer

The theory of the hypsometer is based on the Clausius–Claperyon equation [10.21, 22], see Chap. 8, even though the instrument was developed earlier

$$e(T) = e_0 \exp \left(\frac{\lambda_w}{R_w T_0} \frac{T - T_0}{T} \right), \quad (10.17)$$

with the water vapor pressure e at the temperature T , the water vapor pressure e_0 at the temperature $T_0 = 273.15 \text{ K}$ (6.112 hPa), the heat of evaporation λ_w , and the gas constant of water vapor R_w , see Chap. 5. It is evident that the hypsometric method is one of the most direct methods of pressure measurements, not requiring any further corrections. For the calculation of the altitude from the pressure measurements, the barometric equation should be used (Sect. 10.3.2).

10.3.6 Electronic Barometers

Electronic barometers convert ambient pressure to an electrical signal. Electronic pressure sensors are available over a wide pressure range from vacuum pressure sensors to heavy industry pressure measurement needs. The variety of the different kinds of electronic pressure sensors is also large. In this section, only barometric sensors and three different pressure measurement methods are discussed more in detail: piezoresistive, capacitive, and resonant sensors.

Piezoresistance

The effect of piezoresistance is similar to the strain gauge effect in a metal material, but there is a fundamental difference: the metal strain gauge effect is caused by geometric deformation of the resistor, whereas the piezoresistance is caused by the change of resistivity of the material. In addition, piezoresistivity is, in general, anisotropic and is typically two orders of magnitude larger [10.34].

In the fabrication of piezoresistive sensor chips of silicon, micromachining technologies are used. Micromachining—referring to the dimensions of the mechanical structures processed—can be controlled to an accuracy of microns. The piezoresistive sensor contains a silicon chip with a thin square, rectangular, or circular diaphragm and four piezoresistors [10.35]. Pressure causes the diaphragm to flex, inducing a stress on the diaphragm and also on buried piezoresistors. The resistors are located near the edge center of the bending film, where the maximum stress occurs.

The change in pressure (mechanical input) is converted to a change in resistance (electrical output). The thickness of the film is chosen to match the required pressure sensor range.

The sensor's resistors can be connected in a Wheatstone bridge configuration or a four-terminal structure. These circuits are chosen because of the small size of

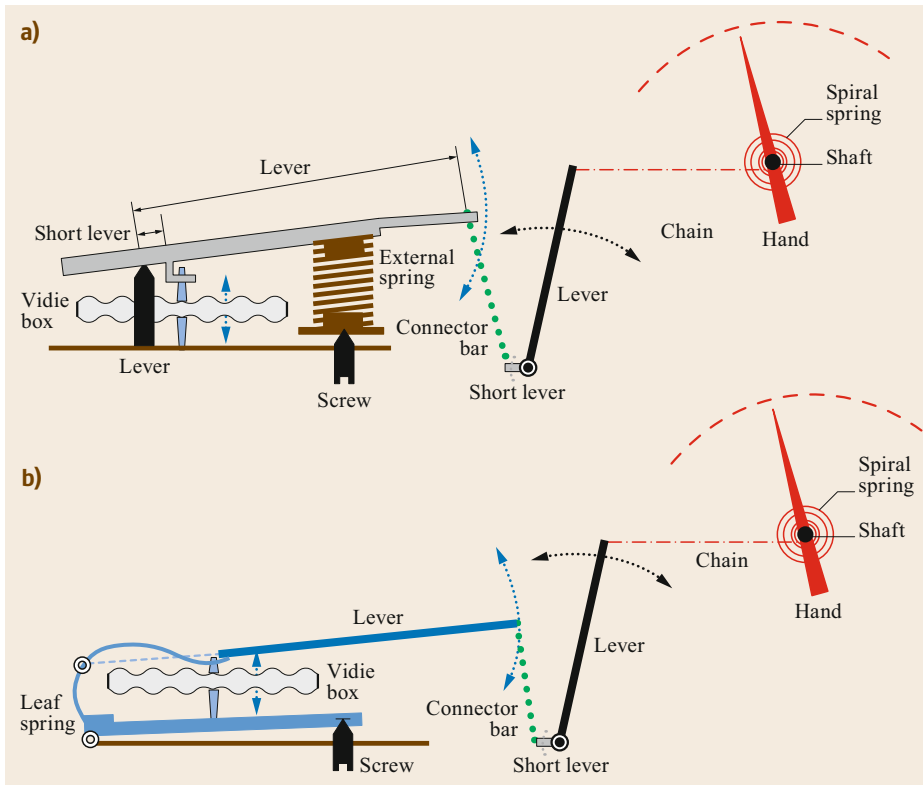


Fig. 10.8a,b The mechanic of the aneroid barometer (after [10.33] with permission of R. Holland): (a) an external spring and (b) a split C-form leaf spring, both according to Vidie

the piezoresistive effect compared with the temperature dependency of a silicon resistor.

The output of this kind of sensor in a Wheatstone bridge is [10.34]

$$V_{out} = 0.51(1 - \nu)p \frac{a^2}{h^2} \pi_{44} V_S, \quad (10.18)$$

where V_S is the supply voltage of the bridge, π_{44} the piezoresistive coefficient of silicon—a function of the doping level of silicon and crystal orientation, a the half width of the diaphragm, h the thickness of the diaphragm, p the applied pressure, and ν the Poisson ratio of silicon.

In general, the output is

$$V_{out} = \frac{\Delta R}{R} V_S, \quad (10.19)$$

where the relative change of piezoresistance depends on the stress on the resistor, material properties, and geometry.

Capacitive Pressure Sensors

The first capacitive pressure sensors had metal diaphragms, but micromechanical sensors with silicon diaphragms are now becoming more popular due to their reliability and good long-term stability. Ceramic

materials like alumina are also used as a material for capacitive pressure sensors, especially in industrial applications.

A commonly used structure for a capacitive pressure sensor has two parallel plates of conductive material, one fixed and the other a flexible diaphragm (Fig. 10.9). Applied pressure causes the diaphragm to deflect and changes the capacitance. The thickness of the bending diaphragm and dielectric material between the plates defines the pressure measurement range. A strength of this technique is the low temperature dependence of the measurement signal compared with piezoresistive sensors.

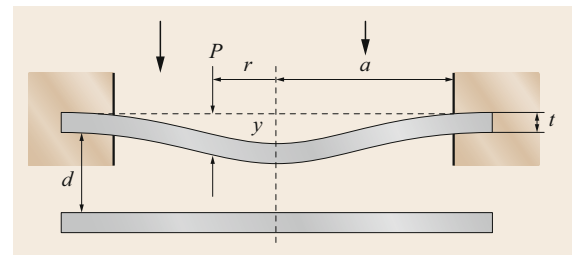
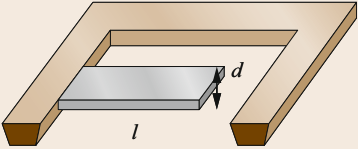
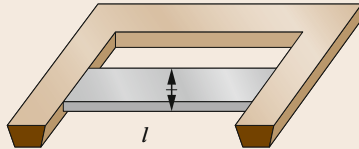
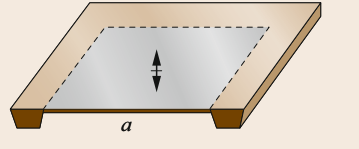


Fig. 10.9 A schematic figure of a capacitive sensor structure; for symbols see text (after [10.36] with permission from Pearson Prentice Hall)

Table 10.6 Three basic resonant structures and their fundamental flexural resonance frequencies f_0 , where E is Young's modulus, ρ the air density, and ν Poisson's ratio (after [10.37] with permission from IOP Publishing)

Beam	Bridge	Diaphragm
		
$f_0 = 0.162 \frac{d}{l^2} \sqrt{\frac{E}{\rho}}$	$f_0 = 0.615 \frac{d}{l^2} \sqrt{\frac{E}{\rho(1-\nu^2)}}$	$f_0 = 1.654 \frac{d}{a^2} \sqrt{\frac{E}{\rho(1-\nu^2)}}$

The relationship between the applied pressure P and the relative capacitance change $\Delta C/C$ due to deflection y of the diaphragm is

$$\frac{\Delta C}{C} = \frac{(1-\nu^2)a^4}{16Edt^3}P, \quad (10.20)$$

where a is the diaphragm radius, t is the diaphragm thickness, $E = \text{Young's}$ modulus, p is the applied pressure, and d is the initial separation of the plates.

The above equation is a first-order estimate of the capacitance change, especially if the size of the capacitor is small as in surface micromachined sensors. For small parallel plate capacitor structures, the so-called edge effect of the electric field becomes remarkable.

Resonant Pressure Sensors

Resonant pressure sensors use a resonating mechanical structure to sense the deflection of the pressure-sensitive structure (e.g., diaphragm, bellow, tube). Applied pressure causes a change in the resonant frequency of the oscillation. There are several different ways to excite and detect the oscillation of the resonator [10.37], Table 10.6.

Single crystal quartz is a common choice of material for resonant pressure sensors due to its good stability and low hysteresis. In academic studies, other piezoelectric materials like PZT (lead zirconate titanate) or ZnO-coated silicon have also been used as res-

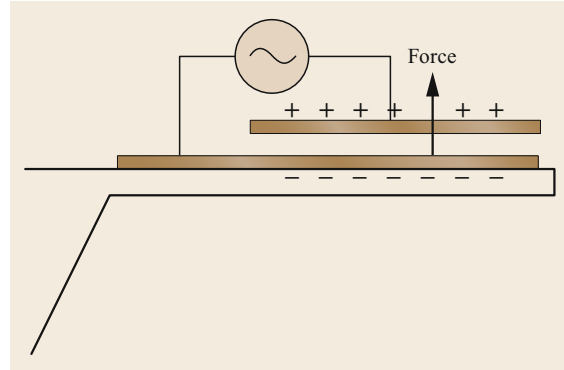


Fig. 10.10 Electrostatic excitation principle for a cantilever beam (electronic excitation and capacitive detection) (after [10.37] with permission from IOP Publishing)

onator materials. For piezoelectric materials like quartz, resonant sensors rely on the piezoelectric effect. In a piezoelectric material, an applied electric field causes a mechanical strain in the material. This effect can be used to excite a resonator (i.e., piezoelectric excitation).

Electrostatic Excitation Principle

Polysilicon and single-crystal silicon are also widely used as resonator materials. For silicon resonators, an electrostatic excitation is used. The principle of excitation and detection of vibration can be seen in Fig. 10.10 for a cantilever.

10.4 Devices and Systems

There is a trend towards the application of electrical sensors, but liquid barometers and aneroid barometers are still in use and are described in the following section as well.

10.4.1 Liquid Barometers

Because of international regulations, instruments with toxic mercury are no longer allowed to be produced,

sold, or applied [10.38, 39]. Only historical instruments may be used as reference instruments or shown for demonstration. Therefore, the following section about mercury barometers is only of interest for historical data. Furthermore, some alternative instruments are shown.

Mercury Barometer

The principle construction of a barometer of the Fortin type is shown in Fig. 10.11 together with a produced

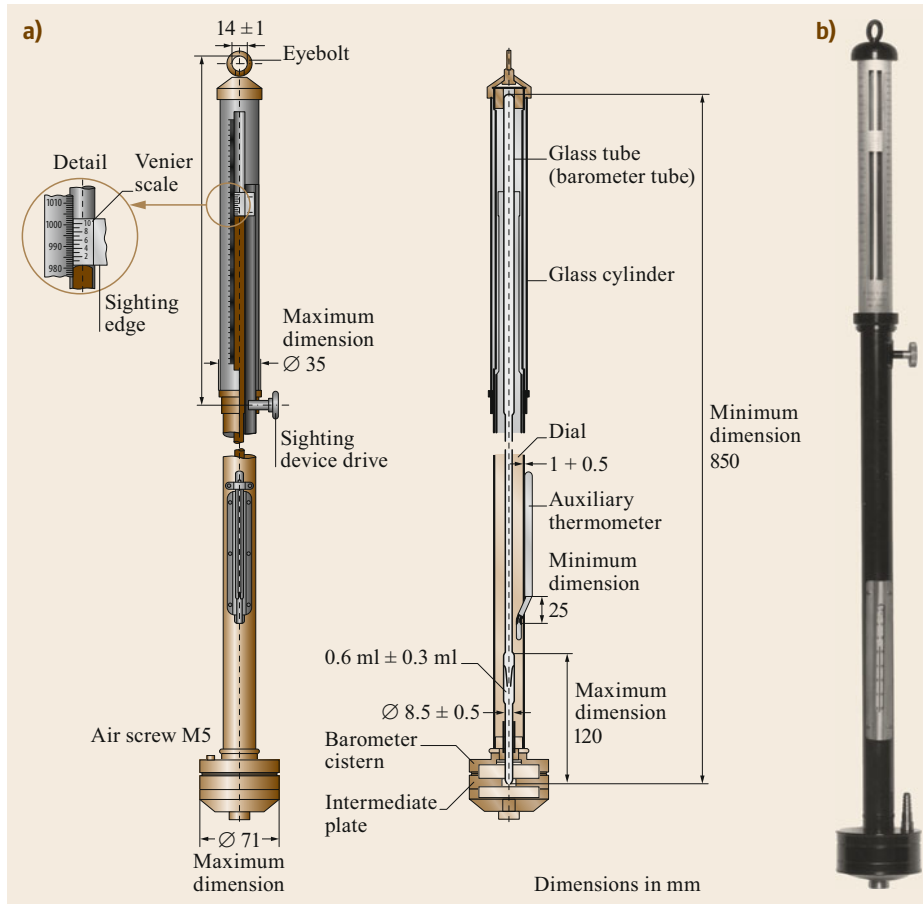


Fig. 10.11a,b Mercury barometer of the Fortin type: (a) schematic view (after [10.30] with permission from VDI e. V., Düsseldorf, Germany); (b) sensor (photo © Theodor Friedrichs & Co., Schenefeld, Germany)

model. Because of the restrictions on application, only the sensor-specific corrections and the pressure reduction to normal conditions (sea level and 0 °C) may be of further relevance.

The pressure readings on the mercury barometer p_m must first be temperature corrected for the cubic thermal expansion of mercury $\alpha = 1.818 \times 10^{-4} \text{ K}^{-1}$ and the linear thermal expansion of the scale (e.g., for alloy of brass and nickel silver, $\beta = 0.184 \times 10^{-4} \text{ K}^{-1}$). Secondly, the volume correction of the mercury must be done with the coefficient of linear thermal expansion of the cistern η and the total volume of mercury in the fixed-cistern barometer V , and the effective cross-sectional area of the cistern A [10.1, 40]; for A and V , see the manufacturer's instructions,

$$p_t = -p_m(\alpha - \beta)t - (\alpha - 3\eta)t \frac{4V}{3A}. \quad (10.21)$$

The reduced pressure for the conditions of the barometer at sea level and 0 °C is

$$p_{\varphi H} = p_t \frac{g_{\varphi H}}{g_n}, \quad (10.22)$$

with the standard acceleration of gravity, $g_n = 9.80665 \text{ m s}^{-2}$ and the acceleration of gravity for a given geographical latitude φ [10.41]

$$g_{\varphi 0} = 9.80620(1 - 2.6442 \times 10^{-3} \cos 2\varphi + 5.8 \times 10^{-6} \cos^2 2\varphi). \quad (10.23)$$

Finally, a correction for the height of the station H is necessary

$$g_{\varphi H} = g_{\varphi 0} - 3.086 \times 10^{-6} H + 1.118 \times 10^{-6} (H - H'), \quad (10.24)$$

where H' is the mean altitude within a radius of 150 km around the station.

For synoptical applications, the pressure must be reduced to sea level according to (10.12) or Table 10.5.

When making an observation with a mercury barometer [10.1], the attached thermometer should be read first. This reading should be taken as quickly as possible. If the barometer is not of a fixed-cistern type, the necessary adjustment should be made to bring the

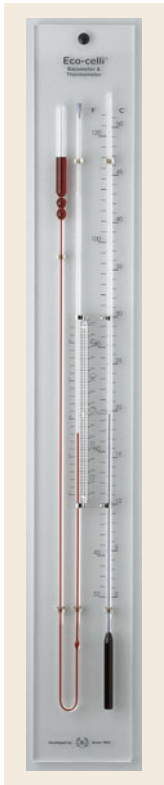


Fig. 10.12 Eco-celli barometer with the barometer on the *left-hand side* with red silicone fluid and a thermometer on the *right-hand side* (photo © Dingens Barometers and Clocks, Hechtel, Belgium)

mercury in the cistern into contact with the fiducial point. The vernier is correctly adjusted when its horizontal lower edge appears to be touching the highest part of the meniscus. The reading should be taken to the nearest 0.1 hPa. Usually, it is not possible to read the vernier to any greater accuracy.

Changes in index errors of mercury barometers may be caused by a drift due to variations in the capillary depression of the mercury surfaces as a result of contamination, due to a rise of air bubbles through the mercury column into the air trap (see Bunten's tip, Fig. 10.3), observer error resulting from failure to tap the barometer before taking the reading, or improper setting of the vernier or fiducial point. A change in correction within 0.1 hPa may be neglected unless persistent; a correction between 0.1 and 0.3 hPa may be provisionally accepted.

Mercury-Free Liquid Barometers

The principle of mercury-free liquid barometers is similar to that of the Goethe barometer (Sect. 10.2.1). The volume above the liquid reservoir is not evacuated and the height of the liquid column can be reduced even for liquids with high density, typically a silicon fluid. As an example, the Eco-celli barometer is shown in Fig. 10.12, with the U-tube of the barometer on the left and a ther-



Fig. 10.13 Ship's aneroid barometer with scales in hPa and in mmHg (photo © Feingerätebau K. Fischer GmbH, Drebach, Germany)

момeter that is necessary for temperature correction on the right. The left limb of the barometer is filled with gas and the liquid, while the right limb has the scale and is connected to atmospheric pressure. The resolution of the scale is larger than for mercury barometers. Such types of barometers are used for education and demonstration but not for science or meteorological observations.

10.4.2 Aneroid Barometers

The chambers of aneroid barometers are made from materials (steel or beryllium copper) that have elastic properties and can themselves act as springs. Typical are mechanical systems with hands (Fig. 10.8) that allow readings better than 0.2 hPa. Alternatively, a ray of light may be deflected over the scale. Instead of these mechanical analog techniques, certain barometers are equipped with a manually operated micrometer whose counter indicates the pressure directly in tenths of a hectopascal [10.1]. Aneroid instruments are portable and robust.

Mechanical aneroid barometers are still in use, but for meteorological stations and research, these instruments are replaced by electrical sensors. An example of a ship barometer is shown in Fig. 10.13. For private use, the instruments are available in many designs. Still in use at climatological stations are barographs using the aneroid principle (Fig. 10.14). The hand is replaced by a recording lever with a pen. For recording, the instru-

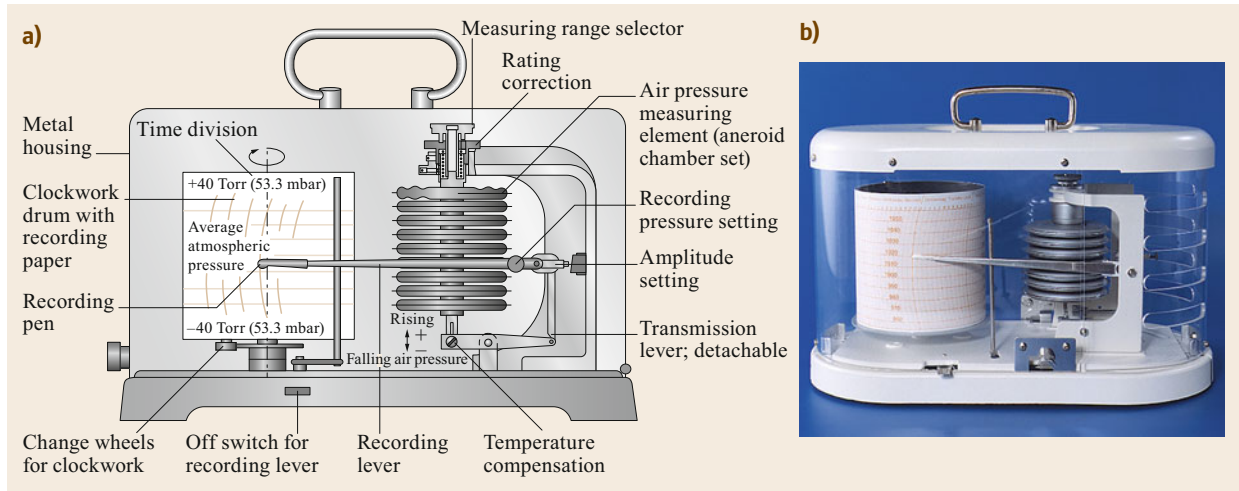


Fig. 10.14a,b Aneroid barograph: (a) schematic view (after [10.30] with permission of VDI e. V., Düsseldorf, Germany); (b) sensor (photo © Feingerätebau K. Fischer GmbH, Drebach, Germany)

ment has a clockwork (e.g., one turn per week) drum with recording paper. To increase the scale, a block of some aneroid chambers can be applied. All aneroid instruments are for indoor use but can also be used in dry conditions outdoors. To reduce errors caused by mechanical levers, optical and digital devices can improve the reading accuracy. The Bourdon tube is no longer applied for meteorological measurements, except for calibrations.

For practical application [10.1] the instrument should always be used in the orientation of the calibration (vertical or horizontal). The sensor should measure the pressure at the level of the instrument. Only over the ocean and for low land stations can a constant difference of the pressure at sea level and at the level of the instrument be assumed and corrected with the screw on the instrument. Temperature compensation can be assumed and a gravity correction is not necessary.

Possible errors [10.1] are a weakened spring or a change of the elasticity of the chamber. The first can be corrected with the bimetallic link in the lever system or by leaving a certain amount of gas inside the aneroid chamber. The second is the reason for hysteresis. Annual comparisons with standard barometers are required. Good instruments do not experience a change of the value within 1 year of more than 0.1 hPa.

The requirements for the barograph (Fig. 10.14) are similar [10.1]. The paper for registration should have a scale of 10 hPa per 1.5 cm so that the scale errors should not exceed 1.5 hPa. The instrument should be fully temperature compensated. The friction between the pen and the paper is important. To reduce errors

related to the pen, barographs have a large aneroid chamber. Good instruments do not experience a change in value within 1 or 2 months of more than 0.2 hPa.

10.4.3 Hypsometer

Since the description of the hypsometer by Wollaston in 1817 [10.13], no significant changes have been made. Figure 10.15 shows a hypsometer employed for balloon flights, with a water reservoir and a heater. The thermometer was placed in the tube, which was filled with water steam after boiling of the water. Above the bulb of the thermometer a small reservoir was included in the capillary to enlarge the scale.

For radiosondes, the hypsometer was miniaturized [10.14]. Instead of mercury-in-glass thermometers, electrical sensors such as thermistors [10.42] or thermocouples [10.43] were used, see also Chap. 46.

10.4.4 Electronic Barometers

The construction of electronic barometers can vary widely. Electronic pressure transmitters offer a wide variety of output options, both digital and analog. Most common analog output range is voltage output $V_{OUT} = 0-5$ V. The variety of digital output protocols used depends on the application field and continent. Displays and data logging features are available, and measurement parameters like sampling rate or averaging can be adjusted. One should check the unit's datasheet and manual for proper output scaling and protocol details.



Fig. 10.15 (a) Hypsometer for balloon investigations with a heater, boiler, and tube for steam; (b) hypsometer thermometer with an enlarged temperature range from 60 to 80 mm Hg (approximately up to heights of 2 km). Photo © Weather Museum, Lindenberg, Germany

Piezoresistive Pressure Transmitters

Silicon piezoresistive pressure sensors have been the most popular MEMS sensor over the past decades. These sensors are small in size, have a good linearity, and do not need any special signal processing (Fig. 10.16). Therefore, pressure transducers based on piezoresistive sensors are cheaper compared to capacitive and resonant sensors. They are widely used in commercial products like small weather stations and watches. A challenge with these sensors is the long-term drift in the resistors due to, for example, surface effects.

Piezoresistive sensors have a temperature dependency that has to be compensated. It is recommended to use transmitters with built-in temperature compensation over the operating temperature range. When the temperature sensor is placed next to the pressure sensor on

the circuit board, no bias error due to temperature difference between the pressure sensor chip and the temperature sensor used for compensation will occur. Note that the compensated temperature range is, in some cases, narrower than the operating temperature range for a transmitter. In choosing an electric pressure transmitter a careful comparison of datasheets is needed.

Overpressure is the maximum pressure applied to the pressure sensor without changing its output characteristics (pressure measurement performance). Piezoresistive sensors withstand an overpressure typically equal to a few times its full-scale pressure.

Capacitive Pressure Sensors

Silicon capacitive pressure sensors have high sensitivity, good long-term stability, and less temperature



Fig. 10.16 A barometric pressure transmitter with a piezo-resistive sensor. Photo © Honeywell Aerospace

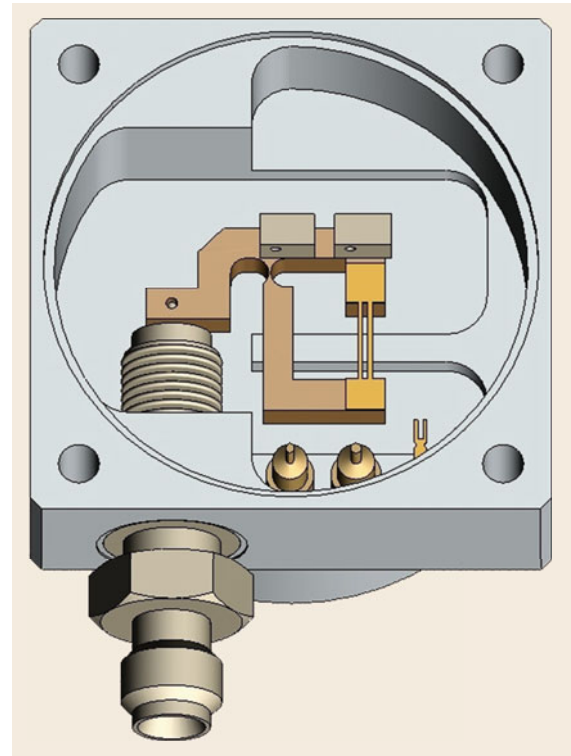


Fig. 10.18 Low-pressure sensor structure with a quartz crystal as a force-sensing element, with permission from Paroscientific, Inc., Redmond, WA, USA



Fig. 10.17 A barometric pressure transmitter with Si capacitive pressure sensors inside. Photo © Vaisala Oyj

dependence than piezoresistive sensors (Fig. 10.17). Capacitive barometric sensors exist with stabilities of 0.01%/year. For reference level measurements, the effect of temperature, although small, has to be compensated with a built-in temperature sensor. The response time of Si capacitive pressure sensors is short. A lower power consumption is a benefit, for example with solar power use in weather stations. Silicon capacitive sensors withstand overpressure well due to the elastic properties of silicon. They also tolerate mechanical shocks or vibration and, therefore, can also be used in buoys, radiosondes, and moving vehicles. Note that for

some transmitters, there is a difference in calibration if the device is mounted vertically or horizontally.

Parallel plate capacitive sensors are also manufactured from ceramic material and metal. Metallic sensors are widely used in heavy industrial applications.

Resonant Pressure Sensors

Several different sensor element technologies can be used in resonant pressure sensors. Piezoelectric-based transducers rely on the piezoelectric effect, which occurs when a crystal reorients under stress forming an internal polarization. These resonant pressure transducers (RPTs) use the piezoelectric effect to drive the quartz sensor into resonance, much like a quartz crystal oscillator (Fig. 10.18). Therefore, a pressure change will change the resonance frequency of the resonating structure. These sensors have high sensitivity and resolution. On the other hand, they can be quite fragile and large in size if there is, for example, a Bourdon tube as a force generating structure.

Silicon (or polysilicon) resonators manufactured using MEMS techniques are smaller in size and not as fragile as those using quartz resonators. One example of a silicon resonator structure in a pressure sensor ele-

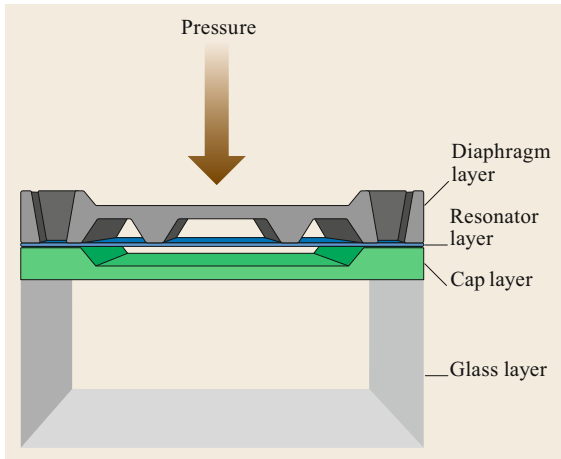


Fig. 10.19 Schematic view of the RPT sensor, a silicon resonator (©DRUCK, a Baker Hughes Business, reprinted with permission)

ment can be seen in Fig. 10.19. In this multilayer sensor structure, there is a pressure sensitive diaphragm and a resonator of single-crystal silicon connected to the diaphragm. A pressure change causes a deflection of the diaphragm, which induces a change in the resonant frequency of the resonator.

These sensors are now the most accurate electronic pressure transducers, with an accuracy of 0.08 hPa at room temperature (15–45 °C). Due to their high sensitivity, these kinds of sensors can be used to detect very small dynamic changes in pressure, for example with infrasound. For instance, tsunamis, vol-

canic eruptions, large explosions, wind mills, and avalanches generate infrasound. Measurement of pressure differences at these frequencies can be used to detect these phenomena or events. A low noise level is also beneficial in these microbarometer applications [10.44].

10.4.5 Piston Gauge

Piston gauges are very accurate instruments with an uncertainty of about 0.05 hPa and can be used as primary standard for calibration. They have a very low drift and the calibration interval is about five years [10.1, 45]. They are available in accredited calibration laboratories or national metrology institutes.

The piston rotates without any lubrication in a cylinder driven by a motor. For absolute pressure measurements a vacuum gauge is necessary. Two systems are available.

Piston Gauges with a Dynamometer Gauge

The sensor undergoing calibration and the piston gauge are connected with a pressure hose. The preselected pressure is generated by the pressure controller and acts on the piston. This is connected to a dynamometer in an evacuated area that measures the force. The very low force due to the residual gas is negligible. The residual pressure of the vacuum is measured with a vacuum gauge and must be taken into account by the piston gauge controller. The pressure can be calculated with a temperature-corrected effective area and the measured force (Fig. 10.20a) [10.1].

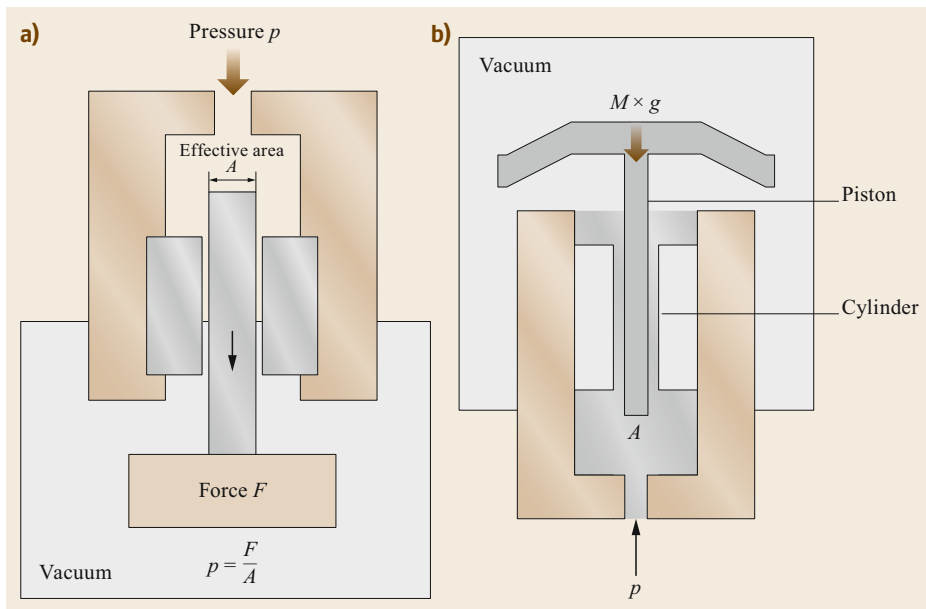


Fig. 10.20 (a) Piston gauge with a dynamometer; (b) loaded piston gauge (after [10.1] with permission from WMO)

Table 10.7 Advantages and disadvantages of the different methods

Devices	Advantages	Disadvantages
Mercury barometer	Accurate reference instrument	Toxic mercury application no longer possible
Aneroid barometer	Easy to handle instrument, moderate accuracy	Normally no electrical output signal
Hypsometer	Accurate system without any corrections	Difficult to use, not for precise measurements near sea level
Piezoresistive pressure sensors	Small electronic sensor	Moderate accuracy, higher power consumption
Capacitive pressure sensors	Accurate electrical sensor with a good stability	
Resonant pressure sensors (quartz or silicon)	Accurate reference instrument	Laboratory size instruments (only quartz resonators)
Piston gauge	Highly accurate	Only for specialized calibration laboratories

Piston Gauges with a Loaded Piston

This piston gauge measures weight and not pressure and is, therefore, directly traceable to SI units. The piston is loaded with weights and, due to the absence of the dynamo, it has the lowest possible uncertainty.

The masses are lifted up by a pressure controller. At a certain height, a motor accelerates the piston with a temporarily connected belt. The motor stops at a certain speed after disconnection of the belt. Due to the low friction, the rotation speed remains nearly constant for up to about half an hour, de-

pending on the weight. The system is covered with an evacuated bell, and the residual pressure must be taken into account by the piston gauge controller (Fig. 10.20b) [10.1].

10.4.6 Comparison of the Methods

Because mercury barometers can no longer be used, and aneroid barometers are not accurate enough, the comparison of the different methods is more or less restricted to the electronic sensors given in Table 10.7.

10.5 Specifications

The range of pressure measurements in the atmosphere is given by the extreme values measured and are within the range from 850 to 1100 hPa at sea level. The local values must be reduced according to the height above

sea level ((10.12) and Table 10.5). Further specification of the measurement methods are given in Table 10.8. For individual devices, see the instructions of the producer.

Table 10.8 Specification of different measurement methods for barometric pressure (typical values)

Method	Uncertainty	Temperature range (°C)	Remark
Mercury barometer	±0.1 hPa	−38 to 50	[10.1]
Aneroid barometer – temperature drift – hysteresis	±0.3 hPa, ±1 hPa ^a 0.3 hPa per 50 K 0.3 hPa, 1 hPa ^a per 50 hPa	−10 to 50	[10.1, 30]
Hypsometer			Dependent on resolution of the thermometer and range of heights
Si piezoresistive sensor	±0.4 hPa	−40 to 85	Long-term stability 0.25 hPa/year not included in accuracy
Si capacitive sensor	±0.1 hPa at 20 °C, ±0.15 hPa	−40 to 60	
Resonant pressure sensor	±0.08 hPa at 15–45 °C, ±0.1 hPa	−40 to 85	Typical temperature range, depends on model and manufacturer
Piston gauge	< ±0.05 hPa		Laboratory calibration instrument

^a barograph

10.6 Quality Control

A good practice is to regularly check the pressure reading of the barometer against a reference barometer. Even the best class of barometers has some long-term drift, and the behavior of the drift can change as the device gets older. The calibration curve provided with a new barometer is not valid many years later. A comparison also indicates if there is a need for maintenance of the barometer.

10.6.1 Reference Barometer

The WMO recommends as the primary standard barometers a precision dead weight tester (piston gauge with loaded piston), producing a calibrated pressure related to the precision weight and the gravity field [10.1, 45].

Electronic barometers, such as silicon diaphragm barometers with long-term stability, are secondary standards [10.45]. Similar devices can be used as working or traveling standards. The WMO organizes international barometer comparisons to compare national working standards with primary or secondary standards [10.1].

10.6.2 Calibration

Electronic pressure transmitters are typically maintenance free but a regular calibration is recommended. A calibration interval of 1 year is a good starting point, depending on air pollution. If the pressure difference in calibration is small compared to specifications, the interval can be lengthened.

Before a comparison with standard barometers or calibration and adjustment, it is important to make sure that no temperature gradients disturb the comparison and that the device under test and the reference device are on the same level (no height correction needed). If the unit cannot be moved to a calibration laboratory, the calibration can be done on site, but the uncertainty of calibration is typically larger due to environmental conditions. The ambient temperature should be stable

within ± 1 K, and the calibration setup should not be in direct sunlight. If the unit is not calibrated at the site, it has to be properly packed for transportation to avoid the effects of mechanical shock on calibration.

A typical calibration setup consists of a pressure controller, a vacuum pump, a pressure supply (e.g., a gas cylinder), and a pressure reference. In some pressure controllers, there is an internal pressure reference. Piston gauges can also act as a reference [10.1, 45, 46]. A requirement for pressure standard uncertainty is 0.1 hPa.

Pressure points in the calibration are chosen from 0 to 100% full scale of the unit under test (e.g., 850–1050 hPa) and should be uniformly distributed over the whole range. Both increasing and decreasing pressure series should be measured in the calibration procedure. For most electric barometers it is possible to make offset and span adjustments based on the calibration results. After the adjustment, the calibration procedure should be repeated (Fig. 10.21). A multipoint calibration and adjustment can be done by the device manufacturer.

In aneroid barometers, there is typically an adjustment screw behind the device. Therefore, it is only possible to do a one-point adjustment. For aneroids, it is important to check whether calibration should be done in a vertical or horizontal position.

10.6.3 Comparison with a Reference Barometer

If a pressure controller is not available, a one-point comparison with a reference barometer can be done at the ambient pressure. This is not a calibration. The comparison should be performed in stable or only slightly changing ambient pressure and at low wind speeds. This is to minimize the uncertainty caused by changing environment conditions. As with laboratory calibrations the unit and reference instrument should acclimate to am-

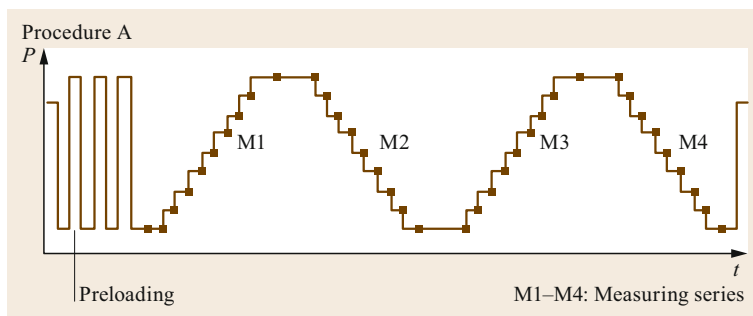


Fig. 10.21 Calibration procedure (after [10.1] with permission from WMO)

bient conditions before the comparison is done. Some aneroids are quite nonlinear and, therefore, it is recommended to do the comparison as close to 1013 hPa as possible [10.47].

10.6.4 Specific Quality Control Methods

With electric barometers a real time quality control can be performed. There are devices that have two or three pressure sensors inside one device. This enables quality control of the measurement data in real time by

comparison of the pressure readings of these pressure sensors.

To identify unrealistic values due to malfunctions of the sensor or data transmission, with the default test the following values should be excluded:

- Negative values
- Reduced values at sea level lower than 940 hPa or larger than 1050 hPa (these values can only be accepted under specific synoptic situations)
- Constancy of the pressure over 6 h.

10.7 Maintenance

The pressure transmitter should be checked regularly, and immediately if, based on quality control of the data, the need for maintenance is suspected. Things to be checked (in addition to calibration or comparison) are:

- Mounting of the barometer to ensure the correct height of the barometer.
- The pressure inlet should be kept clean and free. Especially in outdoor assemblies there is a risk that the barbed fitting is stuck due to bugs or droplets,

for example. This can be also judged based on data, if the pressure output seems not to follow the pressure trend (comparison with another barometer close by).

Typical maintenance intervals are given in Table 10.9. At sites where the environmental conditions are harsher (air pollution, smog, large temperature variations, vibration (on a vehicle)), the maintenance intervals have to be considered on a case-by-case basis.

Table 10.9 Maintenance of pressure measurement systems. If the check reveals a possible malfunction, the instrument is to be replaced

Maximum interval	Aneroid barometer	Piezoresistive	Capacitive	Quartz crystal resonator	Piston gauge
2 months	Barograph: Comparison with standard barometer	Pressure inlet should be kept clean and free (no droplets, bugs)	Pressure inlet should be kept clean and free (no droplets, bugs)	Pressure inlet should be kept clean and free (no droplets, bugs)	
1 year	Comparison with standard barometer	Comparison with standard barometer	Comparison with standard barometer	Comparison with standard barometer	
5 years					Recalibration

10.8 Application

Pressure measurements are not only related to meteorology. Many technical disciplines and medicine need accurate pressure measurements. Electronical sensors are included in many instruments. Two applications will be highlighted, the use in meteorology and climatology and for air navigation.

10.8.1 Meteorology and Climatology

Typical averaging intervals for pressure are 10 min, with 30 or 60 min also being possible. Recently, the sampling rate is much higher, at 1–10 s. For standard meteoro-

logical measurements in Central Europe (for other time zones, the data must be changed accordingly), the true daily mean is calculated from the 24 single pressure values p_i , recorded at 1-hour intervals between 23:50 Coordinated Universal Time (UTC) of the previous day and 22:50 UTC of the current day [10.48]

$$\overline{p_{\text{day}}} = \frac{1}{24} \sum_{i=0}^{23} p_i \quad (10.25)$$

The climatological daily mean is calculated according to (10.25), analogously to the true daily mean.

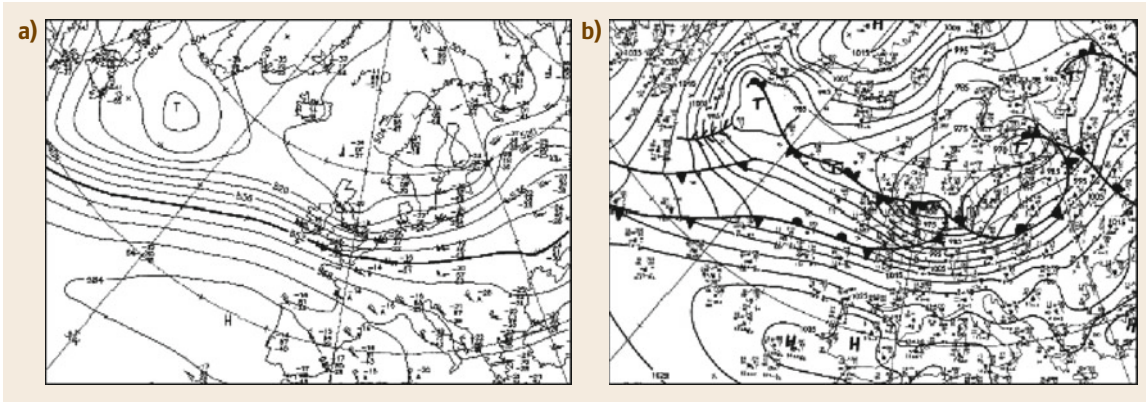


Fig. 10.22a,b Weather charts. (a) geopotential heights in gpdm for the 500 hPa isobaric layer; (b) pressure at sea level; Central Europe, January 18, 2007, 12 UTC, heavy storm *Kyrill* (after [10.49])

The typical meteorological application is for weather charts, with the first being constructed by *Heinrich Wilhelm Brandes* (1777–1834) in 1826 [10.50]. These are geographical maps with isobars for a particular time of measurements (Fig. 10.22b) and indicate low and high-pressure areas. Frontal systems are also analyzed. This type of chart is only used for sea level. For levels in the troposphere, charts with the geopotential height in geopotential dekameters (gpdm) of a layer with constant pressure are constructed. The typical pressure layers are 925, 850, 700, 500, and 300 hPa. According to (10.12), large heights are related to warm air below the isobaric layer and low heights to cold air (Fig. 10.22a).

10.8.2 Pressure Measurements for Aircrafts

Exact pressure measurements are essential for aircraft navigation. The relevant pressure values are given with the typical Q-codes used by the ICAO (International Civil Navigation Aviation) based on Morse telegraphy and introduced by the International Radiotelegraph Convention in 1912. The QFE code is referred to as *atmospheric pressure at aerodrome elevation (or at runway threshold)*. This pressure can differ from that of

the barometer, which differs in altitude by several meters. The QFE pressure is calculated by linear correction of the barometric pressure.

To make pressure measurements at different airports comparable, the QFE pressure is reduced to sea level using the ICAO standard atmosphere [10.25, 51] (ISA) with a constant air temperature of 15 °C (Chaps. 1, 5). This value is referred to as QNH pressure (*the altimeter subscale setting to obtain elevation when on the ground*), and is used for setting the altimeter to indicate the flying height above sea level. With *standard pressure* (1013.2 hPa) set, the altimeters indicate *pressure altitude (flight level)*. This value is applied above the transition altitude that is 18 000 ft in Northern America and different for each airport in Europe and most of the other countries.

According to the ISA the mean pressure gradient is 27 ft hPa^{-1} . Under real conditions, because cold air is denser than warm air, the actual altitude may be different from the readings of the altimeter, with the altimeter overestimating the altitude in cold air and underestimating the altitude in warm air with respect to ISA levels. Because all aircrafts fly with altimeters based on the ISA, this is only a problem over high mountains in cold air, where the true altitude should be used.

10.9 Future Developments

Pressure measurement instruments have changed a lot over the last 100 years as electronic barometers have replaced mercury barometers. The level of automation has increased, enabling installation of barometers in remote sites or, for example, on unmanned ships.

The internet of things (IoT) is now a hot topic and offers more ways to transfer data. This technology megatrend also sets some new requirements for measuring instruments. IoT could offer a larger number of measurement instruments and a denser network of measurement data that would improve local weather forecasting (Chap. 44).

10.10 Further Reading

A thorough introduction into the history and physics of pressure sensors can be found in:

- WMO: Guide to Instruments and Methods of Observation, WMO-No. 8, Volume I – Measurement of Meteorological Variables (World Meteorological Organization, Geneva, 2018)
- VDI: Umweltmeteorologie, Meteorologische Messungen, Druck (Environmental Meteorology, Meteorological Measurements, Pressure, in German and English), VDI 3786 Blatt(Part) 16, (Beuth-Verlag, Berlin 2021)
- T. P. DeFelice: An Introduction to Meteorological Instrumentation and Measurement, (Prentice Hall, Upper Saddle River 1998)
- F. V. Brock, S. J. Richardson: Meteorological Measurement Systems, (Oxford University Press, New York 2001)
- G. Harrison: Meteorological Measurements and Instrumentation, (John Wiley & Sons, Chichester 2015)

References

- 10.1 WMO: *Guide to Instruments and Methods of Observation*, WMO-No. 8, Volume I – Measurement of Meteorological Variables (World Meteorological Organization, Geneva 2018)
- 10.2 H. Moritz: *Geodetic Reference System 1980*, Paper presented at XVII General Assembly of the IUGG (IUGG Canberra, 1980)
- 10.3 H.-G. Körber: *Vom Wetteraberglauben zur Wetterforschung* (Edition Leipzig, Leipzig 1987)
- 10.4 W.E.K. Middleton: *Invention of the Meteorological Instruments* (The Johns Hopkins Press, Baltimore 1969)
- 10.5 R. Holland, G. Stöhr: *Quecksilber-Barometer Handbuch* (Freunde alter Wetterinstrumente, Riedlingen 2012)
- 10.6 S. Nath sen.: *On the Design of the Kew Pattern Barometer*, Geophysical Memoirs, Vol. 27 (Meteorological Office, London 1925) pp. 201–225
- 10.7 G. Stöhr: *Aneroid-Barometer, Die robuste Alternative* (Freunde alter Wetterinstrumente, Riedingen 2016)
- 10.8 D. Botting: *Humboldt and the Cosmos* (Harper & Row, New York 1973)
- 10.9 J.W. Gintl: *Das Höhenmessen mit dem Thermometer* (J. G. Heubner, Wien 1835)
- 10.10 R. Bogue: Mems sensors: past, present and future, *Sens. Rev.* **27**, 7–13 (2007)
- 10.11 D.G. Fahrenheit: *Barometri Novi Descriptio*, *Philos. Trans. R. Soc. London* **33**, 179–180 (1724)
- 10.12 T. Cavallo: An account of some thermometrical experiments; containing, I. Experiments relating to the cold produced by the evaporation of various fluids, with a method of purifying ether. II. Experiments relating to the expansion of mercury. III. Description of a thermometrical barometer, *Philos. Trans. R. Soc. London* **71**, 509–525 (1781)
- 10.13 F.J.H. Wollaston: XIII. Description of a thermometrical barometer for measuring altitudes, *Philos. Trans. R. Soc. London* **107**, 183–196 (1817)
- 10.14 G. Müller: Über die Messung des Luftdrucks durch Bestimmung der Siedetemperatur mit dem Hypsometer, *Ber. Dtsch. Wetterd.* **8**, 1–13 (1954)
- 10.15 C.S. Smith: Piezoresistance effect in germanium and silicon, *Phys. Rev.* **94**, 42–49 (1954)
- 10.16 W.G. Pfann, R.N. Thurston: Semiconducting stress transducers utilizing the transverse and shear piezoresistance effects, *J. Appl. Phys.* **32**, 2008–2019 (1961)
- 10.17 O.N. Tufte, P.W. Chapman, D. Long: Silicon diffused-element piezoresistive diaphragms, *J. Appl. Phys.* **33**, 3322–3327 (1962)
- 10.18 H.A. Waggener, R.C. Kragness, A.L. Tyler: Anisotropic etching for forming isolation slots in silicon beam leaded integrated circuits, *Int. Electron Devices Meet.* **13**, 68–69 (1967)
- 10.19 S.K. Clark, K.D. Wise: Pressure sensitivity in anisotropically etched thin-diaphragm pressure sensors, *IEEE Trans. Electron Devices* **26**, 1887–1896 (1979)
- 10.20 C.S. Sander, J.W. Knutti, J.D. Meindl: A monolithic capacitive pressure sensor with pulse-period output, *IEEE Trans. Electron Devices* **27**, 927–930 (1980)
- 10.21 N. Mölders, G. Kramm: *Lectures in Meteorology* (Springer, Cham 2014)
- 10.22 M.L. Salby: *Physics of the Atmosphere and Climate* (Cambridge Univ. Press, Cambridge 2012)
- 10.23 R.B. Bird, W.E. Stewart, E.N. Lightfoot: *Transport Phenomena* (Wiley, New York 2007)
- 10.24 H. Eckelmann: *Einführung in die Strömungsmesstechnik* (Teubner, Stuttgart 1997)
- 10.25 International Civil Aviation Organization: *Manual of the ICAO Standard Atmosphere: Extended to 80 Kilometres (262,500 Feet)*, ICAO Doc 7488-CD, 3rd edn. (ICAO, Montréal 1993)
- 10.26 H. Liu, G.L. Darkow: Wind effect on measured atmospheric pressure, *J. Atmos. Ocean. Technol.* **6**, 5–12 (1989)
- 10.27 G.R. Harrison: *Meteorological Measurements and Instrumentations* (Wiley, Chichester 2015)
- 10.28 R.W. Miksad: An omni-directional static pressure probe, *J. Appl. Meteorol.* **15**, 1215–1225 (1976)
- 10.29 R.T. Nishiyama, A.J. Bedard: A “quad-disc” static pressure probe for measurement in adverse atmospheres: with a comparative review of static

- pressure probe designs, *Rev. Sci. Instrum.* **62**, 2193–2204 (1991)
- 10.30 VDI: *Umweltmeteorologie – Meteorologische Messungen – Luftdruck (Environmental Meteorology – Meteorological Measurements – Atmospheric Pressure)*, VDI 3786 Blatt 16 (Part 16) (Beuth, Berlin 2021)
- 10.31 E.O. Doebelin: *Measurement Systems: Application and Design* (McGraw-Hill, New York 1983)
- 10.32 F.V. Brock, S.J. Richardson: *Meteorological Measurement Systems* (Oxford Univ. Press, New York 2001)
- 10.33 R. Holland: *Die Techniken der Aneroid-Barometer* (Siegloch, Blaufelden 2017)
- 10.34 M.-H. Bao: *Micro Mechanical Transducers: Pressure Sensors, Accelerometers and Gyroscopes* (Elsevier, Amsterdam 2000)
- 10.35 G. Harman: Pressure sensors. In: *Sensor Technology Handbook*, ed. by J.S. Wilson (Elsevier, Burlington 2005) pp. 411–456
- 10.36 J.P. Bentley: *Principles of Measurement Systems*, 4th edn. (Pearson Prentice Hall, Harlow 2005)
- 10.37 G. Stemme: Resonant silicon sensors, *J. Micromech. Microeng.* **1**, 113–125 (1991)
- 10.38 UNEP: The Minamata Convention on Mercury, <http://mercuryconvention.org> (2014), Accessed 05 July 2021
- 10.39 EU: Commission regulation (EU) no 847/2012 of 19 September 2012 amending annex xvii to regulation (EC) No 1907/2006 of the European Parliament and of the Council on the registration, evaluation, authorisation and restriction of chemicals (REACH) as regards mercury, *Off. J. Eur. Union L* **253**, 1–4 (2012)
- 10.40 T.P. DeFelice: *An Introduction to Meteorological Instrumentation and Measurement* (Prentice Hall, Upper Saddle River 1998)
- 10.41 C. Morelli: *The International Gravity Standardization Net 1971 (I.G.S.N. 71); Final Scientific Report 1 Nov 1962–30 Sep 1970* (Bureau Central de l'Association Internationale de Geodesie, Munich 1974)
- 10.42 J. Rink: Thermistore und ihre Anwendung in der Meteorologie, *Abh. Meteorol. Hydrol. Dienstes DDR* **63**, 1–58 (1961)
- 10.43 H. Richner, J. Joss, P. Ruppert: A water hypsometer utilizing high-precision thermocouples, *J. Atmos. Ocean. Technol.* **13**, 175–182 (1996)
- 10.44 P.K. Kinnell, R. Chaddock: Advances in silicon resonant pressure transducers, *Proc. Eurosensors XXIII Conf., Procedia Chem.* **1**, 104–107 (2009)
- 10.45 D. Groselj: Guidance on instrumentation for calibration laboratories including Rics, WMO, Instrum. *Observ. Methods* **101**, 1–43 (2010)
- 10.46 EURAMET: *Guidelines on the Calibration of Electromechanical and Mechanical Manometers*, EURAMET Calibration Guide No. 17 (EURAMET, Braunschweig 2017)
- 10.47 D. Burch: *The Barometer Handbook* (Starpath, Seattle 2009)
- 10.48 VDI: *Umweltmeteorologie, Meteorologische Messungen, Luftfeuchte (Environmental Meteorology, Meteorological Measurements, Air Humidity)*, VDI 3786 Blatt(Part) 4 (Beuth, Berlin 2013)
- 10.49 A. Bott: *Synoptische Meteorologie* (Springer Spektrum, Berlin, Heidelberg 2016)
- 10.50 M. Börngen: *Heinrich Wilhelm Brandes (1777–1834)* (Edition am Gutenbergplatz, Leipzig 2017)
- 10.51 ICAO: *Procedure for Air Navigation Services, Aircraft Operations, Fly Procedures*, Vol. 1, 5th edn. (ICAO, Québec 2006)

Anni Torri

Vaisala Oyj
Vantaa, Finland



Anni Torri is senior scientist working at Vaisala Oyj, a global company manufacturing and marketing products and services for environmental and industrial measurement. She received a PhD in Physics at the University of Helsinki.

Thomas Foken

University of Bayreuth
Bayreuth, Germany
thomas.foken@uni-bayreuth.de



Thomas Foken is a retired Professor of Micrometeorology at the University of Bayreuth. He was the head of Laboratories at the meteorological observatories at Potsdam (1981–1994) and Lindenberg (1994–1997). His research interests include the interaction between the Earth's surface and the atmosphere and the measurement and modeling of energy and matter fluxes, with a strong focus on experimental meteorology. His scientific contributions have been recognized through various international awards.



Jens Bange

Centre for Applied Geo-Science
University of Tübingen
Tübingen, Germany
jens.bange@uni-tuebingen.de

Jens Bange is a Professor for Environmental Physics at the University of Tübingen since 2010. He received a PhD in meteorology in 1998 and a diploma in physics in 1992 at the University of Hannover. His research interests include atmospheric turbulence, boundary-layer meteorology, wind-energy research, airborne meteorology, and environmental measurement technology. He is a founding member of the research networks ISARRA and WindForS.

Radiation Se

11. Radiation Sensors

Klaus Behrens

Instruments for measuring various characteristics of broadband solar and terrestrial radiation have been developed and used for just over 100 years. While in the early years nearly all possible measurement methods were tested and applied, nowadays mainly thermoelectric and (only for solar radiation) photoelectric detectors are adopted. Currently, only these methods can offer output signals with low uncertainties as well as a high degree of automatic data recording in loggers or even preprocessing in the instruments themselves followed by data transmission using different protocols. The investigation of special spectral regions, e.g., ultraviolet (UV) and photosynthetically active radiation (PAR), requires instruments with photoelectric detectors and filters. The separation of solar radiation into its direct and diffuse components requires additional devices. In addition to these subjects, different calibration methods, maintenance measures, and quality control are also described in this chapter.

11.1	Measurement Principles and Parameters	298	11.3	Theory	315
11.1.1	Measured Parameters	298	11.3.1	Optical Spectrum of Solar and Terrestrial Radiation	315
11.1.2	Measurement Principles	300	11.3.2	Thermoelectric Method	317
11.1.3	Measurement Sites	300	11.3.3	Photodiode-Based Method	318
11.2	History	303	11.3.4	Separation of Solar and Terrestrial Radiation	319
11.2.1	Pyrheliometers	303	11.4	Devices and Systems	320
11.2.2	Pyranometers	308	11.4.1	Pyrheliometer	320
11.2.3	Pyrgeometers	311	11.4.2	Pyranometers	323
11.2.4	Pyrradiometers	312	11.4.3	Pyrgeometers	327
11.2.5	Pyrheliometric Scales	313	11.4.4	Pyrradiometers	328
			11.4.5	Net Radiometers	329
			11.4.6	Multi Radiometers	332
			11.4.7	Sunshine Duration Instruments	335
			11.4.8	Supplementary Equipment	337
			11.4.9	Comparison of Devices to Measure Radiation Parameters	339
			11.5	Specifications	339
			11.6	Quality Control	341
			11.6.1	Calibration of Radiation Instruments	341
			11.6.2	Specific Quality Control of Measured Data	345
			11.7	Maintenance	348
			11.8	Applications	349
			11.8.1	Climatology of Radiation	349
			11.8.2	Daily and Annual Cycles	349
			11.8.3	Radiation on Tilted Surfaces	350
			11.8.4	Radiation Temperature	352
			11.9	Future Developments	352
			11.10	Further Reading	353
			References		353

Radiation processes dominate the Earth's weather and climate as well as life on our planet. The Sun delivers the necessary energy in the form of electromagnetic radiation in the so-called thermal-optical region at wavelengths between 200 and 25 000 nm at the top of the atmosphere, being primarily responsible for driving the physical, chemical, and biological processes that occur within the atmosphere as well as at its bound-

aries with the hydro-, litho-, cryo-, and biosphere. As it passes through the atmosphere, solar radiation suffers extinction processes, such that the solar spectrum at the surface only extends over the region between about 300 and 3000 nm. Furthermore, because of the temperature of the Earth, heat exchange with space occurs in the thermal or terrestrial spectral region (about 3000 to 50 000 nm), resulting in radiative equilibrium.

These boundary wavelengths vary depending on the atmospheric composition and constituents as well as its temperature.

Firstly, important astronomical effects such as the inclination of the Earth's axis, the changing distance from the Earth to the Sun as it moves around its orbit, and the rotation of our planet around its own axis generate steady changes in the solar radiation fluxes received by the Earth. Secondly, different atmospheric constituents, which are unequally distributed in space and time, change the incoming solar radiation on its way from the top of the atmosphere to the ground and the part that is reflected back into space, as well as the thermal radiation emitted by the surface and the atmospheric gases, constituents, and clouds. Radiation fluxes that change in both space and time are thus found at every point on the Earth's surface as well as within the atmosphere, contributing to the exchange of energy.

Furthermore, the interaction of solar radiation with atmospheric constituents and clouds on its path

through the atmosphere, which are highly wavelength-dependent effects, allows the remote derivation of changing atmospheric features (e.g., the optical thickness of aerosols and/or atmospheric gases such as water vapor, ozone, etc.).

Therefore, it is absolutely essential to monitor the integral/broadband as well as spectral radiation fluxes in space and time at different scales for atmospheric physics, climate, and applied sciences (agriculture, energy, environment, etc.). Investigations of broadband radiation are mainly used when considering the radiation and energy balance, while it is necessary to apply spectral data for the investigation of atmospheric features and biological processes.

As a result of these diverse effects, radiation-measuring devices are considered in different chapters of this handbook (e.g., Chaps. 29, 34, 37, 38).

This chapter deals with classical in-situ instruments used from the ground. Furthermore, instruments used to acquire sunshine duration are also described.

11.1 Measurement Principles and Parameters

Before introducing the measured parameters, it is necessary to make some basic remarks regarding radiometric terminology. Table 11.1 presents the radiometric quantities according to [11.1].

The irradiance and the radiant flux density are the quantities most widely used in the field of radiation measurements from the ground, describing the radiation power of processes related to an area, while the radiant exposure or irradiation represents the integral or sum over time of the irradiance, thus indicating the global radiation (energy) received during a day. These quantities must be considered as functions of wavelength if they are applied for special spectral regions.

11.1.1 Measured Parameters

Radiation measurements are highly complex, because they have to cover a wide spectral range with different features and components. Furthermore, it is necessary to consider, depending on the goals of the investigation, wide parts of the spectrum using broadband measurements, or in other cases highly resolved spectral measurements. Hence, many different parameters are measured, as summarized in Table 11.2 and deduced as given in Table 11.3.

Investigations in many disciplines of atmospheric physics, including meteorology as well as climatology and applied sciences, require the acquisition of dif-

ferent solar and terrestrial broadband radiation fluxes near the surface from the upper half-space (sky) and lower half-space (ground) as components of the radiation balance. Because biological, human, technical, and chemical processes and their surfaces, respectively, act partially selective, it is necessary to consider the corresponding quantities in narrow spectral regions or even at single wavelengths.

The terms *short-wave* and *long-wave* radiation are also used for solar and terrestrial radiation, respectively. The use of the terms *solar* and *terrestrial* has the advantage that there is a clear link with the origin of these radiative quantities. The terrestrial spectral range is part of the whole infrared spectral region (Sect. 11.3.1). Furthermore, the potential confusion with *short* and *long* radio waves is thus excluded.

(Extraterrestrial) direct solar radiation is scattered and absorbed on its way to the Earth's surface by air molecules, atmospheric constituents, and clouds in the Earth's atmosphere. Therefore, it is necessary to measure the remaining direct solar radiation (E) and the diffuse solar radiation ($E_d\downarrow$) originating from the sky at the Earth's surface. In most cases, the total solar radiation or global radiation ($E_g\downarrow$) is measured as the sum of the vertical component of the direct solar radiation ($E \cos(z)$) and the diffuse component ($E_d\downarrow$), because this is easier technically

$$E_g\downarrow = E \cos(z) + E_d\downarrow, \quad (11.1)$$

Table 11.1 Radiometric quantities

Name	Symbol	Unit	Relation	Remarks
Radiant energy	Q	J = W s	–	–
Radiant flux	Φ	W (J s ⁻¹)	$\Phi = \frac{dQ}{dt}$	Power
Radiant flux density	$(M), (E)$	W m ⁻²	$\frac{d\Phi}{dA} = \frac{d^2Q}{dAdt}$	Radiant flux of any origin crossing an area element
Radiant exitance	M	W m ⁻²	$M = \frac{d\Phi}{dA}$	Radiant flux from any origin emerging from an area element
Irradiance	E	W m ⁻²	$E = \frac{d\Phi}{dA}$	Radiant flux from any origin incident onto an area element
Radiance	L	W m ⁻² sr ⁻¹	$L = \frac{d^2\Phi}{d\Omega dA \cos \vartheta}$	The radiance is a conserved quantity in an optical system
Radiant exposure (irradiation)	H	J m ⁻²	$H = \frac{dQ}{dA} = \int_{t1}^{t2} E dt$	May be used for, e.g., hourly or daily sums of global radiation, etc.
Radiant intensity	I	W sr ⁻¹	$I = \frac{d\Phi}{d\Omega}$	May be used only for radiation outgoing from <i>point sources</i>

Table 11.2 Parameters measured by radiation instruments at the ground

Parameter	Description	Unit ^a	Symbol ^a
Direct solar radiation ^b	Radiation incident with irradiance E on a plane perpendicular to the radiation's direction from the solid angle of the solar disc solar energy application: direct normal irradiance (DNI)	W m ⁻²	E, E_λ
Diffuse solar radiation	Radiation incident on a horizontal plane with irradiance $E_d \downarrow$ from the upper half-space, excluding the solar disc (2π sr) solar energy application: diffuse horizontal irradiance (DHI)	W m ⁻²	$E_d \downarrow, E_{d,\lambda} \downarrow$
Global solar radiation	Sum $E_g \downarrow$ of the vertical component of the direct $E \cos(z)$ and diffuse solar radiation $E_d \downarrow$ incident on a horizontal plane from the upper half-space (2π sr) solar energy application: global horizontal irradiance (GHI)	W m ⁻²	$E_g \downarrow, E_{g,\lambda} \downarrow$
Upward solar radiation	Reflected solar radiation $E_r \uparrow$ impinging from the lower half-space on a horizontal plane (2π sr)	W m ⁻²	$E_r \uparrow, E_{r,\lambda} \uparrow$
Downward terrestrial radiation	Thermal radiation of the atmosphere $E_1 \downarrow$ from the upper half-space (2π sr)	W m ⁻²	$E_1 \downarrow, E_{1,\lambda} \downarrow$
Upward terrestrial radiation	Thermal radiation of the surface $E_1 \uparrow$ from the lower half-space (2π sr)	W m ⁻²	$E_1 \uparrow, E_{1,\lambda} \uparrow$
Net solar radiation	Difference between the global and reflected solar radiation on a horizontal plane $E_s^* = E_g \downarrow - E_r \uparrow$	W m ⁻²	$E_s^*, E_{s,\lambda}^*$
Net terrestrial radiation	Difference between the downward and upward terrestrial radiation on a horizontal plane $E_1^* = E_1 \downarrow - E_1 \uparrow$	W m ⁻²	$E_1^*, E_{1,\lambda}^*$
Downward (total) radiation	Total of the global solar and atmospheric/downward terrestrial radiation $E \downarrow = E_g \downarrow + E_1 \downarrow$	W m ⁻²	$E \downarrow, E_\lambda \downarrow$
Upward (total) radiation	Total of the reflected solar and upward terrestrial radiation $E \uparrow = E_r \uparrow + E_1 \uparrow$	W m ⁻²	$E \uparrow, E_{1,\lambda} \uparrow$
Radiation balance	Sum of the solar and terrestrial net radiation $E^* = E_s^* + E_1^* = E \downarrow - E \uparrow = (E_g \downarrow + E_1 \downarrow) - (E_r \uparrow + E_1 \uparrow)$	W m ⁻²	E^*, E_λ^*

^a The symbol E with the corresponding unit W m⁻² is chosen here because radiation E measurements at the ground are typically carried out as measurements of irradiance

^b For space-based measurements, this parameter is called the total solar irradiance (TSI)

Table 11.3 Other relevant parameters for radiation measurements

Parameter	Description	Unit	Symbol
Albedo	Ratio of the reflected solar radiation $E_r\uparrow$ impinging from the lower half-space on a horizontal plane (2π sr) to the total or global solar radiation incident on a horizontal plane from the upper half-space (2π sr)	dimensionless	ρ, ρ_λ

where z is the solar zenith angle. The solar upward radiation ($E_r\uparrow$) is the result of reflection of the incoming global radiation at the surface.

The downward terrestrial radiation or downwelling infrared radiation ($E_1\downarrow$) is emitted by atmospheric gases, constituents, and clouds in the atmosphere according to their temperature, while the upward terrestrial radiation or upwelling infrared radiation ($E_1\uparrow$) is mainly emitted by the Earth's surface according to its temperature (thermal radiation). Only a small part of the downward terrestrial radiation is reflected by the surface, and it is included in the upward terrestrial radiation. The downward and upward terrestrial radiation components lie within the same spectral region, so it is impossible to separate the measured upward terrestrial radiation into the parts that are emitted versus reflected by the surface.

Considering that nearly all radiation processes are wavelength sensitive, it is also necessary to consider and measure the corresponding spectral quantities or parameters in special cases, e.g., $E_{g,\lambda}\downarrow$. Some examples include photosynthetically active radiation (PAR) and ultraviolet (UV) radiation.

11.1.2 Measurement Principles

Instruments suitable for measuring radiation have been developed since about 1850. Because radiant energy and radiant power cannot be measured directly, one uses detectors that transform radiation into the energy of another type of response, e.g., thermal, electrical, chemical, or pyroelectric. The wide spectral region from about 300 to 50 000 nm (Sect. 11.3.1) to be explored, together with the wide range of radiation flux densities and (as noted in Sect. 11.1.1) the necessity to investigate broadband and spectrally resolved radiation separately, lead to great challenges regarding the development of radiation instruments. Because of the possibility of rapid changes in the radiation flux density, especially in the solar part of the spectrum, such sensors must also exhibit quick response times. A further challenge is to meet the requirement to measure the radiation quantity of interest as accurately as possible whilst the sensor has to be applied in a certain way or placed within the body of the instrument. Mainly, nonselective thermal detectors are applied to investigate

broadband radiation in the solar and terrestrial parts of the spectrum, while photoelectric sensors are only used to measure spectral regions of the solar radiation. Especially at the beginning, nearly all methods to make radiation measurements were tried out. However, nowadays, mainly methods where the sensor signal enables automatic acquisition of the quantity and the results are reproducible and traceable to the International System of Units (SI) are applied.

In general, radiation instruments are also called radiometers. Meteorological radiation instruments can be separated into several types according to the parameter they measure (Table 11.4).

Generalizing, it can be stated that the classical radiation instrument, being used for continuous field measurements covering the solar or/and terrestrial spectral region, has a thermopile as the receiver, protected by glass or a silicon dome that is coated with a special cutoff filter. Meanwhile, instruments that are applied to investigate only a smaller, special part of the solar spectrum use photodiodes as sensors. Details concerning the main types of instruments and their typical and different features are discussed in Sect. 11.4.

11.1.3 Measurement Sites

Considering that the environmental conditions at a site may influence the measurement results, the World Meteorological Organization (WMO) has performed [11.1, Annex 1.D.] *siting classifications for surface observing stations on land*, which are valid in general, and also published the text of the common ISO/WMO standard [11.2]. A site as a whole does not have a single classification number; rather, each parameter measured at a site has its own class, which may sometimes be different from the others.

Table 11.5 summarizes the classification regarding the measurement of solar radiation parameters from the upper half-space, which may help to classify a site.

In general, the selection of a measurement site depends on the goal of the investigations. It should be representative for the problem to be solved. For example, a site that is representative for the description of a larger region should not be influenced by small-scale topographic or local features (hills or industry), while a site typical for a special microclimate may have

Table 11.4 Classification of radiation instruments

Type of instrument	Parameter measured	Viewing angle (sr)	Remarks
Pyrheliometer	Direct solar radiation	5×10^{-3}	Used as: – Primary standard (absolute pyrheliometer) Receiver: cavity – Secondary standard (for calibration) – Field instrument Receiver: thermopile protected by glass (Sect. 11.4.1) Spectral pyrheliometer: with broad- or narrow-band filters Special case: sun photometer (Chap. 29), spectral radiometer Receiver: photodiode
Pyranometer	Upward looking: global or diffuse solar radiation Downward looking: reflected solar radiation	2π	Used as: – Working standard – Field instrument Receiver: thermopile protected by (a) glass dome(s) (Sect. 11.4.2) (spectral) pyranometer: Receiver: photodiode (Sect. 11.4.2; Chaps. 29, 37)
Pyrgeometer	Upward looking: downward terrestrial radiation Downward looking: upward terrestrial radiation	2π	Used as: – Working standard – Field instrument Receiver: thermopile protected by a silicon dome coated by a special cut on filter blocking the solar radiation (Sect. 11.4.3)
Pyrradiometer	Upward looking: total (global solar + downward terrestrial) radiation Downward looking: total (reflected solar + upward terrestrial) radiation	2π	Used as: – Working standard – Field instrument Receiver: thermopile protected by a polyethylene dome (Sect. 11.4.4)

Table 11.5 Classification of sites where solar radiation parameters from the upper-half space are measured [11.1] (φ : geographical latitude, h_S : altitude of Sun)

Class	Global and diffuse radiation	Direct radiation and sunshine duration
General	Close obstacles must be avoided. Shading due to natural relief is not taken into account for the classification. Nonreflecting obstacles below the visible horizon can be neglected. An obstacle is considered as reflecting if its albedo is greater than 0.5. The reference position for elevation angles is the sensing element of the instrument	Close obstacles must be avoided. Shading due to natural relief is not taken into account for the classification. Obstacles below the visible horizon can be neglected. The reference position for angles is the sensing element of the instrument
1a	$\varphi < 60$: $h_S > 5^\circ$: no shade onto the sensor $\varphi \geq 60$: $h_S > 3^\circ$: no shade onto the sensor	$h_S > 3^\circ$: no shade onto the sensor
1b	No nonshading reflecting obstacles with angular height above 5° and total angular width above 10° .	
2a	$\varphi < 60$: $h_S > 7^\circ$: no shade onto the sensor $\varphi \geq 60$: $h_S > 5^\circ$: no shade onto the sensor	$h_S > 5^\circ$: no shade onto sensor
2b	No nonshading reflecting obstacles with angular height above 7° and total angular width above 20°	
3a	$\varphi < 60$: $h_S > 10^\circ$: no shade onto the sensor $\varphi \geq 60$: $h_S > 7^\circ$: no shade onto the sensor	$h_S > 7^\circ$: no shade onto the sensor
3b	No nonshading reflecting obstacles with angular height above 15° and total angular width above 45°	
4	No shade for more than 30% of daytime, or any day of the year	No shade for more than 30% of daytime, or any day of the year
5	Shade projected during more than 30% of the daytime, for at least one day of the year	Shade projected during more than 30% of the daytime, for at least one day of the year

such characteristics. If measurement of upward radiation fluxes is required, it is also essential to select a site with a typical and representative surface to fulfill this objective.

In the case of planned long-term measurements, it is important that the surroundings of the chosen site should not be changed, to ensure the homogeneity of the time series to be acquired. Therefore, regular supervision of the station and its surroundings and documentation thereof are of major importance. Panoramic cameras or all-sky images are very helpful to accomplish horizon mapping.

According to [11.1], the following general requirements can be formulated:

The site should be readily accessible for construction and dismantling, but mainly for maintenance of all the equipment. The instruments should be securely attached and horizontally leveled if it is not intended to take special measurements, e.g., on tilted surfaces.

Upper Half-Space (Direct and Diffuse Solar Radiation, Global Radiation, and Downward Terrestrial Radiation)

In the ideal case, the site will be free from any obstructions above the sensor. If finding such a site is impracticable, the site must be as free as possible of obstructions that could shadow the receiver at any time of the year.

The horizon should not be limited by buildings, vegetation (trees or bushes), etc. above an elevation angle of 5° , especially within the azimuthal range between sunrise and sunset during the year, to record mainly direct solar radiation. Antennas and similar slender objects can be tolerated if their azimuthal angle is small ($< 1^\circ$) and they do not block the direct beam of radiation. Because light-colored walls or other objects (e.g., large window areas or photovoltaic panels) cause reflections that will enhance the solar diffuse radiation, pyranometers should not be installed close to them. Furthermore, it must be ensured that no strong local emitters of exhaust gases or dust lie in the direct vicinity of the site. Also, note that solar and terrestrial instruments should not be exposed to artificial radiation sources of light and heat, respectively.

Lower Half-Space (Reflected Solar Radiation and Upward Terrestrial Radiation)

In principle, the same conditions and precautions considered appropriate for the upper-half space also apply for down-facing pyranometers and pyrgeometers. How-

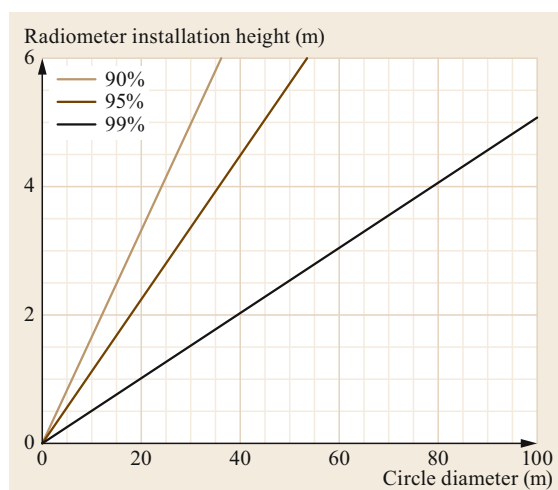


Fig. 11.1 Diameter of the area influencing the measurements of a down-facing pyranometer or pyrgeometer as a function of the installation height of the sensor (after [11.4] reprinted with permission from VDI – The Association of German Engineers)

ever, one must especially bear in mind that the ground should be appropriate to solve the task, considering the field of view of the instrument. According to [11.3], a sensor installed at a height 2 m above the surface will receive 90% of the radiation from a circle of 12 m diameter, and 95% from an 18-m circle. Figure 11.1 shows the diameter of the area influencing such measurements as a function of the installation height of the sensor. To ensure that the mounting rod disturbs the measurements as little as possible, it should be as thin as possible and with a polar position when the instrument points to the equator.

In regions with a lot of snow, there should be a mechanism to adjust the height of the pyranometer or pyrgeometer to keep the distance between the instrument and the snowpack as constant as possible. Furthermore, it should be ensured that maintenance of down-facing equipment is realized such that the reflecting features of the surface will not have an influence, too.

Radiation measurements on towers, special platforms, and ships require specific precautions (see also Chap. 7). In particular, for measurements from research vessels and ships, which are subject to continuous tilting motions, simple gimbal mountings may diminish such disturbances. Nowadays, computer-controlled roll–pitch–yaw angle-compensating systems or platforms are available.

11.2 History

Although, nowadays, solar and terrestrial radiation are of fundamental importance for meteorological processes and life in relation to other quantities, when their measurement started, the thermometer and barometer had been in use for about 200 years in physics and were already applied in regional meteorological networks.

The first, poor measurements were made around the middle of the 19th century. By the end of that century, about a dozen, highly specialized institutes and observatories around the globe were studying radiation and its measurements from the meteorological and climatological points of view.

Only the International Geophysical Year (IGY) 1957/58, one aim of which (among a lot of geophysical objectives) was to promote radiation measurements, encouraged homogenization of such measurements and the enlargement of the number of stations, although the Commission for Instruments and Methods of Observation (CIMO) of the WMO had already demanded a general improvement and extension of radiation measurements in its first session in 1953 [11.5]. The publishing of the *IGY Instruction Manual* [11.6] accomplished this highly valuable contribution. Thereafter, the World Radiation Data Center (WRDC) (<http://wrdc.mgo.rssi.ru/>, Accessed 05 July 2021) was established in St. Petersburg in 1964.

Around the start of the 1990s, the ongoing development of radiation measurements received an impetus from the climate community, resulting in the establishment of the Baseline Surface Radiation Network (BSRN) as a project of the Global Energy and Water Cycle Experiment (GEWEX) under the auspices of the World Climate Research Program (WCRP) ([11.7], see Chap. 63). Distinct targets mainly in terms of accuracy and rules for data acquisition and handling as well as maintenance were presented and summarized in the *BSRN Operations Manual* [11.8, 9], leading to investigations and improvements of such instruments. It highlighted the generation of high-quality and comprehensive datasets from sites representing a typical climate and/or atmospheric conditions such as aerosols or clouds. In 2004, the BSRN was designated as the global baseline network for surface radiation measurements for the Global Climate Observing System (GCOS). These data are gathered and provided by the World Radiation Monitoring Center (WRMC) operated by the Alfred Wegener Institute (AWI) (<https://bsrn.awi.de/>, Accessed 05 July 2021).

The first comprehensive reviews on radiation instruments were published by *Fritz Albrecht* (1896–1965) in 1935 [11.10] and *Walter Mörkofer* (1892–1976) in 1939 [11.11]. About 30 years later, in 1969, the book entitled *Solar Radiation* by *Nathan Robinson* [11.12]

came out. In 1986, *Claus Fröhlich* (1936–2019) and *Julius London* (1917–2009) edited on the request of WMO a *Revised Instruction Manual on Radiation Instruments and Measurements* [11.13], an updated guide of the IGY manual. Furthermore, Chap. 7 of the so-called WMO–CIMO Guide [11.1], which has since become a *living document*, provides a good overview on how to conduct radiation measurements in the framework of the WMO.

11.2.1 Pyrheliometers

A pyrheliometer measures direct solar radiation in a full opening angle of 5° , although in the past this angle was not standardized and older instruments may deviate from this. In some cases, rectangular apertures were applied, too (e.g., the Ångström and Michelson–Marten pyrheliometers) (see also Tables 11.2–11.4).

Nowadays, all instruments for measuring direct solar radiation at the ground are called pyrheliometers, independently of whether they require calibration, while previously pyrheliometers that required calibration were called actinometers.

Pouillet's Pyrheliometer (1838)

According to different sources [11.10, 11, 14], the first measurements of direct solar radiation with absolute albedo crude results were carried out by *Claude Servais Mathias Pouillet* (1790–1868) in 1838 using his pyrheliometer (Fig. 11.2). This pyrheliometer consisted of a flat, water-filled cylindrical capsule made from sheet silver with capacity of about 100 cm^3 . The front side, which was directed towards the Sun, was blackened with soot. The bulb of a thermometer extended into the capsule from the back side. The measurement was made by the so-called dynamical method. A 5 min period of irradiating the front side of the capsule was sandwiched between shading periods of 5 min at the beginning and end of the measurements. The temperatures were determined at the beginning and end of the measurements (t_0 , t_3) as well as at the switching points (t_1 , t_2) from shade to irradiation and vice versa. Knowing the heat capacity of the water-filled capsule c (which is difficult to determine and therefore highly error prone), the irradiance E_1 can then be calculated as

$$E_1 = \frac{c}{\tau} \left[t_2 - t_1 + \frac{(t_1 - t_0) + (t_3 - t_2)}{2} \right]. \quad (11.2)$$

Later, this instrument was improved by *Violle* (1874) and *Crova* (1877) as well as other scientists. However, irradiances measured using all these pyrheliometers were incorrect because of the negative influ-

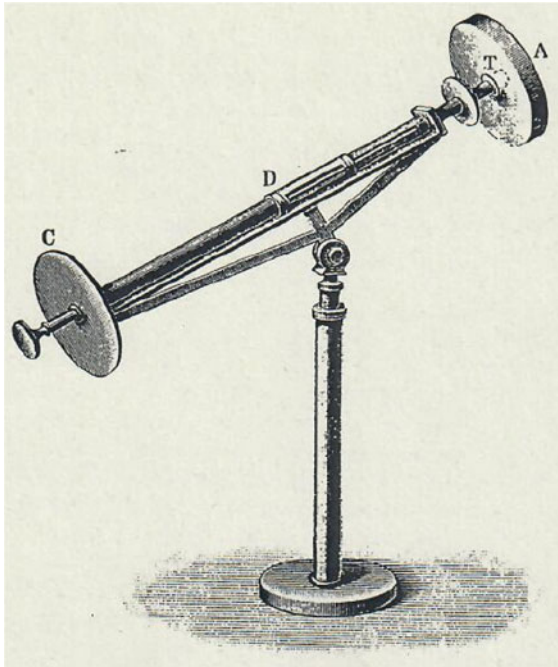


Fig. 11.2 Pouillet's pyrheliometer. A: blackened receiver (metallic container filled with water); D, C: alignment checks; T: thermometer bulb (after [11.15] © Bureau international des Poids et Mesures. Reproduced by permission of IOP Publishing. All rights reserved)

ences of, e.g., wind, convection, and large inertia, which could not be eliminated.

Around the end of the 19th century, a breakthrough was achieved with the development of the Ångström compensation pyrheliometer in 1893 by *Knut Ångström* (1857–1910) [11.16] and the water-flow pyrheliometer by *Charles Greeley Abbot* (1872–1973) in 1905 [11.17].

Ångström Compensation Pyrheliometer (1893)

Ångström used two identical thin, blackened Manganin strips, arranged in parallel at the end of a tube, each bearing on its back an electrically insulated but thermally contacted thermocouple. Both strips were placed in an electrical circuit, which was linked to a flexible shutter situated at the front of the tube. While the tube with the strips, behind two rectangular apertures, was directed perpendicular to the sunbeams, this shutter alternately shaded one strip. During the measurement, the shaded strip was heated by an electrical current while the other strip was irradiated by the Sun. When the thermocouples are connected differentially in a galvanometer circuit, this instrument shows zero if the power of the controlled heater current equals the power of the Sun. However, this equality is only valid if the left- and right-hand strips and their thermocouples are

identical. Because this is difficult to achieve, in practice the left- and right-hand sides are alternately heated and irradiated to overcome any possible asymmetry and the mean current i_m is computed as

$$i_m = \frac{i_{L1} + i_{L2} + 2i_R}{4}, \quad (11.3)$$

where i_{L1} , i_{L2} , and i_R the current readings of the left- and right-hand strips, respectively.

Finally, the direct solar irradiance (E) can be calculated as

$$E = ki_m^2, \quad (11.4)$$

where k is a constant related to the particular instrument. In the case of an absolute instrument, k can be determined from various parameters of the instrument such as the absorptivity and length of the strips as well as the electrical resistance per unit length of the strips. In practice, this difficult task was only carried out for the first accurately built pyrheliometer, while the value of k for other sensors was determined by side-by-side comparison with the Sun as the radiation source. Figure 11.3 shows the schematic circuit and a photograph of the Ångström pyrheliometer.

The method of compensation of the power of the Sun by electrical power, which can be determined very exactly, was first applied by Ångström in meteorology, while independently *Ferdinand Kurlbaum* (1857–1927) used this principle in experimental physics.

In 1905, at the Conference of the Directors of Meteorological Services in Innsbruck, the Ångström pyrheliometer was recommended for observation of solar radiation. One of the original Ångström pyrheliometers (A-70) situated in Sweden was adopted as a reference and established a link to the Ångström scale, the first scale for solar radiation measurements in the world [11.15].

Even nowadays, the compensation of heat fluxes generated by the absorption of radiant flux by a precisely determined electrical flux forms the basis for the construction of absolute pyrheliometers. This crucial development became successful with the transition from the use of direct to comparative calorimetry [11.18].

Water-Flow Pyrheliometer (1905), Water-Stir Pyrheliometer (1913), Silver-Disk Pyrheliometer (1909)

Based on its working principle, Abbot's water-flow pyrheliometer (Fig. 11.4) is actually a calorimeter, because the irradiance is computed based on exact knowledge of the amount of water, the difference in temperature between the water at the inlet and outlet, and the time of exposure. The water flows between the walls of an irradiated conical receiver. However, after

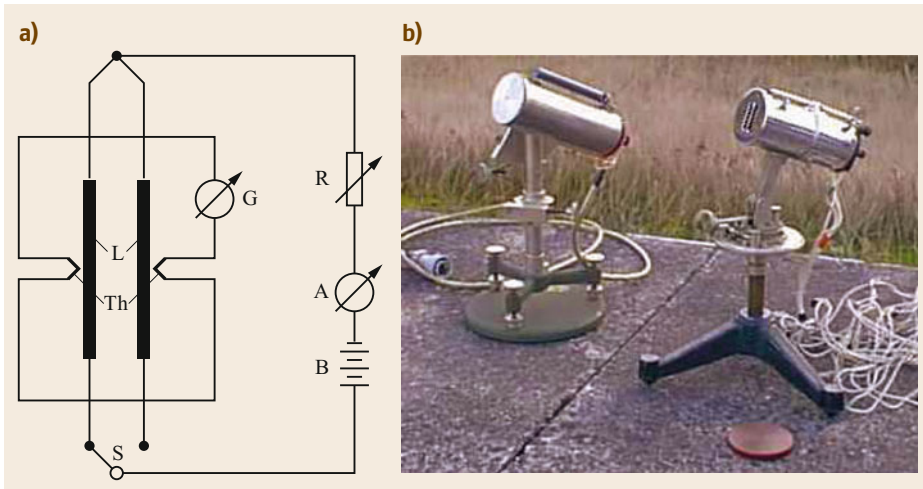


Fig. 11.3 (a) Circuit of Ångström pyr heliometer: L: blackened Manganin strips; Th: thermocouples; G: null galvanometer; A: amperemeter; R: resistance controlling the heater current; B: battery; S: switch to change between heating and shading or irradiating the corresponding strip (after [11.14] with permission from John Wiley and Sons). (b) Two Ångström pyr heliometers of different generations (*right*: A-584; *left*: A-140) manufactured in Sweden without any auxiliary equipment (photo: K. Behrens)

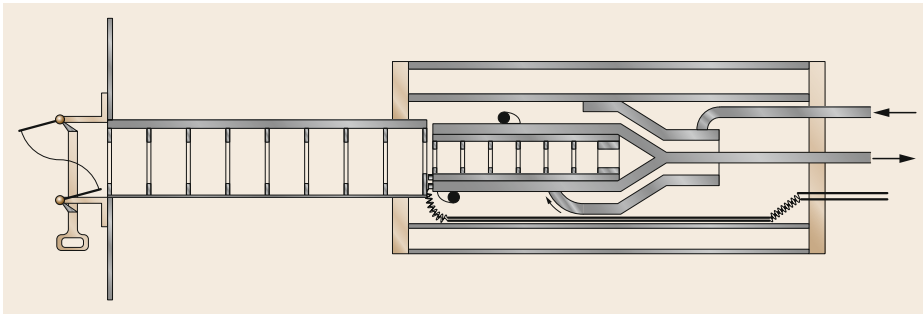


Fig. 11.4 Cross-section of Abbot's water-flow pyr heliometer (after [11.10])

the radiation measurement, a coil of known resistance in the instrument is used to generate the same amount of heat as produced by the solar radiation and thereby verify the result. In this regard, the process of compensation is again applied. In contrast to the Ångström pyr heliometer, the receiver of the water-flow pyr heliometer is constructed using an advantageous type of cavity. Later [11.19], the water-stir pyr heliometer was developed at the Smithsonian Institute to confirm the measurement results of the water-flow pyr heliometer. This new instrument had a similar design and operating principle to the water-flow pyr heliometer, but instead of a continuous water flow, a closed system was used and the water was stirred during the solar heating. Furthermore, it was again possible to verify the results using a coil based on the compensation principle.

As early as 1902, based on the above-described Pouillet pyr heliometer and its modification by Tyn-

dall, Abbot constructed the silver-disk pyr heliometer (Fig. 11.5), which was improved and led in 1909 to the type described in [11.20]. This instrument was very stable and used as a secondary standard which had to be calibrated by comparison with a standard (a water-flow or water-stir pyr heliometer). Because it was impossible to use these water-flow and water-stir pyr heliometers at other locations, Abbot [11.20] in 1911 wrote:

The purpose of the silver disk pyr heliometer is merely to furnish readings proportional to the intensity of radiation of the sun, and comparable one with another at all times and places, but not to furnish independent means of reducing these readings to true heat unit. [...] They must therefore be regarded as secondary instruments, useful only for relative readings, unless standardized by comparison with true standard pyr heliometers.

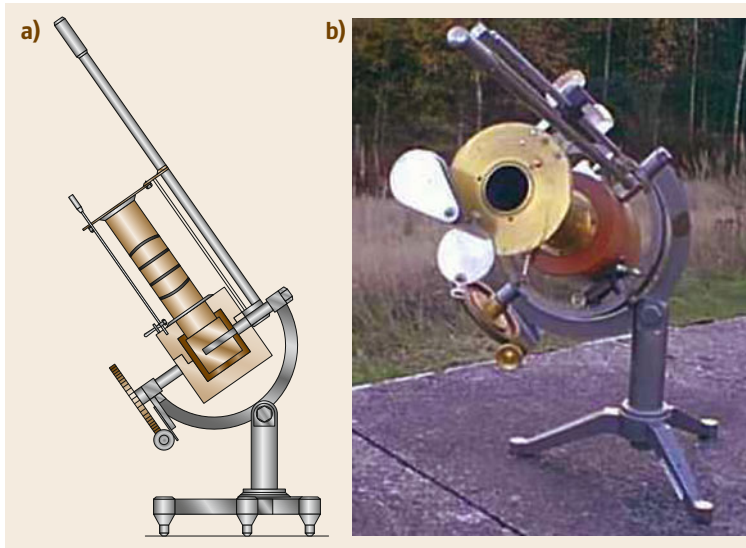


Fig. 11.5 (a) Cross-section of the silver-disk pyrheliometer (after [11.10]). (b) View of the silver-disk pyrheliometer SI 19 with its open circular entrance and shutter (photo: K. Behrens)

Comparisons between water-flow and water-stir pyrheliometers as well as different silver-disk pyrheliometers led to the definition of the revised Smithsonian scale of 1913 [11.21], which was disseminated all over the world with the help of silver-disk pyrheliometers.

Marvin Pyrheliometer (1910)

The Marvin pyrheliometer resembles the silver-disk pyrheliometer in its construction, but instead of a mercury-in-glass thermometer, it uses a resistance wire for temperature determination. Furthermore, in contrast to the silver-disk pyrheliometer, it is fixed on a clock-driven equatorial mount that allows automatic tracking of the Sun. A shutter is mounted on the end of the tube and opened or closed alternately using magnets activated by a clock at the end of each minute. Instruments with this configuration were used by the US Weather Bureau for several years [11.22].

Pyrheliometers with a Thermopile Sensor

This subsection describes various pyrheliometers with one common feature, viz. they all use a thermopile (Sect. 11.3) as a sensor to convert the received radiant energy into electrical energy. According to [11.10, 11], Crova applied a thermopile for radiation measurements for the first time as early as 1885. However, because of the use of copper–iron thermoelements, which generated only a small thermovoltage, this principle did not gain wide acceptance.

Later, *Sawinoff* (1912), *Dorno-Thilenius* (1920), and *Linke* (1921) also developed pyrheliometers that used different thermopiles with better features as detectors, but these instruments also did not receive

wide acceptance for other reasons [11.10]. The instrument constructed by *Sawinoff* was refined by *Yanishkevsky* [11.23] and furthermore applied in the USSR.

A breakthrough was achieved by *Wladyslaw Gorczynski* (1879–1953) in 1924 [11.24] by implementing the thermopile engineered by *Willem Jan Henri Moll* (1876–1947) [11.25] to construct a new pyrheliometer. It was set in a

solid cylinder which was closed at one end by an ebonite plate with two terminals, and at the other end by a heavy brass lid, into which a protecting window is fixed. [11.24]

In contrast to the thermopile used by Crova, the new type developed by Moll using Constantan–Manganin strips offers several advantages: it was free from zero errors, had a rugged form, fast operation, and high sensitivity. In combination with an appropriate recording millivoltmeter and a clock-driven equatorial mount, it was possible to gather daily profiles of direct solar radiation (Fig. 11.6). Furthermore, Gorczynski note that he could apply various filters to investigate different parts of the solar spectrum and that it was easy to use after calibration, especially because of the ability to record measurements at ordinary stations.

In 1932, *Franz Linke* (1878–1944) together with *Karl Feussner* (1902–1982) used also the Moll thermopile but embedded in a copper block with five internal diaphragms. This massive block served as a heat sink and stabilized the temperature conditions for the whole instrument. This instrument (Fig. 11.7), known as the the Linke–Feussner pyrheliometer (or also the *Panzeraktinometer* in German because of the massive

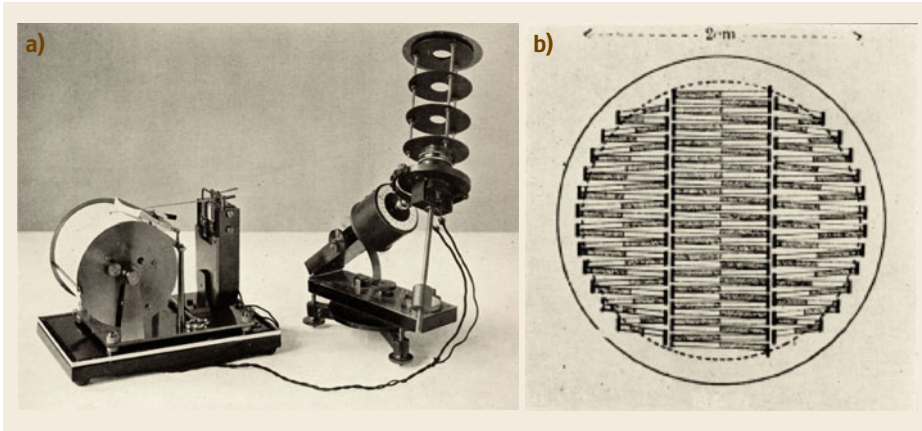


Fig. 11.6 (a) The Moll–Gorczyński pyrheliometer equatorially mounted on a clock drive and connected to a recording drum. (b) The implemented large thermopile (after [11.24])

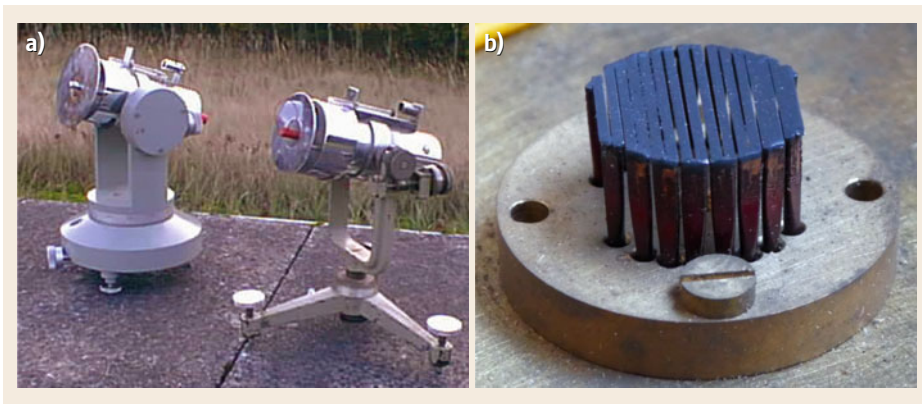


Fig. 11.7 (a) Two Linke–Feussner pyrheliometers of different generations. The one on the left was manufactured by Kipp and Zonen in the 1950s and later, while that on the right is from the first generation from the 1930s. (b) A thermopile from a first-generation instrument (photos: K. Behrens)

block [11.14]) was manufactured more than 30 years by Kipp and Zonen in the Netherlands.

At the beginning of the 1950s, a further pyrheliometer named the Eppley normal incidence pyrheliometer (NIP) was developed. It has a copper–Constantan thermopile with a circular receiver mounted in a brass tube with two view-limiting baffles. The tube is closed by a quartz window in front, filled with dry air, and sealed [11.12].

Measurements by all of these thermoelectric pyrheliometers show a dependence on the ambient temperature. The Linke–Feussner pyrheliometer is equipped with a mercury-in-glass thermometer to enabling correction for this effect. Later, the NIP was changed several times to reduce its dependence on the ambient temperature by employing a new thermopile, a temperature-compensating circuit, and a double-walled tube. These changes led to measurements with

improved uncertainty related to the ambient temperature dependence. Furthermore, an embedded thermistor could be used to determine the temperature of the instrument for such corrections.

The NIP and Moll–Gorczyński pyrheliometer are typically closed by a front window, mounted on an equatorial tracker, connected to corresponding recorders, and used as *all-weather* instruments, while all the other instruments had to be operated manually and only under fair weather.

Because of the interest in obtaining information about the spectral distribution of the solar radiation, a wheel fit with colored glass filters could be mounted in front of the entrance of the Moll–Gorczyński pyrheliometer or NIP, or included as a standard feature in the Linke–Feussner pyrheliometer. Frequently, the internationally recommended bandpass filters OG1, RG2, and RG8 manufactured by Schott and Gen. (Germany)

with respectively cut-on values of 525, 630, and 710 nm and cut-off values of 2800, 2800 and 2700 nm were used [11.6].

It is important to mention that, to obtain accurate results, the reading voltmeter, usually a moving-coil instrument, had to be selected very carefully because of the different sensitivity and resistance values of thermopiles. Similarly, this also applied in the past to the instrument selected for the rarely performed recordings of direct solar radiation.

Michelson Bimetallic Actinometer (Pyrheliometer)

In 1905, *Vladimir Alexandrovitsch Michelson* (1860–1927) in Moscow developed a pyrheliometer with a rectangular aperture which used a very thin blackened strip made of iron and nickel steel as the sensor [11.26]. In contrast to the several Smithsonian instruments, it was very sensitive, because of its low heat capacity. The strip located in a metal block with a small hole was alternately shaded and irradiated, causing it to bend. The resulting change in position, observed using a microscope, corresponds to the change of temperature and therefore amount of irradiance.

This instrument was changed and improved by various scientists. Probably the most well-known changes were made by *Wilhelm Marten* (1874–1949) and later *Konrad Büttner* (1903–1970), because the resulting instruments are mentioned, for instance, in the *IGY Instruction Manual* [11.6]. Marten improved this instrument (Fig. 11.8) several times between 1912 and 1928 [11.27], and it was equipped with different recommended [11.6] colored glass filters for the measurement of separate spectral regions. The device constructed by Michelson and Marten depends on the ambient tem-

perature, leading to changes in the zero point (shaded phase), while *Büttner* [11.28] added a second strip to compensate for this effect.

11.2.2 Pyranometers

A pyranometer, mounted upward facing, can measure the global or—when additionally equipped with a shadow band/ring or a disc—the diffuse solar radiation with a viewing angle of 2π sr. When looking downward it measures the reflected solar radiation (see also Tables 11.2–11.4). If upward- and downward-facing pyranometers are combined into a single unit, the result is sometimes called an *albedometer*. However, this name is incorrect, because the albedo is defined as the ratio of the total reflected solar irradiance to the global irradiance. Indeed, this quantity cannot be measured directly. In contrast, it is possible to measure the solar net radiation immediately by applying a differencing circuit between an upward- and downward-looking pyranometer using thermopiles as detectors, for instance. This type of instrument is called a *net radiometer*. A second way to calculate the solar net radiation is as the difference between the downward- and upward-directed fluxes. Using these fluxes, it is of course also possible to calculate the albedo, too (Tables 11.2–11.4).

The first adequate and properly functioning pyranometer was that of *Hugh Longbourne Callendar* (1863–1930), a British physicist. Its first version was described in a paper by *Callendar* and *Fowler* in 1906 [11.30], in which they reported on the total solar eclipse in August 1905.

The horizontal bolometer was of the usual type designed for recording the vertical component of sun and sky radiation. It consisted simply of a pair of platinum thermometers wound on a horizontal mica plate fixed in a sealed glass bulb. One of the thermometers being coated with black enamel is raised to a higher temperature than the other by exposure to radiation. The difference is very nearly proportional to the intensity of the radiation, and is automatically recorded on an electrical recorder of the usual type. It is, of course, necessary for an instrument intended to be exposed in all weathers that the surface receiving radiation should be protected by a glass bulb [11.30].

Later on, this was called the *Callendar pyrheliometer* [11.31] or *Callendar bolometric sunshine receiver* [11.32], and an improved version with two black and two shiny platinum grids was mainly applied in the USA and Great Britain over a number of years. Simple



Fig. 11.8 Michelson–Marten pyrheliometer with the rectangular entrance, that can be seen in the photo (photo: K. Behrens)

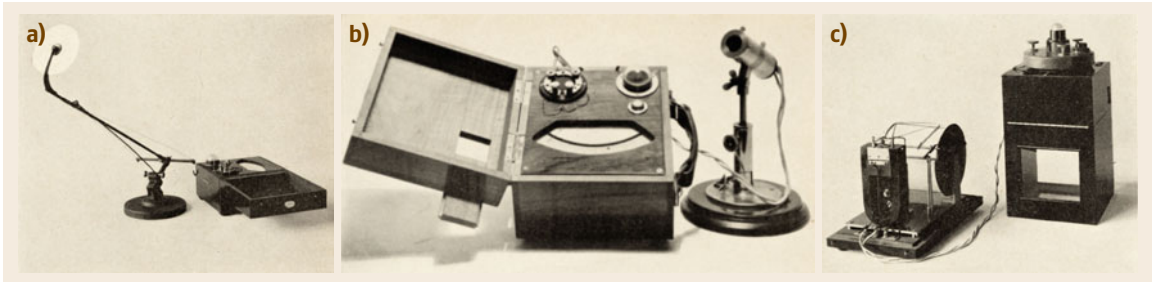


Fig. 11.9a–c The Moll–Gorczyński *solarimeter* as described in the text. (a) Pyranometer with screen measuring diffuse solar radiation. (b) Pyrheliometer on a holder together with a pyranometer in a wooden box. (c) (Weatherproof) pyranometer with recording drum prepared for continuous measurements (after [11.29])

recording with the help of a self-adjusting Wheatstone bridge enabled its easy and successful use, although some important shortcomings were presented as early as 1915 [11.32].

Further pyranometers were developed by *Abbot and Aldrich* (1884–1965) in 1916 [11.33, 34] and *Anders Ångström* (1888–1981) in 1919 [11.35], who tried to apply the idea of *Knut Ångström*, viz. the method of electrical compensation as applied in his well-known and successful pyrheliometer, to pyranometers. It is of some interest to indicate here that US instruments were also able to measure the thermal radiation during nighttime if operated without the glass hemisphere, blocking wavelengths greater than about 3000 nm. However, because of various shortcomings and other factors, these instruments did not gain permanent acceptance.

It is important to note that *Abbot and Aldrich* devised the term *pyranometer* for an instrument measuring the solar radiation from the Sun and sky and applied it for the first time in [11.33].

Pyranometers with Thermopile Sensors

As already mentioned in the section on pyrheliometers, thermopiles have proved to be nearly ideal sensors for the measurement of irradiance.

In contrast to pyrheliometers, which only use *black* thermopiles, in the case of pyranometers it is possible to use *black* as well as *black-and-white* thermopiles. The most well-known and only historically relevant pyranometer with a black thermopile is the instrument developed by *Gorczyński* [11.29], frequently called a *solarimeter* (Fig. 11.9). The original thermopile as used in the pyrheliometer was specially adapted for use in the pyranometer to avoid the influence of the changing angle of incidence of the solar beam. This new thermopile was embedded in a brass cylinder covered by a glass hemisphere. The version designed primarily for direct readings consisted of a solarimeter combined with a millivoltmeter in a wooden box. The same type of thermopile arranged in a pyrheliometric tube closed by a spher-

cylindrical lens or flat glass disc and mounted on a special holder could also be connected to the millivoltmeter. This set was completed by a circular sunscreen. This system allowed alternate measurements of the global, diffuse, and direct solar radiation. A second version applied for continuous recording consisted of the same weatherproof solarimeter mounted on a special holder for permanent outdoor installation and connected to a recorder. Extensive investigations, especially of the recording system, soon revealed various deficiencies, which led to improvements. One of the most important points was the introduction of the pyranometer with a second glass hemisphere to stabilize the nighttime zero points, as mentioned in [11.11]. The *solarimeter* was manufactured by Kipp and Zonen (the Netherlands) and consequently advanced to one of today's state-of-the-art pyranometers.

As early as 1923, the US Weather Bureau in cooperation with the US Bureau of Standards [11.36] developed “a very convenient form of a thermoelectric recording pyrheliometer” consisting of an annular black inner and a white outer ring with thermocouples arranged behind them, covered by a glass dome (Fig. 11.10a). Later, this instrument was manufactured and improved by Eppley Laboratory Inc. It was known as the 180° *pyrheliometer* (Fig. 11.10b) and, despite known shortcomings, was applied in US networks for decades thereafter.

Also, *black-and-white* thermopiles were used in a checkerboard configuration. According to [11.10], Sawinoff in 1922 and later *Volochine* in 1932 developed this kind of sensor [11.37]. While in the construction of Volochine the checkerboard was surrounded by a black area, the thermopile of Sawinoff was embedded in a white surface. The instrument made by Sawinoff, after a refinement by *Yanishevsky* [11.23], was later applied in the USSR.

A further possibility is the radial arrangement of the *black-and-white* thermopiles like a star. According to [11.11], an early representative of this type is the pyranometer introduced by Linke in 1934 (Fig. 11.11).

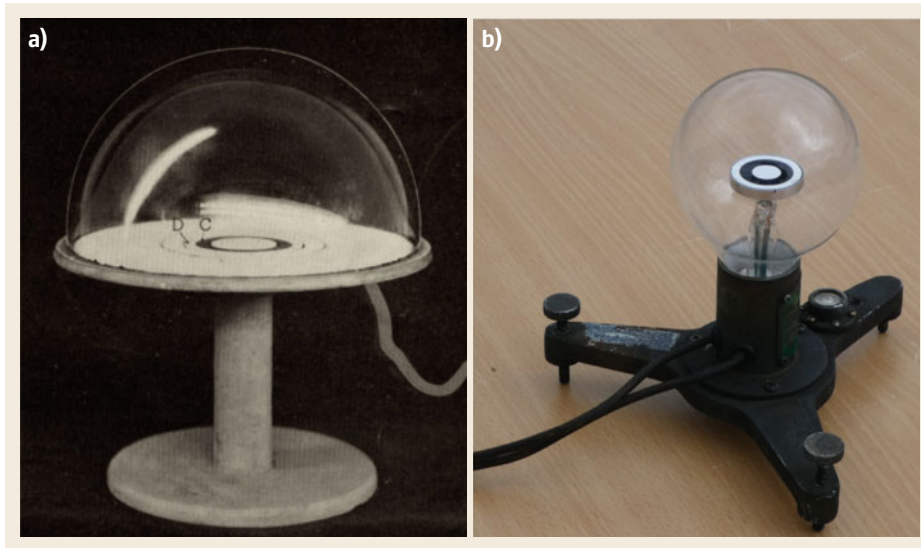


Fig. 11.10a,b 180° pyrheliometer – US Weather Bureau version (a) (after [11.36]) and Eppley Laboratory Inc. version (b), widely known as the *light bulb* (photo: K. Behrens)



Fig. 11.11 Two star pyranometers from different generations: *Left* a modern one manufactured by Fa. Ph. Schenk, Wien and *right* a historical version from the 1930s (photo: K. Behrens)

Robitzsch Bimetallic Pyranometer

As early as 1915, *Max Robitzsch* (1887–1952) [11.38] first reported an instrument based on two nearly equal bimetallic thermometers, one blackened and the other polished, arranged coaxially such that end A of the first was fixed to a ground plate while end B was free. End B' of the second thermometer was rigidly connected to end B, while excluding thermal conduction. The free end A' of the second thermometer held a transfer lever to record on a rotating drum. Because of its construction, this *thermograph* does not show any deflection if both thermometers have the same temperature. However, insolation results in a temperature difference between the blackened and polished thermometers, being proportional to the irradiance. Because the system is sensitive to air movement, it was protected using a glass cuvette. This paper was entitled *Vorläufige Mitteilung über einen neuen Sonnenscheinautographen* (Preliminary information about a new sunshine recorder), because it was his intention to develop an improved sunshine recorder that could also record

the changing irradiance, a feature that existing sunshine recorders did not offer. In the following years, *Robitzsch* improved this instrument step by step based on its known imperfections [11.39]. In 1930, in cooperation with the Fuess company of Berlin, which manufactured the instrument (Fig. 11.12), great progress was achieved. Meanwhile, the application of available thermometers made from industrial welded bimetallic sheet metal which did not exhibit any individual differences, improved spectrally stable paints, and the use of three instead of two stripes (bimetallic thermometers) led to an instrument which fulfilled the demands for a simple and easy-to-use pyranometer with the ability to record the changing irradiance using an ink pen on a chart mounted on a clock-driven drum. The system consisting of the bimetallic sensor, transfer lever, and recording drum was placed in a weatherproof metal case. An aperture over the sensor was protected by a glass dome, enabling the transmission of solar but excluding thermal radiation. He described this instrument in depth in the paper [11.40]. Later, in a paper from 1938 [11.41],

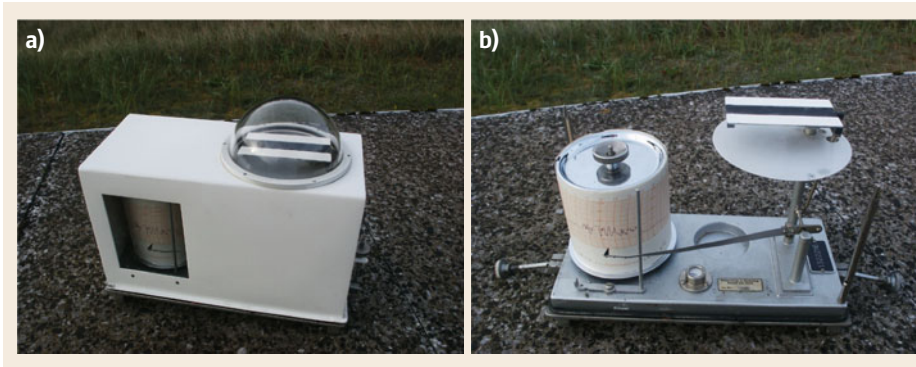


Fig. 11.12a,b
Robitzsch pyranograph manufactured by Fuess. (a) Instrument in working mode, (b) cover removed, showing details of the bimetallic receiver and recording drum (photos: K. Behrens)

Robitzsch reported on the calibration of this instrument as well as its imperfections (e.g., dependence on temperature, and azimuth and altitude of the Sun) and the impossibility of eliminating these effects as well as the resulting uncertainty in such measurements.

Despite its weak spots, this type of instrument was widely used and manufactured, not only in Germany but also in Great Britain and Italy, mainly because of its simplicity and possible use at remote stations.

11.2.3 Pyrgeometers

A pyrgeometer measures the terrestrial downward or upward radiation with a viewing angle of 2π sr (Tables 11.2–11.4). Transferring his successful idea of electrical compensation from the solar to terrestrial spectral region, in 1905 *Knut Ångström* [11.42] constructed a compensation pyrgeometer (Fig. 11.13), which is only usable at night. In contrast to the pyr heliometer, where one strip is irradiated and heated by the Sun while the other is shaded and heated by an electrical current, two blackened and two blank metallic strips with different emissivity, mainly in the thermal spectral region, were applied in the case of the pyrgeometer.

In this design, the distinct sky-facing strips emit different amounts of energy, leading to a temperature difference between the blackened and blank strips. This difference in temperature is determined by thermoelements at the back of the strips and equalized using an electrical current as in the pyr heliometer. Furthermore, it was possible to use a mercury-in-glass thermometer to determine the instrument (body) temperature, which is required to calculate the atmospheric downward radiation.

However, it proved very difficult to determine the value of the constant of the pyrgeometer that is required to calculate the terrestrial downward radiation. Therefore, *Ångström* decided to calibrate the pyrgeometer with the help of a black body, finally resulting in good results.



Fig. 11.13 Ångström pyrgeometer (photo: K. Behrens)

Because the sensor strips are freely exposed to the sky, measurements with this pyrgeometer are only possible in fair weather. Furthermore, it is very sensitive to changes in wind speed. Therefore, proper measurements can only be obtained on clear and calm nights.

As mentioned above in the section on pyranometers, in 1916 *Abbot* and *Aldrich* [11.33, 34] developed pyranometers which could measure downward terrestrial radiation without their glass domes only during the nighttime. In 1922, *Aldrich* [11.43] described a special instrument named after the Greek word *Melikeron*, meaning *honeycomb*. Because of doubt regarding whether the absorbers (sensors, black paints) used in previously applied methods were also good enough in the terrestrial spectral region, an approximately *black body* absorber was tried as the sensor. Honeycomb-like tubes were formed into a relatively large sensor area of about 3×3 cm². A temperature difference arose between the *honeycomb* sensor

and the instrument body when the sensor was exposed to the night sky and was measured by thermoelements. The loss of heat by radiation from the sensor was compensated by an electrical current. Comparisons between the Ångström pyrgeometer and the Melikeron showed differing results, so it was stated [11.43] that further investigations were necessary.

The above-mentioned limitations concerning the dependence of the Ångström pyrgeometer on weather conditions also apply to the described Smithsonian instruments. Therefore, recording terrestrial radiation using these instruments is impossible.

11.2.4 Pyrradiometers

A pyrradiometer measures the downward total (global solar + downward terrestrial) or upward total (reflected solar + upward terrestrial) radiation in a viewing angle of 2π sr (see also Tables 11.2–11.4). If a downward- and an upward-facing pyrradiometer are combined into one unit, it is called a *total net radiometer*. It is possible to determine the total net radiation in three ways:

- Directly measuring the total net radiation using only one thermopile with hot upward-facing and cold downward-facing junctions, because the difference in temperature is proportional to the net irradiance
- Measure the total net radiation immediately by applying a differentiating circuit between a downward- and upward-looking pyrradiometer using two thermopiles as detectors
- Calculate it as the difference between the measured downward- and upward-directed fluxes (Tables 11.2–11.4).

Like pyranometers, pyrradiometers also use thermopiles as sensors. The first suitable instruments were constructed in the late 1940s and the beginning of the 1950s. Because of the urgent need for information regarding the downward and upward terrestrial radiation fluxes for use in the atmospheric sciences prior to the

planned IGY, an *intercomparison of longwave radiation instruments* was organized in Hamburg, Germany. Sixteen different models participated in these comparisons, which were carried out for two weeks in each of September 1955 and May 1956. Most of them were still under development or suffered from other restrictions that did not allow continuous measurements under all weather conditions [11.6]. As a result, it was stated that it was not possible “to publish formal recommendations on the reliability and the value of the different designs” [11.44]. Some instruments, for instance the Gier and Dunkle ventilated radiometer [11.45], worked with unprotected receivers, where the constant airflow over the sensors should avoid the effect of changing wind speed on the detector plates. However, such basic approaches did not finally gain acceptance.

Another instrument that participated was the Schulze radiation balance meter ([11.47], Fig. 11.14). Two thermopiles, one upward and one downward facing, enabled separate measurements of the radiation fluxes from the upper and lower half-spaces. Because of this, the upper and lower part of the balance meter can be considered to represent single pyrradiometers. When the receivers are connected in opposition, the total net radiation (radiation balance) is measured. At that time, the most important innovation made by *Rudolf Schulze* (1906–1974) was the introduction of Lupolen-H (polyethylene). Lupolen has the outstanding feature of transmitting radiation between 300 and 50 000 nm, i.e., the solar and terrestrial regions of the spectrum, which is important for atmospheric physics. As seen in Fig. 11.15, the transmission curve of Lupolen-H is quite stable over the whole region at about 80%, with the exception of three bands in the thermal region. This results in distinct sensitivities for the solar and thermal areas. Therefore, it is necessary to conduct separate calibrations for these two regions. The thermopiles, each protected by a weatherproof hemispherical Lupolen shield, are located at the center of a white-coated cylinder. Air is blown into the cylinder from one side and continuously flows around both hemispheres.



Fig. 11.14 Schulze radiation balance meter with blower (photo: K. Behrens)

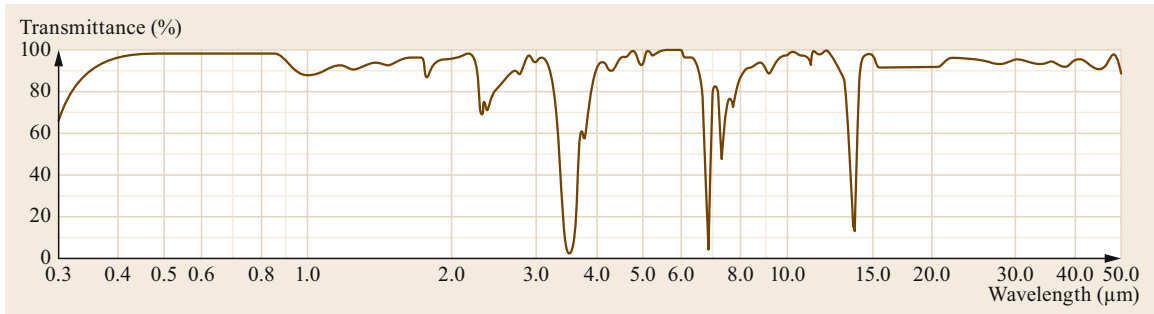


Fig. 11.15 Transmission of Lupolen-H (after [11.46])

A thermocouple measuring the body temperature allowed the calculation of the atmospheric downward and upward radiation, assuming that the global and reflected radiation were additionally measured using separate pyranometers. At that time, such shielded instruments were highly advantageous for continuous measurements of solar and terrestrial irradiance. Their disadvantage was the requirement to use pyranometers during daytime in parallel with separate solar and terrestrial fluxes, which inevitably leads to greater uncertainties in the determination of the thermal radiation. The Schulze radiation balance meter, which later achieved acceptance and widespread use, was frequently investigated and its imperfections improved as far as possible. Furthermore, similar instruments were developed by other scientists [11.48] and manufactured, too.

11.2.5 Pyrheliometric Scales

Comparisons between Ångström and silver-disk pyrheliometers (Sect. 11.2.1), representing the Ångström scale and the Smithsonian scale (revised 1913), respectively, made at different sites and institutions showed various nonnegligible differences, which should not exist. As a consequence, the Commission for Solar Radiation (CSR), which was established by the Conference of Directors of Meteorological Services in 1905 in Innsbruck, solved the problem of these differences between the two scales by the adaption of a 3.5% difference at their meeting in 1923. From this moment, radiation values were to be reported on the Smithsonian scale by using a silver-disk pyrheliometer or by augmenting results from an Ångström pyrheliometer by 3.5% [11.15]. The discussions and comparisons went on thereafter, and two further pyrheliometers were developed. In cooperation between the Potsdam Meteorological Observatory and the Physikalisch-Technische Reichsanstalt in Berlin, a double water-stir pyrheliometer was developed [11.49], while in 1932 *Abbot* and *Aldrich* [11.50] at the Smithsonian Institution constructed after a proposal by *Shulgin* in 1927 [11.51]

an improved double water-flow pyrheliometer based on the 1905 instrument. Both new instruments used cavities as receivers and applied the compensation method of electrically generated heat. However, the problems and reasons for the differences between these two scales could not be solved [11.15].

In preparation for the International Geophysical Year (IGY) 1957/58, one aspect of which was the organization of worldwide radiation measurements, it was necessary, because of the parallel use of the two pyrheliometric scales, to homogenize the measurements. Experts participating at the International Radiation Conference at Davos in 1956 found a *solution* by defining the International Pyrheliometric Scale 1956 (IPS 1956) based on the following relations:

$$\begin{aligned} \text{IPS 1956} &= \text{Ångström scale} && + 1.5\% \\ \text{IPS 1956} &= \text{Smithsonian scale rev. 1913} && - 2.0\% \end{aligned}$$

This definition was adopted by the Commission for Instruments and Methods of Observation (CIMO) of the WMO and introduced as mandatory by the WMO effective 1 January 1957 [11.6].

Furthermore, the CIMO organized the First International Pyrheliometer Comparison (IPC I) with the goal of implementing IPS 1956 worldwide. IPC I in 1959 and later IPC II in 1964 took place at the Physikalisch-Meteorologisches Observatorium Davos (PMOD). During these comparisons, the Swedish Ångström pyrheliometer A-158 was chosen as the reference instrument because it was directly traceable to A-70, which represented the Ångström scale. Hence, applying the given correction value, it was simple to relate measurements to the IPS 1956 level as desired. As a result of these comparisons, the calibration factors for all the participating pyrheliometers were adjusted to give the same readings as the A-158. In 1969 at Carpentras, France, the Regional Pyrheliometer Comparison of the Regional Association VI (RA VI) of the WMO took place. As a result of this comparison and of IPC III, which took place one year later again at Davos, a malfunction

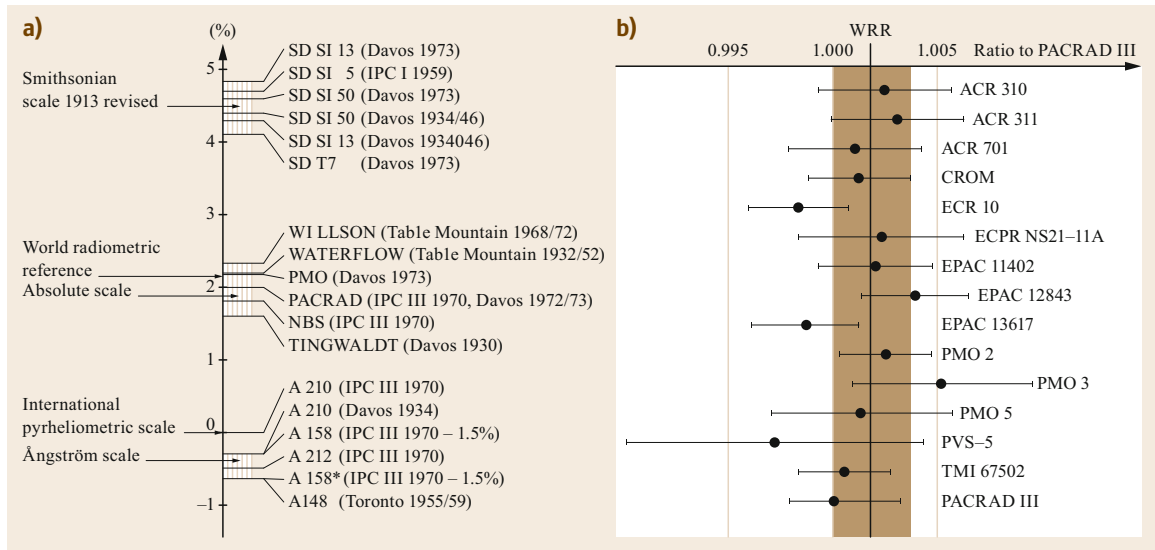


Fig. 11.16 (a) Summary of relations between different scales used for meteorological radiation measurements. (b) Summary of results of 15 absolute radiometers with different designs and origins and the definition of the WRR (after [11.13])

of the A-158 was ascertained, meaning that the defined IPS 1956 was not in conformity with its definition, leading to some confusion.

In several institutions in the USA, Belgium, the USSR, and Switzerland, a new generation of so-called absolute radiometers (pyrheliometers) was developed during the late 1960s and early 1970s by applying the compensation principle with electrically calibrated cavity receivers. This type of instrument is still in use and makes up the backbone of the traceability and comparability of worldwide solar radiation measurements. (For further information see Sect. 11.4.1.)

The results of IPC III in 1970, in which two of these new cavity radiometers already participated, and the increasing number of different absolute radiometers introduced in the following years enabled new investigations to answer open questions concerning the true radiation scale. At PMOD, where the World Radiation Center (WRC) was established in 1971, many comparisons between Ångström and silver-disk pyrheliometers as well as radiometers of the new type were carried out between 1971 and 1974 and during IPC IV, which took place in 1975. Additionally, old pyrheliometer measurements back to the 1930s were critically reviewed. These actions led to better understanding of the discovered problems [11.13]. Finally, the findings shown in Fig. 11.16a led to the definition of the World Radiometric Reference (WRR). Conversion from IPS 1956 to WRR can be realized by applying the relation

$$\frac{\text{WRR}}{\text{IPS}_{1956}} = 1.022. \quad (11.5)$$

WRR was enforced as mandatory by the WMO effective 1 January 1981.

The WRR was defined based on measurements by 15 cavity radiometers of 10 different types (Fig. 11.16b), which were absolutely characterized, while a subgroup of at least four of these of different types form the World Standard Group (WSG). The WRR represents the SI units of solar irradiance, with an estimated accuracy of better than $\pm 0.3\%$ [11.52]. The instruments of the WSG have to fulfill several criteria, first defined in [11.52] and later improved on in [11.1]. The WSG is kept at the WRC at PMOD, to enable intercomparison with the other members of the WSG at least once a year [11.1]. At the request of the CIMO, in 1970 the Executive Committee (EC) of the WMO decided to conduct IPCs every 5 years. Indeed, it is now difficult to imagine correct worldwide solar radiation measurements without the IPCs, because they represent the only opportunities to ensure worldwide traceability and comparability of solar radiation measurements versus the WRR, which is highly important when analyzing climate records gathered at different locations. Furthermore, IPCs are important for checking the long-term stability of the WSG. This is firstly realized by comparison within the WSG, and secondly with the help of the regular participation of regional and national standard pyrheliometers in the IPCs, mostly being cavity radiometers in recent times. Furthermore, the IPCs provide very good opportunities for capacity building regarding all questions related to radiation measurements. A report from the latest IPC-XII in 2015 as well as its results are given in [11.53].

The National Metrology Institutes (NMI) maintain the SI scale of radiant power, which is implemented using cryogenic absolute radiometers and also applies the compensation principle. Currently, these instruments are restricted to narrow beams of laser light and work at much lower power levels than solar radiometers and thus cannot measure solar irradiance. In 1991, an indirect comparison of the WRR as the solar irradiance scale versus the SI scale of radiant power took place in London, where using a special transfer standard, the cryogenic radiometer of the National Physical Laboratory (NPL) of the UK and a WSG radiometer were compared for the first time [11.54]. This intercomparison was repeated in 1995 and 2008 with improved general setups. In all three cases, agreement of both scales within the uncertainty of the comparisons was confirmed [11.55, 56].

The problems occasionally arising with single instruments of the WSG since 2005, which had been used at that time for more than about 30 years, indicated that they were approaching the end of their lifetime. The need to overcome these problems as well as other imperfections that were already known led in 2007 to a joint project of the PMOD/WRC, NPL, and Federal Office of Meteorology of Switzerland (METAS) to develop a cryogenic solar absolute radiometer (CSAR) [11.57], allowing the measurement of solar irradiance as well as radiant power. According to [11.57, p. 7], the main goal of this project was “to design and build a cryogenic radiometer suitable to replace the WRR as standard for solar irradiance

measurements” and secondly “to design and build the CSAR for space flight.” Replacing the WRR by CSAR will enable direct traceability of solar irradiance measurements to the SI radiant power scale, because this instrument may be incorporated into the corresponding and very important key comparisons of the Bureau international des Poids et Mesures (BIMP), which is mandatory for primary SI standards. Because the CSAR operates on the ground in a vacuum, for measuring solar irradiance it is absolutely essential to close the entrance with a material which transmits the solar spectrum reaching the Earth’s surface, preferably without hindrance. A detailed description of the CSAR is provided in [11.58], while a monitor to measure the integral transmittance (MITRA) and its characterization are depicted explicitly in [11.57]. CSAR participated in the IPC for the first time in 2010, resulting in minor improvements.

In 2010, the WMO formally signed the International Committee for Weights and Measures (CIPM) Mutual Recognition Arrangement (MRA) and designated PMOD/WRC to represent the measurement quantity of solar irradiance, meaning that the WRR has been accepted within the SI system.

The fourth comparison between the WRR irradiance scale and SI power scale took place as previously at the NPL and also for the first time at the Laboratory for Atmospheric and Space Physics (LASP) in Boulder, USA, which is equipped with a TSI radiometer facility (TRF) [11.59]. The comparison with the TRF showed that the WRR is 0.34% higher than the SI scale [11.60].

11.3 Theory

Radiation processes are responsible for the radiative equilibrium of the Earth, balancing the incoming solar with the outgoing terrestrial energy at the top of the atmosphere (TOA). A recent study on the global energy balance implies a subtle effect of radiative energy entering the subsurface of the Earth, albeit with some uncertainty (Fig. 11.17). It is very important to measure the radiation at the surface of the Earth as addressed within this chapter to reduce such uncertainty. To understand the physical processes and reasons behind the change of the radiation fluxes between the TOA and ground, it is necessary to measure these fluxes at the TOA and all levels in the atmosphere. These quantities are determined by special radiometers onboard satellites and airplanes at the TOA and intermediate levels, respectively (Chaps. 37, 38) as well as by radiosondes for vertical sounding and near the surface, and by spectral radiometers (Chaps. 28, 29, 34).

11.3.1 Optical Spectrum of Solar and Terrestrial Radiation

Measurements of the spectral distribution of solar radiation show a maximal irradiance at about 500 nm. Applying Wien’s displacement law with this wavelength, the temperature of the Sun’s surface can be estimated as about 5800 K. On the other hand, using the Stefan–Boltzmann law and knowledge about the solar irradiance at the mean Sun–Earth distance outside the atmosphere (solar constant), it is also possible to derive a temperature for the surface of the Sun of about 5800 K. Figure 11.18 shows the blackbody irradiance at 5800 K considering the Sun–Earth distance, and at 300 and 250 K corresponding to temperatures on the Earth’s surface. Furthermore, the solar irradiance at the TOA and at the surface at the solar zenith angle (SZA) of 30° are shown, revealing the well-known textbook

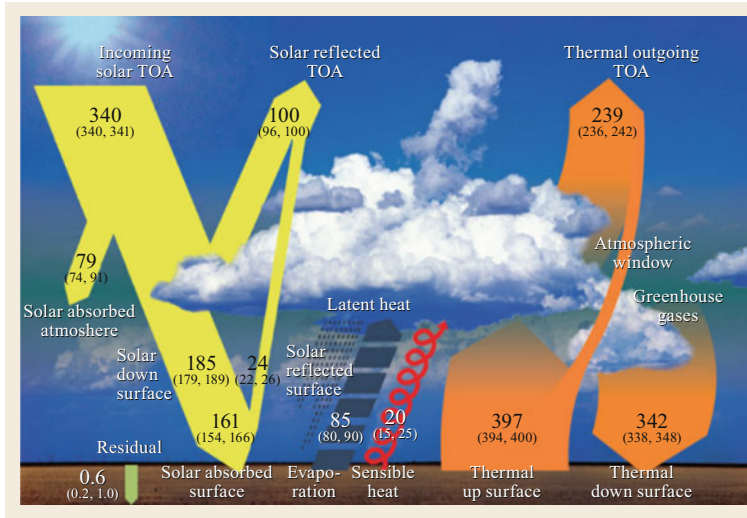


Fig. 11.17 Mean global energy balance of Earth and solar and terrestrial radiation fluxes (in W m^{-2}) on their paths through the atmosphere, as well as the influencing processes of absorption and scattering and latent and sensible heat fluxes also transferring energy from the surface to the atmosphere (after [11.61])

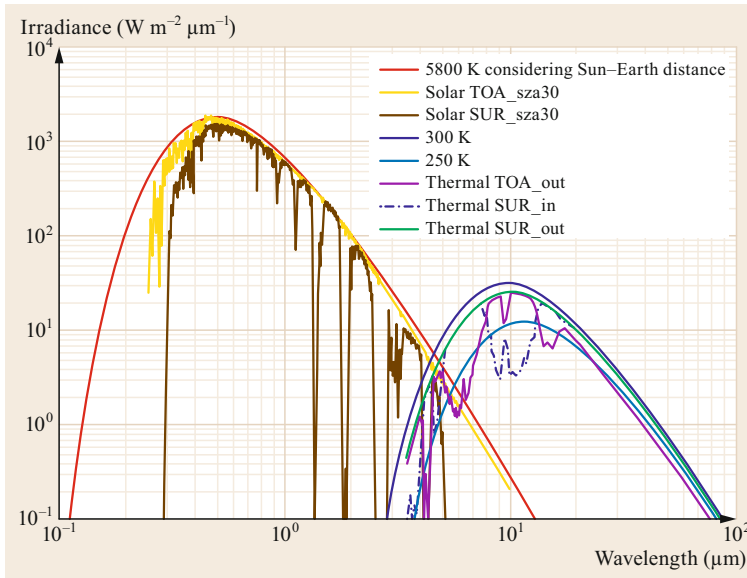


Fig. 11.18 Irradiances of solar and terrestrial spectrum at sea level calculated with libRadtran (after [11.62, 63]) using data of US standard atmosphere at sea level (Chap. 1)

structure due to absorption by atmospheric gases. Additionally, the atmospheric downward radiation at the surface (labeled *thermal SUR_in*), the terrestrial upward radiation at the surface (denoted *thermal SUR_out*), and at the TOA (indicated *thermal TOA_out*) in the thermal (terrestrial) region are plotted on the same figure. The *thermal SUR_out* plot is similar in shape to the blackbody irradiance at 300 and 250 K, and lies between them, meaning that the surface in this special case is irradiating like a blackbody at about 288 K (about 15 °C), while the features of the plots of *thermal TOA_out* and *thermal SUR_in* are not so smooth because of the effects of emission and absorption by the atmosphere. All these calculations were carried out with libRad-

tran2.0.1 [11.62, 63], using the data for the US standard atmosphere (Chap. 1) profile between sea level and the upper bound of the atmosphere as input data. These results show that, as mentioned above (Sect. 11.1.1), it is necessary to investigate the spectral region from about 300 to about 50 000 nm. It is seen that the blackbody curves at the temperatures of the Sun and the Earth overlap at a low level of irradiance at the long- and short-wave end, respectively. Also, the irradiances of solar and thermal radiation calculated by libRadtran overlap more or less at the surface level, depending on the atmospheric conditions, in the spectral area between about 3 and 4 μm . The following conclusions can thus be drawn regarding the conduction of radiation measurements:

- A spectrally nonselective detector covering the whole wide region is preferred.
- It is possible to distinguish between the solar and terrestrial part.
- It is impossible to distinguish between the origin of radiation in the spectral area between about 3 and 4 μm , resulting in imperfect measurements.

Based on past experience as described in Sect. 11.2, and considering the urgent need for automatic data acquisition, only sensors delivering an electrical output are currently considered. These are based on the thermoelectric method (Sect. 11.3.2), mainly applying the approved thermopile and covering the whole solar and terrestrial spectral range, and for special cases in the solar area the more recent photodiode-based method (Sect. 11.3.3), as described below.

11.3.2 Thermoelectric Method

The thermoelectric method was first applied available after the discovery of the thermoelectric effect by Thomas Johann Seebeck (1770–1831) in 1821 (Chap. 8). According to the thermoelectric or Seebeck effect, a voltage originates in an electric circuit consisting of two different conductors (A, B) whose junctions are at different temperatures T_1 and T_2 (Fig. 11.19).

The resulting thermovoltage or electromotive force (EMF) depends on the Seebeck coefficients S of the dissimilar conductors and the temperature difference between the junctions. The greater the difference between the materials and thus their Seebeck coefficient in the electrothermal series, the greater the resulting EMF for a given temperature difference. For frequently used, e.g., copper-Constantan, junctions (Constantan is a copper-nickel alloy), the Seebeck coefficient is $41.5 \mu\text{V K}^{-1}$ at 273 K (see also Chap. 8) for a single thermocouple. Because a single junction generates a very low EMF, they are usually interconnected as a series of several thermocouples. Thermopiles can be designed with different shapes, depending on the location and realization of the active (hot) or passive (cold) junctions (Fig. 11.20).

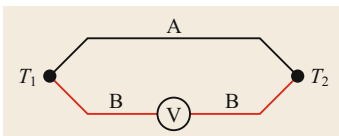


Fig. 11.19 Schematic of thermocouple consisting of two dissimilar wires (A, B) whose junctions are at different temperatures T_1 and T_2 , generating an electromotive force (EMF)

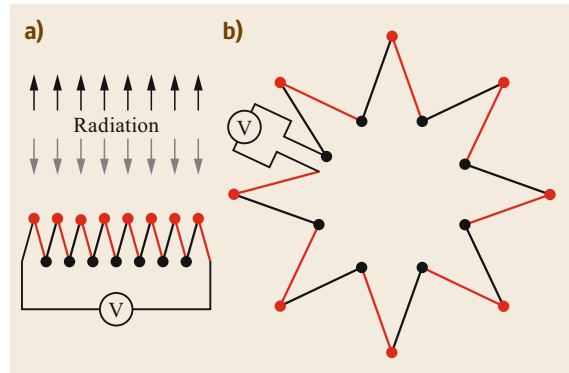


Fig. 11.20 (a) Thermopile, where the active (hot) junctions (red dots) are irradiated, while the passive ones (black dots) are shielded and at a more or less stable reference temperature level. Applied in black thermopiles (see, e.g., Sect. 11.2.2). (b) Active (red dots) and passive (black dots) junctions are located at the same level. The temperature difference between the hot and cold junctions is realized by achieving different levels of absorption, mainly using different paints, applied in black-and-white thermopiles (see, e.g., Sect. 11.2.2). In both pictures the thick red and black lines represent dissimilar wires

Thermopiles are, as suggested by their name, thermal sensors that transform radiant into thermal energy. The resulting temperature increase or difference between the active and passive junctions is finally converted into a measurable voltage.

There are two types of black thermopiles and one type of black-and-white thermopile. While black-and-white thermopiles are only used in pyranometers, black thermopiles are applicable in all broadband radiation instruments. In any case, the active junctions are blackened and irradiated, while the passive ones remain at a *reference* level, which can be realized in three different ways:

- Different absorption
- Different heat conduction (heat sink)
- No interaction with the radiation source.

For each type, the temperature difference originating between the hot and cold thermocouples generates an EMF that is proportional to the irradiance.

For a black-and-white thermopile, the thermocouples are typically located at the same level (Fig. 11.20b; Sect. 11.2.2). The hot junctions are in close thermal contact to blackened circular plates or segments, or arranged in a checkerboard configuration, while the cold junctions are thermally spliced with the corresponding white ones. The differential absorption of the black

and white surfaces ensures a temperature difference between the junctions and generates a voltage that is proportional to the irradiance.

The two types of *black* thermopiles (Fig. 11.20a) differ in how the temperature difference between the active and passive thermocouples is generated. In the case of the classical Moll thermopile (Sects. 11.2.1 and 11.2.2), the different heat capacity of the hot and cold junctions (heat sink) is used, while in the second case, the active junctions are irradiated by the incident solar or terrestrial radiation while the passive ones are facing toward the bottom of the instrument and are in close thermal contact with it, forming the heat sink. In this case, the passive junctions do not interact with the radiation source.

The Moll design uses very thin (0.005 mm) strips of soldered Manganin and Constantan, which are blackened. The ends of these strips are soldered to copper bars, which are fastened with electrical isolation but good thermal contact to a thick brass plate (see, e.g., Figs. 11.6, 11.7). In this way, a minimal heat capacity of the hot junctions in relation to the maximal heat capacity of the passive one can be realized. An advantage of these thin, nearly massless elements is that they instantaneously reach an equilibrium temperature [11.24].

Beside the frequently used copper-Constantan and Manganin-Constantan, combinations of other alloys are also applied. Constantan and Manganin are trade names. Constantan consists of 55% Cu, 44% Ni, and 1% Mn, while Manganin is composed of about 84% Cu, 12% Mn, and 4% Ni.

Also, over the course of time, different paints and lacquers have been tested and improved. For several years now, paints that exhibit flat and nonselective absorption over the whole spectral region of interest from about 300 to 50 000 nm have been applied.

In recent years, rapid development has occurred in microsystems engineering, enabling the fabrication of novel thermopiles with tiny dimensions in comparison with classical devices. Like the classic ones, these thermopiles are still based also on the effect discovered by Seebeck. Furthermore, they work like the described black thermopiles. In these new thermopiles, the hot junctions are located in the center and are irradiated while the cold ones are located at the perimeter and connected to the heat sink. The thermopile itself is a thin film encapsulated in a can (Fig. 11.21b). Also, these detectors exhibit a flat spectral response across the relevant region from the ultraviolet up to the far infrared. Because of their small dimensions and tiny thermal mass as well as thermal conductivity, they offer essentially improved performance parameters, for instance, response time [11.64, 65].

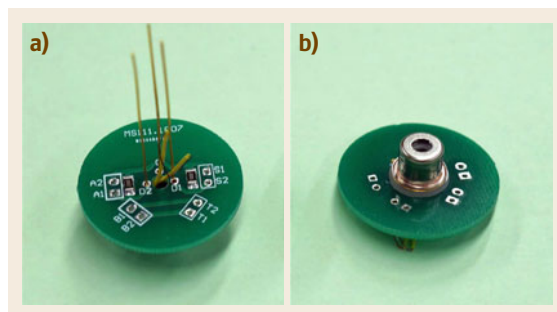


Fig. 11.21a,b Novel sensor with thermopile located inside a can (b), and the back of the sensor (a) of the new pyranometer ER08-S from Middleton Solar, Australia (see also Fig. 11.29) (photo courtesy of D. Mathias, Middleton Solar)

11.3.3 Photodiode-Based Method

Compared with thermopiles, photodiode-based sensors are a recent introduction to the field of radiation measurements. Based on semiconducting material such as silicon, the internal photoelectric effect becomes important. A photodiode is based on a semiconducting n-p junction formed between a material with electron vacancies (p-type semiconductor) and a material with excess electrons (n-type semiconductor). If such a system is illuminated, an electrical current arises, being roughly proportional to the incoming irradiance. Photodiode-based sensors respond to the number of incident photons of a specific wavelength and not to the energy, resulting in a difference between the external quantum efficiency and the irradiance, which causes wavelength dependence and a spectral mismatch.

The advantages of photodiodes include their very low production cost and very fast response times of about 10^{-5} s, depending on the thickness of the n-p junction. One disadvantage is their spectral response, as seen in Fig. 11.22, which is not flat and only covers the range from 400 to 1100 nm, typical for silicon photodiodes, resulting in a spectral mismatch, especially on clear days, when Rayleigh scattering is significant. However, also under a cloudy sky, the agreement with measurements taken using thermopiles is still not good. Nevertheless, photodiodes are applied for special tasks in the solar range, especially if the demands regarding uncertainty are not high, for instance when measuring sunshine duration. Furthermore, when used with special filters, they become highly suitable, for instance for PAR measurements. In contrast to thermopiles, photodiodes transform the incoming radiant energy directly into electrical energy, thus enabling the use of automatic data acquisition systems.

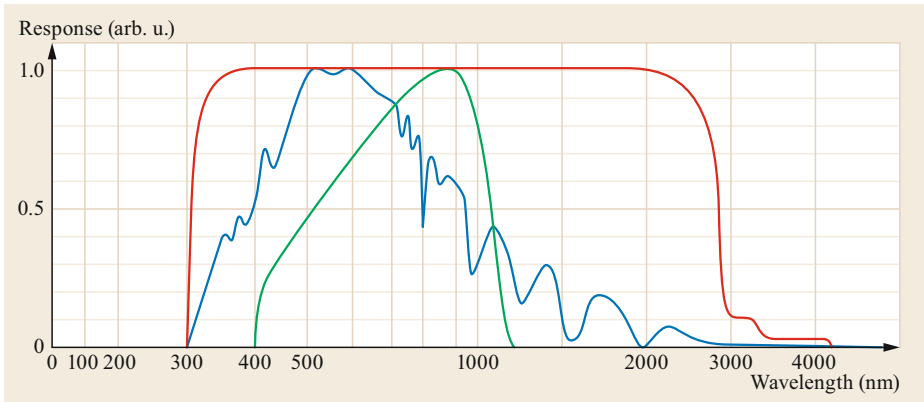


Fig. 11.22 Spectral response of photodiode-based silicon pyranometer and thermopile pyranometer as well as the solar radiation spectrum at sea level. *Blue*: Solar radiation spectrum at sea level, *green*: spectral response of silicon pyranometer, *red*: spectral response of thermopile pyranometer (after [11.66])

11.3.4 Separation of Solar and Terrestrial Radiation

As is generally known and as described in Sect. 11.3.2 from the theoretical point of view, model calculations show that the solar and terrestrial spectra overlap in the range between 3 and 4 μm . However, it is necessary for many reasons to investigate the solar and terrestrial separately.

It was already known in the past that glass is a suitable material to achieve this requirement to distinguish the solar from thermal spectral region. However, this cannot achieve exclusive measurement of the terrestrial part of the spectrum.

In the late 1960s, Eppley Laboratory Inc., USA, a manufacturer of radiation instruments, first commercially offered a dome made from KRS-5 (thallium bromide-iodide) combined with a vacuum-deposited interference filter to block solar radiation, resulting in gray transmission from 4 to 50 μm [11.13].

As an example, the transmission of a glass dome typically used for pyranometers to measure solar radiation and the transmission of a silicon dome together with its special coatings applied to the CG4 pyrgeometer of Kipp and Zonen B.V., the Netherlands [11.67] are shown in Fig. 11.23 and 11.24, respectively.

The results shown in Fig. 11.23 reveal that the transmission of the glass dome for pyranometers is flat at a level above 90% between about 350 and 2000 nm with a steep edge at the cut-on, while at the cut-off it first shows a steep slope up to the 30% level, then a rather gentle slope up to about 4000 nm. The 50% points are given as 305 and 2800 nm by the EKO Instruments Co., Ltd. Japan [11.68], when applied to, e.g., the MS-802

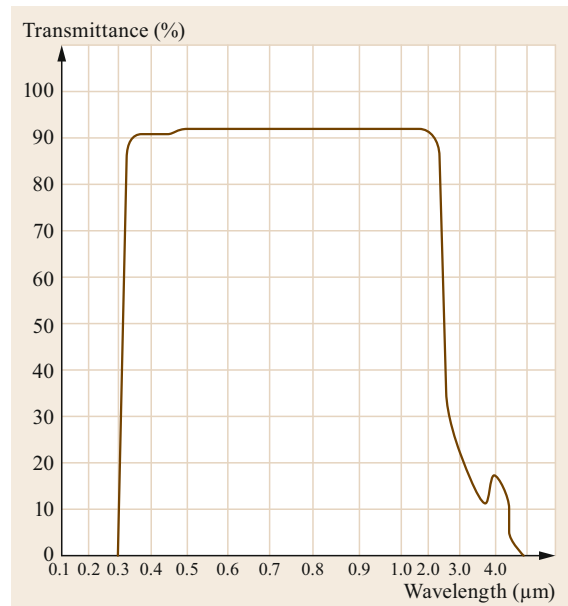


Fig. 11.23 Typical spectral transmission of glass as used with several EKO pyranometers (e.g., MS802) (after [11.68])

pyranometer. Depending on the kind of glass that is chosen, which is frequently not specified, other manufacturers state values between 285 and 2800 nm or 300 and 2800 nm. Kipp and Zonen B.V. [11.69] and Hukseflux Thermal Sensors B.V. [11.70] have specified their use of quartz domes with 50% points of 200 to 3600 nm and 20% points of 190 to 4000 nm. These pyranometers equipped with quartz domes can measure the total solar spectral range reaching the surface of the Earth.

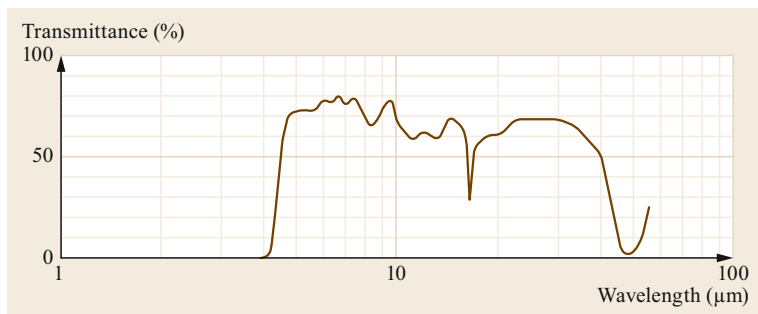


Fig. 11.24 Spectral transmittance of dome applied on CG4 pyrgeometer of Kipp and Zonen (after [11.67])

In contrast to the transmission curve of glass (Fig. 11.23), the example curve of the pyrgeometer dome shown in Fig. 11.24 is not flat unfortunately, which depends on the features of the silicon dome and the special coating applied. Kipp and Zonen B.V. [11.67] specifies its pyrgeometer domes with 50% points from 4.5 to 42 μm , while Hukseflux Thermal Sensors B.V. [11.71] state nominal transmission from

4.5 to 40 μm , with specific values given in the product certificate. Nevertheless, pyrgeometers with such domes can measure terrestrial radiation in the thermal spectral range without sunlight even in daytime. Note that all pyrgeometers currently available on the market use similar materials, all of which do not offer flat spectral transmission, resulting in uncertainties in the measurement of terrestrial irradiance (Sect. 11.4.3).

11.4 Devices and Systems

In principle, radiation measurement instruments are single devices which can be categorized according to the origin of the radiation and the spectrum they cover. Such devices can also be categorized according to their opening or viewing angle, or according to the target of such measurements in the case of solar radiation. Furthermore, one can also consider whether the instrument is single or combined, and pointing to the upper or lower hemisphere. For the measurement of specific quantities such as direct or diffuse solar radiation, supplementary equipment such as a solar tracker is necessary. Other devices, such as ventilation and heating units, have also been developed to improve the quality of such measurements in combination with the radiation instrument. All of the radiation devices described below offer an electrical interface for direct measurements or recording, although these instruments are not considered here.

11.4.1 Pyrheliometer

A pyrheliometer measures the direct solar irradiance on a surface perpendicular to the rays from the Sun (see also Tables 11.2–11.4). This means that their receivers have to follow the path of the Sun continuously. Nowadays, this is achieved by modern computer-controlled trackers, while in the past such alignment was done manually or was clock driven. A pyrheliometer consists of a sensor (a thermal detector such as a thermopile

or a cavity absorbing the incident radiation) mounted in a view-limiting device. In most cases, this is a tube or diaphragm tube, defining the field-of-view geometry. As noted in Sect. 11.2.1, pyrheliometers with different opening angles were constructed and applied in the past, because there were no rules defining this important feature. Typical opening half-angles covered the range between 2.5° and 7.5°. Referring to [11.13], the opening half-angle of 2.5° and slope angle of 1° recommended for all new pyrheliometer designs in [11.72] represent a compromise to minimize the measurement of circumsolar radiation while remaining consistent with sufficient tracking tolerances (Fig. 11.25).

Because the apparent solid angle of the Sun is only about 0.5°, there is an additionally contribution due to the acquisition of the Sun's aureole. This circumsolar radiation depends on the atmospheric turbidity and changes continuously depending on changing atmospheric constituents and conditions.

As stated in [11.73], three different types of device can be distinguished:

- Absolute pyrheliometers
- Compensation pyrheliometers
- Pyrheliometers without self-calibration capability.

Absolute Pyrheliometers

According to [11.72], an absolute pyrheliometer is principally a realization of the scale of irradiance. In this

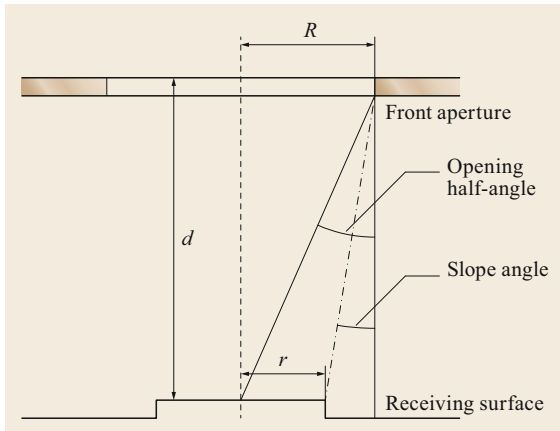


Fig. 11.25 View-limiting geometry: The opening half-angle is $\arctan R/d$; the slope angle is $\arctan(R-r)/d$. (Adapted from [11.1])





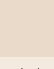

case, the instrument's constant is determined by a so-called characterization. The physical properties of all the parts of the instrument influencing the measurement

result must be determined using laboratory experiments, model calculations, or typical values, to finally describe the deviations from ideal behavior. The resulting reduction factor enables the calculation of the irradiance from the output signal of the instrument. Blackbody receivers and electrically calibrated differential heat flux meters are typical features in the design of absolute pyrheliometers used today.

As already mentioned in Sect. 11.2.5, in the late 1960s and at the beginning of the 1970s, a number of absolute pyrheliometers, also called *self-calibrating pyrheliometers*, were developed at several institutions in the USA, Belgium, the USSR, and Switzerland. They can mainly be distinguished based on the sensors, cavity type, and operation mode applied, as presented in Table 11.6.

A comprehensive description of the construction, functionality, and features of these absolute pyrheliometers, also called cavity radiometers, is provided in [11.18]. Detailed information about each type of instrument is available in special papers published by those who constructed these pyrheliometers [11.74–79].

Table 11.6 Summary of self-calibrating cavity pyrheliometers (after [11.13])

Identification	Sensor and mode	Cavity type	Cavity–heat flow meter arrangement ^a	Aperture area (cm ²)	Characterization ^b
ACR: active cavity radiometer developed by R.C. Willson, Jet Propulsion Laboratory, Pasadena, CA, USA	Resistance thermometer sensor operated in active mode	Classical cone modified to remove meniscus at bottom point, specular paint		0.5	E and M
CROM: developed by D. Crommelynck, Institut Royal Meteorologique de Belgique, Bruxelles	Flux meter with integrated thermopile operated in active mode	Cylindrical in each of two cavities with flat bottom and diffuse paint		0.5	E
H–F: developed by J. Hickey and R. Frieden, The Eppley Laboratory, Inc., Newport, RI, USA	Circular plated and wire-wound thermopile operated in passive mode	Inverted cone within a cylinder, specular paint		0.5	E and T
PACRAD: primary absolute cavity radiometer, developed by J.M. Kendall, Jet Propulsion Laboratory, Pasadena, CA, USA	Discrete junction thermopile, operated in passive mode	Classical cone with truncated inverted cone above, diffuse paint		1.0	M
PMO: developed by R.W. Bruss and C. Fröhlich, Physikalisch-Meteorologisches Observatorium, Davos, Switzerland	Mark 2 has a discrete thermopile, mark 6 a resistance thermometer, both operated in active mode	Inverted cone within a cylinder, specular		0.2	E
TMI: developed by J.M. Kendall, Technical Measurements Inc.	Discrete junction thermopile, usually operated in passive mode	Inverted cone in cylinder, semispecular paint		1.0	E and T

^a The drawings illustrate the cavity–heat flow meter arrangements:

— cavity, = heat flow meter, // heat sink

^b E: characterization by experimental methods

M: characterization based on model calculations

T: characterization based on typical values

According to Table 11.6, absolute pyrheliometers are operated in either *active* or *passive* mode. Operation in active mode means that, during the whole measuring period consisting of alternately closed (shaded) and open (irradiated) phases, a constant heat flux is maintained, while in the passive mode electrical heating is only provided in the shaded phase at the beginning of each measurement series. In the active mode, the difference in electrical power during the two phases is proportional to the radiative power.

As mentioned in Sect. 11.2.5, the cryogenic solar absolute radiometer (CSAR) [11.57, 58] embodies the state of the art in absolute pyrheliometry, because it establishes a link between the self-calibrating cavity pyrheliometers of the 1970s, satellite radiometers, and the (laboratory) radiometers of the National Metrology Institutes (NMI) representing the SI.

Typically, absolute pyrheliometers are only used in fair weather for calibration purposes as reference instruments because they have open apertures (Sect. 11.6.1). Additionally, Eppley Laboratory, Inc. offers H-F-type absolute pyrheliometers with a window that closes the aperture for use in all weather conditions and realize continuous, highly precise measurements of direct solar radiation.

Compensation Pyrheliometers

A typical and the most well-known compensation pyrheliometer is that of Knut Ångström [11.16] described in Sect. 11.2.1, so it is not necessary to repeat its description here. This device applies the compensation technique, meaning that the incident radiation flux is equalized by a corresponding electrically generated heat flux. It has an ambiguous position historically, because the constant of the first instrument was derived from the properties of the pyrheliometer (as for an absolute pyrheliometer) and later the constants of other instruments of the same type were determined by side-by-side comparison. By today's standards, the derivation of the constant for this first compensation pyrheliometer is not comparable to the characterization achieved with current absolute pyrheliometers. The Ångström compensation pyrheliometer is inferior in quality compared with recently introduced self-calibrating pyrheliometers, but it remains a stable instrument that has served as a standard for many years.

Pyrheliometers Without Self-Calibration Capability

Pyrheliometers without a self-calibration capability include typical station or field pyrheliometers. Very stable instruments such as the silver disk pyrheliometer, Michelson bimetallic actinometer, Linke–Feussner pyrheliometer, and Eppley NIP (see also Sect. 11.2.1)

have been used to calibrate other *lower*-class pyrheliometers or pyranometers (Sect. 11.6). Furthermore, pyrheliometers in this group have been applied to determine the Linke turbidity factor T [11.6, 12, 80] or if equipped with colored glass filters (Sect. 11.2.1) to calculate the Ångström turbidity coefficient β [11.6, 12, 81, 82], assuming that the Sun and its vicinity of not less than 15° are not covered by any clouds. These kinds of measurement are spot measurements which are mainly carried out by manual alignment of the pyrheliometer to the Sun. With the availability of sun photometers (Chap. 29), the derivation of the optical depth, which provides more information, gradually replaced these kinds of turbidity determinations. Continuous measurement of direct solar radiation requires a weatherproof pyrheliometer with a sensor delivering an output signal suitable for recording and which is mounted on an equatorial tracker that steadily follows the Sun's path. Currently, these demands are only fulfilled by pyrheliometer instruments equipped with thermopiles. In the past, such trackers were clock or electromechanically driven. However, because of the lack of suitable pyrheliometers (between the 1950s and 1990s, only the NIP was available commercially) and trackers, only a few stations worldwide measured direct solar radiation continuously.

This situation changed at the beginning of the 1990s, when microelectronics had become established and computer-controlled solar trackers and data recording systems became available. Additionally, the demand for improved, accurate all-weather pyrheliometers for science (e.g., BSRN) and industry (e.g., solar industry) emerged. As a result, manufacturers developed new instruments, whereas the imperfections of known devices were mainly eliminated or ameliorated by the addition of various new features.

Pyrheliometers without self-calibration capability that are currently available on the market share the following characteristics: They all use thermal detectors (thermopiles) as receivers, located at the end of a tube, and these are all black thermopiles (Sect. 11.3.2). The (front) aperture of the tube is covered by glass. Concerning the opening angle, they all fulfill the important criteria recommended by the WMO (Sect. 11.4.1), so that direct solar radiation is measured uniformly worldwide.

Available pyrheliometers (see Fig. 11.26 for examples) differ in terms of the detector selected and/or their internal setup, which in most cases is proprietary. Furthermore, the covering front glasses are different but span the spectral region from at least 300 to 3000 nm. In many cases, types of glass with somewhat wider spectral coverage are applied. Pyrheliometers with novel thermopile sensors and very short time constants of about ≤ 0.5 s are now available (Sect. 11.3.2), fulfill-

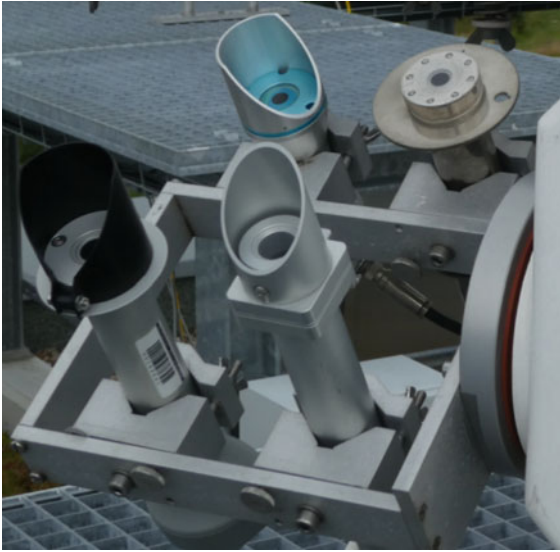


Fig. 11.26 Tracker with different modern pyrheliometers without self-calibration capability. *Top row:* EKO MS-56 and Eppley sNIP, *bottom row:* Kipp and Zonen CHP1 and Hukseflux DR01 (from left to right) (photo: K. Behrens)

ing the new criteria for so-called *fast response pyrheliometers* [11.73]. The temperature dependence of the receivers is, for instance, compensated using electronic compensation circuits. Furthermore, some instruments are equipped with thermistors or Pt-100 thermometers to measure the temperature of the instrument and thus enable subsequent temperature correction (for specifications, see Table 11.9).

Not only have the performance properties regarding direct measurements been improved, but other devices for pyrheliometers, such as ventilation and heating systems for the window to avoid the effects of dew, rime, and raindrops on the front glass, have also been manufactured. Some of these instruments also offer ingress protection against dust and water (IP67). While in the past, pyrheliometers only offered a classical analog voltage output, in some cases the user can now additionally select between different output methods or communication protocols such as Modbus or RS-485. Also, so-called smart instruments are available, allowing a direct link to a personal computer (PC) with the possibility of collecting different types of data and controlling many parameters.

Because this development, especially concerning so-called smart features, has been very fast, it is recommended to check the specification to select a pyrheliometer with the desired features. Furthermore, the statements regarding the deployment and measurement site given in Sect. 11.1.3 are valid and should be considered, too.

Nearly all instruments currently on the market still offer the classical analog voltage output (U) generated by the detector. In this case, the direct solar irradiance (E_1) can be calculated using the known sensitivity (S) as

$$E_1 = \frac{U}{S}. \quad (11.6)$$

Because the sensitivity of most sensors lies in the range between about 7 and $15 \mu\text{V} (\text{W m}^{-2})^{-1}$, they generate voltages of about 10 mV at an irradiance of 1000 W m^{-2} , assuming a sensitivity of the pyrheliometer of $10 \mu\text{V} (\text{W m}^{-2})^{-1}$. In the case when corrections are necessary to calculate the direct solar irradiance, e.g., due to temperature dependence, the manuals of each instrument should contain corresponding instructions.

In the framework of the BSRN, the Variable Conditions Pyrheliometer Comparison (VCPC) was organized at the Solar Radiation Research Laboratory (SRRL) of the National Renewable Energy Laboratory (NREL) in Golden, Colorado. It took place from November 2008 to September 2009, during which 29 pyrheliometers (all the types of thermopile instrument available on the market at that time, plus some experimental types) and three all-weather absolute pyrheliometers of H-F type participated. The goal was to determine how commercial pyrheliometers performed under different real weather conditions. The results were, as expected, that the windowed cavity radiometers showed the smallest uncertainty of about 0.5%, followed by a group with better than 0.9%, while the remaining pyrheliometers still performed better than 1.4% at a 95% confidence level. Two of the 29 pyrheliometers could not be included in this analysis because of their too large deviations. Details including the experimental setup and results were published in [11.83].

The specifications regarding the different types of pyrheliometer are given in Sect. 11.5, while their calibration is described in Sect. 11.6.

11.4.2 Pyranometers

A pyranometer measures the solar radiation incident from a viewing angle of 2π sr on a flat surface (Tables 11.2–11.4). A pyranometer consists of a sensor, usually implemented in a metallic body. The detector faces the radiation source, which is normally the sky with the Sun, or other surfaces reflecting the sunlight such as the ground if it looks downward, or a mixture of both in the case of an inclined installation. Nowadays, only sensors with an electrical output are applied in pyranometers (Sects. 11.3.2 and 11.3.3). These detectors transform the incident radiant energy into either thermal energy, generating a temperature difference between the active and passive junctions of a thermopile which is converted into

an electromotive force (EMF), or directly into electric energy in the case of photodiodes.

Like other types of instrument, pyranometers are nonideal and their output signal is influenced by several parameters, allowing to classify the quality of the different pyranometers. These specification lists are given by WMO in the CIMO-Guide [11.1] as recently updated by the ISO [11.73] (Sect. 11.5, Table 11.8). Some of these points are considered below.

Depending on their construction, thermopiles are protected against wind, precipitation, and dust by one or two glass domes, as well as to prevent heat losses and exchange of thermal radiation with their surroundings. The use of cut-glass hemispheres is important for the observance of the cosine law, while the use of simple and not appropriately treated flat glass would yield a dependence on the angle of incidence of the radiation, influencing the directional response. Recently, thermopiles with receivers that are additionally covered by a diffusor have also become available, while most photodiodes are also situated behind a diffusor, too. Pyranometers are generally all-weather instruments and therefore robust in design. Furthermore, thermopile instruments are equipped with a sun shield to prevent heating of the pyranometer body. In many cases, pyranometers have a drying cartridge filled with silica gel to absorb humidity inside the body and thus prevent condensation. The newer types also offer ingress protection against dust and water (IP67) and are almost sealed, thus not requiring such a drying cartridge.

While in the past pyranometers offered only the classical analog voltage output, in some cases the user can now additionally select between different output methods or communication protocols such as Modbus or RS-485. Also, so-called smart instruments are available, allowing a direct link to a PC with the possibility of collecting different data and controlling many parameters.

Because this development, especially concerning so-called smart features, has been very fast, it is recommended to study the specification to select a pyranometer with the desired features.

Currently, nearly all instruments on the market, independent of their type as discussed below, still offer the classical analog voltage output (U) generated by the detector. In this case, the global solar irradiance ($E_{g\downarrow}$) can be calculated from the known sensitivity (S) as

$$E_{g\downarrow} = \frac{U}{S}. \quad (11.7)$$

Because the sensitivity of most sensors lies in the range between about 7 and 15 $\mu\text{V} (\text{W m}^{-2})^{-1}$, they generate voltages of about 10 mV for an irradiance of 1000 W m^{-2} , assuming a sensitivity of the pyranometer of 10 $\mu\text{V} (\text{W m}^{-2})^{-1}$. If it is necessary to apply corrections, e.g., due to temperature dependence, the manuals of each instrument contain corresponding instructions.

The specifications for different pyranometers are given in Sect. 11.5, while their calibration is described in Sect. 11.6.

As seen above, only thermopiles or photodiodes are applied as sensors in pyranometers, where the former can be divided into black and black-and-white types (Sect. 11.3.2). Furthermore, the statements given in Sect. 11.1.3 regarding the deployment and measurement site are valid and should be considered, too.

Pyranometers with Black Thermopiles

Typically, pyranometers based on black thermopiles include two glass domes, because these thermopiles are particularly sensitive to the impact of changes in their heat balance (for an example, see Fig. 11.27). In the case of a black thermopile, the passive junctions pointing inside the body of the instrument are in close thermal contact with it, functioning as the heat sink. In contrast to the *undisturbed action* of the passive junctions, the active ones are influenced by the target incident solar radiation and the resulting heating. However, the ideal heat conduction from the active to passive junctions (heat sink) is disturbed by the loss of heat via advection and convection as well as radiative exchange in the thermal spectral region. The two glass domes are thus necessary to reduce these processes, especially the



Fig. 11.27 Two different pyranometers of black thermopile type: SR12 (left) and SR22 (right), here without ventilation unit (manufacturer: Hukseflux Thermal Sensors B.V., the Netherlands, photo: K. Behrens)

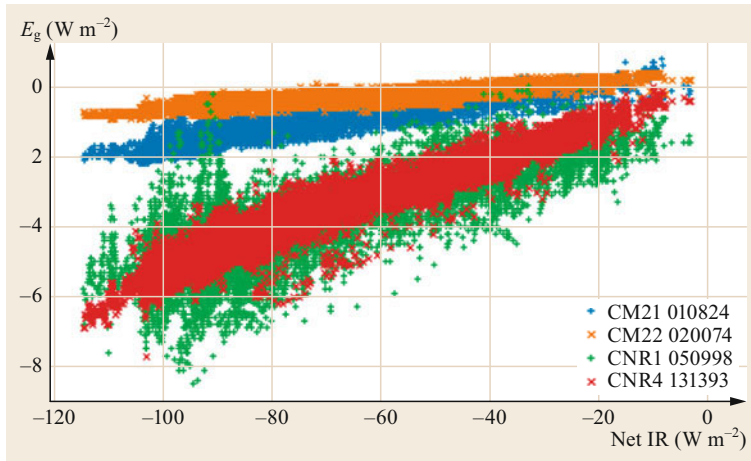


Fig. 11.28 Irradiance of pyranometers from Kipp and Zonen B.V. depending on the net thermal radiation at nighttime ($\text{sza} > 95^\circ$) from 1 to 30 April 2016 at the Meteorological Observatory Lindenberg – Richard-Aßmann Observatory, Germany. (The red marks cover big central parts of the green ones, and the marks of the CM22 partly cover the marks of the CM21)

radiative exchange, which results in the so-called thermal offset. This arises because, in most cases, the sky is colder than the pyranometer body and especially the glass domes [11.84]. Therefore, this thermal radiative flux diminishes the temperature of the active junctions. This process is always active but can be masked by greater incoming solar radiation [11.85]. In particular, at nighttime, they can cool down below the passive ones or the corresponding body temperature, resulting in negative readings. The magnitude of this thermal offset (or so-called zero offset) is proportional to the net thermal radiative flux. This zero offset is one parameter of the specifications on the pyranometer classification list (Sect. 11.5, Table 11.8), and all manufacturers try to minimize it for their instruments.

This feature is exemplarily demonstrated for Kipp and Zonen pyranometers (Fig. 11.28) of different types and quality, although it applies to all pyranometers with black thermopiles of all makes. The CM22 has the highest quality, because of the inclusion of two quartz domes and their special manufacturing with the pyranometer body, while the other instruments have only glass domes. The CM21 is also equipped with two domes, while the other two instruments of CM3 type are only furnished with one dome. The CM3 forms part of the net radiometers CNR1 and CNR4. Both single pyranometers CM21 and CM22 as well as the CNR4 are ventilated and heated. The CNR4 is the successor to the CNR1, which has not been produced for several years now. This figure shows the typical features of these different quality classes. The CM22 and CM21 show almost no scatter or dependence on the thermal radiative flux, while the CNR4 and especially the unventilated CNR1 exhibit a lot of scatter as well as some outliers, indicating the strong influence of the exchange processes as well as the dependence on the thermal radiative flux.

The above-described features are typical of pyranometers with black thermopiles from all manufacturers. However, in recent years, pyranometers and/or thermopiles have been improved using various methods that are partly invisible to the user because of proprietary technologies, mainly in relation to the sensors. For instance, careful ventilation of the pyranometer body and domes in combination with appropriate heating can diminish thermal offsets. Moreover, good ventilation protects against or reduces the effects of dew, rime, dust, and precipitation that in general disturb radiation measurements and represent error sources.

Pyranometers with Novel Black Thermopiles

As mentioned in Sect. 11.3.2, novel thermopiles based on the principles of black ones are now available. The EKO MS-80 and Middleton Solar ER08-S (Fig. 11.29) are pyranometers that use this new type of thermopile. In contrast to the classic black thermopile type, they have only one glass dome. This is sufficient, because these novel thermopiles have some interesting new features. One is the absence of thermal offsets. This is achieved because the thermopile is encapsulated in a can while the sensor (Sect. 11.3.2, Fig. 11.21) is implemented in the pyranometer body. Because of their small dimension, they react very fast and can be optimized regarding other features. Ventilation and heating are only needed to prevent dew, rime, dust etc. from attaching to the glass dome. The sensors are located behind a quartz diffusor in the case of the MS-80, and underneath a diffusor made from PTFE (polytetrafluoroethylene, better known by the trade name *Teflon*) in the case of the ER08-S. By this means, the directional response lies within the range of class A of the ISO specifications (Sect. 11.5, Table 11.8). A further important and impressive feature is the quick response time of less than 0.5 s for both instruments.

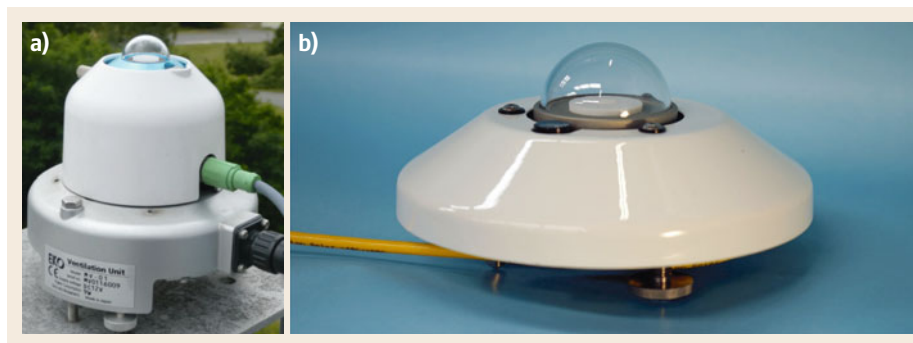


Fig. 11.29a,b Two pyranometers with novel black thermopiles. (a) The EKO MS-80 in use with ventilation unit (photo: K. Behrens). (b) Middleton Solar ER08-S (photo: D. Mathias, courtesy of Middleton Solar)

Pyranometers with Black-and-White Thermopiles

As the name implies, in this type of pyranometer, visible black-and-white circular plates or segments are typically arranged in a star or checkerboard configuration. Currently, only three types of black-and-white thermopile pyranometer are manufactured: the star pyranometer by Schenk in Austria, the black-and-white model 8-48 pyranometer by Eppley Laboratory Inc., USA (Fig. 11.30), and the checkerboard-type SF-06 pyranometer (a refinement of the Yanishevsky M-80 pyranometer) by Peleng company in Belarus.

In contrast to black thermopile pyranometers, these sensors are only protected by one dome. A second dome is not necessary because the active and passive junctions underneath the distinctly colored surfaces (Sect. 11.3.2) are at the same level and it is assumed that the thermal radiation is equally absorbed by the black and white paints. Furthermore, both types of junction are subjected to the same ambient influences. Hence, zero off-set is not a problem for this type of pyranometer. Pyranometers with black-and-white thermopiles show a slow response to changes in irradiance, while their directional response only fulfills the specifications of ISO class C [11.73] (Sect. 11.5, Table 11.8).



Fig. 11.30 Star pyranometer (left) and black-and-white pyranometer (right) (photo: K. Behrens)

Photodiode-Based Pyranometers

Photodiode-based pyranometers use a photoelectric receiver, being a silicon photodiode in most cases (Sect. 11.3.3), thus they are frequently called Si pyranometers. The sensors are mainly placed in small metallic cylinders whose aperture is closed by a cone-shaped diffusor made of a synthetic material. This diffusor ensures that the directional response demands are met, and its shape ensures that rain will run off. In the case of heating, the deposition of dew or rime can be prevented. In general, photodiodes have a restricted spectral response from about 400 to 1100 nm (Sect. 11.2.2, Fig. 11.22), a range in which about 70% of solar energy is incident. Nevertheless, important ranges below and above these limits are not covered. Consequently, photodiodes may only be applied for measurements of solar radiation, while the terrestrial spectral range is excluded. Moreover, the sensitivity of these detectors depends on the wavelength and is not spectrally flat, like that of a thermopile. The subsampling of the solar spectrum together with this nonflat spectral response result in a spectral mismatch on both cloudless and cloud-covered days, resulting in greater uncertainty. Furthermore, they also exhibit temperature dependence.

Nevertheless, photodiode-based pyranometers have gained wide acceptance, especially in the photovoltaic sector, because the spectral features of Si pyranometers and photovoltaic cells are very similar. The production costs of these instruments are low, hence they can be applied in applications where great accuracy is not strictly required. In comparison with the classic thermopile, a photodiode has a very short response time of only a few milliseconds. Therefore, photodiodes are preferred sensors for use in rotating shadowband radiometers, too (Sect. 11.4.6). Furthermore, it should be mentioned that photodiode pyranometers are explicitly considered in the latest ISO update [11.73] (Sect. 11.5), in contrast to its predecessor.

11.4.3 Pyrgeometers

A pyrgeometer (for an example, see Fig. 11.31) measures the terrestrial downward or upward radiation in a viewing angle of 2π sr on a planar surface (Tables 11.2–11.4). Typically, it has the same construction as a pyranometer, with the important difference that the glass dome is replaced by a special filter that blocks solar radiation (Sect. 11.3.4). Black thermopiles are applied as the sensor in all recent pyrgeometers.

Except for the first steps described in Sect. 11.2.3, the successful development of pyrgeometers started with the advent of the Eppley precision infrared pyrgeometer (PIR) first described in [11.86]. This pyrgeometer consisted of a wire-wound plated copper–Constantan thermopile embedded in an aluminum casting acting as the heat sink within copper. The thermopile was protected by a 50-mm-diameter hemisphere of KRS-5 (thallium bromide-iodide) on whose internal surface an interference filter was deposited to block solar radiation. The cut-on was between 3 and 4 μm , with a cut-off at 50 μm [11.86]. Over time, this instrument underwent various improvements, including the replacement of the KRS-5, which deteriorated under the influence of environmental exposure, by a silicon dome. Furthermore, beside the body temperature (the temperature of the cold junctions of the thermopile), the dome temperature was also measured using a thermistor, located at the rim of the dome and used to include the influence of the incident irradiance [11.87].



Fig. 11.31 Two Eppley PIRs (*center*) flanked by two Kipp and Zonen CG4 pyrgeometers within a ventilation unit on an Eppley SMT tracker modified at Meteorological Observatory Lindenberg – Richard-Aßmann Observatory for the use of four instruments to shade and protect the pyrgeometer domes for additional solar beam heating (photo: K. Behrens)

Again, within the goals of the BSRN, it was necessary to improve the measurements of the atmospheric and terrestrial radiation fluxes. Further important steps forward in this regard were made at the Physikalisch-Meteorologisches Observatorium Davos/World Radiation Center (PMOD/WRC). First, the measurement of the dome temperature of the PIR was changed by replacing the thermistor on the rim by three glued at 45°, pointing to the north, southeast, and southwest. In a second step, an improved pyrgeometer equation based on the formula of [11.88] was derived, and thirdly the PIR was characterized as a blackbody [11.89]. The new formula for the calculation of the atmospheric downward irradiance ($E_1\downarrow$) is

$$E_1\downarrow = \left(\frac{U_1\downarrow}{S_1\downarrow} \right) (1 + k_1\sigma T_b^3) + k_2\sigma T_b^4 - k_3\sigma (T_d^4 - T_b^4), \quad (11.8)$$

based on the voltage generated by the thermopile ($U_1\downarrow$) and its sensitivity ($S_1\downarrow$). k_i ($i = 1, 2, 3$) are specific correction factors, σ is the Stefan–Boltzmann constant, and T_d and T_b are the temperatures of the dome and body of the pyrgeometer, respectively. In contrast to the formula given in [11.88], this one is more complete and takes into account higher-order terms. Like the sensitivity for each pyrgeometer, the correction factors k_i must be derived using an elaborate procedure by changing the dome and body temperatures of the pyrgeometer as well as the radiation temperature of the blackbody. This extended pyrgeometer equation (11.8) can only be applied if at least one dome thermistor is present and if the correction factors k_i have been determined as just mentioned. In all other cases, the atmospheric downward irradiance ($E_1\downarrow$) of the Eppley PIR is calculated using the known sensitivity ($S_1\downarrow$) with the simpler equation

$$E_1\downarrow = \frac{U_1\downarrow}{S_1\downarrow} + \sigma T_b^4 - K\sigma (T_d^4 - T_b^4). \quad (11.9)$$

This formula (11.9), often called the Albrecht equation, may also be obtained from (11.8) by considering special assumptions and equals the formula given in [11.88].

At the beginning of the 2000s, Kipp and Zonen B. V. presented a new pyrgeometer called the CG4. It has a similar construction to other Kipp and Zonen pyranometers, but the thermopile is covered by a meniscus-shaped silicon dome that blocks the solar spectral range (Sect. 11.3.4, Fig. 11.24). This dome is in good thermal connection with the pyrgeometer body and thus at the same temperature, so it is not necessary to measure the dome temperature explicitly. Its field of view is 180° like the PIR.

Later, pyrgeometers also became available from other manufacturers, sometimes with a flat filter above the thermopile to block solar radiation, but a restricted viewing angle between 150° and 170° , resulting in greater uncertainty. Some of these pyrgeometers are equipped with a dome or window thermistor, while others are not. It is thus important for the user to study the specifications of each instrument. Typically, this information is also given in the calibration certificate. In the case in which a dome thermistor is available, (11.9) has to be used to determine the atmospheric downward irradiance ($E_{1\downarrow}$). In the absence of a dome thermistor, this quantity is calculated more simply as

$$E_{1\downarrow} = \frac{U_{1\downarrow}}{S_{1\downarrow}} + \sigma T_b^4. \quad (11.10)$$

Since, as mentioned above, a pyrgeometer is very similar in construction to a pyranometer, it is obvious that ventilation and heating units will also improve the data quality, because they prevent dew, rime, and other disturbing deposits from forming on the dome.

Pyrgeometers are general all-weather instruments and therefore robust in design. Furthermore, they are equipped with a sun shield to prevent heating of the pyrgeometer body. In many cases, pyrgeometers have a drying cartridge filled with silica gel to absorb humidity inside the body to prevent condensation. Newer types offer ingress protection against dust and water (IP67) and are virtually sealed, thus not needing such a drying cartridge.

While in the past pyrgeometers only offered the classical analog voltage output, in some cases the user can now additionally select between different output methods or communication protocols such as Modbus or RS-485. Also, so-called smart instruments are available, allowing a direct link to a PC with the possibility of collecting different data and controlling many parameters.

Because this development, especially concerning so-called smart features, has been very fast, it is recommended to study the specification to select a pyranometer with the desired features. Furthermore, the statements given in Sect. 11.1.3 regarding the deployment and measurement site are valid and should be considered, too.

The calibration of pyrgeometers and their traceability to SI is described in Sect. 11.6.

11.4.4 Pyrradiometers

A pyrradiometer measures the total (global solar + terrestrial downward) radiation or total (reflected solar + terrestrial upward) radiation incident from a viewing angle of 2π sr on a flat surface depending on where

the receiver is facing (Tables 11.2–11.4). Combining a downward- and upward-looking pyrradiometer allows the measurement in a viewing angle of 4π sr, and such an instrument is called a *total net radiometer*. The sensors in pyrradiometers are black thermopiles, in most cases embedded in metallic cylinders that nowadays are generally covered by Lupolen-H (polyethylene) hemispheres. The thickness varies between about 0 and 0.05 mm. The thicker ones are self-supporting, while the others are continuously filled with dry compressed air or nitrogen. Frequently, these instruments are offered as total net radiometers. Their status is almost the same as already described in Sect. 11.2.4 and has not really changed or improved. Such instruments are still manufactured by a handful manufacturers around the globe and are used where the demands regarding uncertainty are not very high.

For these instruments, the classical analog output voltage (U) generated by the detector is still typical. The total irradiance (E_{\downarrow}) from the upper hemisphere can then be simply calculated using the known sensitivity (S_{\downarrow}) as

$$E_{\downarrow} = \frac{U_{\downarrow}}{S_{\downarrow}} \quad (11.11)$$

and for the lower hemisphere as

$$E_{\uparrow} = \frac{U_{\uparrow}}{S_{\uparrow}}, \quad (11.12)$$

assuming that the sensitivity in the solar and terrestrial spectral ranges are equal. However, this is typically not the case because of the different transmission of the Lupolen-H hemispheres in the solar and terrestrial regions (Sect. 11.2.4, Fig. 11.15). These differences result from the distinct kinds of polyethylene used and also depend on the thickness and aging of the hemispheres. The transmission in the terrestrial region may be lower by up to 20% compared with that in the solar range. Several methods have been applied to solve this problem. Assuming that there is only a small difference, only one factor is used and (11.11) and (11.12) can be applied as normal. A second option is to determine the sensitivities for the solar and terrestrial regions and assume that these values are valid in general for a particular type of radiometer and polyethylene. In one approach, the blackened surface of the thermopile is partly covered with white paint to equalize the different sensitivities for the solar and terrestrial range [11.48, 90]. However, the best solution to this problem is the individual determination of each sensitivity through a corresponding calibration. The total irradiance (E_{\downarrow}) can then be calculated as

$$E_{\downarrow} = \left(\frac{U_{\downarrow}}{S_{1\downarrow}} \right) + E_{g\downarrow} \left(1 - \frac{S_s\downarrow}{S_{1\downarrow}} \right) \quad (11.13)$$

for the upper hemisphere, and correspondingly for the lower hemisphere as

$$E_{\uparrow} = \left(\frac{U_{\uparrow}}{S_{\uparrow}} \right) + E_r \uparrow \left(1 - \frac{S_s \uparrow}{S_{\uparrow}} \right), \quad (11.14)$$

where S_{\downarrow} , $S_s \downarrow$, $S_s \uparrow$, and S_{\uparrow} are the corresponding sensitivities. However, this clean solution requires measurements of the global and reflected solar irradiance in parallel using pyranometers.

If the pyradiator is additionally equipped with a temperature sensor like a Pt-100 or thermistor to measure the body temperature (T_b in K) of the pyradiator, it also becomes possible to determine the atmospheric downward radiation (E_{\downarrow}) albeit only during nighttime by applying the relation

$$E_{\downarrow} = \frac{U_{\downarrow}}{S_{\downarrow}} + \sigma T_b^4. \quad (11.15)$$

Assuming equal transmission in the solar and terrestrial regions of the polyethylene and measuring also the global radiation separately, the atmospheric downward radiation (E_{\downarrow}) can be calculated as

$$E_{\downarrow} = \left(\frac{U_{\downarrow}}{S_{\downarrow}} \right) - E_{g \downarrow} + \sigma T_b^4 \quad (11.16)$$

during the whole day. The terrestrial upward radiation can then be calculated by applying (11.16) in an equivalent manner for an upward-facing pyradiator. The addition of the term σT_b^4 in (11.15) and (11.16) includes the emission from the instrument itself, because the thermopile gives only the *net radiation* corresponding to the temperature difference between the sky and the surface of the instrument.

The preceding remarks already reveal the problems and uncertainties related to the use of pyradiometers. Another critical point is the aging of the polyethylene hemisphere, which influences its transmissivity, mainly depending on its exposure to ultraviolet (UV) radiation. Currently, polyethylene seems to be the only material available to protect the sensor over the whole spectral region covering the solar and terrestrial regions. Further influences have not yet been considered. The calibration of a pyradiator is not simple and has to be done separately for the solar and terrestrial ranges (Sect. 11.6.1).

11.4.5 Net Radiometers

According to Table 11.2 (Sect. 11.1.1), net radiometers are instruments that allow the measurement of the solar net ($E_s^* = E_g \downarrow - E_r \uparrow$), terrestrial net ($E_l^* = E_{\downarrow} - E_{\uparrow}$), and total net radiation ($E^* = E_s^* + E_l^*$). Therefore, the four main components are measured by pyranometers

(Sect. 11.4.2) in the solar range and by pyrgeometers (see Sect. 11.4.3) in the terrestrial range, as well as by pyrrometers across the whole spectral region, with the corresponding down- and upward radiation fluxes. Because a single radiometer captures a hemisphere of 2π sr, net radiometers cover the whole sphere of 4π sr. From a technical point of view, the net radiation can be realized in the following three ways:

- Directly measuring the net radiation using only one thermopile with hot upward-facing and cold downward-looking junctions, because the difference in temperature is proportional to the net irradiance (single sensor)
- Directly measuring the net radiation by applying a differencing circuit between a downward- and upward-looking radiometer with two thermopiles as detectors (two sensors)
- Calculating it as the difference between the measured downward- and upward-directed fluxes, or in the case of the total net radiation as the total of all four components (four-sensors).

In practice, all of these versions are realized, whereby the uncertainty of the results improves but the cost increases from the first to third solution, a statement that is valid in general.

Normally, all such instruments are equipped with a bubble level so that they can be leveled horizontally. They are mainly mounted at about 2 m above the ground. During the setup, the remarks in Sect. 11.1.3 must be taken into account, and one must additionally ensure that the area below a down-facing instrument is free of the instrument itself and other obstacles.

Solar Net Radiation and Albedo

In most cases, manufacturers combine two thermopiles or two pyranometers (upward and downward facing) into one instrument. Depending on the application requirements, instruments are available in which the thermopiles are covered by only one glass dome or by two domes for higher quality, reaching the criteria for class A pyranometers (Sect. 11.5, Table 11.8). Frequently, these instruments are not ventilated or heated, thus the problems of zero offsets as well as of dew, rime, and dust debris mentioned in Sect. 11.4.3 increase the uncertainty and may diminish the quality of the measurements. Often the thermopiles are selected or adjusted such that their sensitivities match, which offers the advantage that the user can decide whether to apply a differencing circuit or not. Usually, a calibration of the single detector is possible.

Most manufacturers use black thermopiles, but instruments with (star-type) black-and-white thermopiles are also available. The combination of a photodiode

pyranometer would lead to unusable results because of the wavelength-dependent spectral response of the receiver and the different wavelength dependences of the reflected solar radiation and that coming from the upper hemisphere. Although by definition both upward- and downward-pointing instruments should receive radiation from a viewing angle of 2π sr, some manufacturers restrict the viewing angle of the downward-looking pyranometer slightly using a special screen. This prevents incidence of the radiation beam during sunrise and sunset, which is not part of the reflected radiation, onto the sensor. Normally, this effect is not very important, but when measurements are to be carried out at a location with lower surroundings (e.g., on the top of a hill) or the instruments are mounted at higher levels on masts, it may influence or even falsify the data. Furthermore, manufacturers offer special kits and rods to support the mounting.

Frequently, this type of instrument is called an *albedometer*, but this name is incorrect because the albedo is the ratio of the upward- and downward-directed solar radiation and cannot be measured. Theoretically, the albedo can be calculated immediately after the measurement, for instance with the help of a microprocessor, but such an instrument providing a direct output of the albedo is still not known.

To meet high demands in terms of uncertainty and quality, it is possible to combine two, upward- and downward-looking high-quality pyranometers equipped with ventilation and heating to determine the solar net radiation or albedo (Fig. 11.33).

Because the measurements of the described quantities are typically carried out using pyranometers, they are calculated from the ratios of the voltage (U) and the sensitivities (S) of the sensors as shown in (11.7), (11.18), and (11.19). Furthermore, the statements made in Sect. 11.1.3 regarding the deployment and measurement site as well as in Sect. 11.4.2 concerning the handling and features of pyranometers are valid and should also be considered.

Terrestrial Net Radiation

As stated above regarding the solar net radiation, in the case of the terrestrial net radiation it is also possible to combine pyrgeometers into a corresponding net radiation instrument. Because this is only a minor requirement, mainly for pure scientific applications, manufacturers do not offer this type of instrument as standard. However, they will be produced on request, as shown in Fig. 11.32 for the case of an Eppley double direction precision infrared radiometer (DDPIR). The reason for this design is to reduce uncertainty. Note that the DDPIR was not operated as a standalone instrument but was rather part of a total net radiation measurement system, being supplemented with



Fig. 11.32 An Eppley DDPIR net radiometer consisting of two PIR fit together in a case, which also contains the ventilation unit with heater (photo: K. Behrens)

two pyranometers to measure the solar net radiation (Fig. 11.33). Two fully equipped (with body and dome thermistors) PIRs were implemented in a special case with heaters and ventilation units to ensure a constant airflow around the pyrgeometer body and dome and provide protection against multiple environmental influences such as dew, rime, dust, etc. Furthermore, in this special case, the downward and upward terrestrial irradiance can be calculated by applying (11.8) (Sect. 11.4.3).

Total Net Radiometers

In contrast to the on-request production of terrestrial net radiometers, manufacturers do provide a wide offering of total net radiometers. This begins with the simple CNR2 Lite from Kipp and Zonen B.V., continues with the net radiometers based on pyrrometers and simple four-component radiometers described and discussed in Sect. 11.4.4, and finishes with systems composed of two high-end pyranometers and pyrgeometers. The latter systems are manufactured only on request or must be assembled by the user.

The CNR2 Lite matches the features described above and is the simplest way of realizing a net radiometer, i.e., a so-called single-sensor net radiometer. The thermopile (active junctions upward pointing, passive ones downward looking) is fit with black PTFE conical absorbers on both sides. Because all environmental influences such as wind, rain, dew, rime, dust, etc. hit the unprotected sensor, deviations from the correct results are unavoidable. Comparisons made between the predecessor of the CNR2 Lite, the similarly constructed NR-Lite, and a four-component system constructed from an Eppley precision spectral pyranometer (PSP) and PIR pyrgeometer revealed systematic deviations concerning the Sun elevation and wind speed with a large scatter of up to 20 W m^{-2} [11.91]. Further single- and two-sensor net radiometers include the pyrrometers mentioned in Sect. 11.4.4.

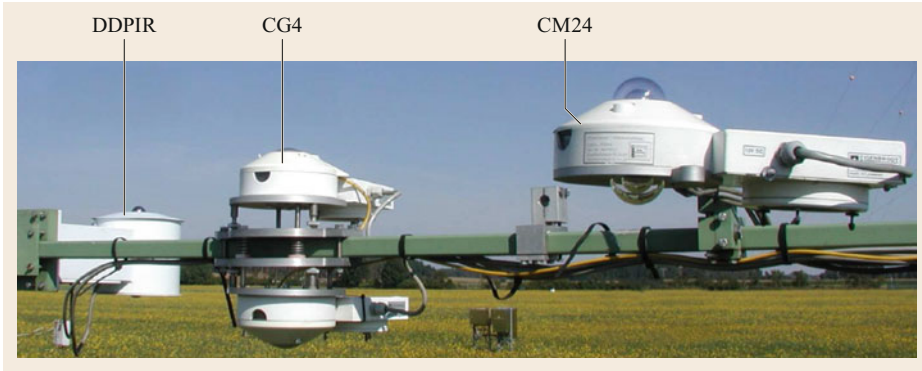


Fig. 11.33 Different net radiometers during a comparison in summer 2013 at the Boundary Layer Measuring Field Falkenberg of the Meteorological Observatory Lindenberg – Richard-Aßmann Observatory, mounted on a special rack about 2 m above the ground. The DDPIR (Eppley Laboratory, Inc. USA), two single CG4 pyrgometers (Kipp and Zonen B. V., the Netherlands) fit in a ventilation unit (with heater) (Eigenbrodt GmbH and Co. KG, Germany) measuring the components of the terrestrial down- and upward irradiance and a CM24 consisting of two CM21 pyranometers (Kipp and Zonen B. V., the Netherlands) also fit in a ventilation unit (with heater) (Eigenbrodt GmbH and Co. KG, Germany) measuring the components of the solar down- and upward irradiance. All instruments including the ventilation units were replaced by successors and will not be produced anymore (photo: K. Behrens)

For a single-sensor detector offering the classical analog voltage output (U) with a known sensitivity (S), the total net irradiance (E^*) can be simply calculated as

$$E^* = \frac{U}{S}. \quad (11.17)$$

Four-sensor net radiometers use a single detector for the acquisition of each of the four different quantities contributing to the total net irradiance (E^*) as follows:

- Global irradiance ($E_g \downarrow$), measured with an upward-facing pyranometer as

$$E_g \downarrow = \frac{U_{g \downarrow}}{S_{g \downarrow}} \quad (11.18)$$

- Reflected solar irradiance ($E_r \uparrow$), measured with a downward facing pyranometer as

$$E_r \uparrow = \frac{U_{r \uparrow}}{S_{r \uparrow}} \quad (11.19)$$

- Atmospheric (terrestrial) downward irradiance ($E_1 \downarrow$), measured with an upward-facing pyrgometer as

$$E_1 \downarrow = \frac{U_{1 \downarrow}}{S_{1 \downarrow}} + \sigma T_b^4 \quad (11.20)$$

- Terrestrial upward irradiance ($E_1 \uparrow$), measured with a downward facing pyrgometer as

$$E_1 \uparrow = \frac{U_{1 \uparrow}}{S_{1 \uparrow}} + \sigma T_b^4. \quad (11.21)$$

All the first terms on the right-hand side of (11.18)–(11.21) consist of the ratio of the voltage (U_x) to the sensitivity (S_x) of the corresponding sensor. In the case of the terrestrial downward and upward irradiance, the term σT_b^4 , where σ is the Stefan–Boltzmann constant and T_b is the temperature of the pyrgometer body in kelvin, has to be added, representing the irradiance of the surface of the thermopile due to its own emissivity. This must be added because the first term contains only the net irradiance, which is proportional to the temperature difference between the irradiating surface (sky or ground) and thermopile.

The following complex quantities can be derived from these individual components

- The solar net irradiance

$$E_s^* = E_g \downarrow - E_r \uparrow. \quad (11.22)$$

- The terrestrial net irradiance

$$E_1^* = E_1 \downarrow - E_1 \uparrow. \quad (11.23)$$

- The total net irradiance

$$\begin{aligned} E^* &= E_s^* + E_1^* \\ &= (E_g \downarrow - E_r \uparrow) + (E_1 \downarrow - E_1 \uparrow). \end{aligned} \quad (11.24)$$

- The albedo

$$\alpha = \frac{E_r \uparrow}{E_g \downarrow}. \quad (11.25)$$

Such measurements of the individual components are the best method to determine these complex quantities of the net irradiance, and manufacturers offer instruments therefor. They consist of two pyranometers, two pygeometers, and a thermometer (Pt-100, thermistor) to measure the instrument's body temperature to form one single net radiometer fit in a common housing, where the four individual voltages and the temperature can be recorded separately. In most cases in these net radiometers, sensors such as black thermopiles covered by only one dome are used, so they cannot measure with the highest quality. Examples include the CNR4 (Kipp and Zonen, B.V.), the NR01 (Hukseflux, B.V.), and the MR-60 (EKO). If a better class is demanded or desired, it becomes necessary to combine single high-end instruments offered by different manufacturers, as shown in Fig. 11.33, for instance. If single radiometers must be applied, that must be mounted close together without hampering the field of view, so that the downward-pointing instruments in particular look at the same area with the same features.

Furthermore, the statements given in Sect. 11.1.3 concerning the measurement site and mounting as well as in Sects. 11.4.2 and 11.4.3 regarding the handling and features of pyranometers and pygeometers are valid for these combined instruments, too.

11.4.6 Multi Radiometers

For years, multi radiometers have been used in applied sciences as well as meteorology. These systems with at least one sensor allow the determination of the three radiation quantities in the solar spectral range from the upper hemisphere, viz. global, diffuse, and direct solar irradiance. The main reason for such a construction is to save money. Ordinarily, this is associated with an increased uncertainty of the measurements. Because multi radiometers are mostly complex instruments, it is recommended to study their datasheets and manuals to obtain information about their usage, signal output, interfaces, etc.

Rotating Shadowband Radiometers (RSRs)

Rotating shadowband radiometers are also called rotating shadowband irradiometers (RSIs) or rotating shadowband pyranometers (RSPs). They consist of a photodiode-based pyranometer and a motorized shadowband that rotates around the pyranometer, e.g., once per minute. During the rotation, the sensor is shaded only for a short time in each circulation, enabling the measurement of the diffuse solar irradiance ($E_d\downarrow$), while in the remaining time the global solar irradiance ($E_g\downarrow$) is recorded. RSRs are subject to the common restrictions already mentioned in Sect. 11.4.2 regarding

the use of photodiode as sensors, especially in terms of a limited, nonflat spectral response and the resulting greater uncertainty. Postprocessing is applied in most models to improve the generated data by correction of known errors caused by shadowband effects and photodiode characteristics.

Two types of RSR are available: A system with *continuous* rotation of the shadowband, and a second one with *discontinuous* rotation. In both types, the rotation occurs once per minute, and both types start their data acquisition with the measurement of the global irradiance with the shadowband in its rest position (nadir) below the sensor. The RSR with continuous rotation, which is also called a burst or sweep type, then starts its full turn of the shadowband, which requires about 1 to 2 s at a constant angular velocity. During this time, data are recorded at a high sampling rate of about 1 kHz. A sensor with a very short response time, such as a photodiode, is thus required. The minimum of this scan is assigned to the moment of shading the detector and corresponds to the diffuse irradiance. The measurement using an RSR with discontinuous rotation proceeds in a similar way, but the shadowband first rotates more slowly, and secondly stops turning immediately before and after the position where the sensor is totally shaded and the diffuse irradiance is measured. These stops last about 1 s each. In this case, only four data points are available. The points before and after covering the sensor are used for specific correction of the diffuse irradiance. Also in the case of a continuous rotation RSR, the data from the so-called shoulders before and after the selected minimum are used to correct the diffuse irradiance. Control of the discontinuously rotating RSR requires greater effort, because exact alignment to shade the sensor completely is required to measure the diffuse irradiance.

The first RSR model was described in 1982 [11.92], being called at that time the dial radiometer and working in the continuous mode, while later in 1986 [11.93], a microprocessor-controlled RSR applying discontinuous rotation was reported. The objective of such constructions is the measurement of the global ($E_g\downarrow$) and diffuse ($E_d\downarrow$) solar irradiance nearly simultaneously using one instrument and the calculation of the third missing but desired quantity, viz. the direct solar irradiance (E), as

$$E = \frac{E_g\downarrow - E_d\downarrow}{\cos(z)}, \quad (11.26)$$

where z is the solar zenith angle. The use of only a single instrument to measure these three quantities allows great cost savings with respect to the classical system consisting of at least two pyranometers equipped

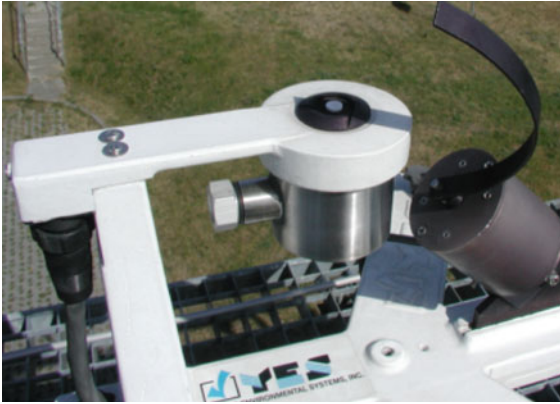


Fig. 11.34 MRF-7 in use (sensor just shaded) at Meteorological Observatory Lindenberg – Richard-Aßmann Observatory (photo: K. Behrens)

with a thermopile as well as a shadowband or solar tracker and a ventilation unit. In particular, RSRs became popular for photovoltaic and concentrating solar power (CSP) applications.

Later, the technique of a discontinuous rotating RSR was applied in the multifilter rotating shadowband radiometer (MFRSR) [11.94] (Fig. 11.34), providing the broadband irradiance of the direct, diffuse, and global solar components as well as the same quantities in six narrow spectral channels at 415, 500, 615, 673, 870, and 940 nm, which allows the derivation of the aerosol optical depth (AOD, see Chap. 29). In the recent version (MRF-7), the broadband irradiance is measured by a micro-thermopile, whereas photodiodes are used for the spectral channels as before.

Improvements regarding the correction of systematic errors, uncertainty analysis based on the *Guide to the Expression of Uncertainty in Measurement* (GUM), and a special calibration method for RSRs are described in [11.95–97].

SPN1 Sunshine Pyranometer

Another multi radiometer is the SPN1 sunshine pyranometer [11.98] (Fig. 11.35). Like the rotating shadowband radiometers, this instrument also enables the measurement of global, diffuse, and direct solar irradiances. However, in contrast to RSRs, it has no moving parts and the sensors are miniature thermopiles. The seven sensors are arranged on a hexagonal grid which is covered by a computer-generated shadow mask so that at least one sensor is always totally irradiated while at least one other is completely shaded. Under the assumption of isotropic diffuse radiation, the completely shaded sensor (that with the minimum reading) receives 50% of the diffuse radiation while the sensor with the maximum reading (that which is fully irradiated) re-



Fig. 11.35 SPN1 at Meteorological Observatory Lindenberg – Richard-Aßmann Observatory (photo: K. Behrens)

ceives the complete direct irradiance at the horizontal surface plus 50% of the diffuse one. Herewith, the readings can be calculated as

$$\begin{aligned} \text{DIFFUSE} &= 2 \cdot \text{MIN} \\ \text{DIRECT} &= \text{MAX} - \text{MIN} \\ \text{GLOBAL} &= \text{DIRECT} + \text{DIFFUSE} = \text{MAX} + \text{MIN} \end{aligned}$$

The single readings of the different thermopiles are internally processed, and the corresponding voltages of the global and diffuse irradiances are available continuously at the analog output interface. Furthermore, there is the possibility of a direct link to a computer via an RS232 serial link, and corresponding software enables access to much information, including the three radiation quantities as well as the derived sunshine duration. Despite the usage of thermopiles, the spectral response (50% points assumed) is restricted to 400 to 2700 nm, covering mainly the UV spectral range, but the response time is short at < 200 ms.

RaZON+

The RaZON+ (Fig. 11.36) also provides the three solar radiation quantities from the upper hemisphere, but in a different way. RaZON+ is an all-in-one smart system consisting of a Global Positioning System (GPS)-controlled solar tracker equipped with a pyrhelimeter PH1 and a pyranometer PR1, which is shaded by a disc, as well as internal data logging with Ethernet and WiFi web access. This means that the system does not have any analog interface and is only connected via the RaZON+ web interface and a standard browser on the owner's system (PC, tablet, or smartphone). The pyrhelimeter PH1 and pyranometer PR1 are specially designed only for use in the RaZON+. The sensors of both radiometers are thermopiles with very short response times of < 0.2 s, and both sensors are located behind a quartz diffusor. In the case



Fig. 11.36 RaZON+ (manufacturer: Kipp and Zonen B.V., the Netherlands): a solar tracker with pyr heliometer and shaded pyranometer measuring direct (E) and diffuse ($E_d\downarrow$) solar irradiance on the roof platform of the Meteorological Observatory Lindenberg – Richard-Abmann Observatory in Lindenberg, Germany (photo: K. Behrens)

of the PH1, a specially designed collimation tube with an open aperture provides the required view-limiting geometry (Sect. 11.4.1, Fig. 11.25), diminishes soiling, and enables drainage of rainwater, being situated in front of the sensor system, while that of the PR1 is covered by a machined and polished glass dome. The PR1 does not show the typical thermal offsets observed for thermopile instruments (Sect. 11.4.2) despite being covered by only one dome. This feature and also the short response time indicate that the sensors are similar to the novel black thermopiles mentioned in Sect. 11.3.2. Despite the usage of a quartz diffusor and thermopile, in both cases the spectral range is limited to 310 to 2700 nm. The data are sampled at 1 Hz, and the built-in processor calculates the 1-min mean irradiances of the direct (E), diffuse ($E_d\downarrow$), and global ($E_g\downarrow$) irradiances as the sum of the two values using (11.1) (Sect. 11.1.1), which is in principle the best solution for determining these three quantities [11.99]. Furthermore, the sunshine duration is additionally derived from the direct (E) solar irradiance (Sect. 11.4.7). All these data are stored locally within the RaZON+ system for 365 days. The RaZON+ offers all-weather ingress protection (IP65), while the PH1 and PR1 offer IP67 protection.

Photosynthetically Active Radiation (PAR) Sensor

PAR is the part of the solar radiation that plants use for photosynthesis, being specific to different plants and crops. Investigations [11.100] have shown that it is best to standardize and define the spectral region from

400 to 700 nm as PAR. Photosynthesis is a quantum process by which photons excite reactions in chlorophyll molecules of plants in a wavelength-dependent fashion. Therefore, the PAR is typically expressed as the photosynthetic photon flux density (PPFD) in units of $\mu\text{mol m}^{-2} \text{s}^{-1}$. Furthermore, photons with shorter wavelengths have higher energy than those with longer wavelengths, resulting in a mismatch between the energy and photon flux densities. However, with the help of weighting functions, the PAR can also be expressed as the irradiance integrated over the wavelength interval between 400 and 700 nm.

Because PAR is defined between 400 and 700 nm, photodiode-based sensors are typically applied in PAR measuring instruments. Therefore, the Si sensor is covered by a combination of a diffusor and special interference filter that approximately emulates the weighting function of PAR. These parts are fixed in a small metallic body, resulting in a weatherproof instrument. Being based on the same detectors, PAR instruments have features similar to those of Si pyranometers (Sect. 11.4.2), or in other words, PAR or quantum sensors are like photodiode-based pyranometers adapted for a special purpose. The quality of such detectors mainly depends on the successful emulation of the weighting function of PAR. The best results in measuring the PPFD are achieved using spectroradiometers (Chap. 28), because they enable detailed acquisition of spectral radiation in the target spectral range of PAR. Concerning the deployment of PAR sensors, the rules and recommendations already mentioned regarding the site for general measurements (see, e.g., Sect. 11.1.3) still apply. In the case of other objectives, for instance, the frequently applied measurement of PAR within plant stands, deviation from these standards is clearly unavoidable.

Further information concerning PAR is summarized in [11.101].

UV Radiation Sensors (see also Chap. 28)

Ultraviolet (UV) radiation lies in the spectral area below 400 nm to about 100 nm. The UV region is subdivided into three parts, amongst which UV-C in the range below 280 nm is not important at the Earth's surface, because radiation with wavelengths < 290 nm is absorbed by ozone in the stratosphere. Consequently, the remaining part reaching the surface strongly depends on the thickness of the ozone layer in the stratosphere. The range between 400 and 315 nm is the so-called UV-A region, while the remaining area (315–280 nm) called UV-B is especially important for humans. On the one hand, it is responsible for sunburn and diseases, while on the other hand it also enables the production of vitamin D. Furthermore, UV-B also influences the change of material properties. Hence, there is great interest in collecting data in this particular spectral range.

As seen in Fig. 11.18, the irradiance between about 290 and 400 nm covers a large dynamic range of about $10^3 \text{ W m}^{-2} \mu\text{m}^{-1}$ but represents a fraction of less than 10% of the total or global solar irradiance, resulting in very high demands for such sensors. A thermopile cannot fulfill these requirements because of its low sensitivity. A detector based on the already considered Si photodiode is also ruled out, because it is not sensitive to wavelengths below 400 nm. However, photodiodes made from other materials such as gallium arsenide phosphide (GaAsP) can be implemented beneath a combination of a diffusor and special filters, mounted in bodies already successfully applied in traditional or Si pyranometers, frequently covered by a dome made from quartz or glass. The diffusor ensures the fulfillment of the cosine law, considering that the sensor receives diffuse radiation, and thereby prevents a dependence of the direct solar radiation on the angle of incidence.

The importance of the distinct spectral UV regions is accommodated by manufacturers by the production of corresponding adapted instruments, including for the special erythral action spectrum. Like the above-mentioned instruments, UV instruments are general all-weather devices and therefore robust in design. Depending on their construction, some instruments are equipped with a drying cartridge filled with silica gel to absorb humidity inside the body to prevent condensation. The newer types offer ingress protection against dust and water (IP67) and are virtually sealed. Furthermore, they are offered with the classical analog output or the possibility to select between different output methods or communication protocols such as Modbus or RS-485, respectively. Also, so-called smart instruments are available, allowing a direct link to a PC with the possibility of collecting different data and controlling many parameters.

Because this development, especially concerning the so-called smart features, has been very fast, it is recommended to study the specifications to select an instrument with the desired features. Furthermore, the statements given in Sect. 11.1.3 regarding the deployment and measurement site are valid and should also be considered.

The best results in measuring UV radiation are achieved by applying spectroradiometers (see also Chap. 28), because they enable high spectral resolution, which is of exceptionally importance in the UV-B range with its large dynamic range.

In contrast to broadband radiometers, in which thermopiles are mainly applied as sensors, the calibration of UV instruments is primarily achieved using standard lamps and is traceable to SI via the National Metrology Institutes (NMIs) (see also Sect. 11.6.).

11.4.7 Sunshine Duration Instruments

Sunshine duration measurements represent one of the oldest methods to indicate solar radiation. According to [11.1],

the term “sunshine” is associated with the brightness of the solar disc exceeding the background of diffuse sky light, or, as is better observed by the human eye, with the appearance of shadows behind illuminated objects. As such, the term is related more to visual radiation than to energy radiated at other wavelengths, although both aspects are inseparable.

From a historical point of view, the Campbell–Stokes sunshine recorder is the most well-known and widespread instrument worldwide for the determination of sunshine duration. As early as 1853, J. F. Campbell (1821–1885) reported for the first time on a sunshine recorder consisting of a glass sphere, which worked like a burning glass, fit in a wooden bowl. It was improved based on a proposal from Sir G. G. Stokes (1819–1903) in 1879, replacing the wooden bowl by a metallic one and applying a card holder, achieving its well-known appearance as shown in Fig. 11.37.

Well-known investigations and comparisons of sunshine duration instruments and measurements have revealed differences of up to 20%, resulting in the recommendation for an *interim reference sunshine recorder* (IRSRR) by the WMO [11.102] in 1962, being of Campbell–Stokes type with defined specifications and the objective of reducing these measurements to a common reference level. Despite the intended improvements, further investigations [11.103] revealed serious deficiencies, including a wide variation of the irradiance threshold to produce a burn on the recorder card of between about 100 and 300 W m^{-2} when using this instrument. Consequently, in 1981, the WMO [11.104] considered among other factors:

- The fact that traditional Campbell–Stokes sunshine recorders do not in fact record the duration of bright sunshine with sufficient consistency
- The difficulty in defining the concept of *sunshine* because of its relationship to physiological effects
- The urgent need to adopt a common threshold value for *sunshine* so that irradiance-based instruments provide compatible data.

and thus recommended:

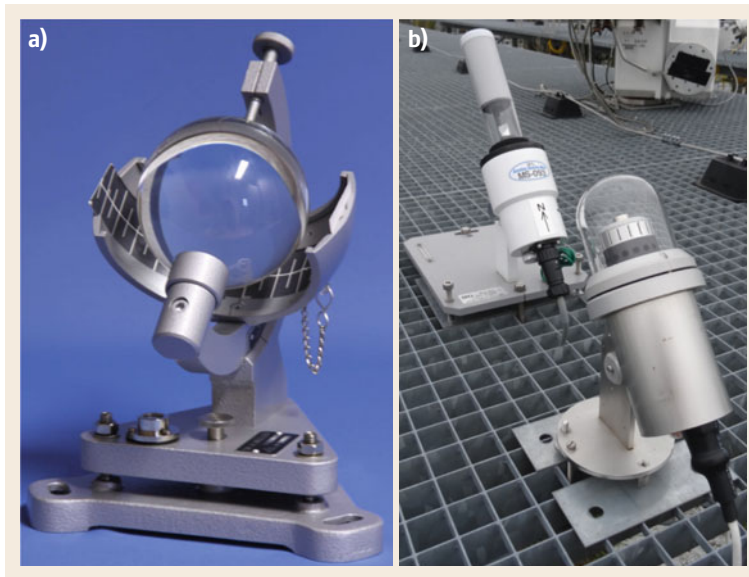


Fig. 11.37a,b The classical Campbell–Stokes sunshine recorder (a) (photo: Dr. Alfred Müller – Meteorologische Instrumente KG – R. Fuess) and (b) two instruments (EKO MS-093 and Meteoservic SD6 digital sunshine detector) applying electrical methods (photo: K. Behrens)

- The adoption of a threshold value for bright sunshine of 120 W m^{-2} of direct solar irradiance
- That (WMO) members incorporate this threshold value in the specification of instruments, with an accuracy of $\pm 20\%$
- That the interim reference sunshine recorder be recognized as merely providing an index of sunshine duration, and that its status as a reference be removed.

Hence, the sunshine duration during a given period is defined as the sum of time for which the direct solar irradiance exceeds 120 W m^{-2} . This new threshold is physically based and metrologically traceable but implies a new precariousness with its wide inaccuracy of $\pm 20\%$.

Like at the beginning of the 1980s with the Eppley NIP (Sects. 11.2.1 and 11.4.1), only one commercial weatherproof pyrheliometer as well as a few expensive solar trackers were available to determine the sunshine duration defined in this way. Even today, this situation has not changed much, because in national meteorological networks sunshine duration is not determined using a pyrheliometer but rather by other methods. Indeed, this development started in the 1970s with the beginning of the automatization of meteorological networks, where the Campbell–Stokes device had to be replaced by sensors providing an electrical output (Fig. 11.37b). For this purpose, manufacturers mainly applied photodiode sensors (Sect. 11.3.3), which can be used in many different ways to measure sunshine duration.

According to [11.1], the WMO distinguishes the following five methods for the determination of sunshine duration:

- Pyrheliometric method
- Pyranometric method
- Burn method
- Contrast method
- Scanning method.

Except for the classical burn (Campbell–Stokes) method, the others are electrical. The pyrheliometric method corresponds to the definition, while the use of two pyranometers to measure the global and diffuse solar radiation allows the direct solar radiation to be calculated with a result that also corresponds with the definition of this quantity. If only one pyranometer measures the global solar radiation, it becomes necessary to apply an algorithm to estimate the sunshine duration [11.105, 106]. The contrast and scanning methods are also electrical and use photodiodes as detectors, albeit in different ways. Corresponding instruments are offered by several manufacturers. Despite the traceable definition of sunshine duration, the use of very different (old and new) methods for its derivation is also possible, with a large but permissible uncertainty. Again as a consequence, problems in data comparability may result [11.107].

In contrast to the methods discussed in previous sections for determining the various radiation quantities that are traceable to SI, it is difficult to accomplish this for sunshine duration. Moreover, it is generally

accepted that sunshine duration contains very little information, viz. only the time during which the direct solar radiation at normal incidence exceeds a (poorly defined) threshold. From this point of view, sunshine duration is only of historical importance as a proxy to prolong time series of global radiation dating back to the 19th century (Sect. 11.8.1). Nevertheless, sunshine duration is still used, for instance, in relation to health resorts or weather forecasts, because humans may simply associate sunshine duration with an impression of climate or weather.

11.4.8 Supplementary Equipment

Supplementary equipment can be categorized into two groups, which may overlap in some cases:

- Necessary equipment for the direct execution of specific measurements (e.g., shadow bands, shadow discs/balls, solar trackers)
- Equipment for improvement and quality assurance of measurements (e.g., ventilation and heating, cleaning, shadow discs).

Measurements of direct solar irradiance are only possible if the corresponding instrument, viz. the pyrheliometer, continuously follows the Sun's path during the day (Sects. 11.2.1 and 11.4.1). While this alignment or tracking was long done manually or using simple clock-driven devices, electromechanical systems based on the frequency of the alternating current (AC) were later applied. The disadvantage of such systems was that they only turned in one direction, so the pyrheliometer cable had to be put back each morning. Moreover, daily adjustment for the changing declination of the Sun was at least necessary for equatorially mounted pyrheliometers, in addition to occasional alignment checks to correct any instability in the AC frequency. The application of step motors and remote control via PCs provided only a short but supporting interim solution, whereas the breakthrough in this regard was achieved in the 1990s when microcontrollers were applied to control the trackers, addressing all the mentioned issues. State-of-the-art solar trackers now also include GPS and Sun sensors (for active tracking) and adopt the plug-and-play principle. Nowadays, many manufacturers offer solar trackers in several configurations and for different applications, including with large payloads. A typical example is shown in Fig. 11.38, demonstrating the complete acquisition of the solar and terrestrial radiation fluxes from the upper hemisphere with a high quality level. The solar tracker is equipped with a pyrhe-



Fig. 11.38 Fully equipped solar tracker (solar tracker and radiation instruments: Kipp and Zonen B.V., the Netherlands; ventilation and heating units: Fa. Eigenbrodt GmbH and Co KG, Germany) at the Boundary Layer Measuring Field Falkenberg of the Meteorological Observatory Lindenberg – Richard-Aßmann Observatory (photo: K. Behrens)

liometer for direct solar radiation, two pyranometers to measure global (unshaded in the center) and diffuse radiation (the shaded one), and a pyrgeometer (also shaded) to measure the downward terrestrial radiation.

Such coincident and independent acquisition of the three solar radiation quantities enables their mutual checking because, according to (11.1) (Sect. 11.1.1), the total of the diffuse irradiance ($E_d \downarrow$) and the vertical component of the direct irradiance ($E \cos(z)$) should equal the global irradiance ($E_g \downarrow$). Therefore, it is important that the geometry of the pyranometer/shade disc (shaded opening angle and slope angle) agree with the field-of-view angle of the pyrheliometer (Sect. 11.4.1). Furthermore, the shading of the pyrgeometer prevents heating of the dome and improves the quality of the atmospheric downward irradiance ($E_1 \downarrow$) measurements. Shade discs may also be replaced by shade balls of an equal diameter.

Regarding measurements of the diffuse irradiance ($E_d \downarrow$), it is appropriate to use a pyranometer with small zero offset because, on very clear days, the diffuse irradiance may represent only about 10% of the global radiation. The thermal offset is of great importance in this regard.

In the past and even now, mainly for economic reasons, trackers are not deployed to cover the area of national networks. Rather, since the early days, shadow bands or shadow rings have been developed and accepted as an alternative to reduce costs, despite their well-known deficiencies as replacements. Shadow rings

block not only the radiation from the desired field-of-view angle corresponding to the pyrheliometer but moreover the irradiance from other parts of the sky, resulting in an underestimation of the diffuse irradiance ($E_d \downarrow$). As early as 1956 [11.108], the following formula was derived to describe the fraction of blocked diffuse solar irradiance in the case of isotropic conditions and for a ring with $b/r < 0.2$

$$\frac{E_{d \downarrow v}}{E_d \downarrow} = \left(\frac{2b}{\pi r} \right) \cos^3 \delta \times \left[\left(t_0 \frac{\pi}{180} \right) \sin \varphi \sin \delta + \cos \varphi \cos \delta \sin t_0 \right], \quad (11.27)$$

where $E_{d \downarrow v}$ is the obscured diffuse irradiance, $E_d \downarrow$ is the unobscured diffuse irradiance, b is the width of the shadow ring, r is the radius of the shadow ring, δ is the declination of the Sun (in degrees), φ is the geographic latitude of the location (in degrees), and t_0 is the hour angle of the Sun (in degrees) between sunrise and noon or sunset and noon, respectively.

Based on this ratio, a correction factor f can be defined as

$$f = \frac{1}{1 - E_{d \downarrow v}/E_d \downarrow}, \quad (11.28)$$

which has to be applied to the measured diffuse irradiance.

In the case of $\varphi = 52.5^\circ$ and $b/r = 0.169$, the correction factor f lies between 1.013 at winter solstice and 1.106 at summer solstice, while at the equinox $f = 1.070$. Unfortunately, the irradiance from the sky is

rarely isotropic. Therefore, to improve on this by considering actual climatological conditions (cloudiness and atmospheric turbidity), it is necessary to determine the correction factor f experimentally by measuring the diffuse irradiance ($E_d \downarrow$) simultaneously using a shadow disc and shadow ring. Unfortunately, no standardization has taken place in this regard to date. However, in [11.109], a method and extended formula based on (11.27) are described to reduce the variation between measurements using different shadow rings and locations.

The shadow ring is mounted on two rails oriented parallel to the Earth's axis, positioned over a pyranometer such that the center of the ring coincides with the sensor at equinox. The ring has to be moved along the rails according to the declination of the Sun. The adjustment of the ring should be checked at least every 2 days, if possible during sunshine. Exact descriptions regarding the mounting and operation are given in the manuals of the various manufacturers.

Because of the increasing demands regarding automatization of stations, a shadow ring controlled by a microcontroller is now also available (Fig. 11.39).

The importance of using ventilation and heating systems, especially for pyranometers and net radiometers using black thermopiles to reduce and stabilize nighttime offsets, was emphasized in Sects. 11.4.2 and 11.4.4. Moreover, such systems also support all kinds of radiation sensors by ensuring and improving the quality of the resulting data by keeping them free of dew, rime, dust, etc., or removing them faster. Typical solutions for external ventilating and heating systems, which are mainly applied for thermopile instruments, are shown in Fig. 11.39.

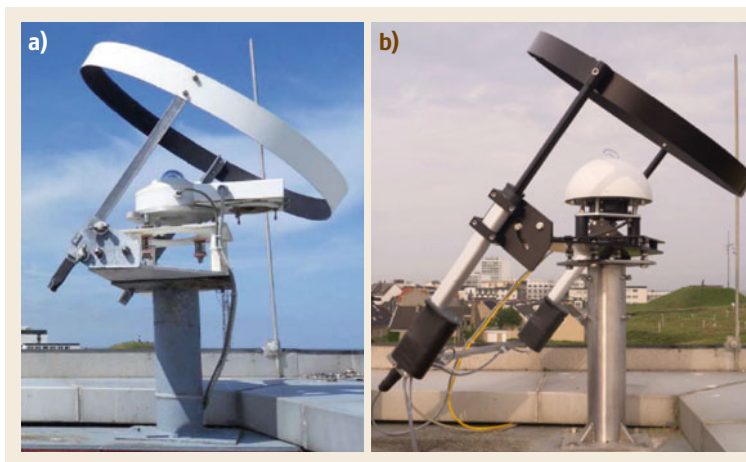


Fig. 11.39a,b Pyranometer assembled in a ventilation and heating unit with shadow ring. (a) Old units with ring manually adjusted along rails. (b) New units with ring remotely controlled by a microcontroller and moved once a day by a stepper motor on each rail. (Ventilation and heating unit as well as shadow ring (old and new systems) Fa. Eigenbrodt GmbH and Co KG, Germany; pyranometer: Kipp and Zonen B.V., the Netherlands (photos: K. Behrens))

Table 11.7 Advantages and disadvantages of different devices

Device	Advantages	Disadvantages
Absolute pyrheliometer	Realization of the irradiance scale, smallest uncertainty	Expensive; very special pyrheliometer
Pyrheliometer without self-calibration capability	Considerably cheaper than absolute pyrheliometer	Calibration is necessary; higher uncertainty than absolute pyrheliometer
Pyranometer with black thermopile	Flat spectral response, available for all classes of uncertainty	Two domes necessary to reduce thermal offset
Pyranometer with novel black thermopile	Limited thermal offset; flat spectral response; very short time response	
Pyranometer with black-and-white thermopile	Limited thermal offset	Not available with smallest uncertainty; responsivity depends on azimuth and temperature
Photodiode-based pyranometer (Si pyranometer)	Very short time response; lightweight, small; considerably cheaper than thermopile pyranometer	Restrictions in spectral response, spectral mismatch; not available with smallest uncertainty
Multi radiometer	At least two quantities with one instrument; very short time response; lightweight, small; cheaper than corresponding pyranometer and/or pyrheliometers systems	Restrictions in spectral response, spectral mismatch; not available with smallest uncertainty
Diffuse solar irradiance ($E_d\downarrow$) measured with a pyranometer on a solar tracker with shadow disc	Best measurement; field-of-view angle of the pyrheliometer and shadow disc agree	Expensive
Diffuse solar irradiance ($E_d\downarrow$) measured with a pyranometer and shadow ring	Considerably cheaper than with tracker	Correction methods can never provide true values
Terrestrial radiation measured with a pyrradiometer		Separation of the terrestrial spectral range is only possible by subtraction of the solar global or reflected radiation measured in parallel; polyethylene domes degrade quickly
Terrestrial radiation measured with a pyrgeometer	Best measurement	

Especially in some Si pyranometers and thus RSR, a heater is included in the body of the instrument. In the case of thermopile pyranometers, an entirely new approach was introduced with the SR30-D1 (Hukseflux B.V., the Netherlands), in which recirculating ventilation and heating (RVH™) technology was applied based on the circulation of slightly warmer air between the inner and outer domes.

Furthermore, for use on ocean platforms, cleaning systems have been developed based on splashing dis-

tilled water over pyranometer and pyrgeometer domes as well as the front glasses of pyrheliometers to wash away salt deposits.

11.4.9 Comparison of Devices to Measure Radiation Parameters

The advantages and disadvantages of the different devices for measuring radiation parameters are presented in Table 11.7.

11.5 Specifications

Specifications of instruments are necessary to compare their features. Concerning broadband radiation instruments, specifications are provided by both the World Meteorological Organization (WMO) and International Organization for Standardization (ISO), being very similar up to the end of 2018, at which time a new ISO stan-

dard [11.73] was published to consider new demands and the state of the art. As always, the ISO standard considers only instruments for measuring hemispherical solar and direct solar radiation but explicitly includes new *photoelectric* sensors. Furthermore, the additional properties of *spectrally flat* and *fast response* were in-

Table 11.8 Pyranometer classification list (excerpt of [11.73])

Parameter Name of the class	Name of the classes, acceptance intervals, and width of the guard bands (in brackets)		
	A	B	C
Response time: time for 95% response	< 10 s (1 s)	< 20 s (1 s)	< 30 s (1 s)
Zero offset: (a) Response to -200 W m^{-2} net thermal radiation	$\pm 7 \text{ W m}^{-2}$ (2 W m^{-2})	$\pm 15 \text{ W m}^{-2}$ (2 W m^{-2})	$\pm 30 \text{ W m}^{-2}$ (3 W m^{-2})
(b) Response to 5 K h^{-1} change in ambient temperature	$\pm 2 \text{ W m}^{-2}$ (0.5 W m^{-2})	$\pm 2 \text{ W m}^{-2}$ (0.5 W m^{-2})	$\pm 8 \text{ W m}^{-2}$ (1 W m^{-2})
(c) Total zero offset including effects (a) and (b) and other sources	$\pm 10 \text{ W m}^{-2}$ (2 W m^{-2})	$\pm 21 \text{ W m}^{-2}$ (2 W m^{-2})	$\pm 41 \text{ W m}^{-2}$ (3 W m^{-2})
Nonstability: percentage change in responsivity per year	$\pm 0.8\%$ (0.25%)	$\pm 1.5\%$ (0.25%)	$\pm 3\%$ (0.5%)
Nonlinearity: percentage deviation from the responsivity at 500 W m^{-2} due to changes in irradiance within 100 to 1000 W m^{-2}	$\pm 0.5\%$ (0.2%)	$\pm 1\%$ (0.2%)	$\pm 3\%$ (0.5%)
Directional response (for beam radiation): range of errors caused by assuming that the normal incidence responsivity is valid for all directions when measuring from any direction (with an incidence angle up to 90° or even from below the sensor) for a beam radiation whose normal-incidence irradiance is 1000 W m^{-2}	$\pm 10 \text{ W m}^{-2}$ (4 W m^{-2})	$\pm 20 \text{ W m}^{-2}$ (5 W m^{-2})	$\pm 30 \text{ W m}^{-2}$ (7 W m^{-2})
Clear sky global horizontal irradiance spectral error	$\pm 0.5\%$ (0.1%)	$\pm 1\%$ (0.5%)	$\pm 5\%$ (1%)
Temperature response: percentage deviation due to changes in ambient temperature within the interval from -10 to 40°C relative to the signal at 20°C	$\pm 1\%$ (0.2%)	$\pm 2\%$ (0.2%)	$\pm 4\%$ (0.5%)
Tilt response: percentage deviation from the responsivity at 0° tilt (horizontal) due to changes in tilt from 0° to 180° at 1000 W m^{-2} irradiance	$\pm 0.5\%$ (0.2%)	$\pm 2\%$ (0.5%)	$\pm 5\%$ (0.5%)
Additional signal processing errors	$\pm 2 \text{ W m}^{-2}$ (2 W m^{-2})	$\pm 5 \text{ W m}^{-2}$ (2 W m^{-2})	$\pm 10 \text{ W m}^{-2}$ (2 W m^{-2})

cluded, and more intuitive names were introduced for the classes (A, B, and C). However, the old names of secondary standard, first class, and second class already differed from those of the WMO, viz. high quality, good quality, and moderate quality. Generally, the ISO specification as well as the WMO characteristics are independent of the technology applied by the manufacturer and are only valid for well-maintained instruments working under the same conditions. Furthermore, the classes express a ranking, but this does not mean that a lower-class instrument will give worse results in corresponding measurement conditions, if the parameter responsible for the lower ranking does not determine the task at

hand. In any case, the selection of an appropriate sensor is important regarding the accordance of its response time with the sampling rate of the data logger, for instance, and similarly for its spectral response.

The corresponding characteristics in the WMO document [11.1] cover pyrheliometers, pyranometers, and pyrrometers. Unfortunately, no equivalent information is available concerning pyrgeometers.

Excerpts from the pyranometer and pyrheliometer classification lists of the ISO standard [11.73] are reproduced in Tables 11.8 and 11.9. For details, including comments regarding the parameters, direct reference to this document is very important and useful.

Table 11.9 Pyrheliometer classification list (excerpt of [11.73])

Parameter	Name of the classes, acceptance intervals, and width of the guard bands (in brackets)			
	AA*	A	B	C
Response time: time for 95% response	See Note 1	< 10 s (1 s)	< 15 s (1 s)	< 20 s (1 s)
Zero offset:				
(a) Response to 5 K h ⁻¹ change in ambient temperature	±0.1 W m ⁻² (0.05 W m ⁻²)	±1 W m ⁻² (0.5 W m ⁻²)	±3 W m ⁻² (0.5 W m ⁻²)	±6 W m ⁻² (1 W m ⁻²)
(b) Complete zero offset including effect (a) and other sources	±0.2 W m ⁻² (0.05 W m ⁻²)	±2 W m ⁻² (0.5 W m ⁻²)	±4 W m ⁻² (0.5 W m ⁻²)	±7 W m ⁻² (1 W m ⁻²)
Nonstability: percentage change in responsivity per year	±0.01% (0.01%)	±0.5% (0.25%)	±1% (0.25%)	±2% (0.25%)
Nonlinearity: percentage deviation from the responsivity at 500 W m ⁻² due to changes in irradiance within 100 to 1000 W m ⁻²	±0.01% (0.01%)	±0.2% (0.1%)	±0.5% (0.2%)	±2% (0.2%)
Clear sky direct normal irradiance spectral error	±0.01% (0.005%)	±0.2% (0.05%)	±1% (0.5%)	±2% (1%)
Temperature response: percentage deviation due to change in ambient temperature within the interval from -10 to 40 °C relative to the signal at 20 °C	±0.01% (0.01%)	±0.5% (0.25%)	±1% (0.5%)	±5% (0.5%)
Tilt response: percentage deviation from the responsivity at 0° tilt (horizontal) due to changes in tilt from 0° to 90° at 1000 W m ⁻² irradiance	±0.01% (0.1%)	±0.2% (0.2%)	±0.5% (0.2%)	±2% (0.5%)
Additional signal processing errors	±0.1 W m ⁻² (0.1 W m ⁻²)	±1 W m ⁻² (0.5 W m ⁻²)	±5 W m ⁻² (2 W m ⁻²)	±10 W m ⁻² (2 W m ⁻²)

Note 1: Pyrheliometers of this class are mainly used as reference instruments for the calibration of other pyrheliometers. They are often absolute pyrheliometers, for which an unambiguous definition of response time is not possible. For instance, it depends on the mode of operation (e.g., active or passive). To avoid confusion and because the response time is of marginal significance for calibration under stable sky conditions, the response is omitted for this class.

* This class was first time introduced in this ISO standard [11.73]

11.6 Quality Control

Quality control is critically important to achieve useful and comparable datasets for scientific analysis. This starts with a reproducible and traceable calibration to SI for the instrument and ends with verification of the generated data, including documentation of any changes throughout the process. In the case of broadband radiation measurements, this traceability to SI does not occur via the National Metrology Institutes but uses the World Radiation Center (WRC) located at the Physikalisch-Meteorologisches Observatorium Davos (PMOD) in Switzerland.

11.6.1 Calibration of Radiation Instruments

Regarding the separation between the solar and terrestrial spectral ranges, see Sects. 11.3.1 and 11.3.4.

Instruments Operating in the Solar Spectral Range

All calibrations in the solar spectral range are based on the World Standard Group (WSG) representing the World Radiation Reference (WRR) (Sect. 11.2.5). Currently, absolute pyrheliometers (Sect. 11.4.1) of the PMO, CROM, TMI, PACRAD and H-F type are members of the WSG (Fig. 11.40). These instruments are operated by the staff of the WRC.

The task of the PMOD/WRC is to disseminate the WRR all over the world, which mainly happens during the international pyrheliometer comparisons (IPCs) that take place every 5 years. During the IPCs, the WRR is transferred to the reference instruments of the regional radiation centers (RRC) and/or national radiation centers (NRC) (Sect. 11.2.5). Corresponding rules and

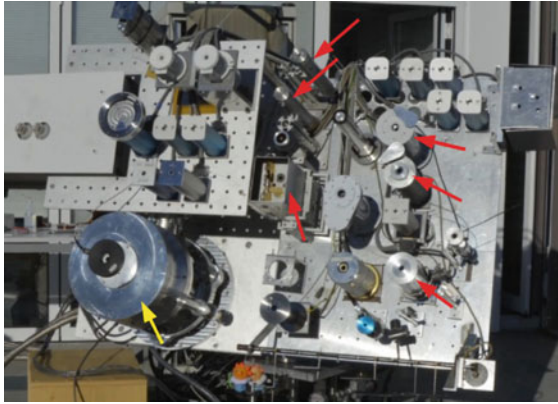


Fig. 11.40 Several absolute pyrheliometers at the PMO Sun tracker during IPC-XII in September/October 2015. *Red arrows* indicate the six absolute pyrheliometers composing the World Standard Group (WSG) and representing the World Radiometric Reference (WRR), while the *yellow arrow* points to the cryogenic solar absolute radiometer (CSAR, Sect. 11.2.5) (photo: K. Behrens)

procedures are governed by the CIMO-Guide [11.1] and ISO standards [11.110–112]. In general, calibrations should only be carried out by special laboratories such as the WRC, RRCs, and NRCs that possess the necessary equipment and well-trained staff. The RRCs are given in [11.1].

Calibration of Pyrheliometers

The calibration of pyrheliometers must be conducted by side-by-side comparison with a reference pyrheliometer and using the Sun as the radiation source. It is important that the reference pyrheliometer be traceability to the WSG and is equal to or better in quality than the pyrheliometers being calibrated in terms of uncertainty. Furthermore, such calibration should take place in clear and stable atmospheric conditions. Detailed procedures are given in [11.1, 110]. The following method may be applied:

- Outdoor – Sun as source
 - *Side-by-side comparison of the reference pyrheliometer and the pyrheliometer being calibrated*
Reference instrument: a pyrheliometer of higher class.
The method can be applied to any type of pyranometer; for details see [11.1, 110].
Execution: Both pyrheliometers are installed side by side on a solar tracker, and the direct irradiance (E) of the reference pyrheliometer and the voltage (U) of the pyrheliometer being calibrated are recorded; the sensitivity (S) of

the pyrheliometer being calibrated is then calculated as

$$S = \frac{U}{E}. \quad (11.29)$$

Calibration of Pyranometers

Several procedures can be used to calibrate a pyranometer. There are some outdoor methods that use the Sun as the source, while others use artificial light sources to provide the radiation for both the reference and test pyranometers. The light source never serves as a reference when calibrating pyranometers. As in the case of pyrheliometers, it is obvious that the reference instrument must be traceable to the WSG. Beside the main goal of calibration, the sensitivity or responsivity, temperature dependence, directional response, and other characteristics of a pyranometer can also be studied. The following methods can be applied:

- Outdoor – Sun as source
 - *Alternating Sun-and-shade method*
Reference instrument: a pyrheliometer.
The method can be applied to any type of pyranometer; calibration should take place during clear and stable atmospheric conditions; for details see [11.1, 111].
Execution: The horizontally adjusted pyranometer being calibrated is alternately shaded and unshaded by a shadow disc, whose field-of-view angle corresponds to that of the pyrheliometer; it is necessary to record the voltage in the unshaded ($U_{\text{un}\downarrow}$) and shaded phase ($U_{\text{s}\downarrow}$) of the horizontally adjusted pyranometer under test as well as the direct solar irradiance (E) determined by the reference pyrheliometer; z is the solar zenith angle of the corresponding time; the sensitivity (S) of the pyranometer under test can then be calculated as

$$S = \frac{U_{\text{un}\downarrow} - U_{\text{s}\downarrow}}{E \cos z}. \quad (11.30)$$

- *Continuous Sun-and-shade method*
Reference instrument: a pyrheliometer and a pyranometer.
The method can be applied to any type of pyranometer; for details see [11.1, 111].
Execution: The horizontally adjusted pyranometer under test and measuring the voltage (U_{\downarrow}) is installed side by side with the reference pyrheliometer and reference pyranometer measuring the solar irradiances E and $E_{\text{d}\downarrow}$, respectively; the field-of-view angle of the shadow disc of the shaded reference pyranometer should

correspond to those of the pyrheliometer; z is the solar zenith angle at the corresponding time; the sensitivity (S) of the pyranometer under test can then be calculated as

$$S = \frac{U\downarrow}{E \cos z + E_d\downarrow} \quad (11.31)$$

- *Side-by-side comparison of the reference pyranometer and pyranometer under test*

Reference instrument: a pyranometer of higher class.

The method can be applied to any type of pyranometer; for details see [11.1, 112].

Execution: The horizontally adjusted reference pyranometer and the pyranometer under test are installed side by side, and the global irradiance ($E_g\downarrow$) of the reference and the voltage ($U\downarrow$) of the pyranometer under test are recorded; the sensitivity (S) of the pyranometer under test can then be calculated as

$$S = \frac{U\downarrow}{E_g\downarrow} \quad (11.32)$$

- Indoor – artificial light source

For any indoor calibration, both the reference pyranometer and the pyranometer under test should be of the same type to prevent a spectral mismatch, because the spectral response of artificial light sources is not the same as that of sunlight:

- *Integrated sphere*

Reference instrument: a pyranometer.

The method can be applied to any type of pyranometer if they are of the same type; for details see [11.1, 112].

Execution: The horizontally adjusted reference pyranometer and the pyranometer under test are installed side by side near the bottom at the same level in the sphere, and the global irradiance ($E_g\downarrow$) and voltage ($U\downarrow$) are recorded; the sensitivity (S) of the pyranometer under test is calculated using (11.32).

- *Direct beam*

Reference instrument: a pyranometer.

The method can be applied to any type of pyranometer if they are of the same type; for details see [11.1, 112].

Execution: In a climatic chamber, the horizontally adjusted reference pyranometer and the pyranometer under test are installed side by side at a certain distance on a rolling table, such that only one of the two is irradiated by a beam; alternately, the reference pyranometer and the pyranometer under test are exposed to the beam, and the global irradiance ($E_g\downarrow$) and the voltage ($U\downarrow$) are recorded, respectively; the zero point between the beam measurements by both instruments is recorded and used in the analysis; the sensitivity (S) of the pyranometer under test can then be calculated using (11.32).

Instruments Operating in the Terrestrial Spectral Range

Currently, all calibrations in the terrestrial spectral range are based on the World Infrared Standard Group of Pyrometers (WISG), representing the interim reference for infrared radiation measurements [11.113, 114]. The WISG consists of two modified Eppley PIR and two Kipp and Zonen CG4 pyrometers (Sect. 11.4.3). Since its establishment, the WISG has been very stable ($\pm 1 \text{ W m}^{-2}$) [11.115]. These instruments are operated by the staff of the WRC.

One of the tasks of the PMOD/WRC is to provide the infrared radiation reference and disseminate the defined infrared scale all over the world. The PMOD/WRC offers a calibration service for pyrometers upon request and provides the opportunity of calibration with the WISG at the prospective international pyrometer comparisons (IPgC). In general, calibrations should be done only by special laboratories such as the PMOD/WRC and/or RRCs that possess the necessary equipment and well-trained staff.



Fig. 11.41 Shaded pyrometers of PIR and CG4 type of the WISG, assembled in a ventilation and heating unit at a Sun tracker during IPgC-II on the roof of PMOD/WRC Davos in September/October 2015 (photo: K. Behrens)

Remarks Regarding the History and Base of Traceability of WISG to SI

Despite the progress concerning improvements of the determination of terrestrial radiation fluxes with pyrgeometers as described in Sect. 11.4.3, deficiencies remained in outdoor measurements due to the calibration by a blackbody emitting a Planck spectrum versus the real atmospheric spectrum (Sect. 11.3.1, Fig. 11.18) as well as the nonflat dome spectrum (Sect. 11.3.4, Fig. 11.24), which is similar for all currently available pyrgeometers. The construction of the windowless absolute sky-scanning radiometer (ASR) at PMOD/WRC, which is described in detail in [11.116], overcame these problems, enabling measurements of atmospheric downward irradiance during nighttime and their traceability via a blackbody to the absolute temperature standard. In this case, the well-calibrated thermistors applied in the blackbody link the irradiance measurements in the terrestrial region to SI [11.116], while, in the solar spectral range, traceability to SI is ensured with the help of substitution of the irradiance by an electrical current (Sects. 11.2.5 and 11.4.1). The ASR, more than 10 pyrgeometers from international institutions (included two pyrgeometers from the later established WISG), an atmospheric emitted radiance interferometer (AERI), and radiative transfer models (MODTRAN, moderate resolution atmospheric transmission, and LBLRTM, line-by-line radiative transfer model) participated in two international radiometer comparisons (IPASRC-I and II) under midlatitude summer and dry Arctic winter conditions. The results of both comparisons showed very good agreement (within $\pm 2 \text{ W m}^{-2}$) between the participating instruments as well as model calculations [11.117, 118].

In 2012, at PMOD/WRC and at the National Renewable Energy Laboratory (NREL) in the USA, two independently designed and calibrated absolute radiometers measuring atmospheric downward irradiance were developed, called the Infrared Integrating Sphere Radiometer (IRIS) [11.119] and Absolute Cavity Pyrgeometer (ACP) [11.120] (Fig. 11.42), respectively. Both instruments are windowless systems and can thus only be operated during nighttime when measuring the atmospheric downward irradiance. They avoid the above-mentioned problems of the classical pyrgeometers whose receivers are covered by a filter. The IRIS radiometer is calibrated to a well-characterized blackbody whose temperature measurements are traceable to SI [11.121], while the ACP uses an in-situ self-calibration technique. Both instruments agree within $\pm 1 \text{ W m}^{-2}$ [11.115] and confirm the present state regarding the WISG and SI, because recalibrations of WISG with ASR no longer take place.

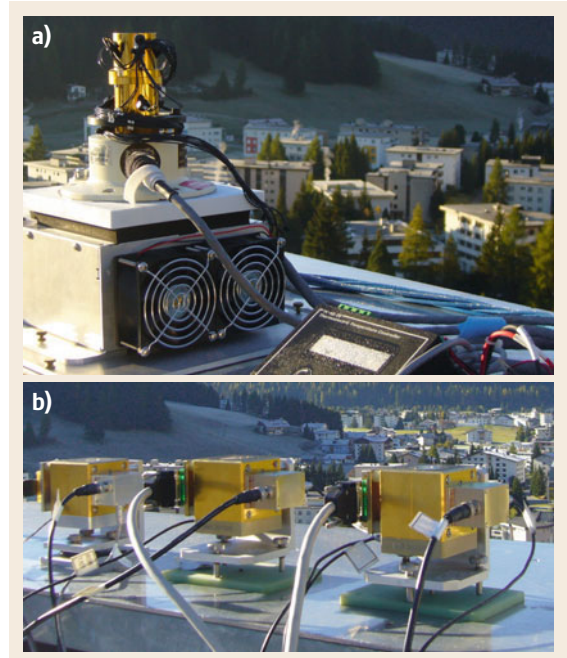


Fig. 11.42a,b ACP (a) and IRIS (b) during IPgC-II on the roof of PMOD/WRC Davos in September/October 2015 (photos: K. Behrens)

In 2018, the CIMO decided to establish a governance framework for WISG and its traceability to the International Standard of Units (SI) [11.122].

Calibration of Pyrgeometers (Check of Sensitivity S_1 of Field Pyrgeometers)

At the moment, there are still no ISO standards or other WMO documents governing or providing sufficient guidance on the calibration of pyrgeometers. However, based on experience obtained in the framework of the BSRN and at the IPgCs that took place at PMOD/WRC in 2010 and 2015 [11.123] as well as the procedure applied at PMOD [11.124], it is possible to provide the following recommendation for the determination of only the sensitivity S_1 of a pyrgeometer:

- The basis of any analysis is (11.8)–(11.10) (Sect. 11.4.3), depending on the type of pyrgeometer used and whether dome temperatures are measured.
- In general, in the presence of dome thermistors, the correction factors k_f or K in (11.8) and (11.9) can only be determined using blackbodies and further supplementary instruments as used in [11.89] or described in [11.121], allowing the characterization of pyrgeometers.

- Comparisons with reference pyrgeometers should be carried out only outdoors during nighttime under a clear sky in stable atmospheric conditions.
- It is mandatory that the reference pyrgeometer be certified as traceable to the WISG.
- The horizontally adjusted reference pyrgeometer and the pyrgeometer under test should be installed side by side, and the atmospheric downward irradiance ($E_1\downarrow$) of the reference and the voltage ($U\downarrow$) of the pyrgeometer under test as well as their body (t_b) and dome (t_d) temperatures are recorded; in the case *without dome thermistors*, the sensitivity (S_1) of the pyrgeometer under test can then be calculated as

$$S_1 = \frac{U_1\downarrow}{E_1\downarrow - \sigma T_b^4}, \quad (11.33)$$

- whereas in the case *with dome thermistors*, the Albrecht equation is used

$$S_1 = \frac{U_1\downarrow}{E_1\downarrow - \sigma T_b^4 + K\sigma(T_d^4 - T_b^4)}. \quad (11.34)$$

- In the case *with dome thermistors* (mainly in the case of PIRs), one uses

$$S_1 = \frac{U_1\downarrow(1 + k_1\sigma T_b^3)}{E_1\downarrow - k_2\sigma T_b^4 + k_3\sigma(T_d^4 - T_b^4)}, \quad (11.35)$$

- where k_i ($i = 1..3$) and K are specific correction factors of the pyrgeometer under test, determined beforehand using a blackbody cavity and available on a certificate, σ is the Stefan–Boltzmann constant, and T_d and T_b are the temperatures of the dome and body of the pyrgeometer in kelvin.

Instruments Operating in Both the Solar and Terrestrial Spectral Ranges

Instruments operating in both the solar and terrestrial spectral ranges are called pyrradiometers (Sect. 11.4.4). They measure the total (global solar + terrestrial downward) radiation or total (reflected solar + terrestrial upward) radiation incident from a viewing angle of 2π sr on a flat surface depending on how the receiver is facing (Tables 11.2–11.4). Combining a downward- and upward-looking pyrradiometer allows measurements in a viewing angle of 4π sr. Such an instrument is called a *total net radiometer*. The calibration of pyrradiometers is extensive and complex, because two totally different spectral ranges are measured simultaneously using one sensor. Therefore, only a brief description is possible here.

Case 1: upward-looking pyrradiometer measuring total (global solar + terrestrial downward) radiation:

- The calibration in the solar spectral range for the determination of the sensitivity $S_s\downarrow$ takes place by applying the *outdoor* methods described for pyranometers (the application of indoor calibrations is not recommended because the very large error sources increase the underlying uncertainties)
- The calibration in the terrestrial spectral range for the determination of the sensitivity $S_1\downarrow$ takes place by applying the *outdoor* methods described for pyrgeometers

Case 2: total net radiometer measuring total (global solar + terrestrial downward) and (reflected solar + terrestrial upward) radiation with one sensor or two sensors applying a differentiating circuit between a downward- and upward-looking radiometer (Sect. 11.4.5):

- The calibration enables only the determination of the sensitivity S ; the best and simplest method is an outdoor comparison of the instrument under test with a four-sensor net radiometer.

11.6.2 Specific Quality Control of Measured Data

Specific quality control of the gathered data is possible at different levels, starting in some cases with verification of the raw data and finishing with its upload to a database or appropriate file system. In most cases, the data acquisition chain including the quality control is automatized. However, the level of automation depends on many factors, such as the computer and programming resources, the number of quantities to be checked, possible redundant and/or complementary measurements, the kind of results to be output (static or interactive), etc. But, independently of the technical capabilities, quality control should start (at least daily) with a visual check of the recorded time series. Furthermore, quality control has to be adapted to local requirements and capabilities.

At all levels, the simplest method to check data is a comparison with physical limits. Because radiation quantities oscillate, it is necessary to check that they remain within appropriate lower and upper bounds. Generally, the measured values of solar radiation quantities (Table 11.2) depend on parameters that vary on an annual and daily basis, viz. the declination of the Sun, the geographical latitude, and the local time. Derived from these parameters, the altitude of the Sun or solar zenith angle (z) determines the upper limit, while the lower limit is zero. The bounds of terrestrial irradiance quantities also depend on the temperature and composition of the atmosphere (gases and clouds, and their base

height) for the upper half-space and mainly the temperature of the underlying surface in the case of the lower half-space. Moreover, such verification of single quantities can be extended to combinations of independently measured quantities.

Additionally, comparisons with modeled and/or satellite data are also helpful methods. Here, of course, it must be ensured that the atmospheric conditions during the measurements indeed correspond to the model input data. In the case of satellite data, the time of the measurements on the satellite and ground should be similar and the atmospheric conditions within the covered satellite pixel should agree as far as possible with those at the station. Good results are particularly available in cloudless conditions at local noon [11.125]. A further, comprehensive method for quality control of global solar radiation measurements at ground level using satellite-based products is given in [11.126]. As the basis of this method are validated satellite products, it is not very suitable for immediate verification processes during data acquisition.

Based on the fundamentals described above, various principles [11.127] were established and successfully applied in the framework of the BSRN [11.128] and also implemented when programming the code of the BSRN Toolbox 2.0 [11.129]. The following equations concerning the solar irradiance given in [11.127] enable the calculation of the upper bounds of *extremely rare limits* (meaning in this context that these bounds may be exceeded in only very rare cases) for the solar quantities

$$\begin{aligned} &\text{Global solar irradiance } (E_g \downarrow) \\ E_g \downarrow &= 1.2E_{0,a} \cos(z)^{1.2} + 50 \end{aligned} \quad (11.36)$$

$$\begin{aligned} &\text{Diffuse solar irradiance } (E_d \downarrow) \\ E_d \downarrow &= 0.75E_{0,a} \cos(z)^{1.2} + 30 \end{aligned} \quad (11.37)$$

$$\begin{aligned} &\text{Direct solar irradiance } (E) \\ E &= 0.95E_{0,a} \cos(z)^{0.2} + 10 \end{aligned} \quad (11.38)$$

$$\begin{aligned} &\text{Reflected solar irradiance } (E_r \uparrow) \\ E_r \uparrow &= E_{0,a} \cos(z)^{1.2} + 50, \end{aligned} \quad (11.39)$$

where $E_{0,a}$ is the direct solar irradiance without the atmosphere (solar constant) adjusted for the Earth–Sun distance and the solar zenith angle z .

The lower bounds for all these mentioned quantities are set to -2 W m^{-2} . This value considers the uncertainty originating if black thermopiles are used for such measurements (Sect. 11.4.2), although solar irradiance during nighttime is exact zero. In the case of downward terrestrial irradiance ($E_1 \downarrow$), the lower and upper bounds are set to 60 and 500 W m^{-2} , respectively.

The corresponding values for the upward terrestrial irradiance ($E_1 \uparrow$) are 60 and 700 W m^{-2} . Examples for the upper limits of global and direct normal irradiance during the diurnal cycle in the course of the year between the equator and 75° N are given in Fig. 11.43, indicating their possible spread. These upper limits are slightly higher in the Southern Hemisphere, because of the shorter distance between the Sun and Earth at the aphelion which takes place in January (summer in the Southern Hemisphere). The pattern of diffuse solar irradiance and reflected solar irradiance are similar to those of the global solar radiation, as can be deduced from (11.36), (11.37), and (11.39). Furthermore, another important aspect of data verification is to check that the diffuse solar irradiance and reflected solar irradiance never exceed the simultaneously measured global solar irradiance, and that in the best case, the maximum reflected solar irradiance (gathered over a fresh snow cover) is about 90% of the global irradiance.

An example of the combination of independently measured quantities is the comparison, based on (11.1), of the global irradiance ($E_g \downarrow$) measured with a pyranometer with the total of the diffuse ($E_d \downarrow$) and the vertical component of the direct solar irradiance ($E \downarrow \cos z$) measured by a shaded pyranometer and a pyrliometer, respectively (Sects. 11.4.6 and 11.4.8 [11.99]). The, in general, good agreement between the independently measured quantities, which are situated at a 1 : 1 line, is displayed in Fig. 11.44. However, some outliers are also visible, which should be checked in detail with the objective of identifying the possible cause.

According to [11.127], the downward ($E_1 \downarrow$) and upward ($E_1 \uparrow$) terrestrial irradiance may be checked simply using the independently measured air temperature by applying (11.40) and (11.42), while in [11.130], slightly different constants are used (11.41), (11.43)

$$\begin{aligned} &\text{Downward terrestrial irradiance :} \\ 0.4\sigma(T_a)^4 &< E_1 \downarrow < \sigma(T_a)^4 + 25 \end{aligned} \quad (11.40)$$

$$\begin{aligned} &\text{Downward terrestrial irradiance :} \\ 0.7\sigma(T_a)^4 &< E_1 \downarrow < \sigma(T_a)^4 \end{aligned} \quad (11.41)$$

$$\begin{aligned} &\text{Upward terrestrial irradiance :} \\ \sigma(T_a - 15)^4 &< E_1 \uparrow < \sigma(T_a + 25)^4 \end{aligned} \quad (11.42)$$

$$\begin{aligned} &\text{Upward terrestrial irradiance :} \\ \sigma(T_a - 10)^4 &< E_1 \uparrow < \sigma(T_a + 10)^4, \end{aligned} \quad (11.43)$$

where σ is the Stefan–Boltzmann constant and T_a is the air temperature in kelvin. It is assumed that the air temperature T_a is measured nearby and at the same height as the pyrgeometer.

The proposed bounds obtained using both relations are shown in Fig. 11.45 to reveal the difference. The

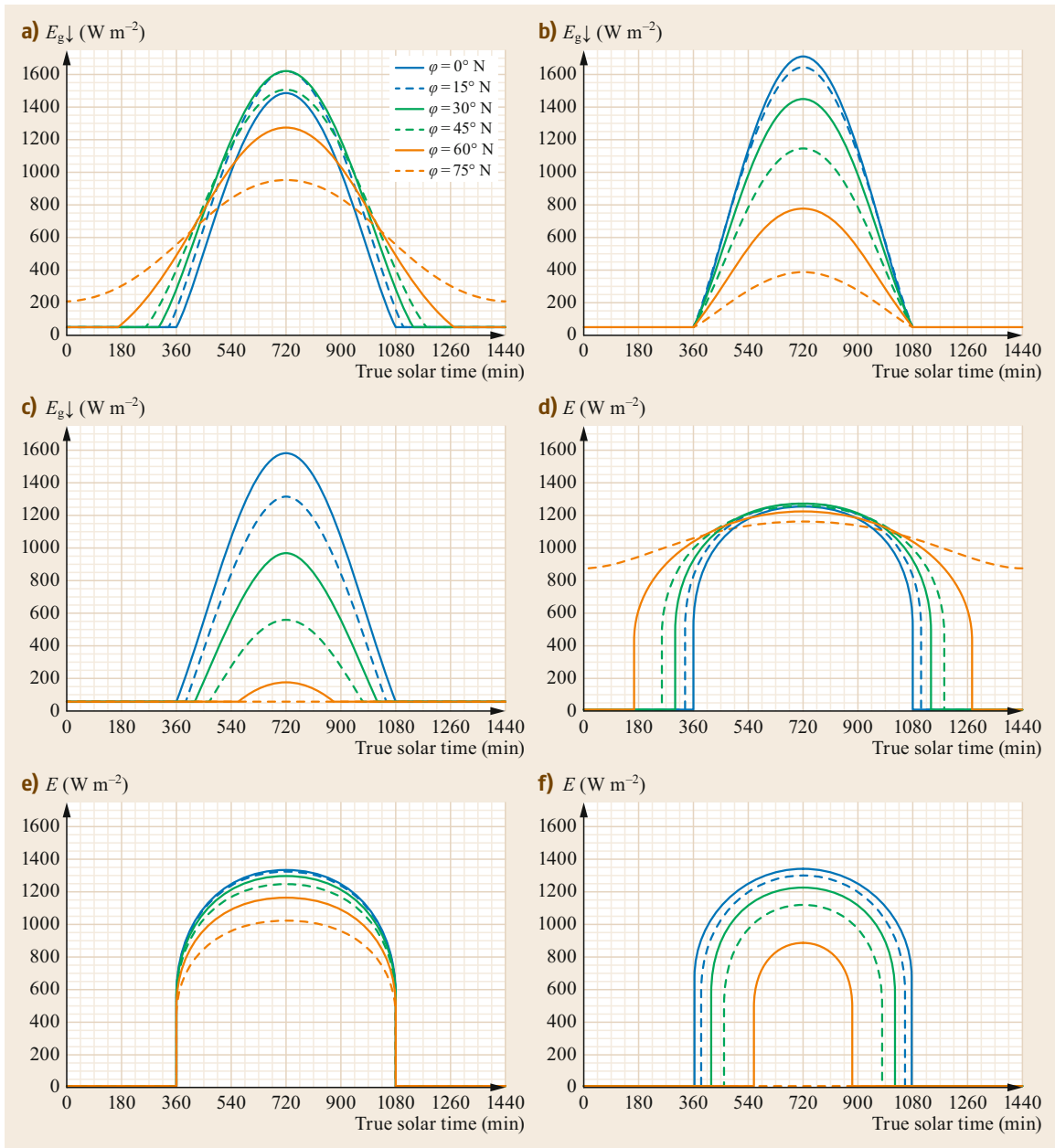


Fig. 11.43a–f Daily courses of global irradiance $E_{g\downarrow}$ (a–c) and direct solar irradiance E at normal incidence (d–f) at extreme rare limits calculated based on (11.36) and (11.38) for six geographic latitudes φ at summer solstice ((a) global solar irradiance; (d) direct normal irradiance), equinox ((b) global solar irradiance; (e) direct normal irradiance), and winter solstice ((c) global solar irradiance; (f) direct normal irradiance) for the Northern Hemisphere

bounds derived from relation (11.40) are labeled *upper and lower bound 1*, while the limits calculated from (11.41) are labeled *upper and lower bound 2*.

In this example, after a nearly overcast night, the clouds dissolved at around 9 UTC and the sky became very clear (Fig. 11.45a). At this time, the downward ter-

restrial irradiance ($E_i\downarrow$) was so low that lower bound 2 was touched. In the summer case (Fig. 11.45b), during approximately the first 4 h, the sky was also overcast but with very low and warm clouds, so that the originating downward terrestrial irradiance ($E_i\downarrow$) was so large that it touched upper bound 2. These examples

Fig. 11.44 Scatter plot of monthly 1-min global irradiance ($E_{g\downarrow}$) measured with a pyranometer (CM 22) on the y-axis and the total of the diffuse ($E_{d\downarrow}$) and the vertical component of the direct solar irradiance ($E_{\downarrow}\cos(z)$) measured by a shaded pyranometer (CM 22) and a pyrhemometer (CH 1), respectively, on the x-axis, from May 2016 at the Meteorological Observatory Lindenberg – Richard-Abmann Observatory, Germany. The assembly of the instruments is similar to that shown in Fig. 11.38 ►

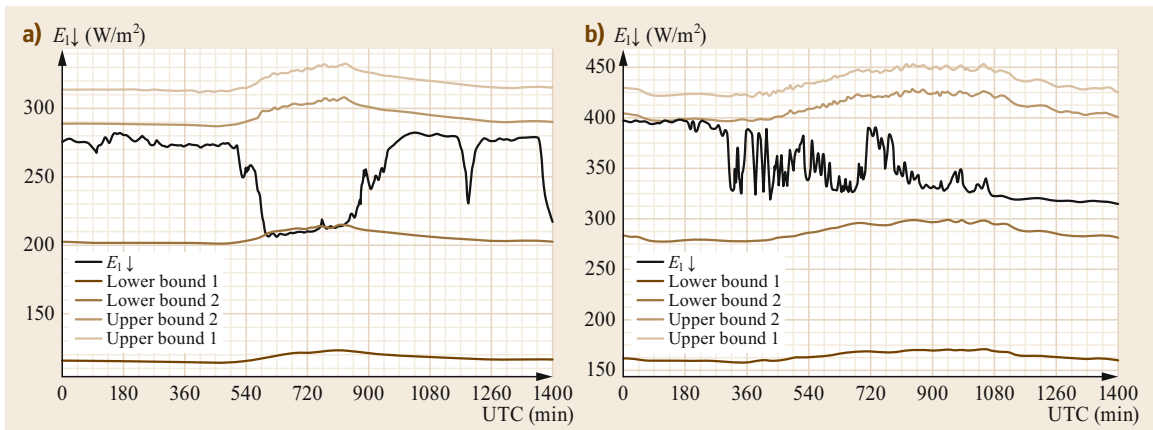
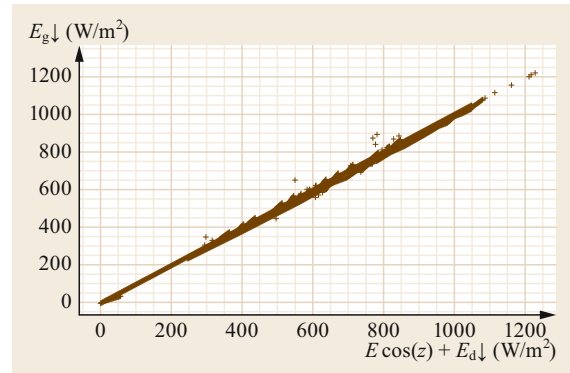


Fig. 11.45a,b Downward terrestrial irradiance ($E_{i\downarrow}$) for (a) a winter (09.02.2017) and (b) a summer case (17.07.2017) measured with a CG4 pyrgeometer at the Meteorological Observatory Lindenberg – Richard-Abmann Observatory (Germany) and the corresponding lower and upper bounds according to (after [11.127, 130]) when applying (11.40) and (11.41)

show that the adopted limits of bound 2 are very close, while lower bound 1 is particularly small in comparison.

Beside the radiation quantities, it is also necessary to check the temperature of the instrument, especially of a pyrgeometer, because this is an important input

quantity determining both the downward ($E_{i\downarrow}$) and upward ($E_{i\uparrow}$) terrestrial irradiances (Sects. 11.4.3–11.4.5). One simple possibility here is a comparison with the air temperature, which is available in most cases. Limits may be derived from climatological data for the corresponding region.

11.7 Maintenance

Generally, maintenance is very important if high-quality data are to be gathered. It starts with on-site maintenance of sensors and the supplementary equipment and continues with data acquisition up to the storage systems. Only well-attended instruments and accessories will enable given standard uncertainties to be attained. It is important to point out that it is necessary to document *all* activities with the instrument and its behavior as well as their time and date. Such compre-

hensive and clear maintenance documentation will facilitate the search for the causes of any deviations from the norm or errors. For detailed and comprehensive maintenance descriptions, the BSRN Operation Manual [11.9] and CIMO-Guide [11.1] are recommended reading. Furthermore, information given in specific instrument and sensor manuals should also be considered.

Nowadays, technical systems such as video cameras may support inspections, especially at remote stations,

Table 11.10 Maintenance requirements for radiation instruments and supplementary equipment

Maximum interval	System	Task
1 week	Radiation sensor	Cleaning dome, front window and check for scratches state/color of thermopile Check for internal condensation Check for horizontal adjustment Check for damage of radiation screen
	Ventilation system	Check for sufficient air stream (rotational speed of motor)
	Cable	Check for damage and loose connections
	Solar tracker	Check for alignment and horizontal adjustment
1 month	Radiation sensor	Check desiccant
	Ventilation system	Check and clean or replace filter
6 months	All instruments	Check to determine aging
	Radiation sensor	Check horizon for possible changes influencing the measurement (e.g., instrument shading (Sect. 11.1.3))
12/24 months	Radiation sensor, voltmeter	Calibration according to the rules given by the manufacturer and/or responsible authorities (e.g., National Metrology Institutes)

and high-performance fans can blow raindrops away from domes and front glasses of pyranometers, pyrgeometers, and pyrhemometers faster, ensuring better results (Sect. 11.4.8). Furthermore, automatic systems enable monitoring of the rotational speed of motors, data loggers, and computers. However, it must be remembered that these systems themselves also need maintenance. In general, maintenance must be adapted by considering the requirements and state of the whole data acquisition process.

If possible, at least daily on-site inspection and maintenance should be performed. If, for instance, a traditional, mechanical shadow band is used for measurements of the diffuse solar irradiance, then it is *mandatory* to check and adjust it daily. This is also the case if a pyrhemometer is fed by a one-axis tracker following the Sun. Likewise, a daily time check of the data acquisition systems and PC is also critical. Table 11.10 presents the minimum verification requirements in certain intervals.

11.8 Applications

As mentioned above, radiation in the so-called thermal-optical region is relevant from every point of view for physical as well as chemical processes within the atmosphere and its interaction at the boundaries with the hydro-, litho-, cryo-, and biosphere. As a consequence, radiation data are used in meteorology and climatology as well as in applied sciences (agriculture, energy, environment, etc.).

11.8.1 Climatology of Radiation

One aspect of climatology is the analysis of time series. As an example, the time series of the annual total global solar radiant exposure ($H_g \downarrow$) at Potsdam (Germany) covering the time span from 1893 to 2018 is shown in Fig. 11.46. It consists of two sections. The first part from 1893 to 1936 is based on measurements of sunshine duration (Sect. 11.4.7), converted to global solar radiant exposure using the well-known regression between global radiation and sunshine duration [11.131]. The second part, starting in 1937, is based

on measurements made with pyranometers. Moreover, since 1937, diffuse solar radiation and direct solar radiation at normal incidence have also been measured in parallel, using a shaded pyranometer and pyrhemometer, which provides a useful verification of the data (Sect. 11.6.2) [11.132].

This figure shows large and fast oscillations in the annual totals, superimposed on an oscillation at lower frequency. The time spans with comparatively low irradiation at the beginning of the 20th century and around the 1980s, well known in literature [11.133, 134] as *global dimming*, are clearly visible. In general, an increasing trend is noticeable, being particularly steep in the last 40 years as a consequence of a cleaner atmosphere and lesser cloudiness.

11.8.2 Daily and Annual Cycles

In most cases, presenting the course of the radiation components over time, e.g., on a daily plot, is based on data compression by means of averaging either in the

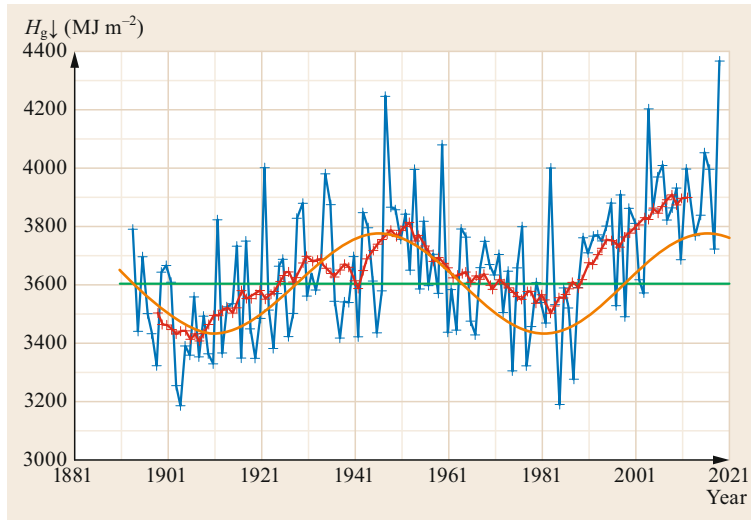


Fig. 11.46 Annual (1893–2018) total global solar radiant exposure ($H_g\downarrow$) in MJ m^{-2} (blue tracks) at Potsdam ($\varphi = 52.4^\circ \text{ N}$, $\lambda = 13.1^\circ \text{ E}$), the 100-year average 1901–2000 (green), 11-year moving averages (red tracks) as well as a curve displaying 70-year oscillation (orange)

data logger or later on in the PC, for instance. Currently, typical sampling rates in the radiation measurement field are 1 Hz, commonly compressed to means over 1 or 10 min or longer, depending on demands (see, e.g., Sect. 11.8.3). An example of two daily courses is shown in Fig. 11.47, displaying a day (02.07.2018) with intermittent cumulus clouds and a cloudless day (03.07.2018) in 2018. After a cloudless night and morning up to 8 UTC (minute 480) at the same irradiance level of about $E_g\downarrow \approx 700 \text{ W m}^{-2}$ on both days, cumulus clouds developed on 02.07.2018. In the left picture, the impact of these clouds is clearly visible in the large oscillation of all four radiation balance components, while the right figure displays the typical diurnal cycle of a cloudless Central European summer day.

In climatological evaluations, in addition to irradiance, another quantity that is often displayed is the irradiation as a sum of the separate measurements or as a product of the mean irradiance and the number of seconds in the interval of interest. The Hovmöller plot (Chap. 1) is one example of how annual variations can be presented (Fig. 11.48).

11.8.3 Radiation on Tilted Surfaces

The use of alternative energy sources and technologies is gaining in importance, leading to increasing interest (e.g., from the energy industry) in knowledge about the solar irradiance received by tilted and vertical surfaces. Usually, only the global solar irradiance on a horizon-

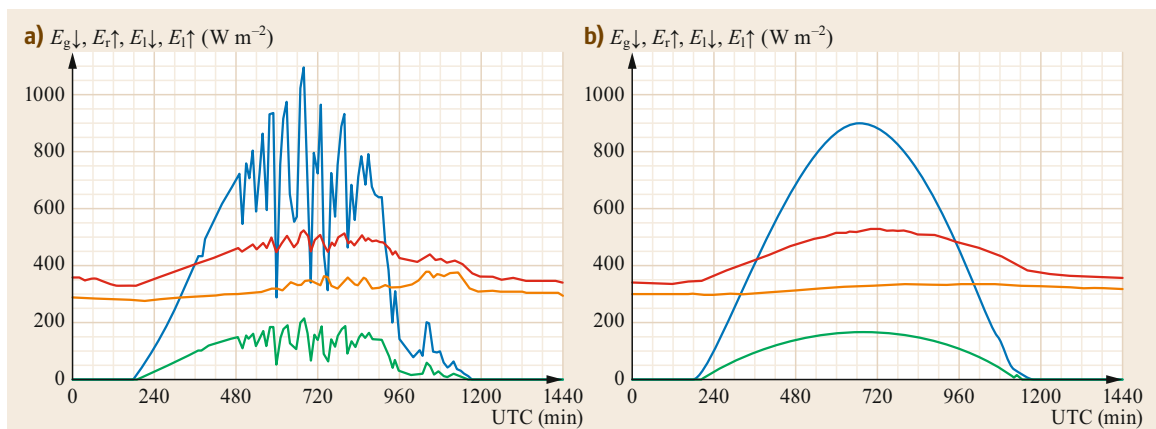


Fig. 11.47a,b Daily courses of 10-min means of radiation balance (Table 11.2) consisting of its components the global solar $E_g\downarrow$ (blue), upward solar $E_r\uparrow$ (green), downward terrestrial $E_l\downarrow$ (orange), and upward terrestrial $E_l\uparrow$ (red) irradiances, measured at the Boundary Layer Measuring Field Falkenberg of the Meteorological Observatory Lindenberg – Richard-Aßmann Observatory on (a) 02.07.2018 and (b) 03.07.2018. Because of the geographical location of this site ($\varphi = 52.16^\circ \text{ N}$; $\lambda = 14.17^\circ \text{ E}$), the true solar noon on these days was at 11:08 UTC

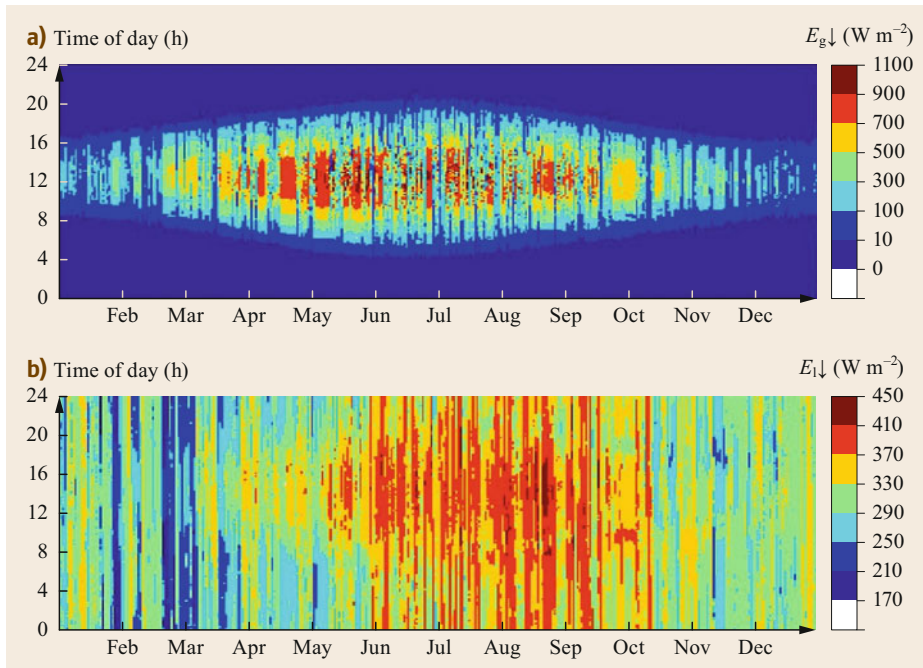


Fig. 11.48a,b
Hovmöller plot of the global solar radiation (a) and the downward terrestrial radiation (b), measured in 2011 (Bayreuth, Ecological–Botanical Garden) (after [11.135])

tal plane is measured in networks. Radiation data for arbitrary inclined surfaces can be derived from the direct and diffuse solar irradiances and relevant azimuthal and inclination angles using an algorithm [11.136]. At Potsdam Meteorological Observatory (Germany), two experimental datasets were obtained from south-facing pyranometers tilted at inclination angles of 30°, 45°, 60°, and 90° and pyranometers mounted vertically (at an inclination angle of 90°) and directed towards the

four main cardinal directions. Figure 11.49 shows example daily courses of the hourly mean global solar irradiance on the tilted and vertical surfaces.

Both plots in Fig. 11.49 show the typical features of inclined and vertically oriented pyranometers measuring global solar irradiance. In the left-hand plot, the global radiation on the surface inclined at 30° significantly exceeds that measured on the horizontal surface, whilst the results for the 45° surface almost reach the

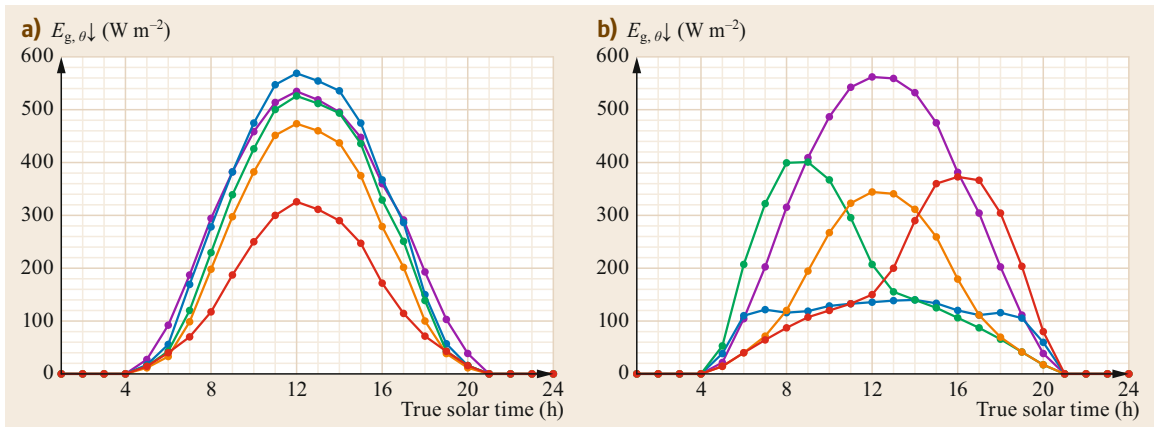


Fig. 11.49 (a) average hourly mean global solar irradiance ($E_{g,\theta\downarrow}$) in W m^{-2} of south-facing pyranometers at different tilt angles θ [$\theta = 0^\circ$ (purple), 30° (blue), 45° (green), 60° (orange), and 90° (red)] (Potsdam, $\varphi = 52.4^\circ \text{ N}$, $\lambda = 13.1^\circ \text{ E}$, June, 1977–1981); (b) average hourly mean global solar irradiance ($E_{g,\theta\downarrow}$) of pyranometers mounted vertically (inclination angle of 90°) and directed to the four main cardinal directions (N (blue), E (green), S (orange), and W (red)) and a horizontally mounted (purple) pyranometer (Potsdam, $\varphi = 52.4^\circ \text{ N}$, $\lambda = 13.1^\circ \text{ E}$, June, 1973–1980)

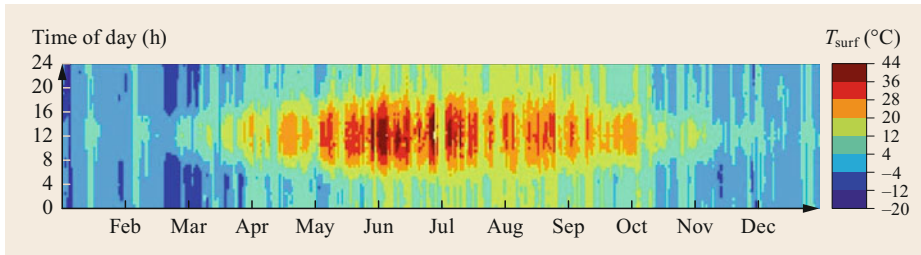


Fig. 11.50 Hovmöller plot of annual variation of surface temperature, measured in 2011 (Falkenberg boundary layer measuring field, Meteorological Observatory Lindenberg – Richard-Abmann Observatory) (after [11.4])

same level. This is a consequence of the angle of incidence of the direct solar radiation. At this geographical latitude of 52.2°N , the sun shines almost perpendicularly onto the 30° surface at noon. In contrast to the averaging period of 8 years for the vertically mounted pyranometers in the left figure, the results for the inclined surfaces obtained over 5 years do not yet display an ideal shape. In the right-hand plot, the curves of the east- and west-facing vertical devices show their maxima at midmorning and midafternoon, respectively, as expected. Because more convective clouds occur in the afternoon during summertime, the maximum irradiance measured by the westward-looking vertical pyranometer is lower than that measured by the eastward-directed device. Again, because of the angle of incidence of the direct solar radiation, the highest value measured by the vertically mounted south-facing sensor is lower than for the eastward- and westward-looking instruments. In the measurements by the vertical pyranometer looking north, the subsidiary maxima in the early morning and late afternoon are due to the direct solar radiation received by this instrument.

11.8.4 Radiation Temperature

Based on the Stefan–Boltzmann law (11.44),

$$E = \varepsilon \sigma T^4, \quad (11.44)$$

describing the relation between the irradiance (E) of an (ideal) blackbody and its temperature (T), with the

emissivity ε and the Stefan–Boltzmann constant σ , it is possible to determine the radiation temperature or rather the so-called effective (equivalent) blackbody radiation temperature, if the irradiance is known. The emissivity ε captures the deviation from an ideal blackbody, for which ε takes a value of 1.

The effective temperature of the sky (T_{sky}) can be calculated from the downward terrestrial irradiance ($E_{1\downarrow}$) as

$$T_{\text{sky}} = \left(\frac{E_{1\downarrow}}{\sigma} \right)^{1/4}, \quad (11.45)$$

while the effective temperature of the surface (T_{surf}) can be derived from the upward terrestrial irradiance ($E_{1\uparrow}$), as measured with upward- and downward-facing pyrgeometers, respectively (Sects. 11.4.3 and 11.4.5). In both cases, it is assumed that the sky or surface emits like an ideal blackbody, which is never actually true, thus the result is called the *effective* temperature.

Furthermore, the radiation temperature can also be determined using radiation thermometers or pyrometers, mainly developed for industrial applications and not discussed in this chapter. These instruments operate preferably in the range between 8 to $12\ \mu\text{m}$, the so-called atmospheric window (Sect. 11.3.1, Fig. 11.19; the plots of *thermal TOA_out* and *thermal SUR_in* at around $10\ \mu\text{m}$). Also in this case, the determined radiation temperature is only approximate because an ideal blackbody radiator or exact knowledge of the emissivity is assumed.

11.9 Future Developments

Classical in-situ radiation instruments for measurements from the ground have been developed for more than 100 years. Nevertheless, as shown by the implementation of novel black thermopiles, new ideas are still being applied. New instruments will be more compact and require less maintenance, as well as offering improved

measurement uncertainty as demanded by modern users, especially in the scientific community. Moreover, instruments will become increasingly smart, which will include different types of communication (from traditional wired to various types of wireless connection) and data handling methods. The individual corrections to a single

sensor based on its characterization can be stored in the instrument and immediately applied to provide a correct result to the user. At the same time, it is necessary to ensure that the processing is and remains traceable.

Traditional radiation measurements will also remain very important for science and many practical applications in the future. The required data quality covers the spread from good and stable data for practical use up to high-quality data with information on the uncertainty for scientific applications. Moreover, the *complete* integration of solar and terrestrial radiation

measurements and corresponding reference instruments into SI will be solved, addressing the remaining questions and problems. This will also be important for atmospheric physics and climatology in terms of obtaining the global radiation budget by combining data from very different origins.

Furthermore, radiation data from ground measurements will be applied in combination with data derived from satellites, using the advantages of both the area coverage of satellites and individually configurable and precise measurements from the ground.

11.10 Further Reading

- F. Hengstenberger (Ed.): *Absolute Radiometry*. Academic (London, San Diego, 1989), 266 pp.
- F. Vignola, J. Michalsky, T. Stoffel: *Solar and Infrared Radiation Measurements*. CRC, 418 pp. (London, New York 2012).
- ISO: *Air quality – Meteorology – Siting classification for surface observing stations on land*. ISO 19289:2015 (Geneva, 2015).
- L. B. J. McArthur: *Baseline Surface Radiation Network (BSRN) operation manual (version 2.0)*. WMO/TD-No 1274. (World Meteorological Organization, Geneva, 2005)
- VDI: *Umweltmeteorologie, Meteorologische Messungen, Strahlung (Environmental Meteorology, Meteorological Measurements, Radiation)* in German and English, VDI 3786 Blatt (Part)5 (Beuth-Verlag, Berlin 2022)
- VDI: *Umweltmeteorologie – Wechselwirkungen zwischen Atmosphäre und Oberflächen – Berechnung der spektralen kurz- und der langwelligen Strahlung (Environmental meteorology – Interactions between atmosphere and surfaces – Calculation of spectral short-wave and long-wave radiation)* in German and English, VDI 3789 (Beuth-Verlag, Berlin 2019)
- WMO: *Guide to Instruments and Methods of Observation*, WMO-No. 8, Volume I - Measurement of Meteorological Variables. (World Meteorological Organization, Geneva, 2018)

References

- | | |
|---|--|
| <p>11.1 WMO: <i>Guide to Instruments and Methods of Observation</i>, WMO-No. 8, Volume I, Measurement of Meteorological Variables (World Meteorological Organization, Geneva 2018)</p> <p>11.2 ISO: <i>Air Quality – Meteorology – Siting Classification for Surface Observing Stations on Land</i>, ISO 19289:2015 (International Organization for Standardization, Geneva 2015)</p> <p>11.3 J.R. Latimer: <i>Radiation Measurement</i>, International Field Year of the Great Lakes, Techn. Manual Series No. 2 (Information Canada, Ottawa 1972) p. 53</p> <p>11.4 VDI: <i>Environmental Meteorology, Meteorological Measurements, Radiation</i>, VDI 3786 Part 5 (Beuth, Berlin 2022)</p> <p>11.5 WMO: <i>Commission for Instruments and Methods of Observation</i>, WMO-No 19. RP. 9 (World Meteorological Organization, Geneva 1953)</p> <p>11.6 CSAGI: <i>Radiation Instruments and Measurements, Part VI</i>, IGY Instruction Manual (Pergamon, London, New York, Paris 1958)</p> | <p>11.7 A. Ohmura, E.G. Dutton, B. Forgan, C. Fröhlich, H. Gilgen, H. Hegner, A. Heimo, G. König-Langlo, B. McArthur, G. Müller, R. Philipona, R. Pinker, C.H. Whitloch, K. Dehne, M. Wild: <i>Baseline Surface Radiation Network (BSRN/WCRP): New precision radiometry for climate research</i>, Bull. Am. Meteorol. Soc. 79, 2115–2136 (1998)</p> <p>11.8 L.B.J. McArthur: <i>Baseline Surface Radiation Network (BSRN) Operation Manual (Version 1.0)</i>, WMO/TD-No. 879 (World Meteorological Organization, Geneva 1998)</p> <p>11.9 L.B.J. McArthur: <i>Baseline Surface Radiation Network (BSRN) Operation Manual (Version 2.0)</i>, WMO/TD-No. 1274 (World Meteorological Organization, Geneva 2005)</p> <p>11.10 F. Albrecht: <i>Die kalorischen Meßmethoden in der atmosphärischen Strahlungsforschung</i>. In: <i>Handbuch der Meteorologischen Instrumente und ihrer Auswertung</i>, ed. by E. Kleinschmidt (Springer, Berlin 1935) pp. 109–185</p> <p>11.11 W. Mörikofer: <i>Meteorologische Strahlungsmeßmethoden</i>. In: <i>Handbuch der biologischen Ar-</i></p> |
|---|--|

- beitsmethoden*, ed. by E. Abderhalden (Urban and Schwarzenberg, Berlin, Vienna 1939) pp. 4005–4245
- 11.12 N. Robinson (Ed.): *Solar Radiation* (Elsevier, Amsterdam, London, New York 1966)
- 11.13 C. Fröhlich, J. London (Eds.): *Revised Instruction Manual on Radiation Instruments and Measurements*, WMO/TD-No. 149 (World Meteorological Organization, Geneva 1986)
- 11.14 L. Foitzik, H. Hinzpeter: *Sonnenstrahlung und Lufttrübung* (Geest and Portig, Leipzig 1958)
- 11.15 C. Fröhlich: History of solar radiometry and the World Radiometric Reference, *Metrologia* **28**, 111–115 (1991)
- 11.16 K. Ångström: Über absolute Bestimmungen der Wärmestrahlung mit dem elektrischen Kompensationspyrheliometer nebst einigen Beispielen der Anwendung dieses Instrumentes, *Ann. Phys. Chem.* **67**, 633–648 (1899)
- 11.17 C.G. Abbot, F.E. Fowle: Apparatus for “solar-constant” determinations, *Ann. Astrophys. Obs. Smithson. Inst.* **2**, 21–49 (1908)
- 11.18 A.A. Kmito, Y.A. Sklyarov: *Pyrheliometry* (A. A. Balkema, Rotterdam 1987)
- 11.19 C.G. Abbot, F.E. Fowle, L.B. Aldrich: Standard pyrheliometer, *Ann. Astrophys. Obs. Smithson. Inst.* **3**, 52–72 (1913)
- 11.20 C.G. Abbot: The silver disk pyrheliometer, *Smithson. Misc. Collect.* **56**(19), 1–11 (1911)
- 11.21 C.G. Abbot, L.B. Aldrich: Smithsonian pyrheliometry revised, *Smithson. Misc. Collect.* **60**(18), 1–7 (1913)
- 11.22 H.H. Kimball: Variations in the total and luminous solar radiation with geographical position in the United States, *Mon. Weather Rev.* **47**, 769–793 (1919)
- 11.23 Y.A. Yanishevsky: *Aktinometricheskie pribory i metody nabliuzdenij* (Gidrometozdat, Leningrad 1957)
- 11.24 L. Gorczynski: On a simple method of recording the total and partial intensities of solar radiation, *Mon. Weather Rev.* **52**, 299–301 (1924)
- 11.25 K. Ruitenbeek, L. van Wehly: Moll’s thermopiles and beyond, *Bull. Sci. Instrum. Soc.* **130**, 11–16 (2016)
- 11.26 W.A. Michelson: Ein neues Aktinometer, *Meteorol. Z.* **25**, 246–253 (1908)
- 11.27 W. Marten: Das Bimetallaktinometer Michelson-Marten in neuester Ausführung mit Gebrauchsanweisung, *Gerlands Beitr. Geophys.* **32**, 69–82 (1931)
- 11.28 K. Büttner: Strahlungsversuche im Flugzeug, *Beitr. Phys. Atmos.* **16**, 156–162 (1930)
- 11.29 L. Gorczynski: Solarimeters and solarigraphs, *Mon. Weather Rev.* **54**, 382–384 (1926)
- 11.30 H.L. Callendar, A. Fowler: Reports on the total solar eclipse of 1905, August 30. (The horizontal bolometer), *Proc. R. Soc. A* **77**, 28 (1906)
- 11.31 H.H. Kimball: The total radiation received on a horizontal surface from the sun and sky at Mount Weather, VA, *Mon. Weather Rev.* **42**, 474–487 (1914)
- 11.32 E.R. Miller: Internal reflection as a source of error in the Callendar bolometric sunshine recorder, *Mon. Weather Rev.* **43**, 264–266 (1915)
- 11.33 C.G. Abbot, L.B. Aldrich: The pyranometer – an instrument measuring sky radiation, *Smithson. Misc. Collect.* **66**(7), 9 (1916)
- 11.34 C.G. Abbot, L.B. Aldrich: On the use of the pyranometer, *Smithson. Misc. Collect.* **66**(11), 9 (1916)
- 11.35 A. Ångström: A new instrument for measuring sky radiation, *Mon. Weather Rev.* **47**, 795–797 (1919)
- 11.36 H.H. Kimball, H.E. Hobbs: A new form of thermoelectric recording pyrheliometer, *Mon. Weather Rev.* **51**, 239–242 (1923)
- 11.37 F.E. Volochine: Quelques appareils du laboratoire actinométrie à Trappes. In: *Internationale Strahlungskommission. Protokolle der Sitzungen in Frankfurt a. M. 15.–17. September 1932*, ed. by Secretariat L’Organisation Meteorologique Internationale No. 15 (Kemink en Zoon N. V., Utrecht 1933) pp. 29–43
- 11.38 M. Robitzsch: Mitteilung über einen neuen Sonnenscheinautographen, *Meteorol. Z.* **32**, 470–471 (1915)
- 11.39 M. Robitzsch: *Die Strahlung in Lindenberg während des Jahres 1920*, Arbeiten des Königlich Preußischen Aeronautischen Observatoriums bei Lindenberg XIV (Vieweg & Sohn, Braunschweig 1922) pp. 128–136
- 11.40 M. Robitzsch: Über den Bimetallaktinographen Fuess–Robitzsch, *Gerlands Beitr. Geophys.* **35**, 387–394 (1932)
- 11.41 M. Robitzsch: Bemerkungen zur Eichung der Robitzsch–Aktinographen, *Meteorol. Z.* **55**, 403–406 (1938)
- 11.42 K. Ångström: Über die Anwendung der elektrischen Kompensationsmethode zur Bestimmung der nächtlichen Ausstrahlung, *Nova Acta Regiae Soc. Sci. Ups. IV I*(2), 11 (1905)
- 11.43 L.B. Aldrich: The Melikeron – An approximately black-body pyranometer, *Smithson. Misc. Collect.* **72**(13), 11 (1922)
- 11.44 H.J. Bolle: *International Radiation Commissions 1896 to 2008: Research into Atmospheric Radiation from IMO to IAMAS*, IAMAS No. 1 (International Association of Meteorology and Atmospheric Sciences, Oberpfaffenhofen 2008) p. 141
- 11.45 J.T. Gier, R.V. Dunkle: Total hemispherical radiometers, *Trans. Am. Inst. Electr. Eng.* **70**, 1–7 (1951)
- 11.46 Fa. B. Lange: *Bedienungsanleitung Bilanzmesser nach Schulze* (Lange, Berlin 1983)
- 11.47 R. Schulze: Über ein Strahlungsmessgerät mit ultrarotdurchlässiger Windschutzhaube am Meteorologischen Observatorium Hamburg, *Geofis. Pur. Appl.* **24**, 107–114 (1953)
- 11.48 L.J. Fritschen: Construction and elevation of a miniature net radiometer, *J. Appl. Meteorol.* **2**, 165–172 (1963)
- 11.49 C. Tingwaldt: Ein neues Pyrheliometer für Absolutmessungen, *Z. Instrumentenk. d.* **51**, 593–599 (1931)

- 11.50 C.G. Abbot, L.B. Aldrich: An improved water-flow pyrheliometer and the standard scale of solar radiation, *Smithson. Misc. Collect.* **87**(15), 1–8 (1932)
- 11.51 W.M. Shulgin: Improved waterflow pyrheliometer, *Mon. Weather Rev.* **55**, 361–362 (1927)
- 11.52 WMO: *Commission for Instruments and Methods of Observation; Abridged Final Report of the Seventh Session, Hamburg, 1–12 August 1977*, WMO–No. 490 (World Meteorological Organization, Geneva 1977)
- 11.53 W. Finsterle: *WMO International Pyrheliometer Comparison IPC–XII 28 September – 16 October 2015 Davos, Switzerland Final Report*, WMO IOM Report No. 124 (World Meteorological Organization, Geneva 2016)
- 11.54 J. Romero, N.P. Fox, C. Fröhlich: First comparison of the solar and an SI radiometric scale, *Metrologia* **28**, 125–128 (1991)
- 11.55 J. Romero, N.P. Fox, C. Fröhlich: Improved comparison of the World Radiometric Reference and the SI radiometric scale, *Metrologia* **32**, 523–524 (1995)
- 11.56 W. Finsterle, P. Blattner, S. Moebus, I. Rüedi, C. Wehrli, M. White, W. Schmutz: Third comparison of the World Radiometric Reference and the SI radiometric scale, *Metrologia* **45**, 377–381 (2008)
- 11.57 A. Fehlmann: *Metrology of Solar Irradiance*, PhD Thesis (University of Zurich, Zurich 2011)
- 11.58 R. Winkler: *Cryogenic Solar Absolute Radiometer – a Potential Replacement for the World Radiometric Reference*, PhD Thesis (University College, London 2012)
- 11.59 G. Kopp, K. Heuerman, D. Harber, G. Drake: The TSI Radiometer Facility: absolute calibrations for total solar irradiance instruments, *Proc. SPIE* (2007), <https://doi.org/10.1117/12.734553>
- 11.60 A. Fehlmann, G. Kopp, W. Schmutz, R. Winkler, W. Finsterle, N. Fox: Fourth World Radiometric Reference to SI radiometric scale comparison and implications for on-orbit measurements of the total solar irradiance, *Metrologia* **49**, S34–S38 (2012)
- 11.61 M. Wild, D. Folini, C. Schär, N. Leob, E.G. Dutton, G. König-Langlo: The global energy balance from surface perspective, *Clim. Dyn.* **40**(11–12), 3107–3134 (2013)
- 11.62 C. Emde, R. Buras-Schnell, A. Kylling, B. Mayer, J. Gasteiger, U. Hamann, J. Kylling, B. Richter, C. Pause, T. Dowling, L. Bugliaro: The libRadtran software package for radiative transfer calculations (version 2.0.1), *Geosci. Model Dev.* **9**, 1647–1672 (2016)
- 11.63 B. Mayer, A. Kylling: Technical note: The libRadtran software package for radiative transfer calculations – description and examples of use, *Atmos. Chem. Phys.* **5**, 1855–1877 (2005)
- 11.64 D. Mathias: Personal communication (2019)
- 11.65 K. Hoogendijk: Personal communication (2019)
- 11.66 Kipp and Zonen: *SP Lite2 Silicon Pyranometer Brochure, Version 1401* (Kipp and Zonen, Delft 2014)
- 11.67 Kipp and Zonen: *CGR4 Pyrheliometer, Instruction Manual, Version 1401* (Kipp and Zonen, Delft 2014)
- 11.68 EKO Instruments: *Pyranometers MS–802, MS–402, MS–602. Flyer EKO–MS802–07E* (2018)
- 11.69 Kipp and Zonen: *Instruction Manual, CMP Series Pyranometer, CMA Series Albedometer*, Manual Doc–No. 1610 (Kipp and Zonen, Delft 2016)
- 11.70 Hukseflux Thermal Sensors: *User Manual SR22, Secondary Standard Pyranometer with Quartz Domes – Extended Spectral Range*, Manual v1506 (Hukseflux, Delft 2015)
- 11.71 Hukseflux Thermal Sensors: *User Manual IR20, Research Grade Pyrheliometer*, Manual v1604 (Hukseflux, Delft 2016)
- 11.72 WMO: *Guide to Meteorological Instruments and Methods of Observation*, WMO–No. 8, 5th edn. (World Meteorological Organization, Geneva 1983)
- 11.73 ISO: *Solar Energy – Specification and Classification of Instruments for Measuring Hemispherical Solar and Direct Solar Radiation*, ISO 9060:2018 (International Organization for Standardization, Geneva 2018)
- 11.74 J.M. Kendall, C.M. Berdahl: Two blackbody radiometers of high accuracy, *Appl. Opt.* **9**, 1082–1091 (1970)
- 11.75 R.W. Brusa, C. Fröhlich: *Entwicklung eines neuen Absolutradiometers*, Technical Note 1 (World Radiation Center, Davos 1972)
- 11.76 R.C. Willson: Active cavity radiometer, *Appl. Opt.* **12**, 810–817 (1973)
- 11.77 D. Crommelynck: Théorie instrumentale en radiométrie absolue, *IRM Publ. A* **81**, 85 (1973)
- 11.78 M.S. Reid, C.M. Berdahl, J.M. Kendall: Calibration standards and field instruments for precision measurements of insolation, *Solar Energy* **20**, 357–358 (1978)
- 11.79 A.R. Karoli, J.R. Hickey, R.G. Frieden: Self-calibrating cavity radiometers at the Eppley Laboratory: Capabilities and applications, *Proc. SPIE* (1983), <https://doi.org/10.1117/12.935917>
- 11.80 F. Linke, K. Boda: Vorschläge zur Berechnung des Trübungsgrades der Atmosphäre, *Meteorol. Z.* **39**, 161–166 (1922)
- 11.81 A. Ångström: On the atmospheric transmission of sun radiation and on dust in the air. I, *Geogr. Ann.* **11**, 156–166 (1929)
- 11.82 A. Ångström: On the atmospheric transmission of sun radiation. II, *Geogr. Ann.* **12**, 130–159 (1930)
- 11.83 J. Michalsky, E.G. Dutton, D. Nelson, J. Wendell, S. Wilcox, A. Andreas, P. Gotseff, D. Myers, I. Reda, T. Stoffel, K. Behrens, T. Carlund, W. Finsterle, D. Halliwell: An extensive comparison of commercial pyrheliometers under a wide range of routine observing conditions, *J. Atmos. Ocean. Technol.* **28**, 752–766 (2011)
- 11.84 E.G. Dutton, J.J. Michalsky, T. Stoffel, B.W. Forgan, J. Hickey, D.W. Nelson, T.L. Alberta, I. Reda: Measurement of broadband diffuse solar irradiance using current commercial instrumentation with correction for thermal offset errors, *J. Atmos. Ocean. Technol.* **18**, 297–314 (2001)

- 11.85 R. Philipona: Underestimation of solar global and diffuse radiation measured at Earth's surface, *J. Geophys. Res.* **107**(D22), 4654 (2002)
- 11.86 A.J. Drummond, W.J. Scholes, J.H. Brown, R.E. Nelson: A new approach of terrestrial long-wave radiation. In: *Radiation Including Satellite Techniques. Proceedings of the WMO/UGG Symposium Held in Bergen, August 1969*, Technical Note No. 104. WMO-No. 248. TP 136, (World Meteorological Organization, Geneva 1970) pp. 383–387
- 11.87 B. Albrecht, S.K. Cox: Procedures for improving pyrgeometer performance, *J. Appl. Meteorol.* **16**, 188–197 (1977)
- 11.88 B. Albrecht, M. Peollet, S.K. Cox: Pyrgeometer measurements from aircraft, *Rev. Sci. Instrum.* **45**, 33–38 (1974)
- 11.89 R. Philipona, C. Fröhlich, C. Betz: Characterization of pyrgeometers and the accuracy of atmospheric long-wave radiation measurements, *Appl. Opt.* **34**, 1598–1605 (1995)
- 11.90 L.J. Fritschen: Miniature net radiometer improvements, *J. Appl. Meteorol.* **4**, 528–532 (1965)
- 11.91 J.A. Brotzge, C.E. Duchon: A field comparison among a domeless net radiometer, two four-component net radiometers, and a domed net radiometer, *J. Atmos. Ocean. Technol.* **17**, 1569–1582 (2000)
- 11.92 M.L. Wesely: Simplified techniques to study components of solar radiation under haze and clouds, *J. Appl. Meteorol.* **21**, 373–383 (1982)
- 11.93 J.J. Michalsky, J.L. Berndt, G.J. Schuster: A micro-processor controlled rotating shadowband radiometer, *Solar Energy* **36**, 465–470 (1986)
- 11.94 L.J. Harrison, J.J. Michalsky, J.L. Berndt: Automated multifilter rotating shadowband radiometer: An instrument for optical depth and radiation measurements, *Appl. Opt.* **33**, 51158–5125 (1994)
- 11.95 F. Vignola, J. Peterson, S. Wilbert, P. Blanc, N. Geuder, C. Kern: New methodology for adjusting rotating shadowband irradiometer measurements, *AIP Conf. Proc.* **1850**, 140021 (2017)
- 11.96 S. Wilbert, S. Kleindiek, B. Nouri, N. Geuder, A. Habte, M. Schwandt, F. Vignola: Uncertainty of rotating shadowband irradiometers and Si-pyranometers including the spectral irradiance error, *AIP Conf. Proc.* **1734**, 150009 (2016)
- 11.97 W. Jessen, S. Wilbert, B. Nouri, N. Geuder, H. Fritz: Calibration methods for rotating shadowband irradiometers and optimizing the calibration duration, *Atmos. Meas. Tech.* **9**, 1601–1612 (2016)
- 11.98 J. Badosa, J. Wood, P. Blanc, C.N. Long, L. Vuilleumier, D. Demengel, M. Haeffelin: Solar irradiances measured using SPN1 radiometers: Uncertainties and clues for development, *Atmos. Meas. Tech.* **7**, 4267–4283 (2014)
- 11.99 C.A. Gueymard, D.R. Myers: Evaluation of conventional and high-performance routine solar radiation measurements for improved solar resource, climatological trends, and radiative modeling, *Solar Energy* **83**, 171–185 (2009)
- 11.100 K.J. McCree: Test of current definitions of photosynthetically active radiation against leaf photosynthesis data, *Agric. Meteorol.* **10**, 443–453 (1972)
- 11.101 J.M. Blonquist, B. Bugbee: Solar, net, and photosynthetic radiation. In: *Agroclimatology: Linking Agriculture to Climate*, Agronomy Monographs, Vol. 60, ed. by J.L. Hatfield, M.V.K. Sivakumar, J.H. Prueger (ASA, CSSA, and SSSA, Madison, WI 2018)
- 11.102 WMO: *Commission for Instruments and Methods of Observation; Abridged Final Report of the Third Session, New Delhi, 29 January–15 February 1962*, WMO-No. 116 (World Meteorological Organization, Geneva 1962)
- 11.103 H.E. Painter: The performance of a Campbell-Stokes sunshine recorder compared with a simultaneous record of normal incidence irradiance, *Meteorol. Mag.* **110**, 102–109 (1981)
- 11.104 WMO: *Commission for Instruments and Methods of Observation; Abridged Final Report of the Eighth Session, Mexico City, 19–30 October 1981*, WMO-No. 590 (World Meteorological Organization, Geneva 1982)
- 11.105 J.C. Olivieri: *Sunshine Duration Measurement Using a Pyranometer*, IOM Report 70, WMO/TD-No. 877 (World Meteorological Organization, Geneva 1998) pp. 357–360
- 11.106 Y.B.L. Hinssen, W.H. Knap: Comparison of pyranometric and pyrhemimetric methods for the determination of sunshine duration, *J. Atmos. Ocean. Technol.* **24**, 835–846 (2007)
- 11.107 D.J. Baumgartner, W. Pötzi, H. Freislich, H. Strutzmann, A.M. Veronig, U. Foelsche, H.E. Rieder: A comparison of long-term parallel measurements of sunshine duration obtained with a Campbell–Stokes sunshine recorder and two automated sunshine sensors, *Theor. Appl. Climatol.* **133**, 263–275 (2018)
- 11.108 A.J. Drummond: On the measurement of sky radiation, *Arch. Meteorol. Geophys. Bioklim. B* **7**, 413–436 (1956)
- 11.109 K. Dehne: *Diffuse Solar Radiation Measured by the Shade Ring Method Improved by a Correction Formula*, IOM Report 15 (World Meteorological Organization, Geneva 1984) pp. 263–267
- 11.110 ISO: *Solar Energy – Calibration of Field Pyrhemimeters by Comparison to a Reference Pyrhemimeter*, ISO 9059:1990 (International Organization for Standardization, Geneva 1990)
- 11.111 ISO: *Solar Energy – Calibration of Pyranometer Using a Pyrhemimeter*, ISO 9846:1993 (International Organization for Standardization, Geneva 1993)
- 11.112 ISO: *Solar Energy – Calibration of Field Pyranometers by Comparison to a Reference Pyranometer*, ISO 9847:1992 (International Organization for Standardization, Geneva 1992)
- 11.113 WMO: *Commission for Instruments and Methods of Observation, Thirteenth Session, Bratislava, 25 September–3 October 2002. Abridged Final Report with Resolutions and Recommendations*, WMO-No. 947 (World Meteorological Organization, Geneva 2003)

- 11.114 WMO: *Commission for Instruments and Methods of Observation, Fourteenth session, Geneva, 7–14 December 2006. Abridged Final Report with Resolutions and Recommendations*, WMO–No. 1019 (World Meteorological Organization, Geneva 2007)
- 11.115 J. Gröbner, I. Reda, S. Wacker, S. Nyeki, K. Behrens, J. Gorman: A new absolute reference for atmospheric longwave irradiance measurements with traceability to SI units, *J. Geophys. Res. Atmos.* **119**, 7083–7090 (2014)
- 11.116 R. Philipona: Sky-scanning radiometer for absolute measurements of atmospheric long-wave radiation, *Appl. Opt.* **40**, 2376–2383 (2001)
- 11.117 R. Philipona, E.G. Dutton, T. Stoffel, J. Michalsky, I. Reda, A. Stifter, P. Wendling, N. Wood, S.A. Clough, E.J. Mlawer, G. Anderson, H.E. Revercomb, T.R. Shippert: Atmospheric longwave irradiance uncertainty: Pyrgeometers compared to an absolute sky-scanning radiometer, atmospheric emitted radiance interferometer, and radiative transfer model calculations, *J. Geophys. Res.* **106**, 28129–28141 (2001)
- 11.118 C. Marty, R. Philipona, J. Delamare, E.G. Dutton, J. Michalsky, K. Stamnes, R. Storvold, T. Stoffel, S.A. Clough, E.J. Mlawer: Downward longwave irradiance uncertainty under arctic atmospheres: Measurements and modeling, *J. Geophys. Res.* **108**, 4358 (2003)
- 11.119 J. Gröbner: A transfer standard radiometer for atmospheric longwave irradiance measurements, *Metrologica* **49**, S105–S111 (2012)
- 11.120 I. Reda, J. Zeng, J. Scheuch, L. Hanssen, B. Wilthan, D. Myers, T. Stoffel: An absolute cavity pyrgeometer to measure the absolute outdoor longwave irradiance with traceability to international system of units, SI, *J. Atmos. Sol. Terr. Phys.* **77**, 132–143 (2012)
- 11.121 J. Gröbner: Operation and investigation of a tilted bottom cavity for pyrgeometer characterizations, *Appl. Opt.* **24**, 4441–4447 (2008)
- 11.122 WMO: *Commission for Instruments and Methods of Observation. Abridged Final Report of the Seventeenth session, Amsterdam, 12–16 October 2018. Part I – Abridged Final Report, Part II – Progress Report*, WMO–No. 1227 (World Meteorological Organization, Geneva 2018)
- 11.123 J. Gröbner, C. Thomann: *Report on the Second International Pyrgeometer Intercomparison (27 Sep–15 Oct 2015, PMOD/WRC)*, IOM Report 129 (World Meteorological Organization, Geneva 2018) p. 52
- 11.124 J. Gröbner, S. Wacker: *Pyrgeometer Calibration Procedure at the PMOD/WRC–IRS*, IOM Report 120 (World Meteorological Organization, Geneva 2015) p. 13
- 11.125 R. Becker, K. Behrens: Quality assessment of heterogeneous surface radiation network data, *Adv. Sci. Res.* **8**, 93–97 (2012)
- 11.126 R. Urraca, A.M. Gracia-Amillo, T. Huld, F.J. Martinez-de-Pison, J. Trentmann, A.V. Lindfors, A. Riihelä, A. Sanz-Garcia: Quality control of global solar radiation data with satellite-based products, *Solar Energy* **158**, 49–62 (2017)
- 11.127 C.N. Long, E.G. Dutton: *BSRN Global Network Recommended QC Tests, V2.0 2002*. <http://hdl.handle.net/10013/epic.38770.d001>, Accessed 05 July 2021
- 11.128 G. König-Langlo, R. Sieger, H. Schmithüsen, A. Bücken, F. Richter, E.G. Dutton: *The Baseline Surface Radiation Network and its World Radiation Monitoring Centre at the Alfred Wegener Institute*, GCOS 174, WCRP Report 24/2013 (World Meteorological Organization, Geneva 2013)
- 11.129 H. Schmithüsen, R. Sieger, G. König-Langlo: BSRN Toolbox – a tool to create quality checked output files from BSRN datasets and station-to-archive files. In: *PANGAEA* (Alfred Wegener Institute, Helmholtz Centre for Polar and Marine Research, Bremerhaven 2012), <https://doi.org/10.1594/PANGAEA.774827>
- 11.130 H. Hegner, G. Müller, V. Nespor, A. Ohmura, R. Steigrad, H. Gilgen: *Technical Plan for BSRN Data Management – 1998 Update*, WMO/TD–No. 882 (World Meteorological Organization, Geneva 1998)
- 11.131 A. Angström: Solar and terrestrial radiation. Report to the international commission for solar research on actinometric investigations of solar and atmospheric radiation, *Q. J. R. Meteorol. Soc.* **50**, 121–125 (1924)
- 11.132 K. Behrens: Recording of solar radiation components for 75 years in Potsdam (Germany), *AIP Conf. Proc.* **1531**, 548–551 (2013)
- 11.133 G. Stanhill, S. Cohen: Global dimming: A review of the evidence for a widespread and significant reduction in global radiation with discussion of its probable causes and possible agricultural consequences, *Agric. For. Meteorol.* **107**, 255–278 (2001)
- 11.134 R.T. Pinker, B. Zhang, E. Dutton: Do satellites detect trends in surface solar radiation?, *Science* **308**, 850–854 (2005)
- 11.135 T. Foken: *Energieaustausch an der Erdoberfläche* (Edition am Gutenbergplatz, Leipzig 2013)
- 11.136 VDI: *Environmental Meteorology – Interactions between Atmosphere and Surfaces – Calculation of Spectral Short-Wave and Long-Wave Radiation*, VDI 3789 (Beuth, Berlin 2019)

Klaus Behrens

Nuthetal, Germany
klaus.behrens@mailbox.org



Klaus Behrens studied meteorology at Humboldt University then worked at Potsdam Meteorological Observatory on radiation climatology and broadband radiation measurements. He worked at the BSRN station in Lindenberg up to his retirement in 2017, being also the scientist responsible for the radiation network of the German Meteorological Service and the Regional Radiation Centre (RA VI of WMO) of Lindenberg Meteorological Observatory. He was also with CIMO of WMO.

In-situ Preci

12. In-situ Precipitation Measurements

Arianna Cauteruccio , Matteo Colli , Mattia Stagnaro , Luca G. Lanza , Emanuele Vuerich

This chapter describes the measuring principles and technological solutions available for in-situ measurements of liquid (rain) and solid (snow) atmospheric precipitation. They can be classified into catching and non-catching precipitation gauges. Instruments belonging to the first family are generally based on gravity-related measuring principles (weighing, tipping buckets, floating devices), while the second group includes instruments based on optical, acoustic, and microwave principles (e.g., disdrometers). All instruments are subject to both systematic (often unknown) biases and measurement uncertainties, depending on the design, the measuring principle, the algorithms used for data interpretation and correction, etc. Moreover, environmental factors affect the measurement accuracy as well, depending on the atmospheric conditions at the collector, the siting characteristics, etc. Typical environmental factors include the gradients of atmospheric temperature, wind speed, and solar radiation and may result in a significant underestimation of accumulated precipitation. The present chapter addresses the achievable accuracy of instruments for in-situ measurement of liquid and solid precipitation, based on both the outcomes of the recent WMO intercomparison initiatives and the accurate laboratory and field tests presently ongoing within the activities of the WMO/CIMO Lead Centre on Precipitation Intensity (Italy).

12.1	Measurement Principles and Parameters	360
12.1.1	Measurement Principles	360
12.1.2	Measured Parameters	360
12.1.3	Requirements	361
12.1.4	Siting Considerations	362
12.2	History	362
12.2.1	History of Precipitation Measurements	362
12.2.2	Evolution of Acquisition Systems	364
12.2.3	Homogeneity of Historical Precipitation Records	365
12.2.4	Instrument Testing and Intercomparisons	366
12.3	Theory	367
12.3.1	Measurement Principles and Accuracy	367
12.3.2	Volumetric Methods	367
12.3.3	Gravimetric Methods	368
12.3.4	Optical Methods	369
12.3.5	Other Methods	370
12.4	Devices and Systems	370
12.4.1	Catching-Type Gauges	370
12.4.2	Non-Catching-Type Gauges	372
12.4.3	Comparison of the Methods	375
12.5	Specifications	375
12.5.1	Specifications for Catching-Type Gauges	375
12.5.2	Specifications for Non-Catching-Type Gauges	376
12.6	Quality Control, Uncertainty, and Calibration	376
12.6.1	Precipitation Measurement Biases and Uncertainties	377
12.6.2	Laboratory Tests and Field Experiments	378
12.6.3	Correction Methods	381
12.6.4	Measurement Uncertainty	387
12.6.5	Specific Quality Control Methods	388
12.6.6	Intercomparison Results	389
12.7	Maintenance	392
12.7.1	Periodic Checks and Maintenance Procedures	392
12.7.2	Field Calibration/Verification	394
12.7.3	Metrological Confirmation	394
12.8	Application	394
12.9	Future Developments	396
12.10	Further Reading	397
	References	397

According to the *Guide to Instruments and Methods of Observation* [12.1] published by the World Meteorological Organization (WMO), precipitation is defined as

the liquid or solid products of the condensation of water vapour falling from clouds. The total amount of precipitation which reaches the ground in a stated period is expressed in terms of the vertical depth of water (or water equivalent in the case of solid forms) to which it would cover a horizontal projection of the Earth's surface.

Precipitation intensity is defined as

the amount of precipitation collected per unit time interval.

Atmospheric precipitation is commonly experienced in our everyday lives and activities, in both business and leisure time, and its impact is manifest in major socioeconomic sectors including transportation, agriculture, safety, tourism, and recreation.

The extraordinary role of atmospheric precipitation in human society (and natural ecosystems as well) justifies the need to obtain accurate quantitative measurements of the amount of water reaching the ground surface and the duration and intensity of precipitation events.

12.1 Measurement Principles and Parameters

Precipitation varies considerably in both space and time. It is erratic and intermittent in nature, and is composed of a large number of hydrometeors, each of them with its own size, shape, density, and fall velocity in reaching the ground, according to specific frequency distributions. Due to the complex processes of nucleation, accretion, melting, and interactions between the hydrometeors (see e.g., [12.2]), the resulting characteristics of precipitation depend on the generating weather phenomenon and climate at any specific location (temperature, humidity, etc.). In addition, the fall trajectories of single particles are affected by local conditions at a site, including wind and shading by obstacles, and by the aerodynamic behavior of the outer body of the measurement instrument itself.

12.1.1 Measurement Principles

Precipitation is among the most challenging environmental measurements, and accurate measurement of the amount of water that would ultimately land on a well-defined portion of the ground surface in undisturbed conditions is a difficult task. This is the aim of the so-called in-situ measurements at the ground, with the instrument located precisely where the information is sought, at a single location immersed in the precipitation process.

Precipitation measured at a single location is representative of a limited area in space,

the size of which is a function of the length of the accumulation period, the physiographic homogeneity of the region, local topography and the precipitation-producing process [12.1].

Weather radar and, more recently, satellites are used to define and quantify the spatial distribution of precipitation from a remote sensing perspective, with the sensor generally located far from the precipitation process. The information is inferred from the observed modifications of other physical quantities due to the interference with the precipitation process (e.g., active/passive microwave, infrared temperature).

In-situ precipitation gauges, however, provide the only direct measurement of precipitation at the ground and are usually referred to as the *ground truth*. Remote sensing techniques for extensive observations (essentially weather radar, aircraft, and satellite-borne radiometers) still require the use of in-situ measurements for calibration and validation purposes. Following [12.3],

measurements at the ground have been proved indispensable, despite advances in several areas of remotely sensing of precipitation. Ground truth seems to be inseparable from any study on precipitation. A better understanding of the behavior of precipitation on the ground with direct measurements can lead to more effective estimations by using other methodologies.

12.1.2 Measured Parameters

The parameters measured by precipitation instruments range quite widely: basic instruments simply inform the status of the rain in that moment, i.e., whether it rains or not, while others detect the particle size distribution of hydrometeors. Traditionally, however, the equivalent volume of water received by a collector through

Table 12.1 Measured parameters of precipitation sensors

Parameter	Description	Unit	Symbol
Rain depth	The total volume of liquid precipitation deposited in a given time interval per unit area of the horizontal projection of the ground surface	mm	RA
Snow depth	The liquid water equivalent of the total volume of solid precipitation deposited in a given time interval per unit area of the horizontal projection of the ground surface	mm	SA
Rainfall intensity	The rain depth per unit time interval	mm h^{-1}	RI
Snowfall intensity	The snow depth per unit time interval	mm h^{-1}	SI
Particle size	The characteristic dimension (usually the diameter assuming spherical shape) of hydrometeors	mm	D
Number of particles	Number of hydrometeors per class of particle size	–	$N(D)$
Particle fall velocity	Velocity of hydrometeors at the ground surface	mm s^{-1}	v

Table 12.2 Other relevant parameters for precipitation measurements

Parameter	Description	Unit	Symbol
Temperature	Ambient temperature	$^{\circ}\text{C}$	T
Wind velocity	Average wind velocity at the sensor's height	mm s^{-1}	U_w
Wind direction	Prevailing wind direction expressed in degrees clockwise from due north	$^{\circ}$	U_d

an orifice of known surface area in a given period is assumed as the reference variable, namely the precipitation depth. The measurement unit of precipitation amount is therefore linear depth, usually expressed in millimeters, obtained as the ratio of the precipitated cumulative water volume over the surface area of the collector.

Under the restrictive hypothesis that precipitation is constant over the accumulation period, a derived variable—the precipitation rate or intensity—can be easily calculated. Using short time intervals ensures that the estimated intensity is close to the real flow of water ultimately reaching the ground. The measurement unit of precipitation intensity is linear depth per unit time, usually expressed in millimeters per hour.

This approximate measure of the precipitation rate has long been accepted as sufficiently accurate to meet the requirements of both scientific and technical applications. Reasons for this are on the one hand that most traditional applications in hydrology operate at the basin scale, thus dealing with aggregated rainfall over large space and timescales, while on the other hand the available technology of measurement instruments—especially in terms of data storage and transmission capabilities—was lower than today.

Although quantitative data regarding the amount (depth) of liquid and solid precipitation are the basis for many practices, the intensity of precipitation has become a variable of almost equal significance. Rainfall and snowfall intensity data are extremely relevant in the case of severe weather. For example, it is clear that events with extremely high precipitation rates affect all types of transportation; they may also destroy crops and vegetation. Precipitation intensity has now been introduced by WMO as a measured parameter, in line with

the present recommendations on weather reporting (Table 12.1).

In addition, most automatic precipitation gauges provide the amount of precipitation at a relatively short time resolution, usually less than 1 min. Users of precipitation measurements typically require information on accumulated rainfall/snowfall for longer time intervals, for example, the hourly, daily, monthly, and even annual total rain depth. Modern non-catching instruments include optical and acoustic principles to derive information including drop size distribution (DSD), fall velocity of single drops, crystal types (Table 12.1) and other relevant parameters (Table 12.2).

12.1.3 Requirements

Research and technological development in the field of precipitation measurements obviously proceed at a different pace, so that the instruments commonly deployed on the territory do not have the same level of accuracy of research-devoted instruments installed at a few experimental sites. Even the research instruments in some cases are used under the blind assumption of a high level of accuracy (because of the physical principle used to measure rainfall), but often no evidence is made available to support this assumption. This is the case, for example, with various types of disdrometers, as it was recently shown that their calibration is still a problem [12.4].

Requirements from the many users of precipitation data are becoming tighter and tighter, and sound research and applications in the geosciences require enhanced quality in precipitation measurement. The interpretation of rainfall patterns, speculation about the nature of the rain field, scaling versus nonscaling issues,

rainfall event modeling and forecasting efforts, everyday engineering applications, etc., are all based on the analysis of precipitation data that are measured at very fine resolution. Therefore, the relevance of precipitation intensity measurements has increased dramatically, and very high values are increasingly recorded, due to the shortening of the reference period. High accuracy is also sought in the upper range of precipitation intensity.

The timescales required for calculation of precipitation intensity at the ground are already much shorter than in traditional applications. The design and management of urban drainage systems, flash flood forecasting and mitigation, transport safety measures, and in general most of the applications where precipitation data are sought in real time, call for enhanced resolution of such information in time (and space), even down to the scale of 1 min in many cases.

The thirteenth session of the WMO Commission for Instruments and Methods of Observation (CIMO-XIII, 2002), as a result of an Expert Meeting held in Bratislava, Slovakia in 2001, noted that significant efforts were necessary to obtain the required information about uncertainties in precipitation intensity measurement. For liquid precipitation, CIMO-XIII adopted the measurement range and related uncertainties recommended by the expert team, published in the *WMO Guide to Instruments and Methods of Observation* (WMO-No. 8) [12.1] and reported in Table 12.4.

Instruments based on modern technology are increasingly deployed as part of or simply to replace traditional monitoring networks, especially in developed countries, where the high cost of such instruments

can more easily be borne. However, little information is available to the user on biases and uncertainties associated with such instruments, and corrections are very seldom applied. Therefore, the quality of the new data sets is not necessarily higher (and is sometime even lower) than what is obtained from traditional networks, while additional inhomogeneities of the time series are added to the picture, with serious consequences, for example, in climate-related studies.

12.1.4 Siting Considerations

Precipitation measurements aim to obtain a sample that is representative of the true amount of water falling over the area that the measurement is intended to represent [12.1]. The quality of the measurement is very sensitive to the exposure of the instrument to the surrounding environment. Appropriate siting is therefore crucial in obtaining accurate precipitation measurements.

The WMO Guide no. 8 [12.1] specifies that

the best sites are often found in clearings within forests or orchards, among trees, in scrub or shrub forests, or where other objects act as an effective windbreak for winds from all directions.

However, the presence of obstacles and other instruments close to the precipitation gauge should be avoided. The [12.1] imposes certain distances for any obstacle, and defines siting classes depending on the slope of the surrounding area and the type and height of obstacles.

12.2 History

In human history, abundant atmospheric precipitation often had a positive acceptance, while the lack of it was sometimes viewed as a visitation from god and a punishment for human sins. The need for the occurrence and recurrence of precipitation is historically evidenced by the presence of dedicated gods in most ancient religions (Chac—Mayan god of rain, Ishkur—god of rain and storm in the Mesopotamian mythology, Baal—god of storm in the Phoenician mythology, Seth—the *Lord of storm* for Egyptians, and many others). As a first reward in response to good conduct by the acolytes, the Torah promises rainfall, “something that is a natural prerequisite for all specific material blessings” (Akeidat Yitzchak 70:1). However, the Book of Amos (4:6–8) reports: “I also withheld rain from you when the harvest was still three months away (. . .), yet you have not returned to me”. Still today, many religions convene the

acolytes to pray for the occurrence of rainfall in periods of intense drought. An exceptional amount of precipitation is equally negative, since it generates floods and inundations, with associated damage and victims, being nowadays among the most common natural disasters on planet Earth.

12.2.1 History of Precipitation Measurements

The early need for measuring atmospheric precipitation in precise quantitative terms in human history seems to be of religious, agricultural, or even taxation-related origins.

Ancient religious texts dated about 400 BCE are often cited in literature as the oldest written documentation of the practice of measuring precipitation in

Palestine [12.2, 5, 6]. The rainfall amount was used to define droughts and the limits of the fast period, thus the question:

How much rain must fall to constitute the first rainfall? 'Enough to fill a utensil three handbreadths in height', the words of R. Meir. I. R. Judah says, 'The first is to be a handbreadth [of rain], the second, two handbreadths, and the final one, three handbreadths' (Jerusalem Talmud, Ta'anit 1, 3).

The utensil mentioned in the text was assumed to be an initial version of a rain gauge, and an estimate of the yearly precipitation in Palestine (divided into three rain periods) was derived from the use of the *handbreadth* (the width of a hand used as an indication of length) by *Julius von Hann* (1839–1921) [12.7]. From the same measurement unit, even the size of the rain gauge was estimated. However, a second version of the same religious text contends:

How long should it continue to rain to warrant the community breaking their fast? [Until the rain has penetrated] as far as the knee of the plough enters the soil; this is the opinion of *R. Meir*. The Sages, however, say: in the case of arid soil one handbreadth, in the case of moderately soft soil two handbreadths, and in the case of cultivated soil three handbreadths. (Babylonian Talmud, Ta'anit 25b).

This second version, as indicated by *Jehuda Feiliks* [12.8] and reported by [12.9], makes it clear that the quantity used to define the limits of the fast period was actually a qualitative measurement of water content in the soil (or infiltration) rather than the rainfall amount, and linked to the penetration of a plough (the actual utensil) into the soil. Therefore, no mention of rainfall measurements is actually contained in such religious texts, although it is clear that the occurrence and amount of rainfall has ruled religious practices since very old times.

An ancient Indian treatise on statecraft, economic policy, and military strategy, called *Arthashastra* and written in Sanskrit, contains clear reference to rainfall measurements in the past [12.10]. Possibly the work of several authors over centuries, its authorship is often attributed to *Kautilya*, a scholar at *Takshashila*, the teacher and guardian of Emperor *Chandragupta Maurya*. Composed, expanded, and redacted between the second century BCE and third century CE, the *Arthashastra* was influential until the twelfth century, when it disappeared. *Shamasastri* rediscovered the text

in 1905 and published it in 1909; the first English translation was published in 1915.

In Book II—The Duties of Government Superintendents, Chapter V—The Duties of the Chamberlain, the *Arthashastra* instructs:

In (front of) the store-house a bowl with its mouth as wide as an *aratni* (the distance from the elbow to the tip of the hand) shall be set up as rain gauge (*varshamána*).

Again, in Chapter XXIV—The Superintendent of Agriculture, it is said that:

the quantity of rain that falls in the country of *Jángala* is 16 dronas [1 drona = $13.2 \times 10^{-3} \text{ m}^3$ of water]; half as much more in moist countries. (...) When one-third of the requisite quantity of rain falls both during the commencement and closing months of the rainy season and two-thirds in the middle, then the rainfall is (considered) very even.

The chapter concludes by indicating the intended use of such measurements, stating:

according as the rainfall is more or less, the superintendent shall sow the seeds which require either more or less water.

In China, the earliest documented memory of rainfall measurement seems to appear in an ancient treatise entitled *Shushu jiu Zhang* (1247), or *Mathematical Writings in Nine Sections*, by *Qin Jiushao* (1202–1261), a Chinese mathematician who first developed a method for solving simultaneous linear congruences. The book is divided into nine *categories*, each containing nine problems related to calendrical computations, meteorology, surveying of fields, surveying of remote objects, taxation, fortification works, construction works, military affairs, and commercial affairs [12.11]. The treatise contains a problem on the shape of rain gauges, discussing the determination of the rain falling on a given area of ground from the depth of rainwater collected in vessels of conical or barrel shape [12.12]. It seems that at that time there was one in each provincial and district capital. The same book shows that snow gauges were also in use. These were large cages made of bamboo, and the author gives sample problems concerning them.

In Korea, the first documented rain gauge measuring rainfall by collecting rainwater in a barrel dates back to 1441 (23rd year of King *Sejong's* reign). However, the only specimen surviving until today was made in 1837 (third year of King *Heonjong's* reign) in the form of a barrel-shaped rain gauge, 31.5 cm high and having

a diameter of 15.3 cm (Treasure 561° of the National Treasures of South Korea, designated within the heritage preservation system of the country). A ruler was used to measure the rainwater depth collected in the barrel. The rain gauge has an associated square stone stand, added when it was on display at the National Gongju Museum. The Korean Meteorological Administration and the National Palace Museum of Korea have also preserved some further rain gauge pedestals made of stone or marble, but the associated rain gauges did not survive.

Father *Benedetto Castelli*, born in Brescia (Italy) in 1578, was an Italian mathematician who entered the Benedictine Order in 1595. He is recognized as the inventor of the rain gauge in 1639 because he was the first to measure rainfall associated with a given interval of time, and therefore the first to measure rainfall intensity (or the average rainfall intensity) at a given site. He designed the first rainfall intensity gauge at the S. Peter Monastery in Perugia (Italy) in order to study the relationship between the observed precipitation and the stages of the Trasimeno Lake in central Italy, following a drought period affecting agriculture in the region.

In a letter to *Galileo Galilei* (1564–1642) in 1639, he writes:

Given a bucket made of glass, with a cylindrical shape one palm high and half a palm wide, after pouring some water in order to cover the bottom of the bucket, I noted accurately the level of water and left it exposed to the rainfall for a period of one hour.

Assuming that the depth of water would have been the same in any similar nearby bucket (and therefore over the lake area), and noting that for a rainfall duration of 8 h at a similar rate the total water would have been eight times the measured one, Castelli managed to predict the water level rise in the Trasimeno Lake.

This is actually the first documented use of the concept of rainfall intensity as measured by a rain gauge, although the simple bucket used is a storage instrument in modern terminology (Sect. 12.3). For this reason, the first WMO/CIMO Lead Centre on Precipitation Intensity established in Italy in 2010 (www.precipitation-intensity.it, Accessed 05 July 2021) is now dedicated to the memory of, and named after, Benedetto Castelli and his historical work on precipitation measurements. Based on refinements of the instrument used by Castelli in the first half of the 17th century in Italy, both *Giovanni Poleni* (1683–1761) in Padova and *Paride M. Salvago* in Genova started regular observations of precipitation, and analogously in many other countries (e.g., B. Franklin since 1725).

According to *Asit K. Biswas* [12.13], *Sir Christopher Wren* (1632–1723), one-time president of the

Royal Society, conceived the earliest English rain gauge in 1662. Unlike the previous instruments, which were all of the nonrecording type, the inventor developed an automatic tipping-bucket rain gauge, which was realized later in 1679. The author notes that reference to the Wren tipping-bucket rain gauge can be seen in the review of the book *De l'origine des Fontaines* by *Pierre Perrault* (1611–1680) in the *Philosophical Transactions* for 1675. The review states that:

the like to which (estimation of the quantity of rain) hath been attempted here, and proposed to the R. Society, some years since, by Sir. Christopher Wren, who by the contrivance of a rain-bucket had taken an account of all the water that fell for a considerable time. By his weather-clock had, among other particulars, not only taken in the measuring of the quantity of rain that falls, but also the time when it falls, and how much at each time.

The invention of the tipping-bucket rain gauge marks the start of modern rainfall intensity measurements, which today are largely obtained using the same measuring principle, although many other instruments based on different principles are also available today, as detailed in Sect. 12.3 below.

12.2.2 Evolution of Acquisition Systems

Similarly to the measuring principles and instrument design, the whole measurement chain has evolved through the years at the pace of technological development. The technological evolution experienced by acquisition systems affects the measurement accuracy and the capability to meet stringent user requirements in terms of resolution, accuracy, sensitivity, etc.

The electronic recording and digital storage of the measured data in the data logger have largely overcome the traditional mechanical transmission of the modifications induced by the accumulated precipitation on the moving parts of the system. Generally, recording was obtained by a moving pen in contact with a paper chart mounted on a rotating cylinder controlled by a clockwise spring mechanism. The resulting charts report the accumulated rainfall, or the number of impulses of the counting mechanism as a function of time, depending on the measuring principle (Sect. 12.3).

The use of electronic circuits allowed the changes induced by precipitation as sensed by the instrument to be transformed into voltage changes and recorded in some digital form. This increased the resolution of the measured data and reduced the uncertainty due to the mechanical recording systems, resulting in a dramatic reduction of the time interval over which changes in the rain signal could be sensed and recorded. The precision

of the temporal labeling of each recorded impulse or voltage change also improved.

One of the major implications is the improved capability of measuring precipitation intensity, since the measured precipitation amount is associated with a much shorter interval than was possible in the past. Since many natural and man-made systems respond to the precipitation intensity forcing rather than to the accumulated water depth (e.g., flash floods, urban drainage systems), the improvement is tangible and valuable for modern applications.

In parallel with the evolution of data acquisition systems, the telemetering capabilities have evolved as well in recent times and are still evolving today. Any need to visit remote gauge stations in order to transfer the recorded measurements to the central archiving site has now vanished thanks to the automated transmission of the data via radio, telephone, or satellite links. In rare cases gauge stations are connected by cable and can transfer data directly over the network. Local storage in the data logger is still preserved for redundancy and safety reasons and can be downloaded, for example, during inspection or maintenance visits.

As an immediate advantage of the data transmission capabilities of modern instruments, the flow of data can now be managed automatically at the archiving station, including the application of quality control procedures, preparation of synthetic reports (e.g., daily average, maximum hourly precipitation intensity, daily accumulation), and data processing in general. This enables failures to be detected in the measurement chain, including instrument problems such as clogging or power supply failures, and timely maintenance to be activated as needed.

The major advantage, however, is the fact that data transmission is made practically instantaneous, so that the information about the ongoing precipitation is obtained at a centralized control station within minutes, and the assessment of impending flooding in urban areas, for example, or level rise in channels can be made in real time. This dramatically improves the efficacy of flood warning systems and the operation of water control systems in a variety of applications.

12.2.3 Homogeneity of Historical Precipitation Records

The technological evolution of the precipitation measurement chain also affects the statistical characteristics of historical records, first of all in terms of the homogeneity of recorded time series. Changes in the instrumentation, acquisition systems, data transmission, and post-processing algorithms indeed introduce both abrupt shifts and smoothed trends in the historical

records. These changes should be extensively documented and the related information made available as metadata, although often—especially for past years—this is not the case. While the most relevant shifts in the time series can be easily identified using suitable statistical tools, detecting smoothed trends may require a long period of measurements, since they are hidden in the natural variability of the precipitation process.

Introducing modern technology is always beneficial, and monitoring networks are continuously updated with more reliable and accurate gauges. However, in the case of precipitation, caution should be exercised and such developments accompanied by the appropriate procedures to ensure homogeneity, or at least to clearly document them in the metadata. Even the progressive introduction of the practice of instrument calibration to ensure the traceability of precipitation measurements is prone to generating inhomogeneity, since the oldest data most probably derive from poorly calibrated instruments.

Calibration issues are evident, for example, with the most common technology used to measure precipitation intensity around the world, i.e., the tipping-bucket rain gauge. As described in Sect. 12.4, this instrument is affected by intrinsic systematic mechanical biases that can be easily adjusted by means of dynamic calibration. Good knowledge of systematic sampling and mechanical errors is available in the literature, with efficient correction methodologies widely tested and discussed (see e.g., [12.14–19]).

This notwithstanding, the errors associated with the tipping-bucket device are often understated by the user, even by national meteorological services (NMS), and data are seldom corrected to account for such errors, with non-negligible consequences in terms of the quality and reliability of the derived data sets (see e.g., [12.20]). Moreover, the time series recorded at each location would experience an artificial climatic trend toward increasing climatological precipitation if mechanical errors affecting historical data were systematically neglected. Since rain gauge manufacturers are progressively distributing dynamically calibrated instruments and smart interpretation algorithms embedded in the data logger, the risk of introducing artificial trends in rainfall time series is far from just academic.

Finally, the reduction of the time resolution of precipitation intensity measurements increasingly allows higher intensity values to be measured that were also present in the past but had been smoothed by the measurement process itself. This might support the false notion that precipitation intensity is increasing at a given location, when in fact the improved measuring capabilities are simply enabling a better representation of the precipitation process at a finer timescale.

12.2.4 Instrument Testing and Intercomparisons

The history of instrument intercomparisons in the case of precipitation measurements dates back significantly to past centuries, experiments in the field being reported by Stow [12.21] and recently by Goodison [12.22]. This is in line with the well-established awareness of the relevance of intercomparison in atmospheric sciences. Father Francesco Denza, member of the Italian Meteorological Society, stated already in 1872 that:

...in order that meteorological studies produce advantages for human beings ...it is not only necessary to have lots of observatories and observations/measurements be done with intelligence and accuracy, but it is moreover requested a meteorological investigation with same methodology and with well compared instruments.

An overview of the list of WMO intercomparisons of precipitation gauges, including the reference standard measurement used and the results obtained, and a short description of each intercomparison was provided by [12.23]. Early international rain gauge intercomparison efforts were focused on accumulated amounts of precipitation, low-intensity events (including solid precipitation), and sometimes only on qualitative rainfall intensity (*RI*) information (light, moderate, and heavy). The *International Comparison of National Precipitation Gauges with a Reference Pit Gauge* [12.24] and the *WMO Solid Precipitation Measurement Intercomparison* [12.22] were conducted comparing only the accumulated amounts of precipitation. Precipitation intensity was first investigated in the *WMO Intercomparison of Present Weather Sensors/Systems* [12.25], but this intercomparison did not focus in particular on quantitative values, and precipitation intensity was reported as a qualitative parameter (light, moderate, heavy).

The latest international intercomparison efforts were designed to assess and compare quantification and catching errors for both catching and non-catching types of rainfall intensity gauges, with an emphasis on high rainfall intensity.

Following the recommendations of the WMO/CIMO Expert Meeting on Rainfall Intensity held in Bratislava, Slovakia, in 2001, the WMO first organized a laboratory intercomparison, followed by a field intercomparison. Only catching-type instruments were considered for the laboratory intercomparisons, while both catching and non-catching types were included in the field intercomparison.

In September 2004, The WMO Laboratory Intercomparison of Rainfall Intensity (*RI*) Gauges was launched simultaneously in the laboratories of the Royal Nether-

lands Meteorological Institute, Météo-France, and the Department of Environmental Engineering (University of Genova, Italy). As recommended by the thirteenth session of the Commission for Instruments and Methods of Observation (CIMO-XIII), Bratislava, Slovakia, 23.09.–03.10.2002, a standardized procedure for generating consistent and laboratory-reproducible flow rates for use as the laboratory reference rainfall intensity was developed for calibration of catching-type gauges. All participating instruments, manufactured in various countries, were catching-type gauges, and a pair of instruments was available for each type. The main objective of the intercomparison was to test the performance of different types of precipitation gauges based on different measuring principles under documented conditions. Results can be found in the final report [12.26].

To ensure the continuity of the performance assessment, a Field intercomparison (2007/2009) was organized, where the instruments already tested in the laboratory were given priority. The results reported an estimation of the overall operational accuracy to be expected in the measurement of *RI* in the field and can be found in the final report of the intercomparison [12.4] and in various published papers [12.27–30].

The WMO/CIMO agreed in 2010 to organize an intercomparison for assessing the impact of automation on the measurement of snowfall, snow depth, and solid precipitation in cold climates, dubbed the WMO Solid Precipitation Intercomparison Experiment (WMO–SPICE). The SPICE objectives focus on the use of automatic instruments for measuring and reporting:

- Precipitation amount, over various time periods (minute, hour, day, season), as a function of the precipitation phase, with a focus on solid precipitation
- Snow on the ground (snow depth); as snow depth measurements are closely tied to snowfall measurements, the intercomparison planned to investigate the linkages between them.

SPICE provides guidance on the use of modern automated systems for measuring solid precipitation amount and snow depth, and recommends appropriate automated field reference system(s) for the unattended measurement of solid precipitation in cold climates. Recommendations are presented for adjustments to account for the undercatch of solid precipitation due to gauge exposure as a function of variables available for an operational site such as wind, temperature, and precipitation type. Additionally, the sources and magnitudes of errors due to instrument characteristics, field exposure, shielding, environmental conditions, and data processing methods are investigated. The final report of SPICE was published by WMO in December 2018 [12.31].

12.3 Theory

Precipitation is measured using various methods, and the theory behind precipitation measurements encompasses basic mechanical, electromechanical, optical, and acoustic principles.

12.3.1 Measurement Principles and Accuracy

Many types of instruments and measurement techniques are in operational use. Because of the extended experience, most of these techniques are well described and understood, but new instruments are appearing and still need deeper testing and investigation [12.26]. Recommendations on standardization of equipment and exposure are well documented [12.1], while procedures for instrument calibration have been proposed in the literature. The basic classification of precipitation gauges is between catching and non-catching instruments. In the first case, precipitation is collected into a container for a given period before water is conveyed to the sensor and measured. They may or may not include a funnel to convey the collected precipitation toward a nozzle for dispensing water to the sensor unit. In non-catching instruments, the precipitation flux is *sensed* when crossing or impacting on a given section, or volume, of the atmosphere in the vicinity of the ground surface. Instruments of the first family are generally based on gravity-related measuring principles (weighing, tipping, floating devices), while the second group includes optical, acoustic, and microwave principles.

All instruments are subject to both systematic (bias) and random measurement errors (Sect. 12.6), depending on the construction of the device, the measuring principle, the algorithms used for data interpretation and correction, etc. The errors themselves can be classified into catching- and counting-type errors.

The errors due to the weather conditions at the collector and those related to wetting, splashing, and evaporation processes are referred to as catching errors. They all indicate the ability of the instrument to collect the total amount of water falling over the projection of the collector's area at ground level. Non-catching instruments (which are based upon a contactless measurement) have no collector and may also show *catching* errors, which in this case implies that the instrument is not able to let the full amount of precipitated water pass through the area or volume where the measurement is taken.

Counting errors are related to the ability of the instrument to correctly quantify the amount of water that is collected or detected by the instrument. They can be experienced in both catching and non-catching types of instruments, although in the latter case, the assessment

of such errors is very difficult and hard to be performed in controlled laboratory conditions. These errors may originate from the very different aspects of the sensing phase, since the available instruments differ, for example, in the measuring principle applied, construction details, or operational solutions.

The impact of such errors on the overall accuracy of precipitation measurements at a site also varies in relation to the type of precipitation (solid, liquid, or mixed) and the range of precipitation intensity. The counting inaccuracies generally have a much stronger impact on the measurement of liquid precipitation, with sampling errors generally affecting low rates and mechanical or dynamic errors mainly affecting higher rain rates. The catching capabilities of the gauge assembly are a major issue in the case of solid precipitation measurements or whenever the rate of liquid precipitation is very low [12.32].

The impact of inaccurate measurements on the results of scientific investigation in precipitation-related fields is not yet fully clear nor quantified [12.33]. With the exception of a few dedicated papers (e.g., [12.20, 34–36]), or papers dealing with the analysis of measurement errors themselves [12.14–17, 37], the issue of how deeply the accuracy of the data sources actually affects the obtained results is rarely addressed. The scarce attention paid to the quality of data often gives rise to serious doubts about the significance of the experimental results made available in the literature. Obviously the effects will not be dramatic in all cases, since the error propagation could be negligible as well, depending on the application.

Nonetheless, scientific soundness requires that all possible uncertainties be properly taken into account, and it is therefore clear that the quality of basic data sources—such as precipitation measurements—should not be an exception. In addition, certified accuracy is needed for meteo-hydrological networks operating within the framework of a quality assurance system.

12.3.2 Volumetric Methods

Precipitation accumulates on the surface of the ground whenever it is not allowed to infiltrate (impervious surfaces) or run away along the terrain slope because of gravity forces (flat or concave surfaces). Accumulation enables the preservation of the water in natural or man-made reservoirs in order to exploit it for various purposes. One such purpose is precipitation measurement, and volumetric methods simply detect how much water is cumulatively collected within a given period in a small reservoir of known geometry.

Water Level

Measurements based on the water level employ a calibrated container, usually a cylinder, used to collect precipitation. The level reached by the water surface is periodically measured to obtain the volume of water accumulated in a given period, based on the known cross section area of the container. Since the method is quite trivial, the earliest measurements of precipitation (Sect. 12.2.1) were based on a direct reading of the water level accumulated in a container.

The measurement can be performed by an operator reading the level directly on a graduated cylinder or by pouring the water collected by the gauge into a reference container of known volume. Usually measurements are performed once or twice a day, then the container is emptied. Depending on the length of time between measurements and the environmental conditions (temperature, humidity), evaporation from the container can significantly affect the measurement accuracy.

An improvement of this method employs a float inside the container to measure the water level and record the data on a strip chart. In automatic precipitation gauges, the measurement of the water level collected in the container is performed by automatic sensors based on conductivity, acoustic distance, or hydrostatic pressure measurements.

Tilting Siphon

A tilting siphon is a particular method that differs from the more traditional water level measurements by employing the automatic emptying principle.

The tilting siphon mechanism consists of a bucket that collects the precipitation and a float connected to a pen that records the signal on graph paper attached to a drum. The float rises with the water level in the container and its movement is recorded by the pen. When the water reaches the top, the bucket tips over one side, and the siphon comes into operation and releases the water outward. The natural siphon recorder consists of two coaxial tubes; when the water reaches the top of the outer tube, the siphon mechanism is activated. The siphoning stops abruptly once the air reaches the top of the tube.

12.3.3 Gravimetric Methods

Gravimetric methods use the action of gravity on the collected water to detect the precipitation amount or intensity. The weight of a given water volume is exploited either directly, by measuring the induced deformation or vibration of sensitive elements, or indirectly by activating the movement of mechanical parts, releasing droplets, etc.

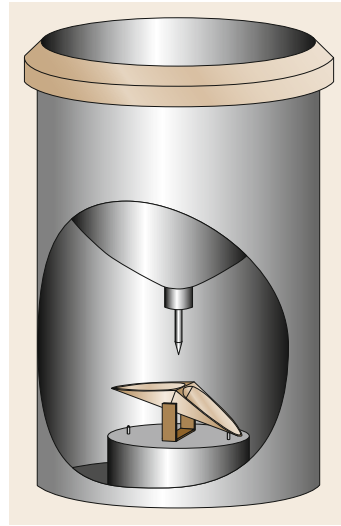


Fig. 12.1 Scheme of the tipping-bucket measuring principle

Tipping bucket

The mechanical principle of tipping-bucket gauges (TBG) was the first used to measure precipitation intensity. It consists of a tilting balance holding a bucket divided into two compartments having the same volume (Fig. 12.1). The compartments are balanced on a horizontal axis in unstable equilibrium, and two stop screws allow the initiation of the movement to be adjusted, i.e., setting the volume of water required to trigger the rotation, and avoid complete tilting on one side. The water mass content of the bucket is constant (M (g)). Therefore, by assuming the density of water $\rho = 1 \text{ g cm}^{-3}$, the corresponding volume (V (cm^3)) is derived, and consequently the corresponding accumulation height (h (cm), usually expressed in mm) is retrieved after dividing by the surface area of the collector (S (cm^2)).

When precipitation occurs, the gauge conveys the water to the twin compartments placed under the funnel through a nozzle. The balance starts moving when one compartment reaches the critical volume. During the rotation the first compartment moves to the emptying position and the second compartment moves below the water flux. The bucket takes a small but finite amount of time to tip, and during the first half of its motion, additional rain may enter the compartment that already contains the calculated amount of rainfall; therefore, this water is lost and not measured (Sect. 12.6.1). The water losses during the tipping movement result into a systematic mechanical error inducing an underestimation bias that increases with the rainfall intensity. This must be corrected by means of suitable calibration procedures (Sect. 12.6.1).

The rotation of the bucket is used to trigger a reed relay (a pen writing on a rotating chart in ancient ver-

sions) and to produce an electrical impulse per each tip as the signal output, which is then recorded by a data logger or an analogue-to-digital converter. This mechanism provides a continuous measurement process without the need of manual interaction. Given the nominal bucket volume, the total volume is calculated from the number of tips in a chosen time interval (1 min is recommended). However, the rainfall intensity is best calculated from the information about inter-tip times, obtained by recording the time stamp of each tip.

Weighing

Precipitation is collected in a bucket and the weight of the container, together with the collected water, is recorded by means of a spring mechanism or using a system of balance weights (Fig. 12.2). The weighing of the container allows the volume of water present in the gauge collector to be measured, and the precipitation rate can be calculated as the difference between the amount of water from two consecutive measurements over a given time interval.

Generally, these gauges do not use any mechanical moving part in the weighing mechanism, and only elastic deformation occurs. The weighing mechanism depends on the sensor employed in the instrument to obtain the water weight of the bucket and usually uses a balance, a load cell, or vibrating wire load sensors.

Recently, fiber Bragg grating (FBG) technology has been developed to measure the rainfall water weight. The FBG has been employed to measure the deformation of a cantilever beam induced by a collecting tilting bucket [12.38] or applied on a rubber thin film with a defined cross section area [12.39]. In the latter case, the rain weight loads the rubber film and causes the deformation of the fiber, changing the grating wavelength.

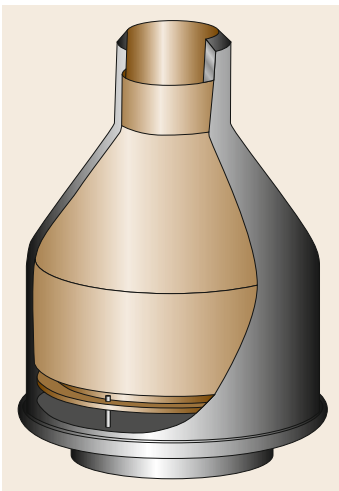


Fig. 12.2 Scheme of the weighing measuring principle

Drop Counting

In the drop-counting catching-type gauge, the precipitation collected by the funnel is conveyed to a calibrated thin nozzle, which starts dispensing droplets with a known volume. A suitable sensor, usually optical, detects the transit of each falling droplet as dispensed by the nozzle and counts the total number of droplets falling within a specific interval.

The size of each droplet depends mainly on the dimensions and characteristics of the dispensing nozzle, but also on the precipitation rate, which affects the frequency of droplets released and the drop formation and detachment process.

The volume of the droplets dispensed by the nozzle requires calibration. By measuring the dropping frequency, and possibly adjusting for the droplet volume changes with frequency, the precipitation depth (or intensity) is obtained.

12.3.4 Optical Methods

Instruments that use optical methods to measure precipitation are typically called disdrometers, and their technology is based mainly on infrared or laser sensors (Fig. 12.3). These methods are able to sense the precipitation particles falling through a measuring area, detect the type of precipitation (rain, snow, hail), measure the number, transit time, and dimensions, and provide the precipitation rate or amount by integrating over the to-

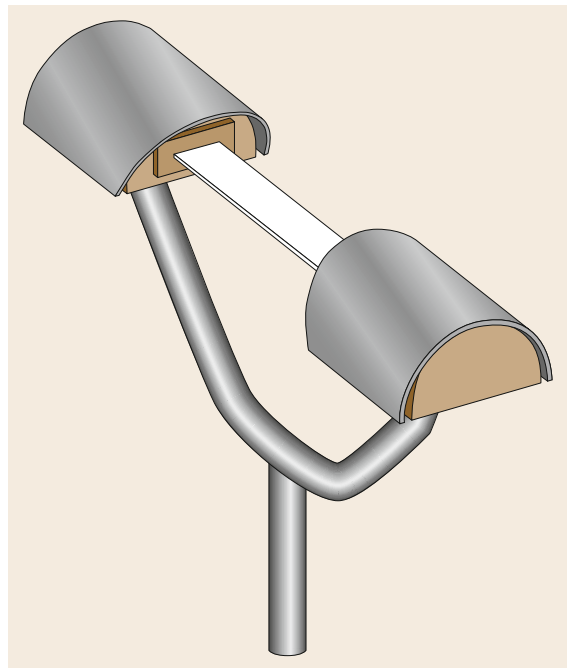


Fig. 12.3 Scheme of the optical measuring principle

tal number of particles in a given time window. The type and size of particles are usually obtained by measuring their fall velocity and assuming a fixed relationship between the fall velocity, size, and density.

Infrared Methods

The infrared gauges measure precipitation by detecting the irregularities in the infrared light beam of the sensor. These irregularities, known as scintillations, are induced by the precipitating particles falling within the infrared sampling volume; by measuring scintillation intensity, the sensors provide precipitation information.

Laser Methods

Optical disdrometers based on laser technology are composed of one or two thin laser light sheets to detect particles crossing the beam. Each particle falling within the laser beam occludes part of the transmitted laser light and decreases the light intensity in proportion to the particle diameter.

12.3.5 Other Methods

Impact Methods

These methods exploit the kinetic energy of the falling droplets impacting on the exposed surface of the instrument. A plastic or metal membrane is used at the measurement surface to sense the impact of single precipitation particles. In some systems, the mechanical movement of the membrane is transduced into an electrical signal by an attached moving coil system. In other solutions, the amplitude and the frequency spectrum of vibrations generated by precipitation particles hitting the membrane are detected and analyzed to determine the number and size of the particles, and therefore the

precipitation amount (or intensity), over a given time window.

Thermodynamic Methods

These methods employ the thermodynamic effect of the latent heat of water to obtain the measurement of both solid and liquid precipitation intensity.

The concept involves monitoring of the electrical power needed to maintain the sensor's temperature constant and high enough to melt and evaporate the snow or rain. The power provided to the sensor depends on the amount of water on the collector, while it is affected by ambient temperature, wind, and humidity conditions. Two sensor surfaces are used, one designated to collect the particles and facing upward, and one serving as the reference, facing downward to avoid collecting any precipitation. The two sensors are influenced by the same temperature, wind, and ambient humidity conditions, but only the upper one is exposed to precipitation. The difference in the power supplied to the twin sensors is attributed to the latent heat absorbed by precipitation, and is employed to determine the precipitation rate.

Microwave Methods

The microwave disdrometers use small radars to acquire the spectrum of the signal backscattered by falling particles. The intensity of the backscattered signal is related to the number of particles, and using a Doppler shift, the fall velocity of particles can be obtained.

Fourier processing of the signal is typically executed by a processor that calculates average spectrum, retrieves drop size distribution from this spectrum, and finally calculates the accumulated precipitation over a given time resolution.

12.4 Devices and Systems

The various measuring principles are exploited by different types of instruments, each of them characterized by specific measurement biases and uncertainties.

12.4.1 Catching-Type Gauges

Catching-type instruments are the traditional and by far the most common type of instrument employed worldwide for the measurement of atmospheric precipitation. They are subject to catching errors, since their capability to collect the amount of precipitation that would reach the equivalent surface area at the ground in the absence of the instrument is seldom guaranteed, and their collection efficiency may be low in the presence of wind. They are also subject to counting errors depending on the measuring principle adopted.

Storage Gauges

The storage gauge consists of a container with a known geometry, and the measuring principle is based on the water level. The most common gauges have a cylindrical shape, but different shapes, especially with reduced section area at the bottom, are used to enhance the measurement of light precipitation events (e.g., see Fig. 12.4).

The gauges are made of metal, glass, or plastic. To permit the reading of the water level by the operator, a transparent gauge is preferable; otherwise a transparent window of glass is provided in many metal buckets. Graduation marks are drawn on the container to allow the reading of the water level.

Since these gauges are able to measure the volume of water inside the collector, they are not suitable in the



Fig. 12.4 Plastic storage gauges developed for agricultural purposes (WMO-METAGRI project; photo © Mattia Stagnaro)

case of solid precipitation. Although deicing liquid may be employed to melt snow precipitation, these instruments are not recommended for use in cold regions.

If the measurement is performed by an operator, the reading of the water level is taken once or twice a day. When automation is employed by introducing different methods to measure the water level inside the gauge, the time resolution increases and can reach the 1 min recording time interval recommended by WMO. The measurements taken by this type of rain gauge are affected by evaporation losses, especially in the case of low recording time resolution.

One particular type of capacitive rain gauge measures the water collected by storing it in a deep cylinder that contains two electrodes acting as the plates of a capacitor, the water between the plates performing the role of dielectric. By including the capacitor in a tuned circuit, the water depth can be measured. It must be emptied periodically.

Tipping-Bucket Gauges

Tipping-bucket rain gauges (TBRs) are widely employed in national meteorological services worldwide to measure rain and snow depth and the associated precipitation intensity. The reasons for extensive use of this type of instrument include their relative ease of maintenance and limited production costs.

The instrument uses a metallic or plastic twin bucket balance to measure the incoming water. It is equipped with a funnel that collects and conveys the water through a nozzle in an alternating manner into the two compartments of the tipping bucket. The gauge typically has a cylindrical shape (Fig. 12.5), although aerodynamic shapes were recently developed to reduce the impact of wind on the collection efficiency of the



Fig. 12.5 Tipping-bucket gauge (photo © Emanuele Vuerich)

gauge (Sects. 12.6.1 and 12.6.3). The tipping of the bucket moves a magnet that triggers a reed relay contact and is recorded by a data logger.

Although there is no standard for the construction of precipitation gauges, recommendations from the WMO and the many years of experience with tipping-bucket instruments have led to typical solutions (now widely accepted), especially for the size of the collector area and the volume of the bucket compartments. Actually, these two construction characteristics are related to each other through the instrument sensitivity, which is generally required to be between 0.1 and 0.5 mm, with 0.2 mm being the most common. The collector area is usually between 200 and 1000 cm². For a tipping-bucket instrument with a 400 cm² collector and sensitivity of 0.2 mm, the bucket size would be 8 cm³.

The shape of the bucket and the collector vary with the manufacturer but the bucket size is quite standardized. It is indeed a sort of compromise between a very small size to limit sampling error during low-intensity precipitation, and a large size to better handle high-intensity events.

The main advantage of tipping-bucket gauges is the automatic emptying principle: when the bucket tips, the water is released outside the instrument body through dedicated apertures. However, the presence of moving parts in the sensor requires periodic maintenance of the instrument (Sect. 12.8).

Weighing Gauges

A weighing gauge (WG) consists of a bucket, usually made of metal or plastic, used to collect and measure liquid and solid precipitation by means of a weighing principle. This type of gauge is widely used to measure solid precipitation because it does not require the snow



Fig. 12.6 Weighing gauge (photo © Emanuele Vuerich)

to be melted before taking the measurement. In the absence of an automatic emptying system, the dimensions of the container are usually larger than for other instruments, and this leads to the common *chimney* shape, with a larger section area at the bottom (Fig. 12.6). The capacity of the bucket can vary with the manufacturer and ranges from 250 to 1500 mm. Low-capacity models should be avoided in areas where large accumulation may occur over a short period of time. The addition of oil or other evaporation suppressants inside the container allows a film to be formed over the water surface to minimize evaporation losses (Sect. 12.6.1).

The large capacity of the bucket has the objective of minimizing the emptying operation, which is manually performed in many cases. Some instruments use an automatic emptying principle based on a siphon. A small automatically emptying weighing gauge has recently been developed, consisting of a balance that measures the weight of the water collected in alternating fashion in the two compartments of a tipping bucket (conveyed through a funnel and a nozzle). When the bucket tips, the water is released outward, and the empty compartment is then placed under the nozzle to be filled and weighed. This automatic emptying principle leads to a reduction in the size of the instrument and ensures that the amount of weighted water is small and constant, therefore increasing the resolution of the gauge. However, these emptying principles result in underestimating precipitation during the emptying process, which can be long when using the siphon or short but frequent in the tilting-bucket gauges. Moreover, the presence of moving parts, typical of tipping-bucket rain gauges, requires additional maintenance operation. Note that the sensitivity of the weighing system can be very high (e.g., 0.01 mm), although the actual gauge sensitivity is generally lower due to the need to eliminate noise from the high-resolution raw signal. The resolution of the transducer affects the noise filtering ef-

iciency, resulting in lower sensitivity that in many cases is comparable to that of tipping-bucket gauges.

Drop Counter

The catching-type drop-counting gauge consists of a funnel that collects the precipitation and conveys water toward a calibrated nozzle, which starts dispensing droplets within an internal chamber before releasing them outside the instrument. An optical sensor is located below the nozzle and detects each falling drop. The rainfall intensity can be calculated from the drop releasing frequency by assuming a constant volume for the calibrated droplets. A recent study [12.40] using dynamic calibration tests (Sect. 12.6.2) revealed that the volume of the released droplets varies with the drop frequency. Traditional calibration of this instrument, assuming a constant volume of the droplets as declared by the manufacturer, is not compliant with WMO requirements. Instead, by using the dynamic calibration curve to adjust the drop size according to the detected frequency, the performance can be improved to meet the WMO recommendations.

The resolution of drop-counting gauges depends on the size of the droplets generated by the nozzle, in the order of 0.005 mm of precipitation, and is suitable for the measurement of light precipitation rates. Indeed, an operational limit of this type of instrument is given by the rainfall intensity at which the water flux from the nozzle starts to be continuous or irregular. The measured frequency then abruptly decreases, and very high inaccuracies result. A stand-alone installation is therefore discouraged, and a collocated rain gauge is required to avoid significant underestimation of severe rainfall intensity.

12.4.2 Non-Catching-Type Gauges

These instruments differ from traditional ones in that the precipitation flux is not collected in any container, but just *sensed* when crossing or impacting a given section, or volume, of the atmosphere in the vicinity of the ground surface. Non-catching instruments are drawing increasing interest from national weather services (NWS) due to the lower maintenance required and unattended operation. They have a number of advantages over the more common catching-type gauges, including the possibility to provide information beyond precipitation intensity alone (e.g., drop size distribution, visibility, etc.), and are especially suitable for automatic weather stations. Having neither a funnel nor a collector, their calibration and uncertainty evaluation are more difficult than for catching-type gauges, since direct comparison with an equivalent reference flow rate is not possible.

Optical Disdrometers

Optical disdrometers consist of a laser or infrared emitter, a receiver, and a digital signal processing unit (Fig. 12.7). The distance between the emitter and the receiver is usually of the order of some tens of centimeters, and the measuring beam is a few centimeters wide. This sensor measures the diameter and velocity of hydrometeors and, from these measurements, identifies the type of precipitation and calculates rainfall rate and amount, reflectivity, visibility, and drop size distribution. The diameter of the particles typically ranges between 0.2 and 8 mm and allows the volume of each droplet to be derived. Consequently, the rainfall intensity can be directly calculated by integrating over the number of particles detected in a given time period, usually ranging from 15 s to 1 min. Depending on the diameter and fall velocity, measurements are grouped into different precipitation classes.

When hydrometeors cross the sensing volume of the disdrometer, the measuring beam is partially obscured. The shadow on the receiver leads to a decrease in the voltage generated by the receiver's photodiode. The digital signal processing unit monitors the photodiode voltage and calculates the diameter of the drop from the minimum observed voltage during the passage of the drop. The velocity is calculated from the duration of the voltage reduction by dividing the sum of the diameter and beam breadth by the drop residence time.

The R resolution is typically between 0.001 and 0.005 mm h⁻¹, so it is possible to measure even very light rain (drizzle events). The maximum detectable precipitation rate varies with the instrument, and ranges from 200 to more than 1000 mm h⁻¹.

The collision of droplets is a possible error source; in that case, droplets are detected as a single *macro-drop*, leading to a systematic overestimation of the water volume. In order to reduce this error, a statistical correction is applied. Measurement errors can also occur when droplets cross the rim of the light sheet; in this case, the droplets are interpreted as smaller particles than they are in reality, causing an underestimation of the volume.

Impact Disdrometers

Impact disdrometers can be divided into two categories: acoustic disdrometers and displacement disdrometers.

Acoustic disdrometers record an electrical signal using a piezoelectric sensor whenever a drop falls on a diaphragm. Based on the relationship between kinetic energy and drop size, this electrical signal is converted into kinetic energy via the measured acoustic energy. The accuracy of drop size estimation is limited due to differences in the acoustic response from the various parts of the diaphragm. The instrument is also limited with regard to measuring small drops, because



Fig. 12.7 Optical non-catching-type gauge (photo © Emanuele Vuerich)

the diaphragm is not sensitive enough and because of the splashing. In addition, higher intensities are hardly measured due to the background noise, which reduces the measurement accuracy.

Displacement disdrometers translate via magnetic induction the energy generated by drops falling on the top surface and estimate the sizes of rain drops by analyzing the associated electrical pulses. The instrument consists of a surface exposed to precipitation and connected to a magnet that, after displacement induced by the raindrop impact, slides within a coil, activating magnetic induction.

Both acoustic and displacement disdrometers are designed to measure liquid precipitation, since the energy of the droplets is directly proportional to the mass and density of the water droplets. Snowflakes and hailstones, on the other hand, have a completely different impact on the sensors, and lead to underestimation or overestimation of the precipitation measurements. A proper calibration of impact disdrometers was recently proposed with the aim of adapting this type of instrument for measuring hail precipitation events [12.41].

Thermodynamic Sensor

The thermodynamic sensor is a new type of instrument recently developed to measure light or solid precipitation [12.42]. The system consists of two identical heated aluminum plates, one facing upward to collect the precipitation, and the other facing downward to serve as a reference. The lower plate is insulated from



Fig. 12.8 Microwave precipitation gauge (photo © Emanuele Vuerich)

the top plate and serves as a reference because it is only affected by wind and ambient temperature and not by precipitation. The two plates are heated to nearly identical constant temperatures (above 75 °C), hot enough to melt large snowflakes in a few seconds. The plates are

maintained at a constant temperature during wind and precipitation conditions by either increasing or decreasing the supplied power. During precipitation, the top plate cools because of the melting and evaporation of the hydrometeors, and the difference between the power required to heat the top plate and the bottom one is proportional to the precipitation rate. The two plates are usually located at a height of 2 m above the ground. The diameter of the plate is large enough to permit collection of falling rain or snow particles and small enough that power demand during heavy precipitation events and high wind speed is not too high.

To convert the power difference to a liquid-equivalent rate, a theoretical conversion factor is calculated, assuming that 100% of the heat of vaporization/sublimation from the precipitation is transferred to the instrument. The conversion factor is based on the area of the plate, the heat capacity of water, the density of water, and the latent heat of sublimation and evaporation. The shape of the instrument body is designed in order to minimize the wind-induced undercatch [12.42], which is however quite low, and was quantified in a recent study [12.43]. This instrument provides precip-

Table 12.3 Advantages and disadvantages of the different methods

Device	Advantages	Disadvantages
Storage gauge (manual)	No power supply, no moving parts, low cost, and easy operation	Not suitable for solid precipitation, reading of the water level only once or twice a day, evaporation losses, operator-related reading uncertainty, limited capacity (requires manual emptying)
Water level gauge	Wide range of intensity, high temporal resolution	Not suitable for solid precipitation, lower sensitivity, limited capacity (requires manual or automatic emptying)
Weighing gauge	No funnel required, no mechanical moving parts. Liquid and solid precipitation. Wide range of intensity, high temporal resolution. High accuracy after dynamic calibration	Influence of dynamic response. Manual emptying: large size, the shape enhances the wind effect on the collection. Periodic emptying maintenance. Automatic emptying: no measure while emptying
Tipping-bucket gauge	High accuracy after dynamic calibration, high temporal resolution. Low cost and simple mechanics. Long-term experience available. No emptying required, small size	Upper intensity limits depending on sensitivity, sampling errors. Heating required to measure solid precipitation. Maintenance of mechanical parts and to prevent clogging
Drop counter	High sensitivity, high accuracy after calibration for low precipitation intensity	Upper intensity limits, not suitable for stand-alone installation. Requires maintenance to prevent clogging
Optical disdrometer	Derives precipitation intensity from particle diameter and velocity measurements and provides additional information such as visibility and particle size distribution (PSD)	High cost. Error due to drop collisions and when particles cross the rim of the light sheet. No standardized calibration available
Impact disdrometer	Small size, low cleaning maintenance	Influence of the drop impact position on the surface. Noise for high precipitation intensity. Not suitable for small drops, snowflakes, and hailstone measurements. No standardized calibration available
Thermodynamic sensor	Small size, suitable only for low precipitation intensity	Additional power consumption. No standardized calibration available
Microwave sensor	Low cleaning maintenance. Provides additional information on columnar profile of vapor content, non-raining cloud liquid water, and temperature	High cost, additional power consumption. No standardized calibration available

itation measurements every minute and can accurately measure rainfall rates up to 35 mm h^{-1} .

Microwave Sensor

Since the 1960s, microwave-based technologies have been developed and improved in both the communication and meteorological fields. Ground-based microwave radiometry (Fig. 12.8) has its traditional applications in meteorology in the estimation of columnar profiles of vapor content, non-raining cloud liquid water, and temperature [12.44].

Precipitation measurements employing microwave sensors have appeared in recent decades, and are based on the signal power reduction through the atmosphere during a precipitation event.

The attenuation and scattering of the sensor emissions are related to the precipitation rate, but also depend on the physics of the precipitation particles, such as the liquid or solid phase and the different particle sizes, but the frequency of the emitting signal also has a fundamental role [12.44, 45]. Radar disdrometers have *RI* resolution up to 0.1 mm h^{-1} .

12.5 Specifications

Following the outcomes of the *WMO Field Intercomparison of Rainfall Intensity Gauges* [12.4, 27] and the decisions of the WMO CIMO (Annex I and II of the CIMO XV Session Report, Helsinki, Finland, 02.–08.09.2010), the CEN (Comité Européen de Normalisation) Technical Report no. 16469 [12.46] recommended the specifications presented below. Terminology and related concepts are also consistent with WMO [12.1], *ISO Guide to the Expression of Uncertainty in Measurement* [12.47] and the *International Vocabulary of Metrology* [12.48].

Specifications for precipitation measurement instruments depend on the intended use of the derived information (Sect. 12.8); therefore, recommendations are reported here with reference to the highest level of performance and do not necessarily apply to all applications. Network managers aiming at a broad spectrum of users may need to conform to such specifications in order to meet the requirements of the most demanding application. Those managing a single station (or a small network) for a specific use may reduce the required performance to fit their need.

12.5.1 Specifications for Catching-Type Gauges

Catching-type gauges should follow the recommendations detailed in the WMO Guide no. 8 [12.1].

12.4.3 Comparison of the Methods

Automatic stations have replaced manual measurements in many developed countries, while manual methods remain common practice in less developed regions of the world. Storage gauges are indeed the most widely used instrument for rain depth measurements, while tipping-bucket gauges are the most common for rainfall intensity measurements. The low cost, easy operation and maintenance, and the many years of experience available with tipping-bucket instruments are the main reasons for their large-scale exploitation. Weighing gauges are mainly used in regions where solid precipitation is expected, but their cost is higher and maintenance is not easy, although the absence of mechanical moving parts is an advantage. Non-catching-type gauges are the new frontier of precipitation measurements and, notwithstanding their high cost, are particularly well suited for automated weather stations, and provide additional valuable parameters such as particle size distribution, precipitation type, and visibility (Table 12.3).

The minimum list of technical parameters provided below should be included in the user manual of each instrument, and sufficient advice on the choice of output values should be provided to the user to meet different applications:

- Measurement range
- Delay time
- Linearity
- Instrumental measurement uncertainty, for the whole measurement range
- Resolution
- Step response time
- Threshold
- Time constant for those instruments classified as first-order response instruments
- Internal calculation cycles (if any) and data reporting interval.

Further recommendations apply to specific instrument technologies. Tipping-bucket rain gauges should be corrected to compensate for the inherent underestimation and the sampling error at high and low precipitation rates, respectively. Software correction algorithms using the time stamp of each tip and applying dynamic calibration curves provide the best results [12.19]. The internal clock (or the clock of the data logger) must be checked and possibly adjusted automatically on a daily basis, at least to the nearest tenth of a second.

For weighing gauges, in the case of precipitation intensity measurements, the time constant should be less than 1 min. Therefore, any filtering algorithm used to reduce the noise in processing the data produced by the weighing device should not increase the response time of the instrument. It is important that the information provided about precipitation intensity and total accumulation be consistent (accumulated precipitation is obtained by integrating precipitation intensity over time), and both values reported separately.

In any case, information about the achievable measurement accuracy must be provided in the technical documentation. For operational rainfall intensity measurements, the achievable accuracy is indicated by WMO [12.1] in the following terms:

- Under laboratory, constant flow conditions: 5% above 2 mm h^{-1} and 2% above 10 mm h^{-1}
- In field conditions: 5 mm h^{-1} up to 100 mm h^{-1} and 5% above 100 mm h^{-1} .

A calibration certificate from an independent third party (possibly a certified or WMO-recognized laboratory) should be included with each individual instrument. The certificate must include a description of the calibration procedure and results to check compliance with the relevant recommendations, and should document the traceability of the reference used, the environmental conditions (such as temperature, humidity, etc.), and the time frame used for averaging the precipitation signal.

In order to reduce the wind-induced undercatch of precipitation particles, the aerodynamic shape of the gauge should minimize the deformation of the wind field above the gauge orifice, as suggested by WMO [12.1] and supported by [12.49] using numerical simulation. The use of windscreens is advisable, especially for solid precipitation, but the positive effect of the shield should be documented by means of wind tunnel measurements or computational fluid dynamics simulations. Correction of the wind-induced undercatch can be applied according to the precipitation intensity, wind speed, and environmental temperature, as sug-

gested by [12.50] and [12.51], but the raw data should be preserved as well.

Precipitation intensity at 1 min should be measured and used for further analysis only if all 1 min data are transmitted and used (1 min intensity should not be used in a temporal sampling scheme, i.e., one synoptic measurement every hour or 3 h, as a single 1 min value is not representative of a longer period of time).

12.5.2 Specifications for Non-Catching-Type Gauges

At the time of writing, no specification for non-catching-type gauges has been provided by WMO. However, the following additional specifications are recommended. The minimum list of technical parameters provided below should be included in the user manual of each instrument, and sufficient advice on the choice of output values should be provided to the user to meet different applications:

- List of the measured quantities, (precipitation particle diameter, terminal velocity, precipitation intensity, etc.)
- Measurement range of each measured quantity
- Delay time of each measured quantity
- Linearity of each measured quantity
- Instrumental measurement uncertainty, for the whole measurement range
- Resolution of each measured quantity
- Step response time of each measured quantity
- Threshold of each measured quantity
- Time constant for those instruments classified as first-order response instruments
- Internal calculation cycles (if any) and data reporting interval of each measured quantity.

Precipitation intensity should be expressed in the usual measurement units (mm h^{-1}), and any classification by intensity intervals should not replace the numerical value. The measurements of the precipitation particle diameter, counting, terminal velocity, precipitation intensity, and the total accumulation should be consistent, and reported separately.

12.6 Quality Control, Uncertainty, and Calibration

The increased need for traceability and comparability of precipitation measurements collected from various sites and monitoring networks worldwide demands greater attention to their overall quality and accuracy. Quality control is the ultimate tool to prevent the propaga-

tion of errors and to ensure the traceability of precipitation measurements to international standards, so that precipitation data from different sources can be soundly compared and used in a variety of applications.

12.6.1 Precipitation Measurement Biases and Uncertainties

Both instrumental and environmental factors may cause biases and uncertainties in precipitation measurements (e.g., the systematic mechanical bias of TBRs, the dynamic response of WGs, the wind-induced undercatch). Calibration and correction may overcome instrumental and environmental measurement biases, but they themselves are subject to uncertainties.

Further sources of uncertainty arise from the field operation of precipitation measurement instruments and can hardly be quantified unless undertaking suitable instrument intercomparison campaigns. In order to support network managers in evaluating the quality of their installations in the field, the Siting Classification for Surface Observing Stations on Land was developed as a common ISO/WMO standard. It was published as ISO standard 19289:2015 (EN) [12.52], and by WMO in the *Guide to Instruments and Methods of Observation* [12.1] (Volume I, Chapter 1, Annex 1.D). The siting classification allows the user to assess how well the siting of an instrument meets the siting recommendations provided in the Guide.

Instrumental Biases

Instrumental biases affect all types of precipitation gauges, with different characteristics depending on the specific measurement principle adopted.

Tipping-bucket gauges are known to suffer from systematic mechanical biases; they underestimate rainfall, especially at high precipitation intensities, because of the amount of water that is lost during the tipping movement of the bucket. Although this can be remedied by dynamic calibration (performed over the full operational range of precipitation intensity values as described below), usual operational practice in hydro-meteorological services and instrument manufacturing companies relies on single-point calibration (obtained at a single reference intensity as described below). This derives from the assumption that dynamic calibration has little influence on the total recorded precipitation amount, although it is essential to reflect the actual pattern of precipitation intensity over time. The related biases, known as systematic mechanical errors, result in an overestimation at lower intensities (depending on the single-point calibration operated) and underestimation at the higher precipitation intensities. To ensure that this bias is independent of the rainfall intensity, some tipping-bucket gauges are equipped with a siphon able to deliver water to the bucket at a constant rate during tilting. This would imply that the bucket is always operated at the same flow rate but with different frequencies depending on the rainfall intensity. In this case, single-point calibration is sufficient to limit the bias.

Tipping-bucket gauges are also subject to the unbalancing of the buckets that can be corrected by reproducing a constant flow rate for a sufficient duration in laboratory conditions and by recording the time between consecutive tips (inter-tip time). If the inter-tip time is not regular, the two buckets are not balanced, and the volume collected in the two buckets is not the same. By acting on the stop screws, the bucket position is adjusted until accurate balancing is obtained.

Finally, tipping-bucket gauges are affected by sampling errors due to the discrete nature of the measurement principle. The hypothesis at the basis of the measurement principle is that precipitation is constant between consecutive tips. Sampling errors strongly influence the assessment of light precipitation events, which commonly results in recording many isolated tips, resulting in substantial overestimation of the precipitation rate at the corresponding time step and underestimation in the contiguous steps. The presence of a certain amount of water previously stored in the bucket before the start of a new event and the amount that remains inside the bucket at the end of the event may affect the measurement of the precipitation rate.

A fundamental characteristic of weighing gauges when measuring precipitation intensity is the response time, which leads to measurement errors (systematic delay due to the filtering algorithm adopted to reduce the signal noise). The response time is of the order of 6 s to a few minutes depending on the gauge design and model. The actual sensitivity of weighing gauges can be very different from gauge to gauge and depends on the transducer resolution.

Catching-type drop-counting gauges are subject to biases due to the changing size of drops generated by the nozzle with precipitation intensity, while the counting system assumes a fixed volume of the droplet. The volume actually varies in a nonlinear fashion with precipitation intensity, and a corresponding bias arises in measurements that may reach 10–20% depending on the instrument design [12.40].

Catching-type rain gauges are affected by so-called catching errors related to wetting and splashing. The associated losses are about 2–10% and 1–2%, respectively, as reported by [12.32]. Wetting losses depend on the geometry and material of the gauge collector and container, the amount and type of precipitation, and the number of events during the time needed to dry the container. For solid precipitation, the loss is smaller than for liquid precipitation, because the collector is usually wetted only once during snowmelt.

The WMO Guide no. 8 [12.1] recommends that the collector be designed to prevent precipitation from splashing in and out. This can be achieved if the vertical wall is sufficiently deep and the slope of the funnel is sufficiently steep (at least 45%).

Environmental Factors

Catching errors also include the effects of evaporation and wind on precipitation measurements.

The first measurements of evaporation losses started in the nineteenth century, as reported by [12.32]. They were based on the difference between the amounts of precipitation simultaneously measured in two storage gauges: one observed daily and the other observed monthly. The annual accumulation was corrected using the difference between the two measures, but the wetting losses from daily emptying of the container were also included; therefore, the method could not be used to single out the evaporation losses. Also, differences in readings from a pit gauge (with the orifice located at the level of the surrounding ground) and an elevated gauge occur due to differences in the temperature of the collected water, and thus the pit gauge is not a good reference for estimating evaporation losses.

Since the end of the nineteenth century, the method employed to assess evaporation losses has involved measuring the evaporation rate of simulated precipitation during precipitation-free periods. As an alternative, comparing the total accumulation from a storage gauge with the time integral of precipitation intensity measurements from a weighing gauge provides a good estimate of the evaporation losses. Weighing gauges may provide measurements of evaporation as negative precipitation values should the weight of the water collected in the container decrease.

Evaporation losses are season-dependent and usually quite low, especially for rain intensity measurements: according to the WMO Guide no. 8 [12.1], they may account for less than 5% of the total precipitation amount. The [12.1] also suggests that, in storage and weighing gauges, errors associated with evaporation are minimized by using an oil surface layer in the container.

Wind is the main environmental factor affecting precipitation measurements. The effects of the immediate surroundings of the measurement site on the wind field can give rise to local variations in precipitation. To reduce the effect of wind on the measured precipitation, the choice of the measurement site, including the location of precipitation gauges within the area of interest, is important. The WMO Guide no. 8 [12.1] reports that objects should not be closer to the gauge than a distance of twice their height above the gauge orifice, and sites on a slope or the roof of a building should be avoided. In general, the best sites are in clearings among trees or where other objects act as an effective windbreak for winds from all directions. The effects of the wind, and of the site on the wind, can be reduced by using a pit gauge for liquid precipitation, or by making

the airflow horizontal above the gauge orifice using homogeneous dense vegetation kept at the same level of the gauge orifice or appropriate fence structures, or by using windscreens around the gauge.

Furthermore, the wind effect on precipitation measurements is due to the interaction between the gauge body and the airflow. Indeed, the airflow surrounding any precipitation gauge is deformed by the presence of the gauge body, resulting in the acceleration of wind above the orifice of the instrument, which deflects the hydrometeors away from the collector, usually resulting in precipitation undercatch. The main factors of influence are the gauge shape, the wind speed, and the type of precipitation. The resulting measurement error is considered the most significant cause of environmental or *catching* bias, and quantification of this error is essential to obtaining accurate measurements. For rainfall and snowfall, the losses relative to the total amount are about 2–10% and 10–50%, respectively [12.32]. At high wind speed ($8\text{--}10\text{ m s}^{-1}$), collection losses of up to 40% and 80% have been reported by [12.53] and [12.51] for liquid and solid precipitation, respectively.

12.6.2 Laboratory Tests and Field Experiments

Counting errors are related to the ability of the instrument to correctly quantify the amount of water that is collected or detected by the instrument. They can be experienced both in catching and non-catching types of instruments, although in the latter case the assessment of such errors is very difficult, and is hard to perform in controlled laboratory conditions. Laboratory calibration is needed to obtain high-quality measurements and may provide a classification of catching-type measurement instruments based on their laboratory performance.

The laboratory calibration is performed under constant equivalent rainfall intensity, obtained by means of steady water flow generation (e.g., using volumetric pumps or gravimetric methods).

The operational status of precipitation gauges can be verified in the field by means of portable calibration devices in order to detect malfunctions, output anomalies, and calibration drifts. Field calibration tests are based on the same principles as laboratory calibration, using the generation of a few constant equivalent precipitation rates within the range of operational use of the instrument.

Catching errors are detectable in the field by comparison with a reference gauge, and intercomparison campaigns lead to their quantification.

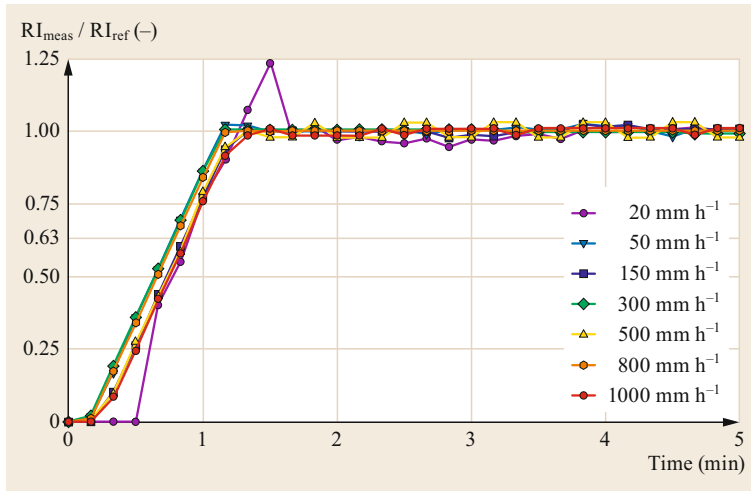


Fig. 12.9 The response time of a weighing gauge: 63.2% of the reference equivalent intensity is measured in less than 1 min

Calibration of Catching-Type Gauges

The CEN/TR 16469:2013 *Hydrometry—Measurement of the Rainfall Intensity (Liquid Precipitation): Requirements, Calibration Methods and Field Measurements* [12.46] reports the procedure for performing the calibration of catching-type gauges as follows. The calibration is performed in a certified laboratory, and a constant water flow, equivalent to a reference precipitation intensity, is conveyed to the funnel of the instrument. The constant flow regime is obtained from a suitable hydraulic device for different precipitation intensity values (dynamic calibration) within the range of operational use declared by the instrument's manufacturer. The flow is measured by weighing the water over a given period after passing through the rain gauge. The output of the instrument under test is recorded when a pulse occurs at regular intervals. The two measurements are compared in order to assess the difference between the actual flow of water conveyed through the instrument and the precipitation intensity measured by the instrument itself. The relative percentage error can be expressed as follows

$$e_{\text{rel}}[\%] = \frac{I_m - I_r}{I_r} \times 100, \quad (12.1)$$

where

I_m is the measured liquid precipitation intensity,
 I_r is the reference equivalent precipitation intensity.

In the case of weighing gauges, the performance is also based on the step response, expressed in terms of the time constant, i.e., the amount of time that is

required by the instrument to measure 63.2% of the reference intensity value (assuming a first-order type of response). Figure 12.9 shows the response time of a weighing gauge for different equivalent precipitation intensity values.

The calibration procedures described above are in agreement with Annex 1 of the report of the fifteenth WMO/CIMO session, where a standardized procedure for laboratory calibration of catching-type gauges is recommended. The result is a calibration certificate presenting the results of the calibration including corrections as required. The Italian standard [12.54] describes the same calibration procedure and, in addition, classifies precipitation gauges into three classes of performance, as follows, according to the calibration results:

- Class A: the maximum deviations are less than or equal to $\pm 3\%$ against the reference precipitation intensity at the temporal resolution of 1 min. Weighing rain gauges shall also have a step response time within the same time interval.
- Class B: the maximum deviations are less than or equal to $\pm 5\%$ against the reference precipitation intensity at the temporal resolution of 1 min. Weighing rain gauges shall also have a step response time within the same time interval.
- Class C: the maximum deviations are less than or equal to $\pm 10\%$ against the reference precipitation intensity at the temporal resolution of 1 min. This also applies to weighing rain gauges where the step response time is less than or equal to 1 min. Where the weighing rain gauge step response is greater than 1 min, the maximum deviations shall be within $\pm 5\%$.

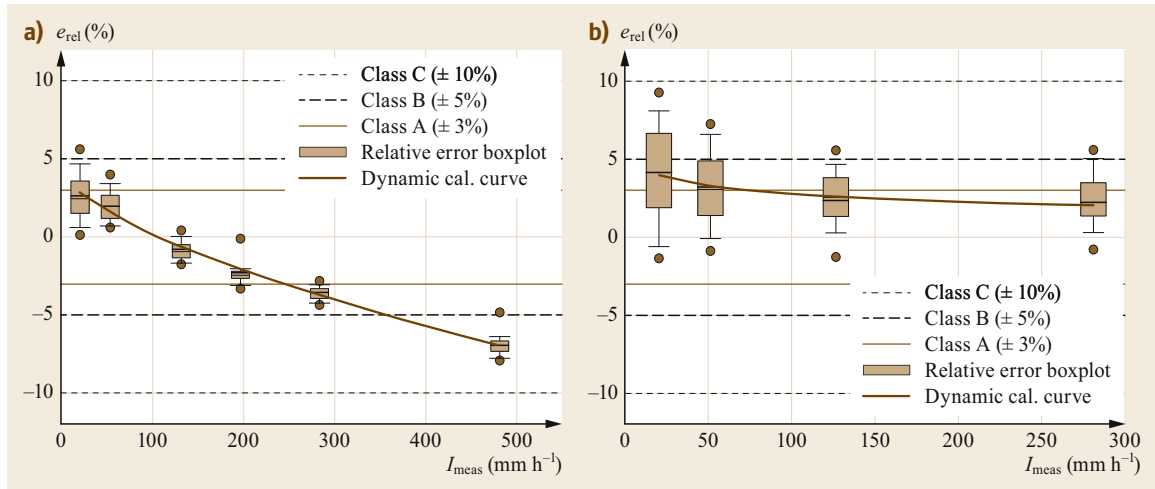


Fig. 12.10a,b Relative percentage errors at various equivalent reference intensities and correction curves for a tipping-bucket gauge (a) and a weighing gauge (b)

If the precipitation gauge tested has a maximum deviation greater than $\pm 10\%$ in measuring the reference precipitation intensity at the temporal resolution of 1 min, it cannot be classified according to this standard.

The same instrument can be assigned to different classes of performance over different measuring ranges.

The calibration certificate must contain the average value and the 10° and 90° percentiles of the percentage relative error distribution e_{rel} (%), for each value of the tested reference precipitation. This is presented in the form of a table. The dynamic calibration curve, obtained by fitting to the relative errors of tested precipitation intensities, must be reported in the certificate to enable correction of the readings. Figure 12.10 shows the performance of a tipping-bucket and a weighing gauge in terms of relative errors e_{rel} (%).

The standard also requires consistency of information. Any inconsistency between the precipitation intensity output at 1 min resolution and other quantities provided by the instrument (e.g., the precipitation amount) must be declared.

Although less efficient, hydro-meteorological services and instrument manufacturers often rely on the single-point calibration. In this case, only one reference precipitation intensity is checked, and the associated adjustment is applied mechanically by operating on the stop screws, so that the error becomes zero at that particular intensity. For any other precipitation intensity, some underestimation or overestimation persists. This is equivalent to assuming a conventional measure for the amount of water associated with each tipping of the bucket, which is different from the actual bucket size.

Calibration of Non-Catching-Type Gauges

No relevant international standard yet exists to define rigorous methods and procedures for calibration of non-catching-type gauges and for the evaluation of the associated uncertainty. As there is no funnel/container to collect precipitation, the calibration and uncertainty evaluation is more difficult than in the catching-type gauges, and the use of an equivalent reference flow rate is not possible. Instead, the actual characteristics of precipitation must be reproduced, including the drop size distribution, drop frequency, and fall velocities.

Laboratory and field tests were used by [12.55] to evaluate the measurement capabilities of an optical disdrometer. In the laboratory tests, high-precision spherical lenses made of silica and sapphire, with known refraction indices, were generated with diameters of 0.5, 1, 3, and 5 mm. These tests provided information on the maximum percentage errors in the diameter measurements. Free-falling water drops of different sizes were also generated using needles connected to a tank maintained at a constant water head. These were collected in a graduated cylinder, and the total volume of the collected water was compared with the cumulative volume of the drops measured by the instrument.

Other authors (e.g., [12.56]) reported that the calibration of optical disdrometers is essentially based on spheres with known diameter falling through the measuring area. A similar principle, based on the fall of small spheres on the sensor membrane, is used to calibrate impact disdrometers.

12.6.3 Correction Methods

Systematic instrumental and environmental biases must be corrected either in real time or in post-processing using calibration curves and suitable algorithms able to maximize the efficiency of the correction. Two examples are reported in detail in this section regarding the correction of systematic mechanical errors of tipping-bucket rain gauges and the wind-induced undercatch.

Correction of Systematic Mechanical Errors

Systematic mechanical biases are corrected using a suitable calibration curve obtained from dynamic calibration tests, as the best-fit regression function. Figure 12.11 shows the performance of the same tipping-bucket and weighing gauges of Fig. 12.10 after correction is applied, thus reporting the residual errors e_{res} (%).

Dedicated post-processing algorithms must be employed to achieve sufficient accuracy and to minimize the impact of sampling errors and the discrete nature of the measurement. Various algorithms have been proposed to this end, as are discussed in the literature [12.19, 57, 58]. However, the operational practice of most users, including national weather services, still relies on the trivial counting of the number of tips occurring in the desired period. The number of tips counted in each 1 min interval (the WMO-recommended time resolution for rain intensity measurements) multiplied by the nominal volume of the bucket provides the 1 min precipitation intensity record.

This method (as already observed by [12.57]) results in a general underestimation of precipitation in-

tensity figures and a high level of uncertainty, due to the random nature of the number of tips per minute within any real-world, highly variable event. Moreover, the correction of systematic mechanical biases is not optimized with this method, since it would be applied to the averaged values only, and most tipping-bucket gauges show a nonlinear correction curve after laboratory calibration [12.29].

A better method employs the inter-tip time algorithm (see, e.g., [12.19, 57]), which is based on the assumption that the nominal volume of each bucket is equally distributed over the inter-tip period. The calculation of precipitation intensity for each minute accounts for the portion of the inter-tip period actually falling into that minute. In this way, the calibration is also the most effective, since the correction applied to the volume of the bucket at the variable inter-tip scale is precisely the one corresponding to the measured precipitation intensity.

The performance of different post-processing algorithms employed in the calculation of rainfall intensity from tipping-bucket gauges is compared and discussed by [12.59] using data recorded at a field test site. Two tipping-bucket gauges using different mechanical designs were compared with a catching-type drop-counting gauge used as the working reference due to its high resolution in both time and volume for the investigated rainfall intensities. The comparison highlights the benefits of employing smart algorithms in post-processing of the raw data and their ability to improve the accuracy of precipitation intensity measurements.

In particular, the results allow comparing the performance of the inter-tip time algorithm with the more

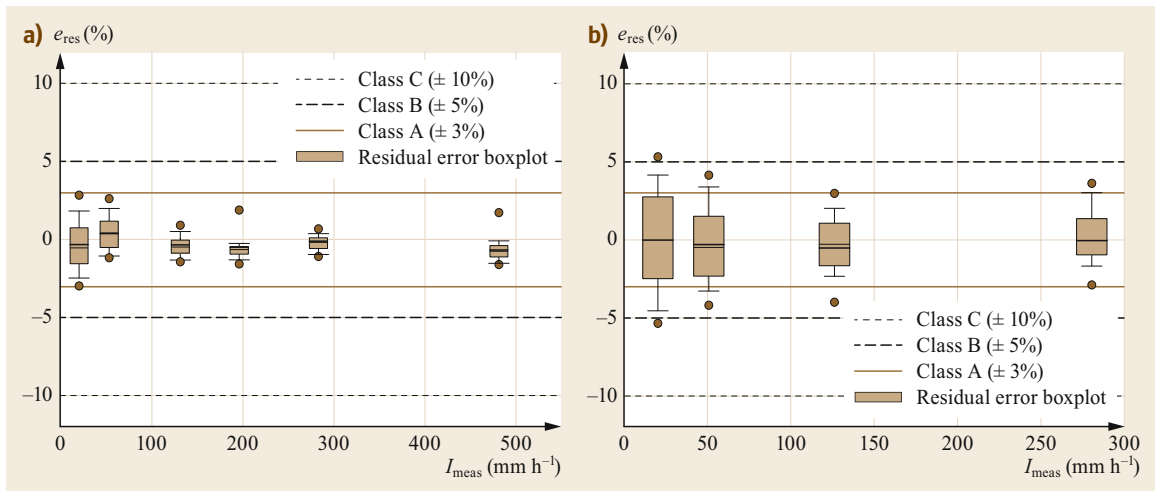


Fig. 12.11a,b Residual errors for a corrected tipping-bucket gauge (a) and a weighing gauge (b). After the correction, the TBR (tipping-bucket rain gauge) falls in Class A, while the WG is in Class B for RI less than 50 mm h^{-1} and in Class A for RI higher than 130 mm h^{-1}



Fig. 12.12a,b The realization of the reference rain gauge pit at Vigna di Valle, Italy (2007) (WMO field intercomparison of rainfall intensity gauges, 2009; photo © Emanuele Vuerich) (a) and a DFIR equipped with a Geonor T-200B weighing gauge located at the experimental site in Marshall (Colorado) (b) (after [12.62] © American Meteorological Society. Used with permission)

common tip-counting method. The main benefit of adopting the inter-tip time method to calculate rainfall intensity resides in a better representation of the inner variability of rainfall events. The measured rainfall intensity series shows an improved correlation coefficient and a lower root-mean-square error (RMSE) with respect to the reference, closely approaching the performance of an ideal gauge, which is not affected by mechanical biases.

Correction of the Wind-Induced Undercatch

The wind-induced undercatch can be approached by using correction curves obtained as a function of wind speed, gauge geometry, type of precipitation (rain or snow), precipitation intensity, and particle size distribution. Correction curves can be derived using data from experimental sites equipped with different precipitation gauges in operational conditions and a reference one. The WMO recommends as a reference for liquid precipitation a gauge placed in a pit (Fig. 12.12a) with the gauge orifice at ground level, sufficiently distant from the nearest edge of the pit to avoid in-splashing. A strong plastic or metal anti-splash grid with a central opening for the gauge should span the pit. Because of the absence of wind-induced error (see e.g., [12.60]), they generally show more precipitation than any elevated gauge. The reference installation for solid precipitation (Fig. 12.12b) is known as the double fence intercomparison reference (DFIR). It has octagonal vertical double fences surrounding a storage or automatic gauge, which itself has a particular form of wind-deflecting shield known as the single Alter shield. Note that this field reference gauge is itself not free

from measurement biases, and its construction could be improved [12.61].

At an experimental site in Haukelisetter (Norway), two Geonor T-200B gauges, one unshielded and one equipped with a single Alter shield, were installed together with the DFIR. Temperature measurements and anemometers at a height of 10 m and at the gauge collector height were also available.

Figure 12.13 shows the catch ratio between the single Alter-shielded gauge and the reference obtained at that site for different temperature classes. For temperatures above 2°C, where the precipitation is mainly

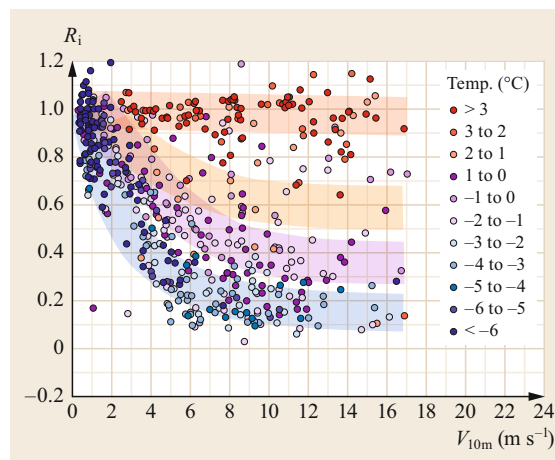


Fig. 12.13 Catch ratio of the Geonor gauge equipped with a single Alter shield when compared with the DFIR for different wind speeds (10 m height), classified according to the air temperature (after [12.63])

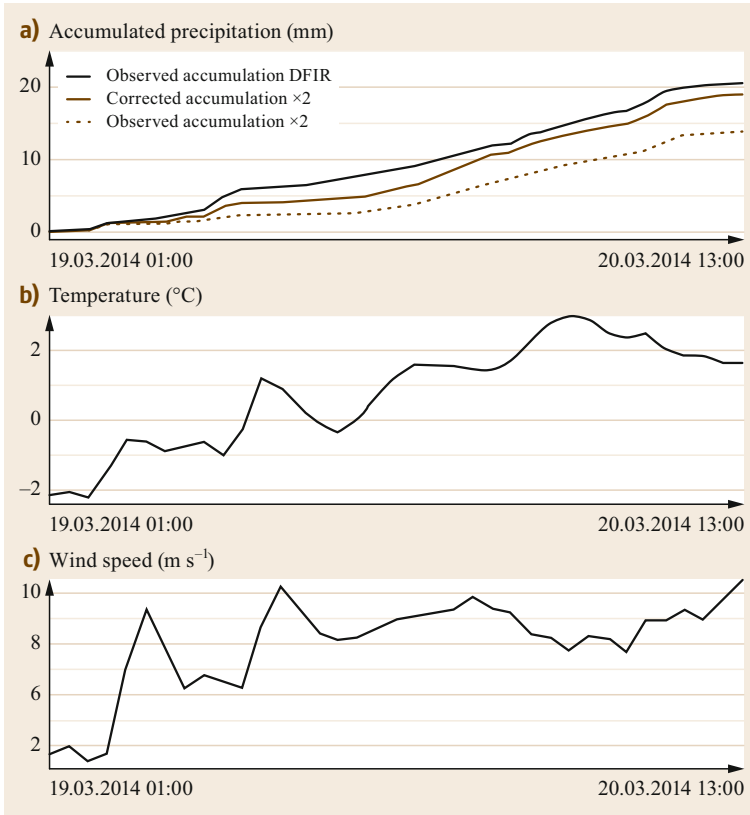


Fig. 12.14 (a) Observed and adjusted accumulation from one precipitation event compared with the accumulation observed by the DFIR. Temperature and wind speed during the event are shown in (b) and (c), respectively

falling as rain, the catch ratio is less influenced by the wind. For temperatures below -2°C , the precipitation is falling mainly as snow, and the catch ratio has a characteristic rapidly decreasing pattern with wind speed. For temperatures between -2 and 2°C , where rain, snow, and mixed precipitation occur, increased scatter appears, depending on the precipitation type. The four temperature classes highlighted as color bands in the figure suggest a continuous change from higher to lower temperature consistent with a gradual change in the distribution of liquid and solid precipitation particles during a mixed-phase event. Based on a three-year data set from the Haukelisetter test site that contains a number of concurrent observations of the catch ratio (R_i), the following correction curve was formulated [12.63]

$$R_i = \left[1 - \tau_1 - (\tau_2 - \tau_1) \frac{e^{\left(\frac{T_i - T_\tau}{s_\tau}\right)}}{1 + \exp\left(\frac{T_i - T_\tau}{s_\tau}\right)} \right] e^{-\left(\frac{V_i}{\theta}\right)^\beta} + \tau_1 + (\tau_2 - \tau_1) \frac{e^{\left(\frac{T_i - T_\tau}{s_\tau}\right)}}{1 + e^{\left(\frac{T_i - T_\tau}{s_\tau}\right)}} + \sigma(T_i) \epsilon_i, \quad (12.2)$$

where β and θ are two fitting parameters, T_τ is the threshold temperature and defines the transition between the two limits above, while s_τ indicates the fuzziness between rain and snow, and $\sigma(T_i)$ is a parameter governing the variance in the measurement error.

The equation was derived from the assumption that the catch ratio is a function of wind speed (V) and air temperature (T) in the form

$$R = f(V, T) = [1 - \tau(T)] e^{-\left[\frac{V}{\theta(T)}\right]^\beta} + \tau(T). \quad (12.3)$$

The parameter $\tau(T)$ goes from one limit, dry snow, to another, mixed precipitation, when the temperature increases/decreases. A sigmoid function fits experimental data reasonably well, yielding the parametric function as follows

$$\tau(T) = \tau_1 + (\tau_2 - \tau_1) \frac{e^{\frac{(T - T_\tau)}{s_\tau}}}{1 + e^{\frac{(T - T_\tau)}{s_\tau}}}. \quad (12.4)$$

An application of the correction curve is shown in Fig. 12.14. Some difference between the adjusted accumulation (brown line) and the reference one (black line) remains, which is probably ascribable to the actual (unknown) particle size distribution.

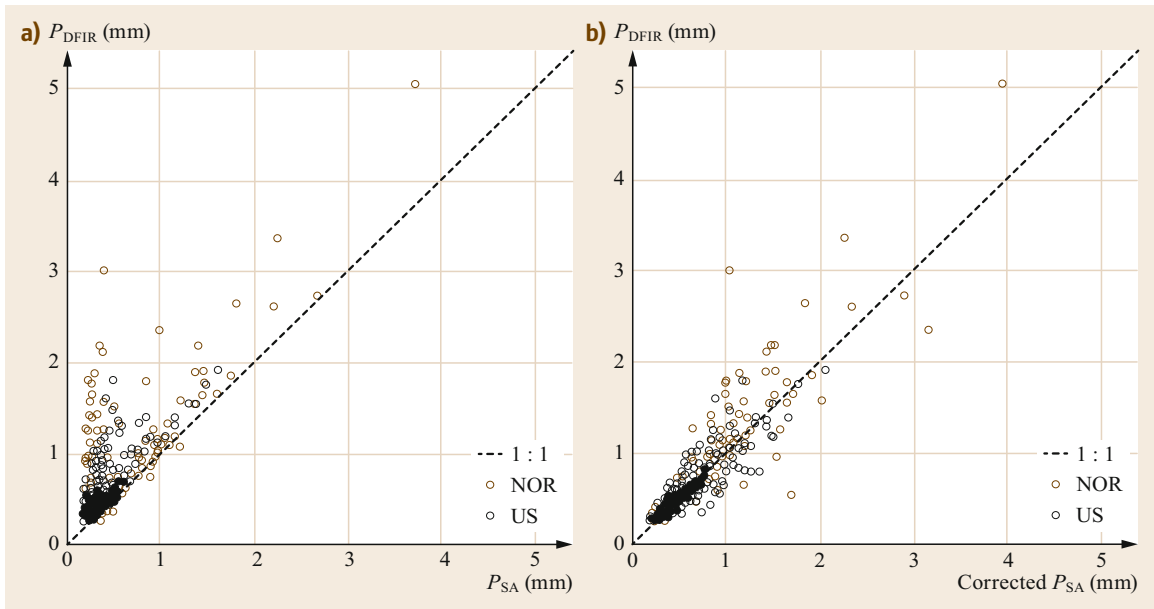


Fig. 12.15a,b Uncorrected (a) and corrected precipitation (b) from a Geonor T-200B weighing gauge equipped with a single Alter shield (P_{SA}) versus the DFIR (P_{DFIR}) for snow events (after [12.64] © J. Kochendorfer et al.)

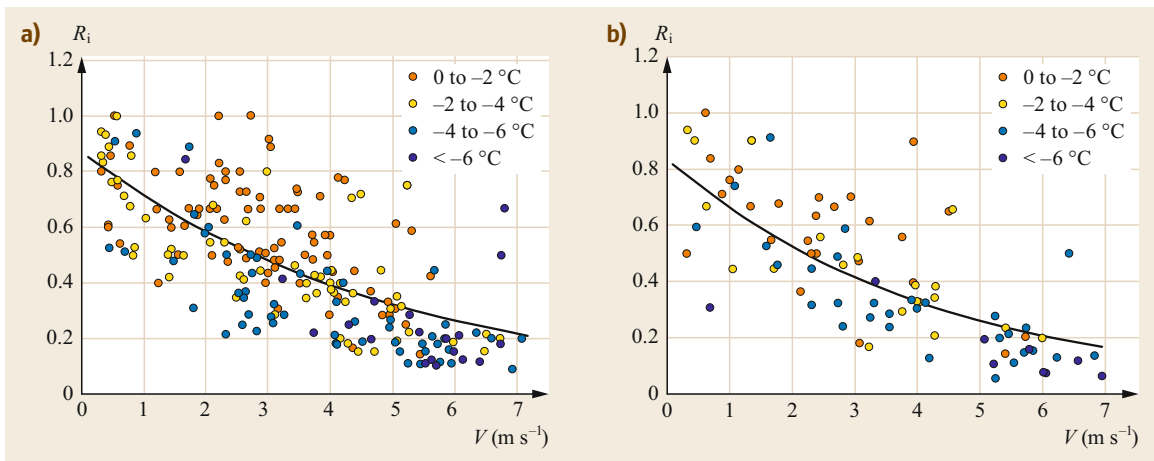


Fig. 12.16a,b The relationship between the catch ratio R_i (TBR/double fence automatic reference) and wind speed V for accumulation periods of (a) 1 h and (b) 3 h. The mean temperature during each accumulation period is color-coded (after [12.66] © S. Buisán et al.)

Data from the 2010 winter in the two experimental sites of Marshall (USA) and Haukeliseter (Norway) were analyzed by [12.64]. The authors proposed a correction function with exponential shape

$$R = e^{-a(U)(1 - [\tan^{-1}(b(T_{air}) + c)])}, \quad (12.5)$$

where the experimental parameters a , b , and c vary with the height of the anemometer and the type of instrument (unshielded, single Alter-shielded, etc.).

The effect of the correction is shown in Fig. 12.15, where the uncorrected and corrected precipitation is compared with the DFIR measurements in Fig. 12.15a and Fig. 12.15b, respectively. After the correction, a significant scatter of the residuals persists, which is probably due to the effect of noise, the spatial variability in precipitation, and the spatial variability in crystal type that are not fully taken into account in this study. With the aim of deriving correction curves that could be extended to other sites, data from eight experimen-

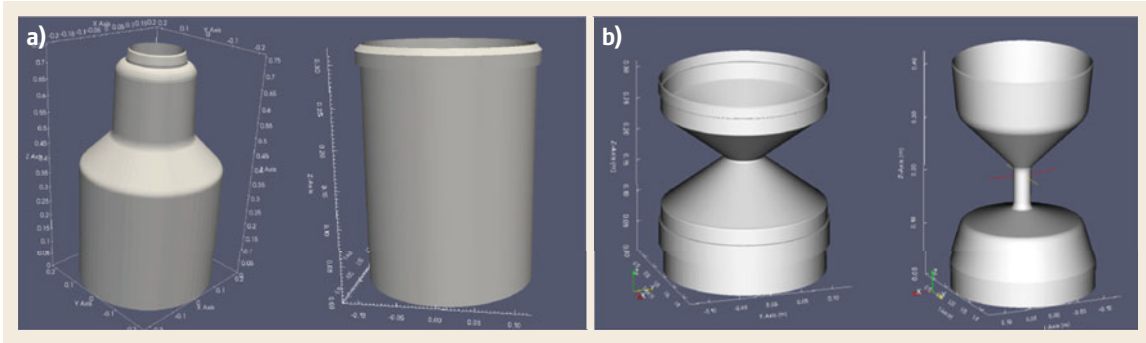


Fig. 12.17a,b 3-D models of the OTT Pluvio2VR weighing gauge and the Casella tipping-bucket rain gauge (a) and models of the EML ARG100VR and the EML SBS500VR tipping-bucket rain gauges (b). The orifice diameters are 160, 228, 254 and 254 mm; their heights are 757, 320 310 and 425 mm. The models are not to scale (after [12.49] with permission from John Wiley and Sons, © American Geophysical Union)

tal sites were analyzed by [12.65]. The study provided the parameters of (12.5) for single Alter-shielded and unshielded chimney-shaped weighing gauges, by separating mixed and solid precipitation, and for wind speed measured at 10 m or at the collector height.

The data set obtained by [12.66] at the Formigal (Spain) experimental site was divided into two samples, and the correction curves derived for TBR rain gauges at 1 and 3 h accumulation scales are shown in Fig. 12.16. For 1 h accumulation, the authors propose (12.6), where a contribution of the melting of snow during the previous hour of accumulation is also included.

$$\text{TrueAcc (1 h)} = \frac{\text{Acc}}{\text{CR}} - 0.095 \frac{\text{Acc}}{\text{CR}} + 0.095 \text{Acc}(\text{prev h}), \quad (12.6)$$

where the catch ratio CR is a function of wind speed and air temperature.

The wind-induced undercatch of precipitation gauges is also addressed in the literature by means of numerical simulations to calculate the flow velocity and turbulence around the gauge collector and the consequences of the aerodynamic disturbance on the hydrometeor trajectories.

This is obtained by performing finite-volume computational fluid dynamics (CFD) simulations based on the solution of Reynolds-averaged Navier–Stokes (RANS) equations or large-eddy simulations (LES) to obtain the airflow patterns close to the gauge collector (e.g., by [12.67, 68]). The computation of the particle trajectories is conducted with a Lagrangian method assuming no influence of particle motion on the airflow [12.69].

CFD simulations based on the RANS model allow for an Eulerian description of the air velocity com-

ponents over the three-dimensional spatial domain in time-averaged terms. The LES simulations allow the time-dependent airflow patterns to be described down to the computational mesh dimension that represents the detached scale.

Particle trajectories are simulated by solving the equation of motion that depends on the relative velocity between air and particles ($v_p - v_a$), the drag coefficient (C_d), and the gravitational contribution, as follows

$$V_p \rho_p \mathbf{a}_p = -C_d A_p \rho_a 0.5 (\mathbf{v}_p - \mathbf{v}_a) |\mathbf{v}_p - \mathbf{v}_a| + V_p (\rho_p - \rho_a) \mathbf{g}, \quad (12.7)$$

where \mathbf{a}_p is the particle acceleration vector, \mathbf{v}_p is the particle velocity vector, ρ_a is the air density, and ρ_p is the particle density.

The physical shape of a gauge has a significant impact on the aerodynamic effect and on the collection efficiency. It has been shown that appropriate *aerodynamic* shapes are able to reduce the deformation of the airflow [12.49]. The authors employed computational fluid dynamics simulations to evaluate the time-averaged airflow realized around *aerodynamic* rain gauge shapes (Fig. 12.17b) when impacted by wind. The results are shown in terms of comparison with the aerodynamic response of two *conventional* rain gauge shapes (chimney and cylindrical shapes, Fig. 12.17a).

Figure 12.18 shows the nondimensional magnitude of velocity (normalized with the undisturbed wind speed) on a stream-wise vertical plane for gauges of different shapes. The white band displayed for all gauges represents the shear layer; the wind speed here equals the undisturbed wind velocity. This layer separates the strong airflow regime above the collector (red shaded colors) from the recirculating airflow zone inside the gauge (blue shaded colors). In the case of aerodynamic

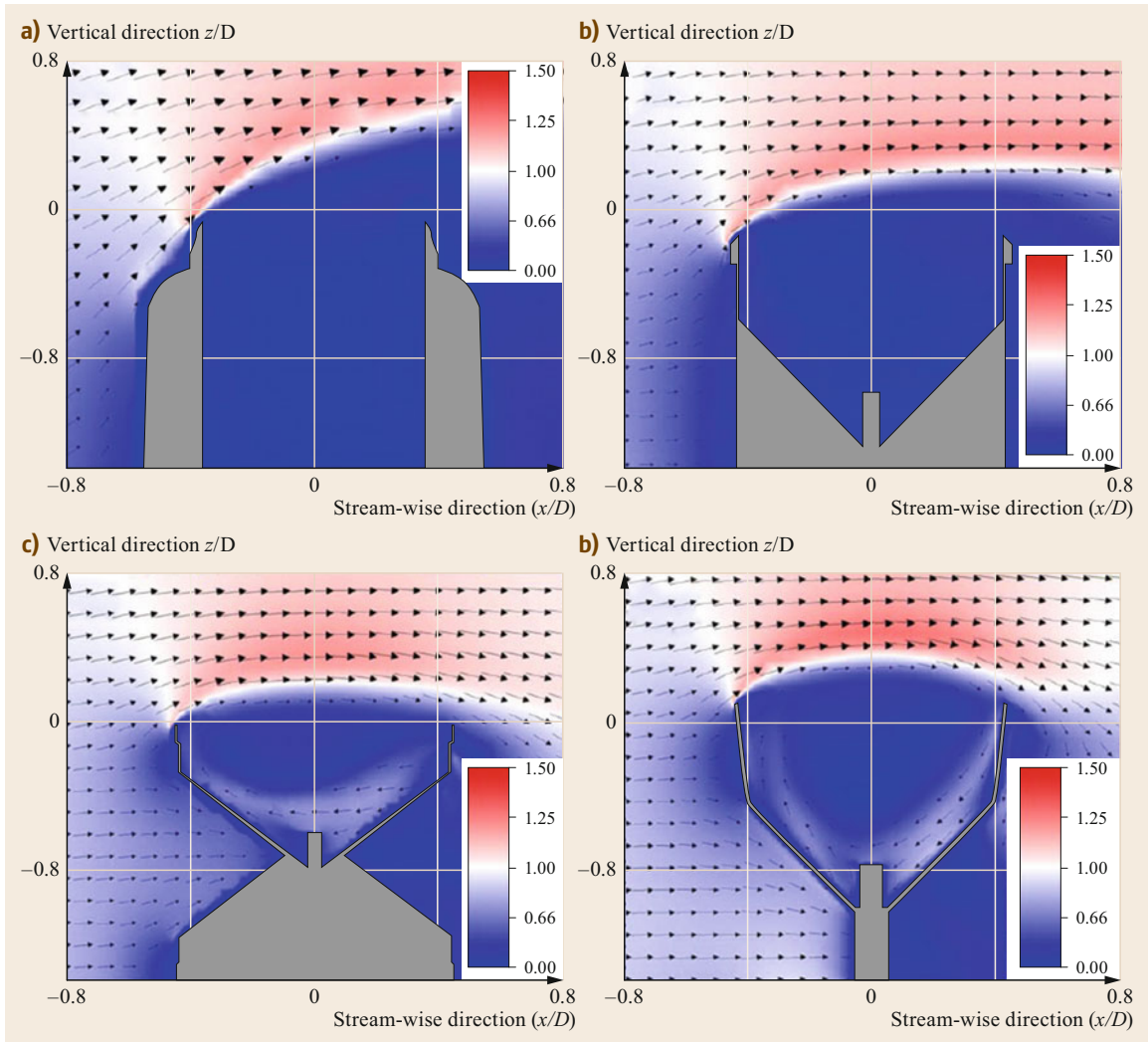


Fig. 12.18a–d Color plots of the vertical stream-wise section of the airflow nondimensional magnitude of velocity for the (a) OTT Pluvio2, (b) Casella, (c) EML ARG100, and (d) EML SBS500 gauges. The velocity fields were computed by executing RANS $k-\omega$ simulations with a horizontal wind speed U_w equal to 2 m s^{-1} . The arrows represent the time-averaged magnitude and direction of the airflow (after [12.49] with permission from John Wiley and Sons, © American Geophysical Union)

rain gauges (Fig. 12.18), the shear layer spans all over the orifice and touches the downwind edge of the collector.

The Lagrangian model of hydrometeor trajectories was improved by dynamically updating the drag coefficient estimation along each trajectory according to the computed particle Reynolds number [12.51, 70]. Figure 12.19 presents a comparison of the simulated collection efficiency for an unshielded (Fig. 12.19a) and a shielded (Fig. 12.19b) gauge for three different particle size distributions of solid precipitation based on field observations.

The impact of wind on the accuracy of non-catching-type gauges is still poorly understood and depends on the specific geometry of the gauge. While for catching-type gauges, three main geometry classes can be easily identified (cylindrical, *chimney*, and *champagne glass* shape), non-catching-type gauges show a broader variety of design and geometric solutions. Most important, they generally lack the axial-symmetric features of catching-type gauges, therefore introducing a new dependence of their measurement accuracy on the wind direction, in addition to wind velocity. Detailed studies are needed to quantify

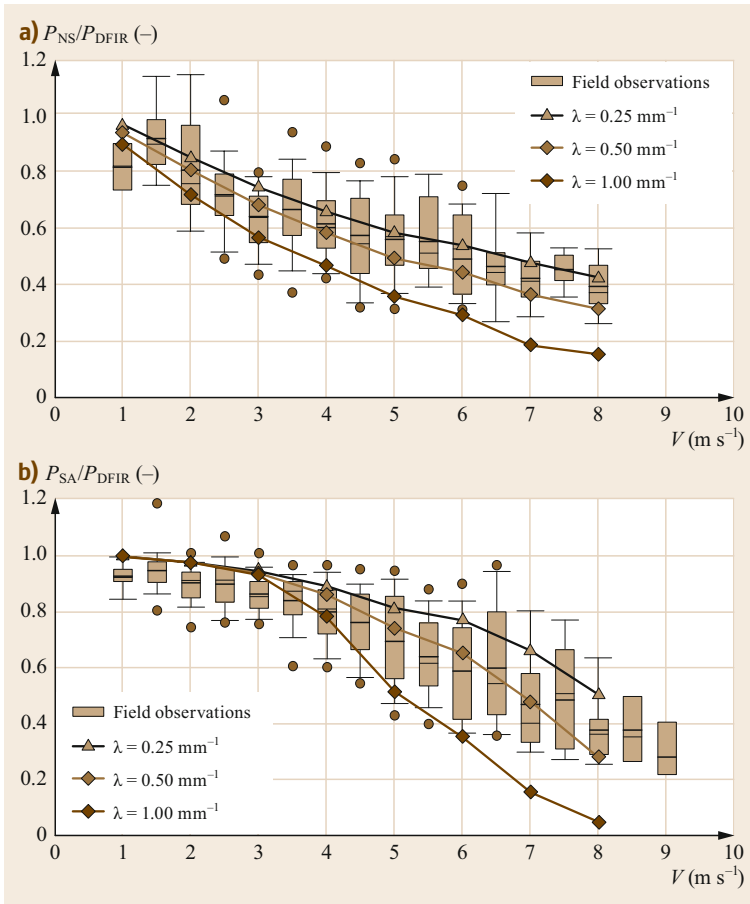


Fig. 12.19a,b Collection efficiency versus horizontal wind speed V (m s^{-1}) for an **(a)** unshielded and **(b)** single Alter-shielded Geonor T-200B gauge computed using a dynamically updated C_d (after [12.51]). Three different particle size distributions for snow are simulated according to the slope parameter λ (mm^{-1}) of the assumed inverse exponential distribution. Experimental data from the Marshall field site are shown in the boxplots (after [12.71] © American Meteorological Society. Used with permission)

such errors and to derive a possible correction curve to account for the aerodynamic performance of the gauge.

12.6.4 Measurement Uncertainty

The measurement result MR can be described as the sum of the raw measurement M , the correction of systematic errors C , and the uncertainty contribution $\pm U$

$$MR = M + C \pm U . \tag{12.8}$$

The measurement uncertainty, which produces the dispersion around the mean value of rainfall intensity measurements (see boxplot in Figs. 12.10 and 12.11), must be estimated. The uncertainty is due to random factors; some sources of uncertainty are observed in the field (wind, evaporation, splashing, etc.), while others may occur during the laboratory calibration [12.72, 73].

The uncertainty of experimental measurements can be synthetically described by (12.9), where the total uncertainty U_T is equal to the sum of field uncertainty U_F , specification uncertainty U_M provided by manufacturer,

and laboratory uncertainty U_L

$$U_T = U_F + U_M + U_L . \tag{12.9}$$

The field uncertainties are estimated to be about -1% for evaporation, $+0.5\%$ for adherence, -0.5% for the inclination of the sensor, $+1\%$ for splashing, and from -5% to $+80\%$ for wind and 0.5% for other sources [12.74]. For U_M , some contributions must be taken into account at the time of calibration, such as drift and nonlinearity. The U_L component varies according to the calibration system. For liquid precipitation, the measuring ranges and the associated uncertainties are reported in Table 12.4, as published in [12.1].

The calibration methods can be classified as input (volumetric) or output (gravimetric) methods. The input method consists in using a calibrated device to drain water into the rain gauge (RG), thus simulating rain with a known amount of water and then verifying the amount of rain measured by the rain gauge under test. The device can be a measuring cylinder, a peristaltic pump, dispensers with interchangeable orifice, etc. The output method consists in using a calibrated weighing to determine the volume of precipitated water after it

Table 12.4 Typical characteristics of precipitation measurements according to WMO Guide no. 8, Volume 1, Chapter 1, Annex 1.A [12.1]

Variable	Range	Required measurement uncertainty	Achievable measurement uncertainty
Rainfall depth (<i>RA</i>)	0–500 mm	0.1 mm for <i>RA</i> ≤ 5 mm 2% for <i>RA</i> > 5 mm	The larger of 5% or 0.1 mm
Snow depth (<i>SA</i>)	0–25 m	1 cm for <i>SA</i> ≤ 20 cm 5% for <i>SA</i> > 20 cm	1 cm
Precipitation intensity (<i>RI/SI</i>)	0.02–2000 mm h ⁻¹	n/a for 0.02–0.2 mm h ⁻¹ (trace) 0.1 mm h ⁻¹ for 0.2–2 mm h ⁻¹ 5% for > 2 mm h ⁻¹	In laboratory: 5% above 2 mm h ⁻¹ 2% above 10 mm h ⁻¹ In field: 5 mm h ⁻¹ 5% above 100 mm h ⁻¹

Note: EN 17277:2019 [12.75] recently published by CEN defines three classes of catching-type instruments based on their measurement uncertainty: ±3%, ±5%, and ±10%.

drains off the rain gauge; the control device is a precision balance.

The uncertainty sources during the calibration can be summarized as follows:

- Repeatability of measurements of air temperature, air relative humidity, atmospheric pressure, and water temperature
- Calibration certificate of thermometer (for air and water), hygrometer, barometer
- Repeatability of measurements of calibrated caliper, resolution of caliper, intra-laboratory measurement with caliper
- Repeatability of measurements of calibrated weighing, calibration certificate of weighing, specification of weighing, calibration certification of standard weight
- Only for input method: repeatability of measurements of calibrated graduated cylinder, resolution of measures of calibrated cylinder, calibration certificate of graduated cylinder, error of parallax and/or meniscus reading using measuring cylinder, specification of measuring cylinder.

The rainfall intensity is obtained indirectly using a rain gauge and a data acquisition system or a data logger to record the times when pulses occur. During a laboratory calibration, the data logger must be calibrated in time and frequency in the pulse channel used for acquisition of the signal from the instrument under calibration, because physical and electrical factors can influence the stability and accuracy of the data logger. The largest contribution to the uncertainty budget may be due to the internal clock of the data logger. Another source of uncertainty for tipping-bucket rain gauges is the repeatability of the time interval between tips (balancing of the buckets).

12.6.5 Specific Quality Control Methods

Quality control (QC) of data is a fundamental component of the measurement chain, used to verify the reliability of data obtained by the user and to prevent the propagation of errors. General guidelines are described in the WMO Guide no. 8 [12.1]. These procedures can be applied in both real time and non-real time for data quality assurance. QC consists of all processes that are used to generate confidence and ensure that the data produced will have the required quality. They also include the examination of data at stations and data centers to verify that the data are consistent with the goals of a quality management system, and to detect errors so that the data can be flagged as unreliable, corrected, or—in the case of gross errors—deleted.

The formal procedures for quality management and quality assurance prescribed by the International Organization for Standardization (ISO) are appropriate for meteorological data. The ISO 9000 [12.76] standard was developed to assist organizations in implementing and operating quality management systems, and describes the fundamentals of quality management systems and gives definitions of the related terms. The ISO 9001 [12.77] standard specifies the requirements for a quality management system that can be certified. The ISO 9004 [12.78] standard gives guidelines for continuous improvement of the quality management system. The ISO 19011 [12.79] standard provides guidance on auditing the quality management system.

In the case of precipitation measurements, suspicious data (doubtful, missing, value beyond the expected limits, etc.) are flagged with a specific number to identify the type of problem and are never deleted.

Typical test criteria for precipitation measurements are summarized in Table 12.5. An example of a suitable

Table 12.5 Typical test criteria for precipitation measurements

Method	Error	Reason
All instruments	Missing data. Value exceeding admissible range	Instrument malfunctioning, power outage, or data transmission error (see instrument diagnostic information)
Tipping-bucket gauges	Low constant value for long periods No value during liquid precipitation No value during solid precipitation	Water storage in the funnel Clogging of the nozzle Snow capping, ice formation (heating failure if present)
Weighing gauges	Spurious values in no-precipitation periods No value during solid precipitation	Vibrations (wind) or temperature induced algorithm error Snow capping, ice formation (heating failure if present)
Non-catching-type gauges	Anomalous number of occurrences in the no-precipitation particles class	Dirt accumulation on the optics (e.g., spider webs, dust). Beam obstruction

quality control procedure for 1 min precipitation data may include the following control actions:

- Number of samples and missing data: for the same sensors the data logging system acquires the raw data on a timescale of less than 1 min. If the number of samples collected in 1 min is less than the expected minimum for each instrument that minute is tagged and the flag is coded.
- Native errors and doubtful/erroneous data: 1 min data can be identified as doubtful or erroneous according to the corresponding diagnostic parameter reported in technical manuals.
- Plausible value check and doubtful/erroneous data: the operational range is declared by the manufacturer; if is not declared or is declared unlimited the 1 min data is assumed plausible if less than the WMO upper limit (2000 mm h^{-1}). A different and bespoke upper limit, related to the local climate conditions, can be assumed. Therefore, if the *RI* value on 1 min exceeds the upper limit it is flagged as doubtful. If the 1 min *RI* value is negative it is flagged as erroneous.
- Data collected during the maintenance actions are flagged to exclude them from data analysis.

Ancillary data can also be controlled by means of a QC procedure. The QC takes into account the working limits of ancillary sensors and the plausible values related to climatic conditions. The maximum and minimum limits for air temperature, relative humidity, atmospheric pressure, wind direction, wind speed, wind gust, and global solar radiation are fixed. Also, the maximum and minimum variability of data in 1 min is checked.

12.6.6 Intercomparison Results

The main objective of the WMO Laboratory Intercomparison of Rainfall Intensity Gauges was to test the performance of catching-type rainfall intensity gauges

of different measuring principles under documented conditions. The involved rain gauges were divided into three groups and were tested in three different laboratories (the Royal Netherlands Meteorological Institute, Netherlands; Météo France, France; University of Genova, Italy) during a period of about 3 months, and the instruments were then rotated from one laboratory to another. Seven fixed reference intensities were tested ($2, 20, 50, 90, 130, 170, 200 \text{ mm h}^{-1}$), and if the maximum declared intensity was larger than 300 mm h^{-1} , further reference intensities were tested between 300 and 500 mm h^{-1} .

The manufacturers of the majority of the tipping-bucket rain gauges did not apply any correction based on dynamic calibration. For some instruments, a single-point calibration was applied at a single rain intensity around $30\text{--}50 \text{ mm h}^{-1}$. On a smaller group of instruments, a correction based on dynamic calibration was applied. Results were presented in the form of two graphs, which report the relative percentage error and the response curve.

Figure 12.20a shows the overall response curves for the uncorrected tipping-bucket gauges, derived by averaging the measured data obtained at all three laboratories for the two identical instruments when applicable. Each curve is therefore representative of the observed behavior of one particular instrument. The deviation from the reference value increases with the equivalent reference rainfall intensity. As for corrected instruments, the correction proposed by the manufacturer and implemented in the data logger was able to reduce the errors in most cases to fall within the limits $\pm 5\%$ defined by WMO for the required uncertainty of rainfall intensity measurements. The performance of instruments after correction is shown in Fig. 12.20b.

For weighing gauges, the bias in terms of relative errors is less than uncorrected tipping-bucket rain gauges over the entire range of intensities. Nevertheless, for this type of instrument, the delay in detecting the variation in the rainfall intensity is sometimes relevant. An assessment of the step response was therefore per-

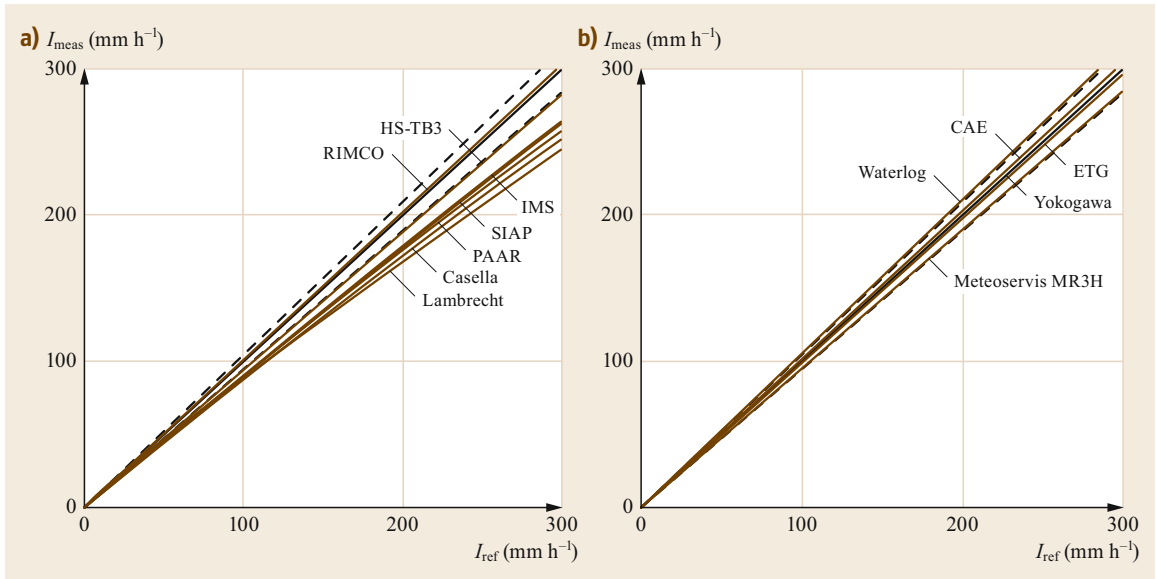


Fig. 12.20a,b Ensemble of response curves for the uncorrected TBRG (a) and those applying some correction for systematic mechanical errors (b). Dashed lines indicate $\pm 5\%$ (after [12.4])

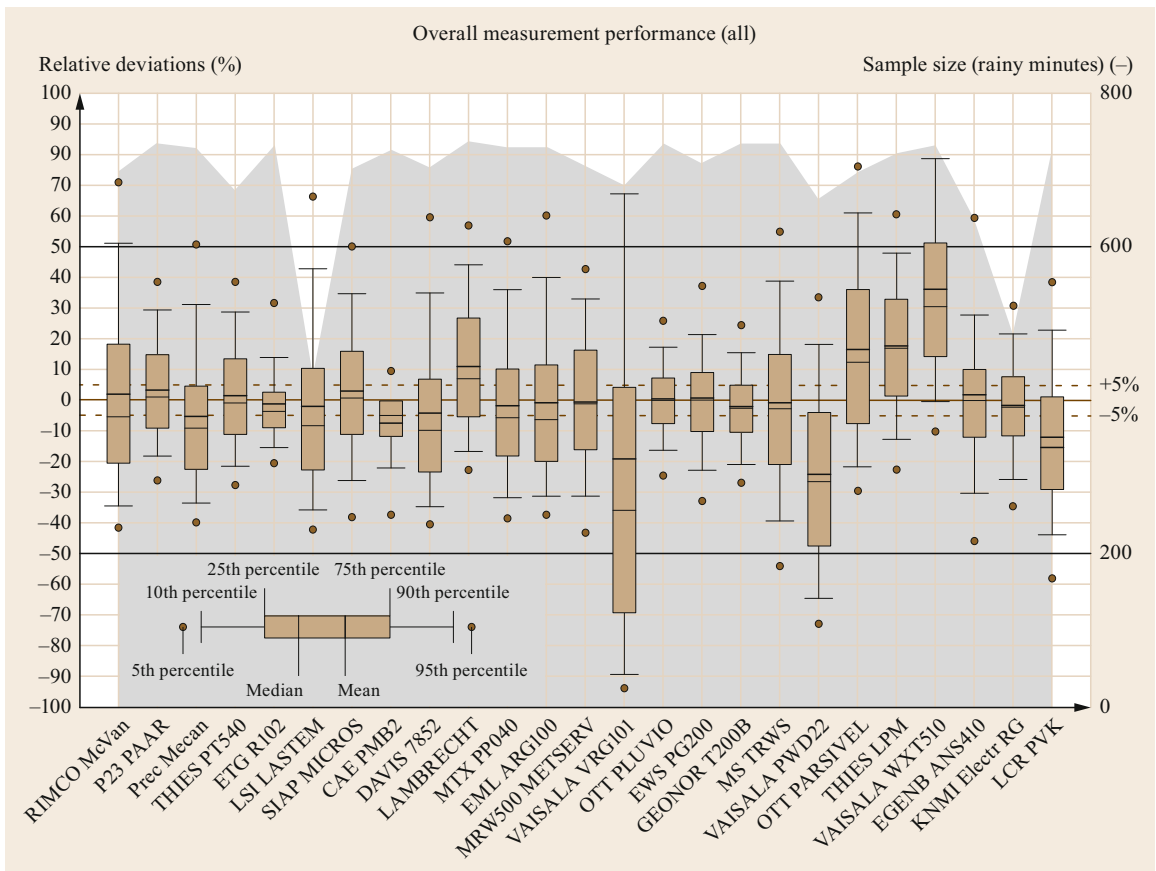


Fig. 12.21 Nonparametric distribution of relative deviations from the reference for all instruments involved, with sample size (number of rainy minutes) indicated in gray background (after [12.28] with permission from Elsevier)

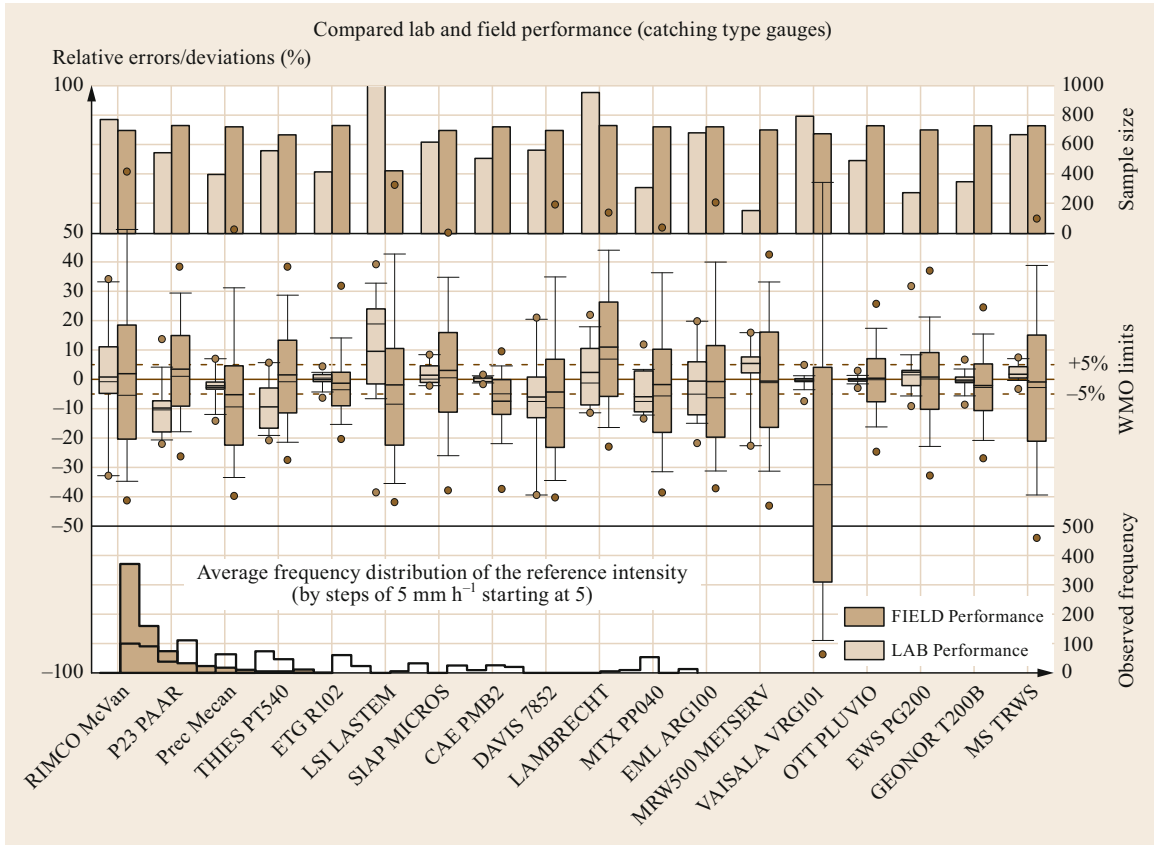


Fig. 12.22 Comparison between relative deviations in the field (dark brown boxplot) and laboratory test results (light brown boxplot) for catching-type gauges. The sample size and the observed frequency distribution are shown at the top and bottom of the graph, respectively

formed by switching the flow rate from 0 to 200 mm h⁻¹ and then back to zero, with the duration of the input flow being determined based on the time needed for stabilization.

The WMO Field Intercomparison of Rainfall Intensity Gauges was carried out in Vigna di Valle, Italy from October 2007 to April 2009. The main objective was to compare the performance of in-situ rainfall intensity instruments of different measuring principles under high rainfall intensity. This experiment enabled the influence of the operational conditions on precipitation measurements to be assessed (e.g., wind effect on precipitation collection, variability of rainfall intensity). Preliminary laboratory tests were carried out on the catching-type rain gauges involved in the field experiment.

Both catching and non-catching types of gauges were involved in the field test, and ancillary instruments were installed (anemometers, wetness sensor, temperature and relative humidity probes, atmospheric pressure

sensor, global irradiance pyranometer). Based on the results of the WMO Laboratory Intercomparison, only some corrected TBRs and WGs with short step response and low residual errors were used as working reference instruments.

The results are summarized in Figs. 12.21 and 12.22. In the first graph, the performance of all instruments (catching and non-catching) are reported in terms of relative deviations, with the associated sample size (number of 1 min rain data). The results show that all catching-type gauges have similar performance in terms of both biases and dispersion (with some outstanding cases), while the non-catching types of gauges have much larger biases and dispersion against the reference. Figure 12.22 shows a comparison between the laboratory and field performance for catching-type rain gauges only. The relative deviations in the field are larger than in laboratory tests, where in some cases the instruments comply with the WMO recommendations of ±5%.

12.7 Maintenance

Although maintenance procedures may be rather expensive and time-consuming, high-quality measurements can hardly be performed in the absence of periodic maintenance and verification of the possible degrading of the instrument performance over time. This is especially true in harsh environments and for instruments employing moving mechanical parts or small orifices that are prone to clogging, such as many catching-type gauges.

12.7.1 Periodic Checks and Maintenance Procedures

The operational status of precipitation gauges in the field is periodically checked in order to detect any malfunction, drift, blockage, etc. Suitable maintenance procedures are adopted to keep the instrument clean and ready to detect and report as soon as precipitation occurs. The frequency of periodic checks and the most suitable maintenance operations depend on the technology and the physical principle exploited to perform the measurement (Table 12.6). Maintenance practices are recommended by WMO [12.1] for the most widely used types of gauges and are reported below. Additional or extraordinary maintenance could be required in the case of different technologies or in locations where the characteristics of the surrounding environment may accelerate ageing or blockage (presence of dust, foliage, ice, etc.).

For any gauge, maintenance and periodic checks should be performed in the absence of precipitation and high wind gusts, and by annotating the period when maintenance is performed and indicating it with a suitable code in the record. For catching-type gauges, checking the conditions of the funnel is a typical maintenance operation and consists of two parts:

- *Clogging*
The maintenance procedure consists in a preliminary visual inspection of the state of the funnel. In case of obstacles, or leaves or sediment accretion along the funnel walls, the operator should remove

the funnel from the gauge and manually clean the walls. In order to verify the conditions of the narrow funnel outlet, the operator could perform one of the following operations. The first is a visual inspection of the funnel outlet, and it may be not possible if the manufacturer applies filters or a sophisticated design of the funnel outlet. The second is pouring a limited amount of water into the funnel and verifying that the water flows through the funnel outlet without accumulating inside the funnel. In any case, the operator should be equipped with a proper pipe cleaner or small brushes in order to clean the narrower parts of the funnel without deformation of the surfaces.

- *Leveling*
The leveling of the funnel orifice should be verified with the help of an electronic or spirit level. If the status is unsatisfactory, the operator can adjust the mounting screws to restore the leveling. Particular attention should be paid to the stability of the supporting pole that must remain in a perfectly steady position; otherwise the operator should plan the execution of a new installation of the supporting pole.

For storage gauges,

the outer container of the gauge and the graduated cylinder should be kept clean, both inside and outside, by using a long-handled brush, soapy water, and a clean water rinse. Worn, damaged, or broken parts should be replaced, as required. The vegetation around the gauge should be kept trimmed to 5 cm (where applicable). The exposure should be checked and recorded. The operation and maintenance of storage gauges in remote areas poses several problems, such as the capping of the gauge by snow or difficulty in locating the gauge for recording the measurement, which require specific monitoring. Particular attention should be paid to assessing the quality of data from such gauges [12.1].

Table 12.6 Maintenance of precipitation instruments

Maximum interval	Water level	Tipping bucket, weighing, and drop counter	Optical	Thermo	Microwave
6 months	Check for clogging and leveling		Sensor cleaning and check of leveling		Check of leveling
1 year	Check of the graduated scale	Field verification of the dynamic calibration curve	No standard calibration procedure available		
3 years	Volumetric calibration	Dynamic calibration in the laboratory	No standard calibration procedure available		

After every extreme/high-precipitation event—check of the instrument status

For weighing gauges, the WMO suggests that routine maintenance be conducted every three to four months, depending on precipitation conditions at the site:

Both the exterior and interior of the gauge should be inspected for loose or broken parts and to ensure that the gauge is level. Any manual read-out should be checked against the removable data record to ensure consistency before removing and annotating the record. The bucket or catchment container should be emptied, inspected, cleaned if required, and recharged with oil for rainfall-only operation or with antifreeze and oil if solid precipitation is expected. The recording device should be set to zero in order to make maximum use of the gauge range. Both the digital memory and power supply should be checked and replaced, if required. Timing intervals and dates of record must be checked [12.1].

Weighing gauges with no automatic emptying devices require regular maintenance in order to maintain the level of the water accumulated in the container below the total capacity. For this reason, the operator must continuously monitor the water level in the gauge and be prepared for a timely intervention according to the magnitude of the precipitation.

Typical checks and maintenance procedures should cover the following aspects:

- Antifreeze solution: every time the operator discharges the container, a minimal amount of liquid must be preserved in a solution of water and antifreeze agent (usually a propylene glycol mixture with alcohol in the quantity specified by the manufacturer) to permit the operation of the gauge when the environmental temperature decreases to -40°C .
- Anti-evaporation agent: every time the operator discharges the container, a given quantity of oil must be added to the solution of water and antifreeze agent (in the quantity specified by the manufacturer). The role of the oil is to reduce the evaporation of volatile antifreeze solutions and precipitation and to reduce splashing, while allowing solid precipitation to penetrate the anti-evaporation film.
- Snow capping and bridging: when long periods of low environmental temperature and solid precipitation occur, the gauges should be monitored regularly in order to detect possible snow accumulation on the gauge orifice rim. Modern gauges are equipped with heating systems to reduce snow capping, but the low electrical power of such devices

does not ensure efficient snow melting in the case of very low temperature. The operator should monitor the power consumption of the heating system (in cases where the information is provided by the data logger) or perform technical inspections to remove any snow/ice residual on the gauge orifice rim.

For tipping-bucket gauges, routine maintenance should include:

cleaning the accumulated dirt and debris from funnel and buckets, as well as ensuring that the gauge is level. It is highly recommended that the tipping mechanism be replaced with a newly calibrated unit on an annual basis. Timing intervals and dates of records must be checked [12.1].

The annual replacement of the mechanism may not be necessary, and is subject to careful checking and/or field verification as detailed below.

The checking of mechanical elements is aimed at verifying the absence of debris inside the buckets and ensuring that the small counting balance rotates without abnormal friction. If the first check fails, the operator should clean the buckets with a small brush. This operation must be performed with great care for the delicate mechanical elements, since the balancing of the bucket could be easily compromised. In the case of abnormal friction during the rotation of the buckets, the operator should return the gauge to the laboratory for an in-depth cleaning of the mechanical components and follow the manufacturer-prescribed procedures if provided, or just replace the bucket assembly. While the verification of the counting performance of the mechanical sensor is not part of the routine maintenance operations, it is good practice to perform a complete field verification after performing any manual intervention on the tipping-bucket balance system.

The characteristics of non-catching-type gauges may differ significantly according to the measuring principle and the design adopted by the manufacturer. It is difficult to provide general maintenance procedures for such gauges; however, many non-catching types of gauges adopt optical elements such as lenses, mirrors, or light/radiation beam orifices that are often subject to occlusion caused by the presence of dirt/dust. The operator should perform periodic checks at intervals depending on the sensor characteristics (usually specified by the manufacturer). In the case of occlusion, the debris must be carefully removed using soft brushes, or the specific products occasionally provided by the manufacturer, in order to prevent damage to the lenses or optical elements of the sensor.

12.7.2 Field Calibration/Verification

For catching-type gauges, the WMO [12.1] suggests that:

a proper field calibration, and field calibration check or field inspection should also be conducted on a regular basis as part of the routine maintenance and check, taking into account site and operational constraints.

For catching-type gauges, a recommended procedure using a portable device to generate reference flow rates is given by WMO [12.1].

The main purpose of the field verification is to detect calibration drifts during operational use, as described by [12.46]. This calibration also provides valuable insights into data analysis and interpretation. The field calibration should be performed using a portable field calibration system (Annex B of [12.46]) based on the same principle as the laboratory calibration, using the generation of constant equivalent rainfall rates within the range of operational use (steady water flow). From the operational viewpoint, the portable field calibrator should permit rapid tests and should not contain any sophisticated components, in order to provide a cost-effective solution. The repeatability of the field calibrator (and its accuracy) should be assessed in a laboratory before operational use and its (expanded) uncertainty determined.

During the WMO Field Intercomparison of Rainfall Intensity Gauges, a dedicated portable calibrator was designed and used for calibration and verification. Its performance and results are described in the final report [12.4].

The field calibrator designed at the University of Genova is a modified Mariotte bottle composed of a cylindrical water container of suitable capacity (about 2 L), a combination of air intakes and output nozzles for generating different rainfall intensities, and an electronic system to detect the emptying time. A suitable combination of air intakes and nozzles can be selected based on the gauge collector size and the reference intensity chosen for the calibration. By opening the top

tap and bottom nozzle, a constant flow is conveyed to the funnel of the gauge, and the reference intensity is determined according to the emptying time and the conversion table (volume–time–intensity). Air intakes provide the pressure compensation, thus maintaining a constant push. The field verification should be performed in operational conditions, in the absence of precipitation or fog and at low wind speed.

12.7.3 Metrological Confirmation

Metrological confirmation is defined as a set of operations required to ensure that measuring equipment conforms to the requirements for its intended use, according to [12.80]. Once the instruments are calibrated and their accuracy certified by an independent third party so that measurements are traceable to the international standards, it is the duty of the station manager to periodically check that the instruments still preserve their original characteristics. This is the role of field inspection, i.e., the practice of testing the performance of an instrument in the field and sending it back to the laboratory for recalibration if needed. Indeed, the instrument performance is subject to deterioration over time due to aging, operating conditions, the surrounding environment, and other random or unexpected events.

For example, in the case of catching-type gauges, a typical procedure would involve periodically checking the performance of the instrument using a suitable field calibrator. The results of the field test are then compared with the expected performance of the gauge, such as from the calibration certificate, and deviations from the expected behavior are calculated. If deviations remain within a satisfactory margin (say $\pm 1\%$), the instrument is still suitable to operate. When deviations are larger, the instrument is either replaced with a new one or sent back to the laboratory for recalibration. The period between two successive field inspections can be set to an initial value (e.g., 1 or 3 years) and then expanded or reduced depending on the results of the first test (if the instrument performance is close to the original behavior, the next inspection can be delayed, and vice versa).

12.8 Application

The use of liquid and solid precipitation measurements covers such a broad spectrum of applications that compiling any detailed list would inevitably fail to be comprehensive. Most of these are based on the observation and investigation of typically measured characteristics of precipitation such as the rainfall

amount, intensity, and duration, in addition to the frequency of intense rainfall events [12.73]. The most common ones include precipitation climatology studies, statistics of extreme events for engineering design, meteo-hydrological warnings and flood protection, optimization of irrigation for agriculture, water resources

management and potable water supply, pollution control, among others.

Since liquid and solid precipitation are the forcing input of the land phase of the hydrological cycle, the knowledge of precipitation, its variability, and the observed patterns of precipitation events in both space and time are of paramount importance for most hydrological studies. The consequences of such studies for the engineering practice are exploited in everyday technical operations for the design, management, and maintenance of any man-made structure that interacts with water in the natural landscape. The *design rainfall* is indeed a common variable used in civil engineering for the realization of urban drainage networks, bridges, levees, erosion control structures, and many other civil works. The design rainfall is obtained from the statistical analysis of long time series of rainfall observations and describes the amount of rain that is expected with a given probability of occurrence at a given location and over a predefined time window.

Measurements of precipitation intensity, and especially long records of measurements extending into the past, are of foremost importance in the management of flood hazard, since the return period of extreme events is derived from the statistical analysis of such time series. Analogously, in water resources management, precipitation measurements are essential for evaluating the availability and variability of freshwater resources (springs, aquifers, etc.) and the management of reservoirs. In addition, precipitation is one of the most important sources of renewable energy, as it releases large amounts of water over high-elevation landscape, providing the potential energy exploited by hydropower plants to obtain sustainable energy.

Agriculture is a major user of precipitation measurements, given the need for adjusting the amount of water provided to crops in order to optimize the growth rate and maximize harvests, especially in regions characterized by a scarcity of precipitation. In addition, the protection of crops from hail and other intense precipitation events requires the availability of direct in-situ observations.

Climatological studies should be based on reliable and accurate data sets of precipitation measurements in order to estimate possible long-term trends and cyclical patterns. The correct measurement of precipitation and other meteorological and hydrological variables, as well as the correct interpretation of historical data, will be of foremost importance in the future for the prediction of changes in weather patterns affecting the earth's climate.

In light of the large demand for precipitation measurements, national or regional agencies in most countries are in charge of deploying, maintaining, and man-

aging precipitation monitoring networks in order to supply the measured data to various types of users. Each application, however, has its own specific requirements in terms of both the measured quantities and the sensitivity, resolution, and accuracy of the measurement instruments.

For example, real-time control of urban drainage networks may require precipitation intensity measurements at a fine temporal resolution (1 min) and with high accuracy, while irrigation control for agricultural purposes may require measurements of the precipitation depth at the daily or weekly scale, with lower accuracy. Measurements used to calibrate precipitation estimates provided by remote sensing tools (e.g., radar or satellite-borne sensors) may require highly accurate knowledge of the particle size distribution and type of hydrometeors at the timescale of minutes. For some users, the accuracy of precipitation measurements is not as crucial as timeliness, and thus amateur networks of low-cost/low-accuracy instruments are successful in that they provide real-time access (within minutes) to the measured data over the Internet.

This broad range of requirements is precisely the reason why the national and international standards on the accuracy of rainfall intensity gauges aim at defining the required performance of measurement instruments according to a small number of classes. Each instrument is assigned to a class based on specified and certified performance, so that the user may decide which class of instruments is required for the application in hand. Once the instrument's class is declared by the station manager, with the associated third-party certification, assessing the suitability of measurements thereof for a specific application would be straightforward.

Although a single station or a small network can be easily developed as a fit-for-purpose technical solution, and instruments thus selected according to the most suitable technology and specifications, measurements from national meteorological networks are made available to the general user with little awareness of the intended use. Adhering to a fit-for-purpose philosophy is therefore very difficult in the case of large networks, which are rather multipurpose services. There is a danger that national agencies may interpret their mission as that of fitting a single purpose (e.g., civil protection), or may try to meet the requirements of one category of users alone (especially if this is the least demanding one). Instead, given the complex nature of the targeted phenomena, for precipitation monitoring networks to provide optimal service they should ideally meet the most demanding requirements of fine temporal resolution and high accuracy, allowing users to possibly degrade the information to the scale they actually need for each application.

12.9 Future Developments

The results of the recent WMO intercomparison initiatives and the ongoing accurate lab/field tests within the activities of the WMO/CIMO Lead Centre B. Castelli on Precipitation Intensity, Italy [12.81], enable the following considerations to be highlighted on the achievable accuracy of currently available instruments for in-situ precipitation measurements.

For liquid precipitation, conventional tipping-bucket rain gauges have the potential to achieve reasonable to high accuracy over the medium to upper range of rainfall intensities. In order to achieve such a high level of accuracy, suitable dynamic calibration is required, and appropriate software corrections for both sampling and mechanical errors must necessarily be applied. Note that the common statistics derived from precipitation intensity records are particularly affected if corrections are not applied (see, e.g., [12.20]). In addition, the catching performance of the gauge is affected by the interaction of the gauge body with the wind, and correction or the use of instruments with an aerodynamic shape are recommended.

Weighing-type gauges are the second most widely employed class of instruments currently in operation for precipitation measurements. Advantages include the absence of mechanical parts, better conveying performance because of the absence of the funnel, and suitability for solid precipitation measurements (snow). However, test results indicate that the influence of the dynamic response (time constant) of the measuring system on the accuracy of time-varying precipitation intensities (including the smoothing algorithm used to deal with the noise) is significant for this kind of instrument and must be taken into account accordingly. Otherwise, the overall accuracy of the weighing gauge can be even lower than that of traditional tipping-bucket rain gauges [12.82]. Again, the statistics on precipitation extremes are particularly sensitive to the associated errors [12.30].

For solid precipitation measurements, the catching performance of the gauge is the key issue, and environmental error sources (especially wind) are the most influential factors. The shape of the gauge body is critical in determining its aerodynamic response when impacted by the wind, and correction curves (either empirically or numerically derived) must be applied to account for the associated undercatch. The use of wind-screens or the practice of burying the instruments with the orifice at the level of the surrounding ground may attenuate this effect.

Non-catching-type instruments are the emerging class of in-situ precipitation gauges. For these

instruments, rigorous testing is more complicated, since rain droplets, crystals, and snowflakes of various size and density should be produced—instead of an equivalent water flow—to provide the reference precipitation. Even the calibration of such instruments is still a problem [12.83], and based on the results of the recent WMO intercomparison of rainfall intensity gauges in the field, caution should be exercised in using the information obtained from non-catching instruments in any real-world application, and even in assessing the results of scientific investigations based on such measurements [12.4].

However, the development of highly accurate non-catching gauges for both liquid and solid precipitation is an increasingly relevant and pressing requirement in the atmospheric and hydrological sciences and their applications. Indeed, national meteorological services and other organizations in charge of the management of monitoring networks over large regions generally prefer such kinds of instruments. This is because of their potential for reducing maintenance costs (by eliminating any moving part or containers to be periodically emptied), the high temporal resolution, and their suitability for use as part of a fully automated monitoring network. Drawbacks can be easily identified in the higher complexity of the exploited technology, such that the user's ability to correctly maintain and calibrate the instrument may be limited.

Whatever the instrumentation employed, the actual requirements for precipitation monitoring networks are primarily their accuracy and reliability. Therefore, the measuring principle alone is insufficient in discriminating between the various types of gauges. Rather, the performance of each instrument over the measuring range of interest for the application in hand should be the focal point, based on well-documented procedures for the assessment and certification of such performance in fully controlled conditions, as well as on the traceability of the measurement to the international standards of mass and time.

This philosophy was the basis for the development of the WMO recommendations on the accuracy of rainfall intensity measurements [12.1], which indicate a range of $\pm 5\%$ as the maximum admissible error (in the laboratory) for *RI* measurements at the time resolution of 1 min. Based on such indications, national standards on the accuracy of precipitation measurements are appearing (e.g., [12.54, 84, 85]), and the standardization process within CEN and ISO has already begun.

12.10 Further Reading

Further information on precipitation measurements can be found in the following publications:

- WMO: Guide to Instruments and Methods of Observation, WMO-No. 8, Volume I - Measurement of Meteorological Variables. (World Meteorological Organization, Geneva, 2018)
- CEN: Hydrometry—Measurement requirements and classification of rainfall intensity measuring instruments, EN 17277:2019
- L. Lanza, C. Leroy, M. Alexandropoulos, L. Stagi, W. Wauben: Laboratory Intercomparison of Rainfall Intensity Gauges, World Meteorological Organisation Instruments and Observing Methods (Rep. No. 84, WMO/TD No. 1304) (2006)
- E. Vuerich, C. Monesi, L.G. Lanza, L. Stagi, E. Lanzinger: WMO field intercomparison of rainfall intensity gauges, World Meteorological Organisation Instruments and Observing Methods (Rep. 99) (2009)
- WMO: WMO Solid Precipitation Intercomparison Experiment (SPICE) (2012–2015), IOM Report-No. 131 (2018).

References

- 12.1 WMO: *Guide to Instruments and Methods of Observation*, WMO-No. 8, Volume I, Measurement of Meteorological Variables (World Meteorological Organization, Geneva 2018)
- 12.2 I. Strangeways: *Precipitation: Theory, Measurement and Distribution* (Cambridge University Press, Cambridge 2006)
- 12.3 S. Michaelides, V. Levizzani, E. Anagnostou, P. Bauer, T. Kasparis, J.E. Lane: Precipitation: Measurement, remote sensing, climatology and modeling, *Atmos. Res.* **94**(4), 512–533 (2009)
- 12.4 E. Vuerich, C. Monesi, L.G. Lanza, L. Stagi, E. Lanzinger: *WMO Field Intercomparison of Rainfall Intensity Gauges*, WMO/TD-No.1504 IOM Report No.99 (World Meteorological Organisation, Geneva 2009)
- 12.5 J.C. Kurtyka: *Precipitation Measurements Study* (University of Illinois, Urbana 1953)
- 12.6 I. Strangeways: A history of rain gauges, *Weather* **65**(5), 133–138 (2010)
- 12.7 J. Hann: Die ältesten Regenmengen in Palästina, *Meteorol. Z.* **12**, 136–140 (1895)
- 12.8 J. Feliks: *Agriculture in Palestine in the Period of the Mishna and Talmud* (Magnes, Jerusalem 1963), (in Hebrew)
- 12.9 Y. Goldreich: *The Climate of Israel: Observation, Research and Application* (Springer, New York 2003)
- 12.10 W.E. Middleton: *Invention of the Meteorological Instruments* (Johns Hopkins Press, Baltimore 1969)
- 12.11 V. Alexei: *Qin Jiushao, Chinese Mathematician*. *Encyclopædia Britannica* (2017). <https://www.britannica.com/biography/Qin-Jiushao>, Accessed 05 July 2021
- 12.12 J. Needham: *Science and Civilization in China. Vol. 3: Mathematics and the Science of the Heavens and the Earth* (Cambridge Univ. Press, Cambridge 1959)
- 12.13 A.K. Biswas: The automatic rain-gauge of Sir Christopher Wren, F.R.S., *Notes Rec. R. Soc. Lond.* **22**(1/2), 94–104 (1967)
- 12.14 I.R. Calder, C.H.R. Kidd: A note on the dynamic calibration of tipping-bucket gauges, *J. Hydrol.* **39**, 383–386 (1978)
- 12.15 J. Marsalek: Calibration of the tipping-bucket rain-gauge, *J. Hydrol.* **53**(3–4), 343–354 (1981)
- 12.16 J. Niemczynowicz: The dynamic calibration of tipping-bucket raingauges, *Hydrol. Res.* **17**(3), 203–214 (1986)
- 12.17 Č. Maksimović, L. Bužek, J. Petrović: Corrections of rainfall data obtained by tipping bucket rain gauge, *Atmos. Res.* **27**(1), 45–53 (1991)
- 12.18 M.D. Humphrey, J.D. Istok, J.Y. Lee, J.A. Hevesi, A.L. Flint: A new method for automated dynamic calibration of tipping-bucket rain gauges, *J. Atmos. Ocean. Technol.* **14**(6), 1513–1519 (1997)
- 12.19 M. Colli, L.G. Lanza, P.W. Chan: Co-located tipping-bucket and optical drop counter RI measurements and a simulated correction algorithm, *Atmos. Res.* **119**, 3–12 (2013)
- 12.20 P. La Barbera, L.G. Lanza, L. Stagi: Tipping bucket mechanical errors and their influence on rainfall statistics and extremes, *Water. Sci. Technol.* **45**(2), 1–9 (2002)
- 12.21 M.H. Stow: Rain gauge experiments at Hawskers, near Whitby, Yorkshire, *Br. Rainfall* **1870**, 9–22 (1871)
- 12.22 B.E. Goodison, P.Y.T. Louie, D. Yang: *WMO Solid Precipitation Measurement Intercomparison – Final Report*, Rep. No. 67, WMO/TD-No. 872 (World Meteorological Organisation, Geneva 1998)
- 12.23 B. Sevruck, M. Ondras, B. Chvila: The WMO precipitation measurement intercomparisons, *Atmos. Res.* **92**(3), 376–380 (2009)
- 12.24 B. Sevruck, W.R. Hamon: *International Comparison of National Precipitation Gauges with a Reference Pit Gauge*, WMO/TD-No. 38, IOM Report No. 17 (World Meteorological Organisation, Geneva 1984) p. 135
- 12.25 M. Leroy, C. Bellevaux, J.P. Jacob: *WMO Intercomparison of Present Weather Sensors/Systems: Canada and France, 1993–1995. Final Report*,

- WMO/TD-No. 887, IOM Report No. 73 (World Meteorological Organisation, Geneva 1998)
- 12.26 L. Lanza, M. Leroy, C. Alexandropoulos, L. Stagi, W. Wauben: *Laboratory Intercomparison of Rainfall Intensity Gauges*, WMO/TD-No. 1304, IOM Report No. 84 (World Meteorological Organisation, Geneva 2006)
- 12.27 L.G. Lanza, E. Vuerich: The WMO field intercomparison of rain intensity gauges, *Atmos. Res.* **94**(4), 534–543 (2009)
- 12.28 L.G. Lanza, E. Vuerich: Non-parametric analysis of one-minute rain intensity measurements from the WMO Field Intercomparison, *Atmos. Res.* **103**, 52–59 (2012)
- 12.29 L.G. Lanza, L. Stagi: High resolution performance of catching type rain gauges from the laboratory phase of the WMO Field Intercomparison of rain intensity gauges, *Atmos. Res.* **94**(4), 555–563 (2009)
- 12.30 L.G. Lanza, L. Stagi: Non-parametric error distribution analysis from the laboratory calibration of various rainfall intensity gauges, *Water. Sci. Technol.* **65**(10), 1745–1752 (2012)
- 12.31 WMO: *WMO Solid Precipitation Intercomparison Experiment (SPICE) (2012–2015)*, IOM Report No. 131 (World Meteorological Organisation, Geneva 2018)
- 12.32 B. Sevruk: *Methods of Correction for Systematic Error in Point Precipitation Measurement for Operational Use*, WMO-No. 589; OHR No. 21 (World Meteorological Organisation, Geneva 1982)
- 12.33 L.G. Lanza, L. Stagi: Certified accuracy of rainfall data as a standard requirement in scientific investigations, *Adv. Geosci.* **16**, 43–48 (2008)
- 12.34 A. Molini, P. La Barbera, L.G. Lanza, L. Stagi: Rainfall intermittency and the sampling error of tipping-bucket rain gauges, *Phys. Chem. Earth C* **26**(10–12), 737–742 (2001)
- 12.35 A. Molini, L.G. Lanza, P. La Barbera: Improving the accuracy of tipping-bucket rain records using disaggregation techniques, *Atmos. Res.* **77**(1–4), 203–217 (2005)
- 12.36 A. Molini, L.G. Lanza, P. La Barbera: The impact of tipping-bucket raingauge measurement errors on design rainfall for urban-scale applications, *Hydrol. Process.* **19**(5), 1073–1088 (2005)
- 12.37 A. Adami, L. Da Deppo: On the systematic errors of tipping bucket recording rain gauges. In: *Proc. Int. Worksh. Correct. Precip. Meas., Zurich* (1985) pp. 1–3
- 12.38 R.M. Lan, Y.Q. Cao: Design and realization of high precision FBG rain gauge based on triangle cantilever beam and its performance research, *Optoelectron. Lett.* **11**(3), 229–232 (2015)
- 12.39 C.Y. Kuo, S.Y. Chen, W.F. Liu, H.Y. Chang: The fiber grating rain gauge. In: *7th Int. Symp. Next Gener. Electron. (ISNE)* (2018) pp. 1–2
- 12.40 M. Stagnaro, A. Cauteruccio, M. Colli, L.G. Lanza, P.W. Chan: Laboratory assessment of two catching type drop-counting rain gauges, *Geophys. Res. Abstr.* **20**, EGU2018–12407 (2018)
- 12.41 M. Löffler-Mang, D. Schön, M. Landry: Characteristics of a new automatic hail recorder, *Atmos. Res.* **100**(4), 439–446 (2011)
- 12.42 R.M. Rasmussen, J. Hallett, R. Purcell, S.D. Landolt, J. Cole: The hotplate precipitation gauge, *J. Atmos. Ocean. Technol.* **28**(2), 148–164 (2011)
- 12.43 A. Cauteruccio, E. Chinchella, M. Stagnaro, L.G. Lanza: Snow particle collection efficiency and adjustment curves for the hotplate precipitation gauge, *J. Hydrometeor.* **22**, 941–954 (2021)
- 12.44 B.E. Sheppard: Effect of rain on ground-based microwave radiometric measurements in the 20–90-GHz range, *J. Atmos. Ocean. Technol.* **13**(6), 1139–1151 (1996)
- 12.45 F.S. Marzano, D. Cimini, M. Montopoli: Investigating precipitation microphysics using ground-based microwave remote sensors and disdrometer data, *Atmos. Res.* **97**(4), 583–600 (2010)
- 12.46 CEN: *Hydrometry – Measurement of the Rainfall Intensity (Liquid Precipitation): Requirements, Calibration Methods and Field Measurements*, CEN/TR 16469:2013 (Comité Européen de Normalisation, Brussels 2013)
- 12.47 ISO: *ISO: Uncertainty of Measurement – Part 3: Guide to the Expression of Uncertainty in Measurement (GUM:1995)*, ISO/IEC Guide 98–3:2008 (International Organization for Standardization, Geneva 2008)
- 12.48 JCGM: *International Vocabulary of Metrology – Basic and General Concepts and Associated Terms (VIM) (Joint Committee for Guides in Metrology, Sèvres 2008)*
- 12.49 M. Colli, M. Pollock, M. Stagnaro, L.G. Lanza, M. Dutton, E. O’Connell: A computational fluid-dynamics assessment of the improved performance of aerodynamic rain gauges, *Water. Resour. Res.* **54**(2), 779–796 (2018)
- 12.50 V. Nešpor, B. Sevruk: Estimation of wind-induced error of rainfall gauge measurements using a numerical simulation, *J. Atmos. Ocean. Technol.* **16**(4), 450–464 (1999)
- 12.51 M. Colli, R. Rasmussen, J.M. Thériault, L.G. Lanza, C.B. Baker, J. Kochendorfer: An improved trajectory model to evaluate the collection performance of snow gauges, *J. Appl. Meteorol. Climatol.* **54**(8), 1826–1836 (2015)
- 12.52 ISO: *Air quality. Meteorology. Siting Classifications for Surface Observing Stations on Land*, ISO 19289:2015 (International Organization for Standardization, Geneva 2015)
- 12.53 A. Cauteruccio, M. Colli, L.G. Lanza: The impact of wind and turbulence on ground-based liquid precipitation measurements. In: *Tech. Conf. Meteorol. Environ. Instrum. Methods Obs. (WMO/CIMO TECO)* (2016)
- 12.54 UNI: *Hydrometry – Measurement of Rainfall Intensity (Liquid Precipitation) – Metrological Requirements and Test Methods for Catching Type Gauges*, UNI 11452:2012 (Ente Nazionale Italiano di Unificazione, Milan 2012)
- 12.55 F.Y. Testik, M.K. Rahman: High-speed optical disdrometer for rainfall microphysical observations, *J. Atmos. Ocean. Technol.* **33**(2), 231–243 (2016)

- 12.56 A. Kruger, W.F. Krajewski: Two-dimensional video disdrometer: A description, *J. Atmos. Ocean. Technol.* **19**(5), 602–617 (2002)
- 12.57 T.A. Costello, H.J. Williams: Short duration rainfall intensity measured using calibrated time-of-tip data from a tipping bucket raingage, *Agric. For. Meteorol.* **57**(1), 147–155 (1991)
- 12.58 E. Habib, W.F. Krajewski, A. Kruger: Sampling errors of tipping-bucket rain gauge measurements, *J. Hydrol. Eng.* **6**(2), 159–166 (2001)
- 12.59 M. Stagnaro, M. Colli, L.G. Lanza, P.W. Chan: Performance of post-processing algorithms for rainfall intensity using measurements from tipping-bucket rain gauges, *Atmos. Meas. Tech.* **9**(12), 5699–5706 (2016)
- 12.60 M.D. Pollock, G. O'Donnell, P. Quinn, M. Dutton, A. Black, M.E. Wilkinson, M. Colli, M. Stagnaro, L.G. Lanza, E. Lewis, C.G. Kilsby, P.E. O'Connell: Quantifying and mitigating wind-induced undercatch in rainfall measurements, *Water. Resour. Res.* **54**(6), 3863–3875 (2018)
- 12.61 J.M. Thériault, R. Rasmussen, E. Petro, J.Y. Trépanier, M. Colli, L.G. Lanza: Impact of wind direction, wind speed, and particle characteristics on the collection efficiency of the double fence inter-comparison reference, *J. Appl. Meteorol. Climatol.* **54**(9), 1918–1930 (2015)
- 12.62 R. Rasmussen, B. Baker, J. Kochendorfer, T. Meyers, S. Landolt, A.P. Fischer, J. Black, J.M. Thériault, P. Kucera, D. Gochis, C. Smith, R. Nitu, M. Hall, K. Ikeda, E. Gutmann: How well are we measuring snow: The NOAA/FAA/NCAR winter precipitation test bed, *Bull. Am. Meteorol. Soc.* **93**(6), 811–829 (2012)
- 12.63 M.A. Wolff, K. Isaksen, A. Petersen-Øverleir, K. Ødemark, T. Reitan, R. Brækkan: Derivation of a new continuous adjustment function for correcting wind-induced loss of solid precipitation: Results of a Norwegian field study, *Hydrol. Earth Syst. Sci.* **19**(2), 951–967 (2015)
- 12.64 J. Kochendorfer, R. Rasmussen, M. Wolff, B. Baker, M.E. Hall, T. Meyers, S. Landolt, A. Jachcik, K. Isaksen, R. Brækkan, R. Leeper: The quantification and correction of wind-induced precipitation measurement errors, *Hydrol. Earth Syst. Sci.* **21**(4), 1973–1989 (2017)
- 12.65 J. Kochendorfer, R. Nitu, M. Wolff, E. Mekis, R. Rasmussen, B. Baker, M.E. Earle, A. Reverdin, K. Wong, C.D. Smith, D. Yang, Y.-A. Roulet, S. Buisan, T. Laine, G. Lee, J.L.C. Aceituno, J. Alastrué, K. Isaksen, T. Meyers, R. Brækkan, S. Landolt, A. Jachcik, A. Poikonen: Analysis of single-Alter-shielded and unshielded measurements of mixed and solid precipitation from WMO-SPICE, *Hydrol. Earth Syst. Sci.* **21**(7), 3525–3542 (2017)
- 12.66 S.T. Buisán, M.E. Earle, J.L. Collado, J. Kochendorfer, J. Alastrué, M. Wolff, C.D. Smith, J.I. López-Moreno: Assessment of snowfall accumulation underestimation by tipping bucket gauges in the Spanish operational network, *Atmos. Meas. Tech.* **10**(3), 1079–1091 (2017)
- 12.67 M. Colli, L.G. Lanza, R. Rasmussen, J.M. Thériault: The collection efficiency of shielded and unshielded precipitation gauges. Part I: CFD airflow modeling, *J. Hydrometeorol.* **17**(1), 231–243 (2016)
- 12.68 M. Colli, L.G. Lanza, R. Rasmussen, J.M. Thériault: The collection efficiency of shielded and unshielded precipitation gauges. Part II: Modeling particle trajectories, *J. Hydrometeorol.* **17**(1), 245–255 (2016)
- 12.69 A. Cauteruccio, L.G. Lanza: Parameterization of the collection efficiency of a cylindrical catching-type rain gauge based on rainfall intensity, *Water* **12**, 3431 (2020)
- 12.70 A. Cauteruccio, E. Brambilla, M. Stagnaro, L.G. Lanza, D. Rocchi: Wind Tunnel Validation of a Particle Tracking Model to Evaluate the Wind-Induced Bias of Precipitation Measurements, *Water Resour. Res.* **57**, e2020WR028766 (2021)
- 12.71 J.S. Marshall, W.M. Palmer: The distribution of raindrops with size, *J. Meteorol.* **5**(4), 165–166 (1948)
- 12.72 M.A.A. Santana, P.L.O. Guimarães, L.G. Lanza, E. Vuerich: Metrological analysis of a gravimetric calibration system for tipping-bucket rain gauges, *Meteorol. Appl.* **22**, 879–885 (2015)
- 12.73 M.A.A. Santana, P.L.O. Guimarães, L.G. Lanza: Development of procedures for calibration of meteorological sensors. Case study: Calibration of a tipping-bucket rain gauge and data-logger set, *J. Phys. Conf. Ser.* **975**(1), 012006 (2018)
- 12.74 M.A.A. Santana, P.L.O. Guimarães, L.G. Lanza: Uncertainty contributions in the calibration of rain gauges. In: *Metrol. Meteorol. Clim. Conf. (MMC)* (2016)
- 12.75 CEN: *Hydrometry – Measurement Requirements and Classification of Rainfall Intensity Measuring Instruments*, EN 17277:2019 (Comité Européen de Normalisation, Brussels 2019)
- 12.76 ISO: *Quality Management Systems – Fundamentals and Vocabulary*, ISO 9000:2015, 4th edn. (International Organization for Standardization, Geneva 2015)
- 12.77 ISO: *Quality Management Systems – Requirements*, ISO 9001:2015, 5th edn. (International Organization for Standardization, Geneva 2015)
- 12.78 ISO: *Quality Management – Quality of an Organization – Guidance to Achieve Sustained Success*, ISO 9004:2018, 4th edn. (International Organization for Standardization, Geneva 2018)
- 12.79 ISO: *Guidelines for Auditing Management Systems*, ISO 19011:2018, 3rd edn. (International Organization for Standardization, Geneva 2018)
- 12.80 ISO: *Measurement Management Systems – Requirements for Measurement Processes and Measuring Equipment*, ISO 10012:2004, 3rd edn. (International Organization for Standardization, Geneva 2018)
- 12.81 WMO-CIMO: Lead Centre “Benedetto Castelli” on Precipitation Intensity, <http://www.precipitation-intensity.it> (2020), Accessed 05 July 2021
- 12.82 M. Colli, L.G. Lanza, P. La Barbera: Performance of a weighing rain gauge under laboratory simulated time-varying reference rainfall rates, *Atmos. Res.* **131**, 3–12 (2013)

- 12.83 L.G. Lanza, A. Merlone, A. Cauteruccio, E. Chinchella, M. Stagnaro, M. Dobre, M.C. Garcia Izquierdo, J. Nielsen, H. Kjeldsen, Y.A. Roulet, G. Coppa, C. Musacchio, C. Bordinanu, M. Parrondo: Calibration of non-catching precipitation measurement instruments: A review, *Meteorol. Appl.* **28**, e2002 (2021)
- 12.84 BSI: *Acquisition and Management of Meteorological Precipitation Data from a Gauge Network*, BS 7843:2012 (British Standards Institution, London 2012)
- 12.85 VDI: *Environmental Meteorology – Meteorological Measurements – Precipitation*, VDI 3786-7 (Beuth, Berlin 2010)

Arianna Cauteruccio

DICCA – Dep. Civil, Chemical and Environmental Engineering
University of Genova
Genova, Italy
arianna.cauteruccio@edu.unige.it



Arianna Cauteruccio, PhD in Civil, Chemical and Environmental Engineering – Fluid-Dynamics and Environmental Engineering at the University of Genova, and Collaborator of the WMO-CIMO Lead Centre “B. Castelli” on Precipitation Intensity. Graduated in Civil and Environmental Engineering (University of Genova, 2016). Research fellow since 2019, conducts research on the uncertainty of precipitation measurements, urban hydrology and flood risk assessment and mitigation, with both numerical (Computational Fluid Dynamics simulations) and experimental (Wind Tunnel and field tests) approaches.

Matteo Colli

DICCA – Dep. Civil, Chemical and Environmental Engineering
University of Genova
Genova, Italy

now at ARTYS s.r.l.
Genova, Italy
m.colli@artys.it



Matteo Colli (M'18) was born in Genova, Italy, in 1983. He received the B.S. and M.S. degrees in Water and Soil Defence Engineering from the University of Genova, Italy, in 2010 and the Ph.D. degree in Fluid Dynamics and Environmental Engineering Processes from the University of Genova, Italy, in 2014. From 2014 to 2017 he was a Research Assistant with the Dep. of Civil, Chemical and Environmental Engineering, University of Genova. Starting from 2017 he is a Research Assistant with the Dep. of Electrical, Electronics and Telecommunication Engineering and Naval Architecture, University of Genova. His research interests include atmospheric measurements, fluid dynamics numerical computation and hydrology.

Mattia Stagnaro



DICCA – Dep. Civil, Chemical and Environmental Engineering
University of Genova
Genova, Italy
mattia.stagnaro@unige.it

Mattia Stagnaro is Research Assistant with the Department of Civil, Chemical and Environmental Engineering, University of Genova. He received the M.Sc. degree in Water and Soil Defense Engineering, and the Ph.D. degree in Fluid-dynamics and Environmental Engineering from the University of Genova, in 2010 and 2014, respectively. Since 2015 he started collaborating with the WMO/CIMO Lead Centre “B.Castelli” on Precipitation Intensity. His research interests include precipitation measurements techniques, numerical simulation to evaluate environmental effects on the measures, and hydrological processes.

Luca G. Lanza



DICCA – Dep. Civil, Chemical and Environmental Engineering
University of Genova
Genova, Italy
luca.lanza@unige.it

Luca G. Lanza is Professor of Hydrology and Hydraulic Structures at the University of Genova, and Scientific Director of the WMO-CIMO Lead Centre “B. Castelli” on Precipitation Intensity. Graduated in Civil Engineering (University of Genova, 1991) with a Ph.D. in Hydro-dynamics (University of Padova, 1995) conducts research on urban hydrology, flood risk assessment and mitigation, environmental monitoring and water resources management, and authored about 400 papers in peer reviewed journals and conference proceedings. He provides technical and technological advisory services for landscape management bodies and private companies.

Emanuele Vuerich

Italian Air Force
Rome, Italy
emanuele.vuerich@aeronautica.difesa.it



Emanuele Vuerich received his M.Sc. Degree of Physics at the University of Roma Tre and the M.Sc. Degree in Leadership and Strategic Analysis at University of Florence. He obtained the qualification in Atmospheric Science and Meteorology and the title of WMO qualified weather Forecaster (Italian Air Force Training Centre in Pratica di Mare – Rome). Chairperson of The WMO CIMO Expert Team in Instrument Intercomparisons (WMO, 2010–2018).

Visibility Sen

13. Visibility Sensors

Martin Löffler–Mang, Klaus Heyn

The main application fields of visibility sensors are traffic safety (air, road, and sea) as well as air quality control. For measurements of the visibility of the atmosphere, a variety of techniques have been used in the past. More recently, optical technologies that utilize transmittance and scattered light measurements have dominated the commercially available instruments, and these are presented in the following. Of special interest are the extinction theory and the deduction of the meteorological optical range. Furthermore, the most important technology limitations are discussed. Besides technical data, the necessary maintenance associated with each method, as well as the methods of quality control and calibration, are presented. Finally, some research developments are described as possible devices for the future.

13.1	Measurement Principles and Parameters	402	13.3.3	Transmissometer	407
13.2	History	403	13.3.4	Instruments Determining the Scatter Coefficient	409
13.2.1	Telephotometric Instruments	403	13.3.5	Forward Scatter Meter	410
13.2.2	Visual Extinction Meters	403	13.4	Devices and Systems	414
13.2.3	Early Analog Visibility Sensors Allowed First Observation Automations	404	13.4.1	Transmissometer	414
13.2.4	First Integrating Nephelometer for Visibility Measurement	405	13.4.2	Scattered Light Sensor	415
13.3	Theory	405	13.4.3	Transmittance Versus Scattered Light Measurements	417
13.3.1	Extinction	405	13.5	Specifications	417
13.3.2	Meteorological Optical Range (MOR) ...	405	13.6	Quality Control	418
			13.6.1	Setup Rules	418
			13.6.2	Data Quality Control	418
			13.6.3	Parasitic Drags and Impact on the Measurement Uncertainty	419
			13.7	Maintenance	421
			13.8	Application	423
			13.8.1	Climatology of Visibility Measurements	423
			13.8.2	Air, Street, and Sea Traffic	423
			13.8.3	Solar and Wind Power Plants	425
			13.8.4	Air Quality Control	425
			13.9	Future Developments	426
			13.9.1	Multiangle Technologies	426
			13.9.2	Multibeam Technologies	427
			13.9.3	Visibility Lidars	427
			13.9.4	Usage of Cameras	427
			13.10	Further Reading	427
			References		428

Visibility is a complex psychophysical phenomenon, governed mainly by the atmospheric extinction coefficient associated with solid and liquid particles held in suspension in the atmosphere; the extinction is caused primarily by scattering rather than by absorption of the light. Its estimation is subject to variations in individual perception and interpretative ability, as well as the light source characteristics and the transmission factor. Thus, any visual estimate of visibility is subjective [13.1].

When visibility is estimated by a human observer (see Chap. 22) it depends not only on the photometric and dimensional characteristics of the object which is, or should be, perceived, but also on the observer's con-

trast threshold. At night, it depends on the intensity of the light sources, the background illuminance and the adaptation of the observer's eyes to darkness and the observer's illuminance threshold [13.1].

Consequently instrumental methods are utilized to measure the extinction coefficient from which the meteorological optical range (MOR) may be calculated. These measurements are based on the assumption that the extinction coefficient is homogeneously distributed and the result of the point measurement can be applied to the entire distance. Some instruments measure the light attenuation directly and others measure the scattering of light to derive the extinction coefficient.

13.1 Measurement Principles and Parameters

Visibility is an optical phenomenon and, therefore, all estimates and measurements of visibility in the past and today use optical methods. Table 13.1 gives an overview of the utilized and measured parameters for visibility. Furthermore, in Table 13.2 the current relevant parameters for visibility measurements are summarized. Air turbidity measurement using the methods listed in this chapter is suitable for air quality monitoring over prolonged periods, e.g., for trend investigations in clean air regions or conurbations.

Basically two categories of instruments for the determination of MOR must be differentiated:

- Instruments that measure the attenuation of the light due to scattering and absorption by particles in the air along a horizontal cylinder of air (transmittance measurement).
- Instruments that measure the intensity of light scattered in specific directions by a small volume of air. From the measured scatter signal (scatter coefficient) the extinction coefficient is directly derived. The absorption of light is often negligible and the scatter signal strength may be considered to represent the extinction coefficient.

Both instrument categories utilize a light transmitter that comprises a collimated light source generating a light beam and a light receiver that comprises a photo detector with lens system to measure the scattered with respect to attenuated light beam.

The typical field of application for transmissometers is along runways in order to provide a precise MOR information for the calculation of the runway visual range (RVR). However, for meteorological stations and/or road or harbor sites the available space does typically not allow to install a transmissometer with 50 or even 100 m baseline length.

The introduced types of instruments that estimate the scatter coefficient require only limited space (1 to 2 m in general). Since the measurement relates only to a very small volume of air, the representativeness of measurements for the general state of the atmosphere at the site may need to be improved by averaging of a number of samples or measurements. In the past the use of this kind of instrument has often been limited to specific applications (for example, highway visibility measurements, or to determine whether fog is present) or when less precise MOR measurements were adequate. However, state-

Table 13.1 Parameters used and measured by visibility sensors

Utilized parameters			
Parameter	Description	Unit	Symbol
Wavelength-dependent spectral radiance (radiant flux)	Radiance of a surface per unit wavelength. This is a directional quantity, sometimes also called <i>spectral intensity</i> .	W sr ⁻¹ m ⁻³	$L_{e,\Omega,\lambda}$
Wavelength		m	λ
Solid angle		sr	Ω
Measured parameters			
Parameter	Description	Unit	Symbol
Spectral directional attenuation coefficient	The attenuation coefficient describes the extent to which the radiant flux of a beam is reduced (absorbed and scattered) as it passes through the atmosphere. It is direction and wavelength-dependent. $\mu_{\Omega,\lambda} = -\frac{1}{L_{e,\Omega,\lambda}} \frac{dL_{e,\Omega,\lambda}}{dz}$	m ⁻¹	$\mu_{\Omega,\lambda}$
Atmospheric transmittance	$T = e^{-\mu l}$ The equation relates the measured atmospheric transmittance to attenuation (extinction) coefficient under consideration of the path length l . In practice the spectral directional transmittance is measured, see below	%	T
Spectral directional transmittance	Transmitted spectral radiance, divided by the received spectral radiance. It is direction and wavelength-dependent. $T_{\lambda,\Omega} = \frac{L_{e,\Omega,\lambda}^t}{L_{e,\Omega,\lambda}^i}$ $L_{e,\Omega,\lambda}^t$ is the transmitted spectral radiance, $L_{e,\Omega,\lambda}^i$ is the received spectral radiance	%	$T_{\Omega,\lambda}$

Table 13.2 Other relevant parameters for visibility measurements

Parameter	Description	Unit	Symbol
Extinction coefficient	Extinction coefficient is an older term for the attenuation coefficient (see Table 13.1) but is still used in meteorology and climatology. In practice the spectral directional attenuation coefficient $\mu_{\Omega,\lambda}$ is measured	m^{-1}	μ
Standard visibility (<i>Normalsichtweite</i>)	Visibility definition by Koschmieder $V_N = -\frac{\ln 0.02}{\mu}$ The distance at which the contrast of a black object against the bright background has reduced to 2%	m	V_N
Meteorological optical range	Operationally used visibility definition incorporates internationally agreed upon contrast safety margin $\text{MOR} = -\frac{\ln 0.05}{\mu}$ The distance at which the contrast of a black object against the bright background has reduced to 5%	m	MOR

of-the-art forward scatter meters are now being used in increasing numbers in automatic meteorological observation systems because of their ability to report MOR over a wide range and their relatively low susceptibility to contamination of optical surfaces compared with transmissometers (see Sect. 13.3.3 for more details).

The siting of visual measuring equipment should be representative; therefore, it should be chosen with the specific measurement task in mind. For aeronautical

purposes, e.g., measurements are to be representative of conditions at the aerodrome or along the runway. In any case the instruments should be installed in accordance with the directions given by the manufacturers and the accessibility for servicing and repairs have to be ensured. The optical axis of a transmissometer with respect to the volume of air in which the extinction coefficient or scatter coefficient is measured should approximately be at the eye level of an observer; 2.0 to 2.5 m above ground level is usual.

13.2 History

For meteorological purposes visibility has traditionally been defined as a quantity to be estimated by a human observer, and observations made in that way had been and are still widely used. However, the human observer estimation of visibility is affected by many subjective and physical factors. The essential meteorological quantity, which is the transparency of the atmosphere, can be measured objectively and nowadays is represented by the MOR. Measurement devices that determine the transparency of the atmosphere have a long history; they have been developed and used since meteorologists started to observe and record visibility.

13.2.1 Telephotometric Instruments

A number of telephotometers have been designed for daytime determination of the extinction coefficient by comparing the apparent luminance of a distant object with that of the sky background. As an example for a historical relevant device a schematic drawing of the

Löhle telephotometer after [13.2] is shown in Fig. 13.1. This relative telephotometer had the advantage that the angular separation of the observation fields could be varied. The last version of this device was produced by Zeiss. Two telescopes F_h and F_z are directed at the horizon sky and the distant object, respectively. A hinge at D permits the adjustment of the separation. There is an adjustable diaphragm in front of the objective of F_h which makes it possible to equate the luminance of the two fields and so measure the ratio B/B_h [13.2].

13.2.2 Visual Extinction Meters

A very simple instrument for use with a distant light at night takes the form of a graduated neutral filter, which reduces the light in a known proportion and can be adjusted until the light is only just visible. The meter reading gives a measure of the transparency of the air between the light and the observer, and from this the extinction coefficient can be calculated. The overall ac-

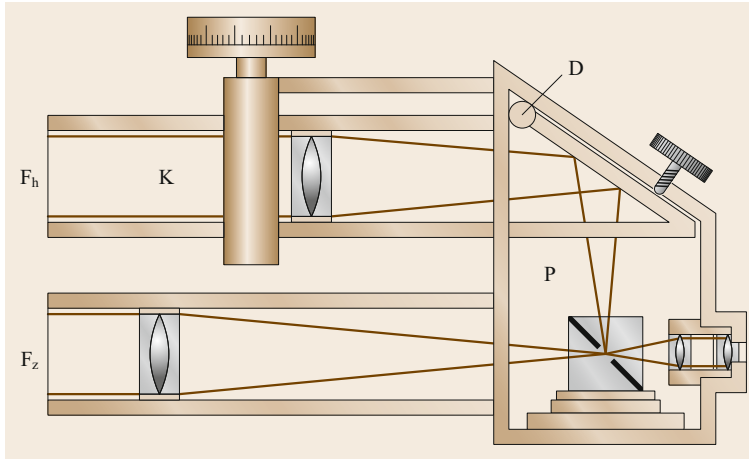


Fig. 13.1 Schematic drawing of the Löhle telephotometer (after [13.2])

curacy depends mainly on variations in the sensitivity of the eye and on fluctuations in the radiant intensity of the light source. The error increases in proportion to MOR.

The advantage of this instrument is that it enables MOR values over a range from 100 m to 5 km to be measured with reasonable accuracy, using only three well-spaced lights, whereas without it a more elaborate series of lights would be essential if the same degree of accuracy were to be achieved. However, the method of using such an instrument (determining the point at which a light appears or disappears) considerably affects the accuracy and homogeneity of the measurements [13.1].

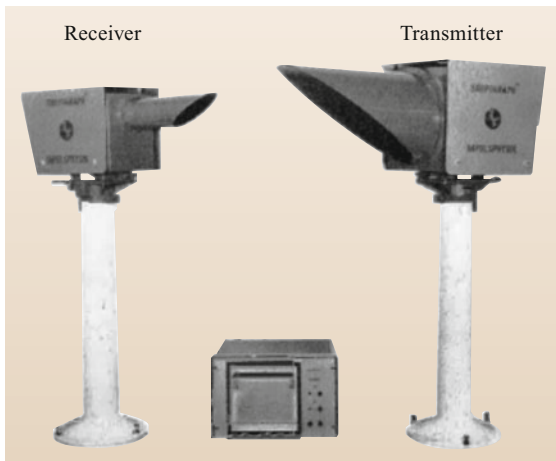


Fig. 13.2 Analog transmissometer SKOPOGRAPH (Impulsphysik, 1960s and 1970s), photo © Impulsphysik, Hamburg, Germany

13.2.3 Early Analog Visibility Sensors Allowed First Observation Automations

By the 1950s, the continuous development in electronics, data distribution and registration technologies had already allowed for the design of the first transmissometers and compact backscatter measurement devices (*F. Friängel*, SKOPOGRAPH and VIDEOGRAPH). Since computer technology at that time was not yet advanced for implementation in customer products (the first 8-bit microprocessor was available in 1975), the measurement, data distribution and recording only had access to analog electronics (analog current data output, chart recorder). Figures 13.2 and 13.3 illustrate the appearance of some exemplary historical devices.

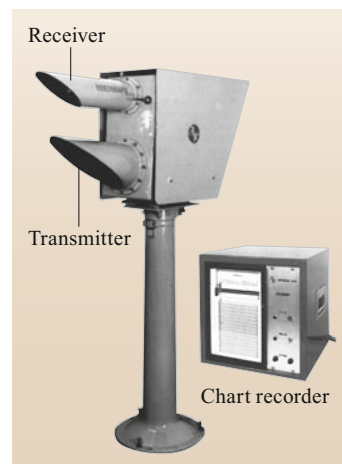


Fig. 13.3 Analog backscatter sensor VIDEOGRAPH (Impulsphysik, 1960s and 1970s), photo © Impulsphysik, Hamburg, Germany

13.2.4 First Integrating Nephelometer for Visibility Measurement

In theory, an integrating nephelometer will give a better estimate of the scatter coefficient than, e.g., a backscatter device like that introduced above. However, in practice it turned out that it was very difficult to prevent the instrument structure from modifying the extinction coefficient in the sample volume. For example, the light beam barrier that is required to avoid optical short cuts between light transmitter and light receiver was located above the measurement volume and provided a significant shadowing for all kinds of precipitation. Consequently, the precipitation-related extinction coefficient was not representatively measured. In Fig. 13.4 a side view of the instrument without mounting pole is shown. Due to their complexity, intense maintenance

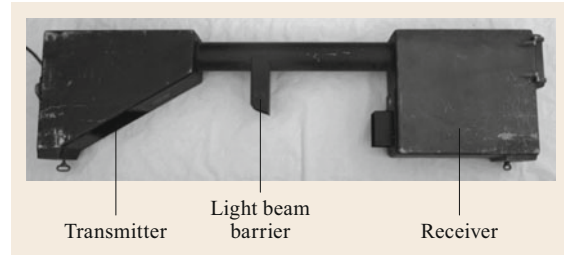


Fig. 13.4 Integrating nephelometer MS04 (AEG/FFM, 1965), photo © Wettermuseum e. V., Museum für Meteorologie und Aerologie, Lindenberg, Germany

requirements, and limitations to determine the extinction coefficient of precipitation particles, this kind of instrumentation achieved no practical relevance for the 24/7 visibility measurement.

13.3 Theory

The following deals with extinction theory, followed by Sect. 13.3.1 on the meteorological optical range (MOR). Furthermore, discussion of transmissometers and instruments determining the scatter coefficient will follow. Finally, details of forward scatter meters are presented.

13.3.1 Extinction

The turbidity of the air is caused by extinction of the visible part of the electromagnetic spectrum by the constituents of the air. Atmospheric air consists of gas molecules plus liquid and solid particles (e.g., cloud and fog droplets, aerosol particles) suspended in the atmosphere. The particles contain, inter alia, water-soluble substances, which give off or take up water vapor depending on the humidity of the surrounding air (evaporation or condensation) and as a result may experience size changes. The size range of the radius from 0.1 to ca. 1 μm is of special significance for the attenuation (extinction) of visible radiation (see Fig. 13.5). Fog typically consists of small water droplets with radii between 2 and max. 10 μm , depending on the fog type (see Fig. 13.6).

There is a relationship between atmospheric turbidity and the visible range. One option for describing the turbidity of the atmosphere is through the MOR, for which one measure is the extinction or attenuation coefficient [13.2–4]. The extinction depends on the wavelength of the radiation and on the thickness and composition of the traversed atmospheric layer. It can

be described by the Bouguer–Lambert–Beer law

$$I = I_0 e^{-b_{\text{ext}}(\lambda)s}, \quad (13.1)$$

where I is the luminous intensity at the end of the traversed atmospheric layer, I_0 the luminous intensity at the beginning of the traversed atmospheric layer, $b_{\text{ext}}(\lambda)$ is the extinction coefficient of the air for the wavelength λ , and s the traversed path length.

Equation (13.1) applies only for monochromatic light of wavelength λ . In practice, the extinction coefficient $b_{\text{ext}}(\lambda)$ is used for polychromatic light in the visible range with adequate accuracy. Equation (13.1) ignores the effect of multiple scattering, which however plays a part only in the case of high extinction values.

13.3.2 Meteorological Optical Range (MOR)

The MOR is the length of path in the atmosphere required to reduce the luminous flux in a collimated beam from an incandescent lamp, at a color temperature of 2700 K, to 5% of its original value [13.1]. The visual range formula proposed by Koschmieder [13.5] is used for an absolutely black visual target in daytime:

$$V = \frac{1}{b_{\text{ext}}} \ln \frac{1}{K'}. \quad (13.2)$$

Koschmieder defined a value of $K' = 0.02$ for the luminance contrast threshold of the eye of a trained observer with normal vision. The range obtained with this value

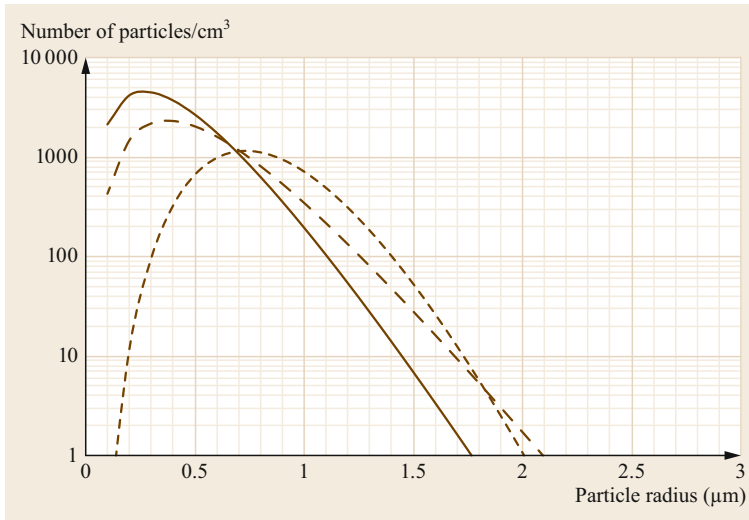


Fig. 13.5 Haze particle size distribution examples for different densities (*dashed lines*) and gamma distribution (*solid line*)

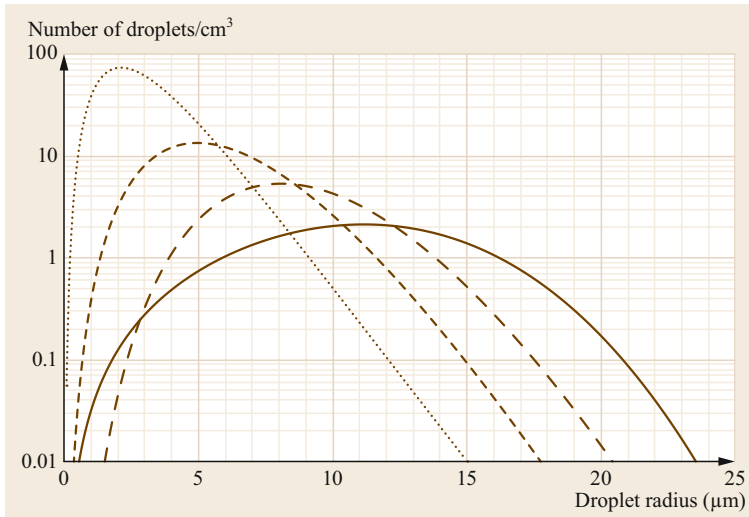


Fig. 13.6 Droplet size distribution examples for radiation (*dotted*), advection (*dashed*) and mature (*solid*) fog

is called the standard visual range V_N :

$$V_N = \frac{1}{b_{\text{ext}}} \ln \frac{1}{0.02} = 3.912 \frac{1}{b_{\text{ext}}} . \quad (13.3)$$

For aviation weather services, a value of $K' = 0.05$ has been recommended due to the special observation conditions. The range obtained with this value is called the meteorological optical range (MOR):

$$\text{MOR} = \frac{1}{b_{\text{ext}}} \ln \frac{1}{0.05} = 2.996 \frac{1}{b_{\text{ext}}} . \quad (13.4)$$

By definition, the standard visual range and the MOR apply only in daytime. It has become customary, however, to apply this relationship regardless of the level of

illumination, i.e., the terms *standard range* and *meteorological optical range* are also used to describe night time ranges. Table 13.3 shows the relationship between MOR, standard visual range, extinction coefficient and transmittance.

The maximum possible MOR in particle-free air is approximately 270 km, being limited by scattering of light by gas molecules (Rayleigh scattering). Since the lower atmosphere always contains water vapor and other pollutants, the extinction coefficient is never zero (or put another way, the MOR is never infinite). It is thus not meaningful to quote a single number for the detection limit, since it depends, inter alia, on the measurement task, the nature of the turbidity-producing particles and the length of the measuring path.

Table 13.3 Meteorological optical range, standard visual range, extinction coefficient and transmittance

Meteorological optical range MOR (km)	0.1	0.2	0.5	1	2	5	10	20
Standard visual range V_N (km)	0.131	0.261	0.653	1.31	2.61	6.53	13.1	26.1
Extinction coefficient $b_{\text{ext}}(\lambda)$ (km^{-1})	29.96	14.98	5.991	2.996	1.498	0.5991	0.2996	0.1498
Transmittance $\tau = e^{-b_{\text{ext}}(\lambda)s}$								
for $s = 100$ m	0.0500	0.2236	0.5493	0.7411	0.8609	0.9418	0.9705	0.9851
for $s = 50$ m	0.2236	0.4729	0.7411	0.8609	0.9287	0.9705	0.9851	0.9925
for $s = 10$ m	0.7411	0.8609	0.9418	0.9705	0.9851	0.9940	0.9970	0.9985

In contrast to human observers, instruments can only observe a small air sample in the direct vicinity of their installation site. This measurement always needs to assure that the determined extinction coefficient will be the same over the entire reported range. This assumption becomes more and more uncertain with increasing visibility range. Since it is possible to *look* in different directions and at very remote targets like a human observer can, camera-based observation systems like those discussed in Sect. 13.9.4 are not meant to replace (due to large uncertainties), but to support the MOR determinations that are naturally locally limited.

13.3.3 Transmissometer

The transmissometer is one of the most commonly used instruments. By measuring the transmittance it determines the mean extinction coefficient in a horizontal cylinder of air between a light transmitter and a light receiver. The light transmitter incorporates a modulated flux light source of constant mean power. The most frequently used light sources are halogen or xenon flash lamps and state-of-the-art transmissometers meanwhile use LED light sources [13.7]. The modulation of the light source prevents disturbance from sunlight and it is

generally recommended that polychromatic light in the visible spectrum should be used to obtain a representative extinction coefficient determination.

Since MOR determinations by transmissometers are based on the loss of light from a collimated beam, which depends on scatter and absorption, they are closely related to the definition of MOR. A good, well-maintained transmissometer working within its range of highest accuracy provides a very good approximation to the true MOR [13.1]. The extinction coefficient within the measurement baseline has to agree with the one within the relevant visual range. This being the case, we obtain the relative errors shown in Fig. 13.7 when determining the MOR for various absolute transmittance errors.

From a metrological perspective, however, the procedure of obtaining the transmittance is impaired not by a constant absolute error, but rather by a combination of a relative error (due especially to misalignments, incorrect calibrations and dirt deposits on the outer optical surfaces), which under some conditions may be of significant magnitude, and a small absolute error (due to the resolution and the signal-to-noise ratio).

Figure 13.8 shows the effect of the relative measurement error, which affects especially the large visual ranges. Limiting the relative transmittance error to, e.g.,

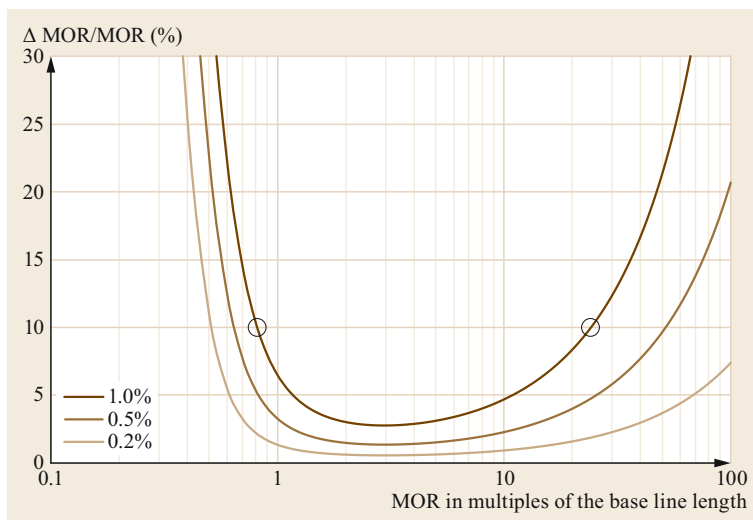


Fig. 13.7 Relative error of the meteorological optical range (MOR) for transmissometers at 1%, 0.5% and 0.2% absolute transmittance error (after [13.6] with permission from VDI e. V., Düsseldorf, Germany)

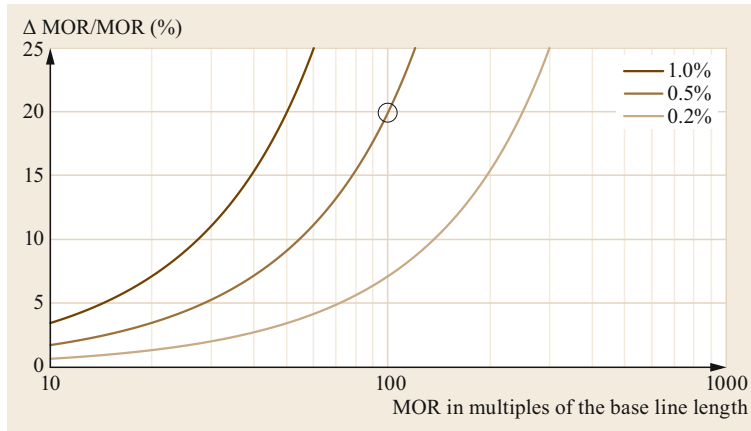


Fig. 13.8 Relative error of the meteorological optical range (MOR) for transmissometers at 1%, 0.5% and 0.2% relative transmittance measurement errors (after [13.6] with permission from VDI e. V., Düsseldorf, Germany)

0.5% allows the range to be determined with a relative error below 20% at meteorological optical ranges up to 100 times the baseline length. If the effects on the procedure of obtaining the transmittance can be reduced even further (to, e.g., 0.2%), measurements are possible up to 250 times the baseline length while maintaining a relative measurement error of 20% for the MOR. The illustrated decreasing measurement uncertainty of a transmissometer with decreasing MOR is an advantage for small meteorological optical ranges, in contrast with forward scatter meters. This is also the reason why one can calibrate a forward scatter meter in fog through transmissometer measurements.

The measurement uncertainties of transmissometers are largely negligible for small ranges, as long as the lower end of the measurement range is matched to the available measurement's dynamic range. The latter is determined by the signal-to-noise ratio, the resolution and any unwanted signal offsets. Figure 13.9 shows the

influence of the measurement error, which affects especially small ranges. A usable dynamic range of 1 : 1000 (60 dB) permits, e.g., a measurement down to 0.4 times the base length at a maximum relative error of 16% for the MOR.

With increasing transmissometer baseline length an increasing impact of the so-called forward scatter error needs to be taken into account. Since the transmitter and receiver optical systems of a transmissometer cannot provide an ideally narrow light beam with respect to field of view, unwanted stray light produces an additional receiver signal, which adds to the measured transmittance signal. The collection of forward-scattered light by the transmissometer receiver leads to a measurement error that is conveniently expressed as a fractional error in extinction coefficient (lower than the true extinction coefficient). The fractional error increases with the radius of the scattering particles but can be considered independent of the baseline.

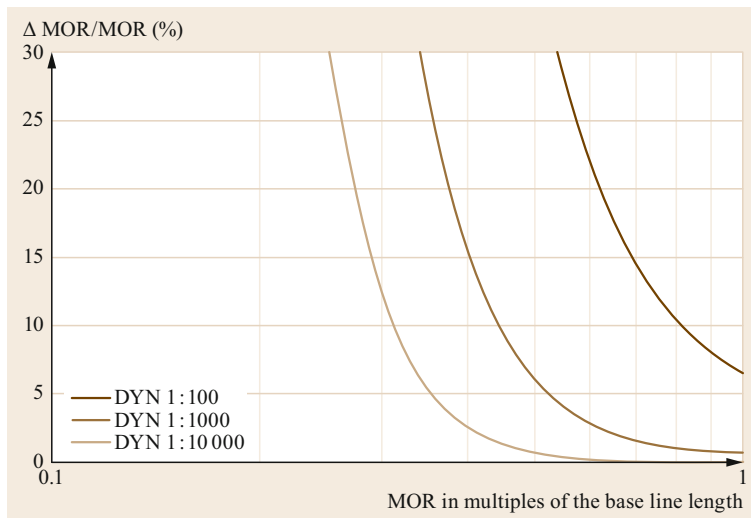


Fig. 13.9 Relative error in the meteorological optical range (MOR) for transmissometers in the presence of different transmittance measurement errors dependent on the dynamic range (DYN) (after [13.6] with permission from VDI e. V., Düsseldorf, Germany)

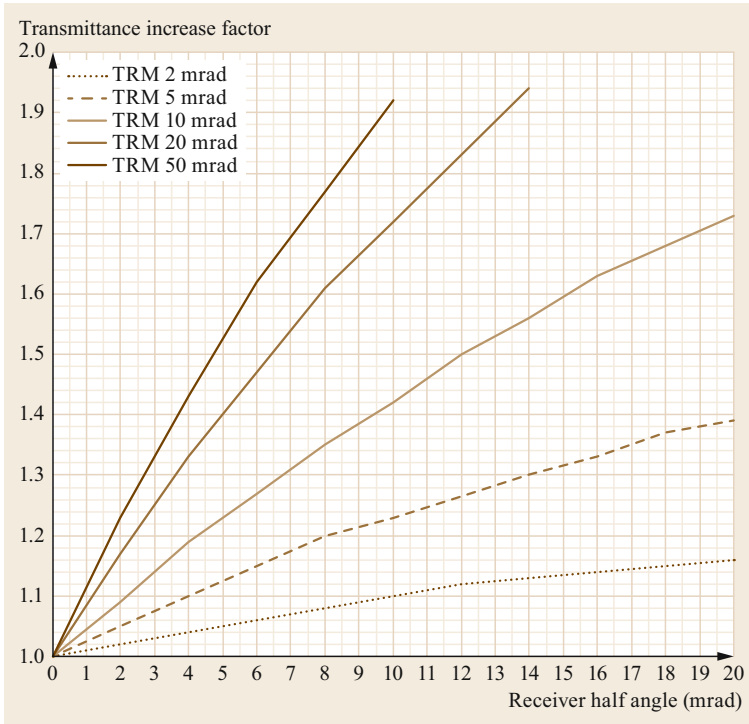


Fig. 13.10 Transmittance measurement value increase due to forward scatter error @ MOR = 0.766 times the baseline length depending on the transmitter and receiver half angles, based on data (after [13.8])

However, the final conversion into the MOR needs to consider the utilized baseline length. Therefore, the resulting MOR error will naturally increase with increasing baseline length. For particles much larger than the wavelength of light, the error is roughly proportional to the particle radius and to the angular width of the receiver. For a particle of $10\ \mu\text{m}$ (i.e., the largest particle radius typically in fogs) and $0.55\ \mu\text{m}$ wavelength (peak in response of human vision), the error will be less than five per cent if the receiver half angle is less than 1 mrad [13.9]. Figure 13.10 illustrates the increase factor for the measured transmittance when different transmitter divergences and receiver fields of view are utilized [13.10].

13.3.4 Instruments Determining the Scatter Coefficient

The attenuation of light in the atmosphere is due to both scattering and absorption. The presence of pollutants in the vicinity of industrial zones or dust may make the absorption term significant. However, in general, the absorption factor is negligible and the scatter phenomena due to reflection, refraction, or diffraction on water droplets constitute the main factor reducing visibility. The extinction coefficient may then be considered as equal to the scatter coefficient, and an instrument for de-

termining the latter can, therefore, be used to estimate MOR. Measurements are typically taken by concentrating a beam of light on a small volume of air and by determining the proportion of light that is scattered in those directions where scattering provides the best estimate of the scatter coefficient in all conditions. Due to the flux modulated light source, an instrument of this type can be used during day and night. The scatter coefficient b is a function that may be written in the following form

$$b = \frac{2\pi}{\Phi_V} \int_0^\pi I(\theta) \sin \theta d\theta, \quad (13.5)$$

where Φ_V is the flux entering the volume of air V and $I(\theta)$ is the intensity of the light scattered in direction θ with respect to the incident beam [13.1]. The accurate determination of b requires the measurement and integration of light scattered out of the beam over all angles. However, practical instruments measure the scattered light over a limited angle range and rely on a high correlation between the limited integral and the full integral (see Sect. 13.4 for further details). Instruments that determine the scatter coefficient use three main measurement methods: backscatter, forward scatter, and scatter integrated over a wide angle.

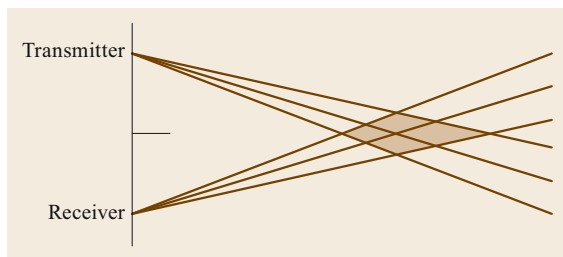


Fig. 13.11 Schematic diagram of a backscatter sensor

Backscatter

In these instruments a light beam is concentrated on a small volume of air in front of the light transmitter. The light receiver is located in the same housing and detects the light that is backscattered from the light beam in the sampled volume of air, see Fig. 13.11. Due to the significantly different response strengths for fog, rain and solid precipitation that cannot be corrected for by conventional backscatter sensors, this technology has up to now been limited to simple fog warning applications with respect to applications that allow larger measurement uncertainties in precipitation.

Forward Scatter

The amount of light scattered by small particles (aerosols, small droplets) is angular-dependent and varies with the chemical composition (e.g., salt concentration), type of nucleus (sand, dust), size and shape of the particles. As a consequence, a scattering angle should be chosen so that the angular dependence is minimal and representative for the scatter coefficient. Instruments determining MOR based on the forward scatter principle are generally called forward scatter sensors or forward scatter meters, see Fig. 13.12.

Scatter over a Wide Angle

Such an instrument, which is usually known as an integrating nephelometer, is based on the principle of measuring scatter over as wide an angle as possible, ideally 0° to 180° , but in practice about 10° to 120° . The light receiver is positioned perpendicularly to the axis of the light transmitter which provides light over

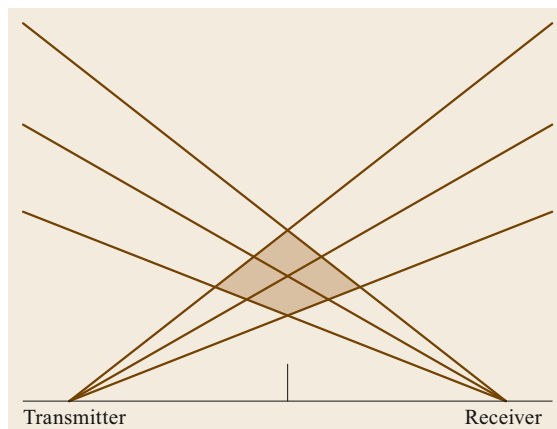


Fig. 13.12 Schematic diagram of a forward scatter sensor

a wide angle, see Fig. 13.13. Although, in theory, such an instrument should give a better estimate of the scatter coefficient than an instrument measuring over a small range of scattering angles, in practice it is more difficult to prevent the presence of the instrument from modifying the extinction coefficient in the air sampled. Integrating nephelometers are not widely used for measuring MOR. This type of instrument is more often used for measuring pollutants.

13.3.5 Forward Scatter Meter

A transmissometer measures the fraction of light (transmittance) that has not been absorbed or scattered out of a light beam after it has travelled a certain distance through the atmosphere. The study of human vision has shown that the transmittance (or the extinction coefficient which is easily computed from transmittance) is the correct parameter to characterize the degradation of vision by precipitation or aerosols. In contrast to the transmissometer, a forward scatter meter measures a small portion of light scattered out of a light beam into a relatively narrow range of scattering angles. The forward scatter meter measurement is then used to estimate the extinction coefficient; the scattered signal is assumed to be proportional to the extinction coefficient.

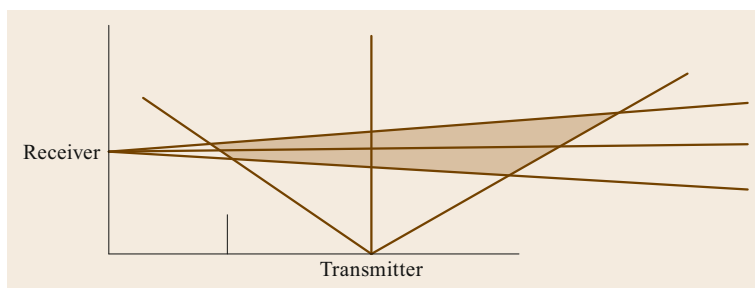


Fig. 13.13 Schematic diagram of an integrating nephelometer

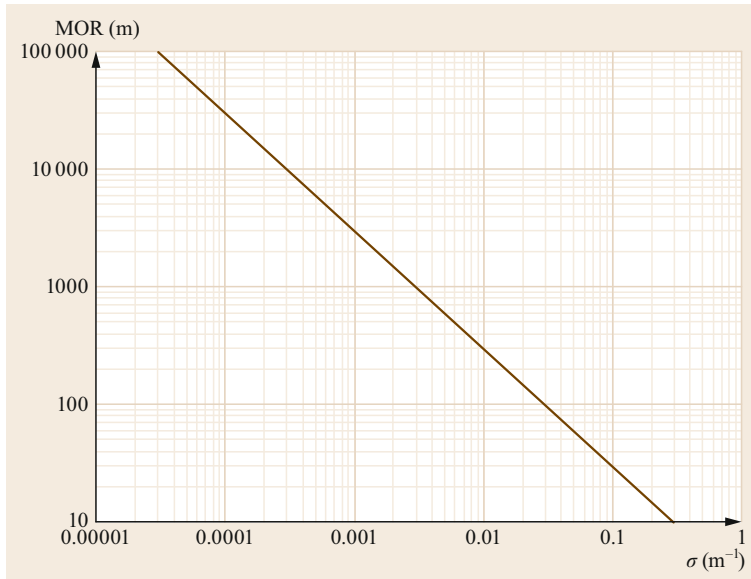


Fig. 13.14 Relation between extinction coefficient σ and MOR according to (13.6)

The validity of the estimate depends upon the physical properties of the scattering particles [13.9]. Since both the forward scatter meter signal and the extinction coefficient are proportional to the particle density, variations in particle density cannot affect the validity of the forward scatter meter measurement.

The response of a forward scatter meter depends upon the fraction of light scattered into the detected range of angles. Since particles of different type have different scatter functions, the ratio of scattered signal to extinction coefficient (i.e., the forward scatter meter calibration factor) can depend upon the type of scattering particles. One way of addressing this problem is to select a scattering angle where scatter function is as closely proportional as possible to the extinction coefficient for the weather phenomena that reduce visibility. Several authors have shown that the best angle is between 20° and 50° [13.10–13]. Another approach is to identify the weather phenomena and apply a different calibration to different weather types.

Particle absorption can be a problem, since a forward scatter meter cannot detect absorption. However, if the amount of absorption is proportional to the amount of scattering, the effect of absorption simply changes the proportionality between scattered signal and total extinction coefficient. Generally speaking, forward scatter meters exhibit larger measurement uncertainties than transmissometers, but due to the smaller effect of deposits on the optical apertures, they are better suited for large ranges than transmissometers. Especially where vision is restricted by precipitation, haze and mist, however, there may occur further particle-type-dependent measurement uncertainties (Mie scat-

tering which depends on the angle, the wavelength and the phenomenon involved).

Influence of the Calibration and the Window Dirt Contamination

The optimal forward scatter angle range was found to be in the range of 40° – 45° when infrared light is utilized. The forward scatter measurement evaluates the light scattering properties of the atmospheric particles but not the absorption by solid particles. It is based on the assumption that the scattered light under the utilized angle range corresponds to the total amount of scattered light and is therefore proportional to the extinction. As a result the following basic aspects apply:

- The forward scatter instrument evaluates the extinction coefficient directly.
- The received signal increases proportional with increasing particle concentration.
- Without any atmospheric extinction, the received signal approaches zero.

Equation (13.6) describes the relationship between the evaluated forward scatter signal (extinction coefficient) and the MOR, as illustrated in Fig. 13.14,

$$\text{MOR} = -\frac{\ln \varepsilon}{\sigma} = -\frac{\ln 0.05}{\sigma}, \quad (13.6)$$

where MOR is the meteorological optical range in meters, σ the extinction coefficient in m^{-1} , and ε the perceptibility contrast threshold (0.05 for MOR).

Due to the inverse proportionality between the measured forward scatter signal (extinction coefficient) and

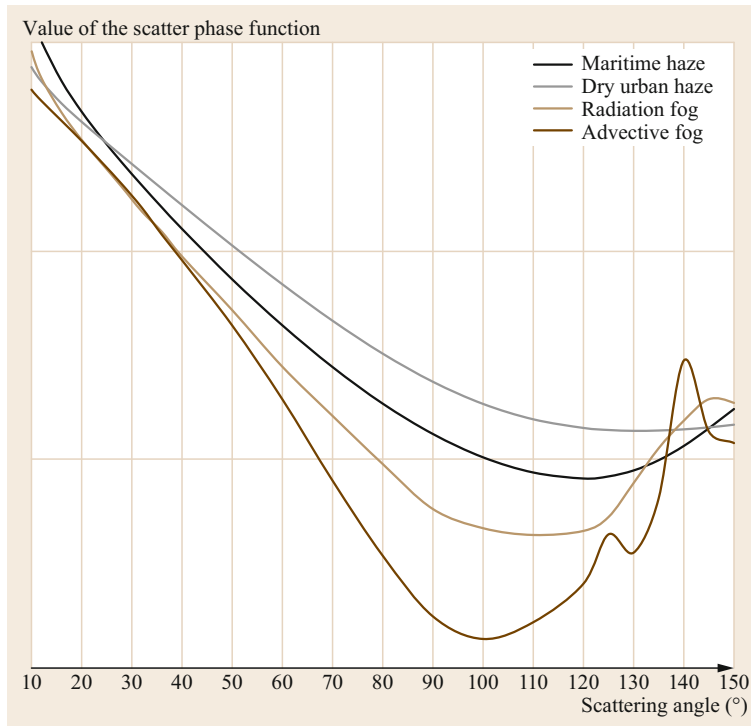


Fig. 13.15 Scatter phase function examples for fog and haze, based on data (after [13.13])

the reported MOR, measurement inaccuracies (e.g., uncorrected window dirt contamination that reduce the measured forward scatter signal or wrong calibration) have the same relative impact (same error percentage) throughout the entire measurement range. These impacts need to be seen as an *unwanted factor* on the extinction coefficient. The target of the calibration for a forward scatter meter is to keep this *unwanted factor* as small as possible.

As already illustrated, the received signal of a forward scatter meter represents the extinction coefficient if the forward scatter angle is selected such that the strength of the scattered light under this angle can represent the entire extinction coefficient,

$$\begin{aligned} \text{FSS (forward scatter signal@40°–45°)} \\ \propto \sigma \text{ (Extinction coefficient in m}^{-1}\text{)}. \end{aligned} \quad (13.7)$$

Depending on the measurement technology and the specific arrangement a sensor type specific conversion factor CF is required to convert the measured forward scatter signal into an extinction coefficient

$$\begin{aligned} \text{FSS (internal units)} \times CF \left(\frac{1}{\text{internal units} \times \text{m}} \right) \\ \propto \sigma \text{ (m}^{-1}\text{)}. \end{aligned} \quad (13.8)$$

Since the unit to unit deviations (including individual parameters like absolute transmitter light intensity with

regards to receiver sensitivity) need to be additionally considered, the forward scatter meter finally needs to be calibrated against a well-known extinction coefficient simulation σ_{CAL} . A fitting calibration factor (CAL) is evaluated

$$\text{CAL} = \frac{\sigma_{\text{CAL}}}{\text{FSS} \times \text{CF}}. \quad (13.9)$$

This calibration factor equalizes the sensor response with the extinction coefficient to be measured

$$\sigma = \text{FSS} \times \text{CF} \times \text{CAL}. \quad (13.10)$$

An unwanted additional influence on the forward scatter signal (FSS), like uncorrected window dirt contamination needs to be seen as an error factor which directly influences the found sensor calibration factor CAL, leading to a proportional under- or overestimation of the true extinction coefficient σ .

Influence of the Scatter Phase Function

So-called scatter phase functions are utilized to describe the relation between scatter angle and scatter strength. The response of a forward scatter meter for different aerosols and droplets can be estimated by utilization of the scatter phase functions. The value of a scatter phase function describes the portion of light that is expected to scatter in a certain direction. To allow direct

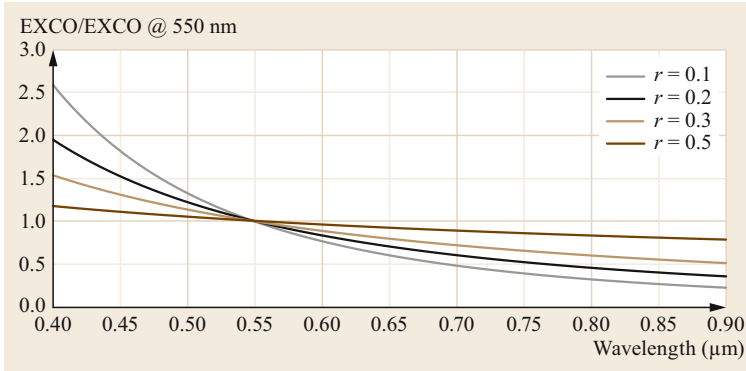


Fig. 13.16 Measurement wavelength impact on relative extinction coefficient (EXCO/EXCO @ 550 nm) for different particle radii

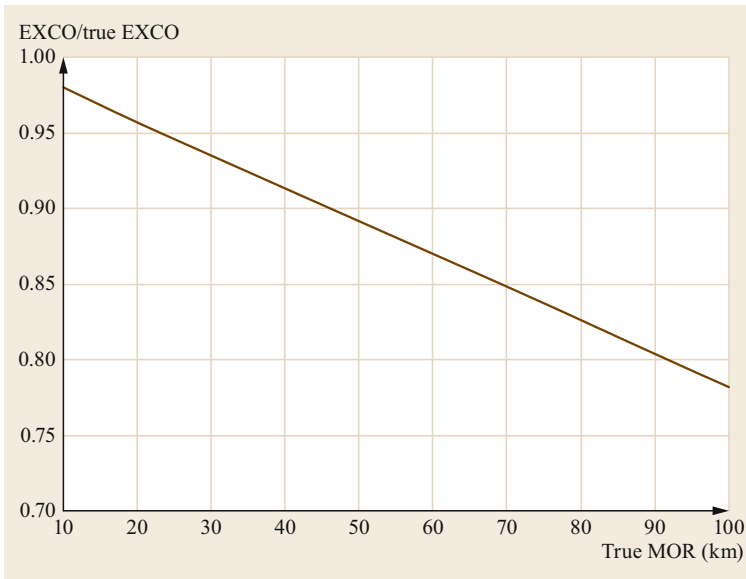


Fig. 13.17 Wavelength impact on the extinction coefficient (EXCO), 785 nm example

value comparisons, a scatter phase function is normalized with respect to the integral value below the curve and the represented extinction coefficient.

One commonly used set of phase functions are contained in LOWTRAN, which is a *low* spectral resolution (20 cm^{-1}) band model radiative transfer algorithm developed by the Air Force Geophysics Laboratories, now the Air Force Research Laboratories (AFRL). LOWTRAN incorporates different aerosol models that are based on measurements and investigations from various sources [13.13]. Figure 13.15 illustrates exemplarily the different expectable scatter signal strengths for some visibility phenomena models over the scatter angle. The response differences between fog and types of hazes are obvious.

Measurement Wavelength Impact

The utilized measurement wavelength also has an impact on the scatter measurement. Due to different scatter

properties, the small non-liquid particles in haze will generate less scattering and will therefore be underestimated. Figure 13.16 illustrates the measurement wavelength impact on the relative extinction coefficient measurement for different particle radii. For smaller particles larger deviations must be expected when other wavelengths than the nominal 550 nm are used.

The general wavelength impact on the extinction coefficient can be described with Ångström's equation

$$\sigma_{\lambda} = \sigma_{550 \text{ nm}} \left(\frac{550 \text{ nm}}{\lambda} \right)^{\text{EXP}} \quad (13.11)$$

In [13.2] different typical exponents EXP are defined to be used with the equation for different high visibility ranges:

- EXP = -1.3 for 30 km standard visibility
- EXP = -1.6 for 90 km standard visibility

- EXP = -2.0 for 150 km standard visibility
- EXP = -4.0 for Rayleigh atmosphere

Figure 13.17 illustrates well the resulting deviation of the measured extinction coefficient at 785 nm versus the true extinction coefficient at 550 nm.

Combined Wavelength and Scatter Phase Function Impacts

For the MOR measurement range beyond 10 km (haze), both the impact of the measurement wavelength and the scatter phase function need to be taken into account, and which fortunately partly compensate for each other when an infrared wavelength is chosen. The combi-

nation of the measurement wavelength and the scatter phase function impact represents the aerosol-dependent measurement uncertainties that need to be taken into account for all forward scatter meters. Depending on the most dominant haze phenomenon (dictated by the installation site) the resulting reporting deviations must be expected to exceed 30% in some cases. Up to a MOR of 10 km, a measurement uncertainty of approximately 10% can be achieved in the best case. Depending on the utilized forward scatter angle and measurement wavelength, the uncertainty can easily become 20% up to more than 30% if all the range-limiting phenomena are taken into account and the entire measurement range up to MOR > 70 km is covered.

13.4 Devices and Systems

Nowadays, MOR can be measured using methods relying on either transmitted or scattered light. Whichever one is applicable depends first and foremost on the type of atmospheric pollutants, which measurement range will be covered and what level of measurement uncertainty is acceptable. The measurement methods described here are applied in visual range measuring instruments which are used predominantly for securing air, road and shipping traffic and for meteorological forecasting. They are commonly calibrated in units of MOR. They can, however, also be used and calibrated accordingly to determine the extinction coefficient, and transmissometers also to determine the transmittance.

13.4.1 Transmissometer

The light from a suitable source is collimated and sent down the required path. It is detected by a photoelectric sensor either directly or after reflection from a triple mirror (see Fig. 13.18). The consistency of the properties of the light source and the sensor has to be ensured. In order to be able to measure in daylight, the interfering effect of the scattering of daylight along the measurement path must be eliminated. This is done by modulating the measured light. The photocurrent (AC) generated in the receiver by the measured light can be separated from the DC part of the daylight signal. In past designs, the transmitter and the receiver were com-

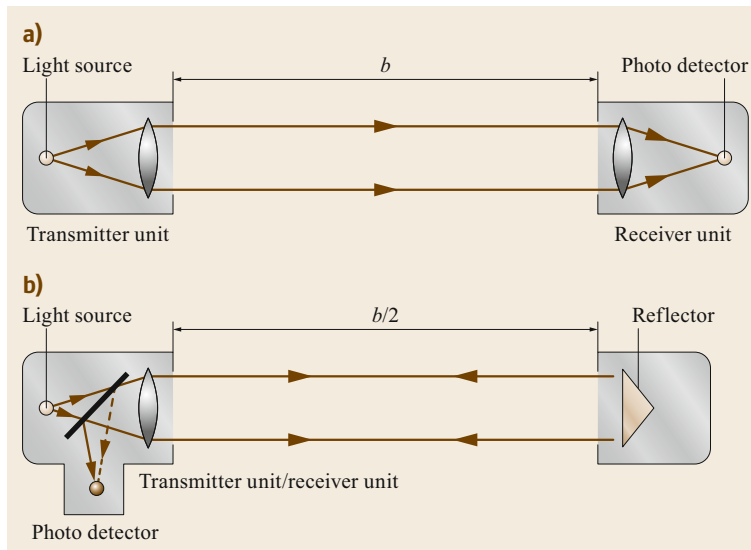


Fig. 13.18a,b Schematic diagram of a transmissometer. **(a)** Single path transmissometer, **(b)** double path transmissometer; b = baseline length (after [13.9] with permission from WMO)

bined into one unit (double path transmissometer) in order to avoid the challenging requirements for the consistency of the properties of the light source and the receiver.

Transmissometers are used preferably for MORs of 10 m to max. 10 km. Due to the principle involved, different baseline lengths might be needed for recording certain ranges. These lengths are typically around 50 to 100 m, and are even longer when dealing with greater ranges. Extinction measurement using the transmissometer principle has the lowest uncertainty. This applies first and foremost to the recording of smoke, soot and dust. In addition to the technical properties of the equipment, however, the MOR measurement uncertainty depends also on the baseline length in relation to the required MOR reporting range. Double path transmissometers (the measurement path is traversed twice) require a triple mirror at the end of the measurement path. Triple mirrors have the property that they reflect an incident light beam in parallel with themselves, without the need for precise adjustment when being setup.

13.4.2 Scattered Light Sensor

Scattered light sensors measure the scattering coefficient $b_{\text{sca}}(\lambda)$ in units of inverse meters. It is possible to determine the MOR directly with the help of scattered light sensors only if the absorption coefficient $b_{\text{abs}}(\lambda)$ is negligible. Otherwise, the results have to be corrected (at a wavelength of 550 nm, the ratio $b_{\text{abs}}/b_{\text{ext}}$ is 0.0 in clouds and in fog, approximately 0.1 to 0.2 in polluted

air)

$$\text{MOR} = \frac{2.996}{b_{\text{sca}}(\lambda)} \left[1 - \frac{b_{\text{abs}}(\lambda)}{b_{\text{sca}}(\lambda)} \right]. \quad (13.12)$$

Due to

$$b_{\text{sca}}(\lambda) = 2\pi \int_0^{180^\circ} p(\vartheta) \sin \vartheta d\vartheta, \quad (13.13)$$

where $p(\vartheta)$ is the scattering function, the measurement of $b_{\text{sca}}(\lambda)$ requires integrating the scattered light over the entire scattering angle range from 0° to 180° , which is not technically possible. Therefore, *integrating* scattered light measurements are restricted to integration over the largest technically feasible angular range (ca. 7° to 170°) and correct the measurement accordingly [13.15]. This concept is utilized in so-called *integrating nephelometers*. However, due to their complexity, high maintenance requirements and limitations to determine the extinction coefficient of precipitation particles, they achieved no practical relevance for the 24/7 visibility measurement. For these reasons the scattered light measurement is conducted exclusively within a selected and limited angle range.

The relationship between scattering and extinction depends on the scattering particles' size distribution and their chemical composition. The amount of light scattered by small particles (aerosols, small droplets) is angular-dependent. The chemical composition (e.g., salt concentration), type of nucleus (sand, dust) and

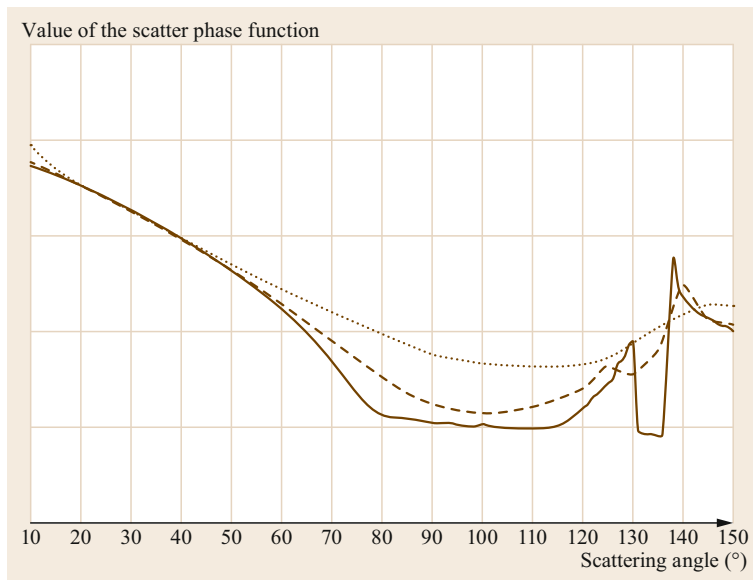


Fig. 13.19 Scatter phase function examples for fog (dashed/dotted lines) and rain (solid line), based on data (after [13.13, 14])



Fig. 13.20 State-of-the-art forward scatter meter example with look down geometry (after [13.16] photo © Vaisala Oyj, Helsinki, Finland)

size and shape of the particles influence the response strength. As a consequence, a scattering angle is chosen so that the angular dependence is minimal and representative for the scatter coefficient. The scatter phase function example in Fig. 13.19 compares the expectable scatter signal strength (logarithmic scaling) for advection fog, radiation fog and rain. The best correlation can be found between 20° and 50°

which is the typical angle range of forward scatter meters.

Compared with transmittance measurements, scattered light measurements have the advantage of compact equipment and a larger measurement range, up to > 70 km. However, they have the drawback of neglecting the absorption, and are therefore unsuitable for recording strongly absorbing particles in polluted air when the absorbing fraction $b_{\text{abs}}(\lambda)$ is unknown. Due to the relatively small measured volume, scattered light measurements in the presence of highly inhomogeneous atmospheric turbidity are representative only for a narrowly confined region. The typical forward scattering angles (Fig. 13.20) are 20° to 50°, preferably 40° to 45°. This angular range ensures the best possible agreement of the values of $b_{\text{sca}}(\lambda)$ for the various different visual range-restricting phenomena, and thus a minimum of any necessary phenomenon-dependent corrections.

Forward scatter meters can be calibrated by comparison with a highly accurate transmissometer, or through measurements with inserted defined scattering discs. However, the consistency of the properties of the light source and of the receiving apparatus has to be ensured (see Sect. 13.7 on maintenance for further reading).

Table 13.4 Advantages and disadvantages of the different measurement methods

Devices	Advantages	Disadvantages
Long baseline transmissometer (≥ 100 m)	Measurement up to MOR > 10 km possible Representative determination of the extinction coefficient for litho- and hydrometeors and all precipitation types	Separate transmitter and receiver units on stable foundations required Measurement down to MOR < 10 m not possible, cannot cover the entire RVR relevant MOR range MOR error due to uncorrected window dirt contamination and miscalibration increases with increasing MOR
Short baseline transmissometer (≤ 30 m)	Measurement down to MOR < 10 m possible Can cover the entire RVR relevant MOR range Representative determination of the extinction coefficient for litho- and hydrometeors and all precipitation types	Separate transmitter and receiver units on stable foundations required MOR error due to uncorrected window dirt contamination and miscalibration increases with increasing MOR
Backscatter meter	Very compact design possible, receiver and transmitter in one common enclosure Measurement volume remote from the instrument	Large measurement uncertainties especially for visibility reductions due to precipitation
Integrating nephelometer	Compact design Measurement under a wide range of scatter angles allows representative determination of the extinction coefficient for litho- and hydrometeors	A disturbance of the measurement volume due to close-by mechanical parts cannot be avoided Shadowing of the measurement volume does not allow representative visibility determination in precipitation
Forward scatter meter	Compact design Optimal forward scatter angle allows visibility determination for fog, mist and precipitation with low uncertainties Large measurement range from < 10 m to > 50 km Internationally agreed measurement method as well for safety relevant air traffic applications (RVR determination)	Measurement uncertainties increase for visibility reductions due to lithometeors

13.4.3 Transmittance Versus Scattered Light Measurements

Compared with transmittance measurements, scattered light measurements have the advantage of compact equipment and a larger measurement range, up to > 70 km. However, they have the drawback of neglecting the absorption, and are therefore unsuitable for recording strongly absorbing particles in polluted air when the absorbing fraction $b_{\text{abs}}(\lambda)$ is unknown. Due to the relatively small measured volume, scattered light measurements in the presence of highly inhomogeneous atmospheric turbidity are representative only for a narrowly confined region. All practical operational instruments for the measurement of MOR sample a relatively small region of the atmosphere compared with that scanned by a human observer. Instruments can pro-

vide an accurate measurement of MOR only when the volume of air that they sample is representative of the atmosphere around the point of observation out to a radius equal to MOR. It is easy to imagine a situation, with patchy fog or a local rain or snow storm, in which the instrument reading is misleading.

Another factor that must be taken into account when discussing representativeness of measurements is the homogeneity of the atmosphere itself. At all MOR values, the extinction coefficient of a small volume of the atmosphere normally fluctuates rapidly and irregularly, and individual measurements of MOR from forward scatter meters, with respect to the short baseline of a transmissometer, might show considerable dispersion [13.1]. Finally, the advantages and disadvantages of different measurement methods are summarized in Table 13.4.

13.5 Specifications

For the measurement of atmospheric turbidity to be representative, bearing in mind the inhomogeneity of the atmosphere, the measuring equipment has to cover a particular minimum volume. The natural atmosphere itself (i.e., without anthropogenic pollution) can cause difficulties when deciding on a volume. In particular where there exist local or regional inhomogeneities or fog banks, the extinction coefficient can vary considerably in space and time, which may render it difficult to obtain a representative value. Generally speaking, in forward scatter meters the covered measurement volume is only a few to a few hundred cm^3 . The representativeness of the measurement results from the equipment's measurement volume and the heterogeneity of the visual range field. Caution is necessary, therefore, when extrapolating from point measurements to a large region. The measurement range of common forward scatter meters is ca. 10 m to 70 km.

Transmissometers always record a spatial average over their baseline length; this depends on the required measurement range and the permitted error magnitude (see Table 13.5). Baseline lengths between 10 and 100 m are common, corresponding to a measurement volume of 0.1 to 1 m^3 . The measurement range of common transmissometers is approximately 10 m to max. 10 km. Theoretically, assuming a constant 1% absolute error in the transmittance measurement, one can expect a relative error of less than 10% for the MOR from approximately 0.8 times to approximately 25 times the baseline length (Fig. 13.7). In case it is not feasible to reduce the error in the transmittance measurement below 1%, it is as well possible to extend the measurement range by using two-range or double-baseline transmis-

someters. In any case it has to be considered that the relationship between the measured transmittance and the reported MOR is not linear.

The measuring equipment is subject to the following general requirements:

- Ideal measurement range of the MOR (depending on the task): 10 m/100 m to 2 km/20 km (10 nmi)/70 km
- Resolution: 1 m according to the World Meteorological Organization (WMO) [13.1]
- Relative standard deviation $\pm 10\%$ (ignoring external influences) for MORs 10 m to 10 km
- Response time: approximately 1 min (for the entire system)
- Averaging time for the measurements: 1 min according to WMO [13.1]
- Data recording: interrogation cycle ≤ 15 s
- Eliminating the adverse effects of daylight, to ensure that the same results are obtained under constant meteorological and physical conditions during daytime and at night
- Independent of atmospheric temperature effects from -30 to 50°C
- The effects of self-heating and heating by solar radiation have to be eliminated
- Preventing the adverse effects of snow clogging, icing and birds/insects disturbances
- Long-term consistency of the light source, the receiver system and the electronics (six months without appreciable deviations), to the extent necessary for the measurement method
- Detecting and correcting for dirt deposits on the optical elements.

Table 13.5 Specification of different measurement methods for visibility. Note: The stated error and uncertainty percentages need to be understood as typical values; they might differ between different instrument types. The development of the MOR error due to uncorrected window dirt contamination over time depends significantly on the local conditions. Instruments with automatic window dirt contamination correction will reach the stated error borders after a much longer maintenance-free operation time. The transmissometers are assumed to be realistically calibrated within an uncertainty of $\pm 20\%$ @ MOR = 10 km. Additionally an uncorrected window dirt contamination of maximally 0.5% is assumed as an example for a 100 m and for a 30 m baseline transmissometer. For the scatter meters a larger uncorrected window dirt contamination of 10% as an example is assumed

Method	Calibration depending MOR error	MOR uncertainty hydrometeors	MOR uncertainty lithometeors	MOR uncertainty precipitation	MOR error due to uncorrected window dirt contamination
Long baseline transmissometer (≥ 100 m)	between 50 and 800 m $\pm 2\%$				-1.3%
	between 800 and 2000 m $\pm 5\%$				-3.2%
	between 2000 and 5500 m $\pm 12\%$				-8.4%
	between 5500 and 10 000 m $\pm 20\%$				-14%
Short baseline transmissometer (≤ 30 m)	between 10 and 800 m $\pm 2\%$				-4.3%
	between 800 and 2000 m $\pm 5\%$				-10%
Backscatter meter	$\pm 3-5\%$	$\pm 20\%$	$\pm 40\%$	$\pm 50\%$	+ 11%
Integrating nephelometer	$\pm 2-3\%$	$\pm 10\%$	$\pm 20\%$	Not usable	+ 11%
Forward scatter meter	$\pm 2-3\%$	$\pm 10\%$	$\pm 30\%$	$\pm 20\%$	+ 11%

13.6 Quality Control

The siting of visual measuring equipment should be representative, which leads to setup rules (Sect. 13.6.1). These are followed by some aspects of data quality control (Sect. 13.6.2). The quality of the reported MOR data from instruments like transmissometers or forward scatter meters are basically influenced by all parasitic drags that are described in the Sect. 13.6.3.

13.6.1 Setup Rules

Whereas in general, transmissometers and forward scatter meters used to determine the MOR are deployed so as to be free from locally limited inhomogeneities due to atmospheric pollution, e.g., smoke, industrial dirt, dusty streets, for the purpose of monitoring air quality they have to be deployed where they are representative for a particular vicinity. This applies especially to their height above ground level. If vertical inhomogeneities have to be recorded a number of vertically staggered instruments might have to be used. In general, it is advisable to avoid deployment at locations highly susceptible to fog, i.e., in the vicinity of bodies of water, streams or rivers or on very wet subsoil.

Particular attention should be paid to the correct alignment of transmissometer transmitters and receivers and to the correct adjustment of the light beam. The poles on which the transmitter/receivers are mounted should be mechanically firm (while remaining frangible when

installed at aerodromes) to avoid any misalignment due to ground movement during freezing and, particularly, during thawing. In addition, the mountings must not distort under the thermal stresses to which they are exposed. Some modern transmissometers can automatically adjust their alignment to compensate for this [13.7].

Furthermore, transmissometers and forward scatter meters should be installed in such a way that the sun is not in the optical field of view of the receiver at any time of the day. Forward scatter meters should also be aligned such that reflecting objects in the optical field of view of the receiver are avoided.

13.6.2 Data Quality Control

Any data quality control needs to be based on a deep understanding of all potential parasitic drags and their technology depending impact on the measurement uncertainty as described in Sect. 13.3.3 in order to find algorithms that can identify and separate unrealistic instruments readings.

Instrumental measurements of MOR must always be interpreted with caution. All practical operational instruments sample a relatively small region of the atmosphere compared with that scanned by a human observer. However, instruments can provide an accurate measurement of MOR only when the volume of air that they sample is representative of the atmosphere

around the point of observation out to a radius equal to MOR. Experience has shown that uncertain situations with patchy fog or local rain or snow events, in which the instrument reading might be misleading are not frequent and that the continuous monitoring of MOR using an instrument will often lead to the detection of changes in MOR before they are recognized by an unaided observer [13.1].

At all MOR values the extinction coefficient of a small volume of the atmosphere will normally fluctuate rapidly and irregularly and individual measurements of MOR from forward scatter meters and short baseline transmissometers will unavoidably show considerable dispersion. In order to obtain a representative MOR value it might therefore be necessary to take many samples and to smooth or average them. The analysis of the results from the *First WMO Intercomparison of Visibility Measurements* [13.17] indicates that, for most instruments, no benefit is gained by averaging over

more than 1 min, but for the *noisiest* instruments an averaging time of 2 min is preferable.

13.6.3 Parasitic Drags and Impact on the Measurement Uncertainty

When measuring MOR, the error sources and perturbations are not exactly quantifiable. The optical apertures (glass surfaces) are exposed to the risk of contamination by atmospheric pollutants. Depending on external conditions, significant transmittance errors can occur even within a few days in conventional transmissometers if the optical apertures are not cleaned regularly. This can, depending on the visibility, lead to considerable errors in the readings of the MOR. Measuring the dirt deposits on the optical apertures, with appropriate correction of the transmittance and/or regular automated recalibration of the transmittance measurement, can reduce the measurement errors. Even with long cleaning intervals,

Table 13.6 Major parasitic drags and countermeasures for transmissometers (after [13.1])

Transmissometers	
Parasitic drag	Countermeasures
Atmospheric pollutants deposited on optical surfaces	Contamination measurement and contamination correction in the frame of the sensor self-diagnostics Regular cleaning in accordance with manufacturer's instructions in the frame of preventive maintenance Reactive maintenance, cleaning only when needed
Instability of system electronics	Regular linearity and calibration check, using a graduated set of attenuation filters under stable, high visibility conditions Change/adjust instrument settings in accordance with manufacturer's instructions
Snow or ice build-up on surfaces near the optical measurement path	Sensor head heaters and hood heaters should be foreseen for instruments at installation sites that usually allow snow and ice conditions
Aging of transmitter light source	Light source intensity measurement and aging warning messages in the frame of the sensor self-diagnostics Replacement of the transmitter light source in the frame of preventive with respect to reactive maintenance
Insufficient rigidity and stability of transmitter and receiver mounting poles and effects of freezing or thawing of the ground	Regular calibration check under stable, high visibility conditions Change/adjust instrument settings in accordance with manufacturer's instructions
Calibration error due to calibration/adjustment being carried out when visibility is low or during unstable atmospheric conditions	Some modern transmissometers can provide automatic calibration corrections, based on the detection of stable high visibility conditions [13.7] Otherwise the calibration with respect to adjustment is to be carried out manually in accordance with manufacturer's instructions
Incorrect alignment of transmitters and receivers	Some modern transmissometers can provide an automatic alignment feature [13.7] Otherwise an alignment check with respect to correction needs to be conducted manually in accordance with manufacturer's instructions
Disturbance when sun is near horizon, or due to reflections from adjacent surfaces	In order to prevent sunlight disturbances, the installation and orientation must be carried out in accordance with manufacturer's instructions

Table 13.7 Major parasitic drags and countermeasures for forward scatter meters (after [13.1])

Forward scatter meters Parasitic drag	Countermeasures
Atmospheric pollutants deposited on optical surfaces	Contamination measurement and contamination correction in the frame of the sensor self-diagnostics A look-down geometry and weather protection hoods for the instrument windows provide a better protection for the optics and enable longer maintenance intervals Regular cleaning in accordance with manufacturer's instructions in the frame of preventive maintenance Reactive maintenance, cleaning only when needed
Instability of system electronics	Regular calibration check, using scatter plates that simulate defined fog conditions Change/adjust instrument settings in accordance with manufacturer's instructions
Snow or ice build-up on surfaces near the optical measurement path	Sensor head heaters and hood heaters should be foreseen for instruments at installation sites that usually allow snow and ice conditions
Aging of transmitter light source	Light source intensity measurement and aging warning messages in the frame of the sensor self-diagnostics Replacement of the transmitter light source in the frame of preventive with respect to reactive maintenance
Atmospheric conditions (for example, rain, snow, ice crystals, sand, local atmospheric pollutants) giving a scatter coefficient that differs from the extinction coefficient	An optimized scattering angle (40° to 45°) will reduce the related uncertainties [13.16] When a discrimination of the atmospheric conditions is possible, related corrections can be applied
Extra absorption by sand, dust and smoke giving a scatter coefficient that underestimates the extinction coefficient	When a discrimination of the atmospheric conditions is possible, related corrections can be applied for the forward scatter meter measurements
Incorrect procedures for calibration/adjustment, or use of incorrect or damaged scatter plates	Calibration and adjustment must be carried out in accordance with manufacturer's instructions Scatter plates must never be used in dense fog, drizzle or rain
Disturbance when sun is near horizon, or due to reflections from adjacent surfaces	In order to prevent sunlight disturbances, the installation and orientation must be carried out in accordance with manufacturer's instructions In the northern hemisphere the light receiver should ideally point toward the northern direction ($\pm 45^\circ$)
Disturbance by cobwebs or individual spider silk in the sample volume	Some modern forward scatter meter designs do not expose any supporting points that would allow a spider web to be placed inside or close to the measurement volume. The disturbance risk is significantly reduced [13.16] Regular cleaning in accordance with manufacturer's instructions in the frame of preventive maintenance Reactive maintenance, cleaning only when needed
Disturbance by flying insects in the sample volume	When a discrimination of the scatter signal that is generated by flying insects is possible, related corrections can be applied for the forward scatter meter measurements [13.16]

the resulting measurement uncertainty can be kept low in this way, including the upper end of the measurement range [13.7].

Rain, especially in conjunction with wind, can give rise to unwanted drops on the glass surfaces. In the case of drifting snow, the protective tubes in front of the optical apertures may become snowed up. Occasionally birds setup residence in these tubes. In order to counteract these effects, forward scatter meters (unlike transmissometers) can benefit from using a look-down

geometry. On the one hand, the downward-directed protective hoods reduce significantly the amount of dirt being deposited on the optical apertures; on the other, they prevent very effectively any kind of blocking of the instrument's optics, e.g., by wind-driven snow (see also [13.9]). Insects (midges), spiders and cobwebs can impair the measurement results of forward scatter meters. A suitable mechanical construction, however, can minimize the number of supporting points for spider webs in or near the measurement volume of forward

scatter meters. Interference by insects can be filtered out from the measured signals.

In transmissometers, mechanical loss of adjustment of the optical axis associated with changes in the state of the ground, ground movements or temperature effects have to be prevented. The possible distortion of transmissometer results, due to the increasing amount of forward-scattered transmitter light when the atmospheric extinction coefficient is very high, can be decreased by using small aperture angles in the transmitter's and receiver's optical systems, but never completely avoided.

In the presence of precipitation, transmissometers and forward scatter meters may produce different readings from the values estimated by an observer, since

these instruments perform point measurements whereas the observer examines a larger volume. Under some conditions, integrating nephelometers hardly respond (or do not respond at all) to precipitation, where due to their construction or deployment the precipitation is prevented from entering the measurement volume. In general, every visual range reduction has to be measured, including a reduction caused by precipitation. Forward scatter meters can be constructed in a way that even under unfavorable wind conditions only negligible shading of the measurement volume can arise [13.16]. A detailed quantification of the impact on the measurement uncertainty is provided in Sects. 13.3.3 and 13.3.5. Tables 13.6 and 13.7 summarize the parasitic drags and the potential countermeasures.

13.7 Maintenance

Systematic inspection and monitoring of the measurement system is required to ensure comparable data. Any contamination of the glass surfaces (light-transmitting areas) due to dirt or precipitation has to be removed before conducting measurements. Some range measuring equipment uses electric heating units and fans at the glass surfaces to guard against precipitation or other deposits. Transmissometers in particular require frequent cleaning or separate measurement of dirt on such surfaces, and appropriate correction of the result and/or automated adjustment of the calibration, since in the upper range they are far more sensitive to contamination of the external optical surfaces than forward scatter meters. Typical maintenance intervals of visibility measurement systems are summarized in Table 13.8.

In all cases of possible loss of adjustment of optical measuring sections, the equipment has to be checked.

Transmissometers in particular are sensitive to loss of adjustment, due to the required collimation of the light. In single path transmissometers (i.e., those without a triple mirror), the luminous intensity of the light sources has to be monitored. In double path transmissometers the individual consistency of the transmitter's luminous intensity and of the receiver's sensitivity is not essential since an internal optical comparison path can be applied in the transceiver that allows an automated compensation. Following any repair or replacement of light sources and other (mechanical, optical, electronic) components, careful adjustment is necessary to ensure that the equipment operates correctly and that the parameters are maintained over the entire measurement range.

For most transmissometers their optical surfaces must be cleaned regularly. Frequent servicing must be

Table 13.8 Maintenance of visibility measurement systems. Note: The above-stated window cleaning intervals are typical for instruments without automatic window dirt contamination correction and depend on the local conditions. For instruments with automatic window dirt contamination correction the cleaning intervals extend significantly and may be carried out exclusively on demand. If related warnings and/or alarms (e.g., window contamination alarm) are generated by the instrument, immediate action will take place independently from the scheduled maintenance interval

Typical interval	Transmissometer	Forward scatter meter Backscatter meter Integrating nephelometer
< 1 week	Immediate windows cleaning after wind driven precipitation contaminated an instrument window	
1 week	Regular windows cleaning	
2–4 weeks		Regular windows cleaning
6 months	General mechanical integrity check and general cleaning Calibration	General mechanical integrity check and general cleaning
1 year	Alignment check/re-alignment and calibration Linearity check with calibrated optical attenuation filters	Calibration check/calibration with scatter meter calibration units (SCU)

planned for, particularly at aerodromes. The instruments should be cleaned during and/or after major atmospheric disturbances, since rain or violent showers together with strong wind may cover the instrument windows with a large number of water droplets and solid particles resulting in major MOR measurement errors. The same is true for snowfall, which could also block the windows. Heating systems are often placed at the front of the optical systems and in the hood to improve instrument performance under such conditions. In some transmissometers air-blowing systems are used to reduce the above problems and the need for frequent cleaning [13.7]. Modern transmissometers and forward scatter meters monitor the contamination on the optical lens or window and produce warnings and errors when the contamination reaches a threshold. Some instruments make a correction for the window dirt contamination [13.1, 7, 16].

The MOR measurement of a forward scatter meter may be affected by cobwebs or even individual spider silk if the mechanical structure allows that these are placed in or close to the sample volume. Additionally, flying insects, which typically swarm around dusk in calm weather conditions can contribute to the scattered signal. Both cause the forward scatter meter to report artificially low MOR values. The reduction of the MOR of a forward scatter meter by cobwebs or flying insects can be very large, whereas these hardly affect a transmissometer measurement. Some forward scatter meters are capable to filter the raw signal for spikes induced by flying insects [13.1, 16].

Each turbidity measurement should be performed with calibrated equipment in accordance with the manufacturer's specifications. Usually the manufacturer specifies and supplies special calibration accessories. The manufacturer's recommended servicing intervals should be observed; they may have to be modified for particular sites. The calibration should be verified regularly (for transmissometers this is normally performed in very good visibility, i.e., over 10 to 15 km) and the instrument should be calibrated and adjusted if necessary. Atmospheric conditions resulting in erroneous calibration must be avoided. When, for example, there are strong up-draughts, or after heavy rain, considerable variations in the extinction coefficient are encountered in the layer of air close to the ground; if several transmissometers are in use on the site (in the case of aerodromes), dispersion may be observed in their measurements. Calibration should not be attempted under such conditions [13.1].

A transmissometer can be calibrated by direct comparison with the distance at which specified objects and lights of known intensity can be seen by an ob-



Fig. 13.21 Forward scatter meter with attached SCU (photo © Vaisala Oyj, Helsinki, Finland)

server. The observation should be as close as possible to MOR, as it is MOR which is used for conversion to obtain transmittance. The unavoidable incorporated observation uncertainties will generate a calibration error for the transmissometer, that decreases with increasing visual range. Instead of a calibration against human observations, the high visibility readings from a well known and maintained forward scatter meter can be utilized for calibration purposes [13.9]. Some state-of-the-art transmissometers conduct a calibration re-adjustment that is based on forward scatter meter readings automatically [13.7]. Additionally a linearity check using traceable optical neutral density filters should be regularly conducted.

The calibration check with regards to adjustment of instruments that measure the scattering coefficient cannot be carried out directly. The calibration has to be traceable and verifiable to a transmissometer standard, the accuracy of which has been verified over the intended operational range [13.9]. The calibration of a scatter meter involves the insertion of scatter plates (scatter meter calibration units, SCU), which simulates a defined MOR value, at a fixed position into the measurement volume. These SCUs are specific and provided by the instrument manufacturer, see Fig. 13.21. For a calibration of the scatter coefficient generally only a SCU simulation that corresponds to a low MOR value is required in combination with blocking the receiver (zero scatter coefficient, high MOR value).

At the visibility calibration facility (typically at the manufacturers premises), the SCU should be regularly checked on a known reference forward scatter meter, and if necessary recalibrated with a new coefficient. The known reference forward scatter meters are themselves regularly calibrated with a reference SCU and they are systematically checked against the reference transmissometers during low visibility episodes [13.1, 16].

13.8 Application

A variety of practical meteorological measurement tasks involve measuring the visual range, e.g., traffic route measurement stations, where the measuring section should be parallel to the road and as close to it as possible. For performing measurements in aviation and for determining various measures for the visual range, see [13.18]. The equipment manufacturer's data should also be adhered to. The temporal sequence of taking the readings should be matched to the relevant measurement task. Averaging intervals should not exceed 30 min, but typically a 1-minute gliding average is required for the MOR reporting according to the WMO and ICAO.

13.8.1 Climatology of Visibility Measurements

The customary representation methods, as used for other meteorological variables, should also be used here. In addition to averaging, however, for further processing only distributions over particular periods (e.g., day, month, year) or corresponding cumulative frequencies are meaningful. Often it is of interest to have information about the frequency distribution of the duration of particular steps of the MOR, especially below 1000 m (fog). In general, it is meaningless to quote extreme values and long-term averages. For the reporting of the MOR in the frame of aviation and roads applications the reporting resolution requirement of 1 m according to the WMO [13.1] needs to be considered. Small MORs below 1 km are of special significance. These should be, as far as possible, investigated for their causes (aerosols, precipitation, etc.), taking the relative humidity into account.

When dividing the MOR into classes for reasons of comparability, they should be chosen in a way that they correspond to the steps specified in the international meteorological codes or can be referred back to them (see Table 13.9 and Chap. 22).

13.8.2 Air, Street, and Sea Traffic

The three traffic types are treated in the following: air traffic (Sect. 13.8.2), street traffic (Sect. 13.8.2), and sea traffic (Sect. 13.8.2).

Air Traffic

The measurement and reporting of the meteorological optical range (MOR) and the runway visual range (RVR) is strictly regulated by the International Civil Aviation Organization (ICAO) with special respect to

installation sites, measurement range, allowed measurement uncertainties, averaging and reporting formats. However, some national Civil Aviation Authority (CAA) standards may modify the ICAO recommendations in a few aspects. Especially the Federal Aviation Authority (FAA) in the United States has defined slightly different requirements. The visibility information is typically required for the RVR calculation and for the reporting of the prevailing visibility. For both applications different visibility ranges, installation sites and/or observation practices are relevant. Whereas the RVR calculation requires MOR measurements up to 2000 m close to the runway, the prevailing visibility reporting requires a much larger observation (or measurement) range since the greatest visibility value which is reached within at least half the horizon circle or within at least half of the surface of the aerodrome needs to be reported.

The tolerable measurement uncertainty for MOR and RVR is specified in [13.1] and [13.19]. The following requirements for the *operationally desirable accuracy of measurement or observation* can be found:

Visibility:

- ± 50 m up to 600 m
- $\pm 10\%$ between 600 and 1500 m
- $\pm 20\%$ above 1500 m

Runway visual range (RVR):

- ± 10 m up to 400 m
- ± 25 m between 400 and 800 m
- $\pm 10\%$ above 800 m

According to ICAO the operationally desirable accuracy is not intended as an operational requirement; it is to be understood as *a goal that has been expressed by the operators*. These limits are only achievable under laboratory conditions but not in the operational practice where all environmental factors need to be considered.

For the operationally achievable measurement uncertainty the related WMO requirements apply. These are based on sensor performance under nominal and recommended exposure that can be achieved in oper-

Table 13.9 Meteorological optical range (MOR) steps to be used, according to the WMO [13.1]

MOR (km)	Steps
0.0–5.0	0.1 km steps
5.0–30.0	1.0 km steps
30.0–70.0	5.0 km steps
> 70.0	No further steps

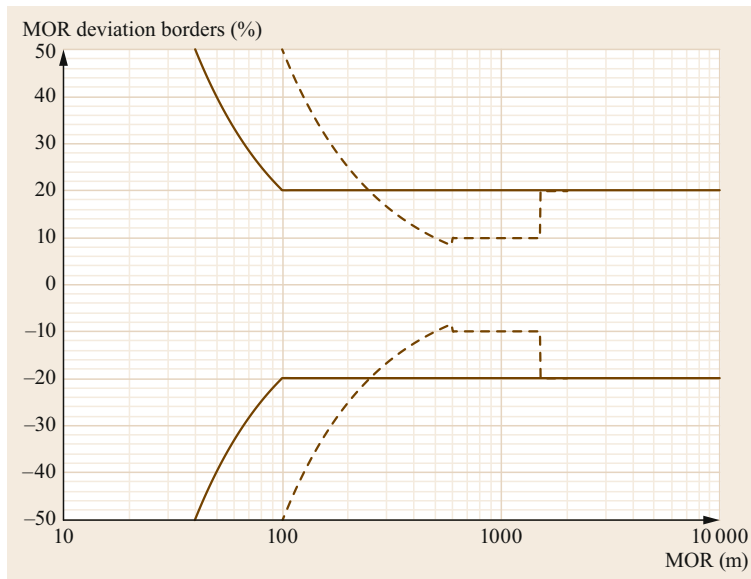


Fig. 13.22 Achievable (solid lines) and desirable (dashed lines) MOR measurement uncertainty (based on numerical ICAO and WMO requirements according to (after [13.1, 9]))

ational practice. The achievable measurement uncertainty according to [13.1] is stated as follows:

MOR: The larger of 20 m or 20%
RVR: The larger of 20 m or 20%

Figure 13.22 illustrates the difference between the desirable and the achievable measurement uncertainties for the MOR measurement. For the RVR reporting even tighter desirable uncertainty borders are relevant (see Fig. 13.23). For the range up to MOR = 2000 m the RVR uncertainty requirements dictate the tolerable measurement uncertainties for a visibility sensor used to determine the RVR (case RVR = MOR). For the MOR range above 2000 m the uncertainty requirements for MOR apply directly.

Special attention needs to be paid on airports close to desert areas. Here the visibility is frequently reduced due to dust and sand. Conventional forward scatter meters will not be capable of reporting the correct MOR (see Sect. 13.3.3) since they are not capable of distinguishing between mist, haze, dust and sand and can therefore not apply any related corrections. For these application areas, transmissometers should still exclusively be used.

Street Traffic

Typically a MOR reporting up to maximally 2 km is required, since the road traffic safety relevant obscurations to vision are fog, dense snow and heavy rain, and therefore mainly the same range that applies for air traffic. Up to now there have not been international standards. Typically the local road authority will de-

fine the requirements. However, the European standard EN 15518-3:2011 [13.20] describes the measurement uncertainty requirements for stationary equipment for road traffic control and orientates on the achievable measurement uncertainty requirements set by the WMO (see above):

Visibility measurement range: 10 to 500 m
Resolution: 10 m
Accuracy: ± 10 m or $\pm 20\%$ of measured value, whichever is greater

Sea Traffic

Visibility information is relevant in all kinds of maritime operations like automatic fog signal and/or fog light control on lighthouses, port entrance marking and protection by harbor authorities, or to secure the vessel traffic in the navigable channel with, e.g., visibility measurements on moored buoys. The distance from which a light can be seen is strictly influenced by the MOR with respect to the atmospheric extinction coefficient. During the early 1970s, the definition of the luminous range was adopted in order to describe the visibility of maritime signal lights.

The luminous range is the maximum distance at which a given signal light can be seen by the eye of the observer at a given time, as determined by the MOR prevailing at that time. It takes no account of elevation, observer's eye level or the curvature of the earth. The luminous range value when the MOR is 10 nmi (18.52 km) is defined as nominal range. A light of an intensity of, e.g., 500 cd, provides a nominal range of approximately 8 nmi. It can be recognized at up to

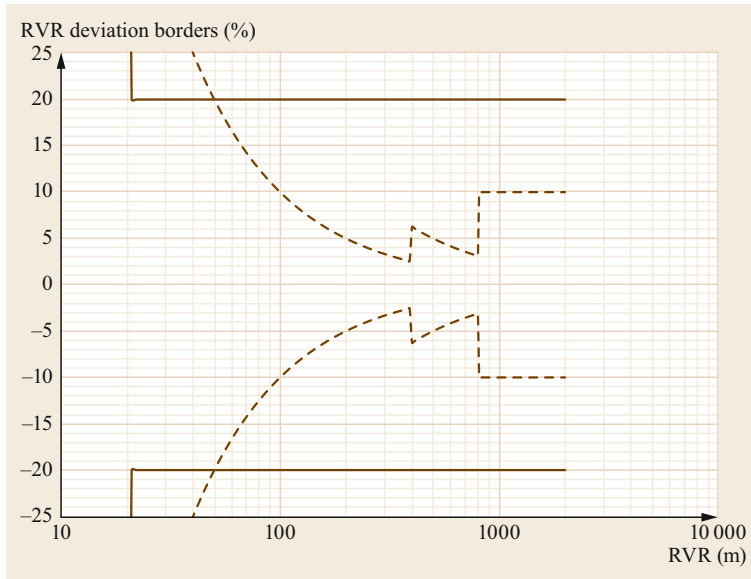


Fig. 13.23 Achievable (solid lines) and desirable (dashed lines) RVR reporting uncertainty (based on numerical ICAO and WMO requirements according to (after [13.1, 9]))

12 nmi when the MOR is 20 nmi, but only at 3 nmi if the MOR is 2 nmi. Figure 13.24 illustrates the relation between the luminous range and the intensity of maritime signal lights for various MOR values.

13.8.3 Solar and Wind Power Plants

Visibility information (as well as the cloud coverage information) may be utilized to support the plant site selection in the planning phase as well as the solar power forecast in the operational phase. The atmospheric extinction between the heliostat field and receiver in solar tower plants is known to cause significant losses of reflected direct normal irradiance (DNI). This phenomenon puts a limitation on the size of the heliostat field and is included in some ray tracing and plant optimization tools. Usually, no detailed information about the local meteorological conditions is available for many sites that are now of interest for tower plant projects [13.22].

Wind turbines are usually equipped with two obstacle lights each. The data of a visibility sensor is used for controlling the intensity of these obstacle lights. The purpose of using the visibility sensor is to keep the disturbance to the neighborhood caused by these lights at a minimum level without risking the safety of air traffic. Related regulations exist in several (mostly European) countries, e.g., in Germany the regulations have been established since 2004 as a general administrative regulation for the marking and lighting of obstacles to air navigation (*Allgemeine Verwaltungsvorschrift zur Kennzeichnung von Luftfahrthindernissen* = AVV Kennzeichnung):

- Obstruction lights are mandatory for 100 m or higher turbines.
- One visibility sensor can observe a range of 1.5 km radius.
- Brightness of obstruction light can be reduced to 30% if the MOR is higher than 5 km and to 10% if the MOR is higher than 10 km.

13.8.4 Air Quality Control

For reasons of air quality control, both scientists and official authorities are displaying increasing interest in measuring the turbidity of the atmosphere due to air pollutants. The turbidity characterizes the atmospheric content of turbid extinguishing particles, and thus the pollution. It provides, therefore, information on long-term changes in air quality. The air quality control has become more and more important since the traffic density in large cities and the related exhausts have increased dramatically during the past years. It is especially important since the measurements of certain gases and the concentrations of small particulates (PM 2.5, PM 10, PM: particulate matter) play a significant role in health. Integrating nephelometers have a certain importance here since the response to small particulates can be expected to be less uncertain than for forward scatter meters (see Sect. 13.3.4).

However, in any case in-situ measurements with transmissometers or scattered light sensors incorporate the problem that they too are highly sensitive to water droplets from mist or fog, yet cannot distinguish between these and the particulates that are relevant for the air quality determination. For that reason the typi-

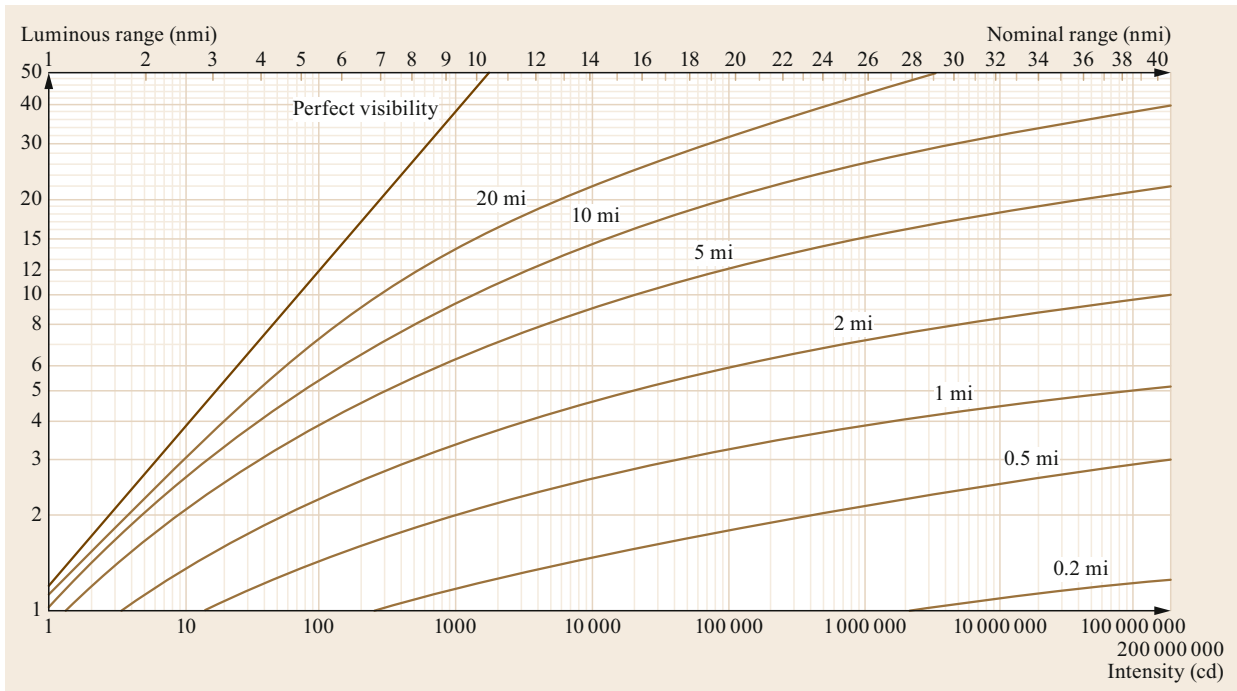


Fig. 13.24 Luminous range in prevailing visibility versus intensity of signal lights for different MORs (after [13.21] © Crown Copyright and/or database rights, reproduced by permission of the Controller of Her Majesty's Stationery Office and the UK Hydrographic Office (www.GOV.uk/UKHO))

cal optical particle concentration measurement devices do not measure directly in the free air like forward scatter meters, but instead utilize a pump in combination with a small measurement chamber in order to monitor the particle concentration for a defined volume of

air with regards to particle stream. One way to reduce the unwanted humidity influence on the particle concentration measurement results is to heat the air sample before it approaches the measurement chamber in order to remove the contained humidity.

13.9 Future Developments

Current developments utilize especially the forward scattering measurement method, but measurements at other scattering angles are used for optimization and correction purposes in order to take the characteristic scatter properties of different hydro- and lithometers into account. More reliable measurements and corrections for any dirt on the light-emitting apertures could allow virtually maintenance-free long-term deployment. New semiconductor light sources offer greater homogeneity of light propagation and longer service life. The sensors' dimensions and weight can be reduced, allowing for simpler operation. Even though its measurement uncertainty does not meet the ICAO and WMO requirements, the lidar (light detection and ranging) technology may be used in supporting applications. Remote measurements allow the detection of local visibility phenomena (like fog banks) in cer-

tain distances from the instrument location. The use of camera systems incorporates the potential for a phenomenon identification and a direct contrast determination of defined targets in order to estimate the MOR in supporting applications that do not need to fulfill the measurement uncertainty requirements according to ICAO and WMO.

13.9.1 Multiangle Technologies

New light scatter measurement arrangements and geometries and the evolving data evaluation techniques may in future allow a better differentiation of the visibility obscuring phenomena and the application of phenomenon-specific calibration corrections if needed. In contrast to conventional forward scatter meters the sample volume may be observed with more than

one receiver and under different optimized scatter angles in order to take advantage of the characteristic scatter properties of different hydro- and lithometeors [13.23, 24]. The different measurement angle-dependent scatter signal responses define a *scatter signature*, which can be beneficially utilized to distinguish between different particle types. As an example, the forward-to-backward ratio of scatter signal responses is significantly lower for solid precipitation particles than for liquid precipitation particles.

13.9.2 Multibeam Technologies

Like all conventional forward scatter meters, the above-mentioned multiangle technologies incorporate the need to correct for window dirt contamination of the transmitter(s) and receivers. There is some on-going research to expand the well-known four-beam technique towards an alternating multibeam technique. This alternating multibeam technique delivers an overestimated system of equations for the measured quantities and thus allows to mathematically reject the unknown parameters of the main disturbances. Consequently, this measurement arrangement and scheme incorporates the potential to automatically correct for window dirt contamination and variations of the transmitter light intensity without dedicated separate measurements.

13.9.3 Visibility Lidars

The lidar (light detection and ranging) technique may be used to obtain visibility when the beam is directed horizontally. The range-resolved profile of the backscattered signal S depends on the output signal S_0 , the distance x , the backscatter coefficient β , and transmission factor T , such that

$$S(x) \approx S_0 \frac{1}{x^2} \beta(x) T^2 \quad \text{where} \quad T = \int -\sigma(x) dx. \quad (13.14)$$

13.10 Further Reading

ICAO and WMO publications are seen as very basic information sources and are highly recommended for further reading. Especially the following two guides are of specific relevance:

- International Civil Aviation Organization, Manual of Runway Visual Range Observing and Reporting Practices (Doc 9328, AN/908), chapters 4, 7, and 8
- WMO, Guide to Instruments and Methods of Observation, WMO-No. 8, Volume I - Measurement

Under the condition of horizontal homogeneity of the atmosphere, β and σ are constant and the extinction coefficient σ is determined from only two points of the profile

$$\ln \left(\frac{S(x)x^2}{S_0} \right) \approx \ln \beta - 2\sigma x. \quad (13.15)$$

In an inhomogeneous atmosphere the range-dependent quantities of $\beta(x)$ and $\sigma(x)$ may be separated with the Klett algorithm [13.25]. As MOR approaches 2000 m, the accuracy of the lidar method becomes poor. More information on the requirements for performing visual-range lidar measurements to determine the direction-dependent MOR can be found in the International Organization for Standardization standard [13.18, 26].

13.9.4 Usage of Cameras

Camera systems are sometimes used as an aid for an observer in order to assess the visibility for an area that is blocked from view by buildings or to make visibility observations for a remote location. Automated determination of the presence of fog and the estimation of visibility from camera images is under development. This is not surprising given that the availability and quality of (web) cameras has increased, the costs of these systems decreased and the images can easily be made available on the Internet. Furthermore, image processing techniques are evolving and are now readily available. Various techniques have been implemented such as determining whether objects at known distances are visible by evaluating the presence of edges or contrast reduction. Other techniques use statistical parameters of an image such as gradients or Fourier analysis and relate these to visibility, or use the results of image enhancement methods such as de-hazing. Often the techniques are limited to daytime, and implementation needs to be tuned to the images/scenes for a specific site [13.27].

of Meteorological Variables. (World Meteorological Organization, Geneva, 2018)

Besides being very detailed description of the different technologies, these guides provide information about the best practices, procedures and the basic capabilities of instruments and systems for assisting Civil Aviation Authorities, National Meteorological and Hydrological Services and other interested users operating observing systems.

References

- 13.1 WMO: *Guide to Instruments and Methods of Observation*, WMO–No. 8, Volume I – Measurement of Meteorological Variables (World Meteorological Organization, Geneva 2018)
- 13.2 W.E.K. Middleton: Vision through the atmosphere. In: *Geophysik II / Geophysics II*, Handbuch der Physik / Encyclopedia of Physics, Vol. 10 / 48, ed. by J. Bartels (Springer, Berlin, Heidelberg 1957)
- 13.3 G. Dietze: *Einführung in die Optik der Atmosphäre* (Akadem. Verlagsges., Leipzig 1957) pp. 211–243
- 13.4 L. Foitzik, H. Hinzpeter: *Sonnenstrahlung und Lufttrübung* (Akadem. Verlagsges., Leipzig 1958)
- 13.5 H. Koschmieder: Theorie der horizontalen Sichtweite. Teil 1 und 2, Beitr. Phys. freien Atmos. **12**, 33–35 (1925), and p. 171–181
- 13.6 VDI 3786 Blatt 6: *Environmental Meteorology – Meteorological Measurements – Turbidity of Ground Level Atmosphere – Meteorological Range* (VDI, Düsseldorf 2018)
- 13.7 Vaisala: Transmissometer LT31, Product Brochure B210416EN–D (2017)
- 13.8 A. Kohnle: *Proceedings of Carl Crantz Gesellschaft* 1987) pp. 1.07–1.09
- 13.9 International Civil Aviation Organization: *Manual of Runway Visual Range Observing and Reporting Practices*, Doc 9328, AN/908, 3rd edn. (ICAO, Montréal 2005)
- 13.10 H.C. Van de Hulst: *Light Scattering by Small Particles* (Wiley, New York 1957), repr. Dover Books on Physics, 1981
- 13.11 O.D. Barteneva: Scattering functions of light in the atmospheric boundary layer, Izv. Akad. Nauk SSSR Ser. Geofiz. **12**, 1237–1244 (1960)
- 13.12 S.-J. Jia, D.-R. Lü: Optimal forward-scattering angles of atmospheric aerosols in North China, Atmos. Ocean. Sci. Lett. **7**(3), 236–242 (2014)
- 13.13 F.X. Kneizys, E.P. Shettle, W.O. Gallery, J.H. Chetwynd, L.W. Abreu, J.E.A. Selby, S.A. Clough, R.W. Fenn: *Atmospheric Transmittance/Radiance: Computer Code LOWTRAN 6, Appendix D*, AFGL–TR–83–0187, Environmental Research Papers No. 846 (Air Force Geophysics Laboratory, Massachusetts 1983)
- 13.14 A. Macke, R. Scheirer, M. Schewski, S. Meyer, I. Schlimme, S. Klotzsche: The publicly available single scattering and radiative transfer codes at IFM–GEOMAR. In: *3rd IBRC Workshop* (Leibniz-Institute for Marine Research, IFM–GEOMAR, Kiel 2005)
- 13.15 J. Heintzenberg, R.J. Charlson: Design and application of the integrating nephelometer: A review, J. Atmos. Ocean. Technol. **13**, 987–1000 (1996)
- 13.16 Vaisala: Forward Scatter FD70 Series, Product Brochure B211755EN–A (2018)
- 13.17 D.J. Griggs, D.W. Jones, M. Ouldridge, W.R. Sparks: *The First WMO Intercomparison of Visibility Measurements: Final Report*, Instruments and Observing Methods Report No. 41, WMO/TD–No. 401 (WMO, Geneva 1990)
- 13.18 DIN ISO 28902–1: *Luftqualität – Umweltmeteorologie – Teil 1: Bodengebundene Fernmessung der Sichtweite mit Lidar* (Beuth, Berlin 2012)
- 13.19 International Civil Aviation Organization: *Meteorological Service for International Air Navigation, Annex 3*, 16th edn. (ICAO, Montréal 2007)
- 13.20 EN 15518–3:2011: *Winter Maintenance Equipment. Road Weather Information Systems. Part 3: Requirements on Measured Values of Stationary Equipments* (Beuth, Berlin 2011)
- 13.21 Admiralty: List of Lights & Fog Signals (ALL) Vol. A: British Isles and North Coast of France (NP74), 2021 Edition (UK Hydrographic Office, Taunton, 2019/20)
- 13.22 N. Hanrieder, F. Wehringer, S. Wilbert, F. Wolfertstetter, R. Pitz–Paal, A. Campos, V. Quaschnig: Determination of beam attenuation in tower plants. In: *SolarPACES Conf., Marrakech* (2012)
- 13.23 S. Engel, K. Heyn: Method for determining visibility, amount of precipitation and type of precipitation, Patent US7122820B2 (2002)
- 13.24 M. Löffler–Mang: Apparatus and method for differentiating types of mist, Patent WO/2008/006578 (2008)
- 13.25 J.D. Klett: Lidar inversion with variable backscatter/extinction ratios, Appl. Opt. **24**(11), 1638–1643 (1985)
- 13.26 International Organization for Standardization: *Air Quality – Environmental Meteorology – Part 1: Ground-Based Remote Sensing of Visual Range by Lidar*, ISO 28902–1:2012 (ISO, Geneva 2012)
- 13.27 W. Wauben, M. Roth: Exploration of fog detection and visibility estimation from camera images. In: *WMO Tech. Conf. Meteorol. Environ. Instrum. Methods Obs. (TECO–2016)*, Madrid (WMO, Geneva 2016), Instruments and Observing Methods Report No. 125

Martin Löffler-Mang

School of Engineering
htw saar, University of Applied Sciences
Saarbrücken, Germany
loeffler-mang@htwsaar.de



Martin Löffler-Mang is Professor of Optical Sensors at the School of Engineering at the University of Applied Sciences in Saarbrücken, Germany. After completing his studies in Physics he received his PhD in Engineering Sciences in 1992 at KIT (Karlsruhe), applying laser measuring techniques to spraying systems. He also spent seven years at the Institute for Meteorology and Climate Research (KIT). Currently, he works on the development of different meteorological sensors, namely for hail, fog, and snow.

Klaus Heyn

Sensing Technologies
Vaisala GmbH
Hamburg, Germany
klaus.heyn@vaisala.com



Klaus Heyn is an industrial expert for optical sensors in meteorological applications. In 1981 he gained his engineering degree in Hamburg, Germany and received a Diploma for his work on probability distribution and distribution density measurements of stochastic ergodic processes. He currently works as a Senior Scientist for the Weather Instruments Business Area of the Finnish company Vaisala and is responsible for current and future measurement technologies.

Electricity M

14. Electricity Measurements

Giles Harrison , Alec Bennett 

Atmospheric electricity concerns the transport of charge in the atmosphere and the resulting effects. Its measurement requires knowledge of several different quantities, each of which spans a wide parameter space. Examples are the range of electric fields present between fair weather conditions and thunderstorms, and the range of charges between that of a single molecular cluster ion to that carried by a hailstone. Methods for measurements of atmospheric electric fields were amongst the first quantitative measurements in atmospheric science, beginning in the mid-eighteenth century. Modern techniques extend to remote detection of lightning from satellites and local monitoring of lightning-induced electric field changes. The measurement of cluster ions is intimately linked to studies of cosmic rays and natural radioactivity and provides a sensitive method of detecting hazardous radioactive releases. Atmospheric electricity measurements have utility for lightning detection, warning, and associated weather forecasting, and in investigating the electrical changes in air associated with aerosol and radioactive pollution. They also have applications to studying electrical effects in the lower atmosphere resulting from changes in the space weather environment.

14.1	Measurement Principles and Parameters	432
14.2	History	432
14.2.1	Early Measurement Technologies	433
14.2.2	Developments in Measurement Technologies	434
14.3	Theory	434
14.3.1	Fair Weather Fundamentals	434
14.3.2	Disturbed Weather Lightning Detection	436
14.3.3	Precipitation Electricity	440
14.3.4	Corona and Point Discharge	441
14.4	Devices and Systems	441
14.4.1	Fair Weather Devices and Systems	441
14.4.2	Disturbed Weather Systems	445
14.5	Specifications	448
14.5.1	Fair Weather Requirements	448
14.5.2	Automatic Recording	448
14.5.3	Disturbed Weather Requirements	448
14.6	Quality Control	448
14.6.1	Fair Weather	448
14.6.2	Disturbed Weather Quality Control	450
14.7	Maintenance	450
14.7.1	Fair Weather Maintenance	450
14.7.2	Disturbed Weather Maintenance	451
14.8	Applications	452
14.9	Future Developments	453
14.10	Further Reading	453
	References	453

Atmospheric electricity is sometimes interpreted as solely concerning the study of lightning, but is more inclusively defined as the study of all electrical phenomena in the atmosphere, regardless of meteorological circumstances. For most purposes, atmospheric electricity can be considered a study of the transport of charge in the stratosphere and troposphere under

a range of meteorological conditions. Thunderstorms are in a sense the exception, as they occur in a restricted range of conditions and regions, in which large charges are separated in the presence of strong turbulent motions. Sufficiently large electric fields are generated to cause electrical breakdown as lightning and the release of acoustic energy as thunder.

Table 14.1 Parameters measured in atmospheric electricity

Parameter	Description	Unit	Symbol
Vertical electric field	Vertical electric force acting per unit charge	V m^{-1}	E_z
Potential gradient	Conventional description of vertical potential difference	V m^{-1}	F (or PG)
Conduction current density	Vertical current flowing per unit area due to conduction	pA m^{-2}	J_c
Air conductivity	Conductivity of air due to both negative and positive ions	fS m^{-1}	σ
Mean ion mobility	Drift speed of a cluster ion per unit electric field	$\text{m}^2 \text{V}^{-1} \text{s}^{-1}$	μ
Mean ion number concentration	Number of ions per unit volume	m^{-3}	n
Ion production rate	Rate of generation of bipolar ions per unit volume	$\text{m}^{-3} \text{s}^{-1}$	q
Space charge	Net concentration of charge per unit volume	C m^{-3}	ρ
Elementary charge	Modulus of the charge carried by an electron	C	e

14.1 Measurement Principles and Parameters

Measurements in atmospheric electricity extend across many different quantities but can be usefully divided into those made for disturbed weather (i.e., thunderstorm) and fair weather conditions. For disturbed weather purposes, a variety of measurement systems have been developed for detection of the lightning discharge itself, optically, electrostatically, or through use of radio frequency emission. In contrast, for fair

weather, when no appreciable charge separation occurs, the vertical electric field and the associated vertical current density are the principal quantities of interest. Fair weather atmospheric electricity has also traditionally included the conduction properties of air, such as the generation, concentration, and properties of the cluster ions it contains. The typical parameters considered are listed in Table 14.1.

14.2 History

Atmospheric electricity is amongst the oldest experimental topics in meteorology, with the globally iconic work of *Benjamin Franklin* (1706–1790) providing a useful date, 1752, with which to define the beginning of the modern era of work. Franklin's international reputation ensured his suggestions for experimental investigations were widely noticed [14.1].

Soon after Franklin's work became known, experimenters found that electrification remained present away from the immediate location of thunderstorms. The astronomer *Pierre Charles Le Monnier* (1717–1799) detected electrification in clear air in 1752 [14.2], and in June 1753, *Guillaume Mazeas* (1720–1775) showed that a silk-insulated 100 m horizontal wire suspended 10 m above the surface would nevertheless acquire charge in dry, nonthunderstorm conditions [14.3]. Later that year, electric charges in a cloudless atmosphere were detected by *John Canton* (1718–1772) [14.4]. Canton developed further apparatus to investigate charges associated with hail, snow, and rain. Remarkable studies were made with the early instrumentation, such as a series of continuous observations by *Giambattista Beccaria* (1716–1781) in Piedmont, north-west Italy [14.5], and 2 years of daily observations made by *John Read* (1726–1814), using a vertical rod mounted above his house in Knightsbridge, London [14.6, 7].

Early measurement instruments often used a flame connected to a mechanical electrometer as a method to acquire the local potential of the air. The need for a method of continuous measurement of the vertical atmospheric electric field was recognized by *Lord Kelvin* (born *William Thomson*, 1824–1907), who developed a continuous recording system based on a *water dropper* sensor for the atmospheric potential with a photographically registering electrometer. The spray of drops generated by the water dropper exchanged charge with its surroundings, ultimately equalizing the potential of the isolated pipe supplying the water spray, which was measured [14.8]. This continuous operation represented a significant advance over the flame probes. The Kelvin water-dropper potential equalizer was widely adopted internationally, including at the top of the Eiffel Tower [14.9], and for use on manned balloons [14.10]. Remarkably, a Kelvin water dropper equalizer is still in routine service at Kakioka Observatory in Japan (Fig. 14.1). Note that the magnitude of the vertical component of the atmospheric electric field E_z is commonly referred to as the *potential gradient* (PG), which is, by convention, regarded as positive in fair weather.

The widespread need for fair weather measurements at many international observatories led to more commonality in the technology used. Kelvin water drop-

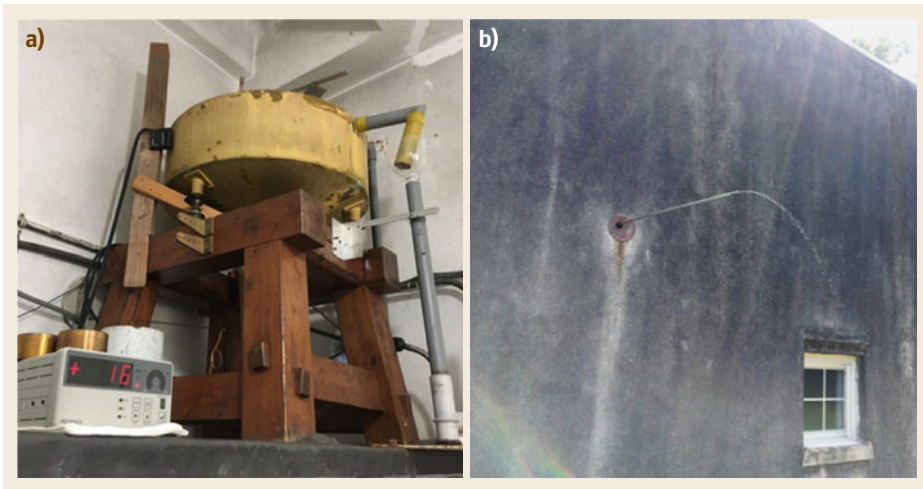


Fig. 14.1a,b Potential gradient measurements made using the Kelvin water-dropper potential equalizer, at Kakioka Observatory, Japan. (a) Electrically isolated water-dropper header tank, with electrometer measuring tank potential and (b) water-dropper spray, falling from an electrically isolated tube emerging from the observatory wall. (photo: R.G. Harrison)

pers were used at some sites for PG, but they were superseded by radioactive probes (e.g., at Porto and Lerwick), which permitted continuous measurements without the need for a water supply and associated frost protection. In the second half of the twentieth century, *field-mill* instruments became increasingly commonly used for PG measurements. These avoid the regulatory issues arising from the use of ionizing radiation on radioactive probe sensors. Many commercial field mills exist and are now in use, and some have proved very durable in hostile atmospheric conditions.

Of particular importance for atmospheric electricity measurements was the lead given by the Carnegie Institution, which developed techniques for use on survey ships, and in particular, the *Carnegie*, an oceanographic and geomagnetic survey ship. The Carnegie's cruises between 1909 and 1928, when the ship was destroyed by fire, included routine measurements of air ion concentration, air ion mobility, and PG. The common diurnal variation in PG found across the planet in fair weather conditions is still known as the *Carnegie curve* [14.11, 12].

14.2.1 Early Measurement Technologies

Electrometers are devices designed to measure small amounts of charge. The earliest electrometers were a pair of pith balls, attached to each other by a thread hung centrally on a hook. When the balls became charged, they repelled by an electrostatic force, with a separation distance which was nonlinearly proportional to the charge carried. Absolute calibration is possible, if the arrangement is described in detail, for

example to allow retrieval of the potential from historical measurements [14.13]. Later designs of mechanical electrometers used gold leaf or straw as the sensing elements, again with the mechanical deflection under an electric force measured to obtain the charge. Using delicate bearings and sensitive torsion measurement, precise measurements of small charges could be made, e.g., in a device made by Kelvin, [14.8]. Attaching a mirror to reflect and move a light beam provided a method of amplification and recording for the small changes detected. This approach was used by the recording part of the Kelvin water-dropper system and for the PG measurements on the final cruise of the *Carnegie*.

During the early twentieth century new technologies were developed, and many geophysical observatories internationally adopted methods for atmospheric electricity measurements. The Nobel Laureate *Charles ("C.T.R.") Wilson* (1869–1959) devised a method to obtain regular measurement of the vertical current density and PG using a horizontal plate system, which was deployed at Kew Observatory from 1909, continuing in regular use for almost 70 years [14.14]. There has also been considerable longevity for the operating principles of a portable (*Gerdien*) device designed for air conductivity measurement [14.15], using an aspirated cylindrical capacitor instrument to determine the air conductivity by rate of decay of charge on an electrode exposed to air.

Some of the first sensors for lightning detection used the response of a capillary electrometer to < 20 Hz changes in atmospheric field, recorded on a photographic plate [14.16]. Wilson's investigations focussed

on determination of lightning charge moment, with the signal authenticity and range determined from acoustic methods, limiting the maximum range to less than 30 km. Similar techniques were used to investigate characteristics of the lightning electrostatic field change such as polarity and shape [14.17]. The arrival of early radio-frequency (RF) lightning detection methods in the mid-twentieth century, combined with an extended human weather observation network, were used to investigate lightning signals beyond audible range [14.18]. As instrumentation and techniques developed during the late twentieth century, the electrostatic field change associated with lightning could be used to estimate the location of charges neutralized by lightning in three dimensions [14.19]. Increased sensitivity of electronics and digital filtering enabled the electrostatic field change (below 50 Hz) associated with lightning to be used by commercial instrumentation to estimate thunderstorm range 100 km from the sensor [14.20].

14.2.2 Developments in Measurement Technologies

Developments in electronics provided alternatives to mechanical electrometers. Between about 1920 and 1960, thermionic valves provided the basis for measuring small charges, or measuring from voltage sources that were unable to supply current (i.e., high impedance voltage sources). The thermionic valve operated by deflecting a current from a heated electrode operating at low pressure, through the action of an electric field. By careful construction, the leakage current of the enclosing glass envelope was small, and the voltage to be measured caused deflection of the current with negligible current drawn. This leakage was further reduced by the use of coatings on the electrodes. Valve electrometers were durable electrically, although physically fragile, and well suited to fair weather measurements [14.21].

14.3 Theory

The description of quantities in atmospheric electricity requires consideration of the fair weather parameters and disturbed weather parameters separately. In the fair weather case, the quantities of electric field, conduction current density, and air conductivity can usually be related by Ohm's law, in the absence of turbulence. In the disturbed weather case, the lightning source position and the flash rate are the primary quantities to be determined for operational meteorology, but the lightning currents and surface electric field changes are important for research.

Transistors replaced thermionic valves in the second half of the twentieth century, with the properties of the semiconductor junction defining the usefulness of a device for measurements. In many ways, the field effect transistor closely replicates the operation of a thermionic valve, but its departure from ideal behavior, from, for example, the effect of leakage currents, restricts its use in electrometry. A major limitation is that the most sensitive semiconductor devices tend to be highly restricted in the dynamic range, which can render them badly damaged by overload conditions. For use in atmospheric electricity, when transient conditions can occur unexpectedly, this can be a severe disadvantage. The overall complexity of a semiconductor measurement circuit may, therefore, be dictated by additional protection devices, which must be included for reliability.

Semiconductor electrometers can be used for measurement of charge, current, and voltage. They typically use a standard integrated circuit element—the operational amplifier—which has been optimized to minimize the sensing current drawn, typically in the range of 1 to 10 fA. Operational amplifiers use feedback to provide close to ideal performance, and the feedback element is chosen for the quantity to be measured. If a capacitor is the feedback element, the device can typically measure charge, and if there is a feedback resistor, current can be monitored [14.22]. Voltage measurements and amplification can also be achieved [14.23], which can be extended over a wide range with additional circuitry [14.24, 25]. One important consideration in electrometry is the size of the feedback resistor required. To provide an output voltage of 1 mV from a 1 pA current, a 1 G Ω resistor is required. Generally, stable resistors in the range from 1 G Ω to 1 T Ω can be difficult to obtain. It is possible to synthesize these large resistor values using more standard components, but other disadvantages arise, depending on the circuit configuration.

14.3.1 Fair Weather Fundamentals

In this section, the fundamental measured parameters of fair weather atmospheric electricity are presented.

The *potential gradient* (PG) is essentially the primary quantity considered in fair weather atmospheric electricity. It is a determination of the vertical component of the atmospheric electric field. In fair weather conditions, the electric potential increases positively with height. If the potential is considered to be zero at the surface, the potential in fair weather at 1 m above

the surface is of the order 100 V. The PG near the surface is conventionally considered to be the difference in potential between a point at 1 m and the surface, i.e.,

$$F = \frac{\Delta V}{\Delta z}, \quad (14.1)$$

for F the potential gradient, Δz the difference in height, and ΔV the associated change in potential. A consequence of this convention is that the vertical electric field E_z differs from the PG by a minus sign, i.e.,

$$F = -E_z. \quad (14.2)$$

In fair weather, the PG is, therefore, positive, and the electric field negative. During disturbed weather, the PG can become large and variable, in magnitude and sign. In these cases, the PG responds to local charge separation and induced effects, whereas, in fair weather, it arises mostly from the conduction current passing through the finite conductivity of atmospheric air.

Atmospheric air has a finite electrical *conductivity* because of the presence of molecular cluster ions, formed by the combined effects of terrestrial radioactivity and cosmic ray ionization. Near the surface over the continents, cluster ions are generated by the ionization of air molecules from high-energy interactions, either from gamma emitting sources in the soil or alpha emitting isotopes of radon released through porous surface materials. There is also a small contribution from cosmic ray ionization, which increases with increasing height. Over the oceans, the principal source of atmospheric ionization is from cosmic rays. The typical surface ionization rate, found by an ionization chamber (a fixed volume device in which the rate of charge generation is measured), q is 10 ion pairs $\text{cm}^{-3} \text{s}^{-1}$, about 20% of which is due to cosmic ray ionization. Cluster ions have traditionally been categorized by their electrical mobility, which is their drift speed in a unit electric field. This has led, historically, to the distinction between small (or fast) ions and large (or slow) ions, and further categories have also been proposed. Small ions have a mobility of about $1 \text{ cm}^{-2} \text{ V}^{-1} \text{ s}^{-1}$, and they provide the greatest contribution to the electrical conductivity of air of atmospheric charged particles. Large ions would now be considered to be aerosol particles that have become charged, for example after a collision with a small ion.

The number concentration of small ions in atmospheric air determines the conductivity of air. If there are n ions per unit volume of mean mobility μ , the total conductivity σ is given by $\sigma = 2n\mu e$, where e is the elementary charge. The factor of 2 accounts for the contribution of the positive and negative ions, which are

assumed to have similar concentrations and values of mobility. If there is appreciable asymmetry in the ion properties, the individual contributions of the bipolar ions can be considered separately.

Air conductivity can also be considered in terms of an Ohm's law relationship for conduction, considering the vertical electric field E_z and vertical current density J_z , as

$$J_z = \sigma E_z. \quad (14.3)$$

This only applies if ohmic conduction occurs and will not be valid in other circumstances, for example if there is a turbulent component contributing to the charge transport. Note that, in this equation, the electric field convention is used: the conduction current density is found to be directed downwards in fair weather.

The air–Earth *current density* J describes the total vertical electric current flowing between the atmosphere and the Earth's surface. This current is measured directly using an electrode—often an isolated flat horizontal plate—exposed to the atmosphere. A sensitive and high impedance ammeter attached between the electrode and ground records the current.

In general, this current has four contributing components [14.2]. Firstly, there is the conduction current [14.26, 27]. This is the near-vertical current, which flows between the lower ionosphere and Earth's surface due to the action the global electric circuit [14.28]. The conduction current component can be found indirectly by measuring the air conductivity and electric field, with current inferred using Ohm's law [14.29, 30]. Turbulent motion of space charge within the atmosphere, charged regions in overhead cloud, and lightning transients combine to induce the second prominent component of the air–Earth current, called the displacement current. Whilst this component is induced on the sensing electrode rather than a flow of charge from the atmosphere, the continuous and broad spectra of variability of the atmospheric electric field means this current must be carefully considered in direct current measurements. The third component is that produced by turbulence, whereby ions and charged particles are transported by the movement of air. During disturbed weather, charged droplets, particles, or pellets falling on the electrode will produce the fourth component, referred to as the precipitation current. If the collecting electrode has sharp edges, an additional disturbed weather component may also be produced under a strong electric field, where point discharge (corona) is initiated. Point discharge can produce currents several orders of magnitude greater than the conduction current [14.19], so electrodes need to be smooth to avoid such contamination from additional current sources.

Of all these components, it is the conduction current (or rather the conduction current density) that is of most significance for the investigation of the global electric circuit, due to its origin from the potential difference between the ionosphere and surface. The small magnitude ($\approx 1 \times 10^{-12} \text{ Am}^{-2}$) of the currents brings with it a requirement for maintenance of extremely good electrical insulation between the electrode and ground under all weather conditions; the need to eliminate other unwanted current components makes the conduction current density a challenging parameter to measure.

14.3.2 Disturbed Weather Lightning Detection

In contrast with the fair weather current, the current that flows as a result of a lightning discharge is very many orders of magnitude greater. Methods of remote detection of lightning are discussed here, using radio frequency, optical and electrostatic techniques, as well as the acoustic energy generated.

The complete process of charge transfer during a single lightning discharge is called a *flash*. A flash neutralizes a portion of charge within a thunderstorm, which can be readily identified by a sharp change in the cloud's electrostatic field over a typical period of 0.2 s, followed by a much slower recovery of the order of 100 s, as electrification mechanisms within the cloud replace the neutralized charge. The complete discharge process during a flash does not produce a smooth current flow, but is, instead, composed of several discrete surges of current lasting a few tens of milliseconds, referred to as strokes. After the initial electrical breakdown of the air, a lightning channel is formed by a trail of electrons, called a leader. These leaders are only weakly luminous and will split and change direction after several meters in steps. These steps in channel propagation give rise to the name of the first stage in a lightning flash—the stepped leader. Once the lightning channel has been formed by the leader, current surges along it in discrete pulses or *strokes*. When the lightning channel is from the cloud to ground (CG), the initial stepped leader creates a pathway for the return stroke. This stroke is often very powerful, generating a typical peak current of the order of 10 000 A and occasionally exceeding 200 000 A. Currents of this magnitude produce a bright channel and quickly heat the air, producing the shockwave that is recognizable as thunder. More commonly, a lightning channel remains within the cloud, and the resulting strokes are termed intracloud (IC) or cloud-to-cloud (CC). Charge transfer between the cloud and nearby cloud-free air also occurs, as well as leaders, which originate from the ground, transferring charge to the cloud overhead and

are consequently termed *upward* or ground-to-cloud lightning. Lightning strokes can be of either positive or negative polarity. The polarity of a cloud-to-ground stroke is determined by the charge it lowers from the cloud to the ground. Since the base of a thundercloud is normally negatively charged, most CG strokes are of negative polarity (–CG). CG strokes with positive polarity tend to originate near the top of the cloud, where a large reservoir of positive charge is often found. A positive cloud to ground stroke (+CG) is, on average, the most powerful type of lightning stroke on Earth, responsible for significant damage and emission of radio signals that can be detected thousands of kilometers away. For radio detection of lightning, it is the stroke that is the fundamental property detected, so the location and count rate of radio-based detection systems will by default relate to strokes, not flashes. Since a single flash is typically composed of 2 to 5 (and occasionally more than 20) strokes, it is important to consider that other detection systems such as human observation or electrostatic techniques will consider lightning discharges in terms of complete flashes. This can, and often does, lead to confusion when comparing the output of different types of lightning detection techniques.

Radio Frequency (ULF to VHF)

Lightning emits a broad spectrum of electromagnetic radiation, which can be used for location and remote determination of the discharge properties [14.31]. Since different components of a lightning flash emit radiation with different effectiveness at different frequencies, researchers can optimize their radio receivers to have greatest sensitivity to bands within the spectrum according to their area of interest [14.31–33] with research on radio emissions spanning ultra low frequency (ULF) to very high frequency (VHF). For example, the initial ground-seeking leader stroke (stepped leader) and short, in-cloud leaders tend to emit most effectively in the VHF band, whereas the subsequent visible, high current surge along the leader's channel associated with the powerful return stroke emits the most strongly in the very low frequency (VLF) band [14.34]. Such differences are important factors in determining the maximum range and detection efficiency of radio-based lightning location instrumentation [14.32].

Whenever electrons are accelerated, electromagnetic radiation is produced. The greater the acceleration and number of electrons involved, the greater the energy radiated. The rapid acceleration of numerous electrons in a lightning channel at the start of a return stroke will, therefore, be expected to generate a signal of high power, albeit for a duration of only a few milliseconds [14.31]. The ionized lightning channel can be

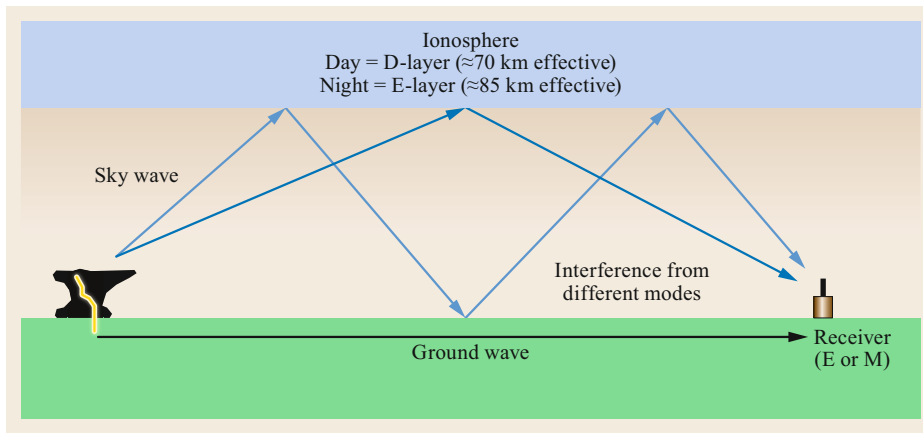


Fig. 14.2 Reflection of VLF waves by the ionosphere

considered as an antenna, the length of which influences what frequency will be most effectively radiated. The ≈ 10 to 100 m steps in a channel of the downward-propagating stepped leader prior to a cloud-to-ground return stroke act as a set of similarly-sized antennas. Such antennas radiate energy most effectively at wavelengths twice their length, equating to typical peak emissions of order 10 MHz in the HF band. Steps energized by weak intracloud strokes can be even smaller, with length scales under 10 m and emitting the most strongly in the VHF band [14.35]. Once a return stroke is initiated by contact with an upward streamer near the ground, a surge of electrons propagate back up the ionized channel of the stepped leader. This channel can be several kilometers long, so will radiate most effectively at much lower frequencies than the stepped leader or intracloud stroke. These near-vertical, long channels act as monopole antennas above the conductive ground, emitting most effectively for wavelengths four times their length, typically around 10 kHz, in the VLF part of the radio spectrum [14.33, 36].

The ionosphere is an electrically conductive layer of the atmosphere beginning at an altitude between 60–90 km, depending on properties such as solar intensity. The ionosphere acts as an effective reflector of very low frequency radio signals such as those from lightning return strokes. Powerful VLF signals can propagate over thousands of kilometers through the atmosphere, since they are reflected between the ionosphere and surface instead of being strongly absorbed or lost to space (Fig. 14.2, [14.34, 37]). Such propagation properties and powerful emissions from return strokes are exploited by long-range lightning location networks, where VLF receivers are deployed across a large region and capable of locating lightning over continent-scale regions, or more [14.38–40]. Lightning is located by comparing the arrival time differences of the same signal received at multiple receivers, some-

times in combination with triangulation using magnetic direction finding (Fig. 14.2). The location accuracy of such long-range VLF arrival time difference (ATD) networks depend on the validity of their signal propagation model, receiver baseline (spatial density of receivers), and how accurate they can time the arrival of the same lightning signal arriving at the receivers (e.g., [14.38]). In reality, median location accuracies of 1–20 km are typical of this long-range location method, although higher density continental-scale networks with higher frequency upper limits (LF/VLF) can achieve median location accuracies of the order of 100 m. The necessity to use VLF for long-range lightning location means that such networks are normally strongly biased to CG lightning stroke detection, although most are also capable of locating strong intracloud activity as well. Shorter baseline, higher density networks incorporating the LF band have been demonstrated to detect, and discriminate between, both CG and IC/CC lightning strokes with peak currents as low as a few hundred amps.

In addition to accurate lightning location using VLF/LF networks, it is possible to detect the shape of individual lightning channels in three dimensions using a short-baseline (of the order of 10 km) network of VHF interferometers [14.35]. Such networks are tuned to the weaker components of the lightning discharge process and cannot exploit ionospheric reflection, so their range is little more than line of sight, at approximately 200 km. The VHF network technique does, however, allow exceptional detection efficiency and location accuracy (of the order of 10 m) over the relatively small area covered, making it popular with lightning research groups. In addition to scientific research, VHF interferometry is also used on some regional-scale lightning location networks for the purpose of total lightning (CG, IC, and CC) detection, especially when detection of weak IC strokes or initiation height is important. The short baselines required normally limit this tech-

nology to coverage of smaller countries or regions compared to the more continental-scale VLF/LF networks, although some near-global network providers incorporate VHF receivers, if they have the capability of deploying a suitably dense network of receivers over a wide geographical area. VHF signals from lightning can propagate through the ionosphere, where they can also be detected by space-based lightning detection instrumentation for scientific research.

The proximity and direction of lightning strokes using a single radio receiver is possible and can be a useful indicator of local thunderstorm activity. The range of such instrumentation is normally limited to a few hundred kilometers, and location accuracy is generally poor compared to using a network due to the assumptions required on lightning signal characteristics and propagation. False alarms can arise due to nearby anthropogenic sources of radio transients (e.g., [14.37]) and can be removed by requiring corroboration from multiple receivers in a network. The presence of ferrous material and conductive paths where currents can be induced at a site can generate systematic and angular-dependent errors in lightning direction estimation from single-site receivers of up to 30°, unless these errors are determined and accounted for by prior comparison with an independent method of lightning location. Range is normally estimated by comparing the amplitude of one or more radio frequency bands, although large uncertainties exceeding 10 km can result from the natural variability of lightning radio emission characteristics.

Given there are typically 2000 active thunderstorms on Earth at any time, the global atmosphere is subject to near-continuous excitation by lightning. Larger lightning strokes radiating strongly below VLF frequencies act to excite the waveguide between the surface and ionosphere, causing it to resonate. The fundamental frequency of this resonance is 7.8 Hz in the extremely low frequency (ELF) band, with six harmonics below 50 Hz [14.41, 42]. These near-continuous peaks are called *Schumann resonances*, and since they are a global signal, they can be measured from any location on Earth [14.43]. Their small amplitude can limit detection to sites with low background electrical noise, where the diurnal cycle of the resonance amplitude can be used to infer general characteristics of global lightning activity, such as diurnal and seasonal variability. Both electric and magnetic field components of Schumann resonances have been used for lightning, ionospheric, and radio propagation research (e.g., [14.37]).

Electrostatic

Neutralization of charge during a lightning flash occurs over a time period of approximately 0.2 s, producing a step-change in the electrostatic field of a thunder-

storm [14.17, 18]. This step is gradually removed as the cloud is re-energized, producing a recovery curve lasting for more than a minute (Fig. 14.3). Due to the image effect of the conductive surface below, the change in charge can be represented as a vertical dipole, of length twice the height of the neutralized charge region above the ground [14.16]. The total charge neutralized by a lightning flash can, therefore, be given in terms of charge moment when using quasi electrostatic measurements. Whilst the change in electric field measured at the surface can exceed 100 kV m^{-1} in the first second after a flash within a few kilometers, this dipole field quickly attenuates with distance, with magnitude proportional to the inverse cube of distance from the dipole. As a consequence, electrostatic lightning detection is usually limited to a range of less than 100 km before any signal is lost to background noise. Such a distance is, however, sufficient for warning of local thunderstorm activity around a site, with automatic electrostatic lightning detection and ranging instrumentation available commercially [14.44]. Every lightning flash will produce a step change of the thunderstorm electric field, so this method of lightning detection from a single sensor is capable of detecting all forms of lightning activity (CG, IC, CC) within a few tens of kilometers from the storm with very high detection efficiency. Providing that the electrostatic field is sampled at a rate of at least 10 Hz (ideally 100 Hz), it is possible to estimate the distance to the lightning flash using the maximum electric field change and an assumption of the charge moment. Note that such sampling frequencies limit the time resolution of the lightning discharge to the flash, not stroke, level. Higher sampling rates risk contamination from the electromagnetic component of the emission, and lower sampling rates risk undersampling of the signal, causing the true magnitude of electric field change immediately following the flash to be underestimated.

Whilst using a fixed value for lightning strength to estimate the distance to a flash based on signal amplitude would produce unacceptably large errors for a radio-receiver, such an assumption is more acceptable when using electrostatic detection. This is due to the inverse-cubed reduction of signal strength with distance for the electrostatic dipole field, which acts to limit the effect of natural variability in lightning charge moment on range uncertainty compared to radio peak amplitude, which reduces by a lower inverse power of distance (between 1 and 2 depending on propagation characteristics). For example, it is possible to estimate the distance of a 20 km flash with a typical uncertainty of 5 km using the electrostatic field change alone. The flash direction cannot be readily determined from the magnitude of the electrostatic signals alone.

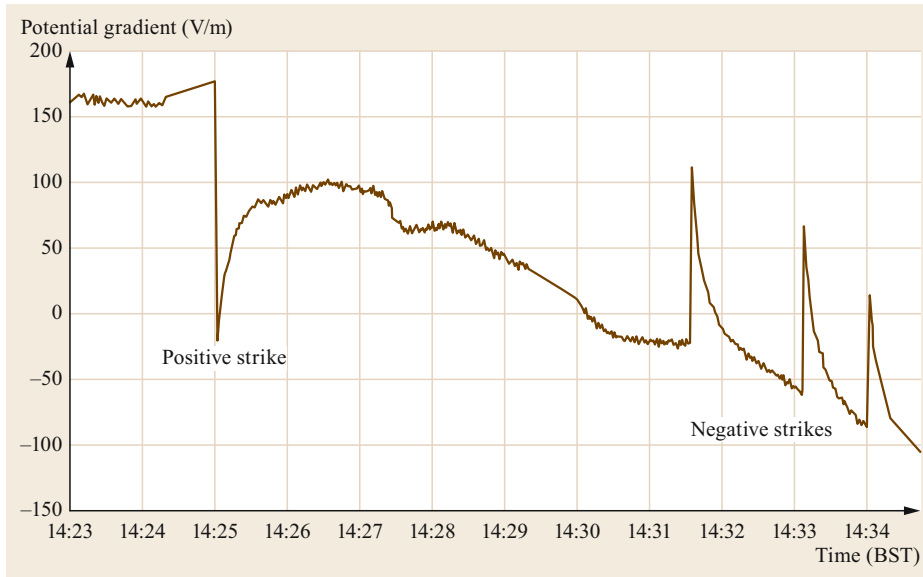


Fig. 14.3 Potential gradient (PG) changes associated with lightning flashes approximately 10 km away, recorded by a JCI 131 field mill on August 25, 2005 (after [14.45])

Optical

In addition to qualitative lightning detection by human observation, optical sensors can be used to monitor lightning activity from the surface, atmosphere or space [14.46]. Selecting a wavelength of strong emission by lightning compared to sunlight allows optical observation of lightning even during the day. The wavelength of choice is at 777.4 nm. This corresponds to the optical emission of oxygen, excited in the plasma of the lightning channel. Optical detection is not generally used in isolation for automated ground-based thunderstorm warning systems but is instead used as an independent confirmation of nearby lightning for single-site detectors, where electric or radio noise can trigger false alarms. Obscuration of the optical signal by nearby objects and cloud limit the effectiveness of ground-based optical detection for distant lightning. An important use of optical lightning detection is on satellites, where the ability of an optical signal to pass through to space largely unaffected by the upper atmosphere is of benefit compared to lower frequency radio signals. Continuous optical lightning detection from polar-orbiting satellites has been available since the mid-1990s, with this proven technology being deployed on geostationary platforms as part of combined atmospheric monitoring missions from the late 2010s. The brightness of the 777.4 nm emission within thunderclouds can be mapped with high resolution cameras on board geostationary satellites to estimate lightning location in realtime over continent-scale regions at a spatial resolution of 5 km for low latitudes, although closer to 30 km at high latitudes due to the less favorable viewing

angle. An advantage of space-based optical detection of lightning is the ability to observe weak intracloud flashes near the top of the cloud, which can sometimes be a precursor for more intense lightning activity. However, the optical signal from strokes nearer the cloud base can be strongly attenuated by the cloud above, leading to the possibility of reduced detection efficiency of such events, especially during bright sunshine.

Acoustic

The explosive heating of air adjacent to the hot plasma within a lightning channel produces the shockwave that is familiar as the sound of thunder. The longest archive of thunderstorm activity extending over two centuries is provided by *thunder day* records, where the occurrence of thunder heard by a human observer was recorded by a weather service or a weather diarist. Thunder can only be heard within approximately 20 km of the lightning flash, if the site is quiet, and the observer is outside, with a maximum range of more like 10 km for indoor environments. Thunder day records are, therefore, of variable quality, depending on the observer's ability to perceive the thunder, but are nonetheless a valuable addition to long-term climatological records, especially prior to the commencement of automated lightning location networks in many developed countries during the 1980s. A particular feature, despite their simplicity, is that the detection sensitivity is constantly providing stable records for climatology, whereas lightning networks are generally regularly upgraded.

The lightning range can be estimated to within a few hundred meters by manually recording the time dif-

ference between the visible flash of lightning and the subsequent arrival of thunder, using the speed of sound in air for the environmental conditions, for example 343 m s^{-1} at 20°C . This range includes the height of the source too, so high-altitude intracloud flashes may be difficult to hear at ground level despite them occurring overhead. Sound propagation effects due to temperature gradients and echoes will introduce uncertainty in range estimation. The short range and difficulty in automatically discriminating between thunder and other sources of similar noise mean that this technique is not used for automatic lightning detection and ranging.

14.3.3 Precipitation Electricity

Convective precipitation is capable of producing strong and rapidly varying electric fields at the surface, due to charge carried to ground on precipitation. Although the total charge transferred between the cloud and ground by precipitation is small relative to other mechanisms, such as lightning and point (corona) discharge [14.47], it is considered as a possible mechanism for the triggering of lightning [14.48].

Raindrop Charging

The first continuous measurements of the electrical charge on rain were conducted over 100 years ago by *George* (later *Sir George*) *Simpson* (1878–1965) [14.49] in Simla, northern India, during the monsoon seasons of 1907–1908. Simpson's apparatus consisted of an electrically insulated rainwater collector connected to a recording electrometer, which registered the charge accumulated on the collector every 2 min. This was converted to a charge per cubic centimeter of rainfall by measuring the collected rainwater volume using a tipping-bucket rain gauge. Simpson reported that 71% of the rainfall associated with monsoon showers and thunderstorms was positively charged, at typically 300 pC cm^{-3} water, generating a typical current density to Earth of the order of 1 nA per square meter. These values are in accordance with more recent observations [14.50]. He also noted that although the heaviest rainfall during the storm was positively charged, there was no clear relationship between charge magnitude and rainfall intensity. The reason for this charge was considered by Simpson to be the result of droplet breakup in strong updrafts, with the falling raindrops retaining a positive charge and the liberated negative ions or smaller droplets traveling upwards in the updraft.

Simpson's explanation for the origin of charged rainfall was contested by C.T.R. Wilson, who instead proposed that the predominant positive charge on convective rainfall resulted from the selective cap-

ture of positive ions by the raindrops as they neared the ground [14.51]. According to Wilson, the negatively charged base of cumulonimbus clouds attracted an upward flow of positive ions. The raindrops falling below this cloud base were polarized by the negative charge above them, resulting in a negative charge on their lowest surface. The positive ions were attracted to the negatively charged drop's underside, causing the drop to acquire an overall positive charge by the time it reached the ground. The charged rainfall measured at ground level was, therefore, considered by Wilson to be the result of the charge distribution within the cloud, rather than the cause, as previously assumed. Nonetheless, Simpson explained his later finding of positively charged regions near thunderstorm cloud bases as being the result of raindrop breakup in strong updrafts [14.52]. The long-standing discussion between Wilson and Simpson on precipitation and thunderstorm charge structure presents one approach to summarizing the development of the subject [14.53].

Wilson's proposed ion-capture mechanism for raindrop charging was recognized by *Simpson* when he discovered that the charge on rainfall at the surface often mirrored that of the electric field, which, in turn, related to the charge near the cloud base [14.54]. This *mirror image effect* was thought to be due to the raindrops charging by scavenging of ions liberated from the surface as a result of point (corona) discharge during the strong electric fields experienced under a cumulonimbus. Since these ions would be of the opposite polarity to the charge of the cloud base and would increase in number with increased electric field, the raindrops they attach to would also be oppositely charged to the cloud base, but of proportionate magnitude. The mirror image effect has been verified by subsequent observations, including ones using modern sensors and techniques (e.g., [14.55, 56]). Although the effect is generally observed, local sources of space-charge can partially mask the inverse correlation under certain circumstances [14.57]. Recent studies indicate that raindrop charge is highly responsive to the ambient electric field, changing within seconds of a field polarity reversal. This calls into question the traditional explanation of selective ion capture by the raindrops as being the primary cause of the mirror image effect [14.54], since a drop is unlikely to scavenge sufficient ions in $\approx 1 \text{ s}$ to significantly affect its charge [14.55].

Precipitation current instrumentation has been based on a conductor shielded from external electric fields by a grounded wire mesh and connected to a sensitive ammeter [14.55, 56, 58]. A funnel-shaped conductor has also been used [14.55, 56], with an effective collection area of 0.2 m^2 . This instrument did not

contain any sharp protrusions to avoid contamination by corona discharge from strong electric fields during overhead thunderstorms. The current from the collector was logged at 50 Hz, with rainfall current, not individual drop charge, being reported. Rainfall intensity and drop size statistics were derived from a nearby distrometer. The direct measurement of precipitation current used by Simpson, and Soula and Chauzy, differs from the induction methods originally devised by [14.59] for measuring the terminal velocity of water drops in the laboratory and later applied to measuring the size and charge of rain drops in the atmosphere [14.60, 61]. The induction method requires the raindrop to pass through a loop conductor, where a current is induced and recorded by a sensitive ammeter. The drop charge is calculated from the induced current and has the advantage of preventing any effect of charge separation from drop breakup on the measurements [14.47].

As the number of charged rainfall observations increased throughout the twentieth century, it was apparent that although the expectation of positive charge during the most intense part of the storm was generally observed, the polarity of convective rainfall can show considerable variability between different rainfall events. This may be due to variability in the strength of updrafts, which have been linked to the polarity associated with graupel, an important charge carrier and common source of rainfall in convective clouds [14.50]. The close association between updraft speed and cloud electrification (and, therefore, precipitation charge) has been established by theoretical and experimental studies (e.g., [14.50, 55, 62, 63]), with heavy rain showers with weak updrafts producing significantly less precipitation current than similarly intense showers containing stronger updrafts.

A further complication in the assessment of rainfall charge is the question of how representative the sampling site is to the spatial distribution of rainfall intensity of the storm. This becomes especially important for complex, multicellular convective systems, with localized anomalies in rainfall intensity or hail shafts being easily missed during their passage over a sampling site.

14.4 Devices and Systems

Fair weather measurements seek to determine the conduction properties of air and the electric field, in the absence of local charge generation. The duration of fair weather conditions varies between sites, and, hence, some durability is required for the apparatus to be continually available for when the fair weather circumstances arise.

Snow Electrification

Early research by [14.64, 65] found that dry snowflakes were usually negatively charged, with rainfall and wet snow found to be generally positively charged. In both cases, increased precipitation rates produced large fluctuations in PG measured at the surface. Ice crystals below the -10°C isotherm height were reported by [14.50] to be of negative charge in the mature stage of a snow shower, with the graupel being positively charged. This is consistent with dry snowflakes reaching the surface with a negative charge. The polarity of ice crystals and graupel reversed at altitudes colder than -10°C .

Measurements of PG by [14.66] during a snow shower found that the PG increased during the heaviest portion of the shower, consistent with a lowering of negative charge to the surface by the snowflakes. Unlike during convective rainfall, the standard deviation of PG sampled at 1 Hz during the snow shower was low; [14.45] interpreted this as primarily due to the lower fall speed of the snowflakes, reducing short-period variability as the flakes moved slower past the sensor compared to raindrops, combined with a greater time for charge exchange with the air (and possibly each other), reducing the spatial and interflake charge variability.

As for sand and dust storms, wind-blown snow can acquire charge through triboelectrification, perturbing the fair weather electric field at snow covered sites, such as Antarctica [14.67].

14.3.4 Corona and Point Discharge

In strong electric fields, such as beneath thunderclouds, vertically-aligned rods and other objects may go in to corona, i.e., the air around the tip of the object may breakdown locally, allowing a large (microamp) current to flow. If the tip of the object is pointed, the electric field will be intensified, and breakdown will occur under a smaller applied field. The current produced can extend over a wide range, so a logarithmic response current ammeter is appropriate (e.g., [14.68]). For atmospheric conditions, temperature compensation is usually required or the possibility of comparison of two techniques [14.69].

14.4.1 Fair Weather Devices and Systems

For fair weather measurements, a typical atmospheric electricity station will include sensors and instruments for some or all of PG, air conductivity, and vertical current density. The PG is commonly obtained with a field mill device, but its calibration depends on having an-

other instrument for comparison. Often, a long wire (or *passive* wire, as there is no active method used to enhance its electrical coupling to the atmosphere) is used for this, as it presents minimal distortion of the electric field. A passive wire works by acquiring the local potential of the air through collision of air ions and falls into the general class of potential equalizer devices.

Potential Equalizers

Measuring the local potential of air requires exchange of charge between a measurement electrode and the air around it, ideally as rapidly as possible. Methods used historically for this include the flame probe, in which the good electrical conductivity of a flame is used to enhance the charge exchange, and the Kelvin water dropper (Sect. 14.2), which increases the area of charge collection by using a large number of small droplets. Radioactive potential equalizers are also effective in greatly increasing the local air conductivity and have been used extensively in the past but are now rarely used because of the radiological hazard they present.

The long or passive wire antenna is probably the most commonly used potential equalizer. In its basic form, it consists of a thin uninsulated horizontal wire stretched at about 1 m above the ground between insulators on two short masts (Figs. 14.4 and 14.5). The use of a thin wire and masts spaced well apart from each other ensures that the distortion of the atmospheric electric field is negligible, and, hence, the passive wire provides a reference method for calibration. For it to operate satisfactorily, considerable attention must be given to the quality of the insulation at each end, in order that the leakage from the antenna is considerably less than the current flowing onto the antenna; [14.70] estimated that the requirement on the leakage current is that it is about 2 fA. With a potential difference across the insulator of typically 100 V, this is a very demanding requirement. However, this can be achieved by using an additional insulator at each end with a short *guard* wire between the main insulator and the secondary insulator. If this guard wire is driven to have a potential close to the measured potential (e.g., to within a few mV), the potential difference across the main insulator is greatly reduced, by a factor of $\approx 10^5$. This approach requires a wide-range bipolar electrometer able to drive an external device to a measured potential, which the [14.21] and [14.70] designs implemented using thermionic valves, and for which the [14.22] design used transistors.

Ion Measurements

Measurements of atmospheric cluster ions typically operate using a deflecting electric field to collect the ions on an electrode and the current flow measured. If the rate of transport of air to the electrode is known, the

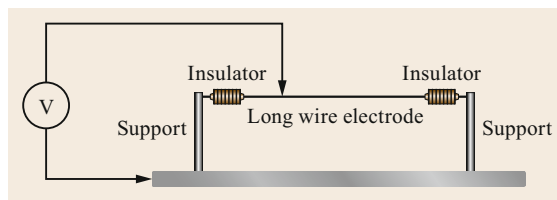


Fig. 14.4 Passive wire antenna. A length of uninsulated wire is stretched between two support masts, using good quality insulators. The potential on the wire is measured using an electrometer voltmeter. (Typical dimensions: length of long wire 20 m, support mast height 1 m)



Fig. 14.5 Passive wire apparatus showing the thin and long sensing wire emerging from a PTFE insulator. (photo: A.J. Bennett)

number concentration of ions can be obtained, under the assumption that the ions are singly charged, due to the difficulty in bringing an additional charge to an existing polarized region around the ion. A cylindrical geometry is well suited to this approach (Fig. 14.6), e.g., following the design of *Hans Gerdien* (1877–1951), as the air can be driven along the cylinder mechanically, with a radial electric field applied to drive the ions to a central coaxial electrode.

The bias voltage is chosen so that, for ions of the mobility required to be measured, an ion can be deflected to reach the central electrode within its transit

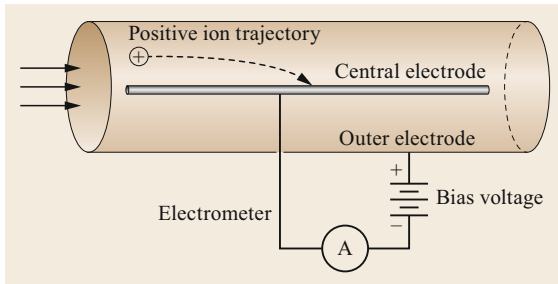


Fig. 14.6 Concept of the operation of a cylindrical ion collector, with the outer electrode grounded. A bias voltage is used to establish a radial electric field. Ion-laden air is driven through the system, and ions are deflected by the electric field and collected at the central electrode, and the integrated current measured

time through the system. Ions with mobility less than the critical value determined by the electric field chosen will also be captured. By switching the polarity of the bias voltage, either positive or negative ions can be collected. There are many variations on the basic principle, for example using a sheath of air to define the capture distance more precisely, or by using a segmented electrode with a range of local electric fields.

The programmable ion mobility spectrometer or PIMS [14.71], allows a range of bias voltages to be programmed to provide a sweep across the positive and negative ion mobility spectra (Fig. 14.7). From these, the bipolar ion concentrations can be determined. Continuous monitoring of the ion mobility spectrum can, therefore, be achieved. In this and many ion counters, it is necessary to compensate for temperature variations and the error currents from the impact of charged particles, which is independent of the deflecting field applied.

Air Conductivity

Air conductivity can be determined using charge relaxation methods or by direct ion counting and calculation. In the relaxation approach, the timescale τ of charging (or discharging) of an electrode exposed to air is related to the total conductivity by $\tau = \epsilon_0/\sigma$, where ϵ_0 is the permittivity of free space. Electrode configurations that have been used for this in the past include a passive wire, which is earthed and then allowed to acquire the local electric potential until it ceases to change, or the central electrode in an aspirated device. The classical device designed by *Gerdien* [14.15] used cylindrical geometry, a manually driven fan, and a mechanical electrometer, for which the charge relaxation time was determined. The PIMS instrument can operate in both conduction and voltage decay modes, allowing internal consistency tests.

Good agreement has been found between a PIMS instrument used to determine the air conductivity by an ion counting method and compared with the relaxation method for a passive wire antenna allowed to charge naturally [14.72, 73].

Current Density

The most direct measurement of the air–Earth current density measurement requires the electrical isolation of a portion of the ground and apparatus to measure the current flow to Earth [14.26]. In reality, the isolated surface can be emulated by a conducting plate electrode mounted flush with flat, open ground, so that the ambient electric field (and, therefore, the air–Earth current) remains unaffected by the presence of the apparatus (Fig. 14.8). The balance between sensitivity and practicality requires that the surface area of this plate is normally between 0.1 and 1.0 m².

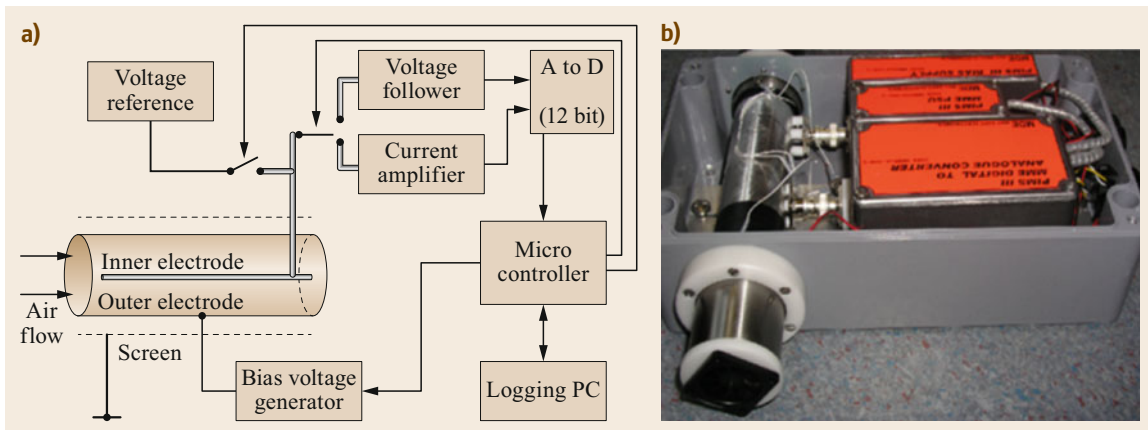


Fig. 14.7a,b Programmable ion mobility spectrometer (PIMS), (a) block diagram form (after [14.71] with permission of AIP Publishing); (b) the fan providing the forced ventilation is at the foreground end of the cylindrical sampling electrodes on the left (photo: R.G. Harrison)

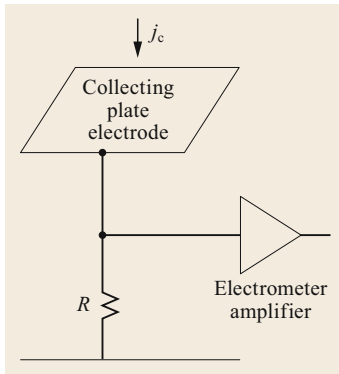


Fig. 14.8 Concept of a plate electrode measurement for the vertical conduction current density. A horizontal plate is positioned slightly above the Earth's surface on insulators and the current flowing from it to the Earth's surface measured

A major challenge in continuous measurements of this current is the need to prevent leakage currents greater than a few tens of fA providing alternative conduction routes, especially in damp conditions. This requires high surface resistivity for all structures supporting the plate and the connection between the sensing electrode and the ammeter. Materials such as PTFE satisfy this requirement, although consideration must be made to the prevention of lower resistivity contaminants and moisture on the surface of the insulators. A guard ring surrounding the sensing electrode may also be used. The guard is electrically isolated from the sensing electrode it encloses but held at the same voltage to prevent leakage currents [14.26, 74]. A temperature-stable (or at least compensated) ammeter is required, which is sensitive to currents of the order of 10 fA, given the typical air–Earth current density of 1 pA m^{-2} . The current flowing can be measured by using a resistor to ground, but it is preferable to keep the plate itself at Earth potential, which can be achieved using a transimpedance amplifier with a high value feedback resistor, usually in the gigaohm range. Depending on the required temporal sensitivity of the measurement, a parallel capacitor may be added to provide passive low pass smoothing.

During fair weather, precipitation and often turbulent components of the air–Earth current density are insignificant, leaving the conduction and displacement components. Whilst the displacement current density is of use when investigating lightning or local variability in the boundary layer, it is the conduction component that is of greatest importance for the study of the global electric circuit [14.2, 26]. As a consequence, air–Earth current density instrumentation needs to eliminate or separate the displacement current component from conduction during fair weather. A method commonly used for continuous measurements due to its simplicity is to select the RC (resistor-capacitor) time constant of the sensor to that of the atmosphere (of order $1 \times 10^3 \text{ s}$) as first described by [14.75]. This allows the displacement current to pass to ground through the capacitor, whilst the conduction current passes through the input resistor



Fig. 14.9 Measurement of the conduction and displacement current densities using the combined two electrodes of different geometry in a GDACCS instrument. (photo: A.J. Bennett)

of the ammeter. Whilst simple to construct, a major disadvantage of this method is the required assumption of constant atmospheric relaxation time and, therefore, air conductivity. In reality, air conductivity varies significantly according to atmospheric aerosol concentration and ionization rate. An alternative method that does not require this assumption is to use two different sensing electrodes of different geometry ([14.72, 76], Fig. 14.9). The magnitude of the displacement current is proportional to the surface area of the electrode, whereas the predominantly vertically flowing conduction current is proportional to the electrode's horizontal cross sectional area. The conduction current component can, therefore, be isolated by subtracting the measurement made by two colocated electrodes of equal surface area but of unequal cross section.

In hostile conditions, it is important to ensure that the insulation is maintained, which is particularly difficult if there is blowing snow; *Burke and Few* [14.77] developed a suspended spherical sensor that allowed the conduction current to flow into its upper hemisphere and out of the lower hemisphere. The electrometer circuit was entirely self-contained within the sphere.

Long-wire (passive) antennas have also been used to measure the conduction current density, but the effective capture area must also be known, either by independent calibration or calculation (e.g., [14.78]).

Electric Field Machines

Electric field machines represent a class of measuring devices that use the motion of an electrode in some way to determine the electric field (Fig. 14.10). This approach is probably most commonly implemented in the electric field mill. A field mill operates by alternately exposing and covering an electrode mechanically. As the electrode is exposed, the change in the electric field

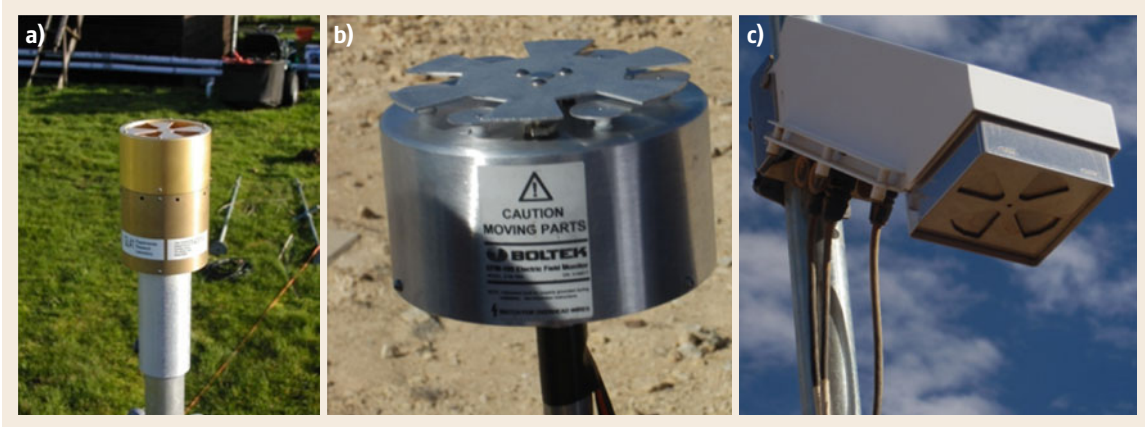


Fig. 14.10a–c Designs of an electric field mill: (a) Chilworth JCI131, (b) Boltek EFM100, (c) Campbell CS110. (photos: R.G. Harrison)

it encounters causes a charge to be induced. If the process is repeated rapidly, the current induced can be measured, which is related to the electric field to which the electrode is exposed. Furthermore, when the electrode is covered by the rotor, it is screened from the field and in a zero field environment. This gives a measure of the various offsets in the electronic system, which can be removed. Using a rotary geometry, a compact and durable instrument can be produced. Phase sensitive detection of the signal is usually employed, with the position of the rotor determined by optical or magnetic switches.

The induced current will be alternating at the frequency of the chopper's exposure to the atmosphere, and the magnitude of the signal is proportional to the atmospheric electric field. The necessity for moving parts makes this instrument relatively high powered compared to other sensors (a few hundred mA from 12 V supply for a rotating chopper) and subject to maintenance. The internal parts need to be kept electrically insulated, as the induced current to be measured is very small (of the order of 1×10^{-12} A). The field mill will measure the DC electric field of the atmosphere and will be sensitive to all variability at frequencies lower than the chopping speed, which is usually ≈ 200 Hz, although single rotations are normally averaged to reduce noise.

The alternate covering and uncovering of the sensing electrode (or stator) is achieved by mounting it beneath a rotating shielding electrode (or rotor), with sufficiently large gaps to prevent water from shorting out the electrode. The instrument can be used facing up or down. There are variations on the basic principle for specific applications, such as cylindrical electrodes rotating around an axis for dust sampling or rotating sampling spheres for use on balloons in thunderstorms,

to minimize instrument corona effects. Durability is improved by modern brushless design [14.79].

14.4.2 Disturbed Weather Systems

Methods for remote lightning detection developed during the later part of the twentieth century, which, through the use of networked systems, allowed the rapid dissemination of information about storm systems. Because a single sensor can detect remote lightning sources and monitor even greater areas in the case of satellite-carried instruments, regional lightning detection systems can be implemented relatively cheaply.

Meteorological Services

Almost all national meteorological services implement lightning detection networks or have access to the data provided by them. Forecasters find the additional information about convective storms useful, as the presence of lightning identifies active convection. For some specific circumstances, notably in Iceland, detection of lightning may provide the first information about the existence of an eruption plume from a volcano.

Stand-Alone Warning Systems

Where a situation requires local thunderstorm detection without the need for an internet connection or data provided by a third party, single-site, stand-alone warning systems are available. Aside from human observation, commercial stand-alone detectors use either radio or (quasi) electrostatic techniques, sometimes combined with an optical receiver.

Lightning is detected mainly by the strong radio-frequency pulse produced by the lightning channel. The pulse covers the entire radio frequency (RF) but has a peak emission at approximately 10 kHz in the

very low frequency (VLF) part of the spectrum. Depending on the frequency chosen, an RF detector may be biased to reporting only cloud-to-ground lightning flashes. A stand-alone RF detector will need to recognize the lightning pulse from background noise and, so, usually incorporates either crude filtering or a microprocessor to distinguish characteristics of the signal, such as pulse length, rise time, etc. The bearing of the emission can be reported using a magnetic induction loop. The simplest RF detectors simply report a suspected lightning pulse and use the signal-to-noise ratio, pulse characteristics, or dual frequency input to estimate the distance to the strike, with no information on bearing. The trend of lightning pulse amplitudes is used to estimate whether the storm is approaching or retreating. These sensors are generally inexpensive and highly portable, although of varied performance. Lightning flash distance estimates using a single site, stand-alone RF sensor are inherently inaccurate due to the natural variability of lightning peak currents and the power falling by only the inverse, or at best square, of distance. Pulse analysis and/or dual antennas of different frequency response provides an improvement to range estimation based on RF amplitude alone.

Sensors that incorporate orthogonal magnetic field antennas to estimate strike bearing from the site generally provide a reasonable estimate of bearing provided that they are located away from strong magnetic field/ferrous sources or not in complex terrain, which can distort the magnetic field of the signal. When magnetic direction finding from a single sensor is combined with the inaccurate distance estimates, the resultant storm location on the map tends to be scattered along the bearing line, making storm location from a single RF sensor rather ambiguous in these situations. RF sensors will always be subject to anthropogenic noise common in the radio spectrum, even down to VLF. Sources of noise originating from sparks from electric motors, power transmission, transportation etc., are particularly troublesome, as they can display similar characteristics to a lightning pulse or raise the noise floor to an unacceptable level. Lightning detectors measuring the magnetic field component (most commonly used) have the advantage that they can operate indoors and when covered, but they may be more subject to anthropogenic noise, as the magnetic component of the electromagnetic radiation will penetrate building walls more effectively than the electric field component. Even the signal from nearby computers and mobile phones has been found to produce false alarms in simple stand-alone RF detectors. Their key advantages over other systems are often related to price, ease of use, and portability rather than performance.

Electrostatic lightning detection is defined here as any measurement technique using variability in the

atmospheric electric field below 100 Hz, where the electromagnetic component of local lightning emission is small compared to the amplitude of the electrostatically generated field change. An electric field change resulting from lightning is the oldest method of quantitative lightning and thunderstorm electrification determination ([14.16, 26]), with its use in thunderstorm research and warning still used in the twenty-first century (e.g., [14.44, 80]). Stand-alone electrostatic methods exploit the large and rapid change in electric field produced by rapid transfer of charge by nearby lightning. The electric field is usually measured by an electric field mill. Except for very close flashes (within 5 km) the signal requires careful interpretation to detect a lightning flash, since lightning signals can appear similar to nonlightning sources of variability such as charged precipitation or even birds flying close by. Electric field mills can be combined with colocated sensors using a different method (e.g., optical) to verify the presence of lightning. As the electric field mill needs to be exposed to the atmosphere, it can only be installed where there is a clear view of the overhead sky (e.g., no overhanging tree branches, cables, etc.) and as far from taller objects as possible, as these will distort the electric field. Electric field mills are capable of detecting lightning to approximately 40 km, depending on their sensitivity, background noise at the site, and the lightning strength. This sensor will not be able to detect the bearing of the lightning, but when calibrated and sampled at a rate of at least 10 Hz will provide a greatly superior indication of distance to the strike compared to a single RF sensor using amplitude alone, as the electrostatic signal reduces by the inverse of the distance cubed. The primary use of an electric field mill is normally to warn of an increased DC atmospheric electric field magnitude indicative of electrified cloud overhead ([14.81]), rather than the detection and range of lightning itself.

An alternative to measuring the DC or slow-varying electrostatic field for stand-alone local thunderstorm detection is to use a displacement current sensor. These sensors work on a similar principle to the chopper in an electric field mill, where a current is induced in a conductor due to the variation of an electric field. Unlike the field mill, however, the sensor does not record the DC electric field but only the changes, so is in this respect the same as a radio receiver and does not require any moving parts. By constructing an antenna and suitable filtering to enable only changes in the atmospheric electric field resulting from lightning to be recorded (e.g., approximately 1–100 Hz) and avoiding the frequencies associated with the RF component of the discharge and artificial transmitters (< 1000 Hz), it is possible to produce an instrument that does not require the moving parts and unwanted slow variability

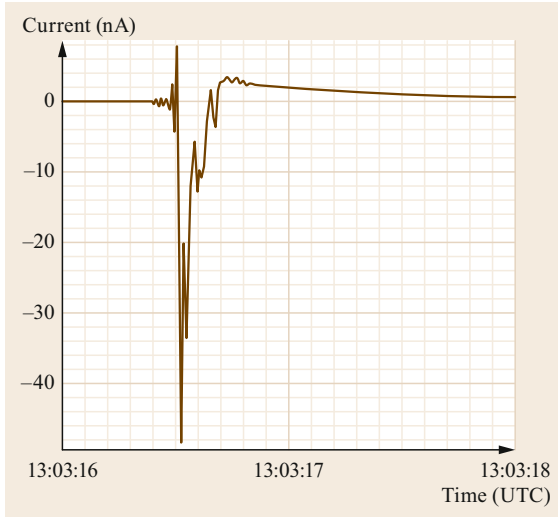


Fig. 14.11 Displacement current induced on the electrode of a BTD-300 thunderstorm detector by a lightning flash approximately 20 km away (recorded on March 21, 2017)

of the DC field characteristic of a field mill yet still retains the ability to detect the electrostatic change associated with a lightning strike ([14.20], Fig. 14.11). Like the field mill, only the distance to the flash can be derived, but again with a much greater sensitivity than RF due to the inverse distance cubed relation for electrostatic signals. A displacement current detector sampling between $\approx 1\text{--}50\text{ Hz}$ can also detect charged precipitation and the increased electric field variability produced by the production of corona ions during the strong electric field beneath a thunderstorm [14.20, 80]. Both signals can be used to warn of increased po-

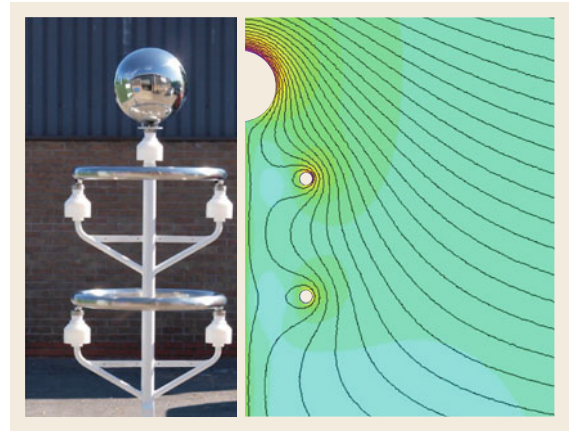


Fig. 14.12 The Biral BTD-300 thunderstorm detector, with modeled lines of equipotential (*black*) compared to ground and electric field magnitude (*colors*) surrounding the three stainless-steel sensing electrodes. *Warmer colors* denote stronger field. (photo and model: A.J. Bennett)

tential for overhead lightning activity. Like field mills, single-site displacement-type detectors cannot be used indoors, are not usually highly portable, their electrodes require good electrical insulation from the ground to be maintained, and they cannot provide flash bearing (Fig. 14.12). Unlike their RF counterparts, they are more resistant to false alarms, very sensitive to all types of local flashes, and are able to detect nonlightning signals such as charged precipitation, which can be used to warn of potential nearby cloud electrification before the first lightning flash has occurred. A summary of the advantages and disadvantages of these detection methods is presented in Table 14.2.

Table 14.2 Comparison of different disturbed weather detection techniques

Technique	Advantages	Disadvantages
RF network	Excellent location accuracy (to a few 100 m) and good detection efficiency if the network is sufficiently dense. Sensor redundancy. Flash type and polarity discrimination. Can provide national or even global coverage.	Expensive to install and maintain. Requires multiple sites, sometimes in different countries. Method of rapid, long-range communication and central processing needed. Can only detect hazard after lightning is produced.
RF stand-alone	Only one sensor and site required. Can have good detection efficiency. Same signal used for range and direction. User-owned and operated.	False alarm rate can be high due to anthropogenic radio interference. Range accuracy can be poor, depending on method. Using VLF only can limit intracloud stroke detection efficiency. Can only detect hazard after lightning is produced.
Displacement current (< 50 Hz)	Only one sensor and site required. Very good flash detection efficiency within 100 km. User-owned and operated. Operates below most anthropogenic noise sources. Can warn of strongly charged cloud overhead before the first flash occurs.	Difficult to determine flash type. Requires exposure to the atmosphere whilst maintaining robust electrical insulation. Range accuracy low compared to RF network. Range limit of $\approx 100\text{ km}$.
Field mill	Only one sensor and site required. Very good flash detection efficiency within 10 km. User-owned and operated. Operates below most anthropogenic noise sources. Can warn of strongly charged cloud overhead before the first flash occurs. Quantifies DC field so can also be used for fair weather atmospheric electrical monitoring.	Cannot determine flash type. Contains moving parts, so liable to mechanical failure. Output can be difficult to interpret due to several sources of atmospheric field change during precipitation. Short range ($\approx 30\text{ km}$ for lightning) and usually unsuitable for flash range determination beyond <i>near</i> and <i>far</i> .

14.5 Specifications

In this section, the typical accuracies and connections for the different instruments are discussed.

14.5.1 Fair Weather Requirements

Generally, the fair weather PG is about 100 V m^{-1} and accurate measurements are possible to a few V m^{-1} , with a dynamic range of $\pm 500 \text{ V m}^{-1}$ usually being desirable to allow nonfair weather data to be identified. However, the limitation on fair weather data is largely that of the local environmental circumstances' exposure, as the surface PG is strongly affected by local meteorological conditions. If the object of the measurements is to obtain globally-relevant information rather than local information, the data has to be selected for that arising under undisturbed conditions. The conventional approach to this is to use data obtained under well-defined fair weather conditions, during which it is regarded that there are no local sources of electrical disturbance.

14.5.2 Automatic Recording

Typical modern field mill instruments provide an analogue output voltage or direct digital data (e.g., via a serial protocol such as RS232 or RS422 or Ethernet). This means that they can be used straightforwardly with data loggers. For fair weather data, sampling rates of 1 s are adequate, with averages computed at 1 or 5 min.

14.6 Quality Control

As with all instruments, the quality of the measurements has to be considered before they are used for a scientific analysis. This has to address the exposure of the instrument, and an assessment has to be made of the validity of the results obtained.

14.6.1 Fair Weather

Depending on the climatology of the site concerned, fair weather circumstances will generally only occur intermittently. The classification of the meteorological conditions is, therefore, an important consideration in determining which measurements to retain for further analysis. For accurate measurement of the electric field, calibration of the installation is required, through a combination of sensor characterization and knowledge of the correction factors to be applied to represent any local distortion of the electric field.

14.5.3 Disturbed Weather Requirements

For the detection of the strong atmospheric electric fields associated with disturbed weather conditions, it is necessary to measure the DC electrostatic field change of magnitude exceeding approximately 500 V m^{-1} , with an upper limit of at least 10 kV m^{-1} , ideally 100 kV m^{-1} , with a resolution and measurement uncertainty of at least 100 V m^{-1} , if quantification of the field is required. Alternatively, detection of electrical changes characteristic of strong electric field conditions, such as strongly charged precipitation (hydrometeors with individual charges typically in excess of 10 pC) and rapid electric field variability associated with wind-blown space charge (of order $10 \text{ V m}^{-1} \text{ s}^{-1}$ or more) or nearby lightning flashes (usually exceeding $1000 \text{ V m}^{-1} \text{ s}^{-1}$) require faster sampling to capture their detail, with a recommended sampling rate of order 100 Hz . As for fair weather measurements, sampling rates of 1 s are acceptable for disturbed weather monitoring, with a sampling rate of at least 20 Hz required to adequately capture electrostatic field changes associated with lightning flashes, using a field mill or displacement current sensor. Radio detection of lightning normally starts at VLF ($3\text{--}30 \text{ kHz}$) for long-range ($< 1000 \text{ km}$), predominately cloud-to-ground strokes, to LF and above (realistically $< 100 \text{ kHz}$) to ensure reasonable detection efficiency of weaker intracloud strokes at ranges exceeding a few 100 km .

Reduction Factor for the Electric Field

When a field mill or other measuring device is installed on a mast, the local electric field encountered will be distorted (Fig. 14.13). This affects the measurements, usually enhancing the field measured. It is necessary to determine a calibration for each installation individually, to allow it to be corrected (or *reduced*) to that of an open flat site with the measurement made flush with the surface. Determining the *reduction factor* to correct the measurements to that of an open surface is, therefore, required. This is achieved by comparison with a calibration measurement that is not affected by distortion, or, theoretically, by using an electrostatic model of the installation in which the distortion can be calculated.

The principle of the experimental approach to this is to run a second set of calibration measurements simultaneously in an undistorted situation and derive the ratio between the two instruments during the same interval,

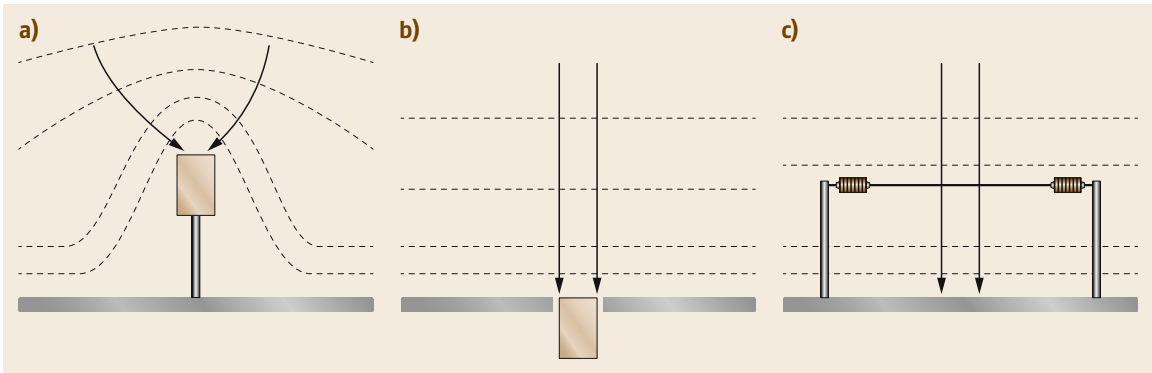


Fig. 14.13 (a) Distortion of the electric field (solid lines, with dashed lines showing equipotentials) for a measuring instrument mounted on a vertical mast. (b) Removal of the electric field distortion by burying the instrument in the ground, with its sensing aperture flush with the ground. (c) A passive wire potential measurement is negligibly affected by the distortion effects (after [14.82])

which need not be very long (\approx minutes to hours), as long as the two instruments show well-correlated values.

One option to remove the distortion is to mount the calibrating instrument so that it is flush with the ground; another is to compare it with a passive wire antenna, which shows negligible distortion of the field because of its small geometry.

Conductivity from Relaxation Time

The air conductivity at the surface is typically in the range of 2 to 30 fS m⁻¹. To establish if an air conductivity measurement is reliable, it should be compared with that from another instrument, or a combination of techniques can be used, thus allowing a consistency check. The PIMS instrument, for example, can operate as a relaxation device as well as a current measurement device, allowing self-consistency checks [14.71]. It is also possible to compare two different techniques, e.g., the comparison of conductivity from an ion counter instrument with that derived from the relaxation time of a passive wire system [14.72].

Removal of Power Line Interference

With sensitive electrometers connected to exposed electrodes there can be difficulties with power line interference. This can be very local and vary with time of day, depending on the loading of the power grid. Corona ions can be generated from breakdown of high-voltage power lines and provide a direct source of interfering ions. For atmospheric electricity applications, when full screening is, almost by definition, impossible, it may be necessary to move the instruments to an electrically quieter site, or one in which saturation of the instruments by power line noise is sufficiently reduced that other filtering techniques become possible. Active com-

pensation of power line interference at 50 Hz has been found to provide some improvements for an exposed plate electrode [14.24], including embedded sharp digital FIR (finite impulse response) filtering stages to produce a low-pass filter below 50 Hz, such as that used by the Biral BTD-300.

Identification of Fair Weather

The selection of fair weather conditions is important in establishing which measurements are suitable for comparison with those from other sites. Various criteria have historically been used to identify fair weather conditions, but those of the UK Met Office (UKMO) originating in the 1950s have established themselves as capable of providing data in which global signals have been detected. The original UKMO criteria [14.83] for fair weather were:

1. The absence of hydrometeors
2. No low stratus cloud
3. Less than three-eighths cumuliform cloud
4. A mean hourly wind speed of less than 8 ms⁻¹.

The UKMO applied these criteria on an hour-by-hour basis to designate hourly PG data values as having *no hydrometeors* (i.e., no rain, hail, or snow), or being *fair weather* [14.83]. Daily and monthly averages were constructed from these hours.

Some refinements to these criteria were suggested by [14.82] to make use of modern automatic measurement systems. These refinements are to ensure that the visual range exceeds 2 km, that no extensive stratus cloud with cloud base below 1500 m is present, and that the surface wind speed is between 1 and 8 m s⁻¹. Taken together with original UKMO requirements, the revised fair weather criteria are:

- (FW1) no hydrometeors, aerosol, and haze, as apparent from the visual range exceeding 2 km
- (FW2) negligible cumuliform cloud and no extensive stratus cloud with cloud base below 1500 m
- (FW3) surface wind speed between 1 and 8 m s⁻¹.

This overall selection approach of identifying fair weather hours can now be implemented using automatic meteorological instrumentation at the same site. It has the merit over daily data selection that, even if the weather is often disturbed at a particular site, it is still possible to make the best use of the available values in forming climatological values.

14.6.2 Disturbed Weather Quality Control

Instruments used for disturbed weather measurements typically require less maintenance than those used for fair weather measurements, as the signals detected are usually larger. Nevertheless, there are quality and reliability considerations for accurate and consistent measurements to be obtained.

Detection Efficiency

The detection efficiency (probability of detection) of a lightning detection system quantifies the amount of lightning activity within a given geographical area that is expected to be detected by the system. The detection efficiency is normally expressed as a percentage and can relate to either lightning strokes or flashes, depending on the technology used. The detection efficiency (DE) is a function of receiver sensitivity, noise, lightning strength, and distance. It is, therefore, common to relate DE to a lower threshold of peak current, type (CG or IC/CC), geographical area (for a lightning location network), or as a function of proximity to individual stand-alone detectors. Reliable *ground truth* data

against which to determine the absolute DE of a system is challenging to obtain, given the challenge of detecting all lightning flashes in a known region during a comparison. The use of video evidence of lightning affecting known locations, lightning damage records, and short-range, high sensitivity VHF mapping arrays are examples of previously used methods to estimate DE from independent observations. Such independent verification has its limitations, especially with respect to weaker intracloud flashes, so DE relative to a high-performance lightning location network is sometimes quoted instead of absolute ground truth data. High-performance VLF/LF networks typically quote a DE of < 95% in their network center for CG flashes with peak currents exceeding a few kA.

False Alarm Rate

The false alarm rate (FAR), also known as the probability of false detection (POFD), of a lightning detection system is commonly expressed as a percentage of cases where an event is falsely detected compared to the total number of strokes or flashes. The false alarm rate is, therefore, sometimes confused with what is more properly determined as the false alarm ratio, since correct negatives are not accounted for. The FAR can also be expressed in terms of false alarms per unit of time (e.g., false alarms per day), which is more likely to be the correct determination of FAR but requires an appropriate time interval to be determined. Like DE, determination of absolute *ground truth* FAR is difficult to obtain due to lack of a reliable method of detecting every electrical discharge affecting an area. False alarm expectations quoted by manufacturers and operators of lightning detection systems are usually less than 2%, although it can be unclear whether the value relates to POFD or the false alarm ratio.

14.7 Maintenance

The operation of atmospheric electricity equipment requires regular attendance and maintenance, depending on the environmental conditions encountered (Table 14.3). Snow and ice, when present, must be removed if the apparatus is not specifically designed for those conditions.

14.7.1 Fair Weather Maintenance

Operation of fair weather equipment is particularly demanding, because of the great sensitivity of the instruments to leakage and degradation.

Insulators and Insulation

Due to the often picoampere currents and high impedances involved in the measurement of fair weather atmospheric electrical parameters, robust, highly resistive insulation is essential. The material used for insulation varies with application and availability, from amber, sulfur, and even heated sapphire in early twentieth century instrumentation, to polytetrafluoroethylene (PTFE) for modern instrumentation. PTFE has many desirable properties for this purpose, including a very high surface resistivity, it is hydrophobic with a low water absorption rate, low chemical and

Table 14.3 Maintenance schedule of instrumentation at mid-latitudes

Maintenance interval	Air conductivity sampling tubes	Plate electrodes	Field Mill	Electrostatic lightning detection
Daily	Surface cleaning and drying of insulators	Debris removal and drying of insulators		
Weekly	Partial dismantling and cleaning of insulators	Clear plants growing near electrodes	Inspect for dead insects	
Annual	Replace insulators. Rebuild and recalibrate	Rebuild electrometer	Clean and rebuild if necessary	Surface cleaning of insulators. Test and recalibrate

UV reactivity, resistance to residue accumulation, and is relatively inexpensive, mechanically robust (aside from creep under pressure), and easy to machine. Nonetheless, if an insulator is to operate reliably when exposed to environmental conditions, slight heating of the surface is normally required to prevent a lowering of surface resistivity in damp conditions, especially when hygroscopic impurities inevitably accumulate on exposed surfaces. The heat source can be placed inside the insulator, warming the surface from the inside (Fig. 14.14). However, as with other plastics, PTFE is a poor thermal conductor, so heater power and material thickness need to be considered to ensure effective surface heating. A rain shield can also be used to physically prevent precipitation from wetting the insulator, which would not be evaporated in sufficient time. Spider webs have always been a problem for very high impedance measurements, such as air–Earth current density, since they can introduce leakage currents to the sensing electrode. There is currently no clearly successful method of preventing spider-web accumulation on sensors, so instrumentation and fieldwork should be designed to minimize this risk. Maintenance for well-designed insulators is normally light, with the occasional (perhaps

6-monthly) check on heater effectiveness and removal of any spider webs and surface impurities.

14.7.2 Disturbed Weather Maintenance

Electrostatic lightning detection instrumentation will have similar insulation requirements for the sensing electrode to those for fair weather equipment (Fig. 14.15). The moving parts of field mill-type electrostatic sensors are subject to mechanical wear and jamming from foreign objects entering the chopper exposure slots. Initial startup may also be problematic in subzero temperatures or heavily contaminated environments if the chopper or motor becomes stuck. It must be ensured that the mechanism moves freely, is free from foreign objects (including insects), and that there are no objects preventing the chopper from being fully exposed to the atmosphere through the slots (e.g., by leaves, snow accumulation, or excessive coverage from spider webs).

For optical lightning detection, a primary requirement is that the optical window remains free from obscuration by opaque material (e.g., leaf debris, snow,

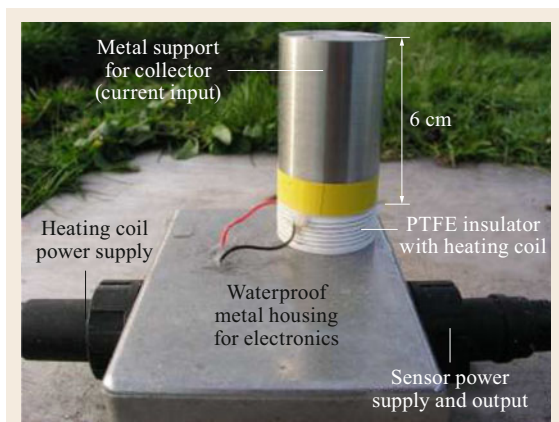


Fig. 14.14 Heated PTFE insulation of the geometrical displacement and conduction current sensor (GDACCS). Ultrahigh quality insulation is required continuously between the sensing electrode and ground (after [14.45])

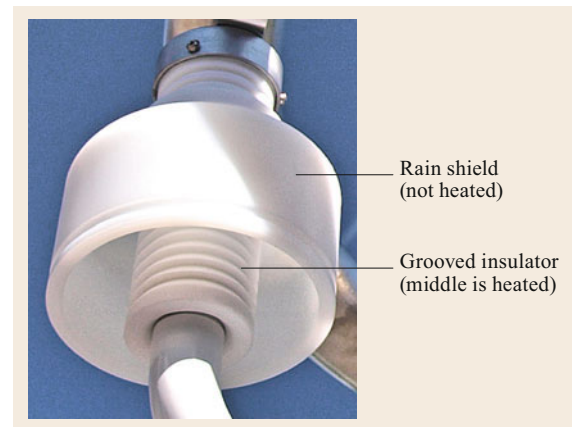


Fig. 14.15 Electrical insulation method for the sensing electrode of a Biral BTD-300 thunderstorm detector, showing the shielded and heated PTFE insulator to prevent water-induced grounding during all weather conditions. (photo: A.J. Bennett)

mud, and spider webs) and gradual reduction of transmittance from accumulation of surface contaminants, including salt and algal growth. Dew and frost on the window will also reduce the window transmittance and, therefore, sensitivity to a lightning signal.

Lightning detection based on radio (RF) signals will generally require less maintenance than instrumentation requiring moving parts and fully exposed electrodes (since electromagnetic radiation is not greatly affected by electrically resistive weather shielding). The background noise should be periodically monitored for any significant increase in noise sources that may obscure or distort the lightning signals. If an increase in noise is detected, the addition of software-defined notch filters can be used to attenuate narrowband noise sources in the listening frequency, such as communication transmitters. Broadband noise sources, such as sparking of electrical equipment, are best avoided during site selection. Electrical shielding of the sensitive (preamplified)

parts of the receiver electronics will reduce noise issues, such as shielded coaxial cables and grounded, metallic shielding on circuit boards. Note that even if a receiver is designed for low-frequency signals, the geometry of the preamplified circuit board tracks may still permit significant interference from microwave signals if left unshielded. It is also important to maintain a good electrical ground on the RF receiving equipment for best performance, which may involve deep ground spikes for sites with low ground conductivity. Appropriate electrical impedance must be maintained for the antenna assembly and RF cabling to keep the standing wave ratio (SWR) as close to unity as possible, optimizing the power transfer. For VHF phase-sensitive radio detection (e.g., interferometry), relative cable length is an especially important consideration, with the short wavelengths involved requiring the maintenance of correctly matched cables to avoid errors in phase-shift calculation.

14.8 Applications

Surface atmospheric electricity measurements have a wide range of applications, including detecting charged clouds overhead and providing lightning warnings.

Atmospheric electricity measurements span a wide parameter space, and accordingly have many uses. The fair weather measurements are chiefly used for studies of the atmosphere's global electric circuit, through which current flows from tropical disturbed weather re-

gions around the planet. It is particularly influenced by space weather and pollution. Space-weather variations and their effects are an active area of study, which the atmospheric electricity data complements. In particular, the possible solar–terrestrial coupling mechanisms with the lower atmosphere can be explored, through, for example, electrical effects in fair weather clouds (Fig. 14.16). The effects of pollution are also sensitively

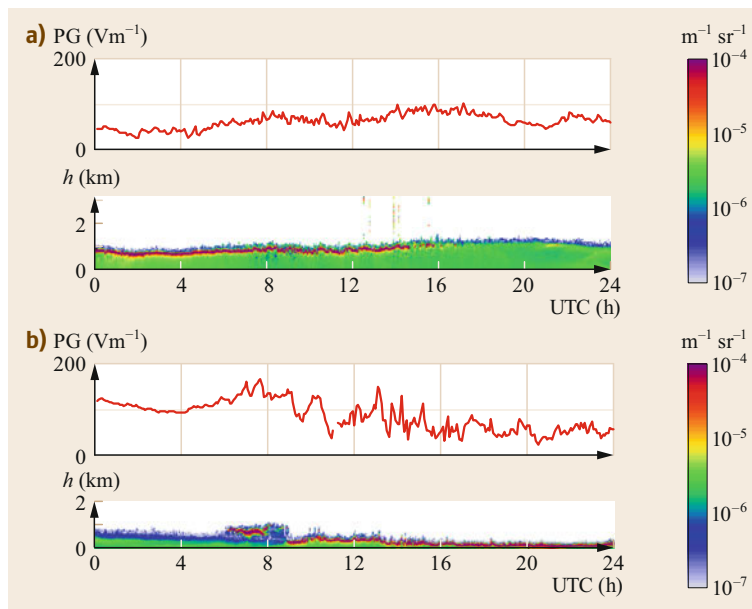


Fig. 14.16a,b Potential gradient (upper panels, red trace) measured under low stratiform cloud at Reading, observed using a colocated JCI131 field mill and Vaisala CL31 ceilometer (lower panels). **(a)** Effect of low clouds on the variability in the surface PG on May 9, 2017, showing the coupling between the cloud base charge and the PG, which ceases when the cloud dissipates at about 16:00 UTC. **(b)** Cloud base charge effect on the surface PG on May 15, 2016, which leads to a reduction in the PG as the negative charge in the cloud base is brought nearer to the surface with reducing cloud base height. (Ceilometer data are colored by the backscatter generated according to the color bar, the cloud base itself yielding the red color)

apparent in air conductivity; aerosol pollution decreases air conductivity, and releases of radioactivity increase the air conductivity. There are associated effects on the potential gradient, with a sharp decrease associated

with radioactivity and a steady increase with increased aerosol pollution. Disturbed weather effects, principally the detection of lightning, have immediate applications to weather forecasting and aviation meteorology.

14.9 Future Developments

Continued miniaturization of atmospheric electricity sensors makes measurements possible on airborne platforms, such as weather balloons and unmanned aircraft systems (UAS). This will allow investigation of the electrical environment within a range of clouds, and, further, regular measurements of the vertical profile of the electric field under fair weather conditions. The vertical integral of the electric field, known as the ionospheric potential, represents a global circuit parameter that has previously been difficult to monitor with continuity beyond that of individual investigators or projects. Improvements to the design of all-weather electrical insulation and cheaper, faster processors will allow more sophisticated and smaller sensors for electrostatic thunderstorm detection. Improved digital storage capacity combined with greater processing speed will

permit lightning monitoring, including raw data logging at higher frequencies, thereby capturing smaller and weaker components of electrical discharge. Continued characterization of the electrical conditions prior to lightning activity will be required to produce robust, reliable preflash warning devices, with associated benefits to lightning safety. Reduced price and increased sensitivity of CCD cameras and photomultipliers can widen the participation of transient luminous events (TLEs) monitoring, with more numerous, detailed, and full-color images of TLEs available across broader regions of the world. The advancement of near-global lightning and TLE monitoring from space will provide a significant addition to ground-based detection methods, especially for weak intracloud activity over the oceans.

14.10 Further Reading

- R.G. Harrison: *Meteorological Measurements and Instrumentation* (John Wiley and Sons, Chichester 2015)
- D.R. McGorman and W.D. Rust: *The Electrical Nature of Storms* (Oxford University Press, Oxford, 1998)

References

- | | |
|---|--|
| <p>14.1 E.P. Krider: Benjamin Franklin and lightning rods, <i>Phys. Today</i>. 59(1), 42–48 (2006)</p> <p>14.2 J.A. Chalmers: <i>Atmospheric Electricity</i>, 2nd edn. (Pergamon Press, Oxford 1967)</p> <p>14.3 J. Parsons, W. Mazeas: Observations upon the electricity of the air, made at the Chateau de Maintenon, during the months of June, July, and October, <i>Philos. Trans. R. Soc.</i> 48, 377–384 (1753)</p> <p>14.4 J. Canton: A letter to the right honourable the Earl of Macclesfield, president of the Royal Society, concerning some new electrical experiments, <i>Philos. Trans. R. Soc.</i> 48, 780–785 (1754)</p> <p>14.5 G. Beccaria: <i>Della Elettricitè Terrestre Atmosferica a Cielo Serno</i> (Turin, 1755)</p> <p>14.6 J. Read: A meteorological journal, principally relating to atmospheric electricity; kept at Knightsbridge, from the 9th of May, 1789, to the 8th of May, 1790, <i>Philos. Trans. R. Soc.</i> 81, 185–212 (1791)</p> | <p>14.7 J. Read: A meteorological journal, principally relating to atmospheric electricity; kept at Knightsbridge, from the 9th of May, 1790, to the 8th of May, 1791, <i>Philos. Trans. R. Soc.</i> 82, 225–256 (1792)</p> <p>14.8 K.L. Aplin, R.G. Harrison: Lord Kelvin's atmospheric electricity measurements, <i>Hist. Geo. Space Sci.</i> 4(2), 83–95 (2013)</p> <p>14.9 A.–B. Chauveau: Sur la variation diurne de l'électricité atmosphérique, observée au voisinage du sommet de la tour Eiffel, <i>C. R. Acad. Sci.</i> 67, 1069–1072 (1893)</p> <p>14.10 J. Tuma: <i>Beiträge zur Kenntniss der atmosphärischen Elektrizität III</i>, Sitzungsberichte (Kaiserlichen Akademie der Wissenschaften, Wien 1899)</p> <p>14.11 R.G. Harrison: The carnegie curve, <i>Surv. Geophys.</i> 34(2), 209–232 (2013)</p> <p>14.12 R.G. Harrison: Behind the curve: A comparison of historical sources for the Carnegie curve of the</p> |
|---|--|

- global atmospheric electric circuit, *Hist. Geo. Space Sci.* **11**, 207–213 (2020)
- 14.13 R.G. Harrison: Two daily smoke maxima in eighteenth century London air, *Atmos. Environ.* **43**, 1364–1366 (2009)
- 14.14 R.G. Harrison, W.J. Ingram: Air–earth current measurements at Kew, London, 1909–1979, *Atmos. Res.* **76**(1–4), 49–64 (2005)
- 14.15 H. Gerdien: Ein neuer Apparat zur Messung der elektrischen Leitfähigkeit der Luft, *Nachr. Ges. Wiss. Göttingen* **1905**, 240–251 (1905)
- 14.16 C.T.R. Wilson: Investigations on lightning discharges and on the electric field of thunderstorms, *Philos. Trans. R. Soc. Lond. A* **221**, 73–115 (1920)
- 14.17 T.W. Wormell: The effects of thunderstorms and lightning discharges on the Earth's electric field, *Philos. Trans. R. Soc. Lond. A* **238**, 239–303 (1939)
- 14.18 E.T. Pierce: Electrostatic field–changes due to lightning discharges, *Q. J. R. Meteorol. Soc.* **81**, 211–228 (1955)
- 14.19 D.R. MacGorman, W.D. Rust: *The Electrical Nature of Storms* (Oxford Univ. Press, New York 1998)
- 14.20 A.J. Bennett: Identification and ranging of lightning flashes using co-located antennas of different geometry, *Meas. Sci. Technol.* **24**, 125801 (2013)
- 14.21 A.W. Brewer: An electrometer valve voltmeter of wide range, *J. Sci. Instrum.* **30**, 91–92 (1953)
- 14.22 R.G. Harrison: An antenna electrometer system for atmospheric electrical measurements, *Rev. Sci. Instrum.* **68**(3), 1599–1503 (1997)
- 14.23 R.G. Harrison: An atmospheric electrical voltmeter follower, *Rev. Sci. Instrum.* **67**(7), 2636–2638 (1996)
- 14.24 R.G. Harrison: A noise-rejecting current amplifier for surface atmospheric ion flux measurements, *Rev. Sci. Instrum.* **68**, 3563–3565 (1997)
- 14.25 R.G. Harrison: A wide-range electrometer voltmeter for atmospheric measurements in thunderstorms and disturbed meteorological conditions, *Rev. Sci. Instrum.* **73**(2), 482–483 (2002)
- 14.26 C.T.R. Wilson: On the measurement of the earth–Air current and on the origin of atmospheric electricity, *Proc. Camb. Philos. Soc.* **13**(6), 363–382 (1906)
- 14.27 A.J. Bennett, R.G. Harrison: A simple atmospheric electrical instrument for educational use, *Adv. Geosci.* **13**, 11–15 (2007)
- 14.28 M.J. Rycroft, R.G. Harrison, K.A. Nicoll, E.A. Mareev: An overview of Earth's global electric circuit and atmospheric conductivity, *Space Sci. Rev.* **137**(1–4), 83–105 (2008)
- 14.29 J.P. Ault, S.J. Mauchly: *Ocean Magnetic and Electric Observations 1915–1921* (Carnegie Institution of Washington, Washington 1926), Publication No. 175
- 14.30 S. Israelsson, H. Tammet: Variation of fair weather atmospheric electricity at Marsta Observatory, Sweden, 1993–1998, *J. Atmos. Sol. Terr. Phys.* **63**, 1593–1703 (2001)
- 14.31 V.A. Rakov, M.A. Uman: *Lightning: Physics and Effects* (Cambridge Univ. Press, Cambridge 2003)
- 14.32 K.L. Cummins, M.J. Murphy: An overview of lightning locating systems: History, techniques, and data uses, with an in-depth look at the US NLDN, *IEEE Trans. Electromagn. Compat.* **51**(3), 499–518 (2009)
- 14.33 H.D. Betz, U. Schumann, P. Laroche: *Lightning: Principles, Instruments and Applications: Review of Modern Lightning Research* (Springer Netherlands, Dordrecht 2008)
- 14.34 K.G. Budden: The propagation of a radio-atmospheric, *Lond. Edinb. Dublin Philos. Mag. J. Sci.* **42**(324), 1–19 (1951)
- 14.35 W. Rison, R.J. Thomas, P.R. Krehbiel, T. Hamlin, J. Harlin: A GPS-based three-dimensional lightning mapping system: initial observations in central New Mexico, *Geophys. Res. Lett.* **26**(23), 3573–3576 (1999)
- 14.36 D.J. Malan: *Physics of Lightning* (English Univ. Press, London 1963)
- 14.37 M. Füllekrug: Wideband digital low-frequency radio receiver, *Meas. Sci. Technol.* **21**(1), 015901 (2009)
- 14.38 A.C. Lee: An operational system for the remote location of lightning flashes using a VLF arrival time difference technique, *J. Atmos. Ocean. Technol.* **3**(4), 630–642 (1986)
- 14.39 R.L. Dowden, J.B. Brundell, C.J. Rodger: VLF lightning location by time of group arrival (TOGA) at multiple sites, *J. Atmos. Sol. Terr. Phys.* **64**(7), 817–830 (2002)
- 14.40 H. Pohjola, A. Mäkelä: The comparison of GLD360 and EUCLID lightning location systems in Europe, *Atmos. Res.* **123**, 117–128 (2013)
- 14.41 M. Balsler, C.A. Wagner: Observations of Earth-ionosphere cavity resonances, *Nature* **188**(4751), 638–641 (1960)
- 14.42 A. Ondrášková, S. Ševčík, P. Kostecký, L. Rosenberg: Simultaneous measurements of low-frequency natural electric field at two neighbouring stations, *Meas. Sci. Rev.* **8**(5), 122–125 (1960)
- 14.43 M. Füllekrug: Detection of thirteen resonances of radio waves from particularly intense lightning discharges, *Geophys. Res. Lett.* **32**(13), L13809 (2005)
- 14.44 A.J. Bennett, R.G. Harrison: Lightning-induced extensive charge sheets provide long range electrostatic thunderstorm detection, *Phys. Rev. Lett.* **111**(4), 045003 (2013)
- 14.45 A.J. Bennett: Measurement of atmospheric electricity during different meteorological conditions, PhD Thesis (Univ. of Reading, Reading 2007).
- 14.46 L. Labrador: The detection of lightning from space, *Weather* **72**(2), 54–59 (2017)
- 14.47 J.A. Chalmers: The electricity of precipitation, *Br. J. Appl. Phys.* **12**(8), 372 (1961)
- 14.48 J.A. Crabb, J. Latham: Corona from colliding drops as a possible mechanism for the triggering of lightning, *Q. J. R. Meteorol. Soc.* **100**, 191–202 (1974)
- 14.49 G.C. Simpson: On the electricity of rain and its origin in thunderstorms, *Philos. Trans. R. Soc. A*, 379–413 (1909)
- 14.50 T. Takahashi: Precipitation particle charge distribution and evolution of east asian rainbands, *Atmos. Res.* **118**, 304–323 (2012)
- 14.51 C.T.R. Wilson: Some thundercloud problems, *J. Frankl. Inst.* **208**(1), 1–12 (1929)

- 14.52 G. Simpson, F.J. Scrase: The distribution of electricity in thunderclouds, *Proc. R. Soc. Lond. A* **161**(906), 309–352 (1937)
- 14.53 E.R. Williams: CTR Wilson versus GC Simpson: Fifty years of controversy in atmospheric electricity, *Atmos. Res.* **91**(2), 259–271 (2009)
- 14.54 G.C. Simpson: Atmospheric electricity during disturbed weather, *Geophys. Mem.* **84**, 1–51 (1949)
- 14.55 S. Soula, S. Chauzy, M. Chong, S. Coquillat, J.F. Georgis, Y. Seity, P. Tabary: Surface precipitation electric current produced by convective rains during the Mesoscale Alpine Program, *J. Geophys. Res.* **108**(D13), 4395 (2003)
- 14.56 S. Soula, J.F. Georgis: Surface electrostatic field below weak precipitation and stratiform regions of mid-latitude storms, *Atmos. Res.* **132**, 264–277 (2013)
- 14.57 I.E. Owolabi: The inverse-relation and the mirror-image effect in precipitation electricity, *J. Atmos. Terr. Phys.* **32**(7), 1205–1213 (1970)
- 14.58 S. Soula, S. Chauzy: Charge transfer by precipitation between thundercloud and ground, *J. Geophys. Res.* **102**(D10), 11061–11069 (1997)
- 14.59 R. Gunn, G.D. Kinzer: The terminal velocity of fall for water droplets in stagnant air, *J. Meteorol.* **6**(4), 243–248 (1940)
- 14.60 T. Takahashi: Measurement of electric charge of cloud droplets, drizzle, and raindrops, *Rev. Geophys.* **11**(4), 903–924 (1973)
- 14.61 S. Chauzy, S. Despiau: Rainfall rate and electric charge and size of raindrops of six spring showers, *J. Atmos. Sci.* **37**(7), 1519–1527 (1980)
- 14.62 C.P.R. Saunders: A review of thunderstorm electrification processes, *J. Appl. Meteorol.* **32**(4), 642–655 (1993)
- 14.63 C. Barthe, J.-P. Pinty: Simulation of a supercellular storm using a three-dimensional mesoscale model with an explicit lightning flash scheme, *J. Geophys. Res.* **112**, D06210 (2007)
- 14.64 C.J. Adkins: The small ion concentration and space charge near the ground, *Q. J. R. Meteorol. Soc.* **85**(365), 237–252 (1959)
- 14.65 E. Gherzi: Atmospheric electricity at Brébeuf college geophysical observatory in Montréal, Canada, *Pure Appl. Geophys.* **67**(1), 239–265 (1967)
- 14.66 A.J. Bennett, R.G. Harrison: Atmospheric electricity in different weather conditions, *Weather* **62**(10), 277–283 (2007)
- 14.67 G.B. Burns, A.V. Frank-Kamenetsky, O.A. Troshichev, E.A. Bering, B.D. Reddell: Interannual consistency of bi-monthly differences in diurnal variations of the ground-level, vertical electric field, *J. Geophys. Res.* **110**, D10106 (2005)
- 14.68 G.J. Marlton, R.G. Harrison, K.A. Nicoll: Atmospheric point discharge current measurements using a temperature-compensated logarithmic current amplifier, *Rev. Sci. Instrum.* **84**, 066103 (2013)
- 14.69 R.G. Harrison, G.J. Marlton, K.A. Nicoll, M.W. Airey, P.D. Williams: A self-calibrating wide range electrometer for in-cloud measurements, *Rev. Sci. Instrum.* **88**, 126109 (2017)
- 14.70 W.D. Crozier: Measuring atmospheric potential with passive antennas, *J. Geophys. Res.* **68**(18), 5173–5179 (1963)
- 14.71 K.L. Aplin, R.G. Harrison: A self-calibrating programmable mobility spectrometer for atmospheric ion measurements, *Rev. Sci. Instrum.* **72**(8), 3467–3469 (2001)
- 14.72 A.J. Bennett, R.G. Harrison: In situ calibration of atmospheric air conductivity measurements, *Rev. Sci. Instrum.* **77**, 016103 (2006)
- 14.73 A.J. Bennett, R.G. Harrison: Surface determination of the air–earth electrical current density using co-located sensors of different geometry, *Rev. Sci. Instrum.* **77**(6), 066104 (2006)
- 14.74 A.J. Bennett, R.G. Harrison: Surface measurement system for the atmospheric electrical vertical conduction current density, with displacement current correction, *J. Atmos. Sol. Terr. Phys.* **70**, 1373–1381 (2008)
- 14.75 H.W. Kasemir: *Measurement of the Air–Earth Current Density*, Heinz-Wolfram Kasemir Collected Works, Vol. 66 (American Geophysical Union, Washington 2012), Special Publication
- 14.76 V.N.R. Mukku: A design for eliminating displacement currents in the air–earth current measurement, *J. Phys.* **17**(E), 629 (1984)
- 14.77 H.K. Burke, A.A. Few: Direct measurements of the atmospheric conduction current, *J. Geophys. Res.* **83**, 3098 (1978)
- 14.78 H. Tammert, S. Israelsson, E. Knudsen, T.J. Tuomi: Effective area of a horizontal long-wire antenna collecting the atmospheric electric vertical current, *J. Geophys. Res.* **101**(D23), 29671–29677 (1996)
- 14.79 J.N. Chubb: Two new designs of “field mill” type fieldmeters not requiring earthing of rotating chopper, *IEEE Trans. Ind. Appl.* **26**(6), 1178–1181 (1990)
- 14.80 A.J. Bennett: Warning of imminent lightning using single-site meteorological observations, *Weather* **73**(6), 187–193 (2018)
- 14.81 D. Aranguren, J. Montanya, G. Sola, V. March, D. Romero, H. Torres: On the lightning hazard warning using electrostatic field: Analysis of summer thunderstorms in Spain, *J. Electrostat.* **67**(2–3), 507–512 (2009)
- 14.82 R.G. Harrison, K.A. Nicoll: Fair weather criteria for atmospheric electricity measurements, *J. Atmos. Sol. Terr. Phys.* **179**, 239–250 (2018)
- 14.83 Meteorological Office: *Observatories’ Year Book* (HMSO, London 1964), Annual volume for 1964

Giles Harrison

Department of Meteorology
University of Reading
Reading, UK
r.g.harrison@reading.ac.uk



Giles Harrison is Professor of Atmospheric Physics at the University of Reading, UK, where he works on atmospheric electricity and scientific sensor development. His PhD is from Imperial College, ScD from the University of Cambridge and he is a member of the Academia Europea. In 2016 he was awarded the Appleton medal of the Institute of Physics, and he is the 2021 recipient of the Christiaan Huygens medal of the European Geosciences Union.

Alec Bennett

Biral
Portishead, UK
alec.bennett@biral.com



Alec Bennett is the Meteorological Products Manager at Biral, UK and a Visiting Research Fellow at the University of Bath. He works on commercial meteorological sensor development and thunderstorm detection research. His PhD is from the University of Reading, and he previously worked for the UK Met Office. In 2017, he was awarded the FitzRoy Prize by the Royal Meteorological Society.

Radioactivity

15. Radioactivity Sensors

Jacqueline Bieringer, Thomas Steinkopff, Ulrich Stöhlker

Radioactive substances in the atmosphere lead to exposure of humans and the environment to radiation. The purpose of monitoring these radioactive substances is to determine the magnitude of the exposure. The primary objective of the various methods of radiation monitoring is to quickly and reliably measure the levels of radioactive substances in the event of an (accidental) release. However, continuous analysis of trace amounts of radioactivity in the atmosphere is also needed to determine long-term trends and identify short-term, low-level increases in atmospheric radioactivity and their causes, for instance to provide proof of underground nuclear weapons tests. Radionuclides can be bound to particles or exist in the atmosphere in the gaseous state or as radioactive noble gases; thus various systems are used for their detection. Furthermore, the different types of radioactive decay require different measurement techniques. National, European, and international measurement networks and programs produce a multitude of data and, in combination with atmospheric transport modeling, enable dose prognosis and source term reconstruction. Here, different measurement techniques and their application are described, as well as methods for quality assurance.

15.1	Measurement Principles and Parameters	458
15.1.1	Monitoring Radioactivity in the Atmosphere	458
15.1.2	Principles of Sampling and Measurements	458
15.2	History	459
15.2.1	History of Radioactivity Measurements in the Atmosphere	459
15.2.2	Measurement Methods	460
15.3	Theory	460
15.3.1	Gamma Dose Rate Measurements	461
15.3.2	Gamma-Ray Spectrometry Using Semiconductors	462
15.3.3	Integrated Measurement of Alpha and Beta Decay	462
15.3.4	Measurement of Noble Gases	463
15.4	Devices and Systems	463
15.4.1	Gamma Dose Rate Probes	463
15.4.2	Alpha/Beta Particulate Monitors	464
15.4.3	High-Purity Germanium (HPGe) Detectors	465
15.4.4	Gaseous Iodine Monitors	466
15.4.5	Noble Gas Measurement	466
15.5	Specifications	467
15.6	Quality Control	468
15.6.1	Calibration	468
15.6.2	Specific Quality Control Methods	468
15.7	Maintenance	469
15.7.1	Gamma Dose Rate Probes	469
15.7.2	Aerosol Sampler	469
15.7.3	Spectrometric Systems	469
15.8	Application	469
15.8.1	Emergency Preparedness	469
15.8.2	Environmental Monitoring	469
15.8.3	Comprehensive Nuclear-Test-Ban Treaty	470
15.9	Future Developments	470
15.10	Further Reading	471
	References	471

The measurement of radioactive substances deposited on the ground and contained in the atmosphere is important for nuclear emergency preparedness, for verification of nonproliferation treaties such as the Comprehensive Nuclear-Test-Ban Treaty (CTBT), and in long-term monitoring of atmospheric radioactivity. Reliable mea-

surement results are essential for all applications: for early warning and implementation of countermeasures in case of a release of radioactive substances into the atmosphere, as part of identifying nuclear testing activity, and for the routine surveillance of atmospheric radioactivity levels. Data exchange at a global level re-

quires harmonized and precise measurement techniques and well-established quality control to enable the assessment and aggregation of available data.

In the following, the examples given are based on the European networks and the international measurement network for the verification of the CTBT.

15.1 Measurement Principles and Parameters

The measurement of radioactive substances in the air and deposited on the ground can be performed with different parameters using various techniques. In general, both the ambient dose/dose rate or activity concentrations in the air and specific activity deposited on the ground can be measured. Activity concentrations can be determined as gross activity concentrations (for alpha, beta, or gamma radiation) or for single radionuclides. Typical parameters of radioactivity sensors are listed in Table 15.1.

15.1.1 Monitoring Radioactivity in the Atmosphere

The primary purpose of continuously monitoring the activity concentrations of radionuclides in the atmosphere is to evaluate and possibly reduce radiation exposure to humans and the environment. For the protection of the population, comprehensive surveillance programs are required:

- To monitor activity concentrations of aerosol-bound and gaseous radionuclides in the atmosphere and to issue alerts in the case of elevated values
- To determine whether administrative and engineering measures for confinement of radioactive substances are effective under routine conditions.

The surveillance strategy chiefly relies on two general techniques:

- The first approach is online monitoring for emergency preparedness, in which activity concentrations and dose rates are monitored continuously and in real time in order to be immediately alerted in the event that a significant release of airborne activity may have occurred.

- The second is retrospective measurement (offline), in which constituents in the air or in precipitation are sampled for a given time span, after which the sample is taken to a radiation detection system and analyzed for radionuclides. Results for activity concentrations are then available after measurement. This is typical, e.g., for radionuclides which require radiochemical separation in the laboratory before analysis.

When implementing an effective surveillance program, it is important to achieve a proper balance between these two general approaches.

15.1.2 Principles of Sampling and Measurements

Locations for *air sampling* sites, in particular for sampling of aerosol-bound radionuclides, must be selected based on the guidelines of the World Meteorological Organization (WMO) [15.1] to ensure representativeness of measurement results for all sampling sites worldwide. In addition, synoptic observations should typically be representative of an area up to 100 km around the station, but for small-scale or local applications, the area may have dimensions of 10 km or less:

- Sampling is preferably conducted at a height between 1.5 and 5 m above ground level, in an undisturbed area so that air can be sampled without obstructions. The distance of the point of sampling to the nearest obstacle should be equal to at least ten times the height of the obstacle [15.2].
- If sampling and measurement equipment are placed in the surroundings of potential sources, e.g., as a part of the monitoring program of nuclear installations, they should be easily accessible for servicing and protected against unauthorized access.

Table 15.1 Measured parameters of radioactivity sensors for atmospheric measurements

Parameter	Description	Unit	Symbol
Ambient dose	Ambient dose equivalent	Sv	$H^*(10)$
Ambient dose rate	Ambient dose rate equivalent $\dot{H}^*(10) = dH^*(10)/dt$	$\mu\text{Sv/h}$ (mostly used)	$\dot{H}^*(10)$
Activity concentration	Activity concentration (activity per sample volume)	Bq/m^3	c
Deposited activity	Activity per area of the radionuclide r	Bq/m^2	$\alpha_{F,r}$

- Samplers are positioned such that their exhaust is directed downwind from the sample collector to avoid sampling their own exhaust air.
- If a sampler is operated on a horizontal surface (e.g., a roof), the exhaust air from the sampler should not be directed to the surface, where it could stir up dust and cause localized elevated activity concentrations from resuspended surface contamination.
- Ideally, 100% of the aerosol particles are deposited on a filter. Alternatively, the collection efficiency of the filter material needs to be accurately determined.
- The area of the filter should be correlated with the air flow, e.g., the sampling volume.
- The air flow and related sampling volume should correlate directly with the achievable detection limits.
- Gaseous components (noble gases, gaseous iodine) need special adsorbents for collection. Due to the limited capacity of the adsorbents, the required contact time between air and adsorbent, and the flow resistance, flow is generally lower than for particulate samplers.

Since buildings and walls in the vicinity of a *gamma dose rate probe* will influence the measured dose rates (e.g. through shielding, in the case of freshly deposited activity after an accidental release), it is recommended that probes be installed according to specific rules. In the *ideal site* approach, gamma dose rate detectors are installed at a height of 1 m on flat natural ground (grassland) without buildings within a distance of 20 m around the station [15.3].

15.2 History

The history of radioactivity measurements in the atmosphere is quite short relative to that of other atmospheric sensors.

15.2.1 History of Radioactivity Measurements in the Atmosphere

With the ignition of the first nuclear bomb, a long series of nuclear weapons tests began. From 1945 to 1962, a total of 345 nuclear weapons were detonated above-ground for experimental purposes. The United States and the former Soviet Union were responsible for the largest share of these, with 83 explosions in 1958 and 77 in 1962 [15.4, 5].

The tests also led to an increase in radioactive particles in the air and precipitation in Europe. Subsequently, monitoring techniques and instrumentation were developed in order to measure these fission products continuously and/or in a nuclide-specific manner. As the nuclear weapons race accelerated, these measurements became increasingly important. For example, the federal government of Germany expanded the area of responsibility of the German Meteorological Service (Deutscher Wetterdienst, DWD) by law in 1955. The DWD was commissioned to monitor radioactivity in air and precipitation and to provide meteorological forecasts of the atmospheric transport of radioactive particles.

The Partial Test Ban Treaty of 1963 banned nuclear testing for both military and peaceful purposes in the atmosphere, underwater, and in space. Although not all countries signed the treaty, it resulted in a significant reduction in radioactivity in the atmosphere,

but did not prevent nuclear testing overall, which moved underground. Underground nuclear testing was banned by the Comprehensive Nuclear-Test-Ban Treaty (CTBT) in 1996, which banned all nuclear explosions on earth [15.6]. For verification of compliance with the CTBT, a worldwide network consisting of seismic, hydroacoustic, infrasound, and radionuclide monitoring stations was installed for the detection and identification of nuclear testing activity. Radionuclide monitoring includes the measurement of both particle-bound radionuclides and the radioactive isotopes of the noble gas xenon [15.7, 8].

As an example, the nuclear weapons tests carried out in 1980 by the People's Republic of China were detected and verified by monitoring. After a test in 1976, a relatively undiluted radioactive cloud reached Central Europe from China, causing an increase in radioactivity levels in air and precipitation.

In order to implement the provisions of the Euratom Treaty of 1957 [15.9], and in the course of the large-scale peaceful use of nuclear energy, monitoring of radionuclides in the environment was extended and increasingly regulated by law.

In parallel with the networks monitoring aerosol-bound radionuclides, gamma dose rate monitoring networks have been established in Europe and internationally for the purpose of protecting people and environment against ionizing radiation. Some of these networks had been established during the Cold War period and were improved after the Chernobyl accident in 1986. Today, the German Federal Office for Radiation Protection (BfS), as an example, operates an early warning network with roughly 1800 ambient dose equivalent

rate (ADER) stations equally distributed over the German territory.

The gamma dose rate monitoring network and the aerosol monitoring network operated in Germany are both part of the German *Integrated Measuring and Information System for the Surveillance of Environmental Radioactivity* (IMIS) [15.10] and the German National Response Plan, which deals with the consequences of a possible large-scale radioactive contamination of the environment. The IMIS stores and distributes the results of predictive atmospheric transport models (in the case of an emergency) and atmospheric monitoring data (under routine conditions) as gamma dose rates, activity concentrations in air and precipitation, and deposited activity on the ground. In addition, data are transmitted to the European Radiological Data Exchange Platform (EURDEP) for aggregation to obtain a full picture of the radiological situation for European decision-makers and the public.

As a consequence of the Fukushima accident in 2011, strategies in Germany for (nuclear) emergency preparedness and monitoring were revised.

15.2.2 Measurement Methods

Radiation measuring devices have been developed to detect ionizing radiation and to determine the type, energy, and intensity of the radiation.

In the early days, only integrated monitoring devices existed for the measurement of gross radiation

15.3 Theory

In general, radioactivity—i.e., ionizing radiation—can be detected because of its interaction with the material of a detection device, which counts and amplifies electric charges. These charges are the result of ionization in the detector material, caused by the transfer of energy from the alpha or beta particles or from gamma radiation.

The measurement conditions must be accurately defined. Due to ionizing radiation emitted from natural radioactive elements (e.g., K-40, Rn-222 and its decay products), it is always necessary to determine the background caused by natural radioactivity.

Detectors must be calibrated for the specific measurement geometry so that measured pulse rates can be converted into activity. Activity concentrations are then determined by division with the amount (volume or mass) of the sample.

These did not discriminate between individual radionuclides and were based on ionization chambers (see e.g. [15.11] and references given therein), proportional counters, or Geiger–Müller tubes (Sect. 15.3.3), and various modifications thereof. One of the first systems able to distinguish between radiation from natural and anthropogenic radionuclides from measurements during sampling is described in [15.12]. NaI scintillation crystals were used from the late 1940s for the monitoring of radiation levels in the environment, but discrimination between individual radionuclides was still not possible. Air sampling and subsequent radiochemical separation was required to identify radionuclides present in the air.

Semiconductor detectors capable of detecting energy-resolved gamma and x-rays and coupled with multichannel analyzers allow real-time monitoring of radionuclide activity levels in air. In-situ liquid nitrogen-cooled high-purity germanium detectors (HPGe detectors) with high energy resolution have been used since the 1970s for the identification of radionuclides in air or deposited on the ground, and the development of new semiconductor materials with good energy resolution at room temperature has enabled the fabrication of compact spectrometric arrays. Today, automated air sampling systems coupled with high-resolution gamma or beta–gamma coincidence spectrometry allow for continuous monitoring of the activity concentrations of various airborne anthropogenic and natural radionuclides at trace levels [15.13–15].

The average activity concentration is determined by the following general equation (15.1)

$$C = \frac{A}{Q_s t_s \varepsilon_c} . \quad (15.1)$$

In this formula, C is the activity concentration given in Bq/m³, A is the activity, given in Bq. The volume flow Q is given in m³/h, and t_s , in h, is the sampling time span. ε_c is the collection efficiency.

In general, the activity at the time the sample was collected is given by equation (15.2). For short-lived radionuclides, corrections for their radioactive decay have to be applied.

$$A = \frac{R_N}{\varepsilon_r \varepsilon_S} . \quad (15.2)$$

R_N is the net count rate from the assay system, in s^{-1} ; ε_r is the counting efficiency of the assay system for a reference standard, in $Bq^{-1} s^{-1}$; and ε_S is the efficiency modification factor for counting (measuring) an actual sample as opposed to the reference standard (e.g., the dimensionless alpha self-absorption factor for particulate alpha on glass fiber filters).

Since temporal variations in activity concentrations during the period of sampling are not known, only average concentrations during the sampling interval can be determined. If individual radionuclides are measured, the radioactive decay during sampling and measurement can be corrected for.

Continuous automatic air monitoring requires more complex calculations of activity concentrations, detection limit, minimum detectable activity, and minimum detectable activity concentration. This is due to the nature of real-time data collection and analysis, in which activity concentrations of both the target radionuclides and interfering background can change over the course of the continuous operation.

Depending on the specific task, different detection devices are used:

- Typical devices for measuring the total amount of activity or the ambient dose rate include ionization chambers, Geiger–Müller tubes, proportional counters, and plastic scintillation counters. The total sum of radiation (alpha (α) and/or beta (β) and/or gamma (γ) radiation) is detected without discriminating between different radionuclides.
- Gamma-ray spectrometry is used for the detection and discrimination of different radionuclides according to the specific energies of their gamma emissions, expressed in kilo-electron volts (keV). This gamma energy can be measured using so-called room-temperature detectors based on semiconductors such as CdZnTe or scintillators such as LaBr₃ (both detector types provide energy resolution on the order of 2%) or thallium-doped sodium iodide (NaI(Tl)) with an energy resolution on the order of 7%. High-purity germanium (HPGe) detectors can be used, providing optimum energy resolution below 1%, but require cooling for operation.
- In laboratories, beta activity is typically measured using liquid scintillation spectroscopy (LSC) or proportional counters. Proportional counters cannot distinguish between different radionuclides. A distinction between certain isotopes is possible using LSC if the system is carefully calibrated and the quench of the sample solution is known. Powerful algorithms are able to distinguish not only between α and β emitters, but also individual radioisotopes.

The sample is mixed with an organic compound (the scintillator), which is stimulated by interaction with the beta (electrons) or alpha (He^{2+} -ions) particles emitted from the sample. The scintillator translates the energy that is transferred by this interaction into visible radiation. The visible radiation is detected by a photomultiplier.

- The measurement of single alpha-emitting radionuclides requires a radiochemical separation of the element. The element of interest is then deposited via electrolysis or auto-deposition on a metal planchet as a very thin layer. A thin layer is necessary to avoid the absorption of the alpha radiation in the sample matrix (self-absorption) and to achieve good energy resolution. The measurement by alpha spectrometry enables the detection of different isotopes due to the specific energies of the alpha particles.
- The sampling of aerosol-bound radionuclides is based on monitoring devices with filter tapes or filter plates. During sampling, the alpha activity can be simultaneously measured with a silicon detector, the beta activity with a GM-tube or plastic scintillation detector, and the gamma radiation by gamma-ray spectrometry, typically using LaBr₃, NaI(Tl), or HPGe detectors.
- The gamma radiation of the precipitation is measured with an in-situ gamma-ray spectrometry system facing downward and detecting the gamma radiation emitted from deposited radionuclides.

In order to reduce the minimum detectable activity and achieve results for very low-activity concentrations, pretreatment of the sample may be necessary before measurement. For example, the filter or the precipitation is measured following a short delay after collection so that the short-lived natural radionuclides (radon decay products) have decayed. The filter may also be charged and then diluted in acid, or precipitation evaporated to concentrate the radioactive material in the residue (e.g., for subsequent alpha and beta spectrometric measurements).

The sensitive measurement of tritium in precipitation requires a different sample preparation method. Separation procedures applied are distillation and electrolytic enrichment.

15.3.1 Gamma Dose Rate Measurements

The Geiger–Müller (GM) tube is the simplest type of measurement device for the detection of ionizing radiation. It consists of a cylinder filled with an inert gas. A high voltage is applied to two electrodes inside the cylinder. Ionizing radiation such as alpha and beta particles or photons interact with the gas inside the cylinder

and generate an electrical charge, which is collected and amplified. The inert gas allows the charged ions to be efficiently neutralized so that the counting of ionizing radiation can be continued. To characterize the performance of this type of detector, the number of output pulses generated by the tube is compared with the number of particles or photons reaching and interacting with the detector material. This depends on the efficiency of the detector, which is dependent on the volume of the cylinder and the pressure of the gas. Secondly, the dead time of the detection device has to be accounted for. This is the time required to collect the charges and neutralize the gas, before counting is continued. A third parameter is the energy response of the detector. Since GM counters detect ionizing radiation independent from the energy of incident particles or photons, the detector housing is designed such that it accounts for photons almost independently from energy.

Proportional counters are similar in design to GM tubes, with the main difference being that the electrical signal generated is proportional to the incident particle or photon energy.

Finally, the obtained count rate has to be converted to a radiation protection quantity. Since these quantities cannot be measured directly, so-called operational quantities are used, which in the case of monitoring external exposure to gamma radiation is the ambient dose equivalent rate ($H^*(10)$). GM tubes are frequently used for the detection of gamma radiation.

It should be noted that efficiency, dead time, and energy response are key parameters of all types of radiation measuring devices. In detectors with energy proportional readings, the energy resolution must be considered as an additional parameter.

Regardless of the type of detector, the operation of gamma dose rate detectors for environmental monitoring requires an understanding that the output of the instrument is the sum of four different components: the detector's inherent background, the natural terrestrial radiation, the secondary cosmic radiation, and the excess dose rate in the case of artificial radiation. The detector response, which is specific for each component, must be known. For this purpose, characterization experiments are required. One example are the intercomparison exercises performed by the European Radiation Dosimetry Group (EURADOS) on an almost annual basis [15.16].

A new development in gamma dose rate detectors in recent years has been initiated by the availability of room-temperature detectors (e.g., LaBr_3) with an energy resolution of approximately 2% at 662 keV. The gamma dose rate is calculated from the total spectrum, but these detectors are also able to determine individual nuclides contributing to the spectrum.

15.3.2 Gamma-Ray Spectrometry Using Semiconductors

Gamma-ray spectrometry measures the energy of gamma radiation emitted from a radioactive source/sample. As gamma rays have specific (discrete) energies characteristic of the respective radionuclide, gamma-ray spectrometry allows for the investigation of radioactive substances in a sample. Radionuclides can be identified, and specific activity or activity concentrations can be determined.

Because solid-state semiconductors and scintillators have much better stopping power than gas-filled ionization chambers, they are better suited for the detection of X- and γ -rays. The energy transfer of the gamma ray to the semiconductor material produces a difference in voltage that is proportional to the transferred energy. The electrical pulses generated by the detector are amplified and fed to a multichannel analyzer for acquisition of a pulse height spectrum.

There are essentially three different processes that can induce a detector pulse [15.17], and even gamma rays of a discrete energy result in a characteristic distribution of pulses across the spectrum. The most important effect is the photoelectric effect: the complete energy of the photon is adsorbed in the detector material. This results in so-called photo-peaks in the spectrum, which have characteristic energies for each radionuclide and are used to evaluate the activity of that particular radionuclide in the sample. The other two processes are e^+e^- annihilation and the Compton background, which comes from interactions involving only partial photon energy loss in the semiconductor material of the detector.

For analysis of the spectra, the system has to be calibrated for energy and detection efficiency. Energy calibration can be done using radiation sources with known radionuclides and energies. Efficiency calibration requires measurements of standards of known activity, ideally of the same geometry and matrix as the sample. Multinuclide solutions can be obtained from metrological institutions. An energy-dependent calibration curve can be obtained from the measured count rates at the various energies. Alternatively, detector responses can be modeled using Monte Carlo techniques.

15.3.3 Integrated Measurement of Alpha and Beta Decay

As a consequence of radioactive decay, a nucleus emits alpha particles (two protons and two neutrons, positively charged) or/and beta particles (electrons). In most cases this coincides with the emission of gamma radiation. For the measurement of the alpha and

beta particles, proportional counters can be used (see Sect. 15.3.1), with a thin entrance window at one end of the cylinder. Differentiation between alpha and beta particles can be achieved taking into account the different stopping power of alpha particles relative to beta radiation.

15.3.4 Measurement of Noble Gases

The activity of the noble gases krypton and xenon can be determined by measuring their beta decay (integrated method) without direct distinction between

the isotopes. They are measured inside a proportional counter (see Sect. 15.3.1), and the noble gas fraction is added to the counting gas [15.18, 19].

Other techniques for the nuclide-specific measurement of xenon use gamma-ray spectrometry (Sect. 15.3.2) or beta–gamma coincidence measurements. Beta–gamma coincidence measurement is based on the fact that a beta decay is accompanied by the emission of a gamma photon of a certain energy. Detecting beta particles in coincidence with gamma radiation enables the discrimination of different isotopes from background radiation [15.13].

15.4 Devices and Systems

The examples of methods, devices, and systems described above are by no means exhaustive. In Tables 15.2, 15.3, 15.4, and 15.5, the types of radiation measured, measuring methods, and sampling intervals and limits of detection are summarized. In addition, the table is divided into normal and emergency modes, respectively. The detection limits indicated are typical values that can vary with respect to the sampled volume, the efficiency of the detector, and the measuring time. For γ -radiation measurements, the detection limits given refer to Cobalt-60.

15.4.1 Gamma Dose Rate Probes

In order to cover an extended dose rate range, gamma dose rate probes are typically equipped with two GM tubes, for low dose (LD) and high dose (HD) rates, pro-

viding a measurement range from 20 nSv/h to 5 Sv/h. They include a high-voltage generation circuit, which needs to be stabilized electronically to cover a temperature range between -20 and $+60$ °C. In spectroscopy dose rate detectors, the LaBr₃ detector is connected to a multichannel analyzer forming a complete spectroscopy unit. Since the dose rate range is typically limited to 3 mSv/h, a GM tube is added to the spectroscopy detector to extend the dose rate range to Sievert per hour.

The probes are installed 1 m above ground level (Fig. 15.1). In the case of a fresh ground deposition, radionuclides deposited in four zones contribute approximately equally (25%) to the final measurement: from a circle of 3 m surrounding the probe, from a circular ring between 3 and 7 m, a circular ring between 7 and 20 m, and a circular ring between 20 and 100 m.

Table 15.2 Sampling and measuring devices for the measurement of radioactivity on aerosol-bound particulates: (a) routine mode, (b) emergency mode

Measured radiation/nuclides	Measurement method	Sampling and measurement interval	Limit of detection (Bq/m ³)
γ -Radiation	Monitoring system, filter tape	a) Daily b) 2 h	a) 0.01 b) 0.1
γ -Radiation	Laboratory method: γ -ray spectrometry after sampling	a) Weekly b) Daily	a) < 0.00001 b) < 1
Artificial α -activity concentration	Monitoring device with alpha spectrometry with a silicon detector	a) Daily/2 h b) 2 h	a) 0.1 b) 0.5
Artificial β -activity concentration	Monitoring device with silicon detector and algorithms to discriminate the count rates from the naturally occurring radionuclides	a) Daily/2 h b) 2 h	a) 1 b) 1
Strontium-89, Strontium-90	Laboratory method: liquid scintillation measurement or proportional counting after chemical separation	a) Monthly b) Daily	a) 0.000001 b) 0.1
Uranium-235, Plutonium-(239+240)	Laboratory method: α -spectrometry after chemical separation	a) Monthly b) Daily	a) 0.0000001 b) 0.1

Table 15.3 Sampling and measuring devices for the measurement of gaseous radionuclides: (a) routine mode, (b) emergency mode

Measured radiation/nuclides	Measurement method	Sampling and measurement interval	Limit of detection (Bq/m ³)
Iodine isotopes	Laboratory method: γ -spectrometry after sampling on charcoal (and molecular sieve)	a) Weekly b) Daily	a) 0.005 b) 1
Iodine-131	NaI(Tl) monitoring device	a) 2 h b) 2 h	a) 0.5 b) 0.5
Krypton-85	Laboratory method: proportional counter	a) Weekly b) Daily	a) 0.01 b) 0.0001
Xenon isotopes	Laboratory method: proportional counter Laboratory method or automated systems: beta–gamma coincidence, gamma-ray spectrometry	a) Weekly b) Daily a) Weekly/daily b) Daily/12 h	0.004 ^a < 0.001 ^a (Xe-133)
Carbon-14	Laboratory method: liquid scintillation spectrometry	Weekly	0.04

^a see [15.19]

Table 15.4 Sampling and measuring devices for the measurement of radioactivity in precipitation: (a) routine mode, (b) emergency mode

Measured radiation/nuclides	Measurement method	Sampling and measurement interval	Limit of detection (Bq/l)
γ -Radiation	Laboratory method: γ -spectrometry a) After evaporation or ion exchange b) Direct	a) Monthly b) Daily	a) 0.005 b) 5
Strontium-89, Strontium-90	Laboratory method: Liquid scintillation spectrometry after evaporation	a) Monthly b) Daily	a) 0.001 b) 1
Uranium-235, Plutonium-(239+240), Americium-241	Laboratory method: α -spectrometry after evaporation	a) Monthly b) Daily	a) 0.00002 b) 0.1
Tritium	Laboratory method: Liquid scintillation counting	a) Monthly b) Daily	a) 1 b) 10
β -Activity	Laboratory method: Counting with Geiger–Müller tube, after evaporation, delayed measurement	a) Daily	0.5
γ -Radiation	In-situ- γ -spectrometry	a) 60 min b) 30 min	a) 700 Bq/m ² b) 1000 Bq/m ²

Table 15.5 Devices for the measurement of ambient dose rate

Measured radiation/nuclides	Measurement method	Measurement interval	Limit of detection (μ Sv/h)
γ -Radiation	Gamma dose rate	10 min	0.02

15.4.2 Alpha/Beta Particulate Monitors

These are automated monitoring devices for the simultaneous measurement of aerosol-bound alpha and beta activity concentrations and gaseous iodine.

Aerosol-bound radionuclides are collected on a filter tape with a typical air flow of about 15 m³/h and measured with a silicon semiconductor. The calcu-

lation of activity concentrations uses a mathematical compensation method, which differentiates between the artificial and natural alpha and beta activity. The sampling interval is adjustable, and after each sampling interval a fresh filter is available for the next measurement. A portion of the air is passed through activated charcoal with a reduced airflow rate of about 3 m³/h. In the activated charcoal the gaseous iodine is separated



Fig. 15.1 A probe of the German gamma dose rate network at a representative measuring site

from the air and simultaneously measured by gamma spectrometry using a NaI(Tl) detector.

15.4.3 High-Purity Germanium (HPGe) Detectors

For most gamma emitters with energies between about 50 keV and a few MeV, semiconductor detectors made of high-purity germanium (HPGe) are the most suitable. HPGe detectors are cooled with liquid nitrogen or electrically during operation to avoid the generation of background signals by thermal processes (*heat noise*). In order to reduce pulses from background radiation during the measurement, lead shielding with copper inlay is recommended.

Laboratory systems consist of an air (or precipitation) sampler that is operated continuously. Sample change is done manually; under routine conditions, sampling intervals of one week are commonly used. The charged filters are then placed on the detector and typically counted for several days. Laboratory detection systems generally consist of an HPGe detector, devices for signal processing—either as NIM (Nuclear Instrumentation Module) standard modules or as digital units—and a computer with control and analysis software. The size of the detector crystal is a benchmark for its efficiency. The combination of sampler and detector is the basis for the minimum detectable activity.

For *continuous monitoring of gamma radiation-emitting aerosol-bound radionuclides*, aerosol-bound radionuclides are collected on a filter tape with a typical volume flow of about 15 m³/h (Fig. 15.2). The gamma

radiation is measured simultaneously by gamma-ray spectrometry. A detection system with an HPGe detector is used. The filter tape is moved after a given sampling interval so that a fresh spot of the filter is available for each sampling interval. The different radionuclides are identified by their specific energies of gamma radiation. The calculation of the true activity concentrations in the given time interval has to take into account the new radioactive particles deposited on the filter during measurement, the decay of radionuclides on the filter, and buildup of their decay products [15.20].

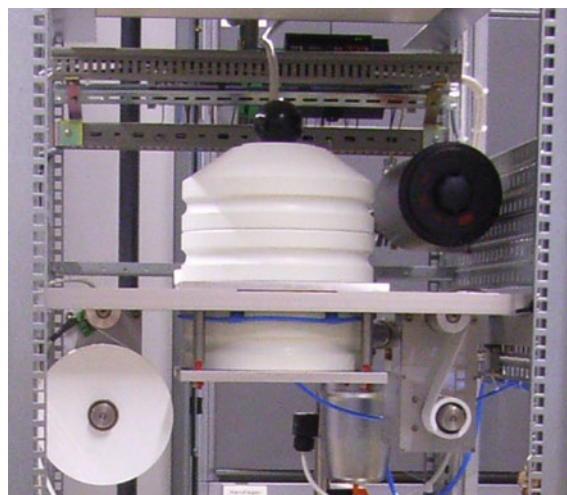


Fig. 15.2 Automated system for aerosol sampling and measurement

Table 15.6 Advantages and disadvantages of the different methods

Measurement method	Monitor/ laboratory	Measured radiation/ nuclides	Advantage	Disadvantage
Dose rate probes	Monitor (network)	Ambient dose equivalent rate	Fast information, good time resolution (10 min), alarm function, robust	Integral measurement, background specific for each installation place, efficiency dependent on type of probe
Alpha/beta particulate monitors	Monitor	Artificial α -activity, artificial β -activity	Moderate time resolution (2 h), alarm function	Integral measurement, no nuclide-specific information
High-purity germanium detectors (HPGe)	Laboratory		Nuclide-specific measurement, high sensitivity	Time delay, well-trained staff needed
High-purity germanium detectors (HPGe)	Monitor	γ -Radiation	Nuclide-specific measurement, moderate time resolution (2 h), alarm function	Lower sensitivity, automatic evaluation needs to be proved
Nuclide-specific measurements after radiochemical treatment	Laboratory	Sr-89, Sr-90, U-235, Pu-(239+240), Am-241, H-3	High sensitivity	Time delay, established methods and well-trained staff needed
Gaseous iodine monitors	Monitor	I-131, I-132, I-133, I-135	Nuclide-specific measurement, moderate time resolution (2 h), alarm function	Adsorbent needs manual exchange
	Laboratory	Kr-85, radioxenon	Kr-85 accessible, established method	Time delay, well-trained staff needed, integral measurement, reduced distinction between different xenon isotopes
Noble gas measurement nuclide-specific measurement	Laboratory	Xe-133, Xe-135, Xe-131m, and Xe-133m	High sensitivity, mostly automated processing	Time delay, well-trained staff needed

15.4.4 Gaseous Iodine Monitors

Elementary iodine I_2 or gaseous compounds with iodine are adsorbed on charcoal and on special adsorption material. This material is either measured directly during sampling, as mentioned above, with a NaI(Tl) detector, or the sample is measured after a certain sample interval, usually with high-resolution gamma-ray spectrometry. With this method, I-131 and the short-lived isotopes I-132, I-133, and I-135 can be easily detected.

15.4.5 Noble Gas Measurement

Noble gases (krypton and xenon) are collected by adsorption on cooled activated charcoal at liquid nitrogen temperature (-197°C). Sampling of xenon only allows for higher temperatures of the activated charcoal, often in combination with other components such as zeolite, molecular sieves, or special membranes. Samples are enriched, purified, and measured using different techniques [15.21]. Since the amount of stable xenon and stable krypton per volume of air is constant worldwide, and the radioactive isotopes of xenon and krypton in the sample are processed along with their stable isotopes, the volume of stable xenon (and krypton) measured by the system can be converted to an effective volume

of air, and thus an activity concentration can be determined.

With *laboratory systems with proportional counters (krypton-85 and radioxenon)*, noble gas measurements in ambient air are performed in the following steps:

1. Sample preparation: enrichment, purification, and separation of the noble gas fractions by cryogenic adsorption and desorption, followed by gas chromatography
2. Measurement of the integral beta activity by gas counting in proportional counters and determination of the stable krypton and xenon volumes by gas chromatography.

In the krypton fraction, only one radioisotope (krypton-85) is present in the sample. For xenon, this counting method determines the integrated activity of all Xe isotopes present in a sample simultaneously, but in most cases originates mainly from the most abundant radionuclide of xenon observed in environmental samples, xenon-133, with a half-life of 5.24 days. Significant amounts of xenon-131m and xenon-135 can be calculated from the measured time-dependent decay rates of the xenon activity of the samples after the completion of counting [15.18, 19].

Laboratory systems with beta–gamma coincidence (xenon) use a different preparation and measurement technique:

1. Sample preparation: enrichment, purification, and separation of the xenon fraction by molecular sieves and activated charcoal
2. Coincidence measurement of beta and gamma radiation with a plastic scintillator (beta) and NaI detector (gamma). Analysis of gamma energy and beta energy spectra.

The energies of the electrons and gamma rays produced in the decay of Xe-133, Xe-135, Xe-131m, and Xe-133m are detected simultaneously. The coincidence technique reduces the ambient background and thus increases the sensitivity of the measurement. The recording of the beta energy allows for high-sensitivity measurement of the meta-stable states [15.20].

Laboratory systems with high-energy-resolution gamma-ray spectrometry (xenon) use a different measuring technique:

1. Sample preparation: enrichment, purification, and separation of the xenon fraction by molecular sieves and activated charcoal
2. Measurement of gamma radiation with a high-energy-resolution HPGe detector. Analysis of gamma energy spectra.

The energy of the gamma rays produced in the decay of Xe-133, Xe-135, Xe-131m, and Xe-133m is detected and resolved with a high-energy-resolution HPGe detector. The xenon isotopes are identified from the known decay energies, and the peak heights in the spectrum are converted into activity. The minimum detectable concentrations are typically around 0.2 mBq/m³ [15.20].

Table 15.6 presents some of the advantages and disadvantages of different devices and methods.

15.5 Specifications

In the following Tables 15.6 to 15.10, the general specifications for different measuring systems are given. They refer to the detection limits given in Tables 15.2 to 15.5, which strongly depend on different parameters as described in Sect. 15.4.

The collection of aerosol particles with an aerosol effective diameter up to 10 μm must be ensured by using filters with corresponding specifications, for example by choosing a glass-fiber filter with a high degree of separation. The choice of the filter medium

Table 15.7 Specifications of typical measuring systems—aerosols

Measured radiation/nuclides	Measurement method	Detection	Sampling medium
γ-Radiation	Automatic system: γ-ray spectrometry	HPGe detector 15%	Filter tape
γ-Radiation	Laboratory method: γ-ray spectrometry after sampling	HPGe detector ≥ 20%	Filter
Artificial α-activity	Monitoring system: alpha spectrometry	Silicon detector	Filter
Artificial β-activity	Monitoring system: integral measurement	Plastic scintillator	Filter
Strontium-89, Strontium-90	Laboratory method: LSC	Photomultiplier	Filter
Alpha-emitting radionuclides	Laboratory method: α-spectrometry	Silicon detector	Filter

Table 15.8 Specifications of typical measurement systems for gaseous radionuclides

Measured radionuclides	Measurement method	Detector	Sampling medium
Iodine isotopes	γ-Ray spectrometry	HPGe detector	Charcoal
Iodine-131	Automatic system: NaI(Tl) monitoring device	NaI(Tl) detector	Charcoal
Krypton-85,	Laboratory method: Beta-counting	Proportional counter	Cryogenic enrichment on charcoal
Xenon isotopes	Laboratory methods: Beta-counting γ-Ray spectrometry Beta–gamma coincidence	Prop. counter, HPGe detector, plastic scintillator	Enrichment on charcoal
Carbon-14 in Carbondioxide	Laboratory method: LSC	Photomultiplier	Enrichment of CO ₂ in NaOH

Table 15.9 Specifications of typical measurement systems in precipitation

Measured radiation/radionuclides	Measurement method	Detector	Sampling medium
γ -Radiation	γ -Ray spectrometry	HPGe detector	Precipitation
Strontium-89, Strontium-90	LSC	Photomultiplier	Precipitation
Uranium-235, Plutonium-(239+240), Americium-241	α -Ray spectrometry	Silicon detector	Precipitation
Tritium	LSC	photomultiplier	Precipitation
β -Activity	Integral beta-counting	Geiger-Müller tube	Precipitation
γ -Radiation	In-situ γ -ray spectrometry	HPGe detector	In-situ; ground

Table 15.10 Specifications for the measurement of ambient dose rate (for GM tubes used in the German gamma dose rate network)

Detector type	Count rate per dose rate ($\text{min}^{-1} \mu\text{Sv}^{-1} \text{h}$)	Intrinsic background rate (min^{-1})	Dose rate range ($\mu\text{Sv h}^{-1}$)	Energy range (keV)	Quantity
Low dose	1000 ± 20	< 15	0.02–1000	$35-1250 \pm 20\%$	$H^*(10)$
High dose	1.0 ± 0.2	< 0.20	20–5 000 000	$60-2000 \pm 20\%$	$H^*(10)$

should also take into consideration that it might need to be suitable for radiochemical processing subsequent to gamma spectrometric analysis, for example for the

identification of alpha and beta emitters. Examples are glass-fiber, cellulose, polypropylene, and PVC filters with cotton support.

15.6 Quality Control

Quality control (QC) for measurement systems is critical for providing reliable results, especially in the event of nuclear emergencies. Internal quality control is conducted by repeated measurements of radioactivity standards and calibration sources. In addition, external quality control is performed through participation in national and international intercomparison and proficiency tests [15.22].

15.6.1 Calibration

Detection systems need to be calibrated with respect to the type and quantity of radiation measured. Calibration sources require well-known composition and activities. Their energies should cover the energy range needed for the measurements. They should be traceable to national standards. Best practice is to use a calibration source in the same measuring geometry and matrix as the samples to be analyzed. If a different medium is used for calibration, corrections for the density and composition of the material must be applied. For γ -ray spectrometry, in some cases a simulation of the detection efficiency is possible using Monte Carlo techniques.

For measurements applied after radiochemical separation, the determination of chemical recovery is necessary. This is done by adding a tracer of another isotope of the same element with known activity to each sample.

Spectrometric systems also need energy calibration to determine the relation between spectrum channel and energy of the radiation. This is done with radiation

sources with radionuclides emitting energies covering the desired energy range.

15.6.2 Specific Quality Control Methods

To ensure high-quality functionality for *gamma dose rate probes* and to uncover possible failures, initial performance tests of newly delivered or repaired probes should be performed. Probes are irradiated at different dose rate levels e.g., 10, 1000 and 100 000 $\mu\text{Sv/h}$, and the observed dose rate is compared with reference values. Initial tests must be complemented by periodic quality assurance tests. Typically these test are performed every 5 years. In these tests, the long-term responses of the probes are compared with their initial parameters.

For *spectrometric measurements*, significant deviations in energy calibration, efficiency, and peak shape may be observed during the measurement. Recurrent measurements of radioactivity standards and calibration sources are used to control the stability of the system with regard to energy calibration, energy resolution, and efficiency. Periodic measurements of the background ensure that possible contamination of the measuring system is identified at an early stage. The time intervals for these checks depend on the tasks of the specific laboratory and vary from daily to semiannually.

For *laboratory filter measurements*, it is also important to measure a blank filter in each new batch to identify potential interfering radionuclides on the filter material.

15.7 Maintenance

Preventive maintenance is recommended to avoid technical failures. The frequency and types of procedures depend on the type of device.

15.7.1 Gamma Dose Rate Probes

Defects in electrical systems and equipment carry an increased risk of accidents and fire. Together with other maintenance tasks, specialists regularly check the safety of the measuring systems, at least every 4 years. Observed failures are removed immediately. Electrical safety tests according to the German Statutory Accident Insurance (DGUV) regulation part 3 and DIN VDE/EN industry standards [15.23–28] are required by law in Germany. These tests improve the electrical safety of the measuring systems and also reduce electromagnetic interference, thus leading to improved overall station performance.

15.8 Application

The described methods and devices are used for nuclear emergency preparedness as well as for environmental monitoring and the verification of the CTBT. In addition, these measurements are used for scientific studies. Measurement are exchanged on an international level to allow for a (more or less) complete assessment of the radiological situation.

15.8.1 Emergency Preparedness

Consistent and appropriate protective measures must be in place before, during, and after radiological emergencies. This requires information about the affected areas, the level of contamination, and the actual and future exposure. For this purpose, online air monitoring and gamma dose rate networks are required, with stationary probes equally distributed over the national territory. In emergency mode, data from all stations will be accessed in almost real time, enabling the population to be informed in an efficient and timely manner.

The operational status of monitoring devices is monitored by experts on a daily basis. For maintenance, technicians are trained to complete repairs as quickly as possible in the case of failures. In both routine mode and emergency mode, all relevant data are transferred to a central location. In the case of offline sampling, the filter and the precipitation samples are collected and transported to central laboratories where measurements (following radiochemical separation procedures, if needed) are conducted.

Along with electrical safety tests, the site conditions of the gamma dose rate stations are checked, and batteries have to be changed every 8 years.

15.7.2 Aerosol Sampler

For aerosol samplers, it is recommended that volume flow and pumps be checked at least semiannually.

15.7.3 Spectrometric Systems

In general, a specific maintenance regime is not necessary. Required maintenance or repair will be identified with the QC measurements. As an example, for HPGe detectors, a continuous degradation of the energy resolution might be caused by a loss of vacuum in the system and will be detected with internal QC measurements.

15.8.2 Environmental Monitoring

Measuring devices used for the detection of radionuclides in the atmosphere are operated in automatic mode. In the case of an emergency, the results for aerosol-bound radionuclides and radioactive iodine isotopes and for ground-deposited radionuclides are available in less than 2 hours.

High-volume filter samples and samples of precipitation have to be collected manually and transferred to a laboratory for further investigation. Sensitive measurements of these filter samples (trace analysis) enable the observation of long-term trends in activity concentrations and investigation of increased activity concentrations in the range of micro-becquerel per cubic meter [15.29]. Possible sources can be identified with information from different sampling sites by applying atmospheric transport models. This is based on a rapid exchange of measurement results between the laboratories performing such measurements with reliable quality.

Precipitation typically must be enriched to measure very low activity concentrations. In the normal mode, this is done by ion exchange systems used in automatic sampling devices. Automation of sampling systems requires precise organization of sample transport to the laboratory and maintenance.

One of the main functions of gamma dose rate networks is to provide immediate alerts if increased radiation levels are detected. If two neighboring stations

(distance less than 30 km) have detected increased radiation levels for a period of a minimum of 1 hour, an officer on duty is notified via cell phone, who then has to analyze the radiological situation within 1 hour [15.30]. Assuming a typical gamma dose rate of $0.08 \mu\text{Sv/h}$, the alert level is approximately $0.11 \mu\text{Sv/h}$. Independent from the alert mechanism, measurement results from the gamma dose rate network are provided every hour in routine mode and every 10 minutes in emergency mode.

The results of environmental monitoring provide continuous information about the present level of radioactivity caused by naturally occurring and man-made radionuclides. In Germany, 41 sampling and measuring sites for the collection and measurement of atmospheric activity concentrations and approximately 1800 stationary gamma dose rate probes are equally distributed over the German territory. The density is increased in the 20 km and 100 km emergency planning zones (according to new recommendations) around nuclear power plants.

All different types of networks provide an overview of the spatial and temporal variability of radionuclide levels deposited on the ground and in the atmosphere. An example of the sensitivity and selectivity of trace survey measurements is the observation of the radioac-

tive cloud from the accident at Fukushima–Daiichi by European networks [15.31].

15.8.3 Comprehensive Nuclear-Test-Ban Treaty

Apart from waveform technologies (seismic, hydroacoustic, and infrasound), continuous monitoring of radionuclides in the atmosphere is part of the worldwide International Monitoring System (IMS) for verification of the CTBT, which was established for the detection and identification of any nuclear test activity. Together with atmospheric transport modeling, the network is designed to detect all kinds of nuclear tests with strength of 1 kT or more at 95% certainty within 10 days. Radionuclide monitoring includes the measurement of both particle-bound radionuclides and the radioactive isotopes of the noble gas xenon, which is of special importance for the detection of underground testing. The radionuclides are detected after atmospheric transport from the source to the CTBT radionuclide stations. To meet the verification requirements, detection limits of $10 \mu\text{Bq/m}^3$ for Ba-140 (aerosol-bound) and 1 mBq/m^3 for Xe-133 (noble gas) must be achieved, along with data availability of 95% [15.7, 15, 32].

15.9 Future Developments

All types of systems used for radionuclide monitoring are under continuous development with respect to the main parameters, including sensitivity, time resolution, and reliability. For example, the CTBTO focuses on improvement in detection limits for the different xenon isotopes of noble gas systems operated in their network [15.14, 33, 34]. Because nuclear tests are not the only source of atmospheric xenon, the reliable determination of the ratio of the different xenon isotopes is important in order to distinguish between civil emissions and a nuclear test.

After the accident at the Fukushima–Daiichi nuclear power plant in March 2011, the application of mobile systems installed in vehicles and drones complemented by mobile gamma spectrometric measurements were found to be the most efficient techniques for monitoring contamination levels and the efficiency of decontamination measures in Japan [15.35]. These measurements were embedded in comprehensive measurement programs that were developed and implemented over a period of several years after the accident. From the lessons learned after the accident at Fukushima–Daiichi in Japan, the development of modern measurement

strategies taking into account recent developments, especially of mobile measurement equipment, will be the focus for improving radiation monitoring systems in the future.

The data exchange platform EURDEP collects and provides data from all European radiation monitoring networks in almost real time on behalf of the European Commission. Today, data are collected from 30 European countries, using a considerable number of different detector and measurement types and following different national policies. The comparability of these data is crucial for a meaningful interpretation, not only in the event of a nuclear accident with transboundary implications, but also for the correct interpretation of the data under natural background conditions. Furthermore, data assimilation techniques used in decision support systems like realtime online decision support system (RODOS) [15.36] strongly depend on harmonized data complemented by an appropriate uncertainty. Therefore, harmonized and metrologically substantiated radiation monitoring data are critical for adequate environmental radiation monitoring in Europe.

15.10 Further Reading

- G. Knoll: *Radiation Protection and Measurement*, Third Edition, Wiley Sons, New York 2007
- D. J. Malcolm-Lawes, *Introduction to Radiochemistry*, Springer Nature Switzerland AG, Part of Springer Nature, 2017
- G. Gilmore: *Practical Gamma-ray Spectrometry*, Wiley, Chichester 2008
- V. Valković (eds.): *Radioactivity in the Environment*, Elsevier Science, 2000
- C. Pilger; L. Ceranna; C. Bönnemann (eds.): *Monitoring Compliance with the Comprehensive Nuclear-Test-Ban Treaty (CTBT)*, Contributions by the German National Data Center, 2017, (*Geologisches Jahrbuch Reihe B, Band B 105*)
- M. L'Annunziata: *Handbook of radioactivity analysis*, Second edition, Elsevier Science Publishers, 2003

References

- 15.1 M. Leroy: Site classification for surface observing stations on land. In: *JMA/WMO Workshop on Quality Management in Surface, Climate and Upper-air Observations in RAIL (Asia), Tokyo, Japan, 27–30 July (2010)*
- 15.2 World Meteorological Organization: *WMO/GAW Aerosol Measurement Procedures, Guidelines and Recommendations*, GAW Report No.227, 2nd edn. (WMO, Geneva 2016), WMO–No.1177
- 15.3 U. Stöhlker, M. Bleher, H. Doll, H. Dombrowski, W. Harms, I. Hellmann, R. Luff, B. Prommer, S. Seifert, F. Weiler: The German dose rate monitoring network and implemented data harmonization techniques, *Radiat. Prot. Dosim.* **183**(4), 405–417 (2019)
- 15.4 UNSCEAR: Report to the General Assembly, with scientific annexes. Vol. 1, http://www.unscear.org/unscear/en/publications/2000_1.html (2000), Accessed 06 July 2021
- 15.5 UNSCEAR: Report to the General Assembly, with scientific annexes. Vol. 2, http://www.unscear.org/unscear/publications/2000_2.html (2000), Accessed 06 July 2021
- 15.6 Preparatory Commission for the Comprehensive Nuclear-Test-Ban Treaty Organization (CTBTO): *Comprehensive Nuclear-Test-Ban Treaty (CTBT)*, <https://www.ctbto.org/the-treaty/> (2012), Accessed 06 July 2021
- 15.7 Special Subject: Monitoring the Nuclear-Test-Ban, *Kerntechnik* **66**(3) (2001)
- 15.8 F. Medici: The IMS radionuclide network of the CTBT, *Radiat. Phys. Chem.* **61**(3–6), 689–690 (2001)
- 15.9 EURATOM: Consolidated version of the treaty establishing the European Atomic Energy Community, *Off. J. Eur. Union* **C 327**, 01 (2012)
- 15.10 W. Weiss, H. Leeb: IMIS—the German integrated radioactivity information and decision support system, *Radiat. Prot. Dosim.* **50**, 163 (1993)
- 15.11 K.M. Miller, R.J. Larsen: The development of field-based measurement methods for radioactive fallout assessment, *Health Phys.* **82**(5), 609 (2002)
- 15.12 H. Stockburger, A. Sittkus: Unmittelbare Messung der natürlichen und künstlichen Radioaktivität in der atmosphärischen Luft, *Z. Naturforsch.* **21a**(7), 1128–1132 (1966)
- 15.13 A. Ringbom, T. Larson, A. Axelsson, K. Elmgren, C. Johansson: SAUNA—a system for automatic sampling, processing, and analysis of radioactive xenon, *Nucl. Instrum. Methods Phys. Res. A* **508**(3), 542–553 (2003)
- 15.14 G. Le Petit, A. Cagniant, P. Gross, G. Douysset, S. Topin, J.P. Fontaine, T. Taffary, C. Moulin: Spalax™ new generation: a sensitive and selective noble gas system for nuclear explosion monitoring, *Appl. Radiat. Isot.* **103**, 102–114 (2015)
- 15.15 R. Werzi, F. Padoani: Verifying the operational setup of a radionuclide air-monitoring station, *Appl. Radiat. Isot.* **65**(5), 557–560 (2007)
- 15.16 H. Dombrowski, M.A. Duch, C. Hranitzky, P. Kleinau, S. Neumaier, M. Ranogajec-Komor, R. Rodriguez: EURADOS intercomparison of passive $H^*(10)$ area dosimeters 2014, *Radiat. Meas.* **106**, 229–234 (2017)
- 15.17 G. Knoll: *Radiation Protection and Measurement*, 3rd edn. (Wiley, New York 2007)
- 15.18 H. Sartorius, C. Schlosser, S. Schmid, W. Weiss: Verfahren zur Bestimmung der Aktivitätskonzentration der atmosphärischen Edelgase Krypton-85 und Xenon-133. In: *Empfehlungen zur Überwachung der Umweltradioaktivität. Loseblattsammlung des Arbeitskreises Umweltüberwachung*, FS-78-15-AKU, ed. by Fachverband für Strahlenschutz e.V. (2002), Blatt 3.4.9
- 15.19 C. Schlosser, A. Bollhöfer, S. Schmid, R. Kraiss, J. Bieringer, M. Konrad: Analysis of radioxenon and Krypton-85 at the BfS noble gas laboratory, *Appl. Radiat. Isot.* **126**, 16–19 (2017)
- 15.20 T. Steinkopff, B. Fay, H. Glaab, I. Jacobsen, A. Klein, M. Mirsch: Early emergency response by means of dispersion forecasting—emergency management of the Deutscher Wetterdienst in the context of national and international agreements, *Kerntechnik* **72**, 172–175 (2007)
- 15.21 M. Auer, A. Axelsson, X. Blanchard, T.W. Bowyer, G. Brachet, I. Bulowski, Y. Dubasov, K. Elmgren, J.P. Fontaine, W. Harms, J.C. Hayes, T.R. Heimbigner, J.I. McIntyre, M.E. Panisko, Y. Popov,

- A. Ringbom, H. Sartorius, S. Schmid, J. Schulze, C. Schlosser, T. Taffary, W. Weiss, B. Wernsperger: Intercomparison experiments of systems for the measurement of xenon radionuclides in the atmosphere, *Appl. Radiat. Isot.* **60**(6), 863–877 (2004)
- 15.22 H. Wershofen, J. Bieringer, S. Frenzel, G. Kanisch, C. Kitzberger, T. Steinkopff, J. Tschiersch, H. Völkle: An inter-laboratory comparison of low-level measurements in ground-level aerosol monitoring, *Appl. Radiat. Isot.* **66**(6/7), 737–741 (2008)
- 15.23 DIN VDE 0100–600: Errichten von Niederspannungsanlagen, Teil 6: Prüfungen (recent version)
- 15.24 DIN VDE 0105–100, Betrieb von elektrischen Anlagen, Teil 100: Allgemeine Festlegungen (recent version)
- 15.25 DIN EN 61557, Electrical safety in low voltage distribution systems up to 1000 V a.c. and 1500 V d.c.—Equipment for testing, measuring or monitoring of protective measures (recent version)
- 15.26 DIN VDE 0701–0702, Prüfung nach Instandsetzung, Änderung elektrischer Geräte – Wiederholungsprüfung elektrischer Geräte (recent version)
- 15.27 DIN EN 62305–5, Protection against lightning—Part 3: Physical damage to structures and life hazard (recent version)
- 15.28 DIN EN 60204–1, Safety of machinery—Electrical equipment of machines—Part 1: General requirements (recent version)
- 15.29 J. Bieringer, C. Schlosser, H. Sartorius, S. Schmid: Trace analysis of aerosol bound particulates and noble gases at the BfS in Germany, *Appl. Radiat. Isot.* **67**(5), 672–677 (2009)
- 15.30 R. Luff, M. Zähringer, W. Harms, M. Bleher, B. Prommer, U. Stöhlker: Open-source hardware and software and web application for gamma dose rate network operation, *Radiat. Prot. Dosim.* **160**, 252 (2014)
- 15.31 O. Masson, A. Baeza, J. Bieringer, K. Brudecki, S. Bucci, M. Cappai, F.P. Carvalho, O. Connan, C. Cosma, A. Dalheimer, D. Didier, G. Depuydt, L.E. De Geer, A. De Vismes, L. Gini, F. Groppi, K. Gudnason, R. Gurriaran, D. Hainz, Ó. Halldórs-son, D. Hammond, O. Hanley, K. Holeý, Z. Homoki, A. Ioannidou, K. Isajenko, M. Jankovic, C. Kitzberger, M. Kettunen, R. Kierepko, R. Kontro, P.J.M. Kwakman, M. Lecomte, L. Leon Vintro, A.–P. Leppänen, B. Lind, G. Lujaniene, P. Mc Ginnity, C. Mc Mahon, H. Malá, S. Marenti, M. Manolopoulou, A. Mattila, A. Muring, J.W. Mietelski, B. Møller, S.P. Nielsen, J. Nikolic, R.M.W. Overwater, S.E. Pálsson, C. Papastefanou, I. Penev, M.K. Pham, P.P. Povinec, H. Ramebäck, M.C. Reis, W. Ringer, A. Rodriguez, P. Rulík, P.R.J. Saey, V. Samsonov, C. Schlosser, G. Sgorbati, B.V. Silobritiene, C. Söderström, R. Sogni, L. Solier, M. Sonck, G. Steinhauser, T. Steinkopff, P. Steinmann, S. Stoulos, I. Sýkora, D. Todorovic, N. Tooloutalaie, L. Tositti, J. Tschiersch, A. Ugron, E. Vagena, A. Vargas, H. Wershofen, O. Zhukova: Tracking of airborne radionuclides from the damaged Fukushima Dai-Ichi nuclear reactors by European Networks, *Environ. Sci. Technol.* **45**, 7670–7677 (2011)
- 15.32 J. Schulze, M. Auer, R. Werzi: Low level radioactivity measurement in support of the CTBTO, *Appl. Radiat. Isot.* **53**(1/2), 23–30 (2000)
- 15.33 A. Cagniant, G. Le Petit, P. Gross, G. Douysset, H. Richard-Bressand, J.–P. Fontaine: Improvements of low-level radionuclide detection sensitivity by a state-of-the art coincidence setup, *Appl. Radiat. Isot.* **87**, 48–52 (2014)
- 15.34 R. Werzi: Improving the sensitivity of radionuclide particulate monitoring stations, *Appl. Radiat. Isot.* **68**(2), 340–344 (2010)
- 15.35 K. Saito, Y. Onda: Preface to a special issue “Japanese national mapping projects on large-scale environmental monitoring and mapping in Fukushima volume 2”, *J. Environ. Radioact.* **166**, 417–418 (2017)
- 15.36 F. Gering, B. Gerich, E. Wirth, G. Kirchner: Potential consequences of the Fukushima accident for off-site nuclear emergency management: a case study for Germany, *Radiat. Prot. Dosim.* **155**, 146–154 (2013)

Jacqueline Bieringer

Atmospheric Radioactivity and Trace Analysis
Federal Office for Radiation Protection
Freiburg, Germany
jbieringer@bfs.de



Jacqueline Bieringer is a physicist and has worked at BfS in Freiburg since 1991 in the field of atmospheric radioactivity and trace analysis for environmental monitoring purposes. Here main focus is on measurements within the Integrated Measuring and Information System (IMIS) and surveillance of the Comprehensive Nuclear-Test-Ban Treaty (CTBT). She is head of the accredited gamma spectrometry laboratory at BfS-Freiburg and works as quality manager in this field.

Thomas Steinkopff

formerly Surveillance of Radioactivity
German Meteorological Service
Offenbach, Germany
tommy_theater@t-online.de



Dr.-Ing. Thomas Steinkopff received a PhD in Chemistry in 1987 from the Technical University of Darmstadt, Department of Inorganic Chemistry and Nuclear Chemistry, under the direction of Prof. Dr. K. H. Lieser. Since 1986 he has been employed at the German Meteorological Service, Surveillance of Radioactivity division, and head of this division since 2009 and retired in 2021. He is also currently a member of the executive board of the German-Suisse Radiation Protection Association.

**Ulrich Stoehlker**

IMIS measurement tasks
Federal Office for Radiation Protection
Freiburg, Germany
ustoehlker@bfs.de

Ulrich Stoehlker is responsible for the German external dose rate monitoring network, with 1800 gamma dose rate measurement posts and mobile equipment. This includes the organization and management of staff and laboratories at six different locations in Germany. From July 2010 until July 2013 he was Senior Radionuclide Officer at the International Data Centre (IDC) of the Comprehensive Nuclear-Test-Ban Treaty Organization (CTBTO) in Vienna.

16. Gas Analysers and Laser Techniques

Dwayne Heard , Lisa K. Whalley , Steven S. Brown 

A range of sensitive and selective analytical techniques are required to perform measurements of the gas-phase composition of the atmosphere, as the lifetimes and concentrations of trace gases in the atmosphere (the analytes) vary widely. This chapter describes in-situ methods where the analyte of interest is quantified either directly via the absorption or emission of radiation by the analyte or indirectly following chemical conversion or photodissociation to another species, which is subsequently detected via absorption or emission spectroscopy or chemiluminescence. Optical excitation is achieved using either a broadband light source or a narrowband laser source.

The techniques covered are differential optical absorption spectroscopy (DOAS), Fourier-transform infrared (FTIR) spectroscopy, cavity-enhanced spectroscopy (CES), tunable diode laser spectroscopy (TDLS), laser-induced fluorescence (LIF) spectroscopy (in particular, LIF at low pressure using fluorescence assay by gas expansion: FAGE), laser-induced phosphorescence (LIP) spectroscopy, and chemiluminescence. A technical description of each method and the underlying theory is presented, together with a discussion of instrument optimization and the parameters that control performance, for example instrument sensitivity and selectivity and possible interference-induced artifacts when operated in the field. Quality assurance is described, including the calibration and inter-comparison of instruments.

Finally, some examples of field measurements of the concentrations of key atmospheric gases (such as short-lived radical intermediates and longer-lived stable gases) using a variety of platforms are presented to illustrate applications of the methods described in this chapter.

16.1	Measurement Principles and Parameters	476	16.2	History	478
16.1.1	Measured Parameters of Gas-Phase Analyzers and Laser Techniques.....	476	16.2.1	Differential Optical Absorption Spectroscopy (DOAS).....	478
16.1.2	Measurement Principles.....	477	16.2.2	Fourier-Transform Infrared (FTIR) Spectroscopy.....	478
			16.2.3	Tunable Diode Laser Spectroscopy (TDLS).....	478
			16.2.4	Cavity-Enhanced Spectroscopy (CES)...	479
			16.2.5	Laser-Induced Fluorescence (LIF) Spectroscopy.....	479
			16.2.6	Chemiluminescence Methods.....	479
			16.3	Theory	480
			16.3.1	Optical Methods: Absorption Spectroscopy.....	480
			16.3.2	Optical Methods: Emission Spectroscopy.....	483
			16.3.3	Chemical Conversion Methods.....	485
			16.4	Devices and Systems	486
			16.4.1	Absorption Spectroscopy Devices.....	486
			16.4.2	Emission (Fluorescence) Spectroscopy Devices.....	487
			16.4.3	Chemical Conversion Devices.....	491
			16.4.4	Comparison of the Methods.....	494
			16.5	Specifications	494
			16.6	Quality Control	495
			16.6.1	Calibration of Gas Analyzers and Laser Techniques.....	495
			16.6.2	Intercomparison of Instruments.....	496
			16.7	Maintenance	496
			16.8	Applications	498
			16.8.1	Measurements of Short-Lived Radical Intermediates and Comparison with Model Calculations.....	498
			16.8.2	Measurements of Halogenated Gases in Remote Regions.....	498
			16.8.3	Measurements of VOC Emissions From Oil and Gas Development.....	498
			16.8.4	Long-Term Monitoring of Climate Gases and Urban Pollutants and Links to Policy.....	499
			16.9	Future Developments	502
			16.10	Further Reading	502
			References	502	

In this chapter, techniques and instruments designed for the in-situ measurement of trace gases in the atmosphere using optical methods are described, together with some examples of their deployment in the field and the results they yield. The chapter covers methods suitable for ground-based measurements from fixed platforms and mobile measurements from ships and aircraft. These techniques can be divided into two main classes. The first involves direct optical excitation of the analyte and quantification via measurement of either the fraction of light absorbed (using the Bouguer–Lambert–Beer’s law) or the intensity of the ensuing emission from the excited state. The second involves the conversion of the analyte to another species via a chemical reaction with an added reagent, with the product being detected optically via its spontaneous chemiluminescence or through absorption or emission spectroscopy.

16.1 Measurement Principles and Parameters

Many trace gases are released directly into the atmosphere at the Earth’s surface from oceans or terrestrial environments via natural processes, or they are emitted during anthropogenic activities. Many others are generated following chemical transformations of those emissions (through the action of sunlight or reactions with a variety of oxidants) to secondary trace gases or aerosols with a very wide range of chemical functionality. With increasing aging of the air mass from the emission source, the oxidation products become less volatile and partition to the aerosol phase. A concern is whether anthropogenic emissions are causing a deterioration of the air that we breathe or are leading to a warming of the atmosphere, with associated impacts.

Gas-phase measurements performed using the techniques covered in this chapter are employed for many purposes. Some are used to monitor long-term trends in gas concentrations (e.g., for gases that have been phased out due to binding international treaties such as the Montreal Protocol) or to quantify human exposure to gases with an identifiable health impact. The resulting data are used by policy regulators. The lifetimes of trace gases span an enormous range, from a few milliseconds for the hydroxyl radical OH in a polluted environment to hundreds of years for some chlorofluorocarbons (CFCs). The lifetimes of short-lived gases such as radicals (which have an unpaired electron) are controlled only by the local in-situ chemistry, not by the transport of these gases. Hence, measurements made at specific times and locations are used as targets for atmospheric models that include our best knowledge of

This chapter is complementary to those on the ground-based sensing of gases (Chap. 1 on atmospheric measurements) and spectroscopic methods (Chap. 28 on spectrometers). Also, as the levels of many trace gases are controlled by solar radiation, this chapter is linked to those on spectrally resolved radiation measurements (Chap. 11 on radiation sensors, Chap. 40 on solar radiation sensors, and Chap. 28 on radiometers).

Local measurements can be made using these instruments at a fixed point in space, and regional measurements can be carried out on an aircraft or ship. Rather than being open-path detectors (like remote sensing instruments), the majority of the instruments described in this chapter have a dedicated inlet to sample the atmosphere.

the chemical mechanisms that transform gas emissions. The level of agreement between the measurements and the models quantifies how well the chemistry is understood. Verifying that the chemistry is understood and correctly represented in models leads to greater confidence in model-based predictions of how the air quality or climate will respond to changes in global emissions. Such predictions have driven policy to combat global warming and deteriorating air quality.

16.1.1 Measured Parameters of Gas-Phase Analyzers and Laser Techniques

The ultimate goal of the methods described in this chapter is to provide a quantitative measurement of the number density (or concentration) of a given trace gas, which can be converted into a mixing ratio if the total density of the air is known at the location of the measurement [16.1]. For a fixed concentration of a trace gas, the mixing ratio increases with altitude as the pressure decreases. One observable is the absorbance, which is a measure of the change in the intensity of radiation at a detector due to absorption by a sample, and is related to the concentration via the Bouguer–Lambert–Beer’s law. For example, the absorbance of a sample present in either a conventional absorption cell or an optical cavity can be measured using differential optical absorption spectroscopy (DOAS). Another observable is the intensity of emission from an excited state, measured either as an analogue voltage from a detector or the number of photons counted by a detector.

Table 16.1 Measured parameters of gas analyzers and laser techniques for trace gases

Parameter	Description	Unit	Symbol
Mixing ratio	Mole fraction of the trace gas in an ambient air sample, often quoted in parts per million (ppmv), parts per billion (ppbv), or parts per trillion (pptv) by volume	mol mol ⁻¹	χ
Concentration as a number density	Number of atoms or molecules of species X per unit volume of air	atom cm ⁻³ or molecule cm ⁻³	[X] or c_n
Concentration as a mass density	Mass of atoms or molecules of species X per unit volume	kg m ⁻³	c_m
Absorption cross-section	Inherent measure of the ability of a molecule to absorb light	cm ² molecule ⁻¹	σ_{abs}
Photodissociation quantum yield	Fraction of the molecules excited via photon absorption that dissociate to form a particular product	No unit	ϕ
Photolysis frequency	Rate of photolysis of a molecule integrated across the atmospheric range of wavelengths	s ⁻¹	J

Table 16.2 Key performance indicators for instruments that are used to measure trace gas concentrations

Parameter	Description	Unit	Symbol
Limit of detection	Lowest concentration or mixing ratio of a trace gas that can be measured, as defined for a given signal-to-noise ratio (or number of standard deviations of the noise) and signal averaging time	Molecule cm ⁻³ or mol mol ⁻¹	[], c_n , c_m , or χ
Precision	Concentration or mixing ratio corresponding to a particular number of standard deviations of the background signal	Molecule cm ⁻³ or mol mol ⁻¹	[], c_n , c_m , or χ
Accuracy	Accuracy of the calibration, cross-section, or path length, usually presented as a percentage of the derived quantity	%	
Degree of interference	Fraction of the observed signal that is due to an unwanted species (sometimes referred to as a bias)	%	

Detectors used in this context include devices such as photodiodes and photomultipliers in which a photocathode converts the emitted photons into electrons. If the path length and absorption cross-section are known, the Bouguer–Lambert–Beer’s law can be used to determine absolute concentrations without the need to perform a calibration, whereas emission methods require calibration (i.e., the signal from a known concentration of analyte is measured). Table 16.1 shows the parameters measured by absorption or emission instruments.

There are also a number of parameters that enable the detection performance of a particular instrument for a particular species to be quantified, as shown in Table 16.2. Which of these is most important depends on the desired application of the data. For example, when determining the trend in methane levels over several years or the emission flux of a given species from a surface, a precision to 1% of the measured concentration may be required. On the other hand, greater accuracy may be required in a comparison of instruments across a network or a comparison with a model [16.1].

It is useful to be able to convert a concentration (number density) [X] into a volumetric mixing ratio χ_X , as both of these quantities are commonly used when reporting abundances of trace gases. The relationships

used to interconvert these two quantities are

$$[X] = \chi_X \frac{p_{\text{air}} N_A}{10^6 RT} \quad (16.1)$$

$$\chi_X = [X] \frac{10^6 RT}{p_{\text{air}} N_A}, \quad (16.2)$$

where p_{air} is the local air pressure (in Pa or Nm⁻¹), N_A is Avogadro’s number (6.022×10^{23} mol⁻¹), R is the gas constant (8.314 J mol⁻¹ K⁻¹), T is the local temperature, and the units of concentration are molecule cm⁻³. In order to convert the mixing ratio into the commonly used units ppmv, ppbv, pptv, and ppqv (parts per million, billion, trillion, or quadrillion by volume, respectively), the mixing ratio is multiplied by 10^6 , 10^9 , 10^{12} , and 10^{15} , respectively.

16.1.2 Measurement Principles

The applications of the different types of measurements (absorption, emission, and chemical conversion with chemiluminescence) that are performed to quantify trace gases are given in Table 16.3. The flux of a gas is the number of molecules of gas that pass through a certain boundary plane (which may be a surface) per

Table 16.3 Principles and applications of gas analyzers

Type of sensor	Measurement principle	Applicability	
		Gas concentration	Gas flux measurements
DOAS, FTIR, CES, TDLs	Absorption	×	×
Laser-induced fluorescence	Emission	×	×
Laser-induced phosphorescence spectroscopy	Emission	×	
Chemical conversion with product detection	Absorption and emission (chemiluminescence)	×	×

unit volume per second. A negative flux corresponds to movement in a downwards direction, which could be due to the deposition of the gas on a surface, whereas

a positive flux corresponds to movement in a upwards direction, which could be due to the emission of the gas from a surface (e.g., a forest canopy).

16.2 History

In this section we provide a short historical account of the main analytical methods discussed in this chapter, mention some of the pioneers in this field, and mention some of the important molecules that can be quantified.

16.2.1 Differential Optical Absorption Spectroscopy (DOAS)

Differential optical absorption spectroscopy (DOAS) is a broadband (i.e., not monochromatic) ultraviolet and visible technique that utilizes the structured electronic absorption features of various small molecules to identify and separate multiple absorbing species. As such, it is often used in remote sensing applications, as described further in Chap. 26. Pioneering DOAS studies include measurements of ozone columns (the highest concentrations of ozone occur in the stratosphere) by *Gordon Dobson* (1889–1975). This technique is also commonly used to measure concentrations of absorbing trace gases over kilometer-scale open paths, in which case it can be considered an in-situ technique. The use of DOAS in closed-path optical cavities is described further in Sect. 16.2.4 below. The first demonstration of this method occurred in the 1970s. *Dieter Perner* and *Ulrich Platt* imaged a frequency-doubled dye laser beam over a 7.8 km path in Jülich, Germany, providing probably the first interference-free measurements of the OH radical [16.2]. Shortly thereafter, those authors used the same technique to measure CH₂O, O₃, NO₂, HONO, and NO₃ at sites in the US and Germany [16.3–5]. This method has since become a standard for measuring these and other trace gases such as halogen oxides [16.6, 7], SO₂, and glyoxal [16.8].

16.2.2 Fourier-Transform Infrared (FTIR) Spectroscopy

Interferometric techniques dating back to the work of *Albert Michelson* (1852–1931) in 1881 form the basis for broadband infrared spectroscopy. FTIR was initially applied as a measurement technique in ambient air in the mid-1950s [16.9], but was first used routinely for air monitoring in polluted regions in the 1970s [16.10, 11]. This method has the advantage of being versatile, as it can provide simultaneous measurements of numerous trace gases (e.g., O₃, H₂O₂, HNO₃, HONO, H₂CO, HCOOH, PAN, HCl, NH₃, NO, and NO₂) based on their mid-infrared absorption bands, but it also has the disadvantage of being less sensitive than other methods. A primary application of FTIR is in the study of biomass burning, as it is used in both laboratory and aircraft measurements of concentrated emissions from fires [16.12–14].

16.2.3 Tunable Diode Laser Spectroscopy (TDLs)

In contrast to DOAS and FTIR, spectroscopy based on tunable diode lasers achieves spectral selectivity through a narrowband light source rather than a dispersive or interferometric detector. This technique is most applicable in the mid- and near-infrared, where narrowband lasers can resolve individual rovibrational features of small, atmospherically relevant molecules. The history of this method is similar to those of the methods described above in that the first applications of this technology occurred in the 1970s and 1980s [16.15] and followed from the development of the laser sources themselves. As with DOAS and FTIR,

the method requires either a long, open atmospheric path or a multipass cell (more typically the latter for TDLS). Whereas White cell optics (invented by *John U. White* in 1942 [16.16]) are most commonly employed with the broadband source used in FTIR, Herriott cells (as demonstrated by *Donald R. Herriott* (1928–2007) in 1964 [16.17]) are appropriate for use with coherent light sources. The development of TDLS methods for atmospheric sensing has been facilitated by the development of these measurement cells [16.18].

16.2.4 Cavity-Enhanced Spectroscopy (CES)

The application of optical cavities to enhance the path lengths of optical detectors is a more recent development than the methods outlined above, although CES does share many attributes with those methods, depending on the specific implementation. In 1988, *O'Keefe and Deacon* [16.19] demonstrated an optical path equivalent to 2–13 km by measuring the decay of light from a pulsed laser light source based on an optical cavity constructed from a pair of visible, high-reflectivity mirrors. A year later, they applied this technique—known as cavity ring-down spectroscopy (CRDS)—to the NO₂ absorption spectrum in laboratory air [16.20]. In 1997, *Romanini et al.* [16.21] demonstrated the use of continuous-wave, narrow-band lasers in CRDS, a breakthrough that has since resulted in the utilization of CRDS and other CES methods in numerous applications, including greenhouse gas measurements. Among the first applications of CRDS (and other CES methods) in atmospheric sampling was the measurement of the nitrate radical NO₃, which has strong visible absorption bands that make it amenable to optical detection [16.22, 23]. It has also rapidly developed into a standard technique for measuring greenhouse gases using inexpensive near-infrared diode lasers [16.24, 25].

16.2.5 Laser-Induced Fluorescence (LIF) Spectroscopy

The hydroxyl radical OH, which is the primary atmospheric oxidant [16.26], was first detected by *James Anderson* in 1971 in the upper stratosphere and mesosphere using solar-induced fluorescence with a rocket-borne instrument. Anderson detected OH in the middle/lower stratosphere in 1975 using resonance fluorescence with gas discharge as a 308 nm light source. The development of LIF spectroscopy began after the invention of the laser in the 1960s [16.27], and measurements of atmospheric concentrations became more

common following the advent of the dye laser, which has a tunable wavelength [16.28]. One of the first attempts to measure tropospheric OH using LIF was undertaken by the Ford Motor Company [16.29]. Unfortunately, subsequent studies demonstrated that the observed signal mainly came from OH generated by the laser pulse itself, rather than from naturally occurring OH. A change of methodology in the 1980s led to the successful measurement of OH in the troposphere. Several other molecules, for example NO₂ and formaldehyde (HCHO), have also been detected directly via LIF at a range of wavelengths [16.30, 31]. Although a number of species have been detected by LIF following their conversion to another species either chemically (e.g., HO₂ → OH via the addition of nitric oxide, NO) or following photolysis (e.g., HONO $\xrightarrow{h\nu}$ OH), LIF is not used as widely as absorption methods to determine atmospheric compositions.

16.2.6 Chemiluminescence Methods

When an excited molecule is produced in an exothermic chemical reaction, it may subsequently spontaneously relax back to its ground state, emitting light in the process. The light emitted from the (usually electronically) excited molecule during this relaxation process is known as chemiluminescence. Detection methods based on chemiluminescence are popular and have been applied to a wide range of molecules, and a large number of commercial instruments that utilize chemiluminescence are in use worldwide. Some of the first atmospheric measurements performed via this method were those of ozone in the 1950s and 1960s; these involved reacting the ozone with a dye molecule [16.32, 33]. Owing to the lightweight nature of instruments that use this technique, chemiluminescence detection has been widely used on airborne platforms. NO is very commonly measured through its chemiluminescent reaction with ozone [16.34], as is NO₂ following its conversion to NO via photolysis or a catalyzed chemical reaction, and instruments that use this method are employed in air quality networks. Total reactive nitrogen (NO_y), which encompasses a number of species such as alkyl nitrates and nitric acid, has also been quantified. Measurement of NO_y is achieved through conversion to NO (usually by heating in the presence of a catalyst) followed by chemiluminescence [16.35], or specific NO_y species can be detected by heating the sample to a controlled temperature and measuring the NO₂ formed after pyrolysis using LIF [16.31].

16.3 Theory

We now outline some of the fundamental concepts and ideas that underpin the analytical techniques described in this chapter, such as the absorption and emission of light and the sensitivity (and therefore the limit of detection) of an instrument.

16.3.1 Optical Methods: Absorption Spectroscopy

Common to all optical absorption spectroscopy methods, regardless of the wavelength region considered or the specific technique used, is the application of the Bouguer–Lambert–Beer’s law. This law relates the change in intensity of a light source over a fixed path length l to the concentration N of an absorbing trace gas and its wavelength-dependent (or frequency-dependent) absorption cross-section $\sigma(\lambda, P, T)$ via

$$I(\lambda) = I_0(\lambda) \exp[-N\sigma(\lambda, P, T)l]$$

$$N = \frac{1}{\sigma(\lambda, P, T)l} \ln \frac{I_0(\lambda)}{I(\lambda)}. \quad (16.3)$$

This expression assumes a uniform gas concentration over the absorption path. If this is not the case, the argument of the exponent must be replaced by an integral over l rather than a product. The expression also assumes that all optical extinction occurs through absorption, which is generally not the case (see later). $I(\lambda)$ and $I_0(\lambda)$ are the intensities at the detector and incident on the sample, respectively, although the latter is often measured in practice as the intensity at the detector in the absence of absorbing trace gases or at a wavelength that is off-resonance with the target absorber. Depending on the type of transition (i.e., electronic, vibrational, or rotational), the absorption cross-section may be dependent on both temperature and pressure, as indicated by the equation. The absorber concentration N is normally given in units of number density (atoms or molecules cm^{-3}), meaning that the argument of the exponential function is unitless (σ is in $\text{cm}^2 \text{ molecule}^{-1}$ and l is in cm). This argument,

$$A(\lambda) = N\sigma(\lambda, P, T)l, \quad (16.4)$$

is referred to as the absorbance.

Absorbance is more commonly defined in terms of base 10 logarithms in the chemical literature, where it is also referred to as the optical density. In atmospheric science, the natural logarithm of the absorbance is considered. With the exception of radical species present at low concentrations, such as OH or Cl, atmospheric trace gas abundances are often expressed in mixing ratio units (pptv, ppbv, or ppmv). The mixing ratio $\chi =$

N/N_{tot} , where N_{tot} is the density of the air sample as a whole and N is the trace gas number density. A related quantity is the path-length-normalized absorbance, also referred to as the absorption or extinction α , which is given by

$$\alpha(\lambda) = \frac{A}{l} = N\sigma(\lambda, P, T), \quad (16.5)$$

and has units of inverse length.

For a typical range of molecular absorption cross-sections ($\sigma = 10^{-17}$ – $10^{-20} \text{ cm}^2 \text{ molecule}^{-1}$) and trace gas mixing ratios of a few tens of pptv to a few ppbv (roughly equivalent to concentrations of 10^9 – $10^{11} \text{ molecule cm}^{-3}$), α is in the range 10^{-11} – 10^{-6} cm^{-1} . Thus, A is not appreciably large unless the optical path length is on the order of 100 m (10^4 cm) or greater. In other words, schemes that increase the optical path using long, open atmospheric paths, multipass cells, or optical cavities are essential when measuring atmospheric trace gases via absorption techniques.

Although the Bouguer–Lambert–Beer’s law is universally applied in optical absorption methods, its implementation varies depending on the technique, as outlined below. Note that each method has a different convention for wavelength or frequency. DOAS often uses the wavelength λ (in nm or μm), FTIR typically uses the wavenumber $\bar{\nu}$ (in cm^{-1}), TDLS commonly uses the frequency ν (in Hz), and CES may use any of these depending on the application. These units are easily interconverted via $\lambda = 1/\bar{\nu} = c/\nu$, where c is the speed of light.

Differential Optical Absorption Spectroscopy (DOAS)

As noted earlier in this chapter, DOAS is an ultraviolet (0.2–0.4 μm) and visible (0.4–0.7 μm) method that is used over long, open atmospheric paths, either in a remote sensing configuration or over a fixed path between an artificial light source and a spectrometer/detector. The application of the latter configuration—referred to as long-path DOAS (LP-DOAS)—for in-situ measurements is described in this section. The first and most obvious modification of the Bouguer–Lambert–Beer’s Law is that the change in intensity from light source to detector over a long open atmospheric path is non-negligibly influenced by Rayleigh (gas-phase) and Mie (particle-phase) scattering, as well as by aerosol absorption. Secondly, the method probes absorption from multiple species simultaneously, such that a sum over the absorbing species must also be included. Expressing (16.3) in terms of extinction and including these terms

yields

$$I(\lambda) = I_0(\lambda) \exp \left[- \left(\sum_i \sigma_i(\lambda, P, T) N_i + \alpha^{\text{Ray}}(\lambda) + \alpha^{\text{Mie}}(\lambda) \right) l \right]. \quad (16.6)$$

Here, $\sigma_i(\lambda, P, T)$ is the absorption cross-section due to trace gas i , while $\alpha^{\text{Ray}}(\lambda)$ and $\alpha^{\text{Mie}}(\lambda)$ are the Rayleigh scattering extinction in air and the Mie scattering extinction by particles, respectively. Rayleigh scattering cross-sections are proportional to the fourth power of the wavelength and thus increase rapidly toward the ultraviolet. For example, the Rayleigh scattering cross-section for dry air at 300 nm (σ^{Ray}) is $5.3 \times 10^{-26} \text{ cm}^2 \text{ molecule}^{-1}$, leading to a 13% attenuation for every 1 km of path length at sea level and 25 °C. Mie scattering by atmospheric aerosols is variable—it depends on the number, size distribution, and composition of the particles involved, but visible optical extinction can easily reach $\alpha^{\text{Mie}} \geq 10^{-6} \text{ cm}^{-1}$ in polluted urban areas.

As it is not possible to record the light intensity in the absence of trace gas absorption or scattering processes in an open path ($I_0(\lambda)$), DOAS separates the trace gas absorption cross-sections into structured (differential) and smoothly varying terms, i.e., $\sigma(\lambda) = \sigma^{\text{diff}}(\lambda) + \sigma^{\text{s}}(\lambda)$, and groups $\sigma^{\text{s}}(\lambda)$ together with Rayleigh and Mie scattering, which also vary smoothly. This separation results in a simplified description of the spectrum,

$$I(\lambda) = I'_0(\lambda) \exp \left[- \left(\sum_i \sigma_i^{\text{diff}}(\lambda, P, T) N_i \right) l \right] \quad (16.7)$$

$$I'_0(\lambda) = I_0(\lambda) \exp \left[- \left(\sum_i \sigma_i^{\text{s}}(\lambda, P, T) N_i + \alpha^{\text{Ray}}(\lambda) + \alpha^{\text{Mie}}(\lambda) \right) l \right]. \quad (16.8)$$

The term $I'_0(\lambda)$ can then be obtained from a smooth fit across the entire spectrum, while the differential structure can be fitted using known differential cross-sections for the target trace gases.

Fourier-Transform Infrared Spectroscopy (FTIR)

Fourier-transform spectroscopy is a common technique for performing broadband mid-infrared (mid-IR, 2.5–25 μm) measurements. Rather than using a dispersive element such as a diffraction grating to achieve

spectral resolution, FTIR records an interferogram by splitting the light from a broadband source and sending it along two paths, one to a fixed and the other to a movable mirror. The two beams are recombined on the same beam splitter and directed through a multipass sample cell to a detector. A scan of the movable mirror leads to sinusoidal variation in the detected light intensity due to alternating constructive and destructive interference of the two beams. The Fourier transform of this interferogram $I(\delta)$, where δ is the mirror displacement (or retardation, in cm), gives the spectrum $B(\bar{\nu})$ as a function of the frequency $\bar{\nu}$ in wavenumbers (cm^{-1}),

$$B(\bar{\nu}) = 2 \int_0^d I(\delta) \cos(2\pi\bar{\nu}\delta) d\delta. \quad (16.9)$$

The limit of spectral resolution (in wavenumbers) is given by $1/d$, where d is the maximum travel in the mirror.

A major advantage of FTIR is the ability to measure wide spectral regions and thus multiple trace gases simultaneously. FTIR instruments achieve this multiplexing at the expense of sensitivity, making the technique generally less applicable to the measurement of low-concentration trace gases. Depending on the spectral resolution and the species detected, analysis of FTIR spectra requires an understanding of spectral line shapes, as described in more detail in the next section.

Tunable Diode Laser Spectroscopy (TDLS)

Tunable diode lasers are typically used in the near-infrared (near-IR, 0.7–2.5 μm) and mid-IR to interrogate individual rovibrational features of small, atmospherically relevant molecules. The linewidths of these light sources are typically narrow compared to the target absorption lines, but their tuning ranges are limited to a single or at most a small number of absorption lines for the target analyte. The absorption cross-section in the Bouguer–Lambert–Beer expression (16.3) is then replaced with the line strength $S(\nu, P, T)$, which is in turn the product of an integrated line strength and a lineshape function. At low pressure, mid- and near-IR absorption lines are Doppler broadened due to the Maxwell–Boltzmann distribution of molecular speeds,

$$\Gamma_{\text{D}} = \sqrt{\frac{4 \ln 2}{\pi}} \frac{1}{\Delta\nu_{\text{D}}} \exp \left[-4 \ln 2 \left(\frac{\nu - \nu_0}{\Delta\nu_{\text{D}}} \right)^2 \right]. \quad (16.10)$$

In this Doppler lineshape function, ν and ν_0 are the frequency and the center of the line, while $\Delta\nu_{\text{D}}$ is the full width at half maximum, which is dependent on the

temperature and molecular mass. At higher pressures of a few hundred millibar or greater, pressure broadening dominates and gives the Lorentzian lineshape

$$\Gamma_L = \frac{1}{2\pi} \left[\frac{\Delta\nu_L}{(v - v_0)^2 + (\Delta\nu_L/2)^2} \right]. \quad (16.11)$$

In practice, the actual lineshape is a convolution of these two functions, referred to as a Voigt lineshape. The optimal sampling pressure is intermediate between the regime where Doppler and pressure broadening dominate, and is determined by the competition between linewidth sharpening and the decrease in analyte number density as the pressure is lowered. This regime is typically in the 50–100 mbar range.

Lineshapes are incorporated into the Bouguer–Lambert–Beer’s law to give a wavelength- or frequency-dependent absorption cross-section using the spectral line intensity, which is integrated over a given molecular rovibrational intensity at a given temperature. Spectral line intensities are available from databases such as HITRAN (high-resolution transmission molecular absorption database) [16.36].

Cavity-Enhanced Spectroscopy (CES)

If the multipass cell that is used to increase the path length and sensitivity for absorption spectroscopy is an optical cavity, the Bouguer–Lambert–Beer’s law still applies, but in a different form due to the lack of a single optical path length within the cavity. There are two methods of extracting an analyte concentration or mixing ratio from a CES signal. The first and most common is to perform time-domain measurements, which involves extinguishing the light source for the optical cavity and then measuring the characteristic time constant τ for single-exponential decay of the light intensity via

$$I(t) = I_0 \exp\left(-\frac{t}{\tau}\right). \quad (16.12)$$

This approach is known as cavity ring-down spectroscopy (CRDS). In the simple case of a two-mirror optical cavity, the time constant is related to the base path of the optical cavity (i.e., the mirror separation L), the speed of light c , and the mirror reflectivity R . Because the optical path lengths can be very long (in some cases in excess of 10 or even 100 km), the time constant is also limited by the Rayleigh scattering in the air at the sample pressure, as well as by Mie scattering by aerosols if an inlet filter is not used, i.e.,

$$\tau(\lambda) = \left[c \left(\frac{1-R}{L} + \alpha^{\text{Ray}}(\lambda) + \alpha^{\text{Mie}}(\lambda) + \sum_i \sigma_i(\lambda, P, T) N_i \right) \right]^{-1}. \quad (16.13)$$

Measurement of the time constants in the presence and absence of an absorber (τ and τ_0 , respectively) yields the absorber number density via

$$N = \frac{1}{c\sigma(\lambda, P, T)} \left(\frac{1}{\tau} - \frac{1}{\tau_0} \right). \quad (16.14)$$

A related time-domain technique, cavity-attenuated phase-shift spectroscopy (CAPS), measures the change in phase between a sinusoidal or square-wave modulated light source at the input and output of an optical cavity [16.37].

Intensity-domain measurements in which the optical cavity is continuously illuminated and the change in output intensity is measured as a function of wavelength or absorber number density are also common. These are referred to as integrated cavity output spectroscopy (ICOS), or simply cavity-enhanced spectroscopy (CES) [16.38], although the latter also refers to all methods that use an optical cavity for path-length enhancements in spectroscopy. In this case, the absorber number density (or densities) is related to the measured intensities at the detector in the presence and absence of the absorbing trace gas(es) via

$$N = \frac{1}{\sigma(\lambda, P, T)} \left[\frac{1-R}{L} + \alpha^{\text{Ray}}(\lambda) \right] \left[\frac{I_0(\lambda)}{I(\lambda)} - 1 \right]. \quad (16.15)$$

In the time domain (CRDS), the relationship in (16.14) is absolute so long as the absorption cross-section is known. In the intensity domain, measurements of I_0 and I are not sufficient to obtain an absolute measurement; the mirror reflectivity (or effective path length in the optical cavity) must also be known. This can be calibrated in laser-based experiments by measuring the ring-down time constant and determining $(1-R)$ from (16.13), or by measuring a known extinction in the case of a light source or detector combination that does not allow for time-resolved measurements. The difference in Rayleigh scattering between two pure gases (e.g., N_2 and He) with strongly contrasting Rayleigh cross-sections has been used for this purpose [16.39].

Cavity-enhanced methods are applicable to all of the wavelength ranges referenced above for the other techniques, from the ultraviolet to the mid-infrared. In the ultraviolet and visible, both CRDS and CES have been used with laser-based and broadband light sources, respectively. In the near- and mid-IR, both approaches have been used for small-molecule spectroscopy in much the same way as TDLS techniques employing multipass cells have. There are only a limited number of examples of the use of CES combined with FTIR.

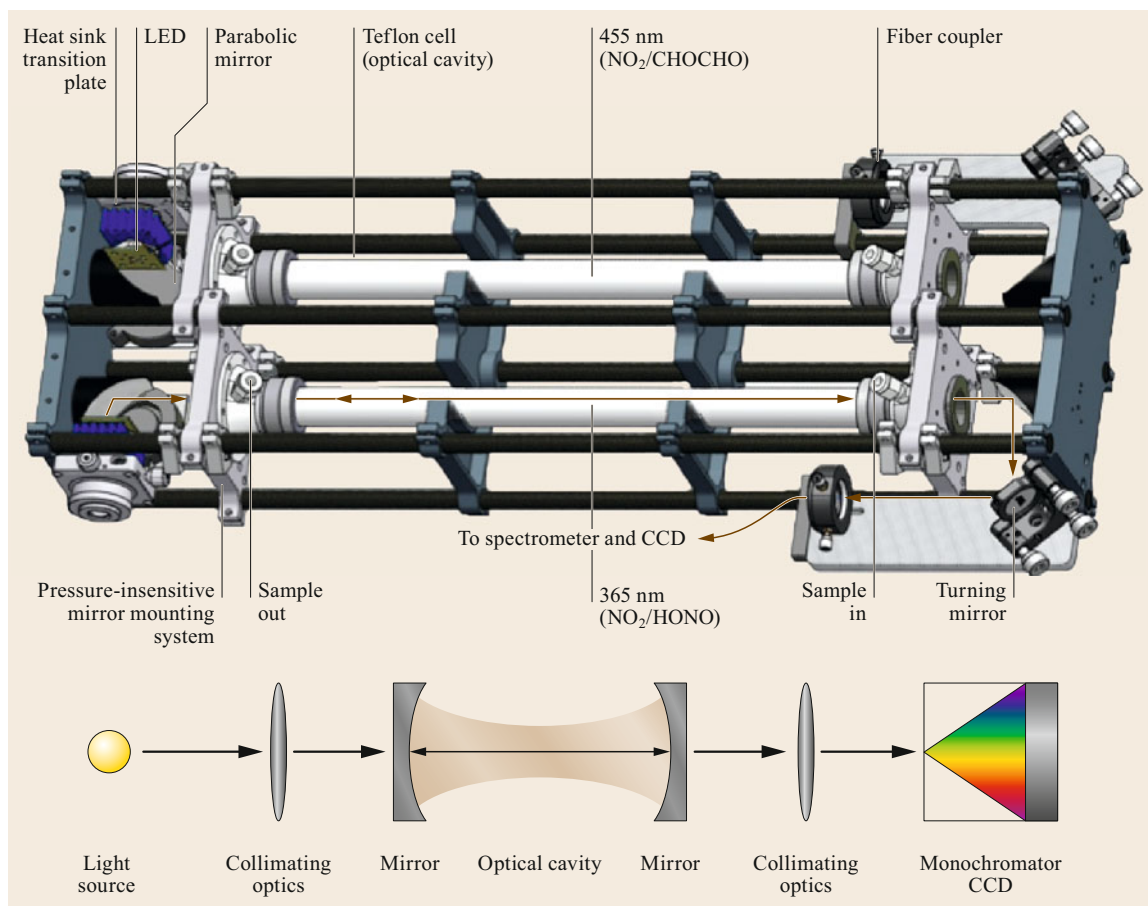


Fig. 16.1 Schematic of a two-channel broadband cavity-enhanced spectrometer (BBCES) that uses LED light sources in the blue (455 nm) and near-UV (365 nm) to measure nitrogen dioxide (NO_2), glyoxal (CHOCHO), and nitrous acid (HONO) (after [16.40] © K.-E. Min et al., licensed under CC-BY)

This combination is not currently in common use in atmospheric sensing.

One other key aspect of the use of CES methods is the coupling between the light source and the optical cavity. Optical cavities are also referred to as optical resonators because they transmit light at discrete wavelengths or frequencies corresponding to the constructive interference that occurs when the cavity length is equal to an integral number of wavelengths. In the case of narrowband laser absorption spectroscopy in the mid- and near-IR, a frequency match between the laser and the optical cavity is required. This can be achieved by a variety of methods that tune the laser frequency and/or the cavity length into resonance with each other. In the visible and UV, it is common to use light sources with a bandwidth exceeding that of the cavity-free spectral range, thus ensuring the coupling of the light source to multiple cavity modes. These light sources may include pulsed lasers or visible diode lasers, or broadband light sources

such as LEDs and Xe arc lamps with emission spectra that span several tens to hundreds of nm. Figure 16.1 shows an example of a broadband cavity-enhanced spectrometer that uses LEDs as the light source.

16.3.2 Optical Methods: Emission Spectroscopy

This section focuses on fluorescence methods, describing the general principles of excitation and fluorescence collection schemes employed in atmospheric instruments. Apparatus design, the sensitivity and selectivity of each technique, and how the sensitivity can be maximized are discussed. Calibration methodology will be covered in Sect. 16.6.1, and examples of fluorescence spectroscopy devices are given in Sect. 16.4.2. All fluorescence instruments rely on an optical cell in which the sampled air, excitation light, and fluorescence detection intersect.

Laser-Induced Fluorescence (LIF) and Fluorescence Assay by Gas Expansion (FAGE)

The most commonly used excitation light source is a laser, although continuous lamps have found success in a number of applications, such as the detection of carbon monoxide [16.41]. Lasers, however, offer advantages in that they can be pulsed, allowing the fluorescence signal to be collected after the laser has been fired. This can greatly reduce the background signal from laser scatter, significantly increasing the signal to noise and the sensitivity of the instrument. The use of low pressures (1–5 Torr in OH and NO₂ cells) can help to extend the lifetime of the fluorescence beyond the duration of the laser pulse by reducing the number of collisions of the excited-state species with bulk gases (typically N₂ and O₂), as such collisions reduce the fluorescence signal through quenching. The fluorescence assay by gas expansion (FAGE) technique [16.42] refers to laser-induced fluorescence (LIF) conducted at low pressure. There is often an optimum pressure for FAGE instruments that balances the number density of the species of interest and the rate of quenching and thus leads to the maximum sensitivity [16.43].

A number of lasers (e.g., dye lasers, fiber lasers, and titanium sapphire lasers) have narrow spectral

linewidths. This property increases the selectivity of the apparatus by reducing the overlap with the excitation windows of other species. These lasers can be spectrally tuned away from an electronic transition, allowing the instrumental background signal to be determined, and making it possible to confirm the identity of the fluorescing species. Background signals originate from laser scatter, solar scatter that enters the cell through the inlet, and detector dark counts.

A single pass of the laser across the detection axis of the fluorescence cell may be performed, or multiple passes of the laser can be achieved using highly reflective mirrors. As the rate of excitation, and therefore the fluorescence signal, increases linearly with photon flux (provided the excited electronic state does not become saturated), multipass arrangements can improve the overall instrument sensitivity. However, the background laser scatter signal emanating from mirror surfaces increases with the number of passes, so the overall limit of detection of the device may be similar for both laser configurations. Also, multipass cells are more difficult to align than a single-pass setup and may increase laser-induced interference. A schematic of a multipass FAGE instrument is shown in Fig. 16.2 [16.43].

The detection of fluorescence may be on-resonance (i.e., excitation and fluorescence occur at the same wavelength) or off-resonance (the fluorescence is

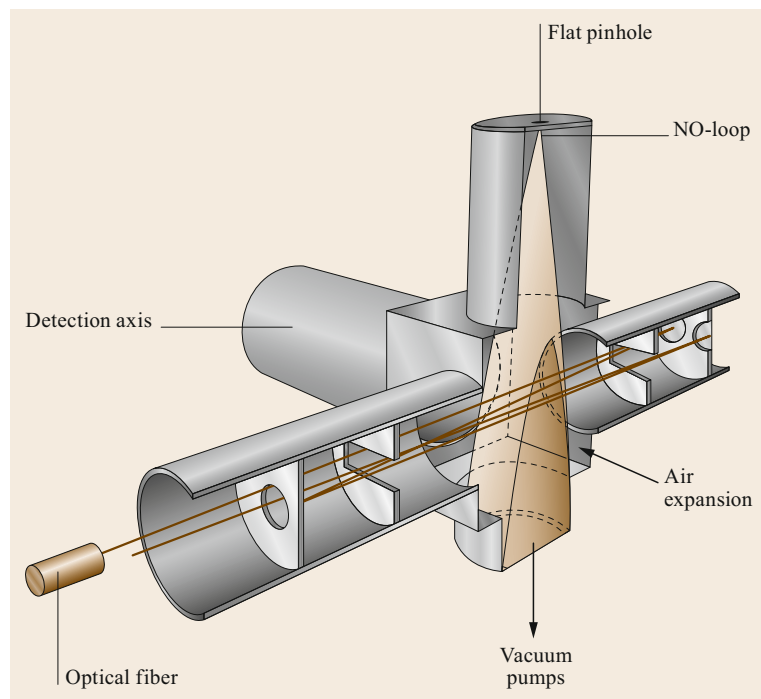


Fig. 16.2 Cross-section of the FAGE instrument at Indiana University (after [16.43] © S. Dusanter et al., licensed under CC-BY)

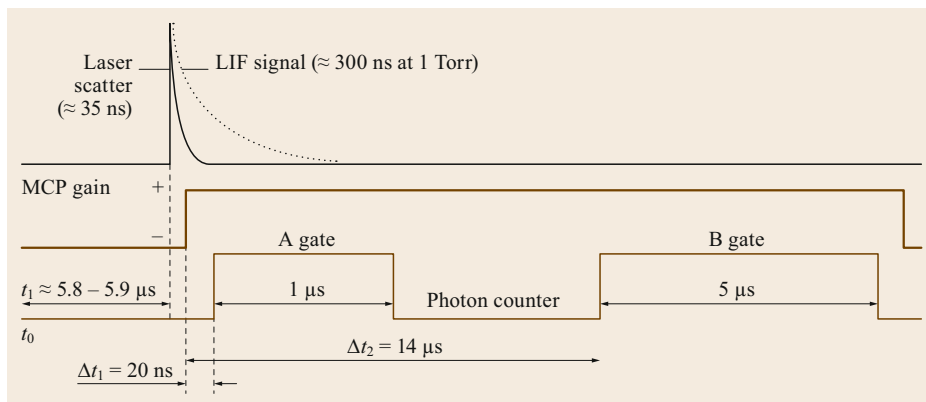


Fig. 16.3 Diagram of the University of Leeds FAGE instrument timings that are used to detect OH fluorescence following laser excitation (*top*). The microchannel plate (MCP) detector gain (*middle*) and photon-counting windows (*bottom*) relative to time zero (t_0) are presented for one 200 μs cycle. The second counter gate, labeled the *B gate*, is used to measure the sum of the photon counts from solar scattered light and detector thermal noise for subtraction from the first counter gate (after [16.44])

shifted with respect to the excitation wavelength). For off-resonance fluorescence, the light that reaches the detector can be optically filtered to distinguish the fluorescence from the laser scatter signal. Bandpass filters (long and short pass) are used. Bandpass filters offer high transmission at the desired wavelengths but considerable attenuation (on the order of 10^{-7}) at other wavelengths, which is sufficient to eliminate Rayleigh scattering and scattering from the cell walls. For on-resonance fluorescence applications, optical filtering to distinguish the fluorescence signal from the laser scatter is not possible. Instead, the detector must be temporally gated to observe the much weaker fluorescence signal once the intense laser scatter pulse has ended; this is the approach adopted for tropospheric OH detection utilizing LIF at 308 nm. On-resonance fluorescence measurements often still employ optical filters to minimize scattered light from other sources (e.g., solar scattered radiation or redshifted laser scattering from the chamber walls).

The gating of the detector from a low-gain state whilst the laser fires to high gain must be rapid in order to maximize the fluorescence detected and thus the instrument sensitivity. Figure 16.3 illustrates the timings used for OH detection with the University of Leeds FAGE instrument [16.44, 45].

LIF techniques include those that detect atoms and molecules directly by electronically exciting the species of interest and then detecting the subsequent fluorescence upon relaxation; examples of such species include OH, HCHO, NO, and NO₂. However, it is also possible to use LIF to detect molecules that do not fluoresce

following excitation by converting those molecules (selectively) into other molecules that do fluoresce. HO₂, for example, is detected using FAGE after it has been chemically converted to OH by reacting it with nitric oxide. Besides chemical conversion, thermal decomposition and photofragmentation techniques are also employed for the indirect detection of molecules using LIF.

16.3.3 Chemical Conversion Methods

In this section, we discuss techniques that permit the detection of atmospheric molecules through chemical conversion. We focus on the use of chemiluminescence, a process that involves the production of light following a chemical reaction. Chemiluminescence is the fundamental process that underpins the methodologies employed for the detection of a variety of atmospherically relevant species. Chemiluminescence can involve heterogeneous reactions between a target gas and a liquid or solid surface, or it can be homogeneous in nature, involving the production of light following a reaction between two gas-phase species. We also cover the process of liquid derivatization, which is used to facilitate the detection of a number of soluble gases by scrubbing the gases into a liquid solution and converting them to another species for detection by either liquid-based techniques such as liquid chromatography, chemiluminescence, or fluorescence detection. Due to the conversion step involved in these types of techniques, we will focus our attention on the sensitivity and selectivity of the chemical conversion methods discussed.

16.4 Devices and Systems

In this section, for each of the major classes of instruments that are used to measure gas-phase compositions, we describe practical aspects of the devices and how they are used in the field to make quantitative measurements. At the end of the section there is a comparison of the devices.

16.4.1 Absorption Spectroscopy Devices

We now introduce a number of examples of the more common applications of absorption spectroscopy devices for atmospheric measurements. The devices include single and multipass instruments and those that exploit optical cavities.

Differential Optical Absorption Spectroscopy (DOAS)

Long-path differential optical absorption spectroscopy (LP-DOAS) was described earlier in this chapter as a method that utilizes ultraviolet/visible absorption over long (typically kilometer-scale) absorption paths. Historically, the method used high-pressure Xe arc lamps as bright broadband light sources that emit across the UV and visible, albeit with some structure due to the presence of atomic emission lines in the source. More recently, light-emitting diodes (LEDs) have been utilized in LP-DOAS as spectrally bright light sources with emission spectra that cover a few tens of nanometers, enough to encompass the absorption bands of specific molecules. These light sources are small, inexpensive, long-lived, and consume barely any power; however, as previously noted, they only emit in specific wavelength regions. The light from the source is collimated by a spherical or parabolic mirror, sent to a retroreflector, and returned to a receiver. This receiver consists of a telescope, grating spectrometer, and detector—most commonly a charge-coupled device (CCD) camera. Situating the light source and receiver at the same location facilitates the recording of reference spectra from the light source. DOAS instruments may also be multiplexed by employing the same light source and receiver combination along multiple light paths and placing retroreflectors at appropriate locations. This arrangement has proven to be very useful for measuring the vertical profiles of trace gases in urban areas, especially for species such as HONO and NO₃ that exhibit characteristic gradients [16.46].

Fourier-Transform Infrared Spectroscopy (FTIR)

As noted above, FTIR spectrometers have the advantage that they can be used to measure multiple small

molecules via broadband measurements throughout the fingerprint region of the mid-IR, where nearly every molecular species (aside from homonuclear diatomics) has strong absorption lines from their fundamental vibrational transitions. Conversely, FTIR suffers from lower sensitivity than laser-based mid- and near-IR absorption spectroscopy. A multipass cell is required for measurements of atmospheric trace gases, and the most common configuration for FTIR instruments involves the use of the White cell [16.16]. White cell optics are appropriate for use with the broadband black-body emission sources used in FTIR instruments. This three-mirror design has the entrance (source) and exit (detector) holes at one end, with a mirror between them, and another two mirrors at the opposite end. Thus, the beam performs four passes through the cell from the source to the detector. This four-pass pattern can be repeated by directing the final pass back onto the second mirror instead, allowing for even more passes and path lengths of up to 100 m.

The strengths of FTIR are well matched to the sampling of biomass burning plumes (forest fires, agricultural fires), which exhibit a large number of trace gases at relatively high concentrations. *Yokelson et al.* have developed an airborne FTIR (AFTIR) system for this application [16.12–14]. The system uses a 0.81 m White cell with 120 passes for a total path length of 97 m. The spectrometer has a resolution of 0.5 cm⁻¹ and a scan time of 1.7 s, although the flush time through the large volume cell is 7–8 s, so sampling is not limited by the scan time. The 1 min limit of detection for absorbance (16.2) is $A < 10^{-3}$, equivalent to a detection limit in optical extinction (16.3) of $\alpha < 10^{-7}$ cm for the ≈ 100 m path length. This is sufficient to measure trace gases with a signal to noise in mixing ratio units of 5–20 ppbv, which permits the characterization of small molecules (CO, CH₄, CH₂O, CH₃COOH, HCOOH, CH₃OH, C₂H₄, NH₃) in fire plumes.

FTIR is also suitable for high-precision, high-accuracy measurements of greenhouse gases, which are present at higher mixing ratios (tenths to hundreds of ppmv) than other trace gases. *Griffith et al.* [16.47] describe a state-of-the-art FTIR instrument for this application that uses a 24 m White cell and a spectrometer with a resolution of 1 cm⁻¹. The 1 min precision (80 scans at 0.75 s each) in absorbance is $A \approx 2 \times 10^{-5}$, or $\alpha \approx 10^{-8}$ cm⁻¹ for a path length of 24 m. The 1 min precisions for CO₂, CH₄, N₂O, CO, and ¹³CO₂ are 20, 0.2, 0.1, 0.2, and 0.07 ppbv, respectively. These specifications meet or exceed standards established by the World Meteorological Organization.

Tunable Diode Laser Spectroscopy (TDLS)

Tunable diode laser spectroscopy measures small regions of the near- or mid-IR with high precision, allowing accurate and sensitive detection of small molecules with well-resolved individual rovibrational transitions. These instruments are typically not multiplexed (i.e., a single or just a few target analytes have transitions in the spectral range of the laser), but they generally yield much more precise measurements than FTIR. In the past, near-IR devices had the distinct advantage that they could make use of readily available, robust, and inexpensive laser sources developed for the telecommunications industry. However, the disadvantage of near-IR devices is that they probe relatively weak absorption lines associated with molecular overtone transitions. While mid-IR light sources that utilize lead salt diode lasers and difference frequency methods are also available [16.48], the recent development of quantum cascade lasers (QCL) and interband cascade lasers (ICL) has led to readily available inexpensive and robust mid-IR sources [16.49].

A common type of multipass cell used in TDLS applications for atmospheric science is the Herriott cell [16.17, 49, 50], which is appropriate for use with coherent light sources. This cell permits several hundred passes utilizing an alignment in which the beam enters through a hole in one mirror and is reflected between the mirrors in the cell. The beam wanders around the surfaces of the mirrors and produces a spot pattern, before eventually exiting through the entrance aperture. The number of passes can be increased through the use of astigmatic, rather than spherical, optics. A Herriott cell can provide path lengths of up to several hundred meters. With a typical precision in absorption of $A = 5 \times 10^{-6}$ for an integration time of 1 s, these instruments can achieve a precision in optical extinction of $\alpha = 5 \times 10^{-10} \text{ cm}^{-1}$, sufficient for the pptv-level detection of numerous atmospherically relevant trace gases in the mid-IR. Examples include CH_4 , N_2O , NO , NO_2 , NH_3 , HNO_3 , HONO , H_2O_2 , OCS , and isotope ratios of greenhouse gases [16.49]. For example, Richter et al. [16.51] report a precision for ethane (C_2H_6) and formaldehyde (CH_2O) of 15 and 40 pptv, respectively, at 1 Hz in airborne measurements.

Cavity-Enhanced Spectroscopy (CES)

Cavity-enhanced spectroscopy encompasses a wide variety of light sources, spectral regions, configurations of the optical cavity/measurement cell, and coupling schemes between the light source and the cavity resonances. Because the multiple passes can occur along a single optical axis, the cell volume can be much smaller in a CES instrument than in a Herriott or White cell.

Ultraviolet and visible CES instruments were originally developed with pulsed laser sources such as tunable dye lasers, but CES instruments based on visible diode lasers, light-emitting diodes (LEDs), and Xe arc lamps (among other sources) have also recently been demonstrated. The target molecules that can be probed in this region are effectively identical to those probed by DOAS and listed above. As an example, Wild et al. [16.52] have reported the measurement of NO_2 by CRDS at 405 nm using a broad-linewidth (0.5 nm) diode laser that passively couples to a 50 cm optical cavity with mirrors of reflectivity $R = 99.995\%$, giving a time constant $\tau_0 = 30 \mu\text{s}$ or an effective path length of 9 km. The precision in optical extinction for a 1 s integration is $\alpha = 2 \times 10^{-10} \text{ cm}^{-1}$, equivalent to a measurement precision of 15 pptv for NO_2 .

CES has found numerous applications in the near-IR due to the previously mentioned advantage of being able to use readily available telecommunications lasers with wavelengths of around $1.5 \mu\text{m}$. Instruments of this type have become a standard measurement technique for the major greenhouse gases CO_2 and CH_4 , which have overtones in that region. These instruments are commercially available. Crosson et al. [16.25] report a three-mirror cavity ring-down instrument with a $1.6 \mu\text{m}$ laser that gives $\tau_0 = 40 \mu\text{s}$ (an effective path length of 12 km) and a sensitivity to extinction of $\alpha = 1.6 \times 10^{-12} \text{ cm}^{-1}$ in 1 s. Application to CO_2 and CH_4 yields measurement precisions of 200 ppbv and 1 ppbv, respectively. Baer et al. [16.24] report an instrument based on an off-axis alignment that is essentially identical to a Herriott cell but does not have a hole through which the laser beam enters and exits. Using ICOS as the detection method and a laser with a wavelength of around $1.5 \mu\text{m}$, they achieved a precision similar to that quoted above of $3 \times 10^{-11} \text{ cm}^{-1}$ in 1 s and similar performance for CO_2 and CH_4 .

Mid-IR CES instruments are a relatively novel development, as robust light sources in that region have only recently become available. As an example, Richard et al. [16.53] demonstrated the measurement of NO to a precision of 20 pptv in 1 s using an interband cascade laser at $5.3 \mu\text{m}$.

16.4.2 Emission (Fluorescence) Spectroscopy Devices

In this section, we provide a number of examples of the more common applications of fluorescence spectroscopy devices for atmospheric measurements. The use of LIF to detect atmospheric molecules such as OH or NO_2 directly is discussed, and the section also includes a summary of how to use these direct techniques to detect nonfluorescing molecules.

FAGE for Tropospheric OH Detection

The hydroxyl radical (OH) is the most important daytime oxidant in the troposphere. OH controls the lifetimes of climate gases such as methane, and—through reactions with volatile organic compounds (VOCs)—governs the production of secondary pollutants such as ozone, acidic gases, and secondary organic aerosols.

Off-resonance fluorescence spectroscopy (excitation at 282 nm followed by fluorescence detection at 308 nm) can be employed for OH detection under dry conditions, such as in laboratory kinetic studies [16.54] or for stratospheric observations [16.28]. In the lower troposphere, however, owing to the high water vapor content, on-resonance detection (excitation and fluorescence at 308 nm) becomes necessary to minimize interference from OH generated during the laser photolysis of ambient ozone. At 282 nm, the ozone absorption cross-section and photolysis quantum yield of O¹D are approximately 25 times greater than those at 308 nm, so high concentrations of OH radicals can be generated along the laser detection axis of the fluorescence cell in the presence of ambient H₂O [16.26].

All current LIF instruments [16.45, 55–60] for tropospheric OH detection utilize low pressures (maintained at 1–4 Torr) achieved through the use of a critical orifice (\approx 1 mm) and a large pumping capacity. 1–10 kHz tunable light at 308 nm is employed, which is generated by a dye or Ti:S laser system operating at laser powers ranging from 1 to 20 mW. The background signal arising from laser scatter, solar scatter, or detector dark counts can be determined by tuning the laser away from a OH transition (typically by a few picometers) to a wavelength region where OH does not absorb. In recent years, however, a number of groups have reported interference from cell-generated OH [16.61, 62]—potentially from the unimolecular decomposition of ozonolysis products (e.g., the stabilized Criegee intermediate, sCI). Therefore, new methods of determining the instrumental background counts that involve the addition of propane or C₃F₆ above the inlet to chemically titrate ambient OH have been developed [16.60, 61, 63–65].

FAGE for Tropospheric HO₂ and RO₂ Detection

HO₂ can be detected by chemically converting it to OH, which is achieved by injecting nitric oxide into the detection cell just below the critical orifice. Although RO₂ radicals also react with NO and can eventually convert to OH in the presence of O₂, this conversion was originally considered to be too slow at the low pressures employed in FAGE cells. In 2011, however, *Fuchs et al.* [16.66] demonstrated that β -hydroxyperoxy radicals (formed following the addition of OH to unsaturated VOCs) could rapidly convert to OH in the

presence of NO within their residence time in a FAGE cell, implying that they could act as an HO₂ interference. Minimizing the FAGE cell residence time and limiting the concentration of NO can reduce this interference to acceptable levels (< 5%) for ambient HO₂ measurements. Alternatively, these RO₂ types can be measured by running under conditions that maximize the conversion [16.67].

The sum of the RO₂ radicals can be measured using LIF by adding a flow reactor that is differentially pumped (held at \approx 30 Torr) to the FAGE cell, in a method that is known as ROxLIF. At these higher pressures in the reactor, the addition of NO efficiently converts all RO₂ species with an extractable H atom to OH. CO is added in excess of the NO to rapidly convert OH to HO₂ and thus minimize radical losses at the walls of the reactor [16.68]. The sum of RO₂ and HO₂ has also been determined using the peroxy radical amplifier (PERCA), in which RO₂ and HO₂ are converted to NO₂ by adding NO and CO [16.33]. Following a chain reaction (which can involve a chain length of several hundred), NO₂ is detected using LIF spectroscopy [16.31]. The original version of the PERCA method detected NO₂ via its chemiluminescent reaction with luminol [16.33]. More recently, a PERCA has been developed that uses ethane instead of CO as the chain initiator [16.69].

Laser-Induced Fluorescence Detection of CH₃O₂ Following Conversion to CH₃O

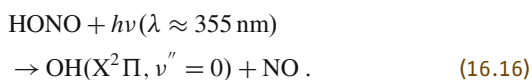
Detailed atmospheric chemistry models predict that methyl peroxy radicals are the most abundant RO₂ radicals present in the atmosphere globally [16.70]. Daytime concentrations in remote regions are predicted to reach the high 10⁸ molecule cm⁻³ level, with the reaction of OH with methane acting as the dominant source of CH₃O₂ radicals. At present, CH₃O₂ is not detected specifically in the atmosphere; it is measured as part of the sum of RO₂ radicals using, for example, ROxLIF. However, *Onel et al.* [16.70] demonstrated that it is possible to sensitively detect CH₃O₂ using LIF by first converting the CH₃O₂ to CH₃O radicals by reaction with NO. The A²A₁($\nu_3 = 3$) \leftarrow X²E($\nu_3'' = 0$) CH₃O transition can be excited at 298 nm, and the resultant redshifted off-resonance fluorescence can be detected between 320 and 430 nm. Pulsed (repetition rate: 5 kHz, pulse width: \approx 25 ns) 298 nm radiation is generated by frequency doubling the output from a YAG-pumped dye laser (the dye DCM is used). Fluorescence is detected orthogonally to the gas flow, which is introduced into the detection cell (operated at low pressure: 2.6 Torr) via a critical orifice. A broad-bandpass filter (> 80% transmission in the region 320–430 nm) can be used to discriminate the laser scatter from the

fluorescence. However, background signals originating from redshifted scattered light from the detection cell walls must be minimized by delaying the fluorescence collection by ≈ 100 ns after the laser pulse. At the pressures employed, the fluorescence lifetime of CH_3O is 0.9–1.5 μs , so delaying the fluorescence detection was found to reduce the fluorescence collected by just $\approx 10\%$. The remaining background signal arising from laser scatter, solar scatter, or detector dark counts can be determined by tuning the laser away from the CH_3O transition to a wavelength at which CH_3O does not absorb (300 nm). The limit of detection for CH_3O_2 radicals using LIF is reported to be 3.8×10^8 molecule cm^{-3} for a 5 min averaging period at 2σ . Thus, LIF looks to be a promising methodology for specifically detecting ambient levels of CH_3O_2 , especially in regions of the globe where concentrations are predicted to be high.

Photofragmentation Laser-Induced Fluorescence Detection of Nitrous Acid

Nitrous acid (HONO) is found in a wide range of environments, ranging from remote oceanic regions to megacities. It plays a central role in tropospheric chemistry, as it is a major source of the hydroxyl radical in urban areas [16.71]. In marine regions, which account for more than 70% of the Earth's surface and are remote from anthropogenic emissions, HONO is one of the few sources of NO_x , which is a key precursor to secondary aerosols [16.72].

HONO is a nonfluorescent molecule, so it cannot be directly detected using fluorescence spectroscopy. However, HONO has a near-UV absorption band involving a $\Pi^* \leftarrow n$ type transition with a progression in the ν_2 stretch [16.73] with the most intense absorption at ≈ 355 nm, and previous investigators [16.74] have obtained a near-unity primary quantum yield for the process



The OH photofragment produced following the photolysis of HONO can readily be detected with high sensitivity and selectivity using either on-resonance (laser excitation at 308 nm) or off-resonance (laser excitation at 282 nm) LIF at low pressures [16.75]. Ambient measurements of HONO using PF (photo-fragmentation) followed by off-resonance LIF detection of the OH fragment were successfully performed by both *Rodgers and Davis* [16.76] and *Liao et al.* [16.75]. In both studies, tests were conducted to assess potential interferences that may arise from species that could photolyze at 282 nm or 355 nm. *Liao et al.* [16.75] report negligible changes to background signals with the addition of

1 ppbv of H_2O_2 , HNO_3 , CH_2O , and HO_2NO_2 . Ozone, however, is readily photolyzed by the 282 nm radiation, generating $\text{O}(^1\text{D})$. This then reacts with a H_2O molecule to give two OH radicals that are excited and detected in the same laser pulse. This is the same O_3 interference that prevents off-resonance LIF being used to make ambient measurements of OH in the troposphere [16.26]. The signal due to the O_3 interference can be accounted for and subtracted from the signal arising from HONO by modulating the photolysis laser on and off. However, the elevated background from the interference increases the limit of detection of the instrument and precludes the detection of ambient OH alongside that of HONO. On-resonance PF-LIF spectroscopic techniques have recently been developed for ambient HONO detection [16.77] as well as laboratory investigations of heterogeneous HONO production from various atmospherically relevant aerosol surfaces [16.78].

A single Nd:YAG laser system was utilized in early PF-LIF HONO instruments. The third harmonic (355 nm) was used to photolyze HONO to OH with typical pulse energies of 100 mJ, whilst the second harmonic (532 nm) was used to pump a dye laser system in order to generate tunable 282 nm radiation; ≈ 0.2 mJ/pulse of the 282 nm light was used for LIF OH detection. Dichroic mirrors were used to delay the OH probe laser by ≈ 14 ns with respect to the photolysis pulse. Both beams were directed into a detection cell along the same axis (orthogonal to the detection axis) in a single-pass configuration. More modern PF-LIF designs that perform on-resonance OH detection use two laser systems for 355 nm and 308 nm wavelength generation. The application of two lasers permits the use of different repetition frequencies, allowing OH to be probed at kHz resolution (at low pulse energies to minimize probe-induced interferences), whilst HONO can be photolyzed at 1–10 Hz (at energies of ≈ 10 –100 mJ/pulse).

Laser-Induced Fluorescence Techniques to Measure NO_2

The NO_2 molecule absorbs photons in the visible region between the $^2\text{A}_1$ and $^2\text{B}_2$ series in a continuum at wavelengths longer than 398 nm (the threshold for dissociation to NO and O), and fluoresces with red-shifted radiation at > 600 nm. Various wavelengths have been used for the LIF detection of NO_2 . *Thornton et al.* [16.79] used excitation of the $\text{A}^2\text{B}-\text{X}^2\text{A}_1$ band at 585 nm, where the NO_2 absorption cross-section is $\approx 1 \times 10^{-19}$ cm^2 molecule $^{-1}$, whereas *Matsumi et al.* [16.80] used 440 nm radiation, where the absorption is a factor of ≈ 6 stronger. Both of these wavelengths are in regions of the continuum where there is enough spectral structure to allow the laser

to be tuned to a peak and trough in the absorption cross-section, thus allowing background laser-scattered signal to be measured. The 585 nm and 440 nm excitation instruments have detection limits of 6 pptv and 30 pptv, respectively. A slightly different method that uses radiation from a single non-tunable laser has been successfully employed by *Matsumoto et al.* [16.81] and *Dari-Salisburgo et al.* [16.82]. These instruments use 523.5 nm and 532 nm radiation, respectively, to excite NO_2 , with the advantage being that only a single wavelength of laser light is required. The tunable sources used in Thornton's and Matsumi's instruments are complicated multilaser systems, meaning that they are expensive and often difficult to align and operate. Also, a large proportion of the laser energy is lost in a multilaser system. For instance, the Matsumi instrument produces $\approx 100 \mu\text{J pulse}^{-1}$ at 440 nm from a pump laser energy of $\approx 170 \text{ mJ pulse}^{-1}$. The disadvantage of the single-wavelength systems is that there is no way to obtain the laser background signal spectrally, so periodic scrubbing of the ambient air to remove NO_2 must be performed.

Thermal Desorption Laser-Induced Fluorescence (TDLIF) for HNO_3 , Alkyl Nitrates, and Peroxy Acetyl Nitrate (PAN)

Upon heating, most NO_y species dissociate to yield NO_2 ($\text{XNO}_2 \rightarrow \text{NO}_2 + \text{X}$, where $\text{X} = \text{RO}_2, \text{RC(O)OO}, \text{RO}, \text{OH}, \text{HO}_2, \text{NO}_3, \text{ClO}, \text{or BrO}$). *Day et al.* [16.83] showed that, for a residence time of 30–90 ms and a pressure of 1 atm, approximate gas temperatures for complete dissociation are as follows: 200 °C for compounds of the form RO_2NO_2 (PANs), 400 °C for compounds of the form RONO_2 (including both alkyl nitrates and hydroxyalkyl nitrates), and 650 °C for HNO_3 . Measured thermal decomposition rates of various compounds within the two organic nitrate classes RO_2NO_2 and RONO_2 exhibit little dependence on the R group.

Detection of Oxygenated VOCs Using Fluorescence Spectroscopy

As well as the detection of reactive small radical intermediates, LIF can also be used to study larger atmospheric intermediates that have a suitable absorption spectrum and a significant fluorescence quantum yield. In this section, we briefly discuss the detection of carbonyl species using LIF and the closely related technique of laser-induced phosphorescence spectroscopy.

Detection of HCHO by LIF. Formaldehyde (HCHO) is one of the most abundant oxygenated VOCs present in the troposphere. It is formed during the oxidation of VOCs that are primarily emitted, and is considered a good target species as it is indicative of recent VOC oxidation activity [16.84]. HCHO is also directly

emitted into the atmosphere from traffic or due to agricultural activities for example [16.84].

HCHO can be detected by fluorescence spectroscopy by exciting the $5_{0,5} \leftarrow 5_{1,4}$ rotational transition of the $4A^1A_2 \leftarrow X^1A_1$ vibronic band at 353.370 nm and collecting the resulting off-resonance broadband fluorescence (typically in the region 390–550 nm). Pulsed frequency-doubled Ti:sapphire lasers (3 kHz; 65 mW; White cell configuration) [16.85] or tunable fiber lasers (300 kHz; a few mW; single-pass configuration) [16.86] have been utilized to excite HCHO in LIF systems.

HCHO LIF detection cells typically run at pressures ≈ 100 –150 Torr; the excited-state lifetime of HCHO is ≈ 200 ns at these pressures. *Hottle et al.* [16.85] report a 3σ limit of detection (LOD) of ≈ 50 pptv for 1 s sampling using the Ti:sapphire HCHO system. A similar LOD (36 pptv, 2σ , 1 s sampling) is achieved with the fiber laser system when it is operated with a laser power of 10 mW [16.86].

The background signal from laser scatter, solar scatter, or detector dark counts can be determined in tunable HCHO LIF instruments by dithering the laser wavelength away from an HCHO rotational transition to a nearby minimum. This background determination ensures that there is no interference from any underlying broadband absorptions.

An UV industrial laser operated at 355 nm was recently developed by the *Hanisco group* [16.87] for the detection of HCHO via LIF. Although this laser system lacks tunability and the narrow linewidth necessary to select a single HCHO absorption feature, selectivity for HCHO can still be achieved through the use of a custom multibandpass optical filter that selectively transmits at the HCHO fluorescence wavelengths between 355 and 550 nm. A typical 1σ instrument precision of 150 pptv at ≈ 0 pptv HCHO can be achieved with 1 s of data collection [16.87].

Laser-Induced Phosphorescence Detection of Glyoxal. Glyoxal, one of the most abundant dicarbonyls in the atmosphere, is produced during the oxidation of acetylene, alkenes, aromatics, and biogenic species, including isoprene [16.88]. Primary emissions of glyoxal are negligible, so measurements of this compound can be used as a marker for oxidation processes involving both anthropogenic and biogenic VOCs [16.88]. Glyoxal also plays an important role in SOA (secondary organic aerosol) formation [16.88].

Away from urban areas, concentrations of glyoxal are typically low (< 200 pptv [16.88]), so techniques for detecting this molecule ideally need to be sensitive and selective. Laser-induced phosphorescence (LIP) detection of glyoxal in the atmosphere was first developed by the *Keutsch group* [16.89]. In their approach, the $8_0^{11}A_u \leftarrow X^1A_g$ transition to the $S_1^1A_u$ state is excited

near 440 nm by a doubled Ti:sapphire laser. The system undergoes complete conversion to the $T_1^3A_u$ state, which phosphoresces for $\approx 10 \mu\text{s}$ at 100 Torr. The design of the LIP detection cell is analogous to that of the NO_2 LIF instrument devised by the *Thornton group* [16.79]; it utilizes a multipass White cell that employs either 32 or 40 passes. The laser operates at 3 kHz and 80 mW of power is generated at 440 nm. Phosphorescence is collected from the 520 nm band, which offers a strong signal and sufficient spectral separation from the excitation wavelength to enable efficient filtering of the scattered laser light. Furthermore, high quantum efficiency detectors are available in this wavelength region. No interference from NO_2 is reported, and there is no requirement to filter the sampled air for particulates or water vapor prior to sampling. Periodically, a 490 nm bandpass filter that is designed to capture N_2 Raman scatter is used instead of the 520 nm bandpass filter to assess any changes in collection efficiency. To minimize the loss of glyoxal, the PTFE or PFA tubing used as the inlet and the detection cell are heated to 35 °C. The sensitivity of the instrument at 3σ was found to be 18 pptv/min during its first deployment on the BEARPEX (biosphere effects on aerosol and photochemistry experiment) field campaign [16.89].

The LIP technique has been developed further to allow the detection of methyl glyoxal alongside glyoxal through the Laser-Induced Phosphorescence of (methyl)GLyOxal Spectrometry (LIPGLOS) technique [16.90]. LIPGLOS exploits the difference between the phosphorescent lifetimes of these two dicarbonyl species, meaning that a single light source can be used to detect both. The method achieves 3σ LODs of 11 pptv and 243 pptv for glyoxal and methyl glyoxal, respectively, for a 5 min measurement point.

16.4.3 Chemical Conversion Devices

Some atmospheric trace gases that are difficult to detect directly using optical methods can be converted using a well-characterized chemical pathway into another species that is easier to measure. There are quite a few examples of the use of chemical conversion to detect atmospheric species [16.33], and in this section we provide a description of a limited selection of these in which the final detection is based on either the absorption or emission of light.

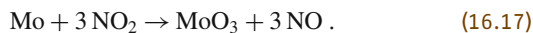
Detection of Nitric Oxide by Chemiluminescence

Reactive nitrogen species ($\text{NO} + \text{NO}_2 = \text{NO}_x$) are important in atmospheric science owing to their role in tropospheric ozone formation. NO_x is primarily emitted as NO, but quickly establishes a steady-state equilibrium with NO_2 during the daytime. By far the most common

detection technique for NO derives from the chemiluminescence reaction between O_3 and NO, which produces excited NO_2 molecules that fluoresce in the visible and IR and can be detected using red-sensitive photomultiplier tubes [16.91]. Interferences from metal carbonyls and ethylene in early NO instruments [16.92] were eliminated in later instruments by applying a red cutoff filter that blocks radiation in the wavelength region $> 648 \text{ nm}$, which is where the chemiluminescence from the interfering species predominantly occurs.

Excess O_3 is employed to maximize the sensitivity of chemiluminescence instruments used for the detection of NO, as the use of excess O_3 ensures that virtually all of the NO present in the sampled air reacts (with the O_3) in the detection region. The region in which the sampled air and ozonated air are mixed is highly reflective (it is often gold plated) to maximize the number of photons from the NO– O_3 reaction that are collected by the detector. Low pressures reduce the rate of quenching of the excited NO_2^* product, whilst slightly elevated temperatures increase the rate of the $\text{NO} + \text{O}_3$ reaction. The H_2O vapor level during ambient sampling can influence the quenching efficiency of NO_2^* and hence the sensitivity of the chemiluminescence instrument, so corrections for the water vapor level may be required in humid environments.

Alongside NO detection, commercial NO_x analyzers offer detection capabilities for NO_2 following its conversion to NO. Heated molybdenum converters are frequently used to carry out the conversion, which proceeds according to the equation



However, studies have highlighted that NO_y species such as PANs, nitrates, nitrites, and nitric acid are also converted to NO. *Winer et al.* [16.93] demonstrated that PAN was converted to NO with the same efficiency as NO_2 , whilst the conversion of nitric acid was less efficient but still significant.

That said, the tendency for NO_y species to convert to NO with similar efficiencies to NO_2 can be exploited to provide a measure of the total reactive nitrogen present. NO_y species have been shown to be efficiently ($> 90\%$) reduced by carbon monoxide on a heated gold catalyst [16.94].

Photolytic conversion of NO_2 using either a xenon lamp or UV-LEDs with an output centered on 395 nm offers a more selective way to convert NO_2 to NO for detection by chemiluminescence [16.95,96]. The conversion efficiency of NO_2 to NO using standard UV-LEDs with an output of 1 W and a sample flow of 1 L/min is up to 42%, which translates to a LOD of 2.5 pptv at 2σ (1 min average) [16.97].

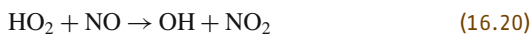
Heat must be removed from the photolytic region to prevent the thermal decomposition of NO_y species such

as PAN, which could then be detected as NO₂. Photolytic cells are typically maintained below 50 °C by coupling heat sinks to cooling fans or Peltier cooling, and short residence times (< 1 s) are employed within the photolytic cell to minimize thermal decomposition. Ryerson *et al.* [16.96] report negligible PAN conversion using a Hg arc lamp converter. Laboratory tests on certain commercially available converters, however, have demonstrated that 8–25% of the PAN can decompose and contribute to the NO₂ signal under normal operating conditions [16.97]. This artifact can be significant, particularly in remote regions where NO_y : NO₂ ratios are elevated.

The spectral output of the UV-LEDs is sufficiently narrow (FWHM = 50 nm) to minimize the photolysis of other species that can yield NO directly or indirectly via NO₂. Reed *et al.* [16.97] demonstrated that there is no overlap of the wavelengths of UV-LEDs used in commercial Air Quality Design NO_x analyzers with the absorption spectrum of PAN. A small overlap of the lamp spectrum with the absorption cross-sections of HONO and NO₃ radicals suggests that these species could interfere with the NO₂ signal to a very small extent.

The use of LEDs with outputs shifted further into the UV (centered at 385 nm, a region where HONO absorbs more strongly) opens up the possibility of actively detecting HONO by photolytic conversion to NO [16.98]. Operating a photolytic cell in a switching mode, where the UV lamps centered at the two different wavelengths (385 nm and 395 nm) are switched on and off alternately, allows HONO to be differentially detected from NO₂ provided the efficiency with which each lamp converts HONO to NO (and NO₂ to NO) can be accurately determined. Reed *et al.* [16.98] determined a difference in HONO conversion efficiency between 385 nm and 395 nm of 6.5%. The back reaction in which OH + NO reforms HONO was noted as a source of uncertainty. Nevertheless, the prototype instrument offered promise, comparing reasonably well ($R^2 = 0.58$, $y = 0.82x$) with a LOPAP (long-path absorption photometer), an established HONO detection technique, during field deployment in a marine environment.

Villena *et al.* [16.99] demonstrated that photolysis of oxygenated VOCs (OVOCs) generates peroxy radicals within NO₂ photolytic instruments. The presence of OVOCs such as glyoxal, (HCO)₂, can lead to a negative artifact from the NO₂ produced in the reaction of NO with RO₂ within the photolysis region, i.e.,



These reactions cause the NO concentration within the photolytic converter to decrease relative to the NO concentration measured in the NO channel of the instrument that does not have a photolytic converter. In extreme situations where OVOC concentrations are high (e.g., at roadside locations), this effect can lead to negative NO₂ concentrations. Interestingly, close to roadside emissions, instruments that catalytically convert NO₂ to NO with molybdenum often suffer less from interferences, as NO_y concentrations close to the source tend to be low relative to NO₂. However, as the air ages and the NO_y : NO₂ ratio increases, the performance of molybdenum converters worsens. Given these reported artifacts for NO₂ instrumentation that rely on conversion to NO for detection, it is crucial to consider the sampling environment (roadside/urban background) when selecting instruments for atmospheric monitoring.

Liquid Derivatization Techniques for the Detection of Soluble Gases

Nitrous Acid Detection. The method most commonly employed to determine the HONO concentrations in ambient air is the long-path absorption photometer (LOPAP) technique, which was developed by Heland and coworkers [16.100]. This instrument was designed to be compact, cheap, and sensitive, making it applicable for long-term air-quality monitoring projects. As shown in Fig. 16.4, it utilizes two channels, with each channel consisting of a stripping coil to extract gaseous HONO into a liquid solution. The first channel extracts most of the gas-phase HONO and a small fraction of interfering species into the stripping solution. The second channel, which is run in series with the first, extracts a similar amount of interfering species, but there is little HONO left to extract. Subtraction of the calibrated signal of the second channel from the first channel provides an interference-free HONO concentration measurement.

The stripping solution used in a LOPAP contains sulfanilamide in HCl, which readily forms a diazonium salt with HONO. Applying a large excess of the sulfanilamide reagent ensures that only a short stripping coil and contact time (≈ 30 ms) between the air sample and stripping solution are required for near-complete (> 99.4%) extraction of gaseous HONO. The addition of *N*-(1-naphthyl)ethylenediamine dihydrochloride solution to this leads to the formation of an azo dye. The detection region of a LOPAP consists of an absorption cell made from Teflon tubing. Visible light is focused into the solution via fiber optics and undergoes multiple internal reflections within the tubing before being detected by a spectrometer. The logarithm of the ratio of the absorption intensities at the azo dye absorption maximum (at 544 nm) and at a wavelength where the azo dye does not absorb ($\lambda > 700$ nm) is linear with re-

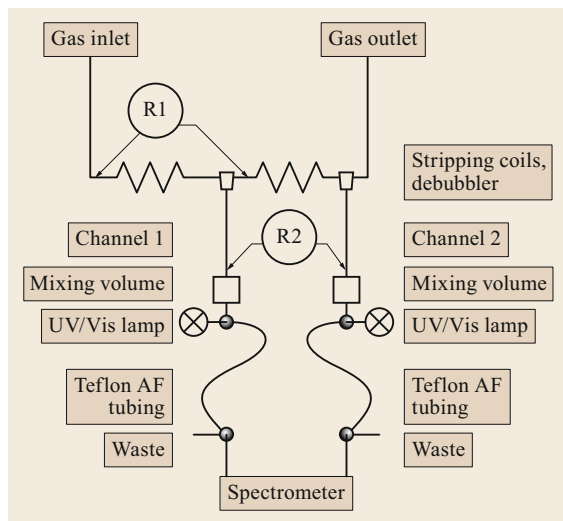


Fig. 16.4 Schematic of the setup of a LOPAP instrument (after [16.100] copyright American Chemical Society 2001)

spect to the HONO concentration present. The HONO concentration (c) can be determined (via the Bouguer–Lambert–Beer’s law (16.3)) using the equation

$$\begin{aligned} \text{Absorbance} &= \log \left(\frac{I_{\text{ref}}}{I_{\text{abs}}} \right) \\ &= \sigma \times l \times c + \log(\text{const}), \end{aligned} \quad (16.21)$$

providing the absorption path length (l) and the absorption coefficient of the azo dye at 544 nm (σ) are known.

The use of two channels in a LOPAP minimizes the occurrence of unknown interferences that are difficult to correct for and were previously observed using wet effluent denuder techniques. Furthermore, the low pH of the stripping solution (pH 0) minimizes known interferences from NO_2 and SO_2 [16.101, 102], NO_2 and phenols [16.103–105], and PAN hydrolysis [16.106], as does the short contact time within the stripping coil.

NO , NO_2 , O_3 , SO_2 , HNO_3 , PAN, a selection of hydrocarbons, HCHO, as well as mixtures of these com-

pounds have given no measurable interference during laboratory tests. However, an intercomparison between the LOPAP technique and DOAS conducted in a large outdoor smog chamber revealed that the LOPAP instrument gave measurements that were $13 \pm 5\%$ higher than DOAS on average [16.100]. Other intercomparisons conducted between DOAS and the LOPAP method under the complex conditions in the atmosphere demonstrated excellent agreement [16.107].

Recent measurements of HONO by a LOPAP at the South Pole highlighted that HO_2NO_2 , which was present at elevated concentrations owing to the low ambient temperatures, could be mistaken for HONO [16.108].

LOPAP is an extremely sensitive technique for HONO detection, with a LOD of 1–2 pptv for a 4 min sampling time [16.109]. The technique has also been extended to permit the detection of NO_2 [16.110] and HNO_3 [16.111].

Hydrogen Peroxide Detection. Hydrogen peroxide is a readily soluble gas and, as such, an important oxidant in the liquid phase. H_2O_2 plays a key role in oxidation processes that take place in cloud water, contributing significantly to secondary sulfate production in clouds and hence acid precipitation. Peroxides are formed in the gas phase in photochemical reactions and act as a temporary OH reservoir. Gas-phase photochemistry is the main source of H_2O_2 in the liquid-phase clouds [16.112]. Due to its high solubility, early attempts to detect H_2O_2 in the gas phase involved first extracting the gas into the aqueous phase by flowing an air sample and distilled water through a coil. The addition of luminol and copper ions to the solution containing H_2O_2 led to chemiluminescence at 450 nm, as detected using a blue-sensitive photomultiplier tube (PMT) [16.113]. Although no significant interferences from other gases such as NO_x , PAN, SO_2 , and O_3 are reported, the high detection limit of this technique (1 ppbv) limits its applicability to polluted regions only.

The reaction of *p*-hydroxyphenylacetic acid with peroxides [16.114] to form a fluorescent dimer that can

Table 16.4 Advantages and disadvantages of the different methods

Devices	Advantages	Disadvantages
Absorption spectrometers	Absolute measurement High specificity for molecular absorption lines Compact and lightweight construction is possible; reduced need for power and vacuum	Insensitive without substantial enhancement of the optical path length May be subject to instabilities and/or noise and drifts in the light source or from optical interference effects
Fluorescence/phosphorescence instruments	High specificity (narrow laser linewidth can excite a specific electronic transition); emission at specific wavelengths High sensitivity, allowing the detection of radical species (e.g., OH) present at very low concentrations	Nonabsolute (calibration is required to determine the ambient concentration of the fluorescing species) Expensive and highly technical instruments that require skill to operate
Chemiluminescence instruments	Compact and easy to operate Sensitive and selective	Nonabsolute (calibration required)

be excited at 320 nm, leading to fluorescence at 400 nm that is detected with a fluorimeter, offers a more sensitive means to detect H₂O₂ originating from the gas phase, with reported detection limits in the low tens of pptv. Much of the methodology outlined by *Lazrus et al.* [16.114] has been employed in all of the liquid derivatization instruments that have subsequently been used in the field to detect gaseous peroxides. An aqueous potassium acid phthalate solution is used to scrub peroxides from the gas phase. A conditioning agent containing formaldehyde and phthalate buffer is added to the scrubbing solution to prevent interference from SO₂, which can also form a fluorescent dimer. Any organic peroxides present also react with *p*-hydroxyphenylacetic acid to form fluorescent dimers. Therefore, to distinguish hydrogen peroxide from higher ROOH species, two-channel instruments are employed, with a H₂O₂-destroying catalase added to one channel to remove > 95% of the H₂O₂.

In more modern instruments, high-performance liquid chromatography (HPLC) is used to separate the peroxides in solution and thus enable speciated detection [16.115, 116]. Sampling resolutions of a few minutes and LODs as low as 5 pptv (for H₂O₂) make the airborne detection of peroxides as well as observations at remote ground locations feasible.

To quantitatively detect peroxides, the formation efficiency of the fluorescent dimer and the sensitivity of the fluorimeter must be determined through the addition of known aqueous-phase concentrations of peroxides. For gas-phase peroxide measurements, the scrubbing efficiency of the stripping coil must also be determined.

16.4.4 Comparison of the Methods

The advantages and disadvantages of the different methods are summarized in Table 16.4.

16.5 Specifications

The specifications for some key performance indicators in various measurement methods that use absorption, emission, or chemiluminescence are given in Table 16.5.

Table 16.5 Specifications for various measurement methods that use absorption, emission, or chemiluminescence

Method	Precision	Accuracy	Limit of detection	Time resolution
DOAS	Similar to LOD	Better than 10%	$\alpha = 1 \times 10^{-10} \text{ cm}^{-1}$ Single-pptv detection for UV/VIS-absorbing gases	10 min–1 h
FTIR		Better than 10%	$\alpha = 1 \times 10^{-7} \text{ cm}$ Single ppbv or tens of ppbv for multiplexed mid-IR-absorbing gases	1–10 min
TDLs		Better than 10%	$\alpha = 5 \times 10^{-10} \text{ cm}^{-1}$ Single pptv for mid-IR-absorbing trace gases Tenths to hundreds of ppbv for near-IR-absorbing trace gases and greenhouse gases	1 s
CES		Better than 10%	$\alpha = 10^{-11}–10^{-9} \text{ cm}^{-1}$, depending on the wavelength region and experimental approach Sub- or single-pptv detection is possible depending on the application	1 s
LIF:				
OH		20–40%	$2–8 \times 10^5 \text{ molecule cm}^{-3}$ (1 min)	1 s
NO ₂		Better than 10%	6–30 pptv	1 s
HCHO		25%	30–50 pptv	1 s
LIP:				
CHOCHO		Better than 10%	18 pptv (1 min)	1 s
Chemical conversion LIF:				
HO ₂		20–48%	$2–340 \times 10^5 \text{ molecule cm}^{-3}$ (1 min)	1 s
CH ₃ O ₂		15–17%	$3.8 \times 10^8 \text{ molecule cm}^{-3}$ (5 min)	1 s
PF-LIF:				
HONO		20–40%	15 pptv (1 min)	1 s
Chemiluminescence:				
NO		5%	7.2 pptv (1 s)	1 s
LOPAP:				
HONO		Better than 10%	1–2 pptv (4 min)	4 min
Liquid derivatization:				
H ₂ O ₂		Better than 10%	5 pptv (3 min)	3 min

16.6 Quality Control

In this section we consider two important aspects of quality control: calibration and intercomparison of instruments.

16.6.1 Calibration of Gas Analyzers and Laser Techniques

Standards can often be purchased for long-lived gases that are chemically stable. Flows of these gases, suitably diluted using a calibrated flow controller, are introduced at the inlet of the instrument. For some gases, the concentration of the gas standard can be traced to a national standard (see Chap. 5 on quality assurance and control).

Permeation Tubes

For other species with much lower vapor pressures, a permeation tube with a critical orifice from which a known quantity of material will effuse per second at a given temperature (often above the ambient temperature) is commonly used. The permeation device is weighed periodically to calibrate its effusion rate. An example of a molecule for which a permeation tube is used for calibration is formaldehyde, which can only be purchased in its trimeric form as a solid.

Short-Lived Species, Radicals, and Intermediates That Must Be Generated In-Situ

Unlike stable gases, short-lived radical species can neither be stored as a gas cylinder standard for calibration nor generated by a permeation tube, meaning that they must be generated in-situ. OH and HO₂ are typically generated by flowing humidified air past a mercury Pen-Ray lamp [16.55]. The 185 nm radiation from the lamp photolyzes water to OH and H (which reacts with O₂ to form HO₂) with a photolysis quantum efficiency of 1. The absorption cross-section of water at 185 nm is known, so if the photon flux F from the lamp and the time t that the air spends within the photolysis region are determined, it is then possible to calculate the generated OH (and HO₂) concentration via

$$[\text{OH}] = [\text{HO}_2] = [\text{H}_2\text{O}] \sigma_{\text{H}_2\text{O}} \phi_{\text{OH}} Ft. \quad (16.22)$$

The lamp flux can be determined using a calibrated photodiode [16.56], or the product Ft is often determined using chemical actinometry [16.55, 56, 117]. Many FAGE groups determine Ft offline using a flow of nitrous acid in either zero air or nitrogen [16.56, 117]. N₂O photolyzes at 185 nm to form NO, which can be detected using a commercial NO_x analyzer. Corrections are applied to account for the reduction in

sensitivity of the NO_x analyzer due to the presence of N₂O, which collisionally quenches a portion of the electronically excited NO₂^{*} molecules (produced in the reaction between NO and supplied O₃). Further corrections are also needed to account for the absorbance of the 185 nm radiation by N₂O. Despite these corrections, NO_x analyzers can sensitively detect just a few pptv of NO arising from the photolysis of N₂O. Applying N₂O actinometry generally permits the use of lower photon fluxes and shorter residence times in the photolysis region, which facilitates the generation of near-ambient levels of radicals (10⁷–10⁸ molecules cm⁻³). When N₂O actinometry is employed, turbulent flow reactors can be used to generate the radicals, which offers advantages over laminar flow reactors in that the flow profile and residence time of the air is better characterized. A faster flow rate also means that losses of radicals between the point of generation and FAGE sampling via radical–radical reactions or reactions with contaminants in the zero air are minimized. The disadvantage of this offline determination of Ft is that any change in the lamp output between actinometry determinations could be misconstrued as a change in the sensitivity of the FAGE instrument.

Ozone actinometry can be used to determine the lamp flux at the same time as a FAGE calibration [16.45, 55]. Oxygen present in the humidified zero air flow is photolyzed at 185 nm, yielding oxygen atoms that react with O₂ to form ozone, which can be detected using a commercial ozone analyzer. The limit of detection of ozone analyzers is ≈ 1 ppbv, which means that when ozone actinometry is employed, slower air flows are typically needed to ensure that sufficient levels of ozone are generated in the photolysis lamp region for detection. This requirement also implies that higher concentrations of radicals (often orders of magnitude higher than typical ambient levels) are generated when O₃ actinometry is used. A further complication arising from reducing the air flow and moving towards a laminar flow regime is that the air at the edges of the calibration tube spends more time passing the lamp than the air at the center. As FAGE instruments typically sample air from the center of the flowtube whereas ozone is typically sampled from the edge of the flowtube, the ratio of Ft at the center of the flowtube to Ft at the edges must be determined. In contrast to the absorption cross-section of H₂O or N₂O, the emission spectrum of the 185 nm Hg band overlaps with several features in the Schumann–Runge band of the O₂ spectrum, meaning that any change in the mercury lamp emission spectrum (e.g., as the lamp ages) can influence the absorption cross-

section. It is prudent, therefore, to determine the O_2 absorption cross-section regularly and for every lamp used [16.118].

Analogous calibration methodologies may be employed for HCHO LIF instruments, where H_2O vapor is replaced with methanol, which photolyzes at 185 nm to form HCHO [16.119].

To produce glyoxal in-situ, excess acetylene can be added to the humidified air flow in an OH calibration flow reactor. Acetylene reacts with the OH produced, generating a known yield of glyoxal [16.120]. Similarly, CH_3O_2 radicals can be generated by adding excess methane to a OH calibration flow reactor [16.70].

16.6.2 Intercomparison of Instruments

Examples of this will be given for the various techniques in relation to sampling the real atmosphere during field campaigns and sampling from within atmospheric simulation chambers. Intercomparisons between different techniques that detect the same chemical species offer a means to test instruments for interferences and assess the accuracy of the calibration method employed, thus increasing confidence in the reliability of those instruments. FAGE instruments used for OH and HO_2 detection have been compared to DOAS and chemical ionization mass spectrometry (CIMS), as well as to other FAGE instruments [16.121–123]. Given that FAGE instruments from around the globe differ significantly in terms of their optical cell designs,

a FAGE–FAGE intercomparison can yield valuable results. Atmospheric simulation chambers are often used for larger multi-instrument comparisons [16.121, 122]. Chambers ensure that instruments are sampling the same air mass and permit control over the chemical environment, thus offering advantages over ambient air intercomparisons. However, intercomparisons run in the real atmosphere offer the opportunity to compare instruments and techniques under more chemically complex conditions; e.g., in aged air masses or in environments where emissions are high and varied. Good agreement between measurements during ambient sampling can provide confidence in the technique and its applicability for use in the field. A drawback to ambient intercomparisons is that differences may arise due to the sampling of heterogeneous air masses.

HOxComp was the first formal blind intercomparison for HO_x measurements. It involved 4 LIF instruments, 1 CIMS, and 1 DOAS instrument [16.121–123]. The comparison took place in Julich, Germany in 2005 and involved 3 days of sampling ambient air and 6 days of sampling from the atmospheric simulation chamber, SAPHIR (Simulation of Atmospheric PHotochemistry in a large Reaction Chamber). All instruments were able to measure OH sensitively and at a time resolution that was sufficient for ambient measurements. However, the intercomparison did identify issues with the stability and accuracy of current calibration devices, and highlighted a potential nighttime artifact in some of the OH LIF instruments that took part [16.121].

16.7 Maintenance

The maintenance tasks for gas analyzers and laser techniques are given in Table 16.6.

Table 16.6 Maintenance of gas analyzers and laser techniques

Maximum interval	DOAS	FTIR	TDLS	CES	LIF	Chemiluminescence
Every measurement	Measure reference spectra	For some IR detectors, the liquid nitrogen typically needs filling every 8 h	Check laser power	Check zero time constant or intensity, align or clean optics as needed	Align laser/optimize power Perform visual check of laser optics Calibrate detection cell Calibrate photodiode against power meter Check cell pressures	Calibrate with known standard gas
Every field campaign	Set up and align retroreflectors	Purge the interior with dry N ₂ and replace desiccant	Align and clean optics Replace inlet lines	Align and clean optics Replace inlet lines	Replace fiber optics Clean detection cells and collection optics Replace nitric oxide cylinder and stainless steel delivery lines Change pump oil and filters Calibrate mass flow controllers used for gas delivery Replace laser chiller water and add fungicide Change dye	Replace inlet lines Calibrate mass flow controllers Replace charcoal trap Change particle filter
1–2 years		Replace the IR source as the intensity decays exponentially; may require alignment afterwards Replace internal HeNe laser if in continuous use			Change flashlamps or pump diodes for solid-state YAG lasers	

16.8 Applications

Some examples of applications are given in this section; please note that the selected examples reflect the interests and expertise of the authors to some extent.

16.8.1 Measurements of Short-Lived Radical Intermediates and Comparison with Model Calculations

One way to assess our understanding of the atmospheric chemistry that occurs in a particular environment is to compare the concentrations of short-lived RO_x radicals predicted by detailed chemistry box models to observations of radicals performed using FAGE instruments. As seen in the schematic provided in Fig. 16.5, OH, HO_2 , and RO_2 all play important roles in the oxidation of primary emissions and the production of secondary species such as ozone, NO_2 , and secondary organic aerosols.

When a model constrained by the concentrations of long-lived species such as VOCs, CO, and NO_x is able to accurately predict observed radical concentrations, it is likely that the radical sources and sinks present and the rate at which the chemical reactions occur are captured well by the model. Conversely, disagreement between a model and observed data can highlight chemical regimes or environments that are not sufficiently well understood. Under clean conditions, where NO_x and VOC concentrations are low and hence the atmospheric chemistry taking place is relatively simple, models tend to capture the observed OH concentrations well [16.125]. In chemically complex environments, however, such as in cities or forested regions (where

the emissions of anthropogenic or biogenic VOCs and, in the case of cities, NO_x are high), models are often unable to reproduce observations of radicals [16.126, 127]. Figure 16.6 highlights the tendency of a model to underestimate RO_2 radicals under high NO_x conditions and HO_2 under low NO_x conditions. The observations of radicals were performed during the 2012 ClearLo project in London, UK [16.127].

16.8.2 Measurements of Halogenated Gases in Remote Regions

The precise quantification of trace levels of halogen radicals is required to understand the global budget for O_3 . Cycling between atomic halogens and their oxides X and XO (X = Cl, Br, I) is an efficient mechanism for O_3 destruction. The magnitude of this mechanism depends on the ambient levels of halogen radicals, which are present at mixing ratios of a few pptv at most in the lower atmosphere. These species, particularly BrO and IO, can be measured by visible absorption spectroscopy. Figure 16.7 shows the diel cycles of measured BrO and IO at the Cape Verde Atmospheric Observatory in the Atlantic Ocean for 8 month periods in 2006 and 2007 [16.128]. Measurements were obtained from UV and visible DOAS at a time resolution of 30 min over a 12 km path, most of which was across a bay (i.e., over water) adjacent to the Cape Verde Atmospheric Observatory. The O_3 loss associated with these levels of halogen oxides, as predicted by a chemical transport model, was about 50% greater than the predictions of the model that was unconstrained by observations of these species.

16.8.3 Measurements of VOC Emissions From Oil and Gas Development

Emissions of methane and volatile organic compounds (VOCs) from oil and gas development strongly influence regional air quality and climate. Particularly in the US, where oil and gas production has increased significantly since 2005, there is considerable interest in quantifying these emissions [16.129]. The development of spectroscopic instruments that can measure ethane (C_2H_6) rapidly and precisely have contributed to this effort. Figure 16.8 shows C_2H_6 measurements over the Barnett Shale, an oil- and gas-producing area in the US state of Texas, in 2013 [16.130]. Measurements were carried out with a Herriott-cell-based tunable diode laser spectrometer operating at $3.3\ \mu\text{m}$. This system produced 1 Hz C_2H_6 data, making it suitable for use in

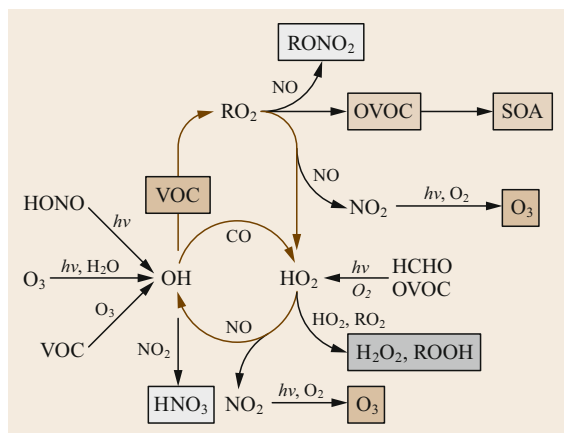
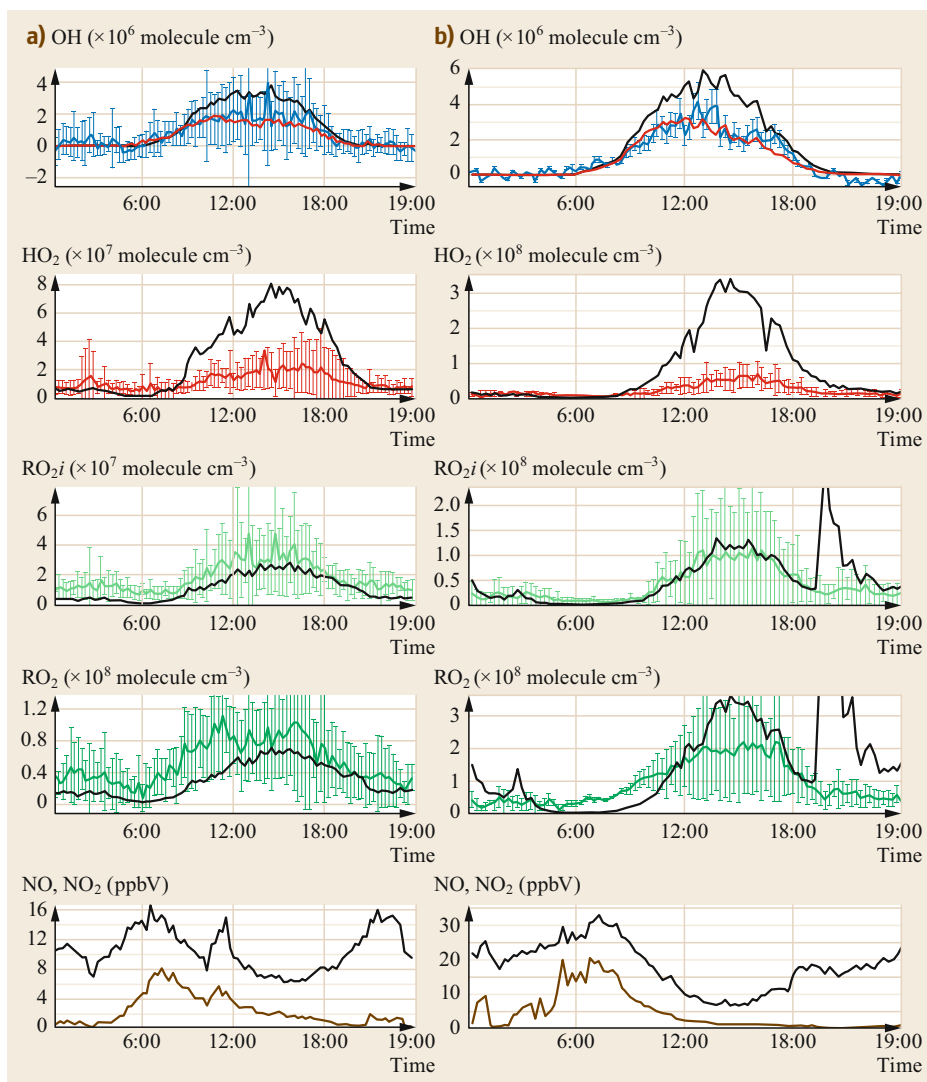


Fig. 16.5 Schematic of the major chemical pathways in the troposphere (after [16.124], Copernicus, licensed under CC-BY 4.0)

**Fig. 16.6a,b**

Average diel observed (*colored lines with error bars*) and MCM (master chemical mechanism) box model (*black line*) OH, HO₂, RO_{2i}, and RO₂ profiles during (a) south-westerly and (b) easterly flows ([OH]_{PSS} is indicated by the orange line). The error bars represent the 1σ variability in the observations. The average diel observed NO (*brown line*) and NO₂ (*green line*) are displayed in the bottom panels. The observations of radicals were performed during the 2012 ClearLo project in London (after [16.127] © L.K. Whalley et al., licensed under CC-BY)

aircraft. Enhanced levels of C₂H₆ and their correlation with CH₄ enables the precise attribution of emissions of both species from various sources, including oil and gas.

16.8.4 Long-Term Monitoring of Climate Gases and Urban Pollutants and Links to Policy

As noted above, CRDS measurements of CO₂ and CH₄ have become a new standard for greenhouse gas mea-

surements globally, augmenting previous networks that were based on lower-frequency measurements such as flask sampling. Figure 16.9 shows one example of aircraft measurements in Alaska performed over three years from 2009–2011 aboard a US Coast Guard C-130 aircraft [16.131]. Comparisons between flask samples, the previous CO₂ standard measurement, and CRDS CO₂ are shown. Results from the assessment suggest that the CRDS measurements are accurate to within 150, 1.4, and 5 ppbv for CO₂, CH₄, and CO, respectively.

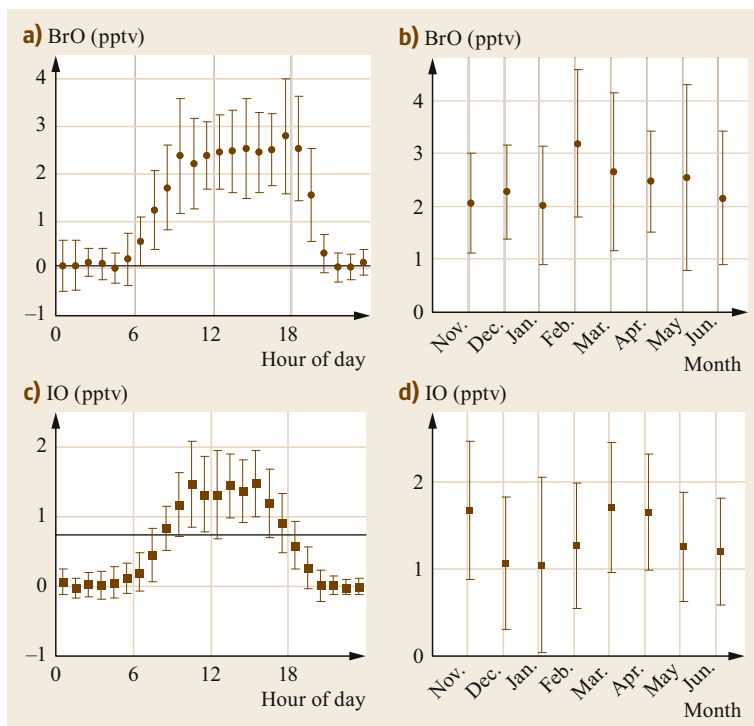


Fig. 16.7 Average diel cycles and seasonal averages of the halogen oxides BrO and IO, as measured at the Cape Verde Atmospheric Observatory in 2006–2007 (after [16.128])

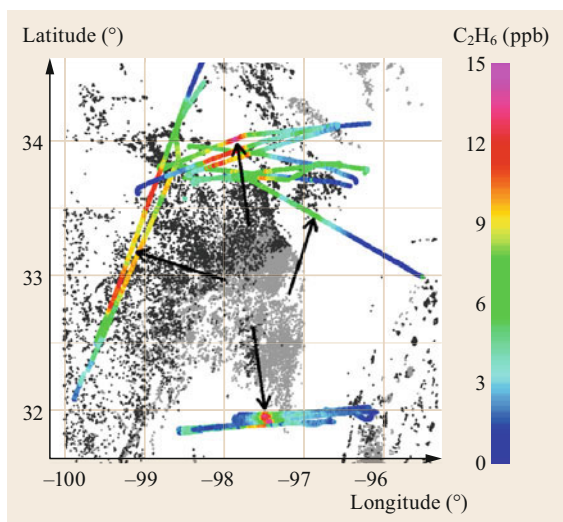


Fig. 16.8 Map of ethane measured along a research aircraft flight track over the Barnett Shale in the US state of Texas in 2013. Ethane mixing ratios along the flight track are color coded according to the key shown on the right, while the dots represent oil and gas wells (after [16.130] reprinted with permission, © American Chemical Society 2015)

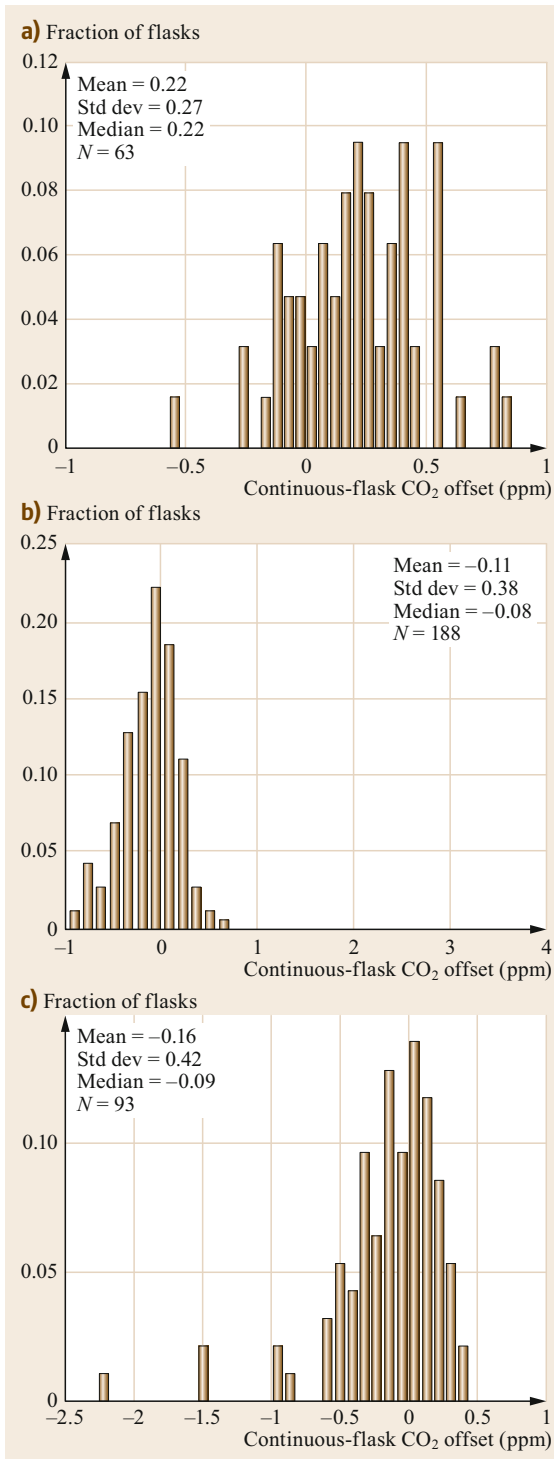


Fig. 16.9 Comparison of CO₂ measurements obtained using a CRDS instrument and flask samples for three years of aircraft sampling (2009–2011) over Alaska (after [16.131] © A. Karion et al., licensed under CC-BY)

16.9 Future Developments

Spectroscopic methods have advanced continuously over the last 50 years, from the onset of routine atmospheric measurements and monitoring in the 1970s to the highly distributed networks and detailed aircraft-based measurements that occur today. This advance is likely to continue with developments in light sources and measurement technology. In recent years, the development of robust mid-IR light sources based on quantum cascade and interband cascade lasers has had a notable impact. New broadband technologies such as optical frequency combs [16.132] may facilitate the next generation of such instruments.

The number of species detected by LIF, either directly or following their conversion to another species, is growing. Laboratory detection of CH_3O_2 by LIF following chemical titration to CH_3O has shown that this method has the sensitivity required for ambient de-

tection [16.70], offering the opportunity to detect an individual organic peroxy radical rather than a measure of the total RO_2 .

The sensitivity, time resolution, and robustness of the latest generation of NO chemiluminescence analyzers facilitates measurements in environments remote from local emissions, thus enabling long-term changes in background concentrations to be studied. In addition, the increasingly high time resolution of these analyzers will permit further flux measurements to be made for a suitable footprint, so that emissions inventories—for example of important pollutants or greenhouse gases—can be validated.

Acknowledgments. Thanks are given to Bob Yokelson (University of Montana) and Scott Herndon (Aerodyne) for helpful discussions.

16.10 Further Reading

The following is a comprehensive textbook that covers the main techniques used to monitor the gas-phase composition of the atmosphere, with substantial chapters on absorption, fluorescence, and chemical conversion with chemiluminescence:

- Heard, D.E. (Ed.), *Analytical Techniques for Atmospheric Measurement*, Blackwell Publishing Oxford, 2006.

For a textbook on differential optical absorption spectroscopy and its methods and applications, please refer to:

- Platt, U. and J. Stutz, *Differential Optical Absorption Spectroscopy*. 2008, Berlin: Springer-Verlag.

The following textbook on cavity-ring down spectroscopy illustrates this technique and a variety of its applications, including those in atmospheric science and other fields:

- Berden, G. and R. Englen, *Cavity Ring-Down Spectroscopy: Techniques and Applications*. 2009, West Sussex, UK: John Wiley & Sons.

References

- | | |
|---|---|
| <p>16.1 D.E. Heard: <i>Analytical Techniques for Atmospheric Measurements</i> (Blackwell Publishing Ltd, Oxford 2006)</p> <p>16.2 D. Perner, D.H. Ehhalt, H.W. Pätz, U. Platt, E.P. Röth, A. Volz: OH-radicals in the lower troposphere, <i>Geophys. Res. Lett.</i> 3, 466–468 (1976)</p> <p>16.3 D. Perner, U. Platt: Detection of nitrous acid in the atmosphere by differential optical absorption spectroscopy, <i>Geophys. Res. Lett.</i> 6, 971–920 (1979)</p> <p>16.4 U. Platt, D. Perner, H.W. Pätz: Simultaneous measurement of atmospheric CH_2O, O_3, and NO_2 by differential optical absorption, <i>J. Geophys. Res. Oceans</i> 84, 6329–6335 (1979)</p> | <p>16.5 U. Platt, D. Perner, A.M. Winer, G.W. Harris, J.N.J. Pitts: Detection of NO_3 in the polluted troposphere by differential optical absorption, <i>Geophys. Res. Lett.</i> 7, 89–92 (1980)</p> <p>16.6 B. Alicke, K. Hebestreit, J. Stutz, U. Platt: Iodine oxide in the marine boundary layer, <i>Nature</i> 397, 572–573 (1999)</p> <p>16.7 M. Hausmann, U. Platt: Spectroscopic measurement of bromine oxide and ozone in the high arctic during polar sunrise experiment 1992, <i>J. Geophys. Res. Atmos.</i> 99, 25399–25413 (1994)</p> <p>16.8 R. Volkamer, L.T. Molina, M.J. Molina, T. Shirley, W.H. Brune: Doas measurement of glyoxal as an indicator for fast VOC chemistry in urban air, <i>Geophys. Res. Lett.</i> 32, L08806 (2005)</p> |
|---|---|

- 16.9 E.R. Stephens: Long-path infrared spectroscopy for air pollution research, *Appl. Spectrosc.* **12**, 80–84 (1958)
- 16.10 P.L. Hanst: Air pollution measurement by Fourier transform spectroscopy, *Appl. Opt.* **17**, 1360–1366 (1978)
- 16.11 E.C. Tuazon, R.A. Graham, A.M. Winer, R.R. Easton, J.N. Pitts, P.L. Hanst: A kilometer Pathlength Fourier-transform infrared system for the study of trace pollutants in ambient and synthetic atmospheres, *Atmos. Environ.* **12**(1967), 865–875 (1978)
- 16.12 R.J. Yokelson, I.T. Bertschi, T.J. Christian, P.V. Hobbs, D.E. Ward, W.M. Hao: Trace gas measurements in nascent, aged, and cloud-processed smoke from African Savanna fires by airborne Fourier transform infrared spectroscopy (AFTIR), *J. Geophys. Res. Atmos.* **108**(D13), 8478 (2003)
- 16.13 R.J. Yokelson, J.G. Goode, D.E. Ward, R.A. Susott, R.E. Babbitt, D.D. Wade, I. Bertschi, D.W.T. Griffith, W.M. Hao: Emissions of formaldehyde, acetic acid, methanol, and other trace gases from biomass fires in North Carolina measured by airborne Fourier transform infrared spectroscopy, *J. Geophys. Res. Atmos.* **104**, 30109–30125 (1999)
- 16.14 R.J. Yokelson, D.W.T. Griffith, D.E. Ward: Open-path Fourier transform infrared studies of large-scale laboratory biomass fires, *J. Geophys. Res. Atmos.* **101**, 21067–21080 (1996)
- 16.15 R.T. Ku, E.D. Hinkley, J.O. Sample: Long-path monitoring of atmospheric carbon monoxide with a tunable diode laser system, *Appl. Opt.* **14**, 854–861 (1975)
- 16.16 J.U. White: Long optical paths of large aperture, *J. Opt. Soc. Am.* **32**, 285–288 (1942)
- 16.17 D. Herriott, H. Kogelnik, R. Kompfner: Off-axis paths in spherical mirror interferometers, *Appl. Opt.* **3**, 523–526 (1964)
- 16.18 J.B. McManus, P.L. Keabian, M.S. Zahniser: Astigmatic mirror Multipass absorption cells for long-path-length spectroscopy, *Appl. Opt.* **34**, 3336–3348 (1995)
- 16.19 A. O’Keefe, D.A.G. Deacon: Cavity ring-down optical spectrometer for absorption measurements using pulsed laser sources, *Rev. Sci. Instrum.* **59**, 2544–2551 (1988)
- 16.20 A. O’Keefe, O. Lee: Trace gas analysis by pulsed laser absorption spectroscopy, *Am. Lab.* **21**, 19–22 (1989)
- 16.21 D. Romanini, A.A. Kachanov, N. Sadeghi, F. Stoekel: CW cavity ring down spectroscopy, *Chem. Phys. Lett.* **264**, 316–322 (1997)
- 16.22 S.M. Ball, I.M. Povey, E.G. Norton, R.L. Jones: Broadband cavity Ringdown spectroscopy of the NO₃ radical, *Chem. Phys. Lett.* **342**, 113–120 (2001)
- 16.23 S.S. Brown, H. Stark, S.J. Ciciora, A.R. Ravishankara: In-situ measurement of atmospheric NO₃ and N₂O₅ via cavity ring-down spectroscopy, *Geophys. Res. Lett.* **28**, 3227–3230 (2001)
- 16.24 D.S. Baer, J.B. Paul, M. Gupta, A.O. O’Keefe: Sensitive absorption measurements in the near-infrared region using off-axis integrated-cavity-output spectroscopy, *Appl. Phys. B* **75**, 261–265 (2002)
- 16.25 E.R. Crosson: A cavity ring-down analyzer for measuring atmospheric levels of methane, carbon dioxide, and water vapor, *Appl. Phys. B* **92**, 403–408 (2008)
- 16.26 D.E. Heard, M.J. Pilling: Measurement of OH and HO₂ in the troposphere, *Chem. Rev.* **103**, 5163–5198 (2003)
- 16.27 W.J. Tango, J.K. Link, R.N. Zare: Spectroscopy of K₂ using laser-induced fluorescence, *J. Chem. Phys.* **49**(4264), 4264–4268 (1968)
- 16.28 P.O. Wennberg, R.C. Cohen, N.L. Hazen, L.B. Lapsion, N.T. Allen, T.F. Hanisco, J.F. Oliver, N.W. Latham, J.N. Demusz, J.G. Anderson: Aircraft-borne, laser-induced fluorescence instrument for the in-situ detection of hydroxyl and hydroperoxyl radicals, *Rev. Sci. Instrum.* **65**, 1858–1876 (1994)
- 16.29 E.L. Baardsen, R.W. Terhune: Detection of OH in the atmosphere using a dye laser, *Appl. Phys. Lett.* **21**, 209 (1972)
- 16.30 D. Stone, L.K. Whalley, D.E. Heard: Tropospheric OH and HO₂ radicals: field measurements and model comparisons, *Chem. Soc. Rev.* **41**, 6348–6404 (2012)
- 16.31 E.C. Wood, R.C. Cohen: Fluorescence methods. In: *Analytical Techniques for Atmospheric Measurement*, ed. by D.E. Heard (Blackwells, Oxford 2006)
- 16.32 A.J. Bernanose, M.G. Rene: Oxyluminescence of a few fluorescent compounds of ozone, *Adv. Chem.* **21**, 7–12 (1959)
- 16.33 A. Weinheimer: Chemiluminescence and chemical methods in analytical techniques for atmospheric measurement. In: *Analytical Techniques for Atmospheric Measurement*, ed. by D.E. Heard (Blackwells, Oxford 2006)
- 16.34 B.A. Ridley, L.C. Howlett: An instrument for nitric oxide measurements in the stratosphere, *Rev. Sci. Instrum.* **45**, 742–746 (1974)
- 16.35 D.W. Fahey, C.S. Eubank, G. Hübler, F.C. Fehsenfeld: Evaluation of a catalytic reduction technique for the measurement of total reactive Odd-nitrogen Noy in the atmosphere, *J. Atmos. Chem.* **3**, 435–468 (1985)
- 16.36 L.S. Rothman, I.E. Gordon, A. Barbe, D.C. Benner, P.F. Bernath, M. Birk, V. Boudon, L.R. Brown, A. Campargue, J.P. Champion, K. Chance, L.H. Coudert, V. Dana, V.M. Devi, S. Fally, J.M. Flaud, R.R. Gamache, A. Goldman, D. Jacquemart, I. Kleiner, N. Lacombe, W.J. Lafferty, J.Y. Mandin, S.T. Massie, S.N. Mikhailenko, C.E. Miller, N. Moazzen-Ahmadi, O.V. Naumenko, A.V. Nikitin, J. Orphal, V.I. Perevalov, A. Perrin, A. Predoi-Cross, C.P. Rinsland, M. Rotger, M. Šimečková, M.A.H. Smith, K. Sung, S.A. Tashkun, J. Tennyson, R.A. Toth, A.C. Vandaele, J. Vander Auwera: The HITRAN 2008 Molecular Spectroscopic Database, *J. Quant. Spectrosc. Radiat. Transf.* **110**, 533–572 (2009)
- 16.37 P.L. Keabian, S.C. Herndon, A. Freedman: Detection of nitrogen dioxide by cavity attenuated

- phase shift spectroscopy, *Anal. Chem.* **77**, 724–728 (2005)
- 16.38 S.E. Fiedler, A. Hese, A.A. Ruth: Incoherent broadband cavity-enhanced absorption spectroscopy, *Chem. Phys. Lett.* **371**, 284–294 (2003)
- 16.39 R.A. Washenfelder, A.O. Langford, H. Fuchs, S.S. Brown: Measurement of Glyoxal using an incoherent broadband cavity enhanced absorption spectrometer, *Atmos. Chem. Phys.* **8**, 7779–7793 (2008)
- 16.40 K.E. Min, R.A. Washenfelder, W.P. Dube, A.O. Langford, P.M. Edwards, K.J. Zarzana, J. Stutz, K. Lu, F. Rohrer, Y. Zhang, S.S. Brown: A broadband cavity enhanced absorption spectrometer for aircraft measurements of Glyoxal, Methylglyoxal, nitrous acid, nitrogen dioxide, and water vapor, *Atmos. Meas. Tech.* **9**, 423–440 (2016)
- 16.41 J.S. Holloway, R.O. Jakoubek, D.D. Parrish, C. Gerbig, A. Volz-Thomas, S. Schmitgen, A. Fried, B. Wert, B. Henry, J.R. Drummond: Airborne Intercomparison of vacuum ultraviolet fluorescence and tunable diode laser absorption measurements of tropospheric carbon monoxide, *J. Geophys. Res. Atmos.* **105**, 24251–24261 (2000)
- 16.42 T.M. Hard, R.J. O'Brien, C.Y. Chan, A.A. Mehrabzadeh: Tropospheric free-radical determination by Fage, *Environ. Sci. Technol.* **18**, 768–777 (1984)
- 16.43 S. Dusanter, D. Vimal, P.S. Stevens: Technical note: measuring tropospheric OH and HO₂ by laser-induced fluorescence at low pressure. A comparison of calibration techniques, *Atmos. Chem. Phys.* **8**, 321–340 (2008)
- 16.44 R. Woodward-Massey: *Observations of Radicals in the Atmosphere, Measurement Validation and Model Comparisons*, PhD Thesis (Univ. of Leeds, Leeds, UK 2018)
- 16.45 D.J. Creasey, P.A. Halford Maw, D.E. Heard, M.J. Pilling, B.J. Whitaker: Implementation and initial deployment of a field instrument for measurement of OH and HO₂ in the troposphere by laser-induced fluorescence, *J. Chem. Soc. Faraday Trans.* **93**, 2907–2913 (1997)
- 16.46 J. Stutz, B. Alicke, R. Ackermann, A. Geyer, A.B. White, E. Williams: Vertical profiles of NO₃, N₂O₅, O₃, and NO_x in the nocturnal boundary layer: 1. Observations during the Texas air quality study 2000, *J. Geophys. Res.* **109**, D12306 (2004)
- 16.47 D.W.T. Griffith, N.M. Deutscher, C. Caldw, G. Kettlewell, M. Riggenbach, S. Hammer: A Fourier transform infrared trace gas and isotope analyser for atmospheric applications, *Atmos. Meas. Tech.* **5**, 2481–2498 (2012)
- 16.48 P. Weibring, D. Richter, J.G. Walega, L. Rippe, A. Fried: Difference frequency generation spectrometer for simultaneous multispecies detection, *Opt. Express* **18**, 27670–27681 (2010)
- 16.49 J.B. McManus, M.S. Zahniser, D.D. Nelson, J.H. Shorter, S.C. Herndon, D. Jervis, M. Agnese, R. McGovern, T.I. Yacovitch, J.R. Roscioli: Recent progress in laser-based trace gas instruments: performance and noise analysis, *Appl. Phys. B* **119**, 203–218 (2015)
- 16.50 E.C. Richard, K.K. Kelly, R.H. Winkler, R. Wilson, R.L. Thompson, R.J. McLaughlin, A.L. Schmeltekopf, A.F. Tuck: A fast response near-infrared tunable diode laser absorption spectrometer for *in situ* measurements of CH₄ in the upper troposphere and lower stratosphere, *Appl. Phys. B* **75**, 183–194 (2002)
- 16.51 D. Richter, P. Weibring, J.G. Walega, A. Fried, S.M. Spuler, M.S. Taubman: Compact highly sensitive multi-species airborne mid-IR spectrometer, *Appl. Phys. B-Lasers Opt.* **119**, 119–131 (2015)
- 16.52 R.J. Wild, P.M. Edwards, W.P. Dubé, K. Baumann, E.S. Edgerton, P.K. Quinn, J.M. Roberts, A.W. Rollins, P.R. Veres, C. Warneke, E.J. Williams, B. Yuan, S.S. Brown: A measurement of total reactive nitrogen, NO_y, together with NO₂, NO and O₃ via cavity ring-down spectroscopy, *Environ. Sci. Technol.* **48**, 9609–9615 (2014)
- 16.53 L. Richard, D. Romanini, I. Ventrillard: Nitric oxide analysis down to ppt levels by optical-feedback cavity-enhanced absorption spectroscopy, *Sensors* **18**, 1997 (2018)
- 16.54 J. Lockhart, M.A. Blitz, D.E. Heard, P.W. Seakins, R.J. Shannon: Mechanism of the reaction of OH with alkynes in the presence of oxygen, *J. Phys. Chem. A* **117**, 5407–5418 (2013)
- 16.55 F. Holland, M. Hessler, A. Hofzumahaus: In-situ measurement of tropospheric OH radicals by laser-induced fluorescence—a description of the KFA instrument, *J. Atmos. Sci.* **52**, 3393–3401 (1995)
- 16.56 I.C. Faloona, D. Tan, R.L. Lesher, N.L. Hazen, C.L. Frame, J.B. Simpas, H. Harder, M. Martinez, P. Di Carlo, X.R. Ren, W.H. Brune: A laser-induced fluorescence instrument for detecting tropospheric OH and HO₂: characteristics and calibration, *J. Atmos. Chem.* **47**, 139–167 (2004)
- 16.57 S. Dusanter, D. Vimal, P.S. Stevens, R. Volkamer, L.T. Molina: Measurements of OH and HO₂ concentrations during the MCMA-2006 field campaign—part 1: deployment of the Indiana university laser-induced fluorescence instrument, *Atmos. Chem. Phys.* **9**, 1665–1685 (2009)
- 16.58 M. Martinez, H. Harder, D. Kubistin, M. Rudolf, H. Bozem, G. Eerdeken, H. Fischer, T. Klupfel, C. Gurk, R. Konigstedt, U. Parchatka, C.L. Schiller, A. Stickler, J. Williams, J. Lelieveld: Hydroxyl radicals in the tropical troposphere over the Suriname rainforest: airborne measurements, *Atmos. Chem. Phys.* **10**, 3759–3773 (2010)
- 16.59 A.E. Parker, D. Amedro, C. Schoemaeker, C. Fittschen: OH radical reactivity measurements by Fage, *Environ. Eng. Manag. J.* **10**, 107–114 (2011)
- 16.60 Z.F. Tan, H. Fuchs, K.D. Lu, A. Hofzumahaus, B. Bohn, S. Broch, H.B. Dong, S. Gomm, R. Haseler, L.Y. He, F. Holland, X. Li, Y. Liu, S.H. Lu, F. Rohrer, M. Shao, B.L. Wang, M. Wang, Y.S. Wu, L.M. Zeng, Y.S. Zhang, A. Wahner, Y.H. Zhang: Radical chemistry at a rural site (Wangdu) in the north China plain: observation and model calculations of OH,

- HO₂ and RO₂ radicals, *Atmos. Chem. Phys.* **17**, 663–690 (2017)
- 16.61 J. Mao, X. Ren, L. Zhang, D.M. Van Duin, R.C. Cohen, J.H. Park, A.H. Goldstein, F. Paulot, M.R. Beaver, J.D. Crouse, P.O. Wennberg, J.P. DiGangi, S.B. Henry, F.N. Keutsch, C. Park, G.W. Schade, G.M. Wolfe, J.A. Thornton, W.H. Brune: Insights into hydroxyl measurements and atmospheric oxidation in a California forest, *Atmos. Chem. Phys.* **12**, 8009–8020 (2012)
- 16.62 A. Novelli, L. Vereecken, J. Lelieveld, H. Harder: Direct observation of OH formation from stabilised Criegee intermediates, *Phys. Chem. Chem. Phys.* **16**, 19941–19951 (2014)
- 16.63 A. Novelli, K. Hens, C.T. Ernest, D. Kubistin, E. Regelin, T. Elste, C. Plass-Dulmer, M. Martinez, J. Lelieveld, H. Harder: Characterisation of an inlet pre-injector laser-induced fluorescence instrument for the measurement of atmospheric hydroxyl radicals, *Atmos. Meas. Tech.* **7**, 3413–3430 (2014)
- 16.64 H. Fuchs, Z.F. Tan, A. Hofzumahaus, S. Broch, H.P. Dorn, F. Holland, C. Kunstler, S. Gomm, F. Rohrer, S. Schrade, R. Tillmann, A. Wahner: Investigation of potential interferences in the detection of atmospheric RO_x radicals by laser-induced fluorescence under dark conditions, *Atmos. Meas. Tech.* **9**, 1431–1447 (2016)
- 16.65 P. Rickly, P.S. Stevens: Measurements of a potential interference with laser-induced fluorescence measurements of ambient OH from the ozonolysis of biogenic alkenes, *Atmos. Meas. Tech.* **11**, 1–16 (2018)
- 16.66 H. Fuchs, B. Bohn, A. Hofzumahaus, F. Holland, K.D. Lu, S. Nehr, F. Rohrer, A. Wahner: Detection of HO₂ by laser-induced fluorescence: calibration and interferences from RO₂ radicals, *Atmos. Meas. Tech.* **4**, 1209–1225 (2011)
- 16.67 L.K. Whalley, M.A. Blitz, M. Desservettaz, P.W. Seakins, D.E. Heard: Reporting the sensitivity of laser-induced fluorescence instruments used for HO₂ detection to an interference from RO₂ radicals and introducing a novel approach that enables HO₂ and certain RO₂ types to be selectively measured, *Atmos. Meas. Tech.* **6**, 3425–3440 (2013)
- 16.68 H. Fuchs, F. Holland, A. Hofzumahaus: Measurement of tropospheric RO₂ and HO₂ radicals by a laser-induced fluorescence instrument, *Rev. Sci. Instrum.* **79**, 084104 (2008)
- 16.69 E.C. Wood, B.L. Deming, S. Kundu: Ethane-based chemical amplification measurement technique for atmospheric peroxy radicals, *Environ. Sci. Technol. Lett.* **4**, 15–19 (2017)
- 16.70 L. Onel, A. Brennan, P.W. Seakins, L. Whalley, D.E. Heard: A new method for atmospheric detection of the CH₃O₂ radical, *Atmos. Meas. Tech.* **10**, 3985–4000 (2017)
- 16.71 J.D. Lee, L.K. Whalley, D.E. Heard, D. Stone, R.E. Dunmore, J.F. Hamilton, D.E. Young, J.D. Allan, S. Laufs, J. Kleffmann: Detailed budget analysis of HONO in central London reveals a missing daytime source, *Atmos. Chem. Phys.* **16**, 2747–2764 (2016)
- 16.72 C.X. Ye, X.L. Zhou, D. Pu, J. Stutz, J. Festa, M. Spolaor, C. Tsai, C. Cantrell, R.L. Mauldin, T. Campos, A. Weinheimer, R.S. Hornbrook, E.C. Apel, A. Guenther, L. Kaser, B. Yuan, T. Karl, J. Haggerty, S. Hall, K. Ullmann, J.N. Smith, J. Ortega, C. Knote: Rapid cycling of reactive nitrogen in the marine boundary layer, *Nature* **532**, 489–491 (2016)
- 16.73 G.W. King, D. Moule: Ultraviolet absorption spectrum of nitrous acid in vapor state, *Can. J. Chem.* **40**, 2057 (1962)
- 16.74 R.A. Cox, R.G. Derwent: Ultraviolet-absorption spectrum of gaseous nitrous-acid, *J. Photochem.* **6**, 23–34 (1976)
- 16.75 W. Liao, A. Hecobian, J. Mastromarino, D. Tan: Development of a photo-fragmentation/laser-induced fluorescence measurement of atmospheric nitrous acid, *Atmos. Environ.* **40**, 17–26 (2006)
- 16.76 M.O. Rodgers, D.D. Davis: A UV-Photofragmentation laser-induced fluorescence sensor for the atmospheric detection of HONO, *Environ. Sci. Technol.* **23**, 1106–1112 (1989)
- 16.77 B. Bottorff, P. Stevens, M. Lew, P. Rickly, S. Dusanter: *Measurements of Nitrous Acid (HONO) in an Indiana Forest by Laser Photofragmentation/Laser-Induced Fluorescence (LP/LIF)* (AGU, Washington DC 2015)
- 16.78 G.A. Boustead: *Measurement of Nitrous Acid Production from Aerosol Surfaces using Photofragmentation Laser Induced Fluorescence*, PhD Thesis (Univ. of Leeds, Leeds, UK 2019)
- 16.79 J.A. Thornton, P.J. Wooldridge, R.C. Cohen: Atmospheric NO₂: in situ laser-induced fluorescence detection at parts per trillion mixing ratios, *Anal. Chem.* **72**, 528–539 (2000)
- 16.80 Y. Matsumi, S. Murakami, M. Kono, K. Takahashi, M. Koike, Y. Kondo: High-sensitivity instrument for measuring atmospheric NO₂, *Anal. Chem.* **73**, 5485–5493 (2001)
- 16.81 J. Matsumoto, J. Hirokawa, H. Akimoto, Y. Kajii: Direct measurement of NO₂ in the marine atmosphere by laser-induced fluorescence technique, *Atmos. Environ.* **35**, 2803–2814 (2001)
- 16.82 C. Dari-Salisburgo, P. Di Carlo, F. Giammaria, Y. Kajii, A. D’Altorio: Laser induced fluorescence instrument for NO₂ measurements: observations at a central Italy background site, *Atmos. Environ.* **43**, 970–977 (2009)
- 16.83 D.A. Day, P.J. Wooldridge, M.B. Dillon, J.A. Thornton, R.C. Cohen: A thermal dissociation laser-induced fluorescence instrument for in situ detection of NO₂, peroxy nitrates, alkyl nitrates, and HNO₃, *J. Geophys. Res. Atmos.* **107**(D6), 4046 (2002)
- 16.84 P. Carlier, H. Hannachi, G. Mouvrier: The chemistry of carbonyl-compounds in the atmosphere—a review, *Atmos. Environ.* **20**, 2079–2099 (1986)
- 16.85 J.R. Hottle, A.J. Huisman, J.P. Digangi, A. Kammrath, M.M. Galloway, K.L. Coens, F.N. Keutsch: A laser induced fluorescence-based instrument for in-situ measurements of atmospheric

- formaldehyde, *Environ. Sci. Technol.* **43**, 790–795 (2009)
- 16.86 M. Cazorla, G.M. Wolfe, S.A. Bailey, A.K. Swanson, H.L. Arkinson, T.F. Hanisco: A new airborne laser-induced fluorescence instrument for in situ detection of formaldehyde throughout the troposphere and lower stratosphere, *Atmos. Meas. Tech.* **8**, 541–552 (2015)
- 16.87 J.M.S. Clair, A.K. Swanson, S.A. Bailey, G.M. Wolfe, J.E. Marrero, L.T. Iraci, J.G. Hagopian, T.F. Hanisco: A new non-resonant laser-induced fluorescence instrument for the airborne in situ measurement of formaldehyde, *Atmos. Meas. Tech.* **10**, 4833–4844 (2017)
- 16.88 T.M. Fu, D.J. Jacob, F. Wittrock, J.P. Burrows, M. Vrekoussis, D.K. Henze: Global budgets of atmospheric glyoxal and methylglyoxal, and implications for formation of secondary organic aerosols, *J. Geophys. Res.* **113**, D15303 (2008)
- 16.89 A.J. Huisman, J.R. Hottle, K.L. Coens, J.P. DiGangi, M.M. Galloway, A. Kammrath, F.N. Keutsch: Laser-induced phosphorescence for the in situ detection of glyoxal at part per trillion mixing ratios, *Anal. Chem.* **80**, 5884–5891 (2008)
- 16.90 S.B. Henry, A. Kammrath, F.N. Keutsch: Quantification of gas-phase glyoxal and methylglyoxal via the laser-induced phosphorescence of (methyl)glyoxal spectrometry (LIPGLOS) method, *Atmos. Tech.* **5**, 181–192 (2012)
- 16.91 M.A.A. Clyne, R.P. Wayne, B.A. Thrush: Kinetics of chemiluminescent reaction between nitric oxide + ozone, *Trans. Faraday Soc.* **60**, 359 (1964)
- 16.92 D.H. Stedman, F. Stuhl, E.E. Daby, H. Niki: Analysis of ozone and nitric-oxide by a chemiluminescent method in laboratory and atmospheric studies of photochemical smog, *J. Air Pollut. Control Assoc., J. Air Waste Manag. Assoc.* **22**, 260 (1972)
- 16.93 A.M. Winer, J.W. Peters, J.P. Smith, J.N. Pitts: Response of commercial chemiluminescent NO–NO₂ analyzers to other nitrogen-containing compounds, *Environ. Sci. Technol.* **8**, 1118–1121 (1974)
- 16.94 D.W. Fahey, C.S. Eubank, G. Hubler, F.C. Fehsenfeld: Evaluation of a catalytic reduction technique for the measurement of total reactive odd-nitrogen NO_y in the atmosphere, *J. Atmos. Chem.* **3**, 435–468 (1985)
- 16.95 B.A. Ridley, M.A. Carroll, G.L. Gregory, G.W. Sachse: NO and NO₂ in the troposphere—technique and measurements in regions of a folded tropopause, *J. Geophys. Res. Atmos.* **93**, 15813–15830 (1988)
- 16.96 T.B. Ryerson, E.J. Williams, F.C. Fehsenfeld: An efficient photolysis system for fast-response NO₂ measurements, *J. Geophys. Res. Atmos.* **105**, 26447–26461 (2000)
- 16.97 C. Reed, M.J. Evans, P. Di Carlo, J.D. Lee, L.J. Carpenter: Interferences in photolytic NO₂ measurements: explanation for an apparent missing oxidant?, *Atmos. Chem. Phys.* **16**, 4707–4724 (2016)
- 16.98 C. Reed, C.A. Brumby, L.R. Crilley, L.J. Kramer, W.J. Bloss, P.W. Seakins, J.D. Lee, L.J. Carpenter: HONO measurement by differential photolysis, *Atmos. Meas. Tech.* **9**, 2483–2495 (2016)
- 16.99 G. Villena, I. Bejan, R. Kurtenbach, P. Wiesen, J. Kleffmann: Interferences of commercial NO₂ instruments in the urban atmosphere and in a smog chamber, *Atmos. Meas. Tech.* **5**, 149–159 (2012)
- 16.100 J. Heland, J. Kleffmann, R. Kurtenbach, P. Wiesen: A new instrument to measure gaseous nitrous acid (HONO) in the atmosphere, *Environ. Sci. Technol.* **35**, 3207–3212 (2001)
- 16.101 D. Littlejohn, Y.Z. Wang, S.G. Chang: Oxidation of aqueous sulfite ion by nitrogen-dioxide, *Environ. Sci. Technol.* **27**, 2162–2167 (1993)
- 16.102 G. Spindler, J. Hesper, E. Brüggemann, R. Dubois, T. Müller, H. Herrmann: Wet annular denuder measurements of nitrous acid: laboratory study of the artefact reaction of NO₂ with S(IV) in aqueous solution and comparison with field measurements, *Atmos. Environ.* **37**, 2643–2662 (2003)
- 16.103 Z.B. Alfassi, R.E. Huie, P. Neta: Substituent effects on rates of one-electron oxidation of phenols by the radicals ClO₂, NO₂, and SO₃, *J. Phys. Chem. US* **90**, 4156–4158 (1986)
- 16.104 R.G. Coombes, A.W. Diggie, S.P. Kempzell: The mechanism of nitration of phenol and 4-methylphenol by nitrogen-dioxide in solution, *Tetrahedron Lett.* **35**, 6373–6376 (1994)
- 16.105 M. Ammann, E. Rossler, R. Strekowski, C. George: Nitrogen dioxide Multiphase chemistry: uptake kinetics on aqueous solutions containing phenolic compounds, *Phys. Chem. Chem. Phys.* **7**, 2513–2518 (2005)
- 16.106 A. Frenzel, S. Kutsuna, K. Takeuchi, T. Ibusuki: Solubility and reactivity of peroxyacetyl nitrate (PAN) in dilute aqueous salt solutions and in sulphuric acid, *Atmos. Environ.* **34**, 3641–3644 (2000)
- 16.107 J. Kleffmann, J.C. Lorzer, P. Wiesen, C. Kern, S. Trick, R. Volkamer, M. Rodenas, K. Wirtz: Intercomparison of the DOAS and LOPAP techniques for the detection of nitrous acid (HONO), *Atmos. Environ.* **40**, 3640–3652 (2006)
- 16.108 M. Legrand, S. Preunkert, M. Frey, T. Bartels-Rausch, A. Kukui, M.D. King, J. Savarino, M. Kerbrat, B. Jourdain: Large mixing ratios of atmospheric nitrous acid (HONO) at Concordia (east Antarctic Plateau) in summer: a strong source from surface snow?, *Atmos. Chem. Phys.* **14**, 9963–9976 (2014)
- 16.109 J. Kleffmann, J. Heland, R. Kurtenbach, J. Lorzer, P. Wiesen: A new instrument (LOPAP) for the detection of nitrous acid (HONO), *Environ. Sci. Pollut. Res.* **9**, 48–54 (2002)
- 16.110 G. Villena, I. Bejan, R. Kurtenbach, P. Wiesen, J. Kleffmann: Development of a new long path absorption photometer (LOPAP) instrument for the sensitive detection of NO₂ in the atmosphere, *Atmos. Meas. Tech.* **4**, 1663–1676 (2011)
- 16.111 J. Kleffmann, T. Gavriloaiei, Y. Elshorbany, M. Rodenas, P. Wiesen: Detection of nitric acid (HNO₃) in the atmosphere using the LOPAP technique, *J. Atmos. Chem.* **58**, 131–149 (2007)

- 16.112 M.R. Hoffmann, J.O. Edwards: Kinetics of oxidation of sulfite by hydrogen-peroxide in acidic solution, *J. Phys. Chem. US* **79**, 2096–2098 (1975)
- 16.113 G.L. Kok, T.P. Holler, M.B. Lopez, H.A. Nachtrieb, M. Yuan: Chemiluminescent method for determination of hydrogen-peroxide in ambient atmosphere, *Environ. Sci. Technol.* **12**, 1072–1076 (1978)
- 16.114 A.L. Lazrus, G.L. Kok, J.A. Lind, S.N. Gitlin, B.G. Heikes, R.E. Shetter: Automated fluorometric method for hydrogen-peroxide in air, *Anal. Chem.* **58**, 594–597 (1986)
- 16.115 M. Lee, B.C. Noone, D. Osullivan, B.G. Heikes: Method for the collection and HPLC analysis of hydrogen-peroxide and C-1 and C-2 hydroperoxides in the atmosphere, *J. Atmos. Ocean Tech.* **12**, 1060–1070 (1995)
- 16.116 R.B. Morgan, A.V. Jackson: Measurements of gas-phase hydrogen peroxide and methyl hydroperoxide in the coastal environment during the PARFORCE project, *J. Geophys. Res. Atmos.* **107**(D19), 8109 (2002)
- 16.117 R. Commane, C.F.A. Floquet, T. Ingham, D. Stone, M.J. Evans, D.E. Heard: Observations of OH and HO₂ radicals over west Africa, *Atmos. Chem. Phys.* **10**, 8783–8801 (2010)
- 16.118 W.J. Bloss, J.D. Lee, C. Bloss, D.E. Heard, M.J. Pilling, K. Wirtz, M. Martin-Reviejo, M. Siese: Validation of the calibration of a laser-induced fluorescence instrument for the measurement of OH radicals in the atmosphere, *Atmos. Chem. Phys.* **4**, 571–583 (2004)
- 16.119 D.R. Cryer: *Measurements of Hydroxyl Radical Reactivity and Formaldehyde in the Atmosphere*, PhD Thesis (School of Chemistry, Univ. of Leeds, Leeds 2016)
- 16.120 H. Walker: *Field Measurements and Analysis of Reactive Tropospheric Species Using the Fage Technique*, PhD Thesis (School of Chemistry, Univ. of Leeds, Leeds 2013)
- 16.121 E. Schlosser, T. Brauers, H.P. Dorn, H. Fuchs, R. Haseler, A. Hofzumahaus, F. Holland, A. Wahner, Y. Kanaya, Y. Kajii, K. Miyamoto, S. Nishida, K. Watanabe, A. Yoshino, D. Kubistin, M. Martinez, M. Rudolf, H. Harder, H. Berresheim, T. Elste, C. Plass-Dulmer, G. Stange, U. Schurath: Technical note: formal blind Intercomparison of OH measurements: results from the international campaign HO_{xcomp}NO, *Atmos. Chem. Phys.* **9**, 7923–7948 (2009)
- 16.122 H. Fuchs, T. Brauers, H.P. Dorn, H. Harder, R. Haseler, A. Hofzumahaus, F. Holland, Y. Kanaya, Y. Kajii, D. Kubistin, S. Lou, M. Martinez, K. Miyamoto, S. Nishida, M. Rudolf, E. Schlosser, A. Wahner, A. Yoshino, U. Schurath: Technical note: formal blind Intercomparison of HO₂ measurements in the atmosphere simulation chamber SAPHIR during the HO_{xcomp}NO campaign, *Atmos. Chem. Phys.* **10**, 12233–12250 (2010)
- 16.123 Y. Kanaya, A. Hofzumahaus, H.P. Dorn, T. Brauers, H. Fuchs, F. Holland, F. Rohrer, B. Bohn, R. Tillmann, R. Wegener, A. Wahner, Y. Kajii, K. Miyamoto, S. Nishida, K. Watanabe, A. Yoshino, D. Kubistin, M. Martinez, M. Rudolf, H. Harder, H. Berresheim, T. Elste, C. Plass-Dulmer, G. Stange, U. Schurath: Comparisons of observed and modeled OH and HO₂ concentrations during the ambient measurement period of the HO_{xcomp}NO field campaign, *Atmos. Chem. Phys.* **12**, 2567–2585 (2012)
- 16.124 K.D. Lu, F. Rohrer, F. Holland, H. Fuchs, B. Bohn, T. Brauers, C.C. Chang, R. Haseler, M. Hu, K. Kita, Y. Kondo, X. Li, S.R. Lou, S. Nehr, M. Shao, L.M. Zeng, A. Wahner, Y.H. Zhang, A. Hofzumahaus: Observation and modelling of OH and HO₂ concentrations in the pearl river delta 2006: a missing OH source in a VOC rich atmosphere, *Atmos. Chem. Phys.* **12**, 1541–1569 (2012)
- 16.125 L.K. Whalley, K.L. Furneaux, A. Goddard, J.D. Lee, A. Mahajan, H. Oetjen, K.A. Read, N. Kaaden, L.J. Carpenter, A.C. Lewis, J.M.C. Plane, E.S. Saltzman, A. Wiedensohler, D.E. Heard: The chemistry of OH and HO₂ radicals in the boundary layer over the tropical atlantic ocean, *Atmos. Chem. Phys.* **10**, 1555–1576 (2010)
- 16.126 L.K. Whalley, P.M. Edwards, K.L. Furneaux, A. Goddard, T. Ingham, M.J. Evans, D. Stone, J.R. Hopkins, C.E. Jones, A. Karunaharan, J.D. Lee, A.C. Lewis, P.S. Monks, S.J. Moller, D.E. Heard: Quantifying the magnitude of a missing hydroxyl radical source in a tropical rainforest, *Atmos. Chem. Phys.* **11**, 7223–7233 (2011)
- 16.127 L.K. Whalley, D. Stone, R. Dunmore, J. Hamilton, J.R. Hopkins, J.D. Lee, A.C. Lewis, P. Williams, J. Kleffmann, S. Laufs, R. Woodward-Massey, D.E. Heard: Understanding in situ ozone production in the summertime through radical observations and modelling studies during the clean air for London project (CLEARFLO), *Atmos. Chem. Phys.* **18**, 2547–2571 (2018)
- 16.128 K.A. Read, A.S. Mahajan, L.J. Carpenter, M.J. Evans, B.V.E. Faria, D.E. Heard, J.R. Hopkins, J.D. Lee, S.J. Moller, A.C. Lewis, L. Mendes, J.B. McQuaid, H. Oetjen, A. Saiz-Lopez, M.J. Pilling, J.M.C. Plane: Extensive halogen-mediated ozone destruction over the tropical atlantic ocean, *Nature* **453**, 1232–1235 (2008)
- 16.129 D. Helmig, S. Rossabi, J. Hueber, P. Tans, S.A. Montzka, K. Masarie, K. Thoning, C. Plass-Duelmer, A. Claude, L.J. Carpenter, A.C. Lewis, S. Punjabi, S. Reimann, M.K. Vollmer, R. Steinbrecher, J.W. Hannigan, L.K. Emmons, E. Mahieu, B. Franco, D. Smale, A. Pozzer: Reversal of global atmospheric ethane and propane trends largely due to us oil and natural gas production, *Nat. Geosci.* **9**, 490–495 (2016)
- 16.130 M.L. Smith, E.A. Kort, A. Karion, C. Sweeney, S.C. Herndon, T.I. Yacovitch: Airborne ethane observations in the Barnett shale: quantification of ethane flux and attribution of methane emissions, *Environ. Sci. Technol.* **49**, 8158–8166 (2015)
- 16.131 A. Karion, C. Sweeney, S. Wolter, T. Newberger, H. Chen, A. Andrews, J. Kofler, D. Neff, P. Tans:

- 16.132 Long-term greenhouse gas measurements from aircraft, *Atmos. Meas. Tech.* **6**, 511–526 (2013)
K.C. Cossel, E.M. Waxman, I.A. Finneran, G.A. Blake, J. Ye, N.R. Newbury: Gas-phase

broadband spectroscopy using active sources: progress, status, and applications [invited], *J. Opt. Soc. Am. B* **34**, 104–129 (2017)

Dwayne Heard

School of Chemistry
University of Leeds
Leeds, UK
d.e.heard@leeds.ac.uk



Dwayne Heard is Professor of Atmospheric Chemistry at the University of Leeds, UK. He received a DPhil in physical chemistry in 1990 from the University of Oxford and was awarded the Royal Society of Chemistry's Environment Prize in 2017. His research focuses on atmospheric chemistry, especially field measurements of hydroxyl and other radicals, reaction kinetics and photochemistry, and aerosols and heterogeneous chemistry, as well as planetary and interstellar chemistry.

Lisa K. Whalley

School of Chemistry
National Centre for Atmospheric Science,
University of Leeds
Leeds, UK
l.k.whalley@leeds.ac.uk



Lisa Whalley is a senior research scientist at the National Centre for Atmospheric Science (NCAS) at the University of Leeds. She received a PhD in atmospheric chemistry in 2004. Her research interests involve atmospheric measurements, modeling studies, and laboratory experiments, and focus on understanding the chemistry responsible for the processing of trace gases in the atmosphere through field observations and comparison of these observations with detailed chemistry models.

Steven S. Brown

NOAA Chemical Sciences Laboratory
Boulder, USA
steven.s.brown@noaa.gov



Steven S. Brown is a Research Chemist at the Chemical Sciences Division of the NOAA Earth System Research Laboratory in Boulder, Colorado, and an Adjoint Professor of Chemistry at the University of Wisconsin-Madison in 1996. His research interests include the chemistry of nitrogen oxides in the Earth's atmosphere and the development of high-sensitivity spectroscopic instruments for atmospheric sensing.

17. Measurement of Stable Isotopes in Carbon Dioxide, Methane, and Water Vapor

Ingeborg Levin , Matthias Cuntz 

Instrumentation for the continuous measurement of stable isotopes in atmospheric trace substances such as carbon dioxide (CO₂), methane (CH₄), and also water vapor (H₂O), has grown tremendously in the last decade. This is due to the development of new highly sensitive infrared spectroscopic techniques such as Fourier transform infrared spectroscopy, or laser-based systems like quantum cascade laser absorption spectroscopy and cavity ring-down spectroscopy. These systems are not only applied for precise continuous concentration measurements, but have also recently been used for high-frequency isotope measurements of net ecosystem-atmosphere exchange fluxes. Similar development of isotope ratio mass spectrometry systems led to successful application of the spectrometers in quasicontinuous mode at field stations. The currently available continuous measurement systems for CO₂, CH₄, and H₂O stable isotopic compositions are described here and information about calibration, maintenance, and quality assurance requirements of these systems is given.

17.1	Measurement Principles and Parameters	510	17.4	Devices and Systems	516
17.2	History of Stable Isotope Measurements in Atmospheric CO₂, CH₄, and H₂O	512	17.4.1	Continuous Isotope Observations with Tunable Diode Laser Absorption Spectroscopy	516
17.2.1	Carbon Dioxide	512	17.4.2	High-Resolution Isotope Observations with Quantum Cascade Laser Absorption Spectroscopy	517
17.2.2	Methane	512	17.4.3	Stable Isotope Observations with Cavity Ring-Down Spectroscopy .	517
17.2.3	Water Vapor	512	17.4.4	Continuous Atmospheric ¹³ C-CO ₂ Observations by Fourier Transform Infrared Spectroscopy	518
17.3	Theory	513	17.4.5	Atmospheric Observations of Methane Isotopologues by Continuous-Flow Mass Spectrometry in Comparison to Quantum Cascade Laser Absorption Spectroscopy	520
17.3.1	Isotope Ratio Mass Spectrometry (IRMS)	513	17.4.6	Overall Evaluation of Available Isotope Measurement Systems	522
17.3.2	Optical Methods	514	17.5	Specifications	523
			17.6	Quality Control	524
			17.6.1	Calibration	524
			17.6.2	Cross-Sensitivities	524
			17.6.3	Specific Quality Assurance Measures ...	525
			17.7	Maintenance	525
			17.8	Application	525
			17.8.1	Ecosystem Observations	526
			17.8.2	Atmospheric Observations	526
			17.9	Future Developments	527
			17.10	Further Readings	527
			References		527

From the classical biogeochemist's point of view, molecules containing different isotopes, known as isotopologues, have equal chemical and biochemical properties. However, tiny differences of often only one mass unit lead to small variations in their physical behavior, such as in molecular diffusion, e.g., dur-

ing uptake of CO₂ through stomata of leaves, or during phase changes, e.g., evaporation or condensation of water vapor [17.1]. These fractionation processes cause measurable differences in the isotope ratios of, most prominently, light atoms, such as hydrogen (²H/¹H), carbon (¹³C/¹²C), nitrogen (¹⁵N/¹⁴N),

or oxygen ($^{17}\text{O}/^{16}\text{O}$, $^{18}\text{O}/^{16}\text{O}$) in the biogeochemically most relevant molecules like H_2O , CO_2 , CH_4 , and N_2O [17.2–5], but also in more rare atmospheric trace substances such as ozone (O_3) or molecular hydrogen (H_2) [17.6–8]. Isotopic fractionation of various processes can be measured in nature or in the laboratory, and may be uniquely associated with one particular process, leaving a so-called fingerprint on the isotope ratio of the molecules involved [17.1]. For example, CO_2 released from ocean surface water is about 16‰ more enriched in the rare ^{13}C isotope than CO_2 respired from the roots or leaves of a tree [17.9]. Also in the case of CH_4 , its production by incomplete combustion car-

ries almost the same isotopic signature as the originally burned carbon, and is thus about 40‰ more enriched in ^{13}C than CH_4 originating from anaerobic decomposition of organic material, e.g., in wetlands [17.10]. As emissions from various sources (and removal by fractionating sinks) cause not only concentration changes but also leave measurable isotopic signals in the atmosphere, the measurement of trace gases' isotopologues, in combination with their concentration measurement in the atmosphere, thus allows for insights into the relevant exchange processes and sometimes even provide quantitative information on their different source components (see Sect. 17.8).

17.1 Measurement Principles and Parameters

Differences in the isotopic composition of natural samples are normally small, i.e., on the order of a few percent; therefore, isotope ratios (R) are measured and reported relative to internationally agreed standard material in the so-called delta notation [17.1],

$$\delta = \frac{R_{\text{Sample}} - R_{\text{Standard}}}{R_{\text{Standard}}} \quad (17.1)$$

with, for example $^2\text{H}/^1\text{H} = ^2R$, $^{13}\text{C}/^{12}\text{C} = ^{13}R$, and $^{18}\text{O}/^{16}\text{O} = ^{18}R$. ^2H is commonly called *deuterium*.

The term δ is most often expressed in per mille. Here, ^2H , ^{12}C , etc. are atom concentrations rather than molecule concentrations. The international standard for hydrogen and oxygen isotope ratios is the Vienna Standard Mean Ocean Water (VSMOW), while for carbon

it is the Vienna Pee Dee Belemnite (VPDB) [17.1] carbonate. All laboratories report their data relative to these standards in order to be comparable to each other. The delta notation is written as the δ symbol followed by the rare isotope, for example $\delta^{18}\text{O}$ for the relative deviation of an $^{18}\text{O}/^{16}\text{O}$ ratio from the VSMOW standard. The substance containing the isotopic composition is often appended to the delta notation, either with a hyphen, e.g., $\delta^{18}\text{O}-\text{H}_2\text{O}$, or in parentheses, e.g., $\delta^{18}\text{O}(\text{H}_2\text{O})$. The hyphen notation is used throughout this chapter.

The classical way to measure isotope ratios is by isotope ratio mass spectrometry (IRMS) [17.20] see Table 17.1. For mass spectrometer (MS) analysis of the isotope ratios in atmospheric carbon dioxide, CO_2 has to be quantitatively separated from the air sample. This

Table 17.1 Principles of continuous atmospheric stable isotope measurements ([17.11–18], and material from Aerodyne Research Inc., Campbell Scientific, Ecotech, Los Gatos Research Inc., Picarro Inc., Thermo Fisher Scientific)

Type of instrument	Measured components							
	$\delta^{13}\text{C}-\text{CO}_2$	$\delta^{18}\text{O}-\text{CO}_2$	$\delta^{17}\text{O}-\text{CO}_2$	$\delta^{13}\text{C}-\text{CH}_4$	$\delta^2\text{H}-\text{CH}_4$	$\delta^{18}\text{O}-\text{H}_2\text{O}$	$\delta^{17}\text{O}-\text{H}_2\text{O}$	$\delta^2\text{H}-\text{H}_2\text{O}$
Isotope ratio mass spectrometry (IRMS)	×	×		×	×			
Tunable diode laser absorption spectroscopy (TDLAS)	×	×	×	×	×	×		×
Quantum cascade laser absorption spectroscopy (QCLAS)	×	×	×	×	×	×		×
Cavity ring-down spectroscopy (CRDS)	×	×	×	×		×	×	×
Off-axis integrated cavity output spectroscopy (OA-ICOS)	×	×	×	×		×	×	×
Difference frequency generation laser spectroscopy (DFG)	×	×						
Fourier transform infrared spectroscopy (FTIR)	×	×				×		×

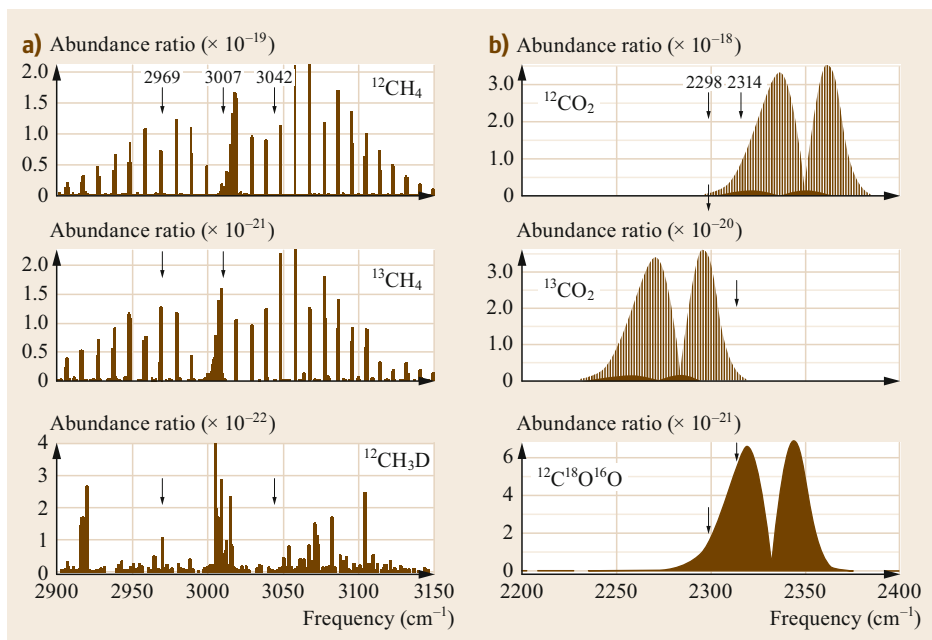


Fig. 17.1a,b Absorption lines for isotopes of CH_4 (a) and CO_2 (b) from the high-resolution transmission molecular absorption database HITRAN. Line strengths are in absorbance units (cm^2 per molecule cm^{-1}), adjusted for the natural abundance of each isotopologue. The y-axes scale with the isotopologue abundance ratios. Possible lines for laser spectroscopy are indicated by *arrows* (after [17.19] with permission from Elsevier)

is done either cryogenically or by gas chromatography. The CO_2 sample is then injected into the ion source of the mass spectrometer, ionized, accelerated, and separated in a magnetic field, with the separated ion beam currents of the different isotopologues measured with three Faraday cups, i.e., for mass 44, 45 and 46 [17.1].

Stable isotope measurements in water vapor by IRMS require preprocessing, firstly as water is condensable and very sticky, sitting as thin films on instrument walls, and secondly as the relevant masses of water overlap with those of oxygen atoms (^{18}O), e.g., originating from traces of dissociated molecular oxygen. The oxygen isotopic composition is often measured via equilibration of the water with CO_2 , measuring then the isotopic composition of CO_2 as above. The water is catalytically reduced to hydrogen gas for hydrogen isotopic measurements using a separate MS with Faraday cups for masses 2 and 3. Therefore, particularly in the case of water isotopologues, optical systems that directly measure both oxygen and hydrogen isotopic compositions create new possibilities to study this important greenhouse gas in the climate system.

Mass spectrometry measurements of the stable isotope ratios in atmospheric methane are often done by separation and preconcentration of CH_4 from other air

constituents and subsequent oxidation of CH_4 to CO_2 and H_2O . Carbon dioxide can then be measured directly in the mass spectrometer while water is reduced to hydrogen before it is injected into the ion source of the mass spectrometer (Sect. 17.2.2).

Optical spectroscopy measurements of isotope ratios use the fact that isotopologues have different characteristic absorption spectra due to small differences in the infrared (IR) rotational–vibrational energy states (see Fig. 17.1). The ratios can thus be measured directly in an air sample without preprocessing, given that the potential overlap of their spectra with those of other trace substances can be corrected for (most prominently absorption lines of water vapor). For CO_2 and CH_4 detection, air samples are therefore most often dried before analysis. Some instruments also measure samples at reduced pressure to limit pressure broadening of the absorption lines. Two principally different methods are in use: Fourier transform infrared spectroscopy (FTIR) and laser-based systems (see also Chap. 28). FTIR uses an infrared light source covering the important range of greenhouse gas (GHG) absorption lines (i.e., from 2000 to 4000 cm^{-1}). An alternative method uses laser systems specifically tuned for the absorption lines of the species to be detected.

17.2 History of Stable Isotope Measurements in Atmospheric CO₂, CH₄ and H₂O

One can determine the source/sink strength of a trace gas when measuring its atmospheric abundance. The atmosphere, however, integrates different sources and sinks and only the net flux density can be determined. The fluxes to and from the atmosphere carry isotopic signatures. This can help disentangle the individual sources and sinks if their isotopic signatures are distinct. A famous example uses the ¹³C-isotopic composition of atmospheric CO₂ to determine ocean versus land uptake of carbon (Sect. 17.8).

17.2.1 Carbon Dioxide

The first systematic stable isotope measurements on atmospheric CO₂ were published by *Charles David Keeling* (1928–2005) in 1958 [17.3]. Carbon dioxide from flask air samples were extracted cryogenically and then measured directly by IRMS. Following this work, isotope measurements were extended to the entire global flask sampling network of the Scripps Institution of Oceanography (SIO). The carbon isotope data provided important new insights into the global distribution of atmospheric CO₂ sources and sinks [17.21–23]. Following that pioneering work, the Commonwealth Scientific and Industrial Research Organisation (CSIRO), the National Oceanic and Atmospheric Administration/Global Monitoring Division (NOAA/GMD), and other groups world-wide extended these flask observations at globally distributed background stations [17.24, 25]. Air drying was introduced, which is essential for maintaining the original CO₂ oxygen isotope ratio in the sample. Now the ¹⁸O isotopic signals can also be used for carbon cycle investigations [17.26–30]. Routine analysis of stable isotope ratios in atmospheric CO₂ from flask samples still uses similar extraction and IRMS analysis methods [17.31–33]; however, sample sizes are now reduced to a few hundred milliliters of air, and extraction and analysis systems in the lab are automated in order to allow for effective measurement of thousands of samples per year from globally distributed networks. Additionally, the newly established European Integrated Carbon Observation System Research Infrastructure (ICOS RI) atmospheric station network uses this methodology for flask analysis [17.32].

17.2.2 Methane

Early stable isotope observations in atmospheric CH₄ are from the 1980s [17.5, 34–37]. They provided important new insights into the relative contributions of natural and anthropogenic sources to the global budget of atmospheric CH₄ [17.10, 38].

Due to the low atmospheric abundance of CH₄, precise measurements in the past used large sample volumes (i.e., CH₄ from several hundreds of liters of air), and special care was needed to fully separate CH₄ from other carbon-containing gases, such as CO₂ and CO, but also trace amounts of hydrocarbons. The purified and preconcentrated CH₄ then had to be converted to CO₂ and H₂O with H₂O being further reduced to H₂ for IRMS measurements [17.37, 39]. An alternative way to extract the hydrogen from CH₄ for IRMS measurement is by pyrolysis [17.32]. As an optical detection method, a tunable diode laser absorption spectrometer was introduced by *Bergamaschi* et al. in the 1990s [17.40] to analyze ¹³C and ²H directly on purified and preconcentrated CH₄ samples without the additional step of conversion to CO₂ and H₂. In particular for $\delta^2\text{H-CH}_4$ this system yielded more precise measurements than IRMS [17.40]. Today, due to the development of continuous-flow mass spectrometry, much smaller sample amounts of a few 100 mL are needed for precise measurements of both stable isotopes in CH₄, so that $\delta^2\text{H-CH}_4$ trends in the atmosphere also become available [17.32, 39, 41–43].

17.2.3 Water Vapor

Atmospheric water vapor stable isotope measurements were traditionally conducted cryogenically on samples collected in-situ [17.44, 45]. As for CO₂ and CH₄, extraction from ambient air must be quantitative in order to avoid isotope fractionation. This is particularly important when sampling in cold areas with ambient dewpoints well below 0 °C. Not much systematic data on water vapor exists in the literature, due to the fact that information on the global water cycle can more readily be obtained from precipitation samples [17.46], which are much easier to collect, e.g., by rain collectors carefully avoiding evaporation [17.47]. Since very sensitive optical systems have recently become available, new systematic quasicontinuous observational records of water vapor isotopologues are established [17.48].

17.3 Theory

The traditional methodology for isotope analysis was by isotope ratio mass spectrometry, which requires the pure substance (CO_2 , CH_4 , H_2O , and others) to be separated from the air sample and, for CH_4 and H_2O , transformation into a measurable molecule, such as CO_2 or H_2 before injection into the mass spectrometer. Respective fractionation-free sample preparation was, therefore, often the most demanding part in the analysis system. Since optical methods have become more sensitive and substance-specific, care has to be taken to avoid spectral interference with other species. For gases with very low abundances, there is also the need for pre-concentration of the component in the sample to be analyzed. Entire analysis systems including sample preparation will be presented in Sect. 17.4. Here we first describe the fundamental background of the different detection systems for atmospheric isotopologue measurements that have been published and are currently in use.

17.3.1 Isotope Ratio Mass Spectrometry (IRMS)

As mentioned earlier, only $\delta^{13}\text{C}\text{-CO}_2$ and $\delta^{18}\text{O}\text{-CO}_2$ can be measured directly on pure CO_2 extracted from whole-air samples. Three Faraday cups are used in the spectrometers, one for collecting mass 44 ($^{12}\text{C}^{16}\text{O}_2$) ion beams, one for mass 45 ($^{13}\text{C}^{16}\text{O}^{16}\text{O}$, $^{12}\text{C}^{16}\text{O}^{17}\text{O}$) and one for mass 46 ($^{12}\text{C}^{16}\text{O}^{18}\text{O}$, $^{13}\text{C}^{16}\text{O}^{17}\text{O}$, $^{12}\text{C}^{17}\text{O}^{17}\text{O}$). Since mass 45 and mass 46 ion beams both contain a mixture of two and three isotopologues, respectively, an assumption of a relation between $^{18}\text{O}/^{16}\text{O}$ and $^{17}\text{O}/^{16}\text{O}$ in ambient samples must be made [17.20]. This is done by assuming that the ratio is only modified by mass-dependent fractionation during related exchange and transformation processes. This then allows for the estimation of accurate $^{13}\text{C}/^{12}\text{C}$ and $^{18}\text{O}/^{16}\text{O}$ ratios of CO_2 . Different correction functions have been suggested ([17.49] and references therein) and were implemented in IRMS software/programs used in individual laboratories, which can lead to biases between measurements in different laboratories that potentially exceed repeatability errors achieved by modern IRMS analytics.

Moreover, when CO_2 is extracted cryogenically at -196°C (with liquid nitrogen) from ambient air samples, atmospheric N_2O is trapped together with the CO_2 and respective N_2O ions generated in the MS ion source are collected on the mass 44 ($^{14}\text{N}_2^{16}\text{O}$) and mass 45 ($^{15}\text{N}^{14}\text{N}^{16}\text{O}$) Faraday cups. This interference also needs to be corrected for; it requires measurement of the N_2O ionization efficiency in the ion source of the IRMS used [17.50].

The $^{17}\text{O}/^{16}\text{O}$ ratio in atmospheric CO_2 (and water) samples, although at first glance assumed to have a fixed relation to its $^{18}\text{O}/^{16}\text{O}$ ratio (see above), has been shown to be anomalously enriched in the stratosphere, due to mass-independent photochemical reactions [17.51]. The measurement of the $^{17}\text{O}/^{16}\text{O}$ ratio of CO_2 , however, requires chemical transformation of the oxygen in the CO_2 , due to the overlap at mass 45 with the relatively large signal of $^{13}\text{CO}_2$. Note that the typical $^{13}\text{C}/^{12}\text{C}$ ratio of CO_2 is on the order of 1%, while the $^{17}\text{O}/^{16}\text{O}$ ratio is only $\approx 0.04\%$. In some applications, the oxygen is fully extracted from the CO_2 [17.52, 53] and then measured as O_2 by IRMS. Alternatively, the $^{17}\text{O}/^{16}\text{O}$ ratio of the CO_2 is modified by isotope exchange with water to a known value to allow for the correct determination of the $^{13}\text{C}/^{12}\text{C}$ ratio of the sample (that stays unchanged during the oxygen equilibration reaction). The $^{17}\text{O}/^{16}\text{O}$ ratio of the original sample can then be determined from the original measurement [17.54, 55].

Quasicontinuous CO_2 isotopologue measurements can be conducted when the mass spectrometer is coupled with a gas chromatograph that separates CO_2 from the ambient air (and N_2O) and subsequently injects the CO_2 peak into the MS [17.56]. This methodology, continuous-flow isotope ratio mass spectrometry (CF-IRMS), although less precise than offline extraction and IRMS analysis, has been applied in the field, for example to study CO_2 exchange processes in ecosystems [17.11].

Mass spectrometric analysis of stable isotopes in atmospheric water vapor (and precipitation) requires well-established preprocessing of the (cryogenically) collected samples. For the ^{18}O isotope ratio, the water sample is equilibrated at a predefined temperature with CO_2 , which is then measured by IRMS. As discussed above for CO_2 , the measurement of ^{17}O on water samples by IRMS is not possible solely via CO_2 equilibration due to mass interference with $^{13}\text{C}\text{-CO}_2$, and this also requires particular preprocessing [17.57]. For hydrogen isotope analysis, the water is catalytically reduced to hydrogen gas, which can then be measured by IRMS on two Faraday cups, one for mass 2 (H_2) and one for mass 3 ($^1\text{H}^2\text{H}$). The measurement is complicated by the fact that in the ion source, H_2 combines with one H^+ and forms an H_3^+ ion, thus contributing to the mass 3 ion beam. A respective instrument-dependent correction needs to be made to account for this effect [17.1].

The development of CF-IRMS has greatly improved the measurement capacity of methane isotopologues [17.32, 42, 43, 58, 59]. Compared to former off-line extraction and preconcentration systems, this methodology requires a smaller sample size and allows automation to be run autonomously in the field [17.18].

Still, the preconcentrated and cryo-focused CH_4 samples need to be converted to CO_2 and H_2 in order to be measured by IRMS.

17.3.2 Optical Methods

The different isotopologues of gaseous species have different absorption lines in the infrared. Hence, one measures absorption strengths at specific wavelengths for heavy and light isotopologues. There are currently two measurement principles in use, either using monochromatic light specific to the species of interest (tunable diode laser absorption spectroscopy, quantum cascade laser absorption spectroscopy, cavity ring-down spectroscopy, off-axis integrated cavity output spectroscopy, difference frequency generation laser spectroscopy), or a broadband light source that passes an interferometer analyzing all wavelengths (Fourier transform infrared spectroscopy).

Tunable Diode Laser Absorption Spectroscopy (TDLAS)

Light in tunable diode laser absorption spectroscopy (TDLAS) comes from tunable diode lasers, which are the most common type of lasers produced. They are semiconductor devices similar to well-known light-emitting diodes. The diode lasers can be tuned by changing the temperature of operation or by changing gain current. The latter allows tuning only in a limited range of only a few cm^{-1} but this can be achieved quickly and with step sizes $< 0.01 \text{ cm}^{-1}$. Different trace gases therefore need different diode lasers because their absorption bands are too far apart. Different absorption bands of isotopologues, however, can be close together so that a small tuning range is sufficient. TDLAS thus tunes its laser through its narrow wavelength range, sampling the absorption spectrum along the wavelengths [17.60] (see Fig. 17.1 for suitable spectral ranges for CH_4 and CO_2 isotope analysis). To limit pressure broadening of the absorption lines, and hence overlap of the lines of the different isotopologues, most systems reduce pressure in the sample gas cell. But, absorption strength depends on the amount of gas the light passes through, which is much less in reduced pressure. These systems therefore use multipass cells, such as White or Herriott cells, where light gets mirrored multiple times, effectively increasing the path length of the light beam through the sample gas by about two orders of magnitude.

Quantum Cascade Laser Absorption Spectroscopy (QCLAS)

Quantum cascade lasers (QCL) are a special kind of semiconductor laser where thin layers of semiconducting materials are periodically stacked. The emitted

wavelength does not depend on the band gap between conduction and valence band of the material, but rather on the physical layer thicknesses. Quantum cascade lasers can therefore be produced for a large variety of wavelengths but also having several emission lines with the same laser system. Using external cavities with later diffraction gratings makes QCLs highly tunable [17.61]. One electron, transitioning from the conduction band to the valence band, can emit more than one photon in QCLs because of the layered organization. QCLs can hence produce higher output powers than laser diodes. Both, the highly tunable wavelengths and the high power output make QCLs very popular in currently available laser spectrometers [17.62].

Cavity Ring-Down Spectroscopy (CRDS)

Cavity ring-down spectroscopy (CRDS) differs from the above absorption techniques in that it uses a time-based measurement rather than an intensity-based measurement. External cavities are used with most absorption spectroscopies. While most systems use multipass cells, extending effective path length by about two orders of magnitude, one can also use resonance cells that have much higher reflectivity, extending the effective path length by about four orders of magnitude. Traditional absorption spectroscopy measures the attenuation of the incident signal given a known path length. CRDS, on the other hand, measures instead the time it takes that a pulsed signal gets attenuated to a threshold level inside the cavity, the so-called ring-down time. This time is in the order of microseconds and depends on the resonance cavity and the amount of trace gas in the cavity (Fig. 17.2). By pulsing different wavelengths with tunable lasers, one samples the wavelengths of the different isotopologues and thus determines their concentrations [17.63]. Laser systems can be any tunable system such as the above diode lasers or quantum cascade lasers used in pulsed mode.

Off-Axis Integrated Cavity Output Spectroscopy (OA-ICOS)

Similar to QCLAS, OA-ICOS uses continuous-wave mid-IR quantum cascade laser absorption spectroscopy. However, the laser enters the measurement cell at an off-axis angle in OA-ICOS, causing excitation of many transverse modes of different orders and a more efficient averaging of the cavity output, thus improving sensitivity through reduced noise [17.65]. Compared to CRDS, OA-ICOS is orders of magnitude less sensitive to internal alignment due to its geometry. Extremely long pathways (kilometers in a cell of a few centimeters length) through multireflection between the two mirrors of the cavity result in high detection sensitivity and precision. OA-ICOS can be operated at any wavelength

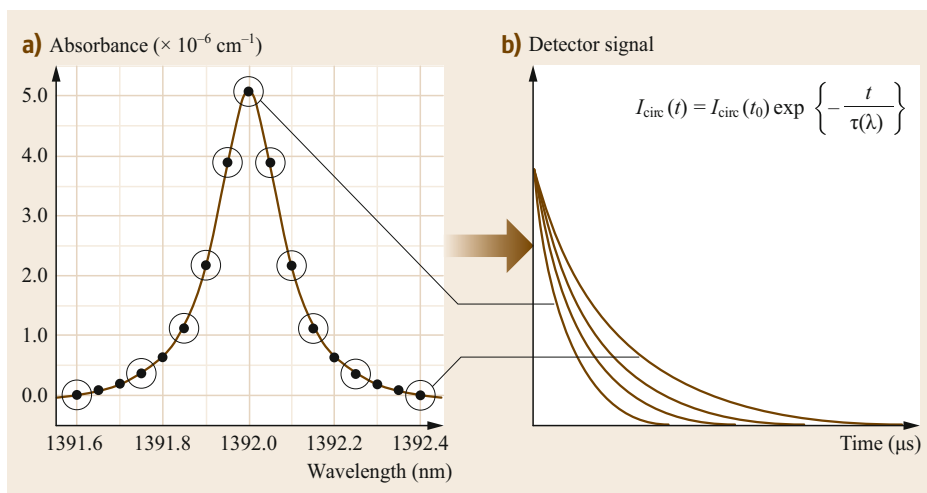


Fig. 17.2a,b Measurement principle of cavity ring-down spectroscopy (CRDS). For each wavelength of the absorption line selected by the wavelength monitor (a), the time development (decay time, (b)) of the beam intensity in the cavity after multireflection is measured (Fig. 17.6). This decay time on the order of microseconds depends on the trace gas concentration in the cavity. The area under the absorbance curve (a) is proportional to the trace gas concentration (after [17.64] with permission from Picarro)

from UV through IR, allowing detection of many different trace gas species and their isotopic ratios.

Difference Frequency Generation (DFG) Laser Spectroscopy

The DFG laser spectrometer of Thermo Fisher Scientific utilizes a simple multipass cell design and laser radiation covering the strong absorption bands in the mid-IR [17.65, 66] (i.e., $2310.1\text{--}2311.0 \text{ cm}^{-1}$, Fig. 17.1). Mid-IR laser radiation is produced by difference frequency generation (DFG) where the beams of two laser diodes are introduced into a nonlinear crystal made from periodically poled lithium niobate (PPLN), generating emission of wavelengths that correspond to the difference of the two fundamentals. One laser is frequency-stabilized, while the other is a tunable distributed feedback laser that is used to tune the difference frequency, in order to cover the spectral range of $2310.1\text{--}2311.0 \text{ cm}^{-1}$. The laser light then enters a multipass cell where it is reflected between two curved mirrors yielding a total effective optical path length of $\approx 5 \text{ m}$. The laser scans over the absorption lines at 500 Hz and the signal is averaged over 1 s before the absorption spectrum is fitted and isotope ratios are calculated from the spectrum fit [17.67].

Fourier Transform Infrared Spectroscopy (FTIR)

Instead of single-wavelength tunable lasers, Fourier transform infrared (FTIR) spectroscopy uses the broadband infrared (IR) radiation from a blackbody light source that covers the entire IR spectrum. The FTIR

uses a Michelson interferometer where the beam of radiation, after having passed the absorption cell, is split with one part directed to a fixed and the other to a movable mirror, introducing a path length difference between the two beams. After recombination of the reflected beam parts, an interference pattern of intensity, depending on the position of the movable mirror is observed at the detector; this is called interferogram [17.14, 68, 69]. Thus, instead of stepwise changing the wavelength of the light source to analyze the transmitted spectrum that has passed the sample cell, the transmission spectrum is calculated via Fourier transformation from the measured interferogram. This way FTIR spectroscopy principally covers the entire mid-infrared (MIR) spectrum of the blackbody light source, where the strong fundamental rotation–vibration bands of many important greenhouse gases, such as H_2O , CO_2 , CH_4 , and N_2O are located. If the interferometer has sufficient resolution to distinguish overlapping absorption bands (e.g., $\leq 0.01 \text{ m}^{-1}$), gas concentrations of several trace gases and, in the case of H_2O and CO_2 also some of their isotopologues, can be measured simultaneously [17.14]. A typical transmission spectrum from an FTIR spectrometer is shown in Fig. 17.3. The relatively weak absorption signals due to the blackbody radiation source being less bright than that of a laser is counteracted by using long multipath sample cells in the interferometer. Precision is also improved by including many absorption lines of the analyzed species. The obtained transmission spectrum is evaluated by a fitting algorithm that calculates

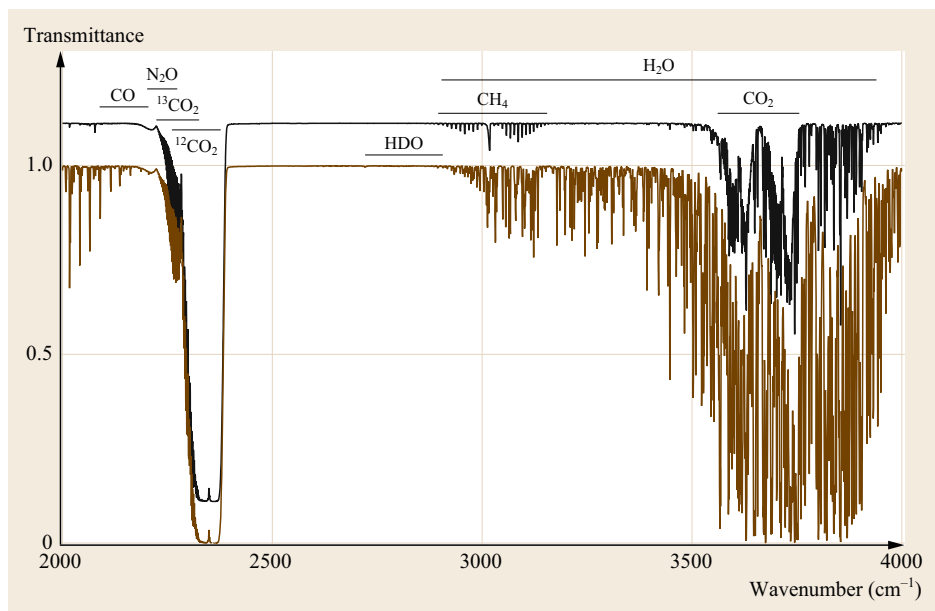


Fig. 17.3 Mid-infrared absorption spectrum of clean air in a 24 m FTIR multipass cell. *Brown:* undried air, *black:* dried air. Positions of main absorption bands of H₂O, CO₂, CH₄, CO, and N₂O are indicated by *horizontal lines* (after [17.14] © D. W. T. Griffith et al., licensed under CC-BY)

the specific absorption coefficients of the different gas components in the sample. Using the individual characteristic absorption bands of the gases (taken from the HITRAN database [17.70]) the algorithm generates a theoretical spectrum based on estimated concentration

values. It then recalculates the concentration values in an iterative way until the best fit to the measured spectrum is achieved [17.71] to determine the final GHG concentrations.

17.4 Devices and Systems

While prototypes of the above-described instrumentation were developed in various research institutions, measurement systems are now commercially available from a number of specialized companies. In many cases, air intake pumping and drying systems are already included in these off-the-shelf devices. Often, however, modifications are introduced by users to reach the required high precision for continuous atmospheric observations. Here we describe some of these dedicated devices, which have been recently or still are successfully applied in the field.

17.4.1 Continuous Isotope Observations with Tunable Diode Laser Absorption Spectroscopy

Tunable diode laser absorption spectroscopy (TDLAS) has been used for trace gas measurements since the late 1980s [17.72, 73]. A classic design of a compact, robust and portable TDLAS monitor was introduced by *Edwards et al.* [17.74] and is now commercialized by Campbell Scientific, Inc., Logan, UT, USA. *Bowling et al.* [17.75] describe the first generation of

Campbell's so-called trace gas analyzer (TGA) and its modifications for atmospheric isotope measurements (Fig. 17.4).

The tunable diode laser is controlled simultaneously for temperature and current to produce a linear wavelength scan centered around single selected absorption lines of the isotopologues of the target gas. The original lead-salt diode lasers needed strong cooling, most often with liquid nitrogen that needed refilling as much as twice per day at the beginning (1993) down to once per week with the TGA200 in 2008. A new room-temperature thermoelectrically cooled interband cascade laser has been used since 2014, making the TGAs more autonomous instruments. The laser beam is split passing through single-pass reference and sample cells. Single-pass cells are chosen to avoid alignment and contamination problems associated with multipath absorption cells. A prepared reference gas having a known composition is flown through the reference cell. The reference signal provides a template for the shape and position of the absorption spectrum, avoiding the need for precise temperature and pressure measurements in the sample cell.

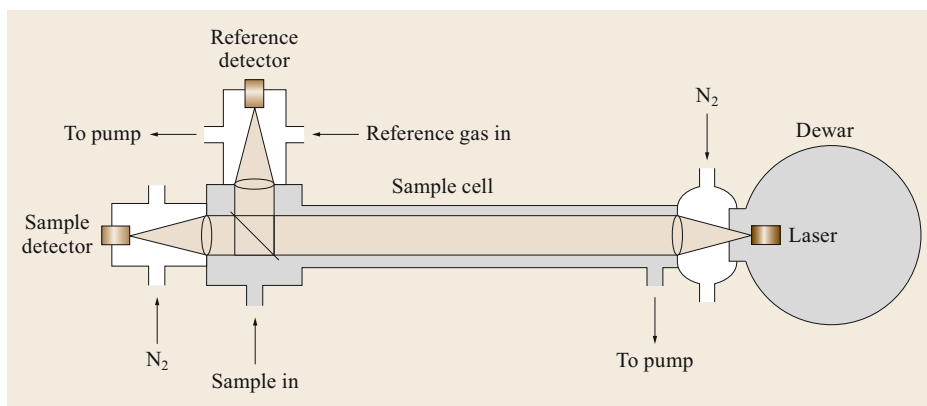


Fig. 17.4 Diagram of Campbell's TGA100 tunable diode laser absorption system (after [17.75] with permission from Elsevier)

17.4.2 High-Resolution Isotope Observations with Quantum Cascade Laser Absorption Spectroscopy

Laser absorption spectroscopy can use principally any laser that can be tuned over a certain wavelength. Popular devices using pulsed quantum cascade lasers (QCL) are the so-called laser trace gas monitors of Aerodyne Research, Inc., Billerica, MA, USA (Fig. 17.5). A key feature of these instruments is a dual-path multipass cell. This is an astigmatic Herriott cell, where the path length depends on the angle the beam enters the cell [17.76]. The ratio of the path lengths is chosen to be similar to the abundance ratio of the different isotopologues, yielding similar absorption depths for both isotopologues [17.19]. For carbon dioxide, the two paths correspond to 2 (e.g., $^{12}\text{CO}_2$) and 174 (e.g., $^{13}\text{CO}_2$) passes within the cell of 0.32 m length. Hence, temperature and pressure are identical for both measurements, i.e., the major and minor isotopologue, because the two measurements are simultaneous within the same cell. Absorption lines are chosen so that they can be detected within a single spectral scan (over 0.5 cm^{-1}) obtained by a current ramp, which modulates laser temperature and thus its spectral frequency. Differences in absorption spectra due to pulse-to-pulse energy variations are reduced by normalizing the pulses via a special reference path within the optical base (Norm. path in Fig. 17.5). Very short pulses ($\approx 10\text{ ns}$) are used to minimize linewidth, but linewidth and associated line shape stability remain precision limiting issues.

The laser trace gas monitors also exist with two QCLs working in parallel. It takes advantage of the astigmatic Herriott cell, which can have not only two but multiple path lengths. The two lasers sweep over two different wavelength ranges, using different angles of attack on the sample cell, which implies different

path lengths within the cell. This allows, for example, measuring methane and carbon monoxide simultaneously, using transitions at 1271 and 2180 cm^{-1} , respectively [17.78].

17.4.3 Stable Isotope Observations with Cavity Ring-Down Spectroscopy

The most common instrument measuring stable isotope ratios with cavity ring-down spectroscopy (CRDS) are manufactured by Picarro, Inc., Santa Clara, CA, USA ([17.12], Fig. 17.6). They use a patented wavelength monitor, which is used threefold:

- (1) It monitors the wavelength from the incoming laser
- (2) It locks the laser to the wavemeter, and
- (3) It can be tuned to different wavelengths, hence actively scanning the absorption line (Fig. 17.2a).

The near-IR laser diode is tuned by changing its drive current and temperature. The relationship between current and wavelength is, however, not stable over time and between individual lasers, which is solved by using the wavelength monitor. The Picarro CRDSs use a ring resonator, i.e., a three-mirror cavity (triangular, Fig. 17.6) resulting in a traveling wave compared to standing waves in two-mirror cavities, providing better signal-to-noise ratio. The cavity is temperature-stabilized to within 20 mK, using active and passive thermal stabilization. The instrument further controls the pressure in the sample cell to within 5 Pa around its nominal pressure of $\approx 187\text{ hPa}$. The stabilization of wavelength, temperature, and pressure allows for precise measurements of isotope ratios [17.15] down to $\approx 0.02\text{ ‰}$ in water and 0.1 ‰ in CO_2 for averages over a few minutes (Table 17.4).

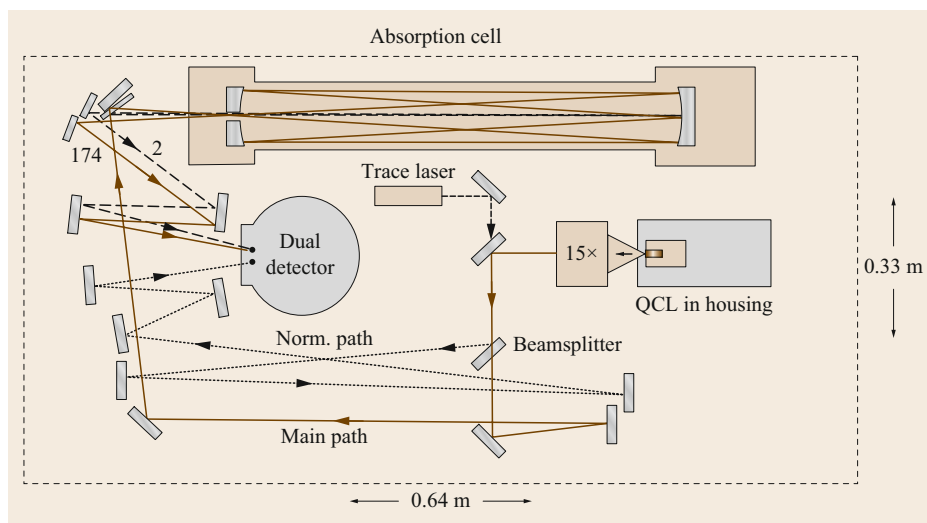


Fig. 17.5 Optical layout of Aero-dyne's single quantum cascade laser instrument (after [17.77] reprinted by permission of Taylor & Francis Ltd.)

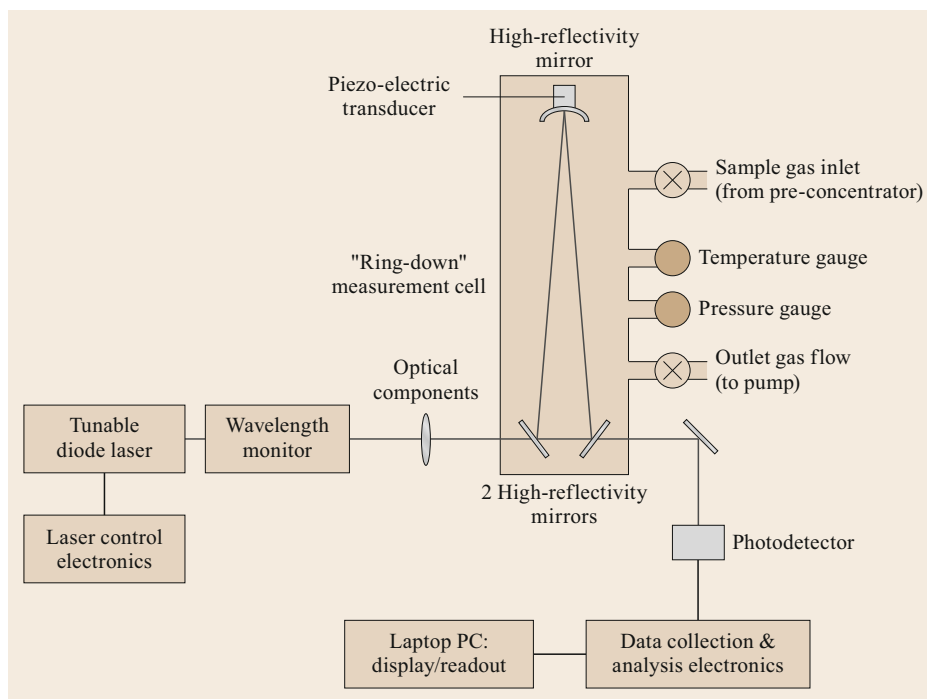


Fig. 17.6 Schematic diagram of Picarro's cavity ring-down instrument (after [17.12] reprinted by permission of Taylor & Francis Ltd.)

17.4.4 Continuous Atmospheric $^{13}\text{C}\text{-CO}_2$ Observations by Fourier Transform Infrared Spectroscopy

After development and publication of a new in-situ FTIR system for precise greenhouse gases concentration and CO_2 (and H_2O) isotopologue measurements by Griffith et al. [17.14], a FTIR system was installed and is still continuously run at the Institut für Umweltphysik, Heidelberg University, to analyze ambient air

on the University campus in Heidelberg, Germany. This system has been slightly modified for better pressure and flow stabilization in the cell and is further equipped with additional air intakes for calibration gases and for regular measurement of so-called target gases for quality assurance [17.79] (Sect. 17.6). A schematic of the Heidelberg in-situ FTIR system is displayed in Fig. 17.7. Ambient or tank air is admitted via a multiport selection valve with the flow rate being stabilized by a mass flow controller (MFC). The sample air then

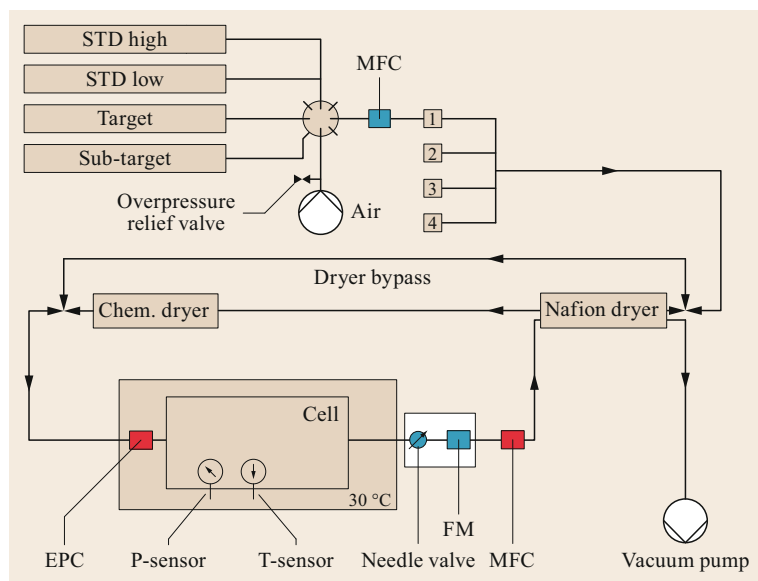


Fig. 17.7 Schematic setup of the in-situ FTIR analyzer of Hammer et al. [17.79]. The blue parts of the original setup of Griffith et al. [17.14] have been replaced with the red parts in the final setup. The modifications include mass flow controllers (MFC) and electronic pressure controllers (EPC) and replace the original needle valve–flow meter (FM) unit (after [17.79] © S. Hammer et al., licensed under CC-BY)

passes a Nafion predrying unit (operated in counter flow mode) and is further chemically dried to an H₂O vapor pressure of < 4 ppm. Excellent drying is necessary to avoid too much overlap of water vapor absorption bands with those of the trace GHGs and CO₂ isotopologues to be monitored (Fig. 17.3). The dry air then passes the 3.5 L multipass cell with 24 m optical path length. An electronic pressure controller at the inlet together with a second MFC at the outlet of the cell keep pressure constant at a slight over-pressure above ambient. A vacuum pump at the air outlet allows evacuation of the cell before admittance of tank air (calibration or target gases). This reduces flushing time of the cell and, thus, the amount of calibration gases needed to fully replace the air of the rather large cell volume (3.5 L). The multipass cell itself is equipped with an in-situ PT100 resistance temperature detector as well as with a pressure sensor. The housing of the cell including the interferometer (IRCube, Bruker Optics, Germany) is temperature stabilized to better than ± 0.1 °C and is permanently flushed with high-purity nitrogen (99.999%) to avoid absorption of GHGs between cell and interferometer.

After modification, Hammer et al. [17.79] performed careful characterization of the entire in-situ FTIR system, including determination of the instrument response function as well as residual interspecies cross-sensitivities. These effects stem from incomplete separation of partly overlapping absorption bands due to imperfect spectral information in the HITRAN [17.70] database as well as from imperfect fitting routines. Further, sensitivity towards residual temperature and pressure variations, i.e., imperfect determination of the sample density in the cell, but also imperfect infor-

mation on these parameters in the HITRAN database determining the line shape required for fitting were determined. Cross-sensitivities turned out to be relevant for CO₂, ¹³C-CO₂, and N₂O, and need to be corrected for if the interlaboratory compatibility goals agreed on by WMO experts (Table 17.3) shall be reached. The instrument was proven to be linear for all GHGs and ¹³C-CO₂ in their ambient air ranges.

The short-term stability of all components was tested with tank air and turned out to be excellent, i.e., reaching the WMO compatibility goals for all GHGs mole fractions and the extended WMO compatibility goal for $\delta^{13}\text{C-CO}_2$ [17.80]. A weekly calibration frequency of the instrument was recommended. $\delta^{18}\text{O-CO}_2$ measurements in ambient air turned out to be possible too, as was shown in a subsequent study by Vardag et al. [17.17]. However, the precision of $\delta^{18}\text{O-CO}_2$ of 0.2–0.3 ‰ turned out not to meet the WMO compatibility goals, neither for regional nor for background air (Table 17.3, from [17.80]).

The FTIR instrument originally developed by the University of Wollongong, Australia, is now commercially available through ECOTECH (Spectronus Trace Gas and Isotope Analyser). In order to reduce the amount of calibration gases, one of the major disadvantages of the instrument, the cell volume was reduced to 2.5 L and it is now manufactured from aluminum and internally gold coated. The latter is to reduce interaction of the measured gases with cell walls. Also, temperature measurement in the cell and its control in the housing was improved. Advantages and disadvantages of FTIR and the other instrumentation presented in this chapter are listed in Table 17.2.

Table 17.2 Comparison of the isotopologue measurement methods

Devices	Advantages	Disadvantages
Isotope ratio mass spectrometry (IRMS)	High sensitivity Applicable to all isotopologues	Pretreatment of air sample required Interfering masses Low temporal resolution
Tunable diode laser absorption spectroscopy (TDLAS)	Availability of wide range of lasers Precise and wide tuning High temporal resolution	Smaller output power than QCL thus less sensitive Some systems do not operate at room temperature
Quantum cascade laser absorption spectroscopy (QCLAS)	Precise tuning with external cavity and diffraction gratings High temporal resolution Large output power High mode purity and wavelength stability	Pulsed mode not optimal and under active development Higher noise thus less sensitive than OA-ICOS
Cavity ring-down spectroscopy (CRDS)	Large range of gas concentrations Insensitive to vibrations Measures and corrects for water vapor	Absolute value of laser wavelength needed Cavity sensitive to temperature and pressure Ring-down time limits sampling frequency Possible interferences of organic molecules
Off-axis integrated cavity output spectroscopy (OA-ICOS)	High sensitivity Large range of gas concentrations Precise beam alignment not critical	No quantitative information on precision and long-term stability available for isotopes in atmospheric CO ₂ and CH ₄
Difference frequency generation laser spectroscopy (DFG)	High precision if referencing is frequently performed Standard gas concentrations adjusted to measured concentration	Standard has different matrix gas than measured sample Frequent referencing strongly reduces time for ambient measurement Current systems have insufficient internal drying units (dewpoint > -20 °C) and not all sample ports are equipped with mass flow controllers
Fourier transform infrared spectroscopy (FTIR)	Many air components measured simultaneously Re-evaluation of spectra possible if interest in additional trace gas or if improved spectral information becomes available	Large sample cell requiring large amounts of sample and calibration gases Low temporal resolution Strong cross-sensitivities of many trace gases with water vapor, requires drying to < 8 ppm for precise measurement of GHGs other than H ₂ O

17.4.5 Atmospheric Observations of Methane Isotopologues by Continuous-Flow Mass Spectrometry in Comparison to Quantum Cascade Laser Absorption Spectroscopy

An interesting study, comparing atmospheric methane isotopologue observations by continuous-flow dual-isotope ratio mass spectrometry with optical measurements by QCLAS at the Cabauw meteorological tower in the Netherlands, has been published by *Röckmann et al.* [17.18]. Both systems use CH₄ preconcentration units but do not require liquid nitrogen, an important advantage for field applications.

Figure 17.8 displays the IRMS setup for $\delta^{13}\text{C}$ and $\delta^2\text{H}$ analysis of atmospheric CH₄, which is based on the integrated System for Analysis of Atmospheric Constituents (ISAAC) developed for flask sample analysis at the Max Planck Institute for Biogeochemistry (MPI-BGC) in Jena, Germany [17.32]. Predried air is collected either from an ambient intake line or from a reference gas tank and is pumped through a preconcentration trap filled with molecular sieve (HaySep D) and cooled down to a temperature below -132 °C.

For cooling, the preconcentration trap is mounted in a copper bloc, cooled with a Polycold compact cooler compressor (Brooks Automation Inc., USA). In the same device a focus trap is mounted. Preconcentration and focus traps can be kept at different temperatures to allow, for example, transfer of the sample from the preconcentration trap (then heated to -30 °C) to the focus trap (kept at below -132 °C).

After complete sample transfer to the focus trap, it is heated up to release the CH₄, which is then either passed on (with He as carrier gas) to a combustion oven, where CH₄ is oxidized to CO₂ and H₂O, then passed through a Nafion dryer for H₂O removal and further through a gas chromatographic column to eliminate interfering co-trapped krypton before it is injected into the MS (Delta plus XP, Thermo Fisher Sci.) for $\delta^{13}\text{C}$ analysis. For $\delta^2\text{H}$ analysis, the CH₄ sample is converted to H₂ and carbon in a pyrolysis tube furnace and, after passing a CarboPLOT column and a Nafion dryer, the H₂ is introduced into the MS for deuterium analysis.

The laser-based QCLAS system run at Cabauw in parallel to the IRMS system introduced above was described in detail by *Eyer et al.* [17.81]. The optimal con-

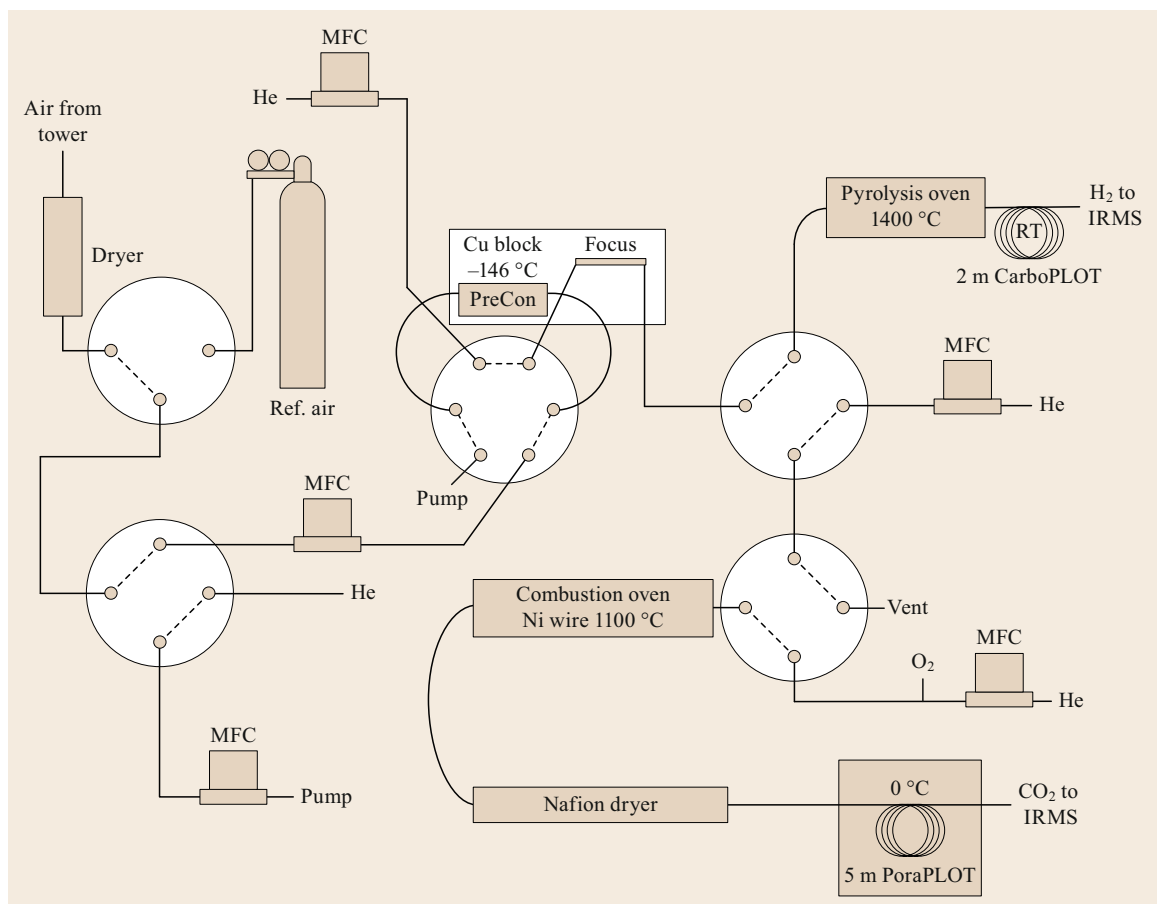


Fig. 17.8 Schematics of the pre-concentration and extraction system developed for the IRMS technique (after [17.18] © t. rückmann et al., licensed under CC-BY)

ditions for analyzing both stable isotope ratios of CH_4 with the commercially available quantum cascade laser system QCL-76-D (Aerodyne Inc., USA) at 20–60 hPa are at a mole fraction range of 600–1000 ppm CH_4 , requiring pre-concentration from ambient mole fraction by a factor of 300–400. A schematic of this trace gas extractor (TRES) is displayed in Fig. 17.9. Similar to the pre-concentration unit used in the IRMS setup above (Fig. 17.8), it requires cooling to very low temperatures. This is achieved with a Stirling cooler. The adsorption trap, filled with HaySep D to selectively retain CH_4 from the air sample, is cooled down to about -175°C (Fig. 17.9, left part) when attached to the copper plate while it gets warmed up stepwise after being detached from the cooler plate (Fig. 17.9, right part) for release of volatile bulk gases. When the temperature reaches -15°C , CH_4 also desorbs from the trap and is transferred to the previously evacuated cell of the QCLAS with synthetic air as purge gas. This process is finished when the pressure in the cell has reached ≈ 40 hPa; the

accumulated sample is then analyzed. The laser spectrometer is based on the QCL-76-D system (Aerodyne Res. Inc., USA) with an optical path length of 76 m and a cell volume of 0.5 L. Hardware electronics have been modified as described by Eyer et al. [17.81] in order to meet the required precision.

Comparability of isotopologue observations between the two systems when measuring ambient air at the Cabauw tower was restricted by lack of synchronization of the analysis cycles (84 min for the IRMS system and 54 min for the TRES-QCLAS system) and air sample integration periods, which were 10 min for the IRMS and 15 min for the TRES-QCLAS. The overall difference between the two systems (QCLAS – IRMS) was $(0.25 \pm 0.04)\text{‰}$ for $\delta^{13}\text{C}$ and $(-4.3 \pm 0.4)\text{‰}$ for $\delta^2\text{H}$. This is slightly outside the extended WMO compatibility goals for stable isotopes in CH_4 (compare Table 17.3) but demonstrates the current state-of-the-art ability of quasicontinuous ambient air CH_4 isotopologue measurements.

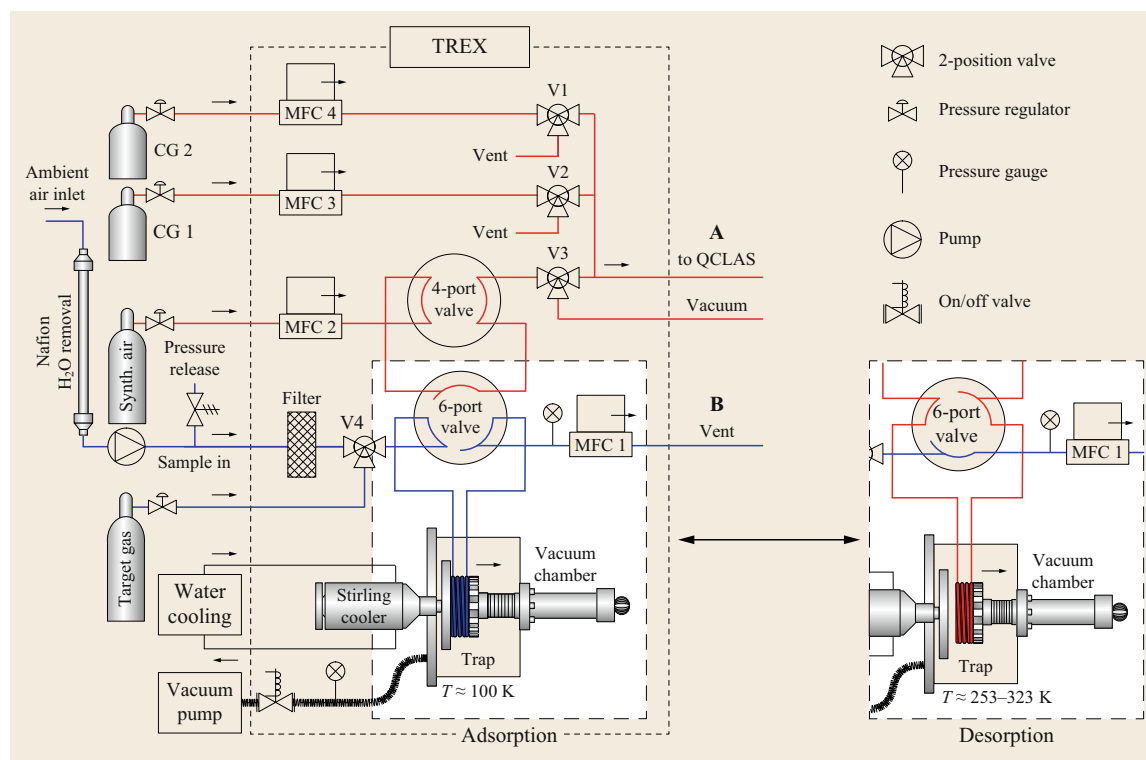


Fig. 17.9 Schematics of the preconcentration unit (TREX) used by Röckmann et al. [17.18]. The blue lines indicate the flow of sample air and target gas, i.e., ambient air CH_4 mole fractions, while red lines represent the flow of calibration gases and desorbed air, i.e., high CH_4 mole fraction (after [17.81] © S. Eyer et al., licensed under CC-BY)

Table 17.3 WMO recommendation for compatibility of measurements of GHGs [17.80]

Component	Compatibility goal 1-sigma	Extended compatibility goal ^{a)}	Range in unpolluted troposphere (approximately range for 2015)	Range covered by the WMO scale
CO_2 (ppm)	± 0.1 (NH ^{b)} ± 0.05 (SH ^{b)})	± 0.2	380–450	250–520
CH_4 (ppb)	± 2	± 5	1750–2100	300–5900
$\delta^{13}\text{C}-\text{CO}_2$ (‰)	± 0.01	± 0.1	–9.5 to –7.5 (VPDB)	
$\delta^{18}\text{O}-\text{CO}_2$ (‰)	± 0.05	± 0.1	–2 to +2 (VPDB-CO2)	
$\delta^{13}\text{C}-\text{CH}_4$ (‰)	± 0.02	± 0.2		
$\delta^2\text{H}-\text{CH}_4$ (‰)	± 1	± 5		

^{a)} Extended compatibility goal is provided as a guideline for studies in which the highest precision and accuracy is not required, for example a regionally focused study with large local fluxes, or services related to urban air quality.

^{b)} NH Northern hemisphere; SH Southern hemisphere.

17.4.6 Overall Evaluation of Available Isotope Measurement Systems

Thanks to the development of new optical instrumentation, precise quasicontinuous field observations of stable isotope ratios in atmospheric CO_2 , CH_4 , and H_2O have become possible. Some characteristics of different commercially available systems are listed in Table 17.2. Continuous isotope measurements are most relevant for

continental or regional applications, where the temporal variability of GHGs is large and where many different source components are associated with different catchments. In the case of CH_4 with atmospheric mole fractions of $< 2 \mu\text{mol mol}^{-1}$, preconcentration is necessary before analysis, which limits time resolution of observations. In some cases, e.g., with FTIR systems, relatively large cell volumes of more than 1 L are also limiting factors for the temporal resolution on one hand,

but also, for example, for their application on stations at tall towers, where fast switching through different levels is required to measure vertical profiles in the atmospheric boundary layer. Although absolute isotope

ratio measurements are principally possible with optical methods, frequent calibration against internationally agreed standards is important for accuracy and compatibility of observations (Sect. 17.6).

17.5 Specifications

Most optical systems have very short response times on the order of milliseconds. One can average several measurements to derive more precise estimations of concentrations. Hence, precision of the different measurement systems depends on the averaging time, which might be given by specific application requirements (high temporal resolution, e.g., for application of eddy-covariance techniques to calculate energy and matter fluxes, see Chap. 55). Atmospheric trace gas concentrations generally do not need temporal resolution of less than one minute and a large number of high-frequency observations can be averaged for more precise mean observations. The averaging time that leads to more precise observations might be limited due to instrument stability such as instrument drifts and temperature effects. This is often investigated with Allan–Werle plots (Fig. 17.10, for $\delta^{13}\text{C-CO}_2$ from [17.17]): the Allan variance (or Allan standard deviation) of the individual high-frequency observation in a certain averaging time interval is plotted against the length of the averaging time [17.82]. The minimum of this curve shows the maximal attainable precision. This is not to be mistaken as the accuracy of the observations. The precisions given in Table 17.4 depend on how the instrument is employed, and which averaging time the specific application demands. Resolutions are given approximately for the fastest instruments in the literature.

Some isotopic species such as deuterated methane are so rare that precise ambient air measurements require preconcentration systems (Sect. 17.4.5) [17.81]. This limits time resolution severely, particularly for continuous-flow IRMS, but even optical instruments might only give one observation per hour (Sect. 17.4.5).

As part of the WMO Global Atmosphere Watch GHG monitoring program (see also Chap. 63), WMO organizes, together with the International Atomic Energy Agency (IAEA), biennial meetings to review the scientific understanding of greenhouse gas sources and sinks, evaluate the network development, review the best practices for quality assurance and quality control, and examine data quality objectives and measurement techniques. The WMO regularly updates their recommendations based on the proceedings from these meetings as WMO Reports [17.80]. These recommen-

ations also include compatibility goals for the various GHGs and their isotopologues, to allow for merging data from different laboratories or networks for global or regional model evaluation. These goals mainly concern compatibility of observations in the background atmosphere where gradients from which, e.g., hemispheric source or sink strengths are deduced, are small (column 2 in Table 17.3). Compatibility goals are slightly relaxed for regional applications named *extended compatibility goal* and listed in column 3 of Table 17.3.

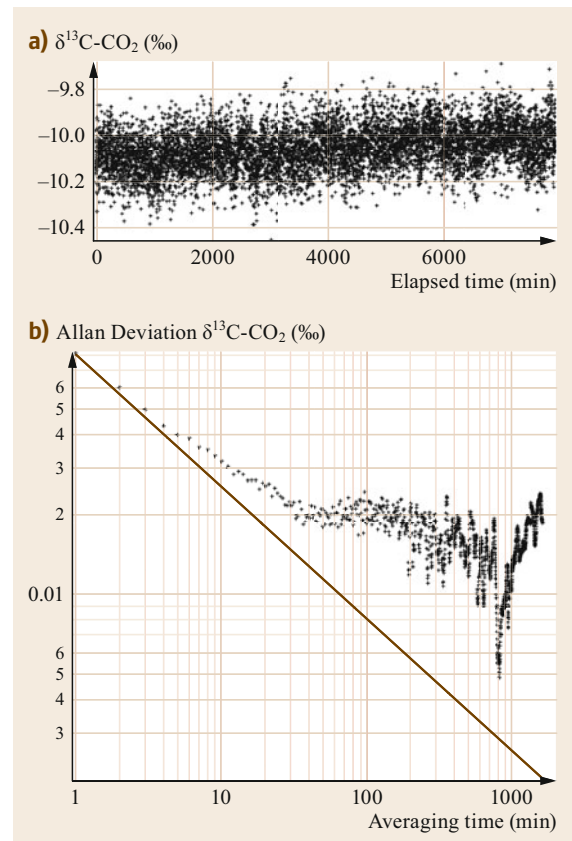


Fig. 17.10a,b Allan–Werle plot (b) of nine-minute mean $\delta^{13}\text{C-CO}_2$ measurements by FTIR of a standard gas over 6 days (a) (after [17.17])

Table 17.4 Specification of different measurement methods for CO₂, CH₄ and H₂O isotopologues. *P* = precision (in ‰), *R* = resolution (in s) ([17.11, 12, 14–16, 18, 62, 66, 81, 83–85]), and material from Aerodyne Research Inc., Campbell Scientific, ECOTECH, Los Gatos Research Inc., Picarro Inc., Thermo Fisher Scientific)

Method	$\delta^{13}\text{C-CO}_2$		$\delta^{18}\text{O-CO}_2$		$\delta^{13}\text{C-CH}_4$		$\delta^2\text{H-CH}_4$		$\delta^{18}\text{O-H}_2\text{O}$		$\delta^2\text{H-H}_2\text{O}$	
	<i>P</i>	<i>R</i>	<i>P</i>	<i>R</i>	<i>P</i>	<i>R</i>	<i>P</i>	<i>R</i>	<i>P</i>	<i>R</i>	<i>P</i>	<i>R</i>
IRMS	0.2	180	0.3	180	0.07	5040	2	5040				
TDLAS	0.5 (10 Hz) 0.1 (1 min)	> 1/10	1.5 (10 Hz) 0.3 (1 min)	> 1/10	0.6	60	5	60				
QCLAS	0.03 (1 min) 0.1 (1 s)	> 1/10	0.03 (1 min) 0.1 (1 s)	> 1/10	1.5 (1 s) 0.1 (5 min)	1	0.5 (5 min)	3000	0.1 (1 s)	> 1/10	0.3 (1 s)	> 1/10
CRDS	0.1 (5 min)	3			1 (5 min)	5			0.02 (1 min)	1	0.1 (1 min)	1
OA-ICOS									0.2	60	1.0	60
DFG	0.04	120	0.06	120								
FTIR	0.04	300	0.4	300					0.2	300	1	300

17.6 Quality Control

As noted above, the very low abundances of some GHG isotopologues and the small spatial and temporal variations of these abundances in the atmosphere require precise measurements. Moreover, data from different laboratories must be highly compatible in order to allow for combining them into global data sets for global GHG budgeting. Calibration relative to internationally agreed standard material as well as ongoing quality control measures are, thus, essential for meaningful data evaluation.

17.6.1 Calibration

As indicated in Sect. 17.1, none of the described instrumentation for stable isotope analysis in GHGs provides accurate absolute isotope ratios from which δ -values can be calculated. Therefore, all instrumentations need calibration gases, which are regularly analyzed to monitor accuracy and long-term repeatability. Depending on instrument response characteristics, two to four calibration points, covering the range of ambient air abundances, are regularly measured for calibration. In many cases, depending on the stability of the instrument, a working gas is frequently analyzed and used as an ongoing reference while the entire response curve for calibration is only measured once per week or even at lower frequency.

The primary standard material was internationally agreed upon during times when (precise) stable isotope measurements were exclusively made by IRMS. In the case of carbon isotopes, the VPDB carbonate standard has to be processed to yield pure CO₂ gas before being analyzed by dual-inlet mass spectrometry [17.20, 50]. Likewise, VSMOW standard water is equilibrated with CO₂ under preset stabilized conditions to allow analysis

as CO₂ gas by IRMS, which carries the ¹⁸O signal, or it has to be reduced to H₂ for deuterium analysis. In the case of CO₂, reference materials, which are linked to the primary scale, are available from the International Atomic Energy Agency [17.86, 87]. This allows for direct calibration of mass spectrometers without chemical processing of the primary carbonate standard VPDB.

As many laboratories in the world that contribute to the global network of atmospheric GHGs isotopologue observations do not have facilities for primary standard preparation, a Central Calibration Laboratory for consistent stable isotope calibrations for CO₂ was established at the Max Planck Institute of Biogeochemistry in Jena, Germany [17.88]. This laboratory provides CO₂-in-air gas mixtures, the so-called JRAS (Jena Reference Air Set) calibration gases that are directly linked to the international stable isotope scale (VPDB for $\delta^{13}\text{C}$) [17.80]. For stable isotopes in CH₄, no such central calibration laboratory currently exists. Laboratories performing these measurements thus have to establish and maintain their own internal standard scale. International compatibility of ambient CH₄ isotopologue measurements is thus not yet fully achieved. Comparison activities are conducted to determine scale offsets between laboratories [17.89] or co-located measurements are compared as an attempt to combine globally distributed observations, e.g., for global modeling efforts [17.90].

17.6.2 Cross-Sensitivities

Precision (and accuracy) may be limited due to the interference of GHGs absorption lines with those of water vapor or other atmospheric components. Moreover, GHGs concentrations are generally reported as mole fractions

Table 17.5 Maintenance of continuous isotopologue measurement systems

Maximum interval	Isotope ratio mass spectrometer (IRMS)	Laser systems (TDLAS, QCLAS, CRDS, OA-ICOS)	Fourier transform infrared spectroscopy (FTIR)
1 day	Full scale calibration of response curve	Target gas analysis for quality control (QC)	Target gas analysis for QC
1 week		Full scale calibration of response curve	Full scale calibration of response curve
1–3 month			Change of chemical drying agent Change of N ₂ flushing gas
1 year	Vacuum pump	Pump	Vacuum pump

in dry air. Therefore, sample air is often dried or corrections need to be made, e.g., based on the parallel analysis of water vapor (or other gases) in the sample air.

As line shape and gas concentrations strongly depend on temperature (and pressure), optical instruments are generally temperature stabilized, and cell pressures and flow rate are controlled (or at least continuously monitored for correction). Typical stabilization requirements are ± 0.01 °C for cell temperature, ± 0.01 hPa for cell pressure, ± 0.2 $\mu\text{mol mol}^{-1}$ for moisture level, and ± 0.01 slpm for sample flow rate. As the air matrix, i.e., the concentration of major air components such as nitrogen, oxygen, and argon, is important for calculating

line shapes, calibration gases need to have the same composition as the ambient air samples. Therefore, standards of artificial gas mixtures should be avoided as they may lead to considerable calibration biases.

17.6.3 Specific Quality Assurance Measures

To monitor the quality of the continuous measurements and the stability of the instrument response, analysis of a so-called target gas, e.g., once per day has been recommended [17.80]. The accuracy and the variability of the target gas results provides an important measure for uncertainty estimates of the ambient air data.

17.7 Maintenance

Instrumentation maintenance for stable isotope ratio measurements mainly involves regular calibration with frequency depending on the stability of the instrument response curve, which itself depends on parameters such as temperature and pressure stabilization in the cell. However, frequent calibration (or referencing) as found in the DFG system (Sect. 17.3.2), even though it has the advantage of avoiding cross-sensitivity or non-linearity over a large concentration range, may take up too much of the time for ambient measurements, in particular if high precision or accuracy are needed [17.66]. Besides temperature and pressure, atmospheric water

vapor is the most influential ambient parameter (if not to be analyzed itself as an unknown variable). To keep water vapor at a constant low level, the drying system requires maintenance such as manual change of cooling traps or drying agent. Furthermore, air pumping systems need to be regularly maintained and checked for leakages, and special care is required to keep all tubing air-tight and free of contamination (e.g., with room air).

In general, optical devices require less maintenance than, e.g., continuous-flow IRMS systems, and are thus often easier and maintained with less effort for continuous observation under field conditions (Table 17.5).

17.8 Application

As introduced in Sect. 17.2, isotopic observations of greenhouse gases can be useful for disentangling contributions of different sources to the total net flux, while the concentration signal or regional gradient alone provide only information on the total net flux.

Principally, two fluxes can be distinguished if their associated isotopic fluxes, so-called isofluxes, are different. The global net ocean and land fluxes of carbon,

for example, have similar magnitudes on the order of 2 Pg C a^{-1} . The ocean flux carries an isotopic signature of around -2% while the land flux is on the order of -18% , leading to very distinct isofluxes [17.91]. Another possibility for different isofluxes is that two large fluxes carry isotopic signatures that are not very different but still distinguishable. The large fluxes then amplify the little differences in the isotopic signatures.

This is the case for ^{18}O in atmospheric CO_2 , where the carbon gross fluxes photosynthesis and respiration are on the order of 100Pg C a^{-1} , globally, and have close isotopic signatures of 14‰ and 15‰, respectively [17.27, 92]. Hence, small variations in the large carbon gross fluxes will lead to rather large differences in the isofluxes of photosynthesis and respiration [17.30].

17.8.1 Ecosystem Observations

The ^{13}C isotopic signature of photosynthesis and respiration have pretty similar magnitudes because the respired CO_2 was fixed by photosynthesis. It was therefore argued that it is impractical to use $\delta^{13}\text{C}$ - CO_2 to determine photosynthesis and respiration separately [17.93]. The tremendous improvements in laser-based spectroscopy, however, have made it possible that one can actually use high-frequency observations of CO_2 together with $\delta^{13}\text{C}$ - CO_2 to disentangle photosynthesis and respiration from the observed net ecosystem exchange [17.94, 95].

$\delta^{18}\text{O}$ - CO_2 , on the other hand, has larger differences in the source signatures of photosynthesis and respiration than $\delta^{13}\text{C}$ - CO_2 . Measuring $\delta^{18}\text{O}$ - CO_2 was therefore projected to have a higher potential for determining the two gross biosphere fluxes [17.93] and the approach was pursued with traditional isotope analysis in the laboratory [17.96]. The enormous potential of in-situ laser-based spectroscopy of $\delta^{18}\text{O}$ - CO_2 has yet to be harvested because of the isotopic equilibration of CO_2 with water, and thus the convolution with a second isotopic cycle.

The water isotopes themselves were, however, used on an ecosystem scale to describe the water cycle in forest ecosystems [17.29, 97]. The isotopic compositions of water evaporated from the soil and transpired by plants are very distinct because evaporating water is fractionated while transpired water is not (in steady state) [17.98]. However, these assumptions have to be tested carefully in the ecosystem because the isotopes will otherwise overpredict the fraction of transpiration in the evapotranspiration signal [17.99]. The obligation to precisely measure two isotopic cycles might be the reason why the considerable potential of $\delta^{18}\text{O}$ - CO_2 has yet to be unleashed.

17.8.2 Atmospheric Observations

Monitoring of GHG isotopologues for global budgeting is still dominated by analysis of grab samples collected at remote stations in the marine realm and analysis in the laboratory at the highest possible precision (Sect. 17.5). Continuous measurements are more fre-

quently applied at continental stations, where the contributions from different regional sources (and sinks) in the immediate catchment shall be identified and quantified on the diurnal time scale, based on their different isotopic signatures.

Concerning atmospheric CO_2 , one important aim is to distinguish regional ecosystem CO_2 fluxes from those of fossil fuel burning. Both CO_2 source categories, ecosystem and fossil, are principally distinguishable by their $\delta^{13}\text{C}$ and $\delta^{18}\text{O}$ signatures [17.1, 100]. Using the Keeling plot approach [17.3, 101] (see also Chap. 56), their varying ^{13}C imprint on atmospheric CO_2 has, for example, been monitored via a significant seasonality of the mean $\delta^{13}\text{C}$ source signature at a polluted station in Germany [17.84]. However, when it comes to quantitatively separating the different source contributions, uncertainties are often large. This is because the fossil fuel and ecosystem CO_2 signatures partly overlap for $\delta^{13}\text{C}$ [17.84, 101]. Additional information might then be necessary such as given by the radioactive isotope ^{14}C [17.102]. For ^{18}O , although the fossil fuel CO_2 has a distinct imprint on the (regional) ^{18}O signature of atmospheric CO_2 [17.17, 103], isotopic equilibration of CO_2 with water reservoirs needs to be additionally modeled for any quantitative CO_2 budget [17.92, 96].

Concerning CH_4 , a number of different source categories, such as emissions from natural wetlands, agriculture, waste management, or energy production and distribution contribute to the continental and global atmospheric methane burden [17.104]. Their individual (regional) share is often mainly estimated from bottom-up inventories. Therefore, top-down source attribution from isotopic observations are a promising application of CH_4 isotopologue measurements [17.105, 106]. An open question concerns, e.g., the causes of the stagnation of the CH_4 concentrations after 1999, following its increase since preindustrial times due to increasing emissions from anthropogenic sources such as agriculture as well as energy production and distribution. Further, since 2006, CH_4 is increasing again at a rate similar to the 1990s. This development in the last two decades has not been fully understood because the CH_4 budget is still largely underconstrained if only $\delta^{13}\text{C}$ - CH_4 trends are taken into account [17.107–109]. More $\delta^2\text{H}$ - CH_4 measurements may help in solving this issue.

A recent proof-of-concept study in the Netherlands at the Cabauw tower site compared a continuous IRMS with a QCLAS-based technique (Sect. 17.4.5) and provided promising results for the regional scale that have a clear potential, together with regional modeling, to test the reliability of bottom-up emission inventories [17.18].

17.9 Future Developments

New and improved measurement techniques for combined ^{18}O and ^{17}O isotopes in CO_2 may allow estimates of carbon exchange fluxes with the biosphere [17.110, 111]: a small signal of the enrichment of rare oxygen isotopes in the stratosphere (due to mass-independent photochemical reactions) should be transferred to the troposphere. To which extent this signal is re-equilibrated with tropospheric water reservoirs, such as leaf water, depends on the gross CO_2 exchange with the terrestrial biosphere. Therefore, triple oxygen isotope observations in tropospheric CO_2 could potentially be used as a tracer for gross primary productivity, an important but not so well-known component in the global carbon cycle [17.110]. Some laboratories, e.g., [17.57] equilibrate CO_2 with water of known composition and then fluorinate CO_2 to produce O_2 . Measuring the masses 36, 37, 38 allows then for the determination of the $\delta^{17}\text{O}$ and $\delta^{18}\text{O}$ isotopic compositions. There are also first optical instruments that allow measuring both oxygen isotopes in CO_2 . Prototypes were delivered to research groups in 2017 and promise improved estimation of photosynthesis on regional scales.

Another interesting development is the measurement of so-called clumped isotopes, with the first optical instrument in its final development. Clumped

isotopes are, for example, double- or triple-substituted CO_2 molecules such as $^{13}\text{C}^{16}\text{O}^{18}\text{O}$ [17.112]. The most prominent example of clumped isotopes applications is the carbonate system, where the clumped isotope signal depends solely on temperature while the individual isotopes such as $\delta^{18}\text{O}$ depend on temperature and on the $\delta^{18}\text{O}$ of waters from which carbonates grew. But clumped isotopes might also constrain the atmospheric budget of trace gases such as CO_2 [17.113]. This signal is not yet fully understood, but might help in the future to improve applications of single isotopes such as $\delta^{18}\text{O}$ [17.114, 115].

In polluted areas, continuous observations of co-located atmospheric CO_2 mole fraction and deuterium excess in atmospheric water vapor [17.116] may be used to estimate combustion-derived water vapor. Measurements at a monitoring station in the Salt Lake City basin in Utah, USA, during winter implied that the particularly low deuterium excess values of water from fossil fuel combustion significantly influenced the isotopic signature of atmospheric water vapor. This effect is most significant during cold temperatures when atmospheric humidity is generally low and stable inversion situations allow combustion-derived emissions (CO_2 and H_2O) to accumulate in a shallow atmospheric boundary layer [17.117].

17.10 Further Readings

- Ehleringer, J.R., Osmond, C.B.: Stable isotopes. In: Plant Physiological Ecology: Field Methods and Instrumentation, ed. by R.W. Pearcy, J.R. Ehleringer, H.A. Mooney, P.W. Rundel. Chapman Hall, London (1989), pp. 281–300.
- Griffiths, H. (Ed.): Stable Isotopes. BIOS Scientific Publishers Ltd., Oxford (1998).
- Ehleringer, J.R., Hall, A.E., Farquhar, G.D. (Eds.): Stable Isotopes and Plant Carbon–Water Relations. Academic Press, San Diego (1993).
- Rundel, P.W., Ehleringer, J.R., Nagy, K.A. (Eds.): Stable Isotopes in Ecological Research. Springer, New York (1989).
- Aggarwal, P.K., Gat, J.R., Froehlich, K.F.O.: Isotopes in the Water Cycle: Past, Present and Future of a Developing Science. Springer, Dordrecht (2006).
- Kendall, C., McDonnell, J.J.: Isotope Tracers in Catchment Hydrology. Elsevier, Amsterdam (1998).

References

- | | | | |
|------|--|------|--|
| 17.1 | W.G. Mook: Environmental isotopes in the hydrological cycle: Principles and applications. Vol. I Introduction. IHP-V, Tech. Doc. Hydrol. 39 (1), SC-2000/WS/58 (2001) | 17.3 | C. Keeling: The concentration and isotopic abundances of atmospheric carbon dioxide in rural areas, <i>Geochim. Cosmochim. Acta</i> 13 , 322–334 (1958) |
| 17.2 | S. Epstein, T. Mayeda: Variation of O^{18} content of waters from natural sources, <i>Geochim. Cosmochim. Acta</i> 4 , 213–224 (1953) | 17.4 | T. Rahn, M. Wahlen: A reassessment of the global isotopic budget of atmospheric nitrous oxide, <i>Global Biogeochem. Cycles</i> 14 , 537–543 (2000) |

- 17.5 C.M. Stevens, F.E. Rust: The carbon isotopic composition of atmospheric methane, *J. Geophys. Res.* **87**, 4879–4882 (1982)
- 17.6 A.M. Batenburg, S. Walter, G. Pieterse, I. Levin, M. Schmidt, A. Jordan, S. Hammer, C. Yver, T. Röckmann: Temporal and spatial variability of the stable isotopic composition of atmospheric molecular hydrogen: Observations at six EUROHYDROS stations, *Atmos. Chem. Phys.* **11**, 6985–6999 (2011)
- 17.7 D.H. Ehhalt: Tritium and deuterium in atmospheric hydrogen, *Tellus* **18**, 249–255 (1966)
- 17.8 K. Mauersberger: Measurement of heavy ozone in the stratosphere, *Geophys. Res. Lett.* **8**, 935–937 (1981)
- 17.9 G.D. Farquhar, J. Lloyd: Carbon and oxygen isotope effects in the exchange of carbon dioxide between terrestrial plants and the atmosphere. In: *Stable Isotopes and Plant Carbon–Water Relations*, ed. by J.R. Ehleringer, A.E. Hall, G.D. Farquhar (Academic Press, San Diego 1993) pp. 47–70
- 17.10 R. Cicerone, R. Oremland: Biogeochemical aspects of atmospheric methane, *Global Biogeochem. Cycles* **2**, 299–327 (1988)
- 17.11 H. Schnyder, R. Schäufele, R. Wenzel: Mobile, outdoor continuous-flow isotope-ratio mass spectrometer system for automated high-frequency ^{13}C - and ^{18}O - CO_2 analysis for Keeling plot applications, *Rapid Commun. Mass Spectrom.* **18**, 3068–3074 (2004)
- 17.12 E.H. Wahl, B. Fidric, C.W. Rella, S. Koulikov, B. Kharlamov, S. Tan, A.A. Kachanov, B.A. Richman, E.R. Crosson, B.A. Paldus, S. Kalaskar, D.R. Bowling: Applications of cavity ring-down spectroscopy to high precision isotope ratio measurement of $^{13}\text{C}/^{12}\text{C}$ in carbon dioxide, *Isot. Environ. Health Stud.* **42**, 21–35 (2006)
- 17.13 C. Dyroff, D. Fütterer, A. Zahn: Compact diode-laser spectrometer ISOWAT for highly sensitive airborne measurements of water-isotope ratios, *Appl. Phys. B* **98**, 537–548 (2010)
- 17.14 D.W.T. Griffith, N.M. Deutscher, C. Caldwell, G. Kettlewell, M. Riggenbach, S. Hammer: A Fourier transform infrared trace gas and isotope analyser for atmospheric applications, *Atmos. Meas. Tech.* **5**, 2481–2498 (2012)
- 17.15 F.R. Vogel, L. Huang, D. Ernst, L. Giroux, S. Racki, D.E.J. Worthy: Evaluation of a cavity ring-down spectrometer for in situ observations of $^{13}\text{CO}_2$, *Atmos. Meas. Tech.* **6**, 301–308 (2013)
- 17.16 O.N. Ulenikov, E.S. Bekhtereva, S. Albert, S. Bauerecker, H.M. Niederer, M. Quack: Survey of the high resolution infrared spectrum of methane ($^{12}\text{CH}_4$ and $^{13}\text{CH}_4$): Partial vibrational assignment extended towards 12 000 cm^{-1} , *J. Chem. Phys.* **141**, 234302 (2014)
- 17.17 S.N. Vardag, S. Hammer, M. Sabasch, D.W.T. Griffith, I. Levin: First continuous measurements of $\delta^{18}\text{O}$ - CO_2 in air with a Fourier transform infrared spectrometer, *Atmos. Meas. Tech.* **8**, 579–592 (2015)
- 17.18 T. Röckmann, S. Eyer, C. van der Veen, M.E. Popa, B. Tuzson, G. Monteil, S. Houweling, E. Harris, D. Brunner, H. Fischer, G. Zazzeri, D. Lowry, E.G. Nisbet, W.A. Brand, J.M. Necki, L. Emmenegger, J. Mohn: In situ observations of the isotopic composition of methane at the Cabauw tall tower site, *Atmos. Chem. Phys.* **16**, 10469–10487 (2016)
- 17.19 J.B. McManus, M.S. Zahniser, D.D. Nelson, L.R. Williams, C.E. Kolb: Infrared laser spectrometer with balanced absorption for measurement of isotopic ratios of carbon gases, *Spectrochim. Acta A* **58**, 2465–2479 (2002)
- 17.20 H. Craig: Isotopic standards for carbon and oxygen and correction factors for mass-spectrometric analysis of carbon dioxide, *Geochim. Cosmochim. Acta* **12**, 133–149 (1957)
- 17.21 C.D. Keeling, W.G. Mook, P. Tans: Recent trends in the $^{13}\text{C}/^{12}\text{C}$ ratio of atmospheric carbon dioxide, *Nature* **277**, 121–123 (1979)
- 17.22 C.D. Keeling, R.B. Bacastow, A.F. Carter, S.C. Piper, T.P. Whorf, M. Heimann, W.G. Mook, H. Roelofzen: A three-dimensional model of atmospheric CO_2 transport based on observed winds: 1. Analysis of observational data. In: *Aspects of Climate Variability in the Pacific and the Western Americas*, Geophysical Monograph Series, Vol. 55 (AGU, Washington 1989) pp. 165–236
- 17.23 C.D. Keeling, T.P. Whorf, M. Wahlen, J. van der Plicht: Interannual extremes in the rate of rise of atmospheric carbon-dioxide since 1980, *Nature* **375**, 666–670 (1995)
- 17.24 P. Ciais, P.P. Tans, M. Trolier, J.W.C. White, R.J. Francey: A large Northern Hemisphere terrestrial CO_2 sink indicated by the $^{13}\text{C}/^{12}\text{C}$ ratio of atmospheric CO_2 , *Science* **269**, 1098–1102 (1995)
- 17.25 T. Nakazawa, S. Morimoto, S. Aoki, M. Tanaka: Time and space variations of the carbon isotopic ratio of tropospheric carbon-dioxide over Japan, *Tellus B* **45**, 258–274 (1993)
- 17.26 P. Ciais, A.S. Denning, P.P. Tans, J.A. Berry, D.A. Randall, G.J. Collatz, P.J. Sellers, J.W.C. White, M. Trolier, H.A.J. Meijer, R.J. Francey, P. Monfray, M. Heimann: A three-dimensional synthesis study of $\delta^{18}\text{O}$ in atmospheric CO_2 : 1. Surface fluxes, *J. Geophys. Res.* **102**, 5857–5872 (1997)
- 17.27 G.D. Farquhar, J. Lloyd, J.A. Taylor, L.B. Flanagan, J.B. Syvertsen, K.T. Hubick, S.C. Wong, J.R. Ehleringer: Vegetation effects on the isotope composition of oxygen in atmospheric CO_2 , *Nature* **363**, 439–443 (1993)
- 17.28 R.J. Francey, P.P. Tans: Latitudinal variation in oxygen-18 of atmospheric CO_2 , *Nature* **327**, 495–497 (1987)
- 17.29 D. Yakir, X. Wang: Fluxes of CO_2 and water between terrestrial vegetation and the atmosphere estimated from isotope measurements, *Nature* **380**, 515–517 (1996)
- 17.30 L.R. Welp, R.F. Keeling, H.A.J. Meijer, A.F. Bollenbacher, S.C. Piper, K. Yoshimura, R.J. Francey, C.E. Allison, M. Wahlen: Interannual variability in the oxygen isotopes of atmospheric CO_2 driven by El Niño, *Nature* **477**, 579–582 (2011)

- 17.31 C.E. Allison, R.J. Francey: $\delta^{13}\text{C}$ of atmospheric CO_2 at Cape Grim: The in situ record, the flask record, air standards and the CG92 calibration scale. In: *Baseline Atmospheric Program Australia*, ed. by J.L. Gras, N. Derek, N.W. Tindale, A.L. Dick (Bureau of Meteorology and CSIRO Atmospheric Research, Melbourne 1999) pp. 45–56
- 17.32 W.A. Brand, M. Rothe, P. Sperlich, M. Strube, M. Wendeberg: Automated simultaneous measurement of the $\delta^{13}\text{C}$ and $\delta^2\text{H}$ values of methane and the $\delta^{13}\text{C}$ and $\delta^{18}\text{O}$ values of carbon dioxide in flask air samples using a new multi-cryo-trap/gas chromatography/isotope ratio mass spectrometry system, *Rapid Commun. Mass Spectrom.* **30**, 1523–1539 (2016)
- 17.33 B.H. Vaughn, J. Miller, D.F. Ferretti, J.W.C. White: Stable isotope measurements of atmospheric CO_2 and CH_4 . In: *Handbook of Stable Isotope Analysis Techniques*, ed. by P.A. de Groot (Elsevier, Amsterdam 2004) pp. 272–304
- 17.34 D.C. Lowe, C.A.M. Brenninkmeijer, S.C. Tyler, E.J. Dlugkencky: Determination of the isotopic composition of atmospheric methane and its application in the Antarctic, *J. Geophys. Res. Atmos.* **96**, 15455–15467 (1991)
- 17.35 P.D. Quay, S.L. King, J. Stutsman, D.O. Wilbur, L.P. Steele, I. Fung, R.H. Gammon, T.A. Brown, G.W. Farwell, P.M. Grootes, F.H. Schmidt: Carbon isotopic composition of atmospheric CH_4 : Fossil and biomass burning source strengths, *Global Biogeochem. Cycles* **5**, 25–47 (1991)
- 17.36 S.C. Tyler: Stable carbon isotope ratios in atmospheric methane and some of its sources, *J. Geophys. Res. Atmos.* **91**, 13232–13238 (1986)
- 17.37 M. Wahlen, B. Deck, R. Henry, N. Tanaka, A. Shemesh, R. Fairbanks, W. Broecker, H. Weyer, B. Marino, J.A. Logan: Profiles of $\delta^{13}\text{C}$ and δD of CH_4 from the lower stratosphere, *EOS Trans. AGU* **70**, 1017 (1989)
- 17.38 I. Fung, J. John, J. Lerner, E. Matthews, M. Prather, L.P. Steele, P.J. Fraser: Three-dimensional model synthesis of the global methane cycle, *J. Geophys. Res.* **96**, 13033–13065 (1991)
- 17.39 A.L. Rice, A.A. Gotoh, H.O. Ajie, S.C. Tyler: High-precision continuous-flow measurement of $\delta^{13}\text{C}$ and δD of atmospheric CH_4 , *Anal. Chem.* **73**, 4104–4110 (2001)
- 17.40 P. Bergamaschi, G.W. Harris: Measurements of stable isotope ratios ($^{13}\text{CH}_4/^{12}\text{CH}_4$; $^{12}\text{CH}_3\text{D}/^{12}\text{CH}_4$) in landfill methane using a tunable diode laser absorption spectrometer, *Global Biogeochem. Cycles* **9**, 439–447 (1995)
- 17.41 M. Brass, T. Röckmann: Continuous-flow isotope ratio mass spectrometry method for carbon and hydrogen isotope measurements on atmospheric methane, *Atmos. Meas. Tech.* **3**, 1707–1721 (2010)
- 17.42 J.B. Miller, K.A. Mack, R. Dissly, J.W.C. White, E.J. Dlugkencky, P.P. Tans: Development of analytical methods and measurements of $^{13}\text{C}/^{12}\text{C}$ in atmospheric CH_4 from the NOAA Climate Monitoring and Diagnostics Laboratory Global Air Sampling Network, *J. Geophys. Res.* **107**, 4178 (2002)
- 17.43 P. Sperlich, C. Buizert, T.M. Jenk, C.J. Sapart, M. Prokopiou, T. Röckmann, T. Blunier: An automated GC–C–GC–IRMS setup to measure palaeoatmospheric $\delta^{13}\text{C}\text{--CH}_4$, $\delta^{15}\text{N}\text{--N}_2\text{O}$ and $\delta^{18}\text{O}\text{--N}_2\text{O}$ in one ice core sample, *Atmos. Meas. Tech.* **6**, 2027–2041 (2013)
- 17.44 H. Jacob, C. Sonntag: An 8-year record of the seasonal variation of ^2H and ^{18}O in atmospheric water vapor and precipitation at Heidelberg, Germany, *Tellus B* **43**, 291–300 (1991)
- 17.45 H. Schoch–Fischer, K. Rozanski, H. Jacob, C. Sonntag, J. Jouzel, G. Östlund, M.A. Geyh: Hydrometeorological factors controlling the time variation of D, ^{18}O and ^3H in atmospheric water vapour and precipitation in the northern westwind belt. In: *Isotope Hydrology 1983* (International Atomic Energy Agency, Vienna 1984) pp. 3–31
- 17.46 L.J. Araguás–Araguás, K.F.O. Froehlich, K. Rozanski: Deuterium and oxygen–18 isotope composition of precipitation and atmospheric moisture, *Hydrol. Process.* **14**, 1341–1355 (2000)
- 17.47 M. Gröning, H.O. Lutz, Z. Roller–Lutz, M. Kralik, L. Gourcy, L. Pölsenstein: A simple rain collector preventing water re–evaporation dedicated for $\delta^{18}\text{O}$ and $\delta^2\text{H}$ analysis of cumulative precipitation samples, *J. Hydrol.* **448/449**, 195–200 (2012)
- 17.48 X. Lee, S.D. Sargent, R. Smith, B.D. Tanner: In situ measurement of the water vapor $^{18}\text{O}/^{16}\text{O}$ isotope ratio for atmospheric and ecological applications, *J. Atmos. Ocean Tech.* **22**, 555–565 (2005)
- 17.49 S.S. Assonov, C.A.M. Brenninkmeijer: On the ^{17}O correction for CO_2 mass spectrometric isotopic analysis, *Rapid Commun. Mass Spectrom.* **17**, 1007–1016 (2003)
- 17.50 C.E. Allison, R.J. Francey, H.A. Meijer: Recommendations for the reporting of stable isotope measurements of carbon and oxygen in CO_2 gas. In: *Reference and Intercomparison Materials for Stable Isotopes of Light Elements* (International Atomic Energy Agency, Vienna 1995) pp. 155–162
- 17.51 M.H. Thiemens, T. Jackson, K. Mauersberger, B. Schueler, J. Morton: Oxygen isotope fractionation in stratospheric CO_2 , *Geophys. Res. Lett.* **18**, 669–672 (1991)
- 17.52 S.K. Bhattacharya, M.H. Thiemens: New evidence for symmetry dependent isotope effects: $0+0\text{C}$ reaction, *Z. Naturforsch. A* **44**, 435–444 (1989)
- 17.53 C. Brenninkmeijer, T. Röckmann: A rapid method for the preparation of O_2 from CO_2 for mass spectrometric measurement of $^{17}\text{O}/^{16}\text{O}$ ratios, *Rapid Commun. Mass Spectrom.* **12**, 479–483 (1998)
- 17.54 S.S. Assonov, C.A.M. Brenninkmeijer: A new method to determine the ^{17}O isotopic abundance in CO_2 using oxygen isotope exchange with a solid oxide, *Rapid Commun. Mass Spectrom.* **15**, 2426–2437 (2001)
- 17.55 S. Kawagucci, U. Tsunogai, S. Kudo, F. Nakagawa, H. Honda, S. Aoki, T. Nakazawa, T. Gamo: An analytical system for determining $\delta^{17}\text{O}$ in CO_2 using continuous flow–isotope ratio MS, *Anal. Chem.* **77**, 4509–4514 (2005)

- 17.56 D.A. Merritt, W.A. Brand, J.M. Hayes: Isotope-ratio-monitoring gas chromatography-mass spectrometry: Methods for isotopic calibration, *Org. Geochem.* **21**, 573–583 (1994)
- 17.57 E. Barkan, B. Luz: High-precision measurements of $^{17}\text{O}/^{16}\text{O}$ and $^{18}\text{O}/^{16}\text{O}$ ratios in CO_2 , *Rapid Commun. Mass Spectrom.* **26**, 2733–2738 (2012)
- 17.58 M. Bock, J. Schmitt, M. Behrens, L. Möller, R. Schneider, C. Spart, H. Fischer: A gas chromatography/pyrolysis/isotope ratio mass spectrometry system for high-precision δD measurements of atmospheric methane extracted from ice cores, *Rapid Commun. Mass Spectrom.* **24**, 621–633 (2010)
- 17.59 R. Fisher, D. Lowry, O. Wilkin, S. Sriskantharajah, E.G. Nisbet: High-precision, automated stable isotope analysis of atmospheric methane and carbon dioxide using continuous-flow isotope-ratio mass spectrometry, *Rapid Commun. Mass Spectrom.* **20**, 200–208 (2005)
- 17.60 D.P. Billesbach, J. Kim, R.J. Clement, S.B. Verma, F.G. Ullman: An intercomparison of two tunable diode laser spectrometers used for eddy correlation measurements of methane flux in a prairie wetland, *J. Atmos. Ocean Tech.* **15**, 197–206 (1998)
- 17.61 A. Hugi, R. Terazzi, Y. Bonetti, A. Wittmann, M. Fischer, M. Beck, J. Faist, E. Gini: External cavity quantum cascade laser tunable from 7.6 to 11.4 μm , *Appl. Phys. Lett.* **95**, 061103 (2009)
- 17.62 J.S. Li, W. Chen, H. Fischer: Quantum cascade laser spectrometry techniques: A new trend in atmospheric chemistry, *Appl. Spectrosc. Rev.* **48**, 523–559 (2013)
- 17.63 B.A. Paldus, A.A. Kachanov: An historical overview of cavity-enhanced methods, *Can. J. Phys.* **83**, 975–999 (2005)
- 17.64 N. Saad, G. Hsiao: *Continuous Flow-Cavity Ring-Down Spectroscopy: A Powerful Tool for Food Origin Analysis and Adulteration Detection. Presented at the Forensic Isotope Ratio Mass Spectrometry FIRMS Conference, Washington, DC* (2010)
- 17.65 A. O'Keefe: Integrated cavity output analysis of ultra-weak absorption, *Chem. Phys. Lett.* **293**, 331–336 (1998)
- 17.66 L. Zipf: *Further development of a $\delta^{13}\text{C}$ spectrometer for small sample analysis*, Master Thesis (Heidelberg Univ., Heidelberg 2017)
- 17.67 R. van Geldern, M.E. Nowak, M. Zimmer, A. Szzybalski, A. Myrtilinen, J.A.C. Barth, H.-J. Jost: Field-based stable isotope analysis of carbon dioxide by mid-infrared laser spectroscopy for carbon capture and storage monitoring, *Anal. Chem.* **86**, 12191–12198 (2014)
- 17.68 S.P. Davis, M.C. Abrams, J.W. Brault: *Fourier Transform Spectrometry* (Elsevier, San Diego 2001)
- 17.69 P.R. Griffiths, J.A. De Haseth: *Fourier Transform Infrared Spectrometry* (John Wiley & Sons, Inc, Hoboken 2007)
- 17.70 L.S. Rothman, D. Jacquemart, A. Barbe, C.D. Benner, M. Birk, L.R. Brown, M.R. Carleer, C. Chackerian Jr., K. Chance, L.H. Coudert, V. Dana, V.M. Devi, J.-M. Flaud, R.R. Gamache, A. Goldman, J.-M. Hartmann, K.W. Jucks, A.G. Maki, J.-Y. Mandin, S.T. Massie, J. Orphal, A. Perrin, C.P. Rinsland, M.A.H. Smith, J. Tennyson, R.N. Tolchenov, R.A. Toth, J. Vander Auwera, P. Varanasi, G. Wagner: The HITRAN 2004 molecular spectroscopic database, *J. Quant. Spectrosc. Radiat. Transf.* **96**, 139–204 (2005)
- 17.71 D.W.T. Griffith: Synthetic calibration and quantitative analysis of gas-phase FT-IR spectra, *Appl. Spectrosc.* **50**, 59–70 (1996)
- 17.72 J. Reid, B.K. Garside, J. Shewchun, M. El-Sherbiny, E.A. Ballik: High sensitivity point monitoring of atmospheric gases employing tunable diode-lasers, *Appl. Opt.* **17**, 1806–1810 (1978)
- 17.73 H.I. Schiff, D.R. Hastie, G.I. Mackay, T. Iguchi, B.A. Ridley: Tunable diode laser systems for measuring trace gases in tropospheric air, *Environ. Sci. Technol.* **17**, 352A–364A (1983)
- 17.74 G.C. Edwards, H.H. Neumann, G. den Hartog, G.W. Thurtell, G. Kidd: Eddy correlation measurements of methane fluxes using a tunable diode laser at the Kinosheo Lake tower site during the Northern Wetlands Study (NOWES), *J. Geophys. Res.* **99**, 1511–1517 (1994)
- 17.75 D.R. Bowling, S.D. Sargent, B.D. Tanner, J.R. Ehleringer: Tunable diode laser absorption spectroscopy for stable isotope studies of ecosystem-atmosphere CO_2 exchange, *Agric. For. Meteorol.* **118**, 1–19 (2003)
- 17.76 J.B. McManus, P.L. Keabian, W.S. Zahniser: Astigmatic mirror multipass absorption cells for long-path-length spectroscopy, *Appl. Opt.* **34**, 3336–3348 (1995)
- 17.77 J.B. McManus, D.D. Nelson, J.H. Shorter, R. Jimenez, S. Herndon, S. Saleska, M. Zahniser: A high precision pulsed quantum cascade laser spectrometer for measurements of stable isotopes of carbon dioxide, *J. Mod. Opt.* **52**, 2309–2321 (2005)
- 17.78 R. Jimenez, S. Herndon, J.H. Shorter, D.D. Nelson, J.B. McManus, M.S. Zahniser: Atmospheric trace gas measurements using a dual quantum-cascade laser mid-infrared absorption spectrometer, *Proc. SPIE* **5738**, 318–331 (2005)
- 17.79 S. Hammer, D.W.T. Griffith, G. Konrad, S. Vardag, C. Caldwell, I. Levin: Assessment of a multi-species in situ FTIR for precise atmospheric greenhouse gas observations, *Atmos. Meas. Tech.* **6**, 1153–1170 (2013)
- 17.80 A. Crotwell, M. Steinbacher: GAW Report No. 242. In: *19th WMO/IAEA Meet. Carbon Dioxide Other Greenh. Gases Relat. Tracers Meas. Tech. (GGMT-2017)* (WMO, Geneva 2017) pp. 27–31
- 17.81 S. Eyer, B. Tuzson, M.E. Popa, C. van der Veen, T. Röckmann, M. Rothe, W.A. Brand, R. Fisher, D. Lowry, E.G. Nisbet, M.S. Brennwald, E. Harris, C. Zellweger, L. Emmenegger, H. Fischer, J. Mohn: Real-time analysis of $\delta^{13}\text{C}$ - and δD - CH_4 in ambient air with laser spectroscopy: Method development and first intercomparison results, *Atmos. Meas. Tech.* **9**, 263–280 (2016)

- 17.82 P. Werle: Accuracy and precision of laser spectrometers for trace gas sensing in the presence of optical fringes and atmospheric turbulence, *Appl. Phys. B* **102**, 313–329 (2011)
- 17.83 C. Dyroff, A. Zahn, S. Sanati, E. Christner, A. Rauthe-Schöch, T.J. Schuck: Tunable diode laser in-situ CH₄ measurements aboard the CARIBIC passenger aircraft: Instrument performance assessment, *Atmos. Meas. Tech.* **7**, 743–755 (2014)
- 17.84 S.N. Vardag, S. Hammer, I. Levin: Evaluation of 4 years of continuous $\delta^{13}\text{C}(\text{CO}_2)$ data using a moving Keeling plot method, *Biogeosciences* **13**, 4237–4251 (2016)
- 17.85 L. Wang, K.K. Caylor, D. Dragoni: On the calibration of continuous, high-precision $\delta^{18}\text{O}$ and $\delta^2\text{H}$ measurements using an off-axis integrated cavity output spectrometer, *Rapid Commun. Mass Spectrom.* **23**, 530–536 (2009)
- 17.86 W.A. Brand, T.B. Coplen, J. Vogl, M. Rosner, T. Prohaska: Assessment of international reference materials for isotope-ratio analysis (IUPAC Technical Report), *Pure Appl. Chem.* **86**, 425–467 (2014)
- 17.87 T.B. Coplen, W.A. Brand, M. Gehre, M. Gröning, H.A.J. Meijer, B. Toman, R.M. Verkouteren: New guidelines for $\delta^{13}\text{C}$ measurements, *Anal. Chem.* **78**, 2439–2441 (2006)
- 17.88 M. Wendeberg, J.M. Richter, M. Rothe, W.A. Brand: Jena Reference Air Set (JRAS): A multi-point scale anchor for isotope measurements of CO₂ in air, *Atmos. Meas. Tech.* **6**, 817–822 (2013)
- 17.89 T. Umezawa, C.A.M. Brenninkmeijer, T. Röckmann, C. van der Veen, S.C. Tyler, R. Fujita, S. Morimoto, S. Aoki, T. Sowers, J. Schmitt, M. Bock, J. Beck, H. Fischer, S.E. Michel, B.H. Vaughn, J.B. Miller, J.W.C. White, G. Brailsford, H. Schaefer, P. Sperllich, W.A. Brand, M. Rothe, T. Blunier, D. Lowry, R.E. Fisher, E.G. Nisbet, A.L. Rice, P. Bergamaschi, C. Veidt, I. Levin: Interlaboratory comparison of $\delta^{13}\text{C}$ and δD measurements of atmospheric CH₄ for combined use of data sets from different laboratories, *Atmos. Meas. Tech.* **11**, 1207–1231 (2018)
- 17.90 I. Levin, C. Veidt, B.H. Vaughn, G. Brailsford, T. Bromley, R. Heinz, D. Lowe, J.B. Miller, C. Poß, J.W.C. White: No inter-hemispheric $\delta^{13}\text{CH}_4$ trend observed, *Nature* **486**, E3–E4 (2012)
- 17.91 R.J. Francey, P.P. Tans, C.E. Allison, I.G. Enting, J.W.C. White, M. Trolrier: Changes in oceanic and terrestrial carbon uptake since 1982, *Nature* **373**, 326–330 (1995)
- 17.92 M. Cuntz, P. Ciais, G. Hoffmann, W. Knorr: A comprehensive global three-dimensional model of $\delta^{18}\text{O}$ in atmospheric CO₂: 1. Validation of surface processes, *J. Geophys. Res.* **108**, 4527 (2003)
- 17.93 J. Ogée, P. Peylin, M. Cuntz, T. Bariac, Y. Brunet, P. Berbigier, P. Richard, P. Ciais: Partitioning net ecosystem carbon exchange into net assimilation and respiration with canopy-scale isotopic measurements: An error propagation analysis with $^{13}\text{CO}_2$ and CO^{18}O data, *Global Biogeochem. Cycles* **18**, GB2019 (2004)
- 17.94 R. Wehr, J.W. Munger, J.B. McManus, D.D. Nelson, M.S. Zahniser, E.A. Davidson, S.C. Wofsy, S.R. Saleska: Seasonality of temperate forest photosynthesis and daytime respiration, *Nature* **534**, 680–683 (2016)
- 17.95 R. Wehr, S.R. Saleska: An improved isotopic method for partitioning net ecosystem-atmosphere CO₂ exchange, *Agric. For. Meteorol.* **214/215**, 515–531 (2015)
- 17.96 U. Langendörfer, M. Cuntz, P. Ciais, P. Peylin, T. Bariac, I. Milyukova, O. Kolle, T. Naegler, I. Levin: Modelling of biospheric CO₂ gross fluxes via oxygen isotopes in a spruce forest canopy: A ^{222}Rn calibrated box model approach, *Tellus B* **54**, 476–496 (2002)
- 17.97 X. Lee, K. Kim, R. Smith: Temporal variations of the $^{18}\text{O}/^{16}\text{O}$ signal of the whole-canopy transpiration in a temperate forest, *Global Biogeochem. Cycles* **21**, GB3013 (2007)
- 17.98 M. Dubbert, M. Cuntz, A. Piayda, C. Werner: Oxygen isotope signatures of transpired water vapor: The role of isotopic non-steady-state transpiration under natural conditions, *New Phytol.* **203**, 1242–1252 (2014)
- 17.99 M. Dubbert, M. Cuntz, A. Piayda, C. Máguas, C. Werner: Partitioning evapotranspiration – Testing the Craig and Gordon model with field measurements of oxygen isotope ratios of evaporative fluxes, *J. Hydrol.* **496**, 142–153 (2013)
- 17.100 M. Schumacher, R.A. Werner, H.A.J. Meijer, H.G. Jansen, W.A. Brand, H. Geilmann, R.E.M. Neubert: Oxygen isotopic signature of CO₂ from combustion processes, *Atmos. Chem. Phys.* **11**, 1473–1490 (2011)
- 17.101 J.B. Miller, P.P. Tans: Calculating isotopic fractionation from atmospheric measurements at various scales, *Tellus B* **55**, 207–214 (2003)
- 17.102 I. Levin, U. Karstens: Inferring high-resolution fossil fuel CO₂ records at continental sites from combined $^{14}\text{CO}_2$ and CO observations, *Tellus B* **59**, 245–250 (2007)
- 17.103 B. Tuzson, S. Henne, D. Brunner, M. Steinbacher, J. Mohn, B. Buchmann, L. Emmenegger: Continuous isotopic composition measurements of tropospheric CO₂ at Jungfrauoch (3580 m a.s.l.), Switzerland: Real-time observation of regional pollution events, *Atmos. Chem. Phys.* **11**, 1685–1696 (2011)
- 17.104 S. Kirschke, P. Bousquet, P. Ciais, M. Saunoy, J.G. Canadell, E.J. Dlugokencky, P. Bergamaschi, D. Bergmann, D.R. Blake, L. Bruhwiler, P. Cameron-Smith, S. Castaldi, F. Chevallier, L. Feng, A. Fraser, M. Heimann, E.L. Hodson, S. Houweling, B. Josse, P.J. Fraser, P.B. Krummel, J.-F. Lamarque, R.L. Langenfelds, C. Le Quéré, V. Naik, S. O’Doherty, P.I. Palmer, I. Pison, D. Plummer, B. Poulter, R.G. Prinn, M. Rigby, B. Ringeval, M. Santini, M. Schmidt, D.T. Shindell, I.J. Simpson, R. Spahni, L.P. Steele, S.A. Strode, K. Sudo, S. Szopa, G.R. van der Werf, A. Voul-

- garakis, M. van Weele, R.F. Weiss, J.E. Williams, G. Zeng: Three decades of global methane sources and sinks, *Nat. Geosci.* **6**, 813–823 (2013)
- 17.105 I. Levin, H. Glatzel–Mattheier, T. Marik, M. Cuntz, M. Schmidt, D.E. Worthy: Verification of German methane emission inventories and their recent changes based on atmospheric observations, *J. Geophys. Res. Atmos.* **104**, 3447–3456 (1999)
- 17.106 P. Bousquet, P. Ciais, J.B. Miller, E.J. Dlugokencky, D.A. Hauglustaine, C. Prigent, G.R. van der Werf, P. Peylin, E.G. Brunke, C. Carouge, R.L. Langenfelds, J. Lathiere, F. Papa, M. Ramonet, M. Schmidt, L.P. Steele, S.C. Tyler, J.W.C. White: Contribution of anthropogenic and natural sources to atmospheric methane variability, *Nature* **443**, 439–443 (2006)
- 17.107 H. Schaefer, S.E.M. Fletcher, C. Veidt, K.R. Lassey, G.W. Brailsford, T.M. Bromley, E.J. Dlugokencky, S.E. Michel, J.B. Miller, I. Levin, D.C. Lowe, R.J. Martin, B.H. Vaughn, J.W.C. White: A 21st-century shift from fossil-fuel to biogenic methane emissions indicated by $^{13}\text{CH}_4$, *Science* **352**, 80–84 (2016)
- 17.108 A.J. Turner, C. Frankenberg, P.O. Wennberg, D.J. Jacob: Ambiguity in the causes for decadal trends in atmospheric methane and hydroxyl, *Proc. Natl. Acad. Sci. U. S. A.* **114**, 5367–5372 (2017)
- 17.109 E.G. Nisbet, M.R. Manning, E.J. Dlugokencky, R.E. Fisher, D. Lowry, S.E. Michel, C. Lund Myhre, S.M. Platt, G. Allen, P. Bousquet, R. Brownlow, M. Cain, J.L. France, O. Hermansen, R. Hossaini, A.E. Jones, I. Levin, A.C. Manning, G. Myhre, J.A. Pyle, B.H. Vaughn, N.J. Warwick, J.W.C. White: Very strong atmospheric methane growth in the 4 years 2014–2017: Implications for the Paris Agreement, *Global Biogeochem. Cycles* **33**, 318–342 (2019)
- 17.110 K. Hoag, C.J. Still, I.Y. Fung, K. Boering: Triple oxygen isotope composition of tropospheric carbon dioxide as a tracer of terrestrial gross carbon fluxes, *Geophys. Res. Lett.* **32**, L02802 (2005)
- 17.111 M.E.G. Hofmann, B. Horváth, L. Schneider, W. Peters, K. Schützenmeister, A. Pack: Atmospheric measurements of $\Delta^{17}\text{O}$ in CO_2 in Göttingen, Germany reveal a seasonal cycle driven by biospheric uptake, *Geochim. Cosmochim. Acta* **199**, 143–163 (2017)
- 17.112 L.Y. Yeung, H. Affek, K.J. Hoag, W. Guo, A.A. Wiegel, E.L. Atlas, S.M. Schauffler, M. Okumura, K.A. Boering, J.M. Eiler: Large and unexpected enrichment in stratospheric $^{16}\text{O}^{13}\text{C}^{18}\text{O}$ and its meridional variation, *Proc. Natl. Acad. Sci. U. S. A.* **106**, 11496–11501 (2009)
- 17.113 J.M. Eiler, E. Schauble: $^{18}\text{O}^{13}\text{C}^{16}\text{O}$ in Earth’s atmosphere, *Geochim. Cosmochim. Acta* **68**, 4767–4777 (2004)
- 17.114 M. Cuntz, P. Ciais, G. Hoffmann, C.E. Allison, R. Francey, W. Knorr, P. Tans, J. White, I. Levin: A comprehensive global three-dimensional model of $\delta^{18}\text{O}$ in atmospheric CO_2 : 2. Mapping the atmospheric signal, *J. Geophys. Res.* **108**, 4528 (2003)
- 17.115 L. Wingate, J. Ogée, M. Cuntz, B. Genty, I. Reiter, U. Seibt, D. Yakir, K. Maseyk, E.G. Pendall, M.M. Barbour, B. Mortazavi, R. Burlett, P. Peylin, J. Miller, M. Mencuccini, J.H. Shim, J. Hunt, J. Grace: The impact of soil microorganisms on the global budget of $\delta^{18}\text{O}$ in atmospheric CO_2 , *Proc. Natl. Acad. Sci. U. S. A.* **106**, 22411–22415 (2009)
- 17.116 W. Dansgaard: Stable isotopes in precipitation, *Tellus B* **16**, 436–468 (1964)
- 17.117 R.P. Fiorella, R. Bares, J.C. Lin, J.R. Ehleringer, G.J. Bowen: Detection and variability of combustion-derived vapor in an urban basin, *Atmos. Chem. Phys.* **18**, 8529–8547 (2018)

Ingeborg Levin

Institut für Umweltphysik
Heidelberg University
Heidelberg, Germany
ingeborg.levin@iup.uni-heidelberg.de



Ingeborg Levin is senior research scientist and professor at the Physics Faculty of Heidelberg University. She received her PhD in Physics in Heidelberg and is head of the Carbon Cycle Group at the Institute of Environmental Physics. Her research interests are studying biogeochemical cycles with help of (radioactive) isotope tracers in the atmosphere and at the soil–atmosphere interface.

Matthias Cuntz

UMR Silva
Université de Lorraine, AgroParisTech,
INRAE
Nancy, France
matthias.cuntz@inrae.fr



Matthias Cuntz is Directeur de Recherche at the Institut National de Recherche pour l’Agriculture, l’Alimentation et l’Environnement (INRAE) in Nancy, France. He received a PhD in physics in 2002, subsequently working in atmospheric physics (Paris), biology (Canberra), biogeochemical cycles (Jena), and hydrology (Leipzig). He combines measurements and modeling to understand and describe mathematically the processes behind the exchanges of the atmosphere with the biosphere.

18. Measurement of Fundamental Aerosol Physical Properties

Andreas Held, Alexander Mangold 

Measurements of physical and optical particle properties are essential for evaluating the impact of atmospheric aerosols on atmospheric chemistry, climate, and health. This chapter describes the fundamental equations and conventions pertinent to particle detection and to the measurement of particle number, size, optical properties, and mass. Optical and electrical detection techniques are presented for particle number measurements. An overview of particle light scattering and absorption measurement methods is given. Various measurement principles for determining particle size are introduced, including those based on the optical interaction, aerodynamic behavior, or electrical mobility of particles. Particle mass measurement methods include gravimetric analysis, the vibration of a piezoelectric crystal, harmonic oscillation, and the attenuation of beta radiation. This chapter introduces sensors for measuring particle number, size, light scattering and absorption, and mass, while analysis of the chemical composition of particles will not be covered. General aspects of calibration and quality control are also described, typical technical specifications of the instrumentation are given, and recommendations for the maintenance of atmospheric particle sensors are presented. Finally, the chapter provides examples of applications and current developments in particle measurement techniques.

18.1	Measurement Principles and Parameters	534
18.1.1	Physical Properties of Atmospheric Particles	534
18.1.2	Principles of Measurements	535
18.1.3	Measurement Site	537
18.2	History	537
18.3	Theory	537
18.3.1	Particle Light Scattering	538
18.3.2	Particle Light Absorption and Extinction	539
18.3.3	Photoacoustic Spectroscopy	539
18.3.4	Electrical Detection and Mobility of Particles	539
18.3.5	Diffusivity of Particles.....	540
18.3.6	Aerodynamic Behavior of Particles....	540
18.3.7	Particle Microbalances	540
18.3.8	Attenuation of Beta Radiation.....	541
18.3.9	Representation of Particle Size Distributions	541
18.3.10	Setup Requirements of the Particle Sampling System.....	541
18.4	Devices and Systems	542
18.4.1	Particle Light Scattering	542
18.4.2	Particle Light Absorption and Extinction	545
18.4.3	Photoacoustic Spectroscopy	546
18.4.4	Electrical Detection and Mobility of Particles	546
18.4.5	Diffusivity of Particles.....	547
18.4.6	Aerodynamic Behavior of Particles....	548
18.4.7	Particle Microbalances	549
18.4.8	Attenuation of Beta Radiation.....	549
18.4.9	Combination of Particle Sensors	549
18.4.10	Comparison of Methods.....	550
18.5	Specifications	552
18.6	Quality Control	553
18.7	Maintenance	555
18.8	Application	556
18.8.1	Secondary Aerosol Formation.....	556
18.8.2	Vertical Particle Flux Measurements ..	557
18.8.3	Atmospheric Particles and Air Quality	557
18.8.4	Climate Effects of Atmospheric Particles	557
18.9	Future Developments	558
18.10	Further Reading	558
	References	559

The atmospheric aerosol is a mixture of solid particles and liquid droplets suspended in air. The nongaseous part of this mixture is typically referred to as particles.

These particles play an important role in atmospheric physics and chemistry. Atmospheric particles are relevant in the climate system because they scatter and ab-

sorb solar radiation, directly influencing the temperature at the surface and within the atmosphere, and exerting a positive or negative radiative forcing. Further, atmospheric particles are essential for the formation of clouds and their microphysical properties and lifetime, which indirectly influence climate. In addition, particles provide surfaces for and take part in (photo)chemical reactions in the atmosphere. A particle size fraction with an aerodynamic diameter $< 10\ \mu\text{m}$ can be readily inhaled and may contain toxicologically relevant substances that can lead to adverse human health effects. Finally, airborne particles contribute to the atmospheric transport

of both nutrients and pollutants, to the advantage or disadvantage of ecosystems. This chapter describes the measurement principles for the fundamental physical and optical properties of atmospheric particles (number, size, mass, light scattering, and absorption) and the respective measurement sensors. Such measurements are essential for assessing the effects of aerosols on climate, health, and atmospheric chemistry. For information about additional aerosol instrumentation and measurement principles, including sensors for the chemical composition of atmospheric particles, the reader is referred to the literature, for example, [18.1, 2].

18.1 Measurement Principles and Parameters

The ability to accurately measure the physical properties of atmospheric particles is essential in order to describe and quantify their impact on climate, atmospheric chemistry, human health, and biogeochemical cycles. This section gives a brief overview of measurement principles for fundamental physical and optical particle parameters (particle number, size, mass, light scattering, and absorption coefficients) and of the respective measurement sensors. The chapter does not cover measuring principles and sensors for the chemical analysis of atmospheric particles, and the reader is referred to the literature, for example, [18.1, 2].

18.1.1 Physical Properties of Atmospheric Particles

Atmospheric particles are produced both by natural sources (e.g., desert dust, biomass burning, sea salt, volcanoes) and anthropogenic sources (e.g., industry, traffic, agriculture) [18.3]. Particles can be emitted directly into the atmosphere as primary emissions (e.g., dust, sea salt, soot) or can be formed by gas-to-particle conversion of precursor gases as secondary emissions (e.g., sulfates, ammonium nitrate, secondary organic aerosol). Once in the atmosphere, particles are transformed by coagulation (i.e., collision and coalescence), condensation growth (gas molecules condense on existing particles) or shrinkage (volatile compounds evaporate from existing particles), are transported by advection and turbulence, and are finally removed from the atmosphere by dry or wet deposition. Accordingly, the particle size range (Fig. 18.1) covers several orders of magnitude and may be subdivided into the *nucleation mode* (diameter $< 20\ \text{nm}$), the *Aitken mode* (diameter $20\text{--}100\ \text{nm}$), the *accumulation mode* (diameter $100\text{--}1000\ \text{nm}$), and the *coarse mode* ($> 1\ \mu\text{m}$). There are various definitions of the exact diameter ranges of

the modes, and the given ranges follow [18.4]. The atmospheric residence time is longest in the accumulation range of $0.1\text{--}1.0\ \mu\text{m}$, because smaller particles quickly grow to larger sizes by condensation and coagulation, and larger particles are efficiently removed by gravitational settling. Depending on the measurement principle, particle size is typically given as an equivalent diameter of a spherical particle with similar behavior as the particle of interest (Sect. 18.3.9).

Due to the high variability of particle sources and sizes, multiple parameters are necessary to comprehensively characterize atmospheric particles (see Tables 18.1–18.4). Measurements of total particle number concentrations and particle sizes are fundamental (Table 18.1). Particle size is measured in specific size bins, covering one or more of the above-mentioned size modes, and is typically connected to a sensor for particle number measurement. This results in particle number size distributions, which are the basis for calculating particle surface, volume, and mass size distributions (Sect. 18.3.9 and Table 18.2). Particle mass concentrations are important for studies in which mass-related particle properties are relevant (e.g., health or mass-specific optical parameters). Particle mass concentrations are typically given for specific size ranges, e.g., PM_{10} as the particle mass concentration of particles $< 10\ \mu\text{m}$ or $\text{PM}_{2.5}$ as the particle mass concentration of particles $< 2.5\ \mu\text{m}$. The highest number concentrations are typically found in the size range $< 100\ \text{nm}$. The highest mass and volume concentrations are found in the coarse mode, because the volume, and thus the mass, of spherical particles scales with the third power of the diameter. The highest surface concentrations are typically found in the accumulation mode.

To further characterize the environmental impact of atmospheric particles, their optical properties must be measured. Radiation will be attenuated by atmospheric

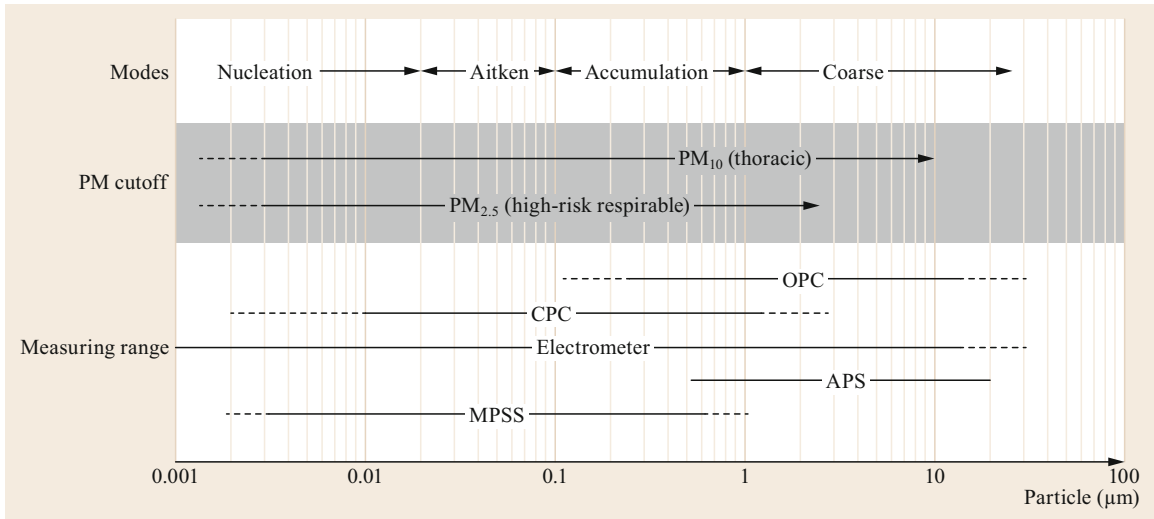


Fig. 18.1 Size ranges of the nucleation, Aitken, accumulation, and coarse modes, the PM₁₀ and PM_{2.5} conventions, and typical measuring ranges of particle instrumentation (OPC: optical particle counter; CPC: condensation particle counter; APS: aerodynamic particle sizer; MPSS: mobility particle size spectrometer). Further details in the text

Table 18.1 Fundamental physical parameters of atmospheric particles; units and symbols are commonly used for atmospheric particles

Parameter	Description	Unit	Symbol
Particle number concentration	Number of particles in a volume of air	cm ⁻³ or m ⁻³	<i>N</i>
Particle mass concentration	Mass of particles in a volume of air	μg m ⁻³	<i>M</i>
Particle size	Particle size typically given as equivalent diameter of a spherical particle	nm or μm	<i>D</i> , <i>D_p</i>

Table 18.2 Derived physical parameters of atmospheric particles

Parameter	Description	Unit	Symbol
Particle surface concentration	Particle surface derived from measurements of particle number and size in a volume of air; shape of particles usually assumed to be spherical	μm ² cm ⁻³	<i>S</i>
Particle volume concentration	Particle volume derived from measurements of particle number and size in a volume of air; shape of particles usually assumed to be spherical	μm ³ cm ⁻³	<i>V</i>
Mass concentration of light-absorbing particles	Particle mass of light-absorbing particles in a volume of air; derived from measurements of particle absorption coefficients and calibration with particles with known mass absorption cross section	μg m ⁻³	<i>M_{LAP}</i>

particles. This attenuation (termed extinction) consists of two parts, particle scattering and absorption (Table 18.3). Based on particle scattering and absorption coefficients, additional optical parameters can be derived (Table 18.4), such as the complex refractive index, the single-scattering albedo, or the particle phase function, which are essential for studies of the radiative forcing of atmospheric particles or for radiative transfer modeling.

18.1.2 Principles of Measurements

Measurement principles for fundamental physical particle properties introduced in Sect. 18.1.1 are summarized in Table 18.5, together with the respective mea-

surement sensors, some of which are also important for sampling trace substances in air (Chap. 19). The particle number can be measured either optically by particle light scattering, or electrically by measuring the electrical charges carried by particles. Particle sizing methods make use of optical properties of particles (light scattering), their aerodynamic behavior, or their electrical mobility. Particle mass is measured by gravimetric methods, absorption of beta radiation, harmonic oscillation of a microbalance, or the vibration of a piezoelectric crystal. Particle light scattering is measured with nephelometers. For the measurement of light absorption, either filter-based instruments are used (which measure the attenuation of light by particles collected on a fil-

Table 18.3 Fundamental optical parameters of atmospheric particles

Parameter	Description	Unit	Symbol
Particle scattering coefficient	Wavelength-dependent attenuation of incident radiation by particle scattering	m^{-1}	σ_{sp}
Particle backscatter coefficient	Wavelength-dependent attenuation of incident radiation by particle scattering, considering only the backward direction	m^{-1}	σ_{bsp}
Particle absorption coefficient	Wavelength-dependent attenuation of incident radiation by particle absorption	m^{-1}	σ_{ap}

Table 18.4 Derived optical parameters of atmospheric particles

Parameter	Description	Unit	Symbol
Particle extinction coefficient	Sum of the particle scattering coefficient and the particle absorption coefficient	m^{-1}	σ_{tot}
Single-scattering albedo	Ratio of the particle scattering coefficient and the particle extinction coefficient	–	ω
Forward scattering coefficient	Attenuation of incident radiation by particle scattering, considering only the forward direction	m^{-1}	σ_{fsp}
Particle phase function	Angular distribution of the particle scattering coefficient	–	p
Asymmetry parameter	Average cosine of the scattering angles, taking into account the scattering intensities of the particle phase function	–	g
Complex refractive index	Optical particle properties with respect to the surrounding medium; consists of a real part (describing scattering) and an imaginary part (describing absorption)	–	m

Table 18.5 Measurement principles and sensors for fundamental physical properties of atmospheric particles

Sections	Measurement principle	Type of sensor	Parameter
Sects. 18.3.1 and 18.4.1 Particle light scattering	Light scattering of individual particles	Optical particle counter (OPC)	Particle number, Particle size
	Light scattering of artificially grown individual particles	Condensation particle counter (CPC)	Particle number
	Light scattering of particle ensemble	Nephelometer	Particle scattering/backscatter coefficient
Sects. 18.3.2 and 18.4.2 Particle light absorption and extinction	Light absorption of particle ensemble	Filter-based absorption sensor	Particle absorption coefficient
Sects. 18.3.3 and 18.4.3 Photoacoustic spectroscopy	Light absorption and conversion into acoustic wave	Photoacoustic sensor	Particle absorption coefficient
Sects. 18.3.4 and 18.4.4 Electrical detection and mobility of particles	Electric charge measurement of particle ensemble Differential electrical mobility of charged particles	Electrometer Mobility particle size spectrometer (MPSS)	Particle number Particle size
Sects. 18.3.5 and 18.4.5 Diffusivity of particles	Size-dependent diffusive deposition of particles	Diffusion battery/diffusion size classifier	Particle size
Sects. 18.3.6 and 18.4.6 Aerodynamic behavior of particles	Time-of-flight measurement of aerodynamic particle diameter	Aerodynamic particle sizer (APS)	Particle size
	Aerodynamic behavior of particles in air flow	Impactor	Particle size, particle mass
Sects. 18.3.7 and 18.4.7 Particle microbalances	Gravimetric analysis of collected particle ensemble	Filter microbalance	Particle mass
	Change in vibration of piezoelectric crystal by collected particle ensemble	Piezoelectric crystal microbalance	Particle mass
	Change in harmonic oscillation of tapered element by collected particle ensemble	Oscillating microbalance	Particle mass
Sects. 18.3.8 and 18.4.8 Attenuation of beta radiation	Attenuation of beta radiation by collected particle ensemble	Beta attenuation monitor	Particle mass

ter), or instruments exploiting the conversion of the energy of light absorbed by particles into an acoustic wave are used. In addition, the particle chemical composition has a distinct impact on their optical properties. Therefore, measurement techniques to determine the chemical composition of particles are highly complementary to the ones described in this chapter.

18.1.3 Measurement Site

Measurements of atmospheric particles are typically colocated with measurements of meteorological parameters such as air temperature, relative humidity, wind speed and direction, precipitation, and solar radiation. In a fixed sampling site, the instrumentation is placed in a temperature-controlled shelter, and the particle sam-

ple is directed to the sensor(s) through an inlet and tubing system. The sampling height for particle measurements close to direct sources such as traffic is between 1.5 and 4 m AGL, while sampling heights of 5–10 m AGL are used for process studies of the undisturbed atmospheric particle population. The sampling location should not be directly influenced by topography, vegetation, or buildings.

Particle measurement sensors are placed not only in laboratory-like setups, but also on platforms such as towers or ships (ground-based, Chap. 6), aircraft (airborne platforms, Chap. 37), or balloons (aerology, Chap. 46), or under extreme conditions with respect to temperature, air pressure, or pollution. It is therefore very important to choose the appropriate instrument and method for the application under question.

18.2 History

Already in historical times, atmospheric particles were linked to air pollution. For example, in 1273 King Edward I prohibited cooking of food over coal fires in England, and proclaimed a ban on coal burning in London in 1306. In 1661, *John Evelyn* (1620–1706) addressed the *inconveniencie of the aer and smoak of London* in his *Fumifugium* tract on air pollution to *King Charles II* [18.5]. The development of particle sensors has its roots in the 19th century with the invention of the nepheloscope, an early cloud chamber, by *James Espy* (1785–1860) in 1841, the discoveries and inventions of *John Tyndall* (1820–1893) in the 1850s and 1860s, and the groundbreaking work on atmospheric condensation nuclei of *Paul-Jean Coulier* (1824–1890) [18.6] and *John Aitken* (1839–1919) [18.7, 8], which led to the development of the first portable particle counter by Aitken. Still today, the design of this instrument is the basis for modern condensation particle counters to measure the number concentration of atmospheric particles by growing individual particles into visible droplets by

condensation of supersaturated water vapor. Only in the 20th century did scientists begin to consider the atmosphere as a colloid, and the term *aerosol* was coined in the early 20th century by *Frederick G. Donnan* (1870–1956) and *August Schmauß* (1877–1954) [18.9]. Seminal work that set the stage for the development of modern aerosol science included *The Mechanics of Aerosols* [18.10] (first published in Russian in 1955 by *Nikolai Fuchs* (1895–1982)), *Air Chemistry and Radioactivity* [18.11] by *Christian Junge* (1912–1996), and *Smoke, Dust and Haze* [18.12] by *Sheldon Friedlander* (1927–2007). Important developments in the field of atmospheric particle measurement techniques were made for example in France by *Jean Bricard* (1907–1988; particle counters and diffusion batteries), in England by *Charles Norman Davies* (1910–1994; particle sampling techniques), in Japan by *Kouichi Iinoya* (1917–1998; particle sampling techniques), and in the USA by *Kenneth Whitby* (1925–1983; electrical aerosol analyzer, differential mobility analyzer).

18.3 Theory

The physical properties of atmospheric particles are measured based on a variety of principles including the interaction of particles with light, electrical mobility, diffusivity, aerodynamic behavior, and particle mass (Sect. 18.1.2 and Table 18.5). Here, we will introduce fundamental equations and conventions pertinent

to particle detection and the measurement of particle optical properties, particle size, and particle mass. This section also describes the specific requirements for the setup of the particle sampling system. Additional theoretical background on particle collection can be found in Chap. 19.

18.3.1 Particle Light Scattering

Due to the interaction of light with molecular dipoles of particles, light is scattered by particles at various scattering angles θ , described as the angle between the direction of propagation of the incident light and the scattered light. For a mathematical description of the scattering process, three different regimes are typically considered, depending on the ratio of particle circumference and wavelength of incident light, $\pi D/\lambda$ (Fig. 18.2). The Rayleigh scattering regime is applicable for particles much smaller than the wavelength of the light ($\pi D/\lambda \ll 1$), the Mie scattering regime for particle sizes of the order of the wavelength of the light, and the geometric scattering regime for particles much larger than the wavelength of the light ($\pi D/\lambda \gg 1$), where scattering is due to diffraction, reflection, and refraction.

Thus, optical detection of individual particles by light scattering strongly depends on particle size and the wavelength of the incident light. This limits the practical use of optical particle detection with visible light to particles $\gtrsim 100$ nm. With condensation particle counters, smaller particles are grown to optically detectable sizes by condensation of a supersaturated vapor. The size of the smallest particles that can still be activated to grow by condensation and the growth rate depend on the vapor supersaturation, which can be evaluated by classical Köhler theory or nano-Köhler theory [18.13].

For an individual particle in the Rayleigh scattering regime, the angular distribution of the scattered light intensity, i.e., the so-called particle phase function $p(\theta)$, is given by

$$p(\theta) = \frac{\lambda^2}{8\pi^2} \left(\frac{\pi D_p}{\lambda} \right)^6 \left| \frac{m^2 - 1}{m^2 + 2} \right|^2 (1 + \cos^2 \theta) I_0, \quad (18.1)$$

with the scattering angle θ , the wavelength of light λ , the particle diameter D_p , the refractive index of the particle m , and the intensity of the incident light I_0 . Obviously, the scattering properties in the Rayleigh regime are strongly dependent on the ratio of the particle diameter and light wavelength as well as the refractive index of the particle. In the Mie scattering regime, the scattering properties are calculated based on approximations of Mie theory [18.14], given for example by [18.15].

Based on Mie theory, dimensionless scattering efficiencies Q_{sp} can be calculated for individual particles. For an ensemble of particles of diameter D_p with number density N , the particle scattering coefficient σ_{sp} is related to Q_{sp} by

$$\sigma_{sp} = N \frac{\pi D_p^2}{4} Q_{sp}. \quad (18.2)$$

The particle scattering coefficient σ_{sp} is given in units of m^{-1} , and can be interpreted as the relative reduction in light intensity per unit length due to scattering.

Optical particle spectrometers directly link the scattering intensity of individual particles to the so-called optical equivalent diameter D_o , defined as the diameter of a spherical particle that exhibits the same optical properties as the studied particle. Therefore, the optical equivalent diameter is particularly useful for characterizing particles in terms of their effect on atmospheric visibility or direct climate effects.

If there is more than one particle in the viewing volume of an optical particle counter, coincidence of particles has to be taken into account. This process can be described by Poisson statistics, and the probability that particle coincidence occurs is

$$P_{\text{coinc}} = 1 - e^{-N_p t_d}, \quad (18.3)$$

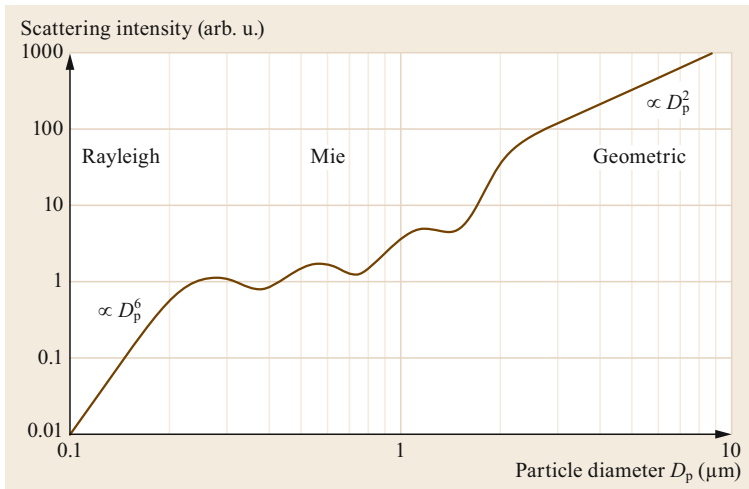


Fig. 18.2 Idealized representation of the relative scattering intensity of light at a wavelength of $\lambda = 0.5 \mu\text{m}$ as a function of particle diameter in the Rayleigh, Mie, and geometric scattering regimes; in the Rayleigh regime, the relative intensity increases in proportion to D_p^6 (18.1); in the Mie regime, the relationship follows a complex, not strictly monotonic pattern; in the geometric regime, the relative intensity is proportional to the particle cross section, i.e., $\propto D_p^2$

with the probability of coincidence P_{coinc} , the particle count rate N_p , and the residence time of an individual particle in the viewing volume t_d . Based on this equation, the actual particle count rate N_a is related to the measured particle count rate N_m [18.16] by

$$N_a = N_m e^{N_a t_d} . \quad (18.4)$$

A common approximation for solving this equation is to substitute N_a with N_m in the exponent on the right-hand side of the equation.

18.3.2 Particle Light Absorption and Extinction

The particle absorption coefficient σ_{ap} characterizes the relative reduction in light intensity due to absorption. Directly measured values of the particle absorption coefficient σ_{ap} can be converted to equivalent mass concentrations of light-absorbing particles M_{LAP} if the mass absorption cross section of the light-absorbing particle population α_{LAP} at the measurement wavelength is known

$$M_{\text{LAP}} = \frac{\sigma_{\text{ap}}}{\alpha_{\text{LAP}}} . \quad (18.5)$$

The particle extinction coefficient σ_{tot} is the sum of the particle scattering coefficient σ_{sp} and the particle absorption coefficient σ_{ap} ,

$$\sigma_{\text{tot}} = \sigma_{\text{sp}} + \sigma_{\text{ap}} . \quad (18.6)$$

The particle extinction coefficient is either calculated from measurements of the scattering and absorption coefficients, or directly measured with extinction meters. The extinction of light by a particle population, including both scattering and absorption of light, can be described by the Bouguer–Lambert–Beer’s law

$$I = I_0 e^{-\sigma_{\text{tot}} L} , \quad (18.7)$$

with the light intensity after interaction with the particle population I , the incident light intensity I_0 , the particle extinction coefficient σ_{tot} , and the path length of interaction L between the particle population and the incident light.

The single-scattering albedo ω , i.e., the ratio of the particle scattering coefficient and the particle extinction coefficient

$$\omega = \frac{\sigma_{\text{sp}}}{\sigma_{\text{tot}}} , \quad (18.8)$$

is a dimensionless measure of the scattering properties with a value of 1 for purely scattering particles, and a value of 0 for purely absorbing particles.

Based on work by [18.17], the particle extinction coefficient at a wavelength $\lambda = 550 \text{ nm}$ can be used to estimate the atmospheric visual range VIS in m,

$$\text{VIS} = \frac{3.9}{\sigma_{\text{tot}}^{550 \text{ nm}}} = \frac{3.9}{\sigma_{\text{sp}}^{550 \text{ nm}}} \omega^{550 \text{ nm}} . \quad (18.9)$$

The complex refractive index of a particle, $m = n + ik$, summarizes the optical properties of a particle. The real part n represents scattering by the particle, while the imaginary part k describes absorption by the particle. The refractive index is not directly measured but rather typically derived from measurements of the particle scattering and absorption behavior.

18.3.3 Photoacoustic Spectroscopy

A direct method for measuring the particle absorption coefficient is photoacoustic spectroscopy. Photoacoustic spectroscopy [18.18] exploits the fact that the absorbed energy of a modulated light source of a specific wavelength will heat up a particle. The dispersed heat of the particle is associated with a thermal expansion of the surrounding gas. The periodic expansion of the gas yields a standing pressure wave that can be detected in an acoustic resonant chamber with a sensitive microphone. The amplitude of the acoustic wave is proportional to the amount of absorbed energy, which again is proportional to the amount of the absorbing particle ensemble.

18.3.4 Electrical Detection and Mobility of Particles

For electrical detection of particles, all particles or a well-defined fraction of the particle population must be electrically charged. Particles are exposed to a high concentration of either positive or negative ions (unipolar charging) or both positive and negative ions (bipolar charging) for a sufficiently long time, typically in the absence of an electric field. For particle detection, unipolar charging with high efficiency is desirable in order to obtain robust electrometer measurements even at low particle concentrations.

In the presence of an electric field, charged particles will migrate through a medium with an electrical mobility Z , defined as the ratio of the velocity of an electrically charged particle in an electric field, v_e , and the electric field strength E that accelerates the particle to that velocity,

$$Z = \frac{v_e}{E} = \frac{neC_c}{3\pi\eta D_m} , \quad (18.10)$$

with the number n of elementary charges e carried by the particle, the slip correction factor C_c that accounts

for noncontinuum effects when considering small particles in the transition regime between free molecular and continuum flow, the dynamic viscosity of air η , and the mobility diameter D_m . Following [18.19], the slip correction factor C_c is calculated as

$$C_c = 1 + \frac{2\lambda_{\text{mfp}}}{D_p} \left[1.165 + 0.483 \times \exp\left(-0.997 \frac{D_p}{2\lambda_{\text{mfp}}}\right) \right], \quad (18.11)$$

with the mean free path at 296.15 K and 1013.25 hPa, $\lambda_{\text{mfp}} = 67.3$ nm, and D_p in nm.

The so-called mobility diameter D_m is defined as the diameter of a spherical particle with the same electrical mobility as the studied particle. D_m is measured with mobility particle size spectrometers, typically in the submicron size range. Particle populations are neutralized by exposing the particle population to a large number of bipolar ions in order to achieve so-called Boltzmann charge equilibrium. Diffusion charging theories as proposed by [18.20, 21] have been experimentally validated for submicron particles [18.22], and are commonly approximated by an empirical polynomial function introduced by [18.23].

18.3.5 Diffusivity of Particles

Diffusion is a key transport and deposition mechanism for atmospheric particles smaller than 100 nm, caused by Brownian motion. Particle diffusivity or the particle diffusion coefficient D_{diff} is given by the Stokes–Einstein equation [18.24]

$$D_{\text{diff}} = \frac{kTC_c}{3\pi\eta D_p}, \quad (18.12)$$

with the Boltzmann constant k , temperature T , the slip correction factor C_c , the dynamic viscosity of air η , and the particle diameter D_p . D_{diff} increases with temperature and is strongly dependent on particle size. For small particles with $C_c \gg 1$, the particle diffusion coefficient is approximately proportional to D_p^{-2} .

18.3.6 Aerodynamic Behavior of Particles

For a particle that is accelerated by the gravitational force, a counteracting drag force described by Stokes' law for the general case of laminar flow around atmospheric particles will lead to a terminal settling velocity v_s in equilibrium [18.24], given by

$$v_s = \frac{\rho_p D_a^2 g C_c}{18\eta}, \quad (18.13)$$

with the gravitational acceleration g , the slip correction factor C_c , the dynamic viscosity of air η , and the aerodynamic equivalent diameter D_a . The aerodynamic equivalent diameter is defined as the diameter of a spherical particle of unit density (particle density $\rho_p = 1 \text{ g cm}^{-3}$) that exhibits the same terminal settling velocity as the studied particle. The aerodynamic diameter is applicable when using the aerodynamic particle sizer or impactors. For an impactor with nozzles of width W (diameter of circular nozzle or half-width of slit) and a particle velocity of v_n through the nozzle, particle collection depends on the dimensionless Stokes number St [18.24] expressed as

$$St = \frac{\rho_p D_a^2 C_c v_n}{9\eta W}. \quad (18.14)$$

Solving this equation for the aerodynamic diameter D_a when the collection efficiency is 50% yields the cutoff diameter of an impactor stage. The resulting size information is directly linked to the deposition behavior of particles in the human body, and therefore, important for the evaluation of particle health effects.

18.3.7 Particle Microbalances

Direct gravimetric measurement of the particle mass concentration after collection of particles with a filter or an impactor requires knowledge of the collection efficiency for different particle sizes. In the case of filtration, collection by molecular diffusion is efficient only for particles < 100 nm, while gravitational settling and sieving is efficient only for supermicron particles. In the range of 100 nm to 1 μm , inertial impaction and interception are the relevant processes for particle collection on the filter. For a quantitative discussion of these collection processes, the reader is referred to Chap. 19 and [18.25].

The deposition of particles on piezoelectric crystals increases the resonant frequency f_0 of the oscillating system. The frequency change Δf (in Hz) of the resonant frequency can be related to the mass change Δm (in kg) using the Sauerbrey equation [18.26],

$$\Delta f = -\frac{2f_0^2}{\sqrt{\rho_c \mu_c A_c}} \Delta m, \quad (18.15)$$

with the density of the crystal ρ_c , the modulus of rigidity of the crystal μ_c , and the deposition area of the crystal A_c .

For quartz crystals, where the quartz is cut at an angle of $\approx 35^\circ$ to the optical axis of the crystal (AT cut), with $\rho_c = 2.648 \times 10^3 \text{ kg m}^{-3}$ and $\mu_c = 2.95 \times$

$10^{10} \text{ kg m}^{-1} \text{ s}^{-2}$, we obtain

$$\Delta f = -2.26 \times 10^{-6} f_0^2 \Delta m. \quad (18.16)$$

Analogously, in a tapered element oscillating microbalance, the particles are deposited on an exchangeable filter, which is part of the microbalance. The sampled air continues through a hollow, tapered tube. The specific design of this tapered element and surrounding component cause the tube to oscillate at its specific frequency. The oscillating frequency changes in proportion to the change in deposited particle mass.

18.3.8 Attenuation of Beta Radiation

Particles attenuate beta radiation (0.01–0.1 MeV energy range) due to inelastic scattering by atomic electrons of particles. The particle mass concentration can be evaluated from an increase in attenuation as more particles are collected on a filter tape.

18.3.9 Representation of Particle Size Distributions

Particle size is typically reported as equivalent diameter, i.e., the diameter of a spherical particle that exhibits the same behavior as the studied particles. Depending on the measurement principle, the frame of reference can be the optical properties of a particle, the aerodynamic behavior of a particle, or the mobility of a particle in an electric field.

For a nonspherical particle, a dynamic shape factor χ [18.10] accounts for the increased drag on the particle due to its irregular shape. It is defined as the ratio of the drag force on the nonspherical particle of interest to the drag force on a volume-equivalent spherical particle moving at the same velocity relative to the surrounding gas. The dynamic shape factor χ allows us to relate the volume-equivalent diameter D_v , the aerodynamic equivalent diameter D_a , and the mobility diameter D_m ,

$$D_v = \sqrt{\chi \frac{\rho_0 C_c(D_a)}{\rho_p C_c(D_v)}} D_a = \frac{1}{\chi} \frac{C_c(D_v)}{C_c(D_m)} D_m, \quad (18.17)$$

with the particle density ρ_p , unit particle density $\rho_0 = 1 \text{ g cm}^{-3}$, and the slip correction factor C_c .

Particle size distribution is measured by parallel or subsequent measurement of the particle number concentration in finite size bins. For atmospheric particles, size distributions show characteristic peaks in certain size ranges, the so-called size modes. Whitby [18.27] proposed that atmospheric particle size distributions can be parameterized by a trimodal model representing the nucleation mode, the accumulation mode, and

the coarse mode, and are mathematically expressed as a superposition of log-normal distributions that represent the different modes,

$$N(\log D_p) = \sum_{i=1}^n \frac{N_i}{\sqrt{2\pi} \log \sigma_i} e^{-\frac{\log D_p - \log \text{GMD}_i}{2 \log^2 \sigma_i}}, \quad (18.18)$$

with the number of particles of diameter D_p N , the number of particles in mode i N_i , the geometric standard deviation σ_i , and the geometric mean diameter (GMD) of each mode i . Thus, each mode of the size distribution is uniquely characterized by the three parameters N_i , σ_i , and GMD_i .

Because atmospheric particles cover a diameter range over several orders of magnitude, the particle size distribution is presented on a logarithmic diameter scale. In order to make graphical representations of particle size distributions independent of the number and width of size bins, the number of particles in each size bin divided by the width of the size bin on a logarithmic scale, $dN/d \log(D_p)$, is plotted against the particle diameter D_p on a logarithmic scale (Fig. 18.3).

Particle surface size distribution dS , particle volume size distribution dV , and particle mass size distribution dM are often calculated from measured particle number size distribution dN assuming spherical particles with a representative diameter D_i in each size bin, and an assumed particle density ρ_p

$$dS = \pi D_i^2 dN, \quad (18.19)$$

$$dV = \frac{\pi}{6} D_i^3 dN, \quad (18.20)$$

$$dM = \rho_p \frac{\pi}{6} D_i^3 dN. \quad (18.21)$$

18.3.10 Setup Requirements of the Particle Sampling System

When sampling atmospheric particles, special attention has to be paid to the design of the inlet and tubing system. The ambient air flow to the inlet must be as free as possible from any disturbance. The inlet itself has to be omnidirectional, i.e., ensuring that ambient air from all wind directions can equally enter the sample tube. If only particles up to a certain size are collected, specific inlets or cyclones with defined cutoffs are needed, which are valid for a specific sample flow only. In order to avoid particle losses to the tubing wall, the tubing should follow a straight path to the measurement chamber, as short as possible, and be of conductive material (e.g., stainless steel, avoiding electrostatic charging and subsequent particle loss). The flow rate should be optimized. High flow rates are advised when sampling

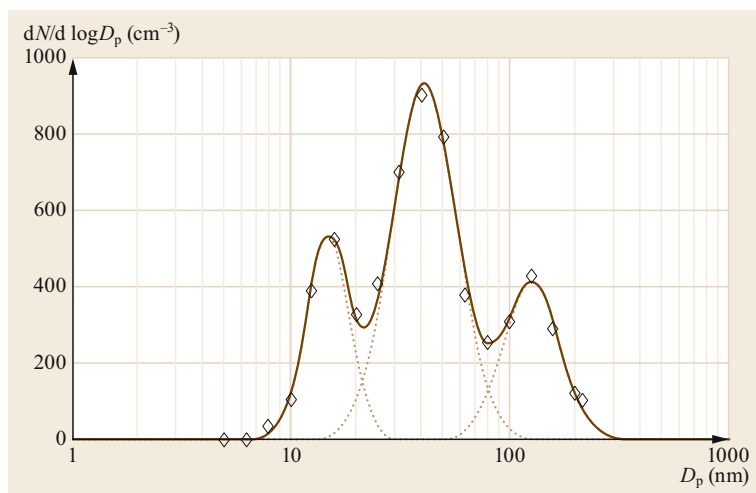


Fig. 18.3 Example of a particle number size distribution; measurement in 18 size bins (*open diamonds*), with three fitted log-normal distributions (*dotted lines*) and the resulting superposition (*solid line*)

low particle concentrations. Low flow rates are recommended for applications that detect single particles in the measurement cell, or in environments with high particle concentrations. According to the sample flow, the tube diameter also has to be adapted. The sample flow should be laminar to avoid losses of small particles due to diffusion and turbulent inertial deposition. To identify an adequate combination of tube diameter and flow rate, the Reynolds number should be calculated [18.28]. Further theoretical background on sampling systems can be found in Chap. 19.

Stable temperature and humidity conditions are very important for atmospheric particle measurement, and therefore temperature and humidity in the measurement cell should be controlled or, if not possible, at least be monitored. For particle sensors operating within the WMO GAW (World Meteorological Organization Global Atmosphere Watch) program, it is recommended that relative humidity in the measurement cell be controlled to < 40% [18.29]. It is important that the temperature of the measurement cell be above

the dewpoint temperature of the sample air in order to avoid contamination by the condensation of water vapor. Drying of the sample air is done by removing water vapor upstream with water traps or dryers, diluting the sample air with dry particle-free air, or heating the tubing system. It must be taken into account that drying might lead to the loss of semivolatile components of the particles. Besides monitoring temperature and humidity, the atmospheric pressure at the measurement site also has to be recorded in order to report particle concentrations at either standard or ambient atmospheric conditions.

Further, the inlet must be protected against the intrusion of insects, rain droplets, or ice crystals. In cold and relatively humid environments, obstruction of the inlet system by riming must be prevented, while taking into account effects of potential heating on the ambient aerosol. For detailed descriptions of inlet system design, including specific applications such as measurements on board aircraft or under extreme environmental conditions, the reader is referred to the literature [18.24, 28].

18.4 Devices and Systems

For the measurement of atmospheric particles, there is no one ideal instrument that can provide information about all relevant properties, but rather a large number of devices and systems that measure one or several specific properties. In the following, relevant instruments for the measurement of particle number, size, mass, and optical properties are summarized according to the respective measurement principles. Due to their widespread use and various specific features, condensation particle counters and mobility particle size

spectrometers are covered in greater detail. Further, the added benefit of particle sensor combinations will be illustrated, and finally, the advantages and disadvantages of the different methods will be compared.

18.4.1 Particle Light Scattering

Optical particle counters (OPC) detect particles by measuring scattered light produced by individual particles crossing a focused light beam (Fig. 18.4). The first

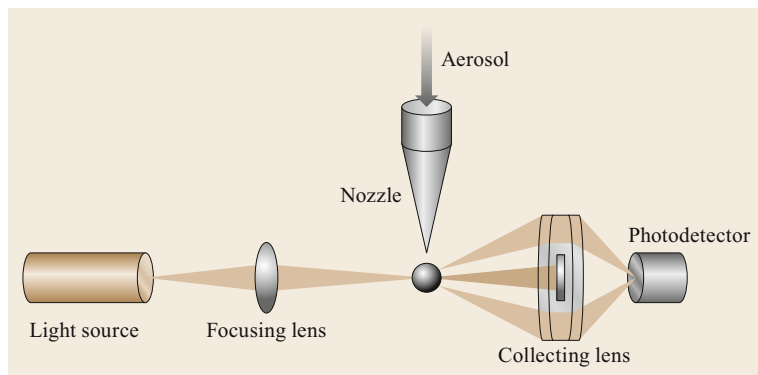


Fig. 18.4 Schematic setup of optical particle detection; particles are focused through a nozzle and illuminated by a light beam; scattered light is directed to a sensitive photodetector through collecting lenses, while the direct light beam is trapped

OPC was introduced by [18.30, 31]. In general, a narrow air sample stream is illuminated by an intense beam of light, which is scattered by individual particles. The scattered light is collected through lenses at a specified angle with respect to the incident light beam, and directed to a photodiode. Here, light is converted into an electric current based on the inner photoelectric effect, and the typical output is a voltage pulse with a magnitude proportional to particle size. Individual pulses are counted for a specified time period, and together with the known sample volume passing through the illuminated region during that time period, the particle number concentration can be calculated.

There is a practical lower detection limit of optical particle detection depending on the wavelength and intensity of illumination and the dark current of the detector. Common OPC light sources operate in the visible wavelength range, including either monochromatic laser light or broadband white light. Laser intensities are typically much larger than those from white light sources and thus preferable for the detection of smaller particles. Most commercially available OPCs use laser diodes, enabling lower-diameter detection limits < 100 nm (but more typically ≈ 200 nm), while white light OPCs typically cannot detect particles with diameters < 300 nm [18.32].

The intensity and angular distribution of the scattered light can also be exploited to determine particle size and shape. Optical particle spectrometers (OPS) evaluate the pulse height of scattered light in order to determine the number concentration in distinct size bins. The relationship between particle size and pulse height is affected by the instrument design and the optical properties of the particle. For practical purposes, a calibration curve for particles of known shape and composition, such as spherical water droplets or polystyrene spheres, is required to determine the optical equivalent diameter. A particle size distribution derived from optical particle spectrometers then describes the

ensemble optical properties of the particle population, i.e., its interaction with light.

The angular distribution of the scattered light intensity exhibits complex patterns (Sect. 18.3.1). In most optical particle spectrometers, scattered light is collected either in an angular range of about 5° – 25° in the forward direction of the incident light (forward-scattering instruments) or in a broad angular range including the perpendicular direction (wide-angle instruments). In both configurations, the relationship between pulse height and particle size is not strictly monotonic, and assigning a particle to a unique size bin is not always possible. Generally, the response of instruments with monochromatic light sources shows stronger oscillations than that of instruments with white light sources. For detailed studies of particle size and shape, the angular distribution of the scattered light intensity can be measured with multiple detectors for various angular regions [18.33].

Condensation particle counters (CPC, also condensation nucleus counters CNC) are widely used for the optical detection of particles < 100 nm. Here, prior to optical detection, individual particles are grown by condensation of a supersaturated vapor to droplets with diameters of several μm , which can be easily detected. There are different methods for producing the supersaturated vapor, including adiabatic expansion, heat transfer, and mixing of warm and cold air streams, as well as different working fluids such as water or *n*-butanol. The earliest instruments, including the original expansion-type instrument [18.8], used water as working fluid and adiabatic volume expansion or pressure release to cool the aerosol sample in a chamber saturated with respect to water vapor, which leads to condensation of water vapor onto the particles, and growth to optically detectable sizes. A major drawback of expansion-type CPCs is the discontinuous measurement cycle. Most modern continuous-flow CPCs use forced convection heat transfer to produce supersaturation, typically with

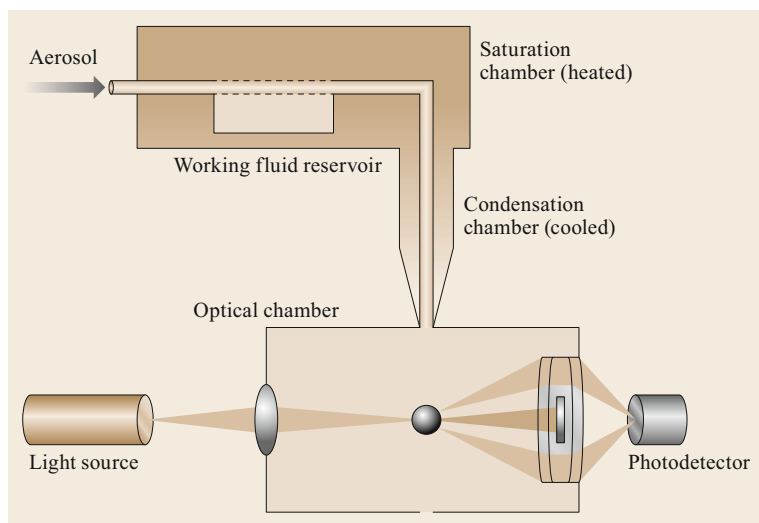


Fig. 18.5 Schematic setup of a condensation particle counter; the aerosol sample is mixed with saturated vapor of the working fluid in a heated saturation chamber, followed by condensation of the vapor onto particles in the cooled condensation chamber and detection of the grown droplets in an optical chamber

n-butanol or water as working fluids. The first instruments of this type were introduced by [18.34–36]. In a butanol-based CPC (Fig. 18.5), the aerosol sample is introduced into a temperature-controlled saturation chamber, which is filled with saturated butanol vapor. Then, the aerosol sample together with the saturated vapor enters a colder, temperature-controlled condensation chamber, where the butanol vapor becomes supersaturated and condenses onto the particles. The temperature conditions in the saturation and condensation chambers determine the supersaturation of the butanol vapor, and thus the smallest size of particles that are still activated to grow by condensation of butanol. High supersaturation is desirable in order to achieve activation of particles insensitive to the chemical composition of the particles. However, nucleation of particles from the butanol vapor, which can occur if the supersaturation is too high, must be avoided. In a water-based CPC, the aerosol sample first flows through a cold, humid chamber, where the particles are cooled and water vapor is saturated. The aerosol then enters a warm, wet-walled growth tube, where water vapor becomes supersaturated and condenses onto the cold particles in the center of the tube, because diffusion of water vapor from the wall to the center is faster than heat transfer and warming of the particles. Another method for achieving supersaturation of the working fluid vapor involves mixing of saturated air streams at different temperatures. While heat transfer instruments are operated in laminar flow and exhibit a limited response to concentration changes, mixing-type instruments have been designed with fast response times [18.37, 38].

Whereas particle detection in early instruments was accomplished by manual counting of droplets under a microscope after collection on a grid, today indi-

vidual particles are automatically detected by light scattering. This direct single-particle counting method is limited to particle number concentrations on the order of 10^4 – 10^5 cm^{-3} , when scattering signals do not overlap. At higher concentrations, coincidence, i.e., the simultaneous detection of multiple particles, occurs and has to be corrected (Sect. 18.3.1). At very high concentrations, particle number concentrations may be derived indirectly by evaluating the light attenuation caused by the particle ensemble in the light path of the instrument.

The working fluid in a CPC should have sufficiently high vapor pressure to grow particles to sizes of several μm within a period of several tenths of a second as the particle population passes through the condensation chamber. At the same time, the supersaturation should not lead to nucleation of particles. In addition to water and butanol, various other working liquids have been used in both research and commercial CPCs, most notably isopropanol, ethylene glycol, and diethylene glycol [18.39].

A key characteristic of each CPC is the lower cutoff diameter, the size of particles that are still activated to grow by condensation of the working fluid. The lower cutoff diameter is defined as the particle diameter with a 50% detection efficiency, which can be derived from detection efficiency curves giving the fraction of activated particles relative to the total particle number as a function of particle size. The nominal lower cutoff diameter of different CPC models depends on various factors including the instrument design, the sampling pressure, and the vapor supersaturation achieved for the specific working fluid. It should be noted that the true lower cutoff diameter may also vary for individual instruments of the same CPC model. Only over the

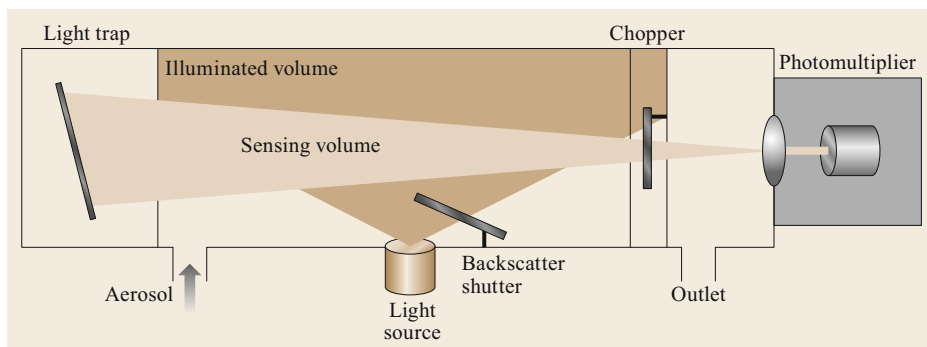


Fig. 18.6 Schematic setup of a nephelometer; particles are pumped through the measuring volume, which is defined by the volume illuminated by a light source and the sensing volume of the detector; the backscatter shutter can restrict the illuminated volume to the backscattering part; a chopper opens and closes the sensing volume to the detector, which may consist of several photomultipliers for different wavelengths selected with bandpass filters

past decade have lower cutoff diameters < 3 nm been achieved. One notable example approaching the molecular regime is the Particle Size Magnifier [18.40], which makes use of diethylene glycol as working fluid to grow particles as small as 1 nm.

Nephelometers (Fig. 18.6) measure light scattering by particles. Integrating nephelometers [18.41, 42] quantify the scattering over all directions, and the signal contribution due to both scattering by gases and instrument noise is subtracted by periodic background measurements of particle-free air. Well-calibrated nephelometers can measure scattering coefficients $< 2 \times 10^{-7} \text{ m}^{-1}$. Commercially available nephelometers include single-wavelength instruments using light in the visible or near-infrared range, as well as multiwavelength instruments that measure scattering of light at different wavelengths (typically 450, 500, 650–700 nm). In addition to the total scattering measurement, some instruments also use a backscatter shutter in the optical path to quantify the hemispheric backscattering. By varying the position of the backscatter shutter, the angular distribution of scattering can be measured with polar nephelometers.

Relative humidity $> 40\%$ strongly influences the scattering measurement due to particle growth and shrinkage, depending on particle composition. It is recommended that nephelometer measurements be performed under *dry* conditions, i.e., at a relative humidity $< 40\%$, and that the measured *dry* value be related to ambient relative humidity by empirical calibration functions. Because of technical limitations, the scattering angles covered for the total and backscatter measurements are truncated. Two commonly used nephelometers, the TSI Model 3563 (TSI Incorporated, St. Paul, MN, USA) and the Ecotech Aurora 3000 (Ecotech, Melbourne, Australia), cover scattering angles from 7° to 170° and 9° to 170° , respectively. Both

humidity effects and truncation must be corrected for accurate scattering measurements.

18.4.2 Particle Light Absorption and Extinction

In *filter-based absorption monitors*, light absorption by particles is characterized by collecting particles on a filter and measuring the transmission or reflection of light with a photometer. Transmission and reflection of light is affected not only by absorption, but also by scattering and multiple scattering of light by both the filter material and the particle sample, which must be accounted for. In the integrating sphere method, a filter is illuminated in an integrating sphere. The difference between light detected with particles on the filter and a clean filter is attributed to the light absorbed by the particles. A simplification of this technique is the integrating plate method [18.43], where a glass plate is placed between the particle filter and the detector. For continuous absorption measurements, particles are collected on a filter or a filter tape and illuminated. In aethalometers [18.44], the light attenuation with particles on the filter tape is measured and compared with the light attenuation by the unloaded filter tape as a reference. The difference is considered to be the absorption due to the collected particles. For automated operation, the filter tape is advanced as soon as the measured attenuation is above a threshold value. Measurements are made either at a single wavelength or at multiple wavelengths. For example, the Magee Scientific aethalometer model AE33 (Magee Scientific, Ljubljana, Slovenia) measures the light attenuation at seven different wavelengths from the UV-A to the near-IR and performs internal corrections for the filter-loading effect (artificial increase in attenuation due to multiple scattering by particles). The particle soot absorption photometer (PSAP, [18.45]) measures

the differential transmittance through a glass fiber filter with and without particle loading, either at a single wavelength of 550 nm or at three wavelengths. The multi-angle absorption photometer (MAAP; [18.46]) measures both the light transmitted through and scattered back in two different angles from particles collected on a glass fiber filter tape. The absorption coefficient is derived with a two-stream approximation radiative transfer model that takes into account multiple scattering and reflection effects. Correction recommendations for the MAAP and the PSAP instruments are given in [18.29], and also for the aethalometer. However, there is presently no consensus on how to correct aethalometer measurements in a consistent way [18.29].

For all filter-based absorption photometers, the absorption coefficient measured at a specific wavelength can be converted to yield the mass concentration of light-absorbing particulate compounds, typically reported as equivalent black carbon, i.e., the mass concentration of black carbon that would yield the measured absorption coefficient.

In a different approach, light extinction can be measured by cavity attenuated phase shift (CAPS) spectroscopy due to a change in the waveform of a square-wave-modulated light-emitting diode coupled to an optical cavity, depending on the particle light extinction in the optical cell [18.47]. Complementing equivalent black carbon measurements by filter-based absorption measurements, the single-particle soot photometer (SP2) measures soot mass in individual particles by laser-induced incandescence [18.48].

18.4.3 Photoacoustic Spectroscopy

An alternative to filter-based absorption measurements is photoacoustic spectroscopy [18.18, 49, 50], where light absorption heats up particles and the surrounding gas. Various photoacoustic sensors have been developed for light absorption measurements of atmospheric particles [18.51–53], including the commercially available three-wavelength photoacoustic soot spectrometer PASS (Droplet Measurement Technologies, Longmont, CO, USA). The photoacoustic extinctions PAX (Droplet Measurement Technologies, Longmont, CO, USA) combines a photoacoustic cell to measure light absorption by particles and a reciprocal nephelometer to measure light scattering by particles in one instrument, yielding particle light extinction.

18.4.4 Electrical Detection and Mobility of Particles

Electrometers are used to determine the number concentration of an ensemble of particles by collecting

electrically charged particles on the electrode of an electrometer and measuring the electric current induced by the deposition of electrical charges. In a Faraday cup electrometer, charged particles are collected on a filter placed in a metal housing (Faraday cup), and the induced charge is measured with a highly sensitive electrometer (0.1–1 fA). For quantitative information, the charging state of the particle ensemble has to be known. In order to charge the sample with high efficiency, unipolar diffusion chargers, where unipolar positive ions are produced by corona discharge, are commonly used. However, the efficiency of the diffusion charging process is dependent on a large number of factors, and the accuracy of the particle number concentration from electrometer measurements is limited by the variability in the particle charging probability as a function of particle size and chemical composition. For example, multiple charged particles deposit more than one elementary charge to the electrometer. Compared with single-particle counting of CPCs, electrometers require a minimum number concentration for reliable quantification, but as an advantage, particles of all sizes will be detected as long as they carry an electrical charge and are captured in the Faraday cup. A typical application of electrometers is the calibration of CPCs by independent measurement of the particle number concentration in a controlled laboratory setup [18.54].

Mobility particle size spectrometers (MPSS) classify submicron particles according to their electrical mobility, i.e., the behavior of charged particles in an electric field. In the first commercial mobility spectrometer, the electrical aerosol analyzer (EAA) [18.55] based on a design developed by [18.56], particles are electrically charged with a unipolar positive charger and then coaxially introduced into a cylindrical classifier with a well-defined electric field. It is recommended that a positive voltage be applied, i.e., measuring the mobility of negatively charged particles. Depending on the flow rate and the electric field, particles with high mobility are removed by deposition to the classifier walls, while larger particles with sufficiently low electrical mobility are detected with a Faraday cup electrometer. By applying different voltages to the classifier, the electric field is adjusted to remove different mobility fractions of the particle population in order to obtain particle size distributions. In typical applications, the EAA covered a size range of about 10 nm to 1 μm in ten size bins.

The differential mobility particle sizer (DMPS) is an improvement over the EAA with much higher size resolution. A DMPS (Fig. 18.7) consists of a particle neutralizer [18.56], a differential mobility analyzer (DMA) [18.57], and a particle detector, e.g., a CPC or an electrometer. In the neutralizer, particles are exposed

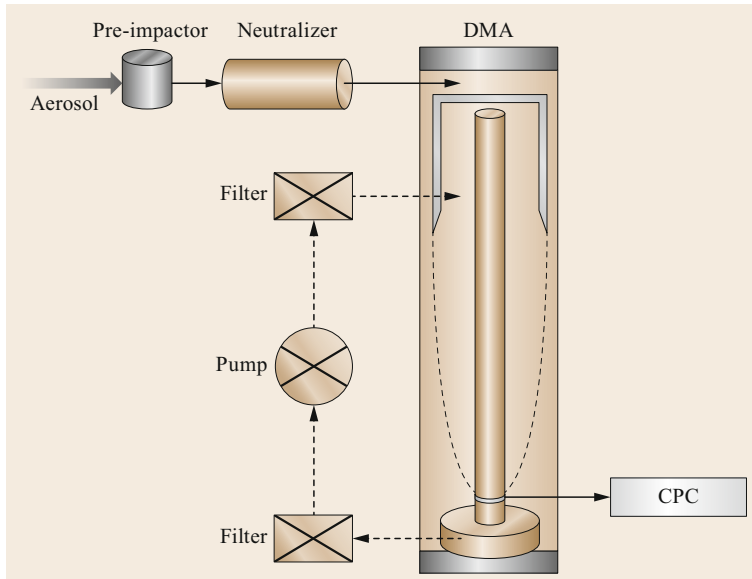


Fig. 18.7 Schematic setup of a mobility particle size spectrometer; the particle sample enters a pre-impactor to remove supermicron particles, a neutralizer to achieve charge equilibrium, and the DMA for mobility classification; the central rod is biased to a variable high voltage to establish an electric field in which particles within a small mobility range are deflected to an annular slit and transferred to a CPC; the *dashed arrows* indicate the particle-free sheath flow

to bipolar ions for a sufficient length of time to achieve Boltzmann charge equilibrium. Most commonly, radioactive neutralizers based on Kr-85, Am-241, or Po-210 are used to establish a bipolar ion cloud. As an alternative, nonradioactive neutralizers based on soft x-ray ionization [18.58] and bipolar corona discharge are available. After passing the neutralizer, the average charge of the particle population is close to zero, and the size-dependent probability of each particle carrying one or multiple positive or negative charges is well defined. A commonly used approximation for particle charge distribution was published by [18.23]. In the DMA, particles are introduced into an electric field between two electrodes. In most cases, a cylindrical design with a metal rod as inner electrode and a metal cylinder as outer electrode is used. The aerosol sample with charged particles enters the annular region between the electrodes in a laminar flow of particle-free sheath air. The geometry of the DMA and the applied voltage determine the trajectory of particles as a function of their electrical mobility. A particle fraction with a defined electrical mobility is deflected to a slit in the inner electrode (which is typically biased to a positive voltage up to several kV), while all other particles are deposited to the walls or removed with the excess air flow. Thus, instead of measuring a particle fraction with an electrical mobility above a certain threshold integrally as in the EAA, the DMA extracts particles differentially within a small range of electrical mobility. To obtain particle size distributions, different voltages are applied in discrete time steps, and the particles are detected with a CPC or an electrometer. A typical measurement cycle for a full DMPS particle size distribution measurement

takes 15–30 min. In order to reduce the time required to complete a full measurement cycle, [18.59] proposed the scanning mobility particle spectrometer (SMPS), where the voltage is ramped up and down continuously instead of applying discrete voltage steps in the DMPS. In addition, various modifications to the design of the cylindrical DMA, and the radial DMA design [18.60] have been developed to improve the DMA transmission efficiency of nucleation mode particles. An overview of the recommended setup and the performance of various currently available MPSS can be found in [18.29, 61].

In order to study fast changes in particle size distribution, e.g., close to particle emission sources or directly in engine exhaust, mobility spectrometers with electrometer detection such as the engine exhaust particle sizer (EEPS) or the fast mobility particle sizer (FMPS) are commercially available. In addition, for size and mobility distribution measurements of molecular clusters and nucleation mode particles, the neutral cluster and air ion spectrometer (NAIS) [18.62] classifies particles and air ions based on their mobility and parallel detection with an array of 21 electrometers. Depending on the operating mode, the NAIS instrument works similarly to the electric aerosol spectrometer [18.63] or to the air ion spectrometer (AIS), which only detects naturally occurring air ions.

18.4.5 Diffusivity of Particles

In a laminar flow field, the diffusivity of ultrafine particles (diameter < 100 nm), and thus the probability of deposition to surfaces, increases with decreasing size. In *diffusion batteries*, this differential diffusion behav-

ior can be exploited to obtain particle size distributions. In practice, there are tube-type (or channel-type) diffusion devices, such as a series of fine capillaries [18.64], and screen-type diffusion devices, where particles flow through a series of fine mesh screens [18.65]. While diffusion batteries have been replaced by MPSS for size distribution measurements, diffusion screens are still in use today for controlling the lower size limit of a particle population, e.g., to modify the lower cutoff diameter of a CPC. Also, *diffusion size classifiers* [18.66], where particles are electrically charged and deposited in consecutive stages depending on their diffusive behavior, have become available as robust portable instruments to infer particle number concentrations, the lung deposited particle surface area concentration, and the mean particle diameter.

18.4.6 Aerodynamic Behavior of Particles

The *aerodynamic particle sizer* (APS) measures the aerodynamic diameter by accelerating the airflow in a nozzle and measuring the time of flight of individual particles after acceleration. Each particle is detected twice by light scattering with two laser beams separated by a fixed distance, e.g., 200 μm . The time delay between the two detection pulses divided by the known distance of the laser beams yields the particle velocity. Due to their inertia, larger particles with a higher mass are accelerated less than smaller particles with lower mass. Thus, the particle velocity and the associated time of flight over a given distance are directly related to particle mass. For a spherical particle of unit density, as used in the definition of the aerodynamic diameter (Sect. 18.3.6), this enables a unique determination of the aerodynamic diameter. Aerodynamic particle sizers cover a nominal aerodynamic diameter range of about 0.5–20 μm , although [18.67] found large instrument-to-instrument variability of up to 60% for particle diameters < 0.9 μm in an intercomparison study of 15 aerodynamic particle size spectrometers. In practice, the aerodynamic diameter derived from the APS is adjusted for particle sphericity, particle and gas density, and air viscosity. For interpretation of the APS, it should also be taken into account that particles may be affected by a pressure and temperature drop after expansion through the nozzle.

Impactors are widely used to collect size-fractionated particle samples based on acceleration of the air flow through nozzles and inertial impaction on collection plates (Chap. 19). The acceleration is determined by the air flow rate and the nozzle size. Depending on the aerodynamic behavior of particles, the fraction of the particle population that cannot

follow the streamlines around the collection plate will impact on the plate. In cascade impactors, size fractions are subsequently collected on several impaction stages with well-characterized cutoff diameters, i.e., the aerodynamic diameter of particles with a collection efficiency of 50%. However, particle bounce effects, potentially leading to a transfer of particles to subsequent stages, have to be avoided, and interstage particle losses have to be characterized. In order to minimize particle bounce-off and transfer to subsequent stages, a thin layer of grease can be applied to the impaction substrates. Each impactor stage is associated with a pressure drop due to expansion through the nozzles. For typical 5-stage or 12-stage cascade impactors such as the Berner-type low-pressure impactor (LPI), covering a diameter range of 50 nm to 10 μm , a pressure drop to ≤ 50 mbar is reached in the final impaction stage.

The electrical low-pressure impactor (ELPI) [18.68] measures particle size distribution by separating particle size fractions according to aerodynamic diameter in a cascade impactor, and electrical detection of the collected particles. Before entering the impactor, the particle population is electrically charged with a unipolar corona charger, and collected particles deposit their charge on the impaction stages, which is measured as electric current with an electrometer. With volume flow rates of 10 or 30 L min^{-1} , the ELPI can provide particle size distribution with high time resolution. The commercial ELPI+ has also been used for size-resolved particle flux measurements [18.69].

A prominent feature of impactors is the physical collection of size fractions of a particle population. The collected particles may be analyzed for particle mass or chemical composition. For gravimetric analysis of the collected particle mass, aluminum impaction substrates are widely used. There are various impactor designs for specific purposes. For example, rotating drum impactors [18.70] collect particle samples continuously on a slowly rotating drum, which allows both size-resolved and time-resolved analysis of the collected particles. In the micro-orifice uniform deposit (MOUDI) impactor [18.71], the collection plates are rotated in order to deposit particles uniformly on the plates. MOUDI impactors can reach a lower cutoff diameter of 10 nm. A quartz crystal microbalance MOUDI has recently been developed, allowing real-time size-resolved mass measurements [18.72] (cf. piezoelectric crystal microbalance in Sect. 18.4.7).

In virtual impactors, the impaction plate is replaced by a second airflow of different velocity, so that the particle population is separated into two size fractions with a specified size cut, and both particle fractions remain suspended. Cyclones also make use of inertial

impaction to separate larger particles from a particle population by deposition on the cyclone wall from the circular path of the airflow in a vortex.

18.4.7 Particle Microbalances

Particle mass concentrations can be directly determined by quantitatively collecting particles from a known volume of air on filters (Chap. 19), and using *microbalances* to measure the particle mass. There is a large variety of filter material for atmospheric particle sampling with well-characterized collection efficiency, including fiber filters made of quartz, glass, cellulose, or metal, and membrane filters [18.73]. Deposition of particles to the filter is caused by different mechanisms, including diffusion (efficient for smaller particles), impaction and interception (important for accumulation mode particles), and gravitational settling and sieving (efficient for larger particles). For collection, filters are placed in filter holders that can be open-faced, integrated in a sampling line (inline), or stacked in filter cassettes. The volume flow rate through the filter holder is typically $> 1000 \text{ L min}^{-1}$ in high-volume samplers, or $< 20 \text{ L min}^{-1}$ in low-volume samplers. Because particle mass concentration is legislatively regulated, it is sometimes necessary to collect a specified size fraction of atmospheric particles on filters by preceding the filter holder with cyclones or impactor-based inlets with a defined cutoff, such as the PM_{10} or $\text{PM}_{2.5}$ standards for particles with diameters < 10 and $2.5 \mu\text{m}$, respectively, with a 50% transmission efficiency for the cutoff sizes. Impactors can also be used for size-resolved particle collection and subsequent gravimetric analysis. Before and after particle collection, the filter is conditioned for 24 h in a temperature- and humidity-controlled room, weighed on a microbalance, and the mass increase is divided by the total volume of sampled air to obtain the particle mass concentration.

A *piezoelectric crystal microbalance* for automated particle mass concentration measurements [18.74] is based on the change in the resonant vibration frequency of a piezoelectric crystal when particle mass is added to the crystal. Typically, quartz crystal microbalances with resonant vibration frequencies of 5–10 MHz are applied, and the change in the vibration frequency due to the deposition of particles from a known volume of air is registered. Piezobalances can resolve absolute mass changes as small as 1 ng, but due to a nonlinear relationship between the change in mass and the change in the vibration frequency, the crystal has to be cleaned when $\gtrsim 10 \mu\text{g}$ of absolute mass has been deposited.

The *tapered element oscillating microbalance* (TEOM) [18.75] consists of a hollow tapered tube with a replaceable particle filter at the narrow tip. Particles

collected on the filter cause a decrease in the natural oscillation frequency of the tapered element. Temperature fluctuations and condensation of water have to be avoided because the oscillation frequency will be affected, and therefore the housing of the microbalance is temperature-controlled, typically to a constant temperature (30 or 50 °C, depending on research objectives or legislative regulations). This can lead to evaporation of volatile or semivolatile compounds, which must be accounted for. With the filter dynamic measurement system (FDMS), the measurement alternates between the sampling of ambient particles and a reference cycle with particle-free air. The mass loss measured during the reference cycle is used as an estimate to compensate for the evaporative mass loss during the ambient measurement.

18.4.8 Attenuation of Beta Radiation

Beta attenuation monitors or beta gauges [18.76] are used for continuous measurement of the particle mass concentration. Particles are collected on a filter tape, and beta radiation (energy range 0.01–0.1 MeV) directed through the filter tape is attenuated due to inelastic scattering by atomic electrons of the filter material and the collected particles. The particle mass concentration is evaluated from the increase in attenuation as more particles are collected on the filter tape. Depending on the ambient particle concentration and the user-selectable intervals of filter tape change, continuous measurements are possible for several months. For the typical composition of atmospheric particles, beta attenuation is only weakly dependent on the chemical composition, and beta gauges are widely used as equivalent methods for the measurement of PM_{10} particle mass concentrations.

18.4.9 Combination of Particle Sensors

The combination of two or more particle sensors allows for additional measuring capabilities, and several examples are briefly presented to illustrate this potential.

Atmospheric measurements of ultrafine particle size distributions typically carried out with mobility spectrometers are limited either by the relatively slow measuring cycle of SMPS or DMPS instruments or by the sensitivity and accuracy of fast mobility spectrometers. In order to measure the temporal evolution of the nucleation mode very quickly and accurately, the condensation particle counter battery and the DMA train have been proposed. The condensation particle counter battery [18.77] is a combination of several separate CPCs with different lower cutoff diameters operated in parallel. The differences in particle number concentration measurements of two CPCs can be attributed to the size

range between the two lower cutoff diameters. In this way, concentration changes in several size bins of the nucleation mode can be measured with the time resolution of the CPCs. For narrower and more precise size bins, the DMA train [18.78] employs six differential mobility analyzers and CPCs in parallel to measure rapid changes in sub-10 nm particles with high time resolution.

The hygroscopic tandem differential mobility analyzer (HTDMA) is a combination of two DMAs, a conditioning unit for humidity and a CPC in order to measure the hygroscopic properties of particles, i.e., how particles respond to changes in relative humidity [18.79]. With the first DMA, a particle size fraction is selected and subsequently exposed to controlled humidity conditions. Depending on size and chemical composition, some or all particles may grow due to water uptake. This size change is measured with the second DMA and the CPC. As a result, HTDMA measurements yield size-resolved hygroscopic growth factors and information about the mixing state of a particle population, i.e., the variability in the chemical composition of individual particles. A variation of this principle is the volatility tandem differential mobility analyzer (VTDMA), where a particle size fraction is selected with the first DMA and exposed to elevated temperatures in a controlled volatility conditioning unit. The loss of volatile compounds at different temperatures can then be determined from the reduced size of the particles measured with the second DMA. Again, by measuring a physical property, i.e., the size change in particles, indirect information about the chemical composition of the particle population can be derived. The hygroscopic growth factors and volatility losses from HTDMA and VTDMA measurements are important in many practical measurement situations, for example when atmospheric particles are sampled through a heated inlet or dried before the measurement.

Considering the relationship between different particle equivalent diameters, the simultaneous measurement for example of aerodynamic and mobility diameters with an electrical low-pressure impactor and an SMPS can be used to estimate particle properties such as the effective density [18.80] or the fractal dimension of particle agglomerates [18.81]. Similarly, a size distribution measurement together with an independent particle mass measurement, for example a combination of SMPS and quartz crystal microbalance measurements [18.82], yields the effective density of a particle population.

18.4.10 Comparison of Methods

For a comprehensive characterization of atmospheric particles, the combination of many complementary

measurement techniques and instruments is necessary. Here, the major advantages and limitations of instrumentation used to measure particle number, particle size, particle mass, and optical properties will be briefly discussed and summarized in Table 18.6.

For particle detection and particle number concentration measurements, single-particle counting is possible with both OPCs and CPCs. However, particle coincidence at high number concentrations has to be taken into account, and the smallest particle size that can be directly detected with an OPC restricts its use for ultrafine particles. In contrast, electrometers can detect particles over a wide size range and with a fast time response, but particles have to be electrically charged, and the sensitivity is not sufficient to count individual particles. Therefore, the CPC is the preferred instrument for accurate measurement of total particle number concentrations over a wide size range. For the determination of the particle number concentration in ambient air according to the technical specification CEN/TS 16976:2016 [18.83], *n*-butanol is required as the working fluid of the CPC.

When evaluating the scattering signal of individual particles in optical particle spectrometers, particle size distributions can be obtained for particles ≥ 100 nm with a time resolution on the order of seconds. The resulting optical equivalent diameter is directly related to the interaction of the particle with light, pertinent to the direct climate effect. When evaluating human health effects and the deposition of particles in the human body, direct measurement of the aerodynamic diameter with the aerodynamic particle sizer or with impactors is more appropriate. An additional benefit of impactor measurement is the physical collection of size-resolved particle samples, which can be analyzed for chemical composition. However, the APS sizes only particles ≥ 0.5 μm , and the size resolution of impactors is limited. For submicron particles, mobility spectrometers such as the DMPS and the SMPS are very popular. These instruments combine good size resolution and sensitive particle detection. However, a minimum scanning time of 2 min is recommended for the SMPS [18.61], and thus the time resolution is typically on the order of minutes. Also, compliance with licensing requirements for radioactive neutralizers in mobility spectrometers typically requires additional administrative effort. Diffusion size classifiers [18.66] are commercially available as portable handheld instruments and yield average size information and particle number concentration. While they are easy to use, their accuracy and fields of application are limited.

Nephelometers can measure the particle scattering coefficient very precisely. When measuring in environments with particles predominantly in the diameter

Table 18.6 Advantages and disadvantages of devices for atmospheric particle measurements

Type of Sensor	Advantages	Disadvantages
OPC	Single-particle counting, information about equivalent diameter	Not applicable for ultrafine particles, size information dependent on particle shape and chemical composition, particle coincidence
CPC	Single-particle counting, wide size range	Particle coincidence
Nephelometer	Direct measurement of particle scattering coefficient	Careful calibration needed
Filter-based absorption sensor	Very low detection limit	Several correction schemes, no definitive standard correction yet; no standard reference calibration material
Photoacoustic sensor	Direct measurement of particle absorption coefficient	Sensitive to noise perturbation; difficulties at low particle concentrations; careful calibration needed
Electrometer	Wide size range, fast response	No single-particle counting, dependent on particle charging probability
MPSS	Mobility diameter measurement in the submicron size range, good size resolution	Limited time resolution (typically several minutes), licensing required for radioactive neutralizers
Diffusion size classifier	Portable instruments, information about ultrafine particles	Limited accuracy
APS	Aerodynamic diameter measurement, no calibration of scattering intensity required	Lower particle diameter cutoff ≈ 500 nm
Impactor	Size-dependent particle collection	Particle bounce in impactor stages, limited size resolution
Filter microbalance	Direct mass measurement, chemical analysis of collected sample possible	Time-consuming due to manual operation
Piezoelectric crystal microbalance	Very low detection limit	Requires frequent routine maintenance
Oscillating microbalance	Continuous measurements of particle mass concentration	Potential loss of (semi)volatile compounds
Beta attenuation monitor	Continuous measurements of particle mass concentration	Particle mass is derived indirectly

range < 100 nm, the scattering intensities are very low. Under these conditions, besides careful calibration, instruments with high flow rates are recommended.

The particle absorption coefficient can be measured by either filter-based methods or the photoacoustic method. Whereas the filter-based photometers require corrections in order to derive the particle absorption coefficient, the photoacoustic photometer yields a direct measurement of the particle absorption coefficient. The photoacoustic method, however, is sensitive to disturbance by noise and vibrations (e.g., pumps) and has a relatively high lower detection limit. With multi-wavelength instruments, the spectral dependency of the particle absorption coefficient can be investigated. Depending on the application, the possible time resolution of the instrument is important. In clean environments, long integration intervals up to 60 min or greater are recommended, while measurement intervals as short as 1 min are typical in polluted environments.

For particle mass concentration measurements, discontinuous techniques, such as sample collection with

filters or impactors and subsequent gravimetric analysis, and continuous techniques with varying degrees of automation exist. Long-term routine measurements are facilitated by continuous techniques such as beta attenuation monitors and piezoelectric crystal or oscillating element microbalances. Here, the quartz crystal microbalance and tapered element oscillating microbalance exploit the direct relationship between a change in vibration frequency and collected particle mass, while beta attenuation monitors rely on the assumption that the attenuation of beta radiation is only a function of particle mass and independent of particle chemical composition. The piezoelectric crystal microbalance requires frequent maintenance, and the oscillating microbalance is prone to loss of semivolatile compounds from the collected sample at the elevated temperatures inside the instrument. Given the limitations of the continuous particle mass measurement techniques, they are often complemented in regular time intervals by filter collection and gravimetric analysis, which is costly in terms of time and labor.

18.5 Specifications

The most important recommendations and general specifications for the different instrument types were described in Sect. 18.4. In this section and in Table 18.7, typical values for accuracy, measurement range, and time resolution are given. For most instrument types, there are several models of several manufacturers available, each with distinct specifications. The values given are therefore guided by the values of standard-quality instruments, installed for example at WMO GAW measurement sites.

For particle number concentration measurements in ambient air, according to [18.83], a condensation particle counter with *n*-butanol as working fluid must provide a lower cutoff diameter (50%) of (7 ± 0.7) nm and counting efficiency $> 90\%$ for $1 \mu\text{m}$ particles. The dynamic range should cover at least three orders of magnitude from $< 100 \text{ cm}^{-3}$ to $> 10\,000 \text{ cm}^{-3}$,

and with a zero filter the zero count rate should be $< 1 \text{ min}^{-1}$. Many commercial CPCs are in compliance with these specifications; however, the actual performance of individual instruments must be checked regularly (Sect. 18.6).

Commercial electrometers for atmospheric particles are sensitive to electrical currents of $\pm 1 \times 10^{-16}$ to 10^{-15} A (0.1–1 fA) at 1 Hz time resolution. This is important in order to quantify small particle number changes even at low particle number concentrations. A comparison of particle size and concentration measurements with electrometers from European national metrology institutes and expert laboratories [18.84] showed a typical instrument-to-instrument variability within $\pm 3\%$ for particle diameters from 20 to 200 nm. For particle diameters < 20 nm and at low concentrations, instrument comparison is more challenging.

Table 18.7 Typical specifications of standard particle sensors; further details in text

Type of sensor	Measurement range	Accuracy	Response time
Sensors detecting particle number			
OPC	Size range: ≈ 0.2 to 10 or $20 \mu\text{m}$; Concentration range: 1×10^{-3} to $1 \times 10^4 \text{ cm}^{-3}$	$< 10\%$ $< 10\%$	< 5 s
CPC	Size range: ≤ 7 nm to $\approx 3 \mu\text{m}$; Concentration range: 1×10^1 to $1 \times 10^5 \text{ cm}^{-3}$;	$< 10\%$; $< 10\%$	< 5 s
Electrometer	Size range: < 10 nm to $\approx 10 \mu\text{m}$; Electric current range: 1×10^{-15} to 1×10^{-11} A	$\pm 1 \times 10^{-15}$ A	< 5 s
Sensors detecting particle size			
MPSS	Several models exist, covering size ranges from < 5 nm to $1 \mu\text{m}$	Depending on size range, e.g., 10% for 20 – 200 nm	2 – 5 min
APS	Size range: ≈ 0.5 to $20 \mu\text{m}$; Concentration range: 1×10^{-3} to $1 \times 10^4 \text{ cm}^{-3}$	$< 2\%$ $< 10\%$	< 5 s
Impactor	Several models exist, covering size ranges from 16 – 56 nm to $10 \mu\text{m}$	$< 10\%$	Depending on sampling interval
Sensors detecting particle light scattering and absorption coefficient			
Nephelometer	2×10^{-7} to $2 \times 10^{-3} \text{ m}^{-1}$	2 to $3 \times 10^{-7} \text{ m}^{-1}$	< 10 s
Filter-based absorption sensor	Lower bound: MAAP: $8 \times 10^{-8} \text{ m}^{-1}$ PSAP: $5 \times 10^{-8} \text{ m}^{-1}$ Aethalometer: $1 \times 10^{-7} \text{ m}^{-1}$ Upper bound: $1 \times 10^{-2} \text{ m}^{-1}$	1 to $5 \times 10^{-7} \text{ m}^{-1}$	1 min
Photoacoustic sensor	1×10^{-6} to $1 \times 10^{-2} \text{ m}^{-1}$	$1 \times 10^{-6} \text{ m}^{-1}$	< 1 min
Sensors detecting particle mass			
Oscillating microbalance	$0.1 \mu\text{g m}^{-3}$ to 1 g m^{-3}	Precision: $0.5 \mu\text{g m}^{-3}$ (24 h average); $2 \mu\text{g m}^{-3}$ (1 h average)	< 1 min; because of reference cycles effectively 6 min
Beta attenuation monitor	$< 1 \mu\text{g m}^{-3}$ to 1 g m^{-3}	Precision: 0.3 – $1.0 \mu\text{g m}^{-3}$ (24 h average); 3 – $5 \mu\text{g m}^{-3}$ (1 h average)	1 min; because of reference cycles effectively ≈ 15 min

Particle number size distributions in the diameter range of 0.2–20 μm are typically measured with aerodynamic or optical particle size spectrometers. Large instrument-to-instrument variability has been reported for concentration measurements in the size range close to the lower cutoff diameter [18.67]. Direct intercomparison in the diameter range around 1 μm often shows lower concentration measurements with optical particle spectrometers compared to aerodynamic particle spectrometers. The number of sizing channels varies between the available models and should be taken into account with respect to the final application.

Following [18.85], number size distribution measurements of particles < 1 μm with carefully calibrated mobility particle size spectrometers should comply with the following specifications. The particle size measurement of a certified polystyrene particle size standard, preferably in the diameter range of 100–350 nm, should be within $\pm 3\%$ of the nominal value of the standard. The particle number size distribution should be within $\pm 10\%$ of a reference mobility particle size spectrometer in the diameter range of 20–200 nm, and within $\pm 20\%$

in the diameter range of 200–800 nm. The particle number concentration derived from the particle size distribution measurement should be within $\pm 10\%$ of a reference CPC. The lower cutoff diameter of the CPC used should be within 1 nm of the nominal value.

Most nephelometers record a measurement value internally each second (or even higher frequency), but integrate to values of 1 min or longer. Depending on the model, the values at high frequency might be accessible. However, the realistic response time is between 1 and 10 s. When choosing a model, the finite bandwidth of each measurement wavelength should be as narrow as possible.

The instrument noise of filter-based light absorption sensors depends on the wavelength, the flow rate, the filter spot size, and the averaging time. In an intercomparison study, [18.86] report typical instrument noise levels for the MAAp, the PSAP, and the aethalometer for different wavelengths and averaging intervals. The lower bounds given in Table 18.7 can vary slightly as a function of wavelength, and longer averaging intervals can yield lower detection limits.

18.6 Quality Control

For most particle sensors mentioned in this chapter, there are standard operating procedure manuals of the scientific community containing guidelines for quality assurance, quality control (QA/QC), and calibration [18.29, 61, 87]. The general QA/QC procedures given in Chap. 3 should be considered. In addition, instructions by the manufacturer for specific calibration procedures should be taken into account. Further, if the particle sensor is used under specific environmental conditions ranging outside the nominal instrument operating conditions, e.g., at high altitude or at very low temperatures, its calibration should take into account these conditions, thus calibrating at low pressure or in a cold chamber. This section summarizes the most important aspects with respect to specific sensor types and presents in Table 18.4 an overview of quality assurance measures.

Instruments for measuring particle number such as CPCs are calibrated by using monodisperse silver particles, size-selected with a DMA. The efficiency of the CPC is then evaluated against a reference electrometer [18.88]. For example, the electrometer used at the World Calibration Center for Aerosol Physics (WCCAP) [18.29] is calibrated to a femtoampere source at the German national metrology institute. Technical specifications for the determination of the number concentration of atmospheric particles in ambient air are given in [18.83].

The accuracy of particle size measurements must be evaluated by providing particles with known or very narrow geometric standard deviation from the particle sizing instrument. Often, polystyrene latex spheres (PLS) are used. They are commercially available in sizes from 20 nm to super-micrometer sizes, and are approved and traceable by the US National Institute of Standards and Technology (NIST). The sizing accuracy can also be validated by producing a quasi-monodisperse particle population (e.g., ammonium sulfate particles with a DMA system). For MPSS, the calibration and QA/QC procedures are described in great detail in [18.29, 61, 85].

Nephelometers are calibrated by sampling a particle-free reference gas with known values of the scattering coefficient for several wavelengths. With this gas, the *span point*, or the upscale part of the calibration curve, is determined. Typically, pure CO₂ (purity grade 4.8 or 5.5) is used. If the nephelometer is applied in environments with very high scattering coefficients, a gas with a higher scattering coefficient is recommended (e.g., heptafluoropropane HFC-227ea, which is however a halocarbon gas). For the zero-point determination, the internal zero-air filter is switched on in order to sample particle-free air. As the zero point defines the effective lower detection limit of the measurements, the quality of the zero-air filter and

Table 18.8 Calibration methods and quality assurance measures of particle sensors; further details in text

Type of sensor	Calibration method; QA/QC measure	Time interval	Remarks
OPC	Application of DMA-size-selected monodisperse particles; Application of NIST-traceable polystyrene spheres; Count efficiency validated with simultaneous CPC measurement	Yearly	See [18.29, 61, 85] for details
CPC	Application of DMA-size-selected monodisperse silver particles and count efficiency validated with reference electrometer	Yearly	See [18.83, 88] for details
Nephelometer	Full calibration with reference gas; Zero-point determination and adjustment of calibration curve	Yearly; Weekly to daily	More often during field campaigns; Zero point determines effective lower detection limit
Filter-based absorption sensor	No standard calibration method available, ongoing research; Application of equivalent black carbon mass; Determination of site-specific mass absorption cross section; Simultaneous scattering measurements	Once at production; Yearly; Yearly	See [18.29, 89]; Includes particle-filter interaction; Chemical analysis necessary; Takes into account particle-filter interaction [18.45, 90]
Photoacoustic sensor	Full calibration with reference gas; Zero-point determination and adjustment of calibration curve	Yearly; Daily to hourly	More often during field campaigns; Zero point determines effective lower detection limit
Electrometer	Calibration to a femtoampere source at reference metrology institutes	Yearly	See also [18.83]
MPSS; Diffusion size classifier; APS; Impactor (size)	Application of DMA-size-selected monodisperse particles; Application of NIST-traceable polystyrene spheres; Count efficiency validated with simultaneous CPC measurement	Yearly	See [18.29, 61, 85] for details
Particle microbalances	Application of NIST-traceable reference weights and standards	Yearly	See [18.29, 87] for details; Filters have to be conditioned before and after collection
Beta attenuation monitor	Application of NIST-traceable reference weights and standards	Yearly	See [18.29, 87] for details

of the zero-point measurement defines the precision with which the instrument's background signal is measured. Therefore, a zero-point measurement should be performed at least weekly to daily, and even hourly when sampling in very clean environments.

The specific characteristics of filter-based particle absorption photometers were described in Sect. 18.4. References [18.29, 87] give more details on potential calibration of these instruments. A calibration of the filter-based methods needs to take into account the interaction of the measurement light beam with the filter media and the deposited particles, which also have scattering properties. References [18.45, 90] describe calibrations with the help of simultaneous nephelometer measurements. For example, the aethalometer has been calibrated using an *equivalent* mass of black carbon with a respective mass absorption cross section, which however includes the particle-filter interaction.

In order to derive mass concentrations representing real ambient air equivalent black carbon concentrations, the respective mass absorption cross sections have to be experimentally derived for each measurement site by chemical analyses. However, there are currently no procedures commonly agreed upon as to how to calibrate filter-based particle absorption photometers and how to convert the attenuation measurements into mass concentrations in a consistent way [18.29, 89].

Photoacoustic absorption sensors can be calibrated using a gas with known absorption coefficients (e.g., NO₂), likewise for nephelometers and the light scattering coefficient. The photoacoustic sensors are sensitive to any disturbance by ambient noise, e.g., from pumps, and the instrument should therefore be insulated. As with nephelometers, a careful zero-point measurement is essential, performed at least daily, and even hourly when sampling in very clean environments.

Calibration and QA/QC procedures for particle mass measurements are described in [18.29, 87] and in the user manuals of the manufacturers. For the calibration of filters to be used with the gravimetric method, NIST-traceable reference weights must be used. The calibration con-

stant of an oscillating microbalance system can be verified with a preweighed calibration filter. Sensors applying the beta attenuation method usually use an internal membrane mass as a reference, which has been calibrated by the manufacturer with NIST-traceable standards.

18.7 Maintenance

The standard operating procedure manuals of the scientific community contain guidelines for the maintenance of particle instruments [18.29, 61, 87]. If available, instructions from the manufacturer (operating manuals) should also be taken into account, in particular concerning specific parts of instruments such as cleaning of optical parts or flow-regulating pieces.

Particle sensors should be calibrated yearly. If the sensor is used within a measurement campaign, it should be calibrated both at the beginning and at the end. When calibrating the instrument, one should not forget to calibrate the internal sensors as well for temperature, relative humidity, and pressure.

A general measure of QA/QC is continuously maintaining and saving log-files of all relevant complementary measurement parameters, such as sample and sheath flow, temperature of housing, sample cell or inlet tubing, relative humidity in the sample cell, the ambient and sample pressure, and current or voltage of light sources. If spurious signals continue to appear, they are a sign that some maintenance is necessary. Most often, the instrument manuals give advice on the type of maintenance required.

For particle concentration measurements, verification of the sample flow rate is essential. The flow rate given by the instrument should be validated with a quality flow meter, which gives the flow rate at both standard atmospheric conditions and the actual volumetric flow. A flow rate check should be done at least every three months, and in the case of measurement campaigns at least once at the beginning.

Many particle sensors apply a specific light source and have an elaborate optical measurement system (e.g., mirrors, filters, windows). Depending on the evolution of the respective parameters in the log-files, replacement of the light source or cleaning of optical parts is necessary.

It is important to check the inlet system regularly and to keep it clean. The inlet and tubing system should

be checked at least weekly with respect to physical integrity and to ensure that the protection against intrusion of insects and water is in good order. The inlet itself and the tubing should be cleaned in regular intervals, including impaction plates in cutoff cyclones and inlets. The time interval of cleaning depends on particle concentrations at the sample location. However, at least a visual check should be done weekly. Cleaning can be done by using lint-free tissues, either dry or wetted with ethanol. For the tubing itself, small, thin brushes can be used or flushing the tubing with purified synthetic air. Tubing parts that are not stainless steel and that are situated outside should be replaced after one to two years, to take into account the aging by the impact of radiation, temperature, and humidity.

Many instruments apply internal filters for regular particle-free reference measurements. These filters should be exchanged in regular intervals, depending on particle concentrations at the sample location. Regular leak checks of the measurement setup are important. The sample flow circuit must not show any leak, in order to avoid potential sample contamination. Typically, absolute particle filters or high-efficiency particulate air (HEPA) filters are placed in front of the instrument and the count rate is observed, which should show zero over at least several minutes. Such a check should be conducted once a month, and in the case of measurement campaigns at least once at the beginning and once in the middle. In addition, an exchange of zero filters or another leak check may be necessary when the zero measurements show a drift. Note that there are different classes of filters for different efficiencies of blocking particles.

It is also important to regularly check the internal clock of each instrument, and adjust it if necessary. If the internal clock or other electronic parts are powered by a separate battery, this battery should be replaced regularly. In Table 18.9, an overview of the most important maintenance procedures is presented.

Table 18.9 Maintenance of particle sensors; further details in text; for devices not explicitly listed, the generally maintenance recommendations apply

Type of sensor	Kind of maintenance	Time interval
All instruments	Full calibration; Calibration of temperature/pressure/humidity sensors; Validation of flow rate (standard and volume flow); Cleaning of inlet system; Zero-air and leak check; Keeping track of metadata log-files	Yearly; Yearly; 3-monthly; Depending on particle concentrations; At least monthly; Weekly
OPC	Replacement of light source and cleaning of optical components	Depending on evolution of respective parameters in log-files
CPC	Exchange of working fluid, also in the internal tubing system; Cleaning or exchange of saturator wick	Yearly; Yearly
Nephelometer	Replacement of light source; Cleaning of optical components	Depending on evolution of respective parameters in log-files
Filter-based absorption sensor	Replacement of filter tape; Precise measurement of filter spot area (PSAP)	Depending on particle concentration; Yearly
Electrometer	Zero measurements compensating for drift in current measurement	Daily – Weekly
MPSS	See [18.29, 61, 85]	
Impactor	Cleaning of impaction plates	Depending on sampling interval, particle concentration
Piezoelectric crystal sensor	Cleaning of piezoelectric crystal	When limit of $\approx 10 \mu\text{g}$ mass deposition is reached
Oscillating microbalance	Replacement of microbalance filter; Replacement of reference filter	Depending on particle concentration

18.8 Application

Atmospheric particle measurements are crucial for a large number of applications in science and technology. This section outlines four examples of particle measurements applied to current atmospheric research challenges, and is neither exhaustive with respect to the many potential applications nor with regard to the various particle sensor types. The choice of the below-mentioned examples is guided by current research about the environmental impact of atmospheric particles, such as the effects on human health and climate. Accordingly, important particle sources such as secondary particle formation and particle removal by dry deposition, air quality impairment due to particles, and the effect of particles on the atmospheric radiation budget must be quantitatively described using particle sensors.

18.8.1 Secondary Aerosol Formation

Particles are emitted into the atmosphere as primary particles from various natural and anthropogenic sources,

such as sea spray or mineral dust, and formed by gas-to-particle conversion in the atmosphere as secondary particles. Until recently, elucidating the reaction mechanisms leading to atmospheric secondary aerosol formation has been limited by the available particle instrumentation. Nucleation, the initial step in secondary aerosol formation, leads to extremely small particles in the size range of 1–20 nm, the nucleation mode. Only over the past 10–15 years, improved condensation particle counters (Sect. 18.4.1) with sufficiently low cutoff diameters to detect freshly nucleated particles and advanced mobility spectrometers to follow the temporal evolution of particle size distributions have been developed, which are capable of characterizing the growth dynamics of the nucleation mode due to coagulation and condensation. New particle formation events are typically identified by a strongly enhanced concentration of nucleation mode particles measured with CPCs, and a characteristic growth behavior as measured with MPSS (Sect. 18.4.4). At the same time, advanced instrumentation for the measurement of the chemical composition of

particles such as the Aerodyne aerosol mass spectrometer (AMS) [18.91], the atmospheric pressure interface time-of-flight mass spectrometer (APi-TOF) [18.92] for atmospheric ions, and the proton-transfer-reaction mass spectrometer (PTR-MS) [18.93] for the measurement of organic precursor gases have provided detailed insight into the mechanisms of atmospheric secondary organic aerosol (SOA) formation. For example, understanding the role of extremely low-volatility organic compounds (ELVOC), which are highly oxidized multifunctional molecules (HOM), in SOA formation helped to better constrain the total contribution of SOA to the atmospheric particle burden. Understanding secondary aerosol formation and SOA properties is also essential for evaluating the impact of atmospheric particles on climate (Sect. 18.8.4).

18.8.2 Vertical Particle Flux Measurements

Dry deposition (Chap. 54) is an important removal process for atmospheric particles. The dry deposition of nutrients and pollutants can be to the advantage or disadvantage of ecosystems, crops, or residential areas. In order to quantify particle dry deposition, vertical particle flux measurements are carried out either directly using CPCs and OPCs (Sect. 18.4.1) in eddy-covariance systems (Chap. 55) or by indirect methods such as flux-gradient relationships. However, there are several limitations to estimating the particle dry deposition. Changes in particle number concentrations occur not only due to turbulent transport but also due to coagulation of particles, particle growth to sizes outside the measuring range of the particle sensor, or secondary aerosol formation, and it is difficult to take into account these processes separate from turbulent transport. For particle number and mass concentration, the assumption of steady-state conditions, which is a requirement for eddy-covariance calculations, is often violated. Also, most particle sensors are not sufficiently fast to provide independent particle number or mass concentration measurements for eddy-covariance with a time resolution of 10 Hz. For example, the response time of laminar-flow condensation particle counters to a number concentration change is typically a few seconds, and the associated loss of high-frequency flux contributions is commonly estimated from a spectral loss model. This is also true for size-segregated particle number flux measurements with optical particle counters [18.94–96] and the electrical low-pressure impactor [18.69, 97]. Particle mass fluxes have been calculated from size-segregated particle number flux measurements or measured directly and

chemically resolved using aerosol mass spectrometers in eddy-covariance measurements [18.98, 99].

18.8.3 Atmospheric Particles and Air Quality

In many studies, airborne particulate matter has been associated with adverse health effects, for example [18.100]. As a result, legislative measures for monitoring and evaluating the PM₁₀ and PM_{2.5} concentrations, i.e., the mass concentrations of all particles with diameters < 10 μm (corresponding to the thoracic convention) or 2.5 μm (corresponding to the high-risk respirable convention) [18.101], have been introduced in Europe and worldwide. Continuous measurements of the particle mass concentration are carried out using oscillating microbalances and beta attenuation monitors (Sects. 18.4.7 and 18.4.8) and validated by filter sampling and gravimetric analysis. However, advanced particle instrumentation is required to identify particle sources and quantify their relative contributions to the atmospheric particle burden, to understand the atmospheric transport and transformation processes of particles, and to evaluate their effect on human health. For example, there is concern that exposure to ultrafine particles with diameters < 100 nm is more detrimental to human health than exposure to larger particles [18.102]. However, the contribution of ultrafine particles to particle mass is negligible due to their small size, and assessing their health effects requires particle number-based metrics and size-resolved measurements. Further, in order to develop effective mitigations strategies in areas with elevated particle concentrations, the identification and evaluation of particle sources and their relative contributions by source apportionment is typically based on measurements of the particle chemical composition [18.103].

18.8.4 Climate Effects of Atmospheric Particles

Atmospheric particles affect the radiation budget both directly, by scattering and absorbing solar radiation, and indirectly by modifying cloud formation and cloud properties. The direct radiative effect of atmospheric particles can be evaluated by characterizing the optical properties of the particles. A key parameter for estimating the direct radiative forcing of particles is the single-scattering albedo (Table 18.4 and Sect. 18.3.2). It is important to note that the scattering and absorption properties of particles exhibit a strong dependence on wavelength. The wavelength dependence of the scattering, absorption or extinction coefficients, and

the single-scattering albedo can be expressed by the Ångström exponent α , which relates the ratio of these parameters at two different wavelengths λ_1 and λ_2 and the ratio of the two wavelengths, for example, for the single-scattering albedo by

$$\frac{\omega_{\lambda,1}}{\omega_{\lambda,2}} = \left(\frac{\lambda_1}{\lambda_2}\right)^{-\alpha} \quad (18.22)$$

This equation can be used to estimate the direct radiative effects of particles from a measurement of scattering and absorption at a single wavelength, and validated by measurements at different wavelengths. In practice, in-situ measurements with nephelometers and filter-based absorption photometers complement remote-sensing techniques such as sun photometers in the Aerosol Robotic Network (AERONET) [18.104, 105] that determine the spectral aerosol optical depth (AOD) and derived products including the refractive index, the particle phase function, and the single-scattering albedo. The AOD is an integral measurement of the combined particle absorption and scattering (thus extinction) over the total atmospheric column and is widely used to represent the atmospheric particle

concentration in global chemistry or transport modeling [18.106, 107].

The indirect climate effect of atmospheric particles, i.e., a change in the formation, distribution, and radiative properties of clouds due to atmospheric particles, is the single largest uncertainty of the global radiative forcing estimate [18.108]. Therefore, major efforts are made to improve our understanding of aerosol–cloud–climate interactions, including in-situ measurements of aerosol–cloud relationships, for example the potential of particles to act as cloud condensation nuclei (CCN) or as ice nuclei (IN). The CCN concentration can be measured with a CCN counter, in which a particle sample is exposed to a well-defined supersaturation of water vapor, and activated particles are detected with an OPC. For size-segregated CCN measurements, a differential mobility analyzer is used to preselect a certain particle size fraction, and then compare the number of activated particles measured with the CCN counter and the total number of particles in this size fraction measured with a CPC. To give an example, based on such measurements, [18.109] suggest that particle size might be more important for the ability of particles to act as CCN than their chemical composition.

18.9 Future Developments

Studying atmospheric particles and their environmental impact is a highly dynamic and interdisciplinary field of research. The development of new measuring capabilities is driven both by fundamental research questions to improve our understanding of the sources, transport, transformation, and sinks of atmospheric particles, and by applied research questions, for example in the fields of nanotechnology and materials sciences. In recent years, miniaturized sensors for atmospheric particles have become very popular. For example, handheld instruments are used for spatially resolved measurements at multiples sites in air quality studies, on mobile platforms such as bicycles and unmanned aerial systems

(Chap. 49), or for personal exposure sampling to assess health risks such as in workplaces. Miniaturized particle sensors are also used in citizen science projects, e.g., studying particle optical properties using low-cost spectropolarimeters attached to smartphones [18.110], or studying urban air quality using low-cost PM_{10} sensors. While the performance of such low-cost sensors is typically not comparable to established particle instrumentation, their development and application promises to open up many opportunities in atmospheric research, as long as the limitations of these sensors are well characterized and taken into account in the interpretation of the resulting data.

18.10 Further Reading

A comprehensive overview of particle measurement techniques, underlying measurement principles, and theory of particle optical properties is provided by:

- C.F. Bohren, D.R. Huffman: *Absorption and Scattering of Light by Small Particles* (Wiley-VCH, Weinheim 2004)
- W.C. Hinds: *Aerosol Technology: Properties, Behavior, and Measurement of Airborne Particles*, 2nd edn. (Wiley, New York 1999)
- P. Kulkarni, P.A. Baron, K. Willeke, K. (Eds.) *Aerosol Measurement: Principles, Techniques, and Applications*, 3rd edn. (John Wiley & Sons, Chichester 2011)

Review articles on atmospheric particle measurements:

- J.C. Chow: Measurement methods to determine compliance with ambient air quality standards for suspended particles, *J. Air Waste Manag. Assoc.* **45**, 320–382 (1995)
- P. McMurry: A review of atmospheric aerosol measurements, *Atmos. Environ.* **34**, 1959–1999 (2000)

Updated information about best practices in atmospheric particle measurement and calibration procedures can be found in:

- WMO: GAW Report No. 200, WMO/GAW Standard Operating Procedures for In-Situ Measurements of Aerosol Mass Concentration, Light Scattering and Light Absorption, ed. by J.A. Ogren (2011)
- World Meteorological Organization GAW Report No. 227, WMO/GAW Aerosol Measurement Procedures, Guidelines and Recommendations, 2nd edn., WMO-No. 1177 (2016)
- <https://actris.nilu.no/Content/SOP>, Accessed 07 July 2021
- <https://www.actris-ecac.eu/measurement-guidelines.html>, Accessed 08 July 2021

References

- 18.1 P.A. Solomon, M.P. Fraser, P. Herckes: Methods for chemical analysis of atmospheric aerosols. In: *Aerosol Measurement: Principles, Techniques and Applications*, 3rd edn., ed. by P. Kulkarni, P.A. Baron, K. Willeke (John Wiley & Sons, Hoboken 2011) pp. 153–177
- 18.2 C.E. Kolb, D.R. Worsnop: Chemistry and composition of atmospheric aerosol particles, *Annu. Rev. Phys. Chem.* **63**, 471–491 (2012)
- 18.3 J.H. Seinfeld, S.N. Pandis: *Atmospheric Chemistry and Physics*, 3rd edn. (Wiley, New York 2016)
- 18.4 A. Wiedensohler, W. Birmili, J.-P. Putaud, J. Ogren: Recommendations for aerosol sampling. In: *Aerosol Science: Technology and Applications*, ed. by I. Colbeck, M. Lazaridis (Wiley, Chichester 2014) pp. 45–59
- 18.5 J. Evelyn: *Fumifugium (1661)* (The Rota at the University of Exeter, Exeter 1976), Reprint, <https://archive.org/details/fumifugium00eveluoft>, Accessed 07 July 2021
- 18.6 P.J. Coulier: Note sur une nouvelle propriété de l'air, *J. Pharm. Chim.* **22**, 165–173 (1875), in French
- 18.7 J. Aitken: On dust, fogs, and clouds, *Proc. R. Soc. Edinb.* **11**, 14–18 (1882)
- 18.8 J. Aitken: On a simple pocket dust-counter, *Proc. R. Soc. Edinb.* **18**, 39–52 (1892)
- 18.9 A. Schmauß, A. Wigand: *Die Atmosphäre als Kolloid* (Vieweg, Braunschweig 1929), in German
- 18.10 N.A. Fuchs: *The Mechanics of Aerosols* (Pergamon, New York 1964)
- 18.11 C.E. Junge: *Air Chemistry and Radioactivity* (Academic Press, New York 1963)
- 18.12 S.K. Friedlander: *Smoke, Dust and Haze: Fundamentals of Aerosol Behavior* (Wiley, New York 1977)
- 18.13 M. Kulmala, V.-M. Kerminen, T. Anttila, A. Laaksonen, C.D. O'Dowd: Organic aerosol formation via sulphate cluster activation, *J. Geophys. Res.* **109**, D04205 (2004)
- 18.14 G. Mie: Beiträge zur Optik trüber Medien, speziell kolloidaler Metallösungen, *Ann. Phys.* **330**, 377–445 (1908), in German
- 18.15 C.F. Bohren, D.R. Huffman: *Absorption and Scattering of Light by Small Particles* (Wiley-VCH, Weinheim 2004)
- 18.16 R. Jaenicke: The optical particle counter: Cross-sensitivity and coincidence, *J. Aerosol Sci.* **3**, 95–111 (1972)
- 18.17 H. Koschmieder: Theorie der horizontalen Sichtweite, *Contrib. Atmos. Phys.* **43**, 33–55 (1924)
- 18.18 A. Rosencwaig: *Photoacoustics and Photoacoustic Spectroscopy* (Wiley, Chichester 1980)
- 18.19 ISO15900:2009: *Determination of Particle Size Distribution – Differential Electrical Mobility Analysis for Aerosol Particles* (International Organization for Standardization, Geneva 2009)
- 18.20 N.A. Fuchs: On the stationary charge distribution on aerosol particles in bipolar ionic atmosphere, *Geofis. Pura Appl.* **56**, 185–193 (1963)
- 18.21 R. Gunn: The hyperelectrification of raindrops by atmospheric electric fields, *J. Meteorol.* **13**, 283–288 (1956)
- 18.22 M. Adachi, Y. Kousaka, K. Okuyama: Unipolar and bipolar diffusion charging of ultrafine aerosol particles, *J. Aerosol Sci.* **16**, 109–124 (1985)
- 18.23 A. Wiedensohler: An approximation of the bipolar charge distribution for particles in the submicron size range, *J. Aerosol Sci.* **19**, 387–389 (1988)
- 18.24 W.C. Hinds: *Aerosol Technology: Properties, Behavior, and Measurement of Airborne Particles*, 2nd edn. (Wiley, New York 1999)
- 18.25 P.C. Raynor, D. Leith, K.W. Lee, R. Mukund: Sampling and analysis using filters. In: *Aerosol Measurement: Principles, Techniques and Applications*, 3rd edn., ed. by P. Kulkarni, P.A. Baron, K. Willeke (John Wiley & Sons, Hoboken 2011) pp. 107–128
- 18.26 G. Sauerbrey: Verwendung von Schwingquarzen zur Wägung dünner Schichten und zur Mikrowägung, *Z. Phys.* **55**, 206–222 (1959), in German
- 18.27 K.T. Whitby: The physical characteristics of sulfur aerosol, *Atmos. Environ.* **12**, 135–159 (1978)
- 18.28 P. Kulkarni, P.A. Baron, K. Willeke (Eds.): *Aerosol Measurement: Principles, Techniques, and Appli-*

- ations, 3rd edn. (John Wiley & Sons, Hoboken 2011)
- 18.29 WMO: *WMO/GAW Aerosol Measurement Procedures, Guidelines and Recommendations*, 2nd edn. (WMO, Geneva 2016), GAW Report No. 227, WMO-No. 1177
- 18.30 F.T. Gucker Jr., C.T. O’Konski, H.B. Pickard, J.N. Pitts Jr.: A photoelectronic counter for colloidal particles, *J. Am. Chem. Soc.* **69**, 2422–2431 (1947)
- 18.31 F.T. Gucker Jr., H.B. Pickard, C.T. O’Konski: A photoelectric instrument for comparing concentrations of very dilute aerosols and measuring very low light intensities, *J. Am. Chem. Soc.* **69**, 429–438 (1947)
- 18.32 P. McMurry: A review of atmospheric aerosol measurements, *Atmos. Environ.* **34**, 1959–1999 (2000)
- 18.33 P.H. Kaye, N.A. Eyles, I.K. Ludlow, J.M. Clark: An instrument for the classification of airborne particles on the basis of size, shape, and count frequency, *Atmos. Environ.* **25**, 645–654 (1991)
- 18.34 D. Sinclair, G.S. Hoopes: A continuous flow condensation nucleus counter, *J. Aerosol Sci.* **6**, 1–7 (1975)
- 18.35 J. Bricard, P. Delattre, G. Madelaine, M. Pourprix: Detection of ultra-fine particles by means of a continuous flux condensation nuclei counter. In: *Fine Particles*, ed. by B.Y.H. Liu (Academic Press, New York 1976) pp. 566–580
- 18.36 J.K. Agarwal, G.J. Sem: Continuous flow, single-particle-counting condensation nucleus counter, *J. Aerosol Sci.* **11**, 343–357 (1980)
- 18.37 J. Wang, V.F. McNeill, D.R. Collins, R.C. Flagan: Fast mixing condensation nucleus counter: Application to rapid scanning differential mobility analyzer measurements, *Aerosol Sci. Technol.* **36**, 678–689 (2002)
- 18.38 B. Wehner, H. Siebert, M. Hermann, F. Ditas, A. Wiedensohler: Characterisation of a new fast CPC and its application for atmospheric particle measurements, *Atmos. Meas. Tech.* **4**, 823–833 (2011)
- 18.39 K. Iida, M.R. Stolzenburg, P.H. McMurry: Effect of working fluid on sub-2 nm particle detection with a laminar flow ultrafine condensation particle counter, *Aerosol Sci. Technol.* **43**, 81–96 (2009)
- 18.40 J. Vanhanen, J. Mikkilä, K. Lehtipalo, M. Sipilä, H.E. Manninen, E. Siivola, T. Petäjä, M. Kulmala: Particle size magnifier for nano-CN detection, *Aerosol Sci. Technol.* **45**, 533–542 (2011)
- 18.41 R.G. Beuttell, A.W. Brewer: Instruments for the measurement of the visual range, *J. Sci. Instrum.* **26**, 357–359 (1949)
- 18.42 J. Heintzenberg, R.J. Charlson: Design and applications of the integrating nephelometer: A review, *J. Atmos. Ocean. Technol.* **13**, 987–1000 (1996)
- 18.43 C.I. Lin, M.B. Baker, R.J. Charlson: Absorption coefficient of atmospheric aerosol: A method for measurement, *Appl. Opt.* **12**, 1356–1363 (1973)
- 18.44 A.D.A. Hansen, H. Rosen, T. Novakov: The aethelometer – An instrument for the real-time measurement of optical absorption by aerosol particles, *Sci. Total Environ.* **36**, 191–196 (1984)
- 18.45 T.C. Bond, T.L. Anderson, D. Campbell: Calibration and intercomparison of filter-based measurements of visible light absorption by aerosols, *Aerosol Sci. Technol.* **30**, 582–600 (1999)
- 18.46 A. Petzold, M. Schönlinner: Multi-angle absorption photometry – A new method for the measurement of aerosol light absorption and atmospheric black carbon, *J. Aerosol Sci.* **35**, 421–441 (2004)
- 18.47 P.L. Kebebian, W.A. Robinson, A. Freedman: Optical extinction monitor using cw cavity enhanced detection, *Rev. Sci. Instrum.* **78**, 063102 (2007)
- 18.48 J.G. Slowik, E.S. Cross, J.-H. Han, P. Davidovits, T.B. Onasch, J.T. Jayne, L.R. Williams, M.R. Canagaratna, D.R. Worsnop, R.K. Chakrabarty, H. Moosmüller, W.P. Arnott, J.P. Schwarz, R.-S. Gao, D.W. Fahey, G.L. Kok, A. Petzold: An inter-comparison of instruments measuring black carbon content of soot particles, *Aerosol Sci. Technol.* **41**, 295–314 (2007)
- 18.49 C.W. Bruce, R.G. Pinnick: In-situ measurements of aerosol absorption with a resonant cw laser spectrophone, *Appl. Opt.* **16**, 1762–1765 (1977)
- 18.50 R.W. Terhune, J.E. Anderson: Spectrophone measurements of the absorption of visible light by aerosols in the atmosphere, *Opt. Lett.* **1**, 70–72 (1977)
- 18.51 K.M. Adams, L.I. Davis Jr., S.M. Japar, W.R. Pierston: Real time, in situ measurements of atmospheric optical absorption in the visible via photoacoustic spectroscopy – II. Validation for atmospheric elemental carbon aerosol, *Atmos. Environ.* **23**, 693–700 (1989)
- 18.52 A. Petzold, R. Niessner: Novel design of resonant photoacoustic spectrophone for elemental carbon mass monitoring, *Appl. Phys. Lett.* **66**, 1285–1287 (1995)
- 18.53 T. Ajtai, A. Filep, M. Schnaiter, C. Linke, M. Vragel, Z. Bozóki, G. Szabó, T. Leisner: A novel multi-wavelength photoacoustic spectrometer for the measurement of the UV-vis-NIR spectral absorption coefficient of atmospheric aerosols, *J. Aerosol Sci.* **41**, 1020–1029 (2010)
- 18.54 B.Y.H. Liu, D.Y.H. Pui: A submicron aerosol standard and the primary, absolute calibration of the condensation nuclei counter, *J. Colloid Interface Sci.* **47**, 155–171 (1974)
- 18.55 B.Y.H. Liu, D.Y.H. Pui: Electrical neutralization of aerosols, *J. Aerosol Sci.* **5**, 465–472 (1974)
- 18.56 K.T. Whitby, W.E. Clark: Electric aerosol particle counting and size distribution measuring system for the 0.015 to 1 μ size range, *Tellus* **18**, 573–586 (1966)
- 18.57 E.O. Knutson, K.T. Whitby: Aerosol classification by electric mobility: Apparatus, theory, and application, *J. Aerosol Sci.* **6**, 443–451 (1975)
- 18.58 L. Tigges, A. Wiedensohler, K. Weinhold, J. Gandhi, H.-J. Schmid: Bipolar charge distribution of a soft X-ray diffusion charger, *J. Aerosol Sci.* **90**, 77–86 (2015)

- 18.59 S.C. Wang, R.C. Flagan: Scanning electrical mobility spectrometer, *Aerosol Sci. Technol.* **13**, 230–240 (1990)
- 18.60 S.H. Zhang, Y. Akutsu, L.M. Russell, R.C. Flagan, J.H. Seinfeld: Radial differential mobility analyzer, *Aerosol Sci. Technol.* **23**, 357–372 (1995)
- 18.61 A. Wiedensohler, W. Birmili, A. Nowak, A. Sonntag, K. Weinhold, M. Merkel, B. Wehner, T. Tuch, S. Pfeifer, M. Fiebig, A.M. Fjåraa, E. Asmi, K. Sellegri, R. Depuy, H. Venzac, P. Villani, P. Laj, P. Aalto, J.A. Ogren, E. Swietlicki, P. Williams, P. Roldin, P. Quincey, C. Hüglin, R. Fierz-Schmidhauser, M. Gysel, E. Weingartner, F. Riccobono, S. Santos, C. Grüning, K. Faloon, D. Beddows, R. Harrison, C. Monahan, S.G. Jennings, C.D. O'Dowd, A. Marioni, H.-G. Horn, L. Keck, J. Jiang, J. Scheckman, P.H. McMurry, Z. Deng, C.S. Zhao, M. Moerman, B. Henzing, G. de Leeuw, G. Löschau, S. Bastian: Mobility particle size spectrometers: Harmonization of technical standards and data structure to facilitate high quality long-term observations of atmospheric particle number size distributions, *Atmos. Meas. Tech.* **5**, 657–685 (2012)
- 18.62 E. Asmi, M. Sipilä, H.E. Manninen, J. Vanhanen, K. Lehtipalo, S. Gagné, K. Neitola, A. Mirme, S. Mirme, E. Tamm, J. Uin, K. Komsaare, M. Attoui, M. Kulmala: Results of the first air ion spectrometer calibration and intercomparison workshop, *Atmos. Chem. Phys.* **9**, 141–154 (2009)
- 18.63 H. Tammet, A. Mirme, E. Tamm: Electrical aerosol spectrometer of Tartu University, *Atmos. Res.* **62**, 315–324 (2002)
- 18.64 P.G. Gormley, M. Kennedy: Diffusion from a stream flowing through a cylindrical tube, *Proc. R. Ir. Acad.* **52**, 163–169 (1949)
- 18.65 D. Sinclair, G.S. Hoopes: A novel form of diffusion battery, *Am. Ind. Hyg. Assoc. J.* **36**, 39–42 (1975)
- 18.66 M. Fierz, H. Burtscher, P. Steigmeier, M. Kasper: *Field Measurement of Particle Size and Number Concentration with the Diffusion Size Classifier (DiSC)* (SAE International, Warrendale 2008), SAE Tech. Paper 2008-01-1179
- 18.67 S. Pfeifer, T. Müller, K. Weinhold, N. Zikova, S. Martins dos Santos, A. Marinoni, O.F. Bischof, C. Kykal, L. Ries, F. Meinhardt, P. Aalto, N. Michalopoulos, A. Wiedensohler: Intercomparison of 15 aerodynamic particle size spectrometers (APS 3321): Uncertainties in particle sizing and number size distribution, *Atmos. Meas. Tech.* **9**, 1545–1551 (2016)
- 18.68 J. Keskinen, K. Pietarinen, M. Lehtimäki: Electrical low pressure impactor, *J. Aerosol Sci.* **23**, 353–360 (1992)
- 18.69 M.J. Deventer, L. von der Heyden, C. Lamprecht, M. Graus, T. Karl, A. Held: Aerosol particles during the Innsbruck Air Quality Study (INNAQS): Fluxes of nucleation to accumulation mode particles in relation to selective urban tracers, *Atmos. Environ.* **190**, 376–388 (2018)
- 18.70 O.G. Raabe, D.A. Braaten, R.L. Axelbaum, S.V. Teague, T.A. Cahill: Calibration studies of the DRUM impactor, *J. Aerosol Sci.* **19**, 183–195 (1988)
- 18.71 V.A. Marple, K.L. Rubow, S.M. Behm: A Microorifice Uniform Deposit Impactor (MOUDI): Description, calibration, and use, *Aerosol Sci. Technol.* **14**, 434–446 (1991)
- 18.72 M. Chen, F.J. Romay, L. Lin, A. Naqvi, V.A. Marple: A novel quartz crystal cascade impactor for real-time aerosol mass distribution measurement, *Aerosol Sci. Technol.* **50**, 971–983 (2016)
- 18.73 J.C. Chow: Measurement methods to determine compliance with ambient air quality standards for suspended particles, *J. Air Waste Manag. Assoc.* **45**, 320–382 (1995)
- 18.74 D.A. Lundgren, L.D. Carter, P.S. Daley: Aerosol mass measurement using piezoelectric crystal sensors. In: *Fine Particles*, ed. by B.Y.H. Liu (Academic Press, New York 1976) pp. 485–510
- 18.75 H. Patashnick, E.G. Rupprecht: Continuous PM-10 measurements using the tapered element oscillating microbalance, *J. Air Waste Manag. Assoc.* **41**, 1079–1083 (1991)
- 18.76 R.B. Husar: Atmospheric particulate mass monitoring with a beta radiation detector, *Atmos. Environ.* **8**, 183–188 (1974)
- 18.77 M. Kulmala, G. Mordas, T. Petäjä, T. Grönholm, P.P. Aalto, H. Vehkamäki, A.I. Hienola, E. Herrmann, M. Sipilä, I. Riipinen, H.E. Manninen, K. Hämeri, F. Stratmann, M. Bilde, P.M. Winkler, W. Birmili, P.E. Wagner: The condensation particle counter battery (CPCB): A new tool to investigate the activation properties of nanoparticles, *J. Aerosol Sci.* **38**, 289–304 (2007)
- 18.78 D. Stolzenburg, G. Steiner, P.M. Winkler: A DMA-train for precision measurement of sub-10 nm aerosol dynamics, *Atmos. Meas. Tech.* **10**, 1639–1651 (2017)
- 18.79 D.J. Rader, P.H. McMurry: Application of the tandem differential mobility analyzer to studies of droplet growth or evaporation, *J. Aerosol Sci.* **17**, 771–787 (1986)
- 18.80 J. Ristimäki, A. Virtanen, M. Marjamäki, A. Rosstedt, J. Keskinen: On-line measurement of size distribution and effective density of submicron aerosol particles, *J. Aerosol Sci.* **33**, 1541–1557 (2002)
- 18.81 A. Virtanen, J. Ristimäki, J. Keskinen: Method for measuring effective density and fractal dimension of aerosol agglomerates, *Aerosol Sci. Technol.* **38**, 437–446 (2004)
- 18.82 B. Sarangi, S.G. Aggarwal, D. Sinha, P.K. Gupta: Aerosol effective density measurement using scanning mobility particle sizer and quartz crystal microbalance with the estimation of involved uncertainty, *Atmos. Meas. Tech.* **9**, 859–875 (2016)
- 18.83 CEN/TS 16976:2016: *Ambient Air – Determination of the Particle Number Concentration of Atmospheric Aerosol* (European Committee for Standardization, Brussels 2016)
- 18.84 R. Högström, P. Quincey, D. Sarantaris, F. Lüönd, A. Nowak, F. Riccobono, T. Tuch, H. Sakurai, M. Owen, M. Heinonen, J. Keskinen, J. Yli-Ojanperä: First comprehensive inter-comparison of aerosol electrometers for particle sizes up to

- 200 nm and concentration range 1000 cm⁻³ to 17000 cm⁻³, *Metrologia* **51**, 293–303 (2014)
- 18.85 A. Wiedensohler, A. Wiesner, K. Weinhold, W. Birmili, M. Hermann, M. Merkel, T. Müller, S. Pfeifer, A. Schmidt, T. Tuch, F. Velarde, P. Quincey, S. Seeger, A. Nowak: Mobility particle size spectrometers: Calibration procedures and measurement uncertainties, *Aerosol Sci. Technol.* **52**, 146–164 (2018)
- 18.86 T. Müller, J.S. Henzing, G. de Leeuw, A. Wiedensohler, A. Alastuey, H. Angelov, M. Bizjak, M. Collaud Coen, J.E. Engström, C. Gruening, R. Hillamo, A. Hoffer, K. Imre, P. Ivanow, G. Jennings, J.Y. Sun, N. Kalivitis, H. Karlsson, M. Kompula, P. Laj, S.-M. Li, C. Lunder, A. Marinoni, S. Martins dos Santos, M. Moerman, A. Nowak, J.A. Ogren, A. Petzold, J.M. Pichon, S. Rodriguez, S. Sharma, P.J. Sheridan, K. Teinilä, T. Tuch, M. Viana, A. Virkkula, E. Weingartner, R. Wilhelm, Y.Q. Wang: Characterization and intercomparison of aerosol absorption photometers: Result of two intercomparison workshops, *Atmos. Meas. Tech.* **4**, 245–268 (2011)
- 18.87 J.A. Ogren (Ed.): *WMO/GAW Standard Operating Procedures for In-Situ Measurements of Aerosol Mass Concentration, Light Scattering and Light Absorption* (WMO, Geneva 2011), GAW Report No. 200
- 18.88 ISO 27891:2015: *Aerosol Particle Number Concentration – Calibration of Condensation Particle Counters* (International Organization for Standardization, Geneva 2015)
- 18.89 D. Baumgardner, O. Popovicheva, J. Allan, V. Bernardoni, J. Cao, F. Cavalli, J. Cozic, E. Diapouli, K. Eleftheriadis, P.J. Genberg, C. Gonzalez, M. Gysel, A. John, T.W. Kirchstetter, T.A.J. Kuhlbusch, M. Laborde, D. Lack, T. Müller, R. Niessner, A. Petzold, A. Piazzalunga, J.P. Putaud, J. Schwarz, P. Sheridan, R. Subramanian, E. Swietlicki, G. Valli, R. Vecchi, M. Viana: Soot reference materials for instrument calibration and intercomparisons: A workshop summary with recommendations, *Atmos. Meas. Tech.* **5**, 1869–1887 (2012)
- 18.90 E. Weingartner, H. Saathoff, M. Schnaiter, N. Streit, B. Bitnar, U. Baltensperger: Absorption of light by soot particles: Determination of the absorption by means of aethalometers, *J. Aerosol Sci.* **34**, 1445–1463 (2003)
- 18.91 J.T. Jayne, D.C. Leard, X. Zhang, P. Davidovits, K.A. Smith, C.E. Kolb, D.R. Worsnop: Development of an aerosol mass spectrometer for size and composition analysis of submicron particles, *Aerosol Sci. Technol.* **33**, 49–70 (2000)
- 18.92 H. Junninen, M. Ehn, T. Petäjä, L. Luosujärvi, T. Kotiaho, R. Kostiainen, U. Rohner, M. Gonin, K. Fuhrer, M. Kulmala, D.R. Worsnop: A high-resolution mass spectrometer to measure atmospheric ion composition, *Atmos. Meas. Tech.* **3**, 1039–1053 (2010)
- 18.93 W. Lindinger, A. Jordan: Proton-transfer-reaction mass spectrometry (PTR-MS): On-line monitoring of volatile organic compounds at pptv levels, *Chem. Soc. Rev.* **27**, 347–354 (1998)
- 18.94 M.W. Gallagher, K.M. Beswick, J. Duyzer, H. Weststrate, T.W. Choularton, P. Hummelshoj: Measurements of aerosol fluxes to Speulder Forest using a micrometeorological technique, *Atmos. Environ.* **31**, 359–373 (1997)
- 18.95 R.J. Vong, I.J. Vong, D. Vickers, D.S. Covert: Size-dependent aerosol deposition velocities during BEARPEX'07, *Atmos. Chem. Phys.* **10**, 5749–5758 (2010)
- 18.96 M. Conte, A. Donato, D. Contini: Characterisation of particle size distributions and corresponding size-segregated turbulent fluxes simultaneously with CO₂ exchange in an urban area, *Sci. Total Environ.* **622/623**, 1067–1078 (2018)
- 18.97 A. Schmidt, O. Klemm: Direct determination of highly size-resolved turbulent particle fluxes with the disjoint eddy covariance method and a 12-stage electrical low pressure impactor, *Atmos. Chem. Phys.* **8**, 7405–7417 (2008)
- 18.98 E. Nemitz, J.L. Jimenez, A. Huffman, I.M. Ulbrich, M.R. Canagaratna, D.R. Worsnop, A.B. Guenther: An eddy covariance system for the measurement of surface/atmosphere exchange fluxes of submicron aerosol chemical species – First application above an urban area, *Aerosol Sci. Technol.* **42**, 636–657 (2008)
- 18.99 R.M. Harrison, M. Dall'Osto, D.C.S. Beddows, A.J. Thorpe, W.J. Bloss, J.D. Allan, H. Coe, J.R. Dorsey, M. Gallagher, C. Martin, J. Whitehead, P.I. Williams, R.L. Jones, J.M. Langridge, A.K. Benton, S.M. Ball, B. Langford, C.N. Hewitt, B. Davison, D. Martin, K.F. Petersson, S.J. Henshaw, I.R. White, D.E. Shallcross, J.F. Barlow, T. Dunbar, F. Davies, E. Nemitz, G.J. Phillips, C. Helfter, C.F. Di Marco, S. Smith: Atmospheric chemistry and physics in the atmosphere of a developed megacity (London): An overview of the REPAR-TEE experiment and its conclusions, *Atmos. Chem. Phys.* **12**, 3065–3114 (2012)
- 18.100 C.A. Pope III, D.W. Dockery: Health effects of fine particulate air pollution: Lines that connect, *J. Air Waste Manag. Assoc.* **56**, 709–742 (2006)
- 18.101 ISO 7708:1995: *Air Quality – Particle Size Fraction Definitions for Health-Related Sampling* (International Organization for Standardization, Geneva 1995)
- 18.102 Health Effects Institute: *HEI Perspectives 3 – Understanding the Health Effects of Ambient Ultra-fine Particles* (HEI, Boston 2013)
- 18.103 J.J. Schauer, W.F. Rogge, L.M. Hildemann, M.A. Mazurek, G.R. Cass, B.R.T. Simoneit: Source apportionment of airborne particulate matter using organic compounds as tracers, *Atmos. Environ.* **30**, 3837–3855 (1996)
- 18.104 NASA: AERONET (Aerosol RObotic NETwork), <https://aeronet.gsfc.nasa.gov/> (2020), Accessed 07 July 2021
- 18.105 B.N. Holben, D. Tanre, A. Smirnov, T.F. Eck, I. Slutsker, N. Abuhassan, W.W. Newcomb, J. Schafer, B. Chatenet, F. Lavenue, Y.J. Kauf-

- man, J. Vande Castle, A. Setzer, B. Markham, D. Clark, R. Frouin, R. Halthore, A. Karnieli, N.T. O'Neill, C. Pietras, R.T. Pinker, K. Voss, G. Zibordi: An emerging ground-based aerosol climatology: Aerosol optical depth from AERONET, *J. Geophys. Res.* **106**, 12067–12097 (2001)
- 18.106 A. Benedetti, J.-J. Morcrette, O. Boucher, A. De-
thof, R. Engelen, M. Fisher, H. Flentje, N. Huneeus,
L. Jones, J. Kaiser, S. Kinne, A. Mangold,
M. Razinger, A. Simmons, M. Suttie: Aerosol anal-
ysis and forecast in the ECMWF Integrated Forecast
System: 2. Data assimilation, *J. Geophys. Res.* **114**,
D13205 (2009)
- 18.107 J. Flemming, A. Benedetti, A. Inness, R.J. Enge-
len, L. Jones, V. Huijnen, S. Remy, M. Parrington,
M. Suttie, A. Bozzo, V.-H. Peuch, D. Akritidis,
E. Katragkou: The CAMS interim reanalysis of car-
bon monoxide, ozone and aerosol for 2003–2015,
Atmos. Chem. Phys. **17**, 1945–1983 (2017)
- 18.108 J.H. Seinfeld, C. Bretherton, K.S. Carslaw, H. Coe,
P.J. DeMott, E.J. Dunlea, G. Feingold, S. Ghan,
A.B. Guenther, R. Kahn, I. Kraucunas, S.M. Krei-
denweis, M.J. Molina, A. Nenes, J.E. Penner,
K.A. Prather, V. Ramanathan, V. Ramaswamy,
P.J. Rasch, A.R. Ravishankara, D. Rosenfeld,
G. Stephens, R. Wood: Improving our fundamen-
tal understanding of the role of aerosol–cloud
interactions in the climate system, *Proc. Natl.
Acad. Sci. U. S. A.* **113**, 5781–5790 (2016)
- 18.109 U. Dusek, G.P. Frank, L. Hildebrandt, J. Curtius,
J. Schneider, S. Walter, D. Chand, F. Drewnick,
S. Hings, D. Jung, S. Borrmann, M.O. Andreae:
Size matters more than chemistry for cloud–nu-
cleating ability of aerosol particles, *Science* **312**,
1375–1378 (2006)
- 18.110 F. Snik, J.H.H. Rietjens, A. Apituley, H. Volten,
B. Mijling, A. Di Noia, S. Heikamp, R.C. Heinsbroek,
O.P. Hasekamp, J.M. Smit, J. Vonk, D.M. Stam,
G. van Harten, J. de Boer, C.U. Keller, and
3187 iSPEX citizen scientists: Mapping atmospheric
aerosols with a citizen science network of smart-
phone spectropolarimeters, *Geophys. Res. Lett.*
41, 7351–7358 (2014)

Andreas Held

Environmental Chemistry and Air Research
Technische Universität Berlin
Berlin, Germany
held@tu-berlin.de



Andreas Held, Professor of Environmental Chemistry and Air Research at Technische Universität Berlin, studied Geoecology at the University of Bayreuth, received his PhD at the University of Münster, and was Junior Professor/Professor of Atmospheric Chemistry at the University of Bayreuth from 2009 to 2018. His research interests include the formation and transport of atmospheric aerosols. He is currently co-chair of the European Aerosol Assembly's Aerosol Measurement Techniques working group.

Alexander Mangold

Scientific Service Observations
Royal Meteorological Institute of Belgium
Brussels, Belgium
alexander.mangold@meteo.be



Alexander Mangold is a Senior Scientist at the Royal Meteorological Institute of Belgium within the Scientific Service Observations. He received the Dipl.-Geoecology degree from the University of Bayreuth and his PhD in Natural Sciences at the University of Wuppertal, Germany. He is responsible for the atmospheric composition research program of his institute at the Belgian Antarctic research station and of the institute's atmospheric aerosol in-situ measurements in Brussels.

19. Methods of Sampling Trace Substances in Air

Christopher Pöhlker , Karsten Baumann , Gerhard Lammerl 

Trace gases are commonly collected via accumulative sampling, employing sorbents and cryotrap that utilize passive (diffusive) or active sampling principles. For semivolatile substances such as ammonium salts as well as oxygenated and halogenated organics, the particulate and gas phases must be collected separately—either side by side or in a sample train. Aerosol particles are collected using a broad spectrum of samplers that rely on physical principles such as inertia-based particle sampling, diffusive particle transport and adsorption to surfaces, particle migration and deposition in external fields, and filter sampling. Dedicated inlet systems with minimized particle losses must be used to ensure that sampling gives representative results, particularly for the particle size distribution. Note that artifact-free sampling is not yet available for a number of target compounds.

19.1	Measurement Principles and Parameters	566
19.1.1	Sampling of Trace Gases	566
19.1.2	Sampling of Semivolatile Substances .	567
19.1.3	Sampling of Aerosol Particles.....	567
19.2	History	568
19.2.1	Sampling of Trace Gases.....	568

19.2.2	Sampling of Semivolatile Substances .	569
19.2.3	Sampling of Aerosol Particles.....	569
19.3	Theory	570
19.3.1	Sampling of Trace Gases.....	570
19.3.2	Sampling of Semivolatile Substances .	571
19.3.3	Sampling of Aerosol Particles.....	571
19.4	Devices and Systems	576
19.4.1	Sampling of Trace Gases.....	576
19.4.2	Sampling of Semivolatile Substances .	579
19.4.3	Sampling of Aerosol Particles.....	580
19.4.4	Comparison of the Methods	587
19.5	Specifications	589
19.6	Quality Control	590
19.6.1	Sampling of Trace Gases.....	590
19.6.2	Sampling of Semivolatile Substances .	590
19.6.3	Sampling of Aerosol Particles.....	591
19.7	Maintenance	592
19.8	Application	593
19.8.1	Sampling of Trace Gases.....	593
19.8.2	Sampling of Semivolatile Substances .	595
19.8.3	Sampling of Aerosol Particles.....	596
19.9	Future Developments	596
19.10	Further Reading	596
	References	596

Poor air quality affects both human and ecosystem health [19.1, 2]. It is therefore important to monitor air quality to ensure that anthropogenic emissions are within the limits specified by national regulations and international agreements. Due to the diversity of natural and anthropogenic emissions, air pollutant concentrations in the atmosphere can vary significantly. In addition to primary pollutants (i.e., those that have long atmospheric lifetimes and remain unaltered after being released), many air pollutants are formed via secondary processes involving photochemical reactions during atmospheric transport. Due to these complexities, it is very difficult and costly to monitor air quality at ad-

equate spatial and temporal resolution. Ground-based monitoring stations provide good temporal coverage in real time but are too expensive to be operated at sufficient spatial resolution. Airborne monitoring via aircraft or satellite platforms provides good regional to global coverage but is extremely costly and very limited in terms of its temporal coverage and the number of pollutant species measured. The integrated sampling methods described here provide a valuable compromise between the two ideals of high spatial and temporal resolution. Furthermore, the sampling of atmospheric trace substances provides the basis for in-depth laboratory investigations of their physical, chemical, and/or biological

cal properties, as well as the changes in their properties upon atmospheric processing. The approaches used to integrate samples of trace substances over prolonged

time periods must be carefully evaluated for systematic artifacts that are quantified in the analytical procedures employed following sample collection.

19.1 Measurement Principles and Parameters

The analysis of trace substances in the atmosphere through sampling occurs indirectly in most cases, namely through a combination of trace substance sampling and the subsequent laboratory analysis of the analyte. The atmospheric abundances of gaseous and semivolatile species are typically quantified as mixing ratios or concentrations (Table 19.1) [19.3]. Since regulations for air pollutants specify limits on mass concentrations or volumetric mixing ratios, the volume of sampled air is the most important quantity aside from the amount of analyte found in the sample. Due to inherent differences in air density at different measurement locations, the atmospheric pressure p and the temperature t must also be known in order to facilitate site comparability and to check for compliance with regulatory standards. In addition, the ambient relative humidity R plays an important role in the partitioning of semivolatile gases, whether they sorb onto droplets or particles, and the hygroscopicity and viscosity of a particle/droplet determine if the sorbed gas stays in the particle phase unaltered or undergoes further chemical transformations.

The abundance of aerosol particles in the atmosphere is typically quantified as a number concentration or mass concentration [19.3]. Mass concentrations are typically obtained from the gravimetric analysis of filter samples [19.4]. It should be noted, however, that a multitude of other properties of the collected particles are also investigated, using various laboratory techniques.

For instance, a wide range of spectroscopic [19.5, 6], microscopic [19.7, 8], chromatographic [19.9, 10], and/or mass spectrometric [19.11, 12] analyses are conducted on aerosol samples. Due to the huge variety of methods used for analyses of aerosol samples, a comprehensive overview of all of the parameters measured in aerosol analysis—such as molecular compositions, aerosol mixing states, light absorbance, and the taxonomic diversity of bioaerosol organisms—is beyond the scope of Table 19.1.

19.1.1 Sampling of Trace Gases

Active and passive sampling are two fundamentally different approaches to the collection of ambient trace gas samples. Passive sampling is based on the molecular diffusion of analyte molecules from the ambient air to a sampling medium due to a gradient in chemical potential. Most passive sampling devices utilize gas diffusion across a well-defined diffusion barrier—in other words, permeation through a membrane, with subsequent deposition onto a sorbent material. This approach is also known as diffusive sampling. Passive sampling is advantageous compared to active sampling in that it requires less operational support (e.g., for flow control and calibration), less maintenance of pumps and other moving parts, and it is more flexible in terms of deployment as it does not require electricity. After sample collection, the analytes are extracted from the

Table 19.1 Parameters measured through the sampling of trace substances in air

Parameter	Description	Unit	Symbol
Molar concentration of gases or semivolatiles	Amount of substance i in a volume of air	mol m^{-3}	c_i
Mass concentration of gases or semivolatiles	Mass of substance i in a volume of air	$\mu\text{g m}^{-3}$	m_i
Mixing ratio or mole fraction of gases or semivolatiles	Ratio of amount of substance i , c_i , in a volume of air to amount of all constituents, c_{total} , in that volume	Parts per million (ppm, $\mu\text{mol mol}^{-1}$), parts per billion (ppb, nmol mol^{-1}), or parts per trillion (ppt, pmol mol^{-1})	ξ_i
Aerosol particle number concentration	Number of aerosol particles in a specified diameter (D) range (e.g., $D > 10 \text{ nm}$ or $D = 1\text{--}10 \mu\text{m}$) in a volume of air	cm^{-3} or m^{-3}	N_D
Aerosol particle mass concentration	Mass of aerosol particles in a specified diameter (D) range (e.g., $D > 10 \text{ nm}$ or $D = 1\text{--}10 \mu\text{m}$) in a volume of air	mg m^{-3} , $\mu\text{g m}^{-3}$, or ng m^{-3}	M_D

sorbent by solvents (usually deionized water for inorganic gases, and often dimethylchloride or alcohols for semivolatile organics) or desorbed thermally, and are then analyzed in the laboratory. Thus, passive sampling methods have a number of advantages: their *small size*, allowing mobile and unobstructed operation in tight spaces such as personal breathing zones; their *low cost* in terms of material and labor, permitting multiple deployments that combine geographical mapping with the capacity to probe long-term data trends; their *integrative nature*, as they provide pollution levels representing weeks, months, or even seasons of accumulation; and their *low impact*, which enables unsupervised operation without any sound or odor emissions, meaning that they can be used in both urban and remote environments. However, passive samples require relatively laborious postprocessing in analytical laboratories, and such sampling typically provides a very low temporal resolution, so it is not possible to access information on dynamic atmospheric relationships or the sensitivities of analytes to changes in the atmosphere or receptor response [19.13]. Active sampling of trace gases requires a pump and flow control to actively draw the ambient air sample over pretreated surfaces that take the form of a tube, multiple concentric tubes (annuli), or a honeycomb structure. These structures are called denuders, and their surfaces are coated with materials that are known to be particularly efficient at retaining (via absorption or adsorption) the specific compounds of interest. In most applications, at least two denuders are used in series to measure compound-specific retaining efficiencies or artifacts. The analytical procedures implemented in the laboratory after active sample collection are the same as those used after passive sampling.

19.1.2 Sampling of Semivolatile Substances

In the two-phase system of an atmospheric aerosol (at ambient temperature and pressure), the semivolatility of the substance causes it to be significantly distributed across both phases, which is known as gas–particle partitioning [19.14].

19.1.3 Sampling of Aerosol Particles

An aerosol is a two-phase system of liquid or solid particles suspended in a gas. Throughout this chapter, we will use the terms *particulate matter* and *aerosol particles* synonymously. Since aerosols are of considerable scientific interest in various research fields [19.15–17],

many techniques for aerosol analysis have been developed, including *offline* techniques, which involve the collection of particles on substrates and subsequent laboratory analysis, and *online* techniques, which allow in-situ and near-real-time particle characterization (Chap. 20). This chapter reviews the principles and applications of aerosol sampling—in other words, the separation and collection of airborne particles from the gas phase, followed by the offline analysis of those particles. However, the gas phase should not be ignored, as the particles typically contain both non-volatile compounds (e.g., salts, mineral dust, and soot) and semivolatile compounds (e.g., nitrates and organics) that partition between the gas and particle phases (Sect. 19.1.2) [19.18].

Particle size plays a key role in the physicochemical properties and atmospheric dynamics of aerosols. Hence, particle size is also highly relevant to the design and application of sampling strategies. In addition to size, the particle shape and density influence the aerodynamic motion of the particles and must therefore be considered in sampling applications. Figure 19.1 provides an overview of the characteristic particle sizes of aerosols from selected sources as well as their health effects. The aerosol particle size range, which spans from ≈ 1 nm to ≈ 100 μm , is typically subdivided into ultrafine (< 0.1 μm), fine (0.1–1 μm), and coarse (> 1 μm) particles. Furthermore, the pronounced modes in the multimodal atmospheric aerosol size distribution are defined as the nucleation mode (1–25 nm), the Aitken mode (25–100 nm), the accumulation mode (0.1–1 μm), and the coarse mode (> 1 μm) [19.3, 19, 20]. Note that different definitions for the thresholds between the modes exist. Particle size is determined by various measurable properties of the particles (e.g., electromobility, aerodynamic mobility, and geometric or optical size); variations in these parameters result in different *equivalent particle diameters* [19.3, 21].

Given the large number and high diversity of commercial and noncommercial devices and systems for aerosol sampling [19.27–29], this chapter cannot provide a comprehensive overview of all of them. Instead, it aims to present the key concepts and characteristics of the most widely used sampling strategies. Moreover, the main designs and operating principles of relevant sampling devices are summarized. The sampling of cloud droplets is treated as a special case of large particle sampling in the relevant sections. Throughout this chapter, we provide multiple references to text books, journal articles and other resources for further reading and in-depth research on this subject.

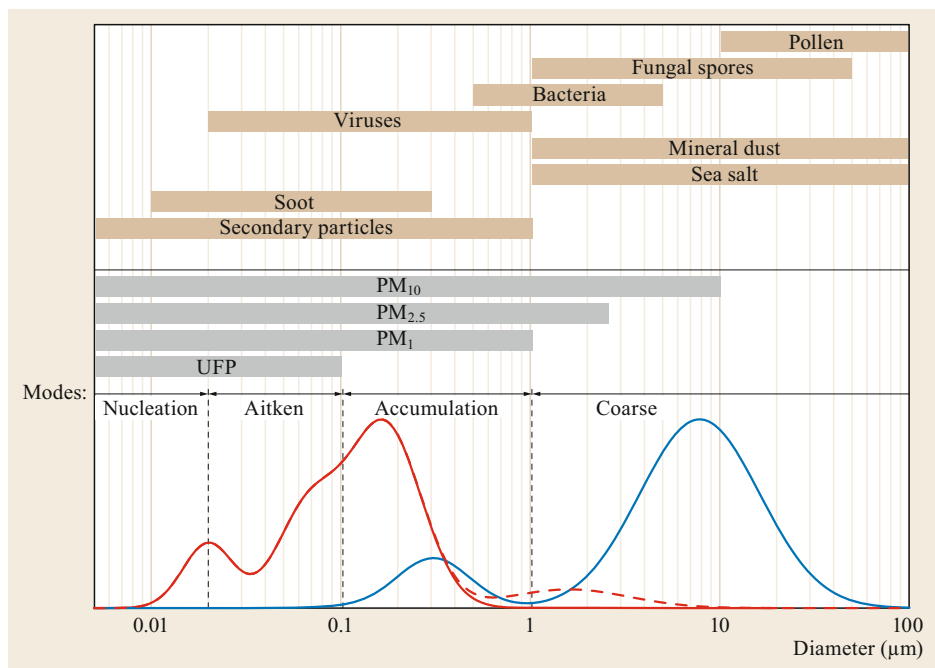


Fig. 19.1 Aerosol particle size scales for selected particle categories and characteristic modes of multimodal particle size distributions. The aerosol particle size distributions (the volume distribution in *blue* is calculated from the number distribution in *red*) are characteristic multimodal cases as frequently observed in the atmosphere. The definitions of the nucleation, Aitken, accumulation, and coarse modes were obtained from [19.3, 19, 20]. Different definitions of the coarse mode exist (> 1 , > 2 , or > 2.5 μm); here, coarse-mode particles have been defined as > 1 μm . The size ranges of the selected particle types (*brown*)—most of which are taken from [19.22]—are generalized and meant for overall orientation here. Typical size ranges for bacteria, fungal spores, and pollen can be obtained from [19.23, 24], the typical size range for mineral dust can be found in [19.25], and that for soot is presented in [19.16, 26]. *Gray bars* refer to the widely monitored particulate matter (PM) mass concentrations PM_1 , $\text{PM}_{2.5}$, and PM_{10} as well as the ultrafine particle (UFP) fraction below 100 nm.

19.2 History

As in most fields of natural science, our current knowledge of aerosol physics and chemistry is based on the curiosity of individual researchers who continuously advanced our understanding through new discoveries. The following summarizes a few highlights of the development of this field without claiming to be a complete reflection of all recent progress made.

19.2.1 Sampling of Trace Gases

The first records of the development and use of a passive sampler date back to the year 1853, when potassium iodide (KI)-impregnated filter papers were used to detect and quantitatively collect ambient ozone (O_3) [19.30]. This method followed on from the discovery of ozone in 1839 by *Christian Friedrich Schönbein* (1799–1868), a professor of chemistry at the Univer-

sity of Basel. He reported to the Swiss National Nature Research Society that a smell developed at the positive electrode during the electrolysis of water, and that this smell was strikingly similar to that obtained when electricity flowed across electrodes [19.31]. By the late 1840s, he had developed Schönbein paper, a mixture of starch, KI, and water spread on filter paper and dried. Ambient ozone oxidizes the KI on the paper, producing iodine (I_2) that reacts with the starch, staining the paper violet. The intensity of the color depends on the amount of ozone present: more ozone leads to a darker color.

Attempts by *Chester S. Gordon* and *James T. Lowe* to quantitatively measure carbon monoxide (CO) using palladium chloride salts as a passive sampler yielded US patent 1644014, filed on 3 December 1925 and granted on 4 October 1927 [19.32]. Early examples of successful passive sampling in outdoor air included the determina-

tion of gaseous oxides of sulfur and nitrogen [19.33, 34]. Several passive samplers were also developed to evaluate and monitor different types of environmental pollution. Most of those studies monitored indoor air pollution [19.35]. *Edward D. Palmes* (1916–2004) and *Albert F. Gunnison* (at the Department of Environmental Medicine, New York University) [19.36] used a mercury chloride sorbent in a Palmes tube to capture sulfur dioxide (SO₂), which was subsequently quantified via colorimetric analysis [19.37]. This design was later modified to trap nitrogen dioxide (NO₂) on a stainless-steel grid coated with triethanolamine [19.34]. The collecting grid was located at the closed end of an acrylic tube that was ≈ 8 cm long and had an inner diameter of 1 cm. Analytical quantification followed spectrophotometric nitrite analysis using sulfanilamide and naphthylethylenediamine as reactants.

The *Swedish Environmental Institute* [19.38] significantly advanced the use of passive sampling of selected air pollutants in remote air quality monitoring applications by demonstrating that high data quality could be attained through the application of dedicated analytical laboratory and rigorous quality control procedures. *Mazur et al.* [19.39] developed one of the first ammonia (NH₃) samplers using an acid-impregnated glass fiber pad resting behind a potassium hydroxide (KOH)-pretreated, charcoal-impregnated glass fiber front filter. The purpose of the charcoal was to remove (adsorb) interfering amines, while the alcoholic KOH with 0.1% wetting agent prevented the occurrence of a negative artifact arising from the irreversible adsorption of NH₃ along its diffusive path to the collecting glass fiber pad. *Christian-Thomas Monn* and *Markus Hangartner* (at ETH Zürich and Dübendorf, respectively) [19.40] developed one of the first passive samplers for ozone, which was based on the Palmes tube mentioned above. The aldehyde resulting from the hydrolysis of the ozonide formed by the reaction of the adsorption medium 1,2-di(4-pyridyl)ethylene with ambient O₃ was measured spectrophotometrically, and the results correlated well with those from collocated reference monitors [19.41]. Parallel applications (which are, however, less widely used) were also developed for carbon dioxide (CO₂) [19.42], hydrogen sulfide (H₂S) [19.43], polyaromatic hydrocarbons (PAHs) [19.44], volatile organic compounds (VOCs) [19.45], and chlorinated semivolatile organic pollutants [19.13, 46].

Researchers from the United States Department of Agriculture (USDA) Forest Service and the University of California (Riverside) developed a passive sampler for atmospheric nitric acid (HNO₃) that was both simple and inexpensive to deploy across USDA-managed landscapes [19.47]. The sampler utilized HNO₃ diffusion through a Teflon filter membrane with a pore size

of 2 μm and a diameter of 47 mm and subsequent adsorption onto a nylon backup filter of the same size (Nylasorb, Pall Corporation). *Bytnerowicz et al.* [19.48] showed that HNO₃ concentrations determined using the nylon filters closely agreed with those measured by a collocated active sampler employing calcium carbonate (CaCO₃)-coated honeycomb annular denuders under both random ambient and controlled experimental conditions. The pair of filters were exposed in a 50 mm round commercial polycarbonate petri dish held in place by Teflon rings and protected from the elements by a generic polycarbonate cap. The original design was susceptible to artifacts from high winds that caused uncontrolled turbulent flow and disrupted the laminar airflow that controls the HNO₃ deposition onto the nylon filter.

19.2.2 Sampling of Semivolatile Substances

Gaseous semivolatile chlorinated organics are not sufficiently retained in adsorbents that are suitable for volatiles. Therefore, since the 1970s, gaseous chlorinated organics have been sampled using polyurethane foam instead [19.49–51]. Since then, polyurethane foam has been employed in many monitoring and research applications across the world to collect various classes of semivolatile organic compounds (SVOCs) [19.52].

19.2.3 Sampling of Aerosol Particles

Historically, the development and application of aerosol sampling strategies were stimulated by increasing awareness of the adverse effects of inhaled aerosols on human health [19.29, 53, 54]. Indeed, the history of the development of sampling strategies for airborne microorganisms stretches back to the work of *Louis Pasteur* (1822–1895), *Christian Gottfried Ehrenberg* (1795–1876), and other pioneers who conducted the first bioaerosol samplings and analyses in the middle of the nineteenth century [19.54–58]. Another strand of development in this field also reaches back to the late nineteenth and early twentieth century, when the protection of public health in the context of increasing industrial and combustion pollution became an important societal issue. Such monitoring is particularly relevant to occupational settings (e.g., workplace exposure for industrial workers and miners) and ambient settings in strongly industrialized and hence particularly polluted cities [19.29, 59]. Evidently, the development of sampling instrumentation is closely linked to the requirements of analytical techniques for subsequent aerosol analysis, such as gravimetric, microscopic, or mineralogical investigations on the one hand and practical and physical constraints on the other.

Moreover, sampling and analytical strategies have developed in concert as knowledge of the physical and chemical properties of aerosols has increased, leading to the definition of criteria for health-relevant sampling standards (e.g., respirable fractions and mass standards such as PM_{10} and $PM_{2.5}$ (particulate matter); see Fig. 19.1) [19.60].

Some milestones in early aerosol sampling include

1. the development of the first impactor by *M.F. Pouchet* in 1860 [19.61],
2. systematic bioaerosol investigations since the 1880s that have been based on sampling with culture media and have focused in particular on the health effects of bioaerosols [19.54],
3. systematic filter sampling for gravimetric analysis to quantify the total mass of collected particulate matter (e.g., in underground mining) [19.62, 63], as performed since the 1900s,

4. the development between the 1900s and 1930s of different designs of thermophoretic precipitators, electrostatic precipitators, and impactors to deposit particles on glass slides or other suitable substrates for subsequent optical microscopy to count smaller, respirable (and hence more relevant to health) particle size fractions [19.64–69],
5. the development of sampling devices with aerodynamic particle size segregation, such as cascade impactors and cyclones, since the 1940s [19.70, 71], and
6. the creation in the 1960s of wearable miniaturized samplers that allowed the exposure of individuals (e.g., miners) to be monitored [19.72].

Since those early days, the developments in this field have progressed rapidly and have yielded a diverse set of partly sophisticated techniques that are now applied routinely in aerosol sampling and analysis.

19.3 Theory

The abovementioned developments and technological progress were achieved largely due to advances in our understanding of their underlying physicochemical principles, which are described below.

19.3.1 Sampling of Trace Gases

The theory behind active and passive sampling has been extensively reviewed elsewhere [19.13, 73–76], so we focus here primarily on issues related to NH_3 and HNO_3 , the two most important reactive gases in the Earth's nitrogen balance. In addition to its acidifying effects, HNO_3 (a member of the reactive nitrogen complex) is involved in the initial soil fertilization process, which increases the growth, productivity, and reproduction of terrestrial plants. It also influences plant community structure, causing shifts from nitrophobic to nitrophilic species and promoting biodiversity. Furthermore, atmospheric deposition of nitrate can result in surface water eutrophication and hypoxia, impacting wildlife habitats and diversity [19.77].

In the context of passive air sampling, diffusional mass transfer through either a static layer of ambient air or across a membrane can be described by Fick's first law of diffusion. This law states that, for a given analyte, the sampling rate v_i (the volumetric amount of analyte collected by the sampler per unit time at constant concentration in the surrounding medium) is given by

$$v_i = D_i \frac{A}{\Delta x}, \quad (19.1)$$

where D_i is the diffusion coefficient and $A/\Delta x$ is the sampler-specific geometric constant.

The $A/\Delta x$ ratios for the Ogawa and Radiello samplers, for example, are specified by the manufacturer as 2.23 and 14.2 cm, respectively. For NH_3 , Radiello [19.78] specifies a constant sampling rate v_{NH_3} of 235 mL min^{-1} for an ambient t of $2\text{--}39^\circ\text{C}$, $R = 10\text{--}90\%$, and a wind speed u of $0.1\text{--}10 \text{ m s}^{-1}$. The NH_3 sampling rate for the Ogawa sampler is 32.3 mL min^{-1} [19.79]. Neither the literature nor the manufacturer provide sampling rates for HNO_3 when utilizing the Ogawa-type passive sampler. Therefore, employing (19.1), a value of 15.8 mL min^{-1} can be used, assuming a constant HNO_3 diffusion coefficient of $0.118 \text{ cm}^2 \text{ s}^{-1}$ [19.80] and an $A/\Delta x$ ratio of 2.23 cm.

In most applications, the D_i values of both HNO_3 and NH_3 vary little within the typical ranges of ambient temperature and pressure, so v_i mainly depends on the sampler geometry, which is given by the effective diffusive surface (cross-section) A and the diffusion path length Δx (the distance between the diffusive and adsorbing surfaces). Knowledge of the relationship between the sampling rate and analyte concentration allows the time-weighted (integrated) average ambient concentration of analyte i to be determined from the difference in mass between the analyte on the exposed sampler (M_i) and a field blank ($M_{i,0}$) divided by the analyte-specific and exposure time (t_{exp})-dependent air volume (V_i), i.e.,

$$C_i = \frac{M_i - M_{i,0}}{V_i}, \quad (19.2)$$

where

$$V_i = v_i t_{\text{exp}} \quad (19.3)$$

At least three main conditions have to be met when using this approach.

1. The receptor medium must act as a so-called *zero sink*; that is, it must not release any of the adsorbed molecules even if the concentration of the analyte in the ambient environment decreases to zero.
2. The trapped molecules must be either inert to variations in the ambient conditions and chemically reactive species, or they must change their state to a measurable quantity consistently and with 100% efficiency.
3. The sampling rate must remain constant throughout the sampling period. This is accomplished when the analyte is absorbed (e.g., into a liquid receiving phase) or *chemisorbed* (e.g., in the case of HNO_3 on a NaCl-coated surface). However, problems occur when physical *adsorption* governs analyte collection, as it does for HNO_3 on nylon. In this case, the linear portion of the adsorption isotherm should be used exclusively throughout the entire sampling process.

This is typically accomplished by using low mass loadings of high-capacity sorbents that are far from thermodynamic equilibrium. However, since adsorption is a competitive process, the linear range of the adsorption isotherm can easily be exceeded whenever other molecules are trapped in large amounts along with the analyte molecules. The adsorption of HNO_2 and NO_2 onto nylon is a good example of this mechanism, as described above.

19.3.2 Sampling of Semivolatile Substances

Many inorganic and organic substances are semivolatile under ambient conditions (i.e., they partition significantly between the particulate and gas phases) [19.81–83]. This behavior corresponds to a vapor pressure in the range 10^{-6} – 10^{-2} Pa (at $t = 293$ K, $p = 1$ bar [19.84]). Higher particulate mass fractions occur at higher altitudes, during the cold season, or at night. The influence of temperature alone is, however, insufficient to explain the partitioning process: it is understood to result from a number of attractive interactions at the molecular level that influence adsorption onto aerosol surfaces and absorption into liquid or semisolid particulate organic matter [19.85, 86]. Accordingly, the slope of the empirical equation

$$\log K_p = -m \log p_L^0 + b, \quad (19.4)$$

which relates the partitioning coefficient $K_p = c_p / (c_g c_m)$ (where c_p and c_g are the substance concentrations in the two aerosol phases, respectively) to the saturation vapor pressure of the supercooled liquid p_L^0 , usually deviates significantly from -1 [19.87].

Observations of the partitioning ($\log K_{\text{oa}} > 11$) of very lipophilic substances indicate that kinetic limitations may cause deviations from phase equilibrium [19.88]. This issue is being addressed in ongoing research. For substances that significantly partition to both aerosol phases, separate sampling media are applied for both phases in parallel. For the respective sampling theory, see Sects. 19.3.1 and 19.3.3.

19.3.3 Sampling of Aerosol Particles

Aerosol samplers are generally active sampling techniques that use a pump to draw air into a device in which aerosol particles within a certain size range are deposited on substrates. The particle deposition process can be governed by different *particle collection mechanisms*, which can be categorized as follows:

1. inertia-based particle separation and sampling;
2. particle transport via Brownian motion and gradient-induced diffusion;
3. particle migration and deposition under the influence of gravitational and electric fields; and
4. particle filtration (which is dominated by the processes of diffusion, impaction, and interception).

All of these processes can be used *intentionally* in aerosol sampling strategies, but they also occur *unintentionally* in aerosol inlets and tubes, leading to sampling artifacts. Thus, the following section summarizes the relevant theoretical background for aerosol sampling techniques, as well as strategies for minimizing aerosol sampling artifacts. More detailed information on the physical background for aerosol properties and dynamics beyond the summary presented below can be found elsewhere [19.3, 27–29].

Inertia-Based Particle Size Separation and Sampling

Inertial sampling is widely used for aerosol particle collection and size separation in numerous devices, such as impactors and cyclones [19.18, 29, 89]. The theoretical basis for inertial sampling presented here is applicable within the Stokes regime, characterized by a Reynolds number $\text{Re} < 1$. The Reynolds number is a dimensionless number that reflects the ratio of inertial forces of the particles to viscous forces of the gas [19.28], and is defined as

$$\text{Re} = \frac{\rho_g U d}{\eta}, \quad (19.5)$$

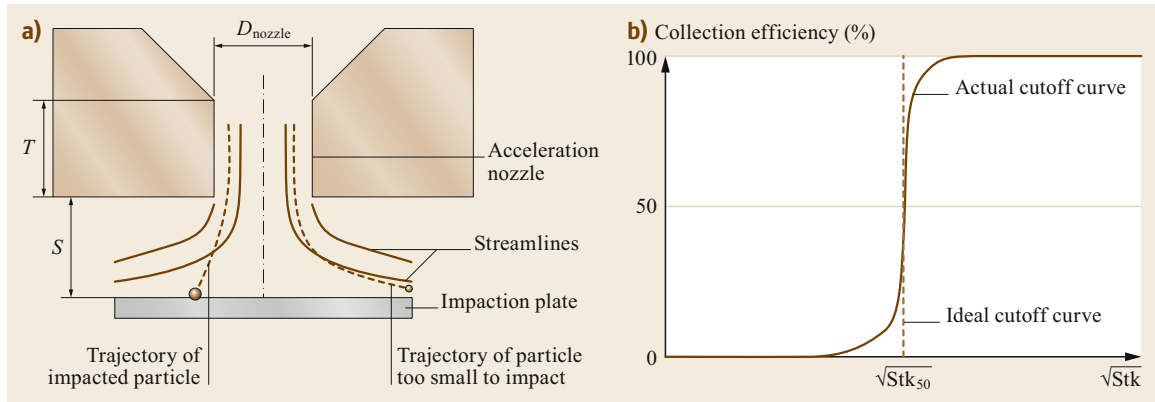


Fig. 19.2 (a) Schematic design of a conventional impactor, showing gas-flow streamlines and characteristic particle trajectories. (b) The corresponding particle collection efficiency curve, showing a comparatively sharp cutoff that approaches an ideal step function. The nozzle diameter D_{nozzle} , the dimensionless jet-to-plate distance S/D_{nozzle} , and the dimensionless nozzle throat length T/D_{nozzle} , as specified in (a), are important parameters in the design of jet impactors [19.90] (after [19.89] with permission from John Wiley & Sons, Inc.)

where ρ_g is the density of the gas, U is the velocity of the gas relative to the object of interest, d is the characteristic dimension of the object, and η is the viscosity of the air.

In aerosol sampling, Re is a key parameter in two fluid flow aspects. First, it describes the fluid flow around a suspended particle (i.e., d is the diameter of the particle and U is the velocity of the gas in relation to the particle), in which case it is called the *particle Reynolds number* Re_p . Second, it describes the fluid flow inside an inlet tube (i.e., d is the diameter of the tube and U is the fluid flow velocity in the tube), in which case it is called the *flow Reynolds number* Re_f . Re is used to predict transitions from laminar to turbulent flow regimes. For a discussion of sampling strategies employed in different Re_f regimes, see Sect. 19.6.3.

The condition $Re_p < 1$ applies to most aspects of aerosol motion, which is predominantly defined by the motion of the gas, given that the inertial forces of particles are relatively weak (because the particle masses and velocities are rather low). Inertial particle classification utilizes the curvilinear motion of the gas flow (e.g., the gas is redirected or deflected using obstacles) to capture the particles with sufficiently high inertia to remain on their original trajectory (or a trajectory close to it). These particles therefore cross the streamlines of the air and collide with a collection body, such as the sampling substrate. On the other hand, smaller particles with less inertia follow the gas flow and remain airborne (Fig. 19.2). The key parameters in inertial deposition are the velocity of the gas, the size of the particles, and the size of the object on which the high-inertia particles are collected. The relevant particle size for inertial techniques is their *aerodynamic equivalent diameter* D_a ,

defined as the diameter of a standard-density (1 g cm^{-3}) sphere with the same terminal velocity as the particle of interest. The ratio of the particle's stopping distance to the size of the collecting body determines whether the particle strikes the body or not. This ratio—a dimensionless parameter—is called the *Stokes number* Stk [19.90, 91]. For typical impactors that accelerate the sample air through a nozzle perpendicularly towards an impaction plate (in conventional impactors, see Fig. 19.2a) or a collecting probe (in virtual impactors), Stk is defined as

$$Stk = \frac{\rho_p D_a^2 C_c U}{9\eta D_{\text{nozzle}}}, \quad (19.6)$$

with

$$U = \frac{Q}{\pi \left(\frac{D_{\text{nozzle}}}{2}\right)^2}, \quad (19.7)$$

where ρ_p is the particle density, C_c is the Cunningham slip correction factor (which accounts for noncontinuum effects that become significant when the value of D_a is comparable to the mean free path λ of the gas molecules), U is the relative velocity of the gas with respect to the body (which, in the present case, is the average air velocity at the nozzle exit), D_{nozzle} is the diameter of the circular nozzle, and Q is the volumetric flow rate through the nozzle.

The relationship of the collection efficiency to D_a is of central importance to the design and characterization of all inertia-based samplers. As an example, the efficiency curve in Fig. 19.2b illustrates the characteristic *cutoff* diameter D_{50} at which 50% of the particles

strike the sampling plate. D_{50} is directly related to Stk_{50} , which depends on the impactor design considered, via

$$D_{50} \sqrt{C_c} = \left(\frac{9\pi D_{\text{nozzle}}^3 Stk_{50}}{4\rho_p Q} \right)^{1/2}. \quad (19.8)$$

As an example, $Stk_{50} = 0.24$, or $(Stk_{50})^{1/2} = 0.49$, is recommended for the design of a circular jet impactor [19.28, 92]. Equation (19.8) indicates that D_{50} can be further decreased by increasing Q , reducing D_{nozzle} (utilized in micro-orifice impactors [19.93, 94]), or enhancing C_c (utilized in low-pressure impactors [19.95, 96]). More detailed information on impactation theory and impactor design can be found elsewhere [19.28, 89, 92, 97, 98]. Other inertia-based sampling devices such as cascade impactors, virtual impactors, cyclones, and aerodynamic lenses are based on the same physical principles [19.99–103]. It should also be noted that inertial particle losses occur in aerosol inlets and tubes when the sample air stream passes through bends or constrictions [19.104]. This effect is particularly pronounced at high gas flow velocities, such as those present in turbulent sampling conditions (Sect. 19.6.3).

Particle Transport Through Brownian Motion and Diffusion Across Gradients

William Hinds [19.28] concisely summarized that

Brownian motion is the irregular wiggling motion of an aerosol particle in still air caused by random variations in the relentless bombardment of gas molecules against the particle. *Diffusion* of aerosol particles is the *net* transport of these particles in a concentration gradient [...] from a region of higher concentration to a region of lower concentration.

The diffusion of aerosol particles and their deposition on surfaces are relevant in various aspects of aerosol sampling. A key parameter is the diffusion coefficient D , which relates the aerosol particle flux J to the particle concentration gradient dn/dx according to Fick's first diffusion law

$$J = -D \frac{dn}{dx}, \quad (19.9)$$

with

$$D = \frac{kTC_c}{3\pi\eta D_p}, \quad (19.10)$$

where k is Boltzmann's constant and T is the absolute temperature.

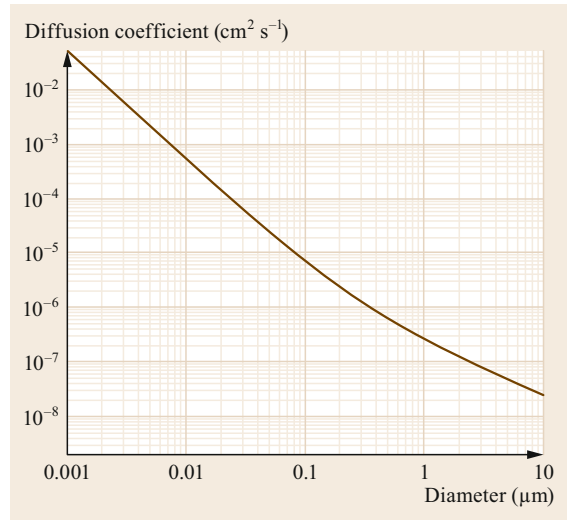


Fig. 19.3 The aerosol diffusion coefficient in air at 20 °C as a function of diameter (after [19.3] with permission from John Wiley & Sons, Inc.)

The parameter D , as a measure of the intensity of Brownian motion and the rate of gradient-driven particle transport, is strongly dependent on size (Fig. 19.3). For larger particles, C_c is approximately unity (meaning that D_p exceeds the mean free path λ of the gas molecules), and (19.10) yields an (approximately) linear relationship: $D \approx D_p^{-1}$. For smaller particles, $C_c = 1 + 1.657(2\lambda/D_p)$, and particle size and diffusivity are related via $D \approx D_p^{-2}$ [19.3]. It is therefore clear that diffusive separation and deposition can be used most effectively for ultrafine particles (those $< 0.1 \mu\text{m}$ in size), which are associated with the largest D values. Net diffusive transport of particles requires a particle concentration gradient and occurs over comparatively short distances. Note that the distances traveled by particles through Brownian motion are negligibly small compared to aerosol transport via atmospheric convection (i.e., wind and large eddies).

Upon colliding with a wall, aerosol particles adhere to it, meaning that the wall acts as a sink and creates a particle concentration gradient that drops to zero (Fig. 19.4). This gradient causes continuous particle diffusion and deposition at the wall and thus a gradual decrease in the overall concentration. This effect can be used in dedicated aerosol sampling strategies. Moreover, diffusional losses are of fundamental importance in the design and operation of aerosol inlets and tubes (Sect. 19.6.3). In particular, when sampling aerosol particles $< 0.1 \mu\text{m}$ in size, measures must be taken to minimize diffusion losses to the walls of the inlet and tubes [19.104].

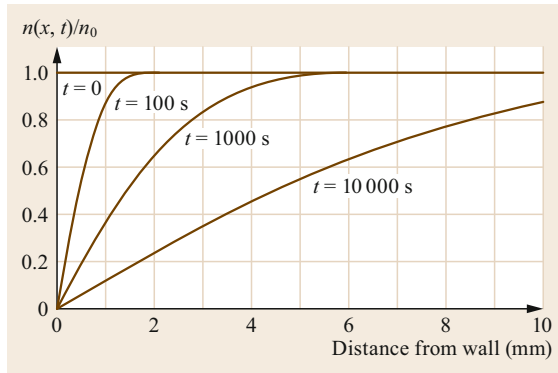


Fig. 19.4 Concentration profile for a stagnant aerosol of $0.05 \mu\text{m}$ particles near a wall in the idealized case of particle deposition at a plane wall from an infinite aerosol particle reservoir. The parameter t is the time since initial mixing. The plot illustrates the formation of a particle concentration gradient and its evolution over time (after [19.28] with permission from John Wiley & Sons, Inc.)

Brownian motion and a gradient-driven net transport of aerosol particles require relatively high particle mobilities in the gas phase. Related weak forces, such as *thermophoresis*, similarly rely on high particle mobilities and have a certain relevance in sampling applications. Thermophoresis is the movement of particles in the gas phase in the direction of decreasing temperature. Mechanistically, this can be explained by the higher velocities of gas molecules in a hotter region than in a cooler region: the faster gas molecules impart more momentum (via collisions) to the particles than the slower gas molecules do. Below $\approx 0.1 \mu\text{m}$, the thermophoretic velocity is independent of particle size, whereas this velocity decreases with increasing particle diameter above a size of $\approx 0.1 \mu\text{m}$ [19.28]. A more detailed description of these processes can be found elsewhere [19.105–107]. In principle, thermophoresis could also cause particle losses upon aerosol sampling, but temperature gradients are typically comparatively small, so thermophoretic losses are negligible [19.104].

Particle Migration and Deposition in Gravitational and Electric Fields

External forces such as gravity and electrostatic attraction cause particle migration and are therefore relevant to aerosol sampling applications. The gravitational force F_G that acts on the particles is

$$F_G = \frac{\pi D_p^3 \rho_p g}{6}, \quad (19.11)$$

where g is the gravitational acceleration.

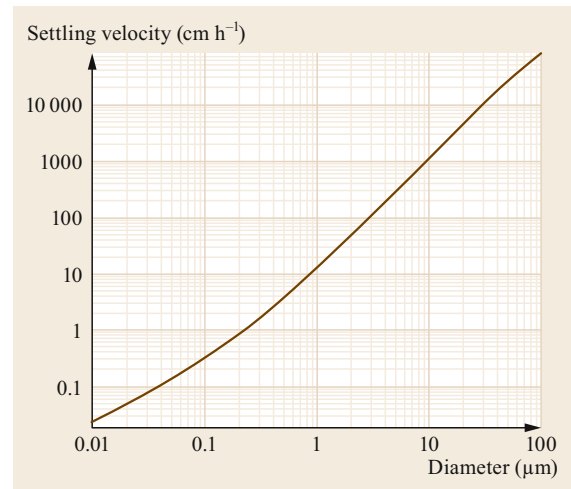


Fig. 19.5 Settling velocity of unit-density spheres in air at 298 K as a function of diameter (after [19.3] with permission from John Wiley & Sons, Inc.)

In the gravitational field, particles instantaneously reach their terminal settling velocity v_G when F_G and the opposing aerodynamic drag force reach equilibrium, i.e.,

$$v_G = \frac{\rho_p D_p^2 g C_c}{18\eta} \quad \text{for } \text{Re}_p < 1. \quad (19.12)$$

Since the gravitational settling velocity increases strongly with size ($v_G \propto D_p^2$), it plays a major role for particles with $D_p > 1 \mu\text{m}$, cannot be neglected for particles with $0.1 \mu\text{m} < D_p < 1 \mu\text{m}$, and is rather insignificant for particles with $D_p < 0.1 \mu\text{m}$ (Fig. 19.5). Gravitational settling is used in dedicated sampling strategies [19.108, 109]. It also plays a critical role in aerosol sampling and transport lines, particularly when supermicrometer aerosols are the focus of the analysis [19.104, 110]. When centrifugal force is used for particle separation and sampling [19.111, 112], the gravitational acceleration g in (19.11) and (19.12) is replaced with the centrifugal acceleration a_c [19.28].

In an electric field, the electrostatic force F_E that acts on a particle is

$$F_E = neE, \quad (19.13)$$

where n is the number of elementary charges e on the particle (i.e., ne is the overall charge on the particle) and E is the intensity of the electric field.

In the electric field, the particles reach their terminal electrical migration velocity v_E when F_E and the opposing aerodynamic drag force reach equilibrium, i.e.,

$$v_E = \frac{neEC_c}{3\pi\eta D_d}. \quad (19.14)$$

The electric migration velocity depends on the overall charge per particle and particle size as ne/D_p . More detailed information on electrostatic sampling strategies can be found elsewhere [19.113]. It should also be noted that the electrostatic charge and the associated electric fields in aerosol inlets and tubes can cause substantial particle losses [19.104]. Accordingly, inlets and tubes are typically made of electrically conductive materials [19.19].

Filtration

Filtration is widely used in aerosol analysis, as it allows simple, flexible, and low-cost aerosol sampling. Because of its popularity and wide range of applications, extended filtration theories for porous membrane, pore membrane, and fibrous filters have been developed [19.114, 115]. These complex filtration theories provide predictive equations that allow the filtration efficiency E (i.e., the fraction of particles retained in the filter) to be quantitatively related to the filter characteristics, air flow velocity, and particle size [19.28, 116]. Generally, filtration involves several particle deposition mechanisms, in particular diffusion, impaction, and interception. Under certain conditions, electrostatic and gravitational settling may also be relevant, but they are not considered in the following theoretical summary. For fibrous filters, the penetration P can be calculated as

$$P = 1 - E = \exp\left(-\frac{4\alpha E_F t}{\pi D_f}\right), \quad (19.15)$$

where α is the filter's packing density (fiber volume/total volume), E_F is the particle deposition efficiency of a single fiber, t is the thickness of the filter, and D_f is the diameter of the fiber.

Equation (19.15) shows that P strongly decreases with increasing filter thickness and also depends on E_F , which can be approximated as the sum of the individual deposition contributions from diffusion (E_D), interception (E_R), and impaction (E_I), i.e.,

$$E_F = E_D + E_R + E_I. \quad (19.16)$$

Especially for small particles, Brownian motion causes the particles to deviate from the air streamlines, increasing the probability that they will strike the fiber (Fig. 19.6a). The efficiency E_D can be calculated as

$$E_D = 2\left(\frac{D_f U_0}{D}\right)^{-2/3}, \quad (19.17)$$

where U_0 is the velocity of the air at the surface of the filter before it enters and D is the diffusion coefficient (19.10).

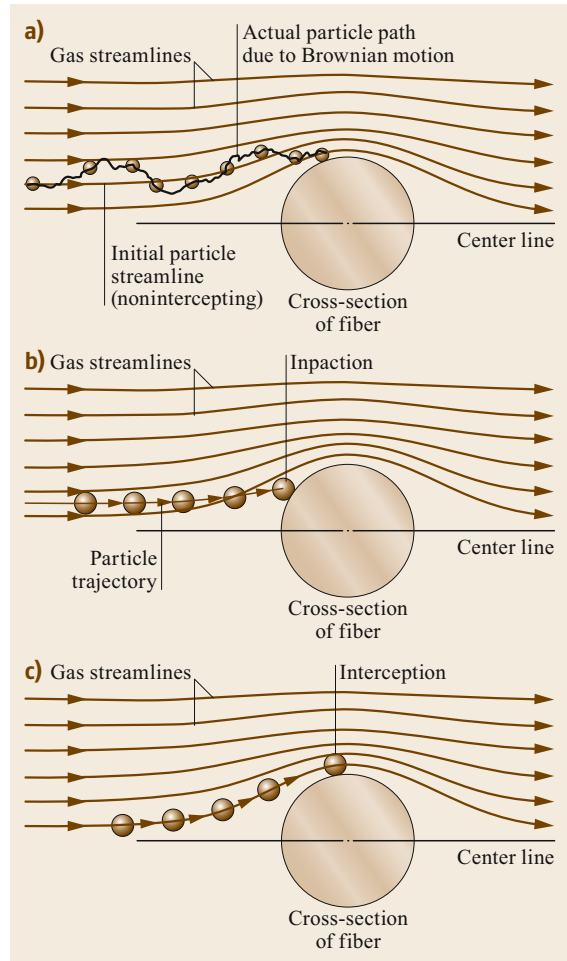


Fig. 19.6a–c Single-fiber particle collection mechanisms: (a) diffusion, (b) impaction, and (c) interception (after [19.28] with permission from John Wiley & Sons, Inc.)

Impaction on the fibers occurs when inertia causes larger particles to deviate from the air streamlines (Fig. 19.6b). The efficiency E_I can be calculated as

$$E_I = \frac{\text{Stk}}{2\text{Ku}^2} [(29.6 - 28\alpha^{0.62})R^2 - 27.5R^{2.8}] \quad (19.18)$$

with

$$\text{Stk} = \frac{\rho_p D_a^2 C_c U_0}{18\eta D_f} \quad (19.19)$$

and

$$\text{Ku} = -\frac{\ln \alpha}{2} - \frac{3}{4} + \alpha - \frac{\alpha^2}{4}, \quad (19.20)$$

where Ku is the Kuwabara hydrodynamic factor [19.117].

Fig. 19.7 Total filter efficiency versus particle diameter calculated from single-fiber efficiency theory for a fibrous filter that has a uniform fiber diameter of $4\ \mu\text{m}$ and a solidity of 0.1 and is operated at an air flow velocity of $0.15\ \text{m s}^{-1}$. The particle density is $1\ \text{g cm}^{-3}$. The diffusion and impaction/interception filtration regimes are indicated in the figure (after [19.116] with permission from John Wiley & Sons, Inc.) ►

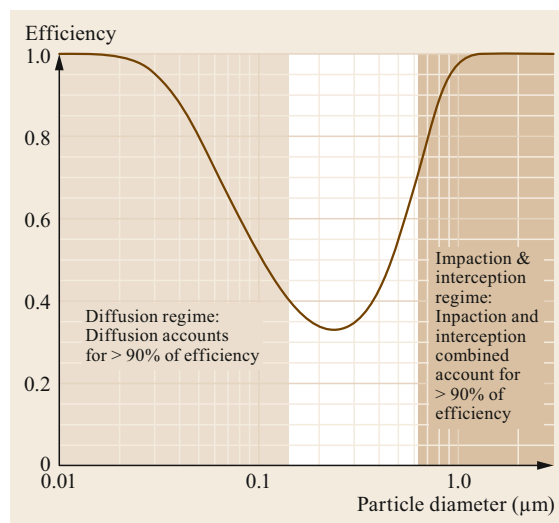
Interception occurs when a particle follows the air streamlines and strikes a fiber because of its finite size (Fig. 19.6c). The efficiency E_R can be calculated as

$$E_R = \frac{(1 - \alpha)R^2}{Ku(1 + R)}, \quad (19.21)$$

where

$$R = \frac{D_p}{D_f}. \quad (19.22)$$

Note that all of the equations shown above have been simplified and are only valid for the following typical conditions: $0.005 < \alpha < 0.2$; $0.001\ \text{m s}^{-1} < U_0 < 2\ \text{m s}^{-1}$; $0.1\ \mu\text{m} < D_f < 50\ \mu\text{m}$, and $\text{Re}_p < 1$. Super-



posing all of the aforementioned processes results in a characteristic efficiency curve for the filter. An example is shown in Fig. 19.7; note that the shape of the efficiency curve changes substantially upon increasing or decreasing the air flow rate [19.28].

19.4 Devices and Systems

This section describes applications of sampler configurations (for trace gases and semivolatile compounds) that are currently employed in various monitoring networks to measure specific compounds around the world. In most cases, the selection of a particular sampler is motivated by the specific objectives and purposes of the respective network. In all applications, the choice of sampler involves a compromise where the advantages outweigh the disadvantages, since no sampler is perfect. These imperfections are illustrated in the following examples. Since a large number of devices and systems have been developed for aerosol particle sampling, it is not possible to cover all of these devices and systems fully here, so only selected examples representing the main sampling principles specified in Sect. 19.3.3 are highlighted.

19.4.1 Sampling of Trace Gases

Four different geometries are used for the passive sampling of inorganic gases: badge [19.118], tube [19.34], radial [19.119], and cartridge [19.13]. These geometries determine the specific sampling rate, an important sampler criterion along with the concentration range

and saturation capacity, which are equally important parameters to consider when selecting a sampler. Due to their relatively short diffusion paths, radial and badge samplers have high uptake rates and are preferred in short-term (daily to weekly) sampling or when low analyte concentrations are expected. Tube samplers with longer diffusion paths tend to be chosen for long-term (weekly to monthly) sampling or when there is a high ambient air concentration. Prevailing environmental factors including wind exposure, temperature, and relative humidity also influence sampler selection.

Table 19.2 summarizes the most common passive sampling methods for the time-integrated collection of atmospheric trace gases, focusing on two of the most frequently targeted gases: ammonia (NH_3) and nitric acid (HNO_3). Both of these trace gases play a critical role in atmosphere–biosphere exchange processes, so their concentrations significantly influence air quality and ecological production. While passive NH_3 samplers have been widely developed and used, the passive sampling of HNO_3 has proven to be more difficult. It was first performed successfully in museums [19.136], where a modified sampler with an open-tube design utilized an appropriately impregnated filter to trap the pollutant. Held

Table 19.2 Overview of passive sampling methods for NH₃ and HNO₃; adapted from [19.131]

Type	Dimensions		Inlet	Collection surface	Collection medium	NH ₃ sam- pling rate (mL min ⁻¹)	HNO ₃ Sam- pling rate (mL min ⁻¹)	Comment, Reference
	L (cm)	A (cm ²)						
Ogawa badge	0.6 × 0.79 (25 holes/0.2 cm in diameter)		Open	Glass fiber or cellulose filter on a stainless steel grid	Citric acid	31.2–32.8	–	Protective cover used outdoors [19.79, 120, 121]
Sigma–Aldrich Radiello	1.8 × 25.6 (via 1.6 × 6 cyl.)		Cylindrical micro- porous PE membrane	5.8 × 60 mm adsorbing cartridge	Phosphorous acid	198–235	–	Protective cover used outdoors [19.78, 122]
USDA petri dish	0.12 × 13.7		Zefluor membrane	47 mm nylon filter behind membrane	Nylon	–	179.1 ^a –239.8 ^b	[19.48]
Teflon pack	0.7 × 7.9 ^c		Open	Cellulose 25/47 mm NH ₃ /HNO ₃	Citric acid/NaCl for NH ₃ /HNO ₃	6.6 ^d	12.1 ^d	[19.123]
Palmer diffusion tube	7.1 × 0.95		Open	Stainless steel grids	Sulfuric acid	1.6	–	With protective cover [19.34, 124]
Palmer diffusion tube	3.5 × 0.95		Membrane	Stainless steel grids	Sulfuric acid	3.4	–	With protective cover [19.125, 126]
Blatter diffusion tube	0.7 × 0.64		Open	Absorbent behind Teflon membrane	Ethylene glycol, HCl	114.0	–	Protective cover used outdoors [19.127]
Ferm badge	1.0 × 3.14		Steel grid + Teflon	Whatman 40	Citric acid	39.3	–	[19.38, 128, 129]
Willems badge	0.2 × 5.31		Polytetrafluoroethylene (PTFE) membrane	Glass fiber filter	Tartaric acid	333.3	–	Additional 0.8 cm inlet in front of mem- brane [19.130]
CEH ALPHA	0.6 × 3.46		PTFE membrane	Schleicher and Schuell 595	Citric acid	72.3	–	Protective cover used for outdoor sam- pling [19.131]
CSPSS badge	8.0 × 17.35		PTFE membrane	Absorbent behind PTFE membrane	–	271.7	–	Not tested for NH ₃ ; protective cover needed [19.132]
Krochmal badge	1.0 × 4.91		Polypropylene (PP) membrane	Whatman 1 or stainless steel grids	–	61.5	–	Not tested for NH ₃ [19.133]
UC Davis badge	1.03 × 8.50		Zefluor membrane	Whatman 41	Citric acid	103.5	–	[19.134]
Kasper and Puxbaum	0.90 × 8.04		Teflon membrane	Stainless steel grids	Phosphoric acid	112.0	–	Protective cover used outdoors [19.135]

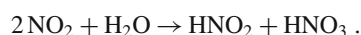
^a Relative to denuders; ^b controlled laboratory environment; ^c assumes 1/3 of filter A; ^d from ppb µg⁻¹ day⁻¹

in position by a stainless steel ring, the filter was placed at the bottom of an inverted glass vial. A fine stainless steel screen protected the open end and suppressed turbulent diffusion inside the vial. Although this sampler was conceptualized for indoor use, outdoor applications of it were also successful as long as the exposure times were short and controlled. The development of designs suitable for long-term outdoor sampling was more difficult. A much improved design employed an aqueous reagent solution of NaCl and glycerin as the impregnating agent on a cellulose filter to collect atmospheric HNO₃ during monthly exposure periods [19.123].

Most of the passive samplers described in the literature and listed in Table 19.2 are planar or axial in shape and have limited sampling rates and sampling capacities. A radial coaxial design, as utilized in the Radiello type employed for NH₃ [19.78], provides an improved geometry that helps to circumvent limitations in sensitivity during short-term sampling (due to improved sampling rates) and long-term sampling (analyte loss due to back diffusion is eliminated due to the high capacity of this technique). This design is superior to planar and axial designs because the NH₃ uptake rate is proportional to the height of the diffusive cylinder and inversely proportional to the logarithm of the ratio of the diffusive to the adsorbing cylinder radii. The radius of the diffusive cylindrical surface can only be determined empirically via exposure experiments, which are yet to be performed successfully for HNO₃ due to difficulties associated with the physical and chemical properties of the microporous layer of the tubular diffusive membrane (distributed via Sigma-Aldrich; more detailed specifications are available from <https://www.sigmaaldrich.com/catalog/product/supelco/rad120?lang=en®ion=US>), Accessed 07 July 2021.

Table 19.3 gives an overview of the most common active sampling methods for the time-integrated collection of HNO₃ and other inorganic gas and aerosol species, along with selected references. The filter-pack method, which usually utilizes Teflon, nylon, or im-

pregnated filters in series, is the least accurate but also the simplest and most commonly used sampling procedure. This technique is labor intensive and suffers from possible interference due to the oxidation of nitrites collected on nylon filters, which positively biases HNO₃ collection. This positive bias was found to be caused by the retention of nitrite (from HNO₂ or NO₂ adsorption) on nylon and the subsequent oxidation of this nitrite to nitrate at almost 100% conversion efficiency during photochemically active sampling periods [19.174]. NO₂ adsorption on nylon involves a heterogeneous surface reaction with H₂O,



This has a removal constant of about $1 \times 10^{-4} \text{ ms}^{-1}$ at a H₂O concentration of 2 vol.%. The Teflon-nylon sampling configuration also suffers from the evaporation of aerosol nitrate from the Teflon front filter [19.137].

Several subsequent studies found that impregnating the surface with sodium carbonate led to similar artifact reactions to those for nylon, albeit with significantly lower reaction rates. This implies that N-containing species (such as NO_x and peroxyacetyl nitrate, PAN) are interfering agents that produce small amounts of nitrite and nitrate on sodium carbonate [19.175, 176]. They also found that the heterogeneous artifact reaction of NO₂ with water vapor contributed to the measured nitrite and nitrate levels, but this contribution was much lower than for nylon. However, based on the penetration efficiency and measured interference from NO₂⁻, NO₂ artifacts occur on both nylon surfaces and Na₂CO₃ coatings and are exacerbated during photochemical smog events, during which up to 100% of the ambient NO₂ may be converted to NO₃ [19.175]. As a consequence, all of the species that are retained on the denuder coating and yield nitrite should be considered potential indirect interferents with the measurement of HNO₃.

In the atmosphere, HNO₃ is mainly formed through the reaction of NO₂ with the hydroxyl radical. Hydrol-

Table 19.3 Overview of active sampling methods for NH₃ and HNO₃; adapted from [19.173]

Method	Measured species	References
Impregnated, Teflon, and nylon filters in series	NH ₃ , HNO ₃ , PM: NH ₄ ⁺ , NO ₃ ⁻ , Cl ⁻ , SO ₄ ²⁻	[19.137–143]
Denuder–filter pack	NH ₃ , HNO ₃ , HONO, HCl, SO ₂ , PM: NH ₄ ⁺ , NO ₃ ⁻ , Cl ⁻ , SO ₄ ²⁻	[19.144–147]
Dry-coated denuder	NH ₃ , HNO ₃ , HONO, HCl, SO ₂	[19.148–150]
Wet effluent denuder	NH ₃ , HNO ₃ , HONO, HCl, SO ₂	[19.151–155]
Parallel-plate denuder	NH ₃ , HNO ₃ , HONO, HCl, SO ₂	[19.156–158]
Thermodenuder	NH ₃ , HNO ₃	[19.159, 160]
Wet annular denuder	NH ₃ , HNO ₃ , HONO, HCl, SO ₂	[19.161–166]
Diffusion scrubber and mist chamber	NH ₃ , HNO ₃ , HONO, HCl, SO ₂	[19.167–172]

ysis reactions involving N_2O_5 and NO_3 radicals also yield HNO_3 , as do NO_2 and NO_3 reactions with O_3 and certain non-methane hydrocarbons (NMHC). All of these reactions may also take place heterogeneously on reactive surfaces such as nylon or surfaces impregnated with sodium carbonate.

Various intercomparison experiments [19.177–179] have revealed significant discrepancies between different HNO_3 measurement techniques, emphasizing the need for artifact-free measurement methods to accurately determine HNO_3 and particulate nitrate in the atmosphere. The approach most widely used to sample a gas in the presence of corresponding aerosol particles is the denuder technique. Dry-coated denuders are reliable but labor intensive and provide only long-term average concentrations (for periods on the order of 24 h) [19.180]. These drawbacks have been overcome by various other developments. Four different designs of systems in which wet effluent diffusion denuders with continuously renewed collection surfaces are coupled to ion chromatography (IC) were developed [19.151]. Efficient retention of trace gases and measurements with high time resolution may be achieved by coupling parallel-plate denuders to online analysis. Another development yielded an automated thermodenuder system for the determination of NH_3 in ambient air [19.159]. A device that enjoys some popularity is the wet annular denuder (WAD), in which near-quantitative collection efficiencies are achieved at high sampling rates in a compact design [19.180]. The continuously rotating WAD is an improvement of the original WAD design [19.162]. Diffusion scrubber and mist chamber techniques also provide measurements with high time resolutions and low artifact sensitivities.

In 2007, the mist chamber technique was employed for the first time to measure water-soluble organic gases (WSOGs) and the impact of particle-bound liquid water on the partitioning of water-soluble organic carbon (WSOC) during the summer in Atlanta, Georgia [19.181]. Their results indicated that partitioning to liquid water may significantly contribute to the formation of secondary organic aerosol and fine PM observed in urban regions with high biogenic emissions (such as Atlanta in the summer). WSOGs were measured with a mist chamber [19.182] that collected organic gases with an effective Henry's law constant $K_H \gtrsim 10^3 \text{ M atm}^{-1}$ [19.183], where M is moles per liter (mol L^{-1}). Filtered sample air entered a glass mist chamber at a flow rate of ≈ 20 LPM. The chamber was initially filled with 10 mL deionized water (DIW) and fitted with a hydrophobic Teflon filter at the chamber exit to enable the DIW to be refluxed. The same technique was employed in a 2012 field study performed in the River Po valley in Italy to measure water-soluble

products from the gas-phase oxidation of VOCs that can partition into atmospheric waters, where they are further oxidized to form low-volatility products [19.184]. These products can remain in the particle phase after water evaporation, forming what is termed aqueous secondary organic aerosol (aqSOA). Duncan et al. [19.185] found that WSOG concentrations in indoor environments were significantly (15 times) higher than those outdoors, implying that surface chemistry significantly affects indoor exposure, although little is known about individual WSOG compounds, their kinetics, and the fate of aqueous products.

During the last two decades, filter-based methods have been replaced with continuous denuder devices and optical measurement techniques that are limited to measuring just one compound or species in a particular physical state (i.e., either a gas or a particulate/droplets). These techniques have evolved into samplers that combine aqueous-phase aerosol collectors with the denuder technique for the simultaneous collection of gas and particulate species. During the USEPA-sponsored Atlanta Super Site Experiment in 1999 [19.186], a breakthrough was made in the development of new semicontinuous aerosol measurement techniques with online IC analysis of the resulting aqueous solution.

19.4.2 Sampling of Semivolatile Substances

While the particulate fraction is collected on a filter, the gaseous mass fraction of the semivolatile trace substance may be collected through irreversible sorption to a filter, a coated wall (denuder), or a polyurethane foam plug.

Filter Packs Used With or Without Denuders

The N(III) species ammonia and ammonium (a cation) as well as the N(V) species nitric acid and nitrate (an anion) can be sampled differentially using denuders in combination with a filter pack, with the latter positioned downstream. While the gaseous mass fraction can be accessed using the denuders (with a selective coating), the particulate mass fraction is derived by subtracting the gaseous fraction from the total [19.187, 188] (Fig. 19.8). The use of denuders in combination with filters is uncommon for organics but has been found to be suitable for semivolatile PAHs with high vapor pressures (up to four-ring PAHs [19.189, 190]). The blow-off from quartz and Teflon filters can be collected on a second (backup) quartz filter [19.191].

Sampling Trains with a Filter and Adsorbent

The differential sampling of organics is commonly achieved using a filter in combination with a down-

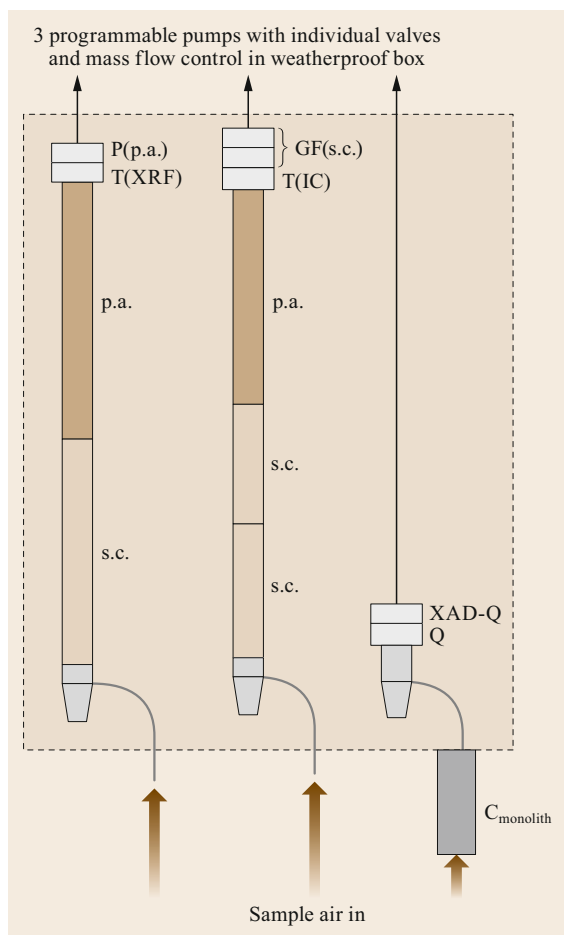


Fig. 19.8 Schematic design of sampling trains including denuders and downstream front and backup filters (p.a. phosphoric acid coating, s.c. sodium carbonate coating, XAD – XAD-4, a porous, macroreticular, nonpolar, polystyrene-divinylbenzene resin with a high specific surface area of $725 \text{ m}^2 \text{ g}^{-1}$). Adapted from [19.192] with permission from John Wiley & Sons, Inc. T(XRF) Teflon filter for x-ray fluorescence analysis upstream of P(p.a.), a p.a.-coated paper filter, in channel 1, T(IC) Teflon filter for ion chromatographic analysis upstream of GF (s.c.), two stacked glass fiber filters coated with s.c., in channel 2, and a quartz fiber filter Q upstream of a XAD-coated quartz fiber filter XAD-Q

stream adsorbent in a glass cartridge (Fig. 19.9). Glass and quartz fiber filters are most common. An oxidant denuder may be employed upstream to prevent oxidative loss during sampling (Fig. 19.9). Polyurethane foam (PUF) is most suitable for apolar and lipophilic organic gases. The specific surface area of PUF is $\approx 0.005 \text{ m}^2 \text{ g}^{-1}$, and its density is $20\text{--}30 \text{ g L}^{-1}$ [19.83]. The PUF material utilizes both adsorption (which depends on the vapor pressure) and

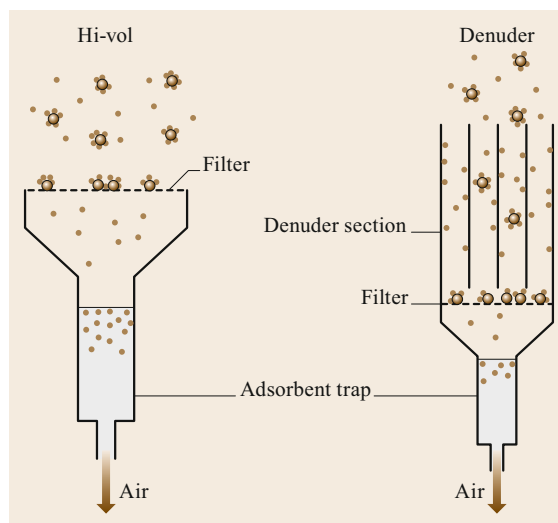


Fig. 19.9 Schematic design of sampling trains that include a filter and adsorbent. High-volume (Hi-vol) sampling occurs typically at flow rates between 200 and 1000 LPM, whereas Denuder sampling is realized at 10 to 200 LPM. (after [19.83] with permission from the American Chemical Society)

absorption (which depends on the PUF–air partitioning coefficient) mechanisms for retention [19.193]. Eventual breakthrough can be controlled by installing a series of plugs [19.194].

Organics that are more polar can be sorbed to XAD. A combination of PUF with XAD-2 or XAD-4 has also been successfully used for pesticides and other more polar target substances [19.51, 195–197]. The specific surface area of XAD is very large: $300\text{--}600 \text{ m}^2 \text{ g}^{-1}$. XAD-2 is a finely ground, porous, macroreticular, nonpolar polystyrene-divinylbenzene resin. To probe a wide spectrum of SVOC classes, mixed sorbent cartridges (e.g., PUF-XAD-2) are used for active sampling and sorbent-impregnated (SIP) PUF disks are employed for passive sampling [19.52, 194].

19.4.3 Sampling of Aerosol Particles

The sampling of aerosol particles requires an inlet setup that draws in the particle-laden air from the environment of interest (e.g., the atmosphere or indoor air) and transports it to the sampling device(s) through a tubing system. Typical components of an ambient aerosol inlet are the *aerosol inlet head* (which often has an impactor or cyclone to define an upper size cutoff or *cut-point*), smooth transport *tubes* made of conductive material (typically stainless steel with smooth inner surfaces), a *dryer* to control the humidity of the sample air (e.g., via diffusion, dilution, or heating), and an (isokinetic) *flow splitter* to distribute the sample air among several

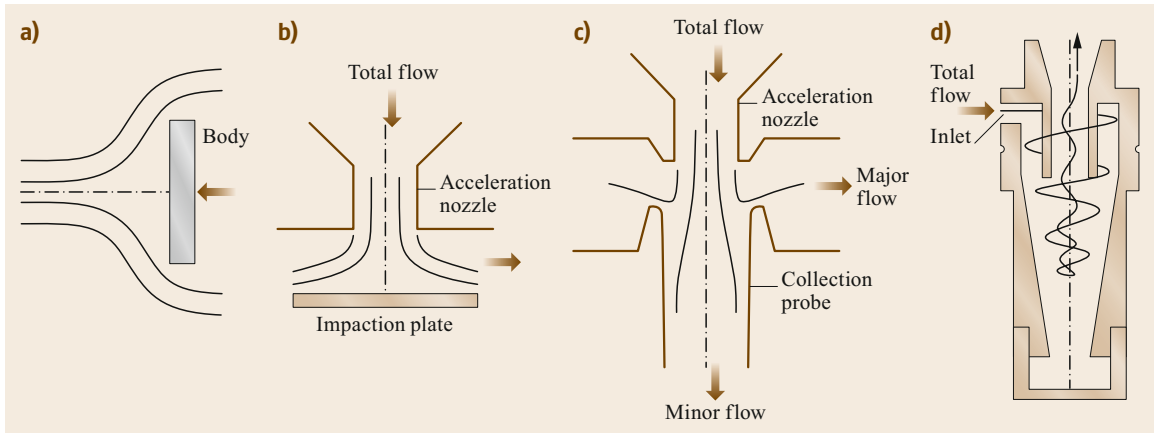


Fig. 19.10a–d Schematics showing the designs of the main types of inertial classifiers: (a) body impactor, (b) conventional impactor, (c) virtual impactor, and (d) cyclone (after [19.89] with permission from John Wiley & Sons, Inc.)

samplers and/or instruments running in parallel [19.19]. Careful design and validation of the inlet system is as crucial to ensuring representative aerosol sampling as the choice of sampling device. The design and construction of inlets for some applications can be challenging (e.g., in tall tower observatories [19.198]) and technically complex (e.g., for aircraft sampling [19.199, 200]). In addition to the design of the setup, the operational settings for the sampling need to be adapted to the targeted size spectrum and the environmental conditions. For example, sampling in fast-moving air should be *isokinetic* (i.e., there should be the same air velocity inside and outside the inlet tube) and *isoaxial* (i.e., the inlet tube should point into the wind) to ensure representative coverage of larger particles, which are prone to inertia-related artifacts. Isokinetic aerosol sampling is particularly challenging on aircraft due to the very high and variable air velocities involved [19.201, 202]. Moreover, *laminar flow* conditions are used in the inlet tubes in most sampling applications, although *turbulent* sampling may also be suitable in certain contexts (see also Sect. 19.6.3). Detailed overviews of inlet construction, validation, and operational settings can be found elsewhere [19.19, 104, 203].

The following section summarizes key aspects of the design and operation of aerosol sampling devices and systems. These aspects are grouped into the following categories:

1. inertia-based particle size separation and sampling,
2. diffusion-based and thermophoretic sampling,
3. particle migration and deposition in gravitational and electric fields, and
4. filter sampling.

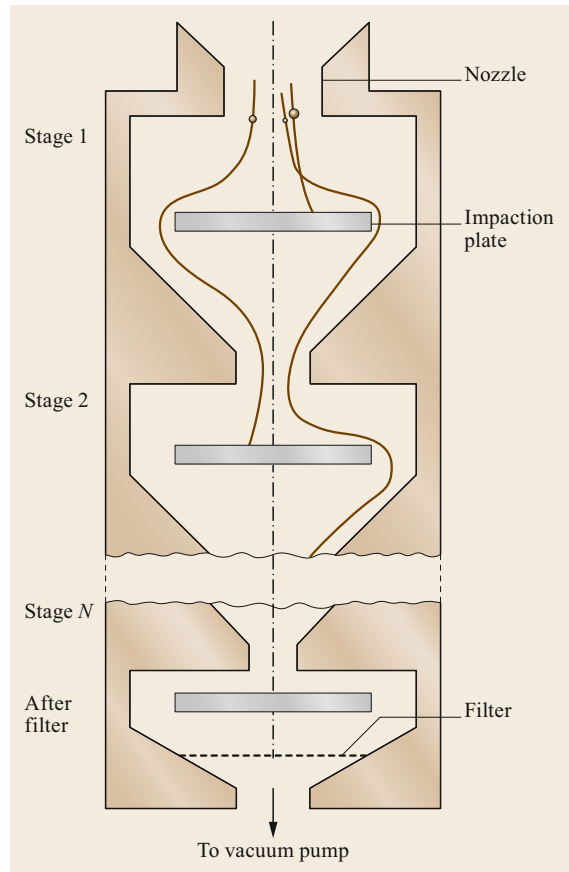


Fig. 19.11 Schematic of a cascade impactor. Moving downstream from stage to stage, the velocity of the accelerated sample air increases and the diameters of the collected particles decrease (after [19.89] with permission from John Wiley & Sons, Inc.)

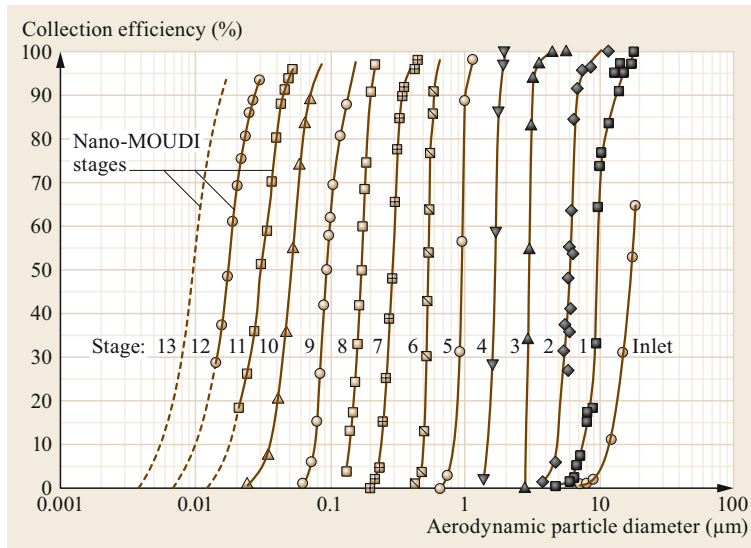


Fig. 19.12 Particle collection efficiency for a micro-orifice uniform deposit impactor (MOUDI) that includes nano-MOUDI stages (after [19.89] with permission from John Wiley & Sons, Inc.)

Inertia-Based Particle Size Separation and Sampling

Inertia-based aerosol samplers have become widely used and almost indispensable tools in atmospheric science. The main types of inertial classifiers are body impactors, conventional impactors, virtual impactors, and cyclones (Fig. 19.10) [19.61, 89].

Body impactors, which are comparatively simple inertial classifiers, either swirl an impaction surface through the air or draw the air past the impaction surface [19.89, 204, 205]. As a result, large particles (typically $\gg 1 \mu\text{m}$ in size) cross the air streamlines around the obstacle in the fluid and strike the impaction surface (e.g., cylinders, ribbons, or slides). The collection efficiency and size cut-point depend on the sizes of the obstacle and particles and the relative velocity of the particles with respect to the obstacle. The main advantages of body impactors are relatively simple handling and the ability to operate them without sample air transport through inlets (thus circumventing the associated aspiration and tube transmission losses of large particles). One example is a rotating arm impactor called the Rotorod[®] (manufactured by IQVIA[™]), which has a rapidly rotating sampling head (2400 rpm) and two plastic rods (1.5 mm by 23 mm) that act as impaction surfaces and are coated with a sticky grease [19.206]. The Rotorod probes $\approx 120 \text{ L min}^{-1}$, and the particles collected on the rods are analyzed via microscopic identification and quantification [19.206]. Rotorod impactors and samplers with comparable designs are routinely used in bioaerosol sampling and aeroallergen monitoring (i.e., pollen and spores) [19.206–208].

Conventional or jet impactors accelerate the sample air through a nozzle perpendicularly towards a flat

impactor surface, which redirects the particle-laden air flow while collecting particles above a certain inertia threshold. Conventional impactors are widely used in aerosol sampling, and there are numerous impactor designs [19.61, 89]. The designs can differ in terms of the geometry of the nozzles (i.e., circular, rectangular, or slit), the number of nozzles (single vs. multiple), single-stage vs. cascade configuration, low-pressure designs, and low- vs. high-volume operation [19.96, 210–212]. The simplest design is a single-nozzle, single-stage impactor that classifies particles into two size fractions. Impaction theory has established design guidelines that allow the prediction and attainment of a sharp particle cut-point (D_{50}) at a precisely known aerodynamic diameter (D_a) [19.90, 210]. For instance, Fig. 19.11 shows the scheme of a cascade impactor with several classification stages. Every stage is characterized by a specific nozzle-to-impaction plate configuration, which defines its collection efficiency and D_{50} . At each stage, particles with $D_a > D_{50}$ are collected, whereas particles with $D_a < D_{50}$ follow the air streamlines and are passed on to the subsequent stage(s). A widely used cascade impactor for which different models are commercially available is the micro-orifice uniform deposit impactor (MOUDI, MSP Corp., Shoreview, USA) [19.89]. The characteristic collection efficiency curves of the 13 MOUDI classification stages are shown in Fig. 19.12. Its wide accessible particle size range and sharp cut-point characteristics make the MOUDI a valuable tool for highly size-resolved aerosol sampling. The particles, which are deposited on dedicated substrates (e.g., filters, aluminum foil, or glass slides) placed on the impaction plates, are then available for subsequent analysis using a variety of methods [19.7,

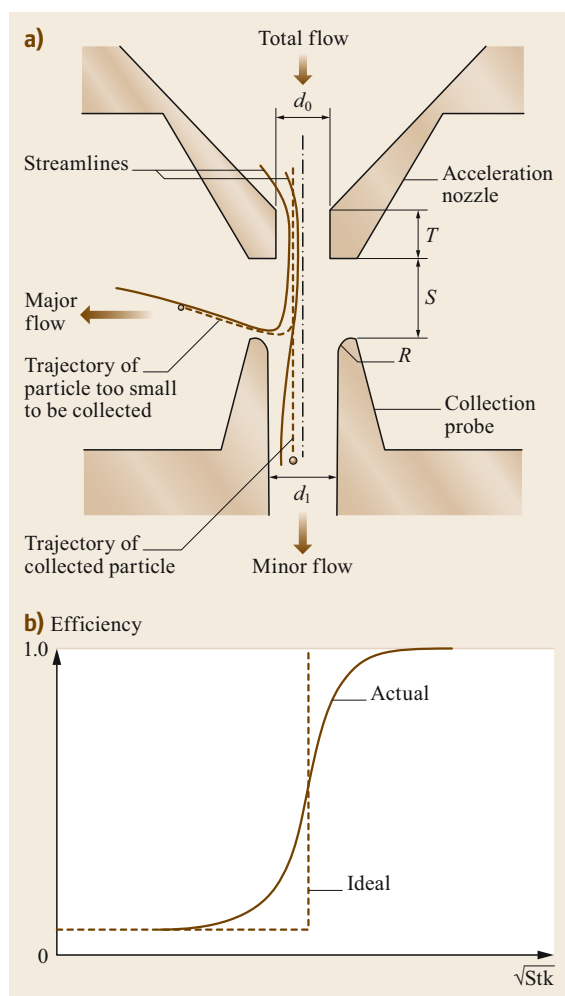


Fig. 19.13 (a) Schematic of a virtual impactor and (b) its particle collection efficiency curve. The overall performance of a virtual impactor (i.e., minimal losses of small particles to the major flow and large particles to the minor flow) is defined by several design parameters, such as the nozzle diameter D_{nozzle} , the dimensionless jet-to-collection probe distance S/D_{nozzle} , the dimensionless nozzle throat length T/D_{nozzle} , the collection probe diameter D_1 , and the collection probe design and symmetry (see (a)) [19.101, 209] (after [19.89] with permission from John Wiley & Sons, Inc.)

213–215]. Note that the relationship between particle rebound at the impaction stages and particle phase state is a major issue in impactor operation, as it can cause substantial size classification biases [19.216]. Particle rebound minimization is addressed in more detail in Sect. 19.6.3. A special form of impaction after air acceleration through a jet is realized in liquid impingers, which collect aerosol particles (mostly bioaerosols) in a liquid (e.g., a buffer) via inertia [19.217].

Virtual impactors are closely related to conventional impactors except that a collecting probe (i.e., a tube that receives the particle-laden air) is employed instead of an impaction plate [19.89, 101, 218]. The scheme in Fig. 19.13a illustrates a typical virtual impactor design. A *minor flow* penetrates into the collecting probe and then follows relatively straight air streamlines in the direction of acceleration of the air through the nozzle, whereas a *major flow* is deflected sideways along a curvilinear flow pattern, typically due to vacuum pumping. Large particles with $D_a > D_{50}$ cross the streamlines due to their high inertia and continue their straight motion into the collecting probe. Smaller particles with $D_a < D_{50}$ tend to follow the air streamlines and thus the major flow perpendicular to the receiving tube. The collection efficiency curves of virtual impactors can be as sharp as those of conventional impactors. However, in a virtual impactor, some particles with $D_a < D_{50}$ remain in the minor flow, so the efficiency curve converges to a finite value that is larger than zero (Fig. 19.13b). The fraction of small particles in the minor flow corresponds to the ratio of the minor flow rate to the major flow rate ($Q_{\text{minor}}/Q_{\text{major}}$). In contrast to body and conventional impactors, the particles in both size fractions remain airborne. As an example, a high-volume (500 L min^{-1}) dichotomous virtual impactor with a single accelerating jet classifies the particles into a coarse size fraction with $D_a \gtrsim 2.5 \mu\text{m}$ and a fine size fraction with $D_a \lesssim 2.5 \mu\text{m}$ [19.219]. After classification, the airborne particles in the major flow and/or minor flow can be analyzed online using instrumentation, directed into further classification devices, or collected on filters [19.220–222]. Virtual impactors can also be used to concentrate airborne particle fractions for subsequent analysis [19.223].

Marple and Olson [19.89] concisely summarized that

in a cyclone, a jet of air impinges tangentially on the inner surface of a cylinder and then swirls downward in a cyclonic fashion inside the cylinder, and into a conical section. In the conical section the air reverses direction and spirals upward [...] to the centrally located exit tube [...]

(see Fig. 19.14a). Particles with D_a above the cyclone cut-point cross the streamlines of the swirling air motion and tangentially strike the inner cyclone walls (Fig. 19.14b). Cyclones are available in a wide range of designs (e.g., cascade configurations), and have been used in a broad spectrum of applications [19.226–228]. Theoretical treatments of air and particle motions inside a cyclone are more demanding than for impactors [19.103, 224, 229]. In aerosol sampling, a cyclone is routinely used as a preclassifier to collect a specific particle size range (e.g., the respirable fraction)

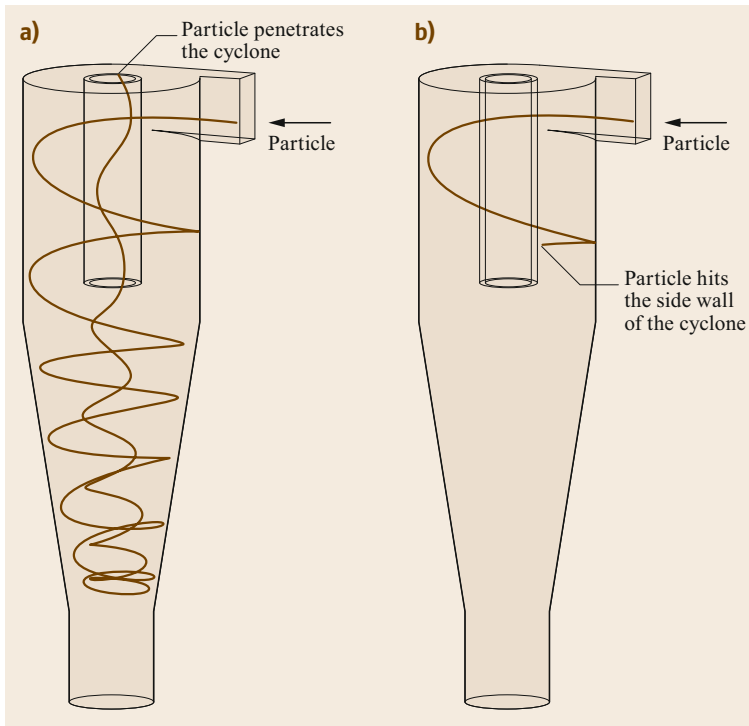


Fig. 19.14a,b Particle trajectories inside a cyclone. **(a)** A particle with $D_a < D_{50}$ follows a swirling trajectory and exits the cyclone. **(b)** A particle with $D_a > D_{50}$ crosses the swirling air streamlines and strikes the cyclone wall (after [19.224] with permission from Elsevier)

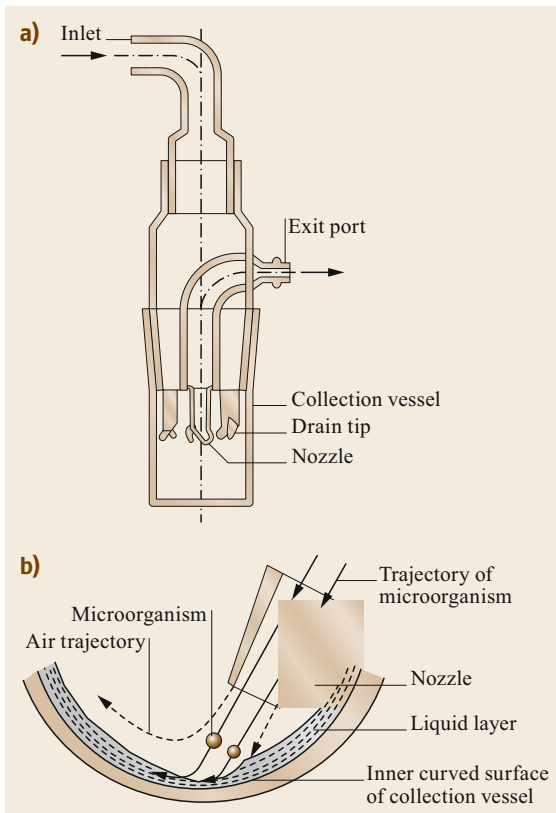


Fig. 19.15a,b Schematic of the BioSampler. **(a)** General design. **(b)** Collection mechanism (after [19.225] with permission from Taylor and Francis) ◀

before a filter sampler [19.230]. In such applications, it is the particle fraction with $D_a < D_{50}$ that remains airborne and is used for subsequent collection and analysis. There are also cyclone designs that collect the large particle fraction with $D_a > D_{50}$ for subsequent analysis. Such wetted wall cyclones that drive the particles into a liquid film are known as tangential impingers, and are widely used in bioaerosol sampling [19.111, 225, 231]. As an example, the BioSampler (SKC Inc., Eighty Four, USA) has become a widely used tangential impinger (Fig. 19.15). Its design utilizes three nozzles to swirl the collection fluid (e.g., a saline solution or buffer) in the collection vessel and propel bioaerosol particles larger than the cut-point at the wetted walls [19.225]. The resulting particle suspension in the collection fluid is available for subsequent analysis [19.232, 233].

Diffusion-Based and Thermophoretic Sampling

Devices that rely on particle separation based on diffusion mobility (i.e., particle diffusion and deposition on surfaces) are used routinely in aerosol sampling. *Diffusion batteries* and *diffusion denuders* are relevant sampling devices in this context. Diffusion denuders—

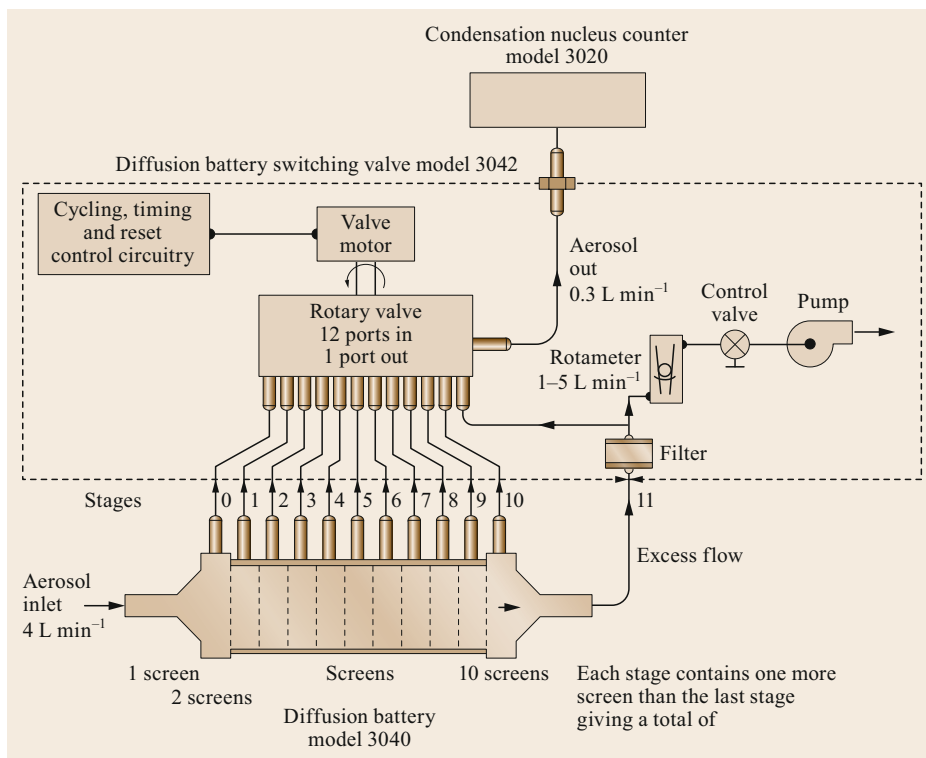


Fig. 19.16 Scheme of a typical ten-stage diffusion battery for the determination of the aerosol particle size distributions in the fine and ultrafine size ranges (after [19.29] with permission from John Wiley & Sons, Ltd.)

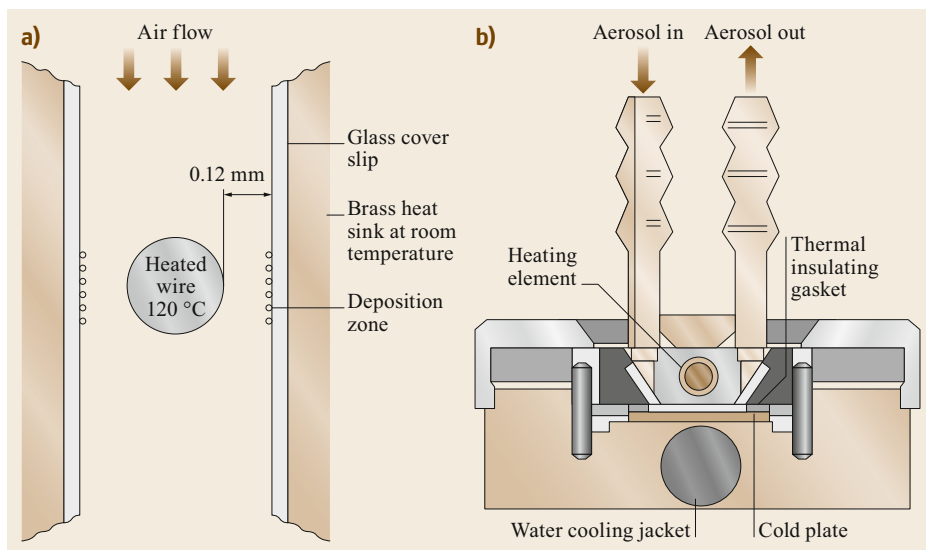


Fig. 19.17a,b Examples of thermal precipitator design. (a) Cross-sectional schematic of a heated wire thermal precipitator (after [19.28] with permission from John Wiley & Sons, Inc.) (b) A more modern thermal precipitator design with heating and cooling of the opposite surfaces to enhance the thermal gradient and the precipitation efficiency (after [19.234] with permission from Taylor and Francis)

which remove specific gases from the sample air without affecting the particle phase (see also Sect. 19.4.1)—are applied, for instance, to account for semivolatiles

that are in aerosol particles but evaporate during the sampling process (see also Sect. 19.6.3) [19.18]. Various designs of diffusion batteries (i.e., tube bundles,

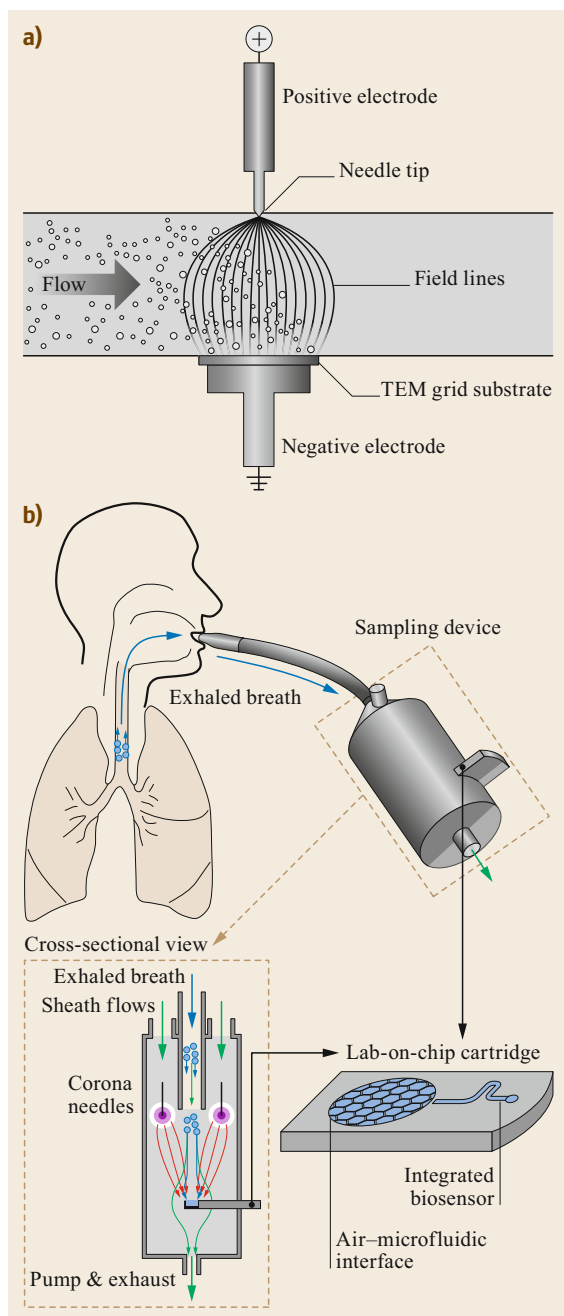


Fig. 19.18a,b Electrostatic precipitator designs. **(a)** Scheme of a point-to-plate electrostatic precipitator for depositing aerosol particles onto electron microscope substrates (a TEM grid here) (after [19.235] with permission from Taylor and Francis). **(b)** Example of a specialized application of an electrostatic precipitator in the analysis of exhaled-breath aerosol, which is enriched via electrostatic deposition at an air–liquid interface on a lab-on-chip cartridge (after [19.236] with permission from Elsevier)

parallel plates, screens, or meshes) can be used to determine the size distribution of aerosol particles that are $\lesssim 0.1 \mu\text{m}$ in size [19.28, 237]. In practice, measurement of the penetration P (i.e., the fraction of the particles that enter the diffusion battery that also exit it) allows the diffusion coefficients and corresponding sizes of the analyzed aerosol population to be determined. By operating multiple units in parallel, as illustrated in Fig. 19.16, the particle size distribution can be obtained through complex data inversions [19.238, 239]. However, there are significant limitations on the quality of the data obtained [19.18]. Detailed information on the design, operation, and performance of diffusion batteries can be found elsewhere [19.238, 240]. Diffusion batteries were widely used prior to the development of online instrumentation for ultrafine particle detection (i.e., electrostatic classification), when aerosol particle sizing $< 100 \text{ nm}$ was particularly challenging [19.238]. However, advanced diffusion battery designs are currently being applied in specific applications as they provide operational advantages over other analytical approaches (e.g., high time resolution, robust operation, and a compact design) [19.241–243].

The instruments based on thermophoresis, *thermal precipitators*, are well-established samplers for collecting rather small amounts of particles in the fine and ultrafine size ranges on dedicated substrates (e.g., glass slides or electron microscope grids), mostly for subsequent light or electron microscopic analysis [19.244, 245]. In a typical design, large temperature gradients (typically 10^4 – 10^5 K m^{-1}) are created within small distances between the heat source and the deposition surface [19.234, 246]. The particles are deposited on the colder surface in the periphery of the heat source, such as a heated wire (Fig. 19.17a). In aerosol sampling, thermal precipitators show several operational advantages, such as robust and inexpensive designs, high collection efficiencies, and low flow rates. They have been widely used as personal samplers in occupational monitoring [19.65, 247]. As an example, a recent design for collecting particles $< 100 \text{ nm}$ in size is shown in Fig. 19.17b [19.234].

Particle Migration and Deposition in Gravitational and Electric Fields

The controlled deflection of aerosol particles in electric fields, which is particularly efficient for the ultrafine size range, is a fundamental principle in aerosol science as it provides the basis for widely used online instruments such as differential mobility analyzers and electrostatic precipitators for particle collection [19.113]. Electrostatic precipitators utilize two main processes: first, charging/ionization beyond the natural charge state of the particles; second, the deposition of the particles on a substrate in a strong electric field. In the design

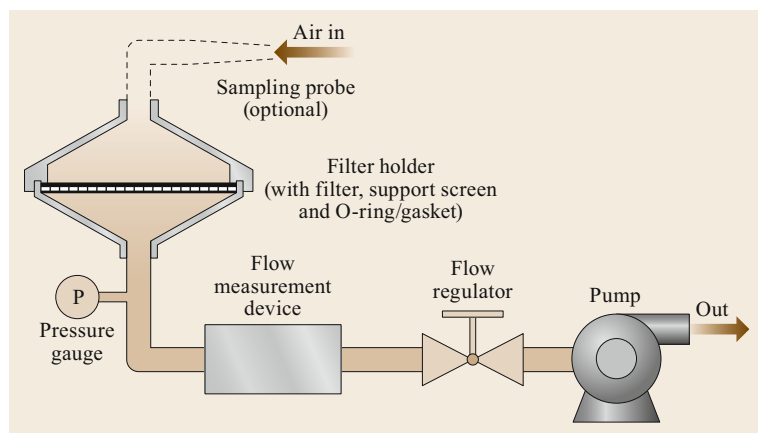


Fig. 19.19 Schematic of a filter collection system typically used for aerosol measurement, comprising a filter holder with a filter medium, a gas flow measurement and control system (e.g., a gas flow meter and a needle valve or gas flow controller), and a pump (after [19.116] with permission from John Wiley & Sons, Inc.)

of so-called point-to-plate precipitators (Fig. 19.18), both processes occur in the same step in a strong electric field (several kV) with corona discharges between a corona needle and the substrate [19.235, 248]. In different designs, the charging and precipitation regions are separated [19.249–251]. Since electrostatic precipitator samples are often used in microscopic analyses (e.g., to retrieve particle size distribution), spatially uniform and representative deposition without a strong size bias is a particularly important performance characteristic [19.252]. Various mobile versions of electrostatic samplers are available [19.235, 250]. Furthermore, dedicated electrostatic precipitators have been used to collect bioaerosols on agar plates, which has the major advantage that the deposition is comparatively gentle, so it conserves organism viability [19.253, 254].

Gravitational deposition has been used for the passive sampling of supermicrometer particles. Most applications of this technique have been from the field of bioaerosol sampling [19.54, 255]; however, coarse-mode mineral dust and sea spray aerosols have also been collected via sedimentation [19.256]. Gravitational sampling is simple and cheap but suffers from several drawbacks, as it is very sensitive to particle size and aerodynamic properties as well as to wind speed and turbulence. Hence, it is prone to sampling bias and a lack of reproducibility. One such device is the so-called Wagner–Leith passive sampler, which is used to collect samples for electron microscopy [19.108, 109]. In this technique, gravitational deposition can be used as an approximation for the overall deposition velocity, although inertial and diffusional processes also provide certain contributions.

Filter Sampling

Filter sampling is the most widely applied method to collect aerosol particles for the subsequent analysis of particle properties such as mass (via gravimetry [19.257]), chemical or isotopic composition (e.g., via spectroscopy, chromatography, mass spectrometry, etc. [19.258, 259]),

taxonomic diversity of bioaerosols (e.g., genome sequencing [19.260]), and for multiple further types of analysis. Filter sampling has the advantages that it is simple, inexpensive, and can be flexibly adapted to the specific requirements of the laboratory analysis (e.g., by adjusting flow rates and sampling times, choosing appropriate filter sizes and materials, and combining it with virtual impactors or cyclones for size fractionation). A scheme of a typical filter sampling setup is shown in Fig. 19.19, and details about the wide range of frequently used systems can be found elsewhere [19.116, 261]. Of central importance is the choice of filter type and material, which has to be adjusted to the intended laboratory analysis. An overview of filter materials, their physical and chemical properties, and their compatibilities with laboratory analysis methods is provided elsewhere [19.261]. Filter characteristics that should be considered when choosing appropriate filters are

1. the particle sampling efficiency,
2. the mechanical, chemical, and temperature stabilities,
3. the blank concentrations of the species of interest,
4. flow resistance and loading capacity, and
5. cost and availability [19.261].

19.4.4 Comparison of the Methods

The major advantages and disadvantages of the various sampling devices and systems highlighted in Sects. 19.4.1–19.4.3 are summarized in Table 19.4. Note that this overview is rather generalized and, in places (i.e., for aerosol particle sampling), simplified, as the advantages and disadvantages strongly depend on the specific requirements of the laboratory analysis of the samples after collection. In fact, some cases may even be ambivalent, since certain aspects of a sampling method may be advantageous in one application and disadvantageous in another.

Table 19.4 Advantages and disadvantages of the different sampling devices and systems

Devices	Advantages	Disadvantages
Sampling of trace gases		
Active	Control over sample volume Artifact correction	Needs electricity Potentially large artifacts under polluted conditions
Passive	Simple, economical, small footprint No electricity required	Uncertain sample volume Prone to artifacts
Sampling of semivolatile substances		
Filter and denuder	Laborious wet chemical technique	Limited mass flow, no high-volume sampling For many substance classes there is no suitable denuder coating available Ultrafine particles (with nonzero sampling efficiencies) are partly misattributed to the gaseous fraction
Filter stack	Simple	Limited mass flow, no high-volume sampling Gas-phase collection limited to acids and bases
Filter and cartridge with sorbent foam plug or sorbent resin	High-volume sampling possible	Limited to hydrophobic and moderately polar trace gases
Sampling of aerosol particles		
Body impactors	Simple operation Collection of coarse particles without inlet lines and associated losses	Low collection efficiencies for fine particles Limited applications
Conventional impactors	Flexible design for many applications Well-defined and sharp size cut-points	Biases from particle rebound Harsh deposition may alter particle morphology and bioaerosol viability
Cascade impactors	Flexible design for many applications Well-defined and sharp size cut-points Coverage of (almost) entire particle size distribution	Biases from particle rebound Harsh deposition may alter particle morphology and bioaerosol viability
Virtual impactors	Flexible design that can be used in combination with many other devices/instruments Particle fractions above and below the cut-point remain airborne for subsequent analysis Application as aerosol concentrator	Some of the particles below the cut-point remain in the minor flow
Cyclones	Flexible design can be used in combination with many other devices/instruments Wetted wall cyclones allow soft bioaerosol collection	Theory of air and particle motions is more demanding than for impactors
Diffusion batteries	Simple and compact design, robust operation Collects ultrafine particles Allows size distribution to be retrieved	Complex data inversions Large uncertainties in results Decreasing collection efficiencies with increasing particle size
Thermal precipitators	Simple, small, robust, and inexpensive design High collection efficiencies for ultrafine particles Low flow rates	Decreasing collection efficiencies with increasing particle size
Electrostatic precipitators	Simple and small High collection efficiencies for ultrafine particles Allows soft bioaerosol collection	Collection efficiency decreases with increasing particle size Deposition is often nonuniform Size distribution is potentially biased
Gravitational samplers	Simple passive sampling No electricity required	Low collection efficiencies for fine and ultrafine particles Prone to sampling biases and a lack of reproducibility
Filter samplers	Simple, flexible, and applicable in various settings Inexpensive and efficient collection over the entire particle size range	Filtration theory is complex

19.5 Specifications

Table 19.5 summarizes the specifications and selected technical details of the trace gas, semivolatile substance, and aerosol particle sampling methods presented above. Since the set of sampling methods presented is very diverse, specifications that are of broad interest (e.g., collected species, sampling times, and flow rates) are summarized. Also note that the experimental uncertainties and errors largely depend on the laboratory analysis of the samples after collection, so

they vary from case to case. To illustrate this case-specific uncertainty, note that cell viability and integrity are important aspects of bioaerosol analysis, but these two parameters may be altered substantially by various sampling methods, such as impaction on solid surfaces with strong desiccation during filter sampling. Accordingly, harsh sampling conditions can lead to major uncertainties in bioaerosol studies, but they are much less significant when sampling nonbiological materials.

Table 19.5 Specifications of and selected technical details for different air sampling methods

Method	Sampling principle and collected species	Operational details (e.g., sampling time/time resolution and flow rates)	Experimental uncertainties and errors
Sampling of trace gases			
Passive	Mostly NH ₃ , HNO ₃ ; less often O ₃ , SO ₂ , CO	Weeks to months Flow rates assumed from diffusional properties	Uncertain sample volume Biased by unquantifiable artifacts
Active	NH ₃ , HNO ₃ , HONO, HCl, SO ₂	Hours to days Controlled flow rate Artifact correction possible	Limited denuder capacity causes breakthrough under certain environmental conditions
Sampling of semivolatile substances			
Filter and denuder	Active Filtration and molecular diffusion followed by an irreversible chemical reaction or sorption	Sampling times: min to h Flow rates: L min ⁻¹	Due to a nonzero sampling efficiency for ultrafine particles, some of these particles are misattributed to the gaseous fraction
Filter stack	Active Filtration, irreversible adsorption	Sampling times: min to h Flow rates: L min ⁻¹	
Filter and cartridge with sorbent foam plug or sorbent resin	Active Filtration, irreversible adsorption	Sampling times: min to h Flow rates: L min ⁻¹ to m ³ min ⁻¹	Sampling artifacts are unavoidable for several substance classes (blow-on, blow-off)
Sampling of aerosol particles			
Inertia-based	Active Deflection of particle-laden air with inertia-driven deviation of particle motion from air streamlines Particle size range: mostly (but not exclusively) $D > 0.5 \mu\text{m}$	Sampling times: min to h Flow rates: L min ⁻¹ to m ³ min ⁻¹ Impactor deposition on 1 to > 10 stages Diverse substrates: e.g., metal foil, glass slides, Si wafers	Particle rebound For microscopy: high substrate loadings create coincidental internal particle mixtures For microscopy: particle morphology altered For bioaerosol analysis: decreased cell viability and altered cell integrity
Diffusion-based	Active Molecular diffusion followed by irreversible adsorption Particle size range: mostly $D < 0.1 \mu\text{m}$	Sampling times: min to h Flow rates: L min ⁻¹ Substrates: tube bundles, parallel plates, screens or meshes	For size distribution retrieval: uncertainties from data inversion
Thermophoretic	Active Diffusion along temperature gradient (10^4 – 10^5 K m^{-1}) followed by irreversible adsorption Particle size range: mostly $D < 1 \mu\text{m}$	Sampling times: min to h Flow rates: L min ⁻¹ Substrates: e.g., glass slides	For microscopy: size biases
Gravitational	Passive Gravitational settling on substrate Particle size range: $D > 1 \mu\text{m}$	Sampling times: h to d Substrates: e.g., glass slides, Si wafers, also agar plates	Large uncertainties due to high dependence on wind speed, particle properties, etc. Sample aging during long sampling runs (days)

Table 19.5 (Continued)

Method	Sampling principle and collected species	Operational details (e.g., sampling time/time resolution and flow rates)	Experimental uncertainties and errors
Sampling of aerosol particles			
Electrostatic	Active Migration in electric field (kV) and deposition on substrate Particle size range: most efficient for $D < 0.1 \mu\text{m}$	Sampling times: min to h Flow rates: L min^{-1} Substrates: e.g., TEM grids	For microscopy: size biases
Filtration	Active Filtration (a combination of diffusional and inertial deposition and interception) Entire particle size range	Sampling times: min to d Flow rates: L min^{-1} to $\text{m}^3 \text{min}^{-1}$ Substrates: porous membrane, pore membrane, and fibrous filters	Blank concentrations of species of interest Sample aging during long sampling runs (days)

19.6 Quality Control

Quality assurance and quality control (QA/QC) are key to ensuring high-quality, reliable sampling and measurement results. The following sections emphasize specific QA/QC aspects of sampling procedures for trace gases, semivolatile substances, and aerosol particles. A detailed overview of QA/QC practices in atmospheric science can be found in Chap. 5.

19.6.1 Sampling of Trace Gases

A valuable QA/QC approach when using passive gas samplers is to collocate two or three samplers at the same site to achieve precise estimates. For active gas samplers, flow control using a critical orifice or temperature-compensated mass flow control ensures accurate measurement of the sample volume. The use of dry gas meters also increases the reliability of the determined sample volume. The treatment of field blanks—samples that accompany the actual sample media (passive sorbents or active denuders) from the lab into the field and back—can be used to determine the overall detection limit of the method employed for passive or active sampling. The capacity of the denuder for the sampled analyte can be estimated from the surface area and the amount of sorbent dissolved in the coating solution, and the maximum operating time of the denuder (i.e., the amount of time that the denuder can operate before the active surface sites on its walls become exhausted and species breakthrough occurs) can be gauged from the flow rate through the denuder and the expected ambient concentrations of the target species.

The Atlanta Super Site Experiment [19.186] provided a quantitative assessment of the performance of a combined denuder-filter technique for time-integrated aerosol measurement. Given the semivolatile character

of HNO_3 , it was recommended that denuders impregnated with sodium carbonate should be used to effectively remove HNO_3 upstream from the Teflon filter that collects fine PM, and that a backup filter impregnated with nylon or sodium carbonate should be employed to collect the volatile fraction of the nitrate aerosol from the front filter in order to accurately measure the nitrate content in $\text{PM}_{2.5}$. However, using the extracts from a tandem denuder setup to quantitatively determine HNO_3 and HONO can cause the HNO_3 to be underestimated and the HONO concentration to be overestimated if the nitrate measured on the second denuder is interpreted as resulting from a secondary heterogeneous reaction of O_3 with nitrite to give nitrate on the denuder walls [19.192].

19.6.2 Sampling of Semivolatile Substances

Absorbent breakthrough can be controlled by using larger cartridges (i.e., a series of sorbent foam plugs) [19.262]. The suitability of PUF can be assessed based on the PUF–air partitioning coefficient $K_{\text{PUF-air}}$ [19.193]. Sampled particulate material can desorb (such material is known as *blow-off*), leading to a positive sampling artifact that is attributed to the gas-phase species. This has been shown to happen for PCBs (polychlorinated biphenyls) [19.263]. Gas molecules may sorb to the filter or sampled particulate material (these sorbed gas molecules are known as *blow-on*), causing a positive sampling artifact that is attributed to the particulate-phase species. This has been observed for polar gas molecules, namely perfluoroalkyl carboxylic acids [19.197]. Organics may be degraded in samplers [19.264]. To prevent the oxidation of particulate PAHs collected on filters, an oxidant denuder is needed upstream during sampling, particularly in the

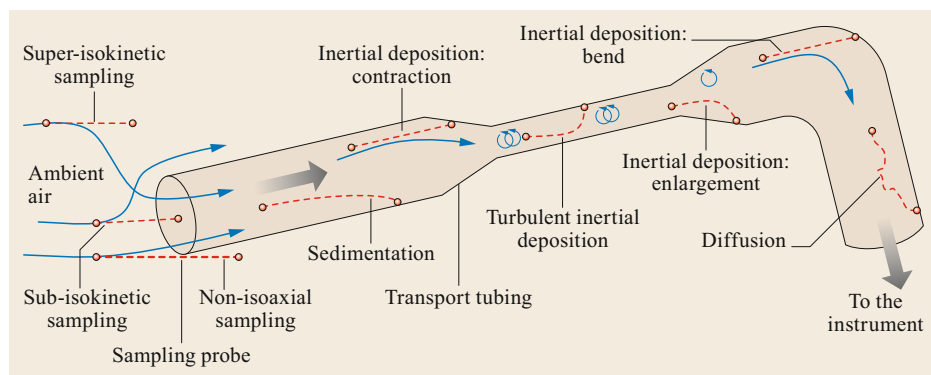


Fig. 19.20 Mechanisms that occur during aerosol sampling and transport in a sampling probe and a transport tube (after [19.104] with permission under CC 3.0)

presence of high oxidant (O_3 , NO_2) concentrations and when using long sampling times [19.265]. This oxidation yields positive sampling artifacts that presumably relate to oxy-PAHs (as-yet unstudied products) and several nitro-PAHs [19.266].

19.6.3 Sampling of Aerosol Particles

Every aerosol sampling protocol and subsequent sample analysis requires dedicated QA/QC practices that cover all relevant working steps in order to ensure that meaningful analytical results are obtained. General guidelines and recommendations for standardized aerosol measurements have been compiled and published for global and long-term measurement programs [19.19, 267, 268]. Moreover, standardized QA/QC protocols have been established for some aerosol analyses [19.19, 269–272]. However, standardized and widely established QA/QC guidelines are not available for most sampling settings. In the following, selected and general QA/QC practices for sampling preparation, the actual sampling process, postsampling sample treatment, sample analysis, and data validation are summarized.

The preparation of a sampling experiment for laboratory analysis (e.g., x-ray microscopy, ion chromatography, or genome sequencing) involves the careful selection of the most appropriate sampling method (see the advantages and disadvantages of each method in Table 19.4) and sampling substrate. Moreover, an appropriate sampling system consisting of an inlet system and sampling device must be set up. Access to recommendations for the design and operation of aerosol inlets and sampling setups is crucial to most (stationary) aerosol sampling efforts, as the recommendations provide a useful reference when attempting to minimize particle losses from imperfect sample air aspiration and/or sample air transport through the tubing system [19.104, 203]. In particular, the particles at both ends of the aerosol size distribution are those that are

most likely to be lost due to diffusional deposition in the ultrafine fraction or sedimentation and impaction losses in the coarse fraction (Fig. 19.20). Accumulation-mode particles are [19.19]

the most long-lived with respect to atmospheric deposition, and they are also the most inert fraction during particle sampling.

The recommendations for representative (stationary) aerosol sampling of reproducible quality according to the second Global Atmosphere Watch (GAW) report [19.267] and Wiedensohler *et al.* [19.19] can be summarized as follows:

- The *overall inlet design* should resemble a vertical stack on the measurement container that shelters the instrumentation. The stack should be high enough to reduce the influences of local effects (e.g., vegetation and buildings). Ideally, the entire setup (inlet, dryer, flow split, and sampler) is aligned vertically to reduce sedimentation losses, but slight bends in the tube are acceptable, and the data obtained can be corrected afterwards [19.104].
- The *aerosol inlet head* excludes precipitation from the sampled aerosols. It should be an omnidirectional inlet head with high transmission efficiency regardless of the wind direction and speed. The inlet head can have a defined particle cutoff (e.g., PM_{10} , $PM_{2.5}$, or PM_1) due to the use of an impactor or cyclone. Total suspended matter (TSP) inlet heads are used for some applications. It may be necessary to heat the inlet head if the site experiences frequent clouds, fog, or freezing.
- The *tubes* of the inlet setup should be as short as possible. They should also be electrically conductive (e.g., longer sections should be made of stainless steel and, if needed, shorter sections should be conductive silicone/polymer tubes) and grounded to avoid electrostatic particle losses. In most sam-

pling applications, laminar flow conditions with Re_f values of up to ≈ 2000 are recommended (Sect. 19.3.3). The flow is turbulent for $Re_f > 4000$, whereas the regime $2000 < Re_f < 4000$ is called the transition regime. Other sources of (local) turbulence such as bends, connectors, and rough inner surfaces should be avoided, as turbulence strongly enhances diffusional losses. Note that turbulent sampling can be acceptable under certain conditions [19.19].

- The sample air must be *dried* if high ambient RH (relative humidity) levels could lead to hygroscopic particle growth and thus biased sizing or even a risk of water condensation in the sampling setup. If drying is performed, the RH is recommended to be $< 40\%$. Note, however, that drying may encourage the volatilization of semivolatile compounds in the particles.
- If the particle-laden air is distributed to several samplers/instruments, an *isokinetic flow splitter* is needed to ensure that the core of the laminar flow profile is sampled and that the velocities of the sample and main flow are comparable. Both measures promote representativeness in the ultrafine and coarse size ranges.

When sampling is performed on moving platforms (i.e., aircraft) or at locations with high wind speeds, isokinetic and isoaxial sample air aspiration are crucial requirements, but they are often difficult to realize (Fig. 19.20). In general, the specifications for the sampling setup have to be adapted to the probed aerosol population as well as the specific environmental conditions of the sampling application. Aside from optimizing the sampling setup, it is necessary to carefully

characterize and document the inlet system in order to correct the data for unavoidable particle losses [19.104].

During sampling, important operational components such as mass flow meters require frequent calibration and validation. Frequent cleaning of parts of the sampler that are in contact with substrates and/or the sample air may be required. Furthermore, sampling blanks are essential (e.g., to assess filter background levels) in most sampling and analysis procedures. After sampling, quality management should specify the treatment of the filters (such as cooling or storage under inert gas) to minimize/avoid sample aging (e.g., oxidation) or alteration (e.g., growth of microorganisms) [19.260].

Sample analysis involves applying the QA/QC practices of the specific analytical technique(s) utilized, such as gravimetry [19.272], x-ray spectroscopy [19.273], or organic and elemental carbon analysis [19.271]. During sample analysis, sampling-related artifacts must be evaluated. Examples are inhomogeneous particle deposition [19.274] and potential volatilization of certain components (e.g., NH_4NO_3 or organics) due to shifts in partitioning between the gas and particle phases upon changes in temperature or pressure in the sampler [19.18, 275, 276]. For impactor sampling, the rebound of solid particles in inertial aerosol sampling (e.g., in cascade impactors) is a major issue that can significantly alter sampling results [19.216]. Performing dedicated rebound experiments and coating the impactor stages can help to assess and minimize this effect [19.277, 278]. Ultimately, a key aspect of the quality management of aerosol sampling results is the comparison with aerosol online data recorded during the sampling period (if available). Consistency of the results from online and offline aerosol techniques is typically a robust indication of high data quality.

19.7 Maintenance

While passive samplers used for the collection of trace gases or semivolatile substances need almost no maintenance, active samplers require frequent flow checks

and maintenance of components of the actively operating flow system, such as the pump and tubing. The more complex the sampling system (e.g., a continuously op-

Table 19.6 Typical maintenance tasks for (active) air sampling devices, particularly when they are continuously operated. Due to the wide range of sampling methods available, only generalized tasks that do not necessarily apply to all methods are shown

Maintenance interval	Maintenance tasks
At every sample change	Visually inspect the sampler for obvious damage or malfunction Check key operational parameters (e.g., the sample air flow rate displayed)
Weekly to monthly	For sensitive samplings: clean (e.g., sterilize) sample holders and critical parts of the sampler Check the electronic and mechanical functions of key components such as the vacuum and flow control systems (e.g., pumps and mass flow controllers) Check that tube connections are tight (leak tests) and check for free passage of the sample air
Annually	Clean or replace components if necessary (e.g., if the tubes become too restrictive or fail flow checks) Calibration of sampler (if applicable)

erated system with automatic sample switching), the more extensive the maintenance needed. The specific maintenance tasks that must be performed depend on

the sampling system utilized and the frequency of sample collection. A generalized overview of typical maintenance tasks is provided in Table 19.6.

19.8 Application

The field of applications of trace substance sampling in the atmosphere is very broad. It ranges, for instance, from the standardized and continuous monitoring of important pollutants within international measurement networks on the one hand to the case-specific sampling of certain substances within dedicated field experiments on the other. Therefore, this section on the applications of trace substance sampling in the atmosphere cannot provide a systematic or even comprehensive overview of all such applications; instead, it presents selected examples to illustrate the broad spectrum of applications.

19.8.1 Sampling of Trace Gases

As part of the International Global Atmospheric Chemistry (IGAC) project, and supported by the GAW program of the World Meteorological Organization (WMO), the international Deposition of Biogeochemically Important Trace Species (DEBITS) program adopted passive sampling to monitor inorganic gaseous species in tropical regions around the world [19.279–281]. The samplers and analytical procedures used in DEBITS were also adopted by other national and international monitoring programs and applied in other continental-scale air quality studies, including the National Atmospheric Deposition Program's Ammonia Monitoring Network (NADP/AMoN) [19.282]. The samplers are based on the Ferm design [19.9], and expose a specifically impregnated paper disk (sorber) that sits 10 mm behind a 1 μ m PTFE filter disk supported by a circular stainless steel mesh. The circular mesh rests on a polypropylene ring with a 21 mm, downward-facing opening through which ambient sample air diffuses. The 10 mm distance between the sorber filter and the PTFE filter is maintained using a plastic ring. The PTFE filter prevents convective air flow and particles from impacting on the impregnated filter above. The type of gas that is trapped depends on the chemical used as the sorber. In DEBITS, NO₂, SO₂, O₃, and NH₃ are captured using absorbing solutions of potassium iodide (KI), potassium carbonate (K₂CO₃), sodium nitrate (NaNO₃), and citric acid (C₆H₈O₇), respectively. *Pienaar et al.* [19.283] gives an excellent overview of the sampling of inorganic and organic gases by passive diffusion in the DEBITS program.

Persistent organic pollutants (POPs) are monitored by passive sampling networks under the auspices of the

Global Monitoring Plan of the Stockholm Convention on POPs [19.284, 285] (Fig. 19.20). Polyurethane foam disk passive air samplers are used [19.286, 287]. As of 2017, the convention lists 24 substances (substance groups) encompassing obsolete pesticides and flame retardants (such as PBDEs (polybrominated diphenyl ethers)), industrial chemicals (such as PCBs), and combustion by-products (such as PCDDs (polychlorinated dibenzodioxins) and PCDFs (polychlorinated dibenzofurans)). The typical sampling (exposure) time is 3 months. Apart from long-term monitoring, passive sampling networks are also used to determine snapshot distributions (exposure times of a few weeks to months) for whole regions or smaller areas (Africa [19.288], Europe [19.289], and the Aegean [19.290]).

As the effective sampling volume of passive samplers is influenced by the wind velocity and temperature, it is usually only estimated, and results are given in units of mass of substance per sample [19.52, 291]. This method is also only semiquantitative for substances that partition to a significant extent into the particulate phase (semivolatiles; see Sects. 19.1.2 and 19.2.2). As most of the samplers used for POPs are not equipped with a diffusion barrier for particles, ultrafine particles are included (albeit with a low sampling efficiency) [19.292]. Given that the diffusion of particles depends strongly on particle size, this sampling efficiency of particles is dependent on the substance's mass size distribution, which varies both temporally and spatially, so it cannot be calibrated. Passive air samplers with a particle diffusion barrier are also used (adsorbent: XAD-2) to monitor levels of POPs and currently used pesticides [19.293], but the time resolution of these samplers is very low (typically 1 year).

In a more recent 17-month study in the Athabasca Oil Sands region of Alberta, Canada, the comparability of passive and active (denuder) systems for monthly integrated measurements of ambient NH₃ and HNO₃ was evaluated [19.294]. The study took place between June 2011 and October 2012 at two urban ambient air monitoring sites (Fort McMurray and Fort McKay) in the network managed by the Wood Buffalo Environmental Association (WBEA). Passive and active (denuder) surfaces coated with citric acid and phosphorous acid were compared for the collection of NH₃, while sodium chloride (NaCl) and nylon were compared for the collection of HNO₃. The passive samplers tested were the Ogawa

PS-100 [19.79] and Radiello RAD-168 (Radiello, 2006; [19.78], www.radiello.com), while 242 mm long annular diffusion tubes (University Research Glassware, Chapel Hill, NC) served as active samplers. This approach allowed the quantitative assessment of differences in performance, especially in the case of HNO_3 , where the difference between the effective stoichiometric, specific chemical absorption of HNO_3 onto NaCl was compared to the nonspecific physical adsorption of HNO_3 onto nylon, which occurs at an unknown rate.

For NH_3 , using citric acid on both the denuder and passive collection surfaces yielded the best agreement with the lowest bias (between 8 and 25%). Using phosphorous acid on the passive sampling media caused NH_3 to be underestimated relative to citric acid by between -13 and -54% . For HNO_3 , using NaCl on passive surfaces yielded HNO_3 concentrations that were highly biased (by 80–92%) relative to when it was used on active denuder surfaces. However, using nylon instead of NaCl as the passive collection surface caused a consistent and very high bias at both sites (a factor of ≈ 7 –8). Using nylon as the passive collection surface yields exceedingly high HNO_3 values relative to all other passive and active collection surfaces, suggesting artifact reactions that are specific to this surface material. Comparison with long-term HNO_3 data collected elsewhere corroborates the finding that the exposed nylon material causes a significant positive artifact. However, the reactions that drive this specific artifact are currently unclear. Simultaneously measured NO_2 , O_3 , and water vapor data indicate that the nylon surface is susceptible to heterogeneous hydrolysis reactions involving NO_2 , N_2O_5 , and NO_3 radicals.

The average HNO_3 results obtained from NaCl surfaces ($0.23 \mu\text{g m}^{-3}$ from active samplers and $0.44 \mu\text{g m}^{-3}$ from passive samplers) compare well with other long-term measurements in the United States and overseas. For example, SEARCH network measurements made in the southeastern US [19.295] during the same period show overall HNO_3 averages ranging from $0.53 \mu\text{g m}^{-3}$ in rural areas to $1.09 \mu\text{g m}^{-3}$ in urban environs. A similar urban–rural gradient in HNO_3 was reported for various locations in Europe, tropical Africa, and tropical Asia [19.296]. Interestingly, a gradient was also observed at much greater spatial scales; that is, tropical low latitudes exhibited an average annual HNO_3 level of about $1.4 \mu\text{g m}^{-3}$ versus roughly $0.3 \mu\text{g m}^{-3}$ at high European latitudes [19.296], similar to the WBEA domain. They also report an increasing urban–rural gradient in the molar HNO_3/NO_2 ratio (from 2.7% urban up to 18% rural), which they attribute to the slow formation of HNO_3 during transport away from its precursor sources. All of these levels are well below the values of almost $3.0 \mu\text{g m}^{-3}$ obtained from the

Ogawa nylon sampler. In other words, not only do nylon surfaces yield HNO_3 concentrations that are higher than those from collocated samplers, they also yield HNO_3 concentrations that are much higher than observed in urban centers in the US and Europe. Taken together, these results indicate there is a significant but as-yet unexplained positive bias when nylon is used for the passive sampling of HNO_3 .

The denuder difference technique has been successfully employed in the SEARCH network for the semi-continuous measurement of atmospheric HNO_3 and NH_3 , as described in detail by Saylor *et al.* [19.297]. For NH_3 , this approach employs a dual-channel nitric oxide-ozone (NO-O_3) chemiluminescence detector (CLD). Ambient air in both channels flows through sodium carbonate (Na_2CO_3)-coated annular denuders (URG Inc., Chapel Hill, USA) at a flow rate of 1.25 L min^{-1} . NH_3 quantitatively passes through the denuders, whereas HNO_3 is removed. The flow in channel 2 passes directly into a 600°C platinum (Pt) mesh converter followed by a 350°C molybdenum (Mo) converter. The Pt converter oxidizes NH_3 and particulate NH_4^+ to NO and nitrogen dioxide (NO_2). The Mo backup converter reduces all NO_x components to NO. The flow in channel 1 is directed through an annular denuder coated with citric acid that removes NH_3 prior to sequential oxidation (Pt) and reduction (Mo) conversion steps. The difference between the channels is therefore operationally defined as NH_3 . Other reduced nitrogen gases that are removed by a citric acid denuder may be included in this operational definition, thus causing a potential positive bias.

Omitting the oxidizing Pt converter, a simpler dual-channel CLD is used for HNO_3 , whereby channel 2 passes ambient air directly into a 350°C Mo converter while channel 1 quantitatively removes HNO_3 via a Na_2CO_3 -coated annular denuder upstream of the Mo converter. Hence, the difference between the channels in this case is operationally defined as HNO_3 . Annular denuder inlets for each channel are exposed directly to the atmosphere and converters are attached to denuder outlets with short (5 cm) lengths of (1/4)" o.d. Teflon® PFA tubing to minimize the potential adsorption of NH_3 on interior instrument surfaces. The residence time upstream of the converters is kept to $< 2 \text{ s}$ to minimize line losses and the decomposition of NH_4NO_3 . Inlet denuders are replaced once per month. Measurements are performed atop the equipment shelter at a height of $\approx 5 \text{ m AGL}$. The CLD is calibrated with NO every other day and zeroed with dry zero air once a day. One-minute averages are acquired from the CLD and used to calculate and report 5-min average, standard deviation, minimum, maximum, and median statistics. The 5-min data can then be used to generate hourly averages and associated statistics.

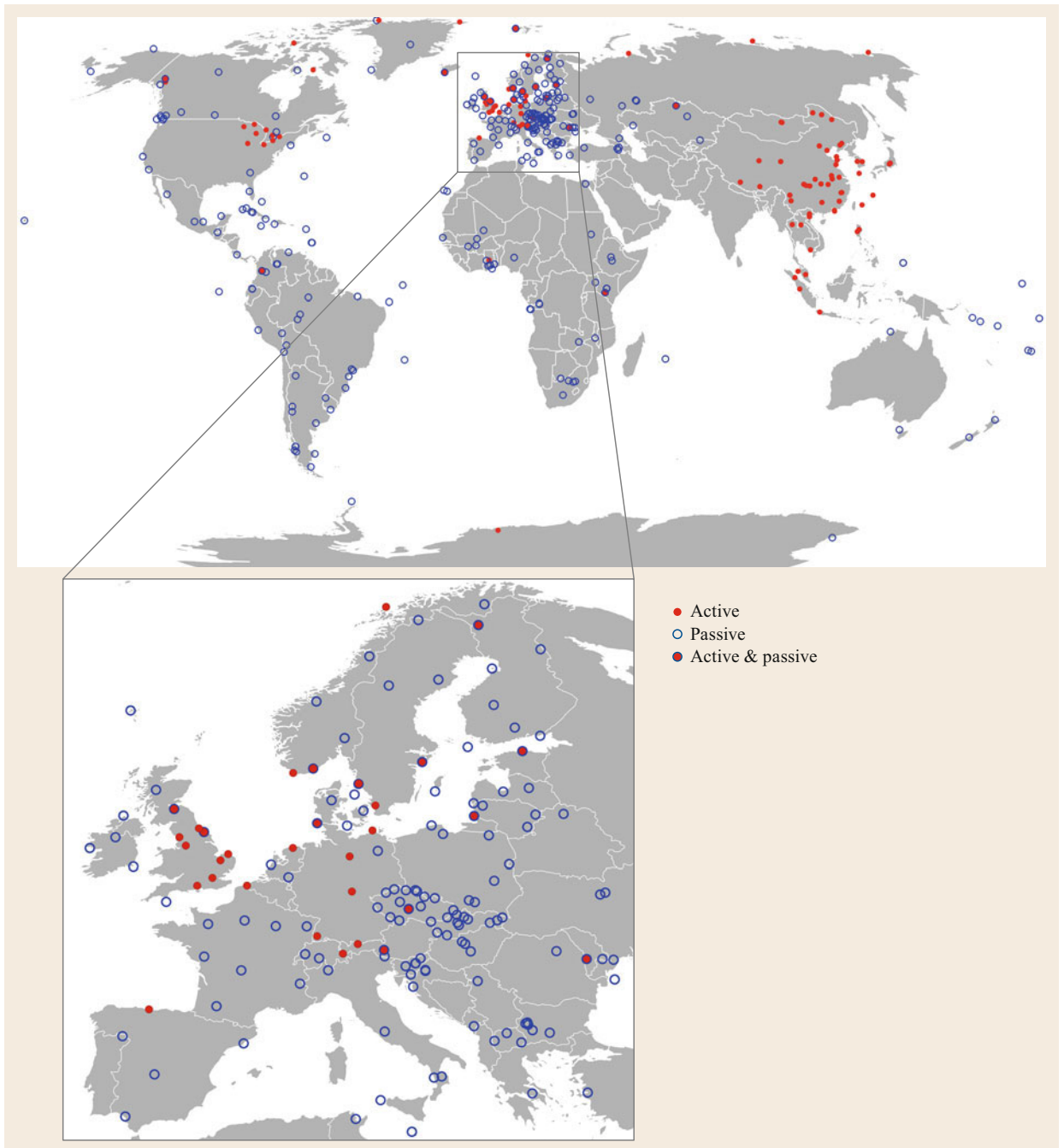


Fig. 19.21 Passive and active air sampling sites for POPs in monitoring networks worldwide [19.298]

19.8.2 Sampling of Semivolatile Substances

Numerous studies on halogenated organic substances and PAHs and their derivatives in continental and ma-

rine atmospheric environments have utilized the separate and simultaneous collection of gases and particles on filters and gases in a downstream adsorbent trap [19.86, 88, 189, 190, 195, 196, 206, 263, 265]. Per-

sistent organic pollutants are monitored by several active sampling networks in Europe, North America [19.299], and the Arctic [19.300] (Fig. 19.21b) using filters and downstream adsorbent traps. The NADP (see also Sect. 19.8.1), EMEP, and AMAP networks are under the auspices of regional conventions on acid deposition (NADP), transboundary air pollution (CLRTAP [19.301]), and the Arctic Council [19.302], respectively.

19.9 Future Developments

Regarding the sampling of trace gases, passive samplers have thus far suffered from undefined sample volumes. However, novel passive samplers for which the relationship of sampling flow to wind speed is known will become available, which will make it possible to calculate the sample volume based on the recorded wind speed.

More chemically specific sampling techniques are desirable for the sampling of semivolatile substances, but such techniques are difficult to implement practi-

19.8.3 Sampling of Aerosol Particles

The range of applications of aerosol sampling is broad, and sampling strategies and setups are diverse. For systematic and comprehensive overviews, we refer the reader to several textbooks as well as review articles that provide detailed information on the broad spectrum of sampling strategies and applications [19.22, 27, 29, 54, 303, 304].

cally due to their generally low reactivities and the huge physicochemical diversity of semivolatile organics. For instance, even substances from the same class show a wide range of polarities (from apolar to highly polar).

The field of aerosol particle sampling and the development of sampling techniques has strongly diversified since its beginnings. Rapid development continues in this field: existing techniques are being modified and optimized further while rather sophisticated novel sampling approaches are being invented.

19.10 Further Reading

Further comprehensive and in-depth information on the topics explored in this chapter can be found in the following textbooks and review papers:

- J.H. Seinfeld, S.N. Pandis: *Atmospheric Chemistry and Physics: From Air Pollution to Climate Change*, 3rd edn. (Wiley, 2016).
- S.V. Krupa, A.H. Legge: *Passive Sampling of Ambient, Gaseous Air Pollutants: An Assessment from an Ecological Perspective*. *Environ. Pollut.* 107, 31–45, 2000.
- J.J. Pienaar, J.P. Beukes, P.G. van Zyl, C.M.B. Lehmann, J. Aherne: Chapter 2 – Passive Diffusion Sampling Devices for Monitoring Ambient Air Concentrations. In: *Comprehensive Analytical Chemistry*, vol 70, ed. by P.B.C. Forbes (Elsevier, 2015.) pp. 13–52.
- P. Kulkarni, P.A. Baron, K. Willeke: *Aerosol Measurement: Principles, Techniques, and Applications*. (Wiley, Hoboken 2011).
- W.C. Hinds: *Aerosol Technology*. (Wiley, New York 1999).
- J.H. Vincent: *Aerosol Sampling: Science, Standards, Instrumentation and Applications*. (Wiley, Chichester 2007).

References

- 19.1 J. Lelieveld, U. Pöschl: Chemists can help to solve the air-pollution health crisis, *Nature* **551**, 291–293 (2017)
- 19.2 M.H. Forouzanfar, A. Afshin, L.T. Alexander, et al.: Global, regional, and national comparative risk assessment of 79 behavioural, environmental and occupational, and metabolic risks or clusters of risks, 1990–2015: A systematic analysis for the Global Burden of Disease Study 2015, *Lancet* **388**, 1659–1724 (2016)
- 19.3 J.H. Seinfeld, S.N. Pandis: *Atmospheric Chemistry and Physics* (John Wiley & Sons, Inc., New York 1998)
- 19.4 J.G. Watson, R.J. Tropp, S.D. Kohl, X. Wang, J.C. Chow: Filter processing and gravimetric analysis for suspended particulate matter samples, *Aerosol Sci. Eng.* **1**, 93–105 (2017)

- 19.5 J. Ofner, T. Deckert-Gaudig, K.A. Kamilli, A. Held, H. Lohninger, V. Deckert, B. Lendl: Tip-enhanced Raman spectroscopy of atmospherically relevant aerosol nanoparticles, *Anal. Chem.* **88**, 9766–9772 (2016)
- 19.6 R.M.B.O. Duarte, C.A. Pio, A.C. Duarte: Spectroscopic study of the water-soluble organic matter isolated from atmospheric aerosols collected under different atmospheric conditions, *Anal. Chim. Acta* **530**, 7–14 (2005)
- 19.7 J.A. Huffman, A.J. Prenni, P.J. DeMott, C. Pöhlker, R.H. Mason, N.H. Robinson, J. Fröhlich-Nowoisky, Y. Tobo, V.R. Despres, E. Garcia, D.J. Gochis, E. Harris, I. Müller-Germann, C. Ruzene, B. Schmer, B. Sinha, D.A. Day, M.O. Andreae, J.L. Jimenez, M. Gallagher, S.M. Kreidenweis, A.K. Bertram, U. Pöschl: High concentrations of biological aerosol particles and ice nuclei during and after rain, *Atmos. Chem. Phys.* **13**, 6151–6164 (2013)
- 19.8 A. Laskin, M.J. Iedema, A. Ichkovich, E.R. Graber, I. Taraniuk, Y. Rudich: Direct observation of completely processed calcium carbonate dust particles, *Faraday Discuss.* **130**, 453–468 (2005)
- 19.9 W. Maenhaut, N. Raes, W. Wang: Analysis of atmospheric aerosols by particle-induced X-ray emission, instrumental neutron activation analysis, and ion chromatography, *Nucl. Instrum. Methods Phys. Res. B* **269**, 2693–2698 (2011)
- 19.10 A.H. Goldstein, D.R. Worton, B.J. Williams, S.V. Hering, N.M. Kreisberg, O. Panić, T. Górecki: Thermal desorption comprehensive two-dimensional gas chromatography for in-situ measurements of organic aerosols, *J. Chromatogr. A* **1186**, 340–347 (2008)
- 19.11 A. Kumar, W. Abouchami, S.J.G. Galer, V.H. Garrison, E. Williams, M.O. Andreae: A radiogenic isotope tracer study of transatlantic dust transport from Africa to the Caribbean, *Atmos. Environ.* **82**, 130–143 (2014)
- 19.12 I. Kourtchev, R.H.M. Godoi, S. Connors, J.G. Levine, A.T. Archibald, A.F.L. Godoi, S.L. Paralo, C.G.G. Barbosa, R.A.F. Souza, A.O. Manzi, R. Seco, S. Sjostedt, J.H. Park, A. Guenther, S. Kim, J. Smith, S.T. Martin, M. Kalberer: Molecular composition of organic aerosols in Central Amazonia: An ultra-high-resolution mass spectrometry study, *Atmos. Chem. Phys.* **16**, 11899–11913 (2016)
- 19.13 S.V. Krupa, A.H. Legge: Passive sampling of ambient, gaseous air pollutants: An assessment from an ecological perspective, *Environ. Pollut.* **107**, 31–45 (2000)
- 19.14 J.F. Pankow: An absorption model of gas/particle partitioning of organic compounds in the atmosphere, *Atmos. Environ.* **28**, 185–188 (1994)
- 19.15 M. Shiraiwa, K. Ueda, A. Pozzer, G. Lammel, C.J. Kampf, A. Fushimi, S. Enami, A.M. Arangio, J. Fröhlich-Nowoisky, Y. Fujitani, A. Furuyama, P.S.J. Lakey, J. Lelieveld, K. Lucas, Y. Morino, U. Pöschl, S. Takaharna, A. Takami, H.J. Tong, B. Weber, A. Yoshino, K. Sato: Aerosol health effects from molecular to global scales, *Environ. Sci. Technol.* **51**, 13545–13567 (2017)
- 19.16 T.C. Bond, S.J. Doherty, D.W. Fahey, P.M. Forster, T. Berntsen, B.J. DeAngelo, M.G. Flanner, S. Ghan, B. Kärcher, D. Koch, S. Kinne, Y. Kondo, P.K. Quinn, M.C. Sarofim, M.G. Schultz, M. Schulz, C. Venkataraman, H. Zhang, S. Zhang, N. Bellouin, S.K. Guttikunda, P.K. Hopke, M.Z. Jacobson, J.W. Kaiser, Z. Klimont, U. Lohmann, J.P. Schwarz, D. Shindell, T. Storelvmo, S.G. Warren, C.S. Zender: Bounding the role of black carbon in the climate system: A scientific assessment, *J. Geophys. Res. Atmos.* **118**, 2169–8996 (2013)
- 19.17 V. Ramanathan, P.J. Crutzen, J.T. Kiehl, D. Rosenfeld: Aerosols, climate, and the hydrological cycle, *Science* **294**, 2119–2124 (2001)
- 19.18 P.H. McMurry: A review of atmospheric aerosol measurements, *Atmos. Environ.* **34**, 1959–1999 (2000)
- 19.19 A. Wiedensohler, W. Birmili, J.–P. Putaud, J. Ogren: Recommendations for aerosol sampling. In: *Aerosol Science: Technology and Applications*, ed. by I. Colbeck, M. Lazaridis (John Wiley & Sons, Chichester 2014)
- 19.20 M. Kulmala, T. Petäjä, T. Nieminen, M. Sipilä, H.E. Manninen, K. Lehtipalo, M. Dal Maso, P.P. Aalto, H. Junninen, P. Paasonen, I. Riipinen, K.E.J. Lehtinen, A. Laaksonen, V.–M. Kerminen: Measurement of the nucleation of atmospheric aerosol particles, *Nat. Protoc.* **7**, 1651–1667 (2012)
- 19.21 M. Lazaridis, I. Colbeck: Introduction. In: *Aerosol Science: Technology and Applications*, ed. by I. Colbeck, M. Lazaridis (John Wiley & Sons, Chichester 2014)
- 19.22 I. Colbeck, M. Lazaridis: *Aerosol Science: Technology and Applications* (John Wiley & Sons, Chichester 2014)
- 19.23 C. Pöhlker, J.A. Huffman, J.D. Förster, U. Pöschl: Autofluorescence of atmospheric bioaerosols: Spectral fingerprints and taxonomic trends of pollen, *Atmos. Meas. Tech.* **6**, 3369–3392 (2013)
- 19.24 V.R. Després, J.A. Huffman, S.M. Burrows, C. Hoose, A.S. Safatov, G. Buryak, J. Fröhlich-Nowoisky, W. Elbert, M.O. Andreae, U. Pöschl, R. Jaenicke: Primary biological aerosol particles in the atmosphere: A review, *Tellus B* **64**, 1–58 (2012)
- 19.25 B. Weinzierl, A. Ansmann, J.M. Prospero, D. Althausen, N. Benker, F. Chouza, M. Dollner, D. Farrell, W.K. Fomba, V. Freudenthaler, J. Gasteiger, S. Groß, M. Haarig, B. Heinold, K. Kandler, T.B. Kristensen, O.L. Mayol-Bracero, T. Müller, O. Reitebuch, D. Sauer, A. Schäfler, K. Schepanski, A. Spanu, I. Tegen, C. Toledano, A. Walser: The Saharan aerosol long-range transport and aerosol–cloud–interaction experiment: Overview and selected highlights, *Bull. Am. Meteorol. Soc.* **98**, 1427–1451 (2017)
- 19.26 J. Ditas, N. Ma, Y. Zhang, D. Assmann, M. Neumaier, H. Riede, E. Karu, J. Williams, D. Scharffe, Q. Wang, J. Saturno, J.P. Schwarz, J.M. Katich, G.R. McMeeking, A. Zahn, M. Hermann, C.A.M. Brenninkmeijer, M.O. Andreae, U. Pöschl, H. Su, Y. Cheng: Strong impact of wildfires on

- the abundance and aging of black carbon in the lowermost stratosphere, *Proc. Natl. Acad. Sci. U. S. A.* **115**, E11595 (2018)
- 19.27 P. Kulkarni, P.A. Baron, K. Willeke (Eds.): *Aerosol Measurement: Principles, Techniques, and Applications*, 3rd edn. (John Wiley & Sons, Hoboken 2011)
- 19.28 W.C. Hinds: *Aerosol Technology* (John Wiley & Sons, New York 1999)
- 19.29 J.H. Vincent: *Aerosol Sampling: Science, Standards, Instrumentation and Applications* (John Wiley & Sons, Chichester 2007)
- 19.30 J. Namiesnik, B. Zabiegała, A. Kot-Wasik, M. Partyka, A. Wasik: Passive sampling and/or extraction techniques in environmental analysis: A review, *Anal. Bioanal. Chem.* **381**, 279–301 (2005)
- 19.31 M.B. Rubin: The history of ozone. The Schönbein period, 1839–1868, *Bull. Hist. Chem.* **26**, 40–56 (2001)
- 19.32 C.S. Gordon, J.T. Lowe: Carbon-Monoxide Detector, Patent US1644014A (1927)
- 19.33 K.D. Reiszner, P.W. West: Collection and determination of sulfur dioxide incorporating permeation and West-Gaeke procedure, *Environ. Sci. Technol.* **7**, 526–532 (1973)
- 19.34 E.D. Palmes, A.F. Gunnison, J. Dimattio, C. Tomczyk: Personal sampler for nitrogen dioxide, *Am. Ind. Hyg. Assoc. J.* **37**, 570–577 (1976)
- 19.35 B. Zabiegała, T. Gorecki, E. Przyk, J. Namiesnik: Permeation passive sampling as a tool for the evaluation of indoor air quality, *Atmos. Environ.* **36**, 2907–2916 (2002)
- 19.36 E.D. Palmes, A.F. Gunnison: Personal monitoring device for gaseous contaminants, *Am. Ind. Hyg. Assoc. J.* **34**, 78–81 (1973)
- 19.37 P.W. West, G.C. Gaeke: Fixation of sulphur dioxide as disulfitomercurate(II) and subsequent colorimetric estimation, *Anal. Chem.* **28**, 1816–1819 (1956)
- 19.38 M. Ferm: *A Sensitive Diffusional Sampler. IVL Report, Vol. 1020* (Swedish Environmental Research Institute, Göteborg 1991)
- 19.39 J.F. Mazur, R.L. Bamberger, G.E. Podolak: Development and evaluation of an ammonia dosimeter, *Am. Ind. Hyg. Assoc. J.* **39**, 749–753 (1978)
- 19.40 C. Monn, M. Hangartner: Passive sampling for ozone, *J. Air Waste Manag. Assoc.* **40**, 357–358 (1990)
- 19.41 R.M. Cox: The use of passive sampling to monitor forest exposure to O₃, NO₂ and SO₂: A review and some case studies, *Environ. Pollut.* **126**, 301–311 (2003)
- 19.42 G. Berton, C. Ciuchini, R. Tappa: Measurement of long-term average carbon dioxide concentrations using passive diffusion sampling, *Atmos. Environ.* **38**, 1625–1630 (2004)
- 19.43 C.J. Horwell, A.G. Allen, T.A. Mather, J.E. Patterson: Evaluation of a novel passive sampling technique for monitoring volcanogenic hydrogen sulfide, *J. Environ. Monit.* **6**, 630–635 (2004)
- 19.44 M.E. Bartkow, J.N. Huckins, J.F. Muller: Field-based evaluation of semipermeable membrane devices (SPMDs) as passive air samplers of polycyclic aromatic hydrocarbons (PAHs), *Atmos. Environ.* **38**, 5983–5990 (2004)
- 19.45 C.W. Chung, M.T. Morandi, T.H. Stock, M. Afshar: Evaluation of a passive sampler for volatile organic compounds at ppb concentrations, varying temperatures, and humidities with 24-h exposures. 2. Sampler performance, *Environ. Sci. Technol.* **33**, 3666–3671 (1999)
- 19.46 H. Paschke, P. Popp: New passive samplers for chlorinated semivolatile organic pollutants in ambient air, *Chemosphere* **58**, 855–863 (2005)
- 19.47 A. Bytnerowicz, P.E. Padgett, M.J. Arbaugh, D.R. Parker, D.P. Jones: Passive sampler for measurements of atmospheric nitric acid (HNO₃) vapor, *Sci. World J.* **1**, 815–822 (2001)
- 19.48 A. Bytnerowicz, M.J. Sanz, M.J. Arbaugh, P.E. Padgett, D.P. Jones, A. Davila: Passive sampler for monitoring ambient nitric acid (HNO₃) and nitrous acid (HNO₂) concentrations, *Atmos. Environ.* **39**, 2655–2660 (2005)
- 19.49 G.R. Harvey, W.G. Steinhauer, J.M. Teal: Polychlorobiphenyls in North Atlantic ocean water, *Science* **180**, 643–644 (1973)
- 19.50 T.F. Bidleman, C.E. Olney: Chlorinated hydrocarbons in the Sargasso Sea atmosphere and surface water, *Science* **183**, 516–518 (1974)
- 19.51 T.F. Bidleman, L. Melymuk: Forty-five years of foam: A retrospective on air sampling with polyurethane foam, *Bull. Environ. Contam. Toxicol.* **102**, 447–449 (2019)
- 19.52 L. Melymuk, P. Bohlin, O. Sanka, K. Pozo, J. Klanova: Current challenges in air sampling of semivolatile organic contaminants: Sampling artifacts and their influence on data comparability, *Environ. Sci. Technol.* **48**, 14077–14091 (2014)
- 19.53 J.H. Vincent: The principles of aerosol samplers and sampling, *Grana* **30**, 409–413 (1991)
- 19.54 P.H. Gregory: *The Microbiology of the Atmosphere* (Leonard Hill Books, Aylesbury 1973)
- 19.55 L. Pasteur: Expériences relatives aux générations dites spontanées, *C. R. Acad. Sci.* **50**, 303–307 (1860)
- 19.56 L. Pasteur: Suite à une précédente communication relative aux générations dites spontanées, *C. R. Acad. Sci.* **51**, 675–678 (1860)
- 19.57 C.G. Ehrenberg: Passat-Staub Und Blut-Regen: Ein großes organisches unsichtbares Wirken und Leben in der Atmosphäre, *Abh. Kgl. Preuss. Akad. Wiss. Berl.* **1847**, 269 (1849)
- 19.58 C.G. Ehrenberg: Neue Beobachtungen über blutartige Erscheinungen in Aegypten, Arabien und Sibirien, nebst einer Uebersicht und Kritik der früher bekannten, *Ann. Phys.* **94**, 477–514 (1830), in German
- 19.59 J.B. Cohen, A.G. Rushton: *Smoke* (Edward Arnold, London 1912)
- 19.60 T.L. Ogden, J.L. Birkett: The human head as a dust sampler. In: *Inhaled Particles IV*, ed. by W.H. Walton (Pergamon, Oxford 1977)
- 19.61 V.A. Marple: History of impactors—The first 110 years, *Aerosol Sci. Technol.* **38**, 247–292 (2004)

- 19.62 R.A. Thomas, W.P.O. McQueen: *The Dust in the Air and the Gases from Explosives in a Cornish Mine (Dolcoath), and the Efficacy of Methods of Dealing with Them* (Royal Commission on the Ventilation and Sanitation of Mines, Perth 1904), Tech. Rep. of the Institution of Mining and Metallurgy (15.12.1904)
- 19.63 J. Boyd: Methods for determining the dust in mine air, as practised on the witwatersrand. In: *Silicosis: Records of the International Conference Held at Johannesburg, 13–27 August 1930*, Studies and Reports: Series F, Vol. 13 (International Labour Office, Geneva 1930)
- 19.64 R. Kotzé: *Final Report of the Miners' Phthisis Prevention Committee* (Union of South Africa, Johannesburg 1916)
- 19.65 H.L. Green, H.H. Watson: *Physical Methods for the Estimation of the Dust Hazard in Industry, with Special Reference to the Occupation of the Stone Mason* (HMSO, London 1935), Medical Research Council, Special Report Series No. 199
- 19.66 L. Greenberg, G.W. Smith: *A New Instrument for Sampling Aerial Dust* (Bureau of Mines, Washington 1922), United States Bureau of Mines Report of Investigations No. 2392
- 19.67 P.H. Kitto, D.G. Beadle: A modified form of thermal precipitator, *J. S. Afr. Inst. Min. Metall.* **52**, 284–306 (1952)
- 19.68 R.J. Hamilton: A portable instrument for respirable dust sampling, *J. Sci. Instrum.* **33**, 395–399 (1956)
- 19.69 R.C. Tolman, L.H. Reyerson, A.P. Brook, H.D. Smyth: An electrical precipitator for analyzing smokes, *J. Am. Chem. Soc.* **41**, 587–589 (1919)
- 19.70 K.L. Rubow, V.A. Marple, J. Olin, M.A. McCawley: A personal cascade impactor – Design, evaluation and calibration, *Am. Ind. Hyg. Assoc. J.* **48**, 532–538 (1987)
- 19.71 K.R. May: The cascade impactor – An instrument for sampling coarse aerosols, *J. Sci. Instrum.* **22**, 187–195 (1945)
- 19.72 R.J. Sherwood, D.M. Greenhalgh: A personal air sampler, *Ann. Occup. Hyg.* **2**, 127–132 (1960)
- 19.73 A. Bailey, P.A. Hollingdale-Smith: Passive sampling and dosimetry from trace organic sample handling. In: *Trace-Organic Sample Handling, Vol. 10*, ed. by E. Reid (E. Horwood, Chichester 1981) pp. 43–50
- 19.74 J. Namiesnik, T. Gorecki, E. Kozłowski, L. Torres, J. Mathieu: Passive dosimeters – An approach to atmospheric pollutants analysis, *Sci. Total Environ.* **38**, 225–258 (1984)
- 19.75 T. Górecki, J. Namieśnik: Passive sampling, *Trends Anal. Chem.* **21**, 276–291 (2002)
- 19.76 A. Kot-Wasik, B. Zabiegała, M. Urbanowicz, E. Dominiak, A. Wasik, J. Namiesnik: Advances in passive sampling in environmental studies, *Anal. Chim. Acta* **602**, 141–163 (2007)
- 19.77 J.N.B. Bell, M. Treshow: *Air Pollution and Plant Life*, 2nd edn. (John Wiley & Sons, Chichester 2002)
- 19.78 Radiello: Product Information and Company Brochure, Edition 01/2006. Fondazione Salvatore Maugeri-IRCCS, Centro di Ricerche Ambientali, Padova 2006
- 19.79 Ogawa: NH₃ Sampling Protocol Using the Ogawa Sampler. Yokohama City Research Institute for Environmental Science, User's Guide 2.0, October 2010
- 19.80 J.L. Durham, L. Stockburger: Nitric acid – Air diffusion coefficient: Experimental determination, *Atmos. Environ.* **20**, 559–563 (1986)
- 19.81 P.B.C. Forbes, E.R. Rohwer: Chapter 5 – Denuders. In: *Monitoring of Air Pollutants – Sampling, Sample Preparation and Analytical Techniques*, Comprehensive Analytical Chemistry, Vol. 70, ed. by P.B.C. Forbes (Elsevier, Oxford 2015) pp. 155–181
- 19.82 A.W. Stelson, S.K. Friedlander, J.H. Seinfeld: A note on the equilibrium relationship between ammonia and nitric acid and particulate ammonium nitrate, *Atmos. Environ.* **13**, 369–371 (1979)
- 19.83 T.F. Bidleman: Atmospheric processes – Wet and dry deposition of organic-compounds are controlled by their vapor particle partitioning, *Environ. Sci. Technol.* **22**, 361–367 (1988)
- 19.84 J. Franklin, R. Atkinson, P.H. Howard, J.J. Orlando, C. Seigneur, T.J. Wallington, C. Zetzsch: Quantitative determination of persistence in air. In: *Criteria for Persistence and Long-Range Transport of Chemicals in the Environment*, ed. by G. Klecka (SETAC, Pensacola 2000) pp. 7–62
- 19.85 K.U. Goss, R.P. Schwarzenbach: Linear free energy relationships used to evaluate equilibrium partitioning of organic compounds, *Environ. Sci. Technol.* **35**, 1–9 (2001)
- 19.86 P. Shahpoury, G. Lammel, A. Albinet, A. Sofuoğlu, Y. Dumanoğlu, S.C. Sofuoğlu, Z. Wagner, V. Zdimal: Evaluation of a conceptual model for gas-particle partitioning of polycyclic aromatic hydrocarbons using polyparameter linear free energy relationships, *Environ. Sci. Technol.* **50**, 12312–12319 (2016)
- 19.87 J.F. Pankow, T.F. Bidleman: Interdependence of the slopes and intercepts from log-log correlations of measured gas-particle partitioning and vapor pressure—I. Theory and analysis of available data, *Atmos. Environ. A* **26**, 1071–1080 (1992)
- 19.88 B. Cetin, M. Odabasi: Atmospheric concentrations and phase partitioning of polybrominated diphenyl ethers (PBDEs) in Izmir, Turkey, *Chemosphere* **71**, 1067–1078 (2008)
- 19.89 V.A. Marple, B.A. Olson: Sampling and measurement using inertial, gravitational, centrifugal, and thermal techniques. In: *Aerosol Measurement: Principles, Techniques, and Applications*, 3rd edn., ed. by P. Kulkarni, P.A. Baron, K. Willeke (John Wiley & Sons, Hoboken 2011), Chap. 8
- 19.90 V.A. Marple, K. Willeke: Impactor design, *Atmos. Environ.* **10**, 891–896 (1976)
- 19.91 N.A. Fuchs: *The Mechanics of Aerosols* (Pergamon, New York 1964)
- 19.92 V.A. Marple, D.L. Roberts, F.J. Romay, N.C. Miller, K.G. Truman, M.V. Oort, B. Olsson, M.J. Holroyd, J.P. Mitchell, D. Hochrainer: Next genera-

- tion pharmaceutical impactor (a new impactor for pharmaceutical inhaler testing). Part 1: Design, *J. Aerosol Med.* **16**, 283–299 (2003)
- 19.93 V.A. Marple, K.L. Rubow, S.M. Behm: A micro-orifice uniform deposit impactor (MOUDI) – Description, calibration, and use, *Aerosol Sci. Technol.* **14**, 434–446 (1991)
- 19.94 R.L.N. Yatarelli, J.A. Thornton: Particulate organic matter detection using a micro-orifice volatilization impactor coupled to a chemical ionization mass spectrometer (MOVI-CIMS), *Aerosol Sci. Technol.* **44**, 61–74 (2010)
- 19.95 J. Keskinen, K. Pietarinen, M. Lehtimäki: Electrical low pressure impactor, *J. Aerosol Sci.* **23**, 353–360 (1992)
- 19.96 R.E. Hillamo, E.I. Kauppinen: On the performance of the Berner low pressure impactor, *Aerosol Sci. Technol.* **14**, 33–47 (1991)
- 19.97 V.A. Marple, B.A. Olson, K. Santhanakrishnan, J.P. Mitchell, S.C. Murray, B.L. Hudson-Curtis: Next generation pharmaceutical impactor (a new impactor for pharmaceutical inhaler testing). Part 2. Archival calibration, *J. Aerosol Med.* **16**, 301–324 (2003)
- 19.98 V.A. Marple, B.A. Olson, K. Santhanakrishnan, D.L. Roberts, J.P. Mitchell, B.L. Hudson-Curtis: Next generation pharmaceutical impactor (a new impactor for pharmaceutical inhaler testing). Part 3. Extension of archival calibration to 15 L/min, *J. Aerosol Med.* **17**, 335–343 (2004)
- 19.99 S. Mertes, B. Verheggen, S. Walter, P. Connolly, M. Ebert, J. Schneider, K.N. Bower, J. Cozic, S. Weinbruch, U. Baltensperger, E. Weingartner: Counterflow virtual impact or based collection of small ice particles in mixed-phase clouds for the physico-chemical characterization of tropospheric ice nuclei: Sampler description and first case study, *Aerosol Sci. Technol.* **41**, 848–864 (2007)
- 19.100 B.T. Chen, H.C. Yeh: An improved virtual impactor – Design and performance, *J. Aerosol Sci.* **18**, 203–214 (1987)
- 19.101 V.A. Marple, C.M. Chien: Virtual impactors – A theoretical study, *Environ. Sci. Technol.* **14**, 976–985 (1980)
- 19.102 X.L. Wang, P.H. McMurry: A design tool for aerodynamic lens systems, *Aerosol Sci. Technol.* **40**, 320–334 (2006)
- 19.103 S. Hu, A.R. McFarland: Numerical performance simulation of a wetted wall bioaerosol sampling cyclone, *Aerosol Sci. Technol.* **41**, 160–168 (2007)
- 19.104 S.L. von der Weiden, F. Drewnick, S. Borrmann: Particle loss calculator – A new software tool for the assessment of the performance of aerosol inlet systems, *Atmos. Meas. Tech.* **2**, 479–494 (2009)
- 19.105 K.H. Leong: Thermophoresis and diffusiophoresis of large aerosol particles of different shapes, *J. Aerosol Sci.* **15**, 511–517 (1984)
- 19.106 B. Sagot: Thermophoresis for spherical particles, *J. Aerosol Sci.* **65**, 10–20 (2013)
- 19.107 F. Zheng: Thermophoresis of spherical and non-spherical particles: A review of theories and experiments, *Adv. Colloid Interface Sci.* **97**, 255–278 (2002)
- 19.108 J. Wagner, D. Leith: Passive aerosol sampler. Part I: Principle of operation, *Aerosol Sci. Technol.* **34**, 186–192 (2001)
- 19.109 D.K. Ott, T.M. Peters: A shelter to protect a passive sampler for coarse particulate matter, PM_{10–2.5}, *Aerosol Sci. Technol.* **42**, 299–309 (2008)
- 19.110 D. Moran-Zuloaga, F. Ditas, D. Walter, J. Saturno, J. Brito, S. Carbone, X. Chi, I. Hrabě de Angelis, H. Baars, R.H.M. Godoi, B. Heese, B.A. Holanda, J.V. Lavrič, S.T. Martin, J. Ming, M.L. Pöhlker, N. Ruckteschler, H. Su, Y. Wang, Q. Wang, Z. Wang, B. Weber, S. Wolff, P. Artaxo, U. Pöschl, M.O. Andreae, C. Pöhlker: Long-term study on coarse mode aerosols in the amazon rain forest with the frequent intrusion of Saharan dust plumes, *Atmos. Chem. Phys.* **18**, 10055–10088 (2018)
- 19.111 K. Willeke, X. Lin, S.A. Grinshpun: Improved aerosol collection by combined impaction and centrifugal motion, *Aerosol Sci. Technol.* **28**, 439–456 (1998)
- 19.112 J. Choi, S.C. Hong, W. Kim, J.H. Jung: Highly enriched, controllable, continuous aerosol sampling using inertial microfluidics and its application to real-time detection of airborne bacteria, *ACS Sensors* **2**, 513–521 (2017)
- 19.113 R.C. Flagan: Electrical mobility methods for sub-micrometer particle characterization. In: *Aerosol Measurement: Principles, Techniques, and Applications*, 3rd edn., ed. by P. Kulkarni, P.A. Baron, K. Willeke (John Wiley & Sons, Hoboken 2011), Chap. 15
- 19.114 K.W. Lee, B.Y.H. Liu: Theoretical study of aerosol filtration by fibrous filters, *Aerosol Sci. Technol.* **1**, 147–161 (1982)
- 19.115 K.R. Spurny: On the chemical-detection of bioaerosols, *J. Aerosol Sci.* **25**, 1533–1547 (1994)
- 19.116 P.C. Raynor, D. Leith, K.W. Lee, R. Mukund: Sampling and analysis using filters. In: *Aerosol Measurement: Principles, Techniques, and Applications*, 3rd edn., ed. by P. Kulkarni, P.A. Baron, K. Willeke (John Wiley & Sons, Hoboken 2011), Chap. 7
- 19.117 S. Kuwabara: The forces experienced by randomly distributed parallel circular cylinders or spheres in a viscous flow at small Reynolds numbers, *J. Phys. Soc. Japan* **14**, 527–532 (1959)
- 19.118 J. Zhou, S. Smith: Measurement of ozone concentrations in ambient air using a badge-type passive monitor, *J. Air Waste Manag. Assoc.* **47**, 697–703 (1997)
- 19.119 P. Bruno, M. Caputi, M. Caselli, G. de Gennaro, M. de Rienzo: Reliability of a BTEX radial diffusive sampler for thermal desorption: Field measurements, *Atmos. Environ.* **39**, 1347–1355 (2005)
- 19.120 J.D. Mulik, R.G. Lewis, W.A. McClenny, D.D. Williams: Modification of a high-efficiency passive sampler to determine nitrogen dioxide or formaldehyde in air, *Anal. Chem.* **61**, 187–189 (1989)

- 19.121 M.J. Roadman, J.R. Scudlark, J.J. Meisinger, W.J. Ullman: Validation of Ogawa passive samplers for the determination of gaseous ammonia concentrations in agricultural settings, *Atmos. Environ.* **37**, 2317–2325 (2003)
- 19.122 National Atmospheric Deposition Program: *Standard Definitions for AMoN Special Study Intercomparison Calculations* (Illinois State Water Survey, Champaign 2009), SOP Number: Da-4065.0
- 19.123 T.T.N. Lan, R. Nishimura, Y. Tsujino, K. Imamura, M. Warashina, N.T. Hoang, Y. Maeda: Atmospheric concentrations of sulfur dioxide, nitrogen oxides, ammonia, hydrogen chloride, nitric acid, formic and acetic acids in the south of Vietnam measured by the passive sampling method, *Anal. Sci.* **20**, 213–217 (2004)
- 19.124 C.H.F. Atkins, D.S. Lee: *The Distribution of Ammonia in the United Kingdom* (Harwell Laboratory, Oxfordshire 1992), Tech. Rep. AEA-EE-0330
- 19.125 T.R. Thijssse, G.P. Wyers, J.H. Duyzer, H.L.M. Verhagen, A. Wayers, J.J. Möls: Measurement of ambient ammonia with diffusion tube samplers, *Atmos. Environ.* **32**, 333–337 (1998)
- 19.126 M.A. Sutton, B.P. Miners, G.P. Wyers, J.H. Duyzer, C. Milford, J.N. Cape, D. Fowler: *National Ammonia Concentration Monitoring in the United Kingdom: Sampling Intercomparison, Network Structure and Initial Network Results* (Institute of Terrestrial Ecology, Edinburgh 1997), Report to the Department of the Environment (EPG 1/3/58)
- 19.127 A. Blatter, M. Fahrni, A. Neftel: A new generation of NH₃ passive samplers. In: *Air Pollution Research Report No. 41*, ed. by I. Allegrini (CEC, Brussels 1992) pp. 171–176
- 19.128 M. Ferm, H. Rodhe: Measurements of air concentrations of SO₂, NO₂ and NH₃ at rural and remote sites in Asia, *J. Atmos. Chem.* **27**, 17–29 (1997)
- 19.129 M. Ferm, P.A. Svanberg: Cost-efficient techniques for urban- and background measurements of SO₂ and NO₂, *Atmos. Environ.* **32**, 1377–1381 (1998)
- 19.130 J.J.H. Willems: *Low-Cost Methods for Measuring Air Pollutants* (Wageningen Agricultural University, Wageningen 1993), Tech. Rep. No. R-635
- 19.131 Y.S. Tang, J.N. Cape, M.A. Sutton: Development and types of passive samplers for monitoring atmospheric NO₂ and NH₃ concentrations, *Sci. World J.* **1**, 513–529 (2001)
- 19.132 H. Tang, T. Lau, B. Brassard, W. Cool: A new all-season passive sampling system for monitoring NO₂ in air, *Field Anal. Chem. Technol.* **3**, 338–345 (1999)
- 19.133 D. Krochmal, A. Kalina: A method of nitrogen dioxide and sulphur dioxide determination in ambient air by use of passive samplers and ion chromatography, *Atmos. Environ.* **31**, 3473–3479 (1997)
- 19.134 N.E. Rabaud, T.A. James, L.L. Ashbaugh, R.G. Flocchini: A passive sampler for the determination of airborne ammonia concentrations near large-scale animal facilities, *Environ. Sci. Technol.* **35**, 1190–1196 (2001)
- 19.135 A. Kasper, H. Puxbaum: Badge-type passive sampler for monitoring ambient ammonia concentrations, *Fresenius J. Anal. Chem.* **350**, 448–453 (1994)
- 19.136 F. De Santis, C. Vazzana, S. Menichelli, I. Allegrini: The measurement of atmospheric pollutants by passive sampling at the Uffizi gallery, Florence, *Ann. Chim.* **93**, 45–53 (2003)
- 19.137 B.R. Appel, Y. Tokiwa, M. Haik: Sampling of nitrates in ambient air, *Atmos. Environ.* **15**, 283–289 (1981)
- 19.138 B.R. Appel, S.M. Wall, Y. Tokiwa, M. Haik: Simultaneous nitric acid, particulate nitrate and acidity measurements in ambient air, *Atmos. Environ.* **14**, 549–554 (1980)
- 19.139 S.H. Cadle, R.J. Countess, N.A. Kelly: Nitric acid and ammonia in urban and rural locations, *Atmos. Environ.* **16**, 2501–2506 (1982)
- 19.140 D.D. Parrish, R.B. Norton, M.J. Bollinger, S.C. Liu, P.C. Murphy, D.L. Albritton, F.C. Fehsenfeld, B.J. Huebert: Measurements of HNO₃ and NH₃ particulates at a rural site in the Colorado Mountains, *J. Geophys. Res. Atmos.* **91**, 5379–5393 (1986)
- 19.141 J.F. Galasyn, K.L. Tschudy, B.J. Huebert: Seasonal and diurnal variability of nitric acid vapor and ionic aerosol species in the remote free troposphere at Mauna-Loa, Hawaii, *J. Geophys. Res.* **92**, 3105–3113 (1987)
- 19.142 P.A. Solomon, S.M. Larson, T. Fall, G.R. Cass: Basin-wide nitric acid and related species concentrations observed during the Claremont Nitrogen Species Comparison Study, *Atmos. Environ.* **22**, 1587–1594 (1988)
- 19.143 B.R. Appel, Y. Tokiwa, V. Povard, E.L. Kothny: The measurement of atmospheric hydrochloric acid in Southern California, *Atmos. Environ. A* **25**, 525–527 (1991)
- 19.144 A.M.N. Kitto, R.M. Harrison: Nitrous and nitric acid measurements at sites in South-East England, *Atmos. Environ. A* **26**, 235–241 (1992)
- 19.145 R.M. Harrison, J.D. Peak, G.M. Collins: Tropospheric cycle of nitrous acid, *J. Geophys. Res.* **101**, 14429–14439 (1996)
- 19.146 D. Danalatos, S. Glavas: Gas phase nitric acid, ammonia and related particulate matter at a mediterranean coastal site, Patras, Greece, *Atmos. Environ.* **33**, 3417–3425 (1999)
- 19.147 M. Possanzini, F. De Santis, V. Di Palo: Measurements of nitric acid and ammonium salts in Lower Bavaria, *Atmos. Environ.* **33**, 3597–3602 (1999)
- 19.148 D.J. Eatough, V.F. White, L.D. Hansen, N.L. Eatough, E.C. Ellis: Hydration of nitric acid and its collection in the atmosphere by diffusion denuders, *Anal. Chem.* **57**, 743–748 (1985)
- 19.149 J.L. Durham, L.L. Spiller, T.G. Ellestad: Nitric acid nitrate aerosol measurements by a diffusion denuder – A performance evaluation, *Atmos. Environ.* **21**, 589–598 (1987)
- 19.150 G.B. Marshall, N.A. Dimmock: Determination of nitric acid in ambient air using diffusion denuder tubes, *Talanta* **39**, 1463–1469 (1992)

- 19.151 P.K. Simon, P.K. Dasgupta, Z. Vecera: Wet effluent denuder coupled liquid ion chromatography systems, *Anal. Chem.* **63**, 1237–1242 (1991)
- 19.152 Z. Vecera, P.K. Dasgupta: Measurement of atmospheric nitric and nitrous acids with a wet effluent diffusion denuder and low-pressure ion chromatography post-column reaction detection, *Anal. Chem.* **63**, 2210–2216 (1991)
- 19.153 M. Taira, Y. Kanda: Wet effluent diffusion denuder for sampling of atmospheric gaseous nitric acid, *Anal. Chem.* **65**, 3171–3173 (1993)
- 19.154 S.M. Buhr, M.P. Buhr, F.C. Fehsenfeld, J.S. Holloway, U. Karst, R.B. Norton, D.D. Parrish, R.E. Sievers: Development of a semicontinuous method for the measurement of nitric acid vapor and particulate nitrate and sulfate, *Atmos. Environ.* **29**, 2609–2624 (1995)
- 19.155 C. Zellweger, M. Ammann, P. Hofer, U. Baltensperger: NO_y speciation with a combined wet effluent diffusion denuder-aerosol collector coupled to ion chromatography, *Atmos. Environ.* **33**, 1131–1140 (1999)
- 19.156 P.K. Simon, P.K. Dasgupta: Wet effluent denuder coupled liquid ion chromatography systems – Annular and parallel-plate denuders, *Anal. Chem.* **65**, 1134–1139 (1993)
- 19.157 C.B. Boring, S.K. Poruthoor, P.K. Dasgupta: Wet effluent parallel plate diffusion denuder coupled capillary ion chromatograph for the determination of atmospheric trace gases, *Talanta* **48**, 675–684 (1999)
- 19.158 G.F. Zhang, S. Slanina, C.B. Boring, P.A.C. Jongejan, P.K. Dasgupta: Continuous wet denuder measurements of atmospheric nitric and nitrous acids during the 1999 Atlanta supersite, *Atmos. Environ.* **37**, 1351–1364 (2003)
- 19.159 M.P. Keuken, A. Wayers-Ijpelaar, J.J. Mols, R.P. Otjes, J. Slanina: The determination of ammonia in ambient air by an automated thermodenuder system, *Atmos. Environ.* **23**, 2177–2185 (1989)
- 19.160 D. Klockow, R. Niessner, M. Malejczyk, H. Kiendl, B. Vomberg, M.P. Keuken, A. Wayers-Ypelaar, J. Slanina: Determination of nitric acid and ammonium nitrate by means of a computer controlled thermodenuder system, *Atmos. Environ.* **23**, 1131–1138 (1989)
- 19.161 M.P. Keuken, C.A.M. Schoonebeek, A. Vansvensenlouter, J. Slanina: Simultaneous sampling of NH₃, HNO₃, HCl, SO₂ and H₂O₂ in ambient air by a wet annular denuder system, *Atmos. Environ.* **22**, 2541–2548 (1988)
- 19.162 G.P. Wyers, R.P. Otjes, J. Slanina: A continuous-flow denuder for the measurement of ambient concentrations and surface-exchange fluxes of ammonia, *Atmos. Environ. A* **27**, 2085–2090 (1993)
- 19.163 J. Slanina, G.P. Wyers: Monitoring of atmospheric components by automatic denuder systems, *Fresenius J. Anal. Chem.* **350**, 467–473 (1994)
- 19.164 M.T. Oms, P.A.C. Jongejan, A.C. Veltkamp, G.P. Wyers, J. Slanina: Continuous monitoring of atmospheric HCl, HNO₂, HNO₃, and SO₂, by wet-annular denuder air sampling with on-line chromatographic analysis, *Int. J. Environ. Anal. Chem.* **62**, 207–218 (1996)
- 19.165 P.A.C. Jongejan, Y. Bai, A.C. Veltkamp, G.P. Wyers, J. Slanina: An automated field instrument for the determination of acidic gases in air, *Int. J. Environ. Anal. Chem.* **66**, 241–251 (1997)
- 19.166 I. Allegrini, A. Febo, C. Perrino, P. Masia: Measurement of atmospheric nitric acid in gas-phase and nitrate in particulate matter by means of annular denuders, *Int. J. Environ. Anal. Chem.* **54**, 183–201 (1994)
- 19.167 P. Matusca, B. Schwarz, K. Bachmann: Measurements of diurnal concentration variations of gaseous HCl in air in the subnanogram range, *Atmos. Environ.* **18**, 1667–1675 (1984)
- 19.168 W.R. Cofer, V.G. Collins, R.W. Talbot: Improved aqueous scrubber for collection of soluble atmospheric trace gases, *Environ. Sci. Technol.* **19**, 557–560 (1985)
- 19.169 D.A. Philips, P.K. Dasgupta: A diffusion scrubber for the collection of gaseous nitric acid, *Sep. Sci. Technol.* **22**, 1255–1267 (1987)
- 19.170 P.F. Lindgren: Diffusion scrubber-ion chromatography for the measurement of trace levels of atmospheric HCl, *Atmos. Environ. A* **26**, 43–49 (1992)
- 19.171 B.L. Lefer, R.W. Talbot, J.W. Munger: Nitric acid and ammonia at a rural northeastern US site, *J. Geophys. Res.* **104**, 1645–1661 (1999)
- 19.172 E. Sanhueza, A. Garaboto: Gaseous HCl at a remote tropical continental site, *Tellus B* **54**, 412–415 (2002)
- 19.173 I. Trebs, F.X. Meixner, J. Slanina, R. Otjes, P. Jongejan, M.O. Andreae: Real-time measurements of ammonia, acidic trace gases and water-soluble inorganic aerosol species at a rural site in the Amazon basin, *Atmos. Chem. Phys.* **4**, 967–987 (2004)
- 19.174 C. Perrino, F. de Santis, A. Febo: Uptake of nitrous acid and nitrogen oxides by nylon surfaces: Implications for nitric acid measurements, *Atmos. Environ.* **22**, 1925–1930 (1988)
- 19.175 C. Perrino, F. de Santis, A. Febo: Criteria of the choice of a denuder sampling technique devoted to the measurement of atmospheric nitrous and nitric acids, *Atmos. Environ. A* **24**, 617–626 (1990)
- 19.176 A. Bari, V. Ferraro, L.R. Wilson, D. Luttinger, L. Husain: Measurements of gaseous HONO, HNO₃, SO₂, HCl, NH₃, particulate sulfate and PM_{2.5} in New York, *Atmos. Environ.* **37**, 2825–2835 (2003)
- 19.177 C.W. Spicer, J.E. Howes, T.A. Bishop, L.H. Arnold, R.K. Stevens: Nitric acid measurement methods – An intercomparison, *Atmos. Environ.* **16**, 1487–1500 (1982)
- 19.178 S.V. Hering, D.R. Lawson, I. Allegrini, A. Febo, C. Perrino, M. Possanzini, J.E. Sickles, K.G. Anlauf, A. Wiebe, B.R. Appel, W. John, J. Ondo, S. Wall, R.S. Braman, R. Sutton, G.R. Cass, P.A. Solomon, D.J. Eatough, N.L. Eatough, E.C. Ellis, D. Grosjean, B.B. Hicks, J.D. Womack, J. Horrocks, K.T. Knapp, T.G. Ellestad, R.J. Paur, W.J. Mitchell, M. Pleasant, E. Peake, A. Maclean, W.R. Pierson, W. Brachaczek,

- H.I. Schiff, G.I. Mackay, C.W. Spicer, D.H. Stedman, A.M. Winer, H.W. Biermann, E.C. Tuazon: The nitric acid shootout – Field comparison of measurement methods, *Atmos. Environ.* **22**, 1519–1539 (1988)
- 19.179 E.J. Williams, S.T. Sandholm, J.D. Bradshaw, J.S. Schendel, A.O. Langford, P.K. Quinn, P.J. Lebel, S.A. Vay, P.D. Roberts, R.B. Norton, B.A. Watkins, M.P. Buhr, D.D. Parrish, J.G. Calvert, F.C. Fehsenfeld: An intercomparison of 5 ammonia measurement techniques, *J. Geophys. Res.* **97**, 11591–11611 (1992)
- 19.180 P.K. Dasgupta: Automated measurement of atmospheric trace gases. In: *Measurement Challenges in Atmospheric Chemistry*, Advances in Chemistry, Vol. 232, ed. by L. Newman (American Chemical Society, Washington 1993) pp. 41–90
- 19.181 C.J. Hennigan, M.H. Bergin, J.E. Dibb, R.J. Weber: Enhanced secondary organic aerosol formation due to water uptake by fine particles, *Geophys. Res. Lett.* **35**, L18801 (2008)
- 19.182 C. Anderson, J.E. Dibb, R.J. Griffin, M.H. Bergin: Simultaneous measurements of particulate and gas-phase water-soluble organic carbon concentrations at remote and urban-influenced locations, *Geophys. Res. Lett.* **35**, L13706 (2008)
- 19.183 R.S. Spaulding, R.W. Talbot, M.J. Charles: Optimization of a mist chamber (cofer scrubber) for sampling water-soluble organics in air, *Environ. Sci. Technol.* **36**, 1798–1808 (2002)
- 19.184 A.P. Sullivan, N. Hodas, B.J. Turpin, K. Skog, F.N. Keutsch, S. Gilardoni, M. Paglione, M. Rinaldi, S. Decesari, M.C. Facchini, L. Poulain, H. Herrmann, A. Wiedensohler, E. Nemitz, M.M. Twigg, J.L. Collett Jr: Evidence for ambient dark aqueous SOA formation in the Po valley, Italy, *Atmos. Chem. Phys.* **16**, 8095–8108 (2016)
- 19.185 S.M. Duncan, K.G. Sexton, B.J. Turpin: Oxygenated VOCs, aqueous chemistry, and potential impacts on residential indoor air composition, *Indoor Air* **28**, 198–212 (2018)
- 19.186 P. Solomon, K. Baumann, E. Edgerton, R. Tanner, D. Eatough, W. Modey, H. Marin, D. Savoie, S. Natarajan, M.B. Meyer, G. Norris: Comparison of integrated samplers for mass and composition during the 1999 Atlanta Supersites Project, *J. Geophys. Res.* **108**, 8423 (2003)
- 19.187 A.G. Allen, R.M. Harrison, J.W. Erisman: Field-measurements of the dissociation of ammonium-nitrate and ammonium-chloride aerosols, *Atmos. Environ.* **23**, 1591–1599 (1989)
- 19.188 M. Possanzini, P. Masia, V. Dipalo: Speciation of ammonium-containing species in atmospheric aerosols, *Atmos. Environ. A* **26**, 1995–2000 (1992)
- 19.189 D.A. Lane, A.J. Peters, L.A. Gundel, K.C. Jones, G.L. Northcott: Gas/particle partition measurements of PAH at Hazelrigg, U.K., *Polycycl. Aromat. Compd.* **20**, 225–234 (2000)
- 19.190 A.J. Peters, D.A. Lane, L.A. Gundel, G.L. Northcott, K.C. Jones: A comparison of high volume and diffusion denuder samplers for measuring semivolatile organic compounds in the atmosphere, *Environ. Sci. Technol.* **34**, 5001–5006 (2000)
- 19.191 T. Novakov, C.E. Corrigan, J.E. Penner, C.C. Chuang, O. Rosario, O.L.M. Bracero: Organic aerosols in the Caribbean trade winds: A natural source?, *J. Geophys. Res. Atmos.* **102**, 21307–21313 (1997)
- 19.192 K. Baumann, F. Ift, J.Z. Zhao, W.L. Chameides: Discrete measurements of reactive gases and fine particle mass and composition during the 1999 Atlanta Supersite Experiment, *J. Geophys. Res. Atmos.* **108**, S05 4–1–S05 4–20 (2003)
- 19.193 I. Kamprad, K.U. Goss: Systematic investigation of the sorption properties of polyurethane foams for organic vapors, *Anal. Chem.* **79**, 4222–4227 (2007)
- 19.194 T.F. Bidleman, M. Tysklind: Breakthrough during air sampling with polyurethane foam: What do PUF 2/PUF 1 ratios mean?, *Chemosphere* **192**, 267–271 (2018)
- 19.195 J.W. Martin, D.C.G. Muir, C.A. Moody, D.A. Ellis, W.C. Kwan, K.R. Solomon, S.A. Mabury: Collection of airborne fluorinated organics and analysis by gas chromatography/chemical ionization mass spectrometry, *Anal. Chem.* **74**, 584–590 (2002)
- 19.196 C. Mai, N. Theobald, G. Lammel, H. Hühnerfuss: Spatial, seasonal and vertical distributions of currently-used pesticides in the marine boundary layer of the North Sea, *Atmos. Environ.* **75**, 92–102 (2013)
- 19.197 H.P.H. Arp, K.-U. Goss: Irreversible sorption of trace concentrations of perfluorocarboxylic acids to fiber filters used for air sampling, *Atmos. Environ.* **42**, 6869–6872 (2008)
- 19.198 W. Birmili, K. Stopfkuchen, M. Hermann, A. Wiedensohler, J. Heintzenberg: Particle penetration through a 300 m inlet pipe for sampling atmospheric aerosols from a tall meteorological tower, *Aerosol Sci. Technol.* **41**, 811–817 (2007)
- 19.199 C.A.M. Brenninkmeijer, P. Crutzen, F. Boumard, T. Dauer, B. Dix, R. Ebinghaus, D. Filippi, H. Fischer, H. Franke, U. Friess, J. Heintzenberg, F. Helleis, M. Hermann, H.H. Kock, C. Koepfel, J. Lelieveld, M. Leuenberger, B.G. Martinsson, S. Miemczyk, H.P. Moret, H.N. Nguyen, P. Nyfeler, D. Oram, D. O’Sullivan, S. Penkett, U. Platt, M. Pupek, M. Ramonet, B. Randa, M. Reichelt, T.S. Rhee, J. Rohwer, K. Rosenfeld, D. Scharffe, H. Schlager, U. Schumann, F. Slemr, D. Sprung, P. Stock, R. Thaler, F. Valentino, P. van Velthoven, A. Waibel, A. Wandel, K. Waschitschek, A. Wiedensohler, I. Xueref-Remy, A. Zahn, U. Zech, H. Ziereis: Civil aircraft for the regular investigation of the atmosphere based on an instrumented container: The new CARIBIC system, *Atmos. Chem. Phys.* **7**, 4953–4976 (2007)
- 19.200 C.A.M. Brenninkmeijer, P.J. Crutzen, H. Fischer, H. Güsten, W. Hans, G. Heinrich, J. Heintzenberg, M. Hermann, T. Immelmann, D. Kersting, M. Maiss, M. Nolle, A. Pitscheider, H. Pohlkamp, D. Scharffe, K. Specht, A. Wiedensohler: CARIBIC–Civil aircraft for global measurement of trace gases and aerosols in the tropopause

- region, *J. Atmos. Ocean. Technol.* **16**, 1373–1383 (1999)
- 19.201 M. Krämer, A. Afchine: Sampling characteristics of inlets operated at low U/U_0 ratios: New insights from computational fluid dynamics (CFX) modeling, *J. Aerosol Sci.* **35**, 683–694 (2004)
- 19.202 J.N. Porter, A.D. Clarke, G. Ferry, R.F. Pueschel: Aircraft studies of size-dependent aerosol sampling through inlets, *J. Geophys. Res. Atmos.* **97**, 3815–3824 (1992)
- 19.203 J.E. Brockmann: Aerosol transport in sampling lines and inlets. In: *Aerosol Measurement: Principles, Techniques, and Applications*, 3rd edn., ed. by P. Kulkaarni, P.A. Baron, K. Willeke (John Wiley & Sons, Hoboken 2011), Chap. 6
- 19.204 K.E. Noll: A rotary inertial impactor for sampling giant particles in the atmosphere, *Atmos. Environ.* **4**, 9–19 (1970)
- 19.205 F. Di-Giovanni: A review of the sampling efficiency of rotating-arm impactors used in aerobiological studies, *Grana* **37**, 164–171 (1998)
- 19.206 E. Levetin: Methods for aeroallergen sampling, *Curr. Allergy Asthma Rep.* **4**, 376–383 (2004)
- 19.207 M.J. Heffer, J.D. Ratz, J.D. Miller, J.H. Day: Comparison of the rotorod to other air samplers for the determination of *Ambrosia artemisiifolia* pollen concentrations conducted in the environmental exposure unit, *Aerobiologia* **21**, 233–239 (2005)
- 19.208 W.R. Solomon, H.A. Burge, J.R. Boise, M. Becker: Comparative particle recoveries by the retracting rotorod, rotoslide and Burkard spore trap sampling in a compact array, *Int. J. Biometeorol.* **24**, 107–116 (1980)
- 19.209 B.W. Loo, C.P. Cork: Development of high-efficiency virtual impactors, *Aerosol Sci. Technol.* **9**, 167–176 (1988)
- 19.210 V.A. Marple, K.L. Rubow, W. Turner, J.D. Spengler: Low flow rate sharp cut impactors for indoor air sampling: Design and calibration, *J. Air Waste Manag. Assoc.* **37**, 1303–1307 (1987)
- 19.211 W.A. Turner, B.A. Olson, G.A. Allen: Calibration of sharp cut impactors for indoor and outdoor particle sampling, *J. Air Waste Manag. Assoc.* **50**, 484–487 (2000)
- 19.212 C. Sioutas, S.T. Ferguson, J.M. Wolfson, H. Ozkaynak, P. Koutrakis: Inertial collection of fine particles using a high-volume rectangular geometry conventional impactor, *J. Aerosol Sci.* **28**, 1015–1028 (1997)
- 19.213 W. Maenhaut, G. Ducastel, R.E. Hillamo, T.A. Pakkanen: Evaluation of the applicability of the MOUDI impactor for aerosol collections with subsequent multielement analysis by PIXE, *Nucl. Instrum. Methods Phys. Res. B* **75**, 249–256 (1993)
- 19.214 L.G. Cena, W.P. Chisholm, M.J. Keane, A. Cumpston, B.T. Chen: Size distribution and estimated respiratory deposition of total chromium, hexavalent chromium, manganese, and nickel in gas metal arc welding fume aerosols, *Aerosol Sci. Technol.* **48**, 1254–1263 (2014)
- 19.215 A. Laskin, R.C. Moffet, M.K. Gilles, J.D. Fast, R.A. Zaveri, B. Wang, P. Nigge, J. Shutthanandan: Tropospheric chemistry of internally mixed sea salt and organic particles: Surprising reactivity of NaCl with weak organic acids, *J. Geophys. Res. Atmos.* **117**, D15302 (2012)
- 19.216 T.G. Dzubay, L.E. Hines, R.K. Stevens: Particle bounce errors in cascade impactors, *Atmos. Environ.* **10**, 229–234 (1976)
- 19.217 T. Reponen, K. Willeke, S. Grinshpun, A. Nevalainen: Biological particle sampling. In: *Aerosol Measurement: Principles, Techniques, and Applications*, 3rd edn., ed. by P. Kulkaarni, P.A. Baron, K. Willeke (John Wiley & Sons, Hoboken 2011), Chap. 24
- 19.218 J.E. Boulter, D.J. Cziczo, A.M. Middlebrook, D.S. Thomson, D.M. Murphy: Design and performance of a pumped counterflow virtual impactor, *Aerosol Sci. Technol.* **40**, 969–976 (2006)
- 19.219 P.A. Solomon, J.L. Moyers, R.A. Fletcher: High-volume dichotomous virtual impactor for the fractionation and collection of particles according to aerodynamic size, *Aerosol Sci. Technol.* **2**, 455–464 (1983)
- 19.220 S.F. Maria, L.M. Russell, B.J. Turpin, R.J. Porcja: FTIR measurements of functional groups and organic mass in aerosol samples over the Caribbean, *Atmos. Environ.* **36**, 5185–5196 (2002)
- 19.221 T.G. Dzubay, R.K. Stevens: Ambient air analysis with dichotomous sampler and X-ray-fluorescence spectrometer, *Environ. Sci. Technol.* **9**, 663–668 (1975)
- 19.222 A. Hoffer, A. Gelencser, P. Guyon, G. Kiss, O. Schmid, G.P. Frank, P. Artaxo, M.O. Andreae: Optical properties of humic-like substances (HULIS) in biomass-burning aerosols, *Atmos. Chem. Phys.* **6**, 3563–3570 (2006)
- 19.223 S. Kim, P.A. Jaques, M. Chang, J.R. Froines, C. Sioutas: Versatile aerosol concentration enrichment system (VACES) for simultaneous in vivo and in vitro evaluation of toxic effects of ultrafine, fine and coarse ambient particles. Part I: Development and laboratory characterization, *J. Aerosol Sci.* **32**, 1281–1297 (2001)
- 19.224 L. Ma, D.B. Ingham, X. Wen: Numerical modelling of the fluid and particle penetration through small sampling cyclones, *J. Aerosol Sci.* **31**, 1097–1119 (2000)
- 19.225 X. Lin, T. Reponen, K. Willeke, Z. Wang, S.A. Grinshpun, M. Trunov: Survival of airborne microorganisms during swirling aerosol collection, *Aerosol Sci. Technol.* **32**, 184–196 (2000)
- 19.226 W.B. Smith, J.R.R. Wilson, D.B. Harris: A five-stage cyclone system for in situ sampling, *Environ. Sci. Technol.* **13**, 1387–1392 (1979)
- 19.227 W. John, G. Reischl: A cyclone for size-selective sampling of ambient air, *J. Air Pollut. Control Assoc.* **30**, 872–876 (1980)
- 19.228 W.G. Lindsley, D. Schmechel, B.T. Chen: A two-stage cyclone using microcentrifuge tubes for personal bioaerosol sampling, *J. Environ. Monit.* **8**, 1136–1142 (2006)

- 19.229 M.E. Moore, A.R. McFarland: Performance modeling of single-inlet aerosol sampling cyclones, *Environ. Sci. Technol.* **27**, 1842–1848 (1993)
- 19.230 R.A. Gussman, L.C. Kenny, M. Labickas, P. Norton: Design, calibration, and field test of a cyclone for PM₁ ambient air sampling, *Aerosol Sci. Technol.* **36**, 361–365 (2002)
- 19.231 E. Carvalho, C. Sindt, A. Verdier, C. Galan, L. O'Donoghue, S. Parks, M. Thibaudon: Performance of the coriolis air sampler, a high-volume aerosol-collection system for quantification of airborne spores and pollen grains, *Aerobiologia* **24**, 191–201 (2008)
- 19.232 J. Kesavan, D. Schepers, A.R. McFarland: Sampling and retention efficiencies of batch-type liquid-based bioaerosol samplers, *Aerosol Sci. Technol.* **44**, 817–829 (2010)
- 19.233 C.W. Haig, W.G. Mackay, J.T. Walker, C. Williams: Bioaerosol sampling: Sampling mechanisms, bio-efficiency and field studies, *J. Hosp. Infect.* **93**, 242–255 (2016)
- 19.234 D. Gonzalez, A.G. Nasibulin, A.M. Baklanov, S.D. Shandakov, D.P. Brown, P. Queipo, E.I. Kaupinen: A new thermophoretic precipitator for collection of nanometer-sized aerosol particles, *Aerosol Sci. Technol.* **39**, 1064–1071 (2005)
- 19.235 A. Miller, G. Frey, G. King, C. Sunderman: A handheld electrostatic precipitator for sampling airborne particles and nanoparticles, *Aerosol Sci. Technol.* **44**, 417–427 (2010)
- 19.236 G. Pardon, L. Ladhani, N. Sandström, M. Ettori, G. Lobov, W. van der Wijngaart: Aerosol sampling using an electrostatic precipitator integrated with a microfluidic interface, *Sens. Actuators B* **212**, 344–352 (2015)
- 19.237 D.S. Ensor, A.S. Viner, E.W. Johnson, R.P. Donovan, P.B. Keady, K.J. Weyrauch: Measurement of ultrafine aerosol particle size distributions at low concentrations by parallel arrays of a diffusion battery and a condensation nucleus counter in series, *J. Aerosol Sci.* **20**, 471–475 (1989)
- 19.238 E.O. Knutson: History of diffusion batteries in aerosol measurements, *Aerosol Sci. Technol.* **31**, 83–128 (1999)
- 19.239 A.A. Onischuk, A.M. Baklanov, S.V. Valiulin, P.P. Moiseenko, V.G. Mitrochenko: Aerosol diffusion battery: The retrieval of particle size distribution with the help of analytical formulas, *Aerosol Sci. Technol.* **52**, 165–181 (2018)
- 19.240 Y. Cheng: Instruments and samplers based on diffusional separation. In: *Aerosol Measurement: Principles, Techniques, and Applications*, 3rd edn., ed. by P. Kulkarni, P.A. Baron, K. Willeke (John Wiley & Sons, Hoboken 2011), Chap. 16
- 19.241 P. Feldpausch, M. Fiebig, L. Fritzsche, A. Petzold: Measurement of ultrafine aerosol size distributions by a combination of diffusion screen separators and condensation particle counters, *J. Aerosol Sci.* **37**, 577–597 (2006)
- 19.242 D.J.H. Vosburgh, T. Klein, M. Sheehan, T.R. Anthony, T.M. Peters: Design and evaluation of a personal diffusion battery, *Aerosol Sci. Technol.* **47**, 435–443 (2013)
- 19.243 M. Fierz, S. Weimer, H. Burtscher: Design and performance of an optimized electrical diffusion battery, *J. Aerosol Sci.* **40**, 152–163 (2009)
- 19.244 A.D. Maynard, L.M. Brown: The collection of ultra-fine aerosol particles for analysis by transmission electron microscopy, using a new thermophoretic precipitator, *J. Aerosol Sci.* **22**, S379–S382 (1991)
- 19.245 S.R. Boddu, V.R. Gutti, T.K. Ghosh, R.V. Tompson, S.K. Loyalka: Gold, silver, and palladium nanoparticle/nano-agglomerate generation, collection, and characterization, *J. Nanopart. Res.* **13**, 6591–6601 (2011)
- 19.246 A. Messerer, R. Niessner, U. Pöschl: Thermophoretic deposition of soot aerosol particles under experimental conditions relevant for modern diesel engine exhaust gas systems, *J. Aerosol Sci.* **34**, 1009–1021 (2003)
- 19.247 N. Azong-Wara, C. Asbach, B. Stahlmecke, H. Fissan, H. Kaminski, S. Plitzko, D. Bathen, T.A.J. Kuhlbusch: Design and experimental evaluation of a new nanoparticle thermophoretic personal sampler, *J. Nanopart. Res.* **15**, 1530 (2013)
- 19.248 P.E. Morrow, T.T. Mercer: A point-to-plane electrostatic precipitator for particle size sampling, *Am. Ind. Hyg. Assoc. J.* **25**, 8–14 (1964)
- 19.249 B.Y.H. Liu, K.T. Whitby, H.H.S. Yu: Electrostatic aerosol sampler for light and electron microscopy, *Rev. Sci. Instrum.* **38**, 100–102 (1967)
- 19.250 M. Fierz, R. Kaegi, H. Burtscher: Theoretical and experimental evaluation of a portable electrostatic TEM sampler, *Aerosol Sci. Technol.* **41**, 520–528 (2007)
- 19.251 J. Zavala, K. Lichtveld, S. Ebersviller, J.L. Carson, G.W. Walters, I. Jaspers, H.E. Jeffries, K.G. Sexton, W. Vizuete: The Gillings sampler – An electrostatic air sampler as an alternative method for aerosol in vitro exposure studies, *Chem. Biol. Interact.* **220**, 158–168 (2014)
- 19.252 J. Dixkens, H. Fissan: Development of an electrostatic precipitator for off-line particle analysis, *Aerosol Sci. Technol.* **30**, 438–453 (1999)
- 19.253 M. Sillanpää, M.D. Geller, H.C. Phuleria, C. Sioutas: High collection efficiency electrostatic precipitator for in vitro cell exposure to concentrated ambient particulate matter (PM), *J. Aerosol Sci.* **39**, 335–347 (2008)
- 19.254 G. Mainelis, K. Willeke, A. Adhikari, T. Reponen, S.A. Grinshpun: Design and collection efficiency of a new electrostatic precipitator for bioaerosol collection, *Aerosol Sci. Technol.* **36**, 1073–1085 (2002)
- 19.255 D. Magyar: Aeromycological aspects of mycotechnology. In: *Mycotechnology: Present Status and Future Prospects*, ed. by M. Rai (International Publishing House Pvt. Ltd., New Delhi 2007) pp. 226–261
- 19.256 K. Kandler, K. Schneiders, M. Ebert, M. Hartmann, S. Weinbruch, M. Prass, C. Pöhlker: Composition and mixing state of atmospheric aerosols determined by electron microscopy: Method de-

- velopment and application to aged Saharan dust deposition in the Caribbean boundary layer, *Atmos. Chem. Phys.* **18**, 13429–13455 (2018)
- 19.257 P. Artaxo, H. Storms, F. Bruynseels, R. Van Grieken, W. Maenhaut: Composition and sources of aerosols from the Amazon basin, *J. Geophys. Res. Atmos.* **93**, 1605–1615 (1988)
- 19.258 A. Kumar, W. Abouchami, S.J.G. Galer, S.P. Singh, K.W. Fomba, J.M. Prospero, M.O. Andreae: Seasonal radiogenic isotopic variability of the african dust outflow to the tropical Atlantic Ocean and across to the Caribbean, *Earth Planet. Sci. Lett.* **487**, 94–105 (2018)
- 19.259 M. Kamruzzaman, S. Takahama, A.M. Dillner: Quantification of amine functional groups and their influence on OM/OC in the IMPROVE Network, *Atmos. Environ.* **172**, 124–132 (2018)
- 19.260 J. Fröhlich–Nowoisky, D.A. Pickersgill, V.R. Després, U. Pöschl: High diversity of fungi in air particulate matter, *Proc. Natl. Acad. Sci. U. S. A.* **106**, 12814–12819 (2009)
- 19.261 J.C. Chow: Measurement methods to determine compliance with ambient air quality standards for suspended particles, *J. Air Waste Manag. Assoc.* **45**, 320–382 (1995)
- 19.262 J.F. Pankow: Overview of the gas–phase retention volume behavior of organic–compounds on polyurethane foam, *Atmos. Environ.* **23**, 1107–1111 (1989)
- 19.263 M. Mandalakis, E.G. Stephanou: Polychlorinated biphenyls associated with fine particles (PM_{2.5}) in the urban environment of Chile: Concentration levels, and sampling volatilization losses, *Environ. Toxicol. Chem.* **21**, 2270–2275 (2002)
- 19.264 J.N. Pitts, K.A. Vancauwenberghe, D. Grosjean, J.P. Schmid, D.R. Fitz, W.L. Belsler, G.B. Knudson, P.M. Hynds: Atmospheric reactions of polycyclic aromatic–hydrocarbons – Facile formation of mutagenic nitro–derivatives, *Science* **202**, 515–519 (1978)
- 19.265 I.G. Kavouras, J. Lawrence, P. Koutrakis, E.G. Stephanou, P. Oyola: Measurement of particulate aliphatic and polynuclear aromatic hydrocarbons in Santiago De Chile: Source reconciliation and evaluation of sampling artifacts, *Atmos. Environ.* **33**, 4977–4986 (1999)
- 19.266 L. Melymuk, P. Bohlin–Nizzetto, R. Prokes, P. Kukucka, P. Pribylova, S. Vojta, J. Kohoutek, G. Lammel, J. Klanova: Uncertainties in monitoring of SVOCs in air caused by within–sampler degradation during active and passive air sampling, *Atmos. Environ.* **167**, 553–565 (2017)
- 19.267 WMO/GAW: *WMO/GAW Aerosol Measurement Procedures, Guidelines and Recommendations* (World Meteorological Organization & Global Atmosphere Watch, Geneva 2016)
- 19.268 ACTRIS: Actris Data Centre – An Atmospheric Data Portal, <http://actris.nilu.no/> (2018), Accessed 07 July 2021
- 19.269 U. Wätjen, H. Cavé: Reference materials in the context of calibration and quality control of PIXE analysis: The case of aerosol analysis, *Nucl. Instrum. Methods Phys. Res. B* **109/110**, 395–401 (1996)
- 19.270 A. Wiedensohler, W. Birmili, A. Nowak, A. Sonntag, K. Weinhold, M. Merkel, B. Wehner, T. Tuch, S. Pfeifer, M. Fiebig, A.M. Fjåraa, E. Asmi, K. Sellegri, R. Depuy, H. Venzac, P. Villani, P. Laj, P. Aalto, J.A. Ogren, E. Swietlicki, P. Williams, P. Roldin, P. Quincey, C. Hüglin, R. Fierz–Schmidhauser, M. Gysel, E. Weingartner, F. Riccobono, S. Santos, C. Grüning, K. Faloon, D. Beddows, R. Harrison, C. Monahan, S.G. Jennings, C.D. O’Dowd, A. Marinoni, H.G. Horn, L. Keck, J. Jiang, J. Scheckman, P.H. McMurry, Z. Deng, C.S. Zhao, M. Moerman, B. Henzing, G. de Leeuw, G. Löschau, S. Bastian: Mobility particle size spectrometers: Harmonization of technical standards and data structure to facilitate high quality long–term observations of atmospheric particle number size distributions, *Atmos. Meas. Tech.* **5**, 657–685 (2012)
- 19.271 J.C. Chow, J.G. Watson, J. Robles, X. Wang, L.W.A. Chen, D.L. Trimble, S.D. Kohl, R.J. Tropp, K.K. Fung: Quality assurance and quality control for thermal/optical analysis of aerosol samples for organic and elemental carbon, *Anal. Bioanal. Chem.* **401**, 3141–3152 (2011)
- 19.272 K.J. Koistinen, A. Kousa, V. Tenhola, O. Hänninen, M.J. Jantunen, L. Oglesby, N. Kuenzli, L. Georgoulis: Fine particle (PM_{2.5}) measurement methodology, quality assurance procedures, and pilot results of the *EXPOLIS* study, *J. Air Waste Manag. Assoc.* **49**, 1212–1220 (1999)
- 19.273 S.M. Almeida, M.A. Reis, M.C. Freitas, C.A. Pio: Quality assurance in elemental analysis of airborne particles, *Nucl. Instrum. Methods Phys. Res. B* **207**, 434–446 (2003)
- 19.274 R.H. Mason, C. Chou, C.S. McCluskey, E.J.T. Levin, C.L. Schiller, T.C.J. Hill, J.A. Huffman, P.J. DeMott, A.K. Bertram: The micro–orifice uniform deposit impactor–droplet freezing technique (MOUDI–DFT) for measuring concentrations of ice nucleating particles as a function of size: Improvements and initial validation, *Atmos. Meas. Tech.* **8**, 2449–2462 (2015)
- 19.275 A.A. May, A.A. Presto, C.J. Hennigan, N.T. Nguyen, T.D. Gordon, A.L. Robinson: Gas–particle partitioning of primary organic aerosol emissions: (1) Gasoline vehicle exhaust, *Atmos. Environ.* **77**, 128–139 (2013)
- 19.276 J.A. Huffman, P.J. Ziemann, J.T. Jayne, D.R. Worsnop, J.L. Jimenez: Development and characterization of a fast–stepping/scanning thermodenuder for chemically–resolved aerosol volatility measurements, *Aerosol Sci. Technol.* **42**, 395–407 (2008)
- 19.277 A.P. Bateman, Z. Gong, T.H. Harder, S.S. de Sá, B. Wang, P. Castillo, S. China, Y. Liu, R.E. O’Brien, B.B. Palm, H.W. Shiu, G.G. Cirino, R. Thalman, K. Adachi, M.L. Alexander, P. Artaxo, A.K. Bertram, P.R. Buseck, M.K. Gilles, J.L. Jimenez, A. Laskin, A.O. Manzi, A. Sedlacek, R.A.F. Souza, J. Wang, R. Zaveri, S.T. Martin: Anthropogenic influences on the physical state of submicron particulate

- matter over a tropical forest, *Atmos. Chem. Phys.* **17**, 1759–1773 (2017)
- 19.278 S.S. Pak, B.Y.H. Liu, K.L. Rubow: Effect of coating thickness on particle bounce in inertial impactors, *Aerosol Sci. Technol.* **16**, 141–150 (1992)
- 19.279 M. Adon, C. Galy-Lacaux, V. Yoboue, C. Delon, J.P. Lacaux, P. Castera, E. Gardrat, J. Pienaar, H. Al Ourabi, D. Laouali, B. Diop, L. Sigha-Nkamdjou, A. Akpo, J.P. Tathy, F. Lavenu, E. Mougin: Long term measurements of sulfur dioxide, nitrogen dioxide, ammonia, nitric acid and ozone in Africa using passive samplers, *Atmos. Chem. Phys.* **10**, 7467–7487 (2010)
- 19.280 G.R. Carmichael, M. Ferm, N. Thongboonchoo, J.H. Woo, L.Y. Chan, K. Murano, P.H. Viet, C. Mossberg, R. Bala, J. Boonjawat, P. Upatum, M. Mohan, S.P. Adhikary, A.B. Shrestha, J.J. Pienaar, E.B. Brunke, T. Chen, T. Jie, D. Guoan, L.C. Peng, S. Dhiharto, H. Harjanto, A.M. Jose, W. Kimani, A. Kirouane, J.P. Lacaux, S. Richard, O. Barturen, J.C. Cerda, A. Athayde, T. Tavares, J.S. Cotrina, E. Bilici: Measurements of sulfur dioxide, ozone and ammonia concentrations in Asia, Africa, and South America using passive samplers, *Atmos. Environ.* **37**, 1293–1308 (2003)
- 19.281 J.J. Martins, R.S. Dhammapala, G. Lachmann, C. Galy-Lacaux, J.J. Pienaar: Long-term measurements of sulphur dioxide, nitrogen dioxide, ammonia, nitric acid and ozone in Southern Africa using passive samplers, *S. Afr. J. Sci.* **103**, 336–342 (2007)
- 19.282 National Atmospheric Deposition Program: NADP Installation Manual, Version 1.9, http://nadp.slh.wisc.edu/lib/manuals/NADP_Site_Selection_and_Installation_Manual_2014_11.pdf (2014), Accessed 07 July 2021
- 19.283 J.J. Pienaar, J.P. Beukes, P.G. Van Zyl, C.M.B. Lehmann, J. Aherne: Chapter 2 – Passive diffusion sampling devices for monitoring ambient air concentrations. In: *Monitoring of Air Pollutants: Sampling, Sample Preparation and Analytical Techniques*, Comprehensive Analytical Chemistry, Vol. 70, ed. by P.B.C. Forbes (Elsevier, Oxford 2015) pp. 13–52
- 19.284 K. Pozo, T. Harner, F. Wania, D.C.G. Muir, K.C. Jones, L.A. Barrie: Toward a global network for persistent organic pollutants in air: Results from the GAPS study, *Environ. Sci. Technol.* **40**, 4867–4873 (2006)
- 19.285 UNEP: *Guidance on the Global Monitoring Plan for Persistent Organic Pollutants* (UNEP, Chatelaine 2015), UNEP/POPS/COP.7/INF/39
- 19.286 C. Rauert, T. Harner, J.K. Schuster, A. Eng, G. Fillmann, L.E. Castillo, O. Fentanes, M. Villa Ibarra, K.S.B. Miglioranza, I. Moreno Rivadeneira, K. Pozo, B.H. Aristizábal Zuluaga: Atmospheric concentrations of new persistent organic pollutants and emerging chemicals of concern in the group of Latin America and Caribbean (GRULAC) region, *Environ. Sci. Technol.* **52**, 7240–7249 (2018)
- 19.287 J. Klánová, P. Ěupr, J. Kohoutek, T. Harner: Assessing the influence of meteorological parameters on the performance of polyurethane foam-based passive air samplers, *Environ. Sci. Technol.* **42**, 550–555 (2008)
- 19.288 J. Klanova, P. Cupr, I. Holoubek, J. Boruvkova, P. Pribylova, R. Kares, T. Tomsej, T. Ocelka: Monitoring of persistent organic pollutants in Africa. Part 1: Passive air sampling across the continent in 2008, *J. Environ. Monit.* **11**, 1952–1963 (2009)
- 19.289 A.K. Halse, M. Schlabach, S. Eckhardt, A. Sweetman, K.C. Jones, K. Breivik: Spatial variability of POPs in European background air, *Atmos. Chem. Phys.* **11**, 1549–1564 (2011)
- 19.290 G. Lammel, O. Audy, A. Besis, C. Efstathiou, K. Eleftheriadis, J. Kohoutek, P. Kukucka, M.D. Mulder, P. Pribylova, R. Prokes, T.P. Rusina, C. Samara, A. Sofuoglu, S.C. Sofuoglu, Y. Tasdemir, V. Vassilatou, D. Voutsas, B. Vrana: Air and seawater pollution and air-sea gas exchange of persistent toxic substances in the Aegean Sea: Spatial trends of PAHs, PCBs, OCPs and PBDEs, *Environ. Sci. Pollut. Res.* **22**, 11301–11313 (2015)
- 19.291 L. Tuduri, M. Millet, O. Briand, M. Montury: Passive air sampling of semi-volatile organic compounds, *Trends Anal. Chem.* **31**, 38–49 (2012)
- 19.292 C. Chaemfa, E. Wild, B. Davison, J.L. Barber, K.C. Jones: A study of aerosol entrapment and the influence of wind speed, chamber design and foam density on polyurethane foam passive air samplers used for persistent organic pollutants, *J. Environ. Monit.* **11**, 1135–1139 (2009)
- 19.293 F. Wania, L. Shen, Y.D. Lei, C. Teixeira, D.C.G. Muir: Development and calibration of a resin-based passive sampling system for monitoring persistent organic pollutants in the atmosphere, *Environ. Sci. Technol.* **37**, 1352–1359 (2003)
- 19.294 S.V. Krupa, K. Baumann, E.S. Edgerton: *HNO₃ Passive Sampler Evaluation Study, Final Report* (Wood Buffalo Environmental Association, Fort McMurray 2012)
- 19.295 D.A. Hansen, E.S. Edgerton, B.E. Hartsell, J.J. Jansen, N. Kandasamy, G.M. Hidy, C.L. Blanchard: The Southeastern Aerosol Research and Characterization Study: Part 1 – Overview, *J. Air Waste Manag. Assoc.* **53**, 1460–1471 (2003)
- 19.296 M. Ferm, F. De Santis, C. Varotsos: Nitric acid measurements in connection with corrosion studies, *Atmos. Environ.* **39**, 6664–6672 (2005)
- 19.297 R.D. Saylor, E.S. Edgerton, B.E. Hartsell, K. Baumann, D.A. Hansen: Continuous gaseous and total ammonia measurements from the Southeastern Aerosol Research and Characterization (SEARCH) Study, *Atmos. Environ.* **44**, 4994–5004 (2010)
- 19.298 R. Hůlek, J. Borůvková, J. Gregor, J. Kalina, Z. Bednářová, K. Šebková, T. Hruban, V. Novotný, M. Ismael, J. Klánová: Global Monitoring Plan Data Warehouse of the Stockholm Convention on Persistent Organic Pollutants: Visualisation and on-line analysis of global levels of chemicals in air, water, breast milk and blood (Masaryk University, Brno, Czech Republic, 2020), <https://www.pops-gmp.org/index.php?pg=gmp-data->

- warehouse and <https://www.pops-gmp.org/index.php?pg=contact>, Accessed 07 July 2021
- 19.299 M. Venier, H. Hung, W. Tych, R.A. Hites: Temporal trends of persistent organic pollutants: A comparison of different time series models, *Environ. Sci. Technol.* **46**, 3928–3934 (2012)
- 19.300 H. Hung, A.A. Katsoyiannis, E. Brorstrom-Lunden, K. Olafsdottir, W. Aas, K. Breivik, P. Bohlin-Nizzetto, A. Sigurdsson, H. Hakola, R. Bossi, H. Skov, E. Sverko, E. Barresi, P. Fellin, S. Wilson: Temporal trends of persistent organic pollutants (POPs) in Arctic air: 20 years of monitoring under the Arctic Monitoring and Assessment Programme (AMAP), *Environ. Pollut.* **217**, 52–61 (2016)
- 19.301 A. Gusev, O. Rozovskaya, V. Shatalov, N. Vuilykh, W. Aas, K. Breivik, F. Couvidat, M.G. Vivanco: *Persistent Organic Pollutants: Assessment of Transboundary Pollution on Global, Regional, and National Scales. Co-Operative Programme for Monitoring and Evaluation of the Long-Range Transmissions of Air Pollutants in Europe* (EMEP, Moscow 2018), Status Report 3/2018
- 19.302 Arctic Monitoring and Assessment Programme: *Arctic Pollution 2009* (AMAP, Oslo 2009)
- 19.303 E.W. Henningson, M.S. Ahlberg: Evaluation of microbiological aerosol samplers – A review, *J. Aerosol Sci.* **25**, 1459–1492 (1994)
- 19.304 J.H. Vincent, G. Ramachandran, Y. Thomassen, G.J. Keeler: Application of recent advances in aerosol sampling science towards the development of improved sampling devices: The way ahead, *J. Environ. Monit.* **1**, 285–292 (1999)

Christopher Pöhlker

Multiphase Chemistry Department
Max Planck Institute for Chemistry
Mainz, Germany
c.pohlker@mpic.de



Christopher Pöhlker leads the aerosol analysis and microspectroscopy group at the Max Planck Institute for Chemistry (Mainz, Germany). He has a PhD in atmospheric science. His research focuses on atmospheric chemistry and physics in the Amazon rainforest, physicochemical analysis of atmospheric aerosol particles in relation to land-use changes, climate change, and public health, as well as the development and application of advanced microscopic and spectroscopic techniques in environmental research.

Karsten Baumann

Environmental Sciences and Engineering
University of North Carolina at Chapel Hill
Chapel Hill, USA
kbaumann@unc.edu



Karsten Baumann is Assistant Professor at the Department of Environmental Sciences and Engineering of the Gillings School for Global Public Health (UNC Chapel Hill, NC, USA). He has a PhD in energy technology and air pollution control. Most recently, his research has focused on multiphase chemical processes of persistent organic pollutants as well as the toxicity of biomass burning pollutants in fresh and photochemically aged emissions.

Gerhard Lammel

Multiphase Chemistry Department
Max Planck Institute for Chemistry
Mainz, Germany
g.lammel@mpic.de,
gerhard.lammel@recetox.muni.cz



Gerhard Lammel is head of the research group Organic Pollutants and Exposure at the Max Planck Institute for Chemistry (Mainz), a professor of environmental chemistry at Masaryk University (Brno), a lecturer at the University of Mainz, and editor of the journal *Environmental Science and Pollution Research*. His research focuses on field and laboratory studies of atmospheric and aerosol chemistry as well as modeling and field studies of multicompartamental chemistry.

20. Optical Fiber–Based Distributed Sensing Methods

Christoph K. Thomas , John Selker 

Optical-fiber-based distributed sensing (OFDS) methods have the potential to bridge the observational gap between single-point-based or networks of in-situ sensors and remote-sensing techniques. By providing thousands of measurements at high spatial resolution at centimeter to decimeter scales at sampling rates of currently up to 1 Hz over distances of several kilometers, they enable a wide range of exciting applications in surface and boundary-layer meteorology, including vertical and horizontal profiling, investigating the spatial structure of the near-surface turbulent flow and scalar fields, evaluating spatially explicit atmospheric modeling techniques, and resolving the response of airflow to land-surface heterogeneity, to name but a few. Since the basic OFDS system measures the temperature inside a fiber-optic cable, the technique is often referred to as distributed temperature sensing (DTS). However, since the current portfolio of applications includes many variables other than temperature, we prefer the more universal terminology OFDS. In contrast to most other in-situ or remote-sensing techniques described in this handbook, a single optical fiber can be used for observations across different media such as air, water, ice, snow, mineral soil, or plant tissue, thus the OFDS technique lends itself to interdisciplinary geosciences research. The field of fiber-optic-based distributed sensing is rapidly evolving, and the combination of fiber-optic cables and existing meteorological sensing approaches has led to an expansion in the range of observable variables beyond the temperature in air, soil, snow, and ice to include also soil moisture, wind speed, air humidity, and solar radiation. This chapter describes the fundamental operating principles and the accuracy, precision, and resolution of such measurements, provides an introduction to calibration routines, and gives an overview over deployed optical fibers. It also provides examples for field and laboratory applications, with a focus on surface-energy balance and turbulent airflow studies.

20.1	Measurement Principles and Parameters	610
20.1.1	Bridging the Gap between In-Situ and Remote-Sensing Techniques	610
20.1.2	Passive and Active Systems	611
20.1.3	Measured Parameters	612
20.1.4	Measurement Principles	612
20.2	History	613
20.3	Theory	614
20.3.1	Temperature Measurement with OFDS Technique	614
20.3.2	Solar Radiation Measurement with OFDS Technique	616
20.3.3	Air Humidity Measurement with OFDS Technique	617
20.3.4	Wind Speed Measurement with OFDS Technique	617
20.3.5	Soil Moisture Measurement with OFDS Technique	619
20.4	Devices	619
20.4.1	Raman-Backscatter Devices	619
20.4.2	Active Heating Systems	620
20.4.3	Fiber-Optic Cables	621
20.4.4	Off-Grid Installations	622
20.4.5	Comparison of Methods	623
20.5	Specifications	623
20.6	Quality Control	624
20.6.1	Single-Ended Configurations	624
20.6.2	Double-Ended Configuration	625
20.7	Maintenance	625
20.8	Applications	626
20.8.1	Atmospheric Profiling	626
20.8.2	Turbulent Airflows	627
20.8.3	Hydrological Applications	627
20.9	Future Developments	629
20.10	Further Reading	629
	References	629

Aerial deployments of optical-fiber-based distributed sensing methods are relevant to all observational applications in meteorology whenever spatial information is useful to resolve a phenomenon or a process, such as when quantifying vertical or horizontal gradients or resolving individual turbulent motions. Unlike any other in-situ meteorological technique, the scales of continuous observations can range from millimeters to thousands of meters in space, and seconds to months in time, thereby enabling the user to determine such quantities at the desired resolution.

Traditional point observations in meteorology assume the validity of Taylor's hypothesis, which states that temporal and spatial scales are related by the mean advective wind speed. This assumption is an important vehicle to translate single-point measurements over time into spatial scales, which forms the basis for similarity theories and weather predictions. In addition, traditional meteorology also requires the spatial ho-

mogeneity of the observational location to fulfill the assumption of ergodicity of the airflow, which states that temporal and spatial averages converge, and therefore observations are representative.

Distributed sensing methods do not a priori require these assumptions due to their simultaneous observations in space and time, and thus can be used to evaluate their validity (e.g., [20.1]). While the user needs to invest substantial experimental effort in constructing a network of fiber-optic cables tailored to the specific measurement task, including a support structure to keep the fiber aloft in the air, continuous referencing of the fiber-optic measurements against traditional thermometers, and careful post-field calibration routines to convert the raw optical signals into environmentally meaningful observations, the rewards of the wealth of observations in space and time at high accuracy are substantial. For these reasons, the range of aerial deployments has grown significantly for meteorological and hydrological applications.

20.1 Measurement Principles and Parameters

Here we briefly introduce optical-fiber-based distributed sensing (OFDS) methods by describing their utility in atmospheric and hydrological applications and their fundamental operating principles. The intention is to provide the reader who is new to these methods with some overview.

20.1.1 Bridging the Gap between In-Situ and Remote-Sensing Techniques

Most studies investigating processes at the interface between air, land, or water surfaces, plants, and the built environment, e.g., addressing questions of air quality, quantifying the urban heat island effect, computing budgets of the surface exchange of energy and matter including carbon, water, and other trace gases, investigating the effects of drought, assessing the impact of cold-air drainage and pooling on agricultural productivity, and forecasting traffic-impairing ground fog, require time-dependent and spatially explicit fields of surface winds and temperatures, humidity, concentrations, etc. as input variables.

While traditional meteorological sensors can provide very accurate and precise point information at high temporal resolution, their time-averaged observations represent spatially averaged information in the proximity of the sensor location described by the scalar concentration or flux footprint. Spatially explicit information on time scales much longer than the averaging

interval can only be derived by relating the point measurements to wind direction, atmospheric stability, sensor height, wind speed, and turbulence strength. These parameters impact the observations' footprint. A sufficient number of time-averaged readings can then be used to assemble a climatological footprint, which can be used to interpret the parameter of interest in a topographic and thus spatially explicit context.

However, even when measurements from several such traditional point sensors are combined into micro- or ecosystem scale using regional or larger networks (e.g., [20.2–5]), the information on vector and scalar quantities can still be considered sparse as the instantaneous footprints of readings from all sensors at the averaging time scale hardly overlap. This lack of time-dependent information on, e.g., air temperature or wind speed, can lead to the masking of passing thermal microfronts, blurring of internal boundary layers defined by changes of surface conditions, or an inability to quantify the momentum and energy contribution of transient boundary-layer-scale eddies. Very dense surface networks, which have the potential to overcome some of these challenges, suffer from increasing observer effects, are cost-prohibitive, or are impractical because of interference from existing surface structures such as trees, lakes, or built infrastructure. Obtaining spatially explicit surface meteorology via satellite or airborne remote-sensing techniques from a variety of platforms (see Chap. 6) may be an elegant and cost-

saving alternative. However, these observations do not only offer benefits, but may also suffer from several challenges: While spatial coverage can be excellent and resolution can be up to the meter scale from, e.g., drone-borne sensors, such measurements are rarely observed simultaneously at all cells within a volume and the reading for each volume element is an implicit spatial average. Hence, only the assembly of spatially explicit information averaged over time will allow an assessment of the process of interest over the desired domain, which sacrifices information on either spatial and temporal variability. Particularly for studies of atmospheric transport by turbulence or under nonstationary conditions, such as process studies during the morning or evening transition, the passage of microfronts, thunderstorms, or other severe weather, these limitations are prohibitive.

Combining measurements from surface sensor networks with those from remote-sensing techniques to synergistically observe vector and scalar fields as input variables raises the unsolved question of whether the explicit time and implicit spatial averages and their variability converge. Hence, there exists an observational gap for many surface meteorological applications, which cannot be filled by either classical technique. In this case, the spatially explicit and very dense readings at high temporal resolution available from distributed sensing methods using arrays of fiber-optic cables can offer a viable alternative to fill this gap with acceptable accuracy and precision if state-of-the-art procedures for quality control are observed. Relatively thin (one to several millimeters in diameter) fiber-optic cables serving as environmental sensors can be installed continuously across air, water, soil, plant, and building material boundaries and thus may provide complete three-dimensional information about the en-

vironment. To date, observations from OFDS systems can be obtained at time scales of up to 1 s, which is sufficient to capture even the most energy-containing and short-lived turbulent eddies for heights outside the dynamic sublayer (approximately 1 m above ground level).

20.1.2 Passive and Active Systems

The basic OFDS system is of passive design, measuring the temperature inside the light-conducting and scattering medium, i.e., in the fiber-optic cable. Hence, these systems are often collectively referred to as distributed temperature sensing (DTS) methods. The reader is referred to Table 20.1 for key references describing the mentioned passive and active sensing applications. The exact procedure to derive temperature from the scattered light depends on the measurement principle of the sensor, which will be described below (Sect. 20.1.4). Even though light is actively injected into the optical fiber by means of discharging a laser diode, which subsequently excites the optical glass core of the fiber-optic cable, these systems are commonly referred to as *passive* as the fiber-optic cable is not actively modified in any other fashion. In contrast, active distributed sensing methods apply time-dependent modifications to the fiber-optic cable to sense environmental state variables other than temperature. The currently available active sensing methods include actively heated and actively wetted systems. The former apply heating to the outer metal jacket of a fiber-optic cable by means of electric resistance with the goal of measuring its heat loss to the surrounding medium, which in combination with a paired passive fiber-optic cable can be used to compute wind speed or soil moisture. The latter apply a thin water film onto the outer jacket of a fiber-optic cable by

Table 20.1 Environmental parameters measured by optical-fiber-based distributed sensing (OFDS) methods using fiber-optic (FO) cables

Quantity	Medium	Type	Basic principle	Reference
Temperature	Water	passive	FO cable in medium	[20.6]
	Ice, snow			[20.7, 8]
	Air			[20.9, 10]
	Soil			[20.11, 12]
	Plant			
Moisture/humidity	Soil	active	Paired passive and actively heated FO cables Paired passive and actively wetted FO cables	[20.11]
	Air			[20.13, 14]
Speed	Air	active	Paired passive and actively heated FO cables	[20.12, 15]
Shortwave radiation	Air	passive	Paired passive FO cables with different albedos (white, black)	[20.16]
	Water			[20.17]
Turbulence – temperature – wind speed – dynamic stability	Air	active	Thin paired passive and actively heated FO cables	[20.10, 12, 15, 18–20]

continuously spraying fine water droplets onto the surface in order to quantify the wet-bulb depression and thus compute air humidity as in classical psychrometry (see Chap. 8). As mentioned above, such distributed sensing methods are currently developing rapidly and their range of application is expanding. The most recent developments include methods that modify the external three-dimensional shape of the outer jacket of a passive or actively heated fiber-optic cable to cause a directionally sensitive heat loss [20.21], which can then be considered as hybrid systems lying somewhere between passive and active distributed sensing systems. The modifications currently under development are discussed in Sect. 20.8.

20.1.3 Measured Parameters

The list of observed environmental parameters derived from passive and active OFDS methods includes the basic temperature measurement in a variety of media as well as other quantities such as wind speed, air humidity, light intensity, soil moisture, and thermal conductivity and capacity (Table 20.1). In this chapter, we distinguish between common hydrometeorological applications requiring time- and space-averaged quan-

ties and geophysical applications studying turbulence by measuring spatiotemporal perturbations of rapidly varying quantities. Even though the basic measurement principles are identical, investigating turbulent geophysical flows using OFDS methods requires a very different design. Such systems are characterized by much finer sampling resolution and greater time response of both the fiber-optic cable and the recording laser of the OFDS system to detect the fingerprint of individual turbulent eddies passing the fiber-optic cable. As mentioned above, this list is expected to expand rapidly as new applications of this novel sensing technique are developed and become available to the user.

20.1.4 Measurement Principles

OFDS measurements can be divided into two categories: those that require light to be drawn from the fiber, which is called *extractive sensing*, and those that report measurements of the properties of the glass itself, referred to as *intrinsic sensing*. In the most extreme form of extractive sensing, a fiber-optic sensor can be made by coating the end of a fiber with an optically responsive paint. Here the light from the fiber acti-

Table 20.2 Principles of optical-fiber-based sensing methods

Name of fundamental principle	Brief explanation	Advantages/limitations	Application examples
Raman backscatter	Observe backscattering of photons at higher and lower energy than those of a narrow injected pulse of light based on Stokes and anti-Stokes (highly temperature dependent) Raman photons	High accuracy possible (0.02 K) Requires detailed calibration Range limited to about 10 km	Ubiquitous in environmental sensing (soil, wells, streams, oceans, aerial) due to excellent accuracy
Brillouin backscatter	Phonons (sound waves) in glass cause a Doppler shift in the backscattered light. The phonon velocity is proportional to the density of the glass and its elasticity, thus being temperature sensitive	Since the Doppler shift has a broad spectrum of values, determining the exact change in shift is difficult, leading to limited accuracy (about 0.1 K) Uses single-mode cable, thus can be employed to about 30 km distances	Can be used to measure physical strain on fiber, and so is commonly employed in mechanical evaluations (e.g., bridges, aircraft wings, etc.)
Rayleigh backscatter	Also known as <i>elastic scattering</i> , Rayleigh backscatter is scattered at the same wavelength as the injected light, and has much higher intensity than the Raman and Brillouin sidebands	Recently shown to be useful for acoustic sensing as well as thermal sensing Can go to very long range (> 30 km) on single-mode fiber High reported accuracy (better than 0.01 K) Equipment tends to be about five times more expensive	Recent products can detect strain, temperature, and acoustic signals with very high spatial resolution (to a few cm)
Bragg gratings	The cladding of the fiber is etched with a series of closely spaced lines which reflect back light of exactly this wavelength. Changes in the fiber density due to strain or temperature change this spacing, which can be used to monitor these factors	Only reports data where the fiber has been etched Loses light at each etching, and each etching must be unique in wavelength, limiting the number of etched points < 200	Mostly used for strain measurements in civil infrastructure

vates/interrogates the paint, and the resulting emitted/reflected light indicates the chemical/physical state of the paint, e.g., its oxygen content, or temperature. In this case, the fiber-optic sensor reports the state of exactly one location. Still considering the extractive approach, if the treatment is applied on the cladding rather than the end of the fiber (see Sect. 20.4.3 for explanation of the terminology), a small fraction of the photons can interact with the treated section, but with most of the photons being retained in the fiber. In such a way, the extractive approach can perhaps interrogate up to on the order of 100 locations along the fiber, making it a *nearly distributed* measurement. The fiber Bragg grating falls into this category, allowing for temperature or strain measurements at up to about 100 locations along a single fiber (Table 20.2). Note that the fiber must be modified at each measurement location.

In contrast, intrinsic OFDS methods employ a fiber that is uniform in its construction and often employ standard telecommunications fibers, so the price of these cables can be much more economical. Intrinsic methods typically employ a single pulse, or a recognizable train of pulses, where location on the fiber is inferred from the time that has passed since the moment the light was injected, assuming that the pulse and response travel at the speed of light after being adjusted for the refractive index of the glass. Note that the optical interaction between the injected light and the glass of the fiber is assumed to be instantaneous, which is generally valid. The modification of the backscattered light indicates the temperature, stress, or local velocity of the glass where the backscatter occurred (cf. methods listed in Table 20.2). The spatial resolution ranging from cen-

timeters to meters depends on either the pulse width of the injected light (for Raman and Brillouin methods, where current instruments have spatial resolution from 0.3 m to 4 m), or the distribution of scattering sites in the glass (for Rayleigh backscatter, with instruments on the market having resolution from 0.03 to 2 m).

Two basic kinds of optical cores are used in fiber-optic cables: single-mode (SM) with a typical core diameter of 9 μm and multimode (MM) typically with a core of 50 μm diameter, but with some cores much larger than this value. Raman and Brillouin scattering produce very faint signals, so having a larger core as provided by MM can provide greater intensity of the backscattered light without moving the process into the nonlinear regime, which occurs at extreme light intensities. On the other hand, since the light can travel along many paths in the fiber, the light disperses into longer pulses as it travels. This typically leads to dispersion on the order of 0.1 m times the square root of the distance from the device, e.g., 0.1 m at 1 km, and 0.2 m dispersion at 4 km. This is a fundamental limitation on the spatial resolution of measurements using MM fibers. SM fibers essentially do not suffer from optical dispersion.

The temporal resolution τ of these methods is purely a function of the measurement precision required, with the precision being equal to $C/\sqrt{\tau}$. In the case of Raman-scattering OFDS, the value of C is about 0.3 K for high-performance instruments set to a spatial resolution of 0.5 m with $\tau = 1$ s (Sect. 20.4.1). Lower-performance instruments have a temporal resolution that is 100 times lower than this value, thus the selection of adequate instruments is very important if high temporal resolution is needed.

20.2 History

OFDS methods were originally developed in parallel in the USA and the UK, as the National Aeronautics and Space Administration (NASA) aimed to understand the temperature dynamics of the Space Shuttle, while in the UK the goal was to provide service to the oil industry for better understanding of the distribution of oil production in wells. Applications in water resources began in the early 2000s with efforts to detect seepage and changes in moisture content in dams. Soon thereafter, applications in environmental monitoring emerged and have since blossomed into a significant portion of the global application of OFDS technology. Use of OFDS in atmospheric measurements has been a more recent domain of activity, led by work such as [20.9] and [20.10] and providing new applica-

tions for actively heated methods [20.15] and humidity measurements [20.13]. The technological requirements of geoscience applications are often much more demanding than those of industrial uses; for example, to identify the flow of groundwater into a stream requires precision of at least 0.02 K, compared with the needs of the petroleum industry, which were satisfied by 1 K resolution. With the move to atmospheric measurements, the demands on OFDS have increased, pushing hard for temporal resolution of < 1 s to allow the resolution of meter-scale turbulent processes. Manufacturers of OFDS instruments have steadily improved their temporal and spatial resolution in response to these needs, though in the past 5 years the rate of improvement has slowed as the technology has encountered fundamen-

tal limits to the fiber light-carrying capacity, the photon efficiency of detectors, and the stability of high-speed amplifiers. While advances in Raman and Brillouin methods have slowed, the interpretation of Rayleigh

scattering for temperature, strain, and acoustic sensing continues to advance rapidly. Tests indicate that, with Rayleigh-scattering OFDS, heretofore unattained levels of spatial and temporal resolution may soon be possible.

20.3 Theory

Here we provide a more detailed quantitative review of the fundamental operating principle of the Raman backscattering OFDS technique for the informed reader, since most commercially available sensors employ this principle for obtaining temperature measurements. Subsequent sections describe the fundamentals of various atmospheric and soil moisture OFDS applications derived from temperature sensing.

20.3.1 Temperature Measurement with OFDS Technique

A good introduction to the theory of OFDS based upon Raman backscatter distributed temperature sensing (DTS) can be found in [20.22] and [20.23]. Here, we review only the basic equations needed to understand and operate such systems. Temperature measurements across individual, but continuously distributed sections along the fiber-optic cable are the fundamental quantity computed from OFDS methods. To a first approximation, the temperature T of a single section of fiber-optic cable located at a mean distance x from the beginning of the measurement section at time step t is proportional to the inverse natural logarithm of the ratio of the power of the Stokes (P_S) to anti-Stokes (P_{AS}) signals resulting from the inelastic Raman scattering of light:

$$T(x, t) \propto \ln \left(\frac{P_{AS}(x, t)}{P_S(x, t)} \right). \quad (20.1)$$

It must be noted that measurements of P_S and P_{AS} for each section represent a spatial average over a cable section of the length given by the sampling resolution Δx of the instrument. The physical resolution of the temperature measurements along the fiber, however, is approximately equal to $3.5\Delta x$ using the *10-90 definition*, as P_S and P_{AS} from directly neighboring sections are statistically not independent (Fig. 20.3). Since the number of Raman photons returned from a single laser pulse is too small to determine its power with sufficient accuracy, OFDS instruments operate at high internal sampling rates between 20 and 50 kHz to compute a temporal average at time step t over the minimum instrument-specific averaging period determining the instrument's temporal resolution τ (for device speci-

cations see Sect. 20.4.1). Hence, each record of $P_{S/AS}$ already represents a statistical quantity that is highly aggregated in both space and time. More precisely, three other quantities are needed to translate the Raman backscatter signals into the desired temperature $T(x, t)$, which results in the following full calibration equation [20.24]:

$$T(x, t) = \frac{\gamma}{\ln \left(\frac{P_S(x, t)}{P_{AS}(x, t)} \right) + C(t) - \int_0^x \Delta\alpha(x') dx'}, \quad (20.2)$$

with γ [K] being considered a constant for each OFDS system, representing the shift in energy between a photon at the incident laser wavelength and the scattered Raman photon; $C(t)$ is a dimensionless specific calibration parameter dependent upon the incident laser and the OFDS instrument. The integral expression in the denominator is a dimensionless quantity representing the differential attenuation of the anti-Stokes and Stokes signals in the optical fiber. The extinction of anti-Stokes and Stokes signals is not identical since they occur at different wavelengths. The effect of such differential attenuation on the temperature measurement is cumulative, which means that this term needs to be integrated over the entire cable length between its start ($x' = 0$) and the measurement location ($x' = x$). If the differential attenuation is constant along the fiber optic cable, then the integral expression simplifies to a single value equal to $\Delta\alpha x$. Since only the quantities $P_S(x, t)$ and $P_{AS}(x, t)$ are directly measured by the instrument, the remaining three quantities need to be obtained indirectly through a matrix inversion using measurements from a physical calibration setup. There now exist open-source software packages including all post-field calibration routines, e.g. [20.25].

The design of the physical calibration setup depends upon the fiber configuration chosen by the user. The four possible configurations include (Fig. 20.1):

- Simple single-ended (Fig. 20.1a)
- Duplexed single-ended (Fig. 20.1b)
- Simple double-ended (not shown)
- Duplexed double-ended (Fig. 20.1c).

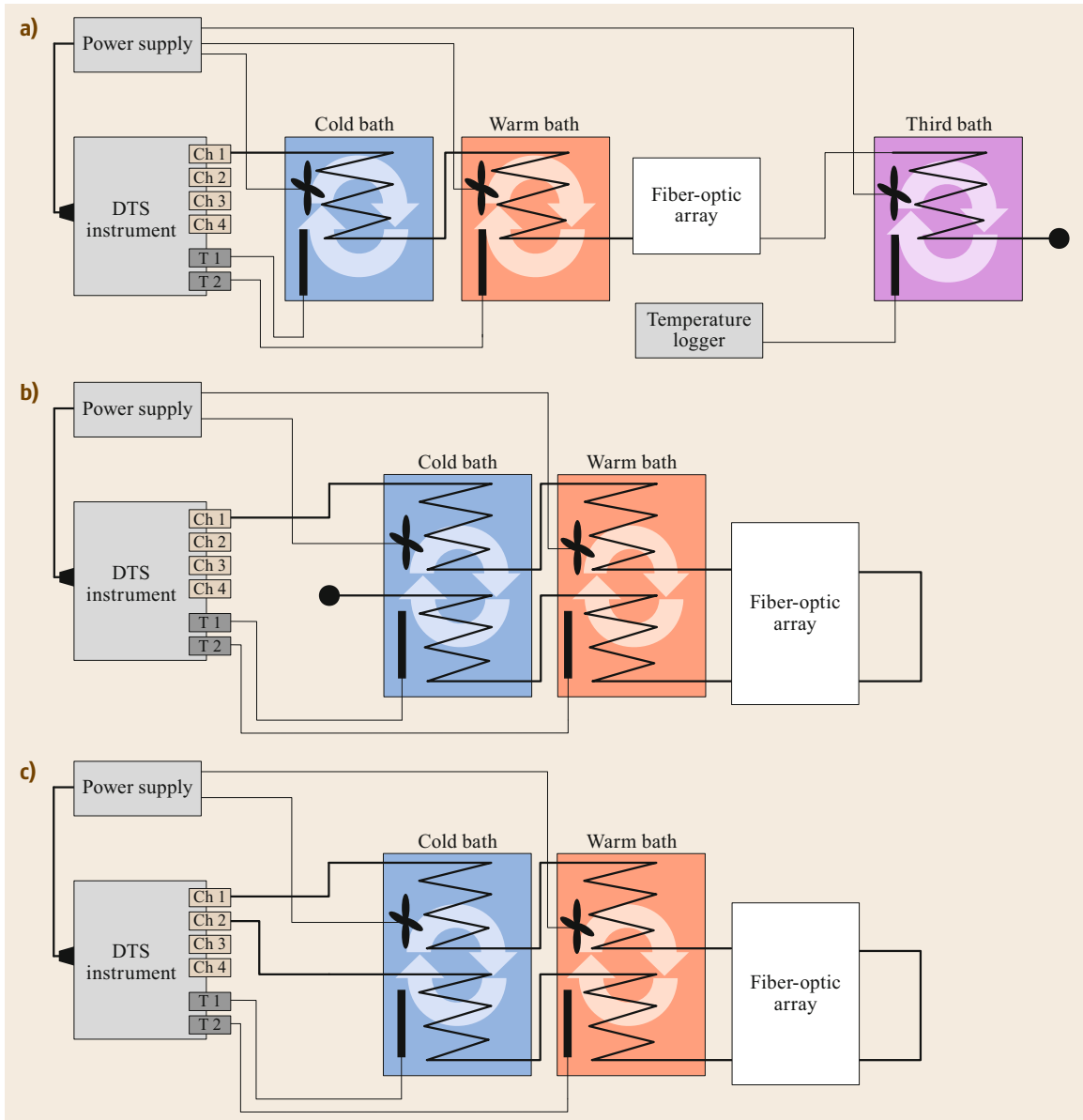


Fig. 20.1a–c Schematic fiber configurations for OFDS technique: (a) simple single-ended, (b) duplexed single-ended, and (c) duplexed double-ended. See text for explanation and limitations and advantages

The terminology of simple or duplexed describes whether each measurement location contains one or two (or more) physically different optical fiber sections. Duplexed configurations allow one to compute a spatial average for each measurement location from either a single fiber-optic cable containing multiple optical SM or MM glass cores or multiple fiber-optic cables with a single glass core. Duplexing may reduce the random and systematic uncertainties of T in certain applications. The terminology of *single- or double-ended*

refers to how the cable is attached to the instrument: either one or both ends of a fiber-optic cable can be attached to the instrument and be used to inject light and receive the backscatter. The latter allows the user to invert the direction in which the light pulse travels and thus reduce the measurement uncertainty in some applications. The advantages and limitations of each configuration are briefly discussed in Sect. 20.6. The simple double-ended fiber configuration differs from its duplexed counterpart only by not routing the fiber

through the fiber-optic array before reconnecting to another optical port of the instrument.

A comprehensive description of how to obtain all the quantities in the calibration equation (20.2) for the single-ended OFDS configuration can be found in [20.26], while [20.27] reviewed this procedure for double-ended configurations. Irrespective of the experimental fiber configuration, a physical calibration setup generally consists of several fiber sections routed through reference environments of known and uniform, but different temperatures. The reference temperatures must be measured independently of OFDS and are commonly obtained using high-grade resistance thermometers (e.g., platinum wire resistance thermometers, see Chap. 7). To date, most OFDS applications use water baths of different temperatures, which are mechanically stirred or mixed by aquarium bubblers to ensure uniform temperatures (see Sect. 20.7 for maintenance recommendations). Due to the requirement of having different temperatures in these reference environments, these baths are often referred to as cold and warm baths. Section 20.6 discusses and recommends practical approaches for how to design and operate reference baths for field and laboratory applications to ensure high-quality temperature measurements.

The theory of using OFDS to measure environmental temperatures in soil, air, water, ice and snow, or plant tissues and across their interfaces is identical and solely depends upon the medium in which the fiber-optic cable is installed. However, for applications in media transmitting solar radiation such as air or clear water, note that temperatures will suffer from radiation errors resulting from the short- and long-wave radiative transfer between the cable and its environment. From simple theoretical considerations, it follows that the error is maximum for peak solar radiation irradiance in still air. Similar to the radiation error for classical single-point thermometers in radiation shields, the radiation error for aerial OFDS deployments is largest for high short-wave radiation loads and low wind speeds and can amount to several degrees kelvin, depending on the cable diameter and its radiative properties [20.28]. An additional source of uncertainty in air temperature measurements by OFDS are errors resulting from conductive heat transport of support structures such as fabrics, pipes, and blocks applied to keep the fiber array in the user-intended configuration aloft in the air. [20.16] reviewed the theory of and quantified both types of errors for aerial OFDS deployments using a coiled fiber-optic cable to obtain air and water temperatures across a vertical pro-

file. They found that, for a thin, 0.9 mm-outer-diameter fiber-optic cable mounted on reinforcement fabric as a mechanical support, the radiation error amounted to between 0.5 and 0.8 K for wind speeds ranging between 2 and 4 ms⁻¹ and short-wave radiation irradiance of $\leq 800 \text{ W m}^{-2}$ above grass. For calm winds and solar irradiances $> 1000 \text{ W m}^{-2}$, the error exceeded 2 K. The effects of solar radiation on fiber-optic cables of different colors and therefore albedos of the outer cable jacket for aquatic installations were investigated quantitatively by [20.10]. They showed that the solar heating error was less than 0.3 K for shallow installation depths of several tens of centimeters below the water surface for clear and very slowly moving streams. With increasing depth or turbidity, the solar heating was less than the measurement resolution of the OFDS even when averaging over longer time periods. In this case, conductive heat transfer from the streambed surface had a much larger impact than solar radiation errors.

20.3.2 Solar Radiation Measurement with OFDS Technique

Theoretically, comparisons of temperature measurements by OFDS techniques using fiber-optic cables with different radiative properties of the outer cable jacket including albedo and emissivity may allow for indirect estimation of short-wave irradiance. This measurement approach would then be identical to that employed in pyranometers using temperature differences between black and white painted surfaces (see Chap. 11). In practice, however, the usefulness of this approach for OFDS methods is limited as the temperature difference between a pair of fiber-optic cables exposed to air is modulated by wind speed and angle of attack, turbulence intensity, and ratio of diffuse to direct-beam solar radiation. These quantities impact the three-dimensional surface radiation of the fiber-optic cable and the turbulent heat transfer coefficient and can be used to compute wind speed and soil moisture (discussed in Sect. 20.3.4). To date, no studies have isolated the effect of solar heating from other confounding processes in order to quantify spatiotemporal variations in solar radiation, while this approach has significant appeal for environmental studies. However, this measurement approach was used qualitatively by [20.29] to estimate shading in streams with varying degrees of vegetation cover. The temperature difference between a pair of helically twisted fiber-optic cables with a white and black outer jacket compared well to independently measured short-wave radiation intensities along the river.

20.3.3 Air Humidity Measurement with OFDS Technique

Since OFDS techniques can precisely measure temperature differences over great extents at high spatial resolution with satisfactory accuracy, they can be used to estimate the air humidity by employing the principle of wet-bulb depression between dry and wetted fiber-optic cable sections as in classic psychrometry (see Chap. 8). [20.13] introduced this measurement approach over a short-statured crop canopy with the intention of using the air temperature and humidity observations from an actively wetted OFDS system at multiple heights to compute sensible and latent heat fluxes based upon Bowen-ratio similarity theory. Their setup consisted of coiled fiber-optic cables in a vertical profile over 6 m in height. One of the cables was wrapped in a cotton cloth and continuously wetted using an irrigation pump at a fixed rate of approximately 41 h^{-1} . The cables were unshielded from solar radiation, which caused a significant increase in cable temperatures by solar heating. [20.14] refined this approach by minimizing the solar heating through shielding the dry and wet cables from direct-beam short-wave radiation with a gauze facing south, while leaving the north face unshielded to allow for sufficient ventilation and evaporation. The sections of the fiber-optic cable to which the water is supplied was excluded from analysis, as their wet-bulb temperature is dominated by the additional heat supplied by the water supply mechanism resulting in an inaccurate determination of the wet-bulb depression and hence air humidity.

20.3.4 Wind Speed Measurement with OFDS Technique

An actively heated OFDS system can be used to measure the wind speed by employing the principle of wind speed-dependent convective heat loss. The underlying basic measurement principle is therefore similar to that used in hot-wire anemometry. [20.15] was the first to propose this measurement approach based upon the temperature difference between two closely co-located fiber-optic cables, one of which is actively heated through electrical resistance while the one is unheated. The unheated fiber-optic cable is expected to be in thermal equilibrium with the surrounding air and thus to report dry-bulb air temperature, assuming that radiative heating errors are negligible. Since the temperature of the actively heated cable will be greater than air temperature, the passing turbulent eddies in-

duce a convective cooling effect proportional to their speed, leading to a response in the cable temperature as sensed by the OFDS device. A small angular dependence of the cooling results from the variation of the efficiency of the energy transfer between the heated cable and the passing eddy with the angle of attack between the cable and the eddy's trajectory [20.19]. The efficiency is largest for airflows orthogonal to the direction of the fiber-optic cable. Hence, this actively heated OFDS technique is most sensitive to the wind component normal to the fiber-optic cable, which needs to be considered by the user when designing the fiber configuration.

A quantitative expression for wind speed can be derived starting from the general energy balance for a section of the fiber-optic cable at distance x , which can be formulated as [20.15]

$$\begin{aligned} Q(x) &= Q_{\text{in}}^{\text{P}}(x) + Q_{\text{in}}^{\text{S}}(x) + Q_{\text{in}}^{\text{L}}(x) + Q_{\text{out}}^{\text{L}}(x) + Q_{\text{out}}^{\text{conv}}(x) \\ &= c_p \rho V \frac{\partial T_s(x)}{\partial t}, \\ \text{I} &= \text{II} + \text{III} + \text{IV} + \text{V} + \text{VI} \end{aligned} \quad (20.3)$$

where Q_{in}^{P} is the energy input from active electric heating, Q_{in}^{S} is the net energy gain from short-wave solar radiative heating, Q_{in}^{L} is the energy gain from long-wave radiative sources (such as the air and surface ground), $Q_{\text{out}}^{\text{L}}$ is the long-wave radiative loss from the cable's surface, $Q_{\text{out}}^{\text{conv}}$ is the convective cooling, c_p is the specific heat at constant pressure, ρ is the mean material density, and T_s is the surface temperature of the fiber section; note that $[Q] = \text{J s}^{-1}$ since all terms are related to the surface area of a fiber section of volume V at measurement resolution Δx . Equation (20.3) is valid under the assumption that energy changes due to mechanical work and conductive heat transfer in both radial and longitudinal directions can be neglected. By convention the sign for energy gain is positive. The expression simplifies when fiber-optic cables with identical properties are used for the heated and unheated sections, which eliminates terms III and IV. Term VI is the key quantity of interest as

$$Q_{\text{out}}^{\text{conv}} \propto h \Delta T \propto \text{Nu} \Delta T \propto \text{Pr}^m \left(\frac{\text{Pr}_a}{\text{Pr}_s} \right)^{\frac{1}{4}} U_N, \quad (20.4)$$

with h being the heat transfer coefficient, Nu the dimensionless Nusselt number, Pr_a and Pr_s the dimensionless Prandtl number evaluated at air $T_a(x)$ and fiber surface temperatures $T_s(x)$, $\Delta T(x) = T_s(x) - T_a(x)$, and U_N the

wind speed component normal to the fiber-optic cable. The exponent $n \approx 0.36$. For the unheated cable, $Q_{\text{out}}^{\text{conv}} = 0 \text{ J s}^{-1}$ since the fiber is assumed to be at air temperature. Applying (20.3) for both fiber-optic cables and solving for wind speed $U_N(x)$ yields a quantitative expression as a function of $\Delta T(x)$

$$U_N(x) = \left(\frac{Q_{\text{in}}^{\text{P}} + Q_{\text{in}}^{\text{S}} + Q_{\text{in}}^{\text{L}} + Q_{\text{out}}^{\text{L}} + \frac{1}{2} c_p \rho r \frac{\partial T_s(x)}{\partial r}}{-C(2r)^{m-1} \text{Pr}^n \left(\frac{\text{Pr}_a}{\text{Pr}_s} \right)^{\frac{1}{4}} K_A \nu^{-m} \Delta T(x)} \right)^{\frac{1}{m}}, \tag{20.5}$$

with r being the radius of the fiber-optic cable, C and m constants with $C = 0.75$ to 0.26 and $m = 0.4$ to 0.6 for $\text{Re} < 20000$, and K_A the thermal conductivity and ν the kinematic viscosity of air. For details of the derivation see [20.15] and the supporting online infor-

mation. Despite the unique spatial information about wind speeds at high resolutions measured continuously along the pair of fiber-optic cables, this measurement approach suffers from two significant shortcomings which limit its utility for observing three-dimensional turbulence and heat fluxes: First, the approach is most sensitive to the wind speed component orthogonal to the fiber-optic cable, as the heat transfer has an angular dependence, but the angle may be poorly defined for stochastic three-dimensional turbulent flows. Secondly, the method cannot determine the direction of the passing eddies and thus the wind direction, which is critical for computing turbulent fluxes as well as properties of the mean airflow. Here, recent research outlined in [20.21] and Sect. 20.8 may overcome these limitations with the goal of constructing a true spatially resolving eddy covariance system able to measure momentum and sensible heat fluxes.

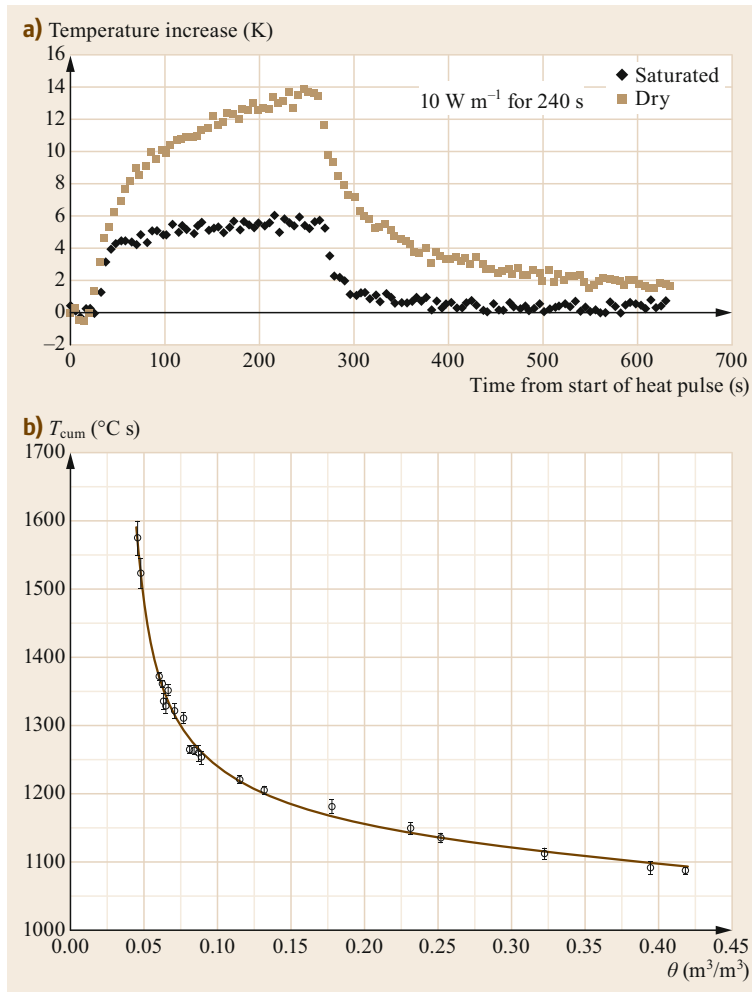


Fig. 20.2 (a) Temperature response of cable embedded in wet and dry sand with a heating rate of 10 W m^{-1} . (b) Cumulative temperature T_{cum} versus soil moisture content θ (after [20.11] with permission from John Wiley and Sons)

20.3.5 Soil Moisture Measurement with OFDS Technique

Soil moisture characterization was the initial application for active OFDS, applying heat to fiber-optic cables to reveal features of the local environment. [20.30] was the first to test this concept, but because of the high noise levels of his instrument and due to the approach taken in data analysis, it was concluded that the technology was not capable of accurate quantification of soil moisture, although it was found to be adequate for determining abrupt changes in the presence or absence of water in soil. [20.11] pointed out that, since wetter soil has both higher thermal heat capacity and higher thermal conductivity, the change in temperature per amount of energy applied is inversely related to the soil moisture content. This gave rise to the so-called T_{cum} -approach to soil moisture measurement, where the total integrated area under a time-temperature plot following the application of a heat pulse can be correlated to moisture content (Fig. 20.2). This approach dramatically improved the signal-to-noise ratio of the heat

pulse signal, and provided accurate and precise soil moisture measurements. The key outstanding issue is how to calibrate this method for each soil, which is an active area of development.

The natural cycles of temperature in the environment can also be used to estimate soil moisture without the need for active heating systems. In this case one may bury one or many fiber-optic cables in the soil, and observe their diurnal and longer-period fluctuations. If one knows the air temperature and net radiation above the site, the dynamics of temperature reveal the thermal properties of the soil, which are in turn a function of the soil moisture content. If one then models not only the energy but also water dynamics of the soil, long-term observations can be used to constrain the hydraulic properties of the soil (permeability and water retention). [20.31] demonstrated the ability to capture both the soil moisture dynamics and the soil characteristics through passive observation of soil temperatures using data assimilation methods. These results are very encouraging for large-scale implementation of this approach.

20.4 Devices

This section summarizes the most important specifications of OFDS instruments, active heating systems, and fiber-optic cables, and relates them to the user's measurement needs and data quality. For active OFDS, we give basic, but important recommendations to maintain safety for humans and machines in close proximity to or in direct contact with the heated fiber-optic array to avoid electric shocks. We also review power recommendations for remote off-grid applications.

20.4.1 Raman-Backscatter Devices

The current commercially available OFDS (DTS) instruments using inelastic Raman backscatter of light in fiber-optic cables can be subdivided into two main categories: standard-performance and high-performance devices.

Standard-performance devices feature a greater minimum spatial sampling resolution and temporal signal integration time, resulting in a lower spatiotemporal resolution of the measurements (Table 20.3). Hence, these devices are best used when the application targets averaged temperature, humidity, and wind speed signals. However, the use of larger and thus more slowly discharging laser diodes allows for higher optical signal intensities, offering an acceptable signal-to-noise ratio of the Raman backscatter photons over a significantly

enhanced maximum cable length exceeding 10 to 20 km per optical port of the device. Since the spatiotemporal aggregation of the temperature measurements in this device category is greater, fewer raw signal computations need to be executed and recorded per unit time, which lessens the need for high-performance central processing units (CPUs) and high-volume onboard data storage. The latter significantly lowers the power needs and makes these units ideally suited for remote and off-grid deployments using batteries in combination with solar panels as a power source. Because of the less resource-demanding components, some devices in the standard-performance category offer ruggedized outdoor enclosures suitable even for an extended environmental temperature range (-40 to $+80^\circ\text{C}$), featuring relatively small outer dimensions and built-in cellphone or radio modems for data transfer to remote servers. These units are well suited for field campaigns even in extreme environments.

High-performance devices use smaller, faster discharging laser diodes, allowing for greater internal sampling rates and a reduced minimum measurement resolution ΔX and integration time Δt , both resulting in observations with much higher spatiotemporal resolution. As a result, these devices are ideal for measuring the fast perturbations of quantities in turbulent flows (see references in Table 20.1). However, the

Table 20.3 Categories of optical-fiber-based distributed sensing devices and their typical characteristics

Characteristic	Category	
	Standard-performance devices	High-performance devices
Minimum spatial sampling resolution Δx (m)	1	0.125
Minimum temporal integration time Δt (s)	30	1
Maximum cable length (km)	10, 20, 50	≤ 5
Typical uncertainty in OFDS temperature measurements at maximum resolution and optimal signal-to-noise ratio (K)	0.2	0.6
Recommended applications	Mean quantities in profiles and transects in air; applications in soil, water, snow, and ice Off-grid applications	Turbulence observations in air and water
Costs per unit (k€) in year 2018	≤ 40	≥ 60

maximum cable length over which physically meaningful measurements can be obtained is reduced compared with the standard-performance devices and is typically < 5 km. Due to the reduced spatiotemporal aggregation, the measurement uncertainty for each $T(x, t)$ is greater since the relative error is proportional to the inverse square root of the number of measurements. These devices require high-performance components, resulting in increased costs and significantly enhanced power requirements that are more suitable for laboratory applications and field deployments with access to line power when sampling over longer periods.

Most standard- and high-performance devices offer multiple optical ports (in most instruments up to four) to which fiber-optic cables can be attached depending on the fiber configuration (Sect. 20.3.1). One device can sample these ports only sequentially at the minimum sampling integration time Δt , while simultaneous observations of multiple cables requires either splicing the individual sections into one long cable whose length is bound by the maximum sampling distance or multiple synchronized OFDS devices. The advantages and disadvantages are briefly discussed in Sect. 20.6. All commercial OFDS devices uses standardized industrial-grade optical connectors of type E2000 for connecting the fiber-optic cables to the optical ports.

20.4.2 Active Heating Systems

Active heating of fiber-optic cables has been shown to be useful in applications in soils, rivers, wells, and atmospheric installations. Active heating of fiber-optic cables is based on converting electrical power into thermal energy via electrical resistance. Heating can be achieved by applying current to metallic armoring concentrically around the fiber, or electrical conductors can be wound around the cable. Required heating rates depend on the application and are typically about 3 W m^{-1} for wind speed measurements [20.12, 15], 5 W m^{-1} for

long-pulse soil water flux, and 10 W m^{-1} for short-pulse soil moisture owing to the differences in heat conductivity and capacity of the medium surrounding the fiber-optic cable. For example, to obtain a heating rate of 1 W m^{-1} along a 1 km cable with a resistance of $10 \Omega \text{ km}^{-1}$ would require 31 V; 10 W m^{-1} would require 100 V, recalling that $P = U^2 R^{-1}$, where P is electric power, U is voltage, and R resistance. Clearly as the heating rate and length of cable increase, so does the voltage required to achieve the goals, and also the risk to safety. Care must be taken to ensure that the insulation provided is adequate to provide for human safety. The safety precautions also apply to the reference baths needed for accurate calibration of the OFDS measurements: one must isolate the actively heated fiber-optic cable sections in the environmental fiber-optic array from those contained in the water baths by mechanically severing the electricity-conducting armoring or wound conductors. Power systems with dedicated device-specific ground fault protection of the heating unit are highly recommended. In case of using heated cables in aerial applications, added electric insulation, e.g., by thin polyethylene (PE) plastic coating of the fiber-optic cable, can greatly slow the thermal response of the cable. The heating approach can be implemented with uninsulated fiber, but we strongly advise against it because of the risk of electrical shock. If used at all, such a system should be implemented so that nonlethal voltages are employed, requiring the use of shorter spans between electrical connections and the use of a floating-ground transformer. This setup ensures that anyone in contact with the heated cable simply establishes a ground for the system, but imposes no current. Any site with actively heated cable needs to have extensive signage to let visitors know to avoid contact between the heated cable and people/machines while the system is active.

The electrical energy delivered to the cable needs to be actively managed to ensure delivery of constant power. Since the electrical resistance of conductors is

a function of temperature, we recommend the use of a data-logging dynamic power controller, where the pulse width of the applied current can be continuously adjusted to obtain the specified power level. Designs for such a system are available from the Center for Transformative Environmental Monitoring Programs [20.32], and some commercial systems are now on the market.

20.4.3 Fiber-Optic Cables

The selection of fiber-optic cables involves balancing many design considerations. Starting from the inside of the cable, the selection of the correct optical core is essential to success. The first requirement is that the fiber matches the requirements of the interrogator, i.e., the OFDS instrument being used. As mentioned above, the device may require 9 μm -core single-mode (SM) fiber, or if multimode (MM) fiber is needed, may employ 50 or 62.5 μm cores. Further, the glass of the fiber can be treated to be *bend insensitive*, wherein the light will stay in the core even if the fiber experiences a significant bend. Generally speaking, bend-insensitive fiber is preferred, since in many applications the cable might be subject to bending, and there is no loss of performance otherwise. Generally, OFDS instruments are designed to be compatible with what is known as Cat 2-fiber, which refers to the bandwidth of the fiber for data communication.

All optical fibers must be protected from degradation by applying an external *buffer* layer to the bare glass. There is a range of materials that may be used to form this buffer, with the most important feature being the range of temperature over which they remain stable. Generally, the buffers are tinted with different colors of coating to help identify each fiber in the cable. Standard telecommunications fibers are coated with material that is stable to long-term exposure to 85 °C, and short-term exposure to slightly over 100 °C. If higher temperatures are expected, a specialized buffer must be employed. Plastic buffering can be obtained with temperature resistance to about 250 °C, with exotic gold- and carbon-coated fibers capable of measurements to over 800 °C. The cost of these fibers is strongly affected by the buffer material choice, starting at around 0.1 € m^{-1} for standard fiber to well above 10 € m^{-1} for high-temperature materials. Further, the operations needed to remove the buffer as required for joining fibers by employing a fusion splicer become very challenging with high-temperature buffers.

Beyond temperature, the glass must be protected from water and hydrogen gas, which if in long-term contact will eliminate the refractive index contrast between the core and jacket glass (referred to as *cladding*), thus leading to light loss from the fiber. Optical fibers

are therefore typically encased in waterproof protection, which can be injection molded directly onto the buffered fiber known as *tight buffering*, or can be placed into a tube known as *loose-tube buffering*. If loose-tube is employed, there is the option of having the fiber embedded in hydrogen-scavenging gel, which eliminates degradation by exposure to this otherwise highly diffusive gas. The loose-tube can be made of many materials, with cables to be exposed to high pressures or other aggressive environments typically employing stainless steel for the tube. Stainless-steel loose-tubes can be constructed with external diameters as small as 0.8 mm for a single fiber, or of several millimeters in diameter if multiple fibers are to be included in the cable. In the oil industry, the stainless tube is often further encased in an aluminum tube, which has much lower gas permeability and further stabilizes the cable against hydrogen ingress.

Generally, further protection is needed outside the buffering to protect the fiber from tensile stress. Tensile elements made of aramid or steel are often employed for this purpose. In the case of actively heated cables, it is sometimes useful to have copper among the metal elements to reduce the electrical resistance of the cable. One must keep in mind that the working tension on a fiber-optic cable is not dictated by the breaking strength of the cable, but rather the tension at which the cable stretch might give rise to tensile stress on the fiber. Should the fiber experience such stresses, this can modify the optical properties of the fiber, which can be problematic if temperature is the target of the measurement. Local stresses from excess tensile load will lead to time-varying local changes in the calibration between backscatter and temperature (see (20.2)), leading to experiments where the temperature is impossible to determine. To avoid this stress, fibers are generally placed in loose-tube buffers with *overstuff* of about 0.1–0.5%, meaning that, for each meter of cable, there is actually 1.001–1.005 m of fiber. In this way a cable can experience 0.1–0.5% change in length without passing stress onto the fiber itself. If the manufacturer puts too much overstuff on the fiber, it can lead to stresses due to the helical bending of the fiber within the loose tube. This problem can sometimes show up only after the cable has been unloaded from the reel, so it is a good idea to obtain optical test reports for the cable both on and off the reel. Most OFDS instruments set an apparent refractive index of the cable to correctly define the relationship between photon timing and location along the cable. This parameter is adjusted until the location of a particular thermal defect matches with the cable markings at that distance. Clearly such an approach intrinsically accounts for the cable overstuff as part of the refractive index. If no such adjustment is

made, the accumulated error in apparent location compared with the actual location can be considerable, e.g., on the order of 5 m error per 1 km of cable.

Many times, a plastic jacketing material will be applied outside the elements that provide crush and tensile protection to give the cable greater environmental resistance, easier handling, and allow for selection of color and markings. This material should be selected with great care to ensure it meets the installation's thermal and mechanical requirements. A common problem in environmental sensing is that the cable markings imprinted by the manufacturer, also known as *meter-marks*, rub off when the cable is guided into the installation. The loss of distance markers can be problematic when it comes to associating specific points along the cable with the data that was obtained from that location. The outer jacket also influences the thermal response time of the system (see discussion in [20.10]). Specifically, if the core of the cable is made up of high-thermal-mass materials while the jacket has low thermal conductivity, the response time of the cable can be on the order of minutes. For many experiments this is not an issue, but especially for actively heated and aerial installations, thermal insulation of the jacket can be essential to resolving the process of interest. If active heating is employed, the jacket must also be mechanically and electrically protective against the possibility of contact between the energized elements and the external environment to prevent electrical shock.

For long-term installations, it is important to consider the stability of the cable components. For example, it is often tempting to use white-jacketed cable to reduce solar heating. While some white plastics are stable, many lack the ultraviolet (UV) stability that darker colored jackets have. Unsuitable cables may deteriorate in a matter of weeks to months, and few plastics that are not specifically designed for outdoor use will be stable in long-term environmental deployments.

In summary, the construction of the nonglass components of cables used for environmental sensing is pivotal to the success of an OFDS deployment. Whether it be exposure to solar radiation, chewing animals, excessive tension, or tight bends, all of these factors must be considered as one selects the cable appropriate to a particular experiment.

20.4.4 Off-Grid Installations

Power is often a key parameter driving the selection of instrumentation for distributed environmental sensing. OFDS instruments have power consumption that generally falls between 5 and 500 W. The ultralow-power systems achieve these efficiencies by powering down the laser and internal data systems for most of

the time, taking data only at prescribed times. Since the signal-to-noise ratio of OFDS measurements is typically inversely related to the square root of the active measurement period, shutting down the instrument has a cost of increasing the noise. For instance, if one were to record for 15 min every 4 h, this would provide an energy savings of 16-fold, but would result in an error four times greater than had the instrument been recording data continuously. Depending on the instrument and length of cable interrogated, the noise could well be acceptable under these conditions, and the energy savings could be pivotal in experimental logistics.

Many installations in remote locations are operated based on solar battery charging. In this case, one must take care to provide ample battery power to sustain operation in the worst weather conditions you expect to see. Many high-quality OFDS instruments are available with a power consumption of 30 to 40 W, which is under 1 kWh d⁻¹. A single 100 Ah 12 V battery with 1.2 kWh can power such an instrument for one day, but such deep discharges dramatically shorten the battery life and do not provide for poor weather conditions. Three such batteries would generally be sufficient, since the batteries should receive some charge each day, which should be able to sustain a week of low-recharge conditions. The power input from the solar panels should be selected to be at least three times the charging capacity so that, on cloudy days, one will obtain a good fraction of the power needed to operate the system, and so one day with good weather will recover a full charge of the batteries. Again, these *rule-of-thumb* values are just listed to give an impression of the trade-offs and considerations at play: budgets, security, feasibility of transporting heavy batteries, and other considerations may dramatically change the design. A small gasoline-powered generator can be a very useful emergency energy source. Beyond pure energy, one should also be mindful of the quality of power. It is preferred to use instruments that can run natively on DC power as this saves the loss of energy in inversion, and generally can be more fully isolated from lightning and other power quality issues. If using an inverter, it is important to verify that the quality of the power is adequate. Some OFDS instruments have large start-up power demands, which can overwhelm systems that would otherwise appear adequate. Also, some inverters have square-wave rather than sine-wave voltages, which can be incompatible with OFDS power supplies. Finally, the reliability of power is not only a matter of convenience, but also potentially important in protecting your instrument: some lasers can be damaged by spontaneous loss of power. In this sense, we recommend inclusion of an uninterruptable power supply for all OFDS installations. Further, we highly recommend

that remote installations be fit with cellphone connection so that the operation of the OFDS system and the status of the power system can be verified regularly without site visits.

20.4.5 Comparison of Methods

The choice between devices of different performance categories, different cable measurement configurations, the use of passive and active systems in combination

with the variety of choices for fiber-optic cables including buffering and power supply makes OFDS an extraordinarily versatile measurement technique. This versatility is reflected in the rapidly expanding range of applications. One cannot say that a high-performance device yields improved measurements compared with a standard-performance device. The opposite may apply. The user needs to select the device which offers optimal performance for a specific observational task (see next section).

20.5 Specifications

Selection of appropriate OFDS instruments for one's application requires quantitative understanding of the spatial and temporal resolution, precision, and accuracy required to achieve the scientific goals. Here, we review the basic issues in instrument specification so that the user can make an informed decision.

We first consider the resolution of changes in temperature in distance along the fiber. The spatial resolution Δx is computed by observing the reported response from a step change in temperature, e.g., the signal generated along a fiber going from warm air into cold water. The distance between where the instrument reports 10 and 90% of this temperature change is taken to be the spatial resolution of the device, which corresponds to approximately 3.5 units (Fig. 20.3). In unpublished data, we have found that the weighting function supporting the reported value is Gaussian, incorporating temperature from a span about the point. It is important to note that many OFDS instruments in their specifications boast sampling at spacings far less than the

reported spatial resolution. As long as the Nyquist requirement of sampling is no more than half the true spatial resolution, sampling at closer spacing provides no advantage.

The effects of the choice of spatial and temporal resolution can be combined into a simple *instrument quality* equation. Taking the temporal resolution to be τ (s) and the spatial resolution to be λ (m), the precision of the measurement will be equal to $C/\sqrt{\tau\lambda}$, where C is the instrument constant. By averaging over longer times and longer distances, the precision is improved. Generally, high-performance instruments have smaller values of C , though this is not universally the case. C is a primary criterion for the identification of the suitability of an instrument for a particular experiment. Manufacturers do not generally state the value of C , but it is easily obtained from their published performance curves.

Suitability for a particular experiment is also a function of the severity of the environmental conditions to which the instrument will be exposed. There are several

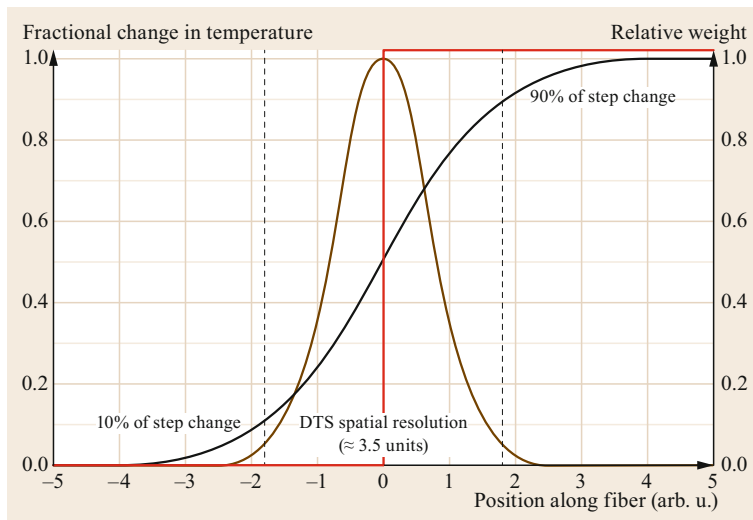


Fig. 20.3 Illustration of 10-90 definition of OFDS spatial resolution and underlying weighting function for photons from a section of cable. The position along the fiber is given in arbitrary units of length with step temperature change at 0. The *thin red line* represents the actual temperature change, the *thick black line* is the reported OFDS temperatures, the *light black line* the Gaussian weighting function over which the OFDS averages in its reported temperature at position 0, and the *dashed lines* indicate the locations along the cable of the 10% and 90% quantiles of change in reported temperature

instruments on the market that are completely sealed, making them more capable of long-term employment in high-dust environments. Different OFDS instruments have very different operating temperature ranges. Indoor-rated machines are generally constrained to use in the +5 to +40°C range, while ruggedized instruments can operate from -40 to +60°C. Low-power instruments with power demands < 40 W can further be sealed into waterproof enclosures, which extends the range of sites where OFDS can be easily deployed.

20.6 Quality Control

As mentioned in Sect. 20.3.1, OFDS requires the use of reference sections with known temperatures to solve for all terms of the full calibration equation (20.2) during post-field data processing. To solve for the three unknown terms, i.e., γ , $C(t)$, and the differential attenuation, a minimum of three reference sections with known $T(x, t)$ is required which vary in at least one dimension: either the position from the start of the fiber x or the temperature T , or both. As a result, all four potential fiber configurations (Fig. 20.1) need to accommodate this requirement by either using three separate water baths (Fig. 20.1a) or routing the fiber-optic cable through at least two baths twice (Fig. 20.1b, c). In practice, each reference section shall contain at least 40 to 50 individual fiber section units at the selected sampling resolution Δx to reduce the calibration uncertainty without using up too much fiber. This full experimental setup is recommended to significantly reduce measurement uncertainty, particularly for applications in which high trueness and accuracy are required. However, all commercially available OFDS instruments also offer simplified calibration setups in which either no external reference sections or only one or two reference sections in form of cold and warm baths are used. This simplified setup works because all instruments have an internal reference coil of fiber-optic cable of approximately 80 m length in combination with a classic internal temperature sensor to perform a crude single-point calibration, and require the user to enter a spatiotemporally fixed value for the differential attenuation into the control software. The ad hoc temperatures obtained from these simplified calibration setups are helpful to obtain a first glance of the environmental temperatures during the experiment and check for potential flaws in the fiber geometry, routing, and support. These flaws commonly lead to unphysical and sudden temperature changes caused by, e.g., applying excessive pressures by pinching the fiber-optic cable and deforming the optical core, using bends with too small radii leading to

We see that OFDS instrument performance has many metrics, including spatial and temporal precision, power consumption, dust resistance, and the range of temperature at which the instrument can operate. Success in using OFDS depends on matching the instrument to the goals and conditions of the experiment, where there is no generally *best* instrument, rather requiring matching of the qualities of the instrument to the characteristics of the application.

excessive light losses, or bad fiber splices resulting in enhanced light reflection and attenuation. Hence, we recommend choosing a calibration setup which combines the advantages of the simplified setup during the experiment with those from the full calibration setup during postprocessing to achieve maximum data quality. Since multiple individual single-core cables with identical or different properties or multiple optical cores of a multicore cable can be combined into one longer optical path by means of an optical fusion splicer, the user needs to ensure that each cable section can be properly calibrated by using the minimum number of reference sections for evaluating the full calibration equation. In particular, the differential attenuation of optical fibers varies across batches, manufacturers, age, and usage history of the fiber-optic cable and leads to skewed temperature signals when incorrectly determined or unknown. Here, we provide some guidance on which fiber configuration to choose depending on the measurement task and resources.

20.6.1 Single-Ended Configurations

These configurations use a smaller amount of fiber-optic cable and offer the remaining optical ports of the OFDS instrument to be used for additional cables. If only a single optical port is used for sampling, these configurations maximize repetition rates and the collected data have the greatest temporal resolution. In case of a simple single-ended configuration (Fig. 20.1a), light is injected in only one direction through the fiber-optic cable, which is routed through two reference baths of different temperatures before the cable enters the experimental fiber-optic array, and a third bath after it. For duplexed single-ended configurations (Fig. 20.1b), a third physical bath is unnecessary as the cable is routed back to the initial set of baths, yielding a total of four reference sections. Having four reference sections allows for independent

verification of the calibration routine by comparing its computed temperature with the independently measured value from the reference sensor as only three baths are used for the matrix inversion. The shortcomings of single-ended configurations are the inability to overcome measurement artifacts resulting from directional light losses, and a heteroscedastic distribution of random measurement error as the signal-to-noise ratio for the Raman backscatter peaks diminishes nonlinearly toward the end of the measurements. In other words, the random error for $T(x, t)$ toward the end of the cable is systematically larger, which is of particular concern for fiber-optic installations using the maximum cable length and duplexed configurations. For duplexed configurations, the cable sections closest to the start of the cable having the smallest random error are combined with those from the far end of the cable suffering from the largest random error. While duplexing reduces the overall uncertainty by a factor of $\sqrt{2}$ through sampling each measurement location twice, it *contaminates* the sections offering the smallest random uncertainty near the beginning of the array. Whether the resulting spatial random error is acceptable or can be partly compensated by greater temporal aggregation depends upon the application.

20.7 Maintenance

While the key to successful application of OFDS is proper design and installation of the system, some maintenance should be expected as well. Particular attention should be paid to the performance of the reference baths and reference thermometers upon which interpretation of the final data collected depends, but breaks in cables, deterioration of power systems, and contamination of connectors are also frequent sources of failure in the field. We review these issues here.

Because the sensitivity of photodetectors, amplifiers, and mechanical connections between fibers depends on their temperature as well as their age, it should immediately be clear that the parameters found in (20.2) should be recalculated frequently. As described above, it is advisable to maintain at least three reference baths along any cable, of which at least one should be at a different temperature from the other two. This means that continuous maintenance of precise reference baths, monitored by high-precision thermometers, will be an ongoing and essential aspect of any installation. All liquid-filled baths must be subject to continuous circulation to avoid stratification, and the cables should be held in the bath without contacting the vessel holding the

20.6.2 Double-Ended Configuration

These configurations use larger amounts of fiber-optic cables and require the use of two optical sampling ports per cable, as the light is sequentially injected from both ends of the cable. The fiber-optic cable is typically routed through two reference baths of different temperatures located close to the start and end of the optical path, yielding a total of four reference sections, which offers the advantage of independent verification of the calibration routine as described in the previous subsections. While double-ended configurations reduce the temporal sampling resolution through sequential sampling of the optical ports of the OFDS instrument, they allow for compensation of directional artifacts by selecting data from the *best* travel direction of the light. As in case of the single-ended configurations, duplexing reduces the overall measurement uncertainty but may introduce a spatially skewed random measurement error. For some applications requiring the highest measurement quality at maximum temporal and spatial resolution, including atmospheric turbulence observations using OFDS, combining the first two halves of the fiber-optic array sampled from each direction of a simple double-ended configuration is the optimum choice.

liquid. For short-term installations, two of the baths might be held at ambient conditions, and the third as an ice bath. For longer-term installations, where power is available, we recommend use of a mechanically cooled chest freezer to act as the cold bath. This must be controlled to avoid fully freezing or fully thawing, which requires active regulation to account for the changing external heat load. For very long-term installations we recommend the use of solid-state references, where the cable is wound around a series of thoroughly isolated thermal masses that provide stable and distinct temperatures.

If any dust is present on the face of a fiber-optic connector, the high-energy light from the laser will likely vaporize this dust, resulting in contamination on both surfaces of the fiber optics being joined. For this reason, whenever fibers are removed or reinserted into an OFDS instrument, the connectors must be cleaned meticulously to ensure that they are completely free of contamination. All outer surfaces of the connectors should be cleaned using an alcohol-wet lint-free towel, while the optical face of the fiber should be cleaned only with a dry-cleaning system designed specifically for this task.

Cables exposed to the insults of natural environments are frequently damaged, either fully eliminating the light path, or causing loss of light that will interfere with calibration. Power systems, many of which depend on batteries and solar charging, are also sub-

ject to deterioration and failure. Hence, we recommend having a schedule for frequent reinspection of the data from an OFDS system to ensure that the system is operating and that the cables remain in-tact.

20.8 Applications

The current range of OFDS applications is already broad and growing rapidly. Here, we focus on providing examples relevant to the scope of this handbook, including atmospheric turbulence, meteorological observations, surface energy balance, and some surface hydrological applications. However, we acknowledge that many other applications exist, including studies of groundwater flows, river discharge, sewerage systems, and slope stability and landslides. The reader is referred to the frequently updated list of OFDS studies found on [20.32] for a broader scope.

20.8.1 Atmospheric Profiling

The vertical distribution of temperature across the air–water interface is of interest to investigate and quantify the process of evaporation and sensible heat exchange to study the formation of surface fog and the impact of water bodies on the microclimate of lake shores. OFDS using fiber-optic cable coiled around a support material can measure these temperature profiles at high spatial resolution on the centimeter scale, resolving the very steep gradient of temperature at the interfacial boundary

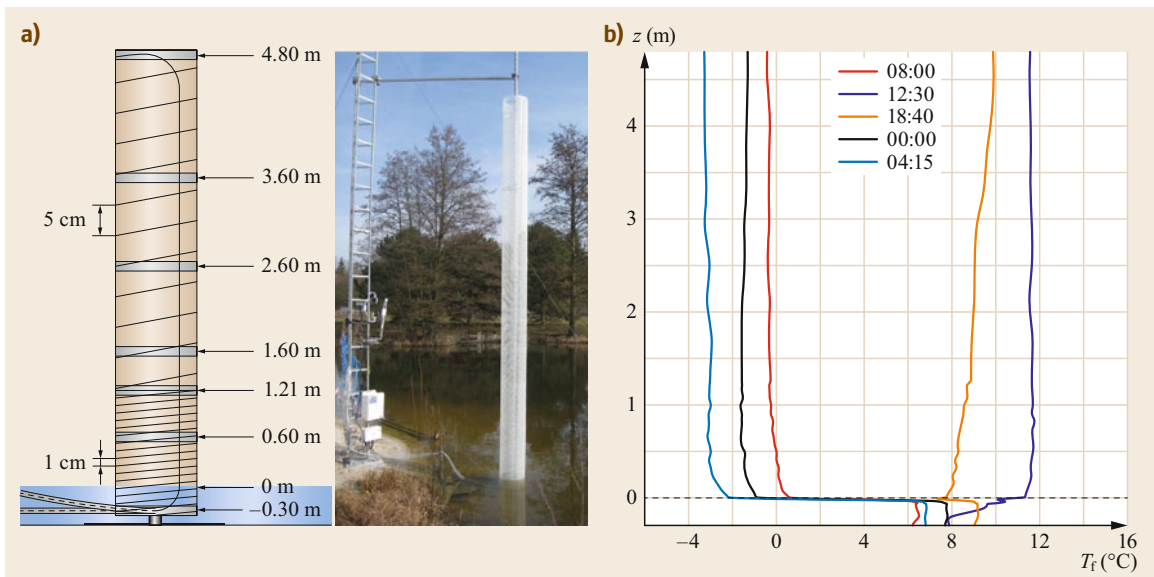


Fig. 20.4a,b Obtaining vertical profiles of temperature at the air–water interface above a lake: The coiled fiber-optic OFDS configuration allowed spatially continuous sampling with up to 0.01 m vertical resolution across 5 m in height using reinforcement fabric as mechanical support material (a). The radiation and conductive errors of the fiber-optic cable and between the support material and the fiber-optic cable were carefully evaluated. OFDS enabled quantification of the very steep temperature gradient near the interfacial boundary, which is greatest in the early morning hours. Temperatures are shown as deviations from the temporal average at the top of the column for a calm night with clear skies and a net radiative forcing of 64 W m^{-2} (b) (after [20.16] © A. Sigmund et al., licensed under CC-BY 3.0)

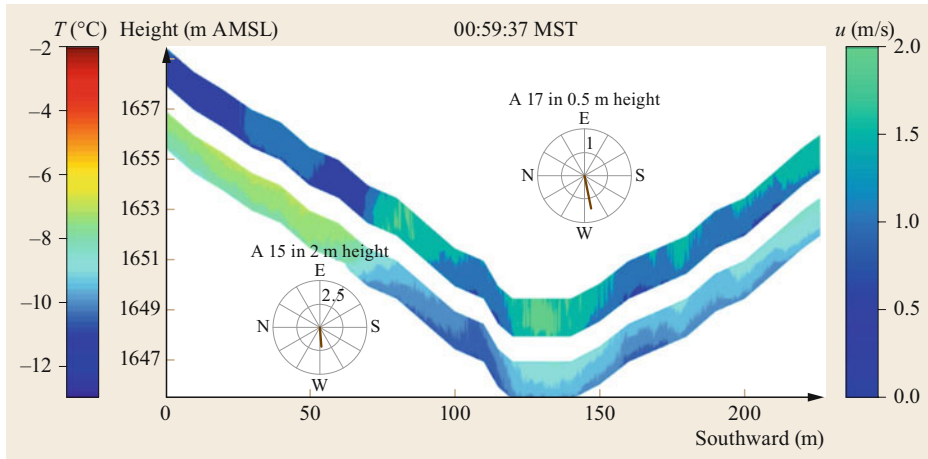


Fig. 20.5 Observing the effects of gentle topography on atmospheric turbulence: Space series of instantaneous wind speeds u (*upper V-shaped graph*) and air temperatures T (*lower V-shaped graph*) across a shallow gully observed at three heights (0.5, 1.0, and 2.0 m above ground, spatially interpolated during postprocessing) sampled by actively heated OFDS during the Shallow Cold Pool experiment. The turbulent temperature perturbations are smallest at the bottom of the gully, but largest on the south-facing slope (*left half* in image) because of lee-turbulence mixing down warm air in this weak-wind boundary layer for northerly flows (from *left to right* in the image). No other experimental technique can map turbulent perturbations at such fine resolutions in the surface layer

(Fig. 20.4). A standard-performance OFDS instrument was used with a minimum temporal aggregation time of $\Delta t = 30$ s at a sampling resolution of $\Delta x = 1$ m. The radius of the column made from the support fabric was chosen such that its circumference was equal to the sampling resolution.

20.8.2 Turbulent Airflows

High-resolution actively heated OFDS allows for observations of the small-scale and short-lived perturbations of atmospheric turbulence in air temperature and wind speed, which may be of interest to investigate the topographic impacts on the formation and behavior of cold-air drainage and pools. A fiber-optic array constructed from a pair of fiber-optic cables consisting of a passive, unheated PVC-jacketed white cable in combination with a resistively heated cable with stainless-steel outer jacket was used to measure air temperature and wind speed at three heights across a 220 m-wide shallow gully during the Shallow Cold Pool experiment [20.12, 19, 20.33] (Fig. 20.5). A high performance-type OFDS instrument was used with a temporal aggregation time of $\Delta t = 1$ s at a sampling resolution of $\Delta x = 0.125$ m using a simple single-ended configuration with three reference baths sampling the passive and heated ca-

bles sequentially, which resulted in records of 0.5 Hz for air temperature and of 0.25 Hz for wind speed. The space series reveal superimposed eddies of varying size for nighttime conditions dominated by cold-air drainage perpendicular to the transect and into the view plane.

20.8.3 Hydrological Applications

Applications of OFDS to environmental sensing were first applied to hydrological processes [20.6, 22, 30]. In this application, temperature is employed as a signature for parcels of water and to identify the structure of turbulence and mixing. The use of actively heated methods in combination with measuring the response time provides an indication of any changes in local heat capacity and thermal diffusivity. Placed in rivers and wells, OFDS was shown to be able to identify the location and intensity of groundwater entry. In lakes and seas, OFDS can identify stratification and thus the presence and magnitude of internal waves (Fig. 20.6; [20.34–36]). In soils, OFDS has allowed for observation of water content and flow of water with unprecedented spatial resolution (e.g., using active heating in [20.11] and using passive observation of profiles of soil temperature by [20.31]).

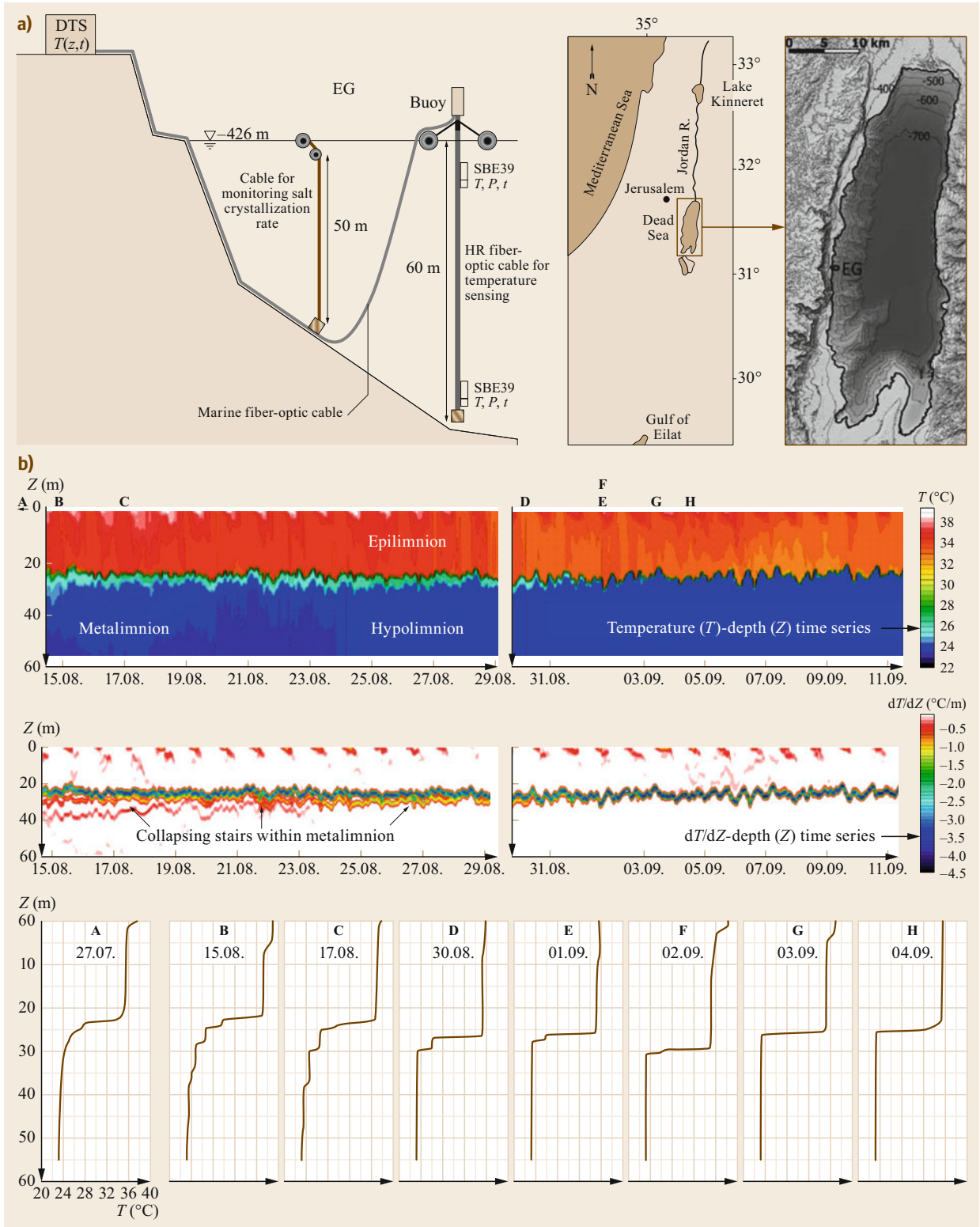


Fig. 20.6 Data from a 55 m vertical profile of high-resolution fiber-optic cable installed in the Dead Sea. The 26 mm-diameter cable had two helically wrapped loose-tube fiber optics which had fiber length of 11 m for each 1 m of cable. The time series of temperature shown illustrate the sharpening of the thermal stratification of the upper 50 m of the Dead Sea from late July to September 2012, overlaid by approximately 5 m excursions of the thermal interface driven by internal waves (after [20.34] with permission from John Wiley and Sons9 ◀

20.9 Future Developments

Here, we briefly present some directions in which OFDS methods are currently evolving. If successful, the resulting applications will greatly enhance the utility of OFDS in cross-disciplinary geosciences research.

Current development of OFDS for atmospheric applications aims at adding wind direction to the parameters which can be obtained at high spatiotemporal resolution. An observational system capable of measuring air temperature, and three-dimensional wind speed and direction at submeter and second resolutions over scales of hundreds and thousands of meters could be used to estimate spatially resolved fluxes of sensible heat and momentum using the spatial eddy covariance method. Such flux estimates would represent true spatial averages without the assumption of ergodicity and avoid the need for spatial homogeneity of the sampling

location and stationarity. The technical approach for adding wind direction to the list of parameters obtained from OFDS is built around the differential directional heat loss from heated fiber-optic cable from small flow obstacles imprinted onto the fiber. First tests of this approach have yielded promising results in controlled laboratory environments [20.21], and first methodological studies are being published at the time of writing.

Other efforts to enhance the sensing capabilities of OFDS aim at extending the wind speed range of the actively heated technique by applying a dynamic heating rate proportional to the wind speed. Such a system would have an optimal signal-to-noise ratio for determining $\Delta T(x, t)$ (see (20.5)) independent of wind speed and would allow for sampling high mean advective velocities during storms and increased gust speeds.

20.10 Further Reading

As mentioned above, a basic review of OFDS methods can be found in:

- J. Selker, N. van de Giesen, M. Westhoff, W. Luxemburg, M. B. Parlange: Fiber optics opens window on stream dynamics. *Geophys. Res. Lett.* **33**, L24401 (2006)
- S. W. Tyler, J. S. Selker, M. B. Hausner, C. E. Hatch, T. Torgersen, C. E. Thodal, S. G. Schladow: Environmental temperature sensing using Raman spectra DTS fiber-optic methods. *Water Resour. Res.* **45**, W00D23 (2009)

A review of calibration equations for single- and double-ended configurations can be found in:

- M. B. Hausner, F. Suárez, K. E. Glander, N. van de Giesen, J. S. Selker, S. W. Tyler: Calibrating single-ended fiber-optic Raman spectra distributed temperature sensing data. *Sensors* **11**, 10859–10879 (2011)
- N. van de Giesen, S. C. Steele-Dunne, J. Jansen, O. Hoes, M. B. Hausner, S. Tyler, J. Selker: Double-ended calibration of fiber-optic Raman spectra distributed temperature sensing data. *Sensors* **12**, 5471–5485 (2012)

An extended and current list of literature on OFDS fundamental principles, techniques, and applications can be found on <https://ctemps.org/publications>, Accessed 07 July 2021.

References

- | | | | |
|------|--|------|--|
| 20.1 | Y. Cheng, C. Sayde, Q. Li, J. Basara, J. Selker, E. Tanner, P. Gentile: Failure of Taylor's hypothesis in the atmospheric surface layer and its correction for eddy-covariance measurements, <i>Geophys. Res. Lett.</i> 44 , 4287–4295 (2017) | 20.2 | D. Belusic, L. Mahrt: Estimation of length scales from mesoscale networks, <i>Tellus A Dyn. Meteorol. Oceanogr.</i> 60 , 706–715 (2008) |
| | | 20.3 | C. Daly, D.R. Conklin, M.H. Unsworth: Local atmospheric decoupling in complex topography alters |

- climate change impacts, *Int. J. Climatol.* **30**, 1857–1864 (2010)
- 20.4 L. Mahrt, C.K. Thomas, J.H. Prueger: Space-time structure of mesoscale motions in the stable boundary layer, *Q. J. R. Meteorol. Soc.* **135**, 67–75 (2009)
- 20.5 C.K. Thomas: Variability of sub-canopy flow, temperature, and horizontal advection in moderately complex terrain, *Bound.-Layer Meteorol.* **139**, 61–81 (2011)
- 20.6 J.S. Selker, L. Thevenaz, H. Huwald, A. Mallet, W. Luxemburg, N.V. de Giesen, M. Stejskal, J. Zeman, M. Westhoff, M.B. Parlange: Distributed fiber-optic temperature sensing for hydrologic systems, *Water Resour. Res.* **33**, L24401 (2006)
- 20.7 S. Kobs, D.M. Holland, V. Zagorodnov, A. Stern, S.W. Tyler: Novel monitoring of Antarctic ice shelf basal melting using a fiber-optic distributed temperature sensing mooring, *Geophys. Res. Lett.* **41**, 6779–6786 (2014)
- 20.8 V. Zagorodnov, S. Tyler, D. Holland, A. Stern, L.G. Thompson, C. Sladec, S. Kobs, J.P. Nicolas: New technique for access-borehole drilling in shelf glaciers using lightweight drills, *J. Glaciol.* **60**, 935–944 (2014)
- 20.9 C.A. Keller, H. Huwald, M.K. Vollmer, A. Wenger, M. Hill, M.B. Parlange, S. Reimann: Fiber optic distributed temperature sensing for the determination of the nocturnal atmospheric boundary layer height, *Atmos. Meas. Tech.* **4**, 143–149 (2011)
- 20.10 C.K. Thomas, A.M. Kennedy, J.S. Selker, A. Moretti, M.H. Schroth, A.R. Smoot, N.B. Tuffillaro, M.J. Zeeman: High-resolution fibre-optic temperature sensing: A new tool to study the two-dimensional structure of atmospheric surface layer flow, *Bound.-Layer Meteorol.* **142**, 177–192 (2012)
- 20.11 C. Sayde, C. Gregory, M. Gil-Rodriguez, N. Tuffillaro, S. Tyler, N. van de Giesen, M. English, R. Cuenca, J.S. Selker: Feasibility of soil moisture monitoring with heated fiber optics, *Water Resour. Res.* **46**, W06201 (2010)
- 20.12 L. Pfister, K. Lapo, L. Mahrt, C.K. Thomas: Thermal Submesoscale Motions in the Nocturnal Stable Boundary Layer. Part 1: Detection and Mean Statistics. *Bound.-Layer Meteorol.* **180**, 187–202 (2021)
- 20.13 T. Euser, W.M.J. Luxemburg, C.S. Everson, M.G. Mengistu, A.D. Clulow, W.G.M. Bastiaanssen: A new method to measure Bowen ratios using high-resolution vertical dry and wet bulb temperature profiles, *Hydrol. Earth Syst. Sci.* **18**, 2012–2032 (2014)
- 20.14 B. Schilperoort, M. Coenders-Gerrits, W. Luxemburg, C. Jimenez Rodriguez, C.C. Vaca, H. Savenije: Technical note: Using distributed temperature sensing for Bowen ratio evaporation measurements, *Hydrol. Earth Syst. Sci.* **22**, 819–830 (2018)
- 20.15 C. Sayde, C.K. Thomas, J. Wagner, J. Selker: High-resolution wind speed measurements using actively heated fiber optics, *Geophys. Res. Lett.* **42**, 10,064–10,073 (2015)
- 20.16 A. Sigmund, L. Pfister, C. Sayde, C.K. Thomas: Quantitative analysis of the radiation error for aerial coiled-fiber-optic distributed temperature sensing deployments using reinforcing fabric as support structure, *Atmos. Meas. Tech.* **10**, 2149–2162 (2017)
- 20.17 B.T. Neilson, C.E. Hatch, H. Ban, S.W. Tyler: Solar radiative heating of fiber-optic cables used to monitor temperatures in water, *Water Resour. Res.* **46**, W08540 (2010)
- 20.18 L. Pfister, A. Sigmund, J. Olesch, C.K. Thomas: Nocturnal near-surface temperature, but not flow dynamics, can be predicted by microtopography in a mid-range mountain valley, *Bound.-Layer Meteorol.* **165**, 333–348 (2017)
- 20.19 L. Pfister, C. Sayde, J. Selker, L. Mahrt, C.K. Thomas: Classifying the nocturnal atmospheric boundary layer into temperature and flow regimes, *Q. J. R. Meteorol. Soc.* **145**, 1515–1534 (2019)
- 20.20 L. Pfister, K. Lapo, L. Mahrt, C.K. Thomas: Thermal Submesoscale Motions in the Nocturnal Stable Boundary Layer. Part 2: Generating Mechanisms and Implications. *Bound.-Layer Meteorol.* **180**, 203–224 (2021)
- 20.21 K. Lapo, A. Freundorfer, L. Pfister, J. Schneider, J. Selker, C.K. Thomas: Distributed observations of wind direction using microstructures attached to actively heated fiber-optic cables, *Atmos. Meas. Tech.* **13**(3), 1563–1573 (2020)
- 20.22 J. Selker, N. van de Giesen, M. Westhoff, W. Luxemburg, M.B. Parlange: Fiber optics opens window on stream dynamics, *Geophys. Res. Lett.* **33**, L24401 (2006)
- 20.23 S.W. Tyler, J.S. Selker, M.B. Hausner, C.E. Hatch, T. Torgersen, C.E. Thodal, S.G. Schladow: Environmental temperature sensing using Raman spectra DTS fiber-optic methods, *Water Resour. Res.* **45**, W00D23 (2009)
- 20.24 M.A. Farahani, T. Gogolla: Spontaneous Raman scattering in optical fibers with modulated probe light for distributed temperature Raman remote sensing, *J. Light. Technol.* **17**, 1379–1391 (1999)
- 20.25 K. Lapo, A. Freundorfer: klapo/pyfocs v0.5 (2020), <https://doi.org/10.5281/zenodo.4292491>
- 20.26 M.B. Hausner, F. Suárez, K.E. Glander, N. van de Giesen, J.S. Selker, S.W. Tyler: Calibrating single-ended fiber-optic Raman spectra distributed temperature sensing data, *Sensors* **11**, 10859–10879 (2011)
- 20.27 N. van de Giesen, S.C. Steele-Dunne, J. Jansen, O. Hoes, M.B. Hausner, S. Tyler, J. Selker: Double-ended calibration of fiber-optic Raman spectra distributed temperature sensing data, *Sensors* **12**, 5471–5485 (2012)
- 20.28 S.A.P. de Jong, J.D. Slingerland, N.C. van de Giesen: Fiber optic distributed temperature sensing for the determination of air temperature, *Atmos. Meas. Tech.* **8**, 335–339 (2015)
- 20.29 A.C. Petrides, J. Huff, A. Arik, N. Van De Giesen, A.M. Kennedy, C.K. Thomas, J.S. Selker: Shade estimation over streams using distributed temperature sensing, *Water Resour. Res.* **47**, W07601 (2011)
- 20.30 J.D. Weiss: Using fiber optics to detect moisture intrusion into a landfill cap consisting of a vegetative

- soil barrier, *J. Air Waste Manag. Assoc.* **53**, 1130–1148 (2003)
- 20.31 J. Dong, S.C. Steele–Dunne, T.E. Ochsner, C.E. Hatch, C. Sayde, J. Selker, S. Tyler, M.H. Cosh, N. van de Giesen: Mapping high-resolution soil moisture and properties using distributed temperature sensing data and an adaptive particle batch smoother, *Water Resour. Res.* **52**, 7690–7710 (2016)
- 20.32 Oregon State University Center for Transformative Environmental Monitoring Programs: <https://ctemps.org>, Accessed 07 July 2021
- 20.33 L. Mahr, C.K. Thomas: Surface stress with non-stationary weak winds and stable stratification, *Bound.-Layer Meteorol.* **159**, 3–21 (2016)
- 20.34 A. Arnon, J.S. Selker, N.G. Lensky: Thermohaline stratification and double diffusion diapycnal fluxes in the hypersaline Dead Sea, *Limnol. Oceanogr.* **61**, 1214–1231 (2016)
- 20.35 A. Arnon, N.G. Lensky, J.S. Selker: High-resolution temperature sensing in the Dead Sea using fiber optics, *Water Resour. Res.* **50**, 1756–1772 (2014)
- 20.36 S.W. Tyler, S.A. Burak, J.P. McNamara, A. Lamontagne, J.S. Selker, J. Dozier: Spatially distributed temperatures at the base of two mountain snowpacks measured with fiber-optic sensors, *J. Glaciol.* **54**, 673–679 (2008)

Christoph K. Thomas

Micrometeorology
University of Bayreuth
Bayreuth, Germany
christoph.thomas@uni-bayreuth.de



Christoph Thomas is Professor of Micrometeorology at the University of Bayreuth in Germany, where he received a PhD in 2005. Awards include the Early Career Award from the US National Science Foundation in 2010, and a Consolidator Grant from the European Research Council in 2017. He was an editor for *Water Resources Research* and *Agricultural and Forest Meteorology*. His research interest include weak-wind turbulence, forest carbon exchange, urban meteorology, and fiber-optic sensing methods.

John Selker

Oregon State University
Corvallis, USA
john.selker@oregonstate.edu



John Selker, OSU Distinguished Professor of Biological and Ecological Engineering at Oregon State University (28 years) and co-Director of both CTEMPs.org and TAHMO.org, and PI of the OPEnS Lab (OpenSensing.org) has worked in more than 20 countries across 5 continents. His focus areas include environmental instrumentation, groundwater processes, and ecohydrology. He served as editor of *Water Resources Research*. Selker has published over 200 peer-reviewed articles. In 2013 he was elected Fellow of the American Geophysical Union, and 2013 received the John Hem Award for Science and Technology from the American Groundwater Association.

Odor Measurements

Ralf Petrich , Axel Delan 

Odor measurements in the atmosphere are carried out using human noses or instruments as sensors. Only human noses are currently able to record an odor impression. To measure odor intensity, distinguish between the presence or absence of odors, or classify odors, instruments can also be used.

From the perspective of typical applications, there are two basic approaches. On one hand, high odor concentrations in the air (several orders of magnitude above the human perception threshold) are measured using olfactometry. This method combines a device for dilution and the evaluation of the diluted odors, usually by human noses. Applications of this method are the determination of odor emitter concentrations in industry or agriculture and, beyond the scope of atmospheric measurements, the characterization of scents. On the other hand, the measurement of low odor concentrations (around or slightly above the human perception threshold) are obtained by means of field inspections. In this case, human assessors breathe the air to be tested and record their odor perception.

Odor concentration, perception frequency, and hedonic impression are typical parameters determined within the scope of odor measurement. Statistical methods play an important role during the evaluation of the raw data obtained from the assessors to finally get representative measurement values.

Measurements of odors in the atmosphere have become more and more important in the last 20 years. In contrast to indoor odor measurements and scent characterization of consumer products, atmospheric odor measurement is usually connected to the assessment of odor nuisances around facilities with odor emissions, such as industrial plants, agricultural operations (livestock), waste and wastewater treatment plants, or composting facilities. There are methods of direct odor

21.1	Measurement Principles and Parameters	634
21.1.1	Measured Parameters	634
21.1.2	Principles of Measurement	634
21.2	History	635
21.3	Theory	635
21.3.1	Derivation of the Odor Unit Concept ...	635
21.3.2	Conventional Measurement Principles	636
21.3.3	Instrument Odor Measurement Systems	637
21.4	Devices and Systems	638
21.5	Specifications	639
21.5.1	Olfactometry Specifications	639
21.5.2	Field Inspection Specifications	640
21.6	Quality Control	640
21.7	Maintenance	641
21.8	Application	641
21.9	Future Developments	642
21.10	Further Readings	642
	References	642

measurement, such as field inspections by panel members who visit the locations where odor measurements are required. Moreover, the concept of odor units was developed to measure the amount of an odor within a unit volume. Thus, it is possible to mathematically describe processes like odor emission, dilution, mixture, or dispersion. Also, direct odor concentration measurements can be carried out using olfactometry.

21.1 Measurement Principles and Parameters

Odor measurements can be carried out for several reasons. For instance, odor annoyances reported by people living near odor emitting facilities are quantified based on odor measurements. Furthermore, if the scents of certain consumer products like perfumes, cars, or food must be characterized, odor measurements (outside the scope of atmospheric measurements) are used.

21.1.1 Measured Parameters

Different kinds of parameters can be obtained from an odor measurement. Odor concentration plays a central role. This concentration describes the amount of odor within a given volume of air. In this context, odor is mathematically treated as an extensive magnitude like, for instance, mass or energy. To accomplish this, the concept of an *odor unit* must first be introduced. An odor unit (OU) is defined as exactly the amount of an odorant (a substance that stimulates the human olfactory sense) within one cubic meter of gas, which constitutes the average human odor perception threshold. Thus, the concentration of one odor unit per cubic meter is the concentration at which the average (regarding her or his odor perception) human starts to perceive the odor. A more detailed representation of the theory behind this concept is given in Sect. 21.3.1.

Once the odor unit and its concentration are defined as quantities, they can be used for calculations and to derive other quantities. For instance, if a gas with an odor concentration of 100 ou m^{-3} is diluted by the factor 20, the resulting concentration is 5 ou m^{-3} . Furthermore, if the amount of time is determined during which a concentration in ambient air, for instance 1 ou m^{-3} , is exceeded, the perception frequency of a specific odor is obtained as another measured parameter.

Other parameters like the hedonic impression of a specific odor, for instance *pleasant* or *unpleasant*, can usually not be treated within the concept of a numerical quantity, but as verbal descriptions. The most relevant measured parameters are summarized in Table 21.1.

21.1.2 Principles of Measurement

As usual, *to measure* means comparing a quantity to a standard. To measure odors is complicated for two reasons. On one hand, the only standard to compare to is the human olfactory perception, which to be precise means the human olfactory perception threshold.

On the other hand, the method to compare a sample of gas to this standard can also be difficult if dilution or a special sample treatment is involved. To accomplish the task of comparison, two basic approaches can be used. The conventional method uses human noses as detectors. Recently, technical instruments have also been used to characterize odors.

Another way to structure measurement principles is based on the odor concentration of the gas under study. On one hand, high odor concentrations in the air (several orders of magnitude above the human perception threshold) are measured using olfactometry. This method combines a device for dilution and the evaluation of the diluted odors, usually by human noses. Applications of this method are the determination of odor concentration of odor emitters in industry or agriculture and, beyond the scope of atmospheric measurements, the characterization of scents. On the other hand, the measurement of low odor concentrations (around or slightly above the human perception threshold) is obtained by means of field inspections. In this case, human assessors (panel members) breathe the air under investigation and record their odor perception. Field inspections can be carried out as grid inspections or plume inspections.

For grid inspections, panel members visit a spatial grid of fixed measurement points over a representative time span (typically one year) and record their odor perceptions, usually every ten seconds over a period of ten minutes at each measurement point. Thus, a spatial distribution of the perception frequency is obtained for the assessment area.

Plume inspections are used to determine the shape and size of the area where an odor plume originating from a given point can be perceived and recognized, with respect to the specific meteorological and odor source conditions. For that, the panel members record the presence or absence of the odor under investigation at different points downwind of a source. They can stay at a fixed measurement point in the assessment area over a certain time (stationary method) or they can move around and follow a plume in the assessment area and record their perception as a function of location and time (dynamic method).

More detailed background information on the measurement principles is given in Sect. 21.3. Table 21.2 shows the sensor types and their respective measurement principles and parameters.

Table 21.1 Measured parameters

Parameter	Description	Unit	Symbol
Odor concentration	Mathematical equivalent to mass concentration, describing the amount of odor within a given volume of air	ou m ⁻³	<i>c</i>
Perception frequency	Percentage of time during which a specific odor is perceived	%	<i>P</i>
Hedonic impression	Verbal description of the type of odor (pleasant, unpleasant, etc.)	–	–

Table 21.2 Principles of odor measurements and applications

Type of sensor	Measurement principle			Parameter		
	Olfactometry	Grid inspection	Plume inspection	Odor concentration	Perception frequency	Hedonic impression
Human nose	×	×	×	×	×	×
Instrument	×	×	×		×	

21.2 History

Olfaction is phylogenetically the oldest sense and man's interest in scents or odors can be traced back into ancient history [21.1]. But only in the nineteenth century were efforts to assess olfaction solidified by *Gabriel Valentin* (1810–1883) in 1842 and *J. Passy* in 1892 [21.2]. Around 1888, *Hendrik Zwaardemaker* developed a device for obtaining olfactory perception thresholds. This device can be regarded as the predecessor for the olfactometers since developed and produced.

The last 20 years of the twentieth century saw development in olfactometry, when interest in the quantification of olfactory perception was promoted by applications in pollution management, environmentalism, and scent management for consumer products. Many test procedures were developed for the human olfactory sense from a medical perspective. Also, studies on the olfactory sense and its statistical parameters (for instance odor perception threshold) were carried out in North America and Europe.

At the end of the twentieth century, a lot of knowledge was available regarding the measurement of the parameters mentioned above.

Sophisticated devices (olfactometers) were developed and built to accurately dilute samples. At first, these olfactometers had simple dilution mechanisms controlled manually; later, computer-controlled dilution mechanisms were introduced. The first olfactometers were able to serve only one panel member; recent devices can serve up to ten panel members at once. Elaborate statistical methods were also developed to accomplish quality management.

With this knowledge and the availability of devices, it was finally possible to handle odor measurements at the same scientific level as the measurements of other atmospheric parameters.

Finally, a set of regulations was developed in Europe and North America to regulate the procedures of olfactometry and field inspections as the most common odor measurement principles [21.3–5].

21.3 Theory

In the following section the concept of odor units is described. Based on this concept, several measurement principles are introduced later in the section.

21.3.1 Derivation of the Odor Unit Concept

As mentioned in Sect. 21.1.2, the basic odor measurement concept is the odor unit. An odor unit is defined as the amount of an odorant within one cubic meter of gas, which constitutes the average human odor perception threshold.

Regarding this definition, several important aspects must be considered. The actual amount of an odorant expressed as its mass in a given volume of air is proportional to the number of odor units within this volume with respect to the specific odorant. The mass concentration of an odorant that corresponds to 1 ou m⁻³ is the specific odor threshold of this odorant. For ammonia, for instance, this value lies between 1 mg m⁻³ and 5 mg m⁻³.

Another aspect in the definition is the term *average human odor perception threshold*. Everyone has

their own (personal) threshold (mass concentration of an odorant within ambient air), above which an odorant becomes perceptible. Below this threshold, the odorant is not perceived, though its mass concentration within the ambient air is not zero. To work with a value averaged over a statistically representative set of people (average threshold), the variation in personal thresholds must be investigated. It was found that even for a mixed population (both genders and ages within the adult range), the personal thresholds do not vary by orders of magnitude. The value can therefore be regarded as stable enough to be used in the definition of odor units. Finally, the *average threshold* can be regarded as the amount of an odorant within ambient air at which half of a statistically representative set of people perceives the odor and the other half does not [21.5]. Thus, *averaging* the perception threshold mathematically corresponds to finding the median value.

In practice, the representative set of people mentioned above is constituted by a panel of assessors. To ensure typical odor perception, the panel members are checked on a regular basis to determine whether their odor perception threshold for certain substances (for instance, *n*-butanol) is within a predefined range. Such a panel of assessors is used for all the measurement principles described below.

Finally, one more aspect must be kept in mind. The amount of odor units within a given volume is always coupled to the one odorant under study. Though odor units offer a convenient way to mathematically handle dilutions, it is not possible to describe the processes if odorants are mixed this way. If an air sample with a certain odor concentration (odor units per volume) is mixed with a sample with another odorant, the odor concentration of the resulting mixture cannot be expressed as a weighted average of the original concentrations. This is because different odors can cover, amplify, or attenuate each other on mixing. The only way to obtain the odor concentration of the mixture is to characterize it with an independent measurement.

21.3.2 Conventional Measurement Principles

As summarized in Table 21.1, different measurement principles are available to determine different measurement parameters. The central measurement principle is olfactometry, which can measure the odor concentration and the hedonic impression of a sample. Other measurement principles like field inspections can yield measurement parameters such as the absence or presence of odors, perception frequency, and the hedonic impression. Instrument-aided measurement principles must be calibrated with measurements based on the

human nose and can then be used to determine odor concentration, the absence or presence of odors, the classification of odors, and perception frequency. However, while nose-based measurements are usually used to study arbitrary odors, instrument-based measurements can only be used to study exactly the odors they were calibrated for, but no other odors.

Olfactometry

Olfactometry as a measurement principle can be used to investigate odor samples with odor concentrations well above the perception threshold of the odor under study. This is caused by the central principle of olfactometry, the sample dilution. For instance, an air sample is diluted and presented to a panel of human assessors until half of the panel members perceives the odor and the other half does not. At this dilution, the air presented to the panel has an odor unit concentration of 1 ou m⁻³ per definition. The dilution factor is recorded and used to derive the odor concentration of the original, undiluted sample. If, for instance, a dilution of 6000 is necessary to reach the panel's odor threshold, the original sample has an odor concentration of 6000 ou m⁻³.

To implement this procedure, a measurement device called an olfactometer is used. An olfactometer usually has two sections. One section consists of the dilution instrument; the other section presents the diluted sample to a panel of assessors and records their odor perception at different dilution levels.

The dilution instrument is the most sophisticated part of an olfactometer. On one hand, it must allow for calibrated dilution in a typical range from 10 to 5000. Even higher dilutions might be reached using predilution. On the other hand, the instrument components must not emit their own odors or modify the odors under study. Thus, typically only materials like glass, stainless steel, or polytetrafluorethylene (Teflon, PTFE) can be used.

Twentieth-century olfactometers were manually controlled to adjust the dilution factor. Current devices usually use automatic control units to adjust the dilution as part of a computerized measurement procedure. Panel sizes to test the diluted sample range from one to ten for common olfactometers.

Usually, the measurement procedure starts with a very high dilution so that the diluted sample presented to the panel is well below the perception threshold of all panel members. Then, the dilution is decreased step by step (for instance, a factor of two at each step) and the odor concentration presented to the panel increases. When the perception threshold of all panel members is reached (perceptions from all members have been recorded), the procedure is finished and will be evaluated. To decrease statistical uncertainty, this procedure

is repeated with the same sample a number of times, for instance three times.

Two common procedures for presenting the diluted sample to the panel members are known [21.5]. In the *yes/no mode*, the assessor is asked to evaluate the presented gas and to indicate if an odor is perceived (yes/no). The assessor is aware that in some cases blanks (only neutral gas) are presented. An additional outlet that always presents neutral gas may be made available to the assessor to provide a reference. Also, neutral reference gas might be presented between the stimulus cycles.

In the *forced choice mode*, the assessor is presented with two or more outlets, of which one presents the stimulus and the other(s) neutral air. The location of the stimulus in consecutive presentations is randomly changed among the two or more outlets. The assessor is asked to indicate which of the outlets presented the stimulus.

By evaluation of the panel member responses over the decreasing dilution factor, it is possible to find the panel's average odor perception threshold. If this threshold is reached, the respective dilution factor is used to determine the sample's odor concentration. Detailed information on olfactometry can be found in [21.5].

Field Inspection – Grid Mode

Grid mode is one of the field inspection methods mentioned in Sect. 21.1.2. Because olfactometry, with its practical lower detection limit of approximately 10 ou m^{-3} , cannot be applied to directly determine odor exposure in the field (faint odors at the concentration where they can just be recognized), grid inspection is not based on the dilution of sample air but brings the panel members to the field for in-place assessment [21.3].

The grid inspection is a statistical survey method carried out over a sufficiently long period of time (typically one year) to provide a representative map of the exposure to recognizable odor, spatially distributed over the assessment area. These measurements are used to determine the distribution of the perception frequency for recognizable odors in ambient air in an assessment area under meteorological conditions that are assumed to be representative for the local meteorology [21.3].

The odor perception frequency can, for instance, be used as an exposure indicator to assess the odor annoyance originating from one or many specific odorant source(s) emitting in a particular area under study.

For grid inspections, the panel members visit a spatial grid of fixed measurement points many times and record their odor perceptions. Usually, the perception is recorded every ten seconds over a total period of ten minutes (60 records) at each measurement point. From these records, a value for the perception frequency can be derived at the respective measurement point.

Typically, the assessment area is inspected with a frequency of approximately twice per week, while the actual time of day for the measurement changes stochastically. Also, the panel member carrying out the measurement is selected stochastically from a pool of at least ten assessors.

Inherently, each inspection represents only a snapshot of the real situation. For that reason, extensive statistical evaluation must be carried out to determine the relevance of the results. The perception frequency usually uses an hour as the time basis (odor hour frequency). By taking two snapshots per week, only 104 samples are available after a typical assessment time of one year. A perception frequency value with respect to the 8760 h of one year derived from only 104 snapshots bears a high statistical uncertainty. This aspect is one of the major disadvantages of grid inspection, besides the immense expense of visiting the assessment area 104 times.

Field Inspection – Plume Mode

Plume inspections are used to determine the shape and size of the area where an odor plume originating from a given point can be perceived and recognized with respect to the specific meteorological and odor source conditions. In contrast to the grid mode, the assessment area is not visited sequentially over a long span of time by the panel members; instead, a snapshot at a specific time is taken by a group of panel members visiting the assessment area simultaneously. The panel members record the presence or absence of the odor under investigation at different points downwind of a source. They can stay at a fixed measurement point in the assessment area over a certain time (stationary method) or they can move around and follow a plume in the assessment area and record their perception as a function of location and time (dynamic method).

The primary parameter measured with this method is the presence or absence of recognizable odors at a specific location downwind of a source, which is recorded by a number of panel members. From these results, the extent of the plume can be assessed as the transition from absence to presence of recognizable odor.

On one hand, the results are typically used to determine a plausible extent of potential exposure to recognizable odors. On the other hand, it is possible to estimate the total emission rate based on the plume extent, using reverse dispersion modelling [21.4].

21.3.3 Instrument Odor Measurement Systems

For instrument odor measurement systems (IOMSs), the human nose as a sensor is replaced by a technical system that can detect odorants in the air. For

a while, these devices were also called *electronic noses*, however all known IOMSs are far from being able to perform similar measurement tasks as the human nose. In particular, the physiological hedonic impression of an odor cannot be measured by an IOMS, but only by the human nose.

Thus, IOMSs are presently restricted to the following measurement tasks:

- Distinguish between the absence and presence of a single specific odor under study
- Classify multiple specific odors under study
- Estimate the odor concentration for a single specific odor under study

Nearly all presently known IOMS rely on a multidimensional sensor system that is sensitive to as many odorants as possible. During measurement, a multidimensional pattern is recorded, where each dimension can be regarded as an indicator for a single odorant concentration. Apparently, most of these sensor systems are not only stimulated by odorants, but also by odorless substances in the air, which leads to adverse cross-sensitivity effects. Conversely, not all odorants that stimulate the human olfactory perception also stimulate the various sensor systems, which leads to the effect that not all the odors perceptible by humans can be detected by the different kinds of IOMSs.

In practice, several kinds of IOMSs are used. For instance, gas chromatography (GC), ion-mobility spectroscopy (IMS), or electrochemical sensor arrays.

While the electrochemical sensor arrays are relatively cheap, they usually suffer from cross-sensitivity, drift effects after some time of exposure to the atmosphere, and the lack of enough independent dimensions to reliably characterize an odor. GC and IMS are well-established measurement principles for gas analysis and thus can also be used as IOMSs. For GC, the resulting chromatogram holds the multidimensional information on as many as possible odorants; for IMS it is the drift-time spectrum. Both GC and IMS are much more expensive than arrays of electrochemical sensors, but also much more effective in odor characterization.

Usually, methods of multivariate data analysis or pattern recognition techniques are applied to evaluate the multidimensional information obtained from the measurement systems.

In general, each IOMS must be calibrated using data obtained from measurements with the human nose, usually with measurement principles involving panel members as explained above. At present, there is no known system that is able to measure odors without a calibration based on human olfactory perception.

IOMS are able or will be able to measure specific odors depending on their training. However, the human nose is much more sensitive than any sensor technique currently available. With human noses, not only can odor concentration or the absence/presence of odors be measured, but the hedonic impression or nuisance level can also be determined. Especially for the determination of hedonic impression and nuisance level, an IOMS will not be usable in the near future.

21.4 Devices and Systems

As explained in the previous sections, the most important sensor system for measuring odors is the human nose. It is either used for direct measurement parameter recording or for calibration of IOMSs.

As technical devices used for odor measurement, the olfactometer plays a central role. IOMSs have recently been used for restricted measurement tasks as stated above. The basic operation principles of the devices were explained in Sect. 21.3.

Table 21.3 summarizes the devices introduced so far. Since IOMSs can only be regarded as supplemental sources of measurement data besides the conventional measurement principles described in Sect. 21.3.2, they are regarded here in general as IOMSs, without respect to the possible measurement principles realized within them. Also, the different kinds of olfactometers are regarded as a device class, without distinguishing between the models of different manufacturers.

Table 21.3 Advantages and disadvantages of the different device classes

Devices	Advantages	Disadvantages
Olfactometer	Direct measurement of any odor concentration using the human nose as sensor	Only batch investigations with relatively high expenditures due to necessary laboratory, device, and human resources
IOMSs	Fast measurement even under field conditions with the possibility of real-time applications	Indirect measurement of a specific odor concentration after calibration with olfactometer measurements



Fig. 21.1 Example for an olfactometer with panel members during a measurement (photo courtesy Olfasense)

Last but not least, it must be kept in mind that the device classes of olfactometers and IOMSs cannot be compared with each aspect of their application scope. IOMSs, for instance, are often used to distinguish between the absence and presence of a specific odor under study or to classify odors at reception level near the human perception threshold. Olfactometers, however,



Fig. 21.2 Example for an IOMS based on ion mobility spectroscopy

are used to investigate samples with much higher odor concentration by dilution to determine the odor concentration in odor units per volume.

Figure 21.1 shows an olfactometer along with the panel members during a measurement and Fig. 21.2 shows an ion-mobility spectrometer as an example of an IOMS.

21.5 Specifications

The measurement principles explained above have different application domains and are used to determine different measurement parameters. Therefore, a comparison of the specifications cannot be easily accomplished, as is possible for other measurement devices described in this book that use tables containing concrete numerical parameters. Here, it is rather useful to discuss the specifications of each measurement principle separately.

For IOMSs, no specifications can be given since the application of these devices is not yet investigated within the usual scope of a measurement principle.

21.5.1 Olfactometry Specifications

Olfactometry is primarily used to determine the odor concentration, though it is also possible to determine the hedonic impression. When describing specifications, it only makes sense for the odor concentration measurement, since the hedonic impression cannot be quantified.

For insight on specifications, especially measurement accuracy, it is important to review the measurement procedure. Starting at a very high dilution well below the perception threshold of the panel members, the concentration of the diluted sample is increased step-wise by a factor of two at each step until the aver-

age perception threshold of the panel is reached. Thus, the inherent resolution of the measurement principle is coupled to this increase step. If only one measurement is carried out, the uncertainty of the measurement result lies between half the result value and double the result value (a factor of two up and down). To reduce this quite large uncertainty, repeated measurements of the same sample are carried out (usually a total of three measurements). From a statistical view, each repetition reduces the statistical uncertainty by the factor 1.41 (square root of 2). In practice, the determination of the total uncertainty must consider the statistical uncertainty of the finite number of panel members (infinity would mean to have the average threshold value without uncertainty) and the systematic errors, for instance due to the precision of the dilution apparatus. A detailed description on handling the different uncertainties during olfactometry is given in [21.5].

The initial inherent uncertainty is of a factor two up and down and seems to be very high compared to the measurement of other atmospheric parameters. However, since according to Weber–Fechner’s law the physiological stimulus perceived by humans is proportional to the logarithm of the physical quantity (odor concentration, in this case), the measurement uncertainty can be expressed as approximately three decibels (correlates to a factor of two) on the logarithmic stim-

ulus scale. While the odor concentration can cover a range of several orders of magnitude between the perceptions *none* and *extremely strong* on the stimulus scale, the uncertainty of a factor of two up and down can be accepted, especially if it is further reduced by repeated measurements.

21.5.2 Field Inspection Specifications

Field inspection measurements are principally based on observations of the absence and presence of an odor under study by the panel members. Though, in special cases, the intensity of the stimulus is also recorded, the numerically useful information remains the panel member's decision between absence and presence. Thus, the resolution of a measurement consisting of these yes/no decisions basically depends on the number of independent single measurements. If just a single perception is recorded, the statistical uncertainty of this measurement is 50% if the panel member is presented with a stimulus near the perception threshold. It is to be expected that the panel member might err on the perception, so the single observation is either right or wrong with a probability of 50% each. To overcome this, repeated measurements are carried out over a certain period of time, typically for ten minutes with one observation every ten seconds (60 in total). If all the observations were independent of each other, the statistical uncertainty would be reduced by a factor of 1.41 (square root of 2) for each observation. So, a total number of 60 observations would significantly reduce the statistical uncertainty if all the observations were independent of each other, which of course they are not, since the conditions causing the absence or presence of an odor are not independent within a time span of ten minutes. So, since the dependency of the single observations from each other is very difficult to express and is different for each measurement, a specific uncertainty value cannot be given.

21.6 Quality Control

For odor measurements, quality control must be implemented in terms of the technical devices, laboratory operations, and panel members involved in the measurements. Detailed information on quality control is given in [21.3–5].

The olfactometer as primary device to measure odor concentration must be continuously checked, with a focus especially on the dilution apparatus. At least once every year the dilution apparatus must be checked or calibrated. This is a special challenge, since the range of the dilution factor covers several orders of magnitude and must be precise over the whole range.

To estimate the measurement uncertainty, an extended approach can be followed. It makes use of the odor hour concept, which by convention declares that an odor hour (time span of one hour, during which a human being has perceived the odor at least once) happens if during the ten-minute measurement period at least six of the 60 single observations stated an odor presence. This concept was introduced to quantify odor nuisance, which was found to be determined primarily by the percentage of odor hours with respect to the number hours in a whole year (perception frequency). If this perception frequency exceeds a certain value, for instance 10%, the overall odor nuisance can be regarded as substantial.

To measure the perception frequency, grid inspections are typically carried out with a total of 104 measurements over one year (two measurements each week). Once again, it can be accepted that the uncertainty of one single measurement is due to the yes/no decision if an odor hour was found or not, especially if the odor concentration in the field is close to the perception threshold. If the panel member doing the measurement is allowed to err in one measurement of the total 104, the overall error due to that single wrong measurement will be almost 1%. If errors happen more often, the yearly error percentage will increase accordingly.

One way to reduce statistical uncertainties is to make sure that the 104 single measurements are equally distributed over as many boundary conditions as possible: over the time of day, days of week, and the four seasons. Also, there should be no correlation between the mentioned boundary conditions and the panel members, meaning that each panel member should cover as much of the other boundary variances as possible. Then, even with the unfamiliar high statistical uncertainties, the results of a field inspection can be used to assess the perception frequency.

A detailed description of uncertainty handling for field inspections can be found in [21.3, 4].

Also, panel members must be checked in certain intervals, for instance every six months, to determine if their odor perception threshold is still within a certain range around the expected average. Since the minimum number of panel members usually is ten, it must be guaranteed that this comparatively (within the statistical context) low number of individuals does not contain members with extraordinary low or high odor perception threshold. The check is usually done by letting the members take part in ordinary olfactometry measurement with samples of known odor concentrations. To eliminate the need for calibrating this procedure, sam-

ples are prepared from neutral air mixed with a suitable amount of a substance with known odor threshold, for instance *n*-butanol.

Quality control on the level of overall laboratory operation includes full documentation of the regular check and maintenance activities and, if possible, the implementation of a recognized quality management system. Another way to ensure quality is to implement collaborative studies, where a uniform set of samples is investigated by different laboratories with the goal of obtaining comparable results.

Quality control for field inspections (grid and plume mode) are implemented on a general level through the

21.7 Maintenance

Maintenance, like quality control, includes activities pertaining to the devices, especially the olfactometer. Besides the activities to calibrate and check the dilution apparatus, cleaning procedures are especially necessary to prevent unwanted odors being emitted from parts of the measurement system itself. This applies not only

21.8 Application

As discussed in the first sections of this chapter, applications of odor measurements are different for the individual measurement parameters.

One of the most common applications of atmospheric odor measurements is the assessment of odor nuisances around facilities with odor emissions, such as industrial plants, agricultural operations (livestock), waste and wastewater treatment plants, or composting facilities. For this purpose, the measurement of perception frequency delivers a parameter to assess the degree of odor nuisance. Even if the expenditures for carrying out a full grid inspection over one year are quite high, this is the only way to obtain an assessment if modelling the odor perception frequency with dispersion models does not lead to reliable results.

Odor concentration measurement is the standard measurement to characterize the odor emission of the facilities mentioned above. If the amount of odor units emitted per unit time is known, this value can be used to assess the processes within the facilities or to act as input parameters for dispersion modeling. Figure 21.3 shows an example of simulated odor hour frequencies in the vicinity of several buildings.

Finally, though not actually within the context of atmospheric measurements, the odor characterization of consumer products (e.g., perfume scents and car smells) can be accomplished by determination of the hedonic impression.

procedures for the panel members described above. Furthermore, quality control on a situation-based level is carried out through plausibility considerations. Thus, for a field inspection, wind direction, for instance, is recorded to be able to decide if an odor source might contribute to an odor stimulus measured during a field inspection. Through these plausibility considerations, erroneous measurements can be sorted out.

Quality control for IOMSs is not currently an issue, however there are activities within the European Committee for Standardization (CEN) to develop standards for quality management for these devices as well.

to the olfactometer, but to all the components for sampling, diluting, and storing samples.

The panel members should not be regarded as being *maintained*, however regularly checking each member's odor threshold can be regarded as a maintenance activity pertaining to the panel as a whole.

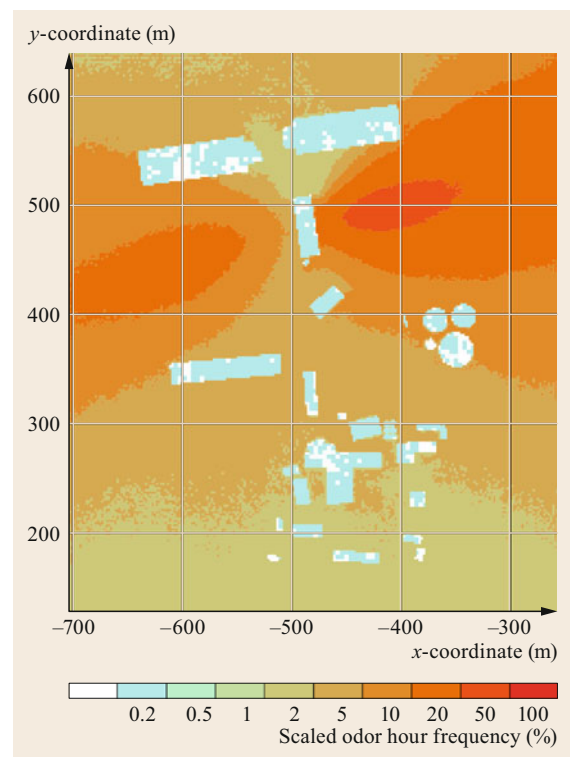


Fig. 21.3 Example of simulated odor hour frequencies obtained from dispersion modeling

21.9 Future Developments

Olfactometry and field inspections are well-established measurement procedures. They deliver reliable results for odor concentration or perception frequency.

Current and future developments should pursue the goals of reducing the expenditures of measurements (field inspections), eliminating the human nose and instead using other sensors to objectify measurements, and obtaining online source monitoring (with odor concentration well above the perception threshold) to obtain an indicator for odor nuisance. For these goals, the development of IOMs plays an important role. As mentioned before, IOMs will become available for special measurement tasks, such as detecting the absence or presence of an odor or to classify odors, for instance to do source apportionment.

Odor concentration measurement with IOMs is still not broadly available and probably will not be in the near future, since changes in odor composition influence the device output the same way or even more than changes to the odor concentration itself.

IMS is currently one of the most promising techniques used for IOMs, since it combines a very sensitive sensor system with long-term stability and very short measurement cycles within the range of seconds.

Especially for IMS, the data handling is very complicated, since complex and nonlinear relationships between raw data (drift time spectra) and measurement parameters (odor concentration) must be evaluated. However, a lot of progress is expected within this field.

21.10 Further Readings

For further information on odors and olfactometric measurements see:

- Hangartner, M., et al.: Improved recommendations on olfactometric measurements, COST 681 working group *Odour Measurement*. In: *Env. Techn. Letters* **10**, 231–236 (1998)
- Buettner, A. (Ed.): *Springer Handbook of Odor*, Springer Handbooks, Springer International Publishing (2017)

Introductory publications on IOMs include:

- Boeker, P.: Elektronische Nasen: Das methodische Konzept und seine Problematik. In: *Gefahrstoffe; Reinhaltung der Luft* **70**(7/8), 314–320 (2010)
- Capelli, L.; Sironi, S.; Del Rosso, R.: *Electronic Noses for Environmental Monitoring Applications. Sensors* **14**, 19979–20007 (2014)

References

- | | |
|---|---|
| <p>21.1 C. Philpott, A. Bennett, G. Murty: A brief history of olfaction and olfactometry, <i>J. Laryngol. Otol.</i> 122(7), 657–662 (2008)</p> <p>21.2 J. Passy: Sur Quelques Minimums Perceptibles d-Odeurs. <i>CR. Hebd. Seances Acad. Sei.</i> 114, 786–788 (1892)</p> <p>21.3 DIN EN 16841-1: <i>Ambient Air – Determination of Odour in Ambient Air by Using Field Inspection – Part 1: Grid Method</i> (Beuth, Berlin 2017)</p> | <p>21.4 DIN EN 16841-2: <i>Ambient Air – Determination of Odour in Ambient Air by Using Field Inspection – Part 2: Plume Method</i> (Beuth, Berlin 2017)</p> <p>21.5 EN 13725: <i>Air Quality – Determination of Odour Concentration by Dynamic Olfactometry and Odour Emission Rate from Stationary Sources</i> (Beuth, Berlin 2019)</p> |
|---|---|

Ralf Petrich

IFU GmbH Privates Institut für Analytik
Frankenberg, Germany
ralf.petrich@ifu-analytik.de



Physicist Ralf Petrich received his PhD in the numerical evaluation of optical spectra. He has worked for NASA, Daimler-Benz, and the environmental office of the state of Saxony in Germany. Currently, he heads the development department at IFU GmbH, a private institute for analytics in Frankenberg, Germany. His primary fields of work are numerical modelling of pollution dispersion in ambient air and the development of technical approaches for odor measurement.

Axel Delan

IFU GmbH Privates Institut für Analytik
Frankenberg, Germany
axel.delan@ifu-analytik.de



Axel Delan is a physicist and managing director of IFU GmbH, a private institute for analytics in Frankenberg, Germany, that performs research and development on technical solutions for olfactometry. He has 25 years of experience managing an accredited and notified monitoring company for emissions and immissions of odors. Due to his wide experience, he works on international olfactometry standardization and is a publicly appointed and sworn authorized expert.

Visual Observations

Thomas Foken , Raymond Rülke

Visual observations of the state of the weather have been made for hundreds and thousands of years. Observers have always been impressed by natural phenomena. Since the beginning of measurements nearly 500 years ago, visual observations have become a relevant part of meteorological observations – even when they only represent empirical relationships. Although electronic sensors and automatization now significantly reduce the importance of visual observations made by direct measurements or the combination of measurements, some observations are still in use and are reported in this chapter. These include the Beaufort wind force scale, the cloud classification scheme, and the atmospheric visibility observation. These observations remain relevant because they cannot be easily replaced, as in the case of cloud classification, or they provide a fast overview of the meteorological situation in the absence of measurements.

22.1	Principles of Visual Observations	645
22.2	History	646
22.2.1	Classification of Visual Observations	646
22.2.2	Diaries and Codes of Visual Observations.....	647
22.3	Theory	647
22.4	Observed Parameters	647
22.4.1	Weather Phenomena	647
22.4.2	Wind Speed and Direction	650
22.4.3	Clouds	650
22.4.4	Visibility	653
22.4.5	State of the Ground	654
22.4.6	Comparison of Visual and Instrumental Observations.....	654
22.5	Quality Control	655
22.6	Application	655
22.7	Future Developments	655
22.8	Further Readings	656
	References	656

Visual observations of the state of the weather and of weather phenomena have been made since ancient times and continue to be part of international and national observation programs [22.1]. With the ongoing automation of meteorological observations, visual observations have been or will be replaced by combinations of dif-

ferent measuring techniques. Nevertheless, visual observations are important when describing the present state of the weather and can also be used for very short-term weather forecasting (nowcasting). This chapter describes different observations and their classification according to international recommendations [22.2].

22.1 Principles of Visual Observations

Visual observations are rarely given in physical units, however the state of the atmosphere can be estimated or approximated in intervals of relevant parameters. Because a description of the state of the atmosphere is often dependent on an individual observer, a classification is made using the international weather code [22.3],

often in units from 0 to 9. Only for wind strength is a special unit employed, the Beaufort, which has been in use for about 200 years and is related to the appearance of the ocean surface, special states of trees, or damage to structures. The most important observed parameters are given in Table 22.1.

Table 22.1 Observed Parameters

Parameter	Description	Unit	Symbol
Weather conditions	Classification of the state of the weather		
Wind speed	Classification of the strength of the wind dependent on the conditions of the sea surface (e.g., waves) or on land (e.g., trees and buildings)	Bft	u
Wind direction	Derived from the movement of plants, etc.	°	
Cloud genera	Application of cloud atlases		
Cloud cover	Visual observation	Octa	C_H, C_M, C_L
Height of clouds	Height of the cloud base and vertical extension	km	
Precipitation	Classification of the amount, duration, and frequency Type of precipitation: rain, snow, hail, etc.	mm, h	R_N
Visibility	Visibility/distance of landmarks	km	
State of surface	Classification of the state of the soil surface or soil		

22.2 History

The beginnings of the visual observations discussed in this section are related to the first classifications of weather phenomena and the use of this information in observation diaries together with measured data. Diaries with visual observations have been kept since ancient times and their information is still apparent in many weather proverbs, like the weather records for Oxford and Driby for 1337–1344 by the cleric *William Merle* (†1347) [22.4]. Since the beginning of aircraft-based measurements, pilots also made visual observations, and until the middle of the twentieth century so-called *weather flights* were carried out. Even today, pilot reports contribute to upper-air monitoring.

22.2.1 Classification of Visual Observations

The classification of visual observations is closely connected with the implementation of the weather code used in telegraphy. However, for clouds and wind speed, useful classifications were developed long before.

Classification of Clouds

Surprisingly, a classification for clouds only dates back to the beginning of nineteenth century based on the early ideas of *Robert Hooke* (1635–1703) [22.5]. The first comprehensive classification was made by the French naturalist *Jean-Baptist Lamarck* (1744–1829) [22.6], who classified five main cloud types with 12 species. But this classification was not successful due to the complicated French descriptions. For a long time, the classification system presented in 1802 by the English chemist and businessman *Luke Howard* (1772–1864) was widely distributed [22.7–9] and used by scientists and even artists and poets (*Alexander von Humboldt*, 1769–1859, *Johann Wolfgang von Goethe*,

1749–1832 [22.10]). Howard used Latin for his classification system, separating the clouds into families (categories), genera (forms), and species, after the classification of plants from *Carl Linnaeus* (1707–1778). He defined four main categories of clouds: cumulus, stratus, cirrus, and nimbus. This system has remained nearly unchanged up to the present day. Howard found that there are forms in between these categories: cumulus-stratus, cirrocumulus, and cirrostratus. Stratocumulus, another cloud type, was described by *Ludwig Friedrich Kämtz* (1801–1867) in 1840 [22.11]. The distinction between cirrostratus and cirrocumulus as well as altostratus and altocumulus was explained by *Émilien Renou* (1815–1902) [22.12] in 1855 and cumulonimbus was described by *Philippe Weilbach* in 1880 [22.13]. Finally, nimbostratus was defined by the International Commission for the Study of Clouds in 1930.

Several classifications that were developed in the nineteenth century are listed in [22.14], but significant progress was made when cloud photographs became available. *Albert Riegenbach* (1854–1921) [22.15] and *Ralph Abercromby* (1842–1897) were pioneers in cloud photography and a selection of their photos was published in [22.14]. Based on this work, Abercromby [22.16] and *Hugo Hildebrand Hildebrands-son* (1838–1920) [22.17] updated Howard's classification and published a classification that was similar to the classification adopted in 1894 by the International Meteorological Conference (see Chap. 1). Two years later, the first International Cloud Atlas was published [22.18]. The first weather satellite of the Television Infrared Observation Satellite (TIROS) program began a new chapter of cloud photography from space in 1960. Of course, the first TIROS pictures [22.14] cannot compare with the high-resolution images from modern satellites.

Scaling of the Wind Speed

In the eighteenth century, wind speed observations were mostly unsatisfactory for sailing ships and windmills. The engineer *John Smeaton* (1724–1792) was probably one of the first to define terms for different classes of wind speeds for wind mill applications. The first hydrographer of the British Admiralty, *Alexander Dalrymple* (1737–1808), combined these terms with those of sea-faring [22.19]. *Francis Beaufort* (1774–1857) included this list of terms in his weather diaries [22.20] in 1806 and used it for his own observations. From 1807 he developed his own scale and first used it on the cruises of the *Beagle* in 1831. Two years prior, in 1829, the Royal Navy had appointed Beaufort as hydrographer. In 1838 the British Admiralty adopted his scale for all ships, as did the International Meteorological Congress in Brussels in 1853 [22.21, 22]. In an instruction of the Smithsonian Institute from 1870, the Beaufort scale was first applied to wind observations on land [22.19].

22.2.2 Diaries and Codes of Visual Observations

In the first manuals for weather observations provided by *Robert Hooke* (1635–1703) [22.5], the coverage and genera of clouds were recommended weather observations in addition to measurements. These observations have been part of weather diaries since that time, together with instrumental observations (see Chap. 1, Sect. 1.2.2). The description of these visual observations was presented in accordance with the experience of the

observer and recordings were still not performed in the standardized manner that became available one to two centuries later. Within the first meteorological network of the *Societas Meteorologica Palatina* [22.23], written descriptions of weather phenomena were replaced by symbols in 1780 to unify the observations. This classification was further enhanced and, in 1873/74, the International Meteorological Conference (see Chap. 1, Sect. 1.2.3) proposed a selection of symbols that has remained valid to the present day (see Sect. 22.4.1).

Karl Kreil (1798–1862), who was Director of the Zentralanstalt für Meteorologie und Erdmagnetismus in Vienna between 1851 and 1862, proposed the use of the electric telegraph, developed between 1833 and 1835 in Göttingen, for the transmission of weather data. About 20 years later during the Crimean War, a heavy storm on 14 November 1854 resulted in the loss of many vessels. Following this, in 1856, the French weather service established the transmission of weather observations by telegraphy to enable the preparation of weather maps [22.4]. From this time it became necessary to make use of numerical codes for visual observations as well. A revised system of these codes was presented at the Conference of Directors of the International Meteorological Organization in Copenhagen in 1929. After the Second World War, the Conference of Directors in Washington D.C., in 1947, and especially a follow-up conference in London, proposed a modified weather code similar to the present form [22.24]. The first edition of the Manual of Codes was issued in 1971 and has been updated regularly until today [22.3].

22.3 Theory

There is no theory behind visual observations, but each observation follows certain international [22.2, 3] or national [22.25] regulations. This makes visual ob-

servations comparable and minimizes the subjective influence of individual evaluations.

22.4 Observed Parameters

Several meteorological elements and phenomena can be observed visually and are described in this section. To make visual observations comparable, code figures are used that are identical to the weather codes listed in the Handbook of Codes [22.3]. The use of code figures facilitates storage and application in digital databases. In the tables of this section the relevant code figures are shown for comparison with the World Meteorological Organization (WMO) regulations. However, the listed tables of code figures contain only a selection of the most common; for more details see the Handbook of Codes [22.3].

22.4.1 Weather Phenomena

The most important visual observations describe the status of present or past weather. The Handbook of Codes [22.3] lists 100 different phenomena and uses the code symbol *ww* representing the numbers 00 to 99. An overview of when one of these numbers applies, is given in Table 22.2; for details see [22.3]. Furthermore, a one-digit code *W* characterizes the weather of the last hour; see Table 22.3. The most important symbols related to *ww* codes are shown in Table 22.4 and

Table 22.2 Present weather phenomena according to the code figure ww [22.3]

Code figure (ww)	Present weather phenomena
00–49	No precipitation at the station at the time of observation
00–19	Fog, ice fog, duststorm, sandstorm, or drifting or blowing snow at the station at the time of observation or during the preceding hour
20–29	Precipitation, fog, ice fog, or thunderstorm at the station during the preceding hour but not at the time of observation
30–39	Duststorm, sandstorm, or drifting or blowing snow
40–49	Fog or ice fog
50–59	Drizzle
60–69	Rain
70–79	Solid precipitation not in showers
80–99	Showery precipitation or precipitation with current or recent thunderstorm

Table 22.3 Weather during past hour according to the code figure W [22.3]

Code figure (W)	Past weather
0	Cloud covering 1/2 or less of the sky throughout the appropriate period
1	Cloud covering more than 1/2 of the sky during part of the appropriate period and covering 1/2 or less during part of the period
2	Cloud covering more than 1/2 of the sky throughout the appropriate period
3	Sandstorm, duststorm, or blowing snow
4	Fog, ice fog, or thick haze
5	Drizzle
6	Rain
7	Snow or mixed rain and snow
8	Shower(s)
9	Thunderstorm(s) with or without rain

the intensities of falling hydrometeors are given in Table 22.5.

The various weather phenomena can be described in the following way [22.25]:

Haze: Relative humidity < 80%. The air contains very fine, solid, or liquid particles (dust, aerosol) that considerably reduce the transparency of air, however the visibility is at least 1 km.

Mist: Relative humidity \geq 80%. Tiny water particles suspended in the atmosphere reduce visibility. Visibility is between 1 and \approx 8 km.

Fog: Very small water droplets are suspended in the air near the Earth's surface, which reduce the horizontal visibility to values < 1000 m. The sky may still be visible above.

Table 22.4 Some selected symbols for ww code figure. The combination of a symbol with] is used for phenomena in the last hour. Symbols after [22.25] with permission from VDI e. V. Düsseldorf, Germany

ww code figure	Symbol	Weather phenomena
05		Haze
10		Mist
13		Lightning visible, no thunder heard
17		Thunderstorm, but no precipitation at the time of observation
31		Slight or moderate duststorm or sandstorm
45		Fog or ice fog, sky invisible
50		Drizzle, not freezing, intermittent, slight at time of observation ^a
53		Drizzle, not freezing, continuous, moderate at time of observation ^a
57		Drizzle, freezing, moderate or heavy (dense)
60		Rain, not freezing, intermittent, slight at time of observation ^a
70		Intermittent fall of snowflakes, slight at time of observation ^a
80		Rain shower(s), slight ^a
89		Shower(s) of hail, with or without rain or rain and snow mixed, not associated with thunder, slight ^a
95		Thunderstorm, slight or moderate, without hail, but with rain and/or snow at time of observation ^a

^a For intensities, see Table 22.5

Dust and sand: Lithometeors can be raised by strong, turbulent wind and reduce visibility. During a duststorm or sandstorm, an extensive area is affected with dust-filled air and visibility < 1 km.

Drizzle: Precipitation consisting of very fine water droplets < 0.3 mm in diameter. Supercooled droplets with a temperature < 0°C may turn into a thin layer of ice or black ice immediately on impact with the ground or other objects.

Rain: Precipitation of falling and clearly visible drops > 0.3 mm in diameter. Supercooled droplets with a temperature < 0°C may turn into a thin layer of ice or black ice immediately on impact with the ground or other objects.

Snow: Precipitation in the form of ice crystals, mainly of intricately branched, hexagonal form and of-

Table 22.5 Intensity of falling hydrometeors (drizzle, rain, snow) [22.2]

Variable	Range (mm h ⁻¹)	Intensity ^a
Drizzle	< 0.1	Light
	0.1 to < 0.5	Moderate
	≥ 0.5	Heavy
Rain (also showers)	< 2.5	Light
	2.5 to < 10.0	Moderate
	10.0 to < 50.0	Heavy
	≥ 50.0	Violent (intense, extreme)
Snow (also showers)	< 1.0 (water equivalent)	Light
	1.0 to < 5.0 (water equivalent)	Moderate
	≥ 5.0 (water equivalent)	Heavy

^a Intensity values based on a 3-min recording period

ten agglomerated into snowflakes, formed directly from the freezing of water vapor in the air. A mixture of snow and rain is called *rain and snow mixed*.

Hail: Showery precipitation consisting of irregular pellets or balls of ice, more or less solid, round to oval, and diameters mostly ranging between 5 and 50 mm. Larger hailstones may also occur.

Showers: Precipitation events characterized by the suddenness with which they start and stop, and by rapid changes of intensity.

Lightning: Visible electrical discharge in association with a thunderstorm. Lightning may occur between clouds (intracloud) or between a cloud and the ground.

Thunderstorm: A local storm produced by a cumulonimbus cloud and accompanied by lightning and thunder. The time gap between lightning discharge and audible thunder is ≤ 10 s (≈ 3 km) for very close thunderstorms.

Table 22.6 Wind force according to the Beaufort scale (Bft) for open sea and 10 m ASL [22.2]

Number (Bft)	Description term	Wind speed range		Maximal wave height (m)	Specification
		(kn)	(m s ⁻¹)		
0	Calm	< 1	0–0.2		Sea like a mirror
1	Light air	1–3	0.3–1.5	0.1	Ripples with the appearance of scales are formed, but without foam crests
2	Light breeze	4–6	1.6–3.3	0.3	Small wavelets; still short but more pronounced; crests have a glassy appearance and do not break
3	Gentle breeze	7–10	3.4–5.4	1.0	Large wavelets; crests begin to break; foam of glassy appearance; perhaps scattered white horses
4	Moderate breeze	11–16	5.5–7.9	1.5	Small waves, becoming longer; fairly frequent white horses
5	Fresh breeze	17–21	8.0–10.7	2.5	Moderate waves, taking a more pronounced long form; many white horses are formed (chance of some spray)
6	Strong breeze	22–27	10.8–13.8	4.0	Large waves begin to form; the white foam crests are more extensive everywhere (probably some spray)
7	Near gale	28–33	13.9–17.1	5.5	Sea heaps up and white foam from breaking waves begins to be blown in streaks along the direction of the wind
8	Gale	34–40	17.2–20.7	7.5	Moderately high waves of greater length; edges of crests begin to break into the spindrift; the foam is blown in well marked streaks along the direction of the wind
9	Strong gale	41–47	20.8–24.4	10.0	High waves; dense streaks of foam along the direction of the wind; crests of waves begin to topple, tumble and roll over; spray may affect visibility
10	Storm	48–55	24.5–28.4	12.5	Very high waves with long overhanging crests; the resulting foam, in great patches, is blown in dense white streaks along the direction of the wind; on the whole, the surface of the sea takes a white appearance; the <i>tumbling</i> of the sea becomes heavy and shock-like; visibility affected
11	Violent storm	56–63	28.5–32.6	16.0	Exceptionally high waves (small and medium-sized ships might be lost to view behind the waves); the sea is completely covered with long white patches of foam lying along the direction of the wind; everywhere, the edges of the wave crests are blown into froth; visibility affected
12	Hurricane	≥ 64	≥ 32.7	–	The air is filled with foam and spray; sea completely white with driving spray; visibility very seriously affected

Table 22.7 Wind force according to the Beaufort scale over land for the standard measurement height of 10 m [22.2]

Number (Bft)	Description term	Wind speed range		Specification	
		(m s ⁻¹)	(km h ⁻¹)	With plants as an indicator	Other indicators
0	Calm	0–0.2	< 1		Calm; smoke rises vertically
1	Light air	0.3–1.5	1–5		Direction of wind shown by smoke drift but not by wind vanes; no noticeable wind; smoke rises nearly vertically
2	Light breeze	1.6–3.3	6–11	Leaves rustle	Ordinary vanes moved by wind; wind felt on face
3	Gentle breeze	3.4–5.4	12–19	Leaves and small twigs in constant motion	Wind extends light flag; hair is disturbed
4	Moderate breeze	5.5–7.9	20–28	Small branches are moved	Dust and loose paper raised, hair disarranged
5	Fresh breeze	8.0–10.7	29–38	Small trees in leaf begin to sway	Crested wavelets form on inland waters; force of wind felt on body
6	Strong breeze	10.8–13.8	39–49	Large branches in motion	Some inconvenience in walking; whistling heard in telegraph wires; umbrellas used with difficulty
7	Near gale	13.9–17.1	50–61	Whole trees in motion	Inconvenience felt when walking against the wind
8	Gale	17.2–20.7	62–74	Breaks twigs off trees	Generally impedes progress; difficulty with balance in walking
9	Strong gale	20.8–24.4	75–88		Slight structural damage occurs (chimney pots and slates removed)
10	Storm	24.5–28.4	89–102	Trees uprooted	Considerable structural damage occurs
11	Violent storm	28.5–32.6	103–117	Very rarely experienced	Widespread damage
12	Hurricane force	≥ 32.7	≥ 118	Devastation	Devastation

22.4.2 Wind Speed and Direction

Wind speed and wind direction can be easily observed by detection of its influence on water surfaces, plants, and obstacles in the surroundings of the observer.

Wind Speed

The wind speed can be observed as wind force according to the *Beaufort* scale (Bft), which is a method that converts the effects of the wind into a scale. The wind forces are still in use in the weather forecast, even when they are not observed, but calculated from the wind speed (Tables 22.6 and 22.7). The scale was developed for effects on the sea surface but was adapted to the effects of wind on land (Table 22.7).

Wind Direction

For observing wind direction, the exact knowledge of the north direction or another direction is essential. In the case of high wind speeds, the observation of the wind direction is relatively easy. The direction should be estimated by observing the drift of smoke, movement of leaves, or the like. At an airport, a wind drogue may be used. Due to the friction in the atmospheric boundary layer (see Chap. 1) the wind direction changes with height, such that the surface wind (usu-

ally measured at a height of 10 m AGL, see Chap. 9), is different from the direction of the geostrophic wind above the atmospheric boundary layer. Therefore the movement of clouds cannot be applied [22.2]. The description of wind directions and their coding is given in Table 22.8.

22.4.3 Clouds

Cloud observation is fascinating with respect to the variety and mutability of cloud appearance and formation. Cloud measurement needs an enormous technical effort and is described in Chaps. 24, 25, 27, 30, 31. For the visual observation of clouds, cloud atlases should be applied as they provide not only descriptions of clouds but also numerous pictures and diagrams. Recently published atlases are [22.26, 27].

Three cloud parameters should be observed: the genera (type) of clouds, the cloud cover of the sky, and the height of cloud base and vertical extension. Furthermore, besides the genera, species and varieties can also be observed, with cloud atlases supplying details. Exact visual determination of the cloud base height in accordance with the present code numbers – up to 3 km in 30 m increments and > 3 km in 100 m increments – is hardly possible.

Table 22.8 Observation of the wind direction (after [22.25] with permission from VDI e. V. Düsseldorf, Germany)

Name of direction	Direction code	Wind rose with direction code and code number
North	N	
Northeast	NE	
East	E	
Southeast	SE	
South	S	
Southwest	SW	
West	W	
Northwest	NW	
Calm	C	C or 00, always combined with wind force 0 Bft

Cloud Genera (Type)

Clouds are grouped into three main categories: high-level, mid-level, and low-level clouds, depending on the height of the respective cloud bases. There are ten main cloud types (genera), which are assigned to these three altitude levels. Clouds with a large vertical extent belong to the low-level cloud section while the nimbostratus becomes part of the mid-level for synoptic reasons. This classification is described in Table 22.9, while Fig. 22.1 shows images of typical clouds for the genera.

The following definitions of the cloud genera are presented according to the WMO [22.26]:

Cirrus (Ci): Detached clouds in the form of white, delicate filaments or white or mostly white patches or narrow bands. These clouds have a fibrous (hair-like) appearance, a silky sheen, or both.

Cirrocumulus (Cc): Thin, white patch, sheet, or layer of cloud without shading; composed of very small elements in the form of grains, ripples, etc., merged or

separate, and more or less regularly arranged; most of the elements have an apparent width of $< 1^\circ$.

Cirrostratus (Cs): Transparent, whitish cloud veil of fibrous (hair-like) or smooth appearance; totally or partly covering the sky; generally produce a halo phenomena.

Alto cumulus (Ac): White or grey, or both white and grey, patch, sheet, or layer of cloud; generally with shading, composed of laminae (a layer or layers), rounded masses, rolls, etc., which are sometimes partly fibrous or diffuse and which may or may not be merged; most of the regularly arranged small elements usually have an apparent width of between 1° and 5° .

Altostratus (As): Greyish or bluish cloud sheet or layer of striated (grooves or channels in cloud formations, arranged parallel to the flow of the air), fibrous, or uniform appearance, totally or partly covering the sky, and having parts thin enough to reveal the Sun at least vaguely, as through ground glass or frosted glass. Altostratus does not show halo phenomena.

Table 22.9 Cloud base height of genera above ground level in temperate regions [22.2]

Code figure	Level	Genera (type)	Genera code	Usual range of height (wider range) (km)	Remarks
0	High (C_H)	Cirrus	Ci	6–12	Ci from dissipating Cb may occur below 6.0
1		Cirrocumulus	Cc	6–12	
2	Middle (C_M)	Cirrostratus	Cs	6–12	Cs may develop in As
3		Alto cumulus	Ac	2–6	
4		Altostratus	As	2–6	As may thicken with progressive lowering of the base to become Ns
5		Nimbostratus	Ns	Surface – 3	Ns is considered a mid-level cloud for synoptic purposes, although it can extend to other levels
6	Low (C_L)	Stratus	St	Surface – 0.6 (1.2)	
7		Stratocumulus	Sc	0.3–1.35 (2.0)	For stations over 150 m ASL the base of low-level clouds will often be less than indicated
8		Cumulus	Cu	0.3–1.5 (2.0)	
9		Cumulonimbus	Cb	0.6–1.5 (2.0)	



Fig. 22.1 Cloud genera (types) according to Table 22.9. Photos © B. Mühr

Nimbostratus (Ns): Grey cloud layer, often dark, the appearance of which is made diffuse by more or less continuously falling rain or snow, which in most cases reaches the ground. It is thick enough throughout to blot out the Sun. Low, ragged clouds frequently occur below the layer, with which they may or may not merge.

Stratocumulus (Sc): Grey or whitish, or both grey and whitish, patch, sheet, or layer of cloud that almost always has dark parts; composed of tessellations, rounded masses, rolls, etc., which are nonfibrous (except for virga) and which may or may not be merged; most of the regularly arranged small elements have an apparent width of $> 5^\circ$.

Stratus (St): Generally grey cloud layer with a fairly uniform base, which may give drizzle, snow, or snow grains. When the Sun is visible through the cloud, its outline is clearly discernible. Stratus does not produce halo phenomena except, possibly, at very low temperatures. Sometimes stratus appears in the form of ragged patches.

Cumulus (Cu): Detached clouds, generally dense with sharp outlines, and developing vertically in the form of rising mounds, domes, or towers, of which the bulging upper part often resembles cauliflower. The sunlit parts of these clouds are mostly brilliant white; their bases are relatively dark and nearly horizontal. Sometimes cumulus is ragged.

Cumulonimbus (Cb): Heavy, dense cloud with a considerable vertical extent in the form of a mountain or huge towers. At least part of its upper portion is usually smooth, fibrous, or striated, and nearly always flattened; this part often spreads out in the shape of an anvil or vast plume. Under the base of this cloud, which is often very dark, there are frequently low ragged clouds either merged with it or not, and precipitation sometimes in the form of virga.

Besides these genera, further classifications are possible such as *species* that characterize special forms of the clouds or *varieties* that characterize, for example, the transparency of a cloud. Furthermore, *supplementary features* or *accessory clouds* and a few *special clouds* are classified [22.26].

Cloud Cover

The coverage of the sky by clouds is measured in oktas, where 0/8 is only given for a totally cloud free sky and 8/8 only if no blue sky is visible at all. Clouds that are present within an elevation angle between the horizon and 5° – 8° are not considered. The scheme is documented in Table 22.10. The value of cloud cover can also be separated for high-level (C_H), mid-level (C_M), and low-level (C_L) clouds.

Table 22.10 Cloud cover observation [22.2]

Code figure (N)	Okta	Meaning in tenths
0	0	0
1	1 okta or less, but not zero	1/10 or less, but not zero
2	2 oktas	2/10–3/10
3	3 oktas	4/10
4	4 oktas	5/10
6	6 oktas	7/10–8/10
7	7 oktas or more, but not 8 oktas	9/10 or more, but not 10/10
8	8 oktas	10/10
9	Sky obscured by fog and/or other meteorological phenomena	
/	Cloud cover is indiscernible for reasons other than fog or other meteorological phenomena, or observation is not made	

Cameras are specifically designed to measure cloud cover. For example, they scan the entire sky using curved mirrors. The image from the sky is analyzed to calculate the proportion of cloud cover [22.2].

22.4.4 Visibility

Visibility was first defined for meteorological purposes as a quantity to be estimated by a human observer, and observations made in that way are widely used [22.2]. This is, of course, a very subjective factor. More objective is the measurement of the transparency of the atmosphere represented by the meteorological optical range (MOR) (see Chap. 13). Visibility observations by a human observer depend on the photometric and dimensional characteristics of the object and the individual contrast threshold of the observer. At night, the intensity of light sources, the sensitivity of the observer's eyes to darkness, and the observer's illuminance threshold are of great importance for the observation of visibility.

Table 22.11 Horizontal visibility [22.3]

Code figure (w_e)	Visibility (m)
0	< 50
1	50–199
2	200–499
3	500–999
4	1000–1999
5	2000–3999
6	4000–9999
7	10 000–19 999
8	20 000–49 999
9	$\geq 50 000$

Table 22.12 State of the ground without snow or measurable ice cover. Numbers 0–2 and 4 apply to representative bare ground and numbers 3 and 5–9 to an open representative area [22.3]

Code figure (E)	State of the ground
0	Surface of ground dry (without cracks and no appreciable amount of dust or loose sand)
1	Surface of ground moist
2	Surface of ground wet (standing water in small or large pools on surface)
3	Flooded
4	Surface of ground frozen
5	Glaze on ground
6	Loose dry dust or sand not covering ground completely
7	Thin cover of loose, dry dust or sand covering ground completely
8	Moderate or thick cover of loose, dry dust, or sand covering ground completely
9	Extremely dry with cracks

For observations, landmarks are necessary for daytime and lamps for nighttime visibility. The following are example landmarks that can be selected:

- For distances up to 1 km: utility poles, traffic signs, trees, bushes, or houses
- For distances up to 5 km: houses, poles, or towers
- For larger distances: mountain ridges, mountain peaks, or towers

The visibility ranges together with the code figure are given in Table 22.11.

22.4.5 State of the Ground

The observation of the conditions near or on the Earth's surface gives information about its state, for example, whether it is wet or dry, or covered by snow or ice. It is an indicator of the recent weather or the weather in the past,

Table 22.13 State of the ground with snow or measurable ice cover for an open representative area [22.3]

Code figure (E')	State of the ground
0	Ground predominantly covered by ice
1	Compact or wet snow (with or without ice) covering less than one half of the ground
2	Compact or wet snow (with or without ice) covering at least one half of the ground but ground not completely covered
3	Even layer of compact or wet snow covering ground completely
4	Uneven layer of compact or wet snow covering ground completely
5	Loose, dry snow covering less than one half of the ground
6	Loose, dry snow covering at least one half of the ground but ground not completely covered
7	Even layer of loose, dry snow covering ground completely
8	Uneven layer of loose, dry snow covering ground completely
9	Snow covering ground completely; deep drifts (50 cm or more above the general snow surface)

and can indicate dangerous situations for agriculture, air travel, ground traffic, etc. Tables 22.12 and 22.13 give an overview of states of the ground and code figures for situations with and without ice and snow cover.

22.4.6 Comparison of Visual and Instrumental Observations

Visual observations have the disadvantage that their results cannot be given in exact numbers and the code figures [22.3] only provide the means to compare and to use these observations for weather prediction or nowcasting. Nevertheless, visual observations can give many details of the state of the weather and weather phenomena that cannot easily be measured with instruments. Table 22.14 is an attempt to show the advantages and disadvantages of visual observations.

Table 22.14 Advantages and disadvantages of visual observations in comparison to direct measurements

Visual observations	Advantages	Disadvantages
Weather phenomena	Very many details on intensities, etc., can be detected	Exact numbers, e.g., for intensities, amounts, or duration, cannot be given
Wind speed (Beaufort scale)	Evaluation of the wind speed and possible damage	Only estimation of possible wind speeds
Wind direction		Might not be very precise
Cloud genera (type)	Cloud genera as well as species and varieties can be observed in great detail (dependent on the observer)	Different observers might not have the same results
Cloud cover	Observation of the whole sky	Accuracy depends on the observer's skills
Cloud base height		Not exact, only rough estimation
Visibility	Visibility information even for sectors possible	Accuracy depends on the observer
State of ground	Very many details possible	

22.5 Quality Control

The quality of visual observations is highly dependent on the experience and abilities of the observer. Observers should therefore compare and discuss their ob-

servations to enable uniform data quality. Where possible, such as for cloud height or wind speed, the observations should also be compared with measured data.

22.6 Application

The reduction in the number of manned meteorological stations, due mainly to their high cost, has resulted in a reduction in the density of visual observations. The amount of data decreases as well as the possibility for the application of these data. Nevertheless, mainly for nowcasting, these observations are still helpful.

Because time series of visual observations are much longer than those of instrumental measurements, it is strongly recommended that these observations, at least at selected meteorological stations, should be continued.

At some very exposed locations like mountain crests or summits, technical equipment and instruments are subjected to very harsh environmental conditions.

At least at certain times, precise measurements cannot be performed or guaranteed at these locations. Particularly at these locations, visual observations are of great importance for obtaining any information about the state of the weather.

In the past, visual observations were used, for example by farmers, for short-term weather forecasts with high precision for a time period of up to 24 h and sometimes even longer under special synoptic situations. Unfortunately, observers with appropriate experience are rarely available. Nevertheless, the general interest in weather phenomena and their documentation still persists. Additionally, continuous and high-quality manual observation is costly.

22.7 Future Developments

Due to the reduction of manned meteorological stations for mainly financial reasons and their replacement by automatic weather stations, there is an urgent need to replace visual observations with instrumental methods. For some meteorological elements this can be easily done (e.g., cloud height), while other parameters re-

quire complex combinations of different sensors (e.g., cloud cover), otherwise valuable and detailed information will no longer be available (e.g., cloud genera). The process of replacing the observations is ongoing and different meteorological services will probably develop their own systems (Table 22.15).

Table 22.15 Meteorological elements that are typically derived from visual observations and possible replacement techniques according to information from the German Meteorological Service

Meteorological element	Visual observation	Replacement technique	Chap.
State of weather	Estimation	Present weather sensor and other techniques	12, 13
Visibility	Estimation with distance marks	Visibility sensors	13
		Lidar	26
Cloud height	Estimation	Ceilometer	24
Cloud coverage	Estimation	Ceilometer	24
		Weather radar	30
		Radar in mm range	32
		Cloud camera	
Cloud genera	Estimation with cloud atlas	Cloud camera	
		Satellite image	42, [22.28]
Snow height	Snow level	Snow height sensor	
Snow water content	Snow scale	Snow and ice accumulation sensor	
Precipitation intensity and type	Estimation	Present weather sensor	12
		Radar in mm range	32
Thunderstorm	Estimation	Lightning and other sensors	14
Soil conditions	Estimation	Imaging techniques	42, [22.28]

Another solution is the implementation of additional available stations (commercial and private) in the meteorological network (see Chap. 43) or even the crowdsourcing of simple measurements (see Chap. 44).

Hopefully, the variability, beauty, and spectacular impression of weather phenomena will still be of interest to enthusiasts even when these observations are not part of the standard meteorological observations.

22.8 Further Readings

A thorough introduction to visual observations can be found in:

- VDI 3786 Part 9: *Environmental Meteorology – Meteorological Measurements – Visual Weather Observations* (Beuth, Berlin 2007)
- WMO: *Guide to Instruments and Methods of Observation*, WMO-No. 8, Volume I - Measurement of Meteorological Variables. (World Meteorological Organization, Geneva, 2018)

- WMO: *Manual of Codes* (World Meteorological Organization, Geneva 2017), WMO-No. 306
- WMO: *International Cloud Atlas: Manual on the Observation of Clouds and Other Meteors* (World Meteorological Organization Geneva 2017), WMO-No. 407

Acknowledgments. The authors acknowledge Bernhard Mühr for his helpful comments.

References

- 22.1 Aristotle: *Meteorology* (Clarendon Press, Oxford 2017), translated by E.W. Webster, first published 350 BCE
- 22.2 WMO: *Guide to Instruments and Methods of Observation*, WMO-No. 8, Volume I - Measurement of Meteorological Variables. (World Meteorological Organization, Geneva 2018)
- 22.3 WMO: *Manual of Codes* (World Meteorological Organization, Geneva 2017), WMO-No. 306
- 22.4 H.-G. Körber: *Vom Wetteraberglauben zur Wetterforschung: Aus Geschichte und Kulturgeschichte der Meteorologie* (Edition Leipzig, Leipzig 1987)
- 22.5 R. Hooke: A method for making a history of the weather. In: *The History of the Royal Society of London, for the Improving of Natural Knowledge*, ed. by T. Sprat (T. R. for 7 Martyn at the Bell, London 1667) pp. 173–179
- 22.6 J.B. Lamarck: Sur la forme des nuages, *Annuaire Meteorol. Repub. Fr.* **3**, 149–164 (1802)
- 22.7 L. Howard: XVIII. On the modifications of clouds, and on the principles of their production, suspension, and destruction; being the substance of an essay read before the Askesian Society in the session 1802–3, *Philos. Mag. Ser. 1* **16**(62), 97–107 (1803)
- 22.8 L. Howard: LXIV. On the modifications of clouds, and on the principles of their production, suspension, and destruction; being the substance of an essay read before the Askesian Society in the session 1802–3, *Philos. Mag. Ser. 1* **16**(64), 344–357 (1803)
- 22.9 L. Howard: I. On the modifications of clouds, and on the principles of their production, suspension, and destruction; being the substance of an essay read before the Askesian Society in the session 1802–3, *Philos. Mag. Ser. 1* **17**(65), 5–11 (1803)
- 22.10 K.H. Bernhardt: Johann Wolfgang v. Goethes Beziehungen zu Luke Howard und sein Wirken auf dem Gebiet der Meteorologie, *Hist. Meteorol.* **1**, 28–40 (2004)
- 22.11 L.F. Kämtz: *Vorlesungen über Meteorologie* (Gebauersche Buchhandlung, Halle 1840)
- 22.12 E. Renou: Instructions météorologiques, *Annuaire Soc. Meteorol. Fr.* **3**, 142–146 (1855)
- 22.13 P. Weilbach: Formes des nuages dans l'Europe septentrionale, *Ann. Bur. Cent. Meteorol. Fr. B* **1**, 11–40 (1880)
- 22.14 H. Völter: *Wolkenstudien – Cloud Studies – Études Des Nuages* (Spector Books, Leipzig 2013)
- 22.15 A. Riggenbach: On a method of photographing cirrus clouds, *Q. J. R. Meteorol. Soc.* **15**, 16–17 (1889)
- 22.16 R. Abercromby: Suggestions for an international nomenclature of clouds, *Q. J. R. Meteorol. Soc.* **13**, 154–166 (1887)
- 22.17 H.H. Hildebrandsson: Remarks concerning the nomenclature of clouds for ordinary use, *Q. J. R. Meteorol. Soc.* **13**, 148–154 (1887)
- 22.18 H.H. Hildebrandsson, A. Riggenbach, L.P. Teissenrenc de Bort: *International Cloud-Atlas* (Gauthier-Villars et Fils, Paris 1896), in French, English, and German
- 22.19 S. Huler: *Defining the Wind* (Crown Publishers, New York 2004)
- 22.20 F. Beaufort: *Diary of Admiral Beaufort* (Met Office, Exeter 1790–1857)
- 22.21 A. Blackadar: Using your computer, the Beaufort wind scale, *Weatherwise* **39**, 278–280 (1986)

- 22.22 H. Crutcher: Wind, numbers, and Beaufort, *Weatherwise* **28**, 260–271 (1975)
- 22.23 Societas Meteorologica Palatina (Ed.): *Ephemerides Societatis Meteorologicae Palatinae. Observationes Anni 1789* (Societas Meteorologica Palatina, Mannheim 1793)
- 22.24 O.M. Ashford, S. Gupta, P.J. Meade, H. Taba, G. Weiss (Eds.): *Forty Years of Progress and Achievement* (World Meteorological Organization, Geneva 1990), WMO–No. 721
- 22.25 VDI 3786 Part 9: *Environmental Meteorology – Meteorological Measurements – Visual Weather Observations* (Beuth, Berlin 2021)
- 22.26 WMO: *International Cloud Atlas: Manual on the Observation of Clouds and Other Meteors* (World Meteorological Organization, Geneva 2017), WMO–No. 407
- 22.27 B. Mühr, W. Berberich: *Der Wolkenatlas und ein Ausflug in die Astronomie* (Kunstschätze Verlag, Gerchsheim 2008)
- 22.28 W. Kresse, D.M. Danko (Eds.): *Springer Handbook of Geographic Information*, 2nd edn. (Springer Nature, Switzerland 2021)

Thomas Foken

University of Bayreuth
Bayreuth, Germany
thomas.foken@uni-bayreuth.de



Thomas Foken is a retired Professor of Micrometeorology at the University of Bayreuth. He was the head of Laboratories at the meteorological observatories at Potsdam (1981–1994) and Lindenberg (1994–1997). His research interests include the interaction between the Earth’s surface and the atmosphere and the measurement and modeling of energy and matter fluxes, with a strong focus on experimental meteorology. His scientific contributions have been recognized through various international awards.

Raymond Rülke

Langendorf, Germany



Raymond Rülke has been a civil servant at the Bundeswehr Geoinformation Service in Germany since 1991. He studied meteorology at Humboldt University Berlin until 1987. After that he was responsible for weather forecasting at various airbases in Germany for 25 years until 2012. Since 2013, he has been responsible for the provision of maritime geoinformatics data for worldwide operations of the German Navy.

Remote **Part C**

Part C Remote-Sensing Techniques (Ground-Based)

- 23 **Sodar and RASS**
Stefan Emeis, Garmisch-Partenkirchen, Germany
- 24 **Backscatter Lidar for Aerosol and Cloud Profiling**
Christoph Ritter, Potsdam, Germany
Christoph Münkel, Hamburg, Germany
- 25 **Raman Lidar for Water-Vapor and Temperature Profiling**
Volker Wulfmeyer, Stuttgart, Germany
Andreas Behrendt, Stuttgart, Germany
- 26 **Water Vapor Differential Absorption Lidar**
Scott M. Spuler, Boulder, USA
Matthew Hayman, Boulder, USA
Tammy M. Weckwerth, Boulder, USA
- 27 **Doppler Wind Lidar**
Oliver Reitebuch, Weßling, Germany
R. Michael Hardesty, Boulder, USA
- 28 **Spectrometers**
Klaus Schäfer, Garmisch-Partenkirchen, Germany
Mark Wenig, Munich, Germany
Mark A. Zondlo, Princeton, USA
Axel Murk, Bern, Switzerland
Konradin Weber, Duesseldorf, Germany
- 29 **Passive Solar and Microwave Spectral Radiometers**
Susanne Crewell, Köln, Germany
Manfred Wendisch, Leipzig, Germany
Ulrich Löhnert, Köln, Germany
- 30 **Weather Radar**
Jörg E.E. Seltmann, Hohenpeissenberg, Germany
- 31 **Radar Wind Profiler**
Volker Lehmann, Lindenberg, Germany
William Brown, Boulder, USA
- 32 **Radar in the mm-Range**
Gerhard Peters, Elmshorn, Germany
- 33 **High Frequency Radar**
Jochen Horstmann, Geesthacht, Germany
Anna Dzvonnkovskaya, Kaltenkirchen, Germany
- 34 **Scintillometers**
Frank Beyrich, Lindenberg, Germany
Oscar K. Hartogensis, Wageningen, The Netherlands
Henk A.R. de Bruin, Bilthoven, The Netherlands
Helen C. Ward, Innsbruck, Austria
- 35 **Acoustic Tomography**
Armin Raabe, Leipzig, Germany
Manuela Starke, Tharandt, Germany
Astrid A. Ziemann, Tharandt, Germany
- 36 **GNSS Water Vapor Tomography**
Michael Bender, Offenbach, Germany
Galina Dick, Potsdam, Germany

Sodar and RASS

Stefan Emeis 

Vertical profiles of the wind speed, turbulence components, and the temperature in the lower regions of the atmospheric boundary layer can be determined by performing active acoustic and radioacoustic sounding with ground-based devices. This chapter introduces two types of instruments—sound detection and ranging (sodar) devices and radioacoustic sounding systems (RASS)—that can be used to carry out such measurements. While sodars can provide quantitative vertical wind and turbulence profiles and qualitative mixed-layer height and inversion height data, RASS can provide that as well as quantitative temperature profiles. Both types of instruments have a typical height range of several hundreds of meters, and their vertical resolution is on the order of 20 m.

23.1	Measurement Principles and Parameters	662	23.3	Theory	666
23.1.1	Relevance of Wind, Turbulence, and Temperature Measurements of the Atmospheric Boundary Layer ...	662	23.3.1	Sound Propagation in the Atmosphere	666
23.1.2	Measured Parameters	662	23.3.2	Doppler Analysis	668
23.1.3	Siting Considerations	662	23.3.3	Principle of Radioacoustic Sounding ..	668
23.1.4	Measurement Principles of Sodars.....	663	23.3.4	Vertical Range.....	669
23.1.5	Measurement Principles of RASS	664	23.3.5	Vertical and Temporal Resolution.....	669
23.2	History	665	23.3.6	Determination of the Mixed-Layer Height and Inversions	669
23.2.1	History of Sodar Measurements	665	23.4	Devices and Systems	670
23.2.2	History of RASS Measurements	666	23.4.1	Sodars and Minisodars	670
			23.4.2	RASS.....	673
			23.4.3	Comparison of the Methods	673
			23.5	Specifications	674
			23.5.1	Measured Parameter Accuracies and Ranges	674
			23.5.2	Permits Required for RASS Operation ..	674
			23.5.3	Compliance with Noise Regulations ...	675
			23.6	Quality Control	675
			23.6.1	Wind Speed Calibration.....	676
			23.6.2	Temperature Calibration.....	676
			23.6.3	Specific Quality Control Methods	676
			23.7	Maintenance	677
			23.8	Applications	677
			23.9	Future Developments	679
			23.10	Further Reading	680
			References		680

Ground-based sonic/sound detection and ranging (sodar) devices and radioacoustic sounding systems (RASS) are active remote-sensing devices that are used to observe boundary-layer wind, turbulence, and—in the case of RASS—temperature profiles (see [23.1] for an overview of all ground-based remote-sensing techniques that are used to investigate and monitor the atmospheric boundary layer). A sodar evaluates the Doppler shifts of sound waves backscattered due to

refraction index fluctuations caused by the small temperature and humidity gradients present in atmospheric turbulence, whereas a RASS emits electromagnetic and acoustic waves and uses one of them (either electromagnetic or acoustic waves) to follow the propagation of the other (acoustic or electromagnetic waves, respectively), which permits the determination of the speed of sound and thus the temperature of the atmosphere.

23.1 Measurement Principles and Parameters

Sodar and RASS devices are used to obtain boundary layer profiles of wind, turbulence, and temperature. Note that, just like many well-established and commonly used abbreviations (such as *radar*), *sodar* and *lidar* are often written in lowercase letters—as they are throughout this chapter. However, the acronym RASS is still generally written in uppercase letters.

23.1.1 Relevance of Wind, Turbulence, and Temperature Measurements of the Atmospheric Boundary Layer

Temperature, humidity, and wind are the main parameters that determine the vertical structure of the atmospheric boundary layer. While the vertical profiles of temperature and humidity are mainly responsible for the static stability of this layer, wind and turbulence dominate the dynamics of the boundary layer.

The static and dynamic states of the boundary layer dictate the strengths and the directions of fluxes of energy, momentum, and other atmospheric constituents (humidity and pollutants) between the Earth's surface and the atmosphere. The strengths of these fluxes correlate with shear and turbulence intensity. The direction is given by the gradient of the mean of the transported property.

The horizontal and vertical dispersions of pollutants correlate with the turbulence intensity. Pollutants that have been dispersed upward by turbulence and are transported upward by thermal convection during the day can undergo considerable horizontal displacement during the night due to stronger winds or even low-level jets [23.2] above the stable near-surface layer.

Wind turbines have become much larger in recent years. Hub heights of between 100 and 150 m are common for modern onshore turbines [23.3]. These turbines operate in the Ekman layer. Remote sensing is the only meaningful way to detect and monitor winds and turbulence at these heights (see Chap. 51 for further details).

23.1.2 Measured Parameters

In contrast to other meteorological variables, the wind is a vector, i.e., it is characterized by a magnitude (the wind speed) and a direction (the wind direction). Generally (except in small-scale and convective processes), the vertical wind component is much smaller than the horizontal wind components, so often only horizontal wind speeds are measured. Furthermore, wind is a highly variable atmospheric parameter; its speed and direction fluctuate strongly. This phenomenon is called the gustiness of the wind.

In the following, x and y are the two horizontal directions (positive towards the east and the north, respectively), z is the vertical direction (positive upward), and $u(t)$, $v(t)$, and $w(t)$ are the three instantaneous time-dependent wind components in the three directions x , y , and z . The following wind speeds can be defined (see Tables 23.1 and 23.2):

- The mean wind speed

$$\bar{u} = \frac{1}{T} \int_0^T \sqrt{u^2(t) + v^2(t) + w^2(t)} dt, \quad (23.1)$$

- The mean horizontal wind speed

$$\bar{u}_h = \frac{1}{T} \int_0^T \sqrt{u^2(t) + v^2(t)} dt, \quad (23.2)$$

- And the mean vertical velocity

$$\bar{w} = \frac{1}{T} \int_0^T w(t) dt, \quad (23.3)$$

where the integral in the following equations is always taken from time $t = 0$ to the end of the time period T over which the speeds are averaged.

Furthermore, sodars and RASS are able to observe the variance of the vertical wind component (see Tables 23.1 and 23.2)

$$\sigma_w = \sqrt{\frac{1}{T} \int_0^T (\bar{w} - w(t))^2 dt}. \quad (23.4)$$

The only turbulence parameter obtained using sodar and RASS is the variance of the vertical velocity component σ_w .

The acoustic temperature T_s (Table 23.2) can be obtained using a RASS. The exact definition of this temperature, which is very similar to the virtual temperature, is given in (23.10) in Sect. 23.3.1 below.

23.1.3 Siting Considerations

Sodars and RASS are sensitive to noise but they also produce noise. This is also true of electromagnetic radiation for RASS. This limits the selection of possible sodar or RASS measurement sites and implies that sodars and RASS cannot be operated close together

Table 23.1 Parameters derived from sodar measurements

Parameter	Description	Unit	Symbol
Radial wind components	Doppler analysis only permits the derivation of radial velocities; sodar detects radial velocities sequentially in at least three different directions using the Doppler beam swinging (DBS) technique	m s^{-1}	u_1, u_2, \dots, u_n
Cartesian wind components	Computed from the radial wind components using trigonometric relations	m s^{-1}	u, v, w
Radial turbulence component	Only the vertical component of the turbulence can be determined using vertical sounding; it is derived from either the broadening of the frequency of the backscattered signal or the temporal fluctuations in the vertical velocity component	m s^{-1}	σ_w
Mixed-layer depth	Determined from the backscatter intensity (mainly the decrease in backscatter intensity with height) using an algorithm	m	MLH
Inversion height	Height of inversion is determined from the secondary maximum in the backscatter intensity	m	

Table 23.2 Parameters that are derived from RASS measurements

Parameter	Description	Unit	Symbol
Acoustic temperature	Vertical profile is determined from a vertically propagating sound pulse	K	T_s
Radial wind components (Doppler RASS only)	Doppler analysis only allows the evaluation of radial velocities; sodar detects radial velocities sequentially in at least three different directions via the Doppler beam swinging (DBS) technique	m s^{-1}	u_1, u_2, \dots, u_n
Cartesian wind components (Doppler RASS only)	Computed from the radial wind components using trigonometric relations	m s^{-1}	u, v, w
Radial turbulence component (Doppler RASS only)	Only the vertical component of turbulence can be determined using vertical sounding; it is derived from either the broadening of the frequency of the backscattered signal or the temporal fluctuation of the vertical velocity component	m s^{-1}	σ_w
Mixed-layer depth (Doppler RASS only)	Determined from the acoustic backscatter intensity (mainly the decrease in the backscatter intensity with height) using an algorithm	m	MLH

(within a few hundreds of meters of each other) because they would interfere with each other. Since these instruments sound mainly in the vertical direction, the chosen measurement site must provide a free sky view. Public access to operational instruments of this type should be prohibited for two reasons. On the one hand, vandalism must be discouraged. On the other hand, the acoustic and electromagnetic radiation emitted from the instruments can be harmful to humans. The noise pressure within the antennae of a three-antenna sodar or the enclosure of a phased-array sodar can damage ear drums. Spending an extended period at distances of up to ≈ 4 m from the sending electromagnetic antenna of a RASS can also be harmful.

Both types of instruments need a steady power supply, which can be provided by either the grid or a system of solar panels connected to an energy storage unit. The transportation of such heavy instrumentation to the intended site requires access roads that are suitable for use by heavy-duty vehicles (this includes sufficient vertical clearance all the way to the measurement site!). Sections 23.3.1 (on fixed echoes), 23.5.2, and 23.5.3 give additional information on the requirements for sites at which these instruments can be operated.

23.1.4 Measurement Principles of Sodars

A sodar consists of a pulsed sound emitter and a receiver [23.4]. Sound waves are scattered by turbulent temperature fluctuations in the atmosphere, since the refractive index for sound waves changes at the boundaries of these fluctuations. The fluctuations that reflect the sound pulses emitted from the sodar are assumed to move with the mean wind. Therefore, acoustic waves that are backscattered in the atmosphere are Doppler shifted in frequency if the air is in motion. Sodars that analyze the Doppler shift of the backscattered sound pulses in order to determine the vertical wind profile are called *Doppler sodars* (see Table 23.3 and Fig. 23.2 for instrument terminology). The Doppler shift is proportional to the radial velocity v_r (see Tables 23.1 and 23.2 and Sect. 23.3.2). The range is dictated by the travel time of the pulse and the backscattered wave. An overview of the basic principle of sounding with a sodar and the history of sodar development are described in [23.5]; a summary of acoustic remote-sensing techniques and their theoretical background was recently provided by Bradley [23.6].

Table 23.3 Measurement principles for wind, turbulence, and temperature, and applications of such measurements

Parameter	Measurement principle			Application	
	Doppler	Backscatter intensity	Sound speed	Mean	Turbulent
Wind	×			×	
Turbulence	×	×			×
Temperature gradient		×			×
Temperature			×	×	

Sodar measurements depend on the state of the atmosphere. If the atmosphere is extremely well mixed (i.e., temperature fluctuations are very small), almost no sound is reflected from the atmosphere, and the signal-to-noise ratio for sodar can be so low that it is not possible to accurately determine the wind speed (via the Doppler shift). Such a scenario tends to occur during the afternoon on days with low mean wind speeds and strong vertical mixing due to thermal heating.

For optimal backscatter, the spatial size of temperature gradients in the atmosphere should be about half the acoustic wavelength (Bragg condition) [23.7]. This condition can be fulfilled by the temperature gradients within turbulence elements as well as those across inversion layers. It is necessary to differentiate between these two possibilities when deducing information on the atmospheric state from the backscattered signal. This can be done by either assessing the general weather conditions or, if a Doppler sodar is used, by analyzing the variance of the simultaneously recorded vertical velocity. High variances indicate thermal forcing, where the backscatter intensity is proportional to the turbulence intensity, whereas low variances indicate stable layering, where the backscatter intensity should be proportional to the mean vertical temperature gradient (i.e., inversion).

For a sodar (just as for radar), the backscattered signal is representative of a certain atmospheric volume. If the duration of the sound pulse is 100 ms, the sodar detects simultaneous backscatter from a volume 33 m deep. If this volume is 500 m AGL, it has a radius of 44 m (assuming that the opening angle of a single emitted sound beam is 5°). Additionally, the three-dimensional wind information must be integrated from a full measurement cycle comprising one vertical and two to four tilted beams (see the description of the Doppler beam swinging technique in Sect. 23.4.1). This implies that the radius of the detected atmospheric

volume at a height of 500 m AGL is about 150–200 m. This means that a sodar performs volume- and time-averaged measurements.

23.1.5 Measurement Principles of RASS

A radioacoustic sounding system (RASS) performs acoustic and electromagnetic sounding simultaneously [23.8, 9]. Two different types of RASS have been developed: the Bragg RASS and the Doppler RASS [23.10].

The *Bragg RASS* (sometimes called a wind-temperature radar) is a wind profiler (see Chap. 31 and [23.11]) with an additional acoustic emitter. When the Bragg condition is fulfilled [23.7] (i.e., the wavelength of the sound waves λ_a is half the wavelength of the electromagnetic waves λ_e , see Tables 23.4 and 23.5), there is optimal backscatter of the electromagnetic waves from the acoustic waves. The electromagnetic signal is emitted at a fixed frequency, but the emitted sound has a continuously varying frequency f_a . The propagation speed of the acoustic signal can be determined from the acoustic wavelength $\lambda_{a,B}$ at which optimal backscatter occurs via the dispersion relation

$$c = \frac{\lambda_{a,B}}{2} f_a. \quad (23.5)$$

A sound frequency of about 100 Hz is used for a VHF wind profiler operating at 50 MHz, while a sound frequency of ≈ 2 kHz optimally fulfills the Bragg condition for an UHF wind profiler operating at 1 GHz. Because the attenuation of sound waves in the atmosphere depends strongly on frequency [23.12], an UHF RASS can detect the temperature profile up to a height of ≈ 1.5 km, whereas a VHF RASS can determine the temperature profile throughout the troposphere.

Table 23.4 Parameters that are measured using sodar

Parameter	Description	Unit	Symbol
Frequency	The mean frequency and the width of the frequency spectrum of the backscattered signal are recorded as functions of propagation time	s^{-1}	f_a
Acoustic backscatter intensity	Parameter is recorded as a function of propagation time	dB	P_R

Table 23.5 Parameters that are measured using a RASS

Parameter	Description	Unit	Symbol
Acoustic frequency (Doppler RASS only)	Mean frequency and width of the frequency spectrum of the backscattered signal are recorded as functions of the propagation time	s^{-1}	f_a
Acoustic backscatter intensity	Parameter is recorded as a function of propagation time	dB	P_R
Electromagnetic frequency	Mean frequency and width of the frequency spectrum of the backscattered signal are recorded as functions of the propagation time	s^{-1}	f_e

Table 23.6 Additional parameters that are required to interpret sodar measurements

Parameter	Description	Unit	Symbol
Atmospheric temperature	Needed to determine the speed of sound, which is then used to derive the distance from the scattering volume	K	T
Orientation, alignment	Orientation with respect to north is needed to convert radial wind velocities into Cartesian wind components; instrument should be aligned horizontally	degrees	
Distance to scattering objects	The distance to possible scattering objects (trees, buildings, electricity cables, ...) must be known in order to identify fixed echoes	m	

A *Doppler RASS* is a sodar with an additional electromagnetic emitter and receiver operating at a frequency of $f_{e,0}$. This instrument is able to detect the acoustic shock fronts of the acoustic pulses and determine their propagation speed from the backscattered electromagnetic waves. This propagation speed is equal to the speed of sound, which is in turn a known function of the air temperature (see also Tables 23.6) and humidity. Using the Doppler shift Δf_e (see Sect. 23.3.3) of the electromagnetic radiation backscattered at the density fluctuations caused by the sound waves, the propagation speed c of the sound waves can be determined as

$$c = 0.5c_1 \frac{\Delta f_e}{f_{e,0}}, \quad (23.6)$$

where c_1 denotes the speed of light. Just like a Bragg RASS, a Doppler RASS emits a *chirp* (a sound signal) to check that the Bragg condition is optimally met, considering that the temperature varies significantly across the entire height interval considered.

The propagation speed c_g is the sum of the speed of sound c and the vertical movement of the air w in which the sound waves propagate, i.e.,

$$c_g = c + w. \quad (23.7)$$

The vertical air speed component w can be determined separately from the Doppler shift of the backscattered electromagnetic clear-air signal when operating a Bragg RASS, or from the Doppler shift of the backscattered acoustic signal when operating a Doppler RASS. The height profile of c can then be converted into a height profile for the acoustic temperature T_s (see Sect. 23.3.1). This acoustic temperature is a sufficiently accurate approximation of the virtual air temperature for many applications.

A Bragg RASS has a greater maximum range than a Doppler RASS but a coarser height resolution. A Doppler RASS is also much easier to implement than a Bragg RASS, meaning that a Doppler RASS is less expensive.

23.2 History

The development of ground-based remote-sensing devices started during World War II with the construction of the first weather radars [23.13]. The first acoustic wind profilers (sodars) were invented shortly after World War II. The idea for a RASS device originated in the early 1970s.

23.2.1 History of Sodar Measurements

Acoustic sounding technology was developed shortly after World War II [23.14]. Most of the theoretical foundations for this field were laid by *Valerian*

Iljitsch Tatarskij [23.15], with the initial development of acoustic sounding technology occurring in the Soviet Union [23.16, 17] and (a decade later) in the United States [23.18]. Analyzing the backscatter intensity was the main focus in the beginning. More recently, the emergence of wind energy applications in the last decade of the twentieth century has fostered renewed interest in this wind measurement technology. The use of Doppler analysis to derive wind speed is now the main application of acoustic sounding technology. However, the rapid development of optical Doppler wind lidars between 2005 and 2010 heavily suppressed

further development in the field of sodar devices. Although optical techniques are much more expensive than acoustic techniques, optical techniques have become more popular because they do not suffer as much from environmental interference and because they have higher data availability during a given time period (see Chap. 27 for further discussion of Doppler wind lidars).

23.2.2 History of RASS Measurements

The acoustic backscatter intensity gives only a very crude estimate of the vertical temperature gradient. This

23.3 Theory

The following sections provide the theoretical background for both sodars and RASS. The theory behind the propagation of acoustic waves in the atmosphere is utilized for both types of instruments, while the theory behind the propagation of radio waves is only employed for RASS.

23.3.1 Sound Propagation in the Atmosphere

Sound waves are elastic vibrations that propagate as longitudinal waves (i.e., the material vibrates in the same direction as the direction of propagation of the sound wave). For ideal gases, the speed of sound c is given by

$$c = (\gamma RT)^{0.5}, \quad (23.8)$$

where γ is the ratio of the specific heats (c_p/c_v), R is the specific gas constant of an ideal gas in $\text{J kg}^{-1} \text{K}^{-1}$, and T is the absolute temperature in K.

The speed of sound in air is mainly a function of the temperature. Nevertheless, changes in the humidity of the air affect both R and γ , so the speed of sound also depends on the humidity. If the humidity is given in terms of the partial pressure e or the specific humidity q , the speed of sound in humid air can be expressed as

$$c = (\gamma_{\text{tr}} R_{\text{tr}} T_s)^{0.5} = 20.048(T_s)^{0.5}, \quad (23.9)$$

where γ_{tr} is the ratio of the specific heats for dry air, R_{tr} is the gas constant of dry air in $\text{J kg}^{-1} \text{K}^{-1}$, and T_s is the acoustic temperature in K, as given by

$$T_s \approx T \left(1 + 0.329 \frac{e}{p} \right) \approx T(1 + 0.531q), \quad (23.10)$$

where p is the air pressure in the same units as e .

led to the development of the RASS nearly 50 years ago [23.8]. RASS were constructed by either adding a radar component to a sodar (Doppler RASS) or by adding a sound component to a wind profiler (Bragg RASS). Although RASS suffer from the same environmental interference as sodar devices, they have not been superseded by optical techniques so far. Passive radiometers (Chap. 29) have come onto the market, but they do not offer the same high vertical resolution as RASS. Raman lidars (Chap. 25) are much more expensive and have poor signal-to-noise ratios during the daytime due to interference from scattered sunlight.

T_s is very similar to the virtual temperature T_v that is commonly used for humid air in meteorology, although it differs from it slightly, as described by

$$T_s = T_v - 0.0489 \frac{eT}{p} \quad (23.11a)$$

or

$$T_s = T_v - 0.079q, \quad (23.11b)$$

where T , T_s , and T_v are in K, e and p are in hPa, and q is in kg kg^{-1} .

Attenuation of Sound Waves in the Atmosphere

The attenuation of sound waves in the atmosphere depends on the frequency, temperature, and humidity. The attenuation-dependent transmittance follows the Bouguer–Lambert–Beer law

$$\tau(x, f) = \exp \left(- \int_0^x \alpha(x', f) dx' \right), \quad (23.12)$$

where the absorption coefficient $\alpha(x, f)$ is in m^{-1} and

$$\alpha = f^2 \left[1.84 \times 10^{-11} \frac{p_r}{p} \left(\frac{T}{T_{20}} \right)^{1/2} + \left(\frac{T}{T_{20}} \right)^{5/2} \times \left(\frac{f_{\text{O}_2} \times 0.01275 \times \exp(-2239.1/T)}{f_{\text{O}_2}^2 + f^2} + \frac{f_{\text{N}_2} \times 0.1068 \times \exp(-3352/T)}{f_{\text{N}_2}^2 + f^2} \right) \right], \quad (23.13)$$

where p_r is a constant pressure (1013.25 hPa), p is the surface pressure at the observation site in hPa, T is the

absolute surface temperature in K, and T_{20} is a constant temperature (293.15 K).

Equation (23.13) requires two relaxation frequencies: f_{O_2} for oxygen, as given by

$$f_{O_2} = \frac{p}{p_r} \left[24 + 4.04 \times 10^4 h \left(\frac{0.02 + h}{0.391 + h} \right) \right], \quad (23.14a)$$

and f_{N_2} for nitrogen, evaluated using

$$f_{N_2} = \frac{p}{p_r} \left(\frac{T}{T_{20}} \right)^{1/2} \left[9 + 280h \times \exp \left(-4.170 \left(\left(\frac{T}{T_{20}} \right)^{-1/3} - 1 \right) \right) \right]. \quad (23.14b)$$

Both of these relaxation frequencies also depend on the relative humidity

$$h = 100 \frac{e}{p}, \quad (23.14c)$$

where h is in %. Further details can be found in [23.12, 19, 20].

Apart from shock waves (described in Sect. 23.3.3), the propagation of electromagnetic waves is only marginally influenced by atmospheric properties, so they can be neglected here.

Backscattering of Sound Pulses in the Atmosphere

Turbulent inhomogeneities of the temperature, humidity, and wind velocity lead to local changes in the speed of sound and thus to the scattering of some of the sound energy. This process is referred to as clear air scattering or Bragg scattering. In backscattering (scattering angle = 180°), only temperature and humidity inhomogeneities (not wind velocity fluctuations) contribute to the scattered signal. Backscattering is most effective when it occurs at turbulent structures with sizes that are half the wavelength of the sound wave (the Bragg condition). Scattering also occurs at precipitation particles.

When an emitting power of ≈ 1 kW is used, a backscattered signal with a power of $\approx 10^{-15}$ W is obtained. This is below the hearing threshold of the human ear (10^{-12} W) but well above the noise produced by the Brownian motion of atmospheric molecules (6×10^{-19} W). The sound frequencies used (1500–4500 Hz) are well within the sensitivity range of the human ear.

The ratio of the emitted to the received power is given by the sodar equation

$$P_R = r^{-2} \left(\frac{c\tau_d A \varepsilon}{2} \right) P_0 \beta_s \exp(-2\alpha r) + P_{bg}, \quad (23.15)$$

where P_R is the received power, P_0 is the emitted power, r is the distance between the sodar and the scattering element, ε is the antenna efficiency, A is the effective antenna area, τ_d is the pulse duration (typically between 20 and 100 ms), β_s is the backscattering cross-section (typically on the order of $10^{-11} \text{ m}^{-1} \text{ sr}^{-1}$), and P_{bg} is the background noise.

The speed of sound c and the absorption coefficient α are defined in (23.8) and (23.13) above. The background noise also includes contributions from ambient noise with the same sound frequency, e.g., traffic noise. The ratio of the two terms on the right-hand side of the sodar equation is called the signal-to-noise ratio (usually abbreviated to SNR). The backscattering cross-section β_s is a function of the temperature structure function C_T^2 [23.15]. When using the wavenumber $k = 2\pi/\lambda$ for a monostatic sodar, we find that

$$\beta_s(180^\circ) = 0.00408 k^{1/3} \frac{C_T^2}{T^2}. \quad (23.16)$$

This equation gives an average over all scattering elements within the atmospheric volume that is hit by the cone-shaped beam [23.21].

Fixed Echoes

Sodar beams also have side lobes. If these side lobes hit highly reflective obstacles, sound energy with a strength that is similar to or even much stronger than the atmospheric return is scattered back towards the instrument. The backscattered signals from these objects are called fixed echoes. Fixed echoes can strongly influence and disturb sodar measurements. Since fixed echoes are reflected from fixed (i.e., stationary) objects, they cause the deduced wind speed to be much lower than it really is. Avoiding fixed echoes requires good measurement site selection for sodar instruments in order to guarantee unbiased wind speed measurements. Sodar must therefore be sited away from obstacles such as buildings, trees, and—most importantly—electric transmission cables. If the sodar has to be sited near such objects, it should be situated such that the distance to the highly reflecting objects does not conflict with the range of the atmospheric layers that are to be investigated. This often means positioning the sodar closer to such objects than the lowest range gate of the instrument (usually ≈ 40 m).

23.3.2 Doppler Analysis

Wind and turbulence are measured with a sodar by analyzing the Doppler shift of the backscattered acoustic pulse that was originally emitted with a frequency f_0 . Assuming that the scattering volume for the sound waves is moving with the wind, the Doppler-shifted sound frequency f_D is given by

$$f_D = f_0 \frac{c - v_r}{c + v_r}, \quad (23.17)$$

where v_r is the radial velocity along the path of the emitted sound beam (positive away from the sodar) and f_0 the emitted acoustic frequency. Solving for the radial velocity v_r gives

$$v_r = c \frac{f_0 - f_D}{f_0 + f_D}. \quad (23.18)$$

23.3.3 Principle of Radioacoustic Sounding

Measurements are achieved using a RASS by modifying the propagation conditions for electromagnetic waves in a controlled manner using sound waves. The scattering of electromagnetic waves from refractive-index modifications generated by acoustic waves differs from scattering due to atmospheric turbulence (such as that used for wind profiler radar measurements) in several respects [23.9]:

1. Modifications of the atmospheric refractive index propagate as spherical waves at the speed of sound, whereas moving refractive-index variations caused by natural turbulence do not show any systematic behavior.
2. The spherical wavefronts focus the scattered electromagnetic waves. Therefore, to obtain a sufficiently high receiver signal, the antenna needs to be located near the focus (*acoustic spot*) formed by the sound waves.
3. Horizontal wind carries sound waves away and causes the focus of the backscatter signal to drift, limiting the maximum range. In a turbulent atmosphere, sound-wave scattering extends the focal area beyond that of the electromagnetic transmitter antenna, reducing the adverse effect of drift on the maximum range.
4. Atmospheric absorption also decreases the sound intensity, leading to a reduction in the maximum range of the RASS, similar to that for a sodar.
5. The backscatter signal is maximized when the ratio of the electromagnetic to the acoustic wavelengths is 2 : 1 ($\lambda_e = 2\lambda_a$, known as the Bragg condition; see Fig. 23.1).

When the Bragg condition is met, the power $P_s(z)$ received at the RASS is described by the RASS equation

$$P_s(z) = 0.588 \times 10^{-14} c_g \frac{\Delta z}{(\lambda_e z)^2} \frac{P_a P_e}{B_a} g \tau I P_{N,N_0}, \quad (23.19)$$

where P_{N,N_0} is the normalized backscatter power for $N = N_0$, N is the number of acoustic waves within the scattering volume Δz (the backscatter power is proportional to N^2), P_a is the transmitted acoustic power, P_e is the transmitted electromagnetic power, B_a is the acoustic bandwidth, g is a gain parameter ($g = g_a$ if $g_e \geq g_a$; otherwise, $g = g_e^2/g_a$), g_a is the gain of the acoustic antenna, g_e is the gain of the electromagnetic antenna, τ is the acoustic transmission due to atmospheric absorption, I is an inhomogeneity parameter that accounts for atmospheric turbulence ($I < 1$ describes a turbulent, agitated, layered atmosphere whereas $I = 1$ is indicative of a stationary, quiet, homogeneous atmosphere), and Δz is the radial extent of the scattering volume.

The equation used to determination c_g depends on the type of RASS employed. For a Doppler RASS, we have

$$c_g = -\frac{\lambda_e}{2} \Delta f_e \approx -\lambda_a \Delta f_e. \quad (23.20)$$

For a Bragg RASS, we have

$$c_g = -\lambda_a f_B. \quad (23.21a)$$

As both Δf_e and f_B are actually equal to the acoustic frequency f_a , we find that

$$c_g = -\lambda_a f_a \quad (23.21b)$$

for both types of RASS.

Finally, the speed of sound and the radial wind component due to atmospheric motion must be separated (see (23.7)). If the effect of a nonzero radial velocity v_r is neglected when deriving the temperature T from the sound velocity c_g , the resulting error is 1.7 K per m s^{-1} of the unknown radial wind v_r . The simplest method of suppressing the effect of the vertical wind consists of pointing the RASS vertically and averaging the speed of sound c_g over a long period of time, as the long-term vertical wind over horizontal terrain tends to zero. This method is usually applied in routine measurements. In a convective atmosphere, however, usual averaging times of between 10 and 30 min may not be sufficient, resulting in a considerable error in the temperature measurement due to the vertical wind. If the terrain is tilted, the average vertical wind may be nonzero, so averaging over long periods of time is not a solution. In these

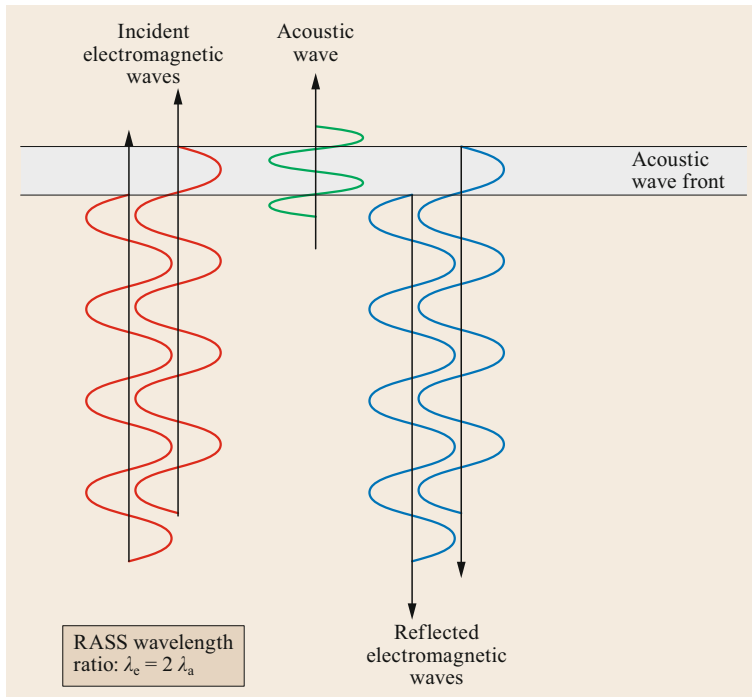


Fig. 23.1 Illustration of the Bragg condition for Doppler RASS instruments. Here, acoustic waves are shown in *green*, whereas emitted and reflected electromagnetic waves are shown in *red* and *blue*, respectively. The electromagnetic waves are reflected at the leading and trailing edges of the sound pulse. For all of the reflected electromagnetic waves to be in phase, the wavelength of the emitted electromagnetic waves must be twice the wavelength of the moving sound pulse

cases, the vertical wind component measured with the sodar (when using a Doppler RASS) or with the wind profile radar (when using a Bragg RASS) can be used for correction. The vertical temperature profile is assessed with a RASS by determining the thermodynamic speed of sound c in each altitude interval.

23.3.4 Vertical Range

The vertical range of the wind and temperature data obtained from a sodar and a Doppler RASS is determined from the travel time of the sound pulses. For a Bragg RASS, the vertical range is determined from the travel time of the electromagnetic waves. The maximum vertical range is influenced by the attenuation of sound waves in the atmosphere (see Sect. 23.3.1).

23.3.5 Vertical and Temporal Resolution

The pulse duration τ_d determines the height resolution of the instrument via the relation

$$\Delta z = 0.5c\tau_d. \quad (23.22)$$

The sodar equation (23.15) shows that the backscatter power is also proportional to the pulse duration. Therefore, the choice of pulse duration is made from a trade-off between height resolution (preferably short pulse durations) and maximum range (preferably long

durations). Equation (23.19) is valid for a perfect rectangular pulse but can also be used as a good first approximation for real pulses.

To avoid unwanted interference, a new pulse cannot be emitted before the backscatter from the previously emitted beam has been received, so a measurement cycle of a sodar lasts six to ten times as long as the time needed for a sound pulse to travel to the maximum vertical range of the instrument. For a sodar or Doppler RASS operating at 1500 Hz, this implies that the duration of a measurement cycle is ≈ 20 s when the range is 1000 m.

23.3.6 Determination of the Mixed-Layer Height and Inversions

The layering of the atmospheric boundary layer due to the vertical temperature and moisture distribution and the existence of inversions within this layer or on top of it strongly influence the development of atmospheric motions and high pollutant concentrations in the air. Well-mixed layers of the atmospheric boundary layer are characterized by enhanced turbulence compared to the stably stratified free troposphere above. For a convective boundary layer (CBL), the mixed-layer height (MLH) is usually identical to the temperature inversion height.

Beyrich [23.22] has listed possible analyses of the MLH and inversions based mainly on acous-

tic backscatter intensities measured by a sodar. Asimakopoulos et al. [23.23] analyzed these methods further and grouped them into three approaches to deriving the MLH from sodar data: the horizontal wind speed (HWS) method, the acoustic received echo (ARE) method, and the vertical wind variance (VWV) method.

The ARE method is the simplest method of determining the MLH from acoustic remote sensing. Most of the methods listed in [23.22] are variants of this type. This method does not require an analysis of the Doppler shift of the backscattered signals. The MLH is derived from either the most negative slope, the change in curvature of the vertical profile of the acoustic backscatter intensity, or the height at which the backscatter intensity decreases below a certain prespecified threshold value. Inversions are found by searching for secondary maxima in the vertical profile of the backscatter intensity.

The ARE method can be enhanced in two ways. The first way is to include further variables for which data are provided by Doppler sodars in the MLH algorithm. For instance, the utilization of the variance of the vertical velocity component is demonstrated in [23.24]. The second way to enhance the ARE method is to determine not only the MLH from sodar measurements but also the heights of lifted inversions. Especially above orographically complex terrain, the vertical structure of the atmospheric boundary layer (ABL) can be very com-

plicated [23.25]. Enhanced ARE methods (and optical methods that use ceilometers and wind lidars) are described in more detail in [23.26].

The HWS method requires an analysis of the Doppler shift of the backscattered signals. It involves analyzing the shape of hourly-averaged vertical wind-speed profiles under the assumption that wind speed and wind direction are almost constant within the mixing layer but the wind speed increases gradually towards the geostrophic value at the top of the mixing layer. Given the underlying assumptions, the applicability of this method is probably limited to well-developed CBLs. Such CBLs are often higher than the maximum range of a sodar. Even if the CBL height is within the range of the sodar, the algorithm used to analyze the Doppler shift often fails above the inversion atop the CBL due to poor signal-to-noise ratios. Therefore, this method is not recommended.

The VWV method also only works for CBLs. It focuses on the vertical profile of the variance of the vertical velocity profile σ_w . In a CBL, σ_w is usually greatest at a height that is between 0.35 and 0.4 times the inversion height. Thus, in principle, this is an extrapolation method. It has been attempted for sodar measurements because it permits MLH detection up to heights that are 2.5 times above the highest that can be probed (usually between 500 and 1000 m) with a sodar. *Beyrich* [23.22] classified this method as unreliable.

23.4 Devices and Systems

This section describes typical configurations of current sodar and RASS systems (see Fig. 23.2 for an overview of different techniques and instruments).

23.4.1 Sodars and Minisodars

The Doppler beam swinging (DBS) technique [23.27] is the standard technique used by sodars. It is different from the usual technique employed by Doppler wind lidars (see Chap. 27), which uses conical scanning to get wind information from different directions. With DBS, at least three—but often five—beams are subsequently emitted in different directions. Two (or four) beams at right angles to each other are emitted at zenith angles of $\approx 15^\circ$; the third (or fifth) beam is emitted vertically. The angle between the slanted beams should be as low as possible to receive the three (or five) different sets of information, which are later used to compute the three orthogonal wind components from air volumes that are close together. If the angle becomes too small, the computation of horizontal wind components

from near-vertical radial velocity components along the beams becomes too uncertain. There is a trade-off between getting information from air volumes that are close together and the certainty with which the horizontal wind components can be computed.

The radial wind component along a beam with a zenith angle δ and an azimuth angle ϕ is composed of all three Cartesian wind components u (towards the east), v (towards north), and w (upwards), i.e.,

$$v_r(\delta, \phi) = u \sin \delta \sin \phi + v \sin \delta \cos \phi + w \cos \delta. \quad (23.23)$$

Inversely, all three Cartesian components can be computed from (at least) three radial velocities in different noncoplanar directions.

Equations (23.12) and (23.13) show that sound attenuation in the atmosphere is strongly frequency dependent. Higher frequencies are attenuated much faster than lower frequencies. Therefore, sodars that are designed to have larger ranges operate at

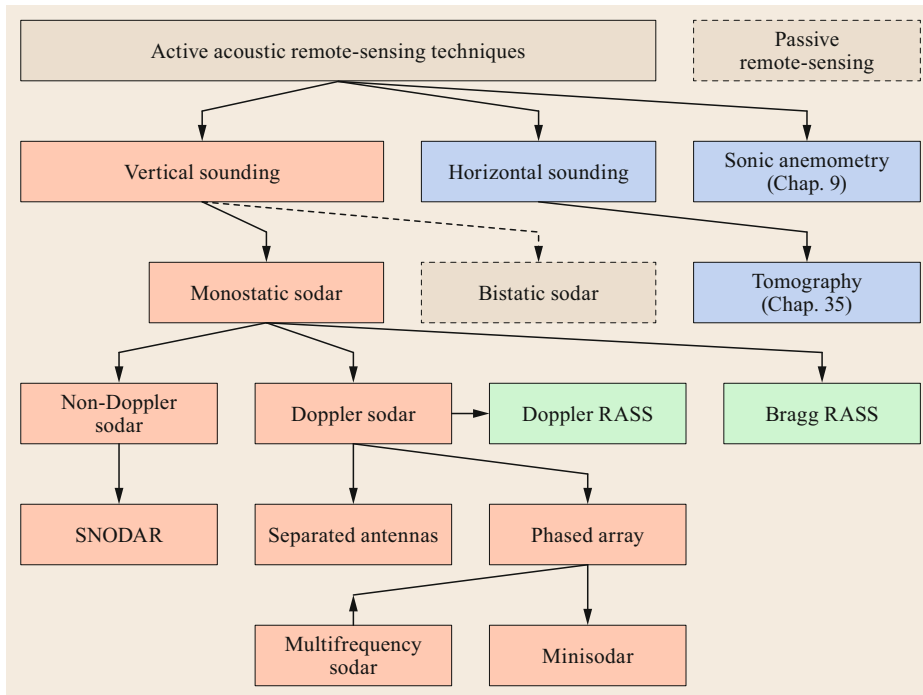


Fig. 23.2 Organigram of acoustic sounding techniques. Techniques in *brown boxes* and *green boxes* are presented in this section. Techniques in *blue boxes* are introduced in other sections. Techniques in *dashed boxes* are not relevant to this chapter

≈ 1500 Hz. However, a second class of sodars has been developed—*minisodars* [23.28]—that are optimized for short-range measurements (up to ≈ 200 m AGL). This shorter range permits more measurement cycles because the time that the sodar must wait to receive the reflected pulse is also shorter. Furthermore, environmental noise is reduced somewhat compared to standard sodars. Minisodars are usually designed for use as phased-array sodars (see Sect. 23.4.1).

Sodars with Antennas

The first Doppler sodars utilized three parabolically shaped antennas (horns) that could be aligned in three different directions (Fig. 23.3). In such systems, the bottom of each antenna has one or a few sound transducers that are operated simultaneously. The transducers first act as loudspeakers and are then switched electronically to act as microphones. The shape of the antenna helps to focus the sound beam. In addition, the antennas at least partially prevent noise interference from reaching the sound transducers and shield the region close to the instrument from excessive sound pulses, which could damage unprotected ear drums. The most suitable and common alignment used in these systems is one where two antennas are inclined by a zenith angle of $\approx 15^\circ$ and have an azimuth angle of 90° between them, while the third antenna is adjusted to be precisely vertical. The sound transducers in the three antennas are oper-



Fig. 23.3 Sodar with three antennas (horns) (photo © Stefan Emeis)

ated sequentially in order to prevent interference from the other antennas. The waiting time between two sound emissions from different antennas must at least be twice the travel time of the sound pulse to the maximum range of the instrument.

Phased-Array Sodars

Phased-array sodars were first constructed in 1989 [23.29]. They are systems in which a field (array) of acoustic transducers is responsible for forming and directing beams (Fig. 23.4). Between 16 and 64 acoustic transducers are usually arranged in a planar array and adjusted to create a defined phase relationship between them. The array of transducers is operated such that sound beams are formed due to interference



Fig. 23.4 Phased-array sodar with 64 sound transducers and no enclosure (photo © Helmut Mayer)

between the sound waves from the individual loudspeakers (Fig. 23.5). These beams are comparable to the beams described above for the systems with antennas. The whole system requires an enclosure that protects the system from environmental noise and ensures that operators and people passing by do not experience dangerous sound levels.

Monostatic and Bistatic Sodars

In a monostatic sodar, the receiver is close to the emitter. The intensity of the backscattered signal depends only on temperature fluctuations in the atmospheric boundary layer. Monostatic sodars have the advantage of compactness, and the instruments are more readily deployed in the field because the instrument package is self-contained. This is the standard configuration of presently available sodars.

In a bistatic sodar, the receiver is deployed away from the emitter. In this case, velocity fluctuations in the atmosphere also contribute to the intensity of the backscattered signal. The Doppler shift and scattering cross-section for bistatic sodars were analyzed by *Thomson and Coulter* [23.30] and *Wesely* [23.31]. Early experiments with bistatic sodars are described in [23.32, 33]. While bistatic sodars have been constructed and used in experiments, there are no commercially available bistatic sodars. Recent studies utilizing these sodars can be found in [23.34, 35].

Other sodar designs [23.36] in which several receivers are arranged around one central sound source (multistatic sodars) have also been proposed. This should allow all three components of the wind to be detected for the same atmospheric volume. Such instruments could be operated in complex terrain without the need to correct for curved streamlines (see Sect. 23.6.3).

Mono- and Multifrequency Sodars

In addition to monofrequency sodars, multifrequency sodars are available. These emit a series of pulses with different frequencies within one shot. Field tests have proven that the multifrequency technique has significant advantages. The use of, say, eight different frequencies halves the minimum acceptable signal-to-noise ratio compared to single-frequency sounding. Moreover, the multifrequency mode improves the accuracy of the instantaneous values of measured parameters and significantly increases the ability to reliably recognize noisy echo signals. Further details regarding multifrequency sodars are given in [23.37].

The principles of pulse code methods that are used to enhance the range and data availability are reviewed and investigated in [23.38]. In particular, detailed simulations are performed using weather-like targets, a comb of frequencies, a chirp, and a phase-encoding method. Three Doppler-adaptive matched filters are described, and two of these are evaluated against the simulated noisy atmosphere. It is found that the comb of frequencies produces the least variance in the estimated Doppler wind speed. A filter based on a single evaluation of a Fast Fourier Transform of the received signal provides Doppler wind measurements to an accuracy of about 1%. The Doppler-adaptive filters add little computational or hardware overhead, and produce a simple output consisting of the best estimate for the wind speed component.

Non-Doppler Sodars

The first sodars were non-Doppler sodars. Later, Doppler sodars became the standard, and now nearly all commercially available sodars are Doppler sodars. Nevertheless, a few non-Doppler sodars do exist. An example is a special sodar developed for use in extremely cold environments. This SNODAR (surface layer non-

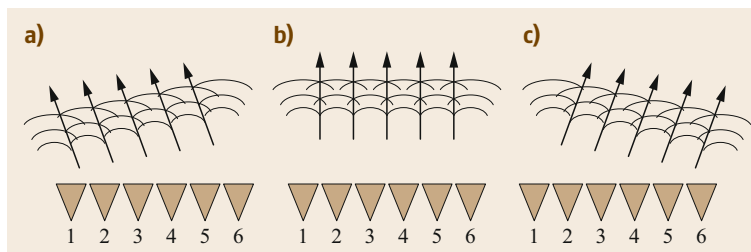


Fig. 23.5a–c Measurement principle of phased-array sodars. (a) Loudspeaker 6 fires first and loudspeaker 1 last, (c) loudspeaker 1 fires first and loudspeaker 6 last, and (b) all loudspeakers operate simultaneously

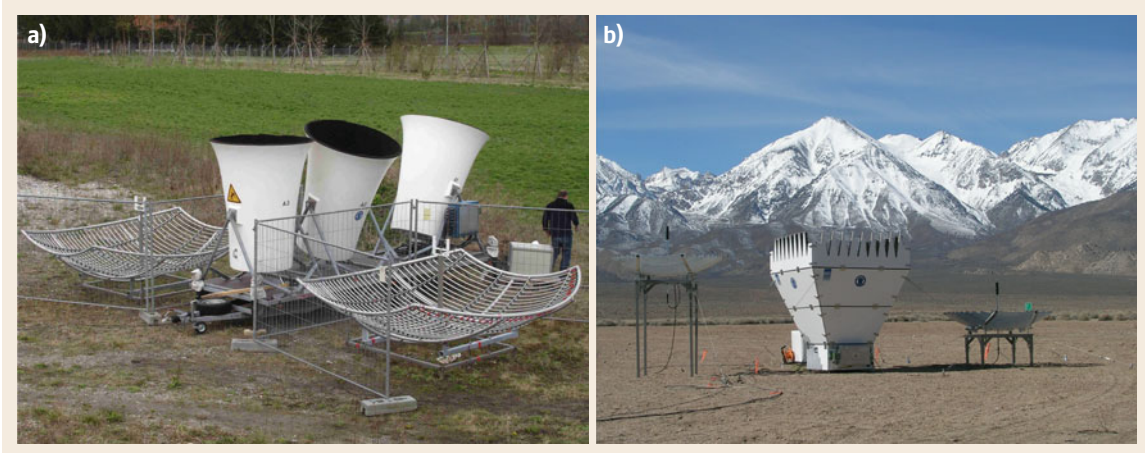


Fig. 23.6a,b Doppler RASS with the acoustic (sodar) instrument at the center and radio antennas to the left and right: (a) 475 MHz system (photo © Stefan Emeis); (b) 1290 MHz system (photo © METEK GmbH, Elmshorn)

Doppler acoustic radar) is designed to measure the height and turbulence intensity of the atmospheric boundary layer above the Antarctic plateau. This is, for example, useful to astronomers who are planning to install future optical telescopes there. SNODAR works by sending an intense acoustic pulse into the atmosphere and listening for backscatter from inhomogeneities resulting from temperature gradients and wind shear. Its operating principle is very similar to that of a well-known underwater sounding technique: SONAR. SNODARs are monostatic sodars with a minimum sampling height of 5 m, a range of at least 200 m, and a vertical resolution of 1 m. They operate at frequencies of between 4 and 15 kHz. Sound waves with such high frequencies propagate relatively well in the low temperatures of the Antarctic atmosphere [23.39].

23.4.2 RASS

There are two types of RASS. One (known as a *Doppler RASS*) is a combination of a sodar with a continuous-wave electromagnetic transmitter and receiver; the other (known as a *Bragg RASS*) is a wind profiler radar (see Chap. 31 and [23.11]) combined with a continuous sound transmitter. The latter combination is sometimes also called a wind-temperature radar (WTR).

Sodar RASS (Doppler RASS)

In today's terminology, the first RASS, which was first designed and built by *Marshall et al.* [23.8], was a Doppler RASS in which acoustic pulses were pursued by continuous electromagnetic radiation emitted from a transmitter (Fig. 23.6). Altitude assignment is achieved for a RASS by measuring the propagation time of the acoustic pulses, much as in a sodar; the time taken for the electromagnetic pulses to return is

negligible. The observed frequency shift of the electromagnetic backscatter signal is interpreted as a Doppler shift. The emitted acoustic pulse is a chirp over a selected sound frequency range that is centered on the Bragg resonance frequency to guarantee that the Bragg condition is met for all temperatures.

Wind Profiler RASS (Bragg RASS)

Adding a sound source to a radar wind profiler yields a Bragg RASS or wind-temperature radar (Fig. 23.7). The first attempts to use such combinations were confronted with the problem that a Stokes shift rather than a Doppler shift was observed [23.40]. *Peters et al.* [23.41] showed that instead of measuring the Doppler frequency, the desired information can be extracted from the Bragg resonance curve. The Bragg resonance is obtained by varying the acoustic frequency and monitoring the backscatter maximum. Whereas the Doppler shift of the backscattered electromagnetic radiation provides information on the speed of sound when using a Doppler RASS, the Bragg resonance provides the acoustic wavelength when using a Bragg RASS (i.e., the acoustic wavelength is measured instead of the speed of sound). To achieve this, a Bragg RASS continuously transmits an acoustic frequency spectrum which is centered on the Bragg resonance frequency. This is in marked contrast to the single pulses transmitted by a Doppler RASS.

23.4.3 Comparison of the Methods

Different types of sodars and RASS have been developed for different measurement purposes, although the presence of various types also reflects the historical development of these instruments. Table 23.7 gives a concise overview of the advantages and disadvantages

Table 23.7 Advantages and disadvantages of the different types of sodars and RASS

Device	Advantages	Disadvantages
Sodar with antennas	Higher vertical range	Heavier instrument—a lorry is needed for deployment
Phased-array sodar	Smaller and lighter instrument—can be transported by a sport utility vehicle (SUV)	Reduced vertical range
Minisodar ($f_a \gtrsim 4000$ Hz)	Higher vertical resolution	Limited vertical range (200–300 m)
Bistatic/multistatic sodar	Velocity fluctuations also produce backscatter when using a multistatic sodar, all three wind components can be measured in the same atmospheric volume	More complicated deployment—all receivers must be connected to the grid and to data transfer, still very experimental
Multifrequency sodar	Higher signal-to-noise ratio, higher range	Enhanced electronics, noise interference
Non-Doppler sodar	Simpler technique and data evaluation	No wind velocity can be obtained
Doppler RASS	Higher vertical resolution, relatively portable, simpler technology, less expensive	Lower range
Wind profiler RASS	Lower vertical resolution	Higher range, not usually portable, more complicated technology, expensive



Fig. 23.7 A Bragg RASS with the radar instrumentation (wind profiler radar) at the center and additional acoustic sources (orange cylinders) next to it. The whole system is surrounded by a fence to prevent interference from other manmade sources of electromagnetic waves (e.g., radar and television emitters) (photo © Stefan Emeis)

of the different types of sodars and RASS. The first six rows refer to sodars, and the last two rows to RASS. Note that the first four rows refer to instruments with

different layouts. The advantages and disadvantages presented in rows 5 and 6 could—at least in principle—apply to any of the sodars referred to in rows 1–4.

23.5 Specifications

This section summarizes information on the measured parameter accuracies and ranges that can be obtained with sodar and RASS measurements. Noise protection rules and electromagnetic permit procedures are also discussed.

23.5.1 Measured Parameter Accuracies and Ranges

The measured parameter accuracies and ranges for sodars and RASS are summarized in Table 23.8. The range of wind speed values is limited by the accu-

racy at the lower end and by environmental noise and noise generated at the edges of the instrument at the upper end. The range of temperature values is only limited by the selected frequency range of the acoustic chirp (Doppler RASS) or the continuous acoustic signal (Bragg RASS).

23.5.2 Permits Required for RASS Operation

RASS devices emit radio waves that can interfere with other telecommunication services. National regulations on the allocation of operating frequencies must

Table 23.8 The accuracies and ranges of wind, turbulence, and temperature measurements obtained using sodars and RASS (based on [23.4, 9])

Parameter	Accuracy	Range
Wind speed (radial wind component)	0.3 m s ⁻¹ for a single measurement; 0.05 m s ⁻¹ for the average of 40 measurements	0.05 to ≈ 20 m s ⁻¹
Wind speed (computed from the radial wind components)	0.3–0.5 m s ⁻¹ for the average of 10 min of measurements	0.3 to ≈ 20 m s ⁻¹
Standard deviation of the vertical wind component	0.16 m s ⁻¹ based on 40 measurements	0.16 to several m s ⁻¹ (no real upper limit)
Temperature	0.5 K; error of 1.7 K per 1 m s ⁻¹ of the unknown vertical wind component (averaging reduces this error; see (23.7))	No principal limit for the temperature range; it depends on the width of the frequency spectrum of the acoustic signal. Doppler RASS: no temperature data for wind speeds ≈ 12–15 m s ⁻¹ because the wind drifts the sound pulse away from the focus of the receiving electromagnetic antenna

therefore be observed when using such systems. In Germany, the standard RegTP 321 ZV 044 [23.42], which references certain international regulations, applies in this context. An application for a permit to operate a RASS must be filed with the Bundesnetzagentur für Elektrizität, Gas, Telekommunikation, Post und Eisenbahnen (RegTP; the Federal Agency for Electricity, Gas, Telecommunication, Post and Railroad Grids).

23.5.3 Compliance with Noise Regulations

In Germany, the operator of a sodar or a RASS must comply with standards and statutory regulations that are relevant to noise, such as the EU's Noise Directive 2003/10/EC [23.43], the German Federal Immission Protection Law (BImSchG [23.44]), or the guideline VDI 2058 Part 2 [23.45]. An a priori application for a permit is not required in Germany.

23.6 Quality Control

General quality assurance and quality control procedures are described in Chap. 3. In this section we focus on quality assurance and quality control procedures that are specific to sodar and RASS devices.

The quality of wind and temperature data from sodar and RASS devices depends mainly on the signal-to-noise ratio (i.e., the intensity ratio of the backscattered signal to the background noise) and the quality of the data evaluation algorithm used. Sodar and RASS devices are usually shipped with built-in data evaluation algorithms. The manufacturers of these devices should

indicate the minimum signal-to-noise ratio that must be attained in order to extract meaningful data from the built-in data evaluation algorithms. The temporal and vertical consistency of the final wind and temperature data provides valuable insight into the reliability of the retrieved data. Table 23.9 gives an overview of common instrument errors.

The signal-to-noise ratio usually decreases with increasing range because the backscattered sound intensity decreases with the square of the range (Sect. 23.3.1). The maximum range is frequency de-

Table 23.9 Typical measurement errors with sodars or RASS

Instrument	Error(s)	Reason(s)
Sodar	No wind data	Antenna is covered with snow, technical failure of instrument
Sodar	Low vertical range, spatially and temporally inconsistent data	Signal-to-noise ratio is too low due to ambient noise (could be caused by rain or very high wind speeds), intensity of atmospheric turbulence is too low to cause sufficient acoustic backscatter
Sodar	Low vertical range in wind data during morning or afternoon	Atmosphere nearly adiabatic
Sodar	Wind speed minima in vertical profiles always occur at the same height (and backscatter intensity is enhanced)	Fixed echo, azimuth angle of antenna must be adjusted or a better measurement site is needed
RASS	No temperature data	Technical failure of instrument
RASS	Missing temperature data for certain heights and for a limited period	Excessive wind speeds (often due to nocturnal low-level jets) have blown the signal away from the focus of the receiving electromagnetic antenna

pendent (Sect. 23.3.1). The signal-to-noise ratio can be strongly influenced by environmental noise at the measurement site. Noise with the same frequency as the emitted sound pulses is especially problematic. Measurement sites in noisy industrial areas or close to motorways or railway lines should be avoided. The signal-to-noise ratio is also degraded by strong winds, as such winds can generate noise in the vicinity of the instrument or even at the edges of the instrument itself.

Some manufacturers also supply data processing software with their instruments. Such software often include visualization tools (e.g., to display time–height cross-sections of the retrieved data), printing options, and data export options. Key parameters that can be entered into the software include temporal and vertical averaging intervals and the start and end dates of the data to be processed.

Some manufacturers provide access to the raw data obtained by the instruments. The analysis of such raw data requires special skills. The processing of raw data may be helpful when attempting to detect and explain inconsistencies in the data sets or to calculate nonstandard output variables.

23.6.1 Wind Speed Calibration

Wind speeds from sodar and RASS devices do not require calibration as long as signal-to-noise ratios are high enough to permit the accurate measurement of the Doppler-induced frequency shift using the built-in data evaluation algorithm. Wind speed data are obtained from Doppler shift analysis using a basic physical principle that does not require any calibration. Nevertheless, it is useful to check the resulting data against the corresponding data provided by a cup anemometer or a sonic anemometer on a mast. Note that it is important to take differences in measurement principles (volume measurements with a sodar or RASS and almost point measurements with a cup or sonic anemometer) into account when comparing data from remote-sensing instruments with in-situ data.

23.6.2 Temperature Calibration

Temperature data from a RASS device do not require calibration as they are derived using a basic physical phenomenon: the detection of the speed of sound in air. This speed is a function of temperature and humidity only (see Sect. 23.3.1). Nevertheless, it may be useful to check the data against that afforded by a thermometer. Again, differences in measurement principles (volume measurements with a RASS and almost point measure-

ments with a cup anemometer) should be taken into account when comparing data from remote-sensing instruments with in-situ data.

23.6.3 Specific Quality Control Methods

The calculation of wind speeds using monostatic remote-sensing devices such as sodars and RASS is based on the assumption that the streamlines are straight (no curvature in any direction) within the measurement volume defined by the separate beams in the Doppler beam swinging technique (see Sect. 23.4.1) or by the walls of the cone in conical scanning. The presence of streamlines that are curved towards the instrument causes the wind speed to be underestimated, whereas the presence of streamlines that are bent away from the instrument leads to an overestimated wind speed [23.46]. Thus, wind data from ground-based remote sensing on a hilltop are lower than the true wind speeds above the instrument, whereas wind data obtained in a valley are higher than the true wind speeds. Some manufacturers claim that they have built-in corrections for streamline curvature in their evaluation algorithms. These corrections cannot be rated here, because the manufacturers do not disclose how their algorithms calculate such corrections. The best way to determine the necessary corrections to the measurements is to run a flow model in conjunction with the instrument. This curvature problem occurs with sodars as well as with wind lidars (Chap. 27).

Measured wind speeds and turbulence data (i.e., the variance of the vertical wind component) must be checked for the impact of fixed echoes (Sect. 23.3.1). Fixed echoes lead to wind speeds that are lower than they should be because reflections from immobile objects are included in the data. Fixed echoes usually occur at a certain height above the ground that corresponds to the direct (diagonal) distance between the remote-sensing device and the object that is generating the fixed echoes. Thus, wind speeds that are consistently lower than expected at a particular height may be indicative of fixed echoes. Another clue that fixed echoes are occurring is the presence of very high backscatter intensities, because most solid objects reflect sound waves much better than the atmosphere does. It is not possible to correct for fixed echoes a posteriori. The best way to deal with them is to discard the flawed wind and turbulence data.

Temperature data are not influenced by curved streamlines because temperature is derived using vertical sound emission only. Temperature sounding also does not suffer from fixed echoes. Thus, for a Doppler

Table 23.10 Maintenance of sodars and RASS

Maximum interval	Sodar (all types)	Doppler RASS	Bragg RASS
Daily	Check incoming data for consistency		
Daily	Perform a visual check of the instrument (unless the site is within a well-guarded and supervised area)		
Every 3 months	Check that all loudspeakers are functioning properly	Check that all loudspeakers and antennas are functioning properly	
Every 2 years	Check all electrical cables and devices		

RASS, the maximum range of the temperature data is usually considerably higher than the maximum range of the wind data.

Temperature determination can be hampered by high wind speeds. In this case, the sound waves emitted from the Doppler RASS are blown outside the

focus of the receiving radio antenna. Thus, it is sometimes impossible to detect the temperature in areas with high wind speeds caused by nocturnal low-level jets. Depending on the size of the instrument, temperature determination can be problematic when wind speeds are $> 10\text{--}15\text{ m s}^{-1}$.

23.7 Maintenance

Just like any device that is connected to the electrical grid and operated outdoors, sodars and RASS devices require technical and electrical maintenance. No additional substances such as gases or liquids have to be supplied during the measurements. The overall amount of maintenance required for such instruments is low (see Table 23.10). Manufacturers' instructions should be followed, and software updates should be uploaded as soon as possible.

A direct connection to the instrument's computer via the internet or mobile telecommunications services is advisable. Error messages issued by the software can give hints about malfunctions. Daily data transfer from the instrument to the operator's institution is recommended. Regular checks of the consistency of the incoming data can provide further insight into potential malfunctions.

23.8 Applications

The most informative data products obtained from ground-based remote-sensing instruments such as sodars and RASS devices are time–height cross-sections of wind speed, wind direction, the vertical component of turbulence, and temperature. The vertical profiles of these parameters can be extracted from time–height cross-sections. Time series of selected parameters (e.g., mixed-layer height) can also be extracted.

An example of real-world data obtained using a sodar is presented in Fig. 23.8, which shows the daily variation in the horizontal wind in an alpine valley during a clear-sky day. Steady southerly to southwesterly winds representing the down-valley flow are seen to occur from 10 p.m. to 8 a.m. (GMT+1), whereas turbulent northerly to northeasterly winds representing the up-valley flow are observed between 10 a.m. and 8 p.m.

Another real-world dataset provided by a sodar is depicted in Fig. 23.9, which shows a perfect example of the measurement of wind speeds in a nocturnal low-level jet. The maximum wind speed along the axis of the jet is $\approx 12\text{ m s}^{-1}$, whereas the wind speed underneath

and above the jet is $\approx 5\text{ m s}^{-1}$. The measurements were performed in a very quiet environment, which made it possible to observe the upper part of the low-level jet, where the wind speed decreases with height (very often, a sodar can only measure wind speeds below the jet axis, not those above it).

A final example (Fig. 23.10) shows the diurnal temperature variation in the lower atmospheric boundary layer on a clear-sky day, as measured with a Doppler RASS. Potential temperature data are presented. In the early morning (between 2 a.m. and 10 a.m. GMT+1), cold air (blue) occurs near the surface. Warmer air (green) occurs above the cold air. At ≈ 10 a.m., vertical mixing starts, and soon afterwards the air is well mixed vertically until ≈ 6 p.m. Then cooling sets in again near the surface while the air remains warm above. The white area in the upper right corner corresponds to missing data. Data are missing from this region because high wind speeds caused by a low-level jet drifted the sound pulse from the Doppler RASS out of the focus of the receiving electromagnetic antenna.

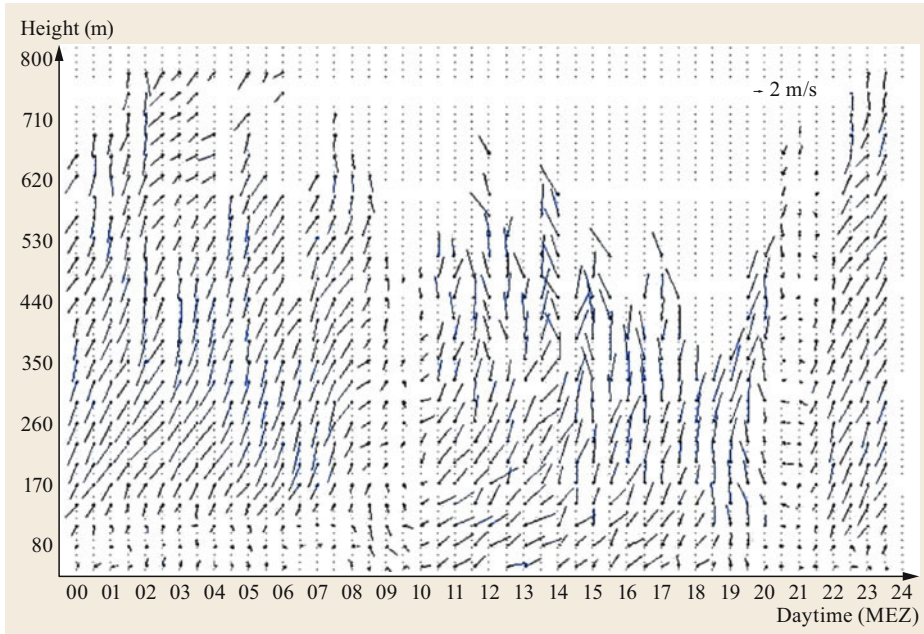


Fig. 23.8 Time–height cross-section of horizontal wind vectors measured over the course of one day (x -axis) for heights of 50–800 m AGL using a three-antenna sodar. Time resolution: 30 min; height resolution: 30 m. Arrow length is proportional to wind speed (see the legend in the *upper right corner*). Arrow direction indicates the wind direction (upward: wind from the south; to the right: wind from the west; etc.). Measurements were performed in an almost north–south-oriented valley on the northern side of the Alps at Oberau (Germany) on 8 May 1998

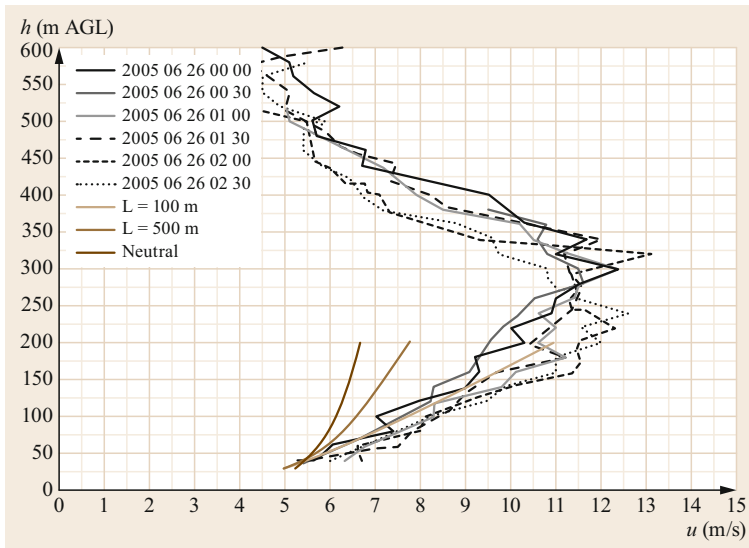


Fig. 23.9 Nocturnal vertical wind-speed profiles obtained with a three-antenna sodar; the profiles show the presence of a low-level jet at ≈ 300 m AGL. Six wind speed profiles (each averaged over 30 min) obtained for heights ranging from 40 to 600 m AGL (vertical resolution: 20 m) are plotted. The measurements were performed at the Charles-de-Gaulle Airport in Paris (France) during the first three hours of 26 June 2005

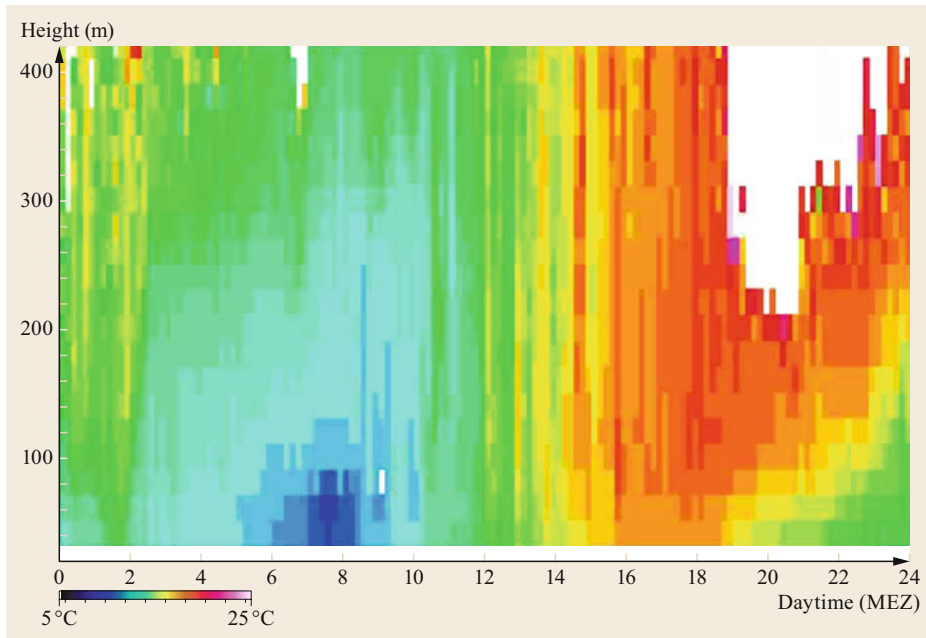


Fig. 23.10 Time–height cross-section of potential temperatures on a clear-sky day measured over a period of 24 h (local time) for heights of 40–420 m (vertical resolution: 20 m) using a Doppler RASS. Colors (see the color bar at the *lower right*) indicate potential temperatures ranging from 5 °C (*dark blue*) to 25 °C (*purple*). The measurements were performed at the northern outskirts of Augsburg (Germany) on 6 April 2009

23.9 Future Developments

Although they are relatively old techniques, there is still a need for these vertical sounding devices that actively emit sound waves. While wind profile measurements are increasingly being performed with wind lidars rather than sodars (because wind lidars offer enhanced data availability and do not suffer from environmental interference), RASS are still the best available devices for measuring the temperature profiles of the lower regions of the atmospheric boundary layer. Passive radiometers have much poorer vertical resolution, meaning that they are generally not well suited to boundary layer studies. Raman lidars also have deficiencies, especially during the daytime, when the intense short-wave solar radiation causes interference.

Apart from classical scientific boundary layer studies, new fields of application for ground-based remote sensing have developed in recent decades, which has reinvigorated the development of acoustic sounders. One of the most important of these new fields of application is wind energy (see Chap. 51 and [23.3]). Wind energy requires highly vertically and temporally resolved wind, turbulence, and temperature profile

data for site assessments, yield forecasts, and load assessments. While site and load assessments are especially valuable for the manufacturers of wind turbines, yield forecasts are mandatory for electrical grid operators and for successful trade actions at energy exchanges.

Another field in which sodars and RASS have been deployed in the last few decades is urban studies. However, in this case, the active emission of sound waves is a disadvantage of these instruments, as it is becoming increasingly difficult to find acceptable measurement sites for sodars and RASS in densely populated areas. Therefore, researchers are attempting to develop measurement configurations that shield urban populations from the emitted sound waves. One such configuration is the bistatic sodar (see Sect. 23.4.1), in which the vertical emission of sound pulses is well shielded and the receiver is located away from the instrument.

Methods of correcting wind profile data from sodars (and wind lidars) located in complex terrain (see Sect. 23.6.3) are still being developed. Some manufacturers offer built-in correction algorithms, although they do not explain how they work. Others suggest running

simple flow models in parallel with the measurements to obtain the necessary corrections. Attempts to produce feasible correction algorithms for ground-based monostatic wind profilers operating in complex terrain will

continue even if sodars start to disappear, because wind lidars have the same problem.

In the long run, the importance of acoustic sounding techniques will decrease.

23.10 Further Reading

A general overview of acoustics can be found in

- Rossing, T.D. (ed.): Springer Handbook of Acoustics, 2nd edn. (Springer, 2014).

The standard resource on sodars is the book by Bradley [23.6]. There is no corresponding book on RASS devices. The bilingual VDI Guideline 3786 Part 18 [23.9] is most probably among the most concise sources of information in this regard.

A general overview of ground-based remote sensing of the atmospheric boundary layer can be found in [23.1].

A short overview of all atmospheric measurement techniques can be found in

- Emeis, S.: Measurement Methods in Atmospheric Sciences. In-situ and remote. (Borntraeger, Stuttgart 2010), XIV + 257 pp.

The 2014 edition of the WMO Guide to Meteorological Instruments and Methods of Observations (WMO No. 8) covers radar in detail but mentions sodars and RASS only briefly (in Chapter 5 of Part II).

References

- 23.1 S. Emeis: Surface-Based Remote Sensing of the Atmospheric Boundary Layer. In: *Atmospheric and Oceanographic Sciences Library*, Vol. 40 (Springer, Berlin, Heidelberg 2011)
- 23.2 S. Emeis: Upper limit for wind shear in stably stratified conditions expressed in terms of a bulk Richardson number, *Meteorol. Z.* **26**, 421–430 (2017)
- 23.3 S. Emeis: *Wind Energy Meteorology – Atmospheric Physics for Wind Power Generation*, Green Energy and Technology, 2nd edn. (Springer, Berlin, Heidelberg 2018)
- 23.4 VDI 3786 Part 11:2015–07: *Environmental Meteorology: Ground-Based Remote Sensing of the Wind Vector and the Vertical Structure of the Boundary Layer – Doppler Sodar* (Beuth, Berlin 2015)
- 23.5 G. Peters: SODAR – Ein akustisches Fernmeßverfahren für die untere Atmosphäre, *Promet* **21**, 55–62 (1991)
- 23.6 S. Bradley: *Atmospheric Acoustic Remote Sensing – Principles and Applications* (CRC Press, Boca Raton 2007)
- 23.7 W.H. Bragg, W.L. Bragg: The reflection of X-rays by crystals, *Proc. R. Soc. A* **88**, 428–438 (1913)
- 23.8 J.M. Marshall, A.M. Peterson, A. Barnes: Combined radar-acoustic sounding system, *Appl. Opt.* **11**, 108–112 (1972)
- 23.9 VDI 3786 Part 18: *Environmental Meteorology: Ground-Based Remote Sensing of Temperature Radio-Acoustic Sounding Systems (RASS)* (Beuth, Berlin 2010)
- 23.10 D.A.M. Engelbart, J. Bange: Determination of boundary-layer parameters using wind profiler/RASS and sodar/RASS in the frame of the LITFASS project, *Theor. Appl. Climatol.* **73**, 53–65 (2002)
- 23.11 VDI 3786 Part 17: *Environmental Meteorology – Ground-Based Remote Sensing of the Wind Vector – Wind Profiler Radar* (Beuth, Berlin 2007)
- 23.12 ISO 9613-1:1993-06: *Acoustics; Attenuation of Sound During Propagation Outdoors; Part 1: Calculation of the Absorption of Sound by the Atmosphere* (International Organization for Standardization, Geneva 1993)
- 23.13 R. Wexler, D.M. Swingle: Radar storm detection, *Bull. Am. Meteorol. Soc.* **28**, 159–167 (1947)
- 23.14 G.W. Gilman, H.B. Coxhead, F.H. Willis: Reflection of sound signals in the troposphere, *J. Acoust. Soc. Am.* **18**, 274–283 (1946)
- 23.15 V.I. Tatarskii: *The Effect of the Turbulent Atmosphere on Wave Propagation* (Kefer Press, Jerusalem 1971)
- 23.16 M.A. Kallistratova: An experimental investigation in the scattering of sound in the turbulent atmosphere, *Dokl. Akad. Nauk. SSSR* **125**, 69–72 (1959)
- 23.17 M.A. Kallistratova, I.V. Petenko, R.D. Kouznetsov, S.N. Kulichkov, O.G. Chkhetiani, I.P. Chunchusov, V.S. Lyulyukin, D.V. Zaitseva, N.V. Vazaeva, D.D. Kuznetsov, V.G. Perepelkin, G.A. Bush: Sodar sounding of the atmospheric boundary layer: Review of studies at the Obukhov Institute of Atmospheric Physics, Russian Academy of Sciences, *Izv. Atmos. Ocean. Phys.* **54**, 242–256 (2018)
- 23.18 L.G. McAllister, J.R. Pollard, A.R. Mahoney, P.J.R. Shaw: Acoustic sounding – A new approach to the study of atmospheric structure, *Proc. IEEE* **57**, 579–587 (1969)

- 23.19 ECMA-108:2010-12: *Measurement of High-Frequency Noise Emitted by Information Technology and Telecommunications Equipment* (European Computer Manufacturers Association, Geneva 2010)
- 23.20 K. Attenborough: Sound propagation in the atmosphere. In: *Handbook of Acoustics*, 2nd edn., ed. by T.D. Rossing (Springer, New York 2014) pp. 117–155
- 23.21 O. Reitebuch: *SODAR-Signalverarbeitung von Einzelpulsen zur Bestimmung hochaufgelöster Windprofile*, Schriftenreihe des Fraunhofer-Instituts Atmosphärische Umweltforschung, Vol. 62 (Shaker, Aachen 1999)
- 23.22 F. Beyrich: Mixing height estimation from sodar data – A critical discussion, *Atmos. Environ.* **31**, 3941–3953 (1997)
- 23.23 D.N. Asimakopoulou, C.G. Helmis, J. Michopoulos: Evaluation of SODAR methods for the determination of the atmospheric boundary layer mixing height, *Meteorol. Atmos. Phys.* **85**, 85–92 (2004)
- 23.24 S. Emeis, M. Türk: Frequency distributions of the mixing height over an urban area from SODAR data, *Meteorol. Z.* **13**, 361–367 (2004)
- 23.25 S. Emeis, C. Jahn, C. Münkel, C. Münsterer, K. Schäfer: Multiple atmospheric layering and mixing-layer height in the Inn valley observed by remote sensing, *Meteorol. Z.* **16**, 415–424 (2007)
- 23.26 S. Emeis, K. Schäfer, C. Münkel: Surface-based remote sensing of the mixing-layer height – A review, *Meteorol. Z.* **17**, 621–630 (2008)
- 23.27 J. Röttger, J. Klostermeyer, P. Czechowsky, R. Ruster, G. Schmidt: Remote sensing of the atmosphere by VHF radar experiments, *Naturwissenschaften* **65**, 285–296 (1978)
- 23.28 R.L. Coulter, T.J. Martin: Results from a high-power, high-frequency sodar, *Atmos. Res.* **20**, 257–269 (1986)
- 23.29 Y. Ito, Y. Kobori, M. Horiguchi, M. Takehisa, Y. Mitsuta: Development of wind profiling sodar, *J. Atmos. Ocean. Technol.* **6**, 779–784 (1989)
- 23.30 D.W. Thomson, R.L. Coulter: Analysis and simulation of phase coherent acdar sounding measurements, *J. Geophys. Res.* **79**, 5541–5549 (1974)
- 23.31 M.L. Wesely: The combined effect of temperature and humidity fluctuations on refractive index, *J. Appl. Meteorol.* **15**, 43–49 (1976)
- 23.32 R.L. Coulter, K.H. Underwood: Some turbulence and diffusion parameter estimates within cooling tower plumes derived from sodar data, *J. Appl. Meteorol.* **19**, 1395–1404 (1980)
- 23.33 K.H. Underwood: *Sodar Signal Processing Methods and the Risø-78 Experiment*, PhD thesis (Pennsylvania State Univ., University Park 1981)
- 23.34 S. Bradley, S. von Hünenbein, T. Mikkelsen: A bistatic sodar for precision wind profiling in complex terrain, *J. Atmos. Ocean. Technol.* **29**, 1052–1061 (2012)
- 23.35 S. Bradley, J. Barlow, J. Lalley, C. Halios: A sodar for profiling in a spatially inhomogeneous urban environment, *Meteorol. Z.* **24**, 615–624 (2015)
- 23.36 A. Strehz, S. Bradley: Mast comparisons for a new bistatic SODAR design. In: *17th Int. Symp. Adv. Bound.-Layer Remote Sens. (ISARS) Auckland* (2014)
- 23.37 R. Kouznetsov: The multi-frequency sodar with high temporal resolution, *Meteorol. Z.* **18**, 169–173 (2009)
- 23.38 S.G. Bradley: Use of coded waveforms for SODAR systems, *Meteorol. Atmos. Phys.* **71**, 15–23 (1999)
- 23.39 C.S. Bonner, M.C.B. Ashley, J.S. Lawrence, J.W.V. Storey, D.M. Luong-Van, S.G. Bradley: Snodar: A new instrument to measure the height of the boundary layer on the Antarctic plateau, *Proc. SPIE* **7014**, 701461 (2008)
- 23.40 A.I. Kon, V.I. Tatarskii: The scattered signal frequency spectrum for radio acoustical atmospheric soundings, *Izv. Atmos. Ocean. Phys.* **16**, 142–148 (1980)
- 23.41 G. Peters, H. Timmermann, H. Hinzpeter: Temperature sounding in the planetary boundary layer by RASS-system analysis and results, *Int. J. Remote Sens.* **4**, 49–63 (1983)
- 23.42 RegTP: Zulassungsvorschrift für Windprofil-Messradaranlagen, RegTP 321 ZV 044, Juli 1999. In: *Amtsblatt der Regulierungsbehörde für Telekommunikation und Post*, Nr. 1 vom 12.01.2000
- 23.43 Directive 2003/10/EC of the European Parliament and of the Council of 6 February 2003 on the Minimum Health and Safety Requirements Regarding the Exposure of Workers to the Risks Arising from Physical Agents (Noise). <https://eur-lex.europa.eu/legal-content/EN/TXT/?uri=CELEX:02003L0010-20081211>, current version (2019), Accessed 08. July 2021
- 23.44 Bundes-Immissionsschutzgesetz: Gesetz zum Schutz vor schädlichen Umwelteinwirkungen durch Luftverunreinigungen, Geräusche, Erschütterungen und ähnliche Vorgänge (BImSchG). (in German http://www.rechtliches.de/info_BImSchG.html) (2017), Accessed 08. July 2021
- 23.45 VDI 2058 Part 2: *Assessment of Noise with Regard to the Risk of Hearing Damages (Draft)* (Beuth, Berlin 2017)
- 23.46 S. Bradley, A. Strehz, S. Emeis: Remote sensing winds in complex terrain – A review, *Meteorol. Z.* **24**, 547–555 (2015)

Stefan Emeis

Institute of Meteorology and Climate Research
 Karlsruhe Institute of Technology (KIT)
 Garmisch-Partenkirchen, Germany
stefan.emeis@kit.edu



Stefan Emeis is an unsalaried Professor of Meteorology at the University of Cologne, group leader at KIT, and editor-in-chief of *Meteorologische Zeitschrift*. His research mainly involves ground-based remote sensing of the atmospheric boundary layer. He has written books on measurement techniques and wind energy, organized conferences (e.g., ISARS 13, METTOOLS VI), and was awarded the Honorary Medal of the VDI and the Reinhard Süring Medal from the German Meteorological Society.

24. Backscatter Lidar for Aerosol and Cloud Profiling

Christoph Ritter , Christoph Münkel 

Backscatter lidars are relatively simple, hence easy to maintain, active remote-sensing instruments, which is why they can be relied upon to continuously detect cloud and aerosol layers and determine the mixing layer height under convective conditions while unattended. In this chapter, the principle of backscatter lidars and their main components are described; this discussion also serves as an introduction to more sophisticated lidar systems. In addition, we examine the extraction of backscatter profiles and basic aerosol properties from lidar data, which normally requires the selection of an appropriate aerosol-type-dependent lidar ratio. Examples of the applications of these instruments are also provided.

24.1	Measurement Principles and Parameters	684	24.3.6	Transition Method	697
24.2	History	686	24.3.7	Importance of the Lidar Ratio.....	697
24.3	Theory	687	24.3.8	The Color Ratio.....	698
24.3.1	Concept and Basic Lidar Equation	687	24.3.9	Depolarization	699
24.3.2	Background Correction and Properties of Lidar Signals	689	24.3.10	Determination of the Boundary Layer Height by Lidar	699
24.3.3	Solution of the Elastic Lidar Equation	690	24.4	Devices and Systems	700
24.3.4	Simplifications	694	24.4.1	Components of the Emission Optics ...	700
24.3.5	Extensions to the Lidar Equation	695	24.4.2	Recording Optics	701
			24.4.3	Design Considerations.....	704
			24.4.4	Ceilmeters.....	705
			24.5	Specifications	706
			24.6	Quality Control	707
			24.6.1	Hardware Quality Control	707
			24.6.2	Error Analysis.....	708
			24.6.3	Depolarization	709
			24.7	Maintenance	709
			24.8	Applications	710
			24.8.1	Using a Ceilometer as an Autonomous Backscatter Lidar	711
			24.8.2	Caveats Regarding the Stable Boundary Layer Height	712
			24.9	Further Reading	714
			References		714

The word *lidar* is an acronym of *light detection and ranging*. A lidar is an active remote-sensing instrument that uses a light source, usually a pulsed laser, to sound the atmosphere. Particles in the atmosphere backscatter some of the light produced by the lidar, and this backscattered radiation is recorded by a telescope near the laser. Knowledge of the time difference between the emission of the laser pulse and the arrival of the backscattered photons at the telescope allows the altitude of the backscattering event to be determined. In other words, when the lidar is operating, a *lidar profile*

is obtained in which the number of photons P is recorded as a function of time t , which is related to the altitude z of the backscatter event via

$$z = \frac{c}{2t}, \quad (24.1)$$

where c is the speed of light in the atmosphere. The factor of 2 is included in this equation because the recorded photons have to travel the distance z twice: they travel to the altitude at which they are backscattered before traveling back to the telescope.

While lidars are versatile instruments that can measure various environmental quantities, such as aerosol properties (e.g., the extinction coefficient) using the Raman effect (Chap. 25), the wind via the Doppler effect (Chap. 27), trace gas concentrations using the ratio of the lidar profiles at colors that are sensitive or insensitive to the species of interest, or the temperature via the Raman effect for rotational states of molecules, we only consider simple backscatter lidars in this chapter. These instruments collect elastically backscattered light that provides information on aerosols, clouds, and—under convective conditions—the boundary layer altitude. One simple example of such an instrument is a ceilometer, which continuously—and unattended—records the altitudes of clouds and atmospheric visibility for airports and weather services.

24.1 Measurement Principles and Parameters

In this section, optical parameters that are frequently encountered when using backscatter lidars for atmospheric science are defined and discussed. The most important of these are the volumetric backscatter β (unit: $\text{m}^{-1} \text{sr}^{-1}$) and the extinction coefficient α (units: m^{-1}). Both of these parameters actually consist of multiple contributions. One of these contributions is due to scattering from particles (which may be cloud or aerosol particles); another is due to Rayleigh scattering from gases in the atmosphere, even when it is clear. As light that is scattered or attenuated by one atmospheric constituent cannot then interact with another atmospheric constituent, the total backscatter and extinction coefficients are simply the sums of the contributions of the individual components, i.e.,

$$\begin{aligned}\beta &:= \beta^{\text{total}} = \beta^{\text{aer}} + \beta^{\text{Ray}} \\ \alpha &:= \alpha^{\text{total}} = \alpha^{\text{aer}} + \alpha^{\text{Ray}} + \alpha^{\text{absorp}}.\end{aligned}\quad (24.2)$$

Here, the superscripts aer and Ray denote the contributions due to scattering from particles and Rayleigh scattering, respectively. The superscript absorp denotes the fraction of the molecules that absorb the light, because α^{Ray} is only the contribution of Rayleigh extinction to the scattering. The molecules that absorb at wavelengths relevant to lidar are mainly trace gases such as ozone (the Chappuis band) [24.5], water vapor [24.6], and carbon dioxide [24.7].

β^{Ray} , α^{Ray} , and α^{absorp} are proportional to the number concentration of air N_{air} or the absorbing trace gas N_x . Therefore, the Rayleigh and aerosol components of the backscatter and extinction coefficients can easily be separated through the use of radio sounding data

The extinction coefficient and the asymmetry parameter of the scattering are generally the most important quantities which determine the (generally unclear) radiative forcing of aerosol [24.1]. Nevertheless, even simple backscatter lidars can provide important information on aerosols. For example, backscatter lidars were used to track the volcanic ash plumes that restricted air traffic in Europe in 2010 [24.2]. Moreover, backscatter profiles from lidar data have been used to improve or constrain cloud properties in climate models; for example, data from the spaceborne CALIPSO lidar were employed in [24.3]. The height of a convective boundary layer can also be derived using backscatter lidar data, as demonstrated in [24.4].

obtained at a nearby site or the density profile of an appropriate atmosphere.

Both the backscatter and extinction are extensive quantities, meaning that they do not depend on the size of the physical system (i.e., the aerosol number concentration in our case). For example, an increased value of the backscatter coefficient at a particular altitude simply means that there is additional scattering at this height. It cannot tell us why this is—it may be that a few particles are scattering the light unusually efficiently, or there could be high abundance of weakly scattering aerosol particles.

The backscatter and extinction coefficients are generally also functions of the wavelength λ of the incoming light. The only important exception arises when the scattering or absorption is due to large particles in clouds. In cirrus clouds, for example, the diameters of ice crystals can exceed $100 \mu\text{m}$ [24.8]. These particles are so large that the *gray approximation* holds for electromagnetic waves in the visible spectrum, which simply means that β and α are independent of wavelength. Aerosol particles are, in contrast, much smaller, so the scattering and absorption depend on the wavelength of the light. The coefficients are frequently assumed (or measured) to have a power-law-like wavelength dependence, such as

$$\begin{aligned}\alpha^{\text{aer}}(\lambda) &= C_1 \lambda^{A_a} \\ \beta^{\text{aer}}(\lambda) &= C_2 \lambda^{A_b},\end{aligned}\quad (24.3)$$

where A_a and A_b are the Ångström exponents for the extinction and backscatter [24.9]. The values of these exponents lie in the interval $[-4. . . 0]$, with the Rayleigh limit (i.e., the particles are much smaller than the wave-

length) as the lower bound and the gray approximation as the upper bound.

Instead of determining A_b from multiwavelength lidar data, sometimes the color ratio (CR) is defined as the ratio of the aerosol backscatter for different colors, i.e.,

$$\text{CR}(\lambda_1, \lambda_2) = \frac{\beta^{\text{aer}}(\lambda_1)}{\beta^{\text{aer}}(\lambda_2)}. \quad (24.4)$$

Here $\lambda_1 < \lambda_2$, meaning that $\text{CR} \geq 1$. The color ratio is an intensive quantity, as it is determined by the size of the particles, not their concentration. Hence, the addition of a second color to a lidar system has the advantage that approximate size information can be obtained. According to the definition of A_b , the color ratio goes to 1 when the grey approximation holds, while $\text{CR} \rightarrow (\lambda_2/\lambda_1)^4$ at the Rayleigh limit.

Using the fact that many lasers emit linearly polarized light, the aerosol linear depolarization ratio δ^{aer} can be defined as the ratio of the aerosol backscatter coefficients for the polarization states perpendicular and parallel to the laser; in other words,

$$\delta^{\text{aer}}(\lambda) = \frac{\beta_{\perp}^{\text{aer}}(\lambda)}{\beta_{\parallel}^{\text{aer}}(\lambda)}. \quad (24.5)$$

Note that δ^{aer} may also be defined as the ratio of the perpendicular polarized backscatter to the sum of the backscatter polarized in the parallel and perpendicular directions [24.10]. Using Mie theory, it can be shown that backscattering by spherical particles does not change the polarization of the light, whereas backscattering from nonspherical particles usually does. Uniformly spatially oriented symmetric ice crystals for which the vertical dimension is the smallest one (e.g., ice plates) are the only exception to this (i.e., backscattering from such crystals results in a negligible change in polarization), but these crystals can be distinguished from spherical particles by pointing the lidar just a few degrees away from the vertical [24.11]. Hence, by inserting an additional recording branch into the lidar to examine the polarization of the light, the shape and thus the state of aggregation (given that liquid particles are almost spherical due to surface tension) of the scattering particles can be determined. The value of δ^{aer} would be expected to be about zero for a liquid aerosol, up to around 30% for desert dust [24.12], and more than 50% for cirrus clouds [24.13]. The aerosol depolarization ratio has the advantage that it depends solely on the properties of the aerosol, not on the molecular contribution (Rayleigh scattering). However, aside from cirrus clouds and desert dust, aerosols always have $\beta_{\perp}^{\text{aer}} < \beta_{\parallel}^{\text{aer}}$, so δ^{aer} can become quite noisy. For this reason, the volume depolarization or total depolarization

ratio δ^{tot} is sometimes used. This is defined as the ratio of the lidar signals in the two orthogonal polarization states [24.14],

$$\delta^{\text{tot}} = \frac{P_s}{P_p}. \quad (24.6)$$

The attenuated backscatter coefficient B may also be used [24.15]. The attenuated backscatter is defined via the simple elastic lidar equation (see Sect. 24.3) as

$$B(z) = \beta(z) \exp\left(-2 \int_{z_0}^z \alpha(\hat{z}) d\hat{z}\right) = \frac{1}{C} P(z) z^2. \quad (24.7)$$

The backscatter coefficient B has units of $\text{m}^{-1} \text{sr}^{-1}$, so it has the advantage of reducing the basic lidar equation to just one unknown, which can be readily derived from the measured signal once the lidar constant C is known. However, the extinction and backscatter coefficients are more useful for constraining the radiative forcing of an aerosol [24.16].

It is also common to denote the product

$$S(z) = P(z) z^2 \quad (24.8)$$

as the range-corrected signal.

A more frequent method of solving the lidar equation is presented in Sect. 24.3. To achieve this, a relation between the backscatter and extinction is required; the *lidar ratio* (LR) is commonly used, which is defined as

$$\text{LR}(\lambda) = \frac{\alpha^{\text{aer}}(\lambda)}{\beta^{\text{aer}}(\lambda)}. \quad (24.9)$$

Values of the the lidar ratio range from < 10 sr for supercooled water droplets [24.17] to ≈ 100 sr for small, highly absorbing aerosols [24.18]. The lidar ratio depends mainly on the refractive index of the aerosol particles, but also on their shape and size (the ratio is higher for smaller and more elongated particles) [24.19, 20]. Due to its importance for evaluating and interpreting lidar data, the LR is discussed further in Sect. 24.3.

The aerosol optical depth τ should also be evaluated to facilitate comparisons with photometers. It is defined via

$$\tau(z) = \int_{z_0}^z \alpha^{\text{aer}}(\hat{z}) d\hat{z}. \quad (24.10)$$

Due to their lack of height resolution, photometers can only measure the integral of the aerosol-induced extinction over the whole atmospheric column, whereas lidars

Table 24.1 Parameters measured using backscatter lidars

Parameter	Description	Unit	Symbol
Attenuated backscatter	A measure of the light that is attenuated and elastically scattered at an angle of 180°	m ⁻¹ sr ⁻¹	<i>B</i>
Backscatter coefficient	A measure of the light that is elastically scattered at an angle of 180°	m ⁻¹ sr ⁻¹	β
Extinction coefficient	A measure of the attenuation of a beam of light	m ⁻¹	α
Range	Distance from the system to the base height (or distance) of interest	m	<i>z</i>

Table 24.2 Intensive properties that can be derived using lidars

Parameter	Description	Unit	Symbol
Lidar ratio	Ratio of the aerosol extinction coefficient to the aerosol backscatter coefficient	sr	LR
Color ratio	Ratio of the aerosol backscatter coefficients for different colors	–	CR
Ångström exponent for backscatter	Spectral dependence of the backscatter coefficient	–	<i>A_B</i>
Ångström exponent for extinction	Spectral dependence of the extinction coefficient	–	<i>A_a</i>
(Linear) depolarization ratio	Ratio of the backscatter coefficients for light that is polarized perpendicular and light that is polarized parallel to the laser	%	δ

provide height-resolved profiles of atmospheric quantities.

Finally, the backscatter ratio *R* is given as

$$R(\lambda) = \frac{\beta(\lambda)}{\beta_{\text{Ray}}(\lambda)} = 1 + \frac{\beta^{\text{aer}}(\lambda)}{\beta_{\text{Ray}}(\lambda)}. \quad (24.11)$$

As can be seen from this definition, the backscatter ratio is dimensionless. An ideal aerosol-free atmosphere would have $R = 1$. Note that the backscatter ratio and backscatter coefficient depend on each other.

Tables 24.1 and 24.2 summarizes the abovementioned parameters.

24.2 History

William E.K. Middleton (1902–1998) and *Athelstan F. Spilhaus* (1911–1998) introduced the acronym *lidar* in 1953 [24.21], 7 years before the invention of the laser. Consequently, the first lidar systems did not resemble those used today. Indeed, the first attempts to measure cloud base heights were made in the 1930s; those experiments involved recording the light scattered from a pulsed or continuous searchlight beam at just one height using an inclined telescope mirror and then applying trigonometry. However, the history of lidar technology is often considered to begin with the invention in 1962 of the *Q*-switched laser, which produces short, high-power laser pulses. A year later, the detection of mesospheric dust using an *optical radar* was reported [24.22]. While a detailed analysis of the lidar signal (see Sect. 24.3) was not yet possible, lidar was soon being utilized to perform ranging measurements, such as tracking the distance to the Moon. The first Apollo missions as well as unmanned Russian spacecraft placed special prisms on the Moon that allowed its distance from the Earth to be tracked with centimeter precision.

Lidar technology rapidly evolved, making it useful for an increasing number of applications, such as digital elevation modeling, the monitoring of agriculture and forest fires, vehicle automation, wind farm optimization, and even biological warfare alarm systems.

Nowadays, almost all analysis of backscatter data is based on the work of *James D. Klett* (1940) [24.23, 24]. However, the first stable analytical inversions of lidar signals were performed in Russia by *Bruno V. Kaul* and *Vladimir E. Zuev* (1925–2003) [24.25, 26]. In the Western world, the *slope method*, a solution of the lidar equation based on simplified assumptions, was used initially (see Sect. 24.3.2) [24.27].

The first spaceborne lidar was flown onboard the space shuttle *Discovery* for almost two weeks in September 1994 [24.28]. This LITE (Lidar In-space Technology Experiment) mission utilized a three-wavelength backscatter lidar and was carried out to demonstrate the feasibility of performing lidar measurements of clouds, aerosols, the planetary boundary height, and stratospheric temperatures from space. In 2006, the CALIPSO satellite was launched. Onboard this satellite is the CALIOP lidar, which delivers valuable information on global aerosol and cloud coverage [24.29]. CALIOP employs a two-wavelength laser that is widely used by the lidar community: a Nd:YAG laser emitting at 1064 and 532 nm (the second harmonic). It also utilizes depolarization separation, allowing some of the intensive quantities defined in Sect. 24.3 to be measured directly. Automatic differentiation between clouds and various types of aerosols has been greatly improved by this mission.

24.3 Theory

In this section, we provide the general solution of the elastic lidar equation. This solution depends on the lidar ratio (24.8), a boundary condition (the value of the backscatter coefficient at a predefined altitude), and of course the lidar profile (along with its noise). Values of the lidar ratio and the aerosol linear depolarization ratio are also given for various types of aerosols.

24.3.1 Concept and Basic Lidar Equation

Here, we denote the range from the lidar system to the point in the atmosphere at which the scattering processes occur by z . However, it is worth remembering that not all backscatter lidars are ground-based; some are used on aircraft and in space (see Chap. 38). Moreover, ground-based backscatter lidars can also be used in horizontal or scanning mode.

The main components of a lidar are a laser with emission optics, a telescope with recording optics, and a signal processing and storage unit, all of which are shown in Fig. 24.1. These components are described in detail in Sect. 24.4.

Typically, a laser is used to emit photons into the atmosphere in short pulses (≥ 10 ns). Some lasers used in lidars emit more than one wavelength simultaneously, which can be achieved by, for example, including additional optical components that double or triple the orig-

inal frequency of the laser. A beam-widening telescope (BWT) is usually employed to decrease the divergence of the laser beam, permitting a smaller, better-defined image of the laser in the sky. Other components such as a plane-parallel mirror may also be necessary to direct the laser beam further into the atmosphere. Particles in the atmosphere can scatter light elastically in the opposite direction to the incoming light; the resulting light is known as *backscatter*. In this section, we use the volumetric backscatter coefficient β , which has units of $\text{m}^{-1} \text{sr}^{-1}$. This backscatter coefficient indicates how well a particular atmospheric layer acts as a mirror, and its value is typically a function of the wavelength λ of the incoming light.

A telescope that collects the backscattered light from the atmosphere is positioned next to the laser or emission mirror. Figure 24.1 depicts this as a Newton-type telescope with a parabolic primary and a plane secondary mirror, but other telescope designs are also used. A field stop that limits the field of view (FOV) of the recording telescope is located in the focal plane of the recording telescope. This field stop increases the signal-to-noise ratio by ensuring that the laser beam is recorded while blocking out as much of the sky background as possible. A collimating lens is employed behind the aperture stop. This lens produces the parallel beam of light needed by optical components as dichroic

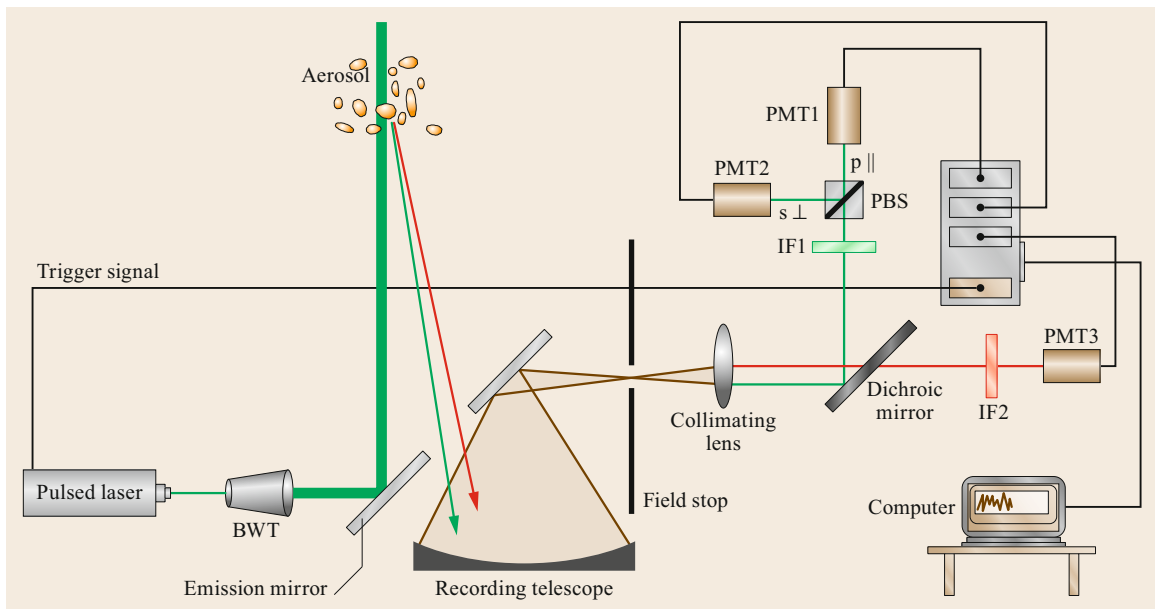


Fig. 24.1 The main components of a lidar system (BWT: beam-widening telescope, IF: interference filter, PBS: polarizing beam splitter, PMT: photomultiplier tube)

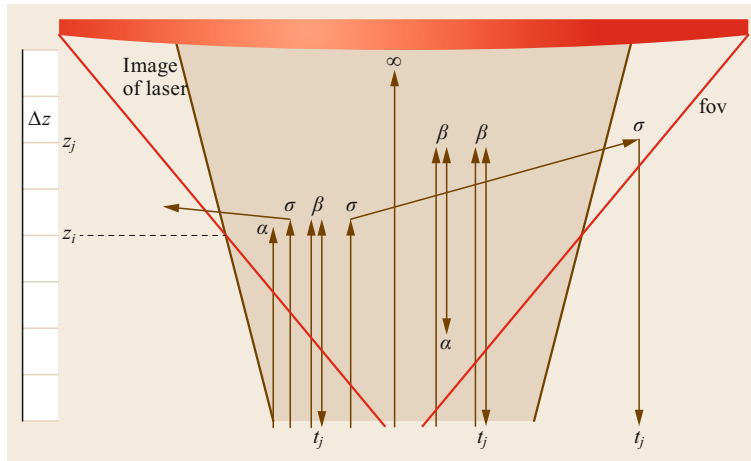


Fig. 24.2 Correct and unwanted events in a lidar system (FOV: field of view of the recording telescope)

mirrors and interference filters (IFs), which utilize multiple beam interference (i.e., the angle of incidence of the beam at the surface is important).

Dichroic beam splitters that reflect or transmit light differentially depending on its wavelength are commonly used in lidars to separate different wavelengths in the laser light or to distinguish between elastically and inelastically scattered light from the atmosphere (see the chapter on the Raman effect). As the number of colors recorded by a lidar is usually small, spectrometers have only rarely been used in lidars. Interference filters are used to eliminate any unwanted stray light before the remaining light is recorded by photomultiplier tubes (PMTs). In some lidars, the light is separated into its polarization states, which are recorded independently because they provide information on the shape of the scattering particles (see below). The light can be separated into its polarization states using polarizing beam splitters (PBSs), which separate the light into components that are polarized parallel (p or \parallel) and perpendicular (s or \perp) to the laser. The measured photocurrent from the PMTs is then counted using transient recorders. Figure 24.1 also shows that the transient recorders (there is normally one for each PMT) require a time stamp to ensure that they are synchronized with the laser flash. Finally, the data are stored in a computer, which can also be used to initially visualize the signal.

Even lidars that are used for meso- and exospheric research [24.30, 31]) will struggle to detect signals > 150 km, meaning that, according to (24.1), the signal must be recorded by a ground-based system within ≈ 1 ms at most. Hence, the lidar profile is recorded such that the flashing of the lidar triggers the transient recorders to start counting the output of the photomultipliers. The sampling frequency is on the order of MHz, which determines the altitude resolution of the lidar. According to (24.1), sampling at 20 MHz yields

an altitude resolution of 7.5 m. A height profile of the measured photocurrent is therefore obtained from each photomultiplier.

Figure 24.1 depicts just one backscatter lidar setup. Some lidars, especially the Raman lidars discussed in Chap. 25, use more colors and photomultipliers. Sometimes the same telescope is used for beam expansion to record the signal.

We will not be discussing continuous-wave (CW) lasers here as they are covered in Chap. 27. White-light femtosecond lidars [24.32, 33] are also omitted from the present discussion because they have only been used in atmospheric research to a very limited extent, even though they are not a new type of lidar [24.34].

Two physical quantities are fundamental to understanding the information content that can be retrieved by a lidar: the previously introduced volumetric backscatter coefficient β (in $\text{m}^{-1} \text{sr}^{-1}$) and the volumetric extinction coefficient α (in m^{-1}). The extinction coefficient describes the energy or the number of photons in the beam that is/are lost as the beam propagates. This loss may due to either scattering σ (in m^{-1}) or absorption a (in m^{-1}); in other words, $\alpha(\lambda, z) = \sigma(\lambda, z) + a(\lambda, z)$.

Figure 24.2 illustrates valid and unwanted events that contribute to the lidar signal. The FOV of the recording telescope is shown in red and the image of the laser beam in light green. The image of the laser is only fully located inside the FOV of the telescope when the altitude z is greater than z_i , which is called the *overlap height*. Evidently, to obtain full overlap, the divergence angle of the laser beam must be smaller than the FOV. Some photons that are scattered or absorbed within the height interval Δz_i are delineated in green in Fig. 24.2. The first photon (i.e., the photon furthest left) is absorbed at this altitude and does not, therefore, yield a signal at the detector. The same is true of the second photon, which is scattered sideways, meaning that

it moves outside of the FOV. However, the third photon is backscattered and is detected by the detector at time t_i , which corresponds to z_i via (24.1). The next photon is scattered to the side; we will come back to this photon later. While most photons are not scattered at all under cloud-free conditions and therefore leave the atmosphere (denoted by the infinity sign in the figure), just as the light from faint stars can be seen at night, some photons are backscattered at z_j . As before, some photons may be absorbed or scattered laterally at this height (not shown in the figure). Among those that are backscattered within the interval Δz_j , only the photons that are not absorbed or scattered laterally on their way down will be recorded at t_j .

So far we have only considered photons in the *single scattering approximation*—in other words, photons that are scattered only once. While this is a justifiable approximation in clear sky conditions and is also widely applied when there are thin clouds, multiple scattering must also be accounted for. This is shown in Fig. 24.2 on the left: one of the photons that is scattered sideways within the interval Δz_i is scattered again within the interval Δz_j and is subsequently recorded by the lidar. This is due to the fact that the final atmospheric scattering event took place within the FOV, even though it occurred outside the image of the laser. Hence, the amount of visible multiple scattering depends on not only the scattering efficiencies below z_j but also the FOV of the recording telescope. Moreover, it is clear from the figure that multiple scattering makes the image of the laser larger (but less defined), similar to the beams from the headlights of an automobile in foggy conditions.

Consider the number of photons per time/height bin $P(z)$ that are received at the detector. This quantity will depend linearly on the number of photons emitted by the laser per pulse P_0 . Moreover, it will depend linearly on the transmission efficiencies of the emission and recording optics: T_{emi} and T_{rec} , respectively. Further, it will depend linearly on the backscatter coefficient $\beta(z)$ at the altitude of interest z as well as the probability that the backscattered photons hit the surface of the recording telescope, A/z^2 . Next, we need to take into account the loss of photons due to extinction α (given by Bouguer–Lambert–Beer’s law) on the way from the lidar (located at z_0) to altitude z and back down to the detector. Hence, we have

$$P(z) = P_0 T_{\text{emi}} T_{\text{rec}} \frac{A}{z^2} \beta(z) \exp\left(-\int_{z_0}^z \alpha(\hat{z}) d\hat{z}\right) \times \exp\left(-\int_z^{z_0} \alpha(\hat{z}) d-\hat{z}\right). \quad (24.12)$$

Combining all of the technical quantities into the lidar constant C and rearranging the terms in the exponentials leads to the normal lidar equation in its simplest form (full overlap, purely single scattering),

$$P(z) = C \frac{1}{z^2} \beta(z) \exp\left(-2 \int_{z_0}^z \alpha(\hat{z}) d\hat{z}\right). \quad (24.13)$$

When using this equation, it is assumed that the height resolution is so high that the variability of the backscatter and extinction coefficients within each altitude step $[z_i, z_{i+1}]$ is negligible and the length of the laser pulse is shorter than the altitude resolution. If these conditions are not fulfilled, a convolution that relates the measured $P(z)$ to the emitted photons that are received from different altitudes should be considered. This is explained in [24.35].

24.3.2 Background Correction and Properties of Lidar Signals

Before solving the elastic lidar equation, we first provide an example of lidar signals in Fig. 24.4. Lidar profiles at 355 and 1064 nm that were obtained simultaneously are shown, with the count rate given in arbitrary units. The raw signals received by the system are shown as dotted functions. These depict an excessive count rate, which occurs for two reasons: first, in the daytime, the signal includes photons from the laser and unwanted photons from the sky. As a whole lidar profile can be obtained in < 1 ms (see (24.1)), it can often be assumed that this background illumination remains constant over this time and can be subtracted from the measured signal. To reduce this background illumination, a small field of view of the recording telescope and interference filters that are as narrow as possible are desirable. Second, the transient recorders can produce an artificial count rate (see Sect. 24.4). Both of these effects need to be corrected for in a process called background correction.

This can be done by subtracting the artificial count rate either at such high altitudes that the laser does not contribute to the signal, or using the count rate before the laser flashes. Hence, we can define a background count rate P_{bg} that is the average of the lidar signal at a background altitude z_{bg} without laser light, i.e.,

$$P_{\text{bg}} = \text{mean}(P_{\text{measured}}(z_{\text{bg}})). \quad (24.14)$$

We can also derive the physical count rate via

$$P(z) = C \frac{1}{z^2} \beta(z) \exp\left(-2 \int_{z_0}^z \alpha(\hat{z}) d\hat{z}\right) = P_{\text{measured}}(z) - P_{\text{bg}}. \quad (24.15)$$

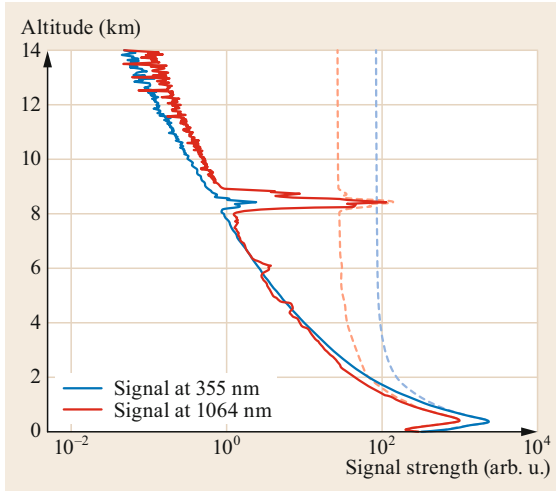


Fig. 24.3 Examples of lidar signals. Note that the molecular contribution from Rayleigh scattering is stronger at shorter wavelengths

These physical count rates at both wavelengths are shown as continuous lines in Fig. 24.3. There are several features of the figure that should be noted. The first noteworthy aspect is the impact of the overlap $\lesssim 500$ m. Below this altitude, the count rate rises with increasing height, as more and more of the laser light contributes to the recorded image. Second, a cloud at ≈ 8 km altitude is much more visible in the IR than in the UV. The reason for this is the Ångström exponent of the backscatter (A_B in (24.3)), which is -4 for Rayleigh scattering but much smaller for particles and especially clouds. Therefore, the molecular contribution is greater in the UV, and the corresponding lidar profile looks *smoother*, and the contrast in count rate between the clouds and the background atmosphere is lower in the UV and higher in the IR. As the contribution from Rayleigh scattering is low in the IR, smaller lidar systems may need some aerosol to be present for a successful evaluation.

Third, it is apparent that the extinction is weaker in the IR and stronger in the UV, as the count rate decays quicker with altitude for the 355 nm channel. This is due to the spectral dependence of A_A in (24.3).

Finally, it can be seen that the count rate decays significantly in the atmosphere. The z^{-2} dependence of the lidar signal is the main reason for this. However, the backscatter coefficient, which is almost proportional to the number density of clear air (scale height: ≈ 8 km), and the exponential term of the extinction also contribute to the deterioration in the count rate with increasing altitude. This imposes some technical constraints on the components in a lidar, as the dynamic range—the difference between the strongest and weakest signals detected by a lidar—may cover more than four orders of magnitude.

24.3.3 Solution of the Elastic Lidar Equation

As already defined above, the elastic lidar equation can be written in the form

$$P(z)z^2 =: S(z) = C\beta(z) \exp\left(-2 \int_{z_0}^z \alpha(\hat{z})d\hat{z}\right), \quad (24.16)$$

where $S(z)$ is the range-corrected lidar signal. The integration is performed from the height of the lidar system z_0 to the altitude of interest z . For a multiwavelength system, (24.16) can be written separately for each color.

This equation links the lidar profile to two physical unknowns: the volume backscatter coefficient β (in $\text{m}^{-1} \text{sr}^{-1}$) and the extinction coefficient α (in m^{-1}). Clearly, a unique solution can only be obtained if we assume a particular relation between α and β . Note that β and α are the total backscatter and extinction coefficients, which contain contributions from the air molecules and aerosol or cloud particles.

The lidar ratio $\text{LR}(z)$, as defined in (24.7), is usually chosen such that (24.16) is transformed into a backscatter equation only. This is achieved by writing

$$\alpha = \alpha^{\text{acr}} + \alpha^{\text{Ray}} = \text{LR}(\beta - \beta^{\text{Ray}}) + \alpha^{\text{Ray}}. \quad (24.17)$$

Hence, we can rewrite (24.15) as

$$\begin{aligned} S(z) \exp\left(2 \int_{z_0}^z (\alpha^{\text{Ray}} - \text{LR}\beta^{\text{Ray}})d\hat{z}\right) \\ = C\beta(z) \exp\left(-2 \int_{z_0}^z \text{LR}(\hat{z})\beta(\hat{z})d\hat{z}\right). \end{aligned} \quad (24.18)$$

If the air density profile and hence α^{Ray} and β^{Ray} are known, all of the terms on the left-hand side are known, leaving one equation for the total backscatter coefficient.

Taking the logarithm and the derivative with respect to height of (24.18), we obtain

$$\begin{aligned} \frac{d}{dz}(\ln S(z)) + 2(\alpha^{\text{Ray}} - \text{LR}\beta^{\text{Ray}}) \\ = \frac{1}{\beta(z)} \frac{d\beta}{dz} - 2\text{LR}(z)\beta(z), \end{aligned} \quad (24.19)$$

from which the nonlinear differential equation

$$\begin{aligned} \frac{d\beta}{dz} = \left[\frac{d}{dz}(\ln S(z)) + 2(\alpha^{\text{Ray}} - \text{LR}\beta^{\text{Ray}}) \right] \beta(z) \\ + 2\text{LR}(z)\beta^2(z) \end{aligned} \quad (24.20)$$

is easily derived.

This is a Bernoulli differential equation of degree 2 (the highest exponent of β), which can be converted into a linear differential equation via the Bernoulli substitution

$$\tilde{\beta} = \beta^{1-n}, \quad (24.21)$$

where n is the degree of the original equation. This substitution yields

$$\frac{d\tilde{\beta}}{dz} = (1-n)\beta^{-n}\frac{d\beta}{dz} \quad (24.22)$$

and

$$\beta^n = \tilde{\beta}^{\frac{n}{1-n}} \quad (24.23)$$

as well as the linear differential equation

$$\begin{aligned} \frac{d\tilde{\beta}}{dz} + \left[\frac{d}{dz}(\ln S(z)) + 2(\alpha^{\text{Ray}} - \text{LR}\beta^{\text{Ray}}) \right] \tilde{\beta}(z) \\ = -2\text{LR}(z). \end{aligned} \quad (24.24)$$

We solve this equation by introducing the integrating factor

$$M(z) := \exp \left[\int \frac{d}{dz}(\ln S(z)) + 2(\alpha^{\text{Ray}} - \text{LR}\beta^{\text{Ray}}) dz \right] \quad (24.25)$$

and by referring to the very important paper written by *James Klett* in 1981 [24.23], which explains that a numerically stable solution can only be found when the integration is performed from the far range back to the system. Hence,

$$\int_{z_{\text{ref}}}^z d\hat{z}, \quad \text{with } z < z_{\text{ref}}, \quad (24.26)$$

so

$$M(z) = \exp \left[\int_{z_{\text{ref}}}^z \frac{d}{dz}(\ln S(z)) + 2(\alpha^{\text{Ray}} - \text{LR}\beta^{\text{Ray}}) d\hat{z} \right] \quad (24.27)$$

$$\begin{aligned} M(z) &= \exp[\ln(S(z_{\text{ref}})) - \ln(S(z))] \\ &\times \exp \left(2 \int_{z_{\text{ref}}}^z \alpha^{\text{Ray}} - \text{LR}\beta^{\text{Ray}} d\hat{z} \right) \end{aligned} \quad (24.28)$$

$$M(z) = \frac{S(z_{\text{ref}})}{S(z)} \exp \left(2 \int_{z_{\text{ref}}}^z \alpha^{\text{Ray}} - \text{LR}\beta^{\text{Ray}} d\hat{z} \right). \quad (24.29)$$

Using this integrating factor and

$$\begin{aligned} N(z) &:= 2 \int_{z_{\text{ref}}}^z M(\hat{z})(-\text{LR}(\hat{z})) d\hat{z} \\ &= 2 \int_z^{z_{\text{ref}}} M(\hat{z})\text{LR}(\hat{z}) d\hat{z}, \end{aligned} \quad (24.30)$$

we can derive

$$\tilde{\beta}(z) = \frac{c + N(z)}{M(z)}, \quad (24.31)$$

and hence

$$\beta(z) = \frac{M(z)}{c + N(z)}. \quad (24.32)$$

To determine the backscatter profile $\beta(z)$ unambiguously, the integrating constant c must be determined. Again, [24.23] suggests that $z = z_{\text{ref}}$ (at the far side of the system) should be selected. The reason for this is simply that $M(z)$ and $N(z)$ are functions that depend on the range-corrected lidar signal and decay with increasing z . If c is chosen to be far away from the lidar and the integration is performed from z_{ref} to z_0 , $M(z)$ and $N(z)$ will become larger, eliminating the influence of an inappropriately chosen integrating constant. In contrast, choosing c to be at z_0 and integrating from z_0 to z would yield unstable results. Therefore, we assume that $\beta(z_{\text{ref}})$ is known for $z < z_{\text{ref}}$. Moreover, we note that

$$\begin{aligned} M(z_{\text{ref}}) &= \frac{S(z_{\text{ref}})}{S(z_{\text{ref}})} \exp \left[2 \int_{z_{\text{ref}}}^{z_{\text{ref}}} (\alpha^{\text{Ray}} - \text{LR}\beta^{\text{Ray}}) d\hat{z} \right] \\ &= 1 \end{aligned} \quad (24.33)$$

and

$$N(z_{\text{ref}}) = 2 \int_{z_{\text{ref}}}^{z_{\text{ref}}} M(\hat{z})\text{LR}(\hat{z}) d\hat{z} = 0, \quad (24.34)$$

from which we derive

$$c = \frac{1}{\beta(z_{\text{ref}})}. \quad (24.35)$$

Thus, the final numerically stable solution for deriving the backscatter profile from the elastic lidar equation

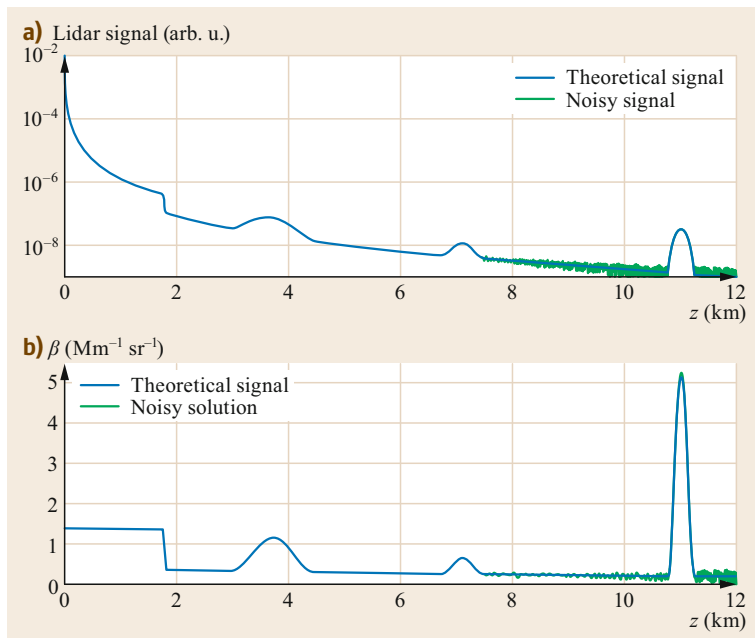


Fig. 24.4a,b Impact of noise in the lidar signal (a) on the retrieval of the backscatter coefficient (b)

(consistently integrating from z to z_{ref} ; note the change of signs!) reads

$$\beta(z) = \frac{\frac{S(z)}{S(z_{\text{ref}})} \text{ST}(z)}{\frac{1}{\beta(z_{\text{ref}})} + \frac{2}{S(z_{\text{ref}})} \int_z^{z_{\text{ref}}} \text{LR}(\tilde{z}) S(\tilde{z}) \text{ST}(\tilde{z}) d\tilde{z}} \quad (24.36)$$

or

$$\beta(z) = \frac{S(z) \text{ST}(z)}{\frac{S(z_{\text{ref}})}{\beta(z_{\text{ref}})} + 2 \int_z^{z_{\text{ref}}} \text{LR}(\tilde{z}) S(\tilde{z}) \text{ST}(\tilde{z}) d\tilde{z}}, \quad (24.37)$$

where

$$\text{ST}(z) = \exp\left(-2 \int_z^{z_{\text{ref}}} (\alpha^{\text{Ray}} - \text{LR} \beta^{\text{Ray}}) d\tilde{z}\right).$$

In honor of James Klett's work in this field, (24.37) is frequently called the *Klett solution*.

In summary, a solution for the elastic lidar equation was pursued by expressing it as a function of the total backscatter coefficient β and introducing the lidar ratio LR. This led to a differential equation that required the backscatter to be calibrated as a boundary value problem. To guarantee the numerical stability of the result, this boundary value had to be applied at the far side of the system, and the integration had to be performed accordingly. Hence, the backscatter profile $\beta(z)$ depends on three quantities:

- The error in the lidar profile $PE(z)$
- The assumed boundary value $\beta(z_{\text{ref}})$
- The chosen profile of $\text{LR}(z)$.

Figure 24.4 shows how the backscatter depends on these quantities.

The dependence of β on the noise in the lidar profile is shown in Fig. 24.4. Figure 24.4b presents an artificial aerosol backscatter profile that shows high and almost height-independent backscatter in the lowest 1.8 km, which could correspond to a well-mixed boundary layer. Above 1.8 km, the backscatter is weaker except for two elevated aerosol layers and some cirrus cloud at an altitude of ≈ 11 km (blue profile in Fig. 24.4b). This aerosol backscatter gives rise to the blue lidar profile shown in Fig. 24.4a. Noise in the lidar signal (green profile in Fig. 24.4a) will produce the backscatter shown in green in Fig. 24.4b. Even with noise present, it is clear that the backscatter can still be retrieved quite reliably.

The dependence of the backscatter profile on the chosen boundary condition is shown in Fig. 24.5. The boundary condition was fixed within the altitude range 11.8–12 km. The green and red functions show the solutions when the boundary condition is lowered or increased by a factor of 1.1, respectively. From Fig. 24.5b, it is apparent that the deviation of the lower/higher solution from the reference solution decreases with altitude. In this respect, the Klett method gives stable results: if the integration is performed from an altitude of 12 km towards the ground, the impact of a wrongly chosen boundary condition slowly decays. This decay becomes stronger as the atmosphere becomes more turbid [24.35]. Nevertheless, the boundary condition does influence the solution, and it is beneficial to have lidar

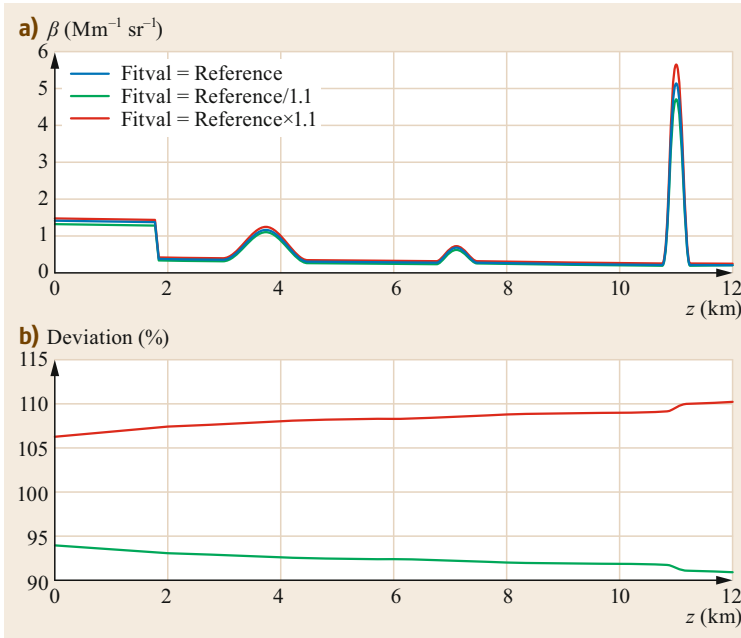


Fig. 24.5a,b Impact of the boundary condition on the retrieval of the backscatter coefficient. **(a)** Shown are three solutions, which differ in the applied boundary condition by 10%. **(b)** The deviation of a too low (green) or too high (red) chosen boundary condition with respect to the reference (blue in **(a)**). It can be seen that the impact of a wrong chosen boundary conditions decays towards the ground

systems that reach the low stratosphere, as this region is normally only slightly affected by aerosols. In this case, the backscatter coefficient at the fitted altitude is only slightly larger than the Rayleigh backscatter, i.e., $\beta^{\text{Fit}} = (1 + \varepsilon)\beta^{\text{Ray}}$ where ε is an arbitrary small number > 0 . These fitting conditions are called *clear sky conditions*. With a little experience, an incorrectly chosen boundary condition is easily spotted—either a peak occurs in the counting rate with altitude (as shown in Fig. 24.4; this must be avoided), or the resulting backscatter profile gives rather low values across the whole troposphere, which indicates that the chosen β^{Fit} is too low.

In a multiwavelength system, the boundary conditions for all the different wavelengths can be estimated consistently by assuming an Ångström exponent for the backscatter (24.3) and then using this to calculate the boundary conditions based on one guess for the first color, as shown in the example below.

Let $\beta^{\text{Fit}}(532 \text{ nm}) = 1.05\beta^{\text{Ray}}$ and $A_B = -1$. This means that, for 532 nm,

$$\beta^{\text{aer}}(z_{\text{Fit}}) = \frac{1}{20}\beta^{\text{Ray}}(z_{\text{Fit}}). \quad (24.38)$$

Therefore, for the doubled wavelength (1064 nm),

$$\begin{aligned} \beta^{\text{Ray}}(1064 \text{ nm}) &= \left(\frac{1064}{532}\right)^{-4} \beta^{\text{Ray}}(532 \text{ nm}) \\ &= \frac{1}{16}\beta^{\text{Ray}}(532 \text{ nm}) \end{aligned} \quad (24.39)$$

and

$$\begin{aligned} \beta^{\text{aer}}(1064 \text{ nm}) &= \left(\frac{1064}{532}\right)^{A_B} \beta^{\text{aer}}(532 \text{ nm}) \\ &= \frac{1}{2}\beta^{\text{aer}}(532 \text{ nm}). \end{aligned} \quad (24.40)$$

Hence, doubling the wavelength reduces the Rayleigh backscatter by a factor of 16, while the aerosol backscatter decreases by only a factor of 2. This means that the fit condition for 1064 nm is

$$\begin{aligned} \beta^{\text{aer}}(z_{\text{Fit},1064\text{nm}}) &= \frac{1}{20} \times 16 \times \frac{1}{2}\beta^{\text{Ray}}(z_{\text{Fit},1064\text{nm}}) \\ &= 1.4\beta^{\text{Ray}}(z_{\text{Fit},1064\text{nm}}), \end{aligned} \quad (24.41)$$

or, more generally,

$$\beta^{\text{Fit}}(\lambda_2) = \left(\frac{\lambda_2}{\lambda_1}\right)^{4-A_B} \varepsilon(\lambda_1). \quad (24.42)$$

This example also shows that clear sky conditions for near-infrared and longer wavelengths must be handled with care.

The influence of a wrongly chosen lidar ratio is demonstrated in Fig. 24.6. It can be seen that lower lidar ratios always lead to higher backscatter values and vice versa. The higher the backscatter and the longer the integration distance, the more pronounced the difference. The lidar ratio is therefore an important parameter

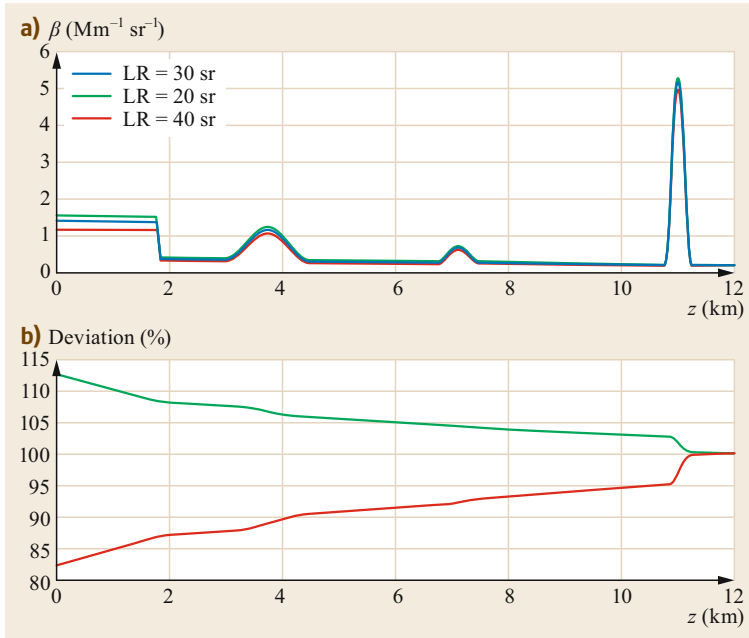


Fig. 24.6a,b Impact of the lidar ratio on the retrieval of the backscatter coefficient. **(a)** Three solutions are shown for different lidar ratios. **(b)** Impact of a too low chosen (green) or too large chosen (red) lidar ratio on the resulting backscatter

for retrieving the backscatter, and it is discussed further in Sect. 24.3.7. Choosing the lidar ratio poorly results in noticeable errors during the retrieval of the backscatter.

In short, determining the backscatter coefficient to a precision of about 10% requires appropriate selection of the boundary condition and (especially) the lidar ratio. Even so, the backscatter coefficient is still the quantity that is easiest to derive from lidar data.

The situation is even worse for the extinction coefficient, as it enters the normal lidar equation (24.2) via the expression

$$\exp\left(-2 \int_0^z \alpha(\hat{z}) d\hat{z}\right), \quad (24.43)$$

which is *infinite smooth*, meaning that there are infinite continuous derivatives with respect to altitude z , regardless of the real extinction profile in the atmosphere.

An example of this is shown in Fig. 24.7. This shows an arbitrary extinction profile (blue curve in the Fig. 24.7a). Just as for the backscatter profile in Fig. 24.4, different maxima can be distinguished, which are due to the presence of an aerosol in the boundary layer, elevated layers, and thin cloud. Figure 24.7b shows the integral of the extinction profile, which is much smoother and increases monotonically. Figure 24.7c shows the variation in (24.43) with height. A tiny amount of noise (barely visible) has been added

to this plot (green curve). This small amount of noise is still relatively minor in Fig. 24.7b (see the green curve), but it is enough to completely destroy the solution for the extinction profile (green curve in Fig. 24.7a). This points to a problem with deriving the profile of the extinction coefficient from lidar data: it enters the lidar equation in an infinite smooth expression behind which an arbitrary extinction profile is hidden. Calculating the derivative d/dz increases the noise dramatically. Hence, the retrieval of the extinction coefficient from lidar data is an ill-posed problem [24.36]. However, it should be noted that the problem is with the position of the extinction in the lidar equation, not the extinction coefficient itself. Instead of using the Klett method as explained above, some authors solve the basic lidar equation for the extinction coefficient. This works as well, but most of the information on the shape of the solution comes from the first term, not the exponential term, in (24.43).

24.3.4 Simplifications

In turbid conditions, or for cloud measurements, the assumptions $\alpha^{\text{aer}} \gg \alpha^{\text{Ray}}$ and $\beta^{\text{aer}} \gg \beta^{\text{Ray}}$ hold true, such that $\alpha \approx \alpha^{\text{aer}}$ and $\beta \approx \beta^{\text{aer}}$. Therefore, we introduce the *total lidar ratio* $L := \alpha/\beta$ and derive (completely analogously to the section above)

$$S(z) = C\beta(z) \exp\left(-2 \int_{z_0}^z L(\hat{z})\beta(\hat{z})d\hat{z}\right). \quad (24.44)$$

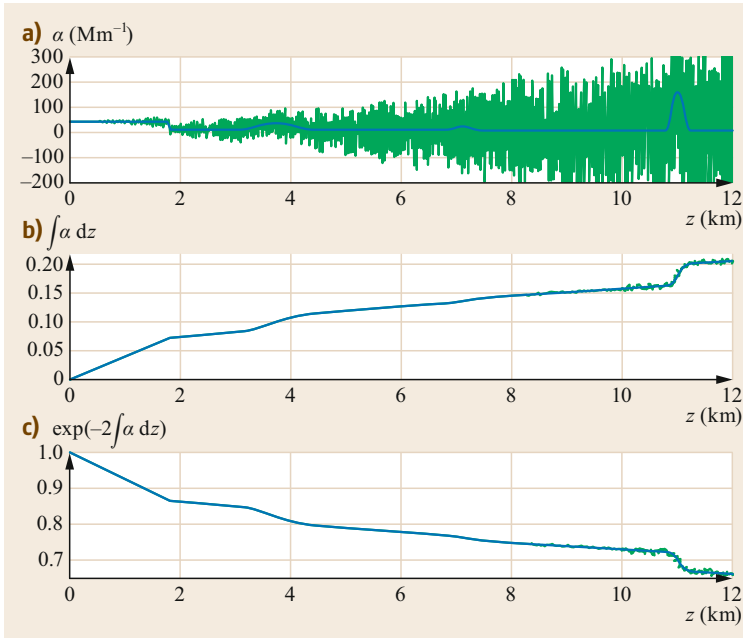


Fig. 24.7a–c Critical impact of noise on the determination of the extinction coefficient. (a) Noise-free (blue) and noisy (green) extinction coefficient, (b) the corresponding profiles of the integral of the extinction coefficient (again blue noise-free and green noisy), (c) the corresponding attenuation term of the lidar equation. It can be seen that only little noise in the lidar profile destroys the solution for the extinction

Hence,

$$\frac{d}{dz} \ln(S) = \frac{1}{\beta} \frac{d\beta}{dz} - 2L\beta. \quad (24.45)$$

As a side note, historically or when using a lidar horizontally in a homogeneous medium, the term $d\beta/dz$ (almost) vanishes and the equation above simplifies accordingly. This is known as the *slope method* [24.23, 27].

Otherwise, using the analog Bernoulli substitution and the guidance supplied by Klett, we obtain the simpler expression

$$\beta(z) = \frac{S(z)}{S(z_{\text{ref}}) / (\beta(z_{\text{ref}}) + 2 \int_z^{z_{\text{ref}}} S(\hat{z})L(\hat{z})d\hat{z})}. \quad (24.46)$$

24.3.5 Extensions to the Lidar Equation

Figure 24.2 illustrates the overlap height—the height above which the field of view (FOV) of the recording telescope contains the full image of the laser beam. This is an important parameter in a lidar system. An overlap occurs even for coaxial lidars in which the outgoing laser beam and the recording telescope share a common optical axis. The reason for this is the field stop in the focal plane of the recording telescope, which is included to reduce the FOV and hence the stray light contamination at daytime operation. This can be seen in Fig. 24.8.

If the laser beam is viewed at a finite distance, its image will form behind the focal plane. While only the rays that pass through the center of the telescope (a) and the ray through the focal point (b) are important when constructing the image in geometrical optics, in reality *all* of the rays that travel from the object through the telescope contribute to the brightness of the image (e.g., the *dashed ray*). Figure 24.8 clearly shows that some of the rays from the edge of the telescope are blocked. Hence, for finite object distances, only part (not the whole) of the telescope contributes to image formation. This reduction in the effective telescope area needs to be accounted for in the lidar equation. The corresponding overlap function, which is often denoted $O(z)$, starts at 0 for $z = z_0$ and approaches a constant value (close to 1) at the altitude z_{overlap} when the overlap is (almost) complete. Hence, the overlap can be included in the lidar equation as

$$\begin{aligned} P(z) &= C \frac{1}{z^2} \beta(z) \exp\left(-2 \int_{z_0}^z \alpha(\hat{z})d\hat{z}\right) O(z) \\ &= C_* \frac{1}{z^2} \beta(z) \exp\left(-2 \int_{z_{\text{Overlap}}}^z \alpha(\hat{z})d\hat{z}\right). \end{aligned} \quad (24.47)$$

In many applications, the lidar data is only evaluated for altitudes $z > z_{\text{overlap}}$. In this case, the lidar has a blind spot close to the system. The overlap problem becomes even more pronounced for larger telescope mirrors that

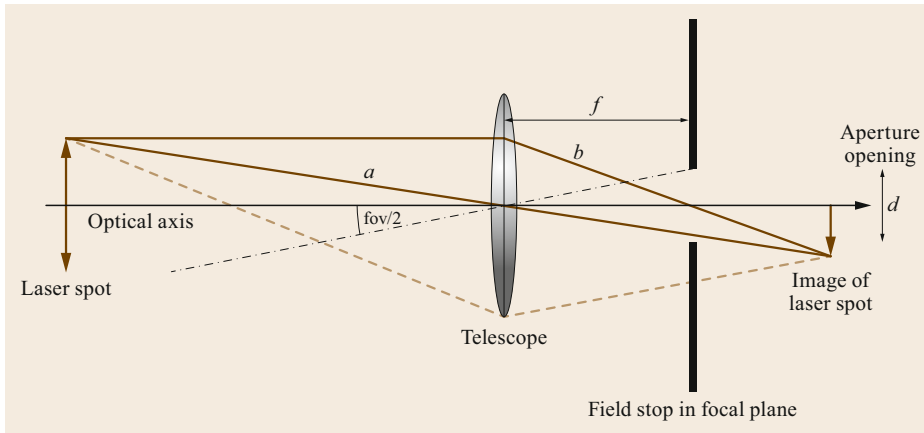


Fig. 24.8 Image formation and the impact of the field stop

may be required to obtain a sufficient return signal from high altitudes. Therefore, lidars with two recording mirrors, in which the smaller mirror collects the light from the near range, are sometimes constructed.

Some approaches for estimating the overlap function from experimental data have been proposed. For example, the scattering of a pure molecular atmosphere with a known expected count rate can be used. In this case, the overlap for each height bin is the ratio of the measured to the expected count rates [24.37]. However, in the real atmosphere, the overlap depends on the number of scattering particles. Turbid conditions lead to an increased probability of scattering events, some of which end up in the FOV of the telescope. In contrast, the count rate is lower in clear conditions, so $O(z, \text{turbid}) > O(z, \text{clear})$.

As shown in previous sections, the lidar ratio, depolarization ratio, and color ratio (all of which are intensive quantities) are derived from the ratios of different lidar signals. If each optical branch (including its interference filter and photomultiplier) had precisely the same alignment, the overlap would be identical for all signals, so it would cancel out. While this is typically hard to achieve, it is clear that lidar properties derived from ratios of different signals are less affected by the overlap.

Given the small FOVs (typically < 1 mrad) of ground-based lidar systems, the assumption of single scattering largely holds for aerosol layers or thin clouds. However, in turbid conditions, some of the photons recorded by the detector have been scattered several times and have therefore zigzagged through the atmosphere. This phenomenon is called multiple scattering (see the photon on the left in Fig. 24.2), and it results in signal count rates behind a cloud that are higher than would be expected from the single scattering lidar equation. An excessive backscatter value translates into a lidar ratio that is too small in and behind clouds (see (24.9)), as pointed out in [24.38].

To compensate for this, a multiple scattering factor η is usually introduced such that the normal lidar equation for single scattering (SS) is generalized to an equation for total scattering (TS), i.e.,

$$P_{\text{SS}}(z) = C \frac{1}{z^2} \beta(z) \exp \left(-2 \int_{z_0}^z \alpha(\hat{z}) d\hat{z} \right) \quad (24.48)$$

and

$$P_{\text{TS}}(z) = C \frac{1}{z^2} \beta(z) \exp \left(-2 \int_{z_0}^z \eta(\hat{z}) \alpha(\hat{z}) d\hat{z} \right). \quad (24.49)$$

This leads to

$$\eta(z) = 1 + \frac{\ln \left(\frac{P_{\text{SS}}(z)}{P_{\text{TS}}(z)} \right)}{2 \int_{z_0}^z \alpha(\hat{z}) d\hat{z}}. \quad (24.50)$$

Values of 0.5–1 for the multiple scattering factor have been estimated [24.38].

Multiple scattering can be treated in different ways—by performing computationally expensive Monte Carlo simulations (see, for example, [24.39]) or by considering the energy distribution in the image of the laser while it is propagating through the atmosphere [24.40].

Also important is a noticeable shift in depolarization: multiple scattering requires a backscatter angle of slightly less than 180° (left ray in Fig. 24.2). It is shown in [24.41] that the plane of polarization—which is conserved for light that is backscattered at 180° from spherical particles—is significantly altered for other backscatter angles, even 179° . This is why water clouds show significant depolarization once multiple scattering sets in.

The amount of multiple scattering rises as the FOV of the lidar system increases [24.39]. It also depends on the geometrical width of the laser beam and the FOV of the recording telescope, because larger surfaces make it more probable that photons scattered roughly in a forward direction remain in the FOV. Thus, multiple scattering is much more severe for spaceborne than for ground-based lidar systems [24.42].

24.3.6 Transition Method

Under favorable conditions, a layer-integrated extinction coefficient and hence also the lidar ratio can be determined from the elastic lidar equation. One of the ways to achieve this is called the transition method, in which we compare the range-corrected lidar signals obtained directly above (z_{top}) and below (z_{bot}) a layer that may contain a cloud or a dense aerosol. We therefore write

$$S(z_{\text{top}}) = C\beta(z_{\text{top}}) \exp\left(-2 \int_{z_0}^{z_{\text{bot}}} \alpha(\hat{z}) d\hat{z}\right) \times \exp\left(-2 \int_{z_{\text{bot}}}^{z_{\text{top}}} \alpha(\hat{z}) d\hat{z}\right) \quad (24.51)$$

$$\Leftrightarrow S(z_{\text{top}}) = \frac{\beta(z_{\text{top}}) S(z_{\text{bot}})}{\beta(z_{\text{bot}})} \exp\left(-2 \int_{z_{\text{bot}}}^{z_{\text{top}}} \alpha^{\text{Ray}}(\hat{z}) d\hat{z}\right) \times \exp\left(-2 \int_{z_{\text{bot}}}^{z_{\text{top}}} \alpha^{\text{aer}}(\hat{z}) d\hat{z}\right). \quad (24.52)$$

The integral in the last term is simply the aerosol optical depth (AOD) of this layer. Hence,

$$\text{AOD}_{\text{Layer}} = \frac{1}{2} \ln \left(\frac{\beta(z_{\text{top}}) S(z_{\text{bot}})}{\beta(z_{\text{bot}}) S(z_{\text{top}})} \right) - \int_{z_{\text{bot}}}^{z_{\text{top}}} \alpha^{\text{Ray}}(\hat{z}) d\hat{z}. \quad (24.53)$$

This method has its value in cases where $\beta(z_{\text{bot}})$ and $\beta(z_{\text{top}})$ can be assumed; for instance, when multiple lidar observations are made that are close to each other in space or time, or—even simpler—when $\beta(z_{\text{bot}})$ and $\beta(z_{\text{top}})$ are assumed to be equal (i.e., for geometrically thin clouds).

The layer-integrated lidar ratio is then given by

$$\text{LR}_{\text{Layer}} = \frac{\text{AOD}_{\text{Layer}}}{\int_{z_{\text{bot}}}^{z_{\text{top}}} \beta^{\text{aer}}(\hat{z}) d\hat{z}}. \quad (24.54)$$

Alternatively, the Klett solution can be applied in an iterative loop with the lidar ratio varying between z_{bot} and z_{top} until the desired $\beta(z_{\text{bot}})$ is obtained.

24.3.7 Importance of the Lidar Ratio

In contrast to the abovementioned special cases or more complex lidar systems such as Raman lidars or high spectral resolution lidars (HSRLs; see, e.g., [24.43]), a backscatter lidar usually cannot determine the extinction coefficient. For this reason, a lidar ratio (see (24.8)) must be assumed in advance when using the Klett method. This lidar ratio is an intensive quantity that does not depend on the aerosol concentration, only on the intrinsic properties of the aerosol particles: their size, shape, and refractive index.

Therefore, we would expect the same type of aerosol to show different LRs depending on its precise chemical composition and age and the water-uptake and meteorological conditions present, even though this issue is largely overlooked in the literature. Nevertheless, long-term experience with different lidar systems has shown that fairly consistent datasets are obtained, with lower LRs observed for clean conditions and cirrus clouds and higher values for absorbing aerosols. Some relevant values are compiled in Table 24.3. These values can be used for orientation when it is possible to identify the type of aerosol seen by the lidar.

To underline that actual LRs may deviate from the values shown in Table 24.3, we should mention the work of Ackermann [24.51], who used Mie theory and assumed some basic aerosol properties (such as the refractive index and a log-normal size distribution) to analyze the hygroscopic behaviors of different aerosol species. Ackermann found, for example, that the LR of continental aerosol strongly increases with relative humidity. Also, it was reported in [24.52] that the LR of sea salt depends on the wind speed: higher winds decrease the observed LR. Moreover, nonspherical particles typically present a higher LR than spherical particles because the backscatter efficiency decreases with increasing particle elongation [24.53].

Again, it should be noted that the values in Table 24.3 are only rough estimates. As changes in photochemistry, coagulation, and water uptake can alter the scattering-relevant microphysical properties (the size, shape, and refractive-index distributions) of real aerosols within minutes, the real lidar ratio will fluctuate over time.

Because the extinction caused by aerosols decreases with wavelength, it is more important to choose an appropriate lidar ratio for short wavelengths than for those in the infrared. Lessening the extinction due to aerosols decreases the difference between the attenuated backscatter and the backscatter coefficient, mean-

Table 24.3 Lidar ratios for different aerosol types (FT: free troposphere, CALIPSO: Cloud-Aerosol Lidar and Infrared Pathfinder Satellite Observations)

Type of aerosol	355 nm	532 nm	1064 nm	Reference	Remarks
Clean continental	–	35 sr	30 sr	[24.44]	CALIPSO
Clean marine	–	20 sr	45 sr	[24.44]	CALIPSO
Marine	–	20–37 sr	–	[24.45]	Higher values in the FT
Dust	–	40 sr	55 sr	[24.44]	CALIPSO
Dust	–	57 sr	–	[24.46]	Tenerife (Sahara)
Dust	49–61 sr	50–70 sr	–	[24.45]	Sahara
Dust	33–43 sr	30–43 sr	–	[24.45]	Gobi, Saudi Arabia
Polluted continental	–	70 sr	30 sr	[24.44]	CALIPSO
Polluted continental	43–70 sr	29–64 sr	–	[24.45]	Europe, N. America
Polluted continental	–	45–64 sr (less during monsoon)	–	[24.18]	China
Polluted dust	–	65 sr	30 sr	[24.44]	CALIPSO
Smoke	–	70 sr	40 sr	[24.44]	CALIPSO
Smoke	33–59 sr	42–64 sr	–	[24.45]	Boreal forests
Volcanic ash	55–65 sr	50–60 sr	–	[24.47]	Europe
Arctic aerosol	25–40 sr	30–55 sr	35–50 sr	[24.48]	European Arctic
Arctic aerosol	48–72 sr	48–72 sr	–	[24.45]	Measured over Europe
Cirrus clouds	–	17–41 sr	–	[24.13]	East Asia
Cirrus clouds	–	28–38 sr	–	[24.49]	CALIPSO (over oceans)
Liquid clouds	18.5 sr	18.5 sr	18.5 sr	[24.50]	

ing that the Klett solution (24.41) does not critically depend upon the choice of LR for long wavelengths. On the other hand, in the UV, any flaw in the choice of the lidar ratio will lead to a major error in the backscatter coefficient.

24.3.8 The Color Ratio

As defined above in (24.4), the CR provides a rough estimate of the size of the aerosol. If we recall the definition of the color ratio and consider two arbitrary wavelengths, 532 and 1064 nm, we have

$$\text{CR}(532 \text{ nm}, 1064 \text{ nm}, z) = \frac{\beta_{532 \text{ nm}}^{\text{aer}}(z)}{\beta_{1064 \text{ nm}}^{\text{aer}}(z)}. \quad (24.55)$$

The small particle limit in scattering theory is given by the Rayleigh limit, the cross-section of which is proportional to λ^{-4} . Hence, in the case of pure Rayleigh scattering, the CR for 532 and 1064 nm would be $(1/2)^{-4} = 16$. In contrast, at the large particle limit, values of around 1 would be expected, as the scattering becomes less dependent on the wavelength. However, it is not possible to classify an aerosol in a straightforward manner based on its color ratio. This is because, for typical aerosol particle sizes that are accessible to lidar (i.e., a radius of 0.1–5 μm), the backscatter coefficient depends strongly on the refractive index [24.54]. Hence, one color ratio does not contain enough information to

determine the size of the scattering aerosol particles. The situation is different for cirrus clouds, for which the refractive index is that of ice. Although they consist of large ice crystals with size and shape distributions that depend on the temperature, altitude, the vertical movement of the air, and possibly other parameters, observations and modeling efforts seem to suggest that $\text{CR} < 1$ are common. For example, in [24.55], cirrus clouds over the US were analyzed and an average color ratio of 0.88 was obtained from a year-long observational cycle. Also, simulations reported in [24.56] indicated that $\text{CR} \approx 0.7$ for hexagonal columns and $\text{CR} \approx 0.8$ for hexagonal plates with wavelengths of 532 and 1064 nm. On the other hand, $\text{CR} \approx 2$ were found for large spherical particles.

Values widely distributed around 2 were also derived using the spaceborne lidar in CALIPSO [24.44]. It was found that the color ratio distribution peaked at $\text{CR} \approx 2$ in different cases involving dust and smoke aerosols over the land and ocean. In cases where the coarse mode contribution is negligible (e.g., for anthropogenic pollution [24.12] or at remote sites such as the polar regions), the color ratio is typically larger. Values of around 5 were found for Arctic haze with wavelengths of 532 and 1064 nm [24.48].

The size of an aerosol in the accumulation range can be estimated quite precisely from multiwavelength Raman lidar; for more on this, please refer to the chapter on Raman lidar (Chap. 25).

Table 24.4 Depolarization ratios for different aerosol types

Type of aerosol	355 nm	532 nm	Reference	Remarks
Fresh desert dust	25%	31%	[24.12]	HSRL lidar, Morocco
Desert dust	–	32%	[24.57]	CALIPSO over the Atlantic
Marine aerosol	2%	3–5%	[24.12]	
Marine aerosol		Max. 22%	[24.14]	Crystalline sea salt
Dust	17%	26%	[24.12]	
Anthropogenic		6%	[24.12]	Europe
Boreal biomass burning		7%	[24.12]	Aged aerosol over Europe
Boreal biomass burning		5%	[24.58]	Aged aerosol over Asia
Tropical biomass burning	16%	16%	[24.12]	
Volcanic	35%	37%	[24.12]	Eyjafjalla, Iceland in 2010
Cirrus		10–100%	[24.13]	Asia; 100% for optically thin cloud

24.3.9 Depolarization

The measurement of aerosol depolarization is a mature technique that provides a reliable scheme to classify and distinguish different aerosol types. As stated above, backscatter at spherical particles preserves the polarization of the light. As liquid particles are almost spherical in shape due to the action of surface tension, depolarization also gives a quick indication of the state of aggregation of the particles. However, the polarization of the light backscattered from hexagonal ice crystals—which are common in cirrus clouds—is also unchanged if the laser beam is perpendicular to the plane with hexagonal symmetry. For this reason, it is convenient to incline the beam of the laser just a few degrees away from the vertical to remove the symmetry of the ice crystals [24.11]. It is also worth bearing in mind that the smallest particles do not depolarize the light effectively [24.14], as the shape becomes less important with decreasing radius. Nevertheless, the depolarization induced by air molecules is nonzero and depends on the spectral resolution. Following the guidance given in [24.59], we assign the (roughly) elastic backscattering from air molecules to the *Cabannes line*, for which the vibrational and rotational states of the molecules remain unchanged. This line is surrounded by a spectrum of rotational Raman lines. Together, the Cabannes line and the rotational Raman spectrum are usually called the *Rayleigh spectrum*. In [24.59], it is stated that the depolarization of the Cabannes line for lidar applications (180° backscatter, linear initial polarization) is 0.363%. This depolarization is therefore expected even in completely aerosol-free layers if narrow interference filters with a bandpass of < 0.3 nm are employed. When filters with a wider bandpass are used, more and more of the rotational Raman lines are recorded too, which increases the depolarization of the clear air to 1.43%.

Table 24.4 compiles depolarization measurements for different aerosol types. The depolarization induced by desert dust, the most abundant type of aerosol on

Earth, is significant. So far, only a few lidar instruments have measured the depolarization in the near-infrared as well. However, the inclusion of an additional depolarization channel in the infrared was shown in [24.60] to facilitate the determination of the effective radius of aerosol particles > 1 μm using multiwavelength lidar systems.

Some of the values in the table are also presented in [24.61], which provides an aerosol classification scheme based on the lidar ratio and depolarization. 100% depolarization for thin and subvisible cirrus clouds over Taiwan, regardless of altitude, have been reported [24.13]. In [24.62], observations performed over North America were used to show that depolarization may increase with decreasing temperature; the same may also be true for China [24.63].

24.3.10 Determination of the Boundary Layer Height by Lidar

Assuming that the main source of aerosols is the ground and that convection lifts the aerosols up and mixes them almost homogeneously within the atmospheric boundary layer (ABL), the altitude of the ABL can easily be derived using a backscatter lidar. There are several slightly different methods of achieving this; these methods are explained in [24.64]. The idea behind all of them is that the profile of the backscatter coefficient $\beta(z)$ or that of the attenuated backscatter $B(z)$ shows higher, almost altitude-independent, values within the ABL and lower values above the ABL. Hence, we require the derivative of $\partial B/\partial z$. In fact, the ABL height H_{ABL} can be determined relatively simply via the gradient method (GM),

$$H_{\text{ABL}}^{\text{GM}} = \min \left(\frac{\partial B(z)}{\partial z} \right). \quad (24.56)$$

Slightly lower values for the ABL height are found by using the inflection point method (IPM), which employs

the second derivative

$$H_{\text{ABL}}^{\text{IPM}} = \min \left(\frac{\partial^2 B(z)}{\partial z^2} \right). \quad (24.57)$$

According to [24.65], this inflection point method gave the best agreement with radiosonde data.

Other methods use either the derivative of the logarithmic attenuated backscatter profile or filter the $B(z)$ profiles with wavelets [24.64, 66].

24.4 Devices and Systems

In this section we discuss the main components of a lidar and some basic design considerations. The complexity of lidar systems will be highlighted and the most important technical parameters for understanding the advantages or disadvantages of a given system are introduced.

All lidar systems can be separated into two parts: the emission optics that produce the outgoing light beam, and the recording branch that retrieves the backscattered light and counts the signal.

The backscattered photons produce an image of the laser at each altitude. This is recorded by a telescope. In lidar systems that use different colors or possess polarization sensitivity, the individual wavelengths or polarization states must be separated and guided onto detectors such as photomultipliers.

24.4.1 Components of the Emission Optics

The emission optics can be divided into the laser and the beam-widening telescope (BWT). The laser is the light source for the lidar, implying that it is a key component. Its most important parameters are:

- **Power.** Measured in watts, the power is the number of photons that the laser emits, meaning that it governs the quantity P_0 in the main lidar equation. The power is the product of the pulse energy (in J) and the repetition rate of the laser (in Hz). Note that for lidar operation it is beneficial to distribute the laser energy into a few strong pulses because the background illumination is added to each shot. Hence, strong pulses with low repetition rates lead to a better signal-to-noise ratio (SNR). Lasers frequently require a warm-up period to obtain their full power.
- **Divergence.** This is the angle by which the diameter of the beam widens as it propagates. It is a very important quantity for lidar operations. The FOV of the recording telescope is normally larger than the

The abovementioned conditions of a well-mixed ABL and dominant aerosol sources on the ground are frequently fulfilled during the day in the low and mid-latitudes, so many publications have reported successful determinations of the ABL height using lidar. However, the situation is more complicated under stable conditions: if the aerosol is advected over long ranges and the atmosphere is stably stratified, the methods mentioned above cannot retrieve the correct ABL height. We will give examples of this in Sect. 24.8.

beam divergence, such that the whole laser beam lies within the FOV of the recording telescope (this corresponds to $O(z) = 1$ in the main lidar equation (24.13)). Hence, a laser with a small beam divergence yields a small FOV and decreased sensitivity to background illumination. When choosing an appropriate laser, it should be noted that the divergence can slowly increase during operation due, for example, to the aging of flash lamps in the laser. Moreover, for lidar applications, the appropriate definition of the divergence is the angle within which all of the laser energy is confined, whereas manufacturers sometimes define it as the angle at which the laser energy drops by 50% of its maximum value (i.e., the *full width at half maximum*, FWHM).

- **Beam point stability.** This refers to any drifting of the direction in which the laser beam is emitted over time, and is normally much smaller than the divergence. However, it is sometimes only calculated when the laser has warmed up.
- **Pulse duration.** This quantity becomes important when a high altitude resolution is required, as the basic lidar equation assumes that the length of the laser beam is smaller than the altitude bins.
- **Polarization accuracy.** Due to optical components behind the laser head, the effective polarization accuracy will be $< 100\%$. In particular, reflections that occur behind the laser to guide the beam into the sky have the potential to deteriorate the polarization accuracy.
- **(Spectral) line width.** This parameter, which has units of cm^{-1} , describes the spectral purity of the laser. It can be increased by injection seeding, which is required for wind measurements performed via coherent detection (see the chapter on wind lidar). In injection seeding, a small spectrally pure laser is used to *seed* the cavity of the main laser, meaning that it determines the mode of the main laser that is

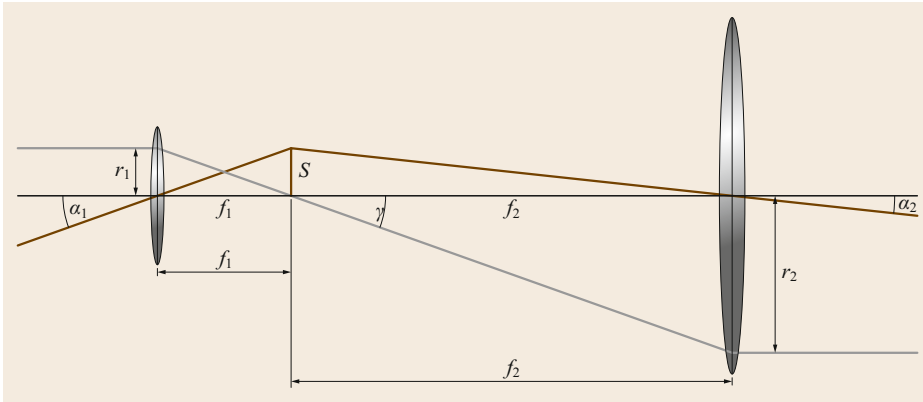


Fig. 24.9 Image formation in a beam-widening telescope

amplified. An extremely small spectral width is not required to determine the visibility or aerosol properties.

- *Energy distribution within the laser beam.* This is not normally an important quantity, as the whole laser beam is detected. However, we mention it here because it relates the beam divergence based on the FWHM to the full divergence.

Aside from the abovementioned parameters, other *soft factors* must also be considered in lidar applications. Long-term stability of the beam properties and the laser energy are generally desired. Therefore, maintenance that changes the optical setup should be minimized; e.g., for flash-lamp-pumped lasers, it is desirable for the laser properties to remain unchanged as the lamp ages, and for flash lamp replacement to be possible without the need to realign the optics. Power consumption, cooling solutions, and sensitivity to temperature changes or vibrations also need to be considered when choosing a laser.

Beam-Widening Telescope

The emission optics frequently also contain elements other than the laser and the mirrors that are needed to guide the laser light into the atmosphere. Many systems use a beam-widening telescope, which increases the diameter of the laser beam but reduces the tangent of the beam divergence by the same factor, as can be seen in Fig. 24.9.

Consider two lenses with focal lengths of f_1 and f_2 and a common focal plane, as seen in Fig. 24.9. The two lenses are arranged as in a reversed Keplerian telescope. The angle γ implies that the laser spot radii before (r_1) and after (r_2) beam widening obey the relation

$$\frac{r_2}{r_1} = \frac{f_2}{f_1}. \quad (24.58)$$

To study the laser beam divergence before (α_1) and after (α_2) beam widening, we consider rays through the center of the lenses and the image scale S , which leads to

$$S = \tan(\alpha_1)f_1 = \tan(\alpha_2)f_2 \quad (24.59)$$

and therefore

$$\frac{\tan(\alpha_2)}{\tan(\alpha_1)} = \frac{f_1}{f_2}. \quad (24.60)$$

The sketch shown in the figure uses geometrical optics, which is justified if all dimensions and spot sizes are much larger than the longest wavelength. Figure 24.9 shows an optical design that should actually be avoided, as a real image of the laser will form at S , producing heat and turbulence within the telescope. To avoid this problem, a Galilean telescope with a virtual image is preferable.

24.4.2 Recording Optics

The detection branch is divided into four systems: the recording telescope, the optics for spectral separation, the recording devices, and the counting electronics.

The Telescope

One of the most important parameters of the telescope is its diameter. Larger mirrors collect more light but also produce longer overlap ranges.

The focal length (f) is not very important. Although the focal length determines the image scale, the most important quantity of a lidar is the FOV of the telescope. When an aperture stop is inserted into the focal plane of a telescope with a diameter of d , the FOV is determined (according to Fig. 24.3) via

$$\text{FOV} = 2 \arctan\left(\frac{d}{2f}\right). \quad (24.61)$$

A smaller FOV reduces the amount of stray light collected during daytime observations. However, a smaller FOV also means a higher overlap altitude.

Another consideration regarding the recording optics is the surface smoothness, for which the criterion introduced by Maréchal in 1943 is relevant (see, e.g., [24.67]). This criterion considers the root mean square (RMS) difference between an ideal wavefront and one deformed by a nonideal telescope surface. Any degradation is negligible if the RMS difference between wavefronts is smaller than 1/14 of a wavelength. If the Maréchal criterion is fulfilled, the optics are as good as they can be for their size, and they are said to be *diffraction limited*. Note that:

- The deviation is measured at the wavefront. A mirror with a defect depth of Δ produces an optical path difference of 2Δ , so the surface roughness of the mirror must be smoother than 1/14 of a wavelength.
- The Maréchal criterion considers the whole surface and is thus superior to the Rayleigh criterion. Consider a perfect mirror with a small defect of depth $\Delta > \lambda/8$. This tiny defect will give rise to a wavefront error of $> \lambda/4$, meaning that the Rayleigh criterion is violated, although it will still deliver good images. More realistically, a mirror with a surface roughness $\Delta \approx \lambda/10$ will produce stray light and will not fulfill the Maréchal criterion.
- As lidar systems consist of many optical surfaces, and as the atmosphere by astronomical seeing further degrades the image quality, it is advisable to have a telescope that is better than simply *diffraction limited*. Ideally, the whole optical path should meet the Maréchal criterion.
- As the deviation is evaluated in comparison to the wavelength, the user should bear in mind the shortest wavelength of the lidar. Optical defects are clearly more severe for UV wavelengths than for infrared ones.

On the other hand, the FOVs of lidar systems are generally small (≤ 1 mrad), meaning that off-center optical aberrations such as comas generated by parabolic mirrors can normally be neglected. It is easier for any optical system to produce a good on-axis image than to image large FOVs.

The thermal stability of the mirror and telescope structure should also be considered. As the temperature at which the lidar is operated will change over time, a system that does not require refocusing due to temperature shifts is desirable. Nowadays, mirrors made from quartz or ceramic glass with very small thermal expansion coefficients are available. The same is true of

telescope tubes made from carbon fibers. Alternatively, the system can be designed such that the telescope structure and the mirror have identical thermal expansion coefficients.

Another issue regarding the thermal stability of the optics is the potential for problematic internal strain in a mirror. Such strain will lead to permanent surface changes as the temperature fluctuates, even when the mirror has been polished to high precision in a lab. This can only be avoided by heating the substrate to a specified temperature and then cooling it so slowly that all internal stress dissipates. This process is called *annealing*, and is mandatory for optical mirrors.

Optics for Wavelength Separation

The main parameters for interference filters (IFs) are the central wavelength (of transmission), the bandwidth, the peak transmission, and the angle at which the filter is to be used. Moreover, the out-of-band suppression—the extent to which light of the wrong wavelength is suppressed—is also important, for two reasons. First, sometimes a very weak signal must be recorded next to a strong signal in a lidar (see the chapter on Raman lidar). Second, glass can fluoresce if it is illuminated with UV light such as the third harmonic of the frequently used Nd:YAG laser at 355 nm [24.68]. Hence, due to the optical components within a lidar, leakage is observed from the strong elastic signal observed at shorter wavelengths to the weaker Raman-shifted light at longer wavelengths. Therefore, it is recommended that weak signals should be separated from strong UV signals as quickly as possible along the optical path in order to strongly suppress the elastic signal in the inelastic branch. An example involving a water vapor system is discussed in [24.69]. Systems that utilize a large amount of light transmission through glass, such as those with fiber optics, are prone to fluorescence.

Finally, the effects of temperature and aging on interference filters should also be accounted for. The peak transmission is a function of temperature; however, as different technologies are used to manufacture IFs, this temperature dependence can vary from IF to IF. While modern IFs last several years without degrading, the application of narrow spectral filters in a changing environment necessitates careful monitoring.

The same considerations outlined above are also valid when choosing dichroic mirrors. Additionally, as these mirrors are normally located in the middle of the optical train, far from the photomultipliers, smooth optical surfaces are required so that they do not degrade the overall optical quality. Also, antireflection coatings can strain optical surfaces, potentially degrading the optics or introducing birefringence.

Recording Devices

In lidar applications, it is not normally necessary to record two-dimensional (2-D) images, only the backscattered light from the laser. This is typically done using devices such as photomultiplier tubes (PMTs) or avalanche photodiodes (APDs). In both of these devices, the photoelectric effect and current amplification are used to obtain an output voltage that is within the linear dynamic range of the device, thus ensuring that the output voltage is proportional to the number of incident photons. A large dynamic range is often required in lidar applications due to the $1/z^2$ dependence of the signal strength with range z (24.13). It should be noted that PMTs show hysteresis, meaning that the recorded photocurrent is a function of the previous photocurrent: if the illumination changes quickly (e.g., rapidly rises), the internal voltage of the PMT is altered (reduced) to adapt to this new situation and keep the output signal constant. However, as real devices require time to adapt to a new voltage, the recorded output signal depends on the previous amount of incident radiation to some extent.

PMT photocathodes can be made from various materials, and the photocathode material determines the range of wavelengths that the PMT is sensitive to. Two important parameters for PMTs are the *quantum efficiency* (QE), which is the number of photoelectrons emitted at the photocathode divided by the number of incident photons, and the *radiant sensitivity*, which is the photoelectric current at the cathode divided by the incident radiant flux. The gain and the noise (sometimes called the dark current) are also important. Dark current can arise in different ways: due to thermal emission at the cathode or the dynodes, ohmic leakage between the anode and other electrodes, cosmic rays or radioactivity, or *scintillation* caused by the collisions of stray photoelectrons with the PMT housing or glass body.

Nevertheless, PMTs are robust, long-lasting devices that show very good performance at UV and visible wavelengths. Infrared photons have lower energy, so it is harder for them to generate a voltage (via the photoelectric effect) that is clearly above the noise limit. Therefore, avalanche photodiodes (APDs) are an alternative for longer wavelengths. APDs work in a similar way to PMTs: they consist of a doped semiconductor material to which a voltage is supplied. Incident photons produce additional charge pairs (electrons and holes) in the material that are accelerated by the supplied voltage, generating a current gain through impact ionization. Hence, APDs are even capable of counting single photons.

The sensitivity of the detection surface may not be constant. As objects from finite and infinite distances will be imaged differently (see Fig. 24.8), the light

should not be focused on the PMT, as this could cause the effective efficiency to become a function of altitude, leading to artificial gradients in the lidar profile. A thorough overview of PMTs is given in documentation provided by Hamamatsu, a PMT manufacturer [24.70].

Counting Electronics

The photocurrent produced by the detector in a lidar system is typically counted using transient recorders. One of the most important parameters of a transient recorder is the digitalization frequency f , which determines the vertical resolution of the lidar signal according to

$$\Delta z = \frac{c}{2f}, \quad (24.62)$$

where Δz is the height resolution and c is the speed of light.

Transient recorders can record the photocurrent from the detector in two different ways. In the photocounting mode, single detection events are counted whenever the photocurrent rises above a predefined threshold value. This is normally the preferred mode for weak signals, but there is a maximum count rate beyond which the current spikes produced by different photons merge together, making them difficult to separate. In contrast, recording in analog mode means that an integrated photocurrent is calculated for each height bin Δz . In this mode, the signal quality depends on the digitization depth (units: bits). In the analog mode, strong signals from the near range or clouds can be retrieved well, but electronic noise presents a challenge when this mode is used to detect weak lidar signals.

This is demonstrated in Figs. 24.10 and 24.11. In these figures, the fictitious output (photocurrent) of the PMT current is given in blue. In the photocounting mode, a threshold photocurrent must be selected. Since the current from a detected photon is normally much stronger than the electronic noise of the detector, choosing the value of this threshold is usually a straightforward task. Hence, almost independent of the threshold value, three photocounting events are detected in the case shown in the figures. Note that, in this mode, the unit of the photocounting channel is Hz. In the analog mode, the photocurrent is integrated over the complete altitude bin, so it is measured in ampere. The output depends critically on the background noise. In the example given in the plot, this background is not even flat—it rises over time (i.e., with altitude). Baselines that exhibit this behavior do actually occur in real signals. For this reason, the photocounting mode is preferable under low light conditions. However, high-intensity conditions are depicted in Fig. 24.11. In this case, a count rate of four would strongly underestimate

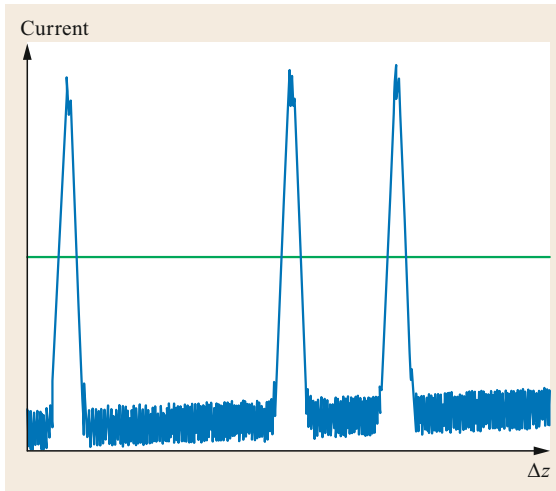


Fig. 24.10 Detector output (blue) and detection threshold (green) for low light levels

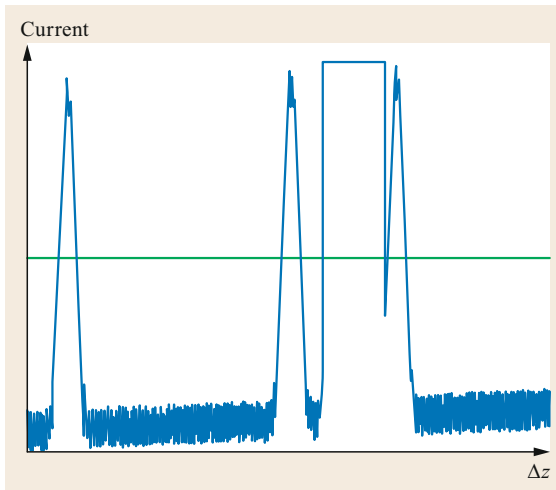


Fig. 24.11 Detector output (blue) for high light levels

the signal: in reality six photons were detected, three of which arrived so close together in time that the detector produced a constant output (i.e., the output becomes saturated) during the interval containing those events. Thus, the analog mode is better suited to retrieving the count rate in this situation.

Some modern transient recorders can record the events from one detector in both photocounting and analog modes simultaneously, meaning that two different lidar profiles (with the same physics) can be retrieved. For some transient recorders, the process of calculating the analog signal introduces a significant time delay, meaning that this signal is shifted in time compared to the photocounting signal (this is particularly apparent for low altitudes).

24.4.3 Design Considerations

Due to the range of environmental monitoring tasks that lidars are used for nowadays, there are various types of backscatter lidars that differ in size, measured quantities, range, ease of use, and eye safety. While small backscatter lidars such as ceilometers have been available commercially for a number of years, meaning that their reliabilities are relatively well known, larger multiwavelength systems are quite new to the market. For this reason, the majority of research instruments are still developed in-house by universities and institutes and therefore vary from type to type. This means that special standards such as algorithm intercomparisons are important for maintaining a reliable standard (see Sect. 24.6).

When choosing a lidar, the first task is obviously to establish the parameters that need to be measured and the altitude to be probed. This influences the selection of the laser and the wavelengths employed. Three designs are possible for the arrangement between the laser and the recording telescope; these are depicted in Fig. 24.12.

In the biaxial configuration, the optical axes of the laser and telescope are different. This design makes it easier to block laser light from low altitudes that could disturb the measurements (e.g., for measurements in the stratosphere or beyond). The other two designs utilize a common optical axis for laser and telescope. In the in-line setup, the same telescope is used to widen and guide the laser beam and record the backscattered signal.

The overlap and hence the starting point for a reliable signal is an important consideration in all designs. Some solutions utilize several telescopes: a smaller one with a wide FOV for the near range and a larger one for longer distances. Given that this requires two telescopes and two recording branches (i.e., filters, multipliers, and transient recorders), adopting this approach will substantially increase the cost, size, and complexity of the lidar.

Another important parameter is the eye safety of the laser. Systems that are not eye safe are subject to regulations such as air traffic or national laws. Lasers are classified into four groups: those in class 1 are not dangerous in normal use, whereas those in class 4 present a high risk to the eyes and skin. The distance from the laser at which the light from it is safe for eyes (skin) is called the *nominal ocular hazard distance* or NOHD (*hazard distance* or HD). These distances depend on various laser parameters: the power, the wavelength, the pulse repetition rate, the beam divergence, and the beam diameter. Widening the laser beam can reduce the NOHD: if the laser diameter becomes larger than a human pupil, the full power of the laser cannot enter the

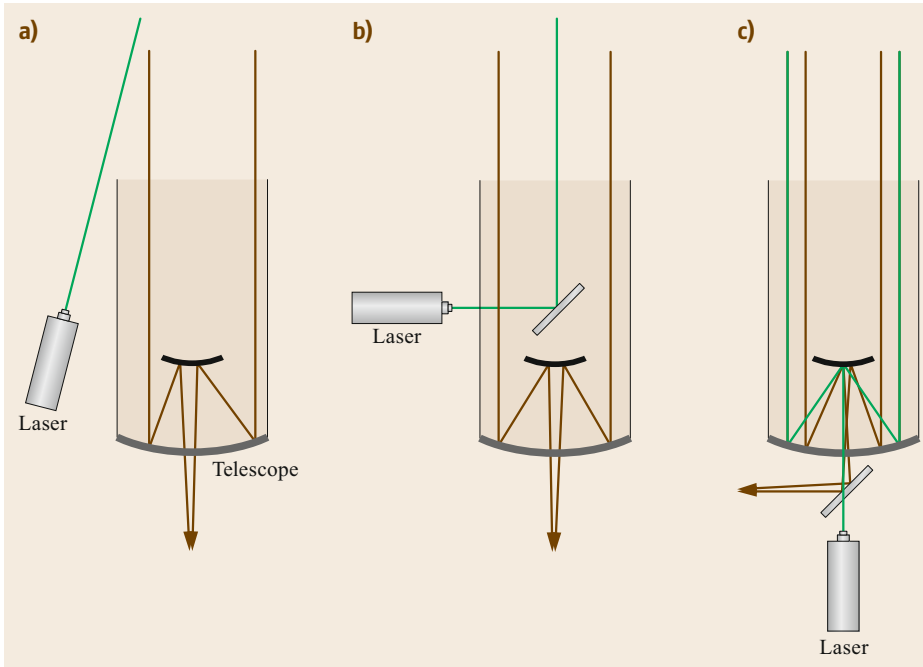


Fig. 24.12a–c The three possible designs of a lidar system: (a) biaxial, (b) coaxial, and (c) in-line

eye, so the risk is reduced. A radar is used in some lidar systems to monitor for any aircraft approaching the FOV, which triggers the deactivation of the laser. This technology has actually existed for a number of years [24.71].

Yet another fundamental criterion is the ease of use of the lidar system. While some of the big multiwavelength Raman systems require regular maintenance (e.g., flash lamp replacement for the laser, or monitoring the spectral positions of the narrow-band filters) and are therefore mainly used for case studies, simple backscatter lidars such as ceilometers or micro pulse lidars can run continuously for years unattended [24.72]. This is obviously a big advantage for environmental monitoring of any kind.

As lidar systems are sometimes installed remotely, grounding can be a concern. Similarly, transient recorders can be disturbed by radio emissions, leading to oscillatory behavior. According to (24.1), a frequency of 10 MHz corresponds to a wavelength of 15 m. Hence, the electronic parts of a lidar must be shielded properly.

24.4.4 Ceilometers

The main tasks of a ceilometer are to determine the cloud base height and vertical visibility and to investigate aerosol layers in the lower troposphere. Unattended 24/7 operation under all meteorological conditions and an eye-safety class of 1M are mandatory

requirements for such lidar systems. Network deployment ability requires that maintenance costs are low and maintenance intervals are long.

Manufacturers of ceilometers must consider all of these points. Therefore, ceilometer designs usually differ significantly from those of lidar systems used for research. Typical design differences are listed below (see keywords in Sects. 24.4.1 and 24.4.2):

- **Laser.** Typical ceilometer lasers operate in the near-infrared region. The most common light sources are therefore laser diodes and Nd:YAG lasers operated at the first harmonic. Lifetime and cost considerations are the main factors to consider when choosing the laser.
- **Telescope.** Most common optical designs of ceilometers use one or two lenses instead of a complex telescope. Lens diameters of ≤ 15 cm are sufficient for ceilometer tasks. This setup allows for a compact, robust, and cost-effective construction, regardless of whether a biaxial or coaxial design is chosen. Biaxial designs use one lens to collimate the laser beam and another to focus the backscattered light onto the receiver; the optical axes are either parallel or slightly inclined. Coaxial designs require one lens only. To avoid optical crosstalk between the transmitter and receiver, the traditional beam splitter setup is replaced with a novel design that divides the lens into separate transmitting and receiving areas [24.4, 73] (Fig. 24.13).

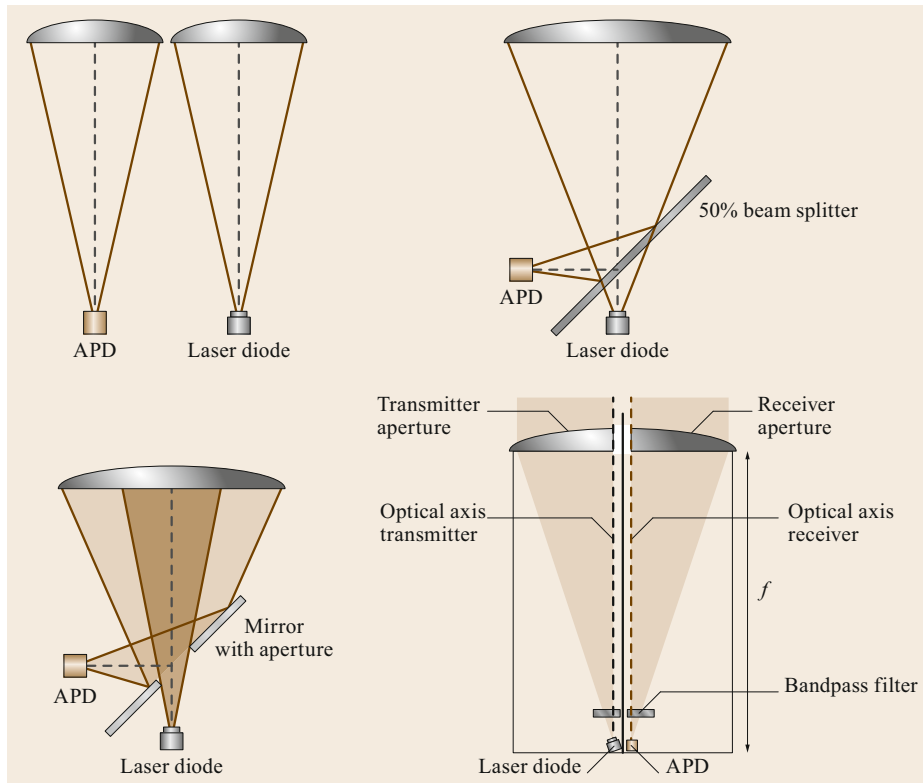


Fig. 24.13 Optical system designs for ceilometers (after [24.73])

- *Optics used for wavelength separation.* Ceilometer IF passbands are chosen to be wide enough to compensate for laser wavelength tolerances or temperature dependences. Current commercial systems use IFs with passbands ranging from about 2–30 nm.
- *Recording devices.* Most ceilometers use APDs, but there are also systems with PMTs.
- *Counting electronics.* Analog digital converters (ADCs) are commonly used in ceilometer electronic design; more sophisticated devices such as transient recorders are generally not required for ceilometer applications.
- *Bird deterrent.* Reliable automatic operation of ceilometers requires the continuous monitoring of all measurement parameters that can affect the performance of the lidar system. This includes the transmission characteristics of the glass window shielding the lens. Animals, in particular birds, are often the reason for reduced transmission. One way to reduce the likelihood of reduced transmission due to birds is to install a deterrent device that encourages birds to perch in an area away from the window.

24.5 Specifications

As with many other remote-sensing instruments, it is not a trivial task to define the *resolution* of a lidar system. The maximum range at which cloud or aerosol layers can be detected depends on the meteorological situation and is therefore dependent on when and where the observations are made. Generally, the laser beam is attenuated in thick cloud. Thus, measurements of regions above clouds can be invalid, although valid lidar signals may be detected from those altitudes on

clear days. In contrast, very clear conditions with low backscatter will lead to a weak lidar signal with more noise. The presence of an aerosol layer at this altitude increases the count rate and the SNR. Moreover, the signal quality also depends on the solar altitude. The quality is best during the night, and some lidar systems even shut down before the sun enters the field of view.

For this reason, statements are sometimes made that a lidar at a specific site can resolve aerosol lay-

Table 24.5 Typical application-dependent resolution and eye-safety class requirements for lidars

Lidar type	Parameter (Table 24.1)	Application	Typical range resolution	Typical temporal resolution	Eye-safety class	Continuous operation?	Remarks
Ceilometer	Attenuated backscatter	Cloud base detection	5–10 m	2–30 s	1M	Yes	
		Detection of aerosol layer boundaries	10–50 m	1–10 min	1M	Yes	
Single-wavelength particle backscatter lidar	Backscatter coefficient Extinction coefficient Lidar ratio	Investigation of elevated aerosol layers	10–200 m	10 s–10 min	1M, 2, 2M, 3B	Typically not required	Includes ceilometer capabilities
Multi-wavelength lidar systems	Color ratio Ångström exponent of backscatter Ångström exponent of extinction	Aerosol classification, optical properties of clouds	7.5–150 m	0.5 s–10 min	1M, 2, 2M, 3B	Typically not required	Includes single-wavelength system capabilities
Polarization lidar	Depolarization	Aerosol classification	10–200 m	10 s–10 min	1M, 2, 2M, 3B	Typically not required	Includes (at least) ceilometer capabilities

ers with a given backscatter at a certain altitude > 50% of the time. The maximum resolution depends on the sampling speed of the electronics and the number of laser shots that are written in each data file. However, in many applications, some of the lidar profiles are

averaged to obtain a SNR that is best suited to the given application. Table 24.5 summarizes some typical specifications of various lidar systems used for cloud and aerosol research, including the required laser class, ranging from 1M (eye safe) to 3B (highly dangerous).

24.6 Quality Control

As it is an active remote-sensing instrument, a lidar collects light. Pointing such a system in the direction of the sun will increase the background light dramatically, and may even harm the recording devices. For this reason, lidars are frequently switched off when the sun is close to the FOV (e.g., at noon in the tropics).

Similarly, thick clouds will reduce the range of a lidar instrument. An example is given in Fig. 24.14. Here, a cloud at an altitude of 2 km presents a count rate at 1064 nm that is almost two orders of magnitude larger than that at the end of the overlap range (about 500 m high). Above the cloud, the signal even has negative values; in other words, count rates below that produced when only the background illumination and electronic noise are recorded. According to (24.23), this phenomenon is unphysical, as is the rise in count rate with altitude seen in Fig. 24.14. A count rate that rises with altitude would mean a negative backscatter or extinction coefficient. Hence, it is clear that the lidar signals above the cloud in Fig. 24.14 cannot be evaluated.

The fact that thick cloud can completely attenuate the lidar signal presents a major challenge to ground-based systems. Hence, ground-based lidar studies of turbulence and the interactions between aerosol, moisture, and clouds above the top of the cloud are very limited.

24.6.1 Hardware Quality Control

As the laser is a critical component of a lidar, its power is monitored in some systems. This can be done by splitting the laser beam and focusing a fraction (on the order of 1%) of its light onto a photodiode. The transmission through the final optical window that separates the lidar from its surroundings (and may therefore be degraded by precipitation, dust, or even scratches) may also be monitored. Of course, it is also necessary to check that switching cooling systems on and off or devices that are only sporadically activated in the system do not produce electronic artifacts in the lidar signal.

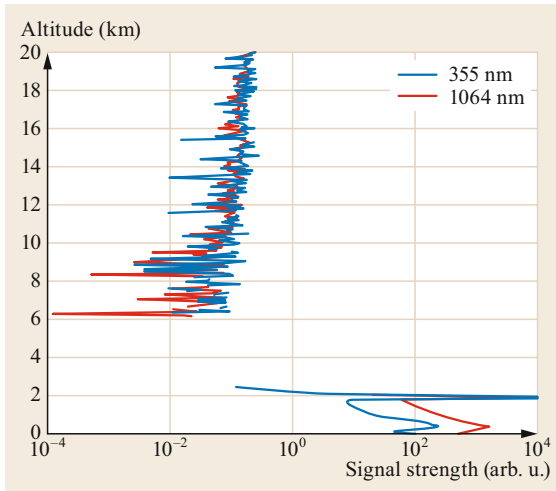


Fig. 24.14 Effects of thick cloud on the lidar signal. Note the negative signal at 2–6 km, and the rising count rate with altitude above the cloud

It is crucial to align the emission and recording optics correctly. Simply recording the altitude corresponding to the maximum lidar signal (i.e., when the full laser beam is recorded by the telescope) is difficult because, as mentioned earlier, environmental variations will affect not only the backscatter coefficient but also the multiple scattering and hence the overlap. Therefore, the altitude at which the signal maximum occurs and the count rate at that maximum will constantly change over time for a backscatter lidar. In systems where the optics are not permanently fixed, it is more convenient to align one branch of the optics (e.g., the emission branch) relative to the other (the recording branch) using a motor and to monitor the measured count rate within a particular height interval as a function of the relative alignment. This is called an overlap scan. As can be seen from Fig. 24.15, the position that gives optimal alignment is easily discerned. Typically, not all of the recording channels share precisely the same optical axis. Nevertheless, as the divergence of the laser beam must be smaller than the FOV of the telescope, there should be a plateau with a constant count rate for different alignment positions. Noise in the data and (especially) variations in the count rate due to changes in the backscatter coefficient within the considered altitude range or in the extinction coefficient below that altitude range lead to an imperfect plateau. For this reason, such an overlap scan can only be performed under cloud-free conditions. Drastic temperature changes that could affect the various optical components or vibrations due to transport may necessitate an overlap

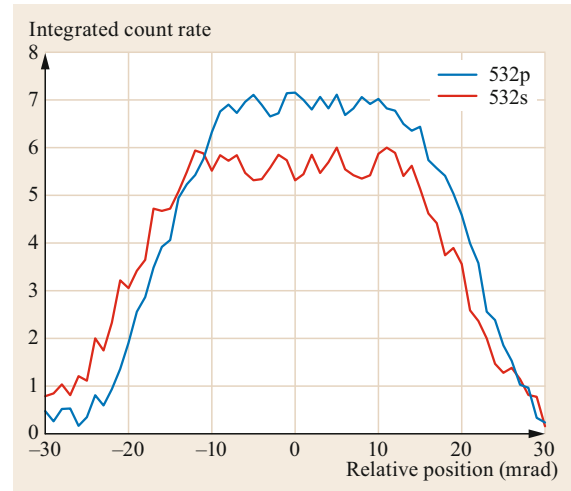


Fig. 24.15 Example of an overlap scan. Height interval: 1000–1500 m

check. Modern systems may track the overlap automatically using a small camera that tracks the image of the laser at the field stop (see Fig. 24.1).

The possible sensitivity of transient recorders to radio emissions or strong and variable electric fields that may originate, for example, from the laser and its power supply has already been mentioned.

When installing a lidar in the field, it is important to include a proper floor, a sufficient electrical supply and appropriate grounding, and effective protection against moisture. Intense sunlight or harsh, cold winds must not shift the system outside its prescribed temperature range, as this could cause the laser to lose power or even fail and the bandpasses of the interference filters to shift. The emission window must be dry and clean all the time.

24.6.2 Error Analysis

The quality of the evaluation process can also be checked, using software. Problems such as that shown in Fig. 24.14 (negative count rates, or, more generally, count rates below that of the background) can be detected by software automatically. In the same way, signals that become saturated or very weak should be identified.

The signal quality is generally gauged via the signal-to-noise ratio (SNR). In its simplest form, this can be written as

$$\text{SNR}(z) = \frac{P(z)}{\sqrt{P_{\text{bg}} + P(z)}}, \quad (24.63)$$

where $P(z)$ is the lidar signal (as above) and P_{bg} is the background count rate. However, this definition is slightly controversial. If we consider that the total measured signal P_{tot} is equal to the sum of the (real) lidar signal and the background count rate [24.74], i.e.,

$$P_{\text{tot}}(z) = P(z) + P_{\text{bg}}, \quad (24.64)$$

and we take P to be in units of photons and assume that the electronic noise can be neglected because it is much smaller than the noise from Poisson statistics, then

$$\Delta P = \sqrt{P_{\text{tot}} + P_{\text{bg}}} = \sqrt{P + 2P_{\text{bg}}}, \quad (24.65)$$

which leads to

$$\text{SNR}(z) = \frac{P(z)}{\sqrt{P(z) + 2P_{\text{bg}}}}. \quad (24.66)$$

Hence, slightly different approaches are found in the literature. In [24.75], the authors start by using (24.63) and then analyze this subject in far more detail. This analysis is not repeated here because it requires detailed knowledge of technical parameters (transmission of the optics, detector characteristics) that an average user of lidar data would not have. On the other hand, a quick check of the quality of raw data can be performed using either (24.63) or (24.66). While the presence of clouds obviously modifies the lidar signal dramatically, the lidar profile should be similar for cloudy and cloud-free conditions, as should the SNR.

Software intercomparisons [24.76] as well as dedicated instrumental intercomparison campaigns [24.77] have been performed for networks of lidar systems, and the results have been reported. Such reports can be useful when selecting a new lidar system.

24.6.3 Depolarization

The importance of having reliable information on the depolarization induced by the scattering particles in order to distinguish ice from water clouds or the main aerosol types was mentioned earlier. Good calibration of the depolarization is therefore also mandatory, including possible crosstalk correction. *Crosstalk* is parallel polarized (with respect to the laser) light that is

erroneously measured in the perpendicular polarized channel, and vice versa. A rather easy method of checking for an alignment error between the emission and receiving branches is to use a half-wave plate [24.78, 79], also called a $\lambda/2$ plate, which consists of birefringent material that introduces a phase shift between perpendicular polarized light. The maximum phase shift is 180° (half a wave). Rotating the $\lambda/2$ plate causes parallel-polarized light to be shifted into perpendicularly polarized light and vice versa. Hence, differential sensitivities and optical misalignment can be determined. Let P_{\perp} and P_{\parallel} be the perpendicular and parallel polarized lidar signals, respectively. If $\delta^{\text{tot}} = \beta_{\perp}/\beta_{\parallel}$ is the total or volume depolarization ratio (as introduced in Sect. 24.3), we can define the gain ratio G of an ideal system as

$$m \equiv \frac{P_{\perp}}{P_{\parallel}} = G\delta^{\text{tot}}. \quad (24.67)$$

Now, if a phase shift angle of Θ occurs due to a phase shift between the emission and receiving optics, we obtain (following [24.79])

$$m = G \left(\frac{\delta + \tan^2(2\Theta)}{1 + \delta \tan^2(2\Theta)} \right). \quad (24.68)$$

If we now rotate the $\lambda/2$ plate by several known angles φ_j , we get

$$m_j(z) = G \left[\frac{\delta(z) + \tan^2(2(\Theta + \varphi_j))}{1 + \delta(z) \tan^2(2(\Theta + \varphi_j))} \right], \quad (24.69)$$

for the altitude of interest z . In (24.69), m_j (the ratio of lidar profiles) and φ_j are known, whereas the gain G , the volume depolarization ratio $\delta(z)$, and the misalignment angle Θ are not known. Hence, if we consider at least three different angles φ_j , the unknowns in (24.69) can be determined, meaning that the system can be calibrated. A detailed work on the calibration of polarization lidars using Mueller matrices [24.80] was recently published. In some lidar systems, this half-wave plate is controlled by a motor so that it can be routinely rotated by different φ_j .

24.7 Maintenance

As lidar systems consist of various rather sophisticated optical and electronic components, care must be taken during either design or operation to assure constant and adequate quality of the system (Table 24.6).

First, the laser requires attention. While some modern diode lasers are robust and easy to operate, even in harsh environmental conditions, other laser types require maintenance (e.g., replacing flash lamps, which

Table 24.6 Maintenance of backscatter lidar systems

Interval	Maintenance activity	Comment
Regularly	Check data flow	
Weekly and after snow or storm events	Check the instrument: is the window clean, is there any visible damage?	
Quarterly	Check that the blower is free from plants and dust	
Yearly (if necessary)	Change dehumidifier	Performed by some manufacturers
3–4 years	Replace laser	Performed by manufacturer
4–8 years	Replace computer	Performed by manufacturer

can necessitate realignment of the emission optics, a cooling system check, and the cleaning of critical optical components, as dust can be burned into glass by intense laser light). This is particularly true of the powerful lasers used in multiwavelength Raman lidars. Generally speaking, however, the weaker lasers used in ceilometers do not require maintenance and last several years in continuous operation.

Some optical components such as laser heads or surfaces that are used in multiple beam interference show a dependence on the temperature. A temperature control system for the whole lidar can therefore be useful. As mentioned earlier, it is also important to check that the (de)activation of cooling systems and the presence of devices that are only active sporadically do not produce electronic artifacts in the lidar signal.

Many other components of a lidar are much sturdier. The transient recorders, dichroic mirrors, interference filters, and photomultipliers are all quite robust and do normally not require special care. Modern IFs age better than older IFs. Old PMTs lose their ability to reliably

record high count rates, so a regular check of the data (see Sect. 24.6.3) is recommended.

As with all instruments installed outside, the lidar should be checked after strong rain or snow events (Is the entrance window clean, and is there any moisture inside the instrument?), frost (Is the window clean, and are the electrical plugs still working?), storms (Is the system firmly anchored?), and lightning (Has the electrical supply been affected?) The window requires the most frequent attention (i.e., cleaning). If the cleaning technique is not specified by the manufacturer, cleaning is typically performed with water and mild soap. Any remnants are removed with distilled water.

Given the cost of a lidar and the fact that smaller units are designed to run unattended even at remote sites for a long time, it may be helpful to install a surveillance camera that monitors the system (including its entrance window) and possibly other parameters such as the cloud cover or visibility. This can also aid the interpretation of the lidar data and help to identify any flaws, especially at new sites.

24.8 Applications

This section presents a few examples of the quantities that can be derived using backscatter lidars.

While this chapter only considers the use of backscatter lidars in atmospheric and environmental research, these lidars are also used for other important applications, including altimetry and remote sensing of vegetation [24.81–83] as well as 3-D distance mapping of autonomous vehicles [24.84–86].

Fig. 24.16 Three ceilometers used during a comparison campaign conducted in 2019 by DWD (Deutscher Wetterdienst) in Hamburg, Germany. The ceilometer *on the left* has a design with a single-lens optical system and a mirror with an aperture (a Vaisala CL31). The ceilometer *in the middle* (behind the power box) is a Lufft CHM 15K double-lens system. The ceilometer *on the right* is another double-lens system, a Vaisala LD-40. Source: DWD ▶

Examples of modern ceilometers are shown in Fig. 24.16. Each instrument weighs ≈ 70 kg and allows continuous, unattended operation.



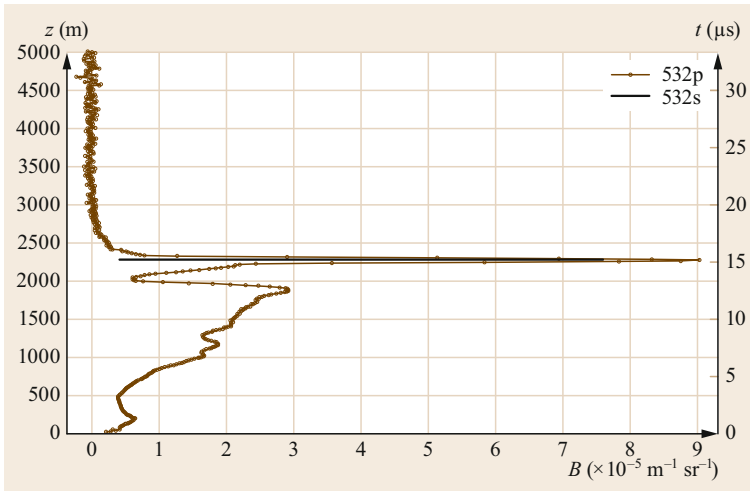


Fig. 24.17 Profile of the attenuated backscatter observed by a ceilometer on 06.06.2012 at 02:14:40

24.8.1 Using a Ceilometer as an Autonomous Backscatter Lidar

Ceilometers are autonomous working backscatter lidars that were originally only used to measure cloud altitudes. However, modern instruments can also detect aerosol layers or precipitation. This is shown in Fig. 24.17. According to the profile, a geometrically

shallow cloud is present at an altitude of ≈ 2.3 km. Directly below the cloud, in the melting layer, a *dark band* is visible at 2050 m. This is a frequently observed layer of decreased backscatter in the melting region of a cloud (e.g., [24.87]). Above a cloud, the attenuated backscatter naturally becomes noisier due to the extinction within the cloud; however, if there is a second cloud layer above the first one, this second layer may

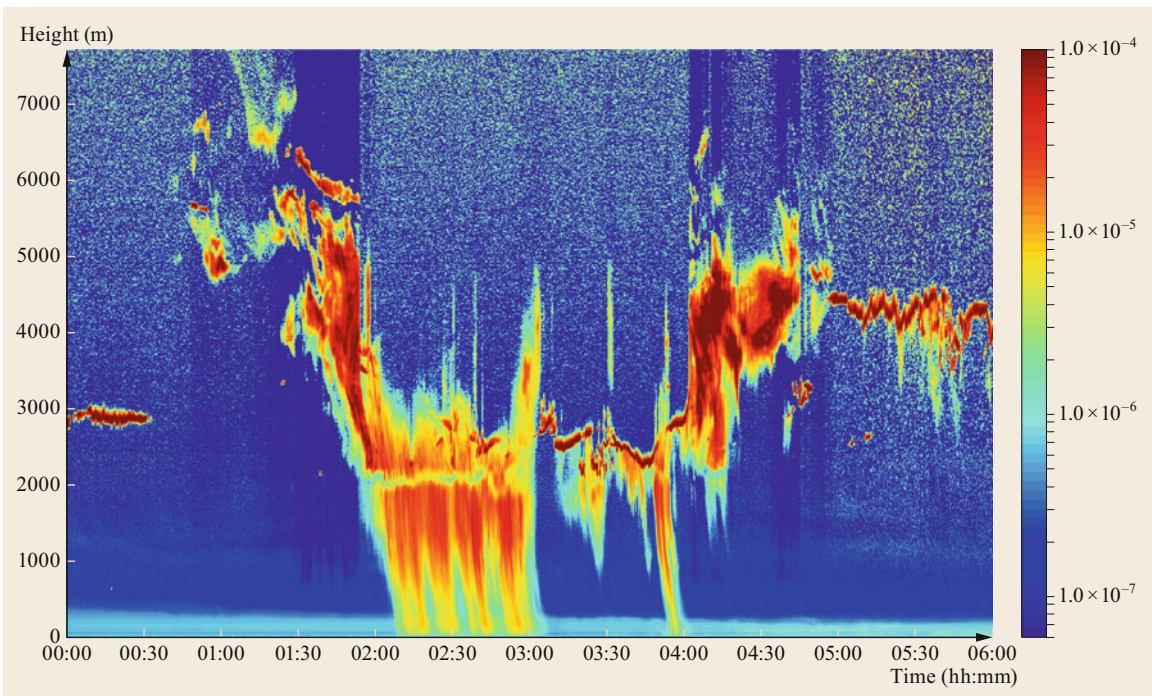


Fig. 24.18 Attenuated backscatter time–height cross-section plot from 06.06.2012, showing clouds, precipitation, and boundary layer properties. Log colorscale: $0.1 = 100.0 \times 10^{-6} \text{ m}^{-1} \text{ sr}^{-1}$ (pixel size = $16 \text{ s} \times 10 \text{ m}$)

be also detected through a significant rise in the count rate. Attenuated backscatter is seen from the ground to ≈ 1950 m; this attenuation increases with altitude. This is due to precipitation from the cloud: the drops start to evaporate once they enter drier air, which decreases the drop size, affecting the scattering efficiency and the backscatter.

To ensure that the system automatically delivers an accurate value for the cloud base, the potential existence of several cloud layers or precipitation should be considered when analyzing lidar retrievals.

Figure 24.18 shows a typical contour plot obtained from lidar data. It shows the time (x -axis), the altitude (y -axis), and the strength of the (attenuated) backscatter (in different colors). Reddish colors refer to large backscatter values. The changes in cloud height and cover are obvious. Moreover, precipitation (occurring from 02:10 to 03:00 and shortly before 04:00) can be discerned, as can a melting layer (which shows less attenuated backscatter than altitudes below or above it, and occurs at 2100 m during the precipitation events). Information on the boundary layer can also be extracted: a nocturnal layer comprising the lowest 300 m, and the residual layer at around 1200 m.

Figure 24.19 shows an example of the successful determination of the boundary layer altitude. The attenuated backscatter $B(z)$ see (24.7) is shown as a time–height cross-section plot. The boundary layer altitude is derived as the minimum of the gradient of $B(z)$. The yellow and black vertical lines denote sunrise and sunset. Before the convective rise triggered by the warmth from the sun, the plot shows a nocturnal layer and a residual layer. The formation of a new nocturnal layer is visible after 22:00.

Figure 24.20 shows an example of the retrieval of water vapor via the differential absorption lidar DIAL approach (Chap. 26). In the near future, commercially available DIAL lidars will monitor the boundary layer for key meteorological quantities. This figure shows the result of an intercomparison between colocated instruments: data from a DIAL water-vapor lidar is compared to that from a Raman lidar (see the chapter on Raman lidar) and a radiosonde. Two typical features can be seen: first, higher concentrations of the measured quantity will generally yield a better retrieval, as the altitudes with low absolute deviations (in green along the y -axis)

correspond to high concentrations. Second, lidar utilization involves compromising between range and data quality: the DIAL system has a small (almost negligible) overlap range but becomes naturally noisy above the boundary layer, whereas the more powerful Raman lidar detects too little water vapor at the lowest altitude (400 m) but exhibits a much better signal-to-noise ratio > 1.5 km.

24.8.2 Caveats Regarding the Stable Boundary Layer Height

As mentioned in Sect. 24.3.10, ABL determination becomes much more difficult if there is no vertical mixing, as this causes the attenuated backscatter needed to determine the ABL to weaken. A relevant example from the Arctic Ocean is shown in Fig. 24.21. A research aircraft flew south from the ice-covered Arctic Ocean towards Spitzbergen. At the end of the plot (around 13:16 UTC), it reached the open ocean, where clouds formed, leading to high values of the attenuated backscatter coefficient measured at 532 nm. Also depicted in Fig. 24.21 is the altitude of the ABL derived by dropsonde, which is a radiosonde that is dropped from an aircraft and parachutes to the ground. The red crosses in the figure mark the height of the ABL from this dropsonde. The criterion that was applied to derive the altitude of the ABL from sonde data under thermally stable conditions was the critical Richardson number. It is apparent that the ABL height already starts to rise around the edge of the ice, probably because leads (i.e., fractures in the ice that allow heat, moisture, and aerosols to rise into the atmosphere) are more frequent in the ice close to the edge. According to the contour plot of the attenuated backscatter, there are some subtle elevated aerosol layers but there is no clear relation between aerosol and the ABL height. Hence, under stable conditions and when aerosol is advected rather than of local origin, attempts to determine the ABL height by lidar can fail. Between 12:58 and 13:05 UTC, the aircraft flew over a region with many open leads, which produced an aerosol load and local convection. During this interval, the attenuated backscatter coefficient within the ABL shows almost no height dependence. Even so, the lidar-derived ABL height and that derived using the sonde only agree fairly well.

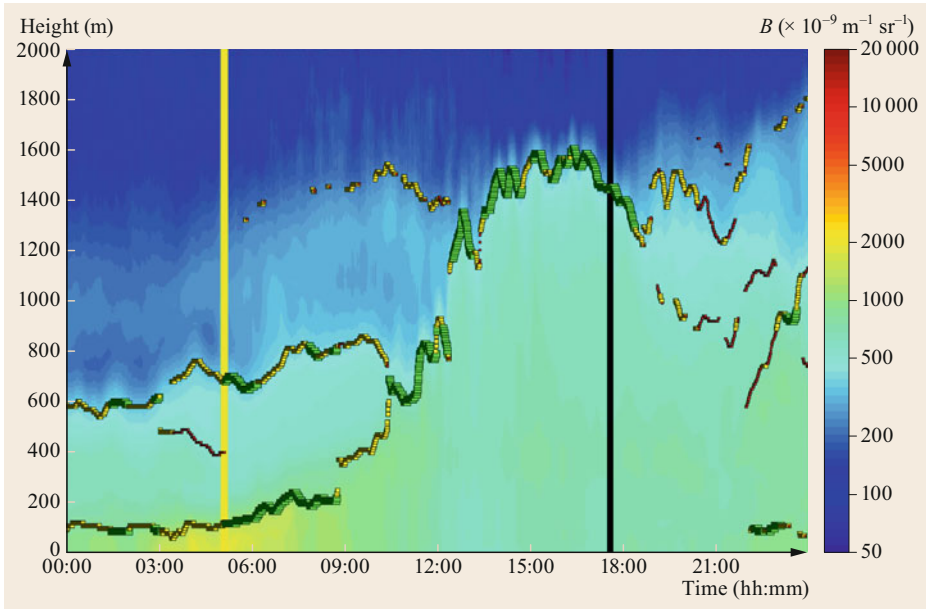


Fig. 24.19 Attenuated backscatter time–height cross-section plot from 30.03.2019, showing layer boundaries derived from gradient minima of nocturnal, residual, and convective layers, as well as the sunrise and sunset (yellow and black vertical lines)

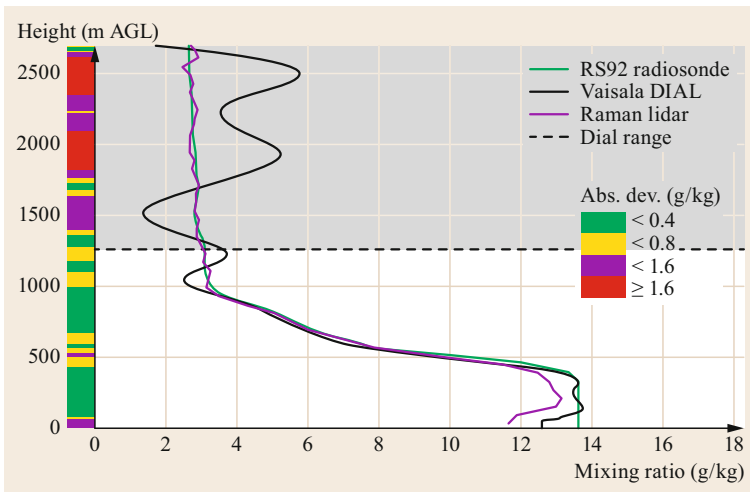


Fig. 24.20 Water vapor mixing ratio profile reported by a radiosonde and determined by two colocated lidar systems: a small commercial DIAL and a large research-type Raman lidar (ARM Southern Great Plains, 18.05.2017, 11:25 UTC)

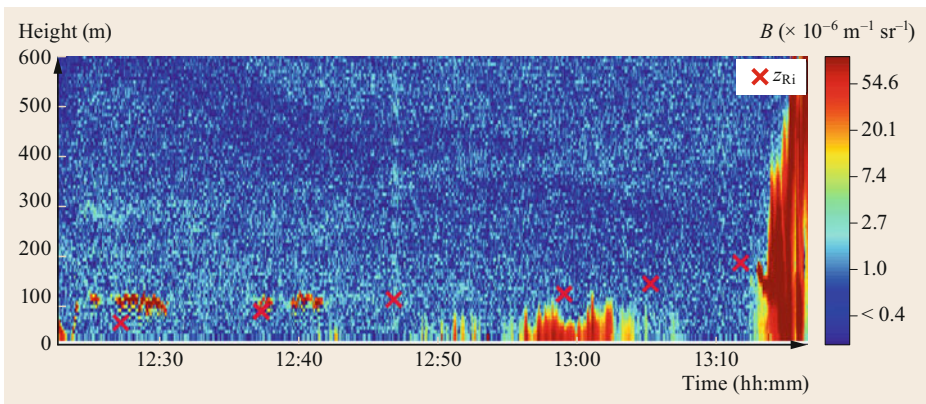


Fig. 24.21 Attenuated backscatter coefficient and ABL height measured by dropsonde (red crosses) over the frozen Arctic ocean under thermally stable conditions (after [24.66])

24.9 Further Reading

Introduction to lidars and their applications:

- C. Weitkamp: Lidar. Range-Resolved Optical Remote Sensing of the Atmosphere. Springer Series of Optical Sciences, Vol. 102 (Springer, Singapore 2005)

Elastic lidar systems:

- V.A. Kovalev, E.W. Eichinger: Elastic Lidar: Theory, Practice and Analysis Methods (John Wiley & Sons, Hoboken 2004)

The Micro Pulse Lidar network (see <https://mplnet.gsfc.nasa.gov/>, Accessed 08 July 2021) utilizes continuously running backscatter lidars for cloud and aerosol research, and the original concept of the MPL system is described in:

- J.D. Spinhirne (1993): Micro pulse lidar. IEEE Trans. Geosci. Remote Sens. **31**(1): 48–55

Information about ceilometer networks, quicklook data interpretation, and further references are provided by https://www.dwd.de/EN/research/projects/ceilomap/ceilomap_node.html, Accessed 09 July 2021

- M. Wiegner, A. Geiß (2012): Aerosol profiling with the Jenoptik ceilometer CHM15kx, Atmos. Meas. Tech. **5**(8): 1953–1964
- E.J. O'Connor, A.J. Illingworth, R.J. Hogan (2003): A technique for autocalibration of cloud lidar. J. Atmos. Ocean. Technol. **21**(5): 777–786

The Global Atmospheric Watch program from the WMO (Chap. 63) is another useful resource.

References

- 24.1 O. Dubovik, B. Holben, T.F. Eck, A. Smirnov, Y.J. Kaufman, M.D. King, D. Tanré, I. Slutsker: Variability of absorption and optical properties of key aerosol types observed in worldwide locations, J. Atmos. Sci. **59**(3), 590–608 (2002)
- 24.2 H. Flentje, B. Heese, J. Reichardt, W. Thomas: Aerosol profiling using the ceilometer network of the German Meteorological Service, Atmos. Meas. Tech. Discuss. **3**(4), 3643–3673 (2010)
- 24.3 H. Chepfer, S. Bony, D. Winker, M. Chiriaco, J.-L. Dufresne, G. Sèze: Use of CALIPSO lidar observations to evaluate the cloudiness simulated by a climate model, Geophys. Res. Lett. **35**(15), L15704 (2008)
- 24.4 C. Munkel, N. Eresmaa, J. Räsänen, A. Karppinen: Retrieval of mixing height and dust concentration with lidar ceilometer, Bound.-Layer Meteorol. **124**(1), 117–128 (2007)
- 24.5 J. Brion, A. Chakir, J. Charbonnier, D. Daumont, C. Parisse, J. Malicet: Absorption spectra measurements for the ozone molecule in the 350–830 nm region, J. Atmos. Chem. **30**(2), 291–299 (1998)
- 24.6 R.M. Pope, E.S. Fry: Absorption spectrum (380–700 nm) of pure water. II. Integrating cavity measurements, Appl. Opt. **36**(33), 8710–8723 (1997)
- 24.7 L.S. Rothman, I.E. Gordon, A. Barbe, D.C. Benner, P.F. Bernath, M. Birk, V. Boudon, L.R. Brown, A. Campargue, J.-P. Champion, K. Chance, L.H. Coudert, V. Dana, V.M. Devi, S. Fally, J.-M. Flaud, R.R. Gamache, A. Goldman, D. Jacquemart, I. Kleiner, N. Lacombe, W.J. Lafferty, J.-Y. Mandin, S.T. Massie, S.N. Mikhailenko, C.E. Miller, N. Moazzen-Ahmadi, O.V. Naumenko, A.V. Nikitin, J. Orphal, V.I. Perevalov, A. Perrin, A. Predoi-Cross, C.P. Rinsland, M. Rotger, M. Šimečková, M.A.H. Smith, K. Sung, S.A. Tashkun, J. Tennyson, R.A. Toth, A.C. Vandaele, J. Vander Auwera: The HITRAN 2008 molecular spectroscopic database, J. Quant. Spectrosc. Radiat. Transf. **110**(9/10), 533–572 (2009)
- 24.8 Y. Takano, K.-N. Liou: Solar radiative transfer in cirrus clouds. Part 1: Single-scattering and optical properties of hexagonal ice crystals, J. Atmos. Sci. **46**(1), 3–19 (1989)
- 24.9 A. Angstroem: The parameters of atmospheric turbidity, Tellus **16**(1), 64–75 (1964)
- 24.10 K. Sassen: Polarization in lidar. In: Lidar – Range-Resolved Optical Remote Sensing of the Atmosphere, Springer Series on Optical Sciences, Vol. 102, ed. by C. Weitkamp (Springer, Singapore 2005) pp. 19–42
- 24.11 C.M.R. Platt, N.L. Abshire, G.T. McNice: Some microphysical properties of an ice cloud from lidar observation of horizontally oriented crystals, J. Appl. Meteorol. **17**(8), 1220–1224 (1978)
- 24.12 S. Groß, M. Esselborn, B. Weinzierl, M. Wirth, A. Fix, A. Petzold: Aerosol classification by airborne high spectral resolution lidar observations, Atmos. Chem. Phys. **13**(5), 2487–2505 (2013)
- 24.13 W.-N. Chen, C.-W. Chiang, J.-B. Nee: Lidar ratio and depolarization ratio for cirrus clouds, Appl. Opt. **41**(30), 6470–6476 (2002)
- 24.14 T. Murayama, H. Okamoto, N. Kaneyasu, H. Kamataki, K. Miura: Application of lidar depolarization measurement in the atmospheric boundary layer: Effects of dust and sea-salt particles, J. Geophys. Res. **104**(D24), 31781–31792 (1999)

- 24.15 R.R. Rogers, C.A. Hostetler, J.W. Hair, R.A. Ferrare, Z. Liu, M.D. Obland, D.B. Harper, A.L. Cook, K.A. Powell, M.A. Vaughan, D.M. Winker: Assessment of the CALIPSO lidar 532 nm attenuated backscatter calibration using the NASA LaRC airborne high spectral resolution lidar, *Atmos. Chem. Phys.* **11**(3), 1295–1311 (2011)
- 24.16 D. Müller, U. Wandinger, A. Ansmann: Microphysical particle parameters from extinction and backscatter lidar data by inversion with regularization: Theory, *Appl. Opt.* **38**(12), 2346–2357 (1999)
- 24.17 I.S. Stachlewska, C. Ritter: On retrieval of lidar extinction profiles using Two-Stream and Raman techniques, *Atmos. Chem. Phys.* **10**(6), 2813–2824 (2010)
- 24.18 W. Wang, W. Gong, F. Mao, Z. Pan, B. Liu: Measurement and study of lidar ratio by using a Raman lidar in Central China, *Int. J. Environ. Res. Public Health* **13**(5), 508 (2016)
- 24.19 S.J. Doherty, T.L. Anderson, R.J. Charlson: Measurement of the lidar ratio for atmospheric aerosol with a 180° backscatter nephelometer, *Appl. Opt.* **38**(9), 1823–1832 (1999)
- 24.20 R.A. Ferrare, D.D. Turner, L. Heilman Brasseur, W.F. Feltz, O. Dubovik, T.P. Tooman: Raman lidar measurements of the aerosol extinction-to-backscatter ratio over the Southern Great Plains, *J. Geophys. Res.* **106**(D17), 20333–20347 (2001)
- 24.21 W.E.K. Middleton, A.F. Spilhaus: *Meteorological Instruments*, 3rd edn. (Univ. Toronto Press, Toronto 1953)
- 24.22 G. Fiocco, L.D. Smulin: Detection of scattering layers in the upper atmosphere (60–140 km) by optical radar, *Nature* **199**(4900), 1275–1276 (1963)
- 24.23 J.D. Klett: Stable analytical inversion solution for processing lidar returns, *Appl. Opt.* **20**(2), 211–220 (1981)
- 24.24 J.D. Klett: Lidar inversion with variable backscatter/extinction ratios, *Appl. Opt.* **24**(11), 1638–1643 (1985)
- 24.25 B. Kaul: *Laser Sensing the Aerosol Pollution in the Atmosphere*, PhD thesis (Institute of Atmospheric Optics, Tomsk State University, Tomsk 1976), in Russian
- 24.26 V.E. Zuev, G.O. Zadde, S.I. Kavkjanov, B.V. Kaul: Interpretation of lidar signals from regions of large optical depths. In: *Remote Sensing in the Atmosphere*, ed. by V.E. Zuev (Nauka, Novosibirsk 1978) pp. 60–68
- 24.27 G.J. Kunz, G. de Leeuw: Inversion of lidar signals with the slope method, *Appl. Opt.* **32**(18), 3249–3256 (1993)
- 24.28 D.M. Winker, R.H. Couch, M.P. McCormick: An overview of LITE: NASA's Lidar In-space Technology Experiment, *Proc. IEEE* **84**(2), 164–180 (1996)
- 24.29 D.M. Winker, M.A. Vaughan, A. Omar, Y. Hu, K.A. Powell, Z. Liu, W.H. Hunt, S.A. Young: Overview of the CALIPSO Mission and CALIOP Data Processing Algorithms, *J. Ocean. Atmos. Technol.* **26**(11), 2310–2323 (2009)
- 24.30 T. Pfrommer, P. Hickson: High-resolution lidar observations of mesospheric sodium and implications for adaptive optics, *J. Opt. Soc. Am. A* **27**(11), A97–A105 (2010)
- 24.31 S.P. Alexander, A.R. Klekociuk, D.J. Murphy: Rayleigh lidar observations of gravity wave activity in the winter upper stratosphere and lower mesosphere above Davis, Antarctica (69° S, 78° E), *J. Geophys. Res.* **116**(D13), D13109 (2011)
- 24.32 M. Petrarca, S. Henin, N. Berti, M. Matthews, J. Chagas, J. Kasparian, J.-P. Wolf, G. Gatti, G. Di Pirro, M.P. Anania, M. Ferrario, A. Ghigo: White-light femtosecond lidar at 100 TW power level, *Appl. Phys. B* **114**(3), 319–325 (2014)
- 24.33 G. Méjean, J. Kasparian, J. Yu, S. Frey, E. Salmon, J.-P. Wolf: Remote detection and identification of biological aerosols using a femtosecond terawatt lidar system, *Appl. Phys. B* **78**(5), 535–537 (2004)
- 24.34 H. Wille, M. Rodriguez, J. Kasparian, D. Mondelain, J. Yu, A. Mysyrowicz, R. Sauerbrey, J.P. Wolf, L. Wöste: Teramobile: A mobile femtosecond-terawatt laser and detection system, *Eur. Phys. J. Appl. Phys.* **20**(3), 183–190 (2002)
- 24.35 V.A. Kovalev, W.E. Eichinger: *Elastic Lidar Theory: Practice and Analysis Methods* (John Wiley & Sons, Hoboken 2004)
- 24.36 P. Pornsawad, C. Böckmann, C. Ritter, M. Rafler: Ill-posed retrieval of aerosol extinction coefficient profiles from Raman lidar data by regularization, *Appl. Opt.* **47**(10), 1649–1661 (2008)
- 24.37 U. Wandinger, A. Ansmann: Experimental determination of the lidar overlap profile with Raman lidar, *Appl. Opt.* **41**(3), 511–514 (2002)
- 24.38 C.M.R. Platt: Lidar and radiometric observations of cirrus clouds, *J. Atmos. Sci.* **30**(6), 1191–1204 (1973)
- 24.39 L.R. Bissonnette: Lidar and multiple scattering. In: *Lidar – Range-Resolved Optical Remote Sensing of the Atmosphere*, Springer Series on Optical Sciences, Vol. 102, ed. by C. Weitkamp (Springer, Singapore 2005) pp. 43–103
- 24.40 R.J. Hogan: Fast approximate calculation of multiply scattered lidar returns, *Appl. Opt.* **45**(23), 5984–5992 (2006)
- 24.41 J.S. Ryan, S.R. Pal, A.I. Carswell: Laser backscattering from dense water-droplet clouds, *J. Opt. Soc. Am.* **69**(1), 60–67 (1979)
- 24.42 A. Garnier, J. Pelon, M.A. Vaughan, D.M. Winker, C.R. Trepte, P. Dubuisson: Lidar multiple scattering factors inferred from CALIPSO lidar and IIR retrievals of semi-transparent cirrus cloud optical depths over oceans, *Atmos. Meas. Tech.* **8**(7), 2759–2774 (2015)
- 24.43 C. Weitkamp (Ed.): *Lidar – Range-Resolved Optical Remote Sensing of the Atmosphere*, Springer Series on Optical Sciences, Vol. 102 (Springer, Singapore 2005)
- 24.44 A.H. Omar, D.M. Winker, M.A. Vaughan, Y. Hu, C.R. Trepte, R.A. Ferrare, K.-P. Lee, C.A. Hostetler, C. Kittaka, R.R. Rogers, R.E. Kuehn, Z. Liu: The CALIPSO automated aerosol classification and lidar ratio selection algorithm, *J. Atmos. Ocean. Technol.* **26**(10), 1994–2014 (2009)
- 24.45 D. Müller, A. Ansmann, I. Mattis, M. Tesche, U. Wandinger, D. Althausen, G. Pisani: Aerosol-

- type-dependent lidar ratios observed with Raman lidar, *J. Geophys. Res.* **112**(D16), D16202 (2007)
- 24.46 C. Cordoba-Jabonero, J.A. Adame, J.R. Campbell, E. Cuevas, J.P. Diaz, F. Exposito, M. Gil-Ojeda: Lidar ratio derived for pure dust aerosols: Multi-year micro pulse lidar observations in a Saharan dust-influenced region. In: *The 27th International Laser Radar Conference (ILRC 27)*, New York, EPJ Web of Conferences, Vol. 119, ed. by B. Gross, F. Moshary, M. Arend (EDP Sciences, Les Ulis 2016)
- 24.47 A. Ansmann, M. Tesche, S. Groß, V. Freudenthaler, P. Seifert, A. Hiebsch, J. Schmidt, U. Wandinger, I. Mattis, D. Müller, M. Wiegner: The 16 April 2010 major volcanic ash plume over Central Europe: EARLINET lidar and AERONET photometer observations at Leipzig and Munich, Germany, *Geophys. Res. Lett.* **37**(13), L13810 (2010)
- 24.48 C. Ritter, R. Neuber, A. Schulz, K.M. Markowicz, I.S. Stachlewska, J. Lisok, P. Makuch, P. Pakszys, P. Markuszewski, A. Rozwadowska, T. Petelski, T. Zielinski, S. Becagli, R. Traversi, R. Udisti, M. Gausa: 2014 iAREA campaign on aerosol in Spitsbergen – Part 2: Optical properties from Raman lidar and in-situ observations at Ny-Ålesund, *Atmos. Environ.* **141**, 1–19 (2016)
- 24.49 D. Josset, J. Pelon, A. Garnier, Y. Hu, M. Vaughan, P.-W. Zhai, R. Kuehn, P. Lucker: Cirrus optical depth and lidar ratio retrieval from combined CALIPSO-CloudSat observations using ocean surface echo, *J. Geophys. Res.* **117**(D5), D05207 (2012)
- 24.50 E.J. O'Connor, A.J. Illingworth, R.J. Hogan: A technique for autocalibration of cloud lidar, *J. Atmos. Ocean. Technol.* **21**(5), 777–786 (2003)
- 24.51 J. Ackermann: The extinction-to-backscatter ratio of tropospheric aerosol: A numerical study, *J. Atmos. Ocean. Technol.* **15**(4), 1043–1050 (1998)
- 24.52 K.W. Dawson, N. Meskhidze, D. Josset, S. Gassó: Spaceborne observations of the lidar ratio of marine aerosols, *Atmos. Chem. Phys.* **15**(6), 3241–3255 (2015)
- 24.53 P. Koepke, J. Gasteiger, M. Hess: Technical note: Optical properties of desert aerosol with non-spherical mineral particles: Data incorporated to OPAC, *Atmos. Chem. Phys.* **15**(10), 5947–5956 (2015)
- 24.54 I. Veselovskii, A. Kolgotin, V. Griaznov, D. Müller, K. Franke, D.N. Whiteman: Inversion of multiwavelength Raman lidar data for retrieval of bimodal aerosol size distribution, *Appl. Opt.* **43**(5), 1180–1195 (2004)
- 24.55 Z. Tao, M.P. McCormick, D. Wu, Z. Liu, M.A. Vaughan: Measurements of cirrus cloud backscatter color ratio with a two-wavelength lidar, *Appl. Opt.* **47**(10), 1478–1485 (2008)
- 24.56 L. Bi, P. Lang, G.W. Kattawar, B.A. Baum, Y.X. Hu, D.M. Winker, R.S. Brock, J.Q. Lu: Simulation of the color ratio associated with the backscattering of radiation by ice particles at the wavelengths of 0.532 and 1.064 μm , *J. Geophys. Res.* **114**, D00H08 (2009)
- 24.57 Z. Liu, A. Omar, M. Vaughan, J. Hair, C. Kittaka, Y. Hu, K. Powell, C. Trepte, D. Winker, C. Hostetler, R. Ferrare, R. Pierce: CALIPSO lidar observations of the optical properties of Saharan dust: A case study of long-range transport, *J. Geophys. Res.* **113**(D7), D07207 (2008)
- 24.58 T. Murayama, D. Müller, K. Wada, A. Shimizu, M. Sekiguchi, T. Tsukamoto: Characterization of Asian dust and Siberian smoke with multi-wavelength Raman lidar over Tokyo, Japan in spring 2003, *Geophys. Res. Lett.* **31**(23), L23103 (2004)
- 24.59 A. Behrendt, T. Nakamura: Calculation of the calibration constant of polarization lidar and its dependency on atmospheric temperature, *Opt. Express* **10**(16), 805–817 (2002)
- 24.60 J. Gasteiger, V. Freudenthaler: Benefit of depolarization ratio at 1064 nm for the retrieval of the aerosol microphysics from lidar measurements, *Atmos. Meas. Tech.* **7**(11), 3773–3781 (2014)
- 24.61 S. Groß, V. Freudenthaler, M. Wirth, B. Weinzierl: Towards an aerosol classification scheme for future EarthCARE lidar observations and implications for research needs, *Atmos. Sci. Lett.* **16**(1), 77–82 (2015)
- 24.62 K. Sassen, S. Benson: A midlatitude cirrus cloud climatology from the facility for atmospheric remote sensing. Part II: Microphysical properties derived from lidar depolarization, *J. Atmos. Sci.* **58**(15), 2103–2112 (2001)
- 24.63 Z. Wang, R. Chi, B. Liu, J. Zhou: Depolarization properties of cirrus clouds from polarization lidar measurements over Hefei in spring, *Chin. Opt. Lett.* **6**(4), 235–237 (2008)
- 24.64 S. Emeis, K. Schäfer, C. Münkel: Surface-based remote sensing of the mixing-layer height – A review, *Meteorol. Z.* **17**(5), 621–630 (2008)
- 24.65 M. Sicard, C. Pérez, F. Rocadenbosch, J.M. Baldasano, D. García-Vizcaino: Mixed-layer depth determination in the Barcelona coastal area from regular lidar measurements: Methods, results and limitations, *Bound.-Layer Meteorol.* **119**(1), 135–157 (2006)
- 24.66 L. Schmidt: *Aerosols and Boundary Layer Structure over Arctic Sea Ice Based on Airborne Lidar and Dropsonde Measurements*, PhD thesis (Univ. Potsdam, Potsdam 2014)
- 24.67 M. Born, E. Wolf: *Principles of Optics – Electromagnetic Theory of Propagation, Interference and Diffraction of Light*, 6th edn. (Pergamon Press, Oxford 2013)
- 24.68 V. Sherlock, A. Garnier, A. Hauchecorne, P. Keckhut: Implementation and validation of a Raman lidar measurement of middle and upper tropospheric water vapor, *Appl. Opt.* **38**(27), 5838–5850 (1999)
- 24.69 D.N. Whiteman, M. Cadirola, D. Venable, M. Calhoun, L. Miloshevich, K. Vermeesch, L. Twigg, A. Dirisu, D. Hurst, E. Hall, A. Jordan, H. Vömel: Correction technique for Raman water vapor lidar signal-dependent bias and suitability for water vapor trend monitoring in the upper troposphere, *Atmos. Meas. Tech.* **5**(11), 2893–2916 (2012)
- 24.70 T. Hakamata: *Photomultiplier Tubes – Basics and Applications*, 3rd edn. (HAMAMATSU PHOTONICS K.K., Hamamatsu 2007), https://www.hamamatsu.com/resources/pdf/etd/PMT_handbook_v3aE.pdf, Accessed 08 July 2021

- 24.71 L. Menut, C. Flamant, J. Pelon, P.H. Flamant: Urban boundary-layer height determination from lidar measurements over the Paris area, *Appl. Opt.* **38**(6), 945–954 (1999)
- 24.72 C.J. Flynn, A. Mendoza, Y. Zheng, S. Mathur: Novel polarization-sensitive micropulse lidar measurement technique, *Opt. Express* **15**(6), 2785–2790 (2007)
- 24.73 J.D. Vande Hey: *A Novel Lidar Ceilometer: Design, Implementation and Characterization* (Springer, Cham 2014)
- 24.74 B. Heese, H. Flentje, D. Althausen, A. Ansmann, S. Frey: Ceilometer lidar comparison: Backscatter coefficient retrieval and signal-to-noise ratio determination, *Atmos. Meas. Tech.* **3**(6), 1763–1770 (2010)
- 24.75 E.G. Lopez, F. Rocadenbosch, J. Tiana-Alsina, A. Comerón, R. Sanz, J.R. Rosell-Polo: Parameter design of a biaxial lidar ceilometer, *J. Appl. Remote Sens.* **6**(1), 063546 (2012)
- 24.76 C. Böckmann, U. Wandinger, A. Ansmann, J. Bösenberg, V. Amiridis, A. Boselli, A. Delaval, F. De Tomasi, M. Frioud, I. Videnov Grigorov, A. Hågård, M. Horvat, M. Iarlori, L. Komguem, S. Kreipl, G. Larchevêque, V. Matthias, A. Papayannis, G. Pappalardo, F. Rocadenbosch, J.A. Rodrigues, J. Schneider, V. Shcherbakov, M. Wiegner: Aerosol lidar intercomparison in the framework of the EARLINET project. 2. Aerosol backscatter algorithms, *Appl. Opt.* **43**(4), 977–989 (2004)
- 24.77 U. Wandinger, V. Freudenthaler, H. Baars, A. Amodeo, R. Engelmann, I. Mattis, S. Groß, G. Pappalardo, A. Giunta, G. D'Amico, A. Chaikovskiy, F. Osipenko, A. Slesar, D. Nicolae, L. Belegante, C. Talianu, I. Serikov, H. Linné, F. Jansen, A. Apituley, K.M. Wilson, M. de Graaf, T. Trickl, H. Giehl, M. Adam, A. Comerón, C. Muñoz-Porcar, F. Rocadenbosch, M. Sicard, S. Tomás, D. Lange, D. Kumar, M. Pujadas, F. Molero, A.J. Fernández, L. Alados-Arboledas, J.A. Bravo-Aranda, F. Navas-Guzmán, J.L. Guerrero-Rascado, M.J. Granados-Muñoz, J. Preißler, F. Wagner, M. Gausa, I. Grigorov, D. Stoyanov, M. Iarlori, V. Rizzi, N. Spinelli, A. Boselli, X. Wang, T. Lo Feudo, M.R. Perrone, F. De Tomasi, P. Burlizzi: EARLINET instrument intercomparison campaigns: Overview on strategy and results, *Atmos. Meas. Tech.* **9**(3), 1001–1023 (2016)
- 24.78 B. Liu, Z. Wang: Improved calibration method for depolarization lidar measurement, *Opt. Express* **21**(12), 14583–14590 (2013)
- 24.79 J.M. Alvarez, M.A. Vaughan, C.A. Hostetler, W.H. Hunt, D.M. Winker: Calibration technique for polarization-sensitive lidars, *J. Atmos. Ocean. Technol.* **23**(5), 683–699 (2006)
- 24.80 V. Freudenthaler: About the effects of polarising optics on lidar signals and the $\Delta 90$ calibration, *Atmos. Meas. Tech.* **9**(9), 4181–4255 (2016)
- 24.81 D.J. Harding, M.A. Lefsky, G.G. Parker, J.B. Blair: Laser altimeter canopy height profiles: Methods and validation for closed-canopy, broadleaf forests, *Remote Sens. Environ.* **76**(3), 283–297 (2001)
- 24.82 K. Lim, P. Treitz, M. Wulder, B. St-Onge, M. Flood: LIDAR remote sensing of forest structure, *Prog. Phys. Geogr.* **27**(1), 88–106 (2003)
- 24.83 X. Liu: Airborne lidar for DEM generation: Some critical issues, *Prog. Phys. Geogr.* **32**(1), 31–49 (2008)
- 24.84 B. Schwarz: Mapping the world in 3D, *Nat. Photonics* **4**(7), 429–430 (2010)
- 24.85 H. Wang, B. Wang, B. Liu, X. Meng, G. Yang: Pedestrian recognition and tracking using 3D Lidar for autonomous vehicles, *Robot. Auton. Syst.* **88**, 71–78 (2017)
- 24.86 H. Gotzig, G.O. Geduld: LIDAR-Sensorik. In: *Handbuch Fahrerassistenzsysteme. Grundlagen, Komponenten und Systeme für aktive Sicherheit und Komfort*, ed. by H. Winner, S. Hakuli, F. Lotz, C. Singer (Vieweg, Wiesbaden 2015) pp. 317–334
- 24.87 K. Sassen, T. Chen: The lidar dark band: An oddity of the radar bright band analog, *Geophys. Res. Lett.* **22**(24), 3505–3508 (1995)

Christoph Ritter

Physics of the Atmosphere
Alfred-Wegener-Institute
Potsdam, Germany
christoph.ritter@awi.de



Christoph Ritter works in the field of atmospheric remote sensing at the Alfred Wegener Institute, the German Institute for Polar and Marine Research, in Potsdam. After studying physics and astronomy, he became interested in the Arctic climate. He has participated in many international aerosol and boundary layer research campaigns in Spitsbergen, and is especially interested in combining remote-sensing and in-situ measurements.

Christoph Münkel

Vaisala GmbH
Hamburg, Germany
cmuenkel@web.de



In 2019, Christoph Münkel retired from his position as senior scientist at Vaisala GmbH, Hamburg. Having attended courses in mathematics, physics, and astronomy, he received a Diplom-Mathematiker (master's degree) from Hamburg University. He develops algorithms for lidar applications, participates in international boundary-layer research campaigns, and participates in standardization bodies for remote sensing. He is a coauthor of the Springer book *Lidar: Range-Resolved Optical Remote Sensing of the Atmosphere*.

Raman Lidar

25. Raman Lidar for Water-Vapor and Temperature Profiling

Volker Wulfmeyer , Andreas Behrendt 

The Raman lidar technique is a refinement of the lidar method and permits, besides the measurement of particle optical properties, the simultaneous profiling of the water-vapor mixing ratio and temperature with high range resolution and accuracy. This technique does not require a laser transmitter with a certain wavelength; it uses standard high-power lasers. Certain portions of the spectrum of the atmospheric backscatter signal are extracted as measurement signals. The noise and systematic errors in each profile can be characterized, which is a fundamental requirement for many applications. Many ground-based Raman lidar instruments that are intended for research have been constructed, some of which are already operational. The first airborne Raman lidar systems are also now in use, and commercial systems have recently become available. This technique has the potential to be used extensively within surface networks for obtaining atmospheric thermodynamic data with regional to global coverage. Spaceborne Raman lidar operation will also be feasible in the near future.

25.1	Measurement Principles and Parameters	720
25.2	History	721
25.3	Theory	722
25.3.1	Raman Lidar Equation	722
25.3.2	Derivation of the Temperature Rotational Raman Lidar Equation	722
25.3.3	Water-Vapor Raman Lidar Equation ...	723
25.3.4	Error Propagation	723
25.4	Devices and Systems	725
25.4.1	Typical Setup of a Water-Vapor and Temperature Raman Lidar	725
25.4.2	The Laser Transmitter	726
25.4.3	The Receiver	726
25.4.4	The Data Acquisition System	727
25.4.5	Processing and Storage of Temperature and Water-Vapor Profiles	727
25.4.6	The Main Features of Raman Lidar Systems	728
25.5	Specifications	728
25.6	Quality Control	729
25.7	Maintenance	731
25.8	Applications	731
25.8.1	Monitoring	731
25.8.2	Model Verification and the Calibration of Other Sensors	732
25.8.3	Data Assimilation	732
25.8.4	Process Studies	732
25.9	Future Developments	733
25.10	Further Reading	733
	References	734

In this chapter, we describe and discuss the use of Raman lidar, a remote-sensing technique for probing the water vapor and temperature distribution in the atmosphere [25.1]. This method is based on the measurement of inelastically backscattered Raman lidar signals. As each type of atmospheric molecules causes a characteristic Raman shift frequency and the intensity of the backscattered radiation is proportional to the number density of the scattering molecules, the cross-sensitivity of this technique to other atmospheric constituents such as aerosol and cloud particles is significantly reduced. Signals that are almost solely dependent on the wa-

ter-vapor mixing ratio or temperature can be obtained by elegant combinations of Raman channels—in other words, by monitoring the Raman scattering of different molecules in different vibrational and rotational energy states. By means of stable calibrations and very robust and efficient receiver setups, water-vapor Raman lidar (WVRL) and temperature Raman lidar (TRL) are currently the only operationally active remote-sensing methods that allow us to probe these fundamental atmospheric variables with high accuracy, resolution, and range.

In the following, after introducing the principle behind the Raman lidar technique, we present the equations that are employed to derive water-vapor and temperature profiles. We explore typical configurations of Raman lidar systems focusing on key elements such as the laser transmitter, the receiver, and the data acquisition system. We consider various applications of the

technique, including atmospheric monitoring, the verification and calibration of models and other observing systems, data assimilation, and process studies. Finally, we discuss the future of water-vapor and temperature Raman lidar systems in terms of their utilization in networks as well as on airborne and spaceborne platforms.

25.1 Measurement Principles and Parameters

A typical Raman scattering spectrum is presented in Fig. 25.1 [25.2]. Either the rotational Raman scattering around the elastic signal (in this case at 354.7 nm) is studied or the vibrational-rotational Raman scattered spectra of water vapor, nitrogen, oxygen, and carbon dioxide are analyzed, or a combination of both.

Observations of water vapor and temperature can be made using a receiver with wavelength-selective elements to extract the different Raman signals from the backscatter signal of a laser pulse transmitted into the atmosphere. Systems that combine WVRL with TRL

are the focus of this chapter; they are termed water-vapor and temperature Raman lidar (WVTRL) systems in the following. An overview of the variables that can be measured directly with WVTRL is presented in Table 25.1.

The performance of a Raman lidar during daytime differs from that during the night due to the significant sensitivity of the signal-to-noise ratios (SNRs) of the water-vapor and temperature signals to the daylight background. However, advanced Raman lidar systems possess resolutions of 1–10 s and 10–100 m for

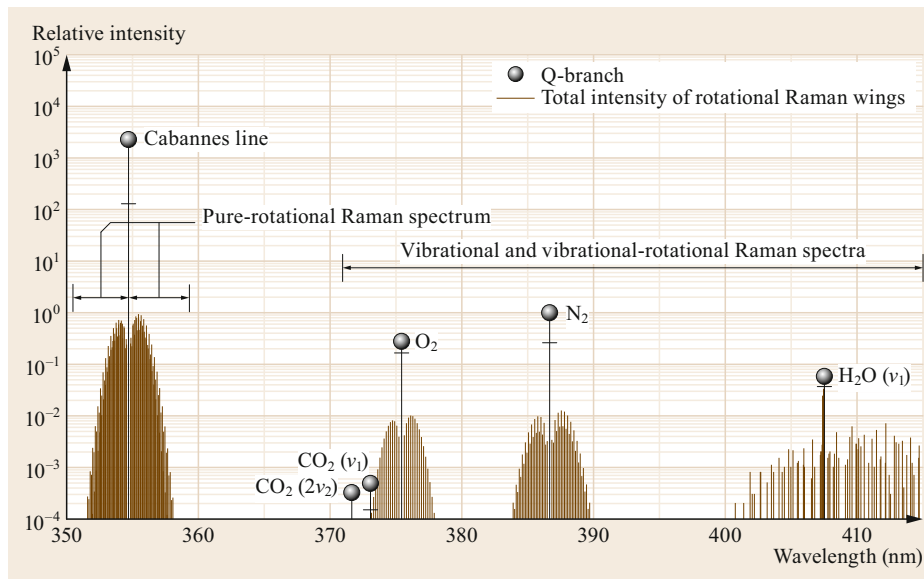


Fig. 25.1 Raman backscatter spectrum (after [25.2]) for a laser wavelength of 354.7 nm. Note that the spectrum is the same for any laser wavelength provided the Raman shifts are calculated in frequency units, as the energies of the transitions are constant

Table 25.1 Atmospheric variables that can be directly measured in dependence of range using WVTRL

Variable	Description	Unit	Symbol
Water-vapor mixing ratio	Ratio of water vapor density to the density of dry air	g kg^{-1}	M
Temperature	Physical air temperature	K	T
Particle backscatter coefficient	Backscattering due to atmospheric aerosols and/or cloud particles	$\text{m}^{-1} \text{sr}^{-1}$	β_{par}
Particle extinction coefficient	Extinction due to aerosol and/or cloud particles	m^{-1}	α_{par}
Lidar ratio	Ratio of the particle extinction coefficient to the particle backscatter coefficient	sr	S

Table 25.2 Further variables that can be derived from combined WVTRL measurements in dependence of range

Variable	Description	Unit	Symbol
Relative humidity	Ratio of the partial pressure of water vapor to the saturation pressure	%	RH
Virtual temperature	Temperature of dry air with the same density as the sampled moist air, assuming both the dry and moist air are at the same pressure (see also Chap. 8)	K	T_V
Buoyancy	Force exerted by a surrounding fluid to an immersed air parcel	N kg^{-1}	B
Convective inhibition	Energy required to overcome lids and stable air levels for deep convection	J kg^{-1}	CIN
Convective available potential energy	Energy available in the atmosphere when deep convection is taking place	J kg^{-1}	CAPE

the lower troposphere and a few hundred meters for the region from the upper troposphere to the lower stratosphere during both the day and night. A detailed overview of system performance is presented in Sect. 25.5.

By combining different Raman channels, it is also possible to determine several derived variables. These variables are summarized in Table 25.2. For water-vapor and temperature measurements, the derived variables include relative humidity, virtual temperature, buoyancy, convective inhibition (CIN), and convective available potential energy (CAPE).

By combining the measured signals in a different way, the scattering and extinction due to particles can be distinguished and measured independently without the need to make any additional assumptions (e.g., [25.2–4]). Therefore, Raman lidar is also a well-established

technique for determining the optical properties of aerosols and cloud particles in dependence of range and relating those properties to aerosol and cloud particle microphysics as well as their interaction.

For a discussion of the principle of backscatter lidar, please refer to Chap. 25. The performance of WVTRL is compared with those of other measurement techniques later in this chapter (Sect. 25.5). WVTRL systems at several sites are currently operational, and their high data qualities demonstrate why WVTRL are extensively used in measurement stations and in proposed ground-based networks (see Chap. 63). WVTRL systems also recently became available commercially. Last but not least, we mention that WVTRL systems are being used on airborne platforms too [25.5, 6], and their inclusion on spaceborne platforms has been proposed [25.7, 8].

25.2 History

The first Raman lidar measurements were performed by *Donald A. Leonard* in 1967 [25.9] using a pulsed nitrogen ultraviolet laser operating at 337.1 nm. The Raman scattered radiations of nitrogen and oxygen were detected in order to demonstrate the use of Raman lidar to observe atmospheric trace gases. In 1968, *John Cooney* [25.10] employed a ruby laser transmitter at 694.3 nm to detect the Raman scattering from nitrogen molecules in order to profile the density of the atmosphere. 1969 saw the first use of a frequency-doubled ruby laser to measure the Raman scattering from both water vapor and nitrogen [25.11], thus enabling the atmospheric profile of the water-vapor mixing ratio M to be derived. The WVRL technique was born. Shortly after, a similar measurement was reported by another group [25.12]. The combination of rotational Raman backscatter signals for atmospheric temperature profiling was pioneered by *John Cooney* in 1972 [25.13]. During the 1980s and 1990s, WVRL measurements were refined through the use of advanced laser transmitters and filter technology, especially for improving the daylight background suppression [25.14–17].

The temperature rotational Raman lidar (TRL) technique was fostered in parallel with work focusing in particular on improving system efficiency and stability and reducing the daylight background, too [25.2, 18–23]. It is noteworthy, that there is another lidar technique using Raman signals for temperature measurements, Raman integration lidar, which must not be confused with the TRL technique which directly measures temperature. The Raman integration technique uses the assumption of hydrostatic equilibrium to estimate the molecular density in the stratosphere and from that a temperature profile [25.24].

These developments resulted in the routine use of WVTRL systems such as those on the Southern Great Plains (SGP) site of the US American Atmospheric Radiation Measurement (ARM) Program [25.25] in the US, in Payerne, Switzerland (operated by Meteo-Swiss [25.26, 27]), in Lindenberg, Germany (operated by the German Meteorological Service (DWD) [25.28]), and in Cabauw, The Netherlands [25.29]. An overview of other research systems is presented in Sect. 25.4.6, too.

25.3 Theory

In the following, we discuss the physical principles of Raman lidar as well as the equations that are used to describe Raman lidar signals.

25.3.1 Raman Lidar Equation

The Raman lidar equation is derived by replacing the elastic backscatter coefficient in the lidar equation (Chap. 25) with the Raman backscatter coefficient and accounting for the transmission at the Raman-shifted wavelengths during the return trip of the Raman signal. The resulting equation relates the photon number P_{Ram} of the received signal to system parameters, atmospheric properties, and the range r . This Raman lidar equation reads

$$P_{\text{Ram}}(r) = \eta \frac{E_0}{h\nu_0} \mathfrak{S}_{\text{las}} \mathfrak{S}_{\text{rec}} O(r) \frac{A}{r^2} \frac{c\Delta t}{2} \mathfrak{S}_{\nu_0}(r) \mathfrak{S}_{\nu_{\text{Ram}}}(r) \times \sum_i F(\nu_i) \beta_{\text{Ram}}(\nu_{\text{Ram},i}, r, T), \quad (25.1)$$

where

$$\beta_{\text{Ram}}(\nu_{\text{Ram},i}, r) = N_{\text{mol},i}(r) \frac{d\sigma_{\text{Ram},i}}{d\Omega}(\nu_{\text{Ram},i}, T) |_{\pi}. \quad (25.2)$$

Here, η is the quantum efficiency of the detector, E_0 is the laser pulse energy, h is Planck's constant, and ν_0 is the laser frequency. $\mathfrak{S}_{\text{las}}$ and $\mathfrak{S}_{\text{rec}}$ are the transmissions of the laser steering and receiver optics, respectively, $O(r)$ is the overlap function between the laser beam and the field of view of the receiver, $A = \pi r_{\text{tel}}^2$ is the area of the telescope (r_{tel} is the radius of the telescope), and Δt is the laser pulse duration. $\mathfrak{S}_{\nu_0}(r)$ and $\mathfrak{S}_{\nu_{\text{Ram}}}(r)$ are the atmospheric transmission functions up to r at the corresponding frequencies. The Raman line number is indicated by the index i . To improve the SNR, it is necessary to insert an interference filter or a grating spectrometer with an effective transmission function $F(\nu)$ into the path of the receiver, as this will constrain the signal to the spectral range of the vibrational and/or rotational Raman scattering lines of interest (Fig. 25.1).

The key to the Raman lidar technique is the information content of the Raman scattering coefficient β_{Ram} . This coefficient is the product of the number density of Raman scatterers $N_{\text{mol},i}(r)$ (e.g., water vapor molecules) and their differential scattering cross-section $d\sigma_i/d\Omega$ in the backward direction. The exact frequencies of the Raman lines depend on the vibrational and rotational quantum numbers of the scatterers.

25.3.2 Derivation of the Temperature Rotational Raman Lidar Equation

In temperature Raman lidar (TRL), the temperature sensitivity of the rotational Raman (RR) lines scattered by nitrogen and oxygen molecules around its fundamental frequency (the frequency of the laser transmitter) is used. In this case, the RR lidar equation can be written [25.22, 30] as

$$P_{\text{RR}}(r) = \eta_{\text{RR}} \frac{E_0}{h\nu_0} \mathfrak{S}_{\text{las}} \mathfrak{S}_{\text{rec}} O(r) \frac{A}{r^2} \frac{c\Delta t}{2} \mathfrak{S}_{\nu_0}(r) \mathfrak{S}_{\nu_{\text{RR}}}(r) \times \sum_i F(\nu_i) \beta_{\text{RR}}(\nu_{\text{RR},i}, r, T) \equiv \eta_{\text{RR}} \frac{E_0}{h\nu_0} \mathfrak{S}_{\text{las}} \mathfrak{S}_{\text{rec}} O(r) \frac{A}{r^2} \frac{c\Delta t}{2} \mathfrak{S}_{\nu_0}(r) \mathfrak{S}_{\nu_{\text{RR}}}(r) \times N_{\text{dry}}(r) \frac{d\bar{\sigma}_{\text{RR}}}{d\Omega}(T), \quad (25.3)$$

where N_{dry} is the number density of dry air and $d\bar{\sigma}_{\text{RR}}/d\Omega$ is the effective differential Raman scattering cross-section after summing over the relevant rotational Raman lines within the filter function.

Since the frequency shifts of the pure rotational Raman spectrum are usually within $\pm 200 \text{ cm}^{-1}$, the atmospheric transmission due to molecular and particle scattering can be considered to be the same for both the upward and downward paths of the photons. Note that WVTRL systems are designed such that there are no molecular absorption lines in the range of the Raman spectrum considered.

In order to eliminate the cross-sensitivity of this Raman measurement to system parameters such as the laser power, the size of the receiving telescope, transmission functions, and other atmospheric properties, two rotational Raman signals are measured at different frequencies. These signals have different temperature sensitivities. Thus, we obtain as TRL equation [25.30]

$$\frac{P_{\text{RR2}}}{P_{\text{RR1}}}(r, T) = \frac{\frac{d\bar{\sigma}_{\text{RR2}}}{d\Omega}[T(r)]}{\frac{d\bar{\sigma}_{\text{RR1}}}{d\Omega}[T(r)]} \equiv Q(r, T). \quad (25.4)$$

This equation can be rearranged to make it a function of the range-dependent temperature. A fit of the form

$$T(r) = f[Q(r), a, b, c] \quad (25.5)$$

is typically applied, which yields highly resolved and very accurate temperature profiles [25.30, 31]. The calibration constants a , b , and c are usually determined through comparison with radio soundings.

25.3.3 Water-Vapor Raman Lidar Equation

Water-vapor (WV) profiles are derived using the water-vapor Raman lidar equation [25.15, 16]

$$\begin{aligned}
 P_{\text{WVRL}}(r) &= \eta_{\text{WV}} \frac{E_0}{h\nu_0} \mathfrak{S}_{\text{las}} \mathfrak{S}_{\text{rec}} O(r) \frac{A}{r^2} \frac{c\Delta t}{2} \mathfrak{S}_{\nu_0}(r) \mathfrak{S}_{\nu_{\text{WV}}}(r) \\
 &\quad \times \sum_i F(\nu_i) \beta_{\text{Ram,WV}}(\nu_{\text{Ram,WV},i}, r) \\
 &= \eta_{\text{WV}} \frac{E_0}{h\nu_0} \mathfrak{S}_{\text{las}} \mathfrak{S}_{\text{rec}} O(r) \frac{A}{r^2} \frac{c\Delta t}{2} \mathfrak{S}_{\nu_0}(r) \mathfrak{S}_{\nu_{\text{WV}}}(r) \\
 &\quad \times N_{\text{WV}}(r) \frac{d\bar{\sigma}_{\text{WVRL}}}{d\Omega}, \quad (25.6)
 \end{aligned}$$

where N_{WV} is the number density of water vapor.

Normalization with a reference signal $P_{\text{mol}}(r)$ for the molecular number density of the atmosphere is performed to eliminate the system parameters and unknown atmospheric variables (similar to TRL). In most WVTRL systems, the nitrogen vibrational Raman signal is used; in some a temperature-independent linear combination of the two RRL channels

$$P_{\text{mol}}(r) = P_{\text{RR1}}(r) + BP_{\text{RR2}}(r) \quad (25.7)$$

to optimize the SNR. Here, the constant B is chosen so that this linear combination of RRL signals is independent of the temperature profile $T(r)$ [25.2]. This permits the derivation of a signal that only depends on the water-vapor mixing ratio M , a system constant C , and a function that corrects for the differential extinction between the laser transmitter and the water-vapor Raman scattering frequencies. The resulting WVRL equation reads

$$\frac{P_{\text{WVRL}}(r)}{P_{\text{mol}}(r)} = C \frac{N_{\text{WV}}(r)}{N(r)} \frac{\mathfrak{S}_{\nu_{\text{WV}}}(r)}{\mathfrak{S}_{\nu_0}(r)} = CM(r) \frac{\mathfrak{S}_{\nu_{\text{WV}}}(r)}{\mathfrak{S}_{\nu_0}(r)}, \quad (25.8)$$

where C combines the system efficiencies at the different frequencies as well as the ratio of the effective Raman scattering cross-sections. $N(r)$ is the molecular number density of the atmosphere at range r .

Depending on the width of the filter used to extract the water-vapor Raman signal, different rotational-vibrational lines of water vapor will be sampled, which may cause the collected signals to be temperature dependent. For instance, for a filter with a Gaussian transmission band that has a full width at half maximum of 18 cm^{-1} (corresponding to 0.3 nm for an initial laser wavelength of 354.7 nm), the temperature sensitivity is found to be 6.7% over the temperature range from 200 to 300 K [25.32, 33]. The temperature sensitivity

increases (decreases) for narrower (wider) filters. For example, a width of at least 120 cm^{-1} (corresponding to 2.0 nm for an initial laser wavelength of 354.7 nm) is needed to reduce the temperature sensitivity to $< 1\%$ over the temperature range $200\text{--}300 \text{ K}$.

Combined WVTRL has the advantage that the simultaneously measured temperature profile can be used to correct for this temperature dependence, thus facilitating the use of narrow filters to extract the water-vapor Raman signals, which in turn reduces the background signal and improves the SNR.

The ratio of the transmissions in (25.8) is readily derived and corrected for. To correct for the molecular contribution to differential extinction, the number density profile is needed, which can be calculated using TRL data, a simultaneously operating and colocated radiosonde, an atmospheric model, or an alternative source of data (as long as its level of accuracy is high enough). The aerosol contribution to the differential extinction can be derived and corrected for using simultaneously obtained and colocated measurements of the particle extinction coefficient provided by a temperature-independent Raman signal—either the vibrational Raman signal of nitrogen [25.4] or a temperature-independent combination of rotational Raman lidar signals [25.2]. After applying these corrections, the remaining uncertainty is small: $< 2\%$ for the water-vapor mixing ratio, even under the unfavorable conditions of a high aerosol load.

In summary, even with the correction operators, it is straightforward to derive $M(r)$ using water-vapor Raman lidar with a combination of two or three Raman lidar signals. The system constant C is usually determined by calibration with other sensors such as radio soundings or water-vapor differential absorption lidar (WVDIAL) [25.34, 35] and is constant for well designed Raman lidar systems over several months or even years. Furthermore, comparisons can be performed with continuously operating passive remote-sensing instruments such as microwave or infrared radiometers. Self calibration methods that do not require external reference water-vapor measurements have also recently been presented. These are based on either the response of the receiver to a lamp [25.36] or the daylight background signal measured by the WVRL [25.37]. Extensive field campaigns and comparisons with soundings have revealed a systematic error of $< 5\%$ for WVRL mixing ratio profiles.

25.3.4 Error Propagation

Errors in TRL and WVRL measurements can arise due to incorrect calibration (resulting in systematic errors) or errors due to system noise (resulting in statistical

errors). Systematic errors have been investigated in a large number of studies where different sensors were compared and the calibration of the WVRL was investigated [25.25, 26, 28, 37–45]. The systematic error in mixing ratio measurements performed throughout the troposphere over several years is generally < 5% if the system is well calibrated using the statistical techniques described in the publications above and state-of-the-art radiosondes or microwave radiometers (MWRs).

Measurement campaigns using TRL are rare because these systems have become available only very recently. However, it was demonstrated that the systematic error in temperature measurements is typically < 1 K [25.2, 22]. More recent studies have confirmed this accuracy as well as the long-term calibration stability [25.23, 31, 46–48]. More information on measurement accuracy will be gathered during the routine operation of WVRL and TRL systems in the years to come.

The statistical uncertainty in the measurements—the so-called noise error—is accurately characterized by the error propagation from Poisson photon statistics based on the Raman lidar equations given above. Using this, the relative noise error in the mixing ratio $\Delta M/M$ is given by

$$\frac{\Delta M}{M} \cong \sqrt{\left(\frac{\Delta P_{\text{WVRL}}}{P_{\text{WVRL}}}\right)^2 + \left(\frac{\Delta P_{\text{mol}}}{P_{\text{mol}}}\right)^2}, \quad (25.9)$$

and the absolute noise error ΔT in the temperature is obtained via

$$\Delta T \cong \frac{dT}{dQ} Q \sqrt{\left(\frac{\Delta P_{\text{RR1}}}{P_{\text{RR1}}}\right)^2 + \left(\frac{\Delta P_{\text{RR2}}}{P_{\text{RR2}}}\right)^2}. \quad (25.10)$$

Equation (25.8) demonstrates that the system noise in water-vapor mixing ratio measurements is mainly determined by photon statistics in the water-vapor Raman lidar channel because these signals are much weaker than the Raman reference signals. The resulting errors vary considerably depending on whether it is nighttime or daytime due to the different levels of daylight background in the water-vapor Raman signal, meaning that it becomes very important to suppress the daylight background. In contrast, (25.10) shows that TRL is less sensitive to the daylight background due to the stronger rotational Raman backscatter signals of nitrogen and oxygen and the much weaker dependence of this signal on the atmospheric conditions.

These errors are typically well described by Poisson statistics, so the 1- σ uncertainty ΔP in the signal P is \sqrt{P} . Consequently,

$$\frac{\Delta P}{P} = \frac{1}{\sqrt{P}}. \quad (25.11)$$

Using this relationship, the roles of individual error sources such as the background photons, which are incorporated into (25.9) and (25.10), can be studied. Hence, it is possible to derive an important equation that describes the relative error in each Raman signal [25.2, 23, 49, 50],

$$\frac{\Delta P_{\text{RL}}}{P_{\text{RL}}} \cong \frac{1}{\sqrt{klP_{\text{RL}}}} \sqrt{1 + \frac{P_{\text{B}}}{P_{\text{RL}}} + \frac{P_{\text{d}}^2 + P_{\text{a}}^2}{BG^2 e^2 P_{\text{RL}}}}, \quad (25.12)$$

where P_{RL} is an arbitrary Raman backscattering photon number, P_{B} is the daylight background photon number, and k and l are the number of range gates and laser shots used to integrate the signal, respectively. The last term in the square root in (25.12) becomes significant if analog signal detection is employed [25.49, 50]. Here, P_{d} and P_{a} are the detector and amplifier noise powers, respectively, e is the charge on an electron, and B and G are the bandwidth and gain of the detector, respectively.

The first three terms under the square root in (25.12) are denoted the *Poisson term*, the *background term*, and the *amplification term*, respectively. Obviously, for any particular laser power, it is better to use a single shot of high pulse energy. However, this approach is limited by the specifications of the laser and eye-safety considerations. The amplification term can be discarded if photon counting is performed, but it must be accounted for if analog detection is used. The number of photons is either measured directly or, if analog detection is used in the near range, the analog signal levels can be calibrated and *glued* to the photon numbers in the far range. Consequently, (25.11) can be applied in real time to derive the statistical error profile for each mixing ratio or temperature profile of the WVTRL. This is an important feature for process studies and data assimilation. State-of-the-art WVTRL systems provide excellent measurements during the daytime in the lower troposphere, even resolving turbulent fluctuations in water vapor and temperature [25.51–53] and, in combination with a Doppler lidar, fluxes [25.54].

25.4 Devices and Systems

A Raman lidar system consists of a laser transmitter, a telescope, a receiver, and a data acquisition system. Until recently, some of these components had limited lifetimes, which is why it has taken until very recently for a WVTRL to become commercially available. Previously, routinely operated WVTRL systems were employed for special research at scientific institutions; examples include those at the ARM SGP site in Billings (Oklahoma, USA), the MeteoSwiss site in Payerne (Switzerland), and the German Meteorological Service Observatory in Lindenberg (Germany).

25.4.1 Typical Setup of a Water-Vapor and Temperature Raman Lidar

The typical design of a WVTRL system is depicted in Fig. 25.2. For measurements performed in the lower tro-

posphere, it is best to operate the laser transmitter in the ultraviolet (UV) [25.30], e.g., at 355 nm, if a frequency-tripled Nd:YAG laser is applied. Wavelengths that are hazardous to the eyes, such as the first and second harmonics of the Nd:YAG laser transmitter at 1064 and 532 nm, can be eliminated during the propagation of the beam into the atmosphere by applying refractive optics such as a Pellin–Broca prism (PBP). The 355 nm beam is expanded to make it eye safe and reduce its divergence, and is transmitted into the atmosphere. Optionally, a 3-D scanner can be used to point the laser beam in different directions and receive the atmospheric backscatter signal from the same direction.

The elastically and Raman backscattered radiation is collected by a telescope and sent to a polychromatic receiver unit. The backscatter signal is separated, e.g., into the elastic signal, the water-vapor Raman chan-

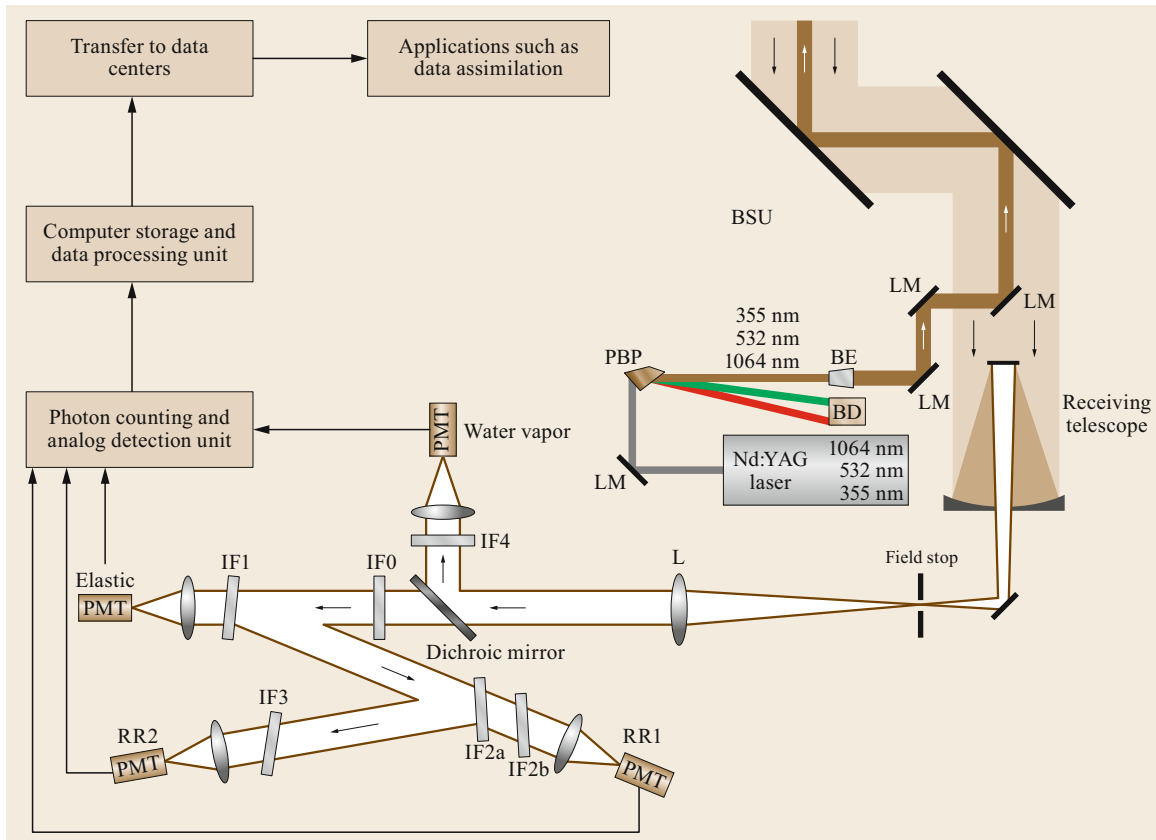


Fig. 25.2 Setup of the WVTRL system of University of Hohenheim: photomultiplier tube (PMT), interference filter (IF), rotational Raman signals (RR1, RR2), lens (L), laser mirror (LM), beam expander (BE), beam dump (BD), and beam steering unit (BSU) (after [25.31] © E. Hammann et al., Creative Commons Attribution 3.0 License)

nel, and the two temperature-sensitive rotational Raman channels (which is the least number of signals needed for the variables listed in Table 25.1). The signals are detected with photomultiplier tubes and sent to a photon counting and/or analog data acquisition unit. The data are transferred to a computer, stored, and processed to give measurements at the selected temporal and spatial resolutions as well as the corresponding noise error profiles.

25.4.2 The Laser Transmitter

For WVTRL, powerful laser transmitters are needed to achieve acceptable photon statistics in the return signals. To perform measurements during the daytime and nighttime, an average power of 10 W is typically used to achieve a high SNR, along with a receiving telescope with a primary mirror diameter of 40 cm. A relatively low laser power can be compensated for to some extent by using a larger telescope; however, since both the background and backscatter signals scale with the telescope area whereas only the lidar backscatter signal scales with the laser pulse energy, a large pulse energy is preferable when there is significant background. Furthermore, the laser should be operated in the UV region, given that the Raman scattering cross-sections increase with the fourth power of the laser frequency (ν_0^4), equivalent to Rayleigh scattering. However, for systems that perform long-distance profiling in the stratosphere and mesosphere, laser wavelengths in the visible are more attractive [25.30].

The present standard laser material is Nd:YAG, as it allows a high pulse energy and reasonable repetition rates to be realized along with efficient frequency tripling to the UV. Commercial flash-lamp-pumped Nd:YAG lasers are available that provide pulse energies of 100–500 mJ and repetition rates of 10–50 Hz at a wavelength of 355 nm. The main drawback of these lasers is their high demand for cooling power, as flash lamps are rather inefficient in laser pumping. The lifetime of a flash lamp is limited to $\approx 10^7$ shots, so the flash lamps must be exchanged quite often, which always necessitates some realignment of the Raman lidar system.

Recently, new diode-laser-pumped Nd:YAG lasers (Fig. 25.3) have become available with a similar average power to the flash-lamp-pumped Nd:YAG lasers. These novel systems operate at high repetition rates such as 200 Hz (due to the duty cycle of the diode lasers) and at a pulse energy of > 100 mJ, leading to an average power of > 20 W in the UV.

Due to the very efficient and direct pumping of the laser material by diode lasers, the size, efficiency, stability, and cooling demand of a diode-laser-pumped

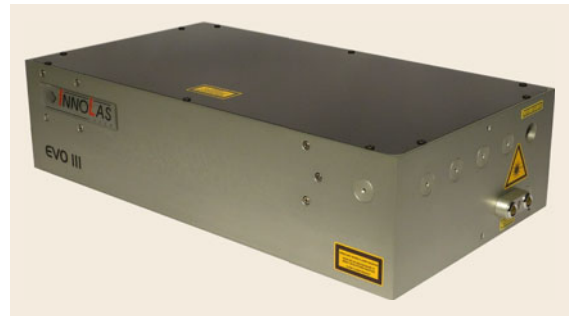


Fig. 25.3 Photo of a diode-laser-pumped, frequency-tripled Nd:YAG laser (photo © Innolas GmbH)

Nd:YAG UV laser make it considerably more attractive than a flash-lamp-pumped Nd:YAG laser for performing WVTRL in the field, on various platforms, and for automatized, unattended operation [25.55].

Since the average power of a diode-laser-pumped Nd:YAG laser is higher than that of a flash-lamp-pumped Nd:YAG laser, significantly better performance in terms of the SNRs of water-vapor and temperature measurements can be achieved with a diode-laser-pumped laser during the night. Its somewhat lower pulse energy increases the noise error during the day, but this effect is relatively small and is also compensated by the larger average power, meaning that the overall performance of a diode-laser-pumped laser transmitter is higher than that of a flash-lamp-pumped laser transmitter. Indeed, the performance of a diode-laser-pumped Nd:YAG laser meets the requirements of the World Meteorological Organization (WMO) for the temperature and humidity profiling needed for nowcasting and very short-range weather forecasts in the lower troposphere ([25.56]; Sect. 25.5). Consequently, the utilization of this new generation of laser transmitters with their improved stability, efficacy, and performance recently resulted in the first commercial WVTRL system [25.55], and should lead to the more widespread application of the WVTRL technique.

25.4.3 The Receiver

The central component of a Raman lidar is its receiver. A receiving telescope with a large primary mirror is typically used to collect the backscatter signal with high efficiency. As the cost of the mirror increases significantly with size, practical values for the diameter of the primary mirror range between 40 and 80 cm. Polychromators with either interference filters or gratings are used to extract the Raman signals from the backscatter signal. Polychromators with state-of-the-art interference filter technology are more common than those with gratings because they are easier to align and

handle, and they offer higher efficiency. Their costs, however, are typically higher.

At least four channels are required for WVTRL: one for the elastic signal, two for the rotational Raman signals with different temperature dependences, and one for the water-vapor Raman signal. Broadband daylight filters are usually combined with narrow-band multicavity interference filters to achieve both high out-of-band blocking and high transmission within the passband. To achieve highly accurate measurements in the presence of aerosol layers and clouds, elastic signal blocking of at least seven and ten orders of magnitude is advised for the rotational Raman channels [25.21] and the water-vapor channel [25.32, 33], respectively.

The optimum frequency bands for the rotational Raman signals depend on the temperature range of interest, the amount of blocking of the elastic backscatter signal in the Raman channels, and the background light conditions. Further details can be found in the literature [25.21, 57].

For the water-vapor signal, the optimum width of the frequency band depends on the background conditions of interest and on the maximum acceptable level of temperature dependence of the signals [25.34, 35]. If temperatures are measured with the same lidar, the measured atmospheric temperature profile can be used to correct for a possible temperature dependence of the water-vapor Raman signals. This means that it may be acceptable to collect several water-vapor Raman lines with high temperature dependences because they yield stronger signals and thus smaller statistical uncertainties in the water-vapor mixing ratio measurements. Typical bandwidths used in WVTRL systems for the water-vapor and temperature channels are 0.2–0.5 nm.

As Raman cross-sections are proportional to ν^4 , the higher the frequency, the stronger the signals for the same laser power. Thus, primary laser frequencies in the UV are preferred for WVTRL. Consequently, the rotational Raman signals are also in the UV, while the water-vapor Raman signals are in the blue part of the visible spectrum. Due to their high quantum efficiency, photomultiplier tubes (PMTs) are generally the preferred detector for these short wavelengths. A further advantage of PMTs is that their photosensitive area is quite large compared to, e.g., avalanche photodiodes.

25.4.4 The Data Acquisition System

Since the Raman signals are typically quite weak, only high-power instruments use analog signal detection. In general, photon counting is the preferred acquisition mode, especially at large ranges and under low-background conditions, because it significantly reduces

the effects of detector noise compared to analog detection. However, combined data acquisition systems that incorporate both modes (and thus their respective advantages) are also available on the market.

Typical resolutions of the raw data are 10–100 laser shots, resulting in one profile every 0.1–10 s, and a few meters for each range bin. Typical maximum ranges are several tens of kilometers, allowing them to reach distances for which the measured signal is nearly only due to the background light. The photon counting and/or analog signals of each range bin are quantified using data acquisition systems connected to computers, where the signals are stored on hard discs or (even more quickly) on solid-state drives.

25.4.5 Processing and Storage of Temperature and Water-Vapor Profiles

Once the raw signals have been stored, higher-level data products can be derived either during postprocessing or even in near real time if the computer is fast enough and the acquisition of raw signals is unaffected by further data processing. The first step in the processing of photon-counting signals is to correct for dead-time effects. Even though the Raman signals are weak (more than two orders of magnitude weaker than the elastic backscatter signals), they may be strong enough to be affected by detector nonlinearities. Depending on the detector and data acquisition system used, either a paralyzable or a nonparalyzable detector model must be applied (for further details regarding this topic, refer to [25.2, 53]).

After correcting for dead-time effects, the background is determined and subtracted from the signals to obtain the atmospheric backscatter signals. These corrected signals are averaged over time and range to reduce their statistical uncertainties. A simple moving box average is usually preferred in order to keep the weighting functions simple.

As described above, for photon counting, the statistical error is mainly due to shot noise. The statistical uncertainties in the temperature and water-vapor measurements of each profile can thus be determined from the measured numbers of photons for the signals using Gaussian error propagation. Of course, the contribution of the background must also be taken into account. As the background is determined over a rather large number of range bins in the far range (typically > 1000), the statistical uncertainty in the background level itself is very small. However, its contribution to the overall error can be significant during the daytime in the far range, as shown in (25.10). In state-of-the-art WVTRLs, data acquisition, signal averaging, and the

derivation of water-vapor mixing ratio and temperature profiles (including their error profiles) are performed routinely, which makes a WVTRL a powerful tool for many applications, such as the derivation of climatologies, model verification, process studies, and data assimilation.

25.4.6 The Main Features of Raman Lidar Systems

A recent overview of WVTRL systems is provided in [25.1], and a summary of operational systems is given in Sect. 25.2. Several other WVRL systems intended for research have been developed and are operated by various international scientific institutions, such as the Goddard Space Flight Center (GSFC) in Greenbelt, USA [25.34, 35], the Leibniz Institute for Tropospheric Research (IfT) in Leipzig, Germany [25.3], the Radio Science Center for Space and Atmosphere (RASC) in Japan [25.2, 22], the Università della Basilicata in Potenza, Italy [25.58, 59], the Max Planck Institute for Meteorology (MPI) in Hamburg, Germany, the Laboratoire des Sciences du Climat et de l'Environnement in Gif-sur-Yvette, France [25.60], the Amazon WVRL in Brazil [25.61], and the high-performance WVRLs with turbulence resolution at the University of Hohenheim (UHOH) in Stuttgart, Germany [25.31, 51, 52, 55]. Many of these systems are mobile and can be transported in special housings such as seatainers, allowing them to be applied in various field campaigns. Airborne systems are oper-

ated at the GSFC [25.5] and at the University of Wyoming [25.6].

TRL measurements have been extended to the daytime through the use of narrowband filters and UV primary wavelengths [25.2, 22, 23, 31, 46, 56, 58, 62]. A 3-D scanning combined WVRL and TRL system has been realized at the Institute of Physics and Meteorology (IPM) of the UHOH in Stuttgart, Germany. A new compact system with even better temperature profiling performance is presented in [25.55]. It was recently shown that convective boundary layer (CBL) turbulence studies are even possible at midday with the IPM TRL [25.51]. Furthermore, scanning ground-based operation has been applied to observe the 3-D structure of the temperature and its gradient at the top of the CBL [25.46] and in the surface layer [25.31]. Other WVTRL systems have also been demonstrated [25.47, 58], though they have considerably less resolution in profiling temperature.

Overall, the straightforward design of a WVTRL in combination with its high accuracy and range resolution makes this instrument very valuable for applications in the weather, climate, and Earth-system sciences. Using a commercially available high-power laser transmitter, well-designed receivers and receiver optics, and standard technology to receive the signals, measurements can be performed with high resolution and accuracy during the nighttime and daytime. Challenges related to calibration and its long-term stability have been solved. Therefore, we can expect applications of water-vapor and temperature Raman lidar techniques to expand significantly in the near future.

25.5 Specifications

When specifying the performance of a WVTRL system, it is important to note that the noise error profiles are range dependent. Furthermore, the error profiles are dependent on the temporal and spatial resolutions employed when deriving the results. Therefore, just specifying an error at a certain height provides misleading information, as the system will perform much better in the near range. The measurement performance is another source of confusion, as previous comparisons with other sensors (such as passive remote sensors) have often overlooked this issue with the noise error profiles. To our knowledge, the first comprehensive comparison of active and passive remote-sensing techniques was carried out in [25.1], where the differences between the methodologies used to derive (active) and retrieve (passive) water-vapor and temperature profiles were accounted for correctly.

A simulation of the expected performance of WVTRL in different climate zones for the least favorable background light conditions at local noon was recently performed [25.55]. The results are presented in Figs. 25.4 and 25.5.

Those results demonstrate that WVTRL can be performed in all climate zones while maintaining the breakthrough requirements of the WMO with respect to high-resolution numerical weather prediction (NWP) in the lower troposphere, which is particularly interesting from a data assimilation perspective. It can also be shown that the WMO breakthrough requirements for water-vapor and temperature profiling are fulfilled (for an overview of these requirements, refer to www.wmo-sat.info/oscar/observingrequirements). Figures 25.5 and 25.6 show that it is important to consider the strong dependence of the error profile on the range.

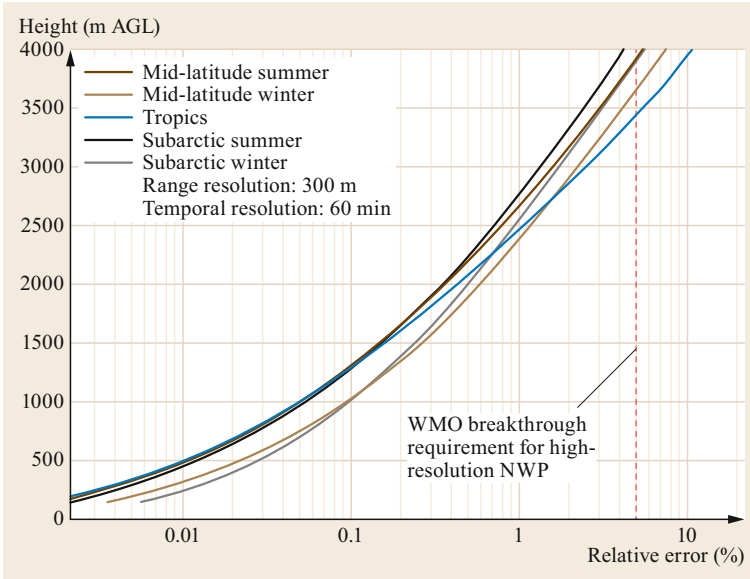


Fig. 25.4 Expected water-vapor mixing ratio measurement performance of WVTRL in different climate zones under the least favorable background light conditions at local noon

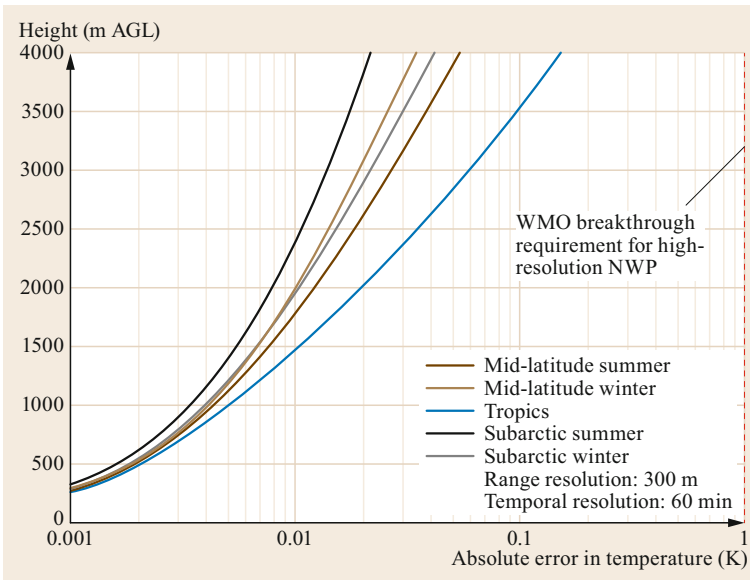


Fig. 25.5 Expected temperature measurement performance of WVTRL in different climate zones under the least favorable background light conditions at local noon

For instance, the errors are two orders of magnitude smaller at a height of 1000 m for water vapor and one order of magnitude smaller for temperature when compared with the errors at 4000 m. This is also why

turbulent moments in the CBL can now be derived with WVTRL. These properties explain why ranges are given for the noise errors in the corresponding spatial and temporal resolutions in Table 25.3.

25.6 Quality Control

In theory, it is possible to determine the calibration constants of moisture and temperature measurements by combining careful inspection of the efficiency of each Raman lidar channel with literature values of the respec-

tive backscatter cross-sections. In practice, however, this approach leads to excessive uncertainties (several tens of percent and several kelvins, respectively) because the uncertainties in the wavelength- and polarization-

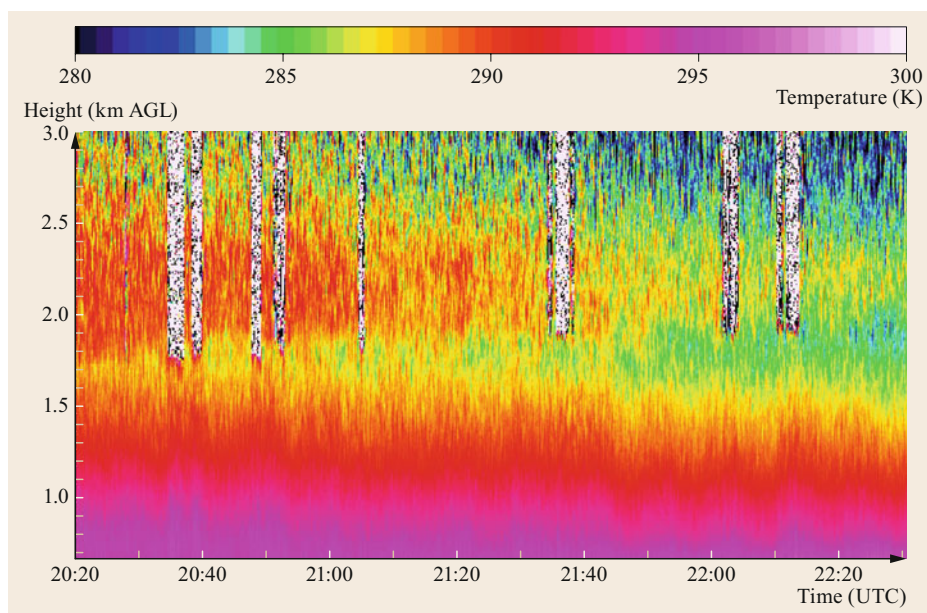


Fig. 25.6 High-resolution temperature profiling with UHOH WVTRL at resolutions of 10 s and 100 m. Using these data, it was possible to study the evolution of the temperature structure in the CBL, including the location and strength of the interfacial layer

Table 25.3 Specification of the daytime performance of state-of-the-art WVTRL for temperature and water-vapor profiling. During nighttime, the specifications will be even better. The typical range of measurements is from the surface layer up to 3000 m in all climate zones. The range is also limited by optically thick clouds

Variable	Noise error	Range resolution (m)	Temporal resolution (s)	Systematic error
Mixing ratio	< 5%	10–300 m	10–600 s	< 5%
Temperature	< 0.2 K	10–300 m	10–600 s	< 0.5 K

dependent transmission of all the optical components as well as those in the detector efficiencies add up. Consequently, other approaches are used. Typically, several local radiosondes are compared with the Raman lidar measurements to determine an average calibration. This comparison is less affected by sampling errors because the measurements are performed at different times and locations and because averaging is carried out spatiotemporally between the drifting radiosonde, which measures along its path, and the lidar, which measures along its thin laser beam. As long as the laser wavelength and the spectral properties of the receiver (filter aging, changes in the incidence angles, etc.) remain constant, the calibration factors are also constant. Note that differences in the laser power cancel and have no effect; the dead-time correction is also unaffected by changes in laser power, as it solely depends on the number of detected photons, which is a known quantity.

Aside from radiosondes, methods used for calibration include comparisons with weather stations on the

ground or towers for scanning WVTRL systems, comparisons with WVDIAL, MWR, and airborne in-situ systems on unmanned aerial systems (UASs) or aircraft.

When assessing the quality of WVTRL data, international comparison campaigns are especially valuable [25.41, 42, 44]. These enable WVTRLs on different platforms to be intercompared directly, not just indirectly via questionable standards such as radiosondes. Airborne WVTRL comparisons are achieved by either designing specific flight modes with crossing points or by performing stacked flights, which result in even more data for comparisons. Such lidar-to-lidar intercomparisons significantly reduce the uncertainty due to sampling error when different types of systems are used for quality control. Upon compiling all of the results from intercomparison campaigns and routine long-term operations, systematic errors of < 5% in water-vapor mixing ratio profiles and < 0.5 K in temperature profiles have been discerned.

The quality of both the accuracy (systematic errors or biases) and the measurement precision (statistical uncertainties) can be controlled. Determining the statistical uncertainty using the Poisson method yields only the shot-noise error, but for each single-photon-counting range bin there is an alternative independent method of determining the mean statistical uncertainties in all error sources (such as the electric noise in the analog signals). This method [25.52, 63] uses the fact that fluctuations due to atmospheric turbulence are temporally correlated whereas the instrumental noise in one profile is uncorrelated with that in the next profile. Therefore, applying an autocorrelation analysis to a high-

resolution data set (temporal resolution of each profile ≤ 10 s; total duration of the data set 30–120 min) allows atmospheric fluctuations to be separated from instrumental noise. Historically, this method was first applied to Doppler lidar and WVDIAL data. These instruments use elastic backscatter signals that are only detected in analog mode, so they typically provide data products with a much higher temporal resolution than afforded by Raman lidars. However, it is not possible to calculate the Poisson error for these systems since no photon counting data are available for them.

The statistical uncertainty in analog signals of WVTRL systems that use combined analog photon-counting data acquisition systems can be estimated using the following approach. First, in a range interval in which both acquisition modes provide reliable

data, the analog data are scaled (*glued*) to the photon counting data. Then the attributed photon-counting numbers for the scaled analog data are used to calculate the uncertainties in the Poisson method. Because the major contributor to the statistical uncertainty is the shot noise, this approach is valid [25.39, 40, 64].

In recent years, WVTRL has reached the performance level required to study atmospheric turbulence in the daytime [25.51, 53, 65]. This allows the instrumental noise errors to be determined precisely and with error estimates for the uncertainties themselves. Using this approach, it is typically found that the photon shot noise is the main contributor ($\approx 75\%$) even to analog signals in the near range in modern high-power WVTRL systems, while other statistical error sources are comparatively small [25.51].

25.7 Maintenance

The maintenance of a Raman lidar mainly involves cleaning the exterior optics (such as the optical window for the transmitter and the receiver) and maintaining the laser. As explained above, the maintenance required for the laser largely depends on the laser technology used. More frequent maintenance is required if a flash-lamp-pumped laser is used. For instance, the lamps must be regularly replaced, which also necessitates subsequent realignment. On the other hand, if

a diode-laser-pumped laser transmitter is used, very little maintenance is required for around 3 years of continuous operation, at which point the diode laser bars will probably start to degrade and ultimately need to be replaced. However, the lifetimes of other optics are not as well known, so the experience gained by monitoring and inspecting currently operational WVTRL systems over the coming years will be important in this respect.

25.8 Applications

In the following, we discuss applications of WVTRL, including process studies, model verification and calibration of other sensors, and the assimilation of measured data into atmospheric models.

25.8.1 Monitoring

There are three main WVRLs that are currently monitoring the lower tropospheric water-vapor distribution. These WVRLs are located at the SGP site in Oklahoma (USA), in Payerne (Switzerland), and in Lindenberg (Germany). Data obtained by the SGP WVRL are available from the ARM data archive (see www.archive.arm.gov) and have been used for various studies of the evolution and variability of the water-vapor field.

The SGP and Payerne WVTRLs can also measure temperature profiles, with the Payerne WVTRL appear-

ing to provide the best resolution and accuracy among the three. The analysis and advanced calibration of these data are ongoing.

A new compact and automatized WVTRL has recently been developed at the UHOH. This system was shown to be capable of unattended 24/7 operation [25.56] and to possess better performance in terms of accuracy, temporal resolution, spatial resolution, and range during the daytime and the nighttime in all climate zones than previous systems (Sect. 25.5). A similar system is now available commercially [25.55]. Due to its capabilities, it is believed that operating and applying this type of WVTRL at individual sites and in networks will revolutionize our knowledge of the structure and evolution of the moisture and temperature fields in the lower to middle troposphere.

Table 25.4 Maintenance of humidity and temperature Raman lidar systems

Maximum interval	Temperature channel	Water-vapor channel	Laser transmitter	Receiver	Data acquisition system
4–8 weeks	None	None	Replace flash lamps if this technology is used	Clean window	None
3 months	None	None	None	None	None
3 years	Check instrument calibration and perform maintenance of diode-laser-pumped laser transmitter			None	None

25.8.2 Model Verification and the Calibration of Other Sensors

The high accuracy and resolution of state-of-the-art WVTRL systems make these systems highly suited to model verification as well as the verification and calibration of other in-situ sensors and remote-sensing techniques. This application was pioneered at the ARM SGP site because the SGP WVTRL was calibrated to a high level of accuracy using a large set of soundings and advanced MWRs that were operated at the site. This cross-referencing considerably increased the trustworthiness of the Raman lidar data and led to the acceptance of WVTRL as a reference standard of the WMO. Thus, WVTRL has been used to study radio soundings [25.25, 36, 37], MWRs [25.38], WVDIAL systems [25.66], and airborne in-situ measurements [25.67]. The accuracies of the WVTRL systems at the Meteo Swiss site in Payerne [25.26, 27] and the DWD site in Lindenberg [25.28] are also high enough to make these systems useful for cross-validating radio soundings and model output. Also, using data collected in field campaigns, WVTRL has been used to calibrate and verify spaceborne passive remote sensors such as the infrared atmospheric sounding interferometer (IASI) [25.68]. However, comprehensive comparisons with model output data obtained under a variety of meteorological conditions are still rare and should therefore be extended [25.69–71].

25.8.3 Data Assimilation

Due to the ability of WVTRL systems to accurately characterize vertical profiles with respect to bias and noise errors, and because of the high temporal and spatial resolutions of these systems, they are excellent candidates for data assimilation (DA). However, only a few impact studies have been performed so far, which is partly due to the limited availability of operational WVTRL data as well as the effort required to conduct DA studies, which depends on the DA method applied and the configuration of the model. To our knowledge, the first four-dimensional variational assimilation study with water-vapor lidar data is reported in [25.72], and the first assimilation of WVRL data is presented in [25.73], which used the MM5 4VAR and a triangle of WVRL systems. A significant positive impact on the analysis of water-

vapor fields was demonstrated through comparison with independent retrievals of integrated water-vapor data obtained by a network of ground-based global navigation satellite system (GNSS) receivers. This work was recently extended by performing the first assimilation of TRL temperature profiles [25.74]. Again, this had very encouraging effects on not only the vertical and horizontal distributions of the temperature field but also the atmospheric boundary layer (ABL) depth and the inversion strength. In that work, the data were assimilated in a 3-D variational (3DVar) rapid update cycle (RUC) using the Weather Research and Forecasting (WRF) model in combination with the land surface model NOAHMP developed at IPM. Recently, MeteoSwiss contributed to these impact studies by using the data of the MeteoSwiss WVTRL in Payerne in combination with the DWD kilometer-scale ensemble data assimilation (KENDA), based on a local ensemble transform Kalman filter (LETKF) [25.75]. IPM advanced those studies by incorporating a new operator for the mixing ratio in the WRF-DA that permits the simultaneous and independent assimilation of absolute humidity, mixing ratio, and temperature profiles [25.76]. In both studies, strong and positive impacts on the water-vapor and temperature field analyses were observed.

Therefore, it is clear that WVTRL data assimilation is a rapidly emerging field of research and applications. WVTRL data have a strong impact because they have high temporal and vertical resolutions, they can be used to resolve the inversion layer and lids, and they are highly accurate. It is expected that the utilization of WVTRL in networks and the assimilation of WVTRL data will have a large positive impact on NWP for now-casting and short-range NWP.

25.8.4 Process Studies

For decades, ground-based WVRLs have been successfully applied in various process studies. Raman lidar systems were utilized during almost all major field campaigns, such as the International Water Vapor Project (IHOP_2002, [25.77]), the Convective Storms Initiation Project (CSIP) during 2004–2005 [25.78], the Convective and Orographically-Induced Precipitation Study (COPS) in 2007 [25.79, 80], the HD(CP)² Observational Prototype Experiment (HOPE) in 2013 [25.81],

the Plains Elevated Convection at Night Field Project (PECAN) in 2015 [25.82], and the Land–Atmosphere Feedback Experiment (LAFE) in 2017 [25.83]. This list is certainly not exhaustive.

Applications of WVTRL systems include investigations of the long-term evolution of the atmospheric water-vapor field [25.25], fronts [25.84, 85], the dry line [25.86], stratospheric intrusion events [25.58], hurricanes [25.87], and convection initiation [25.88, 89]. Additionally, the combined use of WVRL and TRL has been exploited to perform measurements of relative humidity [25.57, 59, 90] (e.g., to characterize cloud condensation levels in the CBL and the microphysical properties of cirrus clouds).

25.9 Future Developments

The ability of WVTRL to measure water-vapor and temperature profiles from the surface to the lower and upper troposphere makes these systems indispensable for applications in the weather, climate, and earth-system sciences. Due to recent success to make these systems more stable, compact, and operational, there is a huge increase in the number of applications of WVTRLs, including the realization of automated, operational, ground-based, combined WVTRL

Due to the advances in daylight background suppression described above [25.52, 65, 67, 91], high-power Raman lidar can even be employed to monitor turbulent moment profiles in the daytime convective atmospheric boundary layer (CBL) up to the third order. This high resolution and accuracy of temperature profiling is demonstrated in Fig. 25.6. More recently, TRL was used to profile turbulent moments of temperature up to the fourth order for the first time [25.51]. Latent and sensible heat flux profiles simultaneously from these data have also been derived with an extensive error analysis [25.54, 83]. In addition, there is great potential to use the data to study L-A feedback [25.92] and its metrics [25.93].

systems designed for continuous operation in networks in all climate zones. Furthermore, WVTRL systems are ready for airborne applications [25.5, 6]. Last but not least, the operation of WVTRL systems on spaceborne platforms has been proposed, which is expected to fill an important gap in global observations of lower-tropospheric water-vapor and temperature fields with high vertical resolution and accuracy [25.7, 8].

25.10 Further Reading

WVRL technique:

- D.N. Whiteman: Examination of the traditional Raman lidar technique: I. Evaluating the temperature-dependent lidar equations, *Appl. Opt.* **42**, 2571–2592 (2003)
- D.N. Whiteman: Examination of the traditional Raman lidar technique: II. Evaluating the ratios for water vapor and aerosols, *Appl. Opt.* **42**, 2593–2608 (2003)

TRL technique:

- A. Behrendt: Temperature measurements with lidar. In: *Lidar: Range-Resolved Optical Remote Sensing of the Atmosphere*, Springer Series in Optical Sciences, Vol. 102, ed. by C. Weitkamp (Springer, New York 2005), pp. 273–305

Land–atmosphere interaction:

- J.A. Santanello Jr, P.A. Dirmeyer, C.R. Ferguson, K.L. Findell, A.B. Tawfik, A. Berg, M. Ek, P. Gen-

tine, B.P. Guillod, C. van Heerwaarden, J. Roundy, V. Wulfmeyer: Land–atmosphere interactions: The LoCo perspective. *Bull. Am. Meteorol. Soc.* **99**(6), 1253–1272 (2017)

- V. Wulfmeyer, D.D. Turner, B. Baker, R. Banta, A. Behrendt, T. Bonin, W.A. Brewer, M. Buban, A. Choukulkar, E. Dumas, R.M. Hardesty, T. Heus, J. Ingwersen, D. Lange, T.R. Lee, S. Metzendorf, S.K. Muppa, T. Meyers, R. Newsom, M. Osman, S. Raasch, J. Santanello, C. Senff, F. Späth, T. Wagner, T. Weckwerth: A new research approach for observing and characterizing land-atmosphere feedback, *Bull. Am. Meteorol. Soc.* **99**(8), 1639–1667 (2018)

Thermodynamic remote sensing and its applications:

- V. Wulfmeyer, R.M. Hardesty, D.D. Turner, A. Behrendt, M.P. Cadeddu, P. Di Girolamo, P. Schliüssel, J. Van Baelen, F. Zus: A review of the remote sensing of lower-tropospheric thermodynamic profiles and its indispensable role for the understanding

and the simulation of water and energy cycles, *Rev. Geophys.* **53**(3), 819–895 (2015)

Status of turbulence research based on high-resolution active remote-sensing systems:

- V. Wulfmeyer, S.K. Muppa, A. Behrendt, E. Hammann, F. Späth, Z. Sorbjan, D.D. Turner, R.M. Hardesty: Determination of convective boundary layer entrainment fluxes, dissipation rates, and the molecular destruction of variances: Theoretical description and a strategy for its confirmation with a novel lidar system synergy, *J. Atmos. Sci.* **73**(2), 667–692 (2016)

Assimilation of TRL temperature profiles:

- S. Adam, A. Behrendt, T. Schwitalla, E. Hammann, V. Wulfmeyer: First assimilation of temperature lidar data into a numerical weather prediction model: Impact on the simulation of the temperature field, inversion strength, and planetary boundary layer depth, *Q. J. R. Meteorol. Soc.* **142**(700), 2882–2896 (2016)

- R. Thundathil, T. Schwitalla, A. Behrendt, S.K. Muppa, S. Adam, V. Wulfmeyer: Assimilation of lidar water vapour mixing ratio and temperature profiles into a convection-permitting model. *J. Meteor. Soc. Japan* **98**, 959–986 (2020)

Importance of thermodynamic profiling from space:

- National Academies of Sciences, Engineering, and Medicine: *Thriving on Our Changing Planet: A Decadal Strategy for Earth Observation from Space* (The National Academies Press, Washington 2018)
- J. Teixeira, J.R. Piepmeier, A.R. Nehrir, C.O. Ao, S.S. Chen, C.A. Clayson, A.M. Fridlind, M. Lebsock, W. McCarty, H. Salmun, J.A. Santanello, D.D. Turner, Z. Wang, X. Zeng: Toward a Global Planetary Boundary Layer Observing System: The NASA PBL Incubation Study Team Report. NASA PBL Incubation Study Team. 134 pp (2021), see <https://science.nasa.gov/earth-science/decadal-pbl>, Accessed 10 July 2021

References

- 25.1 V. Wulfmeyer, R.M. Hardesty, D.D. Turner, A. Behrendt, M.P. Cadetdu, P. Di Girolamo, P. Schlüssel, J. Van Baelen, F. Zus: A review of the remote sensing of lower-tropospheric thermodynamic profiles and its indispensable role for the understanding and the simulation of water and energy cycles, *Rev. Geophys.* **53**(3), 819–895 (2015)
- 25.2 A. Behrendt, T. Nakamura, M. Onishi, R. Baumgart, T. Tsuda: Combined Raman lidar for the measurement of atmospheric temperature, water vapor, particle extinction coefficient, and particle backscatter coefficient, *Appl. Opt.* **41**(36), 7657–7666 (2002)
- 25.3 D. Althausen, D. Müller, A. Ansmann, U. Wandinger, H. Hube, E. Clauer, S. Zörner: Scanning 6-wavelength 11-channel aerosol lidar, *J. Atmos. Ocean. Technol.* **17**(11), 1469–1482 (2000)
- 25.4 A. Ansmann, U. Wandinger, M. Riebesell, C. Weitkamp, W. Michaelis: Independent measurement of extinction and backscatter profiles in cirrus clouds by using a combined Raman elastic-backscatter lidar, *Appl. Opt.* **31**(33), 7113–7131 (1992)
- 25.5 D.N. Whiteman, K. Rush, S. Rabenhorst, W. Welch, M. Cadirola, G. McIntire, F. Russo, M. Adam, D. Venable, R. Connell, I. Veselovskii, R. Forno, B. Mielke, B. Stein, T. Leblanc, S. McDermid, H. Vömel: Airborne and ground-based measurements using a high-performance Raman lidar, *J. Atmos. Ocean. Technol.* **27**(11), 1781–1801 (2010)
- 25.6 B. Liu, Z. Wang, Y. Cai, P. Wechsler, W. Kuestner, M. Burkhart, W. Welch: Compact airborne Raman lidar for profiling aerosol, water vapor and clouds, *Opt. Express* **22**(17), 20613–20621 (2014)
- 25.7 P. Di Girolamo, A. Behrendt, V. Wulfmeyer: Spaceborne profiling of atmospheric temperature and particle extinction with pure rotational Raman lidar and of relative humidity in combination with differential absorption lidar: Performance simulations, *Appl. Opt.* **45**(11), 2474–2494 (2006)
- 25.8 P. Di Girolamo, A. Behrendt, V. Wulfmeyer: Spaceborne profiling of atmospheric thermodynamic variables with Raman lidar, *Opt. Express* **26**(7), 8125–8161 (2018)
- 25.9 D.A. Leonard: Observation of Raman scattering from the atmosphere using a pulsed nitrogen ultraviolet laser, *Nature* **216**(5111), 142–143 (1967)
- 25.10 J.A. Cooney: Measurement of the Raman component of laser atmospheric backscatter, *Appl. Phys. Lett.* **12**(2), 40–42 (1968)
- 25.11 S.H. Melfi, J.D. Lawrence, M.P. McCormick: Observation of Raman scattering by water vapor in the atmosphere, *Appl. Phys. Lett.* **15**(9), 295–297 (1969)
- 25.12 J. Cooney: Remote measurements of atmospheric water vapor profiles using the Raman component of laser backscatter, *J. Appl. Meteorol.* **9**(1), 182–184 (1970)
- 25.13 J. Cooney: Measurement of atmospheric temperature profiles by Raman backscatter, *J. Appl. Meteorol.* **11**(1), 108–112 (1972)
- 25.14 D. Renaut, J.C. Pourny, R. Capitini: Daytime Raman-lidar measurements of water vapor, *Opt. Lett.* **5**(6), 233–235 (1980)

- 25.15 D.N. Whiteman, S.H. Melfi, R.A. Ferrare: Raman lidar system for the measurement of water vapor and aerosols in the Earth's atmosphere, *Appl. Opt.* **31**(16), 3068–3082 (1992)
- 25.16 A. Ansmann, M. Riebesell, U. Wandinger, C. Weitkamp, E. Voss, W. Lahmann, W. Michaelis: Combined Raman elastic-backscatter LIDAR for vertical profiling of moisture, aerosol extinction, backscatter, and LIDAR ratio, *Appl. Phys. B* **55**(1), 18–28 (1992)
- 25.17 J.E.M. Goldsmith, F.H. Blair, S.E. Bisson, D.D. Turner: Turn-key Raman lidar for profiling atmospheric water vapor, clouds, and aerosols, *Appl. Opt.* **37**(21), 4979–4990 (1998)
- 25.18 Y.F. Arshinov, S.M. Bobrovnikov, V.E. Zuev, V.M. Mitev: Atmospheric temperature measurements using a pure rotational Raman lidar, *Appl. Opt.* **22**(19), 2984–2990 (1983)
- 25.19 D. Nedeljkovic, A. Hauchecorne, M.L. Chanin: Rotational Raman lidar to measure atmospheric temperature from the ground to 30 km, *IEEE Trans. Geosci. Remote Sens.* **31**(1), 90–101 (1993)
- 25.20 G. Vaughan, D.P. Wareing, S.J. Pepler, L. Thomas, V. Mitev: Atmospheric temperature profiles made by rotational Raman scattering, *Appl. Opt.* **32**(15), 2758–2764 (1993)
- 25.21 A. Behrendt, J. Reichardt: Atmospheric temperature profiling in the presence of clouds with a pure rotational Raman lidar by use of an interference-filter-based polychromator, *Appl. Opt.* **39**(9), 1372–1378 (2000)
- 25.22 A. Behrendt, T. Nakamura, T. Tsuda: Combined temperature lidar for measurements in the troposphere, stratosphere, and mesosphere, *Appl. Opt.* **43**(14), 2930–2939 (2004)
- 25.23 P. Di Girolamo, R. Marchese, D.N. Whiteman, B.B. Demoz: Rotational Raman lidar measurements of atmospheric temperature in the UV, *Geophys. Res. Lett.* **31**(1), L01106 (2004)
- 25.24 G. Fiocco, G. Benedetti-Michelangeli, K. Maischberger, E. Madonna: Measurement of temperature and aerosol to molecule ratio in the troposphere by optical radar, *Nat. Phys. Sci.* **229**, 78–79 (1971)
- 25.25 D.D. Turner, J.E.M. Goldsmith: Twenty-four-hour Raman lidar water vapor measurements during the Atmospheric Radiation Measurement Program's 1996 and 1997 water vapor intensive observation periods, *J. Atmos. Ocean. Technol.* **16**(8), 1062–1076 (1999)
- 25.26 E. Brocard, R. Philipona, A. Haeferle, G. Romanens, A. Mueller, D. Ruffieux, V. Simeonov, B. Calpini: Raman lidar for meteorological observations, RALMO – Part 2: Validation of water vapor measurements, *Atmos. Meas. Tech.* **6**(5), 1347–1358 (2013)
- 25.27 T. Dineov, V. Simeonov, Y. Arshinov, S. Bobrovnikov, P. Ristori, B. Calpini, M. Parlange, H. van den Bergh: Raman lidar for meteorological observations, RALMO – Part 1: Instrument description, *Atmos. Meas. Tech.* **6**(5), 1329–1346 (2013)
- 25.28 J. Reichardt, U. Wandinger, V. Klein, I. Mattis, B. Hilber, R. Begbie: RAMSES: German Meteorological Service autonomous Raman lidar for water vapor, temperature, aerosol, and cloud measurements, *Appl. Opt.* **51**(34), 8111–8131 (2012)
- 25.29 A. Apituley, K.M. Wilson, C. Potma, H. Volten, M. de Graaf: Performance assessment and application of Caeli – A high-performance Raman lidar for diurnal profiling of water vapour, aerosols and clouds. In: *Proc. 8th Int. Symp. Tropospheric Profiling, Delft*, ed. by A. Apituley, H.W.J. Russchenberg, W.A.A. Monna (2009)
- 25.30 A. Behrendt: Temperature measurements with lidar. In: *Lidar: Range-Resolved Optical Remote Sensing of the Atmosphere*, Springer Series in Optical Sciences, Vol. 102, ed. by C. Weitkamp (Springer, New York 2005) pp. 273–305
- 25.31 E. Hammann, A. Behrendt, F. Le Mounier, V. Wulfmeyer: Temperature profiling of the atmospheric boundary layer with rotational Raman lidar during the HD(CP)² Observational Prototype Experiment, *Atmos. Chem. Phys.* **15**(5), 2867–2881 (2015)
- 25.32 D.N. Whiteman: Examination of the traditional Raman lidar technique: I. Evaluating the temperature-dependent lidar equations, *Appl. Opt.* **42**(15), 2571–2592 (2003)
- 25.33 D.N. Whiteman: Examination of the traditional Raman lidar technique: II. Evaluating the ratios for water vapor and aerosols, *Appl. Opt.* **42**(15), 2593–2608 (2003)
- 25.34 D.D. Turner, B.M. Lesht, S.A. Clough, L.C. Liljegren, H.E. Revercomb, D.C. Tobin: Dry bias and variability in Vaisala RS80–H radiosondes: The ARM experience, *J. Atmos. Ocean. Technol.* **20**(1), 117–132 (2003)
- 25.35 R.A. Ferrare, R. Ferrare, R. Turner, M. Clayto, B. Schmid, J. Redemann, D. Covert, R. Elleman, J. Ogren, E. Andrews, J.E.M. Goldsmith, H. Jonsson: Evaluation of daytime measurements of aerosols and water vapor made by an operational Raman lidar over the Southern Great Plains, *J. Geophys. Res.* **111**(D5), D05S08 (2006)
- 25.36 D.D. Venable, D.N. Whiteman, M.N. Calhoun, A.O. Dirisu, R.M. Connell, E. Landulfo: Lamp mapping technique for independent determination of the water vapor mixing ratio calibration factor for a Raman lidar system, *Appl. Opt.* **50**(23), 4622–4632 (2011)
- 25.37 C. Muñoz-Porcar, A. Comerón, M. Sicard, R. Barragan, D. Garcia-Vizcaino, A. Rodríguez-Gómez, F. Rocadenbosch, M.J. Granados-Muñoz: Calibration of Raman lidar water vapor mixing ratio measurements using zenithal measurements of diffuse sunlight and a radiative transfer model, *IEEE Trans. Geosci. Remote Sens.* **56**(12), 7405–7414 (2018)
- 25.38 D.D. Turner, R.A. Ferrare, L.A. Heilman Brasseur, W.F. Feltz, T.P. Tooman: Automated retrievals of water vapor and aerosol profiles over Oklahoma from an operational Raman lidar, *J. Atmos. Ocean. Technol.* **19**(1), 37–50 (2002)
- 25.39 D.N. Whiteman, B. Demoz, K. Rush, G. Schwemmer, B. Gentry, P. Di Girolamo, J. Comer, I. Veselovskii, K. Evans, S.H. Melfi, Z. Wang, M. Cadirola, B. Mielke, D. Venable, T. Van Hove: Raman lidar measurements during the International H₂O Project. Part I:

- Instrumentation and analysis techniques, *J. Atmos. Ocean. Technol.* **23**(2), 157–169 (2006)
- 25.40 D.N. Whiteman, B. Demoz, G. Schwemmer, B. Gen-
try, P. Di Girolamo, D. Sabatino, J. Comer,
I. Veselovskii, K. Evans, R.-F. Lin, Z. Wang,
A. Behrendt, V. Wulfmeyer, E. Browell, R. Ferrare,
S. Ismail, J. Wang: Raman water vapor lidar mea-
surements during the International H₂O Project.
Part II: Case studies, *J. Atmos. Ocean. Technol.* **23**(2),
170–183 (2006)
- 25.41 A. Behrendt, V. Wulfmeyer, P. Di Girolamo,
C. Kiemle, H.-S. Bauer, T. Schaberl, D. Summa,
D.N. Whiteman, B.B. Demoz, E.V. Browell, S. Ismail,
R. Ferrare, S. Kooi, G. Ehret, J. Wang: Intercompari-
son of water vapor data measured with lidar during
IHOP_2002. Part 1: Airborne to ground-based lidar
systems and comparisons with chilled-mirror hy-
grometer radiosondes, *J. Atmos. Ocean. Technol.* **24**(1),
3–21 (2007)
- 25.42 A. Behrendt, V. Wulfmeyer, C. Kiemle, G. Ehret,
C. Flamant, T. Schaberl, H.-S. Bauer, S. Kooi, S. Is-
mail, R. Ferrare, E.V. Browell, D.N. Whiteman: In-
tercomparison of water vapor data measured with
lidar during IHOP_2002, Part 2: Airborne to airborne
systems, *J. Atmos. Ocean. Technol.* **24**(1), 22–39
(2007)
- 25.43 T. Leblanc, I.S. McDermid: Accuracy of Raman li-
dar water vapor calibration and its applicability to
long-term measurements, *Appl. Opt.* **47**(30), 5592–
5603 (2008)
- 25.44 R. Bhawar, P. Di Girolamo, D. Summa, C. Flamant,
D. Althausen, A. Behrendt, C. Kiemle, P. Bossler,
M. Cacciani, C. Champollion, T. Di Iorio, R. En-
gelmann, C. Herold, S. Pal, A. Riede, M. Wirth,
V. Wulfmeyer: The water vapour intercomparison
effort in the framework of the convective and oro-
graphically-induced precipitation study: Airborne-
to-ground-based and airborne-to-airborne lidar
systems, *Q. J. R. Meteorol. Soc.* **137**(S1), 325–348
(2011)
- 25.45 A. Foth, H. Baars, P. Di Girolamo, B. Pospichal: Wa-
ter vapour profiles from Raman lidar automatically
calibrated by microwave radiometer data during
HOPE, *Atmos. Chem. Phys.* **15**(14), 7753–7763 (2015)
- 25.46 M. Radlach, A. Behrendt, V. Wulfmeyer: Scanning
rotational Raman lidar at 355 nm for the measure-
ment of tropospheric temperature fields, *Atmos.
Chem. Phys.* **8**(2), 159–169 (2008)
- 25.47 R.K. Newsom, D.D. Turner, J.E.M. Goldsmith: Long-
term evaluation of temperature profiles measured
by an operational Raman lidar, *J. Atmos. Ocean.
Technol.* **30**(8), 1616–1634 (2013)
- 25.48 P. Di Girolamo, B. De Rosa, C. Flamant, D. Summa,
O. Bousquet, P. Chazette, J. Totems, M. Cacciani:
Water vapor mixing ratio and temperature inter-
comparison results in the framework of the
Hydrological Cycle in the Mediterranean Experi-
ment—Special Observation Period 1, *Bull. Atmos.
Sci. Technol.* **1**, 113–153 (2020)
- 25.49 V. Wulfmeyer, C. Walther: Future performance of
ground-based and airborne water vapor differen-
tial absorption lidar. I: Overview and theory, *Appl.
Opt.* **40**(30), 5304–5320 (2001)
- 25.50 V. Wulfmeyer, C. Walther: Future performance of
ground-based and air-borne water vapor differen-
tial absorption lidar. II: Simulations of the preci-
sion of a near-infrared, high-power system, *Appl.
Opt.* **40**(30), 5321–5336 (2001)
- 25.51 A. Behrendt, V. Wulfmeyer, E. Hammann,
S.K. Muppa, S. Pal: Profiles of second- to fourth-
order moments of turbulent temperature fluc-
tuations in the convective boundary layer: First
measurements with rotational Raman lidar, *Atmos.
Chem. Phys.* **15**(10), 5485–5500 (2015)
- 25.52 V. Wulfmeyer, S.K. Muppa, A. Behrendt, E. Ham-
mann, F. Späth, Z. Sorbjan, D.D. Turner, R.M. Hard-
esty: Determination of convective boundary layer
entrainment fluxes, dissipation rates, and the
molecular destruction of variances: Theoretical de-
scription and a strategy for its confirmation with
a novel lidar system synergy, *J. Atmos. Sci.* **73**(2),
667–692 (2016)
- 25.53 P. Di Girolamo, M. Cacciani, D. Summa, A. Scoccione,
B. De Rosa, A. Behrendt, V. Wulfmeyer: Characteri-
sation of boundary layer turbulent processes by the
Raman lidar BASIL in the frame of HD(CP)² Obser-
vational Prototype Experiment, *Atmos. Chem. Phys.*
17(1), 745–767 (2017)
- 25.54 A. Behrendt, V. Wulfmeyer, C. Senff, S.K. Muppa,
F. Späth, D. Lange, N. Kalthoff, A. Wieser: Observa-
tion of sensible and latent heat flux profiles with
lidar, *Atmos. Meas. Tech.* **13**, 3221–3233 (2020)
- 25.55 V. Wulfmeyer, A. Behrendt, D. Lange: High profiles,
Meteorol. Technol. Int. **9**(2018), 62–65 (2018)
- 25.56 D. Lange, A. Behrendt, V. Wulfmeyer: Compact
operational tropospheric water vapor and tem-
perature Raman lidar with turbulence resolution,
Geophys. Res. Lett. **46**(24), 14844–14853 (2019)
- 25.57 E. Hammann, A. Behrendt: Parametrization of
optimum filter passbands for rotational Raman
temperature measurements, *Opt. Express* **23**(24),
30767–30782 (2015)
- 25.58 P. Di Girolamo, D. Summa, R. Ferretti: Multiparam-
eter Raman lidar measurements for the charac-
terization of a dry stratospheric intrusion event,
J. Atmos. Ocean. Technol. **26**(9), 1742–1762 (2009)
- 25.59 P. Di Girolamo, D. Summa, R.-F. Lin, T. Maestri,
R. Rizzi, G. Masiello: UV Raman lidar measurements
of relative humidity for the characterization of cir-
rus cloud microphysical properties, *Atmos. Chem.
Phys.* **9**(22), 8799–8811 (2009)
- 25.60 P. Chazette, F. Marnas, J. Totems: The mobile Water
vapor Aerosol Raman Lidar and its implication in
the frame of the HyMeX and ChArMEX programs: Ap-
plication to a dust transport process, *Atmos. Meas.
Tech.* **7**(6), 1629–1647 (2014)
- 25.61 H.M.J. Barbosa, B. Barja, T. Pauliquevis, D.A. Gou-
veia, P. Artaxo, C.G. Cirino, R.M.N. Santos,
A.B. Oliveira: A permanent Raman lidar sta-
tion in the Amazon: Description, characterization,
and first results, *Atmos. Meas. Tech.* **7**(6), 1745–1762
(2014)

- 25.62 Y. Arshinov, S. Bobrovnikov, I. Serikov, A. Ansmann, U. Wandinger, D. Althausen, I. Mattis, D. Müller: Daytime operation of a pure rotational Raman lidar by use of a Fabry–Perot interferometer, *Appl. Opt.* **44**(17), 3593–3603 (2005)
- 25.63 D.H. Lenschow, V. Wulfmeyer, C. Senff: Measuring second-through fourth-order moments in noisy data, *J. Atmos. Ocean. Technol.* **17**(10), 1330–1347 (2000)
- 25.64 R.K. Newsom, D.D. Turner, B. Mielke, M. Clayton, R. Ferrare, C. Sivaraman: The use of simultaneous analog and photon counting detection for Raman lidar, *Appl. Opt.* **48**(20), 3903–3914 (2009)
- 25.65 V. Wulfmeyer, D.D. Turner, S. Pal, E. Wagner: Can water vapour Raman lidar resolve profiles of turbulent variables in the convective boundary layer?, *Bound.-Layer Meteorol.* **136**(2), 253–284 (2010)
- 25.66 R.A. Ferrare, E.V. Browell, S. Ismail, S.A. Kooi, L.H. Brasseur, V.G. Brackett, M.B. Clayton, J.D.W. Barrick, G.S. Diskin, J.E.M. Goldsmith, B.M. Lesht, J.R. Podolske, G.W. Sachse, F.J. Schmidlin, D.D. Turner, D.N. Whiteman, D. Tobin, L.M. Miloshevich, H.E. Revercomb, B.B. Demoz, P. Di Girolamo: Characterization of upper-troposphere water vapor measurements during AFWEX using LAASE, *J. Atmos. Ocean. Technol.* **21**(12), 1790–1808 (2004)
- 25.67 D.D. Turner, R.A. Ferrare, V. Wulfmeyer, A.J. Scarino: Aircraft evaluation of ground-based Raman lidar water vapor turbulence profiles in convective mixed layers, *J. Atmos. Ocean. Technol.* **31**(5), 1078–1088 (2014)
- 25.68 G. Masiello, C. Serio, T. Deleporte, H. Herbin, P. Di Girolamo, C. Champollion, A. Behrendt, P. Bosser, O. Bock, V. Wulfmeyer, M. Pommier, C. Flamant: Comparison of IASI water vapour products over complex terrain with COPS campaign data, *Meteorol. Z.* **22**(4), 471–487 (2013)
- 25.69 J. Milovac, K. Warrach-Sagi, A. Behrendt, F. Späth, J. Ingwersen, V. Wulfmeyer: Investigation of PBL schemes combining the WRF model simulations with scanning water vapor differential absorption lidar measurements, *J. Geophys. Res. Atmos.* **121**(2), 624–649 (2016)
- 25.70 P. Di Girolamo, C. Flamant, M. Cacciani, E. Richard, V. Ducrocq, D. Summa, D. Stelitano, N. Fourrié, F. Saïd: Observation of low-level wind reversals in the Gulf of Lion area and their impact on the water vapour variability, *Q. J. R. Meteorol. Soc.* **142**(S1), 153–172 (2016)
- 25.71 R. Heinze, A. Dipankar, C. Carbajal Henken, C. Moseley, O. Sourdeval, S. Trömel, X. Xie, P. Adamidis, F. Ament, H. Baars, C. Barthlott, A. Behrendt, U. Blahak, S. Bley, S. Brdar, M. Brueck, S. Crewell, H. Deneke, P. Di Girolamo, R. Evaristo, J. Fischer, C. Frank, P. Friederichs, T. Göcke, K. Gorges, L. Hande, M. Hanke, A. Hansen, H.-C. Hege, C. Hoose, T. Jahns, N. Kalthoff, D. Klocke, S. Kneifel, P. Knippertz, A. Kuhn, T. van Laar, A. Macke, V. Maurer, B. Mayer, C.I. Meyer, S.K. Muppa, R.A.J. Neggers, E. Orlandi, F. Pantillon, B. Pospichal, N. Röber, L. Scheck, A. Seifert, P. Seifert, F. Senf, P. Siligam, C. Simmer, S. Steinke, B. Stevens, K. Wapler, M. Weniger, V. Wulfmeyer, G. Zängl, D. Zhang, J. Quaas: Large-eddy simulations over Germany using ICON: A comprehensive evaluation, *Q. J. R. Meteorol. Soc.* **143**(702), 69–100 (2017)
- 25.72 V. Wulfmeyer, H.-S. Bauer, M. Grzeschik, A. Behrendt, F. Vandenberghe, E.V. Browell, S. Ismail, R. Ferrare: Four-dimensional variational assimilation of water-vapor differential absorption lidar data: The first case study within IHOP_2002, *Mon. Weather Rev.* **134**(1), 209–230 (2006)
- 25.73 M. Grzeschik, H.-S. Bauer, V. Wulfmeyer, D. Engelbart, U. Wandinger, I. Mattis, D. Althausen, R. Engelmann, M. Tesche, A. Riede: Four-dimensional variational analysis of water-vapor Raman lidar data and their impact on mesoscale forecasts, *J. Atmos. Ocean. Technol.* **25**(8), 1437–1453 (2008)
- 25.74 S. Adam, A. Behrendt, T. Schwitalla, E. Hammann, V. Wulfmeyer: First assimilation of temperature lidar data into a numerical weather prediction model: Impact on the simulation of the temperature field, inversion strength, and planetary boundary layer depth, *Q. J. R. Meteorol. Soc.* **142**(700), 2882–2896 (2016)
- 25.75 A. Haeefe, D. Leuenberger, G. Martucci, M. Arpagaus, R. Thundathil, T. Schwitalla, A. Behrendt, V. Wulfmeyer: Assimilation of temperature and humidity profiles from a Raman lidar into convective-scale NWP models and the impact on the forecast. In: *9th Symp. Lidar Atmos. Appl., Phoenix* (2019)
- 25.76 R. Thundathil, T. Schwitalla, A. Behrendt, S.K. Muppa, S. Adam, V. Wulfmeyer: Assimilation of lidar water vapour mixing ratio and temperature profiles into a convection-permitting model, *J. Meteorol. Soc. Japan* **98**(5), 959–986 (2020)
- 25.77 T.M. Weckwerth, D.B. Parsons, S.E. Koch, J.A. Moore, M.A. LeMone, B.B. Demoz, C. Flamant, B. Geerts, J. Wang, W.F. Feltz: An overview of the International H₂O Project (IHOP_2002) and some preliminary highlights, *Bull. Am. Meteorol. Soc.* **85**(2), 253–278 (2004)
- 25.78 K.A. Browning, A.M. Blyth, P.A. Clark, U. Corsmeier, C.J. Morcrette, J.L. Agnew, S.P. Ballard, D. Bamber, C. Barthlott, L.J. Bennett, K.M. Beswick, M. Bitter, K.E. Bozier, B.J. Brooks, C.G. Collier, F. Davies, B. Deny, M.A. Dixon, T. Feuerle, R.M. Forbes, C. Gaffard, M.D. Gray, R. Hankers, T.J. Hewison, N. Kalthoff, S. Khodayar, M. Kohler, C. Kottmeier, S. Kraut, M. Kunz, D.N. Ladd, H.W. Lean, J. Lenfant, Z. Li, J. Marsham, J. McGregor, S.D. Mobbs, J. Nicol, E. Norton, D.J. Parker, F. Perry, M. Ramatschi, H.M. Ricketts, N.M. Roberts, A. Russell, H. Schulz, E.C. Slack, G. Vaughan, J. Waight, D.P. Wareing, R.J. Watson, A.R. Webb, A. Wieser: The Convective Storm Initiation Project, *Bull. Am. Meteorol. Soc.* **88**(12), 1939–1956 (2007)
- 25.79 V. Wulfmeyer, A. Behrendt, H.-S. Bauer, C. Kottmeier, U. Corsmeier, A. Blyth, G. Craig, U. Schumann, M. Hagen, S. Crewell, P. Di Girolamo, C. Flamant, M. Miller, A. Montani, S. Mobbs,

- E. Richard, M.W. Rotach, M. Arpagaus, H. Russchenberg, P. Schlüssel, M. König, V. Gärtner, R. Steinacker, M. Dorninger, D.D. Turner, T. Weckwerth, A. Hense, C. Simmer: The Convective and Orographically-induced Precipitation Study: A research and development project of the World Weather Research Program for improving quantitative precipitation forecasting in low-mountain region, *Bull. Am. Meteorol. Soc.* **89**(10), 1477–1486 (2008)
- 25.80 V. Wulfmeyer, A. Behrendt, C. Kottmeier, U. Corsmeier, C. Barthlott, G.C. Craig, M. Hagen, D. Althausen, F. Aoshima, M. Arpagaus, H.-S. Bauer, L. Bennett, A. Blyth, C. Brandau, C. Champollion, S. Crewell, G. Dick, P. Di Girolamo, M. Dorninger, Y. Dufournet, R. Eigenmann, R. Engelmann, C. Flamant, T. Foken, T. Gorgas, M. Grzeschik, J. Handwerker, C. Hauck, H. Höller, W. Junkermann, N. Kalthoff, C. Kiemle, S. Klink, M. König, L. Krauss, C.N. Long, F. Madonna, S. Mobbs, B. Neininger, S. Pal, G. Peters, G. Pigeon, E. Richard, M.W. Rotach, H. Russchenberg, T. Schwitalla, V. Smith, R. Steinacker, J. Trentmann, D.D. Turner, J. van Baelen, S. Vogt, H. Volkert, T. Weckwerth, H. Wernli, A. Wieser, M. Wirth: The Convective and Orographically Induced Precipitation Study (COPS): The scientific strategy, the field phase, and first highlights, *Q. J. R. Meteorol. Soc.* **137**(S1), 3–30 (2011)
- 25.81 A. Macke, P. Seifert, H. Baars, C. Barthlott, C. Beekmans, A. Behrendt, B. Bohn, M. Brueck, J. Bühl, S. Crewell, T. Damian, H. Deneke, S. Düsing, A. Foth, P. Di Girolamo, E. Hammann, R. Heinze, A. Hirsikko, J. Kalisch, N. Kalthoff, S. Kinne, M. Kohler, U. Löhnert, B.L. Madhavan, V. Maurer, S.K. Muppa, J. Schween, I. Serikov, H. Siebert, C. Simmer, F. Späth, S. Steinke, K. Träumner, S. Trömel, B. Wehner, A. Wieser, V. Wulfmeyer, X. Xie: The HD(CP)² Observational Prototype Experiment (HOPE) – An overview, *Atmos. Chem. Phys.* **17**(7), 4887–4914 (2017)
- 25.82 B. Geerts, D. Parsons, C.L. Ziegler, T.M. Weckwerth, M.I. Biggerstaff, R.D. Clark, M.C. Coniglio, B.B. Demoz, R.A. Ferrare, W.A. Gallus, K. Haghi, J.M. Hanesiak, P.M. Klein, K.R. Knupp, K. Kosiba, G.M. McFarquhar, J.A. Moore, A.R. Nehrir, M.D. Parker, J.O. Pinto, R.M. Rauber, R.S. Schumacher, D.D. Turner, Q. Wang, X. Wang, Z. Wang, J. Wurman: The 2015 Plains Elevated Convection at Night Field Project, *Bull. Am. Meteorol. Soc.* **98**(4), 767–786 (2017)
- 25.83 V. Wulfmeyer, D.D. Turner, B. Baker, R. Banta, A. Behrendt, T. Bonin, W.A. Brewer, M. Buban, A. Choukulkar, E. Dumas, R.M. Hardesty, T. Heus, J. Ingwersen, D. Lange, T.R. Lee, S. Metzendorf, S.K. Muppa, T. Meyers, R. Newsom, M. Osman, S. Raasch, J. Santanello, C. Senff, F. Späth, T. Wagner, T. Weckwerth: A new research approach for observing and characterizing land-atmosphere feedback, *Bull. Am. Meteorol. Soc.* **99**(8), 1639–1667 (2018)
- 25.84 S.H. Melfi, D. Whiteman, R. Ferrare: Observation of atmospheric fronts using Raman lidar moisture measurements, *J. Appl. Meteorol.* **28**(9), 789–806 (1989)
- 25.85 B.B. Demoz, D. Starr, K.D. Evans, A.R. Lare, D.N. Whiteman, G. Schwemmer, R.A. Ferrare, J.E.M. Goldsmith, S.E. Bisson: The cold front of 15 April 1994 over the central United States. Part I: Observations, *Mon. Weather Rev.* **133**(6), 1525–1543 (2005)
- 25.86 B. Demoz, C. Flamant, D. Miller, K. Evans, F. Fabry, P. Di Girolamo, D. Whiteman, B. Geerts, T. Weckwerth, W. Brown, G. Schwemmer, B. Gentry, W. Feltz, Z. Wang: The dryline on 22 May 2002 during IHOP_2002: Convective-scale measurements at the profiling site, *Mon. Weather Rev.* **134**(1), 294–310 (2006)
- 25.87 D.N. Whiteman, K.D. Evans, B. Demoz, D.S. O’C, E.W. Eloranta, D. Tobin, W. Feltz, G.J. Jedlovec, S.I. Gutman, G.K. Schwemmer, M. Cadirola, S.H. Melfi, F.J. Schmidlin: Raman lidar measurements of water vapor and cirrus clouds during the passage of Hurricane Bonnie, *J. Geophys. Res.* **106**(D6), 5211–5225 (2001)
- 25.88 U. Corsmeier, N. Kalthoff, C. Barthlott, A. Behrendt, P. Di Girolamo, M. Dorninger, F. Aoshima, J. Handwerker, C. Kottmeier, H. Mahlke, S. Mobbs, G. Vaughan, J. Wickert, V. Wulfmeyer: Processes driving deep convection over complex terrain: A multi-scale analysis of observations from COPS IOP 9c, *Q. J. R. Meteorol. Soc.* **137**(S1), 137–155 (2011)
- 25.89 A. Behrendt, S. Pal, F. Aoshima, M. Bender, A. Blyth, U. Corsmeier, J. Cuesta, G. Dick, M. Dorninger, C. Flamant, P. Di Girolamo, T. Gorgas, Y. Huang, N. Kalthoff, S. Khodayar, H. Mannstein, K. Träumner, A. Wieser, V. Wulfmeyer: Observation of convection initiation processes with a suite of state-of-the-art research instruments during COPS IOP 8b, *Q. J. R. Meteorol. Soc.* **137**(S1), 81–100 (2011)
- 25.90 I. Mattis, A. Ansmann, D. Althausen, V. Jaenisch, U. Wandinger, D. Müller, Y.F. Arshinov, S.M. Bobrovnikov, I.B. Serikov: Relative humidity profiling in the troposphere with a Raman lidar, *Appl. Opt.* **41**(30), 6451–6462 (2002)
- 25.91 D.D. Turner, V. Wulfmeyer, L.K. Berg, J.H. Schween: Water vapor turbulence profiles in stationary continental convective mixed layers, *J. Geophys. Res.* **119**(19), 11151–11165 (2014)
- 25.92 D.D. Turner, V. Wulfmeyer, A. Behrendt, T.A. Bonin, A. Choukulkar, R. Newsom, W.A. Brewer, D.R. Cook: Response of the land-atmosphere system over north-central Oklahoma during the 2017 eclipse, *Geophys. Res. Lett.* **45**(3), 1668–1675 (2018)
- 25.93 J.A. Santanello Jr, P.A. Dirmeyer, C.R. Ferguson, K.L. Findell, A.B. Tawfik, A. Berg, M. Ek, P. Gentine, B.P. Guillod, C. van Heerwaarden, J. Roundy, V. Wulfmeyer: Land-atmosphere interactions: The LoCo Perspective, *Bull. Am. Meteorol. Soc.* **99**(6), 1253–1272 (2017)

Volker Wulfmeyer

Institute of Physics and Meteorology
University of Hohenheim
Stuttgart, Germany
volker.wulfmeyer@uni-hohenheim.de



Volker Wulfmeyer is Professor and Chair of Physics and Meteorology at the University of Hohenheim. The research goals of his team include: high-resolution, seamless weather and seasonal forecasting as well as climate projections; understanding of land-atmosphere feedback and turbulent transport processes in the planetary boundary layer; and the development and application of 3D scanning active remote sensing systems for water-vapor, temperature, and wind measurements.

Andreas Behrendt

Institute of Physics and Meteorology
University of Hohenheim
Stuttgart, Germany
andreas.behrendt@uni-hohenheim.de



Andreas Behrendt is Akademischer Oberrat (roughly equivalent to an associate professor) at the Institute of Physics and Meteorology, University of Hohenheim, Stuttgart. He heads the Remote Sensing Group, is Associate Editor of *Optics Express*, and coordinates the Earth and Climate System Science masters program. His current research focuses on the development and use of lidar systems for studying land-atmosphere feedback processes, boundary-layer turbulence, cloud formation, and convection initiation.

26. Water Vapor Differential Absorption Lidar

Scott M. Spuler, Matthew Hayman, Tammy M. Weckwerth

Water vapor is one of the fundamental thermodynamic variables that define the state of the atmosphere. It is highly variable in space and time and influences many important processes related to weather and climate. For more than two decades the importance of water vapor profiling has been underscored by the research and operational weather communities. The ability to measure the spatial and temporal variability of moisture in the lower troposphere is necessary to improve our understanding of many atmospheric processes, improve numerical weather prediction forecasting skills, study weather phenomena, and study regional climate variability. Differential absorption lidar can provide accurate, continuous high-resolution measurements of water vapor. The technique spans from complex research systems capable of 3-D scanning to truly autonomous field-deployable profiling devices.

26.1	Measurement Principles and Parameters	742
26.2	History	743
26.3	Theory	744
26.3.1	Rayleigh–Doppler Broadening	745
26.3.2	Broadband versus Narrowband DIAL ..	746
26.3.3	Accuracy and Precision	747
26.4	Devices and Systems	749
26.5	Specifications	751
26.6	Quality Control	751
26.7	Maintenance	752
26.8	Applications	752
26.9	Future Developments	753
26.9.1	Networks	753
26.9.2	Temperature Profiling	753
26.10	Further Readings	754
	References	754

Water vapor differential absorption lidar (DIAL) is an application of absorption spectroscopy. The technique isolates absorption by water vapor in the atmosphere from all other atmospheric constituents and instrument terms. With a known and quantifiable absorption coefficient, the number density of water vapor molecules can be inferred based on knowledge of the water vapor absorption spectrum and assumed, measured, or modeled temperature and pressure profiles.

When a lidar's transmission wavelength is tuned precisely to a water vapor absorption feature, the laser light will be attenuated according to the Bouguer–Lambert–Beer law, where the coefficient of absorption is proportional to the number of water vapor molecules seen by the transmitted light.

The challenge of obtaining absorption characteristics with a lidar is establishing a reliable reference for each point in range, where variations in backscatter, aerosol, and cloud extinction, and variability in instrument effects such as the geometric overlap function, all contribute to the observed profile. By itself, observations with a laser tuned to a water vapor absorption line are hopelessly entangled with the complex characteristics of the atmosphere and the instrument. However, the elegance of the DIAL technique is that by adding one wavelength that is largely not affected by water vapor absorption, all of these additional terms may be removed (the absorbing and nonabsorbing wavelengths are traditionally referred to as the *online*, and *offline* wavelengths, respectively).

26.1 Measurement Principles and Parameters

Ground-based water vapor DIAL uses elastic scatter as a distributed backscatter reflector, often referred to as Rayleigh scattering and Mie scattering—both of these scattering processes are several orders of magnitude stronger than inelastic Raman scattering (Table 26.1). A DIAL can therefore operate at significantly less laser power than a Raman lidar (Chap. 25) with similar performance assuming similar optical efficiency. Additionally, the DIAL technique benefits from enhanced aerosol loading in the atmosphere as the elastic scatter signal increases, whereas Raman Lidar gleans no benefit. However, a limitation of DIAL is that it can only operate at specific wavelengths, where a suitable water vapor absorption line exists.

Most modern ground-based water vapor DIAL instruments target specific absorption features within rotational–vibrational overtone bands in the near-infrared. The lines, shown in Fig. 26.1, are spectrally centered in bands (e.g., 730, 820, 940 nm) and have an overall trend toward stronger absorption as the wavelength increases. Developing a narrowband water vapor DIAL requires, first and foremost, a suitable laser source with narrow laser linewidth, high-frequency stability, and high spectral purity. The requirements to keep the systematic errors below 10% are a linewidth of < 400 MHz, a spectral purity of $> 99.5\%$ and a wavelength stability of $< \pm 200$ MHz [26.2, 3]. The availability of detectors with high sensitivity, or quantum efficiency, at the chosen absorption band is also important. Care in the specific absorption line selection is critical to DIAL performance. The chosen line should be free of interfering species, preferably isolated from other water vapor lines, and have an adequate line strength (e.g., to allow measurements in dry conditions). Additionally, to minimize temperature sensitivity, a water vapor DIAL typically targets an absorption feature with a line strength that is insensitive

to atmospheric temperature variations (e.g., the lower ground-state energy for the water vapor line should be ≈ 225 cm^{-1} to minimize sensitivity to temperature variations in the lower troposphere). These spectroscopic values, along with other parameterizations such as the air-broadened and self-broadened linewidth and spectral shift with pressure, are obtained via molecular spectral databases such as the high-resolution transmission molecular absorption database (HITRAN) [26.4]. The a priori spectral knowledge at both of the closely spaced, transmitted wavelengths allows a DIAL system to be disentangled from atmospheric effects, and, in that sense, it is a self-calibrating technique. A water vapor DIAL can achieve measurement errors of a few percent when utilizing surface measurements of pressure and temperature and assuming hydrostatic equilibrium and standard lapse rate. If real-time processing is not needed, improved accuracy can be achieved using atmospheric model reanalysis data.

The only way to obtain an independent measurement of water vapor is via narrowband DIAL, which requires a spectrally narrow, frequency stable (and agile), and high spectral purity laser source. Broadband DIAL is a simpler technological approach; however, it comes with the significant drawback of needing ancillary measurements (e.g., radiosondes or radiometers) for calibration. Narrowband DIAL is a unique active remote sensing technique in that it is self-calibrating and relies only on fundamental theory for its retrievals. In addition, by actively adjusting the wavelength pair for optimal atmospheric absorption, narrowband DIAL has the ability to make high-quality water vapor measurements over a wide range of atmospheric conditions (humid to dry).

Table 26.1 Measured parameters of water vapor DIAL

Parameter	Description	Unit	Symbol
Absolute humidity	Mass water vapor per volume moist air	g m^{-3}	a
Relative backscatter	Attenuated backscatter	arb. u.	β, α^a

^a Although the backscatter (β) and extinction (α) are intertwined, and cannot be separated without a high spectral resolution channel in the receiver [26.1], the qualitative information is useful for understanding the relative location of aerosols and clouds.

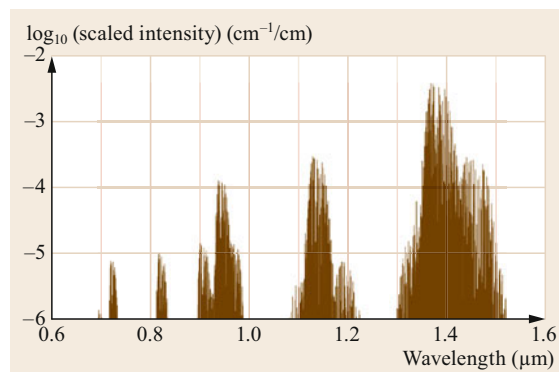


Fig. 26.1 Water vapor rotational–vibrational overtone absorption lines in the near-infrared spectrum

26.2 History

Water vapor DIAL was initially demonstrated in 1964 by *Richard M. Schotland* (1927–2006), with a temperature-tuned ruby laser just four years after its invention [26.5]. Schotland also performed the first error analysis of the technique in 1974, using the acronym DASE (differential absorption of scattered energy) for what would later become DIAL [26.6]. Progress since its inception has been continuous yet slow due to limited availability of suitable laser sources. In 1979, *Browell et al.* [26.7] had access to stronger absorption lines with a ruby-pumped dye laser, and in the early 1980s the groups of *Mégie* and *Cahen* [26.8, 9] advanced to using Nd:YAG-pumped dye lasers. CO₂ lasers, operating in the mid-infrared at 10 μm wavelength, were used from the mid-1970s to mid-1980s to demonstrate water vapor DIAL in both direct detection [26.10–12] and coherent detection [26.13]. In the near-IR $\approx 1.9 \mu\text{m}$ wavelength, there were efforts to develop a combined temperature and water vapor DIAL with a Nd:YAG-pumped optical parametric oscillator (OPO) [26.14, 15], and a water vapor DIAL with a tunable eye-safe Ho laser [26.16]. Ultimately, however, water vapor DIAL instruments for routine operation were built as direct detection systems based on injection-seeded solid-state lasers operating in the 720–940 nm wavelength region. The first such systems used Ti:sapphire and alexandrite lasers as described in [26.17, 18] in the mid-1990s. These efforts led to the modern ground-based water vapor DIAL systems, which use Nd:YAG and/or OPO-pumped Ti:sapphire lasers [26.19–22].

For the last two decades, these high-power solid-state laser water vapor DIAL systems have been used in research and provided valuable measurements. However, they are large, complex, and expensive instruments, which require highly trained people to continuously monitor and operate them. Efforts to develop a more autonomous, lower complexity, and lower-cost instrument were initiated in 2004 [26.23]. This early work used high pulse-rate, low pulse energy diode lasers—in what is known as a *micropulse* lidar architecture. The effort was followed by seminal research on semiconductor-based

lasers for water vapor DIAL from 2009–2012 [26.24–26]. These diode lasers inherently offer the advantage of low-cost and long lifetimes—years of unattended operation, compared to months obtainable with flashlamp-pumped solid-state lasers. (Note, diode-pumped solid-state lasers have become the choice of high-power DIAL systems because they offer much longer lifetimes compared to flashlamp-pumped systems; however, they have very high initial investment costs.) The first truly autonomous field-deployable diode laser-based water vapor DIAL was demonstrated in 2015 [26.27]. When compared to the high-power solid-state laser DIAL systems, diode laser micropulse systems have reduced temporal resolution due to the lower transmitter power, but are better-suited for large networks, e.g., they are cheaper to build, operate, and maintain.

Although this chapter is focused on ground-based water vapor DIAL, we briefly mention the history of two airborne systems. Airborne water vapor DIAL allows for the ability to probe the whole atmosphere—an instrument above the high humidity in the lower troposphere can measure very dry upper-tropospheric and lower-stratospheric air by targeting stronger absorption lines; however, it cannot provide the temporal continuity of ground-based systems. The first, developed at the NASA Langley Research Center, was initially discussed [26.28] in 1983 as utilizing two separate Nd:YAG-pumped dye laser systems. Later, as discussed in 1994, the airborne instrument used a solid-state alexandrite laser to generate its online wavelength and an Nd:YAG laser-pumped dye laser for its offline wavelength [26.29]. Finally, the DIAL used a double-pulsed Nd:YAG-pumped Ti:sapphire laser system [26.30]. The second airborne water vapor DIAL was developed by the German Aerospace Center (Deutsches Zentrum für Luft- und Raumfahrt; DLR). The instrument is described in [26.31, 32] in 1993 as a Nd:YAG-pumped dye laser that later evolved into a Nd:YAG-pumped OPO in the 940 nm wavelength region. DLR also demonstrated a Nd:YGG laser, with direct radiation at 935 nm, for possible future space-borne or airborne water vapor DIAL applications [26.33].

26.3 Theory

Approximating the lidar signal as perfectly elastic backscattered light, the detected photon counts in a narrowband DIAL system is described by

$$N(\lambda, r) = N_0(\lambda)G(r)\frac{A}{r^2}\eta(\lambda)(\beta_a(r, \lambda) + \beta_m(r, \lambda)) \times \exp \left[-2 \int_0^r (\alpha_a(R, \lambda) + \alpha_m(R, \lambda) + \alpha_{wv}(R, \lambda)) dR \right] + b(\lambda), \quad (26.1)$$

where N_0 is the transmitted number of photons, λ is the laser wavelength, $G(r)$ is the geometric overlap function of the instrument, A is the receiver collection aperture, r is the range between the instrument and sample volume, $\eta(\lambda)$ is the receiver system efficiency, $\beta_a(r, \lambda)$ is the aerosol backscatter coefficient, $\beta_m(r, \lambda)$ is the molecular backscatter coefficient, $\alpha_a(r, \lambda)$ is the aerosol absorption coefficient, $\alpha_m(r, \lambda)$ is the molecular absorption coefficient, $\alpha_{wv}(r, \lambda)$ is the water vapor (WV) absorption coefficient, $b(\lambda)$ is the background noise (from the sun, detector dark signal, etc.) and R is a variable for range integration in the exponent. The water vapor concentration is contained in the water vapor absorption term and given by

$$\alpha_{wv}(r, \lambda) = \sigma_{wv}(r, \lambda)n_{wv}(r), \quad (26.2)$$

where $\sigma_{wv}(r, \lambda)$ is the water vapor absorption cross section, and $n_{wv}(r)$ is the number density of water molecules. When near an absorption line this term is highly wavelength sensitive. The range dependence is a result of the absorption spectrum being temperature and pressure dependent. The pressure dependence of these features is generally small but the temperature dependence can be quite pronounced. Typically estimates of temperature from model reanalysis data, radiosondes or inferences based on an assumed lapse rate with ground station data are used. In order to mitigate inaccuracies in these estimates, water vapor lines with weak temperature dependence are generally used in water vapor DIAL.

For brevity, the analysis presented here will sometimes substitute the exponential term in (26.1) with atmospheric transmission given by

$$T_{atm}(\lambda, r) = \exp \left[-2 \int_0^r (\alpha_a(R, \lambda) + \alpha_m(R, \lambda) + \alpha_{wv}(R, \lambda)) dR \right]. \quad (26.3)$$

From (26.1) it becomes apparent that while we are only interested in one optical parameter, $\alpha_{wv}(r, \lambda)$, nature and the instrument are likely to throw any number of variable terms into the observation. Disentangling all of these other terms, which are varying across different time scales, is anything but trivial with a single observation channel. By operating at two closely spaced wavelengths, however, one can assume that all of the nonresonant terms are effectively the same (by closely spaced, we typically mean < 1 nm). Only the spectrally narrow components differ. By subtracting background returns at the separate wavelengths and taking their ratio, the water vapor retrieval is greatly simplified

$$\frac{N(\lambda_1, r) - b(\lambda_1)}{N(\lambda_2, r) - b(\lambda_2)} = \frac{N_0(\lambda_1)\eta(\lambda_1)}{N_0(\lambda_2)\eta(\lambda_2)} \times \exp \left[-2 \int_0^r (\alpha_{wv}(R, \lambda_1) - \alpha_{wv}(R, \lambda_2)) dR \right]. \quad (26.4)$$

All extraneous atmospheric terms are eliminated in this operation and we assume the geometric overlap is the same between the two observations (e.g., the same receiver channel is used for both online and offline wavelengths). Substituting (26.2) into (26.4) and solving for the water vapor number density reveals that the remaining instrument terms are eliminated after a derivative operation. The water vapor is obtained analytically by

$$n_{wv}(r) = -\frac{1}{2} \frac{1}{\sigma_{wv}(r, \lambda_1) - \sigma_{wv}(r, \lambda_2)} \frac{d}{dr} \times \ln \frac{N(\lambda_1, r) - b(\lambda_1)}{N(\lambda_2, r) - b(\lambda_2)}. \quad (26.5)$$

The derivative operation effectively eliminates the retrieval's remaining dependence on instrument parameters. This means, in principle, the two wavelengths can operate at very different transmit power regimes and the retrieval is still valid, but in practice, the two channels should be in roughly the same regime to help mitigate the effects of nonlinearities in detector response. From (26.5) we see that this water vapor retrieval depends on the assumed knowledge of the water vapor spectrum with instrument terms generally assumed to cancel in the ratio between the two observation channels. For this reason, narrowband water vapor DIAL is often described as being *self-calibrating* because no ancillary observations are used to tune or adjust the retrieval.

The approach to performing a derivative in (26.5) on what is generally discrete observational data varies. Often a standard difference approximation is used, but even then it is not clear if the derivative should be propagated to the observations or performed directly on the natural log (our own testing has suggested the two approaches give different answers in noisy regions, but one is no more accurate than the other). Savitzky–Golay filters can be employed to provide a derivative over a window region of three or more points [26.34]. The filters act as polynomial fits over a sliding window region, which have analytically defined derivatives. However, the window size and polynomial orders have to be tuned and the filter inherently acts to limit the bandwidth of the signal (which is not necessarily a bad thing). Also these filters have edge effects near profile edges that can be challenging to deal with. In general, however the derivative is obtained, the result from (26.5) needs low-pass filtering to sufficiently eliminate noise (though Savitzky–Golay filters do this implicitly where the bandwidth is reduced by increasing the window size or decreasing the order).

It should be emphasized that the equations used for this derivation (starting with (26.1) and ending with the result in (26.5)) assume a narrowband transmitter with a narrowband receiver (note that narrowband being defined as a laser linewidth or receiver bandwidth significantly narrower than the absorption feature of interest). In any DIAL system, this is an approximation. Molecular scattering causes spectral broadening that cannot always be ignored. This is called the Rayleigh–Doppler effect and is the principal factor in dismissing DIAL as a solution for measuring temperature. Although we refer to the spectral shape as simply Rayleigh–Doppler herein, the Rayleigh scattered light has a Doppler broadened central peak (called the Cabannes line), which is split into a triplet (from pressure or Brillouin shifts) and sidebands due to pure rotational Raman scattering [26.35]. A model of this temperature and pressure-dependent molecular scattering spectrum is found in [26.36].

26.3.1 Rayleigh–Doppler Broadening

The DIAL equation assumes that the backscattered light collected by the receiver is unchanged by the scattering event. However, scattering by particles in motion results in a momentum transfer between the particle and the incident photons, so a Doppler shift is imparted onto the backscattered light. For large particles (e.g., aerosols and clouds) this has a negligible effect, but for atmospheric molecules (i.e., nitrogen, oxygen and water vapor) their random thermal motion results in a significantly broadened backscatter spectrum with a width

approximated as

$$\Delta\nu_D = 4\nu_0 \sqrt{\frac{2N_A k_B T_{\text{air}} \ln(2)}{M_{\text{air}}}}, \quad (26.6)$$

where $\Delta\nu_D$ is the Doppler broadened backscatter at full width half max (FWHM), ν_0 is the optical frequency of the incident light and related to wavelength through $\nu = c/\lambda$ where c is the speed of light and λ is wavelength, N_A is Avogadro’s number, k_B is the Boltzmann constant, T_{air} is the temperature of the parcel of air, and the M_{air} is the average mass of air, or 28.84 g mol^{-1} .

Observations of the backscattered spectrum received by a narrowband DIAL show two distinct distributions (Fig. 26.2). The spectrum of backscattered light from clouds and aerosols is unchanged from the incident narrowband laser spectrum, but the molecular backscatter is significantly widened (on the order of gigahertz or a couple of picometers wavelength in the near-IR). This effect is directly leveraged by high spectral resolution lidar (HSRL) that separates measurements of molecular and combined (molecular and particle) backscatter signals, allowing one to directly disentangle extinction from backscatter and produce quantitative retrievals of cloud and aerosol scatter-

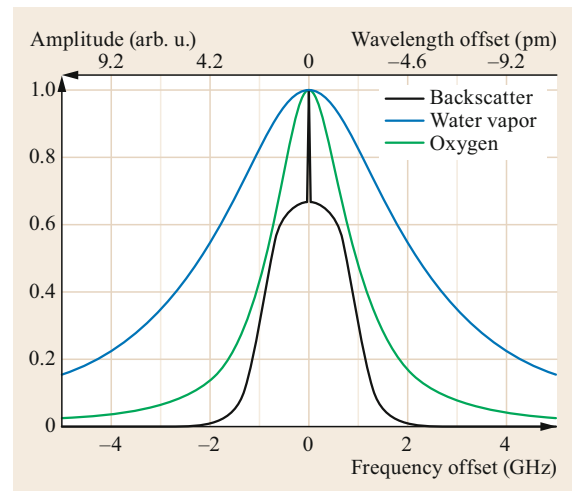


Fig. 26.2 Spectral distribution of backscatter at 828 nm (*black solid*) from a narrowband DIAL. In this case, the distribution is made up of an arbitrary mixture of two components: backscatter from clouds and/or aerosols (the spectrally narrow component) and backscatter from air molecules (the significantly broader component). The water vapor absorption line near 828 nm (*blue line*) and oxygen absorption line near 769 nm (*green line*) are overlaid for reference. All three spectra are for an atmosphere at 1 atm and 300 K. The wavelength offset is approximate for the near-infrared

ing properties [26.37–40]. In narrowband DIAL, the Rayleigh–Doppler effect can mean that the water vapor extinction characteristics are different on the return trip when observing light scattered by molecules.

The definitions in (26.1) ignore this effect, but this is not always a valid assumption. Omitting other constants that lack frequency dependence, the spectrum of photons on a detector is approximated by a convolution of the incident laser spectrum, the backscattered Rayleigh–Doppler spectrum and the particle spectrum after the initial trip up to the scattering volume

$$N(\nu, r) \propto \eta(\nu) T_{\text{atm}}(\nu, r) \{[\beta_{\text{m}}(\nu, r) + \beta_{\text{a}}(\nu, r)] * T_{\text{atm}}(\nu, r) I_0(\nu)\}, \quad (26.7)$$

where ν is the optical frequency, r is range from the instrument, $I_0(\nu)$ is the transmitted laser spectrum representing a frequency normalized $N_0(\lambda)$ in (26.1), $T_{\text{atm}}(\nu, r)$ is the atmospheric transmission as a function of optical frequency and range, $\beta_{\text{m}}(\nu, r)$ is the molecular backscatter coefficient with spectral shape determined by the local pressure and temperature, $\beta_{\text{a}}(\nu, r)$ is the aerosol and cloud backscatter coefficient with a spectral shape typically approximated as a delta function, $\eta(\nu)$ describes the transmission of the receiver as a function of optical frequency (e.g., filter functions) and $*$ is the convolution operator in frequency. If $\eta(\nu)$ is sufficiently narrow, the effects of Doppler broadening can be ignored because the broadened light that sees a different water vapor extinction never makes it to the detector.

Note that in (26.7) we include the laser linewidth term. For narrowband DIAL, this term becomes a delta function, but in broadband DIAL, we must account for this term.

The effect of the change in spectrum upon scattering breaks some of the relationship that cancels many of the atmospheric and instrument terms in (26.4). Now we are forced to account for the relative scattering contribution from molecules (causing Rayleigh–Doppler broadening) and particles (negligible effect).

Since all the other terms cancel when we take the ratio of the two wavelength channels, we are left with

$$N(r, \lambda_1) \propto \eta\left(\frac{c}{\lambda_1}\right) \beta_{\text{a}}(r) T_{\text{atm}}^2\left(\frac{c}{\lambda_1}, r\right) + \eta\left(\frac{c}{\lambda_1}\right) T_{\text{atm}}\left(\frac{c}{\lambda_1}, r\right) \times \int_{-\infty}^{\infty} \eta(\nu) T_{\text{atm}}(\nu, r) \beta_{\text{m}}(\nu, r) d\nu. \quad (26.8)$$

With some algebra we are able to remove the absolute scattering amplitudes and obtain a measurement dependence on the relative contributions of aerosols and molecules, most often described using the backscatter ratio $B(r)$.

$$N(r, \lambda_1) \propto \eta\left(\frac{c}{\lambda_1}\right) (B(r) - 1) T_{\text{atm}}^2\left(\frac{c}{\lambda_1}, r\right) + \eta\left(\frac{c}{\lambda_1}\right) T_{\text{atm}}\left(\frac{c}{\lambda_1}, r\right) \times \int_{-\infty}^{\infty} \eta(\nu) T_{\text{atm}}(\nu, r) \hat{\beta}_{\text{m}}(\nu, r) d\nu, \quad (26.9)$$

where $\hat{\beta}_{\text{m}}(\nu, r)$ is the frequency normalized molecular backscatter spectrum that describes the spectrum shape independent of amplitude.

Errors from Rayleigh–Doppler in water vapor retrievals can largely be mitigated, although in regions with strong gradients (e.g., cloud edges) one should be careful [26.41]. It has been shown that selecting an inflection point on the absorption line can effectively eliminate this error [26.42, 43], although operation at only an inflection point would limit a DIAL's ability to adapt to different environments. Note also that if the receiver passband is much narrower than the water vapor absorption line ($T_{\text{atm}}(\nu, r)$ is approximately constant over the passband of the receiver), the molecular term in (26.9) will approximate the aerosol atmospheric transmission within a constant. Thus operating with a narrow receiver system helps mitigate this error.

Our experience has been that Rayleigh–Doppler correction in water vapor DIAL is largely unnecessary for relatively narrow receiver systems (≈ 1 GHz FWHM or 2.5 pm bandwidth at 828 nm) compared to a broad water vapor line. However this effect is line specific and, more significantly, species specific. DIAL for molecules with higher mass will suffer more from its effect due to the decreased thermal broadening. This can be seen from Fig. 26.2, where the more massive oxygen (32 u) spectrum is of similar width to the Rayleigh–Doppler backscatter spectrum, while the water vapor (18 u) spectrum is considerably broader.

26.3.2 Broadband versus Narrowband DIAL

Where narrowband DIAL approximates aerosol backscatter as a delta function in frequency, broadband DIAL assumes the laser spectrum is so broad, that convolution with the molecular spectrum in (26.7) produces a negligible change in the laser spectrum. Applying this as-

sumption to (26.7) we obtain

$$N(r, \lambda_1) \propto (\beta_a(r) + \beta_m(r)) \times \int_{-\infty}^{\infty} \eta(v) l_0(v) T_{\text{atm}}^2(v, r) dv. \quad (26.10)$$

The assumption that the laser spectrum is much broader than the molecular spectrum allows the molecular and aerosol backscatter terms to be combined into a single spectroscopy term. However, the water vapor concentration is in the atmospheric transmission term behind the frequency integral. This prevents an analytic solution for the water vapor number density, requiring development of a different approach [26.44]. If the laser spectrum is known, the broadband DIAL equation can be solved numerically. This is often easier said than done because accurate knowledge of a broadband laser is not easily obtained without active monitoring. Diode laser mode structures tend to drift depending on environmental conditions and age. Even thermal instability outside of the laser diode itself can cause drifts in mode structure due to changes in feedback path lengths resulting from scattering on optic surfaces [26.45]. Multimode (broadband) lasers also suffer from mode-partition noise where the power in particular modes can vary considerably from pulse-to-pulse even though the total laser power may remain constant [26.46, 47]. In general, it is difficult to know the laser spectrum to sufficient accuracy to directly calibrate its effect. Instead, one uses other *a priori* data to nudge the retrieval into consistency with ancillary observations (such as radiosondes). Because of this, broadband DIAL retrievals are more akin to Raman lidar, which do not provide a truly independent retrieval of other observations.

The assumption that the backscatter spectrum is unaffected by molecular broadening (Rayleigh–Doppler) is key to retrieving water vapor with a broadband DIAL since it allows the collapse of molecular and aerosol terms into a one common spectrum solely dictated by the laser. Without this simplification the errors in the solution to the broadband DIAL equation compound at increasing range. The validity of this assumption will depend somewhat on the laser mode structure. The term *broadband* can be used to describe a variety of laser mode structures but they are rarely spectrally continuous. Very often broadband diode lasers lase at a large number of spectrally narrow frequency modes within a larger envelope. Depending on the mode spacing of the particular laser, Rayleigh–Doppler effects could change the evaluation of the frequency integral in (26.7). For any implementation of a broadband

DIAL, the designers should still confirm that the particular system is immune to Rayleigh–Doppler effects rather than just assume it is the case.

26.3.3 Accuracy and Precision

While the narrowband DIAL technique has the benefit of being self-calibrating, there are a series of factors that can still influence the instrument’s performance in terms of both accuracy and precision. The need and method to mitigate these effects will depend on the specifications for a particular system.

The precision of the instrument is influenced by a variety of noise sources where the dominant terms are system specific. The most common reduction in precision is caused by shot noise in low-power DIAL, which employ photon counting detectors. In high-power systems with analog detectors, detector noise can be significant. For systems with very narrowband transmitters, laser speckle can also be a source of random uncertainty. The complicating factor with zero mean noise sources is that the water vapor calculation requires a derivative operation, which is a high-pass filter and therefore a noise amplifier. Thus, there needs to be a cutoff frequency in the derivative operation (either low-pass filtering afterward or using a bandpass filter that approximates a derivative at low frequencies) to suppress noise and obtain a useful water vapor profile.

High-power DIAL systems are well suited to resolve power spectra at the necessary frequencies for estimating precision directly [26.48, 49]. This technique has the advantage of delivering statistical error estimates without needing to consider specific noise sources, but the system needs to have high enough signal at short time scales to resolve spectral features from atmospheric variability. Low-power micropulse DIAL systems typically do not have sufficient signal and therefore time resolution to employ this technique. Given their tendency to operate in photon counting regimes, shot noise is generally assumed to dominate the precision, which is well described by Poisson statistics. Given an observation of k photons in a bin, the associated variance in the estimate of the underlying signal is $k + 1$. Note that the variance in photon counting lidar signals is often incorrectly assumed to be k ; but if we observe $k = 0$ photons, this would suggest the variance is also zero, which is not the case because there is a nonzero probability of observing zero photons when the underlying signal is not zero. Framing the estimation problem correctly—what is the mean photons given an observation of k photons—results in a variance of $k + 1$. Thus the shot noise error is estimated from

the signal. Using first-order error propagation, the signal variances can be used to estimate the water vapor precision,

$$u_{n_{\text{wv}}}^2(r_i) = \frac{1}{4\Delta\sigma_{\text{wv}}^2\Delta r^2} \left(\frac{u_{N(\lambda_1, r_i)}^2}{N(\lambda_1, r_i)^2} + \frac{u_{N(\lambda_2, r_i)}^2}{N(\lambda_2, r_i)^2} + \frac{u_{N(\lambda_1, r_{i-1})}^2}{N(\lambda_1, r_{i-1})^2} + \frac{u_{N(\lambda_2, r_{i-1})}^2}{N(\lambda_2, r_{i-1})^2} - 2\frac{u_{N(\lambda_1, r_i)N(\lambda_1, r_{i-1})}}{N(\lambda_1, r_i)N(\lambda_1, r_{i-1})} - 2\frac{u_{N(\lambda_2, r_i)N(\lambda_2, r_{i-1})}}{N(\lambda_2, r_i)N(\lambda_2, r_{i-1})} \right), \quad (26.11)$$

where we use the notation u_x^2 for variance of x and u_{xy} to represent the covariance of x and y .

Typically, we assume all bins are independent, but if any prefiltering in range has occurred, a nonzero covariance needs to be accounted for in the error estimate. Background subtraction also creates nonzero covariance terms, but often times this is small enough to be ignored.

The limitation of (26.11) is that it is based on a first-order Taylor expansion, linearizing the nonlinear water vapor inversion formula in (26.2) about the estimated signals. When the argument of the log is noisy, this variance estimate will almost certainly incorrectly estimate water vapor uncertainty. Thus, uncertainty estimates using (26.11) are often the least reliable where signal-to-noise is the lowest. To mitigate this, we typically set a minimum signal threshold in our photon counting lidar, below which the data is masked.

Beyond random uncertainty, there are points where biases can come into DIAL estimates. The treatment we provide below is meant to provide some concept of how these errors fold into the water vapor estimates, the exact estimation methods will depend on the specifics of the system operation.

In order to estimate the water vapor absorption cross section in (26.5), we typically must assume a temperature and pressure for the given altitude. Pressure has the potential to impact the absorption feature shape. Temperature can impact both the spectrum shape and its strength. Obtaining accurate measurements from a DIAL requires that the selected water vapor line has a low temperature sensitivity within the expected temperature range. Typically, a well-designed DIAL can mitigate this error with proper line selection. In isolation, the error in estimated water vapor, $\Delta\sigma$, due to error in the assumed absorption feature is given by

$$\delta n_{\text{wv}} = -n_{\text{wv}} \frac{\delta\sigma}{\Delta\sigma + \delta\sigma}, \quad (26.12)$$

where $\delta\sigma$ is the error in the estimated online absorption term (the offline estimate typically does not have a significant dependence on temperature or pressure) and n_{wv} is the actual water vapor concentration.

As with most lidar products, we assume that the observed signal is linearly proportional to incident optical intensity. Regions of high signal can result in nonlinear detector responses, which generate biases in the retrieved water vapor. If the nonlinear response curve is monotonic and well known, this effect can be corrected to some extent, but additional uncertainties fold into the error analysis [26.50]. For example, dead-time corrections are often made in photon counting lidar systems, but that presumes the dead-time characteristics of the system are well known and the parameterization is a good fit to actual response behavior. The best parameterizations for nonlinear correction tend to be system specific. Data reported in [26.51] tended to fit one parameterization at low count rates but another at high count rates. The dominance of those curves will depend on the hardware employed in the instrument. Because of these uncertainties, nonlinear correction generally does not dramatically extend the dynamic range of the system. Overall, the effect of detector nonlinearities tend to be problematic around clouds and at low altitudes, which is a common theme in water vapor DIAL errors.

In some cases there are range-dependent differences in optical efficiency between the online and offline observations. Some of these are related to the optical system overlap function, which can result from different laser beam properties (e.g., pointing deviations, divergence or intensity distribution) between online and offline channels or slight differences in detector alignment (if separate detectors are used between the two channels). It has also been observed that narrowband filters may have range-dependent transmission spectra [26.3]. A well-designed optical system should have a field stop designed to limit the extent of this filter error, but the effect is certainly possible if the instrument has too wide of a field-of-view (FOV) or too small an etalon for the designed transmission bandwidth.

In all cases of differential overlap errors, the significance of the error depends more on the range gradient than its overall magnitude. An extreme example of this is a mismatch in scalar gain between online and offline channels, which contributes no error to the retrieved product irrespective of its magnitude (as long as detector nonlinearity is not an issue). The error contribution of any range-dependent term can easily be calculated from (26.1) and (26.5) and summarily described by

$$\delta n_{\text{wv}} = -\frac{1}{2\Delta\sigma} \frac{\partial}{\partial r} \ln \frac{\eta_{\text{on}}(r)}{\eta_{\text{off}}(r)}, \quad (26.13)$$

where δn_{wv} is the error in the water vapor concentration and $\eta_{\text{on}}(r)$ and $\eta_{\text{off}}(r)$ are the range-dependent efficiencies of the optical system for the online and offline channels, respectively. Notably, if the range-dependent efficiencies in the two channels are proportional to each other, they still contribute no error.

Many instances of the lidar equation (including that in (26.1)) omit the low-pass filtering effect of the laser pulse. In general, the ideal atmospheric signal needs to be convolved with the laser pulse (more generally called the instrument response function, which also includes receiver system effects) to capture the inherent smoothing operation resulting from a nonzero laser pulse width. Unfortunately, the convolution operation does not commute with the division operation we usually use for retrieving water vapor so the standard signal processing scheme is actually an approximation that assumes the filter operation has an insignificant impact on the return signal. This means that areas of significant backscatter gradient that have high frequency (relative to the laser pulse width) will poorly approximate the true signals and the retrieval will be biased (it should be noted that banded data collection and signal processing techniques also have this effect). Systems with relatively long pulse lengths are poorly suited for estimating water vapor near cloud edges where biases can be very large. Even worse is this effect is quite difficult to quantify without knowing the *unsmoothed* scene. At present we are not aware of a clear analytic definition for this effect, so the user needs to maintain some awareness of the backscatter scene when using DIAL data.

In many DIAL instances, the instrument switches between performing measurements at online and offline

wavelengths, but the DIAL retrievals assume that the atmosphere is unchanged between these observations. If the instrument dwells at one wavelength too long, biases will develop in regions where the atmosphere is changing. A well-designed instrument typically alternates wavelengths at time scales much faster than the variation of the atmosphere. Errors in the retrievals are not so much a result of variability as *inhomogeneous* variability. That is, when variations in backscatter are uncorrelated between range gates. That error is characterized by

$$\delta n_{\text{wv}} = -\frac{1}{2\Delta\sigma} \frac{\partial}{\partial r} \ln \left(\frac{\Delta\beta}{\beta(r)} + 1 \right), \quad (26.14)$$

where $\Delta\beta$ is the difference in observed backscatter coefficient in the online channel compared to the offline channel. For a given covariance spectrum, one can potentially estimate the error due to the interleave times of the wavelengths, but the rough estimate provided by Schotland [26.6] that interleave times should be < 8.5 ms, is often used as the standard. Observations performed by [26.52] suggest that the atmosphere is safely frozen for time periods $< 1\text{--}3$ ms, with decorrelation occurring in the $10\text{--}100$ ms range. Those measurements were performed on kilometer range scales though, so it is less obvious how short range correlations might be impacted. It is important to note that integration times used to generate the water vapor profiles can be much longer than these switching times. The transmitter and data acquisition system need to switch rapidly between wavelengths, but those channels can accumulate over much longer time scales without creating significant biases.

26.4 Devices and Systems

There are two basic types of ground-based water vapor DIAL devices in use currently in the atmospheric science community—*high-power* instruments that utilize Ti:Sapphire laser transmitters and *low-power* instruments that are semiconductor or diode laser-based systems (Table 26.2). Both are highly specialized research instruments and neither type of DIAL is commercially available at the time of this writing. However, industry is actively researching ways to develop commercially viable water vapor DIAL instruments. For example, ventures are underway to develop a $1.5\text{ }\mu\text{m}$ coherent DIAL system [26.53], exploring a broadband DIAL that operates in the near-infrared [26.54], and investigating short-range continuous wave DIAL via the Scheimpflug principle [26.55].

The high-power research DIAL systems in use today output several watts of average power and are capable of time resolutions of $1\text{--}10$ s with range resolutions of $30\text{--}300$ m while maintaining an error of $< 10\%$. Although complex laser transmitters are required, long-term measurements can be made with such systems [26.21, 56]. The fast temporal resolution of a high-power DIAL allows scanning for three-dimensional (3-D) water vapor field studies within the atmospheric boundary layer, which is required to improve our understanding of land atmosphere exchange processes. The current state-of-the-art 3-D high-power system is represented by the University of Hohenheim (UHOH) system [26.42, 57] and shown in Fig. 26.3.

Table 26.2 Advantages and disadvantages of the different methods

Device	Advantages	Disadvantages
High-power (narrowband)	Fast temporal resolution ^a Self-calibrating High range resolutions ^b	Expensive to build and maintain Not eye-safe Large and complex ^c
Low-power (narrowband)	Inexpensive to build and maintain Eye-safe Self-calibrating Compact	Coarse temporal resolution ^d Coarse range resolution ^e
Low-power (broadband)	Inexpensive to build and maintain Eye-safe Compact	Very coarse temporal resolution ^f High background ^g Requires periodic calibration

^a Approximately 1–10 s while maintaining an error of < 10%;

^b approximately 30–300 m while maintaining an error of < 10%; ^c typically requires highly trained staff to operate, and liquid cooling for laser; ^d approximately 1–5 min while maintaining an error of < 10%; ^e approximately 150–300 m while maintaining an error of < 10%; ^f approximately 20 min based on [26.54]; ^g no benefit to using a receiver filter narrower than transmitter width, which may limit range



Fig. 26.3 The current state-of-the-art high-power ground-based water vapor DIAL is represented by the UHOH 3-D-scanning WVDIAL. The instrument is housed inside a mobile trailer. The 80-cm 3-D scanner can be seen protruding out of the top left of the trailer (photo by Andreas Behrendt; used with permission)

Low-power research DIAL instruments in use today are designed for vertical profiling, output a few tens of milliwatts and have time resolutions of 1–5 min with range resolution of 150–300 m in both day and night while maintaining an error of < 10%. Compared to high-power DIAL, the instruments can be made more



Fig. 26.4 The current state-of-the-art low-power ground-based water vapor DIAL is represented by the micropulse DIAL (MPD) developed by NCAR and Montana State University. Photo taken March 2016, Boulder CO, USA (photo by Rich Erickson; used with permission)

compact, are lower cost to build, operate and maintain, and can run autonomously. These qualities make low-power water vapor DIAL promising candidates for large-scale networks. Future networks could be used to advance knowledge in the areas of measuring water vapor concentration and distribution, convection initiation, and could lead to improving our weather and climate forecasting skills. The current state-of-the-art low-power ground-based water vapor DIAL is represented by the MicroPulse DIAL (MPD) [26.27, 58] developed by National Center for Atmospheric Research (NCAR) and Montana State University (Fig. 26.4).

Both *high*-power and *low*-power water vapor DIAL instruments in use today are narrowband—they measure water vapor concentration with a narrow laser spectrum (e.g., ≤ 10 MHz or 0.02 pm at 828 nm). However, a broadband DIAL prototype has been demonstrated with a source much broader than a single water vapor absorption line [26.54]. Note that here broad-

band DIAL is distinguished from the differential optical atmospheric spectroscopy (DOAS) lidar hybrid technique [26.59, 60] as it does not spectrally resolve the backscattered light, e.g., with some type of fast gate spectrometer as a function of range. The broadband DIAL approach has the benefit of simplifying a number of the design constraints on the system with reduced need to actively control and stabilize the source wavelength and enabling the use of lower cost components. Furthermore, conventional thought is that the broadband DIAL is mostly insensitive to Rayleigh–Doppler effects. However, there is a performance cost to relaxing spectral requirements of the source. The spectrally broad source effectively limits our best tool for solar background rejection—narrowband filters in the receiver—so higher pulse energies are needed for day-

time operation, particularly when clouds are present. With broadband lasers, narrowing the receiver spectrum becomes a zero sum game, where reducing receiver bandwidth serves to equally attenuate background and signal. In that case, the only way to overcome this issue of detectability is to move to higher pulse energies and give up the eye-safe classification.

For practical implementations, as outlined in Sect. 26.3, the broadband DIAL retrieval requires calibration to a reference (e.g., radiosondes or radiometers) like Raman lidar. In that sense, a broadband DIAL is not considered self-calibrating and cannot provide independent observations. This means they typically agree quite well with the ancillary observations to which they are calibrated and are poorly suited to identifying the biases in those ancillary observations.

26.5 Specifications

Due to the lack of a commercial instrument, there are not well-defined performance parameters for ground-based water vapor DIAL. In general, the research DIAL systems currently in use are able to profile the entire lower troposphere (4–6 km range) in both day and night conditions. The high-power systems are capable

of temporal resolutions of 1–10 s and range resolutions of 30–300 m while maintaining an error of < 10%; whereas, low-power research DIAL instruments have time resolutions of 1–5 min with range resolution of 150–300 m while maintaining an error of < 10%.

26.6 Quality Control

For the narrowband DIAL technique, knowledge of the laser frequency is paramount, so it is continuously validated against a reference standard (e.g., a stabilized HeNe laser in a wavelength meter, or an absorption cell). The monitoring is typically done in near real time, on either the pulsed output or the injection seed laser, where the spectral conditions are preserved when amplified [26.17]. A second quality control factor for narrowband DIAL instruments is actively adjusting the laser frequency to minimize errors for the atmospheric conditions. The most straightforward method is via sideline tuning—adjusting the absorption cross section by changing the laser frequency away from line center—using accurate knowledge of the absorption lineshape from spectral databases (e.g., a Voigt profile can be used to estimate the absorption lineshape as a function of altitude). In this manner, the laser frequency is optimized for a wide range of moisture conditions. Note, that a one-way column optical depth (OD) of ≈ 1.1 is often used as rule of thumb for maximizing resolution in photon counting DIAL [26.61], although in practice the optimal OD will depend on a number of instrument and atmospheric factors. Only a small amount of wavelength tuning is typically re-

quired to optimize the DIAL; for example, at 828 nm, ≈ 5 GHz (or several picometers in the infrared) of sideline tuning adjusts the absorption cross section by an order of magnitude. Other quality control techniques involve identification of regions of high error, as defined in Sect. 26.3.3, such as low signal regions, regions with high gradients (cloud edges, lowest altitude range bins where the overlap function is changing rapidly), and regions with known nonlinear detector response (e.g., for photon-counting modules, count rates $> 5 \times 10^6 \text{ s}^{-1}$). These regions of high error are typically flagged or masked out of the data products for quality control.

Comparisons with radiosonde humidity profiles, infrared radiometer humidity profiles, or total water vapor column measurements from microwave radiometers, can also be useful tools for quality control. These comparisons can either identify quality control issues that originate from the narrowband DIAL or biases in the ancillary measurement. This is not the case for broadband DIAL—since it is not self-calibrating, it cannot provide truly independent observations or be used to identify biases in the techniques required for its calibration.

26.7 Maintenance

Due to the lack of a commercial instrument, there are not well-defined maintenance parameters for ground-based water vapor DIAL. In general, the high-power systems that use flashlamp-pumped lasers will require

maintenance every month. High-power systems that use diode-pumped solid-state laser and low-power systems are theoretically capable of operations for several years.

26.8 Applications

Standard observations of water vapor are obtained from the world-wide operational radiosonde network. Radiosondes are launched typically twice a day and are separated by hundreds of kilometers or more. This temporal and spatial resolution is not sufficient for many weather and climate research and forecasting applications. Satellite retrievals provide global coverage but are limited in terms of temporal and vertical resolution, particularly in the lower atmosphere where atmospheric moisture variability is most pronounced. Retrievals from ground-based global positioning system (GPS) receivers provide column-integrated precipitable water vapor without important range-resolved height information. Ground-based passive remote sensors include microwave and infrared radiometers. These can provide good profile information in the lowest 1.5 km but suffer from reduced resolution above that height. Active remote sensing systems are the most promising tools to close these observational gaps. Both DIAL and Raman lidar provide accurate range-resolved water vapor profiles; yet, to make a significant scientific impact, these systems need to be distributed on a wide scale [26.62].

Due to the limitations in water vapor measurement techniques described above, severe gaps in the observation of water vapor aloft exist [26.62–64]. The atmospheric research and operational weather forecasting communities have been advocating strongly for an instrument that can continuously profile water vapor at high temporal and vertical resolution in the lower troposphere (i.e., the lowest 3–4 km of the atmosphere). Furthermore, observations of the horizontal variability of water vapor are also important for both improved understanding of atmospheric processes and improved forecasting skill [26.65]. The measurements of small variations in the spatial, vertical, and temporal distribution of water vapor have been shown to be critically important for understanding and improving forecasts of, e.g., convection initiation and evolution, boundary layer processes, orographic precipitation, and tornadic storms [26.66–68].

An example of a vertical range-height indicator (RHI) scan of absolute humidity is shown in Fig. 26.5. This figure shows how the horizontal and vertical structure of water vapor can be measured over a range of

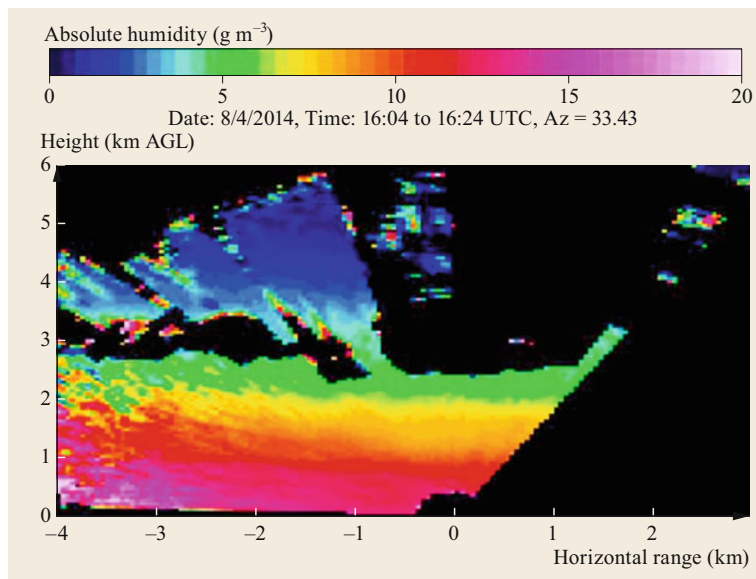


Fig. 26.5 RHI scan of absolute humidity obtained with the UHOH WVDIAL on 04.08.2014. The temporal and spatial resolution of the derived water-vapor field are 10 s and 300 m, respectively. Masked areas are in black (after [26.63] with permission from Wiley and Sons)

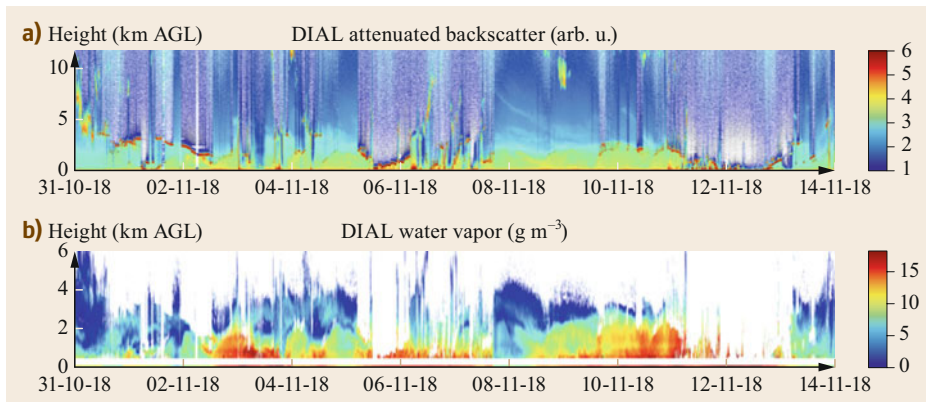


Fig. 26.6a,b Time series of relative aerosol **(a)** in arbitrary units (arb. u.) and absolute humidity in g m^{-3} **(b)** measured with the NCAR MPD. The temporal and spatial resolution of the derived WV field are 5 min and 150 m, respectively. The vertical profiles taken in Pilar, Argentina span two weeks starting 31.10.2018. Masked areas are in *white* and typically signify attenuated signal due to optically thick clouds

several kilometers. This example illustrates pronounced vertical stratification and moisture variability.

Figure 26.6 shows the continuous data collected by an MPD for two weeks during a field project in central Argentina. The top panel of the figure shows the relative aerosol backscatter—corrected for both range and geometric overlap—from near the surface to 12 km. The bottom panel of the figure shows the water vapor absolute humidity profiles from 300 m up to 6 km AGL. The red regions of relative backscatter illustrate cloud bases. Water vapor measurements via the DIAL are not possible through optically thick clouds, and these regions are masked white. These continuous observations reveal dramatic moisture variability, elevated moist and dry layers and moisture variations associated with the diurnal cycle.

While one instrument will not satisfy all of the measurement gaps inhibiting scientific understanding of atmospheric processes that are impacted by water vapor, combinations of sensors are highly valuable. For example, the collocated combination of DIAL with Atmospheric Emitted Radiance Interferometers (AERI) [26.69, 70] holds promise for providing complete clear-air profiles from the ground to the mid-troposphere. This combination will combine the high accuracy, high resolution AERI measurements at low levels with the extended range of DIAL measurements up to 3–5 km AGL [26.58]. Furthermore, the combination and integration of multiple water vapor sensors via data assimilation methods may provide 3-D moisture fields, which would likely benefit short-term convective weather forecasting skill.

26.9 Future Developments

26.9.1 Networks

Large-scale networks of ground-based passive and active remote sensing systems provide the most promising results to close the observational gap of water vapor aloft and are essential for continued progress in weather and climate research [26.62, 63]. Both DIAL and Raman lidar provide accurate range-resolved water vapor profiles; however, future networks need to be comprised of low-cost instruments to provide a sufficient density that is economically feasible. For a significant scientific impact, it is anticipated that several hundred instruments would be required to adequately cover an area the size of the continental United States [26.62].

Semiconductor laser-based DIAL instruments—with a reduced cost and enhanced simplicity, safety, and reliability, while still providing accurate quantitative data products—show promise to enable an autonomous and continuously operated large-scale network of water vapor profiling.

26.9.2 Temperature Profiling

The combination of water vapor and temperature profiles from the same instrument would provide atmospheric stability profiles and be valuable to the weather forecasting and severe weather communities. To date, the most successful active remote sensing temperature

profiling is provided by the rotational Raman technique [26.71, 72]. However, DIAL inherently has two significant advantages over Raman lidar: (1) in practical application, it requires no external calibration and (2) the elastic scattering cross section is several orders of magnitude larger than the Raman scattering cross section. This second advantage has opened the door to using low-power semiconductor lasers for the historically challenging DIAL laser transmitter. It is therefore a tantalizing prospect to investigate the potential of adapting the diode laser-based DIAL technique to include temperature profiling.

The potential to obtain atmospheric temperature profiles with the DIAL technique has been known for several decades [26.73–75]. The concept is to perform a DIAL measurement on the absorption of a line in the oxygen A-band that has a high ground-state energy. The number density of the O₂ profile can be estimated from surface temperature and pressure, and corrected for water vapor concentration (i.e., the water vapor profile needs to be simultaneously measured). The observed temperature-dependent absorption coefficient can then be solved for temperature. However, as outlined in the literature [26.76, 77], the major stumbling

block to implementing this technique stems from the Doppler broadened Rayleigh backscatter. In the oxygen A-band, at 770 nm wavelength, the Rayleigh–Doppler spectrum has a linewidth comparable to the O₂ absorption feature, while, the Mie backscattered linewidth maintains the same narrowband linewidth of the laser (Fig. 26.2). To accurately retrieve temperature profiles, the Rayleigh–Doppler broadened backscatter must be accounted for in the return leg of the optical path. The difficulty of how to adequately correct for this term has stymied O₂ DIAL-based temperature measurements.

One possible solution is to combine the high spectral resolution lidar (HSRL) technique into the micropulse DIAL architecture. The HSRL technique is capable of resolving the molecular to aerosol backscatter ratio without significant assumptions. A simplified version of an HSRL, based on the diode laser-based lidar architecture, was recently demonstrated [26.1]. In the future, a combined diode laser-based lidar—with HSRL, O₂ DIAL, and water vapor DIAL capabilities—may provide temperature profiling opportunities [26.78]. A retrieval technique based on a perturbative solution to the DIAL equation using such a system has been outlined by [26.79].

26.10 Further Readings

- R.M. Measures: *Laser Remote Sensing: Fundamentals and Applications* (John Wiley and Sons, New York 1984)
- F.J. Duarte (Ed.): *Tunable Laser Applications*, 3rd edn. (CRC Press, Boca Raton 2016)
- V.A. Kovalev, W.E. Eichinger: *Elastic Lidar* (John Wiley and Sons, New Jersey 2004)
- C. Weitkamp (Ed.): *Lidar – Range-Resolved Optical Remote Sensing of the Atmosphere* (Springer, New York 2005)

References

- 26.1 M. Hayman, S. Spuler: Demonstration of a diode-laser-based high spectral resolution lidar (HSRL) for quantitative profiling of clouds and aerosols, *Opt. Express* **25**(24), A1096 (2017)
- 26.2 S. Ismail, E.V. Browell: Recent lidar technology developments and their influence on measurements of tropospheric water vapor, *J. Atmos. Ocean. Technol.* **11**(1), 76–84 (1994)
- 26.3 V. Wulfmeyer: Ground-based differential absorption lidar for water-vapor and temperature profiling: Development and specifications of a high-performance laser transmitter, *Appl. Opt.* **37**(18), 3804–3824 (1998)
- 26.4 L.S. Rothman, I.E. Gordon, Y. Babikov, A. Barbe, D.C. Benner, P.F. Bernath, M. Birk, L. Bizzocchi, V. Boudon, L.R. Brown, A. Campargue, K. Chance, E.A. Cohen, L.H. Coudert, V.M. Devi, B.J. Drouin, A. Fayt, J.M. Flaud, R.R. Gamache, J.J. Harrison, J.M. Hartmann, C. Hill, J.T. Hodges, D. Jacquemart, A. Jolly, J. Lamouroux, R.J. Le Roy, G. Li, D.A. Long, O.M. Lyulin, C.J. Mackie, S.T. Massie, S. Mikhailenko, H.S. Müller, O.V. Naumenko, A.V. Nikitin, J. Orphal, V. Perevalov, A. Perrin, E.R. Polovtseva, C. Richard, M.A. Smith, E. Starikova, K. Sung, S. Tashkun, J. Tennyson, G.C. Toon, V.G. Tyuterev, G. Wagner: The HITRAN2012 molecular spectroscopic database, *J. Quant. Spectrosc. Radiat. Transf.* **130**, 4–50 (2013)
- 26.5 R.M. Schotland: Some observations of the vertical profile of water vapor by means of a laser optical radar. In: *4th Symp. Remote Sens. Environ.* (Univ. Michigan, Ann Arbor 1964)
- 26.6 R.M. Schotland: Errors in the lidar measurement of atmospheric gases by differential absorption, *J. Appl. Meteorol.* **13**(1), 71–77 (1974)

- 26.7 E.V. Browell, T.D. Wilkerson, T.J. McIlrath: Water vapor differential absorption lidar development and evaluation, *Appl. Opt.* **18**(20), 3474–3483 (1979)
- 26.8 G. Mégie, J. Pelon, J. Lefrère, C. Cahen, P.H. Flamant: Ozone and water vapor monitoring using a ground-based lidar system. In: *Optical and Laser Remote Sensing*, ed. by D.K. Killinger, A. Mooradian (Springer, Berlin, Heidelberg 1983) pp. 223–228
- 26.9 C. Cahen, G. Megie, P. Flamant: Lidar monitoring of the water vapor cycle in the troposphere, *J. Appl. Meteorol.* **21**(10), 1506–1515 (1982)
- 26.10 E.R. Murray, R.D. Hake, J.E. van der Laan, J.G. Hawley: Atmospheric water vapor measurements with an infrared ($10\ \mu\text{m}$) differential, absorption lidar system, *Appl. Phys. Lett.* **28**(9), 542–543 (1976)
- 26.11 P.W. Baker: Atmospheric water vapor differential absorption measurements on vertical paths with a CO_2 lidar, *Appl. Opt.* **22**(15), 2257–2264 (1983)
- 26.12 W.B. Grant, J.S. Margolis, A.M. Brothers, D.M. Tratt: CO_2 DIAL measurements of water vapor, *Appl. Opt.* **26**(15), 3033–3042 (1987)
- 26.13 R.M. Hardesty: Coherent DIAL measurement of range-resolved water vapor concentration, *Appl. Opt.* **23**(15), 2545–2553 (1984)
- 26.14 M. Endemann, R.L. Byer: Remote single-ended measurements of atmospheric temperature and humidity at $1.77\ \mu\text{m}$ using a continuously tunable source, *Opt. Lett.* **5**(10), 452–454 (1980)
- 26.15 M. Endemann, R.L. Byer: Simultaneous remote measurements of atmospheric temperature and humidity using a continuously tunable IR lidar, *Appl. Opt.* **20**(18), 3211–3217 (1981)
- 26.16 S. Cha, K.P. Chan, D.K. Killinger: Tunable $2.1\text{-}\mu\text{m}$ Ho lidar for simultaneous range-resolved measurements of atmospheric water vapor and aerosol backscatter profiles, *Appl. Opt.* **30**(27), 3938–3943 (1991)
- 26.17 V. Wulfmeyer, S. Schmitz, J. Bösenberg, S. Lehmann, C. Senff: Injection-seeded alexandrite ring laser: Performance and application in a water-vapor differential absorption lidar, *Opt. Lett.* **20**(6), 638–640 (1995)
- 26.18 V. Wulfmeyer, J. Bösenberg: Single-mode operation of an injection-seeded alexandrite ring laser for application in water-vapor and temperature differential absorption lidar, *Opt. Lett.* **21**(15), 1150–1152 (1996)
- 26.19 K. Ertel, H. Linné, J. Bösenberg: Injection-seeded pulsed Ti:sapphire laser with novel stabilization scheme and capability of dual-wavelength operation, *Appl. Opt.* **44**(24), 5120–5126 (2005)
- 26.20 J. Bösenberg, H. Linné: Continuous ground-based water vapour profiling using DIAL. In: *23rd Int. Laser Radar Conf., Nara* (2006) pp. 679–682
- 26.21 H. Vogelmann, T. Trickl: Wide-range sounding of free-tropospheric water vapor with a differential-absorption lidar (DIAL) at a high-altitude station, *Appl. Opt.* **47**(12), 2116–2132 (2008)
- 26.22 A. Behrendt, V. Wulfmeyer, A. Riede, G. Wagner, S. Pal, H. Bauer, M. Radlach, F. Späth: Three-dimensional observations of atmospheric humidity with a scanning differential absorption lidar, *Proc. SPIE* **7475**, 747504 (2009)
- 26.23 J.L. Machol, T. Ayers, K.T. Schwenz, K.W. Koenig, R.M. Hardesty, C. Senff, M.A. Krainak, J.B. Abshire, H.E. Bravo, S.P. Sandberg: Preliminary measurements with an automated compact differential absorption lidar for the profiling of water vapor, *Appl. Opt.* **43**(15), 3110–3121 (2004)
- 26.24 A.R. Nehrir, K.S. Repasky, J.L. Carlsten, M.D. Obland, J.A. Shaw: Water vapor profiling using a widely tunable, amplified diode-laser-based differential absorption lidar (DIAL), *J. Atmos. Ocean. Technol.* **26**(4), 733–745 (2009)
- 26.25 A.R. Nehrir, K.S. Repasky, J.L. Carlsten: Eye-safe diode-laser-based micropulse differential absorption lidar (DIAL) for water vapor profiling in the lower troposphere, *J. Atmos. Ocean. Technol.* **28**(2), 131–147 (2011)
- 26.26 A.R. Nehrir, K.S. Repasky, J.L. Carlsten: Micropulse water vapor differential absorption lidar: Transmitter design and performance, *Opt. Express* **20**(22), 25137–25151 (2012)
- 26.27 S.M. Spuler, K.S. Repasky, B. Morley, D. Moen, M. Hayman, A.R. Nehrir: Field-deployable diode-laser-based differential absorption lidar (DIAL) for profiling water vapor, *Atmos. Meas. Tech.* **8**(3), 1073–1087 (2015)
- 26.28 E.V. Browell: Remote sensing of tropospheric gases and aerosols with an airborne dial system. In: *Optical and Laser Remote Sensing*, ed. by D.K. Killinger, A. Mooradian (Springer, Berlin, Heidelberg 1983) pp. 138–147
- 26.29 N.S. Higdon, E.V. Browell, P. Ponsardin, B.E. Grossmann, C.F. Butler, T.H. Chyba, M.N. Mayo, R.J. Allen, A.W. Heuser, W.B. Grant, S. Ismail, S.D. Mayor, A.F. Carter: Airborne differential absorption lidar system for measurements of atmospheric water vapor and aerosols, *Appl. Opt.* **33**(27), 6422–6438 (1994)
- 26.30 A.S. Moore, K.E. Brown, W.M. Hall, J.C. Barnes, W.C. Edwards, L.B. Petway, A.D. Little, W.S. Luck, I.W. Jones, C.W. Antill, E.V. Browell, S. Ismail: Development of the lidar atmospheric sensing experiment (LASE)—An advanced airborne DIAL instrument. In: *Advances in Atmospheric Remote Sensing with Lidar*, ed. by A. Ansmann, R. Neuber, P. Rairoux, U. Wandinger (Springer, Berlin Heidelberg 1997) pp. 281–288
- 26.31 G. Ehret, C. Kiemle, W. Renger, G. Simmet: Airborne remote sensing of tropospheric water vapor with a near-infrared differential absorption lidar system, *Appl. Opt.* **32**(24), 4534–4551 (1993)
- 26.32 G. Ehret, A. Fix, V. Weiß, G. Poberaj, T. Baumert: Diode-laser-seeded optical parametric oscillator for airborne water vapor DIAL application in the upper troposphere and lower stratosphere, *Appl. Phys. B* **67**(4), 427–431 (1998)
- 26.33 A. Fix, G. Ehret, J. Löhring, D. Hoffmann, M. Alpers: Water vapor differential absorption lidar measurements using a diode-pumped all-solid-state laser at $935\ \text{nm}$, *Appl. Phys. B* **102**(4), 905–915 (2010)
- 26.34 A. Savitzky, M.J.E. Golay: Smoothing and differentiation of data by simplified least squares procedures, *Anal. Chem.* **36**(8), 1627–1639 (1964)

- 26.35 C. She: Spectral structure of laser light scattering revisited: Bandwidths of nonresonant scattering lidars, *Appl. Opt.* **40**(27), 4875–4884 (2001)
- 26.36 C.D. Boley, R.C. Desai, G. Tenti: Kinetic models and Brillouin scattering in a molecular gas, *Can. J. Phys.* **50**(18), 2158–2173 (1972)
- 26.37 R.J. Alvarez, L.M. Caldwell, P.G. Wolyn, D.A. Krueger, T.B. McKee, C.Y. She: Profiling temperature, pressure and aerosol properties using a high spectral resolution lidar employing atomic blocking filters, *J. Atmos. Ocean. Technol.* **10**(4), 546–556 (1993)
- 26.38 P. Piironen, E.W. Eloranta: Demonstration of a high-spectral-resolution lidar based on an iodine absorption filter, *Opt. Lett.* **19**(3), 234–236 (1994)
- 26.39 J. Hair, L. Caldwell, D. Krueger, C.Y. She: High-spectral-resolution lidar with iodine-vapor filters: Measurement of atmospheric-state and aerosol profiles, *Appl. Opt.* **40**(30), 5280–5294 (2001)
- 26.40 J.W. Hair, C.A. Hostetler, A.L. Cook, D.B. Harper, R.A. Ferrare, T.L. Mack, W. Welch, L.R. Isquierdo, F.E. Hovis: Airborne high spectral resolution lidar for profiling aerosol optical properties, *Appl. Opt.* **47**(36), 6734–6752 (2008)
- 26.41 A. Ansmann: Errors in ground-based water-vapor DIAL measurements due to Doppler-broadened Rayleigh backscattering, *Appl. Opt.* **24**(21), 3476–3480 (1985)
- 26.42 F. Späth, A. Behrendt, S.K. Muppa, S. Metzendorf, A. Riede, V. Wulfmeyer: 3D water vapor field in the atmospheric boundary layer observed with scanning differential absorption lidar, *Atmos. Meas. Tech.* **9**(4), 1701–1720 (2016)
- 26.43 F. Späth, A. Behrendt, V. Wulfmeyer: Sensitivity of the Rayleigh-Doppler effect with respect to wavelength and backscatter coefficient. In: *27th Int. Laser Radar Conf., New York* (2015)
- 26.44 V.V. Zuev, V.E. Zuev, Y.S. Makushkin, V.N. Marichev, A.A. Mitsel: Laser sounding of atmospheric humidity: Experiment, *Appl. Opt.* **22**(23), 3742–3746 (1983)
- 26.45 P.C.D. Hobbs: *Building Electro-Optical Systems*, Wiley Series in Pure and Applied Optics, Vol. 1 (John Wiley & Sons, New York 2000)
- 26.46 K. Ogawa, R.S. Vodhanel: Measurements of mode partition noise of laser diodes, *IEEE J. Quantum Electron.* **18**(7), 1090–1093 (1982)
- 26.47 K. Ogawa: Analysis of mode partition noise in laser transmission systems, *IEEE J. Quantum Electron.* **18**(5), 849–855 (1982)
- 26.48 C. Senff, J. Bösenberg, G. Peters: Measurement of water vapor flux profiles in the convective boundary layer with lidar and radar-RASS, *J. Atmos. Ocean. Technol.* **11**(1), 85–93 (1994)
- 26.49 D.H. Lenschow, V. Wulfmeyer, C. Senff: Measuring second- through fourth-order moments in noisy data, *J. Atmos. Ocean. Technol.* **17**(10), 1330–1347 (2000)
- 26.50 D.P. Donovan, J.A. Whiteway, A.I. Carswell: Correction for nonlinear photon-counting effects in lidar systems, *Appl. Opt.* **32**(33), 6742–6753 (1993)
- 26.51 R. Stillwell, R. Neely, J. Thayer, M. Shupe, D. Turner: Improved cloud-phase determination of low-level liquid and mixed-phase clouds by enhanced polarimetric lidar, *Atmos. Meas. Tech.* **11**(2), 835–859 (2018)
- 26.52 N. Menyuk, D.K. Killinger: Temporal correlation measurements of pulsed dual CO₂ lidar returns, *Opt. Lett.* **6**(6), 301–303 (1981)
- 26.53 M. Imaki, R. Kojima, S. Kameyama: Development of wavelength locking circuit for 1.53 micron water vapor monitoring coherent differential absorption LIDAR, *EPJ Web Conf.* **176**, 05039 (2018)
- 26.54 R. Roininen, C. Münkel: Results from continuous atmospheric boundary layer humidity profiling with a compact DIAL instrument. In: *8th Symp. Lidar Atmos. Appl., Seattle* (American Meteorological Society, Washington 2017)
- 26.55 L. Mei, M. Brydegaard: Continuous-wave differential absorption lidar, *Laser Photonics Rev.* **9**(6), 629–636 (2015)
- 26.56 H. Vogelmann, R. Sussmann, T. Trickl, T. Borsdorff: Intercomparison of atmospheric water vapor soundings from the differential absorption lidar (DIAL) and the solar FTIR system on Mt. Zugspitze, *Atmos. Meas. Tech.* **4**(5), 835–841 (2011)
- 26.57 G. Wagner, A. Behrendt, V. Wulfmeyer, F. Späth, M. Schiller: High-power Ti:sapphire laser at 820 nm for scanning ground-based water-vapor differential absorption lidar, *Appl. Opt.* **52**(11), 2454–2469 (2013)
- 26.58 T.M. Weckwerth, K.J. Weber, D.D. Turner, S.M. Spuler: Validation of a water vapor micropulse differential absorption lidar (DIAL), *J. Atmos. Ocean. Technol.* **33**(11), 2353–2372 (2016)
- 26.59 A.M. South, I.M. Povey, R.L. Jones: Broadband lidar measurements of tropospheric water vapor profiles, *J. Geophys. Res. Atmos.* **103**(D23), 31191–31202 (1998)
- 26.60 G.M. Krekov, M.M. Krekova, A.Y. Sukhanov: Estimation of the broadband lidar potential for remote sensing of the molecular atmosphere, *Atmos. Ocean. Opt.* **22**(3), 346–358 (2009)
- 26.61 E.E. Remsburg, L.L. Gordley: Analysis of differential absorption lidar from the space shuttle, *Appl. Opt.* **17**(4), 624–630 (1978)
- 26.62 National Research Council: *Observing Weather and Climate from the Ground Up* (National Academies Press, Washington 2009)
- 26.63 V. Wulfmeyer, R.M. Hardesty, D.D. Turner, A. Behrendt, M.P. Cadeddu, P. Di Girolamo, P. Schlüssel, J. Van Baelen, F. Zus: A review of the remote sensing of lower tropospheric thermodynamic profiles and its indispensable role for the understanding and the simulation of water and energy cycles, *Rev. Geophys.* **53**(3), 819–895 (2015)
- 26.64 R.E. Carbone, R.J. Serafin, R.M. Hoff, R.M. Hardesty, F. Carr, T. Weckwerth, S. Koch, A. Benedetti, S. Crewell, D. Cimini, D. Turner, W. Feltz, B. Demoz, V. Wulfmeyer, D. Sisterson, T. Ackerman, F. Fabry, K. Knupp: *Thermodynamic Profiling Technologies Workshop Report to the National Science Foundation and the National Weather Service*. Tech. Rep. NCAR/TN-488 (2012)

- 26.65 T.M. Weckwerth, V. Wulfmeyer, R.M. Wakimoto, M.R. Hardesty, J.W. Wilson, R.M. Banta: NCAR-NOAA Lower-Tropospheric Water Vapor Workshop, *Bull. Am. Meteorol. Soc.* **80**(11), 2339–2357 (1999)
- 26.66 N.A. Crook: Sensitivity of moist convection forced by boundary layer processes to low-level thermodynamic fields, *Mon. Weather Rev.* **124**(8), 1767–1785 (1996)
- 26.67 T.M. Weckwerth, J.W. Wilson, R.M. Wakimoto: Thermodynamic variability within the convective boundary layer due to horizontal convective rolls, *Mon. Weather Rev.* **124**(5), 769–784 (1996)
- 26.68 T.M. Weckwerth: The effect of small-scale moisture variability on thunderstorm initiation, *Mon. Weather Rev.* **128**(12), 4017–4030 (2000)
- 26.69 W. Feltz, W.L. Smith, R.O. Knuteson, H.E. Revercomb, H.M. Woolf, H.B. Howell: Meteorological applications of temperature and water vapor retrievals from the ground-based atmospheric emitted radiance interferometer (AERI), *J. Appl. Meteorol.* **37**(9), 857–875 (1998)
- 26.70 D.D. Turner, U. Löhnert: Information content and uncertainties in thermodynamic profiles and liquid cloud properties retrieved from the ground-based atmospheric emitted radiance interferometer (AERI), *J. Appl. Meteorol. Climatol.* **53**(3), 752–771 (2014)
- 26.71 J. Cooney: Measurement of atmospheric temperature profiles by Raman backscatter, *J. Appl. Meteorol.* **11**(1), 108–112 (1972)
- 26.72 A. Behrendt: Temperature measurements with lidar. In: *Lidar – Range-Resolved Optical Remote Sensing of the Atmosphere*, Springer Series in Optical Sciences, Vol. 102, ed. by C. Weitkamp (Springer, New York 2005), Chap. 10, pp. 273–305
- 26.73 C.L. Korb, C.Y. Weng: A theoretical study of a two-wavelength lidar technique for the measurement of atmospheric temperature profiles, *J. Appl. Meteorol.* **21**(9), 1346–1355 (1982)
- 26.74 C.L. Korb, G.K. Schwemmer, M. Dombrowski, C.Y. Weng: Atmospheric pressure and temperature profiling using near ir differential absorption lidar. In: *Optical and Laser Remote Sensing*, ed. by D.K. Killinger, A. Mooradian (Springer, Berlin, Heidelberg 1983) pp. 120–127
- 26.75 F. Theopold, J. Bösenberg: Differential absorption lidar measurements of atmospheric temperature profiles: Theory and experiment, *J. Atmos. Ocean. Technol.* **10**(2), 165–179 (1993)
- 26.76 J. Bösenberg: Ground-based differential absorption lidar for water-vapor and temperature profiling: Methodology, *Appl. Opt.* **37**(18), 3845–3860 (1998)
- 26.77 J. Bösenberg: Differential-absorption lidar for water vapor and temperature profiling. In: *Lidar – Range-Resolved Optical Remote Sensing of the Atmosphere*, Springer Series in Optical Sciences, Vol. 102, ed. by C. Weitkamp (Springer, New York 2005), Chap. 8, pp. 213–239
- 26.78 R.A. Stillwell, S.M. Spuler, M. Hayman, K.S. Repasky, C.E. Bunn: Demonstration of a combined differential absorption and high spectral resolution lidar for profiling atmospheric temperature, *Opt. Express* **28**, 71–93 (2020)
- 26.79 C.E. Bunn, K.S. Repasky, M. Hayman, R.A. Stillwell, S.M. Spuler: Perturbative solution to the two-component atmosphere DIAL equation for improving the accuracy of the retrieved absorption coefficient, *Appl. Opt.* **57**(16), 4440–4450 (2018)

Scott M. Spuler

Earth Observing Laboratory
National Center for Atmospheric Research
Boulder, USA
spuler@ucar.edu



Scott Spuler is a Research Engineer in the Earth Observing Laboratory at the National Center for Atmospheric Research. He received MS and PhD degrees in Applied Optics/Engineering Systems from Colorado School of Mines in 1999 and 2001, respectively. His research interests include the development of innovative optical and laser-based instrument systems that can be applied to enhance the understanding of the atmosphere.

Matthew Hayman

Earth Observing Laboratory
National Center for Atmospheric Research
Boulder, USA
mhayman@ucar.edu



Matthew Hayman is an Engineer and Scientist in the Earth Observing Lab at the National Center of Atmospheric Research. He received his PhD in Electrical Engineering and Optics from the University of Colorado at Boulder in 2011. His research focuses on developing optical sensor and signal processing algorithms for environmental sensing applications.



Tammy M. Weckwerth

Earth Observing Laboratory
National Center for Atmospheric Research
Boulder, USA
tammy@ucar.edu

Tammy Weckwerth is a Scientist III in the Earth Observing Laboratory at the National Center for Atmospheric Research. She received a PhD in Atmospheric Sciences from the University of California Los Angeles in 1995. Her scientific research efforts are aimed at using observational data to understand mesoscale convective processes, in particular the initiation and evolution of precipitating convection.

Doppler Wind Lidar

Oliver Reitebuch , R. Michael Hardesty 

Wind lidars use the optical Doppler effect to measure atmospheric wind with high spatial and temporal resolution. In contrast to scalar quantities, such as temperature or humidity, the atmospheric wind is a vector quantity consisting of three components – usually referred to as vertical wind speed, horizontal wind speed, and the horizontal direction. This requires specific techniques for the measurement of each component, taking into account their different temporal and spatial variability in the atmosphere. Principles of wind lidars, including two complementary techniques using coherent and direct-detection approaches and their application for atmospheric research are discussed. Doppler wind lidars offer a wide range of applications from aircraft wake vortex detection and characterization to the measurement of turbulent quantities to resolving mesoscale atmospheric flows, and even global wind profiling from space with the Aeolus mission launched in August 2018.

27.1	Measurement Principles and Parameters	760	27.3.3	Principle of Wind Measurement and Scanning	767
27.2	History	762	27.3.4	Lidar Basics Relevant for Doppler Wind Lidar	768
27.2.1	History of Direct-Detection Wind Lidar	762	27.3.5	Coherent-Detection Doppler Wind Lidar	768
27.2.2	History of Coherent-Detection Wind Lidar	762	27.3.6	Direct-Detection Doppler Wind Lidar ..	772
27.3	Theory	765	27.4	Devices and Systems	773
27.3.1	The Doppler Effect	765	27.4.1	Coherent-Detection Techniques and Systems	773
27.3.2	Spectral Lineshape from Molecular and Particle Backscatter	766	27.4.2	Direct-Detection Techniques and Systems	777
			27.4.3	Comparative Overview of Coherent and Direct Detection	780
			27.5	Specifications	782
			27.6	Quality Control	783
			27.6.1	Calibration and Validation with a Nonmoving Target	783
			27.6.2	Validation by Vertical Pointing Measurements	784
			27.6.3	Quality Control for Line-of-Sight Wind Speeds and Vector Winds	784
			27.7	Maintenance	784
			27.8	Applications	785
			27.8.1	Hazard Detection at Airports	785
			27.8.2	Wind Energy	786
			27.8.3	Gravity Waves in the Stratosphere	789
			27.9	Future Developments	790
			27.10	Further Readings	791
			References		791

This chapter introduces the principles and applications of measuring atmospheric wind speed with lidars (light detection and ranging) based on using the Doppler frequency shift – called Doppler wind lidar (DWL) as the most common approach. Other techniques for measuring wind speeds with lidars as cross-correlation techniques for aerosol and cloud movements or Doppler resonance fluorescence lidar used in the mesosphere are not

covered here. Both coherent and direct-detection DWL principles are discussed based on their physical principle of using spectrally narrow bandwidth aerosol and cloud returns, as well as broad bandwidth molecular returns. Both techniques are discussed with respect to their technical implementation and their specifications. Some applications for DWL are illustrated and potential new technologies and application areas are outlined.

27.1 Measurement Principles and Parameters

Optical remote sensing allows the observations of spatially resolved winds without disturbing the flow for all altitudes of the atmosphere, and, thus, complements conventional in-situ techniques (Chap. 9). Wind observations with lidars are used to study atmospheric flow on a large variety of temporal and spatial scales. Different types of wind lidars allow measurements in different altitude regions of the atmosphere from the atmospheric boundary layer with high aerosol content to the upper troposphere, stratosphere, and even mesosphere with molecules as backscattering targets [27.1, 2]. Optical remote sensing with lidars is a very powerful method for measuring the three-dimensional (3-D) atmospheric wind vector. It is possible to measure the horizontal wind vector as well as the vertical wind component with different viewing geometries. Wind lidars are operated from the ground, balloons, ships, or aircrafts and were deployed for the first time on a satellite platform within the Aeolus mission in 2018 [27.3, 4] (see Chap. 37 for airborne and satellite platforms).

The movement of the air is described by the wind vector $\mathbf{V} = (u, v, w)$, which is composed of three components. Usually, the wind vector is described by a vertical component w (positive for an updraft wind) and two horizontal components u, v . The horizontal wind vector (called *velocity* for a vector quantity) can be either described by the magnitude of the vector M (typically called *speed* for a scalar quantity; $M = \sqrt{u^2 + v^2}$)

and by the wind direction θ (angle between the horizontal wind vector and north; $\theta = \arctan(u/v)$; $\theta = 0^\circ$ for northerly wind, wind from north towards south, $\theta = 90^\circ$ for easterly wind, wind from east to west). Or it is decomposed into the two components along the west–east axis u (zonal wind component, positive if wind is blowing from west towards east, which is a westerly wind) and along the south–north axis v (meridional wind component, which is positive if the wind is blowing from south to north, which is a southerly wind).

The principal measurement from a DWL is the wind speed along the instrument viewing direction LOS (line-of-sight) similar to sodar (sound detection and ranging, Chap. 23) and wind profiler radar (radio detection and ranging, Chap. 31), called LOS wind speed or radial wind speed. The LOS wind speed is the component of the wind vector \mathbf{V} projected onto the pointing direction of the laser beam and the viewing direction of the telescope. In the following, only instruments are considered where both laser and telescope LOS directions are identical – typically called monostatic lidar instruments. By deploying different scanning strategies (Sect. 27.3.3), all components of the wind vector can be derived, which are listed in Table 27.1. Besides the derived LOS wind speeds, also the backscattered intensities, signal-to-noise ratio (SNR), or carrier-to-noise ratio (CNR), are derived from Doppler wind lidars and used for atmospheric scene classification similarly as

Table 27.1 Measured parameters of a Doppler wind lidar

Parameter	Description	Unit	Symbol
LOS speed	Wind speed in direction of the laser line-of-sight (LOS) or radial wind speed	m s^{-1}	v_{LOS}
Wind speed	Magnitude of horizontal wind speed	m s^{-1}	M
Wind direction	Angle for horizontal wind direction with respect to North, where wind is blowing from	$^\circ$	θ
Wind velocity components	Components of the wind vector with zonal wind speed (East–West) u , meridional wind speed (North–South) v , vertical wind speed w (up–down)	m s^{-1}	u, v, w
Signal intensity	Signal intensity of the backscattered signal	arb. u. or dB	I
Signal-to-noise ratio, carrier-to-noise ratio	Ratio of signal intensity (or carrier) to noise intensity for the relevant spectral bandwidth	arb. u. or dB	SNR, CNR

Table 27.2 Derived parameters from DWL measurements

Parameter	Description	Unit	Symbol
Backscatter coefficient	Aerosol and cloud backscatter coefficients	$\text{m}^{-1} \text{sr}^{-1}$	β
Boundary layer height	Height of the atmospheric boundary layer with respect to aerosol mixing or turbulence	m	z_i
Fluctuations of wind component	Fluctuations of the wind components around its mean value	m s^{-1}	u', v', w'
Turbulent quantities	Turbulent energy dissipation rate	$\text{m}^2 \text{s}^{-3}$	ε
	Turbulent kinetic energy	$\text{m}^2 \text{s}^{-2}$	TKE

Table 27.3 Principles of DWL and height range from boundary laser (BL), free troposphere (FT), to stratosphere (ST) and mesosphere (MS)

Type of DWL	Atmospheric backscatter		Altitude range		
	Aerosol, clouds	Molecules	BL	FT	ST/MS
Coherent DWL	×		×	× ^a	
Direct-detection DWL	×	×	×	×	×

^a in the case of clouds or elevated dust layers, e.g., desert dust or volcanic ash.

for backscatter lidars (Chap. 24). Thus, also the vertical extent and boundaries of aerosol and cloud layers, as well as the height of the atmospheric boundary layer are determined from Doppler wind lidars (Table 27.2).

In addition to the mean component of the wind vector, also its turbulent fluctuations around the mean can be derived from DWL measurements with high temporal resolution (Table 27.2). This is mainly the case for turbulent vertical wind fluctuations, where vertical pointing instruments are used. Also, quantities such as the turbulent energy dissipation rates can be determined with a DWL. An excellent review about the measurement and the derivation of turbulent quantities is provided in [27.5] and within a textbook about coherent DWL [27.6].

Through numerous deployments over the past four decades, the efficacy of wind lidars for a variety of atmospheric applications has been demonstrated. Here, only a selection of some references is provided as a first overview:

- Wind energy sector for site assessment, research on turbine wakes, wind turbine control, or power curve verification Chap. 51; [27.7–10] (Sect. 27.8.2)
- Airport surveillance for low-level wind shear and wake vortex detection for a number of airports, e.g., Hong Kong, Frankfurt, and Munich [27.11, 12] (Sect. 27.8.1)
- Aircraft safety and control: wake vortex characterization from ground and aircraft [27.6, 13–15] with applications for clear-air turbulence (CAT) detection and mitigation of gusts and turbulence by active control [27.16, 17]
- Long-range transport, dispersion monitoring, and determination of boundary layer heights [27.18–20]
- Research on atmospheric dynamics with flows in complex terrain, verification of boundary layer parameterization, e.g., recently within the Perdígão field campaign in 2017, where 26 DWL were deployed [27.21, 22], or vertical exchange processes for trace gases [27.23]
- Validation of numerical models from small scales (large eddy simulations), medium scales [27.24], and global scales for numerical weather prediction including assimilation of observations [27.25]

- Routine measurements of wind profiles at meteorological stations [27.26], e.g., German Meteorological Service, Richard-Aßmann-Observatory (DWD RAO) (Chap. 47)
- Research on stratospheric and mesospheric dynamics including gravity wave propagation [27.27, 28] (Sect. 27.8.3)
- Global wind profiling from space for improvement of weather forecasts [27.4, 29].

A DWL determines the wind speed of the air by using the collective motion of a large number of aerosols, cloud particles, and molecules within the air volume as tracers. Different methods are applied for using aerosol and cloud particles as tracers with a coherent-detection DWL and molecules as tracers with a direct-detection DWL. A direct-detection lidar relies on the measurement of the signal intensity or number of photons, whereas a coherent lidar additionally measures the phase and frequency of the backscattered signal. Overviews of DWL principles, techniques, and applications can be found in [27.1, 2, 6, 30–32].

Whereas coherent-detection DWL are applied for wind measurements in the aerosol-rich atmospheric boundary layer and for cloud movements in the boundary layer and troposphere (Table 27.3), direct-detection wind lidars using molecular backscatter allow the determination of wind speeds in the troposphere, stratosphere, and even up to the mesosphere. Thus, the direct-detection approach offers a unique capability to measure higher-altitude winds.

Coherent DWL are commercially available today and can be very compact and reliable, and high temporal resolution and high precision can be achieved, which even allows the determination of vertical winds, turbulent quantities, or aircraft wake vortices. Direct-detection DWL using molecular backscatter are the systems of choice for wind measurements in the upper troposphere and stratosphere but are considered as research instruments, which need qualified lidar experts for development and operation. A more comparative overview of both principles is discussed in Sect. 27.4.

As coherent DWLs rely on the measurement of the spectrally narrowband aerosol and cloud returns, they can, in principle, achieve higher precision for the

same SNR as direct-detection DWL, which rely on the backscatter of broad bandwidth molecular returns. Coherent DWL are usually operated with a pulsed laser source to achieve vertically resolved measurements for longer ranges. However, especially for shorter ranges

(< 500 m) also continuous-wave (CW) laser sources are in use, where the range resolution is achieved by focussing the laser beam for different ranges [27.33]. The principle and setup of coherent DWL are further elaborated on in Sects. 27.3.5 and 27.4.1.

27.2 History

First Doppler wind lidar techniques were pioneered for both direct and coherent-detection methods in the 1960s and early 1970s, shortly after the invention of the laser by *Theodore Maiman* (1927–2007) in 1960 [27.34].

27.2.1 History of Direct-Detection Wind Lidar

The principle of wind measurement with direct-detection Doppler lidar was pioneered by the group of *Giorgio Fiocco* (1931–2012) using a frequency-stabilized argon-ion laser emitting at 488 nm and a spherical Fabry–Pérot interferometer as the spectral analyzer [27.35]. These first atmospheric wind lidar observations (the authors used the term *optical radar*) were performed in 1971 at the European Space Research Institute (ESRIN) in Frascati, Italy. Today, ESRIN is part of the European Space Agency (ESA) and is responsible for the operational phase of the first wind lidar in space, *Aeolus*, which was successfully launched in August 2018. Measuring global atmospheric winds from space was initially proposed in the 1970s and its performance simulated for coherent detection at 10.6 μm using CO_2 lasers by *Milton Huffaker* (1934–2019) [27.36, 37] and for the direct-detection technique by *Vincent Abreu* [27.38] using frequency-doubled Nd:YAG lasers at 532 nm.

Direct-detection Doppler lidar make use of one or more narrowband filters and determine the Doppler frequency shift from the transmitted signal strength through this filter, called the *edge* technique, or from the radial-angular distribution or spatial movement of the interference patterns (*fringes*) of an interferometer, called the *fringe imaging* technique or interferometric techniques.

The commonly used double-edge technique – also applied on *Aeolus* – using two filters was pioneered by *Marie-Lise Chanin* in 1989 [27.39, 40] for stratospheric winds at the observatory of Haute-Provence, France, using the broadband molecular return with a laser wavelength of 532 nm. In parallel, it was exploited for tropospheric winds using laser wavelengths of 1064 and 532 nm for the narrowband aerosol return and 355 nm for the molecular return by *Laurence Korb* [27.41], and *Bruce Gentry* [27.42], respectively, at NASA. The first

airborne direct-detection Doppler lidar was developed by *Oliver Reitebuch* and his coworkers at DLR [27.43] as the airborne prototype for the satellite wind lidar on *Aeolus*. In 1999, the European Space Agency (ESA) decided to establish a DWL mission named Atmospheric Dynamics Mission ADM-*Aeolus* (nowadays called *Aeolus*) to fill the gap in the global observing system [27.4, 44], which is based on a direct-detection wind lidar operating with an ultraviolet wavelength of 355 nm [27.3].

The use of broadband molecular Rayleigh returns with a single Fabry–Pérot interferometer as a spectral filter to measure winds up to 65 km was first applied at the Arecibo Observatory, Puerto Rico, in 1990 by *Craig Tepley* [27.45, 46]. Another approach using only one filter, called the single-edge technique, can be realized by using iodine molecular absorption lines as narrowband filters for both molecular and aerosol backscatter at 532 nm. This technique was pioneered in the 1990s by *Jonathan Friedman* and *Craig Tepley* at the observatory Arecibo for stratospheric winds [27.47], and by *Zhishen Liu* for tropospheric winds [27.48]. These techniques were applied to measure sea-surface winds during the 2008 Olympic sailing games in Qingdao, China [27.49].

Other techniques for direct-detection DWL were also demonstrated in the 1990's. The fringe imaging technique was first proposed and realized by the group of *Vincent Abreu* [27.50, 51]. The use of the two-beam Mach–Zehnder interferometers as spectral analyzer was proposed by *Takao Kobayashi* [27.52] and in parallel by *Ronald Schwiesow* [27.53] for the narrowband aerosol signal and for the broadband molecular signal by *Didier Bruneau* [27.54, 55].

27.2.2 History of Coherent-Detection Wind Lidar

Prior to the development of the laser, coherent, or heterodyne, detection was utilized in receivers for radio and microwave systems. However, very soon after the invention of the laser, the potential application of optical heterodyning to estimate the spectral characteristics of optical radiation was suggested by *Theodore Forrester* (1918–1987) [27.56], who noted that:

the advent of oscillators generating visible or near infrared radiation with spectral widths and angular spreads much smaller than available from ordinary light sources makes possible the application of radio frequency receiver technology to the field of optics ...

Although the initial investigations of optical heterodyne detection involved the application of a single laser source and specular reflectors to generate the signal and local oscillator beams, *Gordon Gould* (1920–2005) [27.57] showed that the technique could also be applied to detection of radiation scattered by a diffuse reflector. Incorporation of coherent detection to observe the movement of particles suspended in air was reported by *Milton Huffaker* [27.58], who employed a continuous-wave (CW) argon laser source and a homodyne receiver to measure the mean velocity and velocity fluctuations of aerosol particles introduced into a wind tunnel. Subsequently, a CW coherent homodyne lidar that incorporated a 25 W CW carbon dioxide CO₂ laser transmitter operating at 10.6 μm was demonstrated for remote atmospheric wind measurements and was shown to compare well with corresponding observations from a cup anemometer [27.59]. From the early 1970s through to the 1980s, CO₂ lasers operating in the thermal infrared spectral region were utilized in most coherent lidar wind systems. Compared to visible wavelength sources, CO₂ lasers possess several advantages over visible wavelength sources, including a greater laser power conversion efficiency and frequency stability, reduced impact on performance from atmospheric turbulence, eye safety, and a superior capability of penetrating haze and fog.

During the 1970s, coherent lidars employing designs similar to the CW technique demonstrated in [27.59] were applied to investigate air motions associated with several dynamic phenomena, including hydrometeors [27.60] and dust devils [27.61]. Demonstrating the potential portability of coherent lidars, a lidar instrument was deployed on a small aircraft for measurements of wind velocities in waterspouts [27.62].

Although CW coherent lidar provides excellent range resolution, aperture size limitations limit the practical range of such systems to a few tens to a few hundreds of meters, which is insufficient to investigate many atmospheric phenomena. To provide measurements at more extended ranges, the development of pulsed coherent lidar systems began in the late 1970s, aided by the development of pulsed coherent laser transmitters and digital signal processing capabilities. Previously, CW lidar systems utilized analogue spectrum analyzers to extract the Doppler signal in the

return. In an early pulsed lidar developed by NASA, the 2 μs-long laser pulses were generated by passing the output of a chopped continuous wave CO₂ laser through a series of optical amplifiers to produce pulses with energies on the order of 5 mJ [27.63]. The atmospheric aerosol-backscattered signals were digitized and range-gated to provide measurements with 330-m-range resolution up to ranges of up to 30 km [27.64]. The NASA system, which was deployed on a Convair 990 aircraft, demonstrated the capability of pulsed lidars to map wind fields under uniform wind field conditions, as well as in the vicinity of thunderstorms and around cumulus clouds.

During the late 1970s, the potential capability to deploy a coherent Doppler lidar in space to measure wind profiles over the entire globe began to attract interest as a way to measure atmospheric winds over poorly sampled regions of the earth. A NOAA study developed concepts, suggested a notional design, and analyzed simulated performance for a proposed space-based lidar system based on a pulsed CO₂ laser [27.65]. Although the results of this study indicated that it was feasible for such a system to provide global winds, the development of frequency-stable high-energy (on the order of 10 J) pulsed lasers suitable for deployment in space was deemed necessary to achieve the performance identified in the study. Also required was an improved understanding of the structure of tropospheric atmospheric backscatter at CO₂ laser wavelengths. To address these issues, in the early 1980s NOAA developed a pulsed lidar system built around a pulsed transverse-excited, atmospheric pressure (TEA) laser that generated 100 mJ pulses at 10.6 μm. Over the next several years, the NOAA system, which was mounted in a mobile trailer, was operated frequently in Boulder, Colorado, and at a number of remote locations to investigate the performance characteristics of TEA Doppler lidars, obtain better information on atmospheric backscatter [27.66], and demonstrate the capability of Doppler lidars to improve the understanding and characterization of atmospheric phenomena. In 1985, the 100 mJ lidar transmitter was upgraded to produce pulses with 2 J of energy at up to 30 Hz pulse repetition rate [27.67], extending the system range to beyond 30 km under favorable aerosol loading. The transportable NOAA lidar was particularly effective in mapping out heterogeneous flows with length scales of several km, such as flows in complex terrain [27.68], severe downslope windstorms in the lee of the Rockies [27.69], and land-sea breeze circulations near Monterey, California [27.70]. Although the system was quite large, it was modified for deployment on a NASA DC-8 to enable both the aerosol characterization and the study of specific phenomena not easily investigated with a ground-based instrument [27.71].

Following the airborne deployments, the NOAA pulsed CO₂ lidar was returned to its container and utilized for field studies intermittently throughout the 1990s, until it was retired following the Vertical Transport and Mixing air quality study in Salt Lake Valley in 2000 [27.72].

During the late 1980s, the development of frequency-stable, coherent solid-state laser transmitters marked a significant advancement in the evolution of coherent lidar for wind measurements. Although the CO₂ laser transmitters used throughout the 1970s and early 1980s were attractive for Doppler lidar applications because of their relatively high gain, versatility, and operation at longer wavelengths where extinction and turbulence are less detrimental, solid-state lasers offered long-term reliability, operation at shorter wavelengths where aerosol backscatter coefficients are typically higher and where room temperature detectors can be employed in the lidar receiver, and the capability of inclusion in compact lidar systems. The first solid-state coherent lidar [27.73] incorporated a laser-diode-pumped Nd:YAG monolithic ring laser as a master oscillator and a flash-lamp-pumped zigzag slab amplifier to produce pulses with a peak power of 2.3 kW. A similar system with pulse energies of 5 mJ [27.74] produced wind-profile measurements to ranges of 3.75 km. Because eye safety issues severely limit lidar operation at 1.06 μm , an important step forward was the demonstration of a coherent lidar employing a Tm,Ho:YAG laser source at 2.1 μm [27.75]. This system transmitted pulses with an energy of about 22 mJ and measured winds in the atmosphere to horizontal ranges beyond 20 km.

Although some CO₂ systems were still operating in the late 1990s and early 2000s [27.76, 77], by this time, the community was well on the way to embracing solid-state sources in coherent lidars for wind measurements. Reliable instruments operating at wavelengths near 2 μm with pulse energies of a few mJ and pulse rates of several hundred Hz, which are capable of unattended, continuous observations to ranges of several km, were developed, e.g., [27.78] and deployed for a range of applications, including characterization of shear flow instability near the surface in the nighttime stable boundary layer [27.79], ship-based observations of the marine boundary layer winds [27.80], and wind shear detection at Hong Kong International Airport [27.11]. A significant advantage of this class of Doppler lidar instruments was the stability and narrow bandwidth of the laser pulse, achieved through injection seeding of a diode-pumped, solid-state power oscillator. This facilitates multipulse accumulation in the receiver to extract the Doppler shift from weak backscattered signals with low carrier-to-noise ratios [27.81]. The Hong Kong airport lidar deployment demonstrated that

a 2 mJ per pulse lidar system could be deployed for unattended operational use on a long-term basis to warn pilots of potentially hazardous wind shear conditions in the airport vicinity. Even though the pulse energy was significantly lower than that in the system described in [27.75], a high pulse rate and efficient signal processing enabled measurements in the range of several km.

The evolution of coherent wind lidars continued in the 2000s with the demonstration of all-fiber systems [27.82] producing tens of μJ of energy at pulse rates of 10 kHz or more. A common version of these low-energy, high-pulse repetition frequency (PRF) systems includes a master-oscillator, power-amplifier configuration with an erbium-doped fiber amplifier producing radiation around 1.55 μm wavelength for the transmitter. Although such systems were limited to a few km of range, the all-fiber design and general use of commercial off-the-shelf parts developed for the telecommunications industry significantly lowered the cost of constructing and operating a Doppler lidar, spawning the formation of private companies focused on producing and selling such instruments to a broader base of academic, government, and industrial users [27.83, 84].

Over the past two decades, the application of Doppler lidar in the wind-power industry has been widespread. Several significant issues associated with wind power are well matched to coherent lidar capabilities, including the characterization of winds to determine the suitability of proposed sites, the measurement of wind-turbine power curves, the warning in advance of wind characteristics such as sudden increases in wind speed and turbulence that can cause damage to turbine blades, the adjustment of wind-turbine blade pitch to mitigate blade fatigue, and the investigation of wake effects on wind properties downwind of large turbines. The synergism between wind energy needs and Doppler lidar capabilities has provided a significant market for small coherent lidars and has contributed substantially to the commercial viability of private companies producing and selling wind lidar systems.

Although much of the development of coherent lidars over the past three decades has been associated with the evolution and variations of pulsed systems, CW instruments also are being deployed. A system operating at 1.55 μm that provides short-range, high-range resolution, high-precision observations, was demonstrated in the early 2000s [27.85]. Instruments incorporating similar designs have found a useful niche to measure winds over scales equivalent to wind turbine rotor diameters. A significant advantage of CW systems, which are typically less expensive than pulsed instruments, in wind energy applications is the capability of measuring at very short ranges not accessible

using monostatic pulsed lidars. Continuous-wave lidar systems have been applied to measure winds and turbulence upwind of turbines [27.86]; instruments mounted at the hub of a spinning wind turbine have been investigated for observing approaching wind and turbulence at ranges and time scales suitable for active control of turbine blades, e.g., [27.87].

Currently, depending on the application, both continuous-wave and pulsed systems are being applied in observational campaigns. Pulsed systems provide maximum ranges up to several km but are limited in range

resolution, while CW instruments provide very high range resolution (a few m) at short ranges, but are limited to ranges of 100 m or so. With respect to the operating wavelength, new coherent lidar development seems to be focused primarily on systems operating in the 1.5 μm wavelength region. Some legacy systems developed earlier at 2 μm , including a high-power Doppler wind lidar designed primarily for airborne deployment but available for ground-based observations [27.88], continue to exist, but a clear trend toward shorter wavelengths in new systems is apparent.

27.3 Theory

This section introduces the physical basis for measuring winds by the Doppler effect and discusses the difference for the spectral lineshape of molecular and aerosol backscatter. Furthermore, the principle of measuring the wind vector and the foundations for coherent and direct-detection DWL are discussed.

27.3.1 The Doppler Effect

Most wind lidars rely on the Doppler effect, which was first described by the Austrian physicist *Christian Doppler* (1803–1853) in 1842 [27.89]. The Doppler effect can be observed for acoustic waves, which is used in remote sensing with a Doppler sodar (Chap. 23), and for electromagnetic waves used for Doppler radar (Chap. 31) and Doppler lidar. It describes the change in frequency (or wavelength) that is present when the source of the wave and the observer are in relative motion to each other. The correspondence of the frequency f_0 and the wavelength λ_0 of an electromagnetic wave is obtained using the speed of light c ($c = 2.99792458 \times 10^8 \text{ m s}^{-1}$ in vacuum)

$$f_0 = \frac{c}{\lambda_0}. \quad (27.1)$$

For a Doppler lidar (and also for any other Doppler remote sensing instrument) the Doppler effect occurs twice. First, when the light wave from the emitting laser

source with a frequency of f_0 is perceived by the moving, scattering particle (aerosol, cloud, and molecule) with f_1 ; the second Doppler effect occurs when the moving particle re-emits the scattered wave, which is perceived by the lidar receiver with f_2 . The Doppler frequency shift Δf or wavelength shift $\Delta \lambda$ is obtained from

$$\Delta f = f_2 - f_0 = 2f_0 \frac{v}{c} = 2 \frac{v}{\lambda_0}, \quad (27.2)$$

$$\Delta \lambda = \lambda_2 - \lambda_0 = -2\lambda_0 \frac{v}{c} = -2 \frac{v}{f_0}. \quad (27.3)$$

With the above definition of the Doppler frequency shift sign, the LOS wind speed is defined such that positive LOS wind speeds describe a movement towards the lidar instrument (*blue shift*, because the wavelength is shifted towards blue colors) and negative LOS wind speeds, when the wind is blowing away (*red shift*). The opposite definition for the sign of the LOS wind speed is also in use; then the above equations need to be multiplied by -1 . Due to this ambiguity in the sign definition, it is important to define the direction of the positive or negative LOS wind speeds.

The relative Doppler shift expressed as $\Delta f/f_0$ or $\Delta \lambda/\lambda_0$ is on the order of 10^{-7} – 10^{-8} for typical atmospheric wind speeds. It is very demanding to detect such small changes in the frequency or wavelength, which imposes high challenges for the laser sources and optical receivers used for a DWL. For illustration purposes, the Doppler shifts for typical wavelengths of a DWL are provided in Table 27.4. A 1 m s^{-1} LOS wind speed would change the wavelength from 2.02 to 2.020000135 μm by only 13.5 fm (1 fm = 10^{-15} m). These wavelength differences are much smaller compared to the size of the hydrogen atom ($\varnothing \approx 50 \text{ pm}$) and are comparable to the size of the hydrogen nucleus ($\varnothing \approx 1.2 \text{ fm}$), especially for wavelengths of 355 nm.

Table 27.4 Doppler shift for a LOS speed of 1 m s^{-1} for typical wavelengths of a DWL

λ_0 (μm)	f_0 (THz)	$\Delta \lambda$ (fm)	Δf (MHz)
0.355	844	2.37	5.63
1.55	193	10.3	1.29
2.02	148	13.5	0.99
10.6	28.3	70.7	0.189

27.3.2 Spectral Lineshape from Molecular and Particle Backscatter

The collective, mean movement of all molecules, aerosol, and cloud particles within a certain atmospheric volume is referred to as wind. This is superimposed by the random, thermal motion of the molecules and particles (*thermal Brownian motion*) and causes so-called Doppler broadening. This motion can be described by the Maxwell–Boltzmann velocity distribution, which is dependent on the atmospheric temperature T and the mass m of a single molecule (or particle). The mean velocity of the air molecules (a mixture of gases with mean mass $m = 4.79 \times 10^{-26}$ kg) is quite high, with a value of 459 m s^{-1} for a temperature of 15°C . If only one component in the LOS direction of the velocity distribution is considered, then it can be described by a Gaussian distribution with a standard deviation in velocity space σ_v or wavelength space σ_λ after applying the Doppler shift equation

$$\sigma_v = \sqrt{\frac{kT}{m}}, \quad (27.4)$$

$$\sigma_\lambda = \frac{2\lambda_0}{c} \sqrt{\frac{kT}{m}}, \quad (27.5)$$

with the Boltzmann constant k ($k = 1.380649 \times 10^{-23} \text{ J K}^{-1}$). The Gaussian approximation is only valid for dilute gases. For typical atmospheric densities, an additional Brillouin scattering effect on moving pressure fluctuations has to be considered, which is described by Rayleigh–Brillouin scattering [27.90–93]. The Gaussian velocity distribution is quite broad for air molecules with $\sigma_v = 288 \text{ m s}^{-1}$ and a full-width at half-

maximum (FWHM) of 678 m s^{-1} for 15°C (FWHM = $2\sqrt{2 \ln(2)}\sigma = 2.355\sigma$ for a Gaussian distribution with unit standard deviation). For aerosol and cloud particles, the width of the velocity distribution is several orders of magnitude smaller due to the larger mass of aerosols and cloud particles. The assumptions of typical particle radii of $0.1\text{--}1 \mu\text{m}$, which are of sizes relevant for Mie scattering at laser wavelengths, and of spherical water particles (density of 10^3 kg m^{-3}) lead to typical masses of 4.2×10^{-18} to 4.2×10^{-15} kg resulting in velocity widths σ_v of $30\text{--}1 \text{ mm s}^{-1}$. Thus, Doppler broadening is a factor of $10^4\text{--}10^6$ smaller for aerosol particles compared to molecules and can be neglected compared to other factors, which influence the line width from aerosol returns, mainly turbulent broadening and the line width of the emitted laser. This results in typical line widths of a few up to 10 m s^{-1} for the narrowband Mie return independent of the laser wavelength chosen, which is still two orders of magnitude smaller than the broad bandwidth molecular returns.

The mean of the Gaussian velocity distribution is given by the mean, collective movement of all molecules, which is referred to as the LOS wind speed. For the case that a laser emits a wavelength λ_0 , the backscattered light from molecules is spectrally broadly distributed, which is illustrated in Fig. 27.1, where the distribution of Doppler shifts is shown for a typical DWL wavelength of 355 nm . A broad bandwidth spectrum is obtained from molecules, whereas a narrow bandwidth spectrum is obtained from aerosol and cloud particles. In the case of a mean wind speed of the air volume, both the aerosol and the molecular spectrum are shifted in parallel along the wavelength axis.

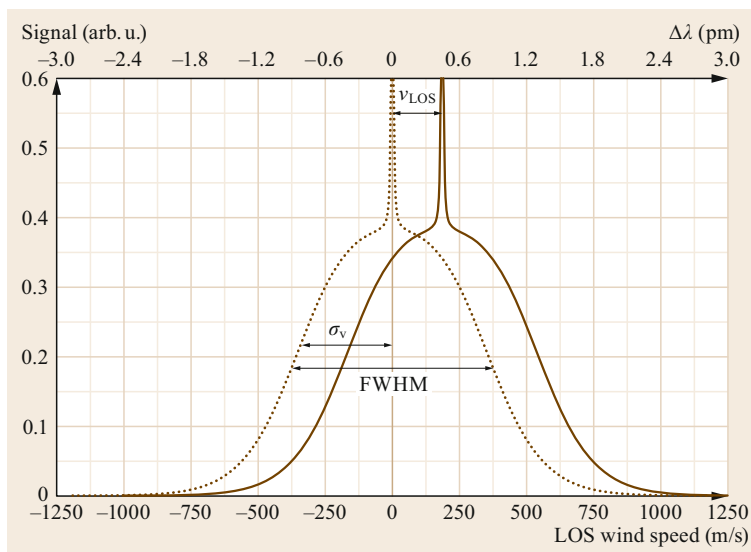


Fig. 27.1 Spectral distribution of LOS wind speed v_{LOS} in m s^{-1} of a broad bandwidth molecular and small bandwidth aerosol signal; corresponding Doppler wavelength shifts in pm for an emitted wavelength of $\lambda_0 = 355 \text{ nm}$ (1 pm equivalent to 422 m s^{-1}), standard deviation σ_v and FWHM are indicated; one spectrum (dotted lines) is shown for a mean LOS wind speed of 0 m s^{-1} , while the other spectrum (bold line) is shown for a 180 m s^{-1} LOS wind speed (equivalent to a Doppler shift of 0.44 pm) (after [27.1])

27.3.3 Principle of Wind Measurement and Scanning

DWL instruments determine the component of the wind vector, which is projected onto the laser beam propagation direction – the so-called LOS with its unit pointing vector \mathbf{D} . The vector \mathbf{D} can be described by the zenith angle α , between the LOS direction and the zenith (for ground DWL, often also the elevation angle ($90^\circ - \alpha$) is used) or nadir (for airborne and spaceborne DWL) and the azimuth angle β between the LOS direction and the north direction in the horizontal plane. This LOS wind speed (or radial wind speed) component v_{LOS} , or v for short (in units of m s^{-1}) is obtained by the projection of the wind vector \mathbf{V} on the LOS direction \mathbf{D}

$$\begin{aligned} v_{\text{LOS}} &= \mathbf{D} \cdot \mathbf{V} \\ &= \sin(\alpha) \sin(\beta)u \\ &\quad + \sin(\alpha) \cos(\beta)v + \cos(\alpha)w, \end{aligned} \quad (27.6)$$

$$v_{\text{LOS}} = \sin(\alpha) V_{\text{h},\parallel} + \cos(\alpha)w. \quad (27.7)$$

When only the horizontal wind speed $M = V_{\text{h},\parallel}$ in the plane of the LOS direction is considered, then v_{LOS} is determined by the off-nadir or off-zenith angle α . Thus, for a measurement of the vertical wind w and its fluctuations, the laser beam has to be directed vertically ($\alpha = 0^\circ$), whereas for the horizontal wind vector, a minimum of two, preferably orthogonal, LOS directions tilted towards the horizontal plane with an angle of α is used. If the LOS direction and the wind vector are perpendicular, then no LOS wind speed is observed. Depending on the pointing direction \mathbf{D} towards zenith from the ground or nadir from space, the sign of the above equations has to be adapted to be consistent with the meteorological definition of the sign for u , v , w , and the sign definition for v_{LOS} in the Doppler shift equations.

The pointing of the laser beam and the receiving telescope is achieved via a combination of several telescopes or an optomechanical scanning device usually composed of two reflecting mirrors or prisms, which can be moved independently and, thus, different scanning patterns are achieved, depending on the application. The scanning device is used to steer the laser beam towards different zenith α and azimuth β angles. For the measurement of the horizontal wind vector the Doppler beam swinging (DBS) method and the velocity azimuth display (VAD) scan techniques are used [27.94, 95]. Both techniques rely on the assumption that the horizontal wind speed is homogenous over the atmospheric volume, which is covered by the scan, and does not vary temporally during the scanning duration. This assumption on homogeneity needs to be verified within the retrieval algorithms, e.g., using cloud

screening for partial cloud coverage or screening on large vertical wind components for some LOS directions.

Doppler beam swinging (DBS): for the determination of the three components of the wind vector, the LOS wind speed needs to be measured in at least three independent, noncollinear directions. Usually up to five directions are chosen for the DBS technique. Here, the beam is pointed with constant zenith angle in four different azimuth directions, which are separated by 90° and, thus, cover four azimuth directions or even the four cardinal directions. In addition, also a fifth vertical pointing direction can be applied. As every other beam is separated by 180° , the difference and the sum of the LOS wind components V_{LOS} are used to derive horizontal and vertical wind speed and directions. The chosen zenith angles are typically between 15° and 30° .

Velocity azimuth display (VAD): here, the beam is pointed with a constant zenith angle, but varying azimuth angle, with a conical scanning pattern covering azimuth angles from 0 to 360° . This is either achieved by continuously steering the beam in different azimuth directions or by step-and-stare scans, where the laser beam is stepped in small angular increments (e.g., $10^\circ - 20^\circ$). Here, the horizontal and vertical wind components are retrieved by least-squares fitting a sinusoidal function to the measured V_{LOS} components, where the phase and the amplitude of the sinus function are related to the horizontal wind direction and speed, respectively. The constant offset from the sinus function from 0 m s^{-1} is related to the mean vertical wind speed over the scanning volume.

Two other principle scanning techniques are applied to sample the atmospheric volume with either high spatial resolution in height for a given direction or horizontally for a given zenith angle.

Range height indicator (RHI): here, the azimuth direction is kept constant, and the zenith angle is varied from 0 to 90° (or even to 180°), which allows sampling of a vertical curtain through the atmosphere.

Plan position indicator (PPI): similarly as for the VAD scan, the azimuth angle is varied for constant zenith angles. In addition to the classical VAD scan, different conical scans using different zenith angles are applied for a PPI.

The limitations of sensing the 3-D wind vector by pointing to different spatial LOS directions for different time periods is obvious. Assumptions about spatial homogeneity and temporal stationarity have to be made, which limits the derivation of turbulent quantities. To overcome these limitations the LOS beams from several DWL instruments can be pointed towards one volume, which is referred to as multiple Doppler techniques [27.19] or virtual towers [27.96]. Significant

progress was achieved with this approach in the past decade due to the widespread use of commercial coherent DWL instruments [27.22, 97], the synchronization of the laser beam pointing of several instruments and analysis techniques for wind retrievals [27.98]. Multiple Doppler techniques allow high temporal sampling of turbulent wind fluctuations [27.99] and resolving structures with high spatial resolution, e.g., wind rotor wakes [27.100] or mountain rotors [27.101]. The use of multiple DWL instruments combined with multiple Doppler techniques enables highly spatial and temporally resolved observations of the atmospheric flow in complex terrain to improve and validate high-resolution numerical models [27.21, 22].

27.3.4 Lidar Basics Relevant for Doppler Wind Lidar

The theory of interaction of laser light with atmospheric constituents as aerosol and cloud particles and molecules is discussed in Chap. 24 for backscatter lidars. This includes Mie scattering on particles (aerosol, clouds) and Rayleigh scattering on molecules, particle and molecular extinction, and absorption by molecules. The received power or energy from the backscattering of laser light in the atmosphere as a function of range R is described by the lidar equation (Chap. 24), which depends on both instrument parameters (laser energy or power, telescope area, instrument efficiency, range gate resolution ΔR) and atmospheric parameters (altitude-dependent backscatter and extinction coefficient).

The range of the atmospheric volume R is determined by the round-trip travel time t of the laser pulse, whereas the range resolution is determined by the temporal resolution T

$$R = \frac{ct}{2}, \quad (27.8)$$

$$\Delta R = \frac{cT}{2}. \quad (27.9)$$

In order to obtain the altitude H of the atmospheric return or the altitude resolution ΔH , the range R or range resolution ΔR needs to be multiplied by the cosine of the elevation angle or sine of the zenith angle, due to the non-zenith pointing for most scanning modes of a DWL.

The range resolution ΔR is usually referred to as the difference of the centers of successive range gates. The resolution T is usually determined by the applied time-gating within the retrieval algorithms, where a number of n digitized values are processed for the information from one range gate. For typical backscatter or differential-absorption lidars (DIAL), this time T is significantly larger than the typical laser pulse length τ

Table 27.5 Range resolution as a function of range gate time for typical laser pulse lengths

$T = \tau$ (ns)	ΔR (m)	Application
5, 10, 20, 30	0.75, 1.5, 3.0, 4.5	Backscatter lidar, DIAL, direct-detection DWL
50, 100, 200, 500	7.5, 15, 30, 75	Coherent DWL

(from several ns to 10–20 ns often determined by the FWHM of the temporal pulse shape). This is not the case for DWL, especially for coherent DWL, where considerably longer pulse lengths are applied (from several 100 ns to μ s). Coherent DWL rely on the spectral narrowband return from aerosol and clouds. The overall spectral width of the return is determined from the convolution of the laser pulse spectral width with the bandwidth of the atmospheric return. Thus, it is necessary for coherent DWL to transmit spectrally narrowband laser lines. In order to achieve this, long pulses are required, because the spectral width of a laser pulse is inversely proportional to its length. Thus, the physical range resolution for DWL is determined by the laser pulse length $T = \tau$. Typical examples of laser pulse lengths and range resolutions are provided in Table 27.5. In coherent lidar systems, the data sampling window for a single range gate is often matched to the pulse length. Because the pulse travels in space during this sampling interval, the range weighting function, given uniform weighting for each sample, has the shape of a triangle extending plus and minus $c\tau/2$ m from the center of the range gate. Therefore, ΔR in Table 27.5 represents the range gate as specified by its half power points. For direct-detection DWL, which derive wind speeds from molecular Rayleigh backscattering, the requirements on the spectral width of the laser pulse are not as strict as for coherent DWL, as the spectral width of the molecular return is significantly larger in any case. Thus, an additional broadening by the laser pulse width is not considered as a significant contributor to the overall spectral width, and shorter laser pulses can be used.

27.3.5 Coherent-Detection Doppler Wind Lidar

The fundamentals of coherent DWL are based on heterodyne techniques developed for radar during the first part of the twentieth century. Figure 27.2 shows a simplified block diagram of a heterodyne receiver. The atmosphere is irradiated by energy from a frequency-stable, single-longitudinal mode, narrowband laser transmitter typically operating in the thermal or near-infrared spectral region at wavelengths $\gtrsim 1.5 \mu\text{m}$, where eye safety issues are less restrictive. A portion of the

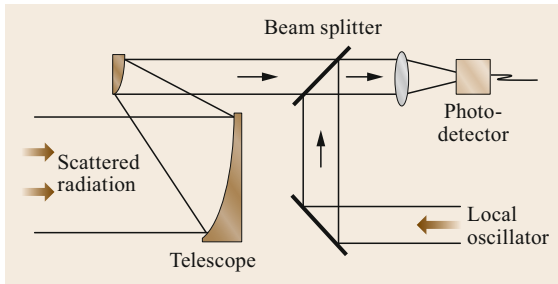


Fig. 27.2 Simplified block diagram of a coherent DWL receiver

energy is scattered back to the receiver by aerosol particles, where it is collected by a telescope and mixed on a photodetector with the field from a local oscillator (LO) laser at the same wavelength as the transmitted signal (homodyne detection) or slightly offset (heterodyne detection). The photodetector converts the resulting optical beat signal to a radio-frequency photocurrent, which frequency is equivalent to the frequency difference between the laser transmitter and the local oscillator laser, plus or minus the Doppler shift resulting from movement of the scatterers in the radial direction. The photocurrent signal is then processed to determine the Doppler shift. Although analogue signal processors, such as filter banks or surface acoustic wave devices, were used during the early years of Doppler lidar, processing today is primarily digital, where the signal from the photodetector is sampled by an analogue-to-digital converter and then analyzed using digital signal processing techniques.

A brief description of the theory of the coherent wind lidar is provided here to illustrate design issues and performance characteristics of coherent systems. For a more detailed theoretical discussion, the reader is directed to [27.31].

The fundamental building blocks of a coherent lidar are the laser transmitter, transmitting optics to direct the laser energy into the atmosphere to collect the backscattered radiation and the heterodyne receiver. As will be shown, coherent lidars achieve best performance when the laser transmitter is single frequency or very narrowband. The transmitted energy, which can be either continuous-wave or pulsed, propagates into the atmosphere, where a portion is scattered back to the lidar by atmospheric aerosols and molecules. Although coherent lidars can, in principle, detect both aerosol and molecular-backscattered radiation, the systems are highly sensitive to aerosol scatter, where spectral broadening of the scattered signal, resulting from the turbulent motions of the aerosol particles irradiated by the beam, is quite small, typically equivalent to a few m s^{-1} . In contrast, the molecular scattered signal band-

width is due to the thermal motions of the particles and is on the order of 300 m s^{-1} . Because the performance of spectral frequency estimation techniques used in coherent receivers improves as the signal bandwidth decreases, coherent wind lidars are primarily used to measure winds based on scatter from aerosol particles.

The radiation scattered by the ensemble of aerosol particles irradiated by the transmitted pulse and collected at the receiver is the superposition of the fields scattered by each particle within the scattering volume illuminated by the transmitted pulse. Because the particles are randomly distributed, and move relatively to each other due to turbulent motions, the field in the receiver plane is represented by a speckle or interference pattern with areas of spatially-correlated amplitude and phase that vary randomly in time and space as a function of the relative motion of the scatterers. Efficient coherent lidar systems are designed such that the backscattered optical field across the receiver aperture is correlated over a region corresponding to the area of the aperture, i.e., a single speckle is roughly the size of the receiver aperture. The backscattered optical signal is mixed with the LO field and focused on the detector. Following [27.31], we can represent the complex optical field resulting from backscattering of the transmitted energy at a point on the detector as

$$U_s(x, y, t) = A_s(x, y, t) \exp(i2\pi ft + i\phi_s(x, y, t)), \quad (27.10)$$

where A_s represents the random, time-varying (t) amplitude of the resultant field at a point (x, y) on the detector, and $\phi(x, y)$ is the random, time-varying phase, f is the frequency ($= c/\lambda$), and $i = \sqrt{-1}$. The wind information in the optical field U_s resulting from the superposition of radiation scattered by each of the scatterers is contained in the time-varying amplitude and phase terms.

Similarly, the local oscillator field at a point (x, y) on the detector is

$$U_L(x, y, t) = A_L(x, y, t) \times \exp(i2\pi(f + \Delta f_L)t + i\phi_L(x, y, t)), \quad (27.11)$$

where Δf is the frequency offset between the transmitter laser and the local oscillator laser. The total field is the sum of the signal and LO fields

$$U = U_s + U_L. \quad (27.12)$$

The photodetector produces a current proportional to the irradiance, which at a point on the detector is

$$I(x, y, t) = |U(x, y, t)|^2. \quad (27.13)$$

For photovoltaic detectors used in contemporary wind lidars, the total photocurrent produced by the spatially integrated irradiance across the detector is

$$i(t) = \iint R(x, y)I(x, y, t)dx dy, \quad (27.14)$$

where

$$R(x, y) = \frac{e\eta_q(x, y)}{hf} \quad (27.15)$$

is the detector responsivity in amperes/watt, $e = 1.602 \times 10^{-19}$ C is the electron charge, and η_q (electrons/photons) is the detector quantum efficiency.

The spatially and temporally varying irradiance has two direct current baseband components: a local oscillator irradiance term and a signal irradiance term, plus a radio frequency (RF) irradiance term resulting from the interference between the backscattered and LO fields. If, for simplicity, spatial variations in the detector response are ignored and complete coherence of the signal and LO fields across the detector is assumed, the heterodyne photocurrent produced by the RF irradiance, which carries the Doppler, is

$$i_H(t) \propto \frac{2e\eta}{hf} \left(\sqrt{I_s(t)I_L(t)} \cos(2\pi\Delta\nu t + \Delta\phi(t)) + I_s + I_L \right), \quad (27.16)$$

where the first term in (27.16) is the time-varying RF heterodyne signal that carries the Doppler signal information, and the second and third terms are baseband signals that are removed by high-pass filtering. Although the DC components of the photocurrent are removed before processing, they still contribute to the total noise in the RF signal current. In a well-designed coherent system, the local oscillator irradiance I_L is much larger than the backscattered signal irradiance I_s , such that the local oscillator shot noise, produced by the random generation of local oscillator-induced photoelectrons, dominates shot noise from both the backscattered signal and heterodyne irradiance terms.

In order to compute the mean Doppler shift in the backscattered signal relative to the transmitted signal frequency, analysis of the heterodyne signal term in (27.16) must be performed. Although some early versions of coherent lidars incorporated analog processing techniques, such as spectrum analyzers, processing in current lidar systems is generally done digitally, taking advantage of the high bandwidth of analog digital converters and high-speed digital processors available today. Because the signal is formed from the superposition of returns from a large number of aerosol particles with random position and motion relative to each other, the heterodyne signal for aerosol atmospheric backscatter takes the form

of a narrowband Gaussian random process with a spectral bandwidth defined primarily by the distribution of velocities within the pulse volume and the spectral characteristics of the transmitted pulse. Figure 27.3 shows the mean power spectra of atmospheric returns from the ≈ 7 km range produced by a low pulse energy, a high pulse-repetition rate coherent Doppler lidar developed at NOAA in Boulder, CO. The spectra are computed by Fourier transformation of the coherent lidar returns from a given range gate and averaged over multiple pulses to smooth out speckle and noise-induced variability. The ratio of signal power to total noise power over receiver bandwidth (carrier-to-noise ratio, or CNR, discussed below) of the return is ≈ -33 dB. The spectra for both 10 000 averages (0.5 s) and 80 000 accumulations (8 s) are shown. The objective of the signal processor is to identify and measure the mean frequency of the atmospheric return, which when adjusted for the LO-transmit pulse frequency difference represents the Doppler shift from which the mean radial component of the wind can be computed. The shape and width of the signal spectra shown in Fig. 27.3 are related to the distribution of velocities within the pulse volume. It is important to note that Fig. 27.3 shows the mean spectra computed by averaging the spectra from multiple pulses. Each spectral component in a single realization of the signal spectrum is a random variable due to the speckle, i.e., the random phases of the backscattered signals from the individual particles moving with velocities that produce the given Doppler shift; only by averaging multiple spectra can the smooth mean spectra shown in Fig. 27.3 be obtained.

Also shown in Fig. 27.3 is a white noise component, resulting from the wideband local oscillator shot noise that is always present in coherent lidar receivers. Both the signal and noise currents can be characterized as complex Gaussian processes, such that the power in a given spectral component for a single realization is an exponentially distributed random variable with a mean equal to the mean signal power plus mean noise power within that spectral region and variance equal to the mean. The randomness in the power spectrum components introduces uncertainty in the detection and estimation of mean signal frequency, which is reduced by accumulating spectra from multiple pulses before performing the estimate.

A key indicator of system performance for coherent receivers is the carrier-to-noise ratio (CNR), defined as the mean signal power delivered to the processor divided by the mean noise power. For an LO shot-noise limited system, a simplified expression for the CNR is [27.31]

$$\text{CNR} = \frac{\eta_r P_s}{hfB}, \quad (27.17)$$

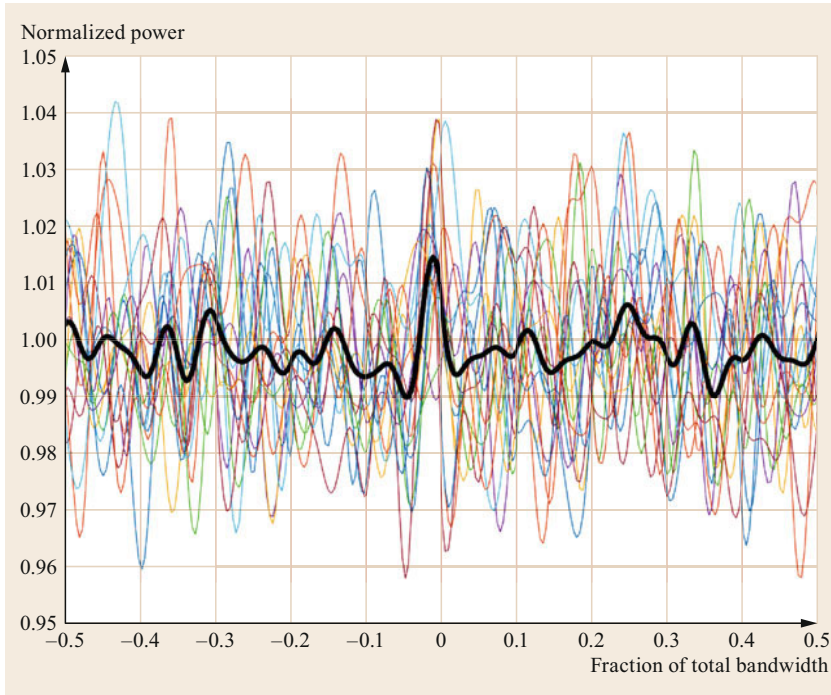


Fig. 27.3 Power spectrum of atmospheric returns showing extraction of a weak Doppler signal by accumulating multiple spectra. Each colored spectrum represents an accumulation of spectra from 10 000 pulses, while the solid black line represents an average of 80 000 pulses (figure courtesy of Alan Brewer, NOAA Chemical Sciences Division)

where P_s is the total received signal power, hf is the photon energy, B is the receiver bandwidth, and η_r represents the receiver efficiency, which accounts for factors such as detector efficiency losses in the receiving optics and components and losses resulting from spatial mode mismatching between the LO and backscattered signal at the detector. The CNR as defined in (27.17) is not a function of the signal bandwidth B_s , which is important in determining the performance of the processor to estimate the mean frequency. The narrowband CNR_n, defined as the ratio of signal power to noise power within the signal bandwidth, is

$$\text{CNR}_n = \frac{\eta_r P_s \tau_s}{hf}, \quad (27.18)$$

where $\tau_s \propto 1/B_s$ is the signal coherence time. The capability of measuring the mean frequency is a function of the signal bandwidth, the total bandwidth, the signal power, and the number of pulses accumulated in the signal processor, and varies somewhat depending on the processing algorithm employed. Detailed examinations of the performance of mean frequency estimators under different CNR regimes are given in [27.102, 103]. In general, the randomness of the backscattered signal due to speckle effects, even at high CNR, impacts the estimate and is a factor in optimizing the design for a given pulsed Doppler system. Under conditions where the narrowband CNR_n is $\gtrsim 2$, increased multipulse accumulation to average out these random fluctuations is more

effective than increasing transmitter pulse energy (thus increasing CNR_n) to improve the precision of a Doppler estimate. This implies that under a constraint of constant average transmitter power output, increasing the pulse rate and decreasing the pulse energy until the expected CNR_n is 2. Conversely, when narrowband CNR_n is $\lesssim 2$, increasing pulse energy to overcome the LO shot noise and increase the CNR_n while decreasing the pulse rate has a greater benefit. This tradeoff becomes important in designing a system when the average power available is somewhat fixed due to, e.g., laser pump power, peak power limitations, etc., but can be partitioned into either pulse energy or pulse rate. Because optimum performance is achieved when narrowband CNR_n ≈ 2 , one should trade off pulse energy and pulse rate to ideally achieve this value. In practice, because CNR_n varies as a function of range for a pulsed system, at best one can only optimize system design for a single range and must accept suboptimal performance at other ranges.

The transmitter pulse bandwidth, pulse energy, pulse repetition frequency, and phase matching between the received signal beam and the local oscillator at the detector are all important in developing design for a coherent system. For a pulsed system, the transmitter should transmit a pulse whose bandwidth, defined both by the frequency characteristics of the laser pulse and the pulse width, is on the order of the bandwidth of the atmospheric return, as computed by converting the anticipated distribution of radial velocities to

Doppler shift ($\delta f \propto 2\sigma_v/\lambda$). This requires a laser transmitter design that incorporates a technique to generate narrowband pulses, such as injection seeding a power oscillator or chopping a continuous-wave master oscillator and directing the chopped signal into a power amplifier. These output pulses have to be temporally long enough to be sufficiently narrowband. The tradeoff between pulse energy and pulse repetition frequency, as discussed earlier, should be carried out so that the CNR_n will approach the optimum value.

An important aspect of transmitter/receiver design is the need for phase coherence of the local oscillator and backscattered signal beam at the detector. Although analysis of system performance can be carried out by theoretically calculating the backscattered field at the detector and applying (27.10)–(27.13), performance has frequently been studied by backpropagating the local oscillator beam from the detector to the target plane and performing the analysis of the mixed signal in that plane, e.g., [27.104]. Backpropagated local oscillator (BPLO) analysis shows that high performance is obtained when the transmit beam spot size at the range of interest approaches the diffraction limit of the telescope and the transmitter and BPLO beam profiles overlap, are both spatially coherent across the telescope aperture, and are roughly matched in size. Modern coherent lidars share several fundamental design properties based on these requirements: highly spatially coherent transmitted and LO beams, high optical quality telescopes and optical components (better than $\lambda/20$ irregularity specification is typical) to maintain that coherence, monostatic design in which the transmitter and BPLO paths are coincident, and implementation of a lens or off-axis telescope to avoid loss of coherence caused by obstruction of an obscuring secondary element [27.105].

Refractive turbulence resulting from atmospheric temperature fluctuations encountered by the propagating beam degrades the performance of coherent wind lidars by introducing random irregularities in the phase front of the propagating transmit beam. Because these irregularities produce scintillation in the irradiance at the target plane and also enlarge the beam relative to the diffraction-limited beam's size, both of which reduce mixing efficiency, system performance is reduced [27.106–108]. The deleterious impact of turbulence is more pronounced at shorter wavelengths and longer ranges, and because it produces a reduction in the transverse coherence of the backscattered signal, turbulence has the practical impact of limiting the effective size of the telescope aperture. Telescopes in contemporary pulsed coherent lidars operating in the 1.5–2 μm wavelength region are typically ≈ 5 –10 cm in diameter. Incorporating larger diameter telescopes

does not generally provide increased performance except under rare zero-turbulence conditions.

The discussion in the previous paragraphs greatly simplifies or does not address many of the issues involved in optimizing the mixing between the received signal and the local oscillator with respect to issues such as the illumination profile of the LO on the detector and the loss of mixing efficiency at near ranges when the telescope is focused at infinity, which is typical for pulsed systems. A more detailed analysis, including more detail on the concept of backpropagating the local oscillator beam to the target plane and doing the analysis in that plane, is presented in [27.31].

27.3.6 Direct-Detection Doppler Wind Lidar

Compared to coherent DWL, where heterodyne detection by optical mixing is used as the principle, the direct-detection approach uses optical bandpass filters or, alternatively, an interferometer as the spectral analyzer. Here, the Doppler frequency shift is not obtained from the spectral analysis of the measured signal as for coherent detection, but a signal that is proportional to the frequency shift is obtained. Thus, a calibration is needed for most types of direct-detection DWL, which determines the relationship between the measured signal or instrument response R to the Doppler frequency shift Δf in the atmosphere. In principle, the Doppler frequency shift Δf is determined as the difference between the frequency of the received atmospheric signal f_a and the transmitted laser pulse signal f_i , usually measured during transmission via an internal optical path (called internal reference),

$$\Delta f = f_a - f_i = 2f_0 \frac{v}{c} = 2 \frac{v}{\lambda_0}. \quad (27.19)$$

Assuming that the measured instrument response $R(f)$ is to a first order linearly dependent on the frequency, the response can be written as

$$R(f) = af + b + \gamma(f), \quad (27.20)$$

where a describes the slope, also called sensitivity, b the intercept (response for frequency differences of 0 MHz), and $\gamma(f)$ contains all higher-order, nonlinear terms. As the instrument response $R(f)$ function depends on both instrument optical parameters (e.g., illumination of interferometers) and atmospheric parameters (e.g., spectral width) the functions are different for the atmospheric return and internal reference path. Thus, the Doppler frequency shift is obtained from

$$\Delta f = f_a - f_i = \frac{R_a - \gamma_a(f) - b}{a_a} - \frac{R_i - \gamma_i(f) - b_i}{a_i}. \quad (27.21)$$

The process of determination the response R as a function of frequency f is called response calibration. This can be achieved by measuring the response R for varying laser frequencies f for atmospheric conditions with zero frequency shifts, e.g., pointing vertically and assuming negligible vertical winds for the measurement period. Or it is achieved by simulation of the response function $R(f)$ using the knowledge of the instrument spectral transmission and spectral properties of the atmospheric signals. This response calibration is not needed for coherent DWL, where this relationship $R(f)$ is obtained via a spectral analysis (e.g., Fourier transformation) of the measured time series from the heterodyne signal. Also some specific implementations of the direct-detection technique (two-beam interferom-

eters) allow the determination of the Doppler frequency shift without the need for regular response calibrations (Sect. 27.4.2).

As the response function for atmospheric signals R_a depends on the spectral width of the signals, the response functions differ for narrowband Mie signals and broad bandwidth Rayleigh signals. In addition, the spectral width of the broad bandwidth Rayleigh signal depends on the atmospheric temperature (Sect. 27.3.2). Thus, the responses measured for broad bandwidth Rayleigh signals depend on the atmospheric temperature (and to a small degree on the atmospheric pressure due to Brillouin scattering), and, thus, this temperature (and pressure) dependency needs to be accounted for in the determination of the derived LOS wind speed [27.109].

27.4 Devices and Systems

Here, the two most common techniques and devices for a DWL applied today are described and a comparative overview is provided.

27.4.1 Coherent-Detection Techniques and Systems

Coherent wind lidar systems can fundamentally be categorized by their operating wavelength and by the form of the transmitted energy, i.e., pulsed or continuous wave (CW). Other characteristics that distinguish different system implementations include output power, optics size, use of free space or fiber coupling, and (for pulsed systems) use of injection-seeded power oscillators or master oscillator-power amplifier configurations (Fig. 27.4). Although these characteristics can vary for different system designs, one common factor among most systems currently used is the average power transmitted to the atmosphere, which tends to be on the order of 1 W, or so. To illustrate differences among implementations, we discuss three currently applied system designs: CW wind lidars for short-range wind measurements; high pulse repetition frequency (PRF ≈ 10 kHz),

very low pulse energy ($\approx 100 \mu\text{J}$) pulsed systems that incorporate commercial off-the-shelf components used in the telecommunications industry, and moderate pulse energy ($\approx 2\text{--}5$ mJ) with moderate pulse repetition frequency (PRF $\approx 200\text{--}500$ Hz).

As was noted earlier, coherent systems have historically operated within three wavelength regions: the 9–11 μm thermal infrared region, and near IR regions around 1.5 and 2 μm . Operation at shorter wavelengths is precluded because eye-safety considerations limit coherent wind lidar operation to wavelengths $> 1.4 \mu\text{m}$, where water absorption in eye tissue blocks light from reaching the retina. Unlike direct-detection wind lidar systems, coherent lidar beams cannot be expanded to reduce energy density without impacting system performance because maximum efficiency is achieved when the beam is focused or collimated at the target. Currently, development of coherent lidar for wind measurements is concentrated at 1.5 μm wavelengths, taking advantage of technological advances in the aftermath of the late 1990's telecommunication revolution, such as coherent optical erbium-doped fiber amplifiers for application in coherent laser transmitters. Incorporation of a fiber architecture offers several advantages, including ease of adjustment, mechanical reliability in a vibrating environment, and the option to spatially separate different subcomponents of the lidar system.

Continuous Wave Coherent Doppler Lidars

CW coherent lidars are highly effective for short-range wind profiling in support of the wind energy industry and other boundary layer applications. Figure 27.5 shows a block diagram of a notional fiber-coupled CW Doppler system incorporating the master oscil-

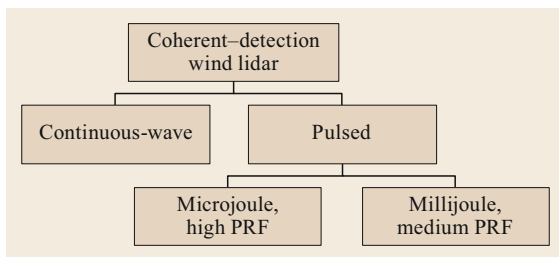


Fig. 27.4 Different implementations for coherent DWL

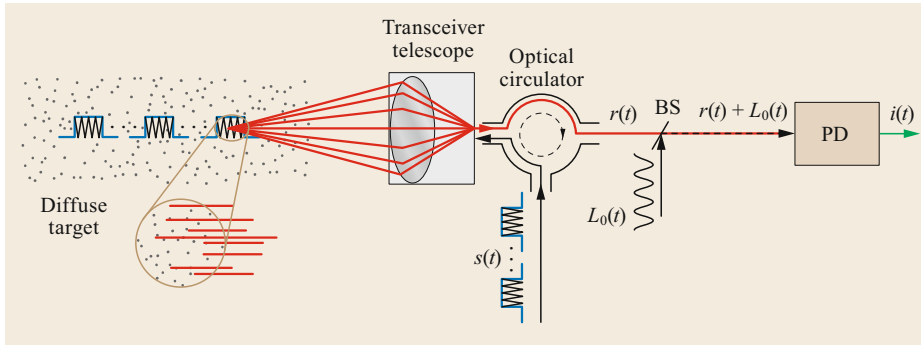


Fig. 27.5 Block diagram of a fiber-coupled CW Doppler system (after [27.110] with permission from the Optical Society of America)

laser power amplifier (MOPA) configuration used in many current CW and pulsed lidars operating at $\approx 1.55 \mu\text{m}$. The CW output from the master oscillator passes through a beam splitter where a small portion of the optical power is split off to form the local oscillator (LO) beam. This beam is coupled to a fiber beam combiner, where it mixes with the signal backscattered from the atmospheric aerosols and is coupled onto the detector. Most of the energy passing through the beam splitter is used to generate the optical beam transmitted to the atmosphere. In order to preserve the sign of the wind, the beam is coupled through a frequency-shifting element, typically an acousto-optic modulator (AOM) that shifts the frequency by f_{if} relative to the LO frequency. For homodyne systems, this element is eliminated, but the sign of the Doppler shift is lost unless a more complex detection scheme is implemented (see [27.110] for a discussion of homodyne detection in CW Doppler systems). The beam from the AOM is coupled onto an erbium-doped fiber amplifier (EDFA) through an optical circulator element that functions as a transmit/receive switch and into the system telescope or lens, where it is expanded and transmitted into the atmosphere. The scattered energy is collected by the telescope, focused, and directed back to the circulator, where it is isolated from the transmitter beam path and directed into the beam combiner for mixing with the LO beam. The combined beam is coupled onto the photodetector, which must have sufficient bandwidth to respond to the backscattered signal/LO beat signal at frequency $f_{\text{if}} \pm \Delta f_{\text{d}}$, where Δf_{d} is the mean Doppler shift due to the motion of the particles (typically in the MHz to tens of MHz range for operation at $1.55 \mu\text{m}$). The photodetector converts the optical signal to electrical current for spectral analysis. In current systems, the detector output is generally digitized for processing using digital signal processing techniques, such as Fourier analysis, to estimate the spectrum and determine the Doppler shift.

A typical signal processing implementation is described in [27.111] for a homodyne CW lidar operating at $1.55 \mu\text{m}$. The detector output signal is digitized at

100 MHz, permitting spectral analysis to maximum frequency of 50 MHz, corresponding to a wind speed of 38.8 m s^{-1} . By applying a 512-point discrete Fourier transform (DFT) to the sampled time series, representing $\approx 5 \mu\text{s}$ of data, each spectral bin has a frequency width of $\approx 200 \text{ kHz}$. To lower the effects of random fluctuation in the shot noise multiple spectra are typically averaged; for a data rate of 20 Hz (corresponding to 20 ms of processing time), ≈ 4000 spectra can be averaged, assuming a 100% duty cycle, which is achievable using field programmable gate arrays (FPGA) technology.

CW coherent lidars transmit coherent energy continuously into the atmosphere, achieving spatial sensitivity by focusing (ideally) the Gaussian beam output from the EDFA at various points in range. Following [27.111], the range-weighting function along the beam is given by a Lorentzian function

$$F = \frac{\Gamma/\pi}{\Delta^2 + \Gamma^2}, \quad (27.22)$$

where Δ is the distance from the focus position along the beam direction, and Γ is the half-width of the weighting function (to the half-maximum). Here, F is normalized such that the integral along the entire beam gives unity. The half-width Γ is approximated by

$$\Gamma = \frac{\lambda R^2}{\pi A^2}, \quad (27.23)$$

where λ is the laser wavelength, R is the distance to the focus from the output lens, and A is the beam radius at the output lens for an axially symmetric two-dimensional (2-D), Gaussian beam. For the commercial system described in [27.111], $A = 24 \text{ mm}$, producing a probe length in the radial direction of 17 m at 100 m range (note that the probe length decreases with decreasing range). A major advantage of CW systems is their very high range resolution at close ranges and their capability of obtaining measurements very close to the lidar transceiver.



Fig. 27.6a,b Photo of commercial CW Doppler lidar systems: (after [27.112] with permission from METEK GmbH) (a) (after [27.113] with permission from ZX) (b)

Figure 27.6 shows two commercially available CW Doppler lidar systems designed to provide near-range measurements in the boundary layer. Per the specifications available from the manufacturer [27.112] the METEK instrument provides measurements in the 10–100 m range, with a range resolution ranging from 0.16 m at 10 m range to 16 m at 100 m range. The lidar beam is offset 10° from the vertical, with wind measurements computed from continuous VAD scans at a rate of 1 revolution/s. Spectra are computed every 0.01 s, providing an angular resolution of 3.6° . The ZX lidar advertises a 10–200 m range with range resolution varying from 0.07 m at 10 m range to 7.70 m at 100 m range, with a 360° scan completed every second [27.113]. Such instruments can be used for wind energy, air quality, and other applications where high resolution wind profiles near the surface are required.

Microjoule Pulsed Coherent Doppler Lidars

Although CW lidars provide excellent measurement at near ranges, their utility decreases for applications where more range is required. Currently, pulsed lidars utilizing erbium fiber technology in the wavelength region around $1.5\ \mu\text{m}$ are available from commercial vendors (HALO Photonics, UK; Leosphere, France; Seaglet, China) and have also been developed for research purposes [27.114]. Conceptually, the instrument design for most systems is similar to that shown in Fig. 27.5, except that the AOM serves to both shift the frequency of the outgoing pulse and to form pulses from the CW output of the master oscillator, while providing

high isolation between the on and off states. Figure 27.7 shows a schematic of a pulsed, microjoule, coherent, polarization-diversity lidar proposed for the investigation of wind turbine properties [27.115]. This lidar utilizes the MOPA configuration common to fiber-based systems operating in this wavelength region. The pulse formed by the AOM from the output of the narrowband CW master oscillator laser is amplified, coupled to the circulator, and expanded and focused (or collimated) by the telescope for transmission into the atmosphere. The scattered signal comes back through the telescope and circulator and is directed to the beam combiner, where it is mixed with the LO beam and directed onto the detector. The detector output, corresponding to a time series of the return for each transmitted pulse, is digitized and spectrally processed to estimate the Doppler shift in the return.

Doppler systems using fiber amplifiers are peak-power limited because stimulated Brillouin scattering (SBS) at powers above a certain threshold in the fiber can cause reflection of the amplified signal back toward the local oscillator and cause damage to the optical components. The SBS threshold can be increased by shortening the fiber length, reducing the laser intensity, or broadening the laser spectrum by lengthening the pulse [27.114]. Presently, both commercial and research microjoule-type Doppler lidar systems typically operate with average power levels $\approx 1\ \text{W}$ at PRF of 10–20 kHz and pulse energies of 50–100 μJ , or so. Although the relatively low pulse energy in these fiber-based coherent lidars results in quite weak backscat-

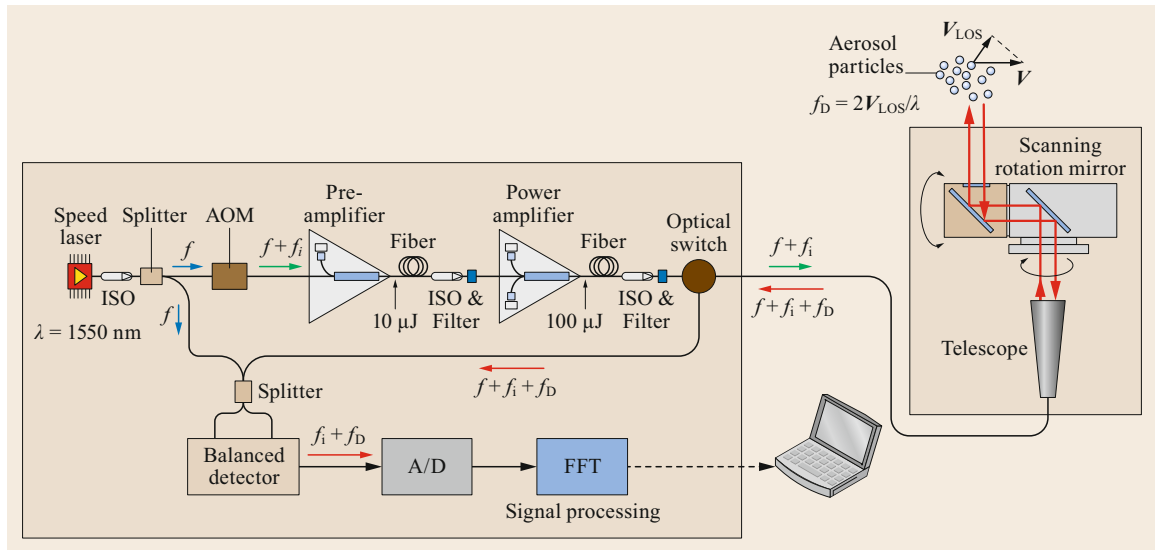


Fig. 27.7 Block diagram of a pulsed, microjoule coherent lidar (after [27.115] with permission from the Optical Society of America)

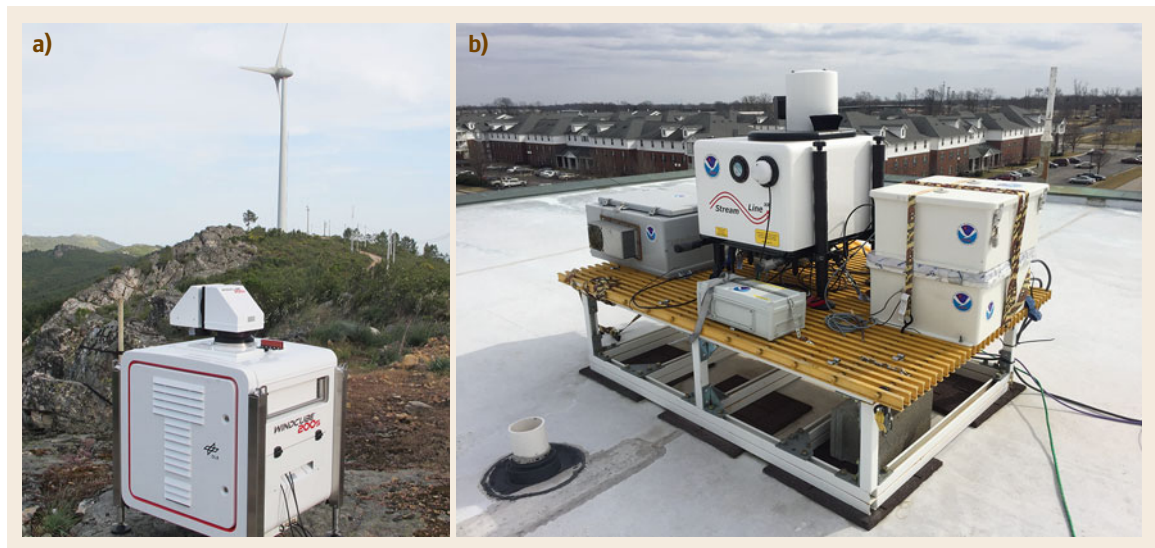


Fig. 27.8 (a) Photo from a coherent Doppler wind lidar from Leosphere (Windcube 200s) operated by DLR during the Perdigo field campaign in Portugal in 2016 (after [27.21, 100]) with a wind turbine (photo © Norman Wildmann, DLR); (b) coherent Doppler wind lidar from HALO Photonics (Streamline) deployed on a building roof for more than 4 years for study of greenhouse gas fluxes in Indianapolis, Indiana (photo © Scott Sandberg, NOAA)

tered signals available at the lidar receiver (carrier-to-noise ratios < 1), even from close ranges, the frequency stability and high PRF enables efficient spectral averaging of multiple pulses. Generally, depending on aerosol conditions, such systems can typically measure out to 3–5 km, in the boundary layer with a time resolution on the order of 1 s and a range resolution of a few tens of m.

Figure 27.8 shows two commercial systems currently available for purchase and deployment. The systems are similar in design and capability. A common, notable feature of these instruments is the availability of a two-axis, full hemispheric scanner that enables the beam to be directed in any direction. This robust scanning capability enables the instruments to be used to profile winds and turbulence using conical (VAD)

scans, vertical (RHI) scans, as well enabling it to be directed and fixed for staring type measurements to measure, e.g., profiles of vertical and horizontal winds and turbulence from a specific direction.

Millijoule Pulsed Coherent Doppler Lidars

Although the microjoule-type lidars described in the previous section are currently widely used because of their robustness, reliability, and affordability, applications exist for which the energy limitations available from these fiber-based laser systems do not provide sufficient range to address the measurement needs. Consequently, systems with pulse energies in the mJ range are used for specific applications, such as wind shear and wake vortex modeling, and for measurements where backscatter coefficients are low, such as from high flying aircraft. An example of an mJ class system is the NOAA High Resolution Doppler Lidar (HRDL) developed in the mid 1990s, which was still being used as recently as in 2016 [27.78, 116]. The primary difference between HRDL and the fiber laser microjoule instruments is in the transmitter design and the output wavelength. The HRDL instrument incorporates a master–slave configuration in which a diode-pumped, Tm,Lu:YAG laser cavity is stabilized using a phase modulation technique to produce 220 ns-long, frequency-stable pulses with 2 mJ of pulse energy at 200 Hz PRF. The 2.022 μm output wavelength of the HRDL instrument is matched to an atmospheric window region to provide maximum range. Although the laser transmitter incorporates free space rather than fiber coupling, frequency stability is sufficient to allow operation from both ship and aircraft platforms.

Operational instruments similar to the HRDL instrument have been developed commercially and applied for airport wind shear [27.11, 12] and airborne lidar applications [27.13, 28]. As low-cost optical components, such as distributed feedback diode master oscillator lasers resulting from advances in optical telecommunications, became more available, mJ-class Doppler lidars followed the path of the microjoule instruments and evolved to operate in the 1.5 μm spectral region [27.117]. A commercially-available pulsed Doppler lidar employs a 1.6 μm Er:YAG power oscillator to produce 2.3 mJ pulses at a 750 Hz pulse repetition rate. A version of this instrument, which has potential applications to wind shear detection and wind energy, utilized a 12.5 cm receiver aperture to demonstrate wind measurements to beyond a 33 km horizontal range [27.117]. Similar results were achieved with a MOPA-based design through the use of an amplifier chain consisting of an EDFA, whose output is coupled into an Er:YAG-doped fiber amplifier followed

by an Er,Yb:glass planar waveguide amplifier [27.118]. This transmitter produced pulses with 1.4 mJ energy at a pulse repetition frequency of 750 Hz and also demonstrated wind measurements to beyond 30 km range using a 15 cm diameter telescope aperture.

27.4.2 Direct-Detection Techniques and Systems

Direct-detection filter techniques make use of one or more narrowband filters and determine the Doppler frequency shift from the transmitted signal strength through this filter, called the *edge* technique [27.40, 119]. In the commonly used double-edge technique, two filters are used, which are often Fabry–Pérot interferometers [27.120]. Single-edge techniques use only one filter, which can be realized by narrowband atomic or molecular absorption lines [27.121–123].

Interferometric techniques can be divided into two principles, using either multiple-path or two-beam interference. For multiple-path interferometers, the radial-angular distribution or spatial movement of the interference patterns (*fringes*) is measured, which is called *fringe imaging*, using either a Fabry–Pérot interferometer [27.124–126] or a Fizeau interferometer [27.1, 43, 127]. Alternatively, two-beam interferometers are used to measure the phase shift between the two beams, which is proportional to the frequency shift. This can be realized by Mach–Zehnder interferometers [27.52, 54, 55, 128, 129] or by Michelson interferometers [27.130, 131].

Due to the difference in the spectral width of the aerosol/cloud and molecular signals by two orders of magnitude, the implementation of direct-detection filters or interferometers must be optimized to either the Mie or Rayleigh spectral line width. From this, it is obvious that a large variety of different direct-detection DWL principles are in use (Fig. 27.9). In the following, the basic principles of filter and interferometric techniques are introduced.

Filter Technique

The filter method is described using a common approach called the double-edge technique [27.40, 42, 119, 132–134], which is also used for the spaceborne DWL on Aeolus [27.3, 4]. The double-edge technique uses two bandpass filters that are placed symmetrically around the maximum of the molecular spectral line with their maximum filter transmission at the edges of the line around the inflexion point (Fig. 27.10a). The signal transmitted through each of these filters is detected, which is proportional to the convolution of the spectral filter transmission and the backscattered

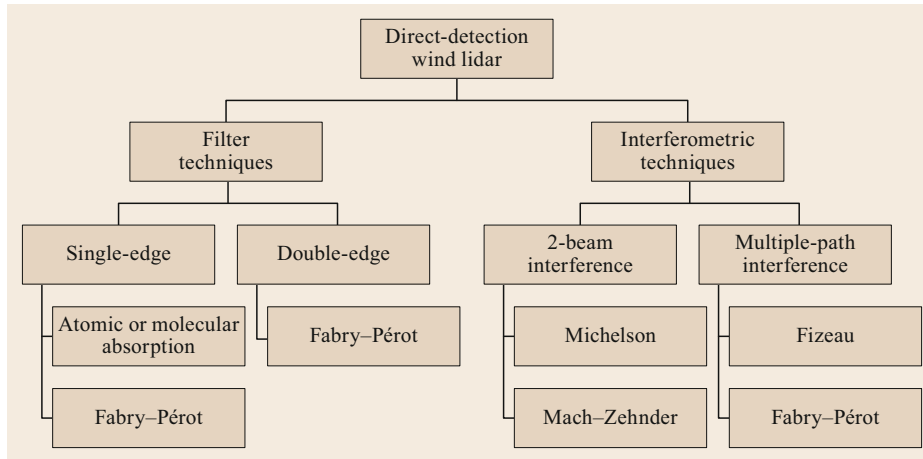


Fig. 27.9 Different implementations for direct-detection DWL

line shape from the atmosphere. In the case that both filters A and B have equal transmission characteristics ($T_A(\lambda) = T_B(\lambda + \Delta\lambda_{A,B})$) and are symmetrically placed around the Rayleigh spectral line with a separation of $\Delta\lambda_{A,B}$, both filters measure the same signal $I_A = I_B$, for a zero LOS wind speed. In the case of a Doppler shift $\Delta\lambda$, the signal transmitted through one filter would be higher than that transmitted through the second one (Fig. 27.10a, bottom). The ratio or contrast of I_A and I_B is used as a measure for the Doppler shift and is called the response R

$$R = \frac{I_A}{I_B} \quad \text{or} \quad R = \frac{I_A - I_B}{I_A + I_B}, \quad (27.24)$$

$$R = f(T_A(\lambda), T_B(\lambda), I_{RBS}(\lambda, \Delta\lambda, T, p)). \quad (27.25)$$

The response R is a function of both filter transmissions $T_A(\lambda)$, $T_B(\lambda)$, and the Rayleigh–Brillouin line-shape from the backscattered signal $I_{RBS}(\lambda, \Delta\lambda, T, p)$ depending on wind-induced Doppler shift $\Delta\lambda$, atmospheric temperature T , and pressure p (Sect. 27.3.2). Exact knowledge of the actual filter transmissions of the instrument is more critical for wind retrieval than the knowledge of the sensitivity to the atmospheric temperature and pressure, which is applied as a correction to the retrieved wind speed or included in the calibration approach [27.109].

The Doppler shift frequency Δf or wavelength $\Delta\lambda$ is to a first approximation linearly proportional to the response measured

$$\Delta f, \Delta\lambda \propto R(f, \lambda). \quad (27.26)$$

Certainly the bandwidth of filters A and B have to be smaller than that of the molecular return signal (e.g., FWHM = 1.6 pm at 15 °C for a wavelength of 355 nm),

which can be realized by a Fabry–Pérot interferometer. A plane Fabry–Pérot interferometer consists of two plane parallel optical plates (called the *etalon*) with high reflectivity and separated by distance d [27.120]. Multiple-beam interference of the incoming light leads to positive interference patterns (called *fringes*), if the wavelength λ is a multiple k of the optical path $\lambda = 2dn \cos(\varphi)/k$ (k : integer, n : refractive index, φ : incidence angle on plates).

When using a Fabry–Pérot interferometer as a filter, only the central ring ($\varphi = 0$) and not the complete, radial interference pattern is used. The two filters can be realized with the same Fabry–Pérot interferometer but with slightly different distances d_A and d_B at different parts of the Fabry–Pérot interferometer (Fig. 27.11a).

Another possibility to realize the filter technique is to use specific, very narrowband molecular or atomic absorption lines. With absorption lines, only one filter can be realized (*single-edge technique*), which relies on the change in absolute intensity through this filter. The technique is limited to spectral regions where narrow bandwidth absorption lines occur at the emission wavelength of lasers. This is realized in the green spectral region at 532 nm and with iodine I_2 absorption lines ([27.48], see the comparative overview in [27.122]). The iodine filter technique is also used for wind and temperature measurements up to 80 km at the Alomar observatory in northern Norway [27.123, 135] using two large 1.8 m diameter telescopes and a powerful laser emitting at 355, 532, and 1064 nm.

Interferometric Techniques – Multiple-Path Interference

Another implementation of the direct-detection DWL uses the spatial location of interference patterns (*fringes*) and its spatial displacement when a Doppler

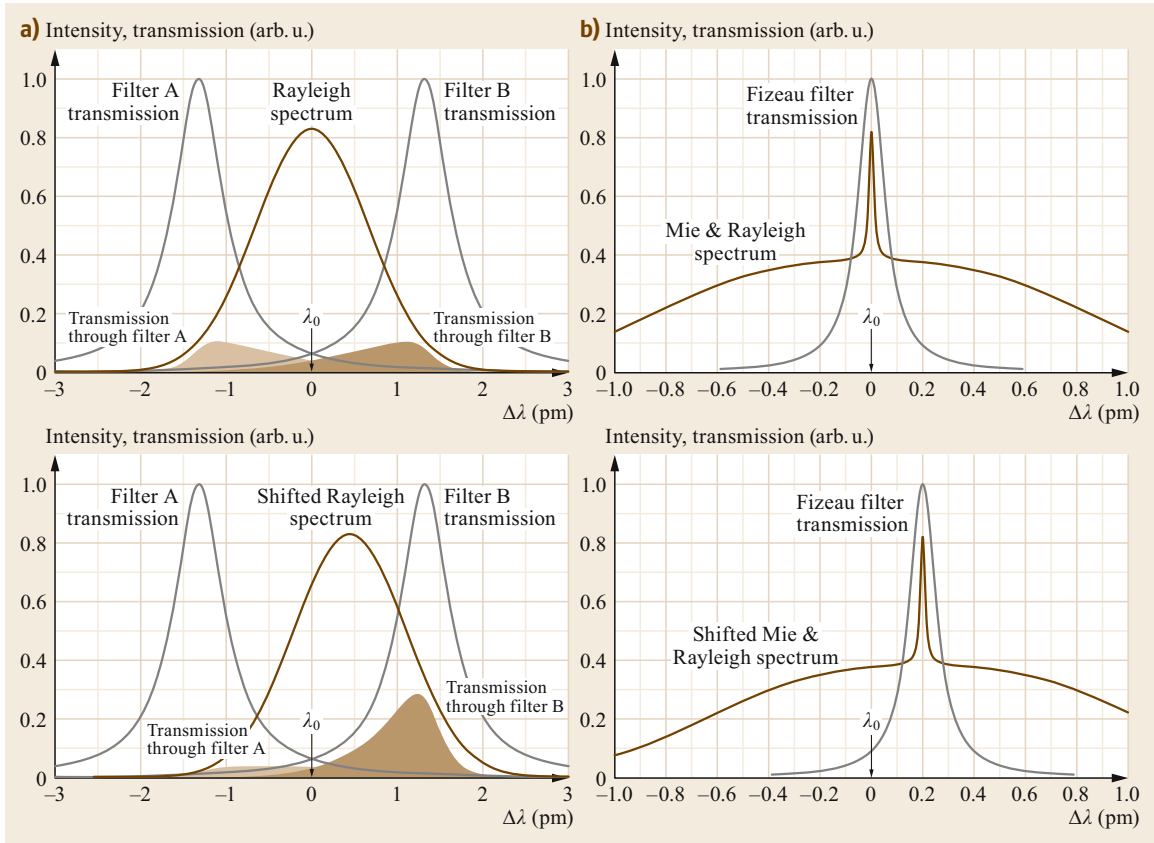


Fig. 27.10a,b Principle of direct-detection DWL with double-edge technique (a) and the fringe-imaging technique (b) used in the spaceborne lidar mission Aeolus; Rayleigh spectrum from molecular backscatter (a, brown line) and double-edge filter A and B transmission (a, gray lines) and additional Mie spectrum from aerosol backscatter (b, brown line) and Fizeau filter transmission (b, gray line) for zero LOS speed (top) and Doppler shifted spectrum (bottom) for a wavelength of 355 nm; note the different wavelength scales on (a) and (b). The different signal levels transmitted through filters A and B (a, light- and dark-brown areas) are used to determine the Doppler shift from molecules; the signal transmitted at different spatial locations of the Fizeau filter transmission (b, gray lines) is used to determine the Doppler shift from aerosols; the spectral transmission for the Fizeau filter is equal for different wavelengths (gray lines), but the maximum of the transmission is located at different spatial locations of the Fizeau filter wedge (b, top and bottom), which needs to be resolved by linear detector array or charge-coupled device (CCD) (after [27.1])

shift is present. Thus, the measured instrument response R is a function of the spatial displacement x of the fringe and a measure of the Doppler shift

$$\Delta f, \Delta\lambda \propto R(x). \quad (27.27)$$

This can be realized by a Fabry–Pérot interferometer, where the movement of the radial-angular pattern of interference rings is used to determine the Doppler shift [27.16, 38, 50, 124–126]. Another approach is based on a Fizeau interferometer, as for the satellite mission Aeolus, to determine the Doppler shift from the narrow bandwidth aerosol return (Fig. 27.11b) [27.3].

A Fizeau interferometer also consists of an etalon, but contrary to a Fabry–Pérot interferometer, where both etalon plates are plane parallel with constant distance d , one of the plates is tilted at a small angle. The resulting variation in distance d results in a distinct spatial location of an interference pattern where the condition for positive interference is fulfilled. A Doppler shift of the signal will result in spatial displacement of the fringe, which is imaged onto a detector (Fig. 27.10b). Therefore, a detector with several sensitive areas (e.g., a charge-coupled device CCD, as is nowadays used in digital cameras) to provide pixel-wise discrete, spectral channels is needed for the fringe-imaging technique [27.136].

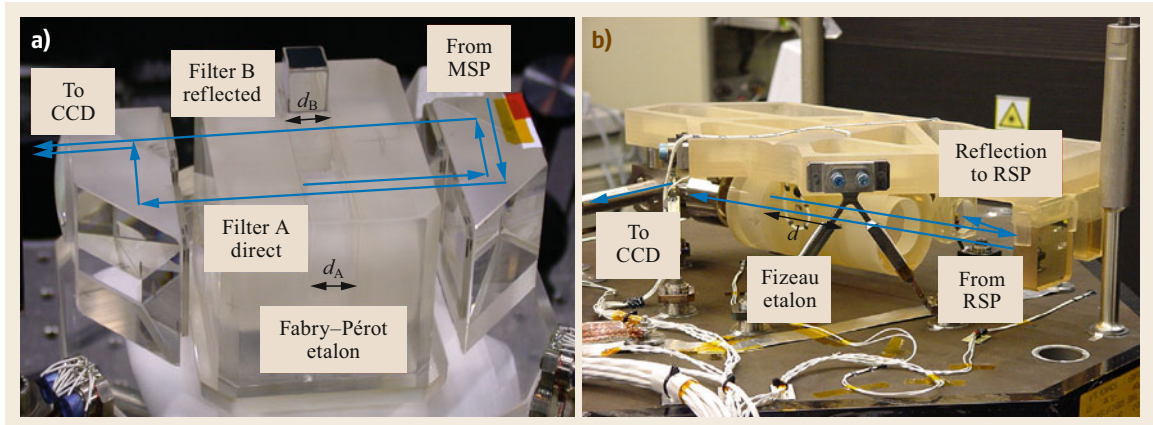


Fig. 27.11a,b Photo of the optical receiver of the ALADIN (atmospheric laser Doppler instrument) airborne demonstrator A2D of the Aeolus satellite mission with (a) a Rayleigh spectrometer (RSP) and its optical paths for filters A and B, and (b) Mie spectrometer (MSP). Optical beam paths towards the CCD detector are indicated by blue lines, the distances d_A and d_B of the Fabry-Pérot etalons (a) and Fizeau etalon (c) are indicated by arrows (after [27.1])

Interferometric Techniques – Two-Beam Interference

The use of a Fabry-Pérot or Fizeau interferometer is based on multiple-beam interference (within the etalon), while two-beam interference is used for both Mach-Zehnder interferometers [27.52, 54, 55, 128, 129] and Michelson interferometers [27.130, 131]. Those are either realized as two-channel or four-channel spectral analyzers or as a fringe-imaging device. Two-beam interferometers are based on the optical interference of the incoming electromagnetic wave with a time-lagged optical copy of the same signal. It is, thus, also referred to as an autocovariance technique, because, essentially, the optical autocovariance function is measured [27.129]. An optical beam splitter essentially creates the optical copy of the signal, while the time lag is introduced by an optical path difference (OPD) between the two arms of the interferometer. This OPD L_{OPD} has to be adapted to the spectral width of either the narrowband aerosol backscatter signal (large OPD on the order of several 10 cm) or the broad bandwidth molecular signal (smaller OPD on the order of several cm). Essentially, this mixing of two waves and measuring the differential phase shift $\Delta\Phi$ is, in principle, comparable to heterodyne detection of the backscatter with the local oscillator signal of a coherent DWL. Thus, this specific implementation of a direct-detection wind lidar does not need a response calibration, especially for optical designs with low sensitivities to angular beam variations. The Doppler frequency Δf shift is determined by the phase shift $\Delta\Phi$ via

$$\Delta f = \frac{c \Delta\Phi}{2\pi L_{OPD}}. \quad (27.28)$$

The phase shift is determined by the difference of the phase or fringe position between the emitted laser beam and the backscattered signal.

27.4.3 Comparative Overview of Coherent and Direct Detection

Due to the large variety of DWL principles and realized instruments, a generalization of differences between the two techniques needs to focus on major aspects. An attempt was made in Table 27.6 to compare a number of relevant differences between coherent and direct-detection DWL with respect to implementation, error characteristics, operation, and its advantages and disadvantages. It is clear that such a condensed overview will need some simplifications, which might not be relevant for all instruments in use. Nevertheless, it provides a generalized discussion of the relevant criteria for the application.

The Cramer Rao lower bound (CRLB), which provides an estimate of the ideal performance of a mean frequency estimator, is often employed to evaluate performance of a given Doppler lidar or to compare performance of different instruments. The CRLB, along with the factors that impact the precision of Doppler lidar velocity estimates, is discussed in [27.137–140]. Exact and approximate expressions for estimating the CRLB for maximum likelihood spectral peak estimators were developed in [27.137], variations of which are employed in most coherent Doppler wind systems currently being used and applied to demonstrate estimated behavior for different signal characteristics and estimator applications. Estimator performance was shown to depend on the wideband signal-to-noise ratio (SNR), the width

Table 27.6 Comparative overview of different wind lidar techniques

	Coherent detection	Direct detection
Wavelengths and lasers	CO ₂ gas lasers 10.6 μm for earlier instruments, solid-state lasers with Tm:LuAG or Tm,Ho:YAG at 2 μm, Er-doped fiber laser at 1.5–1.6 μm	Nd:YAG at 1064 nm, frequency-doubled at 532 nm, and -tripled at 355 nm
Laser operation	Continuous wave or pulsed with repetition rate of 200–500 Hz (solid-state laser) and up to 10–40 kHz (fiber laser)	Pulsed with repetition rate of 10–100 Hz
Laser eye safety	Achieved outside instrument housing for applied infrared wavelengths and laser power	Typically not achieved for green wavelength (532 nm) within some km; achieved for ultraviolet (355 nm) after some km range
Atmospheric backscatter	Aerosol and cloud particles with narrow bandwidth line shape	Molecules with Rayleigh–Brillouin lineshape (broad bandwidth), aerosol, and cloud return (narrow bandwidth)
Altitude range	Boundary layer and clouds or elevated aerosol layers in the troposphere	Troposphere, stratosphere, mesosphere
Receiver	Mainly heterodyne detection some earlier systems used homodyne detection	a) Filter techniques, e.g., double-edge or iodine filter b) Multiple-path interferometer, e.g., Fizeau c) Two-beam interferometer, e.g., Mach–Zehnder
Dominating noise sources	Photon noise of local oscillator, speckle noise, atmospheric turbulence, receiver sensitive to phase distortions	Solar background light and signal photon noise, receiver sensitive to intensity distortions, e.g. angular fluctuations
Calibration	No calibration needed, as relation between Doppler frequency shift and detected signal is obtained by spectral analysis (e.g., Fourier transformation), no bias introduced by approach	Calibration needed to obtain relationship between Doppler frequency shift and detected signal or instrument response (except for some specific instrument implementations), constant and wind-speed-dependent bias introduced by calibration
Random error for LOS speed	Low random errors ($< 0.5 \text{ m s}^{-1}$) achieved due to small spectral bandwidth	Low random errors ($< 0.5 \text{ m s}^{-1}$) for aerosol/cloud; higher random errors of 1–3 m s^{-1} for broad bandwidth molecular returns
Systematic errors for LOS speed	Low systematic errors ($< 0.1 \text{ m s}^{-1}$) as no calibration is needed	Typically 0.5–1 m s^{-1} determined by accuracy of response calibration
Need for additional parameters	No additional parameters needed for wind retrieval	Atmospheric temperature and pressure needed for retrieval of wind from molecular backscatter
Operation	Instrument commercially available from several suppliers, autonomous with 24/7 operation	Research instruments usually only with lidar expert operator, autonomous for satellite lidar on Aeolus
Platforms	Ground, wind rotors, trucks, ships, aircrafts	Ground, aircraft, satellite
Main applications	Need for high precision and high temporal resolution, aircraft wake vortex, turbulence, wind turbines; boundary layer winds, vertical wind speed, and turbulent fluxes	Wind sensing for higher altitudes of upper troposphere, stratosphere and mesosphere, global wind observations from space
Advantages	Higher precision and accuracy possible, higher temporal resolution achievable for turbulent quantities, autonomous, commercial instruments available for 24/7 operation, eye-saving laser wavelengths in IR	Unique method for sensing winds for higher altitudes with molecular backscatter
Disadvantages	Limited to altitude regions with aerosol and clouds, mainly for boundary layer and tropospheric clouds	Need for calibration for most instrument implementations, which is suspicious to systematic errors, potentially lower precision and accuracy for molecular DWL, issues with eye-safety for laser wavelengths in use, additional temperature profile needed for retrieval of winds from molecular backscatter; complex research instruments operated by lidar experts

of the Doppler signal, the number of spectral bins in the frequency estimate, and the number of pulse returns accumulated. Figure 27.12 shows a comparison of the standard deviation in mean frequency estimates computed after averaging 10 000 returns from a microjoule-type coherent lidar system operating at a 20 kHz pulse

rate. The estimate precision, computed using two different methods, versus wideband SNR follows the CRLB curve fairly closely until the CNR drops below -20 dB but then diverges rapidly with further decrease in CNR. At signal-to-noise ratios above -15 dB the velocity precision exceeds 0.05 m s^{-1} . Figure 27.12 illustrates the

value of the multipulse averaging employed in high pulse rate systems to improve the estimate precision and extending the range. The -20 dB threshold corresponds to approximately one photon detected for every four pulses transmitted, illustrating the sensitivity of coherent systems.

The CRLB for a direct-detection system utilizing optical techniques, such as Fabry–Pérot or Fizeau interferometers that provide estimates of energy in spectral bins by developing fringes on imaging detectors, is also addressed in [27.137]. Their expression, aimed at providing a method of comparison between coherent and direct-detection systems, assumes a Gaussian shaped detected signal spectrum in a photon-limited direct-detection system. They show that for equal number of detected photons, and equivalent signal spectral width the CRLB is lower for the direct-detection implementation. In practice, the equivalence of signal and spectral width for direct comparisons is not met because the transmitted laser bandwidth, the presence of additional noise sources, and the system throughput tend to differ significantly for direct and coherent systems. In the infrared region beyond $1.5\ \mu\text{m}$, where eye-safety issues permit higher pulse energies, coherent systems are preferred for aerosol backscatter applications because of their high throughput and lack of susceptibility to background and detector noise. However, a major advantage of direct-detection systems is their capability to provide measurements from both aerosol and molecular backscatter through the use of a single laser operating in the visible or UV spectral regions and separate

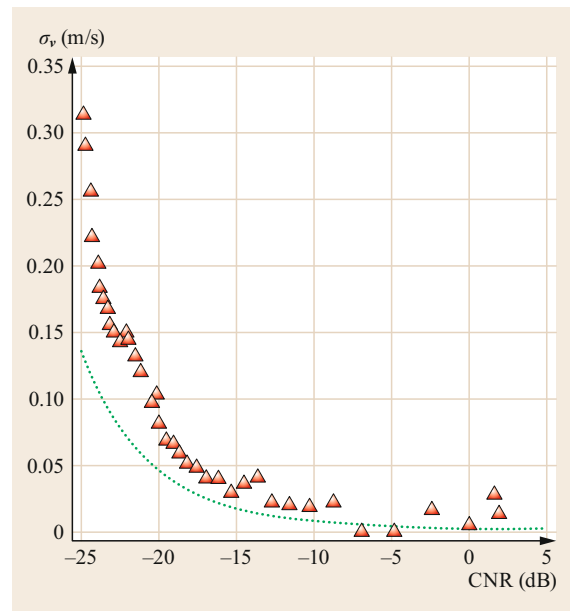


Fig. 27.12 Comparison of standard deviation of mean frequency estimates after averaging 10 000 returns from a microjoule-type coherent, 20-kHz pulse rate lidar (triangles) with CRLB (dots) (courtesy of Paul Schroeder, NOAA)

direct-detection receivers. This approach is used in the Aeolus mission [27.3], which employs a lidar operating in the ultraviolet at 355 nm and two direct-detection receivers to measure winds from space.

27.5 Specifications

The requirements for wind measurement precision, accuracy, and temporal and spatial resolution vary widely depending on the application. The specifications achievable for the random error depend on the vertical and temporal resolution applied, as well as the atmospheric properties, mainly backscatter and extinction coefficients, and the influence of turbulence. Typical values for a number of specifications for DWL instruments are listed in Table 27.7. The relevant ISO norm [27.32, annex D] defines three classes of accuracy of horizontal wind velocity with better than $0.1\ \text{m s}^{-1}$ (wind energy), from 0.1 to $0.5\ \text{m s}^{-1}$ (meteorological applications) and from 0.5 to $1\ \text{m s}^{-1}$ numerical weather prediction (NWP).

To derive horizontal wind speed and direction different scanning strategies are applied (Sect. 27.3.3), resulting in an additional error source related to the atmospheric homogeneity for the sampling of a larger

volume. The atmospheric sampling error adds a contribution, which mainly depends on atmospheric properties (e.g., homogeneity, turbulence, cloudiness) and the sampling volume (range resolution, elevation angle). On the other hand, the error for the horizontal wind speed decreases with the square root of the number of LOS wind speeds. Therefore, longer temporal periods are needed to measure horizontal wind speeds (if no multiple-Doppler techniques are applied).

High precision and accuracy are needed for wind-energy site assessments (Chap. 51), which are comparable to in-situ wind sensors (Chap. 9) or even traceable to standards. Other applications require mainly high temporal resolution for turbulence measurements, e.g., vortex characterisation for aircrafts and wind energy rotors. On the other hand, the requirements for global wind profiling is not that stringent for random errors [27.141], as the current satellite and ground-based observations

Table 27.7 Typical values for coherent (continuous-wave (CW) and pulsed) and direct-detection DWL

Method	Coherent DWL	Direct-detection DWL
Random error LOS (m s^{-1})	0.1–0.5	0.5–3
Systematic error LOS (m s^{-1})	< 0.1	0.5–1
Random error horizontal wind speed (m s^{-1})	0.1–1	0.5–3
Vertical resolution (m)	0.1–20 (cw), 20–100 (pulsed)	100–2000
Temporal resolution LOS (s)	0.1–1	1 to several 10
Wind speed range (m s^{-1})	30–100	150
Temperature operation range ($^{\circ}\text{C}$)	–25 to +45 for commercial DWL	Instruments operated in temperature stabilized container or housing
Scanning device common for both techniques		
Scan speed ($^{\circ}/\text{s}$)	up to 360 (cw), up to 30–40 (pulsed)	
Scan angle range ($^{\circ}$)	360 (in azimuth), –10 to 190 (in elevation)	

for NWP show a large gap in wind-profile observations [27.142]. On the other hand, the requirements for systematic errors are strict for NWP applications, because these would be detrimental for forecast quality.

The maximum range of a DWL is both determined by instrumental parameters (e.g., laser energy, telescope diameter, and optical efficiency), the method used (coherent DWL with aerosol backscatter or direct detec-

tion with aerosol and/or molecular backscatter), and the atmospheric properties. Thus, typical values for maximum ranges are not provided here, because they depend strongly on atmospheric properties and the temporal and spatial resolutions applied. Typical values for the availability of measurements as a function of range and the maximum range for a defined availability (e.g., for 50 or 80%) are discussed in [27.32, 143] for coherent DWL.

27.6 Quality Control

The quality of the wind measurements for LOS winds or vector winds depends on the DWL instrument hardware and retrieval algorithms, as well as on the pointing accuracy of the scanning device. The instrument performance of the DWL hardware, as well as the scanning device, needs to be regularly assessed (Sect. 27.7), including the leveling of the instrument to ensure the quality of the wind product retrieved.

In contrast to in-situ wind sensors (Chap. 9), which are calibrated and validated using wind tunnels, this is not possible for remote-sensing instruments due to their range resolution and volume-sensing approach.

27.6.1 Calibration and Validation with a Nonmoving Target

For calibration and validation, a target with known properties can be used for remote-sensing devices. This is achieved by nonmoving targets for wind lidars, where the LOS wind speed measured should be 0 m s^{-1} . This can be performed for an initial assessment of the performance of the instrument but can be repeated once the instruments are set up in the field.

In addition to validation of the zero-wind measurement by using a hard target, also the pointing accuracy of the scanning device can be calibrated and validated using hard targets in a known distance. Here, the knowl-

edge of the geographical position of the lidar instrument and the position of the hard target is used to infer the azimuth angle for the pointing direction, as well as the range.

Some care needs to be taken with the calibration or validation of the zero-wind measurement capability by using a nonmoving target. The target should ideally fill the complete sensing volume to avoid contamination with atmospheric returns, which would add a contribution from moving particles. Hard targets can be buildings or landmarks as hills (ideally without vegetation, which can move with the wind).

As for any remote-sensing instrument the sampled signal from a certain range is composed of a volume of a conical section with diameter D and a length depending on the range gate resolution ΔR . Thus, it needs to be assured that the hard target is ideally larger in size than the diameter D of the beam, which is approximated by the range R and the laser divergence or instrument field-of-view θ with $D = R\theta$; for a typical laser divergence of 1 mrad and a range of 1 km, this will result in a beam diameter of only 1 m. The range gate resolution for the analysis needs to be set such that the reflection of the laser pulse at the hard target is ideally centered in the range gate in order to avoid the effects of a possible laser chirp (changing laser frequency within the laser pulse). The range gate resolution should ideally be optimized

such that it covers only the laser pulse length and avoids atmospheric volume backscatter before the target.

The derived mean wind speed of the target return provides an assessment of the systematic error (bias), while the standard deviation of the target return provides an assessment of the random error (precision) for high signal-to-noise ratios.

27.6.2 Validation by Vertical Pointing Measurements

The measurement of the vertical wind is performed by pointing the laser beam to the vertical. Here, the assumption can be used that the vertical winds should be close to 0 m s^{-1} in the atmospheric boundary layer for sufficiently long averaging periods, which depends on the atmospheric conditions. Situations with nonzero vertical winds need to be avoided, e.g., the presence of gravity waves, orographically induced vertical movements, or synoptic scale vertical winds.

The advantage of the vertical pointing measurement compared to a hard target is that several altitude ranges can be assessed and also atmospheric volume backscatter is used with more representative SNR values. The derived mean vertical wind speed from the DWL should be zero for longer averaging periods over the altitude range.

For the case that high temporal resolution vertical wind measurements can be performed, the random error of the instrument can be assessed without any other instruments for comparison [27.6, 32, 144]. From the time series of the vertical wind measurements, the power spectra can be derived for each altitude. For the case of well-developed turbulence in the boundary layer, the power spectrum should follow a $f^{-5/3}$ law for a Kolmogorov spectrum (at least over the *inertial spectral range*). In the case of uncorrelated instrument noise, the power spectrum will show a constant, nonfrequency-dependent offset (white noise) for higher frequencies,

which is equivalent to the variance of the instrument wind speed random error.

These vertical pointing measurements are used for validating the performance of coherent DWL in the boundary layer but are used in addition to calibrate the instrument response for direct-detection DWL throughout the troposphere and stratosphere (Sect. 27.3.6.)

27.6.3 Quality Control for Line-of-Sight Wind Speeds and Vector Winds

The main purpose of the control of the quality of the derived LOS wind speeds or the derived wind vectors should be to flag or filter gross outliers, which deviate from a Gaussian distribution. Typically, they occur for values larger than $\pm 3\sigma_v$ (σ_v : random error) from the mean.

As both the probability of gross errors and the instrument random error depend on the SNR or CNR [27.140], this quantity can be used for quality assessment. Both flagging as invalid LOS winds that are below a certain SNR threshold or weighting LOS wind speeds with SNR^{-1} for further processing (e.g., during VAD least-squares fit) can be applied. One should be aware that also the derivation of SNR or CNR from the digitized signal itself is prone to systematic and random errors, especially for low SNR or CNR conditions.

Other quality control (QC) methods come into place when deriving horizontal wind vectors from VAD or DBS using the consistency checks for single LOS winds in different azimuthal direction (e.g., deviation from the sinusoidal fit). They can be used to check the assumption on horizontal homogeneity for situations with partial cloud coverage affecting only a fraction of the LOS winds.

As a final step also QC can be applied to the derived horizontal wind vector (speed and direction) by applying consistency or continuity approaches as performed for radar wind profilers [27.145] (Chap. 31).

27.7 Maintenance

The maintenance efforts for wind lidar instruments strongly depend on its maturity and complexity. On the one hand, there are commercial instruments, which are operable 24/7, unattended, and require only a minimum of maintenance. Also, these instruments are usually operable without any restrictions on laser eye safety. On the other hand, there are research instruments that require expert users for lasers and/or lidars and specific operations and maintenance procedures, which strongly vary for each instrument.

Thus, only some basic maintenance operations for commercial instruments, which are all based on coherent-detection technology, are summarized in Table 27.8. They include visual, functional, and performance inspections, and automatic or semiautomatic checks on instrument parameters (e.g., laser energy, temperatures).

The instrument performance of the lidar instrument is influenced by the cleanliness of the output window, which is used to separate the outside envi-

Table 27.8 Maintenance intervals of autonomous, commercial DWL systems

Interval	Visual inspection	Functional inspection	Performance verification
1–4 weeks		Check instrument housekeeping data, e.g., laser, temperatures, operation flags	Check typical measurement range and data quality
1–3 months	Inspect window, scanning device, electrical power supply, cooling, site and environment with respect to laser viewing direction, desiccants in housing	Check mechanical scanner, laser pointing verification (leveling, and north direction)	Verify laser power and receive path alignment
6–12 months	Lubricants or greasing for mechanical parts of scanner need to be checked and refilled; check of sealing of instrument housing		
1–2 years	Performance verification by manufacturer: laser power, receive path alignment, subunit performance, overall performance		

ronment from the delicate optics inside and to allow thermal control of the units. This window is contaminated by dust, precipitation, snow, and ice from the outside or condensed humidity from the inside. Usually, commercial DWL are equipped with a device to automatically clean this window (e.g., by a wiper). Nevertheless, visual inspections should check the cleanliness of the protecting output window. Furthermore, the site should be inspected regularly with respect to visibility for the laser beam (e.g., blocking by growing vegetation), the conditions of the ground site and instrument setup, leveling (horizontally, vertically), and alignment with respect to the north direction. This includes verification of the laser beam pointing – as is usually performed when setting up the instrument, e.g., by use of returns from hard targets (e.g., buildings) from a known azimuthal direction. Furthermore, a proper electrical power supply, lightning protection, and clearance of the opening for blowers and cooling devices needs to be ensured. Some suppliers use cleaning agents for the window, whose tanks need to be checked. In order to preserve low humidity conditions inside the housing, specific desiccants are used, which need to be checked.

27.8 Applications

A variety of applications of DWL is listed in Sect. 27.1. Here, three typical examples are discussed in more detail, from coherent wind lidars towards the observation of gravity waves in the stratosphere with direct-detection methods.

27.8.1 Hazard Detection at Airports

Doppler lidar techniques are well matched for detecting and characterizing air motions, such as low-level wind shear, wake vortices, and turbulence at airports that can

Functional verifications mainly include the mechanical parts of the scanning device (including lubricants, greasing), the instrument housing, temperature stabilization, or electrical power supply. Basic functional verifications of the lidar instrument should include measurements of the outgoing laser power. Automatic monitoring of instrument parameters is a prerequisite for autonomous operation but should also be verified regularly by the user. The verification of the performance of the instrument is mainly based on the assessment of the typical measurement range and quality of the observations. As this strongly depends on the atmospheric conditions (e.g., the presence of clouds and aerosol as backscatter targets), it varies strongly during the course of the day and from day to day. Thus, experience in assessing the range performance is needed.

Optical performance verifications, such as optical transmission, laser performance, or alignment verifications, should primarily be performed in a laboratory environment. This includes the verification of the performance and functions of the scanning device. Thus, the lidar instrument's optical performance and the scanning device need to be verified by the supplier, typically every year or every other year.

represent a threat to arriving and departing aircraft. Because wind shear encountered on takeoff or landing can result in a sudden change in airspeed necessitating corrective action to maintain lift and aircraft control, timely and accurate reporting of significant shear is important. Significant low-level wind shear is defined as a change in headwind of 15 kn (knots) or more at an altitude < 1600 ft (feet) within 3 nmi (nautical miles) from the runway threshold [27.146]. Because such conditions are ideally observed by Doppler lidar, these have been installed and operated at a number of airports

where local conditions are conducive to the generation of hazardous shear conditions, including Hong Kong, Munich, Sendai, Beijing, Frankfurt, and Las Vegas.

One of the earliest installations of a Doppler lidar intended for operational use was at Hong Kong International Airport (HKIA) in 2002 [27.11]. The orography at HKIA, especially the presence of the Lantau island to the south, is conducive to generation of wind shear in a variety of different weather conditions, including the generation of gravity waves under stable conditions, terrain-induced disruption of airflow under northeast and southwest flow, sea breeze, and severe convection and tropical cyclone events. At the beginning of 2002, a 2 mJ per pulse, 500 Hz pulse repetition frequency commercial Doppler lidar operating at 2 μm wavelength was installed on a rooftop near the center of HKIA. The lidar operated with high reliability (> 98%) over several years, with brief interruptions of a few hours for servicing. Long-term assessment of lidar performance showed that the lidar provided measurements to beyond 6 km range at least 70% of the time. Comparisons of the lidar measured wind with a tower-mounted cup anemometer showed negligible bias in the mean line-of-sight wind measurements and standard deviations on the order of 1 m s^{-1} . In October 2006, a second lidar was installed to provide better coverage along the north runway, where most aircraft approaches are made.

Characterizations of wind shear flow patterns observed by the HKIA lidar superimposed on a map of terrain and showing airport runways can be seen in Fig. 27.13 for different generating phenomena. The measurements show the capability of the lidar to detect potentially hazardous shear events. Lidar observations were also used to develop and test a lidar-based wind-shear alerting system intended to provide automatic wind-shear detection and alerts, based on the observation of a sustained change in headwind along the glide path. The lidar warning system at HKIA was recently upgraded by installing a new pulsed system based on a 1.5 μm fiber-based lidar transmitter and a high power planar waveguide laser [27.147]. The new instrument has demonstrated measurement to ranges of 30 km and heights of 12 km, which should significantly extend the range for wind-shear detection. Similar commercial instruments are scheduled for installation over the next few years at Nice, Beijing, and Antalya, Turkey, airports.

Application of both CW and pulsed coherent lidars to observe aircraft wake vortices has been demonstrated in several studies [27.13, 148]. Currently, the need to avoid wake vortices establishes separation distances between leading and following aircraft during takeoff and landing. Because the persistence of wake vortices is a function of local atmospheric conditions and can vary

significantly, information on vortex behavior under different atmospheric conditions can aid in updating separation distances and evaluating the impacts of implementing changes in operational procedures. Lidar investigations of wake vortices have typically focused on detection of the vortices and characterization of key parameters, including horizontal and vertical position and information on the strength of the vortex circulation.

Although CW lidars can provide excellent range resolution when a wake vortex is located close to the lidar, the lack of ranging capability precludes the use of a single CW lidar to track evolution of vortices as they move away from the lidar. In [27.13], the use of a scanning 2 μm , 2 mJ pulsed coherent lidar with a range resolution of 88 m was investigated to characterize vortex pairs, including trajectory, core separation, tilt angle, and circulation from large transport aircraft. Although the pulse duration defined a range resolution of 88 m, computation of a periodogram at 3 m intervals facilitated identification of the vortex core at higher spatial resolution. The range capability of the pulsed instrument enabled observation and tracking of the vortex pair over a time interval from generation by the aircraft to decay. Recently, in [27.149] a microjoule-type instrument with an average power of 1 W and 18 kHz pulse repetition frequency to observe vortices produced by a Boeing 767 aircraft was demonstrated by applying a retrieval method based on iterative optimization of the state variables describing vortex properties to a Doppler spectrum computed from scanning lidar observations. Field studies at Narita International Airport showed the capability of the technique to estimate the horizontal and vertical positions and radii-averaged circulation of the vortices observed.

Coherent Doppler lidars have also been proposed as part of an observing system to measure wind and turbulence at airports for better mitigation of wake vortex hazards [27.150]. The concept combines a pulsed lidar and X-band radar to estimate wind vectors and the eddy dissipation rate, key parameters for predicting wake vortex evolution after generation. Experiments at Toulouse airport demonstrated the potential capability of the proposed instrument combination to provide the necessary measurements for both wake vortex mitigation and for assimilation into NWP models to improve short-term forecasts.

27.8.2 Wind Energy

Over the past decade, the availability of compact, reliable commercial coherent Doppler lidar systems has contributed to their widespread use for a variety of diverse applications in the wind energy industry, including the evaluation of potential energy yield of wind

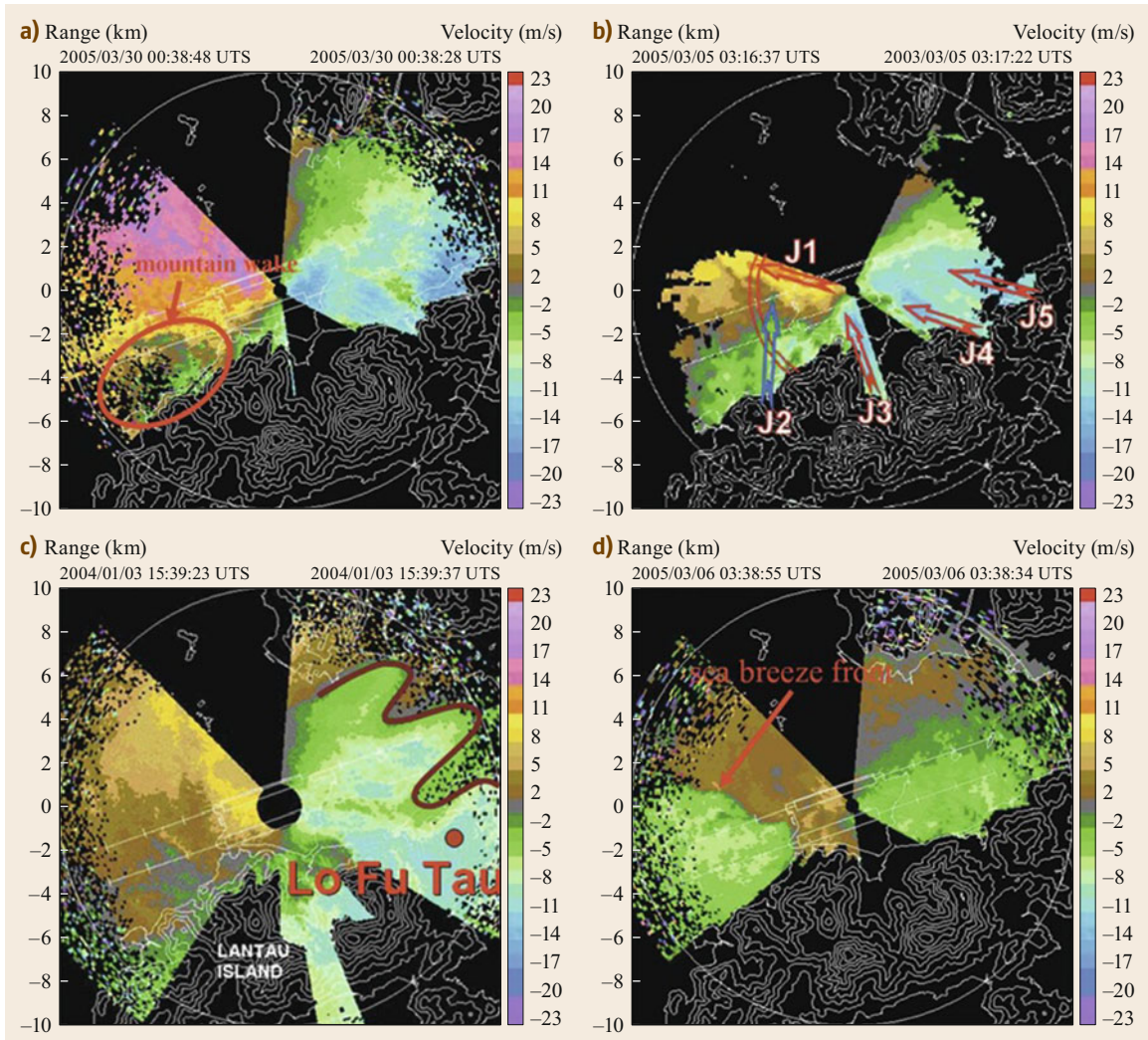


Fig. 27.13a–d Characterizations of wind shear flow patterns observed by the HKIA lidar superimposed on a map of terrain and showing airport runways, for (a,c) mountain waves; (b) accelerated gap flow; (d) westerly sea breeze against easterly winds (after [27.11] © American Meteorological Society; used with permission)

energy sites, the investigation of the effects of turbine wakes on power production of turbines downwind, and active turbine control to reduce blade load and increase energy capture. Both pulsed and CW instruments have been extensively applied and are becoming widely accepted in the industry as a reliable source of wind information.

Effective decisions on the development of new wind farms and optimization of their design require reliable measurement of winds and turbulence, which can be provided by lidar techniques. Traditionally, the wind energy industry has relied on in-situ instruments, such as the cup and vane anemometers deployed on mete-

orological masts to provide these wind measurements (Chaps. 9 and 51). However, as turbines have become larger, the application of in-situ instruments on high masts has become increasingly impractical due to cost and safety issues. Doppler lidars are well suited to remotely characterize winds for the assessment of the wind-energy power generation potential. A study in which a CW lidar was deployed for 1 year at an onshore site near Lake Erie to measure winds at the hub height of two potential wind turbines is described in [27.151]. Following the study, two commercial wind turbines were constructed at the site and provided power capacity data for comparison with the power capacity

estimated from the lidar measurements. The year-long study revealed strong seasonal variabilities in wind speed, with higher wind energy potential available in the winter. The lidar measurements also indicated the general presence of a high level of turbulence at the test site, with more turbulence observed at the greater height. A comparison of capacity factors, defined as the average power output to the rated power output of a generator, estimated from the lidar data with those from the actual in-service turbines showed agreement to within 10%, demonstrating the effectiveness of lidar for predicting energy output at a given site.

Because a CW lidar measures the wind profile above a single location, effectively duplicating measurements from a fixed tower, the representativeness of profile measurements observed by a single lidar for potential wind farm assessment is limited in regions of complex terrain. A scanning pulsed lidar system, which can survey winds over a significant area, addresses the representativeness issue by observing the horizontal variability of the wind across a potential farm site. The capability of a single scanning Doppler lidar to measure spatial and diurnal variability of winds for wind farm assessment by evaluating results on terrain following surfaces at multiple heights across a region of complex terrain was demonstrated in [27.152]. The authors applied an optimal interpolation algorithm to estimate the 2-D wind field from lidar radial velocity measurements. From this, wind power production at every location across the region was predicted (Fig. 27.14)

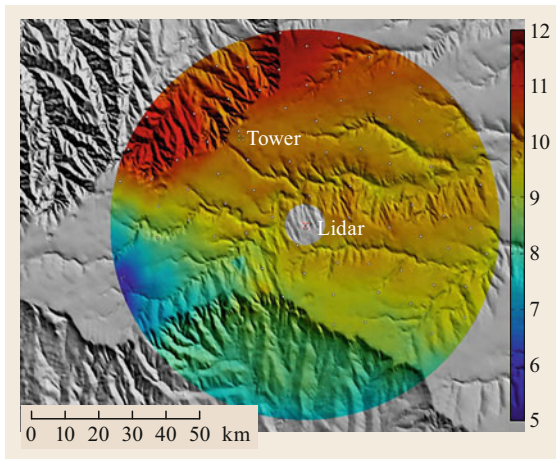


Fig. 27.14 Estimated wind power production across a region of complex terrain estimated from Doppler lidar scans. The color bar represents the power in kilowatts (after [27.152] reprinted with permission from John Wiley & Sons)

based on the average wind at 80 m hub height and was used to develop the layout for a notional wind farm.

A key issue in optimizing power output from large wind farms is minimizing the effects of turbine wakes on downwind turbines because the reduced wind speeds and increased turbulence in turbine wakes affects power generation from the downwind turbines. Doppler lidars are very well matched to study the properties of turbine wakes and have been employed in several studies in recent years [27.10, 153–155]. In one study [27.154], a ground-based scanning lidar was used to investigate wakes from a row of four turbines on a wind farm deployed in central Iowa. Figure 27.15 shows an example of wakes as observed by the lidar, where the velocity deficits in the wakes are clearly observed. Because wakes erode quickly under unstable conditions, wakes in this study were observed primarily under stable conditions. The lidar was used to estimate wake parameters, such as velocity deficits, the size of the wake boundaries, and wake centerlines. The measurements showed the effects of wind veer on the wake centerline location and the vertical structure of the wakes, and also revealed significant differences between the wakes from turbines in the center of the row compared to those at the edge.

Turbine wake characterization can also be addressed with nacelle-mounted lidars [27.153]. In this study, two lidars were mounted on the nacelle of a 2.5 MW wind turbine, with one pointed upstream to characterize the inflow, while the other looked downstream to characterize the wake. Observations from various scan patterns were processed to study the relationships between wake growth rate, wake width at the rotor plane, wake length, and turbulence intensity, which were compared with predictions from an analytic wake mode. In a different study [27.156], results from deployment of an upwind looking, nacelle-mounted CW Doppler lidar are described to detect the presence of upstream wakes for use in yaw steering of the wind turbine.

Wind information from Doppler lidars can be potentially utilized for wind turbine control, whereby the lidar-measured wind data provides information used in a feed-forward loop to improve turbine power output and increase reliability and lifetime. A CW Doppler lidar mounted at the tip of a rotating spinner to measure winds and turbulence ≈ 100 and 45 m upwind of the turbine blade is described in [27.87]. The spinner-mounted lidar observed the line-of-sight wind field in the rotor plan, revealing substantial variation in the rotor plane inflow under some conditions. The lidar-measured *pre-view* of the wind field provided potentially useful information for the optimization of yaw, blade pitch, and

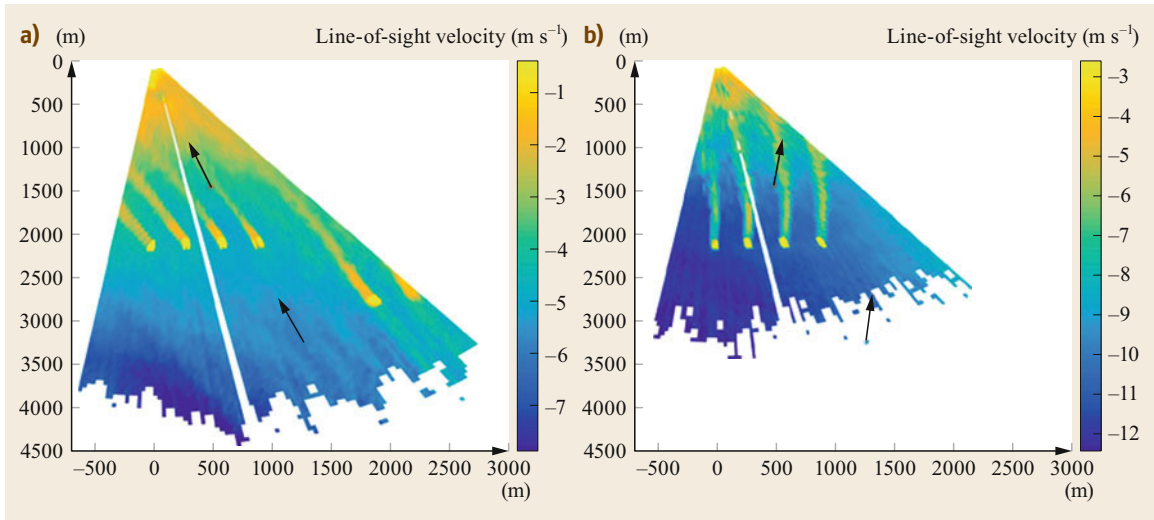


Fig. 27.15a,b Color maps showing line-of-sight wind velocities and wake effects from a line of wind turbines as measured by a scanning Doppler lidar: **(a)** 23.08.2013, 11:57:40, elevation angle = 1.50°; **(b)** 26.08.2013, 02:33:34, elevation angle = 2.80°. Arrows indicate wind direction (after [27.154] © Bodini et al., Creative Common Attribution Licence 3.0)

speed control to improve power output and mitigate the effects of strong wind shear and yaw errors.

27.8.3 Gravity Waves in the Stratosphere

Atmospheric gravity waves describe a perturbation of the atmospheric state in temperature, density, pressure, and wind, which are not of pure random nature and show some periodic behavior with temporal (minutes to hours), vertical (2–30 km), and horizontal (10–1000 km) spatial structures. Gravity waves, where gravity and buoyancy act as restoring forces, are characterized by their wavelength, dispersion relation, and propagation in the atmosphere. These are ubiquitous in the atmosphere and play important roles in influencing its state by transporting energy and momentum between widely separated regions and generating turbulence by breaking of the waves and dissipation of energy. These waves can be generated via different mechanisms, e.g., orographically by disturbances of the atmospheric flow by mountains or islands, by convection, or by instabilities and wind shear within regions of high wind speeds (*jet streams*).

Depending on the atmospheric stability, they propagate vertically and horizontally from their origin, are damped or filtered within atmospheric layers, or break at certain levels. The major wave influences occur in the stratosphere and mesosphere between 10 and 110 km (denoted as the *middle atmosphere*), because of increasing wave amplitude with altitude for vertically

propagating waves due to decreasing density. Thus, gravity waves of large amplitudes are observed in the stratosphere and even mesosphere, and are observed by lidars for the atmospheric temperature as well as wind. An extensive review of gravity wave dynamics and observations is provided in [27.157].

While numerous case studies and climatologies on gravity waves using Rayleigh lidars for measurement of the atmospheric temperatures up to the mesosphere are reported, only few wind lidar observations of gravity waves have been reported for the stratosphere [27.27, 158–160]. Here, an example of the temperature and wind lidar deployed at the ALOMAR (Arctic Lidar Observatory) observatory in northern Norway is discussed, which is operated by the Leibniz Institute of Atmospheric Physics, Germany [27.123, 135]. Figure 27.16 shows zonal and meridional winds retrieved from measurements between 21.01.2012 09:00 UT and 23.01.2012 11:00 UT with clear signatures of gravity waves for both the mean flow as well as the perturbations. These perturbations are calculated by subtracting a representative value for the mean wind speed for each altitude. Between 21.01.2012 16:00 UT and 22.01.2012 10:00 UT, the zonal and meridional winds in the altitude range of 60–70 km show both downward phase progression with $\approx 0.2 \text{ m s}^{-1}$ ($\approx 0.8 \text{ km h}^{-1}$), a vertical wavelength of 8 km, and an observed period of $\approx 11 \text{ h}$. The wave signatures are very similar in the two wind components with comparable vertical wavelengths and phase speeds [27.27].

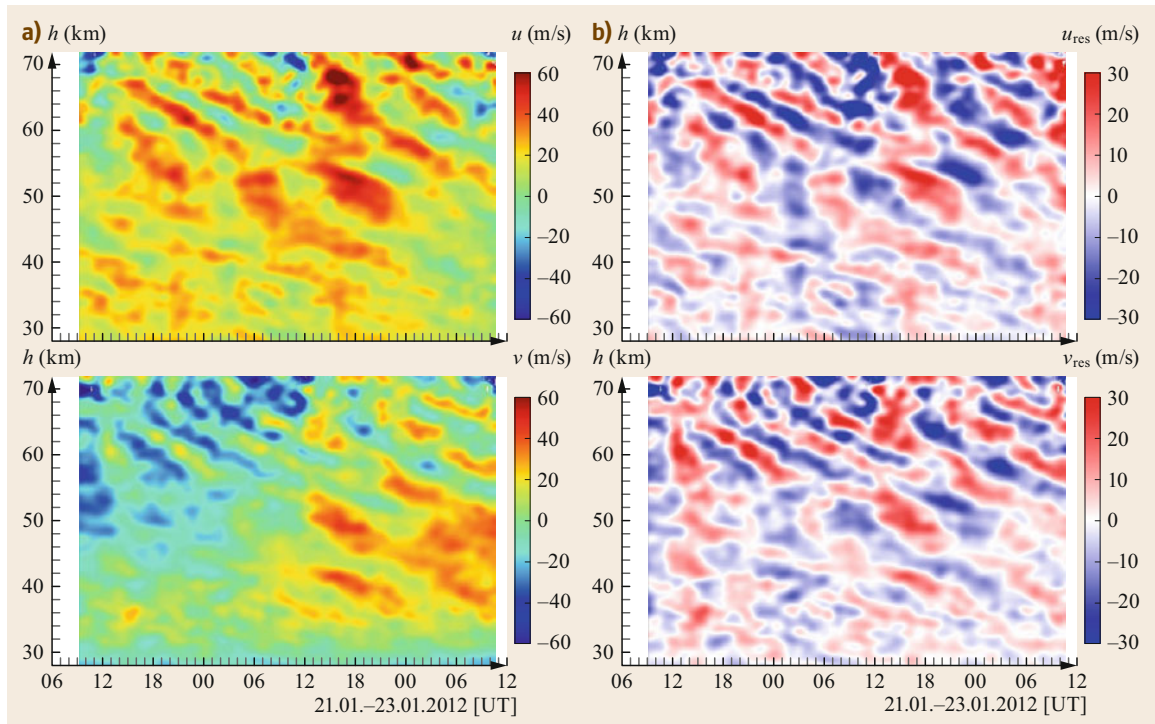


Fig. 27.16a,b Zonal (*top*) and meridional wind (*bottom*) measured between 21.01.2012 and 23.01.2012 at the Alomar observatory for total winds: **(a)** data are smoothed with a Gaussian kernel of 2 km and 2 h FWHM and **(b)** their perturbations from the mean flow (after removing low-frequency observations) (figure courtesy of G. Baumgarten, IAP, Kühlungsborn)

27.9 Future Developments

In the past decade coherent wind lidar instruments matured significantly and were widely applied in the wind energy sector. This was driven by developments for fiber laser technologies emerging from the telecommunications sector. Coherent DWL are operable unattended and continuously by trained persons, and are affordable, with lower investment and maintenance costs. This trend continues with smaller instruments (weight, volume) and lower investment costs, especially with instruments for specific applications, e.g., lower ranges of only up to 100 m for wind turbine control.

Small and cheap lidar instruments for ranging application are developed for the automotive sector, enhancing the capabilities of autonomous driving. Technology concepts are currently being studied to enhance these ranges with Doppler capabilities for speed detection. It can be anticipated that also the atmospheric wind-sensing application would benefit from these developments in the future.

The demands from air traffic for monitoring of low-level wind shears and wake vortex in the vicinity of airport runways during clear air conditions will foster the further application of wind lidars. Research on wind lidar sensors onboard aircraft has been ongoing for more than two decades. Long-range wind lidars with a range of ≈ 10 km could be used for the detection of clear air turbulence (CAT), while short-range wind lidars for ranges of around 50–300 m could be used for active control of aircraft in the future.

Atmospheric monitoring networks for meteorological or pollution transport purposes will make growing demands on wind lidars in combination with other remote sensing sensors. These would be used to measure horizontal transports of gases or particles, as well as turbulent fluxes for vertically pointing instruments for research applications.

Besides deployment of wind lidars on the ground, these instruments have already been used on a num-

ber of different platforms for research purposes, such as on ships, truck-mounted systems (e.g., for tornado research), and aircrafts. With further ruggedizing of these instruments, these research applications will expand to new platforms, e.g., balloons, UAS (unmanned aircraft systems), or even commercial aircraft.

The exploitation of global wind profiling by the use of spaceborne wind lidars just started with the launch of Aeolus in August 2018 [27.161]. Several space lidar mission concepts have been studied and developed,

mainly in Europe, the USA, Japan, and China. Aeolus is considered as a demonstration mission for future operational missions, serving the need for global wind profile observations for numerical weather prediction. Future operational capabilities of global wind profiling will, ideally, require a number of two to three polar-orbiting wind lidar satellites to achieve sufficient horizontal and temporal coverage [27.162]. International collaboration among meteorological satellite agencies will be needed to achieve this objective and fill the gap in the global observing system for wind profiles.

27.10 Further Readings

A comprehensive textbook including theory and application for turbulence research is recommended for readers interested in coherent DWL:

- V. Banakh and I. Smalikho: *Coherent Doppler Wind Lidars in a Turbulent Atmosphere* (Artech House, Boston, London 2013)

An ISO guideline for coherent DWL for the commonly used pulsed systems has been established (and replaces the earlier VDI 3786, part 14, 2001):

- ISO 28902-2:2017: *Air Quality—Environmental Meteorology—Part 2: Ground-Based Remote Sensing of Wind by Heterodyne Pulsed Doppler Lidar* (International Standard Organization, Geneva 2017)

Both coherent and direct-detection wind lidars are covered in an extensive book chapter by:

- S.W. Henderson, P. Gatt, D. Rees, R.M. Huffaker: Wind lidar. In: *Laser Remote Sensing*, ed. by T. Fujii and T. Fukuchi (CRC Press, Boca Raton 2005), pp. 487–740

Shorter introductions to coherent and direct-detection wind lidars can be found in:

- M. Hardesty: Lidar: Doppler. In: *Encyclopedia of Atmospheric Sciences*, 2nd edn., Vol. 3, ed. by G.R. North, J.A. Pyle, F. Zhang (Academic Press, London 2015), pp. 289–295
- O. Reitebuch: Wind lidar for atmospheric research. In: *Atmospheric Physics – Background, Methods, Trends*, ed. by U. Schumann. Springer Series on Research Topics in Aerospace (Springer, Berlin, Heidelberg 2012), pp. 487–507
- C. Werner: Doppler Wind Lidar. In: *Lidar – Range-Resolved Optical Remote Sensing of the Atmosphere*, ed. by C. Weitkamp (Springer, New York 2004)

References

- | | |
|--|--|
| <p>27.1 O. Reitebuch: Wind lidar for atmospheric research. In: <i>Atmospheric Physics – Background, Methods, Trends</i>, Research Topics in Aerospace, ed. by U. Schumann (Springer, Berlin, Heidelberg 2012) pp. 487–507</p> <p>27.2 M. Hardesty: Lidar: Doppler. In: <i>Encyclopedia of Atmospheric Sciences</i>, 2nd edn., Vol. 3, ed. by G.R. North, J.A. Pyle, F. Zhang (Academic Press, London 2015) pp. 289–295</p> <p>27.3 O. Reitebuch: The space-borne wind lidar mission ADM-Aeolus. In: <i>Atmospheric Physics – Background, Methods, Trends</i>, Research Topics in Aerospace, ed. by U. Schumann (Springer, Berlin, Heidelberg 2012) pp. 815–827</p> | <p>27.4 European Space Agency: <i>ADM-Aeolus – Science Report</i>, ed. by P. Clissold (ESTEC, Noordwijk 2008), ESA SP-1311</p> <p>27.5 A. Sathe, J. Mann: A review of turbulence measurements using ground-based wind lidars, <i>Atmos. Meas. Tech.</i> 6(11), 3147–3167 (2013)</p> <p>27.6 V. Banakh, I. Smalikho: <i>Coherent Doppler Wind Lidars in a Turbulent Atmosphere</i> (Artech House, Boston, London 2013)</p> <p>27.7 A. Clifton, P. Clive, J. Gottschall, D. Schlipf, E. Simley, L. Simmons, D. Stein, D. Trabucchi, N. Vasiljevic, I. Würth: IEA Wind Task 32: Wind lidar identifying and mitigating barriers to the adoption of wind lidar, <i>Remote Sens.</i> 10(3), 406 (2018)</p> |
|--|--|

- 27.8 T. Mikkelsen: Lidar-based research and innovation at DTU wind energy – A Review, *J. Phys. Conf. Ser.* **524**, 012007 (2014)
- 27.9 S. Emeis, M. Harris, R. Banta: Boundary-layer anemometry by optical remote sensing for wind energy applications, *Meteorol. Z.* **16**(4), 337–347 (2007)
- 27.10 Y. Käsler, S. Rahm, R. Simmet, M. Kühn: Wake measurements of a multi-MW wind turbine with coherent long-range pulsed doppler wind lidar, *J. Atmos. Ocean. Technol.* **27**(9), 1529–1532 (2010)
- 27.11 C.M. Shun, P.W. Chan: Applications of an infrared Doppler lidar in detection of wind shear, *J. Atmos. Ocean. Technol.* **25**(5), 637–655 (2008)
- 27.12 A. Weipert, S. Kauczok, R. Hannesen, T. Ernsdorf, B. Stiller: Wind shear detection using radar and lidar at Frankfurt and Munich airports. In: *8th Eur. Conf. Radar Meteorol. Hydrol. (ERAD)* (2014), Abstract-ID 058
- 27.13 F. Köpp, S. Rahm, I. Smalikho: Characterization of aircraft wake vortices by 2- μm pulsed Doppler lidar, *J. Atmos. Ocean. Technol.* **21**(2), 194–206 (2004)
- 27.14 I.N. Smalikho, S. Rahm: Lidar investigations of the effects of wind and atmospheric turbulence on an aircraft wake vortex, *Atmos. Ocean. Opt.* **23**(2), 137–146 (2010)
- 27.15 S. Rahm, I. Smalikho: Aircraft wake vortex measurement with airborne coherent Doppler lidar, *J. Aircr.* **45**(4), 1148–1155 (2008)
- 27.16 N.P. Schmitt, W. Rehm, T. Pistner, P. Zeller, H. Diehl, P. Navé: The AWIATOR airborne LIDAR turbulence sensor, *Aerosp. Sci. Technol.* **11**(7/8), 546–552 (2007)
- 27.17 H. Inokuchi, H. Tanaka, T. Ando: Development of an onboard Doppler lidar for flight safety, *J. Aircr.* **46**(4), 1411–1415 (2009)
- 27.18 F. Chouza, O. Reitebuch, A. Benedetti, B. Weinzierl: Saharan dust long-range transport across the Atlantic studied by an airborne Doppler wind lidar and the MACC model, *Atmos. Chem. Phys.* **16**(18), 11581–11600 (2016)
- 27.19 C.G. Collier, F. Davies, K.E. Bozier, A.R. Holt, D.R. Middleton, G.N. Pearson, S. Siemen, D.V. Willetts, G.J.G. Upton, R.I. Young: Dual-Doppler lidar measurements for improving dispersion models, *Bull. Am. Meteorol. Soc.* **86**(6), 825–838 (2005)
- 27.20 S.C. Tucker, C.J. Senff, A.M. Weickmann, W.A. Brewer, R.M. Banta, S.P. Sandberg, D.C. Law, R.M. Hardesty: Doppler lidar estimation of mixing height using turbulence, shear, and aerosol profiles, *J. Atmos. Ocean. Technol.* **26**(4), 673–688 (2009)
- 27.21 H.J.S. Fernando, J. Mann, J.M.L.M. Palma, J.K. Lundquist, R.J. Barthelmie, M. Belo-Pereira, W.O.J. Brown, F.K. Chow, T. Gerz, C.M. Hocut, P.M. Klein, L.S. Leo, J.C. Matos, S.P. Oncley, S.C. Pryor, L. Bariteau, T.M. Bell, N. Bodini, M.B. Carney, M.S. Courtney, E.D. Creegan, R. Dimitrova, S. Gomes, M. Hagen, J.O. Hyde, S. Kigle, R. Krishnamurthy, J.C. Lopes, L. Mazzaro, J.M.T. Neher, R. Menke, P. Murphy, L. Oswald, S. Otarola-Bustos, A.K. Pattantyus, C. Veiga Rodrigues, A. Schady, N. Sirin, S. Spuler, E. Svensson, J. Tomaszewski, D.D. Turner, L. van Veen, N. Vasiljević, D. Vassallo, S. Voss, N. Wildmann, Y. Wang: The Perdigão: Peering into microscale details of mountain Winds, *Bull. Am. Meteorol. Soc.* **100**(5), 799–819 (2019)
- 27.22 N. Vasiljević, J.M.L.M. Palma, N. Angelou, J.C. Matos, R. Menke, G. Lea, J. Mann, M. Courtney, L.F. Ribeiro, V.M.M.G.C. Gomes: Perdigão 2015: Methodology for atmospheric multi-Doppler lidar experiments, *Atmos. Meas. Tech.* **10**(9), 3463–3483 (2017)
- 27.23 C. Kiemle, M. Wirth, A. Fix, S. Rahm, U. Corsmeier, P. Di Girolamo: Latent heat flux measurements over complex terrain by airborne water vapour and wind lidars, *Q. J. R. Meteorol. Soc.* **137**(S1), 190–203 (2011)
- 27.24 O. Reitebuch, H. Volkert, C. Werner, A. Dabas, P. Delville, P. Drobinski, P.H. Flamant, E. Richard: Determination of air flow across the Alpine ridge by a combination of airborne Doppler lidar, routine radio-sounding and numerical simulation, *Q. J. R. Meteorol. Soc.* **129**(588), 715–727 (2003)
- 27.25 M. Weissmann, C. Cardinali: Impact of airborne Doppler lidar observations on ECMWF forecasts, *Q. J. R. Meteorol. Soc.* **133**(622), 107–116 (2007)
- 27.26 E. Päsche, R. Leinweber, V. Lehmann: An assessment of the performance of a 1.5 μm Doppler lidar for operational vertical wind profiling based on a 1-year trial, *Atmos. Meas. Tech.* **8**(6), 2251–2266 (2015)
- 27.27 G. Baumgarten, J. Fiedler, J. Hildebrand, F.-J. Lübken: Inertia gravity wave in the stratosphere and mesosphere observed by Doppler wind and temperature lidar, *Geophys. Res. Lett.* **42**(24), 10929–10936 (2015)
- 27.28 B. Witschas, S. Rahm, A. Dörnbrack, J. Wagner, M. Rapp: Airborne wind lidar measurements of vertical and horizontal winds for the investigation of orographically induced gravity waves, *J. Atmos. Ocean. Technol.* **34**(6), 1371–1386 (2017)
- 27.29 W.E. Baker, R. Atlas, C. Cardinali, A. Clement, G.D. Emmitt, B.M. Gentry, R.M. Hardesty, E. Källen, M.J. Kavaya, R. Langland, Z. Ma, M. Masutani, W. McCarty, R.B. Pierce, Z. Pu, L.P. Riishojgaard, J. Ryan, S. Tucker, M. Weissmann, J.G. Yoe: Lidar-measured wind profiles: The missing link in the global observing system, *Bull. Am. Meteorol. Soc.* **95**(4), 543–564 (2014)
- 27.30 C. Werner: Doppler Wind Lidar. In: *Lidar – Range-Resolved Optical Remote Sensing of the Atmosphere*, Optical Sciences, Vol. 102, ed. by C. Weitkamp (Springer, Singapore 2005) pp. 325–354
- 27.31 S.W. Henderson, P. Gatt, D. Rees, R.M. Huffaker: Wind lidar. In: *Laser Remote Sensing*, ed. by T. Fujii, T. Fukuchi (CRC Press, Boca Raton 2005) pp. 487–740
- 27.32 ISO 28902-2:2017: *Air Quality—Environmental Meteorology—Part 2: Ground-Based Remote Sensing of Wind by Heterodyne Pulsed Doppler Lidar*

- (International Organization for Standardization, Geneva 2017)
- 27.33 C. Hill: Coherent focused lidars for Doppler sensing of aerosols and wind, *Remote Sens.* **10**(3), 466 (2018)
- 27.34 T.H. Maiman: Stimulated optical radiation in ruby, *Nature* **187**(4736), 493–494 (1960)
- 27.35 G. Benedetti-Michelangeli, F. Congeduti, G. Fiocco: Measurement of aerosol motion and wind velocity in the lower troposphere by Doppler optical radar, *J. Atmos. Sci.* **29**(5), 906–910 (1972)
- 27.36 R.M. Huffaker (Ed.): *Feasibility Study of Satellite-Borne Lidar Global Wind Monitoring System* (Wave Propagation Laboratory, Boulder 1978), NOAA Tech. Memo. ERL WPL-37
- 27.37 R.M. Huffaker, T.R. Lawrence, M.J. Post, J.T. Priestley, F.F. Hall, R.A. Richter, R.J. Keeler: Feasibility studies for a global wind measuring satellite system (Windsat): Analysis of simulated performance, *Appl. Opt.* **23**(15), 2523–2536 (1984)
- 27.38 V.J. Abreu: Wind measurements from an orbital platform using a lidar system with incoherent detection: An analysis, *Appl. Opt.* **18**(17), 2992–2997 (1979)
- 27.39 M.L. Chanin, A. Garnier, A. Hauchecorne, J. Porteneuve: A Doppler lidar for measuring winds in the middle atmosphere, *Geophys. Res. Lett.* **16**(11), 1273–1276 (1989)
- 27.40 A. Garnier, M.L. Chanin: Description of a Doppler Rayleigh lidar for measuring winds in the middle atmosphere, *Appl. Phys. B* **55**(1), 35–40 (1992)
- 27.41 C.L. Korb, B.M. Gentry, C. Weng: The edge technique: Theory and application to the lidar measurement of atmospheric winds, *Appl. Opt.* **31**(21), 4202–4213 (1992)
- 27.42 B.M. Gentry, H. Chen, S.X. Li: Wind measurements with 355-nm molecular Doppler lidar, *Opt. Lett.* **25**(17), 1231–1233 (2000)
- 27.43 O. Reitebuch, C. Lemmerz, E. Nagel, U. Paffrath, Y. Durand, M. Endemann, F. Fabre, M. Chaloupy: The airborne demonstrator for the direct-detection Doppler wind lidar ALADIN on ADM-Aeolus: I. Instrument design and comparison to satellite instrument, *J. Atmos. Ocean. Technol.* **26**(12), 2501–2515 (2009)
- 27.44 A. Stoffelen, J. Pailleux, E. Källén, J.M. Vaughan, L. Isaksen, P. Flamant, W. Wergen, E. Andersson, H. Schyberg, A. Culoma, R. Meynart, M. Endemann, P. Ingmann: The atmospheric dynamics mission for global wind field measurements, *Bull. Am. Meteorol. Soc.* **86**(1), 73–88 (2005)
- 27.45 C.A. Tepley, S.I. Sargoytchev, C.O. Hines: Initial Doppler Rayleigh lidar results from Arecibo, *Geophys. Res. Lett.* **18**(2), 167–170 (1991)
- 27.46 C.A. Tepley, S.I. Sargoytchev, R. Rojas: The Doppler Rayleigh lidar system at Arecibo, *IEEE Trans. Geosci. Remote Sens.* **31**(1), 36–47 (1993)
- 27.47 J.S. Friedman, C.A. Tepley, P.A. Castleberg, H. Roe: Middle-atmospheric Doppler lidar using an iodine-vapor edge filter, *Opt. Lett.* **22**(21), 1648–1650 (1997)
- 27.48 Z.S. Liu, W.B. Chen, T.L. Zhang, J.W. Hair, C.Y. She: An incoherent Doppler lidar for ground-based atmospheric wind profiling, *Appl. Phys. B* **64**(5), 561–566 (1997)
- 27.49 Z.-S. Liu, B.-Y. Liu, S.-H. Wu, Z.-G. Li, Z.-J. Wang: High spatial and temporal resolution mobile incoherent Doppler lidar for sea surface wind measurements, *Opt. Lett.* **33**(13), 1485–1487 (2008)
- 27.50 V.J. Abreu, J.E. Barnes, P.B. Hayes: Observation of winds with an incoherent lidar detector, *Appl. Opt.* **31**(22), 4509–4514 (1992)
- 27.51 K.W. Fischer, V.J. Abreu, W.R. Skinner, J.E. Barnes, M.J. McGill, T.D. Irgang: Visible wavelength Doppler lidar for measurement of wind and aerosol profiles during day and night, *Opt. Eng.* **34**(2), 499–511 (1995)
- 27.52 Z. Liu, T. Kobayashi: Differential discrimination technique for incoherent Doppler lidar to measure atmospheric wind and backscatter ratio, *Opt. Rev.* **3**(1), 47–52 (1996)
- 27.53 R.L. Schwiesow, S.D. Mayor: Coherent optical signal processing for a Doppler lidar using a Michelson interferometer. In: *Coherent Laser Radar. Summaries of the Papers Presented at the Topical Meeting*, OSA Technical Digest Series, Vol. 19 (Optical Society of America, Washington 1995) pp. 212–215
- 27.54 D. Bruneau: Mach-Zehnder interferometer as a spectral analyzer for molecular Doppler wind lidar, *Appl. Opt.* **40**(3), 391–399 (2001)
- 27.55 D. Bruneau, A. Garnier, A. Hertzog, J. Porteneuve: Wind-velocity lidar measurements by use of a Mach-Zehnder interferometer, comparison with a Fabry-Perot interferometer, *Appl. Opt.* **43**(1), 173–182 (2004)
- 27.56 A.T. Forrester: Photoelectric mixing as a spectroscopic tool, *J. Opt. Soc. Am.* **51**(3), 253–259 (1961)
- 27.57 G. Gould, S.F. Jacobs, J.T. LaTourrette, M. Newstein, P. Rabinowitz: Coherent detection of light scattered from a diffusively reflecting surface, *Appl. Opt.* **3**(5), 648–649 (1964)
- 27.58 R.M. Huffaker: Laser Doppler detection systems for gas velocity measurement, *Appl. Opt.* **9**(5), 1026–1039 (1970)
- 27.59 T.R. Lawrence, D.J. Wilson, C.E. Craven, I.P. Jones, R.M. Huffaker, J.A.L. Thomson: A laser Doppler velocimeter for remote wind sensing, *Rev. Sci. Instrum.* **43**(3), 512 (1972)
- 27.60 N.L. Abshire, R.L. Schwiesow, V.E. Derr: Doppler lidar observations of hydrometeors, *J. Appl. Meteorol.* **13**(8), 951–953 (1974)
- 27.61 R.L. Schwiesow, R.E. Cupp: Remote Doppler measurements of atmospheric dust devil vortices, *Appl. Opt.* **15**(1), 1–2 (1976)
- 27.62 R.L. Schwiesow: Horizontal velocity structure in waterspouts, *J. Appl. Meteorol.* **20**(4), 349–360 (1981)
- 27.63 J.W. Bilbro, W.W. Vaughan: Wind field measurement of the nonprecipitous regions surrounding severe storms by an airborne pulsed Doppler lidar system, *Bull. Am. Meteorol. Soc.* **59**(9), 1095–1100 (1978)

- 27.64 J. Bilbro, G. Fichtl, D. Fitzjarrald, M. Krause, R. Lee: Airborne Doppler lidar wind field measurements, *Bull. Am. Meteorol. Soc.* **65**(4), 348–359 (1984)
- 27.65 R.M. Huffaker, T.R. Lawrence, M.J. Post, J.T. Priestly, F.F. Hall, R.A. Richter, R.J. Keeler: Feasibility studies for a global wind measuring satellite system (Windsat): Analysis of simulated performance, *Appl. Opt.* **23**(15), 2523–2536 (1984)
- 27.66 M.J. Post, F.F. Hall, R.A. Richter, T.R. Lawrence: Aerosol backscattering profiles at $\lambda = 10.6 \mu\text{m}$, *Appl. Opt.* **21**(13), 2442–2446 (1982)
- 27.67 M.J. Post, R.E. Cupp: Optimizing a pulsed Doppler lidar, *Appl. Opt.* **29**(28), 4145–4158 (1990)
- 27.68 M.J. Post, W.D. Neff: Doppler lidar measurements of winds in a narrow mountain valley, *Bull. Am. Meteorol. Soc.* **67**(3), 274–281 (1986)
- 27.69 P.J. Neiman, R.M. Hardesty, M.A. Shapiro, R.E. Cupp: Doppler lidar observations of a downslope windstorm, *Mon. Weather Rev.* **116**(11), 2265–2275 (1988)
- 27.70 J.M. Intrieri, C.G. Little, W.J. Shaw, R.M. Banta, P.A. Durkee, R.M. Hardesty: The Land/Sea Breeze Experiment (LASBEX), *Bull. Am. Meteorol. Soc.* **71**(5), 656–664 (1990)
- 27.71 J. Rothermel, D.R. Cutten, R.M. Hardesty, R.T. Menzies, J.N. Howell, S.C. Johnson, D.M. Tratt, L.D. Olivier, R.M. Banta: The multi-center airborne coherent wind sensor, *Bull. Am. Meteorol. Soc.* **79**(4), 581–600 (1998)
- 27.72 R.M. Banta, L.S. Darby, J.D. Fast, J.O. Pinto, C.D. Whiteman, W.J. Shaw, B.W. Orr: Nocturnal low-level jet in a mountain basin complex. Part 1: Evolution and effects on local flows, *J. Appl. Meteorol.* **43**(10), 1348–1365 (2004)
- 27.73 T.J. Kane, W.J. Kozlovsky, R.L. Byer, C.E. Byvik: Coherent laser radar at $1.06 \mu\text{m}$ using Nd:YAG lasers, *Opt. Lett.* **12**(4), 239–241 (1987)
- 27.74 M.J. Kavaya, S.W. Henderson, J.R. Magee, C.P. Hale, R.M. Huffaker: Remote wind profiling with a solid-state Nd:YAG coherent lidar system, *Opt. Lett.* **14**(15), 776–778 (1989)
- 27.75 S.W. Henderson, C.P. Hale, J.R. Magee, M.J. Kavaya, A.V. Huffaker: Eye-safe coherent laser radar system at $2.1 \mu\text{m}$ using Tm, Ho:YAG lasers, *Opt. Lett.* **16**(10), 773–775 (1991)
- 27.76 O. Reitebuch, C. Werner, I. Leike, P. Delville, P.H. Flamant, A. Cress, D. Engelbart: Experimental validation of wind profiling performed by the airborne $10\text{-}\mu\text{m}$ heterodyne Doppler lidar WIND, *J. Atmos. Ocean. Technol.* **18**(8), 1331–1344 (2001)
- 27.77 F. Davies, C.G. Collier, K.E. Bozier, G.N. Pearson: On the accuracy of retrieved wind information from Doppler lidar observations, *Q. J. R. Meteorol. Soc.* **129**(587), 321–334 (2003)
- 27.78 C.J. Grund, R.M. Banta, J.L. George, J.N. Howell, M.J. Post, R.A. Richter, A.M. Weickmann: High resolution Doppler lidar for boundary layer and cloud research, *J. Atmos. Ocean. Technol.* **18**(3), 376–393 (2001)
- 27.79 R.K. Newsom, R.M. Banta: Shear-flow instability in the stable nocturnal boundary layer as observed by Doppler lidar during CASES-99, *J. Atmos. Sci.* **60**(1), 16–33 (2003)
- 27.80 V. Wulfmeyer, T. Janjić: Twenty-four-hour observations of the marine boundary layer using shipborne NOAA high-resolution Doppler lidar, *J. Appl. Meteorol.* **44**(11), 1723–1744 (2005)
- 27.81 R. Frehlich, S.M. Hannon, S.W. Henderson: Coherent Doppler lidar measurement of winds in the weak signal regime, *Appl. Opt.* **36**(15), 3491–3499 (1997)
- 27.82 G.N. Pearson, P.J. Roberts, J.R. Eacock, M. Harris: Analysis of the performance of a coherent pulsed fiber lidar for aerosol backscatter applications, *Appl. Opt.* **41**(30), 6442–6450 (2002)
- 27.83 G. Pearson, F. Davies, C. Collier: An analysis of the performance of the UFAM pulsed Doppler lidar for observing the boundary layer, *J. Atmos. Ocean. Technol.* **26**(2), 240–250 (2009)
- 27.84 J.-P. Cariou, L. Sauvage, L. Thobois, G. Gorju, M. Machta, G. Lea, M. Duboué: Long range scanning pulsed coherent lidar for real time wind monitoring in the planetary boundary layer. In: *Proc. 16th Coherent Laser Radar Conf., Long Beach* (Universities Space Research Association, Huntsville 2011)
- 27.85 C.J. Karlsson, F.Å.A. Olsson, D. Letalick, M. Harris: All-fiber multifunction CW $1.55 \mu\text{m}$ coherent laser radar for range, speed, vibration and wind measurements, *Appl. Opt.* **39**(21), 3716–3726 (2000)
- 27.86 S. Lang, E. McKeogh: LIDAR and SODAR measurements of wind speed and direction in upland terrain for wind energy purposes, *Remote Sens.* **3**(9), 1871–1901 (2011)
- 27.87 T. Mikkelsen, N. Angelou, K. Hansen, M. Sjöholm, M. Harris, C. Slinger, P. Hadley, R. Scullion, G. Ellis, G. Vives: A spinner-integrated wind lidar for enhanced windturbine control, *Wind Energy* **16**(4), 625–643 (2013)
- 27.88 M.J. Kavaya, J.Y. Beyon, G.J. Koch, M. Petros, P.J. Petzar, U.N. Singh, B.C. Trieu, J. Yu: The Doppler aerosol wind (DAWN) airborne, wind-profiling coherent-detection lidar system: Overview and preliminary flight results, *J. Atmos. Ocean. Technol.* **31**(4), 826–842 (2014)
- 27.89 C. Doppler: Ueber das farbige Licht der Doppelsterne und einiger anderer Gestirne des Himmels. In: *Christian Doppler – Leben und Werk: Der Dopplereffekt*, Salzburger Portraits, Schriftenreihe des Landespressebüros Salzburg, Vol. 76, ed. by A. Eden (Amt der Salzburger Landesregierung, Salzburg 1988) p. 23, in German
- 27.90 G. Tenti, C.D. Boley, R.C. Desai: On the kinetic model description of Rayleigh–Brillouin scattering from molecular gases, *Can. J. Phys.* **52**(4), 285–290 (1974)
- 27.91 B. Witschas, M.O. Vieitez, E.-J. van Duijn, O. Reitebuch, W. van de Water, W. Ubachs: Spontaneous Rayleigh–Brillouin scattering of ultraviolet light in nitrogen, dry air, and moist air, *Appl. Opt.* **49**(22), 4217–4227 (2010)

- 27.92 B. Witschas: Analytical model for Rayleigh–Brillouin lineshapes in air, *Appl. Opt.* **50**(3), 267–270 (2011), Errata in *Appl. Opt.* **50**(29): 573
- 27.93 B. Witschas: Light scattering on molecules in the atmosphere. In: *Atmospheric Physics – Background, Methods, Trends*, Research Topics in Aerospace, ed. by U. Schumann (Springer, Berlin, Heidelberg 2012) pp. 69–83
- 27.94 K.A. Browning, R. Wexler: The determination of kinematic properties of a wind field using Doppler radar, *J. Appl. Meteorol.* **7**(1), 105–113 (1968)
- 27.95 G. Teschke, V. Lehmann: Mean wind vector estimation using the velocity–azimuth display (VAD) method: An explicit algebraic solution, *Atmos. Meas. Tech.* **10**(9), 3265–3271 (2017)
- 27.96 R. Calhoun, R. Heap, M. Princevac, R. Newsom, H. Fernando, D. Ligon: Virtual towers using coherent Doppler lidar during the Joint Urban 2003 Dispersion Experiment, *J. Appl. Meteorol. Climatol.* **45**(8), 1116–1126 (2006)
- 27.97 N. Vasiljević, G. Lea, M. Courtney, J.–P. Cariou, J. Mann, T. Mikkelsen: Long-range WindScanner system, *Remote Sens.* **8**(11), 896 (2016)
- 27.98 S. Drechsel, G.J. Mayr, M. Chong, M. Weissmann, A. Dörnbrack, R. Calhoun: Three-dimensional wind retrieval: Application of MUSCAT to dual Doppler lidar, *J. Atmos. Ocean. Technol.* **26**(3), 635–646 (2009)
- 27.99 F. Carbajo Fuertes, G.V. Iungo, F. Porté-Agel: 3D turbulence measurements using three synchronous wind lidars: Validation against sonic anemometry, *J. Atmos. Ocean. Technol.* **31**(7), 1549–1556 (2014)
- 27.100 N. Wildmann, N. Vasiljević, T. Gerz: Wind turbine wake measurements with automatically adjusting scanning trajectories in a multi-Doppler lidar setup, *Atmos. Meas. Tech.* **11**(6), 3801–3814 (2018)
- 27.101 M. Hill, R. Calhoun, H.J.S. Fernando, A. Wieser, A. Dörnbrack, M. Weissmann, G. Mayr, R. Newsom: Coplanar Doppler lidar retrieval of rotors from T-REX, *J. Atmos. Sci.* **67**(3), 713–729 (2010)
- 27.102 B.J. Rye, R.M. Hardesty: Estimate optimization parameters for incoherent backscatter heterodyne lidar, *Appl. Opt.* **36**(36), 9425–9436 (1997)
- 27.103 R.G. Frehlich, M.J. Yadlowski: Performance of mean frequency estimators for Doppler radar and lidar, *J. Atmos. Ocean. Technol.* **11**(5), 1217–1230 (1994)
- 27.104 B.J. Rye: Antenna parameters for incoherent backscatter heterodyne lidar, *Appl. Opt.* **18**(9), 1390–1398 (1979)
- 27.105 W.R. Leeb, P.J. Winzer, K.H. Kudielka: Aperture dependence of the mixing efficiency, the signal-to-noise ratio, and the speckle number in coherent lidar receivers, *Appl. Opt.* **37**(15), 3143–3148 (1998)
- 27.106 S.F. Clifford, S. Wandzura: Monostatic heterodyne lidar performance: The effect of the turbulent atmosphere, *Appl. Opt.* **20**(3), 514–516 (1981)
- 27.107 R. Frehlich: Simulation of laser propagation in a turbulent atmosphere, *Appl. Opt.* **39**(3), 393–397 (2000)
- 27.108 A. Belmonte: Feasibility study for the simulation of beam propagation: Consideration of coherent lidar performance, *Appl. Opt.* **39**(30), 5426–5445 (2000)
- 27.109 A. Dabas, M.L. Denneulin, P. Flamant, C. Loth, A. Garnier, A. Dolfi–Bouteyre: Correcting winds measured with a Rayleigh Doppler lidar from pressure and temperature effects, *Tellus A* **60**(2), 206–215 (2008)
- 27.110 C.F. Abari, A.T. Pedersen, J. Mann: An all-fiber image-reject homodyne coherent Doppler wind lidar, *Opt. Express* **22**(21), 25880–25984 (2014)
- 27.111 M. Harris, M. Hand, A. Wright, S. Schreck (2006): Lidar for Turbine Control. Tech. Rep. NREL/TP–500–3914
- 27.112 METEK: *Lidar Wind Sensor Wind Scout. Product Data Sheet* (METEK GmbH, Elmshorn 2019), https://metek.de/wp-content/uploads/2018/05/20180521_Datenblatt_WindScout.pdf, Accessed 10 July 2021
- 27.113 ZX Lidars: *ZX 300 Onshore Wind Lidar. Product Guide* (ZX Lidars, Ledbury 2018), <https://www.zxlidars.com/wind-lidars/zx-300/>, Accessed 10 July 2021
- 27.114 A. Dolfi–Bouteyre, G. Canat, M. Valla, B. Augère, C. Besson, D. Goular, L. Lombard, J.–P. Cariou, A. Durecu, D. Fleury, L. Bricteux, S. Brousmiche, S. Lugan, B. Macq: Pulsed 1.5 μm LIDAR for axial aircraft wake vortex detection based on high-brightness large-core fiber amplifier, *IEEE J. Sel. Top. Quantum Electron.* **15**(2), 441–450 (2009)
- 27.115 S. Wu, B. Liu, J. Liu, X. Zhai, C. Feng, G. Wang, H. Zhang, J. Yin, X. Wang, R. Li, D. Gallacher: Wind turbine wake visualization and characteristics analysis by Doppler lidar, *Opt. Express* **24**(10), A762–A780 (2016)
- 27.116 V. Wulfmeyer, M. Randall, A. Brewer, R.M. Hardesty: 2- μm Doppler lidar transmitter with high frequency stability and low chirp, *Opt. Lett.* **25**(17), 1228–1230 (2000)
- 27.117 P. Gatt, K. Barr, M. Margulis: WindTracer® evolution and recent measurement results. In: *Imaging and Applied Optics 2015*, OSA Technical Digest (online), (Optical Society of America, Washington 2015), paper LT3D.2
- 27.118 S. Kameyama, T. Sakimura, Y. Watanabe, T. Ando, K. Asaka, H. Tanaka, T. Yanagisawa, Y. Hirano, H. Inokuchi: Wind sensing demonstration of more than 30 km measurable range with a 1.5 μm coherent Doppler lidar which has the laser amplifier using Er,Yb:glass planar waveguide, *Proc. SPIE* **8526**, 85260E (2012)
- 27.119 C. Flesia, C.L. Korb: Theory of the double-edge molecular technique for Doppler lidar wind measurement, *Appl. Opt.* **38**(3), 432–440 (1999)
- 27.120 J.M. Vaughan: *The Fabry–Perot interferometer: History, Theory, Practice and Applications*, Adam Hilger Series on Optics and Optoelectronics (IOP Publishing, Bristol 1989)

- 27.121 Z.S. Liu, B.Y. Liu, Z.G. Li, Z.A. Yan, S.H. Wu, Z.B. Sun: Wind measurements with incoherent Doppler lidar based on iodine filters at night and day, *Appl. Phys. B* **88**, 327–335 (2007)
- 27.122 C.Y. She, J. Yue, Z.-A. Yan, J.W. Hair, J.-J. Guo, S.-H. Wu, Z.-S. Liu: Direct-detection Doppler wind measurement with a Cabannes–Mie lidar: A. Comparison between iodine vapor filter and Fabry–Perot interferometer methods, *Appl. Opt.* **46**(20), 4434–4443 (2007)
- 27.123 G. Baumgarten: Doppler Rayleigh/Mie/Raman lidar for wind and temperature measurements in the middle atmosphere up to 80 km, *Atmos. Meas. Tech.* **3**(6), 1509–1518 (2010)
- 27.124 M. Hirschberger, G. Ehret: Simulation and high-precision wavelength determination of noisy 2D Fabry–Pérot interferometric rings for direct-detection Doppler lidar and laser spectroscopy, *Appl. Phys. B* **103**(1), 207–222 (2011)
- 27.125 M.J. McGill, W.R. Skinner, T.D. Irgang: Analysis techniques for the recovery of winds and backscatter coefficients from a multiple-channel incoherent Doppler lidar, *Appl. Opt.* **36**(6), 1253–1268 (1997)
- 27.126 M.J. McGill, J.D. Spinhirne: Comparison of two direct detection Doppler lidar techniques, *Opt. Eng.* **37**(10), 2675–2686 (1998)
- 27.127 J.A. McKay: Assessment of a multibeam Fizeau wedge interferometer for Doppler wind lidar, *Appl. Opt.* **41**(9), 1760–1767 (2002)
- 27.128 D. Bruneau, A. Garnier, A. Hertzog, J. Porteneuve: Wind-velocity lidar measurements by use of a Mach–Zehnder interferometer, comparison with a Fabry–Perot interferometer, *Appl. Opt.* **43**(1), 173–182 (2004)
- 27.129 S.C. Tucker, C.S. Weimer, S. Baidar, R.M. Hardesty: The optical autocovariance wind lidar (OAWL). Part I: Instrument development and demonstration, *J. Atmos. Ocean. Technol.* **35**(10), 2079–2097 (2018)
- 27.130 N. Cézard, A. Dolfi–Bouteyre, J.-P. Huignard, P.H. Flamant: Performance evaluation of a dual fringe-imaging Michelson interferometer for air parameter measurements with a 355 nm Rayleigh–Mie lidar, *Appl. Opt.* **48**(12), 2321–2332 (2009)
- 27.131 J. Herbst, P. Vrancken: Design of a monolithic Michelson interferometer for fringe imaging in a near-field, UV, direct-detection Doppler wind lidar, *Appl. Opt.* **55**(25), 6910–6929 (2016)
- 27.132 M. Imaki, T. Kobayashi: Ultraviolet high-spectral-resolution Doppler lidar for measuring wind field and aerosol optical properties, *Appl. Opt.* **44**(28), 6023–6030 (2005)
- 27.133 C. Flesia, C.L. Korb, C. Hirt: Double-edge molecular measurement of lidar wind profiles at 355 nm, *Opt. Lett.* **25**(19), 1466–1468 (2000)
- 27.134 H. Xia, X. Dou, D. Sun, Z. Shu, X. Xue, Y. Han, D. Hu, Y. Han, T. Cheng: Mid-altitude wind measurements with mobile Rayleigh Doppler lidar incorporating system-level optical frequency control method, *Opt. Express* **20**(14), 15286–15300 (2012)
- 27.135 J. Hildebrand, G. Baumgarten, J. Fiedler, U.-P. Hoppe, B. Kaifler, F.-J. Lübken, B.P. Williams: Combined wind measurements by two different lidar instruments in the Arctic middle atmosphere, *Atmos. Meas. Tech.* **5**(10), 2433–2445 (2012)
- 27.136 T.D. Irgang, P.B. Hays, W.R. Skinner: Two-channel direct-detection Doppler lidar employing a charge-coupled device as a detector, *Appl. Opt.* **41**(6), 1145–1155 (2002)
- 27.137 B.J. Rye, R.M. Hardesty: Discrete spectral peak estimation in incoherent backscatter heterodyne lidar. I: Spectral accumulation and the Cramer–Rao lower bound, *IEEE Trans. Geosci. Remote Sens.* **31**(1), 16–27 (1993)
- 27.138 R. Frehlich: Cramer–Rao bound for Gaussian random processes and applications to radar processing of atmospheric signals, *IEEE Trans. Geosci. Remote Sens.* **31**(6), 1123–1131 (1993)
- 27.139 B.J. Rye: Comparative precision of distributed backscatter Doppler lidars, *Appl. Opt.* **34**(36), 8341–8344 (1995)
- 27.140 A. Dabas: Semiempirical model for the reliability of a matched filter frequency estimator for Doppler lidar, *J. Atmos. Ocean. Technol.* **16**(1), 19–28 (1999)
- 27.141 World Meteorological Organization: *User Requirements for Observation (OSCAR/Requirements)* 2019), <https://www.wmo-sat.info/oscar/observingrequirements>, Accessed 10 July 2021
- 27.142 World Meteorological Organization: *Statement of guidance for global numerical weather prediction (NPW)*, approved 11 May 2018, <https://old.wmo.int/extranet/pages/prog/www/OSY/GOS-RRR.html#SOG>, Accessed 11 July 2021
- 27.143 M. Boquet, P. Royer, J.-P. Cariou, M. Machta, M. Valla: Simulation of Doppler lidar measurement range and data availability, *J. Atmos. Ocean. Technol.* **33**(5), 977–987 (2016)
- 27.144 R. Frehlich: Estimation of velocity error for Doppler lidar measurements, *J. Atmos. Ocean. Technol.* **18**(10), 1628–1639 (2001)
- 27.145 B.L. Weber, D.B. Wuertz, D.C. Welsh, R. McPeck: Quality controls for profiler measurements of winds and RASS temperatures, *J. Atmos. Ocean. Technol.* **10**(4), 452–464 (1993)
- 27.146 ICAO: *Manual on Low-level Windshear and Turbulence*, 1st edn. (International Civil Aviation Organization, Montréal 2005)
- 27.147 I. Kakimoto, T. Harada, S. Kameyama, J.-S. Ha, H.-I. Kim: Up to 12 km vertical wind profiling using Mitsubishi Electric's long range lidar. In: *19th Coherent Laser Radar Conf., Okinawa* (2018), paper P31
- 27.148 M. Harris, R.I. Young, F. Köpp, A. Dolfi, J.P. Cariou: Wake vortex detection and monitoring, *Aerosp. Sci. Technol.* **6**(5), 325–331 (2002)
- 27.149 E. Yoshikawa, N. Matayoshi: Aircraft wake vortex retrieval method on lidar lateral range-height indicator observation, *AIAA Journal* **55**(7), 2269–2278 (2017)

- 27.150 A.C.P. Oude Nijhuis, L.P. Thobois, F. Barbaresco, S. De Haan, A. Dolfi-Bouteyre, D. Kovalev, O.A. Krasnov, D. Vanhoenacker-Janvier, R. Wilson, A.G. Yarovoy: Wind hazard and turbulence monitoring at airports with lidar, radar, and Mode-S downlinks: The UFO Project, *Bull. Am. Meteorol. Soc.* **99**(11), 2275–2293 (2018)
- 27.151 J. Li, X. Yu: LiDAR technology for wind energy potential assessment: Demonstration and validation at a site around Lake Erie, *Energy Convers. Manag.* **144**, 252–261 (2017)
- 27.152 R. Krishnamurthy, A. Choukulkar, R. Calhoun, J. Fine, A. Oliver, K.S. Barr: Coherent Doppler lidar for wind farm characterization, *Wind Energy* **16**(2), 189–206 (2013)
- 27.153 F. Carbajo Fuertes, C.D. Markfort, F. Porté-Agel: Wind turbine wake characterization with nacelle-mounted wind lidars for analytical wake model validation, *Remote Sens.* **10**(5), 668 (2018)
- 27.154 N. Bodini, D. Zardi, J.K. Lundquist: Three-dimensional structure of wind turbine wakes as measured by scanning lidar, *Atmos. Meas. Tech.* **10**(8), 2881–2896 (2017)
- 27.155 R.M. Banta, Y.L. Pichugina, W.A. Brewer, J.K. Lundquist, N.D. Kelley, S.P. Sandberg, R.J. Alvarez II, R.M. Hardesty, A.M. Weickmann: 3D volumetric analysis of wind turbine wake properties in the atmosphere using high-resolution Doppler lidar, *J. Atmos. Ocean. Technol.* **32**(5), 904–914 (2015)
- 27.156 D.P. Held, A. Larvol, J. Mann: Detecting wind turbine wakes with nacelle lidars, *J. Phys. Conf. Ser.* **854**, 012020 (2017)
- 27.157 D.C. Fritts, M.J. Alexander: Gravity wave dynamics and effects in the middle atmosphere, *Rev. Geophys.* **41**(1), 1003 (2003)
- 27.158 F.-J. Lübken, G. Baumgarten, J. Hildebrand, F.J. Schmidlin: Simultaneous and co-located wind measurements in the middle atmosphere by lidar and rocket-borne techniques, *Atmos. Meas. Tech.* **9**(8), 3911–3919 (2016)
- 27.159 J. Hildebrand, G. Baumgarten, J. Fiedler, F.-J. Lübken: Winds and temperatures of the Arctic middle atmosphere during January measured by Doppler lidar, *Atmos. Chem. Phys.* **17**(21), 13345–13359 (2017)
- 27.160 R. Zhao, X. Dou, D. Sun, X. Xue, J. Zheng, Y. Han, T. Chen, G. Wang, Y. Zhou: Gravity waves observation of wind field in stratosphere based on a Rayleigh Doppler lidar, *Opt. Express* **24**(6), A581–A591 (2016)
- 27.161 O. Reitebuch, C. Lemmerz, O. Lux, U. Marksteiner, S. Rahm, F. Weiler, B. Witschas, M. Meringer, K. Schmidt, D. Huber, I. Nikolaus, A. Geiss, M. Vaughan, A. Dabas, T. Flament, H. Stieglitz, L. Isaksen, M. Rennie, J.D. Kloe, G.-J. Marseille, A. Stoffelen, D. Wernham, T. Kanitz, A.-G. Straume, T. Fehr, J. von Bismarck, R. Floberghagen, T. Parrinello: Initial assessment of the performance of the first wind lidar in space on Aeolus, *EPJ Web Conf.* **237**, 01010 (2020)
- 27.162 A. Stoffelen, A. Benedetti, R. Borde, A. Dabas, P. Flamant, M. Forsythe, M. Hardesty, L. Isaksen, E. Källén, H. Körnich, T. Lee, O. Reitebuch, M. Rennie, L.-P. Riishøjgaard, H. Schyberg, A.G. Straume, M. Vaughan: Wind profile satellite observation requirements and capabilities, *Bull. Amer. Meteorol. Soc.* **101**, E2005–E2020 (2020)

Oliver Reitebuch

Institut für Physik der Atmosphäre
Deutsches Zentrum für Luft- und
Raumfahrt e. V. (DLR)
Weßling, Germany
oliver.reitebuch@dlr.de



Oliver Reitebuch is Senior Scientist with the Institute of Atmospheric Physics of the German Aerospace Center DLR, Oberpfaffenhofen. He received his PhD in Physics from the University Regensburg, Germany (1999). His research interests focus on the development and exploitation of airborne and spaceborne wind lidar instruments and observations for atmospheric research. He is currently scientific coordinator of the Data Innovation and Science Cluster (DISC) for the first wind lidar in space on Aeolus.

R. Michael Hardesty

Cooperative Institute for Research in
Environmental Sciences
University of Colorado Boulder
Boulder, USA
r.michael.hardesty@colorado.edu



R. Michael Hardesty is a Senior Research Scientist with the Cooperative Institute for Research in Environmental Sciences at the University of Colorado Boulder, where he serves as Associate Director for Environmental Modeling, Observations, and Forecasting. He received his PhD in Electrical Engineering and Meteorology from the Naval Postgraduate School (1985). He is a recipient of the NOAA Distinguished Career Award. His research interests focus on the development and application of lidar techniques for remotely sensing the atmosphere.

Spectrometers

28. Spectrometers

Klaus Schäfer , Mark Wenig , Mark A. Zondlo , Axel Murk , Konradin Weber 

Spectrometers are used to determine the chemical composition and temperature of the atmosphere, exhausts, and gas releases. A relevant part of the electromagnetic spectrum is detected via absorption spectroscopy by means of artificial (e.g., lamps and lasers) or natural light sources (e.g., the Sun), as well as via emission spectroscopy using temperature differences or atmospheric radiation. The currently preferred spectrometer techniques are Fourier transform infrared spectroscopy (FTIR) in the infrared (IR) and visible (VIS), differential optical absorption spectroscopy (DOAS) in the VIS and ultraviolet (UV), as well as microwave radiometry (MWR). To achieve high sensitivity, tuned or broadband lasers are employed in laser spectrometers. Radiation absorption and scattering can be detected using spectrometers by an open-path configuration either through a single pass or multiple passes by steering optics in the atmosphere or exhausts. Analysis of the measured spectral features can be used to detect atmospheric gas concentrations, temperature, pressure, as well as aerosol scattering and absorption. The basic theory with equations and retrieval algorithms for processing measured spectra is described. In addition to characteristic parameters, quality assurance and quality control, calibration, and the necessary maintenance associated with the different measurement principles are presented.

28.1	Measurement Principles and Parameters	800
28.1.1	Measured Parameters	801
28.1.2	Principles of Measurements	801
28.2	History	801
28.2.1	FTIR Measurement Methods	801
28.2.2	DOAS Measurement Methods	801
28.2.3	Laser Spectrometer Measurement Methods	802
28.2.4	Microwave Spectrometer	802
28.3	Theory	803
28.3.1	FTIR	803
28.3.2	DOAS	804
28.3.3	Laser Spectrometer	804
28.3.4	Microwave Spectrometer	805
28.4	Devices and Systems	805
28.4.1	FTIR	805
28.4.2	DOAS	805
28.4.3	Laser Spectrometer	807
28.4.4	Microwave Spectrometer	808
28.4.5	Comparison of Methods	808
28.5	Specifications	809
28.6	Quality Control	810
28.6.1	Quality Control Principles	810
28.6.2	Quality Control Procedures	811
28.7	Maintenance	811
28.8	Applications	812
28.8.1	Measurement of Gas Concentrations and Emissions by FTIR	812
28.8.2	Measurement of Gas Concentrations and Emissions by DOAS	812
28.8.3	Measurement of Gas Concentrations and Emissions by Laser Spectrometers	812
28.8.4	Measurement of Gas Concentrations, Temperature and Wind by Microwave Spectrometers	813
28.9	Future Developments	813
28.10	Further Readings	813
	References	814

This chapter deals with ground-based spectrometers for in-situ or remote sensing measurements of trace gases, aerosols, and atmospheric state parameters such as temperature and pressure. Ground-based remote sensing (Chap. 1) using spectrometers enables highly sensitive, spectrally resolved radiation measurements

(Chaps. 11, 29, and 40) and provides chemical compositions and temperature distributions of the atmosphere, exhausts, and gas releases. Path-averaged and vertical distributions of chemical compound concentrations and temperature can be detected. When coupled with meteorological conditions, the concentrations are used to

derive emission source strengths of air pollutants and greenhouse gases as well as their changes due to anthropogenic and natural influences.

Most important is the capability to detect the sought-after parameters simultaneously from measured spectra. Furthermore, nonintrusive detection is advantageous because several tasks of atmospheric and environmental investigations cannot be solved by air sampling through an inlet or sampling manifold because it is technically impossible or not representative. Samples

of air can change chemically within the probe extraction system before reaching the analytical equipment, and perturbations of the flow of exhausts by the sampling manifold are often degraded or lost.

Temperature measurements provide essential information for transport processes and stability of the atmosphere. The temperature information of exhausts and gas releases allows conclusions about the originating emission processes and provides data for calculation of pollution transport and dilution.

28.1 Measurement Principles and Parameters

Spectrometers are used to detect relevant parts of the electromagnetic spectrum via absorption spectroscopy by means of artificial (e.g., lamps and lasers) or natural light sources (e.g., the Sun) as well as via emission spectroscopy using temperature differences or atmospheric radiation (Chaps. 29 and 40). Fourier transform infrared spectroscopy (FTIR) is currently the preferred method

in the infrared (IR) and visible (VIS) (Chap. 37), and differential optical absorption spectroscopy (DOAS) in the VIS and ultraviolet (UV) (Chap. 37). To make high-sensitivity absorption measurements, tuned or broadband lasers can also be employed in an open-path configuration as laser spectrometers (Chap. 16). Radiation absorption and scattering can be detected via open-path

Table 28.1 Measured parameters by open-path absorption measurements

Parameter	Description	Unit	Symbol
Gaseous compounds	Path-integrated mixing ratio	ppm m, ppb m, ppt m	X
Gaseous compounds	Path-integrated mass concentration	kg m^{-2}	C_m
Gaseous compounds	Path-integrated number density	molecules m^{-2}	C_n
Gaseous compounds	Mixing ratio by volume	ppmv, ppbv, pptv	x
Gaseous compounds	Mass concentration	kg m^{-3}	c_m
Gaseous compounds	Number density	molecules m^{-3}	c_n
Aerosol	Path-integrated mass concentration	kg m^{-2}	C_m
Aerosol	Path-integrated number density	particles m^{-2}	N
Aerosol	Mass concentration	kg m^{-3}	c_m
Aerosol	Number density	particles m^{-3}	n

Table 28.2 Measured parameters by emission measurements

Parameter	Description	Unit	Symbol
Temperature	Temperature of atmosphere, exhausts, released gases	K	T
Gaseous compounds, aerosol	Mass column density	kg m^{-2}	S_m
Gaseous compounds, aerosol	Number column density	molecules m^{-2} , particles m^{-2}	S_n

Table 28.3 Principles of gas and aerosol concentration, as well as temperature measurements and applications

Type of sensor	Measurement principle	Application			
		Gas conc.	Aerosol conc.	Temp.	Pressure
FTIR	Absorption	\times	\times	\times	\times
	Emission	\times		\times	
DOAS	Absorption	\times	\times		
	Scattering	\times	\times		
Laser spectrometer	Absorption	\times	\times	\times	\times
	Dispersion	\times			
Microwave spectrometer	Absorption	\times			
	Emission	\times		\times	

configurations (directed or folded) in the atmosphere (Chap. 1). Spectrally high-resolved microwave radiometers (MWR) (Chaps. 29 and 41) provide the line shape of the pressure-broadened emission lines so that by using inversion techniques, vertical profiles of trace gas concentrations in the middle atmosphere are determined.

28.1.1 Measured Parameters

The fundamental measurand in spectrometers is the change of intensity of electromagnetic radiation, typically given by a detector voltage or current. For trace gases, the change of light intensity is converted into an optical absorption or emission, which is then converted into a concentration (e.g., molecules per volume) or column abundance (e.g., molecules per area) through the Bouguer–Lambert–Beer law directly or as a part of radiative transfer codes. For aerosol measurements,

the extinction by scattering is fit to complex aerosol radiation transfer codes (e.g., Mie scattering) to yield information on particle size, phase, and composition. For measurements of state parameters (e.g., temperature, pressure), the spectral data are fit to complex line shape/line strength codes for the species of interest. Tables 28.1 and 28.2 describe absorption measurements by open-path measurements and by emission measurements, respectively. The measured parameters are described and the units and symbols are also provided (Chap. 5).

28.1.2 Principles of Measurements

The applications of different techniques (FTIR, DOAS, microwave and laser spectrometer) that detect gas and aerosol concentration, as well as temperature, are given in Table 28.3.

28.2 History

Scientific applications of spectroscopic methods increased rapidly with more and more remote sensing of the atmosphere. As radiation is the sounding method for atmospheric composition and meteorological parameters, spectrometers allow for nonintrusive task monitoring.

28.2.1 FTIR Measurement Methods

In 1881 *Albert A. Michelson* (1852–1931), the first US Nobel Prize winner in physics in 1907, invented the interferometer and in 1949 *Peter Fellgett* (1922–2008) measured the first IR spectrum by using a FTIR spectrometer: the spectral determination by Fourier transformation of the measured interferogram. The application of FTIR spectrometry was limited in that time by computer capacity and carried out by research scientists only.

In the late 1960s, commercial FTIR spectrometers and DOAS systems were developed on the basis of microcomputers and used in the atmosphere because these methods enabled remote sensing and provided lower detection limits. In 1966 *James William Cooley* (1926–2016) and *John Wilder Tukey* (1915–2000) developed an algorithm for quickly calculating the Fourier transform of interferograms to determine spectra. Further technological developments like imaging spectrometers using scanning mirror systems or detector arrays increased the availability and enhanced the capabilities of FTIR spectrometers. During the

1990s, very high-resolution FTIR spectrometry well below the molecular (Doppler-broadened and pressure-broadened) line width of atmospheric trace gases became applicable, both from the experimental and theoretical side.

28.2.2 DOAS Measurement Methods

Alfred Pérot (1863–1925) and *Charles Fabry* (1867–1945) invented the Fabry–Pérot interferometer in 1899 using a transparent plate with two reflecting surfaces, or two parallel highly reflecting mirrors (also called etalon) to study interference fringes in the transmission spectrum. Later in 1913 *Charles Fabry* and *Henri Buisson* (1873–1944) discovered the ozone layer using a Fabry–Pérot interferometer. In 1924 the Dobson spectrometer was invented by *Gordon Dobson* (1889–1975), allowing column as well as profile measurements of atmospheric ozone by measuring the relative intensity of UVA and UVB radiation [28.1]. He used his invention together with *Paul Götz* (1883–1962) and *Alfred Roger Meetham* (1910–1994) in 1930 to determine the height of the ozone layer using the Umkehr effect, which is based on the dependency of the ratio of radiances of scattered sunlight at two ultraviolet wavelengths, where the shorter one is more strongly absorbed by ozone than the longer one, on the solar zenith angle. This dependency exhibits a minimum at a certain zenith angle that allowed them to determine the ozone layer height to be about 25 km. *Erich Regener* (1881–1955) used UV

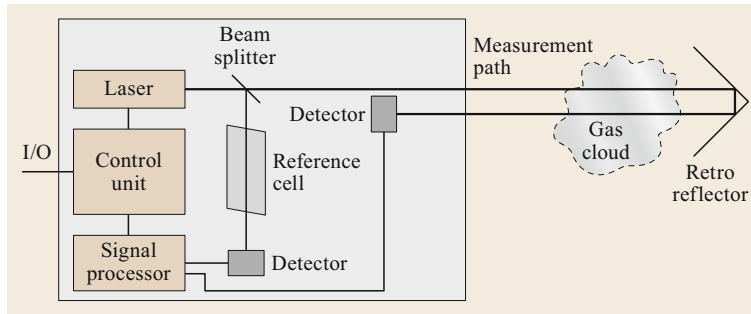


Fig. 28.1 Schematic of laser and optical system for open-path monitoring of atmospheric pollutant gases

spectrographs on balloon sondes to measure the vertical distribution of the ozone layer. In 1948 *Marcel Migeotte* (1912–1992) discovered the presence of methane in the Earth's atmosphere by its infrared absorption band in the solar spectrum [28.2].

John F. Noxon (1928–1985) used visible spectroscopy to measure stratospheric and tropospheric nitrogen dioxide NO_2 [28.3] and started in 1975 to map the latitudinal variability of NO_2 . He discovered a sharp decrease towards the Arctic, a phenomenon now called the Noxon Cliff in his honor. *Dieter Perner* (1934–2012) and *Ulrich Platt* refined the spectroscopic measurement technique towards the DOAS technique to measure OH in the atmosphere [28.4], as well as nitrous acid HNO_2 [28.5]. Since then the DOAS technique has been applied in numerous different setups, both ground-based, airborne and satellite-based (Chap. 37), to measure a variety of different trace gases.

28.2.3 Laser Spectrometer Measurement Methods

Open-path laser spectrometers were first developed in the 1970s [28.6, 7]. Figure 28.1 shows a schematic of laser and optical system for open-path monitoring of atmospheric pollutant gases with laser diode. With the widespread availability of lasers in the 1990s, open-path laser spectrometers blossomed. Methods like tunable diode laser absorption spectroscopy (TDLAS) became common because laser pricing, availability, and reliability rapidly improved (Chap. 16). Initial systems used Pb-salt lasers that required cryogenic cooling, followed by room-temperature telecommunication lasers, and now interband cascade and quantum cascade lasers.

28.2.4 Microwave Spectrometer

The measurement principles and history of MWR are described in Chaps. 29 and 41. All MWR instruments

for atmospheric remote sensing include a microwave spectrometer, which allows observations in more than one frequency channel. For the profiling of tropospheric temperature or humidity a small number of channels (3–12) with a relatively coarse frequency resolution (≈ 100 –2000 MHz) is enough. These are typically realized in the form of a discrete filter bank. The retrieval of trace gas concentration or temperature profiles in the middle atmosphere requires spectrometers with more channels and a significantly higher frequency resolution. The first ground-based and spaceborne limb-sounding MWR instruments for this altitude region were still using conventional filter bank spectrometers as described in Sect. 29.4.2. For practical reasons they have typically less than 100 individual channels with a resolution on the order of 0.1–1 MHz close to the center of the emission lines, and between 10–100 MHz on the line wings. The first ground-based microwave radiometers were all based on filter bank spectrometers, as well as many spaceborne radiometers for atmospheric measurements such as the microwave limb sounder (MLS) [28.8].

Starting in the 1980s acoustooptical spectrometers (AOS) [28.9], chirp transform spectrometers (CTS) [28.10], and auto-correlation spectrometers (ACS) [28.11] became available for atmospheric remote sensing. They provide a much higher frequency resolution with a few thousand channels over a bandwidth between 50 MHz to 1 GHz. They were widely used in ground-based microwave radiometers [28.11, 12], as well as on several space instruments such as the Swedish Odin satellite [28.13].

Today digital fast Fourier transform spectrometers (FFTS) are the preferred high-resolution spectrometers for microwave radiometry. They started to become commercially available in 2005 with 16k channels over a bandwidth of 1 GHz [28.14, 15]. In the meantime, they can provide more than two times higher resolution and bandwidth [28.16].

28.3 Theory

Remote sensing by application of spectrometers is an indirect task and the challenge is the measurement data analysis. It requires numerical simulations that are adapted to source characteristics.

28.3.1 FTIR

IR spectroscopy of gases and vapors makes use of the physical principle that these molecules exhibit characteristic spectral structures in the IR, originating from energy transitions between specific vibrational and rotational levels, and the corresponding absorption and emission of radiation. Radiation scattering occurs for both molecules and aerosols. Elastic scattering of light by molecules is called Rayleigh scattering, which may be neglected in most cases in the infrared spectral range. Aerosol scattering is wavelength-dependent for small aerosols and nearly wavelength-independent for large aerosols. This is called Mie scattering and can influence infrared radiation transfer. Inelastic scatter results in a wavelength shift between incident and scattered radiation. One type is Raman scattering with an efficiency that is proportional to the inverse fourth power of wavelength as Rayleigh scattering.

The propagation of monochromatic infrared radiation in the atmosphere and in exhaust plumes is described by the equation of radiative transfer [28.17].

In the case of homogeneous absorption measurement the radiation damping of a broadband infrared light source is used. In this case of active measurements, the incoming radiation $I_{\Delta\nu}$ in a certain spectral interval $\Delta\nu$ is given by the Bouguer–Lambert–Beer law

$$I_{\Delta\nu} = \varepsilon B_{\Delta\nu}(T_{GB})\tau_{\Delta\nu}(l), \quad (28.1)$$

where T_{GB} is the temperature of the radiation source (e.g., a globar with emissivity ε), ν the wavenumber and $B_{\Delta\nu}$ the radiation of the source as the Planck function in the spectral interval $\Delta\nu$. The term $\tau_{\Delta\nu}$ is the transmittance along the path l from the radiation source to the

detector in the spectral interval $\Delta\nu$, and so

$$\tau_{\Delta\nu}(l) = \int_{\Delta\nu} \prod_{i=1}^N e^{-k_i(\nu)n_i l} d\nu e^{-k_a(\Delta\nu)n_a l}. \quad (28.2)$$

Here k_i is the monochromatic absorption coefficient of the trace gas i , n_i the corresponding number density, N the number of trace gases, k_a the aerosol extinction coefficient, and n_a the aerosol number density.

The basic optical configuration for the emission measurements is illustrated in Fig. 28.2. The radiative transfer through an exhaust plume can be approximated as a three-layered radiative transfer problem: The radiation of the background I_B is transmitted through ambient air (transmittance τ_F and temperature T_F), the plume (τ_P , T_P) and another ambient air layer (τ_F , T_F) to the spectrometer. For those passive measurements the radiation transfer has the index $\Delta\nu$ removed

$$I = I_B \tau_P \tau_F + I_P \tau_F + I_F. \quad (28.3)$$

The plume radiation I_P is given by

$$I_P = B(T_P)(1 - \tau_P). \quad (28.4)$$

The plume as well as the foreground transmittances are calculated according to (28.2) and the foreground radiation according to (28.1), using the assumption that the foreground is a homogenous layer. Only in the case of very hot plumes such as from aircraft engines can the background radiation be neglected. Additionally, it was shown on the basis of a successive order multiple-scattering scheme that aerosol scattering and precipitation contributions to radiation are not important for the infrared spectral signatures of gases [28.18].

A radiometric calibration of the measured raw spectra to absolute radiation units is necessary for further data interpretation of emission measurements [28.19, 20]. This calibration follows the conventional procedure of recording spectra of a blackbody at different

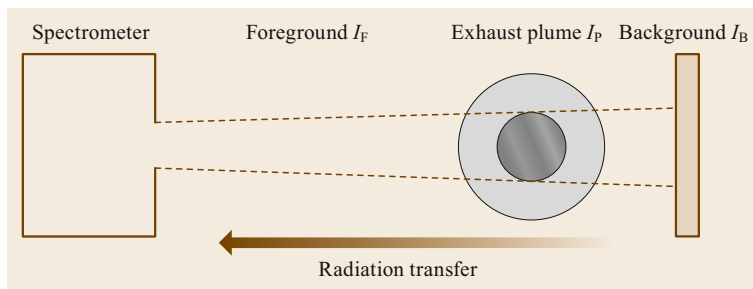


Fig. 28.2 Setup for emission measurements. The radiation of the background I_B is transmitted through ambient air with transmittance τ_F and temperature T_F , the plume (τ_P , T_P), and another ambient air layer (τ_F , T_F) to the spectrometer

temperatures. Also, the instrumental line shape (ILS) function can be determined by measurement of absorption lines of a well-known gas. The ILS must be known for folding calculated transmittances as given in (28.2) [28.21, 22].

The retrieval of measured spectra to determine gas concentrations is performed normally by using reference spectra from a library [28.23]. More than 100 inorganic gases (i.e., HCN, HF, SF₆) and VOCs are available in these libraries. But comparing a spectrum recorded from an instrument with one from a reference database requires knowledge of the instrument's spectral resolution and other factors (e.g., detector sensitivity), all of which cause the observed spectrum to deviate from the true spectra line shape derived from a spectra database. This ILS is challenging to deduce theoretically, and spectra at high resolution are not necessarily available, such that the accuracy of these retrievals is not very high by just comparing the databases with the observed spectra.

The most common approach is to measure a set of reference spectra acquired by the same instrument. This set is then used in comparison to the observed spectra to deduce concentrations. In this way, the instrument response function is fully normalized through the collection of the reference spectra. Different algorithms for calculation of gas concentrations from measured spectra with reference spectra are applied, including classical least-squares fitting and partial least-squares fitting. One drawback of this method is the capability to acquire measured reference spectra in a carefully controlled environment (concentration, pressure, and temperature). For open-path spectrometers that sample over a range of conditions, or for highly reactive species, this may not always be readily feasible.

An alternative approach is a radiative transfer and retrieval software with algorithms based upon a line-by-line calculation procedure using a molecular spectral line database and considering the ILS function [28.20, 24–26]. Furthermore, these algorithms are necessary for the interpretation of spectra from IR spectroscopy of gas plumes with inhomogeneous temperature distribution as warm exhausts, as well as from solar absorption spectroscopy, which cannot be retrieved with reference spectra because the necessary spectra for different temperatures are not available. Commercially available, modified, or self-written line-by-line computer codes are used to derive absorption coefficients in dependence from gas concentration, temperature, and pressure [28.18, 26, 27] with molecular line parameters (position of line center, line intensity, line half width, and energy of the lowest energy transition) [28.28]. These data are then used to calculate synthetic spectra that are fitted to the measured spectra by fitting

routines or nonlinear regression algorithm. Continuum absorption by H₂O and CO₂ as well as aerosol and rain contributions should be included. In the simplest case the gas plume is considered as one homogeneous gas layer, whereas the most sophisticated models use Gaussian profiles or calculate profiles of temperatures and species from flow fields and use validated approximations to ensure fast radiative transfer calculations with maximum accuracy.

28.3.2 DOAS

The DOAS technique is another widely used spectroscopic technique for the measurement of stratospheric and tropospheric trace gases [28.3, 5, 29–31].

The DOAS technique measures the absorption of multiple trace gases. It is based on a modified version of the Bouguer–Lambert–Beer law (Sect. 28.3.1)

$$I(\lambda) = I_0(\lambda)e^{-\sum_i \sigma_i(\lambda) \text{SCD}_i} g(\lambda) \quad (28.5)$$

with the sum in the exponential running over all trace gases i , σ_i being the absorption coefficient of each gas i , λ the wavelength, c_i being the concentration of the gas i , integrating over all possible light paths l , and $g(\lambda)$ describing additional attenuation by the optical system, as well as by Rayleigh and Mie scattering in the atmosphere and all other broadband-structured influences, like the reflection on the ground. SCD _{i} (slant column density) is

$$\text{SCD}_i = \int c_i(l) dl. \quad (28.6)$$

Equation (28.5) is linearized with respect to the SCDs and $\ln g(\lambda)$ is modeled by a polynomial, allowing linear retrieval of the SCDs of the involved gases. Eventually, for uncertain wavelength mapping, or utilizing an additive polynomial modeling of other instrument characteristics, the fit becomes a nonlinear optimization. This may introduce error sources, like the undersampling effect [28.32], which have to be corrected for. For a comprehensive description of the DOAS technique see [28.33].

28.3.3 Laser Spectrometer

Laser-based spectrometers are becoming increasingly common due to the narrow spectral bandwidth of a laser (\ll line widths at atmospheric pressures), fast spectral tuning capabilities (kilohertz to megahertz), and high optical powers (one to hundreds mW). These attributes allow for high-resolution and high-sensitivity detection schemes that generally exceed those of broadband FTIR

spectrometers [28.34]. By scanning the laser at high frequencies (f , typically kilohertz to megahertz) across a narrow spectral region (e.g., on the order of an absorption line width at STP), characteristic flicker ($1/f$) noise can be reduced significantly. Improvements in optical absorption detection limits over FTIR spectrometers of one to two orders of magnitude are generally obtained. Typical optical detection limits are one part in 10^5 absorption for a one second integration period for field-based instruments. These detection levels are about an order of magnitude or two better than typical broadband FTIR-based spectrometers but are still about two orders of magnitude above the shot-noise limits of infrared detectors [28.7, 34]. Other sources of error such as optical interference fringes, temperature stabilities of the laser and detector, inhomogeneities of the atmospheric state and concentrations, and accurate measurements of state parameters across the optical path (temperature, water vapor, pressure) practically limit field-based observations to this one in 10^5 level. Indeed, these significant, real-world field issues distinguish this chapter of laser spectrometers in open-path configurations from those described previously in Chap. 16. Because the techniques themselves for closed-path (i.e., one containing a sampling cell) laser spectroscopy are identical, the governing equations will not be repeated in this chapter but instead focus on challenges for laser spectrometers in the atmosphere.

28.4 Devices and Systems

The relevant characteristics of devices and systems will be shown.

28.4.1 FTIR

To detect trace gases in the near-surface atmosphere and exhausts, the minimum required spectral resolution is 0.2 cm^{-1} due to the line width of the absorption lines in the lower atmosphere and the spectral range is $600\text{--}4500\text{ cm}^{-1}$. To obtain high sensitivity, detectors made from mercury cadmium telluride and indium gallium arsenide must be used, which are cooled by liquid nitrogen, gaseous nitrogen via the Joule–Thomson effect or Stirling coolers.

A spectrometer with telescope is necessary to receive radiation from a source or exhaust plume (distances up to 500 m) or on long open paths (50 up to 1000 m) [28.18]. The diameter of exhaust plumes is determined from the inner diameter of the smoke stack or another exit of the plume release. For that reason and to avoid high optical thickness due to water condensation

28.3.4 Microwave Spectrometer

The physical principles of microwave radiative transfer are described in Chaps. 29 and 41. The combination of a microwave radiometer with a high-resolution spectrometer allows to resolve the line shape of pressure-broadened emission lines. Using the optimal estimation method or other inversion techniques it is possible to derive from the line shape vertical profiles of trace gas concentrations in the middle atmosphere.

The altitude range over which vertical profiles can be retrieved from ground-based measurements depends on different factors. The total bandwidth of the spectrometer must be wider than the line width at the lowest pressure level of interest. The frequency resolution of the spectrometer needs to be small enough to resolve the line center at the highest altitudes. The maximum altitude is also fundamentally limited by the thermal Doppler broadening of the emission lines. Above a certain pressure level, it exceeds the pressure broadening and prevents the retrieval of vertical profiles above that altitude. The Doppler broadening increases with the frequency, and for that reason emission lines at lower frequencies allow retrievals at higher altitudes. This limitation does not exist for limb-sounding observations from a satellite platform, where the vertical information is obtained by pointing the antenna to different tangent heights (Sect. 41.4.3).

in the exhaust plume, the field-of-view of the telescope is orientated near the top of the smoke stack, the nozzle exits of a turbine, or the top of the flame of a flare by use of a tracking mirror (Fig. 28.2) [28.35].

The spectrometers can be coupled with a White cell or multipass-reflection mirror system of up to several 100 m absorption path length for the investigation of trace gases.

The vertical distribution of trace gases can be retrieved from the shape of solar absorption lines by using software [28.36, 37] (Chap. 63) to analyze atmospheric multilayer problems (solar absorption) with input files for pressure–temperature, volume mixing ratios, and optical path parameters.

28.4.2 DOAS

There are many different configurations for DOAS instruments ranging from active DOAS instruments with their own light source to passive instruments sampling the sky or scanning the Earth from space.

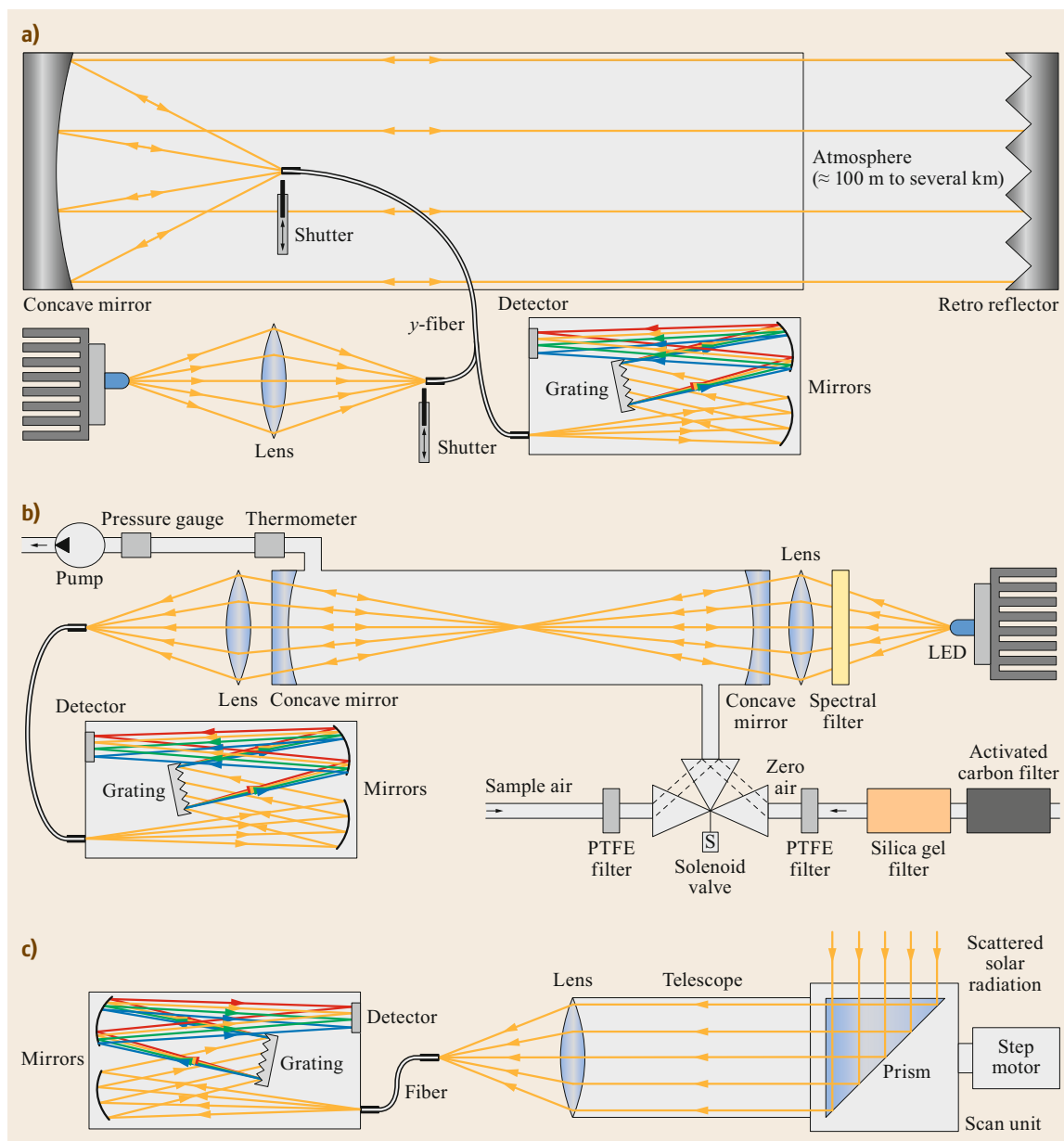


Fig. 28.3a–c Schematic diagram of the experimental setup of the (a) long-path DOAS, (b) cavity-enhanced DOAS, and (c) multi-axis DOAS instrument

A long-path DOAS (LP-DOAS, see Fig. 28.3a) instrument has a light source that sends out a light beam using a telescope. A xenon-arc lamp used to be very popular as a light source, covering the ultraviolet and visible spectral range. However, in recent years LEDs have become powerful enough, at least in the limited spectral range used for a DOAS fit, to be useful for DOAS measurements. Another recent DOAS innovation is the use of y-fibers instead of mirrors to send the

signal from the light source to the telescope and then the reflected signal to the spectrometer. A shutter in front of the y-fiber is used to measure the lamp spectrum (I_0 in (28.5)).

Another active DOAS-type instrument that has recently been developed is the cavity-enhanced DOAS (CE-DOAS, see Fig. 28.3b), which is a cavity-assisted device to provide long absorption paths necessary for the detection of ambient atmospheric trace gases by

multiple reflections in a small optical resonator composed of two highly reflective concave mirrors between a concentric and confocal setup [28.38–40]. Using this technique in combination with a continuous light source allows applying the DOAS retrieval method to in-situ measurements [28.41, 42].

A passive DOAS method using sunlight as the light source is the multi-axis DOAS (MAX-DOAS, see Fig. 28.3c) measurement technique introduced by [28.43]. The authors in [28.44] showed that this technique represents a significant advance on the well-established zenith scattered sunlight DOAS technique, which is mainly sensitive to stratospheric absorbers. Ground-based MAX-DOAS, however, is highly sensitive to absorbers in the lowest few kilometers of the atmosphere and vertical profile information can be retrieved by combining the measurements with radiative transfer model calculations. Those calculations depend on aerosol parameters and [28.45] showed how DOAS retrievals of the oxygen dimer O_4 can be used to derive the needed vertical aerosol profile information. However, most inversion scenarios consist of an underdetermined system; therefore, regularization techniques which are typically based on a priori profile information are needed.

The MAX-DOAS has become a widely and successfully used technique for the remote sensing of tropospheric trace gases and aerosols, e.g., by [28.45–52].

Typical MAX-DOAS observations are performed at fixed locations, which allow retrieving the diurnal variation of tropospheric species at that location, but MAX-DOAS measurements can also be made on mobile platforms like aircrafts [28.53], ships [28.54], or cars [28.55, 56].

28.4.3 Laser Spectrometer

Depending upon the application, common lasers used in open-path spectrometers include near-IR telecommunication lasers, vertical cavity surface emitting lasers (VCSELs), antimonide (Sb) lasers, interband cascade lasers (ICLs), and quantum cascade lasers (QCLs). Telecommunication lasers are readily fiberized (for cases where the laser is not located at the point of sampling location), relatively inexpensive, and have mature optical technologies associated with them. Their downside is the fairly weak linestrengths that can be probed in the near infrared spectral region. VCSELs have large current tuning ranges (15 cm^{-1}) for multiple absorption lines to be probed and consume lower power (e.g., lower-power applications), but their low optical power ($\approx 1\text{ mW}$) and narrow wavelength ranges ($< 3\text{ }\mu\text{m}$) limit their widespread field use. Anti-

monide lasers probe the $2\text{--}4\text{ }\mu\text{m}$ region not accessible by telecommunication lasers but still near the lower limit of the cascade lasers. For highest sensitivity, probing the mid-infrared spectral region is critical, and advances in interband cascade ($3\text{--}6\text{ }\mu\text{m}$) and quantum cascade lasers ($> 4\text{ }\mu\text{m}$) have allowed sampling of trace gases at unprecedented sensitivities. Interband cascade lasers consume lower power ($< 1\text{ W}$) than quantum cascade lasers (with lower but sufficient optical power generally in the milliwatt range), but their spectral range is still limited at the higher end. Quantum cascade lasers probe the fundamental rovibrational bands of trace gas species and also have high optical powers ($> 100\text{ mW}$). The downsides of ICLs and QCLs are the less mature optical technologies (packaging, lenses, coatings, fibers) for the mid-infrared spectral region compared to the near-infrared lasers. Advances in the optical efficiencies (power consumption versus optical power), tuning rates, and wavelength ranges continue for both ICLs and QCLs, in particular.

Direct absorption spectroscopy (DAS) is often employed for laser spectrometers. At fast sweep rates ($> \text{kilohertz}$), laser excess noise can achieve detection sensitivities in the 10^{-4} range [28.57]. DAS is particularly advantageous because if laser/detector systems are well characterized, a direct and accurate measurement of concentration can be derived from the Bouguer–Lambert–Beer law based upon first principles of spectroscopy. In contrast, modulation techniques such as wavelength modulation (WMS) and frequency modulation (FMS) employ a rapid (tens of kilohertz to megahertz) modulation of the laser frequency while scanning across a selected absorption feature at slower rates (kilohertz) [28.58]. The detector signal is demodulated at different harmonics of the modulation frequency to yield much better detection sensitivities over DAS by about an order of magnitude. The drawback of WMS and FMS systems are that they often require calibrations in field environments as tracing back to first principles of spectroscopy employs more difficult to characterize transfer functions.

Optical cells include single path lengths (laser shining to a detector), a retroreflector/mirror arrangement (laser to mirror back to the instrument), perimeter monitoring with a configuration of mirrors, and in-situ sensors with folder optical cavities (e.g., White cells, Herriott cells, astigmatic cells) [28.59–61]. Because in all cases, at least some components of the optical system are always exposed to the environment, the optical qualities of those surfaces are of primary concern (e.g., cleanliness, alignment) and can introduce deleterious measurement artefacts (e.g., increased noise from low signal on the detector due to degraded optics, drifting in calibration due to optical fringing).

Finally, because laser spectrometers are exposed to the changing atmospheric environments, care must be taken to ensure that other influences on the spectroscopy are well characterized. For example, measurements of greenhouse gases such as methane or carbon dioxide require a precision and accuracy of one part in 1000 which is desirable in many cases. While open-path laser spectrometers often exceed the precision metric, other factors will influence the overall accuracy. First, one needs to ensure that calibrations taken in the laboratory and field conditions accurately represent the instrument at all other conditions. Allan variance plots [28.62, 63] may show a system is stable in the laboratory up to a certain length of time, but the same system outdoors may not show the same level of stability due to changes in temperature on electronic components, laser and detector temperature control, and optical alignment issues (e.g., fringes).

Even if the system characteristics remain stable, one needs to consider changing environmental conditions during a measurement. A change of one degree in temperature at ambient conditions will change the retrieved concentrations by about one part in 300 simply because of the ideal gas law. Dilution effects such as changes in water vapor also need to be included (e.g., H₂O mole fraction change from 1% to 1.5% also changes the retrieved concentrations by 0.5%). Spectroscopic effects from water vapor broadening, linestrength temperature dependences, and line shapes from pressure also need to be considered. Even with accurate measurements of these state parameters, it is necessary to know how representative such measurements are over the path-integrated domain of the laser spectrometer (e.g., one measurement over a 500 m path length may or may not be representative). Finally, there are few truly isolated absorption features in the atmosphere that are not influenced by other trace gases, and these effects need to be accounted for, not just under typical conditions but also more extreme cases (e.g., very polluted, atypical temperatures, high humidity, etc.). In summary, to achieve high stability and precision for open-path laser spectrometers, great attention to system performance and environment variables is needed over the wide range of environmental conditions in which one samples.

28.4.4 Microwave Spectrometer

The basic setup of a microwave radiometer with a single channel or a filter bank spectrometer is described in

Sect. 29.4.2. In an acoustooptical spectrometer (AOS) a piezoelectric transducer converts the radio frequency signal into a sound wave propagating in an optical crystal. This leads to a spatial variation of the refractive index with a periodicity that is given by the radio frequency. A collimated laser beam that illuminates this Bragg cell is diffracted by the resulting phase grating. The intensity distribution of the diffracted light is observed with a linear charge-coupled device (CCD) detector array and represents the microwave spectrum.

A chirp transform spectrometer (CTS) multiplies the radio frequency signal with a chirped waveform. The down-converted signal is compressed by a second chirp filter with matching slope, which converts each Fourier component of the incoming signal to a pulse in the time domain. The complete spectrum can be sampled directly by an analog digital converter (ADC) without the need for further digital signal processing. The chirp filters are usually realized with surface acoustic wave devices.

In a digital FFT spectrometer the radio frequency signal is sampled directly with an ADC. The data stream is processed in real-time with a discrete FFT algorithm implemented on a field programmable gate array (FPGA) processor. A standard FFT without apodization window results in a channel response of $|\sin(x)/x|^2$. The channel selectivity can be improved by applying different window functions to the waveform, but this leads to a loss of resolution and sensitivity. Modern digital spectrometers use a polyphase filter-bank (PFB) algorithm instead of the FFT. This requires more computational resources, but results in an almost ideal top-hat channel response with a much smaller spectral leakage and without loss of sensitivity.

The main advantages of the digital spectrometers compared to AOS or CTS are the higher frequency resolution, the improved stability, as well as the uniform and well-defined channel response. In addition, they are readily available since they are based on commercial off-the-shelf hardware.

28.4.5 Comparison of Methods

The advantages and disadvantages of the different methods are described in Table 28.4. This refers to typical applications of the extractive and open-path spectrometer techniques.

Table 28.4 Advantages and disadvantages of the different methods

Devices	Advantages	Disadvantages
Active FTIR	Detection of the relevant gas concentrations for atmospheric radiation budget and for air pollution	No required measurement quality (signal typically too small) to derive relevant aerosol parameters
Passive FTIR	Detection of gas concentrations and temperature	Higher detection limit of concentrations than active FTIR (up to a factor of 10)
Active DOAS	Detection of the relevant gas concentrations for air pollution	No significant spectral features for detection of gases relevant for atmospheric radiation budget like N ₂ O
Passive DOAS	Vertical profiling of gas concentrations	Higher detection limits than active DOAS, limited to daytime measurements as sunlight is used
Laser spectrometer	Better detection limits than FTIR and DOAS	Laser system characteristics must be known very precisely and with high stability. Generally limited to a few spectral features and so one or a few compounds per sensor
Passive microwave spectrometer	Vertical profiles of gas concentrations and temperature, independent of sunlight, not affected by clouds or fog	Only molecules with a dipole moment can be observed (e.g., H ₂ O, O ₃ , ClO, HCl)

28.5 Specifications

The use of gas cells for quality assurance and quality control (QA/QC) is required according to the German or US Environmental Protection Agency (EPA) guideline for FTIR absorption spectroscopy [28.64, 65] and DOAS [28.66] (Chaps. 3 and 4). Also, the relationship to well-known conventional air pollution monitoring stations in networks and to laboratory analysis by gas-chromatography and NDIR instruments of canister sampling along the open-path measurement were investigated [28.18]. The retrieval results from ambient air measurements were compared also with experimental setups of a White cell and calibration gases using a FTIR spectrometer or DOAS (Table 28.5). Furthermore, the passive measurement method was evaluated with in-situ measuring methods (continuous emission

monitoring) in smoke stacks, experiments with gas burner, and laboratory analysis of exhausts [28.27, 67]. The temperature and pressure dependences of spectral lines or features are also considered in these QA/QC studies.

The specifications of different measurement methods for gas and aerosol concentrations and atmospheric temperature under real-world conditions, including error, concentration range, and temperature range, are given in Table 28.5 (provided by producers and in papers). Under ideal conditions, all methods can produce lower uncertainties than stated in the table. The errors of laser spectrometers are for instance limited by the ability to precisely control laser and detector temperatures.

Table 28.5 Typical specification of different measurement methods for gas and aerosol concentrations and temperature

Method	Error ^a in %	Range of concentration detection	Range of atmospheric temperature detection
Active FTIR	± 5	ppb up to vol%	Ambient up to 1300 K (corresponding to HITEMP ^b)
Passive FTIR	± 20	ppb up to vol%	Ambient up to 1300 K (corresponding to HITEMP ^b)
Active DOAS	± 5	ppt up to vol%	Not
Passive DOAS	± 20	ppb up to vol%	Not
Laser spectrometer	± 5	ppt up to vol%	Ambient up to 1300 K (corresponding to HITEMP ^b)
Passive microwave spectrometer	± 5–30	ppt up to ppm	Ambient

^a Total accuracy dominated by the limitations in trueness not precision. ^b <https://hitran.org/hitemp/>, Accessed 13 July 2021

28.6 Quality Control

Quality control is an important measurement, and so the relevant international guidelines are cited. The methods change depending on the technical development of devices and systems.

28.6.1 Quality Control Principles

A well-characterized ILS is a prerequisite for accurate results of FTIR retrieval algorithms [28.22] because the instrument cannot be perfectly aligned or the ILS is degraded by aberrations. This is realized by insertion of a short-path gas cell into the optical path in front of the interferometer. The experimental setup for measurements of absorption spectra includes a thermal radiation source, the gas cell filled with, e.g., CO at ambient air temperature, and the interferometer. Using this setup, the cell measurement provides gas absorption spectra with the current status of the interferometer. It is not necessary for the retrieval of the ILS to open the spectrometer. A software module includes the model for the inherent apparatus function and the fitting algorithm on the basis of the measured spectra with the gas cell to determine the real ILS of the spectrometer.

For most DOAS systems, no classical calibration is needed, since the cross sections of the molecules

only have to be measured once (which has the role of the basic calibration here) and the ILS as the second part of the procedure can be determined correctly. Neglecting classical calibration is possible if the absorption coefficient of each component for the selected wavelengths, the ILS, and the length of the monitoring path are known (as for FTIR, see above). The differential absorption technique, applied for all retrieval algorithms of spectrometers, provides the advantage that all instrumental effects depending on changes in the environment or aging of the instrument, as well as the background influence, will be modeled by the broadband fit function and therefore taken out of the equation. The only exception is the CE-DOAS because the retrieval results are influenced by the effective length of the measurement path generated in the cavity, which depend on the reflectivity and alignment of the mirrors, so that the output of the cavity does not follow the Bouguer–Lambert–Beer law directly as it is a mixture of different path lengths. Although, the DOAS fitting technique may be identical under certain conditions to the other DOAS instruments. Since all the aerosols are filtered out of the incoming air, the effective path length without absorbers can be determined using clean air and helium as two reference gases with different Rayleigh scattering coefficients [28.68].

Table 28.6 Typical test criteria

Method	Error	Reason/Action
Active FTIR	Too low radiation intensity or too high signal noise	Misalignment/adjustment of instrument radiation throughput and ILS determination
Passive FTIR	Too low radiation intensity or too high signal noise	Misalignment of optics/adjustment of instrument radiation throughput and ILS determination
Active DOAS	No convergence in the DOAS fit	Too high SNR or interfering spectral structures by the optical components/adjustment of instrument radiation throughput and ILS determination
Passive DOAS	No convergence in the inversion scheme	Inadequate a priori profile used for the regularization/selection of adequate a priori profile
Laser spectrometer	Degraded accuracy from the calibration condition	Changes in temperature, pressure, water vapor, or other trace gases not representative of calibration conditions; drifting due to changes in the magnitude and phase of optical interference fringes from alignment or scattering of beam/calibration under real conditions
	Degraded precision	Low light due to misalignment of optics or degraded optical surfaces/adjustment of instrument radiation throughput and ILS determination
Microwave spectrometer	Degraded precision	Degradation of microwave components in the radiometer or contamination of windows or reflectors/replace defective parts or cleaning
	Degraded accuracy	Baseline errors on the calibrated spectra and fit residuals, mostly caused by reflections on the blackbody calibration targets/improve calibration targets

For laser spectrometers, because the ambient environment changes, the metrics of instrument noise, precision, and calibration are often obtained through a separate optical channel where a beam splitter sends part of the signal to the sample path and a small fraction to a separate reference channel. The reference channel may contain an equivalent absorption signal as that expected in the sample environment or be replaced with a similar optical path length as the sample path length through a multipass optical cell. Similar procedures are noted as above, which use gas cells and calibration standards. For long-path measurements, care must be taken to ensure that the introduction of a cell or separate optical path has the same optical characteristics (e.g., fringing) as the long path in the field. Allan deviation

experiments [28.62, 63] are often conducted in the laboratory under controlled environments to identify noise and system drift, but the same controlled conditions in the laboratory are rarely duplicated in the outdoor field environment and extrapolating them to field environments are often not representative.

28.6.2 Quality Control Procedures

Table 28.6 gives some sensor-specific criteria that may be applied in quality control procedures (Chap. 3). If the reason for invalid data can be determined and rectified, then a corresponding troubleshooting action is required, and if not, the sensor and measurement setup should be checked.

28.7 Maintenance

The maintenance tasks for spectrometers are given in Table 28.7.

Table 28.7 Maintenance of spectrometers

Maximum interval	Active FTIR	Passive FTIR/MW spectrometer	Active DOAS	Passive DOAS	Laser spectrometer
Every measurement	Check of all internal parameters like wavelength, radiation intensity. Plausibility check of key compounds depending on the spectrometer type like CO ₂ , CH ₄ , N ₂ O, NO ₂ or water vapor. Effective path-length calibration has to be performed before and after every measurement campaign				
	If required from techniques – internal optical adjustment	Radiometric calibration	Wavelength calibration using reference lines is only necessary if there is a large deviation, smaller uncertainties can be corrected during the fit	Wavelength calibration using reference lines is only necessary if there is a large deviation, smaller uncertainties can be corrected during the fit	Optical light reaching the detector needs to be sufficient to achieve desired signal-to-noise
Every measurement campaign	Check of optical windows and mirrors for dirt or damage – cleaning if necessary				Calibrations prior to, during, and after the campaign to identify potential changes in system performance
	Determination of ILS				
1 year	Check of all hygroscopic components				

28.8 Applications

The applications of spectrometers for remote sensing tasks are very broad; therefore, only a few applications are presented and these are the most typical.

28.8.1 Measurement of Gas Concentrations and Emissions by FTIR

FTIR spectrometers are used to determine the chemical composition of the atmosphere, exhausts, and gas releases by active absorption measurements, i.e., by means of a global on open paths. The chemical composition and temperature of the atmosphere, exhausts, and gas releases are determined by passive measurements also using natural light sources (e.g., the Sun) as well as via emission spectroscopy using temperature differences in the atmosphere, exhausts, or atmospheric radiation.

FTIR spectroscopy works for different weather conditions with the exception of fog, strong rain, or snow fall not influenced by turbulence.

The emission source strengths of (1) diffuse sources (industry, traffic, agriculture, waste disposals) and of (2) remote sources (smoke stacks, aircraft engines, flares, fires, volcanoes, mobile sources) are difficult to determine by single in-situ measurements. Remote sensing methods are necessary to quantify emission source strengths without any contact to the source. To determine emission source strengths of diffuse sources, inverse dispersion modeling is adapted to this objective [28.69–71]. The emission indices of compounds in aircraft engine exhausts are calculated with the simultaneously measured CO₂ concentration by stoichiometric calculation of total kerosene combustion [28.20].

Solar absorption spectrometry is not only applied for long-term observation of atmospheric composition in international networks [28.36, 37], but for the determination of diffuse emission source strengths as well [28.72–74]. Measurements of profiles are often validated by aircraft-based measurements through much of the column [28.75].

28.8.2 Measurement of Gas Concentrations and Emissions by DOAS

There are numerous applications of the DOAS techniques for the measurement of trace gas concentrations, ranging from satellite-based monitoring of the Earth over ground-based remote sensing stations to mobile in-situ measurements. The first satellite instrument using the DOAS retrieval was the Global Ozone Monitoring Experiment (GOME) [28.31] on the ESA remote sensing satellite ERS-2, mapping the global

distribution of O₃, NO₂, SO₂, BrO, OClO and H₂O since 1996. Several successor satellite instruments have been launched into space since then: Scanning Imaging Absorption Spectrometer for Atmospheric Cartography (SCIAMACHY) [28.76], GOME-2 [28.77], Ozone Monitoring Instrument (OMI) [28.78] and TROPospheric Monitoring Instrument (TROPOMI) [28.79] to name a few. Those instruments use scattered sunlight that has been traversing the Earth's atmosphere and the DOAS retrieval described in Sect. 28.3.2. DOAS derives the SCDs, which is an ensemble mean of the path distribution. In order to obtain a more comparable quantity that is independent from the viewing direction and solar zenith angle (SZA), the air mass factor (AMF) concept [28.80] is applied to convert the SCDs into vertical column densities (VCDs) or path-integrated mass concentration. This conversion requires the calculation of box air mass factors, which is the sensitivity of the measurement to the different layers, using radiative transfer simulations and additionally a profile shape of the trace gas under investigation. Those are typically taken from chemical transport model simulations. The AMF calculation is the main error source of satellite derived VCDs in addition to the DOAS fit error.

MAX-DOAS instruments are ideal for satellite validation, since they not only provide column measurements, but profile information as well, so that the main retrieval error cancels out in the comparison.

In order to study emission sources, top-down emission inventories of various trace gases can be produced by inverting chemical transport simulations. Common inversion techniques make use of adjoint models or the 4D-Var method [28.81]. Also, individual sources can be analyzed using inverse transport modeling, for example to estimate vertical profiles from SO₂ emissions from volcanic eruptions [28.82]. Ground-based DOAS measurements can be used for source estimation as well, e.g., when a MAX-DOAS instrument is mounted on a car for column measurements around a city, the total emissions of the encircled course can be determined in combination with information on wind speed and direction [28.55].

28.8.3 Measurement of Gas Concentrations and Emissions by Laser Spectrometers

Open-path laser spectrometers are widely used in field environments. Aircraft-based measurements of water using near-IR lasers [28.57, 83–85] have been made routinely for over a decade. Open-path measurements of methane (using a 1.65 μm VCSEL for

low-power applications) [28.86] and ammonia (9.06 μm QCL) [28.87] have been conducted for eddy covariance fluxes, where small changes in concentrations are correlated with high-frequency (10 Hz) updrafts and downdrafts. Long-path measurements and perimeter monitoring using telecommunication lasers and QCLs [28.88] are also common. Methane emission rates from landfills were estimated using open-path TDL measurements combined with dispersion models [28.89]. Volcanic emission investigations and flux determinations of volcanic gases were performed by TDL measurements in different configurations [28.90–93]. Mobile measurements with open-path sensors avoid power-hungry pumps and can be mounted on common passenger vehicles, avoiding expensive generators and custom vehicles [28.94]. Finally, drone-based sensors for methane show great potential in detecting methane emissions [28.95, 96].

28.8.4 Measurement of Gas Concentrations, Temperature and Wind by Microwave Spectrometers

The international Network for the Detection of Atmospheric Composition Change (NDACC) [28.97] includes more than 18 globally distributed microwave spectrom-

eters. They provide long-term measurements of vertical trace gas profiles in the stratosphere and mesosphere. This includes H_2O observed around 22 GHz [28.98], O_3 observed at either 110 or 142 GHz [28.99], as well as ClO around 278 GHz [28.100].

Measurements of the Doppler shift of ozone emission lines allow to derive profiles of horizontal winds in the upper stratosphere and lower mesosphere [28.101]. This is the only measurement technique that can provide continuous wind measurements at these altitudes. Another application for high-resolution microwave spectrometers is to resolve the weak emission lines of stratospheric oxygen on the wing of the saturated oxygen absorption band around 60 GHz. These are used to retrieve temperature profiles in the stratosphere [28.102].

The ground-based microwave radiometers described above can operate nearly continuously and under most weather conditions. This includes clouds, fog, and light rain, where optical and IR instruments will fail. They provide information on trace gas concentrations and dynamic processes on diurnal to multidecadal timescales that are relevant for different applications. This includes the validation of satellite observations or model predictions, as well as long term trend studies of the atmospheric composition.

28.9 Future Developments

Further developments include the determination of spectroscopic parameters or absorption cross sections of more atmospheric compounds so that the detection of these compounds in the atmosphere becomes possible. Also, miniaturization of spectrometers is under development so that smaller, lighter and cheaper instruments will be available [28.103].

For laser spectrometers, new advances in optical detection technologies offer new applications in trace gas detection. For example, frequency combs are now being demonstrated in field environments for methane detection at long distances [28.104], and chirped laser dispersion spectroscopy [28.105] also shows promise for high linearity over a wide range

of returned (backscattered) light. Optical heterodyne methods with a quantum cascade laser to derive vertical profiles from sunlight also show great promise for ground-based measurements [28.106]. Finally, laser-based measurements of line shapes to derive atmospheric pressure have also been accomplished on aircraft [28.107].

Newest application of FTIR is an unattended detection of gas releases or leakages from kilometers away by imaging spectroscopy [28.108–110] which has the potential of early warning prior to hazardous incidences. Chemical composition of gas clouds can be determined including retrieval algorithms of passively measured thermal emission spectra.

28.10 Further Readings

A thorough introduction into the history and physics of DOAS can be found in:

- U. Platt, J. Stutz: Differential Optical Absorption Spectroscopy – Principles and Application, first ed. (Springer, Heidelberg, Germany 2008).

A comprehensive review of the diverse sensors, applications and maintenance of FTIR and DOAS is given in

- EN: Luftqualität – Messungen in der bodennahen Atmosphäre mit FTIR-Spektroskopie (Air quality –

Atmospheric measurements near ground with FTIR spectroscopy), EN 15483:2008, DIN EN 15483, (European Committee for Standardization, Brussels November 2008).

- EN: Luftqualität – Messungen in der bodennahen Atmosphäre mit aktiver Differentieller Optischer Absorptionsspektroskopie (DOAS) – Immissionsmessungen und Messungen von diffusen Emissionen (Air quality – Atmospheric measurements near ground with active Differential Optical Absorption Spectroscopy (DOAS) – Ambient air and diffuse emission measurements), EN 16253:2013, DIN EN 16253, (European Committee for Standardization, Brussels July 2013).
- VDI: Fernmessverfahren. Messungen in der Atmosphäre nach dem Passiv-FTIR-Prinzip. Messen gasförmiger Emissionen und Immissionen (Remote sensing – Atmospheric measurements using passive FTIR spectroscopy – Emission and ambient air measurements), VDI 4211, (Verein Deutscher Ingenieure, Düsseldorf November 2018).
- VDI: Fernmessverfahren. Messen in der Atmosphäre nach dem Passiv-DOAS-Prinzip Messen von Emissionen und Immissionen (Remote sensing – Atmospheric measurements with passive DOAS – Gaseous emissions and ambient air measurements), VDI 4212, (Verein Deutscher Ingenieure, Düsseldorf August 2019).

References

- 28.1 G.M.B. Dobson, D.N. Harrison: Measurements of the amount of ozone in the Earth's atmosphere and its relation to other geophysical conditions, Part 1, Proc. R. Soc. **110**, 660–693 (1926)
- 28.2 M. Migeotte: Spectroscopic evidence of methane in the Earth's atmosphere, Phys. Rev. **73**, 519–520 (1948)
- 28.3 J.F. Noxon: Nitrogen dioxide in the stratosphere and troposphere measured by ground-based absorption spectroscopy, Science **189**, 547–549 (1975)
- 28.4 D. Perner, D.H. Ehhalt, H.W. Pätz, U. Platt, E.P. Röth, A. Volz: OH-radicals in the lower troposphere, Geophys. Res. Lett. **3**, 466–468 (1976)
- 28.5 D. Perner, U. Platt: Detection of nitrous acid in the atmosphere by differential optical absorption, Geophys. Res. Lett. **6**, 917–920 (1979)
- 28.6 R.T. Ku, E.D. Hinkley, J.O. Sample: Long-path monitoring of atmospheric carbon monoxide with a tunable diode laser system, Appl. Opt. **14**, 854–861 (1975)
- 28.7 R.S. Eng, A.W. Mantz, T.R. Todd: Improved sensitivity of tunable-diode-laser open-path trace gas monitoring systems, Appl. Opt. **18**, 3438–3442 (1979)
- 28.8 J.W. Waters, W.G. Read, L. Froidevaux, R.F. Jarnot, R.E. Coffield, D.A. Flower, G.K. Lau, H.M. Pickett, M.L. Santee, D.L. Wu, M.A. Boyles, J.R. Burke, R.R. Lay, M.S. Loo, N.J. Livesey, T.A. Lungu, G.L. Manney, L.L. Nakamura, V.S. Perun, B.P. Ridenoure, Z. Shippony, P.H. Siegel, R.P. Thurstans, R.S. Harwood, H.C. Pumphrey, M.J. Filipiak: The UARS and EOS microwave limb sounder (MLS) experiments, J. Atmos. Sci. **56**(2), 194–218 (1999)
- 28.9 A. Lecacheux, C. Rosolen, D. Michet: Space-qualified, wide-band and ultra-wide-band acousto-optical spectrometers for millimetre and submillimetre radioastronomy, Proc. SPIE **3357**, 253–256 (1996)
- 28.10 P. Hartogh, G.K. Hartmann: A high-resolution chirp transform spectrometer for microwave measurements, Meas. Sci. Technol. **1**, 592–595 (1990)
- 28.11 A. Emrich: A flexible hybrid spectrometer for balloon borne and ground based (sub)millimeter wavelength astronomy, Exp. Astron. **1**(4), 227–235 (1990)
- 28.12 H. Jost, N. Kämpfer, A. Lecacheux, C. Rosolen: Broadband acousto-optical spectrometer used as backend for remote sensing of trace gases in the atmosphere, IEEE Trans. Geosci. Remote Sens. **34**(4), 927–935 (1996)
- 28.13 U. Frisk, M. Hagström, J. Ala-Laurinaho, S. Andersson, J.-C. Berges, J.-P. Chabaud, M. Dahlgren, A. Emrich, H.-G. Florén, G. Florin, M. Fredrixon, T. Gaier, R. Haas, T. Hirvonen, Å. Hjalmarsson, B. Jakobsson, P. Jukkala, P. Kildal, E. Kollberg, J. Lassing, A. Lecacheux, P. Lehtinen, A. Lehto, J. Mallat, C. Marty, D. Michet, J. Narbonne, M. Nexon, M. Olberg, O. Olofsson, G. Olofsson, A. Origné, M. Petersson, P. Piironen, R. Pons, D. Pouliquen, I. Risticelli, C. Rosolen, G. Rouaix, A.V. Räisänen, G. Serra, F. Sjöberg, L. Stenmark, S. Torchinsky, J. Tuovinen, C. Ullberg, E. Vinterhav, N. Wadefalk, H. Zirath, P. Zimmermann, R. Zimmermann: The Odin satellite: I. Radiometer design and test, Astron. Astrophys. **A 402**, 27–34 (2003)
- 28.14 A.O. Benz, P.C. Grigis, V. Hungerbühler, H. Meyer, C. Monstein, B. Stuber, D. Zardet: A broadband FFT spectrometer for radio and millimeter astronomy, Astron. Astrophys. **442**(2), 767–773 (2005)
- 28.15 S.C. Müller, A. Murk, C. Monstein, N. Kämpfer: Intercomparison of digital fast Fourier transform and acousto optical spectrometers for microwave radiometry of the atmosphere, IEEE Trans. Geosci. Remote Sens. **47**(7), 2233–2239 (2009)
- 28.16 B. Klein, S. Hochgürtel, I. Krämer, A. Bell, K. Meyer, R. Güsten: High-resolution wide-band fast Fourier transform spectrometers, Astron. Astrophys. **542**(L3), 1–6 (2012)
- 28.17 R.M. Goody, Y.L. Yung: *Atmospheric Radiation: Theoretical Basis* (Oxford Univ. Press, New York 1989)

- 28.18 R. Haus, K. Schäfer, W. Bautzer, J. Heland, H. Mosebach, H. Bittner, T. Eisenmann: Mobile FTIS-monitoring of air pollution, *Appl. Opt.* **33**, 5682–5689 (1994)
- 28.19 E. Lindermeir, P. Haschberger, V. Tank, H. Dietl: Calibration of a Fourier transform spectrometer using three black-body sources, *Appl. Opt.* **31**, 4527–4533 (1992)
- 28.20 J. Heland, K. Schäfer: Analysis of aircraft exhausts using FTIR-emission-spectroscopy, *Appl. Opt.* **36**, 4922–4931 (1997)
- 28.21 F. Hase, T. Blumenstock, C. Paton-Walsh: Analysis of the instrumental line shape of high-resolution Fourier transform IR spectrometers with gas cell measurements and new retrieval software, *Appl. Opt.* **38**, 3417–3422 (1999)
- 28.22 R. Harig: Passive remote sensing of pollutant clouds by FTIR spectrometry: Signal-to-noise ratio as a function of spectral resolution, *Appl. Opt.* **43**, 4603–4610 (2004)
- 28.23 National Institute of Standards and Technology: <https://www.nist.gov> (2019), Accessed 10 July 2021
- 28.24 Z. Bacsik, J. Mink, G. Keresztury: FTIR spectroscopy of the atmosphere, I. Principles and methods, *Appl. Spectrosc. Rev.* **39**, 295–363 (2005)
- 28.25 Z. Bacsik, J. Mink, G. Keresztury: FTIR spectroscopy of the atmosphere, II. Applications, *Appl. Spectrosc. Rev.* **40**, 327–390 (2005)
- 28.26 E. Lindermeir: Evaluation of infrared emission spectra of aircraft exhaust with the FitFas software, *Ann. Geophys.* **12**, 417–421 (1994)
- 28.27 J. Heland, K. Schäfer: Determination of major combustion products in aircraft exhausts by FTIR emission spectroscopy, *Atmos. Environ.* **32**, 3067–3072 (1998)
- 28.28 L.S. Rothman, I.E. Gordon, Y. Babikov, A. Barbe, D.C. Benner, P.F. Bernath, M. Birk, L. Bizzocchi, V. Boudon, L.R. Brown, A. Campargue, K. Chance, E.A. Cohen, L.H. Coudert, V.M. Devi, B.J. Drouin, A. Fayt, J.-M. Flaud, R.R. Gamache, J.J. Harrison, J.-M. Hartmann, C. Hill, J.T. Hodges, D. Jacquemart, A. Jolly, J. Lamouroux, R.J. LeRoy, G. Li, D.A. Long, O.M. Lyulin, C.J. Mackie, S.T. Massie, S. Mikhailenko, H.S.P. Müller, O.V. Naumenko, A.V. Nikitin, J. Orphal, V. Perevalov, A. Perrin, E.R. Polovtseva, C. Richard, M.A.H. Smith, E. Starikova, K. Sung, S. Tashkun, J. Tennyson, G.C. Toon, V.G. Tyuterev, G. Wagner: The HITRAN2012 molecular spectroscopic database, *J. Quant. Spectrosc. Radiat. Transf.* **130**, 4–50 (2013)
- 28.29 G.M.B. Dobson: Observers Handbook for the Ozone Spectrophotometer. In: *Annals of the international geophysical year*, Vol. V (Pergamon Press, New York 1957) pp. 46–89
- 28.30 M.W. Sigrist: *Air Monitoring by Spectrometric Techniques* (John Wiley & Sons Inc., New York 1994)
- 28.31 J.P. Burrows, M. Weber, M. Buchwitz, V. Rozanov, A. Ladstätter-Weißmayer, A. Richter, R. Debeek, R. Hoogen, K. Bramstedt, K.-U. Eichmann, M. Eisinger: The Global Ozone Monitoring Experiment (GOME): Mission concept and first scientific results, *J. Atmos. Sci.* **56**, 151–175 (1999)
- 28.32 M. Wenig, B. Jähne, U. Platt: Operator representation as a new differential optical absorption spectroscopy formalism, *Appl. Opt.* **44**, 3246–3253 (2005)
- 28.33 U. Platt, J. Stutz: *Differential Optical Absorption Spectroscopy – Principles and Application* (Springer, Berlin, Heidelberg, New York 2008)
- 28.34 F.K. Tittel, D. Richter, A. Fried: Mid-infrared laser applications in spectroscopy, *Top. Appl. Phys.* **89**, 445–510 (2003)
- 28.35 R. Haus, R. Wilkinson, J. Heland, K. Schäfer: Remote sensing of gas emissions on natural gas flares, *Pure Appl. Opt.* **7**, 853–862 (1998)
- 28.36 Network for the Detection of Atmospheric Composition Change: <http://www.ndacc.org> (2019), Accessed 10 July 2021
- 28.37 Total Carbon Column Observing Network: <http://www.tccon.caltech.edu> (2019), Accessed 10 July 2021
- 28.38 P. Zalicki, R.N. Zare: Cavity ring-down spectroscopy for quantitative absorption measurements, *J. Chem. Phys.* **102**(7), 2708–2717 (1995)
- 28.39 S.S. Brown: Absorption spectroscopy in high-finesse cavities for atmospheric studies, *Chem. Rev.* **103**(12), 5219–5238 (2003)
- 28.40 S.M. Ball, J.M. Langridge, R.L. Jones: Broadband cavity enhanced absorption spectroscopy using light emitting diodes, *Chem. Phys. Lett.* **398**, 68–74 (2004)
- 28.41 U. Platt, J. Meinen, D. Poehler, T. Leisner: Broadband Cavity Enhanced Differential Optical Absorption Spectroscopy (CE-DOAS) – Applicability and corrections, *Atmos. Meas. Tech.* **2**, 713–723 (2009)
- 28.42 J. Meinen, J. Thieser, U. Platt, T. Leisner: Using a high finesse optical resonator to provide a long light path for differential optical absorption spectroscopy: CE-DOAS, *Atmos. Chem. Phys.* **10**, 3901–3914 (2010)
- 28.43 G. Hönninger, U. Platt: Observations of BrO and its vertical distribution during surface ozone depletion at alert, *Atmos. Environ.* **36**(15–16), 2481–2489 (2002)
- 28.44 G. Hönninger, C. von Friedeburg, U. Platt: Multi-axis differential optical absorption spectroscopy (MAX-DOAS), *Atmos. Chem. Phys.* **4**, 231–254 (2004)
- 28.45 T. Wagner, B. Dix, C. von Friedeburg, U. Frieß, S. Sanghavi, R. Sinreich, U. Platt: MAX-DOAS O₄ measurements: A new technique to derive information on atmospheric aerosols – Principles and information content, *J. Geophys. Res. Atmos.* **109**, D22205 (2004)
- 28.46 H. Leser, G. Hönninger, U. Platt: MAX-DOAS measurements of BrO and NO_x in the marine boundary layer, *Geophys. Res. Lett.* **30**(10), 1537 (2003)
- 28.47 F. Wittrock, H. Oetjen, A. Richter, S. Fietkau, T. Medeke, A. Rozanov, J.P. Burrows: MAX-DOAS measurements of atmospheric trace gases in Ny-Alesund – Radiative transfer studies and their application, *Atmos. Chem. Phys.* **4**, 955–966 (2004)

- 28.48 G. Hönninger, H. Leser, O. Sebastian, U. Platt: Ground-based measurements of halogen oxides at the Hudson Bay by active long path DOAS and passive MAX-DOAS, *Geophys. Res. Lett.* **31**(4), L04111 (2004)
- 28.49 U. Frieß, P.S. Monks, J.J. Remedios, A. Rozanov, R. Sinreich, T. Wagner, U. Platt: MAX-DOAS O₄ measurements: A new technique to derive information on atmospheric aerosols: 2. Modelling studies, *J. Geophys. Res. Atmos.* **111**, D14203 (2006)
- 28.50 H. Irie, Y. Kanaya, H. Akimoto, H. Tanimoto, Z. Wang, J.F. Gleason, E.J. Bucselo: Validation of OMI tropospheric NO₂ column data using MAX-DOAS measurements deep inside the North China Plain in June 2006: Mount Tai Experiment 2006, *Atmos. Chem. Phys.* **8**, 6577–6586 (2008)
- 28.51 K. Clémer, M. Van Roozendael, C. Fayt, F. Hendrick, C. Hermans, G. Pinardi, R. Spurr, P. Wang, M. de Mazière: Multiple wavelength retrieval of tropospheric aerosol optical properties from MAXDOAS measurements in Beijing, *Atmos. Meas. Tech.* **3**, 863–878 (2010)
- 28.52 K.L. Chan, M. Wiegner, M. Wenig, D. Pöhler: Observations of tropospheric aerosols and NO₂ in Hong Kong over 5 years using ground based MAX-DOAS, *Sci. Total Environ.* **619/620**, 1545–1556 (2018)
- 28.53 K.-P. Heue, A. Richter, M. Bruns, J.P. Burrows, C. von Friedeburg, U. Platt, I. Pundt, P. Wang, T. Wagner: Validation of SCIAMACHY tropospheric NO₂-columns with AMAXDOAS measurements, *Atmos. Chem. Phys.* **5**, 1039–1051 (2005)
- 28.54 T. Wagner, O. Ibrahim, R. Sinreich, U. Frieß, R. von Glasow, U. Platt: Enhanced tropospheric BrO over Antarctic sea ice in mid winter observed by MAX-DOAS on board the research vessel Polarstern, *Atmos. Chem. Phys.* **7**, 3129–3142 (2007)
- 28.55 O. Ibrahim, R. Shaiganfar, R. Sinreich, T. Stein, U. Platt, T. Wagner: Car MAX-DOAS measurements around entire cities: quantification of NO_x emissions from the cities of Mannheim and Ludwigshafen (Germany), *Atmos. Meas. Tech.* **3**, 709–721 (2010)
- 28.56 T. Wagner, T. Deutschmann, U. Platt: Determination of aerosol properties from MAX-DOAS observations of the Ring effect, *Atmos. Meas. Tech.* **2**, 495–512 (2009)
- 28.57 B. Buchholz, A. Afchine, A. Klein, C. Schiller, M. Kramer, V. Ebert: HAI, a new airborne, absolute, twin dual-channel, multi-phase TDLAS-hygrometer: Background, design, setup, and first flight data, *Atmos. Meas. Tech.* **10**(1), 35–57 (2017)
- 28.58 D.S. Bomse, A.C. Stanton, J.A. Silver: Frequency modulation and wavelength modulation spectroscopies: Comparison of experimental methods using a lead-salt diode laser, *Appl. Opt.* **31**, 718–731 (1992)
- 28.59 D.R. Herriott, H. Kogelnik, R. Kompfner: Off-axis paths in spherical mirror interferometers, *Appl. Opt.* **3**, 523–526 (1964)
- 28.60 D.R. Herriott, H.J. Schulte: Folded optical delay lines, *Appl. Opt.* **4**, 883–889 (1965)
- 28.61 J.A. Silver: Simple dense-pattern optical multipass cells, *Appl. Opt.* **44**, 6545–6556 (2005)
- 28.62 P. Werle, R. Mücke, F. Slemr: The limits of signal averaging in atmospheric trace-gas monitoring by tunable diode-laser absorption-spectroscopy (TDLAS), *Appl. Phys. B* **57**, 131 (1993)
- 28.63 P. Werle: Accuracy and precision of laser spectrometers for trace gas sensing in the presence of optical fringes and atmospheric turbulence, *Appl. Phys. B* **102**, 313 (2011)
- 28.64 U.S. EPA: *Method T0-16, Long-Path Open-Path Fourier Transform Infrared Monitoring of Atmospheric Gases. Compendium of Methods for the Determination of Toxic Organic Compounds in Ambient Air*, 2nd edn. (Center for Environmental Research Information, Office of Research and Development, U.S. Environmental Protection Agency, Cincinnati 1999), EPA/625/R-96/010b
- 28.65 EN: *Air quality – Atmospheric measurements near ground with FTIR spectroscopy* (European Committee for Standardization, Brussels 2008), EN 15483:2008, DIN EN 15483
- 28.66 EN: *Air quality – Atmospheric measurements near ground with active Differential Optical Absorption Spectroscopy (DOAS) – Ambient air and diffuse emission measurements* (European Committee for Standardization, Brussels 2013), EN 16253:2013, DIN EN 16253
- 28.67 K. Schäfer, J. Heland, D.H. Lister, C.W. Wilson, R.J. Howes, R.S. Falk, E. Lindermeir, M. Birk, G. Wagner, P. Haschberger, M. Bernard, O. Legras, P. Wiesen, R. Kurtenbach, K.J. Brockmann, V. Kriesche, M. Hilton, G. Bishop, R. Clarke, J. Workman, M. Caola, R. Geatches, R. Burrows, J.D. Black, P. Hervé, J. Vally: Non-intrusive optical measurements of aircraft engine exhaust emissions and comparison with standard intrusive techniques, *Appl. Opt.* **39**, 441–455 (2000)
- 28.68 R.A. Washenfelder, A.O. Langford, H. Fuchs, S.S. Brown: Measurement of glyoxal using an incoherent broadband cavity enhanced absorption spectrometer, *Atmos. Chem. Phys.* **8**, 7779–7793 (2008)
- 28.69 A. Feitz, I. Schroder, F. Phillips, T. Coates, K. Negandhi, S. Day, A. Luhar, S. Bhatia, G. Edwards, S. Hrabar, E. Hernandez, B. Wood, T. Naylor, M. Kennedy, M. Hamilton, M. Hatch, J. Malos, M. Kochanek, P. Reid, J. Wilson, N. Deutscher, S. Zegelin, R. Vincent, S. White, C. Ong, S. George, P. Maas, S. Towner, N. Wokker, D. Griffith: The Ginninderra CH₄ and CO₂ release experiment: An evaluation of gas detection and quantification techniques, *Int. J. Greenh. Gas Control* **70**, 202–224 (2018)
- 28.70 K. Schäfer, I. Steinecke, S. Emeis, M. Stockhause, R. Sussmann, T. Trickl, O. Reitebuch, K. Hoehstetter, A. Sedlmaier, G. Depta, A. Gronauer, A. Seedorf, J. Hartung: Inverse modelling on the basis of remote sensing to determine emission rates, *Meteorol. Z.* **7**(1), 7–10 (1998)
- 28.71 P. de Donato, O. Barres, J. Sausse, N. Taquet: Advances in 3-D infrared remote sensing gas

- monitoring. Application to an urban atmospheric environment, *Remote Sens. Environ.* **175**, 301–309 (2016)
- 28.72 F. Hase, M. Frey, T. Blumenstock, J. Groß, M. Kiel, R. Kohlhepp, G. Mengistu Tsidu, K. Schäfer, M.K. Sha, J. Orphal: Application of portable FTIR spectrometers for detecting greenhouse gas emissions of the major city Berlin, *Atmos. Meas. Tech.* **8**, 3059–3068 (2015)
- 28.73 M. Frey, F. Hase, T. Blumenstock, J. Groß, M. Kiel, G. Mengistu Tsidu, K. Schäfer, M.K. Sha, J. Orphal: Calibration and instrumental line shape characterization of a set of portable FTIR spectrometers for detecting greenhouse gas emissions, *Atmos. Meas. Tech.* **8**, 3047–3057 (2015)
- 28.74 C. Viatte, T. Lauvaux, J.K. Hedelius, H. Parker, J. Chen, T. Jones, J.E. Franklin, A.J. Deng, B. Gaudet, K. Verhulst, R. Duren, D. Wunch, C. Roehl, M.K. Dubey, S. Wofsy, P.O. Wennberg: Methane emissions from dairies in the Los Angeles Basin, *Atmos. Chem. Phys.* **17**, 7509–7528 (2017)
- 28.75 D. Wunch, G.C. Toon, P.O. Wennberg, S.C. Wofsy, B.B. Stephens, M.L. Fischer, O. Uchino, J.B. Abshire, P. Bernath, S.C. Biraud, J.-F.L. Blavier, C. Boone, K.P. Bowman, E.V. Browell, T. Campos, B.J. Connor, B.C. Daube, N.M. Deutscher, M. Diau, J.W. Elkins, C. Gerbig, E. Gottlieb, D.W.T. Griffith, D.F. Hurst, R. Jimenez, G. Keppel-Aleks, E. Kort, R. Macatangay, T. Machida, H. Matsueda, F. Moore, I. Morino, S. Park, J. Robinson, C.M. Roehl, Y. Sawa, V. Sherlock, C. Sweeney, T. Tanaka, M.A. Zondlo: Calibration of the Total Carbon Column Observing Network using aircraft profile data, *Atmos. Meas. Tech.* **3**, 1351–1362 (2010)
- 28.76 H. Bovensmann, J. Burrows, M. Buchwitz, J. Frerick, S. Noël, V. Rozanov, K. Chance, A. Goede: SCIAMACHY: Mission objectives and measurement modes, *J. Atmos. Sci.* **56**, 127–150 (1999)
- 28.77 J. Callies, E. Corpaccioli, M. Eisinger, A. Hahne, A. Lefebvre: GOME-2 – Metop’s second-generation sensor for operational ozone monitoring, *ESA Bull.* **102**, 28–36 (2000)
- 28.78 P. Levelt, G.H.J. Van den Oord, M. Dobber, A. Malkki, H. Visser, J. de Vries, P. Stammes, J. Lundell, H. Saari: The ozone monitoring instrument, *IEEE Trans. Geosci. Remote* **44**, 1093–1101 (2006)
- 28.79 J.P. Veefkind, I. Aben, K. McMullan, H. Förster, J. De Vries, G. Otter, J. Claas, H.J. Eskes, J.F. De Haan, Q. Kleipool, M. Van Weele, O. Hasekamp, R. Hoogeveen, J. Landgraf, R. Snel, P. Tol, P. Ingmann, R. Voors, B. Kruizinga, R. Vink, H. Visser, P.F. Levelt: TROPOMI on the ESA Sentinel-5 Precursor: A GMES mission for global observations of the atmospheric composition for climate, air quality and ozone layer applications, *Remote Sens. Environ.* **120**, 70–83 (2012)
- 28.80 M. Perlicki, S. Lori-Solomon: On the evaluation of air mass factors for atmospheric near-ultraviolet and visible absorption spectroscopy, *J. Geophys. Res. Atmos.* **98**(D6), 10319–10825 (1993)
- 28.81 M. Cooper, R.V. Martin, A. Padmanabhan, D.K. Henze: Comparing mass balance and adjoint methods for inverse modeling of nitrogen dioxide columns for global nitrogen oxide emissions, *J. Geophys. Res. Atmos.* **122**(8), 4718–4734 (2017)
- 28.82 S. Eckhardt, A.J. Prata, P. Seibert, K. Stebel, A. Stohl: Estimation of the vertical profile of sulfur dioxide injection into the atmosphere by a volcanic eruption using satellite column measurements and inverse transport modeling, *Atmos. Chem. Phys.* **8**, 3881–3897 (2008)
- 28.83 R.D. May: Open-path, near-infrared tunable diode laser spectrometer for atmospheric measurements of H₂O, *J. Geophys. Res. Atmos.* **103**(D15), 19161–19172 (1998)
- 28.84 J.R. Podolske, G.W. Sachse, G.S. Diskin: Calibration and Data Retrieval Algorithms for the NASA Langley/Ames Diode Laser Hygrometer for the NASA Transport and Chemical Evolution over the Pacific (TRACE-P) mission, *J. Geophys. Res. Atmos.* **108**(D20), 8792 (2003)
- 28.85 M.A. Zondlo, M.E. Paige, S.M. Massick, J.A. Silver: Vertical cavity laser hygrometer for the National Science Foundation Gulfstream-V aircraft, *J. Geophys. Res. Atmos.* **115**, D20309 (2010)
- 28.86 D. McDermitt, G. Burba, L. Xu, T. Anderson, A. Komissarov, B. Riensche, J. Schedbauer, G. Starr, D. Zona, W. Oechel, S. Oberbauer, S. Hastings: A new lower power, open-path instrument for measuring methane flux by eddy covariance, *Appl. Phys. B* **102**, 391 (2012)
- 28.87 K. Sun, L. Tao, M.A. Zondlo, K. Shonkwiler, C. Nash, J.M. Ham: Open-path eddy covariance measurements of ammonia fluxes from a beef cattle feedlot, *Agric. For. Meteorol.* **213**, 193–202 (2015)
- 28.88 A.P.M. Michel, D.J. Miller, K. Sun, L. Tao, L. Stanton, M.A. Zondlo: Long-path quantum cascade laser-based sensor for methane measurements, *J. Atmos. Ocean. Technol.* **33**(11), 2373–2384 (2016)
- 28.89 A. Hensen, H. Scharff: Methane emission estimates from landfills obtained with dynamic plume measurements, *Water Air Soil Pollut. Focus* **1**, 455–464 (2001)
- 28.90 M. Pedone, A. Aiuppa, G. Giudice, F. Grassa, C. Cardellini, G. Chiodini, M. Valenza: Volcanic CO₂ flux measurement at Campi Flegrei by tunable diode laser absorption spectroscopy, *Bull. Vulcanol.* **76**(4), 812 (2014)
- 28.91 M.L. Carapezza, F. Barberi, M. Rinaldi, T. Ricci, L. Tarchini, J. Barrancos, C. Fischer, N. Perez, K. Weber, A. Di Piazza, A. Gattuso: Diffuse CO₂ soil degassing and CO₂ and H₂S concentrations in air and related hazards at Vulcano Island (Aeolian arc, Italy), *J. Volcanol. Geoth. Res.* **207**, 130–144 (2011)
- 28.92 M.L. Carapezza, F. Barberi, L. Tarchini, M. Ranaldi, T. Ricci, J. Barrancos, C. Fischer, C. Lucchetti, G. Melian, N. Perez, P. Tuccimei, A. Vogel, K. Weber: Hazardous gas emissions from the flanks of the quiescent Colli Albani volcano (Rome, Italy), *Appl. Geochem.* **27**(9), 1767–1782 (2012)
- 28.93 L. Gianfrani, P. de Natale, G. de Natale: Remote sensing of volcanic gases with DFB-laser-based fiber spectrometer, *Appl. Phys. B* **70**, 467 (2000)

- 28.94 L. Tao, K. Sun, D.J. Miller, D. Pan, L.M. Golston, M.A. Zondlo: Low-power, open-path mobile sensing platform for high-resolution measurements of greenhouse gases and air pollutants, *Appl. Phys. B* **119**, 153 (2015)
- 28.95 B.J. Nathan, L.M. Golston, A.S. O'Brien, K. Ross, W.A. Harrison, L. Tao, D.J. Lary, D.R. Johnson, A.N. Covington, N.N. Clark, M.A. Zondlo: Near-field characterization of methane emission variability from a compressor station using a model aircraft, *Environ. Sci. Technol.* **49**(13), 7896–7903 (2015)
- 28.96 L.M. Golston, L. Tao, C. Brosy, K. Schäfer, B. Wolf, J. McSpirt, B. Buchholz, D.R. Caulton, D. Pan, M.A. Zondlo, D. Yoel, H. Kunstmann, M. McGregor: Lightweight mid-infrared methane sensor for unmanned aerial systems, *Appl. Phys. B* **123**, 170 (2017)
- 28.97 M. De Mazière, A.M. Thompson, M.J. Kurylo, J.D. Wild, G. Bernhard, T. Blumenstock, G.O. Braathen, J.W. Hannigan, J.C. Lambert, T. Leblanc, T.J. McGee, G.E. Nedoluha, I. Petropavlovskikh, G. Seckmeyer, P.C. Simon, W. Steinbrecht, S.E. Strahan: The Network for the Detection of Atmospheric Composition Change (NDACC): History, status and perspectives, *Atmos. Chem. Phys.* **18**, 4935–4964 (2018)
- 28.98 R.M. Gomez, G.E. Nedoluha, H.L. Neal, I.S. McDermid: The fourth-generation water vapor millimeter-wave spectrometer, *Radio Sci.* **47**(1), RS1010 (2012)
- 28.99 L. Moreira, K. Hocke, E. Eckert, T. von Clarmann, N. Kämpfer: Trend analysis of the 20-year time series of stratospheric ozone profiles observed by the GROMOS microwave radiometer at Bern, *Atmos. Chem. Phys.* **15**, 10999–11009 (2015)
- 28.100 G.E. Nedoluha, B.J. Connor, J. Barrett, T. Mooney, A. Parrish, I. Boyd, J.E. Wrotny, R.M. Gomez, J. Koda, M.L. Santee, L. Froidevaux: Ground-based measurements of ClO from Mauna Kea and intercomparisons with Aura and UARS MLS, *J. Geophys. Res.* **116**, D02307 (2011)
- 28.101 R. Rüfenacht, A. Murk, N. Kämpfer, P. Eriksson, S.A. Buehler: Middle-atmospheric zonal and meridional wind profiles from polar, tropical and midlatitudes with the ground-based microwave Doppler wind radiometer WIRA, *Atmos. Meas. Technol.* **7**(12), 4491–4505 (2014)
- 28.102 O. Stähli, A. Murk, N. Kämpfer, C. Mätzler, P. Eriksson: Microwave radiometer to retrieve temperature profiles from the surface to the stratopause, *Atmos. Meas. Technol.* **6**(9), 2477–2494 (2013)
- 28.103 M. Erfan, A.A. Elsayed, Y.M. Sabry, B. Mortada, K. Sharaf, D. Khalil: Environmental mid-infrared gas sensing using MEMS FTIR spectrometer. *Proc. SPIE* **10116**, 101160L (2017)
- 28.104 G.B. Rieker, F.R. Giorgetta, W.C. Swann, J. Kofler, A.M. Zolot, L.C. Sinclair, E. Bauman, C. Cromer, G. Petron, C. Sweeney, P.P. Tans, I. Coddington, N.R. Newbury: Frequency-comb-based remote sensing of greenhouse gases over kilometer air paths, *Optica* **1**(5), 290–298 (2014)
- 28.105 M. Nikodem, G. Plant, D. Sonnenfroh, G. Wysocki: Open-path sensor for atmospheric methane based on chirped laser dispersion spectroscopy, *Appl. Phys. B* **119**, 3 (2015)
- 28.106 T.R. Tsai, R.A. Rose, D. Weidmann, G. Wysocki: Atmospheric vertical profiles of O₃, N₂O, CH₄, CCl₂F₂, and H₂O retrieved from external-cavity quantum-cascade laser heterodyne radiometer measurements, *Appl. Opt.* **51**, 8779–8792 (2012)
- 28.107 B. Buchholz, A. Afchine, V. Ebert: Rapid, optical pressure measurement of the atmospheric pressure on a fast research aircraft using open-path TDLAS, *Atmos. Meas. Tech.* **7**, 3653–3666 (2014)
- 28.108 W. Stremme, A. Krueger, R. Harig, M. Grutter: Volcanic SO₂ and SiF₄ visualization using 2-D thermal emission spectroscopy – Part 1: Slant-column and their ratios, *Atmos. Meas. Tech.* **5**, 275–288 (2012).
- 28.109 A. Krueger, W. Stremme, R. Harig, M. Grutter: Volcanic SO₂ and SiF₄ visualization using 2-D thermal emission spectroscopy – Part 2: Wind propagation and emission fluxes, *Atmos. Meas. Tech.* **6**, 47–61 (2013).
- 28.110 N. Höfert, K. Schäfer, A. Richter, K. Weber, P. Maas: Standards VDI 4211 and VDI 4212 on passive FTIR and DOAS remote sensing techniques, *Proc. SPIE* **10786**, 107860W–1–107860W–17 (2018).

Klaus Schäfer

Atmospheric Physics Consultant
Garmisch-Partenkirchen, Germany
schaefer@atmosphericphysics.de



Klaus Schäfer is a Professor at Atmospheric Science College of the Chengdu University of Information Technology, China since 2016. He retired from the Karlsruhe Institute of Technology, Institute of Meteorology and Climate Research, Atmospheric Environmental Research in Garmisch-Partenkirchen on 03/2016. In 1988 he became Professor of atmospheric physics at the Academy of Sciences of GDR in Berlin. Research interests are air quality studies by remote sensing and in-situ.

Mark Wenig

Department of Physics, Meteorological
Institute Munich
Ludwig-Maximilians-University Munich
Munich, Germany
mark.wenig@lmu.de



Mark Wenig is a Professor at the Ludwig-Maximilians-University Munich, Germany. His research interests are on remote sensing of air pollutants with the aim to further the understanding of the anthropogenic impact on the environment, especially the climate system and the atmospheric composition. He attended the University of Heidelberg for his studies, where he received his PhD degree in environmental physics focusing on satellite retrieval algorithms to determine the global distribution of atmospheric pollutants. He continued to work with space-born spectroscopic measurement techniques at the NASA Goddard Space Flight Center. When he took up a professorship at City University of Hong Kong, he broadened his research area and developed different ground-based instrumental setups to analyze urban air quality.

Mark A. Zondlo

Civil and Environmental Engineering
Princeton University
Princeton, USA
mzondlo@princeton.edu



Mark A. Zondlo is an Associate Professor of Civil and Environmental Engineering at Princeton University. He leads the Atmospheric Chemistry and Composition Group that focuses on optical measurements of trace gases important to climate change and air quality. Zondlo received a B.A. in chemistry from Rice University (1994), a Ph.D. in physical and atmospheric chemistry from the University of Colorado (1999), and was an Advanced Study Program Postdoctoral Fellow at the National Center for Atmospheric Research from 1999–2002. Before joining the Princeton faculty in 2008, he was a Senior Research Scientist at Southwest Sciences, Inc., where he developed new laser-based instrumentation for the atmospheric sciences.

Axel Murk

Institute of Applied Physics
University of Bern
Bern, Switzerland
axel.murk@iap.unibe.ch



Axel Murk is leading the Microwave Physics Division at the Institute of Applied-Physics at the University of Bern. He received a PhD in Physics from the University of Bern in 1999, and a MSc in Physics from Technical University of Munich. His research interests include remote sensing of the atmosphere using ground-based or space-born microwave radiometers.

Konradin Weber

Laboratory for Environmental
Measurement Techniques
Duesseldorf University of Applied Sciences
Duesseldorf, Germany
konradin.weber@hs-duesseldorf.de



Konradin Weber is a Professor at the University of Applied Sciences (HSD) in Duesseldorf. He leads the Laboratory for Environmental Measurement Techniques at HSD. He got his PhD degree in Physics 1988 at the University of Marburg. He is involved since many years in atmospheric research of air pollutants in the troposphere, especially using different optical remote sensing techniques with application of FTIR, DOAS and TDL-based instruments. Recently he expanded his research to mobile measurements of air pollutants using light aircraft, measurement cars and measurement drones.

29. Passive Solar and Microwave Spectral Radiometers

Susanne Crewell , Manfred Wendisch , Ulrich Löhnert 

Radiation sensors operating from the ultraviolet to the microwave spectral range are widely used for passive remote sensing of a large variety of atmospheric properties (gases, aerosol particles, clouds). In general, radiometers measure radiant energy (in physical units of joule). The different types of radiometers are defined by instrument specifications, such as detector area, opening solid angle, spectral bandpass, and integration time. Remote-sensing techniques commonly make use of special spectral features to infer atmospheric parameters, which can be deduced from spectrally resolved measurements at a limited number of wavelengths. Here, we introduce two typical groups of passive remote-sensing instruments, which are frequently applied to retrieve aerosol parameters (sun photometers) and thermodynamic profiles, as well as liquid water paths (microwave radiometers). Sun photometers and microwave radiometers measure spectral radiances in the ultraviolet, the visible to near-infrared (photometer), and the microwave spectral ranges, respectively. Sun photometers detect spectral radiation in about 5–15 wavelength channels in different geometries (direct sun direction, zenith, nadir, fixed values of zenith distance or azimuth angle), from which the aerosol optical depth is derived, and further properties of the aerosol particle ensemble (such as size distribution, single scattering albedo, scattering phase function, index of refraction), as well as precipitable water vapor (or other path-integrated gas species) are derived. Microwave radiometers (also called microwave profilers) with several spectral channels along water vapor and oxygen emission features at frequencies < 100 GHz allow the retrieval of air temperature and humidity profiles with coarse vertical resolution. Both instruments, sun photometers and microwave radiometers, also provide information on the microphysical properties of clouds by either using spectral extinction (sun photometer) or the emission by cloud droplets

29.1	Measurement Principles and Parameters	822
29.1.1	Measured Parameters	822
29.1.2	Principles of Measurements	823
29.1.3	Siting Conditions	825
29.2	History	825
29.3	Theory	826
29.3.1	Sun Photometers	826
29.3.2	Microwave Radiometers	827
29.4	Devices and Systems	830
29.4.1	Sun Photometers	830
29.4.2	Microwave Radiometers	830
29.5	Specifications	832
29.5.1	Sun Photometers	832
29.5.2	Microwave Radiometers	832
29.6	Quality Control	833
29.6.1	Calibration of Sun Photometers	833
29.6.2	Microwave Radiometers	833
29.7	Maintenance	834
29.7.1	Sun Photometers	834
29.7.2	Microwave Radiometers	835
29.8	Application	835
29.9	Future Developments	837
29.10	Further Readings	837
	References	838

(microwave radiometer). The sun photometer is the standard instrument to measure aerosol optical depth, and the microwave radiometer is the most suitable device to observe the liquid water path of clouds. An advantage of these passive sensors is their simple operation, which requires only little maintenance and a low power supply, which makes them well suited for continuous network operation from the ground but also on research aircraft.

From the early days of the development of useful satellite-based remote-sensing observations in the 1960s, radiometers have been the backbone for Earth observations. Imaging radiometers operating from ultraviolet (UV) to microwave (MW) spectral ranges provide comprehensive information on the state of the atmosphere, including aerosol particle size distribution and microphysical characteristics, cloud optical and microphysical properties, as well as water vapor and temperature profiles. This chapter is dedicated to radiometers and the associated techniques used for remote sensing of the above-mentioned parameters and is not concerned with broadband radiation measurements (Chap. 12 *Radiation Sensors*). Only instruments

with a limited number of spectral bandpass filters are dealt with here, in contrast to spectrometers, which employ a large number of channels over a given wavelength band with high spectral resolution (Chap. 28 *Spectrometers*). Furthermore, this chapter focusses on instrumentation operated on the ground, while later chapters deal with radiation measurements from aircraft and satellites (Chap. 37 *Solar Radiation Sensors*, Chap. 39 *Microwave Radiometry*, and Chap. 42 *Imaging Techniques*).

Two examples are discussed in detail: sun photometers and microwave radiometers (MWRs). These instruments are easy to handle and suitable for long-term monitoring within larger observational networks.

29.1 Measurement Principles and Parameters

Solar spectral radiation measurements offer plenty of information on atmospheric constituents, such as gas concentrations (e.g., water vapor), or aerosol particles, and cloud properties. Sun photometers are a widespread instrument type to derive, in particular, aerosol properties. Different observation geometries of sun photometers include direct sun (looking into the direction of the sun for optical depth retrieval), as well as almucantar (keeping the zenith angle constant during observations) and principal plane (constant azimuth angle) constellations (for retrievals of aerosol particle size distribution, refractive index, shape of particles). Sun photometers are widely used in global networks, for example in the Aerosol Robotic Network (AERONET) [29.1], the Japanese SKYNET [29.2], or the Sun/sky-radiometer Observation Network (SONET) in China. Recently, polarization measurements were added to the sun photometer measurement program. The Global Atmosphere Watch–Precision Filter Radiometer (GAW-PFR) network was started in 1999; it conducts long-term aerosol optical depth (AOD) measurements at remote background sites. In 2015, in Germany (Lindenberg) AERONET photometers were modified to observe aerosol optical depth at night on an automatic and quasi continuous basis.

Ground-based MWRs measure atmospheric thermal emission by gases and hydrometeors, allowing the retrieval of air temperature and trace gas profiles, as well as the amount of liquid water in clouds. These measurements are useful in a variety of environmental and engineering applications, including meteorological observations and weather forecasting, communications, astronomy, radio-astronomy, geodesy and long-baseline interferometry, satellite validation, climate changes, air–sea interaction, and fundamental molecular physics.

Here, we focus on ground-based MWRs for deriving tropospheric air temperature and humidity profiles, and clouds, which, similarly to the sun photometers, become organized in networks, e.g., the microwave radiometer network (MWRnet) [29.3].

29.1.1 Measured Parameters

Sun photometers and MWRs measure spectral radiances in physical units of $\text{W m}^{-2} \text{sr}^{-1}$ per wavelength or per frequency/wavenumber unit. Sun photometers typically employ wavelength channels from the ultraviolet (340 nm) to the solar near-infrared (2000 nm) spectral ranges. In the microwave spectral range with wavelengths between 1 mm and 1 m (corresponding to frequencies of 0.3–300 GHz), the spectral location is typically given in terms of frequency. The measured radiances result either from the solar emission and subsequent scattering/absorption events within the atmosphere (sun photometer) or from thermal emission by atmospheric and surface constituents. Radiances measured by the sun photometer are calibrated either using reference standards (provided by accepted standards from, e.g., the National Institute for Standards and Technology) or by applying the so-called Langley plot method (Sect. 29.6.1). MWRs are calibrated to brightness temperatures (T_B in kelvin) using *Planck's law* (Table 29.1, (29.3)), which allows a direct conversion from spectral radiance to an equivalent brightness temperature T_B . Note, that the same nomenclature is used for infrared radiometers operating in the atmospheric window $\approx 10 \mu\text{m}$ wavelength. Here, the advantage of using T_B becomes evident by considering a cloud with no further atmospheric emission below it. As liquid water clouds can be treated as blackbodies in the infrared

Table 29.1 Measured parameters by spectral radiometers

Parameter	Description	Unit	Symbol
Spectral radiance (direct solar radiation, scattered skylight)	Radiance, as a function of wavelength and field of view (FOV)	$\text{W m}^{-2} \text{sr}^{-1} \text{nm}^{-1}$	I_λ
Brightness temperature	Radiances detected by microwave receivers in a limited frequency interval (bandwidth) and a certain polarization state, calibrated to <i>Planck</i> equivalent brightness temperatures	K	T_B

spectral range, the brightness temperature measured, T_B , directly corresponds to the cloud base temperature [29.4].

Sun photometers are usually adjusted into the direction of the sun to derive the AOD from atmospheric extinction of solar radiation. However, partly, these instruments scan the atmospheric hemisphere to measure scattered radiation from which several additional aerosol particle parameters besides AOD can be retrieved. MWRs typically detect the thermally emitted radiation in zenith direction, although elevation scanning is required to improve the vertical resolution of the retrieved temperature profiles [29.5]. Combined azimuth and elevation scanning by MWRs can be used to map the hemispheric environment in terms of water vapor and cloud liquid water [29.6, 7].

29.1.2 Principles of Measurements

In order to retrieve atmospheric parameters, spectral radiometers use different wavelength channels to measure a set of radiances I_λ (sun photometer) or brightness temperatures T_B (MWR). The basic target of sun photometer measurements is the total optical depth τ , which is a measure of the opacity of the atmosphere; τ is a function of wavelength λ and is derived as the vertical integral of the volume extinction coefficient σ_{ext} from the ground to the top of the atmosphere (TOA)

$$\tau(\lambda) = \int_0^{\text{TOA}} \sigma_{\text{ext}}(\lambda, z) dz; \quad (29.1)$$

σ_{ext} combines the extinction of radiation due to absorption and scattering by atmospheric gases, aerosol particles, and hydrometeors (clouds, precipitation). The total optical depth τ , as a function of λ , can be decomposed into the individual components. Retrieval algorithms (Sect. 29.1.3) exploit the wavelength-dependence to infer aerosol particle (Sect. 29.2 for the sun photometer) and atmospheric parameters (Table 29.3 for MWRs). The interaction between atmospheric radiation and gas molecules, as well as aerosol particles and hydrometeors (scattering/absorption/emission) is a distinct function of the ratio between the size of the interacting agent and the wavelength. While the measurement principle

of sun photometers and microwave radiometers can be described by similar physical principles, due to their different wavelength ranges, they can provide complementary information on atmospheric constituents.

The basic principle of the operation of a sun photometer is widely described in the literature, for example by [29.8]. Knowing the amount of incoming solar radiation at the TOA and measuring the direct solar radiation at the surface, the Bouguer–Lambert–Beer law quantifies the extinction of solar radiation when penetrating through the atmosphere as a function of the total optical depth τ . The total optical depth is determined by Rayleigh scattering on air molecules, as well as by absorption through specific atmospheric gas components, primarily water vapor, ozone, oxygen, and nitrogen dioxide. Furthermore, aerosol particles and hydrometeor extinction (scattering plus absorption) contribute to τ . Because it is difficult to point the photometer's opening solid angle precisely into the direction of the sun in cloudy conditions, sun photometers are preferably operated in cloud-free atmospheric conditions. Retrievals of cloud properties using sun photometer measurements during cloudy sky conditions are also carried out; however they mostly use sun photometer measurements at different observation geometries, other than into the direct sun. While the contribution of Rayleigh scattering can be approximated by common parameterizations, gaseous absorption and the aerosol particle extinction are highly variable. However, in the 940-nm water vapor absorption band, the total optical depth is dominated by water vapor and, thus, the columnar precipitable water vapor (PWV) can be derived from the total optical depth.

The aerosol particle optical depth τ_A can be retrieved by subtracting the contributions by gas and hydrometeor (in the case of clouds and/or precipitation) scattering and absorption. Exploiting the spectral dependence of τ_A can be used to invert the aerosol particle size distribution. The spectral slope of τ_A can be parameterized by the Ångström exponent α defined by

$$\frac{\tau_A(\lambda)}{\tau_A(\lambda_0)} = \left(\frac{\lambda}{\lambda_0} \right)^{-\alpha}. \quad (29.2)$$

The Ångström exponent α is inversely related to the average size of the aerosol particles: the smaller the

Table 29.2 Parameters retrieved from measurements by the sun photometer

Parameter	Description	Unit	Symbol
AOD	Aerosol optical depth at wavelength λ	–	τ_A
Ångström exponent	Wavelength dependence of τ	–	α
Volume particle size distribution	Differential particle volume per differential logarithmic size bin	$\mu\text{m}^3 \mu\text{m}^{-2}$	$dV/d \ln D_p$
Complex particle refractive index	Real and imaginary parts of particle refractive index, real part describing scattering, imaginary part the absorption properties	–	$n = n_{re} - i n_{im}$
Single scattering albedo	Ratio of particle scattering and extinction coefficient. The cosingle-scattering albedo is represented by $1 - \omega$	–	ω
Particle scattering phase function	Angular distribution of normalized differential scattering intensity	–	P
Precipitable water vapor	Column integrated amount of water vapor	kg m^{-2}	PWV

particles, the larger α . More detailed information on the size distribution of aerosol particles, their scattering phase function, and their refractive index can be derived by inversion of multiwavelength measurements in almucantar or principal plane mode together with τ [29.9–11]. Within AERONET, also the cloud optical depth is retrieved from zenith pointing measurements [29.12]. An overview of different possible retrieval products from sun photometer measurements is given in Table 29.2, along with the underlying measurement principles (Table 29.4).

In the MW frequency range, < 100 GHz, extinction is almost exclusively caused by absorption, since scattering at these frequencies plays a role for large precipitation particles only. Under cloud-free conditions, extinction is dominated by water vapor, i.e., the rotational water vapor absorption line at 22.235 GHz and continuum absorption, as well as oxygen absorption (Fig. 29.1). For the latter, the absorption in the center of the 60 GHz absorption complex is so dominant that a ground-based MWR receives radiation emitted

in its immediate neighborhood only and, thus, measures the temperature very close to the instrument. Frequency channels further away also receive radiation from higher atmospheric layers, the further the frequency channel is separated from the absorption complex center. Therefore, multiple measurements along the wing of the absorption band provide information on the vertical temperature profile.

The water vapor line at 22.235 GHz is much weaker than the oxygen complex, and its pressure broadening (≈ 3 MHz/Pa) provides approximate information on the vertical distribution of atmospheric moisture. To cover the relevant pressure range of the troposphere down to 1000 hPa, typically, seven channels are spaced along the wing of the line covering ≈ 7 GHz. This way, the channel at the outer wing of the line is hardly affected by line absorption and can be considered a window channel, i.e., a frequency channel that is only very weakly influenced by gaseous emission. Around 23.8 GHz, the water vapor extinction is roughly constant with the height, making measurements propor-

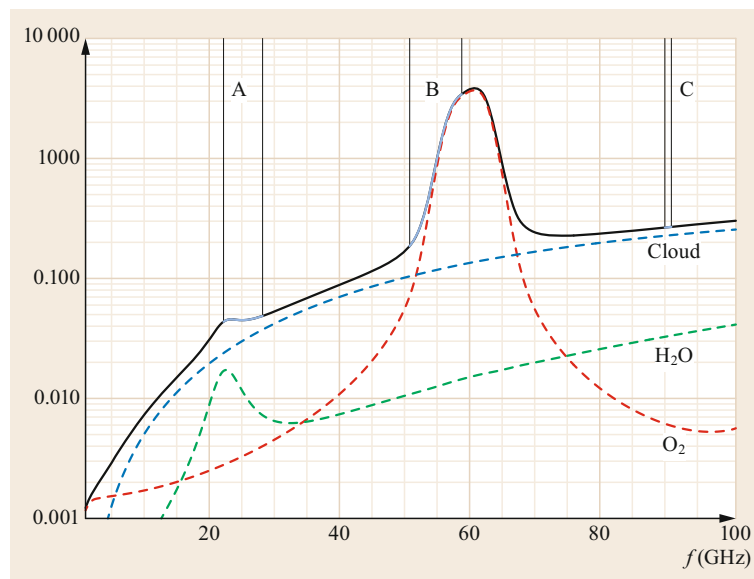


Fig. 29.1 Extinction coefficient in the MW spectral range for a cloudy atmosphere with liquid water content of 0.2 g m^{-3} at 900 hPa. The different contributions by water vapor (green dashed line), oxygen (red dotted line), and cloud water (blue dash-dotted line) are shown. Typical frequency bands used by state-of-the-art microwave radiometers are indicated by the thick lines (after [29.13] with permission from John Wiley and Sons)

Table 29.3 Parameters retrieved from measurements of brightness temperatures in different frequency channels for ground-based microwave radiometers

Parameter	Description	Unit	Symbol
Temperature profile	Vertically resolved atmospheric temperature	K	T
Precipitable water vapor	Column integrated amount of water vapor	kg m^{-2}	PWV
Humidity profile	Vertically resolved mixing ratio	kg kg^{-1}	q
Liquid water path	Column integrated amount of liquid water	kg m^{-2}	LWP

tional to PWV. Cloud liquid water extinction increases strongly with frequency, which allows us to simultaneously retrieve PWV and the liquid water path (LWP) by measuring at two wavelengths: one dominated by water vapor (often 23.8 GHz) and the other one dominated by cloud droplet emission in an atmospheric window, e.g., at 31.4 GHz, whereby a higher LWP accuracy can be achieved by using a 90 GHz channel [29.14]. An overview of the different atmospheric parameters, which are routinely derived from a set of measured brightness temperatures, is given in Table 29.3. Less established retrieval techniques to derive hydrometeor properties including drizzle [29.15], separation of cloud and rain water [29.16], and snow [29.17] exist. These techniques partly use different frequencies, observing geometries, and polarimetric measurements. Note that trace gas profiles observed from spectrometers are described in more detail in Chap. 28.

29.2 History

Hand-held sun photometers were introduced by *Fredrick E. Volz* in 1959 [29.19]. In 1957, he developed a simple photometer that measured AOD with a selenium detector and a green-transmitting 500-nm spectral filter. The photocurrent produced by the device was displayed on a small analog meter. *Volz* subsequently improved his instrument by adding filter channels and replacing the selenium cell with a silicon photodiode and amplifier. His photometers were used in various atmospheric haze studies and networks. Unfortunately, filter drift and the lack of calibrations contaminated the data from the networks. *Volz*'s photometers also served as models for *Glenn Shaw*, who developed hand-held and automated instruments and traveled to Mauna Loa many times to calibrate them [29.20].

Originally, sun photometers used narrow-bandpass filters (with a spectral full width at half maximum,

29.1.3 Siting Conditions

Both instruments (sun photometer and MWR) require an obstacle-free hemispheric view into the atmosphere, and, therefore, a position at an elevated location, e.g., a roof top, is recommended. The sun photometer needs to directly view the sun during daylight hours (unless no cloud observations are intended), in particular during calibration using so-called Langley plots (Sect. 29.6.1). If different observational geometries are considered (almucantar or principal plane), the complete hemisphere should be free of obstacles. In principle, a microwave radiometer can operate in zenith mode only and, thus, is less constrained to a specific location. However, the accuracy of brightness temperature measurements is improved when the so-called sky tipping method [29.18] exploiting elevation scans at principal plane geometry can be applied (Sect. 29.6.2). This is even improved if scans in two opposing directions, i.e., bilateral sky tipping calibrations, are performed to cancel out atmospheric inhomogeneity and instrument leveraging. Furthermore, elevation scanning adds information to the spectral information and can improve the accuracy of the temperature profile retrieval in the boundary layer.

With a typical weight of a few kilograms, a sun photometer is much lighter than an MWR, which weighs between 30 and 60 kg. For unattended continuous operation, a firm fixation to the ground is fundamental, which typically includes the addition of weights to the microwave stand to prevent damage due to very strong wind.

FWHM, of a few nm), but these filters are expensive, fragile, and subject to unpredictable failure. Therefore, light-emitting diodes (LEDs) have been introduced. LEDs as detectors have some disadvantages (their spectral FWHM is relatively large, in the range of a few tens of nm), on the other hand they are cheap and stable over time [29.21].

First MWR observations were intended for extraterrestrial applications, e.g., the sun and cosmic background radiation. During World War II *Robert H. Dicke* (1916–1997) developed an MWR consisting of an antenna connected to a crystal balanced mixer by a rectangular waveguide, which was able to detect a minimum power level of 10^{-16} W [29.22]. Using this radiometer [29.23] he measured the atmospheric absorption at three frequencies around the 22.235 GHz line and showed differences of $\approx 50\%$ to theoretical consider-

ations. It should also be noted that in parallel MWRs were developed in Russia; these, however, are difficult to trace in the open literature.

Early MWR measurements were aimed at a better understanding of microwave propagation in the atmosphere. The possibility to retrieve the atmospheric temperature profile from ground-based measurements along 60 GHz oxygen using a highly directive microwave antenna was first discussed by *Ed R. Westwater* in 1965 [29.24]. Later, he suggested the use of dual channel radiometers operating at ≈ 20 and 31 GHz to accurately derive PWV and LWP simultaneously [29.25].

29.3 Theory

In order to interpret sun photometer and microwave radiometer measurements, basic knowledge of atmospheric radiative transfer is required. The main ideas of radiative transfer and thermal emission are described, for example, by [29.29–31]. Their application to microwave radiometric remote sensing is outlined in [29.32, 33].

Thermal radiation, which is emitted by a blackbody, is described by *Planck's law* (29.3) in terms of spectral radiance, i.e., the emitted power per unit projected area, per unit solid angle, and per unit frequency ν (or wavelength λ), with h the *Planck* and k the *Boltzmann* constant. An ideal blackbody absorbs all incident radiation and re-emits all of the absorbed radiation as a function of its temperature and frequency (or wavelength). To indicate blackbody radiation the emitted spectral radiance is termed *brightness* and can be expressed either as a function of frequency B_ν or wavelength B_λ

$$B_\lambda(\lambda, T) = \frac{2hc^2}{\lambda^5} \frac{1}{\exp(hc/(\lambda kT)) - 1}, \quad (29.3a)$$

$$B_\nu(\nu, T) = \frac{2h\nu^3}{c^2} \frac{1}{\exp(h\nu/(kT)) - 1}. \quad (29.3b)$$

With an approximate blackbody temperature of ≈ 5780 K, the spectral radiance emitted by the sun has its maximum in the visible spectral range ≈ 500 nm. Sun photometers use this as a source and measure spectral radiance in typically less than 15 channels between 300 and 1100 nm wavelength.

The lower the temperature, the lower the emitted spectral radiance. With temperatures between 200 and 300 K, atmospheric constituents show an emission maximum in the thermal infrared. MW radiances

The potential for continuous monitoring of the troposphere using MWRs was quickly recognized, and *D.C. Hogg* [29.26] developed an automatic profiler for temperature, humidity, and wind combining a six-channel MWR for humidity and temperature with a wind profiler. With the technological developments in the last decades, in particular the use of microwave and millimeter-wave integrated circuit (MIMIC) technology, the size of microwave instruments decreased, while their stability increased. First commercial systems specifically designed for continuous and unattended operation have now been available for two decades [29.27, 28].

emitted by the atmosphere are seven orders of magnitude lower than those of solar radiation at TOA in the visible part of the spectrum. Nevertheless, current MWRs detect radiances with sufficient accuracy to retrieve atmospheric moisture, humidity, and temperature measured in typically less than 20 channels between 10 and 100 GHz.

Both sun photometer and MWRs basically measure voltages, and the calibration of these into radiances is one of the largest challenges for accurate measurements.

29.3.1 Sun Photometers

The basic principle of operation of a sun photometer is described, for example, by [29.8]. It is based on the Bouguer–Lambert–Beer law that formulates the exponential attenuation of direct solar radiation as it penetrates through the atmosphere

$$I_\lambda(\lambda, \theta) = I_{0,\lambda}(\lambda, \theta) \exp[-\tau(\lambda, \theta)m(\theta)], \quad (29.4)$$

where $I_\lambda(\lambda, \theta)$ is the radiance of the direct solar radiation measured at wavelength λ , and solar zenith angle θ , $I_{0,\lambda}(\lambda, \theta)$ is the radiance of the direct solar radiation incident at the TOA, τ is the total optical depth of the atmosphere defined by (29.1) at the given wavelength λ , and $m(\theta)$ is the relative optical airmass at the given solar zenith angle θ . In the following, the wavelength dependence of I_λ and τ will not be indicated explicitly.

A measure of the opacity of the atmosphere is τ , which gives the amount of attenuation of direct solar radiation at the given wavelength due to absorption and scattering by atmospheric gases and aerosol particles. It can be expanded into the individual components

that contribute to the extinction of solar radiation

$$\tau = \tau_A + \tau_R + \sum_i \tau_i, \quad (29.5)$$

where the subscript A represents aerosol particles (absorption plus scattering), R stands for *Rayleigh* scattering due to air molecules, and the subscript i indicates the various atmospheric gas components (primarily ozone, water vapor, and nitrogen dioxide) causing absorption of solar radiation.

The relative optical airmass, $m(\theta)$, is given as the slant path length for a given solar zenith angle, θ , relative to the slant path length in the vertical direction. When the sun is directly overhead, the relative optical airmass is equal to unity, and for most solar zenith angles ($\theta < 60^\circ$), the relative optical airmass can be expressed by

$$m(\theta) = \frac{1}{\cos \theta}. \quad (29.6)$$

However, for increasingly larger solar zenith angles ($\theta > 60^\circ$), when the sun gets closer to the horizon, the length of the slant path deviates from that approximated by (29.6), mainly due to the sphericity of the Earth's atmosphere and the effects of refraction. Various formulas and approximations have been developed to account for these effects [29.34]. Furthermore, the airmass depends on the vertical distribution of the scattering and absorbing components in the atmosphere, and for highest accuracies, the airmass for each component (aerosol particles, Rayleigh scattering, ozone, etc.) should be determined individually.

The instruments that measure direct solar radiation do not originally detect solar radiation but record a corresponding wavelength-dependent spectral voltage, V_λ . When this voltage is within the linear region of the given detector, it is directly proportional to the spectral radiance I_λ

$$V_\lambda(\theta) = CI_\lambda(\theta), \quad (29.7)$$

where C is a wavelength-dependent calibration constant characteristic to each detector. Using the above equations and incorporating the airmass factors for each attenuator, (29.7) can be rewritten as

$$V_\lambda(\theta) = V_{0,\lambda} \exp \left[-\tau_A m_A(\theta) - \tau_R m_R(\theta) - \sum_i \tau_i m_i(\theta) \right], \quad (29.8)$$

where $V_{0,\lambda}$ is the voltage that the instrument would read at the TOA at wavelength λ , and the calibration constant C has factored out. The spectral aerosol optical depth can then be obtained by rearranging

$$\tau_A = \frac{1}{m_A(\theta)} \left[\ln(V_{0,\lambda}) - \ln(V_\lambda(\theta)) - \tau_R m_R(\theta) - \sum_i \tau_i m_i(\theta) \right]. \quad (29.9)$$

When retrieving τ_A , the wavelength channels typically chosen for sun photometers are purposely located in regions of the spectrum where aerosol particles and Rayleigh scattering are dominant, and absorption by trace gases is of secondary importance. Most of the terms on the right-hand side of (29.8) can, therefore, be directly calculated or sufficiently estimated; V_λ is the measured signal, the Rayleigh optical depth τ_R can be accurately calculated [29.35], and the optical depths for the various atmospheric gases can be estimated using satellite or climatology data combined with radiative transfer calculations [29.36]; $V_{0,\lambda}$ represents the voltage that the instrument would read at the TOA; it is the one component on the right-hand side of (29.8) that needs to be determined through calibration (Sect. 29.6.1).

29.3.2 Microwave Radiometers

Microwave radiometers (MWRs) measure the thermal emission of atmospheric constituents along the path given by their antenna characteristics. Most microwave emitters show a lower emission compared to that of a blackbody at the same temperature, i.e., the so-called *graybody*. According to *Kirchhoff's* law, a graybody in thermodynamic equilibrium (at temperature T), which absorbs a fraction of incident energy α_ν (or α_λ) at a specified frequency (or wavelength) from a certain direction, will emit the amount $\alpha_\nu B_\nu(\nu, T)$ (or $\alpha_\lambda B_\lambda(\lambda, T)$) into the same direction. For a perfect blackbody, the absorptance α_ν is one for all $\nu \in [0, \infty]$. If a graybody is completely nonabsorbing at a distinct frequency, α_ν is zero, and, thus, in the case of a nonscattering medium, radiation will propagate without any interaction with the medium.

In order to model the microwave signal received by a MWR for a given atmospheric state, the radiative transfer equation (RTE) [29.32] is needed. For a nonscattering medium, it can be derived from the Bouguer–Lambert–Beer law (29.4) in its differential form by adding thermal emission $S = \sigma_a B_\nu ds$ as a source term along the infinitesimal path increment ds (29.10). Also, in a nonscattering atmosphere, the extinction coefficient

Table 29.4 Physical principles of spectral radiometer measurements and applications

Type of sensor	Measurement principle	Application
Sun photometer	Attenuation of direct solar radiation Wavelength dependence of τ_A Inversion of measurements for solar almuquantar, and principal plane geometries, and τ at multiple wavelengths Attenuation of direct solar radiation in 940 nm absorption band	Aerosol optical depth (AOD) Ångström exponent Aerosol microphysical aerosol particle properties (size distribution, refractive index, shape information, single scattering albedo, scattering phase function) Precipitable water vapor
Microwave radiometer (MWR)	Emission along oxygen absorption complex ≈ 60 GHz Emission along water vapor rotation line at 22.235 GHz Continuum emission of liquid water	Temperature profiling Water vapor profiling Liquid water path

σ_{ext} can be reduced to the absorption coefficient σ_a (in m^{-1}), so that we can write for the monochromatic case

$$\frac{dI_v}{ds} = \sigma_a (B_v - I_v). \quad (29.10)$$

Under the assumption of a plane-parallel horizontally homogeneous atmosphere, we may replace the path increment ds by $dz = ds \cos \theta_{\text{gb}}$ with θ_{gb} , the zenith angle of the ground-based observation. Integrating (29.10) the monochromatic radiance actually observed by a ground-based MWR in zenith mode can be described by

$$I_v = I_{v,\text{TOA}} e^{-\tau} + \int_0^{\text{TOA}} \sigma_a(z) B_v [T(z)] e^{-\tau_z} dz, \quad (29.11)$$

where the first term describes the contribution of the cosmic background ($I_{v,\text{TOA}}$) to the signal observed, which is attenuated within the atmosphere according to the total optical depth τ . The second term considers the thermal emission of the atmosphere at all heights z , which are also subject to attenuation

$$\tau_z = \int_0^z \sigma_a(z') dz'$$

on the way from its origin ($z' = z$) to the microwave antenna ($z' = 0$).

In order to simplify the units of (29.11) for measurement applications, *Planck's law* (29.3) can be solved for temperature. At low microwave frequencies and typical atmospheric temperatures, the radiance becomes nearly linearly related to temperature (*Rayleigh–Jeans approximation*). In the case of a gray emitter, T will no longer be equal to the physical temperature of the emitter. In this case, *Planck's law* is used to define an equivalent brightness temperature T_B , so that, applying the

Rayleigh–Jeans approximation, (29.11) can be rewritten to

$$T_B = T_{B,\text{COS}} e^{-\tau} + \int_0^{\text{TOA}} \sigma_a(z) T(z) e^{-\tau_z(z)} dz, \quad (29.12)$$

where $T_{B,\text{COS}}$ is the brightness temperature of the cosmic background radiation of 2.73 K.

Besides frequency, the absorption coefficient σ_a in (29.12) is a function of pressure, temperature, water vapor, and cloud liquid, which strongly varies with frequency (Fig. 29.1). The gaseous contribution can be calculated given the atmospheric state from widely used absorption models, e.g., [29.37, 38], however, improving these models is currently still an ongoing process. The absorption coefficient for liquid hydrometeors, such as cloud droplets, drizzle, or rain drops, which are assumed to be spherical, are calculated using Mie theory. It depends on the complex permittivity of liquid water, which is well known for temperatures $> 0^\circ\text{C}$. However, the refractive index of supercooled liquid water (i.e., liquid water at temperatures below freezing) is less certain, as laboratory data are extremely sparse, but new refractive index models have been developed recently that also take field measurements into account [29.39].

From (29.12), the dependence of the measured brightness temperatures on the vertical temperature profile is obvious, while other dependencies, e.g., towards humidity and liquid water are hidden in the absorption coefficient. Retrieval algorithms are needed to obtain atmospheric parameters from measurements of T_B as a function of frequency in selected bands (Table 29.4). In the case of boundary layer temperature profiles, additional information from measurements at multiple elevation angles can be exploited.

Retrieval algorithms are often developed as multivariate regression or neural network frameworks. Moderately nonlinear problems or composite profiling techniques using the synergy of different ground-based

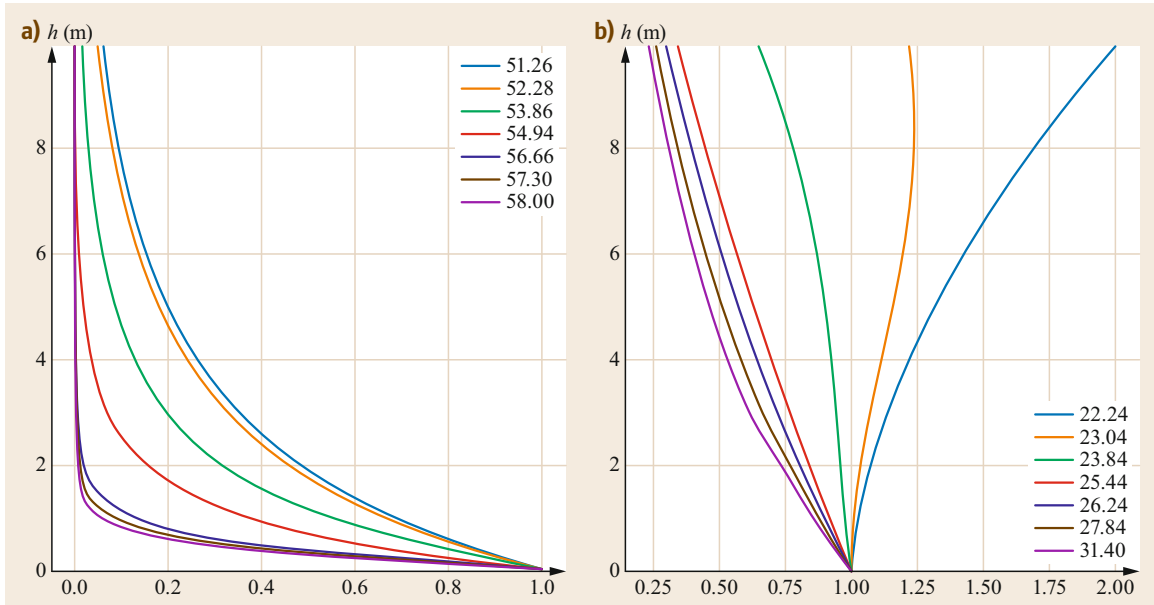


Fig. 29.2a,b Normalized weighting functions for typical frequencies of ground-based microwave radiometers. **(a)** Temperature weighting functions for the center frequencies of typical V-band channels located on the left side of the 60 GHz absorption complex. **(b)** Water vapor density weighting functions at center frequencies of typical K-band channels (on the right side of the 22.235 GHz water vapor absorption line and window channel 31.4 GHz)

sensors (Chap. 47) can be solved within variational approaches that allow the uncertainty specification for each derived quantity. Regression-type algorithms are based on a large, representative data set of concurrent T_B and atmospheric variables, which are related to each other by means of a minimization algorithm (i.e., least-squares or neural network approach). One example is the use of radiosonde profiles measured in parallel to MWR measurements, e.g., [29.40]. Most of the time, such data are not available to cover the full range of atmospheric states, and, therefore, (29.12) is used to calculate brightness temperatures given a climatology of atmospheric profiles, e.g., from radiosondes or reanalysis, for the location of the radiometer. The synthetic data set of consistent T_B and atmospheric parameters is then used to derive the statistical relations.

In contrast, a variational algorithm finds a solution such that for each case, the measured brightness temperatures are sufficiently close to the ones simulated from the retrieved atmospheric state. In general, a large number of atmospheric states can satisfy each combination of T_B , so that physical constraints have to be applied, which will lead to a converged solution. Variational approaches use so-called weighting functions that describe at which altitudes the atmospheric parameters of interest contribute to which degree to the measured brightness temperature. For the standard atmosphere,

Fig. 29.2 illustrates the strong nonlinear function of the temperature weighting function along the oxygen absorption complex. The innermost channels only receive radiation from the lowest layers, while channels further away subsequently receive information also from higher layers. In general, very little information from the upper troposphere is contained in the measurements, which make them highly complementary to satellite observation where the opposite behavior occurs. For moisture, the 23.8 GHz channel weighting function is nearly constant with height, making T_B measurements an ideal proxy for PWV. Due to pressure broadening, frequency channels at frequencies further away from the line center receive higher contributions from the lower layers, while the innermost channels are sensitive to higher altitudes.

The smoothness of the weighting functions already indicate why MWRs only need a limited number of frequency channels along the absorption features. By calculating the number of degrees of freedom for signal following [29.41], it can be shown that typical zenith pointing temperature profilers contain only two independent pieces of information for temperature profiling, which can be increased up to four by adding elevation scans [29.42]. For humidity profiling, the information content increases for moister atmospheres, but the number of degrees of freedom for signal is generally below three.

29.4 Devices and Systems

Both sun photometers and MWRs are commercially available. In the past decade, much effort has been put into optimizing sensitivity and calibration accuracy, as well as unattended, reliable operations for network-suitable applications.

29.4.1 Sun Photometers

Sun photometers consist of a telescopic opening angle, a wavelength selective unit (interference filters, optical gratings) for spectral discrimination, and a detector unit producing an output voltage, which is processed further on. There are handheld instruments for easy application in the frame of field campaigns. Their disadvantage is related to issues of finding the precise sun position and keeping it constant for the time the data are taken. More sophisticated versions are installed in permanent ground-based networks (see example in Fig. 29.3). These instruments are calibrated regularly and follow standard measurement protocols. The data are centrally collected and inversion procedures are applied using unified software and analysis methods. Permanent sun photometers are installed such that they run automatically and that they additionally allow measurements in almucantar and principal plane geometries. Recently, some of the photometers have additionally been equipped with polarization measurement capabilities.

29.4.2 Microwave Radiometers

Microwave radiometers are usually total power instruments, i.e., they measure the signal power that is received by the antenna within the channel bandwidth

$\Delta\nu$ and over the integration time Δt . In the simplest configuration, an MWR consists of an antenna, an amplification chain, and a detection unit (Fig. 29.4). The recorded voltage is then converted to brightness temperatures using calibration information (Sect. 29.6.2). The measurements at the different frequency channels are taken either sequentially or synchronously, depending on the design of the radiometer.

The microwave antenna needs to be highly directive in order to treat the observation as a single (*pencil*) beam in which no horizontal inhomogeneities occur. The beam width of the antenna is commonly defined from its FWHM angular receiving characteristics and is typically on the order of a few degrees. For a given beam width, the diffraction limit causes the size of the antenna to become relatively large, e.g., to 0.5 m for < 10 GHz. Because retrieval algorithms combine channels with different frequencies, and each channel needs to see the same part of the atmosphere, radiometers employing a wide frequency range might need different antennas to match the beam size. The antenna is often connected to a scanning mechanism to adjust the azimuth and elevation angle, either for atmospheric scanning or to view calibration targets. Many designs use an offset parabolic mirror that focuses the microwave radiation onto a classical horn antenna connected to a waveguide. Here, corrugated feed horns provide symmetric beam patterns of a nearly Gaussian characteristic.

As pointed out before, microwave radiances are extremely low and, therefore, microwave radiometers need to amplify the signal received at the antenna by ≈ 80 dB. While lately low-noise amplifiers (LNA) have become available for frequencies up to ≈ 100 GHz, many microwave radiometers still employ the heterodyne technique, and only a few radiometers are based on direct detection techniques. In a heterodyne receiver (Fig. 29.3), the radio frequency (RF) is down converted to an intermediate frequency (IF) by a mixer using a frequency-stable local oscillator (LO). In principle, two side bands with $\nu_{\text{RF}} = \nu_{\text{LO}} \pm \nu_{\text{IF}}$ are converted to the IF. This has the advantage that signal amplification and detection can be performed at a lower frequency, where technology is widely established. Double-sideband measurements are advantageous when observations along a single symmetric absorption line are performed. In this case, the LO is set to the line center frequency, and contributions from equally distant frequencies on both sides of the line are combined into a single channel. This means that a single LO can be used for several frequency channels along the line and, thus, respectively, for pro-



Fig. 29.3 Photo of a sun photometer at the Jülich Observatory for Cloud Evolution (JOYCE) (photo © Birger Bohn)

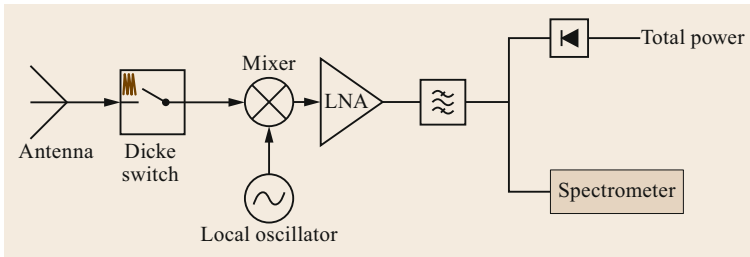


Fig. 29.4 Block diagram of a Dicke type microwave radiometer using the heterodyne principle. After the radio frequency has been down converted, the interim frequency is amplified and bandpass filtered. Afterwards, the signal can be split up and detected either within single-frequency channels or input into a spectrometer

filig. This technique is frequently applied to satellite microwave measurements or at the 183 GHz line for ground-based water vapor profiling. For window channels or along nonsymmetric lines, very low IF center frequencies have to be used to realize typical channel bandwidths of about a GHz or less. If only one frequency band will be received, a single sideband filter needs to be used. Within some radiometers, the LO is tuned, and different frequencies are measured sequentially.

Multichannel MWRs typically split the IF signal into the different channels by bandpass filters in a so-called filter bank approach. Each channel's signal is further amplified, detected, and finally converted to digital counts. For profiling of upper atmospheric gases, the pressure broadened line shape needs to be observed with a frequency resolution of ≈ 1 MHz. In this case, instead of a filter bank, back-end spectrometers are used (Chap. 28).

The sensitivity of a microwave radiometer is mainly determined by its system noise temperature T_{sys} , which is the sum of the receiver's internal noise contribution

and the atmospheric signal. The minimum T_B fluctuations that can be resolved by the radiometer depend on the bandwidth and integration time

$$\Delta T_B \approx \frac{T_{\text{sys}}}{\sqrt{\Delta\nu\Delta t}} \quad (29.13)$$

and are typically ≈ 0.1 K. Due to the high amplification required, microwave radiometers are very sensitive to temperature changes, and, therefore, a good thermal insulation is key. In order to avoid drifts most radiometers employ a gain adjustment by frequently observing a reference signal. This is classically achieved by a Dicke switch, which directs the view to a termination with well-known temperature (Fig. 29.4). However, also different designs that make use of noise injection from a well-characterized noise diode or observation of an external target are used. Absolute accuracy is mostly determined by the absolute calibration, which is either performed using liquid nitrogen or sky tipping [29.18].

Different commercial MWRs are available (Fig. 29.5). Radiometrics Inc. (radiometrics.com) offers the

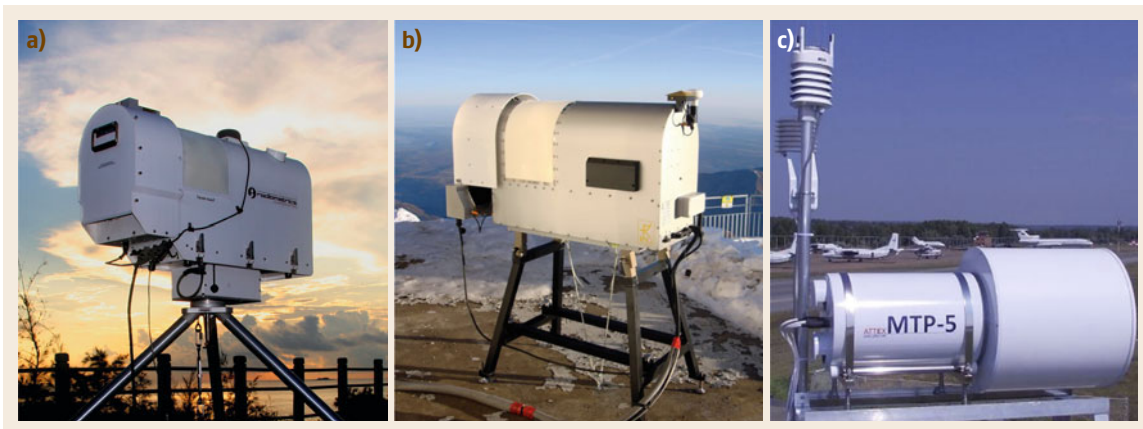


Fig. 29.5a–c Examples of commercially available microwave profiling radiometers. (a) MP-Series profiler by Radiometrics Inc. (photo © Radiometrics Inc.), (b) HATPRO by Radiometer Physics GmbH (photo © Radiometer Physics GmbH), (c) MTP-5 by ATTEX (photo © ATTEX). Photos by permission

MP-Series Profiler [29.27, 43], which performs sequential measurements along the water vapor and oxygen absorption features for profiling (Fig. 29.1). Similar bands are covered by Radiometer Physics GmbH's (RPG; radiometer-physics.de) Humidity and Temperature Profiler (HATPRO, [29.28]), which uses direct-detection and parallel measurements of the different frequency channels. Both Radiometrics Inc. and RPG also offer dual channel radiometers for PWV and LWP measurements only. Optionally, RPG includes higher-frequency channels, like 90 GHz, to achieve higher LWP accuracy. The Russian company ATTEX (attex.net) offers the Microwave Temperature Profiler (MTP), which exploits elevation scanning at a single frequency along the oxygen complex to derive boundary-layer temperature profiles mainly for air pollution studies.

Operational instruments make use of a radome to shield the internal components of the microwave

radiometer (Fig. 29.4) from external disturbances (Fig. 29.5). The radome is made from microwave transparent material, which is often treated such that it repels rain drops. As liquid on the radome affects T_B measurements, a rain sensor helps to identify rainy situations. To keep the radome dry under light drizzle and to enable a quick recovery after a rain event a blower can be used. Radiometer observations are often combined with 2 m meteorological station data, whose temperature and humidity measurements can also serve as input to the retrieval algorithms, taking into account the different spatial representativeness of the point and radiometer measurements. Similarly, infrared radiometers mounted along the side can provide information on cloud occurrence and cloud base height. A global positioning system (GPS) receiver gives the exact time and can also be used to synchronize scans with satellite orbits for exact attenuation measurements.

29.5 Specifications

The retrieval accuracies of sun photometers and MWRs need to be carefully specified and communicated. In addition to instrument performance, these are limited by the physical principles of radiative transfer and remote sensing.

29.5.1 Sun Photometers

Procedures to determine measurement errors and inversion accuracy (depending on the product levels) have been extensively described for the AERONET [29.44] measurements [29.1]. AERONET also derives absorption properties, such as the imaginary refractive index and single-scattering albedo of aerosol particles from the sun photometer data, however, in this case, larger uncertainties have to be taken into account [29.45]. The degree of sphericity of aerosol particles can also be obtained [29.46]. Water vapor column measurements

by sun photometers have frequently been compared to those by other instruments, including MWRs showing an accuracy of $\approx 1 \text{ kg m}^{-2}$ [29.47].

29.5.2 Microwave Radiometers

In the last two decades, commercial MWRs have matured to robust instruments providing continuous and unattended operations. They can be operated at temporal resolutions down to a second and give accurate atmospheric observations under nearly all-weather conditions, except when rain contaminates the microwave window. Commercial MWR units are usually offered with azimuth and elevation-angle scanning capability. The absolute accuracy of well-calibrated microwave radiometers is $\approx 0.3\text{--}0.5 \text{ K}$ with an even lower noise level. Vendors typically include retrieval algorithms for a specific location. Their typical accuracies are given in Table 29.5.

Table 29.5 Specification of the accuracy of the sun photometer and microwave radiometer for different retrieval products

Retrieval product	Error	Limitations
Sun photometer		
AOD	≈ 0.02	Completely cloud-free conditions
Ångström exponent	≈ 0.1	Completely cloud-free conditions
Precipitable water vapor	$\approx 1 \text{ kg m}^{-2}$	Only during clear sky conditions
Microwave radiometer		
Precipitable water vapor	$0.5\text{--}1 \text{ kg m}^{-2}$	Not under precipitating conditions
Liquid water path	$\approx 20 \text{ g m}^{-2}$	Offsets can cause LWP < 0, these can be corrected for by using LWP variability
Temperature profile	$0.5\text{--}2.0 \text{ K}$	Accuracy decreases rapidly with distance from instrument, best performance < 500 m
Humidity profile	$0.2\text{--}1.5 \text{ g m}^{-3}$	Low resolution, typically only two degrees of freedom for signal

Profiles of liquid water content (LWC) are sometimes provided as an additional product by manufacturers. Because information on the vertical position of liquid water is only indirectly contained in the measurements via the temperature dependence of the liquid water absorption, [29.48] conclude that microwave ra-

diometer measurements alone do not contain enough information to retrieve LWC profiles. Additional constraints can be provided by simultaneous measurements of an infrared radiometer or ceilometer for cloud base height and cloud radar for cloud top and vertical structure.

29.6 Quality Control

Applying standardized, well-defined and regular calibrations is essential to obtain sufficiently quality-controlled data for passive radiometers. This will correct for the possible offsets and drifts that can occur within these systems.

29.6.1 Calibration of Sun Photometers

The *Langley* plot method is the primary technique used to determine the TOA calibration voltage constant, V_0 , for a given sun photometer. This method, originally developed in the early 1900s to obtain estimates of the solar constant [29.49], is also based on the Bouguer–Lambert–Beer attenuation law following the notation of [29.36]

$$V_{A\lambda}(\theta) = V_{0,\lambda}(\theta) \exp[-\tau_A(\theta)m_A(\theta)], \quad (29.14)$$

where

$$V_{A,\lambda}(\theta) = V_{\text{meas},\lambda}(\theta) \exp \left[\tau_R(\theta)m_R(\theta) + \sum_i \tau_i(\theta)m_i(\theta) \right], \quad (29.15)$$

is the measured voltage corrected for Rayleigh scattering and gas absorption, that is, the voltage that would be measured if aerosols were the only attenuating component, and $V_{0,\lambda}$ is the voltage the instrument would read at the top of the atmosphere at the time of the calibration.

Taking the natural logarithm of both sides of (29.14) yields the linear equation

$$\ln(V_{A,\lambda}(\theta)) = \ln(V_{0,\lambda}) - \tau_A m_A(\theta), \quad (29.16)$$

which states that for a given wavelength channel, a plot of the natural logarithm of a series of measurements, V_A , over a range of aerosol air mass values, m_A , will give a straight line with a slope that is equal to the aerosol optical depth, τ_A , and a y-intercept that is equal to $\ln(V_0)$. The *Langley* plot method takes advantage of this linear relationship and consists of measuring V_A

as the sun rises or sets (i.e., over a range of air mass values), plotting the $\ln(V_A)$ versus m_A , and then extrapolating the data to zero air mass (i.e., the y-intercept) to determine $\ln(V_0)$, from which the TOA-atmospheric calibration voltage constant, V_0 , can be obtained.

While theoretically straightforward, care must be taken while performing *Langley* plot calibrations to minimize various sources of error. The primary assumption of this technique is that the aerosol optical depth remains constant over the time span of the calibration measurements. For this reason, these calibrations are usually done at high-altitude locations, both to get above the majority of any aerosol particles in the atmosphere, and because the aerosol loading at higher altitudes is typically more temporally stable than that at lower altitudes. A discussion of various modifications and refinements to the *Langley* plot method have been suggested to better account for a variable atmosphere and to improve on the accuracy of these calibrations. A description of these techniques can be found in the literature [29.20, 50–52]. Practical information for obtaining high-quality AOD measurements within AERONET is given at https://aeronet.gsfc.nasa.gov/new_web/system_descriptions_calibration.html, Accessed 20 July 2021.

29.6.2 Microwave Radiometers

For accurate observations of brightness temperatures, signal calibration is of utmost importance. Classically, two blackbody calibration targets of well-known temperature and emissivity are used to derive the gain (receiver sensitivity to input signal change) and noise temperature (T_R , receiver offset), which are subsequently used to calculate brightness temperatures. In order to take system nonlinearities into account, an additional reference, such as a noise diode, is necessary. For absolute calibration, the full system, including the antenna and the scanning unit, needs to be characterized, which is realized either by the automatic sky tipping procedure or by external calibration involving a liquid-nitrogen (LN₂) cooled target. A thorough review concerning the uncertainties of both approaches is given in [29.18, 53].

Absolute calibration employs a warm (typically ambient temperature) and a cold (typically liquid nitrogen (LN₂) cooled) target, whose blackbody temperatures are known to a high accuracy. Assuming a linear detector, the two calibration parameters, i.e., gain and T_R , can be calculated from the voltages recorded with the radiometer pointing to the hot and the cold target, respectively. The temperatures of the targets are chosen such that the observed atmospheric brightness temperatures do not require a strong extrapolation from the calibration range. Nonlinearities can be taken into account by performing two additional measurements, adding a stable noise diode signal when pointing at the targets. From the four voltages measured, the noise diode temperature and the nonlinearity factor can be derived. The major challenge lies in the design of the calibration target and the exact characterization of its temperature. Here, avoiding reflections at the LN₂ interface, mixing oxygen into the LN₂, and the realization of a homogeneous temperature across the calibration target are important to obtain absolute accuracies < 1 K.

An alternative technique realizes the cold calibration point from scene observations, assuming a horizontally homogenous atmosphere. In a similar fashion to the *Langley* plot approach (29.16), atmospheric elevation scanning provides opacities for non-opaque frequency channels. These can be plotted as a function of airmass, and the opacity for an airmass factor of zero can be derived, which needs to correspond to the one of

the cosmic background. Typically, quality check thresholds are applied to the tipping curve in order to detect atmospheric inhomogeneities. Other systematic effects can be avoided by considering the antenna beam width and the Earth's curvature along the slant observation path.

For high-quality observations, the microwave window of the system must be clean of water/ice/dirt at all times. Continuous visual inspection via webcam is highly recommended to detect any disturbances, e.g., by birds, precipitation, or deterioration of the radome material. Communication technology is increasingly making use of higher microwave channels, which can lead to radio frequency interference (RFI) strongly disturbing individual or, in the case of broadband sources, even several channels. Therefore, quality control of brightness temperature time series for unphysical spikes, variability, and spectral inconsistency is necessary. In addition, procedures for checking the physical consistency of the retrieved products are also mandatory. Automatic quality control procedures have been developed by manufacturers as part of the data acquisition software. Also, within MWRnet, experienced operators have developed an online postprocessing tool that can be used to continuously monitor T_B time series against numerical weather prediction models. Last but not least, a regular visual inspection of the obtained T_B time series can often increase the data quality as well.

29.7 Maintenance

In addition to regular calibration, continuous maintenance procedures must be carried out in order to minimize the possibility of external and other instrumental factors deteriorating the radiometers' performance (Table 29.6).

29.7.1 Sun Photometers

NASA suggests a weekly procedure to maintain and service the sun photometers involved in AERONET (<https://aeronet.gsfc.nasa.gov/Operational/pictures/Checklist.html>, Accessed 10 July 2021). To verify system integrity, the following points should be accommodated: check battery connections, untangle zenith/azimuth cables, check sensor data cable, check enclosure box for leaks (remove water, repair leaks as necessary), and check rain detection. Heated rain detectors ensure that also snowfall is detected below freezing temperatures. Moreover, without active heat-

ing suitable measurement periods may be missed by formation of dew, in particular in the early morning.

Furthermore, the battery status and the solar panel connections, as well as the instrument clocks, need to be checked. An important point is to control the leveling procedures and automatic positioning of the sensor head. Instrument tracking and collimator obstructions require some attention. The ability of the instrument to track the sun and automatically scan the sky hemisphere (almucantar and principal plane) needs to be controlled. It is suggested that to remove the collimator (the double tubes on the sensor head) and to look through it toward the sun or a bright light to verify that there are no spider webs and other foreign matter. The collimator needs to be cleaned and obstructions need to be wiped away with soft cloth. However, the inlet optics should remain untouched to make sure that successive calibrations trace any drifts in sensitivity accurately.

Table 29.6 Maintenance of ground-based sun photometer and microwave radiometer systems

Maximum interval	Procedure
Sun photometer	
Daily	Check operation and data transfer
Weekly	Check wet sensor operation, collimator free from obstructions, sun-tracking, battery, and clock
Yearly	Calibration at least every 12 months
Microwave radiometer	
Daily	Automatic checking of the data for inconsistent values of brightness temperature as well as retrieved products to detect possible malfunctions.
Weekly	In spite of using different automatic quality controls, a visual inspection of the T_B time series is recommended in order to assure a complete quality control of data that can identify also nonmeteorological disturbances such as RFI, humans, birds, sun, moon or aircraft
Monthly	Pure water should be used to periodically clean the radome window of the MWR to prevent the reduction of the radome hydrophobic behavior
6-monthly	Absolute calibration using liquid nitrogen, exchange microwave window

29.7.2 Microwave Radiometers

Commercial microwave radiometers have been designed for continuous unmanned operation, and remote access allows data transfer and monitoring of instrument performance. Thus, daily automatic checking of the data quality is recommended to detect any malfunctions quickly (Table 29.6). This concerns continuous quality checks of the brightness temperatures measured for thresholds and spectral consistency, as well as the quality of retrieved products, e.g., by continuous comparisons with numerical weather prediction output or, if available, radiosonde ascents.

Although most commercial MWRs are equipped with rain sensors warning of the presence of rain, it is advisable to compare these data weekly to monthly with other measurements such as webcam, infrared camera, or rain gauge data. This is important to avoid flagging too many measurements as unusable, i.e., in the case of a too-sensitive or malfunctioning rain detector. However, also the opposite case can occur: e.g., after a heavy rain event has ended, the radome dries too

slowly, so that measurements are not yet useable. This can be due to the deterioration of the radome material or a malfunctioning blower/heater system. Also, non-meteorological signals from RFI, humans, birds, the sun, moon, or aircraft should be corrected for. Here, visual inspection of the time series is currently the best way to guarantee reliable data. Objective spectral consistency checks are currently still under development.

In order to guarantee that no artificial signals due to disturbances in the field of view or, particularly, on the microwave transparent radome, occur, the use of a webcam is strongly suggested. Environmental conditions (sunlight, precipitation, etc.) deteriorate the radome material of the microwave window, reducing its hydrophobic characteristic. Depending on the location, the window should be replaced about every 3–6 months. An absolute calibration with LN_2 is recommended every 6 months and can be combined with the exchange of the microwave window. In general, radiometer manufacturers suggest thorough system inspections by the company approximately every 2 years.

29.8 Application

Sun photometers and MWRs typically measure in continuous automated mode providing comprehensive information on the atmospheric state (Tables 29.2 and 29.3), which can be used for many applications. Figure 29.6 shows an example measurement from 26.06.2018 at the Jülich Observatory for Cloud Evolution (JOYCE) [29.54, 55]. The LWP from the microwave radiometer indicates the presence of stratiform clouds starting shortly past midnight and lasting until noon. These clouds strongly influence the thermody-

namic stability. First, the typical nighttime surface-based inversion weakens slowly. Further, the transition from stable to well-mixed conditions only happens around noon, when the cloud layer disappears. The transition to neutral conditions in the boundary layer is rather abrupt and within 1 h the conditions at the surface even change from neutral to superadiabatic. AOD and PWV observations by the sun photometer only become available after cloud disappearance, as a free view of the sun is necessary. At first, only isolated measurements

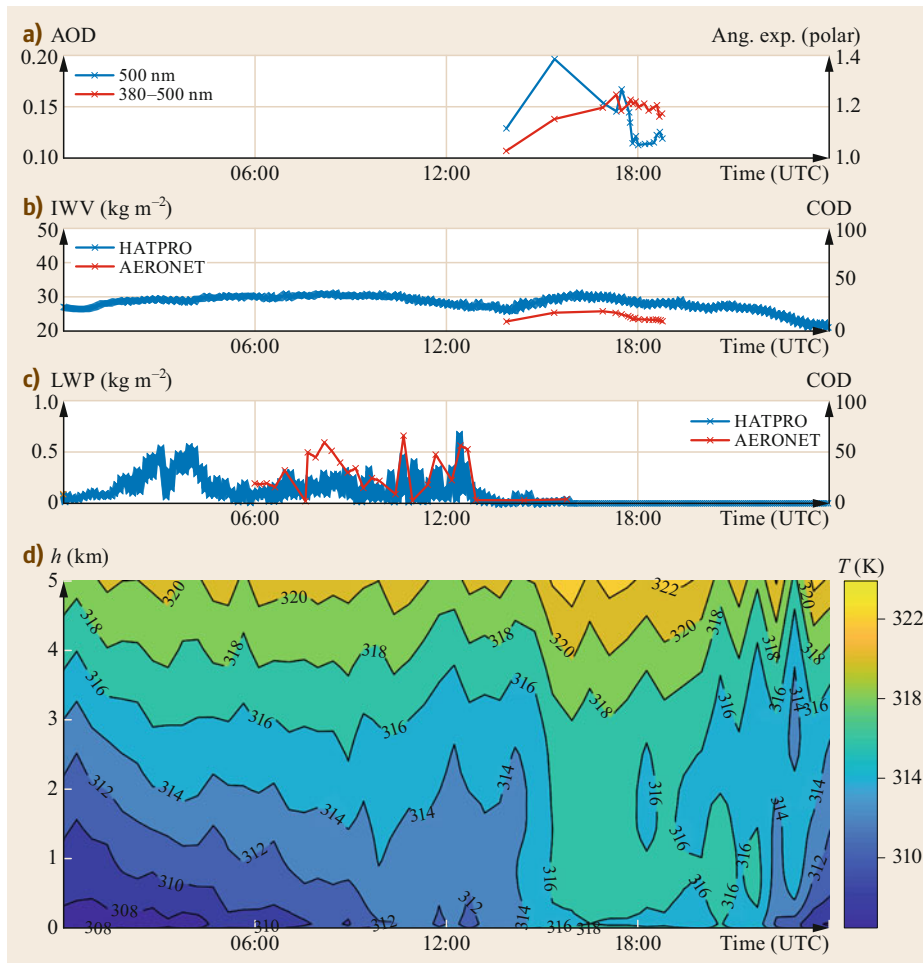


Fig. 29.6a–d
Time series of different measurement quantities on 25.06.2018 at JOYCE: (a) aerosol optical depth at 500 nm (blue) and Ångström exponent between 380 and 500 nm (red), (b) precipitable water vapor from microwave radiometer (blue) and sun photometer (red), (c) liquid water path (blue), and cloud optical depth (red), (d) time-height series of potential temperatures from microwave radiometer HATPRO. COD refers to the cloud optical depth

are available, as some isolated low LWP values still indicate broken cloud conditions, but they become more frequent in the 2–3 h before sunset. Close to sunset an AOD at 500 nm of 0.12 and an Ångström exponent (between 380 and 500 nm) indicate rather typical conditions at JOYCE, which is located in an agricultural area and sometimes under the influence of plumes originating from the cities of Düsseldorf or Cologne. Immediately after sunset a surface-based inversion develops again due to long-wave cooling.

When PWV from both the sun photometer and the microwave radiometer are available, their temporal behavior agrees rather well, however, a systematic offset occurs, which is a bit higher than that identified by [29.47]. Biases between different PWV data sets are frequently found, and the identification of reference measurements is an ongoing challenge for the

community, i.e., as carried out in the Global Climate Observing System (GCOS) Reference Upper Air Network (GRUAN, Chap. 63). Under overcast conditions, the sun photometer turns into zenith staring, the so-called cloud mode of AERONET, and a cloud optical depth retrieval is performed, which shows some correlation with microwave radiometer derived liquid water path. The latter is available with 1 second temporal resolution, while for the sun photometer, the frequency of a valid retrieval is much lower, i.e., 15 min.

The example shows the synopsis of sun photometer and microwave radiometer measurements to capture the atmospheric state with respect to atmospheric stability, aerosol burden, PWV, and clouds. This information is of particular interest for air quality applications and can be enriched by using more details on the aerosol composition, e.g., fine and coarse mode occurrence.

29.9 Future Developments

Within Europe, AERONET is already, and will continue to be, integrated into the ACTRIS (Aerosols, Clouds, and Trace Gases Research Infrastructure) project (<https://www.actris.eu>). The strategic aim of ACTRIS is to secure long-term coordinated aerosol, cloud, and trace gas observations. Within this framework, calibration activities, software upgrades, and new station setups (including new instrument purchases) will be increasingly coordinated. Data analysis will be harmonized in workshops and other meeting activities. These future developments on a European level are closely linked with international projects worldwide.

In France, there are new instrumental developments for mobile photometry, in particular for airborne observations and also for marine applications on board ships. First successful tests have been reported for ship-borne observations. This development opens the path to future automatic marine observations. Another new development is lunar photometry. Furthermore, several low-cost photometer versions are under development, which will enable us to obtain more data on aerosol optical depth.

In the past decades, MWRs have matured into commercially available systems that are able to provide autonomous estimates of temperature and humidity profiles, as well as liquid water paths in nearly all weather conditions. In the United States (US), the Climate Research Facility of the US Department of Energy's Atmospheric Radiation Measurement (ARM) Program operates a network of ground-based MWRs, which provides long-term measurements with a focus on LWP in different climate zones [29.56].

In Europe, different COST (European Cooperation in Science and Technology) actions (EG-CLIMET (European Ground-Based Observations of Essential Variables for Climate and Operational Meteorology) and

TOPROF (Towards Operational Ground Based Profiling with Ceilometers, Doppler Lidars and Microwave Radiometers for Improving Weather Forecasts) [29.57]) have fostered the development of the MWRnet advocating joint standards for operation and processing of microwave radiometer data. First attempts have been made to assimilate MWR profiles of temperature and humidity into numerical weather prediction models [29.58] where benefits in accumulated precipitation forecasts up to 12–18 h, in particular for larger accumulations, have been found. Also, the potential for directly assimilating microwave radiometer brightness temperatures into numerical weather prediction models is currently being explored, which has become possible by the development of the forward operator RTTOV-gb [29.59]. This is of special interest as microwave radiometers provide continuous information on the temperature profile in the boundary layer, which is difficult to assess from satellites. For data assimilation, but also to obtain accurate retrievals of thermodynamic profiles and clouds, stringent quality assurance and accurate uncertainty characterization are of high importance, and efforts to harmonize on the European scale are underway within the European research infrastructure ACTRIS. Within ACTRIS and funded by Deutsche Forschungsgemeinschaft (DFG), a center for MWR calibration and quality assurance is currently installed at JOYCE.

This article has presented standard instrumentation, however, special developments like small-scale networks, tomography, or higher-frequency radiometers for use under low water vapor conditions are explored as well. This is not restricted to the meteorological community as microwave radiometry is also a valuable tool for astronomy, geodesy, and communication studies.

29.10 Further Readings

Radiative transfer theory is explained in detail by:

- C.F. Bohren, E.E. Clothiaux: *Fundamentals of Atmospheric Radiation* (Wiley-VCH, Berlin 2006)
- R.M. Goody, Y.L. Yung: *Atmospheric Radiation, Theoretical Basis* (Oxford University Press, New York 1995)
- M. Wendisch, P. Yang: *Theory of Atmospheric Radiative Transfer – A Comprehensive Introduction* (Wiley-VCH, Weinheim 2012)
- C. Mätzler (Ed.): *Thermal Microwave Radiation: Applications for Remote Sensing*. IET Electromagnetic Waves Series, Vol. 52 (The Institution of Engineering and Technology, London 2006)
- E.R. Westwater, S. Crewell, C. Mätzler: A review of surface-based microwave and millimeter-wave radiometric remote sensing of the troposphere. *Radio Sci. Bull.* **3010**, 59–80 (2004)
- E.R. Westwater, S. Crewell, C. Mätzler, D. Cimini: Principles of surface-based microwave and millimeter wave radiometric remote sensing of the troposphere, *Quad. Soc. Ital. Elettromagn.* **1**(3), 50–90 (2005)

A thorough introduction into microwave radiometry is given by:

A comprehensive guide into the principles and operation of ground-based microwave measurements has been prepared as part of the ESSEM Action COST ES0702 EG-CLIMET and is available online at http://cfa.aquila.infn.it/wiki/eg-climet.org/index.php5/Microwave_radiometer, Accessed 10 July 2021.

Acknowledgments. The authors like to thank Mario Mech for the microwave radiative transfer calculations and Nils Kuchler for producing Fig. 29.6. Birger Bohn is especially acknowledged for his support with respect to his expertise in sun photometer operation and for providing the photograph shown in Fig. 29.3.

References

- 29.1 NASA Goddard Space Flight Center: AERONET, Aerosol Robotic Network, <https://aeronet.gsfc.nasa.gov>, Accessed 10 July 2021
- 29.2 International SKYNET Data Center (ISDC), <https://skynet-isdc.org>, Accessed 10 July 2021
- 29.3 MWRnet – An International Network of Ground-based Microwave Radiometers, <http://cetemps.aquila.infn.it/mwrnet>, Accessed 10 July 2021
- 29.4 A. van Lammeren, A. Feijt, J. Konings, E. van Meijgaard, A. van Ulden: Combination of ground-based and satellite cloud observations on a routine basis, *Meteorol. Z.* **9**(2), 125–134 (2000)
- 29.5 S. Crewell, U. Löhnert: Accuracy of boundary layer temperature profiles retrieved with multi-frequency, multi-angle microwave radiometry, *IEEE Trans. Geosci. Remote Sens.* **45**(7), 2195–2201 (2007)
- 29.6 J.H. Schween, S. Crewell, U. Löhnert: Horizontal-humidity gradient from one single-scanning microwave radiometer, *IEEE Geosci. Remote Sens. Lett.* **8**(2), 336–340 (2011)
- 29.7 M. Schneebeli, C. Mätzler: Spatiotemporal behavior of integrated water vapour, *IEEE Geosci. Remote Sens. Lett.* **8**(5), 948–952 (2011)
- 29.8 M. Wendisch, P. Pilewskie, B. Bohn, A. Bucholtz, S. Crewell, C. Harlow, E. Jäkel, K.S. Schmidt, R. Shetter, J. Taylor, D.D. Turner, M. Zöger: Atmospheric radiation measurements. In: *Airborne Measurements for Environmental Research: Methods and Instruments*, Chap. Vol. 7, ed. by M. Wendisch, J.-L. Brenguier (Wiley-VCH, Weinheim 2013) pp. 343–411
- 29.9 M. Wendisch, W. von Hoyningen-Huene: Possibility of refractive index determination of atmospheric aerosol particles by ground-based solar extinction and scattering measurements, *Atmos. Environ.* **28**(5), 785–792 (1994)
- 29.10 O. Dubovik, M.D. King: A flexible inversion algorithm for retrieval of aerosol optical properties from Sun and sky radiance measurements, *J. Geophys. Res.* **105**(D16), 20673–20696 (2000)
- 29.11 O. Dubovik, A. Smirnov, B.N. Holben, M.D. King, Y.J. Kaufman, T.F. Eck, I. Slutsker: Accuracy assessment of aerosol optical properties retrieval from AERONET Sun and sky radiance measurements, *J. Geophys. Res.* **105**(D8), 9791–9806 (2000)
- 29.12 J.C. Chiu, C.-H. Huang, A. Marshak, I. Slutsker, D.M. Giles, B.N. Holben, Y. Knyazikhin, W.J. Wiscombe: Cloud optical depth retrievals from the aerosol robotic network (AERONET) cloud mode observations, *J. Geophys. Res. Atmos.* **115**(D14), D14202 (2010)
- 29.13 S. Crewell, H. Czekala, U. Löhnert, C. Simmer, T. Rose, R. Zimmermann, R. Zimmermann: Microwave radiometer for cloud cartography: A 22-channel ground-based microwave radiometer for atmospheric research, *Radio Sci.* **36**(4), 621–638 (2001)
- 29.14 U. Löhnert, S. Crewell: Accuracy of cloud liquid water path from ground-based microwave radiometry. Part I. Dependency on cloud model statistics, *Radio Sci.* **38**(3), 8041 (2003)
- 29.15 M.P. Cadeddu, R. Marchand, E. Orlandi, D.D. Turner, M. Mech: Microwave ground-based retrievals of cloud and rain liquid water path in drizzling and precipitating clouds: Challenges and possibilities, *IEEE Trans. Geosci. Remote Sens.* **99**, 1–14 (2017)
- 29.16 H. Czekala, S. Crewell, C. Simmer, A. Thiele: Discrimination of cloud and rain liquid water path by ground-based polarized microwave radiometry, *Geophys. Res. Lett.* **28**(2), 267–270 (2001)
- 29.17 X. Xie, U. Löhnert, S. Kneifel, S. Crewell: Snow particle orientation observed by ground-based microwave radiometry, *J. Geophys. Res.* **117**(D2), D02206 (2012)
- 29.18 G. Maschwitz, U. Löhnert, S. Crewell, T. Rose, D.D. Turner: Investigation of ground-based microwave radiometer calibration techniques at 530 hPa, *Atmos. Meas. Tech.* **6**(10), 2641–2658 (2013)
- 29.19 F.E. Volz: Photometer mit Selen-Photoelement zur spektralen Messung der Sonnenstrahlung und zur Bestimmung der Wellenlangenabhängigkeit der Dunsttrübung, *Arch. Meteorol. Geophys. Bioklimatol. B* **10**(1), 100–131 (1959)
- 29.20 G.E. Shaw: Sun photometry, *Bull. Am. Meteorol. Soc.* **64**(1), 4–10 (1983)
- 29.21 D.R. Brooks, F.M. Mims: Development of an inexpensive handheld LED-based Sun photometer for the GLOBE program, *J. Geophys. Res. Atmos.* **106**(D5), 4733–4740 (2001)
- 29.22 R.D. Dicke: The measurement of thermal radiation at microwave frequencies, *Rev. Sci. Instrum.* **17**(7), 268 (1946)
- 29.23 R.H. Dicke, R. Beringer, R.L. Kyhl, A.B. Vane: Atmospheric absorption measurements with a microwave radiometer, *Phys. Rev.* **70**(5/6), 340–348 (1946)
- 29.24 E.R. Westwater: Ground-based passive probing using the microwave spectrum of oxygen, *Radio Sci.* **69**(9), 1201–1211 (1965)
- 29.25 E.R. Westwater: The accuracy of water vapor and cloud liquid determination by dual-frequency

- ground-based microwave radiometry, *Radio Sci.* **13**(4), 677–685 (1978)
- 29.26 D.C. Hogg, M.T. Decker, F.O. Guiraud, K.B. Earnshaw, D.A. Merritt, K.P. Moran, W.B. Sweezy, R.G. Strauch, E.R. Westwater, C.G. Little: An automatic profiler of the temperature, wind and humidity in the troposphere, *J. Appl. Meteorol.* **22**(5), 807–831 (1983)
- 29.27 F. Solheim, J.R. Godwin, E.R. Westwater, Y. Han, S.J. Keihm, K. Marsh, R. Ware: Radiometric profiling of temperature, water vapor and cloud liquid water using various inversion methods, *Radio Sci.* **33**(2), 393–404 (1998)
- 29.28 T. Rose, S. Crewell, U. Löhnert, C. Simmer: A network suitable microwave radiometer for operational monitoring of the cloudy atmosphere, *Atmos. Res.* **75**(3), 183–200 (2005)
- 29.29 R.M. Goody, Y.L. Yung: *Atmospheric Radiation – Theoretical Basis* (Oxford University Press, New York 1995)
- 29.30 C.F. Bohren, E.E. Clothiaux: *Fundamentals of Atmospheric Radiation* (Wiley-VCH, Berlin 2006)
- 29.31 M. Wendisch, P. Yang: *Theory of Atmospheric Radiative Transfer – A Comprehensive Introduction* (Wiley-VCH, Weinheim 2012)
- 29.32 M.A. Janssen: An introduction to the passive remote sensing of atmospheres. In: *Atmospheric Remote Sensing by Microwave Radiometry*, ed. by M.A. Janssen (John Wiley & Sons Inc., New York 1993) pp. 1–36
- 29.33 G.W. Petty: *A First Course in Atmospheric Radiation* (Sundog Publishing, Madison 2006)
- 29.34 F. Kasten, A.T. Young: Revised optical air mass tables and approximation formula, *Appl. Opt.* **28**(22), 4735–4738 (1989)
- 29.35 A. Bucholtz: Rayleigh-scattering calculations for the terrestrial atmosphere, *Appl. Opt.* **34**(15), 2765–2773 (1995)
- 29.36 P.B. Russell, J.M. Livingston, E.G. Dutton, R.F. Pueschel, J.A. Reagan, T.E. DeFoor, M.A. Box, D. Allen, P. Pilewskie, B.M. Herman, S.A. Kinne, D.J. Hofmann: Pinatubo and pre-Pinatubo optical-depth spectra: Mauna Loa measurements, comparisons, inferred particle size distributions, radiative effects, and relationship to lidar data, *J. Geophys. Res.* **98**(D12), 22969–22985 (1993)
- 29.37 P.W. Rosenkranz: Water vapor microwave continuum absorption: A comparison of measurements and models, *Radio Sci.* **33**(4), 919–928 (1998)
- 29.38 H.J. Liebe, G.A. Hufford, M.G. Cotton: Propagation modeling of moist air and suspended water/ice particles at frequencies below 1000 GHz. In: *Atmospheric propagation effects through natural and man made obscurants for visible to MM-wave radiation*, AGARD Conf. Proc., Vol. 542, ed. by D.L. Jordan, G.D. Lewis (1993)
- 29.39 D.D. Turner, S. Kneifel, M.P. Cadeddu: An improved liquid water absorption model in the microwave for supercooled liquid water clouds, *J. Atmos. Ocean. Technol.* **33**(1), 33–44 (2016)
- 29.40 J. Güldner, D. Spänkuch: Remote sensing of the thermodynamic state of the atmospheric boundary layer by ground-based microwave radiometry, *J. Atmos. Ocean. Technol.* **18**(6), 925–933 (2001)
- 29.41 C.D. Rodgers: *Inverse Methods for Atmospheric Sounding: Theory and Practice*, Series on Atmospheric, Oceanic and Planetary Physics, Vol. 2 (World Scientific, Singapore 2000)
- 29.42 U. Löhnert, D. Turner, S. Crewell: Ground-based temperature and humidity profiling using spectral infrared and microwave observations: Part 1. Simulated retrieval performance in clear sky conditions, *J. Appl. Meteorol. Climatol.* **48**(5), 1017–1032 (2009)
- 29.43 R. Ware, R. Carpenter, J. Güldner, J. Liljegren, T. Nehr Korn, F. Solheim, F. Vandenberghe: A multichannel radiometric profiler of temperature, humidity, and cloud liquid, *Radio Sci.* **38**, 4 (2003)
- 29.44 B.N. Holben, T.F. Eck, I. Slutsker, D. Tanré, J.P. Buis, A. Setzer, E. Vermote, J.A. Reagan, Y.J. Kaufman, T. Nakajima, F. Lavenu, I. Jankowiak, A. Smirnov: AERONET—A federated instrument network and data archive for aerosol characterization, *Remote Sens. Environ.* **66**(1), 1–16 (1988)
- 29.45 O. Dubovik, B. Holben, T.F. Eck, A. Smirnov, Y.J. Kaufman, M.D. King, D. Tanré, I. Slutsker: Variability of absorption and optical properties of key aerosol types observed in worldwide locations, *J. Atmos. Sci.* **59**(3), 590–608 (2002)
- 29.46 O. Dubovik, B.N. Holben, T. Lapyonok, A. Sinyuk, M.I. Mishchenko, P. Yang, I. Slutsker: Non-spherical aerosol retrieval method employing light scattering by spheroids, *Geophys. Res. Lett.* **29**(10), 54–1–54–4 (2002)
- 29.47 S. Steinke, S. Eikenberg, U. Löhnert, G. Dick, D. Klocke, P. Di Girolamo, S. Crewell: Assessment of small-scale integrated water vapour variability during HOPE, *Atmos. Chem. Phys.* **15**(5), 2675–2692 (2015)
- 29.48 S. Crewell, K. Ebell, U. Löhnert, D.D. Turner: Can liquid water profiles be retrieved from passive microwave zenith observations?, *Geophys. Res. Lett.* **36**(6), L06803 (2009)
- 29.49 S. Langley: The “Solar Constant” and related problems, *Astrophys. J.* **17**, 89–99 (1903)
- 29.50 M. Tanaka, T. Nakajima, M. Shiobara: Calibration of a Sun photometer by simultaneous measurements of direct-solar and circumsolar radiation, *Appl. Opt.* **25**(7), 1170–1176 (1986)
- 29.51 M. Shiobara, J. Spinhirne, A. Uchiyama, S. Asano: Optical depth measurements of aerosol, cloud and water vapor using Sun photometers during FIRE Cirrus IFO II, *J. Appl. Meteorol.* **35**(1), 36–46 (1991)
- 29.52 B. Schmid, C. Wehrli: Comparison of Sun photometer calibration by use of the Langley technique and the standard lamp, *Appl. Opt.* **34**(21), 4501–4512 (1995)
- 29.53 N. Küchler, D.D. Turner, U. Löhnert, S. Crewell: Calibrating ground-based microwave radiometers: Uncertainty and drifts, *Radio Sci.* **51**(4), 311–327 (2016)
- 29.54 U. Löhnert, J.H. Schween, C. Acquistapace, K. Ebell, M. Maahn, M. Barrera-Verdejo, A. Hirsikko, B. Bohn, A. Knaps, E. O’Connor, C. Simmer, A. Wahner, S. Crewell: JOYCE: Jülich Observatory for Cloud

- Evolution, *Bull. Am. Meteorol. Soc.* **96**(7), 1157–1174 (2015)
- 29.55 CPEX-LAB: Jülich Observatory for Cloud Evolution (JOYCE), <http://www.joyce.cloud>, Accessed 10 July 2021
- 29.56 M.P. Cadetdu, J.C. Liljegren, D.D. Turner: The atmospheric radiation measurement (ARM) program network of microwave radiometers: Instrumentation, data, and retrievals, *Atmos. Meas. Tech.* **6**(9), 2359–2372 (2013)
- 29.57 A.J. Illingworth, D. Cimini, A. Haeffele, M. Haeffelin, M. Hervo, S. Kotthaus, U. Löhnert, P. Martinet, I. Mattis, E.J. O'Connor, R. Potthast: How can existing ground-based profiling instruments improve European weather forecasts?, *Bull. Am. Meteorol. Soc.* **100**(4), 605–619 (2019)
- 29.58 O. Caumont, D. Cimini, U. Löhnert, L. Alados-Arboledas, R. Bleisch, F. Buffa, M.E. Ferrario, A. Haeffele, T. Huet, F. Madonna, G. Pace: Assimilation of humidity and temperature observations retrieved from ground-based microwave radiometers into a convective-scale model, *Q. J. R. Meteorol. Soc.* **142**(700), 2692–2704 (2016)
- 29.59 F. De Angelis, D. Cimini, J. Hocking, P. Martinet, S. Kneifel: RTTOV-gb – Adapting the fast radiative transfer model RTTOV for the assimilation of ground-based microwave radiometer observations, *Geosci. Model Dev.* **9**(8), 2721–2739 (2016)

Susanne Crewell

Institute for Geophysics and Meteorology
University of Cologne
Cologne, Germany
susanne.crewell@uni-koeln.de



Susanne Crewell is a Professor for Meteorology at the University of Cologne (Germany). She received her PhD at the University of Bremen in 1993. She has been active in the field of microwave remote sensing, including instrument development for more than two decades, covering ground-based, airborne, and satellite measurements for different applications emphasizing a better understanding of atmospheric water cycle processes.

Manfred Wendisch

Physics and Earth Sciences
University of Leipzig
Leipzig, Germany
m.wendisch@uni-leipzig.de



Manfred Wendisch is a Professor at the University of Leipzig (Germany) and Director of the Leipzig Institute for Meteorology. He is involved in airborne field observations, studying the influence of clouds on the atmospheric radiative energy budget with a focus on cirrus and Arctic mixed-phase clouds, as well as on subtropical trade wind cumuli.

Ulrich Löhnert

Institute for Geophysics and Meteorology
University of Cologne
Cologne, Germany
ulrich.loehnert@uni-koeln.de



Ulrich Löhnert is a Professor at the University of Cologne (Germany). His research focuses on the use of ground-based atmospheric remote sensing for a better understanding of the physical processes within the atmospheric boundary layer as well as for improving weather forecast models. For this, he leads JOYCE – the Jülich Observatory for Cloud Evolution (www.joyce.cloud).

Weather Rad

30. Weather Radar

Jörg E.E. Seltmann

Of all ground-based instruments measuring the atmosphere, weather radar is the only one that can deliver volumetric data over large areas at a high spatiotemporal resolution. Born as a byproduct of military development during the Second World War, weather radar has evolved from analog *intensity only* radar over Doppler radar to present-day digital multiparameter radar with a wide use in both research and operational atmospheric measurement.

Being a very intricate active and indirect remote-sensing device, weather radar relies on a plethora of theoretical assumptions and simplifications. Interferences from nonmeteorological targets (*clutter*), unwanted radiation sources, as well as technical limitations and compromises add to the overall error of a radar. The radar receiver measures only a few parameters describing the returned electromagnetic wave. A variety of observables is then being derived via dedicated signal processing. Some of them may directly be related to useful local meteorological information, such as rain rate or radial wind speed.

Radar data are not confined to point measurements but yield areal precipitation fields over wide areas, covering whole countries, if networked. At a (range-dependent) high resolution, spatial structures allow us to detect characteristic meteorological features, such as the vertical extent of convection, wind shear, hook echoes, tornado vortex signatures, and many more.

On a temporal scale, radar observation is quasi continuous at a high temporal resolution of a few minutes, typically. Thus, the rain rate may be integrated to yield hourly or daily precipitation sums. Cell displacement and evolution may be tracked and extrapolated permitting categorical, as well as quantitative nowcasting in automated procedures.

All this makes weather radar the most versatile, powerful, and complex of all instruments probing the atmosphere.

30.1	Measurement Principles and Parameters	842
30.2	History	843
30.3	Theory	845
30.3.1	Radar Basics	846
30.3.2	Doppler Radar Principles	851
30.3.3	The Multiparameter Approach	853
30.3.4	Radar Observables	854
30.4	Radar Systems	858
30.4.1	Transmitters	859
30.4.2	Antenna, Pedestal, and Radome	860
30.4.3	Receivers	862
30.4.4	Signal Processing	864
30.4.5	IT Structure	866
30.4.6	Auxiliary Components	867
30.4.7	Siting, Radar Infrastructure, and Regulations	867
30.4.8	Radar Networks	868
30.5	Specifications	869
30.6	Quality Control	871
30.6.1	Calibration, Parametrization, and Monitoring	871
30.6.2	Error Sources	874
30.6.3	Correction Algorithms	876
30.6.4	Thresholding and Postprocessing	879
30.7	Maintenance	882
30.8	Applications	883
30.8.1	Radar Products and Presentations	883
30.8.2	Interpretation of Weather-Radar Products	886
30.8.3	Automated Weather Radar Algorithms	888
30.9	Future Developments	895
30.9.1	Rapid Update	895
30.9.2	Electronic Scanning	895
30.9.3	Denser Networks	895
30.9.4	Radar Allocation	895
30.9.5	Data Processing	895
30.9.6	Homogeneous Data	895
30.9.7	Internationalization	896
30.9.8	Fully-Integrated Observing Systems	896
30.10	Further Reading	896
	References	896

Weather radar, through volume scanning with high areal coverage in the order of 100 000 km² and with a typical resolution of presently 1°, 250 m, provides information about the spatial distribution of precipitation over large areas, even in inaccessible regions. The precipitation amount can be quantified locally, areally, and vertically integrated. The hydrometeor type, such as rain, drizzle, snow or hail, can be classified and separated to some extent from unwanted targets, called clutter. Observation over time enables monitoring, tracking, and extrapolation of the temporal development of convection and precipitation fields (*nowcasting*). Information on areal wind fields and on small-scale wind phenomena, such as gusts, downbursts, mesocyclones, and even tornadoes, may be gained using standard Doppler radar.

Severe weather alerts and warnings, including natural hazards, such as flash floods or tornadoes, depend heavily on automated radar data processing.

Thus, weather radar represents an indispensable tool not only in the daily work of meteorologists and hydrologists, but also for media, fire fighters, emergency management and services, water authorities, local event organizers, farmers, and, very importantly, aviation, including military. Lately, radar data have even become available to individual users through weather apps on smartphones.

Radar reflectivity and wind data are routinely assimilated into numerical hydrological and weather forecast models. Radar climatology and hindcast is used by experts reporting to court or insurance companies.

30.1 Measurement Principles and Parameters

Weather radar is an active (having a transmitter of its own) and commonly monostatic (transmitter and receiver in the same place) remote-sensing instrument. Unlike optical or IR devices (see Chaps. 13, 24–27, 40), radar works reliably even under unfavorable weather conditions, as microwaves exhibit low absorption. This chapter is about ground-based scanning weather radar; for airborne, millimeter and high frequency radars, or radar wind profiler see Chaps. 31–33, 39.

A typical weather radar sends out a train of short ($\approx 1 \mu\text{s}$) microwave pulses at a pulse repetition frequency typically between 200 and 2000 Hz. Each pulse travels out at the speed of light to meet some rain droplets (or any kind of refraction discontinuities), which backscatter an *echo* that is collected by the radar antenna. The

incoming signal is eventually fed to the radar receiver and is digitized at some point, measuring the exact return time to yield the exact target distance. Together with the known antenna azimuth and elevation there are three coordinates to define the position of the measuring volume in space. Unlike air traffic control and military radar, a weather radar does not only detect and range the target, but it also infers its qualitative and quantitative properties measuring the absolute magnitude of received power.

Tables 30.1 and 30.2 summarize some of the most important technical and measurable parameters of a weather radar. For a detailed description of observables see Sect. 30.3.4. From these relatively few observables, a wealth of meteorologically relevant products may be calculated, such as rain rate and rain accumu-

Table 30.1 Important technical radar parameters

Parameter	Symbol	Unit	Typical value
Number of elevations	n_{el}	–	10–20
Antenna azimuth rate	ω_{az}	rpm	0.1–10 rpm
Antenna size	\varnothing	m	1–8 m
Antenna beam width	θ	deg	1°
Wavelength	λ	cm	3, 5, 10 cm
Pulse width (pulse duration)	τ	μs	1 μs (64 with pulse compression)
Pulse repetition time (interpulse period)	PRT	ms	1 ms
Pulse repetition frequency $\text{PRF} = \text{PRT}^{-1}$	PRF	Hz	200–2500 Hz
Pulse peak power	P_t	W; dBm	10 kW–1 MW
Pulse energy	τP_t	Ws = J	1 J
Average transmitted power $P_{ave} = f P_t$	P_{ave}	W; dBm	10–1000 W
Duty cycle $f = \tau \text{PRT}^{-1} = P_{ave} P_t^{-1}$	f	1; dB	10 ⁻³ ; –30 dB
Received power	P_r	W; dBm	10 ⁻¹² W = 1 pW
Dynamic range		dB	100 dB
Sensitivity	MDS	dBm	–110 dBm
Calibration constant	C	$\text{mm}^6 \text{m}^{-3} \text{mW}^{-1} \text{m}^{-2}$	7 $\text{mm}^6 \text{m}^{-3} \text{mW}^{-1} \text{m}^{-2}$
Calibration reflectivity	Z_0	dBZ	–40 dBZ

Table 30.2 Some radar observables

Parameter	Symbol	Description	Unit
Equivalent reflectivity factor	$z; Z, Z_H, Z_V$	Sum of D_i^6 per unit volume for Rayleigh spheres of equivalent radar cross section	$\text{mm}^6 \text{m}^{-3}$; dBZ
Mean radial velocity	V, V_H, V_V	Weighted mean of Doppler spectrum	deg, rad, m s^{-1}
Spectral width	W, W_H, W_V	Width of Doppler spectrum	deg, rad, m s^{-1}
Differential reflectivity	ZDR	Ratio of copolar reflectivities	dB
Differential (propagation) phase	PHIDP	Phase difference between H and V $\text{PHIDP} = \text{PHIHH} - \text{PHIVV}$	deg
Specific differential phase	KDP	PHIDP per km $\text{KDP} = \Delta\text{PHIDP}/\Delta r$	deg km^{-1}
Depolarization ratio	LDR, CDR	Linear or circular depolarization ratio (crosspolar over copolar)	dB
Copolar correlation	RHO_{co}	Correlation between copolar time series, e.g., $\text{RHO}_{\text{Hr}}, \text{RHO}_{\text{Hv}}$	
Co-crosspolar correlations	$\text{RHO}_{\text{H}}, \text{RHO}_{\text{V}}$	Correlations between copolar and crosspolar time series	

lation, vertically integrated liquid water and ice, echo top height, radial wind fields, vector wind fields and wind profiles, hydrometeor classification, detection and warnings of severe weather, hail, gusts, wind shear, mesocyclones, and tornadoes, see Sect. 30.8.

The volume coverage, high update rate, high representativity, and good resolution are a weather radar's unquestioned strengths. This uniqueness may render verification difficult. Resolution is still better than satellite or numerical weather prediction (NWP) resolution and is usually considered satisfactory, even though for

some features (e.g., TVS, Sect. 30.8.3) a higher resolution might be desirable. Most target parameters are measured indirectly, calling for inversion techniques and models introducing uncertainties larger than the absolute measurement errors. Sometimes, but not always, not being able to measure close to the ground due to beam elevation and Earth curvature may be a disadvantage. Weather radar is complex and expensive causing high initial, operation, and maintenance effort and cost.

30.2 History

Isidor Isaac Rabi (1898–1988), Nobel laureate in physics and one of the leaders in the development of both radar and the atomic bomb, emphasized that the technological advance that contributed most to victory in World War II was not the bomb but microwave radar [30.1].

Radar is based on the theoretical foundation of electromagnetic wave propagation given in 1864/65 by the Scotsman *James Clerk Maxwell* (1831–1879) and experimentally proven some 20 years later (1885–88) by the German *Heinrich Rudolph Hertz* (1857–1894). The Russian *Alexander Stepanovich Popov* (1859–1906) and the Italian *Guglielmo Marconi* (1874–1937) both worked on radio telegraphic transmission by radio waves. In 1904, the German engineer *Christian Hülsmeier* (1881–1957) was the first to make use of electromagnetic waves to remotely detect ships (on the Rhine river in Cologne) by what might today be called a monostatic pulse radar and to patent this *telemobiloskop* (remote motion viewer) in Germany [30.2] and in Great Britain, and a trigonometric method for ranging shortly after. Note that there were no narrowband – let alone microwave – wave sources, no real directional antennas, no frequency filters, no detection or amplifi-

cation tubes, and no measuring of wave travel speed. At the time, the German navy failed to recognize the importance of Hülsmeier's invention, as did the US navy with the bistatic experiment of *Albert H. Taylor* (1879–1961) and *Leo C. Young* (1891–1981) from the US Naval Research Laboratory on the Potomac river in 1922 and their proposal of a *burglary prevention* for navy ports, but its capability was eventually recognized by air forces trying to detect long-range large bombers. At the beginning of the 1930s, Germany, France, Great Britain, Italy, Japan, The Netherlands, the Soviet Union, and USA were all investigating the topic.

“Britain started radar research for aircraft detection in 1935” [30.3], and the Scotsman *Robert Wattson Watt* (1892–1973), a descendent of James Watt and “the inventor of British radar” [30.3], patented the detection and location of aircraft by radio waves that same year, resulting in the construction of the *Chain Home* line of early warning radars (operating at 30 MHz!) starting from 1937 (operational September 1938, continuous operation since Easter 1939), and its German counterpart, the *Kammhuberlinie*, stretching more than 1000 km between Denmark and France.

In Germany, *Rudolf Kühnhold* (1903–1992) was able to range ships in 1934 using something that today

is known as a traveling wave tube, and he presented the first fully functional *Funkmess* device in 1935 [30.4]. “At the beginning of World War II, Germany had progressed farther in the development of radar than any other country”, and “radar was installed on a German pocket battleship as early as 1936” [30.3]. Germany also pioneered the PPI presentation (invented by *Hans E. Hollmann* (1899–1960) and first used it, even remotely, on *Jagdschloß FuG 404*, [30.5]) and the use of shorter wavelength (375 and 560 MHz) radar. In 1942, Telefunken built the passive *Kleinheidelsberg* radar eavesdropping on the British Chain Home [30.6], and Gema built the world’s first phased array radar *FuMG 41/42 Mammuth* in 1944 or 1945 with an azimuth coverage of $2 \times 100^\circ$, a range of 325 km, and a resolution of 300 m [30.7].

Driven by the contest of the belligerent nations, a variety of radar equipment was hastily developed during WW II, and ironically, the US American SCR 270 detected the Japanese bomber attack approaching Pearl Harbour in 1941 but was not believed [30.3].

One decisive step was the development of the high-frequency cavity magnetron that is usually attributed to *John T. Randall* (1905–1984) and *Henry Boot* (1917–1983) of the University of Birmingham, UK, in 1939/40 [30.8]. This invention was shared with MIT Radiation Lab (RL) in the USA, where over 100 radar systems were developed by the end of WW II. After the war, developments were completed by the victorious allies, and the civil use of radar, in the beginning mostly converted military, extended to atmospheric remote sensing. The superheterodyne receiver had been developed as early as WW I.

Even during WW II, weather echoes were sometimes seen to interfere with (to *clutter*) echoes from aircraft. In Great Britain, the first 10 cm-radar was deployed and operated by the General Electric Company GEC in July 1940, and it has been concluded [30.9] that the “first detection of precipitation on radar” was probably accomplished by this radar. In [30.10] a photograph is presented of “thunderstorm conditions” in MIT’s vicinity, detected with a 10 cm-radar on 14 July 1942. While a nuisance in military use, it soon became obvious that radar may be used to guide airplanes around severe weather.

The theoretical foundations to describe the backscattering of electromagnetic waves by small spherical particles had been given by *Lord Rayleigh* (*John W. Strutt*, (1842–1919)) in 1871 [30.11], and for spheres of arbitrary size by *Gustav Mie* (1868–1957) in 1908 [30.12]. Comprehensive basic theoretical work was done by *John Walter Ryde* (1898–1961) and his wife *Dorothy* in Great Britain, also of GEC, between 1946 and 1948 [30.13], in order to determine the effect of weather on military radar, including handwork computation on the re-

lation of radar return and rain rate, i.e., the first *Z/R*-relation [30.9]. In the 1950s, more theoretical concepts evolved, such as signal detection in noise, the matched filter, and Doppler filtering. *Hooper* and *Kippax* from Telecommunications Research Establishment were later able to prove the wavelength and range dependencies of radar echoes, and *J.R. Probert-Jones* derived what is now known as the Probert-Jones factor in the radar equation in 1962 [30.14].

In the USA, radar meteorology can be tracked back to 1941/1942 at MIT RL. MIT also investigated clear air and *angel* echoes, as well as ground and sea clutter and ducting, fluctuations caused by turbulence, and variable polarization, and offered tuition as well. The Army Air Forces conducted the AW-MET-8 project in late 1945 to “investigate the use of airborne radar in meteorology . . .” [30.15].

A weather radar program was initiated as early as 1945 by *J.O. Fletcher* and *E.J. Istvan*, who ordered specification of “three weather radars: a wind finding radar, a storm detection radar, and a cloud base and top detection radar”. The U.S. Air Force (USAF) Weather Service CPS-9 X-band radar of 1954 is considered to be the first specifically designed weather radar [30.16]. In 1953, the Severe Local Storms Forecast Unit (SELS) was created conducting the National Severe Local Storms Research Project later that decade, renamed *National Severe Storms Project NSSP* in 1960, and *National Severe Storms Laboratory NSSL*, in 1964 [30.17].

In Canada, the *Stormy Weather Group* around *J.S. Marshall* and *W.M. Palmer* was set up in 1943, from 1945 at Montreal’s McGill University, who created the famous Marshall–Palmer *Z/R* relationship [30.18].

In postwar Germany, Italy, and Japan radar development had to be stopped, but the Berlin weather radar of 1957 boasts an interesting first-day success story [30.19].

In Japan, the first operational weather radar was established in 1954. A network of typhoon warning radars was initiated soon after, and by the beginning of the 1980s, all radar data output was digital and collected in realtime by the Japan Meteorological Agency [30.20].

In the Soviet Union, the dual-wavelength meteorological radar MRL-5 was designed in the 1960s and is being used to date in different upgraded versions in several parts of the world [30.21].

While MTI (moving target indicator) radars making use of the Doppler effect were developed during the war to suppress stationary targets, the first meteorological application of pulsed Doppler radar and the first weather observation by continuous wave Doppler radar seem to have been described only in 1953 and 1957 [30.22]. Full operational Doppler processing became feasible with computerization in the eighties.

In the 1950s, the US Weather Bureau started replacing weather adapted war radars by specifically designed WSR-57 S-band weather radars creating the first dedicated national weather radar network [30.17]. In the 1960s, electronically steered phased arrays made their reappearance, and in the 1970s, the advance of digital technology enabled data processing in radar. In the 1970s and early 80s, a couple of dual polarization research weather radars were deployed around the world (Colorado State University/University of Chicago-Illinois (CSU-CHILL), Chilbolton, Deutsches Zentrum für Luft- und Raumfahrt (DLR)) [30.23].

Computer control had started to replace the hand-wheel of early days, facilitating operator access and even automated operation without operator involvement. While cathode ray tubes as the first ever radar screens may occasionally still be met, computerization soon led to the development of digital data processing, including product generation, presentation, output, and archiving. This was a tremendous step ahead, even though in the beginning, signal processors were hardwired and wire wrapped, programs hardcoded, projection was through lookup tables (precalculated by a program aptly called *iworm*), presentation based on sixel graphics on VT 100, and archiving on 10.5" tapes.

Around the 1990s, increasing computing power and disk memory provided resources for more challenging techniques, such as realtime Fourier transforms, product calculation and projection on the fly, and storage on disk and configurable templates. Internal and external networking facilitated automated and remote monitoring and messaging and data exchange. National radar networks were equipped with Doppler capability. Solid-state technology, as well as integrated microwave circuitry, enabled digital receivers and solid-state transmitters.

Also in the 1990s, the US WSR-57 radar network was replaced by WSR-88D (D stands for Doppler capability) and called next generation radar (NEXRAD), and radar networks evolved in Europe and many countries around the world as well. International collaboration and exchange even induced harmonization and

supernetworking of national networks, in Europe starting with several COST (European Cooperation in the Field of Scientific and Technical Research) actions, the GORN (Liaison Group on Radar Networking) group and its followup EUMETNET (European Meteorological Network) OPERA (Operational Programme for the Exchange of Weather Radar Information) programs. The OPERA Data Center ODC (*Odyssey*) [30.24] has been collecting radar data from major parts of Europe creating a large-scale pan-European composite covering most of Europe every 15 min. To date, over 120 radars contribute to the OPERA composite. OPERA has also developed the OPERA Data Information Model ODIM for use with WMO (World Meteorological Organization) BUFR (binary universal form for the representation of meteorological data) and HDF5 (hierarchical data format) formats and has recently entered phase V (2019–2023).

With the dawn of the new millennium, the current type of commercial dual-pol radars became available. A *bolt-on* antenna-mounted dual-pol upgrade of an analog Doppler-radar was tested at Hohenpeissenberg Observatory in 2005 using a commercial digital receiver mounted *piggyback* over the antenna elevation shoulder.

With the availability of fast processors and converters digitization has extended into formerly analog receiver parts. Solid-state techniques have been developed to replace electron tubes, and analog as well as rotating parts of a radar by solid-state modulators or transmitters, and – so far in research – electronically steered antennas. Today, networked mass storage media and telecommunications enable archiving of huge data amounts and broadcasting even to cell phone apps.

By now, weather radar has greatly contributed to our understanding of atmospheric processes, to nowcasting, hazard warning, and aviation safety, and radar principles have been adopted by similar sounding technologies, such as lidar, sodar, and sonar. While the weather-radar community is constantly growing, it keeps gathering at the now biannual series of the American Meteorological Society (since 1947) and European (since 2000) conferences on weather radar.

30.3 Theory

As a ground-based remote-sensing instrument, weather radar is sounding the atmosphere indirectly: meteorological phenomena and quantities are targeted, sending out electromagnetic waves to interact with precipitation at a large range of distances. This interaction occurs by way of scattering, and the energy scattered back towards the radar carries characteristic information on the location and properties of the respective scattering tar-

gets. As absorption is largely negligible at microwave frequencies, and scattering is a weak effect, the atmosphere is well transparent to the radar even under cloudy and rainy conditions.

Weather radars are commonly designed as monostatic systems, using the same antenna for transmission and reception. Furthermore, the antenna is usually permanently rotating while stepping through several dis-

crete elevation angles in order to scan the atmosphere. Target location is readily determined in radar-centered polar coordinates.

Using a pencil-beam antenna, the pointing direction of the antenna yields two angles (azimuth and elevation). Distance is derived measuring the round trip time of the echo from a specific range gate, knowing the propagation speed c of electromagnetic radiation to be $c_{\text{vac}} = 299\,792\,458\text{ m s}^{-1}$ in vacuum. In order to measure propagation time, some marker is needed to match transmitted and received radiation. A simple continuous sine wave does not carry any distinguishing information to discriminate the time difference between transmission and echo arrival of a certain target. The easiest marker is to start/stop the radiation in the form of a pulse whose rising (or falling) edge may serve as a marker. Frequency or phase coding represent further options that are also feasible with continuous-wave (CW) radars.

A predefined number of echo pulses may be collected at each range gate to form one batch or time series as a basis for signal processing. More often, however, these batches are synchronized with the antenna movement. For example, one batch is collected between azimuths of 0.5° and 1.5° and is assigned to a position of 1° east of north. This is tolerable, as the antenna azimuth rate is slow compared to the pulse repetition frequency.

Electromagnetic waves are characterized by only a few parameters, such as amplitude, phase, or polarization. These are the parameters that need to be decoded within the receiver and the digital signal processor (DSP). However, they are not the aim of the indirect measurement. The target properties *coded* in the received radiation may be retrieved from intensity, and Doppler and polarization properties of the echo, as well as from the spatiotemporal behavior (e.g., texture) of these parameters. Retrieval calls for model assumptions about the target and the measurement. The desired information may still be altered by propagation effects on its way back to the receiving antenna.

The choice of radar wavelength depends on technical and logistic aspects: short wavelengths (X-band (9.4 GHz, $\lambda = 3.2\text{ cm}$)) are stronger attenuated in heavy rain, and, therefore, longer wavelengths (S-band (3 GHz, $\lambda = 10\text{ cm}$)) are preferred in the (sub)tropics and wherever high-range coverage is desired (USA *tornado alley*). Longer wavelengths also offer larger unambiguous velocities (Sect. 30.3.2). On the other hand, X-band antennas are smaller, so higher directivity and gain may be obtained at lower cost. Short wavelength is, therefore, preferred for short range (regional catchment coverage, sewerage plants) and mountainous areas, or as gap fillers in networks of larger radars. Large parts of

Europe prefer the intermediate C-band (5.6 GHz, $\lambda = 5.4\text{ cm}$), which also offers better frequency protection.

From conventional and Doppler radar, echo strength (reflectivity factor) and Doppler radial velocity are obtained. Adding geometrical and textural characteristics (height extent, echo structure) and physical knowledge (e.g., on coherency and homogeneity), information may indirectly be derived on severe convection, hail, wind profiles, or ground clutter. To better capture and parameterize the physical properties of scatterers and to discriminate between them, more radar observables are necessary, which can be provided by multiparameter (dual wavelength, dual polarization) radars. Multiparameter multiradar observations are employed to describe the full precipitation process from hydrometeor formation to precipitation.

30.3.1 Radar Basics

Weather radar is a pulse radar with a limited unambiguous range. The radar beam propagates through the atmosphere and is bent due to refraction. An *echo* is returned due to scattering by raindrops, etc. The main observable is the radar reflectivity factor. It is related to the properties of the scatterers and is expressed in logarithmic units of dBZ.

Pulse Radar

A short microwave pulse of pulse width (PW) τ is sent out at a pulse repetition frequency PRF, i.e., at a pulse repetition time $\text{PRT} = \text{PRF}^{-1}$, and the radar *listens* to the incoming echo during $\text{PRT} - \tau$ until the next pulse is sent out. The antenna is switched to the transmitter during τ and to the receiver during $\text{PRT} - \tau$ by the T/R-switch (Sect. 30.4.1). This is called time multiplexing and allows for a monostatic setup avoiding crosstalk. Short pulses offer high resolution but call for large bandwidth ($B = \tau^{-1}$) as the time-bandwidth product equals 1.

Range and Cross-range Resolution. Targets are range resolvable if their echoes do not overlap: $t_1 - t_2 > \tau$, i.e., the minimum distance that can be resolved is

$$\Delta r = \frac{c\tau}{2} = \frac{c}{2B}. \quad (30.1)$$

For instance, with $\tau = 1\text{ }\mu\text{s}$, $\Delta r = 150\text{ m}$. This range resolution is not to be confused with the sampling resolution (Sect. 30.4.4), which may be higher (oversampling) or (rarely) lower (undersampling). Range resolution may be increased applying pulse compression techniques (Sect. 30.4.4).

The cross range (= azimuth) resolution depends on the antenna beam width (very often 1°), i.e., on the an-

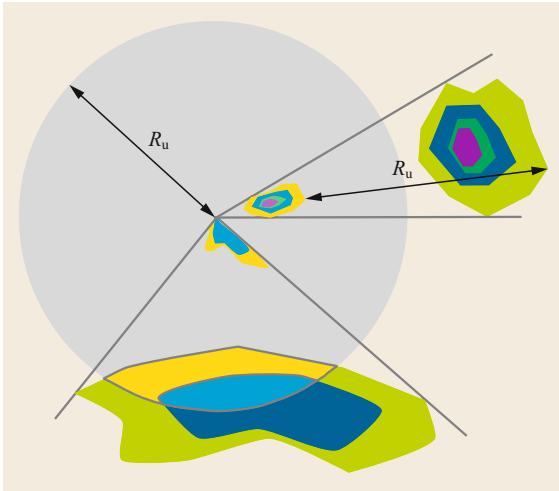


Fig. 30.1 Illustration of range aliasing: echoes of the previous pulse are folded into the unambiguous range R_u (image © J. Seltmann, used by permission)

tenna size and wavelength, and on the number of pulses that are integrated and assigned to a specific azimuth direction (angle syncing, see Sect. 30.4.4). Crossbeam resolution in linear units degrades progressively with increasing range and is thus poor at a distance, as compared to range resolution.

Unambiguous Range and Range Folding. The return time of the echo is measured relative to the pulse that has been sent out last. If the echo originates from a previous pulse, the range assignment becomes ambiguous or *folded*, as illustrated by Fig. 30.1. The maximum unambiguous range R_u is, therefore, determined by a two-way return time smaller than PRT, i.e.,

$$R_u = \frac{c\text{PRT}}{2} = \frac{c}{2\text{PRF}}. \quad (30.2)$$

Thus, a PRF of 1000 Hz corresponds to $R_u = 150$ km. A target at $R = 185$ km appears *folded* at 35 km. Range-folded echoes are called second (third, multiple)-trip echoes or second (third, multiple)-time around echoes. If standalone, they may be recognized by their compressed shape due to the intercept theorem, their weak power (because of wrong range correction, see Sect. 30.6.3), and their incoherency (if incoherent pulses are sent by a magnetron or on purpose, see Sect. 30.6.3). If a second-trip echo overlaps a first-trip echo, its reflectivity adds to the first trip reflectivity, which is consequently overestimated, and its radial velocity estimate may be biased and noisy. Unambiguous ranges between 50 and 250 km are common; the US WSR-88D (NEXRAD) even ranges to 460 km in surveillance scans.

Beam Propagation

Radiation propagation follows Fermat's extremum principle that extremizes the optical path through the atmosphere described by the refractive index $n := c_{\text{vac}}/c_{\text{medium}}$. Under ITU standard conditions, $n = 1.000315$ is very close to unity, giving rise to the definition of refractivity $N = (n - 1) \times 10^6$. In a homogeneous medium $n = \text{const.}$, resulting in propagation along a straight line. In a layered atmosphere,

$$N = \frac{77.6}{T} \left(p + 4810 \frac{e}{T} \right), \quad (30.3)$$

where p is the barometric pressure in hPa (= mbar), e in hPa is the water vapor pressure (important for microwaves), and T in K is the absolute temperature. As the variables p , e , and T usually decrease with height (p , e even rapidly), so does N (c_{medium} increases with height), and the radar beam is bent downward by refraction.

In an exponential model, the refractivity height profile in the lowest kilometers of a standard atmosphere is

$$N(h_{\text{asl}}) = N_0 \exp \left(\frac{-h_{\text{asl}}}{h_{\text{scale}}} \right), \quad (30.4)$$

where h_{asl} is measured above sea level, $h_{\text{scale}} = 7.35$ km is the global average scale height, and $N_0 = 315$ is the average atmospheric refractivity at sea level (values according to [30.25]).

In a linear approximation, $dN/dh \approx \text{const.}$ ($\approx -40 \text{ km}^{-1}$) in the relevant height range so that beam curvature is also constant. Then, the radius of the Earth R_E may be replaced by an effective radius kR_E , where $k = 1/(1 + R_E dn/dh) \approx 4/3$. Over a fictitious Earth surface with radius kR_E , the radar beam would be a straight line. This *four-thirds Earth radius* holds under standard refraction. A nonstandard refractivity profile leads to anomalous beam propagation called *anaprop*. *Subrefraction* occurs if the gradient dN/dh is weaker than the standard or even positive, so that the radar beam is bent less or even upward. If dN/dh is more negative than -40 km^{-1} , as under temperature inversion (nocturnal cooling), the beam curvature is stronger than the standard. This is called *superrefraction*; Fig. 30.2 shows an example. The radar beam may even be trapped within an inversion layer creating an atmospheric dielectric wave guide (like in a glass fiber), which is called *ducting* or *trapping* and occurs when $dN/dh \leq -157 \text{ km}^{-1}$. Anaprop conditions are particularly common if warm air masses are advected over cold water or landmasses.

Scattering and Reflectivity

For many purposes, the energy sent out by one pulse may be considered to be contained in a truncated cone

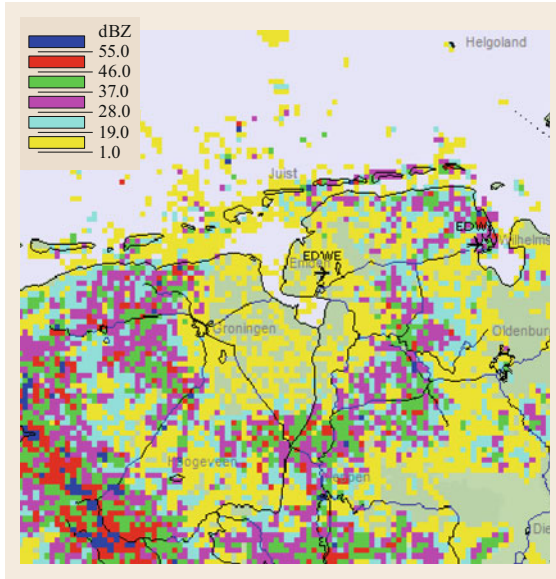


Fig. 30.2 Example of a pronounced anaprop situation at the Emden radar, Germany. There is no precipitation in this case (after [30.26], © DWD)

of length $c\tau$. The total energy scattered back by any drops contained within this pulse volume ΔV – usually a very large number of drops with an unknown drop-size distribution (DSD) – will be measured; ΔV should be large enough to be statistically representative and small enough so that the scattering particles can be approximately considered to fill the beam completely and homogeneously. In reality, ΔV is given by the range-dependent beam broadening. Therefore, it is useful to take to quantities normalized to unit volume (intensive quantities).

For a monostatic radar, the characteristic target parameter is the radar backscattering cross section σ_b , which depends on wavelength λ , refractive index n , and particle diameter D . As there are very many targets in the measuring volume of a weather radar, each individual backscattering cross section $\sigma_{b,i}$ contributes to the sum of all scatterers in a unit volume. This sum is called the reflectivity $\eta = \sum \sigma_{b,i}$.

Assuming spherical scatterers, the scattering process is described by Mie theory [30.12]. A few non-spherical symmetric shapes may be calculated as well, e.g., rotational ellipsoids [30.27] or Chebyshev particles [30.28]. Most scatterers, however, exhibit a complicated backscatter that cannot be solved analytically. Numerical methods have been developed, such as the EBCM (extended boundary condition method), also called the T-matrix method, for rotation-symmetric particles of arbitrary size [30.29], layered multiphase particles [30.30], and tumbling particles [30.31], or the discrete dipole approximation of [30.32].

Table 30.3 Radar backscattering cross sections σ_b of typical targets

Target	Typical σ_b (m^2)
A 380, B26	100
Light aircraft	3
Human being	1
Stealth plane	0.1
Bird	0.01
Raindrop $D = 1$ mm	10^{-11}

The radar backscattering cross sections of different targets comprise many orders of magnitude (cf. Table 30.3). If the sphere is large compared to the wavelength, $D \gg \lambda$ (e.g., $D > 10\lambda$ or $D > \pi\lambda$), the backscattering cross section approaches the geometrical cross section, where $\sigma_b = \pi D^2/4$. This is referred to as the geometric region.

The range where target size is of the order of the wavelength $D \approx \lambda$ ($\pi D \approx \lambda$) is the Mie or resonance region with the full Mie theory applicable. The backscattering cross section $\sigma_b(D)$ is not a monotonous function of D in the Mie region.

Often (but not always), however, the scattering particles can – in addition to being spherical – be considered small compared to the wavelength, $D \ll \lambda$ (e.g., $D < 0.1\lambda$ or $\pi D < \lambda$). This condition is more critical with shorter wavelengths (X-band) but is notwithstanding usually assumed. In this case the Rayleigh approximation applies and

$$\sigma_b = \pi^5 |K|^2 D^6 \lambda^{-4}, \quad (30.5)$$

where $K = (m^2 - 1)/(m^2 + 2)$, and $m = n - jk$ is the complex index of refraction with $N \approx 9$, $k = 0.63 - 1.47$ ($20 - 0^\circ\text{C}$, $\lambda = 10$ cm) in liquid water, and $n \approx 1.78$, $k = 2.4 \times 10^{-3}$ to 5.5×10^{-4} ($0 - 20^\circ\text{C}$) in ice, so that the factors $|K|^2 \approx 0.93$ (water), 0.197 (ice), differ by 7 dB (see Sect. 30.3.1, subsection *Calculation in Decibels*, for decibel and Sect. 30.6 for bright band).

In the case of rain or clouds, billions of individual point targets are assumed to be spherical and small. Integrating over all scatterers in a unit volume to calculate reflectivity yields

$$\eta = \sum \sigma_{b,i} = \pi^5 |K|^2 \lambda^{-4} \sum D_i^6, \quad (30.6)$$

where D_i is the diameter of the i -th droplet, and the sum is over the unit volume. As the radar wavelength is fixed, the important feature here is not the dependence of $\sigma_{b,i}$ on λ^{-4} (which accounts for the blue sky), but the proportionality to D_i^6 . It states that *a million droplets are needed to produce the same reflectivity as one single drop only ten times as large!* The factor $\sum D_i^6$ (sum over unit volume) is determined by the DSD $n_j(D_j)$ (where j

Table 30.4 Correspondence reflectivity – rain intensity

Z (dBZ)	Presumable target
-10	Clouds, clear air
0	Clear air, snow
10	Snow; drizzle
20	Light rain
30	Rain
40	Rain, graupel
50	Hail, rain
60	Hail

numbers size classes) and is called the (radar-)reflectivity factor

$$z = \sum D_i^6 \quad (\text{mm}^6 \text{m}^{-3}, \text{ sum over unit volume}). \tag{30.7}$$

The reflectivity factor is the most important observable of a weather radar and the only one of a classical intensity-only radar. It is correlated with precipitation activity so that a radar image represents something like a weather chart, cf. Figs. 30.13, 30.17, and 30.22. As, unlike η , the reflectivity factor is independent of wavelength, z values are comparable between X, C, and S-band radars. However, in linear units of $\text{mm}^6 \text{m}^{-3}$, the values of z are cumbersome, easily stretching over 12 orders of magnitude. This is why radar meteorologists invented the unit of dBZ (see below). Often z is used to refer to linear units, and Z indicates log units of dBZ. Whenever the drop-size distribution is known, (e.g., from disdrometer measurement), Z may be calculated.

In the real world it is difficult to know if the Rayleigh condition is met for real targets with unknown distribution of composition, number, size, shape, orientation, and velocity. Therefore, the echo power measured by the radar is related to an *effective* reflectivity factor z_e ; one that would result in the same radar return if the Rayleigh condition were fulfilled. Table 30.4 gives some typical observed values.

The Radar Equation

What parameters determine the echo power P_r received by the radar? The radar equation anatomizes the dependence of received power P_r on radar and target properties.

If the radar were an isotropic source of radiation transmitting the pulse power P_t into space, the total inner surface of any sphere concentric around the radar would receive exactly this power, due to conservation of energy, irrespective of the radius of the sphere. As the sphere’s surface $4\pi r^2$ increases with distance r from the radar, the irradiance or power density decreases propor-

tionately: $P_t/(4\pi r^2)$. This decrease is sometimes called the spreading loss or free-space path attenuation.

A real radar, however, is built to radiate as much energy as possible into a preferred direction at the cost of all other directions. The energy is no longer evenly distributed on the imaginary sphere’s inner surface, but the irradiance in forward direction is increased by a factor G called the antenna gain. A rain drop at distance r is, thus, irradiated by $P_t G/(4\pi r^2)$, scattering a (very) small portion of the incident power into all directions. From a distance, the raindrop may itself be seen as a point source of radiation sending the power $P_t G \sigma(\theta, \varphi)/(4\pi r^2)$ into the direction of θ, φ . In the usual monostatic configuration, the portion $\sigma(\theta = 180^\circ, \varphi = 0^\circ) = \sigma_b$ goes back to the radar antenna and is called the radar backscattering cross section, as it must have the dimension of an area, according to the equation.

The resulting irradiance at the receiving antenna decreases with $4\pi r^2$ again and, thus, amounts to $P_t G \sigma_b/(4\pi r^2)^2$. The power received by the effective area $A_e = G \lambda^2/(4\pi)$ [30.33] of the radar antenna is therefore

$$P_r = \frac{P_t G^2 \lambda^2}{4\pi} \frac{\sigma_b}{(4\pi r^2)^2} = \frac{P_t G^2 \sigma_b \lambda^2}{(4\pi)^3 r^4}. \tag{30.8}$$

This is the radar equation for a point target located in the middle of the radar beam (where the gain is G). Note the proportionalities to the target property σ_b and to the fourth power of the distance r .

However, there may be billions or trillions of distributed point targets (rain drops) in one radar sample volume, which is defined by the pulse length and beam cross sections at a given distance. Under a geometric beam approximation, the sample volume is a truncated cone (frustum) of volume

$$V = \pi r \frac{\theta_0}{2} \frac{r \Phi_0}{2} \frac{c\tau}{2}, \tag{30.9}$$

where r is the distance to the radar, θ_0 and Φ_0 are the horizontal and vertical beam widths in rad (typically, $\theta_0 \approx \Phi_0$ for a weather radar), and $c\tau$ is the pulse length and receives a factor of 1/2 for the leading edge of the radar volume to go out and come back in order to arrive simultaneously with the trailing edge. As a figure to remember, the diameter of a 1° beam is about 1 km at a distance of 57 km. With a raindrop density of 100 drops per 1 m^3 , one sample volume may contain 10^9 – 10^{12} droplets.

Provided that the sample volume is completely and homogeneously filled and evenly illuminated by the radar, the backscattering cross sections $\sigma_{b,i}$ of all point targets (numbered by i) contribute linearly to the total backscatter, yielding a total backscattering cross section

of

$$\begin{aligned} \sigma_{\text{tot}} &= \sum \sigma_i \quad (\text{sum over } V) \\ &= V \sum \sigma_i \quad (\text{sum over unit volume}). \end{aligned} \quad (30.10)$$

In reality, the sample volume is not homogeneously irradiated, as there is no radar beam but an antenna diagram (Sect. 30.4.2). The decrease of gain within the 3-dB beam width may, in a first approximation, be described by a Gaussian, leading to an average over the beam width or shape factor of $1/2 \ln(2) \approx 72\%$ [30.34]

$$V = \frac{\pi}{16 \ln(2)} r^2 \theta_0 \Phi_0 c \tau. \quad (30.11)$$

As σ_{tot} is an extensive quantity, it is convenient to normalize to the unit volume, making use of the (radar-) reflectivity $\eta = \sum \sigma_{b,i} = \sigma_{\text{tot}}/V$, where the sum is over the unit volume and is measured in units of m^2/m^3 or cm^{-1} . Letting $\theta_0 = \Phi_0$ for a circular beam,

$$\sigma_{\text{tot}} = \frac{\pi}{16 \ln(2)} r^2 \theta_0^2 c \tau \sum \sigma_{b,i} \quad (30.12)$$

$$\begin{aligned} P_r &= \frac{1}{1024 \ln(2) \pi^2 r^2} P_t G^2 \lambda^2 \theta_0^2 c \tau \sum \sigma_{b,i} \\ P_r &= \frac{\pi^3}{1024 \ln(2) \lambda^2 r^2} P_t G^2 \theta_0^2 c \tau |K|^2 z_e \end{aligned} \quad (30.13)$$

This is the radar equation for distributed (volume) targets. Note that for volume targets, P_r (dBm) is proportional to r^{-2} : $P_r \propto z_e \lambda^{-2} r^{-2}$, so that $z_e = CP_r r^2$ or, in logarithmic form,

$$Z_e = 10 \log_{10} P_r + 20 \log_{10}(r) + 10 \log_{10}(C). \quad (30.14)$$

C ($\text{mm}^6 \text{m}^{-3} \text{mW}^{-1} \text{m}^{-2}$) or ($\times 10^{-15} \text{mm mW}^{-1}$) is called the radar constant and contains all coefficients and parameters that are not functions of r or Z_e . The system-specific radar constant is determined during calibration (Sect. 30.6.1). Once C is known, a target's Z_e may be determined measuring its range and return power.

As droplets within the sample volume move around, successive radar pulses produce identical echoes only if $\text{PRT} \rightarrow 0$. Hydrometeors need to reshuffle for the radar to obtain statistically independent samples. The time needed to decorrelate (e.g., to 0.01) is called the decorrelation time or time to independence and decreases with decreasing wavelength and increasing turbulence. Experimentally, $t_{0.01}$ (ms) $\approx 2.5\lambda$ (cm) in the range of 3.5–30 ms [30.33]. In reality, this condition is not met because under operational conditions the dwell time is

too short. Instead, more pulses are collected at higher PRF, and independence is increased by averaging over azimuth and range.

Calculation in Decibels

There are a couple of variables in radar science that span a very large dynamic range. The radar reflectivity factor for small particles increases with D^6 and easily spans more than ten orders of magnitude. The received power of a radar is up to 18 orders smaller than its transmit power. In cases like these, it is convenient to take the logarithm in order to avoid writing many digits. Thus, it is considered more convenient to write $-30 \text{ dB}\sigma$ and $+90 \text{ dBZ}$, instead of 0.001 cm^2 and $10^9 \text{ mm}^6 \text{m}^{-3}$.

The unit of decibels is defined as a logarithmic power ratio $10 \log_{10} P_1/P_0$. A power ratio of 1 results in 0 dB.

Calculation in dB follows the laws of exponentiation and logarithm, e.g., $\log_{10} 10^{a-b} = \log_{10}(10^a/10^b) = a - b$. Keeping in mind that $\log_{10} 10 = 1$, $\log_{10} 2 \approx 0.3$ and $\log_{10} \pi \approx 0.5$, it turns out that a factor of 2, 3, 10, 100 corresponds to 3, 5, 10, 20 dB. Then, it is easy to estimate the following useful examples (Table 30.5).

Thus, *decibel* is a dimensionless power ratio. However, it may be agreed upon to refer this ratio to a given absolute value x , which is subsequently indicated in the unit of dBx. For instance, the unit of dBm refers to $P_0 = 1 \text{ mW}$ by convention, so that $0 \text{ dBm} = 1 \text{ mW}$, and $33 \text{ dBm} = 2 \text{ W}$. Table 30.6 shows a couple of examples.

It should be kept in mind that any power calculation, such as averaging or Fourier transformation, must be performed on linear values; e.g., Z (dBZ) must not

Table 30.5 Useful dB values

Factor of	Write as	dB
0.1	10^{-1}	-10
0.5	$1/2$	$0 - 3 = -3$
1	10^0	0
2	$10 \log 2$	3
3	$10 \log 3$	5
4	2×2	$3 + 3 = 6$
5	$10/2$	$10 - 3 = 7$
10	10^1	10
250	$10^3/4$	$30 - 6 = 24$

Table 30.6 Some absolute logarithmic quantities

Log unit	Refers to	Typical value
dBZ	$z = 1 \text{ mm}^6 \text{m}^{-3}$	-31.5 to +95 dBZ
dBm	$P = 1 \text{ mW}$	84 dBm = 250 kW
dBi	$G = 1$ (isotropic radiator)	45 dBi
dBσ	$\sigma = 1 \text{ cm}^2$	-30 to +80 dBσ
dBsm	$\sigma = 1 \text{ m}^2$	-40 to +20 dBsm
dBRR	$RR = 1 \text{ mm h}^{-1}$	-1 to +2.5 dBRR

be averaged. (Even though it has been pointed out that interpolation in log units may produce smaller errors.)

30.3.2 Doppler Radar Principles

Doppler radar is based on the Doppler effect that is well known in daily life (the siren of a passing police car) and science (the Hubble effect). The movement of a precipitating cloud is such that there is no relativistic effect but only a linear radial Doppler effect. It describes the change of frequency in dependence of a moving light (or sound) source's velocity by

$$f' = f_0 \left(1 \mp \frac{V_r}{c} \right), \quad (30.15)$$

where f' is the observed frequency and f_0 is the transmitted frequency, c its wave propagation velocity, and V_r the velocity of the moving source relative to the observer; V_r is counted as negative (positive) if directed towards (away from) the radar and creates a positive (negative) Doppler shift. In a monostatic radar, the effect occurs twice as the target acts as a moving receiver and as a moving backscatterer at the same time, so the Doppler frequency shift f_{DOP} becomes

$$f_{\text{DOP}} = \frac{-2V_r}{\lambda} = -2V_r \frac{f_0}{c}. \quad (30.16)$$

The Doppler shift is, thus, 62.5, 36.4, or 20.0 Hz for every 1 m s^{-1} of radial velocity at X-band, C-band, or S-band, respectively. It must be kept in mind that only the radial wind component V_r can thus be measured, and nothing can be said about the magnitude and direction of the real wind vector \mathbf{V} , even if the subscript r is sometimes dropped.

Each droplet k within the radar volume contributes to the echo according to its radar backscattering cross section σ_k and Doppler frequency $f_{\text{DOP},k}$, the whole ensemble giving rise to the Doppler power spectrum $S(f_k)$. The individual contributions are conveniently described as complex pointers or vectors $\mathbf{a}_k = a_k \exp(-j\omega_{\text{DOP},k}t)$, using the echo amplitude a_k and angular frequency $\omega_{\text{DOP},k} = 2\pi f_{\text{DOP},k}$ of each droplet. As all droplets in the radar volume are illuminated by a coherent wave, their contributions add coherently (vectorially) to $\mathbf{A} = \sum \mathbf{a}_k = \sum a_k \exp(-j\omega_{\text{DOP},k}t)$, which, in turn, represents a complex number $\mathbf{A}_i = a_i \exp(-j\omega_{\text{DOP},i}t)$. Here, k counts the droplets in the radar volume and i the irradiating pulses. Each pulse i returns a complex echo at every range bin. The index of the range bin is usually suppressed, where appropriate.

Phase Measurement

According to the above formula, the frequency shift between transmitted and received waves is in the or-

der of 1 kHz (often less) at meteorological velocities and is, thus, very small compared to the radar transmit frequency f (e.g., 5 GHz), which makes it difficult to calculate the frequency difference. The phase shift $\Delta\phi$ due to target displacement between two consecutive pulses is measured instead and divided by PRT to obtain the target radial velocity. Thus, the (double) target interpulse displacement is measured in units (as a fraction $\Delta\lambda$) of the transmitted wavelength λ modulo integer multiples of λ or as $\Delta\phi$ in radians modulo 2π . Division by the pulse repetition time PRT (or multiplication by PRF) yields the mean target velocity

$$v(\Delta\lambda) = \frac{\Delta\lambda \text{PRF}}{2}, \quad (30.17)$$

$$v(\Delta\phi) = \frac{\Delta\phi \lambda \text{PRF}}{4\pi}. \quad (30.18)$$

Mathematically, if the transmitted phase is ϕ_0 , and the distance to target is r , then the distance traveled by the wave is $2r$ or, measured in wavelengths, $2r\lambda^{-1}$, or $2\pi 2r\lambda^{-1}$ if measured in radians, so that the phase of the echo wave incident at the radar is $\phi_0 + 4\pi r\lambda^{-1}$. Its derivative with respect to time t is

$$\frac{d\phi}{dt} = \frac{4\pi}{\lambda} \frac{dr}{dt}, \quad (30.19)$$

where $d\phi/dt = 2\pi f_{\text{DOP}} (= \omega_{\text{DOP}}$, the angular Doppler frequency), and $dr/dt = -V_r$, the radial target velocity (counted negative if approaching), so that $f_{\text{DOP}} = -2V_r/\lambda$, as before. The differential quotient $d\phi/dt$ is approximated by the difference quotient $\Delta\phi/\Delta t$, where Δt is the time difference between pulses, i.e., PRT, and $\Delta\phi$ is the respective pulse-to-pulse phase difference. In order to compare the phases of consecutive pulses, their phase must be corrected for the initial transmit phase ϕ_0 if the latter is not constant (as in a magnetron system, see Sect. 30.4.1, or in a whitening procedure, see Sect. 30.6.3).

The Doppler Dilemma

Due to Nyquist's sampling theorem ([30.35] or Chap. 2), f_{DOP} has to be sampled twice (by different radar pulses) in order to be recovered correctly. If the pulse repetition frequency is PRF, then $|f_{\text{DOP}}|$ may not be larger than $\text{PRF}/2$, yielding

$$V_{r,\text{max}} = \pm \text{PRF} \frac{\lambda}{4}. \quad (30.20)$$

Thus, the maximum unambiguous Doppler velocity that can be measured by a radar depends on its wavelength λ and pulse repetition frequency PRF.

Table 30.7 Product of unambiguous velocity and unambiguous range

Band	λ (cm)	$V_{r,\max}R_{\max}$ (km m s ⁻¹)
X	3	1125
C	5	1875
S	10	3750

The range $[-V_{r,\max}, +V_{r,\max}]$ of unambiguous velocities is also called the Nyquist interval $[-V_N, +V_N]$ and is expressed in either absolute velocities (m s⁻¹), in phase units (deg or rad), or normalized to $[-1, +1]$. Velocities lower than $-V_N$ or higher than $+V_N$ will appear aliased or *folded* into the unambiguous interval. That is, $V_r = V_N + \partial V$ will be erroneously interpreted as $-V_N + \partial V$, which is $2V_N$ away from the real value V_r , see Fig 30.16 for an example. Combined with (30.2) this yields

$$V_{r,\max}R_{\max} = \pm\lambda \frac{c}{8}. \quad (30.21)$$

The equation shows that there is a tradeoff between $V_{r,\max}$ and R_{\max} , each one can only be extended at the cost of the other. This is called the Doppler dilemma. Obviously, an S-band radar is capable of simultaneously measuring larger unambiguous velocities and ranges than an X-band radar. This is shown in Table 30.7. Methods exist to extend the unambiguous range (Sect. 30.6.3).

Complex Signals in Time and Frequency Domains

For each single pulse, echoes are returned from targets along the propagation path. The return time defines the target distance. In modern computerized radars, the incoming echo is digitized at certain range gates (range bins). This is done for every single transmitted pulse, yielding a time series of returned pulse signals at each range gate. For an operational radar, the length of the time series is defined by the time on the target (dwell time), which is a function of antenna beam width and angular (usually azimuth) rate.

In an intensity-only radar, the measured time series is just a real time series representing the echo intensity, and nothing is known about phase. In a Doppler radar, the echo phase complements each measurement to form a complex number in either Cartesian, trigonometric, or exponential representation. A dual-polarization radar measures two complex time series, one for each polarization. All meteorological information is contained in and must be derived from these signals in either the time or the frequency (spectral) domain using filters, correlations, and Fourier transforms for every single range gate. This is performed in realtime by a digital signal processor DSP (Sect. 30.4.4).

The echo amplitude A_i and phase ϕ_i of the i -th pulse at a certain range bin (the range index is dropped) are considered as a complex signal in the exponential notation

$$A_i = A_i \exp -j\phi_i, \quad (30.22)$$

which may be equally well described in its algebraic form

$$A_i = I_i + jQ_i, \quad (30.23)$$

where $I_i = A_i \cos \phi_i$ and $Q_i = A_i \sin \phi_i$ constitute the Cartesian components. These are the (real) signals measured in a radar, possibly for each polarization, after I/Q demodulation by an analog or digital quadrature detector. The pulse (or time) index i runs from the first usable pulse to the last one in a batch, so that A_i forms a time series. Note that a time series is obtained at each (raw) range bin, whose index has been dropped for simplicity. The time series may be processed either in the time domain or in the frequency domain; the equivalency is guaranteed by the Wiener–Khinchin theorem, which states that the autocorrelation function $R(t)$ and the power spectrum $S(f)$ of a signal form a pair of Fourier transforms cf. Chap. 2.

The Doppler spectrum is commonly modelled to consist of three parts: a Gaussian weather spectrum of width W around the mean velocity V and a narrow clutter spectrum centered at zero velocity, above a white noise floor; S , C , and N are the powers (the areas under the respective curves) of the Gaussian weather spectrum, the (Gaussian) clutter spectrum and the white noise; S , V , and W are the zeroth, first and second moments of the Doppler spectrum in a mathematical sense.

Time-domain or Pulse-pair Processing (PPP)

Time-domain processing is based on correlation calculation. As per definition, the autocorrelation of the filtered (superscript “f”; cf. Sect. 30.6.3) or unfiltered complex radar time series $A_i^{(f)}$ is

$$R_l^{(f)} = \frac{1}{n-l} \sum_{i=1}^{n-l} A_i^{(f)*} A_{i+l}^{(f)}, \quad (30.24)$$

where n is the number of available pulses (the length of the time series), l is the lag index, and the asterisk (*) denotes the complex conjugate. Commonly, unfiltered R_0 is denoted T_0 , and (f) is omitted for filtered autocorrelations, so that R_0 , R_1 , and R_2 are understood to be filtered; T_0 and R_0 are real numbers, all other R_l are complex.

The desired information – weather echo power S , mean radial velocity V , and spectral width W – is concentrated in the first lags ($l = 0, 1, 2$) of R_l and extracted during signal processing, cf. Sect. 30.4.4.

Table 30.8 Autocorrelations and moments

	Formula	Physical model
T_0	$\frac{1}{n} \sum_{i=1}^n A_i^* A_i$	$\frac{S+C+N}{2\pi}$
R_0	$\frac{1}{n} \sum_{i=1}^n A_i^{(f)*} A_i^{(f)}$	$\frac{S+N}{2\pi}$
R_1	$\frac{1}{n-1} \sum_{i=1}^{n-1} A_i^{(f)*} A_{i+1}^{(f)}$	$\frac{S}{2\pi} \exp\left(j\pi V - \frac{(\pi W)^2}{2}\right)$
R_2	$\frac{1}{n-2} \sum_{i=1}^{n-2} A_i^{(f)*} A_{i+2}^{(f)}$	$\frac{S}{2\pi} \exp(j2\pi V - 2(\pi W)^2)$

Table 30.8 gives an overview of this. The mean velocity V and spectral width W are normalized to $V_N = [-1, +1]$.

Frequency-domain Processing.

The discrete Fourier transform (DFT) of a periodic signal x_n is

$$X_k = \sum_{n=0}^{N-1} x_n \exp -\frac{2\pi jkn}{N}, \quad (30.25)$$

and the inverse DFT is

$$x_n = \frac{1}{N} \sum_{k=0}^{N-1} X_k \exp \frac{2\pi jkn}{N}.$$

As the radar signal A_i is *not* periodic, it must be made periodic by tapering it with a periodic window, which, on the downside, produces unwanted sidelobes and a higher variance (reducing the effective number of independent samples). This is why several windows, such as rectangular, von Hann, Hamming, and Blackman, have been designed for tradeoff. A rectangular window exhibits a narrow pulse response but high sidelobes masking weak targets, while a Blackman window shows a broad pulse response but very low sidelobes, which can only be exploited in very low-phase noise systems. In a magnetron radar, a Hamming window is usually considered appropriate.

A fast Fourier transform (FFT) requires a power-of-two number of samples, which cannot be guaranteed under a free-running antenna with dynamic angle synchronization DAS (Sect. 30.4.4). As a workaround, the number N of samples available within one batch (ray) may be split into two overlapping groups of 2^n pulses each, where $2^n < N$. FFT is performed on each group separately, and the results are averaged. Once the Fourier spectrum has been obtained, adaptive clutter filtering is performed (Sect. 30.6.3).

The Doppler moments may then be directly derived from the spectrum (e.g., adding up the spectral components to find the filtered and unfiltered powers and finding the strongest Fourier component to determine the mean velocity). Often, however, the spectrum

is converted back to the time domain via an inverse Fourier transform to make use of the autocorrelation processing.

In the end, T_0 , R_0 , R_1 , and R_2 are available. Time-domain processing is faster and less intensive, as all correlations may be calculated incrementally simply by adding each new pulse, and only few lags need to be calculated. It can also work with lower SNR. Doppler filtering (Sect. 30.6.3), however, as well as scientific analysis, is more efficient in the frequency domain.

It may be noted that the assumption of a Gaussian weather spectrum is appropriate if one mean velocity and one spectral width is calculated for the whole Doppler spectrum by the above standard algorithms. If, however, there is a high enough spectral resolution, which is the case for a long underlying time series (e.g., 1024 pulses), then several modes may be detected, and their corresponding mean velocities and spectral width calculated in order to discriminate between different groups of hydrometeors within the radar detection volume.

The physical moments and parameters that may be calculated from Doppler measurements are integrated into Sect. 30.3.4.

30.3.3 The Multiparameter Approach

As there is only one radar observable in a reflectivity-only radar, and three in a Doppler radar, it is desirable to measure more independent observables in order to describe the distributions of size, shape, aggregate state, and velocity of the ensemble of scattering particles. Polarization or frequency diversity radars are promising candidates.

Compared to dual polarization, dual frequency has received considerably less attention so far, except for the Russian MRL-5, which features two nested parabolic antennas. The COST-75 study [30.36] opted against dual-wavelength radars mainly because of beam matching challenges. Existing dual-frequency radars mostly operate at higher frequencies (Ku-W-band) [30.37]. Measuring the frequency-differential reflectivity, also called differential frequency ratio (DFR), which is defined as the difference of radar reflectivity factors between the respective frequency bands, it is expected that hail may be detected making use of the resonances of the radar backscattering cross section in the Mie region.

Dual-Polarization Principles

Besides wavelength, amplitude, and phase, polarization of an electromagnetic wave is one more parameter that may be measured to gain additional information. Polarization is defined as the direction of the electric field vector – if there is any predominant direction. The

most general polarization state would be elliptical, with circular and linear polarization as special cases. The instantaneous polarization state is usually described as a vector in an arbitrary orthogonal basis $\{e_1, e_2\}$, most often circular (left/right-handed $\{e_l, e_r\}$) or linear (horizontal/vertical $\{e_h, e_v\}$).

Any action on the polarization state is then described by a left matrix multiplication, e.g.,

$$\begin{bmatrix} E_h^r \\ E_v^r \end{bmatrix} = \begin{pmatrix} S_{hh} & S_{hv} \\ S_{vh} & S_{vv} \end{pmatrix} \begin{bmatrix} E_h^t \\ E_v^t \end{bmatrix} \frac{\exp(-2jkr)}{2r} \quad (30.26)$$

represents the transformation of the transmitted wave (superscript t) into the received wave (superscript r) due to backscattering only. The complex 2-D vectors are called Jones vectors and characterize the electric field vector orthogonal to the direction of propagation (so that the third field component is zero). The complex elements (*scattering amplitudes*) of the backscattering matrix \mathbf{S} are directly connected to the scattering-related polarization observables (Sect. 30.3.4). The Jones formalism is applicable to fully polarized transversal waves. Partially polarized waves are described by the 4-D Stokes formalism combining 4-D Stokes vectors by Mueller matrices. The Stokes–Mueller formalism may be represented by the Poincaré sphere [30.38] but is related to intensity only (no phase information).

Classical and Doppler radars are not *unpolarized*; rather, their polarization can neither be altered during transmission nor differentiated while receiving. The polarization of such a radar is usually chosen horizontally to maximize the return of large, oblate raindrops.

Fully polarization-agile weather radar systems (e.g., CSU-CHILL, Chilbolton, DLR) are mostly research systems whose full capabilities (to measure the full covariance matrix in different polarization bases) cannot be adequately valued here, see [30.38] instead for a thorough theoretical discussion of polarization and its measurement. They are capable of changing the polarization state on a pulse to pulse basis, e.g., alternating between horizontal and vertical polarization, making use of a fast polarization switch. This mode is called the alternate or switched mode.

Operational dual-polarization weather radars usually invoke a linear polarization base (i.e., horizontally and vertically) in the so-called hybrid (or STAR, or SIDPOL©) configuration. STAR stands for simultaneous transmit and receive of *H* and *V*, (*not* transmitting and receiving at the same time). Transmitting equal power in *H* and *V* simultaneously results in transmitting at 45° (vector addition). Two transmitters may (rarely) be used to produce *H* and *V*, or a power splitter (*magic tee*) may be applied. Phase measurement accuracy (correlation) is higher with hybrid mode because *H*

Table 30.9 Pros and cons of switched and hybrid dual-pol modes

Switched mode	Hybrid mode
Full polarization matrix measurable	No cross-polar measurements
Vulnerable ferrite switch	Robust power divider
Expensive	Cheaper
Full power available	Half power each channel
Only every second pulse coherent	Pulses less decorrelated

and *V* measurements are obtained simultaneously for each pulse, while in alternate mode, only every other pulse is to be used. The hybrid mode is easy and robust to set up using a splitter, while pulse-to-pulse ferrite switches are prone to failure. While halving the transmit power by splitting into *H* and *V* does not pose a real problem (at least in magnetron and klystron systems), no cross-polar measurement can be performed in hybrid mode, and there is a small error in the copolar measurement due to the depolarized component of the other (cross polar) channel. Therefore, some radars may be able to switch off one (usually the vertical) channel temporarily so as to enable measurement of the cross polar components. These are still much weaker than copolar backscatter and are, therefore, difficult to measure because of low SNR and possible crosstalk in antenna and receiver. In Europe, only the MetOffice seems to operate their radars using both hybrid and LDR mode operationally. Table 30.9 summarizes advantages and drawbacks of both approaches.

30.3.4 Radar Observables

Based on the echo time series available (intensity only, Doppler, dual pol), the following observables or *moments* may be calculated.

The Reflectivity Factor

An intensity-only weather radar measures just the received power P_r , commonly in logarithmic units. It may also calculate a clutter correction CCOR from the amplitude fluctuation, see Sect. 30.6.3. Based on (30.14) the effective reflectivity factor Z_e (dBZ) is calculated as

$$Z_e = 10 \log P_r + 20 \log r + ar + Z_0(+CCOR), \quad (30.27)$$

where the prefix C or U is commonly added to indicated the corrected or uncorrected moment, so that:

- UZ is the uncorrected (unfiltered and without adding CCOR) reflectivity.
- CZ (CCOR added) is the (clutter and, if required, second-trip) corrected reflectivity.

- r (km) is the target range, and $20 \log r$ is the r^2 range correction (Sect. 30.6.3).
- a (dB km⁻¹) is the two-way specific gas attenuation (Sect. 30.6.3).
- Z_0 (dBZ) is the calibration reflectivity determined during calibration (Sect. 30.6.1).
- P_r is the pulse-averaged (linear) received power (including clutter) after subtraction of (measured) noise and biases.
- In the case of a Doppler radar, $P_r = (T_0 - N)N^{-1}$ is calculated from the unfiltered unlagged autocorrelation and the noise measurement.
- CCOR is the clutter correction (Sect. 30.6.3).

If applicable, the reflectivity factor is calculated separately for both polarizations (e.g., h and v) and denoted Z_h and Z_v , with the above prefixes.

Doppler Moments

Many more parameters can be derived using a Doppler radar. Note that all of these are obtained twice in a dual-pol radar.

Mean Radial Velocity V . For a symmetric Doppler spectrum V may be calculated from formula (Table 30.8)

$$V = \frac{\lambda \arg(R_1)}{4\pi\tau} \quad (30.28)$$

R_1 is the complex autocorrelation (30.24) at lag $l = 1$, whose argument is the phase difference between the two pulses. In the case of a magnetron system, the phases of the individual pulses must first be corrected for the transmitted initial phase sampled from the burst pulse prior to correlating in order to be comparable; V may be calculated from filtered and unfiltered time series and, in a dual-pol radar, for both polarizations yielding V_h , V_v , UV_h , and UV_v ; V may be output by DSP in absolute units of m s⁻¹ or normalized to the Nyquist intervals $[-V_N, +V_N]$, $[1, +1]$, respectively.

Spectrum Width W . In a Gaussian model, this parameter is the spectral width of the Doppler spectrum. It is indicative of shear, turbulence, or a radial component of the fall velocity distribution and subject to broadening effects, such as system (particularly magnetron) phase instability and antenna rotation. As a side note, the spectral width of clutter also depends on phase stability and antenna speed, and, in addition, on natural fluctuations, such as moving leaves. This broadening influences the clutter filter width to be chosen (Sect. 30.6.3).

In signal processing, an effective spectral width will be estimated, as real spectra are sometimes not Gaus-

sian or even not monomodal. There are two algorithms to estimate the Doppler spectrum width. The faster one,

$$W = \frac{\sqrt{2 \ln(R_0)/|R_1|^{-1}}}{\pi} \quad (30.29)$$

uses only R_0 and R_1 and requires a Gaussian spectrum and large SNR (e.g., SNR > 10 dB), as clarified by (30.32), when SNR/(SNR + 1) → 1.

The more accurate one,

$$W = \frac{\sqrt{\frac{2}{3} \ln(|R_1|)/|R_2|^{-1}}}{\pi} \quad (30.30)$$

makes use of R_0 , R_1 , and R_2 and can work with lower SNR (e.g., SNR > 0 dB);

W may be calculated from corrected and uncorrected time series and, in the case of a dual-pol radar, for both polarizations yielding W_h , W_v , UW_h , and UW_v . The output format may be normalized to [0–1] or absolute m s⁻¹.

Signal Quality Index SQI . The power normalized amplitude of lag 1 autocorrelation is called the signal quality index

$$SQI = \frac{|R_1|}{R_0} \quad (30.31)$$

where R_0, R_1 are the autocorrelations at lag 0 and lag 1 of the filtered time series according to Table 30.8. Its value is zero for white noise and one for a single spectral line. In the Gaussian model,

$$SQI = \frac{SNR}{SNR + 1} \exp\left(-\frac{(\pi W)^2}{2}\right) \quad (30.32)$$

SQI may, thus, be considered as an indicator of the Doppler signal quality, and $SQI < SQI_{thr}$ may be used as a threshold criterion thereof. In a digital receiver of a magnetron (or of a pulse coded klystron) radar second or third-trip SQI may also be calculated cohering to the phase of the previous or earlier pulses, see Sect. 30.6.3.

Clutter Phase Alignment CPA . CPA is the absolute value of the complex (vectorial) addition of the A_i time series, normalized to the sum of A_i magnitudes,

$$CPA = \frac{|\sum A_i|}{\sum |A_i|} \quad (30.33)$$

CPA is an indicator of the phase variability within (over N samples of) the received complex time series. The echo phase is constant for stationary targets but

changes deterministically in weather echo, if the mean velocity is not zero, and randomly for noise. Thus, CPA ranges between 0 and 1 and is low if the resulting vector is *short* due to rapid phase shifts, and approaches 1 (e.g., CPA > 0.95) if all A_i point to the same direction, indicating no Doppler shift as an evidence of a stationary target (ground clutter). Azimuthal super resolution may be used to capture the maximum CPA under strong reflectivity gradients, but the reliability of CPA decreases if N is too small.

Amplitude STD. The normalized standard deviation STD of the received signal amplitude $|A_i|$

$$\text{STD} = \sqrt{1 - \frac{\sum |A_i|^2}{\sum |A_i|^2}} \quad (30.34)$$

is a stability indicator. Low STD is indicative of stable signals with low amplitude variance. On the contrary, interference from pulsed foreign transmitters exhibits high STD. A typical value for noise would be STD \approx 0.5. This property may be applied to detect pulsed RF interference, cf. Sect. 30.6.3.

Signal-to-noise Ratio SNR. This standard parameter is calculated as

$$\text{SNR} = 10 \log \frac{T_0 - N}{N}, \quad (30.35)$$

where the total power is T_0 (Table 30.8) in a Doppler radar and the average of squared unfiltered amplitudes (linearized log samples) in an intensity-only radar. The noise power N is determined from noise measurement (Sect. 30.6.1). SNR is typically used for quality control and can easily be converted to the received power simply adding the minimum detectable signal (MDS) in dBm that is determined during calibration. The power estimate can then be related to an external reference, such as the sun to monitor the receiver calibration.

Clutter Correction CCOR. Clutter correction CCOR is defined as

$$\text{CCOR} = 10 \log \frac{S}{C+S} = 10 \log \frac{1}{\text{CSR} + 1}, \quad (30.36)$$

where the antilogarithm is related to the clutter-signal ratio CSR = CS^{-1} but is calculated differently in intensity-only, analog and digital Doppler radar, see Sect. 30.6.3.

When SNR is large enough,

$$\text{CCOR} = 10 \log \frac{R_0}{T_0} \quad (30.37)$$

(cf. Table 30.8) approaches (30.36). Using T_0 , R_0 , R_1 , and additionally R_2 , signal and clutter powers may be

calculated independently by

$$C = \frac{T_0 - R_0}{2\pi}, \quad (30.38)$$

$$S = \frac{|R_1|}{2\pi} \exp \frac{\pi^2 W^2}{2}, \quad (30.39)$$

even with low SNR.

Note that CCOR is *negative* by definition, as it will be *added* in (30.27). The calculated CCOR is usually tested against a predefined threshold CCOR_{thr}, cf. Sect. 30.6.4.

Weather Signal Power WSP. This parameter (sometimes called SIG or SIGPOW) estimates the SNR of the weather signal in dB after clutter correction. WSP may be calculated from T_0 , R_0 , R_1 alone by

$$\text{WSP} = 10 \log \frac{T_0 - N}{N} + 10 \log \frac{R_0}{T_0}, \quad (30.40)$$

which represents the total SNR plus CCOR by (30.35) and (30.37). If R_2 is available,

$$\text{WSP} = 10 \log \frac{S}{R_0/2\pi - S}, \quad (30.41)$$

with S as before (30.39).

WSP is mainly used for thresholding; the pertaining threshold is WSP_{thr} (Sect. 30.6.4).

Polarization Observables

Several observables may be derived from the complex copolar and cross-polar dual-pol time series. First, all moments known from a Doppler radar may be obtained in h and v versions: Z_h/Z_v , UZ_h/UZ_v , V_h/V_v , W_h/W_v , SQI_h/SQI_v , and $CCOR_h/CCOR_v$. Second, several ratios, differences, and correlations may be formed:

Differential Reflectivity ZDR. Differential reflectivity is the ratio z_{hh} over z_{vv} of horizontal over vertical copolar reflectivity factors measured in $\text{mm}^6 \text{mm}^{-3}$ (noise subtracted) – or their dBZ difference

$$\text{ZDR} = 10 \log_{10} \left(\frac{z_{hh}}{z_{vv}} \right) = Z_h - Z_v \quad (\text{dB}). \quad (30.42)$$

Intuitively, ZDR describes the shape or axis ratio of the scattering targets, so that for spheres (raindrops smaller than 0.3 mm) ZDR = 0, while for oblate particles (large drops falling against air drag) ZDR = 0–6 dB. This may be used as a measure of drop size in quantitative precipitation estimation QPE and hydrometeor classification HMC. Depending on temperature (measurement height), ZDR larger than 1 may also be indicative of

supercooled water drops in strong storm updrafts. Prolate (aligned ice) particles exhibit negative ZDR. ZDR is around 0 in hail, because falling hail is usually not aligned. Thus, ZDR may be used to differentiate between hail and large raindrops. Small reflectivity combined with larger ZDR may indicate insects.

Although ZDR may be calculated from both filtered and unfiltered reflectivities, it is preferred to use uncorrected input to avoid clutter filter artifacts. ZDR must be calibrated for any offset and will be biased by differential attenuation.

ZDR may also be calculated using the autocorrelations at first lags

$$\text{ZDR}_1 = 10 \log_{10} \left(\frac{|R_{1h}|}{|R_{1v}|} \right). \quad (30.43)$$

A differential Doppler velocity is sometimes calculated according to

$$\text{DDV} = V_h - V_v. \quad (30.44)$$

It may be used as an indicator in bird watching [30.39].

Depolarization Ratio LDR. Not all of the energy is scattered back at the same polarization as it was transmitted. Some part may be depolarized into the cross-polar channel. The depolarization ratio relates this cross-polar received power to the copolar received power. For example, transmitting horizontally in a linear polarization base, the cross-polar reflectivity factor Z_{vh} measured in the vertical channel is related to the copolar reflectivity factor Z_{hh} . (By convention, the first index refers to the receive channel, the second one to the transmit channel.) Hence, the *linear depolarization ratio* is

$$\text{LDR}_{vh} = 10 \log_{10} \left(\frac{z_{vh}}{z_{hh}} \right) = Z_{vh} - Z_{hh} \quad (\text{dB}) \quad (30.45)$$

and is, thus, negative by definition. LDR depends on the shape, orientation, and fall behavior of particles and is, therefore, used to identify particles that are rotated against the plane of polarization, e.g., the melting layer (*bright band*) or wet hail/graupel, tumbling asymmetric melting particles exhibiting high copolar and cross-polar reflectivities, as well as ground clutter and non-met echoes. LDR may be calculated from filtered or unfiltered reflectivities and must be calibrated for any offsets, usually by pointing at the sun. LDR cannot be measured under the hybrid (STAR) setup as no cross-polar channel is available.

Under a circular polarization base transmitting, say, lefthanded circular (LHC) and receiving both LHC (copolar) and RHC (cross polar), the *circular depolarization ratio* is defined as

$$\text{CDR}_{rl} = 10 \log_{10} \left(\frac{z_{rl}}{z_{ll}} \right) = Z_{rl} - Z_{ll} \quad (\text{dB}). \quad (30.46)$$

Compared to ZDR and LDR, CDR can be measured more easily and depends only weakly on the orientation of scatterers. CDR is mainly conducive of their shape and phase composition and is, therefore, used to study ice microphysics and hail size. On the other hand, CDR is prone to corruption due to differential attenuation and phase shift to a degree of turning positive, particularly behind strong precipitation [30.40].

Both LDR and CDR tend to $-\infty$ for spheres, but very low values are limited by the radar overall crosstalk, mainly caused by the antenna assembly including the feed. As depolarization will also occur in forward scattering, the polarization purity of the incident wave may be affected when passing through a depolarizing medium.

Copolar Cross Correlation RHOHV. The copolar cross correlation is the correlation between the copolar complex time series, usually horizontal $A_{hh,i}$ and vertical $A_{vv,i}$, or between the corresponding elements of the backscattering matrix \mathbf{S} . Its absolute value at lag zero is designed RHOHV,

$$\begin{aligned} \text{RHOHV} &= |\rho_{hv}(0)|, \\ \rho_{hv}(0) &= \frac{\sum S_{vv} S_{hh}^*}{\sqrt{\sum S_{vv}^2 \sum S_{hh}^2}} = |\rho_{hv}(0)| \exp j\delta. \end{aligned} \quad (30.47)$$

RHOHV is very close to 1 (e.g., 0.99) with spherical and uniformly falling particles and decreases in unevenly falling nonspherical particles, such as hail, graupel, or melting snow. Clutter may be expected to the range below 0.6. RHOHV is, therefore, used to discriminate between different hydrometeors. Figure 30.10 shows an example of a *bright band*. As RHOHV is phase sensitive, it is best calculated from the unfiltered time series to avoid filter phase errors. The phase angle δ in (30.47) is the differential backscattering phase. In the absence of propagation effects it describes the phase change upon (non-Rayleigh) scattering.

If the full polarization measurement is available, or if the radar is in LDR mode, the cocrosspolar cross correlation coefficient RHOH (or RHOV, if V is transmitted) may be computed similarly to RHOHV, even

though these correlations have so far rarely been used in routine operation. For example,

$$\text{RHOH} = |\rho_h(0)|, \quad \rho_h(0) = \frac{\sum S_{vh} S_{hh}^*}{\sqrt{\sum S_{vh}^2 \sum S_{hh}^2}}. \quad (30.48)$$

Differential Phase PHIDP. While all of the above observables describe target properties within the respective range bin, there are a number of cumulative parameters representative of the two-way propagation path. For example, oblate and prolate raindrops lead to different attenuations of the H and V polarized waves. This is called *differential attenuation* but cannot be measured directly using a monostatic radar. Also, the microwaves experience a phase shift on their way through the atmosphere, which may be different for H and V waves [30.41]. The differential phase PHIDP is the integral (cumulative with range) two-way phase shift between H and V returns measured in units of deg or rad, including the intrinsic differential propagation phase φ_{DP} , the differential backscattering phase, and any measurement errors

$$\text{PHIDP} = \Phi_{hh} - \Phi_{vv}. \quad (30.49)$$

PHIDP can be calculated from the hybrid or from the alternating mode. It is usually smoothed over some distance and must be corrected for system offset $\text{PHIDP}_{\text{offset}}$, mainly introduced by different H and V path lengths.

PHIDP is a reliable indicator of oblate or prolate scatterers and, therefore, of heavy rain with large drops,

as large drops are increasingly oblate. Intuitively, the horizontally polarized wave travels slower than the V component. PHIDP is a monotonically increasing function of range in rain and finds a major application in rainfall attenuation correction (Sect. 30.6.3). Also, PHIDP of meteorological echoes exhibits a smooth structure, whereas clutter or clear air echoes show a noisy pattern. This feature is commonly used to separate clutter and weather echoes.

The one-way local slope (range derivative) of PHIDP is called the *specific differential propagation phase*

$$\text{KDP} = \frac{1}{2} \frac{d\text{PHIDP}}{dr}, \quad (30.50)$$

and describes the differential phase shift per unit range, and as such may be very susceptible to the noisiness of PHIDP. Measures have to be taken to smooth, unfold, and interpolate PHIDP. Practically, it must be calculated as a difference quotient over a certain range, e.g., $\Delta r = 5$ (or 10) km to smooth PHIDP. Its unit is deg km^{-1} or rad km^{-1} with typical values of $0\text{--}8^\circ \text{ km}^{-1}$ in rain (in the C-band). KDP is a function of target size, shape, and orientation. Statistically isotropic (randomly oriented) targets result in $\text{KDP} \approx 0$. KDP is positive (negative) for oblate (prolate) targets, e.g., large raindrops (conical graupel). Any system phase offset cancels in KDP and it does not depend on calibration and transmit power errors or beam blockage errors. KDP is used to parameterize rain-rate relations (Sect. 30.8.3) and to correct for attenuation effects (Sect. 30.6.3). All differential polarization parameters LDR, CDR, PHIDP, and KDP are immune to errors in absolute calibration.

30.4 Radar Systems

As was mentioned above, most radars, particularly pulse radars, measure the return time of the echo as well as the antenna pointing direction in order to locate a target. A weather radar additionally measures at least echo intensity (reflectivity factor Z).

Doppler radar offers additional phase measurement; this calls for coherency. Depending on the transmitter type (see Sect. 30.4.1), the system may be fully coherent (e.g., klystron, travelling wave tube (TWT), solid-state power amplifier) or coherent on receive (magnetron). In an analog receiver (Sect. 30.4.3), coherency cannot be achieved in the logarithmic channel LOG, because the logarithm introduces phase distortions. This is why an additional linear channel LIN is needed.

A dual-pol radar is able to discern at least two orthogonal polarizations on reception, and it may be able to transmit two different (orthogonal) polarization states. Polarization diversity refers to the measurement of polarization variables at fixed transmit polarization, while polarization agility means a radar's ability to change the transmitted polarization state on a pulse-to-pulse basis. Dual-polarization, thus, adds differences and correlations between at least two polarization states. Weather radars may, therefore, be classified to be intensity-only (classical, conventional), Doppler, and multiparameter (dual-pol, dual-frequency). Most principles, components, and features used in a classical radar are also used in the more complex ones and are well described in the standard tutorials, e.g., [30.42] or [30.43].

Dual-frequency radars are too rare to be treated in extenso here, suffice it to point out that two transmitters are needed as well as matched receivers, and two antennas either collocated side by side, or the smaller one (X-band) inset into the larger one (S-band) (as e.g., MRL5, [30.21]).

The introductory remarks to Sect. 30.3.3 define some of the main components of a radar, most of which are represented in more detail in Fig. 30.5. A transmitter creates the high-power microwave waveform that is radiated into the atmosphere by the antenna. The antenna movement and position are controlled by the servo. Usually a weather radar is monostatic in that it uses the same antenna to collect the energy backscattered by the target. This is why a duplexer switches the antenna to the transmitter or to the receiver, accordingly. During transmit, the duplexer in conjunction with the T/R-limiter protects the receiver from the high-power transmit pulse. The received energy is amplified and sent to a superheterodyne receiver, as is common at radio frequencies to demodulate the high frequency. The receiver output signal is digitized and fed to a digital signal processor, DSP. The DSP calculates the parameters of interest and outputs them to a realtime display and to the host computer.

The host computer calculates special radar products and/or distributes the data and status messages via an external network. Via an internal network and the radar control unit RCU, it is also in control of the whole radar, including servo, DSP, and BITE. This is the built-in test equipment capable of automatically checking most radar components and supplementary devices. In the case of power failure, computer, and sometimes even transmitter, operation is temporarily maintained by an uninterruptible power supply UPS and possibly by an emergency generator.

30.4.1 Transmitters

The transmitter (TX) consists of either a high-power oscillator like a magnetron or a power amplifier, such as a klystron, a travelling wave tube (TWT), or a solid-state power amplifier (SSPA). Oscillator and amplifier tubes need a high voltage supply. High-voltage components are enclosed in a safe enclosure called a hotbox. Key parameters of the transmitter are efficiency, peak power, pulse length(s) PW, duty cycle (maximum PRF depending on PW), coherency, (phase) noise, long time stability, and maintainability, and size/weight may be an issue in mobile radars.

Power Amplifiers

Klystrons, TWT, and SSPA are high-power amplifiers magnifying precision low-power signals that contain

the desired waveform (frequency, phase, PRF, pulse coding . . .), e.g., supplied by the DSP. Therefore, radars applying power amplifiers inherently turn out to be coherent.

Klystrons are efficient and stable. Their size and weight and their need for high voltage (around 90 kV) usually do not pose a problem in ground-based systems. The klystron bandwidth increases with output power, while the TWT bandwidth decreases. Amplifier tubes are rugged and tolerant towards heat, overpower, antenna mismatch, and the environment.

Solid-state power amplifiers consist of many low-power amplifier modules. Even if a few elements fail, the transmitter as a whole continues working. Redundant elements increase the failure resistance and render entire backup transmitters (as with the US terminal Doppler weather radar, TDWR) unnecessary. SSPA offer high reliability and a long life (millions of hours) and are easy to maintain; modules are sometimes hot swappable. They dispense with a high-voltage power supply, thus decreasing noise and increasing safety. Their efficiency is even better than that of tube transmitters.

With the advent of GaN monolithic microwave-integrated circuits (MMICs) capable of 100 W each, the limited peak power of early (GaAs) SSPA is no longer a real issue. SSPA with 12 kW peak power are available, which achieve a sensitivity comparable to a conventional 500 kW magnetron transmitter. As solid-state modules feature low peak power, they are well suited for flexible waveforms of long pulses (pulse compression). Long (e.g., 64 μ s), low-power frequency or phase-coded waveforms are transmitted to obtain independent samples, and both the required sensitivity and range resolution. SSPA are still costly, but radars with solid-state transmitters are already being operated at X and C-bands.

Solid-state amplifier modules feature a relatively wide bandwidth and easily lend themselves to frequency agility, as well as to being arranged in an active array permitting electronic beam steering.

Magnetrons

The magnetron is a high-power self-oscillator that bursts into free oscillation with an unpredictable phase each time high voltage is applied. Its pulses are, therefore, not coherent, but may be cohered-on-receive (COR, Sect. 30.4.3). Active pulse coding is not feasible. A changing thermal regime, external or due to a changing load, primarily after a cold start, causes a frequency drift in a magnetron. Its waveform is not flexible and must be provided by a modulator.

The classical modulator consists of a pulse forming network (PFN) and a thyratron. The PFN consists of at least one set of condensers and coils immersed in oil for

high-voltage isolation that buffer energy and, thus, define the pulse width. If there are several sets for several pulse widths, they must be de-energized for switching, which takes a couple of seconds. The thyatron is a high-voltage switch that is sparked by the system trigger. Once the thyatron opens, it cannot be closed until the charge buffered in the PFN has completely discharged into a transformer that provides the necessary high-voltage pulse (25–40 kV) to the magnetron.

A more recent type of modulator is the solid-state modulator (SSM) based on field-effect transistors (FET) or insulated gate bipolar transistors (IGBT). The storage capacitors of an IGBT SSM are charged at ca. 800 V. When triggered, a one-shot oscillator gates the IGBT switch array, which, in turn, enables discharge of the capacitor energy into a pulse transformer, similarly to a thyatron, and the magnetron fires. The resulting pulse characteristics are, thus, defined by the modulator setting and the tuning of the magnetron.

More Devices in the Transmit Path

To transport the high-power high-frequency pulse from the transmitter to the antenna using a *thick cable* will not do. Due to the skin effect, all energy is transported in a thin surface layer (the *skin*) of the conductor. The skin becomes thinner, as the effect becomes more pronounced with higher frequency. No energy would be transported in the center of such cable at microwave frequencies. That is why only a conducting skin is needed and is built in the form of a hollow, often rectangular tube, called *waveguide*. The cross dimension of a waveguide is in the order of the wavelength.

The wave guide must be dehydrated in order to avoid arcing. Electrically, the wave guide must be impedance matched so that no energy is reflected back. This is achieved using a *double-stub tuner* to minimize the voltage standing wave ratio (VSWR), which is usually checked by RF sensors measuring the transmitted and reflected pulse powers at the *bidirectional coupler's* forward and reverse ports. VSWR should be close to 1. Usually, waveguide RF harmonic and bandpass filters will be necessary to suppress out of band transmission.

The transmit RF pulse is routed to the antenna through azimuth and elevation *rotary joints*. In a monostatic system, the *duplexer* or transmit–receive switch alternately switches the antenna onto transmitter or receiver. While formerly branched or balanced duplexers, nowadays mostly ferrite circulators are in use. They feature insertion losses of ≈ 0.3 dB and isolation of ≈ 20 dB.

In the case of a dual-pol radar, there may be two transmitters, or the transmit pulse may be split by a *power divider* in the transmitter cabinet. In this case, there are two circulators in the cabinet, two waveguides and dou-

ble rotary joints for azimuth and elevation in the pedestal, one for each polarization channel, and the received signal comes back the same way. The preferred setup, however, is to route the RF through single azimuth and elevation rotary joints to the antenna, as in a single-polarization radar. The power divider or ferrite switch and two circulators are then placed on the antenna. There may also be a *waveguide switch* to bypass the power divider and transmit only H (or rarely V) to enable measurement of the cross-polar component of the return signal in order to calculate LDR. As there is only one waveguide below the power divider in this case, the dual-pol receiver must be placed on the antenna as well. This configuration is called antenna-mounted receiver (AMR) or receiver-over-elevation (gear) (ROE); a schematic is shown in Fig. 30.3. It features smaller waveguide losses, and there is no need for double rotary joints (for h, v) that might cause additional imbalance. However, air conditioning and maintenance may be more demanding than in the traditional setup.

30.4.2 Antenna, Pedestal, and Radome

The antenna facilitates radiation transition from waveguide to free space or vice versa. In weather radar, reflector antennas are the most common, consisting of a parabolic *dish* with a feed in its focus. If applicable, a four-port orthomode transducer (OMT) serves as a polarization duplexer, combining orthogonal polarizations h, v for transmission through one feed. Weather radar antennas are highly focussed into a main beam (*pencil beam*) in order to facilitate high resolution sampling of the atmosphere. In reality, there is no strictly bounded geometric beam, but a 3-D radiation pattern $P(\theta, \varphi)$ (W sr^{-1}) and a normalized pattern: $P_{\text{norm}}(\theta, \varphi) = P(\theta, \varphi)P_{\text{max}}^{-1}(\theta = 0, \varphi = 0)$ that resembles the (Mie) scattering function of a scattering sphere and indicates the antenna sensitivity in every direction in space. The integral over all angles θ, φ is the total radiated power P_{tot} . As can be seen from Fig. 30.4, this pattern shows a strong forward lobe that is considered Gaussian and is taken to represent the radar beam, which is most often defined in terms of the half-power beam width (HPBW), i.e., within the -3 dB points off maximum, and is typically of the order of 1° . The first minima occur around 2.5° on both sides and define the first null beam width (FNBW), while sidelobes should be down 40 dB from the main beam maximum. The feed design is critical to sidelobe performance and polarization purity. Sidelobes are also affected by the strut design (Fig. 30.4), as center-fed antennas require struts to keep the feed in focus.

$P_{\text{max}}(\theta = 0, \varphi = 0)$ relative to isotropic radiation $P_{\text{tot}}/(4\pi)$ is the antenna gain G usually expressed in

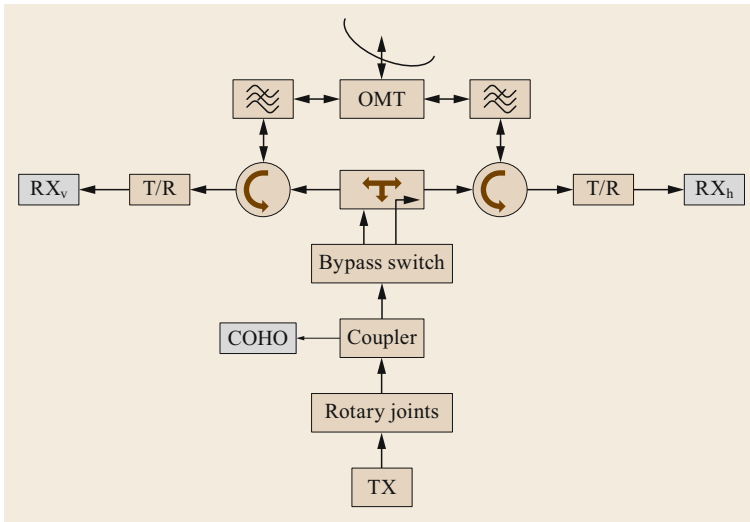


Fig. 30.3 Transmitter schematics with transmitter (TX), splitter, circulators, and antenna with orthomode transducer (OMT) in a dual-pol hybrid mode setup with an antenna-mounted receiver. Receivers (RX_h, RX_v) are also indicated (image © J. Seltmann, used with permission)

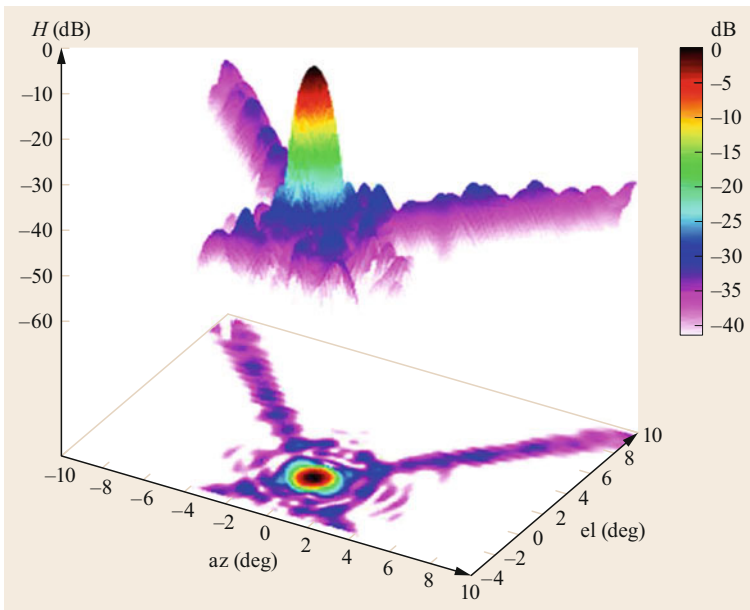


Fig. 30.4 Detail from measured 3-D antenna diagram showing the main lobe and part of the side lobes. Sidelobe deterioration due to feed supports is clearly visible (*diagonals*). Image © M. Frech, DWD, modified from [30.44]

logarithmic units of dBi (Table 30.6) and is used in the radar equation (30.8). Gain values of 40–45 dBi are common in weather radar. Antenna gain, beam width, and the number of sidelobes depend on the ratio of antenna diameter D to wavelength λ , so that larger and more expensive antennas are needed for higher resolution (smaller beam width) and for higher wavelengths. As a rule of thumb, the beam width BW (rad) is

$$BW = 1.22 \frac{\lambda}{D}. \quad (30.51)$$

Weather radar antennas used to be parabolic dishes, which may be center or offset fed or of some special

design, such as the Cassegrain or Gregory type. Early antenna dishes used to be deep-drawn from solid metal, then cut for transport, and flanged for reassembly. Nowadays, paraboloids consist of compound materials, such as carbon graphite. Larger antennas are sometimes made from metal grids.

Phased array antennas, although they have been in military use since WW II and have been under testing in research weather radar for a while, have long been deemed an investment that does not pay in weather radar [30.36] and are only recently being reconsidered as an option for (operational) weather radar to answer the increased demand for rapid scanning. Further

research is needed in order to achieve the same performance as a standard radar using a parabolic dish. While earlier issues of power and focusing seem to have been solved, 360° round view and polarization purity, beam shaping, and sidelobe control pose the major challenges presently. Multiple beam designs so far suffer from insufficient beam isolation and sensitivity. Electronically steerable antennas may also help suppress antenna sidelobes [30.45]. Antenna characteristics are decisive for the overall performance of a system and have to be carefully specified (Sect. 30.5), particularly in a dual polarization radar.

The antenna is mounted on a *pedestal* and should be well balanced by counterweights and have its balance point close to the axes in order to keep accelerating moments low. High-precision servo amplifiers, motors, and gears are required to rotate and position the antenna in azimuth and elevation. The motion must be appropriately damped to avoid oscillating overshooting on the one hand, as well as asymptotic positioning on the other hand. Lubrication (depending on wear) must be supplied manually or by an automated pumping system. There should be hardware and software breakers to limit elevation e.g., at 0° or -2° and possibly at 90° (depending on the design). The actual antenna position is read by angle encoders (*syncros*). If safety sector blanking (TX is turned off for safety reasons) is required, encoders must be safety approved (fault-tolerant and redundant). The pedestal must be stable and level (this should be specified); inclinometers and a vibration sensor may be provided to check that the pedestal is upright.

Waveguides have to be routed through the stationary pedestal, the rotating azimuth gear, and the up-and-down swinging elevation gear to the antenna dish. This is effected by special *rotary joints*, which must exhibit isotropy, low insertion loss (< 0.1 dB), and low VSWR. Depending on the receiver/DSP setup, it may include a (fiber) optical data channel using an optical rotary joint. The azimuth rotary joint is usually supplemented by a slip ring to transfer power supply and signals. Rotating parts must exhibit isotropic characteristics (not a function of direction); isotropy should also be specified.

With most operational weather radars, the antenna and any collocated system parts (e.g., an antenna-mounted receiver) are protected from severe environmental conditions by a *radome*, mainly to alleviate the wind load (deformation). The radome is usually a self-supporting or air-inflated geodesic sphere panelized for ease of transport. However, due to absorption and anisotropy, the radome interferes with the antenna radiation [30.46]. Particularly with dual polarization, identical RF performance for both horizontal

and vertical polarizations is essential. Therefore, special construction types (“orange peel”, quasi random, ...) made of sandwich panels with hydrophobic coatings as well as electrically seamless, impedance-matched *stealth* radomes are offered by manufacturers. To reduce snow load and icing and absorption thereby, and to climatize AMR, the radome interior may be heated.

30.4.3 Receivers

The radio frequency (RF) signal (*echo*) received by the antenna is coupled into the waveguide(s) by the antenna feed (separately for H and V, in the case of a dual-pol radar). It is then circulated (Sect. 30.4.1) to the receiving channel(s) and coupled out (usually by a waveguide to a type *N* adaptor) after passing the T/R limiter (see below).

Classically, the receiver used to be mounted in a receiver cabinet (e.g., 19" rack) next to the transmitter cabinet, way down from the antenna tower. As a consequence, the RF signal had to pass waveguides and rotary joints twice. In the wake of miniaturization and digitalization, antenna-mounted receivers (AMR, also called receiver over elevation (gear), ROE) have become a preferred setup.

During transmit time, the duplexer protects the sensitive receiver from the high-power burst pulse. Its isolation of ca. 20 dB is, however, by far not sufficient, and further receiver protection is needed, also against damaging high power by way of duplexer failure, mismatch of VSWR, abnormal operation (arcing), or external transmitters. *Receiver protectors* (RP) need to feature minimum insertion loss (e.g., 0.3 dB) and a maximum receive power (lower protection limit) around 10 dBm, and low waveform distortion. They may be active switches (e.g., all solid state), or passive, self-activating (T/R tubes). While each one has its own advantages and disadvantages, a T/R tube is often the optimum overall tradeoff, as it is robust and protective even out of band or under radar failure. This is why T/R limiters are the preferred choice in weather radar.

Superheterodyne Receivers

A radar receiver, much as any current radio receiver, is a superheterodyne receiver that provides high sensitivity and frequency selectivity and easily meets nearly all performance requirements. After passing an initial low-noise amplifier (LNA) and an RF bandpass filter, the incoming RF is downconverted by multiplicative mixing with the signal of an internal high-frequency oscillator (called stable local oscillator (STALO)) that keeps a constant difference from the transmitter frequency. The mixing product of received RF and STALO frequencies contains the sum and difference and higher-

order frequencies and is, therefore, filtered to keep only the difference frequency, which serves as an intermediate frequency (IF, often 30 or 60 MHz in a radar) and contains all necessary information but is much easier to process than RF. In a dual-pol system, the STALO signal is split to mix independently with the incoming H and V RF signals.

The STALO must exhibit low noise, low phase noise, and high stability, as it sets the reference frequency. Current STALOs will consist of a quartz oscillator and a digital synthesizer. Downconverters are also designed to suppress the image frequency (image rejection mixers; the image frequency is the RF mirrored by the STALO frequency so that incoming signals at image frequency are downconverted to the same IF).

Because in a magnetron system frequency keeps drifting depending on the duty cycle, the transmitter burst pulse is sampled and fed to an automatic frequency control (AFC) controlling the STALO to keep the IF stable. The AFC may be analog (typically via SMA) or digital (typically via RS-232) and may be hard to set manually. AFC is not necessary in a klystron system. Furthermore, shifting the STALO frequency by AFC introduces small phase errors, so that a magnetron radar's coherency is slightly inferior to that of a klystron or solid-state transmitter.

So far, this has to be analog technology, even today. Depending on the type of radar, the following stages may be digital or analog. In both cases, the receiver setup depends on the type of radar (intensity-only, Doppler, dual polarization/dual frequency) and on the type of transmitter (fully coherent or not).

Coherent Receivers

In a classical, non-Doppler weather radar only the echo intensity z is measured, the phase information is lost. A Doppler radar needs to keep track of the transmitted and echo phases in addition to the amplitude. In a fully coherent (amplifying, e.g., klystron) system, the transmit phase is a-priori known because it is coupled to the injected small signal (e.g., from STALO). It is either constant or actively modulated and may, thus, be used for a phase reference.

A magnetron, however, is a free oscillator, and the phase of each burst pulse must be measured in order to later correct (cohere) the echo phase. This is sometimes called *coherent on receive* (COR). To this end, in an analog COR system, the phase of an appropriately attenuated RF burst sample is also downconverted to IF and injected into another, highly coherent oscillator (COHO) that is phaselocked to the current pulse over its echo return time and started anew with the next burst pulse. This reference phase is routed to the quadrature detector together with the amplified echo IF.

Analog and Digital Receivers

With the advent of fast processors and analog digital converters (ADC) with a wide dynamic range, digitization has extended far into the formerly all-analog receiver.

Dynamic Range. The dynamic range of radar signals is tremendous: 12 orders of reflectivity magnitude are easily obtained for realistic drop size ranges, plus 5 orders for range dependence (recall that $P_r \approx D^6 r^{-2}$, Sect. 30.3.1). As it is difficult to build a linear receiver with that large a dynamic range, a logarithmic analog receiver (LOG) is used instead, which, however, introduces phase distortions. Therefore, there needs to be an additional linear receiver (LIN) in an analog Doppler radar.

The dynamic range of a digital receiver is largely determined by the ADC's number of bits, as the least significant (LSB) and the highest bits set the low and high limits of the converter range. One additional bit increases the voltage range by a factor of 2 and the power range by a factor of 4 (6 dB). Currently, 16-bit high-speed IFD are standard. An ideal 16-bit (12-bit) ADC yields a dynamic range of 98 dB (74 dB). As this is not quite sufficient in radar application, the dynamic range of each channel may be extended in current digital receivers by splitting the input signal and using two or more ADCs with different attenuation in parallel. This is sometimes called *stacked ADC* architecture.

Analog Receivers. In an analog receiver, the signal is first passed to a filter that is optimally adapted to the transmitted waveform and, thus, maximizes the signal-to-noise ratio. For a simple rectangular pulse of length τ , this is a bandpass filter of band width $B = \tau^{-1}$. There have to be several physical filter banks if there are several pulse widths. Depending on the type of radar, the resulting narrowband IF is then fed into a logarithmic (LOG) amplifier (in an intensity-only radar) or split into a LOG and a linear (LIN) channel (in a Doppler-radar). The LIN channel provides true-phase signals for Doppler processing and must, therefore, maintain symmetry in both amplitude and phase over a certain limited range (e.g., 30–40 dB). In order to keep the current signal within this linear range, a gain control is needed, which may be based on range time (sensitivity time control, STC), the intensity of the previous batch/ray (automatic gain control, AGC), or on the instantaneous power (instantaneous AGC, IAGC) and must not distort amplitude or phase characteristics. The IF is then input to a quadrature detector, which is additionally fed the COHO reference phase and its replica shifted by 90° to produce the I and Q signals (30.23). In a fully coherent (klystron) system, this is the signal of a coher-

ent oscillator (COHO), the same one that is amplified by the klystron. In an analog COR (magnetron) system, the COHO is phase locked to every single transmitted pulse using the analog burst sample. This phase locking and its stability is a limiting factor in COR systems. While in an analog magnetron system the burst phase is thus corrected for, its value is not known. In a digital receiver, the phase is measured digitally and stored for further advanced processing (Sect. 30.6.3).

Digital Receivers. In a digital receiver, the echo phase (and amplitude) is directly digitally sampled from the echo IF and corrected for the transmitted phase. The burst IF is sampled as well in order to determine the transmit power and PW, and its phase is used to digitally cohere the incoming radar signal in a digital COR system. Unlike with an analog COHO, it is easy to digitally store the transmit phase over several pulses and cohere to or correct for previous pulses (multiple-trip echoes, Sect. 30.6.3.).

In a digital receiver, most analog IF components (such as matched bandpass filters, COHO, LOG and LIN amplifiers, including AGC, quadrature phase detector, and analog AFC) are redundant or replaced by controllable digital modules: IF bandpass, IQ calculation, measurement of and correction for transmitter phase and amplitude (the latter was not feasible earlier), and measurement of burst frequency and output for AFC of STALO. Essentially, a digital receiver needs only STALO and downconverters, and, in the case of a magnetron, AFC. After downconversion, the IF is directly digitized. This also renders maintenance simpler, as there are fewer spare parts, which in addition are easy to replace. Also, a digital receiver is well suited to transform an intensity-only radar into a Doppler radar, possibly even with some dual-pol functionality.

The IF digitizers (IFD) are located exactly where there are the LOG (and LIN) amplifiers in an analog radar, traditionally in the receiver cabinet under the antenna or on the back of the antenna dish in an antenna-mounted receiver AMR. The IFD ingests analog IF (typically 30 or 60 MHz) and outputs digital I/Q data.

There are one or two IFDs for one or two polarizations and, in the case of a magnetron transmitter, also for the burst sample. The IFDs usually come with the signal processor (DSP) due to their tight internal connection, while hooking the IFDs to an analog signal of adequate power level is pretty simple. IFDs connect to DSP (in a narrow sense) via a fiber optics link that allows for about 100m distance if routed through an optical rotary joint. However, an antenna-mounted receiver greatly facilitates the connection between IFDs and DSP, even though there are systems that bring the waveguide (H, or both H and V) down the rotary joints.

While an analog LIN receiver hardly exceeds a dynamic range of 40dB and depends on sensitive bias control (AGC), present-day digital linear receivers feature almost the same dynamic range as earlier analog logarithmic receivers without sensitive circuitry. In an analog receiver, the signal IF must be switched to the appropriately matched filter depending on the pulse width, while in a digital receiver, the corresponding filters may be digitally controlled. The matched filter is realized digitally either in the IFD or in the DSP, e.g., as a decimating complex digital FIR filter. The digital phase lock provides a better coherency as a function of range than an analog COHO, thus enabling distant second-trip handling.

A digital receiver is stable, robust, and long-lived and provides monitoring and control algorithms (e.g., COHO and burst-sample gate adjustment) that improve overall performance, which, together with simpler troubleshooting and replacement, provide better maintainability and availability compared to an analog receiver.

30.4.4 Signal Processing

Signal processing in radar refers to the creation and processing of the scalar (X_i) or complex time series (A_i) in order to calculate certain observables (moments) for each range bin. This is performed by the digital signal processor DSP, the main steps being:

- Data ingest and filtering.
- Processing of X_i and/or A_i time series for each raw range bin. Time (= azimuthally) averaged power \bar{X} and/or lag 0, 1, and 2 autocorrelations both Doppler filtered and unfiltered for each polarization, as well as cross correlations are obtained and range averaged. Full spectra may also be calculated and output.
- Calculation of observables or *moments* (Sect. 30.3.4) from (averaged) correlations and subsequent quality screening by thresholding.
- Conversion of all data to the required output format, e.g., 8 bit or 16 bit integer or 32 bit float, and output to the radar host computer.

In a wider sense, the DSP also performs a couple of auxiliary processes: The DSP usually provides the radar master clock, trigger and several slave triggers, pulse width switch, AFC and possibly AGC, signal output to klystron, depending on the radar system. Modern DSPs are even capable of direct digital waveform synthesis (DDS) with frequency or phase pulse modulation for digital output to state-of-the-art transmitters. All configuration parameters necessary to the DSP are uploaded from the radar host computer.

Digital weather radar signal processors may be proprietary but there is a clear tendency worldwide towards open source (Linux-based) systems. Algorithms are pipelined and lend themselves to parallel bin processing allowing near-realtime performance on a nonrealtime operating system.

Data Ingest

The DSP is hooked to the radar receiver output channels and ingests its data in a first step. Depending on the receiver type, the LOG, I , and Q video channels of the analog LOG and LIN receivers are acquired and digitized and sampled into range gates, or the digitized IF of a digital receiver is acquired, separately for H and V, in a dual-pol radar.

In this case, the DSP receives digitized (sampled) IF data together with the necessary meta data, such as antenna position (azimuth and elevation), angle syncing flag, sampled burst IF, AFC status, etc. for each pulse.

A modern DSP receives and digitally bandpass filters (e.g., by an FIR-matched filter) the IF time series if this has not been performed in the IFD already. The digital matched filter must be adapted to the pulse width and may usually be designed interactively by a skillful user. Time samples are then assigned to the correct range gates (raw bins). For each raw range bin, the appropriate number of pulse returns is stored, forming the time series X_i or $A_i = A_i^{\text{raw}} - \bar{A}_{\text{noise}} = I_i + jQ_i$ after noise subtraction to give the time-series zero mean. The appropriate number of pulses in each range bin is determined according to an angle syncing flag set for each pulse if either the required number of pulses has been collected (e.g., 32 or 1024 pulses) or a synchronizing condition has been met. A common syncing condition is the dynamic angle syncing DAS, synchronizing on the antenna position, usually spaced every 1° . From the digital receiver of a COR system, the DSP also receives the magnetron burst sample IF signal. Data acquisition needs to take place in near realtime in order to avoid losses. Sometimes the I/Q data stream may be tapped via a high-speed connection for storage or third-party processing.

Pulse Processing

In a second step, range-gate-based time series are processed in the time or frequency domains including Doppler or statistical filtering, possibly staggered PRT, and multiple-trip handling (Sect. 30.6.3), to obtain spectra or, commonly, autocorrelations. As this is performed on each individual raw range bin, the range index is usually dropped.

Realtime pulse processing for thousands of range bins is computationally demanding, even today. Whereas accumulation of T_0 , R_0 , R_1 , and R_2 can be

performed while collecting the pulses, DFT/FFT processing needs to wait for a time series (batch) to be complete.

Log Processing. The analog signal of an intensity-only logarithmic receiver is digitized by the DSP. In order to perform any linear processing, such as adding and averaging, the A/D log power readings P_i of a single pulse i must be linearized according to

$$X_i = 10^{\frac{SP_i}{10}}, \quad (30.52)$$

where S is the slope of the calibration curve, and relogarithmized for calibration and output. Unlike a Doppler measurement, the LOG time series is real, not complex, because no phase is retained. Therefore, LOG processing takes place in the time domain. The time series is then split: one branch is highpass filtered (Sect. 30.6.3), while the other one is not. The filtered, as well as the unfiltered, scalar amplitudes X_i^f and X_i are each squared and time averaged, yielding the filtered and unfiltered power estimates \bar{X}^f and \bar{X} .

The measured noise \bar{X}_N is subtracted, and the result quality checked against the (linearized) noise threshold. Any bias (X_{offset}) is then corrected, and the result is applied as P_r in (30.27), so that

$$Z_c = 10 \log_{10}(\bar{X} - \bar{X}_N) - 10 \log_{10}(X_{\text{offset}}) + Z_0 + 20 \log_{10}(r) + ar + \text{CCOR}. \quad (30.53)$$

Doppler Processing. Pulse processing of a coherent time series A_i may take place in the time or frequency domains, or both, in order to extract the correlation and spectral moments described in Sects. 30.3.2 and 30.3.4. Prior to this, some special processing and corrections (Sect. 30.6.3) must also be performed at this stage if selected, viz. pulse compression, second-trip and staggered PRT velocity unfoldings, and clutter filtering.

Burst Sample Processing: In a digital COR (magnetron) system, the DSP also receives and analyzes IF samples of the magnetron burst. The burst amplitude is used in order to monitor and automatically correct pulse-to-pulse power variability. The burst phase is applied to cohere the echo phase for coherent processing.

This phase correction may be performed to an accuracy of about 1° independently of range (while an analog COHO tends to drift with range time). The difference between burst sample and STALO frequencies is calculated, D/A-converted if necessary, and uplinked via IFD to control the STALO/AFC. In a fully coherent (klystron) system, the DSP commonly provides the waveform (pulse width, frequency/phase control) that is input to the power amplifier.

Pulse-pair Processing (PPP): time-domain processing calculates the desired lags of the complex autocorrelation following its definition (30.24), adding up complex products of (conjugate complex) amplitudes of the current pulse i with the complex amplitude of the same ($l = 0$), the previous ($l = 1$), or the antepenultimate ($l = 2$) pulse. Consequently, for each moment, only one pair of pulses has to be kept in memory at any time; hence the name of pulse-pair processing (PPP). With PPP, the accumulation of T_0 , R_0 , R_1 , and R_2 can be efficiently performed while collecting the pulses.

Fourier Transform Processing: frequency-domain processing is launched by Fourier transforming the A_i time series into the corresponding Doppler spectrum for each raw range bin. A discrete Fourier transform (DFT) or a fast Fourier transform (FFT; forcing a power of two number of pulses for computational efficiency) may be applied.

After clutter filtering and second-trip processing in the frequency domain, the spectra are commonly retransformed to the time domain for ease of pulse-pair autocorrelation processing.

Pulse Compression. Range resolution and/or sensitivity may be increased by transmitting wideband waveforms to boost the time-bandwidth product τB using pulse compression. For example, in linear intrapulse frequency modulation between low and high frequencies f_1 and f_2 , $B = \Delta f = f_2 - f_1$. Frequency changes may also be digitally coded (Barker, Costas, and Frank codes).

Bandwidth can also be increased using phase coding where a long pulse of duration τ is divided into N short subpulses (*chips*) of duration τ/N . The phase of each subpulse is set to either 0 or 180° (0 or π , + or -), following some binary phase code, such as a Barker code [30.47]. Phases may also be a multivalued function, e.g., of the SZ(8/64) code [30.48] designed to minimize range sidelobes; N defines the compression ratio. The new bandwidth will be $B = N\tau^{-1}$, the compressed pulse width $\tau N^{-1} = B^{-1}$, and the pulse energy increased N times. Thus, pulse compression benefits from the energy of a long pulse and the resolution of a short pulse at the same time.

Range Averaging. As a last substep, the correlation data is range sampled, if so required. The raw range bins (e.g., spaced every 25 m) are sampled or averaged to form larger output bins, e.g., 1 km long. The optional clutter microsuppression CMS (Sect. 30.6.3) is applied at this stage as well.

Moment Estimation

In a next step, physical moments as well as parameters of interest for QA/QC are calculated from the correla-

tions according to their definitions in Sect. 30.3.4. They are then usually passed to a correction stage including (Sect. 30.6.3) range and (both gas and precipitation) attenuation corrections, velocity unfolding by dual PRF, and spectral width correction. Some QC algorithms usually follow (Sect. 30.6.4), including thresholding and flagging for various interferences, and a speckle remover.

Data Output and Recording

The output of an operational DSP to the host computer consists of the calculated moments on a ray basis and is called preprocessed base data or level II data. For research purposes, data may be tapped for offline processing and storage as soon as they are digitized, even on the IF level (I/Q data). This may be useful to test new pulse-processing algorithms. Even Fourier spectra may be recorded and displayed. Some processors offer data output to a realtime display (time series, spectra, A-scope, etc.).

30.4.5 IT Structure

In the digital age, radar is no longer controlled by manual switches and cranks but by computers, and it delivers digital data to computers instead of analog signals to a cathode ray tube. In fact, a modern radar is largely a computer of its own, called the radar control unit RCU; its console is the closest one can get to control the radar manually.

Thus, radar operation may be attended by an operator or may be fully automatic and remote controlled even for a whole network. In continuous operation, the RCU is slave to a host computer that runs the radar control software. It stores all necessary data and parametrization in templates and sends them to the RCU according to a configurable scheduler.

Within the radar, many components and sensors are networked using IP addresses and optical, ethernet, USB, and wireless communications. Their data are fed to the BITE system (Sect. 30.4.6). The RCU also collects BITE and other internal messages and status information and passes them on to the host computer. The host distributes the data to the operator, a user help desk, or some archive, according to selectable severity levels. This greatly facilitates troubleshooting. The system can take predefined action automatically, e.g., restart certain processes or devices, or shutdown in case of emergency.

The host computer also collects the data produced by the DSP. Under normal operation, the DSP processes the bin-based I/Q time series and outputs processed rays of tagged *moments* (Sects. 30.3.4 and 30.4.4) over the appropriate range. The host computer ingests these rays and packs them into sweeps at a given elevation or

Table 30.10 Data rates at different stages of radar processing

Data stream	1980s: Analog Z-only radar	1990s: Analog Doppler radar	Present: Digital dual-pol radar
Bit resolution	8	8; 16	8; 16; 32 float
Number output moments	1	4	50
One ray (kB)	0.256	0.512	> 20
One sweep (kB)	92.160	368	3200
Sweeps per update interval	21	26	13
One volume (MB)	2	9.5	75
Volume update rate (min)	15	15	5
GB per day	0.185	0.912	21

at a fixed azimuth (PPI or RHI, Sect. 30.8.1) that are subsequently sent to product generation by either the host computer itself (nowadays often called *legacy* production) or by centralized processing.

All processing has to be performed in near real-time so that no incoming data is being lost. In internal processing, the number of available pulses N is determined by PRF, the azimuthal sampling resolution, and the antenna azimuth rate ω_{az} , e.g., 55 pulses at realistic values of 1° resolution, $\omega_{az} = 3$ rpm, and PRF = 1000 Hz. This number (maybe reduced by a few filter stabilizing pulses) is identical for each raw range bin. Depending on computing power, the DSP may perform pulse processing (Sect. 30.4.4) on a limited number of raw range bins, e.g., 2048 bins. Raw bin data are often averaged to e.g., 1 km, yielding output rays of 256 range bins at a range of 256 km. This range resolution has a large impact on data rate; increasing the output range resolution from 1 km to 250 m (50 m) increases the data rate by a factor of 4 (20). The number of output moments is another influential parameter that multiplies the data rate in proportion. While operational azimuth resolution is commonly 1° over one full revolution of 360° (one sweep), oversampling is possible and easily increases the data amount by a factor of 10. Lastly, the volume definition and update rate determine the number of sweeps with a recent tendency of faster update at the cost of fewer elevations.

Table 30.10 gives an example of the approximate data throughput for one single radar under operational conditions in the past and presently. Data may vary largely.

30.4.6 Auxiliary Components

There are a couple of auxiliary components and devices that are necessary to successfully operate and maintain a radar. A weather radar has a variety of monitoring and test devices that are jointly referred to as built-in test equipment (BITE). The BITE checks and measures around 250 system states and parameters such as voltages, currents, and temperatures that are collected by the RCU and forwarded to the host computer message

system. BITE messages are used to continuously monitor the radar state, to check the proper operation, and diagnose system failures.

Depending on the type of radar, more test and safety equipment is necessary or desirable to perform calibration and maintenance, such as power meters, attenuable and phase shiftable test signal generators, interface devices, spectrum and network analyzers, in addition to standard tool kits and user utilities. A test signal generator (TSG) is usually built into the radar and may be controlled through RS 232 for remote access or automated test procedures, even under operation.

For safety purposes, there is a system-wide interlock circuit including radome hatch and *hotbox* contactors to prevent radome or hotbox access under operation, as well as emergency switches and labels marking radioactivity and radiation according to regulations.

As a provision for the case of power failure, an uninterrupted power supply (UPS) is commonly provided to keep the system alive and accessible. At least computers are not to be switched off in an uncontrolled manner. Sometimes, the whole system, including the transmitter, may be run on UPS for a couple of minutes until an emergency generator engages or power returns.

Air conditioning is necessary for a couple of reasons: the transmitter needs to be cooled, and the receiver is to be kept at a stable (preferably low) temperature in order to avoid drift. This is true even under favorable climatic conditions. Often, the radome is also climatized to keep a snow cap and icing away and to create bearable working conditions.

30.4.7 Siting, Radar Infrastructure, and Regulations

An unfavorable radar site can create many and uncorrectable problems. An unobstructed view is one obvious condition that usually calls for an elevated position with no higher mountains situated nearby. Buildings, towers, bridges, and wind parks should be far enough away, which may be difficult to achieve in flat terrain. In a radar network, high areal coverage and near equal radar distances should be aimed for.

Infrastructure is another issue to be considered, as it must be able to accommodate the radar size, weight, and wind load and to provide the operating requirements and environmental conditions (temperature, humidity classes for normal, emergency, and stopped operation) defined by the radar manufacturer. What will be the necessary height and stability of the radar tower? Vibration under strong winds and tilting due to solar irradiation may become a problem. Accordingly, a concrete tower and/or guying may be considered. Safety considerations should be kept in mind as well, such as protection against falling ice and against vandalism. Is an escape exit mandatory?

A certain site development may be necessary. Must a road be built and maintained, or supply of telecommunications, power (e.g., 10 kW, 3×18 A, possibly UPS/generator), sanitary facilities, water, and sewerage? Can those requirements be met at the site under consideration, particularly if situated in a nature sanctuary or if the radar operator is not the land owner?

Laws on radio and telecommunications, safety, and construction will be applicable. What authorizations must be obtained under the operator's specific legislation? In Europe, a radar station must be compliant with the EC machinery directive and CE conformity, and national technical inspection certificates, local building regulations, and governmental priority regulations. As radar emits strong radiation, a radiation permit must be obtained from the respective authorities that limits transmit and out-of-band power and bandwidth, and sets safety distances and possibly certain angular sectors that must – safe against any failure – be blanked. Moreover, a radar usually contains radioactive substances (T/R limiter, Sect. 30.4.3), which must also be authorized and sometimes notified to local disaster management and firefighters. In addition, radars supplying data to air traffic require an EC test report with regard to the implementation of the European regulations on interoperability defined in regulation (EC) No. 549/2004, Article 2. The procurement process itself must comply with applicable laws. All permits granted, may citizens' initiatives overthrow radar construction plans?

Operators usually establish additional safety instructions of their own, e.g., decide on authorized staff or a two person rule. On the other hand, little-thought-of regulations may seriously degrade data quality (four lightning poles around the radar) and coverage (priority construction of obstacles) or even preclude deployment (frequency allocation).

The following list gives some specific regulations that apply in Germany:

- Location permit (Federal Emission Protection Law) by the Federal Radio Authority (BNetzA)

- Permit as per the Radiation Protection Regulation (StrlSchV)
- Permit according to the X-Ray Protection Regulation (RöV)
- Technical inspection certificates (TÜV)
- Lighting protection and potential equalization according to DIN V VDE 0185 or its equal
- Procurement regulation (UfAB).

30.4.8 Radar Networks

The main reason to combine individual weather radars to form a network is the complete coverage of a certain area, often a nation's whole territory. Most networks are, therefore, operated and their data shared by national or federal authorities, even though operation may be outsourced, or local networks may be operated by research groups and syndicates. NEXRAD data, although not completely covering the contiguous USA, is used by the US National Weather Service (NWS), Federal Aviation Administration (FAA), and the Department of Defense (DoD), the media, and private institutions.

A network may, depending on its density, mitigate some of the problems in single radars, such as data gaps due to radar maintenance and failure, incomplete elevation coverage including the *cone of silence*, beam blockage, beam elevation over the Earth surface and beam overshoot, cross-beam resolution increasing with range, or thresholding due to poor data quality. It, thus, enhances the detection of low-altitude and small-scale phenomena and facilitates object-based automated algorithms. Moreover, multiple overlap enables calculation of dual and multiple Doppler wind vectors (Sect. 30.8.3).

Functionally, the network may be considered to represent one measuring instrument with the individual radars as sensors sending their data to some central facility via telecommunication, preferably with guaranteed bandwidth, as timely transmission and data supply is crucial. The central facility collects and processes all the data in near real time and distributes them to users. It may also remotely control each radar sending predefined parameter templates. In a centralized network, it is easier to maintain data homogeneity using identical and well-documented scanning and processing. Data quality may automatically be assessed and error statistics derived by identical algorithms.

The US NEXRAD system is run by operators who adjust offsets, select a scan pattern according to the weather situation, etc. Germany operates a network of fully automated, identical weather radars running at identical scan strategies (Fig. 30.6).

30.5 Specifications

Radar manufacturers report a very wide span in the depth of customer specifications. Some customers may just specify “the best possible radar for their money”, others may take a more thorough approach. In the USA, for instance, extended joint experiments were conducted over several years to establish the capabilities and requirements of Doppler (JDOP experiment 1976–1978) and dual-polarization (JPOLE, 2000–2004) techniques. Germany affords the Hohenpeissenberg re-

search radar to evaluate upcoming new features prior to final operational specification.

Besides the general type of radar (X, C, or S-band, klystron/magnetron, dual-pol, AMR), internal and remote network capabilities and functionalities, control and access structure (e.g., reboot performance, remote version inquiry and upload/upgrade), data output formats, interfaces, maximum maintenance intervals and line replaceable units (LRU), including LRU interfaces,

Table 30.11 Overall specification

Wavelength	3.2–10.7 cm
Continuous operation	24/7/365
Availability excluding maintenance	98%
MTBF	E.g., 6 months
Maintenance interval and downtime	E.g., 9 months and 6 h down
Internal and external time synchronization	E.g., NTP
AMR	Dual-pol splitter and IFD or DSP above elevation gear
Product generation	(specify products, Sect. 30.8)
Local product storage	E.g., 14-day ring buffer. Fault logging
Fault logging	Selectable transmission and storage
Min and max operation temperatures	–40 to +50 °C outdoors, 0 to 40 °C transmitter and receiver
Power supply: mains voltage and frequency, number of phases	110/115/120/127/230/240/400 V AC 50/60 Hz + 5 Hz, 3 phases evenly loaded
Documentation requirements	Operations, maintenance, and SW manuals in native language, up to date, including safety instructions, digital (PDF) and print (3×)
Range coverage	60–460 km
System overall coherency	E.g., 1° to 180 km
Clutter suppression	E.g., 40 or 50 dB
Safety appliances and precautions	Emergency interlocks and latches; selective system protection (fuses, circuit breakers); warning and danger signs; safety directions; and interference immunity

Table 30.12 Antenna and radome specification

Antenna type	Parabolic (center-fed; offset; Cassegrain etc.) Electronically steered (planar phased array, <i>crow nest</i>)
Angular ranges	Elevation 0–90°, azimuth 0–360° cont.
Azimuth/elevation rotation rate	0.1–3–10 rpm (0.6–18–60° s ⁻¹)
Max azimuth/elevation acceleration	E.g., 15° s ⁻²
Safe sector blanking	Radiation safety, e.g., for close buildings (even in the case of system failure!)
Feed	Single or dual-pol corrugated horn. OMT
Diameter	0.7–8.5 m and larger
Gain	45 dBi
Beam width horiz. and vert.	0.5° or 1° both
Sidelobe suppression	–25 to –35 dB
Pointing error and dual pol beam squint	0.05°
Polarization crosstalk	–35 dB
Radome construction type	Orange peel; quasi random panel; air-inflated structure; hydrophobic coating
Radome diameter	4–12 m and more
Maximum wind speed	250 km h ⁻¹
Maximum snow/ice load	250 kg m ⁻²
Dry radome oneway transmission loss; delta ZDR; differential attenuation	< 0.2 dB; < 0.005 dB; < 0.005 dB

Table 30.13 Transmitter specification

Transmitter type	Magnetron, klystron, TWT, SSPA
Frequency	X, C, or S-band, rarely X+S-band
Pulse power	0.1–1 MW
Pulse widths	0.2–4.5 μ s, often switchable; 64 μ s with pulse coding
PRF	200–4000 Hz
Max. duty cycle	E.g., 30 dB
Safety sector blanking	Yes/no
Polarization base and setup	Single (mostly linear); dual pol H/V (pulse-to-pulse or hybrid); LHC/RHC; arbitrary

Table 30.14 Receiver specification

Type	Analog or digital Intensity-only (LOG) or coherent/COR LIN Optional dual-pol dual channel
IF	30 MHz, 60 MHz
IF bandwidth	0.2–5 MHz depending on pw
MDS	E.g., –114 dBm
Dynamic range	90 dB
Noise figure	E.g., 2 dB
Image rejection	E.g., 56 dB

and expected lifetimes (maybe expenditure estimation), as well as safety and emergency appliances should also be specified according to technical and legal conditions. Some special construction features may be dictated by existing infrastructure.

All radar data and messages must be time stamped (if appropriate, on a pulse-to-pulse basis) based on synchronized (e.g., by ntp daemon) time (master clock) and logged and flagged according to severity. Ray data must be tagged with start and stop timestamps, angles (az and el start and stop) and mean antenna velocity, housekeeping information, and metadata, such as radar settings and DSP parameters.

Tables 30.11–30.15 are just examples and are not intended to be a complete or consistent real specification.

An uncertainty estimation (according to the laws of error propagation) may be stipulated for certain observables. Alternatively or additionally, measurable ranges and error limits may be specified (Table 30.16).

Overall signal detection capabilities, such as minimum sensitivity and a minimum large signal detection at various ranges may also be benchmarked (Table 30.17).

For the sake of clarity in testing, the operation parameters should be given with these specs, e.g., $PW = 0.8 \mu$ s, $\omega_{az} = 18^\circ \text{ s}^{-1}$, $PRF = 600 \text{ Hz}$, range averaged to 1 km. Note that double pulse width PW will increase MDS by 3 dB. If MDS can be lowered by a factor of 4 (6 dB), the same target can still be detected at double range.

Procedures and utilities to prove compliance with specs during acceptance tests, including test software, may or may not be left to the tenderer. Depending on the buyer's legislature and procurement regulations it may be necessary to define acceptance procedures as early as the call for tender. Special scan definitions may be devised to test overall performance under certain ranges and stress combinations of interrelated parameters.

When specifying a new radar network, it appears useful to include identity of all systems at some end-point, as manufacturers will beta-test and systems will evolve over the production process. Unlike in a first

Table 30.15 DSP specification

Signal Processor	Options/typical values (examples)
Maximum number of range bins per ray	E.g., 4000
Minimum sampling resolution	E.g., 25 m
Basic processing modes	PPP, FFT, dual pol, pulse compression, phase coding/random phase processing
IIR Clutter filter depth and halfwidth	30–60 dB; 5–25% V_N
Meteorological moments (depending on transmitter/receiver setup)	$Z_h, Z_v, V_h, V_v, W_h, W_v$ ZDR, LDR, PHIDP, KDP, RHOV
Quality moments and thresholds	LOG, SNR, SQI, WSP, CPA, CCOR
Correction algorithms	Range averaging, CMS, Doppler filter, GMAP, CMD, thresholding, velocity unfolding, attenuation and second-trip correction
Define adjustable offsets to account for any power and phase imbalances	$\Delta ZDR, \Delta LDR, \Delta PHI$ and $\Delta PHIDP$
Ray header information	Operation mode, # of pulses used; time + Az and El start/stop and rate; AFC and sector blanking status; burst av. power, STD, frequency, etc.
Storage capability of raw I/Q data	E.g., 4 TB

procurement, in a replacement, usually not all radar components are specified at the same time, particularly in a network. Often, it is deemed appropriate to change just one module, such as software or signal processors, or to replace an analog receiver by a digital one. While modular system architecture is current state of the art, module interfaces must be specified precisely to every relevant detail. Also, it may be necessary to specify communication structure and interfaces so that they conform to the customers IT and SW. SW source codes and/or special licenses may be required.

Keeping in mind legal requirements and specification of infrastructure (Sect. 30.4.7), specifying a weather radar is sufficiently complex, and it is highly recommendable to profit from the know-how of an experienced weather radar operator.

30.6 Quality Control

Weather radar data quality plays a major role in data interpretation and sales processes. European weather services supplying data to air traffic control and airports even have to be ISO certified according to ISO 9001 to fulfill the requirements of Single European Sky (SLS), including the process of radar data acquisition. Therefore, quality assessment QA and quality control QC are important throughout the data acquisition chain, starting with proper specifications (30.5), accurate calibration, appropriate parametrization, and monitoring (Sect. 30.6.1).

Radar data quality is greatly influenced by interferences and nonmeteorological targets and also by the degree to which underlying model assumptions are fulfilled (Sect. 30.6.2). Some of the shortcomings can, at least in principle, be overcome (Sect. 30.6.3), others can only be detected (Sect. 30.6.4), or are not accessible at all.

30.6.1 Calibration, Parametrization, and Monitoring

There are about 5000 tuneable parameters in a radar to optimize its performance. Some of them – such as trigger timing, transmit frequency adjustment, and receiver calibration – harmonize the proper functioning of the system. Some of them optimize performance to some specific purpose, such as pulse repetition frequency, which defines an unambiguous range versus unambiguous velocity (Sect. 30.3.2), calling for either a compromise or targeted optimization, e.g., special parametrization in research radars.

Table 30.16 Accuracies and measurement ranges

Observable	Range	Max error
Z	−32 to 96 dBZ	±1 dB
V	±32 or ±48 m s ^{−1}	±0.5 m s ^{−1}
ZDR	±6 dB	±0.1 dB
RHOHV	0 to > 0.995	±0.005
LDR	< −35 dB	±1 dB
PHIDP	±180°	±0.5°

Table 30.17 Detection benchmarks

Large signal detection	$Z_e = +64$ dBZ	4 km
MDS	$Z_e = -45$ dBZ	1 km
MDS	$Z_e = -25$ dBZ	10 km
MDS	$Z_e = -5$ dBZ	100 km
MDS, long pulse	$Z_e = +7$ dBZ	250 km
Point target detection	$\sigma = 4$ cm ²	100 km
Rainfall of 0.01 mm hr ^{−1}	−10 dBZ _e	50 km

Calibration

A full system end-to-end calibration includes the transmitter, antenna, receiver, and DSP, and is astonishingly difficult to perform. Although calibration with a sphere of known backscatter cross section suspended at some height and distance may seem straightforward, keeping the sphere motionless in the center of the radar beam poses a major problem. In most cases, radar calibration refers to the calibration of the receiver making use of independent transmitter and system measurements.

Receiver Calibration. Receiver calibration may be performed manually or by automated utilities injecting a TSG signal of known power into the antenna coupler and stepping through the calibration curve (to detect nonlinearities, otherwise a two-point calibration will suffice). On a log/log scale there will be a linear part of the calibration curve that defines the dynamic range between noise and saturation roll-off.

During receiver calibration the calibration reflectivity $Z_0 = 10 \log(Cr_0^2 P_0)$ is determined from (30.14) at $r_0 = 1$ km, where P_0 is the intercept of the calibration curve with the noise level; Z_0 is, thus, the minimum detectable reflectivity factor at range $r_0 = 1$ km. Some typical values are: $C = 6.8 \times 10^6$ mm⁶ m^{−3} mW^{−1} km^{−2}, $P_0 = 3 \times 10^{-11}$ mW = −105 dBm, and $Z_0 = -37$ dBZ [30.49].

Once linearity and dynamic range have been established, calibration may even be checked *on the fly*, placing a TSG signal at some distant range bin during normal operation or by monitoring the sun whose position and solar constant are very well known. Sun

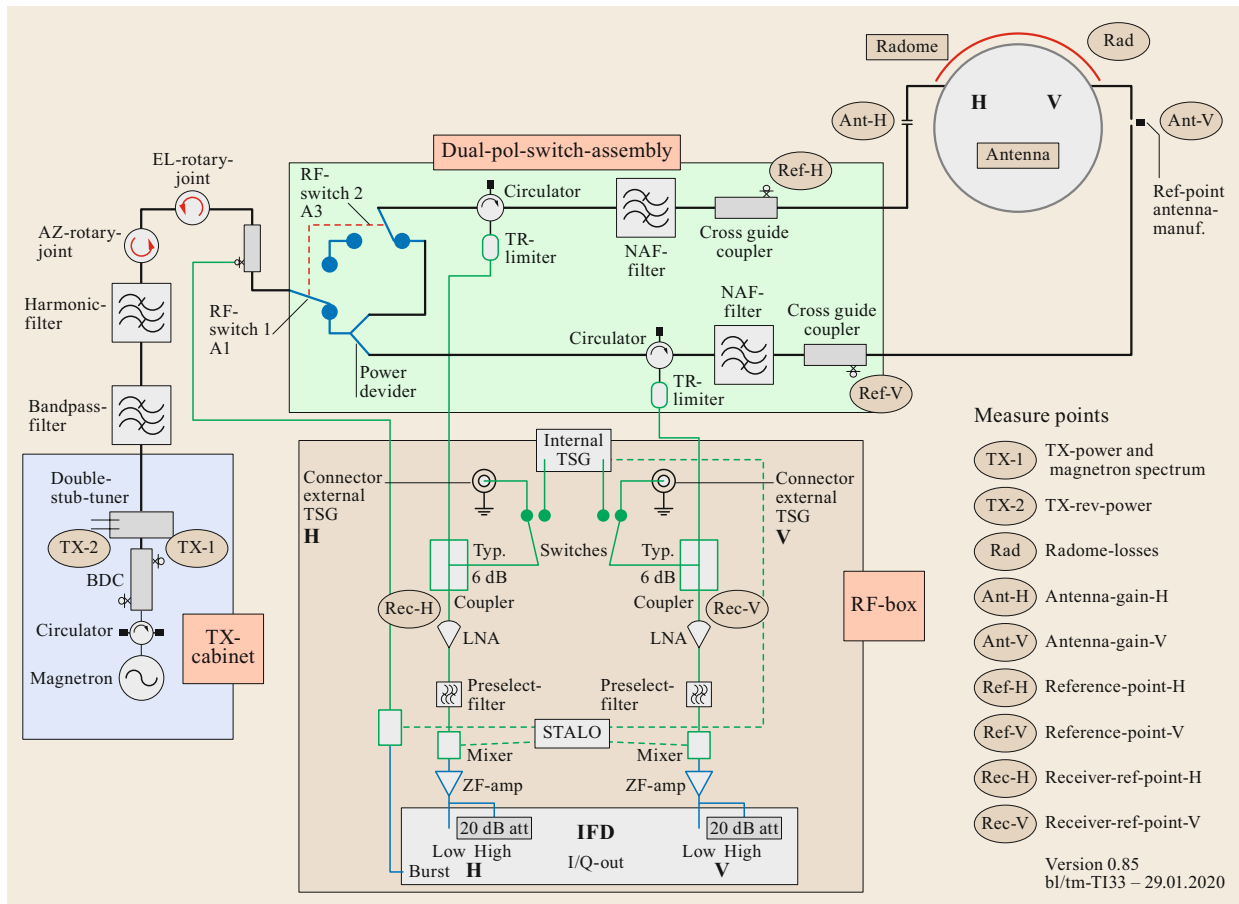


Fig. 30.5 A typical hardware calibration diagram of polarimetric weather radar, indicating all relevant elements to be considered and characterized in the transmit and receive paths (image © T. Mammen, DWD)

calibration can be performed by tracking the sun (interrupting operation) or fitting occasional hits during volume scanning over a day.

Noise Sample. In order to estimate the noise floor of the calibration curve, a noise measurement is performed to determine the current noise power plus any biases in receiver and ADC. The noise value is determined by pointing the antenna away from the ground and taking a certain number of samples at a distance sufficient to ensure that no thermal noise or target is present. (The rare chance of hitting aircraft may be handled by an outlier check.) Noise samples are taken not only during calibration but are repeated periodically (e.g., every hour) during regular operation to check for any drift.

Losses. Care must be taken to account for any power losses, such as waveguide, cable, and coupler insertion losses. Some fraction L_t of the energy (factor < 1) is lost between the transmitter (where P_t is specified) and

antenna feed (radiated power), as L_r is lost between antenna and receiver input (where P_r is measured). Losses of spectral components in the limited bandwidth receiver filter (dependent on the pulse width), as well as any amplifier gains G_r must also be accounted for. Figure 30.5 gives the idea of this. These losses will appear as constant linear factors or summands in the linear or logarithmic form of the radar equation and are commonly integrated into the radar constant.

ZDR Calibration. ZDR is calculated as $Z_h - Z_v$ according to (30.42), where imbalances between the horizontal and vertical channels in the transmit, antenna, and receiver parts may occur and produce a bias in ZDR. In order to get rid of any system imbalances, an end-to-end ZDR calibration is best carried out on symmetric targets that do not generate intrinsic differences between H and V, e.g., raindrops appearing circular when seen from below. Therefore, it is common practice to observe falling rain by pointing the antenna vertically and

rotating over a full circle in the azimuth [30.50]. ZDR calibration methods, including an *engineering method* for WSR88D (not capable of 90° elevation) are summarized in [30.51].

Parametrization

Once a radar is ready to run it needs to be configured so that it can operate in a predefined state. Some of the necessary parameters are static, site or type specific. Most of them are variable and define the operational properties of the radar (*scan definition*), such as the sequence of antenna elevations, the azimuth rate, the polarization state, PRF, thresholds, etc. Configuration parameter sets are combined into templates that are stored in the host computer and uploaded to the RCU and DSP according to a configurable scheduler.

Scanning of a radar (of operational radar, at least, and even more so of networked operational radars) is a trade-off between dense volume coverage, accuracy, and fast update rate. For some applications, slow scanning is required for higher accuracy, while rapid surveying can be faster. Applications related to air traffic, severe convection, and vertical profiles need extended height coverage even close to the radar. Early investigations showed that the quality of (Z-only) precipitation estimation dropped if updated after 6 min or slower. The same has proved true for cell tracking, cf. Fig. 30.22. Thus, the selection of scan parameters depends on priority tasks.

Unlike earlier radars, current systems are capable of pointing vertically in order to measure time–height profiles over the radar. High elevations close the *cone of silence* above a radar site, but the radar beam will soon be beyond any weather phenomena taking place in the lowest layers of the atmosphere only, particularly in winter. Relatively, lower elevation leads to more information, but ground proximity is still limited by the Earth's curvature and orography.

In routine 24/7 operation of a radar, parameters may be different for different sweeps according to a predefined time schedule describing the scan strategy or volume coverage pattern (VCP). While with earlier patterns it was deemed necessary to cover a dense volume (e.g., 18 elevations in 10 min), rapid update has been given priority in recent years at the cost of thinned-out volume coverage. The so-called *Swiss scan* [30.52] to speed up volume coverage using two interleaved *half volumes* of 10 elevations each within 5 min is a famous example.

In a network, radar parametrization may be strictly identical for all radars at all times (e.g., in the German radar network) or dependent on season, orography, and climate region (in very large networks, e.g., USA), or may be adapted to the prevailing weather conditions (*adaptive scanning*) by an operator or automatically.

NEXRAD operators may currently choose from 13 different VCPs [30.53].

DWD has been running identical volume scans at every radar consisting of 10 elevations, plus a prioritized terrain-following sweep optimized for precipitation measurement, plus a 90° vertical scan, every 5 min since 2013 [30.54], as is shown in Fig. 30.6. DWD is presently experimenting with a lowest (0.5°) sweep every minute. Faster update rates will only be available with future electronic scanning and beam steering.

Monitoring

Besides calibration, parametrization, and regular maintenance, it is good practice to monitor proper radar operation, data quality, and data availability for timely detection of any problems in order to keep availability and data quality high. The notion of monitoring refers to the observation, characterization, and tracking over time of parameters, status, availability, and any undue alteration thereof. Thus, monitoring helps achieve and maintain specified conditions and performance.

Firstly, it is desirable to detect any problems as early as possible in order to keep the duration of any radar failure or of degraded data quality at a minimum. This is particularly true for radars operated in remote areas with low accessibility. Continuous monitoring of all elements of a radar system is necessary to achieve an in-time detection of a radar system component failure.

There are also some elements in a radar system that tend to creepingly degrade with time, such as a TR-limiter. Such degradation does not cause instantaneous failure but may affect data quality. If it is possible to detect trends or unusual changes of radar parameters early enough, preventive maintenance may be scheduled, so that an actual system failure can be avoided. The BITE system supplies continuous information that may be monitored and analyzed.

Secondly, based on user requirements, radar data are subject to high-quality standards concerning absolute accuracy and associated uncertainty. The latter is mainly determined by the sampling strategy (e.g., acquiring a sufficient number of pulses) and must be optimized/traded off in a proper design of a scan definition. Observed variations in the measurements (e.g., related to the scatter of ZDR) beyond what can be expected theoretically may indicate a hardware issue and should be monitored.

The absolute accuracy of a radar moment is determined by all components of its transmit and receive chains, which are typically characterized during calibration. Obviously, any changes in the transmit path (e.g., transmit losses due to a wet radome or a degrading circulator) will affect the absolute accuracy of all radar moments that rely on the received power measurement.

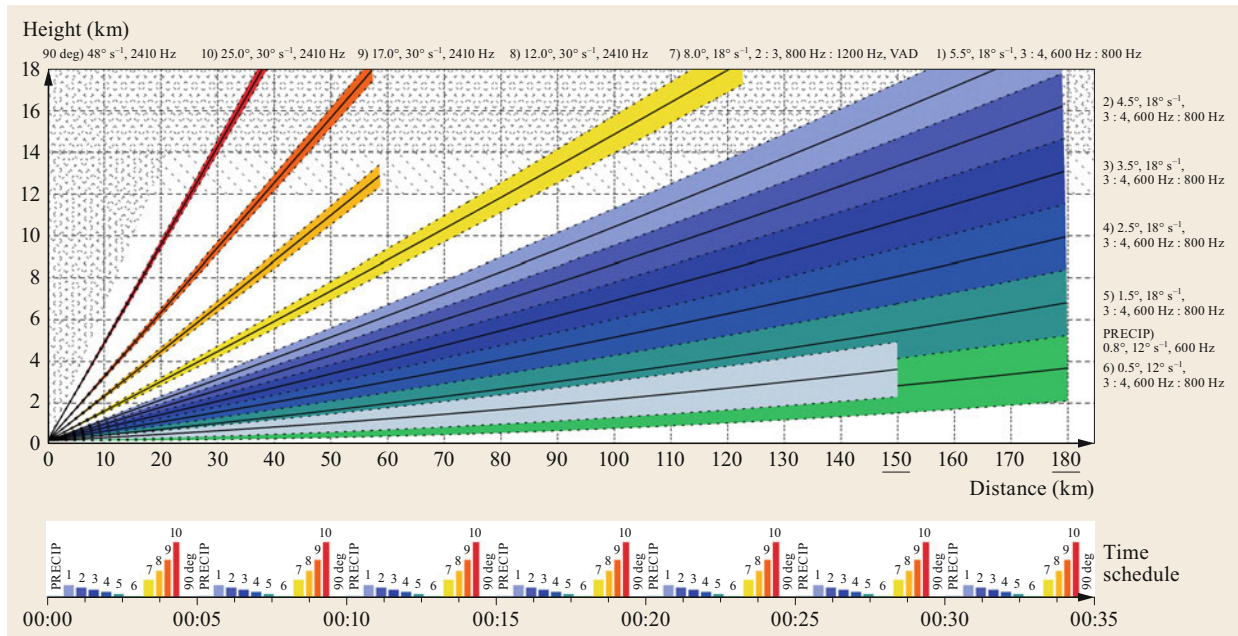


Fig. 30.6 Current scan sequence at DWD. The pattern starts at hh:mm with a coarsely terrain-following lowest sweep optimized for QPE. It continues with a sweep at an elevation of 5.5°, moving downwards by 1°-steps to cover the lower atmosphere without gaps in such way that at hh:mm +2.5 there is another lowest sweep at 0.5°. The volume finishes upward with elevations at 8, 12, 17, and 25°. A vertical scan is added for calibration of ZDR and as a meteorological profiler scan, so that the complete volume is finished before hh:mm +5. Values for numbers 1 to 10 (and PRECIP and 90°) in given order: elevation (°), azimuth rate (° s⁻¹), dual PRF ratio, PRF1 (Hz) : PRF2 (Hz) (image © P. Tracksdorf, DWD)

All components of the radar that may affect data quality need to be identified and monitored.

However, the uncertainty of engineering measuring techniques is too large when it comes to quantifying all relevant elements in the transmit and receive paths within an accuracy of 1 dB for Z, or 0.1 dB for ZDR. Therefore, integral end-to-end assessments of the system performance have to be considered. An end-to-end radar system monitoring may be performed including well characterized targets or reference measurements, so that all elements of the radar equation are taken into account.

Data-based monitoring approaches have been established, where well-characterized targets or reference measurements are used to quantify the accuracy of radar moments and to detect issues in the radar hardware. For instance, the sun may be used to monitor the pointing accuracy of a weather radar [30.55] as well as its power and ZDR calibration [30.56, 57], as the sun's position and radiation properties are well known. Receiver calibration may also be monitored with the radar operating and placing a test signal at some remote range bin, where there is no weather. The noise level is monitored periodically during operation; weather permitting, the same is feasible for 90° ZDR calibration. A digital receiver provides data to monitor the transmit pulse

power and frequency. Single radar end-to-end monitoring may be performed using external devices, such as rain gauges, disdrometers, or another radar. Radar-radar comparisons may be performed in the overlapping areas of a radar network to check consistency. However, due to different radar positions, beam propagations, and beam heights/widths, a pointwise comparison is difficult, and a statistical evaluation is necessary instead.

Beyond the technical and observed parameters of a radar itself, system load, network performance, data completeness (a check for missing rays), data transmission (a check for missing sweeps), and product generation (check timely production) are usually also monitored in order to ensure high data availability.

30.6.2 Error Sources

The accuracy of radar interpretation largely depends on the underlying model assumptions, as given in Sects. 30.3 and 30.8. Some of them are readily met under normal conditions, while others are known to be critical, if only under extreme weather conditions. On the other hand, there are interferences from external error sources, such as nonmeteorological targets and active emitters.

Model Assumptions

There are several assumptions underlying the radar equation (30.13) and its constituents, such as antenna properties:

- No unknown losses, misadjustments, or undiscovered malfunctions are assumed to occur in the radar system; the radar is considered to run according to specifications and parametrization.
- A geometric radar beam is usually assumed to hit the target at a certain direction, while in reality, there is an antenna pattern transmitting and receiving via both the main lobe and sidelobes. The assumption relies on a more rapid decrease of the main lobe flanks than a possible gradient in off-beam reflectivity. If this is not the case, measurement and interpretation may go grossly wrong, as strong echoes will be collected over the side lobes or flanks of the main lobe and projected into the direction of the main beam.
- Beam propagation is assumed to occur in standard atmosphere and to follow a $4R_E/3$ curvature. Anaprop and multipath scattering are sometimes detected but not usually corrected for.
- Increasing beam broadening and increasing beam height with increasing range make measurements essentially incomparable.
- In routine operation, at least in single-polarization radars, target droplets are commonly assumed to consist of water, using a K^2 -factor of 0.93 in the radar equation. If real measurement occurs in ice, K^2 should be 0.176, i.e., 7 dB less, and reflectivity is overestimated by this amount.
- Moreover, targets are considered to be Rayleigh scatterers, i.e., small spheres. Liquid droplets may be considered spherical, if small, but large drops are oblate, ice crystals are symmetric, hail and graupel and nonmeteorological scatterers are irregular, canting, tumbling and often large. In the latter respect, a larger wavelength (S-band) can help at a cost.
- Also, complete and homogeneous beam filling is assumed, while in reality, overshooting and large reflectivity gradients (such as hail shafts, bright band, wind turbines) may occur.
- In a real radar, several parameters will deviate from their specification, such as the transmit power, pulse form, phase stability, polarization purity, and antenna squint.
- Signal-processing assumptions, such as a monomodal Doppler spectrum, will not always be fulfilled.
- Range and/or velocity folding may go unrecognized.
- Radar parametrization and scan strategy introduce sampling gaps and a cone of silence.

Even with a perfect measurement, some more assumptions are related to data interpretation:

- Classical QPE relies on an average Z/R -relation, which is based on an average drop-size distribution (e.g., Marshall–Palmer) with a very large spread.
- Some interpretations of Doppler radial wind depend on the assumptions of wind field homogeneity, continuity, and, maybe, horizontality.
- Some correction procedures may themselves turn out to introduce new errors, such as Doppler filtering, thresholding, dual-PRF unfolding, or range correction in the second trip, or the comparison of radar volume measurement to gauge-point measurements.
- The vertical reflectivity profile VRP may not be an error in itself but commonly causes errors in QPE because the (maybe correct) radar measurement from aloft is extrapolated to the ground not taking into account drop-sorting effects due to size/velocity distribution, or evaporation (virga), or the *bright band*.
- The bright band appears as a height region of enhanced reflectivity caused by the melting layer just below the zero isotherm. It is caused by melting particles, e.g., snow flakes or graupel, which due to their water cover appear to be large solid raindrops (remember K^2 in (30.5) and (30.13) is 7 dB larger for water than for ice). The bright band is more conspicuous at higher antenna elevations than close to the ground.

External Error Sources and Interferences

There are more things between heaven and earth than are dreamt of in pure rain. Besides precipitation and other meteorological phenomena, other targets are also seen by a weather radar, such as (Fig. 30.7) mountains, buildings, ships, wind parks, birds, and chaff (anaprop was mentioned before). Sometimes, a careless radar setup may produce additional errors, such as obstacles in the antenna near-field.

Any unwanted echoes are collectively called clutter. Clutter affects not only reflectivity, but also biases Doppler wind [30.58] and dual pol moments.

Clear air echoes from insects or turbulent fluctuations in the refractive index [30.59–61] may be considered clutter or may be used as wind tracers. External interference is caused by active emitters, such as the sun and foreign narrow or broadband transmitters, such as other radars, WiFi, or (thermal) noise. Figure 30.7 allegorizes most of these error sources. Many error sources may to some degree be corrected for, as is shown below.

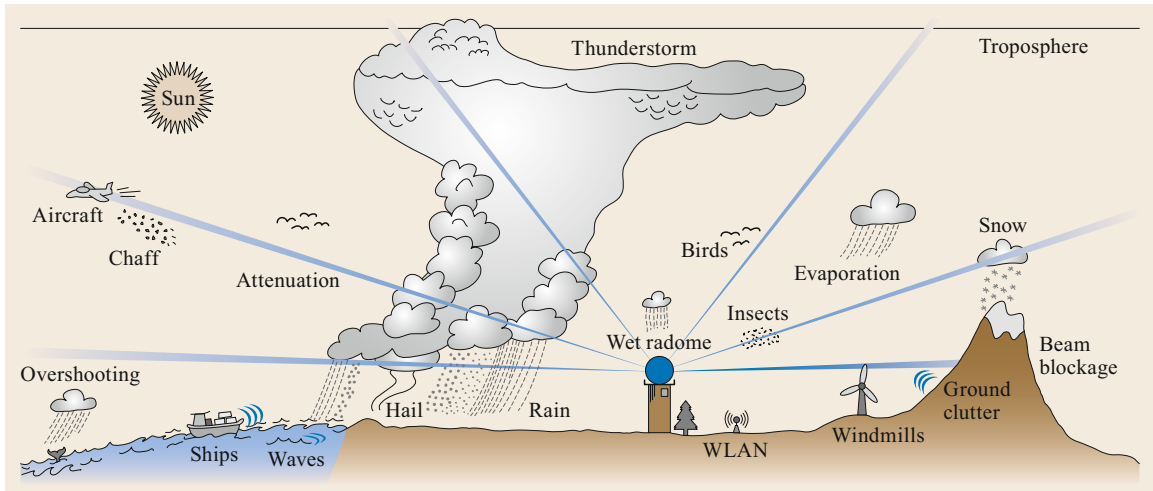


Fig. 30.7 Graphic depiction of external error sources in a weather radar (image © N. Rathmann, DWD, inspired by M. Peura, FMI)

30.6.3 Correction Algorithms

Some correction algorithms may be run in realtime on the DSP, where maximum radar information but limited external information is available. The following algorithms are commonly applied to the moment estimates of Sect. 30.3.4. External postprocessing/QC has all possible weather and technical information available, but maybe not all of the radar internals. This is presented in Sect. 30.6.4 together with DSP thresholding algorithms.

Range and Noise Correction

According to the radar equation (30.13) the received power decreases with the square of the distance. This must be corrected for in the calculation of the reflectivity factor by a term of $-20 \log(r)$. For example, 40 dB must be added for a volume target 100 km away. This may seem simple, but will only be correct if applied to a target at range r .

If, for instance, the signal contains system noise (which does *not* depend on range–time), the noise will nonetheless be corrected by $\sim r^2$ together with the signal, causing the noise to increase with range. Even though this may be detected, the data will be useless and must be excluded from causing problems. Therefore, noise is measured periodically – often at the beginning of every scan – and subtracted from the signal in the radar equation. If in reality the target is *not* located at range r , e.g., originating from second or higher trips (Sect. 30.3.1), range correction goes wrong, and second-trip echoes are represented too weakly and in the wrong place, if no specific measures are taken (see Sect. 30.6.3, *Second-trip Unfolding – Range Dealiasing*).

Attenuation and Beam Blockage

In addition, the received power has been attenuated by atmospheric gases, depending on wavelength and distance, and by precipitation. Part of the radar beam may be blocked by obstacles.

Atmospheric *gas attenuation* is taken into account as a tunable parameter in the radar equation. A two-way attenuation of $a = 0.016 \text{ dB km}^{-1}$ is considered standard at the C-band and is applied as the $-ar$ -term in (30.27). Even though the radar wavelength is chosen not to be attenuated even by large precipitation fields, the radiation field may be noticeably damped by strong rain or hail.

Attenuation by precipitation is usually not corrected for in classical radar. In dual-pol radars, the dependence of PHIDP on attenuation by large drops allows for an attenuation correction of the horizontal and differential reflectivities. Attenuation losses by heavy rain are intuitively assumed to be proportional to K_{DP} (Sect. 30.3.4), $A_h(r) = \alpha K_{DP}(r)$ and may be corrected for, e.g.,

$$\begin{aligned} {}^A Z_h(r) &= {}^U Z_h(r) + 2 \int_0^r A_h(r'; \alpha) dr' \\ &= {}^U Z_h(r) + \alpha \Delta \text{IDP}, \end{aligned} \quad (30.54)$$

where A_h is the attenuation factor in dB km^{-1} , K_{DP} in deg km^{-1} is approximated as $\Delta \phi_{DP}/2\Delta r$, the left superscripts indicate uncorrected (U) and attenuation corrected (A) reflectivity factors Z_h in dBZ, and the parameter α is around 0.08 in the C-band. The same reasoning holds for differential reflectivity

$$\begin{aligned} {}^A Z_{DR}(r) &= {}^U Z_{DR}(r) + 2 \int_0^r A_{dp}(r'; \beta) dr' \\ &= {}^U Z_{DR}(r) + \beta \Delta \text{PHIDP}, \end{aligned} \quad (30.55)$$

based on the effect of differential attenuation $A_{dp}(r) = \beta K_{DP}(r)$ with a parameter β 0.02 in the C-band. The crux of the matter lies in the parameters α and β , see [30.38] for details. PHIDP must be unfolded and possibly interpolated first.

Shadowing/beam blockage is best avoided by choosing an appropriate radar site with free round view. Methods have been proposed to correct precipitation measurements from intensity-only radars [30.62] and to take beam blockage into account in dual polarization radars [30.63].

Clutter Correction

The main starting point for the treatment of stationary clutter is that clutter does not move or is in some way more stable than weather echoes. In olden times, one or several measurement sweeps were taken when there was no precipitation. Any remaining echo was considered clutter and stored in a so-called static clutter map, which was used to flag suspicious range bins later with precipitation present. Because of varying propagation conditions, it is difficult to set the sensitivity of the clutter map so that no clutter goes unrecognized and not more weather echo is flagged than necessary. Better results are achieved using a dynamic clutter map, e.g., based on radial velocity output. Anyway, the clutter can only be recognized; the weather echo is lost and cannot be restored. Nowadays, dynamic clutter maps based on more sophisticated approaches are used to decide on adaptive filtering (see CMD below).

Realtime clutter suppression started with analog filters called moving target indicator (MTI) which essentially subtract the previous pulse or, in a more sophisticated way, subtract not only the most recent pulse but also a few earlier pulses with corresponding weights a_i . In recursive filters, filtered pulses (weighted b_i) are fed back as well resulting in an infinite impulse response (IIR) filter. The same technique is applied in digital filters, cf. (30.56) below.

Statistical Clutter Filters. In a radar without Doppler capability, a recursive (IIR, e.g., third order) highpass filter called a *statistical filter* may be applied to the fluctuating LOG *amplitude* time series following [30.64]. Low amplitude variance due to stable returns from clutter is filtered out. Therefore, unlike Doppler processing, samples should be taken at low PRF in order to not be correlated. In principle, CCOR (30.36) is calculated as the difference of filtered and unfiltered powers (averaged squares of amplitudes) but includes some subtleties, such as a correction factor due to Poisson statistics and a gamma-bias correction depending on the estimated CSR. Statistical filters are the only clutter filters available in intensity-only radars and

are less effective than Doppler filters. Notwithstanding, they are sometimes also used in Doppler radars as a makeshift, e.g., with staggered PRT where filters requiring equally spaced samples cannot be used. In this case, the amplitude time series is calculated from IQ as $A_i = \sqrt{I_i^2 + Q_i^2}$. Statistical filters may improve reflectivity measurements but, of course, cannot correct Doppler and dual-pol moments.

Doppler Clutter Filters. In a Doppler radar, clutter filtering is achieved by applying either time series IIR or frequency-domain (*Fourier*) filters, usually in a second channel parallel to an unfiltered one. CCOR is then calculated as the difference in the reflectivity factor between the two. For time-series (IIR) filters with fixed coefficients, CCOR is limited by the fixed filter depth. In an analog Doppler radar, CCOR is transferred to the LOG receiver channel for application in the logarithmic radar equation (30.53).

Doppler clutter filters rely on zero radial clutter velocity or a sufficiently narrow clutter spectrum around zero velocity. These spectral components are filtered out by a digital high-pass filter, which may be implemented in the time or spectral domains. In fact, the superior performance of its clutter filters is one of the main reasons to choose FFT processing.

Time-domain Doppler filters are usually implemented as recursive or infinite impulse-response (IIR) filters, e.g., a Chebyshev filter of order $n = 4$,

$$A_k^f = \sum_{i=0}^n a_i A_{k-i} - b_i A_{k-i}^f, \quad (30.56)$$

where $b_0 = 0$. The choice of coefficients determines the width and depth of the filter. In modern signal processors, predefined filters are available but may also be customized using graphical tools and downloaded to the DSP. Clutter filters of different depth/width may be set depending on range and elevation (the more aggressive filters at closer range and lower elevation). An example of effective clutter correction is shown in Fig. 30.8.

Besides being an effective means of clutter removal, there are some drawbacks to IIR filters. Due to the theoretically infinite impulse response, any perturbations (strong gradients, changing PRF) practically propagate over many pulses, possibly into subsequent rays. This effect can largely be mitigated by a filter delay that lets the filters stabilize at the beginning of each new ray, possibly after reinitializing (zeroing), by skipping the closest (say, three) pulses without using them.

Filters must also be reset if PRF changes, e.g., with staggered PRF (Sect. 30.6.3), or if AGC (Sect. 30.4.3) is applied. This loss of pulses may be critical with a fast

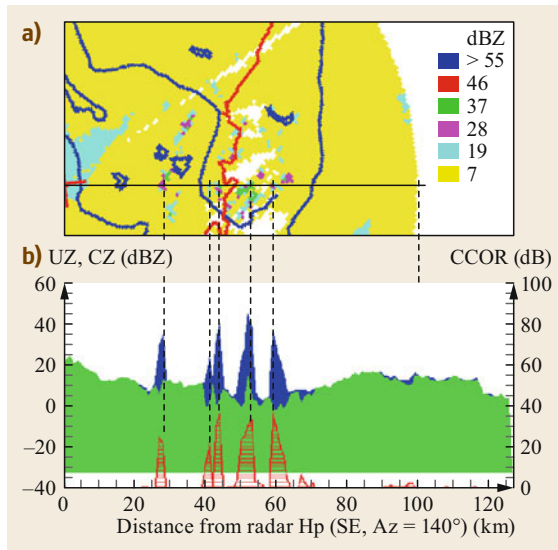


Fig. 30.8a,b The effect of successful quantitative clutter filtering. (a) Cutout of a PPI of UZ over the Karwendel mountains, BY, Germany. The DWD Hohenpeissenberg radar is located to the left (red cross). (b) Cross section of CZ (green) plotted over UZ (blue) along the black line in (a). CCOR is indicated in red (right scale), mountains are filtered by up to 40 dB, precipitation is left unchanged (after [30.65], © J. Seltmann, DWD)

rotating antenna. Furthermore, as the filter coefficients are fixed, so are its stopband depth and width. Therefore, a clutter peak stronger or wider than the filter will be attenuated but not completely removed. On the other hand, weather echoes around zero velocity (with no or only weak clutter present) may be attenuated as well, losing signal power in Z with a chance of SQI falling below the threshold (Sect. 30.6.4) and losing Doppler moments, too.

Frequency-domain Clutter Filter. The Fourier transform of such IIR time-domain filter is a spectral highpass filter with a notch around zero velocity. If the Doppler Fourier spectrum $S_i = |FFT(A_j)|^2$ is available, a highpass notch filter (laxly called a Fourier filter) may be designed in an even more effective way. The idea is to remove and subsequently interpolate a certain uneven number $2k - 1$ of spectral components around zero velocity

$$S_i^f = S_{-k-1} + (S_{-k-1} + S_{k+1}) \frac{k+i+1}{2(k+1)},$$

$$i = -k \text{ to } +k. \quad (30.57)$$

This makes the filter adaptive (no predefined filter depth) and particularly effective removing the clutter

signal while reconstructing the weather signal, even if it overlaps with the weather. Interpolation may be linear as in (30.57) or use an (iterative) Gaussian model. The Gaussian model adaptive processing GMAP [30.66] fits a Gaussian to the three central spectral taps of the clutter spectrum (centered around zero) and removes all taps under this curve. The remaining weather spectrum is then fitted to another Gaussian. This procedure is repeated until the resulting power and mean velocity of the signal stabilize within 0.2 dB and $0.005 V_N$. Finally, the optimum tapering window is decided upon based on CSR.

Clutter-mitigation Decision System CMD. IIR clutter filters and even adaptive spectral filters still remove weather power when the weather spectrum is narrow, and its mean V is close to zero. Therefore, the clutter-mitigation decision system CMD [30.67] applied by NEXRAD identifies clutter prior to filtering. To this end, CPA (Sect. 30.3.4) plus three internal parameters are calculated:

- The texture reflectivity TDBZ of a range bin is defined as the mean of squared differences between reflectivities on both sides of that bin.
- The SPIN parameter tells how often the reflectivity gradient changes sign in a certain neighborhood of a bin, normalized by the number of neighbors used.
- Clutter ratio narrow (CRN) is computed dividing the power contribution of the three spectral lines centered at $V = 0$ by the power of four adjacent lines (two on each side).

CMD is then calculated in a fuzzy logic from weighted membership functions of TDBZ, SPIN and CPA, and CMD. The decision flow is IF SNR > 3 dB THEN IF CRN > 6 dB THEN IF CMD > 0.5 THEN set clutter flag and apply clutter filter. An excellent skill of CMD has been reported [30.67]. An update to CMD is described in [30.68], including two dual-pol membership functions based on the standard deviation of ZDR and PHIDP.

An internal dynamic clutter map may be created within the DSP based on CMD or CPA alone. Doppler filtering is only applied to range bins that are flagged as clutter. This works also for PPP (except for CRN) rendering IIR filtering, in a sense, adaptive. If the parameters mentioned above are output as additional moments by the DSP, CMD may even be performed a posteriori in a centralized QC (Sect. 30.6.4).

Clutter Microsuppression CMS. CMS excludes raw range bins exceeding a predefined clutter/signal ratio estimated by $(T_0 - R_0)/R_0$ from range averaging auto-correlations, i.e., at a very early processing stage. This

improves subclutter visibility in the presence of strong, isolated clutter targets.

Unfolding, Dealiasing

Range or velocity folding (aliasing) or both may occur due to the Doppler dilemma (Sect. 30.3.2). There are several techniques to recognize and even correct them.

Second-trip Unfolding – Range Dealiasing. In order to resolve the range ambiguity, i.e., to differentiate between first and second (or higher)-trip echoes in a pulse radar, pulses must in some way be *labeled* to be distinguishable. To this end, phase coding or alternate dual-pol mode are feasible under the appropriate hardware setups.

COR (magnetron) systems offer a simple approach to range unfolding as they perform, so to say, an involuntary random phase coding. Second trips are not coherent to the first trip and appear as white noise in the (first trip) Doppler spectrum, as a traditional receiver is phase locked to the most recent pulse. On the other hand, the random magnetron phase of each pulse is measured. It may be stored in a digital receiver and be used to rotate each A_i vector (using matrix multiplication) to cohere to the second trip; the first trip will now turn incoherent and show up as white noise in the (second-trip) Doppler spectrum. The coherent second trip (and its coherent clutter) may now be removed from the spectrum by an adaptive whitening filter, leaving the first trip as white noise, which will now be recovered to the first trip. This way, both signals may be retrieved. Comprising Fourier transforms, matrix multiplications, autocorrelations, and filtering, second-trip processing imposes a substantial computational load on the DSP. In fully coherent radars, the method will only work when coding the transmitter phase on a pulse-to-pulse basis.

Velocity Unfolding. As unambiguous velocity and velocity folding depend on PRF, different folded velocities will show up under different pulse repetition times. For instance, if the real radial velocity is $V = +20 \text{ m s}^{-1}$, then at $\text{PRF} = 800 \text{ Hz}$ ($V_{\text{max}} = 10.6 \text{ m s}^{-1}$) the radar detects $V'_{800} = -1.2 \text{ m s}^{-1}$, while at $\text{PRF} = 1200 \text{ Hz}$ ($V_{\text{max}} = 16 \text{ m s}^{-1}$) $V'_{1200} = -12 \text{ m s}^{-1}$. This may be exploited to detect and correct for velocity folding.

One method called staggered or dual PRF alternates transmit PRF between adjacent rays (consecutive batches), i.e., one high PRF_h and one low PRF_l , so that the measured velocities are $V'_{1/h} = \theta_{1/h} \lambda \text{PRF}_{1/h} / 4$, resulting in an enlarged unambiguous velocity, $V_{\text{max}} = \lambda / 4 (\text{PRT}_h - \text{PRT}_l)$. With a stagger ratio of $\text{PRF}_h : \text{PRF}_l = 4 : 3$ (3 : 2), an extended unambiguous $V_{\text{max}} = 3V_{\text{max};h}$ ($2V_{\text{max};h}$) is obtained. In the above example

of 1200/800 Hz an unambiguous velocity of $V_{\text{max}} = 32 \text{ m s}^{-1}$ results. The method assumes that the radial velocity is constant over adjacent azimuthal rays. If this is not the case, e.g., with small-scale clutter targets or at the edge of a precipitation field, staggered PRF unfolding will go wrong. As PRF is changing between rays, clutter filters need to stabilize at the beginning of each ray. This filter delay is configurable but diminishes the effective number of available pulses (the length of the time series). Still more serious, the filter notches at the center of the original, narrower Nyquist intervals of $\pm V_{\text{max};l}$ and $\pm V_{\text{max};h}$ now appear several times in the extended interval $\pm V_{\text{max}}$ (four times at a 3 : 2 ratio, three of them unwanted).

The same principle may be applied to changing pulse repetition time pulsewise within one ray (batch), which is referred to as staggered (dual, triple, ...) or random PRT [30.69, 70]. As IIR filters and FFT processing assume equidistant pulses, neither of them may be used under staggered PRT; statistical clutter filter may be applied instead.

Spectral Width Correction. A rotating antenna causes the Doppler spectrum width to broaden. A formula has been proposed for the variance σ_r^2 ($\text{m}^2 \text{ s}^{-2}$)

$$\sigma_r^2 = 0.017 \left(\frac{\omega_{\text{az}} \lambda}{\theta} \right)^2, \quad (30.58)$$

where ω_{az} is the antenna azimuth rate in deg s^{-1} , θ the horizontal beamwidth in deg, and λ the radar wavelength in m. The spectrum width W calculated by (30.29) or (30.30) may be corrected for this spectral widening.

30.6.4 Thresholding and Postprocessing

Quality control occurs throughout the data generation chain. Quality checks may be performed as a last step within DSP before data are output, but also by means of postprocessing or as an entrance test to follow-up meteorological algorithms (Sect. 30.8.)

Thresholding

The validity and quality of individual moments measured in certain range bins may be checked by screening against nonmeteorological values of some adequate parameters. Output moments are subjected to a logical combination of configurable thresholds usually stored in a binary bit mask. Different threshold combinations may be applied to different moments. Range bins and moments that do not pass these tests are flagged as invalid. For instance, radar measurements are usually discarded if the signal-to-noise ratio SNR is consid-

Table 30.18 Common thresholds

Threshold	Typical value	Typically applied to
CMS	35 dB	R_i^f
CPA	0.95	Filter yes/no?, CMD
CMD	0.5	Clutter filter yes/no?
$CCOR_{thr}$	-25 dB	CZ, V, W
LOG (NOISE)	1 dB	SNR, UZ, CZ, ZDR
STD_{thr}	0.5	RF interference
SQI_{thr}	0.5	V, W
$SQI2_{thr}$	0.3	Second trip
$RHOHV_{thr}$	0.8 rain, 0.5 clutter	CZ
WSP_{thr}	10 dB	W

ered too low, the clutter correction $CCOR$ too high, the spectrum width too wide, etc. Setting thresholds too stringent will result in a loss of sensitivity, setting them too loose may pass interference/noise. Table 30.18 shows the most commonly used thresholds.

Noise Power Threshold, LOG . The SNR parameter is tested against the noise threshold in order to suppress data with an SNR lower than the selected threshold. The noise threshold is usually set visually so that no noise is visible, commonly around 0.5–1 dB above the noise floor measured during the noise sample, thus defining the system MDS. Averaging in time (i.e., a longer time series) or range allows lower LOG values. LOG should be set high enough to eliminate noise and low enough not to lose sensitivity. Low-reflectivity range bins above the noise threshold will be considered as valid *no rain* bins.

Clutter-correction Threshold, $CCOR_{thr}$. The $CCOR$ parameter is the clutter correction obtained from LOG , IIR, or FFT filtering. A threshold $CCOR_{thr}$ may be used to reject data where very strong clutter is present, i.e., $|CCOR|$ is large, as it may not be desirable to trust corrections that are very much (e.g., by a factor 100) larger than the weather signal.

Recalling that $CCOR$ is negative, setting a threshold $CCOR_{thr}$ means that more negative corrections (with a larger absolute value) will be rejected. As $CCOR_{thr}$ approaches zero *less* corrections will pass.

$CCOR_{thr}$ should be chosen to eliminate the strongest clutter targets but leave headroom to filter and correct for the weaker ones. The measured $CCOR$ and the pertaining threshold $CCOR_{thr}$ depend on system coherency and the clutter filter chosen. To optimize $CCOR_{thr}$ watching a realtime reflectivity PPI, the absolute value of the threshold should be increased starting from a value close to zero (thresholding nearly all clutter), until the number and size of clutter targets no longer increase. The threshold absolute value should be set approximately 5 dB lower (closer to zero).

Signal-quality Index Threshold, SQI_{thr} . As SQI (Sect. 30.3.4) is a measure of coherency, noncoherent echoes, such as the sun, foreign transmitters, or second-trip echoes may effectively be thresholded. An SQI threshold is usually applied to Doppler data V and W at values around 0.5. A second, lower threshold may be used to screen against second trip. If second-trip processing is available, the time series may be cohered to the previous pulses, so that second or even third-trip signal quality may be calculated for the previous pulses. Storing and applying the phase information of the respective pulses in a digital receiver, $SQI2$ (and $SQI3$) may be calculated to be coherent with the second and third-trip echoes.

SQI_{thr} should be set to the lowest value eliminating noise in the velocity display. A higher value will pass less valid range bins. Averaging fewer pulses or range bins will force a higher value of SQI_{thr} .

RF Interference. Frequency assignment has become an increasing issue as more and more radiation sources fill the ether. There may be authoritative regulations, but many RLAN devices are not compliant to dynamic frequency selection (DFS) requirements. External RF emitters within the receiver bandwidth of the radar, such as the sun, or radio links, or other radars, will cause artifacts in the data. The interfering radiating source may be broadband or narrowband, continuous or pulsed, local or moving. A cw interferer, such as the sun will cause a spike of typically 1° width in the data and its intensity will increase with range because it is wrongly r^2 -corrected. Pulsed interferers (e.g., radio links) are not synchronized with the radar pulses, so that the standard deviation STD (30.34) of a pulsed interferer will be high, and no well-defined distance can be made out. The pattern of a moving pulsed interferer (aircraft, a neighboring radar reflected from a mountain) may be complicated. In any case, an external source will not be coherent, so that a low SQI is measured. These properties may be used to detect and flag external RF.

Speckle Handling. Range bins left isolated after thresholding are called speckles. Valid (= not thresholded so far) but isolated range bins are considered to be of nonmeteorological origin and may be flagged or removed by a speckle filter. Likewise and independently, isolated invalid (= thresholded earlier) bins may be recovered by interpolation, depending on the number of valid neighbors. Speckle handling may be performed on a 1-D or 2-D (or even 3-D) basis, the notions of *isolated* and of *neighbors* (their number) must be defined accordingly in order to decide on the speckle property of each bin.

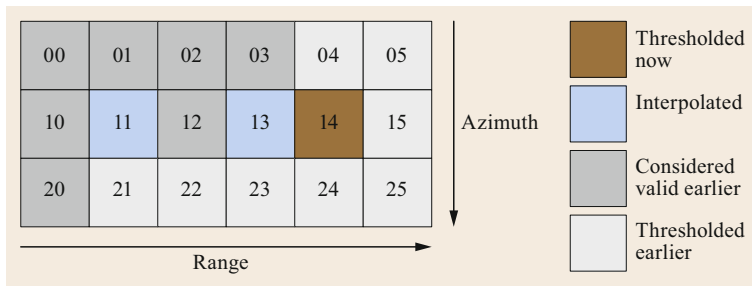


Fig. 30.9 Demonstration of the handling of speckle bins #11, #12, #13, #14 after range averaging and thresholding

In Fig. 30.9, a so-far valid bin is defined as speckle if surrounded by less than three valid neighbors. Bin #14 is, hence, flagged invalid. Thresholded bins #11 and #13 are considered isolated, as they have three or more valid neighbors that are consequently used as interpolation boundaries. Bin #12 is not a speckle and left unchanged (valid). Speckle removal may be applied for any output parameters. As a consequence, some earlier thresholds might be relaxed iteratively/in retrospect to increase sensitivity. Interpolation should be used with caution. A 2-D speckle remover will lag the quasi real-time output by 1° while waiting for the subsequent ray.

Postprocessing Quality Control

Fixed thresholds have long been used within DSPs to output only valid data for the sake of computational effectiveness. However, the results of threshold tests and classifications (such as CMD, second trip, RF interference) may be also stored and output as additional moments (sensor map) by the DSP. With fast processors and broadband data transmission, it is presently possible to calculate and output virtually all parameters and moments. Knowing for each output range bin what thresholds were not passed offers greater flexibility in choosing different threshold values and combinations for different applications and complex offline user quality control.

For example, a clutter-detection algorithm similar to CMD has been realized in the form of a centralized postprocessing QC [30.71] using fuzzy logic classification plus the texture of PHIDP to detect stationary and variable clutter (birds, insects, chaff, etc.) and to recover data that should not have been filtered, replacing them with uncorrected data.

Some more corrections and quality checks are possible outside the DSP when volume radar data and external information, such as model or satellite data are available.

Vertical Reflectivity Profile (VRP). Growth, melting (bright band!), riming, evaporation, coagulation, break up, and drop sorting due to size-dependent fall velocity are the main reasons for a vertical profile of reflectivity to exist and to be highly variable in space and time. Depending on the elevation angle and distance, the radar beam often measures rain at close range, and snow of lower reflectivity at greater distance/height. Crossing the bright band inbetween gives rise to a ring/layer of increased reflectivity in a PPI/RHI (Sect. 30.8.1). VRP has been considered the main problem in radar precipitation estimation [30.72]. Therefore, VRP correction aims at extrapolating radar measurements at height to yield precipitation fields at the ground, and several approaches have been proposed. Mean climatological profiles may be derived from several years of radar volume data, possibly differentiated by location, season, or weather type. Updated profiles may be obtained averaging local volume radar data at ranges where many elevations scan the volume, or from radiosonde or vertically pointing radar [30.73, 74]. As RHOHV and LDR have proved to be good indicators, polarimetric weather radars offer new ways of bright-band detection [30.75].

Quality Products. QC is continued when products are being generated from base data (sweeps collected ray by ray from DSP). A literature review of radar QC techniques is given in [30.76]. In DWD, a quality index field [30.77] is produced that contains flags of several data contaminations for every range bin. Simple algorithms are used to detect gross errors/corrupt data sets (no transmitter, no noise sample ...) as well as artefacts, such as spikes (sun/external emitters, beam blockage) and rings (sidelobes), clutter remnants and speckles. Similar approaches have been proposed [30.78] or realized [30.71] for polarimetric and Doppler moments.

30.7 Maintenance

Weather radar is an instrument designed to operate 24/7 with a low downtime and a very high availability, usually above 95% including, or 98% excluding maintenance. In order to meet the high quality standards and availability requirements, careful maintenance is imperative. (Unless the radar operator chooses to maximize availability reducing downtime due to maintenance.) Maintenance may be split into two categories, preventive and corrective.

Corrective maintenance becomes necessary in the case of failure. Waveguides have been seen sparking, antenna gears broken, magnetrons dead, electronics gone faulty, radomes damaged by lightning stroke, and whole radar towers unbolted. Obviously, serious breakdowns can easily thwart high availability, especially if broken parts have to be brought from overseas or are no longer available at all. This calls for stocks of spare parts, logistics and prevention.

The BITE and message systems facilitate active or on-demand distribution of selected information. Automated messages containing predefined status reports may be sent to configurable addresses, e.g., a user help desk or a technician on duty, by the radar host computer. Remote access to modern radars allows us to read out, check and control system functions and processes, such as BITE messages, scan definition and scheduler, log-files, product generation and data distribution, etc. In the case of failure, an operator may assess and possibly evaluate any problems at home and take correct spare parts to the repair site. This greatly reduces downtime.

Preventive maintenance is performed to avoid unforeseeable failures. It includes definition and stock-keeping (regional, national, or continental) of line replaceable units (LRU) as well as maintenance plans; maintenance contracts may be bought if technical service cannot be provided by the operator and is to be outsourced. Likewise, a midlife refurbishment may be negotiated with the manufacturer, or a service life extension program (SLEP, as is presently planned in NEXRAD) may be initiated.

Maintenance plans have to be thought of. If, for instance, a complete maintenance takes more than one working day, then monthly maintenance does not fit an overall availability requirement of 97%. Maintenance intervals may be stretched using solid-state, optical, and digital units instead of analog and mechanical ones, defining LRUs that are fast to replace, and by making use of automated and/or remote BITE, monitoring, calibration, validation, and messaging techniques. Rou-

time maintenance intervals have increased from earlier monthly to presently 6 or 9 months.

Many preventive maintenance tests are quite cumbersome and need to be performed more often with an analog radar, even though there may be special maintenance utilities with graphic frontends to facilitate (remote) maintenance, such as asscopes, spectrum presentation, AFC checks, calibration tools, sun trackers etc. Some maintenance checks turn out to be more easy or even unnecessary or become automated in digital parts of the radar. As digital devices and solid-state parts are very reliable and easily manageable, very low MTTR (mean time to repair, e.g., 1 h) and fairly high MTBF (mean time between failure, e.g., 50 000 h) may be expected under nonextreme operation conditions.

The following example of a maintenance checklist is neither complete nor consistent. Checks with an asterisk* lend themselves to automated monitoring (depending on the radar type), whereas a caret^ refers to high-maintenance analog components that are not present in a digital receiver. Some checks have to be performed twice on a dual-pol system:

- Overall system: check safety switches and indicators; air conditioning; leak tightness of waveguides; screws and cables; voltages*; BITE* and log messages*; USV*. Clean flies, air filters, lubrication, slip rings, radome etc.
- Antenna/radome: check motors, servos, gears, lubrication; 2-D levelling of pedestal; antenna pointing* (e.g., sun position*); servo velocities* and accelerations*; slippings/brushes; antenna safety breakers; radome water tightness and hydrophobicity; obstruction lights.
- Transmitter: Check transmit power*, stability*, frequency* and bandwidth; klystron current*, waveform*, RF input level*; PW*, PRF*, duty cycle*; VSWR*; trigger*; thyatron and burst pulse gates; any waveguide switches*; safety sector blanking
- Receiver: check T/R limiter dead time; COHO window^, frequency^ and phase locking^; AFC locking; burst sample gate^; oscillator and AFC outputs; noise figure*; gain*, MDS and dynamic range; known intensity and velocity target*, e.g., sun power*

Continuous radar monitoring (Sect. 30.6.1) presents another way to prevent failure, enable timely corrections (e.g., of biases), and ensure the required data quality.

30.8 Applications

Weather radar data are used in many fields. In atmospheric research, an operating scientist may still sit in front of the radar watching a realtime display. External users will be supplied with standard or tailored radar products. Increasingly, radar data are evaluated by computer algorithms and are integrated into complex automated procedures.

30.8.1 Radar Products and Presentations

Prior to the advent of digital signal processing, the analog video signals coming from the receiver were just displayed on a cathode ray tube (CRT). From DSPs hooked to analog receivers, the LOG, I and Q , and maybe AGC signals are still tee'd off for check on an oscilloscope. For digital receivers, there are no real baseband videos but they may be generated by the DSP for visual inspection. In an analog receiver, analog signals may still be viewed on a realtime display prior to digitization as in the past on a CRT. A-scope (intensity, etc., over range), plan position indicator (PPI), and range–height indicator (RHI) are typical presentations of this type but may also be generated on a digital base.

A PPI is one of the oldest and still one of the most common presentations of radar data. It shows the radar echoes in two-dimensional radar-centered polar coordinates (range, azimuth) with a brightness or color-coded intensity, or any other measured parameter.

An RHI is obtained by vertical antenna scanning at a fixed azimuth. It is well suited to investigate the inner structure of thunderstorms. For instance, an automated

or operator-induced RHI may be performed through the strongest echo in an operational azimuth scan. As there is a fixed volume scan schedule in most operational weather radars, a pseudo or soft-RHI may be produced from the volume data with a much coarser resolution and with some distortion due to the time delay between elevations. Figure 30.10 shows an example of a real (hardware) RHI. Note that due to the presentation scales the vertical is largely exaggerated.

For data presentation, radar data may be referred to GIS-based digital maps, warped to Google Earth®, or provided with vector under- and overlays. While radar data are intrinsically measured in radar-centered polar coordinates (range, azimuth, elevation), many radar products are projected to some geographic grid based on an earth-centered (e.g., stereographic projection) or geodetic datum (e.g., WGS 84 flat map). There are several issues with sampling in this type of projection, as the data density is large close to the radar and scarce at a distance, depending on the range bin and pixel size. For example, at near range, the range bin closest to the Cartesian pixel center may be chosen to represent the pixel, or the maximum or mean value, and range bins flagged for interference (Sect. 30.6.4) may be excluded.

Many more products may be generated from volume data. For instance, a CAPPI (constant altitude PPI) is a horizontal cut at a certain height. Obviously, a cut in a strict sense would just produce concentric rings, as measurement occurs on cones of constant elevation. To close gaps between different elevations, data are usually *zigzag*-sampled from a layer around the nominal CAPPI

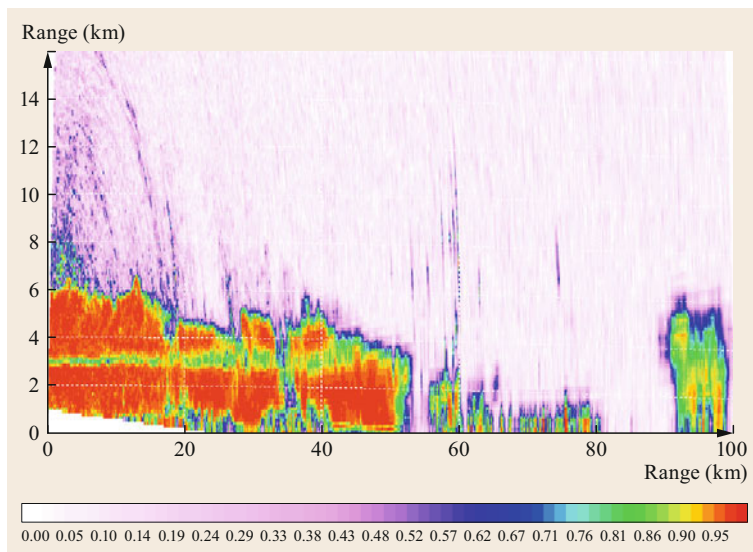


Fig. 30.10 Range–height indicator RHI of RHOHV through summer noon precipitation. The bright band and ground clutter are clearly discernible, illustrating RHOHV to be a potent hydrometeor discriminator (image © J. Seltmann, DWD)

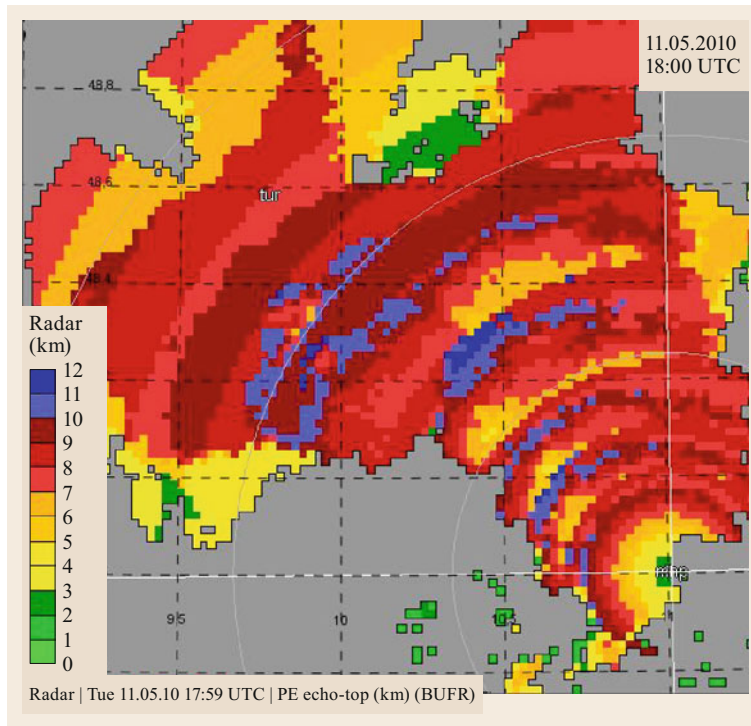


Fig. 30.11 Echo-top product indicating the height of the 10 dBZ isoreflectivity surface (in km). Rings are due to discrete elevation sampling (image © DWD)

height. The layer thickness depends on the elevation spacing as a tradeoff between the desired accuracy versus data completeness. A thicker layer produces more data less accurately located and more visible rings. Figure 30.16 shows an operational product containing 12 CAPPs at heights between 1 and 12 km.

An echo-top product (Fig. 30.11) is a color-coded height indication of a certain iso-reflectivity level, e.g., the maximum height where 18 dBZ are encountered. Visible rings occur due to the *elevation jump*, as before. Special considerations lead to more specific products, such as a top-down maximum projection, or the lowest *clean* (= not thresholded) voxel bottom-up.

A 2.5-D presentation is a very useful tool to locate severe convection or hail shafts. It may be created using a ground view (e.g., a low CAPPI or a maximum projection top-down) together with two maximum projections west–east and south–north through the data cube, as shown in Fig. 30.12.

A maximum projection makes sense only with reflectivity, while for radial wind data, two real cross sections E–W and S–N through the radar would be appropriate.

The aforementioned *legacy products* may all be (and traditionally are) generated by the radar software on site. In a weather radar network or compound, product generation may be centralized. This is particularly true for products based on several radars.

Multiradar Products

While research facilities sometimes run their own radars for research purposes, the national weather services in many countries operate networks of weather radars, often covering all of their country's territory. Water management facilities and national and supranational associations generate composites (mosaics) over certain regions, such as catchment areas, individual countries (Fig. 30.13), or (part of) Europe.

Not only may the individual radars be mosaicked, thereby making up for beam blockage or attenuation and reducing the effect of beam broadening as a positive side-effect, but due to some overlap the data volume may be densified in space and time, closing elevation gaps and possibly filling each other's cone of silence, resulting in faster updates and information condensation for meteorologists and vertically sampling algorithms. Echo top, maximum-column reflectivity, or vertically integrated liquid water content (Sect. 30.8.3) are examples of products that will profit from multiradar data. Thus, products of networked radars are more robust than single-radar products. However, even with identical calibration, two radars may not see the same thing. Differences of several dB have been reported.

If several radar data sets are being composited, in addition to the projection considerations above, it must now be decided how to handle overlapping areas.

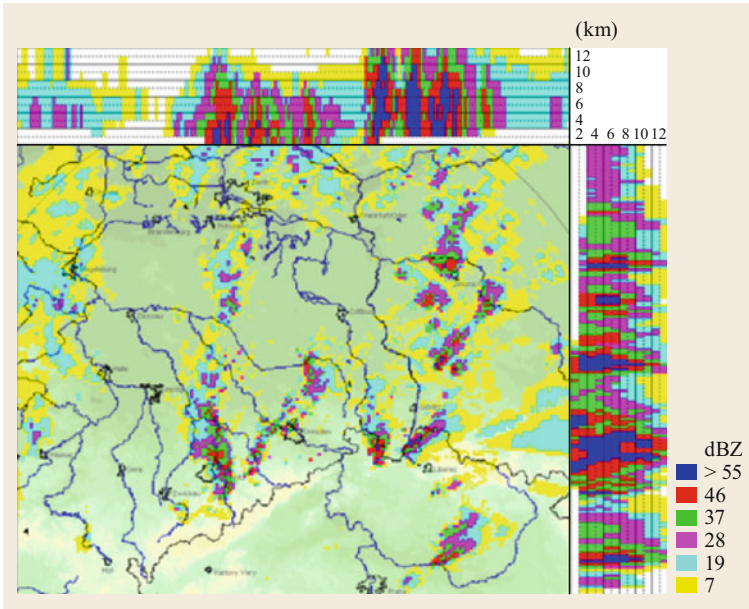


Fig. 30.12 2.5-D product showing a severe weather case that was to cause damage in Saxony, Germany, on 14 May 2007, here as seen by the Dresden radar at 16:41 UTC. The vertical maximum projections S→N and W→E show several high-reaching cells that may easily be located in the ground projection (image © DWD)

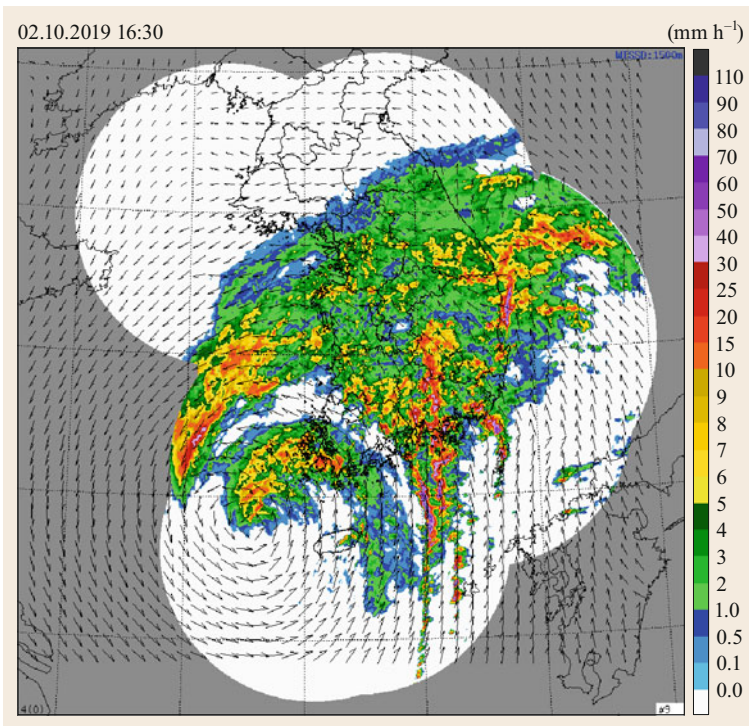


Fig. 30.13 Korea nationwide mosaic of rain rate estimation during typhoon Mitag, the 18th tropical storm in 2019 and the 7th to hit Korea, causing 9 casualties due to drowning and landslides (image © Korea Meteorological Administration)

Again, minimum, maximum, average, or closest-to-ground values may be chosen, or the decision may be based on some quality information that comes along with the data, choosing the higher quality [30.77]. This impacts pixel origin and availability and, hence, any climatological interpretation.

Several countries (Canada, Denmark, Germany, and Switzerland) are conducting a common project *NinJo* [30.79] to help process and display meteorological data, combining data of several sources (*layers*), such as synoptic observations, aerological soundings, lightning, satellite, and radar data into a common

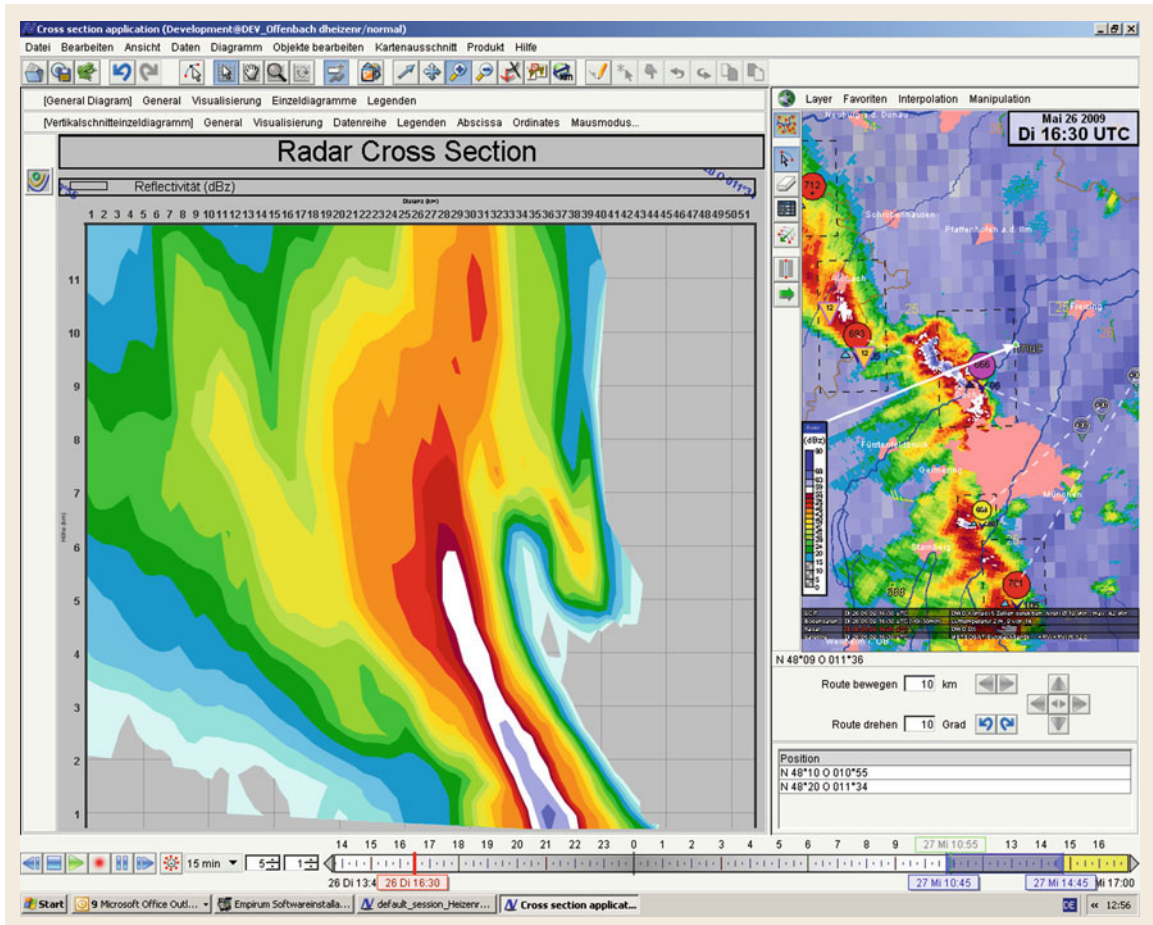


Fig. 30.14 Interactive cross section (indicated by a *white arrow, right*) through a squall line, NinJo presentation (image © DWD)

database. This allows interactive presentations, such as arbitrary cross sections through a thunderstorm, as shown in Fig. 30.14, or along a flight path.

30.8.2 Interpretation of Weather-Radar Products

The easiest way to use weather radar is visual image interpretation. Widespread precipitation, its areal distribution and patterns, including strong local gradients, are readily detected. Specific features typical of certain meteorological phenomena can sometimes be seen, as well checking the local data structure for high-resolution (e.g., 250 m, 5 min) products. For instance, echoes about 57 dBZ and above are usually associated with a high chance of hail even in a single PPI, and the more so if extending high (Fig. 30.12). Hook echoes (Fig. 30.17) are considered typical of mesocyclones with a high risk of tornado, a so-called hail spike is sometimes visible behind strong hail, and conver-

gence/divergence or velocity dipoles may be detected in radial wind patterns. The same is true with 3-D data: hailshafts or overhanging precipitation may be detected from vertical cross sections or projections, the vertical extension of precipitation may be read from echo top presentations, and jet streams may be seen in velocity PPIs at medium elevation. Observation over time will help in nowcasting storm movement and development. Time–height presentations may help investigation into the vertical structure of precipitation, e.g., the detection of a descending *bright band* (Fig. 30.15).

Negative differential propagation phase and negative ZDR may betray cloud regions where ice crystals are aligned by electric fields, even when there is no lightning [30.81, 82]. In combination with satellite images radar also helps monitor tropical cyclones (Fig. 30.13) and issue hurricane landfall warnings.

The following considerations may help to interpret Doppler radial wind products: velocity folding is easiest recognized by abrupt color jumps between $+V_N$

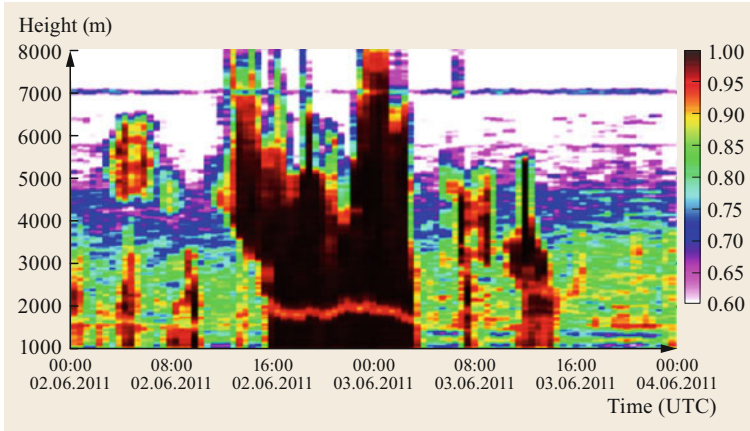


Fig. 30.15 Time series of vertical scans with a bright band descending over time clearly visible in RHOHV. Hohenpeissenberg radar, 02–04 June 2011 (after [30.80], © M. Frech, DWD)

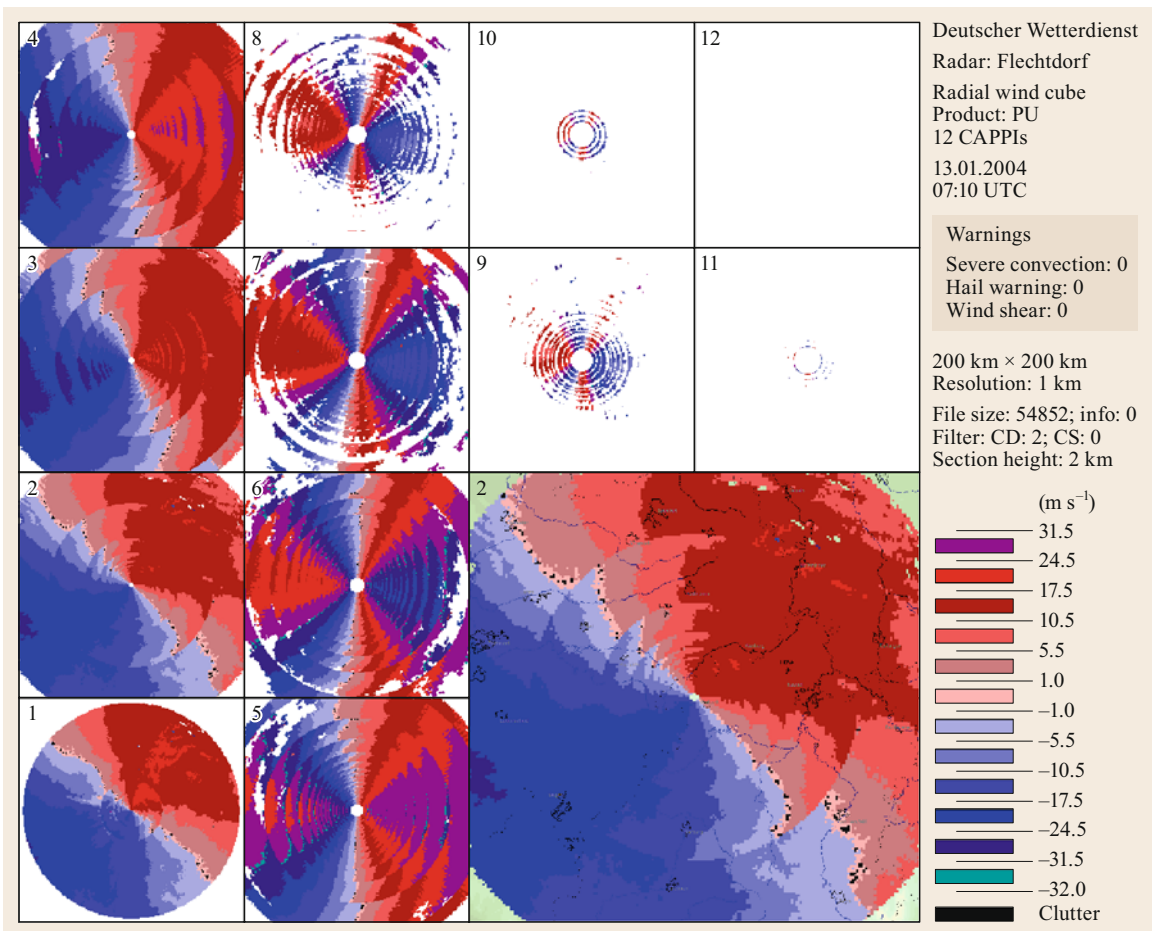


Fig. 30.16 Radar product with CAPPIs at several altitudes, small numbers indicate heights in km. The wind is veering clockwise from SW at 1 km to W at 5 km (advection of warm air). A slight divergence seems to occur at midaltitudes. Folding occurs starting from 4 km upwards. Elevation jumps are visible due to the CAPPI sampling process (image © DWD)

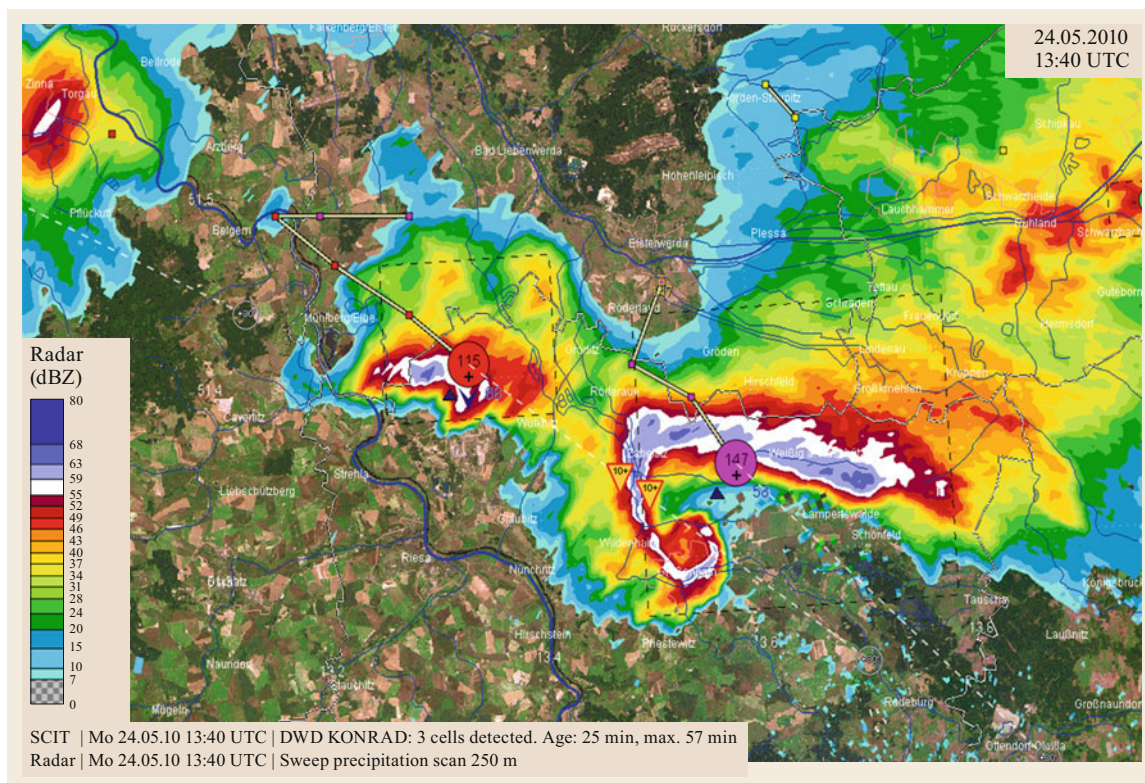


Fig. 30.17 A hook echo is indicative of a supercell that may potentially produce a tornado, exemplified here by the disastrous Grossenhain tornado (F3) of 24 May 2010 in Germany (image © 2018, NinJo-Consortium/DWD)

and $-V_N$ in continuous precipitation fields (red and blue in Fig. 30.16). Searching for the (central) zero isodop (the line of zero radial velocity) and moving against or with the wind (maybe crossing another – folded – zero isodop), the real radial velocity may be estimated. On the (unfolded) zero isodop, the real wind vector is a tangent to any circle around the radar. This helps recognize regions of convergence or divergence. Also, looking at the elevation of a PPI, something can be said about the vertical wind profile, e.g., vertical wind velocity or directional shear (veering). Even a low-level jet may be detected this way (velocity first increasing, then decreasing again with height/slant distance). Warm air advection is accompanied by a clockwise rotation with height (Northern Hemisphere), whereas cold fronts may be detectable by a cyclonic wind jump. Azimuthally closely spaced pixels of opposite wind direction (called a dipole) indicate rotation, as in a mesocyclone (Fig. 30.21).

The temporal development of some radar objects may occur very rapidly. This is not only true for the movement of tornadoes. *Normal* thunderstorms can develop from nonexistent to a full-grown hailstorm within less than 10 min (Fig. 30.18).

30.8.3 Automated Weather Radar Algorithms

While visual interpretation may be intelligent and complex, there are strong reasons even besides the cutdown of human resources to automatically derive interesting features, such as rain accumulation over a catchment area or weather warnings. For example, difficult situations may arise for a meteorologist if large-area networks have to be monitored in critical situations. Some characteristics may not be accessible to the human eye at all or can only be estimated roughly. Lately, a weather radar's increased ability to detect and possibly warn of short-lived local weather hazards has become one of its most important applications. Integrations, thresholding, BOOLEAN decision trees, or fuzzy logic, as well as image processing, are typical automated algorithms. Products from integrated data of several networked radars facilitate faster update, denser data, and greater robustness than single-radar products and may help with beam blockage, beam broadening, and the cone of silence. Verification may turn out to be difficult if no observation is available.

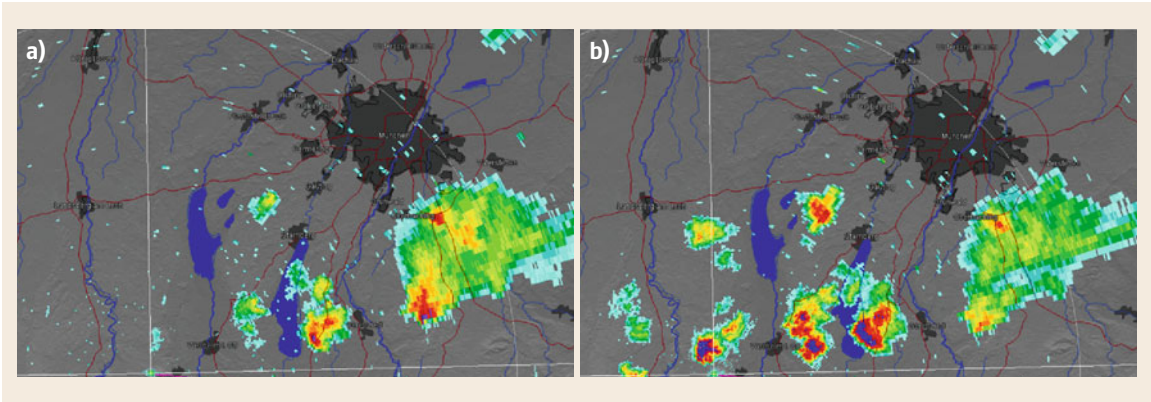


Fig. 30.18a,b Extremely rapid development of several convective cells over the lakes Ammersee and Starnberger See, close to Munich, Germany, detected by Hohenpeissenberg radar on 1 August 2018, at 18:57 (a) and 19:04 UTC (b). Within 7 min, at least two additional convective cells, one of them with a high probability of hail ($Z \geq 55$ dBZ), appear out of nowhere (image © J. Seltmann, DWD)

Quantitative Precipitation Estimation

Radar quantitative precipitation estimation QPE and quantitative precipitation forecast QPF have long received high priority consideration in most national hydromet authorities and by WMO [30.83].

One of the earliest and simplest methods to estimate precipitation intensity is the conversion of the measured echo strength (reflectivity factor z) into rain rate R by a so-called Z/R -relation. Its empirical determination is straightforward, if Z and R are observed, plotted, and fitted to an analytical function. The same may be effected semi-empirically if the raindrop size distribution is measured by a disdrometer and z and R are calculated integrating over the observed size spectra according to

$$z = \int_0^{\infty} N(D)D^6 dD \tag{30.59}$$

$$R = \frac{\pi}{6} \int_0^{\infty} N(D)D^3 v(D) dD \approx \frac{\pi}{6} \int_0^{\infty} N(D)D^{3.7} dD . \tag{30.60}$$

In an attempt to reduce the coincidence mismatch in space and time between individual samples of rain gauge and radar, pairs of z_i and R_i showing equal cumulative probabilities (CDFs): $\int p(z) dz = \int p(R) dR$ (pairs of equal CDF percentiles) are matched in the probability matching method [30.84], where the integrals run from 0 to z_i and R_i , respectively. In [30.85], it was proposed to confine radar data to a spatiotemporal window about the gauges in the window PMM (WPMM).

Marshall et al. [30.86] fitted their data to $z = aR^b$, resulting in a straight line in a log-log plot and in the

Marshall–Palmer relation

$$z = 200R^{1.6} , \tag{30.61}$$

which is the most famous among hundreds of Z/R -relations derived locally, climatologically, and for specific weather conditions (stratiform, convective, northern, tropical ...). Ambiguities arise trying to express the strongly nonlinear and multiparameter relation between z and R by only one measured parameter. As this type of Z/R -relation usually overestimates high rain rates, a partwise linear approach has been proposed [30.87, 88].

With the advent of dual-polarization radar, more observables are available to parameterize the highly nonlinear relationship. Again, many individual relations have been proposed; many of them of the type $cZ^a ZDR^b$, $cZ^a 10^{0.1bZDR}$, or $cKDP^a ZDR^b$.

As an example, the following prototype NEXRAD algorithm (tuned for Oklahoma) was published [30.38]

$$\left. \begin{aligned} R(z) &= 0.017Z^{0.714} , \\ R(K_{dp}) &= 45.3|KDP|^{0.786} \text{sign}(KDP) \\ R &= \frac{R(z)}{0.4 + 5.05(ZDR - 1)^{1.17}} \\ &\quad \text{if } R(z) < 6 \text{ mm h}^{-1} , \\ R &= \frac{R(KDP)}{0.4 + 3.48(ZDR - 1)^{1.72}} \\ &\quad \text{if } 6 < R(z) < 50 \text{ mm h}^{-1} , \\ R &= R(KDP) \\ &\quad \text{if } R(z) > 50 \text{ mm h}^{-1} . \end{aligned} \right\} \tag{30.62}$$

It has been established that ZDR needs to be accurate within 0.1 dB for light rain and 0.2 dB for heavy

rain in order to perform better than a nonpolarimetric estimator [30.51]. Moreover, polarimetric target classification (see Sect. 30.8.3, *Hydrometeor Classification HMC*) can help select the correct QPE regime and avoid biases in precipitation estimation due to snow, bright band, and non-met targets.

Once fields of rain rate have been obtained from radar data, they are usually validated against or adjusted to *ground truth*. There are many different ways to accomplish gauge adjustment, such as a constant average factor derived from a comparison of radar and gauge average areal precipitations, updated Z/R -relations, kriging including co-kriging and external-drift kriging, as well as a geostatistical merging procedure, which are all described in [30.89].

Vertically Integrated Products: VIL, VILD, VII

Using 3-D volume measurements, vertically integrated liquid water (VIL) or ice (VII) content in a vertical column over a certain area are easily obtained by adding and possibly interpolating measurements at different radar elevations within the column after conversion to rain amount. VIL yields the mass of water over 1 m^2 and is typical between 0 and 100 kg m^{-2} . Following [30.90],

$$\text{VIL} = \sum 3.44 \times 10^{-6} \left(\frac{Z_i + Z_{i+1}}{2} \right)^{\frac{4}{7}} \Delta h, \quad (30.63)$$

where the layer mean reflectivity (the round bracket) is capped at 56 dBZ to screen against ice. If possible, the bright band should be removed from the Z profile. High values are typical of heavy rain or hail. Convective events typically exhibit $\text{VIL} > 10 \text{ kg m}^{-2}$ [30.91]. VIL is used to estimate storm potential and, thus, serves as a warning indicator of storm severity.

VIL density (VILD) is defined as VIL normalized by its column depth at each grid point. For precipitation reaching the ground, the echo-top height h_{ET} may be used

$$\text{VILD} = \text{VIL} h_{\text{ET}}^{-1} \quad (\text{g m}^{-3}). \quad (30.64)$$

The 18 dBZ echo top is applied in [30.92]. VILD is considered to be more useful than a VIL-of-the-day threshold to assess storm severity.

Similarly, an estimate of vertically integrated ice VII may be derived from the VRP $Z(h)$ within the ice growth layer determined by sounding or model analysis. VII may be used as an indicator of initiating convective storms, cell growth, and electrical activity, of storm severity and potential for hail, and of increasing/decreasing updraft intensity. One formula is given

in [30.93] and [30.94]

$$\text{VII} = 10^3 \pi \rho_i N_0^{\frac{3}{7}} \left(\frac{5.28 \times 10^{-18}}{720} \right)^{\frac{4}{7}} \int_{H(-10^\circ)}^{H(-40^\circ)} Z(h) dh, \quad (30.65)$$

with the ice density $\rho_i = 917 \text{ kg m}^{-3}$ and the parameter $N_0 = 4 \times 10^6 \text{ m}^{-4}$; the integration here is performed between the -10 and -40°C isotherms.

Hail Detection

Due to its high potential for damage, hail has always received special attention in the interpretation of weather radar. Several criteria and algorithms have been developed even for intensity-only radars using characteristics such as high-reaching strong echoes and strong horizontal gradients (Fig. 30.12), *hail spike*, and special polarization signatures:

- In the CAPPI method, a reflectivity threshold is defined at a certain height, e.g., $Z_{\text{thr}} = 55 \text{ dBZ}$ at a height of $H = 0.8, 1.5$ or 2 km .
- In the ZMAX-method, the maximum reflectivity in a vertical column is checked, e.g., $Z_{\text{max}} = 55 \text{ dBZ}$.
- In the VIL method, the vertically integrated liquid water content VIL is used as a hail indicator, e.g., $25\text{--}35 \text{ kg m}^{-2}$ and $50\text{--}60 \text{ kg m}^{-2}$ in cold and warm air masses, respectively.
- In the VIL density method, VILD is used instead, e.g., $\text{VILD}_{\text{thr}} = 3.5 \text{ g m}^{-3}$.
- The Waldvogel method [30.95] checks for a certain reflectivity at a certain height above freezing level, e.g., $H_{45\text{dBZ}} \geq H_{0^\circ} + 1.4 \text{ km}$.
- The severe hail index SHI is calculated using a Z/\dot{E} relation (instead of Z/R in VIL). In this sense, SHI is complementary to VIL, making use only of higher reflectivities and leaving out lower ones.

$$\text{SHI} = 0.1 \int_{H_0}^{H_T} W_T(H_T) \dot{E} dH \quad (\text{J m}^{-1} \text{ s}^{-1}) \quad (30.66)$$

$$\dot{E} = 5 \times 10^{-6} \times 10^{0.084Z} W(Z) \quad (\text{J m}^{-2} \text{ s}^{-1}) \quad (30.67)$$

[30.96], where H_T is the storm cell top height, \dot{E} is the kinetic energy flux of hail, and $W(Z)$ is a weight function that increases linearly from 0 to 1 between certain reflectivity limits, e.g., between 40 and 50 dBZ. The vertical integration is further weighted by temperature, excluding heights below the freezing level at 0°C and increasing to 1 around the -20°C height obtained by sounding or NWP. SHI is primarily used in the following methods.

- The POSH method estimates the probability of severe hail. An SHI warning threshold WT was empirically found in [30.96] as a function of the melting layer height $H_{0^\circ\text{C}}$ (km) above radar: $WT = \max\{20; 57.5H_{0^\circ\text{C}} - 121\}$ ($\text{J m}^{-1} \text{s}^{-1}$). POSH (%) is then calculated as

$$\text{POSH} = \min \left\{ \max \left\{ 0; 29 \ln \frac{\text{SHI}}{\text{WT}} + 50 \right\}; 100 \right\}, \quad (30.68)$$

so that there is a 50% chance of severe hail if SHI meets the warning threshold. POSH is used to describe the probability of 1.9 cm (3/4", the former US weather service's NWS severe hail criterion) diameter hail; 70% POSH is also considered equivalent to a 50% probability of 1" (2.54 cm) hail.

- Maximum estimated size of hail (MESH) in cm. This parameter is calculated from SHI as

$$\text{MESH} = \sqrt{\text{SHI}} \times 2.54 \text{ cm} \quad (30.69)$$

and is used to estimate the maximum expected hailstone size as well as areal hail distribution [30.96].

- The hail signal according to [30.97] is based on Z_h and ZDR

$$\text{HDR} = Z_h - \begin{cases} 27 \\ 19\text{ZDR} + 27 \\ 60 \end{cases} \cdot \begin{cases} \text{ZDR} < 0 \text{ dB} \\ 0 \text{ dB} \leq \text{ZDR} \leq 1.74 \text{ dB} \\ \text{ZDR} > 1.74 \text{ dB} \end{cases}. \quad (30.70)$$

- Fuzzy logic hydrometeor classifiers usually feature a hail class of their own.

Hydrometeor Classification HMC

Differentiation of targets within the radar volume according to their aggregate state has been one of the main goals in radar observation and one of the main reasons for deploying multiparameter radars. Interestingly, some estimation is possible even with Z-only radars using empirical intensity and/or height extension thresholds and possibly external (temperature) information (see the description of hail detection above).

As dual-pol observables (Sect. 30.3.4) depend on phase, shape, orientation, and the number distributions of the targets, the former are well suited to classify different types of hydrometeors and nonmeteorological targets. Several techniques have been proposed [30.38],

such as a Boolean decision logic [30.98], statistical decision theory, or neural networks. Fuzzy logic is commonly considered one of the most promising approaches; [30.99, 100], and different types of membership functions, such as triangular, trapezoidal, ramp, or beta functions have been used. Classification categories may be just a few, or more than a dozen. Hydrometeor classification at radar beam height may then be extrapolated to the ground. Figure 30.19 shows an example.

Wind Products

While interpreting radial wind patterns may give the meteorologist a clue to the mesoscale wind regime, there are also automated procedures to derive wind vector fields or profiles or to detect shear, mesocyclones, or even tornado signatures.

Velocity Azimuth Display (VAD) and Volume Velocity Processing (VVP)

Assuming a horizontally homogeneous horizontal wind field over the radar site [30.101], the radar measurement over a circle at constant radius (height) may be fitted to a sine over the azimuth. Its amplitude yields the wind speed, and the argument of the minimum is the wind direction. VAD may be performed at several heights over one conical elevation scan with increasing circle diameter, or at constant circle diameter over several elevations. The method fails if the homogeneity assumption is violated, leading to an insufficient number or a large spread of measuring points. The VVP technique [30.102] uses volume data in a multidimensional regression.

Uniform Wind Method UW. As the above-mentioned sine over azimuth is theoretically defined by two values, the homogeneity condition may be relaxed. In the uniform wind (UW) technique, homogeneity is stipulated only over certain areas of, e.g., $20 \text{ km} \times 20 \text{ km}$. A sine is then fitted in each of these areas, resulting in a coarse wind field estimate as shown in Fig. 30.20.

Dual Doppler. While one radar is capable of measuring only one – the radial – component of the wind vector field, suitably positioning two or more radars offers the possibility to measure two different radial components. The latter will be orthogonal only on a circle (sphere) through both radars, but useful wind fields can be constructed as long as the components are not near collinear.

If more than two radars overlap in a network, a multiple-Doppler technique may be applied to increase areal coverage and data quality. The distance between radars must not be too large because of beam elevation and beam broadening (decreasing resolution).

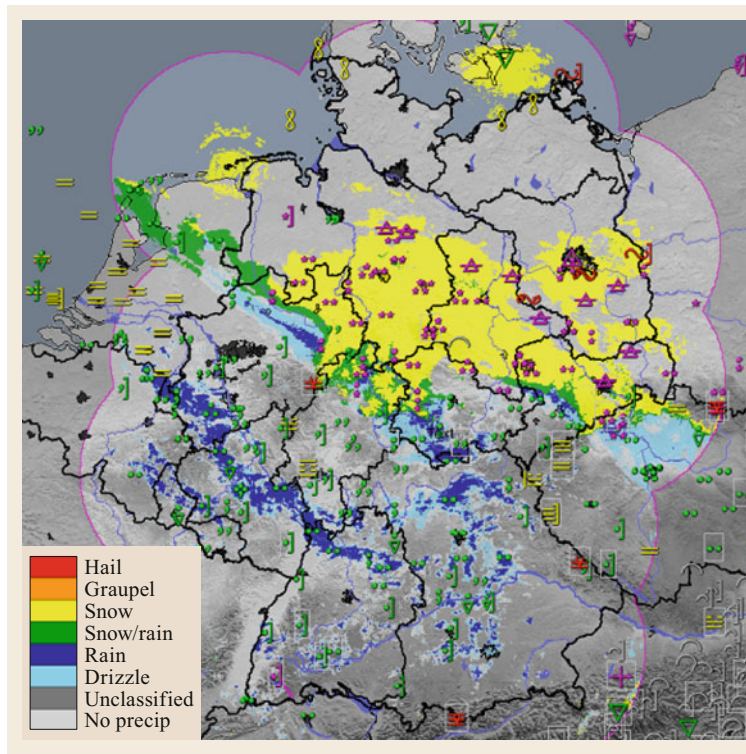


Fig. 30.19 DWD final product of hydrometeor type estimation at 2 m AGL, preoperational state. Polarimetric fuzzy logic classification of radar measurement aloft has been extrapolated to the ground using model and ground temperature information. NinJo presentation of German composite overlaid with ground observations (image © DWD)

Multistatic Doppler. More than one wind component may also be cost-efficiently measured by deploying additional receivers around a transmitting radar in a so-called bistatic or multistatic configuration [30.103]. Strict synchronization between transmitter and receivers is necessary.

Mesocyclone Detection and Tornadoes. Automated mesocyclone detection relies on the existence of a cyclonic rotation dipole in high-resolution polar radial wind data [30.104]. In order to estimate the risk of a tornado once a mesocyclone has been detected, the mesocyclonic rotation is scrutinized to find a *tornado vortex signature* (TVS), which is defined as a three-dimensional circulation with its base at 0.5° elevation or below 600 m above radar [30.105]. It indicates a region where the rotational shear is further intensified, representing the transition to a tornado, as shown in Fig. 30.21. The detection of a TVS may initiate a tornado warning.

Multitemporal and Tracking Products, Nowcast, and Forecast

The notion of nowcasting refers to a very short mesoscale forecast (2 h) using extrapolation methods (e.g., *optical flow*). In addition to quantitative extrapolation of precipitation fields, tracking and extrapolation of convective cell motion, including potential cell development, has

gained particular focus. Radar data also help in nowcasting the potential for icing through supercooled large drops in air traffic, and freezing in road traffic.

VIL Track. A VIL track is accumulated over some span of time, say 3 h, each pixel representing the sum or the maximum VIL over this span of time. VIL tracks are another way to visually track storm cell movements over time, see Fig. 30.22.

MESH tracks are calculated similarly from the maximum values of MESH and simultaneously show history and trends in the motion and development of a storm, particularly its hail core, as well as regions of large hail fall, over a certain period of time.

The operational DWD nowcasting product CONRAD (convection development in operational radar products) [30.107] detects, analyzes, and evaluates cell cores with respect to echo strength, areal extension, and direction of past movement. This is extrapolated, and warnings are given for heavy rain, hail, and wind gusts.

Assimilation into NWP Models

Radar data may be assimilated into high-resolution numerical weather prediction (NWP) models, thus forcing the model into realistic initial conditions. Especially cloud-resolving models may benefit, as those models are designed to simulate severe weather conditions

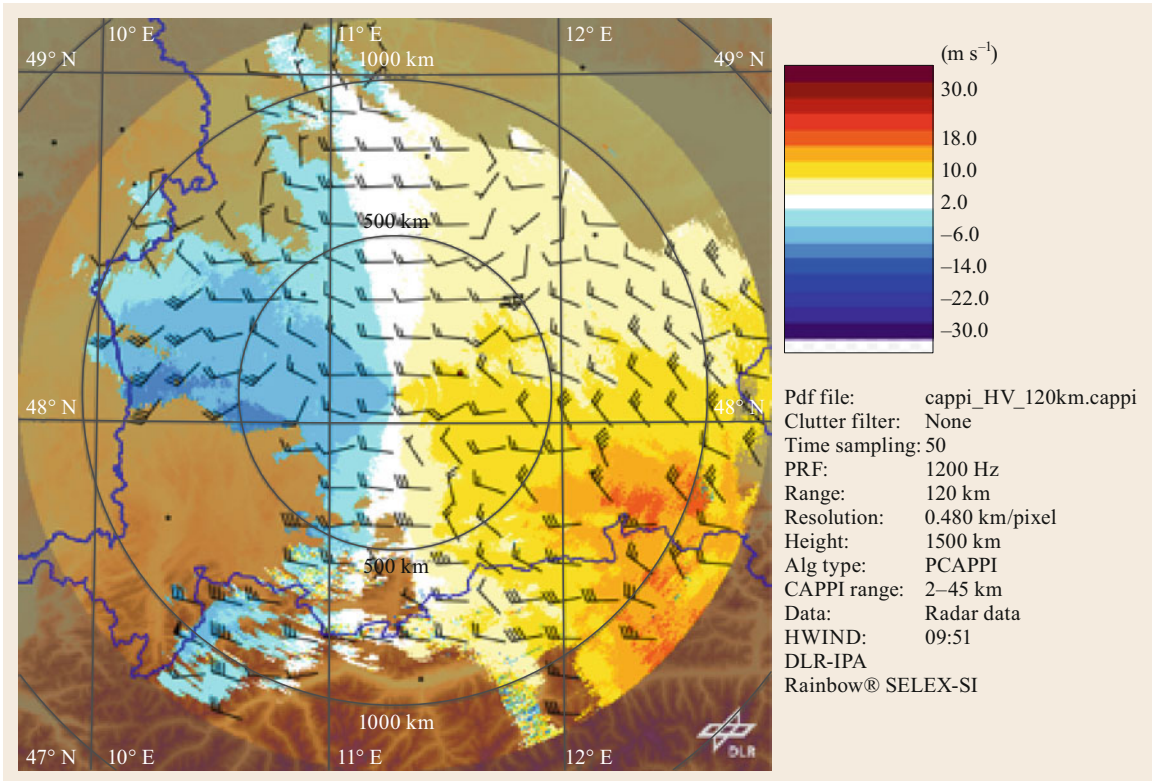


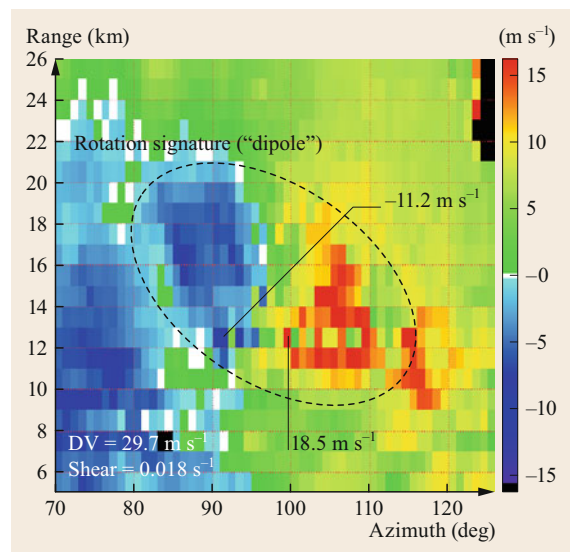
Fig. 30.20 CAPPI at 2 km ASL of radial wind, overlaid with wind barbs according to the UW method. DLR POLDIRAD, Germany, on 15 February 2013 at 09:51 UTC (image © DLR, reprinted with permission)

in near-realtime. Several approaches have been developed to assimilate different kinds of radar observations and related products. Latent heat nudging, as well as variational approaches 3-D-Var and 4-D-Var are used and have been demonstrated to improve short-range forecast scores. A survey is given in [30.108]. High-quality radar wind and precipitation fields including error statistics are needed to improve initial conditions for NWP models [30.109]. In any case, the model has to provide information comparable to the radar observation. Some of the following approaches are already running successfully in operational applications.

The simplest approach is assimilation of 2-D composites of derived precipitation rates using the so-called

latent heat nudging (LHN) approach [30.110, 111]. The model state will instantaneously respond by simulating a precipitation rate very close to the observation. LHN is

Fig. 30.21 Rotation structure of a mesocyclone (Glas-huette, Germany, 13 May 2015 at 19:15 UTC) as detected by the Feldberg radar at an elevation of 1.5° after subtraction of the cell displacement velocity. The dipole is slightly rotated due to convergence. There is a marked TVS signal according to Mitchell (pixel pairs and velocities indicated). The mesocyclone was detected 15 min prior to the occurrence as per ESWD entry (modified from [30.106], © T. Hengstebeck, DWD) ▶



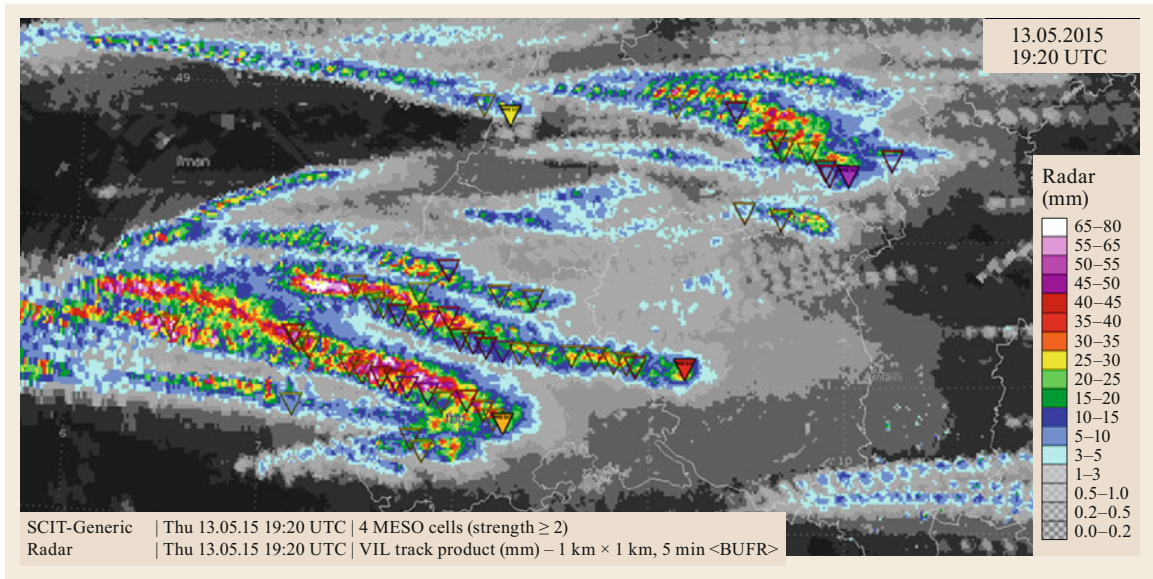


Fig. 30.22 VIL track composite product showing trails of several eastwards moving convective cells with high columnar water contents. Cell splittings and a right mover are visible. Fast movement produces discontinuous tracks, depending on the volume update rate (image © 2018, NinJo-Consortium/DWD)

operational at the United Kingdom Met Office (UKMO) and Consortium for Small-Scale Modelling (COSMO) consortia; Canada decided on implementation recently.

In order to assimilate 3-D radar reflectivity, a model forward operator is required to calculate a radar equivalent model parameter. This provided, reflectivity can be applied in any kind of variational assimilation methods or in ensemble-based methods. At Meteo France, reflectivity is assimilated indirectly within a 3-D-Var scheme, whereas UKMO uses reflectivity directly in 4-D-Var. 3-D radar radial wind is operationally assimilated at UK Metoffice and at Meteo France. Given the radar location, radial velocity can easily be obtained within the model. However, aliasing turned out to cause problems.

Vertical profiles of horizontal radar wind (e.g., VAD) have also long been assimilated into global models. The benefit of this suffers from quality issues of the VAD approach. First approaches have been developed and tested to assimilate 3-D polarimetric parameters and refractivity (see below).

Special Applications

Refractivity and Moisture Fields. A method was proposed in [30.112] to estimate the refractivity and, hence, the near-ground moisture fields using the principle explained in Sect. 30.3.2. The phase of the incoming echo from many fixed ground targets is monitored. Knowing that such a target is not moving, and assuming that the radar frequencies and phases are known, any phase changes are attributed to changes in refractiv-

ity along the radar path and may be used as a proxy to mesoscale air humidity patterns. The method is relative (measuring only phase changes) but may be coupled to absolute refractivities determined independently. It is limited by phase aliasing and by the curvature of Earth.

Bird Observation. Weather radar has also been used by ornithologists and entomologists using Doppler data [30.113], the differential Doppler velocity $DDV = V_h - V_v$ [30.39], and polarimetric data [30.114].

Radar Statistics and Climatology. Weather radar data are, in principle, well suited for climatology studies because they cover weather phenomena from micro to macro scale with a spatiotemporal resolution exceeding the demands of climatology. However, due to frequent changes in radar hardware, calibration, parametrization, and maintenance state, as well as differences (including availability) between network radars, the homogeneity and duration of radar time series used to be insufficient. Lately, with digital hardware becoming more stable, demanding less frequent repair and maintenance, and with quality standards for maintenance, unified calibration, parametrization, and scan strategies being agreed upon, reliability and availability have been increasing. First cautious steps have already been taken to climatologically exploit radar data [30.115] using statistics of severe convection, hail, or mesocyclones. Radar statistics may also be used for correction of beam blocking and beam height [30.62, 116].

30.9 Future Developments

Over the past three or four decades, the use of weather radar data has tremendously increased worldwide and will continue to do so. Radar has been revolutionized by solid-state technology, miniaturization, digitization, computerization, and networking. This process is still ongoing and, in turn, facilitates elimination of moving mechanics, sensitive analog electronics, and critical high voltage, leaving an all-digital all-solid-state fast scanning radar on today's horizon.

30.9.1 Rapid Update

The need to catch and understand rapidly developing phenomena, or tornadoes and microbursts, and to produce timely warning, has produced a demand on data update rate that cannot yet be fully satisfied. Speeding-up antenna rotation meets its limits, even though experiments are underway to combine 5 min volumes with lowest sweeps every minute using a standard mechanical parabolic antenna. Weather adaptive scanning may be an option to save scan time and gain more information from high priority targets and regions, e.g., taking RHIs through convective storms. The main effort, however, is concentrated on electronic scanning and adaptive waveform selection.

30.9.2 Electronic Scanning

Only recently are electronically steered antennas being tested and evaluated for operational meteorological purposes. When the remaining difficulties are overcome, large and heavy rotating paraboloids, and even all mechanically rotating parts, will eventually be replaced, which will allow fast and flexible scanning and system stability. Under benefit–cost considerations, mechanical rotation in the azimuth of a vertically scanning plane phased array will likely be a first step.

30.9.3 Denser Networks

Densification of existing networks using more network radars or smaller (e.g., X-band) radars will close network coverage gaps and improve radar overlap, as well as boundary layer coverage due to the lower radar beam. A gap-filling network of short-range radars offers many of the advantages of a dense network if data fusion models are available. Gap-filler radars will start to be deployed near metropolitan areas and airports or in fast reacting drainage systems using low-power solid-state transmitters. Solid-state technology may also open the way to multifrequency radar.

30.9.4 Radar Allocation

Unfortunately, in heavily populated countries, such as within the European Union, siting new radars is becoming an increasing problem due to the lack of unused areas fulfilling the requirements of unobstructed sight and of radiation regulations, and possible movements against electromog. Frequency allocation may turn out to be next to impossible in the future. Some upcoming technologies (e.g., pulse compression) result in wider bandwidth waveforms, increasing problems with frequency allocation and (wideband) external jammers.

30.9.5 Data Processing

Nowadays, DSPs are ready to handle SSPAs, pulse coding and pulse compression, and adaptive waveforms. Open-source processing is becoming more widespread in radar signal processing, too. What was an exclusive domain of commercial DSPs, even pulse processing, will increasingly be handled by common PCs.

With increasing transmission rates and bandwidths available, near-realtime distribution of undreamt-of data amounts is close at hand. In radar networks, this will further increase centralized processing, exploiting the benefits of multiradar data-based object-oriented processing and quality control instead of product generation at the radar site. Instead of waiting for complete data volumes, sweepwise dissemination will enable processing of intervolumetric products (a new product with each new sweep), so that the product update rate will be increased beyond the radar volume update rate. More raw and base data, as well as complex and comfortable archives, will be available for research, climatology, and hindsight expertise.

30.9.6 Homogeneous Data

Faster updates, denser data, and improved quality monitoring will produce more homogeneous data. Radar climatology will become more meaningful, as continuous and quality controlled data become available from standardized and homogeneous radar networks. This process is being worked upon by WMO, Eumetnet, and national authorities.

On the one hand, hardware, software, and data processing chains, including scan strategy, will be harmonized within national networks and beyond. On the other hand, there is a tendency to adapt scanning according to geographic and climatic environment, particularly in large countries, such as Russia or the USA, and to the imminent weather situation.

30.9.7 Internationalization

International data exchange is still on the rise, promoting standardization of data models and formats (HDF5), as well as radar data centers. Multinational supernetworks, such as OPERA, are evolving to harmonize future national development and are supplying support to emerging nations.

30.9.8 Fully-Integrated Observing Systems

However, the future of radar will not be confined to the development of radar technology and specialized processing alone. It is believed that future weather radars will be embedded into integrated observing systems merging data from sources facilitating as manifold

a description of the atmosphere/hydrosphere system as possible. Likewise, quality control and processing of radar data will be in synergy with complex analysis and processing techniques, such as complex interpretation schemes as input into a seamless 4-D data assimilation in combined numerical models.

As all these processes continue, they will, on the one hand, further push the cutting edge in radar meteorology. On the other hand, an increasing number of high technology radars will level the gap between frontline development and (sometimes older) operational systems to very high average standards. Above all, with increasing data availability and quality, radar remote sensing will continue to contribute to man's understanding of the atmosphere and play an important role in the preservation of life and property.

30.10 Further Reading

- Ronald E. Rinehart: *Radar for Meteorologists*, 4th edn. (Rinehart, Columbia 2004).
- Henri Sauvageot: *Radar Meteorology* (Artech House Publishers, New York 1992), 384 pp.
- Richard J. Doviak and Dusan S. Zrnic: *Doppler Radar and Weather Observations*, 2nd edn. (Academic Press, Cambridge 1993), 562 pp.
- V.N. Bringi, and V. Chandrasekar: *Polarimetric Doppler Weather Radar: Principles and Applications* (Cambridge University Press, Cambridge 2001).
- Peter Meischer: *Weather Radar: Principles and Advanced Applications* (Springer, Berlin, Heidelberg 2004).
- Frédéric Fabry: *Radar Meteorology: Principles and Practice* (Cambridge University Press, Cambridge 2015).
- Merrill Skolnik: *Introduction to radar systems* 3rd edn. (McGraw-Hill, New York 2001).
- Merrill Skolnik: *Radar Handbook* (MacGraw-Hill, New York 2008).

References

- | | | | |
|------|---|-------|--|
| 30.1 | J.O. Fletcher: Early developments of weather radar during World War II. In: <i>Radar in Meteorology: Battan Memorial and 40th Anniversary Radar Meteorology Conference</i> , ed. by D. Atlas (American Meteorological Society, Boston 1990) pp. 3–6 | 30.6 | Wikipedia: <i>Klein Heidelberg</i> , https://en.wikipedia.org/wiki/Klein_Heidelberg , Accessed 11 July 2021 |
| 30.2 | C. Hülsmeier: Verfahren, um entfernte metallische Gegenstände mittels elektrischer Wellen einem Beobachter zu melden, Reichspatent Nr. 165546 (1904) | 30.7 | Wikipedia: <i>Mammut radar</i> , https://en.wikipedia.org/wiki/Mammut_radar , Accessed 11 July 2021 |
| 30.3 | Encyclopædia Britannica: <i>History of Radar</i> , http://www.britannica.com/technology/radar/History-of-radar , Accessed 11 July 2021 | 30.8 | Y. Blanchard, G. Galati, P. van Genderen: The cavity magnetron: not just a British invention, <i>IEEE Antennas Propag. Mag.</i> 55 (5), 244–254 (2013) |
| 30.4 | Wikipedia: <i>Rudolf Kühnhold</i> , https://de.wikipedia.org/wiki/Rudolf_Kühnhold , Accessed 11 July 2021 | 30.9 | D. Atlas, C.W. Ulbrich: Early foundations of the measurement of rainfall by radar. In: <i>Radar in Meteorology: Battan Memorial and 40th Anniversary Radar Meteorology Conference</i> , ed. by D. Atlas (American Meteorological Society, Boston 1990) pp. 86–97 |
| 30.5 | Wikipedia: <i>Jagdschloss radar</i> , https://en.wikipedia.org/wiki/Jagdschloss_radar , Accessed 11 July 2021 | 30.10 | I. Katz: Radar meteorology at radiation laboratory, MIT, 1941 to 1947. In: <i>Radar in Meteorology: Battan Memorial and 40th Anniversary Radar Meteorology Conference</i> , ed. by D. Atlas (American Meteorological Society, Boston 1990) pp. 16–21 |

- 30.11 Lord Rayleigh: On the light from the sky, its polarization and color, *Philos. Mag.* **41**, 107–120 (1871), 274–279
- 30.12 G. Mie: Beiträge zur Optik trüber Medien, speziell kolloidaler Metallösungen, *Ann. Phys.* **25**, 377–445 (1908)
- 30.13 J.W. Ryde: Attenuation of centimeter radio waves and the echo intensities resulting from atmospheric phenomena, *J. IEEE* **93**(3A), 101–103 (1946)
- 30.14 J.R. Probert-Jones: A history of radar meteorology in the United Kingdom. In: *Radar in Meteorology: Battan Memorial and 40th Anniversary Radar Meteorology Conference*, ed. by D. Atlas (American Meteorological Society, Boston 1990) pp. 54–60
- 30.15 J.I. Metcalf, K.M. Glover: A history of weather radar research in the U.S. Air Force. In: *Radar in Meteorology: Battan Memorial and 40th Anniversary Radar Meteorology Conference*, ed. by D. Atlas (American Meteorological Society, Boston 1990) pp. 32–43
- 30.16 D.M. Swingle: Weather radar in the United States Army's Fort Monmouth Laboratories. In: *Radar in Meteorology: Battan Memorial and 40th Anniversary Radar Meteorology Conference*, ed. by D. Atlas (American Meteorological Society, Boston 1990) pp. 7–15
- 30.17 E. Kessler: Radar meteorology at the National Severe Storms Laboratory, 1964–1986. In: *Radar in Meteorology: Battan Memorial and 40th Anniversary Radar Meteorology Conference*, ed. by D. Atlas (American Meteorological Society, Boston 1990) pp. 44–53
- 30.18 R.H. Douglas: The Stormy Weather Group (Canada). In: *Radar in Meteorology: Battan Memorial and 40th Anniversary Radar Meteorology Conference*, ed. by D. Atlas (American Meteorological Society, Boston 1990) pp. 61–68
- 30.19 G. Warnecke: *Der denkwürdige Beginn der Radarbeobachtungen in Berlin vor 50 Jahren am 7. Juli 1957. In Memoriam Richard Scherhag*, Beiträge des Instituts für Meteorologie der Freien Universität Berlin zur Berliner Wetterkarte (Berliner Wetterkarte, Berlin 2007)
- 30.20 N. Kodaira, J. Aoyagi: History of radar meteorology in Japan. In: *Radar in Meteorology: Battan Memorial and 40th Anniversary Radar Meteorology Conference*, ed. by D. Atlas (American Meteorological Society, Boston 1990) pp. 69–76
- 30.21 O.L. Rodríguez, L.L. Fernández, R.A. Naranjo, A. Barreiras, A.A. Peña, M. Diez, W. Pozas, M.O. Aguiar, J.L. Perez: *The Cuban Weather Radar Network: current status and trends* (2005), <https://ams.confex.com/ams/pdfpapers/97206.pdf>, Accessed 11 July 2021
- 30.22 R.R. Rogers: The early years of Doppler radar in meteorology. In: *Radar in Meteorology: Battan Memorial and 40th Anniversary Radar Meteorology Conference*, ed. by D. Atlas (American Meteorological Society, Boston 1990) pp. 122–129
- 30.23 A.C. Schroth, M.S. Chandra, P.F. Meischner: A C-band coherent polarimetric radar for propagation and cloud physics research, *J. Atmos. Ocean. Technol.* **5**, 803–822 (1988)
- 30.24 D. Harrison, R. Scovell, H. Lewis, S. Matthews: *The development of the EUMETNET OPERA radar data hub* (2006) <http://www.crahi.upc.edu/ERAD2006/proceedingsMask/00103.pdf>, Accessed 11 July 2021
- 30.25 ITU: *The radio refractive index: its formula and refractivity data, Recommendation ITU-R P453-1* (2016) https://www.itu.int/dms_pubrec/itu-r/rec/p/R-REC-P.453-11-201507-S1!PDF-E.pdf, Accessed 11 July 2021
- 30.26 J. Seltmann: Radarforschung im DWD: Vom Scan zum Produkt, *Promet* **26**(1/2), 32–42 (1997)
- 30.27 R. Gans: Über die Form ultramikroskopischer Goldteilchen, *Ann. Phys.* **37**, 881–900 (1912)
- 30.28 A. Mugnai, W.J. Wiscombe: Scattering from nonspherical Chebyshev particles. 3: Variability in angular scattering patterns, *Appl. Opt.* **28**(15), 3061–3073 (1989)
- 30.29 P.C. Waterman: Matrix formulation of electromagnetic scattering, *Proc. IEEE* **53**, 805–812 (1965)
- 30.30 B. Peterson, S. Ström: T-matrix formulation of electromagnetic scattering from multilayered scatterers, *Phys. Rev. D* **10**(8), 3274–3285 (1974)
- 30.31 I. Dölling: *Modellrechnungen für polarimetrische Radarparameter im C-Band für Ensembles taumelnder und schmelzender Eisparkeln und Vergleich mit Messungen*. Dissertation. DLR-Forschungsbericht 97–29 (1997)
- 30.32 E.M. Purcell, C.R. Pennypacker: Scattering and absorption of light by nonspherical dielectric grains, *Astrophys. J.* **186**, 705–714 (1973)
- 30.33 R.E. Rinehart: *Radar for Meteorologists*, 4th edn. (Rinehart, Columbia 2004)
- 30.34 J.R. Probert-Jones: The radar equation in meteorology, *Q. J. R. Meteorol. Soc.* **88**, 485–495 (1962)
- 30.35 H. Nyquist: Certain topics in telegraph transmission theory, *AIEE Trans.* **47**, 617–644 (1928)
- 30.36 C.G. Collier (Ed.): *COST-75: Advanced weather radar systems 1993–1997. Final Report* (Office of Publication of European Communities, Brussels 2001)
- 30.37 N. Majurec, S.M. Sekelsky, S.J. Frasier, S.A. Rutledge: The Advanced Multi-Frequency Radar (AMFR) for remote sensing of clouds and precipitation. In: *Proc. AMS Radar Conf., Albuquerque* (2005), <https://ams.confex.com/ams/pdfpapers/96284.pdf>, Accessed 11 July 2021
- 30.38 V.N. Bringi, V. Chandrasekar: *Polarimetric Doppler weather radar: principles and applications* (Cambridge Univ. Press, Cambridge, New York 2001)
- 30.39 V. Melnikov, M. Leskinen, J. Koistinen: Doppler velocities at orthogonal polarizations in radar echoes from insects and birds, *IEEE Geosci. Remote Sens. Lett.* **11**(3), 592–596 (2014)
- 30.40 J. Tan, A.R. Holt, A. Hendry, D.H.O. Bebbington: Extracting rainfall rates from X-band CDR radar data by using differential propagation phase shift, *J. Atmos. Ocean. Technol.* **8**, 799–801 (1991)
- 30.41 J.A. Morrison, M.J. Cross, T.S. Chu: Rain-induced differential attenuation and differential phase

- shift at microwave frequencies, *Bell Syst. Tech. J.* **52**(4), 599–604 (1973)
- 30.42 M. Skolnik: *Radar Handbook*, 3rd edn. (McGraw-Hill, New York 2008)
- 30.43 C. Wolff: *Radartutorial* 1998). <http://www.radartutorial.eu/index.en.html>, Accessed 11 July 2021
- 30.44 M. Frech, T. Mammen, B. Lange, J. Seltmann, J. Rowan, C. Morehead: Onsite dualpol antenna performance verification. In: *35th AMS Radar Conf., Pittsburgh* (2011), https://ams.confex.com/ams/35RADAR/webprogram/handout/Paper191389/ams_2011_frech_antenna_performance_poster_78.pdf, Accessed 11 July 2021
- 30.45 M. Sachidananda, R. Doviak, D. Zrnic: Whitening of sidelobe powers by pattern switching in radar array antenna, *IEEE Trans. Antennas Propag.* **33**(7), 727–735 (1985)
- 30.46 M. Frech, B. Lange, T. Mammen, J. Seltmann, C. Morehead, J. Rowan: Influence of a radome on antenna performance, *J. Atmos. Ocean. Technol.* **30**, 313–324 (2013)
- 30.47 R.H. Barker: Group synchronizing of binary digital sequences. In: *Communication Theory*, ed. by W. Jackson (Butterworths, London 1953) pp. 273–287
- 30.48 M. Sachidananda, D.S. Zrnic: Systematic phase codes for resolving range overlaid signals in a Doppler weather radar, *J. Atmos. Ocean. Technol.* **16**, 1351–1363 (1999)
- 30.49 Sigmet: *RVP7 Doppler Signal Processor User's Manual* (Sigmet, Westford 1998)
- 30.50 E. Gorgucci, S. Gianfranco, V. Chandrasekar: A procedure to calibrate multiparameter weather radar using properties of the rain medium, *IEEE Trans. Geosci. Remote Sens.* **37**(1), 269–276 (1999)
- 30.51 R.L. Ice, A.K. Heck, J.G. Cunningham, W.D. Zittel: Challenges of polarimetric weather radar calibration. In: *8th Eur. Conf. Radar Meteorol. Hydrol., Garmisch-Partenkirchen* (2014), https://www.pa.op.dlr.de/erad2014/programme/ExtendedAbstracts/117_Ice.pdf, Accessed 11 July 2021
- 30.52 J. Joss, R. Lee: The application of radar-gauge comparisons to operational precipitation profile corrections, *J. Appl. Meteorol.* **34**, 2512–2630 (1995)
- 30.53 Radar Operations Center: *Current VCP in use for each Site*, <https://www.roc.noaa.gov/WSR88D/Operations/VCP.aspx>, Accessed 11 July 2021
- 30.54 J.E.E. Seltmann, T. Hohmann, M. Frech, P. Tracksdorf: DWD's new operational scan strategy. In: *36th AMS Radar Conf., Breckenridge* (2013), https://ams.confex.com/ams/36Radar/webprogram/Handout/Paper229003/AMS_2013_ScanStrategie_shft_v1.1.pdf, Accessed 11 July 2021
- 30.55 A. Huuskonen, I. Holleman: Determining weather radar antenna pointing using signals detected from the sun at low elevations, *J. Atmos. Ocean. Technol.* **24**, 476–483 (2007)
- 30.56 I. Holleman, A. Huuskonen, M. Kurri, H. Beekhuis: Operational monitoring of weather radar receiving chain using the sun, *J. Atmos. Ocean. Technol.* **27**, 159–166 (2010)
- 30.57 I. Holleman, A. Huuskonen, R. Gill, P. Tabary: Operational monitoring of radar differential reflectivity using the sun, *J. Atmos. Ocean. Technol.* **27**, 881–887 (2010)
- 30.58 J. Seltmann: Clutter versus radar winds, *Phys. Chem. Earth B* **25**(10–12), 1173–1178 (2000)
- 30.59 J.W. Wilson, T.M. Weckwerth, J. Vivekanandan, R.M. Wakimoto, R.W. Russell: Boundary layer clear-air radar echoes: Origin of echoes and accuracy of derived winds, *J. Atmos. Ocean. Technol.* **11**, 1184–1206 (1994)
- 30.60 E.E. Gossard: Radar research on the atmospheric boundary layer. In: *Radar in Meteorology: Battan Memorial and 40th Anniversary Radar Meteorology Conference*, ed. by D. Atlas (American Meteorological Society, Boston 1990) pp. 477–527
- 30.61 R.J. Serafin, W. Wilson: Operational weather radar in the United States: Progress and opportunity, *Bull. Am. Meteorol. Soc.* **81**, 501–518 (2000)
- 30.62 J. Bech, U. Gjertsen, G. Haase: Modelling weather radar beam propagation and topographical blockage at northern high latitudes, *Q. J. R. Meteorol. Soc.* **133**, 1191–1204 (2007)
- 30.63 S.E. Giangrande, A.V. Ryzhkov: Calibration of dual-polarization radar in the presence of partial beam blockage, *J. Atmos. Ocean. Technol.* **22**, 1156–1166 (2005)
- 30.64 J. Aoyagi: Ground clutter rejection by MIT weather radar. In: *Prepr. 18th Conf. Radar Meteorol., Atlanta* (1978) pp. 358–363
- 30.65 J.E.E. Seltmann: Quantitative aspects of clutter highpass filtering as used by DWD. In: *30th AMS Radar Conf., Munich* (2001), <https://ams.confex.com/ams/pdfpapers/21902.pdf>, Accessed 11 July 2021
- 30.66 A. Siggia, R.E. Passarelli Jr.: Gaussian model adaptive processing (GMAP) for improved ground clutter cancellation and moment calculation. In: *Proc. 3rd Eur. Conf. Radar Meteorol. Hydrol. (ERAD), Visby* (2004) pp. 67–73, https://www.copernicus.org/erad/2004/online/ERAD04_P_67.pdf, Accessed 11 July 2021
- 30.67 J.C. Hubbert, M. Dixon, S. Ellis: *Real time mitigation of ground clutter* (2008) <https://www.eol.ucar.edu/system/files/Realtimemitigationofgroundclutter.pdf>, Accessed 11 July 2021
- 30.68 S. Ellis, M. Dixon, J. Hubbert, G. Meymaris: *CMD: Improvements and Transition to Dual Polarization* (2011) https://www.roc.noaa.gov/WSR88D/PublicDocs/TAC/2011/CMD_Improve_Trans_to_Dual_Polarization_March_2011.pdf, Accessed 11 July 2021
- 30.69 S. Torres: Processing of staggered PRT sequences on the KOUN research radar. In: *Preprints 31st Int. Conf. Radar Meteorol., Seattle* (2003) pp. 746–748, <https://ams.confex.com/ams/pdfpapers/63620.pdf>, Accessed 11 July 2021
- 30.70 P. Tabary, F. Guibert, L. Perier, J. Parent-du-Chatelet: An operational triple-PRT Doppler

- scheme for the French radar network, *J. Atmos. Ocean. Technol.* **23**(12), 1645–1656 (2006)
- 30.71 M. Werner: A new radar data post-processing quality control workflow for the DWD weather radar network. In: *8th Eur. Conf. Radar Meteorol. Hydrol., Garmisch-Partenkirchen* (2014), http://www.pa.op.dlr.de/erad2014/programme/ExtendedAbstracts/079_Werner.pdf, Accessed 11 July 2021
- 30.72 J. Joss, A. Waldvogel: Precipitation measurement and hydrology. In: *Radar in Meteorology: Battan Memorial and 40th Anniversary Radar Meteorology Conference*, ed. by D. Atlas (American Meteorological Society, Boston 1990) pp. 577–606
- 30.73 B. Vignal, G. Galli, J. Joss, U. Germann: Three methods to determine profiles of reflectivity from volumetric radar data to correct precipitation estimates, *J. Appl. Meteorol.* **39**, 1715–1726 (2000)
- 30.74 R. Sánchez-Diezma, I. Zawadzki, D. Sempere-Torres: Identification of the bright band through the analysis of volumetric radar data, *J. Geophys. Res.* **105**(D2), 2225–2236 (2000)
- 30.75 S.E. Giangrande, J.M. Krause, A.V. Ryzhkov: Automatic designation of the melting layer with a polarimetric prototype of the WSR-88D radar, *J. Appl. Meteorol. Climatol.* **47**, 1354–1364 (2008)
- 30.76 C. Golz, T. Einfalt, G. Galli: Radar data quality control methods in VOLTAIRE, *Meteorol. Z.* **15**, 497–504 (2006)
- 30.77 K. Helmert, B. Hassler, J.E.E. Seltmann: An operational tool to quality control 2D radar reflectivity data for assimilation in COSMO-DE, *Int. J. Remote Sens.* **33**(11), 3456–3471 (2012)
- 30.78 K. Friedrich, M. Hagen, T. Einfalt: A quality control concept for radar reflectivity, polarimetric parameters and Doppler velocity, *J. Atmos. Ocean. Technol.* **23**, 865–887 (2006)
- 30.79 D. Heizenreder, S. Haucke: Das meteorologische Visualisierungs- und Produktionssystem *NinJo*, *Promet* **35**(1–3), 57–69 (2009)
- 30.80 J.E.E. Seltmann, T. Hohmann, M. Frech, P. Tracksdorf: DWD's new operational scan strategy. In: *36th AMS Radar Conf., Breckenridge* (2013), https://ams.confex.com/ams/36RADAR/webprogram/Handout/Paper229003/AMS_2013_ScanStrategie_shft_v1.pdf, Accessed 11 July 2021
- 30.81 I.J. Caylor, V. Chandrasekar: Time varying ice crystal orientation observed with multi-parameter radar, *IEEE Trans. Geosci. Remote Sens.* **34**(4), 847–858 (1996)
- 30.82 L.D. Carey, S.A. Rutledge: Electrical and multiparameter radar observations of a severe hailstorm, *J. Geophys. Res.* **103**, 13979–14000 (1998)
- 30.83 T.J. Keenan, P. Joe, J. Wilson, C. Collier, B. Goldring, D. Burgess, P. May, C. Pierce, J. Bally, A. Crook, A. Seed, D. Sills, L. Berry, R. Potts, I. Bell, N. Fox, E. Ebert, M. Eilts, K. O'Loughlin, C. Mueller: The Sydney 2000 World Weather Research Programme Forecast Demonstration Project: Overview and Current Status, *Bull. Am. Meteorol. Soc.* **84**, 1041–1054 (2003)
- 30.84 R.V. Calheiros, I.I. Zawadzki: Reflectivity rain-rate relationships for radar hydrology in Brazil, *J. Appl. Meteorol. Climatol.* **26**, 118–132 (1987)
- 30.85 D. Rosenfeld, D.B. Wolff, E. Amitai: The window probability matching method for rainfall measurements with radar, *J. Appl. Meteorol.* **33**, 683–693 (1994)
- 30.86 J.S. Marshall, R.C. Langille, W.M. Palmer: Measurement of rainfall by radar, *J. Atmos. Sci.* **4**(6), 186–192 (1947)
- 30.87 H. Bartels, E. Weigl, T. Reich, P. Lang, A. Wagner, O. Kohler, N. Gerlach: *Projekt RADOLAN – Routineverfahren zur Online-Aneicherung der Radarniederschlagsdaten mit Hilfe von automatischen Bodenniederschlagsstationen (Ombrometer)* (Deutscher Wetterdienst, Offenbach 2004)
- 30.88 A. Marx, H. Kunstmann, A. Bárdossy, J.E.E. Seltmann: Radar rainfall estimates in an alpine environment using inverse hydrological modelling, *Adv. Geosci.* **9**, 25–29 (2006)
- 30.89 U. Ehret: *Rainfall and Flood Nowcasting in Small Catchments Using Weather Radar*, *Mitteilungen/Institut für Wasserbau, Universität Stuttgart*, Vol. 121 (Universität Stuttgart, Stuttgart 2003)
- 30.90 D.R. Greene, R.A. Clark: Vertically integrated liquid water – A new analysis tool, *Mon. Weather Rev.* **100**, 548–552 (1972)
- 30.91 D.H. Kitzmiller, W.E. McGovern, R.F. Saffle: The WSR-88D severe weather potential algorithm, *Weather Forecast.* **10**, 141–159 (1995)
- 30.92 S.A. Amburn, P.L. Wolf: VIL density as a hail indicator, *Weather Forecast.* **12**, 473–478 (1997)
- 30.93 L.D. Carey, S.A. Rutledge: The relationship between precipitation and lightning in tropical island convection: A C-band polarimetric study, *Mon. Weather Rev.* **128**, 2687–2710 (2000)
- 30.94 R.M. Mosier, C. Schumacher, R.E. Orville, L.D. Carey: Radar nowcasting of cloud-to-ground lightning over Houston, Texas, *Weather Forecast.* **26**, 199–212 (2011)
- 30.95 A. Waldvogel, B. Federer, P. Grimm: Criteria for the detection of hail cells, *J. Appl. Meteorol.* **18**, 1521–1525 (1979)
- 30.96 A. Witt, M.D. Eilts, G.J. Stumpf, J.T. Johnson, E.D. Mitchell, K.W. Thomas: An enhanced hail detection algorithm for the WSR-88D, *Weather Forecast.* **13**, 286–303 (1998)
- 30.97 K. Aydin, T.A. Seliga, V. Balaji: Remote sensing of hail with a dual linear polarisation radar, *J. Appl. Meteorol.* **25**, 1475–1484 (1986)
- 30.98 H. Höller, V.N. Bringi, J. Hubbert, M. Hagen, P.F. Meischner: Life cycle and precipitation formation in a hybrid-type hailstorm revealed by polarimetric and Doppler radar measurements, *J. Atmos. Sci.* **51**, 2500–2522 (1994)
- 30.99 J. Vivekanandan, D.S. Zrnic, S.M. Ellis, R. Oye, A.V. Ryzhkov, J. Straka: Cloud microphysics retrieval using S-band dual polarization radar measurements, *Bull. Am. Meteorol. Soc.* **80**, 381–388 (1999)
- 30.100 H. Al-Sakka, A. Boumahmoud, B. Fradon, S.J. Frasier, P. Tabary: A New fuzzy logic hydrom-

- eteor classification scheme applied to the French X-, C-, and S-band polarimetric radars, *J. Appl. Meteorol. Climatol.* **52**, 2328–2344 (2013)
- 30.101 K.A. Browning, R. Wexler: The determination of kinematic properties of a wind field using Doppler radar, *J. Appl. Meteorol.* **7**, 105–113 (1968)
- 30.102 P. Waldteufel, H. Corbin: On the analysis of single-Doppler radar data, *J. Appl. Meteorol.* **18**, 532–542 (1979)
- 30.103 J. Wurman: Vector winds from a single transmitter bistatic dual-Doppler radar network, *Bull. Am. Meteorol. Soc.* **75**, 983–994 (1994)
- 30.104 T. Hengstebeck, K. Wapler, D. Heizenreder, P. Joe: Radar network-based detection of mesocyclones at the German weather service, *J. Atmos. Ocean. Technol.* **25**, 299–321 (2018)
- 30.105 E.D. Mitchell, S.V. Vasiloff, G.J. Stumpf, A. Witt, M.D. Eilts, J.T. Johnson, K.W. Thomas: The National Severe Storms Laboratory tornado detection algorithm, *Weather Forecast.* **13**, 352–366 (1998)
- 30.106 J.E.E. Seltmann, T. Böhme: Wind turbine issues in Germany. In: *38th AMS Radar Conf., Chicago* (2017), https://ams.confex.com/ams/38RADAR/webprogram/Manuscript/Paper320410/2017_AMS_38Radar_Chicago_Seltmann-Boehme.pdf, Accessed 11 July 2021
- 30.107 P. Lang: Cell tracking and warning indicators derived from operational radar products. In: *30th Int. Conf. Radar Meteorol., Munich* (2001) pp. 245–247, <https://ams.confex.com/ams/pdfpapers/21678.pdf>, Accessed 11 July 2021
- 30.108 B. Macpherson, M. Lindskog, V. Ducrocq, M. Nuret, G. Gregorič, A. Rossa, G. Haase, I. Holleman, P.P. Alberoni: Assimilation of radar data in numerical weather prediction (NWP) models. In: *Weather Radar: Principles and Advanced Applications*, ed. by P. Meischner (Springer, Berlin, Heidelberg 2004) pp. 255–279
- 30.109 R.J. Keeler, S.M. Ellis: Observational error covariance matrices for radar data assimilation, *Phys. Chem. Earth B* **25**(10–12), 1277–1280 (2000)
- 30.110 C.D. Jones, B. Macpherson: A latent heat nudging scheme for the assimilation of precipitation data into an operational mesoscale model, *Meteorol. Appl.* **4**, 269–277 (1997)
- 30.111 K. Stephan, S. Klink, C. Schraff: Assimilation of radar derived rain rates into the convective-scale model COSMO-DE at DWD, *Q. J. R. Meteorol. Soc.* **134**, 1315–1326 (2008)
- 30.112 F. Fabry, C. Frush, I. Zawadzki, A. Kilambi: On the extraction of near-surface index of refraction using radar phase measurements from ground targets, *J. Atmos. Ocean. Technol.* **14**, 978–987 (1997)
- 30.113 A.M. Dokter, F. Liechti, H. Stark, L. Delobbe, P. Tabary, I. Holleman: Bird migration flight altitudes studied by a network of operational weather radars, *J. R. Soc. Interface* **8**, 30–43 (2011)
- 30.114 P.M. Stepanian, K.G. Horton, V.M. Melnikov, D.S. Zrnić, S.A. Gauthreaux Jr.: Dual-polarization radar products for biological applications, *Ecosphere* **7**(11), e01539 (2016)
- 30.115 A.M. Haberlie, W.S. Ashley: A radar-based climatology of mesoscale convective systems in the United States, *J. Clim.* **32**(5), 1591–1606 (2019)
- 30.116 A. Wagner, J. Seltmann, H. Kunstmann: Joint statistical correction of clutters, spokes and beam height for a radar derived precipitation climatology in southern Germany, *Hydrol. Earth Syst. Sci.* **16**, 4101–4117 (2012)

Jörg E.E. Seltmann

Hohenpeissenberg Observatory
German Meteorological Service (DWD)
Hohenpeissenberg, Germany
joerg.seltmann@yandex.com



Jörg E.E. Seltmann is a physicist and senior radar scientist at the German Meteorological service (DWD). He has conducted and supervised several radar projects and was responsible for the system design and technological innovation of the current German weather radar network, including the introduction of the dual-polarization technique. He led DWD's research unit on radar meteorology and precipitation process at the Hohenpeissenberg Observatory up to 2020 and is teaching radar meteorology at Augsburg University.

Radar Wind

31. Radar Wind Profiler

Volker Lehmann, William Brown 

Radar wind profilers (RWPs) are meteorological radars that are used to determine the vertical profile of the wind vector in the atmosphere. RWPs typically use wavelengths ranging from about 20 cm to about 6 m. The scattering processes that occur at such wavelengths give these instruments a unique ability to obtain detectable echoes in both the optically clear, as well as in the particle-laden, atmosphere (i.e. in the presence of clouds, fog, or precipitation). The height coverage of RWPs varies, mainly due to the wavelength dependence of the clear air scattering process: boundary-layer RWPs (which operate at frequencies of around 1 GHz) typically probe the lowest 3–5 km of the atmosphere, while (markedly larger) systems in the 50 MHz band can provide data on the atmospheric region up to about 20 km above the ground.

31.1	Measurement Principles and Parameters	902
31.2	History	903
31.2.1	Puzzling Radar Echoes from the Clear Air	903
31.2.2	Jicamarca and Follow-On Research	903
31.2.3	Development of RWP for Meteorology	903
31.2.4	Operational Use of RWP Networks	904
31.3	Theory	904
31.3.1	Scattering Processes for RWP	904
31.3.2	Clear-Air Scattering	905
31.3.3	Signal Processing	908
31.3.4	Wind Vector Estimation: Doppler Beam Swinging	912
31.3.5	Wind Vector Estimation: Spaced-Antenna Systems	913
31.4	Systems	916
31.4.1	Spectrum Allocation	916
31.4.2	Doppler Systems	917
31.4.3	Spaced-Antenna Systems	919
31.4.4	Comparison of the Methods	920
31.5	Specifications	920
31.5.1	Measurement Range	920
31.5.2	Accuracy	921
31.6	Quality Control	923
31.6.1	Signal Processing: Clutter and RFI Filtering	923
31.6.2	Consistency Checks	923
31.6.3	Numerical Weather Prediction: 0–B statistics, FS01	923
31.7	Maintenance	924
31.8	Applications	925
31.9	Future Developments	926
31.10	Further Reading	926
	References	927

Gravity causes the atmosphere to stratify in a distinct manner that is reflected in significant vertical variations in atmospheric variables. One such variable is the wind—the velocity vector that describes the motion of the air [31.1]. Structures such as jet streams (both low-level jets and those near the tropopause) as well as shear

zones at frontal boundaries are prominent examples of the rich three-dimensional (3-D) flow structure of the Earth's atmosphere. Quantitative knowledge of the vertical profile of the wind vector is crucial for various reasons, but most obviously for weather forecasting and aviation.

31.1 Measurement Principles and Parameters

A radar wind profiler (RWP) is essentially a coherent radar that operates at long wavelengths ranging from about 20 cm to about 6 m. Electromagnetic waves in this range are scattered at fluctuations in the refractive index of particle-free *clear air*, which are almost omnipresent due to the turbulent state of the atmosphere. This clear-air scattering allows a RWP to obtain measurable echoes even when there are no hydrometeors in the radar resolution volume.

The fundamental radar measurables are the amplitude and phase (relative to the transmitted signal) of the signal received at the output port of the antenna. During signal processing, important properties such as the reflected power and Doppler information are extracted from the demodulated receiver signal in a range-resolving fashion. It should be noted that even these fundamental radar variables are obtained through often rather complex mathematical operations. It is therefore useful to structure the data obtained by a RWP into hierarchical data levels that correspond to the various stages of processing. At each stage, a particular algorithm implemented by a software module converts the data from a lower to a higher data level. The ultimate aim of signal processing is to convert the received electrical signals into meteorological quantities.

RWP architectures fall into two broad categories: Doppler systems that use a single receiving antenna and spaced-antenna systems that use multiple receiving antennas. Doppler systems steer the radar beam in various near-zenith directions. The Doppler shift arising from the movement of the atmospheric medium in each of these line-of-sight directions can then be measured directly. An explicit wind vector retrieval operation is then performed to transform the radial Doppler shifts into a 2-D or even 3-D wind vector. In contrast, spaced-antenna systems use an arrangement

of three or more horizontally spaced and vertically directed receiving antennas to measure the diffraction pattern due to atmospheric scattering. This diffraction pattern shifts due to the horizontal drift of the scatterers, allowing the movement of the atmospheric medium to be inferred from a cross-correlation analysis of the signals obtained by the different antennas. The vertical component is derived directly through the Doppler method.

The main variable determined by a RWP is the vertical profile of the horizontal wind vector, i.e., the wind speed and direction as a function of altitude. These quantities can be estimated in a fully automated way under almost all meteorological conditions. The radar hardware as well as the signal and data processing algorithms needed for this task can nowadays be regarded as mature.

Measurement of the vertical wind component is more difficult. Since cloudy air is a complex multiphase, multivelocity, and multitemperature physical system [31.2, 3], there is generally a need to distinguish between the velocity of the gaseous phase (wind in the strictest sense) and the velocity of liquid and solid water particles with respect to the surrounding air. While the horizontal displacement of the rather small water particles is usually dictated by the horizontal wind, the terminal velocity of the hydrometeors needs to be taken into account when estimating the vertical wind. Especially at shorter wavelengths, such as in the 1 GHz band and even in the 400 MHz band, Doppler measurements obtained with a vertically directed beam often reflect an unknown combination of the vertical wind and the terminal speed of the hydrometeors, unless the particle scattering can be unambiguously separated from the clear air scattering component.

RWP signals contain more information than just the Doppler shift, so enabling quantities other than the wind

Table 31.1 Signals measured by RWP and important derived properties

Variable	Description	Unit	Symbol
RX time series	Time series of the demodulated receiver voltage	arb. u.	$I/Q(t)$
Doppler spectrum	Power spectrum of the I/Q time series	arb. u.	$S(f)$
Signal power	Zeroth moment of the signal component in the power spectrum	arb. u.	P_s
Mean Doppler frequency	First moment of the signal component in the power spectrum	Hz	f_D
Spectral width	Second moment of the signal component in the power spectrum	Hz	σ

Table 31.2 Meteorological quantities that can be extracted from RWP data

Variable	Description	Unit	Symbol
Radial wind velocity	Atmospheric motion along the line of sight of the antenna beam	m s^{-1}	v_r
Horizontal wind vector	Horizontal components (u, v) of the 3-D wind vector (u, v, w)	m s^{-1}	\mathbf{v}_h
Vertical wind	Vertical component w of the 3-D wind vector (u, v, w)	m s^{-1}	w

to be determined. For instance, atmospheric properties such as the structure constant of the refractive index C_n^2 [31.4] can be derived, although the extraction of such parameters requires a tailored data analysis using specialized algorithms to account for the complexity of the measurement process. It is therefore difficult to fully automate algorithms for these quantities as they can usually be only be applied for a limited range of atmospheric conditions.

31.2 History

This section provides a brief overview of the main phases in the evolution of RWP. More comprehensive historical overviews of the development of clear-air radars or RWPs are given in [31.5–7].

31.2.1 Puzzling Radar Echoes from the Clear Air

The story of radar-based wind profiling began in 1939, when *Albert Wiley Friend* (1910–1972) published a letter in the *Bulletin of the American Meteorological Society* [31.8] that described a radio wave propagation experiment in which he related reflections from the troposphere to temperature inversions and the associated changes in the dielectric constant of the atmosphere. He even went as far as suggesting a monitoring of these discontinuities in between profile measurements obtained with radiosondes. Such echoes were later called *angels* by the radar community [31.9], which directed considerable effort into understanding this intriguing phenomenon. The autobiography of *David Atlas* (1924–2015) gives an interesting personal account of that period of research [31.10]. By the end of the 1960s, it was theoretically and experimentally established that dot echoes from clear air originate from point targets such as insects and birds, whereas diffuse echoes are caused by sharp gradients in the refractive index. The theoretical foundations for radar wind profiling were laid by *Valerian Tatarskii* (born 1929), who utilized a combination of Maxwell’s electromagnetic theory and statistical turbulence theory [31.11]. The state of knowledge at that time is summarized in [31.12].

31.2.2 Jicamarca and Follow-On Research

Another decisive development was triggered by incoherent radar scattering investigations of the upper atmosphere. Radio observatories with large and powerful radar systems such as Jicamarca [31.13] and Arecibo [31.14] were founded for this purpose in the

Obviously, the site at which a RWP is installed must have an electrical power supply as well as data transmission infrastructure and should be accessible for maintenance. Furthermore, such RWPs should preferably be sited at locations that minimize potential problems with ground or sea clutter, external electromagnetic interference, corrosion, and lightning damage. As with all radars, a proper license for radio spectrum use is a prerequisite for legal operation.

early 1960s. It is interesting to note that the breakthrough experiment performed at the Jicamarca Observatory under the direction of *Ronald Woodmann* (born 1934) was the consequence of pure curiosity-driven research: when the USA and Peru quarreled about fishing grounds off the coast of Peru, American funding was withheld for a period, freeing the Jicamarca group to look more closely at radar echoes from the neutral atmosphere using unconventional processing methods [31.7]. New findings from this research were published in 1974 in a seminal paper by *Woodman* and *Guillen* [31.15]. These results spurred comprehensive follow-on research, including the construction of specialized radars for sounding the upper atmosphere (mesosphere-stratosphere-troposphere (MST) radars) [31.16]. The findings were reviewed in early 1980 [31.17] with a focus on the resulting theoretical understanding of the clear-air returns and some aspects of the capabilities of the hardware and signal processing used. The paper also listed a variety of atmospheric phenomena that the new technique could be employed to observe. Considering operational applications, it was concluded that “large pulsed radars can provide continuous vector wind measurements throughout the troposphere under all weather conditions”.

31.2.3 Development of RWP for Meteorology

The potential of the MST radar technique was brought to the attention of the meteorological community [31.18], which led to the development and testing of prototypes of dedicated wind-profiling Doppler radars [31.19]. Soon after, the *Colorado Wind-Profiling Network*, an experimental network of five radars, was constructed as a means to evaluate the long-term viability of the method [31.20]. At about the same time, small boundary-layer radars probing with higher frequencies (around 1 GHz) were developed for wind profiling [31.21, 22]; these were subsequently commercialized through technology transfer to the private sector.

31.2.4 Operational Use of RWP Networks

The first truly operational network, initially termed the Wind Profiler Demonstration Network (WPDN) and later denoted the NOAA National Profiler Network, was completed in May 1992 [31.23–25]. This network was routinely operated until the NOAA announced that it would be decommissioned in 2014, mainly due to management issues and funding difficulties within

the NWS. In Europe, the first demonstration of radar wind profiler networking, the COST WIND Initiative for a Network Demonstration in Europe (CWINDE) project [31.26], was organized in early 1997 as part of COST Action 76. Other operational networks followed, in particular the outstanding WINDAS network of the Japanese Meteorological Administration [31.27] and the network of the Australian Bureau of Meteorology [31.28, 29].

31.3 Theory

The aim of RWP instrument theory is to derive sufficiently accurate but tractable functional relationships between the properties of the atmosphere and the signal received by a RWP [31.30]. This theory incorporates scattering physics to describe the interaction of the (artificially generated) wave with the atmosphere, the reception of the scattered wave, its transformation into a measurable function (receiver voltage), and finally the extraction of the desired atmospheric information from this signal using adequate mathematical signal processing methods.

31.3.1 Scattering Processes for RWP

The fundamental physical process for scattering is the interaction of an electromagnetic wave with the discrete electric charges in matter, that is protons and electrons. Those charges are set in oscillatory (accelerated) motion by the wave which leads to secondary radiation that superposes with the incident field. This fundamental microscopic process manifests itself in macroscopic effects such as diffraction, refraction, reflection, scattering, changes in propagation speed, polarization, and absorption [31.31], depending on the properties of the medium. It is impossible to describe these macroscopic effects at an elementary (microscopic) level for any practical problem, even with the aid of modern computers [31.32, 33], so macroscopic electrodynamics is used instead, and the electromagnetic properties of matter are described using bulk parameters [31.34, 35].

The atmosphere below the thermosphere can be assumed to be an electrically neutral continuum, i.e., a dielectric gas mixture, although short-lived ionization can occur in meteor trails or lightning channels. Furthermore, a suspension of a broad range of liquid and solid particulates (hydrometeors and aerosols) may be embedded in this continuum. Airborne objects such as insects, birds, and airplanes must also be considered. The following idealized scattering models can be formulated:

- Scattering at refractive index inhomogeneities in particle-free air
- Scattering at particle ensembles in an otherwise homogeneous medium
- Scattering at plasma in lightning channels
- Echoes from airborne objects
- Echoes from the ground surrounding the RWP (through antenna sidelobes).

Instrument theory for RWP is typically restricted to scattering at inhomogeneities in the refractive index of air. Since the atmosphere is almost permanently in a turbulent state, the link between electrodynamics and turbulence theory is key. For the idealized case of exclusive clear air scattering, the theory that maps the atmospheric properties of interest (implicitly contained in the field of refractive-index fluctuations) to the signal measured by the RWP is relatively well developed [31.36].

The very nature of turbulence makes theoretical analysis an extremely challenging task, as our understanding of turbulence and refractive-index structure at the meter and submeter scales in the free atmosphere is still very limited. Numerical simulations of realistic turbulent flows are increasingly being used in lieu of high-resolution in-situ measurements to investigate various aspects of RWP measurements in unprecedented detail [31.37–40].

The second atmospheric scattering process relevant for RWPs is scattering at small particles, such as hydrometeors. While the Rayleigh approximation can be used for simplification because the particle diameter is always much smaller than the wavelength, this approximation assumes that the particles are randomly positioned, which is open to debate. Thus, there is also the possibility of coherent scattering effects from non-randomly positioned particles [31.31, 41–43].

Often, both scattering processes act in tandem, and separating the simultaneous contributions from particulate scattering and clear-air scattering poses a practical problem if the data are to be used to extract

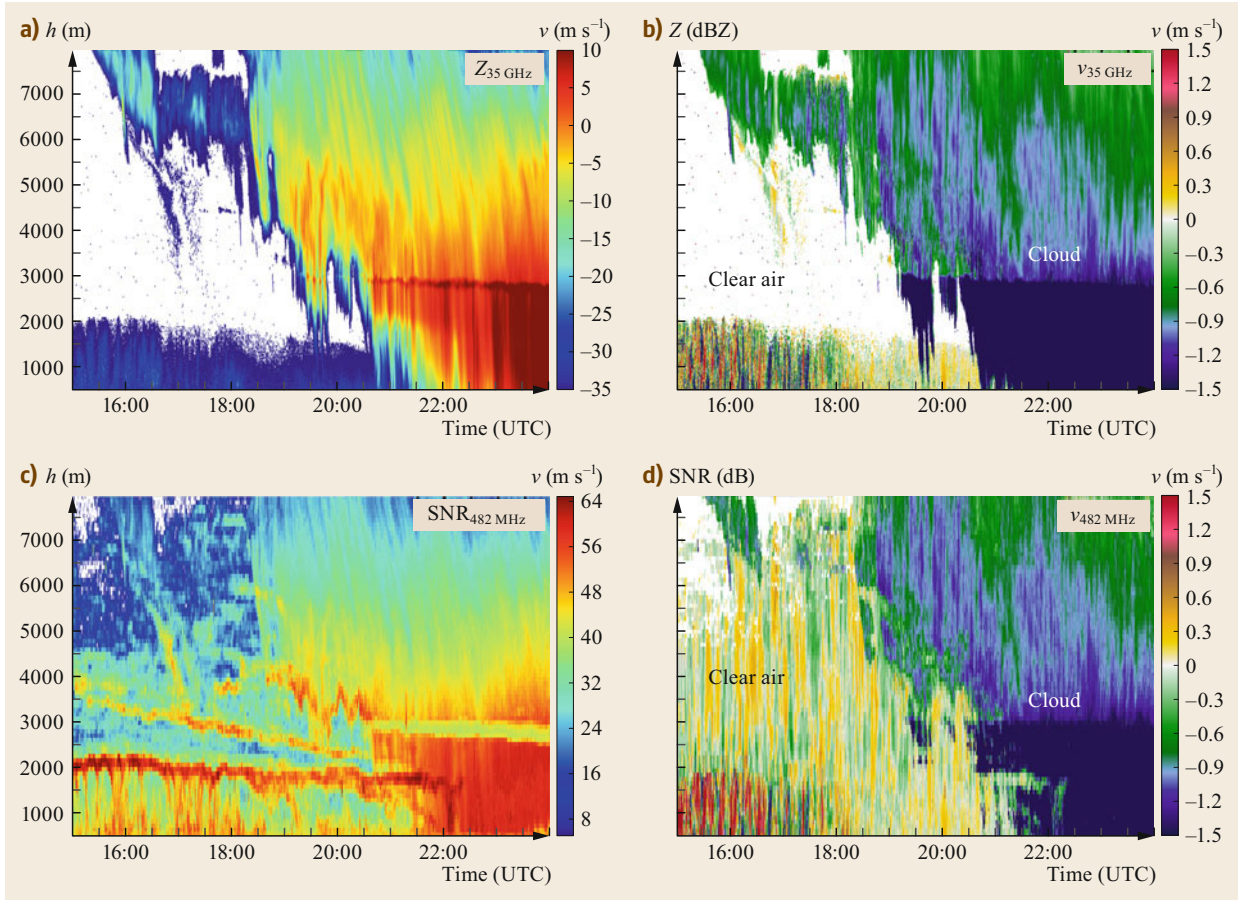


Fig. 31.1a–d Cloud radar reflectivity (a), RWP SNR (c), cloud radar velocity (b) and RWP velocity (d) at Lindenberg (Germany) on 17 June 2015, illustrating simultaneous clear-air and particle scattering. When the particle return dominates (i.e., there is high reflectivity in the 35 GHz cloud radar), the clear-air signal in the RWP is dominated by falling particles (after [31.44] © Authors Creative Commons Attribution 4.0 License)

information other than the estimated horizontal wind components [31.44–54]. An example of this so-called Bragg–Rayleigh ambiguity is shown in Fig. 31.1.

All remaining scattering or echoing mechanisms are considered to be clutter: unwanted echoes. This includes scattering at plasma in lightning channels [31.55–58], scattering by airplanes [31.19, 20] and birds [31.24, 59], as well as ground clutter echoes received through the ubiquitous sidelobes of finite-aperture antennas [31.15, 60–64].

31.3.2 Clear-Air Scattering

There is a considerable amount of literature on clear-air scattering [31.4, 30, 31, 36, 65–67], and this topic continues to attract new research [31.36, 68–70]. Due to its unique relevance to RWP systems, an overview of the theory of clear-air scattering is provided below.

The macroscopic polarization properties of air are described through a material parameter, the relative permittivity ϵ . By using different expressions for the atomic polarizability of dry air (nonpolar gases) and water vapor (a polar gas), ignoring carbon dioxide, and noting that by definition the relative permittivity is related to the refractive index via $n^2 = \epsilon$, it can be shown [31.71] that

$$(n-1)_{\text{Air}} = \frac{k_1 p}{z_a T} + \frac{k_2 e}{z_w T} + \frac{k_3 e}{z_w T^2}, \quad (31.1)$$

where e is the partial pressure of water vapor and the parameters k_i relate to the molecular polarization. z_a and z_w are corrections to the ideal state equation for gases. In radar meteorology, it is common to use the refractivity N [31.66], defined as $N = (n-1)10^6$. Using the

constants given by [31.66],

$$N = c_1 \frac{p}{T} + c_2 \frac{e}{T} + c_3 \frac{e}{T^2}, \quad (31.2)$$

with

$$c_1 = 0.776 \frac{\text{K}}{\text{Pa}}, \quad c_2 = 0.716 \frac{\text{K}}{\text{Pa}}$$

and $c_3 = 3.7 \times 10^3 \frac{\text{K}^2}{\text{Pa}}.$

The ubiquitous variations in temperature, humidity, and pressure in the turbulent atmosphere result in variations in the refractive index of the atmospheric medium [31.4, 66], which in turn cause the macroscopic scattering of electromagnetic waves propagating through the atmosphere.

The first step when analyzing the scattering problem is to utilize the macroscopic Maxwell equations. If we only consider a harmonic time dependence of the fields by separating a factor $e^{i\omega t}$ from the electric and magnetic field vectors $\mathbf{E}(\mathbf{r}, t)$ and $\mathbf{H}(\mathbf{r}, t)$, respectively [31.72], we obtain the vector Helmholtz equation

$$\Delta \mathbf{E}(\mathbf{r}) + \epsilon_0 \mu_0 \omega^2 \epsilon(\mathbf{r}) \mathbf{E}(\mathbf{r}) = -\nabla[\mathbf{E}(\mathbf{r}) \cdot \nabla \ln(\epsilon(\mathbf{r}))], \quad (31.3)$$

which implicitly assumes that the phenomenon under consideration is monochromatic. This is a good approximation whenever the medium varies over a much longer timescale than the propagation time of the wave. The permittivity of the atmosphere fluctuates around a value of 1, so

$$\epsilon(\mathbf{r}, t) = \langle \epsilon(\mathbf{r}, t) \rangle + \epsilon'(\mathbf{r}, t) = 1 + \epsilon'(\mathbf{r}, t). \quad (31.4)$$

The ansatz for the total electric field is written $\mathbf{E} = \mathbf{E}_0 + \mathbf{E}_s$, where \mathbf{E}_0 is the solution of the homogeneous version of (31.3), i.e., the field in the absence of permittivity fluctuations. For single scattering, all products of the two small quantities \mathbf{E}_s and ϵ' are neglected (Born approximation), which leads to an equation for the scattered electric field \mathbf{E}_s ,

$$\Delta \mathbf{E}_s(\mathbf{r}) + \epsilon_0 \mu_0 \omega^2 \mathbf{E}_s(\mathbf{r}) = \epsilon_0 \mu_0 \omega^2 \epsilon'(\mathbf{r}) \mathbf{E}_0(\mathbf{r}) - \nabla[\mathbf{E}_0(\mathbf{r}) \cdot \nabla \ln(\epsilon'(\mathbf{r}))] \quad (31.5)$$

The solution to this equation when there are no additional boundary conditions for \mathbf{E}_s (except for the radiation condition) in the far field is known to be [31.4, 69]

$$\mathbf{E}_s(\mathbf{r}) = \frac{k^2}{4\pi} \iiint_V \frac{e^{ik|\mathbf{r}-\mathbf{r}'|}}{|\mathbf{r}-\mathbf{r}'|} \epsilon'(\mathbf{r}') [\mathbf{o} \times [\mathbf{E}_0(\mathbf{r}') \times \mathbf{o}]] d^3 \mathbf{r}'. \quad (31.6)$$

The unit vector $\mathbf{o} = (\mathbf{r} - \mathbf{r}')/|\mathbf{r} - \mathbf{r}'|$ is directed from the variable scattering point to the observation point. Equation (31.6) is fairly general because it only assumes that the observation point lies in the far field of the scatterer.

For any concrete problem, the exact scattering geometry (e.g., the location of the transmitting and receiving antenna) and the incident field $\mathbf{E}_0(\mathbf{r})$ must be specified. To obtain closed-form expressions, it is customary to simplify the treatment by assuming that the transmitted electromagnetic pulse has a Gaussian shape and that the antenna radiation pattern (the beam geometry) is also Gaussian [31.36, 69]. This model for \mathbf{E}_0 together with the term $e^{ik|\mathbf{r}-\mathbf{r}'|}/|\mathbf{r}-\mathbf{r}'|$ essentially defines the instrument sampling function. A comprehensive theoretical analysis of the measurement process for clear-air Doppler radars based on explicit formulations for the instrument sampling function is presented in [31.36]. Two levels of approximation are used to simplify this instrumental sampling function analytically. These are obtained by expanding $|\mathbf{r} - \mathbf{r}'|$ in a Taylor series and retaining terms up to first order (i.e., linear; this is known as the Fraunhofer approximation) or up to second order (i.e., quadratic; this is termed the Fresnel approximation).

The Fraunhofer diffraction or small-volume scattering approximation assumes that the phase fronts of the incident wave are planar over the scattering volume. In this case, (31.6) simplifies to

$$\mathbf{E}_s(\mathbf{r}, t) = \mathbf{E}_0 \frac{k^2}{4\pi} \frac{e^{ikr}}{r} \iiint_V \epsilon'(\mathbf{r}', t) e^{-i2k\mathbf{r}' \cdot \mathbf{r}} d^3 \mathbf{r}', \quad (31.7)$$

which explicitly allows for a refractive index variation with a timescale that is much longer than the propagation time of the wave. Equation (31.7) shows that the field of permittivity fluctuations is sampled at twice the wavenumber k of the incident electromagnetic wave. Therefore, refractive index fluctuations at the half-wavelength scale play a prominent role in clear-air backscattering. This is essentially a condition for constructive interference, which leads to detectable backscattered signal levels.

Current radar theory builds upon the Fresnel approximation, which is applicable under much weaker assumptions and includes additional relevant effects [31.36, 65, 69]. However, the Fresnel approximation leads to the same final radar equation as the traditional Fraunhofer approximation if the refractive index perturbations are statistically isotropic at the Bragg wavenumber [31.36].

It is convenient to choose a coordinate system with the origin centered on the scattering area (Fig. 31.2). Assume that the scattering region is illuminated by

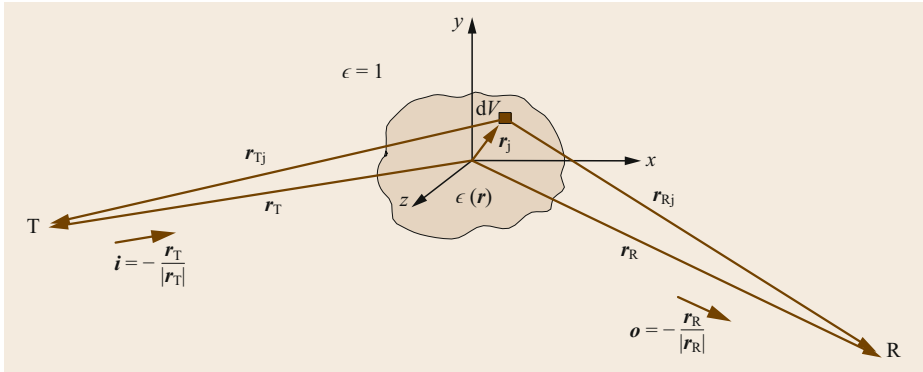


Fig. 31.2 Geometry of the general scattering problem

a monochromatic and linearly polarized plane wave of normalized (to unity) amplitude

$$E(\mathbf{r}, t) = e_i e^{i(\mathbf{k}\mathbf{r} - \omega t)}, \quad \text{where } k = \omega \sqrt{\mu_0 \epsilon_0}. \quad (31.8)$$

In this case, at a sufficiently large distance R from the scattering area, the scattered wave can be formally written as

$$E_s(\mathbf{r}, t) = f(\mathbf{o}, \mathbf{i}) \frac{e^{i\mathbf{k}\mathbf{R}}}{R}. \quad (31.9)$$

This equation introduces the *scattering amplitude* $f(\mathbf{o}, \mathbf{i})$, a parameter that is commonly used in the theory of scattering processes [31.73] and ignores the harmonic time dependence. It describes the amplitude, phase, and polarization of the scattered wave in the far field. In radar meteorology, the cross-section is defined as “the area intercepting that amount of (incident) power, which, if scattered isotropically, would return to the receiver an amount of power equal to that actually received” [31.74], see also [31.31, 66]. Mathematically, this can be expressed as [31.73]

$$\sigma(\mathbf{o}, \mathbf{i}) = \lim_{R \rightarrow \infty} \frac{4\pi R^2 S_s(\mathbf{o}, R)}{S_i(\mathbf{i})}, \quad (31.10)$$

where $S_s(R)$ is the scattered power flux density at a distance R in direction \mathbf{o} from the scatterer and S_i is the incident power flux density. The Poynting vector $\mathbf{S} = \mathbf{E} \times \mathbf{H}^*$ for an electromagnetic wave progressing in unit direction \mathbf{n} is

$$\mathbf{S} = \frac{|\mathbf{E}|^2}{\sqrt{\eta}} \mathbf{n}, \quad (31.11)$$

where $\eta = \sqrt{\mu_0 / (\epsilon \epsilon_0)}$ is the wave impedance. Upon inserting (31.11) and (31.9) into (31.10) and noting that E_i has an amplitude of unity by definition, we obtain

$$\sigma(\mathbf{o}, \mathbf{i}) = 4\pi |f(\mathbf{o}, \mathbf{i})|^2. \quad (31.12)$$

For distributed targets, the volume reflectivity η is defined as the radar cross-section per unit volume

$$\eta = \frac{d\sigma}{dV}. \quad (31.13)$$

By definition, the backscattering cross-section is given by

$$\sigma_b = \sigma(-\mathbf{i}, \mathbf{i}) = 4\pi |f(-\mathbf{i}, \mathbf{i})|^2. \quad (31.14)$$

The field of fluctuations in the dielectric number ϵ' is a random function, meaning that the scattering amplitude is also a random function [31.66, 73],

$$\sigma_b = \frac{k^4}{4\pi} \iiint_V \iiint_V \langle \epsilon'(\mathbf{r}'_1) \epsilon'(\mathbf{r}'_2) \rangle e^{i2\mathbf{k}\mathbf{i}(\mathbf{r}'_1 - \mathbf{r}'_2)} d^3\mathbf{r}'_1 d^3\mathbf{r}'_2. \quad (31.15)$$

The function $B_\epsilon = \langle \epsilon'(\mathbf{r}_1) \epsilon'(\mathbf{r}_2) \rangle$ is the correlation function for dielectric fluctuations. If we introduce the new coordinates [31.75] $\boldsymbol{\sigma} = 1/2(\mathbf{r}_1 + \mathbf{r}_2)$ and $\boldsymbol{\delta} = (\mathbf{r}_1 - \mathbf{r}_2)$, then

$$\sigma_b = \frac{k^4}{4\pi} \iiint_V \iiint_V B_\epsilon(\boldsymbol{\sigma}, \boldsymbol{\delta}) e^{i2\mathbf{k}\mathbf{i}\boldsymbol{\delta}} d^3\boldsymbol{\delta} d^3\boldsymbol{\sigma}. \quad (31.16)$$

The last integral can be interpreted as a Fourier transformation of B_ϵ with respect to $\boldsymbol{\delta}$. According to statistical turbulence theory, this gives the variance spectrum Φ of ϵ [31.76]. Thus,

$$\sigma_b = 2\pi^2 k^4 \iiint_V \Phi_\epsilon(\boldsymbol{\sigma}, 2\mathbf{k}\mathbf{i}) d^3\boldsymbol{\sigma} \quad (31.17)$$

and

$$\eta_b = 2\pi^2 k^4 \Phi_\epsilon(\boldsymbol{\sigma}, 2\mathbf{k}\mathbf{i}). \quad (31.18)$$

The volume reflectivity is directly proportional to the 3-D spectrum of refractivity for the wavenumber corresponding to half the radar wavelength. The sampling of Φ at just one wavenumber is the Bragg condition, which is required for constructive interference. Note that the variance spectrum is sampled at wavevector $2ki$. Obviously, there is a dependence of the volume reflectivity on the direction of the incident wave in case of an anisotropic variance spectrum of the permittivity at the wavenumber $2k$. This phenomenon is indeed observed with radars in the 50 MHz band and is termed *aspect sensitivity*. It is very difficult to derive the statistical properties of a stratified and therefore anisotropic medium, so heuristic models are commonly used [31.77].

For locally isotropic fluctuations in the dielectric number (i.e., in the inertial subrange), (31.18) reduces to

$$\eta_b = 8\pi^2 k^4 \Phi_n(\sigma, 2k). \quad (31.19)$$

If the corresponding variance spectrum for the refractive index is used, $\Phi_\epsilon = 4\Phi_n$ [31.31].

Kolmogorov's statistical theory predicts that the 3-D variance spectrum in the inertial range has a typical wavenumber dependence of $k^{-11/3}$ and can therefore be written as

$$\Phi_n(\sigma, k) = 0.0330 C_n^2(\sigma) k^{-11/3}, \quad (31.20)$$

where C_n^2 is the structure parameter for the refractive index [31.76]. Thus, we finally arrive at

$$\eta_b = 0.3787 C_n^2(\sigma) \lambda^{-1/3}, \quad (31.21)$$

an important equation that is used in radar meteorology to determine the volume reflectivity caused by fluctuations in the refractive index (see for example [31.75, 78–80] and references cited therein).

Such a scattering process is often termed *Bragg scattering*. It is clearly the most relevant scattering model for RWPs [31.31, 80].

31.3.3 Signal Processing

The RWP antenna receives the backscattered electromagnetic wave and converts it into a measurable electrical signal S at the antenna output port, where

$$S(\mathbf{r}, t) = \iint_F \mathbf{E}_s(\mathbf{r} + \boldsymbol{\rho}, t) f_A(\boldsymbol{\rho}) d^2 \boldsymbol{\rho}. \quad (31.22)$$

Here, f includes the antenna radiation pattern [31.81].

The voltage at the output port of the antenna $S(\mathbf{r}_0, t) = S(t)$ is the physical carrier of all of the information about the atmosphere that is made available by the scattering process. The purpose of signal processing is therefore to convert the measured electrical signal into meteorological parameters [31.82].

In signal analysis, it is useful to find a mathematical representation of the signal that facilitates physical interpretation. The signal is typically transformed into another representation (e.g., from the time domain to the frequency domain) in order to study the same piece of information from a different perspective [31.83]. It is important to pick an appropriate new representation for subsequent signal processing tasks such as detection, classification, and estimation. The representation is well adapted to the problem if only a few coefficients reveal the information contained in the signal. This is called a sparse representation [31.84]. A typical radar echo is sparse in the frequency domain; hence the prominent role of the Doppler spectrum. The suppression or filtering of unwanted echoes is also more efficient if a sparse representation of the clutter signal component can be found.

RWP signal processing was initially developed for an idealized setting where the receiver signal was assumed to consist of only the atmospheric signal of interest and the ubiquitous thermal noise of the receiver electronics. The idealized properties of the receiver signal at the antenna output port of a pulsed single-frequency RWP are [31.85]:

- $S(t)$ is a continuous real-valued random voltage signal
- $S(t)$ is narrowband, with the information contained in the slowly varying signal envelope [31.86]
- $S(t)$ has a large dynamic range, with strong signal power for some clutter echoes and extremely low power signals typically occurring at the uppermost range gates.

The detection of weak signals in noise or—equivalently—optimization of the SNR requires a matched filter approach [31.66, 87].

Demodulation, Range Gating, and A/D Conversion

The narrowband RWP signal at the output port of the low-noise amplifier can be written

$$S_{rx}(t) = A(t) \cos[\omega_c t + \Phi(t)]. \quad (31.23)$$

Information about the scattering process is contained in the amplitude and phase modulation of the received signal $S_{rx}(t)$. A demodulation step is first

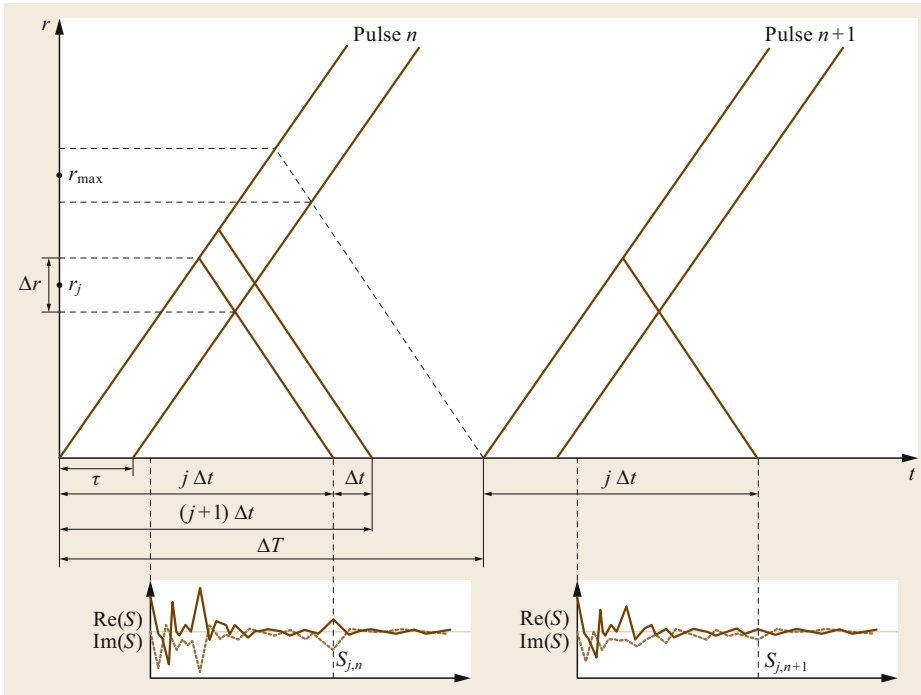


Fig. 31.3 Simplified schematic of range-time sampling for two successive pulses

performed to remove the carrier frequency ω_c while retaining the modulation information contained in the instantaneous amplitude $A(t)$ and the instantaneous phase $\Phi(t)$. This yields the complex baseband signal

$$\tilde{S}(t) = I(t) + iQ(t), \quad (31.24)$$

where the real part $I(t)$ is called the in-phase component and the imaginary part $Q(t)$ is termed the quadrature-phase component of the signal [31.86]. The implementation details of this demodulation depend on the particular receiver architecture of the RWP.

RWPs transmit a series of short electromagnetic pulses. The backscattered signal is sampled during the time interval ΔT between successive pulses. Knowledge of the propagation speed of the wave group (i.e., the speed of light) allows the radial distance of the measurement to be determined, as illustrated in Fig. 31.3. The maximum distance that can be determined unambiguously (known as the maximum unambiguous range h_{\max}) is of course limited by the pulse separation or interpulse period ΔT , with $h_{\max} = c\Delta T/2$.

The vertical resolution is determined by the pulse width τ , with $\Delta r = c\tau/2$. It is customary to perform range sampling with a frequency of at least $1/\tau$. Note that it is not possible to increase the vertical resolution by range sampling more densely [31.87].

Range gating is usually done during A/D conversion. If the range sampling frequency is given by $1/\Delta t$

and N_h is an integer that denotes the number of range gates with $\Delta T > N_h\Delta t$, then the signal $\tilde{S}(t)$ is obtained at the discrete grid

$$\begin{aligned} \tilde{S}[j, n] &= \tilde{S}(t_0 + j\Delta t + n\Delta T), \\ j &= 0, \dots, N_h - 1, \quad n = 0, \dots, N_T - 1. \end{aligned} \quad (31.25)$$

For each range gate j at height $c/2j\Delta t$, a discrete (complex) time series of the signal is obtained with a sampling interval of ΔT . This can be written in a simplified notation as

$$S[n] = S_I[n] + iS_Q[n], \quad n = 0, \dots, N_T - 1. \quad (31.26)$$

The Digitized Raw Signal

The theoretical basis for RWP signal processing is the mathematical model of stationary Gaussian random processes. Specifically, the model for the digitized and range-gated RWP signal is

$$S[n] = I[n]e^{i\omega n\Delta T} + N[n], \quad (31.27)$$

where $I[n] \propto \mathcal{N}(0, \mathbf{R}_I)$ and $N[n] \propto \mathcal{N}(0, \mathbf{R}_N)$ are independent, complex, zero-mean, Gaussian random vectors that describe the atmospheric signal and the receiver noise, respectively [31.88], ΔT is the sampling interval of the sequence and ω is the mean Doppler frequency. Furthermore, $I[n]$ is narrowband compared to the receiver bandwidth and $|\omega| \leq \pi/\Delta t$ (the Nyquist criterion).

Since $S[n]$ results from the demodulation of a real-valued, zero-mean, stationary Gaussian random process, the resulting complex random process is also stationary, has a mean of zero, and is proper; that is, the sequence has vanishing pseudo-covariance $E(S[p]S[q]) = 0$ [31.89]. The underlying random process of the realization $S[n]$ is completely characterized by its covariance matrix \mathbf{R} , where [31.85]

$$\begin{aligned} (\mathbf{R})_{p,q} &= \text{Cov}(S[p], S[q]) \\ &= \sigma_I^2 \boldsymbol{\varrho}[p-q] e^{i\omega(p-q)\Delta T} + \sigma_N^2 \delta_{p-q,0}, \end{aligned} \quad (31.28)$$

The autocorrelation sequence $\boldsymbol{\varrho}$ is typically assumed to be Gaussian as well, and therefore corresponds to a Gaussian signal peak in the power spectrum. If the spectral width of the signal is σ_v , then [31.88, 90]

$$\boldsymbol{\varrho}[n] = e^{-2\pi^2 \sigma_v^2 n^2 \Delta T^2}. \quad (31.29)$$

This Gaussian correlation model must not be confused with the characterization of the random process as Gaussian, which encompasses a much wider class of signals. To completely describe such a random process, it is sufficient to consider either the autocovariance function or—according to the Wiener–Khinchine theorem—the power spectrum. In radar meteorology, the latter is usually referred to as the Doppler spectrum.

This signal model provides the theoretical justification for why only the first three moments of the Doppler spectrum are usually estimated. Note that stationarity must be assumed over typical dwell times of $O(1 \text{ min})$.

Real-world effects such as clutter or radiofrequency interference make it necessary to extend the simple model (31.27) by adding an additional clutter component with potentially very diverse properties, i.e.,

$$S[n] = I[n]e^{i\omega n \Delta T} + N[n] + C[n]. \quad (31.30)$$

Furthermore, atmospheric scattering is of course not limited to only clear-air echoes. This modifies the general properties of the signal as follows:

- $S(t)$ becomes multicomponent due to the possibility of simultaneously acting atmospheric scattering mechanisms, internal (electronic) noise, and external (artificial) effects
- $S(t)$ can be nonstationary due to the transient nature of bird, airplane, or lightning echoes.

Strictly speaking, only the clear-air scattering mechanism is of interest in radar wind profiling. However, from a practical point of view, it has become customary to include the scattering at hydrometeors as a non-

clutter component too, provided that the particles can be considered tracers for wind measurements. Multiple signal components from different scattering processes or other effects need to be separated and classified using additional information provided a priori. The presence of several independent stationary signal components will give rise to a Doppler spectrum with multiple signal peaks, which will necessitate more sophisticated target classification.

While the receiver signal is intrinsically nonstationary due to the impulsive character of the transmitted signal (a pulse) and the inhomogeneous vertical structure of the atmosphere, this property changes significantly during range gate sampling. The assumption of stationarity is usually valid for atmospheric scattering, ground clutter, and noise. However, intermittent clutter introduces nonstationarity at the level of the range-gated I/Q data. This nonstationary signal character requires the application of nonstationary signal analysis to obtain the problem-adapted (sparse) signal representation required for efficient filtering [31.91].

Time Domain Processing: Digital Filtering

Digital time-domain processing includes all the operations applied to the signal \mathbf{S} before a Doppler spectrum is estimated. This includes coherent integration, which essentially allows the data rate to be reduced at the expense of the analyzable Nyquist interval and introduces unwanted digital filtering [31.92], as well as specially designed linear FIR (finite impulse response) [31.93] and sophisticated nonlinear (clutter) filtering algorithms [31.85, 91, 94]. An example of a coherently integrated time series is shown in Fig. 31.4.

Frequency Domain Processing: Spectral Estimation

For a stationary Gaussian random process, the power or Doppler spectrum provides a sparse representation. A modified periodogram is typically used as a classical nonparametric estimator of the power spectrum [31.95, 96] since it does not need any further information a priori and produces reasonable results for a large class of relevant processes, including ground clutter and simple types of radio-frequency interference (RFI). It can easily be implemented using a discrete Fourier transform (DFT).

The (leakage) bias of the periodogram estimate is reduced through data tapering [31.97]. Welch's overlapped segment averaging [31.96, 98] is a popular method for reducing the variance of the estimate due to its ease of implementation. This is known as spectral or incoherent averaging [31.20]. Other methods such as multitaper estimators can also be applied [31.99].

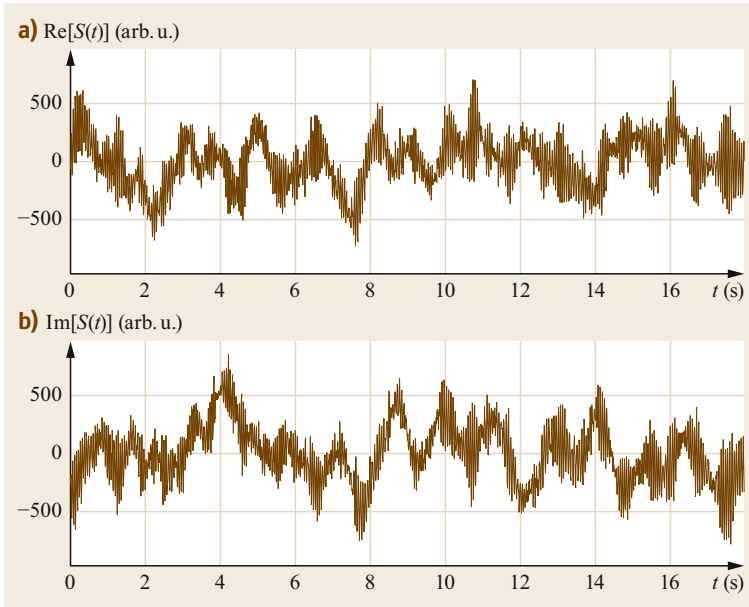


Fig. 31.4a,b Example of a coherently integrated I/Q time series obtained from a 482 MHz RWP at 08:24:59 UTC on 1 Dec. 1999 (Beam East, height 3035 m): **(a)** real component, **(b)** imaginary component (after [31.70] with permission)

The Doppler spectrum is usually given as a function of velocity rather than frequency. Interconversion between the frequency shift f and the radial velocity v_r is achieved using the well-known relation $f = 2v_r/\lambda$, where λ denotes the radar wavelength.

An example of a Doppler spectrum is shown in Fig. 31.5.

Signal Detection, Classification, and Moment Estimation

To discriminate between the noise and the signal, an objective noise level is estimated using the method proposed by *Hildebrand and Sekhon* [31.100]. The next step is the identification of the signal peak caused by the atmospheric return. A simple method that selects the signal peak with the highest power density as the atmospheric signal works very well for single-peak spectra and is furthermore robust [31.20, 101]. A number of multiplex algorithms have been proposed for more complex situations, including rather simple ground-clutter algorithms and more sophisticated techniques [31.93, 102, 103]. Unfortunately, only a few of these algorithms have been comprehensively validated [31.104–106]; most methods remain experimental.

Since the power spectrum of the atmospheric signal is often assumed to be Gaussian in form, the first three moments (power, mean frequency, and frequency spread) are sufficient to describe the signal [31.15]. They are well defined even when the assumption that the power spectrum is Gaussian is violated [31.62]. For spectra with sufficient frequency resolution, it may therefore be useful to estimate higher-order moments.

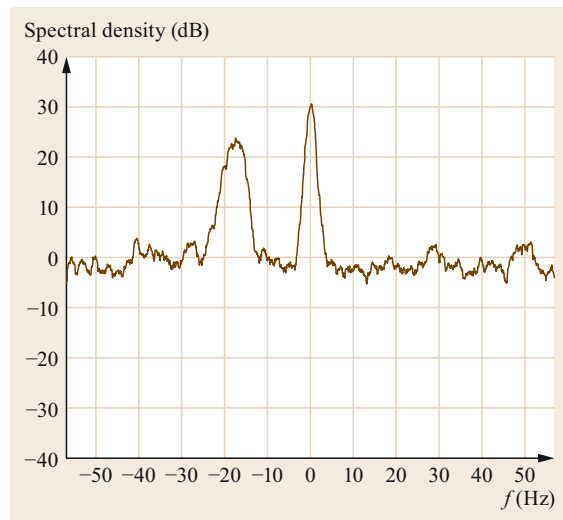


Fig. 31.5 Example of an incoherently averaged Doppler spectrum obtained from a 482 MHz RWP at 08:24:59 UTC on 1 Dec. 1999 (Beam East, height 3035 m). The clear-air echo peak is visible at about -18 Hz, whereas an unusually strong ground-clutter peak is centered around 0 Hz. The signal contribution from the noise is spread evenly across the Nyquist frequency range. The spectral density of the noise level has been normalized to zero as the radar was not calibrated (after [31.70] with permission)

Small SNR values are typical of RWPs, at least for the uppermost range gates. Consequently, one is faced with a statistical detection task that leads to a binary decision problem with two hypotheses (H_0 : no atmo-

spheric signal is present; H_1 : an atmospheric signal is present). A simple but powerful method known as consensus averaging is often used to discriminate between (false) Doppler estimates caused by random noise peaks and (correct) estimates that are due to stationary atmospheric returns. The technique essentially provides a homogeneous (nonlinear) estimator for the Doppler velocity that includes outlier suppression [31.20, 90, 107].

31.3.4 Wind Vector Estimation: Doppler Beam Swinging

In so-called Doppler systems, the frequency shift of the scattered waves is used to measure the motion of the scattering medium directly. However, the velocity can only be determined along the line of sight or radial direction of the antenna beam. Most RWPs use a simple method known as Doppler beam swinging (DBS) to determine the wind vector [31.108–110]. Three linearly independent beam directions are required to transform the measured line-of-sight radial velocities into the wind vector using additional assumptions concerning the wind field. Measurements are usually taken in more than three directions to minimize errors.

For a given azimuth α and zenith angle ϕ , the beam direction can be described mathematically by a unit vector $\mathbf{e} = (\sin \alpha \sin \phi, \cos \alpha \sin \phi, \cos \phi)^T$. The wind vector \mathbf{v} is retrieved from projections of \mathbf{v} onto a set of different beam vectors $\{\mathbf{e}_k\}_{k=1}^N$, which defines the spatial sampling. These projections are described by the inner product of the wind vector and the beam unit vectors.

For a stationary and horizontally homogeneous wind field, i.e., $\mathbf{v}(x, y, z, t) \approx \mathbf{v}(z)$, and for N beams, the N inner products can be expressed as a linear system of equations

$$\mathbf{A}\mathbf{v} = \mathbf{V}_r, \quad (31.31)$$

where $\mathbf{v} = (uvw)^T$ and $\mathbf{V}_r = (V_{r1} V_{r2} V_{r3} \dots V_{rn})^T$.

The rows of matrix \mathbf{A} consist of the beam unit vectors, i.e.,

$$\mathbf{A} = \begin{pmatrix} \sin(\alpha_1) \sin(\phi) & \cos(\alpha_1) \sin(\phi) & \cos(\phi) \\ \sin(\alpha_2) \sin(\phi) & \cos(\alpha_2) \sin(\phi) & \cos(\phi) \\ \sin(\alpha_3) \sin(\phi) & \cos(\alpha_3) \sin(\phi) & \cos(\phi) \\ \dots & \dots & \dots \\ \sin(\alpha_n) \sin(\phi) & \cos(\alpha_n) \sin(\phi) & \cos(\phi) \end{pmatrix}. \quad (31.32)$$

System (31.31) is obviously an overdetermined set of equations. If the azimuth angles α_i (with $i = 1, \dots, n$) and the elevation angle ϕ are chosen properly, \mathbf{A} is a matrix with full column rank: $\text{rank}(\mathbf{A}) = 3$. The solution is unique and exact when it does exist; otherwise,

an approximate solution that minimizes $\|\mathbf{V}_r - \mathbf{A}\mathbf{v}\|_2^2$ can be obtained using the method of least squares,

$$\mathbf{v} = (\mathbf{A}^T \mathbf{A})^{-1} \mathbf{A}^T \mathbf{V}_r = \mathbf{A}^+ \mathbf{V}_r, \quad (31.33)$$

where \mathbf{A}^+ denotes the Moore–Penrose pseudoinverse of \mathbf{A} . However, this solution tends to worsen the condition of the matrix, i.e., $\text{cond}(\mathbf{A}^T \mathbf{A}) = (\text{cond}(\mathbf{A}))^2$. It may be ill conditioned or even numerically singular, i.e., small errors in the (measured) data may produce large errors in the solution. It is therefore useful to employ the singular value decomposition (SVD) of matrix \mathbf{A} , namely $\mathbf{A} = \mathbf{U}\mathbf{D}\mathbf{V}^T$, where \mathbf{U} is an orthogonal matrix, \mathbf{V} is a 3×3 orthogonal matrix, and \mathbf{D} is a diagonal matrix whose elements σ_i are called the singular values of \mathbf{A} . The least squares solution can then be expressed as

$$\mathbf{v} = \mathbf{A}^+ \mathbf{V}_r = \mathbf{V}\mathbf{D}^{-1}\mathbf{U}^T \mathbf{V}_r. \quad (31.34)$$

This method provides stable numerical solutions in the general case and can therefore be implemented in operational Doppler systems, whether they utilize radar or lidar [31.111]. Obviously, an explicit solution of (31.31) would provide more insight into error propagation and possibly also the optimal sampling conditions. Such an explicit solution can be obtained for a symmetric VAD-like sampling scenario; see [31.112].

With preassigned equispaced azimuth angles $\alpha_k = 2\pi k/N$, $k = 0, \dots, N-1$ and a constant zenith angle ϕ , the explicit solution for the wind vector is obtained as

$$\mathbf{v} = \begin{pmatrix} u \\ v \\ w \end{pmatrix} = \begin{pmatrix} \frac{2}{N \sin \phi} \sum_{k=0}^{N-1} \sin \alpha_k V_k \\ \frac{2}{N \sin \phi} \sum_{k=0}^{N-1} \cos \alpha_k V_k \\ \frac{1}{N \cos \phi} \sum_{k=0}^{N-1} V_k \end{pmatrix}. \quad (31.35)$$

Assuming a Gaussian error model for the radial wind $\Delta V \propto \mathcal{N}(\boldsymbol{\beta}, \boldsymbol{\Sigma})$, where $\mathcal{N}(\boldsymbol{\beta}, \boldsymbol{\Sigma})$ is the N -dimensional normal distribution with expectation vector $\boldsymbol{\beta}$ and variance matrix $\boldsymbol{\Sigma}$, and that the components β are constant ($\beta_i = \beta$ for $i = 0, \dots, N-1$) and $\boldsymbol{\Sigma} = \text{diag}(\sigma^2, \dots, \sigma^2)$, error propagation yields

$$E(\Delta \mathbf{v}) = \frac{\beta}{\cos \phi} \begin{pmatrix} 0 \\ 0 \\ 1 \end{pmatrix}. \quad (31.36)$$

A constant bias in the radial wind estimates only affects the estimation of the vertical wind component; the horizontal wind vector components remain free from bias. This is due to the symmetry of the sampling, which leads to the cancellation of any existing bias in the radial winds.

The RMS error can be estimated as

$$E \begin{pmatrix} (\Delta u)^2 \\ (\Delta v)^2 \\ (\Delta w)^2 \end{pmatrix} = \begin{pmatrix} \frac{2\sigma^2}{N \sin^2 \phi} \\ \frac{2\sigma^2}{N \sin^2 \phi} \\ \frac{\sigma^2}{N \cos^2 \phi} \end{pmatrix} + \begin{pmatrix} 0 \\ 0 \\ \frac{\beta^2}{\cos^2 \phi} \end{pmatrix}. \quad (31.37)$$

In the presence of wind field inhomogeneities, the RMS error in the wind retrieval is reduced by increasing the number of off-vertical beams used in the Doppler beam-swinging technique. Note, however, that for the vertical wind component, increasing N only reduces the random error.

The assumption of a horizontally homogeneous and stationary wind field appears to be fairly restrictive, but the goal is not to determine the instantaneous wind vector in an arbitrary turbulent wind field but rather the mean (horizontal) wind vector over an averaging time of $O(10\text{--}30 \text{ min})$. For the average wind field, horizontal homogeneity must be assumed over the area encompassed by the beams (typically $O(1\text{--}10 \text{ km})$ for Doppler radar profilers), and stationarity must be assumed to hold during the averaging time. In the vertical direction, the wind field is assumed to be piecewise constant within layers that are approximately as thick as the radial resolution of the RWP, namely $O(100 \text{ m})$. An experiment with a volume-imaging multisignal radar wind profiler in a convective boundary layer indicated that the assumptions inherent in the DBS retrieval method can indeed be valid for a wind field that is averaged over 10 min [31.113].

However, deviations from these assumptions can easily lead to wind retrieval errors of $O(1 \text{ m s}^{-1})$. Wind retrievals are particularly error-prone during strong gravity-wave activity [31.109], patchy precipitation [31.114], and of course over complex terrain [31.115]. Errors can also occur in convective boundary layers if they are not horizontally homogeneous in the statistical sense. While the assumptions of statistical (local) homogeneity and quasi-steadiness are applied quite often in boundary-layer meteorology [31.116], it is clear that violations will occur when larger-scale (coherent) structures are present [31.117]. More work is required to quantitatively appraise the effects of this nonhomogeneity and nonstationarity on wind retrieval for various types of convective boundary layers.

31.3.5 Wind Vector Estimation: Spaced-Antenna Systems

Spaced-antenna (SA) wind profilers address the homogeneity problem by using multiple receiving antennas with overlapping sampling volumes. SA profilers only transmit pulses vertically, i.e., there is no steering, in contrast to DBS profilers. The backscattered signal is

then sampled by receivers on multiple closely spaced receiving antennas (Figs. 31.6 and 31.7).

As the atmosphere moves overhead, so does the backscattered signal at the ground. The time series of signals received by the spaced antennas are slightly temporally displaced in a manner that can be related to the motion of the atmosphere. As can be surmised by tracing the rays in Fig. 31.7, the velocity of the diffraction pattern at the ground is twice that of the atmosphere. Historically, SA techniques have primarily been used to observe the upper atmosphere [31.118, 121], although they are now used in some tropospheric and boundary-layer radar systems [31.28, 122, 123]. SA radars sample the drift of backscattered signals over the ground to derive wind velocities, so this method is sometimes called *spaced antenna drift*.

A variety of techniques are used to analyze the backscattered signals and thus determine the wind velocity. Many techniques use cross-correlation analysis, in which the time series of signals from the receivers are cross-correlated. Ideally, the sampling volumes of the receiving antennas overlap, so there is a significant degree of correlation between the time series from the receivers. The temporal difference between the time series obtained from a pair of neighboring receivers is determined by examining the cross-correlation function for a sequence of time offsets (or *lags*),

$$\rho(\varepsilon_{ij}, \eta_{ij}, \tau) = \frac{\langle E_i(t) E_j^*(t + \tau) \rangle}{\sqrt{\langle E_i(t) E_i^*(t) \rangle \langle E_j(t) E_j^*(t) \rangle}}, \quad (31.38)$$

where ε_{ij} and η_{ij} indicate the eastward and northward spacing of a pair of receivers (i, j) and τ indicates the time lag.

The cross-correlation function (31.38) shows a peak at the time lag corresponding to the average temporal difference between the time series of the neighboring receivers. Note that, as it moves, the atmosphere is continually changing (due to turbulence for instance), so there is never perfect cross-correlation.

The distance vector between the neighboring antennas is divided by the displacement time to obtain the component of motion along that vector. The *apparent* velocity can be determined by considering multiple pairs (at least three nonorthogonal pairs) of neighboring antennas and their cross-correlation functions. Note that this is denoted the apparent velocity because it is distorted by changes in the atmosphere as it moves. The more the atmosphere evolves, the more the received signals become temporally decorrelated. The effect of this decorrelation is that the cross-correlation functions become biased towards shorter time lags, which in turn means that the apparent velocity is always an overesti-

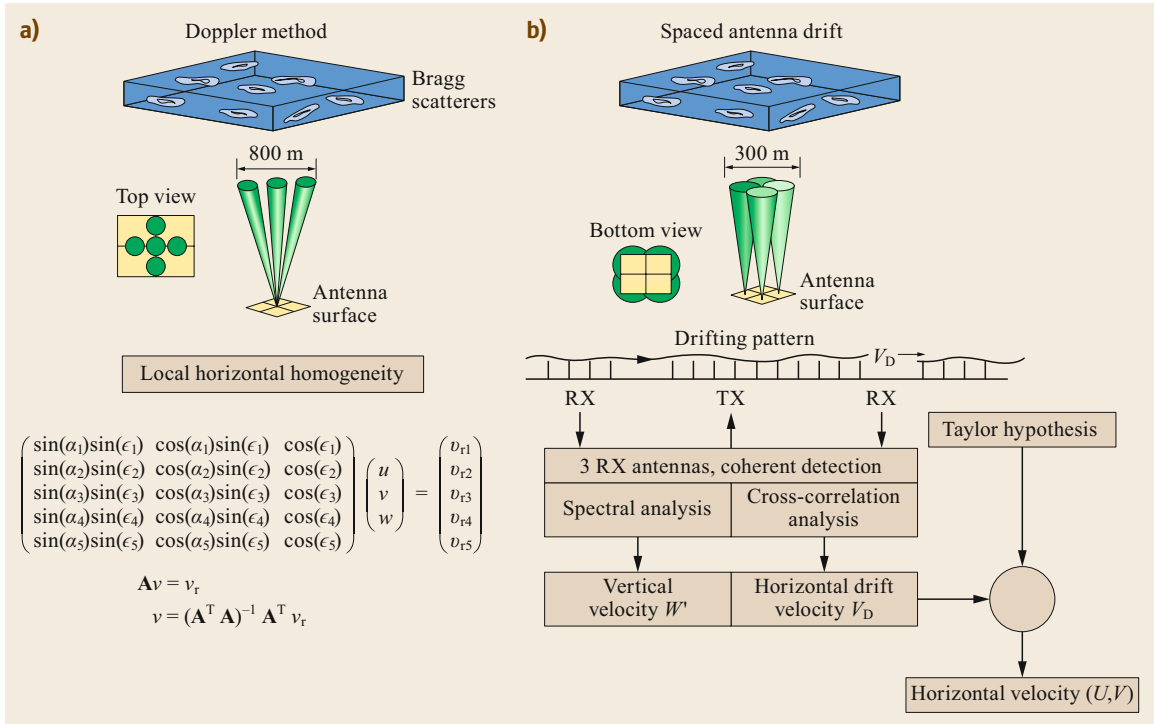


Fig. 31.6a,b Comparison of the Doppler (a) and spaced-antenna (b) RWP methods (after [31.118] reproduced with the permission of NCAR/EOL)

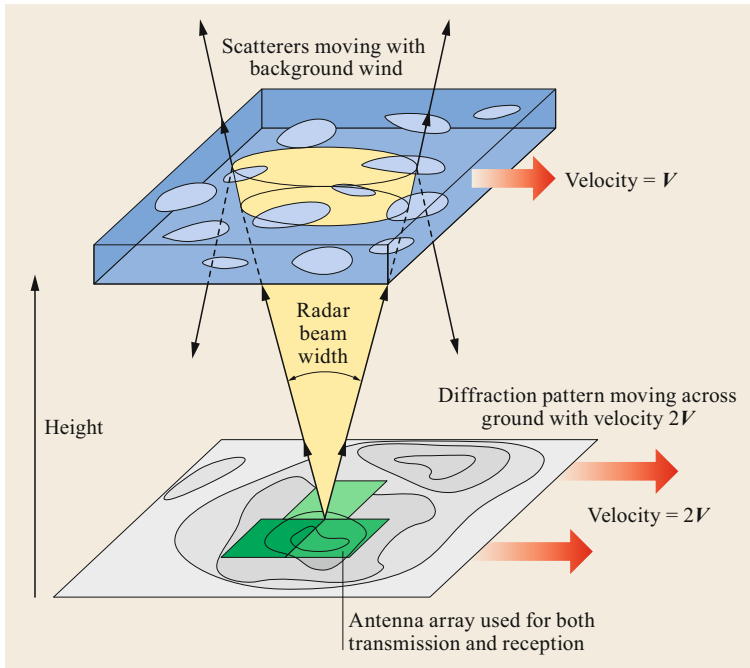


Fig. 31.7 Schematic representation of the SA method. The *three green squares* denote the spaced receiving antennas. Note that the diffraction pattern moves across the ground at a velocity of $2V$ due to the point source effect (after [31.119, 120])

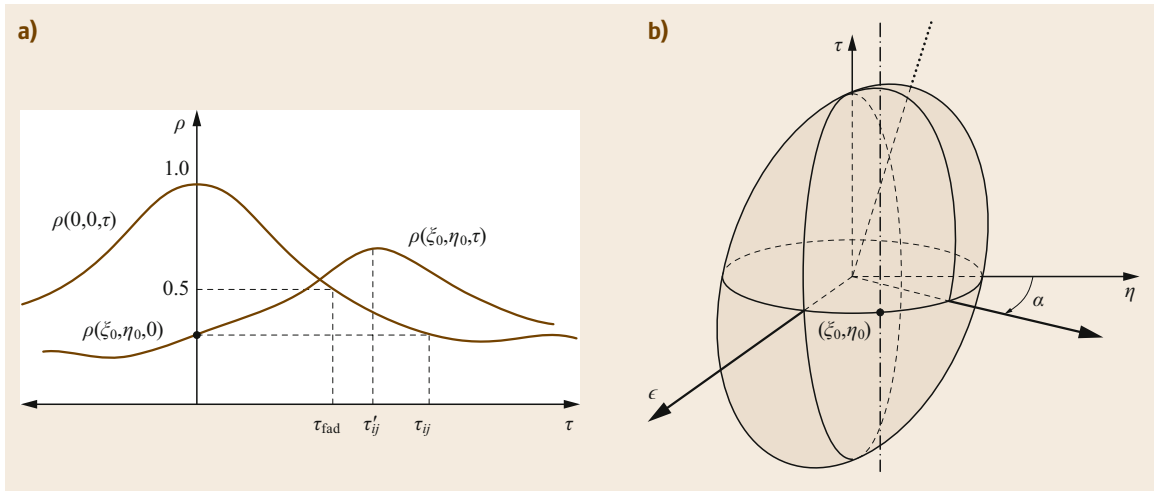


Fig. 31.8 (a) Idealized auto- and cross-correlation functions. The time lag of the peak of the cross-correlation function (τ_{ij}) is used to determine the apparent velocity. (b) A correlation ellipsoid surface indicating surfaces of constant correlation in the temporal and spatial domains. A surface of 0.5 is typically considered, meaning that the time lags τ for the auto- and cross-correlation functions to fall to 0.5 are determined then mapped onto the ellipsoid. The vertical axes intersect at τ_{fad} (often called the fading time). The ellipsoid can then be parameterized geometrically, and the tilt—which is directly related to the wind velocity—can be determined

mate of the true motion of the atmosphere. In addition, if the backscatter is anisotropic due to waves or rolls, the direction of the apparent velocity can be similarly biased.

Many points in both the time and spatial domains would need to be sampled with a suitably large number of receivers to precisely characterize these distortions. While SA profilers typically do collect many samples in the time domain, most radars can only deploy a small number of receivers (a minimum of three are required), so the spatial variability of the scattering is not well characterized. Several approaches can be used to parameterize the distortions and estimate a corrected wind; the most commonly used method is known as *full correlation analysis* (FCA) [31.124].

FCA was developed by *Briggs* [31.124, 125] among others. The basic assumption of FCA and other correlation techniques is made that to first order, the variability in the time domain has a similar functional form to the variability in the spatial domain. For example, some correlation techniques make the assumption that the temporal variability can be described as Gaussian, and thus the spatial variability is also Gaussian. In FCA [31.124], the actual function is not important, but it must take the same form in the spatial and temporal domains. An ellipsoidal surface of constant correlation is considered in the spatial and temporal correlation space (Fig. 31.8). This surface can be parameterized by examining key points for the auto- and cross-correlation functions. The ellipsoid can be considered an average

representation of the backscatter in the spatial and time domains. Further details of this method are beyond the scope of this review, but essentially the tilt of the ellipsoid is related to a corrected velocity that is referred to in FCA as the *true velocity* [31.7, 124].

Other correlation techniques take different approaches, such as considering the intersection point of the auto- and cross-correlation functions (assuming Gaussian behavior) or the slopes of the cross-correlation functions. Error analyses of various correlation techniques have been performed by *Doviak et al.* [31.126], who found that FCA compared well with other techniques in this respect.

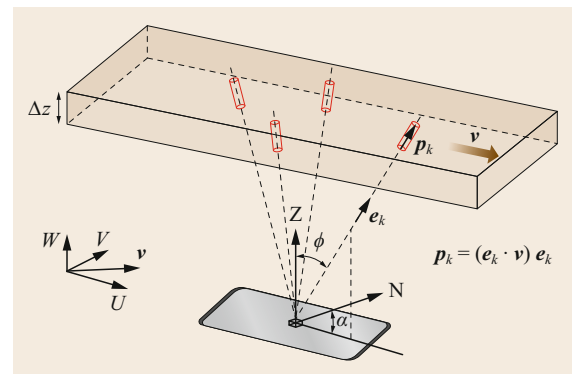


Fig. 31.9 Schematic showing the sampling performed for $N = 4$ (after [31.112] © Authors Creative Commons Attribution 3.0 License)

Interferometric techniques represent another approach to SA wind analysis. Consider Fig. 31.9 and the case in which all four samples are within a broad transmit pulse and the broad sampling volumes of multiple receivers. The backscattered signals from each of the four samples would have differing Doppler shifts. In addition, the backscatter would differ in phase at each receiver due to differences in the angle of arrival from that sample. SA interferometry techniques utilize the variation in the Doppler shift with respect to the angle of arrival to derive the estimated wind velocity. Typically, the cross-spectrum of signals received

at pairs of adjacently spaced receivers is analyzed. The phase of the cross-spectrum contains the angle of arrival information and, in the ideal case, varies uniformly across the spectrum. It was shown in [31.127] that interferometric techniques are equivalent to correlation techniques, as might be expected from the Fourier transform relationship between spectra and correlation functions, and that the wind velocity derived using interferometry is equivalent to the apparent velocity from correlation techniques. This led to the development of an analysis that allowed the wind velocity to be corrected in a similar manner to FCA.

31.4 Systems

RWPs come in many shapes and sizes. However, operationally relevant radars employ either the Doppler or the spaced-antenna method, so our discussion will be limited to these configurations. There are specialized research systems with additional sampling capabilities, such as those that use two [31.128] or multiple carrier frequencies to facilitate frequency-domain interferometry (FDI) or range imaging (RIM) [31.129–131], or those that employ a bistatic combination of a single transmit antenna and a multitude of receiving antennas to perform digital beamforming [31.132, 133]. The vast majority of RWPs are land-based, but there have been interesting technical developments relating to moving platforms such as ships, where the motion of the platform is compensated for during real-time operation [31.134].

31.4.1 Spectrum Allocation

A radar wind profiler can only be operated within a legal frequency allocation. Such allocations are defined

in resolutions COM5-5 and footnotes S5.162A and S.5.291A of the World Radiocommunication Conference 1997 (WRC-97). These documents assign RWP frequency allocations for the 50, 400, and 1000 MHz bands for each ITU region. A notable exception is the national allocation at 205 MHz for India [31.135, 136]. However, the radio spectrum is a precious resource, and the competition for frequencies continues to grow tremendously [31.137]. For this reason, all RWP spectrum allocations are constantly under pressure from other potential users of the respective bands. The importance of being able to utilize parts of the RF spectrum has been outlined in a number of official documents by the WMO and other international organizations [31.138, 139]. It is likely that this *spectrum congestion problem* will lead to changes in frequency management in the future [31.140]. Even today, it is already necessary to share profiler frequency bands with other services. One particular advantage of RWP is the near-vertical direction of the profiler beams, which helps to protect against horizontally propagating waves. Another is the relative flexibility in the selection of the operating frequency, as the clear-air scattering mechanism works across a broader range of wavelengths. This is in contrast to the rather strict constraints typical for passive remote-sensing instruments.

Nevertheless, the high sensitivity of RWPs makes them vulnerable to any sufficiently strong external radio-frequency interference that is in-band. RWP signal processing and quality control procedures must account for RFI to eliminate the spurious data which may otherwise occur in such cases.



Fig. 31.10 482 MHz radar wind profiler of the Deutscher Wetterdienst. A 1.5 μm Doppler lidar is visible in the foreground (photo © R. Leinweber) ◀

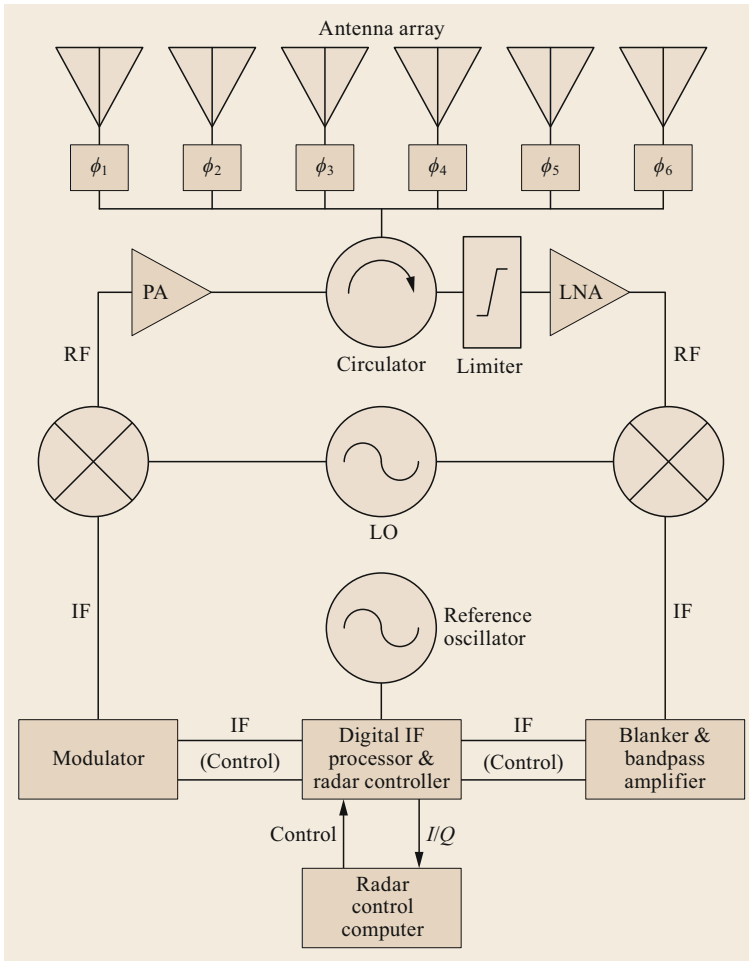


Fig. 31.11 Simplified block diagram of a single-signal radar wind profiler

31.4.2 Doppler Systems

The following discussion of the main RWP hardware components will be restricted to single-signal systems. Clearly, we can only describe the basic functionality here due to the great variety of possible hardware solutions for specific systems. More details about the general hardware aspects of radar can be found in [31.141–144].

A block diagram of the general architecture is given in Fig. 31.11. The central unit is the radar controller, which uses a highly stable oscillator as the single reference for all signals. This controller generates all of the timing and control signals needed to operate the radar, such as the transmit time, receiver blanking, A/D conversion (ADC) sample timing, and antenna control. It also generates the local oscillator (LO) signal and the transmit waveform, usually at an intermediate frequency (IF) that makes it easy to perform digital-to-analog conversion. The envelope of the transmit signal is often

shaped to minimize the occupied bandwidth of the transmitted wave group. Many radars are also capable of pulse compression; binary phase modulation using complementary codes is frequently used [31.145–149].

An additional modulator module is used to gate and amplify the pulse envelope before it is upconverted by mixing with the LO to give the transmitted radio frequency. The mixer is a three-port device with a non-linear component that ideally produces the sum and difference frequencies of two input signals at the output port [31.144]. The resulting low-level RF signal is passed to a linear power amplifier, which is generally a solid-state device nowadays. Finally, the transmit signal is delivered to the antenna and converted into an electromagnetic wave that is radiated into free space.

The antenna is typically designed as a phased array [31.81], although some simpler systems do use reflector antennas at shorter wavelengths [31.150]. The performance of the RWP is essentially determined by the antenna radiation pattern, which describes the an-

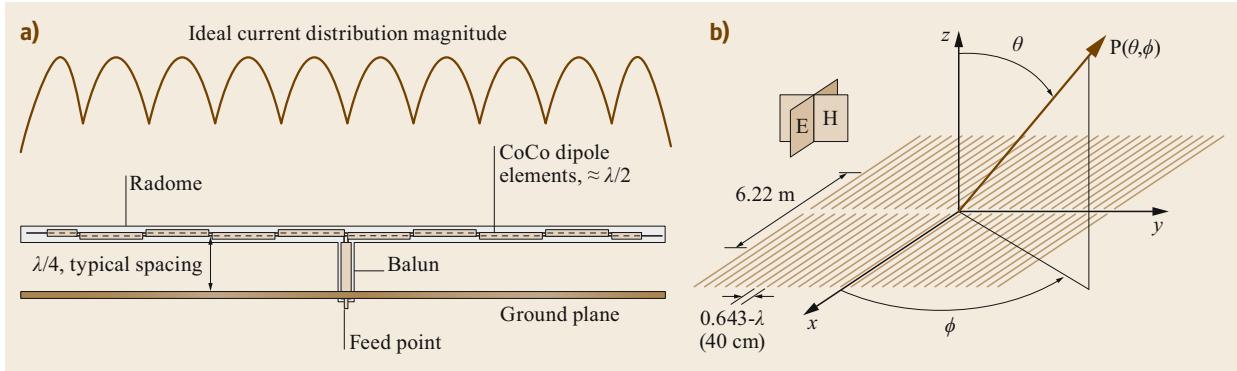


Fig. 31.12a,b Single coaxial-collinear antenna element with an ideal current amplitude distribution (a), and an array of such antenna elements (b). The planar CoCo array generates a linear polarized electromagnetic wave, with the electric and magnetic field vectors oscillating in the so-called E-plane and H-plane, respectively. The antenna beam can be steered in the H-plane by controlling the phasing of the CoCo lines

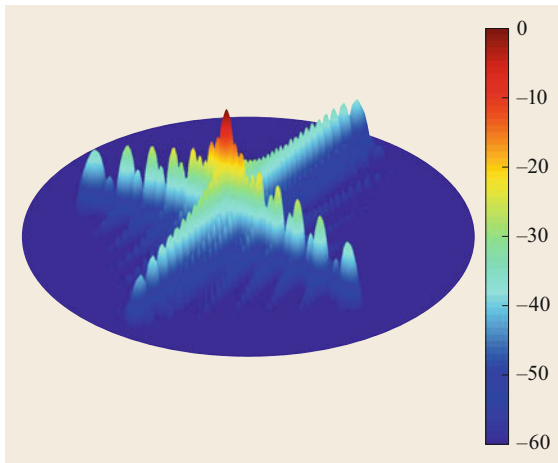


Fig. 31.13 Normalized radiation pattern $P(\theta, \phi)/P_{\max}$ of a coaxial-collinear phased array antenna in [dB]

gular dependence of the radiated energy as a function of the spherical antenna coordinates θ and ϕ (in contrast to an isotropic antenna). A simple and proven RWP antenna based on a planar array of coaxial-collinear antenna elements is shown in Fig. 31.12. The beam can be steered in the H-plane by imposing a linear phase progression between the CoCo rows. Figure 31.13 shows the ideal radiation pattern for this array, as calculated using the method described in [31.151]. The transmit energy is typically concentrated in a narrow angular region called the radar beam. The key performance parameters are the beam width and the gain of the antenna.

Due to the finite extent of the antenna array, the beam can not be made infinitely narrow. A phase-shifting unit generates the individual element phasing required to steer the beam in several directions. However, the electromagnetic wave is also radiated in direc-

tions other than that of the boresight through so-called sidelobes, which can be minimized but not eliminated completely. The sidelobes are influenced by the spatial distribution of the electric field across the antenna aperture, which can be tailored to some extent (this is known as tapering). The sidelobes are actually stronger and less regular in reality due to unavoidable (stochastic) differences in excitation between array elements resulting from hardware imperfections [31.81].

As the same antenna is used for signal reception, a duplexer is needed to protect the sensitive receiver electronics from the strong transmit signal. This typically incorporates a ferrite circulator and receiver-protecting limiters to achieve the isolation required to avoid transmitter leakage into the highly sensitive receiver. The scattered wave intensity has a rather large dynamic range of more than 100 dB, including signals that are well below -150 dBm (10^{-18} W) at the low end (close to the sensitivity limit of the radar receiver) as well as some types of clutter that induce receiver saturation. The receiver itself is of the classical superheterodyne type [31.152]. A broadband, high-gain, low-noise amplifier (LNA) is necessary to raise the signal level of the weak atmospheric return for further processing. For small input signals, LNA performance is fundamentally limited by microphysical processes, whereas the effects of nonlinearities need to be minimized for very strong signals. After frequency downconversion to the IF, a blanker and bandpass amplifier are used to provide additional protection against leakage during transmission and for signal amplification and filtering during the receive phase. In modern systems, the received signal is digitized at the IF by so-called digital IF receivers, which have largely replaced the analog quadrature detectors at baseband that were previously used. The IF signal undergoes A/D conversion and digital demodu-



Fig. 31.14 The NCAR Modular Profiler is an example of a spaced antenna radar. This 449 MHz radar uses a number of hexagonal antennas—three are employed in the boundary-layer configuration shown, but the system can also be deployed in a seven-panel configuration for higher altitude measurements. All of the antenna panels are used for transmission and each panel has its own receiver system

31.4.3 Spaced-Antenna Systems

The basic architecture of a SA radar is similar to that of a DBS radar except that there are at least three receiver channels that typically share a single transmitter system. SA radars do not tend to include a steering mechanism but they do have the additional complexity associated with the inclusion of multiple receiver channels. Figure 31.14 shows an example of a SA radar, the NCAR Modular Wind Profiler [31.153, 154]. The three hexagonal antennas are driven together for transmission, but the antennas have individual receivers and data channels. One unique feature of the Modular Profiler is its scalability—additional antennas can be added to increase the aperture of the antenna and thus its sensitivity.

lation. To maximize the per-pulse signal-to-noise ratio (SNR) and thus optimize signal detection, the bandwidth of the digital FIR bandpass filter is matched to the width of the transmitted pulse [31.87]. Further processing steps are performed in the radar processor.

SA profilers are capable of very rapid wind measurements, and Fig. 31.15 provides an illustration of this capability. A highly convective storm observed by the NCAR Modular Wind Profiler during the PECAN (Plains Elevated Convection at Night) field campaign [31.155] is shown. A very strong updraft (the red region) is apparent in the upper panel. At the same time, in the lower panel, strong circulating wind gusts with timescales of just a minute or two can be seen. The ability to record such brief wind gusts while simultane-

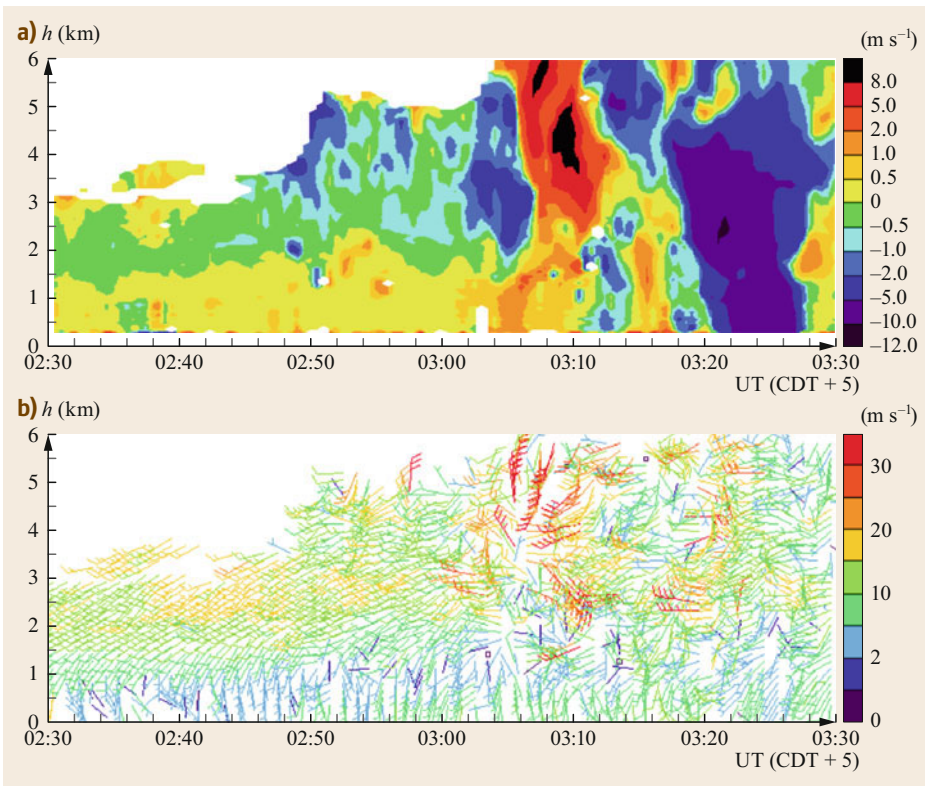


Fig. 31.15a,b Example demonstrating the rapid wind measurement capability of SA radars. The NCAR Modular Wind Profiler recorded the passage of a storm over a site in Kansas for the PECAN field campaign: **(a)** vertical velocity, with red areas indicating updrafts, green areas representing downdrafts, and blue areas corresponding to precipitation; **(b)** simultaneous one-minute wind measurements

Table 31.3 Comparison of the Doppler and spaced-antenna methods

	Advantages	Disadvantages
Doppler	Sensitivity across a wide range of scattering conditions, including weak SNR Single-channel transmit and receive system	Statistical homogeneity required over the area spanned by the beams Phase switches or steerable antenna can have undetected failures
SA	Higher time resolution due to less stringent homogeneity constraints No antenna steering required	Requires a higher SNR than DBS Three or more receiver chains required

ously measuring vertical velocities enabled the radar to capture the rapidly evolving dynamics of the storm.

One disadvantage of a SA radar is its need for increased transmit power to achieve the same altitude coverage as a DBS radar of the same size. The receiving antenna is divided among at least three receiver channels. In addition, the information content in the backscattered signals used by a DBS radar is in the first moment of the data, and can still be extracted at SNR levels of around -12 dB or even lower. For a SA radar, the information used to derive winds is present in higher-order moments, requiring SNR levels that are around $6-10$ dB more than those needed by a DBS radar [31.122].

SA radars are not as common as DBS radars, but there are some notable SA radars in operation. The Australian Bureau of Meteorology operates a network of ten SA boundary-layer radars scattered around Australia [31.28, 29]. These radars are also unusual boundary-layer radars in that they operate in the 50 MHz band rather than the more commonly used 1 GHz band. Another notable SA-capable radar is the

MU (Middle and Upper Atmosphere) Radar operated by Kyoto University in Japan [31.156]. This highly capable MST radar can operate in SA or DBS mode, leading to interesting comparison studies of the two techniques. In general, the results obtained using the MU Radar indicate that the two techniques produce comparable results [31.157].

31.4.4 Comparison of the Methods

From a user perspective, the most important consideration when selecting a particular RWP instrument is obviously the operating frequency, as it strongly influences the measurement range. However, the available operating frequencies are of course constrained by a number of practical factors, such as frequency allocation options, resources available for installation and long-term support, and (last but not least) the availability of real estate. When choosing the technique (either DBS or SA), it is important to consider the intended use of the radar system. Table 31.3 summarizes the advantages and disadvantages of both methods.

31.5 Specifications

The achievable altitude coverage and the accuracy of the wind data are key when selecting a RWP. It is important to appreciate that these performance parameters depend not only on the radar instrument and its properties but also on the state of the atmosphere itself. A theoretical appraisal is therefore difficult but nevertheless useful to understand the essential factors, at least in a qualitative way.

31.5.1 Measurement Range

The achievable measurement range or altitude coverage is determined by the lowest backscattered wave intensity that can be correctly analyzed by the radar. That is, the signal-to-noise ratio (SNR) must be above a certain level. The SNR depends on a number of factors that are present in the so-called radar equation. The general

form of this equation is [31.66]

$$P(\mathbf{r}_0) = \int_V I(\mathbf{r}_0, \mathbf{r}) \eta(\mathbf{r}) d^3\mathbf{r}, \quad (31.39)$$

where η denotes the volume reflectivity and

$$I(\mathbf{r}_0, \mathbf{r}) = \frac{P_t g^2 \lambda^2 f^4 (\Theta - \Theta_0, \Phi - \Phi_0)}{(4\pi)^3 l^2(\mathbf{r}) r^4} |W_s(\mathbf{r}_0, \mathbf{r})|^2 \quad (31.40)$$

is the radar instrument weighting function, which essentially depends on the antenna radiation pattern described by f , and the range weighting function W , and is furthermore scaled by the transmit power as well as by all gains and losses of the radar. I is essentially an integral kernel and (31.39) can be regarded as an inverse

Table 31.4 Simplified classification of RWPs based on typical parameters

	Stratospheric	Tropospheric	Lower tropospheric	Boundary layer
Frequency (MHz)	50	400–500	400–500	1000
Height range (km)	2–20	0.5–16	0.3–10	0.2–3
Vertical resolution (m)	150–500	150–500	150–300	50–300
Antenna size (m ²)	100 × 100	15 × 15	6 × 6	3 × 3
Peak transmit power (kW)	100–1000	10–20	1–5	1

problem, with all of the associated challenges. The advantage of active remote sensing is the ability to tailor this kernel function within the relevant technical limits.

The instrument function describes the capabilities of the radar; its main parameters are:

- The transmit power
- The antenna directivity and gain
- The receiver efficiency, including losses in the antenna feed
- The pulse width (expressed through the range weighting function)
- The distance from the radar to the sampled volume.

The first three items are determined by the technical design of the radar and are therefore subject to the principal physical limits that affect the components. The pulse width used has direct consequences for the altitude coverage. Since the pulse width also determines the range resolution, there is a direct tradeoff between range resolution and range coverage. For this reason, many RWPs are operated in two modes: a low mode that uses a short pulse to achieve the best possible vertical resolution at the expense of vertical range, and a high mode that employs a longer pulse to maximize height coverage at the expense of resolution. The choice of mode is dictated by the intended use of the measurements.

The other important factor is the state of the atmosphere, as expressed by the volume reflectivity η . For RWPs, both the clear-air scattering caused by inhomogeneities in the refractive index at a scale of half the radar wavelength (the Bragg scale, $\lambda/2$) and the scattering induced by hydrometeors must be considered.

If the Bragg scale lies within the inertial subrange of fully developed turbulence (i.e., $l_0 \leq \lambda/2 \leq L_0$, where l_0 denotes the inner scale and L_0 the outer scale of the turbulence), the volume reflectivity of clear air η_{ca} can be related to the refractive index structure parameter by the Ottersten equation (31.21). For scales smaller than l_0 , the viscous dissipation of kinetic energy dominates and the turbulence spectrum is extremely small or zero [31.73]. This is crucial to understanding why the height coverage of a RWP decreases towards smaller wavelengths.

When hydrometeors are present in the radar resolution volume, it is safe for the RWP to assume that the particles are much smaller than the radar wavelength. If the particles are also randomly distributed in the radar resolution volume, the volume reflectivity for incoherent particle or Rayleigh scattering is

$$\eta_p = \int \sigma_\lambda(D)N(D)dD = \pi^5 |K|^2 \lambda^{-4} Z, \quad (31.41)$$

where $\sigma_\lambda(D)$ is the backscattering cross-section of particles of diameter D at wavelength λ , $N(D)$ is the particle size distribution, Z is the radar reflectivity factor, and $|K|^2$ describes the refractive index of the particle [31.66].

It is customary to restrict the discussion of RWP altitude coverage to the case of clear-air scattering [31.158, 159], which means that the vertical and temporal statistics of C_n^2 must be taken into account [31.17, 160, 161]. For a boundary-layer RWP, it is also important to consider Rayleigh scattering effects, which can drastically improve the maximum attainable height of useful radar returns.

Given the large number of factors that affect RWP performance, it is useful to group these radars into four main categories, as shown in Table 31.4.

There are, however, notable exceptions to these classes, such as the 55 MHz boundary-layer wind profilers in the Australian Wind Profiler network [31.28].

31.5.2 Accuracy

Estimating the accuracy of the meteorological parameters determined by RWP is a difficult task due to the large number of factors that influence the measurement process. For a monostatic pulsed RWP, the accuracy of the final wind data depends on:

1. The accuracies of the position and shape of the measurement volume determined by the radar hardware (antenna radiation pattern and range weighting function defined by the envelope of the transmit pulse and the receiver filter properties).
2. The correct identification of the scattering process that generates the receiver voltage signal, as this ensures that the motion of the air (i.e., the wind) is

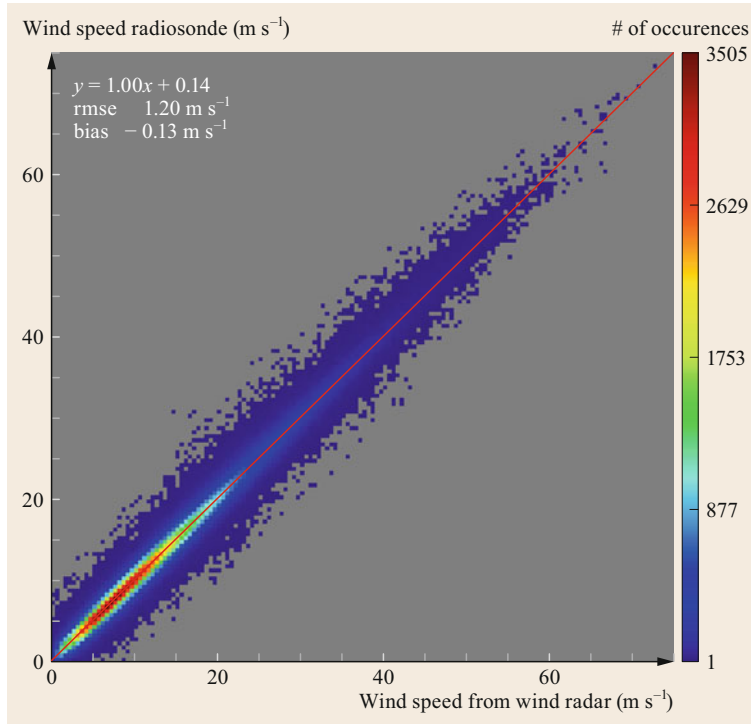


Fig. 31.16 Long-term intercomparison of wind speed measurements obtained from a 482 MHz RWP and a collocated radiosonde

indeed inferred from an atmospheric echo, and any clutter or RFI signal component is sufficiently suppressed.

3. The accuracies of the estimates for the Doppler shift (the first moment of the Doppler spectrum).
4. The validity of the assumptions implicitly used in the wind retrieval algorithm, such as horizontal homogeneity and stationarity.

A problem with any of these factors will propagate and increase the uncertainty in the wind vector. It is possible to verify the accuracies of items (1) and (3) with well-defined test measurements using calibrated RF instruments. Indeed, such tests should be performed as part of regular maintenance activities to verify the correct operation of the radar hardware and possibly also some low-level signal processing algorithms. Item (2) needs to be addressed with proven, validated, and robust signal processing algorithms, assuming their correct implementation in software. The last item (4) is dependent on the (unknown) state of the atmosphere, which needs to be assessed by appropriate consistency checks in the wind retrieval algorithm.

A large number of publications have discussed the accuracy and precision of RWP data based on compar-

isons with independent wind measurements from meteorological towers, tethered balloon sounding systems, radiosondes, aircraft measurements, and Doppler lidars [31.18, 45, 111, 114, 122, 162–164]. Furthermore, numerical weather prediction assimilation systems are increasingly being used to estimate the quality of RWP data [31.106]. The latter method is especially important for operational quality monitoring.

A statistical intercomparison of more than 10 000 vertical profiles of the horizontal wind obtained with a 482 MHz RWP and a collocated radiosonde at Lindenberg during 2010–2018 is shown in Fig. 31.16. The absolute wind speed difference bias was found to be less than 0.2 m s^{-1} up to a height of about 10 km (the wind speeds obtained from the profiler were slightly smaller than the wind speeds provided by the sonde). For the tropopause region, the values increased but were generally less than 0.8 m s^{-1} . The RMSE was smaller than 1.3 m s^{-1} up to a height of 10 km, but above that the values steadily increased to almost 3 m s^{-1} in the tropopause region. The bias in direction was smaller than 1° for the full depth of the troposphere and peaked at about 5° near the tropopause. These values are comparable to or even better than the results of an intercomparison of data obtained in 1997 [31.165].

31.6 Quality Control

For early RWPs, quality control for clear-air radar measurements involved a subjective edit of the data performed by experts who were familiar with the instrument. While this could indeed identify and partially remedy many of the deficiencies of those early systems, it was usually limited to special research applications. Even today, this technique may be included in the training of new radar operators. However, this methodology is clearly impossible to apply to operational radars, so fully automated algorithms that remove clutter or RFI effects from the data and identify unreliable wind retrievals have been developed. It is interesting to note that these algorithms were first developed for the final wind data, before increasing computational power allowed spectral or even I/Q data to be processed in real time.

31.6.1 Signal Processing: Clutter and RFI Filtering

Ignoring the clutter term leads to errors during parameter estimation, the severity of which varies with the type, strength, and duration of the clutter. This became obvious soon after the installation of the NOAA-WPDN [31.24, 59], and the need for improved signal processing methods was quickly recognized, so work began to develop new algorithms. These algorithms fall into two main groups:

- Those that improve the estimation of Doppler moments [31.102, 166, 167]
- Those that improve the estimation of Doppler spectra [31.85, 93, 168].

However, not all of these algorithms have achieved widespread acceptance. Some overly complex moment estimation algorithms remain experimental, as they were found to be error-prone due to the excessive use of weakly justified a-priori assumptions, like constraint for the vertical continuity of the estimated Doppler values, especially under conditions of low SNR.

31.6.2 Consistency Checks

Quality control postprocessing was initially developed as a way to address issues that quickly became apparent with the very first operational RWP [31.23, 24]. Today, the importance of these postprocessing methods is greatly diminished due to significant improvements in signal processing methods that have resolved most of the practically relevant issues. However, a notable exception is the test for the homogeneity of the wind field during the retrieval process.

31.6.3 Numerical Weather Prediction: O-B Statistics and the FSOI

An important practical way of a statistical quality control for RWP data is provided by numerical weather prediction (NWP). During the assimilation step, it is useful to compare the measurements with the background of the model, which is a short-term forecast from a previous analysis. While the difference between the measurements and the background is also affected by model issues, these so-called observation minus background (O-B) statistics offer a convenient way to identify problems with the observing system [31.169]. An example is shown in Fig. 31.17.

Yet another interesting way to gauge the the data quality is through forecast sensitivity methods in variational or ensemble-based assimilation systems [31.170–172]. This approach is even more indirect than O-B statistics, but it has the advantage of being estimated at the end of the weather prediction process. The forecast sensitivity to observations index (FSOI) measures the relative contribution of the observation to the reduction in the forecast error. This parameter actually depends on many factors, not just the quality of the measurement; however, when the results from different observation systems of the same type are compared, this parameter can be used together with all the other quality control measures to assess the usefulness of a particular RWP system in a holistic way.

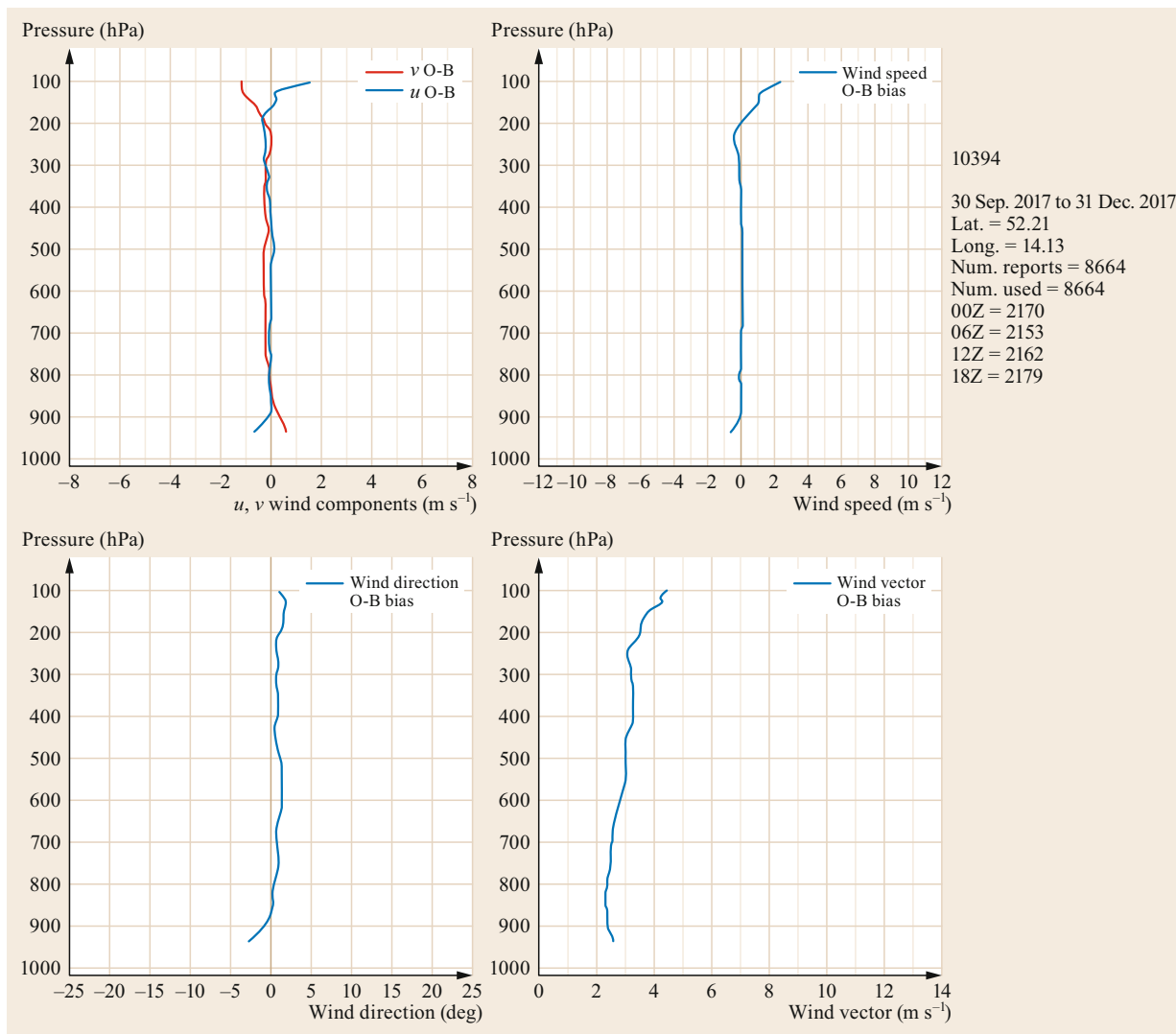


Fig. 31.17 O-B statistics from the UK Met Office for the Lindenberg 482 MHz RWP (© Crown copyright Met Office)

31.7 Maintenance

RWPs are complex technical instruments, and regular maintenance of all subsystems is needed to guarantee a high level of data quality. While the systems are typically specified to operate for 10–20 years without requiring major technical upgrades, the mean time between failures (MTBF) is less than this for various system components. It is therefore necessary for the user to develop, implement, and document policy and procedures for routine maintenance, both preventive and corrective. Competent staff are of the utmost

importance if all maintenance requirements and responsibilities are to be met.

Regular preventive maintenance of all essential system components is typically specified by the manufacturer of the radar system as well as by the vendors of the specific subsystems. This includes hardware, software, telecommunications, and ancillary systems such as the air conditioning or uninterruptible power supply. The typical interval between regular on-site preventive inspections is a year, but this depends on factors

such as the age of the instrument and the environmental conditions. Preventive maintenance is especially important for components that can degrade or even partially fail without obvious consequences for the data quality. Such incidents often remain undetected by quality monitoring systems. A prominent candidate for such a degradation is a phased array antenna: as it is an outdoor element, the antenna is exposed to humidity, precipitation, and radiation, and needs to withstand temperature changes of at least 50 K over the course of the year. On the other hand, the failure of a single antenna in a phased array is extremely difficult to detect in the final meteorological data. Although the overall array performance degrades, such subtle changes in performance characteristics typically remain hidden

31.8 Applications

RWPs are mainly used to measure the local vertical profile of the horizontal wind vector (Fig. 31.18), although there is a great deal of other information about the state of the atmosphere bound up in RWP data too. Wind profiling can be done as part of a local atmospheric analysis [31.173], to monitor the vertical wind shear at airports [31.174, 175], to facilitate the launch of space vehicles [31.176], to assess local air quality [31.177], to continuously monitor the dispersion conditions near potential sources of hazardous substances such as nuclear power plants [31.178], or even for hydrological purposes (e.g., the atmospheric river observatories [31.179] on the west coast of the USA).

However, most of the RWPs used in operational meteorology perform continuous monitoring of the vertical profile of the horizontal wind, which is used to initialize numerical weather prediction models [31.27, 180–183]. The particular advantage of these systems is their ability to provide data at a high temporal resolution under almost all weather conditions around the clock.

Beyond this standard application, special measurements can be performed for a wide variety of other purposes ranging from basic meteorological research to ornithology. There are a huge number of scientific questions that RWPs can help to answer, especially when the information they provide aside from the Doppler shift—such as the echo power or spectral width—is utilized. Examples include research into mesoscale upper-air wind structures [31.184], turbulence research [31.185],

behind the high variability of atmospheric scattering processes.

Remote monitoring and diagnostic systems can significantly increase the effectiveness of inspection and supervision activities, and can trigger on-site corrective maintenance. This monitoring should include technical parameters of the radar and its subsystems, ideally supported by built-in test equipment as well as the radar data at various stages of the processing. The ability of qualified staff to perform at least some diagnostic tasks remotely can significantly increase the efficiency of on-site visits, thereby helping to achieve greater overall system uptime and operational quality.

A comprehensive discussion of the various aspects of RWP maintenance can be found in [31.165].

estimating the boundary-layer depth [31.186, 187], investigating atmospheric waves [31.188], upper-air wind climatology [31.189], measuring the vertical wind component when investigating cloud dynamics [31.190], and quantitatively assessing bird migration for ornithological research [31.191, 192]. Many more examples can be found in topical reviews such as [31.193–195].

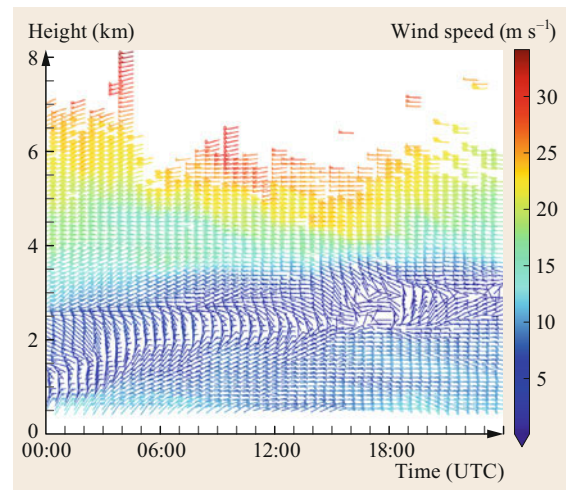


Fig. 31.18 Measurement of the wind profile by the Lindenberg 482 MHz RWP on 7 Jan. 2018 using a pulse width of 1000 ns

31.9 Future Developments

The longterm operational use of RWPs is demanding, but has been successfully demonstrated. However, it should be emphasized that this rather complex technology needs to be understood and managed correctly. In particular, users must have enough organizational and budgetary flexibility to ensure that the systems can be operated according to the state of the art. Unfortunately, there have been cases where a lack of commitment or even knowledge has led to embarrassing failures followed by disappointment. In hindsight, it is probably safe to say that most of these unsuccessful cases could have been avoided with greater consideration of the research-to-operations problem [31.196]. As stated in [31.197] the “transitions from development to implementation are frequently difficult, and, if done improperly, these transitions often result in ‘skeletons in Death Valley’.”

From a purely physical point of view, the future of RWPs is bright because there is no other remote-sensing method that can provide wind data for a significant vertical range regardless of the atmospheric conditions. Given the importance of the wind vector in meteorology, it is hard to imagine that radar wind profiling will become obsolete in the future.

However, as with every nontrivial problem, a few research questions remain also for RWP, some of which will be briefly touched upon below.

Although the theory of clear-air scattering is fairly well developed, it remains an area of active research [31.36, 40, 68]. This is not surprising, given

the involvement of the notoriously difficult turbulence problem. Discussions focus on issues such as the applicability of simplifying assumptions (e.g., the Fraunhofer versus the Fresnel approximation [31.69]) and the (vertical) velocity bias of RWPs [31.198]. It would also be desirable to extend the existing theory to include particle scattering effects.

Increasing interest in renewable energy has led to the rapid development of large wind turbines, which unfortunately produce peculiar clutter echoes with a rather complex time–frequency signal structure. These clutter echoes are received through the sidelobes of antennas, and the width of the spectrum is significantly increased by the rotation of the propeller blades. There is currently no standard signal processing algorithm that can suppress or filter out this type of clutter. However, new methods such as adaptive clutter suppression using array processing methods appear to be quite promising [31.199–201] and may have the potential to overcome these difficulties.

A prerequisite for the successful operation of a radar wind profiler is the existence of uncontaminated frequency bands, as the high sensitivity of RWPs make them vulnerable to any sufficiently strong external in-band radio-frequency interference. Frequency management therefore remains an important issue, as available regions of the frequency spectrum have become scarce. Effective protection of allocated frequency bands is needed to maintain the quality of radar wind profiler data.

31.10 Further Reading

RWPs are rather complex instruments, so an in-depth discussion of all technical and scientific aspects of RWPs is obviously beyond the scope of this handbook.

Even though the book *Radar Observations of Clear Air and Clouds* by Earl Gossard and Dick Strauch [31.31] was published more than 35 years ago, it still provides a fairly comprehensive yet concise overview of the science of clear-air radar observations. More detailed and interesting in terms of a historical perspective on MST radars are the contributions from Jürgen Röttger and Michael Larsen (*UHF/VHF radar techniques for atmospheric research and wind profiler applications*) [31.118] and Ken Gage (*Radar observations of the free atmosphere: Structure and dy-*

namics) [31.202] in the AMS monograph *Radar in Meteorology* edited by David Atlas and published in 1990.

As far as textbooks are concerned, *Doppler Radar and Weather Observations* by Dick Doviak and Dusan Zrnić [31.66] is considered a classic, although it is not easily accessible for the novice. The more recent book *Radar for Meteorological and Atmospheric Observations* by Sho Fukao and Kyosuke Hamazu [31.80] covers many important aspects of clear-air radars in considerable detail.

Finally, the monograph *Atmospheric Radars* by Wayne Hocking et al. [31.7], which focuses exclusively on MST radars, is an essential resource for researchers as well as practitioners.

References

- 31.1 J.A. Dutton: *The Ceaseless Wind* (Dover, Mineola 1986)
- 31.2 W.R. Cotton, G.H. Bryan, S.C. van den Heever: *Storm and Cloud Dynamics*, 2nd edn. (Academic Press, Burlington 2011)
- 31.3 A. Makarieva, V.G. Gorshkov, A.V. Nefiodov, D. Sheil, A.D. Nobre, P. Bunyard, P. Nobre, B.-L. Li: The equations of motion for moist atmospheric air, *J. Geophys. Res. Atmos.* **122**, 7300–7307 (2017)
- 31.4 V. Tatarskii: *The Effects of the Turbulent Atmosphere on Wave Propagation* (Israel Program for Scientific Translations, Jerusalem 1971) p. 471
- 31.5 K.R. Hardy, K.S. Gage: The history of radar studies of the clear atmosphere. In: *Radar in Meteorology*, ed. by D. Atlas (American Meteorological Society, Boston 1990) pp. 130–142, Chap. 17
- 31.6 T. Van Zandt: A brief history of the development of wind-profiling or MST radars, *Ann. Geophys.* **18**(7), 740–749 (2000)
- 31.7 W.K. Hocking, J. Röttger, R.D. Palmer, T. Sato, P.B. Chilson: *Atmospheric Radar* (Cambridge Univ. Press, Cambridge 2016)
- 31.8 A.W. Friend: Continuous determination of air-mass boundaries by radio, *Bull. Am. Meteorol. Soc.* **20**, 202–205 (1939)
- 31.9 D. Atlas: Meteorological 'angel' echoes, *J. Meteorol.* **16**, 6–11 (1959)
- 31.10 D. Atlas: *Reflections—A Memoir* (American Meteorological Society, Boston 2001)
- 31.11 V.I. Tatarskii: *Wave Propagation in a Turbulent Medium* (McGraw-Hill, New York 1961) p. 285
- 31.12 K.R. Hardy, I. Katz: Probing the clear atmosphere with high power, high resolution radars, *Proc. IEEE* **57**(4), 468–480 (1969)
- 31.13 K. Bowles: Measuring plasma density of the magnetosphere, *Science* **139**(3553), 389–391 (1963)
- 31.14 L. LaLonde: The upgraded Arecibo observatory, *Science* **186**(4160), 213–218 (1974)
- 31.15 R.F. Woodman, A. Guillen: Radar observation of winds and turbulence in the stratosphere and mesosphere, *J. Atmos. Sci.* **31**, 493–505 (1974)
- 31.16 K. Gage, B. Balsley: Doppler radar probing of the clear atmosphere, *Bull. Am. Meteorol. Soc.* **59**, 1074–1093 (1978)
- 31.17 P. James: A review of radar observations of the troposphere in clear air conditions, *Radio Sci.* **15**(2), 151–175 (1980)
- 31.18 M. Larsen, J. Röttger: VHF and UHF Doppler radars as tools for synoptic research, *Bull. Am. Meteorol. Soc.* **63**(9), 996–1008 (1982)
- 31.19 D. Hogg, M. Decker, F. Guiraud, K. Earnshaw, D. Merritt, K. Moran, W. Sweezy, R. Strauch, E. Westwater, C. Little: An automatic profiler of the temperature, wind and humidity in the troposphere, *J. Clim. Appl. Meteorol.* **22**, 807–831 (1983)
- 31.20 R.G. Strauch, D.A. Merritt, K.P. Moran, K.B. Earnshaw, D. van de Kamp: The Colorado Wind Profiling Network, *J. Atmos. Ocean. Technol.* **1**, 37–49 (1984)
- 31.21 W.L. Ecklund, D.A. Carter, B.B. Balsley: A UHF wind profiler for the boundary layer: brief description and initial results, *J. Atmos. Ocean. Technol.* **5**, 432–441 (1988)
- 31.22 D. Carter, K. Gage, W. Ecklund, W. Angevine, P. Johnston, A. Riddle, J. Wilson, C. Williams: Developments in UHF lower tropospheric wind profiling at NOAA's aeronomy laboratory, *Radio Sci.* **30**, 977–1001 (1995)
- 31.23 B.L. Weber, D.B. Wuertz, R.G. Strauch, D.A. Merritt, K.P. Moran, D.C. Law, D. van de Kamp, R. Chadwick, M. Ackley, M. Barth, N.L. Abshire, P.A. Miller, T.W. Schlatter: Preliminary evolution of the first NOAA demonstration network wind profiler, *J. Atmos. Ocean. Technol.* **7**, 909–918 (1990)
- 31.24 M. Barth, R. Chadwick, D. van de Kamp: Data processing algorithms used by NOAA's wind profiler demonstration network, *Ann. Geophys.* **12**, 518–528 (1994)
- 31.25 T.W. Schlatter, F.S. Zbar (Eds.): *Wind Profiler Assessment Report* (NOAA, Silver Spring 1994)
- 31.26 J. Nash, T.J. Oakley: Development of COST-76 wind profiler network in Europe, *Phys. Chem. Earth B* **26**, 193–199 (2001)
- 31.27 M. Ishihara, Y. Kato, T. Abo, K. Kobayashi, Y. Izumikawa: Characteristics and performance of the operational wind profiler network of the Japan Meteorological Agency, *J. Meteorol. Soc. Jpn.* **84**, 1085–1096 (2006)
- 31.28 B.K. Dolman, I.M. Reid: Bias correction and overall performance of a VHF Spaced Antenna boundary layer profiler for operational weather forecasting, *J. Atmos. Sol. Terr. Phys.* **118**, 16–24 (2014)
- 31.29 B.K. Dolman, I.M. Reid, C. Tingwell: Stratospheric tropospheric wind profiling radars in the Australian network, *Earth Planets Space* **70**, 170 (2018)
- 31.30 R.F. Woodman: A general statistical instrument theory of atmospheric and ionospheric radars, *J. Geophys. Res.* **96**(A5), 7911–7928 (1991)
- 31.31 E.E. Gossard, R.G. Strauch: *Radar Observation of Clear Air and Clouds, Developments in Atmospheric Science* (Elsevier, Amsterdam 1983) p. 280
- 31.32 R.B. Laughlin, D. Pines: The theory of everything, *Proc. Natl. Acad. Sci. U. S. A.* **97**, 28–31 (2000)
- 31.33 M.I. Mishchenko, L.D. Travis, A.A. Lacis: *Scattering, Absorption and Emission of Light by Small Particles* (Cambridge Univ. Press, Cambridge 2002) p. 448
- 31.34 C.F. Bohren, D.R. Huffman: *Absorption and Scattering of Light by Small Particles* (Wiley, New York 1983) p. 530
- 31.35 G.L. Stephens: *Remote Sensing of the Lower Atmosphere* (Oxford Univ. Press, New York, Oxford 1994) p. 523
- 31.36 A. Muschinski: Local and global statistics of clear-air Doppler radar signals, *Radio Sci.* **39**, RS1008 (2004)
- 31.37 A. Muschinski, P.P. Sullivan, D.B. Wuertz, R.J. Hill, S.A. Cohn, D.H. Lenschow, R.J. Doviak: First synthesis of wind-profiler signals on the basis of

- large-eddy simulation data, *Radio Sci.* **34**(6), 1437–1459 (1999)
- 31.38 D.E. Scipion, P.B. Chilson, E. Fedorovich, R.D. Palmer: Evaluation of an LES-based wind profiler simulator for observations of a daytime atmospheric convective boundary layer, *J. Atmos. Ocean. Technol.* **25**, 1423–1436 (2008)
- 31.39 D. Scipion, R. Palmer, P. Chilson, E. Fedorovich, A. Botnick: Retrieval of convective boundary layer wind field statistics from radar profiler measurements in conjunction with large eddy simulation, *Meteorol. Z.* **18**, 175–187 (2009)
- 31.40 P.M. Franke, S. Mahmoud, K. Raizada, K. Wan, D.C. Fritts, T. Lund, J. Werne: Computation of clear-air radar backscatter from numerical simulations of turbulence: 1. Numerical methods and evaluation of biases, *J. Geophys. Res.* **116**, D21101 (2011)
- 31.41 E.E. Gossard: A fresh look at the radar reflectivity of clouds, *Radio Sci.* **14**(6), 1089–1097 (1979)
- 31.42 J.S. Erkelens, V.K.C. Venema, H.W.J. Russchenberg, L.P. Ligthart: Coherent scattering of microwaves by particles: Evidence from clouds and smoke, *J. Atmos. Sci.* **58**, 1091–1102 (2001)
- 31.43 K. Matsuda, R. Onishi, M. Hirahara, R. Kurose, K. Takahashi, S. Komori: Influence of microscale turbulent droplet clustering on radar cloud observations, *J. Atmos. Sci.* **71**(10), 3569–3582 (2014)
- 31.44 M. Radenz, J. Bühl, V. Lehmann, U. Görsdorf, R. Leinweber: Combining cloud radar and radar wind profiler for a value added estimate of vertical air motion within clouds, *Atmos. Meas. Tech.* **11**, 5925–5940 (2018)
- 31.45 D.B. Wuertz, B.L. Weber, R.G. Strauch, A.S. Frisch, C.G. Little, D.A. Merritt, K.P. Moran, D.C. Welsh: Effects of precipitation on UHF wind profiler measurements, *J. Atmos. Ocean. Technol.* **5**, 450–465 (1988)
- 31.46 A. Steiner, H. Richner: Separation of clear-air echoes from precipitation echoes in UHF wind profiler measurements, *Ann. Geophys.* **12**, 497–505 (1994)
- 31.47 F.M. Ralph: Using radar-measured radial vertical velocities to distinguish precipitation scattering from clear air scattering, *J. Atmos. Ocean. Technol.* **12**, 257–267 (1995)
- 31.48 F.M. Ralph, P.J. Neimann, D.W. van de Kamp, D.C. Law: Using spectral moment data from NOAA's 404-MHz radar wind profilers to observe precipitation, *Bull. Am. Meteorol. Soc.* **76**, 1717–1739 (1995)
- 31.49 S.A. Cohn, R.R. Rodgers, S. Jascourt, W.L. Ecklund, D.A. Carter, J.S. Wilson: Interactions between clear-air reflective layers and rain observed with a boundary-layer wind profiler, *Radio Sci.* **30**, 323–341 (1995)
- 31.50 F.M. Ralph, P.L. Neiman, D. Ruffieux: Precipitation identification from radar wind profiler spectral moment data: Vertical velocity histograms, velocity variance, and signal power-vertical velocity correlation, *J. Atmos. Ocean. Technol.* **13**, 545–559 (1996)
- 31.51 B.W. Orr, B.E. Martner: Detection of weakly precipitating winter clouds by a NOAA 404-MHz wind profiler, *J. Atmos. Ocean. Technol.* **13**, 570–580 (1996)
- 31.52 K.S. Gage, C.R. Williams, W.L. Ecklund, P.E. Johnston: Use of two profilers during MCTEX for unambiguous identification of Bragg scattering and Rayleigh scattering, *J. Atmos. Sci.* **56**, 3679–3691 (1999)
- 31.53 C.R. Williams, W.L. Ecklund, P.E. Johnston, K.S. Gage: Cluster analysis techniques to separate air motion and hydrometeors in vertical incident profiler observations, *J. Atmos. Ocean. Technol.* **17**, 949–962 (2000)
- 31.54 A.J. McDonald, T.K. Carey-Smith, D.A. Hooper, G.J. Fraser, B.P. Lublow: The effect of precipitation on wind-profiler clear air returns, *Ann. Geophys.* **22**, 3959–3970 (2004)
- 31.55 W.D. Rust, R.J. Doviak: Radar research on thunderstorms and lightning, *Nature* **297**, 461–468 (1982)
- 31.56 E.R. Williams, S.G. Geotis, A.B. Bhattacharya: A radar study of the plasma and geometry of lightning, *J. Atmos. Sci.* **46**, 1173–1185 (1989)
- 31.57 M.C. Lee, Y.R. Dalkir, E.R. Williams: Radar reflectivity of lightning-induced plasmas, *J. Atmos. Sol. Terr. Phys.* **60**, 941–949 (1998)
- 31.58 M. Petitdidier, P. Laroche: Lightning observations with the strato-tropospheric UHF and VHF radars at Arecibo, Puerto Rico, *Atmos. Res.* **76**, 481–492 (2005)
- 31.59 J. Wilczak, R. Strauch, F. Ralph, B. Weber, D. Merritt, J. Jordan, D. Wolfe, L. Lewis, D. Wuertz, J. Gaynor, S. McLaughlin, R. Rogers, A. Riddle, T. Dye: Contamination of wind profiler data by migrating birds: Characteristics of corrupted data and potential solutions, *J. Atmos. Ocean. Technol.* **12**, 449–467 (1995)
- 31.60 B. Balsley, N. Cianos, D. Farley, M. Baron: Winds derived from radar measurements in the arctic troposphere and stratosphere, *J. Appl. Meteorol.* **16**, 1235–1239 (1977)
- 31.61 T. Sato, R.F. Woodman: Spectral parameter estimation of CAT radar echoes in the presence of fading clutter, *Radio Sci.* **17**(4), 817–826 (1982)
- 31.62 R.F. Woodman: Spectral moment estimation in MST radars, *Radio Sci.* **20**(6), 1185–1195 (1985)
- 31.63 B.E. Martner, D.B. Wurtz, B.B. Stankov, R.G. Strauch, K. Westwater, K.S. Gage, W.L. Ecklund, C.L. Martin, W.F. Dabberdt: An evaluation of wind profiler, RASS, and microwave radiometer performance, *Bull. Am. Meteorol. Soc.* **74**, 599–613 (1993)
- 31.64 P.T. May, R.G. Strauch: Reducing the effect of ground clutter on wind profiler velocity measurements, *J. Atmos. Ocean. Technol.* **15**, 579–586 (1998)
- 31.65 R.J. Doviak, D.S. Zrnić: Reflection and scatter formula for anisotropically turbulent air, *Radio Sci.* **19**(1), 325–336 (1984)

- 31.66 R.J. Doviak, D.S. Zrnić: *Doppler Radar and Weather Observation* (Academic Press, San Diego 1993) p. 562
- 31.67 A. Monin, A. Yaglom: *Statistical Fluid Mechanics*, Vol. II (Dover Publications, Mineola 2007) p. 874
- 31.68 V.I. Tatarskii, A. Muschinski: The difference between Doppler velocity and real wind velocity in single scattering from refractive index fluctuations, *Radio Sci.* **36**(6), 1405–1423 (2001)
- 31.69 V.I. Tatarskii: Theory of single scattering by random distributed scatterers, *IEEE Trans. Antennas Propag.* **51**, 2806–2813 (2003)
- 31.70 A. Muschinski, V. Lehmann, L. Justen, G. Teschke: Advanced radar wind profiling, *Meteorol. Z.* **14**, 609–626 (2005)
- 31.71 J.C. Owens: Optical refractive index of air: Dependence on pressure, temperature and composition, *Appl. Opt.* **6**(1), 51–59 (1967)
- 31.72 W. Hoffman: Electromagnetic wave propagation in a random medium, *Radio Sci.* **68D**, 455–459 (1964)
- 31.73 A. Ishimaru: *Wave Propagation and Scattering in Random Media* (Academic Press, San Diego 1978) p. 600
- 31.74 L.J. Battan: *Radar Observation of the Atmosphere* (Univ. of Chicago Press, Chicago 1973)
- 31.75 A. Muschinski: *The First Moments of the Variance- and Cross-Spectra of Standard and Interferometric Clear-Air-Doppler-Radar Signals*, NCAR Tech. Note NCAR/TN-441+STR (NCAR, Boulder 1998)
- 31.76 U. Frisch: *Turbulence. The Legacy of A.N. Kolmogorov* (Cambridge Univ. Press, Cambridge, New York 1996)
- 31.77 F. Dalaudier, A.S. Gurvich: A scalar three-dimensional spectral model with variable anisotropy, *J. Geophys. Res.* **102**(D16), 19449–19459 (1997)
- 31.78 K.R. Hardy, D. Atlas, K.M. Glover: Multiwavelength backscatter from the clear atmosphere, *J. Geophys. Res.* **71**, 1537–1552 (1966)
- 31.79 H. Ottersten: Radar backscattering from the turbulent clear atmosphere, *Radio Sci.* **4**, 1251–1255 (1969)
- 31.80 S. Fukao, K. Hamazu: *Radar for Meteorological and Atmospheric Observations* (Springer, Tokyo 2014)
- 31.81 R.J. Mailloux: *Phased Array Antenna Handbook* (Artech House, Norwood 1994) p. 536
- 31.82 D.S. Zrnić: Signal processing: Panel report. In: *Radar in Meteorology*, ed. by D. Atlas (American Meteorological Society, Boston 1990) pp. 230–234, Chap. 20b
- 31.83 P. Flandrin: *Time-Frequency/Time-Scale Analysis* (Academic Press, San Diego 1999) p. 386
- 31.84 S. Mallat: *A Wavelet Tour of Signal Processing—The Sparse Way* (Academic Press, Burlington 2009)
- 31.85 V. Lehmann, G. Teschke: Advanced intermittent clutter filtering for radar wind profiler: Signal separation through a Gabor frame expansion and its statistics, *Ann. Geophys.* **26**, 759–783 (2008)
- 31.86 R.N. McDonough, A.D. Whalen: *Detection of Signals in Noise* (Academic Press, San Diego 1995) p. 495
- 31.87 D.S. Zrnić, R.J. Doviak: Matched filter criteria and range weighting for weather radar, *IEEE Trans. Aerosp. Electron. Syst.* **AES-14**(6), 925–929 (1978)
- 31.88 D.S. Zrnić: Estimation of spectral moments for weather echoes, *IEEE Trans. Geosci. Electron.* **17**, 113–128 (1979)
- 31.89 F.D. Neeser, J.L. Massey: Proper complex random processes with applications to information theory, *IEEE Trans. Inf. Theory* **39**, 1293–1302 (1993)
- 31.90 R. Frehlich, M. Yablowsky: Performance of mean-frequency estimators for Doppler radar and lidar, *J. Atmos. Ocean. Technol.* **11**, 1217–1230 (1994)
- 31.91 V. Lehmann: Optimal Gabor frame expansion based intermittent clutter filtering method for radar wind profiler, *J. Atmos. Ocean. Technol.* **29**, 141–158 (2012)
- 31.92 G. Schmidt, R. Rüster, P. Czechowsky: Complementary code and digital filtering for detection of weak VHF radar signals from the mesosphere, *IEEE Trans. Geosci. Electron.* **GE-17**, 165–161 (1979)
- 31.93 T.L. Wilfong, D.A. Merritt, R.J. Latatits, B.L. Weber, D.B. Wuertz, R.G. Strauch: Optimal generation of radar wind profiler spectra, *J. Atmos. Ocean. Technol.* **16**, 723–733 (1999)
- 31.94 L. Bianco, D. Gottas, J.M. Wilczak: Implementation of a Gabor transform data quality-control algorithm for UHF wind profiling radars, *J. Atmos. Ocean. Technol.* **30**, 2697–2703 (2013)
- 31.95 S.M. Kay, S.L. Marple: Spectrum analysis—A modern perspective, *Proc. IEEE* **69**(11), 1380–1491 (1981)
- 31.96 D.B. Percival, A.T. Walden: *Spectral Analysis for Physical Applications* (Cambridge Univ. Press, Cambridge 1993) p. 583
- 31.97 F.J. Harris: On the use of windows for harmonic analysis with the discrete Fourier transform, *Proc. IEEE* **66**(1), 51–83 (1978)
- 31.98 P.D. Welch: The use of fast Fourier transform for the estimation of power spectra: A method based on time averaging over short, modified periodograms, *IEEE Trans. Audio Electroacoust.* **AU-15**, 70–73 (1967)
- 31.99 V.K. Anandan, C. Pan, T. Rajalakshmi, G.R. Reddy: Multitaper spectral analysis of atmospheric radar signals, *Ann. Geophys.* **22**, 3995–4003 (2004)
- 31.100 P.H. Hildebrand, R. Sekhon: Objective determination of the noise level in Doppler spectra, *J. Appl. Meteorol.* **13**, 808–811 (1974)
- 31.101 P.T. May, R.G. Strauch: An examination of wind profiler signal processing algorithms, *J. Atmos. Ocean. Technol.* **6**, 731–735 (1989)
- 31.102 L.B. Cornman, R.K. Goodrich, C.S. Morse, W.L. Ecklund: A fuzzy logic method for improved moment estimation from Doppler spectra, *J. Atmos. Ocean. Technol.* **15**, 1287–1305 (1998)
- 31.103 C.S. Morse, R.K. Goodrich, L.B. Cornman: The NIMA method for improved moment estimation from Doppler spectra, *J. Atmos. Ocean. Technol.* **19**, 274–295 (2002)
- 31.104 S.A. Cohn, R.K. Goodrich, C.S. Morse, E. Karplus, S.W. Mueller, L.B. Cornman, R.A. Weekly: Radial velocity and wind measurement with NIMANWCA: Comparisons with human estimation and

- aircraft measurements, *J. Appl. Meteorol.* **40**, 704–719 (2001)
- 31.105 C. Gaffard, L. Bianco, V. Klaus, M. Matabuena: Evaluation of moments calculated from wind profiler spectra: A comparison between five different processing techniques, *Meteorol. Z.* **15**, 73–85 (2006)
- 31.106 D.A. Hooper, J. Nash, T. Oakley, M. Turp: Validation of a new signal processing scheme for the MST radar at Aberystwyth, *Ann. Geophys.* **26**, 3253–3268 (2008)
- 31.107 M.A. Fischler, R.C. Bolles: Random sample consensus: A paradigm for model fitting with applications to image analysis and automated cartography, *Commun. ACM* **24**, 381–395 (1981)
- 31.108 A.J. Koscielny, R.J. Doviak, D.S. Zrnic: An evaluation of the accuracy of some radar wind profiling techniques, *J. Atmos. Ocean. Technol.* **1**, 309–320 (1984)
- 31.109 B. Weber, D. Wuertz, D. Law, A. Frisch, J. Brown: Effects of small-scale vertical motion on radar measurements of wind and temperature profiles, *J. Atmos. Ocean. Technol.* **9**(3), 193–209 (1992)
- 31.110 R.K. Goodrich, C.S. Morse, L.B. Cornman, S.A. Cohn: A horizontal wind and wind confidence algorithm for Doppler wind profilers, *J. Atmos. Ocean. Technol.* **19**, 257–273 (2002)
- 31.111 E. Päschke, R. Leinweber, V. Lehmann: An assessment of the performance of a 1.5 μm Doppler lidar for operational vertical wind profiling based on a 1-year trial, *Atmos. Meas. Tech.* **8**(6), 2251–2266 (2015)
- 31.112 G. Teschke, V. Lehmann: Mean wind vector estimation using the velocity–azimuth display (VAD) method: An explicit algebraic solution, *Atmos. Meas. Tech.* **10**, 3265–3271 (2017)
- 31.113 B.L. Cheong, T.-Y. Yu, R.D. Palmer, K.-F. Yang, M.W. Hoffman, S.J. Frasier, F.J. Lopez-Dekker: Effects of wind field inhomogeneities on Doppler beam swinging revealed by an imaging radar, *J. Atmos. Ocean. Technol.* **25**, 1414–1422 (2008)
- 31.114 A. Adachi, T. Kobayashi, K.S. Gage, D.A. Carter, L.M. Hartten, W.L. Clark, M. Fukuda: Evaluation of three-beam and four-beam profiler wind measurement techniques using a five-beam wind profiler and collocated meteorological tower, *J. Atmos. Ocean. Technol.* **22**, 1167–1180 (2005)
- 31.115 S. Bradley, A. Strehz, S. Emeis: Remote sensing winds in complex terrain—A review, *Meteorol. Z.* **24**(6), 547–555 (2015)
- 31.116 J.C. Wyngaard: *Turbulence in the Atmosphere* (Cambridge Univ. Press, Cambridge 2010)
- 31.117 V. Maurer, N. Kalthoff, A. Wieser, M. Kohler, M. Mauder, L. Gantner: Observed spatiotemporal variability of boundary-layer turbulence over flat, heterogeneous terrain, *Atmos. Chem. Phys.* **16**, 1377–1400 (2016)
- 31.118 J. Röttger, M.F. Larsen: UHF/VHF radar techniques for atmospheric research and wind profiler applications. In: *Radar in Meteorology*, ed. by D. Atlas (American Meteorological Society, Boston 1990)
- 31.119 A.D. MacKinnon, R.A. Vincent, I.M. Reid: Boundary layer radar measurements during DAWEX. In: *Int. Symp. Equat. Process. Incl. Coupling (EPIC, Kyoto)* (2002) pp. 478–480
- 31.120 I.M. Reid: MF and HF radar techniques for investigating the dynamics and structure of the 50 to 110 km height region: A review, *Prog. Earth Planet. Sci.* **2**(1), 33 (2015)
- 31.121 M. Larsen, J. Röttger: The spaced antenna technique for radar wind profiling, *J. Atmos. Ocean. Technol.* **6**, 920–938 (1989)
- 31.122 S.A. Cohn, W.O.J. Brown, C.L. Martin, M.E. Susedik, G.D. Maclean, D.B. Parsons: Clear air boundary layer spaced antenna wind measurement with the Multiple Antenna Profiler (MAPR), *Ann. Geophys.* **19**(8), 845–854 (2001)
- 31.123 R.A. Vincent, S. Dullaway, A. MacKinnon, I.M. Reid, F. Zink, P.T. May, B.H. Johnson: A VHF boundary layer radar: First results, *Radio Sci.* **33**, 845–860 (1998)
- 31.124 B.H. Briggs: The analysis of spaced sensor records by correlation techniques. In: *Ground-Based Technique*, Middle Atmosphere Program, Handbook for MAP, Vol. 13, ed. by R.A. Vincent (SCOSTEP, Urbana 1984) pp. 166–186
- 31.125 B.H. Briggs: On the analysis of moving patterns in geophysics—I. Correlation analysis, *J. Atmos. Sol. Terr. Phys.* **30**, 1777–1788 (1968)
- 31.126 R.J. Doviak, G. Zhang, S.A. Cohn, W.O.J. Brown: Comparison of spaced-antenna baseline wind estimators: Theoretical and simulated results, *Radio Sci.* **39**(1), R51006 (2004)
- 31.127 B.H. Briggs, R.A. Vincent: Spaced-antenna analysis in the frequency domain, *Radio Sci.* **27**(2), 117–129 (1992)
- 31.128 E. Kudeki, G. Stitt: Frequency domain interferometry: A high resolution technique for studies of atmospheric turbulence, *Geophys. Res. Lett.* **14**, 198–201 (1987)
- 31.129 R.D. Palmer, T.-Y. Yu, P.B. Chilson: Range imaging using frequency diversity, *Radio Sci.* **34**(6), 1485–1496 (1999)
- 31.130 P.B. Chilson, T.-Y. Yu, R.G. Strauch, A. Muschinski, R.D. Palmer: Implementation and validation of range imaging on a UHF radar wind profiler, *J. Atmos. Ocean. Technol.* **20**, 987–996 (2003)
- 31.131 P.B. Chilson: The retrieval and validation of Doppler velocity estimates from range imaging, *J. Atmos. Ocean. Technol.* **21**, 1033–1043 (2004)
- 31.132 J.B. Mead, G. Hopcraft, S.J. Frasier, B.D. Pollard, C.D. Cherry, D.H. Schaubert, R.E. McIntosh: A volume-imaging radar wind profiler for atmospheric boundary layer turbulence studies, *J. Atmos. Ocean. Technol.* **15**, 849–859 (1998)
- 31.133 B.D. Pollard, S. Khanna, S.J. Frasier, J.C. Wyngaard, D.W. Thomson: Local structure of the convective boundary layer from a volume-imaging radar, *J. Atmos. Sci.* **57**(14), 2281–2296 (2000)
- 31.134 D. Law, S. McLaughlin, M. Post, B. Weber, D. Welsh, D. Wolfe, D. Merritt: An electronically stabilized phased array system for shipborn atmospheric

- wind profiling, *J. Atmos. Ocean. Technol.* **19**, 924–933 (2002)
- 31.135 A. Kottayil, K. Mohanakumar, T. Samson, R. Rebello, M.G. Manoj, R. Varadarajan, K.R. Santosh, P. Mohanan, K. Vasudevan: Validation of 205 MHz wind profiler radar located at Cochin, India, using radiosonde wind measurement, *Radio Sci.* **51**(3), 106–117 (2016)
- 31.136 K. Mohanakumar, A. Kottayil, V. Anandan, T. Samson, L. Thomas, K. Satheesan, R. Rebello, M. Manoj, R. Varadarajan, K. Santosh, P. Mohanan, K. Vasudevan: Technical details of a novel wind profiler radar at 205 MHz, *J. Atmos. Ocean. Technol.* **34**, 2659–2671 (2017)
- 31.137 A. Clegg, A. Weisshaar: Future radio spectrum access, *Proc. IEEE* **102**(3), 239–241 (2014)
- 31.138 National Academies of Sciences, Engineering, and Medicine: *A Strategy for Active Remote Sensing Amid Increased Demand for Radio Spectrum* (The National Academies Press, Washington DC 2015)
- 31.139 WMO, ITU: *Handbook on Use of Radio Spectrum for Meteorology: Weather, Water and Climate Monitoring and Prediction* (WMO, Geneva 2017)
- 31.140 H. Griffiths, L. Cohen, S. Watts, E. Mokole, C. Baker, M. Wicks, S. Blunt: Radar spectrum engineering and management: technical and regulatory issues, *Proc. IEEE* **103**(1), 85–102 (2015)
- 31.141 M.I. Skolnik: *Radar Handbook*, 2nd edn. (McGraw-Hill, New York 1990)
- 31.142 M.I. Skolnik: *Introduction to Radar Systems* (McGraw-Hill, New York 2001) p. 772
- 31.143 M.A. Richards, J.A. Scheer, W.A. Holm: *Principles of Modern Radar* (SciTech, Raleigh 2010)
- 31.144 D.M. Pozar: *Microwave Engineering* (Wiley, Hoboken 2012)
- 31.145 O. Ghebrebrehan: Sidelobe properties of complementary codes, *Meteorol. Rundsch.* **42**, 109–114 (1990)
- 31.146 O. Ghebrebrehan, M. Crochet: On full decoding of truncated ranges for ST/MST radar applications, *IEEE Trans. Geosci. Remote Sens.* **30**(1), 38–45 (1992)
- 31.147 E. Spano, O. Ghebrebrehan: Pulse coding techniques for ST/MST radar systems: A general approach based on a matrix formulation, *IEEE Trans. Geosci. Remote Sens.* **34**(2), 304–316 (1996)
- 31.148 E. Spano, O. Ghebrebrehan: Complementary sequences with high sidelobe suppression factors for ST/MST radar applications, *IEEE Trans. Geosci. Remote Sens.* **34**(2), 317–329 (1996)
- 31.149 E. Spano, O. Ghebrebrehan: Sequences of complementary codes for the optimum decoding of truncated ranges and high sidelobe suppression factors for ST/MST radar systems, *IEEE Trans. Geosci. Remote Sens.* **34**(2), 330–345 (1996)
- 31.150 E. Lau, S. McLaughlin, F. Pratte, B. Weber, D. Merritt, M. Wise, G. Zimmerman, M. James, M. Sloan: The DeTect Inc. RAPTOR VAD–BL radar wind profiler, *J. Atmos. Ocean. Technol.* **30**, 1978–1984 (2013)
- 31.151 D. Law, J. Khorrami, W. Sessions, M. Shanahan: Radiation patterns of a large UHF phased-array antenna: A comparison of measurements using satellite repeaters and patterns derived from measurements of antenna current distributions, *IEEE Antennas Propag. Mag.* **39**(5), 88–93 (1997)
- 31.152 J.B.–Y. Tsui: *Digital Microwave Receivers: Theory and Concepts* (Artech House, Norwood 1989) p. 389
- 31.153 B. Lindseth, W.O.J. Brown, J. Jordan, D. Law, T. Hock, S.A. Cohn, Z. Popovic: A new portable 449-MHz spaced antenna wind profiler radar, *IEEE Trans. Geosci. Remote Sens.* **50**(9), 3544–3553 (2012)
- 31.154 W.O. Brown, S. Cohn, B. Lindseth, J. Jordan: The NCAR 449 MHz modular wind profiler—Prototype deployment and future plans. In: *35th Conf. Radar Meteorol.* (2011)
- 31.155 B. Geerts, D. Parsons, C.L. Ziegler, T.M. Weckwerth, M.I. Biggerstaff, R.D. Clark, M.C. Coniglio, B.B. Demoz, R.A. Ferrare, W.A. Gallus Jr., K. Haghi, J.M. Hanesiak, P.M. Klein, K.R. Knupp, K. Kosiba, G.M. McFarquhar, J.A. Moore, A.R. Nehrir, M.D. Parker, J.O. Pinto, R.M. Rauber, R.S. Schumacher, D.D. Turner, Q. Wang, X. Wang, Z. Wang, J. Wurman: The 2015 plains elevated convection at night field project, *Bull. Am. Meteorol. Soc.* **98**(4), 767–786 (2017)
- 31.156 S. Fukao, T. Sato, T. Tsuda, M. Yamamoto, M.D. Yamamaka, S. Kato: MU radar: New capabilities and system calibrations, *Radio Sci.* **25**(4), 477–485 (1990)
- 31.157 J.S. Van Baelen, T. Tsuda, A.D. Richmond, S.K. Avery, S. Kato, S. Fukao, M. Yamamoto: Comparison of VHF Doppler beam swinging and spaced antenna observations with the MU radar: First results, *Radio Sci.* **25**(04), 629–640 (1990)
- 31.158 A. Frisch, B. Weber, R. Strauch, D. Merritt, K. Moran: The altitude coverage of the Colorado wind profilers at 50, 405 and 915 MHz, *J. Atmos. Ocean. Technol.* **3**, 680–692 (1986)
- 31.159 A. Frisch, B. Weber: The distribution of C^2_n as measured by 50-, 405-, and 915 MHz wind profilers, *J. Atmos. Ocean. Technol.* **9**, 318–322 (1992)
- 31.160 R. Chadwick, K. Moran: Long-term measurements of C^2_n in the boundary layer, *Radio Sci.* **15**(2), 355–361 (1980)
- 31.161 A. Frisch, B. Weber, D. Wuertz, R. Strauch, D.A. Merritt: The variations of C^2_n between 4 and 18 km above sea level as measured over 5 years, *J. Appl. Meteorol.* **29**, 645–651 (1990)
- 31.162 R.G. Strauch, B.L. Weber, A.S. Frisch, C.G. Little, D.A. Merritt, K.P. Moran, D.C. Welsh: The precision and relative accuracy of profiler wind measurements, *J. Atmos. Ocean. Technol.* **4**, 563–571 (1987)
- 31.163 B.L. Weber, D.B. Wuertz: Comparison of Rawinsonde and wind profiler radar measurements, *J. Atmos. Ocean. Technol.* **7**(1), 157–174 (1990)
- 31.164 W.M. Angevine: Errors in mean vertical velocities measured by boundary layer wind profilers, *J. Atmos. Ocean. Technol.* **14**(3), 565–569 (1997)
- 31.165 J. Dibern, W. Monna, J. Nash, G. Peters: *Development of VHF/UHF Wind Profilers and Vertical Sounders for Use in European Observing Systems*,

- Final Report COST Action 76, EUR 20614 (European Commission, Luxembourg 2001) pp. 225–258
- 31.166 E. Clothiaux, R. Penc, D. Thomson, T. Ackerman, S. Williams: A first-guess feature-based algorithm for estimating wind speed in clear-air Doppler radar spectra, *J. Atmos. Ocean. Technol.* **11**, 888–908 (1994)
- 31.167 T. Griesser, H. Richner: Multiple peak processing algorithm for identification of atmospheric signals in Doppler radar wind profiler spectra, *Meteorol. Z.* **7**(6), 292–302 (1998)
- 31.168 D.A. Merritt: A statistical averaging method for wind profiler Doppler spectra, *J. Atmos. Ocean. Technol.* **12**, 985–995 (1995)
- 31.169 W. Lahoz, B. Khattatov, R. Menard (Eds.): *Data Assimilation. Making Sense of Observations* (Springer, Berlin, Heidelberg 2010)
- 31.170 R.H. Langland, N.L. Baker: Estimation of observation impact using the NRL atmospheric variational data assimilation adjoint system, *Tellus A* **56**, 189–201 (2004)
- 31.171 C. Cardinali: Monitoring the observation impact on the short-range forecast, *Q. J. R. Meteorol. Soc.* **135**, 239–250 (2009)
- 31.172 M. Sommer, M. Weissmann: Ensemble-based approximation of observation impact using an observation-based verification metric, *Tellus A* **68**(1), 27885 (2016)
- 31.173 A. Hiscott: Exploiting wind profiler information, *Weather* **74**(1), 8–19 (2019)
- 31.174 M.K. Politovich, R.K. Goodrich, C.S. Morse, A. Yates, R. Barron, S.A. Cohn: The Juneau terrain-induced turbulence alert system, *Bull. Am. Meteorol. Soc.* **92**, 299–313 (2011)
- 31.175 A. Boilley, J.-F. Mahfouf: Wind shear over the Nice Cote d’Azur airport: Case studies, *Nat. Hazards Earth Syst. Sci.* **13**, 2223–2238 (2013)
- 31.176 R.E. Barbré Jr.: Quality control algorithms for the Kennedy Space Center 50-MHz-Doppler radar wind profiler winds database, *J. Atmos. Ocean. Technol.* **29**, 1731–1743 (2012)
- 31.177 A.B. White, C.J. Senff, A.N. Keane, L.S. Darby, I.V. Djalalova, D.C. Ruffieux, D.E. White, B.J. Williams, A.H. Goldstein: A wind profiler trajectory tool for air quality transport applications, *J. Geophys. Res.* **111**, D23S23 (2006)
- 31.178 B. Calpini, D. Ruffieux, J.-M. Bettems, C. Hug, P. Huguenin, H.-P. Isaak, P. Kaufmann, O. Maier, P. Steiner: Ground-based remote sensing profiling and numerical weather prediction model to manage nuclear power plants meteorological surveillance in Switzerland, *Atmos. Meas. Tech.* **4**, 1617–1625 (2011)
- 31.179 A.B. White, M.L. Anderson, M.D. Dettinger, F.M. Ralph, A. Hinojsa, D.R. Cayan, R.K. Hartman, D.W. Reynolds, L.E. Johnson, T.L. Schneider, R. Cifelli, Z. Toth, S. Gutman, C. King, F. Gehrke, P. Johnston, C. Walls, D. Mann, D. Gottas, T. Coleman: A twenty-first-century California observing network for monitoring extreme weather events, *J. Atmos. Ocean. Technol.* **30**, 1585–1603 (2013)
- 31.180 W.A. Monna, R.B. Chadwick: Remote-sensing of upper-air winds for weather forecasting: Wind-profiler radar, *Bull. World Meteorol. Organ.* **47**, 124–132 (1998)
- 31.181 F. Bouttier: The use of profiler data at ECMWF, *Meteorol. Z.* **10**(6), 497–510 (2001)
- 31.182 J.S. St-James, S. Laroche: Assimilation of wind profiler data in the Canadian Meteorological Centre’s analysis system, *J. Atmos. Ocean. Technol.* **22**, 1181–1194 (2005)
- 31.183 S. Soldatenko, C. Tingwell, P. Steinle, B.A. Kelly-Gerrey: Assessing the impact of surface and upper-air observations on the forecast skill of the ACCESS numerical weather prediction model over Australia, *Atmosphere* **9**(1), 23 (2018)
- 31.184 P. Clark, S. Gray: Sting jets in extratropical cyclones: A review, *Q. J. R. Meteorol. Soc.* **144**, 943–969 (2018)
- 31.185 K. McCaffrey, L. Bianco, J.M. Wilczak: Improved observations of turbulence dissipation rates from wind profiling radars, *Atmos. Meas. Tech.* **10**, 2595–2611 (2017)
- 31.186 L. Bianco, J.M. Wilczak: Convective boundary layer depth: Improved measurement by Doppler radar wind profiler using fuzzy logic methods, *J. Atmos. Ocean. Technol.* **19**, 1745–1758 (2002)
- 31.187 L. Bianco, J.M. Wilczak, A.B. White: Convective boundary layer depth estimation from wind profilers: Statistical comparison between an automated algorithm and expert estimations, *J. Atmos. Ocean. Technol.* **25**, 1397–1413 (2008)
- 31.188 T. Böhme, T. Hauf, V. Lehmann: Investigation of short-period gravity waves with the Lindenberg 482 MHz tropospheric wind profiler, *Q. J. R. Meteorol. Soc.* **130**(603), 2933–2952 (2004)
- 31.189 T. Sakazaki, M. Fujiwara: Diurnal variations in lower-tropospheric wind over Japan part I: Observational results using the wind profiler network and data acquisition system (WINDAS), *J. Meteorol. Soc. Jpn.* **88**(3), 325–347 (2010)
- 31.190 J. Bühl, R. Leinweber, U. Görzdorf, M. Radenz, A. Ansmann, V. Lehmann: Combined vertical-velocity observations with Doppler lidar, cloud radar and wind profiler, *Atmos. Meas. Tech.* **8**(8), 3527–3536 (2015)
- 31.191 N. Weisshaupt, J. Arizaga, M. Maruri: The role of radar wind profilers in ornithology, *Ibis* **160**, 516–527 (2017)
- 31.192 N. Weisshaupt, V. Lehmann, J. Arizaga, M. Maruri: Radar wind profilers and avian migration: A qualitative and quantitative assessment verified by thermal imaging and moon watching, *Methods Ecol. Evol.* **8**, 1133–1145 (2017)
- 31.193 R. Rodgers, W. Ecklund, D. Carter, K. Gage, S. Ethier: Research applications of a boundary-layer wind profiler, *Bull. Am. Meteorol. Soc.* **74**(4), 567–580 (1993)
- 31.194 S. Fukao: Recent advances in atmospheric radar study, *J. Meteorol. Soc. Jpn.* **85B**, 215–239 (2007)
- 31.195 W.K. Hocking: A review of mesosphere-stratosphere-troposphere (MST) radar developments

- and studies, circa 1997–2008, *J. Atmos. Sol. Terr. Phys.* **73**, 848–882 (2011)
- 31.196 R.J. Serafin, A.E. MacDonald, R.L. Gall: Transition of weather research to operations, *Bull. Am. Meteorol. Soc.* **83**, 377–392 (2002)
- 31.197 National Research Council: *From Research to Operations in Weather Satellites and Numerical Weather Prediction: Crossing the Valley of Death* (The National Academies, Washington DC 2000)
- 31.198 S. Cheinet, P. Cumin: Local structure parameters of temperature and humidity in the entrainment-drying convective boundary layer: A large-eddy simulation analysis, *J. Appl. Meteorol. Climatol.* **50**, 472–481 (2011)
- 31.199 K. Kamio, K. Nishimura, T. Sato: Adaptive sidelobe control for clutter rejection of atmospheric radars, *Ann. Geophys.* **22**(11), 4005–4012 (2004)
- 31.200 T. Hashimoto, K. Nishimura, T. Sato: Adaptive sidelobe cancellation technique for atmospheric radars containing arrays with nonuniform gain, *IEICE Trans. Commun.* **E99.B**(12), 2583–2591 (2016)
- 31.201 M.K. Yamamoto, S. Kawamura, K. Nishimura: Facility implementation of adaptive clutter suppression to an existing wind profiler radar: First results, *IEICE Commun. Express* **6**(9), 513–518 (2017)
- 31.202 K.S. Gage: Radar observations of the free atmosphere: Structure and dynamics. In: *Radar in Meteorology*, ed. by D. Atlas (American Meteorological Society, Boston 1990) pp. 534–565

Volker Lehmann

Meteorologisches Observatorium
Lindenberg
Deutscher Wetterdienst
Lindenberg, Germany
volker.lehmann@dwd.de



Volker Lehmann is head of the Remote Sensing Group of Lindenberg Observatory of the Deutscher Wetterdienst (DWD). He received a diploma degree in meteorology from Humboldt University of Berlin in 1990 and a PhD from Bayreuth University in 2010. His research focuses on the operational use of ground-based remote-sensing systems.

William Brown

Earth Observing Laboratory
National Center for Atmospheric Research
Boulder, USA
wbrown@ucar.edu



William Brown is a project scientist in the Earth Observing Laboratory at the National Center for Atmospheric Research in Boulder, CO, USA. He leads the Atmospheric Profiling Group, which deploys the Integrated Sounding System suites of profiling instruments such as wind profilers, lidars, soundings, and other instrumentation for the National Science Foundation. His research focuses on the development and applications of radar wind profilers.

Radar in the

32. Radar in the mm-Range

Gerhard Peters 

Part C | 32.1

Although the potential of mm-wave radar for cloud observation was demonstrated already in the 1950s, it took another 30 years before the technological development of microwave components and of digital signal processing allowed the realization of polarimetric Doppler radars, which became a crucial tool for cloud observations in various applications from climate modeling to weather services. This chapter provides an outline of cloud detection with radar, the historical development, contemporary cloud radar technology, and approaches for retrieving quantitative cloud parameters. The following refers to ground-based systems. The role of cloud radar in airborne applications and in upcoming space missions is addressed in Chap. 39 and Part D of this book.

32.1	Measurement Principles and Parameters	935
32.2	History	938
32.3	Theory	938
32.3.1	Reflectivity Factor	938
32.3.2	Attenuation	939
32.3.3	Doppler	940
32.3.4	Polarimetry	942
32.3.5	Multifrequency	942
32.3.6	Combination of Methods and Synergy with Other Remote-Sensing Techniques	944
32.4	Devices and Systems	946
32.5	Specifications	946
32.6	Quality Control	947
32.7	Maintenance	947
32.8	Application	948
32.9	Future Developments	948
32.10	Further Reading	948
	References	949

Here, clouds are understood as areas with enhanced concentration of suspended particles causing reduced visibility. They play an important role in meteorology due to their impact on the radiation budget, the hydrological cycle, and atmospheric dynamics. While the composition of particles can be very different, we focus

here on the most prevalent, namely water in the liquid and solid phases. Clouds are complex objects that defy a stringent general definition. Nevertheless, depending on the scientific question, it is often possible to define sets of variables that are relevant for describing certain cloud properties and that are observable by cloud radar.

32.1 Measurement Principles and Parameters

Why are mm-waves favorable for cloud observations? Clouds are nearly invisible for weather radars in the centimetric or decimetric range due to the small size of cloud particles. Just increasing the radar sensitivity would not help, because other scattering mechanisms, such as ground clutter or clear-air scattering would obscure the weak cloud signal. Since the scattering cross section of particles, which are small compared to the wavelength λ , is proportional to λ^{-4} , the use of shorter

waves specifically increases the scattering cross section of small particles, while the above-mentioned obscuring effects tend to become weaker. The typical wavelength of cloud radars is one order of magnitude shorter compared with weather radars. This corresponds to 40 dB enhancement of the cloud particle scattering cross section. Even more intense scattering at cloud particles would occur in the optical range, but optical waves cannot penetrate clouds. Thus, the mm-range is a tradeoff

Table 32.1 Measured primary variables of a mm-wave cloud radar

Variable	Description	Unit	Symbol
Received power	Backscattered power collected by the radar receiving antenna	W	P_r
Doppler spectrum	Spectral backscattered power as function of frequency f	W s	$s(f)$
Line-of-sight or radial velocity	First moment of spectrum	m s^{-1}	v_r
Spectral width	Standard deviation of spectrum	m s^{-1}	σ_v
Skewness	Deviation from symmetry of spectrum	–	SK
Kurtosis	Tailedness of spectrum	–	KU
Linear depolarization ratio	Ratio between received power in the cross-polarized and copolarized receiving channel	–	LDR

Table 32.2 Selection of secondary variables

Variable	Description	Unit	Symbol
Volume reflectivity	Backscatter cross section per volume	m^{-1}	η
(Equivalent) reflectivity factor	In the case of small water droplets: 6-th moment of drop-size distribution	$\text{mm}^6 \text{m}^{-3}$	Z_e, Z
Attenuation	Dissipation of wave energy per unit path due to interaction with matter divided by the local energy flux	m^{-1}	κ, κ_{wc}
Path-integrated attenuation	Relative reduction of energy flux after passing an attenuating medium	–	PIA
Liquid water content	Mass of condensed water per volume	kg m^{-3}	LWC
Ice content	Mass of ice per volume	kg m^{-3}	IWC
Particle size	Diameter of an equivolumic sphere	m	D
Radial wind velocity	Projection of velocity on the radar beam of tracers carried with the wind	m s^{-1}	w
Terminal fall velocity	Fall velocity of particles, when equilibrium of gravity acceleration and drag has been reached	m s^{-1}	v_t
Cloud thickness	Distance between cloud base and top	m	
Target class	Qualitative description of the type of targets (e.g., cloud drops, rain drops, ice crystal type, type of agglomerate, insects, seeds, ash)		

between scattering strong enough to be detectable and weak enough to allow penetration of clouds. Thus, mm-wave radars allow the observation of the inner structure of clouds, including multiple cloud layers.

Primary measured variables of a cloud radar do not contain any assumptions on the wave propagation or the scattering process. They comprise the received scattered power, its frequency distribution (spectrum), and spectral parameters. In the case of a dual-polarization receiver, these variables can be measured in different polarization states. In the case of linear polarization, one plane coincides with the transmitter polarization (cochannel) and the other one is orthogonal to it (cross channel). Full polarimetric radars can measure these variables also as function of the transmitter polarization. All variables are measured as functions of range.

A not-exhaustive list of primary variables, measured by a mm-wave cloud radar, is shown in Table 32.1. The actual set of variables can be much more comprehensive and depends on the design and complexity of the radar.

Secondary variables represent physical cloud properties and are derived from the primary variables using the physical relations of wave propagation, scattering processes, and target properties. They comprise volume reflectivity, cloud extension, cloud particle characteri-

zation, including their phase, turbulence intensity, and cloud water content. A selection of secondary variables is shown in Table 32.2.

A basic secondary variable is the equivalent reflectivity factor Z_e . It is related to P_r by

$$Z_e = \frac{1}{C} \frac{P_r}{P_t} \text{PIA} \frac{\lambda^4}{\pi^5 |K_w|^2} r^2, \quad (32.1)$$

where C = radar calibration constant, P_t = transmitted power, PIA = path-integrated attenuation (two-way), $K_w = (n_w^2 - 1)/(n_w^2 + 2)$, n_w = complex refractive index of water, and r = range. The idea behind the introduction of Z_e is the comparability of radars with different wavelengths; Z_e is in the Rayleigh range (drop diameter D small compared to λ) and, in the case of liquid phase, a descriptor of the drop-size distribution $N(D)$, which does not depend on the wavelength

$$Z_e = Z \equiv \int_0^\infty N(D) D^6 dD \quad \text{for } D \ll \lambda. \quad (32.2)$$

The subscript of Z_e is a reminder that the Rayleigh approximation is not always valid in case of mm-waves.

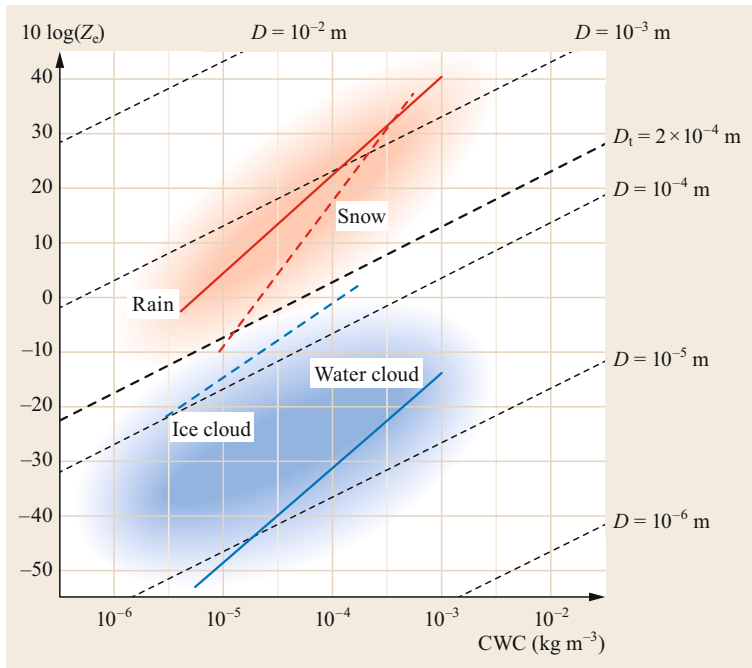


Fig. 32.1 Range of reflectivity (Z_e in $\text{mm}^6 \text{m}^{-3}$) for precipitation and clouds versus condensed water content. *Red area*: precipitation (rain [32.1] and snow [32.2]); *blue area*: clouds (water cloud [32.3] and ice cloud [32.4])

The range of Z_e -values expected for precipitation (red) and clouds (blue) is shown in Fig. 32.1 as a function of the condensed water content, referred to as CWC. It may be liquid water LWC, ice water content IWC, or a mixture of both. The thin dashed lines indicate the functions for monodisperse liquid particle sizes with diameters from $1 \mu\text{m}$ to 10mm .

Although there is no sharp distinction between clouds and precipitation, there is a conventional threshold of particle size at $D_t = 0.2 \text{mm}$ (thick black dashed line in Fig. 32.1). The rationale for this choice is the transition between dominating particle growth processes at this size. Smaller cloud particles tend to grow primarily by condensation, while larger particles grow by capturing smaller (more slowly falling) particles. The fall velocity of droplets with $D = D_t$ is $\approx 0.75 \text{m s}^{-1}$.

The thick colored lines represent the mean empirical relations between Z and CWC:

- Rain: $Z_e = 11\,080\text{LWC}^{1.75}$ [32.1]
- Snow: $Z_e = 14\,027\text{ICW}^{2.57}$ [32.2]
- Water cloud: $Z_e = 0.068\text{LWC}^{1.9}$ [32.3]
- Ice cloud: $Z_e = 25.5\text{ICW}^{1.44}$ [32.4].

The slopes of the empirical functions are always steeper than for the monodisperse case. This reflects the fact that higher values of CWC are correlated with a shift of the particle-size distribution $N(D)$ towards larger diameters.

It is obvious – particularly for clouds – that CWC cannot be retrieved with reasonable accuracy from Z_e without further knowledge about the particle habits. In the cloud domain, CWC varies by up to two orders of magnitude, depending on the phase for a given value of Z_e . The liquid and solid phases may coexist in clouds with any partitioning. Moreover, clouds may contain precipitation. In that case, the reflectivity tends to be dominated by the larger precipitation particles, even if their contribution to CWC is small. The range of ambiguity can be narrowed by analysis of the Doppler spectra structure, by use of multiple frequencies, by polarimetric measurements, and by combination with other observation techniques, such as, for example, lidar or radiometry. These techniques will be outlined in Sect. 32.3. A more in-depth introduction to the use and potential of mm-wave radars for cloud research can be found in [32.5], and a general overview of remote-sensing technologies for cloud studies is given in [32.6].

32.2 History

The first systematic survey of the capability of radar for cloud observation was carried out by *Vernon G. Plank* and coworkers in 1951–1952 [32.7]. It was based on existing knowledge of cloud particle-size distributions [32.8–10] and on radar data, collected for a period of 3 years with a 12.5 mm radar operated by the US Air Force Cambridge Research Center in the Boston, Massachusetts, area. The data were supplemented by sky-camera pictures, human observations, and aircraft missions. A correlation between detectability and internationally defined cloud types was established. It was concluded that nonprecipitating water clouds have the lowest scattering cross sections, while the ice phase is more favorable to being detected by radar. The visual and radar observations of the cloud base were often found to disagree. This was attributed to drizzle falling through the cloud base and evaporating at some distance below the cloud. The detection threshold of that early radar was -22 dBZ at a 1 km range. The authors were aware that most nonprecipitating clouds could not be detected with this modest sensitivity (Fig. 32.1). Recording techniques were still in an embryonic stage. The time–height cross section of signal power was stored on paper tape in gray-scale values produced by a facsimile recorder. Records of quantitative signal power were made by a *pulse integrator*-hardware, which was applied to selected range gates. Digital signal acquisition techniques and spectral analysis of radar signal time series were still far off the

horizon. Nevertheless, the main findings of this study are still valid.

In view of the missing Doppler capabilities of radars, it was suggested in [32.11] to use relations between the (unobserved) spectral width of the radar signal and statistical properties of the observable signal power time series (referred to as *audio signal*). In [32.12, 13], the performance of dedicated hardware devices was analyzed to estimate the spectral width (R-meter) and the mean Doppler velocity (frequency tracker) of weather echoes. These early steps towards Doppler radar techniques were prone to large systematic errors, depending on the signal-to-noise ratio and on the spectral width of the signals [32.13]. The first radars with satisfying sensitivity for cloud observation with 8.5 mm wavelength (K-band) were operated by the US Air Force in the late 1960s and early 1970s [32.14]. Nevertheless, the gain of insight into cloud physics remained limited by these one-parameter observations. A K-band system with all contemporary features of a cloud radar, including pulse-pair and Fourier analysis, as well as the retrieval of polarimetric variables, was developed at the NOAA Wave Propagation Laboratory [32.15]. It stimulated the development of increasingly sophisticated cloud radars in the mm-range at various laboratories in the 1980s, mainly in the United States. The introduction of a 3.5 mm-wavelength (W-band) cloud radar in 1987 [32.16] opened the path towards multifrequency mm-wave cloud observations.

32.3 Theory

In the following sections, some secondary variables and the corresponding retrieval schemes are described. They are arranged in the order of increasing complexity, which approximately agrees with the historical development.

32.3.1 Reflectivity Factor

The received power is related to the volume reflectivity η by the radar equation according to

$$\eta = \frac{1}{C} \frac{P_r}{P_t} \text{PIA} r^2; \quad (32.3)$$

η is converted into the equivalent reflectivity factor Z_e by

$$Z_e = \frac{\lambda^4}{\pi^5 |K_w|^2} \eta. \quad (32.4)$$

The combination of and (32.3) and (32.4) yields (32.1); K_w is nearly constant and by convention is set equal to 0.93 in (32.4). For some applications (e.g., [32.4]), the reflectivity of ice clouds is converted in Z_i , which is obtained by using the complex refractive index of ice in (32.4). This leads to

$$Z_i \cong 5.28 Z_e. \quad (32.5)$$

The exact relation depends on frequency and temperature.

An example for a high reaching cloud is shown in Fig. 32.2. At 16:50 UTC precipitation reaches the ground, and the melting layer becomes visible at 3.5 km height (bright band). The dotted ground-based layer of weak reflectivity (-30 dBZ) reaching up to 2 km is caused by insects and organic debris, sometimes referred to as atmospheric plankton.

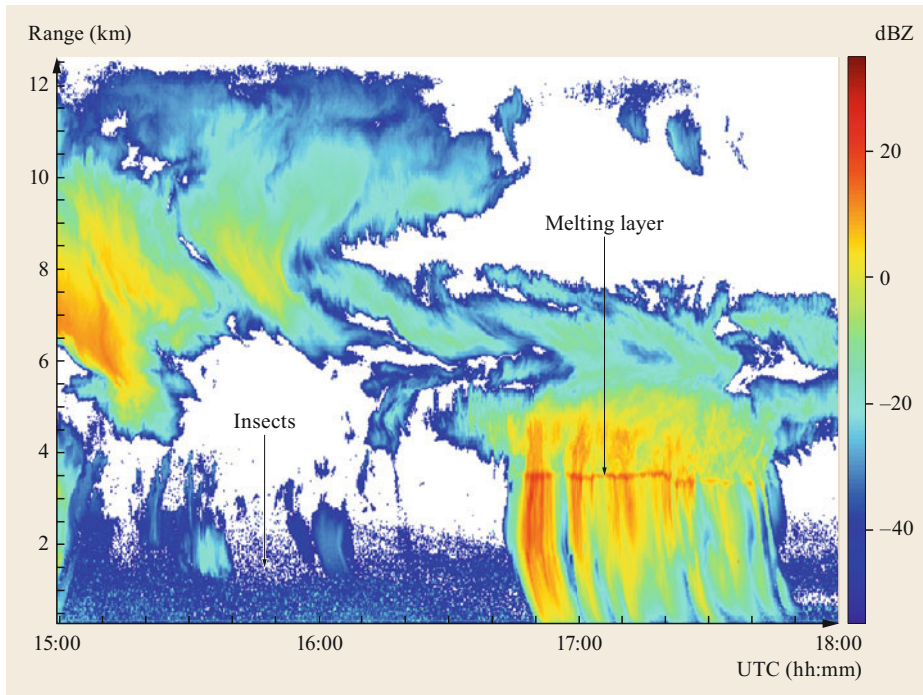


Fig. 32.2 Equivalent reflectivity factor from high reaching clouds (Date: 27.07.2006, 14:59–18:00)

32.3.2 Attenuation

Millimeter waves are attenuated in the atmosphere by gaseous absorption and by hydrometeors. Particularly, the attenuation by rain imposes a limitation to the range of mm-wave radars and prevents their use as universal weather radars. The local attenuation is defined as

$$\kappa(r) = \frac{1}{2} \left. \frac{\partial \text{PIA}(r')}{\partial r'} \right|_r. \quad (32.6)$$

At vertical incidence, attenuation is less important, because the range is anyway limited due to the depth of the troposphere, but nevertheless attenuation must be considered for all retrievals, which are based on calibrated values of radar reflectivity. Therefore, so-called window frequencies are preferred for cloud radars. They are between attenuation peaks at 23, 60, and 118 GHz, caused by molecular absorption of atmospheric water vapor and oxygen [32.17].

The attenuation κ_{CWC} by small particles increases monotonically with frequency and is a combined effect of scattering and absorption. In the case of water clouds, which are free of precipitation, absorption is the dominating contribution to attenuation. In the Rayleigh domain, it is linearly related to the liquid water content and can be described analytically (e.g., [32.18]) by

$$\kappa_{\text{LWC}} = \frac{82}{\lambda} \text{Im}(K_w) \text{ dB km}^{-1} \text{ kg}^{-1} \text{ m}^3, \quad (32.7)$$

κ_{LWC} can be calculated as a function of frequency and temperature by using, for example, the model in [32.19]. The attenuation is not only a disturbing mechanism, but it can also be exploited for estimating cloud-LWC. The strong attenuation of mm-waves allows its retrieval on reasonably short path lengths and at moderate values of LWC. An attractive feature of κ_{LWC} is its weak dependence on the drop-size distribution, which avoids uncertainties in retrieval schemes based on the reflectivity (Fig. 32.1). A further advantage of estimating attenuation is the independence of radar calibration, because only ratios of reflectivity are considered. While some drizzle is allowed for the application of (32.7) in clouds, it is not valid for rain, because the Rayleigh approximation is not applicable for larger rain drops in the mm-wave range. Nevertheless, relations between attenuation and rain rate, based on field data and on simulations, also show only weak dependence on the drop-size distribution at mm-wave frequencies [32.20]. Consequently, this property was exploited for estimating rain rates from attenuation retrievals of a vertically pointing K-band radar [32.21]. The application of the method is limited because it crucially depends on the homogeneous reflectivity on the attenuation path. This limitation can be overcome by using more than one radar frequency (Sect. 32.3.5). Typical values of attenuation by atmospheric gas molecules, liquid clouds, and rain for two frequencies are shown in Table 32.3.

Table 32.3 Attenuation for two frequencies (35 and 94 GHz) according to [32.22]

Parameter	Attenuation (dB km ⁻¹)	
	for 35 GHz	for 94 GHz
Atmospheric gas molecules		
Water vapor density = 2.5 × 10 ⁻⁴ kg m ⁻³	0.04	0.042
Water vapor density = 2.5 × 10 ⁻² kg m ⁻³	0.35	2.1
Liquid clouds		
LWC = 0.3 × 10 ⁻³ kg m ⁻³	0.3	1.47
LWC = 5 × 10 ⁻³ kg m ⁻³	0.96	24.5
Rain		
Rain rate = 0.3 mm h ⁻¹	0.06	0.35
Rain rate = 10 mm h ⁻¹	2	7

The absorption by ice particles is negligible. So – within some limits – the attenuation is a specific indicator of the liquid phase. The main effect of ice crystals on the propagation of mm-waves is scattering. If scattering becomes so strong that it contributes significantly to the total attenuation of the direct wave, attenuation-based retrieval methods may become impractical.

Multiple scattering can be an issue at W-band frequencies for airborne and space-borne applications in the case of strong precipitation, where the size of the radar footprint may become comparable with the free photon path length [32.23]. This introduces additional complication, because the basic radar equation is no longer applicable for converting received power versus time into reflectivity versus range.

32.3.3 Doppler

If the scattering targets move with respect to the radar, the frequency of the backscattered signal is shifted (nonrelativistic approximation) by

$$f_D = -2\frac{v}{\lambda}, \quad (32.8)$$

with v = the radial velocity component (positive away from the radar); f_D is derived from the phase shift $\Delta\phi$ between subsequent echoes separated by the pulse repetition time t_p according to

$$f_D = \frac{1}{2\pi} \frac{\Delta\phi}{t_p}. \quad (32.9)$$

Combining (32.8) and (32.9)

$$v = -\frac{\lambda}{4\pi} \frac{\Delta\phi}{t_p}. \quad (32.10)$$

Application of (32.10) requires that t_p be shorter than the coherence time τ of the scattered signal. For

ground-based radar, this condition is generally satisfied. (This is not the case for lidar wavelengths.) Then, the spectral resolution is ultimately limited by the analysis time T ($\delta f \propto 1/T$), and δf can be chosen small enough such that the observed spectral width σ is dominated by physical processes in the scattering volume. The most important contributions (inertial forces are neglected) to σ are

$$\sigma^2 = \frac{4}{\lambda^2} \sigma_t^2 + \frac{4}{\lambda^2} \sigma_p^2 + \frac{4}{\lambda^2} \sigma_m^2 + \frac{4}{\lambda^2} \sigma_s^2 + \sigma_d^2, \quad (32.11)$$

σ_t and σ_p are the spreads of turbulent velocity and of particle fall velocity distribution in the scattering volume; σ_m is the beamwidth broadening; $\sigma_m = u\sigma_\phi$ with u = transversal wind and σ_ϕ = beam-width; σ_s is caused by the horizontal and vertical shear of the radial wind component, and σ_d is the so-called dwell time broadening. In the case of a vertical beam $\sigma_d \propto u/(\sigma_\phi h)$, with h = height above the radar.

The motion of airborne particles is controlled by the drag of the ambient air and by gravitation. On a horizontal beam, the Doppler velocity is not affected by gravitation and indicates the horizontal wind component in the beam direction. At vertical incidence, the Doppler shift depicts the vertical motion of particles. The fall velocity – relative to ambient medium – represents an equilibrium between the drag and gravitational force, which is called terminal particle fall velocity v_p . For cloud drops ($D < 0.1$ mm) Stokes' law applies

$$v_p(D) = -\frac{1}{18} \frac{(\rho_w - \rho_a) D^2 g}{\mu}, \quad (32.12)$$

with ρ_w the density of water, ρ_a the density of air, μ the dynamic viscosity of air, and g gravity acceleration. For larger drops, the relation becomes more complicated; v_p of rain drops [32.24] has been determined in laboratory measurements as a function of the equivolumic diameter D at standard atmospheric surface conditions. The use of $v_p(D)$ for the retrieval of drop-size distributions from Doppler spectra was suggested in [32.25], and this concept was adopted in [32.26] to design a compact low-power rain radar at 24 GHz.

The observed vertical velocity v of particles is the sum of the vertical wind component v_t and v_p , $v = v_t + v_p$. For small and other slowly falling particles, v_t can be the dominating contribution to v . This is demonstrated in Fig. 32.3. for the same example as Fig. 32.2. Before the onset of precipitation and above the melting layer, the velocities (Fig. 32.3a) are close to zero with upward and downward excursions. We assume that these velocities are dominated by v_t , so that (a slightly biased) map of the turbulent vertical wind component is provided here. After onset of precipitation, the motion

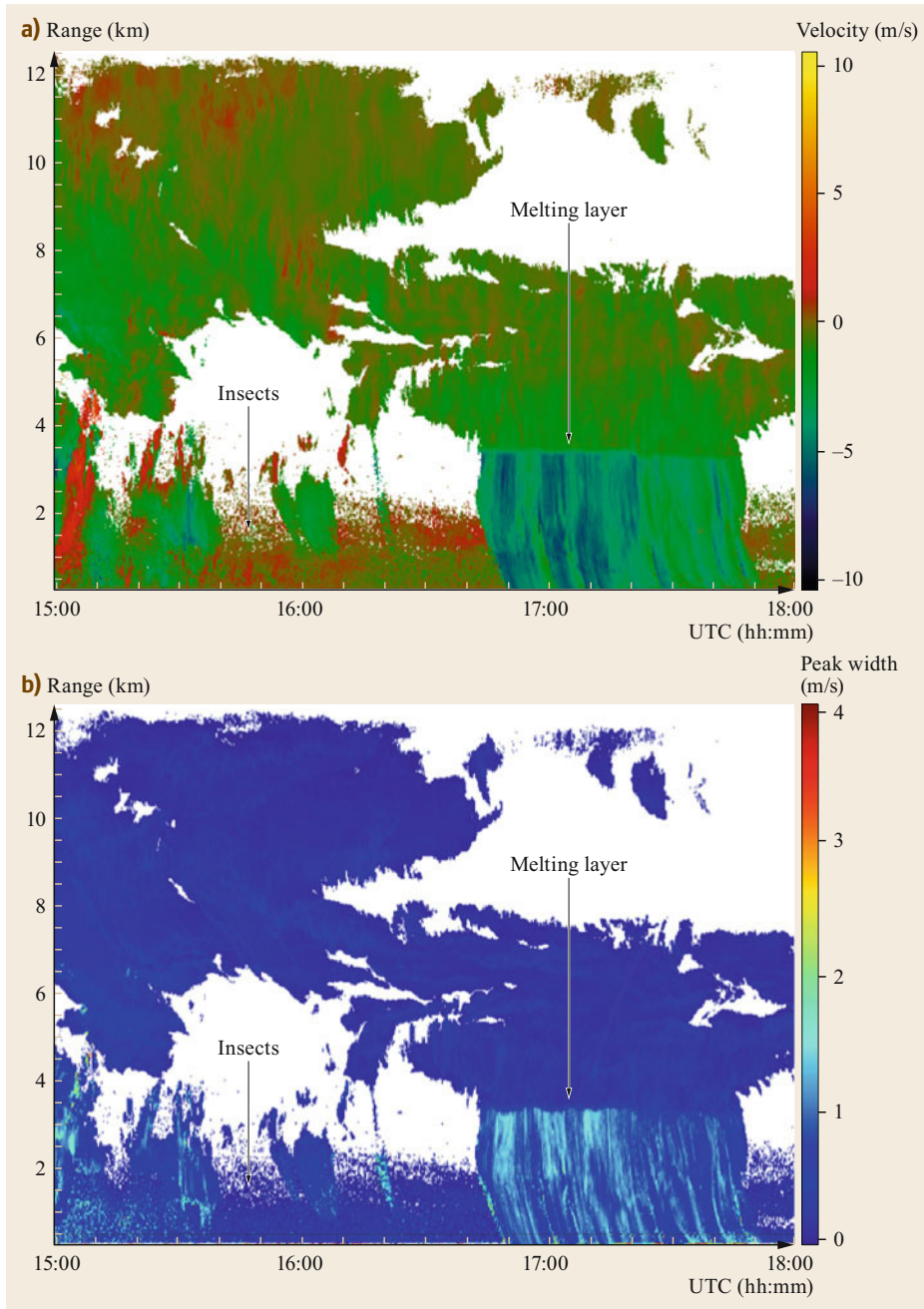


Fig. 32.3a,b The same example as in Fig. 32.2 but with (a) Doppler velocity and (b) spectral width (Date: 27.07.2006 14:59–18:00)

below the melting layer is consistently downward, with $|v|$ up to 6 m/s. Here, the fall velocity v_p is the dominating contribution to v . This interpretation is supported by the spectral width (in terms of velocity) shown in the Fig. 32.3b. We assume that σ is dominated by the first two terms of (32.11). The sudden increase from 0.1 to 1.5 m/s can be explained by the spread of fall velocity related to the rain drop-size distribution. The enhanced

values of σ in the left lower corner coincide with strong shear accompanying updrafts (Fig. 32.3a).

A scheme for deconvolution of Doppler spectra with respect to turbulence and particle-size distribution was described in [32.27] and demonstrated in [32.28] for K-band cloud radar data. It was applied in [32.29] to cirrus clouds and used for establishing a climatology of microphysical cirrus cloud properties [32.30]. These

schemes were based on pulse-pair analysis [32.31], which provides the first three moments of the Doppler spectrum. With the advent of affordable realtime spectrum analyzers, it was possible to observe more features of Doppler spectra. The multippeak structure occurring in mixed phase clouds and in drizzling clouds was exploited in [32.32] by using the slow-motion peak for estimating the vertical wind component and for retrieving v_t from $v_t = v - w$. Even overlapping cloud and drizzle spectra were separated in [32.33] by analyzing higher spectral moments in cloud regions, where drizzle is initially produced and does not yet dominate the reflectivity. Often, only the first two terms of (32.11) need to be retained. For these conditions, [32.34] proposed a scheme to separate σ_t and σ_p in (32.11) by independent estimation of turbulence via the time series of v . This way, σ_p may be retrievable in precipitating clouds to validate microphysical model parameterizations.

The potential of applying optimal estimation techniques to higher spectral moments for retrieving microphysical properties and turbulence parameters in ice clouds was demonstrated in [32.35]. The use of the structures of the Doppler spectra of rain echoes, which are caused by non-Rayleigh scattering, to separate v_t and w was suggested in [32.36]. The method works at W-band frequencies or higher, if sufficiently large rain drops exist.

A side-application of scanning mm-wave Doppler radars is the retrieval of wind profiles using Doppler beam-swinging methods, as was described in earlier chapters for other wavelengths. Albeit disturbing for the observation of clouds, particle targets in cloud-free regions are helpful tracers for this application.

32.3.4 Polarimetry

Polarization techniques as described in Chap. 30 are also used in mm-wave radars for target classification and quantitative estimation of cloud contents. A standard application is the distinction of biological targets (insects, seeds) from clouds using the linear depolarization ratio, referred to as LDR. The shape of biological targets tends to deviate from circular symmetry, and the particles are relatively large. Therefore, biological targets show much higher values of LDR than cloud particles do. This can be used for target separation, as is shown in Fig. 32.4. The time–height cross sections of the signal-to-noise ratio, referred to as SNR, and LDR were measured with a vertically pointing K-band radar (MIRA 36) at the German Meteorological Service in Lindenberg [32.37]. Figure 32.4a shows the SNR of the backscattered signal, which is dominated here by biological targets reaching up to 3 km AGL. This is suggested by LDR values of more than -10 dB, shown in

Fig. 32.4b. The black dotted lines indicate the cloud base detected by an optical ceilometer. After removing all pixels exceeding a certain threshold of LDR, in Fig. 32.4c only structures above the ceilometer-detected cloud base remain (with a few exceptions), which reveals the passage of thin boundary layer clouds.

The observation of other polarimetric parameters requires the transmission of two polarization states or at least hybrid mode operation [32.38] (this is explained in Chap. 30). They provide additional information about the microphysical habit, based on preferred particle orientations with respect to the radar pointing axis [32.39]. Deviations from uniform orientation distribution are typically related to gravitational forces and are, therefore, observable only on nonvertical beams.

32.3.5 Multifrequency

Under some conditions the combination of two or more radar frequencies can provide more information than the sum obtained by using the individual frequencies. While numerous studies consider the synergy of wavelengths ranging from meter to millimeter, we restrict the discussion to the combination of mm-waves.

In Fig. 32.5, the two-way path-integrated attenuation PIA for a 1 km range is shown as function of LWC for two window frequencies in the case of nonprecipitating water clouds (solid lines) based on (32.7) and for rain (dashed lines) based on empirical relations compiled in [32.40]. The rain rate corresponding to the liquid water content assuming exponential drop-size distributions according to [32.41] is indicated by the black dotted line.

LWC of stratocumulus clouds can be retrieved with reasonable accuracy according to [32.42] by combining vertically pointing radars at 35 and 94 GHz and evaluating the dual-wavelength ratio DWR_i (dB) $\equiv Z_{35,i}$ (dBZ) $- Z_{94,i}$ (dBZ) at two heights h_i ($i = 1, 2$) using the equation

$$LWC = \frac{1}{\kappa_{LWC94} - \kappa_{LWC35}} \times \left[\frac{DWR_2 - DWR_1 - \beta}{2(h_2 - h_1)} - \alpha_{94} + \alpha_{35} \right], \quad (32.13)$$

where

$$\beta = 10 \log_{10} \left[\frac{|K_{35}(T_2)|^2 |K_{94}(T_1)|^2}{|K_{35}(T_1)|^2 |K_{94}(T_2)|^2} \right] \quad (32.14)$$

is a small correction accounting for the temperature dependence of K , and α is the gaseous absorption. In

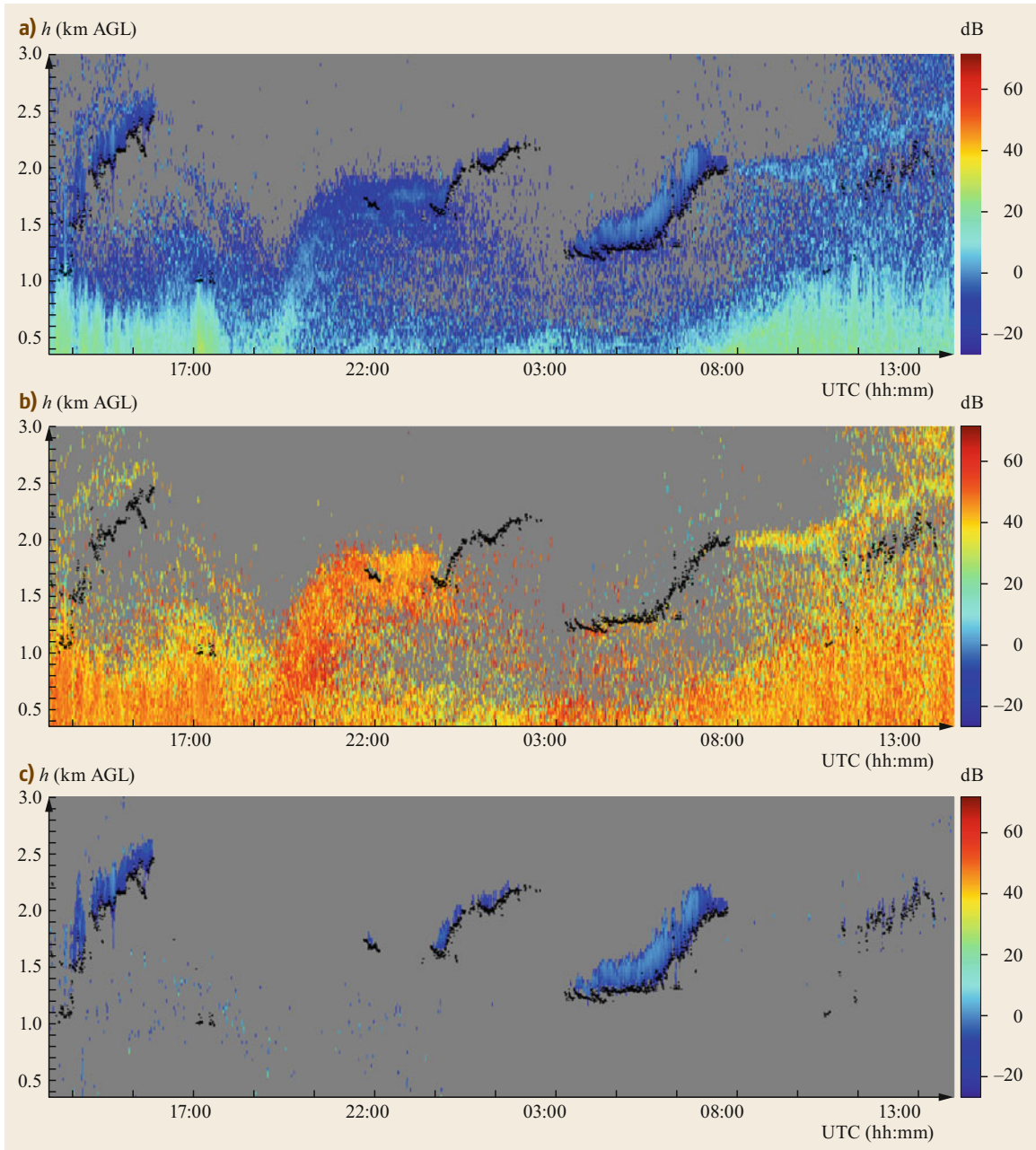


Fig. 32.4 (a) K-band echoes (SNR) from thin boundary layer clouds and from biological targets, (b) linear depolarization ratio, (c) all pixels removed where LDR exceeds a certain threshold (removal of biological targets). (a–c) Black dots indicate cloud base, detected by optical ceilometer (after [32.37])

Fig. 32.5, we recognize that significant differences of PIA exist between the two frequencies. It is also obvious that the result of (32.13) would be biased, if there were rain instead of cloud droplets between h_1 and h_2 . In rain clouds, rain and cloud drops coexist, and it depends on the partitioning whether the bias is acceptable.

The authors pointed out that some light drizzle is tolerable, even if it is the dominating backscatter source due to the D^6 proportionality.

An attractive feature of attenuation-based retrieval of LWC is its independence of the drop-size distribution for cloud droplets and only weak dependence in the

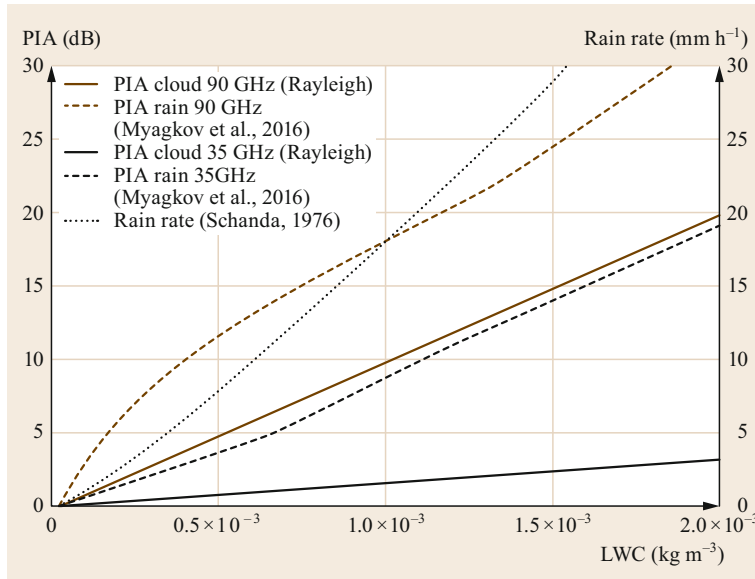


Fig. 32.5 Two-way path integrated attenuation PIA (for a 1 km range) and rain rate as function of liquid water content

case of rain. At higher rain rates, the attenuation is not only caused by absorption, but also scattering at larger particles extracts energy from the original wave.

If particle sizes are above the upper limit of the Rayleigh regime at least for the shorter wavelength, the ratio of the observed reflectivities at two frequencies allows inferences on the particle-size distribution (referred to as PSD). This was demonstrated in [32.43] for the crystal size of cirrus clouds observed with K- and W-bands. Snow PSDs and pertinent bulk parameters were estimated successfully in a similar approach in [32.44], combining reflectivities observed in Ka(35 GHz)- and Ku(13.6 GHz)-bands.

An extension of dual-frequency analysis to rain was demonstrated in [32.45]. The authors used the Mie oscillations of the scattering cross section at the W-band to separate the vertical wind from the (size-dependent) particle fall velocity, as proposed earlier in [32.46]. The novel element of this method [32.47] is the use of the Rayleigh part of the spectra (small particles) to estimate the differential attenuation and to use this information for correcting the reflectivity ratio in the non-Rayleigh part of the spectra. The result is a self-calibrated drop-size distribution including an estimate of vertical wind and turbulent broadening.

The potential benefit of a third radar frequency (combination of Ku-, Ka-, and W-bands) for separating snowflake classes, like aggregates and spheroidal particles, and for retrieving basic PSD parameters was discussed in [32.48]. Observational evidence for a direct

link of these model-based scattering regimes to bulk snowfall density, habit, and particle size was shown in [32.49, 50]. These studies suggest that traditional scattering calculations based on medium refractive index approximations are insufficient to explain the observed Z_e -variability in the triple frequency space. More advanced scattering schemes using discrete-dipole approximation seem to be significantly superior in linking the observed triple-frequency signatures with snowflake aggregation [32.51] and riming [32.52].

The upper three panels in Fig. 32.6 show simultaneous W-, Ka-, and X-band reflectivities measured during TRIPEX in the winter season of 2015, together with isolines of temperature (0 and -15°C). The corresponding differential reflectivities are shown in the lower two panels. In [32.53], methods how microphysical processes in the ice phase, such as, for example, aggregation and riming, can be deduced from such data are described.

32.3.6 Combination of Methods and Synergy with Other Remote-Sensing Techniques

While radar provides excellent spatial resolution, the quantitative relation between radar observables and physical variables of interest is often ambiguous. The characteristics of microwave radiometry are complementary to some extent. The spatial resolution is poor, but the retrieval of path-integrated values of physi-

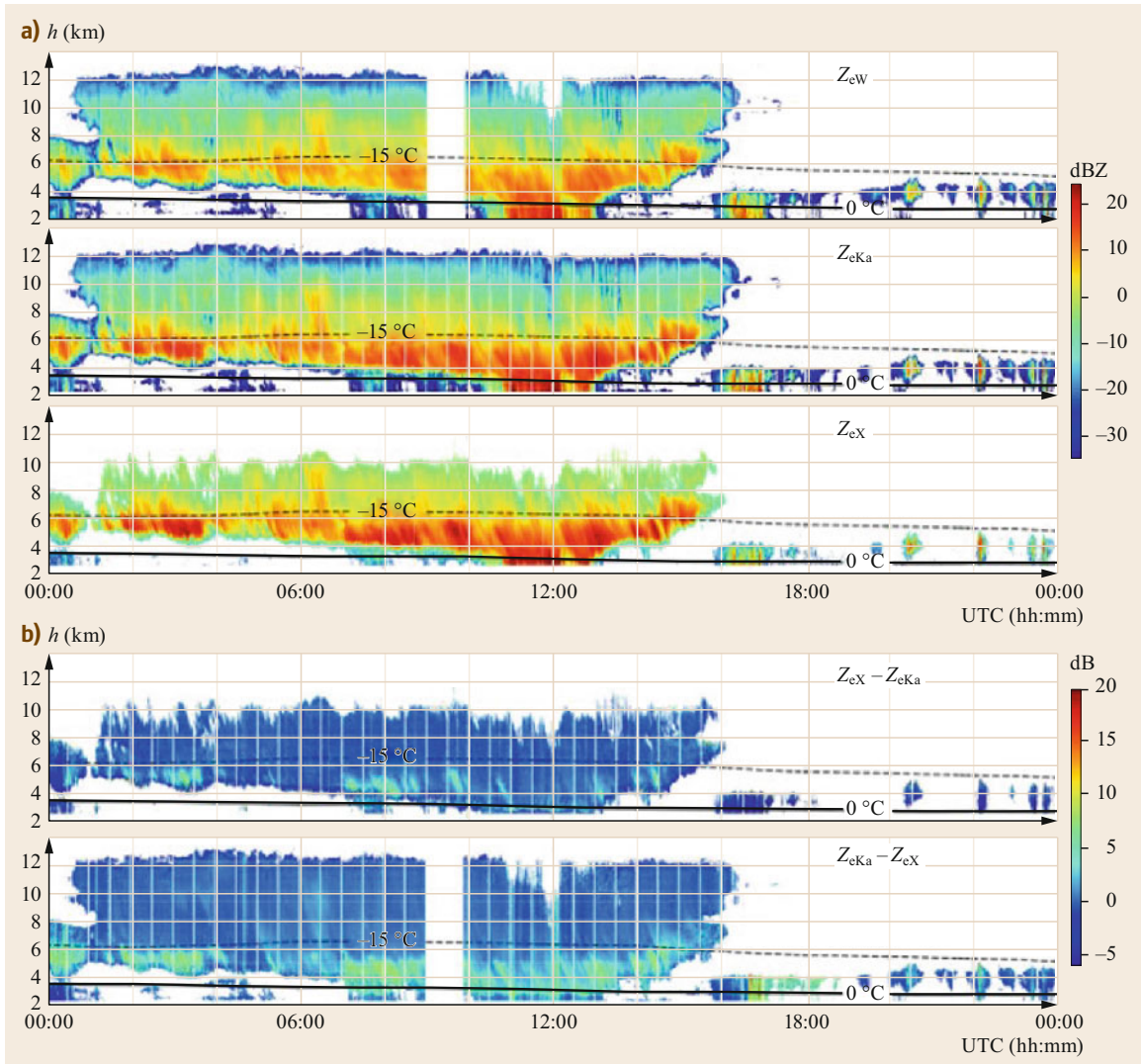


Fig. 32.6a,b Triple-frequency reflectivities measured on 20.11.2015 during TRIPEX (triple-frequency and polarimetric radar experiment). (a) Z_{eW} , Z_{eKa} , Z_X . (b) $Z_{eX} - Z_{eKa}$, $Z_{eKa} - Z_{eW}$ (courtesy: J. Dias Neto and S. Kneifel, Emmy-Noether Group OPTIMIce, University of Cologne)

cal variables, such as, for example, the liquid water path, are sometimes straightforward. Therefore, the combination of radiometers and mm-wave radar was suggested to describe the content distribution of water clouds [32.54, 55]. An optimal estimation framework that includes ceilometer cloud base information to retrieve physically consistent profiles of temperature, humidity, and cloud LWC was developed and demonstrated in [32.56]. The algorithms for operational cloud

characterization in the European CLOUDNET program using data from mm-radars in combination with microwave radiometers, lidars, and models are described in [32.57]. Continuing research aims at improving the quality and extending the range of retrieved variables within CLOUDNET, such as, for example, the quantitative separation of mixed-phase cloud contents using a suite of active and passive ground-based remote-sensing devices, including mm-wave radar [32.58].

32.4 Devices and Systems

The basic design of mm-wave cloud radars does not differ from that of weather radars. Most systems use pulsed transmitters, which can be divided into two classes. One uses magnetron transmitters, where the pulse-to-pulse coherence is achieved on the receiver side by storage of the phase of each transmitted signal [32.59]. The range resolution δr is related to the pulse width τ by $\delta r = c\tau/2$. The other class uses phase-stable continuous sources and switched transmit amplifiers with typically lower peak power than magnetrons. Here, the mean transmit power can be

increased by using longer transmit pulses, which are phase or frequency-coded, such that $\delta r \ll c\tau/2$ can be achieved [32.60]. The most efficient use of transmit power is made by continuous transmission. Here, the ranging is achieved by frequency modulation of the transmitted signal and frequency analysis of the heterodyne signal (FMCW radar (frequency-modulated continuous-wave radar)). Except for radars with very low transmit power, as used in [32.61], a separate antenna is needed for the receiver. A very sensitive FMCW W-band cloud radar is described in [32.62].

32.5 Specifications

In Table 32.4, specifications of some commercially available mm-wave radars are compared. Based on the radar equation for beam-filling water droplets in the Rayleigh range, the minimum detectable reflectivity was estimated. For all radars, the same range, resolution, averaging time, and losses in wave guides and T/R-switch were assumed. In addition to the Rayleigh dependence $\propto \lambda^4$, a factor $\lambda^{-0.5}$ was introduced, which describes the effects of wavelength-dependent coherence time on the SNR after some time of incoherent averaging. The most sensitive radar was used as a reference system for normalization of a *figure of merit*

(FOM), which is here defined as follows

$$\text{FOM} = 10 \log \left[\left(\frac{\lambda_0}{\lambda} \right)^{3.5} \frac{A_e \bar{P}_t}{A_{e0} \bar{P}_{t0}} \right] - \text{NF}, \quad (32.15)$$

with $A_e \equiv G\lambda^2/(4\pi)$ effective antenna area and \bar{P}_t mean transmit power and NF noise figure of the receiver. The index 0 indicates the reference system. Insertion losses in waveguides etc., are assumed identical in all systems.

The calculation is based on specifications as published in the documents [32.59, 62–64].

Table 32.4 Specifications of some commercial cloud radars (EIKA: Extended Interaction Klystron Amplifier; TWTA: Extended Interaction Klystron Amplifier)

Radar trade name	WACR	KAZR	MIRA36	RPG-FMCW-94	MRR
Manufacturer	ProSensing	ProSensing	Metek	RPG radiometer physics	Metek
Ranging method	Pulse compression	Pulse compression	Pulse	FMCW	FMCW
Mean transmitted power \bar{P}_t (W)	1.5	50	30	1.5	0.03
Frequency (GHz)	95	35	35	94	24
Transmitter type	EIKA	TWTA	Magnetron	Solid state	Solid state
Antenna type	Monostatic	Monostatic	Monostatic	Bistatic	Monostatic
Antenna gain G (dBi)	59.5	57.5	54.5	51.5	40.1
Effective antenna area A_e (m ²)	0.71	3.3	1.6	0.11	0.13
Noise figure NF (dB)	5.5	2.4	3	3	18
FOM (dB)	0	−2	−6	−16	−62

32.6 Quality Control

The quality of radar products can be deteriorated by various categories of influences. Generally, retrieval algorithms imply disregard or only first-order consideration of influencing physical variables (e.g., attenuation, target class, ground clutter). The management of such uncertainties should be an integral part of the retrieval algorithm, while the purpose of quality control is to monitor all relevant technical specifications of the radar system.

The most demanding is the validation of the absolute whole-system calibration S , which includes all system-related factors of the radar (32.1)

$$S = \frac{1}{C} \frac{P_r}{P_t} \quad (32.16)$$

Usually, cloud radars contain sensors, which monitor the transmit power, the impedance match of the antenna, and the transmit frequency and transmit pulse envelope. These and other housekeeping data should be stored in a log file. Often, the operation scheme of the radar includes a periodic recalibration mode, where the receiver gain and system noise figure are measured by switching the receiving channels to a calibrated noise source. These results can be compared with the noise level measured in clear air conditions to detect potential drifts of the noise source calibration. The stability of transmit power measurement is checked either by redundant sensors or by manual inspections. Verification of the antenna efficiency is the most difficult element of quality control. The degradation of sensitivity due to mechanical deformation increases with increasing antenna gain.

For scanning radars, antenna pattern measurements using a calibrated radio source or receiver yield SP_t or S/P_t . The sun can serve as a well-defined radio source. While the above-mentioned procedures provide only subgroups of factors constituting S , direct determination of S is possible by scanning an artificial, calibrated target. If the position of the target with respect to the radar is determined by an independent survey, also the ranging accuracy of the radar can be verified.

In some applications (e.g., multifrequency, polarization diversity, or radar network operation), a degree of agreement between participating systems is required, which is difficult to achieve by independent absolute calibration. Here, one may resort to a relative calibration, which is achieved by evaluating simultaneous measurements in common scattering volumes. In the case of multifrequency or polarization diversity, suitable meteorological conditions that allow a most accurate interpretation must be selected (e.g., negligible PIA, weak drizzle with spherical drops in the Rayleigh regime for all frequencies, exclusion of ice phase, absence of other contaminating targets, ...). For network homogenization, various methods are applied or under discussion from statistical evaluation over movable ground-based reference systems to comparisons with space-borne radars [32.65].

The general difficulty of absolute radar calibration calls for auxiliary observations. Constraints can be provided by radiometers via the path-integrated liquid water content (LWP) and/or by distrometers measuring the mass flux in the case of precipitation.

32.7 Maintenance

The antenna dish surface (or radome) must be kept clean. Wet leaves and, particularly, wet snow act as efficient absorbers compromising the radar calibration. Component lifetimes and maintenance schedules depend on the type of radar. If the radar uses vacuum

tubes (magnetron, traveling-wave tube, klystron, etc.), their lifetimes are to be specified by the manufacturer. If the transmit power is monitored, an alert should be issued, if some threshold – as specified by the manufacturer – is crossed. In the case of pressurized wave

Table 32.5 Maintenance schedule

Recommended interval	Transmitter type	
	Vacuum tube	Solid state
1 week	Check log file for drifts of transmit power and other tube related parameters and events	–
Depending on installation site and weather conditions:	Clean antenna dish	
1 month	Check log file for anomalies according to manufacturer's instructions Check air drying device	
2 years	Perform antenna calibration	

guides, the pump and air-drying device require regular inspection. Scanning radars require more maintenance than radars with fixed beam direction due to wear and tear of bearings and, possibly, of slip rings. Since the

technology and complexity of radar systems is very diverse, only a few general maintenance steps are listed in Table 32.5. A concrete maintenance schedule should be agreed upon with the manufacturer.

32.8 Application

At present, cloud radars are primarily used in various atmospheric research areas and in climatologic studies. Research areas include cloud physical processes such as particle growth, shape, interaction, phase, phase-mixture, phase transitions, habits, and the role of clouds in dynamics, cloud entrainment, and the cloud life cycle. Climatologic studies concern statistics of cloud coverage, including multilayer clouds, overlap factor, cloud height, cloud phase, and particle habit. Cloud radars are the backbone of several corresponding observation

networks. The Atmospheric Radiation Measurement (ARM) program, established in 1992 by the US Department of Energy, provides freely available cloud radar observations and various higher-level products for various sites and time periods. CloudNet [32.57] is another international long-term cloud observation program, which is going to become an EU research infrastructure. It aims to demonstrate the potential of operational cloud radar-based observation networks to improve the representation of clouds in weather prediction and climate models.

32.9 Future Developments

The potential benefit of combining cloud radars at different frequencies and with other sensing techniques has already been demonstrated in numerous studies. Some of them were mentioned above, but much more effort will be devoted to the exploration of synergistic effects with other sensing techniques. Cloud radar data are not yet used to support weather prediction. Although the benefit could be significant, the development of adequate tools in weather prediction models for ingesting cloud radar data is still a major task. The observation of fog develop-

ment – particularly in airport areas – may become a major practical and straightforward application. The ongoing progress of solid-state electronics will lead to cost reductions, increased sensitivity, and the availability of higher frequencies for cloud radars. The added value of using frequencies up to 300 GHz in atmospheric-window regions is discussed in [32.66]. First attempts of water vapor density retrieval in clouds by differential absorption using frequencies close to the water vapor absorption line at 182 GHz were published in [32.67].

32.10 Further Reading

A comprehensive review of the present state of the art of remote-sensing techniques, including mm-wave radar for clouds and precipitation, is given by:

- J. Bühl, S. Alexander, S. Crewell, A. Heymsfield, H. Kalesse, A. Khain, M. Maahn, K. van Tricht, M. Wendisch: Remote sensing. In: *Ice Formation and Evolution in Clouds and Precipitation: Measurement and Modeling Challenges*, AMS Monograph, Vol. 58 (2017), Chap. 10.

A general up-to-date introduction into meteorological radar, including a dedicated chapter on spaceborne and cloud radars can be found in:

- F. Fabry: *Radar Meteorology: Principles and Practice*. (Cambridge University Press, Cambridge 2015).

A basic introduction to mm-wave radar technology for cloud observation and its potential for climate research can be found in:

- K.P. Moran, B. E. Martner, M. J. Post, R. A. Kropfli, D. C. Welsh, K. B. Widener: *An Unattended Cloud-Profiling Radar for Use in Climate Research*, Bull. Am. Meteorol. Soc., **79**(3), 443–455 (1998).

References

- 32.1 J.S. Marshall, W. Palmer: The distribution of raindrops with size, *J. Meteorol.* **5**(4), 165–166 (1948)
- 32.2 R.S. Sekhon, R.C. Srivastava: Snow size spectra and radar reflectivity, *J. Atmos. Sci.* **27**(2), 299–307 (1970)
- 32.3 H. Sauvageot, J. Omar: Radar reflectivity of cumulus clouds, *J. Atmos. Ocean. Technol.* **4**(2), 264–272 (1987)
- 32.4 K. Sassen: Ice cloud content from radar reflectivity, *J. Clim. Appl. Meteorol.* **26**(8), 1050–1053 (1987)
- 32.5 P. Kollias, E.E. Clothiaux, M.A. Miller, B.A. Albrecht, G.L. Stephens, T.P. Ackerman: Millimeter-wavelength radars: New frontier in atmospheric cloud and precipitation research, *Bull. Am. Meteorol. Soc.* **88**(10), 1608–1624 (2007)
- 32.6 J. Bühl, S. Alexander, S. Crewell, A. Heymsfield, H. Kalesse, A. Khain, M. Maahn, K. van Tricht, M. Wendisch: Remote sensing. In: *Ice Formation and Evolution in Clouds and Precipitation: Measurement and Modeling Challenges*, AMS Monograph, Vol. 58 (2017), Chap. 10
- 32.7 V.G. Plank, D. Atlas, W.H. Paulsen: The nature and detectability of clouds and precipitation as determined by 1.25-centimeter radar, *J. Meteorol.* **12**(4), 358–378 (1955)
- 32.8 M. Diem: Messung der Größe von Wolkenelementen, *Ann. Hydrogr. Mar. Meteorol.* **32**, 142–150 (1942)
- 32.9 M. Diem: Messung der Größe von Wolkenelementen II, *Meteorol. Rundsch.* **1**(9/10), 261–273 (1948)
- 32.10 A.C. Best: Drop-size distribution in cloud and fog, *Q. J. R. Meteorol. Soc.* **77**(333), 418–426 (1951)
- 32.11 S. Bartnoff, D. Atlas: Microwave determination of particle-size distribution, *J. Meteorol.* **8**, 130–131 (1951)
- 32.12 R.R. Rogers: Radar measurement of velocities of meteorological scatterers, *J. Atmos. Sci.* **20**(2), 170–174 (1963)
- 32.13 R.R. Rogers, B.R. Tripp: Some radar measurements of turbulence in snow, *J. Appl. Meteorol.* **3**, 603–610 (1964)
- 32.14 K.P. Moran, B.E. Martner, M.J. Post, R.A. Kropfli, D.C. Welsh, K.B. Widener: An unattended cloud-profiling radar for use in climate research, *Bull. Am. Meteorol. Soc.* **79**(3), 443–456 (1998)
- 32.15 F. Pasqualucci, B.W. Bartram, R.A. Kropfli, W.R. Moninger: A millimeter-wavelength dual-polarization Doppler radar for cloud and precipitation studies, *J. Clim. Appl. Meteorol.* **22**(5), 758–765 (1983)
- 32.16 R. Lhermitte: A 94-GHz Doppler radar for cloud observations, *J. Atmos. Ocean. Technol.* **4**(1), 36–48 (1987)
- 32.17 H.J. Liebe: An updated model for millimeter wave propagation in moist air, *Radio Sci.* **20**(5), 1069–1089 (1985)
- 32.18 F.T. Ulaby, R.K. Moore, A.K. Fung: *Microwave Remote Sensing—Active and Passive*, Vol. I (Addison-Wesley, Reading 1981)
- 32.19 T. Meissner, F.J. Wentz: The complex dielectric constant of pure and sea water from microwave satellite observations, *IEEE Trans. Geosci. Remote Sens.* **42**(9), 1836–1849 (2004)
- 32.20 R.J. Doviak, D.S. Zrnić: *Doppler Radar and Weather Observations* (Academic Press, San Diego, London 1993)
- 32.21 S.Y. Matrosov: Attenuation-based estimates of rainfall rates aloft with vertically pointing K_a -band radars, *J. Atmos. Ocean. Technol.* **22**(1), 43–54 (2005)
- 32.22 G. Peters, U. Goersdorf: Wolkenradar – Prinzipien und Messungen, *Promet* **36**(3/4), 144–153 (2010)
- 32.23 A. Battaglia, S. Tanelli, S. Kobayashi, D. Zrnić, R.J. Hogan, C. Simmer: Multiple-scattering in radar systems: A review, *J. Quant. Spectrosc. Radiat. Transf.* **111**(6), 917–947 (2010)
- 32.24 R. Gunn, G.D. Kinzer: The terminal velocity of fall for water droplets in stagnant air, *J. Meteorol.* **6**(4), 243–248 (1949)
- 32.25 D. Atlas, R.C. Srivastava, R.S. Sekhon: Doppler radar characteristics of precipitation at vertical incidence, *Rev. Geophys.* **11**(1), 1–35 (1973)
- 32.26 G. Peters, B. Fischer, T. Andersson: Rain observations with a vertically looking micro rain radar (MRR), *Boreal Environ. Res.* **7**(4), 353–362 (2002)
- 32.27 E.E. Gossard: Measurement of cloud droplet size spectra by Doppler radar, *J. Atmos. Ocean. Technol.* **11**(3), 712–726 (1994)
- 32.28 E.E. Gossard, J.B. Snider, E.E. Clothiaux, B. Martner, J.S. Gibson, R.A. Kropfli, A.S. Frisch: The potential of 8-mm radars for remotely sensing cloud drop size distributions, *J. Atmos. Ocean. Technol.* **14**(1), 76–87 (1997)
- 32.29 M. Deng, G.G. Mace: Cirrus microphysical properties and air motion statistics using cloud radar Doppler moments. Part I: Algorithm description, *J. Appl. Meteorol. Climatol.* **45**(12), 1690–1709 (2006)
- 32.30 M. Deng, G.G. Mace: Cirrus microphysical properties and air motion statistics using cloud radar Doppler moments. Part II: Climatology, *J. Appl. Meteorol. Climatol.* **47**(12), 3221–3235 (2008)
- 32.31 D.S. Zrnić: Spectral moment estimates from correlated pulse pairs, *IEEE Trans. Aerosp. Electron. Syst.* **13**(4), 344–345 (1977)
- 32.32 M.D. Shupe, P. Kollias, S.Y. Matrosov, T.L. Schneider: Deriving mixed-phase cloud properties from Doppler radar spectra, *J. Atmos. Ocean. Technol.* **21**(4), 660–670 (2004)
- 32.33 E.P. Luke, P. Kollias: Separating cloud and drizzle radar moments during precipitation onset using Doppler spectra, *J. Atmos. Ocean. Technol.* **30**(8), 1656–1671 (2013)
- 32.34 P. Borque, E. Luke, P. Kollias: On the unified estimation of turbulence eddy dissipation rate using Doppler cloud radars and lidars, *J. Geophys. Res. Atmos.* **121**(10), 5972–5989 (2016)
- 32.35 M. Maahn, U. Löhnert: Potential of higher order moments of the radar Doppler spectrum for retrieving microphysical and kinematic properties of

- Arctic ice clouds, *J. Appl. Meteorol. Climatol.* **56**(2), 263–282 (2017)
- 32.36 R. Lhermitte: Observation of rain at vertical incidence with a 94 GHz Doppler radar, an insight on Mie scattering, *Geophys. Res. Lett.* **15**(10), 1125–1128 (1988)
- 32.37 M.R. Bauer-Pfundstein, U. GÖrsdorf: Target separation and classification using cloud radar Doppler spectra. In: *33rd Int. Conf. Radar Meteorol., Cairns* (2007), 11B.2
- 32.38 A. Myagkov, P. Seifert, M. Bauer-Pfundstein, U. Wandinger: Cloud radar with hybrid mode towards estimation of shape and orientation of ice crystals, *Atmos. Meas. Tech.* **9**(2), 469–489 (2016)
- 32.39 A. Myagkov, P. Seifert, U. Wandinger, J. Bühl, R. Engelmann: Relationship between temperature and apparent shape of pristine ice crystals derived from polarimetric cloud radar observations during the ACCEPT campaign, *Atmos. Meas. Tech.* **9**(8), 3739–3754 (2016)
- 32.40 E. Schanda: *Remote Sensing for Environmental Sciences* (Springer, Berlin, Heidelberg, New York 1976)
- 32.41 J.S. Marshall, W.M. Palmer: The distribution of raindrops with size, *J. Meteorol.* **5**, 165–166 (1948)
- 32.42 R.J. Hogan, N. Gaussiat, A.J. Illingworth: Stratocumulus liquid water content from dual-wavelength radar, *J. Atmos. Ocean. Technol.* **22**(8), 1207–1218 (2005)
- 32.43 R.J. Hogan, A.J. Illingworth, H. Sauvageot: Measuring crystal size in cirrus using 35- and 94-GHz radars, *J. Atmos. Ocean. Technol.* **17**(1), 27–37 (2000)
- 32.44 L. Liao, R. Meneghini, A. Tokay, L.F. Bliven: Retrieval of snow properties for Ku- and Ka-band dual-frequency radar, *J. Appl. Meteorol. Climatol.* **55**(9), 1845–1858 (2016)
- 32.45 F. Tridon, A. Battaglia, E. Luke, P. Kollias: Rain retrieval from dual-frequency radar Doppler spectra: Validation and potential for a midlatitude precipitating case-study, *Q. J. R. Meteorol. Soc.* **143**(704), 1364–1380 (2017)
- 32.46 R. Lhermitte: Attenuation and scattering of millimeter wavelength radiation by clouds and precipitation, *J. Atmos. Ocean. Technol.* **7**(3), 464–479 (1990)
- 32.47 F. Tridon, A. Battaglia: Dual-frequency radar Doppler spectral retrieval of rain drop size distributions and entangled dynamics variables, *J. Geophys. Res. Atmos.* **120**(11), 5585–5601 (2015)
- 32.48 S. Kneifel, M.S. Kulie, R. Bennartz: A triple-frequency approach to retrieve microphysical snowfall parameters, *J. Geophys. Res.* **116**(D11), D11203 (2011)
- 32.49 S. Kneifel, A. von Lerber, J. Tiira, D. Moisseev, P. Kollias, J. Leinonen: Observed relations between snowfall microphysics and triple-frequency radar measurements, *J. Geophys. Res. Atmos.* **120**(12), 6034–6055 (2015)
- 32.50 S. Kneifel, P. Kollias, A. Battaglia, J. Leinonen, M. Maahn, H. Kalesse, F. Tridon: First observations of triple-frequency radar Doppler spectra in snowfall: Interpretation and applications, *Geophys. Res. Lett.* **43**(5), 2225–2233 (2016)
- 32.51 J. Leinonen, D. Moisseev: What do triple-frequency radar signatures reveal about aggregate snowflakes?, *J. Geophys. Res. Atmos.* **120**(1), 229–239 (2015)
- 32.52 J. Leinonen, W. Szyrmer: Radar signatures of snowflake riming: A modeling study, *Earth Space Sci.* **2**(8), 346–358 (2015)
- 32.53 J. Dias Neto, S. Kneifel, D. Ori, S. Trömel, J. Handwerker, B. Bohn, N. Hermes, K. Mühlbauer, M. Lenefer, C. Simmer: The triple-frequency and polarimetric radar experiment for improving process observations of winter precipitation, *Earth Syst. Sci. Data* **11**(2), 845–863 (2019)
- 32.54 A.S. Frisch, C.W. Fairall, J.B. Snider: Measurement of stratus cloud and drizzle parameters in ASTEX with a Ka-band Doppler radar and a microwave radiometer, *J. Atmos. Sci.* **52**(16), 2788–2799 (1995)
- 32.55 M.K. Politovich, B.B. Stankov, B.E. Martner: Determination of liquid water altitudes using combined remote sensors, *J. Appl. Meteorol.* **34**(9), 2060–2075 (1995)
- 32.56 U. Löhnert, S. Crewell, C. Simmer: An integrated approach toward retrieving physically consistent profiles of temperature, humidity, and cloud liquid water, *J. Appl. Meteorol.* **43**(9), 1295–1307 (2004)
- 32.57 A.J. Illingworth, R.J. Hogan, E.J. O'Connor, D. Bouniol, M.E. Brooks, J. Delanoé, D.P. Donovan, J.D. Eastment, N. Gaussiat, J.W.F. Goddard, M. Haefelin, H. Klein Baltink, O.A. Krasnov, J. Pelon, J.-M. Piriou, A. Protat, H.W.J. Russchenberg, A. Seifert, A.M. Tompkins, G.-J. van Zadelhoff, F. Vinit, U. Willén, D.R. Wilson, C.L. Wrench: Cloudnet: Continuous evaluation of cloud profiles in seven operational models using ground-based observations, *Bull. Am. Meteorol. Soc.* **88**(6), 883–898 (2007)
- 32.58 J. Bühl, P. Seifert, A. Myagkov, A. Ansmann: Measuring ice- and liquid-water properties in mixed-phase cloud layers at the Leipzig Cloudnet station, *Atmos. Chem. Phys.* **16**(16), 10609–10620 (2016)
- 32.59 U. GÖrsdorf, V. Lehmann, M.G. Bauer-Pfundstein, G. Peters, D. Vavriv, V. Vinogradov, V. Volkov: A 35-GHz polarimetric Doppler radar for long-term observations of cloud parameters – Description of system and data processing, *J. Atmos. Ocean. Technol.* **32**(4), 675–690 (2015)
- 32.60 N. Bharadwaj, V. Chandrasekar: Wideband waveform design principles for solid-state weather radars, *J. Atmos. Ocean. Technol.* **29**(1), 14–31 (2012)
- 32.61 G. Peters, B. Fischer, H. Münster, M. Clemens, A. Wagner: Profiles of raindrop size distributions as retrieved by microrain radars, *J. Appl. Meteorol.* **44**(12), 1930–1949 (2005)
- 32.62 N. Küchler, S. Kneifel, U. Löhnert, P. Kollias, H. Czekala, T. Rose: A W-band radar-radiometer system for accurate and continuous monitoring of clouds and precipitation, *J. Atmos. Ocean. Technol.* **34**(11), 2375–2392 (2017)
- 32.63 N. Bharadwaj, K.B. Widener, K.L. Johnson, S. Collis, A. Koontz: ARM radar infrastructure for global and regional climate study. In: *35th Conf. Radar Meteorol., Pittsburgh* (2011)

- 32.64 METEK: Micro Rain Radar MRR-PRO, http://metek.de/de/wp-content/uploads/sites/6/2018/01/20180206_Datenblatt_MRR-PRO.pdf (2018), Accessed 11 July 2021
- 32.65 A. Protat, D. Bouniol, E.J. O'Connor, H. Klein Baltink, J. Verlinde, K. Widener: *CloudSat* as a global radar calibrator, *J. Atmos. Ocean. Technol.* **28**(3), 445–452 (2011)
- 32.66 A. Battaglia, C.D. Westbrook, S. Kneifel, P. Kollias, N. Humpage, U. Löhnert, J. Tyynelä, G.W. Petty: G band atmospheric radars: New frontiers in cloud physics, *Atmos. Meas. Tech.* **7**(6), 1527–1546 (2014)
- 32.67 R.J. Roy, M. Lebsock, L. Millán, R. Dengler, R. Rodriguez Monje, J.V. Siles, K.B. Cooper: Boundary-layer water vapor profiling using differential absorption radar, *Atmos. Meas. Tech.* **11**(12), 6511–6523 (2018)

Gerhard Peters

Metek, Meteorologische Messtechnik
GmbH
Elmshorn, Germany
peters@metek.de



Dr Gerhard Peters has been R&D consultant at METEK GmbH since his retirement from the University Hamburg in 2010. He received a PhD in Geophysics in 1978. He has developed ground-based remote-sensing methods for the atmosphere, participated in numerous field projects dealing with the arctic and maritime boundary layer, and contributed to VDI and ISO standards for measuring meteorological variables.

High Frequency Radar

33. High Frequency Radar

Jochen Horstmann , Anna Dzvонkovskaya 

High frequency (HF) radars operate at radio frequencies between 3 and 30 MHz, where electromagnetic waves have the ability to propagate along the ocean surface and therefore to obtain information beyond the horizon. All the information measured by a HF radar corresponds to physical parameters of the upper couple of meters of the ocean surface. Today, HF radar systems are typically used along the coast, as they offer the unique opportunity to monitor the coastal area within a distance of 40–200 km. A HF radar system transmits electromagnetic waves and measures the backscatter intensity and speed of ocean waves. This information is primarily used to estimate surface currents and ocean wave properties. However, in the last decade, HF radars have also been shown to be extremely useful for several other applications such as surface wind measurements and tsunami monitoring, as well as vessel traffic support.

33.1	Measurement Principles and Parameters	953
33.2	History	954
33.3	Theory	955
33.4	Devices and Systems	956
33.5	Specifications	959
33.6	Quality Control	961
33.7	Maintenance	961
33.8	Applications	962
33.8.1	Surface Wind Measurements.....	962
33.8.2	Waves	963
33.8.3	Surface Currents	963
33.9	Future Developments	965
33.10	Further Reading	965
	References	965

With respect to the atmosphere, HF radars give a direct measure of the upper ocean response to lower marine atmospheric boundary layer forcing, and therefore the air–sea interaction. In this context, the main parameters retrieved from HF radar measurements are surface winds [33.1, 2], the sea state [33.3, 4], surface currents [33.5, 6], and tsunamis [33.7, 8]. Today, they

are utilized for the coastal monitoring of these parameters [33.9, 10], the short-term prediction of surface currents [33.11], search and rescue operations [33.12], and oil spill monitoring [33.13], as well as for the improvement and data assimilation of numerical circulation models [33.14, 15].

33.1 Measurement Principles and Parameters

HF radar systems utilize radio frequency transmission between 3 and 30 MHz, which correspond to electromagnetic wavelengths between 100 and 10 m. The electromagnetic waves are transmitted from an antenna, propagate as a ground wave along the electrically conductive ocean surface, and enable the measurement of radar backscatter beyond the line of sight. Therefore, these radars can measure the surface beyond the hori-

zon, which is why they are also named over-the-horizon radars. To first order, the transmitted radio waves are resonantly backscattered by ocean surface waves that are propagating along the radar look direction and have a wavelength equal to half the electromagnetic wavelength. These so-called Bragg waves lead to Doppler shifts, resulting in first-order and second-order peaks in the backscatter frequency spectrum. The measured

Table 33.1 Main parameters extracted from HF radar measurements

Parameter	Description	Unit	Symbol
Current speed	Current speed at the ocean surface	m s^{-1}	v
Current direction	Current direction at the ocean surface	$^{\circ}$	Φ_c
Wind speed	Wind speed at the ocean surface (similar to a 10 min mean wind speed at 10 m height)	m s^{-1}	u_{10}
Wind direction	Wind direction at the ocean surface (similar to a 10 min mean wind speed at 10 m height)	$^{\circ}$	Φ_w
Significant wave height	Mean wave height (trough to crest) of the highest third of the waves (defined as four times the standard deviation of the surface elevation)	m	H_S
Tsunami probability	Probability of a tsunami	%	

frequency spectrum is analyzed with respect to the location and shape of these peaks, allowing the retrieval of the parameters listed in Table 33.1.

Since a radar can measure the distance and angle to an ocean wave patch, it becomes possible to generate a map within the radar-covered range and azimuth (radar look directions) and obtain the frequency spectra at each grid point. The simplest way of measuring the range distance with a radar is to measure the time difference between the transmitted and received signals. To obtain high range resolution, a short pulse is needed, which in turn leads to a decrease in range. Therefore, the transmitted power has to be increased in order to get a sufficient signal-to-noise ratio, in particular at longer ranges. To overcome this drawback, HF radars transmit a linear chirped signal, where the frequency shift between the transmitted and received signals contains the distance information. With this chirped signal, also named frequency-modulated continuous wave (FMCW), the range resolution is related to the frequency bandwidth of the chirp and is independent of the transmitted power. Alternatively, the HF radar can be operated with a frequency-modulated interrupted continuous wave (FMICW). With the latter concept, the transmitter is switched off during the reception phase of the backscattered signal and operation is similar to that of a pulsed radar. If the transmit and receive anten-

nas are too close to each other, the transmitting antenna can saturate the receive antennas even before the signal reflected from the ocean arrives. Turning off the transmit antennas after one chirp, as in a pulsed radar, will prohibit this saturation and allow a smaller separation distance between the transmit and receive antennas. However, turning off the transmitter during the reception time also reduces the amount of transmitted energy and therefore the energy content of the received echo signals, which in turn reduces the maximum range distance of the radar. To get azimuthal coverage over the ocean surface, it is necessary to point the radar in different azimuth directions. Several systems for resolving the azimuth direction of the radar have been developed, which will be introduced in Sect. 33.4.

The measured frequency spectrum of the sea echoes at every range–azimuth grid point is subjected to a comprehensive spectral analysis to extract meteorological and oceanographic parameters. Today, HF radars are operationally utilized to measure ocean surface current fields [33.16, 17]. However, they have also been shown to be useful for measuring ocean wave parameters such as the wave spectrum [33.3] and the significant wave height [33.18] as well as surface winds [33.19]. Furthermore, they have been shown to be valuable for the detection of tsunami [33.20, 21] as well as for maritime surveillance [33.22, 23].

33.2 History

The era of HF radar for meteorological and oceanographic applications started in 1955 with *D.D. Crombie* [33.24], who observed Doppler shifts of the returned signal from the ocean surface with respect to that transmitted at HF frequency (3–30 MHz). The reproduction and analysis of the signal spectrum showed two narrow resonant peaks that corresponded to the ocean waves, had exactly half the radio wavelength, and moved along the radar look direction. A tentative explanation of these peaks included an assumption that the sea waves acted as a diffraction grating containing several wave crests. This occurrence was

later called resonant Bragg scattering, following the discovery of the scattering of x-rays in crystals by the English physicist *William Lawrence Bragg* (1890–1971) [33.25]. In 1966, Crombie's observations were analytically verified by examining the reflection of electromagnetic waves from a gently rippled ocean surface [33.26]. In 1972, *Donald E. Barrick* [33.27] derived a model for the first-order radar cross-section of the ocean surface that is consistent with *Crombie's* observations, and he presented the first surface current maps in 1977 [33.28]. In addition to surface currents, it was found that the HF radar backscatter can be used

to extract information on the wind [33.29] and sea state [33.30].

The first commercial HF radar was the Coastal Ocean Dynamics Applications Radar (CODAR) system introduced in 1977 at the National Oceanic and Atmospheric Administration (NOAA), USA [33.28]. This groundwave radar system was initially designed for the mapping of ocean surface current fields. The overall advantages and disadvantages of the system have been examined over the years, and many new ideas were

33.3 Theory

When the sea surface is illuminated by a HF radar, a portion of the incident energy is backscattered from the ocean surface waves that are propagating along the radar look direction. When the wavelength λ_{gr} of the ocean gravity wave is equivalent to half the transmitted electromagnetic wavelength λ_{el} , the so-called Bragg resonance phenomenon occurs [33.25] (echoes from successive crests of this oscillation are in phase). Ocean waves leading to Bragg resonant scattering are therefore called Bragg waves.

In deep water, the phase velocity of surface gravity waves is given by

$$C_p = \sqrt{\frac{g\lambda_{gr}}{2\pi}}, \quad (33.1)$$

where g is the acceleration due to gravity and λ_{gr} is the wavelength of the surface gravity wave.

The roughness of the ocean surface is a combination of waves of different wavelengths and directions. When the radar operates at different frequencies, the corresponding Bragg wavelength varies as well. Thus, if $\lambda_{gr} = \lambda_{el}/2$, a resonance Bragg frequency appears, which is defined as

$$f_{Bragg} = \pm \sqrt{\frac{g}{\pi\lambda_{el}}}, \quad (33.2)$$

where a positive Bragg frequency is associated with waves propagating radially towards the radar and a negative Bragg frequency is associated with waves propagating away from the radar.

Spectral analysis of the backscattered signal results in a Doppler frequency spectrum, as depicted in Fig. 33.1. In the Doppler frequency spectrum, the Bragg waves lead to Doppler shifts (33.2) that show up as two predominant peaks, the so-called first-order peaks. In the absence of currents, the frequency of the first-order

developed. These resulted in the development of the Ocean Surface Current Radar (OSCR) by Marconi in the United Kingdom [33.31], the SeaSonde by CODAR in the USA, and the Wellen Radar (WERA) by the University of Hamburg, Germany [33.6]. Developments independent of the first CODAR were made in Canada in 1991 (C-CORE (Centre for Cold Ocean Resources Engineering) Northern Radar), the UK in 1988 (University of Birmingham, PISCES), France in 1990 (University of Toulon), as well as in Australia and Japan.

peak has a Doppler shift caused by the phase velocity of Bragg waves (33.1) in the radial direction of the transmitting antenna (the radar look direction). In the presence of a surface current along the radar look direction, the first-order peaks are shifted with respect to the transmitting frequency. To determine the current velocity, it is necessary to find the central frequency of the two Bragg peaks. From the frequency shift, the radial current velocity can be calculated as

$$v_r = (f_o - f_{Bragg}) \frac{\lambda_{el}}{2}, \quad (33.3)$$

where f_o is the observed resonant frequency in the radar spectra.

The surface current estimated by HF radars has been suggested to include all or part of the wave-induced Stokes drift [33.32–35]; however, other researchers

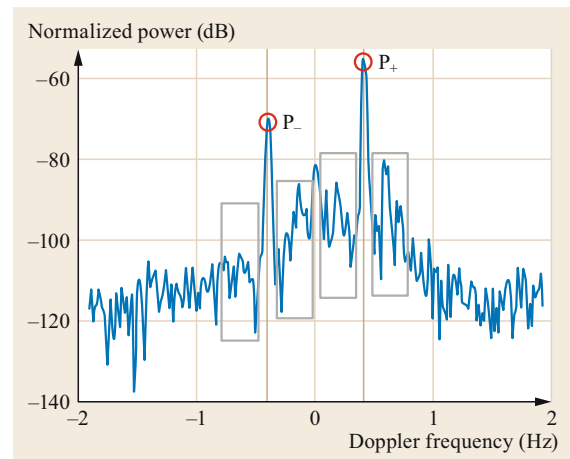


Fig. 33.1 Normalized measured HF Doppler frequency spectrum for a selected range-azimuth cell. First-order peaks P_+ and P_- (red circles) and the second-order return (gray boxes) are indicated

have provided evidence against this assumption [33.36]. In any case, the magnitude of this component is typically smaller than the uncertainties in the HF-radar-retrieved surface currents [33.34, 37].

To obtain highly accurate radial velocities, a high-resolution frequency spectrum has to be measured by the HF radar. This is achieved by repeating the range measurements at a regular rate and performing a time-series analysis of each individual range measurement. The coherent integration time t provides a Doppler frequency resolution of $\Delta f_D = 1/t$, which consequently gives a velocity resolution of $\Delta v = \Delta f_D \lambda_{el}/2$. Due to its long integration time, an ocean radar is capable of measuring a radial velocity of a few centimeters per second.

As mentioned before, the positive first-order peak is associated with waves approaching the radar site, whereas the negative first-order peak is associated with waves receding from the radar site. The amplitudes of these peaks are directly related to the energy within the approaching and receding wave components. Under the assumption that the Bragg waves are locally wind driven and aligned with the wind, the relative ratio of the two first-order peaks contains information on the wind direction [33.37],

$$\frac{P_+}{P_-} = \tan^s \left(\frac{\beta}{2} \right), \quad (33.4)$$

where β is the angle between the wind direction and the receding Bragg waves and s is the spreading parameter (commonly, $s = 4$). Given the radar beam direction Φ , the wind at a selected grid point and the directional spreading pattern of the Bragg waves determine the strengths of the wave components receding from and approaching the radar site; hence, the wind direction Φ_w

is calculated via

$$\Phi_w = \Phi \pm \beta. \quad (33.5)$$

Several different models are available for extracting wind directions from HF radar backscatter. However, all of them require the power ratio of the two first-order peaks (33.4) combined with a directional distribution function for the Bragg waves. Although details of the various techniques differ, the principle is well established. However, most researchers simplify the calculation by setting the directional spreading parameter s to be a constant value.

Bragg scattering also leads to the second-order return in the radar frequency spectrum (Fig. 33.1). However, within these bands, the backscatter is from nonlinear ocean waves, which propagate at different speeds and hence result in different Doppler shifts. In addition, the second-order return contains backscatter from multiple surface scattering. Therefore, the second-order return is proportional to the wave-height nondirectional temporal spectrum [33.30]. A solution to this scattering problem has been given in the form of a two-dimensional nonlinear integral equation based on a perturbation expansion and the assumption that the sea surface is a perfect conductor [33.38, 39]. By inverting this integral equation, a two-dimensional wave height spectrum can be obtained from the HF-radar measurements [33.3, 40]. A further approach is based on an empirically obtained power law relating the wave height (e.g., as measured by a buoy) to the ratio of the power in the second-order return to that of the stronger first-order peak [33.41]. Other researchers have performed similar empirical approaches [33.4, 42] that, in general, relate the amplitude of the second-order return to wave buoy measurements.

33.4 Devices and Systems

The simplest antenna system is a phased array consisting of identical receiving elements spaced equal distances ($\leq \lambda_{el}/2$) along a line perpendicular to the center of the desired look directions [33.6]. The time delay between antennas on the receive array is used to sequentially point the radar in different directions. An alternative to the beamforming method is the so-called direction-finding technique [33.43]. It is based on comparing the relative amplitudes of the returned energy on the collocated antennas. When the beam pattern of each antenna is known, the direction of the received signal can be retrieved via the ratio of the antenna signal strengths. In contrast to the phased-array method,

where a sequential set of spectra are used to get information over the azimuth, a single combined spectrum is utilized in the direction-finding method.

Conventional beamforming is usually applied in HF radar systems where receive antennas are operated as uniform linear arrays of antenna elements, for example, WERA ocean radar systems [33.6]. After the received signal has undergone down conversion and fast Fourier transformation (FFT), the time delays between antenna elements are phase shifted. To maximize the output power from a certain direction Φ , the weighted signal at each array element is summed to steer a narrow beam in a desired direction, so that signals from partic-

Table 33.2 HF radar systems and the techniques utilized to obtain the range and azimuth of the sea echo

HF radar system	Range Radar waveform	Angle	
		Direction finding	Beamforming
CODAR/NOAA [33.28]	Pulse	+	–
CoSRad (Colorado software radar) [33.44]	Pulse	–	+
PISCES [33.45]	FMCW	–	+
OSCR [33.46]	Pulse	–	+
C-CORE [33.47]	FMCW	–	+
SeaSonde [33.48]	FMCW	+	–
WERA [33.6]	FMCW	+	+
LERA (least expensive radar)	FMCW	+	+

ular directions sum constructively while signals from other directions sum destructively. The weighted and summed signal $S(\Phi)$ for the azimuthal look direction Φ is given by

$$S(\Phi) = a(C)^H x, \\ a(\Phi) = \left[1 e^{-ik_{el}d \sin(\Phi)} \dots e^{-ik_{el}d(N-1) \sin(\Phi)} \right]^T, \quad (33.6)$$

where x is the fast-Fourier-transformed vector signal of the antenna elements, d is the spacing between antenna elements, and N is the total number of elements in the uniform linear array. The term H represents the conjugate transpose and $a(\Phi)$ is the steering vector with the beamformer weights equal to the inner product of the steering vector and the gain function of each antenna element. Sidelobes of the formed beam are generally reduced at the expense of beamwidth through the application of an amplitude taper over the elements, e.g., the Hamming window function.

Here, the classical spatial beamformed spectrum is obtained as

$$P(\Phi) = S(\Phi)S^H(\Phi), \quad (33.7)$$

and its local maxima yield the directions of incoming signals.

Direction-finding systems utilize a direction of arrival determination algorithm, e.g., Multiple Signal Classification (MUSIC) [33.44], which has been widely investigated in conjunction with antennas with a compact configuration (typically a single antenna) such as the Coastal Ocean Dynamics Applications Radar (CODAR) [33.43]. The CODAR system consists of two collocated cross-loop antennas and one monopole antenna. Antenna patterns of each element are utilized that can distinguish the directions of the incoming signals. The MUSIC algorithm determines the signal space (assuming the number of signal arrival directions is M) by diagonalizing the covariance matrix formed by the measured signals at each antenna. Projecting all the bearings associated with a particular range cell onto the

signal space allows the most likely bearing of the signal to be determined. In practice, an estimate of the covariance matrix of measurements is obtained and split into the signal and noise eigenvectors U_s and U_n , respectively. The orthogonal projector onto the noise subspace defines the MUSIC *spatial spectrum* as

$$P(\Phi) = \frac{a^H(\Phi)a(\Phi)}{a^H(\Phi)U_n U_n^H a(\Phi)}. \quad (33.8)$$

The main disadvantage of MUSIC is that it requires the number of signal components M to be known in advance, so the original method cannot be used in more general cases. The number of source components M is estimated from the statistical properties of the autocorrelation matrix under the assumption that coexistent sources are not correlated. For HF-radar surface sensing, the number of signal components for current estimation is usually assumed to be less than three, which means that the number of Doppler spectra to be averaged must be at least three.

The major HF radar developments that are being utilized in oceanography today are listed in Table 33.2, together with operational concepts—the waveform utilized to obtain a large range with high resolution and the techniques applied to obtain the azimuth direction of the sea echo return.

Phased-array and direction-finding systems differ significantly in antenna design and setup. Figure 33.2 shows a typical setup of a phased-array system on the island of Wangerooge in the North Sea off the German coast, which consists of a transmit (Tx) and a receive (Rx) antenna array. Each individual antenna is a pole with a height that typically varies from 1 to 3 m depending on the manufacturer and the transmission frequency utilized. The Tx array consists of 4 antennas, which are set up in a rectangle ($0.45\lambda_{el} \times 0.15\lambda_{el}$) with a distance of at least 100 m to the Rx array. The Rx array extends over a distance of $0.45\lambda_{el}(n-1)$, where n is the number of antennas. Distances below $0.5\lambda_{el}$ are preferably used to reduce the effect of side lobes. Typical Rx setups include between 8 and 16 antennas; increasing the number of

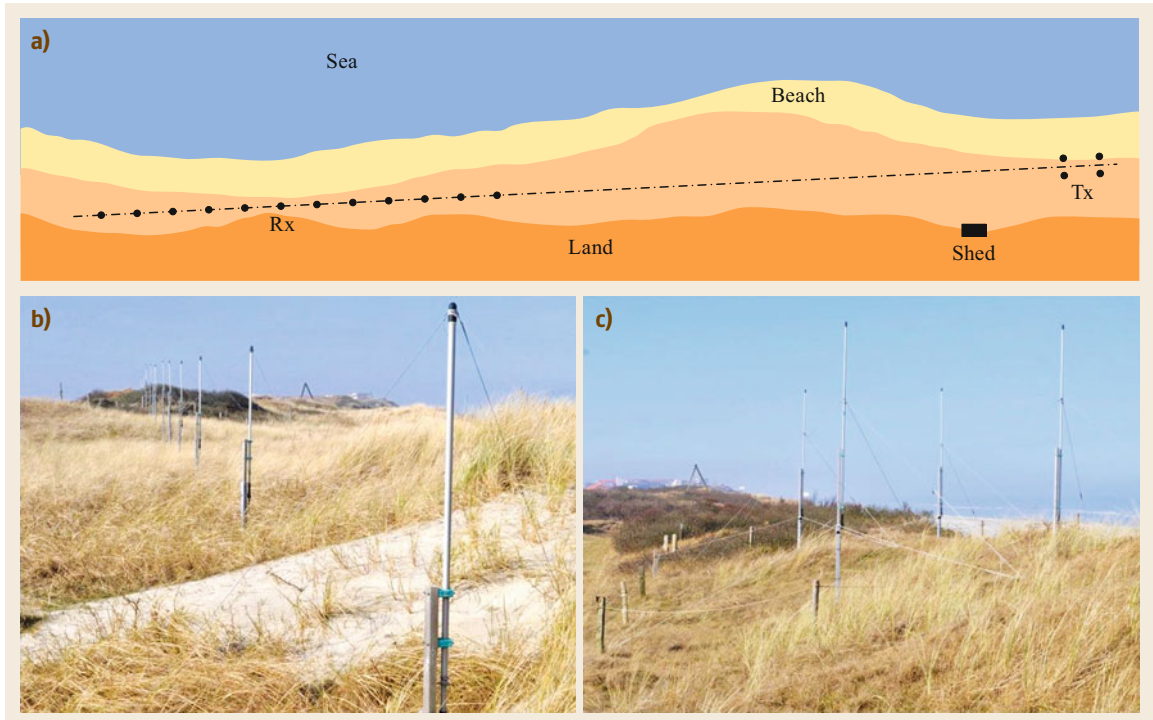


Fig. 33.2a–c Typical setup of a phased-array system (a). The photos show a phased-array setup of a WERA system on the island of Wangerooge in the North Sea off the German coast: (b) receive array (Rx) and (c) transmitter antenna array (Tx)

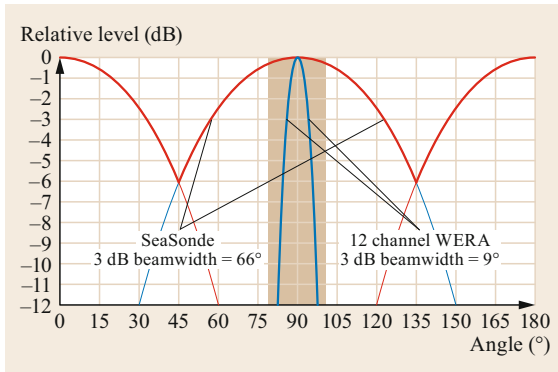


Fig. 33.3 Antenna beam patterns for a 12-element phased array with 0.45λ spacing (blue line) and a crossed-loop antenna (\sin^2 and \cos^2 function, red line)

antennas leads to higher azimuthal resolution. A phased-array antenna array consisting of 12 antenna elements spaced $0.45\lambda_{el}$ apart forms a beam width of 9° (at 3 db), while the beam pattern of a crossed-dipole antenna has a beam width of 66° (at 3 db), as shown in Fig. 33.3.

Figure 33.4 depicts the setup of a direction-finding system that consists of one Tx antenna (or two for larger ranges). The antenna length is between 8 and 15 m (de-

pending on the radar frequency) and one Rx antenna system typically separated by 80 m. The receive antenna system consists of one dome loopstick antenna unit and a vertical element with a total height of approximately 7 m. Some systems operating at shorter wavelengths (above 24 MHz) use a single-pole antenna system that combines the Tx and Rx antennas. The older direction-finding systems operate with four antennas set up in a rectangle, similar to the Tx of a phased-array system. The photo in Fig. 33.4b shows the main antenna of a SeaSonde system operating at 4.5 MHz, which is part of the Basque Operational Oceanography System (EUSKOOS) HF-Radar system at Cape Matxitxako (northern coast of Spain), operated by Basque Meteorological Agency (EUSKALMET).

A phased-array system requires a significant property for installation. However, since each backscattered power spectrum is from a single range–azimuth cell (the range and azimuth resolutions are determined by radar parameters), it is a straightforward measurement. Direction-finding systems require only a very small property, but the use of direction-finding methods can lead to limitations; for instance, if two different surface current patterns are located within one range cell and their components in the direction to the radar hap-

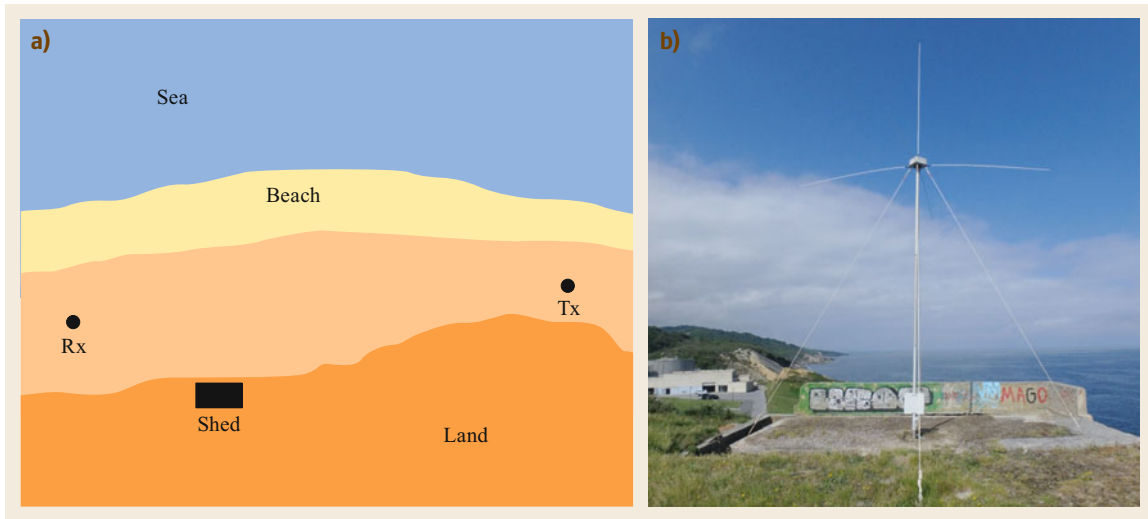


Fig. 33.4 (a) A typical setup of a direction-finding HF radar system. (b) This photo shows a direction-finding system from SeaSonde installed at Cape Matxitxako (northern coast of Spain). This system is one of the two EUSKOOS HF radars that were set up in 2009 to monitor sea surface currents within the coastal area of the Spanish Basque Country (photo courtesy of AZTI Marine Research)

pen to be equal. The spectra for compact systems are from separate range cells but contain information from all directions simultaneously. Current measurements are resolved using direction-finding techniques, and better directional accuracy can be achieved. However, longer integration times (about an hour) are usually required to gather current data covering the whole area of interest using such methods. This can become a problem in rapidly varying marine environments. Furthermore, at higher radio frequencies and higher wave heights, the resonant peaks used for both current and wind measurements are less easily separated from the second-order return of the spectra, which yields the sea state information. This is likely to be a more serious problem with a direction-finding system, but it can be solved by operating the radar at lower frequencies. For more details on the pro and cons of the different systems, refer to [33.49].

HF radars can measure surface winds, waves, and currents spatially and temporally, while most other in-

struments can only obtain point measurements, albeit typically with higher accuracy. With respect to surface winds, only satellite-borne scatterometers [33.50], synthetic aperture radars [33.51], and platform-based marine radars [33.52] enable the measurement of two-dimensional surface wind fields. All other instruments typically measure a profile or at a single point over time. With respect to waves, there are a few systems that allow the two-dimensional wave field information to be measured. Those systems are either based on radars [33.53] or light detection and ranging (lidar) technology [33.54]. The main application of HF radar is the measurement of two-dimensional surface current fields over time. So far, only systems with significantly smaller spatial coverage, such as marine radars [33.55] or a video-based system [33.56], have given results of similar quality. However, a lot of effort goes into the development of satellite-based radar systems for obtaining surface currents [33.57].

33.5 Specifications

The working range of a HF radar depends on the attenuation of the electromagnetic wave between the transmitter and surface scatter elements and on the noise, such as that due to the atmosphere or radio interference. The operating range of groundwave-based HF radar systems is strongly dependent on the transmitted frequency and the conductivity (salinity) of the seawater.

High salinity results in high conductivity and therefore optimum range performance, while strong attenuation limits the use of HF radars for remote sensing, particularly in freshwater lakes and over ice-covered areas. In Fig. 33.5, the working ranges for a beamforming system with respect to surface current retrieval are shown as functions of the radar frequency and the water salin-

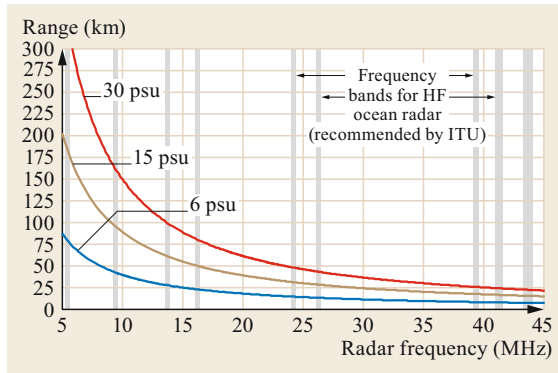


Fig. 33.5 Dependence of the maximum working range for surface current measurements by a typical beamforming system on the radar frequency and water salinity. The ranges for a direction-finding system are approximately 75% of those for a beamforming system if both systems utilize the same transmission frequency and sampling time. Data are valid for a phased-array-type WERA

Table 33.3 Typical specifications for a phased-array HF radar system operating at 16 and 24/26 MHz

Operating frequency (MHz)	16	24/26
Working ranges (km) using beamforming for:		
– Currents	80	50
– Wind direction	55	35
– Wave height	35	20
– Wave spectrum	25	15
Typical range (km) resolution	1.5	1.0
Azimuthal accuracy (°) using beamforming:		
– 4 antennas	±5	±5
– 8 antennas	±2	±2
– 16 antennas	±1	±1
Temporal resolution (min) for:		
– Currents	5–10	5–10
– Wind	5–10	5–10
– Waves	20	20

ity. The ranges for wind retrieval are between 25–100% of those ranges, depending on the local wind direction with respect to the radar look direction. The range for wave measurements is approximately 50% of that shown in Fig. 33.5. The working ranges for direction-

finding systems with the same operating frequency are approximately 75% of those of beamforming systems. Typical specifications for beamforming HF radar systems are listed in Table 33.3.

The availability of different types of HF radar systems allows the marine science and engineering community to select the system that best covers their needs with respect to the characteristics of the area, the parameters to be measured, and the required performance. Direction-finding systems require a significantly smaller antenna footprint and offer, due to their full azimuthal coverage, the option of chaining stations to achieve continuous coverage along a coastline. However, these benefits come at the cost of a reduced operating range as well as coarser azimuthal and temporal resolution [33.49].

Furthermore, direction-finding systems are more sensitive to atmospheric noise, necessitating longer time integration (≈ 90 min) to achieve a similar working range to phased-array systems. In addition, the direction-finding algorithm has a coarser azimuth resolution (18°). However, the main disadvantage of direction-finding systems relates to the extraction of sea state information, as first-order peaks associated with other directions mask the second-order return in certain directions. Another disadvantage arises from the assumption that different radial velocities come from different directions (with respect to the radar), which is invalid in the case of a current field that varies strongly at subradar resolution. Phased-array HF radars have a lower-noise antenna system that, for the same operating range, offers a higher temporal resolution (≈ 5 – 10 min) and, in the case of an 16-element receive array, has a higher azimuthal resolution ($\pm 4^\circ$ for a 16-element array).

The accuracies of the parameters retrieved with HF radar, e.g., wind, waves, and currents, are strongly dependent on the environmental conditions, on the HF radar frequency utilized, as well as on the setup system. Typical accuracies of beamforming systems are listed in Table 33.4. For details on the performance of an individual radar system at a specified operating frequency, please refer to the manufacturer’s specifications and scientific literature.

Table 33.4 Typical accuracies of HF radar systems operating at 16 and 24/26 MHz

Operating frequency (MHz)	16	24/26
Radial surface current speed ($m\ s^{-1}$)	0.04	0.03
Wind direction (°)	10–40 (depends on wind speed)	10–40 (depends on wind speed)
Wave height (%)	< 10	< 10
Mean wave direction (°)	< 5	< 5
Mean wave period (s)	±1.1	< ±0.6
Directional wave spectra (Hz)	0.01	0.01
Limits for wave height measurements (m)	0.3–7	0.25–4

33.6 Quality Control

The use of HF radar systems for monitoring ocean surface current fields is now widely accepted; however, quality assessment and control is an area of ongoing research. With respect to the proper technical operation of the system, many internal checks have been designed and implemented by manufacturers to make sure that the measurements are performed by a fully functioning system. However, there are several other sources that can lead to uncertainties in the retrieved parameters. From a technical point of view, these can be simplifications and errors within the analysis, such as a wrong determination of the first-order peaks or the utilization of an incorrect antenna pattern. However, they are most commonly due to noise in the spectral radar data, which can be induced by radio frequency interferences, ship echoes, ionospheric clutter, or other environmental noise induced by power lines or electromagnetic activity. Further sources of error are variations in the current speed or direction within the spatial resolution of the radar as well as variations during the integration time of the measurement. In particular, these

have to be taken into consideration in coastal areas with strongly changing bathymetry or strong tidal currents. One method of identifying such errors is to measure the width of the first-order peak, which will be wider for measurements affected by these variations than for those not affected by such variations [33.58]. Other approaches observe the likelihood of a measurement to be correct with respect to its location (in space and time) as well as with its direct neighborhood (meaning consistency with respect to space and time). Furthermore, there are methods that take into account measurements obtained over a certain amount of time and flag outliers accordingly [33.58]. Over the years, a great number of validation studies have been carried out to estimate the error in HF-radar-retrieved surface currents, and those studies have come up with errors of between 0.08 and 0.15 m s^{-1} [33.17, 59]. This huge span of error estimates is due to differences in radar setups, in particular with respect to frequency, resolution, and location, as well as due to differences in the accuracies of the systems utilized for comparison.

33.7 Maintenance

With respect to maintenance, HF radar systems are fairly easy to deal with. Nevertheless, it is useful to check the status of the system on a daily basis to identify any system components that are failing or degrading, in particular the outdoor components (antenna arrays). In general, HF radar sites operate in a fully automated manner. The systems perform daily self-checks and send reports to the operator (assuming remote access is available). In addition, many of the other units integrated on-site, such as air conditioning, the uninterruptible power supply (UPS), and the backup system, should be checked remotely on a daily basis. Besides the on-site checks, the creation and archiving of files containing results and—if applicable—the functionality of the web server should be investigated daily.

However, these daily checks should not replace on-site inspections and maintenance, which should be performed at least every 3 months. In the case of severe weather events such as strong storms, thunderstorms, or flooding, an immediate on-site visit is highly recommended. Typical on-site maintenance consists of

careful inspection of the antennas with respect to their condition, alignment, mounting, and guying, as well as to check that they are properly connected. The latter includes checking the cables and, in particular, the connection points. If any antenna or cable needs to be repaired or replaced, a new calibration of the antenna array may be required. It is also very helpful to monitor the levels and phase values of all antennas (especially for a phased-array setup), as any changes in these parameters give an indication of problems with the installation, such as bad connectivity of the antenna or broken radials or antennas. Furthermore, in the enclosure (typically a container), the functionality of the air conditioning should be checked, as should the electronics for corrosion, the UPS for battery status and functionality, and the backup systems and their hard drives. However, every individual HF radar system and site has its own characteristics, so each will require an adjusted maintenance plan. Typically, a quarter-yearly check of a 16 antenna phased-array system requires half a day of work, which includes some smaller repairs and adjustments.

33.8 Applications

As mentioned above, HF radars are well suited to monitoring the coastal zone within a range of 40–300 km, depending on their operating frequency. In the following, some examples of the application of HF radars to measuring surface winds, waves, and currents in the coastal zone are given.

33.8.1 Surface Wind Measurements

Although the main application of HF radar is the mapping of surface currents, the ability to map the wind direction at scales of one to several kilometers and over many hundreds [33.1, 2] to millions of square kilometers in the case of skywave HF radars [33.19, 60] offers huge potential. Maps of HF-radar-retrieved wind directions have shown variations in wind direction over horizontal scales of just a few kilometers. This enables the investigation of wind stress divergences and curl, as well as their impacts on coastal mixing and circulation, over time and space at scales on the order of a couple of minutes and kilometers [33.1]. Furthermore, HF-radar-retrieved maps of wind direction can be utilized to detect frontal boundaries (sudden changes in direction) and small-scale storms (e.g., waterspouts, thunderstorms) [33.61]. A typical map of HF-radar-retrieved wind directions is shown in Fig. 33.6. In this case, the wind directions result from simultaneous measurements by the phased-array radar systems located

on Wangerooge (12.1 MHz) and at Büsum (10.8 MHz), both of which are part of the German HF radar network for monitoring the German Bight located in the southern North Sea [33.62]. Note that only wind direction measurements are presented here; however, HF radars have also been shown to resolve information on the wind speed [33.2, 63, 64]. However, there are limitations on the minimum and maximum measured wind speeds and there are large errors in the retrieved wind speeds.

In contrast to ground wave radars, the capabilities of skywave HF radars have been demonstrated through their application to the monitoring of tropical cyclones [33.19, 60]. Two US Air Force over-the-horizon radar systems operating at 15.8 MHz were utilized to monitor large areas of the North Atlantic and northeastern Pacific Ocean. The systems were huge in size; their antenna arrays occupied a few kilometers of coastline. However, their ability to monitor a large portion of the ocean surface was demonstrated by tracking the wind directions of Hurricane Claudette in September 1991 and Hurricane Andrew in August 1992 at a distance of 2400 km [33.60]. Similar observations of Hurricane Hortense were made in September 1996 by a pair of relocatable over-the-horizon radar systems operating at 14.7 and 18.5 MHz. Simultaneous coverage of the area by both radars led to an unambiguous surface wind direction field and a surface current field with a spatial resolution of 15 km over a large portion of the

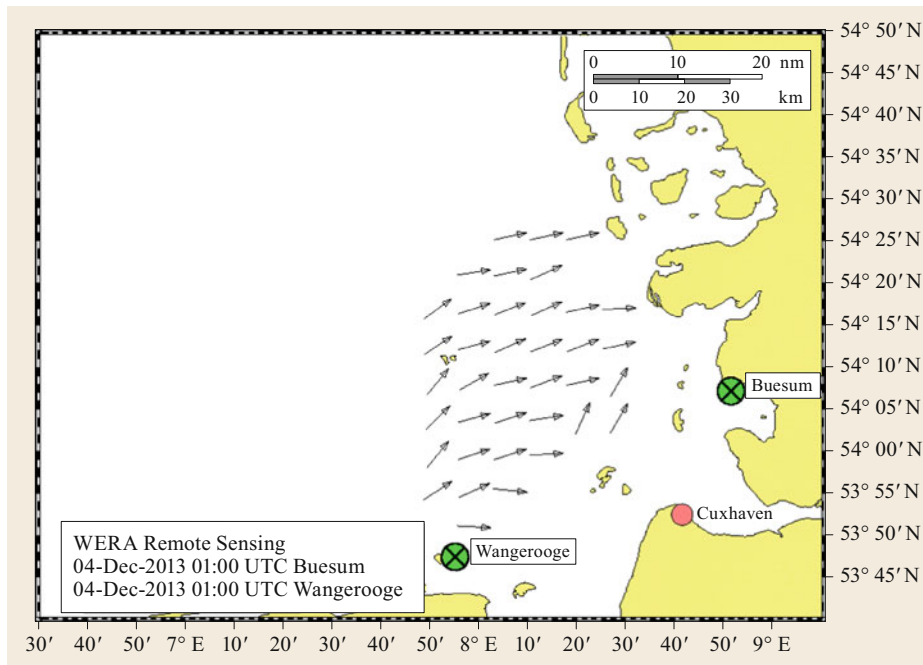


Fig. 33.6 Surface wind directions in the German Bight in the North Sea on December 4, 2013 at 01:00 UTC. The results were obtained from simultaneous measurements by the phased-array systems located on Wangerooge and Büsum, which are part of the German HF radar network for monitoring the German Bight in the North Sea. (© HZG 2018)

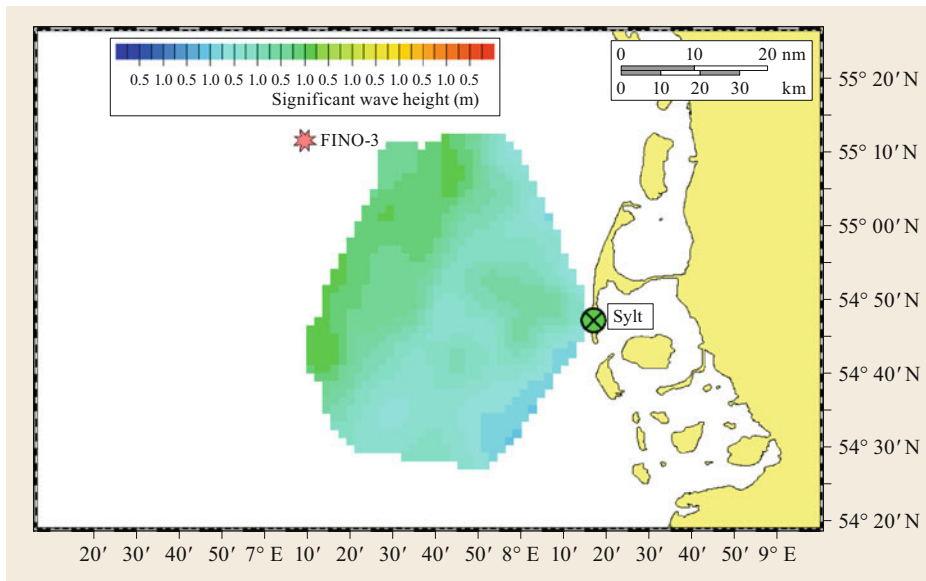


Fig. 33.7 Map of significant wave heights in front of the island of Sylt in the North Sea off the German coast on January 17, 2019 at 13:19 UTC. The results were obtained from measurements from the phased-array systems located on Sylt, which are part of the German HF radar network

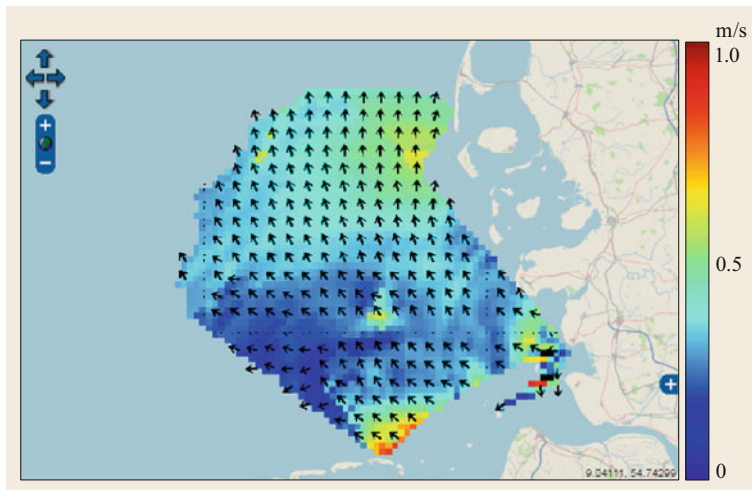


Fig. 33.8 Surface current field in the German Bight in the North Sea on December 4, 2013 at 01:00 UTC. The results were obtained from simultaneous measurements using the phased-array systems of the German HF radar network in the southern North Sea

storm [33.19]. These measurements can help to improve the forecasting of tropical cyclones as well as our understanding of their intensities and propagation directions.

33.8.2 Waves

As mentioned above, the second-order return contains information on the sea state and can be utilized to retrieve sea state information such as the significant wave height, mean wave direction, and other spectral information. Therefore, two main approaches are followed: a theoretical approach that obtains the wave directional spectrum through the inversion of an equation describing the sea surface scattering [33.3] and empirical approaches [33.4, 42]. Nevertheless, as both

methods are based on information within the second-order return, which has a lower signal-to-noise ratio than the first-order peak, the range covered by the resulting wave fields is less than that covered by the corresponding current fields (Table 33.3). A typical HF-radar-retrieved wave field is depicted in Fig. 33.7. This shows the significant wave heights in the German Bight on January 17, 2019 at 13:19 UTC, as retrieved by the beamforming HF radar located on the island of Sylt, which was operating at a frequency of 10.8 MHz.

33.8.3 Surface Currents

Today, most installed HF radars are used for monitoring coastal ocean surface currents. A large number of

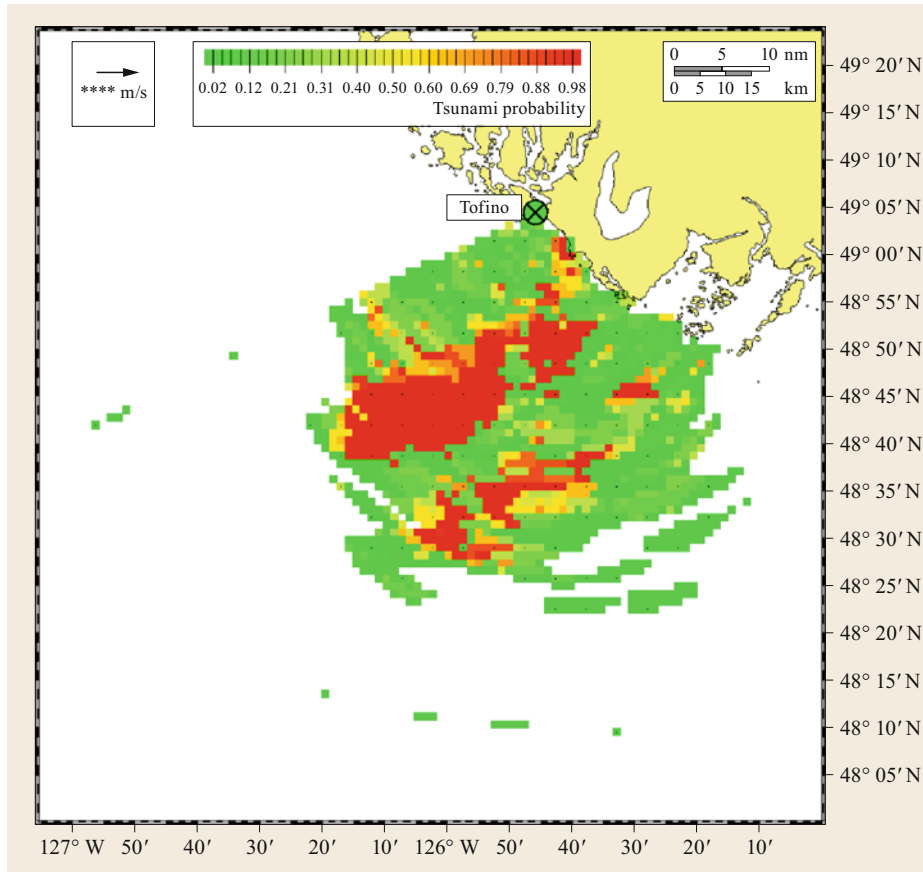


Fig. 33.9 Tsunami probability map of the west coast of Vancouver Island, Canada from October 14, 2016, at 06:12 UTC. The results were obtained by a phased-array system located at Tofino, Canada. (© Helzel Messtechnik GmbH 2015)

HF radars are being operated around the world, and most of the networks from Europe, North America, and Australia provide near real-time ocean surface current fields and make them available via the World Wide Web [33.10].

Figure 33.8 shows an example of a current field from the German Bight acquired on November 5, 2010 at 07:00 UTC. The current map was retrieved utilizing all radial currents from the three radar sites of the German HF radar network. The network resolves surface currents every 20 min. These currents are made available within 30 min of acquisition and are assimilated into a numerical simulation model [33.58] to improve the surface current forecast. Today, HF-radar-retrieved current fields are used in various applications such as search and rescue [33.12], oil spill monitoring [33.13], assimilation into numerical circulation models [33.14, 15], and marine traffic information [33.65].

One specific application of HF-radar-retrieved currents is the real-time detection and monitoring of tsunami [33.21]. In order to identify tsunami-like waves, the HF-radar-retrieved current fields are filtered. In general, the tsunami-induced velocity features

are extracted from the surface current fields measured by the HF radar by removing background current velocities, e.g., tidal currents. In contrast to direction-finding systems, phased-array systems require significantly shorter integration times to obtain an accurate surface current velocity that can be utilized to generate tsunami probability maps [33.21]. Figure 33.9 shows a tsunami probability map off the coast of Vancouver Island (Canada) during a tsunami event on October 14, 2016 at 06:12 UTC [33.66]. On that occasion, Vancouver Island was hit by a so-called meteotsunami, which is typically generated by a rapid change in barometric pressure that leads to the displacement of the water body. Meteotsunamis are restricted to local effects because they lack the energy available to significant seismic tsunamis. Although meteotsunamis are not as catastrophic as seismically induced events, they can become hazardous when amplified by resonance [33.67]. Several HF radar observations of tsunami have shown that phased-array radar technology is highly applicable for the monitoring of seismic and nonseismic tsunami, regardless of the generating mechanism, i.e., an underwater earthquake, a submarine landslide, or me-

teological conditions. Therefore, HF-radar-retrieved tsunami probability maps that become available sec-

onds after the acquisition provide valuable information for decision makers with respect to tsunami warnings.

33.9 Future Developments

From a technical point of view, a lot of effort is going into the development of active antennas (in particular for beamforming systems) as well as new antenna array concepts such as multiple-input multiple-output (MIMO) radar waveform designs [33.68]. Today, HF-radar current retrieval is well accepted, and such systems are being used on an operational basis along various coasts around the globe. Most HF radar networks are also made available to the public via the World Wide Web and gathered on platforms such as the EMODnet portal of the European Global Ocean Observing System (EuroGOOS).

Most developments in parameter retrieval are focused on improving sea state parameters such as the wave directional spectrum [33.3] or on improvements in tsunami detection [33.21] and ship detection [33.23] aimed at producing operational applications. Also, with regards to wind field retrieval, HF radar systems are not yet well suited for operational use. However, in particular with respect to wind field retrieval, satellite-borne scatterometers offer reliable wind fields with global coverage, which have been available on an operational basis for the last two decades from the European Organization for the Exploitation of Meteorological Satellites (Eumetsat).

33.10 Further Reading

A special issue on high frequency radars for coastal oceanography was published in *Oceanography* **10**(2), (1997). This can be accessed via the World Wide

Web at <http://tos.org/oceanography/issue/volume-10-issue-02>. Accessed 11 July 2021.

References

- 33.1 M. Heron, R. Rose: On the application of HF ocean radar to the observation of temporal and spatial changes in wind direction, *IEEE J. Ocean. Eng.* **11**(2), 210–218 (1986)
- 33.2 W. Shen, K.W. Gurgel, G. Voulgaris, T. Schlick, D. Stammer: Wind-speed inversion from HF radar first-order backscatter signal, *Ocean Dyn.* **62**(1), 105–121 (2012)
- 33.3 L.R. Wyatt: A relaxation method for integral inversion applied to HF radar measurement of the ocean wave directional spectrum, *Int. J. Remote Sens.* **11**(8), 1481–1494 (1990)
- 33.4 K.-W. Gurgel, H.-H. Essen, T. Schlick: An empirical method to derive ocean waves from second-order Bragg scattering: Prospects and limitations, *IEEE J. Ocean. Eng.* **31**(4), 804–811 (2006)
- 33.5 J.D. Paduan, L.K. Rosenfeld: Remotely sensed surface currents in Monterey Bay from shore-based HF radar (coastal ocean dynamics application radar), *J. Geophys. Res. Oceans* **101**(C9), 20669–20686 (1996)
- 33.6 K.-W. Gurgel, G. Antonischki, H.-H. Essen, T. Schlick: Wellen Radar (WERA): A new ground-wave HF radar for ocean remote sensing, *Coast. Eng.* **37**(3/4), 219–234 (1999)
- 33.7 D.E. Barrick: A coastal radar system for tsunami warning, *Remote Sens. Environ.* **8**(4), 353–358 (1979)
- 33.8 K.-W. Gurgel, A. Dzvankovskaya, T. Pohlmann, T. Schlick, E. Gill: Simulation and detection of tsunami signatures in ocean surface currents measured by HF radar, *Ocean Dyn.* **61**(10), 1495–1507 (2011)
- 33.9 L.R. Wyatt, J.J. Green, A. Middleditch, M.D. Moorhead, J. Howarth, M. Holt, S. Keogh: Operational wave, current and wind measurements with the pisces HF radar, *IEEE J. Ocean. Eng.* **31**(4), 819–834 (2006)
- 33.10 A. Rubio, J. Mader, L. Corgnati, C. Mantovani, A. Griffa, A. Novellino, C. Quentin, L. Wyatt, J. Schulz-Stellenfleth, J. Horstmann, P. Lorente, E. Zambianchi, M. Hartnett, C. Fernandes, V. Zervakis, P. Goringe, A. Melet, I. Puillat: HF radar activity in European coastal seas: Next steps toward a pan-European HF radar network, *Front. Mar. Sci.* **4**, Article 8 (2017)
- 33.11 A. Orfila, A. Molcard, J.M. Sayol, J. Marmain, L. Bel-lomo, C. Quentin, Y. Barbin: Empirical forecasting of HF-radar velocity using genetic algorithms, *IEEE Trans. Geosci. Remote Sens.* **53**(5), 2875–2886 (2015)

- 33.12 D.S. Ullman, J. O'Donnell, J. Kohut, T. Fake, A. Allen: Trajectory prediction using HF radar surface currents: Monte Carlo simulations of prediction uncertainties, *J. Geophys. Res. Oceans* **111**(C12), C12005 (2006)
- 33.13 A.J. Abascal, S. Castanedo, R. Medina, I.J. Losada, E. Álvarez-Fanjul: Application of HF radar currents to oil spill modelling, *Mar. Pollut. Bull.* **58**(2), 238–248 (2009)
- 33.14 J.D. Paduan, I. Shulman: HFR data assimilation in the Monterey Bay area, *J. Geophys. Res. Oceans* **109**(C7), C07S09 (2004)
- 33.15 A. Barth, A. Alvera-Azcárate, R.H. Weisberg: Assimilation of high-frequency radar currents in a nested model of the West Florida Shelf, *J. Geophys. Res. Oceans* **113**(C8), C08033 (2008)
- 33.16 R.D. Chapman, L.K. Shay, H.C. Graber, J.B. Edson, A. Karachintsev, C.L. Trump, D.B. Ross: On the accuracy of HF radar surface current measurements: Intercomparisons with ship-based sensors, *J. Geophys. Res.* **102**(C8), 18737–18748 (1997)
- 33.17 C. Ohlmann, P. White, L. Washburn, B. Emery, E. Terrill, M. Otero: Interpretation of coastal HF radar-derived surface currents with high-resolution drifter data, *J. Atmos. Ocean. Technol.* **24**(4), 666–680 (2007)
- 33.18 S.F. Heron, M.L. Heron: A comparison of algorithms for extracting significant wave height from HF radar ocean backscatter spectra, *J. Atmos. Ocean. Technol.* **15**(5), 1157–1163 (1998)
- 33.19 J.A. Harlan, T.M. Georges: Observations of hurricane Hortense with two over-the-horizon radars, *Geophys. Res. Lett.* **24**(24), 3241–3244 (1997)
- 33.20 B.J. Lipa, D.E. Barrick, J. Bourg, B.B. Nyden: HF radar detection of tsunamis, *J. Oceanogr.* **62**(5), 705–716 (2006)
- 33.21 A. Dzvонkovskaya: HF surface wave radar for tsunami alerting: From system concept and simulations to integration into early warning systems, *IEEE Aerosp. Electron. Syst. Mag.* **33**(3), 48–58 (2018)
- 33.22 A.M. Ponsford, L. Sevgi, H.C. Chan: An integrated maritime surveillance system based on high-frequency surface-wave radars. 2. Operational status and system performance, *IEEE Antennas Propag. Mag.* **43**(5), 52–63 (2001)
- 33.23 S. Maresca, P. Braca, J. Horstmann, R. Grasso: Maritime surveillance using multiple high-frequency surface-wave radars, *IEEE Trans. Geosci. Remote Sens.* **52**(8), 5056–5071 (2014)
- 33.24 D.D. Crombie: Doppler spectrum of sea echo at 13.56 Mc./s., *Nature* **175**(4459), 681–682 (1955)
- 33.25 W.H. Bragg, W.L. Bragg: The reflexion of x-rays by crystals, *Proc. R. Soc. A* **88**(605), 428–438 (1913)
- 33.26 J.R. Wait: Theory of HF ground-wave backscatter from sea waves, *J. Geophys. Res.* **71**(20), 4839–4842 (1966)
- 33.27 D.E. Barrick: First-order theory and analysis of MF/HF/VHF surface from the sea, *IEEE Trans. Antennas Propag.* **20**(1), 2–10 (1972)
- 33.28 D.E. Barrick, M.W. Evans, B.L. Weber: Ocean surface currents mapped by radar, *Science* **198**(4313), 138–144 (1977)
- 33.29 A.E. Long, D.B. Trizna: Mapping of North Atlantic winds by HF radar sea backscatter interpretation, *IEEE Trans. Antennas Propag.* **21**(5), 680–685 (1973)
- 33.30 K. Hasselmann: Determination of ocean wave spectra from Doppler radio return from the sea surface, *Nat. Phys. Sci.* **229**(1), 16–17 (1971)
- 33.31 D. Prandle, D.K. Ryder: Measurement of surface currents in Liverpool Bay by high-frequency radar, *Nature* **315**(6015), 128–131 (1985)
- 33.32 H.C. Graber, B. Haus, R.D. Chapman, L.K. Shay: HF radar comparisons with moored estimates of current speed and direction: Expected differences and implications, *J. Geophys. Res. Oceans* **102**(C8), 18749–18766 (1997)
- 33.33 K. Law: *Measurements of Near Surface Ocean Currents Using HF Radar*, PhD thesis (Univ. California, Santa Cruz 2001)
- 33.34 F. Ardhuin, L. Marie, N. Rasclé, P. Forget, A. Roland: Observation and estimation of Lagrangian, Stokes and Eulerian currents induced by wind and waves at the sea surface, *J. Phys. Oceanogr.* **39**(11), 2820–2838 (2009)
- 33.35 C. Chavanne: Do high-frequency radars measure the wave-induced Stokes drift?, *J. Atmos. Ocean. Technol.* **35**(5), 1023–1031 (2018)
- 33.36 J. Röhrs, A.K. Sperrevik, K.H. Christensen, G. Broström, Ø. Breivik: Comparison of HF radar measurements with Eulerian and Lagrangian surface currents, *Ocean Dyn.* **65**(5), 679–690 (2015)
- 33.37 D.M. Fernandez, H.C. Graber, J.D. Paduan, D.E. Barrick: Mapping wind direction with HF radar, *Oceanography* **10**(2), 93–95 (1997)
- 33.38 D.E. Barrick, B.L. Weber: On the nonlinear theory for gravity waves on the ocean's surface. Part II: Interpretation and applications, *J. Phys. Oceanogr.* **7**(1), 11–21 (1977)
- 33.39 B.J. Lipa, D.E. Barrick: Extraction of sea state from HF radar sea echo: Mathematical theory and modelling, *Radio Sci.* **21**(1), 81–100 (1986)
- 33.40 D.E. Barrick: The ocean waveheight nondirectional spectrum from inversion of the HF sea-echo Doppler spectrum, *Remote Sens. Environ.* **6**(3), 201–227 (1977)
- 33.41 J.W. Maresca, T.M. Georges: Measuring RMS waveheight and the scalar ocean wave spectrum with HF skywave radar, *J. Geophys. Res.* **85**(C5), 2759–2771 (1980)
- 33.42 L.R. Wyatt: An evaluation of wave parameters measured using a single HF radar system, *Can. J. Remote Sens.* **28**(2), 205–218 (2002)
- 33.43 B. Lipa, D. Barrick: Tidal and storm-surge measurements with single-site CODAR, *IEEE J. Ocean. Eng.* **11**(2), 241–245 (1986)
- 33.44 R.O. Schmidt: Multiple emitter location and signal parameter estimation, *IEEE Trans. Antennas Propag.* **34**(3), 276–280 (1986)
- 33.45 M.L. Heron, P.E. Dexter, B.T. McGann: Parameters of the air-sea interface by high frequency ground-wave HF Doppler radar, *Aust. J. Mar. Freshw. Res.* **36**(5), 655–670 (1985)
- 33.46 E.D.R. Shearman, M.D. Moorhead: Pisces: A coastal ground-wave HF radar for current, wind and wave

- mapping to 200 km ranges. In: *Int. Geosci. Remote Sens. Symp. 'Remote Sensing: Moving Toward the 21st Century'*, Edinburgh (1988) pp. 773–776, <https://doi.org/10.1109/IGARSS.1988.570433>
- 33.47 D. Prandle, S.G. Loch, R. Player: Tidal flow through the straits of Dover, *J. Phys. Oceanogr.* **23**(1), 23–37 (1992)
- 33.48 K. Hickey, R.H. Khan, J. Walsh: Parametric estimation of ocean surface currents with HF radar, *J. Ocean. Eng.* **20**(2), 139–144 (1995)
- 33.49 M.L. Heron: Comparisons of different HF ocean surface-wave radar technologies. In: *2015 IEEE/OES 11th Curr. Waves Turbul. Meas., St. Petersburg, FL* (2015) pp. 1–4, <https://doi.org/10.1109/CWTM.2015.7098121>
- 33.50 H. Hersbach: Comparison of C-band scatterometer CMOD5.N equivalent neutral winds with ECMWF, *J. Atmos. Ocean. Technol.* **27**(4), 721–736 (2010)
- 33.51 J. Horstmann, S. Falchetti, C. Wackerman, S. Maresca, M.J. Caruso, H.C. Graber: Tropical cyclone winds retrieved from C-band cross-polarized synthetic aperture radar, *IEEE Trans. Geosci. Remote Sens.* **53**(5), 2887–2898 (2015)
- 33.52 H. Dankert, J. Horstmann: A marine radar wind sensor, *J. Atmos. Ocean. Technol.* **24**(9), 1629–1642 (2007)
- 33.53 H. Dankert, J. Horstmann, S. Lehner, W. Rosenthal: Detection of wave groups in SAR images and radar image sequences, *IEEE Trans. Geosci. Remote Sens.* **41**(6), 1437–1446 (2003)
- 33.54 P.A. Hwang, W.B. Krabill, W. Wright, R.N. Swift, E.J. Walsh: Airborne scanning lidar measurement of ocean waves, *Remote Sens. Environ.* **73**(2), 236–246 (2000)
- 33.55 B. Lund, B.K. Haus, J. Horstmann, H.C. Graber, R. Carrasco, N.J.M. Laxague, G. Novelli, C.M. Guigand, T. Özgökmen: Near-surface current mapping by shipboard marine X-band radar: A validation, *J. Atmos. Ocean. Technol.* **35**(5), 1077–1090 (2018)
- 33.56 M. Streßer, R. Carrasco, J. Horstmann: Video-based estimation of surface currents using a low-cost quadcopter, *IEEE Geosci. Remote Sens. Lett.* **14**(11), 2027–2031 (2017)
- 33.57 F. Ardhuin, P. Brandt, L. Gaultier, C.J. Donlon, A. Battaglia, F. Boy, T. Casal, B. Chapron, F. Collard, S. Cravatte, J.-M. Delouis, E. De Witte, G. Dibarboure, G. Engen, H. Johnsen, C. Lique, P. Lopez-Dekker, C. Maes, A. Martin, L. Marié, D. Menemenlis, F. Nougier, C. Peureux, P. Rampal, G. Ressler, M.-H. Rio, B. Rommen, J.D. Shutler, M. Suess, M. Tsamados, C. Ubelmann, E. van Sebille, M. van den Oever, D. Stammer: SKIM: The sea surface kinematics multiscale monitoring satellite mission, *Front. Mar. Sci.* **6**, Article 209 (2019)
- 33.58 E.V. Stanev, F. Ziemer, J. Schulz-Stellenfleth, J. Seemann, J. Staneva, K.-W. Gurgel: Blending surface currents from HF radar observations and numerical modeling: Tidal hindcasts and forecasts, *J. Atmos. Ocean. Technol.* **32**(2), 256–281 (2015)
- 33.59 S. Cosoli, A. Mazzoldi, M. Gačić: Validation of surface current measurements in the northern Adriatic sea from high frequency radars, *J. Atmos. Ocean. Technol.* **27**(5), 908–919 (2010)
- 33.60 T.M. Georges, J.A. Harlan, L.R. Meyer, R.G. Peer: Tracking hurricane Claudette with the U.S. Air Force over-the-horizon radar, *J. Atmos. Ocean. Technol.* **10**(4), 441–451 (1993)
- 33.61 A. Dzvonkovskaya, T. Helzel: WERA HF ocean radar performance during severe storm Xaver. In: *2015 16th Int. Radar Symp., Dresden* (2015) pp. 846–851, <https://doi.org/10.1109/IRS.2015.7226385>
- 33.62 B. Baschek, F. Schroeder, H. Brix, R. Riethmüller, T.H. Badewien, G. Breitbach, B. Brügge, F. Colijn, R. Doerffer, C. Eschenbach, J. Friedrich, P. Fischer, S. Garthe, J. Horstmann, H. Krasemann, K. Metfies, L. Merckelbach, N. Ohle, W. Petersen, D. Pröfrock, R. Röttgers, M. Schlüter, J. Schulz, J. Schulz-Stellenfleth, E. Stanev, J. Staneva, C. Winter, K. Wirtz, J. Wollschläger, O. Zielinski, F. Ziemer: The coastal observing system for northern and Arctic seas (COSYNA), *Ocean Sci.* **13**(3), 379–410 (2017)
- 33.63 P. Dexter, S. Theodorides: Surface wind speed extraction from HF sky-wave radar Doppler spectra, *Radio Sci.* **17**(3), 643–652 (1982)
- 33.64 D. Green, E. Gill, W. Huang: An inversion method for extraction of wind speed from high-frequency ground-wave radar oceanic backscatter, *IEEE Trans. Geosci. Remote Sens.* **47**(10), 3338–3346 (2009)
- 33.65 Ø. Breivik, Ø. Sætra: Real time assimilation of HF radar currents into a coastal ocean model, *J. Mar. Syst.* **28**(3/4), 161–182 (2001)
- 33.66 A. Dzvonkovskaya, L. Petersen, T.L. Insua: Real-time capability of meteotsunami detection by WERA ocean radar system. In: *18th Int. Radar Symp., Prague* (2017) pp. 1–10, <https://doi.org/10.23919/IRS.2017.8008096>
- 33.67 S. Monserrat, I. Vilibić, A.B. Rabinovich: Meteotsunamis: Atmospherically induced destructive ocean waves in the tsunami frequency band, *Nat. Hazards Earth Syst. Sci.* **6**(6), 1035–1051 (2006)
- 33.68 J.O. Hinz, U. Zölzer: A MIMO FMCW radar approach to HFSWR, *Adv. Radio Sci.* **9**, 159–163 (2011)

Jochen Horstmann

Ocean Surface Dynamics
Helmholtz-Zentrum hereon
Geesthacht, Germany
jochen.horstmann@hereon.de



Jochen Horstmann is a Department Head at the Institute of Coastal Ocean Dynamics of the Helmholtz-Zentrum hereon, Germany. Since 2007, he is also Adjunct Professor at the Rosenstiel School of Marine and Atmospheric Science, University of Miami. He has extensive experience in developing applications for radar- and video-based sensors, with a particular focus on ocean surface and subsurface processes, and has published more than 80 scientific papers in international peer-reviewed journals.

Anna Dzvonkovskaya

Helzel Messtechnik GmbH
Kaltenkirchen, Germany
dzvonkovskaya@gmail.com



Dr. Anna Dzvonkovskaya was an algorithm developer at Helzel Messtechnik GmbH, Germany (left in 2019). Her research interests include radar-based remote sensing of the marine environment and tsunami detection, signal processing algorithms, data fusion, and statistical analysis. An IEEE Senior Member and recipient of the Young Engineer Award at the international conference RADAR 2009 (Surveillance for a Safer World), she has authored more than 40 publications in highly rated journals and conference proceedings.

Scintillometers

34. Scintillometers

Frank Beyrich, Oscar K. Hartogensis , Henk A.R. de Bruin, Helen C. Ward 

Scintillometers consist of a transmitter–receiver pair for electromagnetic radiation separated from each other by a distance of 10^2 – 10^4 m. As the emitted radiation travels through the atmosphere, it is scattered by turbulent eddies of different density. At the receiver, the resulting high-frequency intensity fluctuations of the electromagnetic signal (*scintillations*) are recorded, from which the turbulent sensible and latent heat fluxes can be derived. Further, the wind component perpendicular to the path (crosswind) and, for a specific system configuration, the turbulent momentum flux can be determined from the correlation of the fluctuation time series between two parallel beams. The signal at the receiver represents an integrated effect of the conditions along the path; scintillometers, therefore, provide area-averaged values of fluxes and crosswind. This is of special relevance for applications like the validation of flux data from numerical weather prediction and climate models or from satellite retrievals, or for the estimation of regional-scale evaporation rates in agricultural management and hydrology. After a brief introduction to the theoretical background, the commercially available scintillometer types are characterized, and the conditions of their use are discussed.

34.1	Measurement Principles and Parameters	970	34.3.2	Turbulence Spectrum	974
34.2	History	971	34.3.3	Scintillometry Equations	975
34.3	Theory	972	34.3.4	Saturation and Absorption	976
34.3.1	The Refractive Index of Air and the Structure Parameters for Refractive Index, Temperature, and Humidity	973	34.3.5	The Derivation of Heat Fluxes Based on Similarity Theory	977
			34.3.6	Determination of Friction Velocity Using Similarity Theory	978
			34.3.7	The Effective Path Height	979
			34.3.8	The Determination of Crosswind	979
			34.4	Devices and Systems	979
			34.4.1	Optical Small-Aperture Scintillometers	980
			34.4.2	Optical Large-Aperture Scintillometers	980
			34.4.3	Microwave Scintillometers	982
			34.4.4	Summary of Assumptions, Advantages and Disadvantages of Scintillometers	983
			34.5	Specifications	984
			34.6	Quality Control	985
			34.7	Maintenance	987
			34.8	Applications	989
			34.8.1	Field-Scale Fluxes Using the Dual-Beam, Small-Aperture Scintillometer	989
			34.8.2	Meso-γ Scale Fluxes from LAS and OMS	990
			34.8.3	Crosswind Determination	991
			34.8.4	Applications in Geodesy and Astronomy	991
			34.9	Future Developments	991
			34.10	Further Readings	992
			References		992

Electromagnetic radiation propagating through the atmosphere experiences scattering by air parcels of different refractive index (i.e., density) which irregularly move in the atmosphere due to turbulence. This leads

to high-frequency intensity fluctuations of the electromagnetic signal detected at any point, so-called scintillations. Astronomers notice these scintillations as a blurring of star images and were among the first to study

them in order to avoid or correct their influence on astronomical observations. Scintillations may also be seen by the human eye as the apparent distortion of the back-

ground over strongly heated surfaces or the twinkling of stars at night. Meteorologists use these scintillations to derive turbulent fluxes of heat and momentum.

34.1 Measurement Principles and Parameters

Scintillometer measurements are based on the line-of-sight propagation of electromagnetic waves through the turbulent atmosphere. A scintillometer consists of a transmitter and a receiver unit, separated from each other over a (basically horizontal) distance of 10^2 – 10^4 m. The transmitter emits electromagnetic radiation of constant intensity at a given wavelength (λ), but turbulent density fluctuations of the air prevent straight propagation and cause a distortion of the wave fronts. These density fluctuations are essentially due to temperature and humidity fluctuations. At the receiver side, the cumulative effect of wave propagation disturbances along the path results in intensity fluctuations of the electromagnetic signal, which are mathematically expressed as variances (σ_λ). These variances can be related to the refractive index structure parameter, C_{nm} , of air; C_{nm} can be written in terms of the structure parameters of temperature and humidity, C_{TT} , C_{qq} , and C_{Tq} (Sect. 34.3.1), where the relative contribution of temperature and humidity fluctuations to the refractive index depends on the wavelength of the electromagnetic radiation. While temperature fluctuations dominate in the visible and near-infrared spectral range (wavelengths typically between 400 nm and 4 μ m), humidity fluctuations become relevant for millimeter waves (wavelength 1–20 mm). This has implications for the choice of a certain scintillometer setup, depend-

ing on the fluxes to be derived (Table 34.1). Using Monin–Obukhov similarity theory (MOST, Chap. 1), the turbulent surface fluxes of heat (Q_H) and moisture (Q_E) can be derived from the structure parameters. Further, analysis of the correlation of the received signal between two parallel beams allows for the determination of the wind component perpendicular to the path (crosswind). Finally, if the sensor geometry and system specifications of the two-beam scintillometer are sensitive to turbulent eddies close to the inner scale length of turbulence (Sect. 34.3.2), the turbulent kinetic energy dissipation rate and therefrom the turbulent momentum flux can be derived. An overview of the atmospheric variables determined from scintillometer measurements is given in Table 34.1. The different scintillometer types are characterized in Sect. 34.4.

As an example of the data processing chain, the steps to derive the turbulent fluxes of sensible and latent heat from the measurements with a combined optical-microwave scintillometer system are illustrated in Fig. 34.1.

As the signal at the receiver represents an integrated effect of the conditions along the path, scintillometers provide area-averaged information about the fluxes upstream of the path. This is of special relevance for applications like the validation of fluxes representing a grid cell in a numerical weather prediction (NWP) or climate

Table 34.1 Atmospheric variables derived from scintillometer measurements

Scintillometer type	Measured variable	Derived atmospheric variable	Symbol and unit
Single-beam optical scintillometer	Variance of electromagnetic signal intensity	Structure parameter of temperature Sensible heat flux density ^a	C_{TT} in $K^2 m^{-2/3}$ Q_H in $W m^{-2}$
Combined optical-microwave scintillometer	Variances and covariance of optical/microwave signal intensities	Structure parameters of temperature and humidity Sensible and latent heat flux densities ^a	C_{TT} in $K^2 m^{-2/3}$ C_{qq} in $kg^2 m^{-6} m^{-2/3}$ C_{Tq} in $K kg m^{-3} m^{-2/3}$ Q_H in $W m^{-2}$ Q_E in $W m^{-2}$
Dual-beam optical scintillometer	Variances and covariance of electromagnetic signal intensities of the two beams	Structure parameter of temperature Dissipation rate of turbulent kinetic energy ^b Sensible heat flux density ^a Crosswind perpendicular to path Momentum flux ^b (friction velocity)	C_{TT} in $K^2 m^{-2/3}$ ϵ in $m^2 s^{-3}$ Q_H in $W m^{-2}$ u_{cross} in $m s^{-1}$ τ in $kg m^{-1} s^{-2}$ (u_* in $m s^{-1}$)

^a Information on momentum flux must be available (Sect. 34.3.6)

^b Possible with optical small-aperture laser scintillometers (*inner-scale scintillometers*), for which the beam distance is of the order of the inner scale length of turbulence (a few mm, Sects. 34.3.2 and 34.4.1)

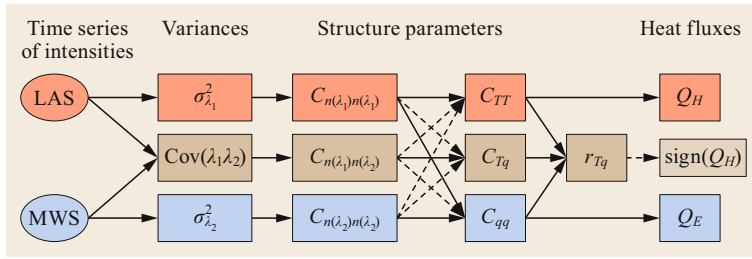


Fig. 34.1 Schematic representation of the data processing for a combined optical-microwave scintillometer (OMS) consisting of an optical large-aperture scintillometer (LAS, operated with an optical wavelength λ_1) and a microwave scintillometer (MWS, operated with a millimeter wavelength λ_2)

model, or a pixel of a satellite picture. Moreover, scintillometers allow for the estimation of regional-scale evaporation rates in agricultural management and hydrology. For these applications, scintillometers are an

easy-to-employ and low-maintenance alternative to networks of eddy-covariance flux stations (Chap. 55) or to airborne flux measurements using aircraft, helicopters, or unmanned aerial systems (Chaps. 47 and 48).

34.2 History

Scintillometry is a relatively young discipline in atmospheric science and measurement technology. First systematic studies of scintillations were performed in the middle of the twentieth century by astronomers, and by engineers and scientists dealing with communication systems (on both ground-based and satellite platforms) and for military purposes (related to the development of laser defense systems). After the theoretical description of wave propagation in a turbulent fluid and a theory to describe surface layer turbulence based on scaling arguments had been worked out in the 1950s and 1960s by *Monin*, *Obukhov*, and *Tatarski* [34.1–3], it was recognized that parameters characterizing atmospheric turbulent flows, notably, the dissipation rate of turbulent kinetic energy (ε) and the structure parameter of the refractive index (C_m) can be obtained from scintillation measurements wherefrom the vertical surface fluxes of momentum, sensible and latent heat can be derived. First prototype research scintillometer systems were built and tested in the 1970s and 1980s in the United States by *Wang*, *Hill*, *Ochs*, and *Frehlich* (e.g., [34.4–11]). These systems were employed to further develop and verify the theoretical concepts and to demonstrate possible applications. However, most of these basic studies found little attention in the meteorological community. In the 1980s *Kohsiek* brought the design idea of a large-aperture scintillometer (LAS) to Europe. Subsequently, he built a first prototype at the Royal Netherlands Meteorological Institute (KNMI) and participated in the EFEDA field campaign in Spain in 1991 [34.12] to determine the sensible heat flux of a sparse vineyard, a strongly heterogeneous surface at meter scale [34.13]. The scintillometer fluxes were shown to compare very well with independent eddy-covariance measurements. This success initiated

a very intense and fruitful period of scintillometer development and applications at the Meteorology and Air Quality Department at Wageningen University and Research (WURMAQ), The Netherlands, driven and guided by *de Bruin* [34.14] and continued by a number of PhD students and scientists [34.15–20]. In the second half of the 1990s, the WURMAQ group built a series of optical LAS, which were operated in several locations all over the world (e.g., in The Netherlands, Germany, Greece, Mexico, Brazil, Marocco, Ghana, South Africa, Indonesia, China, and New Zealand), where the potential of the method and the robustness of the instruments were demonstrated under different climate and surface conditions and for a wide range of applications in meteorology, ecology, hydrology, and agriculture [34.21–28]. A WURMAQ scintillometer setup in Lindenberg for the LITFASS project in 1998 [34.29–31] has been in almost continuous operation by the German Meteorological Service (Deutscher Wetterdienst, DWD) for about 20 years. In parallel, the WURMAQ group made important theoretical contributions to qualify the scintillometry method and to define algorithms for data analysis and quality assurance/quality control. This contributed significantly to the design and realization of the commercial scintillometers presently available from Kipp & Zonen and the Radiometer Physics Group (Sect. 34.4).

Independently of the work in the US and the Netherlands, a double-beam laser scintillometer (DBLS) was designed and tested in Germany in 1990 by *Thiermann* [34.32–34]. A modified version of this instrument was the first scintillometer introduced commercially to the market by Scintec AG, Germany, in 1991 for measurements in the surface layer and over distances of 50–250 m (Sect. 34.4.1). About 10 years later, Scintec

AG developed a multiple-LED LAS, which they called boundary-layer scintillometer (BLS) directing towards its application at larger spatial scales (Sect. 34.4.2).

Already in the early 1980s, *Kohsiek* and *Herben* [34.35] had shown that evaporation can be estimated from a combination of an optical LAS and a microwave scintillometer (MWS). Several prototypes of MWS were later built at Eindhoven University in The Netherlands [34.15, 25], at Rutherford Appleton Laboratory in the UK [34.36–38], and at the University of Bern, Switzerland [34.39]. Due to the more complex (and expensive) microwave technology it took

until 2014 before the first MWS became commercially available on the market (manufactured by Radiometer Physics GmbH, Meckenheim, Germany; Sect. 34.4.3).

Important contributions to the improvement of commercial scintillometer systems and their data processing software resulted from a number of instrument intercomparison experiments performed in New Mexico, USA, Chilbolton, UK, and Lindenberg, Germany [34.40–44].

Although this is still not a standard measurement technique, scintillometers are currently in wide use for a variety of applications (Sect. 34.8).

34.3 Theory

Scintillometry relies on the theory of electromagnetic wave propagation in the turbulent atmosphere, relating the measured intensity fluctuations of an electromagnetic signal to the characteristics of atmospheric turbulence, quantified by the structure parameters of refractive index, temperature, and humidity. Monin–Obukhov similarity theory (MOST) is then used to derive the surface fluxes of momentum, sensible and latent heat from these structure parameters. This implies a series of assumptions, such as weak scattering of the emitted light beam, sensitivity to frequencies in the inertial subrange of turbulence, homogeneous and locally isotropic turbulence, homogeneous surface and stationary atmospheric conditions (see the discussion in the following subsections). The principle of scintillometry is illustrated in Fig. 34.2.

Electromagnetic radiation of wavelength λ is emitted at the transmitter with constant strength and propagates over a distance X towards the receiver where the time series of its intensity (i.e., the intensity fluctuations) is recorded with a sampling frequency of

10^3 – 10^4 Hz. Along the propagation path, turbulent eddies of different size and thermodynamic characteristics cause scattering of the electromagnetic signal, which is, therefore, highly variable in time. Figure 34.2 also shows a number of length scales that are important in connection with the analysis and interpretation of scintillometer measurements. These are:

- The length of the scintillometer path (X)
- The (effective) height of the path above ground (z , see Sect. 34.3.7)
- The outer and inner scale lengths of turbulence (L_0 and l_0 , respectively, where L_0 marks the transition between the production and inertial ranges of the turbulence spectrum that usually scales with z , and l_0 marks the transition between the inertial and dissipation ranges of the turbulence spectrum, it typically amounts to a few mm; Sect. 34.3.2).
- The aperture of the transmitter and receiver units (in principle, they might be different, but for most systems $D(\text{transmitter}) = D(\text{receiver})$).

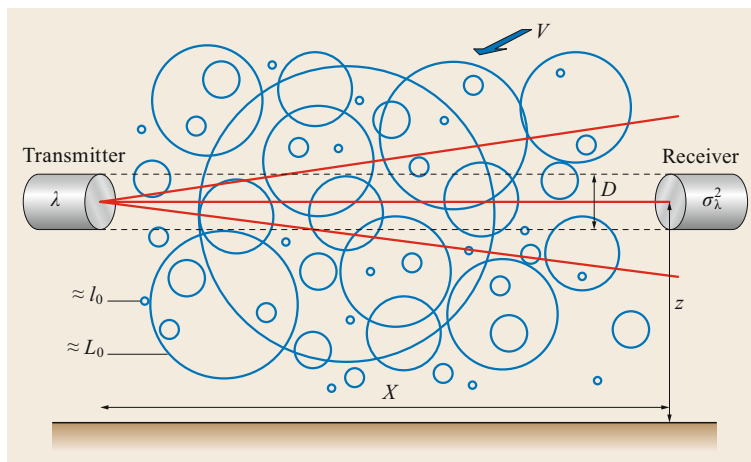


Fig. 34.2 Schematic representation of the scintillometer principle (after [34.16] modified)

Table 34.2 Exemplary values of the A_T and A_q coefficients in the optical and microwave ranges for typical atmospheric conditions according to [34.45]

Scalar y (unit)	Mean (y)	Fluctuation y'	Relative fluctuation y'/y	Optical range ($\lambda = 880 \text{ nm}$)		Microwave range ($\lambda = 3.4 \text{ mm}$)	
				A_y	$A_y y'/y$	A_y	$A_y y'/y$
T (K)	288	1	3×10^{-3}	-2.70×10^{-4}	-9×10^{-7}	-4.13×10^{-4}	-1.4×10^{-6}
q (kg kg^{-1})	10^{-2}	10^{-4}	10^{-2}	-6.85×10^{-7}	-6.9×10^{-9}	7.14×10^{-5}	7.1×10^{-7}
p (Pa)	10^5	10^{-1}	10^{-6}	2.70×10^{-4}	2.7×10^{-10}	3.40×10^{-4}	3.4×10^{-10}

Another important length scale is the Fresnel length $F = (\lambda X)^{1/2}$. F is the maximum diameter of the first Fresnel zone, an ellipsoid with the transmitter and receiver units at its focal points. Most of the scintillation signal originates from inside this region. Therefore, an undisturbed signal can only be recorded if the first Fresnel zone is free of obstacles.

It is the maximum of either F or D that determines the size of those eddies that contribute most to the measured intensity fluctuations. If $D < F$, the light source can be considered as a point source, and F defines the relevant eddy size. These systems are called small-aperture scintillometers. For $D > F$, the dominant eddies are of the dimension of the instrument aperture; the system is called a large-aperture scintillometer (LAS).

34.3.1 The Refractive Index of Air and the Structure Parameters for Refractive Index, Temperature, and Humidity

Scintillations detected by the receiver of a scintillometer are caused by fluctuations of the refractive index of air (n), which is generally a function of air pressure (p), air temperature (T), and water vapor content (q). Here, specific humidity is used to express the water vapor content of air, as q is a conservative variable invariant to changes of height and air temperature. The refractive index n at a given point and time can be expressed as $n = \bar{n} + n'$, where \bar{n} represents an ensemble mean value and n' the deviation of the actual value from the mean. For an individual eddy, n' is given by

$$\begin{aligned} n' &= \frac{\partial n}{\partial T} T' + \frac{\partial n}{\partial q} q' + \frac{\partial n}{\partial p} p' \\ &= A_T \frac{T'}{\bar{T}} + A_q \frac{q'}{\bar{q}} + A_p \frac{p'}{\bar{p}}, \end{aligned} \quad (34.1)$$

where A_T , A_q and A_p are functions of pressure, temperature, and humidity, and can generally be expressed as $A_y = \bar{y}(\partial n / \partial y)$ with $y = (p, T, q)$. In addition, they depend on the wavelength λ of the electromagnetic

radiation. Details on the determination of these coefficients are discussed, e.g., in [34.45, 46]. Typical values are given in Table 34.2.

It becomes obvious from the values given in Table 34.2 that the contribution of temperature fluctuations to the refractive index fluctuations dominates by two orders of magnitude for near-infrared radiation, while temperature and humidity fluctuations are similarly important for microwave radiation. The contribution of pressure fluctuations can generally be neglected. As a consequence, an optical scintillometer system alone may be used to derive the sensible heat flux, while a microwave scintillometer and an optical scintillometer operated simultaneously are needed to determine the latent heat flux (evaporation) from scintillation measurements. In many applications, just an optical scintillometer is operated to derive an area-representative value of the sensible heat flux from scintillation measurements while the latent heat flux is determined as a residual of the energy budget equation or with the Bowen ratio method using measurements or reasonable estimates of net radiation and soil heat flux (and the gradients of temperature and humidity for the latter method). Note that the latter data are usually of a very different spatial representativeness, adding additional uncertainties to the derived latent heat flux.

A key atmospheric variable considered in scintillometry is the refractive index structure parameter, C_{nn} . For homogeneous and isotropic turbulence, it is given by (e.g., [34.48])

$$C_{nn} = \overline{[n(x, t) - n(x + \Delta x, t)]^2} \Delta x^{-2/3}. \quad (34.2)$$

This definition indicates that the mean difference of the instantaneous values of n at position $x + \Delta x$ from a reference value at position x only depends on the distance Δx , which must be within the inertial subrange of the turbulence spectrum. This definition of a turbulent structure parameter can be formulated in the same way for any atmospheric variable, including T and q . With (34.1), the refractive index structure parameter can be expressed as a combination of the structure parameters for temperature, C_{TT} , humidity, C_{qq} , and

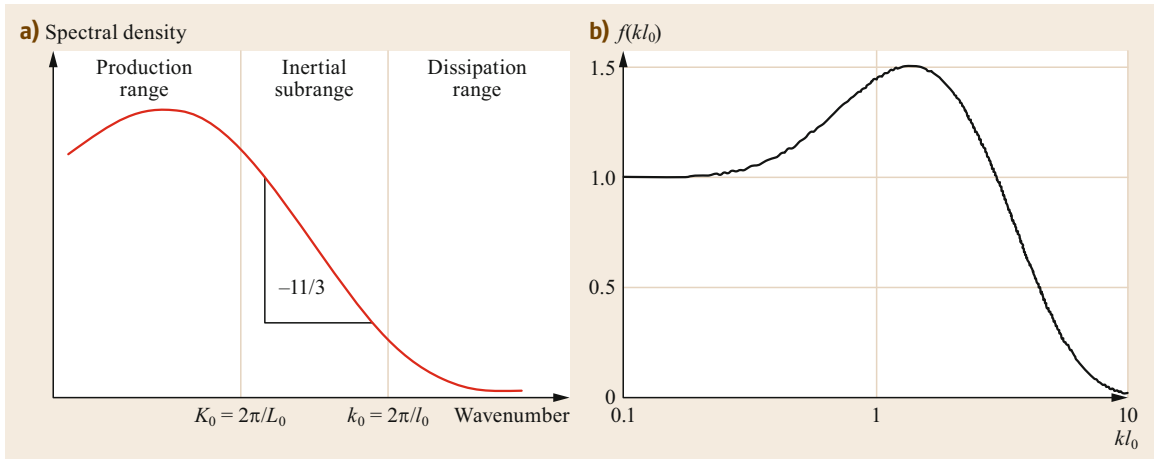


Fig. 34.3 (a) Schematic representation of the power spectrum of turbulence (courtesy of Radiometer Physics GmbH) and (b) the correction function $f(kl_0)$ for the power spectrum of turbulence for wavelengths around l_0 according to the model proposed (after [34.47])

of the temperature-humidity cross-structure parameter, C_{Tq} , [34.49]

$$C_{nn} = \frac{A_T^2}{\bar{T}^2} C_{TT} + 2 \frac{A_T A_q}{\bar{T} \bar{q}} C_{Tq} + \frac{A_q^2}{\bar{q}^2} C_{qq}; \quad (34.3)$$

C_{Tq} is related to the correlation between temperature and humidity fluctuations (e.g., [34.46])

$$r_{Tq} = \frac{C_{Tq}}{\sqrt{C_{TT} C_{qq}}}. \quad (34.4)$$

As discussed above, the first term on the right-hand side of (34.3) is dominant for visible and near-infrared wavelengths, such that C_{TT} can be directly related to C_{nn} with a correction factor accounting for the humidity effects via the Bowen ratio, Bo [34.46, 50]

$$C_{TT} = \frac{\bar{T}^2}{A_T^2} C_{nn} \left[1 + \frac{0.03}{\text{Bo}} \right]^{-2}. \quad (34.5)$$

The correction factor exceeds 10% for Bowen ratio values $\text{Bo} < 0.3$. Equation (34.5) is an approximation to the exact solution (presented in [34.46]) resulting in increasing errors for Q_H with decreasing absolute Bo values for $|\text{Bo}| < 1$. This, however, corresponds to situations where Q_H is small compared to Q_E , such that the absolute errors in Q_H and the impact on the total energy budget are reasonably small.

In order to derive both the sensible and latent heat fluxes from the simultaneous operation of a LAS and an MWS, r_{Tq} has to be either determined directly from correlating the fluctuation measurements at the two wavelengths (the so-called *bichromatic* method, [34.39])

or prescribed by a reasonable value [34.51]. Typical values are $r_{Tq} = 0.8$ for unstable conditions and $r_{Tq} = -0.5$ for stable conditions (see [34.52] for a summary).

34.3.2 Turbulence Spectrum

A schematic illustration of the power spectrum of turbulence is given in Fig. 34.3. The spectrum can be subdivided into three typical regions (Chap. 1):

- The production range where turbulent energy is generated by buoyancy and shear.
- The inertial subrange over which the energy is transferred from larger to smaller eddies.
- The dissipation range where turbulent energy is dissipated into heat.

Kolmogorov [34.53] provided a model for the three-dimensional refractive index spectrum for homogeneous and isotropic turbulence in the inertial subrange, $\phi_{nn}(k)$, as a function of the turbulent wavenumber, k ,

$$\phi_{nn}(k) = 0.033 C_{nn} k^{-11/3}. \quad (34.6)$$

In the inertial subrange, the intensity of turbulence decreases with $k^{-11/3}$. Close to L_0 or close to l_0 , outer and inner scale effects have to be considered, and the spectral shape deviates from the inertial subrange behavior. When operating a scintillometer, certain requirements regarding l_0 and L_0 must be matched. In any case, D and F should both be much smaller than L_0 . Except for inner-scale scintillometers, it is required that D or F is much larger than l_0 . Both conditions are usually fulfilled for optical LAS and MWS systems (although

for large values of l_0 , around 15 mm, $D \approx 10l_0$ holds for some LAS systems which makes a correction necessary, this correction amounts to about 10% for C_{mn} , see [34.17]).

For the spectral range around l_0 , which is of relevance for the operation of Scintec's dual-beam laser scintillometers (Sect. 34.6), Hill [34.47] has proposed a model to parameterize the deviations from the inertial subrange behavior (Fig. 34.3b). It describes a small increase in spectral energy (often referred to as the *Hill bump*) at the transition from the inertial subrange to the dissipation range, followed by a rapid decrease (with a slope exceeding the $k^{-11/3}$ behavior in the inertial subrange) towards very small values. Different analytical approximations to this model have been described in the literature [34.11, 17, 54].

34.3.3 Scintillometry Equations

Refractive index inhomogeneities along the propagation path cause a signal of electromagnetic radiation to exhibit both amplitude and phase fluctuations; in scintillometry it is the amplitude fluctuations that are analyzed. Amplitude fluctuations in the weak-scattering turbulence regime follow a log-normal distribution. However, what is usually recorded is not the amplitude but the intensity, I , of the electromagnetic signal (or a voltage that is proportional to the intensity). The conversion from intensity fluctuations to amplitude fluctuations assuming a log-normal distribution is given by

$$\sigma_{\ln(A)}^2 = \frac{1}{4} \ln \left(\frac{\sigma_I^2}{\bar{I}^2} + 1 \right). \quad (34.7)$$

The fundamental scintillometer equation is given by the solution of the wave propagation equation in a turbulent medium [34.3] using Rytov's perturbation method. For spherical waves propagating from a point source to a point detector through a statistically homogenous and locally isotropic turbulence field it was presented by [34.55]

$$\sigma_{\ln(A)}^2 = 4\pi^2 k_\lambda^2 \int_0^X \int_0^\infty k \phi_{mn} \sin^2 \left(\frac{k^2 x(X-x)}{2k_\lambda X} \right) dk dx, \quad (34.8)$$

where k_λ is the wavenumber of the electromagnetic radiation ($k_\lambda = 2\pi/\lambda$), and x is the distance along the path between transmitter and receiver (0– X).

This equation relates the variance of the log-amplitude fluctuations, $\sigma_{\ln(A)}^2$, to the three-dimensional spectrum of turbulence, ϕ_{mn} . The other parameters in (34.8) are determined by the measurement setup (λ, X).

With (34.6) for ϕ_{mn} , and (34.7) to convert from signal intensities to amplitudes, integration of (34.8) provides the relation between the refractive index structure parameter and the variance of the logarithmic signal intensities measured by a scintillometer.

Additional terms in the fundamental equation (34.8) have to be considered in order to account for aperture averaging at the transmitter and the receiver (in the case of the LAS), for inner and outer scale contributions (if applicable, depending on the system characteristics), as well as for saturation effects, and to describe the covariances between two scintillometer beams (for the dual-beam laser scintillometer and for the optical-microwave scintillometer). For a LAS and for an MWS, the following relations result [34.4]

$$C_{mn}(\text{LAS}) = 4.48 \sigma_{\ln(A)}^2 D^{7/3} X^{-3}, \quad (34.9a)$$

$$C_{mn}(\text{MWS}) = 8.06 \sigma_{\ln(A)}^2 k^{-7/6} X^{-11/6}. \quad (34.9b)$$

The integral over x in (34.8) represents the path-weighting function; it shows to what extent fluctuations at the relative position x/X along the path contribute to the measured scintillation signal. Path-weighting functions for a typical configuration of an optical LAS combined with an MWS are presented in Fig. 34.4.

Figure 34.4 illustrates that the path-weighting functions for a symmetric scintillometer setup are symmetric and have a clear peak in the middle of the path. They decrease towards the edges of the path, indicating that fluctuations close to the transmitter/receiver do not contribute significantly to the measured signal. This implies that flow distortion effects by the mount-

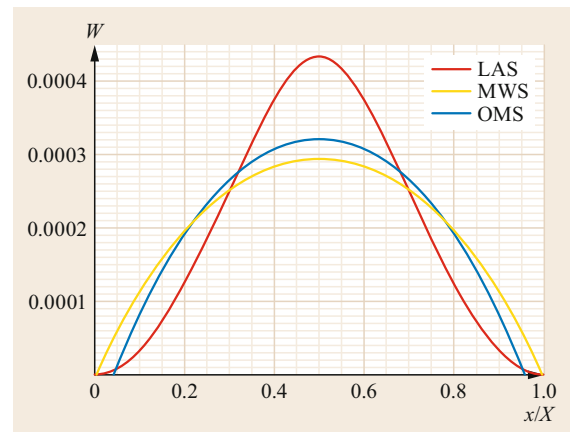


Fig. 34.4 Normalized path-weighting function W , vs. normalized path position x/X , for a combined LAS/MWS system with symmetric setup. Here, OMS means optical-microwave scintillometer (Sect. 34.4) and stands for the crosscorrelated signal between the LAS and the MWS systems (courtesy of Radiometer Physics GmbH)

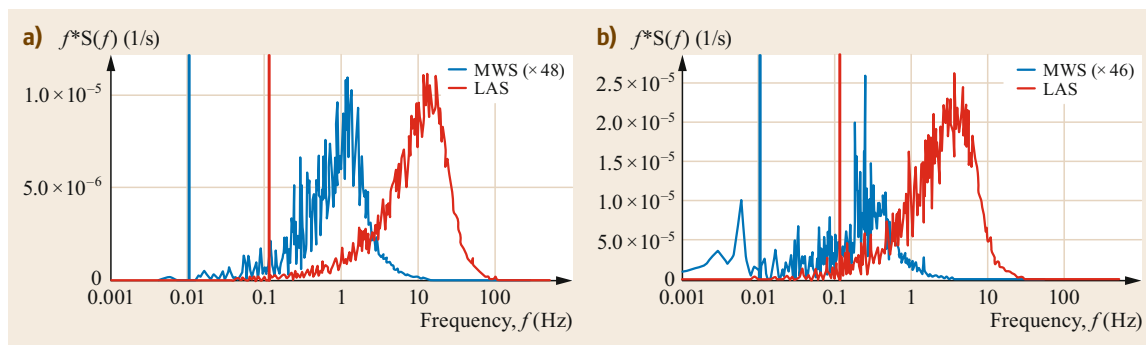


Fig. 34.5a,b Scintillation spectra from simultaneous LAS and MWS measurements with a Wageningen University and Research LAS (WURLAS) and an RPG-MWSC-160 (for the instruments, Sect. 34.4) measured at Lindenberg and visualized with the MWSC.exe software (Radiometer Physics GmbH) for realtime system watch. (a) 26.09.2018 00:00–00:17 UTC (moderate crosswind), (b) 30.09.2018, 00:00–00:17 UTC (low crosswind) – the vertical red and blue solid lines mark the cut-off frequencies of the high-pass filters

ing structures of the scintillometer units are not an issue for scintillometer measurements. This can be an advantage when selecting the positions where to install the scintillometer units, since it allows installation on, e.g., church towers or the roofs of buildings. The peak in the center of the path is broader for the MWS, while the curve for the optical LAS exhibits a sharp drop already at $x \approx X/2 \pm X/6$. This different behavior has to be kept in mind for the interpretation of combined optical-microwave scintillometer measurements over a heterogeneous land surface.

34.3.4 Saturation and Absorption

The proportionality between the measured scintillometer signal intensity fluctuations and the refractive index structure parameter as described by (34.9) is based on the theory of weak scattering, assuming that each wavefront of the electromagnetic signal coming from the transmitter is distorted only once before reaching the receiver. A criterion for the weak-scattering regime is given by the relation $\sigma_A^2 < 0.3$ [34.56]. Beyond this limit, when turbulence becomes stronger, the signal variance gets saturated and no longer increases with C_{nn} . In a transition region between both regimes, saturation effects cause deviations from the linear proportionality given by (34.9), but there is still an increase of the signal variance with C_{nn} , and models have been proposed to correct for these deviations from the single-scattering theory (e.g., [34.56–58]). The saturation issue is particularly relevant for the LAS. In practice, the effects of saturation can be reduced by increasing the LAS aperture, i.e., employing an extra large-aperture scintillometer (XLAS) instead of a LAS (Sect. 34.4), by reducing the scintillometer path length and/or by increasing the path height.

Scintillometers often operate at wavelengths where electromagnetic radiation is absorbed by water vapor or aerosols. Absorption fluctuations, however, typically occur at lower frequencies than the scintillations. In practice, they are often removed through a suitable high-pass filtering of the received signal. However, the position of the scintillation-caused spectral peak in the frequency domain is different for optical waves and microwaves (Fig. 34.5). Moreover, it depends on the crosswind (a property that allows to derive the crosswind speed from scintillation spectra, see Sect. 34.3.7), for low crosswind speeds, the spectrum is shifted towards lower frequencies. It is, thus, strongly recommended to allow for a variable high-pass-filter cutoff frequency when analyzing scintillometer data. If fixed filters are applied, different values should be allowed for the raw signal from an optical LAS and from an MWS. For the examples presented in Fig. 34.5, the LAS filter applied to the MWS signal would cut a significant part of the spectrum. In practice, the scintillation signal is often bandpass filtered in order to additionally remove unwanted electronic noise in the high-frequency range. Further unwanted contributions to the scintillation spectrum may result from vibrations of the mounting platforms; these are difficult to filter because their appearance may vary with wind speed, wind direction, or human activities around the site (traffic, building activities, tower maintenance, etc.). It should be noted that any filter has to be applied to the raw signal time series before calculating the variances.

Water droplets or dust may lead to additional extinction, in particular for visible and near-infrared radiation, such that only a weak or no detectable signal reaches the receiver. As a rule of thumb one may assume that optical scintillometers can only be operated if the visibility surpasses X , the scintillometer path length (Sect. 34.6).

34.3.5 The Derivation of Heat Fluxes Based on Similarity Theory

Monin–Obukhov similarity theory (MOST) is used to derive the surface fluxes of sensible heat, latent heat, and momentum from the structure parameters and from the eddy dissipation rate derived from the scintillation measurements. MOST represents a framework to parameterize the vertical profiles of atmospheric variables (temperature, humidity, and wind speed, but also variances and structure parameters) using a limited number of scaling parameters and a set of universal functions (Chap. 1). It has been developed to describe the structure of the atmospheric surface layer over a homogeneous surface under stationary atmospheric conditions. These assumptions should be kept in mind when defining a scintillometer setup and when interpreting the results of the measurements. In practice, MOST is often routinely applied to nonideal surfaces and under nonideal conditions. The surface layer is generally assumed to roughly cover the lowest 10% of the atmospheric boundary layer (ABL); hence, under daytime convective conditions scintillometer measurements with typical path heights < 50 m can be assumed to represent surface-layer turbulence. For stable conditions, this assumption may be violated, particularly in situations with weak winds and strong near-surface inversions. However, heat fluxes are usually small under these conditions, and even large relative errors often cause only rather small absolute errors. Quasi stationarity can usually be assumed over reasonably short averaging intervals, and it is a clear advantage of scintillometer measurements (when compared to, e.g., eddy-covariance measurements; Chap. 55) that statistically stable results can be obtained for averaging intervals down to a few minutes (1–10). The homogeneity assumption is usually fulfilled for a typical scintillometer setup at field scale. For a LAS setup at several decameters above ground (intended to provide regional-scale fluxes), it may be assumed that the path height is above the blending height where the varying signatures of small surface patches are blended by turbulent mixing.

MOST relates the nondimensional temperature and humidity structure parameter profiles to the surface fluxes via [34.48]

$$\frac{C_{TT}(z-d)^{2/3}}{\bar{T}_*^2} = f_{TT} \left(\frac{z-d}{L} \right), \quad (34.10a)$$

$$\frac{C_{qq}(z-d)^{2/3}}{\bar{q}_*^2} = f_{qq} \left(\frac{z-d}{L} \right), \quad (34.10b)$$

where T_* and q_* are the turbulent temperature and humidity scales (Chap. 1) defined through

$$T_* = -\frac{Q_H}{\rho c_p u_*}, \quad (34.11a)$$

$$q_* = -\frac{(1-\bar{q})Q_E}{\rho L_V u_*}, \quad (34.11b)$$

and f_{TT} and f_{qq} are universal functions of the height, reduced by the displacement height d , and nondimensionalized by L , the Obukhov length, which is given by

$$L = -\frac{\rho c_p u_*^3}{\frac{g}{T} \kappa Q_H}. \quad (34.12)$$

Here, κ is the von-Kármán constant, for which a value of $\kappa = 0.4$ is commonly accepted.

Most of the universal functions f_{TT} and f_{qq} proposed in the literature are of the general form

$$f_{XX} = a \left[1 - b_1 \left(\frac{z-d}{L} \right) + b_2 \left(\frac{z-d}{L} \right)^{c_1} \right]^{c_2} \quad (34.13)$$

The coefficients a , b_1 , b_2 , c_1 , and c_2 were determined by various authors based on data from field experiments; for an overview, see [34.59, 60]. Both the coefficients and the functional form differ for stable and unstable conditions. Some of the most common sets of coefficients that have been used to derive the sensible heat flux from scintillometer data are given in Table 34.3.

Depending on the choice of the similarity functions and their coefficients, the fluxes derived may differ substantially (Fig. 34.6). It has been demonstrated that the values of a and b_1 in the most common function used for unstable conditions (with b_2 not determined, $c_2 = -2/3$) depend on the observation height, on the stability range covered by the data, and on the regression approach used to fit the data [34.67].

The coefficients for the universal functions should, therefore, be carefully selected based on either recommended mean values [34.60] or on values that were determined for surface and climate conditions comparable to the actual application. In any case, a methodical uncertainty of the derived fluxes of about 10–20% must be assumed based on the uncertainty of the similarity coefficients. In practice, the same coefficients are often used for the universal functions f_{TT} and f_{qq} . This implies that temperature and humidity behave similarly and are perfectly correlated ($r_{Tq} = 1$) in the surface layer, which is, again, a simplifying assumption. There are a very few studies available only that have experimentally determined the coefficients for the humidity function f_{qq} [34.60, 64].

Table 34.3 Commonly used values for the coefficients in the universal functions for C_{TT} (see (34.13)), empty cells indicate that the model fitted by the authors to their data did not consider this specific coefficient/term

Reference	Unstable conditions					Stable conditions				
	a	b_1	b_2	c_1	c_2	a	b_1	b_2	c_1	c_2
Wyngaard et al. [34.48] ^a	4.9	6.1			-2/3	4.9		2.2	2/3	
Hill et al. [34.61]	8.1	15			-2/3					
Thiermann and Grassl [34.34]	6.34	7	75	2	-1/3	6.34	-7	20	2	1/3
de Bruin et al. [34.62]	4.9	9			-2/3					
Hartogensis and de Bruin [34.63]						4.7		1.6	2/3	
Li et al. [34.64]	6.7	14.9			-2/3	4.5		1.3	2/3	
Kooijmans [34.65]	6.15	12.0			-2/3	4.84		1.05	2/3	
Kooijmans and Hartogensis [34.60]	5.6	6.5			-2/3	5.5		1.1	2/3	

^a corrected for $\kappa = 0.4$ by Andreas [34.66].

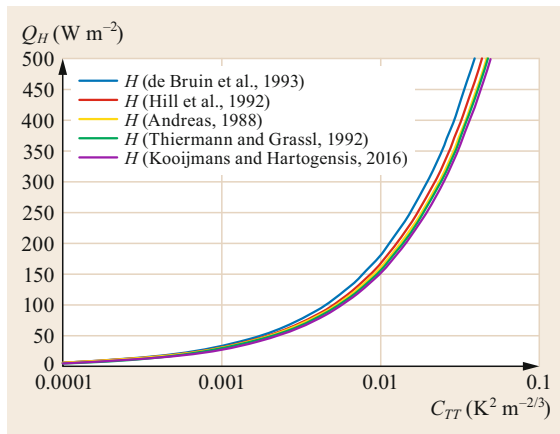


Fig. 34.6 Sensitivity of the derived sensible heat flux, Q_H , to the similarity coefficients in (34.13) for unstable stratification used by different authors (Table 34.3; the calculations were done assuming $z = 43$ m, and $u_* = 0.2$ m s⁻¹)

For the calculation of the sensible and latent heat fluxes via MOST based on (34.10)–(34.12), friction velocity is additionally needed in order to determine L , θ_* , and q_* . Methods to derive u_* are discussed in Sect. 34.3.6.

In the special case of free convection (weak wind conditions, unstable stratification above the surface layer), friction velocity no longer plays a role as a scaling velocity, and the similarity relationship between Q_H and C_{TT} is given through (e.g., [34.2, 48])

$$\frac{Q_H}{\rho c_p} = c C_{TT}^{3/4} \left(\frac{\bar{T}}{\kappa g} \right)^{-1/2} (z - d). \tag{34.14}$$

This equation allows for a direct estimation of the surface sensible heat flux from C_{TT} without the need for additional data on wind speed or friction velocity. The constant c depends on the choice of the similarity

constants for unstable stratification ((34.12) and Table 34.3), it is related to a and b_1 through

$$c = \frac{(b_1)^{1/2}}{a^{3/4}}$$

for the most common similarity model with no b_2 term and $c_2 = -2/3$.

34.3.6 Determination of Friction Velocity Using Similarity Theory

The dual-beam laser scintillometer (Sect. 34.4) is sensitive to eddy sizes close to the inner length scale of turbulence, l_0 ; it operates with two parallel laser beams a few millimeters apart from each other. For this specific setup, a scintillometer equation analogue to (34.8) can be formulated for the covariance between the signal amplitudes of the two beams. It can be shown that the correlation coefficient, r , calculated from this covariance and from the amplitude variances of the two beams becomes a function of l_0 only such that l_0 can be directly determined from r . The inner scale length is related to the dissipation rate of turbulent kinetic, ε , energy via

$$\varepsilon = \nu^3 \left(\frac{7.4}{l_0} \right)^4, \tag{34.15}$$

where ν is the kinematic viscosity of air, which depends on temperature, humidity, and pressure. MOST relationships can be formulated to link ε to the surface flux of momentum (represented by the friction velocity, u_*) using universal functions f_ε , which, again, have the general form given in (34.13)

$$\frac{\varepsilon \kappa (z - d)}{u_*^3} = f_\varepsilon \left(\frac{z - d}{L} \right). \tag{34.16}$$

For the calculation of the sensible and latent heat fluxes via MOST from the measurements with a single-beam and/or large-aperture scintillometer (Eqs. (34.10)–(34.12)), friction velocity is normally derived from independent representative wind measurements. Based on MOST, horizontal wind speed, V , and friction velocity are related through

$$u_* = \frac{\kappa V}{\ln\left(\frac{z-d}{z_0}\right) - \psi_M\left(\frac{z-d}{L}\right) + \psi_M\left(\frac{z_0}{L}\right)}, \quad (34.17)$$

where z_0 is the roughness length, and ψ_M is the integral of the universal function f_M , which, again, is given by a functional relationship of the type described by (34.13) with different forms for stable and unstable stratification, respectively (Chap. 1). The equation system defined by (34.10)–(34.12) has to be solved iteratively.

34.3.7 The Effective Path Height

The derivation of surface fluxes from scintillometer measurements using similarity theory as described in the previous sections always involves the height z as a key variable. Determination of the representative scintillometer path height above the surface is, therefore, an important issue. For a short path (magnitude 10^2 m) at low heights over a basically flat and homogeneous surface, the mean geometric height of the transmitter and receiver units, possibly reduced by the displacement height d (which can be roughly estimated as $2/3$ of the vegetation height), usually provides a reasonable value. For longer paths (10^3 – 10^4 m, the typical path length of LAS and MWS systems), over heterogeneous or very rough surfaces (e.g., cities) and over orographically structured terrain (e.g., across valleys with the transmitter and receiver units installed on the valley slopes or ridges), an effective path height has to be determined from a convolution of the variable geometric height above ground with the scintillometer path-weighting function [34.68]. In the case of strong surface or oro-

graphic variability perpendicular to the path, the height above ground should not be determined just from below the path but for the footprint area upstream of the path [34.24]. For a combined optical-microwave system, the different path-weighting functions of the two scintillometers have to be taken into account [34.69]. The estimation of representative values for displacement height and roughness length is important (since uncertainties in d and z_0 may cause appreciable uncertainties in the fluxes) but challenging in particular above strongly structured surfaces (e.g., heterogeneous forest or urban areas).

34.3.8 The Determination of Crosswind

In addition to the turbulent fluxes of heat and momentum, scintillometers also allow for the determination of the so-called crosswind, i.e., the component of the horizontal wind vector perpendicular to the scintillometer path. Basically, two types of method are available for this application [34.70–73]. The first type (e.g., [34.73]) is based on scintillation measurements with two parallel beams. Assuming Taylor's frozen turbulence hypothesis to be fulfilled, the turbulent eddy field does not change while being transported through the two scintillometer beams. The fluctuation time series recorded for the two beams should, therefore, show the same signatures, but with a time shift that depends on the mean wind perpendicular to the path. This crosswind can, thus, be derived from the time lag of maximum correlation between the two signals. This method is implemented with Scintec's dual-beam instruments (Sect. 34.4). The second type of method can be applied to single-beam large-aperture scintillometers [34.72]. It makes use of the fact that the position on the frequency axis of a characteristic inflection point in the scintillation spectrum depends on the crosswind speed. This approach cannot determine the sign (direction) of the crosswind and has so far not been implemented in the software of any of the commercially available scintillometer systems.

34.4 Devices and Systems

The scintillometer types in use mainly differ with respect to the wavelength of the radiation emitted, the beam configuration, and the geometrical dimensions of the transmitters and receivers. These instrument characteristics also determine the setup of a system (e.g., path length, path height). Scintillometers operating at wavelengths $\lambda \approx 400$ nm– 4 μ m are called optical scintillometers; systems using a wavelength

$\lambda \approx 1$ – 10 mm are called microwave (or millimeter-wave or radiowave) scintillometers (MWS). Most scintillometers emit one beam of electromagnetic radiation. The optical systems manufactured by Scintec AG (Sects. 34.4.1 and 34.4.2) use two parallel beams (dual-beam system or dual-disk system). This allows for an estimation of the crosswind (Sect. 34.3.8) and—for the laser scintillometers (Sect. 34.4.1)—the friction

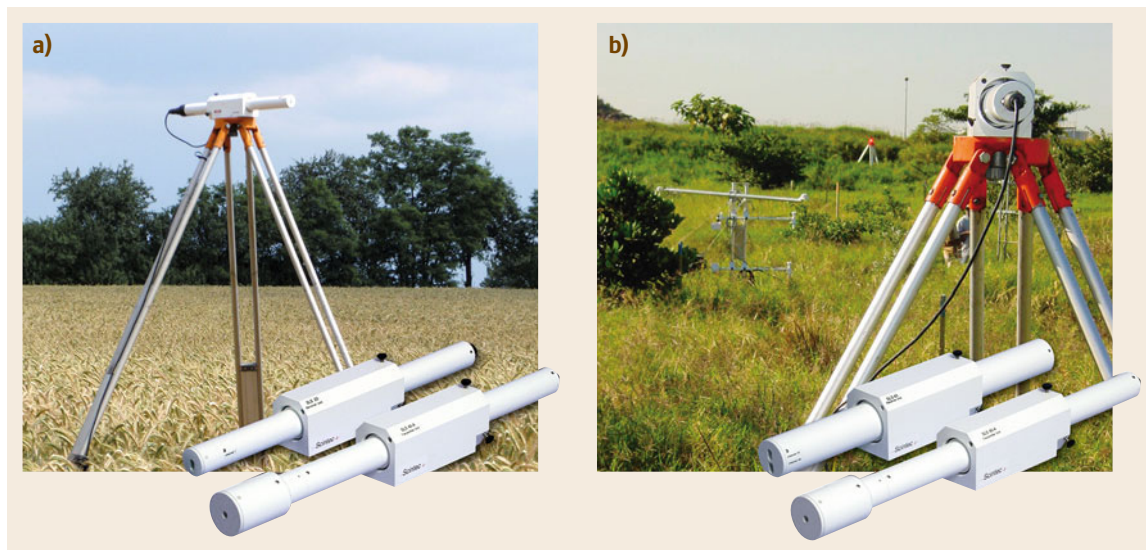


Fig. 34.7 (a) The SLS20/SLS40-A and (b) SLS40/SLS40-A units by Scintec AG (courtesy of Scintec AG; the right background photo was kindly provided by C. Jarman – South Africa)

velocity (Sect. 34.3.6) from analyzing the correlation between the two scintillation signals that are distinguished at the receiver side by a different polarization of the two beams. The following sections give a brief description of the scintillometer types widely applied and/or commercially available.

34.4.1 Optical Small-Aperture Scintillometers

The German manufacturer Scintec AG introduced to the market a series of optical dual-beam, small-aperture laser scintillometers (DBLS), called surface-layer scintillometers (SLS). Their basic application is the determination of the turbulent fluxes of sensible heat and momentum at field scale. They are generally operated within the atmospheric surface layer. A crosswind option is available. Scintec's SLS systems operate with visible laser light at 670 nm wavelength (red light); the laser is categorized as class 2M (IIIa).

There are four system versions available, the SLS20 and SLS40, and an A type of both systems (Fig. 34.7). The SLS20 is the basic version, the SLS40 has implemented special features to correct for possible vibrations of the mounting platforms (e.g., towers), while the A-version of both types offers automatic beam steering, a feature especially suited for operation on soft ground.

A careful calibration of the transmitter and receiver beam separations (which is offered by the manufacturer) is highly recommended, since specifically the calculated momentum flux is rather sensitive with respect to small deviations from preset standard values [34.43].

Special features implemented with the system hardware and software include:

- Window heating to prevent dew and ice deposition
- Radiation modulation for background elimination and interference filter for use in direct sun light
- Background noise and crosstalk measurement and correction options
- Amplitude and statistics tests on the mean and scintillation signals resulting in an internal data quality assessment
- Realtime data monitoring, including raw data and fluxes, and special display for alignment purposes
- Viewing and postprocessing options for previously recorded data.

Auxiliary pressure and temperature sensors can be directly connected to the system data acquisition unit to provide the meteorological input parameters necessary for the flux calculations and stability estimation.

34.4.2 Optical Large-Aperture Scintillometers

A series of research LAS was built by the Meteorology and Air Quality Department at Wageningen University and Research (WURMAQ) at the end of the 1990s. These instruments use a wavelength of 940 nm. The signal is emitted from an LED placed in the focal point of a concave mirror with a diameter of 15 cm. At the receiver side the same type of mirror is used to focus the scintillation signal on a photodiode (Fig. 34.8).



Fig. 34.8 The WURMAQ LAS transmitter mounted at the Falkenberg tower of DWD

In 2001, Kipp & Zonen adopted elements of the WURMAQ scintillometer design with its LAS MkI instrument, in which the signal is created by one single LED, and a Fresnel lens is used both at the transmitter and receiver sides to form the beam and to focus the received signal on a photodiode. This instrument was redesigned in 2012, resulting in the LAS MkII (a change of the infrared LED emitter and detector to improve range and performance, the addition of an infrared (IR) bandpass filter with a center wavelength at 850 nm to improve the signal-to-noise ratio, a larger detector area for easier instrument setup and alignment in the field, a change of the housing and internal optical mounting to allow outdoor alignment by hand and easy focusing of the LED and detector at the factory, replacement of the analogue electronics with internal

digital processing). The LAS MkII (Fig. 34.9) can be easily installed and configured using its built-in display and keypad without the need for any extra equipment. The receiver has a built-in data logger and digital outputs for direct PC connection. Realtime measurements are shown on the display. The C_{nm} data and demodulated signal are also available as an analogue output to be recorded using virtually any type of data acquisition system. The internal clock is automatically synchronized with a global positioning system (GPS) antenna. All systems are tested outdoors for 2 weeks and compared against reference instruments before being shipped to customers to ensure consistency and high data quality.

The EVATION[®] software included with the LAS MkII scintillometer is a fully featured configuration, monitoring and data processing program. The scintillometer can be controlled using EVATION[®] and it offers many data processing options and real time data display. The processing parameters are customizable for more advanced or application-specific processing options. Data files can be read to process data from LAS MkII analogue or serial outputs recorded on virtually any type of external data logger. The standard operating range of the LAS is 0.25–4.5 km, but this can be reduced to 0.1–1 km using the included reduction aperture set.

In 2018, a new version of the extra-large aperture scintillometer (XLAS) MkII was released with all the benefits of LAS MkII but extending the range to 12 km (Fig. 34.9). An additional design feature is the lightweight carbon fiber housing, which provides increased stiffness and reduced thermal expansion of the enclosure to maintain optical alignment.

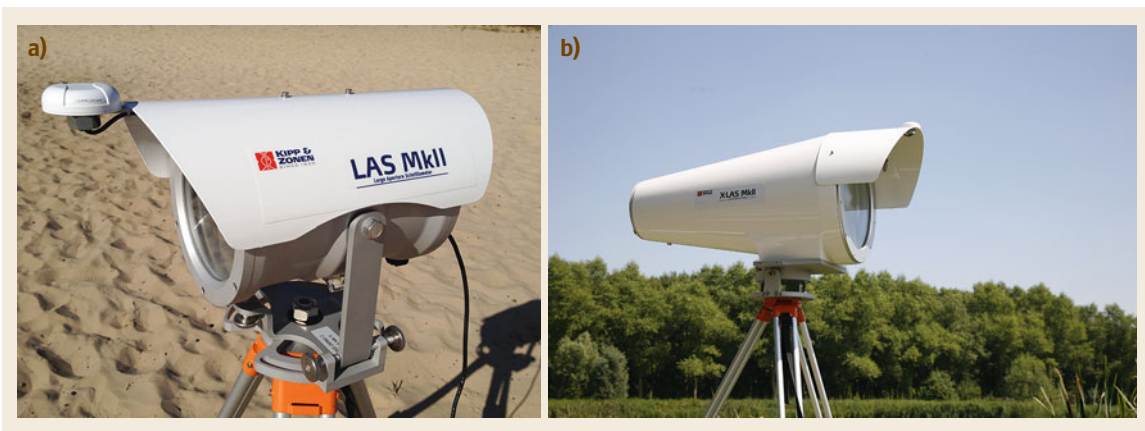


Fig. 34.9a,b The receiver units of the LAS MkII (a) and XLAS MkII systems (b) by Kipp & Zonen (courtesy of Kipp & Zonen B.V.)

Special features of the system include:

- Low maintenance and low power consumption
- Integrated data logger with analogue and digital outputs
- Stand-alone operation or direct PC connection
- Modulated IR beam and narrowband filter to avoid interference from surrounding light sources and sunlight
- Internal configuration option for high and low-pass filters
- Optional meteorological sensor (wind speed, air temperature and pressure sensors) plugs directly in the sensor port.

The system is also available as a LAS MkII ET (Evapo-Transpiration) system, which comes complete with scintillometer, meteorological sensors, and data acquisition capability.

Scintec AG offers three types of LAS, which are called boundary-layer scintillometers (BLS, to be distinguished from their surface-layer scintillometers, SLS): the BLS450, the BLS900, and the BLS2000. The transmitter signal originates from a large number of LEDs (444, 888, and 1756, respectively; these numbers also determine the system names) arranged on one (BLS450) or two disk(s) (BLS900, BLS2000 – Fig. 34.10), the transmitter divergence is 16° , resulting in a quite large illuminated area with increasing path length. This reduces the sensitivity to misalignment or instability of the mounting structures. At the receiver side, a glass (BLS450



Fig. 34.10 The BLS-900 transmitter and receiver units (courtesy of Scintec AG; background photo kindly provided by C. Jarman – South Africa)

and BLS900) or Fresnel lens (BLS2000) acts to focus the signals on two photodiodes. The BLS450 and the BLS900 are classified as LAS systems; the BLS2000 is an extra-large aperture scintillometer (XLAS). An aperture-reduction is available for operation of the BLS over paths shorter than the specified lower limit (500 m and 1 km, respectively – Table 34.6). The dual disk transmitter of the BLS900 and BLS2000 emits two parallel beams allowing both the determination and correction of possible contributions from absorption fluctuations to the scintillation signal and the determination of the cross-wind perpendicular to the path.

Special features implemented with the system hardware and software include:

- A selectable transmitter pulse repetition rate (which is of relevance in particular if available transmitter power is limited for operation with batteries or solar panels).
- A series of 18 red-light LEDs in each transmitter LED row to indicate the transmitter status.
- Radiation modulation for background elimination and interference filter for use in direct sunlight.
- Optical alignment aid for the receiver using two detectors.
- Automatic corrections for saturation, absorption fluctuations, and outer scale effects.
- Error identification based on the received signal characteristics.
- Comprehensive realtime data monitoring, including raw data and fluxes, and special display for alignment purposes.
- Viewing and postprocessing options for previously recorded data files.

Auxiliary pressure, temperature, and wind sensors can be directly connected to the system data acquisition unit to provide the meteorological input parameters necessary for the flux calculations.

34.4.3 Microwave Scintillometers

Several noncommercial microwave scintillometers have been built over the last three decades; they have mainly been used within research projects. An overview on these systems is given in Table 34.4.

Due to the large wavelength (when compared to optical scintillometers), all microwave scintillometers are so-called small-aperture systems for which the diameter of the first Fresnel zone determines the size of the eddies that contribute to the scintillation signal detected at the receiver.

In 2014, the commercial microwave scintillometer MWSC-160 was introduced to the market by Radiome-

Table 34.4 Research type microwave scintillometers used over the last 30 years

Manufacturer	Frequency (GHz)	Wavelength (mm)	Transmitter/receiver aperture (m)	References
Eindhoven University of Technology	27	11	0.6	Green et al. [34.23], Meijninger et al. [34.25]
University of Bern	94	3.2	0.4	Lüdi et al. [34.39], Meijninger et al. [34.74]
Rutherford Appleton Laboratory	94	3.2	0.25	Evans [34.36], Ward et al. [34.37, 38]
Monash University	26/38	12/8		Mei Sun Yee et al. [34.75]



Fig. 34.11a–c The RPG MWSC-160 combined with different LAS systems; **(a)** with a WURMAQ LAS at the tower at Lindenberg Meteorological Observatory – Richard-Aßmann-Observatory, **(b,c)** with a Kipp & Zonen LAS MkII system (photos courtesy of DWD and Kipp & Zonen B.V., respectively)

ter Physics GmbH (RPG). The system combines the experience from previous design versions with the theoretical expertise from WURMAQ and the experience in microwave technology available at RPG. It can be combined with each of the commercially available optical LASs and even with the noncommercial WURMAQ LAS to form an optical-microwave scintillometer system (OMS) suitable for estimating both the sensible and latent heat fluxes (Fig. 34.11). A standard WXT-5xx (Vaisala Oy) weather station can be directly connected to the system data acquisition unit to provide the meteorological input parameters necessary for the flux calculations. It also gives a rain flag to remove data during precipitation when the assumptions of scintillometer theory are violated.

Special features implemented in the system software include:

- Comprehensive realtime data monitoring, including raw data, spectra, derived fluxes, and system internal (housekeeping) data.
- Corrections for saturation and absorption fluctuations.
- User-selectable configuration of high-path filters; A_T and A_q coefficients (34.1), similarity function coefficients (34.13)
- Internal calculation of the effective path height based on prescribed topography along the path and on the mounting heights of the transmitter/receiver units.
- Viewing and postprocessing options for previously recorded data files.

34.4.4 Summary of Assumptions, Advantages and Disadvantages of Scintillometers

Table 34.5 gives a brief overview of the basic assumptions behind scintillometry methods and applications and of the advantages and disadvantages of scintillometers to derive the turbulent fluxes of sensible heat, latent heat, and momentum.

Table 34.5 Assumptions, advantages and disadvantages of scintillometry

<p>Assumptions and limitations</p> <ul style="list-style-type: none"> • Weak scattering ($\sigma_A^2 < 0.3$, otherwise saturation may occur) • Log-normal frequency distribution of instantaneous measured signal intensities • Relevant eddy size within the inertial subrange of turbulence, for $(D, F) \approx l_0$ a model parameterization for the turbulence spectrum of refractive index must be applied • Prescribed values for r_{Tq} to determine C_{TT} and C_{qq} from C_{mm} (except for the bichromatic method) • Parameterization of the humidity contribution to C_{mm} for a stand-alone optical scintillometer with increasing uncertainty for $Bo < 0.3$ • Effective path height above the blending height (above heterogeneous surfaces) • Applicability of Monin–Obukhov similarity theory (horizontal homogeneity, stationarity) 	
<p>Advantages</p> <ul style="list-style-type: none"> • Provides line-/area-averaged flux values at scales of 10^2–10^4 m resulting in an improved spatial representativeness, especially over heterogeneous surfaces • No absolute calibration of signal strength required because relative intensity fluctuations are evaluated • Statistically stable results even for short averaging times (since the size of sampled eddies is more than three magnitudes smaller than the path length and the wind fetch, i.e., the product of effective crosswind speed and averaging time) allowing to study fast processes • Low maintenance requirements • No flow distortion (since the path weighting function goes to zero at the transmitter and receiver positions) • Operation at (very) low heights possible (for the DBLS: $F \ll z$ is fulfilled for $z > 0.1$ m, for a LAS $D \ll z$ is fulfilled for $z > 1.5$ m) 	<p>Disadvantages</p> <ul style="list-style-type: none"> • Need for additional temperature and pressure data for the flux calculations (default values may be used but increase uncertainty) • Need for additional wind data (except for the DBLS) and estimates of d and z_0 for the flux calculations, derived fluxes linearly depend on uncertainties in d and z_0 • Need for additional measurements/assumptions to distinguish between stable/unstable stratification • Large relative uncertainty due to pronounced minima of C_{mm} at near-neutral stratification (but low fluxes under these conditions) • Water vapor absorption at optical and mm wavelengths (absorption fluctuations can be removed by spectral separation and filtering or by the dual-beam technique) • Reduced signal strength (and data availability) in case of precipitation, haze/fog and strong turbidity because of heavy smoke or dust due to particle/droplet extinction of radiation • Uncertainty of the derived fluxes due to different MOST stability functions and coefficient values available

Part C | 34.5

34.5 Specifications

Table 34.6 gives an overview of the basic system specifications, the typical setup conditions, and the basic output variables of the scintillometer systems commercially available at present.

Most commercial scintillometers are specified for environmental conditions between -20 and $+40$ °C for temperature and between 0 and 100% for relative humidity.

Table 34.6 Basic specifications of scintillometer systems commercially available in 2018

Instrument	SLS20/SLS40	BLS450	BLS900	LAS MkII ^a	BLS2000	XLAS MkII ^a	MWSC-160
Manufacturer	Scintec	Scintec		Kipp & Zonen	Scintec	Kipp & Zonen	RPG
Specifications							
Number of beams	2	1	2	1	2	1	1
Wavelength	670 nm	880 nm	880 nm	850 nm	880 nm	850 nm	1.86 mm
Aperture size ^b	(2 mm)	14 cm	14 cm	(10) 15 cm	26.5 cm	(15) 32.8 cm	30 cm
Signal power	1 mW	7.5 W (peak)	15 W (peak)	0.5–6 W	28 W (peak)	0.5–6 W	25 mW (peak)
Typical setup							
Height	0.5–5 m	1.5–50 m	1.5–50 m	1.5–50 m	3–100 m	3–100 m	3–100 m
Path length ^b	0.05–0.25 km	(0.1) 0.5–6 km	(0.1) 0.5–6 km	(0.1) 0.25–(1) 4.5 km	1–12 km	(0.25) 1–(4.5) 12 km	1–10 km
$F = (\lambda X)^{1/2}$	8 mm	3 cm	3 cm	3 cm	7 cm	7 cm	3 m
Dimensions	$D < F \propto l_0$	$l_0 < F < D$	$l_0 < F < D$	$l_0 < F < D$	$l_0 < F < D$	$l_0 < F < D$	$D < F$
Derived variables	Q_H, u_*, u_{cross}	Q_H	Q_H, u_{cross}	Q_H	Q_H, u_{cross}	Q_H	Q_E

^a The given specifications also apply to the Kipp & Zonen LAS MkI upgrade and XLAS MkI upgrades to MkII

^b Values in brackets apply to the reduced-aperture versions

34.6 Quality Control

Scintillometers measure intensity fluctuations of electromagnetic radiation around a mean value, hence no (absolute) calibration is needed against any standard or reference instrument (except of the internal analogue system electronics, in the case of the WURMAQ design, but this is probably a historical aspect). Geometrical dimensions (e.g., aperture size of a LAS/XLAS, transmitter and receiver beam separations of Scintec's dual-beam surface-layer scintillometer) have to be accurately prescribed, and instrument-specific values should be used instead of default values [34.43].

When interpreting the derived fluxes, the assumptions behind the method should always be kept in mind (Sect. 34.4.4). Commercial scintillometer systems have often implemented certain corrections in their software (e.g., for saturation, absorption, inner/outer scale effects), as well as some quality tests (e.g., mean signal strength, statistical distribution of the fluctuations). Correction factors and quality flags given in the output files should always be considered during data interpretation. Figure 34.12 illustrates the frequency distribution of correction factors applied to two types of BLS systems. The correction for high-pass filter effects is almost negligible except under low crosswind conditions. The corrections for inner scale effects and saturation are less relevant for the BLS2000 because of the larger aperture diameter when compared with the BLS900. However, the different corrections may partly compensate for each other such that the total effect (Fig. 34.12b) is smaller than $\pm 10\%$ in more than 2/3 of the cases. When using the bichromatic method to derive the sensible and latent heat fluxes from a combined optical-microwave scintil-

lometer, the r_{Tq} values determined from the correlation between the two signals should always be critically examined for unphysical values ($|r_{Tq}| > 1$); in the case of $|r_{Tq}| < 0.3$, the fluxes should be interpreted with caution, since low values of the correlation indicate a violation of the assumptions behind MOST.

The definition of structure parameters (34.2) is based on the absolute differences of atmospheric variables at positions x and $x + \Delta x$ without taking into account the sign of the differences. Therefore, scintillation measurements alone generally do not allow for a determination of the sign of the heat fluxes. Since different MOST functions have to be applied to derive the surface fluxes under stable and unstable conditions, the software of commercial systems often provides calculated fluxes for both stability regimes in the output data files. Alternatively, ad-hoc assumptions might be implemented, such as a prescribed change of the heat flux sign in relation to sunrise and sunset. If fluxes for both stable and unstable conditions are reported, the decision as to their choice has to be made by the user. Gradient measurements of mean temperature and humidity in the vicinity of the scintillometer path may support this decision. Moreover, with a clear diurnal cycle of ABL development, in particular C_{TT} exhibits pronounced minima in the case of (near-)neutral stratification indicating the change from stable to unstable conditions and vice versa (Fig. 34.13). The occurrence of these minima can be taken as an indicator for the change of flux signs directly from the scintillometer measurements. An assessment of various methods to determine the stability transition can be found in [34.76].

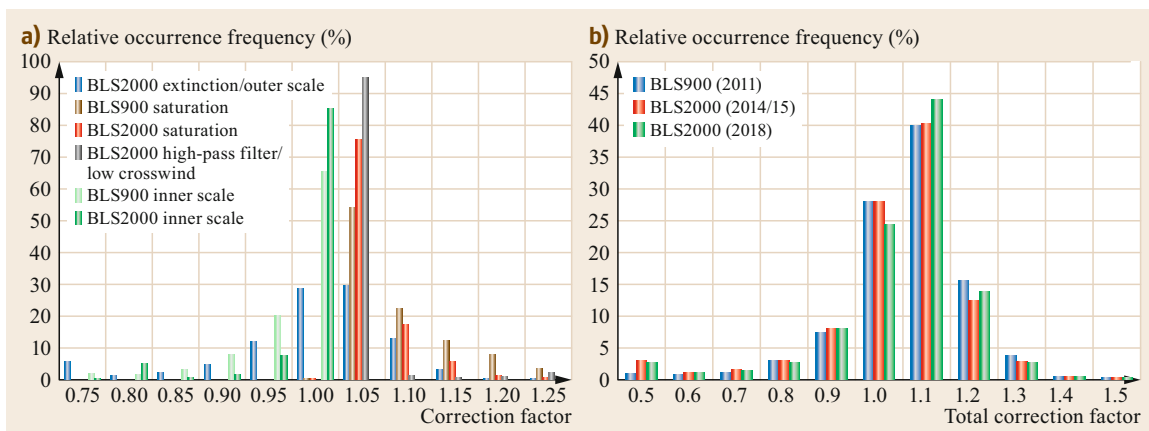


Fig. 34.12a,b Frequency distribution of correction factors to the measured signal intensity variances for BLS900/BLS2000 measurements: (a) Single corrections and (b) total correction. Measurements were performed in 2011 (BLS900), 2014/2015, and 2018 (BLS2000) over a distance of 4.8 km at Lindenberg Meteorological Observatory, Richard-Aßmann-Observatory, Germany

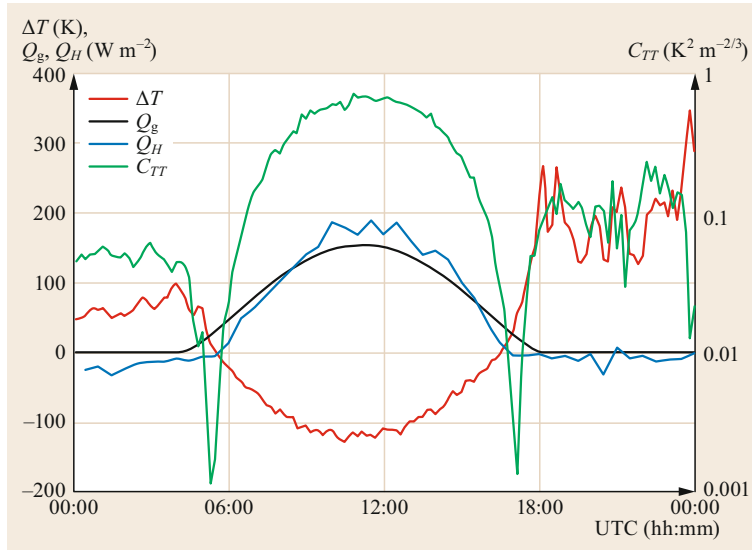


Fig. 34.13 Diurnal cycle of the temperature structure parameter C_{TT} , global radiation Q_g , sensible heat flux Q_H , and the temperature difference ΔT near ground ($T_{2m}-T_{0.5m}$) on 26.08.2016 at Falkenberg (Germany) under clear-sky conditions. Pronounced minima in C_{TT} occur when the gradients and fluxes change sign in the morning/evening (note that global radiation is multiplied by a factor of 0.2 and the temperature difference by a factor of 100, respectively, for scaling purposes)

Part C | 34.6

As with all measurement techniques, it is recommended to check the derived meteorological variables for plausibility. This should include a consistency check between the flux sign and the sign of the gradients of temperature and humidity below the path (if these gradients are not used earlier to decide on the flux sign). Note also that for operation heights of several decameters AGL of LAS, MWS, and OMS systems, MOST links the surface fluxes to elevated measurements of the structure parameters, which only holds if the gradients do not change sign between the surface and the scintillometer path height; this makes scintillometer fluxes uncertain during morning and evening transition in the near-surface layer. In addition, the sum of sensible and latent heat fluxes determined from LAS and MWS measurements should be critically compared versus measurements (or estimates) of net radiation and soil heat flux not to exceed the energy available for turbulent exchange processes over longer time periods.

A summary of the different steps of quality control recommended for scintillometer measurements is given in Table 34.7.

Based on the performance of these tests, the availability of good-quality derived flux values can be expected for about 60–90% of the operation time, which is comparable to the eddy-covariance method (Fig. 34.14).

Results of scintillometer intercomparison experiments have been reported, e.g., in [34.40–44]. These studies reveal that the instrumental differences result in a flux uncertainty of typically 3–10%. A larger uncertainty may be due to methodical issues, i.e., the application/realization of certain corrections within the system software, the difficulty in determining representative values of roughness length and displacement height, and the choice of the similarity coefficients; these aspects may lead to flux uncertainties of about 15–25%.

Table 34.7 Quality control criteria for scintillometer measurements

Category	Test
Mean and scintillation signal (tests are usually implemented in the system software provided by the manufacturer, but can be applied by the user if the scintillation raw data are recorded) Assumptions behind the methodology	<ul style="list-style-type: none"> • Mean signal intensity above a certain threshold minimum value • No singular spikes in the signal intensity time series • Statistical distribution of the scintillation signal close to log-normal • No pronounced/broad peaks in the spectra (due to vibrations or electronic noise) • No saturation ($\sigma_A^2 < 0.3$) • No precipitation • $Bo > 0.3$ (for LAS, to ensure applicability of (34.5)) • $0.3 < r_{Tq} \leq 1$ • Consistency of the gradients below the scintillometer path height
Resulting fluxes	<ul style="list-style-type: none"> • Flux sign in agreement with gradients or rule-of-thumb assumptions • Sum of the derived turbulent fluxes should not exceed available energy (i.e., the sum of net radiation and soil heat flux)

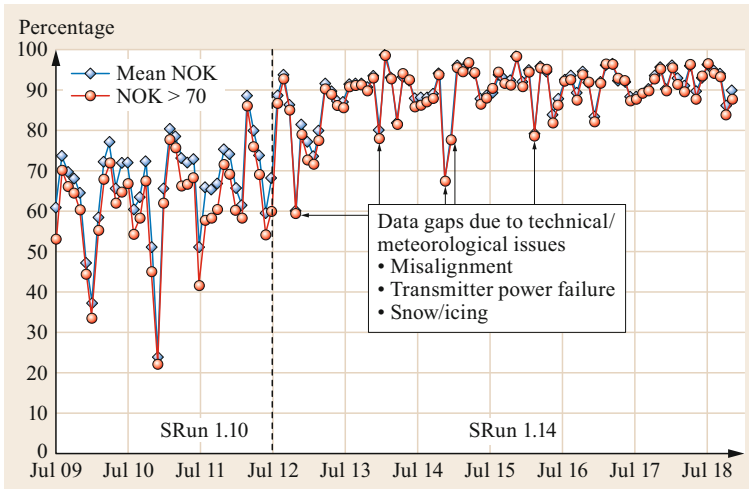


Fig. 34.14 Monthly mean values of data availability of heat and momentum fluxes from SLS-40 measurements at Falkenberg (Germany) (the NOK parameter indicates the percentage of sampling intervals with good statistics of the scintillation signal; a value of 70% has been found as a reasonable threshold for good quality fluxes – note the change in system software in July 2012)

34.7 Maintenance

Scintillometer systems are generally well-suited for unattended long-term operation and require only a minimum of maintenance efforts, basically a cleaning of the units depending on the environmental conditions.

A number of different aspects has to be taken into account in connection with the installation of a scintillometer system; these include scientific (path should be centered around the flux source area of interest and preferably oriented perpendicular to the prevailing mean wind direction), logistic (mounting structures, power supply, LAN availability, accessibility for maintenance, security), and methodical aspects (path height well above the roughness sublayer, path height in relation to path length to avoid frequent saturation, no obstacles within the first Fresnel zone, for optical systems: receiver should be positioned such that it does not receive direct sunlight). For the operation of microwave scintillometers, a frequency allocation permission has to be obtained from the responsible national agency. Care has to be taken during installation and set up with respect to mounting stability and optimum alignment. Path length, path height, and (in the case of a combined optical-microwave system) the relative distances of the transmitter and receiver units with respect to each other in both y and z -directions should be determined with an accuracy of 2% or better, since these geometric variables directly enter the internal calculations of the spectral filter and path-weighting functions. Bird protection measures of the scintillometer units and/or connected meteorological sensors might be required, depending on the site conditions.

The formation and accumulation of water droplets or ice crystals at the transmitter and receiver windows or antenna surfaces under humidity conditions close to saturation and during precipitation is normally prevented by transmitter/receiver heating. However, water or ice may temporarily accumulate on the surfaces if the wind acts on the windows during heavy precipitation or snow drift. Strong wind load on the transmitter and receiver units may cause some misalignment, and regular checks of the signal strength and of the optimum alignment are thus recommended; these should include checking the proper fixing of the positioning screws. Moderate to strong winds may also cause vibrations of the mounting structures, which might add additional variance to the measured scintillation spectra, although not all vibration frequencies are necessarily seen or are inside the relevant frequency range of the scintillation spectra (e.g., [34.77]). Single narrow peaks in the scintillation spectra might be removed in data processing by fitting a model spectrum to the measured one (e.g., [34.28]).

Regular system supervision should be performed according to the user's request for data availability and completeness to be able to rapidly react on a persisting drop or breakdown of the receiver signal that might occur as a result of an instrument fault, of mechanical (misalignment due to mechanical forces, e.g., strong wind), electrical (power failure, empty batteries, broken cables, overvoltage), or weather-related (e.g., snow/ice on the transmitter/receiver windows/antenna surfaces) events. Note that precipitation or fog generally reduce the re-

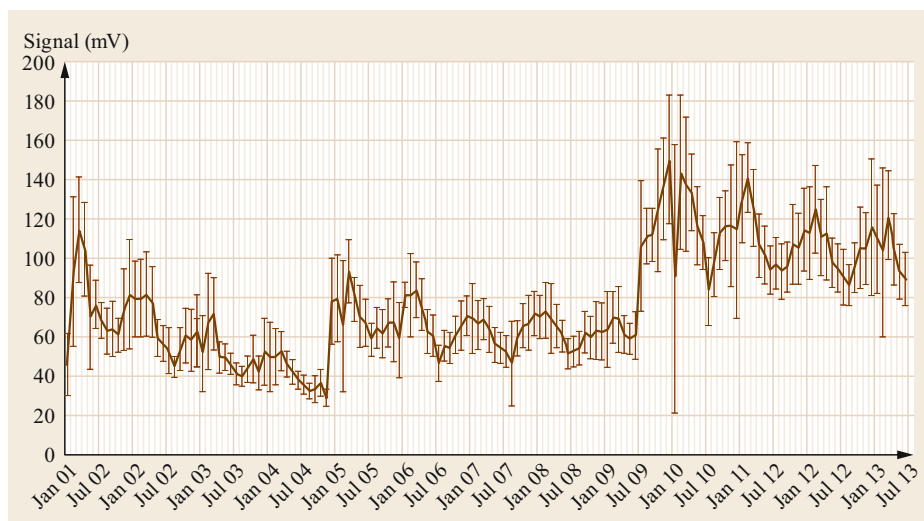


Fig. 34.15 Long-term behavior of monthly mean receiver signal intensity and its standard deviation for a WURMAQ LAS system operated at Lindenberg, Germany. A mean annual cycle and phases of gradual decrease can be clearly seen; in spring 2005, the transmitter light source was replaced, and in summer 2009, the transmitter power was increased

ceived signal (normally below an acceptance threshold, resulting in no output data) without the need for user-specific action. Supervision should include an inspection of error flags given in the data files or error messages contained in the system log files, and attention to the messages related to time synchronization.

It is recommended to check the status of the transmitter and receiver windows/surfaces, the transmitter output power (control LED status in case of the Scintec BLS disk systems), and the alignment of the transmitter and receiver units at monthly to yearly intervals. For the SLS instruments, a background/crosstalk measurement should be performed at the same time. The frequency of these checks (in particular of the (re)alignment) strongly depends on the mounting and surface conditions. For concrete roof or tower mountings, annual alignment control might be sufficient; with tripods on soft ground, monthly control might be necessary.

For long-term operation (several years to decades) the mean received signal intensity should be calculated

as a monthly block or moving average in order to detect a possible slow degradation of the transmitter source (Fig. 34.15). Initial reduction of the emitted radiation intensity can usually be compensated by an increase of transmitter power.

Note that a pronounced annual cycle in mean signal intensity – depending on the site conditions – can often be observed, which is related to the mean water vapor content in the atmospheric surface layer. Such seasonal variations are particularly pronounced for microwave scintillometers. For these systems, it might be recommended to change transmitter power regularly in spring and autumn to ensure optimum signal strength both in humid summer and in dry winter conditions. A summary of supervision and maintenance activities is given in Table 34.8. The frequency of the single measures strongly depends on the user's need and on the site conditions. The recommended regular control activities listed in the first row can be done remotely with no site access needed.

Table 34.8 Recommended supervision and maintenance activities for scintillometers

Frequency	Activity
Regularly (daily to weekly)	<ul style="list-style-type: none"> • Check for data availability and reasonable mean signal behavior • Check for system error messages and time synchronization
From time to time (monthly to seasonally)	<ul style="list-style-type: none"> • Check status of units/windows, cleaning if necessary • Check/optimize alignment (soft ground)
Occasionally (seasonally to annually)	<ul style="list-style-type: none"> • Check/optimize alignment (stable mounting) • Check/adjust transmitter power

34.8 Applications

Scintillometers have demonstrated their value for a great variety of applications for which area-averaged meteorological quantities over short averaging times are of special relevance. The following sections provide some examples without the claim of completeness.

34.8.1 Field-Scale Fluxes Using the Dual-Beam, Small-Aperture Scintillometer

The dual-beam, small-aperture scintillometer is typically operated at installation heights of 1–5 m AGL and over path lengths of 100–200 m. It thus allows for the determination of the turbulent fluxes of sensible heat and momentum at field scale; the latent heat flux can be estimated as the residuum of the energy budget equation or by using the Bowen ratio method (Chap. 58), if the scintillometer is supplemented by measurements of net radiation, soil heat flux, and the gradients of temperature and humidity. For the determination of sensible heat and momentum fluxes at field scale, scintillometers can be seen as an alternative to turbulence measurements using the eddy-covariance method (Chap. 55). Compared to the latter, scintillometry has several advantages:

- Due to the path averaging of the scintillation signal, the footprint area of a scintillometer-based flux is considerably larger than for a point measurement using a sonic anemometer-thermometer; resulting fluxes may thus be more representative, especially over locally heterogeneous surface patches.
- The light beam is influenced by thousands of eddies along the propagation path sampled at frequencies of 10^3 – 10^4 Hz, which results in statistically stable

results even for short averaging times, down to the order of a minute, while the eddy-covariance method always requires averaging times of 10–30 min to obtain reasonable spectral coverage. This is of special relevance in nonstationary conditions, e.g., with rapidly changing cloud cover (Fig. 34.16).

- The dominant eddy size seen by the laser scintillometer is ≈ 1 cm, which allows for very low measurement heights above ground (even < 1 m is possible over flat surfaces with no or short vegetation) and, thus, for flux measurements over small surface patches of a rather limited upstream extension, where the fetch requirements of the eddy-covariance method are often not met.

Numerous examples of laser-scintillometer-based fluxes can be found in the literature for various types of natural and managed surfaces, preferably over low vegetation and in different climate regions [34.34, 79–82]. A few studies also report on fluxes over urban surfaces [34.83, 84]. The path-averaging effect becomes of particular relevance over sparse vegetation, where a suitable averaging over patches with plants and patches of bare soil can be achieved. Comparisons of the scintillometer-based fluxes versus eddy-covariance data usually give comparable statistics to eddy-covariance intercomparison experiments, i.e., typical deviations around 10–15%.

A special application is the derivation of trace gas fluxes (water vapor, carbon dioxide) for short averaging times (1 min) over a homogenous agricultural surface using scintillometry in combination with the variances derived from the raw data of a fast-response infrared gas analyzer (Fig. 34.16) [34.78].

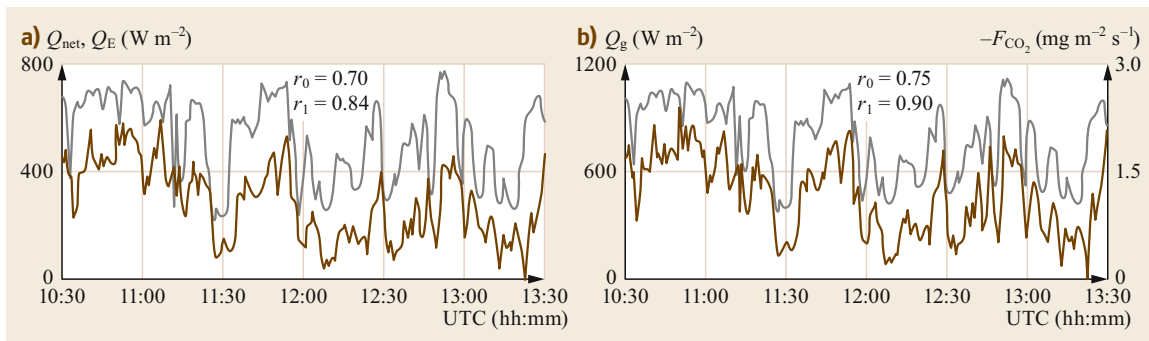


Fig. 34.16a,b Time series of net (global) radiation (grey lines) and of the fluxes of water vapor (a) and carbon dioxide (b) derived with 1 min resolution from a combination of scintillometer and infrared gas analyzer measurements. Data were collected at Merken (Germany) on 14.08.2008, r_0 and r_1 are the correlation coefficients between the time series of the radiation and the trace gas fluxes for a time delay of 0 and 1 min, respectively (after [34.78] with permission from Elsevier)

34.8.2 Meso- γ Scale Fluxes from LAS and OMS

LAS and OMS systems are typically operated over a path length of several kilometers, thus providing surface fluxes at regional scale; such fluxes are of special interest for a variety of applications, including:

- The development and validation of parameterizations in numerical weather prediction and climate models, the grid resolution of which matches well with the scintillometer path length (e.g., [34.29, 85])
- The validation of flux retrieval schemes from satellite data – again the pixel resolution is similar to the scintillometer path length (e.g., [34.22, 85, 86])
- The determination of evaporation at the scale of small catchments for hydrological applications (e.g., [34.76, 87, 88])
- The determination of evaporation over agricultural farmland in connection with irrigation management (e.g., [34.26, 27, 89])
- The determination of heat and water vapor transport over cities in connection with the management and development of urban structures (e.g., [34.37, 38, 90]).

With an OMS, both the sensible and latent heat fluxes can be determined directly from the scintillometer measurements. A single LAS only provides the sensible heat flux; evaporation is then usually determined as the residual of the energy budget, which additionally requires radiation measurements and a reasonable assumption for the soil heat flux representative for the LAS path.

Heat fluxes from LAS and OMS systems have been demonstrated to be reliable over various types of un-

derlying surface and in different climate regions of the world, including heterogeneous midlatitude farmland [34.24, 25, 31, 36, 74, 91], Mediterranean dry landscape and irrigated farmland [34.13, 21, 27], sparse steppe and desert vegetation [34.22, 92–94], wetlands and rice paddies [34.95], and over both midlatitude and tropical forests [34.28, 57]. A few experiments were realized over moderately complex terrain, along mountain slopes and across valleys [34.36, 68]. Over the last two decades LAS and OMS measurements were increasingly performed over cities [34.37, 38, 90, 96–99]. For these two types of surfaces, complex terrain and urban regions, special attention has to be paid to the determination of the effective path height taking into account the considerable variability across the footprint area and variations in the displacement and roughness heights as well as potential issues with MOST.

Considering heterogeneous land surfaces, scintillometry appears to be the only method suited for routine operational estimation of area-averaged surface fluxes. Alternative methods such as airborne flux measurements, the application of budget considerations to observed boundary layer evolution or the operation of eddy-covariance systems at all relevant surface types occurring in a certain region are either too expensive from the point of instrumentation and operation, not suited for continuous operation or limited to specific situations because of certain methodical assumptions. An assessment of scintillometer fluxes compared to aggregated surface layer measurements using more than ten eddy-covariance systems operated over different types of farmland and to airborne flux measurements within the LITFASS-2003 experiment [34.74, 91] demonstrated their reliability (Fig. 34.17). With the same data set, it could be shown that a better closure of the surface energy budget could be achieved

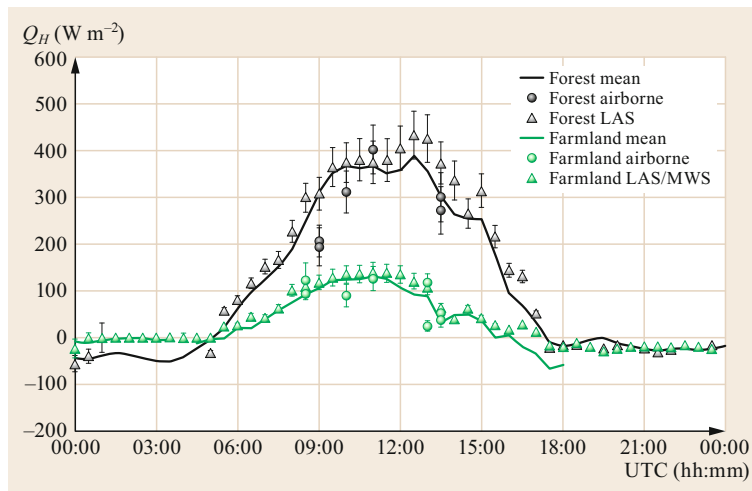


Fig. 34.17 Diurnal cycle of sensible heat fluxes over farmland and forest as determined from eddy-covariance measurements (lines, over farmland data from 11 eddy-covariance systems provided the *farmland mean*), LAS (triangles), and airborne measurements (circles) on 25.05.2003 over the LITFASS area (after [34.91])

when compared to eddy-covariance data [34.74], which is still an open issue in micrometeorological research (e.g., [34.100] and Chap. 55).

34.8.3 Crosswind Determination

Dual-beam scintillometry allows for the determination of the line-averaged crosswind component perpendicular to the path. This capability is of special interest for a number of applications including:

- The determination of bulk transport in regions with dominant wind directions, e.g., along valleys (e.g., [34.101, 102])
- The determination of the source strength of trace gases or aerosols at the borders of farms or waste disposal sites [34.18]

34.9 Future Developments

Very reliable and stable scintillometer systems – from a technical point of view – are nowadays commercially available for the different applications described above. Their operation and data analysis relies on a profound theoretical basis, and on often evaluated methods and algorithms. Scintillometers can be seen as advantageous over classical turbulence measurement techniques, e.g., eddy-covariance systems, for the determination of representative flux values above structured terrain, such as valleys, urban areas, and heterogeneous land surfaces. Despite this potential, scintillometers are still rarely employed beyond the research community. Further qualification of the data analysis and presentation software of commercial scintillometers for non-

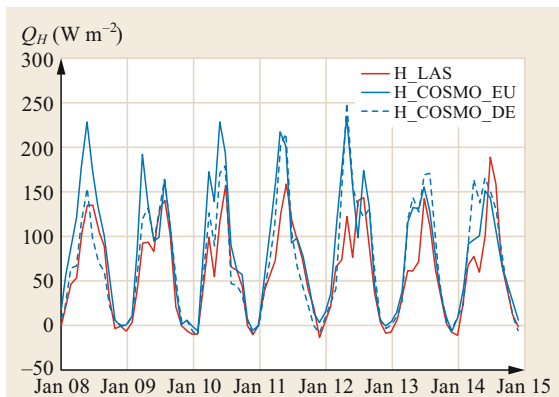


Fig. 34.18 Monthly mean values of the 12 UTC sensible heat fluxes from LAS measurements and from the regional operational numerical weather prediction models at DWD

- The determination of the wind component perpendicular to the runway at airports [34.20, 103].

34.8.4 Applications in Geodesy and Astronomy

Refractive index fluctuations in the atmosphere deteriorate the straight propagation of any electromagnetic signal coming from a star to be detected by a telescope; they cause the typical shimmering of star light and, thus, represent an unwanted disturbance for astronomical measurements and observations. In order to quantify these disturbances, the refractive index structure parameter as a direct primary output of scintillometer measurements is of special interest in connection with astronomical measurements and in precision geodesy using optical methods [34.104].

science applications is considered necessary to result in a significantly broader use. This should include features such as the automatic and reliable distinction between stable and unstable stratification or the direct presentation of derived parameters, e.g., the daily evaporation sum for the scintillometer footprint area, together with some uncertainty and quality information.

Further perspectives are seen in the use of scintillometers for operational validation of turbulent flux parameterization schemes implemented in NWP and climate models (Fig. 34.18) and for an operational validation and coupling of models to derive the surface heat fluxes from satellite data. A continental-scale scintillometer network with instruments operated routinely over different surface types and in different climate regions could provide a reasonable number of reference points to operationally calibrate satellite-based flux estimation algorithms (as was already suggested in [34.105]).

It should also be mentioned that some theoretical ideas behind scintillometry still call for further refinement; this does concern, e.g., the possible effect of saturation on r_{Tq} , the uncertainty of the latent heat flux estimates from an MWS for $Bo \approx 2$ (when the contributions from C_{TT} , C_{qq} and C_{Tq} almost cancel out), the applicability of the footprint and blending height concepts (which have been developed for fluxes, see Chap. 1) to structure parameters, the determination of representative values of the roughness length and displacement height, the possible impact of temperature-humidity dissimilarity on the derived fluxes using the bichromatic method, the interpretation of scintillometer

data for intermittent turbulence, or the relation between area-averaged and local similarity functions and the applicability of surface-layer scaling to measurements at a few decameters above ground, particularly under stable conditions. Important results that may support the interpretation of scintillometer data can be obtained from large-eddy simulations [34.106, 107].

Concerning the methodology, a successful proof of the reliability of the path-averaged values of C_{TT} , C_{Tq} , and C_{qq} derived from scintillometer measurements is still missing. An experiment on this issue has been performed at Lindenberg, Germany, by flying with an un-

manned aerial vehicle along a 4.8 km LAS path [34.77], the authors were able to correctly reproduce the diurnal cycle qualitatively but they could not achieve quantitative agreement better than a factor of two in many situations [34.108].

Another interesting perspective, for which first research and demonstration results have already been presented, is the use of telecommunication links as scintillometers to monitor precipitation and evaporation (e.g., [34.109, 110]). Broad application of these methods is presently hampered by commercial and data security/privacy restrictions.

34.10 Further Readings

- R.J. Hill: Review of optical scintillation methods of measuring the refractive-index spectrum, inner scale, and surface fluxes, *Waves Random Media* **2**, 179–201 (1992)
- R.J. Hill: Algorithms for obtaining atmospheric surface-layer fluxes from scintillation measurements, *J. Atmos. Ocean. Technol.* **14**, 456–467 (1997)
- H.A.R. de Bruin: Time to think – Reflections of a pre-pensioned scintillometer researcher, *Bull. Amer. Meteorol. Soc.* **90**, ES17–ES26 (2009)
- A.F. Moene, F. Beyrich, O.K. Hartogensis: Developments in scintillometry, *Bull. Amer. Meteorol. Soc.* **90**, 694–698 (2009)
- H.C. Ward: Scintillometry in urban and complex environments: A review, *Meas. Sci. Technol.* **28** 064005 (2017)

Acknowledgments. The authors gratefully acknowledge the comments of Eileen Päsche, Thomas Foken, Gerrit Maschwitz, Volker Thiermann, and Keith Wilson on the draft version of this text.

References

- | | |
|--|---|
| <p>34.1 A.S. Monin, A.M. Obukhov: Basic laws of turbulent mixing in the surface layer of the atmosphere, <i>Tr. Akad. Nauk SSSR Geofiz. Inst.</i> 24(151), 163–187 (1954)</p> <p>34.2 A.M. Obukhov: O strukture temperaturnogo polja i polja skorostej v uslovijach konvekcii (Structure of the temperature and velocity fields under conditions of free convection), <i>Izv. AN SSSR Ser. Geofiz.</i> 9, 1392–1396 (1960)</p> <p>34.3 V.I. Tatarski: <i>Wave Propagation in a Turbulent Medium</i> (McGraw-Hill, New York 1961), translated by R.A. Silverman</p> <p>34.4 T. Wang, G.R. Ochs, S.F. Clifford: A saturation-resistant optical scintillometer to measure C_n^2, <i>J. Opt. Soc. Am.</i> 68(3), 334–338 (1978)</p> <p>34.5 R.J. Hill: Saturation resistance and inner-scale resistance of a large-aperture scintillometer: A case study, <i>Appl. Opt.</i> 20(22), 3822–3824 (1981)</p> <p>34.6 R.J. Hill: Comparison of scintillation methods for measuring the inner scale of turbulence, <i>Appl. Opt.</i> 27(11), 2187–2193 (1988)</p> <p>34.7 G.R. Ochs, W.D. Cartwright: An optical device for path-averaged measurements of C_n^2, <i>Proc. SPIE</i> 277, 2–5 (1981)</p> | <p>34.8 G.R. Ochs, R.J. Hill: Optical scintillation method of measuring turbulence inner scale, <i>Appl. Opt.</i> 24(15), 2430–2434 (1985)</p> <p>34.9 E.L. Andreas: Two-wavelength method of measuring path-averaged turbulent surface heat fluxes, <i>J. Atmos. Ocean. Technol.</i> 6(2), 280–292 (1989)</p> <p>34.10 E.L. Andreas: Three-wavelength method of measuring path-averaged turbulent surface heat fluxes, <i>J. Atmos. Ocean. Technol.</i> 7(6), 801–814 (1990)</p> <p>34.11 R. Frehlich: Laser scintillation measurements of the temperature spectrum in the atmospheric surface layer, <i>J. Atmos. Sci.</i> 49(16), 1494–1506 (1992)</p> <p>34.12 H.-J. Bolle, J.-C. Andre, J.L. Arrue, H.K. Barth, P. Bessemoulin, A. Brasa, H.A.R. de Bruin, J. Cruces, G. Dugdale, E.T. Engman: EFEDA: European field experiment in a desertification-threatened area, <i>Ann. Geophys.</i> 11, 173–189 (1993)</p> <p>34.13 H.A.R. de Bruin, B.J.J.M. van den Hurk, W. Kohsiek: The scintillation method tested over a dry vineyard area, <i>Bound.-Layer Meteorol.</i> 76(1/2), 25–40 (1995)</p> |
|--|---|

- 34.14 H.A.R. de Bruin: Introduction: Renaissance of scintillometry, *Bound.-Layer Meteorol.* **105**(1), 1–4 (2002)
- 34.15 A.E. Green: *The Practical Application of Scintillometers in Determining the Surface Fluxes of Heat, Moisture and Momentum*, PhD thesis (Wageningen Univ., Wageningen 2001)
- 34.16 W.M.L. Meijninger: *Surface Fluxes Over Natural Landscapes Using Scintillometry*, PhD thesis (Wageningen Univ., Wageningen 2003)
- 34.17 O.K. Hartogensis: *Exploring Scintillometry in the Stable Atmospheric Surface Layer*, PhD thesis (Wageningen Univ., Wageningen 2006)
- 34.18 B.J.H. van Kesteren: *Measuring Water-Vapour and Carbon-Dioxide Fluxes at Field Scales with Scintillometry*, PhD thesis (Wageningen Univ., Wageningen 2012)
- 34.19 M. Braam: *Aspects of Atmospheric Turbulence Related to Scintillometry*, PhD thesis (Wageningen Univ., Wageningen 2014)
- 34.20 D. van Dinther: *Measuring Crosswind Using Scintillometry*, PhD thesis (Wageningen Univ., Wageningen 2015)
- 34.21 W.M.L. Meijninger, H.A.R. de Bruin: The sensible heat fluxes over irrigated areas in western Turkey determined with a large aperture scintillometer, *J. Hydrol.* **229**(1/2), 42–49 (2000)
- 34.22 C.J. Watts, A. Chehbouni, J.-C. Rodriguez, Y.H. Kerr, O.K. Hartogensis, H.A.R. de Bruin: Comparison of sensible heat flux estimates using AVHRR with scintillometer measurements over semi-arid grassland in northwest Mexico, *Agric. For. Meteorol.* **105**(1–3), 81–89 (2000)
- 34.23 A.E. Green, M.S. Astill, K.J. McAneney, J.P. Nieveen: Path-averaged surface fluxes determined from infrared and microwave scintillometers, *Agric. For. Meteorol.* **109**(3), 233–247 (2001)
- 34.24 W.M.L. Meijninger, O.K. Hartogensis, W. Kohsiek, J.C.B. Hoedjes, R.M. Zuurbier, H.A.R. de Bruin: Determination of area-averaged sensible heat fluxes with a large aperture scintillometer over a heterogeneous surface – Flevoland field experiment, *Bound.-Layer Meteorol.* **105**(1), 37–62 (2002)
- 34.25 W.M.L. Meijninger, A.E. Green, O.K. Hartogensis, W. Kohsiek, J.C.B. Hoedjes, R.M. Zuurbier, H.A.R. de Bruin: Determination of area-averaged water vapour fluxes with large aperture and radio wave scintillometers over a heterogeneous surface – Flevoland field experiment, *Bound.-Layer Meteorol.* **105**(1), 63–83 (2002)
- 34.26 J.C.B. Hoedjes, R.M. Zuurbier, C.J. Watts: Large aperture scintillometer used over a homogeneous irrigated area, partly affected by regional advection, *Bound.-Layer Meteorol.* **105**(1), 99–117 (2002)
- 34.27 J. Ezzahar, A. Chehbouni, J.C.B. Hoedjes, S. Er-Raki, A. Chehbouni, G. Boulet, J.M. Bonnefond, H.A.R. de Bruin: The use of the scintillation technique for monitoring seasonal water consumption of olive orchards in a semi-arid region, *Agric. Water Manag.* **89**(3), 173–184 (2007)
- 34.28 C. von Randow, B. Kruijt, A.A.M. Holtslag, M.B.L. de Oliveira: Exploring eddy-covariance and large-aperture scintillometer measurements in an Amazonian rain forest, *Agric. For. Meteorol.* **148**(4), 680–690 (2008)
- 34.29 F. Beyrich, H.A.R. de Bruin, W.M.L. Meijninger, J.W. Schipper, H. Lohse: Results from one-year continuous operation of a large aperture scintillometer over a heterogeneous land surface, *Bound.-Layer Meteorol.* **105**(1), 85–97 (2002)
- 34.30 F. Beyrich, H.-J. Herzog, J. Neisser: The LITFASS project of DWD and the LITFASS-98 experiment: The project strategy and the experimental setup, *Theor. Appl. Climatol.* **73**(1/2), 3–18 (2002)
- 34.31 F. Beyrich, S.H. Richter, U. Weisensee, W. Kohsiek, H. Lohse, H.A.R. de Bruin, T. Foken, M. Göckede, F. Berger, R. Vogt, E. Batchvarova: Experimental determination of turbulent fluxes over the heterogeneous LITFASS area: Selected results from the LITFASS-98 experiment, *Theor. Appl. Climatol.* **73**(1/2), 19–34 (2002)
- 34.32 V. Thiermann: *Optische Messung turbulenter Flüsse und Vorhersage der optischen Turbulenz aus einfachen Grenzschichtparametern*, PhD thesis (Hamburg Univ., Hamburg 1990)
- 34.33 V. Thiermann: A displaced-beam scintillometer for line-averaged measurements of surface layer turbulence. In: *Proc. 10th Symp. Turb. Diff* (AMS, Boston 1992)
- 34.34 V. Thiermann, H. Grassl: The measurement of turbulent surface-layer fluxes by use of bichromatic scintillation, *Bound.-Layer Meteorol.* **58**(4), 367–389 (1992)
- 34.35 W. Kohsiek, M.H.A.J. Herben: Evaporation derived from optical and radio-wave scintillation, *Appl. Opt.* **22**(17), 2566–2570 (1983)
- 34.36 J.G. Evans: *Long-Path Scintillometry Over Complex Terrain to Determine Areal-Averaged Sensible and Latent Heat Fluxes*, PhD thesis (Univ. Reading, Reading 2009)
- 34.37 H.C. Ward, J.G. Evans, C.S.B. Grimmond, J. Bradford: Infrared and millimetre-wave scintillometry in the suburban environment – Part 1: Structure parameters, *Atmos. Meas. Tech.* **8**(3), 1385–1405 (2015)
- 34.38 H.C. Ward, J.G. Evans, C.S.B. Grimmond: Infrared and millimetre-wave scintillometry in the suburban environment – Part 2: Large-area sensible and latent heat fluxes, *Atmos. Meas. Tech.* **8**(3), 1407–1424 (2015)
- 34.39 A. Lüdi, F. Beyrich, C. Mätzler: Determination of the turbulent temperature–humidity correlation from scintillometric measurements, *Bound.-Layer Meteorol.* **117**(3), 525–550 (2005)
- 34.40 J. Kleissl, J. Gomez, S.-H. Hong, J.M.H. Hendrickx, T. Rahn, W.L. Defoor: Large aperture scintillometer intercomparison study, *Bound.-Layer Meteorol.* **128**(1), 133–150 (2008)
- 34.41 J. Kleissl, C.J. Watts, J.C. Rodriguez, S. Naif, E.R. Vivoni: Scintillometer intercomparison study continued, *Bound.-Layer Meteorol.* **130**(3), 437–443 (2009)

- 34.42 B. van Kesteren, O.K. Hartogensis: Analysis of the systematic errors found in the Kipp & Zonen large aperture scintillometer, *Bound.-Layer Meteorol.* **138**(3), 493–509 (2011)
- 34.43 B. van Kesteren, F. Beyrich, O.K. Hartogensis, A.C. van den Kroonenberg: The effect of a new calibration procedure on the measurement accuracy of Scintec's displaced-beam laser scintillometer, *Bound.-Layer Meteorol.* **151**(2), 257–271 (2014)
- 34.44 B. van Kesteren, F. Beyrich, O.K. Hartogensis, M. Braam: Long-term evaluation of the Scintec boundary layer scintillometer and the Wageningen large-aperture scintillometer: Implications for scintillometer users, *Bound.-Layer Meteorol.* **156**(2), 303–323 (2015)
- 34.45 H.C. Ward, J.G. Evans, O.K. Hartogensis, A.F. Moene, H.A.R. de Bruin, C.S.B. Grimmond: A critical revision of the estimation of the latent heat flux from two-wavelength scintillometry, *Q. J. R. Meteorol. Soc.* **139**(676), 1912–1922 (2013)
- 34.46 A.F. Moene: The effects of water vapour on the structure parameter of the refractive index for near-infrared radiation, *Bound.-Layer Meteorol.* **107**(3), 635–653 (2003)
- 34.47 R.J. Hill: Models of the scalar spectrum for turbulent advection, *J. Fluid Mech.* **88**(3), 541–562 (1978)
- 34.48 J.C. Wyngaard, Y. Izumi, S.A. Collins: Behavior of the refractive index structure parameter near the ground, *J. Opt. Soc. Am.* **61**(12), 1646–1650 (1971)
- 34.49 R.J. Hill, S.F. Clifford, R.S. Lawrence: Refractive-index and absorption fluctuations in the infrared caused by temperature, humidity, and pressure fluctuations, *J. Opt. Soc. Am.* **70**(10), 1192–1205 (1980)
- 34.50 M.L. Wesely: The combined effect of temperature and humidity fluctuations on refractive-index, *J. Appl. Meteorol.* **15**(1), 43–49 (1976)
- 34.51 R.J. Hill: Algorithms for obtaining atmospheric surface-layer fluxes from scintillation measurements, *J. Atmos. Ocean. Technol.* **14**(3), 456–467 (1997)
- 34.52 H.C. Ward: Scintillometry in urban and complex environments: A review, *Meas. Sci. Technol.* **28**(6), 064005 (2017)
- 34.53 A.N. Kolmogorov: The local structure of turbulence in an incompressible viscous fluid for very large Reynolds numbers, *Dokl. Akad. Nauk* **30**, 299–303 (1941)
- 34.54 J.H. Churnside: A spectrum of refractive turbulence in the turbulent atmosphere, *J. Mod. Opt.* **37**(1), 13–16 (1990)
- 34.55 R.S. Lawrence, J.W. Strohbehn: A survey of clear air propagation effects relevant to optical communications, *Proc. IEEE* **58**(10), 1523–1545 (1970)
- 34.56 S.F. Clifford, G.R. Ochs, R.S. Lawrence: Saturation of optical scintillation by strong turbulence, *J. Opt. Soc. Am.* **64**(2), 148–154 (1974)
- 34.57 W. Kohsiek, W.M.L. Meijninger, H.A.R. de Bruin, F. Beyrich: Saturation of the large aperture scintillometer, *Bound.-Layer Meteorol.* **121**(1), 111–126 (2006)
- 34.58 J. Kleissl, O.K. Hartogensis, J.D. Gomez: Test of scintillometer saturation correction methods using field experimental data, *Bound.-Layer Meteorol.* **137**(3), 493–507 (2010)
- 34.59 T. Foken: *Micrometeorology*, 2nd edn. (Springer, Berlin, Heidelberg 2017)
- 34.60 L.M.J. Kooijmans, O.K. Hartogensis: Surface-layer similarity functions for dissipation rate and structure parameters of temperature and humidity based on eleven field experiments, *Bound.-Layer Meteorol.* **160**(3), 501–527 (2016)
- 34.61 R.J. Hill, G.R. Ochs, J.J. Wilson: Measuring surface-layer fluxes of heat and momentum using optical scintillation, *Bound.-Layer Meteorol.* **58**(4), 391–408 (1992)
- 34.62 H.A.R. de Bruin, W. Kohsiek, B.J.J.M. van den Hurk: A verification of some methods to determine the fluxes of momentum, sensible heat, and water vapour using standard deviation and structure parameter of scalar meteorological quantities, *Bound.-Layer Meteorol.* **63**(3), 231–257 (1993)
- 34.63 O.K. Hartogensis, H.A.R. de Bruin: Monin-Obukhov similarity functions of the structure parameter of temperature and turbulent kinetic energy dissipation rate in the stable boundary layer, *Bound.-Layer Meteorol.* **116**(2), 253–276 (2005)
- 34.64 D. Li, E. Bou-Zeid, H.A.R. de Bruin: Monin-Obukhov similarity functions for the structure parameters of temperature and humidity, *Bound.-Layer Meteorol.* **145**(1), 45–67 (2012)
- 34.65 L.M.J. Kooijmans: *Testing the Universality of Monin-Obukhov Similarity Functions*, M.Sc. thesis (Wageningen Univ., Wageningen 2013)
- 34.66 E.L. Andreas: Estimating C_n^2 over snow and sea ice from meteorological data, *J. Opt. Soc. Am.* **78**(4), 481–495 (1988)
- 34.67 M. Braam, A.F. Moene, F. Beyrich, A.A.M. Holtslag: Similarity relations for C_T^2 in the unstable atmospheric surface layer: Dependence on regression approach, observation height and stability range, *Bound.-Layer Meteorol.* **153**(1), 63–87 (2014)
- 34.68 O.K. Hartogensis, C.J. Watts, J.-C. Rodriguez, H.A.R. de Bruin: Derivation of an effective height for scintillometers: La Poza experiment in north-west Mexico, *J. Hydrometeorol.* **4**(5), 915–928 (2003)
- 34.69 J.G. Evans, H.A.R. de Bruin: The effective height of a two-wavelength scintillometer system, *Bound.-Layer Meteorol.* **141**(1), 165–177 (2011)
- 34.70 R.S. Lawrence, G.R. Ochs, S.F. Clifford: Use of scintillations to measure average wind across a light-beam, *Appl. Opt.* **11**(2), 239–243 (1972)
- 34.71 T. Wang, G.R. Ochs, R.S. Lawrence: Wind measurements by the temporal cross-correlation of the optical scintillations, *Appl. Opt.* **20**(23), 4073–4081 (1981)
- 34.72 D. van Dinter, O.K. Hartogensis, A.F. Moene: Crosswinds from a single-aperture scintillometer using spectral techniques, *J. Atmos. Ocean. Technol.* **30**(1), 3–21 (2013)

- 34.73 D. van Dinter, O.K. Hartogensis: Using the time-lag correlation function of dual-aperture scintillometer measurements to obtain the crosswind, *J. Atmos. Ocean. Technol.* **31**(1), 62–78 (2014)
- 34.74 W.M.L. Meijninger, F. Beyrich, A. Lüdi, W. Kohsiek, H.A.R. de Bruin: Scintillometer-based turbulent fluxes of sensible and latent heat over a heterogeneous land surface – A contribution to LITFASS-2003, *Bound.-Layer Meteorol.* **121**(1), 89–110 (2006)
- 34.75 M.S. Yee, V.R.N. Pauwels, E. Daly, J. Beringer, C. Rüdiger, M.F. McCabe, J.P. Walker: A comparison of optical and microwave scintillometers with eddy-covariance derived surface heat fluxes, *Agric. For. Meteorol.* **213**, 226–239 (2015)
- 34.76 B. Samain, W. Defloor, V.R.N. Pauwels: Continuous time series of catchment-averaged sensible heat flux from a large-aperture scintillometer: Efficient estimation of stability conditions and importance of fluxes under stable conditions, *J. Hydrometeorol.* **13**(2), 423–442 (2012)
- 34.77 F. Beyrich, J. Bange, O.K. Hartogensis, S. Raasch, M. Braam, D. van Dinter, D. Gräf, B. van Kesteren, A.C. van den Kroonenberg, B. Maronga, S. Martin, A.F. Moene: Towards a validation of scintillometer measurements: The LITFASS-2009 experiment, *Bound.-Layer Meteorol.* **144**(1), 83–112 (2012)
- 34.78 B. van Kesteren, O.K. Hartogensis, D. van Dinter, A.F. Moene, H.A.R. de Bruin, A.A.M. Holtslag: Measuring H₂O and CO₂ fluxes at field scales with scintillometry: Part II – Validation and application of 1 min flux estimates, *Agric. For. Meteorol.* **178/179**, 88–105 (2013)
- 34.79 H.A.R. de Bruin, W.M.L. Meijninger, A.-S. Smedman, M. Magnusson: Displaced-beam small aperture scintillometer test. Part I: The wintex data-set, *Bound.-Layer Meteorol.* **105**(1), 129–148 (2002)
- 34.80 O.K. Hartogensis, H.A.R. de Bruin, B.J.H. van de Wiel: Displaced-beam small aperture scintillometer test. Part II: CASES-99 stable boundary layer experiment, *Bound.-Layer Meteorol.* **105**(1), 149–176 (2002)
- 34.81 J.-P. Lagouarde, J.-M. Bonnefond, Y.H. Kerr, K.J. McAneny, M. Irvine: Integrated sensible heat flux measurements of a two-surface composite landscape using scintillometry, *Bound.-Layer Meteorol.* **105**(1), 5–35 (2002)
- 34.82 G. Pozniková, M. Fischer, B. van Kesteren, M. Orság, P. Hlavinka, Z. Žalud, M. Trnka: Quantifying turbulent energy fluxes and evapotranspiration in agricultural field conditions: A comparison of micrometeorological methods, *Agric. Water Manag.* **209**, 249–263 (2018)
- 34.83 M. Kanda, R. Moriwaki, M. Roth, T. Oke: Area-averaged sensible heat flux and a new method to determine zero-plane displacement length over an urban surface using scintillometry, *Bound.-Layer Meteorol.* **105**(1), 177–193 (2002)
- 34.84 J.A. Salmond, M. Roth, T.R. Oke, A. Christen, J.A. Voogt: Can surface-cover tiles be summed to give neighborhood fluxes in cities?, *J. Appl. Meteorol. Climatol.* **51**(1), 133–149 (2012)
- 34.85 A. Marx, H. Kunstmann, D. Schüttemeyer, A.F. Moene: Uncertainty analysis for satellite derived sensible heat fluxes and scintillometer measurements over savannah environment and comparison to mesoscale meteorological simulation results, *Agric. For. Meteorol.* **148**(4), 656–667 (2008)
- 34.86 N.A. Brunsell, J.M. Ham, K.A. Arnold: Validating remotely sensed land surface fluxes in heterogeneous terrain with large aperture scintillometry, *Int. J. Remote Sens.* **32**(1), 6295–6314 (2011)
- 34.87 B. Samain, B.V.A. Ferket, W. Defloor, V.R.N. Pauwels: Estimation of catchment averaged sensible heat fluxes using a large aperture scintillometer, *Water Resour. Res.* **47**(5), W05536 (2011)
- 34.88 S.M. Liu, Z.W. Xu, Z.L. Zhu, Z.Z. Jia, M.J. Zhu: Measurements of evapotranspiration from eddy-covariance systems and large aperture scintillometers in the Hai River Basin, China, *J. Hydrol.* **487**, 24–38 (2013)
- 34.89 M.J. Savage: Estimation of evaporation using a dual-beam surface layer scintillometer and component energy balance measurements, *Agric. For. Meteorol.* **149**(3/4), 501–517 (2009)
- 34.90 H.C. Ward, J.G. Evans, C.S.B. Grimmond: Multi-scale sensible heat fluxes in the urban environment from large aperture scintillometry and eddy covariance, *Bound.-Layer Meteorol.* **152**(1), 65–89 (2014)
- 34.91 F. Beyrich, J.-P. Leps, M. Mauder, J. Bange, T. Foken, S. Huneke, H. Lohse, A. Lüdi, W.M.L. Meijninger, D. Mironov, U. Weisensee, P. Zittel: Area-averaged surface fluxes over the LITFASS region based on eddy-covariance measurements, *Bound.-Layer Meteorol.* **121**(1), 33–65 (2006)
- 34.92 J. Asanuma, K. Iemoto: Measurements of regional sensible heat flux over Mongolian grassland using large aperture scintillometer, *J. Hydrol.* **333**(1), 58–67 (2007)
- 34.93 G.O. Odhiambo, M.J. Savage: Surface layer scintillometry for estimating the sensible heat flux component of the surface energy balance, *S. Afr. J. Sci.* **105**(5/6), 208–216 (2009)
- 34.94 J. Kleissl, S.-H. Hong, J.M.H. Hendrickx: New Mexico scintillometer network supporting remote sensing and hydrologic and meteorological models, *Bull. Am. Meteorol. Soc.* **90**(2), 207–218 (2009)
- 34.95 A.E. Green, Y. Hayashi: Use of the scintillometer technique over a rice paddy, *J. Agric. Meteorol.* **54**(3), 225–234 (1998)
- 34.96 J.-P. Lagouarde, M. Irvine, J.-M. Bonnefond, C.S.B. Grimmond, N. Long, T.R. Oke, J.A. Salmond, B. Offerle: Monitoring the sensible heat flux over urban areas using large aperture scintillometry: Case study of Marseille city during the ESCOMPTE experiment, *Bound.-Layer Meteorol.* **118**(3), 449–476 (2006)
- 34.97 C.R. Wood, R.D. Kouznetsov, R. Gierens, A. Nordbo, L. Järvi, M.A. Kallistratova, J. Kukko-

- nen: On the temperature structure parameter and sensible heat flux over Helsinki from sonic anemometry and scintillometry, *J. Atmos. Ocean. Technol.* **30**(8), 1604–1615 (2013)
- 34.98 M. Zielirski, K. Fortuniak, W. Pawlak, M. Siedlecki: Turbulent sensible heat flux in Łódź, Central Poland, obtained from scintillometer and eddy covariance measurements, *Meteorol. Z.* **22**(5), 603–613 (2013)
- 34.99 S.-H. Lee, J.-H. Lee, B.-Y. Kim: Estimation of turbulent sensible heat and momentum fluxes over a heterogeneous urban area using a large aperture scintillometer, *Adv. Atmos. Sci.* **32**(8), 1092–1105 (2015)
- 34.100 T. Foken: The energy balance closure problem: An overview, *Ecol. Appl.* **18**(6), 1351–1367 (2008)
- 34.101 L.P. Poggio, M. Furger, A.S.H. Prévôt, W.K. Graber, E.L. Andreas: Scintillometer wind measurements over complex terrain, *J. Atmos. Ocean. Technol.* **17**(1), 17–26 (2000)
- 34.102 M. Furger, P. Drobinski, A.H. Prévôt, R.O. Weber, W.K. Graber, B. Neininger: Comparison of horizontal and vertical scintillometer crosswinds during strong foehn with lidar and aircraft measurements, *J. Atmos. Ocean. Technol.* **18**(12), 1975–1988 (2001)
- 34.103 D. van Dinter, O.K. Hartogensis, A.A.M. Holtslag: Runway wake vortex, crosswind, and visibility detection with a scintillometer at Schiphol airport, *Bound.-Layer Meteorol.* **157**(3), 481–499 (2015)
- 34.104 A.I. Weiss, M. Hennes, M.W. Rotach: Derivation of refractive index and temperature gradients from optical scintillometry to correct atmospherically induced errors for highly precise geodetic measurements, *Surv. Geophys.* **22**(5/6), 589–596 (2001)
- 34.105 H.A.R. de Bruin, A.F. Moene, F.C. Bosveld: An integrated MSG-scintillometer network system to monitor sensible and latent heat fluxes. In: *Proc. 2nd MSG RAO Workshop, Salzburg* (2004) pp. 137–142
- 34.106 B. Maronga, A.F. Moene, D. van Dinter, S. Raasch, F.C. Bosveld, B. Gioli: Derivation of structure parameters of temperature and humidity in the convective boundary layer from large-eddy simulations and implications for the interpretation of scintillometer observations, *Bound.-Layer Meteorol.* **148**(1), 1–30 (2013)
- 34.107 B. Maronga: Monin-Obukhov similarity functions for the structure parameters of temperature and humidity in the unstable surface layer: Results from high-resolution large-eddy simulations, *J. Atmos. Sci.* **71**(2), 716–733 (2014)
- 34.108 M. Braam, F. Beyrich, J. Bange, A. Platis, S. Martin, B. Maronga, A.F. Moene: On the discrepancy in simultaneous observations of the structure parameter of temperature using scintillometers and unmanned aircraft, *Bound.-Layer Meteorol.* **158**(2), 257–283 (2016)
- 34.109 H. Leijnse, R. Uijlenhoet, J.N.M. Stricker: Hydro-meteorological application of a microwave link: 1. Evaporation, *Water Resour. Res.* **43**(4), 04416 (2007)
- 34.110 R. Uijlenhoet, J.-M. Cohard, M. Gosset: Path-average rainfall estimation from optical extinction measurements using a large-aperture scintillometer, *J. Hydrometeorol.* **12**(5), 955–972 (2011)

Frank Beyrich

Meteorologisches Observatorium
Lindenberg –
Richard-Aßmann-Observatorium
Lindenberg, Germany
frank.beyrich@dwd.de



Frank Beyrich has been Head of the Boundary Layer Processes Group at the Meteorological Observatory Lindenberg of the German Meteorological Service (DWD) since 1997. He organized the LITFASS field experiments in 1998, 2003, and 2009 that focused on the area-averaging of energy fluxes over a heterogeneous land surface. He has been performing atmospheric research with scintillometers since 1994, when he received his PhD at Freie Universität Berlin.

Oscar K. Hartogensis

Environmental Sciences – Meteorology
and Air Quality
Wageningen University
Wageningen, The Netherlands
oscar.hartogensis@wur.nl



Oscar Hartogensis works as a researcher at the Meteorology and Air Quality Group of Wageningen University in the Netherlands. He received a PhD in Meteorology in 2006 and works in the field of (turbulent) exchange processes between the atmosphere and the land surface. He has a special interest in developing new measurement methodologies for estimating fluxes at the land–surface interface, in particular related to the scintillometry technique.

**Henk A.R. de Bruin**

Bilthoven, The Netherlands
hardb@xs4all.nl

Henk de Bruin obtained his MSc in Physics at the University of Amsterdam and his PhD in Agricultural Sciences at Wageningen University. In 1985 he was appointed as Associate Professor at Wageningen University and worked there until his retirement. His research focused on micrometeorology with a special emphasis on turbulence and evapotranspiration. In the 1990s, he was one of the initiators of the "renaissance of scintillometry", which led to a broader application of scintillometers in many countries around the globe.

**Helen C. Ward**

Department of Atmospheric and
Cryospheric Sciences
University of Innsbruck
Innsbruck, Austria
helen.ward@uibk.ac.at

Helen Ward studied physics at Oxford University and received her PhD in urban micrometeorology from King's College London (2013). She carried out postdoctoral research at the Centre for Ecology and Hydrology, Reading University and Yonsei University and is currently based at Innsbruck University, Austria. Her research focuses on improving understanding of turbulent exchange, particularly in complex environments (e.g., urban areas and mountainous terrain), through measurements (eddy covariance, scintillometry) and modeling.

Acoustic Tomography

Armin Raabe , Manuela Starke , Astrid A. Ziemann 

Remote sensing techniques supply valuable observations from distant regions, which should not be disturbed or cannot otherwise be monitored. These observations often provide integrated information along the whole signal path. Thus, particular data analysis is necessary in order to generate a spatial mapping of the observed quantities. If a sufficiently large number of line-integrating or beam-integrating observations is available, tomographic techniques can be applied to combine these quantities to a spatially resolved two-dimensional or three-dimensional field according to output data of numerical atmospheric models. That way, for example, atmospheric temperature and wind fields can be derived by a special application of tomography presented in this chapter: acoustic travel-time tomography. This method uses the propagation speed of acoustic waves in air to estimate temperature and wind fields within the atmospheric surface layer.

The basic setup for acoustic travel-time tomography is a configuration of sound sources and sound receivers that are placed around an area under investigation. Knowing their exact positions, travel-time measurements provide information on the speed of sound along the acoustic propagation path between the sources and receivers. A subsequent joint analysis of the sound wave travel times, the tomographic inversion, gives the spatially resolved temperature field and the wind field. The technical setup of the method is described together with the required calibration and quality control procedures. Furthermore, selected results and an estimate of the achieved quality are presented.

Tomography is a noninvasive measurement technique combined with a special analysis algorithm and an imaging method. It is used to remotely monitor distributions of physical quantities without installing sensors in the area under investigation. For this purpose, influences on a probing energy, for example electromagnetic or acoustic waves, are analyzed. The waves

35.1	Measurement Principles and Parameters	1000
35.2	History	1001
35.2.1	Tomography in General	1001
35.2.2	Tomography in Air	1001
35.3	Theory	1001
35.3.1	General Procedures	1002
35.3.2	Sound Speed in Air	1003
35.3.3	Acoustic Travel Time	1004
35.3.4	Separation of Temperature and Flow from Sound Speed	1006
35.3.5	Uncertainty	1007
35.3.6	Experimental Setup	1009
35.3.7	An Example of Inverse Tomographic Reconstruction	1010
35.4	Devices and Systems	1012
35.4.1	Travel-Time Recording	1012
35.4.2	Sound Sources and Receivers	1012
35.4.3	Scalability	1014
35.5	Specifications	1015
35.6	Quality Control	1015
35.7	Maintenance	1017
35.8	Application	1017
35.9	Future Developments	1020
35.10	Further Readings	1021
	References	1021

pass through an area under investigation along different paths and are changed by the properties of the medium. In most tomographic applications, the energy used for investigation is emitted and received by transducers which are placed around the area or volume of interest. It must be ensured that sources and receivers are arranged such that the signals pass through all parts of

the measurement domain on crossing paths. On their way they encounter different physical conditions of the medium. Thus, all recorded signals carry information about the medium from their individual ways through it. The observed modifications along all propagation paths are then used, to draw conclusions about the spatial distribution of properties within the investigation area. To do this, tomographic inversion algorithms are used. The mathematical algorithms used for this inversion aim at generating spatial distributions of physical quantities

within the measurement domain, which enable computation of synthetic signals that match optimally with the observed values.

Tomographic techniques require an enormous amount of measured data, which must then be handled and processed. The development of computer-based tomography is closely linked with an increase in the computing capacity which, in turn, leads to an increasing number of tomographic applications in science and technology.

35.1 Measurement Principles and Parameters

One special implementation of tomography for meteorological applications is the acoustic travel-time tomography (A-TOM). This technique is based on the dependency of effective sound speed on air temperature and the flow field (Tables 35.1–35.3). The values of the relevant physical constants (R_a , γ) can be found in Chap. 5. The warmer (and moister) the air is, the faster acoustic signals travel through it. Furthermore, the effective speed of acoustic signals that travel in the wind direction is increased, while it is decreased in upwind direction (Table 35.3). Sound speed measurements, which are based on the travel-time measurements between points whose positions relative to each other are known, contain information about the air temperature and the wind vector component along the sound propa-

gation paths. If sound sources (speakers) and receivers (microphones) are placed around the measurement area or volume in such a way that acoustic signals travel along different directions through this region, it is possible to reconstruct the spatial distribution of wind and temperature in the region spanned by the sound paths using tomographic inversion algorithms.

The A-TOM method is scalable and thus suitable for observing wind and temperature distributions at several spatial scales and application areas (e.g., over natural landscapes, detecting the flow conditions in a wind tunnel, or controlling the air conditioning in rooms). Subsequent descriptions concentrate on tomographic measurements within the atmospheric surface layer.

Table 35.1 Measured parameters

Parameter	Description	Unit	Symbol
Geometric distance	Geometric distance between all transmitter and receiver positions	m	D
Travel time	Travel time of sound signal between transmitters and receivers	s	τ

Table 35.2 Output parameters

Parameter	Description	Unit	Symbol
Wind vector	Flow velocity of air	m s^{-1}	$\mathbf{v}(u, v, w)$
Relative wind speed	Flow component in sound propagation direction (wind component along the sound ray path)	m s^{-1}	v_r
Acoustic virtual temperature	Moisture-dependent air temperature including the influence of air temperature T and air humidity q on the adiabatic sound speed: $T_{\text{av}} = T(1 + 0.513q)$	K	T_{av}

Table 35.3 Other relevant parameters and relationships

Parameter	Unit	Symbol and description
Signal path between transmitter and receiver	m	L
Effective sound speed (depends on temperature and the movement of the fluid)	m s^{-1}	$c_{\text{eff}}(T_{\text{av}}, \mathbf{v}) = c_L(T_{\text{av}}) + \mathbf{v} \cdot \mathbf{s} = c_L(T_{\text{av}}) + v_r$
Unit vectors in direction of sound propagation and normal to the acoustic wave front		\mathbf{s}, \mathbf{n}
Laplace (adiabatic) sound speed (sound propagation = adiabatic process)	m s^{-1}	$c_L = \sqrt{\gamma R_a T_{\text{av}}}$
Inverse sound speed (slowness)	s m^{-1}	$s = 1/c_L$
Absolute air temperature	K	T
Specific moisture of air	kg kg^{-1}	q

35.2 History

The theoretical basis for tomographic reconstruction techniques is connected with *Johann Radon's* (1887–1956) derivation of what is now called the Radon transform (1917) [35.1], a special form of the Fourier transformation. The Radon transform mathematically describes the line-integrated value of a function at a plane if this function changes spatially along the considered line. The result of the integral is called a projection. If one knows several projections from different imaging directions, one can inversely recalculate the distribution of this function.

35.2.1 Tomography in General

The Radon transformation is one important mathematical basis for the development of technically applicable tomographic reconstruction algorithms. Tomographic techniques are used to estimate cross sections of an object from line-integrated measurements [35.2]. Such methods are widely used in medicine, for example, to examine the interior of the human body without surgical intervention. For the development of x-ray computer-assisted tomography (CT, *Allan M. Cormack* (1924–1998), *Godfrey Hounsfield* (1919–2004)) and magnetic resonance tomography (MRT, *Paul C. Lauterbur* (1929–2007), *Peter Mansfield* (1933–2017)), the Nobel Prize was awarded in 1979 and 2003, respectively.

Since the development of the CT, tomographic techniques are developing and becoming more and more attractive for several applications in science and technology. Consequently, sonic tomography devices have also been developed for medical purposes (e.g., [35.3]).

Compared with developments in medicine (CT overview, e.g., in [35.4]), geophysics, (overview in [35.5, 6]) and oceanography (overview [35.7]), where acoustic tomography methods have been standardized and used routinely for many years, acoustic tomography in meteorology is still at a research state. Tomography of the atmosphere focuses on analyzing boundary layer structures (overview, e.g., in [35.8, 9]) and depicting flow and temperature fields in fluid dynamics [35.10] (see also Chap. 36).

35.3 Theory

Even if the mathematical tomographic method can theoretically reconstruct a temperature or flow field from an observed sound speed field, a reasonable reconstruction is only possible if the measurements are able to observe this velocity distribution with

35.2.2 Tomography in Air

The experiments of *Spiesberger* and *Fristrup* around 1990 [35.11] provided the basic ideas underlying recent developments in acoustic tomography for meteorology. At the time, they combined acoustic measurement methods with tomographic algorithms to improve the accuracy of location of chirping birds in complex surroundings. A few years later, *Wilson* and *Thomson* [35.12] used an acoustic array of loudspeakers and microphones to record wind and temperature fields over a homogeneous flat terrain. Similar developments were done by *Raabe*, *Arnold* and *Ziemann* [35.13, 14] to observe the structure of turbulent transport over a nonhomogeneous landscape. Special experiments and observational campaigns were implemented (e.g., [35.15]). The observed datasets are used to apply different tomographic algorithms [35.16, 17] that employ statistic, algebraic, or filter-procedures to invert the line-integrated information to a two-dimensional (2-D) or three-dimensional (3-D) distribution of meteorological quantities, which affect the sound propagation. An assessment of the meteorological potential of acoustic tomographic methods for atmospheric research is given in [35.9]. Note that signals of sound propagating through the atmosphere have long been used to obtain information about vertical and horizontal structure of the atmosphere within the troposphere up to the stratosphere, using natural and artificial sources of sound [35.9].

In our case the measurements use artificial sound sources and they are positioned within the atmospheric surface layer. The size of investigation areas or volumes includes scales of >100 m down to some meters. Acoustic tomographic methods are also used in wind tunnels [35.10] or inside of rooms to detect flow and temperature fields [35.18, 19]. An air stream tomograph, which was tested in laboratories [35.20], is another example of actual developments. The applications go down in spatial extent to record turbulent structures at the scale of an acoustic anemometer [35.21]. A newly developed tomographic application is the use of unmanned aerial vehicles as a sound source at different heights of the atmosphere, and an array of receivers at the surface, to reconstruct vertical structures in the boundary layer [35.22].

sufficient accuracy. The tomographic inversion techniques provide a useful result only if the measurement of the parameters are performed in sufficient spatial density and sufficient temporal sampling.

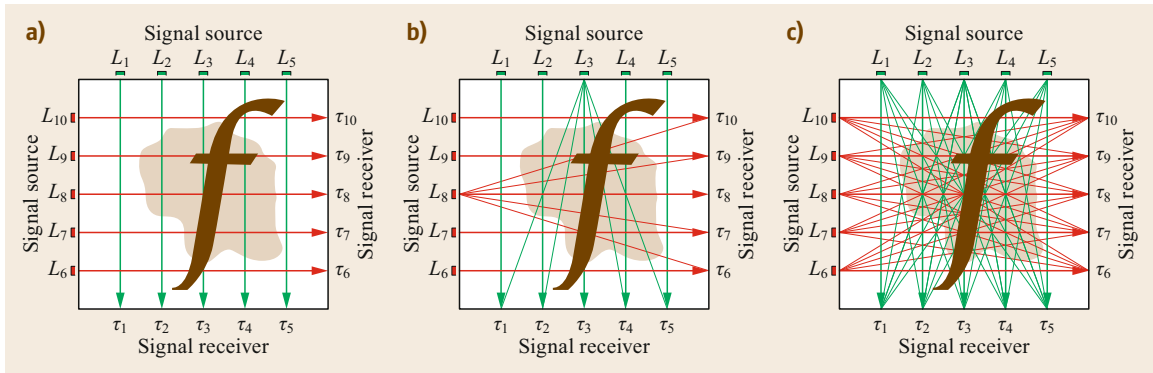


Fig. 35.1a–c Schematic view of a simultaneous or successive observation of signal travel times $\tau_i(1-10)$ at different paths $L_j(1-10)$, which cross the area characterized by a field f which in turn influences the propagation times and paths. The first example (a) shows schematically a single sound path between one fixed source and one fixed receiver. The number of paths throughout the field f increases due to the fact that the signal of one sound source can be detected by several receivers (b,c). With an increased number of sound paths a spatially higher resolved tomographic reconstruction of the field f is possible

35.3.1 General Procedures

The tomographic reconstruction of a spatial distribution of a quantity within a region, which can be described by a model function f , is based on measurements taken along different paths L through the medium (theoretically first described in [35.1]). The measurements take place along certain propagation paths, which are characterized by the position of the signal sources and signal receivers, and by the properties of the medium. Because such measurements contain information about the integral conditions along the entire propagation path, the measured data are referred to as line integral values or projections. The tomographic inversion is then an algorithm that can deduce the distribution f from the knowledge of the line integral values illuminating the medium from different view directions.

In the case of acoustic tomography described here, these line-integrated values are travel-time measurements. The observed quantity is the signal travel time τ between the transmitter and the receiver, which is related to the propagation medium by the line integral

$$\tau = \int_L f dL, \quad (35.1)$$

where L is the signal path length through the medium and f is a scalar field that describes the speed of the propagating wave in the medium. For acoustic waves in a non-moving medium, $f = s = 1/c_L$ is the slowness, the reciprocal of the Laplace sound speed c_L . In refractive media, the signal path is in general a curved path, which depends on the field f . The observed travel time τ does not provide information about the exact signal

path L or the distribution of f along L and is therefore a nonlocal path-integrated quantity.

The basic idea of atmospheric tomography is to combine a large number of travel-time observations that scan the investigated region from many directions in order to obtain a well-resolved approximation of the field f . For a given set of observations τ_i , a set of equations

$$\tau_i = \int_{L_i} f dL_i, \quad (35.2)$$

has to be solved for the unknown function f (scheme is shown in Fig. 35.1). As the corresponding curved signal paths L_i depend on f , this is a nonlinear inverse problem. It is also an ill-posed problem as (1) there may be no solution in a strict mathematical sense, especially if real noisy observations are considered, (2) the solution is usually not unique, and (3) the solution is not stable (Chap. 36). In real applications, the problem is also globally underdetermined as the number of observations is in general insufficient to describe the field f .

The extension of field f is determined by the propagation paths between the positions of the signal sources and signal receivers. In the case of acoustic tomography, the source is a sound transmitter and the receiver is a microphone. The reconstruction of the f field is possible because different paths cross different parts of the field leading to different travel times, when the signals interact with different parts of f . An inversion algorithm searches for such a distribution of f that the observed travel times can be reproduced. To solve this inverse problem, numerous algorithms have been developed. These can be subdivided into four main groups. A solu-

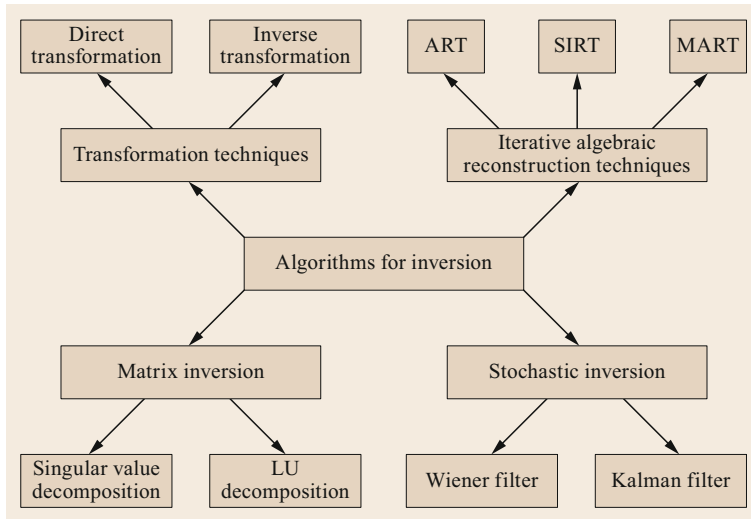


Fig. 35.2 Classification of inversion techniques (ART – algebraic reconstruction technique, SIRT – simultaneous iterative reconstruction technique, MART – multiplicative algebraic reconstruction technique, LU – lower-upper matrix decomposition) (after [35.23] © G. Fischer, with kind permission of the author). In the literature, examples for all the methods can also be found in the field of meteorology (Sect. 35.10)

tion method cannot be favored and should be chosen depending on the specific application of tomography (Fig. 35.2).

35.3.2 Sound Speed in Air

If the composition of air is constant, the effective speed of sound in air depends on the air temperature and the wind vector. In nature, the composition of air is constant for the ratio of nitrogen, oxygen and argon, but it is variable with respect to the proportion of water vapor. That means, the sound speed is influenced by water vapor concentration which is accounted for by use of acoustic virtual temperature instead of air temperature (Table 35.2). Under average conditions, the sound speed increases by 0.6 m s^{-1} if the absolute air temperature increases by 1 K. In the same manner, the sound speed increases by 0.1 m s^{-1} if specific moisture increases by $10^{-3} \text{ kg kg}^{-1}$.

Under normal atmospheric conditions, the air temperature can vary in time or from position to position by $\approx 10 \text{ K}$ over a day (a moderate value). Hence, the sound speed changes by $\approx 6 \text{ m s}^{-1}$. The moisture can vary maximally by 10 g kg^{-1} (a very big value) followed by sound speed changes by 1 m s^{-1} . That is the reason for the assumption applied in the following: the sound speed based on the acoustic virtual temperature is only slightly influenced by air moisture variability. Of course, the individual gas constant and specific heat ratio must be known for another gas composition to calculate the sound speed (Table 35.3).

Regardless of the exact composition of the air mixture, the movement of the medium always influences the speed of sound as follows. The sound speed decreases if sound waves are traveling against the flow

direction (i.e., against wind direction), increases in downwind direction and does not change under cross-wind conditions. This statement is limited to a flow speed $|v|$, which is much smaller than the sound speed c_L (Fig. 35.3). This limitation must be taken into account when describing the propagation of sound waves in a moving medium.

In a medium at rest, the sound wave propagates with a speed c_L in a direction \mathbf{n} normal to the acoustic wave front

$$c_L = c_L \mathbf{n} .$$

The sound velocity along the sound propagation in a moving medium point in a different direction \mathbf{s} tangent to the sound ray path

$$c_{\text{ray}} = c_{\text{ray}} \mathbf{s} .$$

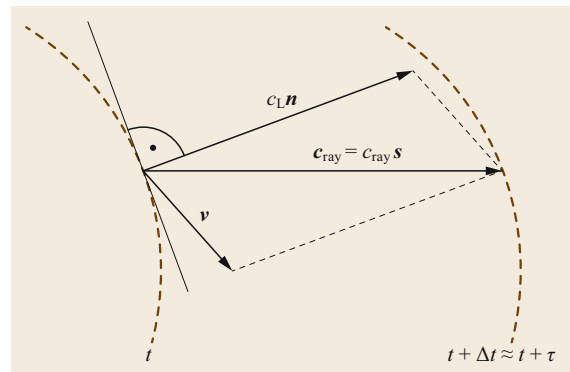


Fig. 35.3 Velocity of acoustic signals propagating in a moving atmosphere illustrated by a relocated wave front (dashed lines) at time t and $t + \Delta t$ (after [35.10] © IOP Publishing, reproduced with permission, all rights reserved)

The sound energy propagates along this vector, which results from the vector sum of the speed of sound vector in the wave front direction and the velocity \mathbf{v} of the moving medium

$$c_{\text{ray}} = c_L \mathbf{n} + \mathbf{v}.$$

Of interest is now the magnitude of the sound speed

$$c_{\text{ray}}(\mathbf{s} \cdot \mathbf{s}) = c_L(\mathbf{n} \cdot \mathbf{s}) + \mathbf{v} \cdot \mathbf{s}.$$

Only under assumption $|\mathbf{v}| \ll c_L$ the direction of \mathbf{n} and \mathbf{s} are near the same.

The resulting sound speed is called effective sound speed

$$c_{\text{ray}} = c_L + v_r = c_{\text{eff}}.$$

A detailed description of the physics of sound propagation in moving media can be found in [35.24, 25]. In history, *J.W.S. Rayleigh* [35.26] introduced this concept of effective sound speed for a small wind speed in comparison to the magnitude of Laplace (adiabatic) sound speed c_L in air, which only depends on acoustic virtual temperature T_{av} , (Tables 35.2 and 35.3). The effective sound speed is then determined by the component of the wind vector, which acts in or against the propagation direction of the sound wave. Using this approximation, methods developed for a motionless medium can be applied to a moving medium. In practice, the applicability of the effective sound speed approximation should be investigated for the individual application [35.27].

35.3.3 Acoustic Travel Time

Measuring sound speed is described in the following from the perspective of a propagation of known sound signals over greater distances (order of magnitude: 50–500 m). The approach was proven in practice with several applications of acoustic tomography inside the atmospheric boundary layer.

The speed of sound between a source and a receiver is estimated as the quotient between the geometric sound path length D and the elapsed time of an acoustic signal, which travels along this path. The assumption of straight-line sound propagation is thereby used, i.e., it is assumed that the influence of spatial sound speed variability is primarily in first order in comparison with the influence on the sound path length due to sound refraction. To neglect the influence of refraction on the sound path, the actual sound speed gradients, especially in the vertical direction, have to be checked and the length of the sound path must be limited.

The distance between transmitter and receiver can be determined relatively simply, e.g., with an electronic

tachymeter, even at distances of > 100 m with an uncertainty of a few millimeters. It is important that the geometric distance also coincides with the positions of the transmitted and received signal, which are not so easy to determine, because of the finite dimensions of the transmitter and receiver.

To analyze the travel time using the record of sound signals between sound source and receiver, a successfully used technique is based on cross correlation between the transmitted and received signal [35.12].

The travel time of the acoustic signals between a sound source and a receiver corresponds to the time delay of the received signal relative to the time of its emission at the source. Assuming that the signal is not changed along its propagation path, the received signal $y(t)$ corresponds to a time-delayed version of the transmitted signal $x(t)$: $y(t) = x(t - \tau_0)$. The time delay τ_0 is estimated by analyzing the cross correlation function $r_{x,y}(\tau)$ between the transmitted and the received signal

$$\begin{aligned} r_{x,y}(\tau) &= \int_{-\infty}^{\infty} x(t)y(t + \tau)dt \\ &= \int_{-\infty}^{\infty} x(t)x(t - \tau_0 + \tau)dt. \end{aligned} \quad (35.3)$$

The cross correlation function reaches its maximum for the delay $\tau = \tau_0$, which corresponds to the travel time of the acoustic signal. This cross correlation technique for estimating the travel time requires special properties of the generated signals. From information technology so-called pseudorandom sequences (MLS: maximum length sequences) are known whose autocorrelation is characterized by an impulse-like function [35.28]. In such a signal, however, all sound frequencies are included similar to white noise, which may not fully be transmitted by the sound sources. Furthermore, the air absorbs sound energy, especially for higher sound frequencies. Hence, it then cannot be ensured that the signals are transmitted along the sound propagation paths without any changes in their signals' signature. However, it should be noted that such MLS signals have been successfully applied for short distances up to a few meters [35.10, 18, 28].

For applications of the method with distances between the sources and receivers of several decameters up to a few hundreds of meters in the atmospheric boundary layer, signals with a fixed sound frequency, two wave trains with a defined number of oscillation periods, and a pause between them are used [35.29, 30]. The chosen frequency has to be adjusted to the hardware (speakers) and a possible high-pass filtering of the received signal has to be taken into account. This,

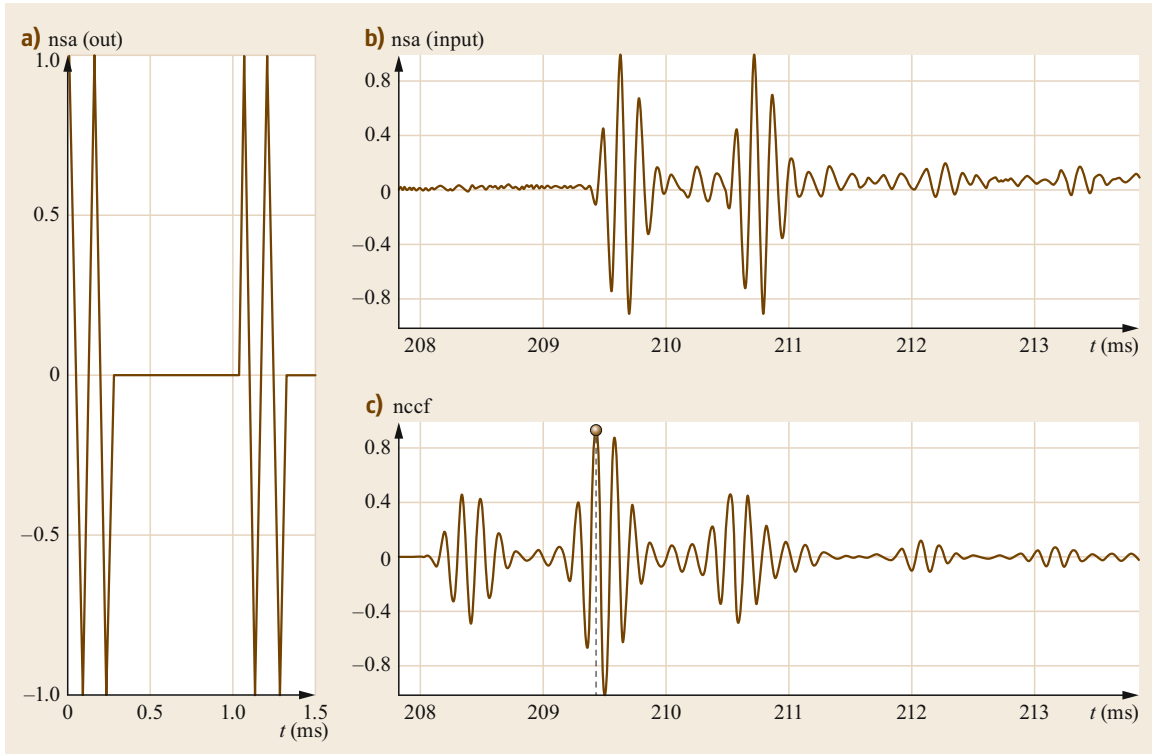


Fig. 35.4 (a) Normalized signal amplitude (nsa) of a theoretical acoustic signal (out) consisting of 2×2 sine periods with a frequency of 7 kHz interrupted by a break, (b) the normalized signal amplitude of the received signal (nsa (input)), and (c) the normalized cross correlation function (nccf) between the generated and the received signal. The nccf maximum is marked with a filled circle. The associated time lag corresponds to the travel time of the acoustic signal (adapted from [35.29])

in turn, is recommended in noisy environments (street noise) to enhance the signal-to-noise ratio (SNR). An upper limit for the sound frequency is given because atmospheric absorption of sound increases for increasing frequency [35.31], which is especially important for long-range sound propagation. The sample rate of the device has to be high enough to ensure that the signal frequency could be represented properly with respect to the sampling theorem, which states that the sample rate has to be at least twice as high as the signal frequency.

It is possible to synthetically increase the sample rate by interpolating the signal to estimate interim values within the sampling time of the data logger using a sinc function. With such a method it is possible to increase temporal resolution by a factor of ≈ 10 [35.28]. This leads to a sharper detection of the maximum using the cross correlation method described above.

Successful experiments have been carried out with sound frequencies of 1 kHz [35.14] and 7 kHz ([35.29, 32], cp. Fig. 35.4). Wilson and Thomson [35.12] worked with a swept-frequency signal (Table 35.4).

Table 35.4 Examples for used sound signal structures to detect travel times by the cross correlation technique

Reference	Data logger sampling rate (kHz)	Sound signal	Interpolation after cross correlation
[35.30]	10	1 kHz double burst of 4 ms duration with a 14 ms pause between the bursts	–
[35.29]	51.2	2×2 sine periods with a frequency of 7 kHz with a break of ≈ 1 ms	Using sinc
[35.12]	16	Sine wave sweep 100–1000 Hz, duration 0.1 s	–
[35.10]	51.2	Pseudorandom sequences (MLS)	Using sinc
[35.18]	51.2	Pseudorandom sequences (MLS)	Using sinc

35.3.4 Separation of Temperature and Flow from Sound Speed

If the distances between transmitters and receivers in the measuring area are known, then the observed sound travel times over the distances between transmitter and receivers can be used to calculate an effective sound speed. This velocity reflects the path-integrated influence of the acoustic virtual temperature and of the wind vector. Because the observed effective sound speed is influenced by temperature and the wind vector, the measurement method itself or the analyzing algorithm must allow to distinguish between temperature and wind if one is interested in the meteorological quantities.

There are examples of the use of bidirectional sound paths, which may be spatially separated in the measurement field [35.33]. In practice the measuring sections do not necessarily have to be arranged at right angles to record the full information for the calculation of the horizontal wind; however, this can be advantageous depending on the inversion scheme (Fig. 35.5) [35.28, 34].

Other methods use stochastic inversion, which is designed from the outset to generate two separate distributions of the direction-independent temperature field and the direction-dependent flow field from the sound speed data. Such procedures have to specify some parameters, which describe the turbulent nature of the underlying meteorological fields of temperature and flow velocity [35.20, 35, 36].

Some methods firstly separate influences of temperature and wind included in the effective sound speed. In a second step, these separated datasets are converted into spatial distributions of wind vector and temperature using inversion algorithms. The most favorable method is probably the use of reciprocal transmission paths.

Examples with consistently reciprocally arranged sound paths are analyzed in [35.37].

In the following, we describe the application of the reciprocal method to separate datasets of temperature-dependent and wind-dependent sound travel time from

the measurements. These data are used after the separation as input data for tomographic algorithms.

This method for separating is based on the fact that scalar temperature influences the speed of sound independently of the direction of sound propagation, while the influence of flow depends on the direction. A flow component in the direction of sound propagation yields an increase of the effective sound speed, while it leads to a decrease in the opposite direction, as is obvious from $c_{\text{eff}} = c_L(T_{\text{av}}) + v_r$ (Table 35.3, Fig. 35.5).

To separate the vectorial and scalar influences, an arrangement consisting of two transmitter–receiver pairs is used in which they are facing each other in opposite directions at a defined distance D (Fig. 35.5).

Two sound sources (loudspeakers) and two receivers (microphones) are mounted at a distance D . Along both directions the travel time of an acoustic signal τ is measured. The effective sound speed in the direction of the flow component along the sound ray path v_r is given as a sum of the adiabatic sound speed c_L and v_r : $c_{\text{eff},1} = c_L + v_r$. In the opposite direction the effective sound speed is given as a difference $c_{\text{eff},2} = c_L - v_r$.

The indices mark the forward (index 1) and backward (index 2) direction. Consequently, c_L or T_{av} as well as v_r along the straight propagation paths between the transmitter–receiver pairs can be calculated

$$c_L = \frac{1}{2} (c_{\text{eff},1} + c_{\text{eff},2}) = \frac{D}{2} \left(\frac{1}{\tau_1} + \frac{1}{\tau_2} \right) = \sqrt{\gamma R_a T_{\text{av}}}, \quad (35.4)$$

$$v_r = \frac{1}{2} (c_{\text{eff},1} - c_{\text{eff},2}) = \frac{D}{2} \left(\frac{1}{\tau_1} - \frac{1}{\tau_2} \right). \quad (35.5)$$

This approach is also used, at a very small scale, by sonic anemometer/thermometer (for an overview see Chap. 9 and [35.38]).

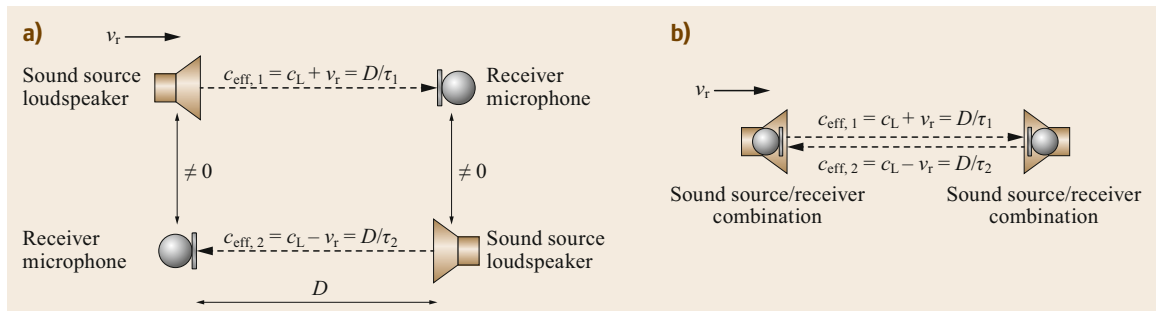


Fig. 35.5a,b Scheme of bidirectional (a) or reciprocal sound propagation (b) used to separate scalar temperature and the vectorial flow influence on the effective speed of sound (sound source: loudspeaker; receiver: microphone)

In this result, two datasets of simultaneous observations exist:

1. A dataset of Laplace sound speed values for each transmitter–receiver pair
2. A further dataset for the wind speed component along the sound propagation path, which influences the speed of sound between each transmitter–receiver pair

A distribution of several such pairs enables probing through an area or volume of air from different directions. Therefore, it is possible to obtain information from mostly all parts of a measuring area or volume. This information consists of averages along lines, which must be understood as projections for using tomographic reconstruction methods. Such precisely recorded datasets create the requirements for the technical developments of acoustic tomography and the experimental setup to reconstruct air temperature and velocity fields.

35.3.5 Uncertainty

The basis for accurate tomographic reconstruction of temperature and flow fields in air is a proper estimation of the speed of sound along different paths through the area. In order to calculate the speed of sound (Table 35.3) between a source and a receiver precisely, the transmission path length and the travel time along this path must be measured or known. Several issues, e.g., technical and signal-dependent, influence the travel-time determination leading to uncertainties due to sampling and signal analysis as well as to possible errors in recalculated wind speed and temperature values [35.29].

To detect the signal within the environmental noise, the SNR should be as high as possible. Thus, sound attenuation effects in air should be minimized. The measured sound pressure level at a microphone depends on the effects of spherical spreading, i.e., geometrical sound attenuation, and attenuation due to air absorption. Atmospheric absorption is primarily dependent upon sound frequency and secondary on air temperature and humidity [35.31]. Additionally, interference from environmental sounds near the microphones should be avoided. Unfortunately, the wind itself creates flow noise on the microphones. Windscreens for microphones are a useful tool to avoid this noise contamination.

The travel-time measurements require application of an acoustic multichannel device, which uses a common temporal basis for all output and input channels. The digital record of a continuous acoustic signal is im-

plemented with an analog digital converter (ADC). The ADC provides discrete values with a time resolution (sampling interval or sample period Δt) that depends on the sampling frequency or sampling rate f_s of the device: $\Delta t = f_s^{-1}$. Thus, an increasing sampling rate results in a decreasing uncertainty of the travel-time estimates. On the other hand, an increasing sampling rate is followed by higher demands on storage space and data processing capacity. Furthermore, a reduction of the time intervals between successive data points can be achieved by interpolating, e.g., using the sinc function [35.28].

The sampling rate f_s must be high enough to record the complete sound frequency range $f_{\text{sound}}^{\text{max}}$ contained in the used sound signal. Here, the sampling theorem and the resulting Nyquist frequency f_v must be kept in mind: $f_s = 2f_v \geq 2f_{\text{sound}}^{\text{max}}$ [35.39].

Further, it is important to take into account that the electronic transmission and reception of the sound signals requires a certain amount of processing time in the electronic device itself. This period is not part of the sound travel time; nevertheless, it must be determined separately to include the inertia time of the electronics in the process of analysis.

Additional uncertainties with respect to travel-time estimation arise from the properties of the signal analyzing method, e.g., of the cross correlation function. The most certain results can be achieved for signals with an impulse-like autocorrelation function, i.e., for an impulse-like signal or white noise. However, both signals are inappropriate for acoustic travel-time applications with path length of more than several meters. Impulse-like signals would require an enormous excitation energy in order to generate a signal. A single impulse is not suitable to drive a speaker appropriately (without any damage). On the other hand, white noise is not bandlimited, which, in turn, would require an infinite sampling rate. Thus, signals are used which hold a special signature as shown in Fig. 35.4 and whose autocorrelation function is characterized by a clearly distinguishable maximum. At the very least, one must estimate the uncertainty of the travel-time measurement $\Delta\tau$, which is $\Delta\tau \geq \Delta t$.

For an estimation of the effective speed of sound, not only the travel-time measurements have to be implemented with a small uncertainty, but also the positions of the sound sources and receivers have to be known exactly. Thus, the measurement of positions should be put into practice using a device, which reaches a very high accuracy, e.g., an electronic tachymeter. With such a device, the geometric distances D along all sound travel paths can be measured within an uncertainty dD of only a few millimeters up to path lengths of several hundred of meters.

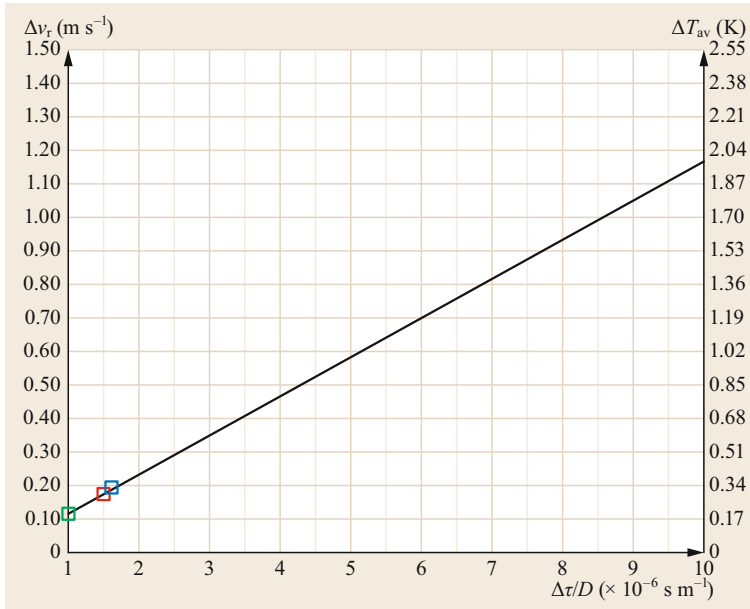


Fig. 35.6 Uncertainty of the derived temperature and wind speed along the propagation path as dependent upon the uncertainty in the determination of acoustic travel time normalized by the distance between the sound source and receiver, applying reciprocal sound propagation. The uncertainties associated with various experiments are marked (red STINHO-1, -2 [35.30]; blue SQuAd [35.29], green [35.12])

When employing reciprocal sound paths, one assumes sound wave propagation along straight rays with measured geometric distances between sources and receivers. However, the geometric distances and the sound path lengths are not identical in any case due to gradients of temperature and wind along the sound propagation path, which cause a refraction of the sound wave. Generally, in the atmosphere, vertically increasing wind speed prevails, while air temperature can decrease or increase with height. In the horizontal direction, all conceivable gradients can exist. As a result, the sound propagates along curved lines. These deviations from the geometric distances produces a systematic uncertainty in the sound speed measurement, which results in uncertainties in determination of temperature and wind speed [35.29, 32].

For practical applications, it is possible to measure with absolute or relative accuracy.

Absolute accuracy means that the distances between all sources and receivers are measured with an uncertainty dD and that acoustic travel times are measured with an uncertainty of $d\tau$. Thus, the resulting uncertainty of the estimated speed of sound depends on both, dD and $d\tau$. Relative accuracy refers to measurements of acoustic travel times, where positions of sources and receivers are calculated using an alternatively measured temperature and wind distribution as an initial calibration of the system. After doing this calibration, changing travel times are only attributed to variations in temperature and wind speed with regard to the initial conditions at the calibration time. Consequently, uncertainties of the positioning of sources and receivers can

be neglected, resulting in higher accuracies of relative measurements. Nonetheless, this approach requires precise knowledge of temperature and wind distribution within the area under investigation at the calibration time.

Ziemann et al. [35.29] show the complete derivation of temperature and wind uncertainty assuming an exact sound path determination for reciprocal sound propagation. The analysis indicates that the uncertainty of the temperature is given by

$$\Delta T_{av} = 2\sqrt{\frac{T_{av}}{\gamma R_a}} \Delta\tau \left[\frac{(\gamma R_a T_{av}) + v_t^2}{D} \right], \quad (35.6)$$

$$\Delta v_t = \Delta\tau \left[\frac{(\gamma R_a T_{av}) + v_t^2}{D} \right]. \quad (35.7)$$

As an illustration, for a travel-time accuracy of $78 \mu\text{s}$ (SQuAd-Project, spatially resolved quantification of the advection influence on the balance closure of greenhouse gases [35.29]) and a path length of 50 m (i.e., travel-time uncertainty normalized by distance of $1.6 \times 10^{-6} \text{ s m}^{-1}$), a maximum temperature uncertainty of $\approx 0.3 \text{ K}$ results for the instantaneous single path measurement (Fig. 35.6). The uncertainty of relative wind measurements depends only on the uncertainty of travel-time measurements. Assuming again a path length of 50 m, a maximum wind uncertainty for the instantaneous single path measurement of $\approx 0.2 \text{ m s}^{-1}$ results. For other experiments (e.g., STINHO, structure of turbulent processes under inhomogeneous surface conditions [35.15, 30]) in the past, a travel-time un-

certainty of $300\ \mu\text{s}$ was achieved applying path lengths of $\geq 200\ \text{m}$ (i.e., normalized, by distance, travel-time uncertainty of $1.5 \times 10^{-6}\ \text{s m}^{-1}$) resulting in similar temperature and wind uncertainties. With increasing path lengths, the uncertainty of temperature and wind components decreases. Otherwise, for a constant distance between sound source and receiver, the uncertainties are lower for a lower uncertainty in the travel time (Fig. 35.6).

35.3.6 Experimental Setup

A tomographic measurement setup using reciprocal sound propagation (Sect. 35.3.4) is based on measurements that determine the speed of sound along one and the same propagation path in the backward and forward directions. This is similar to a sonic anemometer which spans long distances (Chap. 9). Conversely, a sonic anemometer can also be understood as a tomographic array [35.21].

For tomography, a number of transmitter/receiver stations must be distributed within the area of investigation (Fig. 35.7). Some experimentally realized transmitter/receiver distributions are presented in Sect. 35.8. To prepare a measuring configuration the following topics are helpful.

Spatial Distribution

Sound paths must pass through all parts of the area spanned by the positions of the transmitter/receiver stations. In order to obtain information about the spatial

distribution of sound velocities within the area of interest, several sound sources and receivers have to be positioned around or inside the area. To reconstruct temperature and flow field using an inversion algorithm, the resultant sound paths should cover the area of interest as homogeneously as possible. The length of sound paths must be known as exactly as possible. Applying reciprocal sound propagation and algebraic reconstruction techniques (Sect. 35.3.7), positions of sources and receivers have to be chosen in such a way that a separation of the influences of temperature and flow on the speed of sound is possible. It would be advantageous if the distance between the transmitter/receiver positions at the border of the measuring field (red line) are chosen in such a way that the sound path lengths differ as far as possible between all positions. In such a case, the sound signals reach the receiver at different times, and the single signals can be easily identified.

Identification of Sound Signals

Sound sources and receivers situated close to the ground make sound propagation more complex. Besides direct sound waves between loudspeaker and microphone, there are also ground-reflected waves [35.40]. This reflected wave integrates the conditions of the air layer between the ground surface and the source/receiver. Additionally, the interference between those sound reflections can lead to considerable effects within the received signal, which should be estimated before starting with the experimental setup.

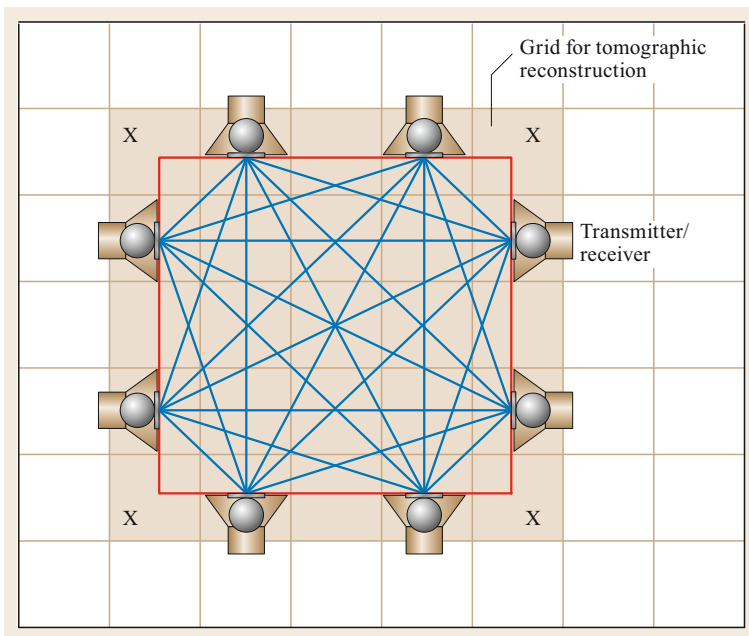


Fig. 35.7 Schematic representation of the measuring principle of acoustic travel-time tomography. An area is scanned along various paths by sound signals (blue lines), which are sent (received) from loudspeakers (microphones) at different locations. The determination of travel times of the signals along known propagation paths allows the calculation of the effective speed of sound and thus provides information about the temperature and flow along the propagation path (X: grid cells without any crossing sound ray)

Furthermore, it has to be ensured that the acoustic signals, which reach the receiver from different transmitters, can be clearly assigned to the source of origin. This can be implemented using a different signal signature for each transmitter or by choosing the distances between all transmitters and receivers in such a way that all paths have different lengths (i.e., clearly distinguishable travel times). In the latter case, a time window can be defined for each sound propagation path, in which the signal is expected to arrive at the receiver. The time window size must be selected so that, during the measurement time, possible wind and temperature changes leading to travel-time changes can also be recorded. By specifying a detection range for air temperature or wind, the time window size can be set.

Resolution of Field Reconstruction

Especially for algebraic reconstruction (inversion) techniques, the area under investigation must be subdivided into distinct grid cells. Within each grid cell, the physical properties (both temperature and wind) are assumed to be constant. After separation of the influences of temperature and flow on the speed of sound (Sect. 35.3.4), the meteorological fields are reconstructed independently using various tomographic inversion methods.

In the example of Fig. 35.7, the area of investigation is divided in $5 \times 5 = 25$ cells. In this example, there is no sound path through the cells at the corners (X) of the tomographic grid. Hence, there is no information available for tomographic inversion within these grid cells (or voxels in 3-D case) and the available information has to be extrapolated from neighboring cells. In the optimal case, the sound paths are traveling through all parts, i.e., all grid cells, of the measuring area.

Before starting with a tomographic field experiment it is appropriate to test the arrangement of sound sources and receivers applying optimization algorithms. This is due to the fact that an acceptable reconstruction of the temperature and velocity fields in the measurement area strongly depends on the arrangement of the sound transmitters and receivers and their number. As a rule, a study area equipped with M transmitters and N receivers can ultimately be decomposed into $(M \times N)/2 = J$ subareas for which temperature and velocity can be identified. The denominator 2 results from the separation of wind and temperature as required for reciprocal sound propagation, which means that each two sound paths are identical. The prerequisite for the use of tomographic procedures is that the positions of the transmitters and receivers and their mutual position are known. The arrangement of transmitters and receivers is limited only by imagination. When

positioning, the above-mentioned influences on sound propagation should be considered.

35.3.7 An Example of Inverse Tomographic Reconstruction

In the following, the reconstruction of temperature and velocity fields from travel-time (sound speed) measurements is explained with an example. The example uses the simultaneous iterative reconstruction technique SIRT (Fig. 35.2), which has proven to be one of the most robust algebraic reconstruction techniques [35.41, 42].

SIRT presupposes that after recording the signal travel times along all paths between sound sources and receivers it is possible to divide the sound speed observation into two parts:

1. Travel times which are only influenced by Laplace sound speed along all paths
2. Velocities v_i that represent the influences of wind component on the sound speed along the paths.

Here we note that the time-dependent stochastic inversion (TDSI) [35.16, 35] exhibits comparable results, with the advantage that the datasets must not be divided into a Laplace sound speed part and a velocity part, but one has to know additional information of the turbulent field structure.

Reconstruction of (Air) Temperature Fields

The following information must be available (see Sect. 35.3.1):

For each transmitter–receiver pair $1 \leq i \leq I$: temperature-dependent travel time of acoustic signal τ_i

$$\tau_i = \int_{L_i} \frac{dL_i}{c_{L,i}} \quad (35.8)$$

and sound path length L_i to estimate the Laplace sound speed at the path $c_{L,i} = L_i/\tau_i$, or the so-called slowness $s_i = \tau_i/L_i$ along L_i .

For a tomographic reconstruction using SIRT the whole area of interest, through which the sound propagates, is subdivided into J grid cells. The path length between transmitter and receiver is then given by

$$L_i = \sum_{j=1}^J l_{ij}, \quad (35.9)$$

where l_{ij} is the path length of the i -th sound ray path through the j -th grid cell.

Each piece l_{ij} can be affected by the individual slowness s_j

$$\tau_i = \sum_{j=1}^J l_{ij} s_j. \quad (35.10)$$

The aim of the tomographic reconstruction is to estimate a set of slowness values for all grid cells $j = 1, \dots, J$ in such a way that, for a given geometry (course of sound paths through a defined grid cell structure), the measured travel-time values along all $i = 1, \dots, I$ rays are well represented.

The calculation of slowness values for all grid cells using algebraic reconstruction techniques requires the following steps [35.10]:

1. Presetting of an initial distribution for the slowness values (e.g., homogeneous distribution)
2. Calculation of travel-time values for all sound ray paths according to (35.10) (forward modeling)
3. Computation of deviations between calculated and measured travel-time values and subsequent calculation of corrections for slowness values within each grid cell
4. Calculation of an improved slowness distribution within the tomographic grid
5. Repetition of steps 2–4 until a termination criterion is reached (maximum number of iterations, maximum deviation between modeled and measured travel-time values)
6. Stop of iterative process, and calculate distributions of acoustic virtual temperatures from slowness values/Laplace's sound speed values using the physical relations from Tables 35.2 and 35.3

For the most applications presented here, SIRT is used to calculate the slowness distribution within the grid cell structure. Advantages of SIRT are its favorable convergence properties, its low computational requirements (which allows for online analyses), and also its low sensitivity with respect to small perturbations of the input data, i.e., the travel-time measurements [35.43]. Furthermore, no additional information on the properties of the distribution is required prior to the reconstruction using SIRT. In contrast to other algebraic methods, SIRT calculates corrections for the slowness values within each grid cell Δs_j but not before all modelled (τ_i^{calc}) and measured travel-time values (τ_i^{meas}) have been treated

$$s_j = L_j^{-1} \sum_{i=1}^I \left(l_{ij} \frac{\tau_i^{\text{meas}} - \tau_i^{\text{calc}}}{L_i} \right). \quad (35.11)$$

Here,

$$L_j = \sum_{i=1}^I l_{ij}$$

represents the length of all sound ray sections within grid cell number j . Hereafter, the new distribution of slowness values (superscript $t + 1$) within the grid can be calculated from the present distribution and correction (superscript t) by $s_j^{t+1} = s_j^t + \Delta s_j^t$.

Reconstruction of Wind Velocity Fields

In order to reconstruct the vector wind field within the area of interest, a vector tomographic algorithm has to be used. An overview on vector tomography is given in [35.44]. As consistent with the temperature reconstruction, an iterative tomographic algorithm is used for flow reconstruction [35.10, 37]. Basic information can be found in [35.45].

To reconstruct the flow field distribution, the area of interest is divided into J grid cells as it is done for temperature reconstruction. The measured flow values v_i along I different propagation paths serve as input data for the tomographic reconstruction of the flow field. Starting from an initial guess for the flow values within each grid cell j (e.g., for a three-dimensional wind vector $\mathbf{v}_j = (u_j, v_j, w_j) = (0, 0, 0)$ – calm) an iterative algorithm is used to improve the grid cell solution up to a termination criterion.

To improve the solution, the projection of the flow field on the i -th sound ray path $v_{r,i}^{\text{calc}}$ is calculated dependent on the grid cell values for the flow for each grid cell j and the fraction of the ray path length of the i -th sound ray within the j -th grid cell l_{ij} , where the total length of the i -th sound ray is L_i

$$v_{r,i}^{\text{calc}} = \frac{1}{L_i} \sum_{j=1}^J l_{ij} [(u_j \cos \alpha_i + v_j \sin \alpha_i) \cos \theta_i + w_j \sin \theta_i], \quad (35.12)$$

$$v_{r,i}^{\text{calc}} = \frac{\sum_{j=1}^J l_{x,ij} u_j + l_{y,ij} v_j + l_{z,ij} w_j}{L_i}. \quad (35.13)$$

In this equation, $l_{x,ij}$, $l_{y,ij}$, $l_{z,ij}$ denote the signed fraction of the i -th sound ray path within the j -th grid cell in the x -direction, y -direction, and z -direction, respectively. The flow vector within each grid cell j is given by its components $\mathbf{v}_j = (u_j, v_j, w_j)$ as before. The angles in (35.12) describe the geometry of the sound ray path within the volume, where α_i is the azimuth angle of the projection of the i -th ray path on the horizontal plane and θ_i is the elevation angle of the i -th sound ray path measured from the horizontal plane (Fig. 35.8).

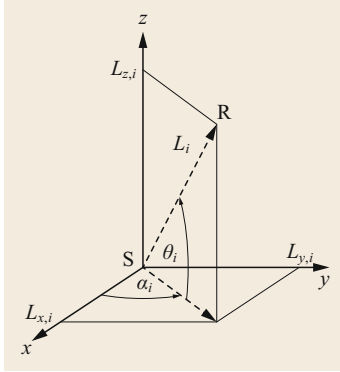


Fig. 35.8 Geometry for the i -th sound ray path, which is defined as a straight connection between a sound source (S) and a receiver (R) within a Cartesian coordinate system. L_i is the total length of the sound ray path, while $L_{x,i}$, $L_{y,i}$ and $L_{z,i}$ are the orthogonal projections of the sound ray onto the x -axis, y -axis, and z -axis of a Cartesian coordinate system, respectively (from [35.10], © IOP Publishing. Reproduced with permission. All rights reserved)

A measure for successive improvements of the solution within all tomographic grid cells is given by

the difference between $v_{r,i}^{\text{calc}}$ and the measured velocity component along the i -th sound ray path $v_{r,i}^{\text{meas}}$

$$\Delta \mathbf{v}_j = \begin{pmatrix} \Delta u \\ \Delta v \\ \Delta w \end{pmatrix}_j = \left\{ \begin{array}{l} \left[\sum_{i=1}^I |L_{x,ij}| (v_{r,i}^{\text{meas}} - v_{r,i}^{\text{calc}}) \cos \theta_i \cos \alpha_i \right] L_{x,j}^{-1} \\ \left[\sum_{i=1}^I |L_{y,ij}| (v_{r,i}^{\text{meas}} - v_{r,i}^{\text{calc}}) \cos \theta_i \sin \alpha_i \right] L_{y,j}^{-1} \\ \left[\sum_{i=1}^I |L_{z,ij}| (v_{r,i}^{\text{meas}} - v_{r,i}^{\text{calc}}) \sin \theta_i \right] L_{z,j}^{-1} \end{array} \right\}. \quad (35.14)$$

In the preceding equation, $|\cdot|$ stands for the absolute value, e.g., $|L_{x,ij}|$ is the absolute length of the i -th sound ray path within the j -th tomographic grid cell in the x -direction and $L_{x,j}$, $L_{y,j}$, and $L_{z,j}$ are the total lengths of all sound ray paths within the j -th grid cell in the x -, y -, and z -direction, respectively.

35.4 Devices and Systems

Standardized equipment for applications of acoustic tomography in atmospheric sciences does not exist at present. Generally, a measurement system consists of a multichannel controlling and recording unit together with sound sources (loudspeakers) and sound receivers (microphones). Additionally, a procedure and a device (e.g., electrooptical device like a tachymeter) to locate the transmitter and receiver at exact positions within the area of investigation is needed (Fig. 35.9).

35.4.1 Travel-Time Recording

The electronic devices must be able to record the sound signal correctly. It is advantageous if the used sound signals have a signature to identify the artificial signal within the environmental noise recorded by the microphone unit. In several implementations (e.g., [35.14, 42]), the acoustic signal consisted of a defined repetition of short pulses. To derive the travel time of the received sound signal, a cross correlation method between transmitted and received signals was successfully used (Sect. 35.3.3). Transmission and reception of signals could be controlled by an acoustic spectrometer card, which has a common time base for all input and output channels. The sample rate of this device has to be

high enough to ensure that the signal frequency is represented properly with respect to the Nyquist sampling theorem (e.g., [35.39] Chap. 2).

35.4.2 Sound Sources and Receivers

Commercial loud speakers of different types are used as sound sources, which are designed for different frequency ranges and a wide angle of sound emission. The sound receivers are commercial microphones. Figures 35.10 and 35.11 show typical sound sources and microphones (with wind screen) that are used during different experiments like STINHO-1 and STINHO-2 [35.15]. Figure 35.10d also shows the distance of microphones and speakers in the landscape. The transmitter–receiver station shown in Fig. 35.11 corresponds almost for reciprocal sound transmission.

The volume of the hardware-generated sound signals has to be adjusted to enable a proper detection at the microphone. It is advantageous if the structure of the transmitted signals is so short that the human ear cannot hear their tonal structure. Long-lasting measurement campaigns with such a signal (Fig. 35.4) were mostly accepted by people in the surrounding neighborhood.

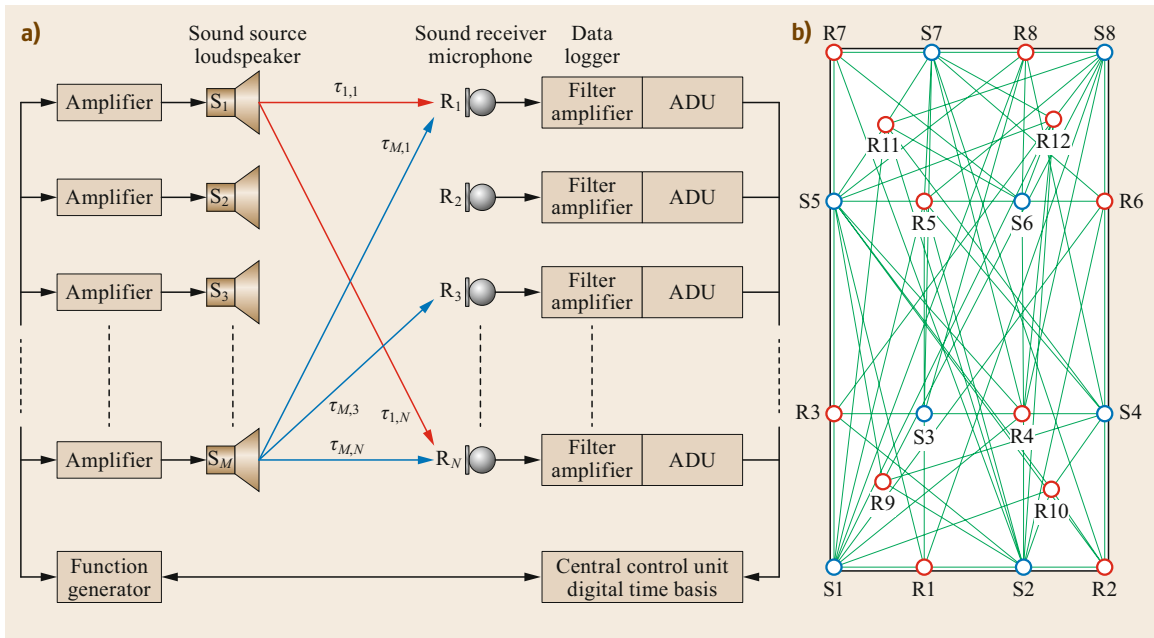


Fig. 35.9 (a) Scheme of a multichannel system to record travel times of sound signals using a bidirectional approach (similar to reciprocal sound propagation, but with a small spatial offset between transmitter/receiver pairs) consisting of M sound sources and N receivers. Each receiver can detect the signal from each sound source. (b) The measurement system records $N \times M$ sound travel times. Each travel time belongs to a different path (green lines) through the measuring area with receivers (R_*) and sources (S_*). These individual paths can be identified in a measurement setup which was realized, e.g., during the STINHO-2 experiment (after [35.15]). In this case, the system consists of 8 sources and 12 receivers distributed within an area of $300 \text{ m} \times 440 \text{ m}$

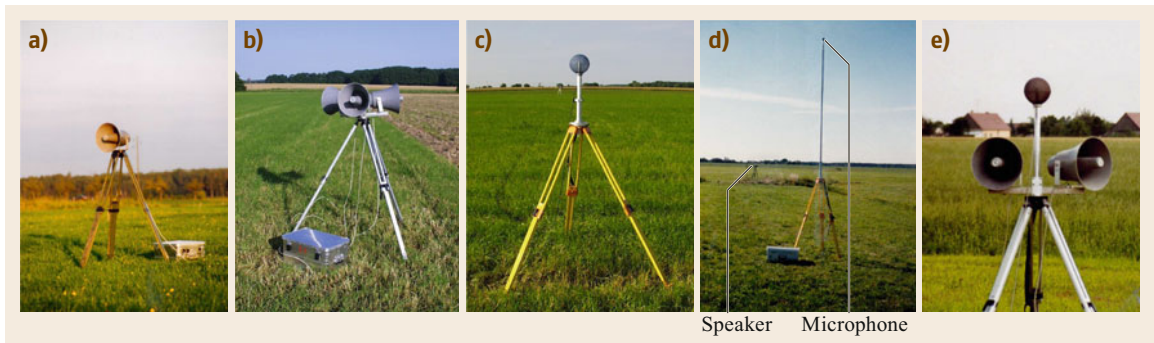


Fig. 35.10a–e Speakers, used as sound sources (a,b) and microphones (c,d) used during different experiments like STINHO-1 and STINHO-2. The equipment implements the travel-time measurement with 1 kHz signals. To obtain a wide angle of sound transmission up to 3° of such loudspeakers are combined into one station (b). A single microphone (a wind screen is necessary (c,d)) is used as a receiver station. To realize reciprocal sound speed measurements, transmitter and receiver must be combined into one station (e). Part (d) shows the distribution of microphones and speakers in the landscape (a) (after [35.30] with permission from © Acta Acustica united with Acustica); (b,c) (after [35.33]); (d,e) (photos © Arnold)

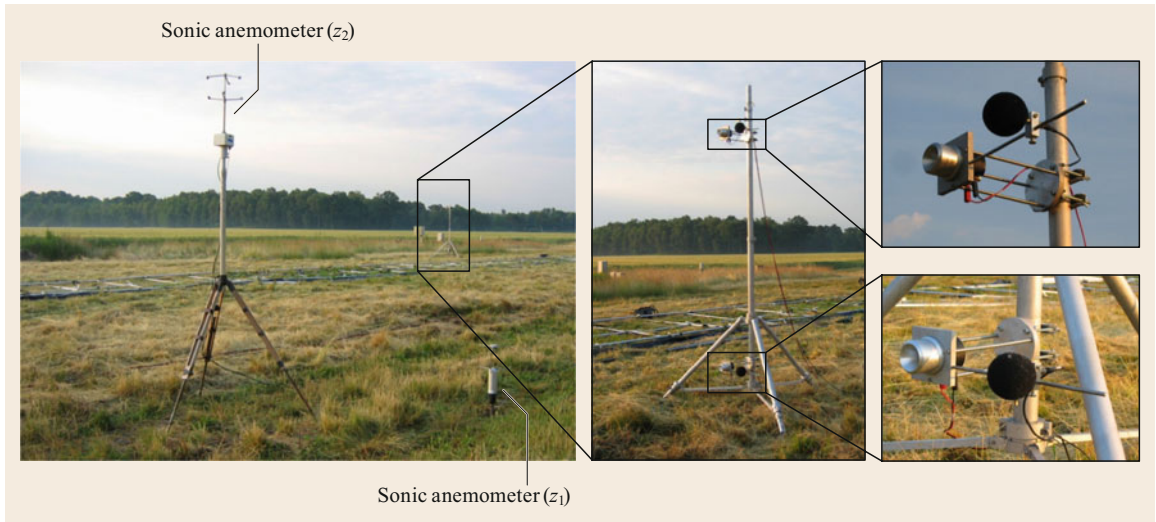


Fig. 35.11 Transmitter/receiver station equipped with Visaton loudspeaker and a 1/4-inch microphone under a wind screen. These travel-time measurements use 7 kHz sound signals. The picture also shows two sonic anemometers, which are used for comparison during the experiment (after [35.32] with permission from E. Schweizerbart'sche Verlagsbuchhandlung OHG)

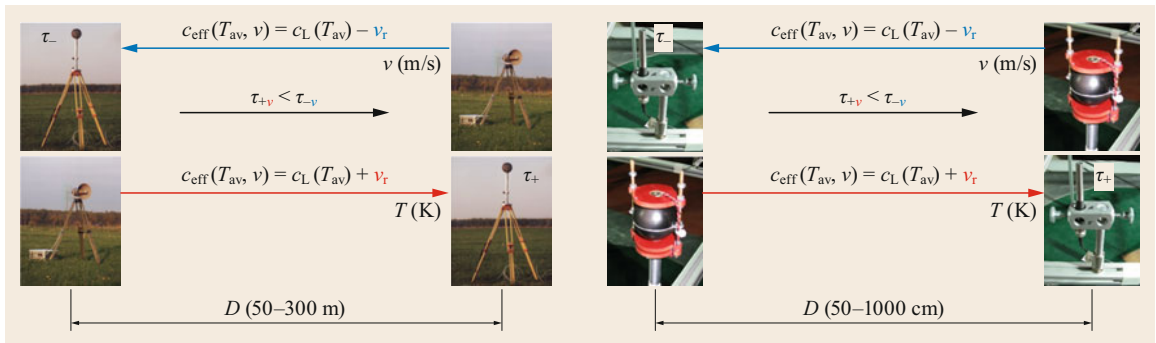


Fig. 35.12 Examples for the scalability of acoustic travel-time measurements

35.4.3 Scalability

An advantage of acoustic methods is their scalability. Depending on the geometric extent of the area of investigation, the physical data analysis methods do not change (Fig. 35.12). This property allows new components to be easily tested under laboratory conditions, as well as to investigate the interaction between an experimental setup, electronic signal transmission and numerical analysis. A change of the extent of the area under investigation may demand an adjustment of the

frequency of the sound signal as well as a corresponding choice of sound sources and receivers to fit to the measurement task. Here, the scalability is limited to measuring sections, for which a straight-line sound propagation under the given temperature gradients or flow gradients must be ensured. Small-scale laboratory setups are used to test types of sound signals [35.28] and tomographic inversion methods [35.20, 37]. The small-scale measurement setups are then again suitable for analyzing the structure of temperature and flow fields (e.g., in wind tunnels [35.10] or indoors [35.18]).

Table 35.5 Example characteristics for temperature and wind speed measurements (instantaneous values) at different spatial scales calculated using (35.6) and (35.7)

Reference	General conditions of the measurement		Uncertainty of target variables		
	Acoustic path length (m)	Travel-time uncertainty (μs)	Uncertainty of travel time ($\times 10^{-6} \text{ s m}^{-1}$) normalized by distance (Fig. 35.6)	Acoustic virtual temperature (K) (35.6)	Wind speed (m s^{-1}) (35.7)
[35.30]	≥ 200	300	1.5	0.3	0.2
[35.29]	50	78	1.6	0.3	0.2
[35.12]	100	100	1	0.2	0.1
[35.10]	1	2	2	0.4	0.25
[35.18]	5	2	0.4	< 0.2	< 0.1

35.5 Specifications

Tomography systems have to be designed to adapt to the structure of the sound signals, their frequency content, and the repetition rate of the measurements to the geometric configuration of the measuring field. Since higher sound frequencies are strongly attenuated over long distances, the use of ultrasound is infeasible when working on a micrometeorological scale. However, under small-scale laboratory conditions, ultrasound may well be the frequency range of choice. The tomographic experiments described in the literature thus also use sound signal structures adapted to the measuring conditions, which are intended above all to ensure unmistakable identification of the sound signal. Differing signal structure of the emitted sound from the various transmitters is to be regarded as an advantage. The

recording of the sound signals is done with data logger technology, which of course has to ensure a sampling rate that can record the frequency content of the used sound signals.

For different implementations of the technique, estimated uncertainties of derived temperature and wind values are given in Table 35.5. As described in Sect. 35.3.5, uncertainties strongly depend on the size of the measurement area as well as on the feasible temporal resolution of travel-time measurements. It is important to note that a maximum error calculation was applied. The received values of uncertainties are higher in comparison to an investigation of purely statistical uncertainties, which can be described, e.g., by the standard deviations of high-frequency measurements.

35.6 Quality Control

If the geometric structure of the measurement array is known, then the recording of the travel times of the sound signals must be controlled for the following reasons:

1. For plausibility of propagation time windows of the sound signals

2. For plausibility of variability of the sound speed field between successive measurements

An overview to parameters which must be controlled in preparation for and during acoustic tomographic measurements can be found in Table 35.6.

Table 35.6 Influences and uncertainties of sound speed measurements for acoustical tomographic purposes and tomographic reconstruction methods

Uncertainty	Influence on the speed of sound and its measurement	Consideration
Composition of the air, different water vapor content	Change of R_a ($\text{J kg}^{-1} \text{K}^{-1}$), γ	Measurement of the acoustic virtual temperature (acceptance of a small influence of moisture on the temperature measurement)
Geometric distance	Measurement of the distance between the transmitter and receiver and their mutual location	Estimation of uncertainty of distance measurements
Travel-time measurements	Time synchronization of electronic devices sampling frequency of received sound signals, used frequency of sound	Estimation of the uncertainty of travel-time measurements. The accuracy is limited at least by the digitizing frequency of the data logger and the frequency of the used sound signal.

Table 35.6 (Continued)

Uncertainty	Influence on the speed of sound and its measurement	Consideration
Deviation from straight sound propagation: curved rays	Vertical and horizontal gradients of wind and temperature Possible formation of acoustic shadow zones. The signal is not detectable (see Sect. 35.3.6, <i>Identification of Sound Signals</i>)	Limitation of the distance between individual transmitters and receivers Monitoring signal level/amplitude of the maximum of the cross correlation function to exclude measurements with insufficient signal strength
Reciprocal sound propagation	Different influence on the sound paths in the up and downwind direction	Determine whether differing path lengths in back and forth direction are a negligible source of uncertainty. The sound levels at these paths are different
Reflections	Reflections of sound signals on the ground (ground dip) or obstacles Superposition of direct sound signal and reflections	Definition of time windows in which the incoming signal is assigned to the known sound source–receiver path. Positioning of equipment in sufficient distance to reflecting obstacles (also to objects which belong to the measuring device)
Identification of the designed/emitted sound signals	Signal-to-noise ratio (SNR) Expected arrival times of the used sound signals at the receiver Signal amplitude too low (acoustic shadow due to refraction, upwind, damping) → cross correlation function no clear maximum → no clear travel time signal	Use of defined signal forms. Defining the time slots for the arriving times of sound signals traveling along the known distances between transmitters and receivers Time window size must be based on the possible signal travel time change during the measurement time (possible wind and temperature change in the study area and during the duration of measurements) Monitoring SNR (e.g., amplitude of maximum of cross correlation function relative to noise) Reduction influence of ambient noise (usually low-frequency) due to (high-pass) filtering of the received signals (corresponding selection of the sound signal frequency required for this)
Superimposition of (identical) sent sound signals	Distances between transmitters and receivers are identical	Measurement setup must be changed so that all distances between transmitters and receivers are of different lengths, so that the sound signals arrive separately at the receiver Not simultaneous emission of sound signals from all positions, but send out the signals at the different transmitters successively. Or each transmitter signal get its own identifier
Separation of wind and temperature influence in the travel-time data	Unfavorable arrangement of sources and receivers with respect to up and downwind	Altering the design of the measurement layout by changing the location of sources and receivers appropriately Use different sound signals to identify each individual sound source
Tomographic reconstruction	Sequence of iterative solution processes, abort criterion for iterative solutions Decomposition of the measurement area into subareas	The structure of the spatial resolution of the tomographic reconstruction must match the number of sound paths. When algebraic reconstruction algorithms are used, this can be determined by the number of transmitter–receiver pairs. The number of grid cells should not be greater than the number of sound paths that cross the study area in different directions
Duration of the measurement cycle or repetition rate of complete cycles of the sound propagation time measurement	Computer processing time Averaging successive measurements	Limits the resolution of temporal changes in temperature and wind field structure, making representation of turbulent structures more difficult
Turbulence	Turbulent structures of smaller spatial extent than the predetermined grid width of tomographic array	Fluctuations in travel time and sound level Adaptation of the repetition time of a measuring cycles to turbulence
Attenuation of sound waves	Sound frequency-dependent	Necessary volume, choice of sound frequency in relation to the distances between source and receiver

35.7 Maintenance

Tomographic arrays for characterization of micrometeorological conditions have so far been operated only during special measurement campaigns.

The aim of those campaigns was:

1. To ensure the comparability of the tomographic results to conventional measurement methods at several spatial scales.
2. To provide temperature and flow field data in a structure comparable to numerical models.
3. To validate various tomographic algorithms for their applicability.

Experiments over an extended duration of time require stability of the measurement equipment (no changes to the source and receiver characteristics unless it is possible to recalibrate the equipment regularly) as well as using speakers and microphones that are suitable for outdoor use. If the measuring positions are connected by cables, then the cable has to be protected from destruction for instance by rodents. It is to ensure that the measurements can be performed continuously, which may require a tremendous amount of storage media as well as a control of a sufficient amplitude of the received signals.

35.8 Application

Various arrangements of transmitters and receivers can be found in the literature.

The arrangement installed at the Larson Agricultural Research Center was aimed at reconstructing horizontal (2-D) wind and temperature fields [35.12]. Later, at the Boulder Atmospheric Observatory (BAO), an arrangement for 3-D A-TOM was installed (Fig. 35.15) [35.9]. Experiments such as STINHO

(Figs. 35.13 and 35.14) [35.15] attempt to capture the horizontal wind and temperature fields over relatively large heterogeneously designed landscape sections (max. $300\text{ m} \times 700\text{ m}$) [35.33], e.g., to apply the observed data for the validation of LES (large eddy simulation) models [35.15, 46]. Specially designed measurements can be found in [35.34, 47]. Integral information about temperature and wind along specific

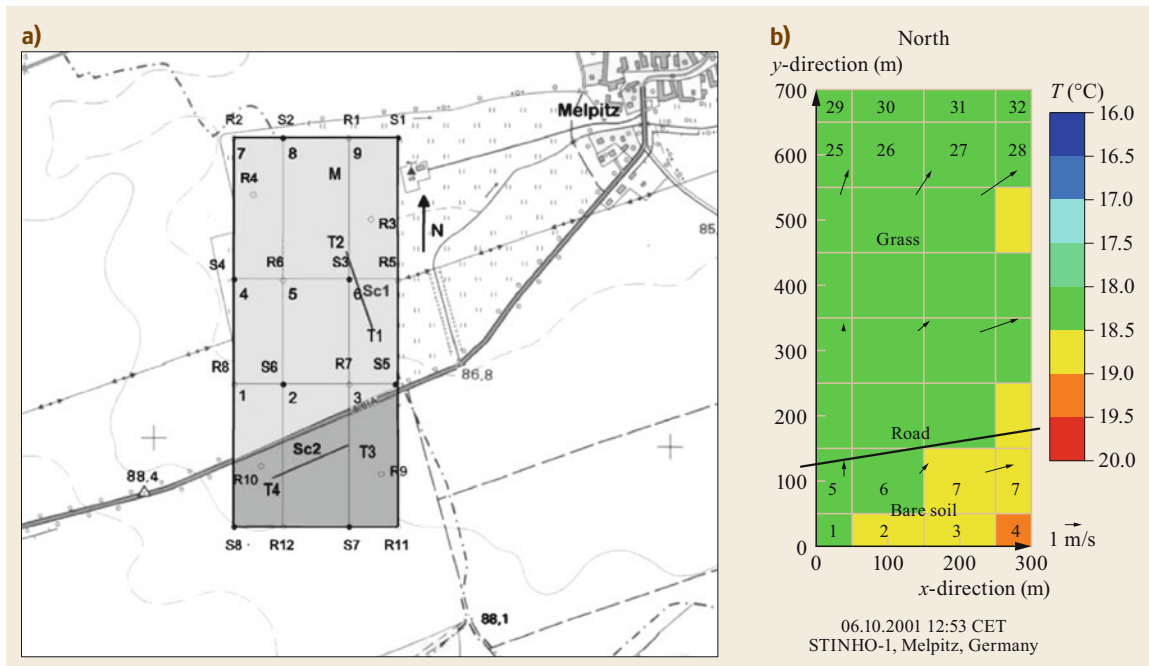


Fig. 35.13a,b STINHO-1: (a) Layout of the area under investigation ($300\text{ m} \times 700\text{ m}$) at the research station Melpitz (after [35.33]); (b) example of a single tomographic temperature and wind field measurement, which provides a grid structure comparable to numeric calculations

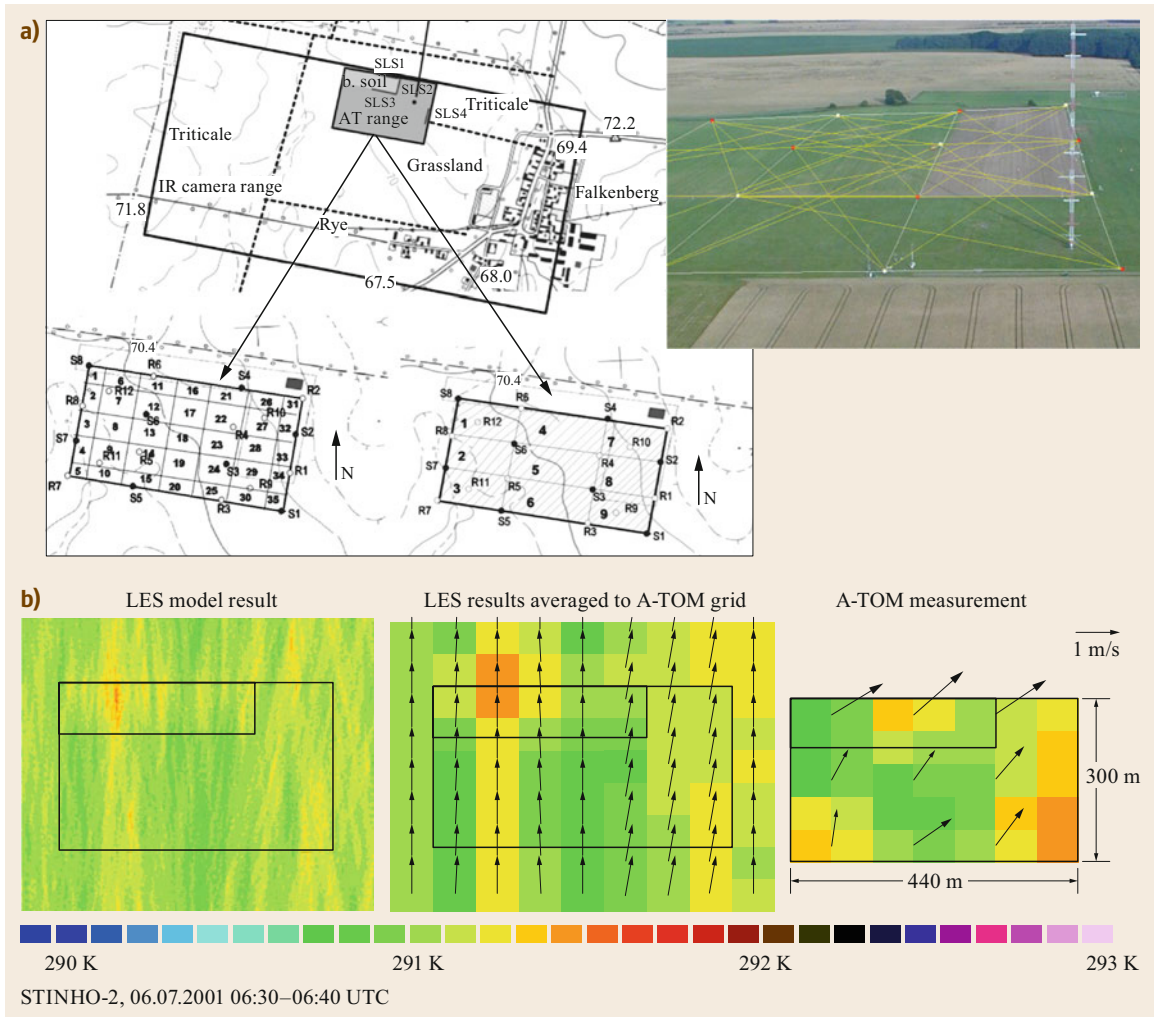


Fig. 35.14a,b STINHO-2: View of the experimental area around the boundary layer field site near the Meteorological Observatory Lindenberg of the German Meteorological Service (DWD). See text for further information. **(a)** Left: map of the measuring field near Lindenberg/Falkenberg: AT marks the area for acoustic tomography measurements. The area was divided for tomographic images into 35 grid cells for temperature and 9 grid cells for wind vector. Right: aerial photo of the landscape around the AT range: yellow lines show schematically the propagation paths of the sound waves between the sound sources and receivers (after [35.15] with permission from E. Schweizerbart'sche Verlagsbuchhandlung OHG.) **(b)** Large-eddy simulation of temperature and wind field (10 min mean) in comparison to the tomographic reconstruction of the acoustic travel-time measurements during this time of the day

propagation paths has been used to provide additional information, e.g., for path-integrated observations like FTIR (Fourier-transform infrared spectroscopy) procedures [35.29, 32]. In [35.22], UASs (unmanned aircraft systems) served as sound sources at different altitudes of the atmospheric boundary layer, with a microphone array on the ground. The aim was to visualize the vertical structure of the boundary layer using sound speed observations. To illustrate the spectrum of experimental designs, three examples are described in more detail.

The STINHO-1 experiment (Fig. 35.13) was carried out at the research station Melpitz of the Institute of Tropospheric Research (TROPOS) near Leipzig, Germany. At this site, a road cuts through the measuring area and separate areas of grassland (northern part) and bare soil (southern part). This indicates the aim to investigate the structure of turbulent processes under inhomogeneous surface conditions (STINHO). The positions of receivers are labelled R1 to R12, the sources S1 to S8. Not all transmitters and receivers are posi-

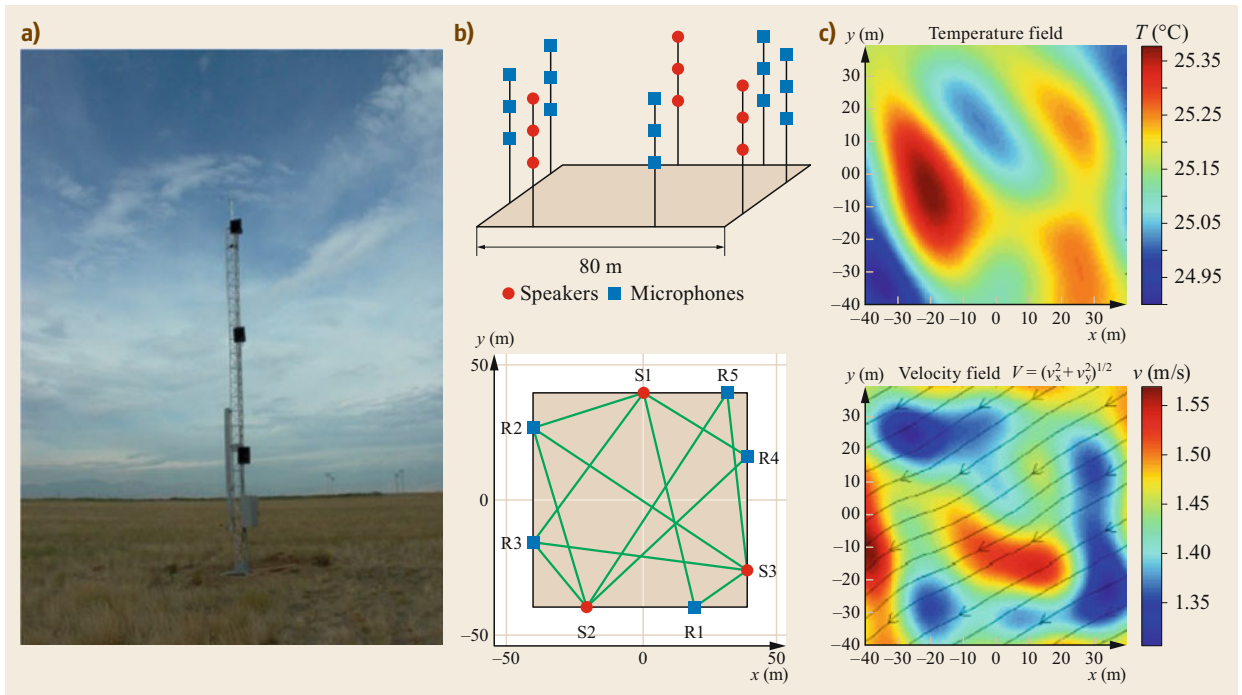


Fig. 35.15a–c The 3-D array for acoustic tomography research built at the Boulder Atmospheric Observatory (BAO), which was designed for reconstruction of 3-D temperature and wind fields. Shown are tomographic reconstructions of the temperature and velocity fields in one of the three levels at 09.07.2008 21:32:30 UTC. **(a)** Photography of arrangement of sound sources and receivers at one mast. **(b) Top:** scheme of experimental setup with 8 masts, 5 masts with microphones, and 3 masts with loudspeakers. **Bottom:** scheme of sound paths used for tomographic reconstruction (method of time-dependent stochastic inversion, TDSI). **(c) Top:** the reconstruction of temperature field using tomographic algorithm. **Bottom:** the reconstruction of wind field using tomographic algorithm (after [35.48, 49] Figure assembled)

tioned at the border of the measuring field. Because of the great distances between the transmitter and receiver positions and the desire to cover all parts of the measuring field with sound paths, some transmitters or receivers are inside the measuring area (e.g., S8, R6). T1 to T4 are positions of conventional temperature and humidity sensors, Sc1 and Sc2 are the scintillometer measurements and M marks the routinely working 12 m profile mast. These additional sensors were used to compare area-averaged measurements (A-TOM) with point or line measurements. All meteorological sensors and acoustic equipment were positioned 2 m above the surface. A horizontal slice of temperature (color scale) and wind (arrows) field at a height of 2 m above the ground on 06.10.2001 at 12:53 CET are shown as an example. This picture is reconstructed from one single measurement cycle, whose duration is given by the sound travel times and represents a snapshot of the temperature and wind field. The legend indicates the achievable resolution for the temperature as well as for the wind vector.

Because it is not entirely possible to have a reciprocal sound path distribution, the method of bidirectional sound paths was applied to obtain the wind field distribution. In this case, the resolution of wind field is reduced (9 cells, number 1–9 in Fig. 35.13a) in comparison to the resolution of temperature (numbering of temperature cells 1–32 in Fig. 35.13b).

The STINHO-2 experiment (Fig. 35.14) was carried out at the boundary layer research field Falkenberg, a part of the Meteorological Observatory Lindenberg (MOL) of the German Meteorological Service (DWD). Around the 99-m meteorological tower (foreground), the tomographic array was built up. To get different surface conditions, the measuring area covers grassland and a plowed field. The yellow lines symbolize the sound propagation paths for acoustic tomography, which covers an area of $300\text{ m} \times 440\text{ m}$ (AT range). Within the A-TOM range different observational systems (e.g., profile masts, eddy covariance, scintillometer) were distributed. The tomographic array is included in an area of an extension of $900\text{ m} \times 2000\text{ m}$ which was observed with an infrared camera to detect sur-

face temperature distributions. Figure 35.14 shows the arrangement of the twelve acoustic receivers (R) and eight sound sources (S) and the resulting temperature and wind cells for tomographic reconstruction. The investigated area is divided into 35 grid cells for the temperature with an extension of $70\text{ m} \times 70\text{ m}$ and nine cells for the wind vector. The lower partitioning of the wind field is due to the bidirectional separation algorithm. Figure 35.14 also shows a large-eddy simulation of an air temperature and wind field with a resolution on $2.5 \times 2.5\text{ m}^2$ aggregated to the grid structure of the tomographic reconstruction. In comparison to the simulation, the A-TOM shows a 10-min average for the same time 06.07.2001, 06:30–06:40 UTC.

The STINHO-2 experiment produced travel-time datasets, which were used by different publications to investigate the capability of tomographic reconstruction schemes [35.16, 36, 48]. The transmitter–receiver configuration used during STINHO only allows reconstruction of 2-D temperature and velocity fields.

In [35.30], a tomographic experiment with an acoustic array comparable to STINHO is introduced. In com-

parison to the STINHO experiment, microphones were positioned at two different heights above the ground. Subsequently, acoustic measurements from different heights were used to analyze horizontal and vertical gradients of temperature and wind fields.

The acoustic array built at the BAO (Fig. 35.15) is the only example of an outdoor tomographic measurement setup, which was used to investigate the 3-D structure of turbulent wind and temperature fields [35.9]. The 8 masts are equipped with 9 transmitters (speaker) and 15 microphones and enclose a volume of $80\text{ m} \times 80\text{ m} \times 10\text{ m}$. In order to represent turbulent structures in the wind and temperature field from the measurements, stochastic tomographic reconstruction methods were used. This acoustic tomography array was intended particularly for developing reconstruction methods suitable to the verification of LES schemes. In its version BAO 2.0, the array consisted of 8 combined transmitter–receiver stations at the positions shown above. With this distribution of the equipment, a perfect reciprocal sound transmission was realized only for one plane parallel to the surface [35.50].

35.9 Future Developments

Acoustic tomography (A-TOM) of the atmospheric surface layer (ASL) has been demonstrated through research as a viable and unique technique for remote sensing of the temperature and wind velocity fields. The method was developed to provide spatially averaged measurement data, e.g., to compare flow field models (LES) with experimental data, where model and experiment achieve the same resolution. All of the tools needed to include A-TOM in continuous monitoring of temporal changes in 2-D and 3-D temperature and wind velocity fields in the ASL were developed. However, currently a long-term monitoring site does not exist. Even tomographic arrays such as the BAO are not operated permanently at the present time. But new applications can always be envisioned. In its version 2.0, the BAO is operated close to wind turbines to measure the turbulent wake flow.

Permanent use of acoustic tomography is difficult because audible sound is typically used for the measurements, which at times can disturb local residents. Furthermore, the measurement positions must be permanently fixed in the landscape very accurately in order to ensure a high quality of sound speed observations. A conceivable solution would be the use of natural or existing sound sources. Such sources could provide information to reconstruct the structure of the velocity and temperature fields where the sound has

traveled through (e.g., sound of airplanes). Then, not only a part of the surface layer, but the entire boundary layer or troposphere, could be the subject of investigation [35.51].

An example of obtaining sound speed information from the entire atmosphere comes from infrasound and seismic stations used for verifying compliance with the Comprehensive Nuclear-Test-Ban Treaty [35.52]. For this purpose, a global observation network is maintained internationally, which also records infrasound [35.53] created by different natural sources (meteors, severe storms, mining explosions, and other human-caused or natural phenomena). By determining the velocities, angles of arrival, and, in some cases, travel times of these waves, one can attempt to solve the inverse problem of reconstructing the temperature and velocity fields in the atmosphere. Such monitoring could allow us to gain new knowledge about the spatial structure of these fields and their temporal evolution in different meteorological regimes [35.9, 48].

Presently, it is still a goal to include observed and analyzed sound field data in continuous and operational meteorological monitoring programs. But experiences with A-TOM provide a helpful example to extrapolate and upscale results of point-like measurements for special measurement campaigns and to deliver consistent data to numerical models across a range of scales.

35.10 Further Readings

Overviews of inverse techniques can be found in the following textbooks:

- For general description of inversion techniques see W. Menke: *Geophysical Data Analysis: Discrete Inverse Theory* (Academic Press, New York 1984).
- Mathematical basics for tomographic and inverse methods are introduced by F. Natterer: *The Mathematics of Computerized Tomography*. Classics in Applied Mathematics, Vol. 32 (SIAM, Philadelphia 2001).
- The fundamentals of computer tomography are summarized in A.C. Kak, M. Slaney: *Principles of Computerized Tomographic Imaging* (IEEE Press, New York 1988) and its specification to geophysics in T. Lo, P.L. Inderwiesen: *Fundamentals of Seis-*

mic Tomography. Geophysical Monograph Series, Vol. 6 (SEG, London 1994).

- Tomographic techniques in combination with oceanographic research are described by W. Munk, P. Worcester, C. Wunsch: *Ocean Acoustic Tomography* (Cambridge Univ. Press, New York 1995).
- Physical effects in atmospheric acoustics and the sound propagation through inhomogeneous, turbulent media are explained and illustrated by V.E. Ostashev, D.K. Wilson: *Acoustics in Moving Inhomogeneous Media*, 2nd edn. (CRC Press, Boca Raton 2016), as well as by E.M. Salomons: *Computational Atmospheric Acoustics* (Springer, Dordrecht 2001) and K. Attenborough, K.M. Li and K. Horoshenkov: *Predicting Outdoor Sound* (Taylor & Francis, London 2007).

References

- 35.1 J. Radon: Über die Bestimmung von Funktionen durch ihre Integralwerte längs gewisser Mannigfaltigkeiten, Ber. Verh. Kgl. Sächs. Ges. Wiss. Leipz. Math. Phys. Kl. **69**, 262–277 (1917)
- 35.2 F. Natterer: *The Mathematics of Computerized Tomography*, Classics in Applied Mathematics, Vol. 32 (SIAM, Philadelphia 2001)
- 35.3 A.C. Kak, M. Slaney: *Principles of Computerized Tomographic Imaging* (IEEE Press, New York 1988)
- 35.4 G.T. Herman: *Image Reconstruction from Projection – The Fundamentals of Computerized Tomography* (Academic Press, New York, London 1980)
- 35.5 T. Lo, P.L. Inderwiesen: *Fundamentals of Seismic Tomography*, Geophysical Monograph Series, Vol. 6 (SEG, London 1994)
- 35.6 W. Menke: *Geophysical Data Analysis: Discrete Inverse Theory* (Academic Press, New York 1984)
- 35.7 W. Munk, P. Worcester, C. Wunsch: *Ocean Acoustic Tomography* (Cambridge Univ. Press, New York 1995)
- 35.8 D.K. Wilson, A. Ziemann, V.E. Ostashev, A.G. Voronovich: An overview of acoustic travel-time tomography in the atmosphere and its potential application, Acta Acust. United Acust. **87**(6), 721–730 (2001)
- 35.9 V.E. Ostashev, S.N. Vecherin, D.K. Wilson, A. Ziemann, G.H. Goedecke: Recent progress in acoustic travel-time tomography of the atmospheric surface layer, Meteorol. Z. **18**(2), 125–133 (2009)
- 35.10 M. Barth, A. Raabe: Acoustic tomographic imaging of temperature and flow fields in air, Meas. Sci. Technol. **22**(3), 035102 (2011)
- 35.11 J.L. Spiesberger, K.M. Fristrup: Passive localization of calling animals and sensing of their acoustic environment using acoustic tomography, Am. Nat. **135**(1), 107–153 (1990)
- 35.12 D.K. Wilson, D.W. Thomson: Acoustic tomographic monitoring of the atmospheric surface layer, J. Atmos. Ocean. Technol. **11**(3), 751–769 (1994)
- 35.13 K. Arnold, A. Ziemann, A. Raabe: Acoustic tomography inside the atmospheric boundary layer, Phys. Chem. Earth B **24**(1/2), 133–137 (1999)
- 35.14 A. Ziemann, K. Arnold, A. Raabe: Acoustic travel time tomography – A method for remote sensing of the atmospheric surface layer, Meteorol. Atmos. Phys. **71**(1/2), 43–51 (1999)
- 35.15 A. Raabe, K. Arnold, A. Ziemann, F. Beyrich, J.-P. Leps, J. Bange, P. Zittel, T. Spieß, T. Foken, M. Göckede, M. Schröter, S. Raasch: STINHO – Structure of turbulent transport under inhomogeneous surface conditions – Part 1: The micro- α scale field experiment, Meteorol. Z. **14**(3), 315–327 (2005)
- 35.16 S.N. Vecherin, V.E. Ostashev, A. Ziemann, D.K. Wilson, K. Arnold, M. Barth: Tomographic reconstruction of atmospheric turbulence with the use of time-dependent stochastic inversion, J. Acoust. Soc. Am. **122**(3), 1416–1425 (2007)
- 35.17 G. Fischer, M. Barth, A. Ziemann: Acoustic tomography of the atmosphere: Comparison of different reconstruction algorithms, Acta Acust. United Acust. **98**(4), 534–545 (2012)
- 35.18 M. Barth, A. Raabe, K. Arnold, C. Resagk, R. Du Puits: Flow field detection using acoustic travel time tomography, Meteorol. Z. **16**(4), 443–450 (2007)
- 35.19 M. Bleisteiner, M. Barth, A. Raabe: Tomographic reconstruction of indoor spatial temperature distributions using room impulse responses, Meas. Sci. Technol. **27**(3), 035306 (2016)
- 35.20 I. Jovanović, L. Sbaitez, M. Vetterli: Acoustic tomography for scalar and vector fields: Theory and application to temperature and wind estimation, J. Atmos. Ocean. Technol. **26**(8), 1475–1492 (2009)

- 35.21 N.S. Vecherin, V.E. Ostashev, C.W. Fairall, D.K. Wilson, L. Bariteau: Sonic anemometer as a small acoustic tomography array, *Bound.-Layer Meteorol.* **149**(2), 165–178 (2013)
- 35.22 A. Finn, K. Rogers: Acoustic atmospheric tomography using multiple unmanned aerial vehicles, *IET Radar Sonar Navig.* **10**(9), 1541–1551 (2016)
- 35.23 G. Fischer: *Invertierungsalgorithmen für die akustische Laufzeitotomographie in der Atmosphäre*, diploma thesis (Institut für Meteorologie an der Universität Leipzig, Leipzig 2008)
- 35.24 A.D. Pierce: *Acoustics – An Introduction to Its Physical Principles and Applications* (ASA, Melville 1989)
- 35.25 V.E. Ostashev: *Acoustics in Moving Inhomogeneous Media* (E & FN SPON Thompson Professional, London 1997)
- 35.26 J.W.S. Rayleigh: *The Theory of Sound* (Dover Publications, New York 1945), first published by MacMillan, London 1896
- 35.27 O.A. Godin: An effective quiescent medium for sound propagating through an inhomogeneous, moving medium, *J. Acoust. Soc. Am.* **112**(4), 1269–1275 (2002)
- 35.28 P. Holstein, A. Raabe, R. Müller, M. Barth, D. Mackenzie, E. Starke: Acoustic tomography on the basis of travel-time measurement, *Meas. Sci. Technol.* **15**(7), 1420–1428 (2004)
- 35.29 A. Ziemann, M. Starke, C. Schütze: Line-averaging measurement methods to estimate the gap in the CO₂ balance closure – Possibilities, challenges, and uncertainties, *Atmos. Meas. Tech.* **10**(11), 4165–4190 (2017)
- 35.30 K. Arnold, A. Ziemann, A. Raabe: Tomographic monitoring of wind and temperature in different heights above the ground, *Acta Acust. United Acust.* **87**(6), 703–708 (2001)
- 35.31 H.E. Bass, L.C. Sutherland, A.J. Zuckerwar, D.T. Blackstock, D.M. Hester: Atmospheric absorption of sound: Further developments, *J. Acoust. Soc. Am.* **97**(1), 680–683 (1995)
- 35.32 M. Barth, G. Fischer, A. Raabe, A. Ziemann, F. Weiße: Remote sensing of temperature and wind using acoustic travel-time measurements, *Meteorol. Z.* **22**(2), 103–109 (2013)
- 35.33 K. Arnold, A. Ziemann, A. Raabe, G. Spindler: Acoustic tomography and conventional meteorological measurements over heterogeneous surfaces, *Meteorol. Atmos. Phys.* **85**(1–3), 175–186 (2004)
- 35.34 A. Ziemann, K. Arnold, A. Raabe: Acoustic tomography as a method to identify small-scale land surface characteristics, *Acta Acust. United Acust.* **87**(6), 731–737 (2001)
- 35.35 S.N. Vecherin, V.E. Ostashev, G.H. Goedecke, D.K. Wilson, A.G. Voronovich: Time-dependent stochastic inversion in acoustic travel-time tomography of the atmosphere, *J. Acoust. Soc. Am.* **119**(5), 2579–2588 (2006)
- 35.36 S. Kolouri, M.R. Azimi-Sadjadi, A. Ziemann: A statistical-based approach for acoustic tomography of the atmosphere, *J. Acoust. Soc. Am.* **135**(1), 104–114 (2014)
- 35.37 M. Barth: *Akustische Tomographie zur zeitgleichen Erfassung von Temperatur- und Strömungsfeldern*, Wissenschaftliche Mitteilungen aus dem Institut für Meteorologie der Universität Leipzig, Vol. 44 (LIM, Leipzig 2009)
- 35.38 J.C. Kaimal, J.J. Finnigan: *Atmospheric Boundary Layer Flows: Their Structure and Measurement* (Oxford Univ. Press, New York 1994)
- 35.39 J.S. Bendat, A.G. Piersol: *Random Data Analysis and Measurement Procedures*, Wiley Series in Probability and Statistics, Vol. 351 (Wiley, New York 2000)
- 35.40 V.E. Ostashev, D.K. Wilson: *Acoustics in Moving Inhomogeneous Media*, 2nd edn. (CRC Press, Boca Raton 2016)
- 35.41 C. Krajewski, L. Dresen, C. Gelbke, H. Rüter: Iterative tomographic methods to locate seismic low velocity anomalies: A model study, *Geophys. Prospect.* **37**(7), 717–751 (1989)
- 35.42 A. Ziemann, K. Arnold, A. Raabe: Acoustic tomography in the atmospheric surface layer, *Ann. Geophys.* **17**(1), 139–148 (1999)
- 35.43 P. Gilbert: Iterative methods for the three-dimensional reconstruction of an object from projections, *J. Theor. Biol.* **36**(1), 105–117 (1972)
- 35.44 G. Sparr, K. Stråhlén: *Vector Field Tomography, an Overview* (Lund Institute of Technology, Lund 1998), Tech. Rep.
- 35.45 A. Hauck: *Tomographie von Vektorfeldern*, Fortschritt-Berichte VDI, Reihe 8, Mess-, Steuerungs- und Regelungstechnik, Vol. 220 (VDI, Düsseldorf 1990)
- 35.46 S. Weinbrecht, S. Raasch, A. Ziemann, K. Arnold, A. Raabe: Comparison of large-eddy simulation data with spatially averaged measurements obtained by acoustic tomography – Presuppositions and first results, *Bound.-Layer Meteorol.* **111**(3), 441–465 (2004)
- 35.47 G. Tetzlaff, K. Arnold, A. Raabe, A. Ziemann: Observations of area averaged near-surface wind- and temperature-fields in real terrain using acoustic travel time tomography, *Meteorol. Z.* **11**(4), 273–283 (2002)
- 35.48 V.E. Ostashev, S.N. Vecherin, D.K. Wilson, A. Ziemann, G.H. Goedecke: Recent progress in acoustic tomography of the atmosphere, *IOP Conf. Ser. Earth Environ. Sci.* **1**(1), 012008 (2008)
- 35.49 V.E. Ostashev, S.N. Vecherin, D.K. Wilson, A.J. Beardard, J.L. Leach, K.A. Clark, C.W. Fairall, D.E. Wolfe: Acoustic travel-time tomography of the atmosphere at the Boulder Atmospheric Observatory. In: *16th Int. Symp. Adv. Bound. Layer Remote Sens* (2012), http://radiometrics.com/data/uploads/2012/12/Ostashev_ISARS_2012.pdf, Accessed 12 July 2021
- 35.50 V.E. Ostashev, S.N. Vecherin, D.K. Wilson: Overview of acoustic tomography of the atmosphere. In: *17th Long Range Sound Propag. Symp., Lyon* (2018)
- 35.51 A. Finn, K. Rogers: An acoustic tomography technique for concurrently observing the structure of the atmosphere and water bodies, *J. Atmos. Ocean. Technol.* **34**(3), 617–629 (2017)

- 35.52 National Academy of Sciences: *Technical Issues Related to the Comprehensive Nuclear Test Ban Treaty* (National Academies Press, Washington 2002)
- 35.53 A. Le Pichon, E. Blanc, A. Hauchecorne (Eds.): *Infrasound Monitoring for Atmospheric Studies* (Springer, Dordrecht 2009)

Armin Raabe

Leipzig Institute for Meteorology (LIM)
University of Leipzig
Leipzig, Germany
raabe@uni-leipzig.de



Armin Raabe studied physics at Leipzig University and obtained his PhD in 1980. As a member of the Leipzig Institute of Meteorology he focused on mesoscale modeling of atmospheric and hydrological processes over a heterogeneous landscape. In 1994 he developed methods to observe temperature and air stream fields of landscape areas, as well as indoors using acoustic sound measurements, especially focusing on acoustic tomographic methods.

Manuela Starke

Chair of Meteorology
Technische Universität Dresden
Tharandt, Germany
manuela.starke@tu-dresden.de



Manuela Starke (Barth) studied meteorology at the University of Leipzig where she also obtained her PhD in 2009. The main focus of her work was the further development and optimization of a method for simultaneous measurements of spatially resolved temperature and flow fields in air using acoustic travel-time tomography. Further research topics include the modeling of atmospheric sound propagation and of atmospheric boundary layer processes.

Astrid A. Ziemann



Chair of Meteorology
Technische Universität Dresden
Tharandt, Germany
astrid.ziemann@tu-dresden.de

Astrid A. Ziemann is a research associate at the Chair of Meteorology at TU Dresden. She studied meteorology at the Humboldt-Universität zu Berlin and received her PhD at the Leipzig University in 2000 for a theoretical study of acoustic tomography. Current research topics include: wind energy, heat resilient cities in changing climate and outdoor sound propagation.

GNSS Water Vapor

36. GNSS Water Vapor Tomography

Michael Bender, Galina Dick

The spatial distribution of the atmospheric humidity is difficult to observe, especially for larger domains with dimensions of tens or hundreds of kilometers. The signals of satellite positioning systems like GPS or Galileo are modified by the atmospheric water vapor, and a combination of a large number of such signals provides an opportunity to observe the humidity distribution with high temporal resolution under all weather conditions. The positioning signals are collected by ground-based receiver networks and processed in a certain way in order to separate the humidity information. The information obtained in this way is a nonlocal path-integrated quantity, and tomographic techniques are required to obtain spatially and temporally resolved humidity fields. The whole processing chain from signal detection and signal processing to the final tomographic reconstruction of the atmospheric humidity distribution is presented.

36.1	Measurement Principles and Parameters	1026
36.2	History	1028
36.3	Theory	1028
36.3.1	Tomography and Inverse Problems	1028
36.3.2	GNSS Tomography	1029
36.3.3	Wet Delay and Integrated Water Vapor	1031
36.3.4	Discrete Spatial Grid	1032
36.3.5	Observation Operator and Design Matrix A	1032
36.3.6	Inversion	1032
36.4	Devices and Systems	1033
36.4.1	GNSS Systems	1033
36.4.2	Ground-Based GNSS Networks for Tomographic Applications	1034
36.4.3	GNSS Processing	1035
36.4.4	Setup of a GNSS Tomography System ..	1036
36.5	Specifications	1039
36.6	Quality Control	1040
36.6.1	GNSS Processing Quality Control	1040
36.6.2	Validation of Meteorological GNSS Products	1040
36.6.3	Validation of 3-D Humidity Fields from GNSS Tomography	1041
36.7	Maintenance	1041
36.7.1	GNSS Stations and GNSS Hardware	1041
36.7.2	GNSS Data Processing and Tomography System	1041
36.8	Application	1042
36.9	Future Developments	1045
36.10	Further Reading	1046
	References	1046

The impact of the atmospheric water vapor on weather and climate, as well as its significance, were highlighted in many of the previous chapters, as were the relevance of reliable humidity observations. Satellite positioning was not designed as a remote-sensing system but is sensitive to atmospheric humidity and can contribute to large-scale humidity monitoring. The information contained in positioning signals and collected by ground-based receiver networks can fill the gap between in-situ observations, such as sensors at synoptic stations or radio soundings and satellite-based remote-sensing instruments. The signals propagate through large parts of the atmosphere and are modified by the amount of

water vapor along each signal path. If the density of the received signals is sufficiently high, tomographic techniques can be used to reconstruct the spatial humidity field from these path-integrated observations. The spatial resolution of such humidity fields is limited by the receiver density and is usually between 10 and 50 km horizontally and between 100 and 1000 m vertically. While the resolution is not very impressive at first glance, the fields extend across large areas of the atmosphere, which would not otherwise be covered. The extension of small networks is usually limited to some tens of kilometers while nation-wide networks are extended over several hundreds of kilometers. The

observations are available continuously for all weather conditions and can be processed within a rather short time. Currently, a near realtime processing with delays

below 30 min is possible, but realtime applications with delays below some minutes are currently under development.

36.1 Measurement Principles and Parameters

Global navigation satellite systems (GNSS) are based on a constellation of satellites that orbit the Earth and transmit navigation signals continuously. GNSS receivers at the Earth's surface decode the navigation messages from several GNSS satellites and compute the receiver position. As of January 2021, there are four GNSS: the US American Navstar Global Positioning System (GPS), the Russian GLONASS, the European Galileo, and the Chinese BeiDou. Each of these systems consists of at least 24 satellites. In total, about 100 satellites are operational, and up to 30 can be tracked simultaneously at any place on Earth.

GNSS was not designed as a remote-sensing device, however the impact of the Earth's atmosphere on the navigation signals deteriorates the quality of positioning and needs to be corrected for. The atmosphere corrections estimated in precise positioning carry valuable information on the atmospheric state, which leads to the special branch of GNSS atmosphere sounding.

GNSS signals are electromagnetic waves in the microwave range, i.e., $\approx 1\text{--}1.5$ GHz, and can be detected in all weather conditions. The Earth's atmosphere leads to a delay of the signals and to curved signal paths as the speed of light in the atmosphere is smaller than in vacuum. The major contribution to the atmospheric delay is caused by the free electrons in the ionosphere but can be corrected by an ionosphere-free linear combination of signals with different frequencies. The neutral atmosphere is a nondispersive medium for microwaves, and other strategies had to be developed.

GNSS determines the signal travel time from the GNSS satellite to the GNSS receiver and estimates the distance between satellite and receiver. The receiver position can be obtained if at least four satellites are in view. Signal delays due to the neutral atmosphere lead to wrong distances and positions. The delays depend on the satellite elevation, i.e., the angle of the satellite above the horizon, which determines the length of the signal path inside the atmosphere, and the atmospheric state. The former leads to a simple geometric expression and can easily be corrected, but the latter leads to a considerable uncertainty for positioning.

To overcome this problem the zenith total delay (ZTD) is estimated by most GNSS data processing techniques. The ZTD is the delay due to the neutral atmosphere obtained for a hypothetical GNSS satellite in

the zenith of the GNSS receiver. ZTDs are estimated using the signals of all visible GNSS satellites and represent the mean atmospheric state above the receiver at a certain time. The signal travel times are corrected with the ZTDs, thereby leading to improved positions, but the ZTD is also the basic quantity for GNSS atmosphere sounding.

The ZTD is related to the pressure, the temperature, and the humidity in the vicinity of the GNSS station. GNSS signals provide no information about the specific contributions of these quantities to the ZTD, and additional meteorological observations are required to get more specific information, e.g., about the humidity. The atmospheric humidity is highly variable in space and time and is less well known than pressure and temperature. Pressure and temperature observations at the GNSS station have, therefore, been used to separate the integrated water vapor (IWV) from the ZTD. The IWV is equivalent to the precipitable water (PW) in a column above the station but provides no information about the vertical profile. The IWV is expressed in kg m^{-2} , while the PW is given in mm (of liquid water). IWV observations from GNSS networks provide valuable information about the horizontal distribution of the atmospheric humidity, and IWV was the first GNSS-derived quantity widely used in meteorology [36.1–3].

ZTD and IWV are rather idealized and simplified quantities, and the true delays along each individual satellite-receiver axis would provide much more detailed information. In recent years, more advanced processing techniques have been developed, which estimate such slant total delays (STDs). Instead of 1 ZTD, about 10 (GPS) or 30 (all GNSS) STDs are now available for each GNSS station and each epoch. The atmosphere over dense ground-based networks of GNSS receivers is scanned by STDs from many directions, and the information about the spatial humidity distribution hidden in large path-integrated STD data sets can be acquired by tomographic techniques.

Tomography requires large data sets of path-integrated quantities observed along intersecting signal paths (Fig. 36.1). Because of the integrated character of the observations it is not possible to locate the information along individual signal paths. In the case of many intersecting paths, the information can to some degree be located near the intersection points. A combined

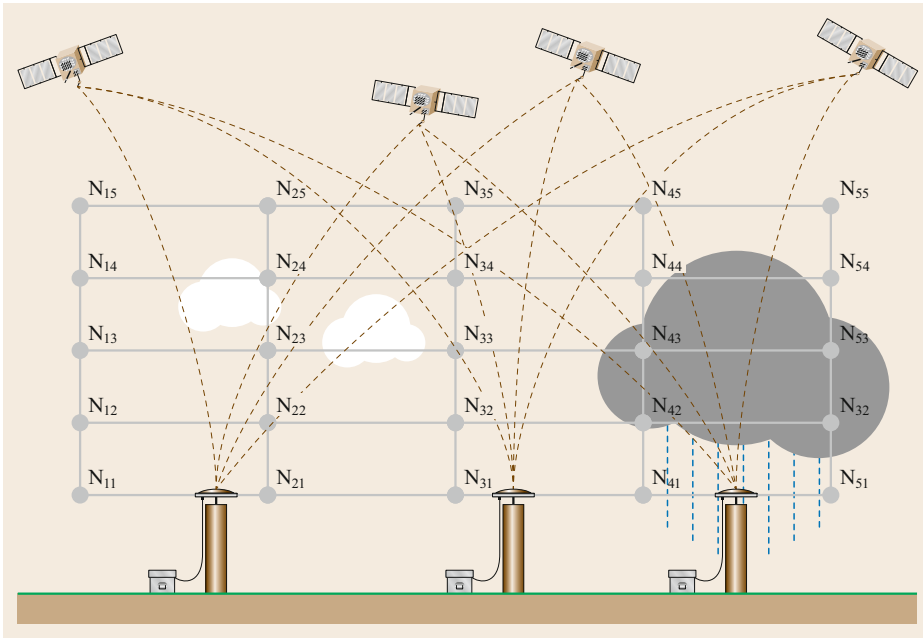


Fig. 36.1 GNSS signals propagating through a spatial grid. The refractivities at the grid nodes can be estimated by tomographic techniques if there is a sufficient number of GNSS signal paths near each node

Table 36.1 GNSS-specific parameters. Most quantities are defined in Sect. 36.3. Physical constants and humidity-related parameters can be found in Chaps. 5 and 8, respectively

Parameter	Description	Unit	Symbol
Parameters relevant for GNSS observations and processing			
Refractive index	$n = c/v$, vacuum speed of light to speed of light in gas	–	n
Observed GNSS parameter			
Optical path length	$t = \int_s n ds$, signal travel time transmitter–receiver	s	t
Output of the GNSS processing			
Slant total delay	$STD = 10^{-6} \int N ds$, delay by neutral atmosphere	m	STD
Slant hydrostatic delay	Approx. delay of dry atmosphere	m	SHD
Slant wet delay	$SWD = STD - SHD$, approx. delay due to water vapor	m	SHD
Integrated water vapor	Vertically integrated amount of water vapor	kg m^{-2}	IWV
Slant-integrated water vapor	Total amount of water vapor along signal path	kg m^{-2}	SIWV
Precipitable water	$IWV = \rho_w PW$ with the density of liquid water ρ_w	mm	PW
Final result of the GNSS tomography			
Refractivity	$N = 10^6(n - 1)$, equivalent to n	–	N
Wet refractivity	Atmospheric refraction due to water vapor	–	N_{wet}
Absolute humidity	Density of water vapor	kg m^{-3}	a

solution for all signals observed leads to a spatially resolved 3-D field, and techniques for solving such systems of equations are summarized under the term *tomography*.

Data sets of real observations are, in most cases, not sufficient to determine the entire field within the scanned volume. The reasons for this are insufficient numbers of observations, inadequate distributions of transmitters and receivers, or large observation errors. This leads to ill-posed inverse problems, which are difficult to solve. In the case of the GNSS tomography a very large vol-

ume, i.e., the whole atmosphere up to the tropopause over regions of several hundred square kilometers, is scanned by a rather limited number of STDs, and additional meteorological observations and some constraints are required to obtain stable tomographic solutions.

The physical quantities obtained by GNSS and some intermediate parameters provided by the GNSS processing are given in Table 36.1. The fundamental quantities for describing the atmospheric humidity are given in Chap. 8, and the physical constants are listed in Chap. 5.

36.2 History

The basic ideas of tomography were already developed at the beginning of the twentieth century, but widespread applications could not evolve until detector and computer technology reached a sufficiently high level. In the beginning of the 1970s, tomographic applications were developed in many different fields, such as radiology, materials science, geophysics, oceanography, and atmospheric science. Atmosphere sounding with acoustic tomography is described in Chap. 35.

The application of tomographic techniques to GPS signals seemed natural and was already suggested in an

early stage of the development of GPS [36.1, 4, 5]. First experiments in 1999 [36.6, 7] and 2000 [36.8–10] led to positive results with small networks of GPS receivers. As a consequence of these early results, many experiments were completed all over the world [36.11–13].

In the meantime, the geodetic agencies of most countries built up nation-wide networks of GPS receivers that could be utilized for the GPS tomography. Attempts were made to establish operational GNSS tomography systems that provide 3-D humidity fields in near realtime for nowcasting or data assimilation [36.14–16].

36.3 Theory

GNSS tomography is an approach to reconstruct large three-dimensional tropospheric fields from a rather limited number of path-integrated GNSS observations. This leads to a demanding inverse problem, which is discussed in Sect. 36.3.1. There is no direct interdependency between GNSS signals and the atmospheric state, and there is some freedom to choose from different GNSS-derived quantities as input to the tomography. The relationship between GNSS observations and different atmospheric quantities is described in Sect. 36.3.2, and some options for reconstructing humidity fields are discussed in Sect. 36.3.3.

36.3.1 Tomography and Inverse Problems

GNSS tomography is based on travel time measurements. The observed quantity is the signal travel time t between the transmitter and the receiver through the Earth's atmosphere with the refractive index n . In the case of electromagnetic waves, t is given by the optical path length

$$t = \int_S n \, ds, \quad (36.1)$$

where S is the signal path within the atmosphere. In refractive media, the signal path is, in general, a curved path that depends on the field n . The observed travel time t does not provide information about the exact signal path S or the distribution of n along S and is, therefore, a nonlocal path-integrated quantity. The basic idea of atmospheric tomography is to combine a large number of travel time observations that scan the investigated region from many directions in order to ob-

tain a well-localized approximation of the field n . For a given set of observations t_j , a set of equations

$$t_j = \int_{S_j} n \, ds_j \quad (36.2)$$

has to be solved for the unknown field n . As the corresponding curved signal paths S_j depend on n , this is a nonlinear inverse problem. It is also an ill-posed problem, as there may be no solution in a strict mathematical sense; especially if real noisy observations are regarded, the solution is usually not unique and not stable. In real applications, the problem is also globally underdetermined, as the observations are, in general, not sufficient to describe the entire field n . To overcome these limitations a number of approximations are made.

In a first step, the continuous field n is discretized by introducing a spatial grid with a discrete set of grid nodes. The field n is defined on the grid nodes only, and the set of equations (36.2) can be described in vector notation. The observations are combined to an observation vector \mathbf{y} , n_i are mapped to a 1-D state vector \mathbf{x} , and the integral equations are expressed by a vector operator \mathbf{F} , which acts on the state vector \mathbf{x}

$$\mathbf{y} = \mathbf{F}(\mathbf{x}). \quad (36.3)$$

Throughout this chapter it is assumed that all observations were taken at the same time and that the field n did not develop during the observation. To observe the temporal evolution of n , several sets of observations may be taken into account, which are processed consecutively but independently. This is equivalent to a temporal discretization of the problem.

The observation operator \mathbf{F} solves the line integrals on a discrete grid. As the signal paths depend on \mathbf{x} , this is still a demanding problem, and a second approximation is made by assuming that the signal paths are known in advance. This linearizes the problem, and the integral can be approximated by the sum

$$\int_S n \, ds \approx \sum_i n_i \Delta s_i. \quad (36.4)$$

The sum can always be rewritten as an array of weights, which are applied to the n_i , i.e., $w_i n_i$. For each observation, such an array is obtained and can be assigned to the row of a matrix \mathbf{A} . This leads to a discretized and linearized form of (36.2)

$$\mathbf{y} = \mathbf{A}\mathbf{x}, \quad (36.5)$$

with one row $y_j = A_{ij}x_i$ for each observation j and the grid nodes i . The properties of \mathbf{A} are defined by the implementation of the discrete observation operator, by the form of the grid, i.e., by the density and distribution of grid nodes, and by the number and distribution of observations; \mathbf{A} is, in general, not a square matrix, and \mathbf{A}^{-1} does not exist. Because of the ill-posed character of the problem, \mathbf{A} is a rank-deficient matrix. In the case of an insufficient number of observations or an irregular distribution of observations, \mathbf{A} may be a sparse matrix with lots of zero elements. The properties of \mathbf{A} are defined by the geometrical setup only, the shape of the field n and the quality of the observations do not affect \mathbf{A} . However, \mathbf{A} determines the amplification of observation errors and the quality of the reconstructed n field, i.e., the stability of the solution.

The properties of \mathbf{A} can be investigated by the singular value decomposition (SVD). For ill-posed problems, a limited number of large singular values and a large number of small singular values, which decay to zero, is obtained. The singular values are used to define the conditioning of the matrix and the degree of ill-posedness of the entire problem. The singular value decomposition of the $m \times n$ matrix \mathbf{A} is given by

$$\mathbf{A} = \mathbf{U}\mathbf{\Sigma}\mathbf{V}^T, \quad (36.6)$$

where \mathbf{U} is a unitary $m \times m$ matrix, \mathbf{V} is a unitary $n \times n$ matrix, and $\mathbf{\Sigma}$ is a diagonal matrix with the singular values σ_i of \mathbf{A} , usually given in descending order. The condition number of \mathbf{A} is defined by the ratio between the largest and the smallest singular value

$$\text{cond}(\mathbf{A}) = \frac{\sigma_{\max}}{\sigma_{\min}} \quad (36.7)$$

and determines the amplification of small variations $\Delta\mathbf{y}$ in the input data

$$\frac{\|\Delta\mathbf{x}\|}{\|\mathbf{x}\|} = \text{cond}(\mathbf{A}) \frac{\|\Delta\mathbf{y}\|}{\|\mathbf{y}\|}. \quad (36.8)$$

Ill-posed problems lead to ill-conditioned matrices \mathbf{A} with large condition numbers. The decay rate of the ordered singular values σ_i is used to define the degree of ill-posedness α [36.17]: if the singular values satisfy

$$\sigma_i = \text{order}(i^\alpha) \quad \text{with } \alpha \in \mathbb{R}^+, \quad (36.9)$$

the problem is mildly ill-posed if $\alpha \leq 1$ and moderately ill-posed if $\alpha > 1$. The problem is severely ill-posed if σ_i decay exponentially

$$\sigma_i = \text{order}(\exp(-\alpha i)) \quad \text{with } \alpha > 0. \quad (36.10)$$

The three-dimensional problem of the GNSS tomography with a highly variable transmitter-receiver geometry leads to moderately or severely ill-posed problems and strong constraints, and additional observations are required to obtain stable and meaningful results.

Because of the ill-posed character the usual linear algebra techniques for solving sets of linear equations, e.g., a least-squares solution, cannot be applied. There is a variety of different approaches for solving these kinds of problems [36.18–21], and it depends very much on the specific problem which ones lead to reliable results. The techniques applied in the GNSS tomography are described in the subsequent sections.

36.3.2 GNSS Tomography

The optical path length (36.1) describes the travel time between the GNSS transmitter on board the GNSS satellite and the GNSS receiver at the ground, which is about 70 ms in the zenith direction. For the GNSS atmosphere sounding only the impact of the atmosphere is important. The neutral atmosphere delays the signals about 10 ns in the zenith direction and up to 100 ns at low elevations. The slant total delay (STD) is the difference between the optical path length (36.1) and the geometric distance G between transmitter and receiver

$$\text{STD} = \int_S n \, ds - \int_G dg = \int_s (n-1) \, ds + (S-G). \quad (36.11)$$

The signal is delayed for two reasons: $n > 1$ along the signal path as described by the integral term, and the curved signal path S is slightly longer than G ,

i.e., $S - G > 0$. As the integral term is the major contribution to the STD it is usually possible to neglect the geometric delay $S - G$ in tomographic applications, and the STD can be expressed by

$$\text{STD} = \int_s (n - 1) ds = 10^{-6} \int_s N ds, \quad (36.12)$$

with the refractivity $N = 10^6(n - 1)$. It is rather cumbersome to deal with small delays on the order of some nanoseconds, and delays are usually expressed in meters by multiplying the delay with the vacuum speed of light. Following this convention, a delay of 7.7 ns is given as a STD of 2.3 m.

Each GNSS receiver tracks all GNSS satellites in view, i.e., all GNSS satellites above the horizon at a given position and a given time. In the case of GPS, about 8–12 satellites can be tracked simultaneously; multi-GNSS receivers can track up to ≈ 30 satellites. A ground network of GNSS receivers provides a large number of different views through the atmosphere, which contains spatial information about the atmospheric state. Due to the almost random distribution of the GNSS satellites and receivers there is no meaningful projection on a 2-D plane, and the full three-dimensional problem needs to be addressed.

The refractivity N can be expressed in atmospheric quantities pressure p , temperature T , and relative humidity R . For a mixture of gases like the Earth's atmosphere, empirical approximations for N are applied [36.22–24]. A widely used expression is the Smith and Weintraub formula

$$N = k_1 \frac{p_d}{T} + k_2 \frac{e}{T} + k_3 \frac{e}{T^2}, \quad (36.13)$$

where p_d is the partial pressure of dry air in hPa, e is the partial pressure of water vapor in hPa, and T is the temperature in kelvin. The empirical constants k_1 , k_2 , and k_3 were determined by several authors and are given in Table 36.2. For geodetic applications, the Rüeger constants are recommended [36.26], while the Bevis constants [36.25] quite often lead to better results in meteorological applications. The first term in (36.13)

Table 36.2 Atmospheric refractivity constants k_1 , k_2 , and k_3 according to different authors

Reference	k_1 (K hPa ⁻¹)	k_2 (K hPa ⁻¹)	k_3 ($\times 10^5$ K ² hPa ⁻¹)
Smith and Weintraub [36.24]	77.6	72.0	3.75
Thayer [36.23]	77.6	64.8	3.776
Bevis [36.25]	77.6	70.4	3.739
Rüeger [36.26]	77.689	71.2952	3.75463

describes the refractivity due to the dry atmosphere, i.e., all atmospheric gases without water vapor, the two remaining terms describe the contribution due to water vapor. The partial pressures p_d and e can be replaced by the ideal gas law

$$p_d = \varrho_d \frac{R^*}{M_d} T \quad \text{and} \quad e = \varrho_w \frac{R^*}{M_w} T, \quad (36.14)$$

where ϱ_d and M_d are the density and molar mass of dry air, ϱ_w and M_w are the density and molar mass of water vapor, and R^* is the gas constant (Chap. 5). This leads to an alternative form of (36.13)

$$N = k_1 \varrho \frac{R^*}{M_d} + \left(k_2 - k_1 \frac{M_w}{M_d} \right) \frac{e}{T} + k_3 \frac{e}{T^2}. \quad (36.15)$$

Here, ϱ is the density of moist air, i.e., $\varrho = \varrho_d + \varrho_w$. Using (36.15) and (36.1) the hydrostatic and the wet delay can be defined: the slant hydrostatic delay (SHD) is given by

$$\text{SHD} = \int_s k_1 \varrho \frac{R^*}{M_d} ds, \quad (36.16)$$

and the slant wet delay (SWD) can be expressed as

$$\begin{aligned} \text{SWD} &= \int_s \left[\left(k_2 - k_1 \frac{M_w}{M_d} \right) \frac{e}{T} + k_3 \frac{e}{T^2} \right] ds \\ &= \int_s \left[k'_2 \frac{e}{T} + k_3 \frac{e}{T^2} \right] ds \end{aligned} \quad (36.17)$$

by introducing a new constant k'_2

$$k'_2 = k_2 - k_1 \frac{M_w}{M_d}. \quad (36.18)$$

The specific form of the SHD was chosen as the integral can be solved in the case of hydrostatic equilibrium (Sect. 36.3.3).

Equation (36.13) can be combined with (36.12) and provides an expression that relates the observed STD to three atmospheric fields, i.e., p , T , and R . However, the GNSS observations provide no information about the individual contributions of these fields to the STD, and it is not possible to reconstruct all three atmospheric fields from STD observations. There are basically two strategies to address this problem. One is the tomographic reconstruction of the refractivity field using the STD observations. The humidity field can later be obtained using N , the p and T observations, and (36.13). Another strategy is the derivation of the SWD or the

Table 36.3 Different options for the application of observations and the tomographic reconstruction

Case	Observations	Tomography	Final field
1	STD \rightarrow	STD $\rightarrow N$	$+p, +T \rightarrow a$
2	STD + $p \rightarrow$	SWD $\rightarrow N_{\text{wet}}$	$+T \rightarrow a$
3	STD + $p, +T \rightarrow$	SIWV $\rightarrow a$	$\rightarrow a$

slant-integrated water vapor (SIWV). The meteorological observations at the GNSS site are used to separate certain contributions to the STD and to reduce the number of fields in (36.13). The GNSS tomography will lead to the wet refractivity, if SWDs are used and to the absolute humidity, if SIWV data are used. The different options to obtain the final humidity field are given in Table 36.3.

In all cases, pressure and temperature profiles are required. In cases 2 and 3 in Table 36.3, the profiles at the GNSS stations need to be known; in cases 1 and 2, one profile for each column of the tomography grid would be required. Usually, only surface observations are available, and attempts have been made to approximate the profile information from the surface data. The STD \rightarrow SWD \rightarrow SIWV conversion strategy is described in the next section. In the case of the grid columns, it is in most cases sufficient to compute profiles based on p_0 and T_0 using, e.g., the US standard atmosphere [36.27] or simple approximations from textbooks.

36.3.3 Wet Delay and Integrated Water Vapor

Most implementations of the GNSS tomography use slant wet delays (SWDs) or the slant-integrated water vapor (SIWV) as input, and a reliable method for converting STDs to SWDs and SIWV is required. These methods make use of the zenith delay, which can be obtained from the slant delay by integrating (36.12) for a vertical signal path, i.e., by replacing $\int_s ds$ with $\int_{h_0}^{h_{\text{sat}}} dz$. Here, the GNSS receiver is located at the height h_0 , and the GNSS satellite is assumed to be at the height h_{sat} above the receiver; z is the vertical coordinate. This leads to the zenith total delay (ZTD), the zenith hydrostatic delay (ZHD), and the zenith wet delay (ZWD).

The zenith hydrostatic delay can be estimated from the surface pressure. This is a standard technique [36.28] based on [36.29, 30], which solves (36.16) for a vertical atmospheric column in hydrostatic equilibrium

$$\text{ZHD} = \frac{0.0022768p_0}{1 - 0.00266 \cos(2\varphi) - 2.8 \times 10^{-7}h_0}, \quad (36.19)$$

where p_0 is the total atmospheric pressure at the antenna reference point in hPa, h_0 is the height above geoid in m, and φ is the geodetic latitude. With the observed ZTD, this leads to the wet delay $\text{ZWD} = \text{ZTD} - \text{ZHD}$. The ZWD can be mapped to the signal path using a mapping function, like the wet global mapping function [36.31]

$$\text{SWD} = m_{\text{wet}}\text{ZWD}. \quad (36.20)$$

In geodesy mapping functions [36.32, 33] are used to compute the projection of the zenith delay on a given signal path with a specific elevation. They are empirical functions that approximate the Earth's curvature at a given latitude and the atmospheric state at a given day of the year.

Regarding (36.16) the term *wet delay* is somewhat misleading. The SHD is not strictly the delay due to the dry atmosphere, as ϱ instead of ϱ_d is used. The SHD is, therefore, somewhat larger than the true dry delay, and the wet delay estimated with $\text{ZWD} = \text{ZTD} - \text{ZHD}$ is smaller than the true wet delay. The error is in the order of a few percent, and the ZWD estimated using (36.19) is a good approximation.

The SIWV is a linear function of the SWD [36.25, 34]

$$\text{SIWV} = \Pi \text{SWD}. \quad (36.21)$$

The factor Π depends on some constants and the temperature profile above the GNSS receiver. In most cases, the temperature profile is not known, and the water vapor weighted mean temperature T_m is used to estimate the impact of the whole profile from the temperature T_0 in kelvin at the GNSS antenna

$$T_m = 72.2 + 0.72T_0. \quad (36.22)$$

The factor Π is given by

$$\Pi = \frac{10^6}{\varrho_w R_w \left(k'_2 + \frac{k_3}{T_m} \right)}, \quad (36.23)$$

where ϱ_w is the density of water vapor, R_w is the gas constant of water vapor (Chap. 5), k_3 is the empirical constant given in Table 36.2, and k'_2 is given by (36.18). There are alternative approaches for estimating the SHD or SIWV, e.g., the Hopfield model [36.35, 36], but as there is no reference for water vapor observations in the free atmosphere, it is difficult to identify the best one.

The procedure described above is based on two assumptions. 1. Surface observations p_0 and T_0 are sufficient to approximate the impact of the pressure and temperature profiles above the GNSS receiver. 2. The

horizontal pressure and temperature gradients are sufficiently small to map the zenith delay on the signal path even at rather low elevations of $\approx 5^\circ$. The error introduced by (36.23) is much larger than the error of (36.19), and the SWDs are a more reliable input to the tomography than the SIWV. However, in severe weather conditions, even (36.19) can introduce serious errors [36.37], and the application of STDs might be the best option.

36.3.4 Discrete Spatial Grid

A spatial and temporal discretization is required to solve (36.5) numerically. Assuming that all observations in \mathbf{y} were taken at the same time is equivalent to temporal discretization, and the choice of the time step Δt depends on many parameters, which are discussed in Sect. 36.4.4. The spatial grid is used to describe the refractivity field on a limited number of grid nodes and defines the number of unknowns that have to be specified by the inversion. The shape of the grid and the distribution of grid nodes is not predefined by (36.5), and any irregular grid can be chosen. However, the GNSS receiver network, which provides the observations, constrains some parameters of the grid (Sect. 36.4.2), and a special grid structure might be recommended by the observation operator, e.g., a regular voxel grid. The grid nodes are usually defined by latitude, longitude, and height and need to be mapped on a vector \mathbf{x} . No specific order is required, but the mapping must be unique, and the same mapping needs to be used when the design matrix \mathbf{A} is defined.

36.3.5 Observation Operator and Design Matrix \mathbf{A}

The slant-delay observation operator computes individual delays based on the observation geometry and the discrete refractivity field defined on a spatial grid. The operator defines the signal path between the satellite and the receiver within the grid, interpolates the refractivities of adjacent grid nodes on the signal path, and estimates the delay by numerical integration of (36.12).

With the approximations described in Sect. 36.3.1, it is assumed that the signal path is known in advance and does not change during the inversion. The signal path might be a straight line between transmitter and receiver, but it could also be a more realistic curved signal path.

The simplest way to define the forward operator is a straight line in a voxel grid, i.e., a direct implementation of $\int N ds \approx \sum N_i \Delta s_i$, where the N_i are the refractivities within the voxels, and Δs_i are the subpaths in the corresponding voxels. This is rather similar to

a nearest-neighbor interpolation combined with a very basic numerical integration. While this can be implemented easily, it leads to a step function along the signal path and a very nonsmooth observation operator. Such an operator will lead to rather large operator errors and to a less stable inversion.

A much better observation operator can be obtained in a two-step approach. A set of supporting points for the numerical integration along the signal path is defined in a first step. A high-quality numerical integration algorithm [36.38, 39] provides the weights of each supporting point. In a second step, the refractivities from the spatial grid are interpolated on the supporting points. The interpolation algorithm determines the contribution of each grid point to each supporting point, i.e., a second set of weights. The observation operator is a combination of both weights [36.40].

An alternative approach is to implement the full nonlinear observation operator. The linearized operator, i.e., the j -th row of \mathbf{A} , is given by the derivatives of the STD operator with respect to N_j

$$a_{ij} = \frac{\partial \text{STD}_i}{\partial N_j}. \quad (36.24)$$

This is equivalent to the adjoint operator used, e.g., in the variational data assimilation. In the case of a voxel grid, the operator is already linearized by the approximation described above, and the derivatives of the sum are the subpaths in each voxel. For a more sophisticated STD operator with a nonlinear interpolation and a numerical integration based on higher-order polynomials, the derivatives must be computed explicitly.

The bending of the signal path needs to be taken into account if STDs at low elevations $\varepsilon \lesssim 30^\circ$ are used. Observation operators developed for numerical weather models show that the STDs computed for straight lines overestimate the delays systematically [36.41], leading to an operator error of $\gtrsim 5$ mm at $\varepsilon = 30^\circ$ and ≈ 100 mm at 5° . A raytracer [36.42] can be used to estimate the curved signal path in a previous refractivity state or even in the standard atmosphere [36.27], and (36.12) can be integrated along this curved path. As the vertical structure of the humidity field is to a large degree determined by STDs at low elevations, the application of a raytracer is recommended.

36.3.6 Inversion

There is a variety of tomographic techniques [36.19, 43], but most of them focus on the solution of isolated static problems. In the case of the GNSS tomography, a continuously developing humidity field is desired, and the atmospheric state needs to propagate in time. The

Kalman filter [36.44] is a reliable approach for estimating the state and the error of continuously developing linear systems. While the Kalman filter is not designed for solving inverse problems, it very often provides stable results. In the case of severely ill-posed problems, it can be combined with regularization techniques that lead to a well-conditioned matrix \mathbf{A} [36.45].

The Kalman filter uses a two-step approach. The forecast step propagates the system in time, and the update step combines the current state with the latest observations. The forecast step from time t_{k-1} to t_k with the previous state $\mathbf{x}_{k-1} = \mathbf{x}(t_{k-1})$, and the forecast $\mathbf{x}_k^- = \mathbf{x}^-(t_k)$ is given by

$$\mathbf{x}_k^- = \mathbf{F}\mathbf{x}_{k-1}, \quad (36.25)$$

$$\mathbf{P}_k^- = \mathbf{F}\mathbf{P}_{k-1}\mathbf{F}^T + \mathbf{Q}_k. \quad (36.26)$$

In the case of tomography, there is no model that propagates the state \mathbf{x} in time, and the forecast is just a copy of the old state \mathbf{x}_{k-1} to \mathbf{x}_k^- ; \mathbf{F} is the unit matrix \mathbf{I} , the forecast error covariance matrix \mathbf{Q} is not time dependent, and the equations simplify considerably

$$\mathbf{x}_k^- = \mathbf{x}_{k-1} \quad \text{and} \quad \mathbf{P}_k^- = \mathbf{P}_{k-1} + \mathbf{Q}. \quad (36.27)$$

The update step combines the forecast \mathbf{x}_k^- with the latest observations \mathbf{y}_k and provides the new state \mathbf{x}_k with the error covariance matrix \mathbf{P}_k . The Kalman gain matrix \mathbf{K}_k is used to compute the increments to \mathbf{x}_k^- and to update the error covariance matrix; \mathbf{K}_k depends on the observation operator \mathbf{A}_k , the forecast error covariance matrix

\mathbf{P}_k^- , and the observation errors \mathbf{R}_k

$$\begin{aligned} \mathbf{K}_k &= \mathbf{P}_k^- \mathbf{A}_k^T (\mathbf{A}_k \mathbf{P}_k^- \mathbf{A}_k^T + \mathbf{R}_k)^{-1}, \\ \mathbf{x}_k &= \mathbf{x}_k^- + \mathbf{K}_k (\mathbf{y}_k - \mathbf{A}_k \mathbf{x}_k^-), \\ \mathbf{P}_k &= (\mathbf{I} - \mathbf{K}_k \mathbf{A}_k) \mathbf{P}_k^-. \end{aligned} \quad (36.28)$$

A continuously running GNSS tomography system would start with an initial state \mathbf{x}_0^- and an error estimate \mathbf{P}_0^- . The state \mathbf{x}_0^- is updated using the latest observations \mathbf{y}_0 which leads to the best estimate of the state \mathbf{x}_0 , i.e., the state with the minimum error covariance \mathbf{P}_0 . The cycle continues with the subsequent application of the equations (36.27) and (36.28). The choice of the time step Δt depends on the respective application and is discussed in Sect. 36.4.4.

There are two fundamental problems with the application of the Kalman filter to GNSS tomography. A reliable estimate of the propagation error \mathbf{Q} is required to obtain a stable system; \mathbf{Q} is the error introduced by the assumption that the state does not change within a period Δt and can be estimated from climatological data. The conditioning of \mathbf{A} is crucial, as \mathbf{A} is not only used for updating the latest state but also for estimating its error covariances. In the case of severely ill-posed problems, the ill-conditioning of \mathbf{A} leads to an instable filter, which diverges quite fast to meaningless results. Regularization techniques like the truncated SVD or Tikhonov regularization can be used to improve the conditioning of \mathbf{A} and to stabilize the filter.

36.4 Devices and Systems

The GNSS tomography is the last step in a rather long and complex processing chain with three almost independent subsystems. The GNSS raw observations with the basic travel time information are collected by ground-based networks of GNSS receivers. The raw observations are processed by complex GNSS processing systems, which provide precise positioning information. The GNSS atmosphere processing is usually done in a second step and determines the STDs together with other tropospheric products. The STDs and some additional meteorological observations are used by the GNSS tomography system in order to estimate spatially resolved humidity fields. The only hardware components of the whole system are the GNSS satellites and receivers. GNSS processing and tomography are done by special software packages that run virtually on any computer and at any place with access to the data.

36.4.1 GNSS Systems

Navigation satellite systems were designed for precise positioning and consist of GNSS satellites that orbit the Earth twice a day at a height of $\approx 20\,000$ km and GNSS receivers at the ground or onboard other satellites. The GNSS satellites carry high-precision atomic clocks and GNSS transmitters that continuously broadcast GNSS signals with precise timing information. There is no communication between the GNSS receivers and the satellites, and there are no remote-sensing instruments onboard the GNSS satellites. Any receiver that can track at least four GNSS satellites is able to compute its position from the timing information coded in the GNSS signals [36.35].

The GNSS satellites and the supporting infrastructure are operated by space agencies that are responsible for guaranteeing continuous uninterrupted availability

of the positioning services. GNSS receivers are available from many companies and in a variety of product types, ranging from on-chip receivers for mobile devices to high-quality geodetic receivers. GNSS atmosphere sounding is based on the signal travel time information, and precise geodetic receivers with high-grade antennas are required to obtain observations of sufficient quality. Different GNSS use slightly different frequencies and special signals, which are not supported by all receivers. However, most geodetic receivers do now support all four GNSS.

Apart from the quality requirements, there are no special demands on receivers for the GNSS tomography. It is not the single receiver but an entire network of receivers that provides the basic data for the GNSS tomography and determines the quality of the final humidity fields.

36.4.2 Ground-Based GNSS Networks for Tomographic Applications

The GNSS tomography requires a large amount of observations from many GNSS receivers. The GNSS receivers and the supporting infrastructure are organized in ground-based GNSS networks. The distribution of the stations within the network has a large impact on the quality of the tomographic reconstruction and needs to be considered when the tomography system is configured.

The basic parameters of a GNSS tomography system are the region covered by the system, the horizontal resolution, and the vertical resolution of the solution. The vertical extension is given by the tropopause height, as almost all of the atmospheric water vapor needs to be considered for a reliable solution. These parameters are to a great extent predetermined by the receiver network.

GNSS delays are integrated along the whole signal path. To get a spatially resolved humidity field, a sufficiently large number of intersecting signal paths is required in order to locate the information on each path. For subsections without any intersecting paths, only some spatial mean value can be obtained. This is the case in the lowest part of the atmosphere, where the minimum elevation of the observed GNSS signals and the Earth's curvature prevent intersections between different signal paths. Another problem are the outer boundaries of the network, where the intersections with outward pointing signal paths decrease significantly.

The vertical resolution of the tomographic solution is limited by the mean interstation distances within the GNSS network. A receiver located at the position B in Fig. 36.2 cannot detect any signals below a given height H_2 at a point A in a distance S_{AB} . The atmosphere be-

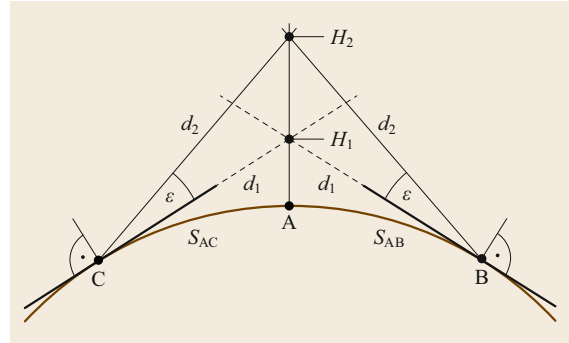


Fig. 36.2 Geometric limitations for atmosphere sounding by GNSS slant paths. GNSS signals detected at a position B cannot cover the atmosphere below the height H_2 at a position A. The vertical range below H_1 is not visible due to the Earth's curvature, and the range between H_1 and H_2 cannot be scanned because of the minimum elevation $\varepsilon = \varepsilon_{\min}$ that is detected by the receiver

low the height H_1 is shaded by the Earth's curvature, and the range between H_1 and H_2 cannot be scanned because of the minimum elevation $\varepsilon = \varepsilon_{\min}$, which is usually between 5° and 10° . An estimate of H_1 and H_2 for a spherical Earth and without regarding the ray bending in the atmosphere is given by [36.46]

$$H_1 = R_0 \left(\sqrt{1 + \tan^2 \left(\frac{S_{AB}}{R_0} \right)} - 1 \right), \quad (36.29)$$

with the radius R_0 of the Earth and the distance S_{AB} between the points A and B. The contribution $H_2 - H_1$ due to ε_{\min} is

$$H_2 - H_1 = R_0 \tan \left(\frac{S_{AB}}{R_0} \right) \left[\sin \left(\frac{\pi}{2} + \frac{S_{AB}}{R_0} \right) \times \left(\tan^{-1} \left(\frac{\pi}{2} + \frac{S_{AB}}{R_0} \right) + \tan^{-1} \varepsilon \right) \right]^{-1}. \quad (36.30)$$

To estimate the vertical resolution it is helpful to compute the distance S on the Earth's surface where a slant with the elevation ε reaches the height H_2

$$S = R_0 \left(\frac{\pi}{2} - \varepsilon - \arcsin \left(\frac{R_0}{R_0 + H_2} \right) \right). \quad (36.31)$$

Some distances S obtained with $\varepsilon = 5^\circ$ are shown in Table 36.4. It turns out that signals below 1000 m can be expected only for stations within a radius of 11.3 km, and stations with distances exceeding 22.4 km provide data above 2000 m. Stations that are farther away than ≈ 100 km cannot contribute any information. The num-

Table 36.4 Station distances S for some heights H_2 according to (36.31) with $\varepsilon = 5^\circ$

H_2 (m)	1000	2000	5000	10000
S (km)	11.3	22.4	54.5	104.4

ber of stations that provide data increases with H_2 until the top height regarded by the tomography is reached. In the case of a large network with a homogeneous station density, the number of stations will grow with S^2 . If the tomography requires a certain number of signals within each layer, the vertical extension of the layers can be reduced, i.e., the vertical resolution increases with height.

The horizontal resolution in the lower troposphere is also limited by the mean receiver distances within the network, as there are almost no GNSS observations between the stations. The situation improves with increasing height, but more than 50% of the water vapor is located below 2 km and increasing the horizontal resolution with height brings no advantage.

Summarizing, there is a rather large gap in the lower troposphere where no intersecting slant paths can be expected and where the vertical resolution is very poor. Above a certain height, the vertical resolution begins to increase. This is exactly the opposite of the desired situation. To obtain a reasonable vertical resolution in the boundary layer, the minimum elevation can be decreased, but only very dense receiver networks will lead to substantial improvements.

So far, a flat terrain has been assumed. In mountainous regions, it might be possible to place some receivers along mountainsides that provide almost horizontal views at different heights and help alleviate the low resolution near the surface.

It depends very much on the density and distribution of GNSS receivers within the network whether the STD data sets are really sufficient for GNSS tomography. If the spatial coverage of the atmosphere by GNSS observations is insufficient, tomographic techniques will lead to instable solutions with many artifacts, and other strategies for combining all available observations might be more productive, e.g., data assimilation techniques [36.47] or least-squares collocation [36.48].

Modern GNSS networks consist of geodetic multi-GNSS receivers which track all visible satellites on several frequencies simultaneously [36.49]. High-quality multi frequency receivers are required to remove the impact of the ionosphere and to achieve the required precision. Existing networks can be further densified with less expensive single-frequency receivers [36.50, 51] in order to reach the high receiver density required by the GNSS tomography.

36.4.3 GNSS Processing

GNSS receivers are able to display their position. However, the coordinates computed by the receiver are rather inaccurate, with errors between ≈ 10 m for budget single-frequency receivers and ≈ 10 cm in the case of high-quality geodetic receivers. In order to obtain high-precision coordinates with sub-cm errors complex GNSS processing packages are required. GNSS atmosphere products can only be derived during the GNSS processing. An overview about GNSS processing in general can be found in [36.52, 53] and about GNSS atmosphere processing in [36.54, 55].

Processing of the GNSS raw data can be done in network mode using undifferenced phase observations [36.56] or double differences (DD) of phase observations [36.57]. The DD approach removes satellite and receiver clock errors by differencing simultaneous observations from two sites and two satellites. Because DD processing eliminates clocks and allows for ambiguity resolution, it is sensitive to small variations in the nonisotropic part of the troposphere. The technique to transform double difference residuals into line-of-sight residual delays (which can then be converted into non-isotropic slant water observations) for an individual ray path between a transmitting satellite to a receiving antenna is described by [36.58].

However, this approach has several disadvantages, especially for operating dense GNSS networks with more than 200 sites, where the processing time increases exponentially with an increasing number of sites/parameters. The disadvantage of DD for STD calculation is that the resulting residual is a combination of four observations instead of one.

The necessity of an efficient operation of large networks within short computation time was one of the main reasons for introducing the precise point positioning (PPP) approach [36.59]. The main idea of the PPP strategy is the processing of each site separately, fixing the high quality GNSS orbits and clocks. The advantage of PPP for slant calculation is that the line-of-sight observations from the receiving antenna to each transmitting satellite are individually modeled, and site specific effects can be investigated. This approach helps to avoid error propagation from poorly functioning stations within the network and even to avoid a complete failure of the solution in the case of problems with one of the fiducial sites of the network.

However, the main advantage of the PPP strategy is the processing time, which increases only linearly with the number of stations and solved parameters (e.g., ZTDs or gradients every 15 min). The possibility to process a large number of the stations in near realtime is of

significant importance for the tomography where dense networks are required.

The main disadvantage of the PPP analysis is that satellite orbit and clock estimates with high accuracy are required. Typically, satellite clock values are computed together with the satellite orbits from a global GNSS tracking network. Thus, the GNSS data processing for PPP has to be split into two steps. Step 1 includes the estimation of high-quality GNSS orbits and clocks from a global network, e.g., from a network of IGS (International GNSS Service) sites. This leads to the most accurate and consistent results and, consequently, to highly reliable STDs. Another possibility is to use accurate final orbit and clock products provided by IGS. However, this may lead to inconsistent results. Step 2 is the actual PPP processing of individual stations. An overview of the PPP strategy can be found in [36.60].

There is a number of software packages for GNSS data processing. The most widely used commercial GNSS software package is Bernese, which can handle both DD and PPP methods [36.57] and is based on a least-squares (LSQ) adjustment. Two other free packages that are typically used for research are GIPSY/OASIS, which is based on a Kalman filter and GAMIT/GLOBK, which uses LSQ. GIPSY/OASIS is often preferred because of its better computational efficiency associated with the PPP approach, while GAMIT/GLOBK does not support PPP and is restricted to DD. These three software packages are used by most GNSS analysis centers that provide tropospheric GNSS products for meteorological projects like E-GVAP (egvap.dmi.dk) or COST Action 1206 [36.61].

Another example of a noncommercial software package that is able to process the STDs automatically using the PPP strategy is the Earth Parameter and Orbit System (EPOS) software developed at the German Research Centre for Geosciences (GFZ). The EPOS software is based on a least-squares adjustment of undifferenced phase observations and makes use of the conventions defined by the International Earth Rotation and Reference Systems Service (IERS) [36.56, 62–64]. EPOS supports both the network mode and the PPP mode. The former is required to calculate high-precision GNSS orbits, clocks, and station coordinates, which are provided to IGS and are required by PPP. The latter is used to process large numbers of stations for different meteorological applications.

Operational GNSS data processing at the GFZ for meteorological applications has provided all kinds of tropospheric products, namely zenith total delays, integrated water vapor, slant total delays, and tropospheric gradients in near realtime for more than 15 years.

The automated processing of GNSS data in PPP mode with EPOS is split into two parts. Part 1 is the so-called *base cluster* analysis in network mode, where

the estimation of high-quality GNSS orbits and clocks from a global network of about 100 IGS sites is performed. Among the estimated parameters at this step are the GNSS orbits, satellite clocks, Earth rotation parameters (ERPs), and ZTDs for 4-h intervals. GFZ ultra rapid IGS products for orbits and clocks as well as GFZ ERPs are used as initial values.

The second part is the PPP analysis itself: estimation of all tropospheric products (ZTDs/IWV/STDs) using parallel processing of stations in clusters based on fixed orbits and clocks from the first step. EPOS adjusts for the ZTDs with a resolution of 15 min, for tropospheric east and north gradients with an hourly resolution, as well as for STDs with 2.5 min time resolution from a sliding 24-h data window. The station coordinates are fixed, once determined with sufficient accuracy within ITRF (International Terrestrial Reference Frame).

36.4.4 Setup of a GNSS Tomography System

A GNSS tomography system is basically a solver for (36.5), and its structure is quite simple. In a first step, the three components of the equation need to be set up for a specific case. The state vector \mathbf{x} is defined by the spatial grid, which is usually a predefined static grid. Equation (36.5) is solved for \mathbf{x} , however most algorithms require an initial state or background, and \mathbf{x}_{ini} needs to be specified, optionally together with some error characteristics or a full background error covariance matrix. All available observations, i.e., the delays and any additional observations that might be required to stabilize the inversion algorithm are mapped to the observation vector \mathbf{y} . In most cases, the observation errors are also required. The size of \mathbf{y} depends on the number of observations available at a certain time and may vary considerably. The linear operator \mathbf{A} maps the state vector on the observation vector. The rows of \mathbf{A} are the linearized observation operators for each observation in \mathbf{y} and need to be redefined for each specific situation. The second step is the numerical solution of (36.5) and provides \mathbf{x} , optionally together with some error estimates. As the problem is ill-posed, and \mathbf{A} is ill-conditioned, some strong constraints are usually required to obtain stable and meaningful solutions. The constraints are an important part of the whole system and need to be carefully tuned. In a last step, the results might be converted to a more convenient quantity, e.g., from a refractivity field to a field of the absolute humidity, and provided to potential users.

Discretization and Approximations

The numerical solution of (36.5) requires a discrete spatial grid. The grid defines the region that is covered by the tomography, and the horizontal and the vertical res-

olution. The total number of grid nodes is the number of unknowns in (36.5) and needs to be sufficiently large to implement realistic observation operators with reasonable operator errors but should be as small as possible, as the ill-conditioning of \mathbf{A} increases with the number of unknowns. The limitations of the grid resolution due to the receiver network were discussed in Sect. 36.4.2.

Another important choice is the kind of delays used by the tomography: STD, SWD, or SIWV. As discussed in Sect. 36.3.2, additional errors are introduced by the conversion to SWDs or SIWV, and it depends on the meteorological observations available at or near each GNSS station whether the conversion leads to reliable results.

In most cases, the signal paths do not cover the whole volume of the atmosphere spanned by the GNSS tomography. This leads to a sparse matrix \mathbf{A} . One strategy for reducing the sparsity of \mathbf{A} is to collect path delays over a longer period of time. Especially rising or setting satellites have a rather high angular velocity and scan different parts of the atmosphere if the period is sufficiently long, e.g., between 15 and 60 min. This leads to a better spatial coverage and more stable results at the expense of a reduced temporal resolution. Increasing the sampling rate of the GNSS receivers is usually not beneficial as signal paths separated by only 30–120 s propagate through almost the same parts of the atmosphere and do not provide additional information.

Modeling of the Observation Operator

The design of the STD observation operator is discussed in Sect. 36.3.5. The implementation used in a specific GNSS tomography system can affect the performance of the whole system, as the operator adds some error to the system of equations. The operator error at low elevations can exceed the observation error if no raytracer is used.

In general, it is a good idea to use all available meteorological observations to stabilize and constrain the tomographic solution. This might be synoptic observations, radiosonde profiles, water vapor radiometer data, satellite observations, or even other GNSS products like ZTDs or the vertically integrated water vapor (IWV). As the GNSS tomography works with just one field, e.g., the refractivity or absolute humidity, all these observations need to be mapped on this field. These observations are appended to the vector \mathbf{y} , and the linearized observation operators need to be in the corresponding rows of the operator \mathbf{A} .

Inversion Strategy

The inversion algorithm is the core of any tomography system and the choice of a specific algorithm has

a significant impact on the whole system. The inversion technique determines the solution strategy for the ill-posed inverse problem and the stability of the solution. It also controls the complexity of the system. A tomography system based on the algebraic reconstruction techniques (ART) can basically work with the observations and the corresponding operator \mathbf{A} . No error information is required or provided, and the iterative algorithm does not require any complex matrix manipulations or inversions. This leads to a much leaner system than, e.g., a Kalman filter, which requires detailed error information and is based on a much more complex and computationally demanding algorithm. A large number of inversion techniques has already been applied successfully to the GNSS tomography [36.11, 43]; some examples are given below.

The many variants of the ART family [36.43, 65] are fast iterative approaches that require little extra information [36.66, 67]. However, a good initialization is very beneficial. The mathematical justification is not very convincing [36.18], and a general criterion for stopping the iteration (index k in (36.32)) does not exist, which may lead to degrading or oscillating solutions. Usually it is possible to find a set of parameters for a specific configuration that leads to fast and rather stable results. Multiplicative ART (MART) is a particularly fast converging variant and was used in Sect. 36.8

$$x_j^{k+1} = x_j^k \left(\frac{y^i}{\langle \mathbf{A}^i, \mathbf{x}^k \rangle} \right)^{\frac{\lambda A_j^i}{\sqrt{\langle \mathbf{A}^i, \mathbf{A}^i \rangle}}}. \quad (36.32)$$

This equation describes three nested loops of the iteration algorithm. The innermost loop, index i , determines the factor that is applied to the j -th element of the state vector \mathbf{x} . The contributions of all observations y^i are added and applied to each single x_j^k . This is repeated for all elements x_j of the state vector, index j . These two loops are repeated until a stable state \mathbf{x} is reached, index k . The relaxation parameter λ determines the weight of the observations with respect to \mathbf{x} . The algorithm shows fast convergence if λ is large but also becomes less stable with an increasing number of artifacts. A large number of iterations k is required if λ is too small, which also leads to instable results. The optimal λ needs to be experimentally determined [36.15].

The pseudo inverse \mathbf{A}^\dagger is an approach to invert \mathbf{A} and to compute the new state \mathbf{x} with $\mathbf{x} = \mathbf{A}^\dagger \mathbf{m}$ [36.66, 68, 69]; \mathbf{A}^\dagger is estimated using the truncated SVD (36.6), i.e., the large number of small singular values that are typical for inverse problems are truncated at a certain threshold in order to obtain a well-conditioned matrix: $\mathbf{A}_p = \mathbf{U}_p \mathbf{\Sigma}_p \mathbf{V}_p^T$. There are algorithms for estimating the threshold, but the exact threshold remains somewhat ar-

bitrary. The solution is obtained in one step

$$\mathbf{x} = \mathbf{A}_p^\dagger \mathbf{m} \quad \text{with } \mathbf{A}_p^\dagger = \mathbf{V}_p \mathbf{\Sigma}_p^{-1} \mathbf{U}_p^T. \quad (36.33)$$

If an initial field \mathbf{x}_0 with some error characteristics \mathbf{B} is available, a weighted, damped least-squares solution leads to an optimal combination of the initial information and the new observations [36.70–72]. A similar approach is used in the variational data assimilation [36.73]. These techniques cannot update the error estimates and work either with a constant background error or need an additional strategy for estimating the errors of the solutions. The solution can be given in incremental form

$$\mathbf{x} = \mathbf{x}_0 + \mathbf{B} \mathbf{A}^T (\mathbf{A} \mathbf{B} \mathbf{A}^T + \alpha^2 \mathbf{R})^{-1} (\mathbf{y} - \mathbf{A} \mathbf{x}_0), \quad (36.34)$$

where α is the damping term, \mathbf{B} is the error covariance matrix of \mathbf{x}_0 , and \mathbf{R} is the observation error covariance matrix as in Sect. 36.3.6. By increasing or decreasing α the weight of the observations can be decreased or increased, which has an impact on the stability of the solution. For $\alpha = 1$, this is equivalent to the 3-D variational solution.

The Kalman filter (Sect. 36.3.6) might be the most consistent technique as long as no specialized inversion strategies that can deal with the highly variable degree of ill-posedness are available. The Kalman filter combines the latest humidity field and the observations using the corresponding error covariance matrices and provides not only an optimal solution but also an updated error covariance matrix for the solution. For numerical reasons, a square-root filter should always be implemented, which is more stable and avoids negative humidities that can easily appear if the original Kalman filter is used. Reliable error estimates are required but may be difficult to obtain.

Especially the error of the forward step, which in case of the GNSS tomography is just a copy of the previous state, is difficult to estimate. A climatology provides some mean error, but the true error of the humidity fields is highly variable in space and time and can lead to strong deviations from the true state. As there is no stabilizing physical model it is difficult for the system to recover from a wrong state, and it may get unstable. Another problem is the ill-conditioned operator \mathbf{A} that enters the Kalman gain matrix and has a degrading effect not only on the solution but also on the error characteristics.

The GNSS tomography systems developed up to now do not run continuously by updating the latest state with newly acquired observations. Even a Kalman filter can become unstable after some time and needs to be restarted from a reliable state. There are many rea-

sons for this. The system runs without a physical model and can easily get into a meteorologically meaningless state. The degree of ill-posedness depends on the satellite constellation and varies heavily, leading to an ill-conditioned operator \mathbf{A} that amplifies small errors to a varying degree. The inversion techniques described above cannot adapt to such a behavior and may become unstable [36.74].

Meteorological Observations, Constraints, and Pseudo Observations

In most cases, (36.5) has an infinite number of solutions \mathbf{x} , and most of them are meteorologically meaningless. Therefore, strategies are required to single out the most realistic humidity field. The best strategy is to add some extra observations to the system of equations. Especially well located observations, e.g., from synoptic stations or radiosondes, constrain the system to a realistic state and stabilize the inversion as the operator \mathbf{A} becomes less ill-conditioned. Especially whole profiles from radiosondes, radiometers, or lidars are very beneficial, but other integrated quantities like satellite data or the GNSS column-integrated water vapor are also helpful.

Synoptic observations can be used to constrain the surface layer to the observed humidities, and the top layer at the tropopause can be constrained to a very small humidity or even be set to zero. Such constraints guarantee that most of the humidity is located in the lower atmosphere. If only the slant delays were regarded, an upside-down atmosphere with most of the humidity near the tropopause would be entirely equivalent, at least in a flat geometry.

Constraints can, in general, be described as

$$c(p(\mathbf{x})) = 0, \quad (36.35)$$

where c is the constraining function, and p is some projection. Most constraints used in GNSS tomography are equality constraints that simplify to $c(\mathbf{x}) = 0$ and can be regarded as pseudo observations

$$\mathbf{y}_c = \mathbf{A}_c \mathbf{x}, \quad (36.36)$$

where the rows of \mathbf{A}_c are the linear(ized) constraints c and $\mathbf{y}_c = 0$. The original system of linear equations (36.5) can be extended by (36.36) and be solved in one step. However, there is also an error related to the constraints that needs to be considered if, e.g., a Kalman filter is used [36.75].

In most cases, the GNSS slant delays are available only for some parts of the atmosphere, while there is no information for other parts. This leads to strong and

unrealistic gradients within the solution. One way to smooth out such gradients are intervoxel constraints. One option is to constrain the humidity at each grid node to the mean humidity of the neighboring nodes, e.g.,

$$0 = x_i - \frac{1}{\sum_j c_j} (c_1 x_{r_1} + c_2 x_{r_2} + \dots + c_M x_{r_M}), \quad (36.37)$$

where the indices r_1, \dots, r_M select the neighbors of node i , the c_j are the weights assigned to each neighbor, and M is the total number of neighbors, e.g., $M = 26$ in a regular 3-D grid. Another option is a Gaussian filter, which takes all grid nodes within a given radius into account. As the humidity usually decreases with height, the weights should be vertically adjusted.

In most cases, the GNSS processing also provides the IWV above each GNSS station, and the vertically

integrated humidity at the corresponding grid columns can be restricted to the observed IWV

$$0 = \text{IWV}_j - \sum_r a_r, \quad (36.38)$$

where IWV_j is observed at station j , and the a_r are the absolute humidities in the grid column next to the station.

A well-tuned combination of these strategies is usually required to obtain a stable GNSS tomography system. Care must be taken to avoid too strong constraints or too much smoothing, as the solutions may look very convincing but are far from reality. An overconstrained system leads to some kind of mean humidity field with only minor fluctuations due to the observations and cannot represent the real atmospheric dynamics.

36.5 Specifications

The final product of the GNSS tomography is a field of the absolute humidity a . Some of the most relevant parameters are the horizontal and vertical resolution and the error of a . The resolution of the final field is to a large degree defined by the mean interstation distances within the GNSS ground network (Sect. 36.4.2) but also depends on the quality and density of the observations. It would be possible to increase the resolution if a large number of STDs, e.g., from multi-GNSS receivers, is available, or if meteorological observations from dense sensor networks can be utilized. The latter is especially important for the lower part of the troposphere, which can hardly be resolved with GNSS observations alone. As there are so many influencing variables, it is a demanding task to estimate the theoretical resolution even for an existing network, and no general statements can be made. However, applications with horizontal resolutions between 10 and 80 km and

vertical resolutions between several hundred meters and ≈ 2000 m exist.

To quantify the error of a is even more difficult, as a is obtained by solving an ill-posed inverse problem with highly variable input data. It is, in general, not possible to propagate errors beyond the solution of an inverse problem, and the validation of the results with independent observations is the only way to estimate the error (Sect. 36.6.2). The situation is comparable to the output of numerical weather models, i.e., analyses and forecasts, which are also provided without any error estimates and can only be validated using the observations.

The humidity fields provided by the GNSS tomography can be related to the requirements of the World Meteorological Organization (WMO) for the specific humidity (Table 36.5). The WMO threshold for the higher and lower troposphere can already be reached by most local GNSS networks and some dense national net-

Table 36.5 WMO requirements for the specific humidity according to the Observing Systems Capability and Review Tool (OSCAR) and feasibility of the targets by the GNSS tomography (<http://www.wmo-sat.info/oscar/variables/view/161>). The uncertainty ε , the horizontal resolution h_{res} , and the vertical resolution v_{res} as specified by the WMO are given

WMO target	ε (%)	h_{res} (km)	v_{res} (km)	GNSS tomography
High troposphere				
Goal	2	2	0.3	Future very dense local networks with additional profile information
Breakthrough	5	10	0.4	Dense (local) networks with interstation distances ≤ 10 km
Threshold	10	30	1	National networks with interstation distances ≤ 30 km
Lower troposphere				
Goal	2	0.5	0.1	Presumably out of reach
Breakthrough	5	5	0.2	Future very dense local networks with additional profile information
Threshold	10	20	1	National or local networks with interstation distances ≤ 20 km

works, if additional surface observations that constrain the profile in the lower troposphere are available. Tomographically reconstructed humidity fields with a horizontal resolution of 10 km are also available for some local networks; however, whole profiles with a vertical resolution of 400 m and a rather small uncertainty are very demanding. As discussed in Sect. 36.4.2, the vertical resolution is limited by the interstation distances and a resolution of 400 m, or even 200 m as required for the lower troposphere, can be obtained only for interstation distances below 2 km. A high vertical resolution with a small uncertainty can presumably be obtained only if

additional observed profiles are available. The temporal resolution and timeliness of tomographic products depend on the GNSS processing strategy and are almost independent of the spatial resolution. The delay due to the tomography is in the order of some minutes, and the tomographic products can be provided almost as fast as the original GNSS products. Most GNSS processing centers are already better than the WMO breakthrough with a 60 min observation cycle and a timeliness of 30 min. There are even some GNSS products that reach the WMO goal of a 15 min cycle. Future realtime products will be supplied significantly faster.

36.6 Quality Control

GNSS products cannot be regarded as true observations but are estimates from rather complex processing systems. Monitoring the quality of such products is a rather complex task. The most important atmospheric GNSS products are humidity estimates such as the IWV or 3-D humidity fields. As there is no high-quality reference system for humidity observations in the free atmosphere, the GNSS humidity products can only be compared to observations from other remote-sensing systems, which have their own peculiarities.

36.6.1 GNSS Processing Quality Control

The basic output of GNSS processing systems are the coordinates of the stations that are used in parallel for quality monitoring. The errors of several input parameters are estimated during the processing, such as the error of the GNSS satellite orbits, the error due to the ionosphere, signal multipath errors, antenna-related errors, and the uncertainties of mapping functions. These errors can be propagated through the least-squares adjustment of the atmospheric parameters and provide a per-epoch and station error of the ZTD and STD [36.55, 76]. While these error estimates to some degree depend on the process-

ing system, they provide valuable information on the temporal variation of errors and can complement the empirically determined errors derived in the next section.

36.6.2 Validation of Meteorological GNSS Products

The basic GNSS atmosphere products are the ZTD, IWV, and STD. These quantities are continuously validated by most processing centers in order to ensure a high quality of the products and to improve the processing strategies. There are few meteorological observation systems that provide these quantities, and additional observations are usually required to obtain comparable quantities, e.g., converting a radiosonde profile into a ZTD or the IWV. It should be emphasized that intercomparison studies provide the bias and standard deviation of the differences between both systems but do not reveal the true error of the GNSS products. It is always the error of both instruments plus the error of the data conversion that contribute to the standard deviation of the differences, and the error estimates can be regarded as an upper limit for the true error of one of the systems.

Table 36.6 Error of GNSS atmosphere products found in different inter-comparison studies. The typical range of the GNSS derived quantity is shown together with the standard deviation σ , the instruments which were used for comparison and references of recent studies. Radiosondes (RS), water vapor radiometers (WVRs), satellite systems like DORIS or geodetic techniques like VLBI are typically used for such studies

GNSS	Range	σ	Instruments
ZTD	1–2.7 m	3–6 mm	DORIS, RS, NWP [36.77, 78]
ZWD	0–250 mm	3–9.5 mm	VLBI, WVR, RS, NWP [36.79], WVR [36.80]
IWV	0–80 kg m ⁻²	0.9–2.7 kg m ⁻²	DORIS, RS, NWP [36.77, 81]
SIWV	0–300 kg m ⁻²	1.76–7.13 kg m ⁻²	WVR [36.82]
STD	1–25 m	10–12 mm	NWP, WVR [36.83]

The errors of some GNSS atmosphere products as found in recent intercomparison studies are shown in Table 36.6. A more comprehensive overview is given in [36.11]. Table 36.6 provides a range of errors because various GNSS products were validated with different instruments.

36.6.3 Validation of 3-D Humidity Fields from GNSS Tomography

The validation of large three-dimensional atmospheric fields is a demanding task because the errors vary spatially and temporally, and the entire quality of the fields is difficult to express. The fields of the wet refractivity or the absolute humidity provided by the GNSS tomography are usually compared to radiosonde profiles or fields from numerical weather prediction models (NWP), which requires a mapping to the observed quantities and also spatial interpolation.

Table 36.7 shows the results of some tomography validation studies. The errors are difficult to compare

Table 36.7 Errors of tomographically reconstructed humidity fields. The number of GNSS stations (N_{stat}), the reconstructed variable (var.), the observations used for validation (obs.) and the reported errors are shown. The error is expressed either by the root mean square (RMS) or the standard deviation σ

Reference	N_{stat}	Var.	Obs.	Error
Benevides, et al., 2018 [36.74]	17	N_{wet}	RS	0.5–3 g m ⁻³ RMS in a
Rohm, et al., 2014 [36.45]	45	N_{wet}	NWP	$\sigma = 4.2\text{--}12.4$
Shangguan, et al., 2013 [36.84]	272	N_{wet}	RS	RMS = 6.5–9.2
Troller, et al., 2006 [36.16]	43	N_{wet}	NWP	RMS = 1.8–6.5

because the tomography experiments differ in many ways. The number of GNSS stations, the extension of the network, the GNSS processing, the inversion strategy, and the regarded period of time vary in a wide range, and only a general impression can be provided.

36.7 Maintenance

The GNSS tomography depends on the STD products provided by GNSS processing systems, which themselves require raw GNSS observations from ground-based receiver networks. Consequently, the maintenance of a GNSS tomography system must take place on the corresponding levels, i.e., maintenance of the GNSS hardware and the data links to the processing centers, and operation and monitoring of the GNSS processing system and the tomography system.

In a strict sense, the GNSS satellites should also be mentioned here, but they are operated by space agencies that ensure almost unlimited availability.

36.7.1 GNSS Stations and GNSS Hardware

Depending on the application, existing permanent networks can be utilized or small temporary networks need to be installed. In the first case, the provider will keep the network up and running, and only the data link needs to be monitored. In the latter case, the major effort is to build up a new network (Sect. 36.4.2). GNSS receivers are basically radio receivers without any moving parts and usually run for many years but require

some infrastructure like power supply, data links, housing, etc., which need some attendance.

36.7.2 GNSS Data Processing and Tomography System

GNSS processing systems and tomography software are both rather complex applications that require continuous supervision, especially if they run operationally. Apart from the computer hardware, the data links and the availability of external products must be monitored. In both cases, data from external sources must be available, e.g., orbits and clocks for GNSS processing or STDs and meteorological observations for tomography. Up to now, the stability of tomographic solutions has been an issue, and continuously cycled tomographic systems require constant monitoring.

The processing of atmospheric products like STDs and the GNSS tomography are fields of active research, and continuous updates of the software systems are required in order to provide state-of-the-art results. The growing interest in GNSS atmospheric products leads to new user requirements, which need to be addressed.

36.8 Application

The GNSS tomography is a valuable tool for monitoring the spatiotemporal variation of water vapor in a specific region. The majority of the applications developed up to now is based on small regional networks with 20–30 receivers [36.12, 66, 70–72, 74]. Large nationwide geodetic networks were utilized to monitor the water vapor distribution on much larger scales of sev-

eral hundred kilometers. Attempts were made to run operational tomography systems that provide spatially resolved humidity fields for nowcasting and assimilation in numerical weather models [36.15, 16]. However, the stability of the inversion and the quality of the results is still an issue, and none of these systems is already operational.

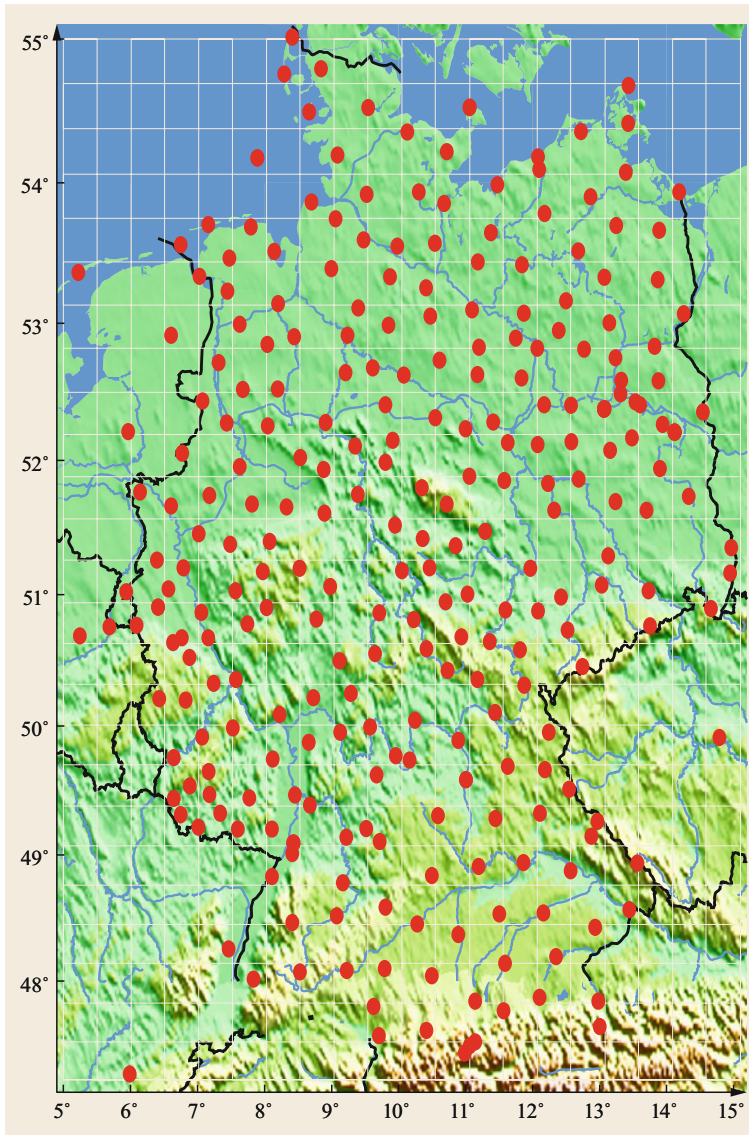


Fig. 36.3 German GNSS network of about 270 stations. Between 8 and 12 GPS satellites could be tracked simultaneously at each station, leading to 2100–3200 STDs. A horizontal 20×25 cell grid was used for the tomographic reconstruction (gray lines)

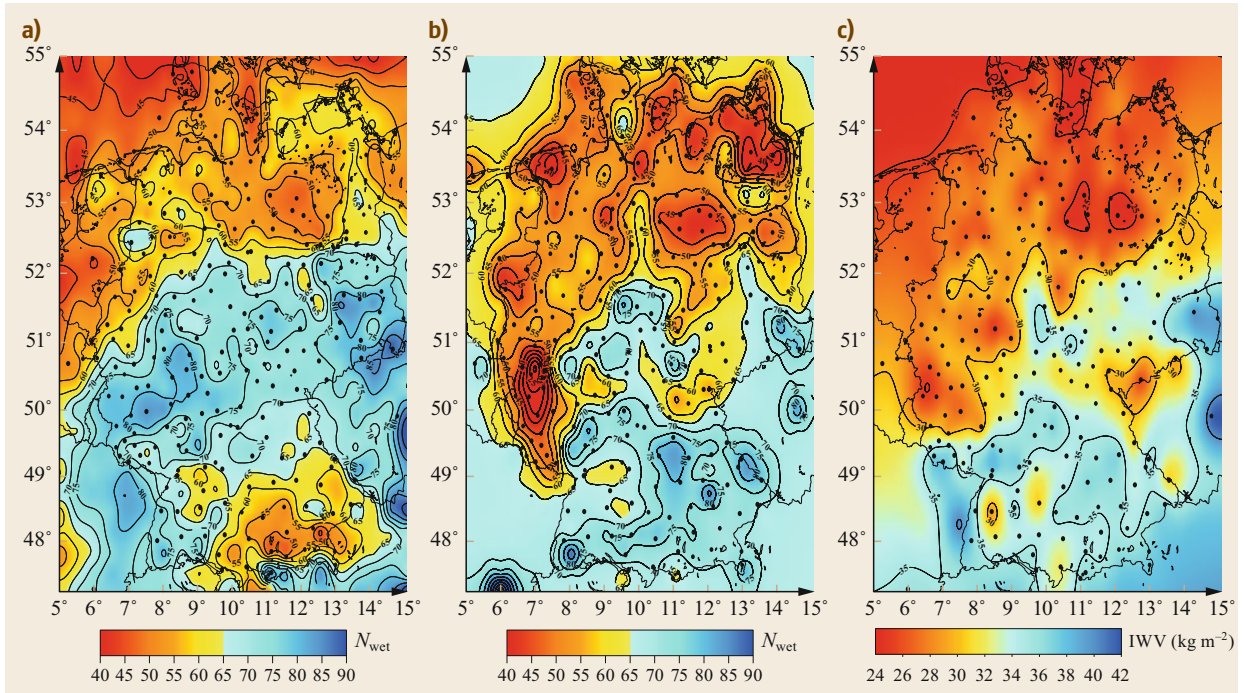


Fig. 36.4a–c Humidity fields from COSMO (a), the tomographic reconstruction (b) and GPS IWV (c) from 14.07.2009, 16:00 UTC and for the region shown in Fig. 36.3. The 1009 m layer of the model and the tomography is shown. The N_{wet} field computed from COSMO fields and interpolated on the tomography grid was used to initialize the tomography. The IWV field of interpolated GPS station observations is shown as a reference

As an example, some results of a German tomography system that was developed at the GFZ in Potsdam are shown [36.15]. The GNSS tomography was designed to run as a part of the near realtime GNSS processing, which already provides STD data from ≈ 300 German stations. Pressure and temperature observations from meteorological sensors at the GNSS stations and from the synoptic stations of the German Weather Service (DWD) were used to obtain SWD data sets (Sect. 36.3.3). A regular spatial grid with 20 grid cells in E–W direction and 25 cells in N–S direction covering 700×930 km was used. STD observations from 30 min were combined in each solution, leading to a total of 30 000–50 000 STDs, depending on the satellite constellation. The vertical range of 10 km was divided into 30 cells leading to a resolution of 35 km horizontally and 330 m vertically (Fig. 36.3). Several inversion algorithms were compared, e.g., different variants of ART, weighted, damped least-squares estimates, or the Kalman filter, but none of them proved to be superior, and most of the experiments used the fast MART algorithm.

The tomography was initialized using N_w fields computed from the surface observations and a simple exponential profile, which was scaled to the GNSS IWV observations or with analyses provided by the operational local weather model COSMO-DE of the DWD. The results shown in Fig. 36.4 were initialized by a COSMO field that differed considerably from the GNSS IWV field. The result of the tomographic reconstruction is much closer to the observed IWV field than the initialization but shows some clustering due to insufficient observations. Smooth areas without any structure are obtained at the outer borders, where no GNSS observations were available. The vertical N_w distribution shown in Fig. 36.5 also differs from the initial COSMO field. As the humidity distribution in numerical weather models is always somewhat uncertain, independent observations are required to validate the vertical humidity structure in the fields. The radiosonde profiles from 12 German radiosondes were compared to the columns of the N_w field near the radiosonde stations. Some results for 12 UTC are shown in Fig. 36.6. The

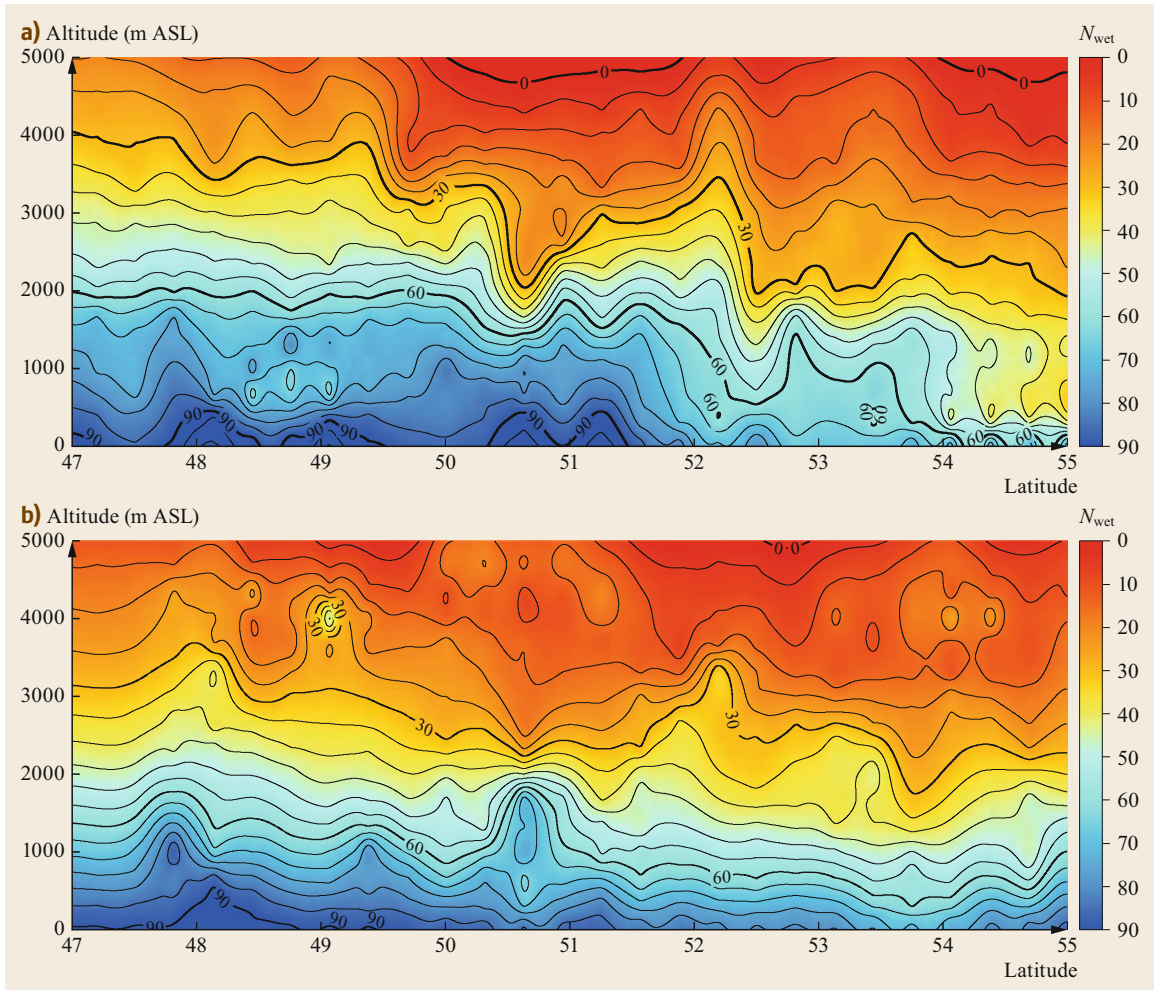


Fig. 36.5a,b Vertical N_{wet} distribution in COSMO (a) and in the tomographic reconstruction (b). The vertical humidity structure in N–S direction at a longitude of 10° is shown

results from the tomography were interpolated on the radiosonde profiles in order to preserve the high vertical resolution of the observations. The tomography solution is based on a spatial grid with a vertical spacing of 330 m and is much smoother than the observations. In general, the tomography profiles try to reproduce the observed vertical structure, but the quality of the pro-

files depends very much on the distribution of the GNSS observations and the initial conditions. While some profiles are in good agreement, others show strong deviations, especially in the lower part of the troposphere up to 3000 m [36.82]. As discussed in Sect. 36.4.2, such a behavior was to be expected because the interstation distances are much too large to obtain reliable results below 3000 m.

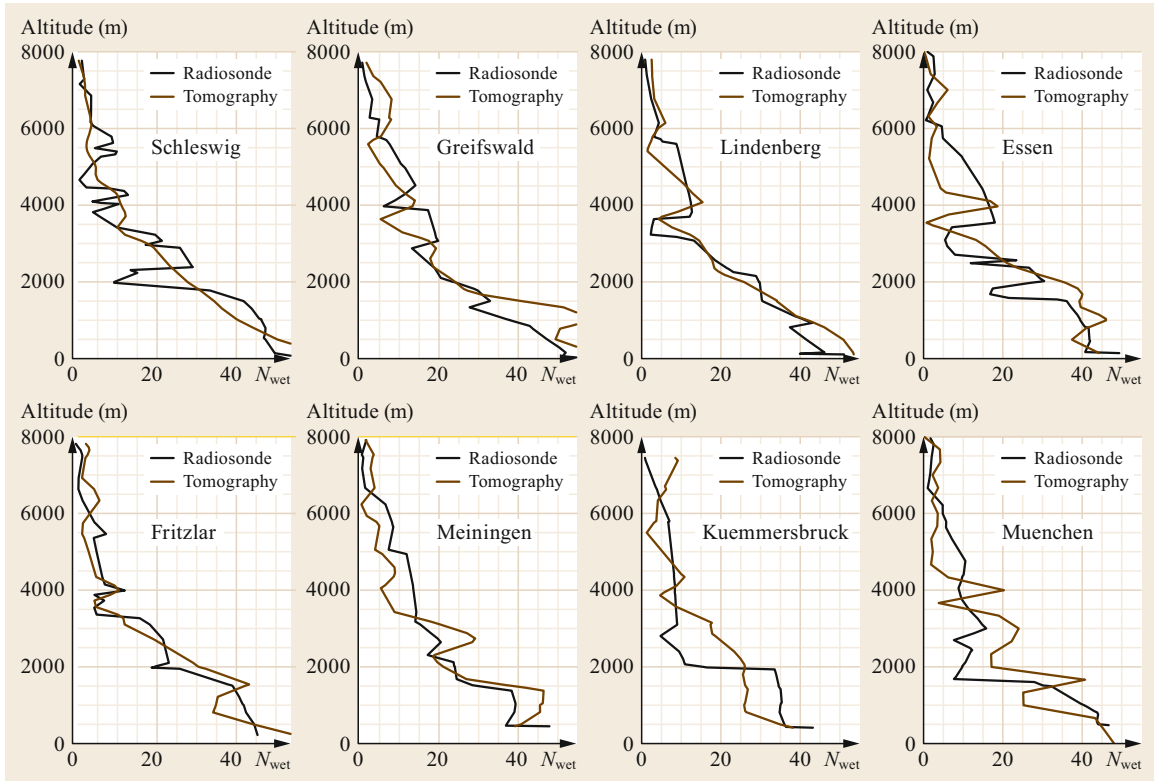


Fig. 36.6 Tomography profiles (brown) interpolated on the observations of some German radiosonde stations (black). The profiles were observed at 14.07.2009, 12:00 UTC

36.9 Future Developments

GNSS atmosphere sounding and GNSS tomography are fields of active research that are developing rapidly. Currently, four satellite positioning systems with more than 120 satellites are available. When Galileo and Bei-Dou become fully operational, more than 30 satellites will be visible at any time and any station. This will lead to about three times more STDs and a much better spatial coverage of the atmosphere than GPS alone. With the new satellites, additional frequencies and signals of improved quality became available and accelerated the development of advanced multi-GNSS receivers. In parallel, more sophisticated multi-GNSS processing techniques have been developed and will be further improved, leading to atmospheric GNSS products of increasing quality.

New processing strategies allow realtime processing of the raw GNSS observations, including atmospheric products, and STDs may in the near future be available within a few minutes. First realtime systems

are already running, and the quality is approaching the quality of currently operational near realtime systems with delays of about 30 min.

In the last decade, the number of national weather services that use GNSS atmosphere products increased constantly and created a common interest with geodetic research. Programs like E-GVAP (egvap.dmi.dk), which combine the efforts of meteorological and geodetic research to improve weather forecasts, are very successful and promote further cooperation. Up to now, the main focus was on cooperation with existing geodetic network providers in order to get access to the GNSS observations. In future, new GNSS networks especially designed for atmosphere sounding might be established.

A combination of these efforts might in the near future lead to nation-wide realtime tomography systems that provide 3-D humidity fields with a high spatial and temporal resolution.

36.10 Further Reading

GPS/GNSS:

- E. Kaplan, C. Hegarty: *Understanding GPS/GNSS: Principles and Applications*, 3rd edn. (Artech House, 2017)
- B. Hofmann-Wellenhof, H. Lichtenegger, E. Wasle: *GNSS – Global Navigation Satellite Systems: GPS, GLONASS, Galileo, and more* (Springer, 2008)
- S. Jin, E. Cardellach, F. Xie: *GNSS Remote Sensing: Theory, Methods and Applications* (Springer, 2016)

Inverse problems and tomography:

- R.C. Aster, B. Borchers, C.H. Thurber: *Parameter Estimation and Inverse Problems*, 2nd edn. (Academic Press, 2012)
- C.D. Rodgers: *Inverse Methods for Atmospheric Sounding: Theory and Practice* (World Scientific, 2000)
- A. Doicu, T. Trautmann, F. Schreier: *Numerical Regularization for Atmospheric Inverse Problems* (Springer, 2010)
- B.P. Gibbs: *Advanced Kalman Filtering, Least-Squares and Modelling* (Wiley, 2011)

References

- 36.1 M. Bevis, S. Businger, T.A. Herring, C. Rocken, R.A. Anthes, R.H. Ware: GPS meteorology: Remote sensing of atmospheric water vapor using the Global Positioning System, *J. Geophys. Res.* **97**(D14), 15787–15801 (1992)
- 36.2 L. Cucurull, F. Vandenberghe, D. Barker, E. Vilaclara, A. Rius: Three-dimensional variational data assimilation of ground-based GPS ZTD and meteorological observations during the 14 December 2001 storm event over the western Mediterranean Sea, *Mon. Weather Rev.* **132**(3), 749–763 (2004)
- 36.3 J. Douša: Towards an operational near real-time precipitable water vapor estimation, *Phys. Chem. Earth A* **26**(3), 189–194 (2001)
- 36.4 H.E. Fleming: Satellite remote sensing by the technique of computed tomography, *J. Appl. Meteorol.* **21**(10), 1538–1549 (1982)
- 36.5 R.H. Ware, D.W. Fulker, S.A. Stein, D.N. Anderson, S.K. Avery, R.D. Clark, K.K. Droegemeier, J.P. Kuetner, J.B. Minster, S. Sorooshian: Suominet: A real-time national GPS network for atmospheric research and education, *Bull. Am. Meteorol. Soc.* **81**(4), 677–694 (2000)
- 36.6 J. Braun, C. Rocken, C. Meertens, R. Ware: Development of a Water Vapor Tomography System Using Low Cost L1 GPS Receivers. In: *Nineth ARM Science Team Meet. Proc* (ARM, San Antonio 1999)
- 36.7 U. Foelsche: *Tropospheric Water Vapor Imaging by Combination of Ground-based and Spaceborn GNSS Sounding Data*, Wissenschaftlicher Bericht No. 10 (Karl-Franzens-Universität, Graz 1999)
- 36.8 A. Flores, G. Ruffini, A. Rius: 4D tropospheric tomography using GPS slant wet delays, *Ann. Geophys.* **18**(2), 223–234 (2000)
- 36.9 K. Hirahara: Local GPS tropospheric tomography, *Earth Planets Space* **52**, 935–939 (2000)
- 36.10 H. Seko, S. Shimada, H. Nakamura, T. Kato: Three-dimensional distribution of water vapor estimated from tropospheric delay of GPS data in a mesoscale precipitation system of the Baiu front, *Earth Planets Space* **52**(11), 927–933 (2000)
- 36.11 G. Guerova, J. Jones, J. Dousa, G. Dick, S. de Haan, E. Pottiaux, O. Bock, R. Pacione, G. Elgered, H. Vedel, M. Bender: Review of the state-of-the-art and future prospects of the ground-based GNSS meteorology in Europe, *Atmos. Meas. Tech.* **9**(11), 5385–5406 (2016)
- 36.12 Z. Adavi, M. Mashhadi-Hossainali: 4D-tomographic reconstruction of water vapor using the hybrid regularization technique with application to the North West of Iran, *Adv. Space Res.* **55**(7), 1845–1854 (2015)
- 36.13 A.E. MacDonald, Y. Xie, R.H. Ware: Diagnosis of three-dimensional water vapor using a GPS network, *Mon. Weather Rev.* **130**(2), 386–397 (2002)
- 36.14 H. Brenot, J. Neméghaire, L. Delobbe, N. Clerbaux, P.D. Meutter, A. Deckmyn, A. Delcloo, L. Frappez, M.V. Roozendaal: Preliminary signs of the initiation of deep convection by GNSS, *Atmos. Chem. Phys.* **13**, 5425–5449 (2013)
- 36.15 M. Bender, G. Dick, M. Ge, Z. Deng, J. Wickert, H.-G. Kahle, A. Raabe, G. Tetzlaff: Development of a GNSS water vapor tomography system using algebraic reconstruction techniques, *Adv. Space Res.* **47**(10), 1704–1720 (2011)
- 36.16 M. Troller, A. Geiger, E. Brockmann, H.-G. Kahle: Determination of the spatial and temporal variation of tropospheric water vapour using CGPS networks, *Geophys. J. Int.* **167**(2), 509–520 (2006)
- 36.17 P.C. Hansen: *Rank-Deficient and Discrete Ill-posed Problems* (SIAM, Salt Lake City 1998)
- 36.18 A.C. Kak, M. Slaney: *Principles of Computerized Tomographic Imaging* (IEEE Press, New York 1999)

- 36.19 F. Natterer: *The Mathematics of Computerized Tomography* (SIAM, Philadelphia 2001)
- 36.20 A. Tarantola: *Inverse Problem Theory and Methods for Model Parameter Estimation* (SIAM, Salt Lake City 2005)
- 36.21 W. Menke: *Geophysical Data analysis: Discrete Inverse Theory*, International Geophysics Series (Academic Press, Cambridge 1989)
- 36.22 J.M. Aparicio, S. Laroche: An evaluation of the expression of the atmospheric refractivity for GPS signals, *J. Geophys. Res.* **116**, D11104 (2011)
- 36.23 G.T. Thayer: An improved equation for the radio refractive index of air, *Radio Sci.* **9**(10), 803–807 (1974)
- 36.24 E.K. Smith, S. Weintraub: The constants in the equation for atmospheric refractive index at radio frequencies, *J. Res. Natl. Inst. Stand.* **50**(1), 39–41 (1953)
- 36.25 M. Bevis, S. Businger, S. Chiswell, T.A. Herring, R.A. Anthes, C. Rocken, R.H. Ware: GPS meteorology: Mapping zenith wet delays onto precipitable water, *J. Appl. Meteorol.* **33**(3), 379–386 (1994)
- 36.26 J.M. Rüeger: Refractive index formulae for radio waves. In: *FIG XXII Int. Congr.* (International Federation of Surveyors (FIG), Washington D.C. 2002)
- 36.27 National Oceanic and Atmospheric Administration: *U.S. Standard Atmosphere, 1976 NOAA-S/T 76-1562* (NOAA, Washington D.C. 1976)
- 36.28 G. Petit, B. Luzum (Eds.): *IERS Conventions*, IERS Technical Note No. 36 (Verlag des Bundesamts für Kartographie und Geodäsie, Frankfurt a. M. 2010) pp. 132–150
- 36.29 J. Saastamoinen: Atmospheric correction for the troposphere and stratosphere in radio ranging of satellites. In: *The Use of Artificial Satellites for Geodesy*, Geophysical Monograph Series, Vol. 15, ed. by S.W. Henriksen, A. Mancini, B.H. Chovitz (AGU, Washington, D.C. 1972) pp. 247–251
- 36.30 J. Davis, T. Herring, I. Shapiro, A. Rogers, G. Elgered: Geodesy by radio interferometry: Effects of atmospheric modeling errors on estimates of baseline length, *Radio Sci.* **20**(6), 1593–1607 (1985)
- 36.31 J. Boehm, A. Niell, P. Tregoning, H. Schuh: Global Mapping Function (GMF): A new empirical mapping function based on numerical weather model data, *Geophys. Res. Lett.* **33**, L07304 (2006)
- 36.32 V. de Brito Mendes: *Modeling the Neutral-Atmosphere Propagation Delay in Radiometric Space Techniques*, Tech. Rep. No. 199 (Univ. New Brunswick, Fredericton 1999)
- 36.33 A.E. Niell: Global mapping functions for the atmosphere delay at radio wavelengths, *J. Geophys. Res.* **101**(B2), 3227–3246 (1996)
- 36.34 J. Askne, H. Nordius: Estimation of tropospheric delay for microwaves from surface weather data, *Radio Sci.* **22**(3), 379–386 (1987)
- 36.35 B. Hofmann-Wellenhof, H. Lichtenegger, J. Collins: *Global Positioning System – Theory and Practise*, 2nd edn. (Springer, Vienna 1993)
- 36.36 J. Saastamoinen: Contributions to the theory of atmospheric refraction Part II. Refraction corrections in satellite geodesy, *Bull. Geod.* **107**, 13–34 (1973)
- 36.37 H. Brenot, V. Ducrocq, A. Walpersdorf, C. Champollion, O. Caumont: GPS zenith delay sensitivity evaluated from high-resolution numerical weather prediction simulations of the 8–9 September 2002 flash flood over southeastern France, *J. Geophys. Res.* **111**, D15105 (2006)
- 36.38 P.E. Gill, G.F. Miller: An algorithm for the integration of unequally spaced data, *Comput. J.* **15**(1), 80–83 (1972)
- 36.39 W.H. Press, S.A. Teukolsky, W.T. Vetterling, B.P. Flannery: *Numerical Recipes in Fortran 90*, Vol. 1, 2nd edn. (Cambridge Univ. Press, New York 2002)
- 36.40 D. Perler, A. Geiger, F. Hurter: 4D GPS water vapor tomography: New parameterized approaches, *J. Geod.* **85**(8), 539–550 (2011)
- 36.41 R. Eresmaa, H. Järvinen: An observation operator for ground-based GPS slant delays, *Tellus A* **58**, 131–140 (2006)
- 36.42 F. Zus, M. Bender, Z. Deng, G. Dick, S. Heise, M. Shang-Guan, J. Wickert: A methodology to compute GPS slant total delays in a numerical weather model, *Radio Sci.* **47**, RS2018 (2012)
- 36.43 V.E. Kunitsyn, E.D. Tereshchenko: *Ionospheric Tomography* (Springer, Berlin, Heidelberg 2010)
- 36.44 G. Welch, G. Bishop: *An Introduction to the Kalman Filter*, SIGGRAPH 2001, Course 8 (Univ. North Carolina, Chapel Hill 2001)
- 36.45 W. Rohm, K. Zhang, J. Bosy: Limited constraint, robust Kalman filtering for GNSS troposphere tomography, *Atmos. Meas. Tech.* **7**(5), 1475–1486 (2014)
- 36.46 M. Bender, A. Raabe: Preconditions to ground-based GPS water vapour tomography, *Ann. Geophys.* **25**(8), 1727–1734 (2007)
- 36.47 A. Carrassi, M. Bocquet, L. Bertino, G. Evensen: Data assimilation in the geosciences: An overview of methods, issues, and perspectives, *WIREs Climate Change* **9**, 1757–7780
- 36.48 F. Hurter, O. Maier: Tropospheric profiles of wet refractivity and humidity from the combination of remote sensing datasets and measurements on the ground, *Atmos. Meas. Tech.* **6**, 3083–3098 (2013)
- 36.49 R. Odolinski, P.J.G. Teunissen: Single-frequency, dual-GNSS versus dual-frequency, single-GNSS: A low-cost and high-grade receivers GPS-BDS RTK analysis, *J. Geod.* **90**(11), 1255–1278 (2016)
- 36.50 Z. Deng, M. Bender, G. Dick, M. Ge, J. Wickert, M. Ramatschi, X. Zou: Retrieving tropospheric delays from GPS networks densified with single frequency receivers, *Geophys. Res. Lett.* **36**, L19802 (2009)
- 36.51 Z. Deng, M. Bender, F. Zus, M. Ge, G. Dick, M. Ramatschi, J. Wickert, U. Löhnert, S. Schön: Validation of tropospheric slant path delays derived from single and dual frequency GPS receivers, *Radio Sci.* **46**, RS6007 (2011)
- 36.52 P.J.G. Teunissen, O. Montenbruck (Eds.): *Springer Handbook of Global Navigation Satellite Systems* (Springer, Cham 2017)
- 36.53 G. Seeber: *Satellite Geodesy*, 2nd edn. (de Gruyter, Berlin, New York 2003)

- 36.54 T. Hobiger, N. Jakowski: Atmospheric signal propagation. In: *Springer Handbook of Global Navigation Satellite Systems*, ed. by P.J. Teunissen, O. Montenbruck (Springer, Cham 2017) pp. 165–193
- 36.55 G. Elgered, J. Wickert: Monitoring of the neutral atmosphere. In: *Springer Handbook of Global Navigation Satellite Systems*, ed. by P.J.G. Teunissen, O. Montenbruck (Springer, Cham 2017) pp. 1109–1133
- 36.56 G. Gendt, G. Dick, W. Söhne: GFZ Analysis Center of IGS – Annual report 1998. In: *IGS 1998 Technical Reports*, ed. by K. Gowey, R. Neilan, A. Moore (IGS, Pasadena 1999) pp. 79–87
- 36.57 R. Dach, S. Lutz, P. Walser, P. Fridez: *Bernese GNSS Software Version 5.2* (Univ. Bern, Bern 2015)
- 36.58 J. Braun, C. Rocken, R. Ware: Validation of line-of-sight water vapor measurements with GPS, *Radio Sci.* **36**(3), 459–472 (2001)
- 36.59 J.F. Zumberge, M.B. Hefflin, D.C. Jefferson, M.M. Watkins, F.H. Webb: Precise point positioning for the efficient and robust analysis of GPS data from large networks, *J. Geophys. Res.* **102**(B3), 5005–5018 (1997)
- 36.60 J. Kouba, F. Lahaye, P. Tétreault: Precise point positioning. In: *Springer Handbook of Global Navigation Satellite Systems*, ed. by P.J.G. Teunissen, O. Montenbruck (Springer, Cham 2017) pp. 723–751
- 36.61 J. Jones, G. Guerova, J. Douša, G. Dick, S. de Haan, E. Pottiaux, O. Bock, R. Pacione, R. van Malderen (Eds.): *COST Action 1206 Final Report – Advanced Global Navigation Satellite Systems Tropospheric Products for Monitoring Severe Weather Events and Climate* (Springer, Cham 2018)
- 36.62 G. Dick, G. Gendt, C. Reigber: First experience with near real-time water vapor estimation in a German GPS network, *J. Atmos. Sol. Terr. Phys.* **63**(12), 1295–1304 (2001)
- 36.63 G. Gendt, G. Dick, C. Reigber, M. Tomassini, Y. Liu, M. Ramatschi: Near real time GPS water vapor monitoring for numerical weather prediction in Germany, *J. Meteorol. Soc. Japan* **82**(1B), 361–370 (2004)
- 36.64 M. Ge, G. Gendt, G. Dick, F.P. Zhang, M. Rothacher: A new data processing strategy for huge GNSS global networks, *J. Geod.* **80**(4), 199–203 (2006)
- 36.65 P.M.V. Subbarao, P. Munshi, K. Muralidhar: Performance of iterative tomographic algorithms applied to non-destructive evaluation with limited data, *NDT & E International* **30**(6), 359–370 (1997)
- 36.66 R. Notarpietro, M. Cucca, M. Gabella, G. Venuti, G. Perona: Tomographic reconstruction of wet and total refractivity fields from GNSS receiver networks, *Adv. Space Res.* **47**(5), 769–912 (2011)
- 36.67 M. Bender, R. Stosius, F. Zus, G. Dick, J. Wickert, A. Raabe: GNSS water vapour tomography – Expected improvements by combining GPS, GLONASS and Galileo observations, *Adv. Space Res.* **47**(5), 886–897 (2011)
- 36.68 W. Rohm: The ground GNSS tomography – Unconstrained approach, *Adv. Space Res.* **51**(3), 501–513 (2013)
- 36.69 A. Flores, J.-G. de Arellano, L.P. Gradinarsky, A. Rius: Tomography of the lower troposphere using a small dense network of GPS receivers, *IEEE Trans. Geosci. Remote Sens.* **39**(2), 439–447 (2001)
- 36.70 J.V. Baelen, M. Reverdy, F. Tridon, L. Labbouz, G. Dick, M. Bender, M. Hagen: On the relationship between water vapour field evolution and the life cycle of precipitation systems, *Q. J. R. Meteorol. Soc.* **137**(S1), 204–223 (2011)
- 36.71 H. Brenot, A. Walpersdorf, M. Reverdy, J. van Baelen, V. Ducrocq, C. Champollion, F. Masson, E. Doerflinger, P. Collard, P. Giroux: A GPS network for tropospheric tomography in the framework of the Mediterranean hydrometeorological observatory Cévennes-Vivarais (southeastern France), *Atmos. Meas. Tech.* **7**, 553–578 (2014)
- 36.72 P. Benevides, J. Catalao, P. Miranda: Experimental GNSS tomography study in Lisbon (Portugal), *Fis. Tierra* **26**, 65–79 (2014)
- 36.73 S. de Haan: *Meteorological Applications of a Surface Network of Global Positioning System Receivers*, Ph.D. Thesis (Wageningen Univ., Wageningen 2008)
- 36.74 P. Benevides, J. Catalao, G. Nico, P.M.A. Miranda: 4D wet refractivity estimation in the atmosphere using GNSS tomography initialized by radiosonde and AIRS measurements: Results from a 1-week intensive campaign, *GPS Solutions* **22**, 91 (2018)
- 36.75 S.J. Julier, J.J. LaViola: On Kalman filtering with nonlinear equality constraints, *IEEE Trans. Signal Process.* **55**(6), 2774–2784 (2007)
- 36.76 T. Ning, J. Wang, G. Elgered, G. Dick, J. Wickert, M. Bradke, M. Sommer, R. Querel, D. Smale: The uncertainty of the atmospheric integrated water vapour estimated from GNSS observations, *Atmos. Meas. Tech.* **9**(1), 79–92 (2016)
- 36.77 O. Bock, P. Willis, J. Wang, C. Mears: A high-quality, homogenized, global, long-term (1993–2008) DORIS precipitable water data set for climate monitoring and model verification, *J. Geophys. Res.* **119**(12), 7209–7230 (2014)
- 36.78 K. Teke, T. Nilsson, J. Böhm, T. Hobiger, P. Steigenberger, S. García-Espada, R. Haas, P. Willis: Troposphere delays from space geodetic techniques, water vapor radiometers, and numerical weather models over a series of continuous VLBI campaigns, *J. Geod.* **87**(10), 981–1001 (2013)
- 36.79 T. Ning, R. Haas, G. Elgered, U. Willén: Multi-technique comparisons of 10 years of wet delay estimates on the west coast of Sweden, *J. Geod.* **86**(7), 565–575 (2012)
- 36.80 M. Kačmařík, J. Douša, J. Zapletal: Comparison of GPS slant wet delays acquired by different techniques, *Acta Geodyn. Geomater.* **9**(4), 427–433 (2012)
- 36.81 R.V. Malderen, H. Brenot, E. Pottiaux, S. Beirle, C. Hermans, M.D. Mazière, T. Wagner, H.D. Backer, C. Bruyninx: A multi-site intercomparison of integrated water vapour observations for climate change analysis, *Atmos. Meas. Tech.* **7**(8), 2487–2512 (2014)
- 36.82 M. Shangguan, S. Heise, M. Bender, G. Dick, M. Ramatschi, J. Wickert: Validation of GPS atmospheric

- water vapor with WVR data in satellite tracking mode, *Ann. Geophys.* **33**(1), 55–61 (2015)
- 36.83 M. Kačmařík, J. Douša, G. Dick, F. Zus, H. Brenot, G. Möller, E. Pottiaux, J. Kapłon, P. Hordyniec, P. Václavovic, L. Morel: Inter-technique validation of tropospheric slant total delays, *Atmos. Meas. Tech.* **10**, 2183–2208 (2017)
- 36.84 M. Shangguan, M. Bender, M. Ramatschi, G. Dick, J. Wickert, A. Raabe, R. Galas: GPS tomography: Validation of reconstructed 3-D humidity fields with radiosonde profiles, *Ann. Geophys.* **31**(9), 1491–1505 (2013)

Michael Bender

FE12 Datenassimilation
German Meteorological Service (DWD)
Offenbach, Germany
michael.bender@dwd.de



Michael Bender is a member of the data assimilation group of the German Meteorological Service (DWD) and works on the assimilation of GNSS atmospheric products and satellite observations into numerical weather models. Previously he was active in the field of GNSS atmosphere sounding and GNSS tomography.

Galina Dick

GFZ German Research Centre for
Geosciences, Department 1: Geodesy
Helmholtz Centre Potsdam
Potsdam, Germany
galina.dick@gfz-potsdam.de



Galina Dick is Group Leader of the GNSS Meteorology at the German Research Center for Geosciences GFZ in Potsdam, Head of the GFZ GNSS Analysis Center for E-GVAP (The EUMETNET GNSS Water Vapor Program) and responsible for the GNSS processing within the GCOS Reference Upper-Air Network (GRUAN). She is a member of several expert teams and working groups related to GNSS atmosphere sounding.

Remote Sensing Part D

Part D Remote Sensing Techniques (Space- and Aircraft-Based)

37 **Satellite and Aircraft Remote Sensing Platforms**

Manfred Wendisch, Leipzig, Germany
André Ehrlich, Leipzig, Germany
Peter Pilewskie, Boulder, USA

38 **Airborne Lidar**

Martin Wirth, Weßling, Germany

39 **Airborne Radar**

Martin Hagen, Weßling, Germany
Julien Delanoë, Guyancourt, France
Scott Ellis, Boulder, USA
Florian Ewald, Weßling, Germany
Jeffrey French, Laramie, USA
Samuel Haimov, Laramie, USA
Gerald Heymsfield, Greenbelt, USA
Andrew L. Pazmany, Amherst, USA

40 **Airborne Solar Radiation Sensors**

K. Sebastian Schmidt, Boulder, USA
Manfred Wendisch, Leipzig, Germany
Bruce Kindel, Boulder, USA

41 **Spaceborne Microwave Radiometry**

Susanne Crewell, Köln, Germany
Catherine Prigent, Paris, France
Mario Mech, Köln, Germany

42 **Imaging Techniques**

Jan Cermak, Karlsruhe, Germany
Isabel F. Trigo, Lisboa, Portugal
Julia Fuchs, Karlsruhe, Germany

37. Satellite and Aircraft Remote Sensing Platforms

Manfred Wendisch , André Ehrlich , Peter Pilewskie 

Instrumented satellites and high/mid-altitude research aircraft equipped with remote sensors are used to derive dynamic, thermodynamic, chemical, and radiative properties of the atmosphere, as well as to characterize atmospheric components (gases, aerosol particles, clouds, and precipitation) and surface properties (e.g., albedo, reflectivity, and temperature). This chapter provides an overview of these air- and spaceborne sensing platforms, especially those that are currently operational. The basic principles of satellite orbits are introduced, some historical milestones in the development of satellite and aircraft platforms for Earth observations are summarized, and special issues and requirements relating to spaceborne and airborne sampling are outlined. Two concise tables included in the chapter are particularly informative. As well as listing the agencies that currently operate Earth observation satellites, Table 37.2 provides detailed information on some of those satellites, such as their orbits and launch dates, selected remote sensing instruments carried

by the satellites, and parameters that are measured or retrieved by them. Furthermore, the table presents some links to more detailed information on current Earth remote sensing satellites. Table 37.3 provides similar information for research aircraft that are utilized to measure atmospheric and surface properties.

37.1	Principles of Platforms	1054
37.2	History	1054
37.3	Issues and Instrumental Requirements	1056
37.4	Available Platforms for Active and Passive Remote Sensing	1056
37.4.1	Satellite Platforms	1057
37.4.2	Aircraft Platforms	1057
37.5	Future Development	1057
37.6	Further Reading	1065
	References	1065

Satellites and aircraft can be used as platforms for instruments to observe the atmosphere and surface of the Earth. These instrumented airborne and spaceborne platforms have revolutionized Earth observations and driven the development of improved remote sensing instruments. The increased use of satellite observations has in turn created a demand for research aircraft with in-situ and remote sensing instruments that can supplement and validate the satellite observations. In this chapter, we present an overview of most of the currently operational spaceborne and aircraft-based measurement platforms equipped with remote sensing instrumentation that are used to derive atmospheric dynamic and state properties, radiative, chemical, and other atmospheric parameters,

and characteristics of the Earth's surface. We restrict our summary to facilities that provide a global view of the Earth system, so we do not discuss:

- Low-flying or ultralight aircraft (i.e., with a single seat, a weight of less than 120 kg, and a top speed of less than 100 km h⁻¹) with ceiling altitudes of less than about 4 km
- Tethered or free balloons
- Unmanned (remotely controlled) aerial vehicles
- Helicopters.

This allows us to focus on remote sensing platforms on satellites and high/mid-altitude aircraft.

Table 37.1 General characteristics of meteorological satellites and research aircraft

	Meteorological satellites		Research aircraft	
	Geosynchronous (e.g., geostationary)	Low Earth orbit (e.g., Sun-synchronous)	Pressurized	Unpressurized
Application	Operational weather forecasts and (increasingly) research	Research and operational	Mostly research; partly for data assimilation into synoptic models	
Altitude (km)	35 800	300–1000	≥ 4	< 4

37.1 Principles of Platforms

Satellites are essential for obtaining a global picture of the Earth system. Spaceborne observations of the Earth are performed from two primary types of satellite orbits: geosynchronous and low Earth orbits.

Geosynchronous satellites orbit the Earth at an altitude of approximately 35 800 km. Each orbit takes one sidereal day (23 h, 56 min, and 4 s), so the satellite moves at a speed that matches the Earth's rotation. Geostationary satellites, a special type of geosynchronous satellite, orbit the Earth in its equatorial plane or at a low angle of inclination (relative to the equatorial plane) above a fixed location on the Earth, so they are ideal for observing diurnal cycles in a specific region. Most currently operational meteorological satellites are geostationary and observe the Earth at different longitudes. They are mostly used to forecast weather, but they are increasingly being utilized in research too.

Low-Earth-orbit satellites are found at altitudes of 300–1000 km. In a special type of low Earth orbit called a *Sun-synchronous orbit*, the satellite passes over a given point on the Earth's surface at the same local mean solar time each day. Satellites in Sun-synchronous orbits circle the Earth in 90–103 min at high angles of inclination of 96–99°, meaning that they pass close to the poles (i.e., a Sun-synchronous orbit is almost a po-

lar orbit around the Earth). A Sun-synchronous orbit is characterized by constant illumination of the Earth on the day side of the orbit, which ensures repeatable solar illumination during specific seasons. Because a Sun-synchronous orbit does not pass directly over the poles, it is difficult for a satellite in such an orbit to acquire data for the central polar regions if it has fixed nadir-viewing instruments. For most Sun-synchronous satellites that perform 14–16 orbits daily, full Earth coverage is achieved anywhere from twice a day to once every 16 days, depending on the scan width of the sensor.

Research aircraft can be categorized into pressurized platforms (with a ceiling altitude of more than 4 km) and unpressurized platforms (low-flying; a ceiling of less than 4 km). Certain complications are encountered when installing sensors within a pressurized aircraft cabin; for instance, the instruments will need to be sealed to avoid drawing in cabin air that will contaminate samples of the free atmosphere. Our discussion of research aircraft is restricted to pressurized high-altitude (above 9 km) platforms and partially-pressurized mid-altitude (between 4 and 9 km) platforms. Table 37.1 lists some of the main characteristics of satellites and aircraft that are used for meteorological observations and research.

37.2 History

A comprehensive overview of the history of Earth observations by satellites is given in [37.1], and the history of aircraft-based measurements is provided in several chapters of [37.2]. The first aerial photographs were probably taken by the French photographer Gaspard Félix Tournachon (1820–1910) at an altitude of about 80 m over Paris on 23 October 1858. Tethered balloon observations were also performed for military purposes during the US Civil War (1861–1865). Airplanes were used to take photos of the Earth's surface during both World Wars. The first cloud photographs were obtained

at altitudes of 110–165 km using rockets built by the US military and the Soviet Union in 1947. Color infrared photography was used for the first time after World War II. The Soviet Union launched the first satellite (Sputnik 1, designed by Sergei Pavlovich Korolev) on 4 October 1957. The US followed with its first satellite, Explorer 1, launched on 31 January 1958. The first weather satellite, Vanguard 2, followed in 1959, although it had limited success. The Television InfraRed Observation Satellite (TIROS-I), launched on 1 April 1960, was the first low-Earth orbit, Sun-synchronous

meteorological satellite. Today there are hundreds of Sun-synchronous satellites in orbit [37.3].

The first geostationary satellite, the Applications Technology Satellite (ATS), was launched on 7 December 1966; it operated for six years. This was followed by a series of six spacecraft launched by the National Aeronautics and Space Agency (NASA) in collaboration with the National Oceanic and Atmospheric Administration (NOAA). In 1974, the Synchronous Meteorological Satellite-1 (SMS-1) became the first operational satellite for measuring meteorological conditions to enter geostationary orbit. SMS-2 followed in 1975 to complement SMS-1. The first Geostationary Operational Environmental Satellite (GOES-1) was launched on 16 October 1975. The first satellites of the GOES series were spin-stabilized and viewed the Earth only 10% of the time; they were in operation from 1975 until 1994. From 1994 on, the GOES series of spacecraft employed three-axis stabilization. GOES-8, the first of those spacecraft, was launched on 13 April 1994. GOES-9 through GOES-12 were launched between 1994 and 2001. These three-axis stabilized satellites were capable of viewing the Earth 100% of the time, continuously acquiring images and atmospheric soundings. GOES-13, launched on 24 May 2006, was the first of the subsequent generation of GOES spacecraft with an advanced attitude control system that uses star trackers and a spacecraft optical bench and has improved instrument pointing performance. Currently, GOES-15 (also called GOES-P) operates as GOES-West and GOES-16 (GOES-R) as GOES-East, in reference to continental North America. The latest in the series, GOES-17 (GOES-S), was launched on 1 March 2018. GOES-T and GOES-U are scheduled for launch in 2020 and 2025, respectively.

Landsat is one of the longest-running programs for acquiring Earth imagery from space. On 23 July 1972, the first Earth Resources Technology Satellite (ERTS-1) was launched. Follow-up satellites in this series were eventually renamed to Landsat. The most recent satellite in this series, Landsat 8, was launched on 11 February 2013.

In Europe, the European Space Agency (ESA) and the European Organisation for the Exploitation of Meteorological Satellites (EUMETSAT) operate geostationary satellites. METEOSAT-1 was launched in November 1977, and METEOSAT-2 was launched in 1981. METEOSAT Second Generation (MSG) is currently operational, and the fourth of the MSG series was launched in 2015. Data continuity will be ensured until the first METEOSAT Third Generation (MTG)

satellites enter service, which is expected to happen in 2022 and 2023. Russia operates the Geostationary Operational Meteorological Satellite (GOMS) series at a longitude of 76° E, first launched in 1994. Three new geostationary spacecraft are planned for operation at longitudes of 14° W, 76° E, and 166° E. Japan utilized the Geostationary Meteorological Satellite (GMS) series at 140° E; the first GMS was launched in 1977, and GMS-5 reached orbit in 1995.

Recent satellite missions by the ESA as part of the EU's Copernicus project include the polar-orbiting Sentinel satellite family. Sentinel-1A was launched in April 2014; Sentinel-1B followed two years later, in April 2016. Both include a C-band synthetic aperture radar (SAR) with a wavelength of 6 cm. Sentinel-2A and B were launched in 2015 and 2017, respectively. They carry a multispectral imaging instrument for high-resolution atmospheric and surface observations, and are considered a continuation of the Landsat program. Sentinel-3A and B (2016, 2018) include different sensors for characterizing land, ocean, and ice surfaces. Sentinel-4 and 5 focus on atmospheric composition measurements. For example, Sentinel-5P (launched in 2017) uses the Tropospheric Monitoring Instrument (TROPOMI) to quantify the atmospheric composition, air pollution, and the ozone layer.

In 1912, *Richard Assmann* (1845–1918) performed the first atmospheric measurements using an aircraft [37.4]. He recorded the atmospheric pressure and temperature up to an altitude of 1100 m. Near-daily temperature soundings by aircraft commenced in the 1920s and continued through World War II. Eventually, these quasi-regular measurements were replaced by routine radiosonde measurements. However, early aircraft profile data were shown to improve synoptic weather forecasts. In 1936, the first aircraft observations of turbulence and thermodynamic properties were carried out in France. In 1944, a series of temperature and humidity soundings of the lowest 300 m of the atmosphere over the ocean were carried out using an aircraft. Further aircraft-based turbulence measurements were conducted in the 1950s. *Wigand* was one of the first to perform cloud measurements from an airborne platform in the early twentieth century [37.5]. Ice crystals were sampled by *Weickman* in 1945 [37.6]. In the 1970s, *Robert Knollenberg* pioneered the development of optical spectrometers to measure the size distributions of cloud and precipitation particles [37.5]. With the development of imaging cameras and spectrometers, as well as radar and lidar, aircraft-borne remote sensing measurements became widespread by the 1980s, and have continued since then.

37.3 Issues and Instrumental Requirements

Spaceborne and aircraft platforms operate in harsh environments, often with rapidly changing conditions, which has consequences for the instruments and the measurements performed on the platforms, and perhaps even the subsequent data analysis. For example, vertical wind or solar radiation measurements from aircraft or satellites require extremely accurate time and position data that are obtained with high frequency in real time for data analysis and interpretation. Therefore, the movement, position, and angular attitude of the quickly moving platform must be measured precisely and then made available immediately during the flight. When performing thermodynamic measurements from an aircraft, corrections must be made for the compressibility of air and dynamic heating. The instruments used must be capable of handling large and sudden pressure variations, as such variations are common (e.g., they occur during take-off and landing). Dramatic temperature changes are possible. Humidification and icing of sensors may occur, especially in the presence of supercooled liquid water clouds. High winds and strong turbulence may occur. Aircraft operation at mid and high altitudes requires fast true air speeds that typically range between 100 and 200 m s⁻¹. As a result, the instruments must have fast response times. The remote sensing devices installed on aircraft need to be robust and insensitive to the mechanical shocks that may occur during take-off and landing; they also need to withstand instant accelerations, heavy vibrations, and sudden altitude and attitude changes. The requirements for satellite sensors are even stricter because they must survive the launch. There are advantages to constructing remote sensing instruments with low weights, volumes,

and power consumptions. This is true for both satellite- and aircraft-mounted sensors. The high measurement sampling rates needed (for both satellite- and aircraft-based instruments) mean that huge amounts of data must be saved.

Aircraft can deliver both in-situ and remote sensing measurements, unlike satellites, which can only provide remote sensing data. The in-situ data are obtained along the track of the aircraft (spaghetti-like or otherwise), but the remote sensing capabilities of an aircraft measurement platform can equal or improve upon (e.g., through better resolution) satellite measurements. Aircraft are also often used for dropping sondes, which are an essential part of both research and operational meteorology.

Aircraft platforms enable data collection at otherwise unreachable altitudes. They also have flexibility in all three spatial dimensions when choosing the flight path. Targeted sampling and Lagrangian measurements can be pursued. Furthermore, detailed process studies can be performed (e.g., characterizing the vertical distribution of cloud particles). Satellite remote sensing measurements can be validated using aircraft platforms. Thus, new satellite sensors are often developed and tested for airborne use before they are launched into space. Satellite sensors are far more sophisticated than aircraft sensors: they need to operate unattended for many years, they must maintain calibration over that period, and they must include systems that can identify sensor degradation. They must also be built to comply with much stricter guidelines which ensure that the sensor will survive the launch load and the harsh radiation that is present in space.

37.4 Available Platforms for Active and Passive Remote Sensing

Remote sensing includes measurements of electromagnetic (EM) radiation, which is the only signal received by satellite sensors. Aircraft measurements may apply both remote sensing and in-situ sampling techniques. Remote sensing is classified as either *passive*, where the natural radiation emitted or scattered by the atmosphere and the Earth's surface is measured, or *active*, where EM waves are emitted by the instrument and the subsequent scattered signal is evaluated. Passive sensors receive either solar EM radiation that has been scattered by atmospheric gases, aerosol particles, hydrometeors, and the Earth's surface, or terrestrial infrared and microwave radiation emitted by atmospheric and surface components. Sensors that actively emit EM radiation and measure the signal that comes back to a receiver

are called active remote sensing instruments (e.g., radar, which is based on microwave radiation, or lidar, which uses solar radiation). Both passive and active sensors evaluate signals in order to retrieve parameters such as air temperature profiles, wind and humidity fields, and aerosol, cloud, and precipitation distributions. Furthermore, the components of the solar and terrestrial radiative energy budget of the climate system are estimated from measurements taken by active and passive sensors installed on satellite and aircraft platforms. All of these applications of remote sensing observations require a detailed knowledge of radiative processes in the atmosphere and the radiative interactions between different components of the climate system.

37.4.1 Satellite Platforms

Table 37.2 provides an overview of the atmospheric and selected surface observation capabilities of the main Earth observation satellites. For more detailed information, the reader is referred to the Observing Systems Capability Analysis and Review Tool (OSCAR), which can be accessed at <https://www.wmo-sat.info/oscar/satellites>, Accessed 12 July 2021. The table only considers satellite platforms that are operated by major international agencies: NASA (see https://eospsa.gsfc.nasa.gov/files/mission_profile.pdf, Accessed 12 July 2021, for the NASA Earth Science Mission Profile) and NOAA from the United States of America (USA) as well as the European Organization for the Exploitation of Meteorological Satellites (EUMETSAT), jointly with the European Space Agency (ESA), from Europe. Today, most of the largest endeavors require close international collaboration. Information included in Table 37.2 includes the satellite constellations, launch years, instrumentation, measured parameters, and some links to further information.

The family of Sun-synchronous A-Train (Afternoon Train or Afternoon Constellation) satellites from NASA fly at an altitude of 705 km along the same orbit. They employ active (lidar, radar) and passive (imag-

ing and polarization spectrometers, limb sounders) remote sensing instruments. Although both CloudSat and CALIPSO are still part of the A-Train, these satellites were both recently (2018) dropped to the same lower orbit, and are now referred to as the *C-Train*. NASA maintains a series of satellites known as the Earth Observing System (EOS), including Terra, Aqua, Aura, and many more. NOAA operates geostationary satellites (GOES) and Sun-synchronous spacecraft such as Jason (which observes hurricanes) and JPSS (partly in collaboration with NASA and other contributors). Europe has a fleet of geostationary (Meteosat) and Sun-synchronous (EPS-MetOp, Sentinel) satellites. Other countries such as Japan, China, and India are also increasingly contributing to the collection of meteorological satellites observing the Earth.

37.4.2 Aircraft Platforms

Table 37.3 lists the main operators of high/mid-altitude aircraft that provide remote sensing observations of atmospheric and, to some extent, surface parameters. The table only considers major agencies and contains information on aircraft types, selected technical parameters, and major instrumentation. It also includes useful links to more detailed information on aircraft facilities.

37.5 Future Development

In January 2018, the Committee on the Decadal Survey for Earth Science and Applications from Space (ESAS) of the US National Academy of Sciences issued the 2017 Decadal Survey [37.16]. This survey also included plans for space-based observations of the Earth by US agencies for the next 10 years.

In Europe, EarthCARE is currently planned for launch in 2022. Its goal is to investigate the role of clouds and aerosol particles in reflecting solar radiation and absorbing/emitting terrestrial thermal infrared radiation. EarthCARE has a prime mission duration of two years. Four major measurement systems are planned: the Atmospheric Lidar (ATLID), Cloud Profiling Radar (CPR), Multispectral Imager (MSI), and Broad Band Radiometer (BBR). The ATLID provides vertical profiles of aerosols and thin clouds. It operates at a wavelength of 355 nm and has a high spectral resolution receiver and a depolarization channel. The CPR is a 94 GHz Doppler radar, while the MSI consists of thermal infrared and visible/near-infrared cameras.

ADM-Aeolus was launched on 22 August 2018. It is the first satellite mission to acquire wind profiles for the Earth on a global scale. The only instrument on this satellite is the Atmospheric Laser Doppler Instrument ALADIN, a lidar that measures the wind in the lowermost 30 km of the atmosphere. ADM-Aeolus is one of the ESA's Earth Explorer missions, which are intended to address key scientific challenges identified by the science community. Besides ADM-Aeolus and EarthCARE, other prominent European missions include: Gravity Field and Steady-State Ocean Circulation Explorer (GOCE), BIOMASS (which carries the first space-based P-band synthetic aperture radar), Soil Moisture and Ocean Salinity (SMOS, launched in 2009), CryoSat-2 (launched in 2010; this measures fluctuations in the thickness of ice on both land and sea), SWARM (launched in 2013; this surveys the geomagnetic field and its temporal evolution), and the Fluorescence Explorer (FLEX) mission (which maps vegetation fluorescence to quantify photosynthetic activity).

Table 37.2 List of operators, constellations, and information on the main satellites currently operated by the US and Europe, including launch years, major instrumentation onboard, measured parameters, and some links to spaceborne applications that perform atmospheric remote sensing, all links Accessed 12 July 2021

Agency, country	Orbit	Satellite	Launch	Remote sensing instrumentation	Measured or retrieved parameters	More information
NASA, USA	Sun-synchronous	Polarization and Anisotropy of Reflectances for Atmospheric Science coupled with Observations from a Lidar (PARASOL) (part of A-Train, Earth Observing System EOS, until 2013) jointly with France	2004	Polarization and Directionality of the Earth's Reflectances (POLDER)	Solar radiation reflected by Earth's atmosphere, including studies of tropospheric aerosols, sea surface reflectance, bidirectional reflectance distribution function of land surfaces, and the Earth Radiation Budget	https://eospspo.nasa.gov/missions/polarization-anisotropy-reflectances-atmospheric-sciences-coupled-observations-lidar https://atrain.nasa.gov/
		Aura (part of A-Train, EOS)	2004	High Resolution Dynamics Limb Sounder (HIRDLS) Microwave Limb Sounder (MLS) Tropospheric Emission Spectrometer (TES) Ozone Monitoring Instrument (OMI)	Infrared limb emission by trace gases and aerosol particles Microwave radiation from ozone-depleting substances Nadir and limb emission by aerosol particles and anthropogenically emitted trace gases Global ozone distribution	https://eospspo.nasa.gov/missions/aura https://atrain.nasa.gov/
		CloudSat (part of A-Train, EOS)	2006	94 GHz Cloud Profiling Radar (CPR)	Cloud macrophysical and microphysical properties	https://eospspo.nasa.gov/missions/cloudsat https://atrain.nasa.gov/ [37.7]
		Cloud-Aerosol Lidar and Infrared Pathfinder Satellite Observation (CALIPSO) (part of A-Train, EOS)	2006	Cloud-Aerosol Lidar with Orthogonal Polarization (CALIOP) Imaging Infrared Radiometer (IIR) Wide Field Camera (WFC)	Vertical aerosol and cloud distribution Spectral radiances, cirrus properties Cloud imagery	https://www-calipso.larc.nasa.gov/ https://atrain.nasa.gov/ [37.7]

Table 37.2 (Continued)

Agency, country	Orbit	Satellite	Launch	Remote sensing instrumentation	Measured or retrieved parameters	More information
NASA, USA	Sun-synchronous	Aqua (part of A-Train, EOS)	2002	Advanced Microwave Sounding Unit (AMSU-A) Atmospheric Infrared Sounder (AIRS) Humidity Sounder for Brazil (HSB) Advanced Microwave Scanning Radiometer-EOS (AMSR-E) Moderate Resolution Imaging Spectroradiometer (MODIS) Clouds and the Earth's Radiant Energy System (CERES) LEOSTar-2 satellite bus	Profiles of temperature and humidity Profiles of temperature and humidity, clouds Humidity profiles Clouds, precipitation, humidity Radiative properties of clouds and aerosols, a variety of other Earth system geophysical parameters Broadband radiation flux densities Carbon dioxide distributions in the atmosphere	https://eosps.nasa.gov/missions/aqua https://atrain.nasa.gov/
		Orbital Carbon Observatory (OCO-2) (part of A-Train, EOS) Terra	2014 1999	Advanced Spaceborne Thermal Emission and Reflection Radiometer (ASTER) Clouds and the Earth's Radiant Energy System (CERES) Multi-angle Imaging SpectroRadiometer (MISR) Moderate-Resolution Imaging Spectroradiometer (MODIS) Measurements of Pollution in the Troposphere (MOPITT) Enhanced Thematic Mapper Plus (ETM+)	Thermal radiances in 14 channels, visible through thermal infrared Broadband radiation flux densities 9 cameras, different observation angles Radiative properties of clouds and aerosols, a variety of other Earth system geophysical parameters Concentrations of methane and CO	https://rsdo.gsfc.nasa.gov/images/catalog/LEOSTar-2.pdf https://eosps.nasa.gov/missions/terra
		Landsat-7	1999	Operational Land Imager (OLI) and the Thermal Infrared Sensor (TIRS)	Land surface properties	https://www.usgs.gov/core-science-systems/hli/landsat
		Landsat-8	2013			https://www.usgs.gov/core-science-systems/hli/landsat

Table 37.2 (Continued)

Agency, country	Orbit	Satellite	Launch	Remote sensing instrumentation	Measured or retrieved parameters	More information
NOAA, USA	Geostationary	GOES-West (GOES-15, -17 GOES-P), 135° W GOES-East (GOES-16, GOES-R) 75.2° W	2010 2016	Imager, Sounder, Solar X-Ray Advanced Baseline Imager (ABI), Solar Ultraviolet Imager (SUI), Extreme ultraviolet (EUV) and X-Ray Irradiance Sensors, Geostationary Lightning Mapper	Weather, clouds, precipitation Aerosol, cloud, land products	https://www.ospo.noaa.gov/Operations/GOES/status.html https://www.goes-r.gov/products/overview.html
	Sun-synchronous	Jason-3	2016	Poseidon-3B Altimeter, Doppler Orbitography and Radiopositioning Integrated by Satellite (DORIS), Advanced Microwave Radiometer-2 (AMR-2)	Hurricane observations, tropical cyclone forecasts	https://www.nesdis.noaa.gov/jason-3/
NOAA and NASA, USA	Sun-synchronous	Joint Polar Satellite System (JPSS), National Polar-orbiting Partnership (Suomi-NPP)	2017	Advanced Technology Microwave Sounder (ATMS), Clouds and the Earth's Radiant Energy System (CERES), Cross-track Infrared Sounder (CRIS), Ozone Mapping and Profiler Suite (OMPS), Visible Infrared Imaging Radiometer Suite (VIIRS)	Sea and land surface temperatures, vegetation, clouds, rainfall, snow and ice cover, fire locations and smoke plumes, atmospheric temperature, water vapor, and ozone	https://www.jpss.noaa.gov/ Suomi NPP https://www.nasa.gov/mission_pages/NPP/main/index.html
EUMETSAT/ESA, Europe	Geostationary	Meteosat MSG (0°)	2002	Spinning Enhanced Visible and Infrared Imager (SEVIRI); twelve channels, eight in thermal infrared Scanning radiometer in the central compartment (GERB)	Permanent visible and infrared imaging of the Earth's disc, with a baseline repeat cycle of 15 min	https://www.eumetsat.int/our-satellites/meteosat-series

Table 37.2 (Continued)

Agency, country	Orbit	Satellite	Launch	Remote sensing instrumentation	Measured or retrieved parameters	More information
EUMETSAT/ESA, Europe	Sun-synchronous	EUMETSAT Polar System (EPS) MetOp-A MetOp-B MetOp-C	2006 2012 2018	Infrared Atmospheric Sounding Interferometer (IASI)	Temperature and humidity profiles	https://www.eumetsat.int/iasi
				Global Ozone Monitoring Experiment-2 (GOME-2) Advanced Scatterometer (ASCAT)	Ozone measurements Wind speed and direction over the ocean	https://www.eumetsat.int/iasi https://www.eumetsat.int/iasi
				Advanced Microwave Sounding Unit-A (AMSU-A) Microwave Humidity Sounder (MHS) Advanced Very High Resolution Radiometer (AVHRR)	Global atmospheric temperature files Atmospheric ice, cloud cover, precipitation, and humidity Cloud cover, sea surface temperature, ice, snow, vegetation cover characteristics	https://www.eumetsat.int/iasi https://www.eumetsat.int/iasi https://www.eumetsat.int/iasi
				GNSS (Global Navigation Satellite System) Receiver for Atmospheric Sounding (GRAS) High-resolution Infrared Radiation Sounder (HIRS/4)	Stratospheric and tropospheric temperature and humidity profiles Vertical profiles of temperature and humidity, cloud cover, cloud top temperature and cloud phase, surface albedo	https://www.eumetsat.int/iasi https://www.eumetsat.int/iasi
		Sentinel-3a/b	2016/ 2018	Ocean and Land Colour Instrument (OLCI) Sea and Land Surface Temperature Radiometer (SLSTR) Synthetic Aperture Radar Altimeter (SRAL)	Sea surface topography and wave height Sea surface temperature Visible and thermal infrared radiances	https://www.eumetsat.int/sentinel-3

Table 37.3 Examples of high/mid-altitude research aircraft used for atmospheric and, to some extent, surface remote sensing purposes (operator acronyms: *AWI* Alfred-Wegener-Institut, Helmholtz-Zentrum für Polar- und Meeresforschung; *DLR* Deutsches Zentrum für Luft- und Raumfahrt; *DOE* Department of Energy; *EMTA* Environmental and Networking Technologies and Applications; *FAAM* Facility for Airborne Atmospheric Measurements; *GFR1* Gromov Flight Research Institute; *GLORIA* Gimballled Limb Observer for Radiance Imaging in the Atmosphere; *GRC* Glenn Research Center; *INCAS* National Institute for Aerospace Research; *INTA* Instituto Nacional de Tecnica Aeroespacial; *MDB* Myasishchev Design Bureau; *NAC* Netherlands Aerospace Centre; *NASA* National Aeronautics and Space Agency; *NCAR* National Center for Atmospheric Research; *NERC* Natural Environment Research Council; *NOAA* National Oceanic and Atmospheric Administration; *NPOESS* National Polar-orbiting Operational Environmental Satellite System; *NSF* National Science Foundation; *PNML* Pacific Northwest National Laboratory; *RAF* Research Aviation Facility; *SAFIRE* Service des Avions Francais Instrumentés pour la Recherche en Environnement), all links Accessed 12 July 2021

Agency, country	Aircraft type (registration number)	Technical parameters		Selected remote sensing instrumentation	More information		
		Ceiling altitude (km)	Range, endurance			Useful payload (t)	
NASA, USA	ER-2	21.3	9260 km 12 h	Airborne Visible/Infrared Imaging Spectrometer (AVIRIS) Enhanced MODIS Airborne Simulator (eMAS) MODIS/ASTER Airborne Simulator (MASTER) Next-Generation Airborne Visible/Infrared Imaging Spectrometer (AVIRIS-NG) NPOESS Airborne Sounder Testbed Interferometer (NAST-I) Cloud Physics Lidar (CPL) High Spectral Resolution Lidar (HSRL) Research Scanning Polarimeter (RSP)	https://airbornescience.nasa.gov/aircraft/ER-2 https://airbornescience.nasa.gov/instrument/facility		
							1.3
							8.8
							30
							6.7
							1.6
	WB-57	18.3	4000 km 6.5 h	AVIRIS MASTER AVIRIS-NG NAST-I MASTER	https://airbornescience.nasa.gov/aircraft/WB-57 https://airbornescience.nasa.gov/instrument/facility		
	DC-8	12.5	10 000 km 12 h 7000 km 14 h	MASTER Cloud Physics Lidar (CPL) High Spectral Resolution Lidar (HSRL) Research Scanning Polarimeter (RSP)	https://airbornescience.nasa.gov/aircraft/DC-8 https://airbornescience.nasa.gov/aircraft/P-3_Orion https://airbornescience.nasa.gov/instrument/facility		
	P-3 Orion	8.5		AVIRIS AVIRIS-NG	https://airbornescience.nasa.gov/aircraft/Twin_Otter_-_GRC https://airbornescience.nasa.gov/instrument/facility		
	Twin Otter – GRC	7.6	830 km 3 h				

Table 37.3 (Continued)

Agency, country	Aircraft type (registration number)	Technical parameters	Useful payload (t)	Selected remote sensing instrumentation	More information
		Ceiling altitude (km)	Range, endurance		
NOAA, USA	Gulfstream IV	12	7000 km 10 h	Tail Doppler radar	http://www.aoml.noaa.gov/hrd/about_hrd/aircraft.html
	Lockheed WP-3D Orion	7.6	4000–6000 km 8.5–10.5 h	Tail Doppler radar Lower fuselage radar	http://www.aoml.noaa.gov/hrd/about_hrd/aircraft.html
	Beechcraft King Air BE350CER (N68RF)	10.7	7–8 h	Digital cameras Multispectral and hyperspectral sensors Lidar	https://www.omao.noaa.gov/learn/aircraft-operations/aircraft/hawker-beechcraft-king-air-350er
	De Havilland DHC-6-300 Twin Otter	7.6	4–6 h	Digital cameras	https://www.omao.noaa.gov/learn/aircraft-operations/aircraft/dehavilland-twin-otter-dhc-6
NSF/NCAR (RAF), USA	Hercules C-130	8.2	5370 km 10 h	C-band Doppler radar Radio altimeter	https://www.eol.ucar.edu/node/139
	High-Performance Instrumented Airborne Platform for Environmental Research (HIAPER) Gulfstream GV	15.5	11 265 km	Cloud radar (millimeter wavelength) High spectral resolution lidar Water vapor differential absorption lidar	https://www.eol.ucar.edu/content/nsfncar-hiaper-0 [37.8]
Univ. of Wyoming, USA	Beechcraft King Air 200T (N2UW)	8.5	4 h	Cloud radar, Lidar	http://flights.uwyo.edu/twka/
PNNL for DOE, USA	Gulfstream-159, G-1	7.5	2800 km 4–5 h		https://www.arm.gov/capabilities/observatories/aaf/manned
FAAM, UK	BAe 146 (G-LUXE)	9.1	3000 km 6 h	Weather Doppler radar Radio altimeter Aerosol lidar	http://www.eufar.net/aircrafts/21
NERC, UK	DHC-6 Twin Otter (VP-FAZ, VP-FBL)	4.6			http://www.eufar.net/aircrafts/84
SAFIRE, France	ATR42 (F-HMTO)	6.4	2200 km 6 h	Broadband radiometer	http://www.eufar.net/aircrafts/41
	Falcon 20 (F-GBTM)	11.9	3200 km 5 h	Broadband radiometer	www.eufar.net/aircrafts/38
ENTA, Greece	Cessna C-208 B Grand Caravan EX (HB-TEN)	4.6	1600–2000 km 7 h	Lidar altimeter Imaging spectrometer Multiband imager	http://www.eufar.net/aircrafts/66

Table 37.3 (Continued)

Agency, country	Aircraft type (registration number)	Technical parameters Ceiling altitude (km)	Range, endurance	Useful payload (t)	Selected remote sensing instrumentation	More information
NAC, Netherlands	Cessna Citation II (PH-LAB)	13.1	3000 km 6 h		Lidar	http://www.eufar.net/aircrafts/16
INCAS, Romania	Hawker Beechcraft King Air C90 GTX (ij2018)	9.1	1200 km 4 h	0.155	Laser scanner	www.eufar.net/aircrafts/86
INTA, Spain	STEMME S15 (EC-LOT)	6.1	1800 km 10 h	0.250		www.eufar.net/aircrafts/87
MDB, Russia	M55—Geophysica (55204)	20.4	2500–3450 km 4–5 h	2	Fourier transform spectrometer (GLORIA)	http://www.eufar.net/aircrafts/31/details/ [37.9]
GFRI, Russia	Tupolev, Tu-154M (RA85317)	12	4000 km 7 h	18		http://www.eufar.net/aircrafts/65 [37.9]
DLR, Germany	HALO Gulfstream G 550 (D-ADLR)	15	10 000 km 8–10 h	3	Aerosol and DIAL-water vapor lidar Ka-band Doppler radar 26-Channel microwave radiometer Passive solar/infrared spectral upward/downward irradiance/radiance, imaging/pointing Fourier transform spectrometer (GLORIA)	https://www.halo.dlr.de/ [37.10, 11]
	Falcon 20E (D-CMET)	12.8	3700 km 5.5 h	1.1	Aerosol lidar Infrared and radar antennas Passive solar/infrared spectral upward/downward irradiance/radiance, imaging/pointing	https://www.dlr.de/pa/en/desktopdefault.aspx/tabid-8857/15304_read-62309/
AWI, Germany	Basler BT-67 Polar 5 (C-GAWI) and Polar 6 (C-GHGF)	7.6	2300 km 6–7 h	2.5	Aerosol lidar 94 GHz radar, microwave radiometer Sun photometer Laser altimeter Passive solar/infrared spectral upward/downward irradiance/radiance, imaging/pointing	https://www.avi.de/en/expedition/aircraft/polar-5-6.html [37.12, 13]
enviscope GmbH, Germany	Learjet 35A (D-CGFD)	13.7	4000 km 5 h	1	Passive solar spectral upward/downward irradiance/radiance	http://www.enviscope.de/enviscope_new/operation/airborne-platforms/learjet-35a [37.14, 15]
Grob Aircraft, Germany	G520T Egret (D-FHHH)	14.9	3000 km 9 h	0.6		http://www.eufar.net/operators/95

37.6 Further Reading

- Kramer, H. J., 2002: *Observations of the earth and its environment: Survey of missions and sensors*. Springer, Berlin Heidelberg
- Wendisch, M., and J.-L. Brenguier (Eds.), 2013: *Airborne Measurements for Environmental Research: Methods and Instruments*. Wiley-VCH Verlag, Weinheim

Acknowledgments. We thank Dr. Steven E. Platnick from the NASA Goddard Space Flight Center (Greenbelt, MD, USA) for his useful comments on Table 37.2.

References

- 37.1 H.J. Kramer: *Observations of the Earth and Its Environment: Survey of Missions and Sensors* (Springer, Berlin, Heidelberg 2002)
- 37.2 M. Wendisch, J.-L. Brenguier (Eds.): *Airborne Measurements for Environmental Research: Methods and Instruments* (Wiley, Berlin 2013)
- 37.3 Pixalytics: How many satellites are orbiting the Earth in 2018? <https://www.pixalytics.com/sats-orbiting-the-earth-2018> (2018), Accessed 12 July 2021
- 37.4 J. Bange, M. Esposito, D.H. Lenschow, P.R.A. Brown, V. Dreiling, A. Giez, L. Mahr, S.P. Malinowsky, A.R. Rodi, R.A. Shaw, H. Siebert, H. Smit, M. Zöger: Measurement of aircraft state and thermodynamic and dynamic variables. In: *Airborne Measurements for Environmental Research: Methods and Instruments*, ed. by M. Wendisch, J.-L. Brenguier (Wiley, Berlin 2013) pp. 7–75
- 37.5 J.-L. Brenguier, W. Bachalo, P.Y. Chuang, B.M. Esposito, J. Fugal, T. Garrett, J.-F. Gayet, H. Gerber, A. Heymsfield, A. Kokhanovsky, A. Korolev, R.P. Lawson, D.C. Rogers, R.A. Shaw, W. Strapp, M. Wendisch: In situ measurements of cloud and precipitation particles. In: *Airborne Measurements for Environmental Research: Methods and Instruments*, ed. by M. Wendisch, J.-L. Brenguier (Wiley, Berlin 2013) pp. 225–301
- 37.6 H. Weickman: Formen und Bildung atmosphärischer Eiskristalle, *Beitr. Phys. Atmos.* **28**, 12–52 (1945)
- 37.7 G. Stephens, D. Winker, J. Pelon, C. Trepte, D. Vane, C. Yuhas, T. L’Ecuyer, M. Lebsock: CloudSat and CALIPSO within the A-train: ten years of actively observing the Earth system, *Bull. Am. Meteorol. Soc.* **99**(3), 569–581 (2018)
- 37.8 K.K. Laursen, D.P. Jorgensen, G.P. Brasseur, S.L. Ustin, J.R. Huning: HIAPER: the next generation NSF/NCAR research aircraft, *Bull. Am. Meteorol. Soc.* **87**, 896–909 (2006)
- 37.9 M.A. Strunin: Investigation of methods of the thermodynamic condition of atmosphere using aircraft-observatory (in Russian) (Central Aerological Observatory) (2020)
- 37.10 M. Wendisch, U. Pöschl, M.O. Andreae, L.A.T. Machado, R. Albrecht, H. Schlager, D. Rosenfeld, S.T. Martin, A. Abdelmonem, A. Afchine, A. Araujo, P. Artaxo, H. Aufmhoff, H.M.J. Barbosa, S. Borrmann, R. Braga, B. Buchholz, M.A. Cecchini, A. Costa, J. Curtius, M. Dollner, M. Dorf, V. Dreiling, V. Ebert, A. Ehrlich, F. Ewald, G. Fisch, A. Fix, F. Frank, D. Fütterer, C. Heckl, F. Heidelberg, T. Hüneke, E. Jäkel, E. Järvinen, T. Jurkat, S. Kanter, U. Kästner, M. Kenntner, J. Kesselmeier, T. Klimach, M. Knecht, R. Kohl, T. Kölling, M. Krämer, M. Krüger, T.C. Krisna, J.V. Lavric, K. Longo, C. Mahnke, A.O. Manzi, B. Mayer, S. Mertes, A. Minikin, S. Molleker, S. Münch, B. Nillius, K. Pfeilsticker, C. Pöhlker, A.-E. Roiger, D. Rose, D. Rosenow, D. Sauer, M. Schnaiter, J. Schneider, C. Schulz, R.A.F. de Souza, A. Spanu, P. Stock, D. Vila, C. Voigt, A. Walsler, D. Walter, R. Weigel, B. Weinzierl, F. Werner, M.A. Yamasoe, H. Ziereis, T. Zinner, M. Zöger: ACRIDICON-CHUVA campaign: studying tropical deep convective clouds and precipitation over Amazonia using the new German research aircraft HALO, *Bull. Am. Meteorol. Soc.* **97**(10), 1885–1908 (2016)
- 37.11 B. Stevens, F. Ament, S. Bony, S. Crewell, F. Ewald, S. Gross, A. Hansen, L. Hirsch, M. Jacob, T. Kölling, H. Konow, B. Mayer, M. Wendisch, M. Wirth, K. Wolf, S. Bakan, M. Bauer-Pfundstein, M. Brueck, J. Delanoe, A. Ehrlich, D. Farrell, M. Forde, F. Gödde, H. Grob, M. Hagen, E. Jäkel, F. Jansen, C. Kleo, M. Klingebiel, M. Mech, G. Peters, M. Rapp, A.A. Wing, T. Zinner: A high-altitude long-range aircraft configured as a cloud observatory – the NARVAL expeditions, *Bull. Am. Meteorol. Soc.* **100**(6), 1061–1077 (2019)
- 37.12 C. Wesche, D. Steinhage, U. Nixdorf: Polar aircraft Polar5 and Polar6 operated by the Alfred Wegener Institute, *J. Large-Scale Res. Facil.* **2**, A87 (2016)
- 37.13 M. Wendisch, A. Macke, A. Ehrlich, C. Lüpkes, M. Mech, D. Chechin, K. Dethloff, C. Barientos, H. Bozem, M. Brückner, H.-C. Clemen, S. Crewell, T. Donth, R. Dupuy, C. Dusny, K. Ebell, U. Egerer, R. Engelmann, C. Engler, O. Eppers, M. Gehrman, X. Gong, M. Gottschalk, C. Gournbeyre, H. Griesche, J. Hartmann, M. Hartmann, B. Heinold, A. Herber, H. Herrmann, G. Heygster, P. Hoor, S. Jafariserajehlou, E. Jäkel, E. Järvinen, O. Jourdan, U. Kästner, S. Kecorius, E.M. Knudsen, F. Köllner, J. Kretschmar, L. Lelli, D. Leroy, M. Maturilli,

- L. Mei, S. Mertes, G. Mioche, R. Neuber, M. Nicolaus, T. Nomokonova, J. Notholt, M. Palm, M. van Pinxteren, J. Quaas, P. Richter, E. Ruiz-Donoso, M. Schäfer, K. Schmieder, M. Schnaiter, J. Schneider, A. Schwarzenböck, P. Seifert, M.D. Shupe, H. Siebert, G. Spreen, J. Stapf, F. Stratmann, T. Vogl, A. Welti, H. Wex, A. Wiedensohler, M. Zanatta, S. Zeppenfeld: The Arctic cloud puzzle: using ALOUD/PASCAL multi-platform observations to unravel the role of clouds and aerosol particles in Arctic amplification, *Bull. Am. Meteorol. Soc.* **100**, 841–871 (2019)
- 37.14 F. Finger, F. Werner, M. Klingebiel, A. Ehrlich, E. Jäkel, M. Voigt, S. Borrmann, P. Spichtinger, M. Wendisch: Spectral optical layer properties of cirrus from collocated airborne measurements and simulations, *Atmos. Chem. Phys.* **16**, 7681–7693 (2016)
- 37.15 M. Klingebiel, A. Ehrlich, F. Finger, T. Röschen-thaler, S. Jakirlić, M. Voigt, S. Müller, R. Maser, M. Wendisch, P. Hoor, P. Spichtinger, S. Borrmann: A tandem approach for collocated measurements of microphysical and radiative cirrus properties, *Atmos. Meas. Tech.* **10**, 3485–3498 (2017)
- 37.16 National Academies of Sciences, Engineering, and Medicine: *Thriving on Our Changing Planet: A Decadal Strategy for Earth Observation from Space* (The National Academies Press, Washington, DC 2018)

Manfred Wendisch

Physics and Earth Sciences
University of Leipzig
Leipzig, Germany
m.wendisch@uni-leipzig.de



Manfred Wendisch is a Professor at the University of Leipzig (Germany) and Director of the Leipzig Institute for Meteorology. He is involved in airborne field observations, studying the influence of clouds on the atmospheric radiative energy budget with a focus on cirrus and Arctic mixed-phase clouds, as well as on subtropical trade wind cumuli.

André Ehrlich

Leipzig Institute for Meteorology (LIM)
University of Leipzig
Leipzig, Germany
a.ehrlich@uni-leipzig.de



André Ehrlich is a Senior Scientist at the Leipzig Institute for Meteorology at the University of Leipzig in Germany. He received a PhD in Meteorology in 2009 from the Johannes Gutenberg University of Mainz, Germany. His research utilizes airborne remote-sensing techniques to characterize Arctic clouds in order to investigate their impact on the enhanced warming of the Arctic climate, also known as Arctic amplification.

Peter Pilewskie

Laboratory for Atmospheric and Space
Physics and Department of Atmospheric
and Oceanic Sciences
University of Colorado Boulder
Boulder, USA
peter.pilewskie@lasp.colorado.edu



Peter Pilewskie is a Professor at the University of Colorado Boulder's Department of Atmospheric and Oceanic Sciences and Laboratory for Atmospheric and Space Physics (LASP). He is Principal Investigator for the Total and Spectral Solar Irradiance Sensor and Lead Scientist at LASP for CLARREO Pathfinder. His research interests include quantifying the Earth's radiative energy budget, surface, airborne, and satellite remote sensing of clouds and aerosols, and atmospheric radiative transfer.

Airborne Lidar

38. Airborne Lidar

Martin Wirth 

Part D | 38.1

The lidar techniques used for ground-based measurements may all, in principle, be implemented on an airborne or spaceborne platform. This chapter describes the techniques and instruments that have been successfully applied on such a platform or are expected to be in operation in the near future. The theory part of the chapter extends the sections in Chaps. 24–27 on ground-based lidar systems with topics that are only relevant for a moving platform.

38.1	Measurement Principles and Parameters	1067	38.3.3	Relation to Meteorological Reference Frames	1078
38.1.1	Measurement Principles	1068	38.3.4	Inclusion of the Doppler Effect	1080
38.1.2	Measured Parameters	1069	38.4	Devices and Systems	1084
38.2	History	1071	38.4.1	Airborne Instruments for Aerosol and Cloud Parameters	1084
38.3	Theory	1072	38.4.2	Airborne Instruments for Trace Gas Measurements	1084
38.3.1	Technical Constraints for Airborne Lidar Instruments	1073	38.4.3	Airborne Instruments for Wind	1086
38.3.2	Reference Frames	1075	38.4.4	Spaceborne Instruments	1087
			38.5	Specifications	1089
			38.6	Quality Control	1089
			38.7	Maintenance	1089
			38.8	Applications	1090
			38.9	Future Developments	1090
			38.10	Further Reading	1091
			References		1091

The lidar techniques described in Chaps. 24–27 may all, in principle, be used not only from the ground but also on an airborne or spaceborne platform. This allows a much larger measurement volume, up to a global scale, to be covered by spaceborne instruments. Applied on an airborne platform, targeted observations become possible, and an air mass can be easily tracked for process studies. Also, these carriers allow a downward-looking geometry, which has advantages such as lower signal dynamics or the possibility to use multiple absorption lines for trace gas retrieval. Furthermore, the blind range near the instrument is moved away from the often very interesting atmospheric ground layer. On the other hand,

the fast-moving platform only allows for low integration times, which lead to a low signal-to-noise ratio, thus limiting the performance of some techniques with very low return signals, such as Raman or fluorescence lidars. Most air- and spaceborne platforms are also limited in terms of electrical power, volume, and weight, but at the same time have to be isolated against vibrations and temperature and pressure gradients in the airborne case and against cosmic radiation in the spaceborne case. For spaceborne lidar systems, the very high velocity of about 7 km s^{-1} for a low Earth orbit forces one to consider aberration and Doppler effects, which can normally be neglected for ground-based or most airborne systems.

38.1 Measurement Principles and Parameters

Most, but not all, lidar techniques have been implemented on fast-moving platforms. The following subsections briefly describe the relevant measurement

principles and the corresponding atmospheric parameters. This section focuses on the benefits and problems associated with an airborne or spaceborne platform.

38.1.1 Measurement Principles

In principle, every lidar measurement that can be done by a stationary system is also possible from a moving platform. Chapters 24 to 27 introduce the basics of lidars for different applications. A more elaborate exposition may be found in the book edited by *Weikamp* [38.1]. The following paragraphs briefly describe the most common lidar types for which aircraft-based operation has been reported.

Simple Backscatter Lidar

Here only the atmospheric backscatter from molecules and aerosol and cloud particles is detected, possibly at several wavelengths and with the option of depolarization measurements. Its advantage is its simplicity and the possibility of building small, robust systems. The main purpose of such systems is to map the geometric distribution of aerosol and cloud layers. If depolarization channels are present, such a system allows for a rough discrimination of the type of particles, e.g., sea-salt aerosol (low depolarization) or mineral dust (high depolarization), or whether an ice cloud or a liquid-phase cloud is being probed. However, in general, due to ambiguities in the backscatter function, more detailed aerosol characterization is not possible. This would require additional extinction channels, as provided by much more complex high spectral resolution lidars (HSRLs) and Raman lidars.

High Spectral Resolution Lidar (HSRL)

This technique requires a single-mode laser source and a very narrow band filter in the receiver to separate the light scattered by molecules from that scattered by aerosol and cloud particles. This is made possible by the fact that the molecular constituents of the air are of much lower mass than the particles and hence their thermal speed is much higher ($v \approx 1/\sqrt{m}$). This higher velocity then leads to higher Doppler broadening of the backscattered light. The total spectrum of the light from a single-mode laser scattered back in the atmosphere is the sum of a broad molecular part and a narrow peak in the middle originating from scattering by aerosol and cloud particles. These two parts are separated with an optical filter of high spectral resolution (hence the name of the method). The molecular part is proportional to the density of air multiplied by the total atmospheric transmission. If the air density is known, e.g., from temperature and pressure data, the signal of the molecular channel of a HSRL system provides a direct method to measure the atmospheric transmission profile. By taking the logarithm and performing numerical differentiation, the extinction profile can be derived without making assumptions about the scattering function—

something not possible with a simple backscatter lidar. The main advantage for airborne use is the relatively low signal integration time that can be achieved when compared to Raman lidars, which provide a similar capability.

Raman Lidar

Raman lidars use the rotational and/or vibrational Raman effect of molecules in the air to derive several parameters. The total Raman signal is proportional to the density of the air multiplied by the atmospheric transmission. Therefore, it is possible to derive particle extinction profiles in the same manner as with the HSRL method. The requirements for the optical filter to separate the Raman scattering from the elastic scattering are even lower than for the HSRL method. The Raman spectrum consists of several lines whose relative intensities depend strongly on temperature. This can be used to retrieve the temperature profile. Up to now, temperature Raman measurements have only been reported for ground-based systems, but airborne applications are expected in the near future. The Raman scattering of H_2O molecules can be used to retrieve humidity profiles. However, the high versatility of the Raman lidar technique is counteracted by low scattering cross-sections, which lead to a signal that is about three orders of magnitude lower than that for a lidar based on elastic backscatter. On an airborne platform, this limits the range and resolution of such systems, so very few applications are reported in the literature (Sect. 38.4).

DIAL/IPDA

The differential absorption lidar (DIAL) principle uses the elastic backscatter for several emission wavelengths to derive trace gas concentrations. This requires a minimum of two laser pulses with wavelengths that show strongly contrasting absorption by the atmospheric trace gas under consideration. Further requirements are that the difference between the wavelengths is small enough to assume the same atmospheric backscatter and that possible interfering trace gases show much lower absorption for these wavelengths (strictly speaking, it is only required that other trace gases show the same absorption cross-sections, which can often be established by clever selection of the wavelength with low absorption—the so-called off-line). Under these assumptions, the derivative of the logarithm of the ratio of the backscatter signals for these two wavelengths with respect to the range only depends on the number concentration of the probed molecule, not on any other component of the atmosphere. All instrumental factors such as the laser pulse energy and the detector sensitivity cancel out, so no calibration is needed.

This makes the DIAL technique ideal for airborne applications, where the rapidly changing environmental conditions could render stable calibration of the system difficult. The integrated path differential absorption (IPDA) method is a simplified version of the DIAL where only the ground or cloud reflex is taken and the upper point of the partial column is replaced with an energy measurement within the instrument. It delivers only column values of the probed trace gas, but the very high hard target return as compared to atmospheric backscatter allows for relatively small systems or very high precision, as needed for CO₂ or CH₄ measurements. Compared to the Raman technique, the DIAL/IPDA is also applicable to trace gases with very low concentrations as long as they have high enough absorption cross-sections, and the averaging time to reach the same precision is much lower because the large elastic backscatter signal is used.

If the concentration of the absorbing gas is known, the DIAL technique can be used to derive the temperature and pressure. For example, [38.2] describes a technique for measuring the pressure profile, surface pressure, and cloud-top pressure height that utilizes the pressure-dependent absorption of trough regions in the wings of two molecular resonant absorption lines of oxygen near 760 nm. The temperature measurements sense the line center absorption of highly temperature-sensitive lines of oxygen. However, because of system complexity and difficulties in handling gradients in particle backscattering, temperature and pressure measurement by DIAL has not found widespread use.

Fluorescence Lidar

This technique uses the fluorescence that emerges from constituents of the air when they are excited by an appropriate laser light pulse to derive their concentrations or quantities such as temperature. There are two totally different applications where this technique is used. One is middle atmosphere research, where atomic metal layers are probed, e.g., the sodium layer (80–105 km). For excitation at the sodium D line, for example, the fluorescence cross-section is 13 orders of magnitude larger than that for Rayleigh scattering, which more than compensates for the low number of sodium atoms present in this layer. The fluorescence in this case is spectrally very narrow, but the spectral width is determined by the temperature. By scanning the fluorescence line, the temperature within the sodium layer can be retrieved. Other metals such as iron (Fe), potassium (K), and calcium (Ca) also form metal layers in the middle atmosphere and may be used in the same way. The other application of a fluorescence lidar is the characterization of aerosols in the troposphere. Organic aerosols in particular show characteristic fluorescence spectra that

may be used to discriminate them. The spectral bandwidth of the fluorescence is broad in this case, which generally makes daylight measurements impossible.

Doppler Wind Lidar

Light scattering by moving particles leads to a shift in the wavelength of the incident light—the so-called Doppler effect (Sect. 38.3.4 for details). This can be used to infer the velocity of the scatterers. For scattering from molecules or small aerosol particles, this is equivalent to the wind velocity. For larger particles, their sedimentation speed is superimposed. To implement a Doppler lidar, a single-mode laser with a very small bandwidth is necessary, as is a receiver system capable of discriminating very small wavelength shifts. For example, for a wind lidar operating at a wavelength of 2 μm, the shift is 1 MHz for a target velocity of 1 m s⁻¹ (expressed here in frequency units; this is 0.0133 pm in wavelength units). To resolve such tiny wavelength alterations, either interferometers (the Fabry–Pérot, Fizeau, and Mach–Zehnder types are commonly used) or a heterodyne technique is implemented. The latter works by superimposing a very stable continuous-wave laser source with a very close wavelength onto the backscattered light and measuring the frequency of the resulting intermodulation signal, which is in the high frequency (HF) range. The accuracy of the heterodyne method is essentially determined by the laser stability, and can be brought down to the mm s⁻¹ range. The downside of the heterodyne method is that only scattering by aerosol or cloud particles that are heavy enough not to show a broadening effect due to thermal motion can be used. In principle, the molecular scattering can also be detected by a heterodyne receiver, but with much higher noise and some as-yet unsolved systematic problems [38.3].

38.1.2 Measured Parameters

Table 38.1 lists the directly measured parameters for the most common airborne lidar types. References are given for systems with a high number of publications in the literature. Special methods that have been demonstrated but have not been applied more broadly, such as temperature and pressure measurements by DIAL, are not included.

Using auxiliary data, further data products may be derived from the primary ones given in Table 38.2.

Compared to ground-based lidars, airborne and spaceborne systems provide several advantages. The most prominent of these are described in the following.

The location of the measurement is freely selectable and optimally adaptable to the measurement problem at hand. There is no need to wait until the atmospheric

Table 38.1 Parameters that are directly measured by airborne lidar

Parameter	Symbol	Unit	Lidar technique	References
Attenuated backscatter coefficient	B	$\text{m}^{-1} \text{sr}^{-1}$	Elastic backscatter lidar	[38.4–9]
Backscatter coefficient	β	$\text{m}^{-1} \text{sr}^{-1}$	HSR (high spectral resolution) lidar, Raman lidar	[38.10–14]
Extinction coefficient	α	m^{-1}	HSR lidar, Raman lidar	[38.10–14]
Linear depolarization	δ		Depolarization lidar	[38.10, 11, 14]
H ₂ O molecular density	$\rho_{\text{H}_2\text{O}}$	m^{-3}	DIAL, Raman lidar	[38.12, 13, 15–20]
O ₃ molecular density	ρ_{O_3}	m^{-3}	DIAL	[38.21–24]
CO ₂ column density	χ_{CO_2}	m^{-2}	IPDA	[38.25–28]
CH ₄ column density	χ_{CH_4}	m^{-2}	IPDA, Raman lidar	[38.17, 28–30]
Wind velocity	v	m s^{-1}	Doppler lidar	[38.31–36]

Table 38.2 Parameters derived from airborne lidar measurements using auxiliary data

Parameter	Symbol	Unit	Primary parameter	Auxiliary data
H ₂ O specific humidity	q	kg kg^{-1}	H ₂ O molecular density	Air density profile
Relative humidity	RH		H ₂ O molecular density	Temperature profile
O ₃ mixing ratio	χ_{O_3}	mol mol^{-1}	O ₃ molecular density	Air density profile

situation of interest occurs at a research station. With a long-range aircraft, it is possible to reach remote locations that are otherwise not accessible given reasonable cost constraints, such as deserts, the open ocean, or the polar regions. Further, it is easily possible to scan larger areas within a short time. Depending on the orbit, a spaceborne lidar may even provide global coverage, but due to the essentially predetermined track, the measurement region is not flexibly selectable with respect to time. For a recurring orbit, which is the baseline for most missions, there are also locations on Earth that never get probed.

The freely selectable measurement location allows for coordinated measurements with satellites or other airplanes. This can be used to perform instrument validation by comparing instruments side-by-side under different measurement conditions, or the synergy with in-situ measurements on a lower-flying aircraft can be used to complement remote sensing measurements. (See [38.37] for a campaign description involving multiple coordinated aircraft.) Flight tracks that connect different ground stations can be chosen, and the airborne instrument can then be used as an intercalibration tool.

With a fast-moving platform, it is possible to perform so-called quasi-Lagrangian measurements, where the flight path is aligned with the motion of the atmosphere. Although, due to vertical wind shear, this is not always possible over large vertical intervals, it nevertheless provides the opportunity to study the evolution of air parcels—something not possible from a single station on ground, where a volume is only probed once. Measurements from ground lidar stations are often hindered by low clouds. With a high-flying aircraft, it is

always possible to perform measurements above clouds or through holes between clouds, thus greatly enhancing the atmospheric situations in which the lidar can be used.

In a downward-looking probing geometry, an airborne lidar has some advantages concerning the signal dynamics. The probed atmosphere gets denser with increasing range, partly compensating for the geometric signal decay (r^2 dependence) and the atmospheric transmission, which both cause the signal to decrease with range. From the ground, both effects work in the same direction. When compared, the downward-looking geometry has signal dynamics that are 1–2 orders of magnitude lower than those for the upward-looking geometry for a range of 10–15 km. For special applications such as an H₂O-DIAL, the advantage is even bigger. Since water vapor decreases by about four orders of magnitude between the ground and the tropopause, absorption measurements of upper layers cannot use strong absorption lines when the lidar is on the ground, since the transmission would be too low. In contrast, for a lidar on a high-flying platform, the water vapor profile allows the use of strong lines for the upper parts of the atmosphere and weak lines for the layers near the ground without incurring transmission problems.

For middle atmospheric research, a high-flying platform has several advantages, such as less atmospheric extinction, less stray-light from the sun, and a shorter distance to the target.

Besides the advantages listed above, there are of course also limitations.

The fast-moving platform only allows for short signal integration times. While ground-based lidars often

accumulate signals over minutes to hours, this would lead to horizontal averaging of 10–1000 km for the typical speed of a jet-engine research aircraft. Usable integration times for most tropospheric applications range up to only 10–20 s. For highly variable situations such as clouds, the integration time should be below 1 s. This puts strong constraints on the power-aperture product of the lidar and limits, for example, the application of a Raman or fluorescence lidar on an airplane. For a spaceborne system with a velocity of about 7 km s^{-1} , this situation is even worse.

Most smaller airplanes have a limited endurance of only 2–3 h. Together with the time needed to reach the target region and fly back afterwards, this limits the us-

able observation time to not much more than 1 h. This is often too short to study atmospheric processes that depend, for example, on the diurnal cycle, or to cover synoptic-scale phenomena.

The limited resources on an aircraft (Sect. 38.3.1) exclude some applications, depending on the aircraft's size and available power. For example, very few Raman lidars are flown on an airplane.

Last but not least, the operation of a research aircraft is expensive. This typically limits its deployment to dedicated field experiments. A long-term, regular monitoring application has not been reported so far, with the possible exception of pipeline monitoring with IPDA from a helicopter [38.29].

38.2 History

This section will give a short account of the history of airborne and spaceborne lidars. Readers interested in further details are referred to [38.38] for airborne and spaceborne lidars. A more recent history of spaceborne lidar can be found in [38.39].

The first ground-based lidar systems emerged during the mid-1960s (shortly after the invention of the laser), and the first attempts to operate such instruments on an airplane were carried out shortly after, in the late 1960s and early 1970s. These early systems were simple backscatter lidars for the detection of clear air turbulence and lower tropospheric aerosol. During the late 1970s, the first airborne upward-pointing lidar [38.40] and the first autonomous system on a high-altitude airplane [38.41] expanded the range of applications. Shortly after these relatively simple instruments, the first O_3 -DIAL [38.42] and the first H_2O -DIAL [38.43] were flown on NASA airplanes. In 1985, there was the first flight of an airborne lidar to measure pressure [38.44] using the DIAL technique. Around the same time, Doppler wind lidar instruments were implemented on aircraft [38.31, 32, 45]. These systems were only sideways-pointing and could not retrieve the full wind vector. The first conical scanning Doppler wind lidar that was able to get full wind information was implemented more than 10 years later [38.34]. Also in the 1980s, the first resonance fluorescence lidar for mesosphere research was flown on an airplane [38.46].

In the 1990s, a few new technologies were reported to have gone airborne for the first time. Existing technologies were made more robust and efficient (mainly due to advances in laser technology), and they found more widespread use [38.18, 20, 34, 47].

The next technological step in aerosol and cloud profiling occurred after the year 2000, with the introduction of more complex airborne backscatter lidars that had several wavelengths, depolarization channels,

and HSRL channels for extinction profiling [38.10, 11, 14]. With these systems, it became possible to discriminate aerosols of different origins without needing to make too many assumptions. This allowed airborne aerosol lidars to keep up with the capabilities of the growing ground-based Raman lidar networks. Raman lidars themselves are still very uncommon on airplanes, mainly because of their limited range, horizontal resolution, and daytime capability.

During the last few decades, growing interest in greenhouse gas monitoring has led to the development of airborne IPDAs for CO_2 and CH_4 monitoring [38.25–28, 30].

Many of the developments in the field of airborne lidars were achieved by national space agencies, with the ultimate goal being to make the technology ready for space. While several studies were conducted to prove the feasibility and usefulness of spaceborne lidar applications in the 1970s and 1980s, it took until 1994 for the first lidar in space, the *Lidar In-Space Technology Experiment* (LITE), to be launched as a short-term (10 day) experiment on a NASA Space Shuttle [38.48]. LITE was a quite sophisticated instrument, with three emission wavelengths, a powerful laser, and a 1 m diameter telescope.

The next three systems, which were placed into orbit during the years 1995–1997, were BAL-KAN-1 [38.49] on the Russian space station MIR, ALISSA (l'atmosphère par lidar sur salioût), [38.50] on the Priroda module docked onto MIR, and BALKAN-2 [38.51] on the Russian ALMAZ-1B satellite. These were much simpler and smaller systems that were mainly used to detect cloud tops and, in some cases, the boundary layer height.

The first long-duration spaceborne lidar was the *Geoscience Laser Altimeter System* (GLAS) on ICE-Sat [38.52]. Although primarily designed as an al-

timer to monitor ice-sheet topography, it featured channels for atmospheric measurements as a secondary goal [38.53]. GLAS used diode-pumped Nd:YAG lasers that were designed to provide the necessary lifetime for a multiyear mission with continuous operation. Unfortunately, however, the first laser failed after 37 days of operation. To fulfill its primary mission objective, the data collection strategy was changed to dedicated campaigns of ice shield mapping, with minimized laser operation. This allowed a 7 year record of polar ice height development to be established before the last of the three lasers ceased operation.

The first mission to be mainly dedicated to aerosol and cloud monitoring was *Cloud–Aerosol Lidar and Infrared Pathfinder Satellite Observation* (CALIPSO), a joint NASA and CNES mission launched in 2006. The lidar instrument on CALIPSO is called the *Cloud–Aerosol Lidar with Orthogonal Polarization* (CALIOP) [38.54]. Based on the experience gained from early laser failures on the GLAS mission, several countermeasures were taken for CALIOP. As a result, this system is still in operation after 12 years of continuous measurement in space. CALIOP is a simple backscatter lidar with 1064 and 532 nm channels. The 532 nm branch incorporates a depolarization channel for enhanced aerosol and cloud type discrimination.

38.3 Theory

This theory section only discusses points relevant to lidar applications where the instrument is mounted on a (fast) moving platform. In terms of physical measurement principles, there is no difference between a lidar operated on the ground and one operated on an airplane or satellite, so the general theory described in Chaps. 24–27 also applies to airborne/spaceborne applications. However, there are several constraints that impose strong limits on the possible realizations of such a system, the most important of which are described in Sect. 38.3.1.

Also, from a purely theoretical standpoint, there are two points that need special attention when the instrument is not stationary.

The first is the accurate determination of the geolocation of the measurement. The fast-moving platform, together with a variation in the pointing of the lidar (which may be caused by a rolling and pitching platform or induced deliberately by a scanning device), makes this much more involved than for a ground-based application. A short introduction containing some basic equations will be given here. For typical applications,

While the spaceborne lidars described up to now only had simple backscatter channels, it is planned that future systems will also incorporate extinction channels, like the more modern ground-based and airborne systems. In 2015, the *Cloud–Aerosol Transport System* (CATS) was installed on the International Space Station (ISS) as a technology demonstrator for such upcoming instruments [38.55]. CATS is a three-wavelength (1064, 532, and 355 nm) system with depolarization and extinction channels. Besides the large number of detection channels, it is also the first spaceborne lidar to use high repetition rate Nd:YVO₄ lasers (4–5 kHz). Since it was designed as a technology demonstrator with limited budget, not all operation modes are available at the same time. In October 2017, the mission ended after about two and a half years.

The latest step in spaceborne lidar happened in August 2018, when ESA (European Space Agency) launched the *Aeolus* mission. *Aeolus* is a single-instrument mission with the *Aladin* wind lidar onboard. *Aladin* implements a direct-detection Doppler wind lidar with one line of sight. Additionally, there will be aerosol and cloud products, but with a limited vertical resolution compared to dedicated aerosol-cloud missions such as CALIPSO.

More technical details regarding the spaceborne lidars mentioned here are given in Sect. 38.4.

It is not only necessary to know the exact geolocation of the measurement but also to relate it to model data in order to extract auxiliary data and for intercomparison and validation purposes. In general, this problem is not specific to a flying platform, but it is much more pressing than for a ground station, where a wealth of meteorological data is typically available from nearby measurements, whereas airborne or spaceborne data are often acquired over remote places.

The second point, which is much more pronounced for a moving platform, is the wavelength shift of the emitted laser light caused by the Doppler effect. From the ground, this effect can almost always be neglected or (in the case of a wind lidar) used for the retrieval, but no corrections for the movement of the platform are needed. The following subsection presents a form of the lidar equation where wavelength shifts are taken into account, and discusses the implications for trace gas measurements with a DIAL or IPDA, for a HSRL (with its narrow-band detection unit), and for wind lidars, based on the Doppler effect.

38.3.1 Technical Constraints for Airborne Lidar Instruments

The main differences when operating a lidar on a moving platform such as an airplane as compared to ground-based operation come from the various limitations, restrictions, and environmental conditions such a platform imposes. These may be the rapidly changing temperature and pressure, accelerations and vibrations, the limited space, electrical power or cooling, or the requirements from certification. These aspects all depend strongly on the type of aircraft, ranging from a helicopter to small propeller-driven machines, small business jets, and large airplanes such as NASA's DC-8. A further category is high-flying airplanes with only one or no pilot, such as the ER-2, M-55 Geophysics, or Global Hawk, for which the system has to run autonomously in a near-vacuum environment. In the following, the major constraints will be discussed, with a focus on small commercial passenger airplanes, as they are the aircraft most commonly used in atmospheric research. Because even this subclass of aircraft is highly diverse, only rough estimates for numbers or examples for a specific airplane will be given. This section should be regarded more as a checklist of things not to forget rather than a definite specification.

For spaceborne systems, other sets of restrictions apply due to their operation in vacuum, the extremely high vibrational load during launch, and cosmic radiation. Readers are referred to special literature on this topic, e.g., [38.39].

The Moving Platform

The roll angle reaches values of up to 30° during normal flight operation (Fig. 38.1a), which changes the range to altitude relation and hence the apparent optical thickness per range gate. This has to be corrected, when possible, or cut out during data processing. When longer signal averaging is required to achieve a good signal-to-noise ratio, the correction of curve flights shorter than the averaging interval can be very difficult or impossible. Therefore, it is advisable to optimize the flight planning for long straight legs. In addition to curve flights, the roll angle oscillates fast with an amplitude of about 1° , even during straight legs and quiet conditions. Besides, for Doppler and high-precision ranging lidars, this is a minor problem (the path length elongation is less than 2 m from an altitude of 10 km). For upward-pointing lidars, there is the possibility that the telescope is pointed towards the sun during turns, even when operated out of the tropics. Since this could damage the detector units, a protection device may be needed—one that blocks the light path in the receiver before it reaches any possibly sensitive component, and is triggered by a sun sensor.

The pitch angle is positive and around $2\text{--}4^\circ$ during level-flight conditions, but changes with speed and fuel loading. This means that the lidar is always looking forward (by ≈ 0.5 km from 10 km) as compared to its nominal pointing with respect to the aircraft fuselage. This has to be taken into account if correlated measurements with nadir-looking instruments are made, e.g., with radiometers.

Roll rates reach peak values of up to 6 deg s^{-1} and pitch rates reach up to 1 deg s^{-1} (Fig. 38.1b). This means that wind and ranging applications need high-rate attitude data for correction. There is also a possible problem for long-range/narrow field-of-view lidars, i.e., upper atmosphere applications. A change rate of 6 deg s^{-1} corresponds to an angle change of $62 \mu\text{rad}$ during the round trip time for a target at 60 km distance. If the receiver field of view is smaller than this $62 \mu\text{rad}$, there is the possibility that no signal from this range is detected at all.

The roll, pitch, and heading data from the inertial reference system of an aircraft has an accuracy of about 0.1° . For some systems, values that are more than ten times better can be reached by postprocessing the raw data. However, it should be noted that there is typically an offset between the zero position of the inertial reference system and the *zero* position of the lidar system, which is referenced to the aircraft floor. This offset has to be calibrated on the ground or determined in-flight though comparison with topographic targets [38.56].

The pressure altitude, which is usually given by the aircraft's data system, can differ from the geometric altitude above sea level by up to 1 km (Fig. 38.2). The alternative is to use data from a GNSS system such as global positioning system (GPS). The precision here is normally about 10 m peak-to-peak if enough satellites close to the local zenith are in view. Higher precisions are possible if additional correction data are used. The geometric altitude from GPS is sometimes referred to the reference ellipsoid of WGS84 and sometimes to the geoid. Care has to be taken to interpret the altitude data correctly. High-accuracy comparisons ($\Delta h < 10 \text{ m}$) with NWP-model data or other data given with pressure as the vertical coordinate should use the geopotential as an intermediate quantity. See Sect. 38.3.3 for a more detailed discussion of this point.

Since the target is rapidly changing at high platform speeds of 200 m s^{-1} or more, the clocks of different instruments on the same platform have to be synchronized if collocated synergistic retrievals are planned.

Non-laboratory Environment

An airplane is an environment with unstable pressure and temperature. Lidar components have to be specially de-

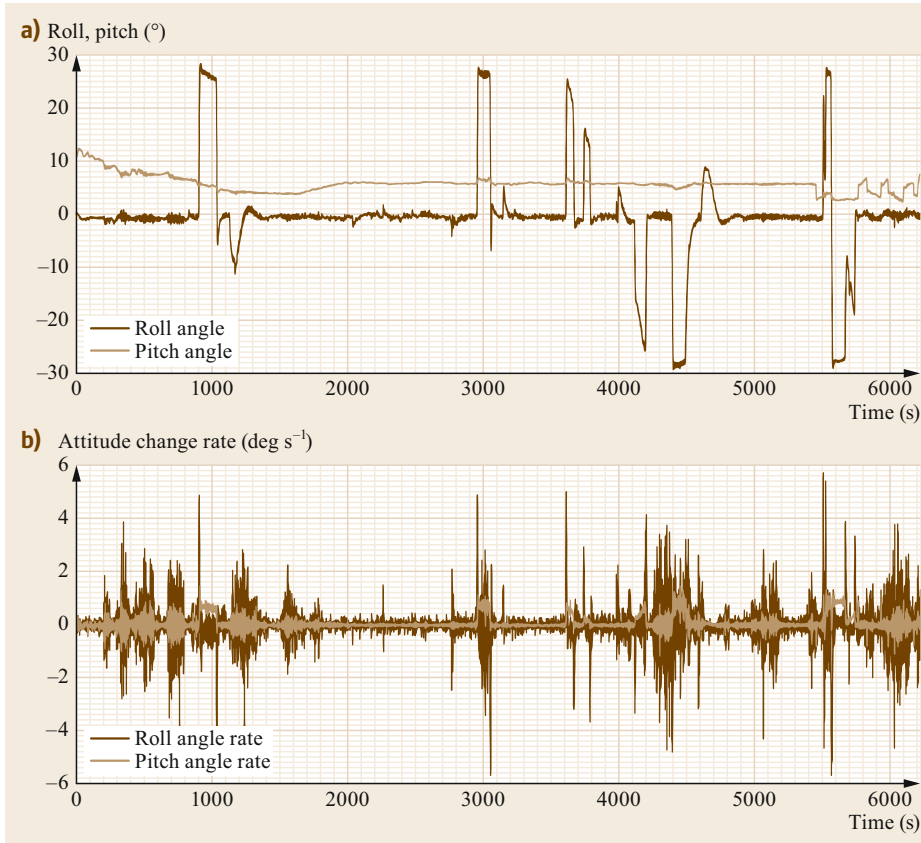


Fig. 38.1a,b Time series of the roll and pitch angles (a) and the rates of change in those angles (b) during a research flight of DLR's Falcon F-20 aircraft

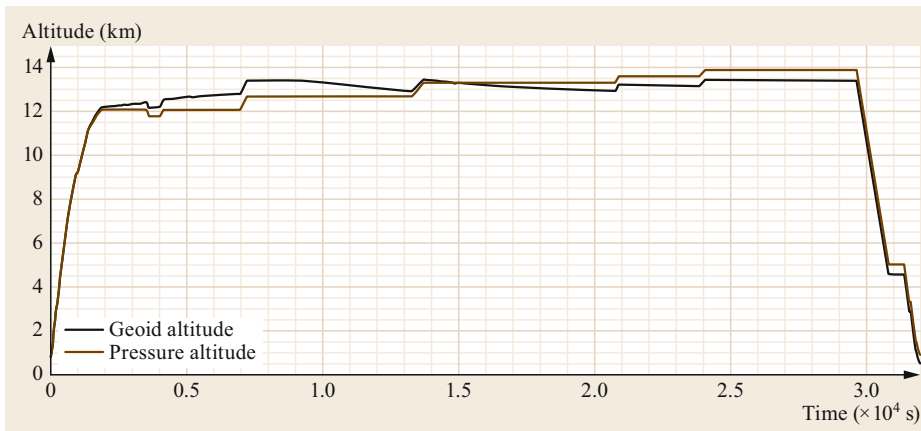


Fig. 38.2 The pressure altitude from the aircraft's air data computer and the geodetic height from a GNSS receiver during a flight of the German research aircraft HALO from southern Germany to Kiruna in Sweden. Differences of up to 1 km are apparent

signed to cope with large spatial temperature gradients and relatively fast changes. For example, on DLR's research aircraft HALO, the air temperature in the middle of the cabin varies between 24 and 28 °C during a normal research flight, making it relatively stable when compared to the cabin air temperature on other airplanes. However, at the same time, the air temperature near the optical lidar window changes from 20 to -10 °C at rates

of about 1 °C min⁻¹. The coldest point in the aircraft is the ring mount of the optical window, which approaches -22 °C with an outer static air temperature of -65 °C. Because the window is the coldest spot in the cabin, there is a risk that water vapor will condense there on the inside. It is often necessary to purge with dry air to avoid this. Condensation from the outside is possible in strongly supersaturated regions, but because of the

large difference between the window temperature and the static air temperature due to the compression of the air caused by the motion of aircraft, this condensation not observed in practice for flights at a constant level. An exception is the special case of a fast descent of a still cold aircraft into warm and moist air.

The cabin pressure normally drops by more than 200 hPa during ascent, even in airplanes with a pressurized cabin. This can provide problems for pressure-tight but unstable housings of optical elements. Further, the associated refractive index change requires fast adaptive laser control for some applications and continuous recalibration of spectrometers and wavemeters, even if they are based on solid-state etalons. Special attention must also be given to the high-voltage circuits used in lasers to drive the Pockels cell or the flashlamps or used in the receiver as bias voltages for photomultipliers. Under reduced-pressure conditions, these devices can produce arcing if they are not specially designed. This is of course much more severe if the lidar is installed in an unpressurized section of the airplane.

Peak accelerations from bumps at the start of the flight can reach several times of the Earth's gravitational acceleration. On a jet aircraft, in-flight vibrations show a broad spectrum up to 2 kHz, with stronger excitation in the vertical direction at low frequencies. On propeller airplanes, the spectrum peaks more at the rotational frequency of the propeller and its harmonics. While such a vibrational environment does not provide problems for a simple backscatter lidar, more sophisticated setups that require single-mode operation of the laser or use very narrow band etalon-based filters in the receiver have to be specially isolated against vibrations or actively stabilized by a fast control loop.

Compared to a laboratory or container environment, many resources are quite limited on most research aircraft. Examples include space and weight. Lidar systems, especially the more powerful ones, are large and heavy. Even when they fit into a small research airplane, they often have to be assembled from smaller parts within the cabin and potentially readjusted afterwards. On most airplanes designed for commercial passenger transportation, the allowable floor load is rather limited. This means that the use of heavy optical tables is not possible and the mechanical structure of the lidar system has to be specially designed to have the required low weight as well as the stiffness necessary for stable optical alignment. Also, the balance constraints of the aircraft have to be met, so heavy items have to be kept close to the center of gravity—typically not a place where large openings for optical windows are located. Another resource that is limited is the electrical power, which often only reaches a few kW on a small aircraft. If commercial components are used to build the lidar

system, adaptation to the power nets used in aviation is necessary. Small airplanes use a 28 V DC based power unit and larger ones a 115 V/400 Hz AC version. However, an often more severe constraint than the available electrical power is the ability to get rid of the heat produced by a high-power lidar. The air conditioners of commercial passenger airplanes are not designed to remove all of the available power if it is dissipated into the cabin. A possible solution is to cool the laser directly against the outside using a heat exchanger mounted in an opening of the aircraft, e.g., a window.

An airplane is not a clean environment. The air conditioner typically does not have fine filtering, and the dust load in the cabin can be much larger than in, e.g., a container. This means that high-power laser optics have to be dust screened as much as possible in order to avoid damage to the optical coatings. If it is impossible to dust screen the light path, a workable solution is to expand the laser beam to a larger diameter in order to reduce the energy density and thus the risk of dust-induced damage to the optics.

38.3.2 Reference Frames

Obtaining the accurate geodetic coordinates of the scattering target for each laser pulse in an Earth-centered reference frame is crucial to successfully interfacing the measured quantity with other real-world or model data. As the airborne or spaceborne platform is moving relatively fast, and the probing direction may change, determining the location of the probed volume is not completely trivial. This is especially true for a satellite in orbit, where even small angles of a few degrees with respect to the nadir lead to a large horizontal offset—large enough that the *flat Earth approximation* does not hold any more and one has to deal with the ellipsoidal shape of the Earth in a more accurate way.

In this section, an outline of the fundamental reference frames and transformations involved is given. A more in-depth exposition can be found in, e.g., [38.57]. The reader should note that different conventions regarding reference-frame axis orientation are in use for different applications. For example, in aeronautics, the z axis is usually pointing downwards in the direction of the Earth's surface; in land vehicle applications, it is pointing upwards. This has to be taken into account when using transformations or relations from different sources. In this section, the conventions from aeronautics are used.

When determining an exact geolocation, four reference frames are involved:

BRF: the Body Reference Frame linked to the platform. Usually, for an airplane, the X_{BRF} axis is

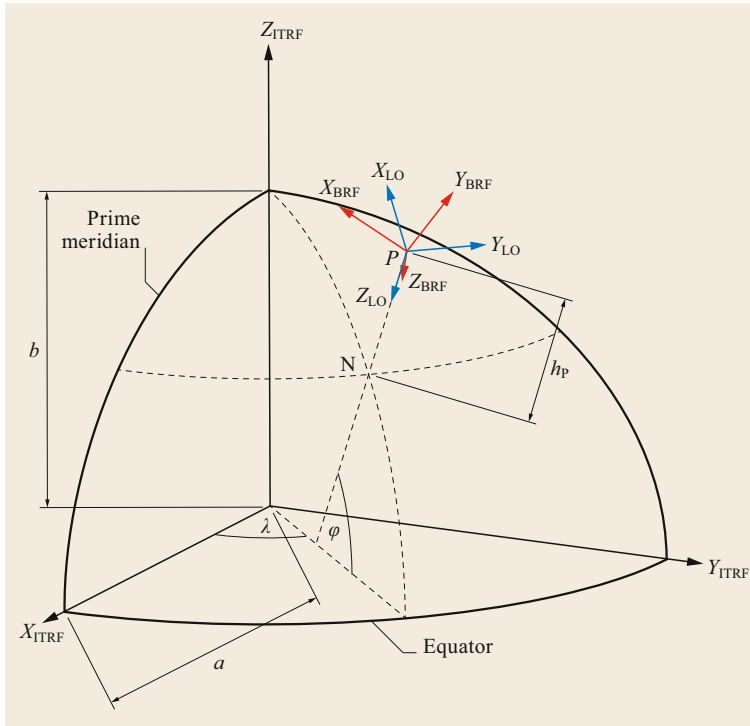


Fig. 38.3 Illustration of the relative positions of the instantaneous ITRF, LO, and BRF reference frames as seen from an inertial reference frame, and of the angles and distances that are relevant for the derivation of the geodetic coordinates of the target in the ITRF reference frame. The flattening of the Earth’s reference ellipsoid and the platform altitude are greatly exaggerated for clarity. See the main text for definitions and more details

aligned with the long axis of the aircraft body, the Y_{BRF} axis is pointing to the right wing, and the Z_{BRF} axis is pointing downwards, such that a right-handed orthonormal reference frame is formed (refer to the red axes in Fig. 38.3).

LO: the LOcal reference frame, with its origin at the platforms’s center of mass P, Z_{LO} directed downwards perpendicular to the reference ellipsoid, Y_{LO} pointing east, and X_{LO} pointing (true) north (refer to the blue axes in Fig. 38.3).

ITRF: the International Terrestrial Reference Frame, which is rigidly linked to the Earth’s reference ellipsoid and thus corotates with the latter during its diurnal motion in space. It has its origin at the Earth’s center of mass, as defined by the International Earth Rotation Service (IERS) [38.58], and is virtually identical to the WGS84 reference frame down to a precision of 10 cm (refer to the black axes in Fig. 38.3).

GCRF: the Geocentric Celestial Reference Frame, which is the inertial reference frame with a fixed orientation with respect to extragalactic radio sources (mostly quasars). The GCRF is also defined by the IERS [38.58]. It has to be used as an intermediate reference frame when applying a physical law that is only valid in an inertial frame, i.e., in the absence of pseudo

forces such as the Coriolis force. (This reference frame is not shown in Fig. 38.3.)

Typically, the position of the platform is given with respect to the ITRF, e.g., based on data from a GNSS such as GPS, whereas the orientation of the platform is given with respect to the LO frame from an inertial reference system based on laser gyros or a star tracker for satellites. To calculate the georeferenced position of a target volume from these data, one has to calculate the position of the platform $(X_P, Y_P, Z_P)_{ITRF}$ and the pointing vector $(X_L, Y_L, Z_L)_{ITRF}$ of the lidar beam in Cartesian ITRF coordinates. If the effect of the atmosphere’s refractive index is neglected, the lidar range from the platform P to the target T, r_T , is the Euclidean distance between P and T, and therefore the target position is given by

$$\begin{pmatrix} X_T \\ Y_T \\ Z_T \end{pmatrix}_{ITRF} = \begin{pmatrix} X_P \\ Y_P \\ Z_P \end{pmatrix}_{ITRF} + \frac{r_T}{\sqrt{X_L^2 + Y_L^2 + Z_L^2}} \cdot \begin{pmatrix} X_L \\ Y_L \\ Z_L \end{pmatrix}_{ITRF} \quad (38.1)$$

See Fig. 38.4 for an illustration of the geometrical setup. Now, if $(X_L, Y_L, Z_L)_{BRF}$ is the direction vector (assumed to be known) of the laser beam with respect

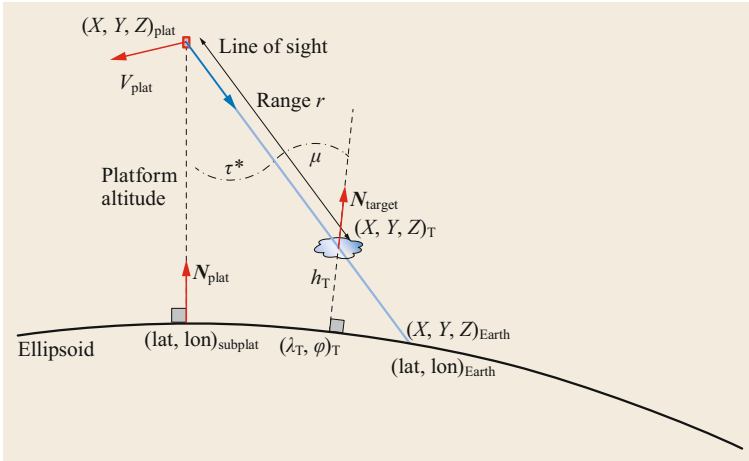


Fig. 38.4 Illustration of the platform position, velocity, and instrument line of sight. The geolocation of the target is computed using the range from the platform to $(X, Y, Z)_T$ as determined by the lidar. Normal vectors to the ellipsoid at the target and platform locations are also shown ($N_{\text{plat}}, N_{\text{target}}$)

to the instrument-fixed BRF system, and the orientation of the platform with respect to LO is given by the roll, pitch, and heading angles θ_{ro} , θ_{pi} , and θ_{he} , respectively, the laser pointing vector with respect to the LO system is given by

$$\begin{pmatrix} X_L \\ Y_L \\ Z_L \end{pmatrix}_{LO} = \begin{pmatrix} c_{pi}c_{he} & s_{ro}s_{pi}c_{he} - c_{ro}s_{he} & c_{ro}s_{pi}c_{he} + s_{ro}s_{he} \\ c_{pi}s_{he} & s_{ro}s_{pi}s_{he} + c_{ro}c_{he} & c_{ro}s_{pi}s_{he} - s_{ro}c_{he} \\ -s_{pi} & s_{ro}c_{pi} & c_{ro}c_{pi} \end{pmatrix} \cdot \begin{pmatrix} X_L \\ Y_L \\ Z_L \end{pmatrix}_{BRF}, \quad (38.2)$$

with the abbreviations

$$\begin{aligned} c_{ro} &\equiv \cos(\theta_{ro}) & s_{ro} &\equiv \sin(\theta_{ro}) \\ c_{pi} &\equiv \cos(\theta_{pi}) & s_{pi} &\equiv \sin(\theta_{pi}) \\ c_{he} &\equiv \cos(\theta_{he}) & s_{he} &\equiv \sin(\theta_{he}). \end{aligned}$$

Finally, to transform the direction vector from the LO system to the ITRF, the matrix

$$\begin{pmatrix} X_L \\ Y_L \\ Z_L \end{pmatrix}_{ITRF} = \begin{pmatrix} -\sin(\phi)\cos(\lambda) & -\sin(\lambda) & -\cos(\phi)\cos(\lambda) \\ -\sin(\phi)\sin(\lambda) & \cos(\lambda) & -\cos(\phi)\sin(\lambda) \\ \cos(\phi) & 0 & -\sin(\phi) \end{pmatrix} \cdot \begin{pmatrix} X_L \\ Y_L \\ Z_L \end{pmatrix}_{LO} \quad (38.3)$$

has to be applied, where λ is the geographical longitude and ϕ the geographical latitude of the point where the local LO frame is referenced to. Conventionally, the coordinates with respect to the ITRF are given as

the longitude, latitude, and altitude above the reference ellipsoid. The transformation from (elliptical) geodetic coordinates (λ, ϕ, h) to Cartesian coordinates is given by

$$\begin{pmatrix} X \\ Y \\ Z \end{pmatrix}_{ITRF} = \begin{pmatrix} (R_N + h)\cos(\phi)\cos(\lambda) \\ (R_N + h)\cos(\phi)\sin(\lambda) \\ ((1 - e^2)R_N + h)\sin(\phi) \end{pmatrix}, \quad (38.4)$$

where $R_N = a/\sqrt{1 - e^2\sin^2(\phi)}$ is the radius of curvature of the prime vertical, $a = 6378137.0$ m is the semi-major Earth axis, and $e^2 = f(2 - f)$ (with $1/f = 298.257223563$) is the flattening of the Earth. The numerical values given here are taken from the definition of WGS84. There is no known simple closed form of the inverse relation that transforms the Cartesian coordinates to geodetic form, but there are numerous iterative solutions; see, for example, [38.59, 60].

In summary, the procedure for target geolocation is as follows. The coordinates of the platform are transferred into Cartesian form using (38.4). The attitude information from the platform (heading, roll, and pitch angles) is used to transform the lidar pointing vector from the BRF (where it is assumed to be known) to the LO via (38.2), and then to the ITRF by applying (38.3), where the geodetic coordinates of the platform also enter. Finally, (38.1) is used to derive the location of the target at range r_T in Cartesian ITRF coordinates. For further use, they have to be transformed back to geodetic form by a suitable inverse of (38.4).

For a low-flying aircraft, or if it is not necessary to know the geolocation to high precision, this procedure can be simplified by using the *flat Earth approximation*. If the lidar is pointing in the direction of the z axis of the BRF, the geolocation of the target can be determined

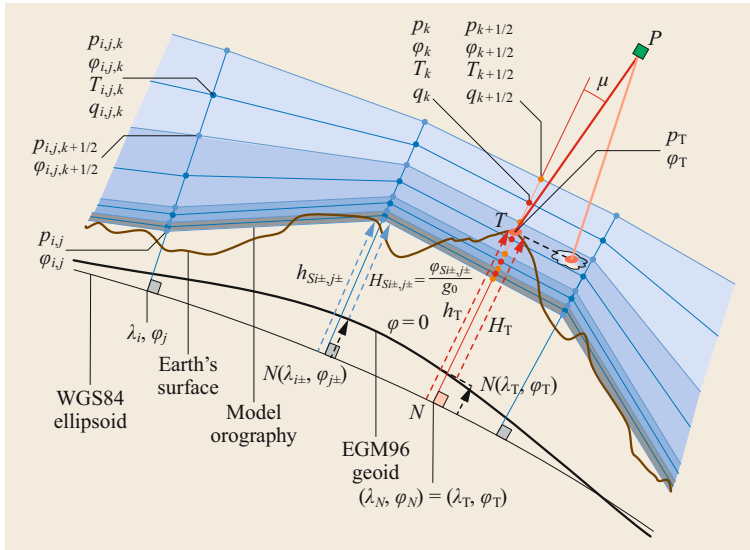


Fig. 38.5 Illustration of the model levels and their relationships to the ellipsoid, the geoid, the Earth’s topography, and the lidar geometry, where indices (i, j) refer to the horizontal grid coordinates and index k refers to the vertical coordinate. See the main text for more details

using the much simpler equations

$$\begin{aligned} \lambda_T &= \lambda_P + \frac{180^\circ r_T}{\pi R_E \cos(\phi_P)} (c_{ro} s_{pi} s_{he} - s_{ro} c_{he}) \\ \phi_T &= \phi_P + \frac{180^\circ r_T}{\pi R_E} (c_{ro} s_{pi} c_{he} + s_{ro} s_{he}) \\ h_T &= h_P - r_T c_{pi} c_{ro} \end{aligned} \quad (38.5)$$

where the same abbreviations for the sines and cosines of the attitude angles are used as in (38.2), and $R_E = 6371000.785\text{ m}$ is the mean radius of the Earth. For an upward-looking lidar, the sign before r_T in the third equation of (38.5) has to be reversed.

38.3.3 Relation to Meteorological Reference Frames

To make use of the data set acquired by an airborne or spaceborne lidar system, it is often necessary to relate the data to numerical weather models (NWM) or climate models. This may be the case when the data have to be assimilated into a model or used for validation purposes, or when the calculation of higher-level products from the lidar requires auxiliary data, e.g., the air density. The previous subsection described how to properly reference lidar data with respect to coordinates in the ITRF. Unfortunately, coordinate systems in NWM are typically not referenced to geodetic coordinates but rather to a coordinate space that is native to the equations describing the physical processes, thereby radically simplifying the formalism and increasing computational efficiency. Most significantly, the vertical discretization at each horizontal grid point is tied to predefined relationships between the pres-

ures at each atmospheric level. As long as the model remains self-consistent, the relationship between the *real-world* coordinates of an air parcel and the coordinates of this air parcel in the model is not of great interest to the NWM community. Furthermore, conventional (i.e., in-situ) observations that are assimilated by the models are already referenced to a model coordinate (e.g., surface weather station measurements or radiosonde profiles, both of which are referenced to the readings from a local pressure sensor), while nonconventional (i.e., remote-sensing-based) observations from passive instruments do not require a fine understanding of the *geometry of the atmosphere* (e.g., assimilation of top-of-the-atmosphere radiances). The assimilation of some relatively new types of altitude-resolved remotely sensed observations does, however, require a better understanding of the geometric relationship between model atmosphere and instrument. Besides lidar instruments, this is notably the case with GNSS meteorological data when making use of the radio occultation principle in a limb-sounding-like configuration. The following considerations show how to proceed, using the Integrated Forecasting System (IFS) of the European Centre for Medium-Range Weather Forecasts (ECMWF) as an example.

Figure 38.5 illustrates the geometry of the model’s idealized atmosphere. In order to account for the effects of the topography, the ECMWF’s model makes use of so-called *hybrid coordinates*, as outlined in [38.61]. The lower levels follow a simplified orographic model of the Earth, while the upper levels are defined by a constant pressure. They are defined dynamically at each horizontal grid point (λ_i, ϕ_j) by fixed relationships between the atmospheric pressures $p_{i,j,k\pm 1/2}$ at

their interfaces (so-called *half-levels*; light blue dots in Fig. 38.5) and the surface pressure $p_{Si,j}$ at the model orography, a model output. The pressure $p_{i,j,k}$ in the middle of the layers (so-called *full levels*; blue dots in Fig. 38.5) is then defined as the arithmetic mean value of $p_{i,j,k+1/2}$ and $p_{i,j,k-1/2}$. In addition to the pressure levels, the model parameters at any grid point that are typically needed for lidar data processing are the temperature and humidity profiles $T_{i,j,k}$ and $q_{i,j,k}$. Even if the humidity itself is not of direct interest, it is required to calculate the virtual potential temperature, which enters the equations for the geopotential given below. For some applications, the dry air mixing ratio is also needed, and hence the water vapor content has to be subtracted appropriately. For DIAL/IPDA applications, water vapor is often an interfering trace gas, and knowledge of its concentration is required to correct the optical thickness values in the retrieval of the species of main interest.

The problem at hand is twofold:

1. to horizontally and temporally interpolate the model profiles to the target location, and
2. to change the vertical variable from lidar range r to the natural vertical coordinate of the model and then interpolate the model variables to this vertical location, which generally lies in between model levels.

For objective (1.), the fact that NWMs widely make use of a spherical model of the Earth suggests an interpretation of the horizontal grid coordinates, from a strictly geometric viewpoint, as the *geocentric* longitude and *geocentric* latitude. However, as the orography of the model is taken from WGS84-referenced data sets [38.62], it is more consistent to interpret the model's latitude as the geodetic latitude ϕ , not the geocentric latitude, when a comparison to the real-world data is made. The question of how to interpolate the NWM profiles to the location of the target (i.e., how to obtain the parameters p_k , T_k , Φ_k , and q_k in Fig. 38.5) then remains. The simplest approach is to carry out a bilinear interpolation of all relevant model parameters using the target's four neighboring grid points at coordinates $(i+1, j+1)$, $(i+1, j-1)$, $(i-1, j+1)$, and $(i-1, j-1)$. This is done for two model outputs that bracket the time of the measurement, and then a linear interpolation in time is used to arrive at a model layer based data set at the time and location of the measurement.

For the second problem, the geopotential is used as an intermediate quantity to reference the model's vertical scale to the geometric altitude of the lidar target. For the reasons discussed above, the normal height h does not actually appear in the fundamental NWM equations as an internal variable nor as a model output.

From a NWM point of view, it is simpler to deal with the effect of the gravitational force through the associated potential energy, the geopotential Φ , defined as the potential energy of a unit mass of air in the Earth's gravity field relative to a reference surface. When combined with the ideal gas law for dry air, the geopotential-based hydrostatic equation takes the form

$$\frac{d\Phi}{dp} = -\frac{R_{\text{dry}}T_v(p)}{p}, \quad (38.6)$$

where R_{dry} is the gas constant for dry air and

$$T_v(p) \equiv T(p) \left(1 + \left(\frac{R_{\text{H}_2\text{O}}}{R_{\text{dry}}} - 1 \right) q(p) \right) \quad (38.7)$$

is the so-called virtual temperature, with $T(p)$ the temperature at pressure level p , $R_{\text{H}_2\text{O}}$ the gas constant for water vapor, and $q(p)$ the specific humidity at level p . The specific humidity is related to the dry air volume mixing ratio of water vapor $x_{\text{H}_2\text{O}}(p)$ through

$$x_{\text{H}_2\text{O}}(p) = \frac{m_{\text{dry-air}}q(p)}{m_{\text{H}_2\text{O}}(1-q(p))}. \quad (38.8)$$

Equation (38.6) is used in [38.61] in the discretized and integrated form

$$\Phi_{i,j,k+\frac{1}{2}} = \Phi_{Si,j} + \sum_{l=k+1}^{N_{\text{LEV}}} R_{\text{dry}}T_{v,i,j,l} \ln \left(\frac{p_{i,j,l+\frac{1}{2}}}{p_{i,j,l-\frac{1}{2}}} \right), \quad (38.9)$$

where N_{LEV} is the number of model levels and $\Phi_{Si,j}$ is the geopotential of the model surface layer (which remains constant over time), to calculate the half-level geopotentials. The geopotential at a full level is then given by

$$\begin{aligned} \Phi_{i,j,k} &= \Phi_{i,j,k+\frac{1}{2}} + R_{\text{dry}}T_{v,i,j,k} \\ &\times \left(1 - \frac{p_{i,j,k-\frac{1}{2}}}{p_{i,j,k+\frac{1}{2}} - p_{i,j,k-\frac{1}{2}}} \ln \left(\frac{p_{i,j,k+\frac{1}{2}}}{p_{i,j,k-\frac{1}{2}}} \right) \right). \end{aligned} \quad (38.10)$$

What remains is the calculation of the geopotential for each target altitude h . Φ is a function of the orthometric height H , i.e., the height above the geoid. Because of the ellipsoidal nature of the Earth, this relation is latitude dependent, and an established and accurate approximation is

$$\begin{aligned} \Phi(\phi, H_T) &= g(\phi)H_T \\ &\times \left(1 - \frac{H_T}{a} (1+f+m-2f \sin^2(\phi)) + \frac{H_T^2}{a^2} \right), \end{aligned} \quad (38.11)$$

where $m = \omega_0^2 a^2 b / (GM)$, a and b are the semi-major and semi-minor axes of the reference ellipsoid, $f = (a - b)/a$ is the ellipsoid flattening, G is Newton's gravitational constant, M is the mass of the Earth, and ω_0 is the Earth's angular velocity. Further, $g(\phi)$ is the magnitude of the normal gravity at the surface of the geoid as a function of geodetic latitude, as given by Somigliana's formula

$$g(\phi) = g_e \frac{1 + k \sin^2(\phi)}{\sqrt{1 - e^2 \sin^2(\phi)}}, \quad k = \frac{b g_p}{a g_e} - 1, \quad (38.12)$$

where g_e and g_p are the theoretical normal gravity values at the equator and the poles, respectively, and $e^2 = f(2 - f)$ is the reference ellipsoid's eccentricity. The orthometric height H is related to the geodetic height by

$$H = h - N(\lambda, \phi), \quad (38.13)$$

where $N(\lambda, \phi)$ is the so-called *geoid undulation*, i.e., the normal height of the geoid above the reference ellipsoid. A commonly used standard for $N(\lambda, \phi)$ is EGM96 [38.63], but there are various refinements from recent high-resolution gravimetric measurements.

The geopotential value of the target given by (38.11) is then transferred to the model world and, via a straightforward search, the level index k_T that satisfies

$$\Phi_{k_T + \frac{1}{2}} \leq \Phi(H_T) \leq \Phi_{k_T - \frac{1}{2}} \quad (38.14)$$

is determined. Finally, once more, a discretized form of (38.6) is used to calculate the target pressure p_T

$$p_T = p_{k_T - \frac{1}{2}} \exp\left(\frac{\Phi_{k_T - \frac{1}{2}} - \Phi(H_T)}{R_{\text{dry}} T_{v k}}\right). \quad (38.15)$$

For other model variables, which are defined at full levels, a similar procedure is used. Again, the full level Φ_k (given by (38.10)) that brackets $\Phi(H_T)$

$$\Phi_{k_T} \leq \Phi(H_T) \leq \Phi_{k_T - 1} \quad (38.16)$$

is found and then a linear interpolation is done; e.g., in the case of temperature,

$$T_T = \alpha T_k + (1 - \alpha) T_{k-1}, \quad \alpha \equiv \frac{\Phi_{k_T - 1} - \Phi(H_T)}{\Phi_{k_T - 1} - \Phi_{k_T}}. \quad (38.17)$$

For variables that tend to show a more linear vertical behavior, when pressure is used as the independent variable, the interpolation may also be done using the full pressure levels p_k .

38.3.4 Inclusion of the Doppler Effect

To discuss the effects of a Doppler shift caused by a rapidly moving platform, a form of the lidar equation that explicitly contains the spectra of the emitted and received light pulses is needed. The signal power from the backscattered laser radiation incident on the detector device of the receiver of the lidar system is described by the simple radiative transfer equation

$$P_D(t) = \int_0^\infty \left(\iint D(\nu_v) \tau_b(\nu_b, r) \frac{O(r)A}{r^2} \times \beta_L(\kappa_b(r) \nu_b, \kappa_f(r) \nu_f, r) \tau_f(\nu_f, r) \times S_L(\nu_f) d\nu_f d\nu_b \right) P_L(t - t_\pi(r)) dr, \quad (38.18)$$

for which the symbols are defined in Table 38.3.

Remarks

- The equation is written, from right to left, in the order of radiative transfer: first the laser spectrum is transformed by the forward transmission; it is then backscattered and possibly spectrally broadened; next, it is again transformed by the backward transmission; finally, it is spectrally filtered by the receiver. The geometrical factor A/r^2 is kept close to the backscatter coefficient because it defines the solid angle that the radiation is scattered into and thus logically belongs to β_L , although it is not frequency dependent and could be pulled out of the integral.
- The equation in the given form allows for inelastic scattering and laser pulses of arbitrary temporal and spectral shape. Simplifications for elastic scattering or short and/or spectrally narrow pulses lead to the usual lidar equation; see Chap. 25.
- This equation holds for all situations where multiple scattering can be neglected, i.e., outside of optically thick clouds. The strong forward scattering caused by large ice crystals in cirrus clouds does not lead to time stretching, and the transmission effects can be taken into account by a suitable modification of the transmission terms, so (38.18) is still applicable.
- The laser radiation is characterized by the frequency ν and not by the wavelength, which makes things simpler in the nonvacuum case and for the discussion of the Doppler effect. Alternatively, the vacuum wavenumber can be used, which is more common in molecular spectroscopy.
- In principle, due to the vectorial nature of the electromagnetic radiation field, the polarization of light

Table 38.3 Explanation of the symbols used in (38.18)

Symbol	Explanation
r	Distance from the lidar system to the scattering volume along the main propagation direction of the laser beam
t	Time coordinate at the receiver system
ν_f, ν_b	Frequency of the forward- or backward-propagating radiation, respectively, in the reference frame of the instrument
$P_D(t)$	Power of the light incident on the detector at time t
$\kappa_f(r), \kappa_b(r)$	Doppler-shift factors between the reference system of the instrument and the reference system of the scattering volume at distance r ; see definition below
$t_{\tau}(r)$	Time taken for the laser pulse to perform a round trip to the scattering volume at distance r and back. If refractive index effects are neglected, $t_{\tau}(r) = 2r/c_0$, where c_0 is the vacuum speed of light
$\tau_f(\nu, r)$	Transmission of the atmosphere from the transmitter to the point at distance r where the light is scattered back
$\tau_b(\nu, r)$	Transmission of the atmosphere from the point at distance r where the light was scattered back to the receiver
$\beta_L(\nu_b, \nu_f, r)$	Backscatter coefficient at range r averaged over the laser beam profile for incident light of frequency ν_f to a possibly shifted frequency ν_b
$S_L(\nu)$	Spectral density of the light source (normalized to $\int S_L(\nu)d\nu = 1$)
$P_L(t)$	Output power of the light source for time t (temporal pulse shape)
$D(\nu)$	Efficiency factor of the detection optics, including spectral filters
A	Effective area of the receiver (essentially given by the telescope aperture)
$O(r)$	Overlap function describing the deviation from a pure $1/r^2$ law

has to be taken into account. This can be achieved by expressing the terms of the lidar equation as Stokes vectors and transforming Mueller matrices. As polarization effects are not discussed in the following, this complication is avoided.

- The integration over frequency runs over the range where the laser emission spectrum is nonzero for ν_f (typically a few hundred MHz for a spectrally pure laser and up to several dozens of GHz if a broadband impurity is present) and over the range generated by the possibly nonelastic backscattering plus the laser bandwidth for ν_b .
- The spectral density $S_L(\nu)$ and the pulse shape $P_L(t)$ of the laser emission are not independent but linked. $P_L(t)$ is proportional to the low-frequency component of the absolute square of the electric field

strength, whereas $S_L(\nu)$ is the power spectrum of the electric field. For a chirp-free laser, they determine each other.

- If the integration over r is changed to integration over the round-trip time, it can be seen that the power incident on the detector is the convolution of the outgoing laser pulse shape with a function determined by atmospheric properties.

In the following, selected terms from the lidar equation are discussed in more detail.

Due to the Doppler effect, the transmission of the atmosphere as viewed from the reference system of the instrument depends on the velocity field of the atmosphere. A velocity component relative to the line-of-sight direction of the lidar system introduces a Doppler shift of the molecular absorption that has opposite signs for the two propagation directions. Since the absorption lines of typical trace gases of interest (e.g., H_2O , CO_2 , or CH_4) are very narrow in the infrared, the effect of Doppler shifting has to be incorporated into the lidar equation. The other reason to consider the Doppler effect is the total frequency shift seen at the receiver after a round trip. This becomes relevant if the receiver bandwidth is very small, as in HSR-lidar applications. In the case of Doppler wind lidars, this shift is also actively used to determine the mean velocity of the scattering volume.

In the reference frame where the lidar is at rest, the Doppler shift can be accounted for by introducing the Doppler factor

$$\kappa_f(r) = 1 - \frac{\mathbf{v}_T(r) \cdot \mathbf{e}_L}{c_0}, \quad (38.19)$$

which *shifts* the light frequency from the value seen at the lidar system to the value valid within the reference frame where the atmospheric scatterer or absorber is at rest. Here, $\mathbf{v}_T(r)$ denotes the velocity of the target air parcel at range r from the lidar, and \mathbf{e}_L is the unit vector pointing in the direction of laser beam emission. The speed of light in vacuum is denoted by c_0 . If, for example, the air parcel moves towards the lidar, the scalar product in (38.19) is negative because the two vectors point in opposite directions. Hence, $\kappa_f(r)$ is bigger than 1, which means a shift to a higher frequency—a blueshift. For applications to the Earth's atmosphere, the nonrelativistic approximation given here is sufficient. Also, the deviation of the speed of light from its vacuum value due to the refractive index of air can be safely neglected. On its way back, the light—which may be absorbed by a molecule—comes from the back, meaning that the direction \mathbf{e}_L has to be reversed. From

(38.19), it follows that

$$\kappa_b(r) = 1 + \frac{\mathbf{v}_T(r) \cdot \mathbf{e}_L}{c_0}. \quad (38.20)$$

These Doppler factors also enter the expression for the backscattering described by the coefficient $\beta_L(\kappa_b(r)v_b, \kappa_f(r)v_f, r)$. For elastic scattering, i.e., $\kappa_b(r)v_b = \kappa_f(r)v_f$, this gives a total frequency shift at the receiver of

$$\begin{aligned} \Delta\nu &\equiv \nu_b - \nu_f = \nu_f \left(\frac{\kappa_f(r)}{\kappa_b(r)} - 1 \right) \\ &\approx -2\nu_f \frac{\mathbf{v}_T(r) \cdot \mathbf{e}_L}{c_0} \\ &= -2\mathbf{v}_T(r) \cdot \frac{\mathbf{e}_L}{\lambda}, \end{aligned} \quad (38.21)$$

the well-known formula for a wind lidar. Note that this doubled shift in (38.21) is the shift seen by the detection unit on the platform, not the relevant one for the calculation of the absorption cross-section for DIAL/IPDA applications, as is explained in the following.

The transmissions from the lidar system to the point at distance r and back may be expressed as a product of a rest atmospheric transmission $\tau_A(r)$ that does not depend strongly on the light frequency ν and a part that comes from narrow absorption lines of trace gases. $\tau_A(r)$ may be caused by aerosol or cloud absorption and scattering or Rayleigh scattering of the air molecules. The induced forward and backward transmissions $\tau_f(\nu, r)$ and $\tau_b(\nu, r)$ then are given by

$$\begin{aligned} \tau_{f/b}(\nu, r) &= \tau_A(r) \prod_G \exp \left(- \int_0^r \rho_G(r') \sigma_G(\nu \kappa_{f/b}(r'), r') dr' \right) \\ &= \tau_A(r) \exp \left(- \sum_G \int_0^r \rho_G(r') \sigma_G(\nu \kappa_{f/b}(r'), r') dr' \right). \end{aligned} \quad (38.22)$$

Here, the index G runs over all trace gases with narrow line absorption features in the frequency region of interest. ρ_G denotes the volume density of the molecular species G and $\sigma_G(\nu, r)$ is the absorption cross-section for G . The cross-section depends on r since it is pressure and temperature sensitive in general. The Doppler factors shift the frequency of the laser to the value seen by a molecule at rest. For example, for a DIAL or IPDA operating at $\nu = 1.6 \mu\text{m}$, a relative line-of-sight wind velocity of 1 m s^{-1} leads to a Doppler shift

of 0.625 MHz between the emitted and absorbed frequencies (or 1.25 MHz for the round trip). Thus, under a slant viewing geometry of 2° , range-dependent shifts of up to 2 MHz may be encountered for an atmospheric wind shear of 100 m s^{-1} , which can typically be neglected for DIAL/IPDA applications.

For a wind lidar, this frequency shift is of course the interesting part that contains the information about the velocity of the air parcel. For this application, the effect is strongly enhanced by using a large off-nadir angle, e.g., 30° , in which case half of the horizontal velocity is in the line of sight, and a sensitivity of $3 \text{ MHz m}^{-1} \text{ s}$ is reached at a wavelength of 355 nm. For a wind lidar, only the frequency offset to the emitted light is measured, and absorption effects do not play any role.

There remains the non-range-dependent Doppler shift caused by the platform velocity in combination with the rotation of the Earth. This shift has to be calculated from the attitude and orbital velocity of the platform and incorporated into the calculation of the absorption cross-section used for the trace gas retrieval or subtracted as an offset in the case of a wind lidar.

As seen above, the velocity component relevant to the calculation of the Doppler shift at range r is the projection of the velocity of an air parcel with respect to the platform $\mathbf{v}_T(r)$ onto the line of sight direction \mathbf{e}_L . In an inertial frame such as the GCRF, the Doppler-shift-relevant velocity component, v_{Doppler} , is given by

$$\begin{aligned} v_{\text{Doppler}} &= ((\mathbf{v}_T - \mathbf{v}_L) \cdot \mathbf{e}_L) = (\mathbf{v}_T \cdot \mathbf{e}_L) - (\mathbf{v}_L \cdot \mathbf{e}_L) \\ &= v_{\text{Doppler,Target}} + v_{\text{Doppler,lidar}}, \end{aligned} \quad (38.23)$$

where it becomes evident that the Doppler shift includes a term associated with the Earth's rotation and air parcel movement, $v_{\text{Doppler,Target}}$, and a term associated with the platform's movement, $v_{\text{Doppler,lidar}}$.

For the part due to the Earth and wind, the worst case is obtained at Equator crossings, where the angle between the across-track plane and the velocity of the target point is smallest (thus maximizing the scalar product) while the magnitude of the nadir point's velocity is highest.

As can be seen from a short calculation, (38.23) still holds if all vectors are expressed with respect to the Earth-fixed and thus rotating ITRF. This is not completely trivial, since the ITRF is a rotating reference system, and hence velocity vectors do not transform simply with the corresponding rotation matrix; terms containing the Earth's angular velocity also appear in the equations. In the Earth-fixed system, \mathbf{v}_T is, by definition, the wind velocity, which can either be neglected in the DIAL/IPDA case (as outlined above) or is the

quantity of interest in the case of a wind lidar. The remaining part, which has to be used in the calculation of absorption cross-sections or subtracted in the wind lidar case, can be calculated from the platform velocity and the target pointing vector alone. Therefore, it is easiest to do the Doppler calculations in the ITRF, i.e.,

$$v_{\text{Doppler}} = v_{\text{wind}}^{\text{ITRF}} \cdot e_L^{\text{ITRF}} - v_L^{\text{ITRF}} \cdot e_L^{\text{ITRF}}. \quad (38.24)$$

DIAL/IPDA

As already noted in Sect. 38.3.4, the Doppler effect is—with the exception of CO₂ systems—mostly negligible for airborne DIALs. It only plays a relevant role for satellite-based systems, and even then, proper orbit and pointing angle selection helps to minimize the Doppler shift. The most stringent requirements come from CO₂ IPDA systems because of the high accuracy requirements for this trace gas and the lack of a suitable wavelength-shift-insensitive trough region in the absorption spectrum, such as that for CH₄; see [38.64]. For carbon dioxide, the Doppler shift caused by the wind will most likely have to be taken into account, as the frequency must be known to an accuracy of 100 kHz, and exact nadir pointing is not possible because it would generate other problems (with specular reflections, for example). For CO₂, even the aircraft case is demanding. During a typical research flight with the CHARM-F IPDA of DLR [38.28], the frequency shift of the carbon dioxide channel ranges from 3 to 9 MHz over all flight conditions, which would result in a retrieval error of 0.1%. Uncorrected, this is already about an order of magnitude too large, since the goal in terms of accuracy is 0.02% and the Doppler shift error is only one of several systematic error sources.

HSRL

High spectral resolution lidars use very narrow band filters in the receiver to separate the molecular backscatter from the scattering by aerosol and cloud particles. The effective transmissions of these filters for the laser wavelength and for the broadened spectrum of the molecular return signal have to be known for the retrieval. These transmissions depend on the central wavelength, which is in turn shifted by the Doppler effect. For example, for an iodine-cell-based HSRL operating at 532 nm [38.10], the emission frequency must be known to an accuracy of a few MHz. Using (38.21), one can see that at a typical aircraft speed of 200 m s⁻¹ and an off-nadir angle of 4° (which is often used to avoid specular reflection by ice cloud particles), the Doppler shift at the receiver is about 52 MHz. This value is too high to be neglected for precision mea-

surements and has to be corrected for in the retrieval. The exact value depends on the pitch and roll angles of the aircraft and on its speed relative to the air in the probed volume, which was assumed to be at rest in the example above. If a nonzero wind, possibly with shear, is present, there are additional uncertainties. For typical atmospheric wind speeds outside of high-level jets, the contribution from the wind can be neglected. The situation gets much worse in curves with high roll angles. If a precise HSRL retrieval during curve flight is required, this can only be done using additional wind information. This additional information can come from an external source or can be measured with the same lidar system through a second channel. The HSRL based on the Mach-Zehnder technology [38.14] provides the opportunity to simultaneously retrieve the wind along the line of sight without additions to the system, and hence a Doppler-shift-insensitive retrieval can be established.

For a spaceborne DIAL with a speed of about 7 km s⁻¹, the Doppler shifts due to the platform's motion are larger by a factor of 35 than those for a typical jet aircraft with a speed of 200 m s⁻¹. At a system level, this can partly be compensated for by pointing as nadir as possible. The small deviation from nadir usually required to avoid specular reflections should be chosen in such a way that the beam direction is perpendicular to the motion direction of the satellite. An active steering mechanism usually has to be implemented to maintain this condition over the whole orbit.

Wind

For a Doppler wind lidar, the frequency shift due to the movement of the target is the raw data quantity of interest. The part coming from the movement of the platform is an offset that has to be subtracted. Unfortunately, the speed of the platform is usually large compared to the accuracy required for wind measurement, which is well below 1 m s⁻¹. Especially for spaceborne Doppler lidars, the offset is several orders of magnitude larger than the part due to the wind. If only one wind component is of interest, it is possible to point the lidar in a direction perpendicular to the flight track, as done for ESA's Aeolus mission (Sect. 38.4.4), but this is not possible if the whole wind vector has to be measured. The velocity and attitude data for the platform are typically not known with high enough accuracy to simply calculate the offset from them. The solution is to use the Doppler shift of the ground, if available. In this way, correction parameters for the platform velocity data can also be established, which allows for a precise wind retrieval in cases where no ground return is available.

38.4 Devices and Systems

This section describes selected airborne and spaceborne lidar systems in more detail. To keep this section within reasonable bounds, only state-of-the-art systems that were or still are in regular use for atmospheric research as documented by peer-reviewed publications are considered.

38.4.1 Airborne Instruments for Aerosol and Cloud Parameters

For aerosol and cloud parameters, there are a number of mostly small systems with limited power and a limited number of channels. We will not list them here, but rather restrict the description to two more powerful systems with extinction channels based on the high-resolution lidar principle, as these systems set the standard upon which future developments will be based.

NASA HSRL

The National Aeronautics and Space Administration (NASA) Langley Research Center (LaRC) airborne High Spectral Resolution Lidar (HSRL) is a compact, nadir-viewing airborne HSRL developed for the accurate measurement of aerosol and cloud properties in the context of radiation- and chemistry-focused field missions and for validating the CALIOP on the CALIPSO satellite [38.11]. The system uses an injection-seeded Nd:YAG laser that is frequency doubled to provide pulse energies of 1.1 mJ at 1064 nm and 2.5 mJ at 532 nm at a repetition rate of 200 Hz. The laser is locked to a J_2 cell by a phase modulation technique. The receiving system uses a 40 cm diameter telescope with an adjustable field of view of 0.25–1.0 mrad. Photo multiplier tubes (PMTs) are used as detectors for the 532 nm channels and Si-APDs (avalanche photo diodes) are used for 1064 nm. The system provides depolarization channels for both wavelengths and a HSRL channel at 532 nm, which uses an iodine cell to suppress the particular backscatter. For each detection channel, the signal is split in the ratio 1 : 20 and fed to a low-signal and a high-signal detector unit to extend the dynamical range. This system was used in several field campaigns to establish a widely used aerosol classification database [38.65].

LNG

The French *lidar aerosols nouvelle génération* (LNG) is a HSRL based on a Mach–Zehnder interferometer [38.14]. A frequency-doubled and -tripled Nd:YAG laser with a 20 Hz repetition rate is used. The emitted pulse energies are 50 mJ at 1064 nm, 10 mJ at 532 nm, and 50 mJ at 355 nm. The pulsed laser is in-

jection seeded to provide stable single longitudinal mode operation with a line width of 70 MHz. The receiver uses a telescope 300 mm in diameter. The channels at 1064 and 532 nm are polarization insensitive, while there are parallel- and cross-polarized channels at 355 nm. The parallel-polarized channel is fiber coupled to a Mach–Zehnder interferometer (MZI). To establish the necessary stability, the MZI design is based on an arrangement of fused silica prisms and air gaps. Using the MZI technique to build a HSRL has several advantages as compared to a molecular absorption filter or an etalon-based system. For example, the laser does not have to be absolutely stabilized; it may drift slowly. Compared to etalons, the acceptance angle of the filter is much larger, and compared to molecular filters, the wavelength is freely selectable. The technique can also be used to infer the wind velocity, although the LNG layout yields lower accuracy than dedicated wind lidars. The downside is that the separation of molecular and particle backscatter is lower than for systems based on molecular filters, and the corresponding errors in extinction retrieval are higher.

38.4.2 Airborne Instruments for Trace Gas Measurements

This subsection covers the latest airborne DIAL instruments for water vapor and ozone and currently operational IPDA systems for greenhouse gas monitoring.

LASE

The latest operational version of NASA's airborne H₂O DIAL systems is the *Lidar Atmospheric Sensing Experiment* (LASE) [38.18, 19]. The transmitter is Ti:sapphire-laser based and emits double pulses with a separation of 300 μ s in the wavelength band 813–818 nm. The pulse-pair repetition frequency is 5 Hz and the pulse energy more than 100 mJ. The receiving telescope has an area of 0.1 m² and uses an APD with 80% quantum efficiency. The covered altitude range is the troposphere with the exception of the tropopause region and the lower stratosphere, where the optical thicknesses of even the strongest absorption lines in the region accessible to the system are too low. LASE has been used in a large number of field and validation campaigns and is thought to have an accuracy of about 5% in the upper troposphere, where accurate measurements are most difficult [38.66]. From a technological point of view, LASE is becoming outdated, so there are currently developments at NASA to replace it with a system using the latest laser and detector technology; see Sect. 38.9.

LEANDRE II

The airborne differential absorption lidar LEANDRE II (lidar pour l'étude des interactions aérosols nuages dynamique rayonnement et du cycle de l'eau) has been developed for tropospheric water vapor profiling by the French Centre National de la Recherche Scientifique (CNRS). The emitter uses a flash-lamp-pumped alexandrite laser, which operates in a double-pulse, dual-wavelength mode in the 727–736 nm spectral domain. Two 50 mJ successive on-line and off-line pulses with an output line width of less than 720 MHz and a spectral purity larger than 99.99% are emitted at a repetition rate of 20 Hz. The emitted wavelength is controlled in real time by a wavemeter with an absolute accuracy of 150 MHz. The receiver is a 30 cm aperture telescope with a 3.5 mrad field of view and a background-light filter bandwidth of 1 nm. A photomultiplier tube with a quantum efficiency of 4% serves as the detector. The precision of the instrument is better than 0.5 g kg^{-1} in the first 5 km of the atmosphere, it has a range resolution of 300 m, it integrates 100 shots, and it has an instrumental systematic error of less than 2% [38.20, 67].

WALES

The German Aerospace Center (DLR) developed a multiwavelength H_2O DIAL with additional channels for aerosol and cloud characterization [38.68] as an airborne demonstrator for a proposal to ESA regarding a spaceborne mission called WALES (water vapour lidar experiment in space) [38.69]. The WALES airborne demonstrator only uses technologies such as diode-pumped solid-state lasers and nonlinear conversion techniques that are suitable for an in-orbit deployment. It operates in the 935 nm region and is capable of emitting at four wavelengths at the same time for water vapor measurement. An optical parametric oscillator (OPO) is used to generate the pulses at 935 nm. Additionally, there are aerosol detection channels operating at wavelengths of 1064 nm and 532 nm, where the depolarization and aerosol extinction (only at 532 nm) in the atmosphere are measured. Output pulse energies are 45 mJ at 935 nm, 75 mJ at 532 nm, and 125 mJ at 1064 nm, with a total repetition rate of 200 Hz. Pulses at all wavelengths have a duration of about 8 ns and are single longitudinal mode, with a bandwidth below 150 MHz and a stability of better than 30 MHz for 935 nm and better than 1 MHz for 1064 nm and 532 nm. The receiver uses a telescope 48 cm in diameter and a field of view of 1.6 mrad. PMTs are used as detectors for the 532 nm channels and Si-APDs for 935 and 1064 nm channels. The raw data range resolution is 15 m. The temporal resolution is reduced to 5 Hz by the onboard averaging of signals. The system

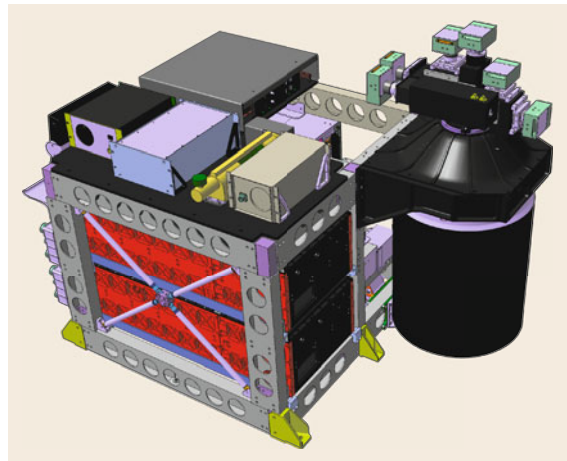


Fig. 38.6 WALES: DLR's airborne demonstrator for a possible future spaceborne water-vapor DIAL system

is very compact for this power class, with a volume of only about 1 m^3 ; see Fig. 38.6. The uniqueness of this system is the possibility of measuring the whole tropospheric profile of water vapor (including the tropopause region and the lower stratosphere) simultaneously by combining the raw data profiles of four close wavelengths at 935 nm. The systematic error in the water vapor retrieval is estimated to be below 2.5% from multi-instrument comparisons [38.70].

TOPAZ

The National Oceanic and Atmospheric Administration (NOAA) developed an airborne DIAL for tropospheric ozone (tunable optical profiler for aerosol and ozone, [38.24]). The system is based on a tunable solid-state Ce:LiCAF laser which is able to generate short light pulses in the wavelength range 283–310 nm. This laser is pumped by a frequency-doubled Nd:YLF laser, which is, in turn, laser-diode pumped. The output energy ranges between 0.2 and 0.8 mJ, depending on the wavelength. The repetition rate is 1 kHz and the pulse length 100 ns. The laser is operated at three wavelengths that are generated sequentially. The third, intermediate, wavelength is used to reduce the retrieval error caused by aerosol. The tunability allows to adapt to different atmospheric conditions, and to reduce the cross-sensitivity to other trace gases such as SO_2 . The receiver uses a 0.5 m diameter telescope and photomultiplier tubes as detectors. To cover the large signal dynamics, a far-field and a near-field channel are implemented. The vertical resolution of O_3 profiles is 90 m, and the horizontal resolution is 600 m (10 s at a typical aircraft speed). The precision is about 5% close to the aircraft and increases to 12–30% at distances of 2.5 km and beyond. The accuracy is estimated to be better than 5% in most cases.

NASA CO₂ Sounder

To prepare for a proposed mission called ASCENDS (active sensing of CO₂ emissions over nights, days and seasons) that aimed to measure CO₂ from space with an active system, NASA developed several candidate airborne demonstrators. The most well developed is the so-called CO₂ Sounder [38.25]. This system has been upgraded over several years. Here we describe the version focused upon in the latest publication [38.71]. The CO₂ Sounder uses a pulsed, multiwavelength (i.e., more than two wavelengths) IPDA approach. In the 1570 nm absorption band of CO₂, a single line is scanned by typically 30 different wavelengths. The laser is operated at a 10 kHz pulse repetition rate and the wavelength is changed from shot to shot so that the line is scanned at about 300 Hz. A single laser pulse has an energy of up to 50 μJ at a pulse width of 1 μs. The laser is implemented as a continuous-wave (CW) master laser that is modulated into pulses 1 μs in duration and amplified in erbium-doped fiber amplifiers. A 20 cm diameter telescope is used as the receiver, and the field of view is 500 μrad. In the latest version, the detector is a HgCdTe APD with a quantum efficiency of 70% and an internal gain of 300. The line scanning approach has several advantages with respect to the detection and elimination of spectroscopic or instrumental effects that depend on the wavelength. The downside is the relatively high laser power needed compared to a two-wavelength system with an optimally selected optical depth. The measurement precision for a 1 s averaging interval is about 0.7 ppm over desert (high reflectivity at 1.6 μm) and 2.5 ppm over snow (low reflectivity) from a flight altitude of 8 km. Comparisons with an in-situ sensor made during vertical profiling with the aircraft led to an estimation of less than 1 ppm for the systematic error.

CHARM-F

CHARM-F is a combined CO₂ and CH₄ IPDA instrument developed by the German Aerospace Center DLR [38.28]. It uses short-duration (20 ns), high-energy (10 mJ) laser pulse pairs at a repetition rate of 50 Hz. To illuminate nearly the same target, the temporal separation within one pair is 500 μs. The laser wavelength is about 1572 nm for CO₂ and 1646 nm for CH₄. To generate these wavelengths, Nd:YAG-laser-pumped OPO are used. They are injection seeded to ensure a spectral width below 50 MHz at a jitter of about 2 MHz root mean square (RMS). The transmitter divergence and receiver field of view are set to 3 mrad to ensure an illuminated ground spot of about 30 m at a typical aircraft altitude. This is favorable since the relative difference in illuminated surface area between the on-line and off-line pulses within one pulse pair gets lower as the spot size increases. For each trace

gas, the receiver has two channels. One uses a 200 mm telescope with a quadrant PIN diode. This allows active monitoring of the overlap of the transmitted beam with the receiver field of view. The other channel uses an InGaAs-APD similar to those intended for future space missions. These devices have a much lower diameter, which forces the use of a much smaller telescope (60 mm) at the prescribed field of view (F-number limited). The APDs have higher sensitivity but may be subject to nonlinearities, so the presence of two detectors enables cross-checking for such effects. The measurement precision is about 1 ppm for CO₂ and 7 ppb for CH₄, both for 10 s of averaging time. Comparisons with in-situ profiles acquired during aircraft dives point to an accuracy of better than 1.5 ppm for CO₂ and 15 ppb for CH₄.

38.4.3 Airborne Instruments for Wind

There are two detection principles for Doppler lidar: direct and heterodyne (Sect. 38.1). Both types are represented in the following list.

A2D

The Aladin Airborne Demonstrator (A2D) [38.72] is a direct-detection Doppler wind lidar developed by the German Aerospace Center (DLR) to very closely resemble the Aladin instrument on ESA's Aeolus mission (Sect. 38.4.4). It uses a very similar frequency-tripled Nd:YAG laser and an engineering model of the receiver of the spaceborne system. Like the spaceborne instrument, it is only capable of measuring one line of sight, so the main purpose of this system is to produce test data and evaluate the processing chain for the space mission. However, since an aircraft is much more free to choose its flight track than a satellite, dedicated atmospheric problems can also be investigated with this lidar, even though it has just one line of sight [38.36].

HRDL

The High Resolution Doppler Lidar (HRDL) is a heterodyne detection system developed by The National Oceanic and Atmospheric Administration (NOAA) [38.35]. It uses a Tm:Lu YAG laser emitting at a wavelength of 2 μm. The pulse length is 200 ns at a repetition rate of 200 Hz and a typical pulse energy of 1.5 mJ. The pulsed laser is injection seeded by a Tm:Lu YAG CW reference laser. The combined transmit/receive telescope has a diameter of 0.2 m. An InGaAs-PIN diode with a quantum efficiency of 60% that is operated at room temperature is used as the detector. By mixing the return pulse with a frequency-shifted (by 100 MHz) part of the light from the ref-

erence laser, a beat note is generated that is digitized after down-mixing to the baseband. The down-mixing is done to avoid high sampling rates and large raw data rates. The velocity measurement range is $\pm 25 \text{ m s}^{-1}$. The velocity precision is close to the theoretical limit for such a system and below 0.1 m s^{-1} for most atmospheric conditions. Systematic errors are estimated to be on the order of 0.01 m s^{-1} .

38.4.4 Spaceborne Instruments

This section on spaceborne systems is limited to lidars that were or still are in orbit. Future developments are briefly described in Sect. 38.9.

LITE

On 9/9/1994, the first lidar in space, LITE, was launched as a 10 day experiment on the NASA Space Shuttle *Discovery* [38.48]. The LITE used a Nd:YAG laser to generate three emission wavelengths: 1064, 532, and 355 nm. The laser was flash-lamp pumped and operated at a repetition rate of 10 Hz. For redundancy, a second laser of the same type was also integrated. The pulse energies were approximately 445 mJ at 1064 nm, 557 mJ at 532 nm, and 162 mJ at 355 nm. The receiver had a telescope diameter of 1 m, which—together with the quite high single pulse energies and the low orbit of 259 km—led to an overall sensitivity that has not been achieved again since. The receiver field of view could be switched between 1.1 mrad, 3.5 mrad, and an annular field stop for multiple scattering measurements. This feature was also unique and allowed the effect of multiple scattering on the retrieval to be estimated. In terms of detectors, photomultipliers (PMTs) were used for the 532 and 355 nm channels and an avalanche photodiode was used for the 1064 nm channel. The analog signals were digitized with a 12 bit A/D converter running at 10 MHz, resulting in a range binning of 15 m. The real range resolution was about 35 m, limited by the bandwidth of the analog electronics. The overlap between transmitter and receiver could be adjusted by a two-axis gimbaled turning prism to steer the direction of the outgoing beam. Part of the return signal at 532 nm was monitored by a microchannel plate quadrant detector, and the resulting signals were used to set up closed-loop beam stabilization.

Although LITE was a simple backscatter lidar without depolarization and extinction channels, it clearly showed the value of globally available two-dimensional curtains of backscatter data to address problems such as desert dust transport, biomass burning, pollution outflows from megacities, and the monitoring of stratospheric aerosol.

GLAS

The first spaceborne lidar on its own satellite was NASA's GLAS on ICESat [38.52]. Although primarily designed as an altimeter to monitor ice-sheet topography, it also featured channels for atmospheric measurements [38.53]. GLAS used three diode-pumped Nd:YAG lasers in a redundant configuration designed to provide the necessary lifetime for a multiyear mission with continuous operation. The laser generated two emission wavelengths, 1064 and 532 nm, at a repetition rate of 40 Hz. The pulse energies were approximately 75 mJ at 1064 nm and 35 mJ at 532 nm. The receiver had a telescope diameter of 1 m. The receiver channel at 1064 nm was optimized for altimeter applications, had a field of view of $500 \mu\text{rad}$, and used two redundant Si-APDs with a bandwidth of approximately 160 MHz. The signals were digitized with a 1 GHz sample rate, corresponding to a 15 cm range resolution. For the atmospheric signals, the 1064 nm channel was simultaneously filtered and digitized at a 2 MHz sample rate or a range resolution of 75 m. For the 532 nm channel, an array of eight APDs operated in Geiger mode was used to implement a photon-counting detection unit. The range gates for the counting were set to 75 m, just as for the infrared channel. For the suppression of stray light from the sun, the 532 nm channel contained a two-stage optical filter with a 0.37 nm bandwidth prefilter and a 30 pm Fabry–Pérot etalon as the second stage. The field of view was limited to $170 \mu\text{rad}$ for further sunlight reduction.

Unfortunately, the first laser failed after 37 days of operation. An analysis by an anomaly review board found an error source common to all three lasers onboard, so it was decided that continuous operation should be abandoned and that the data collection strategy should be changed to three 33 day campaigns per year dedicated to ice shield mapping. In this way, a 7 year record of polar ice height development was established before the last of the three lasers ceased operation.

Due to the limited operation times, the impact of GLAS on atmospheric studies was not as expected. Nevertheless, the mission was able to collect a large data set of aerosol height structure, cloud top heights and layering, and cloud optical depths down to very low values of 0.02.

CALIOP

The GLAS system described in the previous paragraph did not implement a depolarization channel, so the ability to discriminate different aerosol types was very limited. This changed with the launch of the joint NASA and CNES mission called *Cloud–Aerosol Lidar and Infrared Pathfinder Satellite Observation* (CALIPSO). The lidar instrument on CALIPSO is

called the CALIOP [38.54]. CALIOP, like all previous spaceborne lidars, uses Nd:YAG lasers to generate the two emission wavelengths, 1064 and 532 nm. The repetition rate is 20.16 Hz and the pulse energy is approximately 110 mJ at each emitted wavelength. Operation of the laser is continuous, and two lasers in a redundant configuration are onboard. The receiver has a telescope diameter of 1 m and a field of view of 130 μ rad. The optical filters for background light suppression have a bandwidth of 35 pm for the 532 nm channel and 400 pm for 1064 nm. CALIOP implements a linear depolarization channel at 532 nm. Photomultiplier tubes (PMTs) were chosen for the 532 nm channel detectors, and an avalanche photodiode (APD) for the 1064 nm channel. All operate in analog detection mode and are digitized at a rate of 10 MHz, resulting in a raw data range binning of 15 m. For each channel, two 14-bit analog digital converters are stacked in a low- and high-sensitivity configuration so that the dynamical range spans about 4×10^6 . The raw data resolution for downlinking is reduced by temporal and vertical averaging, depending on the altitude region covered. For example, the highest resolution is available for the altitude region between -0.5 and 8.2 km, with an along-range gridding of 30 m for the 532 nm channel and 60 m for 1064 nm, and no coaddition of shots. For higher layers, several shots and more range bins are added; see [38.73] for details.

The standard data products from CALIOP are attenuated (i.e., not extinction corrected) backscatter for 1064 nm and for the parallel and perpendicularly polarized channel at 532 nm; cloud geometry, such as top and bottom altitudes, and optical depth and phase (ice or water); aerosol layer geometry, optical depth, and aerosol type; profiles of backscatter coefficients and extinction for clouds and aerosol; and finally a feature mask for cloud phase and aerosol type. It should be emphasized that CALIOP does not have a channel to directly measure the extinction (HSRL or Raman), so the attenuation-corrected products and the extinction profiles depend on assumptions about the scattering properties of the aerosol or cloud under investigation. In the case of vertically isolated layers, the transmission is estimated by comparing the signals above and below the layer. Where this is not possible, prescribed values for the lidar ratio are assumed; see [38.54] for details. So, while the data set of CALIOP is quite complete for a cloud and aerosol lidar, there is some basic uncertainty for uncommon scenes where the type classification fails.

Besides standard backscatter lidar products, CALIPSO enables more indirect retrievals, such as sea surface wind inferred from the sea surface roughness [38.74]. CALIPSO is part of the A-Train, a con-

stellation of satellites for Earth observation that fly in the same orbit with close temporal spacing. The original A-Train consisted of the satellites Aqua, CloudSat, CALIPSO, PARASOL (polarization & anisotropy of reflectance for atmospheric sciences coupled with observations from a lidar), and Aura, all flying with a separation of less than 15 minutes. The temporal separation between CALIPSO and CloudSat with its cloud radar is only 15 s. This near-collocation enables synergistic retrievals using data from several instruments [38.75].

CATS

Simple backscatter lidars show deficiencies in the discrimination of different aerosol types. For ground-based systems, this has been overcome by using Raman or HSRL lidars, which provide additional extinction channels, so the logical step would be to use one of these methods from space. In 2015, the CATS was installed on the ISS as a technology demonstrator for such upcoming instruments [38.55]. CATS had two Nd:YVO₄ lasers. The first laser generated pulses of about 1 mJ at 1064 and 532 nm at a repetition rate of 5 kHz. The second laser produced three wavelengths (1064, 532, and 355 nm) with an output of 2 mJ at a repetition rate of 4 kHz. This second laser was injection seeded to produce single longitudinal mode radiation, as necessary for a HSRL. The receiver had a telescope 60 cm in diameter with a field of view of 110 μ rad. The photon-counting detectors were fiber coupled to the telescope. The mission ended in October 2017, after about two and a half years [38.55, 76].

Aeolus

On August 22, 2018, ESA launched the Aeolus satellite. Aeolus is a single-instrument mission with the Aladin wind lidar on board. Aladin implements a direct-detection Doppler wind lidar with one line of sight [38.77]. It uses two frequency-tripled Nd:YAG lasers in a redundant configuration that produce pulses of 120 mJ at a wavelength of 355 nm and with a repetition rate of 50 Hz. The lasers are injection seeded to run at a stable single longitudinal mode. The receive/transmit telescope is a SiC structure 1.5 m in diameter with a field of view of only 19 μ rad.

To simplify the instrument concept, only one component of the wind vector is sensed. This line of sight (LOS) direction is perpendicular to the satellite velocity in order to nullify the contribution of the satellite ground speed to the Doppler frequency shift. Additionally, yaw steering of the complete satellite is applied to compensate for the Earth's rotation. Only the projection of the wind vector to the LOS is obtained, for which an off-nadir angle of 35° was chosen.

The optical receiver consists of two spectrometers: a Rayleigh spectrometer measures the Doppler frequency shift from molecular backscatter and a Mie spectrometer measures the Doppler frequency shift from aerosol and cloud particles backscatter. Separation of the molecular and aerosol backscatter requires significantly different spectral bandwidths of the two signals—the broad bandwidth signal from the molecular scattering in the atmosphere and the narrow bandwidth from aerosol scattering. Rayleigh–Brillouin scattering on molecules causes a broad bandwidth signal with a FWHM of 1.6 pm due to the thermal motions of the molecules. The aerosol scattering has a bandwidth that is a factor of almost 80 lower: 0.021 pm (or 50 MHz at 355 nm). A double-edge technique is used for the molecular backscattered signal and a fringe

imaging technique for the aerosol return. The imaging detector needed for the Mie spectrometer is realized by a charge-coupled device (CCD). The CCD allows the accumulation of backscattered signal from a number of laser pulse returns directly on the CCD itself, a novel concept for lidar instruments. The minimum vertical resolution of the Aladin instrument is limited by the CCD detector to 250 m, and only a limited number (24) of atmospheric altitude ranges can be acquired. The number of laser pulses accumulated directly on the detector is typically set to 20–35. Further averaging of 600–700 laser pulses (12–14 s) is needed to reach the random error requirement of 1 or 2 m s⁻¹.

Additionally, there will be aerosol and cloud products, but with a limited vertical resolution as compared to dedicated aerosol-cloud missions such as CALIPSO.

38.5 Specifications

The most prominent error source for lidar systems is photon noise. Because of this, the resolution and precision of a lidar system depend on each other and are determined by size of the instrument, which is roughly described by the power-aperture product, i.e., the product of the emitted mean laser power and the effective area of the receiving telescope. For a prescribed precision, a certain number of photons have to be collected. Here, the power-aperture product determines the total number of photons received from a certain range interval for one laser pulse. The nec-

essary photon count can be reached if the single pulse performance is not sufficient by adjusting the range interval (i.e., the vertical resolution) and coadding the signals from several laser pulses. From the list of systems discussed in Sect. 38.4, it can be seen that, for example, the range resolution covers the interval from below 1 m to more than 1 km, depending on the system layout and technology. Therefore, it is not possible to give simple specification tables for certain types of lidars. Details about individual systems can be found in Sect. 38.4.

38.6 Quality Control

The procedures for quality control do not differ for an airborne/spaceborne lidar when compared to

a ground-based system, so all the measures described in Chaps. 24–27 also apply here.

38.7 Maintenance

The necessary maintenance procedures for an airborne lidar differ quite significantly between systems, as they depend on system complexity and size, the technology used, the quality standards applied during the development and manufacturing process, etc. Some research-grade systems need maintenance actions after every flight, while spaceborne systems are designed to have minimal maintenance needs. It is therefore not possible to give standard check intervals here, even if the same basic technology is implemented.

However, for airborne systems, all maintenance actions must be laid down during aircraft certification. For the certification of a lidar system on an airplane, it has to be shown that, among other things, the system is electrically safe and has no electromagnetic interference (EMI) with other systems, that it is mechanically stable enough to withstand crash load conditions (typical values are 9g forward, 6g downward, and 3g sideways for several seconds), that it is made of nonflammable material, and that the risks posed by other potentially dan-

gerous components (such as those from water systems, gases under pressure, toxic/radioactive substances, hot components, etc.) are under control. This all means that it is not possible to use standard laboratory components without modification. Typically, special housings have to be designed, and the cables and hoses have to be replaced with those conforming to aviation standards. It can also be difficult for pulsed lasers to meet the EMI requirements without additional screening and line filtering.

It has to be shown that the laser system is eye-safe for the crew, for people on the ground, and for other airplanes. This often places strong limits on the pulse

energy and/or the minimum divergence of the transmitter. For Europe, the European Aviation Safety Agency (EASA) has published guidelines on how a laser that is operated on an aircraft can be certified [38.78].

After the lidar system has been certified, maintenance actions are only possible according to the procedures described in the maintenance manual, which is part of the certification documentation. In particular, this means that parts may only be replaced by those of the exact same type. Thus, gradual upgrading of the lidar, as often practiced for ground-based research systems, is not possible. Every alteration requires a recertification.

38.8 Applications

Airborne lidars have been applied to various topics in atmospheric research. The first applications of backscatter lidar systems were dedicated to the monitoring and analysis of the origin and transport of aerosol and pollution in the troposphere [38.5, 6, 8, 79, 80]. More complex systems with several wavelengths and depolarization and extinction capabilities are used to retrieve the optical properties of aerosol, which are then used to classify the aerosol type and possible mixtures [38.9, 65, 81, 82].

Although lidar cannot penetrate most tropospheric clouds, it is successfully applied in research into optically thin clouds, e.g., cirrus [38.83, 84]. Even if it is not possible to penetrate the cloud, the downward looking geometry allows the detection of the cloud top height [38.85], which can then be used in combination with passive remote sensing.

In boundary layer research, airborne lidar is used to map the geometric structure of the layer, especially the top of the layer, using aerosol as a tracer [38.7, 86, 87]. Using a combination of water vapor and wind lidars, it is even possible to determine latent heat flux profiles in the boundary layer [38.88].

Understanding water vapor transport in the upper troposphere lower stratosphere (UTLS) leading to stratosphere/troposphere exchange is crucial to under-

standing and modeling the radiation budget of the atmosphere. Airborne water vapor measurements are used to study the large-scale isentropic mixing processes that dominate the transport of humidity into the lowermost stratosphere at higher latitudes [38.37, 89].

The possibility of collecting long-range two-dimensional cross-sections of the atmospheric humidity and wind field by airborne DIAL makes it an ideal tool to validate numerical weather models [38.90]. In a further step, such data can be assimilated into the model to increase the forecast skill [38.91–95].

From early on, airborne lidar has been used to investigate stratospheric aerosol [38.40, 96, 97], clouds [38.4, 98–100], and ozone [38.21], especially in connection with the winter time polar vortex. The remote locations of these phenomena often make them only accessible from airborne platforms.

Airborne lidar is even used to provide insight into the physics of the mesosphere, where the propagation of gravity waves and their momentum deposition are the main targets [38.46, 101].

For climate research, the monitoring of greenhouse gases by airborne IPDA instruments has become a valuable tool to investigate the emissions from point and distributed sources in recent years [38.28, 30].

38.9 Future Developments

For airborne lidar, advances in laser technology will allow more compact and robust systems to be built. In this way, the capabilities of current large, research-grade systems will become the standard for future airborne lidars. The higher average laser powers that are possible for Raman lidars will allow them to be used for more airborne applications than currently possible.

Over the years, there have been several proposals for new spaceborne lidar missions, such as DIAL or Raman systems to measure water vapor or ozone. However, currently only two lidar projects are advanced enough to have mission status: EarthCARE and Merlin, which is described briefly below.

To continue and extend the dataset on aerosol and clouds gathered by NASA's Calipso and Cloudsat missions, ESA is developing a satellite mission called EarthCARE that implements an advanced lidar and a radar on the same platform [38.102]. The EarthCARE lidar will have an extinction channel based on the high spectral resolution principle, and the cloud radar will have a Doppler capability giving information on convective motions as well as ice and rain fall speeds.

The other space project under development that uses the lidar technique is the French–German methane monitoring mission Merlin [38.103]. This will use the IPDA principle to measure column-integrated values of CH₄, which will then be used for the inverse modeling of surface sources and sinks of this, the second most important greenhouse gas. Due to the low bias of Merlin data, the error budget for methane emissions is expected to be considerably smaller than currently possible with passive remote sensing data [38.104].

38.10 Further Reading

A more detailed review of airborne and spaceborne lidar is given by:

- M. Patrick McCormick: Airborne and Spaceborne Lidar, in Lidar—Range-Resolved Optical Remote Sensing of the Atmosphere, edited by C. Weitkamp, Springer New York 2005, ISBN 0-387-40075-3

A general introduction to lidar with a focus on spaceborne applications can be found in:

- Juan Carlos Fernandez Diaz et al., Lidar Remote Sensing, in Handbook of Satellite Applications, edited by J. N. Pelton and S. Madry and S. Camacho-Lara, Springer New York 2017

References

- 38.1 C. Weitkamp: *Lidar: Range-Resolved Optical Remote Sensing of the Atmosphere*, Vol. 102 (Springer, New York 2005)
- 38.2 G.K. Schwemmer, M. Dombrowski, C.L. Korb, J. Milrod, H. Walden, R.H. Kagann: A lidar system for measuring atmospheric pressure and temperature profiles, *Rev. Sci. Instrum.* **58**(12), 2226–2237 (1987)
- 38.3 F. Chouza, B. Witschas, O. Reitebuch: Heterodyne high-spectral-resolution lidar, *Appl. Opt.* **56**(29), 8121–8134 (2017)
- 38.4 E.V. Browell, C.F. Butler, S. Ismail, P.A. Robinette, A.F. Carter, N.S. Higdon, O.B. Toon, M.R. Schoeberl, A.F. Tuck: Airborne lidar observations in the wintertime Arctic stratosphere: Polar stratospheric clouds, *Geophys. Res. Lett.* **17**(4), 385–388 (1990)
- 38.5 P. Mörl, M.E. Reinhardt, W. Renger, R. Schellhase: The use of the airborne lidar system ALEX F 1 for aerosol tracing in the lower troposphere, *Beitr. Phys. Atmos.* **54**(4), 403–410 (1981)
- 38.6 E.E. Uthe, B.M. Morley, N.B. Nielsen: Airborne lidar measurements of smoke plume distribution, vertical transmission, and particle size, *Appl. Opt.* **21**(3), 460–463 (1982)
- 38.7 J.L. McElroy, T.B. Smith: Vertical pollutant distributions and boundary layer structure observed by airborne lidar near the complex southern California coastline, *Atmos. Environ.* (1967) **20**(8), 1555–1566 (1986)
- 38.8 R.M. Hoff, M. Harwood, A. Sheppard, F. Froude, J.B. Martin, W. Strapp: Use of airborne lidar to determine aerosol sources and movement in the Lower Fraser Valley (LFV), BC, *Atmos. Environ.* **31**(14), 2123–2134 (1997)
- 38.9 M.J. McGill, D.L. Hlavka, W.D. Hart, E.J. Welton, J.R. Campbell: Airborne lidar measurements of aerosol optical properties during SAFARI-2000, *J. Geophys. Res. Atmos.* **108**(D13), 1–12 (2003)
- 38.10 M. Esselborn, M. Wirth, A. Fix, M. Tesche, G. Ehret: Airborne high spectral resolution lidar for measuring aerosol extinction and backscatter coefficients, *Appl. Opt.* **47**(3), 346–358 (2008)
- 38.11 J.W. Hair, C.A. Hostetler, A.L. Cook, D.B. Harper, R.A. Ferrare, T.L. Mack, W. Welch, L.R. Izquierdo, F.E. Hovis: Airborne high spectral resolution lidar for profiling aerosol optical properties, *Appl. Opt.* **47**(36), 6734–6752 (2008)
- 38.12 D.N. Whiteman, K. Rush, S. Rabenhorst, W. Welch, M. Cadirola, G. McIntire, F. Russo, M. Adam, D. Venable, R. Connell, I. Veselovskii, R. Forno, B. Mielke, B. Stein, T. Leblanc, S. McDermid, H. Vömel: Airborne and ground-based measurements using a high-performance Raman lidar, *J. Atmos. Ocean. Technol.* **27**(11), 1781–1801 (2010)
- 38.13 B. Liu, Z. Wang, Y. Cai, P. Wechsler, W. Kuestner, M. Burkhart, W. Welch: Compact airborne Raman lidar for profiling aerosol, water vapor and clouds, *Opt. Express* **22**(17), 20613–20621 (2014)
- 38.14 D. Bruneau, J. Pelon, F. Blouzon, J. Spatazza, P. Genau, G. Buchholtz, N. Amarouche, A. Abchiche, O. Aouji: 355-nm high spectral resolution airborne lidar LNG: system description and first results, *Appl. Opt.* **54**(29), 8776–8785 (2015)

- 38.15 S. Ismail, E.V. Browell: Airborne and spaceborne lidar measurements of water vapor profiles: A sensitivity analysis, *Appl. Opt.* **28**(17), 3603–3615 (1989)
- 38.16 N.S. Higdon, E.V. Browell, P. Ponsardin, B.E. Grossmann, C.F. Butler, T.H. Chyba, M.N. Mayo, R.J. Allen, A.W. Heuser, W.B. Grant, S. Ismail, S.D. Mayor, A.F. Carter: Airborne differential absorption lidar system for measurements of atmospheric water vapor and aerosols, *Appl. Opt.* **33**(27), 6422–6438 (1994)
- 38.17 W.S. Heaps, J. Burris: Airborne Raman lidar, *Appl. Opt.* **35**(36), 7128–7135 (1996)
- 38.18 A.S. Moore, K.E. Brown, W.M. Hall, J.C. Barnes, W.C. Edwards, L.B. Petway, A.D. Little, W.S. Luck, I.W. Jones, C.W. Antill, E.V. Browell, S. Ismail: Development of the Lidar Atmospheric Sensing Experiment (LASE) – an advanced airborne DIAL instrument. In: *Advances in atmospheric remote sensing with lidar*, ed. by A. Ansmann, R. Neuber, P. Rairoux, U. Wandinger (Springer, Berlin, Heidelberg 1997) pp. 281–288
- 38.19 E.V. Browell, S. Ismail, W.B. Grant: Differential absorption lidar (DIAL) measurements from air and space, *Appl. Phys. B* **67**(4), 399–410 (1998)
- 38.20 D. Bruneau, P. Quaglia, C. Flamant, M. Meissonnier, J. Pelon: Airborne lidar LEANDRE II for water-vapor profiling in the troposphere. I. System description, *Appl. Opt.* **40**(21), 3450–3461 (2001)
- 38.21 M. Wirth, W. Renger: Evidence of large scale ozone depletion within the Arctic Polar Vortex 94/95 based on airborne LIDAR measurements, *Geophys. Res. Lett.* **23**(8), 813–816 (1996)
- 38.22 R.J. Alvarez, C.J. Senff, R.M. Hardesty, D.D. Parrish, W.T. Luke, T.B. Watson, P.H. Daum, N. Gillani: Comparisons of airborne lidar measurements of ozone with airborne in situ measurements during the 1995 Southern Oxidants Study, *J. Geophys. Res. Atmos.* **103**(D23), 31155–31171 (1998)
- 38.23 G. Ancellet, F. Ravetta: Compact airborne lidar for tropospheric ozone: description and field measurements, *Appl. Opt.* **37**(24), 5509–5521 (1998)
- 38.24 R.J. Alvarez, C.J. Senff, A.O. Langford, A.M. Weickmann, D.C. Law, J.L. Machol, D.A. Merritt, R.D. Marchbanks, S.P. Sandberg, W.A. Brewer, R.M. Hardesty, R.M. Banta: Development and application of a compact, tunable, solid-state airborne ozone lidar system for boundary layer profiling, *J. Atmos. Ocean. Technol.* **28**(10), 1258–1272 (2011)
- 38.25 J.B. Abshire, H. Riris, G.R. Allan, C.J. Weaver, J. Mao, X. Sun, W.E. Hasselbrack, S.R. Kawa, S. Biraud: Pulsed airborne lidar measurements of atmospheric CO₂ column absorption, *Tellus B* **62**(5), 770–783 (2010)
- 38.26 J.T. Dobler, F.W. Harrison, E.V. Browell, B. Lin, D. McGregor, S. Kooi, Y. Choi, S. Ismail: Atmospheric CO₂ column measurements with an airborne intensity-modulated continuous wave 157 micron fiber laser lidar, *Appl. Opt.* **52**(12), 2874–2892 (2013)
- 38.27 A.K. Ramanathan, J. Mao, J.B. Abshire, G.R. Allan: Remote sensing measurements of the CO₂ mixing ratio in the planetary boundary layer using cloud slicing with airborne lidar, *Geophys. Res. Lett.* **42**(6), 2055–2062 (2015)
- 38.28 A. Amediek, G. Ehret, A. Fix, M. Wirth, C. Büdenbender, M. Quatrevalet, C. Kiemle, C. Gerbig: CHARM-F – a new airborne integrated-path differential-absorption lidar for carbon dioxide and methane observations: Measurement performance and quantification of strong point source emissions, *Appl. Opt.* **56**(18), 5182–5197 (2017)
- 38.29 A. Fix, G. Ehret, A. Hoffstädt, H.H. Klingenberg, C. Lemmerz, P. Mahnke, M. Ulbricht, M. Wirth, R. Wittig, W. Zirnig: CHARM-A helicopter-borne lidar system for pipeline monitoring. In: *22nd International Laser Radar Conference (ILRC 2004)*, Vol. SP-561, ed. by G. Pappalardo, A. Amodeo (European Space Agency, Noordwijk 2004) p. 45
- 38.30 H. Riris, K. Numata, S. Li, S. Wu, A. Ramanathan, M. Dawsey, J. Mao, R. Kawa, J.B. Abshire: Airborne measurements of atmospheric methane column abundance using a pulsed integrated-path differential absorption lidar, *Appl. Opt.* **51**(34), 8296–8305 (2012)
- 38.31 J. Bilbro, G. Fichtl, D. Fitzjarrald, M. Krause, R. Lee: Airborne Doppler lidar wind field measurements, *Bull. Am. Meteorol. Soc.* **65**(4), 348–359 (1984)
- 38.32 J.W. Bilbro, C. DiMarzio, D. Fitzjarrald, S. Johnson, W. Jones: Airborne Doppler lidar measurements, *Appl. Opt.* **25**(21), 3952–3960 (1986)
- 38.33 R. Targ, B.C. Steakley, J.G. Hawley, L.L. Ames, P. Forney, R. Swanson, R. Stone, R.G. Otto, V. Zarifis, P. Brockman, R.S. Calloway, S.H. Klein, P.A. Robinson: Coherent lidar airborne wind sensor II: flight-test results at 2 and 10 μm, *Appl. Opt.* **35**(36), 7117–7127 (1996)
- 38.34 P.H. Flamant, C. Werner, F. Koepp, C. Loth, P. Delville, O. Reitebuch, C. Boitel, D. Bruneau, P. Drobinski, R. Haering, H. Herrmann, M. Klier, M. Lopez, M. Meissonnier, E. Nagel, B. Romand, L. Sauvage, M. Schrecker, J. Streicher, G. Wildgruber: WIND: the joint French-German airborne Doppler lidar, *Proc. SPIE* **3865**, 1–8 (1999)
- 38.35 C.J. Grund, R.M. Banta, J.L. George, J.N. Howell, M.J. Post, R.A. Richter, A.M. Weickmann: High-resolution doppler lidar for boundary layer and cloud research, *J. Atmos. Ocean. Technol.* **18**(3), 376–393 (2001)
- 38.36 O. Lux, C. Lemmerz, F. Weiler, U. Marksteiner, B. Witschas, S. Rahm, A. Schäfler, O. Reitebuch: Airborne wind lidar observations over the North Atlantic in 2016 for the pre-launch validation of the satellite mission Aeolus, *Atmos. Meas. Tech.* **11**(6), 3297–3322 (2018)
- 38.37 A. Schäfler, G. Craig, H. Wernli, P. Arbogast, J.D. Doyle, R. McTaggart-Cowan, J. Methven, G. Rivière, F. Ament, M. Boettcher, M. Bramberger, Q. Cazenave, R. Cotton, S. Crewell, J. Delanoë, A. Dörnbrack, A. Ehrlich, F. Ewald, A. Fix, C.M. Grams, S.L. Gray, H. Grob, S. Groß, M. Hagen, B. Harvey, L. Hirsch, M. Jacob, T. Kölling,

- H. Konow, C. Lemmerz, O. Lux, L. Magnusson, B. Mayer, M. Mech, R. Moore, J. Pelon, J. Quinting, S. Rahm, M. Rapp, M. Rautenhaus, O. Reitebuch, C.A. Reynolds, H. Sodemann, T. Spengler, G. Vaughan, M. Wendisch, M. Wirth, B. Witschas, K. Wolf, T. Zinner: The North Atlantic waveguide and downstream impact experiment, *Bull. Am. Meteorol. Soc.* **99**(8), 1607–1637 (2018)
- 38.38 M.P. McCormick: Airborne and spaceborne lidar. In: *Lidar: Range-Resolved Optical Remote Sensing of the Atmosphere*, Vol. 102, ed. by C. Weitkamp (Springer, New York 2005) pp. 355–397
- 38.39 J.C. Fernandez Diaz, W.E. Carter, R.L. Shrestha, C.L. Glennie: LiDAR remote sensing. In: *Handbook of Satellite Applications*, ed. by J.N. Pelton, S. Madry, S. Camacho-Lara (Springer, New York 2017) pp. 757–808
- 38.40 M.P. McCormick, P. Hamill, T.J. Pepin, W.P. Chu, T.J. Swisler, L.R. McMaster: Satellite studies of the stratospheric aerosol, *Bull. Am. Meteorol. Soc.* **60**(9), 1038–1047 (1979)
- 38.41 J.D. Spinhirne, M.Z. Hansen, L.O. Caudill: Cloud top remote sensing by airborne lidar, *Appl. Opt.* **21**(9), 1564–1571 (1982)
- 38.42 E.V. Browell, A.F. Carter, S.T. Shipley, R.J. Allen, C.F. Butler, M.N. Mayo, J.H. Siviter, W.M. Hall: NASA multipurpose airborne DIAL system and measurements of ozone and aerosol profiles, *Appl. Opt.* **22**(4), 522–534 (1983)
- 38.43 E.V. Browell: Remote sensing of tropospheric gases and aerosols with an airborne DIAL system. In: *Optical and Laser Remote Sensing*, ed. by D.K. Killinger, A. Mooradian (Springer, Berlin, Heidelberg 1983) pp. 138–147
- 38.44 C.L. Korb, G.K. Schwemmer, M. Dombrowski, C.Y. Weng: Airborne and ground based lidar measurements of the atmospheric pressure profile, *Appl. Opt.* **28**(15), 3015–3020 (1989)
- 38.45 E.W. McCaul, H.B. Bluestein, R.J. Doviak: Airborne Doppler lidar techniques for observing severe thunderstorms, *Appl. Opt.* **25**(5), 698–708 (1986)
- 38.46 K.H. Kwon, D.C. Senft, C.S. Gardner: Airborne sodium lidar observations of horizontal and vertical wave number spectra of mesopause density and wind perturbations, *J. Geophys. Res. Atmos.* **95**(D9), 13723–13736 (1990)
- 38.47 G. Poberaj, A. Fix, A. Assion, M. Wirth, C. Kiemle, G. Ehret: Airborne all-solid-state DIAL for water vapour measurements in the tropopause region: system description and assessment of accuracy, *Appl. Phys. B* **75**(2), 165–172 (2002)
- 38.48 D.M. Winker, R.H. Couch, M.P. McCormick: An overview of LITE: NASA's Lidar In-space Technology Experiment, *Proc. IEEE* **84**(2), 164–180 (1996)
- 38.49 Y.S. Balin, V.E. Mel'nikov, A.A. Tikhomirov, I.V. Znamenskii, S.V. SamoiloVA, V.E. Zuev: Spaceborne aerosol lidar BALKAN-1, *Proc. SPIE* **2310**, 144–151 (1994)
- 38.50 M.-L. Chanin, A. Hauchecorne, C. Malique, D. Nedeljkovic, J.-E. Blamont, M. Desbois, G. Tulinov, V. Melnikov: Premiers résultats du lidar Alissa embarqué à bord de la station Mir, *C. R. Acad. Sci. Ser. IIA Earth Planet. Sci.* **328**(6), 359–366 (1999)
- 38.51 G.G. Matvienko, V.E. Zuev, V.S. Shamanaev, G.P. Kokhanenko, A.M. Sutormin, A.I. Buranskii, S.E. Belousov, A.A. Tikhomirov: Lidar BALKAN-2 for the space platform ALMAZ-1B, *Proc. SPIE* **2310**, 161–163 (1994)
- 38.52 J.B. Abshire, X. Sun, H. Riris, J.M. Sirota, J.F. McGarry, D. Palm, S. Yi, P. Liiva: Geoscience Laser Altimeter System (GLAS) on the ICESat Mission: On-orbit measurement performance, *Geophys. Res. Lett.* **32**(21), 1–4 (2005)
- 38.53 J.D. Spinhirne, S.P. Palm, W.D. Hart, D.L. Hlavka, E.J. Welton: Cloud and aerosol measurements from GLAS: Overview and initial results, *Geophys. Res. Lett.* **32**(22), 1–5 (2005)
- 38.54 D.M. Winker, M.A. Vaughan, A. Omar, Y. Hu, K.A. Powell, Z. Liu, W.H. Hunt, S.A. Young: Overview of the CALIPSO mission and CALIOP data processing algorithms, *J. Atmos. Ocean. Technol.* **26**(11), 2310–2323 (2009)
- 38.55 M.J. McGill, J.E. Yorks, V.S. Scott, A.W. Kupchock, P.A. Selmer: The Cloud-Aerosol Transport System (CATS): a technology demonstration on the International Space Station, *Proc. SPIE* **9612**, Lidar Remote Sensing for Environmental Monitoring XV, 96120A (2015)
- 38.56 A. Amediak, M. Wirth: Pointing verification method for Spaceborne Lidars, *Remote Sens.* **9**(56), 1–8 (2017)
- 38.57 A. Noureldin, T.B. Karamat, J. Georgy: *Fundamentals of Inertial Navigation, Satellite-based Positioning and their Integration* (Springer, Berlin, Heidelberg 2013)
- 38.58 D.D. McCarthy, G. Petit: *IERS Conventions (2003)*, Vol. 32, 1st edn. (International Earth Rotation and Reference Systems Service, Frankfurt am Main 2003)
- 38.59 M. Ligas, P. Banasik: Conversion between Cartesian and geodetic coordinates on a rotational ellipsoid by solving a system of nonlinear equations, *Geod. Cartogr.* **60**(2), 145–159 (2011)
- 38.60 L.O. Lupash: A new algorithm for the computation of the geodetic coordinates as a function of Earth-Centered Earth-Fixed coordinates, *J. Guidance Control Dyn.* **8**(6), 787–789 (1985)
- 38.61 ECMWF: *IFS Documentation – Cy43r3: Part III: Dynamics and Numerical Procedures* (European Centre for Medium-Range Weather Forecasts, Reading 2017)
- 38.62 ECMWF: *IFS Documentation – Cy43r3: Part IV: Physical Processes* (European Centre for Medium-Range Weather Forecasts, Reading 2017)
- 38.63 F.G. Lemoine, S.C. Kenyon, J.K. Factor, R.G. Trimmer, N.K. Pavlis, D.S. Chinn, C.M. Cox, S.M. Klosko, S.B. Luthcke, M.H. Torrence, Y.M. Wang, R.G. Williamson, E.C. Pavlis, R.H. Rapp, T.R. Olson: *The Development of the Joint NASA GSFC and the National Imagery and Mapping Agency (NIMA) Geopotential Model EGM96* (National Aeronautics and Space Administration, Greenbelt 1998)

- 38.64 C. Kiemle, M. Quatrevalet, G. Ehret, A. Amediek, A. Fix, M. Wirth: Sensitivity studies for a space-based methane lidar mission, *Atmos. Meas. Tech.* **4**(10), 2195–2211 (2011)
- 38.65 S.P. Burton, R.A. Ferrare, C.A. Hostetler, J.W. Hair, R.R. Rogers, M.D. Obland, C.F. Butler, A.L. Cook, D.B. Harper, K.D. Froyd: Aerosol classification using airborne High Spectral Resolution Lidar measurements – methodology and examples, *Atmos. Meas. Tech.* **5**(1), 73–98 (2012)
- 38.66 R.A. Ferrare, E.V. Browell, S. Ismail, S.A. Kooi, L.H. Brasseur, V.G. Brackett, M.B. Clayton, J.D.W. Barrick, G.S. Diskin, J.E.M. Goldsmith, B.M. Lesht, J.R. Podolske, G.W. Sachse, F.J. Schmidlin, D.D. Turner, D.N. Whiteman, D. Tobin, L.M. Miloshevich, H.E. Revercomb, B.B. Demoz, P. Di Girolamo: Characterization of upper-troposphere water vapor measurements during AFWEX using LASE, *J. Atmos. Ocean. Technol.* **21**(12), 1790–1808 (2004)
- 38.67 D. Bruneau, P. Quaglia, C. Flamant, J. Pelon: Airborne lidar LEANDRE II for water–vapor profiling in the troposphere. II. First results, *Appl. Opt.* **40**(21), 3462–3475 (2001)
- 38.68 M. Wirth, A. Fix, P. Mahnke, H. Schwarzer, F. Schrandt, G. Ehret: The airborne multi-wavelength water vapor differential absorption lidar WALES: system design and performance, *Appl. Phys. B* **96**(1), 201 (2009)
- 38.69 ESA: *WALES – Water Vapour Lidar Experiment in Space*, Vol. ESA SP–1279(3) (European Space Agency, Noordwijk 2004)
- 38.70 R. Bhawar, P. Di Girolamo, D. Summa, C. Flamant, D. Althausen, A. Behrendt, C. Kiemle, P. Bosser, M. Cacciani, C. Champollion, T. Di Iorio, R. Engelmann, C. Herold, D. Müller, S. Pal, M. Wirth, V. Wulfmeyer: The water vapour inter-comparison effort in the framework of the Convective and Orographically-induced Precipitation Study: airborne-to-ground-based and airborne-to-airborne lidar systems, *Q. J. R. Meteorol. Soc.* **137**(S1), 325–348 (2011)
- 38.71 J.B. Abshire, A.K. Ramanathan, H. Riris, G.R. Allan, X. Sun, W.E. Hasselbrack, J. Mao, S. Wu, J. Chen, K. Numata, S.R. Kawa, M.Y.M. Yang, J. DiGangi: Airborne measurements of CO₂ column concentrations made with a pulsed IPDA lidar using a multiple-wavelength-locked laser and HgCdTe APD detector, *Atmos. Meas. Tech.* **11**(4), 2001–2025 (2018)
- 38.72 O. Reitebuch, C. Lemmerz, E. Nagel, U. Paffrath, Y. Durand, M. Endemann, F. Fabre, M. Chaloupy: The airborne demonstrator for the direct-detection doppler wind lidar ALADIN on ADM–Aeolus. Part I: Instrument design and comparison to satellite instrument, *J. Atmos. Ocean. Technol.* **26**(12), 2501–2515 (2009)
- 38.73 W.H. Hunt, D.M. Winker, M.A. Vaughan, K.A. Powell, P.L. Lucker, C. Weimer: CALIPSO Lidar Description and Performance Assessment, *J. Atmos. Ocean. Technol.* **26**(7), 1214–1228 (2009)
- 38.74 Y. Hu, K. Stamnes, M. Vaughan, J. Pelon, C. Weimer, D. Wu, M. Cisewski, W. Sun, P. Yang, B. Lin, A. Omar, D. Flittner, C. Hostetler, C. Trepte, D. Winker, G. Gibson, M. Santa-Maria: Sea surface wind speed estimation from space-based lidar measurements, *Atmos. Chem. Phys.* **8**(13), 3593–3601 (2008)
- 38.75 G.L. Stephens, D.G. Vane, R.J. Boain, G.G. Mace, K. Sassen, Z. Wang, A.J. Illingworth, E.J. O’connor, W.B. Rossow, S.L. Durden, S.D. Miller, R.T. Austin, A. Benedetti, C. Mitrescu, the CloudSat Science Team: The CloudSat mission and the A–train, *Bull. Am. Meteorol. Soc.* **83**(12), 1771–1790 (2002)
- 38.76 J.E. Yorks, M.J. McGill, S.P. Palm, D.L. Hlavka, P.A. Selmer, E.P. Nowottnick, M.A. Vaughan, S.D. Rodier, W.D. Hart: An overview of the CATS level 1 processing algorithms and data products, *Geophys. Res. Lett.* **43**(9), 4632–4639 (2016)
- 38.77 O. Reitebuch: The Spaceborne wind Lidar mission ADM–Aeolus. In: *Atmospheric Physics: Background – Methods – Trends*, ed. by U. Schumann (Springer, Berlin, Heidelberg 2012) pp. 815–827
- 38.78 EASA: *CM–AS–006 Issue 01: Certification of Airborne Systems Using Light Amplification by Stimulated Emission of Radiation (LASER) With High Energy* (European Aviation Safety Agency, Cologne 2016)
- 38.79 E.E. Uthe, W. Viezee, B.M. Morley, J.K.S. Ching: Airborne Lidar Tracking of Fluorescent Tracers for Atmospheric Transport and Diffusion Studies, *Bull. Am. Meteorol. Soc.* **66**(10), 1255–1262 (1985)
- 38.80 C. Flamant, J. Pelon, P. Chazette, V. Trouillet, P.K. Quinn, R. Frouin, D. Bruneau, J.F. Leon, T.S. Bates, J. Johnson, J. Livingston: Airborne lidar measurements of aerosol spatial distribution and optical properties over the Atlantic Ocean during a European pollution outbreak of ACE–2, *Tellus B* **52**(2), 662–677 (2000)
- 38.81 B. Weinzierl, D. Sauer, M. Esselborn, A. Petzold, A. Veira, M. Rose, S. Mund, M. Wirth, A. Ansmann, M. Tesche, S. Gross, V. Freudenthaler: Microphysical and optical properties of dust and tropical biomass burning aerosol layers in the Cape Verde region – an overview of the airborne in situ and lidar measurements during SAMUM–2, *Tellus B* **63**(4), 589–618 (2011)
- 38.82 S. Groß, M. Esselborn, B. Weinzierl, M. Wirth, A. Fix, A. Petzold: Aerosol classification by airborne high spectral resolution lidar observations, *Atmos. Chem. Phys.* **13**(5), 2487–2505 (2013)
- 38.83 S. Groß, M. Wirth, A. Schäfler, A. Fix, S. Kaufmann, C. Voigt: Potential of airborne lidar measurements for cirrus cloud studies, *Atmos. Meas. Tech.* **7**(8), 2745–2755 (2014)
- 38.84 B. Urbanek, S. Groß, A. Schäfler, M. Wirth: Determining stages of cirrus evolution: a cloud classification scheme, *Atmos. Meas. Tech.* **10**(5), 1653–1664 (2017)
- 38.85 J.D. Spinhirne, M.Z. Hansen, L.O. Caudill: Cloud top remote sensing by airborne lidar, *Appl. Opt.* **21**(9), 1564–1571 (1982)

- 38.86 S. Nyeki, M. Kalberer, I. Colbeck, S. De Wekker, M. Furger, H.W. Gäggeler, M. Kossmann, M. Lugauer, D. Steyn, E. Weingartner, M. Wirth, U. Baltensperger: Convective boundary layer evolution to 4 km asl over High-alpine terrain: Airborne lidar observations in the Alps, *Geophys. Res. Lett.* **27**(5), 689–692 (2000)
- 38.87 K.J. Davis, N. Gamage, C.R. Hagelberg, C. Kiemle, D.H. Lenschow, P.P. Sullivan: An objective method for deriving atmospheric structure from airborne lidar observations, *J. Atmos. Ocean. Technol.* **17**(11), 1455–1468 (2000)
- 38.88 C. Kiemle, G. Ehret, A. Fix, M. Wirth, G. Poberaj, W.A. Brewer, R.M. Hardesty, C. Senff, M.A. LeMone: Latent heat flux profiles from collocated airborne water vapor and wind lidars during IHOP_2002, *J. Atmos. Ocean. Technol.* **24**(4), 627–639 (2007)
- 38.89 E.V. Browell, E.F. Danielsen, S. Ismail, G.L. Gregory, S.M. Beck: Tropopause fold structure determined from airborne lidar and in situ measurements, *J. Geophys. Res. Atmos.* **92**(D2), 2112–2120 (1987)
- 38.90 A. Schäfler, A. Dörnbrack, C. Kiemle, S. Rahm, M. Wirth: Tropospheric water vapor transport as determined from airborne lidar measurements, *J. Atmos. Ocean. Technol.* **27**(12), 2017–2030 (2010)
- 38.91 R. Kaminen, T.N. Krishnamurti, R.A. Ferrare, S. Ismail, E.V. Browell: Impact of high resolution water vapor cross-sectional data on hurricane forecasting, *Geophys. Res. Lett.* **30**(5), 1–4 (2003)
- 38.92 M. Weissmann, R. Busen, A. Dörnbrack, S. Rahm, O. Reitebuch: Targeted observations with an airborne wind lidar, *J. Atmos. Ocean. Technol.* **22**(11), 1706–1719 (2005)
- 38.93 F. Harnisch, M. Weissmann, C. Cardinali, M. Wirth: Experimental assimilation of DIAL water vapour observations in the ECMWF global model, *Q. J. R. Meteorol. Soc.* **137**(659), 1532–1546 (2011)
- 38.94 A. Schäfler, F. Harnisch: Impact of the inflow moisture on the evolution of a warm conveyor belt, *Q. J. R. Meteorol. Soc.* **141**(686), 299–310 (2014)
- 38.95 F. Chouza, O. Reitebuch, M. Jähn, S. Rahm, B. Weinzierl: Vertical wind retrieved by airborne lidar and analysis of island induced gravity waves in combination with numerical models and in situ particle measurements, *Atmos. Chem. Phys.* **16**(7), 4675–4692 (2016)
- 38.96 D.M. Winker, M.T. Osborn: Airborne lidar observations of the Pinatubo volcanic plume, *Geophys. Res. Lett.* **19**(2), 167–170 (1992)
- 38.97 M. Wirth, G. Ehret, P. Mörl, W. Renger: Two dimensional stratospheric aerosol distributions during EASOE, *Geophys. Res. Lett.* **21**(13), 1287–1290 (1994)
- 38.98 K.S. Carslaw, M. Wirth, A. Tsias, B.P. Luo, A. Dörnbrack, M. Leutbecher, H. Volkert, W. Renger, J.T. Bacmeister, E. Reimer, T. Peter: Increased stratospheric ozone depletion due to mountain-induced atmospheric waves, *Nature* **391**(6668), 675 (1998)
- 38.99 G.S. Kent, L.R. Poole, M.P. McCormick: Characteristics of arctic polar stratospheric clouds as measured by airborne lidar, *J. Atmos. Sci.* **43**(20), 2149–2161 (1986)
- 38.100 C. Voigt, A. Dörnbrack, M. Wirth, S.M. Groß, M.C. Pitts, L.R. Poole, R. Baumann, B. Ehard, B.-M. Sinnhuber, W. Woiwode, H. Oelhaf: Widespread polar stratospheric ice clouds in the 2015–2016 Arctic winter – implications for ice nucleation, *Atmos. Chem. Phys.* **18**(21), 15623–15641 (2018)
- 38.101 C.S. Gardner: Introduction to ALOHA-90: the airborne lidar and observations of the Hawaiian airglow campaign, *Geophys. Res. Lett.* **18**(7), 1313–1316 (1991)
- 38.102 A.J. Illingworth, H.W. Barker, A. Beljaars, M. Ceccaldi, H. Chepfer, N. Clerbaux, J. Cole, J. Delanoë, C. Domenech, D.P. Donovan, S. Fukuda, M. Hiraoka, R.J. Hogan, A. Huenerbein, P. Kollias, T. Kubota, T. Nakajima, T.Y. Nakajima, T. Nishizawa, Y. Ohno, H. Okamoto, R. Oki, K. Sato, M. Satoh, M.W. Shephard, A. Velázquez-Blázquez, U. Wandinger, T. Wehr, G.-J. van Zadelhoff: The EarthCARE satellite: the next step forward in global measurements of clouds, aerosols, precipitation, and radiation, *Bull. Am. Meteorol. Soc.* **96**(8), 1311–1332 (2015)
- 38.103 G. Ehret, P. Bousquet, C. Pierangelo, M. Alpers, B. Millet, J.B. Abshire, H. Bovensmann, J.P. Burrows, F. Chevallier, P. Ciais, C. Crevoisier, A. Fix, P. Flamant, C. Frankenberg, F. Gibert, B. Heim, M. Heimann, S. Houweling, H.W. Hubberten, P. Jöckel, K. Law, A. Löw, J. Marshall, A. Agustí-Panareda, S. Payan, C. Prigent, P. Rairoux, T. Sachs, M. Scholze, M. Wirth: MERLIN: a French-German space lidar mission dedicated to atmospheric methane, *Remote Sens.* **9**(10), 1–29 (2017)
- 38.104 P. Bousquet, C. Pierangelo, C. Bacour, J. Marshall, P. Peylin, P.V. Ayar, G. Ehret, F.-M. Bréon, F. Chevallier, C. Crevoisier, F. Gibert, P. Rairoux, C. Kiemle, R. Armante, C. Bès, V. Cassé, J. Chinaud, O. Chomette, T. Delahaye, D. Edouard, F. Estève, A. Fix, A. Friker, A. Klonecki, M. Wirth, M. Alpers, B. Millet: Error budget of the MEthane Remote Lidar mission and its impact on the uncertainties of the global methane budget, *J. Geophys. Res. Atmos.* **123**, 11766–11785 (2018)

Martin Wirth

Institut für Physik der Atmosphäre
Deutsches Zentrum für Luft- und
Raumfahrt e. V. (DLR)
Weßling, Germany
martin.wirth@dlr.de



Martin Wirth received his PhD in Physics in 1996 from the LMU in Munich. He is currently a research scientist at the Lidar Department at the German Aerospace Centre (DLR) in Weßling, where he has developed several airborne lidar systems for measuring aerosols and atmospheric trace gases (e.g., ozone and water vapor). He is also a member of the Science Advisory Group for MERLIN, the French-German methane lidar space mission.

Airborne Radar

39. Airborne Radar

Martin Hagen , Julien Delanoë , Scott Ellis, Florian Ewald , Jeffrey French , Samuel Haimov , Gerald Heysmsfield , Andrew L. Pazmany 

Ground-based radar systems have been used to observe clouds and precipitation since the 1940s. While weather radars that use centimeter waves can observe precipitation several hundred kilometers away, radars that are dedicated to cloud observations use millimeter waves and have limited ranges of just a few tens of kilometers. Airborne radars have the advantages that they can perform measurements close to the region of interest and they provide radar information on regions that ground-based radars cannot access. There is no such thing as a standard airborne radar system; all systems are tailored for use on specific research aircraft, although some of them are designed to be modular so that they can be mounted on various aircraft. Airborne radar systems use frequencies ranging from those in the X band to those in the W band. Radars that use shorter wavelengths are preferred due to spatial restrictions on antenna size in aircraft, but C-band systems are also being considered for installation in large aircraft. Besides reflectivity (the backscatter signal), the radial motions of scattering particles can be measured and used to retrieve atmospheric motion. In addition, several airborne radars are able to measure dual-polarization backscatter signals that can be employed to identify different types of hydrometeors.

39.1	Measurement Parameters and Principles	1098
39.1.1	Measurement Principles	1098
39.1.2	Measured Parameters	1098
39.2	History	1100
39.2.1	The Wyoming Cloud Radar (WCR)	1100
39.2.2	ELDORA	1101
39.2.3	NASA High-Altitude Radars (EDOP, CRS, HIWRAP, EXRAD)	1101
39.3	Theory	1102
39.3.1	Radar Principle	1102
39.3.2	Wavelength Selection	1103
39.3.3	Technology	1105
39.3.4	Airborne Doppler Measurement	1105
39.3.5	Multi-Doppler Principle	1106
39.3.6	Dual Polarization	1108
39.4	Devices and Systems	1108
39.4.1	W-Band Wyoming Cloud Radar (WCR)	1108
39.4.2	W-Band HIAPER (HCR)	1109
39.4.3	W-Band RASTA	1109
39.4.4	Ka-Band HALO (HAMP)	1110
39.4.5	HIWRAP (Ku, Ka), CRS (W), EXRAD (X)	1111
39.4.6	Ka-Band Precipitation Radar (KPR)	1113
39.5	Specifications	1114
39.6	Calibration and Quality Control	1114
39.6.1	Radar Calibration	1115
39.6.2	Pointing Direction Calibration	1115
39.6.3	Quality Control	1116
39.7	Maintenance	1117
39.8	Applications	1117
39.8.1	Cumulus Cloud Observations	1117
39.8.2	Observations of Synoptic-Scale Frontal Systems	1117
39.8.3	Deep Convection	1118
39.8.4	Stratocumulus Observations	1118
39.8.5	Wind Field Retrieval in Stratiform Precipitation	1120
39.8.6	Synergetic Retrieval of Cloud Microphysics Using Radar and Lidar ...	1122
39.9	Future Developments	1123
39.9.1	C130 C-Band Phased Array Radar	1123
39.9.2	Quadratic Phase Coding with Solid-State Weather Radars	1124
39.10	Further Reading	1124
	References	1125

Clouds and precipitation play an important role in atmospheric science. While detailed studies of microphysical properties such as particle concentration, shape, phase, and density can only be achieved through airborne or ground-based in-situ observations, the three-dimensional structures of cloud and precipitation systems can only be accessed by radar and, to some extent, lidar observations. The measurements ranges of ground-based radar systems are limited, meaning that phenomena of interest (e.g., hurricanes) are not within range. In contrast, airborne radars have the advantage that they can provide targeted radar measurements in regions—such as over oceans—that cannot be probed by ground-based radars.

A number of research aircraft can be equipped with additional remote-sensing instruments or in-situ cloud probes. It is difficult to achieve the optimal combina-

tion of in-situ cloud probes [39.1] and remote-sensing observations if the probes are mounted on the same aircraft because measurements of the same location in the cloud cannot be performed by both systems at the same time. Remote-sensing instruments such as microwave radiometers (Chap. 41) and lidars (Chap. 38) provide additional information about clouds and precipitation and can be used for synergistic retrievals of microphysical parameters.

This chapter does not discuss the weather radar systems used by commercial and private aircraft to avoid severe weather, even though these systems have occasionally been used for meteorological research. Such systems are poorly suited to providing quantitative measurements, as they are intended for the detection and localization of regions in the atmosphere (such as thunderstorms) that are not suitable for aircraft.

39.1 Measurement Parameters and Principles

The measurement parameters and principles of meteorological radars are described in much more detail in Chaps. 30 and 32 of this Handbook and in other textbooks such as [39.2, 3]. Further details on airborne measurement systems can be found in the book by *Wendisch and Brenguier* on airborne measurements [39.4]; Chap. 9 of that book describes airborne radar and lidar systems in detail [39.5]. Radar techniques are described in depth in [39.6].

39.1.1 Measurement Principles

Radar, an acronym for *radio detection and ranging*, is the technique of detecting a target using the electromagnetic waves reflected from that target. Meteorological

radar systems also use these reflected waves to quantify the target. Typically, a radar system transmits a short electromagnetic pulse towards the target, and the range of the target is evaluated by measuring the transit time of the radar pulse. Provided the direction in which the narrow beam was emitted by the radio antenna is known, the direction of the target can also be estimated (Fig. 39.1).

The power of the backscattered signal depends on the size and number of the targets (i.e., cloud and precipitation particles) within the measurement volume. A number of radar pulses are typically averaged to get a more stable signal from the randomly distributed targets within the measurement volume. If the radar is coherent (which can be achieved through various techniques), it is possible to estimate the Doppler shift of the backscattered signal. This allows the motion of the particles relative to the radar beam to be estimated. The design of the antenna and its components determine the polarization plane of the transmitted and received pulses. Different techniques allow the target to be measured using different polarizations of the electromagnetic wave. Since the backscattered signal of a target can differ for different polarized waves, target classification is possible.

39.1.2 Measured Parameters

A number of radar parameters are measured by airborne radars. Typical measured parameters are summarized in Table 39.1, and are described in more detail in the following sections.

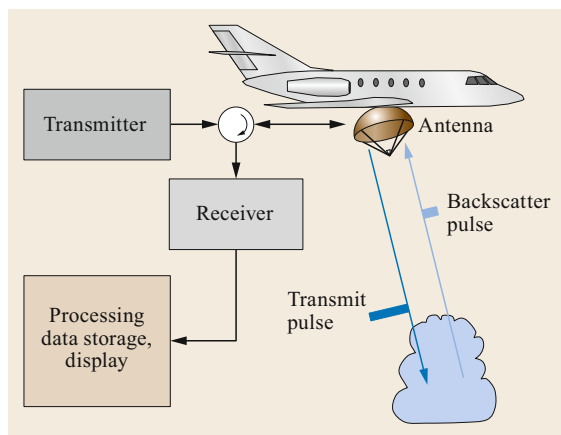


Fig. 39.1 Measurement principle of radar

Table 39.1 Parameters measured by airborne radars (note that some radar systems cannot measure all of the parameters shown)

Parameter	Description	Unit	Symbol
Reflectivity	Backscatter signal	$\text{mm}^6 \text{m}^{-3}$	z
	Logarithm of the backscatter signal	dBz	Z
Doppler velocity	Radial velocity of particles	m s^{-1}	V or v_r
Spectral width	Width of the Doppler spectrum	m s^{-1}	W or σ_v
Linear depolarization ratio	Ratio of the copolar and crosspolar backscatter signals	dB	LDR

Radar Reflectivity Factor

Radar reflectivity is a synonym for the magnitude of the reflected radar pulse. The relationship between the received signal P_r and the scattering cross-section σ of the target is given by the radar equation for volume targets,

$$P_r = \frac{P_t g^2 \lambda^2}{64 \pi^3 r^4} \frac{\pi r^2 \theta_0^2 h}{8} \frac{1}{2 \ln(2)} \sum_{i=1}^n \sigma_i, \quad (39.1)$$

where P_t is the transmitted power, g is the antenna gain, λ is the wavelength, θ_0 is the beamwidth, h is the pulse length, r is the distance to the targets, and σ_i is the scattering cross-section of the targets within the measurement volume. It is assumed that the measurement volume is uniformly filled with scattering targets. The first term of the equation is the radar equation for a single-point target, the second gives the measurement volume, and the third term accounts for the fact that only part of the transmitted power is within the measurement volume bounded by the half-power beamwidth θ_0 .

For particles that are large compared to the wavelength (diameter $D > 10\lambda$), the scattering cross-section σ of the target is given by its geometric cross-section. For particles that are much smaller than the wavelength ($D < 1/10\lambda$), the scattering cross-section can be approximated by Rayleigh scattering, i.e.,

$$\sigma = \frac{\pi^5}{\lambda^4} |K|^2 D^6, \quad (39.2)$$

where $K = (m^2 - 1)/(m^2 + 2)$ represents the complex refractive index m of the scattering particle ($|K|^2 \approx 0.93$ for water and $|K|^2 \approx 0.2$ for ice). Note that the value of $|K|^2$ for water is dependent on the temperature and frequency. Assuming that the targets are water particles that are much smaller than the wavelength, the radar reflectivity factor z is defined as the sum of D^6 for all particles within the unit volume V ,

$$z = \frac{1}{V} \sum_{i=1}^n D_i^6. \quad (39.3)$$

The unit of z is $\text{mm}^6 \text{m}^{-3}$. It is common in radar meteorology to express the reflectivity factor as a logarithmic ratio with respect to the reflectivity factor ($z = 1 \text{ mm}^6 \text{m}^{-3}$) of a single water sphere with a diameter of 1 mm per unit volume,

$$Z = 10 \log_{10} \left(\frac{z}{1 \text{ mm}^6 \text{m}^{-3}} \right). \quad (39.4)$$

The unit of the logarithmic quantity Z is dBz (decibel z). Informally, but also in a large number of publications, the term *reflectivity* is used instead of reflectivity factor. This should not be confused with the wavelength-dependent reflectivity η , defined as the sum of the scattering cross-sections (39.7), which must account for Mie scattering in the case of a cloud radar.

Doppler Velocity and Spectral Width

If there is relative motion with velocity v between the radar and the target, a frequency shift of the reflected wave is observed by the radar. This frequency shift is given by

$$f_D = \pm \frac{2v}{\lambda}, \quad (39.5)$$

as the Doppler effect occurs twice: once on the way to the target and once on the way back to the radar.

Even though a radar cannot measure the frequency shift directly (it actually measures phase differences between subsequent pulses), the term *Doppler velocity* or radial velocity is widely used in radar meteorology, whereas scientists working on lidar systems prefer the term *line-of-sight component* (or *velocity*). Only motion towards or away from the radar (the radial or line-of-sight component) can be detected based on the Doppler effect. If the target moves perpendicular to the radar beam, no Doppler effect is visible.

The standard deviation of the phase measurements is termed the spectral width since it describes the width of the Doppler velocity spectrum. The spectral width is a measure of the turbulence within the measurement volume or—in the case of a radar viewing vertically—a measure of the diversity in the fall speeds of different particle types and sizes.

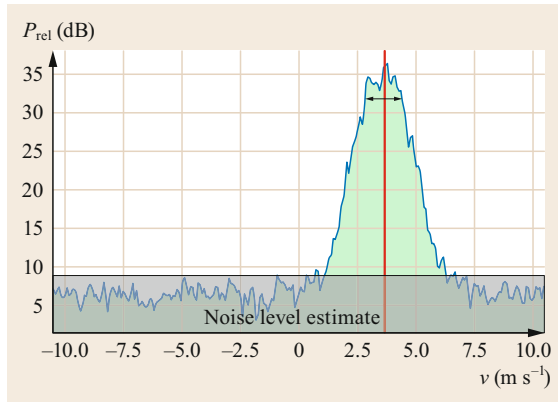


Fig. 39.2 Example of a measured Doppler spectrum (blue line). The gray area indicates the noise level, the green area above the noise level is the signal-to-noise power, the red line is the mean Doppler velocity, and the line with black arrows indicates the spectral width

Doppler Spectrum

Besides using the technique described above, the phase measurements can be transferred by a Fourier transform into the frequency domain. Frequency is equivalent to Doppler velocity in this case; see (39.5). The Doppler spectrum gives the backscatter power or reflectivity for each Doppler velocity bin. Figure 39.2 shows an example of a Doppler spectrum from a vertically pointing ground-based cloud radar. The green area is the signal-to-noise ratio (SNR) after the noise has been subtracted. Noise levels can be estimated using the Hildebrand and

Sekhon algorithm [39.7]. The reflectivity can be estimated from the SNR using the radar equation. The mean Doppler velocity is the first moment of the spectrum, which is indicated by the red vertical line in Fig. 39.2. The horizontal line with arrows indicates the estimated spectral width (the second moment of the spectrum).

Linear Depolarization Ratio

The linear depolarization ratio (LDR) describes how much of the energy of the transmitted polarized wave is scattered back in the orthogonal crosspolar scattering plane (Sect. 39.3.6). It is given by

$$\text{LDR} = 10 \log \left(\frac{z_{\text{cx}}}{z_{\text{co}}} \right), \quad (39.6)$$

where z_{cx} is the reflectivity factor (in $\text{mm}^6 \text{m}^{-3}$) for the crosspolar backscatter signal when a signal with copolar polarization z_{co} is transmitted. The unit of the LDR is dB. Depolarization is caused by irregularly shaped particles that are canted or that tumble or rotate heavily while falling. These are often particles that are coated in water, such as melting snowflakes, wet graupel, or hail. The LDR is about -35 dB for weak rain, -25 dB for graupel, and -15 dB or higher for melting hail, meaning that the LDR can be used to identify hydrometeors. The LDR is also a good indicator of ground clutter returns. The lower limit of the LDR is given by technical constraints such as the isolation between the two receiver channels and the purity of the antenna shape and feed horn.

39.2 History

In the late 1960s and early 1970s, several groups discussed the need for aircraft equipped with weather radar systems as well as the technical feasibility of installing such systems on aircraft. An airborne radar investigation of Hurricane Debbie was performed in 1969 [39.8], and the installation of meteorological Doppler radars on aircraft was proposed in [39.9]. Although the main aim of these systems was to probe the motion of particles at vertical incidence, it was also proposed that they could be used to measure the horizontal wind field of a storm. At that time, radars used long wavelengths (3 or 10 cm) to study precipitation processes. During the Battan Memorial and 40th Anniversary Radar Meteorology Conference in 1987, airborne cloud radars were proposed and discussed by several groups [39.10, 11]. These discussions led to the development of the Wyoming Cloud Radar and ELDORA.

39.2.1 The Wyoming Cloud Radar (WCR)

The WCR was developed as a collaboration between the University of Wyoming (UW) Department of Atmospheric Science and the University of Massachusetts Microwave Remote Sensing Laboratory (MIRSL). Development work commenced in 1989. After some ground-based tests at the UW Elk Mountain Observatory, the MIRSL W-band radar was mounted on the University of Wyoming King Air Research aircraft (UWKA) in October 1992, leading to the first cloud measurements performed with airborne radar [39.12, 13]. By June 1995, the first version of the WCR was built by Quadrant Engineering (now ProSensing Inc.) and installed on the UWKA. It was a fully polarimetric radar with Doppler capabilities that utilized a single dual-polarization antenna oriented horizon-

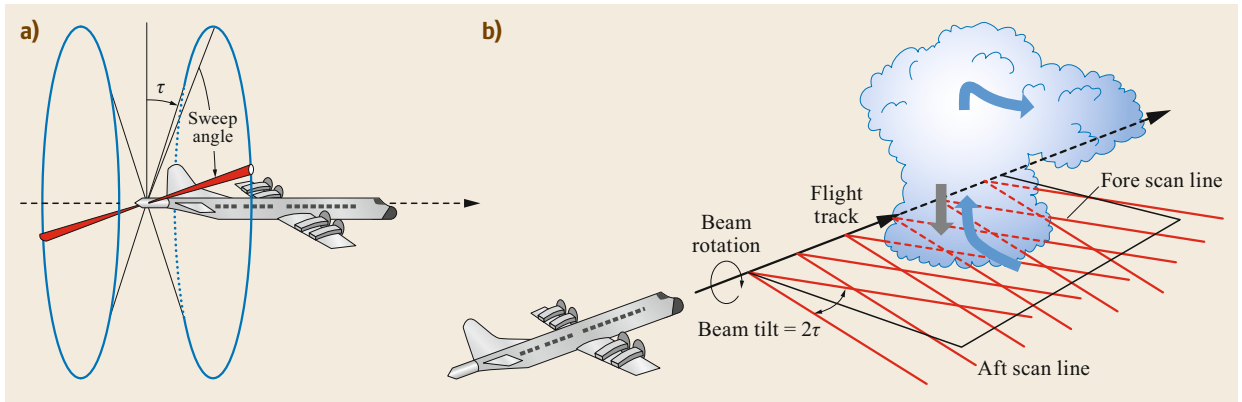


Fig. 39.3a,b Illustration of the ELDORA sampling strategy and geometry. The fore and aft beams swept out conical helices (a). These helices provided two separate viewing angles for locations within the echo as the aircraft flew by, illustrated in (b)

tally and laterally with respect to the aircraft track or that vertically profiled the atmosphere above the aircraft. The WCR was first deployed in the Small Cumulus Microphysics Study (SCMS) in 1995 [39.14, 15]. Since then, the WCR has undergone several major upgrades and now has the capabilities described in Sect. 39.4. The WCR has participated in numerous field campaigns that have studied marine clouds and precipitation, ice clouds, cumulus clouds, convection initiations, and many more phenomena, allowing the collection of unique high-resolution cloud microphysics and cloud dynamics data.

39.2.2 ELDORA

The Electra Doppler Radar (ELDORA) was an X-band, dual-beam, airborne research radar that was operated by the National Center for Atmospheric Research (NCAR) Atmospheric Technology Division (ATD, now EOL) as a National Science Foundation Lower Atmospheric Observing Facility. ELDORA made groundbreaking observations of high-societal-impact weather, including severe thunderstorms, tornadoes, and hurricanes [39.16]. The radar was mounted on the tail of an aircraft. One of its two beams pointed about 16° forward of vertical; the other pointed about 16° aft (Fig. 39.3a). The two beams were produced by two flat-plate, slotted-waveguide antennas that were mounted back-to-back. These antennas were then rotated along the longitudinal axis of the aircraft to sweep out two conical helices. This configuration permitted two viewing angles of the same location within the echo of interest as the aircraft passed by (Fig. 39.3b), enabling two-dimensional (2-D) and three-dimensional (3-D) wind retrievals (Sect. 39.3.5). The antennas were scanned very quickly (about 24 revolutions per minute, RPM)

in order to sample the atmosphere with the required resolution. Such rapid scanning, however, necessitated the use of advanced waveforms to acquire a sufficient number of independent samples to achieve the required Doppler velocity accuracy ($< 1 \text{ m s}^{-1}$). The approach taken for ELDORA was a four-element stepped chirp, with each element distinguished by discrete shifts in transmit frequency. This enabled the received signals to be processed individually by separate radar receivers, increasing the number of independent samples and thus improving the sampling statistics of the radar measurements.

The ELDORA research radar was designed based on input from the user community via workshops, town halls, and surveys. The development was a joint effort between NCAR and France's Centre de Recherches en Physique de l'Environnement Terrestre et Planétaire (CRPE). The radar was first deployed in Toga Core in 1993 on the NCAR Electra aircraft [39.17]. After the Electra was retired in 2000, the radar was moved to the NRL P-3. ELDORA supported nine major field campaigns between 1993 and 2008, resulting in more than 145 publications.

39.2.3 NASA High-Altitude Radars (EDOP, CRS, HIWRAP, EXRAD)

NASA has conducted radar measurements from high-altitude (18–20 km) aircraft since the early 1990s to address various scientific questions and to provide simulators for satellite missions such as CloudSat and Global Precipitation Measurement (GPM). Several radars that operate at different frequencies with both fixed-nadir and scanning beams have been developed. The primary aircraft used have been the ER-2, WB-57, and the Global Hawk Unmanned Aerial System, all of which

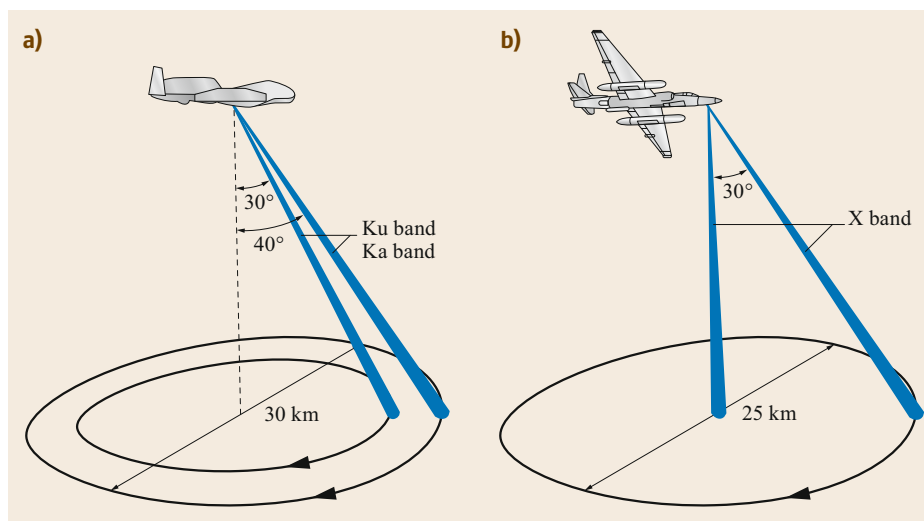


Fig. 39.4a,b
Illustration of
(a) the HIWRAP
and (b) EXRAD
conical sampling
strategies

are capable of altitudes of > 18 km. These aircraft have flight durations of 8, 6, and 26 h, respectively.

The X-band ER-2 Doppler Radar (EDOP, 9.6 GHz) was developed to study severe deep convection, but its emphasis rapidly shifted to tropical precipitation after the launch of the Tropical Rainfall Measuring Mission (TRMM) satellite [39.18]. EDOP has two fixed beams, one at nadir and the other 30° forward of nadir, to provide data on horizontal (along-track) and vertical winds below the aircraft. The first EDOP flights occurred in 1993, and subsequent flights until 2007 were field experiments with a particular focus on tropical convection and hurricanes [39.19].

Development on the W-band (94 GHz) Cloud Radar System (CRS) for cloud measurements was initiated in 1991. CRS first flew in 2001 [39.20, 21]. In combination with X-band measurements from EDOP, CRS provides information on snow and rain properties from dual-frequency retrievals [39.22, 23].

The High-Altitude Imaging Wind and Rain Airborne Profiler (HIWRAP) is a conical-scanning, dual-beam (30° and 40° off-nadir), Ku- and Ka-band (≈ 13.5

and 35.5 GHz) radar that was developed for long-duration, high-altitude operation on the NASA Global Hawk unmanned aircraft [39.24]. HIWRAP provides wind measurements within hurricane precipitation regions as well as ocean surface winds from ocean scatterometry. The scan geometry is shown in Fig. 39.4. The conical scans provide Doppler velocities from both the Ku and Ka bands at two incidence angles and from multiple azimuth angles (forward- and backward-looking as the aircraft flies over the region), from which the three components of the wind are retrieved [39.25].

The ER-2 X-Band Radar (EXRAD) is a new scanning and nadir-pointing radar that is intended to replace the EDOP system. EXRAD has a single conical/cross-track scanning beam and a dedicated nadir beam to provide the versatility needed to study all types of deep precipitation systems. The X-band conical scanning beam provides similar information to HIWRAP at the Ku band, but with less attenuation from hydrometeors. The nadir beam provides high-resolution measurements of vertical hydrometeor motions similar to those provided by the retired EDOP radar.

39.3 Theory

The basic principle of radar and the theory behind it are described in Sect. 39.1.2 and Chaps. 30 and 32 of this Handbook as well as in other relevant textbooks listed above. For completeness, some points that are relevant to airborne systems will be discussed in the following sections.

39.3.1 Radar Principle

Meteorological radars are typically pulsed systems that transmit a short (on the order of $0.1\text{--}2\ \mu\text{s}$) electromagnetic pulse using a high-power (kW to MW) transmitter such as a magnetron or klystron or a less power-

Table 39.2 Frequency bands used for airborne meteorological radars

Band	Frequency (GHz)	Wavelength (cm)	Antenna diameter for a 0.6° beam (m)	Remarks
C	5.2–5.7	5.2–5.7	6.4	Sect. 39.9.1
X	9.3–9.5	3.1–3.2	3.6	
Ku	13.6–13.8	2.2	2.6	Also used by meteorological satellites such as TRMM, GPM, CloudSat, and EarthCARE
Ka	35.2–35.5	0.8	1.0	
W	94–95	0.3	0.4	

ful (10–100 W) solid-state transmitter. Short pulses allow for high spatial resolution along the range; on the other hand, a short pulse contains less power than a long one. Since meteorological scatterers are distributed randomly, the backscatter signal is stochastic, so it is necessary to average over a number of independent pulses to achieve stable and representative measurements. A relevant factor in this context is the pulse repetition frequency (PRF). A high PRF enables frequent measurements and short observation times, which are important considering that airborne systems fly at high speeds. A high PRF is also necessary for a high Nyquist velocity and for high spectral resolution of the Doppler velocity. On the other hand, the PRF is limited by the duty cycle of the transmitter and the maximum range of unambiguous radar measurements. The duty cycle is the proportion of the time that the transmitter can transmit within a given time interval, and is typically on the order of 1 : 100 to 1 : 1000 for tube transmitters and up to 1 : 10 for solid-state transmitters. A PRF of 5000 Hz limits the unambiguous range to 30 km.

A few radar systems use frequency-modulated continuous wave (FMCW) technology. In such systems, the transmit frequency is modulated by several MHz in a sawtoothed manner. This is advantageous because it only requires low power. However, some complexity arises from the unambiguous frequency shift due to the Doppler velocity and ranging. Hard targets such as ground echoes for airborne systems are spread over several range bins for a FMCW radar.

While the depth of the measurement volume of a pulsed radar is given by the pulse duration, the width of the measurement volume is given by the beamwidth or the half-power width of the antenna. The beamwidth is defined as the angular difference between the half-power (–3 dB) points on the main lobe. For a radar, the beamwidth is on the order of 0.2°–3°. A narrow beam (pencil beam) gives high spatial resolution but requires large antennas. A beamwidth of 0.6° gives a spatial resolution of 50 m at a range of 5 km, or 100 m at 10 km. See later sections for a discussion of the influence of wavelength on the beamwidth and constraints on airborne systems. For example, a W-band ($\lambda \approx 0.3$ cm) cloud radar with a 50 cm antenna has a beamwidth of about 0.5°. Side lobes are not generally relevant,

although they must be considered for airborne radars when the side lobe for a tilted beam hits the ground before the main lobe. In this case, the measurements from the main lobe will be contaminated by side-lobe echoes. Multiple scattering effects (see below) are relevant for a wide beam. Due to the large measurement volume of a wide beam, the measurement range should be limited to close to the aircraft.

39.3.2 Wavelength Selection

Various frequency bands are assigned for use by meteorological radars. Table 39.2 gives some characteristics of the bands used for airborne radars. For further detailed discussion of millimeter (mm) waves, see also Chap. 32. The utilization of bands with higher frequencies, such as the G band (≈ 200 GHz), to observe small ice particles is also under discussion [39.26]. Constraints due to antenna size and installation on an aircraft are discussed in Sect. 39.5. Table 39.3 gives pros and cons of the different wavelengths.

Backscatter and Attenuation

Centimeter waves are used to observe precipitation particles, while mm waves are used to observe cloud particles. The backscatter signal (39.1) or reflectivity

$$\eta = \frac{\pi^5}{\lambda^4} |K|^2 \sum_{\text{Vol}} \sigma_i^6 \quad (39.7)$$

is inversely proportional to the wavelength. This indicates that less transmit power is needed to receive a signal above the noise floor for short wavelengths, so mm waves are more suitable for the observation of small cloud droplets and ice crystals. On the other hand, shorter wavelengths suffer from greater attenuation by precipitation and the atmosphere (oxygen and water vapor).

The scattering cross-section depends on the ratio of the wavelength to particle size. If the particles are small compared to the wavelength, the Rayleigh approximation $\sigma \approx D^6$ can be assumed. If the particle size is similar to the wavelength, Mie resonance makes a significant contribution to the backscatter signal. Mie computations for water spheres are shown in Fig. 39.5. Especially for the Ka and W bands, strong Mie effects are visible with rain, complicating the process of esti-

Table 39.3 Some pros and cons of different radar wavelengths

Frequency band, frequency, wavelength	Pros	Cons
C band, 5.5 GHz, 5.5 cm	<ul style="list-style-type: none"> • High TX power available • Mainly sensitive to precipitation • Less attenuated by rain • Rayleigh scattering 	<ul style="list-style-type: none"> • Huge antenna required for a narrow beam
X band, 9.4 GHz, 3.2 cm	<ul style="list-style-type: none"> • High TX power available • Mainly sensitive to precipitation • Mainly Rayleigh scattering 	<ul style="list-style-type: none"> • Large antenna required for a narrow beam • Some attenuation by precipitation
Ku band, 13.5 GHz, 2.2 cm	<ul style="list-style-type: none"> • Sensitive to clouds and precipitation • Used by the TRMM and GPM spaceborne radars 	<ul style="list-style-type: none"> • Large antenna required for a narrow beam • Attenuated by precipitation
Ka band, 35.5 GHz, 0.8 cm	<ul style="list-style-type: none"> • High sensitivity to (ice) clouds and precipitation • Used by the GPM spaceborne radar 	<ul style="list-style-type: none"> • Attenuated by precipitation • Pure water clouds cannot be observed at far ranges • Mie scattering
W band, 95 GHz, 0.3 cm	<ul style="list-style-type: none"> • High sensitivity to clouds • Small antennas • Used by the CloudSat and EarthCARE spaceborne radars 	<ul style="list-style-type: none"> • Strongly attenuated by precipitation • Multiple scattering can occur when using wide beams • Mie scattering

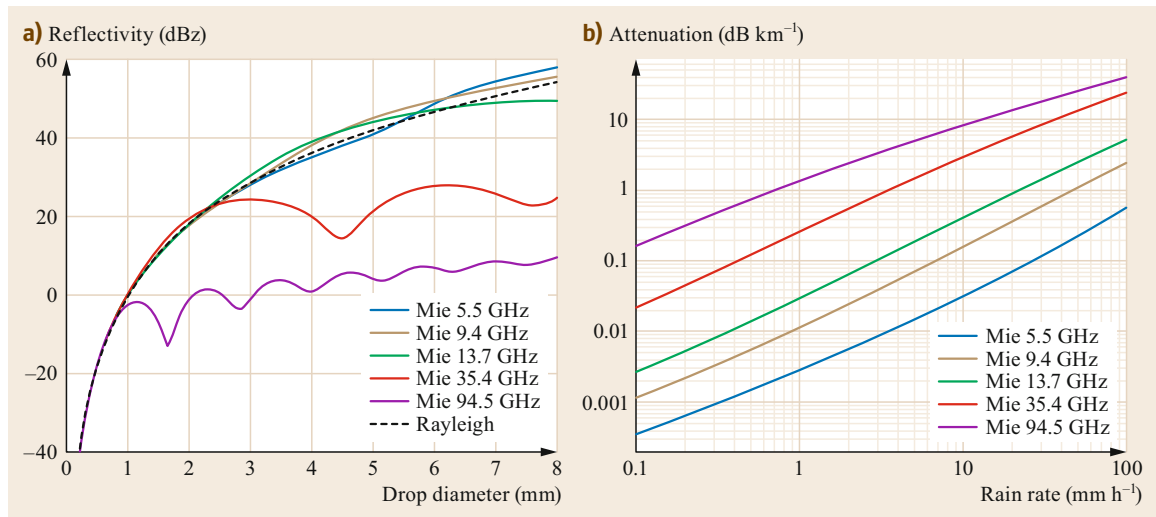


Fig. 39.5 (a) Backscatter from single water spheres at 5 °C for different radar frequencies; (b) attenuation by rain at 5 °C assuming Mie scattering with a particle size distribution that follows the Marshall and Palmer parameterization (after [39.27])

mating the rain rate or other microphysical properties from the reflectivity. For shorter wavelengths, the particle shape should also be considered in simulations, necessitating more complex algorithms.

Multiple Scattering

One effect that is often discussed in the context of spaceborne cloud radars is multiple scattering [39.28, 29]. This can be neglected for precipitation radars with centimeter (cm) wavelengths (S band to X band) and a narrow beam. The effects are even considered to be

small for the Ka band (e.g., the GPM satellite). In the Rayleigh scattering regime, lateral scattering will occur. If a narrow beam is used, it is quite unlikely that the laterally scattered signal will reach the radar via multiple scattering. For larger particles or short wavelengths, Mie forward scattering dominates, so the scattered signal will stay within the beam and will therefore be received by the radar. This effect is mainly visible for lidar systems. For radar systems, multiple scattering at mm waves occurs mainly in regions with strong attenuation. Strong forward scattering reduces

the visible effects of attenuation, such that the attenuation appears to be relatively low. The presence of irregularly shaped ice particles can enhance multiple scattering. In general, multiple scattering is expected for spaceborne systems with large footprints, but it is generally negligible for airborne systems with narrow beamwidths [39.29]. Data from airborne radars emitting in the W- to Ku-band region have recently shown that multiple scattering can be a serious problem in deep convective hailstorms [39.30]. It was found that the LDR (if available) can be used to identify regions with multiple scattering [39.29].

Multiple Wavelengths

The different scattering and attenuation behaviors observed for different particle sizes and shapes at different radar frequencies can be utilized in multiple-wavelength systems. This is common for atmospheric radiation measurement (ARM) sites [39.31], but also for spaceborne applications such as the GPM satellite [39.32, 33]. GPM uses a combination of the Ku and Ka bands to improve rain rate estimation. As will be shown in Sect. 39.4.5, airborne combinations are also available. A number of coordinated flights of the HAMP (HALO Microwave Package; Ka band; Sect. 39.4.4) and RASTA (Radar System Airborne; W band; Sect. 39.4.3) radar systems have been performed to investigate the potential of the Ka and W bands. The HIWRAP system uses the Ku and Ka bands, similar to the GPM satellite. HIWRAP has been combined with CRS and EXRAD (Sect. 39.4.5) to provide four frequencies: X, Ku, Ka, and W [39.30].

The power received depends on the wavelength of the radar system due to the backscatter properties of the particles (Rayleigh or Mie scattering) and the two-way attenuation between the radar and the target. For Rayleigh scattering, the backscatter is proportional to D^6 , whereas the attenuation is proportional to D^3 . This property can be used to improve rain rate estimation, as exemplified by the GPM dual-frequency precipitation radar (DPR) system [39.32], for which attenuation due to rain is present at the Ka band but negligible at the Ku band. Because of their complex shapes and densities, retrievals of the microphysical properties of ice particles are based on a number of assumptions. A number of algorithms that use the scattering properties of ice particles at different frequencies to probe their microphysical properties have been proposed [39.34, 35].

39.3.3 Technology

The significant advances made in radar technology in recent years are driving the development of airborne research radars that are smaller, lighter, more power

efficient, and possess enhanced performance. Two advances that have recently had a profound impact on airborne radars are the improved signal processing capabilities facilitated by field-programmable gate arrays (FPGAs) and solid-state power amplifiers (SSPAs). FPGAs and their implementations continue to improve, and they have come to the forefront of radar signal processing. They are well suited to airborne radar processing and enable the use of advanced signal processing algorithms employing complex pulse waveforms. Airborne radar transmitters that use tube-based transmitters such as magnetrons, extended-interaction klystrons (EIKs), and traveling-wave tubes (TWTs) can be problematic on an aircraft as they use high-voltage modulators and only permit low duty cycles (typically up to 5–10%). These modulators are heavy and fairly large in size, require significant input power, and run at very high voltages, which could lead to arcing for some airborne installations. Nevertheless, non-SSPA radars have been used successfully in a number of flight campaigns. On the other hand, SSPAs are well suited to airborne systems. They do not use high voltages, they are small, lightweight, and reliable, and they allow a duty cycle of 100%. While SSPAs have lower output powers than tube systems, they generally make use of their high duty cycle to achieve pulse compression such that the average transmit power of a SSPA-based radar is roughly comparable to that of a high-power radar. Several airborne radars use FPGA and SSPA technologies at frequencies in the Ku- to W-band region [39.24, 36, 37]. SSPA technology continues to improve in terms of both transmit power and power efficiency. The drawback of using pulse compression is that range side lobes are produced, which can bias radar returns around high reflectivity gradients, such as near the surface or within strong convective storms. Range side lobe contamination requires special attention and can be minimized in most cases. In addition, the ability to run a SSPA at a high duty cycle allows new techniques to be explored (Sect. 39.9.2).

39.3.4 Airborne Doppler Measurement

Airborne Doppler radars measure the reflectivity-weighted radial (i.e., along the radar beam direction) Doppler velocity using the same principle as weather Doppler radars on the ground. The main difference is that the radar is installed on a moving platform with a velocity vector that is not necessarily orthogonal to the radar beam-pointing vector (Fig. 39.6). This means that a component of the aircraft motion may be present (in fact, it almost always is present) in airborne radar Doppler measurements.

An airborne Doppler measurement for a given radar resolution volume along the beam can be expressed

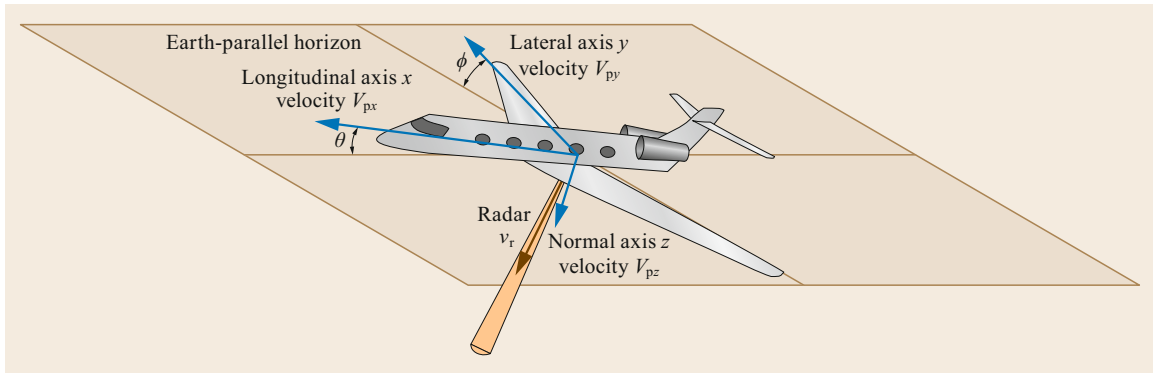


Fig. 39.6 Coordinate system relative to the aircraft, and the attitude angles (roll ϕ and pitch θ)

as the scalar product $v_r = \mathbf{b} \cdot (\mathbf{V}_s + \mathbf{V}_p)$, where $\mathbf{b} = (b_x, b_y, b_z)$ is the unit vector of the radar beam-pointing vector

$$|\mathbf{b}| = \sqrt{b_x^2 + b_y^2 + b_z^2} = 1,$$

\mathbf{V}_s is the mean three-dimensional 3-D velocity vector of the scatterers within the radar resolution volume, and $\mathbf{V}_p = (V_{px}, V_{py}, V_{pz})$ is the 3-D velocity vector of the aircraft at the radar antenna. v_r is the reflectivity-weighted mean velocity along the radar beam and relative to the aircraft. All vectors are referenced in their native aircraft coordinate system [39.38]. To retrieve the mean radial velocity of the scatterers in the resolution volume, i.e., $v_s = \mathbf{b} \cdot \mathbf{V}_s$, the aircraft motion contribution $\mathbf{b} \cdot \mathbf{V}_p$ must be removed. Only then can airborne radar Doppler measurements be used to estimate atmospheric winds and/or to study the motions of the scatterers in the atmosphere. Removal of the contribution due to aircraft motion requires the precise determination of the radar beam-pointing vector (Sect. 39.6.2) and the aircraft velocity vector.

A further effect of the moving platform is the broadening of the Doppler spectrum caused by the finite beamwidth of the radar [39.9, 39]. For an antenna pattern with a half-power beamwidth θ_0 in radians, the broadening of the Doppler spectrum can be estimated as $\sigma \approx 0.3V_x\theta_0$, where σ is the spectral width that describes the broadening of the spectrum and V_x is the motion of the platform perpendicular to the beam-pointing vector. In this context, the spectral width represents the uncertainty in the Doppler velocity. For the HALO cloud radar (Sect. 39.4.4) with a beamwidth of 0.6° on an aircraft flying at a typical speed of 210 m s^{-1} , σ is on the order of 0.7 m s^{-1} . The results of simulations are shown in Fig. 39.7. Note that the Mie notch ($v \approx 9.4 \text{ m s}^{-1}$) arising from raindrops 4.4 mm in diameter is smoothed over and cannot be used to estimate the vertical air motion [39.40].

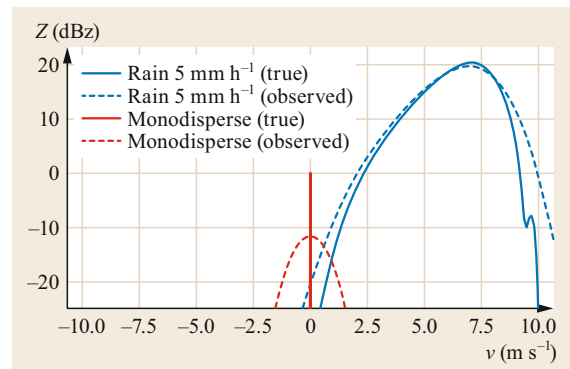


Fig. 39.7 Simulated Doppler spectra for a monodisperse distribution of particles with no fall speed, and raindrop size distributions for a Ka-band radar with a beamwidth of 0.6°

39.3.5 Multi-Doppler Principle

In the multi-Doppler technique, multiple radial Doppler velocities of a volume of atmospheric scatterers are measured at a given location and time from different aspect angles. If three accurate and orthogonal velocity measurements can be made simultaneously, the 3-D mean velocity vector of the scatterers in the resolution volume can be determined in the desired reference frame (e.g., the ground coordinate or storm/cloud-relative coordinate system). In practice, such idealized 3-D measurements cannot be achieved. Constrained multi-Doppler measurements can be performed with an airborne radar from several noncollinear directions by taking advantage of the motion of the aircraft and scanning or fixed-pointing antennas.

The ability to retrieve the 2-D or 3-D velocity field using multi-Doppler measurements has important applications, such as the estimation of 3-D winds, hydrometeor trajectories, hydrometeor fall velocities, cloud kinematics/dynamics, and turbulence [39.42–47].

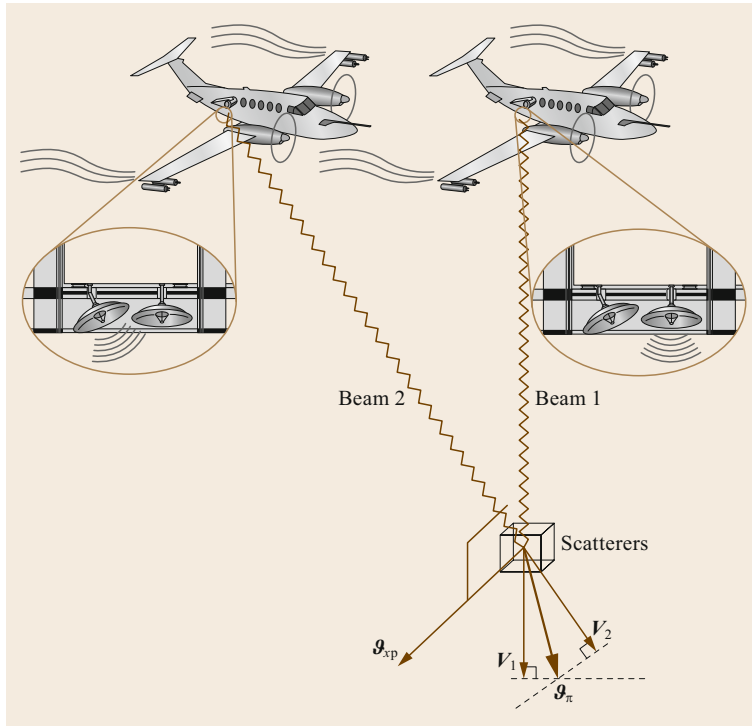


Fig. 39.8 Dual-Doppler concept: a given scatterer volume is illuminated by two beams separated by a short time interval. V_1 and V_2 are the mean Doppler radial velocities, ϑ_{π} is the cross-plane component (i.e., the unmeasured component of the velocity normal to the plane of the beams), and v_{xp} is the retrieved scatterer velocity in the plane of the beams (after [39.41] © 2006 IEEE)

Depending on the radar antenna configuration employed, multi-Doppler measurements can be acquired in several ways. For a radar with a single non-scanning (fixed) antenna or an antenna scanning normal to the aircraft flight track, various flight patterns that allow the same atmospheric phenomenon to be illuminated from different directions are used (e.g., an L pattern). This approach was used in the early days of airborne weather Doppler radar (e.g., the National Oceanic and Atmospheric Administration (NOAA) P-3 tail radar [39.48, 49]). This leads to large time lags between illuminations of the same atmospheric volume, and is therefore the least accurate approach. Radars that use scanning dual antennas (e.g., ELDORA [39.17]) or fixed multi-antennas (e.g., WCR [39.41, 50] and RASTA [39.51]) collect multi-Doppler data from several antennas that illuminate nearly the same volume but with a slight time lag between them while the aircraft is flying straight and level legs. The time lag is range dependent. For example, if the aircraft speed is 100 m s^{-1} and almost nadir-pointing and a 30° slant-pointing illumination of targets is performed, the time delay is 1.2 and 17.3 s for target ranges of 0.2 and 3 km, respectively.

The most typical application of multi-Doppler measurements is the dual-Doppler technique, which involves measuring radial Doppler velocities from two or more different angles that are usually separated by between 25° and 45° and aligned in a plane (Fig. 39.8).

These measurements then are used to determine the two orthogonal velocity components in the plane of the measurements, thus providing estimates of 2-D hydrometeor motion and the wind (Fig. 39.8). Dual-Doppler measurements can only resolve the 2-D velocity field. In order to determine the 3-D velocity field, additional information in the third dimension is needed. Multiantenna configurations (scanning or fixed) that provide multi-Doppler data in the vertical and horizontal directions can improve the retrieval of the 3-D dynamics [39.42, 51].

All multi-Doppler retrieval techniques involve some uncertainties. For instance, the mean 3-D velocity vector of the hydrometeors in the resolution volume must be stationary longer than the time lag or an error will occur. The magnitude of this error depends on the time lag, the scale of the observations, and the scale of the observed phenomenon, and is difficult to estimate. The uncertainties due to errors in the beam-pointing direction (Sect. 39.6.2), the mismatch between the volumes illuminated by the different beams, errors in the advection scheme, a low signal-to-noise ratio (SNR), and differences in attenuation all affect the accuracy of the retrieval. Note that this is not a complete list of all possible uncertainties. In addition, there are errors specific to the retrieval technique that must be taken into account [39.41]. It is also implicitly assumed that any folding in the Doppler measurements is resolved be-

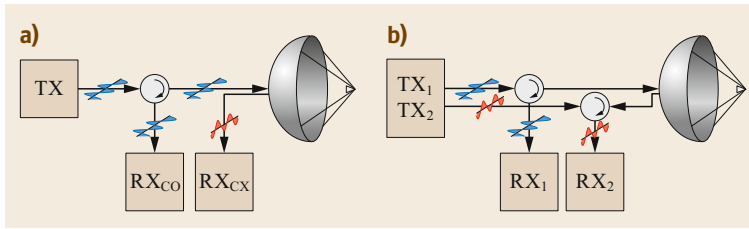


Fig. 39.9a,b Technical realizations of a dual-polarization radar (TX = transmitter, RX = receiver; *blue* and *red* waves indicate horizontal and vertical polarization, respectively): (a) measurement of copolar and crosspolar signals; (b) measurements at two orthogonal polarization planes using two transmitters or a power splitter

fore a multi-Doppler synthesis of the velocity field is applied. Notwithstanding all possible errors, airborne multi-Doppler retrieval techniques can provide good results with reasonable overall uncertainty [39.41, 42, 50].

39.3.6 Dual Polarization

Most meteorological radars use linearly polarized waves; in other words, the electric field vector and the (orthogonal) magnetic field vector (\mathbf{E} and \mathbf{H} , respectively) remain in the transmitted plane (Chap. 30) [39.3]. The orientation of the polarization is defined by the orientation of \mathbf{E} . The signal received with the same polarization as the transmitted wave is the copolar signal, whereas the signal received by the orthogonal polarization is the crosspolar signal. Different technical realizations are in use (Fig. 39.9). If the crosspolar signal LDR is of interest, one transmitter and two receivers are necessary. More complex realizations are possible for measurements of differential reflectivity and differential phases. The power from a single transmitter can

be split into the two polarization planes (STAR mode: simultaneous transmit and receive); two independent transmitters with similar frequencies can be used; or the power from one transmitter can be fed alternately into the two polarization planes (AHV mode: alternating H and V transmit). The latter mode allows the full backscatter matrix to be measured, whereas the STAR mode measures the principal diagonal only.

Good isolation (> 25 dB) of the crosspolar from the copolar signal is necessary to measure the crosspolar signal. Depolarization is caused by aspherical particles, which present irregular falling behavior. These are irregularly shaped ice particles or any melting ice particles. Cloud droplets and raindrops do not cause depolarization. The LDR values observed with rain are an indicator of the channel isolation. Depolarization cannot be measured using the STAR mode, and depolarization causes crosstalk between the two polarizations. Due to the preferred orientation of falling particles, differential reflectivity or differential phase measurements are preferred in a horizontal or slanting beam orientation.

39.4 Devices and Systems

A wide selection of current (as of the year 2018) systems are described in this section. Note that these are research systems that undergo regular modifications and upgrades.

39.4.1 W-Band Wyoming Cloud Radar (WCR)

The Wyoming Cloud Radar (WCR) is a 95 GHz pulsed Doppler radar. It is designed for installation inside an aircraft cabin and is mount-ready for the University of Wyoming King Air (UWKA) and NCAR/NSF C-130 research aircraft. The transmitter is a klystron-based extended-interaction amplifier (EIA) from CPI that delivers a peak power of up to 1.8 kW and a maximum duty cycle of 3%. The transceiver front end can accommodate up to five antennas. The current configuration used for the UWKA and C130 utilizes two single-polarization antennas and one dual-polarization

antenna (Fig. 39.10a). The two down antennas are aligned in a near-vertical plane for dual-Doppler data acquisition below the aircraft [39.41]. The third antenna points laterally on the starboard side of the UWKA and near to the zenith on the NCAR/NSF C-130. On the UWKA, there is also an external reflector for redirecting the side-pointing beam to near the zenith. Another configuration with four antennas can be used for the UWKA; this employs an additional lateral forward (beam WCR 3 in Fig. 39.10b) pointing antenna for dual-Doppler measurement in a horizontal plane (Fig. 39.10b). The transceiver includes two receiver channels that provide full polarimetric measurement capabilities. The receiver back end utilizes a 16-bit dual-channel digital receiver, and the data system is capable of recording the signal in-phase and quadrature (I&Q) components as well as processing, displaying, and recording the received power, pulse-pair products, and full Doppler spectra in real-time. WCR data are

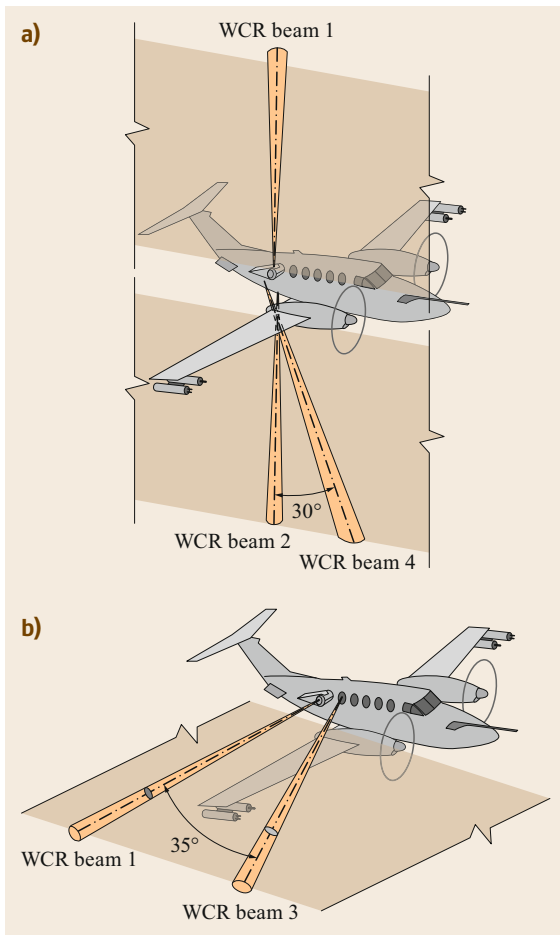


Fig. 39.10a,b Multiple beam configuration of the Wyoming Cloud Radar mounted on the Wyoming King Air research aircraft. **(a)** Measurements in the vertical plane, **(b)** measurements in the lateral horizontal plane. For further details, see the main text

integrated with the new Ka-Band Precipitation Radar (Sect. 39.4.6), the UWKA's other remote sensors, and its extensive suite of in-situ probes [39.52].

39.4.2 W-Band HIAPER (HCR)

The National Center for Atmospheric Research (NCAR) operates a 95 GHz pulsed, dual-polarization, Doppler research radar on its High-Performance Instrumented Airborne Platform for Environmental Research (HIAPER) Gulfstream V (GV) aircraft [39.53]. The HIAPER Cloud Radar (HCR) operates from an underwing pod, as shown in Fig. 39.11, and uses a single standard instrument rack in the cabin of the GV. The transmitter is an extended-interaction klystron amplifier (EIKA) which, together with the modulator, can

operate at maximum duty cycle of 5%. The lens antenna illuminates the rotating reflector (Fig. 39.11), resulting in a 3 dB beamwidth of 0.68° that is transmitted perpendicular to the longitudinal axis of the pod. The beam can be scanned in the cross-track plane or operated at a constant pointing angle (staring mode) such as the nadir or zenith. In staring mode, the beam is stabilized with respect to changes in platform orientation that occur during flight. This stabilization is accomplished by adjusting the reflector pointing at a rate of 10 Hz using the position measurements of the dedicated inertial navigation system (INS)/Global Positioning System (GPS) unit mounted at the front of the pod. The stabilization keeps the pointing angle within about 0.1° of the requested angle, mitigating errors at vertical incidence from horizontal winds. The HCR data system is capable of recording the full suite of dual-polarization moment data as well as the raw I&Q time series data. The HCR is commonly deployed in conjunction with a high spectral resolution lidar (HSRL) [39.54] that detects aerosols, ice crystals, and cloud droplets, and can determine regions of supercooled liquid water. HCR and HSRL measurements are often complementary and can be used together to characterize clouds, precipitation, and aerosols in much greater detail than is possible with a single instrument (Sect. 39.8.5).

39.4.3 W-Band RASTA

The French research aircraft fleet operated by SAFIRE (Service des Avions Français Instrumentés pour la Recherche en Environnement) can be equipped with a multibeam 95 GHz Doppler radar, RASTA [39.55, 56]. This system was developed by LATMOS (Laboratoire Atmosphères, Milieux, Observations Spatiales), and is flown on the SAFIRE Falcon 20 and ATR 42. It is combined with a HSRL in order to retrieve cloud microphysical properties.

RASTA measures the Doppler velocity and reflectivity at 95 GHz along a radial defined by the pointing direction of the antenna. The RASTA radar includes three downward-looking and three upward-looking beams (nadir, 28° off-nadir and opposite to the direction of travel, 20° off-nadir and perpendicular to the direction of travel, zenith, 25° off-zenith and in the direction of travel, and 20° off-zenith and perpendicular to the direction of travel; see Fig. 39.12). The antennas are installed in the cabin of the aircraft, and the radar beams are directed through bottom and top windows. This unique configuration permits the retrieval of the three-dimensional wind beneath the aircraft by combining the independent Doppler radial velocities from the multibeam antenna system (Sect. 39.3.5). Raw data are

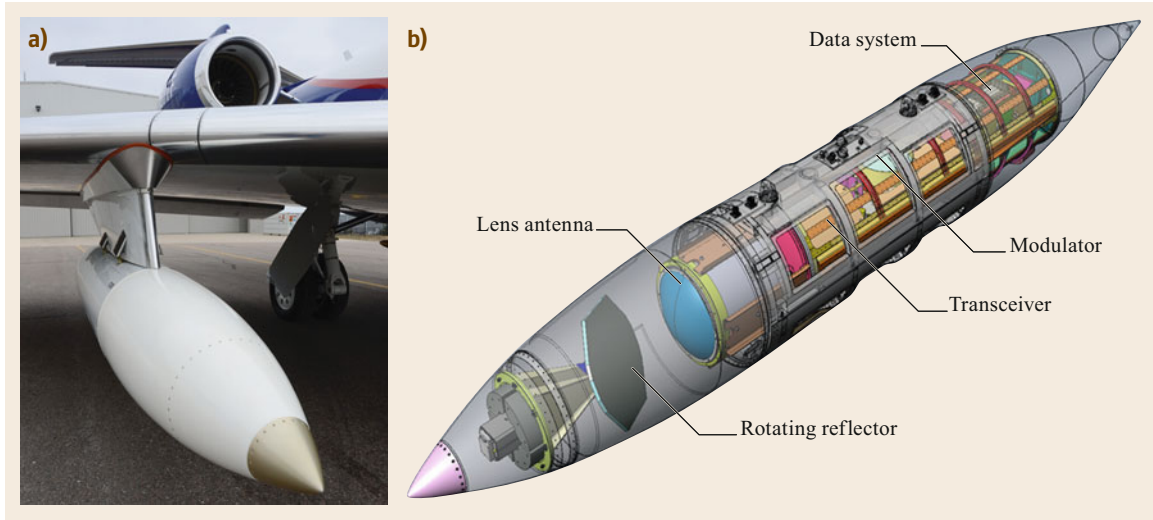


Fig. 39.11 (a) Photo and (b) diagram showing the HCR underwing pod configuration; the reflector is located forward of the wing (photo © S. Ellis)

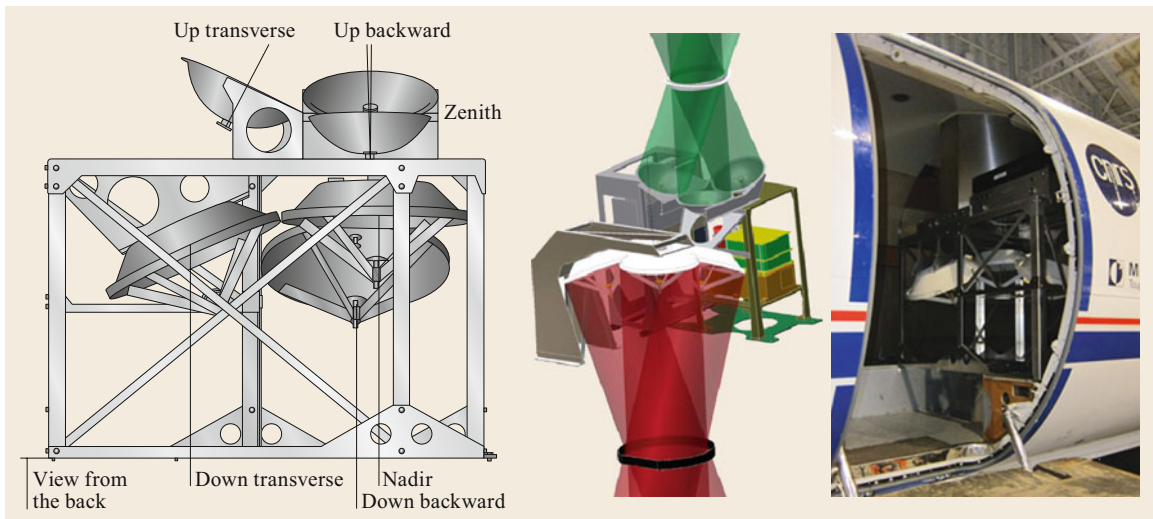


Fig. 39.12 RASTA configuration onboard a SAFIRE Falcon 20 (photo © J. Delanoë)

recorded for each beam, allowing radar moments and Doppler spectra to be reprocessed.

Since 2000, RASTA has been flown in a number of campaigns for various scientific missions. An example of a wind field retrieved by RASTA is shown in Sect. 39.8.5.

39.4.4 Ka-Band HALO (HAMP)

The German research aircraft HALO (High Altitude and Long Range Research Aircraft; [39.57])—a modified Gulfstream G550—can be equipped with an ac-

tive and passive microwave package, HAMP [39.58]. HAMP consists of a high-power (30 kW) Ka-band cloud radar (a MIRA35 radar manufactured by METEK GmbH) that is tailored for aircraft integration and five microwave radiometers that operate between 22 and 183 GHz. Together with HAMP, a high spectral resolution lidar for water vapor (WALES; see Chap. 38) is also flown. The radar and radiometers were jointly provided and integrated by the Max Planck Institute for Meteorology, the Meteorological Institute of the University of Hamburg, and the DLR Institute of Atmospheric Physics.



Fig. 39.13 Images showing the installation of the cloud radar antenna, including the clutter fence, lidar window, and microwave radiometers, in the HALO research aircraft belly pod (photos © M. Hagen)

The radar electronics are installed within the aircraft cabin and the radar antenna is mounted beneath the fuselage in the external belly pod (Fig. 39.13). The Cassegrain antenna has a diameter of 1 m, resulting in a beamwidth of 0.6° , and has a clutter fence to minimize lateral scatter and reflections within the belly pod. The antenna is fixed at the fuselage but not to the direction of motion of the aircraft, meaning that the pitch and roll angles of the aircraft must be considered when evaluating the Doppler velocity. During signal processing, Doppler spectra are recorded for both the co- and crosspolar polarizations, and the average reflectivity, Doppler velocity, spectral width, and LDR are available in real time. A recent upgrade of the radar has made in-flight recording of raw I&Q data possible, which can be used for off-line signal processing. A detailed calibration of the radar and a comparison with other radar systems are reported in [39.59].

So far, HAMP has spent about 300 h in the air during four campaigns focusing on the Atlantic trade wind region (out of Barbados) and the North Atlantic (out of Iceland) in 2013, 2014, and 2016 (the Next-Generation Aircraft Remote Sensing for Validation (NARVAL) and North Atlantic Waveguide and Downstream Impact Experiment (NAWDEX)) campaigns [39.60, 61]. Some results are shown in Sect. 39.8.2.

39.4.5 HIWRAP (Ku, Ka), CRS (W), EXRAD (X)

The High-Altitude Radar (HAR) Group at the Goddard Space Flight Center developed the EDOP, CRS, EXRAD, and HIWRAP radars using a variety of commercial and custom parts. These radars require special thermal and high-altitude design considerations since they use high-voltage transmitters and numerous heat-producing components. In addition, these high-altitude radars must be compact and lightweight due to the limited space available on an aircraft, they require turn-key operation, and (more recently) they must allow remote operation and data transmission to the ground using high-speed satellite data links. HIWRAP (Fig. 39.14) is the most advanced of the HAR radars, as it was designed for the NASA Global Hawk, a developmental version of the US Air Force version of the unmanned plane. It has also been flown on NASA's WB-57 high-altitude aircraft with a similar conical scan configuration, and with a fixed nadir beam on the ER-2 aircraft. The HIWRAP hardware uses solid-state transmitters (≈ 40 W at the Ka band and ≈ 90 W at the Ku band) along with pulse compression to improve sensitivity. It employs a FPGA-based processor and a unique transmit waveform with a sequence of 2, 20, and $2\mu\text{s}$ pulses (for returns near the surface and in the blind zone near the aircraft)—where each pulse has a slightly different frequency for

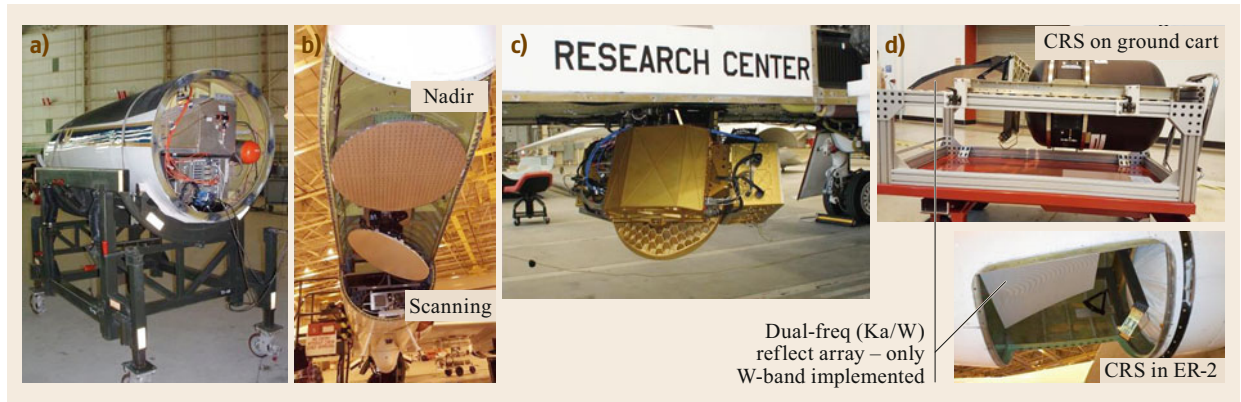


Fig. 39.14a–d Images showing the (a) EDOP in ER-2 nose, (b) EXRAD in ER-2, (c) HIWRAP, and (d) CRS radars (photos © G.M. Heymsfield)

improved isolation—to mitigate range sidelobe contamination associated with pulse compression, which is particularly problematic near the surface for down-looking radars [39.24, 62]. HIWRAP operates with dual PRFs (≈ 4000 and 5000 Hz) to mitigate Doppler aliasing. Calibration is performed using an internal calibration loop on a pulse-to-pulse basis. This accurately accounts for variations in radar stability associated with large environmental temperature changes from the surface to the flight altitude and the fact that SSPA outputs can vary by 1–2 dB due to these temperature changes. Calibration is performed using both the internal calibration loop and the ocean surface, similar to the approaches used by precipitation satellites and airborne radars [39.21, 63]. The weight of HIWRAP on the Global Hawk is ≈ 160 kg due to its heavy scanner mechanism; its weight is only ≈ 100 kg when it is installed on the ER-2.

The current CRS (version 2.0) and the version that is under development (version 3.0) incorporate many of the advances in solid-state transmitter and pulse compression technology used in HIWRAP. It has a single nadir beam and Doppler and polarimetric (LDR) capabilities. CRS version 1.0 [39.21] used an EIK-based transmitter, but it was upgraded in 2014 to utilize a 30 W SSPA-based transmitter and pulse compression, yielding comparable performance to the EIK-based transmitter used in version 1.0 while allowing the size and weight of the system to be reduced by $\approx 50\%$. This version of CRS (2.0) used a custom reflectarray antenna that was a subscale prototype of a dual-wavelength spaceborne radar with W-band nadir and Ka-band electronic scanning [39.64]. However, only the W-band antenna is currently used. CRS version 3.0 will be a complete repackaging of version 2.0 with increased



Fig. 39.15 The Ka-Band Precipitation Radar mounted on the Wyoming King Air research aircraft. The radar is mounted on the right wing (see the *inset* showing a close-up image of the wing tip). The *inset* in the top left corner shows the internal components of the radar, including the two flat-plate antennas (photos © A. Pazmany)

transmit power (50 W) for better sensitivity, improved calibration (similar to HIWRAP’s calibration loop), and a further size reduction due to the use of a newer FPGA-based compact digital processor. The total weight of CRS version 3.0 will be less than ≈ 70 kg.

EDOP is a conventional Doppler radar that uses a 25 kW TWT-based transmitter [39.18]. It has been replaced with EXRAD (Fig. 39.14), which has two slotted-waveguide antennas with beamwidths of $\approx 3^\circ$, one of which is conically scanned at $\approx 24^\circ \text{ s}^{-1}$ and at an incidence of 30° , while the other performs fixed nadir pointing. It uses a 10 kW TWT-based transmitter that alternates between the two beams, has dual PRFs (≈ 4000 and 5000 Hz) and a pulse width of $2 \mu\text{s}$, and oversamples at 4 MHz . EXRAD has flown in both the ER-2 and the Global Hawk with similar hardware; its weight is ≈ 90 kg.

39.4.6 Ka-Band Precipitation Radar (KPR)

The weight that can be carried by an aircraft and the space and electrical power available on it are always limited. Advances in microwave technology (Sect. 39.3.3), especially in mm-wave range solid-state transmitters, have made it possible to develop compact, lightweight, low-power, but sensitive cloud and precipitation radars [39.37]. ProSensing Inc., in collaboration with the University of Wyoming (UW), developed the Doppler Ka-Band Precipitation Radar (KPR), which is operated from a standard Particle Measuring Systems (PMS) canister [39.36, 65]. Key components of this radar system include an arbitrary transmit pulse waveform generator, a 10 W solid-state power amplifier, and a pair of 14 cm diameter flat-plate slotted-waveguide array antennas for interleaved profiling above and below the aircraft. The KPR is installed on the right wing tip of the UW King Air research aircraft (Fig. 39.15). The specifications of the KPR are listed in Table 39.4. The radio frequency (RF) components and the front end of the receiver are installed in a pod-mounted insert. The total weight of the insert and the canister is less than 20 kg. The power consumption of the unit is about 130 W. A small form-factor computer located in the aircraft cabin houses a 16-bit dual-channel digital receiver and executes radar control, data acquisition, and real-time display software. A miniature GPS-aided inertial measurement unit can be installed in the KPR head cone for more accurate Doppler measurements. The transmitted waveform consists of a linear frequency-modulated long pulse segment followed by an offset-frequency short RF pulse. Pulse compression is used to enhance the sensitivity of the radar to cloud and precipitation at far ranges (the typical maximum range is about 10 km), and the short pulse can be used

Table 39.4 Specifications of the airborne radars described in Sect. 39.4

Acronym	WCR	HCR	RASTA	HAMP	HIWRAP	CRS	EXRAD	KPR
Full name	Wyoming Cloud Radar	HIAPER Cloud Radar	Radar System Airborne	HALO Microwave Package	High-Altitude Imaging Wind and Rain Airborne Profiler	Cloud Radar System	ER-2 X-Band Radar	Ka-Band Precipitation Radar
Operator	U. of Wyoming	NCAR	LATMOS	MPI Met./DLR	NASA	NASA	NASA	U. of Wyoming
Frequency	94.9 GHz	94.0 GHz	95.0 GHz	35.5 GHz	13.5 GHz 35.5 GHz	94.2 GHz	9.6 GHz	35.6 GHz
Antenna	Up to 5 antennas, multiple beams	1 antenna, variable beam direction	Up to 6 antennas, multiple beams, nadir and zenith	1 antenna, nadir	Conical scan: 1 antenna, two dual-freq. feeds, nadir: 1 lens polarimetric	1 antenna, nadir	2 antennas, nadir and conical/cross-track	2 antennas, nadir and zenith
Beamwidth	0.8°	0.7°	0.5°	0.6°	3° (Ku) 1.2° (Ka)	0.46°	3.3°	4.2°
Transmit power	1.8 kW klystron	2 kW klystron	1.8 kW klystron	30 kW magnetron	0.090 kW (Ku) 0.040 kW (Ka) solid state	0.050 kW solid state	9 kW klystron	0.010 kW solid state
Sensitivity	-40 dBz at 1 km	-22 dBz at 10 km	-35 dBz at 1 km	-25 dBz at 10 km	0 dBz (Ku) -5 dBz (Ka) at 10 km	-30 dBz at 10 km	-15 dBz at 10 km	-18 dBz at 1 km
Typical unambiguous velocity	$\pm 15.8 \text{ m s}^{-1}$	$\pm 7.75 \text{ m s}^{-1}$	$\pm 6 \text{ m s}^{-1}$	$\pm 12.67 \text{ m s}^{-1}$	$\pm 96 \text{ m s}^{-1}$ (Ku) $\pm 38 \text{ m s}^{-1}$ (Ka)	$\pm 15.914 \text{ m s}^{-1}$	$\pm 156 \text{ m s}^{-1}$	$\pm 42.1 \text{ m s}^{-1}$
Polarization diversity	Alternating H, V; one or two antennas	Alternating H, V	-	LDR	Nadir mode: LDR	LDR	-	-

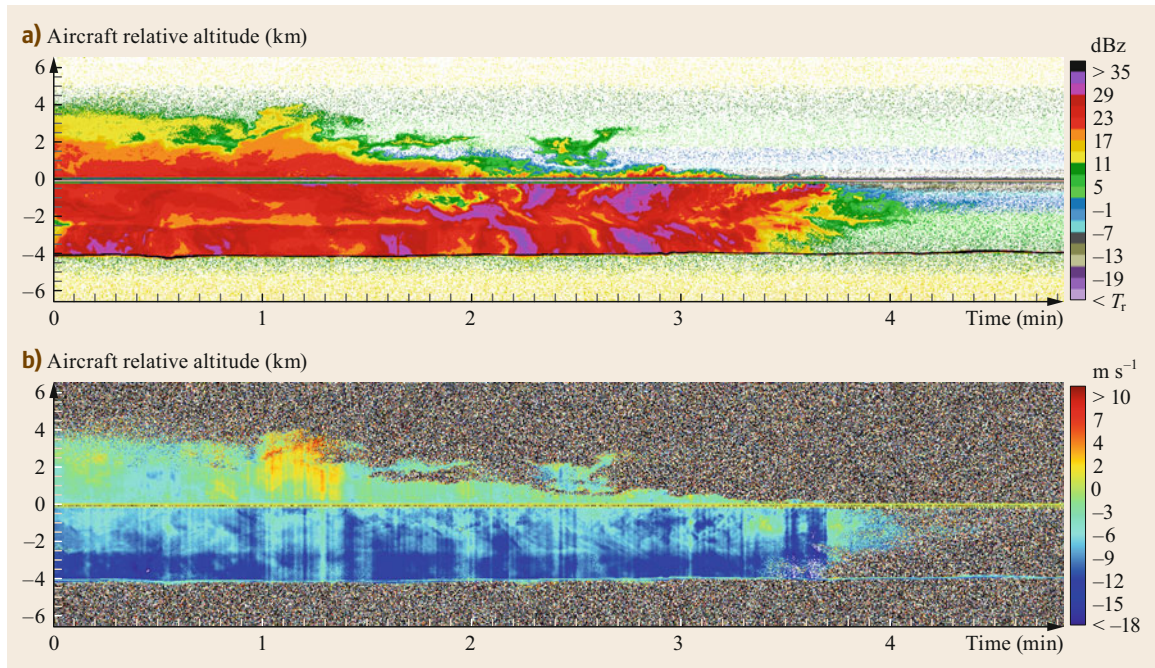


Fig. 39.16 (a) Ka-band reflectivity and (b) Doppler velocity measurements

to measure precipitation closer to the aircraft (at ranges of 100 m to about 1 km). An additional improvement in sensitivity is achieved by utilizing a high pulse repetition frequency (PRF) of up to 20 kHz, which provides a large number of pulses to average during a typical dwell time of 200 ms. The radar reflectivity factor can

be estimated directly from the received power or from the lag-1 and lag-3 coherent power for optimal detection [39.36].

Sample measurements of reflectivity and Doppler velocity are shown in Fig. 39.16. Note that Doppler velocity has not been corrected for aircraft motion.

39.5 Specifications

It is not possible to provide general specifications for airborne cloud and precipitation radar systems. These radar systems are tailored by the various research groups involved to the aircraft available. The systems presented above as well as other systems listed in [39.4] show great diversity in terms of aircraft integration, technical properties, and signal processing. Table 39.4 provides a summary of the technical properties of the radar systems described in Sect. 39.4.

Various radar configurations are used, depending on the size and type of the aircraft employed as well as

the scientific missions that the radar is anticipated to be utilized for. The space available for the antenna is the most important influence on the selection of the radar wavelength and beamwidth. Wavelength selection is discussed in Sect. 39.3.2. A wide beamwidth and thus a small antenna can be used when the clouds of interest occur close to the aircraft and the aircraft is flying relatively slowly. If the aircraft is flying quickly at high altitude, a narrow beam is needed to achieve high spatial resolution.

39.6 Calibration and Quality Control

In principle, the calibration and quality control of airborne radar systems are similar to those of ground-based radars. However, direct calibration using fixed targets is often not possible. While the sun can be used

as an external reference for the pointing direction of a ground-based radar, a different approach is needed for an airborne system.

39.6.1 Radar Calibration

The power or reflectivity of a cloud radar system is typically calibrated using a budget approach. In this, the gain or loss of system components like transmitter, receiver, waveguides, antenna, and radome are characterized in the laboratory first. All gains and losses are subsequently combined into an overall radar calibration. Furthermore, variable system parameters need to be continuously logged for subsequent drift correction. In addition, an external calibration source should be used to check for systematic errors in this budget approach (e.g., [39.59]).

For ground-based radars equipped with a scanning antenna, trihedral corner reflectors or calibration spheres are established calibration methods for the radar reflectivity [39.66]. In contrast, the radiometric calibration of airborne cloud radar instruments remains a difficult task. Comparing fixed, nadir-pointing cloud radars on aircraft with external calibration sources is almost impossible.

One of the remaining external references is the well-defined ocean surface backscatter [39.21, 63, 67]. For this technique, roll maneuvers of the aircraft are used to measure the normalized radar cross-section (NRCS) of the ocean surface at different incidence angles. Measurements and simulations have shown that the NRCS becomes very stable and almost independent of the wind speed and wind direction for an incidence angle of 10° from the nadir [39.68, 69]. Various airborne cloud radar instruments such as the Ku/Ka-band cloud radar APR-2 [39.69], the W-band cloud radar RASTA [39.70], and the HAMP MIRA35 [39.59] have been successfully calibrated using this technique.

Further calibration verification can be carried out during campaigns when two or more airborne radars observe the same cloud systems. Another possibility is to fly beneath the track of a satellite that carries a cloud radar [39.59].

Note that the Doppler velocity does not need to be calibrated.

39.6.2 Pointing Direction Calibration

For any weather radar, ground or mobile, it is important to precisely determine the direction of the radiation. At a minimum, this allows the returned echo to be correctly assigned to a given frame of reference. For airborne radars, as discussed in Sect. 39.3.4, the direction of the radiation must be known before the contribution of the aircraft's motion to the measured Doppler velocity can be removed. Moreover, a change in the beam-pointing direction affects the magnitudes of the contributions of the vertical and horizontal components of the 3-D

velocity vector of the weather echo (winds and hydrometeor fall velocity) to the radial Doppler measurement. Therefore, accurate knowledge of the radar beam pointing direction is crucial to correctly interpreting the measured Doppler velocity.

Any aircraft frequently changes its attitude during flight. Even under the best meteorological conditions (flying straight and level in clear air with no winds and turbulence), there are small changes in the roll, pitch, and yaw of the aircraft. Aircraft are not perfectly rigid bodies and are prone to mechanical vibrations and airframe distortions. This can affect the mounting and the beam pointing of the radar antenna. It also means that there is always a level of uncertainty in the direction of the beam—at least a small fraction of a degree. A beam-pointing error of 0.1° in the direction of the velocity vector of an aircraft flying at 100 m s^{-1} will affect the Doppler measurement by about 0.2 m s^{-1} . For a vertically pointing airborne radar that measures vertical velocities, a deviation of the beam-pointing vector from vertical will also add a contribution from the horizontal wind [39.71]. Using a stabilized radar platform to maintain a fixed pointing direction helps to counter variations in the attitude of the aircraft, but cannot completely eliminate small deviations. Airborne scanning radars that mechanically or electronically steer the beam have additional beam-pointing uncertainty due to the limited accuracy of scanning angle measurements.

To estimate a beam-pointing vector of an airborne radar in flight in the ground coordinate system at the sampling rate of the radar data, the following measurements must be performed at a rate equal to or higher than the radar data rate:

- Aircraft ground velocity vector
- Aircraft attitude, attitude rate, and position
- Antenna beam-pointing vector.

The first two sets of required measurements are provided by an inertial reference system (IRS), also known as an inertial measurement unit (IMU), which is either used by the aircraft for navigation (an INS) or is specifically dedicated to the radar. The third required measurement is a beam-pointing calibration. All of the measurement components have uncertainties associated with them. Data from global navigation satellite systems (GNSSs) are used to reduce errors in the aircraft position, velocity, and attitude measurements from the IRS. Even modern high-accuracy hybrid IMU/GNSS devices that employ sophisticated Kalman filters suffer from drifts in accuracy during a flight, particularly for yaw. This is due to the fact that the heading measurement is only well measured during lateral accelerations (i.e., turns); it is poorly constrained for straight and

level flight. These yaw errors can also impact pitch and roll. It is therefore recommended that the aircraft should perform turns periodically during flight to constrain the heading measurements and minimize errors due to drift. Detailed information about IRSs and GNSSs can be found in [39.4, Sect. 2.3].

There are techniques that can correct the Doppler data for the aircraft motion contribution and are applicable to scanning radars (ELDORA and the NOAA P-3 tail radar). Variational and optimization procedures that utilize Doppler measurements of the Earth's surface are used to minimize the errors in the antenna-pointing and navigational data [39.72–75]. However, beam-pointing calibration is not performed in advance for these techniques since they are developed to correct errors in the antenna scanning position and the navigational data collected during research flights.

A different approach is to first calibrate the antenna-pointing beam vector at a fixed position by flying prescribed aircraft maneuvers while collecting surface Doppler data. An airborne Doppler return from the Earth's surface is equal to the component of the aircraft velocity vector into the radar beam assuming that the target within the radar resolution volume has zero velocity (see Fig. 39.8; $v_r = \mathbf{b} \cdot (\mathbf{V}_s + \mathbf{V}_p)$ where $\mathbf{V}_s = \mathbf{0}$). Thus, if the aircraft's velocity and attitude at the radar antenna are known, one can solve for the unknown beam-pointing vector \mathbf{b} . A nonlinear least-squares method can be used to minimize the residual velocity of the ground. The result of this procedure is the fixed-position beam-pointing vector in the aircraft coordinate system. Given the presence of random errors in the IMU/GNSS and radar Doppler data, the solution for the beam vector is a probability distribution with a mean value and a standard deviation that represents the uncertainty in the pointing direction [39.38].

The calibrated fixed mean beam-pointing vector and the aircraft's navigational data from a research flight are used to determine the radar data beam-pointing vectors in ground coordinates and correct the Doppler measurements for this flight.

With the advent of inexpensive and highly accurate IMU/GNSS devices, this approach does not typically require corrections for the IMU/GNSS data during a research flight, and is simpler. It can be used for airborne radars with scanning antennas (e.g., the HCR) for which the offset of the scanning beam from its calibrated fixed position is measured and the offset error is small.

This approach to calibration and Doppler correction was used for the WCR on UWKA and the HCR on NCAR/NSF GV aircraft. The results for the WCR on UWKA indicated that there was a root mean square error in the antenna beam-pointing vector of less than

0.03° and a residual error in the corrected Doppler measurements of less than 0.1 m s^{-1} [39.38]. The results for the HCR [39.53] were similarly encouraging. The HCR has a dedicated IMU/GNSS unit with a reported pitch error of 0.06° . Using a calibration based on the method described in [39.38], the antenna pointing bias was found to be smaller than 0.05° . It is important to have well-calibrated pointing angles during radar operation because the HCR employs beam stabilization in the nadir and zenith staring modes in order to reduce the errors in the measured vertical motion from the horizontal wind. The stabilization is accomplished by moving the beam in response to the changes in aircraft attitude reported by the IMU/GNSS, and any pointing bias will cause Doppler measurement errors. A final correction is applied to the nadir-pointing data from the HCR that utilizes the stationary surface echo as a reference [39.76]. This surface-reference correction was shown to result in Doppler velocity errors of less than 0.05 m s^{-1} for data collected during the Nor'easter research flight [39.77].

39.6.3 Quality Control

Quality control for radar systems involves regular calibration of the system and monitoring system performance during measurements or inspecting system-generated log files.

As described above, power measurements can be calibrated either on the ground or when airborne. Some systems are difficult to calibrate on the ground due to technical constraints. Airborne calibration of reflectivity often requires dedicated maneuvers that must be planned in advance during campaigns. In addition to power calibration, it is also important to verify the pointing direction of the radar beam, especially after modifying the mounting of the antenna or the IMU. The pointing direction needs to be verified during special maneuvers or during regular measurement flights. It should always be possible to correct the Doppler velocity of the surface to zero; if it is not, the estimation of the attitude of the aircraft—and thus the radar antenna—is erroneous.

During the flight, or at least before the next flight, all radar parameters (reflectivity, dual-polarization parameters, Doppler velocity) should be inspected for plausibility and related to other observations such as visual impression, satellite images, and lidar or radiometer data.

More quality control can be applied during postprocessing or data evaluation. This includes estimating the noise level or identifying multiple peaks in the Doppler spectrum.

39.7 Maintenance

Unlike radars that are operated continuously (Chap. 30), fixed maintenance intervals are not applicable to airborne radar systems. Due to the high costs of airborne campaigns, it is advisable to perform technical maintenance according to the instructions of the manufacturers of the radar system before each campaign. It will also be necessary to perform calibration, especially if the radar system is removed from the aircraft between campaigns.

39.8 Applications

To demonstrate the potential of airborne radars and their applications, some examples from recent campaigns are discussed in this section.

39.8.1 Cumulus Cloud Observations

The WCR (Sect. 39.4.1) has been used extensively to investigate the microphysical and kinematic structure (and the interplay between these two) within cumulus and cumulus congestus cloud systems. Aspects studied include the development of drizzle within shallow, warm cumulus [39.78], the initial development of ice through primary and secondary mechanisms in marine and continental environments [39.79–81], the detailed kinematic structure of developing cumulus [39.82] (including compelling evidence for toroidal circulations [39.83–85]), and the pulsating nature of cumulus growth with successive thermals, which can act to precondition the environment and promote further convective growth [39.84, 86, 87].

The data shown in Fig. 39.17 demonstrate the powerful synergy between airborne in-situ measurements and high-resolution reflectivity and velocity radar observations in a vertical curtain directly above and below aircraft flight level. In this example (taken from [39.79]), cloud tops are at -8°C , the top of the so-called Hallett–Mossop zone. Slightly elevated LDRs measured by the WCR directly beneath the aircraft (black boxes in Fig. 39.17b) indicate regions of mixed hydrometeor populations, suggesting the presence of graupel. Indeed, observations from particle imaging probes reveal some small ($D \approx 500\ \mu\text{m}$), lightly rimed graupel at the center of the core updraft. The presence of strong downward Doppler velocities in the same region (Fig. 39.17c) suggests the presence of even larger graupel particles that are falling from higher in the cloud through a region with a strong updraft and significant cloud liquid water, while near-zero Doppler velocities indicate a region where graupel particles

are balanced within the updraft. These conditions are expected to be highly conducive to ice production through rime splintering [39.88], and likely account for the high ice concentrations found in relatively warm cumuli.

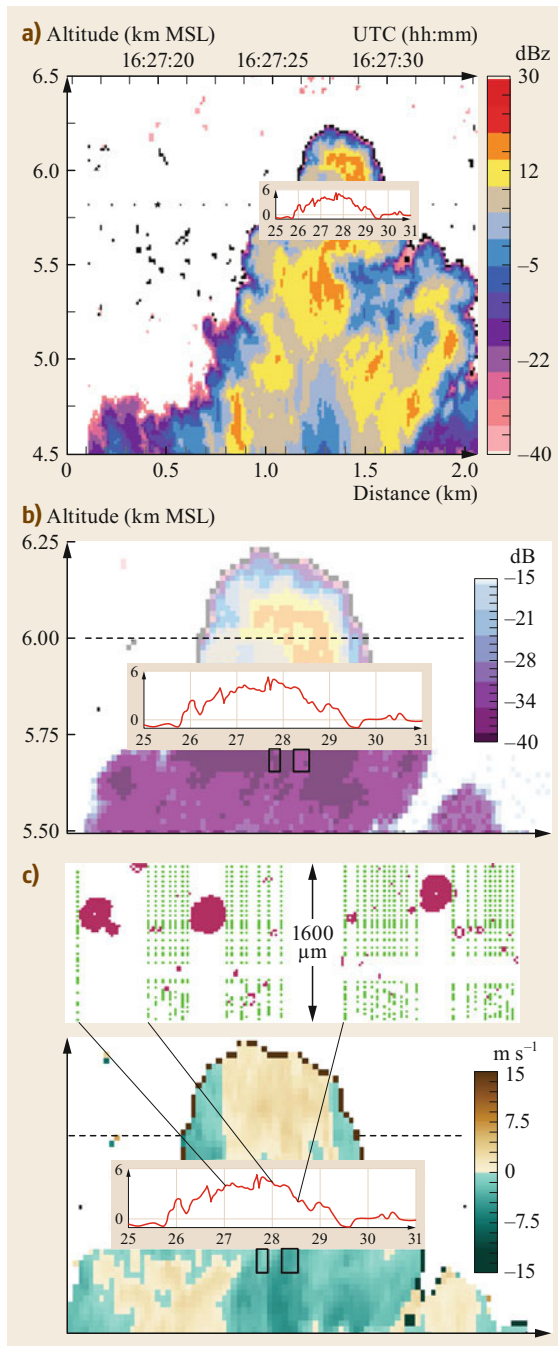
In cases such as that described above, interpretations of the detailed in-situ microphysical measurements from the aircraft are aided by high-resolution radar measurements that provide the context of the cloud. Likewise, interpretations of the radar observations rely on measurements from the aircraft to (in this instance) deconvolve the particle fall velocity from the vertical air motion.

In cases such as that described above, interpretations of the detailed in-situ microphysical measurements from the aircraft are aided by high-resolution radar measurements that provide the context of the cloud. Likewise, interpretations of the radar observations rely on measurements from the aircraft to (in this instance) deconvolve the particle fall velocity from the vertical air motion.

39.8.2 Observations of Synoptic-Scale Frontal Systems

During the NARVAL North campaign in January 2014 [39.60, 89] and the NAWDEX campaign in September and October 2016 [39.61], a number of synoptic-scale frontal cloud and precipitation systems were investigated over the North Atlantic. The HALO aircraft equipped with the HAMP payload (Sect. 39.4.4) was based at Keflavik Airport in Iceland.

Figure 39.18 shows the flight track and the radar observations for a mature extratropical cyclone on 12 January 2014. The occlusion and cold front of the cyclone produced a spiraling convective cloud and precipitation band with partly deep convection. During the 6 h 38 min flight, the band was crossed several times. The flight was performed at FL 270 ($\approx 7900\ \text{m}$ above sea level (ASL)) in order to obtain permission to release dropsondes. The radar operation was started about 40 min after take-off, and the radar was switched off about 15 min prior to landing. The precipitation area of the occlusion was crossed after take-off and before landing. Also, the southern turns were within the spiraling band with deep convection. At about 11:00 UTC, the center of the cyclone was crossed, and low post-



frontal showers were observed at about 13:30 UTC. The aircraft flew through the cirrus clouds of the cold front during the eastern turn at about 14:00 UTC.

Though this was a relatively short flight (other flights lasted for up to 9 h), the long range of HALO facilitates detailed studies of synoptic-scale cloud and precipitation systems. Since the radar is flown together

with the microwave radiometers and the water-vapor lidar, additional information on water vapor, ice, and the liquid water path is available. Dropsondes also provide thermodynamic background information.

Dropsondes also provide thermodynamic background information. **Fig. 39.17a–c** Observations of a cumulus tower that was penetrated near the cloud top at 5.75 km above mean sea level (MSL) ($\approx -6^\circ\text{C}$) during the ICE-T experiment. **(a)** Radar reflectivity from the WCR above and below the aircraft flight level. **(b)** Radar reflectivity above and LDR below the aircraft flight level, and vertical particle velocity above and below. For all graphs, the *inset* shows aircraft-measured vertical winds at flight level. **(c)** Images showing hydrometeors measured at flight level during cloud penetration (after [39.79] © 2016 American Meteorological Society (AMS)) ◀

with the microwave radiometers and the water-vapor lidar, additional information on water vapor, ice, and the liquid water path is available. Dropsondes also provide thermodynamic background information.

39.8.3 Deep Convection

The NASA ER-2 with EXRAD (Sect. 39.4.5) flew over intense hailstorms during the Integrated Precipitation and Hydrology Experiment (IPHEX) during 2014. EXRAD provided unique conical scan and nadir-pointing measurements from a group of deep convective storms that propagated across North Carolina into South Carolina and produced up to 5 cm of hail. Measurements from EXRAD's nadir beam, HIWRAP, and CRS are presented in [39.30] and attest to the large ice hydrometeors present in these storms. Figure 39.19 shows horizontal winds derived from EXRAD's conical scan beam during one aircraft pass, obtained using the approach presented in [39.25]. The images show a high-reflectivity (> 60 dBZ) core at the 6 km level, strong low-level inflow from the south-southeast at the 1 km level, and strong divergent outflow above the 6 km level. These images are typical of the swath provided by the conical scan, which was ≈ 25 km wide at the surface and 12.5 km wide at an altitude of 10 km. The conical scan provided reasonably accurate horizontal winds over the swath, but vertical winds were less reliable away from the nadir. When the nadir Doppler velocities (essentially reflectivity-weighted vertical hydrometeor motions) were combined with modest estimates for the hail fall speed, vertical air velocities were estimated to exceed $30\text{--}40$ m s $^{-1}$ in the convective core at the north-west end of this line.

39.8.4 Stratocumulus Observations

Their long ranges and endurance make airborne research platforms with integrated remote and in-situ measurements a critical tool for studying large, remote cloud systems over the world's oceans, including stratocumulus. These cloud systems are important to re-

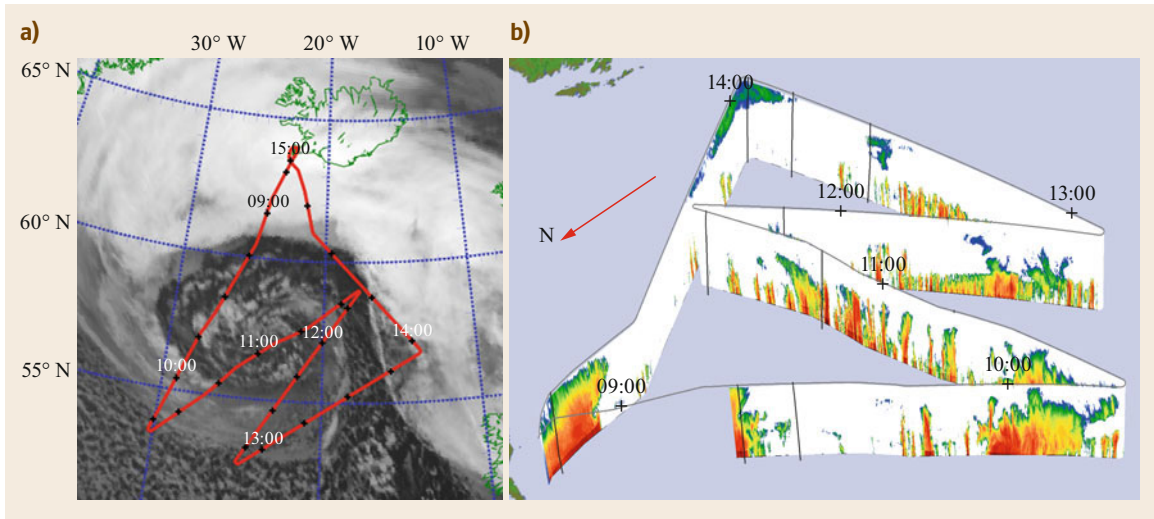


Fig. 39.18a,b Extratropical cyclone on 12 January 2014. **(a)** HALO flight pattern overlaid on a SEVIRI infrared (10.8 μm) satellite image. **(b)** Observations (reflectivity) from a downward-looking cloud radar; vertical black lines indicate the paths of dropsondes (image courtesy of M. Wirth, DLR)

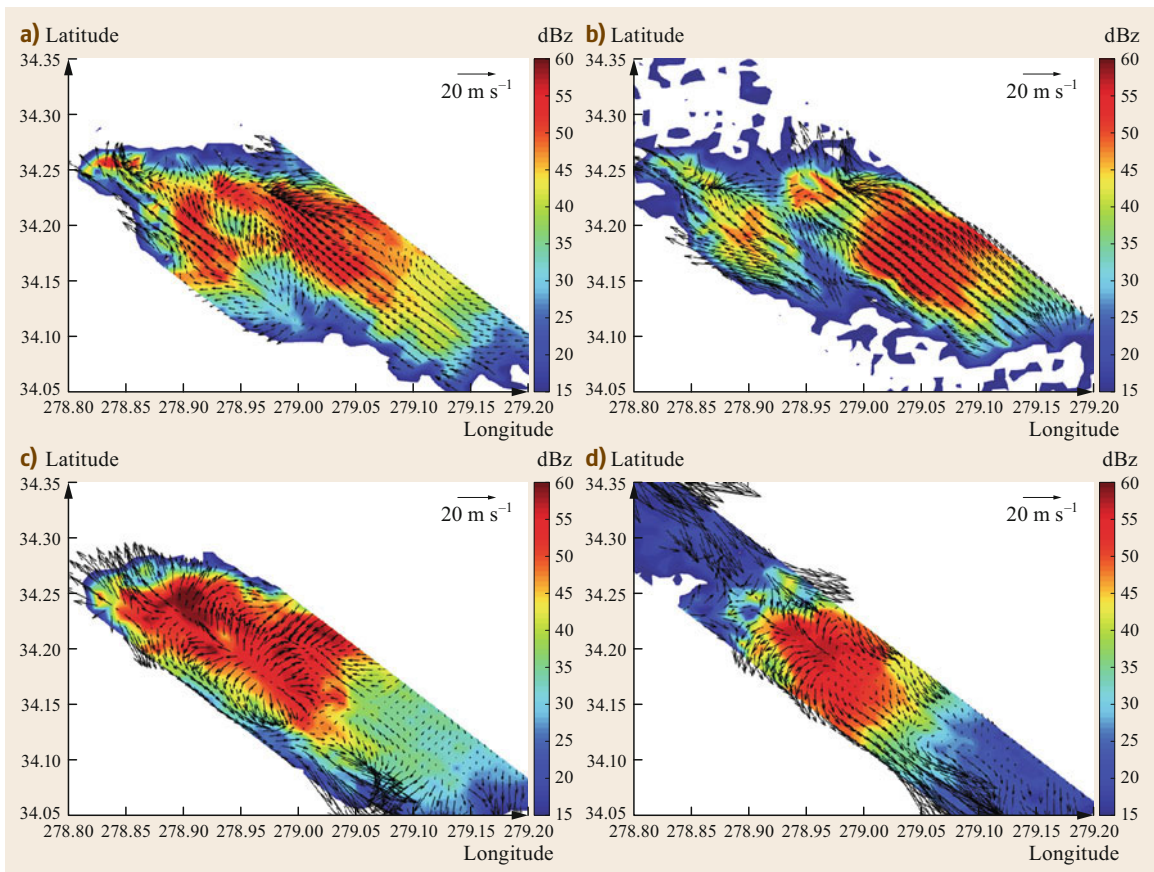


Fig. 39.19a-d Horizontal wind vectors and reflectivity at heights **(a)** 6 km, **(b)** 10 km, **(c)** 1 km, and **(d)** 3 km above ground level (AGL), as derived from the EXRAD conical scan radar during the IPHEX field experiment on 23 May 2014

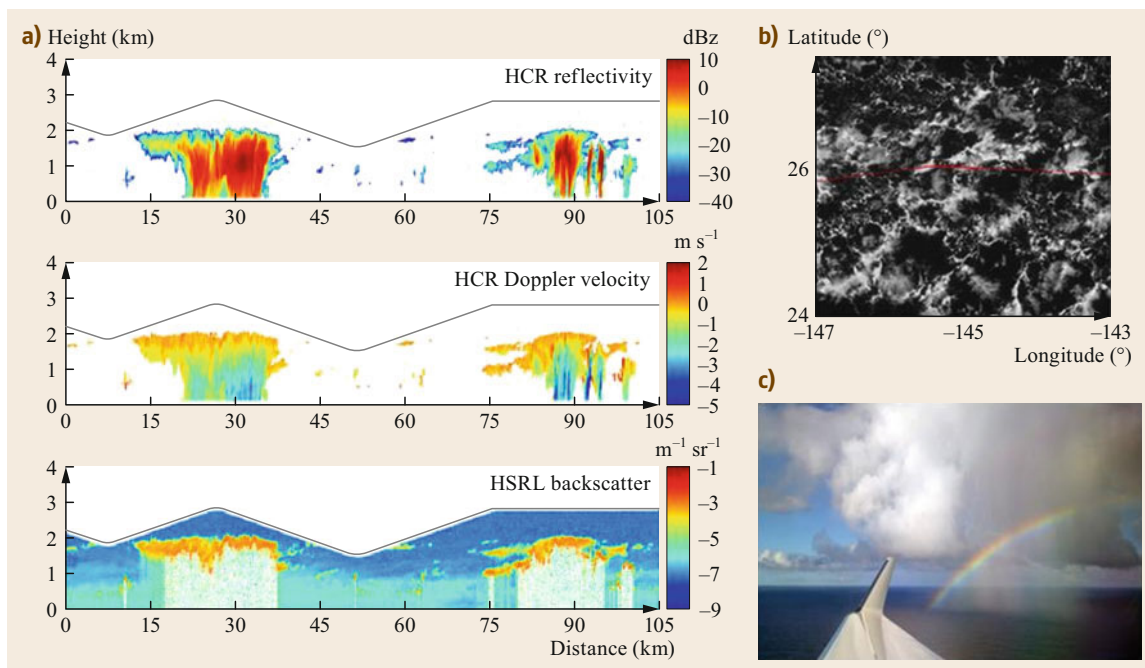


Fig. 39.20a–c Radar and lidar observations from the CSET study. **(a)** HCR and HSRL returns from mesoscale cloud and precipitation complexes observed on 19 July 2015 at 19:10–19:20 UTC. **(b)** A GOES high-definition visible image showing the location of the aircraft near the time of the sampling. **(c)** A photo of drizzle falling from the cumulus and a rainbow that was taken during a 500 ft leg at 18:02 UTC (after [39.90] © 2018 American Meteorological Society (AMS))

gional weather and climate as well as the global climate system, but are often poorly represented by numerical weather and climate models [39.90–94]. Airborne radars are an important component of the measurements that can be used to study these complicated cloud systems.

The NCAR HIAPER Cloud Radar, used in combination with the HSRL and onboard in-situ probes, has been an important tool for studying the microphysics, aerosol interactions, and evolution of large-scale oceanic stratocumulus cloud systems. The Cloud System Evolution in the Trades study (CSET) [39.90], which took place in the summer of 2015, investigated the evolution of boundary-layer aerosol, cloud, and precipitation as well as the thermodynamic structure of stratocumulus clouds in the Pacific Ocean. The associated missions consisted of two legs: a flight from Sacramento (California) to Kona (Hawaii) and the return flight. The outbound flights were planned using the Global Forecast System forecast trajectories to ensure that the return flight could sample the evolution of the same cloud population in a Lagrangian fashion two days later. Each leg included segments above, below, and within the clouds, and the radar and lidar were operated at nadir or were zenith-pointing.

Figure 39.20 shows the synergy of the radar and lidar observations. The radar measures the structures throughout the cloud and precipitation, while the lidar is highly sensitive to the clouds and aerosols but the signal is quickly completely attenuated by liquid clouds. However, as reported in [39.91] (and following [39.95]), the HCR and HSRL were used in combination to retrieve the liquid water content and effective droplet radii in the optically thin veil clouds in the zone of transition from stratocumulus to cumulus during CSET. They found that the veil clouds had few relatively large droplets, making their albedo highly sensitive to changes in concentration.

39.8.5 Wind Field Retrieval in Stratiform Precipitation

The RASTA cloud radar [39.56] is capable of retrieving the 3-D wind field. The three components of the wind field in a vertical plane below and above the aircraft are retrieved using the six-antenna configuration by combining independent measurements of the projected wind on radar radials. This is achieved by using a variational approach [39.96] and a Doppler velocity forward model to iteratively adjust the estimated wind field and

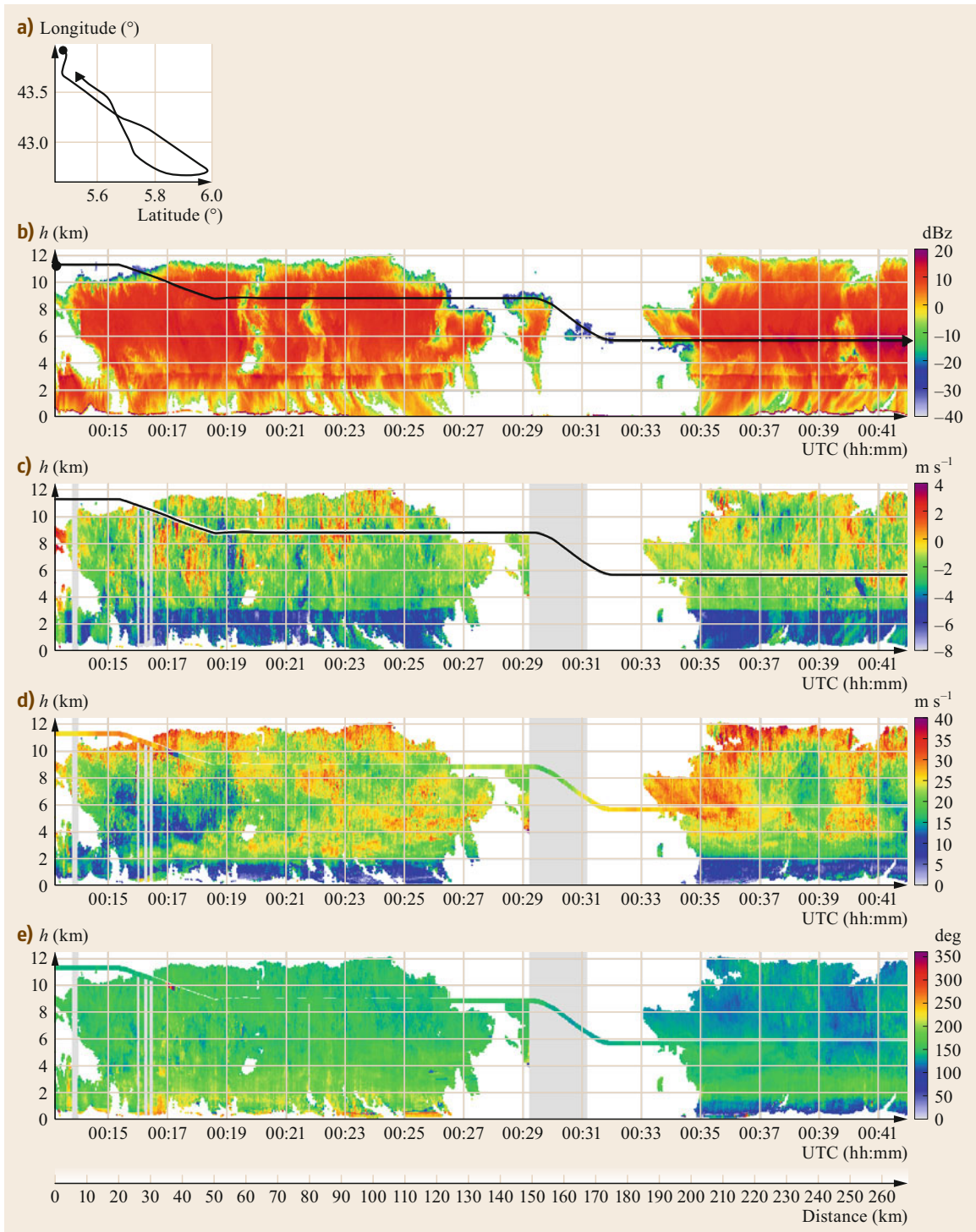


Fig. 39.21a–e Example of airborne multi-Doppler cloud radar retrieval (RASTA) based on a combination of data from three antennas looking down and three antennas looking up during the HYMEX campaign on 21 October 2012 (see the main text for more details): **(a)** The aircraft track, **(b)** nadir and zenith reflectivities, **(c)** retrieved vertical velocity, **(d)** horizontal wind speed, and **(e)** wind direction

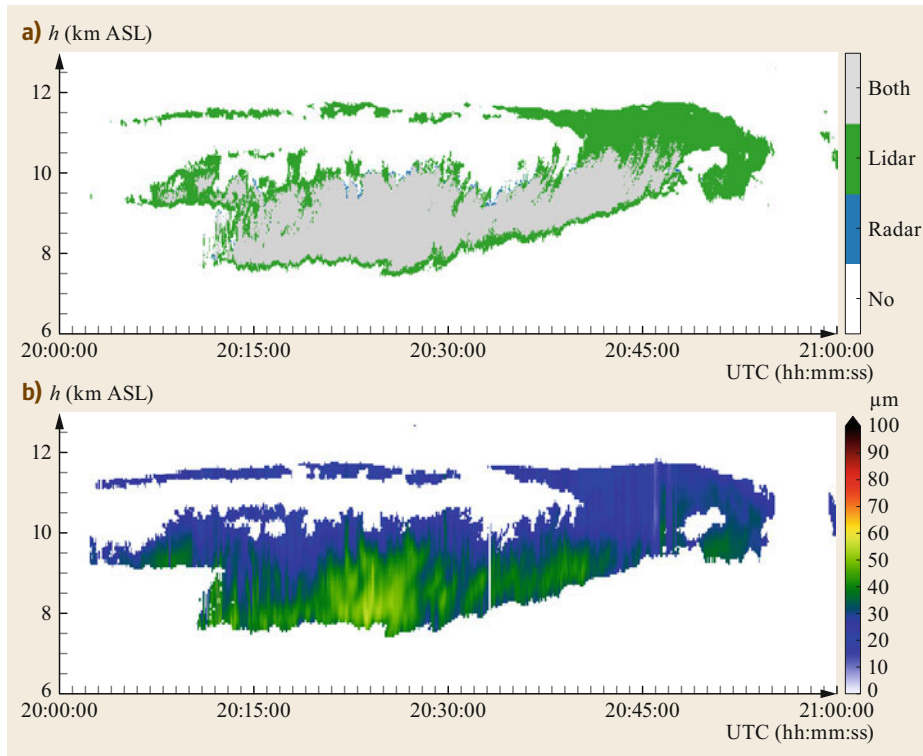


Fig. 39.22a,b
Cirrus measured by the HALO research aircraft on 16 December 2013. **(a)** Instrument mask showing the sensitivity overlap of radar and lidar (gray) and the lidar-only (green) region. **(b)** Retrieved effective ice crystal radius obtained by the synergistic VarCloud algorithm

particle fall velocities to the measured Doppler velocities. The six antenna measurements are assimilated to retrieve the vertical velocity (the sum of the terminal fall velocity of the hydrometeors and the vertical air motion) and the along- and cross-track wind speeds, based on precise knowledge of the attitude of the aircraft and the pointing angles. Along- and cross-track wind velocities can be converted into meridional and zonal winds or the horizontal wind speed and direction.

Figure 39.21 shows the wind retrievals derived from measurements collected during the Hydrological Cycle in the Mediterranean Experiment (HyMeX) field campaign [39.51] on 21 October 2012 above the Marseille region in France (the aircraft track is presented in Fig. 39.21a). Nadir and zenith reflectivities are presented in Fig. 39.21b. The blind zone (240 m) was assigned interpolated values of the reflectivity between the upward and downward domains. The retrieved vertical velocity (a combination of the terminal fall velocity of the hydrometeors and the vertical air motion V_z) and the horizontal wind speed and direction are presented in Fig. 39.21c–e respectively. The sharp gradient observed in the vertical velocity is due to the conversion from ice crystals to rain drops, thus highlighting the melting layer. Clear-sky data are excluded and appear white in the panels. Areas where the retrieval cannot be used or where the algorithm does not converge and therefore

leads to unrealistic winds are shown in gray. For instance, the vertical component of the wind cannot be retrieved above and below the aircraft when the aircraft is turning to the right and the left, respectively. The in-situ horizontal wind speed and direction measured by the aircraft at flight level are plotted over the path of the aircraft. This example shows that the retrievals above and below the aircraft are in good agreement.

39.8.6 Synergetic Retrieval of Cloud Microphysics Using Radar and Lidar

Lidar and cloud radar instruments are sensitive to different ice crystal sizes. In order to retrieve profiles of ice cloud microphysics by remote sensing, it is necessary to combine cloud radar and lidar measurements. Since the radar wavelength used is normally larger than the ice crystals, interactions with radar signals can be described by Rayleigh scattering. In contrast, the interaction of ice crystals with laser light that has a much shorter wavelength is described by Mie scattering. This leads to complementary sensitivities: the radar is sensitive to the larger ice crystals in optically thicker regions whereas the lidar provides information on the optically thinner regions found at the top of an ice cloud. These complementary sensitivities are illustrated by the instrument mask shown in Fig. 39.22a for a cirrus cloud

measured by the HALO research aircraft on 16 December 2013 during the NARVAL South campaign [39.89]. Here, the gray-colored cloud region shows the overlap of the radar and lidar measurements, while the green-colored cloud region is solely contributed by the lidar.

When radar and lidar instruments are flown on the same platform, their complementary sensitivities can be exploited to retrieve profiles of ice cloud microphysics.

An optimal estimate approach such as VarCloud [39.97] can be used to combine both sets of measurements. This algorithm starts with assumed climatological profiles of ice cloud microphysics and iteratively tries to converge forward-simulated instrument signals with the actual measured signals. Figure 39.22b shows that the synergistically retrieved ice crystal sizes decrease with height.

39.9 Future Developments

Besides the radar systems mentioned in Sect. 39.4, there are a number of developments that are currently under investigation. Two examples are discussed below.

39.9.1 C130 C-Band Phased Array Radar

At the NCAR Earth Observing Laboratory, a collaborative effort to design and build a new airborne research radar that takes advantage of modern phased-array radar technology is underway. The proposed system consists of four removable active electronically scanned array (AESA) antennas with Doppler and dual-polarimetric capabilities that are operated in the C band from the NCAR C-130 aircraft (Fig. 39.23). The planned 3 dB beamwidth of the four radars is $< 2^\circ$, and their along-track resolution will be approximately 130 m. The peak transmit power will be about 12 kW and the pulse width will range from 0.5 to 40 μ s, resulting in a minimum detectable signal of around -15 dBz at a range of 10 km, depending on the specific operating parameters.

Several airborne research radar strengths could be realized with the airborne phased array radar (APAR) design. C-band radars generally require larger antennas than traditional airborne radars that use shorter

wavelengths. However, the size and robust flight characteristics of the C-130 enable the use of larger antennas, making the C band a feasible choice. Attenuation at the C band is substantially less than that at the X band and shorter wavelengths. For example, attenuation from liquid drops that satisfy the Rayleigh scattering approximation is greater at the X, Ka, and W bands than at the C band by factors of about 3.9, 46.7, and 272.2, respectively. Thus, the C band is highly advantageous for observing the heavy precipitation associated with tropical storms, severe convection, and mesoscale convective complexes, among other phenomena. The electronic beam steering of the proposed APAR antennas enables flexible scanning that can be optimized for the particular phenomena observed and sampling strategies employed. Each of the four panels depicted in Fig. 39.23 will be able to scan fore and aft beams at various elevation angles, enabling dual-Doppler wind estimates (Sect. 39.3.5). Surveillance scanning is also enabled by APAR, which, combined with the nose-cone radar, provides near-complete coverage around the aircraft. The combination of C-band dual-polarimetric scanning with dual-Doppler scanning will provide simultaneous precipitation microphysics and kinematic

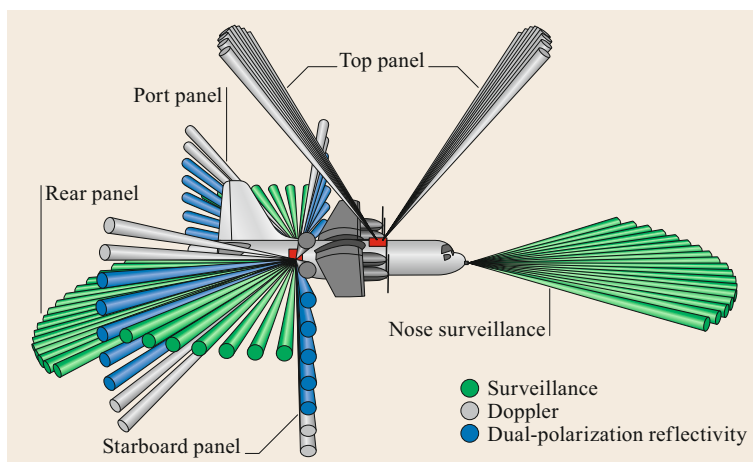


Fig. 39.23 APAR scanning geometry and configuration on the NCAR C-130 aircraft. Courtesy of NCAR/EOL

measurements when airborne. This promises to be a powerful tool for studying precipitation and storms in remote regions.

39.9.2 Quadratic Phase Coding with Solid-State Weather Radars

Over the past decade, advances in solid-state technology have led to the development of a new generation of high duty cycle amplifiers (SSPAs) with peak powers that are still less than, but average powers that are comparable to, those of many vacuum tubes. The challenge to radar engineers has been how to utilize this higher duty cycle capacity to match the sensitivity of conventional radars that employ transmitters with similar average powers, lower duty cycles, but much higher peak powers.

The typical method of increasing the operating duty cycle of a radar is to implement some form of pulse compression. FMCW radars can operate at 100% duty and achieve very fine range resolution at all ranges, but they usually require two antennas, which significantly increases the size and complexity of the system. Also, at mm wavelengths, it is difficult to keep narrow beam-width antennas reliably aligned. Another method that is commonly used to increase the operating duty cycle is to transmit a long, frequency-modulated pulse compression waveform. However, the duty cycle of the pulse

compression waveform is typically 5–20%, and it is operated well below the average power capacity of most SSPA-based transmitters, meaning that it is much less sensitive.

One potential technique for dramatically boosting the duty cycles of single-antenna weather radars is quadratic phase coding (QPC) [39.98]. The QPC technique uses the Chu sequence to separate (but not spread) the ambiguous return signals in the spectral domain, so the radar PRF can be on the order of 1000 times higher than is used with conventional radar systems. This high PRF has several advantages, the most significant being that the duty cycle can approach 50%, yielding a sensitivity comparable to that of a continuous-wave radar at all ranges but without the need for two antennas.

ProSensing Inc. developed the QPC technique in 2016–2017 [39.98], and has demonstrated QPC-mode operation at PRFs of up to 3.1 MHz using X-, Ka-, and W-band radar systems running at duty cycles of approximately 45%. When compared to a conventional pulsed radar operating at the same maximum target range, the QPC-coded radar will exhibit much higher sensitivity, with the improvement equal to the ratio of the PRF of the QPC radar to the PRF of the conventional radar. Initial tests indicated a ≈ 20 dB improvement in sensitivity for a QPC-mode radar operating at a PRF of 3.1 MHz as compared to a conventional short-pulse radar operating at a PRF of 10 kHz.

39.10 Further Reading

A thorough introduction to airborne measurements in general is given by:

- Wendisch, M. and Brenquier, J.-L., 2013: *Airborne Measurements for Environmental Research: Methods and Instruments*, Wiley-VCH Verlag GmbH & Co. KGaA, Weinheim, Germany, 655 pp

Of particular interest is Chap. 9 of that book, on lidar and radar measurements:

- J. Pelon, G. Vali, G. Ancellet, G. Ehret, P.H. Flamant, S. Haimov, G. Heymsfield, D. Leon, J.B. Mead, A.L. Pazmany, A. Protat, Z. Wang, M. Wolde: Lidar and radar observations. In: *Airborne Measurements for Environmental Research: Methods and Instruments*, ed. by M. Wendisch, J.-L. Brenguier (Wiley-VCH, Weinheim 2013), Chap. 9, pp. 457–526

Further details on meteorological radars can be found in Chaps. 30 and 32 of this Handbook and in textbooks such as:

- V.N. Bringi, V. Chandrasekar: *Polarimetric Doppler Weather Radar* (Cambridge Univ. Press, Cambridge 2001)
- F. Fabry: *Radar Meteorology: Principles and Practice* (Cambridge Univ. Press, Cambridge 2015)
- R.M. Rauber, S.W. Nesbitt: *Radar Meteorology: A First Course* (Wiley, Chichester 2018)

Finally, radar technology is described in detail in:

- M. Skolnik: *Radar Handbook*, 3rd edn. (McGraw-Hill, New York 2008)

References

- 39.1 J.-L. Brenguier, W.D. Bachalo, P.Y. Chuang, B.M. Esposito, J. Fugal, T. Garrett, J.-F. Gayet, H. Gerber, A. Heymsfield, A. Kokhanovsky, A. Korolev, R.P. Lawson, D.C. Rogers, R.A. Shaw, W. Strapp, M. Wendisch: *In situ* measurements of cloud and precipitation particles. In: *Airborne Measurements for Environmental Research: Methods and Instruments*, ed. by M. Wendisch, J.-L. Brenguier (Wiley-VCH, Weinheim 2013) pp. 457–526, Chap. 5
- 39.2 R.M. Rauber, S.W. Nesbitt: *Radar Meteorology: A First Course* (Wiley, Chichester 2018)
- 39.3 V.N. Bringi, V. Chandrasekar: *Polarimetric Doppler Weather Radar* (Cambridge Univ. Press, Cambridge 2001)
- 39.4 M. Wendisch, J.-L. Brenguier (Eds.): *Airborne Measurements for Environmental Research: Methods and Instruments* (Wiley-VCH, Weinheim 2013)
- 39.5 J. Pelon, G. Vali, G. Ancellet, G. Ehret, P.H. Flamant, S. Haimov, G. Heymsfield, D. Leon, J.B. Mead, A.L. Pazmany, A. Protat, Z. Wang, M. Wolde: Lidar and radar observations. In: *Airborne Measurements for Environmental Research: Methods and Instruments*, ed. by M. Wendisch, J.-L. Brenguier (Wiley-VCH, Weinheim 2013) pp. 457–526, Chap. 9
- 39.6 M. Skolnik: *Radar Handbook*, 3rd edn. (McGraw-Hill, New York 2008)
- 39.7 P.H. Hildebrand, R.S. Sekhon: Objective determination of the noise level in Doppler spectra, *J. Appl. Meteorol.* **13**(7), 808–811 (1974)
- 39.8 P.G. Black, H.V. Senn, C.L. Courtright: Airborne radar observations of eye configuration changes, bright band distribution, precipitation tilt during the 1969 multiple seeding experiments in hurricane Debbie, *Mon. Weather Rev.* **100**(3), 208–217 (1972)
- 39.9 R.M. Lhermitte: Probing of atmospheric motion by airborne pulse-Doppler radar techniques, *J. Appl. Meteorol.* **10**(2), 234–246 (1971)
- 39.10 P.H. Hildebrand, R.K. Moore: Meteorological radar observations from mobile platforms. In: *Radar in Meteorology*, ed. by D. Atlas (AMS, Boston 1990) pp. 287–315, Chap. 22a
- 39.11 D.P. Jorgensen, R. Meneghini: Airborne/spaceborne radar: Panel report. In: *Radar in Meteorology*, ed. by D. Atlas (AMS, Boston 1990) pp. 315–322, Chap. 22b
- 39.12 A. Pazmany, R.E. McIntosh, R.D. Kelly, G. Vali: An airborne 95 GHz dual polarized radar for cloud studies, *IEEE Trans. Geosci. Remote Sens.* **32**(4), 731–739 (1994)
- 39.13 G. Vali, R.D. Kelly, A. Pazmany, R.E. McIntosh: Airborne radar and in-situ observations of a shallow stratus with drizzle, *Atmos. Res.* **38**(1–4), 361–380 (1995)
- 39.14 J. French, G. Vali, R.D. Kelly: Evolution of small cumulus clouds in Florida: Observations of pulsating growth, *Atmos. Res.* **52**(1/2), 143–165 (1999)
- 39.15 J. French, G. Vali, R.D. Kelly: Observations of microphysics, pertaining to the development of drizzle in warm, shallow cumulus clouds, *Q. J. R. Meteorol. Soc.* **126**(563), 415–443 (1994)
- 39.16 P.H. Hildebrand, C.A. Walther, C.L. Frush, J. Testud, F. Baudin: The ELDORA/ASTRAIA airborne Doppler weather radar: Goals, design, and first field tests, *Proc. IEEE* **82**(12), 1873–1890 (1994)
- 39.17 P.H. Hildebrand, W.-C. Lee, C.A. Walther, C. Frush, M. Randall, E. Loew, R. Neitzel, R. Parsons, J. Testud, F. Baudin, A. LeCornec: The ELDORA/ASTRAIA airborne Doppler weather radar: High-resolution observations from TOGA COARE, *Bull. Am. Meteorol. Soc.* **77**(2), 213–232 (1996)
- 39.18 G.M. Heymsfield, S.W. Bidwell, I.J. Caylor, S. Ameen, S. Nicholson, W. Boncyk, L. Miller, D. Vandemark, P.E. Racette, L.R. Dod: The EDOP radar system on the high-altitude NASA ER-2 aircraft, *J. Atmos. Ocean. Technol.* **13**(4), 795–780 (1996)
- 39.19 G.M. Heymsfield, J.B. Halverson, J. Simpson, L. Tian, T. Paul Bui: ER-2 Doppler radar investigations of the eyewall of hurricane Bonnie during the Convection and Moisture Experiment-3, *J. Appl. Meteorol.* **40**(8), 1310–1330 (2001)
- 39.20 L. Li, G.M. Heymsfield, P.E. Racette, L. Tian, E. Zenker: A 94 GHz cloud radar system on a NASA high-altitude ER-2 aircraft, *J. Atmos. Ocean. Technol.* **21**(9), 1378–1388 (2003)
- 39.21 L. Li, G.M. Heymsfield, L. Tian, P.E. Racette: Measurements of ocean surface backscattering using an airborne 94-GHz cloud radar – Implication for calibration of airborne and spaceborne W-band radars, *J. Atmos. Ocean. Technol.* **22**(7), 1033–1045 (2005)
- 39.22 L. Tian, G.M. Heymsfield, L. Li, R.C. Srivastava: Properties of light stratiform rain derived from 10 and 94 GHz airborne Doppler radar measurements, *J. Geophys. Res.* **112**(D11), D11211 (2007)
- 39.23 M. Grecu, L. Tian, G.M. Heymsfield, A. Tokay, W.S. Olson, A.J. Heymsfield, A. Bansemmer: Non-parametric methodology to estimate precipitating ice from multiple-frequency radar reflectivity observations, *J. Appl. Meteorol. Climatol.* **57**(11), 2605–2622 (2018)
- 39.24 L. Li, G. Heymsfield, J. Carswell, D.H. Schaubert, M.L. McLinden, J. Creticos, M. Perrine, M. Coon, J.I. Cervantes, M. Vega, S. Guimond, L. Tian, A. Emory: The NASA high-altitude imaging wind and rain airborne profiler (HIWRAP), *IEEE Trans. Geosci. Remote Sens.* **54**(1), 298–310 (2015)
- 39.25 S.R. Guimond, L. Tian, G.M. Heymsfield, S.J. Frasier: Wind retrieval algorithms for the IWRAP and HIWRAP airborne Doppler radars with applications to hurricanes, *J. Atmos. Ocean. Technol.* **31**(6), 1189–1215 (2014)
- 39.26 A. Battaglia, C.D. Westbrook, S. Kneifel, P. Kollias, N. Humpage, U. Löhnert, J. Tyynelä, G.W. Petty: G band atmospheric radars: New frontiers in cloud physics, *Atmos. Meas. Tech.* **7**(6), 1527–1546 (2014)
- 39.27 J.S. Marshall, W.M. Palmer: The distribution of raindrops with size, *J. Meteorol.* **5**, 165–166 (1948)
- 39.28 A. Battaglia, M.O. Ajewole, C. Simmer: Multiple scattering effects due to hydrometeors on precip-

- itation radar systems, *Geophys. Res. Lett.* **32**(19), L19801 (2005)
- 39.29 A. Battaglia, M.O. Ajewole, C. Simmer: Evaluation of radar multiple scattering effects in Cloudsat configuration, *Atmos. Chem. Phys.* **7**(7), 1719–1730 (2007)
- 39.30 A. Battaglia, K. Mroz, T. Lang, F. Tridon, S. Tanelli, L. Tian, G.M. Heymsfield: Using a multiwavelength suite of microwave instruments to investigate the microphysical structure of deep convective cores, *J. Geophys. Res. Atmos.* **121**(16), 9356–9381 (2016)
- 39.31 P. Kollias, E.E. Clothiaux, M.A. Miller, B.A. Albrecht, G.L. Stephens, T.P. Ackerman: Millimeter-wavelength radars: New frontier in atmospheric cloud and precipitation research, *Bull. Am. Meteorol. Soc.* **88**(10), 1608–1624 (2007)
- 39.32 A.Y. Hou, R.K. Kakar, S. Neeck, A.A. Azarbarzin, C.D. Kummerow, M. Kojima, R. Oki, K. Nakamura, T. Iguchi: The global precipitation measurement mission, *Bull. Am. Meteorol. Soc.* **95**(5), 701–722 (2014)
- 39.33 G. Skofronick-Jackson, W.A. Petersen, W. Berg, C. Kidd, E.F. Stocker, D.B. Kirschbaum, R. Kakar, S.A. Braun, G.J. Huffman, T. Iguchi, P.E. Kirstetter, C. Kummerow, R. Meneghini, R. Oki, W.S. Olson, Y.N. Takayabu, K. Furukawa, T. Wilheit: The global precipitation measurement (GPM) mission for science and society, *Bull. Am. Meteorol. Soc.* **98**(8), 1679–1695 (2017)
- 39.34 S.Y. Matrosov: A dual-wavelength radar method to measure snowfall rate, *J. Appl. Meteorol.* **37**(11), 1510–1521 (1998)
- 39.35 S. Kneifel, M.S. Kulie, R. Bennartz: A triple-frequency approach to retrieve microphysical snowfall parameters, *J. Geophys. Res.* **116**(D11), D11203 (2011)
- 39.36 A.L. Pazmany, S.J. Haimov: Coherent power measurements with a compact airborne Ka-band precipitation radar, *J. Atmos. Ocean. Technol.* **35**(1), 3–20 (2018)
- 39.37 A.L. Pazmany, J.B. Mead: Millimeter-wave solid-state cloud and precipitation radars and signal processing. In: *IEEE Radar Conf., Oklahoma* (2018) pp. 0104–0109
- 39.38 S. Haimov, A. Rodi: Fixed-antenna pointing-angle calibration of airborne Doppler cloud radar, *J. Atmos. Ocean. Technol.* **30**(10), 2320–2335 (2013)
- 39.39 P.W. Sloss, D. Atlas: Wind shear and reflectivity gradient effects on Doppler radar spectra, *J. Atmos. Sci.* **25**(6), 1080–1089 (1968)
- 39.40 P. Kollias, B.A. Albrecht, F. Marks Jr.: Why Mie?, *Bull. Am. Meteorol. Soc.* **83**(10), 1471–1484 (2002)
- 39.41 R. Damiani, S. Haimov: A high-resolution dual-Doppler technique for fixed multiantenna airborne radar, *IEEE Trans. Geosci. Remote Sens.* **44**(12), 3475–3489 (2006)
- 39.42 O. Bousquet, J. Delanoë, S. Bielli: Evaluation of 3D wind observations inferred from the analysis of airborne and ground-based radars during HyMeX SOP-1, *Q. J. R. Meteorol. Soc.* **142**(S1), 86–94 (2016)
- 39.43 J.R. French, S.J. Haimov, L.D. Oolman, V. Grubišić, S. Serafin, L. Strauss: Wave-induced boundary-layer separation in the lee of the Medicine Bow Mountains. Part I: Observations, *J. Atmos. Sci.* **72**(12), 4845–4863 (2015)
- 39.44 B. Geerts, Y. Yang, R. Rasmussen, S. Haimov, B. Pokharel: Snow growth and transport patterns in orographic storms as estimated from airborne vertical-plane dual-Doppler radar data, *Mon. Weather Rev.* **143**(2), 644–665 (2015)
- 39.45 D.E. Kingsmill, P.O.G. Persson, S. Haimov, M.D. Shupe: Mountain waves and orographic precipitation in a northern Colorado winter storm, *Q. J. R. Meteorol. Soc.* **142**(695), 836–853 (2015)
- 39.46 L. Strauss, S. Serafin, S. Haimov, V. Grubišić: Turbulence in breaking mountain waves and atmospheric rotors estimated from airborne *in situ* and Doppler radar measurements, *Q. J. R. Meteorol. Soc.* **141**(693), 3207–3225 (2015)
- 39.47 R. Damiani, G. Vali, S. Haimov: The structure of thermals in cumulus from airborne dual-Doppler radar observations, *J. Atmos. Sci.* **63**(5), 1432–1449 (2006)
- 39.48 D.P. Jorgensen, P.H. Hildebrand, C.L. Frush: Feasibility test of an airborne pulse-Doppler meteorological radar, *J. Clim. Appl. Meteorol.* **22**(5), 744–757 (1983)
- 39.49 P.H. Hildebrand, C.K. Mueller: Evaluation of meteorological airborne Doppler radar. Part I: Dual-Doppler analyses of air motions, *J. Atmos. Ocean. Technol.* **2**(3), 362–380 (1985)
- 39.50 D. Leon, G. Vali, M. Lothon: Dual-Doppler analysis in a single plane from an airborne platform, *J. Atmos. Ocean. Technol.* **23**(1), 3–22 (2006)
- 39.51 O. Bousquet, A. Berne, J. Delanoë, Y. Dufournet, J.J. Gourley, J. Van-Baelen, C. Augros, L. Besson, B. Boudevillain, O. Caumont, E. Defer, J. Grazioli, D.J. Jorgensen, P.-E. Kirstetter, J.-F. Ribaud, J. Beck, G. Delrieu, V. Ducrocq, D. Scipion, A. Schwarzenboeck, J. Zwiebel: Multifrequency radar observations collected in southern France during HyMeX-SOP1, *Bull. Am. Meteorol. Soc.* **96**(2), 267–282 (2015)
- 39.52 Z. Wang, J. French, G. Vali, P. Wechsler, S. Haimov, A. Rodi, M. Deng, D. Leon, J. Snider, L. Peng, A.L. Pazmany: Single aircraft integration of remote sensing and *in situ* sampling for the study of cloud microphysics and dynamics, *Bull. Am. Meteorol. Soc.* **93**(5), 653–668 (2012)
- 39.53 J. Vivekanandan, S. Ellis, P. Tsai, E. Loew, W.-C. Lee, J. Emmett, M. Dixon, C. Burghart, S. Rauenbuehler: A wing pod-based millimeter wavelength airborne cloud radar, *Geosci. Instrum. Methods Data Syst.* **4**(2), 161–176 (2015)
- 39.54 E.E. Eloranta: High spectral resolution lidar. In: *Range-Resolved Optical Remote Sensing of the Atmosphere*, Springer Series in Optical Sciences, Vol. 102, ed. by C. Weitkamp (Springer, New York 2005) pp. 143–163, Chap. 5
- 39.55 A. Protat, J. Pelon, N. Grand, P. Delville, P. Laborie, J.-P. Vinson, D. Bouniol, D. Bruneau, H. Chepfer, J. Delanoë, M. Haeffelin, V. Noël, C. Tinel: Le projet RALI – Combinaison d’un radar et d’un lidar pour l’étude des nuages faiblement précipitants, *Météorologie* **47**, 23–33 (2004)

- 39.56 J. Delanoë, A. Protat, O. Jourdan, J. Pelon, M. Pappozoni, R. Dupuy, J.-F. Gayet, C. Jouan: Comparison of airborne in situ, airborne radar–lidar, and spaceborne radar–lidar retrievals of polar ice cloud properties sampled during the POLARCAT campaign, *J. Atmos. Ocean. Technol.* **30**(1), 57–73 (2013)
- 39.57 M. Krautstrunk, A. Giez: The transition from FALCON to HALO era airborne atmospheric research. In: *Atmospheric Physics. Research Topics in Aerospace*, ed. by U. Schumann (Springer, Berlin, Heidelberg 2012) pp. 609–624
- 39.58 M. Mech, E. Orlandi, S. Crewell, F. Ament, L. Hirsch, M. Hagen, G. Peters, B. Stevens: HAMP – The microwave package on the high altitude and long range research aircraft (HALO), *Atmos. Meas. Tech.* **7**(12), 4539–4553 (2014)
- 39.59 F. Ewald, S. Groß, M. Hagen, L. Hirsch, J. Delanoë, M. Bauer–Pfundstein: Calibration of a 35 GHz airborne cloud radar: Lessons learned and intercomparisons with 94 GHz cloud radars, *Atmos. Meas. Tech.* **12**(3), 1815–1839 (2019)
- 39.60 B. Stevens, F. Ament, S. Bony, S. Crewell, F. Ewald, S. Gross, A. Hansen, L. Hirsch, M. Jacob, T. Kölling, H. Konow, B. Mayer, M. Wendisch, M. Wirth, K. Wolf, S. Bakan, M. Bauer–Pfundstein, M. Brueck, J. Delanoë, A. Ehrlich, D. Farrell, M. Forde, F. Gödde, H. Grob, M. Hagen, E. Jäkel, F. Jansen, C. Klepp, M. Klingebiel, M. Mech, G. Peters, M. Rapp, A.A. Wing, T. Zinner: A high–altitude long–range aircraft configured as a cloud observatory – The NARVAL expeditions, *Bull. Am. Meteorol. Soc.* **100**(6), 1061–1077 (2019)
- 39.61 A. Schäfler, G. Craig, H. Wernli, P. Arbogast, J.D. Doyle, R. McTaggart–Cowan, J. Methven, G. Rivière, F. Ament, M. Boettcher, M. Bramberger, Q. Cazenave, R. Cotton, S. Crewell, J. Delanoë, A. Dörnbrack, A. Ehrlich, F. Ewald, A. Fix, C.M. Grams, S.L. Gray, H. Grob, S. Groß, M. Hagen, B. Harvey, L. Hirsch, M. Jacob, T. Kölling, H. Konow, C. Lemmerz, O. Lux, L. Magnusson, B. Mayer, M. Mech, R. Moore, J. Pelon, J. Quinting, S. Rahm, M. Rapp, M. Rautenhaus, O. Reitebuch, C.A. Reynolds, H. Sodemann, T. Spengler, G. Vaughan, M. Wendisch, M. Wirth, B. Witschas, K. Wolf, T. Zinner: The North Atlantic Waveguide and Downstream Impact Experiment, *Bull. Am. Meteorol. Soc.* **99**(8), 1607–1637 (2018)
- 39.62 M.L. Mclinden, J. Carswell, L. Li, G. Heymsfield, A. Emory, J.I. Cervantes, L. Tian: Utilizing versatile transmission waveforms to mitigate pulse compression range sidelobes with the HIWRAP radar, *IEEE Geosci. Remote Sens. Lett.* **10**(6), 1365–1368 (2012)
- 39.63 I.J. Caylor, G.M. Heymsfield, R. Meneghini, L.S. Miller: Correction of sampling errors in ocean surface cross-sectional estimates from nadir-looking weather radar, *J. Atmos. Ocean. Technol.* **14**(1), 203–210 (1997)
- 39.64 T. Hand, M. Cooley, G. Kempic, D. Sall, P. Stenger, S. Woodworth, R. Park, P.E. Racette, G. Heymsfield, L. Li: Dual-band shared aperture reflector/reflectarray antenna: Designs, technologies and demonstrations for NASA's ACE radar. In: *IEEE Int. Symp. Phased Array Syst. Technol., Waltham* (2013) pp. 352–358
- 39.65 S. Haimov, J. French, B. Geerts, Z. Wang, M. Deng, A. Rodi, A. Pazmany: Compact airborne Ka-band radar: A new edition to the University of Wyoming aircraft for atmospheric research. In: *IEEE Int. Geosci. Remote Sens. Symp., Valencia* (2018) pp. 897–900
- 39.66 S.M. Sekelsky: Near-field reflectivity and antenna boresight gain corrections for millimeter-wave atmospheric radars, *J. Atmos. Ocean. Technol.* **19**(4), 468–477 (2002)
- 39.67 I.J. Caylor, G.M. Heymsfield, S.W. Bidwell, S. Ameen: NASA ER-2 Doppler Radar Reflectivity Calibration for the CAMEX Project (Goddard Space Flight Center, Greenbelt 1994), NASA-TN-104611, <https://ntrs.nasa.gov/search.jsp?R=19940033279>, Accessed 19 July 2021
- 39.68 S.L. Durden, E. Im, F.K. Li, W. Ricketts, A. Tanner, W. Wilson: ARMAR: An airborne rain-mapping radar, *J. Atmos. Ocean. Technol.* **11**(3), 727–737 (1994)
- 39.69 S. Tanelli, S.L. Durden, E. Im: Simultaneous measurements of ku- and ka-band sea surface cross sections by an airborne radar, *IEEE Geosci. Remote Sens. Lett.* **3**(3), 359–363 (2006)
- 39.70 D. Bouniol, A. Protat, A. Plana–Fattori, M. Giraud, J.-P. Vinson, N. Grand: Comparison of airborne and spaceborne 95-GHz radar reflectivities and evaluation of multiple scattering effects in spaceborne measurements, *J. Atmos. Ocean. Technol.* **25**(11), 1983–1995 (2008)
- 39.71 G.M. Heymsfield: Accuracy of vertical air motions from nadir-viewing Doppler airborne radars, *J. Atmos. Ocean. Technol.* **6**(6), 1079–1082 (1989)
- 39.72 J. Testud, P.H. Hildebrand, W.-C. Lee: A procedure to correct airborne Doppler radar data for navigation errors using the echo returned from the Earth's surface, *J. Atmos. Ocean. Technol.* **12**(4), 800–820 (1995)
- 39.73 J.F. Georgis, F. Roux, P.H. Hildebrand: Observation of precipitating systems over complex orography with meteorological Doppler radars: A feasibility study, *Meteorol. Atmos. Phys.* **72**(2–4), 185–202 (2000)
- 39.74 B.L. Bosart, W.-C. Lee, R.M. Wakimoto: Procedures to improve the accuracy of airborne Doppler radar data, *J. Atmos. Ocean. Technol.* **19**(3), 322–339 (2002)
- 39.75 H. Cai, W.-C. Lee, M.M. Bell, C.A. Wolff, X. Tang, F. Roux: A generalized navigation correction method for airborne Doppler radar data, *J. Atmos. Ocean. Technol.* **35**(10), 1999–2017 (2018)
- 39.76 S. M. Ellis, P. Tsai, C. Burghart, U. Romatschke, M. Dixon, J. Vivekanandan, J. Emmett, E. Loew: Use of the Earth's Surface as a Reference to Correct Airborne Nadir=Looking Radar Radial Velocity Measurements for Plattform Motion, *J. Atmos. Oceanic Technol.* **36**, 1343–1360 (2019)
- 39.77 R.M. Rauber, S.M. Ellis, J. Vivekanandan, J. Stith, W.-C. Lee, G.M. McFarquhar, B.F. Jewett, A. Janiszewski: Finescale structure of a snowstorm

- over the northeastern United States: A first look at high-resolution HIAPER cloud radar observations, *Bull. Am. Meteorol. Soc.* **92**(2), 253–269 (2017)
- 39.78 J.R. French, G. Vali, R.D. Kelly: Observations of microphysics pertaining to the development of drizzle in warm, shallow cumulus clouds, *Q. J. R. Meteorol. Soc.* **126**(563), 415–443 (2000)
- 39.79 S. Lasher-Trapp, D.C. Leon, P.J. DeMott, C.M. Villanueva-Birriel, A.V. Johnson, D.H. Moser, C.S. Tully, W. Wu: A multisensor investigation of rime splintering in tropical maritime cumuli, *J. Atmos. Sci.* **73**(6), 2547–2564 (2016)
- 39.80 R. Jackson, J.R. French, D.C. Leon, D.M. Plummer, S. Lasher-Trapp, A.M. Blyth, A. Korolev: Observations of the microphysical evolution of convective clouds in the southwest of the United Kingdom, *Atmos. Chem. Phys.* **18**(20), 15329–15344 (2018)
- 39.81 J.W. Taylor, T.W. Choullart, A.M. Blyth, Z. Liu, K.N. Bower, J. Crosier, M.W. Gallagher, P.I. Williams, J.R. Dorsey, M.J. Flynn, L.J. Bennett, Y. Huang, J. French, A. Korolev, P.R.A. Brown: Observations of cloud microphysics and ice formation during COPE, *Atmos. Chem. Phys.* **16**(2), 799–826 (2016)
- 39.82 R. Damiani, J. Zehnder, B. Geerts, J. Demko, S. Haimov, J. Petti, G.S. Poulos, A. Razdan, J. Hu, M. Leuthold, J. French: The cumulus, photogrammetric, in situ, and Doppler observations experiment of 2006, *Bull. Am. Meteorol. Soc.* **89**(1), 57–74 (2008)
- 39.83 R. Damiani, G. Vali, S. Haimov: The structure of thermals in cumulus from airborne dual-Doppler radar observations, *J. Atmos. Sci.* **63**(5), 1432–1450 (2006)
- 39.84 R. Damiani, G. Vali: Evidence for tilted toroidal circulations in cumulus, *J. Atmos. Sci.* **64**(6), 2045–2060 (2007)
- 39.85 Y. Wang, B. Geerts: Vertical-plane dual-Doppler radar observations of cumulus toroidal circulations, *J. Appl. Meteorol. Climatol.* **54**(10), 2009–2026 (2015)
- 39.86 J.R. French, G. Vali, R.D. Kelly: Evolution of small cumulus clouds in Florida: Observations of pulsating growth, *Atmos. Res.* **52**(1/2), 143–165 (1999)
- 39.87 Y. Wang, B. Geerts: Observations of detrainment signatures from non-precipitating orographic cumulus clouds, *Atmos. Res.* **99**(2), 302–324 (2011)
- 39.88 J. Hallett, S.C. Mossop: Production of secondary ice particles during the riming process, *Nature* **249**(5452), 26–28 (1974)
- 39.89 C. Klepp, F. Ament, S. Bakan, L. Hirsch, B. Stevens: *NARVAL Campaign Report*, Reports on Earth System Science, Vol. 164 (Max Planck Institute for Meteorology, Hamburg 2014), <http://hdl.handle.net/11858/00-001M-0000-0026-A620-1>, Accessed 19 July 2021
- 39.90 B. Albrecht, V. Ghate, J. Mohrmann, R. Wood, P. Zuidema, C. Bretherton, C. Schwartz, E. Eloranta, S. Glienke, S. Donaher, M. Sarkar, J. McGibbon, A.D. Nugent, R.A. Shaw, J. Fugal, P. Minnis, R. Pali-knoda, L. Lussier, J. Jensen, J. Vivekanandan, S. Ellis, P. Tsai, R. Rilling, J. Haggerty, T. Campos, M. Stell, M. Reeves, S. Beaton, J. Allison, G. Stossmeister, S. Hall, S. Schmidt: Cloud system evolution in the trades (CSET): Following the evolution of boundary layer cloud systems with the NSF/NCAR GV, *Bull. Am. Meteorol. Soc.* **100**(1), 93–121 (2019)
- 39.91 R. Wood, K.-T. O, C.S. Bretherton, J. Mohrmann, B.A. Albrecht, P. Zuidema, V. Ghate, C. Schwartz, E. Eloranta, S. Glienke, R.A. Shaw, J. Fugal, P. Minnis: Ultraclean layers and optically thin clouds in the stratocumulus-to-cumulus transition. Part I: Observations, *J. Atmos. Sci.* **75**(5), 1631–1652 (2018)
- 39.92 J. Teixeira, S. Cardoso, M. Bonazzola, J. Cole, A. DelGenio, C. DeMott, C. Franklin, C. Hannay, C. Jakob, Y. Jiao, J. Karlsson, H. Kitagawa, M. Köhler, A. Kuwano-Yoshida, C. LeDrian, J. Li, A. Lock, M.J. Miller, P. Marquet, J. Martins, C.R. Mechoso, E. v. Meijgaard, I. Meinke, P.M.A. Miranda, D. Mironov, R. Neggers, H.L. Pan, D.A. Randall, P.J. Rasch, B. Rockel, W.B. Rossow, B. Ritter, A.P. Siebesma, P.M.M. Soares, F.J. Turk, P.A. Vaillancourt, A. Von Engel, M. Zhao: Tropical and subtropical cloud transitions in weather and climate prediction models: The GCS/WGNE Pacific cross-section intercomparison (GPCI), *J. Clim.* **24**(20), 5223–5256 (2011)
- 39.93 K.D. Williams, A. Bodas-Salcedo, M. Déqué, S. Ferme-pin, B. Medeiros, M. Watanabe, C. Jakob, S.A. Klein, C.A. Senior, D.L. Williamson: The Transpose-AMIP II Experiment and its application to the understanding of southern ocean cloud biases in climate models, *J. Clim.* **26**(10), 3258–3274 (2013)
- 39.94 A. Bodas-Salcedo, K.D. Williams, M.A. Ringer, I. Beau, J.N.S. Cole, J.-L. Dufresne, T. Koshiro, B. Stevens, Z. Wang, T. Yokohata: Origins of the Solar radiation biases over the southern ocean in CFMIP2 models, *J. Clim.* **27**(1), 41–56 (2014)
- 39.95 E.J. O'Connor, R.J. Hogan, A.J. Illingworth: Retrieving stratocumulus drizzle parameters using Doppler radar and lidar, *J. Appl. Meteorol.* **44**(1), 14–27 (2005)
- 39.96 C.D. Rodgers: *Inverse Methods for Atmospheric Sounding: Theory and Practice*, Series on Atmospheric, Oceanic and Planetary Physics, Vol. 2 (World Scientific, Hackensack 2000)
- 39.97 J. Delanoë, R.J. Hogan: A variational scheme for retrieving ice cloud properties from combined radar, lidar, and infrared radiometer, *J. Geophys. Res.* **113**(D7), D07204 (2008)
- 39.98 J.B. Mead, A.L. Pazmany: Quadratic phase coding for high duty cycle radar operation, *J. Atmos. Ocean. Technol.* **36**(6), 957–969 (2019)

Martin Hagen

Institut für Physik der Atmosphäre
Deutsches Zentrum für Luft- und
Raumfahrt e. V. (DLR)
Weßling, Germany
martin.hagen@dlr.de



Dr. Martin Hagen, leader of the Radar Team at the DLR Institute of Atmospheric Physics, has over 25 years of experience in the operation and development of the polarimetric C-band Doppler radar POLDIRAD. His focus is on the development of radar methods that use dual-polarization and Doppler techniques to analyze mesoscale phenomena. He is involved in radar training for meteorological services and teaching at universities at national and European levels.

Julien Delanoë

LATMOS/IPSL, UVSQ Université Paris-Saclay,
Sorbonne Université, CNRS
Guyancourt, France
julien.delanoë@latmos.ipsl.fr



Julien Delanoë is an associate professor in LATMOS (Laboratoire Atmosphères, Milieux, Observations Spatiales) at the University of Versailles Saint-Quentin—Paris Saclay. He received his PhD in remote sensing in 2005. The main focus of his research is cloud and light precipitation mechanisms and observational strategies for studying them. He develops cloud radars and elaborates methodologies for combining radar and lidar.

Scott Ellis

Research Applications Laboratory
National Center for Atmospheric Research
Boulder, USA
sellis@ucar.edu



Scott Ellis is a Project Scientist in the Research Applications Laboratory (National Center for Atmospheric Research, Boulder, CO, USA). He received his PhD in 2010, and his research interests focus on radar data quality and retrievals of physical quantities from airborne and ground-based radar data. Dr. Ellis has participated in over 20 major field campaigns in various roles ranging from science support to principal investigator.

Florian Ewald

Institut für Physik der Atmosphäre
Deutsches Zentrum für Luft- und
Raumfahrt e. V. (DLR)
Weßling, Germany
florian.ewald@dlr.de



Florian Ewald received his PhD in 2016 from Ludwig Maximilian University (LMU) in Munich for his research on cloud remote sensing using passive cloud side measurements. He is currently working as a postdoc at the Institute of Atmospheric Physics of the German Aerospace Center (DLR). His research focuses on the synergistic use of active and passive techniques for the remote sensing of cloud microphysics.

Jeffrey French

Department of Atmospheric Science
University of Wyoming
Laramie, USA
jfrench@uwyo.edu



Jeffrey French is a Professor of Atmospheric Science at the University of Wyoming, USA. He is also Facility Manager for the Wyoming King Air Research Aircraft, a National Science Foundation-funded Lower Atmospheric Observing Facility. He received his PhD in Atmospheric Science from the University of Wyoming in 1998. Dr. French's expertise is in airborne measurements of clouds and precipitation.

Samuel Haimov

Atmospheric Science Department
University of Wyoming
Laramie, USA
haimov@uwyo.edu



Samuel Haimov is Senior Research Scientist at the Atmospheric Science Department, University of Wyoming, USA. He received his PhD in electrical systems engineering in 1982 from Sofia Technical University, Bulgaria. He is a senior member of the IEEE. Dr Haimov's expertise is in signal processing and radars. His current interest is the remote sensing of the atmosphere using millimeter-wave radars.

Gerald Heymsfield

Mesoscale Atmospheric Processes
Laboratory
Goddard Space Flight Center
Greenbelt, USA
gerald.heymsfield@nasa.gov



Gerald Heymsfield is a Senior Research Scientist in the Mesoscale Atmospheric Processes Laboratory at the NASA Goddard Space Flight Center. He has a PhD in meteorology from the University of Oklahoma. He leads the High Altitude Radar Group at Goddard, which has developed several airborne Doppler radar systems and performs scientific studies with their data. His scientific interests include deep convection, hurricanes, and winter storms.



Andrew L. Pazmany

ProSensing Inc.
Amherst, USA
pazmany@prosensing.com

Andrew L. Pazmany is a Senior Engineer and Managing Partner at ProSensing Inc. He received a BS, a MS, and a PhD in electrical and computer engineering from the University of Massachusetts Amherst in 1982, 1986, and 1993, respectively. After graduation, he stayed at UMass as a Research Professor until 2005. His research interests are signal processing and designing and developing novel remote sensing instruments.

Airborne Solar

40. Airborne Solar Radiation Sensors

K. Sebastian Schmidt , Manfred Wendisch , Bruce Kindel 

This chapter gives an overview of airborne radiometry, specifically solar spectral and broadband radiation (irradiance, radiance, actinic flux) measurements and their use for quantifying the radiative effects of atmospheric constituents (clouds, aerosols, gases), photochemistry, and surface properties. Crucially, airborne radiometers establish a link between the properties of atmospheric constituents as retrieved from remote sensing and their radiative impact on weather and climate. The chapter addresses important advances in instrumentation, motivated by challenging problems in radiation science and examines remaining challenges and expected developments.

40.1	Measurement Principles and Parameters	1132
40.2	History	1132
40.3	Theory	1134
40.4	Devices and Subsystems	1135
40.5	Specifications	1138
40.6	Calibration and Quality Control	1139
40.6.1	Radiometric Calibration	1139
40.6.2	Angular Calibration	1140
40.6.3	Wavelength Calibration	1140
40.6.4	Field Data Processing and Error Assessment	1140
40.7	Maintenance	1141
40.8	Applications	1141
40.8.1	Energetics and Remote Sensing	1141
40.8.2	Combination of Cloud/Aerosol Microphysics and Radiation	1142
40.8.3	Surface Characteristics	1145
40.9	Future Developments	1146
40.10	Further Readings	1146
	References	1147

Airborne measurements of solar radiation complement ground-based monitoring (Chap. 12) and spaceborne remote sensing of atmospheric constituents (clouds, aerosols, gases) by providing information on atmospheric radiative energetics and photochemistry that is not directly accessible from orbit or from surface stations. Neither irradiance (F , also known as flux density, Table 40.1) nor actinic flux density (F_{act} , also known as mean intensity or mean radiance) can be measured remotely because they are defined via the angular integration of the radiance field at a given point in the atmosphere ([40.1]; Sect. 40.3). A sensor measuring irradiance weights incoming radiance by the cosine of the incidence angle; actinic flux density sensors weight in-

coming radiance isotropically. The distinct advantage of airborne radiometers is that they acquire simultaneous measurements of upward (nadir-viewing) and downward (zenith-viewing) radiative energy flux densities at any level in the troposphere and the lower stratosphere (depending on the aircraft), providing validation for radiative quantities derived from remote-sensing data directly quantifying radiative effects (e.g., absorption and heating rate) of atmospheric constituents. After discussing measurement principles and parameters, theory, and history, this chapter describes the current instrumentation, as well as applications of aircraft solar radiation measurements.

Table 40.1 Radiometric quantities for airborne solar radiation sensors

Name	Symbol	Unit	Relation	Notes
Flux	Φ	W	$\frac{dE}{dt}$	Radiated power (energy/time)
Solid angle	Ω	sr	$d\Omega = \sin(\vartheta)d\vartheta d\varphi$ ϑ : polar angle; φ : azimuth angle	In spherical coordinates
Radiance	L	$\text{W m}^{-2} \text{sr}^{-1}$	$\frac{d\Phi}{dA_{\perp}d\Omega}$	Area \perp beam direction
Downward irradiance	F^{\downarrow}	W m^{-2}	$\int_0^{2\pi} \int_0^{\pi/2} L(\vartheta, \varphi) \cos(\vartheta) d\Omega$	Integration over upper hemisphere
Upward irradiance	F^{\uparrow}	W m^{-2}	$\int_0^{2\pi} \int_{\pi/2}^{\pi} L(\vartheta, \varphi) \cos(\vartheta) d\Omega$	Integration over lower hemisphere
Actinic flux density	F_{act}	W m^{-2}	$\int_0^{2\pi} \int_0^{\pi} L(\vartheta, \varphi) d\Omega$	Also known as mean radiance
Net irradiance	F_{net}	W m^{-2}	$F^{\downarrow} - F^{\uparrow}$	
Albedo	α	–	$\frac{F^{\uparrow}}{F^{\downarrow}}$	

40.1 Measurement Principles and Parameters

Because the measurement parameters and principles for airborne solar radiation sensors are similar to those used on the ground, the reader is referred to Chap. 12 for a detailed description of ground-based instruments. Table 40.1 defines only those quantities that are relevant

to this chapter. For simplicity, only broadband quantities are listed. In this chapter, their spectral equivalent is denoted by a λ subscript (e.g., F_{λ}^{\uparrow} , with units of $\text{W m}^{-2} \text{nm}^{-1}$).

40.2 History

Aircraft solar irradiance measurements began in the 1920s, with pyranometers that had been adapted for airborne use in an ad hoc fashion. Although not specifically designed for flight, they allowed direct observations of parameters driving radiative energetics of atmospheric layers and provided a tool to survey surface albedo (1929 in Germany [40.2]; 1948 in the USA [40.3]—Fig. 40.1; 1951 in the USSR [40.4]; and 1961 in the UK [40.5]). The first flux divergence (absorption) measurements were made in the 1940s and 1950s, with blimps [40.6], tethered balloons [40.7], and stacked aircraft [40.5, 8]. These early studies suggested that the atmosphere might absorb considerably more solar radiation than theoretical estimates, and they proposed absorbing aerosol particles as the likely cause [40.9]. This problem—never fully resolved—motivated a series of new instruments and dedicated

aircraft campaigns. While substantial progress has been made, questions remain.

As in most fields, progress in understanding has required new observational strategies. During the 1969 Barbados Oceanographic and Meteorological Experiment (BOMEX), for example, National Aeronautics and Space Administration's (NASA) CV990 aircraft was instrumented with two pairs of nadir and zenith-viewing pyranometers, of which one was equipped with commercial long-pass filters that had been previously explored for surface observations [40.10]. By separating partial-band (wavelengths less than $0.7 \mu\text{m}$) from broadband solar irradiances in this way, the aerosol signal (largest in the visible range) could be observationally isolated from that of water vapor, which absorbs almost exclusively in the wavelength range greater than $0.7 \mu\text{m}$ [40.11]. Follow-on research, such



Fig. 40.1 Early aircraft irradiance measurement (after [40.3] with permission of the American Meteorological Society)

as the 1972 Global Atmospheric Aerosol and Radiation Study (GAARS [40.12]) used more elaborate filter combinations alongside in-situ aerosol instrumentation and airborne sun photometers for multispectral aerosol optical thickness (AOT) retrievals, which had advanced considerably by the 1970s.

The first solar irradiance spectrometers, developed in the late 1960s for the Soviet Aerosol and Radiation Research Program, capitalized on photomultiplier tubes as detectors. Spectra were acquired in as little as 10 s using motor-controlled dispersion devices in three wavelength ranges simultaneously [40.13]. Spectral absorption measurements during the 1970 Complete Atmospheric Energetics Experiment (CAENEX), conducted with an IL-18 research aircraft in the Karakum desert, revealed the spectral dependence of dust optical thickness and enabled the rigorous separation of gas and particulate contributions to atmospheric absorption in the solar range [40.7].

With the adaptation of pyroelectric detectors for airborne radiation science, broadband and partial-band radiometers with a faster response time relative to traditional thermopiles entered the field [40.14]. This type of device is ideally suited for aircraft measurements because it also mitigates thermal drift and feedback. However, it requires an optical chopper—a moving part that introduces some complexity. The original radiometer was designed to measure upward and downward irradiance with the same sensor by periodically inverting the assembly, thus minimizing the calibration error when deriving net irradiance and subsequently absorption from flux divergence [40.14]. This is important because the absorption is small relative to the quantities from which it is derived (Sect. 40.3, (40.5)).

For fast-response multispectral measurements, silicon photodiodes, combined with narrow-band filters, were used in the *total direct and diffuse radiometer* (TDDR). It measured global (total) and diffuse solar irradiance at several discrete spectral bands (≈ 10 nm full-width half maximum, FWHM) by rotating a shadow band over the detector surface, thereby blocking the direct beam of the Sun periodically for a diffuse sample [40.15]. From the direct irradiance (difference of global and diffuse), the AOT was derived at seven wavelengths ranging from 0.50–1.75 μm , similarly to methods later applied to the surface-based multifilter rotating shadowband radiometer (MFRSR, [40.16]). While not providing the same accuracy as sunphotometers, which determine the direct solar beam attenuation by pointing at the Sun, the TDDR did not require a Sun tracker.

Broadband, partial-band, and multispectral radiometers were combined to make up an instrument package that was specifically optimized for aircraft [40.17]. This package was deployed in aircraft campaigns throughout the 1980s and 1990s [40.15, 18, 19]. During that time, clouds had come into renewed focus as atmospheric absorbers because clear-sky absorption caused by aerosol particles and gases was understood, at least in principle. However, observations beginning with the first flux divergence experiments [40.6] continued to suggest absorption by clouds that exceeded theoretical estimates. Hypothesized explanations for this discrepancy (e.g., absorption by aerosols, unknown gases, or large cloud drops) called for spectrally resolved observations to test them [40.20]. Surprisingly, the first flux divergence flights with a combination of broad-band and partial-band radiometers [40.21, 22] suggested that clouds absorb in the visible (where water does not absorb). To investigate the issue of apparent (also called enhanced or anomalous) cloud absorption, several campaigns were conducted. They largely confirmed the model-measurement discrepancy with a range of instruments, but ruled out absorption by aerosol particles [40.23].

By the end of the 1990s, commercially available compact grating spectrometers with silicon (Si) and indium–gallium–arsenide (InGaAs) linear detector arrays (Sect. 40.4) began to replace multispectral instruments such as TDDR and photomultiplier scanning spectrometers, offering contiguous spectral measurements at fast sampling frequencies (1 Hz) and high signal-to-noise ratio. In photochemical applications, actinic flux density measurements with spectrometers enabled the simultaneous photolysis rate derivation of multiple reactions with varying spectral dependencies of the molecular absorption cross sections and quantum

efficiencies (Sect. 40.3, (40.8)), replacing dedicated filter radiometers for individual reactions that had been common before. Previous to the advent of filter or spectrometer systems for measuring actinic flux, photochemical reactions themselves were used, so-called *actinometers*. These date back to the nineteenth century. The new generation of instruments, first flown around the year 2000 [40.23–28], is still used today.

Subsequent field campaigns gave insights into spectral aerosol particle optical properties and radiative effects throughout various regions of the world (review by [40.29]), informing the NASA A-Train era aerosol satellite retrieval algorithms. These measurements explained apparent cloud absorption as a sampling artefact under inhomogeneous cloud conditions due to net horizontal radiation transport [40.30], and parameterized its spectral dependence [40.31] (Sect. 40.8).

About the same time (early 2000s), actively controlled leveling platforms were introduced [40.24] to counteract aircraft attitude changes in flight. They increased the measurement accuracy and data yield, enabling measurements during vertical aircraft maneuvers

(e.g., spirals) for radiation science [40.32]. Flying actively leveled irradiance spectrometers and actinic flux density spectrometers in tandem gave insights into the enhancement of photochemistry reaction rates in the presence of aerosol particles and clouds (especially near the cloud top: [40.28]).

When paired with airborne imagers, leveled irradiance spectrometers (also called albedometers) proved useful in deriving surface-leaving upwelling radiance from flight level measurements (atmospheric correction) even under partially cloudy conditions [40.33], enabling the remote sensing of ecosystems with frequent cloud cover. They are also increasingly successful in isolating fairly small radiative perturbations in complex scenes with large background variations, for example, aerosol radiative effects above clouds [40.34] or cloud radiative effects over bright snow and ice [40.35, 36]. Recent new instrument developments, such as the Sunshine Pyranometer (SPN-1: [40.37], Sect. 40.4) for simultaneous diffuse and global irradiance measurements will augment existing capabilities and pave the way toward miniaturization and deployment of solar radiation sensors on autonomous airborne vehicles.

40.3 Theory

Airborne radiometers acquire simultaneous measurements of upward (nadir-viewing) and downward (zenith-viewing) radiative energy flux densities within the altitude range of the aircraft at nearly any vertical resolution, providing validation for radiation quantities derived from remote sensing and directly quantifying radiative effects of an atmospheric constituent. An overview of the primary quantities and derived parameters is given in Table 40.1. The flight level albedo

$$\alpha = \frac{F^\uparrow}{F^\downarrow} \quad (40.1)$$

is frequently used to infer surface albedo through atmospheric correction [40.24, 33, 38, 39]. The instantaneous radiative forcing (radiative effect, RE) is defined as the change of the net irradiance

$$F_{\text{net}} = F^\downarrow - F^\uparrow \quad (40.2)$$

in the presence of an atmospheric constituent

$$\text{RE} = F_{\text{net}}^{\text{with constituent}} - F_{\text{net}}^{\text{without constituent}} \quad (40.3)$$

The net irradiance, which quantifies the radiative energy flux density into the atmospheric column below the flight altitude, is directly accessible to airborne

measurements, serving as a starting point for studying radiative effects as a function of scene conditions, such as surface albedo, aerosol or cloud properties, and water vapor concentration.

The absorbed radiative flux per volume (units of W m^{-3}) can be derived from vertical profile flight patterns or collocated flight legs at the top z_{top} and base z_{base} of an atmospheric layer through flux divergence as

$$\frac{d\Phi}{dV} = -\nabla F = -\left(\frac{\partial F_x}{\partial x} + \frac{\partial F_y}{\partial y} + \frac{\partial F_z}{\partial z}\right), \quad (40.4)$$

if the vertical term $\nabla F_V = \partial F_z / \partial z$, measured as the vertical gradient of net irradiances

$$\nabla F_V \approx \frac{\Delta F_V}{\Delta z} = \frac{F_{\text{net}}^{\text{top}} - F_{\text{net}}^{\text{base}}}{z_{\text{top}} - z_{\text{base}}}, \quad (40.5)$$

is much larger than the combined horizontal terms $\partial F_x / \partial x + \partial F_y / \partial y$ (i.e., $\nabla F_H \ll \nabla F_V$), a condition that is often not met for horizontally inhomogeneous scenes (see Sect. 40.5 and [40.34]). In this case, $\Delta F_V \approx F_{\text{abs}}$ is the absorbed irradiance of the layer, with a corresponding instantaneous heating rate [40.40]

$$\frac{\Delta T}{\Delta t} = \frac{1}{\rho c_p} \frac{\Delta F_V}{\Delta z} = -\frac{g}{c_p} \frac{\Delta F_V}{\Delta p}, \quad (40.6)$$

where the Δp is the pressure differential corresponding to Δz (g , c_p , and ρ are the gravitational acceleration, constant pressure specific heat capacity and density of air). If both absorption and actinic flux density are measured, the layer absorption coefficient k_{abs} (m^{-1}) can be obtained from

$$F_{\text{abs}} = k_{\text{abs}} F_{\text{act}} \Delta z, \quad (40.7)$$

establishing a connection between actinic flux density and absorbed irradiance [40.41]. The primary use of actinic flux density measurements is the determination of photo-dissociation rates (also called photolysis frequencies or simply j -values) as

$$J \left(\text{AB} \xrightarrow{h\nu} \text{A} + \text{B} \right) = \int_0^{\infty} \sigma_{\text{AB}}(\lambda, T, p) \Phi_{\text{AB} \rightarrow \text{A} + \text{B}}(\lambda, T, p) \frac{F_{\text{act}}(\lambda)}{hc/\lambda} d\lambda, \quad (40.8)$$

where

$$\frac{F_{\text{act}}(\lambda)}{hc/\lambda} = \frac{F_{\text{act}}(\lambda)}{h\nu} \quad (40.9)$$

is the photon flux density at a given wavelength or frequency ν (h : Planck constant; c : speed of light). Most reactions with relevance for air quality studies are driven by ultraviolet (UV) and visible radiation, with a distinct wavelength dependence of the absorption cross section σ_{AB} of molecule AB and the reaction's quantum efficiency $\Phi_{\text{AB} \rightarrow \text{A} + \text{B}}$ (both known

from laboratory spectroscopy). In order to determine the photodissociation rates of multiple molecular species, measurements of actinic flux density are now performed with spectrometers. The measurement is challenging due to low signal levels in the ultraviolet wavelength range.

Irradiance measurements are also increasingly performed spectrally because this facilitates the partitioning of observables such as heating rates into contributions from atmospheric constituents. For instance, strong water vapor absorption occurs in distinct bands in the near-infrared spectral range, whereas aerosol absorption decreases smoothly with wavelength, enabling the direct spectral decomposition with few assumptions. At the same time, discrepancies between directly measured and model-derived irradiances can be attributed to errors arising from:

1. Inaccurate model input (cloud, aerosol particles, gas, or surface properties as obtained from remote sensing)
2. Three-dimensional (3-D) radiative transfer effects not captured by most models
3. Measurement artefacts [40.42–44].

In some cases, spectral irradiance measurements are used for remote sensing, for example to determine aerosol-intensive optical properties [40.34, 45]. Despite their versatility for a range of applications as described in Sect. 40.8, spectral instruments cannot replace their broadband counterparts because they usually do not encompass the whole solar wavelength range and tend to be less accurate than broadband radiometers when integrated over wavelength.

40.4 Devices and Subsystems

Airborne radiation measurements impose unique demands on instrument design and function that are not encountered with ground-based operations. They experience an extreme and rapidly varying temperature, pressure, and moisture environment, along with vibrations mostly during takeoff and landing of the aircraft that adversely affects instrument stability, functioning, and signal-to-noise ratio. These circumstances limit the types of instruments that can be deployed on a flying platform. For example, standard sun-tracking shades (Chap. 12) for separating diffuse and global (total) irradiance are impractical, given the aerodynamic drag on externally moving parts and the varying solar geometry. The rapidly changing radiation fields for spatially variable scene types (e.g., broken clouds and hetero-

geneously vegetated surfaces) must be sampled at high frequency, which requires detectors with a fast response time and low inertia or hysteresis.

In atmospheric applications, irradiance is defined with respect to a horizontally aligned surface. Therefore, an irradiance sensor needs to be actively leveled, or correction procedures need to be applied—one of the major difficulties unique to aircraft radiation observations. For sensors that are fix-mounted to the aircraft fuselage, significant measurement errors (especially in downward irradiance measurements) arise under turbulent conditions and changes in aircraft attitude (turns, spirals, etc.) [40.24, 32].

These aircraft-specific errors exceed common sources of uncertainty for ground-based operations,

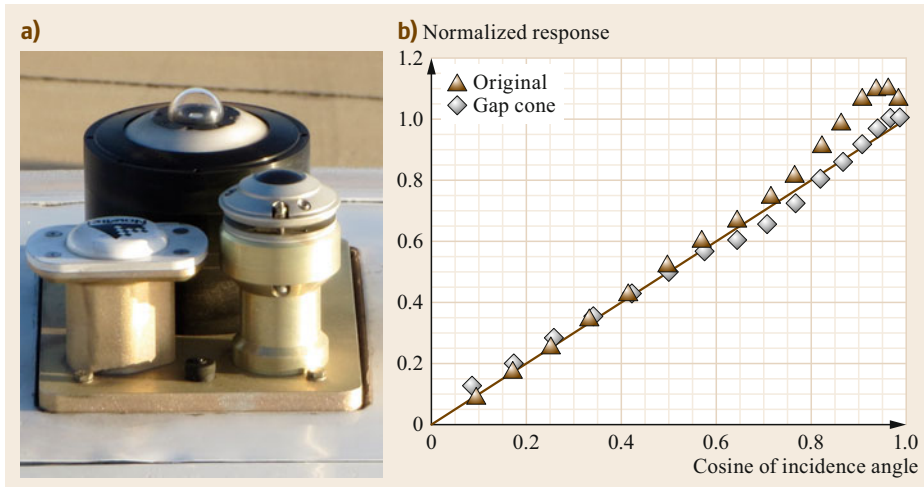


Fig. 40.2 (a) Solar spectral irradiance light collector mounted on a leveling platform (*back*), along with antenna for leveling platform subsystem; pyrometer for thermal irradiance (*front, right*). (b) Angular response of a typical light collector (integrating sphere), normalized by normal incident irradiance, before and after improvements (after [40.46] with permission of B.C. Kindel)

and generally cannot be corrected adequately after the flight. Therefore, it has become common to mount sensors on active leveling platforms, greatly increasing data return and accuracy. Despite such improvements, accurate airborne observations are far more challenging to make than at the surface. Accuracy and precision depend on the specific instrument constellation on the host platform, but often the error budget is dominated by terms that do not factor into fixed installations on the ground. Recent campaigns with radiation science goals have transitioned to redundant or mutually complementary instruments to reduce uncertainty—an approach that has long been standard practice for surface observations.

Here, we only cover non-imaging devices (irradiance and actinic flux density radiometers and spectrometers) that are commonly flown on aircraft, keeping general sensor descriptions at a minimum (details in Chap. 12). Sun photometers are described in Chap. 29.

Figure 40.2a shows a typical irradiance radiometer installation mounted on top of a research aircraft. The pedestal on the right carries a broadband radiometer (in this case, for thermal irradiance) that is fix-mounted to the interface plate and combines the aperture, sensor, and electronics in a single, compact enclosure. Analogue or digitized signals are transmitted by a signal harness to a data logger in the body of the aircraft. For measuring spectrally resolved radiation, the required dispersive devices (usually monolithic grating spectrometers) need to be connected to a light collector, often an integrating sphere, that appropriately weights the incident radiance (Table 40.1) and transmits suffi-

cient signal to the sensors. In most cases, such systems are distributed; the light collector is mounted externally on the aircraft fuselage, the detector (spectrometer) and data acquisition assembly are housed inside the cabin. The light is transmitted from the light collector to the spectrometer with fiber optics. For pressurized aircraft, the optical cable and any signal or power harnesses connecting to externally mounted components have to pass through a pressure seal.

The light collector contained in the black cylinder in Fig. 40.2a (*back*) is mounted on a leveling platform. In this case, the light collector is an integrating sphere. Other subdevices are described below (see Table 40.3 for a summary). The platform includes a GPS (GNSS) antenna (*front, left*) connected to an inertial navigation system (INS) mounted on the underside of the interface plate. Several such systems with various form factors exist [40.24, 32]. Common elements include the INS for accurate determination of the attitude angles of the aircraft (pitch and roll), and a dual-axis tip/tilt stage. No single design works for all aircraft, which have different space, weight, and environmental limitations (altitude range, vibrations, etc.). Leveling platforms are important ancillary systems on aircraft because they actively stabilize light collectors or compact radiometers and keep them horizontally aligned during pitch and roll changes. They are especially useful for radiometers with nonideal angular response (see below). Also, they prevent radiation from the lower hemisphere (for instance, in the presence of clouds) to affect downward irradiance measurements (and vice versa). Design considerations are response time, an-

Table 40.2 Airborne solar radiation sensors—advantages and drawbacks

Sensors	Advantages	Drawbacks
Thermopile pyranometer	Simple, off-the-shelf design; no moving parts	Slow/temperature-induced biases
Pyroelectric radiometers	Fast response time; no thermal inertia issues	Moving parts; not commercially available
Spectrometers	Fast response time; no thermal inertia; allows remote sensing and attribution of radiative effects	Straylight; detector nonlinearities; requires separate light collector; does not cover full solar spectrum

gular range, and system latency. A dedicated INS, mounted in close proximity to the light collector can be costly and impractical because of space requirements. Alternatively, aircraft INS can be used if their signal can be transmitted with a low latency. Since the mechanical components are externally mounted, the enclosure needs to be weatherized. Water vapor condensation often occurs after rapid altitude changes, especially after cold-soaking of metal parts, requiring a desiccant or purge gas mechanism.

Figure 40.2b shows the angular response of an integrating sphere used for spectral solar irradiance radiometers [40.46] with respect to the cosine of the incidence angle ϑ (1: overhead, 0: horizontal radiance). An almost ideal response (a straight line) is typically only achieved by broadband radiometers with a flat receptor area (Chap. 12). Even those do not have an ideal response as the incidence angle exceeds 70° . It is difficult to correct the measured irradiance for a nonideal angular response because it requires knowledge of the radiance distribution. Therefore, the diffuse and direct irradiance are typically corrected separately [40.32], which requires a few assumptions (e.g., isotropy of the diffuse component). Without a leveling platform, it becomes very difficult if not impossible to apply a correction after the fact, especially when clouds are present.

Spectral radiometers require either transmissive diffusers (such as Delrin[®] or flashed opal [40.47]) or integrating spheres made of highly reflective Spectralon[®] or Fluorilon-99W[®] with a circular aperture (Fig. 40.2, [40.46]). Which system is used for a specific application depends on the predominant incidence angles for an aircraft campaign and on the wavelength range of the radiometer. For example, integrating spheres have an almost spectrally flat transmittance over a wide wavelength range, but their optical throughput is low, and they exhibit a *hotspot* close to normal incidence. It can be minimized with modification of the internal baffle guided by optical component modeling [40.46], but the response at steep incidence angles has not been made completely linear with respect to the cosine of the incidence angle (Fig. 40.2b). Transmissive diffusers, on the other hand, usually have a better response at near-normal incidence, but dete-

riorate for shallow incidence angles. Specially shaped surfaces are in use to improve the shallow incidence angle response. While transmissive diffusers have a larger optical throughput than integrating spheres, most materials have spectrally variable scattering (diffusing) or absorbing properties, limiting their use to certain wavelength regions. For instance, flashed opal acts as a good diffuser, but only works up to $1\ \mu\text{m}$. Delrin works for longer wavelengths, but exhibits absorption in some wavelength regions, resulting in large deviations from an ideal cosine response. Whatever the diffusing element, the throughput and cosine response needs to be carefully characterized, as does the fiber optics cable that transmits the light to the spectrometer subsystem. In some cases, the throughput depends on the bending radius. Thus, once installed and calibrated, the cables should be fixed in place.

Table 40.2 lists the advantages and drawbacks of broadband and spectral sensors that have been commonly used. For aircraft operations with rapidly changing signals, the slow response time of thermopiles is not ideal, especially when flying sensors with a large mass and, therefore, a large thermal inertia. Pyroelectric radiometers [40.14] have a response that is adequate for aircraft operations, but they require a moving part (chopper). Both of these radiometers have a near-ideal angular response up to 70° incidence angle—superior to those of spectrometers with their imperfect light collectors as described previously.

Spectrometers are more complicated in their design than broadband radiometers. They may suffer from straylight and detector nonlinearities, as well as temperature-dependent dark currents. Typical systems are described by [40.24, 25]. They consist of commercially available single-enclosure units with optical fiber pigtailed that are coupled with the optical fibers from the externally mounted light collector through optomechanical shutters. The shutters enable periodic measurements of the dark signal. After the dispersion of the light by a diffraction grating, the spectrum is measured by a linear photodetector array. Order sorting filters are included, typically placed directly above the detector array, if the wavelength range spans more than one octave. The detector signal is preamplified, digitized, and

Table 40.3 Subsystems and ancillary components

Component	Comment
Irradiance transmissive diffuser	Diffusive properties are wavelength dependent
Irradiance integrating sphere	Flat spectral response over wide range; nonideal response at near-zenith incidence
Actinic flux density diffuser	Provide isotropic angular response (frosted quartz)
Radiance baffle system	Narrow field-of-view aperture with lenses and baffles
Domes and optical filters	Provide protection from the elements and limit radiation to fractional or narrow bands
Fiber optic cables (optical shutters)	Transmit (block) radiation from light collector to spectrometer; sensitive to bending radius
Shadow mask (SPN)	Used in conjunction with thermopiles or spectrometers to separate global/diffuse radiation
Leveling platforms	Actively stabilize light collectors with tip/tilt stages
Inertial navigational system	Provides aircraft pitch and roll to leveling platform

recorded (typically at 1 Hz, with an integration time ranging from 50–500 ms). To cover most of the solar wavelength range, two off-the-shelf spectrometers with overlapping subranges are used: spectrometers with silicon detector arrays from the UV to the near-infrared (about 1 μm), and spectrometers with InGaAs detector arrays from about 1–2 μm . Identical spectrometer pairs are used for zenith and nadir light collectors. For the InGaAs spectrometers, the temperature of the detector array needs to be stabilized, and the spectrometer enclosure and preamplifier should also be kept at a constant temperature.

The recently commercialized sunshine pyranometer (SPN-1) [40.37] provides broadband global and diffuse downwelling irradiances. This is accomplished by an array of seven detectors under a shadow mask, which is designed such that at least one detector is shaded and measures the diffuse radiation, whereas the unshaded detectors measure the global irradiance component. The detectors are miniature diffuser-covered thermopiles with low thermal inertia; their angular response is similar to that of pyranometers. Their stated measurement accuracy is somewhat lower than that of traditional pyranometers (Table 40.4). A new spectral prototype instrument based on the same shadow mask design measures spectrally resolved global and diffuse irradiance from 350–1000 nm. It was recently tested on an aircraft field campaign and will enable new remote sensing applications once it is commercially available.

Ideally, a combination of solar irradiance radiometers should be flown as *canonical payload*:

1. Pyranometers (high accuracy, full spectral coverage of the solar range, and near-ideal angular response up to 70°)
2. Spectrometers (spectrally resolved irradiance for physical interpretation of signals and no thermal inertia)
3. Diffuse/global radiometers (correction of angular response; new remote sensing opportunities).

These three instruments can be used synergistically to ensure high-fidelity spectral irradiance measurements even in difficult environments such as the Arctic [40.36], with extremely low sun angles (zenith angles up to 85° are feasible).

Table 40.3 summarizes the components that go along with the radiometers themselves. In addition to the two types of irradiance light collectors, there are diffusers for collecting isotropically weighted radiance (actinic flux) with a series of elongated frosted quartz domes. Because the hemispheres are measured separately, the instrument horizon (field-of-view cutoff at 90°) for the two subsystems needs to be defined carefully to minimize artifacts due to reflections from the aircraft and to avoid signal contamination from the opposing hemisphere. This is done with a black artificial horizon under the diffuser. Otherwise, the design of the actinic flux radiometer systems (fiber optic cables linking light collectors to spectrometers) is similar to irradiance instruments [40.28]. The grating spectrometers that are now commonly used are prone to straylight contamination, especially in the UV-B range, more so than the older scanning double-monochromator systems [40.48]. However, scanning systems use moving parts and require more time to complete a scan than fixed-grating spectrometers with a photodiode array or CCD (charge-coupled device). Therefore, they are rarely used operationally today. Filter radiometers, once the mainstay instrument, are no longer widely used either [40.49].

40.5 Specifications

The radiometric accuracy and instrument precision of commonly used radiometers is provided in Table 40.4. The overall accuracy of broadband irradiance is higher

than that of spectral radiometers, mainly because of the better angular response of broadband radiometers. The error sources include: radiometric uncertainty, imper-

Table 40.4 Specifications of precision and accuracy for solar range aircraft radiometers

Quantity	Accuracy/Precision	Notes
Downward spectral solar irradiance	7%/1% of dynamic range	With leveling platform
Upward spectral solar irradiance	3–5%/1% of dynamic range	Varies with wavelength
Broadband solar irradiance	2–5%/1–3%	Excludes attitude correction
Global/diffuse BB irradiance	8%/1–3% of dynamic range	SPN-1
Actinic flux density	3–5%	UV-B: stray light cont.
Spectral radiance	7%/1% of dynamic range	Calibration limited

fect angular response, aircraft attitude stabilization (or postflight correction), straylight contamination, calibration drift, and thermal effects. Additional specifications are wavelength range (330–4000 nm for pyranometers, depending on quartz dome transmittance cutoff; 400–2700 nm for SPN-1, 350–2150 nm for spectral irradiance, > 295 nm for spectral actinic flux density), spectral sampling (4–8 nm for spectral irradiance, 1–2 nm for spectral actinic flux density) and spectral response (Sect. 40.6). For a broadband sensor, the spectral response should be constant (flat) across the full wavelength range; a spectral sensor's response varies with wavelength and is determined through the radiometric calibration (Sect. 40.6).

For radiance light collectors, the field-of-view needs to be specified (typically 1–4°); for irradiance and actinic flux density, obstructions by the aircraft (e.g., tail,

propellers, protruding antennae, or landing gear) need to be assessed on a case-by-case basis (by calculating the fractional solid angle they occupy). In some cases, reflections by the aircraft can lead to a high-bias in the measurements. This is usually quantified empirically for a given installation; occasionally, wingtip-by-wingtip comparisons of different aircraft help quantify such effects.

Finally, the instrument line shape or *slit function* determines the wavelength resolution of a spectrometer (8–12 nm FWHM for commonly used systems). The wavelength uncertainty is usually about 0.5–1 nm. Wavelength registration is determined in the laboratory (Sect. 40.6) and can be verified in the field with low-pressure line sources. Mercury, for example, provides a good assortment of isolated emission lines in the visible and near-infrared.

40.6 Calibration and Quality Control

Calibration procedures for airborne radiometers (described in detail by [40.47]) include the characterization of their radiometric, angular, and wavelength response (Sects. 40.6.1–40.6.3). Any uncertainties propagate into the final product, requiring careful error assessment (Sect. 40.6.4).

40.6.1 Radiometric Calibration

There are various different methods for establishing the radiometric response of airborne solar radiometers. One method is to reference the radiometer to a primary or secondary standard that is traceable to the World Radiation Reference (WRR, Davos, Switzerland), the National Institute of Standards and Technology (NIST, USA), or to other national standards. Broadband radiometers are run side by side with such standards to transfer the calibration under a wide range of insolation conditions from a calibration source. During this transfer, it is important to calibrate the instrument across the full dynamic range expected during flight to ensure the linearity of the response. Also, since the spectral composition during measurements may deviate from that

during calibration, the spectral response should be flat. A research-grade instrument's data sheet should provide this information, but it needs to also be measured in the laboratory—for example with a monochromator [40.50]. More details on the radiometric calibration of broadband radiometers can be found in Chap. 12.

An alternate calibration source for broadband radiometers is a cavity pyrheliometer, which serves as an absolute standard for direct irradiance. To transfer the calibration from such an instrument, the diffuse radiation needs to be subtracted from the global irradiance (it is obtained by periodically obstructing the direct beam). Global/diffuse radiometers (SPN-1) can also be calibrated by the Langley method, where the Sun serves as the calibration source. This is only possible when flying extended legs at high altitude, during which the solar zenith angle and thus the airmass factor $m = 1/\cos(\vartheta)$ change significantly.

Spectral radiometers are calibrated with incandescent calibration lamps that are also traceable to a standard (NIST or otherwise). They come with a data sheet that provides the spectral irradiance at a distance of 50 cm, at a specified current. Since these primary stan-

dards degrade with burn time due to changes to the filament and optical elements, it is advisable to keep their usage at a minimum. This is done by transferring their calibration to secondary lamps. Installed in portable field calibrators, the secondary standards can be taken to field campaigns for on-site calibration of radiometers and be recalibrated after a field campaign in the laboratory. Radiance calibrations are done in a similar fashion. In this case, a Spectralon[®] panel with known reflectance is placed at 50 cm from the primary standard, and the radiance light collector is pointed at its center on the optical axis. The nonlinearity of a system can be characterized by either varying the integration time constant of the spectrometers or by varying the distance to the calibration source. The latter method requires an absolute reference measurement (either broadband or at a single wavelength) alongside the spectrometer light collector. For integrating spheres, the effective receiving plane does not necessarily coincide with the location of the aperture, but is slightly inside the sphere. This slight offset (about 1/10 of the diameter of the integrating sphere) can be determined by recording the instrument counts for a varying distance to the light source while also recording the signal from a reference radiometer. For the absolute calibration, the 50 cm distance from the light source needs to be measured against the effective receiving plane.

40.6.2 Angular Calibration

The angular calibration is done by illuminating the light collector by a collimated light source at normal incidence (for reference), and then rotating it about its receiving plane. Noncollimated light sources, such as the radiometric calibration lamps (point sources), may lead to an incorrect characterization of the instrument's angular response. Care needs to be taken to rotate the light collector about the accurate location of the receiving plane (aperture). This is straightforward for pyranometers with a physical surface but challenging for an integrating sphere or transmissive diffusers, where the location of the effective receiving plane may depend on the angle of incidence. However, collimated light minimizes these biases. Outdoor tests under clear-sky conditions [40.37] are only effective if the direct and diffuse irradiance can be separated. The angular response needs to be assessed spectrally, since the properties of the transmissive or reflective material may change. Temperatures should be held close to the operating conditions if possible; overheating of the optical elements in the characterization process may change their response.

The *azimuthal* response of a sensor or light collector is usually fairly constant for a given polar incidence

angle. However, at shallow incidence, it may vary due to imperfections of the sensor surface. For integrating spheres, any internal impurities of the reflector material that are asymmetric will lead to azimuthal asymmetry, even at steeper incidence angles. The calibration in the laboratory can be accomplished with rotating tables.

40.6.3 Wavelength Calibration

The spectrometer wavelength registration is typically provided by the manufacturer. However, wavelength shifts sometimes occur, even for fixed-grating devices, and may require recalibration at least once before a field campaign. This is accomplished with line sources with gas lamps (Ar, Hg, Ne, Kr) and with lasers. Tabulated line positions are compared with their reported location in the literature [40.51], and the wavelength coefficients for the spectrometer channels are adjusted with this information. At the same time, the apparent line width in the measurement provides information on the instrument spectral resolution (slit function). At least once per lifetime of a spectrometer, the slit function should be measured with a monochromator, with representative samples across the full wavelength range. Straylight and order-sorting errors are best diagnosed with measurements of laser light because monochromators output higher-order light that may be mistaken for spectrometer artifacts. The wavelength calibration is the first step in the calibration of a spectrometer system (followed by radiometric/nonlinearity and angular calibration).

40.6.4 Field Data Processing and Error Assessment

Calculating irradiance from the raw data first requires bias corrections for any thermal offsets (pyranometers) or subtraction of dark counts (spectrometers). Next, the instrument raw counts are divided by the spectral response function (obtained from the radiometric calibration). For a nonlinear instrument response, this step may also entail a correction based on laboratory measurements as described in Sect. 40.6.1. The resulting irradiance is often archived as field data, based on the most recent radiometric field calibration. The aircraft attitude and angular correction is usually performed after a campaign, at which point diffuse and direct irradiance undergo separate correction steps before they are recombined. If no global-diffuse radiometer is available, radiative transfer calculations are used to separate the global irradiance into diffuse and direct components. Specific correction steps are described by [40.32]. For low-elevation Sun angles, it is especially difficult to correct for changing attitude angles

in the absence of a leveling platform. It is essential to measure the angular offset between the aircraft INS and the horizon of the fix-mounted sensor or light collector at least once during the mission. With a leveling platform, only the angular correction for the light collector is required. After completing all processing steps, the measurements are compared with radiative transfer calculations. This step facilitates data quality and error assessment. Uncertainties may arise from all system components and processing steps, and they may depend on the specific aircraft configuration, temperature environment, and Sun-sensor geometry. Quick in-field data quality control helps to identify instrument issues and

the optimization of instrument settings, such as integration time, acquisition frequency, and temperature set points. For example, some instruments have dual gain (or integration time) settings, which are alternated to adequately capture low and high signal levels and require adjustment early in the mission to maximize the signal-to-noise ratio. As noted above, mutually complementary and partially redundant measurements (broadband, spectral, and global/diffuse radiometers) lead to high-fidelity results. Unlike in operational ground-based observations, standards for processing joint data sets systematically have yet to be established by the airborne community.

40.7 Maintenance

Routine tasks during field operations include regular radiometric calibrations, angular offset measurements between the INS and the horizon of the instruments, and cleaning of external optical components (domes) with alcohol or water (especially after flying through dust or soot aerosol plumes). For spectrometers, optical fibers need to be monitored; partially broken fiber strands can lead to errors that are difficult to correct after the fact (even with regular radiometric field cal-

ibrations). Any moving parts (optical shutters, leveling platform actuators) need to be inspected. Those system components that may be exposed to the elements need to be checked for water or ice intrusion, and heaters in these areas need to be monitored during flight. Integrating spheres are either operated under vacuum or with a purge line to keep water vapor and condensation out. This requires checking the vacuum with a pump or adjusting the purge air with a flow meter.

40.8 Applications

Current applications of airborne solar radiometry focus on atmospheric energetics (absorption, heating rates), remote sensing of atmospheric constituents, and surface characterization (albedo, atmospheric correction), with a growing emphasis on the connection between remote sensing and radiation measurements. This linkage is necessary when considering complex atmospheric and surface scenes with inhomogeneous clouds, variable surface properties, or aerosols co-occurring with clouds.

40.8.1 Energetics and Remote Sensing

Many field campaigns now include airborne remote sensing instrumentation. These observations provide 3-D radiative transfer calculations with the necessary input to put radiation measurements into context. Figure 40.3 illustrates this approach for the 2007 TC⁴ (Tropical Composition, Cloud and Climate Coupling) campaign [40.52], where two research aircraft (ER-2 and DC-8) flew collocated legs above, below, and within cloud fields to sample their microphysical and radiative properties. In this case, 3-D irradiance fields were calculated from the cloud products generated by

an imager aboard the ER-2 (swath width: about 20 km; length of the leg: 200 km), embedded in the larger context of geostationary imagery, and validated with the spectral irradiance measurements on both aircraft. The visible-range vertical flux divergence ∇F_V from the net flux difference between the ER-2 and DC-8 spectral radiometers compares fairly well with the 3-D calculations. Since clouds do not significantly absorb solar radiation in the visible, the observed positive (negative) areas of ∇F_V are entirely due to net horizontal loss (gain) of radiation. This kind of transport is not always tied to the cloud optical thickness distribution as the plot suggests. Rather, photon *donor* and *recipient* regions (red and blue in Fig. 40.3a) exchange radiation over a range of scales that are distinct from the cloud structure (Fig. 40.3b). When measured with broadband radiometers, ∇F_V in the visible (related to net horizontal photon transport) cannot be distinguished from true absorption in the near-infrared spectral range. In this case, apparent and true absorption have similar magnitudes at many points along the flight track with a net loss of visible radiation into the surrounding areas. Unless these are equally sampled over adequate scales, the net export from the cloud field of inter-

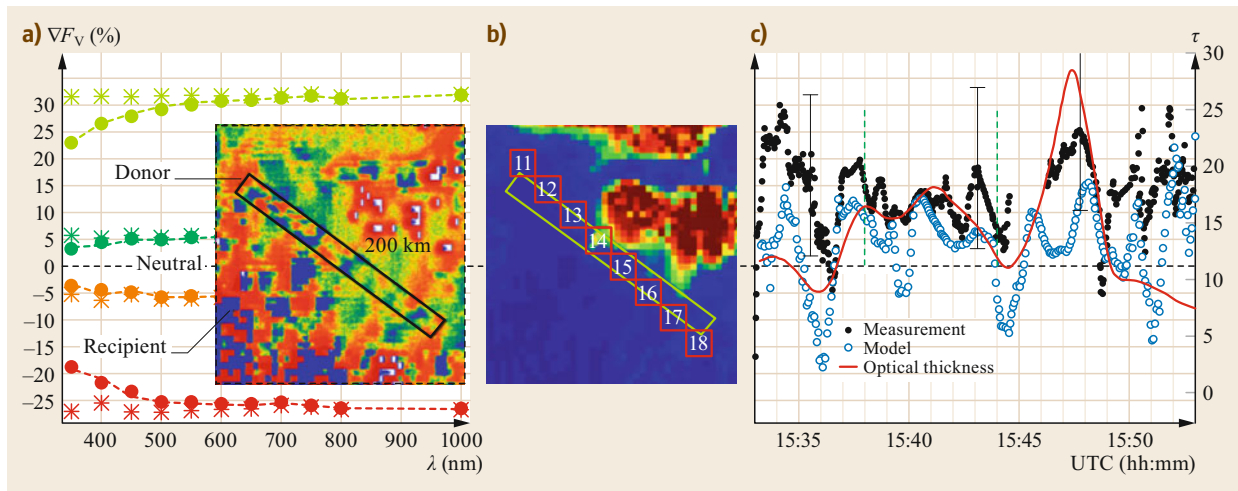


Fig. 40.3a–c Radiation measurements and cloud passive imagery of an inhomogeneous cloud scene observed during the 2007 Tropical Composition, Cloud and Climate Coupling (TC⁴) campaign in Central America. The images in (b) and (a) show the optical thickness τ and net horizontal photon transport, obtained from geostationary and airborne imagery (200 km \times 20 km domain along the flight track of two collocated aircraft) through 3-D radiative transfer calculations (after [40.31]). (a) Vertical flux divergence ∇F_V spectra for representative points in the domain (full symbols/stars: calculations with/without molecular scattering). (c) Point-by-point 500 nm observations along the flight track along with the calculations and the optical thickness τ within the field-of-view of the radiometers (after [40.30]). (a,b) (after [40.31] © Author Creative Commons license 3.0) and (c) (after [40.28] with permission of the American Geophysical Union)

est is insufficiently compensated by recipient regions. This is interpreted as cloud absorption in broadband measurements, explaining the longstanding problem of enhanced absorption [40.30].

Separate measurements in the visible subrange provide information on the contribution of horizontal flux to the overall observed vertical flux divergence [40.21]. The correct way of using this information for mitigating the apparent absorption bias is the conditional sampling of net irradiance pairs along collocated legs above and below a layer of interest [40.43, 53]. This is done by selecting those points where ∇F_V in the visible is close to zero and averaging their broadband ∇F_V . If spectral observations are made, another method is to use the spectral slope of the mid-visible ∇F_V , which is proportional to its magnitude [40.31]. Neither of these filtering methods work in the presence of aerosol particles, which commonly do absorb in the visible, with a distinct spectral dependence. In this case, spiral measurements are more appropriate than collocated legs (Figs. 40.5b and 40.6; Sect. 40.8.2). For pure cloud layers, accurate sampling allows the direct spectral partitioning of absorption by contributions from clouds, water vapor, and other atmospheric constituents of the layer. In many cases, cloud absorption accounts for a fraction of the total layer absorption. For a marine stratus layer case, [40.43] attributed 25% to liquid water, 59% to water vapor, and the rest to enhanced

absorption due to multiple scattering (increased photon path length) of various gases in clouds.

Absorption and other radiation parameters can also be obtained *indirectly* by using irradiance measurements at various flight levels to validate imagery-based 3-D radiative transfer calculations and then deriving the parameters of interest from the calculations. This method is particularly useful for single-aircraft campaigns, where radiation fields above and below a layer are sampled sequentially. Because the cloud field changes on time scales smaller than the sampling time, its radiative properties are best obtained from the measurement-constrained model output—provided that imagery is available to drive the model. This does not work if the imagery-derived cloud properties are themselves biased by 3-D effects. In this case, calculated and measured irradiances will be inconsistent. For example, the optical thickness of broken clouds tends to be underestimated by passive imagery retrievals, translating in an underestimation of a cloud's absorption and an overestimation of its transmission [40.31].

40.8.2 Combination of Cloud/Aerosol Microphysics and Radiation

When imagery is unavailable, the link between cloud microphysics (sampled by in-situ instruments) and macroscopic distribution to the associated radiation

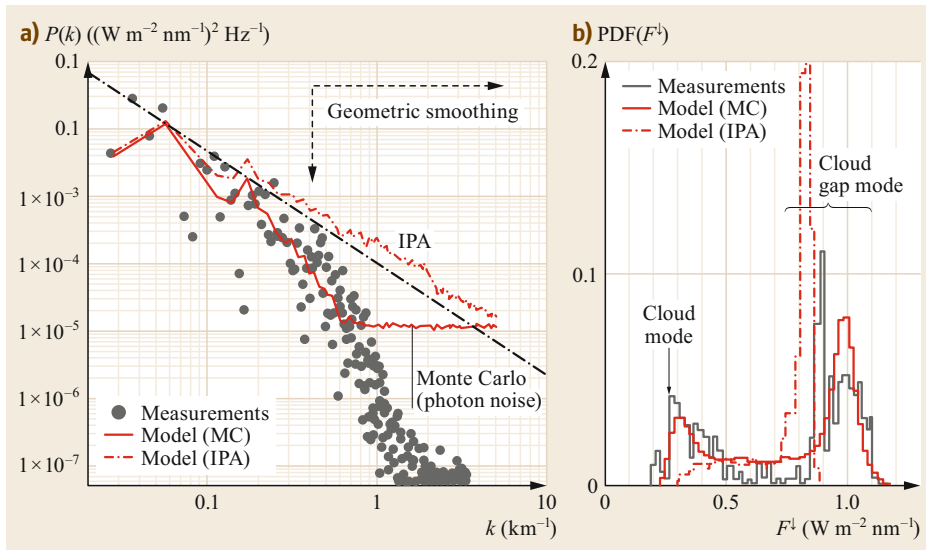


Fig. 40.4a,b Downward irradiance measurements and calculations below a broken cloud field (500 nm wavelength (after [40.54])). **(a)** Power spectrum $P(k)$ (calculations with horizontal photon transport (MC: Monte Carlo 3-D radiative transfer model) and without (IPA: independent column approximation)). The $k^{-5/3}$ scaling law of the underlying liquid water field is included (dash-dotted line). **(b)** Histogram with two primary modes: 0.3 and $1.0 \text{ W m}^{-2} \text{ nm}^{-1}$ under clouds and cloud gaps. The *left* (cloud) mode is only reproduced when horizontal photon transport is enabled in the 3-D radiative transfer model (MC) (after [40.54] with permission of the Royal Meteorological Society (Great Britain))

fields can be achieved through cloud simulators [40.55]. These generate synthetic 3-D distributions of parameters, such as liquid water content from measured mean profiles, and two-point statistics, such as power spectra. While not placing individual clouds accurately, the statistical properties of a cloud field are sufficiently well reproduced to match measured radiation fields when feeding the synthetic cloud fields into a 3-D radiative transfer model [40.54]. Figure 40.4b shows the downward irradiance below a broken cloud field. Two modes can be distinguished, one corresponding to gaps between clouds (direct and diffuse irradiance), the other to the irradiance transmitted through clouds. If the modes are as well separated as in this example, the area under the left mode can be interpreted as *radiative* cloud fraction. *Radiative closure* in this case can be understood as the consistency between the cloud micro- and macrophysics-driven 3-D calculations and the observations—individually for the two modes. In the traditional sense, radiative closure between measured and calculated cloud transmittance, reflectance, and absorptance is achieved if the radiative cloud fraction and therefore the domain average (from cloud and gap mode) irradiance fields are consistent between observations and calculations. This is harder to achieve, and a mode-by-mode assessment is often preferable.

Beyond closure itself, the power spectrum (Fig. 40.4a) is a metric for characterizing horizon-

tal structure. It relates cloud microphysical scaling laws (the $k^{-5/3}$ Kolmogorov eddy dissipation) to the associated radiation fields. Irradiances mirror the microphysical scaling down to a characteristic scale, below which radiative smoothing decreases the spatial variability of the radiation fields relative to the microphysical structure.

A persistent challenge for airborne radiation science is the isolation of aerosol radiative effects in the presence of clouds. Figure 40.5a illustrates a strategy using measurements on horizontal legs below scattered clouds embedded in an aerosol layer. Here, the locations of the two modes discussed in the previous figure are plotted as a function of wavelength, along with calculations (in this case, based on large-eddy simulations) with and without considering aerosols [40.56]. The direct aerosol radiative effect (DARE) in the presence of clouds can simply be derived from the measurement-constrained modeled net irradiance fields in the presence and absence of the aerosol layer. Figure 40.5a shows that the aerosol perturbation for the downward irradiance (the difference between closed and open symbols) decreases with the wavelength, as expected. The aerosol radiative effect in the presence of clouds is not necessarily the same as in the absence of clouds. Consequently, quantifying DARE as a function of the cloud context is one of the ongoing themes in radiation science.

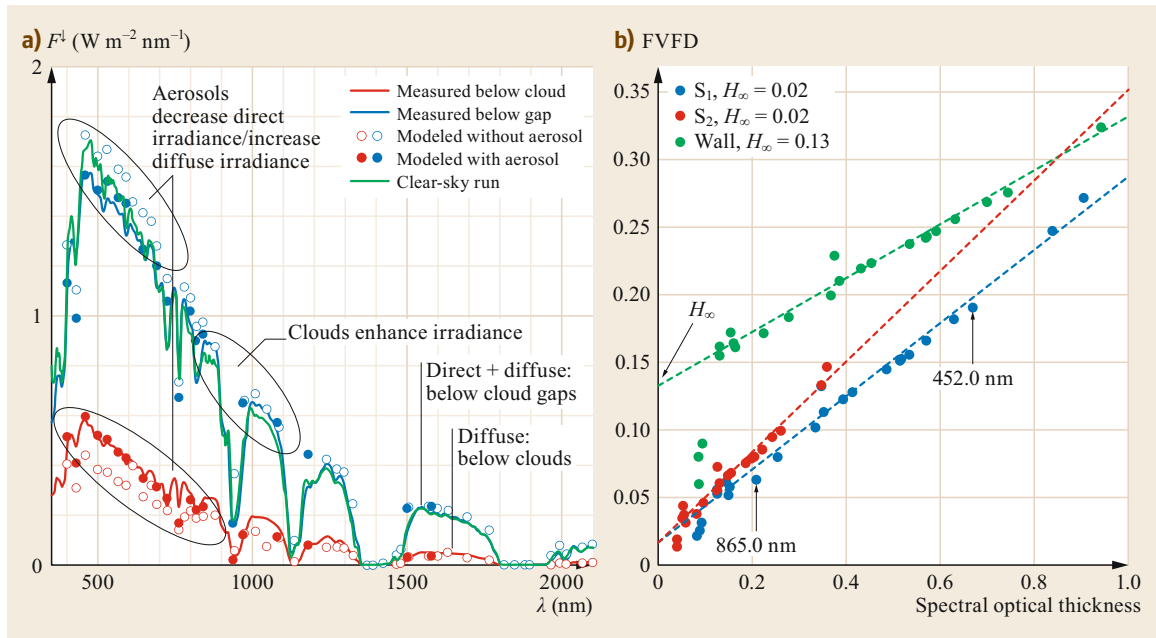


Fig. 40.5 (a) Measured and modeled downward irradiance below a scattered cloud field embedded in an aerosol layer, sampled separately under clouds and cloud gaps. The model results show that the addition of the aerosol decreases the global (direct and diffuse) irradiance in cloud gaps and increases the diffuse irradiance under clouds (after [40.56] with permission of the American Geophysical Union). (b) FVFD, vertical flux divergence normalized by incident irradiance (fractional) plotted as a function of spectral optical thickness. In the limit of large wavelengths (zero aerosol optical thickness, AOT), this reveals the contribution of horizontal flux divergence. The example shows the vertical flux divergence obtained for an aerosol layer above clouds from two (vertical) spirals (S_1 and S_2) and collocated (horizontal) legs (so-called wall). For the spirals, horizontal flux has a negligible impact on the absorption measurements (2%, in contrast to 13% from wall measurements) (after [40.34] © Author Creative Commons license 3.0)

The absorption and heating rate of an aerosol layer above various surfaces (including cloud fields) is best obtained from vertical profiles through the layer, ideally in so-called square spiral patterns with four short level legs per full circle, provided that a leveling platform is available enabling this sampling pattern. These spirals have the advantage of minimizing the variability in the underlying scene while maintaining a constant descent rate of, e.g., 1000 ft min^{-1} . More importantly, they provide a large number of irradiance measurements that can be regressed against altitude or the AOT (obtained from other measurements) as vertical coordinates. The change of net irradiance throughout the layer (i.e., the layer absorption) is obtained from the slope of the linear fit and incorporates multiple samples from the full profile, rather than the two samples above and below the aerosol layer as available from stacked legs. In addition to providing more robust absorption estimates than stacked legs, spiral profiles are also less prone to sampling biases associated with net horizontal photon transport. Its contribution to the measured vertical flux divergence ∇F_V , and thus the bias

in the derived absorption, can be determined by plotting $\nabla F_{V,\lambda}$ against the spectral optical thickness of the aerosol layer, as done in Fig. 40.5b for a NASA field campaign in the Southeast Atlantic that targeted aerosols above low-level clouds (ORACLES: Observations of Aerosols above Clouds and Their Interactions).

In the limit of large wavelengths, and therefore negligible aerosol absorption, one can interpret H_{∞} as a metric for net horizontal photon transport, as the intercept (AOT $\rightarrow 0$). A reasonable measurement of the true absorption and heating rate can be expected if $\nabla F_V \gg H_{\infty}$. In this case, the two spirals meet this condition much better than the wall measurements, even for wavelengths into the near-infrared where AOT becomes small [40.34].

Figure 40.6 shows the measured irradiance profile from such a spiral (Fig. 40.6a) along with the heating rate profile (Fig. 40.6b). In principle, the total heating rate can be directly obtained from profile measurements of broadband solar irradiance (as shown for clouds in [40.40] using ramp descents and ascents) if the scene is homogeneous. With spectral measurements, one can

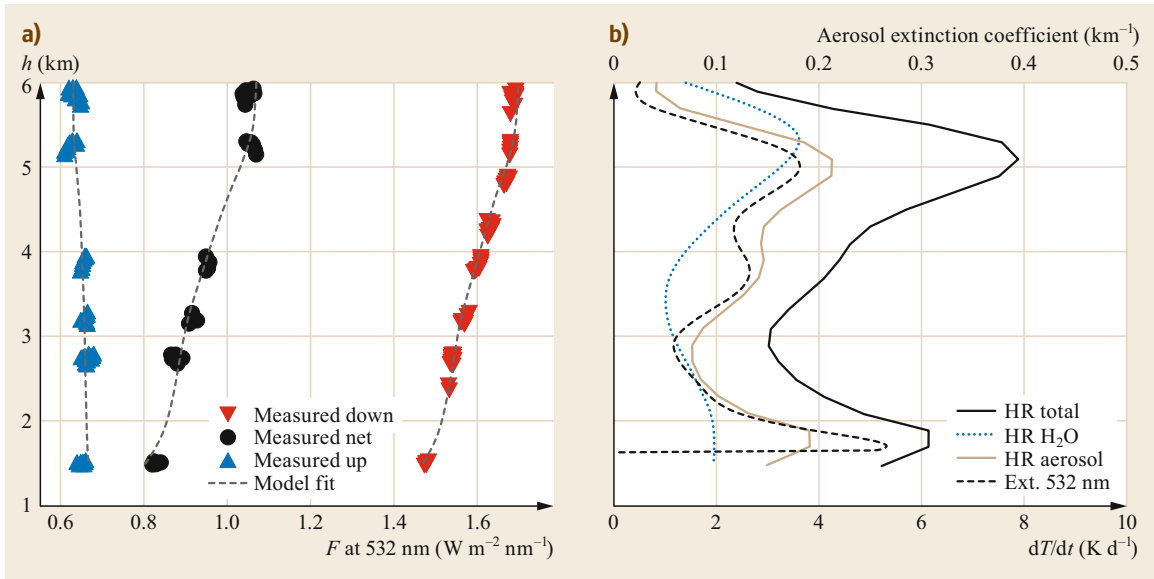


Fig. 40.6 (a) Spiral profile measurements (532 nm wavelength) through aerosol layer above clouds, along with radiative transfer calculations based on AOT and retrieved intensive aerosol optical properties (single-scattering albedo, asymmetry parameter) as dashed lines (model fit). (b) Heating rate dT/dt profile (total and for aerosol and water vapor). The aerosol extinction coefficient profile is also shown

also segregate by absorbers, as shown in Fig. 40.6b, and derive the aerosol single-scattering albedo (SSA) and scattering asymmetry parameter (ASY) by varying them in a radiative transfer model until the calculations match the observed profiles [40.34, 57, 58].

The resulting spectra of aerosol SSA and ASY are shown in Fig. 40.7a, up to a wavelength where H_∞ becomes too large relative to the true absorption (black line Fig. 40.7a) for a meaningful retrieval [40.34]. AOT and absorption are both smooth functions of wavelength; the local maxima are due to atmospheric gases (mainly oxygen in the plotted wavelength range). From AOT, SSA, and ASY, DARE at any level can easily be calculated for any scene albedo. For ORACLES, the top-of-layer DARE switches from negative (cooling) to positive (warming) at 0.25 ± 0.05 , the so-called critical albedo. Similar studies have been made for various aerosol and surface types (for example, dust in the Sahara [40.59]). The systematic study by [40.29], summarizing results from multiple aircraft campaigns, emphasizes that aerosol single-scattering albedo in conjunction with scene albedo largely determines whether a layer has an overall warming or cooling top-of-atmosphere effect.

40.8.3 Surface Characteristics

Figure 40.7b shows a collection of surface albedo spectra for various scene types. Because of its importance

for aerosol and cloud radiative effects, aircraft surface albedo measurements are routinely acquired. They are used to validate surface albedo derived indirectly from spaceborne imagers via the bidirectional reflectance distribution function (BRDF, e.g., [40.60]). For dark surfaces (e.g., water), the atmospheric correction of radiances from spaceborne imagery leads to substantial errors in the derived surface-leaving radiance. To avoid atmospheric correction errors, airborne surface albedo legs should be conducted at a low altitude [40.24, 39, 58]. When flown under clouds, aircraft can acquire so-called white-sky (diffuse) albedo, which may differ from blue-sky (global) albedo [40.33]. Figure 40.7b illustrates the diversity of surface types from multiple aircraft campaigns: ASTAR (Arctic Study of Tropospheric Aerosol and Radiation, 2000: [40.61]), SAMUM (Saharan Mineral Dust Experiment, 2006: [40.62]), MELTEX (Impact of Melt Ponds on Energy and Momentum Fluxes between Atmosphere and Sea Ice, 2008: [40.63]), and ARISE (Arctic Radiation IceBridge Sea and Ice Experiment, 2014: [40.36, 64]). It shows, for example, that vegetation is dark in the visible and becomes bright in the very near infrared; the opposite is true for ice and snow. Characterizing spatially and temporally variable surfaces, such as sea ice and snow in the Arctic, is difficult for both spaceborne and airborne observations, yet important for filling gaps in our understanding of the surface radiation budget. Recent campaigns in the region have led to innovative approaches to simultaneously re-

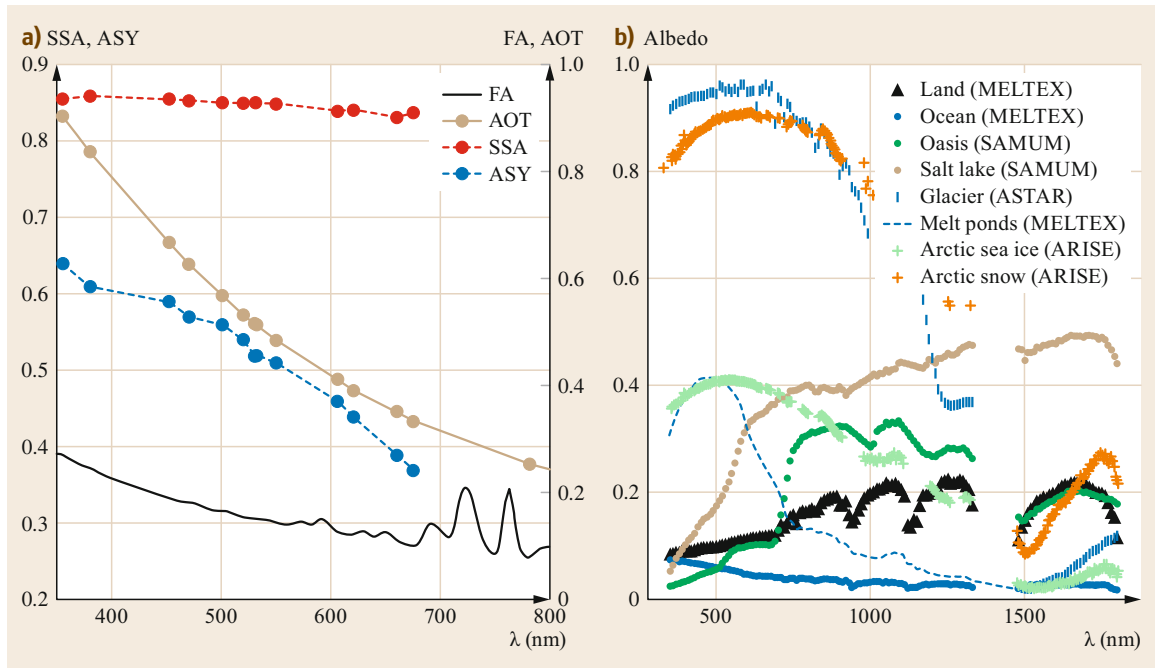


Fig. 40.7 (a) Spectral AOT and absorption normalized by the incident irradiance (fractional absorption, FA) and retrieved SSA and ASY; (b) various different surface albedo spectra from multiple field campaigns

trieve cloud and surface properties [40.35] and to validate imagery-derived cloud radiative effects over snow and ice [40.36]. Such developments and validation ac-

tivities ultimately improve spaceborne observations and therefore our understanding of the radiation budget of the globe.

40.9 Future Developments

Currently, a *canonical* radiometer payload is emerging that maximizes accuracy and information content with spectrally resolved radiation measurements on heritage aircraft. Meanwhile, the future necessitates standalone sensors on small platforms. This calls for innovative instrumentation and calibration techniques to achieve an acceptable level of accuracy. Recently, miniaturized subsystems have become available (e.g., spectrometers,

mini-INS systems), and they may soon fly on remotely piloted aircraft and on autonomous platforms taking observations in regions inaccessible to traditional aircraft. For example, routine surface observations in the high Arctic may be achieved by dropping disposable sondes from a helicopter or aircraft that collect and transmit surface data for part of a season, filling one of the remaining gaps in the global radiation observation system.

40.10 Further Readings

A thorough review of ground-based radiometers is provided by F.J. Vignola et al.: *Solar and Infrared Radiation Measurements, Energy and the Environment* (CRC, Boca Raton 2012). Aircraft radiometers and calibration techniques are described by M. Wendisch et al.: *Atmospheric radiation measurements*. In: *Airborne Measurements for Environmental Research – Methods and*

Instruments, ed. by M. Wendisch and J.-L. Brenguier (Wiley-VCH Weinheim, 2013), while K.S. Schmidt, P. Pilewskie: *Airborne measurements of spectral short-wave radiation*. In: *Cloud and Aerosol Remote Sensing and Energy Budget Studies*, Light Scattering Reviews, Vol. 6, ed. by A. Kokhanovsky (Springer, 2011) show cases applications.

Acknowledgments. We thank Anthony Bucholtz (Naval Postgraduate School, Monterey, CA, USA) and Sam Hall (National Center for Atmospheric Research, Boulder, CO, USA) for their valuable contributions to

this chapter. The first author was supported by NASA grant NNX14AP72G. Irradiance data collection for NASA ARISE [40.36, 64] and ORACLES [40.34] was supported through NNX12AC11G and NNX15AF62G.

References

- 40.1 M. Wendisch, P. Yang: *Theory of Atmospheric Radiative Transfer – A Comprehensive Introduction* (Wiley-VCH, Weinheim 2012)
- 40.2 K. Büttner: Messungen der Sonnen- und Himmelstrahlung im Flugzeug, *Meteorol. Z.* **525** (1929), in German
- 40.3 S. Fritz: The albedo of the ground and atmosphere, *Bull. Am. Meteorol. Soc.* **29**, 303–312 (1948)
- 40.4 L.I. Zubenok: Airborne albedo measurements of various vegetation surfaces. In: *Trudy glavnoy geofizicheskoy observatorii – teplovoiy balans*, 18, Vol. 80, ed. by M.I. Budyko (Gidrometeorologicheskoye Izdatel'stvo, Leningrad 1949) pp. 56–60, in Russian.
- 40.5 W.T. Roach: The absorption of solar radiation by water vapour and carbon dioxide in a cloudless atmosphere, *Q. J. R. Meteorol. Soc.* **87**, 364–373 (1961)
- 40.6 M. Neuberger: Reflection, absorption and transmission of insolation by stratus clouds, *J. Meteorol.* **6**, 98–104 (1949)
- 40.7 K.Y. Kondratyev, O.B. Vassilyev, V.S. Grishechkin, L.S. Ivlev: Spectral radiative flux divergence and its variability in the troposphere in the 0.4–2.4 μm region, *Appl. Opt.* **13**(3), 478–486 (1974)
- 40.8 S. Fritz, T.H. MacDonald: Measurements of absorption of solar radiation by clouds, *Bull. Am. Meteorol.* **32**, 205–209 (1951)
- 40.9 G.D. Robinson: Some determinations of atmospheric absorption by measurement of solar radiation from aircraft and at the surface, *Q. J. R. Meteorol. Soc.* **92**, 263–269 (1966)
- 40.10 A.K. Ångström, A.J. Drummond: Transmission of “cut-off” glass filters employed in solar radiation research, *J. Opt. Soc. Amer.* **49**, 1096–1099 (1959)
- 40.11 A.J. Drummond, G.D. Robinson: Some measurements of the attenuation of solar radiation during BOMEX, *Appl. Opt.* **13**(3), 487–492 (1974)
- 40.12 J.J. deLuisi, P.M. Furukawa, D.A. Gillette, B.G. Schuster, R.J. Charlson, W.M. Porch, R.W. Fegley, B.M. Herman, R.A. Rabinoff, J.T. Twitty, J.A. Weinman: Results of a comprehensive atmospheric aerosol-radiation experiment in the southwestern United States part I: size distribution, extinction optical depth and vertical profiles of aerosols suspended in the atmosphere, *J. Appl. Meteorol.* **15**, 441–454 (1976)
- 40.13 K.Y. Kondratyev, L.S. Ivlev, V.F. Krapivin, C.A. Varostos: *Atmospheric Aerosol Properties – Formation, Processes and Impacts* (Springer, Berlin Heidelberg 2006)
- 40.14 F.P.J. Valero, W.J.Y. Gore, P.M. Giver: Radiative flux measurements in the troposphere, *Appl. Opt.* **21**, 831–838 (1982)
- 40.15 F.P.J. Valero, T.P. Ackerman, W.J.Y. Gore: The effects of the Arctic haze as determined from airborne radiometric measurements during AGASP II, *J. Atmos. Chem.* **9**, 225–244 (1989)
- 40.16 F.J. Vignola, J. Michalsky, T. Stoffel: *Solar and Infrared Radiation Measurements, Energy and the Environment* (CRC, Boca Raton 2012)
- 40.17 F.P.J. Valero, A. Bucholtz, B.C. Bush, S.K. Pope, W.D. Collins, P. Flatau, A. Strawa, W.J.Y. Gore: The atmospheric radiation measurements enhanced shortwave experiment (ARESE): Experiment and data details, *J. Geophys. Res.* **102**, 29929–29937 (1997)
- 40.18 C.S. Zender, B. Bush, S.K. Pope, A. Bucholtz, W.D. Collins, J.T. Kiehl, F.P.J. Valero, J. Vitko Jr.: Atmospheric absorption during the Atmospheric Radiation Measurement (ARM) Enhanced Shortwave Experiment (ARESE), *J. Geophys. Res.* **102**(D25), 29,901–29,915 (1997)
- 40.19 P. Pilewskie, F.P.J. Valero: Direct observations of excess solar absorption by clouds, *Science* **267**, 1626–1629 (1995)
- 40.20 G.L. Stephens, S.C. Tsay: On the cloud absorption anomaly, *Q. J. R. Meteorol. Soc.* **116**(493), 671–704 (1990)
- 40.21 S.A. Ackerman, S.K. Cox: Aircraft observations of shortwave fractional absorptance of non-homogeneous clouds, *J. Appl. Meteorol.* **20**, 11510–11515 (1981)
- 40.22 F. Rawlins: Aircraft measurements of the solar absorption by broken cloud fields: A case study, *Q. J. R. Meteorol. Soc.* **115**, 365–382 (1989)
- 40.23 W. O'Hirok, C. Gautier: Absorption of shortwave radiation in a cloudy atmosphere: Observed and theoretical estimates during the second Atmospheric Radiation Measurement Enhanced Shortwave Experiment (ARESE), *J. Geophys. Res.* **108**(D14), 4412 (2003)
- 40.24 M. Wendisch, P. Pilewskie, E. Jäkel, S. Schmidt, J. Pommier, S. Howard, H.H. Jonsson, H. Guan, M. Schröder, B. Mayer: Airborne measurements of areal spectral surface albedo over different sea and land surfaces, *J. Geophys. Res.* **109**, D08203 (2004)
- 40.25 P. Pilewskie, J. Pommier, R. Bergstrom, W. Gore, S. Howard, M. Rabbette, B. Schmid, P.V. Hobbs, S.C. Tsay: Solar spectral radiative forcing during the Southern African Regional Science Initiative, *J. Geophys. Res.* **108**(D13), 8486 (2003)
- 40.26 R.E. Shetter, M. Müller: Photolysis frequency measurements using actinic flux spectroradiometry during the PEM-Tropics mission: Instrumentation description and some results, *J. Geophys. Res.* **104**(D5), 5647–5661 (1999)

- 40.27 A. Hofzumahaus, A. Kraus, M. Müller: Solar actinic flux spectroradiometry: a technique for measuring photolysis frequencies in the atmosphere, *Appl. Opt.* **38**, 4443–4460 (1999)
- 40.28 E. Jäkel, M. Wendisch, A. Kniffka, T. Trautmann: Airborne system for fast measurements of upwelling and downwelling spectral actinic flux densities, *Appl. Opt.* **44**, 434–444 (2005)
- 40.29 P.B. Russell, R.W. Bergstrom, Y. Shinozuka, A.D. Clarke, P.F. DeCarlo, J.L. Jimenez, J.M. Livingston, J. Redemann, O. Dubovik, A. Strawa: Absorption Angstrom Exponent in AERONET and related data as an indicator of aerosol composition, *Atmos. Chem. Phys.* **10**, 1155–1169 (2010)
- 40.30 K.S. Schmidt, P. Pilewskie, B. Mayer, M. Wendisch, B. Kindel, S. Platnick, M.D. King: Apparent absorption of solar spectral irradiance in heterogeneous ice clouds, *J. Geophys. Res.* **115**, D00J22 (2010)
- 40.31 S. Song, K.S. Schmidt, P. Pilewskie, M.D. King, A.K. Heidinger, A. Walther, H. Iwabuchi, G. Wind, O.M. Coddington: The spectral signature of cloud spatial structure in shortwave irradiance, *Atmos. Chem. Phys.* **16**, 13791–13806 (2016)
- 40.32 A. Bucholtz, R. Bluth, B. Kelly, S. Taylor, K. Batson, A. Sarto, T. Tooman, R. McCoy Jr.: The Stabilized Radiometer Platform (STRAP) – An actively stabilized horizontally level platform for improved air-craft irradiance measurements, *J. Atmos. Oceanic Technol.* **25**, 2161–2175 (2008)
- 40.33 L.A. Wright, B.C. Kindel, P. Pilewskie, N. Leisso, T. Kampe, K.S. Schmidt: Below-cloud atmospheric correction of airborne hyperspectral imagery using simultaneous solar spectral irradiance observations, *IEEE Trans. Geosci. Remote Sens.* **59**, 1392–1409 (2020)
- 40.34 S.P. Cochrane, K.S. Schmidt, H. Chen, P. Pilewskie, S. Kittelman, J. Redemann, S. LeBlanc, K. Pistone, M. Kacenenbogen, M. Segal Rozenhaimer, Y. Shinozuka, C. Flynn, S. Platnick, K. Meyer, R. Ferrare, S. Burton, C. Hostetler, S. Howell, A. Dobracki, S. Doherty: Above-cloud aerosol radiative effects based on ORACLES 2016 and ORACLES 2017 aircraft experiments, *Atmos. Meas. Tech.* **12**, 6505–6528 (2019)
- 40.35 A. Ehrlich, E. Bierwirth, L. Istomina, M. Wendisch: Combined retrieval of Arctic liquid water cloud and surface snow properties using airborne spectral solar remote sensing, *Atmos. Meas. Tech.* **10**, 3215–3230 (2017)
- 40.36 H. Chen, K.S. Schmidt, M.D. King, G. Wind, A. Bucholtz, E.A. Reid, M. Segal-Rozenhaimer, W.L. Smith, P.C. Taylor, S. Kato, P. Pilewskie: Shortwave radiative effect of Arctic low-level clouds: Evaluation of imagery-derived irradiance with aircraft observations, *Atmos. Meas. Tech.* **14**, 2673–2697 (2021)
- 40.37 J. Badosa, J. Wood, P. Blanc, C.N. Long, L. Vuilleumier, D. Demengel, M. Haeffelin: Solar irradiances measured during SPN1 radiometers: uncertainties and clues for development, *Atmos. Meas. Tech.* **7**, 4267–4283 (2014)
- 40.38 A.R. Webb, A. Kylling, M. Wendisch, E. Jäkel: Airborne measurements of ground and cloud spectral albedos under low aerosol loads, *J. Geophys. Res.* **109**, D20205 (2004)
- 40.39 O. Coddington, K.S. Schmidt, P. Pilewskie, W.J. Gore, R.W. Bergstrom, M. Román, J. Redemann, P.B. Russell, J. Liu, C.C. Schaaf: Aircraft measurements of spectral surface albedo and its consistency with ground-based and space-borne observations, *J. Geophys. Res.* **13**, D17209 (2008)
- 40.40 A. Bucholtz, D.L. Hlavka, M.J. McGill, K.S. Schmidt, P. Pilewskie, S.M. Davis, E.A. Reid, A.L. Walker: Directly measured heating rates of a tropical sub-visible cirrus cloud, *J. Geophys. Res.* **115**, D00J09 (2010)
- 40.41 E. Bierwirth, M. Wendisch, E. Jäkel, A. Ehrlich, K.S. Schmidt, H. Stark, P. Pilewskie, M. Esselborn, G.P. Gobbi, R. Ferrare, T. Müller, A. Clarke: A new method to retrieve aerosol layer absorption coefficient from airborne flux density and actinic radiation measurements, *J. Geophys. Res.* **115**, D14211 (2010)
- 40.42 B.C. Kindel, K.S. Schmidt, P. Pilewskie, B.A. Baum, P. Yang, S. Platnick: Observations and modeling of ice cloud shortwave spectral albedo during the Tropical Composition, Cloud and Climate Coupling Experiment (TC⁴), *J. Geophys. Res.* **115**, D00J18 (2010)
- 40.43 B.C. Kindel, P. Pilewskie, K.S. Schmidt, O. Coddington, M.D. King: Solar spectral absorption by marine stratus clouds: Measurements and modeling, *J. Geophys. Res.* **116**, D10203 (2011)
- 40.44 K.S. Schmidt, P. Pilewskie: Airborne Measurements of Spectral Shortwave Radiation. In: *Cloud and Aerosol Remote Sensing and Energy Budget Studies*, Light Scattering Reviews, Vol. 6, ed. by B.A. Kokhanovsky (Springer, Berlin Heidelberg 2011)
- 40.45 J.J. Michalsky, P.W. Kiedron: Comparison of UV-RSS spectral measurements and TUV model runs for clear skies for the May 2003 ARM aerosol intensive observation period, *Atmos. Chem. Phys.* **8**, 1813–1821 (2008)
- 40.46 B.C. Kindel: *Cloud shortwave spectral radiative properties: Airborne hyperspectral measurements and modeling of irradiance*, PhD Thesis (University of Colorado, Boulder 2010), https://scholar.colorado.edu/atoc_gradetds/4, Accessed 15 July 2021
- 40.47 M. Wendisch, P. Pilewskie, B. Bohn, A. Bucholtz, S. Crewell, C. Harlow, E. Jäkel, K.S. Schmidt, R. Shetter, J. Taylor, D. Turner, M. Zöger: Atmospheric radiation measurements. In: *Airborne Measurements for Environmental Research – Methods and Instruments*, ed. by M. Wendisch, J.-L. Brenguier (Wiley-VCH, Weinheim 2013)
- 40.48 R. Shetter, L. Cinquini, B. Lefer, S. Madronich: Comparison of airborne measured and calculated spectral actinic flux and derived photolysis frequencies during the PEM Tropics B mission, *J. Geophys. Res.* **108**(D2), 8234 (2003)
- 40.49 B. Bohn, A. Kraus, M. Müller, A. Hofzumahaus: Measurement of atmospheric O₃ → O(1-D) photolysis frequencies using filterradiometry, *J. Geophys. Res.* **109**, D10S90 (2004)

- 40.50 J. Schreder, J. Grobner, A. Los, M. Blumthaler: Intercomparison of monochromatic source facilities for the determination of the relative spectral response of erythemal broadband filter radiometers, *Opt. Lett.* **13**, 1455–1457 (2004)
- 40.51 H.J. Kostkowski: *Reliable spectroradiometry* (Spectroradiometry Consulting, La Plata 1997)
- 40.52 O.B. Toon, D.O. Starr, E.J. Jensen, P.A. Newman, S. Platnick, M.R. Schoeberl, P.O. Wennberg, S.C. Wofsy, M.J. Kurylo, H. Maring, K.W. Jucks, M.S. Craig, M.F. Vasques, L. Pfister, K.H. Rosenlof, H.B. Selkirk, P.R. Colarco, S.R. Kawa, G.G. Mace, P. Minnis, K.E. Pickering: Planning, implementation, and first results of the Tropical Composition, Cloud and Climate Coupling Experiment (TC4), *J. Geophys. Res.* **115**, D00J04 (2010)
- 40.53 A. Marshak, W. Wiscombe, A. Davis, L. Oreopoulos, R. Cahalan: On the removal of the effect of horizontal fluxes in two-aircraft measurements of cloud absorption, *Q. J. R. Meteorol. Soc.* **125**, 2153–2170 (2007)
- 40.54 K.S. Schmidt, V. Venema, F. Di Giuseppe, R. Scheirer, M. Wendisch, P. Pilewskie: Reproducing cloud microphysical and irradiance measurements using three 3-D cloud generators, *Q. J. R. Meteorol. Soc.* **133**, 765–780 (2007)
- 40.55 V. Venema, F. Ament, C. Simmer: A stochastic iterative amplitude adjusted Fourier transform algorithm with improved accuracy, *Nonlinear Processes in Geophysics* **13**(3), 321–328 (2006)
- 40.56 K.S. Schmidt, G. Feingold, P. Pilewskie, H. Jiang, O. Coddington, M. Wendisch: Irradiance in polluted cumulus fields: Measured and modeled cloud-aerosol effects, *Geophys. Res. Lett.* **36**, L07804 (2009)
- 40.57 R.W. Bergstrom, K.S. Schmidt, O. Coddington, P. Pilewskie, H. Guan, J.M. Livingston, J. Redemann, P.B. Russell: Aerosol spectral absorption in the Mexico City area: results from airborne measurements during MILAGO/INTEX B, *Atmos. Chem. Phys.* **10**, 6333–6343 (2010)
- 40.58 K.S. Schmidt, P. Pilewskie, R. Bergstrom, O. Coddington, J. Redemann, J.M. Livingston, P. Russell, E. Bierwirth, M. Wendisch, W. Gore, M.K. Dubey, C. Mazzoleni: A new method for deriving aerosol solar radiative forcing and its first application within MILAGO/INTEX-B, *Atmos. Chem. Phys.* **10**, 7829–7843 (2010)
- 40.59 S. Otto, M. de Reus, T. Trautmann, A. Thomas, M. Wendisch, S. Borrmann: Atmospheric radiative effects of an in situ measured Saharan dust plume and the role of large particles, *Atmos. Chem. Phys.* **7**, 4887–4903 (2007)
- 40.60 J.V. Martonchik, D.J. Diner, B. Pinty, M.M. Verstraete, R.B. Myneni, Y. Knyazikhin, H.R. Gordon: Determination of land ocean reflective, radiative, and biophysical properties using multiangle imaging, *IEEE Trans. Geosci. Remote Sens.* **36**(4), 1266–1281 (1998)
- 40.61 T. Yamanouchi, R. Treffeisen, A. Herber, M. Shiobara, S. Yamagata, K. Hara, K. Sato, M. Yabuki, Y. Tomikawa, A. Rinke, R. Neuber, R. Schumacher, M. Kriews, J. Ström, O. Schrems, H. Gernandt: Arctic Study of Tropospheric Aerosol and Radiation (ASTAR) 2000: Arctic haze case study, *Tellus B Chem. Phys. Meteorol.* **57**, 141–152 (2005)
- 40.62 E. Bierwirth, M. Wendisch, A. Ehrlich, B. Heese, M. Tesche, D. Althausen, A. Schladitz, D. Müller, S. Otto, T. Trautmann, T. Dinter, W. von Hoyningen-Huene, R. Kahn: Spectral surface albedo over Morocco and its impact on radiative forcing of Saharan dust, *Tellus B* **61**, 252–269 (2009)
- 40.63 G. Birnbaum, W. Dierking, J. Hartmann, C. Lüpkes, A. Ehrlich, T. Garbrecht, L. Sellmann: *The campaign MELTEX with research aircraft "POLAR 5" in the Arctic in 2008, Reports on Polar and Marine Research 593* (Alfred Wegener Institute for Polar and Marine Research, Bremerhaven 2009), https://doi.org/10.2312/BzPM_0593_2009
- 40.64 W.L. Smith, C. Hansen, A. Bucholtz, B.E. Anderson, M. Beckley, J.G. Corbett, R.I. Cullather, K.M. Hines, M. Hofton, S. Kato, D. Lubin, R.H. Moore, M. Segal Rosenhaimer, J. Redemann, S. Schmidt, R. Scott, S. Song, J.D. Barrick, J.B. Blair, D.H. Bromwich, C. Brooks, G. Chen, H. Cornejo, C.A. Corr, S. Ham, A.S. Kittelman, S. Knappmiller, S. LeBlanc, N.G. Loeb, C. Miller, L. Nguyen, R. Palikonda, D. Rabine, E.A. Reid, J.A. Richter-Menge, P. Pilewskie, Y. Shinozuka, D. Spangenberg, P. Stackhouse, P. Taylor, K.L. Thornhill, D. van Gilst, E. Winstead: Arctic Radiation-IceBridge Sea and Ice Experiment: The Arctic Radiant Energy System during the Critical Seasonal Ice Transition, *Bull. Am. Meteorol. Soc.* **98**, 1399–1416 (2017)

K. Sebastian Schmidt

Laboratory for Atmospheric and Space Physics
University of Colorado at Boulder
Boulder, USA
sebastian.schmidt@lasp.colorado.edu



Sebastian Schmidt is an Associate Professor at the Department of Atmospheric and Oceanic Sciences and at the Laboratory for Atmospheric and Space Physics at the University of Colorado in Boulder. He received his PhD in 2005 from the University of Leipzig, Germany. His research focuses on atmospheric remote sensing and energy budget studies using aircraft, ground-based, and spaceborne observations. He is a member of the International Radiation Commission.

Manfred Wendisch

Physics and Earth Sciences
University of Leipzig
Leipzig, Germany
m.wendisch@uni-leipzig.de



Manfred Wendisch is a Professor at the University of Leipzig (Germany) and Director of the Leipzig Institute for Meteorology. He is involved in airborne field observations, studying the influence of clouds on the atmospheric radiative energy budget with a focus on cirrus and Arctic mixed-phase clouds, as well as on subtropical trade wind cumuli.

Bruce Kindel

Laboratory for Atmospheric and Space Physics
University of Colorado at Boulder
Boulder, USA
bruce.kindel@lasp.colorado.edu

Bruce Kindel is a research scientist at the Laboratory for Atmospheric and Space Physics (LASP) at the University of Colorado, Boulder. He received his PhD in Atmospheric and Oceanic Sciences from the University of Colorado, Boulder in 2010. His research focuses on remote sensing of the Earth's atmosphere and surface from satellite, aircraft, and surface instrumentation, with an emphasis on hyperspectral measurements.

41. Spaceborne Microwave Radiometry

Susanne Crewell , Catherine Prigent , Mario Mech 

Since several decades, microwave radiometers have been an essential component of the satellite observation system, enabling the retrieval of a multitude of parameters. Conical scanning imagers are mainly dedicated to deriving characteristics of the Earth's surface, e.g., soil moisture, sea-surface temperature, salinity, and sea ice. For this purpose, they make use of channels at low frequencies where the atmosphere is relatively transparent. By exploiting the differential absorption along pressure-broadened rotational lines, coarse resolution vertical profiles of water vapor and temperature can be derived from microwave sounders observing along the wings of atmospheric absorption lines. Furthermore, clouds and precipitation produce distinct spectral signatures in the microwave region, which can be best used over ocean surfaces that have a lower surface emissivity than land. Due to the rather long wavelengths, the spatial resolution of microwave satellite instruments is relatively poor, of the order of 10 km or more. By deploying microwave radiometers onboard aircrafts, much finer resolution can be achieved, which allows dedicated process studies. Microwave instruments flown on several polar orbiting satellites are an essential ingredient into today's numerical weather prediction, and their measurements are assimilated directly as radiances by several meteorological services worldwide. With measurements having been available for more than three decades, microwave observations are starting to play an important role

41.1	Measurement Principles and Parameters	1152
41.1.1	Measured Parameters	1152
41.1.2	Principles of Measurements	1153
41.2	History	1155
41.3	Theory	1156
41.3.1	Surface Emissivity	1156
41.3.2	Atmospheric Gases	1157
41.3.3	Atmospheric Hydrometeors	1158
41.4	Devices and Systems	1159
41.4.1	Microwave Imagers	1159
41.4.2	Nadir Sounders	1160
41.4.3	Limb Sounders	1161
41.5	Specifications	1162
41.6	Quality Control	1163
41.7	Maintenance	1163
41.8	Application	1164
41.8.1	Numerical Weather Prediction (NWP) ..	1164
41.8.2	Earth System and Climate Monitoring ..	1164
41.9	Future Developments	1167
41.10	Further Readings	1167
	References	1167

in monitoring and understanding the effects of climate change, such as the melting of the polar ice caps. With the upcoming new generation of satellites, the frequency range of the measurements is expanded into the submillimeter range to better capture ice clouds.

This chapter deals with spaceborne and airborne microwave radiometers operating in the spectral range between 1 and 300 GHz, which are utilized in a variety of environmental and engineering applications, including weather forecasting and climate monitoring. Using microwave radiation provides complementary information to the visible and infrared spectral range (Chap. 42). Compared to visible and infrared observa-

tions, passive microwaves are less affected by clouds and can, to some extent, provide *all-weather* surface and atmospheric information. The general design of microwave radiometers is similar to that of ground-based radiometers (Chap. 29), however, the antenna design and scanning concept become highly important for reaching global coverage with reasonable spatial and temporal resolutions.

41.1 Measurement Principles and Parameters

The microwave spectral range offers some distinct advantages for remote sensing of geophysical parameters. First, the high transmittance of the atmosphere ($> 80\%$ below 40 GHz) provides possibilities for the observation of surface properties for downlooking geometry, i.e., from space and aircraft. Second, the fact that wavelengths are relatively large compared to atmospheric particles allows scattering processes to be neglected for most applications, simplifying the retrieval and allowing observations under nearly all weather situations. The semitransparency of clouds and precipitation also allows us to determine information on atmospheric hydrometeors.

Today, various microwave instruments are flown on polar orbiting instruments and provide key information for data assimilation in numerical weather prediction (NWP) centers [41.1]. Microwave radiometers on research aircraft have served as prototypes for upcoming satellite missions and also within calibration and validation (CAL/VAL) activities. Compared to satellite missions, they allow finer scale observations than satellites in remote areas, such as the tropical trade wind region [41.2].

41.1.1 Measured Parameters

Microwave radiometers (MWR) are passive remote sensing instruments that measure the natural thermal emission by atmospheric components and from the ground. Typically, microwave radiation is measured in several spectral channels and is provided as the brightness temperature (BT), i.e., the temperature a blackbody producing the same radiance would have according to Planck's law (Table 41.1). Note that this is the typical nomenclature of the satellite community, while the ground-based community typically uses TB as an acronym for brightness temperatures (Chap. 29). The reflection of microwave radiation at the surface, as well as scattering by hydrometeors in the atmosphere, can lead to polarization and serves as an additional information source. The MWRs are polarization sensitive, and BT are often measured in vertical and horizontal polarizations. To observe the wind vector over the ocean even the full Stokes vector is used [41.3].

For NWP, BT are directly assimilated at most operational centers by using forward operators, including the description of radiative transfer. By applying retrieval algorithms to sets of different spectral regions, a variety of atmospheric and surface variables can be derived (Table 41.2).

Table 41.1 Measured parameters of microwave radiometers

Parameter	Description	Unit	Symbol
Brightness temperature	Radiances detected by microwave receivers in a limited frequency interval (bandwidth) and a certain polarization state are calibrated to the Planck equivalent brightness temperatures	K	BT

Table 41.2 Parameters retrieved from measurements of brightness temperatures in different frequency channels

Parameter	Description	Unit	Symbol
Temperature profile	Vertically resolved atmospheric temperature	K	T
Precipitable water vapor	Column integrated amount of water vapor	kg m^{-2}	PWV
Humidity profile	Vertically resolved water vapor mixing ratio	kg kg^{-1}	q
Liquid water path	Column integrated amount of liquid water	kg m^{-2}	LWP
Precipitation	Precipitation rate at the surface	mm h^{-1}	R
Ice water path	Column integrated amount of frozen hydrometeors	kg m^{-2}	IWP
Snowfall rate	Liquid equivalent of frozen precipitation rate	mm h^{-1}	S
Ocean wind speed	Wind speed at the ocean surface	m s^{-1}	OWS
Soil moisture	Volumetric soil moisture	%	SM
Land surface temperature	Skin temperature of the land surface	K	LST
Sea surface temperature	Skin temperature of the sea	K	SST
Sea surface salinity	Percentage of salt in sea water at the sea surface	PSU	SSS
Sea ice concentration	Area covered with sea ice relative to the total area	%	SIC
Sea ice type	Classification of sea ice into first-year and multiyear ice		
Snow water equivalent	Equivalent height of melted snowpack	mm	SWE
Stratospheric trace gases	Vertically resolved concentrations of different gases such as ozone, ClO, BrO, HCl, HNO ₃	ppm	

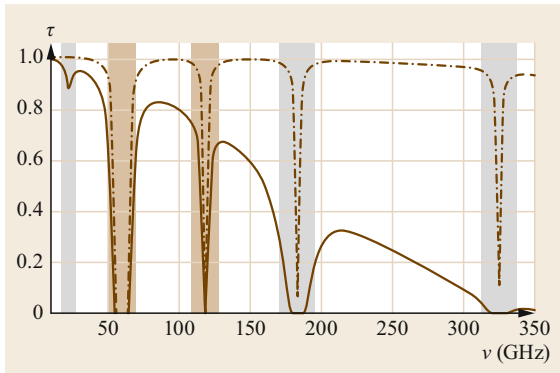


Fig. 41.1 Atmospheric transparency at sea level (solid line) and at 5 km elevation (dotted-dashed line) in the microwave spectrum for the clear-sky standard atmosphere showing the absorption features related to water vapor (grey) and oxygen (brown)

41.1.2 Principles of Measurements

All natural objects emit thermal radiation in the microwave spectral region. The transparency of the atmosphere is rather high at low microwave frequencies and generally decreases with increasing frequency (Fig. 41.1). The emissivity ε of the surface strongly depends on the surface roughness and dielectric properties of the material, varying roughly between 0.3 for ocean surfaces to 1 over vegetated land surfaces (Fig. 41.2). When the emissivity is known and the atmosphere is highly transparent, i.e., at low frequencies (< 20 GHz), the thermal radiation received at the satellite is closely proportional to the surface brightness temperature, and sea and land surface temperatures (SST and LST) can be derived. Sea-surface emissivity depends on surface roughness, temperature, and salinity. As the land emis-

sivity depends on the water content, especially at low frequencies, the soil moisture content can be derived. The strong contrast between the emissivity of sea water and sea ice allows us to distinguish open ocean from sea ice. The emissivity of snow and ice strongly depends on their morphologies allowing us to retrieve more details on the age and thickness of sea ice (Table 41.2).

Several atmospheric gases exhibit rotational transitions (Fig. 41.1), which allows us to derive information about their abundance and vertical structure. Examples of such absorption features are the oxygen absorption complex (caused by magnetic dipole transitions) around 60 GHz, which is used to derive temperature profiles or the water vapor absorption line at 183.31 GHz (dipole rotational transition). Other significant absorption lines are found at 118.75 GHz (oxygen absorption) and at 22.235 GHz (water vapor absorption). The 183.31 GHz line is much stronger than the 22.235 GHz one and is used for spaceborne moisture profiling [41.7] as the strong atmospheric absorption masks the surface. Weak absorption features of trace gases like ozone, nitrous dioxide, or chlorine monoxide are also used for profiling of these species. To derive their stratospheric profiles, limb sounding is employed and spectrally resolved measurements around the center of the pressure broadened absorption lines are performed (Chap. 28 Spectrometry).

In addition to the distinct absorption features of molecular transition lines, there are also nonresonant contributions by hydrometeors (liquid drops and frozen particles). Liquid water emission increases with frequency. Hence, measurements at window channels dominated by liquid water emission (typically 37 GHz), together with those close to the water absorption line (22.235 GHz), are used to observe the vertically in-

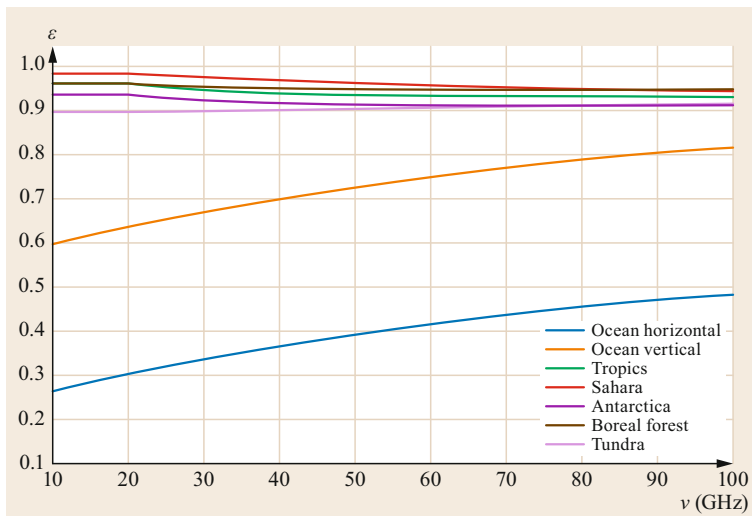


Fig. 41.2 Microwave emissivity ε for vertical polarization (unless otherwise stated) between 10 and 100 GHz at 53° incidence angle for different surface types derived from FASTEM calculations for ocean [41.4] and emissivity atlas TESSEM² for the continental surfaces (after [41.5, 6])

Table 41.3 The most important microwave instruments, their acronyms, satellite platforms, and operation time periods

Acronym	Instrument	Primary Usage	Platform	Time frame
AMSR AMSR-E AMSR-2	Advanced Microwave Scanning Radiometer	Sea ice and snow, SST, precipitation, PWV, LWP	ADEOS-2, EOS-AQUA, GC-COM-W, GOSAT-3	Since 2002
AMSU-A	Advanced Microwave Sounding Unit – A	Temperature profiling, PWV, LWP	Since NOAA-15, AQUA, MetOp	Since 1998
AMSU-B	Advanced Microwave Sounding Unit – B	Specific humidity profile	NOAA-15 to NOAA-17	1998–2004
ATMS	Advanced Technology Microwave Sounder	Precipitation, sea ice, wind speed, PWV, LWP, water vapor and temperature profiles	NOAA NPP	Since 2011
GMI	Global Precipitation Mission (GPM) Microwave Imager	Precipitation, PWV, LWP	GPM Core Satellite	Since 2014
MHS	Microwave Humidity Sounder	Specific humidity profile	Since NOAA-18, MetOp	Since 2005
MLS	Microwave Limb Sounder	Ozone, chlorine monoxide, nitric acid	UARS, EOS-AURA	1991–2018
SMOS	Soil Moisture and Ocean Salinity	Soil moisture, sea surface salinity	SMOS	Since 2009
SMAP	Soil Moisture Active–Passive	Soil moisture	SMAP	Since 2015
SSM/I	Special Sensor Microwave/Imager	Precipitation, sea ice, wind speed, PWV, LWP	Since DMSP-F08 until DMSP-F15	Since 1987
SSMIS	Special Sensor Microwave Imager/Sounder	Precipitation, sea ice, wind speed, PWV, LWP, temperature, water vapor and temperature profiles	Since DMSP-F16	Since 2003
TMI	Tropical Rainfall Measuring Mission (TRMM) Microwave Imager	Precipitation	TRMM	1997–2015
WindSat	WindSat	Sea surface wind vector	Coriolis	Since 2003

Table 41.4 Principles of microwave remote sensing for different applications and most important satellite instruments

Applications	Measurements		Instrument
	Principle	Frequencies used (GHz)	
Temperature profile	Sounding along oxygen absorption complex	50–60	AMSU-A, ATMS
Precipitable water vapor	Emission above radiatively cold ocean with correction for liquid water	19/24 & 31/36	SSM/I, AMSR, GMI
Humidity profile	Sounding along water vapor line	183	AMSU-B, MHS, ATMS
Liquid water path	Emission in window channels corrected for water vapor	31/36/90 & 24	SSM/I, AMSR, GMI
Precipitation	Emission algorithms over ocean and	19, 22, 36	SSM/I, AMSR, GMI
	scattering algorithms over land	90, 150	
Ice water path and snowfall rate	Scattering signature	90, 150, 183	AMSU, MHS, GMI
Wind speed	Surface roughness, polarization signal at the ocean surface	10, 19, 36	SSM/I, AMSR, GMI, WindSat
Soil moisture	Surface emission	1.4	SMOS, SMAP
Land surface temperature	Surface emission	19, 36	SSM/I, AMSR, GMI
Sea surface temperature	Surface emission	6	AMSR
Ocean (or sea) salinity	Surface emission	1.4	SMOS, SMAP
Sea ice concentration	Surface emission	6, 10, 19, 36, 90	SSM/I, AMSR, GMI
Sea ice type	Surface emission	6, 10, 19, 36, 90	SSM/I, AMSR, GMI
Snow water equivalent	Surface emission	19, 36, 90	SSM/I, AMSR, GMI

tegrated liquid water path (LWP) and simultaneously the precipitable water vapor (PWV) over ocean surfaces. The so-called *water vapor continuum* increases strongly with frequency with a nearly opaque atmo-

sphere in the far-infrared part of the electromagnetic spectrum.

Large rain drops, as well as large frozen hydrometeors (snow, graupel, hail), also scatter microwave

radiation, especially at higher frequencies (> 90 GHz). [41.8] first suggested a scattering index to identify and subsequently derive precipitation also above land surfaces. Furthermore, the scattering signal is exploited in integrated retrieval algorithms to obtain the snowfall rate [41.9].

Several satellite missions employ microwave instruments to measure land surface and atmospheric parameters for different applications. The World Meteorological Organization (WMO) keeps an inventory of the different satellite instruments on their webpage <https://www.wmo-sat.info/oscar/instruments#>, Accessed 15 July 2021. Information on the most important ones is

provided in Table 41.3 and the measurement principles for the different applications are given in Table 41.4. Here, the focus is on routine measurements performed from polar orbiting satellites operated by the European Organization for the Exploitation of Meteorological Satellites (EUMETSAT), the Defense Meteorological Satellite Program (DMSP), the Japan Aerospace Exploration Agency (JAXA), and the National Oceanic and Atmospheric Administration (NOAA). Furthermore, Earth Observation System (EOS) satellites (AQUA, AURA, TERRA) by the National Aeronautics and Space Administration (NASA) dedicated to Earth Observations are included.

41.2 History

Microwave radiometry was developed in the field of astronomy and extraterrestrial applications. In 1962, the Mariner-2 mission to Venus was launched by NASA and included a two-channel radiometer at 16 and 22 GHz to investigate water vapor and temperature. In 1972, the first systematic microwave observations of the Earth, between 22 and 58 GHz were made aboard the NASA operated Nimbus 5 missions in polar low Earth orbit. These microwave data produced for the first time temperature profiles in the presence of clouds and provided the vapor and liquid water contents of the Earth's atmosphere over the ocean [41.10]. Within the Nimbus series, radiometers advanced further, and in 1978 the nine-channel scanning multichannel microwave radiometer (SMMR, [41.11]) was launched into space. This demonstrated the considerable potential of passive microwave measurements for meteorology and their complementarity with visible and infrared observations.

These Nimbus satellite missions were mainly dedicated to research and paved the way for low-orbit operational meteorological satellites as we know them today. Starting in 1979, low-orbit meteorological satellites managed by NOAA were equipped with microwave sounders. The MSU radiometer (Microwave Sounding Unit) was first placed in orbit aboard the TIROS-N satellite at the end of 1978. The MSU radiometers (nine in total) included four channels between 50 and 60 GHz to provide measurements of atmospheric temperature down to the lower troposphere, with a ground spatial resolution of about 250 km.

With the operational deployment of the SSM/I instrument, a follow-up of SMMR, on the DMSP satellite series in 1987, global precipitation observations over ocean became possible. Their data built the backbone of global precipitation records in the satellite era [41.12].

For the tropics, TRMM provided a milestone, as for the first time, microwave passive (from radiometers) and active (from radar) observations were combined to improve the accuracy of precipitation estimates. Geostationary satellites allow temporal resolutions of the order of 15 min. However, these satellites are still not equipped with passive microwave instruments, as large antenna systems would be required even for moderate spatial resolution (Sect. 41.4). The temporal repeatability of microwave measurements is, therefore, limited by the number and temporal spacing of low-orbiting satellites within a constellation, such as GPM, currently providing observations at the same location every 3 h.

In the 1980s, thanks to advances in microwave radiometer technology, more accurate observations at higher frequencies were possible, up to 200 GHz. This opened the possibility of analyzing the water vapor profile in the atmosphere by measurements in the 183 GHz water vapor line. In 1998, the Advanced Microwave Sounding Unit (AMSU) instrument was launched onboard of NOAA-15, the first satellite of the NOAA fifth generation/Polar Operational Environmental Satellites, which was specifically designed for temperature profiling but also for providing information on water vapor and hydrometeors. Launched on nine satellites in total, the AMSU instrument provides core information for numerical weather prediction.

With the detection of the Antarctic ozone hole in 1995, the need to monitor stratospheric trace gases became apparent. MLS onboard the Upper Atmospheric Research Satellite (UARS) launched in 1991 for the first time provided global observations of species involved in the catalytic cycle of ozone depletion, e.g., chlorine monoxide, and nitric acid. The follow-up mission on the Earth Observation System (EOS) Aura satellite expanded spaceborne microwave mea-

measurements into the submillimeter range to observe the hydroxyl radical (OH) at 2.5 THz.

For the next generation of Meteorological Operation satellites (MetOp-SG, for the Second Generation, after 2020), Europe decided to strengthen the passive microwave observations, with the addition of two instruments, the Microwave Imager (MWI) and the Ice

Cloud Imager (ICI), in addition to the temperature and humidity sounder (Microwave Sounder (MWS)). With the ICI instrument, observations up to 664 GHz will be made for the first time for operational meteorology. These measurements will have a high sensitivity to ice in the clouds and will allow an estimate of the ice water content, a variable that is currently poorly known.

41.3 Theory

The basics of microwave radiative transfer in the atmosphere are described in the literature [41.13–15], as well as in Chap. 29. While ground-based microwave radiometers observe the atmospheric contribution against the cold cosmic background ($T_{\text{cos}} = 2.7$ K), the Earth's surface emission becomes the background for the airborne and satellite perspective. For simplicity, we assume an atmosphere with constant vertical properties that has the optical depth τ_{atm} and the blackbody brightness temperature BT_{atm} . The simplified monospectral radiative transfer equation then consists of four different contributions to the brightness temperature at the satellite

$$BT = BT_{\text{atm}} + \varepsilon BT_{\text{surf}} e^{-\tau_{\text{atm}}} + (1 - \varepsilon) BT_{\text{atm}} e^{-\tau_{\text{atm}}} + (1 - \varepsilon) BT_{\text{cos}} e^{-2\tau_{\text{atm}}}. \quad (41.1)$$

In addition to the direct atmospheric BT (first term), the satellite senses the emission of the surface according to the emissivity ε times blackbody brightness temperature of the surface (second term) attenuated by the atmosphere. The third term describes how downwelling atmospheric radiation is reflected by the surface and attenuated by the atmosphere on its path to the satellite. The fourth term becomes important only for rather low-opacity conditions and for reflective surfaces, in which case the cosmic background signal is reflected and attenuated twice by the atmosphere. For sounding channels with high opacity, only the first term is important, while for land surface missions, frequencies with low τ_{atm} are chosen to avoid atmospheric contributions such that the second term dominates. Knowing the surface properties and the vertical profiles of thermodynamical variables and all absorbing gases, synthetic satellite measurements of BT can be calculated using radiative transfer models.

Equation (41.1) describes the simplified case of a nonscattering atmosphere. However, in the presence of large hydrometeors and especially frozen hydrometeors, scattering cannot be neglected. Thus, scattering must be considered, and the effects from all directions need to be included. Furthermore, in order to treat po-

larization effects from the surface or hydrometeors, the Stokes formalism needs to be used. The atmospheric radiative transfer simulator (ARTS; [41.16]) is an example of a complex community model that can treat these effects, as well as different geometries. For many applications, a fast model is necessary. In Europe, the radiative transfer for ATOVS (RTTOV) [41.17] is frequently used to calculate synthetic satellite measurements from NWP or climate model output (Sect. 41.8.1).

41.3.1 Surface Emissivity

In principle, the Fresnel equations that describe the reflection and transmission of light at an interface can be used to calculate the frequency dependent emissivity ε_v of a flat water surface for any incidence angle and orthogonal polarization with the water permittivity calculated as a function of temperature and salinity. However, over the oceans, the effects of near surface winds on surface roughness and foam production, as well as the appearance of larger-scale waves and swell influence emissivity. Efficient models have been set up to estimate the emissivity as a function of surface wind speed and direction, sea-surface temperature, and salinity. These models are based on a two-scale approach combining the small-scale effect of ripples and those of large-scale waves that can be treated as an ensemble of facets, for which the Fresnel reflection applies. Estimating the surface coverage of foam and its emissivity is difficult, and several models exist. The dielectric properties of sea water depend upon its temperature and salinity. Salt is a good conductor and contributes to the imaginary part of the dielectric constant for low frequencies. Above 20 GHz, the effect of salinity becomes negligible. Double Debye models have been developed to fit observations [41.18]. The Fast Microwave Emissivity Model (FASTEM) [41.4] is adopted in RTTOV and in the Community Radiative Transfer Model (CRTM). Herein, a two-scale model is parameterized, which is optimized for the frequencies up to 200 GHz that are currently observed. Recently, the Tool to Estimate Sea

Surface Emissivity from Microwave to Submillimeter waves (TESSEM²; [41.19]) became available to handle frequencies above 200 GHz.

Over continental surfaces, the physical modeling of the microwave emissivity is very challenging. First, the interaction of electromagnetic waves with the surface components is very difficult to model, and different schemes have to be developed, depending on the surface types. Second, the land surface emissivity is sensitive to a large number of parameters (e.g., soil moisture, topography, as well as the presence and physical properties of vegetation or snow) and shows a broad spatial and temporal variability. Specific emissivity models have been developed for different surface types, taking into account more or less complex processes. A major obstacle is the limited availability and/or reliability of model inputs (such as soil moisture, snow grain size, vegetation water content). Given the difficulty to model the emissivities of land surfaces and sea ice, they have also been derived directly from satellite observations. The satellite measurements have been exploited to analyze spectral, angular, and polarization dependence of satellite-derived emissivities. The Tool to Estimate the Land Surface Emissivity from the Microwaves to the Millimeter Waves (TELSEM²; [41.5, 6]) provides a parameterization of the emissivity for all observing conditions and for all continental surfaces, given the surface location and month of the year, for frequencies from 6 to 700 GHz.

41.3.2 Atmospheric Gases

In the microwave spectral range, absorption by atmospheric gases can be separated into contributions by resonant transitions (by gases like H₂O, O₂, O₃) and nonresonant absorption. The latter is commonly known as continuum absorption and is less well understood, as the relative contributions of bimolecular absorption and far-wing effects are unclear [41.20]. To describe the absorption coefficient α leading to atmospheric opacity in (41.1), frequently used absorption models describing both resonant and continuum absorption are the one by [41.21] or the Microwave Propagation Model (MPM) by [41.22]. These models only include the major effects of oxygen, nitrogen, and water vapor, while trace gases important for atmospheric chemistry, e.g., O₃, N₂O, or ClO, are not considered. For these gases, whose main absorption features occur above 100 GHz, line catalogues like the high-resolution transmission molecular absorption database (HITRAN; [41.23]) are available. The improvement of absorption models is an ongoing process and is pursued by performing laboratory measurements and radiative closure studies using field measurements. A thorough review on microwave

spectroscopy relevant for the remote sensing of water vapor can be found in [41.24].

The strong absorption features of oxygen and water vapor, around 60 and 183 GHz, respectively (Fig. 41.1), are frequently used by satellite instruments to profile temperature and water vapor, respectively. Within these bands, the atmosphere becomes opaque, and due to the low transmission of the atmosphere, all terms in (41.1), except the first one, can be neglected. However, the temperature of the atmosphere is not constant with altitude, and instead of a simplified BT_{atm} , we need to consider the thermal emission in each height z , depending on its temperature and absorption coefficient, which is subject to attenuation along its path to the satellite. This leads to the definition of the temperature weighting function W_T , which relates the brightness temperature at a frequency ν at the satellite to the atmospheric temperature profile

$$BT_\nu \approx \int_0^\infty W_{T,\nu}(z)T(z)dz, \quad (41.2)$$

with

$$W_{T,\nu}(z) = \alpha_\nu(z)e^{-\int_z^{\text{TOA}} \alpha_\nu(z')dz'}. \quad (41.3)$$

The weighting function at a given frequency describes the contribution of each height to the total signal; W_T is equal to the change in transmission with height [41.25]. As shown in Fig. 41.3, frequency channels in the center of the absorption feature, e.g., 57 GHz, have a strong contribution from the upper atmosphere. In fact, the absorption is so high that emission by lower layers is completely absorbed by higher layers. Therefore, a clear maximum in the weighting function at a certain height is observed. This height constantly moves to lower altitudes the more transparent the atmosphere becomes, i.e., the further the frequency moves away from the center of the absorption feature. For very transparent frequencies, e.g., 31.4 GHz, the maximum contribution stems from the surface.

The broad vertical range of the weighting functions illustrates that temperature profiles can only be retrieved with coarse vertical resolution. Furthermore, the relation between BTs measured at a set of microwave frequencies and the temperature profile is ambiguous. Therefore, retrieval algorithms do not perform a direct matrix inversion but rather stabilize the solution by introducing prior knowledge on the structure of the atmosphere. The simplest algorithms make use of a database of synthetic BTs calculated from a set of typical atmospheric states, for example from radio soundings or NWP output. Statistical algorithms based on linear regressions or neuronal networks are then trained with

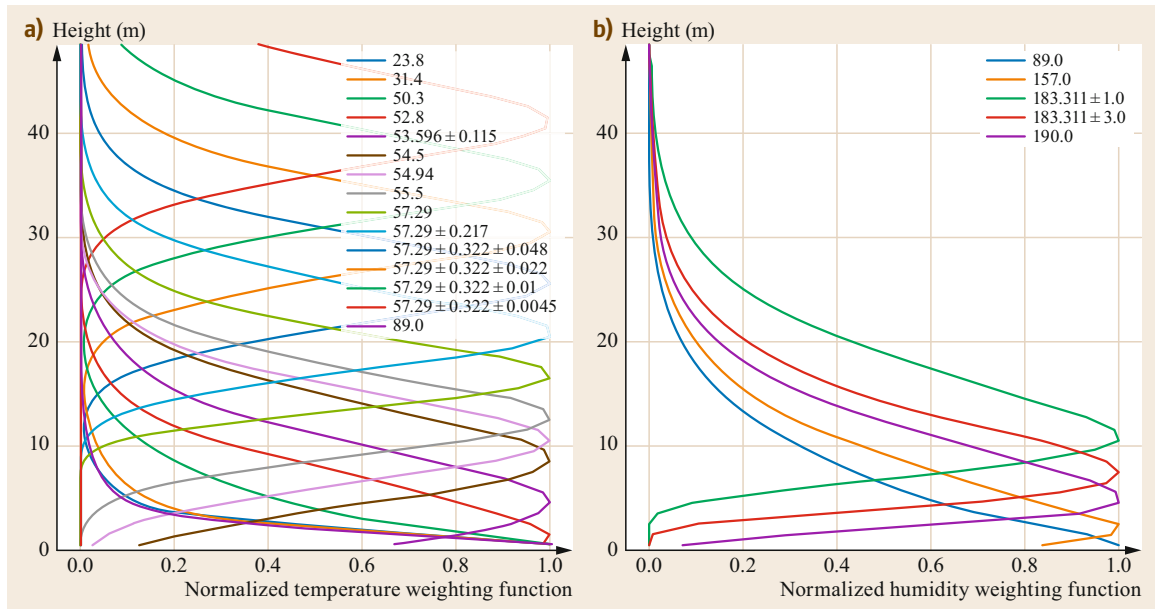


Fig. 41.3a,b Normalized weighting functions for the different frequency channels used by AMSU-A (a) and MHS (b)

the data set. More physically based algorithms employ Bayesian methods for the retrieval.

41.3.3 Atmospheric Hydrometeors

Atmospheric hydrometeors, e.g., cloud droplets, rain drops, ice particles, and graupel, show a large variety in terms of size, shape, density, etc., which determines how they interact with radiation. Cloud droplets with a size of about $10 \mu\text{m}$ are small compared to microwave wavelengths, and, therefore, no significant scattering occurs. Their mass absorption coefficient can be calculated using the Rayleigh approximation, and it increases with frequency. It depends on the dielectric permittivity that is accurately known for temperatures above zero degree Celsius but it is more uncertain for supercooled liquids [41.26].

In general, absorption and scattering of spherical particles can be calculated using Mie theory. With larger rain drops, the shape deviates more and more from a sphere as they become flattened. Therefore, more complex methods to calculate the single-scattering properties are needed. The T-matrix method [41.27] can handle homogeneous, rotationally symmetric, nonspherical particles in fixed and random orientations,

which is suitable to describe absorption and scattering by rain drops. With the axis ratio parameterized as a function of particle size, polarization effects due to the nonspherical shape can be described.

For frozen hydrometeors, particle absorption is mostly negligible compared to scattering, but the situation becomes more complex due to the enormous variety of individual particles in terms of size, shape, density, and orientation. Still, the T-matrix method is frequently employed in the assumption that the single-scattering properties of a spheroid to some extent approximate the ensemble-averaged properties of more realistically shaped particles. For a more accurate description of the single-scattering properties of complex ice particles, the discrete dipole approximation (DDA; [41.28]) can be used. However, besides it being computationally expensive, the problem lies in the realistic description of the size and composition of the particles. To overcome the high computational demand, databases have been generated that contain the single-scattering properties for common shapes and frequencies [41.29–31]. These databases still do not cover the full frequency range, especially for the higher frequencies, as well as more complex particles, such as the ones found in the melting layer.

41.4 Devices and Systems

Microwave radiometers onboard satellites have a similar design to those operated from the ground (Chap. 29). The major difference is in the antenna system, as narrow beams are needed to achieve useful resolution at the Earth's surface. Narrow beams are obtained through large apertures, and therefore the antenna system often becomes the driver in the design of the satellite payload. Currently, microwave radiometers are only employed in low-Earth orbits with typical flight altitudes of about 800 km above the Earth's surface. For example, the EUMETSAT MetOp series is in Sun-synchronous orbit at 827 km passing the Equator at 09:30 LT on its descending branch. With an orbital period of 101 min, about 14 orbits per day are performed. To obtain a broad swath and good global coverage, cross track or conical antenna scanning is exploited. In the following, more details for the three geometries used by microwave instruments are given, together with their advantages and disadvantages (Table 41.5).

41.4.1 Microwave Imagers

The passive microwave imagers are equipped with a conical scanning mechanism that makes it possible to observe with a constant incidence angle, over a set of selected frequencies. Figure 41.4 schematically depicts the scanning configuration of a conically scanning imager like SSM/I or AMSR. For example, AMSR-2, a large-frequency range imager launched in 2012, has an antenna main reflector with a 2 m-diameter and a fixed off-nadir angle of $\theta = 46.5^\circ$ providing an incidence angle of 55° at the surface. It rotates at 40 rounds per minutes to provide successive fields of view (FOV) over a 1450 km swath. AMSR-2 observes at seven frequencies (6.9, 7.3, 10.65, 18.7, 23.8, 36.5, and 89 GHz) in both orthogonal polarizations. The FOV, defined as the intercept between the half-power beam width and the Earth's surface, has an elliptical shape and is largest (35×62 km) at 6 GHz. With a constant antenna size, it is smallest (3×5 km) at 89 GHz, i.e., the shortest wavelength. The receivers are regularly calibrated using hot

and cold references. The cold reference is provided by the deep space, whereas the hot loads are blackbodies at a controlled temperature.

Sun-synchronous passive microwave polar imagers provide a quasi-full coverage of the globe each day, with ≈ 14 orbits. Figure 41.5 presents the descending orbits for half a day from SSMIS on the DMSP-F17 satellite, on 11 November, 2007, for two frequencies (19 and 91 GHz) and both vertical and horizontal polarizations. One can immediately note the difference in atmospheric absorption at these two frequencies: the surface structures appear very clearly at 19 GHz, whereas 91 GHz is clearly more sensitive to the atmospheric features, such as water vapor, cloud, and rain. The polarization difference at 19 GHz is rather large over the ocean and depends upon the wind-induced surface roughness; this effect is exploited to estimate the wind speed of the ocean. Over the poles, the large variability of the surface emissivity at these frequencies is analyzed to extract the ice cover, which can be seen especially well in the Southern Hemisphere.

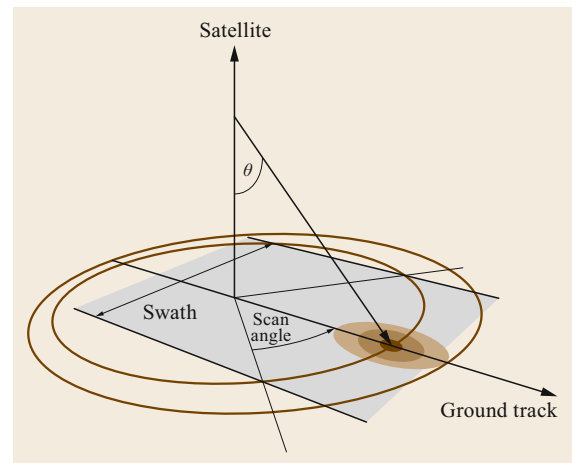


Fig. 41.4 Conical scanning configuration. The color shading illustrates the different FOV sizes at different frequencies, i.e., darker areas indicate higher frequencies

Table 41.5 Advantages and disadvantages of different viewing geometries

Devices	Advantages	Disadvantages
Conical scanning by microwave imagers	<ul style="list-style-type: none"> • Always the same geometry with respect to the surface, and as a consequence, possibility to build an image • Possibility to measure the different polarizations 	<ul style="list-style-type: none"> • Large incidence angle (around 53°) that provides lower spatial resolution than close to nadir views • Calibration issues
Cross track scanning by microwave sounders	<ul style="list-style-type: none"> • Good spatial resolution close to nadir 	<ul style="list-style-type: none"> • Varying observing conditions (incidence angle, polarization) that makes retrieval more complicated
Limb sounders	<ul style="list-style-type: none"> • Good vertical resolution • No impact of the Earth's surface background 	<ul style="list-style-type: none"> • Poor horizontal spatial resolution

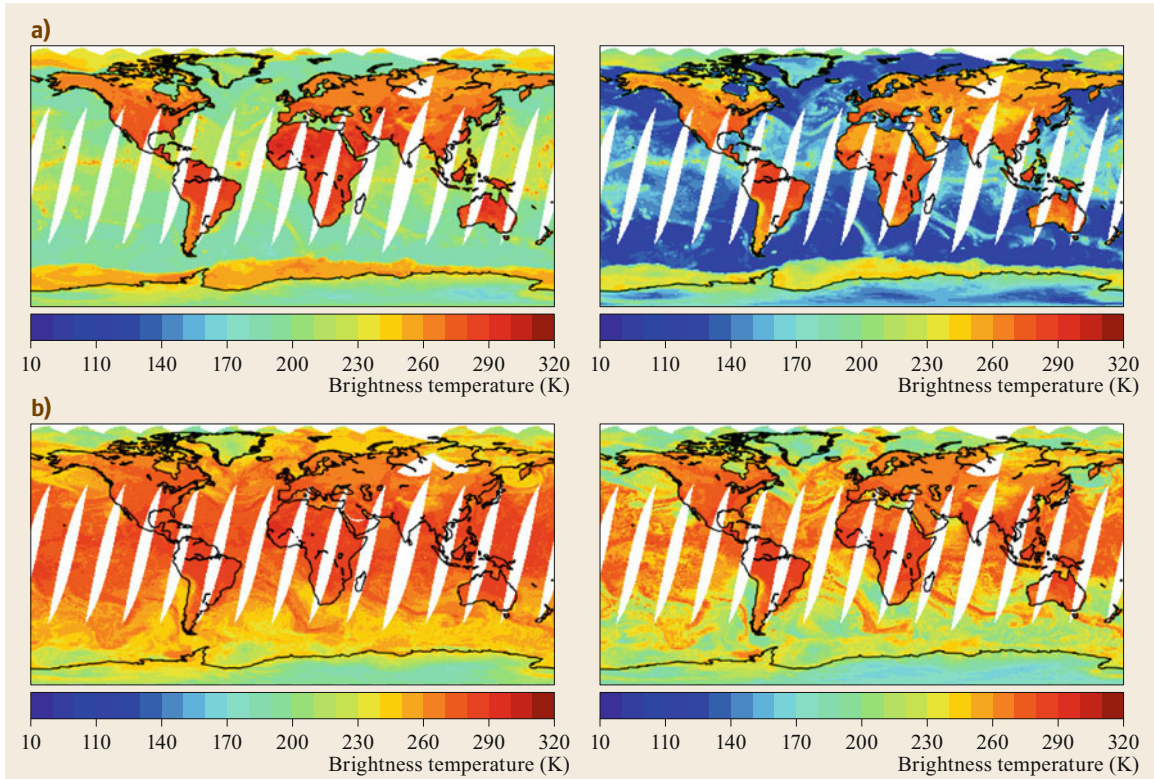


Fig. 41.5a,b Examples of passive microwave images over half a day on 11 November, 2007, from SSMIS (F17) descending orbits, at 19 GHz (a) and 91 GHz (b) for both vertical (*left*) and horizontal (*right*) polarizations

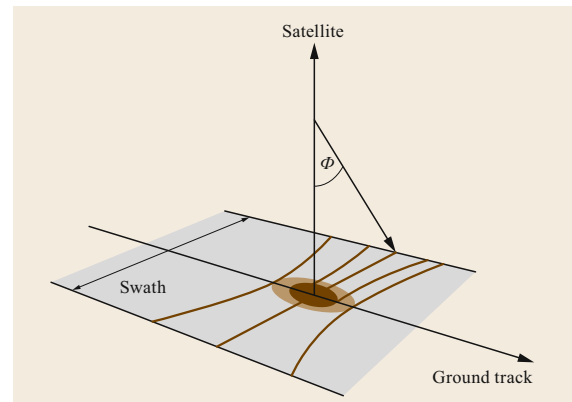
41.4.2 Nadir Sounders

Because nadir sounders like AMSU aim at vertical profiling, the fixed incidence angle at the surface is not necessary and cross-track scanning is employed. AMSU is a cross-track step-scan instrument and executes one complete revolution every 8 s period. The AMSU-A antenna systems have a nominal beamwidth of 3.3° covering a 48 km-diameter FOV at nadir. In each cross-track scan (see Fig. 41.6 for illustration), 30 Earth FOVs within an angular range of $\Phi = \pm 48.3^\circ$ from nadir are performed, as well as one cold calibration towards deep space and one view of the warm blackbody. With 837 km nominal orbital altitude, the swath width is 2074 km. The FOV size increases towards the outermost scan positions of the Earth views. AMSU-A has been mainly designed for temperature profiling with 12 frequency channels along the 60 GHz oxygen absorption complex. Additional channels are located along the weak water vapor line at 23.8 GHz and in two windows,

at 31.4 and 89 GHz, providing information on water vapor and clouds.

AMSU-B and its successor MHS are self-calibrating, cross-track scanning, five-channel microwave, full-power radiometers, operating in the 89 to 190 GHz region dedicated to water vapor profiling. AMSU-A and AMSU-B (or MHS) share the same antenna. Therefore, due its shorter wavelengths AMSU-B/MHS channels have a narrower beamwidth (1.1°), yielding a 15 km

Fig. 41.6 A cross-track scanning configuration. The *color shading* illustrates the different pixel sizes at different frequencies ▶



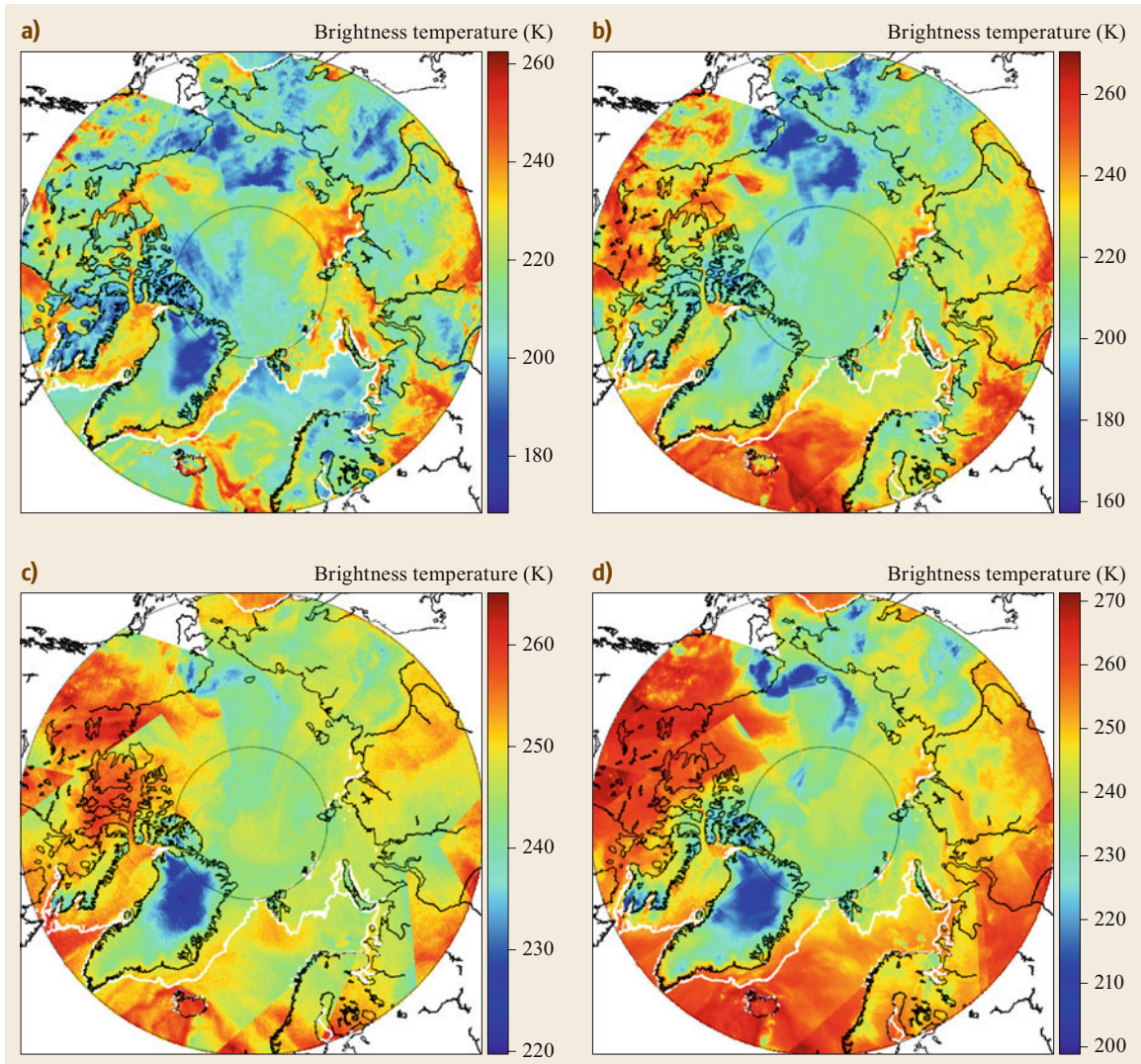


Fig. 41.7a–d Example of the brightness temperatures at 89 (a), 150 (b), (183.31 ± 7) GHz (c), and (183.31 ± 3) GHz (d) for the whole Arctic domain (coverage north of 60°) measured by all AMSU-B/MHS instruments in orbit on the first 6 h (00:00–06:00 UTC) of an individual day (31 March, 2011). The *white contours* mark the area with sea-ice concentration $> 15\%$

resolution at nadir. The instrument is able to scan through 90 Earth views once every 2.667 s.

Polar orbiting satellites have best coverage at high latitudes. Figure 41.7 shows that already within 6 h the whole Arctic is well covered. The example of the brightness temperatures measured by all AMSU instruments in orbit on March 31, 2011 illustrates the strong influence of surface characteristics at the relatively transparent frequency of 89 GHz. Especially the sea-ice margin can be detected well, due to its higher emissivity compared to the open ocean, which is why these measurements are used

to derive sea-ice concentration. At the higher frequency of (183.31 ± 3) GHz surface effects become less apparent, and the higher temporal variability of atmospheric compared to surface features can be seen in the stronger changes between different orbits.

41.4.3 Limb Sounders

Limb sounders avoid the influence of the surface by viewing the Earth's atmosphere along a path that has its closest point to the Earth in the so-called tan-

gent point (Fig. 41.8). By scanning measurements, the

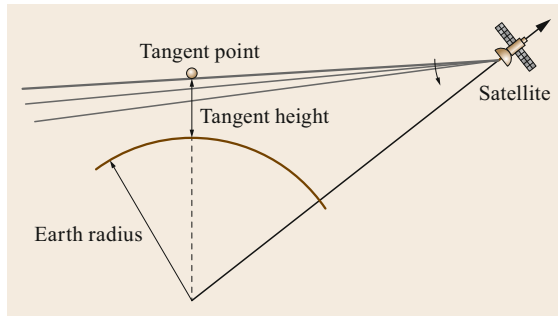


Fig. 41.8 Limb sounding geometry

tangent height can be varied to achieve profile information. This observation technique allows a good vertical resolution, however, at the cost of a relatively large horizontal resolution. The method is therefore best suited for stratospheric and mesospheric measurements with tangent heights typically between 10 and 50 km that can give profile information with about 3 km vertical resolutions. MLS, first launched on UARS in Septem-

41.5 Specifications

Depending on the characteristics of the individual satellite instruments and their observing geometry, the uncertainty in the retrieved parameters is variable. Ta-

ber 1991 and later with spectrally enhanced capabilities on the Aura satellite, has provided vital information for the understanding of stratospheric ozone chemistry and the interaction of atmospheric composition and climate [41.32]. Several atmospheric chemical species (e.g., ClO, BrO, HCl, HNO₃, HO₂, H₂O, N₂O, O₃, OH, and volcanic SO₂) were measured from spectrally highly resolved measurements around absorption lines between 118 GHz and 2.5 THz. Measurements at low tangent heights were used to measure cloud ice to investigate pollution in the upper troposphere.

The joint Swedish, Canadian, Finnish, and French Odin satellite was launched in February 2001 with the submillimeter radiometer (SMR) on board. SMR performed measurements at 486–504 and 541–581 GHz, and one fixed band at 118.75 GHz with spectral resolutions from 150 kHz to 1 MHz [41.33]. The mission served both the astronomical and the atmospheric communities. It provided information on stratospheric ozone, nitric acid, and water vapor, as well as measurements of the upper tropospheric cloud ice.

ble 41.6 gives a rough estimate of these uncertainties and describes the limitations of the products.

Table 41.6 Specification of microwave satellite measurement methods for different parameters

Method	Uncertainty	Limitations
Temperature profile	1–2 K	Coarse vertical resolution
Precipitable water vapor path	1–2 mm	Over ocean surfaces only
Humidity profile	15% RH	Coarse vertical resolution Not possible under low humidity conditions No information on lower atmosphere under moist conditions.
Liquid water path	25 g m ⁻²	Over ocean surfaces only Difficult to distinguish cloud and rain water
Precipitation	20%	Strongly depending on intensity and aggregation time period or region
Ice water path	20%	Not sensitive to very low amounts Depends on the assumptions of particle habit
Ocean wind speed	1 m s ⁻¹	Good sensitivity at rather high wind speeds, less sensitivity at low wind speed Limited sensitivity to wind direction (as compared to the scatterometer)
Soil moisture	< 0.04 m ³ m ⁻³	Rather low spatial resolution (40 km at best), especially when using low microwave frequencies at 1.4 GHz
Land surface temperature	> 2 K	Low spatial resolution and precision as compared to infrared (IR) estimates, but <i>all-weather</i> capability
Sea surface temperature	< 0.5 K	Low spatial resolution and precision as compared to IR estimates, but <i>all-weather</i> capability
Sea surface salinity	< 0.3 PSU (weekly product)	Low spatial resolution due to the necessary use of the 1.4 GHz observations
Sea-ice concentration	15%	Compromise between high spatial resolution (using frequencies > 30 GHz) and high precision (using lower frequencies)
Snow-water equivalent	20% (monthly means)	Significant retrieval errors for individual measurements due to the large variety in snow morphology

41.6 Quality Control

Space agencies employ various quality checks to ensure high accuracy of observed brightness temperatures. In the last years, the degradation of microwave satellite observations due to radio frequency interference (RFI) is becoming more problematic as modern telecommunication systems exploit higher microwave frequencies more and more as they enable higher data rates. The radio regulations at the International Telecommunication Union (ITU) define the frequency bands that are primarily allocated for the passive Earth Exploration Satellite Service (EESS). The intensity of natural microwave radiation from terrestrial and atmospheric sources is generally much lower compared to the intensity from man-made emitters on the ground, on aircraft, or spaceborne systems. Therefore, even an emission outside an allocated band can potentially affect the measurements, as the receiver passband might not completely suppress the external signal. Furthermore, not all satellite frequencies are protected, e.g., 36 GHz, the protected bandwidths are small, and commercial interests threaten even existing protected bands.

The situation is worst at low microwave frequencies due to the high occurrence of RFI sources and the large satellite footprints, which enhance the likelihood for disturbances. SMOS and SMAP (Table 41.3), operating in the passive L band at 1.4 GHz to measure soil moisture and sea salinity, have been particularly severely affected by RFI over continental areas [41.34]. To reduce the effects of RFI, the elimination of illegal sources is attempted, and algorithms to minimize the interference, for example by pulse, frequency or spectrogram blanking have been developed. However, all these techniques reduce observation time. For future missions, RFI resistant receivers are planned for channels that are especially exposed to RFI.

Satellite measurements are mostly used for near-realtime use. However, with the record of conical microwave imagers now covering more than 30 years, climate monitoring is gaining increasing importance. For this purpose, the brightness temperature data from different satellites need to be harmonized, quality controlled, and corrected for different issues to create fundamental climate data records (FCDR). This in-

cludes corrections for cross-track biases, view angle and geolocation errors, emissive reflector issues, solar and lunar intrusions into the warm load, antenna pattern spillover effects, and intercalibration of the instruments. Recently, Berg [41.35] published a > 30 year FCDR using data from a total of 14 research and operational conical-scanning microwave imagers. The data by the SSM/I and SSMIS instruments are available at <http://rain.atmos.colostate.edu/FCDR/>, Accessed 15 July 2021. An interim climate data record is updated in near realtime, and updates to the FCDR are done once a year. With the advent of the GPM, also NASA developed a Level 1C FCDR dataset, available at <https://pmm.nasa.gov/data-access/downloads/gpm>, Accessed 15 July 2021, which has been extended back in time to the SSM/I on board DMSP F08 in July 1987. The imager observations have recently been carefully intercalibrated at the Climate Satellite Application Facility (Climate SAF) under EUMETSAT support and are provided to the community with a quality compatible with climate applications (https://wui.cmsaf.eu/safira/action/viewDoiDetails?acronym=FCDR_MWI_V002, Accessed 15 July 2021).

For nadir sounders, AMSU-A, AMSU-B, and MHS have been in operation since 1998, starting with the launch of NOAA-15 (Table 41.3). In order to arrive at a consistent FCDR, the thorough treatment of cross-scan asymmetry of AMSU-A window channels is of high importance. Ferraro [41.36] utilized a brightness temperature CDR for these satellites to create a dataset called the *Hydrological Bundle* which consists of thematic CDRs (TCDRs) for precipitable water, cloud liquid water, sea-ice concentration, land surface temperature, land surface emissivity for 23, 31, and 50 GHz, rain rate, snow cover, ice-water path, and snow-water equivalent.

Since 2011, ATMS has been combining the capacity of AMSU-A and B in a single compact instrument on board the Suomi National Polar-Orbiting Partnership (NPP) program, with performances superior to AMSU. Based on pitch manoeuvre, a physical model has been developed to correct the scan bias that is often an issue with cross-track scanners [41.37].

41.7 Maintenance

Before launch, satellite instruments are thoroughly tested to check whether they fulfill the requirements, and preliminary calibrated parameters are derived. Past launch a systematic calibration and validation

(CAL/VAL) phase takes place to check the instrumental performances with real orbit data before official data are released. The cold space with the well-known cosmic background serves as the most reliable reference target

and can be used to check whether the radiometric temperature sensitivity (noise equivalent differential temperature, NEDT), i.e., the minimum change in a scene radiometric temperature that can be detected, agrees with prelaunch values. Several checks like systematic differences between ascending and descending overpasses, the spectral dependence of different channels over well-defined surfaces like the ocean, or the variation of long-

term brightness temperature means across track are studied [41.38] for the CAL/VAL assessment of MetOp AMSU instrument. During the lifetime of the satellite instrument, long-term trends in NEDT and housekeeping parameters are continuously monitored to track the instrument performance and system stability. Any maintenance, e.g., the orbit adjustment, is performed by space agencies and depends on the individual mission.

41.8 Application

Microwave satellite measurements are used for a manifold of applications. Here, we only provide a few examples with respect to numerical weather prediction and climate monitoring.

41.8.1 Numerical Weather Prediction (NWP)

Both conical imagers (Sect. 41.4.1) and nadir sounders (Sect. 41.4.2) have become essential ingredients for NWP worldwide. Measurements made by microwave temperature and humidity probes are used in global and regional scale weather forecast models within the *assimilation* process [41.39]. At first, retrieval products from microwave measurements, e.g., temperature profiles, were assimilated. *Gerard and Saunders* [41.40] first used a 1-D variational retrieval for total columnar water vapor from SSM/I measurements at the European Center for Medium-Range Weather Forecasts (ECMWF) forecast model. In a second step, the retrievals were then assimilated using the operational, 4-D variational (4DVar) analysis at ECMWF.

In order to directly assimilate microwave measurements into an NWP model, a fast-forward model is needed to calculate the measurements from the NWP model output. As shown in Fig. 41.9, by using the prognostic temperature, moisture, hydrometeor, and further information from model output, synthetic brightness temperatures can be calculated. Herein it is important that similar assumptions to those in the NWP model are made in the radiative transfer (RT), e.g., the size and shape of hydrometeor particles. However, in order to be computationally efficient fast models are needed, which, for example, employ simplified approaches to scattering. To improve the NWP model using the difference between the synthetic and the real measurements, most assimilation schemes need an adjoint version of the fast RT model. An example for this is the RT-TOV model [41.17], which is used by many operational weather centers.

Together with other satellite measurements and in addition to classical synoptic data, microwave measure-

ments describe the atmospheric column with more precision and allow an improvement of the meteorological forecast. In fact, observations from microwave temperature sounders like AMSU-A are those contributing the most to the improvement of weather prediction, among all the observations assimilated [41.41]. This important impact comes not only from the high information content of each microwave observation, but also from the fact that more data are assimilated, since they are less contaminated by clouds than other satellite observations. This is despite the low intrinsic data volume provided by AMSU compared to high spectral resolution infrared sounders, such as the Atmospheric Infrared Sounder (AIRS) or the Infrared Atmospheric Sounding Interferometer (IASI) (Fig. 41.10).

41.8.2 Earth System and Climate Monitoring

The fact that microwave satellite observations of sufficient quality have now been available for three decades offers the opportunity to build climatological records and to investigate trends of different variables. Most frequently, retrievals from conical imagers, e.g., SSM/I, are used as they provide homogeneous records since 1987. However, for atmospheric parameters they are limited to open water surfaces.

In a warmer climate, it is expected that with constant relative humidity the water vapor increases, and due to its strong greenhouse gas effect, the water vapor feedback amplifies warming. Recently, *Mears* [41.43] combined measurements from 11 satellites and found an increase of about 1.5% in precipitable water vapor per decade over the global ice-free oceans for the time period from 1988 to 2017. In absolute numbers, the trend is highest in the deep tropics (20° S–20° N) with 0.63 kg m⁻² per decade.

Passive microwave observations from conical imagers are also playing a key role in the quantification of the decline of the Arctic sea-ice cover over the last decades. The methodology to estimate the ice cover is based on the large difference in emissivity between the

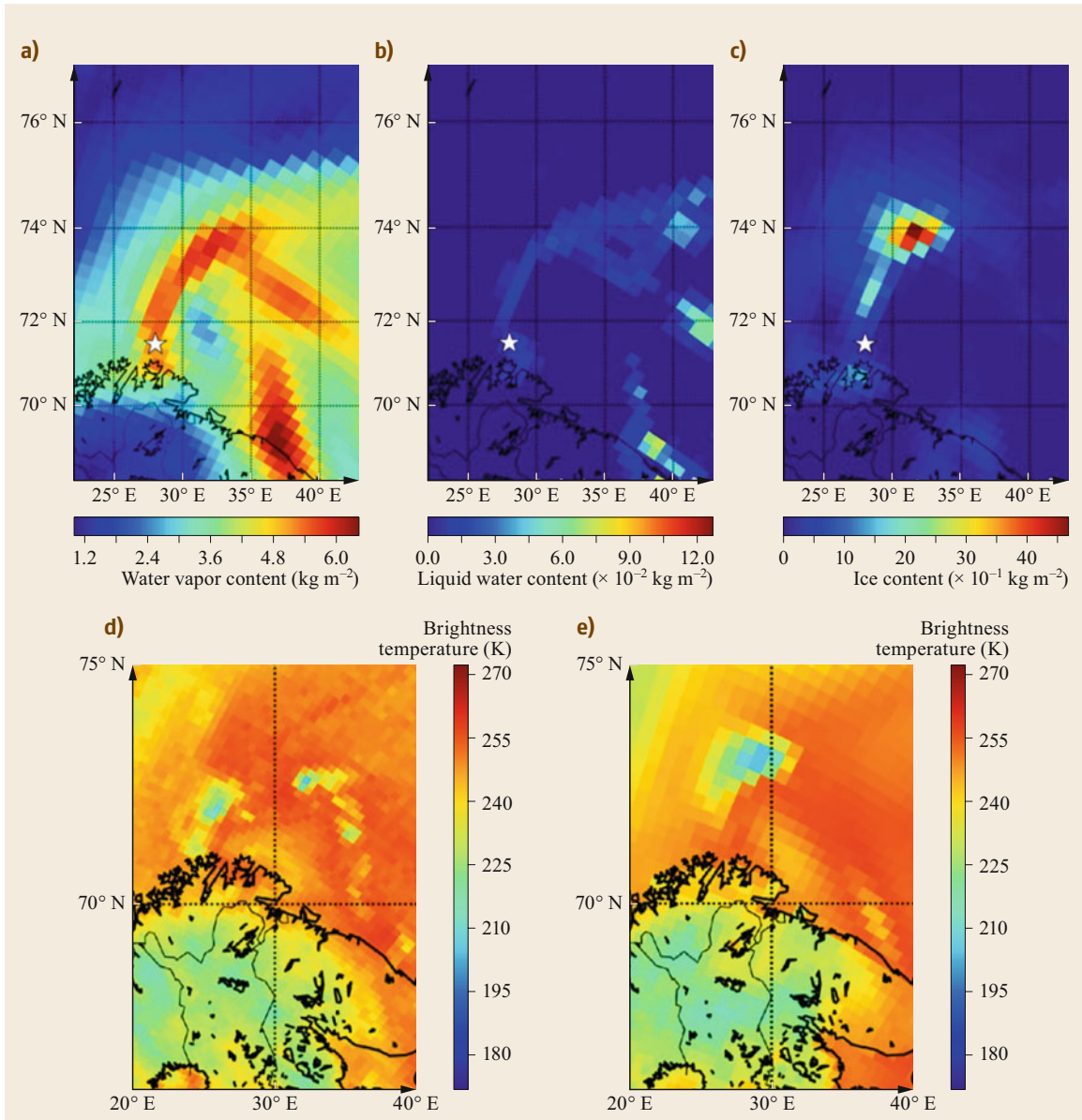


Fig. 41.9 (a) Vertically integrated water vapor; (b) sum of cloud and rain liquid water content, (c) sum of cloud ice, graupel, and snow, all from the Arctic System Reanalysis (ASR); the *star* marks the center of the polar low in (a–c); (183.31 ± 7) GHz BT observed by AMSU-B (d) and simulated BT based on ASR (e)

open ocean and the ice, from 6 and 90 GHz. The higher the frequency, the better the spatial resolution but at the expense of the uncertainty in the ice cover. A continuous series of consistent passive microwave observations from SMMR, SSM/I, and SSMIS have been available since 1978 to provide sea-ice cover over the poles. Fig-

ure 41.11 shows the monthly anomalies in ice area in the Northern Hemisphere, from 1978 to 2016, as estimated from different algorithms [41.44]. Regardless of the retrieval methodology, a similar significant decline in the ice cover is observed, giving rise to a strong confidence in these passive microwave estimates.

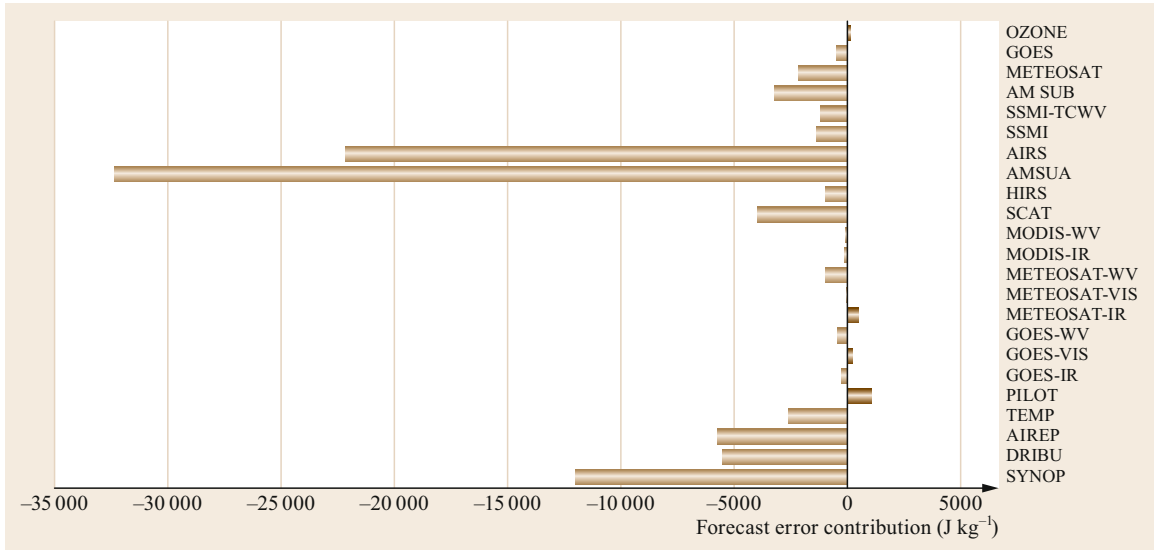


Fig. 41.10 The contribution of different data sources, satellite and in-situ, to the ECMWF assimilation system. The error reduction for each type of data is indicated: the more the number is negative, the more the data contribute to the reduction of error (after [41.42] with permission from Wiley and Sons)

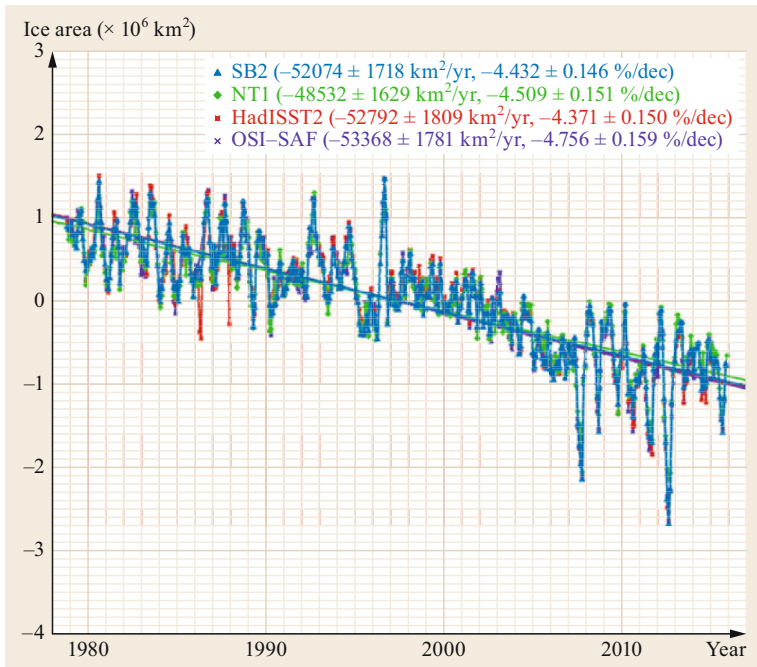


Fig. 41.11 Monthly anomaly in the sea-ice area in the Northern Hemisphere, as estimated from different algorithms from a series of passive microwave instruments (SMMR, SSM/I, SSMIS) (after [41.44] with permission from Wiley and Sons)

41.9 Future Developments

Microwave measurements are sensitive to a wide range of atmospheric and surface parameters. Contrary to infrared observations that are blocked by clouds, passive microwave observations at low frequencies can, for example, provide estimates of SST in all weather conditions except rain. The merging of the infrared and passive microwave SST estimates are today used for operational purposes not only for SST but also for precipitation.

The potential of miniaturized satellites to provide more flexible and higher resolved observations is currently investigated within different projects. The Time-Resolved Observations of Precipitation structure and storm Intensity with a Constellation of Smallsats (TROPICS) mission [41.45] is scheduled for launch in 2022 by NASA. It will combine six CubeSats, each equipped with radiometers between 90 and 205 GHz to provide a median refresh rate better than 60 min in the tropics to observe thermodynamics and precipitation structure over the entire storm lifecycle. In the framework of the Temporal Experiment for Storms and Tropical Systems – Demonstration [41.46] six CubeSats were deployed from the International Space Station in July 2018 observing at 5 millimeter-wave frequencies from 89 to 182 GHz. In order to reduce the sensitivity to RFI the CubeRRT (CubeSat Radiometer Radio Frequency Interference Technology Validation)

mission [41.47] investigates on-board realtime RFI processing.

The next generation of European operational meteorological satellites planned after 2020 (Metop-SG) will be equipped with two passive microwave instruments MWI and ICI, in addition to MWS sounder for temperature and humidity. With the ICI instrument, observations above 200 GHz will be made for the first time for operational meteorology. These measurements will have a high sensitivity to ice in the clouds and will allow an estimate of the ice content in the clouds, a variable that is currently poorly known. Currently, an aircraft demonstrator has been developed and installed on a British aircraft, and the community is analyzing these new observations, between 183 and 700 GHz.

In addition, a conical scanning radiometer between 1.4 and 37 GHz and a large antenna (ca. 7 m) are under study in Europe, for high-resolution *all-weather* observations of the polar regions, within the Copernicus program: the Copernicus Imaging Microwave Radiometer (CIMR) [41.48]. With no guarantee of successors to AMSR2, SMOS, and SMAP, the CIMR mission will provide continuity in the observations of low-frequency microwave measurements with much improved radiometric and/or spatial characteristics for all-weather observations of key surface parameters over all surface types.

41.10 Further Readings

A thorough introduction into microwave radiometry is given by:

- M.A. Janssen (Ed.): Atmospheric Remote Sensing by Microwave Radiometry (Wiley, New York 1993)
- F.T. Ulaby and D.G. Long: Microwave Radar and Radiometric Remote Sensing, (Artech House, Boston 2015)
- C. Maetzler, (Ed.): Thermal Microwave Radiation: Applications for Remote Sensing, (The Institution of Engineering and Technology, Stevenage 2006)
- The Microwave Remote Sensing Topics Distance Learning Course provided by COMET (https://www.meted.ucar.edu/training_course.php?id=15, Accessed 15 July 2021) gives insights into theory and application.

Acknowledgments. The authors would like to thank the reviewer for the helpful suggestions and Ana Radovan for producing Fig. 41.7.

References

- 41.1 A.J. Geer, B. Fabrizio, N. Bormann, S. English: *All-Sky Assimilation of Microwave Humidity Sounders*, European Centre for Medium-Range Weather Forecasts Newsletter 2014). <https://www.ecmwf.int/sites/default/files/elibrary/2014/17339-all-sky-assimilation-microwave-humidity-sounders.pdf>, Accessed 15 July 2021
- 41.2 S. Schnitt, E. Orlandi, M. Mech, A. Ehrlich, S. Crewell: Characterisation of water vapor and clouds during the next-generation aircraft remote-sensing for validation (NARVAL)-south studies, IEEE

- J. Sel. Top. Earth Obs. Remote Sens. (JSTARS) **10**(7), 3114–3124 (2017)
- 41.3 P.W. Gaiser, K.M. St. Germain, E.M. Twarog, G.A. Poe, W. Purdy, D. Richardson, W.L. Jones, D. Spencer, G. Golba, J. Cleveland, L. Choy, R.M. Bevilacqua: The windsat Spaceborne polarimetric microwave radiometer: sensor description and early orbit performance, *IEEE Trans. Geosci. Remote Sens.* **42**(11), 2347–2361 (2004)
- 41.4 Q. Liu, F. Weng, S. English: An improved fast microwave water emissivity model, *IEEE Trans. Geosci. Remote Sens.* **49**, 1238–1250 (2001)
- 41.5 F. Aires, C. Prigent, F. Bernardo, C. Jimenez, R. Saunders, P. Brunel: A tool to estimate land-surface Emissivities at microwave frequencies (TELSEM) for use in numerical weather prediction, *Q. J. R. Meteorol. Soc.* **137**, 690–699 (2011)
- 41.6 D. Wang, C. Prigent, L. Kilic, S. Fox, C. Harlow, C. Jimenez, F. Aires, C. Grassotti, F. Karbou: Surface emissivity at microwaves to millimeter waves over polar regions: parameterization and evaluation with aircraft experiments, *J. Atmos. Ocean. Technol.* **34**(5), 1039–1059 (2017)
- 41.7 H. Brogniez, S. English, J.-F. Mahfouf, A. Berendt, W. Berg, S. Boukabara, S.A. Buehler, P. Chambon, A. Gambacorta, A. Geer, W. Ingram, E.R. Kursinski, M. Matricardi, T.A. Odintsova, V.H. Payne, P.W. Thorne, M.Y. Tretyakov, J. Wang: A review of sources of systematic errors and uncertainties in observations and simulations at 183 GHz, *Atmos. Meas. Tech.* **9**, 2207–2221 (2016)
- 41.8 N.C. Grody: Classification of snow cover and precipitation using the Special Sensor Microwave Imager, *J. Geophys. Res.* **96**, 7423–7435 (1991)
- 41.9 H. Meng, J. Dong, R. Ferraro, B. Yan, L. Zhao, C. Kongoli, N. Wang, B. Zavadsky: A 1DVAR-based snowfall rate retrieval algorithm for passive microwave radiometers, *J. Geophys. Res.* **122**, 6520–6540 (2017)
- 41.10 D.H. Staelin, A.H. Barrett, J.W. Waters, F.T. Barath, E.J. Johnston, P.W. Rosenkranz, N.E. Gaut, W.B. Lenoir: Microwave spectrometer on the Nimbus 5 satellite: meteorological and geophysical data, *Science* **182**(4119), 1339–1341 (1973)
- 41.11 P. Gloersen, F.T. Barath: A scanning multichannel microwave radiometer for Nimbus-G and SeaSat-A, *IEEE J. Ocean. Eng.* **2**, 172–178 (1977)
- 41.12 R.F. Adler, G. Gu, M. Sapiano, J.J. Wang, G.J. Huffman: Global precipitation: A review, variations and trends during the satellite era (1979–2014), *Surv. Geophys.* **38**(4), 679–699 (2017)
- 41.13 F.T. Ulaby, D.G. Long: *Microwave Radar and Radiometric Remote Sensing* (ARTECH House, Boston 2015)
- 41.14 R.M. Goody, Y.L. Yung: *Atmospheric Radiation, Theoretical Basis*, 2nd edn. (Oxford Univ., Oxford 1995) p. 544
- 41.15 G.W. Petty: *A First Course in Atmospheric Radiation*, 2nd edn. (SunDog Publishing, Madison 2006) p. 459
- 41.16 S.A. Buehler, J. Mendrok, P. Eriksson, A. Perrin, R. Larsson, O. Lemke: ARTS, the Atmospheric Radiative Transfer Simulator—Version 2.2, the Planetary Toolbox edition, *Geosci. Model Dev.* **11**(4), 1537–1556 (2018)
- 41.17 R. Saunders, J. Hocking, E. Turner, P. Rayer, D. Rundle, P. Brunel, J. Vidot, P. Roquet, M. Matricardi, A. Geer, N. Bormann, C. Lupu: An update on the RTTOV Fast Radiative Transfer Model, *Geosci. Model Dev.* **11**, 2717–2737 (2018)
- 41.18 W.J. Ellison, A. Balana, G. Delbos, K. Lamkaouchi, L. Eymard, C. Guillou, C. Prigent: New permittivity measurements of seawater, *Radio Sci.* **33**(3), 639–648 (1998)
- 41.19 C. Prigent, F. Aires, D. Wang, S. Fox, C. Harlow: Sea surface emissivity parameterization from microwaves to millimeter waves, *Q. J. R. Meteorol. Soc.* **143**, 596–605 (2017)
- 41.20 V.H. Payne, E.J. Mlawer, K.E. Cady-Pereira, J.-L. Moncet: Water vapor continuum absorption in the microwave, *IEEE Trans. Geosci. Remote Sens.* **49**(6), 2194–2208 (2011)
- 41.21 P.W. Rosenkranz: Water vapor microwave continuum absorption: A comparison of measurements and models, *Radio Sci.* **33**(4), 919–928 (1998)
- 41.22 H.J. Liebe, G.A. Hufford, M.G. Cotton: Propagation modeling of moist air and suspended water/ice particles at frequencies below 1000 GHz. In: *AGARD, Atmospheric Propagation Effects Through Natural and Man-Made Obscurants for Visible to MM-Wave Radiation*, 542,1993 pp. 3.1–3.11
- 41.23 L.S. Rothman, A. Barbe, D.C. Benner, L.R. Brown, C. Camy-Peyret, M.R. Carleer, K. Chance, C. Clerbaux, V. Dana, V.M. Devi, A. Fayt, J.-M. Flaud, R.R. Gamache, A. Goldman, D. Jacquemart, K.W. Jucks, W.J. Lafferty, J.-Y. Mandin, S.T. Massie, V. Nemtchinov, D.A. Newnham, A. Perrin, C.P. Rinsland, J. Schroeder, K.M. Smith, M.A.H. Smith, K. Tang, R.A. Toth, J. Vander Auwera, P. Varanasi, K. Yoshino: The HITRAN Molecular Database: Editions of 1991 and 1992, *J. Quant. Spectrosc. Radiat. Transf.* **48**, 469–507 (1992)
- 41.24 M.Y. Tretyakov: Spectroscopy underlying microwave remote sensing of atmospheric water vapor, *J. Mol. Spectrosc.* **328**, 7–26 (2016)
- 41.25 M.A. Janssen: *Atmospheric Remote Sensing by Microwave Radiometry* (J. Wiley & Sons, New York 1993) pp. 1–36
- 41.26 D.D. Turner, S. Kneifel, M.P. Cadeddu: An improved liquid water absorption model at microwave frequencies for Supercooled liquid water clouds, *J. Atmos. Oceanic Technol.* **33**, 33–44 (2016)
- 41.27 M.I. Mishchenko, L.D. Travis, D.W. Mackowski: T-matrix computations of light scattering by nonspherical particles: A review, *J. Quant. Spectrosc. Radiat. Transf.* **55**, 535–575 (1996)
- 41.28 M.A. Yurkin, A.G. Hoekstra: The discrete dipole approximation: An overview and recent developments, *J. Quant. Spectrosc. Radiat. Transf.* **106**(1–3), 558–589 (2007)
- 41.29 P. Eriksson, R. Ekelund, J. Mendrok, M. Brath, O. Lemke, S.A. Buehler: A general database of Hydrometeor single scattering properties at microwave and sub-millimetre wavelengths, *Earth Syst. Sci. Data* **10**, 1301–1326 (2018)
- 41.30 G. Hong, P. Yang, B.A. Baum, A.J. Heymsfield, F. Weng, Q. Liu, G. Heygster, S.A. Buehler: Scatter-

- ing database in the millimeter and Submillimeter wave range of 100–1000 GHz for nonspherical ice particles, *J. Geophys. Res.* **114**, D06201 (2009)
- 41.31 G. Liu: A database of microwave single-scattering properties for nonspherical ice particles, *Bull. Amer. Met. Soc.* **89**(10), 1563–1570 (2008)
- 41.32 J.W. Waters, W.G. Read, L. Froidevaux, R.F. Jarnot, R.E. Cofield, D.A. Flower, G.K. Lau, H.M. Pickett, M.L. Santee, D.L. Wu, M.A. Boyles, J.R. Burke, R.R. Lay, M.S. Loo, N.J. Livesey, T.A. Lungu, G.L. Manney, L.L. Nakamura, V.S. Perun, B.P. Ridenoure, Z. Shippony, P.H. Siegel, R.P. Thurstans, R.S. Harwood, H.C. Pumphrey, M.J. Filipiak: The UARS and EOS microwave limb sounder (MLS) experiments, *J. Atmos. Sci.* **56**(2), 194–218 (1999)
- 41.33 U. Frisk, M. Hagström, J. Ala-Laurinaho, S. Andersson, J.-C. Berges, J.-P. Chabaud, M. Dahlgren, A. Emrich, H.-G. Florén, G. Florin, M. Fredrixon, T. Gaier, R. Haas, T. Hirvonen, Å. Hjalmarsson, B. Jakobsson, P. Jukkala, P. Kildal, E. Kollberg, J. Lassing, A. Lecacheux, P. Lehikoinen, A. Lehto, J. Mallat, C. Marty, D. Michet, J. Narbonne, M. Nexon, M. Olberg, O. Olofsson, G. Olofsson, A. Origné, M. Petersson, P. Piironen, R. Pons, D. Poulliquen, I. Ristocelli, C. Rosolen, G. Rouaix, A.V. Räisänen, G. Serra, F. Sjöberg, L. Stenmark, S. Torchinsky, J. Tuovinen, C. Ullberg, E. Vinterhav, N. Wadefalk, H. Zirath, P. Zimmermann, R. Zimmermann: The Odin satellite: I. radiometer design and test, *Astron. Astrophys.* **402**, 27–34 (2003)
- 41.34 R. Oliva, E. Daganzo, Y.H. Kerr, S. Mecklenburg, S. Nieto, P. Richaume, C. Gruhier: SMOS radio frequency interference scenario: status and actions taken to improve the RFI environment in the 1400–1427 MHz passive band, *IEEE Trans. Geosci. Remote Sens.* **50**(5), 1427–1439 (2012)
- 41.35 W. Berg, R. Kroodsma, C. Kummerow, D. McKague: Fundamental climate data records of microwave brightness temperatures, *Remote Sens.* **10**(8), 1306 (2018)
- 41.36 R. Ferraro, B. Nelson, T. Smith, O. Prat: The AMSU-based hydrological bundle climate data record—description and comparison with other data sets, *Remote Sens.* **10**(10), 1640 (2018)
- 41.37 E. Kim, C.H. Lyu, K. Anderson, R.V. Leslie, W.J. Blackwell: S-NPP ATMS instrument prelaunch and on-orbit performance evaluation, *J. Geophys. Res. Atmos.* **119**(9), 5653–5670 (2014)
- 41.38 T. Mo: Post-launch calibration of the METOP-A advanced microwave sounding unit-A, *IEEE Trans. Geosci. Remote Sens.* **46**(11), 3581–3600 (2008)
- 41.39 J.R. Eyre, G.A. Kelly, A.P. McNally, E. Andersson, A. Persson: Assimilation of TOVS radiance information through one-dimensional variational analysis, *Q. J. R. Meteorol. Soc.* **119**(514), 1427–1463 (1993)
- 41.40 E. Gerard, R. Saunders: Four-dimensional variational assimilation of special sensor microwave/imager total column water vapour in the ECMWF model, *Q. J. R. Meteorol. Soc.* **119**(514), 1427–1463 (1993)
- 41.41 P. Bauer, A. Geer, P. Lopez, D. Salmond: Direct 4D-Var assimilation of All-Sky radiances. Part I: Implementation, *Q. J. R. Meteorol. Soc.* **136**(652), 1868–1885 (2010)
- 41.42 C. Cardinali: Monitoring the observation impact on the short-range forecast, *Q. J. R. Meteorol. Soc.* **135**(638), 239–250 (2009)
- 41.43 C.A. Mears, D.K. Smith, L. Ricciardulli, J. Wang, H. Huelsing, F.J. Wentz: Construction and uncertainty estimation of a satellite-derived total precipitable water data record over the world's oceans, *Earth Space Sci.* **5**, 197–210 (2018)
- 41.44 J.C. Comiso, W.N. Meier, R. Gersten: Variability and trends in the arctic sea ice cover: Results from different techniques, *J. Geophys. Res. Oceans* **122**(8), 6883–6900 (2017)
- 41.45 W.J. Blackwell, S. Braun, R. Bennartz, C. Velden, M. DeMaria, R. Atlas, J. Dunion, F. Marks, R. Rogers, B. Annane, R.V. Leslie: An overview of the TROPICS NASA Earth Venture Mission, *Q. J. R. Meteorol. Soc.* **144**(Suppl. 1), 16–26 (2018)
- 41.46 Colorado State University: Temporal Experiment for Storms and Tropical Systems (TEMPEST): <https://tempest.colostate.edu/>, Accessed 15 July 2021
- 41.47 Jet Propulsion Laboratory: CubeSat Radiometer Radio Frequency Interference Technology Validation mission <https://www.jpl.nasa.gov/cubesat/missions/cuberrt.php>, Accessed 15 July 2021
- 41.48 L. Kilic, C. Prigent, F. Aires, J. Boutin, G. Heygster, R.T. Tonboe, H. Roquet, C. Jimenez, C. Donlon: Expected performances of the Copernicus Imaging Microwave Radiometer (CIMR) for an all-weather and high spatial resolution estimation of ocean and sea ice parameters, *J. Geophys. Res. Ocean.* **123**(10), 7564–7580 (2018)

Susanne Crewell

Institute for Geophysics and Meteorology
University of Cologne
Köln, Germany
susanne.crewell@uni-koeln.de



Susanne Crewell is a Professor for Meteorology at the University of Cologne (Germany). She received her PhD at the University of Bremen in 1993. She has been active in the field of microwave remote sensing, including instrument development for more than two decades, covering ground-based, airborne, and satellite measurements for different applications emphasizing a better understanding of atmospheric water cycle processes.

Catherine Prigent

LERMA
CNRS, Observatoire de Paris
Paris, France
catherine.prigent@obspm.fr



Catherine Prigent is a researcher at the Centre National de la Recherche Scientifique (CNRS, Paris). She received a PhD in Physics from Paris University (1988) and worked at the NASA/Goddard Institute for Space Studies (1995–2000). Her research covers satellite microwave remote sensing of the Earth, for both surface and atmosphere characterization, for global applications. She is involved in the preparation of several satellite instruments with ESA, EUMETSAT, and CNES.

Mario Mech

Institute for Geophysics and Meteorology
University of Cologne
Köln, Germany
mario.mech@uni-koeln.de



Mario Mech is Senior Research Scientist of Meteorology at the Institute for Geophysics and Meteorology at the University of Cologne in Germany. He received his PhD in Meteorology in 2008 from the University of Cologne. His research focus is airborne remote sensing of clouds and precipitation and the simulation of active and passive radiative transfer in cloudy atmospheres for the microwave wavelength region.

Imaging Tech

42. Imaging Techniques

Jan Cermak , Isabel F. Trigo , Julia Fuchs 

This chapter introduces techniques for characterizing the properties of the Earth's surface and atmosphere using satellite sensors. The utilization of passive imagers to measure visible and infrared radiation is at the focus of this chapter.

42.1	Measurement Principles and Parameters	1171	42.4	Devices and Systems	1177
42.2	History	1172	42.4.1	Satellite Systems and Orbits	1177
42.2.1	Surface Parameters	1173	42.4.2	Product Suites and Comparisons	1178
42.2.2	Atmospheric Quantities	1174	42.5	Specifications	1179
42.3	Theory	1175	42.6	Quality Control	1180
42.3.1	Surface Parameters	1175	42.7	Maintenance	1180
42.3.2	Atmospheric Quantities	1176	42.8	Applications	1180
			42.9	Future Developments	1180
			42.10	Further Reading	1182
			References		1182

Earth observation satellites are among the most important means of gathering information about our planet, as they can be used to monitor the various physical, chemical, and biological states and processes that drive the climate and influence the environment. Imaging techniques are methods of creating two-dimensional spatial representations of geophysical parameters, i.e., *images*.

In this chapter, we discuss imaging techniques used by passive-sensor satellite systems that observe the visible (solar) and infrared (terrestrial) ranges of the electromagnetic spectrum. These techniques can be used to characterize either the Earth's surface or its atmosphere. Both of these aims are considered in detail in this chapter.

42.1 Measurement Principles and Parameters

In a classical satellite imaging approach, a sensor mounted on an Earth observation (EO) satellite measures radiation from a target. This radiation reaches the sensor from a variety of directions and angles. The measurements are then mapped onto a data array in a very similar way to the sensor of a digital camera. If the sensor performs *passive* imaging, the radiation from the target was originally generated by a natural source (in contrast to *active* imaging, where the radiation from the target was originally produced by an artificial source on the satellite platform). Thus, passive sensor systems observe radiation that originated from the Sun (visible radiation) or the Earth's surface (infrared radiation). The measurements obtained by these sensors are used to evaluate surface and atmospheric parameters such

as the surface temperature, vegetation and snow cover, cloud properties, aerosol optical depth, and radiation fluxes [42.1]. Satellite imagers provide measurements of large areas, ranging up to the global scale. Depending on the imaging width (swath width) of the sensor and the orbit of the satellite, sampling can be performed at temporal frequencies that complement in-situ observations [42.2]. Geophysical parameters can be extracted from top-of-atmosphere radiances measured by a satellite-based sensor by exploiting the interaction between electromagnetic radiation and the atmosphere and/or the surface via absorption, scattering, emission (thermal or not), or refraction, as further discussed in Sect. 42.3.

A wide range of parameters pertaining to atmospheric or surface properties are retrieved from satellite

Table 42.1 Parameters associated with the Earth's surface (a nonexhaustive list)

Parameter	Description	Unit	Symbol
Land or sea surface temperature	The radiometric temperature of the land or sea surface, corresponding to an aggregated value within the sensor's field of view.	K	LST and SST
Albedo	The ratio of the radiation flux reflected by the surface in all directions to the incoming solar irradiance.	–	AL
Vegetation indices	Combination of radiances measured in two or more channels in the visible and near-infrared that is utilized to identify vegetated areas and the spatiotemporal variability of these areas. This chapter considers the normalized difference vegetation index (NDVI) and the enhanced vegetation index (EVI).	–	NDVI and EVI
Leaf area index	One-half of the total leaf area per unit ground area, accounting for the leaf surface present in a vertical column normalized to its cross-sectional area.	$\text{m}^2 \text{m}^{-2}$	LAI
Fraction of the photosynthetically active radiation absorbed	Fraction of the solar energy incident on the surface that is absorbed by vegetation for photosynthesis.	–	FAPAR
Snow cover/fraction	At the pixel level, this usually corresponds to a yes/no classification for presence of snow. The corresponding aggregation allows the snow cover to be estimated at a lower spatial resolution.	%	SC
Fire radiative power	The total rate at which identified fires are emitting thermal radiation, integrated over all wavelengths and directions.	W m^{-2}	FRP

Table 42.2 Atmospheric parameters (a nonexhaustive list)

Parameter	Description	Unit	Symbol
Shortwave incoming surface radiation	The flux density of solar radiation reaching the Earth's surface	W m^{-2}	SIS
Aerosol optical depth/thickness	Integral of the radiation extinction due to atmospheric aerosols along the satellite sensor's line of sight	–	AOD/AOT
Fractional cloud cover	Fraction of a given satellite pixel covered by cloud	–	CF
Cloud type	Categorization of the clouds detected into common types	–	CT
Cloud optical depth/thickness	Integral of the radiation extinction caused by a cloud along the satellite sensor's line of sight	–	COD/COT
Cloud droplet effective radius	Area-weighted radius of cloud droplets (usually near the cloud top)	μm	DER (also: r_e , a_e)
Cloud liquid water path	Column-integrated liquid water mass per area	g m^{-2}	LWP
Cloud top height	Altitude of the cloud top with respect to a reference level (typically sea level or terrain elevation)	m	CTH

imaging data. This chapter provides an overview of the parameters that are most commonly evaluated through remote sensing, as well as the underlying algorithms employed to derive the values of the surface and atmospheric variables detailed in Tables 42.1 and 42.2. This set of variables cover the satellite products most

commonly applied for climate and environmental monitoring or numerical weather prediction (NWP) model assessment and improvement.

While the abbreviations and symbols used for parameters vary in the scientific literature, those employed in this chapter are widely used.

42.2 History

The history of using spaceborne sensors to retrieve parameters pertaining to the Earth's surface is closely linked to the history of extracting information about the atmosphere using satellites. Many of the sensors that have been used on satellites are identical, and the various methods that have been applied to retrieve useful

images of the Earth's surface and the atmosphere from satellite-based sensors are also related—some surface retrievals require the removal (and thus knowledge) of atmospheric conditions, and some atmospheric retrievals require information on the radiative properties of the surface (such as the *background signal*).

42.2.1 Surface Parameters

The Advanced Very High Resolution Radiometer (AVHRR), which was originally launched into space on TIROS-N in October 1978, is arguably the oldest sensor design still in use by the remote-sensing community. Originally designed as a 4-channel radiometer, it evolved into a 5-channel instrument (AVHRR/2) that was carried by many of the National Oceanic and Atmospheric Administration (NOAA) family of satellites (NOAA-7 to NOAA-14, with launch dates between 1981 and 1994), and later into a 6-channel instrument (AVHRR/3) that was fitted to NOAA-15 (1998) and subsequent NOAA satellites as well the MetOp satellites (Meteorological Operational Satellite; first launched in 2006) operated by the EUMETSAT. This radiometer was designed to allow multispectral analysis of the Earth in the visible to thermal infrared domain as a means to infer cloud cover, surface temperatures, and surface reflectances, which could in turn be used to probe the surface vegetation. The AVHRRs have been, and continue to be, an important source of continuous measurements of our planet at the global scale.

Many algorithms for deriving surface temperatures based on data from AVHRR/2 and later sensors have been proposed since the 1970s and early 1980s. Surface temperature estimation relies on measurements of top-of-atmosphere radiances (converted to brightness temperatures) by channels sensitive to the radiation emitted from the surface; these radiances are then corrected for atmospheric absorption and emission and surface emissivity. Sea surface temperatures (SSTs) have been derived from clear-sky AVHRR observations using the split-window theory (atmospheric absorption can be partially accounted for by analyzing the differences between measurements from split-window channels) and assuming that sea and water surfaces have emissivities that are equal or very close to 1 [42.3–8]. Similar methodologies have also been applied to derive SSTs using other instruments, including the Along Track Scanning Radiometer (ATSR-1 and ATSR-2 on the satellites ERS-1 and ERS-2, respectively)—later replaced by the Advanced Along Track Scanning Radiometer (AATSR) launched on the Envisat satellite [42.9]—and the Moderate Resolution Imaging Spectroradiometer (MODIS).

Strategies to estimate land surface temperatures (LSTs) from satellites have often utilized the split window approach first developed for SST measurements, except that infrared measurements within the thermal window channels provided by the sensors referred to above are analyzed instead [42.10–12]. However, the uncertainty in the surface emissivity and the spatial and temporal variabilities are significantly higher when

attempting to estimate LSTs rather than SSTs. The pronounced diurnal cycle of the LST favors the use of top-of-atmosphere observations acquired by geostationary platforms instead of (or as well as) those obtained by the abovementioned sensors, all of which are installed on polar orbiters. Sensors onboard geostationary satellites, such as the Meteosat Visible and Infrared Imager (MVIRI) on the Meteosat First Generation (first launched in 1977), the Spinning Enhanced Visible and Infrared Imager SEVIRI on the Meteosat Second Generation (launched in 2002), and the imager onboard the North American GOES series (Geostationary Operational Environmental Satellite), have the advantage of providing a higher observation frequency (from 30 to 10 min full disk) at the cost of lower spatial resolution when compared to optical instruments in lower orbits.

It has long been acknowledged that the green vegetation cover can be estimated by comparing the surface reflectance in the visible (red, e.g., AVHRR channel 1) with that in the near-infrared (e.g., AVHRR channel 2). For instance, the normalized difference vegetation index (NDVI), which has been used since the 1970s to monitor vegetation cover [42.13, 14], is estimated as the normalized difference between the reflectances in the red and near-infrared, i.e.,

$$\text{NDVI} = \frac{\text{NIR} - R}{\text{NIR} + R}, \quad (42.1)$$

where NIR is the reflectance in the near-infrared band and R is the reflectance in the red band, and normalized by the sum of both. The NDVI was traditionally estimated using top-of-atmosphere reflectances; however, to compensate for perturbing factors such as the different reflectance attenuations of the channels due to variations in aerosol optical depth and water vapor content, and to reduce the impact of the directional effects atmospheric correction is performed.

Combining various surface reflectance measurements in the visible and near-infrared domains allows the surface bidirectional reflectance distribution function (BRDF), and therefore the surface albedo [42.15, 16], to be estimated. Analyzing the BRDF signatures of surface vegetation within the main biomes allows vegetation variables such as the leaf area index (LAI) and the fraction of absorbed photosynthetically active radiation (FAPAR) to be inferred [42.17–20].

A critical aspect of the retrieval processes for all surface variables that are derived from visible and infrared observations is cloud screening [42.21]. Clouds partially or completely mask the window channels within this domain of the electromagnetic spectrum, often severely hampering attempts to measure the radiation reflected or emitted by the surface.

Table 42.3 Milestones in satellite imaging [42.22–24]

Platform	Launch	Milestone in parameter retrieval
Rocket flight	1929	First meteorological instruments on a rocket
Rocket flights	Late 1940s	Cloud formation photographed by cloud cameras
Explorer 6 and 7	1959	First successful use of a meteorological instrument on an orbiting satellite First coarse maps of solar and infrared radiation obtained using an imaging system and a Suomi-type radiometer
TIROS-1 to -10 (Television Infrared Operational Satellite)	1960–1965	TIROS-1: First satellite completely dedicated to satellite meteorology First integrated view of the Earth and its weather systems using radiometers TIROS-9 and -10: First polar-orbiting meteorological satellites
Nimbus 1–7	1964–1978	First use of spaceborne microwave radiometers, atmospheric sounders, ozone mappers, and infrared radiometers First quantitative use of satellite data in numerical weather prediction First spaceborne ultraviolet instrument to measure ozone Paved the way for the Landsat program
ESSA-1 to -9 (Environmental Science Service Administration)	1966–1969	First operational meteorological satellite Advanced vidicon camera systems and Suomi-type radiometers
ATS-1 to -3 (Applications Technology System)	1966–1967	First rapid imaging of the Earth and clouds First of six spacecraft that were used to test the feasibility of placing a satellite into geosynchronous orbit (GSO) First high-quality images of cloud cover and continuous observation of global weather patterns ATS 3: First color images of the Earth
SMS-1 and -2 (Synchronous Meteorological Satellite)	1974–1975	Specifically tasked with atmospheric observations
GOES	Since 1975	Series of US geostationary weather satellites
Himawari	Since 1977	Series of Japanese geostationary weather satellites
Meteosat	Since 1977	Series of European geostationary weather satellites
NOAA ITOS (Improved TIROS Operational System) TIROS-N/NOAA program (TIROS Next-generation)	1978–1981	High-resolution imaging (AVHRR) Improved observations and expanded operational capabilities Climate data record
POLDER (Polarization and Directionality of the Earth's Reflectances)	1996–2013	First remote-sensing instrument designed for aerosol measurements and surface anisotropy
A-Train	2006	Combination of active and passive instruments dedicated to aerosol–cloud interactions
MetOp	Since 2006	European polar-orbiting weather satellite system Improved accuracy of temperature, humidity, and wind measurements

42.2.2 Atmospheric Quantities

The development of satellite-based sensors for atmospheric measurements has resulted in significant progress in weather and climate prediction.

Remote sensing of atmospheric quantities dates back to the first rocket flights performed in 1946, as the rockets were equipped with cloud cameras (Table 42.3). However, a short rocket flight is not a suitable platform for weather observations [42.22]. After its launch in 1960, TIROS-1, the first successful weather satellite, provided the first complete pictures of clouds and synoptic weather systems from space using television cameras and infrared sensors. The series of satellites known as the TIROS Operational System (TOS) became operational in 1966. It was superseded by a new

series of spaceborne scanning radiometers in the 1970s, including the AVHRR series, which have contributed an important data record (Sect. 42.2.1). The Nimbus series, launched a few years after TIROS-1, was a testbed for atmospheric remote-sensing systems and facilitated various Earth system applications such as observations of the ozone hole and storm forecasting [42.23].

The first retrievals of cloud optical thickness and effective particle radius were achieved by performing visible and infrared measurements using airborne and spaceborne instruments [42.25, 26]. Methods that are employed to derive cloud optical depth and effective particle radius are typically based on their relationships to the nonabsorbing band of the visible spectrum and the absorption band of water in the near-infrared, respectively [42.27]. Retrieval methods and satellite instrumen-

tation are continually being refined and upgraded in order to improve the precision, the temporal resolution, and the spatial resolution of atmospheric observations [42.28].

42.3 Theory

In this section, we introduce the theory behind the algorithms applied in satellite-based imaging. These algorithms utilize spectral information provided by the various types of satellite-based sensors used for surface and atmospheric imaging. An overview of common applications of particular wavelength regions is given in Table 42.4. The channel characteristics of two passive imaging sensors are shown as examples in Tables 42.5 and 42.6.

42.3.1 Surface Parameters

We now examine the main concepts behind the estimation of surface variables, focusing on the medium- to low-resolution sensors that are typically installed on meteorological satellites. Although microwave instru-

Table 42.4 Typical wavelength regions probed by passive imaging sensors, and the atmospheric or surface parameters or properties that can be derived from measurements of those regions

Wavelength region (μm)	Parameters
0.5–0.8	Land surface properties, e.g., albedo, vegetation Aerosol optical thickness Cloud optical thickness (atmospheric window)
1.6	Snow, cloud phase
2.1	Cloud droplet size
3.9	Cloud droplet size
6–7	Water vapor
9–12	Temperature of the surface and atmospheric features (atmospheric window)

Table 42.5 Sensor example 1: channels of the Advanced Very High Resolution Radiometer 3 (AVHRR/3)

Channel	Wavelength (μm)	Resolution at nadir (km)
1	0.58–0.68	1.09
2	0.725–1.00	1.09
3A	1.58–1.64	1.09
3B	3.55–3.93	1.09
4	10.30–11.30	1.09
5	11.50–12.50	1.09

A brief summary of the milestones in the history of satellite imaging by spaceborne sensors is provided in Table 42.3.

ments have also been used to infer surface temperatures and vegetation properties, here we consider the measurements most commonly used to evaluate the parameters identified in Table 42.1, which are confined to the optical domain.

Visible and Shortwave Observations

One of the first applications of spaceborne remote-sensing observations was to estimate the NDVI in order to monitor vegetated areas. The simplicity of this index, which relies on the fact that healthy plants absorb photosynthetically active radiation (PAR) and reflect near-infrared (NIR) radiation, has facilitated the creation of a long NDVI time series that started in the late 1970s and is still being added to today. While plants use PAR for photosynthesis, they would overheat if they absorbed longer wavelengths. NDVI, the normalized difference between the reflectances in the NIR and the visible (VIS) or red channels, is high for green healthy vegetation and low for surfaces that are good reflectors of both wavelengths (e.g., dry vegetation, bare ground, clouds, snow). As noted earlier, although the NDVI was initially derived from top-of-atmosphere reflectances, it is now commonly obtained from top-of-canopy (i.e., atmospherically corrected) reflectances instead. However, NDVI estimates can be sensitive to the viewing angle and illumination geometry of the observations [42.29], so satellite NDVI products are often presented as composites (8-day, 10-day, or monthly).

Table 42.6 Sensor example 2: channels of the Spinning Enhanced Visible and Infrared Imager (SEVIRI)

Channel	Wavelength (μm)	Resolution at nadir (km)
1	0.56–0.71	3
2	0.74–0.88	3
3	1.50–1.78	3
4	3.48–4.36	3
5	5.35–7.15	3
6	6.85–7.85	3
7	8.30–9.1	3
8	9.38–9.94	3
9	9.80–11.80	3
10	11.00–13.00	3
11	12.40–14.40	3
12	≈ 0.4 –1.1 (broadband)	1

The NDVI presents saturation problems for densely vegetated areas, as it does not accurately reflect changes in green biomass across regions with dense vegetation [42.30, 31]. Other indices have therefore been proposed to overcome this and other limitations of the NDVI. One of the most common is the enhanced vegetation index (EVI), which uses the reflectance in the blue band (e.g., available with MODIS) as well as a canopy background adjustment term that enhances its sensitivity to green vegetation [42.32].

As widely demonstrated by the many indices that have been created to monitor vegetation (and also soil) properties based on relatively simple relations between the reflectances of channels within the shortwave domain (visible to near-infrared), detailed knowledge of the surface reflection properties for any combination of illumination and viewing angles within this domain (i.e., knowledge of the surface BRDF) is highly beneficial when attempting to retrieve more complex vegetation properties, including the LAI and FAPAR. Furthermore, the BRDF is intrinsically linked to the surface albedo, which in turn crucially influences the radiation balance and hence the energy balance at the surface.

To estimate the surface BRDF, it is usually necessary to accumulate a sufficient number of satellite observations of the same surface scene from different viewing angles (as provided by MODIS, MISR (Multi-angle Imaging SpectroRadiometer), or AVHRR instruments on polar orbiters) and/or different sun zenith angles (as provided by MVIRI, SEVIRI, ABI (Advanced Baseline Imager), or AHI (Advanced Himavari Imager) sensors on geosynchronous platforms). The most popular procedures [42.33, 34] assume that the BRDF can be modeled as a sum of weighted kernels, each associated with a basic aspect of surface reflection (e.g., an isotropic component, volumetric scattering, and a geometric shadow-driven component) [42.16].

The kernel weights may be estimated by fitting the clear-sky top-of-canopy (i.e., atmospherically corrected) reflectances for bands within the solar domain, although the approach was also successfully transposed to the thermal infrared (TIR) domain [42.35]. Hemispherical integration of the BRDF provides the spectral (or channel) albedo; empirical (often linear) regression of this spectral albedo yields a broadband value for the whole shortwave region (e.g., 0.3–3 μm). The albedo can be defined for a given solar illumination or the integral of the solar illumination during a day. If the BRDF is known, the directional hemispherical reflectance (black-sky albedo) can be generated for any solar zenith angle of interest, as can the bihemispherical reflectance (white-sky albedo). Both are operationally derived from measurements provided by instruments on polar orbiters after accumulating observations over

periods ranging from about 1 week to 1 month [42.33, 36–38]. Given the higher temporal frequency of geostationary observations, albedo values can be estimated from Meteosat or GOES series as often as daily [42.34, 39].

LAI and FAPAR are more tangible vegetation variables than vegetation indices. The former can, for instance, be incorporated into land surface schemes within NWP or climate models. Several authors have proposed that the specific spectral and directional reflectance signatures of vegetation should be explored so that the BRDF can be used to derive those vegetation variables [42.17, 20].

42.3.2 Atmospheric Quantities

In order to retrieve atmospheric properties from passive sensor measurements in the visible and infrared spectral ranges, it is necessary to interpret the signal received at the satellite appropriately. This signal is either a terrestrial signal that has been modified by one transition through the atmosphere, or a signal of solar origin that has been modified by two atmospheric transitions and a reflection at the Earth's surface. In both cases, two unknowns need to be disentangled: the radiative properties of the Earth's surface and atmospheric features [42.1]. Since the focus is on the retrieval of the latter, reliable information on the former is required before attempting almost any atmospheric retrieval. Some relevant surface retrievals were covered in the previous section. This section addresses the second set of problems: deriving information on the presence and properties of atmospheric features.

In general, passive retrieval algorithms for the properties of atmospheric features such as aerosols and clouds use the transmission, emission, and scattering of electromagnetic radiation [42.28].

Aerosol optical depth (AOD), the integral of the extinction due to aerosols along the atmospheric path, varies with the wavelength of the radiation measured. It is thus usually reported for a particular wavelength. In general, the contribution of the AOD to the signal received at the satellite sensor decreases with wavelength, whereas the contribution of the Earth's surface increases. Therefore, short wavelengths are particularly useful for retrieving the AOD, as are dark, relatively homogeneous surfaces in the background such as the oceans and large continental water bodies. Upon discarding cloudy pixels from further analysis, a radiative transfer scheme is applied to retrieve the AOD. Most of the time, this involves assuming that an idealized aerosol is present and making assumptions about the shape and size distributions. Other aerosol parameters such as the Ångström coefficient, fine-mode fraction,

aerosol indices, and single-scattering albedo are also retrieved in some cases, but these are either less robust or more specific in terms of their scientific context [42.40].

The solar radiation received at the Earth's surface is a direct function of the solar signal and the modification of this signal by the atmosphere. A commonly used technique, Heliosat [42.41], makes use of this insight. The clear-sky solar signal is derived from radiative transfer calculations, and the solar radiation that actually reaches the Earth's surface is estimated by scaling the clear-sky solar signal by the relative cloudiness in a given location. This relative cloudiness is expressed as a *cloud index*, which is computed for each pixel by comparing the observed reflectivity at that pixel to the minimum and maximum observed reflectivities for the same location.

Cloud presence and cloud properties are derived in a number of ways, and the following discussion only touches on the main principles. Visible measurements play a central role for many of the parameters considered here, but such measurements are, of course, only available during the daytime.

Cloud presence and fraction are commonly detected in either a single channel (especially in older systems and for continuity purposes) or a combination of channels. As clouds tend to be cooler than the Earth's surface, they can often be identified in the thermal infrared. Low clouds and cold surfaces (e.g., fog over snow) are not, however, suited to this approach. The same type of situation can be problematic when using visible-range information. Introducing additional channels, e.g., the mid-infrared $\approx 1.6\ \mu\text{m}$, as well as in the thermal IR $\approx 9\ \mu\text{m}$, leads to increased accuracy in delineating clouds. The cloud fraction is often defined as either the fraction of an area of several pixels

that is covered by cloud or a fraction of an individual pixel based on scaling radiative signals in a predefined range [42.42, 43].

Cloud-type determination utilizes spectral and textural features [42.43, 44]. Clouds are typically classified by altitude, opacity, and cloud family (i.e., stratiform, cumuliform, or cirrus). Classifications are usually based on predefined thresholds.

Cloud optical thickness and droplet effective radius are commonly derived in a dual-channel approach based on the knowledge that visible-range reflectivity increases with cloud optical thickness whereas the mid-infrared signal is determined by droplet effective radius [42.43, 45]. Both signals are modeled using a radiative transfer code and then inverted. The droplet effective radius reflects the conditions near the cloud top, with smaller wavelengths (e.g., $1.6\ \mu\text{m}$) representing greater penetration depth into the cloud than larger wavelengths (e.g., $3.9\ \mu\text{m}$). The liquid-water path is usually computed as the product of COT and DER scaled by a constant [42.27, 43]. This approach involves assuming that there is an adiabatic or slightly subadiabatic increase in cloud liquid-water content with altitude, and different values have been used in different studies [42.46].

Finally, cloud top height can be obtained by either comparing an atmospherically and emissivity-corrected cloud-top temperature to a (standard) atmospheric profile or using a split-window approach. In the latter, one channel is at a wavelength that is strongly absorbed by a gas with a well-known atmospheric distribution (e.g., oxygen) while the other is at a nearby wavelength unaffected by this absorption. The difference in signal between the channels can be interpreted as the length of the atmospheric path above a cloud and thus the cloud top height.

42.4 Devices and Systems

This section highlights the fundamental differences between existing satellite systems and discusses selected product suites that are available to users.

42.4.1 Satellite Systems and Orbits

Most satellite systems that are used to image parameters associated with the Earth's surface or the atmosphere allow for both types of retrievals, and are therefore treated jointly here (Chap. 34).

As mentioned above, this chapter focuses on passive-sensor satellite systems that generally probe the visible and infrared ranges of the electromagnetic spectrum. Since a comprehensive analysis of the at-

mosphere and how it is changing is of great interest in many applications, wide-area coverage—up to the global scale—is desirable. At the same time, monitoring patterns and changes to the climate requires repeated measurements obtained at intervals determined by the specifics of the desired application or study. In general, the main choice to be made when selecting an adequate system for the scientific problem at hand is between satellite platforms on polar orbits and geostationary platforms. The former orbit the Earth at altitudes of a few hundred kilometers and provide observations at spatial resolutions of between a few tens of meters and a few kilometers. The swath (the area covered on both sides of a satellite's nadir) of a polar orbiter ranges up



Fig. 42.1 The MetOp-C satellite is the newest of the first generation of Europe’s EUMETSAT Polar System series (following Metop-A and -B) that orbit at 817 km (© ESA)

to a few hundred kilometers (e.g., for MODIS [42.45]). The main disadvantage of a polar orbiter is its low repeat rate—it only images a given location at specific times of the day, and therefore takes a number of orbits (which often corresponds to days) to completely observe the entire Earth (Fig. 42.1). Geostationary satellite systems, on the other hand, are placed at an altitude of around 36 000 km above the Earth and at a fixed longitude along the equator. At this location, they can monitor wide areas at spatial resolutions of between 500 m and a few kilometers. Given the constant position and very high altitude of a geostationary satellite relative to the Earth’s surface, the sensors on such a platform can provide coverage of a very wide, approximately circular area (the *full disk*) at a high repeat rate. Depending on the sensor characteristics, full-disk scans can be achieved every 5 min (e.g., GOES [42.47]), while selected smaller areas can be imaged at 30 s intervals (Fig. 42.2).

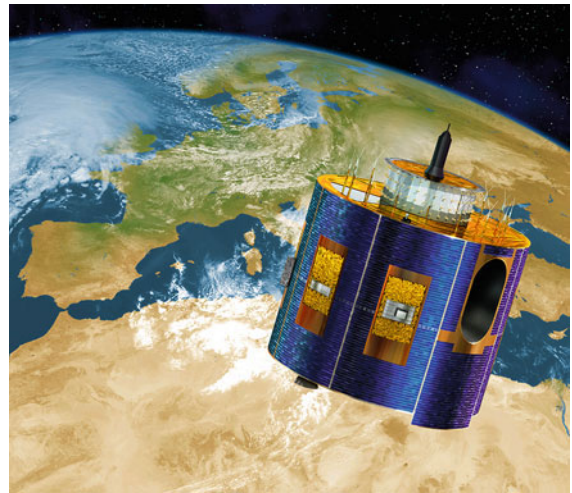


Fig. 42.2 The Meteosat Second Generation satellites monitor weather systems over Europe and Africa (© ESA: D. Ducros)

A summary of the main advantages and disadvantages of various observation systems is given in Table 42.7.

42.4.2 Product Suites and Comparisons

A large number of algorithms for retrieving geophysical parameters have been developed for numerous satellite sensors. Many of the associated products are generated operationally and distributed freely or commercially by government, private, and academic institutions around the world. In the following, two examples of coordinated efforts to produce, compare, and distribute information derived from satellite imagers are introduced.

Table 42.7 Advantages and disadvantages of various observation systems

Observation systems	Advantages	Disadvantages
Imagers on geostationary platforms, e.g., – SEVIRI/MSG – ABI/GOES-R – AHI/Himawari	Temporal resolution ranging from 5 to 15 min. Variables with strong diurnal cycles (surface temperature, solar radiation) or those that change rapidly (cloud cover) to be monitored	Coarse spatial resolution Limited vertical information
Imagers on polar orbiters, e.g., – AVHRR/3/MetOp – MODIS/Aqua, Terra – MSI/Sentinel-2 – SLSTR/Sentinel-3 – VIIRS/Suomi NPP – OLI/Landsat-8 – MISR/Terra	Near-global coverage of various meteorological, cloud, and aerosol properties is provided Moderate to high spatial resolution	Coarse temporal resolution Limited vertical information

MSI: Multispectral Instrument; NPP: National Polar-orbiting Partnership; OLI: Operational Land Imager; SLSTR: Sea and Land Surface Temperature Radiometer; VIIRS: Visible Infrared Imaging Radiometer Suite

Moderate Resolution Imaging Spectroradiometer (MODIS) Product Suite

The Moderate Resolution Imaging Spectroradiometer (MODIS) is installed on the Terra satellite (in orbit since 2000) as well as on the Aqua satellite (launched in 2002). A range of operational products have been developed by scientists at various institutions that comprise the MODIS Science Team. The data produced are jointly distributed via the National Aeronautics and Space Administration (NASA, atmospheric products) and the United States Geological Survey (USGS, Earth's surface products).

Network of Satellite Application Facilities (SAFs)

The European Organization for the Exploitation of Meteorological Satellites (EUMETSAT) operates a network of Satellite Application Facilities (SAFs) that develop, maintain, and in some cases distribute products based on mostly European satellite systems. Most SAF contributors are European national meteorological and hydrological services, although some are academic and private institutions. The Land Surface Analysis SAF (LSA SAF) and the Ocean and Sea Ice SAF (OSI SAF) provide and distribute a number of products relating to Earth's surface parameters. The Climate Monitoring SAF (CM SAF) and the support to Nowcasting and Very Short Range Forecasting SAF (NWC SAF) produce and distribute products and software for atmospheric properties.

42.5 Specifications

Accuracy targets are usually defined before developing a satellite product and evaluations are performed afterwards. Since the potentials and requirements of sensor systems vary markedly, the targeted and obtained accuracies also vary substantially. Providing general-

ized estimates of the accuracy would not, therefore, be very meaningful. Instead, Table 42.8 lists the reference measurements that are usually taken to assess the quality of the satellite-derived parameters considered here.

Table 42.8 Specifications for different measurement methods

Parameter	Reference measurement	Details
LST	In-situ radiometers (broadband or thermal infrared)	e.g., ARM (Atmospheric Radiation Measurements) sites [42.48] (Chap. 63), LSA-SAF validation sites [42.49]
Albedo	Two pyranometers measuring downward & upward radiation in-situ	e.g., NETWORK of FLUX measurement sites (FLUXNET), LSA-SAF validation sites [42.49]
Vegetation index (VI)	Characterization of VI sensitivity to actual vegetation conditions; assessment of long-term stability	Reference sites, e.g., FLUXNET, Chap. 64, Aerosol RObotic NETWORK (AERONET, Chap. 63), Enviro-Net (Chap. 64)
LAI	In-situ foliage sampling	Integrated Carbon Observation System (ICOS network)
FAPAR	(direct radiation measurement)	ICOS network
SC	Ground-based station observations	Networks of national hydrological and meteorological services
FRP	Ground-based event observations	
SIS	Pyranometers	Baseline Surface Radiation Network (BSRN, see Chap. 63) [42.50]
AOD	Sun photometers	Most belong to the global AERONET and MPL networks [42.51] (Chap. 63)
CF	Human observers, ground-based, airborne, and spaceborne lidar and radar observations	Observation networks of ground-based stations, e.g., SYNOP (surface SYNOptic observation) [42.43]; validation campaigns, e.g., Atlantic Stratocumulus Transition Experiment (ASTEX) [42.52], Arctic High-Spectral Resolution Lidar (AHSRL), Cloud Physics Lidar (CPL), and Geoscience Laser Altimeter System (GLAS) [42.53]
CT	Human observers, ground-based and space-based lidar and radar observations	
COT	Ground-based and space-based lidar and radar observations	Observation networks of ground-based stations, e.g., SYNOP [42.43] (Chap. 63); validation campaigns, e.g., ASTEX [42.52]
DER	In-situ droplet probes, spectrometer, particulate volume monitor	Validation campaigns, e.g., ASTEX [42.52]
LWP	Microwave radiometers, spectrometer, particulate volume monitor	e.g., CloudNET observations [42.54]
CTH	Spaceborne lidar and radar observations	e.g., CloudSat and Cloud-Aerosol Lidar and Infrared Pathfinder Satellite Observation (CALIPSO) [42.43]

42.6 Quality Control

To ensure consistency, and to aid further product development, systematic comparisons of existing products are organized by various organizations. A notable international example of such efforts is the Climate Change Initiative (CCI) of the European Space Agency (ESA). The CCI examines the present-day ability to derive selected essential climate variables (ECVs) from satellite data by systematically evaluating existing products

(e.g., LST, aerosol, and cloud products). This quality control process adheres to norms such as the Q4ECV, which is employed as a reference to appraise the quality of C3S products. The World Meteorological Organization (WMO) also supports initiatives through the Global Climate Observing System (GCOS), which establishes specifications and provides directions for future initiatives relating to long-term ECV data series.

42.7 Maintenance

The satellite products and algorithms presented here are constantly being developed and improved, and adjustments are made when new platforms become available. Satellite sensors are often calibrated in space by comparing their data with synchronous observations from other

sensors (intersatellite calibration), measuring an object (blackbody) onboard the satellite, or pointing the sensor at a background object with well-established properties (e.g., open space or the Moon). For more on this topic, please refer to the chapter on remote-sensing platforms.

42.8 Applications

The amount of information obtained from satellite-based imaging is immense, so applications of satellite products span a wide range of fields. These include:

- *Environmental monitoring.* Near-real-time evaluation of imaging observations provides a sound basis for monitoring changes in parameters that are relevant to society and ecology (e.g., air quality, vegetation health, and weather systems).
- *Climate change monitoring.* By examining long homogenized time series, it is possible to gain insights into how components of the global climate system develop over time as a basis for studying climate change.
- *Evaluation of climate and weather models.* To assess their applicability, numerical models of climate and weather need to be evaluated against independent observations. With its spatial component, satellite imaging is a crucial and commonly used source of such measurements.
- *Earth system analysis.* Satellite imaging datasets facilitate systematic studies of components of the Earth–atmosphere system. Such studies frequently use statistical methods ranging from bivariate correlation analysis to machine learning.
- *Communicating science.* Finally, satellite imaging produces spatial datasets, which can easily be presented as maps, which are useful tools for communicating scientific insights.

42.9 Future Developments

Future satellite missions will take advantage of advances in satellite detector technology, optical sensor properties, and electronics. Continuous monitoring of essential climate and environmental variables, the op-

erational use of research instruments, and the implementation of low-cost missions will be core activities. A few planned satellite missions are listed in Table 42.9.

Table 42.9 Planned satellite missions and primary instruments

Future mission	Mission description	Primary instrument(s)
CLARREO (Climate Absolute Radiance and Refractivity Observatory)	Solar and Earth radiation characteristics for understanding climate forcing	Broadband radiometer Absolute spectrally resolved interferometer
GPSRO (Operational GPS Radio Occultation)	High-accuracy, all-weather temperature, water vapor, and electron density profiles for weather, climate, and space weather	GPS receiver
XOVWM (Extended Ocean Vector Winds Mission)	Sea surface wind vectors for weather and ocean ecosystems	Backscatter radar
SMAP (Soil Moisture Active–Passive)	Soil moisture and freeze–thaw for weather and water cycle processes	L-band radar, L-band radiometer
ICESat-II (Ice, Cloud, and Land Elevation Satellite II)	Ice sheet height changes for climate change diagnosis	Laser altimeter
DESDynI (Deformation, Ecosystem Structure, and Dynamics of Ice)	Surface and ice sheet deformation for understanding natural hazards and climate; vegetation structure for ecosystem health	L-band InSAR Laser altimeter
HypIRI (Hyperspectral Infrared Imager)	Land surface composition for agriculture and mineral characterization; vegetation types for ecosystem health	Hyperspectral spectrometer
ASCENDS (Active Sensing of CO ₂ Emissions over Nights, Days, and Seasons)	Day/night, all-latitude, all-season CO ₂ column integrals for climate emissions	Multifrequency laser
SWOT (Surface Water and Ocean Topography)	Ocean, lake, and river water levels for ocean and inland water dynamics	K _a - or K _u -band radar K _u -band altimeter Microwave radiometer
GEO-CAPE (Geostationary Coastal and Air Pollution Events)	Atmospheric gas columns for air quality forecasts; ocean color for coastal ecosystem health and climate emissions	High-spatial-resolution hyperspectral spectrometer Low-spatial-resolution imaging spectrometer IR correlation radiometer
ACE (Aerosol–Cloud–Ecosystem)	Aerosol and cloud profiles for climate and water cycle; ocean color for open ocean biogeochemistry	Backscatter lidar Multiangle polarimeter Doppler radar
LIST (Lidar Surface Topography)	Land surface topography for landslide hazards and water runoff	Laser altimeter
PATH (Precipitation and All-Weather Temperature and Humidity)	High-frequency, all-weather temperature and humidity soundings for weather forecasting and sea surface temperature	Microwave array spectrometer
GRACE-II (Gravity Recovery and Climate Experiment II)	High-temporal-resolution gravity fields for tracking large-scale water movement	Microwave or laser ranging system
SCLP (Snow and Cold Land Processes)	Snow accumulation to monitor freshwater availability	K _u - and X-band radars K- and K _a -band radiometers
GACM (Global Atmospheric Composition Mission)	Ozone and related gases for intercontinental air quality and stratospheric ozone layer prediction	UV spectrometer IR spectrometer Microwave limb sounder
3D-Winds (Three-Dimensional Tropospheric Winds)	Tropospheric winds for weather forecasting and pollution transport	Doppler lidar
MTG (Meteosat Third Generation)	Next generation of geostationary satellites; continuous observation in the visible and IR spectrum with improved spatial, temporal, and radiometric resolutions	Flexible combined and lightning imagers Infrared and ultraviolet sounders
EUMETSAT Polar System—Second Generation (EPS-SG)	Climate monitoring and nowcasting	Infrared and microwave imagers and sounders
Copernicus Satellites (Europe’s Copernicus program: Sentinel-4 to -6)	Measurements of atmospheric composition and global sea-level (Sentinel 6)	Instruments of the MTG and EPS-SG programs, Radar altimeter
EarthCare (the ESA’s cloud, aerosol and radiation mission)	Across-track information on clouds and aerosols	Atmospheric lidar, cloud profiling radar, multispectral imager, broadband radiometer
FLEX (Fluorescence Explorer)	Map vegetation fluorescence to quantify photosynthetic activity	High-resolution imaging spectrometer
Biomass	Accurate maps of tropical, temperate and boreal forest biomass	P-band synthetic aperture radar

42.10 Further Reading

Technical details on active and passive scanning methods can be found in

- W., Kresse and D.M. Danko: Springer Handbook of Geographic Information (Springer, Berlin Heidelberg 2012)

A visual overview of satellite applications in atmospheric and Earth science is given in Sect. 3 of

- J.N., Pelton, S. Madry and S. Camacho-Lara: Handbook of Satellite Applications, Volume 1 (Springer, New York 2013)

A comprehensive introduction to meteorological satellites and technologies is given by

- S.-Y., Tan: Meteorological Satellite Systems, SpringerBriefs in Space Development (Springer, New York 2014)

A compilation of relevant basic equations and measurement principles can be found in

- R. Rizzi, R. Saunders: Principles of remote sensing of atmospheric parameters from space, ECMWF Meteorological Training Course Lecture Series (Reading, 2002)

References

- 42.1 K.N. Liou: *An Introduction to Atmospheric Radiation*, 2nd edn. (Academic Press, Cambridge 2002)
- 42.2 G. Balsamo, A. Agustí-Parareda, C. Albergel, G. Arduini, A. Beljaars, J. Bidlot, N. Bousserez, S. Boussetta, A. Brown, R. Buizza, C. Buontempo, F. Chevallier, M. Choulga, H. Cloke, M. Cronin, M. Dahoui, P. De Rosnay, P. Dirmeyer, M. Drusch, E. Dutra, M. Ek, P. Gentile, H. Hewitt, S. Keeley, Y. Kerr, S. Kumar, C. Lupu, J.-F. Mahfouf, J. McNorton, S. Mecklenburg, K. Mogensen, J. Muñoz-Sabater, R. Orth, F. Rabier, R. Reichle, B. Ruston, F. Pappenberger, I. Sandu, S. Seneviratne, S. Tetsche, I. Trigo, R. Uijlenhoet, N. Wedi, R. Woolway, X. Zeng: Satellite and in situ observations for advancing global Earth surface modelling: A review, *Remote Sens* **10**(12), 2038 (2018)
- 42.3 L.M. McMillin: Estimation of sea surface temperatures from two infrared window measurements with different absorption, *J. Geophys. Res.* **80**(36), 5113–5117 (1975)
- 42.4 I.J. Barton: Dual channel satellite measurements of sea surface temperature, *Q. J. R. Meteorol. Soc.* **109**(460), 365–378 (1983)
- 42.5 L.M. McMillin, D.S. Crosby: Theory and validation of the multiple window sea surface temperature technique, *J. Geophys. Res.* **89**(C3), 3655–3661 (1984)
- 42.6 D.T. Llewellyn-Jones, P.J. Minnett, R.W. Saunders, A.M. Zavody: Satellite multichannel infrared measurements of sea surface temperature of the N.E. Atlantic Ocean using AVHRR/2, *Q. J. R. Meteorol. Soc.* **110**(465), 613–631 (1984)
- 42.7 E.P. McClain: Multi-channel sea surface temperatures from the AVHRR on NOAA-7, Proceedings of the Satellite-Derived Sea Surface Temperature: Workshop-II, JPL Publ. **84**(5), 1–8 (1984)
- 42.8 P.J. Minnett: The regional optimization of infrared measurements of sea surface temperature from space, *J. Geophys. Res.* **95**(C8), 13497–13510 (1990)
- 42.9 I.J. Barton, A.J. Prata: Satellite derived sea surface temperature data sets for climate applications, *Adv. Space Res.* **16**(10), 127–136 (1995)
- 42.10 J. Sobrino, C. Coll, V. Caselles: Atmospheric correction for land surface temperature using NOAA-11 AVHRR channels 4 and 5, *Remote Sens. Environ.* **38**(1), 19–34 (1991)
- 42.11 F. Becker, Z.-L. Li: Surface temperature and emissivity at various scales: Definition, measurement and related problems, *Remote Sens. Rev.* **12**(3–4), 225–253 (1995)
- 42.12 Z. Wan, J. Dozier: A generalized split-window algorithm for retrieving land-surface temperature from space, *IEEE Transact. Geosci. Remote Sens.* **34**(4), 892–905 (1996)
- 42.13 J.W. Rouse, R.H. Haas, J.A. Schell, D.W. Deering: Monitoring vegetation systems in the Great Plains with ERTS. In: *Proc. Third Earth Res. Technol. Satellite-1 Symp.* (1974) pp. 301–317
- 42.14 R.B. Myneni, F.G. Hall, P.J. Sellers, A.L. Marshak: The interpretation of spectral vegetation indexes, *IEEE Transact. Geosci. Remote Sens.* **33**(2), 481–486 (1995)
- 42.15 B. Pinty, M.M. Verstraete, R.E. Dickinson: A physical model for predicting bidirectional reflectances over bare soil, *Remote Sens. Environ.* **27**(3), 273–288 (1989)
- 42.16 J.-L. Roujean, M. Leroy, P.-Y. Deschamps: A bidirectional reflectance model of the Earth's surface for the correction of remote sensing data, *J. Geophys. Res.* **97**(D18), 20455–20468 (1992)
- 42.17 J.-L. Roujean, F.-M. Breon: Estimating PAR absorbed by vegetation from bidirectional reflectance measurements, *Remote Sens. Environ.* **51**(3), 375–384 (1995)

- 42.18 P. Bicheron, M. Leroy: A method of biophysical parameter retrieval at global scale by inversion of a vegetation reflectance model, *Remote Sens. Environ.* **67**(3), 251–266 (2000)
- 42.19 N. Gobron, B. Pinty, M.M. Verstraete, J.-L. Widlowski: Advanced spectral algorithm and new vegetation indices optimized for upcoming sensors: Development, accuracy and applications, *IEEE Transact. Geosci. Remote Sens.* **38**(6), 2489–2505 (2000)
- 42.20 J.-L. Roujean: Global mapping of vegetation parameters from POLDER multiangular measurements for studies of surface-atmosphere interactions: A pragmatic method and its validation, *J. Geophys. Res.* **107**(D12), 1–14 (2002)
- 42.21 W.B. Rossow, R.A. Schiffer: Advances in understanding clouds from ISCCP, *Bull. Am. Meteorol. Soc.* **80**(11), 2261–2287 (1999)
- 42.22 S.-Y. Tan: *Meteorological Satellite Systems*, Springer Briefs in Space Development (Springer, New York 2014)
- 42.23 E. Parlow: Meteorological satellites – A brief historical review, *EARSeL Newsl.* **67**, 5–10 (2006)
- 42.24 S.Q. Kidder, T.H. Vonder Haar: *Satellite Meteorology: An Introduction* (Academic Press, Cambridge 1995)
- 42.25 J.E. Hansen, J.B. Pollack: Near-infrared light scattering by terrestrial clouds, *J. Atmos. Sci.* **27**(2), 265–281 (1970)
- 42.26 R.J. Curran, H.L. Kyle, L.R. Blaine, J. Smith, T.D. Clem: Multichannel scanning radiometer for remote sensing cloud physical parameters, *Rev. Scientific Instrum.* **52**(10), 1546–1555 (1981)
- 42.27 M. D. King, S.-C. Tsay, S. E. Platnick, M. Wang, K.-N. Liou: Cloud Retrieval Algorithms for MODIS: Optical Thickness, Effective Particle Radius, and Thermodynamic Phase, MODIS Algorithm Theoretical Basis Document No. ATBD-MOD-05, MOD06 Cloud product, version 5, 1–79 (1997)
- 42.28 G.L. Stephens, C.D. Kummerow: The remote sensing of clouds and precipitation from space: A review, *J. Atmos. Sci.* **64**(11), 3742–3765 (2007)
- 42.29 B.N. Holben: Characteristics of maximum-value composite images from temporal AVHRR data, *Intern. J. Remote Sens.* **7**(11), 1417–1434 (1986)
- 42.30 J. Townshend, C. Justice, W. Li, C. Gurney, J. McManus: Global land cover classification by remote sensing: Present capabilities and future possibilities, *Remote Sens. Environ.* **35**(2–3), 243–255 (1991)
- 42.31 A.A. Gitelson, Y.J. Kaufman, M.N. Merzlyak: An atmospherically resistant “green” vegetation index (ARGI) for EOS-MODIS, *Remote Sens. Environ.* **58**, 289–298 (1997)
- 42.32 H.Q. Liu, A. Huete: A feedback based modification of the NDVI to minimize canopy background and atmospheric noise, *IEEE Transact. Geosci. Remote Sens.* **33**(2), 457–465 (1995)
- 42.33 C.B. Schaaf, F. Gao, A.H. Strahler, W. Lucht, X. Lia, T. Tsang, N.C. Strugnell, X. Zhang, Y. Jin, J.-P. Muller, P. Lewis, M. Barnsley, P. Hobson, M. Disney, G. Roberts, M. Dunderdale, C. Doll, R.P. d’Entremont, D. Roy: First operational BRDF, albedo nadir reflectance products from MODIS, *Remote Sens. Environ.* **83**(1–2), 135–148 (2002)
- 42.34 B. Geiger, D. Carrer, L. Franchistéguy, J.-L. Roujean, C. Meurey: Land surface albedo derived on a daily basis from Meteosat second generation observations, *IEEE Transact. Geosci. Remote Sens.* **46**(11), 3841–3856 (2008)
- 42.35 W.C. Snyder, Z. Wan: BRDF models to predict spectral reflectance and emissivity in the thermal infrared, *IEEE Transact. Geosci. Remote Sens.* **36**(1), 214–225 (1998)
- 42.36 F. Gao, C.B. Schaaf, A.H. Strahler, A. Roesch, W. Lucht, R. Dickinson: MODIS bidirectional reflectance distribution function and albedo climate modeling grid products and the variability of albedo for major global vegetation type, *J. Geophys. Res.* **110**(D1), 1–13 (2005)
- 42.37 M. Sütterlin, C.B. Schaaf, R. Stöckli, Q. Sun, F. Hüsler, C. Neuhaus, S. Wunderle: Albedo and reflectance anisotropy retrieval from AVHRR operated onboard NOAA and MetOp satellites: Algorithm performance and accuracy assessment for Europe, *Remote Sens. Environ.* **168**(10), 163–176 (2015)
- 42.38 Y. Liu, Z. Wang, Q. Sun, A.M. Erb, Z. Li, C.B. Schaaf, X. Zhang, M.O. Román, R.L. Scott, Q. Zhang, K.A. Novick, M.S. Bret-Harte, S. Petroy, M. San-Clements: Evaluation of the VIIRS BRDF, Albedo and NBAR products suite and an assessment of continuity with the long term MODIS record, *Remote Sens. Environ.* **201**(11), 256–274 (2017)
- 42.39 D. Carrer, J.-L. Roujean, C. Meurey: Comparing operational MSG/SEVIRI land surface albedo products from land SAF with ground measurements and MODIS, *IEEE Transact. Geosci. Remote Sens.* **48**(4), 1714–1728 (2010)
- 42.40 Y.J. Kaufman, D. Tanré, O. Boucher: A satellite view of aerosols in the climate system, *Nature* **419**(6903), 215–223 (2002)
- 42.41 D. Cano, J.M. Monget, M. Albuissou, H. Guillard, N. Regas, L. Wald: A method for the determination of the global solar radiation from meteorological satellite data, *Solar Energy* **37**(1), 31–39 (1986)
- 42.42 S. Ackerman, R. Frey, K. Strabala, Y. Liu, L. Gumley, B. Baum, P. Menzel: Discriminating clear-sky from cloud with MODIS algorithm theoretical basis document (MOD35), 1–114 (2010)
- 42.43 M.S. Stengel, A.K. Kniffka, J.F.M. Meirink, M.L. Lockhoff, J.T. Tan, R.H. Hollmann: CLAAS: the CM SAF cloud property data set using SEVIRI, *Atmos. Chem. Phys.* **14**(8), 4297–4311 (2014)
- 42.44 M. Derrien, H. Le Gléau: MSG/SEVIRI cloud mask and type from SAFNWC, *Intern. J. Remote Sens.* **26**(21), 4707–4732 (2005)
- 42.45 S. Platnick, M.D. King, S.A. Ackerman, W.P. Menzel, B.A. Baum, J.C. Riédi, R.A. Frey: The MODIS cloud products: Algorithms and examples from Terra, *IEEE Transact. Geosci. Remote Sens.* **41**(2), 459–472 (2003)
- 42.46 R. Wood, D.L. Hartmann: Spatial variability of liquid water path in marine low cloud: the importance of Mesoscale cellular convection, *J. Climate* **19**(9), 1748–1764 (2006)

- 42.47 T.J. Schmit, M.M. Gunshor, W.P. Menzel, J.J. Gurka, J. Li, A.S. Bachmeier: Introducing the next-generation advanced baseline imager on GOES-R, *Bull. Am. Meteorol. Soc.* **86**(8), 1079–1096 (2005)
- 42.48 J.H. Mather, J.W. Voiles: The arm climate research facility: A review of structure and capabilities, *Bull. Am. Meteorol. Soc.* **94**(3), 377–392 (2013)
- 42.49 F.-M. Göttsche, F.-S. Olesen, I. Trigo, A. Bork-Unkelbach, M. Martin: Long term validation of land surface temperature retrieved from MSG/SEVIRI with continuous in-situ measurements in Africa, *Remote Sens* **8**(5), 410 (2016)
- 42.50 K.G. Karlsson, K. Anttila, J. Trentmann, M. Stengel, J.F. Meirink, A. Devasthale, T. Hanschmann, S. Kothe, E. Jaäskeläinen, J. Sedlar, N. Benas, G.J. Van Zadelho, C. Schlundt, D. Stein, S. Finkensieper, N. Häkansson, R. Hollmann: CLARA-A2: The second edition of the CM SAF cloud and radiation data record from 34 years of global AVHRR data, *Atmos. Chem. Phys.* **17**(9), 5809–5828 (2017)
- 42.51 B.N. Holben, T.F. Eck, I. Slutsker, D. Tanré, J.P. Buis, A. Setzer, E. Vermote, J.A. Reagan, Y.J. Kaufman, T. Nakajima, F. Lavenu, I. Jankowiak, A. Smirnov: AERONET-A federated instrument network and data archive for aerosol characterization, *Remote Sens. Environ.* **66**(1), 1–16 (1998)
- 42.52 S. Platnick, F.P.J. Valero: A validation of a satellite cloud retrieval during ASTEX, *J. Atmos. Sci.* **52**(16), 2985–3001 (1995)
- 42.53 S.A. Ackerman, R.E. Holz, R. Frey, E.W. Eloranta, B.C. Maddux, M. McGill: Cloud detection with MODIS. Part II: Validation, *J. Atmos. Ocean. Technol.* **25**(7), 1073–1086 (2008)
- 42.54 R.A. Roebeling, H.M. Deneke, A.J. Feijt: Validation of cloud liquid water path retrievals from SEVIRI using one year of CloudNET observations, *J. Appl. Meteorol. Climatol.* **47**(1), 206–222 (2008)

Jan Cermak

Institute of Meteorology and Climate Research and Institute of Photogrammetry and Remote Sensing Karlsruhe Institute of Technology (KIT) Karlsruhe, Germany
jan.cermak@kit.edu



Jan Cermak has been Professor of Geophysical Remote Sensing at the Karlsruhe Institute of Technology, Germany, since 2016. Before that, he was a professor at Ruhr-Universität Bochum, Germany. He received his PhD from the University of Marburg, Germany, in 2006, after which he performed postdoctoral research at ETH Zurich, Switzerland. His main research interest is satellite climatology, focusing on clouds, fog, aerosols, and exchange processes in the boundary layer.

Isabel F. Trigo

Portuguese Institute for the Sea and the Atmosphere (IPMA) Lisboa, Portugal
isabel.trigo@ipma.pt



Isabel F. Trigo is a senior researcher at the Portuguese Institute for Sea and Atmosphere (IPMA), where she leads the Earth Observation Group. Her research focuses on applications of satellite observations to derive land surface variables, and on their use to better understand and model land surface processes. She coordinates the EUMETSAT LSA SAF, and has been involved in several international projects funded by ESA and European programs.

Julia Fuchs

Institute of Meteorology and Climate Research and Institute of Photogrammetry and Remote Sensing Karlsruhe Institute of Technology (KIT) Karlsruhe, Germany
julia.fuchs@kit.edu



Julia Fuchs is a research scientist at the Institute of Meteorology and Climate Research and the Institute of Photogrammetry and Remote Sensing at the Karlsruhe Institute of Technology (Germany), where she investigates the effects of urban areas on the lower atmosphere and the application of machine learning techniques to remote-sensing datasets. During her PhD, she used satellite remote sensing to map and quantify processes within the aerosol–cloud–meteorology system.

Complex

Part E

Part E Complex Measurement Systems – Methods and Applications

- 43 Atmospheric Measurements for Different Purposes**
Bodo Wichura, Potsdam, Germany
Thomas Foken, Bayreuth, Germany
- 44 Crowdsourcing**
Matthias Budde, Karlsruhe, Germany
- 45 Mesometeorological Networks**
Jerald A. Brotzge, Albany, USA
Christopher A. Fiebrich, Norman, USA
- 46 Aerological Measurements**
Holger Vömel, Boulder, USA
Masatomo Fujiwara, Sapporo, Japan
- 47 Composite Atmospheric Profiling**
Christoph Kottmeier, Karlsruhe, Germany
Bianca Adler, Boulder, CO, USA
Norbert Kalthoff, Karlsruhe, Germany
Ulrich Löhnert, Köln, Germany
Ulrich Görtdorf, Lindenberg, Germany
- 48 Aircraft-Based Flux Density Measurements**
Raymond L. Desjardins, Ottawa, Canada
Devon E. Worth, Ottawa, Canada
Ian MacPherson, Ottawa, Canada
Matthias Mauder, Dresden, Germany
Jens Bange, Tübingen, Germany
- 49 Unmanned Aircraft Systems**
Jens Bange, Tübingen, Germany
Joachim Reuder, Bergen, Norway
Andreas Platiss, Tübingen, Germany
- 50 Ground-based Mobile Measurement Systems**
Eberhard Parlow, Basel, Switzerland
Thomas Foken, Bayreuth, Germany
- 51 Measurement Systems for Wind, Solar and Hydro Power Applications**
Stefan Emeis, Garmisch-Partenkirchen, Germany
Stefan Wilbert, Almeria, Spain
- 52 Urban Measurements and Their Interpretation**
Sue Grimmond, Reading, UK
Helen C. Ward, Innsbruck, Austria
- 53 Fog Deposition**
Shih-Chieh Chang, Hualien, Taiwan
Robert S. Schemenauer, Kamloops, Canada
- 54 Immission and Dry Deposition**
Ivonne Trebs, Belvaux, Luxembourg
Christof Ammann, Zürich, Switzerland
Jürgen Junk, Belvaux, Luxembourg
- 55 Eddy-Covariance Measurements**
Matthias Mauder, Dresden, Germany
Thomas Foken, Bayreuth, Germany
Marc Aubinet, Gembloux, Belgium
Andreas Ibrom, Lyngby, Denmark
- 56 Alternative Turbulent Trace Gas Flux Measurement Methods**
Janne Rinne, Lund, Sweden
Christof Ammann, Zürich, Switzerland
Elizabeth Pattey, Ottawa, Ontario, Canada
Kyaw Tha Paw U, Davis, CA, USA
Raymond L. Desjardins, Ottawa, Canada

57 Evapotranspiration Measurements and Calculations

Richard Allen, Kimberly, USA
Thomas Foken, Bayreuth, Germany
Ayse Kilic, Lincoln, USA
Ricardo Trezza, Sacramento, USA
Samuel Ortega-Farias, Talca, Chile

58 Lysimeter

Sascha Reth, Hallbergmoos, Germany
Oscar Perez-Priego, Sydney, NSW, Australia
Heinz Coners, Göttingen, Germany
Reinhard Nolz, Wien, Austria

59 Plant Chamber Measurements

Oscar Perez-Priego, Sydney, NSW, Australia

60 Soil Chamber Measurements

Jens-Arne Subke, Stirling, UK
Lars Kutzbach, Hamburg, Germany
David Risk, Antigonish, Canada

61 Soil Measurements

Bernd Huwe, Bayreuth, Germany
Christina Bogner, Cologne, Germany
Thomas Foken, Bayreuth, Germany

62 Water Measurements

Volker Mohrholz, Rostock, Germany
Anita Flohr, Southampton, UK

43. Atmospheric Measurements for Different Purposes

Bodo Wichura, Thomas Foken 

Meteorological measurements are performed by various types of stations, including synoptic weather and climate monitoring stations, agrometeorological stations, and stations that require meteorological data for other purposes, such as to monitor traffic or air pollution or for private use. This chapter describes the history of stations that carry out atmospheric measurements, as well as recent developments in this field, mostly involving the use of new technologies to measure meteorological parameters. The specifics of the installation of stations for different purposes and the main parameters measured are summarized. The accuracy of the atmospheric measurements and the sensor system maintenance required vary depending on the intended application of the data. Therefore, the requirements for the measured meteorological parameters may differ from those defined in the corresponding parameter-specific chapters of this Handbook.

43.1	Principles of Atmospheric Measurement Station Classification ..	1188
43.1.1	General Overview of Station Types.....	1188
43.1.2	Classification of Atmospheric Measurement Stations According to Purpose.....	1189
43.1.3	Networks of Different Station Types....	1189
43.2	History	1190
43.3	Theory	1190
43.3.1	Recommendations for Synoptic Weather and Climate Monitoring Stations.....	1190
43.3.2	Parameter Requirements for Different Station Types	1191
43.4	Devices and Systems	1192
43.4.1	Single-Sensor Stations.....	1192
43.4.2	Stations with Compact Sensors	1193
43.4.3	Sensors for Networks of Different Station Types	1193
43.4.4	Sensor Comparison	1193
43.5	Specifications	1195
43.6	Quality Control	1195
43.7	Maintenance	1195
43.8	Applications	1196
43.9	Future Developments	1196
43.10	Further Reading	1197
	References	1197

Besides being used as classic weather stations, atmospheric measurements are utilized for many other purposes as well. Such data are used, for example, in research, by industry, in building services engineering, by public authorities, and by private users. Furthermore, some of the sensors in a variety of electronic devices (e.g., smartphones), can be used to measure meteorological parameters (see Chap. 44). Recommendations for the accuracy and availability of these measurements and for the maintenance of

the system that performs them may differ from those given in the corresponding parameter-specific chapters of this Handbook. Consequently, the quality and the areas of application of the resulting meteorological data differ from those of classical meteorological measurements performed at weather stations. This chapter aims to categorize the large number of applications of atmospheric measurements, and demonstrates how such data can be used for a range of purposes.

43.1 Principles of Atmospheric Measurement Station Classification

A general classification of the various types of stations used for atmospheric measurements is not yet available; indeed, such a classification could be rendered meaningless by the fast-growing number of reasons for performing atmospheric measurements and applications of them. Atmospheric measurement stations may be categorized according to the purpose of the station, the types of measurements performed, and the quality and availability of

the data. The representativeness of the measurements at various time and spatial scales can also be used as a criterion, as mentioned in Chap. 1.

43.1.1 General Overview of Station Types

A general overview of the quality of the measurements provided by various types of stations is shown in Ta-

Table 43.1 Proposed rough classification of station types; see Table 43.10 for data quality classification (high or extremely high for single sensors; medium or low for compact sensors; low or extremely low for simple sensors)

Station type	Data quality	Source of regulations
Synoptic weather and climate monitoring stations	High or extremely high	[43.1], this Handbook
Stations used for various purposes (see Sect. 43.1.2)	Medium to high	Partly [43.1, 2], this Handbook
Networks (combinations of different station types, possibly including crowdsourcing stations)	Low to high	Network internal regulations, partly defined in this Handbook
Industry, building services engineering	Low to medium	Internal regulation, partly defined in this Handbook
Crowdsourcing stations	Extremely low to low	No general regulations, partly defined in this Handbook (Chap. 44)

Table 43.2 Classification of atmospheric measurement stations [43.2, 9]

No.	Classification type	Features and recommendations	Relevant Handbook chapters
1	Microclimatological or micro-meteorological station	Miscellaneous applications with different instrumentations (e.g., biometeorological measurements)	Chapters in Part B
2	Micrometeorological station with turbulence measurements	Including eddy-covariance measurements for research purposes	Chapters in Part B and Chap. 55
3	Station for monitoring air pollution conditions	Determination of meteorological and boundary-layer parameters	Chapters in Parts B and C, Chap. 46
4	Station for immission measurements	Determination of air pollutant concentrations, along with additional meteorological measurements	Chapters in Part B and Chap. 54
5	Deposition measuring station	Determination of air pollutant concentrations in air and precipitation water, along with additional meteorological measurements	Chapters in Part B and Chap. 54
6	Landfill measuring station	Mainly for the determination of the water balance	Chapters in Part B and Chap. 57
7	Hydrological station	Mainly precipitation measurements	Chap. 12
8	Agricultural meteorological station	Miscellaneous applications with different instrumentations, (e.g., parameters for determining evapotranspiration [43.3–5])	Chapters in Part B and Chap. 57
9	Forest climate station	Measurement of meteorological elements in clearings and below trees [43.6]	Chapters in Part B
10	Urban climate station	Measurement of meteorological elements in urban locations such as street canyons, parks, etc.	Chapters in Parts B and C and Chaps. 50, 52
11	Spa climate station	Measurement of climate elements that are relevant to spa conditions	Chapters in Part B
12	Icing measurement station	Measurement of relevant meteorological elements (e.g., icing of power lines)	Chapters in Part B
13	Energy meteorological station	Measurement of parameters relevant to renewable energy (wind, solar, water)	Chapters in Parts B and C and Chap. 51
14	Noise pollution measuring station	Determination of meteorological parameters (mainly wind) that influence sound propagation [43.7]	Chapter in Part B
15	Traffic route measuring station	Measurement of meteorological elements that may affect traffic [43.8]	Chapters in Part B
16	Nowcasting station	Measurement of the current state of the weather, e.g., with present weather sensors	Chapters in Part B
17	Crowdsourcing	Measurement of meteorological elements with simple sensors (and usually not according to relevant installation instructions)	Chapters in Part B

ble 43.1. According to the data quality criteria given in Chap. 3, high and extremely high data quality are defined by a working or secondary standard established by the World Meteorological Organization (WMO) [43.1]. Medium data quality is defined according to the specifications given in the specific chapters of this Handbook. Low and extremely low data quality imply that the sensors and/or the installation do not comply with the quality specification for the specific parameter.

Furthermore, the WMO [43.1], Annex 1.B classifies stations into five classes depending on whether they fulfill the recommended siting conditions for temperature and humidity, precipitation, global and diffuse radiation, direct radiation and sunshine duration, and surface wind speed (for more in-depth discussions of siting conditions, please refer to the relevant chapters). According to this classification, a station may be assigned to different classes for different parameters (see also Chap. 45).

Data availability is high for most station types (Sect. 43.1.2) and most networks. It is still good in

industry and building engineering. However, for building engineering purposes, the sensors are often used to determine operating conditions only (by the use of corresponding limit values of meteorological parameters).

43.1.2 Classification of Atmospheric Measurement Stations According to Purpose

Classical weather stations that perform synoptic and climate monitoring measurements are described in detail by the WMO [43.1]. Other types of measurement stations can be categorized according their purpose, as shown in Table 43.2 (for more on this topic, see Sect. 43.3.1).

43.1.3 Networks of Different Station Types

The networks considered in this section are not mesoscale networks (Chap. 45) or specific atmospheric

Table 43.3 Some networks that were created to overcome deficiencies in atmospheric measurements

Name	Description	Links, references
Weather Observation Website (WOW)	WOWs are repositories for citizen weather data. They collect and share weather observations and weather impact information. WOWs are currently hosted in the UK, Netherlands, Australia, and New Zealand. Data from around the world are available. A site station description is required for continuous data upload. A basic level of data quality is ensured by community-driven reporting.	www.wow.metoffice.gov.uk , Accessed 15 July 2021
Citizen Weather Observer Program (CWOP)	CWOP is a network of private electronic weather stations that are mostly located in the United States, but data from around the world are also available. Network participants send automated surface weather observations to the National Weather Service (NWS). Temporal and spatial consistency checks are performed, and quality flags are stored.	www.wxqa.com , Accessed 15 July 2021
Community Collaborative Rain, Hail and Snow Network (CoCoRaHS)	CoCoRaHS is a network of volunteer weather observers in the United States, Canada, and the Bahamas. They report daily precipitation readings to a central data store. CoCoRaHS aims to provide accurate, high-quality precipitation data for end users.	www.cocorahs.org , Accessed 15 July 2021
Urban Meteorological Networks	There are a large number of urban meteorological networks with a wide range of research or operational objectives.	See [43.10] for a summary of these networks, including their objectives, data availability, management, and quality.
Aircraft-derived data (ADD): Automatic Dependent Surveillance (ADS)	ADS is a messaging regime used by aircraft (the standards are defined by the International Civil Aviation Organization, ICAO). ADS-Contract (ADS-C) data can be used to receive and/or derive both wind and temperature information at the aircraft's location. Additional parameters may also be available. Cooperation with either air traffic control (ATC), airlines, aircraft, or engine manufacturers is required to obtain the data, which involves data communication costs.	See [43.11] for a summary of data derivation, collection, and quality.
ADD: Mode-Selective Enhanced Surveillance Data (MODE-S EHS)	Mode-S EHS is a messaging regime used by aircraft (the standards are defined by the ICAO). Mode-S EHS data can be used to derive both wind and temperature information at the aircraft's location. Such data can be obtained using a local ADS-B/Mode-S receiver, and does not involve data communication costs.	See [43.11] for a summary of data derivation, collection, and quality.
ADD: Aircraft Meteorological Data Relay (AMDAR)	AMDAR uses the Aircraft Communications Addressing and Reporting System (ACARS) and the Aircraft Condition Monitoring System (ACMS) to provide meteorological datasets. The data is obtained through cooperation with airlines, which involves data communication costs.	See [43.11] for a summary of data derivation, collection, and quality.

(Chap. 63) or ecological (Chap. 64) networks, but networks that were created to overcome deficiencies in atmospheric measurements or to provide all available

information to another network (e.g., for nowcasting or warning systems). Table 43.3 lists a selection of some of these networks.

43.2 History

The history of synoptic weather and climate monitoring stations (as well as networks of them) is closely connected with the development of sensors (see Chap. 1 and the brief description provided in the following section). The first instructions for performing weather observations were given by *Robert Hooke* (1635–1703) [43.12], and the first stations were realized around 1660. These stations monitored the temperature, humidity, and pressure, carried out visual observations of cloud coverage (amount) and genera (type), and made other observations. Aided by *Karl Theodor*, Elector of Bavaria (1724–1799), who founded the first meteorological society—the *Societas Meteorologica Palatina* [43.13]—in Mannheim, *Johann Jakob Hemmer* (1733–1790) established a network comprising 36

stations in Europe, two in North America, and one at Greenland. Regular measurements were commenced in 1872 under the recommendation of the International Meteorological Conference at Leipzig. In 1951, the Commission for Instruments and Methods of Observation (CIMO) was founded [43.14]. The CIMO became responsible for international coordination and standardization in the field of atmospheric measurements, continuing activities that began in Leipzig 80 years earlier.

By contrast, no accounts of the historical development of other station types are available. However, the timelines of national and international recommendations or guidelines for implementing atmospheric measurements for various purposes may provide some historical information about these station types.

43.3 Theory

There is no general theory that can be applied to any meteorological station. Recommendations for the installation of a meteorological station are based upon the representativeness of meteorological parameters near the surface as well as upon experience (see Chap. 1). Some recommendations are given in [43.1], and lists of relevant parameters for different types of stations are compiled for instance in [43.2].

43.3.1 Recommendations for Synoptic Weather and Climate Monitoring Stations

The classical weather station with a Stevenson (or similar) temperature screen (see Chap. 7) comprising visual observations and a few instruments for measuring the wind, temperature, humidity, and precipitation has been widely replaced by automatic weather stations (AWS), which perform and transmit observations automatically. The general requirements, types, and locations of synoptic weather and climate monitoring stations as well as the composition, frequency, and timing of the measurements performed by them are described in [43.15, 16]. The meteorological elements required for manned and automatic surface synoptic weather stations are listed in Table 43.4. For other WMO station types, such as aeronautical or agricultural meteorological stations, see [43.16]. The specific requirements for measurements, site conditions, and measured data quality are given in [43.1] as

well as in the relevant chapters of this Handbook. In general, fewer meteorological parameters can be measured by an AWS than by a manned station. Therefore, there is a tendency to replace particular parameters with others, or to combine parameters (see Chap. 22).

Classical meteorological observing stations are designed to perform representative measurements. Thus, synoptic weather stations should permit observations that are representative for the synoptic scale, whereas stations used for other purposes can also determine values that are representative for more local conditions [43.1]. Synoptic weather or climate monitoring stations typically cover an area of at least 25 m × 25 m, covered with grass or a surface that is representative of the locality, and are surrounded by open fencing. Within this area, a patch of bare ground approximately 2 m × 2 m in size is reserved for soil-related measurements (see Chap. 61). All instruments should be installed according to the recommendations [43.1] given in the relevant chapters of this Handbook. Further recommendations for the siting of meteorological stations are provided in [43.17], and an example of such a station is shown in Fig. 43.1.

In general, the site for a particular type of observing station should be chosen based on the most stringent requirements for that station type [43.1, Sect. 1.3.3]. This means that requirements regarding the siting, the area, the surface conditions, and the area surrounding the station may differ from the corresponding requirements for

Table 43.4 Meteorological elements that are monitored by manned and automatic surface synoptic weather stations [43.16] (observables marked with a × are required, while those marked with a 0 are desirable but not required)

Meteorological element	Manned station	Automatic station	Relevant chapter
Present weather	×	× ^a	Chap. 22
Past weather	×		Chap. 22
Wind direction and speed	×	×	Chap. 9
Amount of clouds	×		Chap. 22
Cloud type	×		Chap. 22
Height of cloud base	×	0	Chaps. 22 and 24
Visibility	×	0	Chap. 13
Air temperature	×	×	Chap. 7
Humidity	×	×	Chap. 8
Atmospheric pressure	×	×	Chap. 10
Pressure tendency	0		Chap. 10
Characteristic of the pressure tendency	0		Chap. 10
Extreme temperature	0		Chap. 7
Precipitation (yes or no)		×	Chap. 12
Amount of precipitation	×	0	Chap. 12
Intensity of precipitation		0	Chap. 12
State of ground	0		Chap. 22
Direction of cloud movement	0		Chap. 22
Special phenomena	0	0	Chap. 22
Snow depth or snow cover	×	0	Chap. 22
Sunshine duration and/or solar radiation ^b		0	Chap. 11
Soil temperature ^b	0	0	Chaps. 7 and 61

^a Present weather sensor, Chaps. 12 and 13

^b Only monitored by climatological stations

**Fig. 43.1** Photo of a meteorological observing station (Station Quickborn, Germany; photo © S. Waas)

classical synoptic weather or climate monitoring stations.

43.3.2 Parameter Requirements for Different Station Types

Each type of station defined in Sect. 43.1.2 (see also Table 43.2) must monitor a specific set of parameters, while measurements of some other parameters are optional. These required and optional parameters are listed

for each station type in Table 43.5. The parameter symbols used in Table 43.5 are explained in Table 43.6, which also points to the Handbook chapters in which each parameter is discussed and to Table 1.1 in Chap. 1. The latter table lists the chapters that describe the in-situ and remote-sensing methods employed to measure the parameters. The set of parameters that are observed by a particular type of station depend on its purpose or the installation recommendations for that station type (Table 43.2).

Table 43.5 Parameters that are measured by different types of stations (station type numbers are defined in Table 43.2; parameter symbols are defined in Table 43.6; parameters marked with a × must be monitored, whereas it is not required but it is desirable to monitor those marked with a 0) [43.2]

Station type number	t_a	R	u_h	dd	R_N	$K\downarrow$	Q_s^*	t_{IR}	PAR	t_s	f_s	Q_G	p	ww	Q_H	Q_E	Q_c	τ
1	×	×	×	×	×	0							0	0				
2	×	×	×	×	×	0	×					0	0		×	×	0	×
3	0	0	×	×		0	0						0	0				0
4	×	×	×	×	0	0												
5	×	×	×	×	0	0												
6	×	×	×	×	×	0	×											
7	0	0	0		×		0											
8	×	×	×	×	×	0	0		0	×	×	0	0					
9	×	×	×	×	×	×	0		0	0	0							
10	×	×	×	×	×	0	0						0					
11	×	×	×	×		0												
12	0	0	×	×	×	×							×	×				
13	×	×	×	×	×									×				
14	×		×	×											0			0
15	×	×	×	×	0			0		0				×				
16	×	×	×	×	×	0							0	×				
17	×	×	0	0									0					

Table 43.6 The parameters measured by each type of station (see also Table 43.5), and sources of further information on each measured parameter

Symbol	Parameter	Refer to
t_a	Air temperature	Chap. 7, Table 1.1
RH	Humidity (relative humidity)	Chap. 8, Table 1.1
u_h	Horizontal wind speed	Chap. 9, Table 1.1
dd	Wind direction	Chap. 9, Table 1.1
R_N	Precipitation	Chap. 12, Table 1.1
$K\downarrow$	Global radiation	Chap. 11, Table 1.1
Q_s^*	Net radiation	Chap. 11, Table 1.1
t_{IR}	Surface (IR) temperature	Chap. 11
PAR	Photosynthetically active radiation	Chap. 11
t_s	Soil temperature	Chaps. 7 and 61, Table 1.1
f_s	Soil moisture	Chap. 61, Table 1.1
Q_G	Ground heat flux	Chap. 61, Table 1.1
p	Air pressure	Chap. 10, Table 1.1
ww	State of the weather	Chap. 22
Q_H	Sensible heat flux	Chap. 55, Table 1.1
Q_E	Latent heat flux (evapotranspiration)	Chaps. 55 and 57, Table 1.1
Q_c	Trace gas flux	Chaps. 54 and 55, Table 1.1
τ	Friction	Chaps. 54 and 55, Table 1.1

43.4 Devices and Systems

Possible sensor combinations that can fulfill the measurement requirements of particular station types are discussed in this section, while the individual sensors are described in the relevant chapters of Part B of this Handbook.

43.4.1 Single-Sensor Stations

In principle, all of the station types listed in Table 43.2 can be implemented using single sensors. Nevertheless, the current trend is to use combined sensors

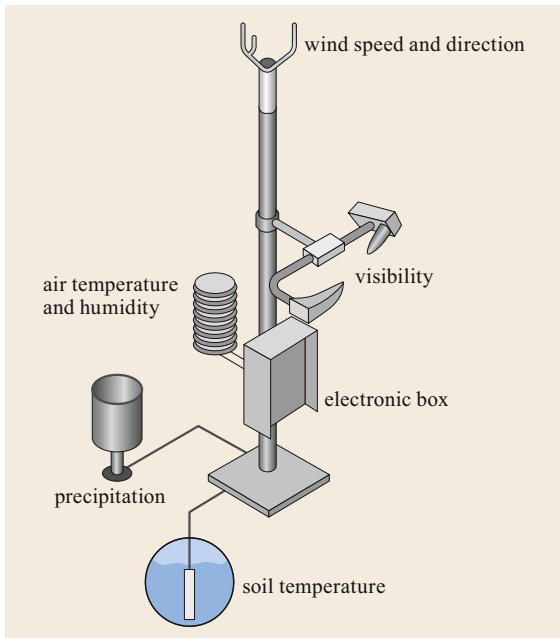


Fig. 43.2 Schematic of an automatic weather station (© Vaisala Oyj, Vantaa, Finland)

or even more specific configurations for some station types (Sect. 43.4.2). Only automatic synoptic weather and climate monitoring stations (i.e., AWS) and micrometeorological stations are typically installed with single sensors. This ensures that the highest data quality requirements of the WMO [43.1] will be achieved, and allows the sensor to be positioned precisely at the specified measurement height (e.g., 10 m for wind, 2 m for temperature and humidity, and 1 m for precipitation). The sensors used in AWS should be selected according to Table 43.4 [43.16] and regional standards. A schematic example of an AWS is shown in Fig. 43.2.

The configuration of a micrometeorological station or agricultural meteorological station is tailored to specific measurement requirements or research programs [43.5, 9]. Such stations are also used in ecological networks with region-dependent standards (see Chap. 64). More on this topic is provided in Chap. 55.

43.4.2 Stations with Compact Sensors

There is a fast-growing market for compact systems (multiparameter sensors) for measuring meteorological parameters. Such systems are easy to handle, mainly due to the fact that only one compact sensor block

must be mounted. The disadvantages of these systems are flow distortion effects on wind measurements and the need for different sensor heights to measure different parameters (e.g., wind and precipitation). In some compact sensor systems, wind and precipitation sensors can be installed separately. Most compact sensor systems are modular and combinable during the configuration process, and the user can select the most suitable sensors for the required measurements. Table 43.7 shows four examples of compact sensors. New compact sensor systems are continually in development. Therefore, the configurations and datasheets should be requested as needed. Measurement principles vary significantly depending on the system. Table 43.8 provides an overview of the most common principles.

For some specific station types the design has been modified to better achieve their aim. For instance, the spatial density of stations may not be high enough to measure the parameter of interest accurately, so mobile sensors are also used (see Chap. 50), e.g., for road and urban measurements.





43.4.3 Sensors for Networks of Different Station Types

A wide variety of sensors are used in networks of different station types. The sensors used depend on the purpose of the network and the participating parties, and vary from highly accurate measurement devices (see Sect. 43.4.1) to compact sensors (see Sect. 43.4.2) and simple sensors (see Chap. 44). In particular, in some networks such as ADS-C or Mode-S EHS (Table 43.3), a sensor is not needed to estimate the meteorological parameters of interest. In these cases, the required meteorological data are deduced from other information, such as aircraft flight parameters. Therefore, it is virtually impossible to summarize the sensors that are used in networks of different station types.

43.4.4 Sensor Comparison

The most appropriate sensor system to use in a station depends on the measurement quality required and the level of maintenance that is feasible. These should be decided upon before any system is applied (see Chap. 3). Quality assurance is therefore very important and should not be underestimated. Some basic information on the advantages and disadvantages of the sensor configurations used for different station types is given in Table 43.9.

Table 43.7 Some compact measurement systems (photos © OTT HydroMet Fellbach GmbH, Germany; Adolf Thies GmbH & Co. KG, Göttingen, Germany; Vaisala Oyj, Vantaa, Finland, Gill Instruments Ltd., Lymington, UK) [43.2]

OTT HydroMet (e.g., WS 800 UMB)	Thiesclima (e.g., Clima-Sensor US)	Vaisala (e.g., WXT530)	Gill (e.g., GMX 531)
Most important measured parameters			
Air temperature, relative humidity, air pressure, wind direction, wind speed, precipitation intensity, amount of precipitation, radiation, lightning	Air temperature, relative humidity, air pressure, wind direction, wind speed, precipitation intensity, amount of precipitation, radiation	Air temperature, relative humidity, air pressure, wind direction, wind speed, precipitation intensity, amount of precipitation	Air temperature, relative humidity, air pressure, wind direction, wind speed, dewpoint, radiation, precipitation intensity, amount of precipitation
Specific features			
Ventilated screen		Acoustic rain gauge	Separated rain gauge
			
photo © OTT HydroMet Fellbach GmbH, Germany	photo © Adolf Thies GmbH & Co. KG, Göttingen, Germany	photo © Vaisala Oyj, Vantaa, Finland	photo © Gill Instruments Ltd., Lymington, UK

Note that the devices shown here were selected to highlight that device construction can vary markedly. These types of devices are sold by many companies, who fit them with various equipment, meaning that this table should not be used for comparison purposes

Table 43.8 Measurement principles used for compact measurement systems [43.2]

Measured parameter	Measurement principle
Temperature	Thermocouple, thermistor, Pt100/Pt1000
Relative humidity	Capacitive
Air pressure	Capacitive
Wind direction	Ultrasound Wind vane
Wind speed	Ultrasound Cup anemometer
Precipitation	Acoustic, radar, tipping bucket (separated)
Global radiation	Semiconductor, thermopile
Brightness	Semiconductor
Lightning	Radio wave detector

Table 43.9 Advantages and disadvantages of the different sensor configurations (for data quality, see Table 43.10)

Configuration	Advantages	Disadvantages
Single sensor	Highly accurate measurements, easy to compare measurements between stations within a network	Expensive sensors, considerable maintenance required
Compact sensor	Easy-to-handle sensors, good price-to-quality ratio	Often do not comply with the WMO recommendations
Simple sensor for crowdsourcing	Inexpensive sensors or devices, readily available in large numbers/quantities	Data can only be used and compared with considerable mathematical effort (see Chap. 44)
Sensors for networks of different station types	Configuration has the advantages and disadvantages of the other sensor configurations (depending on the purpose of the network and the participating parties)	

Table 43.10 Measurement uncertainties and recommended installation heights for standard measurements performed using various station configurations (based on Table 1.5, Chap. 1)

Parameter	Typical sensor(s)	Recommended installation height (m) ^a	Typical measurement uncertainty		
			Single sensor	Compact sensor	Simple sensor ^b
Air temperature	Pt resistance with a radiation screen	2.0	1 K	1 K	2 K
	Pt resistance, ventilated with a radiation screen	2.0	0.1 K	0.3 K	
Humidity	Capacitive sensor	2.0	1%	5%	10%
Wind speed and direction	Cup anemometer with wind vane	10.0	0.2 m s ⁻¹ 3°		
	Sonic anemometer	10.0	0.1 m s ⁻¹ 2°	0.3 m s ⁻¹ 3°	
Pressure	Piezoelectronic sensor	Fixed height ASL	0.1 hPa	0.5 hPa	1 hPa
Precipitation	Rain gauge	1.0	0.1 mm resolution ≈ 10%	0.1 mm resolution ≈ 10%	
Global radiation	Pyranometer	≈ 2.0	5 W m ⁻²	20 W m ⁻²	

^a For standard measurements

^b Note that measurement uncertainties for simple sensors are estimated values (see Chap. 44)

43.5 Specifications

The general specifications for single sensors are described in the relevant chapters in Part B and Table 1.5 (Chap. 1) of this Handbook. The accuracies of compact sensors are slightly lower than those of single sensors (Table 43.10). A comparison of data from compact sensors with standard meteorological measurements is only possible if the recommendations for the measurement height and location are fulfilled when using compact sensors. Since these sensors are used in measurement stations for specific applications (Table 43.2), the specifications for standard meteorological mea-

surements are often not relevant for compact sensors. A common additional source of error for simple sensors used in crowdsourcing is inaccurate sensor installation, e.g., no radiation screen for temperature and humidity measurements, or different installation heights. Therefore, the main problem with these sensors is generally not their accuracy (see Table 43.10) but their installation. In principle, this issue can be resolved by selecting appropriate data from a large number of sensors (see Chap. 44) through the application of adequate filter techniques.

43.6 Quality Control

The principles of quality assurance and quality control (see Chap. 3) are valid for stations with single and compact sensors. The procedures followed for

the various meteorological parameters of interest are described in the relevant chapters in Part B of this Handbook.

43.7 Maintenance

The maintenance requirements are identical for stations with single and compact sensors, and similar for specific networks and industrial applications. The maintenance recommendations for specific sensors are given in the chapters of Part B of this Handbook. Table 43.11 provides a general overview of the maintenance re-

quirements for the station types listed in Table 43.1. For sensors used in specific networks (Table 43.3), for industrial applications, and for crowdsourcing, it is often cheaper to replace the sensor than to carry out costly maintenance work.

Table 43.11 Sensor maintenance for different types of stations (see Table 43.1)

Maximum interval	Single-sensor station	Station with compact sensors	Sensors in networks	Sensors used in industry and building engineering	Sensors for crowdsourcing ^a
1 week	Maintenance of special sensors if required				
	Check function and plausibility; if the sensor is not operating correctly, it must be serviced, replaced, or excluded from the network				
3 months	Check mechanical function, perform maintenance on special sensor types if required				Replace sensors with a permanent malfunction or exclude them from the network
2 years	Sensor calibration; replace sensors if necessary				
If a sensor check reveals a significant malfunction, the instrument should be replaced.					
^a Data need to be quality checked and corrected or deleted before further application					

43.8 Applications

Examples of how data for various meteorological parameters are used are described in the relevant chapters of Part B of this Handbook. The station types described in this chapter (see Table 43.1) cover practically every conceivable field of application of atmospheric measurements. Starting with classical weather stations for synoptic and climate monitoring measurements, Table 43.2 categorizes a large number of atmospheric

measurement station types according to their utilization in different areas of meteorology, hydrology, and environmental science. More recent applications include collecting and transferring all available information from atmospheric measurements to new networks or estimating atmospheric data from other networks. See Table 43.3 and Chaps. 63 and 64 for examples that can be accessed online.

43.9 Future Developments

Recently, there has been a trend for customers to choose less expensive sensors with medium to high data quality and data availability (see Table 43.10) and low maintenance costs. In order to comply with these requirements, manufacturers have been developing compact sensors (Sect. 43.4.2) that combine sensors and reduce the number of measurement principles utilized. This trend is likely to continue in the near future.

Single sensors will only be used in synoptic weather and climate monitoring stations or for research purposes due to their high accuracy, their specific requirements for maintenance, and their larger scope of measurements. It is likely that compact sensors will be increasingly used for atmospheric measurements at other stations. Due to their modular layout, they can be tailored to specific uses.

Networks that combine different station types (i.e., stations with private users, those with industrial users, and those with users from building services) will likely develop more rapidly due to the availability of inexpensive sensors with reasonable data quality and low maintenance costs. The ability to access the data generated

by many stations online, along with meta-information on their geographical locations, the characteristics of their surroundings, and sensor and installation heights, offers the ability to monitor atmospheric parameters to a much greater spatial density than some national monitoring networks can. In these cases, the accuracy of the sensors at the various locations is not the primary problem. The challenge is to develop software solutions for quality assurance and quality control that can distinguish between good and biased data, thus allowing a representative and sufficiently accurate spatial distribution of the atmospheric parameters to be derived and subsequently applied.

Nevertheless, climate monitoring stations, stations used for research purposes, and stations used for other purposes will continue to be utilized too, as only those stations can meet the requirements for data quality, long time series, and the collection of specific atmospheric data, respectively. Combining data from classical atmospheric measurement stations with atmospheric data measured and collected in new ways via inhomogeneous networks and crowdsourcing will be the most challenging and exciting task in the near future.

43.10 Further Reading

- VDI: Umweltmeteorologie, Meteorologische Messungen, Meteorologische Stationen (Environmental Meteorology, Meteorological Measurements, Meteorological stations, in German and English), VDI 3786 Blatt(Part) 13, (Beuth-Verlag, Berlin 2019)
- WMO: Guide to Instruments and Methods of Observation, WMO-No. 8, Volume I - Measurement of Meteorological Variables. (World Meteorological Organization, Geneva, 2018)

References

- 43.1 WMO: *Guide to Instruments and Methods of Observation, WMO-No. 8, Volume I - Measurement of Meteorological Variables* (World Meteorological Organization, Geneva 2018)
- 43.2 VDI 3786 Part 13: *Environmental Meteorology, Meteorological Measurements, Measuring Station* (Beuth, Berlin 2019)
- 43.3 R.G. Allen, L.S. Pereira, D. Raes, M. Smith: *Crop Evaporation: Guidelines for Computing Crop Water Requirements. Irrigation Drainage Paper 56* (Food and Agriculture Organization of the United Nations, Rome 1998)
- 43.4 R.G. Allen, I.A. Walter, R. Elliott, T. Howell, D. Itenfisu, M. Jensen: *The ASCE Standardized Reference Evapotranspiration Equation* (ASCE-EWRI Task Committee, Reston, VA 2005)
- 43.5 J.L. Hatfield, J.M. Baker, M.K. Viney (Eds.): *Micrometeorology in Agricultural Systems*, Agronomy Monographs, Vol. 47 (ASA, CSSA, SSSA, Madison 2005)
- 43.6 H.-P. Dietrich, S. Raspe, C. Schulz: Waldklimastationen – Säule Forstlicher Umweltbeobachtung, *AFZ/Der Wald* **18**, 972–974 (2006)
- 43.7 ISO 9613-2: *Acoustics – Attenuation of Sound During Propagation Outdoors – Part 2: General Method of Calculation* (Beuth, Berlin 1996)
- 43.8 EN 15518-3: *Winter Maintenance Equipment – Road Weather Information Systems – Part 3: Requirements on Measured Values of Stationary Equipment* (Beuth, Berlin 2011)
- 43.9 T. Foken: *Micrometeorology*, 2nd edn. (Springer, Berlin, Heidelberg 2017)
- 43.10 C.L. Muller, L. Chapman, C.S.B. Grimmond, D.T. Young, X. Cai: Sensors and the city: A review of urban meteorological networks, *Int. J. Climatol.* **33**, 1585–1600 (2013)
- 43.11 EUMETNET: *Final Report of the EUMETNET Aircraft Derived Data Feasibility Study Expert Team on the Feasibility to Initiate a New EUMETNET Activity for Aircraft Derived Observations under the EUMETNET Observation Program* (EUMETNET ADD FS ET, Brussels 2017)
- 43.12 N.R. Dalezios, P.T. Nastos: Milestones of the diachronic evolution of meteorology, *Int. J. Glob. Environ. Issues* **15**, 49–69 (2016)
- 43.13 Societas Meteorologica Palatina (Ed.): *Ephemerides Societatis Meteorologicae Palatinae. Observationes Anni 1789* (Societas Meteorologica Palatina, Mannheim 1793)
- 43.14 O.M. Ashford, S. Gupta, P.J. Meade, H. Taba, G. Weiss (Eds.): *Forty Years of Progress and Achievement* (World Meteorological Organization, Geneva 1990), WMO-No. 721
- 43.15 WMO: *Manual of Codes, Part A, B, C* (World Meteorological Organization, Geneva 2011), WMO-No. 306, updated version 2017
- 43.16 WMO: *Manual on the Global Observing System, Volume I – Global Aspects* (World Meteorological Organization, Geneva 2015), WMO-No. 544, updated version 2017
- 43.17 WMO: *Siting and Exposure of Meteorological Instruments (J. Ehinger)* (World Meteorological Organization, Geneva 1993), WMO/TD No. 589, IOM No. 55

Bodo Wichura

Climate and Environment Consultancy,
Regional Office Potsdam
German Meteorological Service (DWD)
Potsdam, Germany
bodo.wichura@dwd.de



Bodo Wichura is a senior scientist and expert in technical meteorology at the German Meteorological Service (DWD), Potsdam. He received his PhD in micrometeorology in 2009 from the University of Bayreuth. He is a member of and actively contributes to various working groups for German and European standards committees (DIN, DKE, VDI, CEN, CENELEC) that focus on aspects of technical meteorology.

Thomas Foken

University of Bayreuth
Bayreuth, Germany
thomas.foken@uni-bayreuth.de



Thomas Foken is a retired Professor of Micrometeorology at the University of Bayreuth. He was the head of Laboratories at the meteorological observatories at Potsdam (1981–1994) and Lindenberg (1994–1997). His research interests include the interaction between the Earth's surface and the atmosphere and the measurement and modeling of energy and matter fluxes, with a strong focus on experimental meteorology. His scientific contributions have been recognized through various international awards.

Crowdsourcing

44. Crowdsourcing

Matthias Budde 

Aside from classical meteorological measurements from a wide variety of weather stations, so-called crowdsourcing approaches have been applied to the collection of meteorological data, as well as generally atmospheric measurements in recent years. The topic of this chapter is crowdsourcing, but it is also a broad overview of sensors applied in crowdsourcing and corresponding projects. This chapter first introduces the definition and typology of the relevant terminology, along with a short history of crowdsourcing. We describe and discuss aspects of both the typically employed low-cost measurement technology, as well as human factors that emerge from laypersons carrying out the measurements. This includes general considerations concerning measurement uncertainty, as well as possible measures to improve the data quality in mobile nonexpert sensing. Devices and sensors, ranging from dedicated devices over do-it-yourself sensors to internal smartphone sensors are discussed, as are a number of applications and projects that illustrate in which ways crowdsourcing approaches have been applied to the measurement of atmospheric parameters and what type of challenges have been addressed and which ones remain.

44.1 Measurement Principles and Parameters	1200
44.1.1 General Overview	1200
44.1.2 Parameters	1200
44.2 History	1201
44.2.1 Evolution of Crowdsourcing	1201
44.2.2 Low-Cost Sensors and Crowdsensing Hardware	1201
44.3 Theory	1202
44.3.1 Definition and Typology	1202
44.3.2 Promises and Criticism	1204
44.3.3 Human Factors in Crowdsourcing	1205
44.3.4 Measurement Uncertainty	1206
44.4 Devices and Systems	1207
44.4.1 Dedicated Devices	1207
44.4.2 Do-It-Yourself Platforms	1207
44.4.3 Smartphone Accessories	1208
44.4.4 Internal Smartphone Sensors	1210
44.4.5 Human Observation	1211
44.4.6 Comparison of Sensors	1211
44.5 Specifications	1212
44.6 Quality Control	1213
44.6.1 Calibration	1214
44.6.2 Mitigating Human Influence	1215
44.7 Maintenance	1217
44.8 Applications	1218
44.9 Future Developments	1227
References	1227

Besides data collection from classical weather stations, gathering meteorological (or generally atmospheric) measurements has become possible with technology operated by nonexperts, as, e.g., citizens. So-called crowdsourcing approaches distribute tasks, such as, for example, data collection, to a group of individuals. This chapter provides an introduction of the general underlying concepts, the history of crowdsourcing, as well as an overview of low-cost measurement technology

and applications in atmospheric measurements. This includes an attempt to classify sensors and devices on the one hand and example projects on the other. In addition to presenting an overview of crowdsourcing in atmospheric measurements, this chapter discusses some specific aspects more deeply, such as measurement uncertainty, possible measures to improve the data quality in mobile nonexpert sensing, challenges and approaches, as well as possible future developments.

44.1 Measurement Principles and Parameters

Crowdsourcing has increasingly been applied in different ways and in different fields over the past two decades. Since the underlying concepts and the terminology employed are almost as diverse as the projects and the measurement technology employed, we begin this chapter by briefly introducing crowdsourcing as a general concept and present an overview of the atmospheric parameters that can be measured using crowdsourcing approaches.

44.1.1 General Overview

There are different notions of what crowdsourcing entails exactly. According to an integrated definition that was proposed in 2012 [44.1], crowdsourcing entails a task that is assigned online and uses the Internet, with a clear goal being carried out by a clearly defined crowd, which receives some form of recompense from a clearly defined crowdsourcer, who in turn receives some sort of compensation from the task being carried out. This definition, along with a typology of crowdsourcing systems, is discussed in more depth in Sect. 44.3.

Other concepts that are related to the notion of crowdsourcing include *citizen science (CS)*, *mobile crowdsourcing (MCS)*, *crowdsensing*, *participatory sensing (PS)* [44.2], *volunteered geographic information (VGI)* [44.3], *public participatory geographic information systems (PPGIS)*, *public–private partnerships (PPP)*, and others. They partially overlap and/or may also have differing definitions. Citizen science is a very broad term as well and does not necessarily include an online activity, and as the name says, it often involves the claim of contributing to science in some way. In this chapter, we include citizen science projects that have reached a certain scale. The concepts of participatory sensing (PS) and (mobile) crowdsensing both entail data collection with personal handheld devices, mostly smartphones. Another important factor in participatory sensing is the focus on the user, as the concept intrinsically involves empowering citizens [44.2].

44.1.2 Parameters

Measurement principles are highly variable for different systems, as are the capabilities in terms of meteorological parameters that can be detected, as well as, of course, the quality of the data provided by different instruments. In principle, any meteorological parameter could be measured with a crowdsourcing approach.

However, crowdsourcing is typically only feasible if the cost of the device is in a range that makes it either affordable for the crowdsourcer to fund it or possible that crowdworkers themselves cover the cost. This usually prohibits collecting data on parameters that can only be measured with intricate and expensive equipment. On the other hand, there are low-cost sensors for many meteorological parameters today.

Table 44.1 gives an overview of the meteorological parameters that can be typically covered with different devices and device classes, which we have roughly divided into five groups: *automatic weather stations (AMS)*, often commercially available *dedicated systems* (e.g., consumer devices), *do-it-yourself (DIY) platforms* that require some technical understanding and possibly assembly by the crowdworkers, and *smartphone accessories* that in some way interface with mobile phones and leverage its processing, storage, and/or communication capabilities. Finally, some approaches try to

Table 44.1 Data sources and meteorological and atmospheric elements of crowdsourcing

Data source	Atmospheric parameter	Relevant chapter
Internal smartphone sensors	Temperature Surface pressure Humidity	This chapter, Chaps. 7, 8, 10
Smartphone add-ons	Temperature Particulate matter Wind speed	This chapter
Cars	Temperature	Chap. 7
Venetian blind	Wind speed Shortwave radiation	Chap. 9, Chap. 11
Automatic weather stations (AMS)	Temperature Humidity Barometric pressure Wind speed Wind direction Precipitation etc.	Chap. 43, this chapter
Dedicated devices/personal weather stations	Temperature Humidity Barometric pressure Wind speed Wind direction Precipitation	This chapter, Chap. 43
Do-it-yourself (DIY) platforms	Temperature Humidity Particulate matter Wind speed	This chapter
Human observation	Qualitative data, e.g., on precipitation Data processing	This chapter

use *internal smartphone sensors* to directly assess parameters, such as temperature or atmospheric pressure. Section 44.4 lists examples of individual devices from each of these classes.

Besides these groups of technical systems, *human observation* is a notable data collection approach in crowdsourcing. This entails crowdworkers directly observing certain meteorological events and creating and submitting according reports. These are typically of a qualitative nature, i.e., observing precipitation events and reporting type and intensity. In addition to direct

observation, crowdworkers can also be employed for crowdanalyzing of tasks, i.e., in some way analyzing, classifying, or annotating existing data.

Whatever the underlying collection approach, crowdsourcing is typically impacted both by the measurement equipment and the humans involved. In the remainder of this chapter, we present possible measures to increase the quality of data collected by nonexpert users and discuss tradeoffs between the data quality of established measurement equipment and the scale of low-cost sensors.

44.2 History

While the term crowdsourcing is little more than a decade old, many related concepts existed before this. This section first briefly introduces the origin of the terminology. Subsequently, it presents a brief history of crowdsourcing, as well as of the hardware typically employed in crowdsensing. While, in principle, any level of device fidelity can be used, in most cases, low-cost sensors or consumer devices are, as other technology is prohibitively expensive and/or not obtainable by crowdworkers. The device history is related to the general development of meteorological sensors, as discussed in Chap. 1.

44.2.1 Evolution of Crowdsourcing

The term crowdsourcing is usually attributed to *Jeff Howe* who originally coined it in his article *The Rise of Crowdsourcing* [44.4] in *Wired magazine* in June 2006. It is a portmanteau of the words *crowd* and *outsourcing*, initially describing the business practice of literally outsourcing an activity to the crowd. It since has evolved and is used for all sorts of tasks being carried out by some group of people.

However, both the idea and the practice of using crowds to solve a challenging problem date back much further. In fact, according to the definition presented in Sect. 44.1.1 above, almost any announcement of a contest could be seen as a (competitive) crowdsourcing call. That is why early examples for crowdsourcing activities often include the Longitude Prize of 1714, the French Food Preservation Prize of 1795, or the Orteig Prize of 1919. An early example that is of a noncompetitive nature is the Oxford English Dictionary, which called for the submission of entries through newspapers in 1884.

However, as current crowdsourcing definitions typically include an activity that in some way involves usage of the Internet, the earliest examples that actually

qualify are probably the first online software sharing communities in the 1980s, in which so-called bulletin board systems (BBS) were used to collaboratively collect and modify source code. The first major crowdsourcing system that uses the Internet in today's sense is probably the community-driven Wikipedia project that was launched in 2001.

In 2004, *James Surowiecki* discussed the opportunities of crowdsourcing – still 2 years before the term was coined by *Jeff Howe* – in his book *The Wisdom of Crowds* [44.5]. Since then, a plethora of projects of different types have been realized. Countless online contests have leveraged the creativity of the crowd. Microwork platforms, such as the *Amazon Mechanical Turk* (launched in 2005) have emerged; some of them developed into general microtask markets, others specialized in tasks, such as software testing or graphical design. Platforms such as *Indiegogo* (2008) or *Kickstarter* (2009) have enabled diverse crowdfunded products, games, and even multimillion dollar movies. Moreover, in academia, countless research projects managed to engage volunteers for various purposes. Common applications of crowdsourcing in citizen science are both data processing as well as data gathering. Through crowdsensing, large volumes of data covering many geographical locations or moments in time can be collected today.

44.2.2 Low-Cost Sensors and Crowdsensing Hardware

In terms of the hardware employed, the origins of low-cost sensors, according communication technology and network intelligence have their roots in the advent of wireless sensor networks (WSNs) and, before that, in telemetric systems. The first academic WSN research was military driven, sponsored by the US Defense Advanced Research Projects Agency (DARPA),

and the first conference on the matter *A Workshop on Distributed Sensor Nets*, was held at Carnegie-Mellon University in December 1978. Back then, sensor nets were conceived differently from today, the emphasis lying mainly on distribution and less on miniaturization, mobility, or self-organization [44.2]. This workshop marks the starting point of approaches to sensor networks taken in the following years.

Over the course of the 1990s, advances in micro-electromechanical systems (MEMS) and system-on-chip (SOC) technologies allowed the development of small, generic, embedded devices with onboard sensors, short-range wireless communication, processing, and storage capabilities. The earliest attempts at developing such devices were the DARPA-sponsored UCLA programs *low-power wireless integrated microsensors (LWIM)* [44.6] and *wireless integrated network sensors (WINS)* [44.7], both initiated in the early 1990s. These projects resulted in the commercial production of the first inexpensive low-power sensor node platforms, which showed the integration of an embedded processor, wireless radio, and multiple sensors into a single device.

44.3 Theory

As already mentioned, crowdsourcing is neither entirely new, nor so well-defined that there would be one theory behind it. Instead, different aspects are of importance. We therefore begin this section with a definition of crowdsourcing and a typology of different classes of crowdsourcing approaches. Subsequently, we will go deeper into the peculiarities of crowdsourcing systems compared to classical measurement approaches, both in terms of challenges as well as potential benefits.

In the remainder of this section, we focus on approaches that involve data collection by nonexperts with nonstandard measurement equipment. The central issue in such systems is data quality, and the two factors that have the most impact on this are the user and low-cost sensing technology. We therefore shortly discuss ways in which humans may affect the quality in a crowdsourcing data collection system. Subsequently, a bit of mathematical theory is presented in order to enable a better understanding of the tradeoffs involved in using low-cost sensors at a large scale.

44.3.1 Definition and Typology

As was already briefly discussed in the introduction, detailed definitions of what exactly crowdsourcing

In 1998, DARPA initiated the *Smart Dust* program with the ambitious task of creating integrated sensor nodes measuring only 1 cubic millimeter by the year 2001. While this goal had not been reached by the end of the project, remarkable miniaturization was achieved, and the project fueled the development of WSN hardware and software outside the immediate scope of the program. In Europe, the EU project *Smart-Its* [44.8] developed a similar but more modular platform in 2000.

Around the same time, first projects that integrated mobile phones with sensor technology ushered in the era of mobile computing. The first one was the EU-project *TEA* (Technology for Enabling Awareness) in 1999 [44.9, 10] that extended a commercial mobile phone with various sensors similar to the ones we find in smartphones today, including, among others, a sensor for ambient temperature measurement.

Today, low-cost sensors, either standalone or available in inexpensive personal devices, enable unprecedented measurement networks and bottom-up citizen science approaches that have also started to influence and change the field of meteorological observations and analysis.

means – and what not – differ. While the term crowdsourcing originated in 2006 [44.4], there are earlier examples of the concept. In 2012, an integrated definition of crowdsourcing was proposed [44.1], which was formulated deliberately wide in order to cover most, if not all, of the (at the time) existing crowdsourcing processes. In verbatim, this definition is [44.1]:

Crowdsourcing is a type of participative online activity in which an individual, an institution, a nonprofit organization, or company proposes to a group of individuals of varying knowledge, heterogeneity, and number, via a flexible open call, the voluntary undertaking of a task. The undertaking of the task, of variable complexity and modularity, and in which the crowd should participate bringing their work, money, knowledge, and/or experience, always entails mutual benefit. The user will receive the satisfaction of a given type of need, be it economic, social recognition, self-esteem, or the development of individual skills, while the crowdsourcer will obtain and utilize to their advantage that what the user has brought to the venture, whose form will depend on the type of activity undertaken.

Table 44.2 Defining elements of crowdsourcing, according to an integrated definition [44.1]

No.	Description	Element
1	There exists a task with a clear goal	E2
2	There is a clearly defined crowd	E1
3	The recompense received by the crowd is clear	E3
4	The crowdsourcer is clearly identified	E4
5	The compensation to be received by the crowdsourcer is clearly defined	E5
6	It uses an open call of variable extent	E7
7	It is an online assigned process of participative type	E6
8	It uses the Internet	E8

Summing this up, the definition entails eight distinguishing elements (originally numbered E1–E8, Table 44.2). A task with (1) a clear goal being (2) carried out by a clearly defined crowd, which (3) receives some form of recompense from (4) a clearly defined crowdsourcer, who in turn (5) receives some sort of compensation from the task being carried out. Three additional constraints concerning the task are defined. First, that (6) the task is assigned via a somehow open call, second, that it (7) is an online assigned participative process, and third that it (8) uses the Internet.

If not interpreted too narrowly, the above definition covers all projects and applications featured in this chapter. However, depending on how strictly one takes the definition, individual ones could be seen as not meeting all of the eight conditions. Especially the latter constraints might exclude interesting systems. We adopt a broad interpretation here. Specifically, we do

not exclude projects that are not assigned online or do not involve an online activity. Passive sharing of meteorological data from personal weather stations could, for example, be seen as not being an online activity (or, for that matter, an activity at all). In addition, we include approaches that may not have a clearly defined crowdsourcer or in which the crowd and the crowdsourcer overlap or are identical. This is, for example, typically the case for bottom-up or grassroots projects that may initially both be started and worked on by the same set of people. Another aspect that may not always be met, especially with academic projects, is that of crowdworkers receiving some sort of recompense, or at least it may be individual rather than universally clear what this recompense entails. Besides money and other extrinsic motivators that may lead to people participating, the crowdworkers might only be intrinsically driven by creating something for their personal utility, expressing themselves, or simply gaining pleasure from their participation. We thus interpret *recompense* as including any such kind of motivation. Overall, if not interpreted too narrowly, we find the presented integrated definition very fitting and, therefore, adopt it here unaltered.

For typologies or taxonomies of crowdsourcing, the situation is a bit less clear. Only few papers have classified crowdsourcing types, one of which [44.11] proposed an integrated typology from individual ones from related work (e.g., [44.12–14]). As we find some of the presented classes ambiguous and/or partially orthogonal, we propose an adjusted typology of crowdsourcing (Fig. 44.1). As the main distinguishing characteristic, we chose the *type of activity* that is being carried out

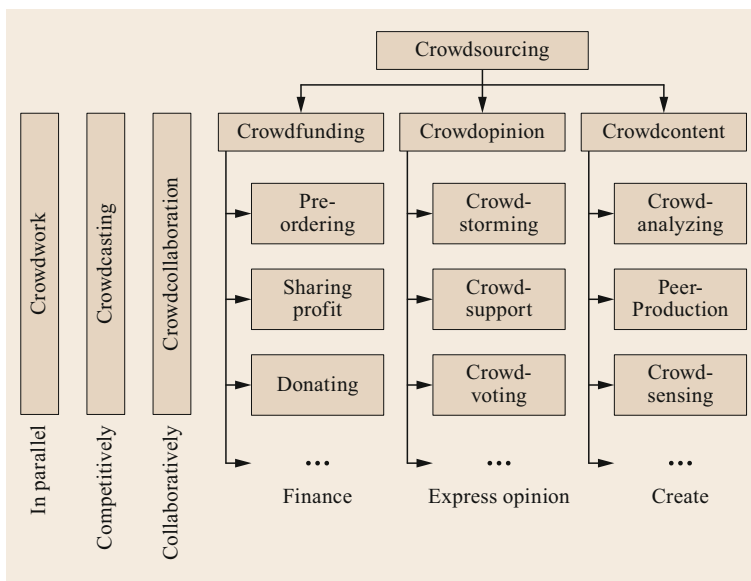


Fig. 44.1 Proposed typology of crowdsourcing. The distinguishing factor between the classes is the *type of activity* being carried out (financing, opinionating, or creating). Three orthogonal classes additionally allow categorization by the *level of collaboration* (in parallel, competitively, or collaboratively). Image © Matthias Budde

by crowdworkers. However, we do recognize that there are other dimensions along which categories could be distinguished. Additionally, we therefore also adopted three orthogonal classes that distinguish tasks by the *level of collaboration*. Any crowdsourcing task can fall in any of the classes, as well as either of the orthogonal classes. Of course, a crowdsourcing activity may also involve different tasks that cover multiple of the classes. This chapter contains multiple examples in which the same crowd, e.g., is involved in crowdfunding a platform and subsequently deploying and operating it (see the applications in Sect. 44.8). There have also been examples of multiple-tier crowdsourcing systems in which, e.g., the task of data acquisition is crowdsourced to one crowd, and the task of analyzing said data is crowdsourced to a different one [44.15, 16].

We would like to point out that while we adopted many of the names for the individual classes and their meaning from related work [44.11], many of the terms, in fact, have no clear definition and may also be defined or denoted differently in related work. As an example, neither *crowdopinion* nor *crowdcontent* are clearly defined terms, and our definitions may differ from those presented in other work.

On the first level of our typology, we distinguish three classes according to the type of activity that is being carried out. In *crowdfunding*, crowdworkers contribute by in some way financing an activity or project, in *crowdopinion*, they contribute something intangible, such as their knowledge or opinion, and in *crowd content*, their contribution is something more tangible, like for instance sensor data, labels, or even some sort of product.

On the second level, we list three exemplary classes each, including the classes from other proposed typologies, and add some that we believe to be important and that were missing before. However, there are literally dozens of other terms that could be used or added (e.g., *crowdrating*, *crowdsearching*, *crowdinvesting*, *crowdprocessing*, *crowdcreating*, *crowdcleaning*, *crowdsolving*, *crowdproduction*, etc.) and, as was pointed out above, many of them lack a clear definition. We do not intend to make this a comprehensive taxonomy, as we feel that this does not make sense or would be beneficial in any way.

Previous work distinguishes crowdfunding approaches as *preordering* and *profit sharing* [44.17]. Additionally, we include *donating* as a third category, in which people do not receive a direct reward (or the promise of one) for their money. Instead, they decide to contribute their funds no matter what, e.g., because they believe in an idea or would like to support some development voluntarily and unconditionally, a model

that was, for instance, common in early public domain (PD) software development.

Under *crowdopinion*, we added the class *crowdvoting*, which entails some rating activity. Additionally, we adopted and moved the two classes *crowdstorming* (online brainstorming sessions in which ideas can be raised) [44.11] and *crowdsupport* (user-to-user customer support systems) [44.11] from previous work into this branch of our revised typology, since we think that the defining factor is that crowdworkers express their opinion in some way, which does not necessarily need to involve working collaboratively.

In the third branch, *crowdcontent*, any activity that involves the creation of something is covered. This may lead from tasks like classifying or labeling a dataset (*crowdanalysis*) over the production of goods and services (*peer production*) to the collection of data using sensors or by making observations (*crowdsensing*). As crowdsourcing for atmospheric measurements often entails collecting data, we strongly focus on this last subcategory in the remainder of this chapter.

Since we think that, in principle, any of the presented activities can be carried out either by individual members of the crowd by themselves, or in competition between each other, or by working together, we included three orthogonal classes that additionally allow categorization by the *level of collaboration*. Depending on whether crowdworkers work on a task individually but in parallel, competitively, or collaboratively, we distinguish the classes *crowdwork*, *crowdcasting*, and *crowdcollaboration*.

44.3.2 Promises and Criticism

Whichever the term and detailed definition, the biggest benefits of crowdsourcing approaches usually named are always the same: scalability and cost effectiveness. Especially in data acquisition, crowdsourcing approaches enable unprecedented spatiotemporal resolution and often also (near) real-time data. This, in turn, allows, e.g., novel meteorological applications such as the identification of so-called urban heat islands and generally a better understanding of the urban climate and its dynamics.

An additional important aspect, especially of bottom-up or grassroots citizen science projects, is that of empowerment. The so-called democratization of technology has, for instance, brought forth open source software, accessible electronics platforms (like, e.g., Arduino), prototyping possibilities through three-dimensional (3-D) printers, and social media channels that facilitate building communities. All of these are tools that enable anyone to invent, design, implement,

and deploy novel systems that might potentially transform the world we live in [44.18].

On the other hand, crowdsourcing approaches have different issues as well. An often criticized aspect of systems that involve laymen carrying out tasks is that of questionable or at least unknown quality of the work result. Also, crowdsourcing approaches are not generally applicable to any problem, especially when trying to leverage the so-called *wisdom of the crowd* [44.5]. Depending on the task, it may, for instance, be difficult or even impossible to find and select appropriate crowdworkers, keep them engaged, and minimize uncertainty concerning the results of their work. A key factor for a successful crowdsourcing application is to always carefully consider the needs of the crowd. In commercial systems, further problems may include low wages, social dumping, and tax evasion. Paid microtasks may, e.g., circumvent minimum wage laws, as crowdworkers act like being self-employed (even if they, in fact, might not be). Apart from the legal and ethical questions involved, this again may have implications on quality.

Quality is especially an issue when the task involves crowdcontent. This is a topic that has been controversially discussed. The quality of content generated by crowdsourcing initiatives is often questioned or challenged, especially when it involves data collection [44.19, 20]. One extreme position even goes so far as to claim that while promising more truth and deeper knowledge, the possibilities of user-generated content and peer production actually destroy professionalism and ultimately lead to their disappearance [44.21]. However, this argument has, in turn, been criticized for being one-sided and suppressing positive examples. As so often in life, the truth is probably somewhere in the middle: crowdsourcing surely neither is the answer to all problems nor is it generally the source of unusable information. An important aspect is to be aware of and to acknowledge the shortcomings and deal with them as necessary for the application at hand. Otherwise, one might – maybe even inadvertently – contribute to the blurring between fact and opinion, especially when the collected data is made publicly available.

44.3.3 Human Factors in Crowdsourcing

Mobile and wearable devices – always being on, always online, always with the user, and context-sensitive – present a perfect platform for crowdsourcing, and, thus, crowdsensing applications. In contrast to the potential of such systems stand the many sources of systematic error that may affect data quality in nonexpert low-cost sensing [44.22]. That is why, as past research points out [44.19],

despite the wealth of information emerging from citizen science projects, the practice is not universally accepted as a valid method of scientific investigation. [...] At the same time, opportunities to use citizen science to achieve positive outcomes for science and society are going unrealized.

This goes to the extreme that data from laypersons is considered to be undesirable by experts or policy makers and may even be prohibited for official use [44.20]. On the other hand, research shows that laypersons can collect data of comparable quality to experts, if properly familiarized with the task [44.23]. The problem is that nonexperts are typically not, and thus cannot ensure standardized sensing processes. They may be [44.24]:

- *Untrained*: unfamiliar with the way the sensing process is intended to be performed
- *Overwhelmed*: uncomprehending or unable to recall the correct measurement procedure
- *Inattentive*: not paying attention to all details of the process (this is especially likely if participation is extrinsically driven, e.g., through monetary incentives or gamification)
- *Digital immigrants*: not digital natives, i.e., have little or no experience with mobile or wearable technology, or even
- *Malicious*: deliberately trying to influence the measurement process or *to play* the system.

We argue that in crowdsourcing applications, it is often neglected that, in fact, the user is often an important part of the technical sensing architecture, directly affecting the quality of the data generated or task performed. Research recognizes that [44.25]

[...] this application domain is poorly understood by most system designers who focus almost exclusively on empowering citizens rather than considering the needs of both citizens and civic authorities and establishing trusted relationships between these stakeholders.

By designing for both adequate data quality and intelligibility, this trust relationship between users and authorities is strengthened.

In previous work [44.24, 26], we studied mobile phone-based environmental sensing approaches and identified six main dimensions of human error in such systems (Fig. 44.2). These dimensions form a compilation of ways in which participants' behavior may adversely affect the eventual data quality. The purpose is to sensitize designers and facilitate the design of

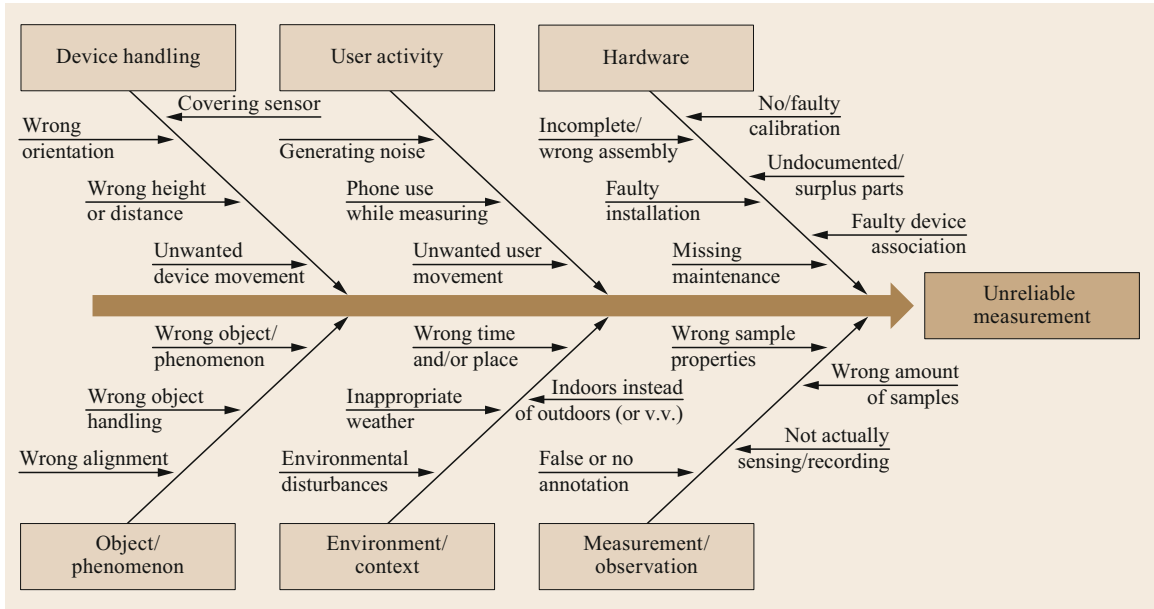


Fig. 44.2 Six dimensions of influence on data quality in nonexpert environmental sensing, as identified by previous research (image after [44.24] with permission from the ACM)

systems that are used by nonexperts to gather environmental data, such that they deliver a higher data quality.

Section 44.6 below discusses measures that can be taken to reduce uncertainty introduced by user error.

44.3.4 Measurement Uncertainty

Aside from the user, the most significant source of uncertainty regarding data quality in crowdsourcing is low-cost instrumentation (that is, for projects that employ sensors to make observations). Despite the often relatively low performance of such instrumentation in direct comparison to sophisticated, established equipment, the low cost allows measurements at a scale orders of magnitude above that of classical measurement grids. This scale in itself carries the potential to trade off uncertainty against spatiotemporal resolution (on the general topic of uncertainty see also Chap. 2).

For some natural number n , consider the data points x_1, \dots, x_n that each carry an error Δx_i . Now calculate the average value

$$\hat{x} = \frac{1}{n} \sum_{i=1}^n x_i. \tag{44.1}$$

The error of \hat{x} can be approximated by the error propagation formula

$$\Delta \hat{x} = \sqrt{\sum_{i=1}^n \left(\frac{\partial \hat{x}}{\partial x_i}\right)^2 \Delta x_i^2}. \tag{44.2}$$

Assuming the same errors for each data point

$$\Delta x_i = \Delta x = \text{const.} \quad \forall i \in \{1, \dots, n\}, \tag{44.3}$$

we get

$$\Delta \hat{x} = \sqrt{\sum_{i=1}^n \left(\frac{1}{n}\right)^2 \Delta x^2} = \frac{\Delta x}{\sqrt{n}}. \tag{44.4}$$

One can see here that any uncertainty in a measurement x_i can be lowered by conducting several independent measurements and averaging all of them. For 100 measurements, a reduction of an order of magnitude can be achieved. Figure 44.3 illustrates this fact.

The thin black line at $y = 5$ is the mean of the Gaussian distribution with $\mu = 5, \sigma = 1$ from which 1000 points (blue dots) were sampled. The colored, thick bars are the averages of batches of 100 points. We can clearly see that the spread of the colored bars around the black line is much smaller than that of the blue dots.

This reflects the strength of a large-scale crowdsourcing scenario with low-cost sensors. The fact that low-cost sensors are, in general, subject to numerous error sources can be alleviated by the sheer amount of sensors that can be deployed due to cost reduction. Statistical errors will be dampened in the average values of the whole sensor network. Systematic errors still need to be addressed differently. One approach to manage this is by calibrating the low-cost sensor network to a few high-cost reference devices, thus spreading high-cost accuracy over the whole network [44.27].

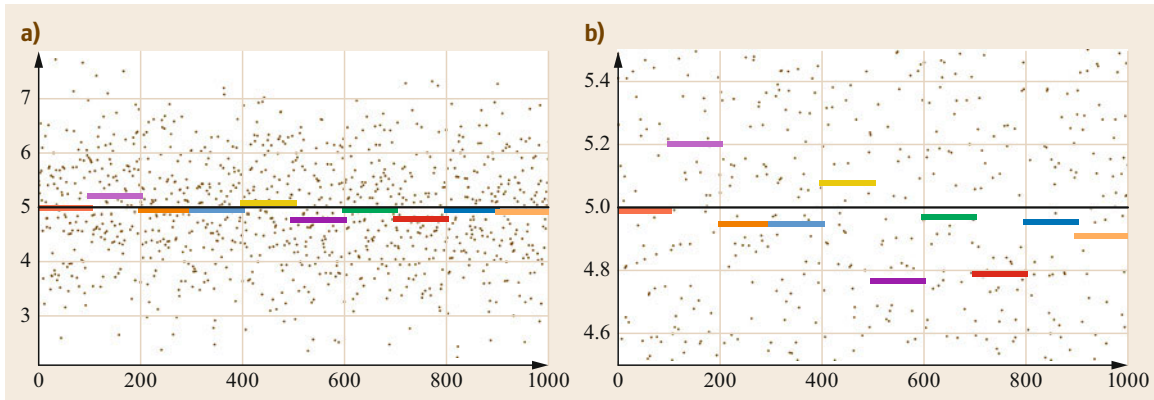


Fig. 44.3a,b Example of how a large scale can compensate for noisy data from low-cost sensors. By averaging over several independent measurements, the uncertainty can be lowered. In this example, averaging over 100 readings leads to a reduction of one order of magnitude (*dots* are readings, *colored bars* are averages; both images **(a)** and **(b)** show the same data on different scales)

As was already mentioned above, this approach still has some disadvantages. The act of averaging not only lowers the uncertainty but may destroy important information, too. For instance, averaging a time series will leave us with a worse time resolution of our (mean)

sensor reading. Similarly, a network average of, e.g., a whole city block will result in a worse spatial resolution. These two facts, reduction of uncertainty and loss of information, have to be thought of as an indisputable tradeoff in the act of averaging.

44.4 Devices and Systems

This section features examples of systems that are typically used in crowdsourcing for atmospheric measurements. We roughly group these devices into five classes: *automatic weather stations (AMS)* were already covered in Chap. 43. *Dedicated systems* cover consumer devices and personal systems, many of which are directly commercially available to the end-user. *Do-it-yourself (DIY) platforms* are usually low-cost for their respective capabilities, but demand some effort and/or technical understanding and possibly assembly on part of the user. *Smartphone accessories* are small add-on devices, often used to sense a single phenomenon, that leverage the processing, storage, and communication capabilities of modern mobile phones. Finally, some approaches try to use *internal smartphone sensors* to directly assess parameters such as temperature or atmospheric pressure. An overview of the meteorological parameters that can be typically covered with different devices or device classes was presented in Table 44.2 at the beginning of this chapter. We would like to point out that the list of devices and systems in this section is exemplary and is not meant to be comprehensive. Especially in the commercial sector, many consumer devices are available, and some of them are very similar.

44.4.1 Dedicated Devices

There are many different sensing platforms that can be used for crowdsourcing applications. The best known measurement devices are typically dedicated small networked weather stations that are designed as consumer products. A prominent example of these are, for example, products from the French company *Netatmo* [44.28], for which different modules exist, even to measure parameters such as wind or precipitation (Fig. 44.4).

There is a fast growing market of such compact systems to measure meteorological parameters. As they are designed for end-users, these systems are typically easy to set up and operate. Many of the systems – like *Netatmo* – are modular, letting the user select the sensors for his personal needs. Well-known examples for the measurement of gases and/or particulate matter include the open source *Air Quality Egg* (which was also crowdfunded and was named a *Best of Kickstarter 2012* project) or the *Laser Egg*.

44.4.2 Do-It-Yourself Platforms

In addition to commercial products, there exists today a wide range of *do-it-yourself (DIY)* projects. The ba-



Fig. 44.4a,b The networked *Netatmo* weather stations can (a) be extended with various modules, among them a rain gauge (b) to measure precipitation (photo © Netatmo. Photos Masaki Okumura, M-Agency, Marion Leflour, Fred Reynaud and 1988)

sis for these are usually single-board computers, such as *RaspberryPi*, *Arduino* platforms, or *ESP32* SOC microcontrollers. The *WeatherPi* project website, for instance, features manuals to set up a networked (optionally solar powered) *RaspberryPi*, which senses 20 different environmental values. *TheWeatherStation.com* shows a similar platform built on an *Arduino Uno*, and many more similar projects can be found on various pages on the Internet. These types of projects usually require users to read at least simple circuit diagrams, connect electronics accordingly – which may or may not include soldering – and load some kind of firmware onto the platform. Depending on the individual project, deeper electronics, operating systems, and/or programming skills may be required.

An example of a simple sensor used in DIY citizen science projects based on an *ESP* platform is the *Novafitness SDS011* particle sensor (Fig. 44.5). The low-cost nephelometer is available for currently just over US \$30 (as are other similar sensors as well), which is orders of magnitude below the cost of professional particle monitoring equipment. As is to be expected, the sensor has its shortcomings, but for its price it performs well under certain conditions [44.29].

Other than ready-to-use plug-in sensors, there is a variety of low-cost sensors available at very low cost due to the rise of smartphones and automotive sensor applications. Among these are inexpensive sensors for phenomena like temperature, humidity, or pressure, and increasingly also for gases. A recent report from the World Meteorological Organization (WMO) provides an overview of low-cost sensors for the measurement of the atmospheric composition [44.30]. In terms of their data quality, single sensors are of varying performance; some are very stable, others more noisy. An equally important aspect with these sensors is the



Fig. 44.5 The \$20-fine dust sensor SDS011 is (among other low-cost sensors of similar design) used in different crowdsensing campaigns around the world, such as the *luftdaten.info* project of the Open Knowledge Foundation Germany (image taken from Wikimedia under *CC0 1.0 Universal* license)

installation [44.24]. A decent temperature sensor, for instance, that is installed in direct sunlight will hardly be able to deliver adequate air temperature readings.

44.4.3 Smartphone Accessories

However, not only dedicated weather stations are available but also sensors and modules that can be used for mobile crowdsensing applications as accessories for or even integrated into smartphones. To realize truly large-scale pervasive sensing systems, it would be beneficial to carry out measurements directly with users' personal devices, especially smartphones. Different companies offer commercial smartphone anemometer apps that either wirelessly transmit data from small external wind meters to the phone or even directly from anemome-

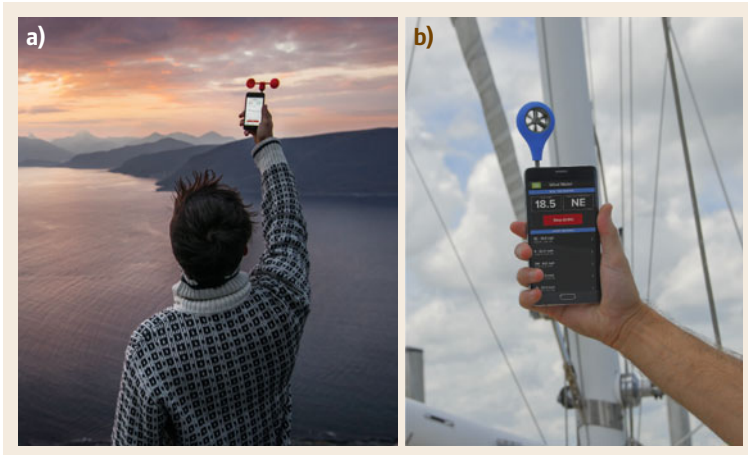


Fig. 44.6a,b The smartphone anemometers from the company *vaavud* (a) and the *WINDmeter* from *WeatherFlow* (b) are plugged into the microphone jack of an Android or Apple phone (photos © *vaavud* (a) and © *WeatherFlow* (b), used here with kind permission)

ter modules that are plugged into the microphone jack of an Android or Apple phone (Fig. 44.6). This allows both powering the accessory as well as sending the sensor data to an app on the phone. An example of this is the smartphone anemometer from the Danish company *vaavud*, which was later acquired by the company *WeatherFlow*, which offers a similar product under the name *WINDmeter*. The same technology approach is used for the *Thermodo* temperature sensing modules. These small plugs are also jacked into the microphone socket.

Other available products include visible light meters (*Lumu Power*), ultraviolet (UV) meters, and even Geiger counter modules (both from *Ftlab*). Some of these are fun gadgets rather than meaningful instruments. A general problem with data quality is again the user, as the measurement context greatly influences the validity of the readings [44.24]. The Geiger module, for example, requires the phone to be switched to airplane mode, as it can give false readings from the phone's own cellular and Wi-Fi radio frequency interference. Even if this is done, because we are today surrounded by many different sources of electromagnetic radiation, it remains hard to believe that meaningful accuracy can be achieved under uncontrolled conditions. For the *Thermodo* system, sensor performance is reportedly much less of an issue. However, as many smartphone users carry their phone in their pants or jacket pocket, body heat plays a role and, of course, influences the measurement results. So again, the correct measurement context is vital for achieving meaningful readings.

Apart from these commercial modules, several approaches that augment smartphones with accessories to measure different environmental parameters have been proposed in academia. These include, for instance, a system to measure black carbon (BC) with cellphones [44.31]. The aethalometry-based approach

involves BC aerosol collection on a quartz filter. The smartphone's camera is then used to capture the coloration of the filter, and the reading is transmitted to an analytics component for real-time evaluation.

Another interesting approach to measuring atmospheric dust in participatory sensing scenarios was presented by the Air Visibility Monitoring [44.32] and the *iSPEX* [44.33] projects. In the former, people use their camera phones to take pictures of the sky and upload them to a central database. The particle pollution then is estimated from the image luminance, the location, and other phone sensor data (such as, e.g., orientation). Cloudy skies and indoor environments present clear limitations to this approach. The *iSPEX* system is an ultra-low-cost (US \$3), mass-producible hardware add-on for the *iPhone* that enables crowdsourced spectropolarimetric measurements (Fig. 44.7). The system aggregates multiple readings for quantitative remote aerosol sensing [44.33]. It has been successfully used in single-day measurement campaigns on a large participatory sensing scale (Sect. 44.8).

The *FeinPhone* [44.26, 34] system is another approach that attempts to enable particulate matter (PM) sensing directly with smartphones using a clip-on module. It uses camera and flashlight functions that are readily available on today's off-the-shelf smartphones together with a passive hardware add-on based on light-scattering particle sensors. This direct, in-situ measurement distinguishes the approach from the former two. However, so far, *FeinPhone* is in a proof-of-concept stage and has not yet been used in realworld deployments.

Aside from modules that are directly (physically) attached to smartphones, there are a number of sensing modules that connect wirelessly to a phone, e.g., via Bluetooth (BT)/Bluetooth low energy (BLE). An example of this is, for instance, the *Qualcomm BLE*

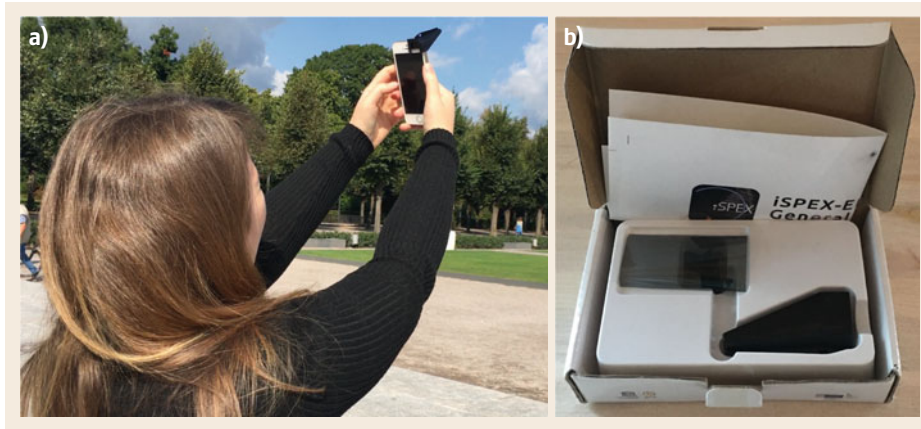


Fig. 44.7a,b A citizen scientist is conducting a measurement (a) with the *iSPEX* clip-on module (b) clipped onto her *iPhone* camera (images after [44.24] with permission from the ACM)

Environmental Sensor Board, which carries different MEMS sensors, among them a temperature, humidity, and pressure sensor. The board is not intended to be an end-user device, but rather a development platform to prototype connected products that enable the Internet of Things (IoT). Dedicated wireless smartphone accessories exist as well: the *Plume Labs Flow* device, for instance, is intended to enable personal exposure tracking of a variety of parameters through a small device. There are many more such platforms of different fidelity available or under development.

44.4.4 Internal Smartphone Sensors

From a pure distribution perspective, the closer sensors come to being integrated into our phones, the better they can be employed for crowdsensing. Internal phone sensors are practically always with the user, inseparably tied to powerful processing and communication capabilities, as well as interfaces for control and visualization. In today's smartphones, a plethora of sensors is installed (Fig. 44.8).

Basically every smartphone has a 3-D accelerometer, gyroscope, magnetometer (compass), multiple microphones, as well as two or more cameras (newer models sometimes include depth sensors). Aside from the global positioning system (GPS) receiver, multiple radio interfaces can be used to obtain absolute or relative position information, through beacons, RF fingerprints, or cell trilateration. Many phones additionally feature pressure sensors and proximity (infrared (IR) light) and ambient light sensors. Smartphone batteries usually have an internal thermistor to monitor their temperature. Modern smartphones come with additional features, such as fingerprint sensors, retina scanners, or heart rate monitors.

Aside from the actual sensors, several so-called virtual sensors are available on today's smartphones. Their

readings are based on data fusion from the physical sensors, especially the inertial sensors. They range from simple ones, such as orientation/gravity sensors, over step counters/pedometers to context information, such as *running*, *standing still*, *on bicycle*, *in vehicle*, etc. While not directly usable for environmental observation, the inferred activities can maybe be used to rate and/or improve the data quality [44.24].

Individual smartphones even feature meteorological sensors. For instance, in 2013, the *Samsung Galaxy S4*, was the first smartphone equipped with ambient temperature and humidity sensors. One year later, the *Samsung Galaxy Note 4* featured the first UV light sensor. The waterproof *Caterpillar CAT S61* phone even includes a sensor to measure volatile organic compounds (VOCs) for indoor air assessment, a laser rangefinder, and a thermal imaging camera.

The most exotic sensor in a smartphone was probably built into the 2012 *Sharp Pantone 5 107SH*. The phone, which was only available in Japan, featured a radiation detector. However, this can probably be considered as serving a short-term niche market after the 2011 Fukushima disaster in Japan. At least, no further developments in this direction have been seen in later phone generations.

Aside from these sensors that are already available in smartphones today, efforts to enable, e.g., particulate matter sensing with small sensors that can be integrated into the housing of a smartphone have been made in the past. Researchers have proposed the design of a capacitive particle sensor that has the potential to be microfabricated and embedded into phones [44.35]. In a different approach, the direct measurement of the mass concentration of particles was enabled with an air-microfluidic microelectrical mechanical systems (MEMS) design [44.36]. These developments show both interesting approaches, as well as a promising performance under laboratory con-

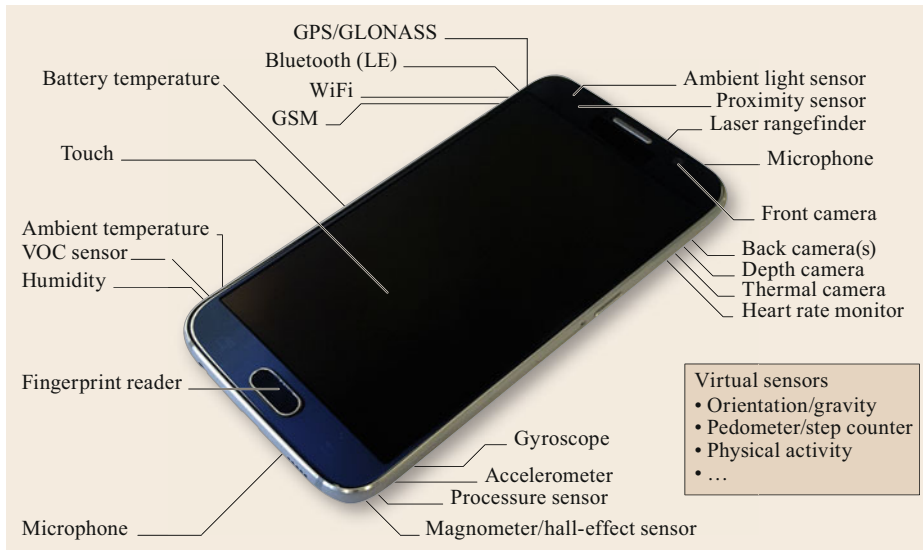


Fig. 44.8 A current smartphone and examples of sensors found in different phones (no single smartphone features all of the listed sensors). Smartphones possess a plethora of integrated sensors, some of which can be (re)purposed for environmental measurements. More exotic ones feature sensors for ambient temperature and humidity, special cameras, or VOC (volatile organic compound) gas sensors

ditions. However, there may be one issue with the general approach of miniaturizing aerosol sensors that far, which is not a question of detection principle but rather one of statistics: the smaller the detector volume, i.e., the smaller the amount of air that can be sampled at a time, the more consecutive measurements need to be taken in order to make a statistically reliable statement concerning the mean concentration. This has implications, for example for air flow and measurement duration and frequency requirements [44.26, 37].

The most notable internal smartphone sensors that have actually been used for meteorological crowdsourcing applications are the battery temperature sensor and the pressure sensor. The respective applications are presented in Sect. 44.8.

44.4.5 Human Observation

Finally, we would like to point out that smartphone users themselves can be the sensor. This human-as-a-sensor approach is actually not uncommon in citizen science projects. Instead of measuring with some kind of device, users contribute qualitative observation(s). This is, in some cases, obligatory, if the information sought after is of a nature that can only – or a least much better – be determined by humans [44.38]. In other cases, it may simply enable a scale of observation that can otherwise be hard to achieve. This may be the case for direct active observation and reporting by the

user. Examples of this are, e.g., user-generated reports on precipitation events [44.39, 40] (Sect. 44.8).

Conversely, information can also be derived from indirect user reports. Through social media analytics (SMAs), public postings on platforms like Twitter can be analyzed to retrieve information. This has been done in the past for various applications in disaster situations, ranging from identifying active entities [44.41] over peer production of accurate maps in the aftermath of disasters [44.42] to real-time mapping applications [44.43].

Also, crowdanalyzing applications can be seen as another kind of human-as-a-sensor systems. In these, the task often involves data review and labeling rather than the collection of new data. Examples of this include the classification of cyclones or the analysis of historical weather reports from ship's logs, both on the *Zooniverse* Citizen Science Platform [44.44] (Sect. 44.8).

44.4.6 Comparison of Sensors

The choice of a sensor system depends on the crowd, the application, its quality requirements, and the effort required for maintenance. This should be decided before any system is applied (Chap. 3). The necessary process of quality assurance is, therefore, very important and should not be underestimated. Some basic information about advantages and disadvantages of the sensor configurations for the different station types is given in Table 44.3.

Table 44.3 Advantages and disadvantages of the different sensor configurations

Devices	Advantages	Disadvantages
Stations set up with single sensors	Highly accurate measurements Easily comparable measurements in networks	Expensive sensors High maintenance efforts
Compact sensors	Easy to handle sensors Good price-quality ratio	Often not in agreement with WMO recommendations
Simple sensors for crowdsourcing	Cheap sensors or devices Available in large amounts Tend to be small and low power and, thus, potentially mobile Possibility of collecting data with unprecedented spatiotemporal resolution accessible to almost anyone through open source drivers and single-board microcontrollers (democratization of technology): inexpensive tool for research purposes Enables novel applications	Often noisy sensors of varying data quality Sometimes cross sensitivity/selectivity Comparable information often only available with high additional effort (mathematical, organizational, etc.) Uncertainty in data quality Higher effort for writing consumer grade software and user interface

However, there are some peculiarities in crowdsourcing that may require looking at sensor performance and quality characteristics in a different way. Crowdsourcing enables unprecedented applications and quantities of data not possible in classical applications. One could argue – and depending on the application we think one should – that the definition of data quality on the device level is not adequate to describe such systems in the first place.

Comparing a single low-cost sensor against gold standard equipment is fine to characterize the short-

comings of cheap sensor technology, but it should not be the sole basis to rate a system using these sensors on a large scale. Taken as a whole, the emergent properties of such systems will likely differ from those of a single sensor, be it simply as an effect of scale (Sect. 44.3.4), or because data fusion and analytics enable new approaches to build models in a data-driven fashion. Therefore, we propose that the logical continuation of crowdsourced data acquisition is the fusion and analytics of this data with high-quality data available from different sources [44.45].

44.5 Specifications

For the specification of the single sensors see the chapters of Part B or Table 1.5 for general values. For compact sensors, the accuracy is slightly lower (Table 43.10). For simple sensors, like the ones typically used in crowdsourcing approaches, a general assertion concerning the uncertainty is difficult. As discussed in Sect. 44.4 above, there are small sensors that deliver little more than indicative readings, while others come close to or even exceed the accuracy of sophisticated equipment. Especially sensors that are used in the automotive sector, or those that are available in today's smartphones, offer remarkable performance characteristics, while being available at very low unit prices, because of the massive scale at which they are produced. An example of this is, for instance, the *Bosch BME280* integrated temperature, humidity, and pressure sensor, which shows high precision according to its data sheet [44.46]. On the other hand, there are many cheap sensors that claim a certain performance in their technical documentation but fail to deliver on that specification in real life. Increasingly, there are also cheap

copies of sensors on the market, mainly shipped from Asia, that are sold for a fraction of the price of the original sensor but under the same name. These imitations are sometimes indistinguishable on the outside but fail to achieve the performance of the original. In order to determine the suitability of a certain sensor, consulting related research or even conducting own validation experiments may be necessary.

For some sensors, characterizing the uncertainty is not a simple task, as they may perform very well under certain conditions, but not generally or in changing environments. An example of this is the *SDS011* particle sensor, which generally shows good correlation with reference equipment but fails to estimate concentrations correctly under high humidity or shifting particle size distribution [44.29].

For simple sensors in crowdsourcing, an additional problem is the often incorrect installation and/or operation of the sensor. This can entail, e.g., a missing radiation screen for temperature and humidity measurements, operation outside of a sensor's specifications,

Table 44.4 Overview of possible measures to improve the data quality in mobile non-expert sensing [44.24, 26]

Approach	Advantages	Disadvantages
Participant selection	Domain expertise/prior knowledge	Usually requires thorough analysis, high resource cost Selection success hard to verify
Training	Best/covers everything Trainer can assess success	High resource cost, experts needed continuously
Instruction (manual)	Clear	Mentally demanding Passive access
Instruction (in-situ)	Very clear Temporally close	Requires some sort of display
Reputation	Good for sorting out single users Helps against malicious intent	Can demotivate users May be hard to build
Verification	Ensures data quality	Infeasible for many tasks After-the-fact
Expert reviews	Ensures data quality	Infeasible for many tasks Experts needed continuously After-the-fact
Redundancy	Very simple	Only robust against statistical error, not systematic May be difficult to achieve Bad readings still contribute
Outlier/anomaly detection	Eliminates implausible readings	Prevents capturing <i>true</i> anomalies Ineffective against systematic error
Bayes filter	Adapts to available data	Needs basic models and multiple readings
Repetition	Simple	Only robust against statistical error, not systematic Needs to be triggered in some way
Context recognition	Potentially fine-grained control over measurements	Only a certain class of errors Maybe technically difficult
Reconstruction	Extremely robust	Only applicable in special cases
Data design	Provides structure	Mostly for textual data
Feedback	Supports user in verifying correct procedure himself Almost always possible	May overwhelm or frustrate user if not carefully balanced
Gamification	Motivates Increases hedonic quality May enhance measurement frequency	May distract from sensing task Can demotivate intrinsically motivated participants May promote quantity over quality

mobile sensing at speeds that compromise ventilation, or measuring background levels too close to a local source, etc. The problem is often not the accuracy of the sensor itself – given in Table 44.4 – but the installation. While incorrect procedure or installment are a problem that is independent of the technology employed, in crowdsourcing it is more likely to occur, because non-experts carry out the measurements.

On the other hand, crowdsourcing scenarios have a set of advantages that may potentially mitigate these drawbacks. The first one is scale. Because of the large

amount of sensors, inadequate measurements have less effect if multiple readings are averaged (Sect. 44.3.2). Additionally, as pointed out in Sect. 44.4.6, the definition of data quality on the device level may not be adequate to describe such systems accurately, because the emergent data quality may exceed that of a single sensor. Secondly, low-cost sensors and crowdsourcing enable novel applications that would not be possible otherwise. The accuracy requirements of these scenarios may differ. Examples are, for instance, hotspot detection or source identification and tracking.

44.6 Quality Control

The principles of quality assurance and quality control (Chap. 3) are valid for stations with single and compact sensors. For the different parameters, the procedures are described in the chapters of Part B.

For crowdsourcing, the situation is somewhat more intricate. As systems and approaches are very diverse, so are requirements and means for quality control. In crowd-based measurements, there usually are no

standard operation procedures (SOPs). There may not even be a clearly defined measurement process at all, or if there is, compliance with it may not be monitored. Apart from the measurement instrumentation employed, which is usually low-cost and in itself a source for unreliable readings, the human is the most important factor. In crowdsourcing projects, especially if they include data collection, the human is not only an operator of measurement equipment, but instead part of the technical sensing infrastructure.

Therefore, we will first discuss sensor calibration in this section, followed by an overview of approaches that can be employed to address issues with data quality that may stem from nonexpert users operating sensing equipment or otherwise contributing observations.

44.6.1 Calibration

As we have seen in Sect. 44.3.4, statistical error of low-cost sensors can be handled by averaging a large number of sensor readings. Suppose we are working now with mean sensor values that possess a low statistical deviation. The remaining relevant sources of error are systematic, i.e., they are stable with respect to different contexts, such as time, place, measurement setup, etc. Due to their stability, one can often apply calibration procedures in order to reduce them.

While research on sensor calibration often addresses the same issues, different terminology is used, some of it interchangeable, some entailing different meanings [44.26].

Generally, there are two main ways of calibrating a device:

- By exposing the device to a defined, often artificially created condition for calibration (usually in a lab environment).
- By comparison against another device in close proximity, typically one with a higher reliability.

As we are concerned with distributed sensing systems, we focus on *device-by-device* calibration, sometimes also known as *comparison calibration* [44.47] or *cross calibration*. Also, device-by-device calibration can either be carried out under factory or laboratory conditions or in the field. Other terms can be found for the distinction between calibration that is carried out by sensors autonomously (*auto* calibration) [44.48] in contrast to calibration that requires manual interaction (*manual* calibration) [44.49].

Regarding calibration with or without the existence of reliable, ground truth measurements, many terms can be found in the literature. So-called *blind* methods achieve calibration gain without ground truth reference

data [44.50]. In line with this, other work uses the term *semiblind* when referring to calibration with partial ground truth data and *nonblind* for calibration with full ground truth data [44.51]. In addition to this, the terminology *off-line* and *on-line* [44.52] can also be found when referring to calibration with or without ground truth data; the latter is sometimes also called *in-place calibration* [44.53]. The terminology *multihop* and *single-hop* [44.27] does not make a distinction regarding the availability of ground truth, but rather the quality of the reference. Single-hop calibration means calibrating directly against reliable reference sensors, while multihop calibration makes use of sensors whose calibration was propagated through several nodes. Another term is *virtual* in-situ calibration [44.54].

Regarding the level on which the calibration is carried out, i.e., whether on the sensing devices themselves or on a central instance that collects all data, also different terms are used. Some authors refer to *device-level* and *system-level* [44.55] calibration, while the terms *micro* and *macro* calibration are also found [44.56]. Calibration schemes without a central instance that use only peer-to-peer (P2P) communication are referred to as *distributed* calibration [44.57]. In addition, *local* calibration is also used in some works for calibration on the sensing devices themselves [44.55].

The general approach for device-by-device calibration is like this: given a set of pairs $(x_1, y_1), \dots, (x_n, y_n)$ of sensor readings x_i and reference values y_i , one tries to find an optimal fit function $f_\theta(x)$, such that a given loss function $L(f_\theta(x), y)$ is minimal. Here, θ are free parameters, e.g., polynomial coefficients or weights of a neural network. Obviously, the quality of calibration greatly depends on the right choice of the fit function f and the loss function L . Most often, a linear fit and a quadratic loss function are well suited

$$f_{a,b}(x) = ax + b, \quad (44.5)$$

$$L(f_{a,b}(x), y) = |f_{a,b}(x) - y|^2. \quad (44.6)$$

By optimizing this loss function, the differences between the calibrated values $f_{a,b}(x_i)$ and the reference values y_i are minimal. Given one value pair (x_i, y_i) we can derive the conditions for a minimum either analytically or by one of the numerous optimization algorithms available today. Because the above functions are so simple, we will do it analytically here

$$\frac{\partial L(f_{a,b}(x_i), y_i)}{\partial a} = 2(ax_i + b - y_i)x_i = 0, \quad (44.7)$$

$$\frac{\partial L(f_{a,b}(x_i), y_i)}{\partial b} = 2(ax_i + b - y_i) = 0. \quad (44.8)$$

The last equation implies the first one. So, in fact we only get a single minimum condition per value

pair. This is a general fact for polynomials and should be considered as a rule of thumb for other fit functions. Furthermore, if we consider all value pairs $(x_1, y_1), \dots, (x_n, y_n)$ we will have more conditions than parameters. The system is overdetermined and almost always unsolvable. Hence, we can try to construct an average solution, i.e., solve subsystems of two conditions and average the parameters over all such subsystems. If the fit function is not linear, a better approach is to minimize the average loss of all value pairs in order to combine the minimum conditions. Again, this corresponds to a specific choice of the loss function.

At the end of this procedure, we will have a set of parameters θ (here a, b), which will most likely not correspond to an exact match $f_\theta(x_i) = y_i$ but rather to some erroneous fit $f_\theta(x_i) = y_i + \Delta y(x_i)$, where $\Delta y(x_i)$ quantifies the error of the calibration at a given sensor reading x_i .

For distributed sensing systems, on-the-fly calibration (as, e.g., in [44.27]) is an interesting approach. If two sensors *meet* each other with respect to a given context, for instance (but not restricted to) time and space, one can apply a calibration method to *synchronize* both sensor readings. The above procedure describes the case where one sensor (the reference) has maximum trust, i.e., whose sensor readings are considered to represent the ground truth. There are different methods based on statistical models that can assign intermediate values of trust to each sensor and still try to match both sensor readings. For these scenarios, one aspect is very important: data dynamics. If the values measured do not vary enough during the meeting process, the scatter plot of points $(x_1, y_1), \dots, (x_n, y_n)$ will form a very narrow area. As has been said before, a single point can usually only determine one of the parameters. Hence, a narrow (point-like) area will most likely not contribute enough information to perform a good calibration [44.26].

44.6.2 Mitigating Human Influence

Numerous approaches have been proposed in the literature to mitigate the problem of low data quality. Some of these approaches are applicable to crowdsourcing, citizen science, and/or participatory sensing scenarios, some only under certain conditions, and some not. Mostly, this is because of one of the two following reasons: either, the approach may, in principle, be applicable, but does not scale to a crowdsourcing level, or the approach cannot be applied because it relies on information that is unobtainable in a practical setting. Still, the general need to ensure the viability of data from cheap sensors is recognized in the literature on mobile sensing [44.58]. However, only seldom, the focus is placed on the effects that the behavior of untrained

users may have on the quality of the collected data. Table 44.4 shows an overview of possible approaches.

Participant selection is an approach that has been used in different fields to identify and separate suitable personnel from such that is unfit for a task. Past research reviewed different methods of identifying people who are likely to perform successfully along with different measures of ability, albeit with a focus on assigning people to jobs [44.59]. However, by definition, crowdsourcing involves an open call and, therefore, often addresses everyday users, which conflicts with a pre-selection step. Additionally, at larger scale, screening may become prohibitively expensive.

The most intuitive approach to ensure that users perform a task correctly is *training* [44.23]. It has been reported that [44.60]

numerous studies have demonstrated that volunteers can successfully perform basic data collection tasks when given a half day or more of practical field training.

Unfortunately, this also highlights the biggest drawback of training sessions: a lot of resources (experts, facilities, etc.) are needed, and the approach does not scale. Slightly different forms of training that do not require the user to keep a mental model of the process are *instructions* (e.g., manuals or tutorials). The key difference to training is that instructions are typically given in writing or otherwise fixed form (video, etc.), which is used to make the nonexperts to understand the measurement process. Understanding is defined as the ability to hold and process all elements that define the measurement process simultaneously in working memory [44.61]. However, working memory is extremely limited in capacity [44.62] and in duration [44.63], in particular for novel information that needs to be processed in a novel way [44.61]. That is, people might fail to understand or completely recall new material if it is sufficiently complex, as may or may not be the case in crowdsourcing, depending on the application context. However, it is reasonable to assume that nonexperts will not have an in-depth understanding concerning the standard measurement procedures for a given meteorological parameter or the effects that deviations from a standard may have.

As a series of simple studies can show [44.24], even a seemingly easy task like recording an audio signal with a smartphone involves a complex measurement process for the user. Also, classic manuals are of little help, as people tend to not read them [44.64], especially if they do not encounter problems, as would be the case in a badly but (from the point of view of the nonexpert) successfully performed measurement

process. On the other hand, instructions can be given much *closer* to the actual task (spatially and temporally). In shorter form and in-situ, instructions provide an advantageous approach, up to providing a complete step-by-step walkthrough.

Another popular approach are *reputation systems* [44.65]. There are different flavors, ranging from picking users based on their reputation or skill level [44.66] over assessing it beforehand [44.67] to building it through data analytics. However, this again requires some kind of ground truth determined by expert users or a series of campaigns, making it an intricate option. In mobile crowdsensing systems, individual readings can usually not be reevaluated, and their classification as being correct or wrong after-the-fact is often infeasible, making reputation levels difficult to build. Additionally, *ranking users can backfire* [44.68], influence the participants' motivation, and paradoxically lead to the best performing participants dropping out, as they would feel they had *won the game*.

Verification of data entries is similar approach to increase data quality. Related work [44.69] differentiates between verified and direct citizen science. Entry verification can either be approached automatically by using some sort of computational recognition or simple sanity tests. The advantage of this sort of verification is that it can be performed in real time, and the user can be prompted before leaving the area, as proposed in past research (*Did you really just see 40 diesel trucks go by in 5 minutes?*) [44.2]. In community-based data validation [44.70], instead of revisiting their own data, participants verify data from their peers. This is obviously infeasible for sensor data, as the exact environmental conditions cannot be verified after the fact, at least not if they do not deviate so much as to become completely implausible (e.g., the observation of heavy rainfall on a completely sunny day). The same is true for *expert reviews* [44.2] of data. They also have the disadvantage that data has already been collected and can only be discarded, as the analysis takes place after the fact.

Computational approaches are diverse. The simplest ones are of a statistical nature: *redundancy* [44.71] and/or *repetition* [44.23] both lead to multiple instances of the same data, which can then, in turn, be processed, e.g., to remove outliers. These approaches only work, if the underlying assumption holds that the overall error is nonsystematic, i.e., people will on average perform the task correctly. However, as the exploratory studies that lead to the taxonomy in Fig. 44.2 indicate [44.24], there may be certain errors that the majority of people tend to make.

More sophisticated approaches like *outlier/anomaly detection* or *Bayes filtering* take the structure of the data

into account. Outlier detection is an approach that today is still largely carried out manually by experts that use their experience in order to remove implausible data sets. One of the drawbacks of automatically filtering out anomalies is that smoothing makes the approach less suitable for highly dynamic phenomena. If only few data points are available or no model can be constructed, filtering is also not applicable.

A different way of computationally addressing procedural errors is *context recognition*. Mechanisms may be as simple as performing simple plausibility checks, e.g., by detecting whether the GPS receiver is turned on, or the acceleration sensors of a device pick-up movement when there should be none, and range to integrating full-fledged activity recognition or applying other artificial intelligence (AI) techniques [44.72]. A robust way to deal with data afflicted with different unknown types of error is signal reconstruction from noise [44.22]. However, it is not generally applicable, as the measured phenomenon must be modelable as particles, among other constraints.

An interesting approach is *data design*, i.e., using methods from the field of human-computer interaction (HCI) not only to design interfaces but also to assess the needs of data consumers to collect reliable, standardized, and overall more useful data [44.73]. However, this works for observations that are reported in a free form (e.g., textual), but not so much for pure sensor data. Additionally, models have been developed to exchange, revise, and merge structured off-line data, e.g., from contributions that are accomplished via paper [44.74]. Finally, one of the most universal mechanisms is *feedback*. Since we can, in many cases, assume that users are actually interested in collecting and submitting high-quality data, it is important to make the measurement process as transparent as possible. Feedback (e.g., on the correct execution of a step, etc.) can greatly contribute to this understanding.

Some of the approaches discussed can be combined with *gamification* techniques. Researchers have, e.g., shown in the context of mobile experience sampling (ESM) that gamification can lead to an increase in amount and quality of participant contributions [44.75]. In other contexts, the location-based game *GeoSnake* [44.76] has been used to boost verification rates, the game *PhotoCity* gamifies training [44.77], and it has been proposed to use game contexts to ensure correct execution of a sensing task [44.78]. However, gamification approaches must be used with care, since they can have unintended side effects, such as perceived pressure that can have a negative effect on data quality [44.79]. It has also been discovered that extrinsic incentives can lessen or even replace intrinsic motivation or discourage certain peo-

ple. Again, knowing the crowd that is engaged in the task or activity is key here.

An underestimated aspect that indirectly may have an effect on data quality in systems involving individuals that collect data is privacy, or rather measures to ensure privacy. When collecting geolocated sensor data, people actually may submit a location trace of themselves along with the measurement data. If the data is made available online in real time, this can even enable live tracking of people. There are several measures that can be taken to ensure privacy, one of them being the obfuscation of the precise position of the measuring person and instead providing only a wider area in which the measurement was collected or artificially adding uncertainty to the location information. However, for some phenomena or analyses, precise location information may be important in terms of data quality. Therefore, it is prudent to determine which measures can be taken to protect the users' privacy while at the same time not sacrificing data quality. Other possibilities than direct obfuscation of the exact location may include only publishing analyzed data rather than raw data or relying on systems without mobility to circumvent the tracking issue. For device-to-device calibration, also several privacy-preserving approaches exist [44.80].

While the measures discussed may help to identify and control possible sources of error in large-scale crowdsensing systems, we already argued above that the definition of data quality on the device level may no longer be adequate to describe such systems in the first place. Instead, we propose that the logical continuation of crowdsourced data acquisition is the fusion and analytics of this data with available high-quality measurement data, as well as other relevant data from different sources, e.g., on traffic or urban topology [44.45]. Poor data quality remains a threat in such systems, as many possible sources of uncertainty potentially accumulate, and well-verified systems are still the exception in the scientific literature today.

On the contrary, increasingly there are systems emerging in which, e.g., machine learning or big data analytics approaches are used on questionable data in

order to produce data products such as animated maps or predictive applications. The danger is that people tend to accept values such systems provide without reflecting on data quality. Another danger is that they may judge the data quality in these systems based on the quality of presentation. If the visualization is professional, people may wrongfully place a higher level of trust in the data. Past research already reported this problem two decades ago: *Computer generated maps, a standard output of geographic information systems (GISs), generally imply an accuracy not warranted by the data* [44.81]. Therefore, a very important aspect of systems that involve users or that communicate observations to end users is that of finding adequate ways to visualize uncertainty and communicate clearly if there are doubts concerning the quality of the data presented.

This adds to the general problem that careful communication and education of users is important, especially in grassroots citizen science projects that may also have a political dimension. The use of low-cost sensors can form an increasing *threat* for the existing measurement infrastructure and the institutions that operate them. As people become aware of their existence and the fact that they are being operated by other citizens, they approach the institutions with queries like *why don't you use this technology?*, *why don't you measure in my street?*, and *why is your value for that parameter so much lower than what I measure here?*. While these are, in principle, legitimate inquiries, it is important that crowdsourcers also educate themselves and their crowdworkers concerning the limitations of the often imperfect technology they may be using, as well as the applications that can be used for and the conclusions that can be drawn from their raw data. Otherwise, they run the risk of their project discrediting itself and other similar efforts.

That being said, the large-scale sensing of environmental phenomena has the potential to bring forth unprecedented measurement systems that reveal previously undiscovered aspects and relationships, especially in urban environments. When properly assessed, actively managed, and properly communicated, data quality need not be an issue in these systems.

44.7 Maintenance

The requirements for maintenance are identical for stations with single and compact sensors and similar for specific networks and industry applications. For specific sensors, the maintenance recommendations are given in the chapters of Part B of this Handbook.

For cheaper sensors in specific networks, industrial applications and crowdsourcing sensors on the other hand, the replacement of the sensor is often cheaper than costly maintenance works. General statements about maintenance intervals are not possible, as

the variety of available sensors does not have uniform specifications (Sect. 44.5). Additionally, the application case also influences both maintenance requirements and feasibility. Besides the requirements for maintenance not being clearly defined, compliance with the requirements is hard to track, validate, and document in crowdsourcing systems. However, it is generally pru-

dent to at least somehow monitor sensor performance, so that the need for either the timely exchange of a sensor can be detected or other action can be taken.

Other maintenance efforts in crowdsourcing applications that may matter include keeping wireless systems powered (e.g., by regularly charging batteries) and ensuring connectivity or data upload.

44.8 Applications

Examples of applications for different parameters are given in the chapters of Part B, as well as in Chap. 43. For most of the station types described in this chapter, a huge amount of applications is available. Therefore, in the following, only a few examples of station types according Table 44.1 are given. All of the projects and applications listed in this section employ crowdsourcing in some way. Table 44.5 shows an overview of projects, indicating for each project which property is observed or which task is performed and which sensors (if any) are used for this. For each entry, the table further shows whether the project is academic, civic, or commercial, which scale the project has reached (in terms of community size and/or data points), and whether extrinsic incentives are offered. Finally, for each row, the type of task is indicated, as well as the interfaces over which the crowdworkers interact with the system.

There have been multiple surveys on crowdsourcing in the past, some general and at least one specific to crowdsourcing in meteorology, presenting a survey on crowdsourcing for climate and atmospheric sciences [44.82]. It features a plethora of atmosphere, weather, and climate-related crowdsourcing projects and techniques. Many of the applications featured in that work are presented here as well. Table 44.5 shows an overview of all projects described in this section. As was already the case with the list of crowdsourcing technology in Sect. 44.4, this is not intended to form a comprehensive list but rather an overview of different projects and approaches.

For each crowdsourcing application, the column *Observed Properties* indicates which data is collected or created in the respective project. The column *Sensors* holds the class of device or system that is used to do this, according to the classification from Sect. 44.4. Under *Purpose*, we list the type of project (academic, public, commercial, grass-roots), and the column *Scale* describes the level the project has reached, in terms of number of devices, volunteers, and/or data points. Under *Incentives*, the table shows whether the application relies on intrinsically motivated participants or features

some kind of incentivization method, monetary or other. The column *Type (task)* indicates the type of activity the crowdworkers are involved in according to the typology presented in Sect. 44.3.1, as well as information on the task itself (e.g., observation, classification, maintenance, prediction, etc.). Finally, the table lists the *Interface(s)* over which the crowdworkers perform the tasks, upload the data, and/or access the results, if applicable.

The *Old Weather* project [44.83] has the goal of making historical weather data that is *hidden* in ships' logs available for research by crowdsourcing the task of extracting, labeling, and digitizing the data. It is hosted on the *Zooniverse* citizen science platform [44.44]. The ultimate goal is to better understand what the weather is going to be like in the future by analyzing how it has been in the past. To this end, crowdworkers extract all kinds of weather data from millions of pages of nineteenth century and World War I ships' logs.

There are two activities crowdworkers can choose from: *marking* and *transcribing*. Marking is used to identify specific pieces of data (like time, date, location, what kind of sea ice happened to be around the ship, etc.) in digital images of each of the logs' pages (Fig. 44.9). Transcribing is the activity of digitizing marked information by typing it into corresponding text input fields, a task in which humans outperform automated approaches handwritten entries.

The project was initially launched in 2010. By 2012, more than one million log pages had been transcribed and in 2016, the project reported that more than 4 million observations had been digitized by a total of more than 20 000 participants [44.84]. In terms of incentives, the platform relies on the intrinsic motivation of participants to contribute to science, as well as, apparently, learn about historical seafaring. *Blaser and Ridge* [44.85] report that

many users have commented in the Old Weather forum that as a result of the project, they were buying books and enrolling in courses to enhance their knowledge further.

Table 44.5 Overview of example crowdsourcing projects and applications that collect meteorological and/or other atmospheric data. While most projects involve data collection (crowdsensing), some entail classifying or annotating existing data (crowdanalyzing)

Project/application	Observed properties	Sensors	Purpose	Scale	Incentives	Type (task)	Interface(s)
Old weather	Historical weather data from ships' logs	Human observation	Academic	> 20,000 volunteers, > 4 million data points (2016)	Intrinsic; extrinsic (gamification)	Crowdsensing (observation), crowdanalyzing (classification)	Website
Cyclone Center	Cyclone classification	Human observation	Academic	> 16,000 active users, > 900,000 data points, > 44,000 images complete (2018)	Intrinsic	Crowdanalyzing (classification)	Website
mPING	Qualitative precipitation (rain, snow, ...), selected events (flood, tornado, mudslide, ...)	Human observation	Academic/public	> 30,000 downloads, > 860,000 reports (2015)	Intrinsic	Crowdsensing (observation)	App, website, application programming interface (API)
RainRadar	Qualitative precipitation	Human observation	Academic	N/A (inactive)	Intrinsic	Crowdsensing (observation)	Twitter, website
UK Snow Map	Qualitative snowfall	Human observation, (camera)	N/A	N/A	Intrinsic	Crowdsensing (observation)	Twitter, website, app
Snow Tweets	Snow depth	Human observation, ruler	Academic	N/A (inactive)	Intrinsic	Crowdsensing (observation)	Twitter, website
CoCoRaHS	RR, qualitative condition reports	Human observation, high quality manual rain gauges	Academic/public	> 20,000 volunteers, \approx 10,000 reports/day (2018), > 31 mio. reports total	Intrinsic	Crowdsensing (observation)	Website, app
Citizen Weather Observer Program (CWOP)	t_a , R, p, RR, dd, u_h (varies)	Automatic stations (AMS); consumer stations; DIY platforms	Public	> 13,000 stations, > 100,000 reports/hour	Intrinsic	Crowdfunding, crowdsensing (observation, maintenance)	API
Netatmo	t_a , R, p, CO ₂ , RR (optional), u_h (optional)	Dedicated commercial consumer stations	Commercial	> 100,000 stations	Extrinsic (service)	Crowdfunding, crowdsensing (observation)	Website, API, app

Table 44.5 (Continued)

Project/application	Observed properties	Sensors	Purpose	Scale	Incentives	Type (task)	Interface(s)
Weather Underground	t_a , R , p , RR , dd , u_h , and others (depends on personal weather stations (PWSs))	Heterogeneous consumer stations/PWS	Commercial	> 250 000 consumer stations	Intrinsic, extrinsic (service)	Crowdfunding, crowdsensing (observation, maintenance)	Website, multiple apps, API
AirBox	PM_{10} , $PM_{2.5}$, t_a , R	Dedicated commercial platform with low-cost sensors	Commercial/civic/grass-roots	> 4000 sensor stations	Intrinsic	Crowdfunding, crowdsensing (observation)	Website, API, app
luftdaten.info	PM_{10} , $PM_{2.5}$, (t_a , R)	Dedicated DIY platform with low-cost sensors	Civic/grass-roots	> 5000 sensors installed worldwide (2018)	Intrinsic	Crowdfunding, peer-production (DIY sensor), crowdsensing (observation, maintenance)	Website, API
SenseBox/OpenSenseMap	t_a , R , p , E_v , UVR, PM_{10} , $PM_{2.5}$	Dedicated DIY platform with low-cost sensors	Academic/civic/commercial	> 3000 sensors	Intrinsic	Crowdfunding, peer-production (DIY sensor), crowdsensing (observation, maintenance)	Website, API
CurieuzNeuzen	NO_2	Diffusion tubes	Academic/public	Campaign with > 20 000 users, > 17 000 data points (2018)	Intrinsic	Crowdfunding, crowdsensing (observation, maintainable)	Snail mail, website
iSPEX	TSP (total suspended particles) (indirect)	Internal smartphone camera with smartphone clip-on module	Academic	Campaign with > 1000 participants in one day, > 6000 data points	Intrinsic	Crowdfunding, crowdsensing (observation)	App
PressureNET	P	Internal smartphone sensors	Academic/commercial	> 100 000 hourly smartphone pressure readings across the USA	Intrinsic, extrinsic (service)	Crowdsensing (observation)	App, website
OpenSignal/Weather Signal	t_a (and others)	Internal smartphone sensors	Academic/commercial	> 270 000 downloads, hundreds of millions of data points	Intrinsic, extrinsic (service)	Crowdsensing (observation)	App(s), website

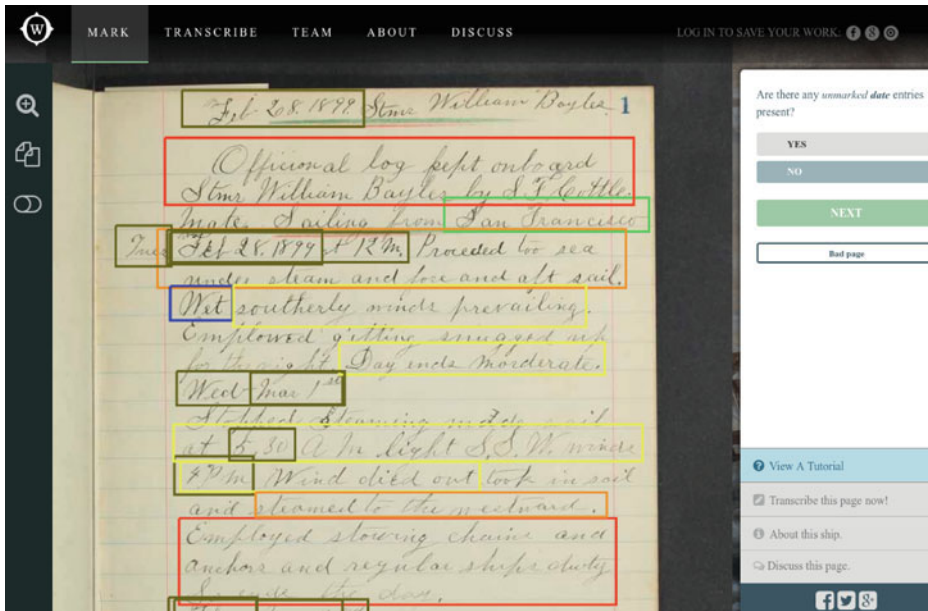


Fig. 44.9 The *Old Weather* project crowdsources the task of digitizing historical ships' logs to extract weather observations by marking and transcribing relevant data (screenshot after [44.83])

As an additional extrinsic incentive, gamification techniques were employed [44.86]. Through a ranking system, participants could earn promotions: when 'joining a ship', i.e., starting to transcribe weather observations for one particular vessel, volunteers started with the rank of cadet, working their way up to lieutenant. The person with the most contributions for that particular ship holds the rank of captain, which can be lost once another volunteer takes the first rank. In some research [44.86], these competitive game elements were partially perceived as being problematic, as they contributed to participants choosing quantity over quality, as well as to the decision of discontinuing participation for some users. They conclude that competitive and personal achievements should be balanced and that, generally, the appeal of game elements varies between participants and over time.

The *Cyclone Center* [44.87] is another *Zooniverse* project that uses crowdworkers to label atmospheric data. In this case, infrared images from weather satellites are analyzed. These images carry information on the cloud-top temperatures, which in turn give an indication of the height of the clouds. Crowdworkers analyze these satellite images according to the so-called *Dvorak Technique* [44.88], developed by *Vernon Dvorak* in the 1970s and early 1980s. For this, two satellite images of whirlwinds are presented to the user at a time, prompting the decision as which one is stronger. Subsequently, the crowdworkers are asked to mark the center of the system and to select which type of cloud pattern best describes it. They are further asked to indicate how organized or intense the cloud pattern is, and whether the

system looks stronger or weaker than on a satellite image from 1 day earlier. From this information, the type and intensity of that tropical cyclone can be approximated.

The *Cyclone Center* project has close to 300 000 satellite images of tropical cyclones dating back as far as 1978 available that need to be analyzed, more than 44 000 of which have been completely analyzed by crowdworkers so far.

While in the former two projects, crowdworkers analyze existing data and create labels for it, most crowdsourcing projects in this section deal with the collection of new data. In the *mPING* project (short for *Meteorological Phenomena Identification Near the Ground*) [44.39] for example, smartphone users collect public weather reports for the *National Severe Storms Laboratory* (NSSL) of the *US National Oceanic and Atmospheric Administration* (NOAA) through a free app. Released in 2012 in collaboration with the University of Oklahoma, by 2015 the app had been downloaded more than 20 000 times, and over 860 000 observations had been collected [44.90]. Users can select the type of observation (rain/snow, hail, wind damage, tornado, flood, mudslide, or reduced visibility), some of them being subcategorized further (e.g., by size). The observations purely report occurrence though, not intensity.

The *RainRadar* project [44.40] of the University at Buffalo and the Ohio State University employed Twitter as a medium through which users could both pose queries to inquire about the precipitation at a certain location (e.g., @RainRadar? Weather Loc:Buffalo, NY), as well as post answers to respective queries relayed

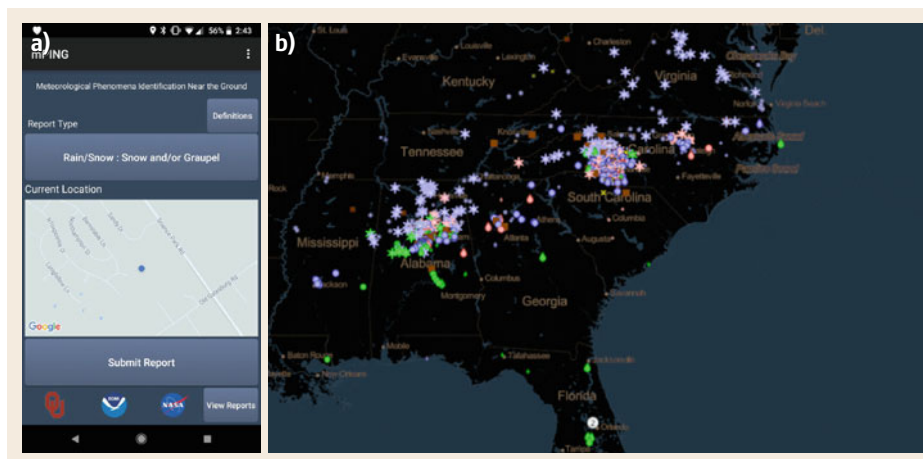


Fig. 44.10a,b In the *mPING* project, crowdworkers report the occurrence and type of precipitation events via an (a) app or (b) web interface (screenshots of (a) mobile app and (b) web interface, after [44.89])

to them based on their current location. The research project also featured a sensing component that automatically read out sensor data and sent it via Twitter. Additional components, such as mining tweets, exploiting social network structures, or adding incentives were envisioned as future work. However, the research project seemed to only have been a case study in 2009, and the respective Twitter account does not show much activity since 2010, so it can be assumed that this project is no longer active.

The *UK Snow Map* project [44.91] follows a similar approach. To indicate that it is snowing, users send a tweet with the hashtag *#uksnow*. The tweet should either be geotagged or contain the first half of the UK postcode of the user's location, as well as a snow intensity rating ($x/10$). A live map is displayed online, along with pictures that users attach to their reports. Another project that works similarly is the *Snow Tweets* project of the University of Waterloo, the difference being that the property observed is not snowfall but snow depth, simply using a ruler. However, since the original website is down, and the current website shows no data points at all, the project can be considered discontinued.

While the previous projects all collect qualitative reports from human observation, many projects use technology to obtain quantitative measurements. The *CoCoRaHS (Community Collaborative Rain, Hail & Snow Network)* [44.92] project ([44.93], Fig. 44.11) is a large citizen science observation network in North America, in which volunteer participants manually submit reports on precipitation and other events. CoCoRaHS volunteers use low-cost, high-quality manual rain gauges to measure precipitation. The project was officially initiated in 1998 at the Colorado Climate Center at Colorado State University (CUS) and has since then been running continuously for more than 20 years, scal-

ing up to more than 20 000 active volunteers who have submitted over 30 million reports in total [44.94].

The *Citizen Weather Observer Program (CWOP)* is a Public Private Partnership that collects data from privately owned electronic weather stations. Unlike CoCoRaHS, measurements are not carried out manually, but instead by automatic stations (AMS, see Sect. 44.4 and Chap. 43). More than 8000 stations are maintained in North America alone, and more than 13 000 across the world. The CWOP originated in the amateur (ham) radio community, but today also includes stations that are connected via the Internet. The connected stations are not all of the same type; any station that implements the APRS (automated packet reporting system) protocol can be configured to connect to the CWOP server. Therefore, the properties observed and the quality of data varies between stations.

A growing number of systems and projects exist that, in contrast to the CWOP program, employs small dedicated Internet of Things (IoT) measurement devices. The technology of the commercial *Netatmo* system was already described in Sect. 44.4. Users can configure whether their data should be made publicly available. If so, the data can be accessed via the public *Netatmo Weathermap* [44.95], as well as an API. Worldwide, more than 100 000 Netatmo personal weather stations transmit their data to the system. This data is freely accessible by anyone.

Data from Netatmo stations has also been analyzed for scientific projects. Researchers have analyzed crowdsourced data from over 1100 Netatmo stations in the city of Berlin and the surrounding area from a period of 6 months (from January to June 2015) [44.96]. Their results indicate that crowdsourced atmospheric data can be valuable for urban climate research, provided faulty data is filtered out. Causes for bad raw data

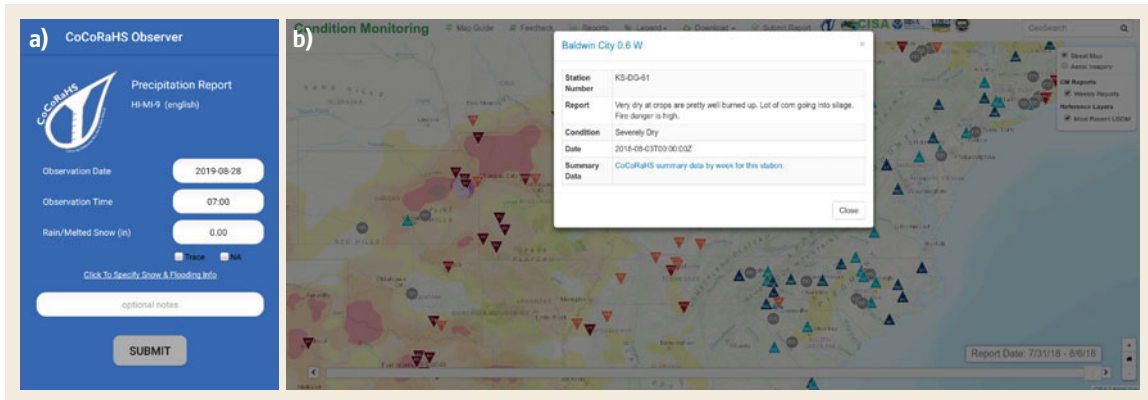


Fig. 44.11a,b The *CoCoRaHS* (*Community Collaborative Rain, Hail & Snow Network*) project has been collecting volunteer precipitation measurements and qualitative condition reports since 1998 (screenshots of **(a)** mobile app and **(b)** web interface (after [44.93] licensed under Creative Commons Attribution 3.0))

were, among others, intermittent connectivity, wrong or incomplete meta data, and faulty installation (e.g., outdoor module operated indoors). After five filtering steps, linear correlation coefficients between reference stations and the *Netatmo* data ranged from 0.80 to 0.99. The daily number of stations that provided data on this quality level dropped to between 350 and 831 stations. For Berlin, this was still sufficient to greatly increase the spatial density of available stations and enable further analysis. However, the authors stress that standardized, calibrated, and quality-checked reference stations are essential in order to validate such systems. An extended version of the research on 1 year of data basically yielded the same conclusions [44.97].

Another scientific project based on *Netatmo* data was conducted in the city of London [44.98]. It characterized the urban heat island effects for a study area from 287 *Netatmo* stations and seven standard reference sites for validation. Among others, the study authors observed a temperature bias probably caused by improper siting of stations, resulting in a systematic deviation of several Kelvin in the temperature readings. Overall, the study concludes that there is clear potential in using crowdsourced data from Internet-connected weather stations for meteorological studies, as long as the challenges of quality assurance and control are properly addressed.

There are other commercial services that integrate data collected by individuals operating personal weather stations, some that sell their own devices, others that integrate data from anyone who registers their station with them. An early example of the latter is the *Weather Underground* (or for short, *Wunderground*; [44.99]). *Wunderground* is a commercial service that evolved from initially being an academic

project at the University of Michigan into a major commercial weather provider. The notable aspect that distinguishes *Weather Underground* from classic weather providers is that it early on integrated data from personal weather stations (PWS) and reached an impressive scale of sensors through that. In 2012, *Weather Underground* was acquired by the *Weather Company*, which in turn sold its B2B, mobile and cloud-based web properties, including *Weather Underground*, to *IBM* in 2015. Also in 2015, *NetAtmo* stations were added to the *Wunderground* map. Today, over 250 000 personal weather stations submit their data into *Weather Underground* [44.100]. *Wunderground* invites people to upload their data but does not distribute their own sensors and, instead, features a PWS buying guide on its website. Incentives to upload one's data were mainly intrinsic in the early days and today include services such as the provision of dashboards and graphs of one's personal station data. Various research papers used weather data from *Wunderground* in their evaluations, either working directly on the dense data (e.g., [44.101]) or using it as supplemental meteorological data (e.g., [44.102, 103]).

Airbox [44.104] is a Taiwanese project for large-scale $PM_{2.5}$ sensing, which started with the deployment of 150 devices in Taipei city in 2016 [44.105]. Since then, a total of more than 4000 devices has been deployed in over 30 countries [44.106], though most of the devices are located in Taiwan (Fig. 44.12). *Airbox* is a mixture of a commercial and a citizen science project. While the *Airboxes* are today manufactured and sold for profit by a company, the project has its roots in a citizen science project LASS (location-aware sensing system [44.107]), the devices of which were directed at makers. The *Airbox* website aggregates both data from

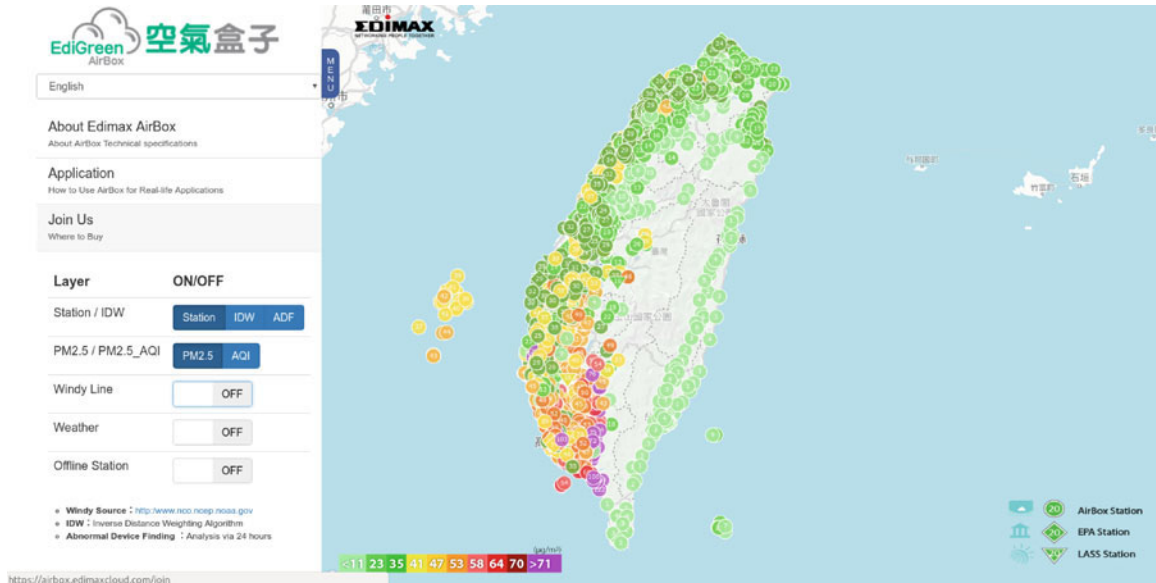


Fig. 44.12 The Taiwanese *Airbox* project provides access via an open API to the data from over 4000 commercially sold *Airbox* devices that measure fine dust (screenshot after [44.104] reprinted with permission from Edimax Technology Co., Ltd)

the LASS devices, as well as from *Airboxes*. Access to the data remains free; it can be accessed either after applying for an access token and downloading the data from the *AirBox* manufacturer's backend database or by using the data API provided by the LASS community to download the measurement data directly [44.105]. Apart from the open data API, the manufacturer donated almost 1000 *Airboxes* to elementary schools in four major Taiwanese Cities, making a substantial contribution to the fine-dust measurement community in Taiwan.

Other notable grass-roots projects have sprung out of citizens' growing consciousness for air quality in the last decade. *Sensor Community* [44.108] is a project affiliated with the Open Knowledge Foundation Germany. Started for the monitoring of PM_{10} in Stuttgart, Germany, sensors are today deployed across the world, though the vast majority is located in central Europe. Luftdaten.info provides a construction manual that describes how to build a PM sensing node out of a low-cost dust sensor, a microcontroller platform, and an external temperature/humidity sensor. Apart from information on which hardware to purchase and how to connect it, open firmware is provided for downloading. After deploying, configuring, and registering the node, it sends PM data to the luftdaten.info servers, from which the raw data is visualized as a heat map on a website (Fig. 44.13). The data is also available through an open API. More than 5000 sensors currently contribute data in this way. This is especially impressive, since the

project is a pure grass-roots effort that has been built and scaled up by a group of environmentally conscious citizens without an institution behind it.

A very similar project is *OpenSenseMap* [44.109], or *SenseBox* [44.110]. In contrast to the grass-roots origin of luftdaten.info, *SenseBox* developed out of an academic project of the Institute for Geoinformatics at the University of Münster, Germany. The *SenseBox* hardware [44.111] developed through several iterations and is today available in two different versions: *SenseBox:home*, which is a modular sensor device directed at citizens, and *SenseBox:edu*, which targets schools, universities, and educational institutions. Both versions are developed and sold by the company *re:edu*, which is a startup that grew out of the *SenseBox* project. A notable aspect of the *SenseBox* project is its strong emphasis on education. Around the hardware and the data platform, many resources on experimentation with sensors, visual programming of the devices, planning workshops, and hackathons, etc., are available. The *OpenSenseMap* platform [44.112] is open not only to data from the *SenseBoxes* but also other registered sensing devices. In total, more than 6000 *SenseBoxes* currently send their data to the *OpenSenseMap* (Fig. 44.14). There are multiple other projects that provide manuals for DIY measurement nodes (Sect. 44.4.2) and open APIs to collect and visualize the data.

In addition to continuous measurements, impressive scales have also been reached by campaign-style

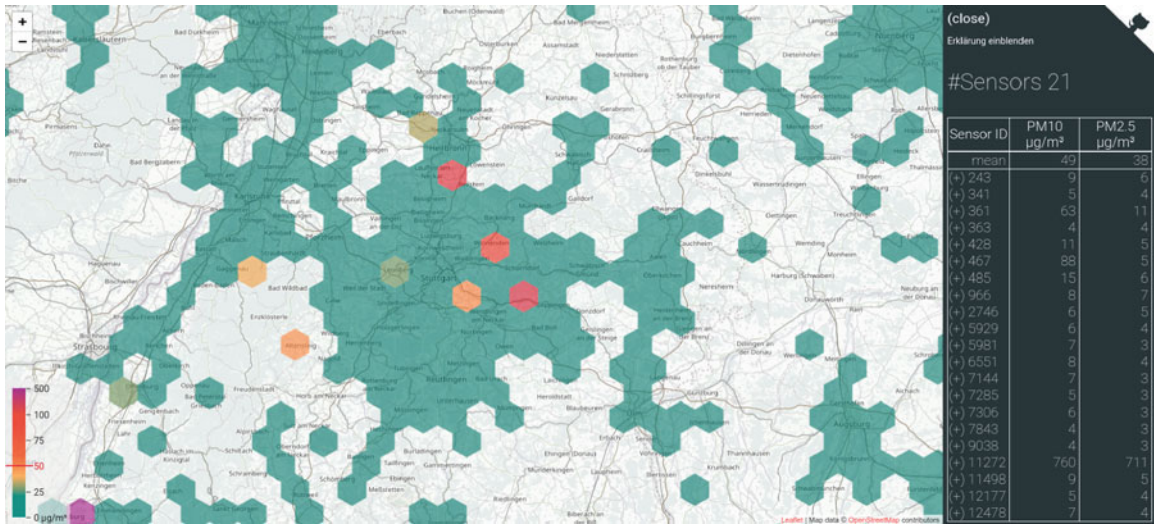


Fig. 44.13 The grass-roots *luftdaten.info* project collects and provides raw data from a network of Citizen Science fine-dust sensors, which are built from off-the-shelf components bought by the users and open software provided by volunteers of *luftdaten.info* (screenshot after [44.108])

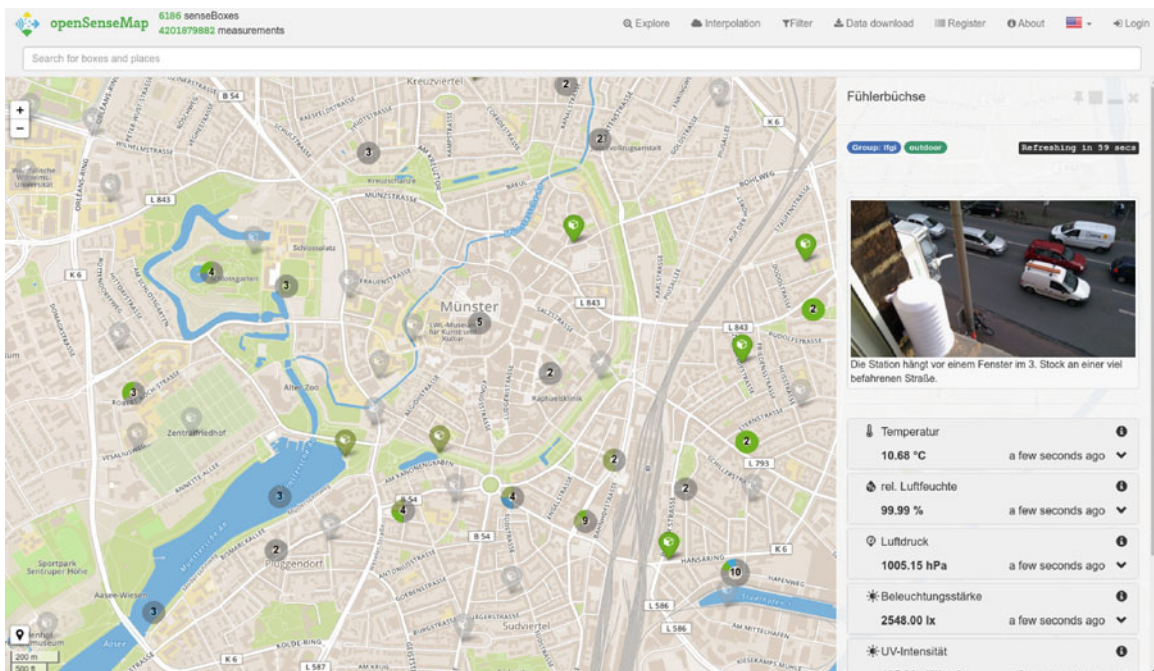


Fig. 44.14 The *SenseBox/OpenSenseMap* project provides an open API that also allows registering devices other than the *SenseBox* hardware to upload and visualize data (screenshot after [44.109])

projects with custom sensor technology. *Curieuzen* [44.113] is a Flemish citizen science project to measure nitrogen dioxide (NO_2) in ambient air. In order to do this, participants are asked to install a pair of diffusion tubes outside their home, on a window facing the street. To ensure a standardized setup for the mea-

surement, the samplers are installed inside a v-shaped window sign, which participants receive as a ready-to-install kit. After a 4-week measurement campaign, they collect the tubes and send them via snail mail to be analyzed in the lab. The results of all measurements are then calibrated against official measurement

stations and jointly analyzed and eventually made public. Two campaigns have been run so far, one in 2016 with 2000 participants (Curieuzeneuzen Antwerp) and one in 2018 with 20 000 participants (Curieuzeneuzen Flanders). The latter eventually managed to collect over 17 000 valid readings and gained interesting insights, e.g., that *the centres of rural villages, which were thought to have pure air, in fact have high levels of traffic-related air pollution* [44.114]. Besides crowdsourcing the measurement, the project also partially uses crowdfunding to cover the cost of the measurement. While 75% of the costs are covered by the project partners, 10 € per measurement are covered by each participant. Additionally, donations are accepted, e.g., to provide free measurement kits to schools.

Another campaign-style citizen science project that reached an impressive scale is the *iSPEX* project [44.33] from Leiden University in The Netherlands. The technology that was developed for and employed in the project was presented above (Sect. 44.4.3). A small clip-on module for the *iPhone* camera enables spectropolarimetric measurements, which are aggregated between multiple users to enable quantitative remote aerosol sensing. The parameter that is derived from the camera recordings is the aerosol optical thickness (AOT). As with other projects we have seen before, users contribute not only the time and effort to make recordings with the system but also part of the cost (only a couple of Euros) of the ultra-low-cost clip-on modules, adding a crowdfunding aspect to the academic *iSPEX* project. Multiple 1-day campaigns have been conducted in The Netherlands, involving up to more than 1000 volunteers in a single day.

While the *iSPEX* project relies on a passive clip-on module in combination with a smartphone camera, some projects attempt to only use the internal sensors of a smartphone. The *PressureNET* project [44.115] collects data on surface pressure from smartphones with internal barometric pressure sensors. The GPS-tagged data from multiple smartphones is sent to a server and processed to support numerical weather prediction. Range and dynamics checks can be used to filter out obviously false data, and movement can be detected through the GPS signal or rapid changes resulting from vertical movement. *PressureNET* experienced some difficulties in the beginning with many users uninstalling the free app quickly after having installed it. When surveying their user base for the reasons, many reported that they did not understand the results the app displayed. One of the problems also seemed to be that in the early phase, *PressureNET* could not yet provide very much direct value to the user and had little more to offer besides the promise to make the weather forecast better. *PressureNET* was acquired by the Sunshine

company in 2016. It is unclear whether *PressureNET* may have been discontinued, as the website no longer seems to be available.

Another project that built on data from internal smartphone sensors concerns itself with deducing urban air temperature based on data from *OpenSignal* [44.116] on smartphone battery temperatures [44.117]. Using mathematical transformations, the battery temperatures from a group of phones in the same vicinity were used to calculate the outdoor air temperature. The research was conducted on a subset of a large worldwide 1-year data set consisting of 220 million battery temperature readings. From this, 2.1 million data points for eight major cities spanning half a year were selected, and after filtering, 1.3 million readings remained. Since many assumptions needed to be made (e.g., people usually carry their phones in their pockets, the majority of readings is recorded outside, etc.), the application of the developed heat transfer model delivered only an estimate of the actual areal average air temperature. Still, the study shows a relatively high accuracy, provided that the number of readings is high enough and model coefficients are adapted to season and location. Following this academic research, *OpenSignal* released *WeatherSignal* in 2013, a specialized Android crowdsourcing app dedicated to collecting information relevant to meteorology in real time from native smartphone sensors, such as barometers, hygrometers, thermometers, magnetometers, and lux meters, with the aim of creating live weather maps. While the app initially seemed to be a success, today neither the website nor the app are available.

In summary, we can see many projects that involve crowdsourcing in atmospheric sciences in some way. The list presented only features examples, with no claim of comprehensiveness. Nevertheless, these examples illustrate the diversity of projects and applications. While most of the crowdsourcing projects focus on data collection and can, thus, be classified as crowdsensing projects, some also involve annotating or classifying existing data, making them fall into the category of crowdanalyzing. Additionally, both academic and commercial projects sometimes involve financial support by the crowd, adding a crowdfunding dimension to them. Some projects entail continuous measurements, others are campaign-style projects that focused the collection period on a short timeframe. Projects may be organized by academic institutions, companies, or bottom-up in a grass-roots fashion by concerned citizens. The technology employed ranges from full-scale automated meteorological stations (AMS) over personal weather stations, both commercial as well as do-it-yourself (DIY) devices, to attempts at gaining useful information from internal smartphone sensors.

Devices can be stationary or mobile, and the sensing procedure may either involve an active role of the user or be rather passive sampling [44.118]. Every project

has its very own challenges, be it scaling up to a certain level, filtering out unwanted data, or creating sustained engagement.

44.9 Future Developments

There is a general trend that people are becoming more concerned and interested in measuring environmental data in the cities they live in, among them the weather and the air quality. For this, they are in need of low-cost sensing equipment with low maintenance effort. Besides individual measurements, the network connection of such devices enables providing novel services such as real-time data visualization, cross calibration, or small-scale exposure assessment and prediction. The possibility to perform individual exposure assessment is particularly interesting for research purposes, potentially complementing, e.g., classical tools of epidemiological researchers, such as regression models to estimate personal exposure. In the long run, the combination of the Internet of Things (IoT) devices and big data analytics has the potential to improve forecasts both in terms of quality and resolution and enable completely novel applications and services.

These developments involve both risks and chances, as well as challenges that need to be addressed. The projects and applications presented in this chapter have shown that low-cost networked sensing systems have the potential to bring science deeper into society. This so-called *democratization* of technology will bring forth new challenges, such as the need to educate citizens concerning the peculiarities of the measurement of certain environmental phenomena, as well as the informative value of the raw data collected. On the other

hand, it is important to collect information on the needs of citizens and user requirements to develop adequate solutions.

This is closely related to the data quality and measurement uncertainty of the measurement technology employed. It remains important to at least document the measurement context and to establish methods to filter out erroneous data. In networked sensing systems that involve big data fusion and real-time analytics, it may be prudent to judge the quality of the data in question not on the single device level but rather view it as data products that are the result of fusing data from heterogeneous sensors, models, etc. Such systems are yet unprecedented, which is why validation strategies are needed that can holistically assess the quality of such systems [44.45].

One of the biggest challenges still seems to be to build sustainable systems that can be maintained over long periods of time, rather than prototypes that are eventually discontinued. Besides appropriately incentivizing participation on the one hand, new business models are needed on the other hand to sustain long-term network operation, data storage, and processing.

Acknowledgments. This chapter was written while during the author's employment at and with the support of the Chair for Pervasive Computing Systems/TECO at Karlsruhe Institute of Technology (KIT), Germany.

References

- 44.1 E. Estellés-Arolas, F. González-Ladrón-De-Guevara: Towards an integrated crowdsourcing definition, *J. Inf. Sci.* **38**(2), 189–200 (2012)
- 44.2 J. Burke, D. Estrin, M. Hansen, A. Parker, N. Ramanathan, S. Reddy, M.B. Srivastava: *Participatory Sensing* (CENS, Los Angeles 2006)
- 44.3 M.F. Goodchild: Citizens as sensors: The world of volunteered geography, *GeoJournal* **69**(4), 211–221 (2007)
- 44.4 J. Howe: The rise of crowdsourcing, *Wired Mag.* **14**(6), 1–4 (2006)
- 44.5 J. Surowiecki: *The Wisdom of Crowds* (Anchor Books, Random House, New York, Toronto 2005)
- 44.6 K. Bult, A. Burstein, D. Chang, M. Dong, M. Fielding, E. Kruglick, J. Ho, F. Lin, T.H. Lin, W.J. Kaiser, H. Marcy, R. Mukai, P. Nelson, F.L. Newburg, K.S.J. Pister, G. Pottie, H. Sanchez, K. Sohrabi, O.M. Stafsudd, K.B. Tan, G. Yung, S. Xue, J. Yao: Low power systems for wireless microsensors. In: *1996 Int. Symp. Low Power Electron. Des., Monterey* (1996), <https://doi.org/10.1109/LPE.1996.542724>
- 44.7 G. Asada, M. Dong, T.S. Lin, F. Newberg, G. Pottie, W.J. Kaiser, H.O. Marcy: Wireless integrated network sensors: Low power systems on a chip. In: *24th Eur. Solid-State Circuits Conf., The Hague* (1998), <https://ieeexplore.ieee.org/document/1470957>, Accessed 17 July 2021
- 44.8 M. Beigl, H. Gellersen: Smart-its: An embedded platform for smart objects. In: *Smart Objects Conf. (sOc)* (2003)

- 44.9 A. Schmidt, K. Asante Aidoo, A. Takaluoma, U. Tuomela, K. Van Laerhoven, W. Van de Velde: Advanced interaction in context, *Lect. Notes Comput. Sci.* **1707**, 89–101 (1999)
- 44.10 A. Schmidt, M. Beigl, H.-W. Gellersen: There is more to context than location, *Comput. Graph.* **23**(6), 893–901 (1999)
- 44.11 E. Estellés-Arolas, R. Navarro-Giner, F. González-Ladrón-de-Guevara: Crowdsourcing fundamentals: Definition and typology. In: *Advances in Crowdsourcing*, ed. by F. Garrigos-Simon, I. Gil-Pechuán, S. Estelles-Miguel (Springer, Cham 2015) pp. 33–48
- 44.12 D. Linders: From e-government to we-government: Defining a typology for citizen coproduction in the age of social media, *Gov. Inf. Q.* **29**(4), 446–454 (2012)
- 44.13 C. Gomes, D. Schneider, K. Moraes, J. de Souza: Crowdsourcing for music: Survey and taxonomy. In: *2012 IEEE Int. Conf. Syst. Man Cybern. (SMC), Seoul* (2012), <https://doi.org/10.1109/ICSMC.2012.6377831>
- 44.14 D. Geiger, M. Rosemann, E. Fieft, M. Schader: Crowdsourcing information systems – Definition, typology, and design. In: *33rd Int. Conf. Inf. Syst., Orlando* (2012)
- 44.15 M. Budde, J. De Melo Borges, S. Tomov, T. Riedel, M. Beigl: Leveraging spatio-temporal clustering for participatory urban infrastructure monitoring. In: *First Int. Conf. IoT Urban Space* (2014), <https://doi.org/10.4108/icst.urb-iot.2014.257282>
- 44.16 J. De Melo Borges, M. Budde, O. Peters, T. Riedel, A. Schankin, M. Beigl: Estavis: A real-world interactive platform for crowdsourced visual urban analytics. In: *Second Int. Conf. IoT Urban Space* (2016), <https://doi.org/10.1145/2962735.2962749>
- 44.17 P. Belleflamme, T. Lambert, A. Schwienbacher: Crowdfunding: Tapping the right crowd, *J. Bus. Ventur.* **29**(5), 585–609 (2014)
- 44.18 T.J. Tanenbaum, A.M. Williams, A. Desjardins, K. Tanenbaum: Democratizing technology: Pleasure, utility and expressiveness in DIY and maker practice. In: *SIGCHI Conf. Hum. Factors Comput. Syst.* (2013), <https://doi.org/10.1145/2470654.2481360>
- 44.19 R. Bonney, J.L. Shirk, T.B. Phillips, A. Wiggins, H.L. Ballard, A.J. Miller-Rushing, J.K. Parrish: Next steps for citizen science, *Science* **343**(6178), 1436–1437 (2014)
- 44.20 S.K. Gibb: Volunteers against pollution, *Chem. Eng. News* **93**(36), 12–17 (2015)
- 44.21 A. Keen: *The Cult of the Amateur: How Today's Internet Is Killing Our Culture* (Crown Business, New York 2007) pp. 70–75
- 44.22 M. Budde, M. Köpke, M. Beigl: Robust in-situ data reconstruction from poisson noise for low-cost, mobile, non-expert environmental sensing. In: *2015 ACM Int. Symp. Wearable Comput.* (2015), <https://doi.org/10.1145/2802083.2808406>
- 44.23 L. See, A. Comber, C. Salk, S. Fritz, M. van der Velde, C. Perger, C. Schill, I. McCallum, F. Kraxner, M. Obersteiner: Comparing the quality of crowd-sourced data contributed by expert and non-experts, *PLoS One* **8**(7), e69958 (2013)
- 44.24 M. Budde, A. Schankin, J. Hoffmann, M. Danz, T. Riedel, M. Beigl: Participatory sensing or participatory nonsense?: Mitigating the effect of human error on data quality in citizen science. In: *ACM Interact. Mob. Wearable Ubiquitous Technol.* (2017), <https://doi.org/10.1145/3131900>
- 44.25 M. Harding, B. Knowles, N. Davies, M. Rouncefield: HCI, civic engagement & trust. In: *33rd Annu. ACM Conf. Hum. Factors Comput. Syst.* (2015), <https://doi.org/10.1145/2702123.2702255>
- 44.26 M. Budde: *Distributed, Low-Cost, Non-Expert Fine Dust Sensing with Smartphones*, Doctoral dissertation (KIT, Karlsruhe 2018)
- 44.27 D. Hasenfratz, O. Saukh, L. Thiele: On-the-fly calibration of low-cost gas sensors, *Lect. Notes Comput. Sci.* **7158**, 228–244 (2012)
- 44.28 Netatmo, <https://www.Netatmo.com>, Accessed 17 July 2021
- 44.29 M. Budde, A. Schwarz, T. Müller, B. Laquai, N. Streibl, G. Schindler, T. Riedel, A. Dittler, M. Beigl: Potential and limitations of the low-cost SDS011 particle sensor for monitoring urban air quality. In: *3rd Int. Conf. Atmos. Dust – DUST2018*, ProScience, Vol. 5 (2018) pp. 6–12
- 44.30 A. Lewis, W.R. Peltier, E. von Schneidemesser: *Low-Cost Sensors for the Measurement of Atmospheric Composition: Overview of Topic and Future Applications* (WMO, Geneva 2018)
- 44.31 N. Ramanathan, M. Lukac, T. Ahmed, A. Kar, P.S. Praveen, T. Honles, I. Leong, I.H. Rehman, J.J. Schauer, V. Ramanathan: A cellphone based system for large-scale monitoring of black carbon, *Atmos. Environ.* **45**(26), 4481–4487 (2011)
- 44.32 S. Poduri, A. Nimkar, G.S. Sukhatme: Visibility monitoring using mobile phones. In: *Annual Report: Center for Embedded Networked Sensing* (2010) pp. 125–127
- 44.33 F. Snik, J.H.H. Rietjens, A. Apituley, H. Volten, B. Mijling, A. Di Noia, S. Heikamp, R.C. Heinsbroek, O.P. Hasekamp, J.M. Smit, J. Vonk, D.M. Stam, G. van Harten, J. de Boer, C.U. Keller: Mapping atmospheric aerosols with a citizen science network of smartphone spectropolarimeters, *Geophys. Res. Lett.* **41**(20), 7351–7358 (2014)
- 44.34 M. Budde, S. Leiner, M. Köpke, J. Riesterer, T. Riedel, M. Beigl: FeinPhone: Low-cost smartphone camera-based 2D particulate matter sensor, *Sensors* **19**(3), 749 (2019)
- 44.35 M. Carminati, L. Pedalà, E. Bianchi, F. Nason, G. Dubini, L. Cortelezzi, G. Ferrari, M. Sampietro: Capacitive detection of micrometric airborne particulate matter for solid-state personal air quality monitors, *Sens. Actuators A* **219**, 80–87 (2014)
- 44.36 F.L. Doering, I. Paprotny, R.M. White: MEMS air-microfluidic sensor for portable monitoring of airborne particulates. In: *2012 Solid-State Sens. Actuators Microsyst. Workshop, San Diego* (2012)
- 44.37 M. Budde, M. Köpke, M. Beigl: Design of a light-scattering particle sensor for citizen science air quality monitoring with smartphones: Tradeoffs

- and experiences. In: *2nd Int. Conf. Atmos. Dust – DUST2016*, ProScience, Vol. 3 (2016) pp. 13–20
- 44.38 H.W. Leibowitz, R.B. Post: Capabilities and limitations of the human being as a sensor. In: *Selected Sensory Methods: Problems and Approaches to Measuring Hedonics*, ed. by J. Kuznicki, R. Johnson, A. Rutkiewicz (ASTM International, West Conshohocken 1982) pp. 3–10
- 44.39 K.L. Elmore, Z.L. Flamig, V. Lakshmanan, B.T. Kaney, V. Farmer, H.D. Reeves, L.P. Rothfusz: mPING: Crowd-sourcing weather reports for research, *Bull. Am. Meteorol. Soc.* **95**(9), 1335–1342 (2014)
- 44.40 M. Demirbas, M.A. Bayir, C.G. Akcora, Y.S. Yilmaz, H. Ferhatosmanoglu: Crowd-sourced sensing and collaboration using twitter. In: *2010 IEEE Int. Symp. World Wirel. Mob. Multim. Netw. (WoWMoM)* (2010), <https://doi.org/10.1109/WoWMoM.2010.5534910>
- 44.41 F. Cheong, C. Cheong: Social media data mining: A social network analysis of tweets during the 2010–2011 Australian floods. In: *PACIS 2011 Proceedings* (2011)
- 44.42 M. Zook, M. Graham, T. Shelton, S. Gorman: Volunteered geographic information and crowd-sourcing disaster relief: A case study of the Haitian earthquake, *World Med. Health Policy* **2**(2), 7–33 (2010)
- 44.43 S.E. Middleton, L. Middleton, S. Modafferi: Real-time crisis mapping of natural disasters using social media, *IEEE Intell. Syst.* **29**(2), 9–17 (2014)
- 44.44 R. Simpson, K.R. Page, D. De Roure: Zooniverse: Observing the world's largest citizen science platform. In: *23rd Int. Conf. World Wide Web* (2014), <https://doi.org/10.1145/2567948.2579215>
- 44.45 M. Budde, T. Riedel, M. Beigl, K. Schäfer, S. Emeis, J. Cyrus, J. Schnelle-Kreis, A. Philipp, V. Ziegler, H. Grimm: SmartAQnet: Remote and in-situ sensing of urban air quality, *Proc. SPIE* **10424**, 104240C (2017)
- 44.46 Bosch GmbH (2018): *BME 280 Combined Humidity and Pressure Sensor – Data Sheet*, document revision 1.6, available from: https://ae-bst.resource.bosch.com/media_tech/media/datasheets/BST-BME280-DS002.pdf, Accessed 17 July 2021
- 44.47 X.-D. Lu, D.L. Trumper: Self-calibration of on-axis rotary encoders, *CIRP Annals* **56**(1), 499–504 (2007)
- 44.48 W. Tsujita, H. Ishida, T. Moriizumi: Dynamic gas sensor network for air pollution monitoring and its auto-calibration, *Proc. IEEE Sens.* **1**, 56–59 (2004)
- 44.49 V. Bychkovskiy, S. Megerian, D. Estrin, M. Potkonjak: A collaborative approach to in-place sensor calibration, *Lect. Notes Comput. Sci.* **2634**, 301–316 (2003)
- 44.50 L. Balzano, R. Nowak: Blind calibration of sensor networks. In: *6th Int. Conf. Inf. Process. Sens. Netw.* (2007), <https://doi.org/10.1145/1236360.1236372>
- 44.51 R. Tan, G. Xing, Z. Yuan, X. Liu, J. Yao: System-level calibration for data fusion in wireless sensor networks, *ACM Trans. Sens. Netw.* **9**(3), 28 (2013)
- 44.52 J. Feng, S. Megerian, M. Potkonjak: Model-based calibration for sensor networks, *Sensors* **2**, 737–742 (2003)
- 44.53 V.L. Bychkovskiy: *Distributed In-Place Calibration in Sensor Networks*, Doctoral dissertation (Univ. California, Los Angeles 2003)
- 44.54 Y. Yu, H. Li: Virtual in-situ calibration method in building systems, *Autom. Constr.* **59**, 59–67 (2015)
- 44.55 R. Tan, G. Xing, Z. Yuan, X. Liu, J. Yao: System-level calibration for fusion-based wireless sensor networks. In: *2010 IEEE 31st Real-Time Syst. Symp.* (2010), <https://doi.org/10.1109/RTSS.2010.29>
- 44.56 K. Whitehouse, D. Culler: Calibration as parameter estimation in sensor networks. In: *1st ACM Int. Workshop Wirel. Sens. Netw. Appl.* (2002), <https://doi.org/10.1145/570738.570747>
- 44.57 E. Miluzzo, N.D. Lane, A.T. Campbell, R. Olfati-Saber: CaliBree: A self-calibration system for mobile sensor networks, *Lect. Notes Comput. Sci.* **5067**, 314–331 (2008)
- 44.58 N.D. Lane, E. Miluzzo, H. Lu, D. Peebles, T. Choudhury, A.T. Campbell: A survey of mobile phone sensing, *IEEE Commun. Mag.* **48**(9), 140–150 (2010)
- 44.59 C.D. Wickens, J. Lee, Y.D. Liu, S. Gordon-Becker: *Introduction to Human Factors Engineering: Pearson New International Edition*, 2nd edn. (Pearson, Harlow 2014)
- 44.60 B.A. Thelen, R.K. Thiet: Cultivating connection: Incorporating meaningful citizen science into Cape Cod National Seashore's estuarine research and monitoring programs, *Park Sci.* **25**(1), 74–80 (2008)
- 44.61 J. Sweller: Visualisation and instructional design. In: *Int. Workshop Dyn. Vis. Learn.* (2002)
- 44.62 G.A. Miller: The magical number seven, plus or minus two: Some limits on our capacity for processing information, *Psychol. Rev.* **63**(2), 81 (1956)
- 44.63 L. Peterson, M.J. Peterson: Short-term retention of individual verbal items, *J. Exp. Psychol.* **58**(3), 193 (1959)
- 44.64 D.G. Novick, K. Ward: Why don't people read the manual? In: *24th Annu. ACM Int. Conf. Des. Commun.* (2006), <https://doi.org/10.1145/1166324.1166329>
- 44.65 K.L. Huang, S.S. Kanhere, W. Hu: Are you contributing trustworthy data? The case for a reputation system in participatory sensing. In: *13th ACM Int. Conf. Model. Anal. Simul. Wirel. Mob. Syst.* (2010), <https://doi.org/10.1145/1868521.1868526>
- 44.66 S. Reddy, D. Estrin, M. Srivastava: Recruitment framework for participatory sensing data collections, *Lect. Notes Comput. Sci.* **6030**, 138–155 (2010)
- 44.67 A. Truskinger, H. Yang, J. Wimmer, J. Zhang, I. Williamson, P. Roe: Large scale participatory acoustic sensor data analysis: Tools and reputation models to enhance effectiveness. In: *2011 IEEE 7th Int. Conf. E-Sci. (e-Science)* (2011), <https://doi.org/10.1109/eScience.2011.29>
- 44.68 E. Kintisch: *How to Grow Your Own Army of Citizen Scientists* (2011), available from: <http://www.sciencemag.org/news/2011/02/how-grow->

- your-own-army-citizen-scientists, Accessed 17 July 2021
- 44.69 M.M. Gardiner, L.L. Allee, P.M.J. Brown, J.E. Losey, H.E. Roy, R. Rice Smyth: Lessons from lady beetles: Accuracy of monitoring data from US and UK citizen-science programs, *Front. Ecol. Environ.* **10**(9), 471–476 (2012)
- 44.70 A. Wiggins, Y. He: Community-based data validation practices in citizen science. In: *19th ACM Conf. Comput. Support. Coop. Work Social Comput.* (2016), <https://doi.org/10.1145/2818048.2820063>
- 44.71 S. Kim, J. Mankoff, E. Paulos: Sensr: Evaluating a flexible framework for authoring mobile data-collection tools for citizen science. In: *2013 Conf. Comput. Support. Coop. Work* (2013), <https://doi.org/10.1145/2441776.2441940>
- 44.72 B. Maag, Z. Zhou, L. Thiele: W-Air: Enabling personal air pollution monitoring on wearables. In: *ACM Interact. Mob. Wearable Ubiquitous Technol.* (2018), <https://doi.org/10.1145/3191756>
- 44.73 S. Kim, C. Robson, T. Zimmerman, J. Pierce, E.M. Haber: Creek watch: Pairing usefulness and usability for successful citizen science. In: *SIGCHI Conf. Hum. Factors Comput. Syst.* (2011), <https://doi.org/10.1145/1978942.1979251>
- 44.74 S.A. Sheppard, A. Wiggins, L. Terveen: Capturing quality: Retaining provenance for curated volunteer monitoring data. In: *17th ACM Conf. Comput. Support. Coop. Work Social Comput.* (2014), <https://doi.org/10.1145/2531602.2531689>
- 44.75 N. Van Berkel, J. Goncalves, S. Hosio, V. Kostakos: Gamification of mobile experience sampling improves data quality and quantity. In: *ACM Interact. Mob. Wearable Ubiquitous Technol.* (2017), <https://doi.org/10.1145/3130972>
- 44.76 S. Matyas, P. Kiefer, C. Schlieder, S. Kleyer: Wisdom about the crowd: Assuring geospatial data quality collected in location-based games, *Lect. Notes Comput. Sci.* **6972**, 331–336 (2011)
- 44.77 K. Tuite, N. Snaveley, D.-Y. Hsiao, N. Tabing, Z. Popovic: PhotoCity: Training experts at large-scale image acquisition through a competitive game. In: *SIGCHI Conf. Hum. Factors Comput. Syst.* (2011), <https://doi.org/10.1145/1978942.1979146>
- 44.78 M. Budde, R. Öxler, M. Beigl, J. Holopainen: Sensified gaming: Design patterns and game design elements for gameful environmental sensing. In: *13th Int. Conf. Adv. Comput. Entertain. Technol.* (2016), <https://doi.org/10.1145/3001773.3001832>
- 44.79 N. van Berkel, M. Budde, S. Wijenayake, J. Goncalves: Improving accuracy in mobile human contributions: An overview. In: *2018 ACM Int. Jt. Conf. 2018 Int. Symp. Pervasive Ubiquitous Comput. Wearable Comput.* (2018), <https://doi.org/10.1145/3267305.3267541>
- 44.80 J.-F. Markert, M. Budde, G. Schindler, M. Klug, M. Beigl: Private rendezvous-based calibration of low-cost sensors for participatory environmental sensing. In: *Second Int. Conf. IoT Urban Space* (2016), <https://doi.org/10.1145/2962735.2962754>
- 44.81 B. Buttenfield, M.K. Beard: Graphical and geographical components of data quality. In: *Visualization in Geographic Information Systems*, ed. by H.M. Hearnshaw, D. Unwin (Wiley, Chichester 1994) pp. 150–157
- 44.82 C.L. Muller, L. Chapman, S. Johnston, C. Kidd, S. Illingworth, G. Foody, A. Overeem, R.R. Leigh: Crowdsourcing for climate and atmospheric sciences: Current status and future potential, *Int. J. Climatol.* **35**(11), 3185–3203 (2015)
- 44.83 Old Weather Blog: Our weather's past, the climate's future, <http://www.oldweather.org>, Accessed 17 July 2021
- 44.84 Old Weather Blog, available from: <https://blog.oldweather.org>, Accessed 17 July 2021
- 44.85 L. Blaser: Old weather: Approaching collections from a different angle. In: *Crowdsourcing Our Cultural Heritage*, ed. by M. Ridge (Ashgate Publishing, Farnham 2014) pp. 45–56, Chap. 2
- 44.86 A. Eveleigh, C. Jennett, S. Lynn, A.L. Cox: "I want to be a Captain! I want to be a Captain!": Gamification in the Old Weather Citizen Science Project. In: *First Int. Conf. Gameful Des. Res. Appl.* (2013), <https://doi.org/10.1145/2583008.2583019>
- 44.87 The Cyclon Center, <http://www.cyclonecenter.org>, Accessed 17 July 2021
- 44.88 V.F. Dvorak: *NOAA Tech. Rep. NESDIS 11: Tropical Cyclone Intensity Analysis Using Satellite Data* (US Department of Commerce, Washington 1984)
- 44.89 National Oceanic and Atmospheric Administration (NOAA): Meteorologica Phenomena Identification Near the Ground (mPING), <https://mping.nssl.noaa.gov>, Accessed 17 July 2021
- 44.90 NOAA: *mPING: Crowdsourcing Weather Reports* (2015), available from: <https://www.citizenscience.gov/assets/files/mping-weather-reports.pdf>, Accessed 17 July 2021
- 44.91 UK Snow Map, <http://uksnowmap.com>, Accessed 17 July 2021
- 44.92 R. Cifelli, N. Doesken, P. Kennedy, L.D. Carey, S.A. Rutledge, C. Gimmestad, T. Depue: The community collaborative rain, hail, and snow network: Informal education for scientists and citizens, *Bull. Am. Meteorol. Soc.* **86**(8), 1069–1078 (2005)
- 44.93 Community Collaborative Rain, Hail & Snow Network (CoCoRaHS), "Because every drops count", <http://cocorahs.org>, Accessed 17 July 2021
- 44.94 H.W. Reges, N. Doesken, J. Turner, N. Newman, A. Bergantino, Z. Schwalbe: COCORAHs: The evolution and accomplishments of a volunteer rain gauge network, *Bull. Am. Meteorol. Soc.* **97**(10), 1831–1846 (2016)
- 44.95 Netatmo Weathermap, <https://weathermap.netatmo.com/>, Accessed 17 July 2021
- 44.96 F. Meier, D. Fenner, T. Grassmann, B. Jänicke, M. Otto, D. Scherer: Challenges and benefits from crowd sourced atmospheric data for urban climate research using Berlin, Germany, as testbed. In: *ICUC9 – 9th Int. Conf. Urban Clim. jt. with 12th Symp. Urban Environ.* (2015)
- 44.97 F. Meier, D. Fenner, T. Grassmann, M. Otto, D. Scherer: Crowdsourcing air temperature from

- citizen weather stations for urban climate research, *Urban Clim.* **19**, 170–191 (2017)
- 44.98 L. Chapman, C. Bell, S. Bell: Can the crowdsourcing data paradigm take atmospheric science to a new level? A case study of the urban heat island of London quantified using Netatmo weather stations, *Int. J. Climatol.* **37**(9), 3597–3605 (2017)
- 44.99 Weather Underground, <https://www.wunderground.com>, Accessed 17 July 2021
- 44.100 TWC Product and Technology LLC (2018): Weather Underground. Personal Weather Station Network, available from: <https://www.wunderground.com/weatherstation/overview.asp>, Accessed 17 July 2021
- 44.101 J. Bruns, J. Riesterer, B. Wang, T. Riedel, M. Beigl: Automated quality assessment of (citizen) weather stations, *GI_Forum* (2018), https://doi.org/10.1553/giscience2018_01_s65
- 44.102 N. Chandra, S. Lal, S. Venkataramani, P.K. Patra, V. Sheel: Temporal variations of atmospheric CO₂ and CO at Ahmedabad in western India, *Atmos. Chem. Phys.* **16**(10), 6153–6173 (2016)
- 44.103 R.A. Atun, Y.A. Samyshkin, F. Drobniowski, S.I. Kuznetsov, I.M. Fedorin, R.J. Coker: Seasonal variation and hospital utilization for tuberculosis in Russia: Hospitals as social care institutions, *Eur. J. Public Health* **15**(4), 350–354 (2005)
- 44.104 Airbox Edimax Cloud, <https://airbox.edimaxcloud.com>, Accessed 17 July 2021
- 44.105 L.-J. Chen, Y.-H. Ho, H.-H. Hsieh, S.-T. Huang, H.-C. Lee, S. Mahajan: ADF: An anomaly detection framework for large-scale PM_{2.5} sensing systems, *IEEE Internet Things J.* **5**(2), 559–570 (2018)
- 44.106 L.-J. Chen: Airbox: A participatory ecosystem for PM_{2.5} monitoring. In: *Mid-term Int. 1st Netw. Workshop SmartAQnet Proj.* (2019)
- 44.107 L.-J. Chen, W. Hsu, M. Cheng, H.-C. Lee: Demo: LASS: A location-aware sensing system for participatory PM_{2.5} monitoring. In: *14th Annu. Int. Conf. Mob. Syst. Appl. Serv. Companion* (2016), <https://doi.org/10.1145/2938559.2938560>
- 44.108 OK Lab: Luftdaten, <https://sensor.community/de/>, Accessed 17 July 2021
- 44.109 OpenSenseMap, <https://opensensemap.org>, Accessed 17 July 2021
- 44.110 Sense Box, <https://sensebox.de/en>, Accessed 17 July 2021
- 44.111 A. Bröring, A. Remke, D. Lasnia: *SenseBox* – A generic sensor platform for the web of things. In: *Mobile and Ubiquitous Systems: Computing, Networking, and Services. MobiQuitous 2011*, Lecture Notes of the Institute for Computer Sciences, Social Informatics and Telecommunications Engineering, Vol. 104, ed. by A. Puiatti, T. Gu (Springer, Berlin, Heidelberg 2011)
- 44.112 M. Pfeil, T. Bartoschek, J.A. Wirwahn: OPENSENSEMAP – A citizen science platform for publishing and exploring sensor data as open data. In: *Free Open Source Softw. Geospat. (FOSS4G) Conf. Proc.* (2015), <https://doi.org/10.7275/R56971SW>
- 44.113 Curieuzeneuzen Vlaanderen, <https://curieuzeneuzen.be>, Accessed 17 July 2021
- 44.114 A. Irwin: Citizen science comes of age – Efforts to engage the public in research are bigger and more diverse than ever. But how much more room is there to grow?, *Nature* **562**(7728), 480–482 (2018)
- 44.115 C.F. Mass, L.E. Madaus: Surface pressure observations from smartphones: A potential revolution for high-resolution weather prediction?, *Bull. Am. Meteorol. Soc.* **95**(9), 1343–1349 (2014)
- 44.116 OpenSignal <https://opensignal.com>, Accessed 17 July 2021
- 44.117 A. Overeem, J.C.R. Robinson, H. Leijnse, G.-J. Steeneveld, B.K.P. Horn, R. Uijlenhoet: Crowdsourcing urban air temperatures from smartphone battery temperatures, *Geophys. Res. Lett.* **40**(15), 4081–4085 (2013)
- 44.118 M.N. Kamel Boulos, B. Resch, D.N. Crowley, J.G. Breslin, G. Sohn, R. Burtner, W.A. Pike, E. Jezierski, K.-Y. Slayer Chuang: Crowdsourcing, citizen sensing and sensor web technologies for public and environmental health surveillance and crisis management: Trends, OGC standards and application examples, *Int. J. Health Geogr.* **10**(1), 67 (2011)

Matthias Budde

Institute of Telematics, TECO / Chair for Pervasive Computing Systems
Karlsruhe Institute of Technology (KIT)
Karlsruhe, Germany

Disy Informationssysteme GmbH
Karlsruhe, Germany
budde@teco.edu,
matthias.budde@disy.net



Matthias Budde is a consultant and senior research scientist at Disy Informationssysteme GmbH in Karlsruhe, Germany. Before that, he was a postdoctoral scholar in the TECO/Pervasive Computing Systems group at Karlsruhe Institute of Technology (KIT), Germany, where he received his PhD degree in Computer Science (2018) for work on low-cost, non-expert environmental sensing and its data quality. Matthias has worked on a variety of projects in ubiquitous computing with the research foci environmental sensing, mobile computing, the Internet of Things (IoT), human-computer-interaction and context and activity recognition.

Mesometeorological Networks

Jerald A. Brotzge , Christopher A. Fiebrich 

Real-time environmental monitoring and numerical weather prediction at high resolutions are now made possible by the deployment of mesometeorological networks. Mesometeorological networks are designed in a manner to optimize sampling across mesospatial (3–100 km) and temporal (minutes to hours) scales. A given number of weather stations are similarly sited, instrumented, and deployed with appropriate spacing across a broad geographic area in order to provide simultaneous, comparable measurements across a region. Each station is comprised of a platform, sensors, and a datalogger, equipped with a power source and communications; the system utilizes centralized software for networking, quality control (QC), and dissemination. Raw data are archived, along with appropriate metadata and QC flags. Ideally, the network operates continuously and indefinitely with routine maintenance including regular sensor cleaning, repair, and calibration. As mesometeorological networks become more widespread and reliable, data from these networks are consumed by emergency management, agriculture, transportation, and utility sectors, among others. Technological advances in computing and networking allow for continued expansion and adoption of these networks worldwide.

45.1	Measurement Principles and Parameters	1234
45.1.1	Purpose	1234
45.1.2	General Description	1235
45.2	History	1235
45.2.1	Growth, Spread of Technology for Communication and Observation ..	1235
45.2.2	Automated Networks – Growth and Examples of Current Networks	1235
45.3	Theory	1235
45.3.1	General Requirements	1235
45.3.2	Siting Requirements	1236
45.3.3	Basic Building Blocks of a Network	1236
45.4	Devices and Systems	1237
45.4.1	Platform	1237
45.4.2	Sensors	1237
45.4.3	Datalogger	1238
45.4.4	Station Power	1238
45.4.5	Station Communication	1238
45.4.6	Operations and Maintenance	1238
45.5	Specifications	1239
45.5.1	General Guidelines for Siting	1239
45.5.2	General Sensor Guidelines for Automated Stations	1239
45.6	Quality Control	1240
45.6.1	Automated Algorithms	1240
45.6.2	Manual Review	1240
45.6.3	Metadata and Documentation	1240
45.7	Maintenance	1240
45.7.1	General Sensor Rotation Rate	1241
45.7.2	Maintenance Schedule	1241
45.8	Applications	1242
45.9	Future Development	1243
45.10	Further Readings	1244
	References	1244

We live in a period of history often referred to as the Information Age where data drives decision-making in all areas of life. In meteorology, weather data is the fundamental building block for understanding the past, analyzing the current state, and predicting the future. Yet in order to use data properly, we must understand its errors and uncertainties. Measurement errors can arise from faulty sensor design, siting issues, and sampling

mistakes, among others. But one way to minimize errors among many measurements is to create a common network with similar siting standards, sampling methods, sensors, transmission, quality control, and archival methods. To satisfy this need, mesometeorological networks have developed across those regions around the world with the greatest requirements for high-quality, real-time weather information.

45.1 Measurement Principles and Parameters

Mesometeorological networks (often abbreviated “mesonets”) are a series of stations deployed in a manner that allows *mesoscale* features (Chap. 1) to be sampled in real time over a relatively large area. Mesoscale phenomena range in size from 3 to > 100 km and may evolve rapidly on the order of minutes. In general, all sites within a network have a common infrastructure, set of sensors, and sampling methodology. All data are collected together, quality controlled, and then archived and disseminated.

45.1.1 Purpose

The unique purpose of a mesometeorological network is to collect similar variable observations simultaneously in time and space across a mesoscale region. For most research and operational applications, these measurements must be done with a high level of accuracy and precision on a continuous, real-time basis. To fulfill these functions, each network must be designed carefully in a way that can best satisfy these requirements (Chaps. 3 and 4).

Table 45.1 Common parameters of a standard mesometeorological network

Parameter	Typical height (m)	Stations per 100 km ²	Chapter
Horizontal spacing			
Temperature	1.5–2	0.1 ^a	Chap. 7 – Temperature Sensors
Humidity	1.5–2	0.1 ^a	Chap. 8 – Humidity Sensors
Wind	10	0.1 ^a	Chap. 9 – Wind Sensors
Precipitation	1	0.1 ^a	Chap. 12 – Precipitation Gauges
Pressure	2	0.1	Chap. 10 – Pressure Sensors
Solar radiation	2	0.1	Chap. 11 – Radiation Sensors
Snow depth	2	0.1 ^a	
Soil temperature and moisture	–5, –10, –25, and –50 cm	0.1 ^a	Chap. 61 – Soil Measurements
Vertical spacing			
Temperature	50–10 000	1	Chap. 29 – Microwave Radiometer (ground-based, air and spaceborn-based, Chap. 41)
Humidity	50–10 000	1	Chap. 29 – Microwave Radiometer (ground-based, air and spaceborn-based, Chap. 41)
Wind	50–7000	1	Chap. 27 – Doppler Wind Lidar Chap. 47 – Vertical Composite Profiling

^a More in very complex terrain, coastal environments, or for specific phenomena such as local circulations or cold air flows



Fig. 45.1 A typical mesonet weather station equipped with a 9.1 m (\approx 30 ft) tower, communications, power, datalogger, and sensors (photo: courtesy of the New York State Mesonet at the University at Albany)

45.1.2 General Description

Specifically, each network configuration must be designed in a way that enables it to observe mesoscale features. In addition, each station should be sited in a way that collects observations most representative of the region, thereby limiting microscale influences. Each site must be equipped with the proper equipment, such as a platform, sensors, power, and communications, installed at standardized heights at high spatial density

45.2 History

The Bureau of Aeronautics in the US Navy began to develop automated weather stations (AWS) in 1939, thereby advancing the technology needed to collect real-time environmental data at numerous locations at high temporal resolution [45.1]. The expansion of automated weather stations continued through the twentieth century, as meteorologists and decision-makers became increasingly reliant on the data.

45.2.1 Growth, Spread of Technology for Communication and Observation

The US Federal Aviation Administration and the National Weather Service developed automated weather stations for widespread use at airports in the 1970s [45.2–4]. With advances in microelectronics, computers, and communication technologies, automated weather stations grew in use throughout the 1980s. By 2001, the National Oceanic and Atmospheric Administration's automated surface observing system

(Table 45.1), and be adequately maintained and calibrated to retain high quality performance with limited down time. A central processing center is needed in order to collect, process, quality control, archive, and disseminate data from the network of stations to users of the data. Extensive metadata should accompany the data and include detailed descriptions of the site locations and characteristics, site configuration, sensor properties, and quality control standards. A typical mesometeorological station is shown in Fig. 45.1.

(ASOS) was the largest network of automated sites in the United States. Many regional to statewide mesonets were established also in the 1980s and 1990s and into the early part of this century [45.5–7]. Many of these mesonets were a result of efforts at colleges and universities [45.8].

45.2.2 Automated Networks – Growth and Examples of Current Networks

By 1992, large-scale networks of automated stations were becoming widespread [45.9]. The Nebraska Automated Weather Data Network, the California Irrigation Management Information System, and the Oklahoma Mesonet constituted some of the earliest, largest networks of stations [45.10]. The Climate Reference Network [45.11] was established nationwide in 2008 with over 100 stations to provide long-term, homogeneous observations to monitor climate change. By 2017, 1619 mesonet stations were active across the US. [45.8].

45.3 Theory

Several features are common to mesometeorological networks to enable them to monitor mesoscale features accurately and in real time. These features include common siting standards, similar instrumentation, automated real-time sampling and communications, and regular quality control, maintenance, and calibration.

45.3.1 General Requirements

An essential element of mesometeorological networks is that local differences are minimized in order to more accurately monitor the evolution of mesoscale features in time and space. To minimize differences between sites, each site should conform to similar sit-

ing standards; these are discussed in more detail in the next section (Chaps. 3 and 43). Furthermore, each site should be designed with the same station configuration, be equipped with the same model and brand of sensors, and have the same signal processing applied [45.12].

A second functional requirement of most mesometeorological networks is the need to provide data in real time. Many networks supply data to weather operations or emergency service providers where real-time analyses are critical for time-sensitive warnings and response. Thus, most networks must have the ability to not only collect observations frequently and repetitively, but also to transmit these data on the order of minutes. A reliable communication network is essen-

tial. In addition, for many applications, data are needed 24 hours a day, 7 days a week, at high frequency intervals (e.g., every 5 min), something few human networks can provide. Importantly, automated sensors have been shown to be more accurate by reducing some types of errors in measurements [45.13].

A final essential element expected from most mesometeorological networks is the ability to produce high-quality data. Regularly applied quality assurance and quality control routines applied to the data can be used to identify sensor errors early and minimize sensor downtime (Chap. 3). Routine preventive and responsive maintenance can ensure the continuity and reliability of the network. Regular calibration of sensors against known international standards can ensure the accuracy and precision of the data. Archiving all operations and maintenance metadata can improve the monitoring of long-term sensor performance. Even field experiments that deploy mesonets on a relatively short-term basis can benefit from site standardization, real-time data access, automated quality control, and attention to sensor calibration.

45.3.2 Siting Requirements

To adequately monitor mesoscale features, mesonet stations must have an average spacing distance between stations on the scale of ≤ 30 km apart. In general, the network topology should be as uniformly distributed as possible to minimize gaps in coverage. Special care should also be taken to include stations across a variety of landscapes as representative of each region. When covering a large area, the variability in topography, vegetation, land use, and soil types common across the region should be well represented by the network. For example, in complex terrain, stations should be placed in both valleys and hills to the extent that these locations can still satisfy World Meteorological Organization (WMO) standards for siting [45.14]. Network spatial density may need to be greater in areas of complex terrain, near large bodies of water, and in urban areas.

One factor that separates many high-quality networks from lesser quality ones is how well each station is sited. Many site-dependent factors can bias otherwise accurate measurements, and this is especially critical in a mesometeorological network where data are to be compared and possibly averaged across multiple stations simultaneously. For example, local terrain features can impact a station's winds, and nearby trees can shade its pyranometer. Nearby concrete surfaces and local bodies of water can bias local temperature and moisture measurements. To help minimize these issues, the

WMO has provided a set of guidelines for station siting [45.14]. Network scientists should work to limit these issues when siting each station, and where possible, all station properties should be captured within exhaustive metadata.

45.3.3 Basic Building Blocks of a Network

The four primary building blocks of a mesonet include the infrastructure and resources associated with data collection, data integration, data dissemination, and network operations and maintenance.

Each network must have the field infrastructure and sensors that measure and collect the sensible weather observations. The network infrastructure may include a tower or mast, power equipment, and weather sensors. Field data are collected automatically and remotely. Often, a sensor will collect a voltage, current, pulse, or digital reading, which is then converted into the correct units, as representative of a weather variable. A datalogger is often used to distribute power, make the necessary conversions, and store data on site. Network infrastructure is discussed in more detail in Sect. 45.4.

Integration of the data is necessary in order to analyze the mesoscale features of interest. Data are collected in real time from all sites and then transmitted to a central processing center. A reliable communication network, such as cellular, radio, or satellite, is necessary for data transmission. Site communications are discussed in more detail in Sect. 45.4.5. One or more servers are needed at the central processing site for the data ingest and subsequent quality control; these servers can be set up for automated retrieval of archived data from field sites when real-time data transmissions are interrupted.

Once processed, data may be disseminated to a variety of users. Data may be disseminated through several avenues, including file transfer protocol (FTP), local data manager (LDM), application program interfaces (APIs), or the Internet. Many networks utilize phone apps and engage users through social networks and other online media. Additional value-added products and displays can be created for specific customers [45.15].

A final but critical building block of a network is the continual operations and maintenance of the system. Continuous monitoring of all data is recommended to flag erroneous data and to alert field technicians of needed repairs. Regular firmware upgrades and sensor calibrations keep sensors within instrument specifications. Software must also be maintained and updated regularly.

45.4 Devices and Systems

Mesometeorological networks vary largely as a function of their original purpose and financial support. Networks may be mobile or fixed, simple or complex. Nevertheless, they have many common elements. These elements include

- (i) A platform
- (ii) Sensors
- (iii) A central processing unit
- (iv) A power source
- (v) Communications
- (vi) Quality assurance and quality control
- (vii) Regular calibration and maintenance.

45.4.1 Platform

A collective suite of sensors that comprises a weather station must be mounted on a platform from which to operate (Chap. 6). A platform provides the mounting structure for the sensors and associated infrastructure, such as a datalogger and access to power and communications. A platform can be mobile or stationary. Many field programs utilize weather instrumentation mounted on vehicles [45.16] (Chap. 50). This provides a flexible network that can move with the feature of interest. For most long-term networks, stationary, fixed towers are used. These towers may vary in height; many are at least 10 m tall in order to collect wind measurements at the 10 m level. Some networks, primarily used for agriculture or transportation, may utilize shorter towers. Some towers are fold-over or hinged to allow easier maintenance without climbing. Some towers are free standing, while others are guyed. Most towers are manufactured using steel or aluminum. Steel towers are sturdier and allow for heavier payloads and greater wind loading. Aluminum towers are cheaper and of lighter weight and are adequate for most purposes, though they may not be climbable. Overall, the platform used should be designed in such a way to minimize overall impact on the variable(s) being measured. For towers, the lattice should be as open and minimal as possible so as not to block or disturb the wind flow. All platforms should be well grounded for lightning protection.

45.4.2 Sensors

A wide variety of sensors are deployed across mesometeorological networks. The most common variables measured include air temperature, relative humidity, wind speed and direction, atmospheric pressure, and precipitation (see the chapters in Part B). Other less common variables include solar radiation, soil temper-

ature and moisture, leaf wetness, snow depth, and snow water equivalent. Some networks measure the surface energy budget, including shortwave and longwave radiation, photosynthetically active radiation (PAR), as well as sensible, latent, CO₂, and ground heat fluxes (see the chapters in Part F). Some networks are beginning to expand beyond surface measurements to collect vertical profiles, such as temperature, moisture, and wind profiles to augment the radiosonde record [45.17] (see the chapters in Part C). Now with high bandwidth available from commercial cellular communications, cameras are being deployed to provide imagery along with standard meteorological data. Photographic data provide important visual verification of sensible weather and act as an excellent quality-control tool for understanding unusual weather events.

All sensors should be mounted in a way that minimizes instrument errors, platform interference, and local siting impacts. While it is not always possible because of power and budgetary constraints, temperature sensors should ideally be mounted in aspirated shields in order to minimize radiational heating errors. This is especially important in areas where sunny, light wind conditions ($< 2 \text{ m s}^{-1}$) are common. Aspiration fan speeds should be monitored to ensure a uniform air flow across the sensor. Humidity sensors should be placed in a radiation shield to prevent direct solar radiation from heating the sensor. Barometers are often mounted in a weatherproof enclosure with a pressure tube extending to the outside of the enclosure to minimize pressure changes and differences with the outside environment. Wind sensors should be mounted on top of a mast or tower such that there are no obstacles impacting the winds impinging upon the sensor. Precipitation is often measured using either a tipping bucket gauge or weighing gauge. Both types of gauges require a single or double Alter shield placed ≈ 1.2 to ≈ 2.4 m around the gauge, designed to minimize the acceleration of air at the gauge orifice, which could lead to an underestimation in precipitation if not used [45.18]. Pyranometers should be mounted level on a cross arm on the south side of a tower, or independently away from a tower on an independent platform, such as a tripod, to minimize shadows or reflectance from the platform. Soil sensors must be installed level in undisturbed soil, and preferably at multiple locations within a site to provide a collective average due to soil inhomogeneities. For most purposes, soil sensors should be placed under naturally occurring vegetation representative of the site area; however for some applications such as agriculture, soil data collected under bare soil may be needed. Soil sensor measurements are often collected

at several depths in order to provide a vertical profile. The WMO recommends soil data collection at 5, 10, 20, 50, and 100 cm. Some networks may collect measurements at 25 or 75 cm. Near-surface rock may inhibit some lower soil depth measurements.

The data collection requirements of most mesonets demand a relatively high data collection rate. Most variables sample at a 1 or 3-second rate; others may sample at a 12 or 60-second rate (e.g., barometer). Typically, these samples are averaged within a central processing unit or datalogger to produce 1-minute and/or 5-minute averages. For some variables, such as maximum rainfall rate and wind gust, a maximum sample is retained. Most sites report 5-minute to hourly averaged observations computed from the higher-frequency sampling.

Redundant sampling yields a more robust data record. Multiple, same type sensors allow for exact, real-time comparisons to ensure good calibration. Multiple sensors that use different measurement techniques, such as the use of a propeller vane and sonic anemometer, can provide even greater confidence in an observation. Extreme weather events can create doubt in a measurement when just one sensor is available. Multiple sensors enable long-term drift to be detected earlier than when just one sensor is used. Whenever sensors are upgraded across a network, it is advisable to collect at least 1 year of simultaneous field measurements with both the old and new sensor at select locations in order to document any unforeseen changes or biases with the upgrade. Furthermore, all networks should be compared against independent network systems whenever possible in order to identify any systematic errors or biases that may be present.

45.4.3 Datalogger

Each station has a central processing unit (CPU), typically referred to as a datalogger (Chap. 2). The datalogger is often multifunctional; it can be used to convert voltages to meteorological units, apply averaging and calibration coefficients, distribute power to sensors, temporarily archive data, and bundle data for transmission. Dataloggers can handle either digital or analog sensors. Dataloggers also provide on-location storage and, depending upon the amount of data generated, can store up to months of data at a time. This is useful whenever communications are interrupted, and archived data can be retrieved once communications are reestablished such that no data are lost in the archive.

45.4.4 Station Power

Siting requirements often limit mesonet stations access to utility power. Many stations are deployed in remote,

wide-open areas away from utility poles. Solar power is now a viable alternative used to power a majority of mesometeorological sites. A solar power system is comprised of one or more solar panels, a charging system, and one or more batteries for power storage. In general, higher-latitude sites require more and larger panels due to the lower winter sun angle and more sensors requiring heating.

One complication with powering a weather station is the distribution of power from the panels to the sensors. Some sensors require 24 V, while others require 12 V. Some sensors are sensitive to the regularity of the current. A distribution system may be needed to regulate and distribute power from the solar panels and datalogger to the sensors and supporting equipment.

45.4.5 Station Communication

At the site, data are bundled by the datalogger and then sent to a modem for transmission. Again, largely due to siting requirements, most stations do not have easy access to line (e.g., Ethernet) communications. As an alternative, many sites use either line-of-sight radio telemetry, or increasingly cellular communications. The proliferation of cellular communications is aiding the collection of data from remote stations; however, the use of cellular requires some costs paid to a third party, private network. For those networks deemed critical for emergency management in the United States, hourly transmissions are allowed free of charge through the geostationary operational environmental satellite (GOES). A limited 30-second transmission is allowed once per hour from each station and provides critical environmental information during emergency situations.

Ideally, all data are collected, processed, and then transmitted in near real time from network stations simultaneously, where data are then collected at a central processing unit. At the receiving end, a single server or cluster will ingest this raw data, where additional processing, such as quality control, may be applied. The entire process, including data collection, transmission, data processing, and dissemination to customers, can ideally be completed in several minutes.

One increasingly critical issue with regards to communications is cyber security. Public internet protocols (IP)s should be used with caution when setting up any communication network.

45.4.6 Operations and Maintenance

Once established, the focus of resources in a mesometeorological network quickly becomes aimed at regular operations and maintenance. Some regular staff should be dedicated to the continuous upkeep of both net-

work field hardware, as well as the central processing center servers and software. A number of automated tools can be utilized for the standard data collection, transmission, quality control, and dissemination steps. Nevertheless, direct human intervention is needed when

problems arise, and a manual review of data is highly recommended even on a daily basis in order to more reliably detect subtle errors or sensor drift that may arise. Site maintenance is discussed in greater detail in Sect. 45.7.

45.5 Specifications

Fortunately, years of study and experience operating mesonets worldwide have now yielded reliable guidelines for station siting and sensing standards. These general recommendations are reviewed below.

45.5.1 General Guidelines for Siting

As discussed in Sect. 45.3.2, the WMO provides a classification scheme for siting guidance based on station site properties [45.14]. These properties include land use type, slope, vegetation height, roughness, and the presence of large bodies of water, heat sources, and obstacles. The ideal site is classified as “Class 1”, which means that the weather measurement incurs minimal, generally insignificant impacts as a function of the site properties. In contrast, station properties at a “Class 5” site overwhelm the measurement to a significant degree. However, note that each site classification is variable dependent. A Class 1 site for measuring rainfall could be a Class 5 site for monitoring solar radiation. For more details, see Chaps. 7, 9, 11, and 12.

Ultimately, the location of a site will depend upon many factors; however, the site properties will have a direct impact on data quality. If very high data quality is required, then a Class 1 site (for as many variables as possible) should be selected. If data quality is less of a concern, then lower class sites can be considered. In general, the more restrictive the class category is, often the fewer the options available for placing a station will be.

45.5.2 General Sensor Guidelines for Automated Stations

As with station siting, many factors determine which sensors are best suited for use in any given mesometeological network. For example, data quality requirements, power constraints, communication availability, and sensor costs may all impact the selection of sensors. In general, high-quality, low-power, robust (low-maintenance) sensors are best for use in mesonets. A list of sensors used in the New York State Mesonet and their corresponding properties is provided in Table 45.2 as an example of a typical system (Chap. 43).

Table 45.2 Sensor specifications for the New York State Mesonet, as an example of a standard mesometeological network

Parameter	Sensor	Operating range	Sampling rate (s)	Accuracy
Temperature	R.M. Young 41342 Platinum RTD	−50 to +50 °C	3	±0.3 °C (at 23 °C)
Humidity	Vaisala HMP155	−80 to +60 °C, (0–100% RH)	3	±1% RH (0–90% RH) ±1.7% RH (90–100% RH)
Pressure	Vaisala PTB330	500–1100 hPa	12	±0.25 hPa (−40 to +60 °C)
Precipitation (weighing gauge)	Pluvio ² 200 by Ott	−40 to +60 °C, (up to 50 m s ^{−1})	60	±0.05 mm (amount) 0.01 mm (resolution)
Wind speed, wind direction (sonic anemometer)	Lufft V200A	0–75 m s ^{−1} , 0–360°	3	±0.3 m s ^{−1} or 3% of reading, wind direction: ±3°
Wind speed, wind direction (vane propeller)	R.M. Young wind propeller 05103	0–100 m s ^{−1} , 0–360°, −50 to +50 °C	3	±0.3 m s ^{−1} or 1% of reading, wind direction: ±3°
Solar radiation	LiCor LI-200SA	−40 to +65 °C	3	Approximately ±5%
Soil temperature and moisture	Stevens Hydra Probe II	−30 to +55 °C	60	±0.1 °C
Snow depth	SR50A	−45 to +50 °C	3	±1 cm, or 0.4% of distance to target
Camera	Hikvision	−30 to +60 °C	5 min	–

RH: relative humidity

45.6 Quality Control

The high-resolution nature of data from mesometeorological networks is often an advantage during the quality control process (Chap. 3). In general, data are tested for internal, spatial, and temporal consistency. The challenging aspect of quality control for mesonets is oftentimes the diversity of observations collected (e.g., soil temperatures, solar radiation) and phenomenon detected (e.g., heat bursts, mesolows; [45.19]). Proper siting (Sect. 45.5), the use of calibrated sensors, and routine maintenance (Sect. 45.7) are considered paramount in the quality-control process. Once those conditions are met (or at least documented in the metadata), a number of automated and manual techniques can further refine the assessment of data quality.

45.6.1 Automated Algorithms

The general automated algorithms for mesometeorological data consist of range tests (both based on sensor specifications and on climate thresholds), temporal tests that evaluate observation-to-observation consistency, and spatial tests that compare data from neighboring stations [45.20]. Range tests based on climatological extremes may need to be updated periodically as a meteorological network's data archive grows. Temporal tests can identify anomalous data that have changed either too rapidly during sequential observations (e.g., a temperature decrease of more than 9 K in 5 min) or too slowly (e.g., a temperature change of less than 0.1 K in 60 min). Spatial tests take advantage of neighboring sites to identify sensor drift, bias, or other quality issues. Automated tests for spatial consistency oftentimes include dynamic thresholds based on the standard deviation of the variable tested. For instance, during stormy weather, greater variability may be allowed than during quiescent times. Depending on the data available, many additional, sensor-specific automated algorithms can be employed. For instance, multiple measurements of the same parameter at various heights can be compared to test for expected gradients. For some measurements such as pressure and relative humidity, it is more appropriate to derive sea-level pressure and dewpoint before performing automated spatial comparisons (Chaps. 8 and 10).

45.7 Maintenance

It has often been remarked that the best performing sensor is the best maintained sensor. In other words, it is possible to get accurate data from a well-maintained,

45.6.2 Manual Review

While automated algorithms are invaluable for screening data in real time, a manual review is required to accurately flag erroneous data in the archive. For instance, an automated spatial check may identify a subtle sensor bias that has finally grown large enough to be detected. In that case, a manual edit to the metadata would be required to accurately flag the observations back to the true start of the sensor problem. Thus, rather than manually reviewing hundreds of thousands of observations that might be collected on a given day, a suite of automated tests can pinpoint the dozen or so observations that require manual review. Oftentimes during manual review, external datasets can be exploited. For instance, visible satellite data can be compared to solar radiation data to identify problematic pyranometers. Likewise, radar data can be used to identify failing precipitation sensors. Because these remotely-sensed observations are not necessarily direct measurements, a subjective eye is often required during these manual comparisons.

45.6.3 Metadata and Documentation

Metadata and documentation are critical to the quality review process. Station properties, such as topography and roughness, can have a major influence on sensible observations. For example, a site's elevation in relation to neighboring stations may explain why temperature observations are anomalously cold (due to a relatively low elevation) or warm (due to a relatively high elevation) on a night with a strong low-level inversion. Likewise, panoramic photos of a station may help explain an anomalously low wind speed at a station when the flow is from a direction that has obstructions (e.g., trees) on the horizon. Real-time photos collected by a station can be especially helpful when determining if and when precipitation, fog, or even human or animal vandalism occurred. A well-documented record of all calibrations, sensor changes and rotations, firmware upgrades, and regular maintenance visits provide data users (and quality control managers!) with a wealth of valuable information.

inexpensive sensor. Likewise, it is possible to get poor data from a neglected, expensive sensor. Regular maintenance of mesometeorological networks typically

Table 45.3 General sensor rotation guidelines for automated stations [45.21]. For more details, see Chaps. 7–12

Sensor	Rotation interval (month)
Temperature	60
Humidity	24
Pressure	48
Precipitation (tipping bucket)	60
Wind (propeller vane)	48 (speed); 60 (direction)
Solar radiation	24–36

consists of performing vegetation maintenance in and around the sensors, performing sensor rotations, cleaning and inspecting sensors, performing in-field sensor tests, and documenting site characteristics with photographs [45.21].

45.7.1 General Sensor Rotation Rate

Optimal sensor rotation rates are dependent on a number of factors. The sensor manufacturer often has general guidance on the typical sensor drift rate or life expectancy. Such intervals vary based on manufacturing quality and environmental exposure. For instance, a humidity sensor may drift faster in a moist, coastal environment in comparison to one deployed in a dry, desert environment. While the manufacturer’s guidelines are a good starting point, each network will likely adopt rotation intervals based on typical drift and time-to-failure rates observed in their particular environmental

conditions. As an example, Table 45.3 lists rotation periods based on sensor drift and failure rates experienced across Oklahoma, a region that spans moist, humid conditions in the southeast and dry, arid conditions in the northwest. Some networks choose not to preventatively rotate soil sensors (e.g., soil temperature, soil moisture, soil heat flux), since disturbing the soil structure is often more damaging to the data archive than simply waiting for the soil sensor to fail before replacing it.

45.7.2 Maintenance Schedule

Routine, scheduled maintenance provides an efficient way to perform standard work at each station, as well as complete sensor rotations and collect and update metadata. Oftentimes, vegetation growth is a driving factor in how often routine maintenance is needed. A survey of maintenance schedules at various networks found a range from monthly to annually [45.21]. Tables 45.4 and 45.5 provide example maintenance schedules for a typical mesometeorological network.

Not all maintenance can be scheduled in advance, and the ability to repair failed sensors quickly is critical to minimizing gaps in the data record. Sites and sensors can fail from a myriad of causes, including normal sensor aging, dirt and dust, vandalism, wildlife (e.g., mice chewing wires), snow and ice buildup, extreme temperatures, rain, wind, and lightning. Table 45.6 lists various precautionary recommendations and common problems often observed by field networks.

Table 45.4 General maintenance schedule for automated weather stations

Maximum interval	Site in general	Temperature	Humidity	Wind (propeller vane)
2–4 weeks (growing seasons)	Cut grass within site area			
6 months	Clean all sensors, inspect wiring, check for bugs and critters	Inspect sensor, aspirator fans	Clean sensor tip	Test speed and direction
1 year	Inspect tower, fencing			
2 years			Rotate, recalibrate	
3 years				
4 years				Rotate propeller, recalibrate
5 years		Rotate, recalibrate		Rotate vane, recalibrate

Table 45.5 General maintenance schedule for automated stations, additional variables

Maximum interval	Pressure	Precipitation (tipping bucket)	Precipitation (weighing gauge)	Solar radiation
2–4 weeks (summer)				
6 months	Inspect pressure port	Clean debris from top	Fill antifreeze (fall); empty antifreeze (spring); test weighing device	Clean sensor, check leveling
1 year				
2 years				Rotate, recalibrate
3 years				
4 years	Rotate, recalibrate			
5 years		Rotate, recalibrate		

Table 45.6 A list of common operational issues often encountered by mesometeorological networks

Variable	Guidance
General site	<ul style="list-style-type: none"> • Vegetation should be maintained such that the vegetation height does not interfere with the measurements. Vegetation type should match vegetation outside the station when possible • Beware of wildlife chewing cabling; consider burying all cabling within rodent-proof conduit. Adequate fencing around site to keep domestic animals and large game away from sensors • Site should be well grounded to minimize damage from lightning
Temperature	<ul style="list-style-type: none"> • Sensors must be protected against radiation, preferably housed within aspirated shielding. Air ventilation within shielding be $\approx 3 \text{ m s}^{-1}$
Humidity	<ul style="list-style-type: none"> • Sensitive to dirt and pollutants; require filtering on most sensors • Sensors must be protected against radiation, preferably housed within shielding
Pressure	<ul style="list-style-type: none"> • Sensitive to temperature, drift, vibration, and exposure • Sensors should be housed within a protected enclosure; if housed within a sealed container, a pressure tube must be used
Precipitation	<ul style="list-style-type: none"> • Tipping bucket gauges must be kept clear of debris • Weighing gauges require antifreeze during the winter months • Portions of some gauges should be heated with temperatures $< 0^\circ \text{C}$ • Wind shielding should be used to reduce under-catchment
Wind	<ul style="list-style-type: none"> • Propeller anemometers are susceptible to ice buildup; recommend heating if possible • Sonic anemometers may fail during moderate to strong winds and precipitation
Solar radiation	<ul style="list-style-type: none"> • Sensitive to dirt accumulating on the sensor • Sensitive to leveling
Soil temperature, soil moisture	<ul style="list-style-type: none"> • Be aware of water channeling along the cabling; include a drip loop in installation • Should be installed in undisturbed soil and remain as undisturbed as possible • Estimates sensitive to the soil properties
Snow depth	<ul style="list-style-type: none"> • Sensitive to snow drifting • Data quality may fail during precipitation

45.8 Applications

Dense networks of observations in the near-surface and lower boundary layer have been shown to improve analysis and short-term prediction [45.22]. Sites in particularly remote areas provide significant value to large-scale numerical weather prediction models [45.23]. Stations in urban areas are critical for decision-makers in transportation, energy, and emergency management. These applications point to the need for more observations, which has driven the proliferation of new and expanded mesonets across portions of the United States, Canada, South Korea, and many parts of the world. A growing number of industries and sectors recognize the value for more accurate, more precise analysis and prediction, as these improved weather output translate to more efficient, more cost-effective services and products.

Many early mesometeorological networks were deployed primarily for research, and many networks still retain a research component. For instance, Oklahoma Mesonet data have been used in over 500 peer-reviewed journal articles and over 400 theses and dissertations [45.24]. Research-oriented networks may be mobile and/or transitory.

Access to highly localized, high-temporal weather information is critical for emergency management. Emergency management is harnessing mesometeorological network data for aiding storm preparation and response [45.25, 26]. Improved short-term prediction allows for more efficient prestaging of resources, and real-time information allows for faster postevent response. Observations of precipitation, snowfall depth, and snow water equivalent aid in hydrological forecasting and flood response. Temperature, wind, and pressure data aid in monitoring severe weather. Temperature, humidity and wind data also help with fire management (e.g., remote automatic weather stations (RAWSS) network; [45.27]). Drastic wind shifts can be a matter of life and death for firefighters on the front lines [45.15].

Local and frequent weather information is critical to many ground transportation operations. Some state and federal transportation agencies operate their own networks, often sited along roadways (roadway weather information systems (RWISs)); e.g., the Iowa State University's environmental mesonet, <https://mesonet.agron.iastate.edu/RWIS/>, Accessed 20 July 2021). Real-time weather data are used for winter

weather operations and road closures, while climate archives can be useful for long-term planning [45.28].

Aviation is highly sensitive to meteorological conditions. While weather radar is the primary tool used by aircraft, surface networks and boundary-layer sensing networks provide necessary ground truth of radar data and improve overall weather analyses and prediction. Furthermore, networks of short-range radars and vertical profiling sensors, such as gap-filling (X-band) weather radars, lidars, and microwave radiometers, fill a void in sampling the lower-level boundary layer (0–3 km) largely missed by large (C- and S-bands) radars. The value of mesometeorological networks can be expected to increase as more localized, frequent data are needed as the operation of near-surface drones becomes more widespread.

Utility companies rely increasingly on local weather networks to optimize power load predictions [45.29]. Energy production costs are lower when peak demands are correctly forecast; access to local weather information can save utilities millions of dollars. Weather data are also used for improving short-term prediction of high-impact weather in order to prestage resources to minimize outage times. Power grids are particularly susceptible to lightning, high winds, and ice storms, and the

analysis and prediction of these can be improved with the use of local, dense weather networks. As utility companies become more dependent on renewable energies, energy production and grid operations will become even more sensitive to weather extremes and variability.

Arguably the most weather savvy community is the agricultural sector, and a majority of current mesometeorological networks have an important agricultural component. Farmers utilize weather data for a variety of uses including planting, fertilizing, and harvesting of crops and modeling of plant disease and pests (e.g., the Network for Environmental and Weather Applications (NEWA); [45.30]). The use of weather information can be economically beneficial [45.31].

Data from mesometeorological networks continue to find many other uses. Public health is beginning to utilize networked data to explore the spread of infectious disease and to monitor public health issues, such as asthma. Criminologists are exploring weather information to predict criminal activity. Forensic meteorologists utilize local weather information for use as evidence in court cases. Data from mesonets are becoming increasingly important as more personalized, more efficient, and autonomous infrastructure is adopted that requires frequent, local weather input.

45.9 Future Development

Several current trends portend future growth and utilization of mesometeorological networks. These trends include:

1. Continued expansion of networks worldwide as resources permit
2. Continued increase in the number of variables measured and the frequency at which they are measured
3. Expansion in observations from the surface to include lower-level boundary layer sensing
4. Increasingly automated end-to-end networks with adaptive sampling features
5. Diversification in how mesometeorological networks are funded and operated.

The last decade has seen a proliferation of mesonets across the US; over 20 states now host some type of mesometeorological network [45.8]. Networks have also expanded in their capabilities as new sensors are developed and made cheaper and more reliable. Sensors to measure snow depth, snow water equivalent, pavement temperatures, PAR, and soil moisture are becoming more common. Cameras may be added to more networks as bandwidth and power become more easily accessible.

To extend measurements into the vertical, the New York State Mesonet hosts a network of 17 profiling stations, each equipped with a lidar, microwave radiometer, and environmental sky imaging radiometer (eSIR). The West Texas Mesonet has several sodars deployed, whereas the Oklahoma Mesonet is experimenting with drone technologies. As the costs of these sensors come down, and as the technology continues to advance, we can expect more of these and other vertically penetrating sensors to be deployed.

Nearly all networks collect data at fixed, regular intervals. However, with increasingly adept artificial intelligence algorithms, more networks will integrate adaptive sampling, which may automatically adapt their scanning strategies as a function of the evolving environment.

Finally, it is an important reality that the deployment and operation of a mesometeorological network is expensive. As the expectations from these networks rise, the cost burden also increases. Increasingly, these costs are shared among the public and private sectors, with some active networks already utilizing a combination of public and private funding.

45.10 Further Readings

Listed below are two overarching papers that describe the need for mesometeorological networks and make recommendations on how they should evolve to facilitate future needs:

- W.F. Dabberdt, T.W. Schlatter, F.H. Carr, E.W.J. Friday, D. Jorgensen, S. Koch, M. Pirone, F.M. Ralph, J. Sun, P. Welsh, J.W. Wilson, X. Zou: Multifunctional Mesoscale Observing Networks, *Bull. Amer. Meteorol. Soc.* **86**, 961–982 (2005)
- National Research Council: *Observing Weather and Climate from the Ground Up: A Nationwide Network of Networks*, Washington D.C., National Academies Press, 250 pp. (2009)

Most mesonets are well documented, and below are several papers describing some exemplary networks:

- R. McPherson, C. Fiebrich, K. Crawford, R. Elliott, J. Kilby, D. Grimsley, J. Martinez, J. Basara, B. Illston, D. Morris, K. Kloesel, S. Stadler, A. Melvin, A. Sutherland, H. Shrivastava: Statewide monitoring of the mesoscale environment: A technical update on the Oklahoma Mesonet, *J. Atmos. Ocean. Technol.* **24**, 301–321 (2007)
- J. Brotzge, J. Wang, C.D. Thorncroft, E. Joseph, N. Bain, N. Bassill, N. Farruggio, J.M. Freedman, K. Hemker Jr., D. Johnston, E. Kane, J.R. Miner, S. McKim, S.D. Miller, P. Naple, S. Perez, J.J. Schwab, M.J. Schwab, J. Sicker: A technical overview of the New York state Mesonet standard network, *J. Atmos. Ocean. Technol.* **37**, 1827–1845 (2020)
- J. Horel, M. Splitt, L. Dunn, J. Pechmann, B. White, C. Ciliberti, S. Lazarus, J. Slemmer, D. Zaff, J. Burks: Mesowest: Cooperative Mesonets in the Western United States, *Bull. Amer. Meteorol. Soc.* **83**, 211–225 (2002)
- H. Jenkins-Smith, J. Ripberger, C. Silva, N. Carlson, K. Gupta, and M. Henderson: The Oklahoma Meso-Scale Integrated Socio-Geographic Network: A Technical Overview, *J. Atmos. Oceanic Technol.* **34**, 2431–2441 (2017)
- S. Kimball, M. Mulekar, S. Cummings, and J. Stamat: The University of South Alabama Mesonet and Coastal Observing System: A Technical and Statistical Overview, *J. Atmos. Oceanic Technol.* **27**, 1417–1439 (2010)
- J. Schroeder, W. Burgett, K. Haynie, I. Sonmez, G. Skwira, A. Doggett, and J. Lipe: The West Texas Mesonet: A Technical Overview, *J. Atmos. Ocean. Technol.* **22**, 211–111 (2005)
- M. Shulski, S. Cooper, G. Roebke, and A. Dutcher: The Nebraska Mesonet: Technical Overview of an Automated State Weather Network, *J. Atmos. Ocean. Technol.* **35**, 2189–2200 (2018)

References

- 45.1 L.E. Wood: Automatic weather stations, *J. Meteorol.* **3**, 115–121 (1946)
- 45.2 E. Mandel: An early look at the development of an unmanned automated surface aviation weather observation system, *Bull. Am. Meteorol. Soc.* **56**, 979–982 (1975)
- 45.3 E. Bromley: Aviation weather forecasts in tomorrow's flight service system, *Bull. Am. Meteorol. Soc.* **56**, 372–374 (1975)
- 45.4 J.A. Lindquist: Automation – Some potential applications to aviation weather, *Bull. Am. Meteorol. Soc.* **58**, 1161–1163 (1977)
- 45.5 F. Beyrich, H.-J. Herzog, J. Neisser: The LITFASS project of DWD and the LITFASS-98 experiment: The project strategy and the experimental setup, *Theor. Appl. Climatol.* **73**, 3–18 (2002)
- 45.6 T. Foken: Erfordernisse der Datengewinnung, –übertragung und –bearbeitung für mesometeorologische Zwecke, *Abh. Meteorol. Dienstes DDR* **141**, 9–17 (1989)
- 45.7 E. Rudel, H. Schwabach, H. Trimmel: *Automatic Measuring System for a Better “Nowcasting” to Protect the Environment* (WMO, Geneva 1985) pp. 221–225, Instruments and Observing Methods Report No. 22, WMO-TD No. 50
- 45.8 R. Mahmood, R. Boyles, K. Brinson, C. Fiebrich, S. Foster, K. Hubbard, D. Robinson, J. Andresen, D. Leathers: Mesonets: Mesoscale weather and climate observations for the United States, *Bull. Am. Meteorol. Soc.* **98**, 1349–1361 (2017)
- 45.9 S.J. Meyer, K.G. Hubbard: Nonfederal automated weather stations and networks in the United States and Canada: A preliminary study, *Bull. Am. Meteorol. Soc.* **73**, 449–457 (1992)
- 45.10 C.A. Fiebrich: History of surface weather observations in the United States, *Earth Sci. Rev.* **93**, 77–84 (2009)
- 45.11 K.P. Gallo: Evaluation of temperature differences for paired stations of the U.S. Climate Reference Network, *J. Clim.* **18**, 1629–1636 (2005)
- 45.12 C. Fiebrich, K. Brinson, R. Mahmood, S. Foster, M. Schargorodski, N. Edwards, C. Redmond, J. Atkins, J. Andresen, X. Lin: Toward the standardization of mesoscale meteorological networks, *J. Atmos. Ocean. Technol.* **37**, 2033–2049 (2020)

- 45.13 C.A. Fiebrich, K.C. Crawford: Automation: A step toward improving the quality of daily temperature data produced by climate observing networks, *J. Atmos. Ocean. Technol.* **26**, 1246–1260 (2009)
- 45.14 World Meteorological Organization: *Guide to Meteorological Instruments and Methods of Observation* (WMO, Geneva 2014), WMO–No. 8
- 45.15 J.R. Ziolkowska, C.A. Fiebrich, J.D. Carlson, A.D. Melvin, A.J. Sutherland, K.A. Kloesel, G.D. McManus, B.G. Illston, J.E. Hocker, R. Reyes: Benefits and beneficiaries of the Oklahoma Mesonet: A multisectoral ripple effect analysis, *Weather Clim. Soc.* **9**, 499–519 (2017)
- 45.16 E.N. Rasmussen, J.M. Straka, R. Davies–Jones, C.A. Doswell, F.H. Carr, M.D. Eilts, D.R. MacGorman: Verification of the origins of rotation in tornadoes experiment: VORTEX, *Bull. Am. Meteorol. Soc.* **75**, 995–1006 (1994)
- 45.17 P. Joe, S. Belair, N. Bernier, V. Bouchet, J. Brook, D. Brunet, W. Burrows, J. Charland, A. Dehghan, N. Driedger, C. Duhaime, G. Evans, A. Filion, R. Frenette, J. de Grandpre, I. Gultepe, D. Henderson, A. Herdt, N. Hilker, L. Huang, E. Hung, G. Isaac, C. Jeong, D. Johnston, J. Klaassen, S. Leroyer, H. Lin, M. MacDonald, J. MacPhee, Z. Mariani, T. Munoz, J. Reid, A. Robichaud, Y. Rochon, K. Shairsingh, D. Sills, L. Spacek, C. Stroud, Y. Su, N. Taylor, J. Vanos, J. Voogt, J. Wang, T. Wiechers, S. Wren, H. Yang, T. Yip: The Environment Canada Pan and ParaPan American Science Showcase Project, *Bull. Am. Meteorol. Soc.* **99**, 921–953 (2018)
- 45.18 C.E. Duchon, G.R. Essenberg: Comparative rainfall observations from pit and aboveground rain gauges with and without wind shields, *Water Resour. Res.* **37**, 3253–3263 (2001)
- 45.19 C.A. Fiebrich, K.C. Crawford: The impact of unique meteorological phenomena detected by the Oklahoma Mesonet and ARS Micronet on automated quality control, *Bull. Am. Meteorol. Soc.* **82**, 2173–2187 (2001)
- 45.20 C. Fiebrich, C.R. Morgan, A.G. McCombs, P.K. Hall Jr., R.A. McPherson: Quality assurance procedures for mesoscale meteorological data, *J. Atmos. Ocean. Technol.* **27**, 1565–1582 (2010)
- 45.21 C. Fiebrich, D.L. Grimsley, R.A. McPherson, K. Kesler, G. Essenberg: The value of routine site visits in managing and maintaining quality data from the Oklahoma Mesonet, *J. Atmos. Ocean. Technol.* **23**, 406–416 (2006)
- 45.22 A. Schenkman, M. Xue, A. Shapiro, K. Brewster, J. Gao: Impact of CASA radar and Oklahoma Mesonet data assimilation on the analysis and prediction of tornadic mesovortices in an MCS, *Mon. Weather Rev.* **139**, 3422–3445 (2011)
- 45.23 D. Tyndall, J. Horel: Impacts of mesonet observations on meteorological surface analyses, *Weather Forecast.* **28**, 254–269 (2012)
- 45.24 B. Van der Veer Martens, B.G. Illston, C.A. Fiebrich: The Oklahoma Mesonet: A pilot study of environmental sensor data citations, *Data Sci. J.* **16**, 47 (2017)
- 45.25 D. Morris, K. Crawford, K. Kloesel, J. Wolfinbarger: OK–FIRST: A meteorological information system for public safety, *Bull. Am. Meteorol. Soc.* **82**, 1911–1923 (2001)
- 45.26 J. Hocker, A. Melvin, K. Kloesel, C. Fiebrich, R. Hill, R. Smith, S. Piltz: The evolution and impact of a meteorological outreach program for public safety officials: An update on the Oklahoma Mesonet’s OK–First program, *Bull. Am. Meteorol. Soc.* **99**, 2009–2024 (2018)
- 45.27 J. Zachariassen, K. Zeller, N. Nikolov, T. McClelland: *A Review of the Forest Service Remote Automated Weather Station (RAWS) Network* (USDA, Forest Service, Fort Collins 2003), Gen. Tech. Rep. RMRS–GTR–119
- 45.28 C.B. Boon, C. Cluett: *Road Weather Information Systems: Enabling Proactive Maintenance Practices in Washington State* (NTIS, Springfield 2002), Gen. Tech. Rep. WA–RD 529.1
- 45.29 E. Gregow, B. Bernstein, I. Wittmeyer, J. Hirvonen: LAPS–LOWICE: A real-time system for the assessment of low-level icing conditions and their effect on wind power, *J. Atmos. Ocean. Technol.* **32**, 1447–1463 (2015)
- 45.30 J. Carroll, D. Olmstead, T. Weigle, A. Seaman, J. Grant: NEWA (Network for Environment and Weather Applications) 2016: A Year in Review. Project Report of the New York State IPM Program (2017), available at <https://ecommons.cornell.edu/handle/1813/65597>, Accessed 19 July 2021
- 45.31 K.E. Klockow, R.A. McPherson, D.S. Sutter: On the economic nature of crop production decisions using the Oklahoma Mesonet, *Weather Clim. Soc.* **2**, 224–236 (2010)

Jerald Brotzge

New York State Mesonet
University at Albany
Albany, USA
jbrotzge@albany.edu



Jerald Brotzge is Program Manager of the New York State (NYS) Mesonet at the University at Albany. Dr. Brotzge obtained his PhD in Meteorology at OU in 2000 where he received the Provost’s Dissertation Award in the Sciences and Engineering for his work with the Oklahoma Mesonet. His multidisciplinary research includes instrumentation, weather networks, severe weather, and emergency management.

Christopher A. Fiebrich

Oklahoma Mesonet/Oklahoma
Climatological Survey
University of Oklahoma
Norman, USA
fiebrich@ou.edu



Christopher A. Fiebrich is the Associate Director of the Oklahoma Climatological Survey and Executive Director of the Oklahoma Mesonet at the University of Oklahoma. He is also Adjunct Faculty with the School of Meteorology at OU. His areas of expertise are in mesoscale meteorology and climatology, meteorological instrumentation, and applied meteorology and climatology.

Aerological M

46. Aerological Measurements

Holger Vömel , Masatomo Fujiwara 

Many aerological measurements rely on compact radiosondes, which are carried into the atmosphere using rubber balloons. Radiosondes measure essential atmospheric state parameters: pressure, temperature, humidity, and winds. Although sensor technology is similar to the sensors used in ground-based measurements, sensors used on radiosondes must be able to measure a much wider range of conditions and to operate in difficult environments. Many different technologies for radiosonde sensors exist. Here, common sensor technology in modern radiosondes is described. Radiosonde pressure measurements either use specialized small solid-state sensors or rely on pressure derived from global navigational satellite system (GNSS) height measurements. Temperature measurements either use small thermistors or wire resistance thermometers. Coatings to minimize solar radiative heating and accumulation of water on the sensor reduce measurement artifacts. Modern humidity sensors are almost exclusively based on thin film polymer sensors, which are optimized for atmospheric observations under a wider range of conditions and may have heaters implemented to reduce icing problems. Wind measurements are based on GNSS signals received onboard the radiosondes. Radiosonde technology is also used on dropsondes, which are deployed from aircraft for targeted observations of severe weather and hurricanes, as well as on tethered systems. Data sharing through international systems is an important component in the distribution and use of global radiosonde data. Technical specifications, quality control, and maintenance considerations, as well as an outlook on applications and future developments are presented.

46.1	Measurement Principles and Parameters	1248
46.1.1	Measured Parameters	1248
46.1.2	Principles of Measurements	1250
46.2	History	1250
46.3	Theory	1254
46.3.1	Temperature	1255
46.3.2	Pressure	1256
46.3.3	Relative Humidity	1257
46.3.4	Winds	1259
46.4	Devices and Systems	1260
46.4.1	Radiosondes	1260
46.4.2	Dropsondes	1262
46.4.3	Tethered Sondes	1264
46.4.4	Balloons	1265
46.4.5	Autolaunching Systems	1267
46.4.6	Data Transmission and Formats	1268
46.5	Specifications	1268
46.6	Quality Control	1270
46.7	Maintenance	1272
46.8	Application	1272
46.8.1	Sounding Networks	1273
46.8.2	Scientific Soundings	1273
46.9	Further Development	1275
46.10	Further Readings	1276
	References	1276

Weather and climate, which we experience on the surface of our planet, are largely controlled by the processes in the air above us. Meteorology started to develop as a specialized discipline of physics, when early

scientists developed the capabilities to observe the state parameters of the atmosphere above us. From the drive to understand the state of our atmosphere and the details of atmospheric processes, these observations led

to a solid foundation of meteorology and atmospheric physics and enabled the important field of weather forecasting, on which we rely every day.

From the humble beginnings of measurements of the lower and middle troposphere on balloons and kites by few dedicated scientists, aerological measurements have developed into a complex system of observations and data sharing. The technology needed to be developed to lift instruments into the air. With balloon technology, which was developed over 100 years ago, soundings today routinely reach altitudes well above 30 km or well into the middle stratosphere. Sensor technology needed to be developed to enable more accurate observations and reduce the environmental influences on the measurements. As remote-sensing technologies were developed, in-situ sensing technologies were required for validation and even calibration of remote-sensing methods. Aircraft meteorological observations complement the observations on small balloons but have not replaced them, due to aviation safety reasons. Simultaneous measurements of pressure, temperature, humidity, and winds are still the core aerological observations, but technological developments now allow observations of many more parameters onboard small balloons.

The large-scale dynamics that drives our atmosphere requires meteorological observations covering large regions, crossing national borders and oceans. With the development of the observation technologies and platforms, a system of cooperation and data sharing needed to be developed to study the processes, which affect everyone. International cooperation started with personal contacts between scientists and developed into the World Meteorological Organization (WMO) within the framework of the United Nations. To share data specialized formats had to be agreed upon, a data-sharing infrastructure had to be built, types and frequencies of observations had to be defined, and developments meeting needs had to be enabled.

Today, aerological observations play a central part in weather forecast, climate studies, and research of atmospheric processes around the globe. Few scientific research areas are as globally interconnected as aerological observations. New observational technologies are being developed, new platforms to carry sensors into the air are built, and new questions arise about how our atmosphere works. Here, we provide an overview of the history and the current state of aerological measurement technology, and how aerological observations fit into the larger field of global meteorology.

46.1 Measurement Principles and Parameters

Aerological observations refer to measurements of the thermodynamic variables pressure, temperature, relative humidity (water vapor), and winds in the free atmosphere, covering the vertical range up to the middle stratosphere. Balloon-borne in-situ measurements have been a core technique since the beginning of aerological observations, and current radiosonde balloon soundings are among the most important technologies to characterize the atmospheric state (Fig. 46.1).

46.1.1 Measured Parameters

Soundings are carried out worldwide, and, therefore, the instruments must to be able to cover a large range of atmospheric conditions. Table 46.1 lists the ranges for pressure, temperature, humidity, water vapor mixing ratio, and wind, which sounding instruments may encounter. The altitude range is assumed to be up to ≈ 35 km, corresponding to ≈ 5 hPa, which is the al-

Table 46.1 Range of atmospheric parameters measured in aerological observations

Parameter	Minimum	Typical region of minimum	Maximum	Typical region of maximum
Altitude (m ASL)	0	Some sounding sites are below sea level	35 000	Typical ceiling maximum for sounding balloons in the middle stratosphere
Pressure (hPa)	5	Typical ceiling maximum for sounding balloons in the middle stratosphere	≈ 1065	Typical pressure at the elevation of the Dead Sea at 430 m BSL
Temperature ($^{\circ}\text{C}$)	≈ -90	Tropical tropopause over the Western Pacific, Antarctic winter stratosphere	> 40	Dry desert regions
Relative humidity (%)	< 1	Stratosphere	≈ 100	Clouds, fog
Water vapor mixing ratio (mg kg^{-1})	< 1	Tropical tropopause	$> 25\,000$	Tropical monsoon region
Wind (m s^{-1})	0		> 100	Jet streams, hurricanes, tornadoes

Fig. 46.1 Radiosonde launch at the DWD Meteorological Observatory Lindenberg, Germany ►

titude range that is easily reached by balloon-borne soundings. The relative humidity (over liquid water) and mixing ratio are two measures of the atmospheric water vapor concentration. Almost all radiosondes report relative humidity, from which the mixing ratio can be calculated (Chap. 8).

All radiosondes are capable of measuring pressure and temperature over the required range (Sect. 46.3). However, radiosonde humidity sensors are limited to tropospheric measurements only, with decreasing capabilities at colder temperatures. Stratospheric humidity is measured with only few scientific sounding instruments at a few select stations (Sect. 46.8.2).

A typical tropical profile of pressure, temperature, relative humidity, and winds is shown in the Skew-T/Log-P diagram shown in Fig. 46.2. The temperature in this example ranges from about 17 °C at the surface to -78 °C at the tropopause. Relative humidity ranges from near saturation in the boundary layer to about 2% RH at 6 km. Typical for tropical wind profiles is the high variability of wind directions across the profile. The boundary layer top is indicated by a very strong thermal inversion ≈ 1.6 km above ground.

Aerological observations are also taken from commercial and research aircraft, which are limited to the ceiling altitude of the aircraft and to weather conditions,



Table 46.2 Atmospheric parameter and current and historic radiosonde sensor technology

Parameter	Sensor	Notes
Temperature	Small bead or disk thermistor	Calibration over the entire temperature range required
	Wire resistance	Current state of technology
	Glass-ceramic capacitor	Thermocap [®] technology of the Vaisala RS80, RS90, and RS92 radiosondes
	Bimetal strip	No longer in use
	Thermocouple	Very rarely used
Pressure	Piezoresistive strain gauge and capacitive sensor	Large relative uncertainty in stratosphere
	GNSS altitude	Larger uncertainty in boundary layer, requires independent surface pressure
	Radar height	Large uncertainties especially at far distances
	Aneroid can and Bourdon tube	No longer in use
	Hypsometer	No longer in use
Humidity	Thin film capacitor	Tropospheric humidity only
	Cryogenic frostpoint hygrometer	Scientific instrument for tropospheric and stratospheric water vapor
	Lyman- α hygrometer	Scientific instrument for stratospheric water vapor only
	Carbon hygristor	Used on only few sondes
	Goldbeater's skin	No longer used on radiosondes
	Hair hygrometer	No longer used on radiosondes
Wind	Psychrometer	No longer used on radiosondes
	GNSS	Current state of technology
	Radar	Large uncertainties especially at far distances
	Radio navigation (LORAN and Omega)	Obsolete
	Optical theodolite	May still be used on pilot balloons

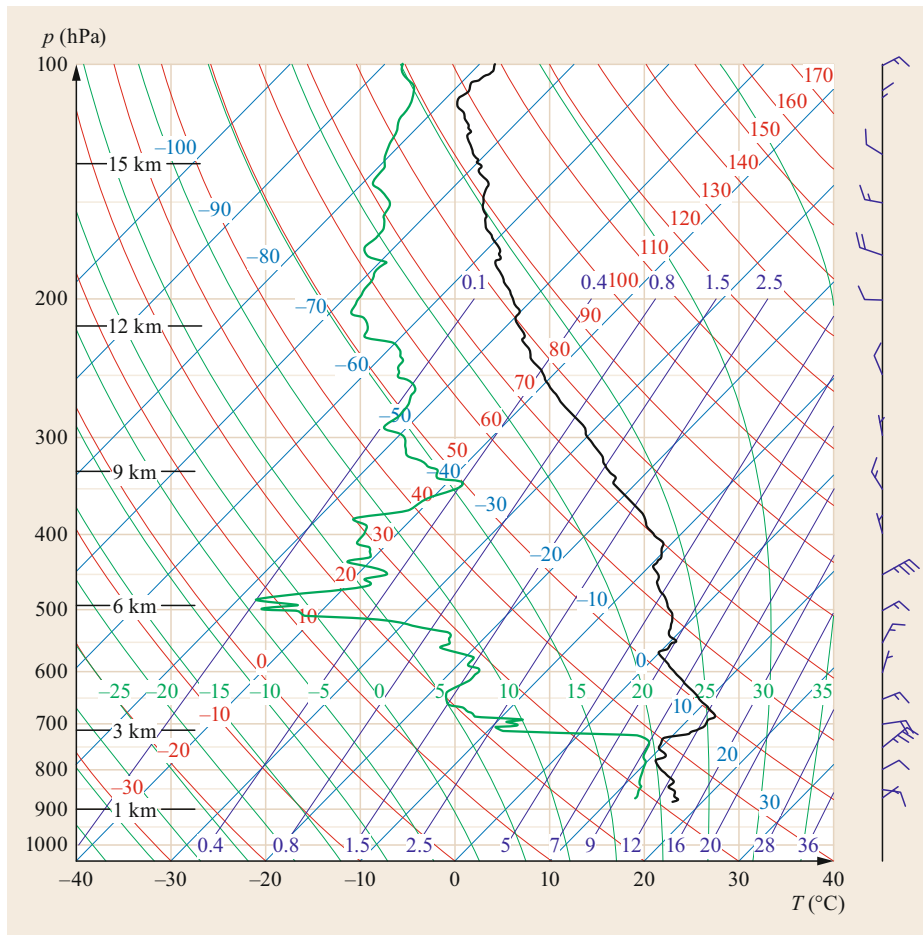


Fig. 46.2 Profile of pressure, air temperature (black), dewpoint temperature (green), and winds (as wind barbs) measured at the Universidad de Costa Rica, San Jose, Costa Rica on 05.02.2016

which are safe for aviation (Chap. 43). Aircraft observations complement the observations by radiosondes and are used in dedicated research projects. Aerological observations are also taken from long duration balloons at constant density. These measurements are used for research purposes only and provide a detailed representation of the dynamics of a single air parcel.

46.1.2 Principles of Measurements

Sensors to measure pressure, temperature, humidity, and winds typically found on current and his-

toric radiosondes are listed in Table 46.2. For pressure measurements, some radiosondes allow combining in-situ measurements with GNSS or radar altitude measurements. Stratospheric humidity currently can only be measured with specialized scientific instruments, such as frostpoint and Lyman- α hygrometers. Some of the technology that is no longer used on radiosondes may still be in widespread use for surface-based measurements. Refer to the respective chapters for more information. A detailed description of historic instrumentation can be found in [46.1].

46.2 History

The term *aerology* refers to the branch of meteorology that uses aeronautical means for the scientific study of the upper air. This term was coined by *Wladimir Köppen* (1846–1940) [46.2] in the early years of the twentieth century and was quickly adopted as scientific

discoveries and technological developments in this field progressed at a rapid pace. Until the end of the nineteenth century, atmospheric observations had been taken largely from the surface, except for few occasional observations from manned hot-air or gas

balloons. In 1894, Abbot *Lawrence Rotch* (1861–1912), who 10 years earlier had founded the Blue Hill observatory near Boston, MA, USA, flew the first kite equipped with a recording instrument to measure a profile of the atmospheric conditions [46.3]. This moment marks the beginning of systematic upper air observations. In 1898, Leon Teisserenc de Bort (1855–1913) founded the observatory at Trappes near Paris, France, where he pioneered gas-filled hydrogen balloons as observational platforms. In 1899, *Richard Assmann* (1845–1918) founded the Aeronautical Observatory at Reinickendorf near Berlin, Germany, which in 1905 was relocated to Lindenberg, Germany, and which has continued until today to be a preeminent institute for atmospheric observations. Assmann used kites and tethered balloons but also free-flying *registering* instruments, for which he had invented rubber balloons [46.4]. The instruments used in these measurements were sophisticated barothermohydrographs, better known at the time as meteorographs. They typically measured pressure using aneroid cans, temperature using bimetal strips, and humidity using hair hygrometers. Measurements were recorded on mechanical strip charts, and in the case of free-flying registering balloons, the instrument had to be recovered to retrieve the data. Registering balloons and the simpler pilot balloons, which did not carry any instruments, were also tracked by one or two optical theodolites to measure wind profiles aloft. The discovery of the stratosphere by *Léon-Philippe Teisserenc de Bort* (1855–1913) and Assmann in 1902 [46.5, 6] constituted a seminal milestone of upper air observations [46.7]. *Arthur Berson* (1859–1942), who worked with Assmann at Reinickendorf and later at Lindenberg, was responsible for almost all of the manned balloon ascents. In 1901 he flew on a gas-filled balloon, taking manual Assmann psychrometer observations to confirm the measurements by a parallel-flying registering balloon. This validation measurement was an essential part in the discovery of the stratosphere [46.8]. With this flight, Berson also set an altitude record of 10.8 km for open-basket balloon ascents, which still holds today.

John Wise (1808–1879), an avid balloonist in the middle of the nineteenth century, noticed very strong winds in the middle troposphere. By the early decades of the twentieth century, a network of upper-air stations had been established in Europe and in the USA performing regular soundings for weather forecasting. In Japan, *Wasaburo Ooishi* (1874–1950) founded the first meteorological upper-air observatory at Tateno, in 1920 [46.9]. Ooishi traveled to Lindenberg in 1911 to learn about upper air observations and returned to Japan in 1913. Due to World War I, the creation of his observatory was significantly delayed; however, by the mid 1920s, Tateno was a well-established observatory.

Between March 1923 and February 1925, Tateno measured 1288 profiles, which is nearly two soundings by kite or pilot balloon per day. *Ooishi* observed unusually strong winds in the upper troposphere, and he published these observations in Esperanto [46.10]. This publication is effectively the first climatology of what 13 years later *Heinrich Seilkopf* (1895–1968) called *Strahlströmung* [46.11] or jet stream in its English translation. In Europe, *Vilhelm Bjerknes* (1862–1951) used the upper-air network and coordinated ascents at 18 stations in a set of four different case studies. The last of these [46.12] also found narrow regions of high wind speeds and put these into a much more theoretical context. Further approaches for a theoretical explanation of the jet stream followed in the 1940s [46.13–15]. *Carl-Gustaf Rossby* (1898–1957) and collaborators [46.16] created 5-day averages of synoptic chart at 3 km over North America over several years to extend weather forecasts by investigating these slower variabilities. They identified and theoretically described upper-level stationary troughs and long waves, which would later be known as Rossby waves.

Profiling by kites was very labor-intensive work. Despite a number of improvements (e.g., *Grund's* self-regulating kite [46.17]), breaking wires and escaping kites were common and dangerous occurrences. Furthermore, observations by kites were limited to the lowest few km of the atmosphere. Typical operational profiling heights done at Lindenberg were generally up to 4 km, with occasional ceilings up to 7.5 km. In 1919, a string of eight kites raised at Lindenberg reached an altitude of 9750 m, a record still standing today [46.18]. To measure the atmosphere above that altitude required flying registering devices on free-flying balloons, which were not always recovered. This motivated the development of instruments that were able to send their data by radio transmission rather than recording data in situ on paper charts, which had to be recovered. Early developments of balloon-borne transmitters for meteorological work started at Lindenberg in the early 1920s, followed by work in the Soviet Union, France, and in the USA [46.1]. In 1924, *William Blair* (1874–1962) at the US Signal Corps laboratory at McCook Field, Ohio, built and flew what can be considered the first radiosonde, which, however, only included a temperature measurement. This work was abandoned when Blair was reassigned and was not published until 1931. The first published radiosonde launch was likely conducted in 1929 by *Robert Bureau* (1892–1965) in France, who also coined the term *radiosonde*. His first sonde also contained only a temperature sensor, but he soon added an aneroid pressure sensor. In 1930, *Pavel Molchanov* (1893–1941) built a similar design in Russia, and *Paul Duckert* (1900–1966) in Lindenberg followed with

a design that was similar to Blair's. Duckert soon added a sensor for humidity to complete the sensors still used in today's radiosondes. In 1930, *Vilho Väisälä* (1889–1969), a Finnish engineer, started a design for a radiosonde after seeing one of Molchanov's radiosondes [46.19]. Väisälä's sonde used capacitive sensors for pressure, temperature, and humidity, and combined these with fixed capacitive references to characterize the transmitter. His design principle was more innovative and could be implemented at lower cost. This basic design principle lasted through most of Väisälä's radiosondes for nearly 80 years.

Many radiosonde designs followed and allowed a significant expansion of the upper-air network. By the late 1940s almost all kite-based profiling had transitioned to observations by radiosondes [46.18]. Measurements of winds, however, still required tracking of the balloon by optical theodolites, which limited wind measurements to fair weather or below cloud base. The invention of radio-theodolites and radar tracking offered two alternative solutions to this problem, which would both be weather independent. Both techniques led to the now outdated term *rawinsonde* (radar-wind sonde) for radiosondes. Both systems for radio wind finding were implemented by different manufacturers, and some are still in use today in Russia and China. Later wind finding systems were based on radio navigation systems such as LORAN and Omega, which have meanwhile been replaced by GNSS, such as the American Global Positioning System (GPS), the European Galileo system, the Russian Global Navigation Satellite System (GLONASS), or the Chinese BeiDou Navigation Satellite System (BDS). These systems allow measurements of temperature and winds well into the stratosphere independent of weather and are one of the backbones of global upper-air observing systems.

In 1908, Berson led an expedition to East Africa to study monsoons. During this campaign, kite observations were taken from several ships, and registering and pilot balloons were launched well into the stratosphere. The soundings launched during this campaign found that the tropopause in the tropics is much higher and colder than at mid latitudes. They also discovered westerly winds in the stratosphere, which were opposite in direction to the easterly winds that had been deduced from the dispersion of ash in the stratosphere following the Krakatoa eruption in 1883. *Clarence. E. Palmer* (1911–1973) [46.20] called these winds *Berson's westerlies* and *Krakatoa winds*, and assumed easterlies overlying westerlies to be a feature of the lower tropical stratosphere, although he pointed out that *technical difficulties of observation are very great, the accumulated data almost insignificant*. With the expansion of the radiosonde network in tropical regions, in particular in

the context of nuclear tests, stratospheric observations became more abundant and provided a better dataset for the analysis of tropical stratospheric dynamics. The analysis of stratospheric winds from radiosonde launches in Nairobi, on Canton Island, and on the Christmas Islands between 1955 and 1960 [46.21, 22] showed that wind reversal descends with time throughout the lower stratosphere in what became known as the quasi-biennial oscillation [46.23–25]. A first theoretical explanation of the QBO was provided by *Lindzen and Holton* [46.26], who proposed a new idea of wave mean-flow interaction, which could generate a reversing wind pattern independent of the annual solar cycle.

A dramatic warming of deep layers of the stratosphere, with temperature increases of several tens of kelvin over a few days, accompanied by a wind reversal from strong westerlies to easterlies was discovered in the 1950s by upper air observations first at Berlin and then over the American radiosonde network [46.27, 28]. These sudden stratospheric warmings (SSW) are occasionally observed over the northern winter polar region and rarely over the southern winter polar region. SSWs are caused by the interaction of the mean flow with planetary scale waves in the troposphere.

In-situ soundings over oceans, which cover 2/3 of our planet, have been notoriously difficult due to the logistical effort to launch soundings away from land and, more importantly, the dangers of launching soundings in storms. Nevertheless, these measurements are most needed when storms threaten populated regions on land. In 1943, *Colonel Joseph B. Duckworth* (1902–1964) flew into the eye of a hurricane near Houston, thereby starting the era of hurricane reconnaissance. However, since flights through severe storms are inherently dangerous for aircraft, measurements were soon done by launching instruments from aircraft into storms. Early dropsondes still used chart recorders and had to be recovered [46.29]. In the late 1960s, the National Center for Atmospheric Research (NCAR) at Boulder, CO, USA, developed a dropsonde system, which could be deployed from aircraft into thunderstorms [46.30]. Wind finding based on the Omega global navigation system was added in the early 1970s [46.31]. LORAN wind finding and later GPS and more advanced sensors were added [46.32]. Dropsondes have become an essential instrument for hurricane surveillance and have significantly improved the ability to forecast how hurricanes develop and which regions they may affect [46.33]. They fill an important gap for many research programs that rely on targeted observations in data-sparse regions.

Ionizing radiation had been discovered by the end of the nineteenth century, and it was well understood that many materials might emit this mysterious radiation. To understand the nature of this ubiquitous radiation,

Victor Hess (1883–1964) tried to measure vertical profiles of this radiation. In the last of his manned balloon flights, which reached an altitude of 5380 m and landed not far from Lindenberg, he found that the radiation increased nearly fourfold over that measured at the surface [46.34]. He had discovered cosmic rays, for which he received the Nobel Prize in Physics in 1936. Most measurements above this altitude required heavier instruments and pressurized gondolas for the observer. In the 1930s, a race to greater heights using manned balloons ensued with programs in Russia, Europe, and the USA. In the early 1930s, balloonist *Auguste Piccard* (1884–1962) used rubberized cotton balloons to fly to altitudes of ≈ 16 km in a steel pressure capsule. One of his scientific goals was to continue the study of cosmic rays. However, most efforts went to sustaining high-altitude life support in the nascent space program with little value for the atmospheric sciences. His twin brother *Jean Piccard* (1884–1963) was first to develop lighter plastic balloons [46.35], which could carry much heavier payloads into the stratosphere. However, World War II interrupted most of these developments. In 1945, the German engineer *Otto C. Winzen* (1917–1979) partnered with Jean Piccard to make plastic balloons using polyethylene for manned stratospheric flights. The development of these balloons culminated in the record-breaking parachute jump from an altitude of 102 800 ft (31 300 m) by *Joseph Kittinger* (*1928) in 1960. However, this work also provided the technology to lift heavy instruments into the stratosphere and to break into a region of the atmosphere that had previously been out of reach. In 1961, the National Scientific Ballooning Facility (NSBF) was founded; it was initially operated by NCAR to provide scientists access to altitudes up to well above 30 km. The same year, the French National Center for Space Studies (Centre national d'études spatiales, CNES) was founded and started a similar ballooning program. Vincent Lally (1922–2005), who was the first NSBF director, initiated the Global Horizontal Sounding Technique (GHOST) balloon program to study tropospheric and stratospheric winds [46.36]. This program demonstrated that specialized superpressure balloons could stay afloat for many months, measuring winds at constant density levels, and led to a number of follow on programs by NASA, NCAR, and CNES. Many hundreds of balloons were launched as part of these programs, and they stayed afloat for many months, with a record of 744 days. Data collected from these balloons provided the first representation of winds covering the tropics and nearly the entire Southern Hemisphere [46.37].

In addition to remote-sensing techniques, monitoring of stratospheric ozone requires frequent in-situ observations. Few instruments for small balloons

were available in the 1960s when *Walter Komhyr* designed the electrochemical concentration cell ozone sonde [46.38]. This instrument has been used extensively on small rubber and plastic balloons and is recognized as the in-situ reference instrument for vertical profiles of ozone in the troposphere and lower to middle stratosphere. It is the only in-situ instrument that provides accurate measurements of the vertical extent of the annual ozone hole.

In the early 1940s, *Alan W. Brewer* (1915–2007) made the first observations of stratospheric water vapor on meteorological research flights of the Royal Air Force over England. These measurements were largely in support of WWII military efforts in understanding the formation of aircraft contrails. However, they revolutionized the understanding for stratospheric dynamics. Brewer and *Gordon M.B. Dobson* (1889–1975) deduced that tropospheric air enters the stratosphere from the tropics [46.39, 40]. Their model was the first description of the general stratospheric circulation. However, it took another 20 years before stratospheric water vapor measurements in the tropics could be taken. In the late 1950s, work on stratospheric frostpoint hygrometers were taking place at a number of locations. *H. John Mastenbrook* (1919–2010) at the Naval Research Laboratory developed a cryogenically cooled frostpoint hygrometer, which was small enough to be launched on rubber balloons [46.41]. Due to the size of the balloon and the instrument, he found that unlike normal temperature measurements, water vapor measurements on ascent were usually contaminated due to the water vapor carried with the balloon and the payload itself. To avoid this issue, he developed a method for the controlled release of gas from small rubber balloons, which allowed water vapor measurements on descent. This instrument flew over several Pacific islands, in India, as well as Trinidad [46.42, 43], where he achieved a 2-year dataset of tropical stratospheric water vapor, which would not be repeated for another 40 years. These measurements confirmed the stratospheric dryness, hypothesized by Brewer and Dobson. In 1980, this instrument was transferred to NOAA in Boulder, CO, USA, where some derivatives of the original instrument are still flown. This continuing program represents the longest data series for stratospheric water vapor worldwide [46.44] and is a sensitive indicator for climate change [46.45].

With the miniaturization of instruments, it is now possible to build lightweight payloads for small sounding balloons, which measure a multitude of parameters. The combination of frostpoint hygrometers and ozone sondes flown across the tropical tropopause provides important measurements on mechanisms for troposphere–stratosphere exchange or Antarctic dehydration [46.46, 47]. Small versions of cloud backscatter

sensors, icing probes, and aerosol counters have been built with sufficient quality to obtain scientific observations with high vertical resolution using small sounding balloons. This technology is highly flexible and can be transported to even the most remote locations.

International coordination was an important step for large-scale meteorological observations. Following a proposal by *Buijs Ballot* (1817–1890) [46.48], the International Meteorological Organization (IMO) was formed in 1873. In 1896, the IMO proposed simultaneous upper-air observations using kites, manned balloons, and unmanned registering balloons at different observatories, and initiated the International Committee for Scientific Aeronautics to coordinate upper-air observations and the exchange of observational data [46.49]. In 1951, the WMO succeeded the IMO as specialized agency within the United Nations (UN). While the IMO was an organization of scientists, the WMO has full support of the governments of all member countries of the UN. Unchanged from the founding periods, measurements are conducted by each national hydro-meteorological service, with coordinating efforts by the WMO, such that measurements follow accepted procedures and data standards and may be best used for regional and global weather prediction and climate monitoring [46.50]. Today, the global radiosonde network coordinated by the WMO Global Observing System comprises about 900 stations, more than two-thirds of which launch soundings twice daily (00:00 UTC and 12:00 UTC). As a subset of this network, the Global Climate Observing System (GCOS) Upper-Air Network (GUAN; Chap. 63) was established in the early 1990s, with 170 stations as of 2014, for long-term high-quality measurements for climate monitoring purposes [46.51]. Furthermore, the GCOS Reference Upper-Air Network (GRUAN; Chap. 63) was established in 2008 with a dedicated Lead Center within the German Meteorological Service, with 26 sites at the end of 2017. The goal of GRUAN is to lay the foundation for long-term climate records based on well-characterized upper-air observations using high-quality instrumentation.

46.3 Theory

In-situ soundings onboard balloons, kites, and unmanned aircraft systems use similar instrumentation and sensors as surface-based measurements. However, due to weight restrictions and the need for low-cost equipment, sensors for these platforms may have different performance characteristics than those used in surface-based measurements. In addition, airborne platforms lift sensors into very different environmental

The question of how well different instruments at different stations provide comparable observations has been a challenge since coordinated observations started. The comparability of upper-air instrumentation was an important topic in the discovery of the stratosphere [46.7], and some simultaneous tests were done early on. The International Aeronautical Congress in 1902 already proposed formal intercomparisons of different instrumentation [46.49], and the WMO has conducted international radiosonde comparison campaigns since 1950 [46.52] to characterize the differences between instruments. The latest of these intercomparisons took place in 2011 at Yangjiang, China [46.53].

In recent years, research groups have developed homogenized radiosonde temperature datasets for climate research purposes by correcting jumps in time series due to instrumental and other changes, using various homogenization methods (a list of such datasets can be found, e.g., in [46.54] for a list of such datasets). Some of these datasets have been used in global atmospheric reanalysis data sets, which combine global *re-analyzed* observations and a fixed, numerical forecast-assimilation system (e.g., [46.55] for a list of reanalysis data sets). The homogenization efforts benefit from efforts such as GRUAN to characterize measurement uncertainties and to avoid artificial jumps in data records to the extent possible.

In-situ upper-air observations using small and large balloons continue to play an important role in atmospheric research, weather forecasting, and climate change studies. In particular, for small sounding balloons, great emphasis is being placed on how changes in sensor technology, data processing, and operating procedures affect time series of upper-air parameters. Standardization of procedures and a detailed quantification of measurement uncertainty are essential elements in providing in-situ upper-air observations. A detailed understanding of the technology, operational procedures, and how data are used is essential for future progress in this field.

conditions and require that sensors cover a larger range of observed parameters, which creates additional challenges that must be considered in aerological measurements.

Operational stations launch radiosondes on fixed schedules under all weather conditions, which do not pose a safety hazard to the observers and the sounding equipment. Radiosonde stations are located in all cli-

mate zones from the southernmost station at the South Pole to the northernmost at Alert, NU, Canada (83° N). Sounding instrumentation needs to be able to operate in surface temperatures exceeding 30 °C and at the tropical tropopause with temperatures well below –80 °C and needs to provide accurate measurements in very dry and very wet conditions. Radiosondes may be launched in rain or snow and may pass any type of clouds as well as icing conditions within supercooled liquid clouds. In-situ soundings are expected to provide an accurate representation of the atmospheric state across this large range of challenging conditions.

Balloon-borne soundings generally last between 1 and 2 h, and typical sounding instrumentation is rarely exposed to the atmosphere for longer than that. This reduces the need for long-term stability under extreme conditions and relaxes some requirements that may exist for surface-based instruments that may be operated continuously for a long time.

Almost all current balloon-borne sounding systems report measurements once per second. At a typical ascent rate of 5 m s^{–1} this represents a vertical resolution of 5 m. For some parameters, the effective vertical resolution may be less due to a slower response time or the need to filter out unwanted signals.

46.3.1 Temperature

In-situ observations of temperature on sounding balloons use electronic sensors similar to some sensors used for surface-based measurements (Chap. 7). Almost all modern radiosondes use resistive temperature sensors, which can be grouped into two categories: thermistors and wire resistors. Capacitive elements, which until recently had a significant market share, and thermocouples are much less common today.

Thermistors are made of semiconductor material, whose resistance changes strongly with temperature. These sensors are typically manufactured as small beads or disks with diameters down to < 1 mm. The temperature dependence is highly nonlinear, and the resistance of these sensors may increase by two to three orders of magnitude between the temperature at the surface and the coldest temperature near the tropopause.

Resistance wires are most commonly made of platinum, but tungsten wires have also been used for atmospheric observations. The resistance of these materials also depends on temperature; however, the temperature dependence is much weaker and highly linear.

The WMO requires an uncertainty of < 0.4 K at two standard deviations for tropospheric temperature measurements and < 0.8 K for stratospheric temperature measurements > 16 km [46.56]. The Global Climate Observing System [46.57] specifies an uncertainty re-

quirement of 0.5 K at two standard deviations for this Essential Climate Variable (ECV) throughout the entire profile. In addition, GCOS specifies a long-term stability requirement of 0.05 K decade^{–1}. These requirements present some challenge for the calibration of in-situ temperature sensors, which should be calibrated to at least this requirement over the entire temperature range.

The calibration of thermistors is typically based on the *Steinhart–Hart* equation [46.58]

$$\frac{1}{T} = A + B \ln(R) + C [\ln(R)]^3, \quad (46.1)$$

where R is the resistance in Ω at temperature T in K. The coefficients A , B , and C are the Steinhart–Hart coefficients, which are determined during calibration, typically at three calibration temperatures spanning the expected temperature range. Higher-order polynomials of $\ln(R)$ may be added to this equation to reduce the deviation of the fit curve from the true temperature between the calibration temperatures. However, using higher-order polynomials leads to larger calibration fit errors outside the range over which the thermistors were calibrated. Therefore, thermistors should be calibrated over the entire temperature range over which they will be used to achieve the required uncertainty and stability requirements.

Platinum and other wire-resistance temperature sensors have a nearly linear dependence of resistance on temperature and are considered more stable [46.59, 60]. For the calibration, the *Callendar–Van-Dusen* equation [46.61]

$$R(t) = R(0) [1 + At + Bt^2 + C(t - 100)t^3] \quad (46.2)$$

may be sufficient to achieve a better calibration fit over the atmospheric temperature range compared to thermistors. Here, t is temperature in °C and R the resistance in Ω .

Unlike in typical surface measurements, temperature sensors on radiosondes are exposed to solar radiation, leading to heating of the sensor, which increases with decreasing pressure. The balloon ascent provides reliable and measurable ventilation, and highly reflective coatings reduce the sensor heating by sunlight as much as possible (Fig. 46.3). At lower pressures, sensor heating is the most significant source of uncertainty. Solar radiation correction algorithms remove most of this measurement error using the solar elevation angle, the ambient pressure, and the ascent rate of the balloon as input parameters. Currently, no manufacturer provides algorithms that consider cloud cover, surface or cloud albedo, and all algorithms assume a climatological radiation field to estimate the amount of radiative heating

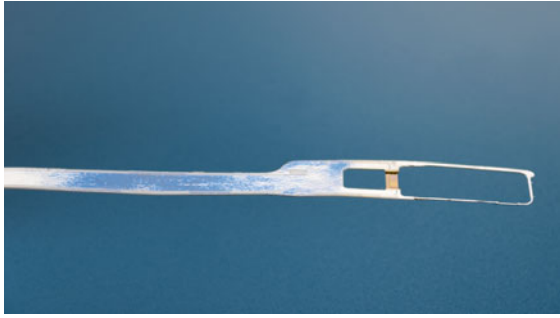


Fig. 46.3 Temperature and humidity sensor of the Vaisala RS41 radiosonde. Note the highly reflective coating of the sensor boom and the temperature sensor to right of the sensor boom

(e.g., [46.62]). Changes in coatings by the manufacturer require changes in the correction algorithm to avoid artificial signals in long-term climate records. Changes in the climatological albedo may also lead to artificial temperature trends, although this effect is generally ignored.

Most modern radiosonde temperature sensors are sufficiently small and at typical balloon rise rates equilibrate with ambient conditions fast enough. At the typical data rate of 1 Hz, a correction for sensor lag may not be needed or may provide only a small correction.

Exposure to moisture inside clouds may cause some temporary bias in atmospheric temperature measurements after a radiosonde exits a cloud. The evaporation of water or ice, which has accumulated around a temperature sensor inside supercooled liquid clouds, will cause evaporative cooling of the temperature sensor and indicate a temperature well below the true atmospheric temperature in the dry layer above the cloud. The bias may be large enough to indicate apparent superadiabatic lapse rates [46.63]. This effect cannot be avoided, but it can be minimized through hydrophobic coatings and by reducing the total surface area around the temperature sensor that may accumulate water or ice. Temperature errors of 2 K or more are possible in layers up to 300 m or more above the top of a cloud [46.53].

The presence of the balloon may also affect the temperature measurement by the radiosonde below the balloon. Solar heating of the balloon can strongly raise the temperature of the lifting gas inside the balloon, while nearly adiabatic expansion without solar heating at night can cool the lifting gas to well below ambient temperature. These effects may create wakes of warmer air during daytime and of colder air during nighttime below the rising balloon [46.59]. The turbulent motion around the balloon may also generate a wake of reduced ventilation. These warm and cold spikes can be detected by fast temperature sensors and may be filtered out by

the radiosonde processing software [46.62]. To minimize these effects, the string separating balloon and radiosonde should be at least 20 m in length in the troposphere and 40 m in the stratosphere [46.56]. Some manufacturers provide unwinder strings longer than the minimum recommended value to reduce the risk of temperature spikes further.

The uncertainty requirements for temperature measurements are a significant challenge, in particular, the stability requirement of $0.05 \text{ K decade}^{-1}$ by GCOS. Small changes in sensor coating and sensor calibration may introduce systematic changes larger than this requirement into the production of radiosondes. Operational procedures such as changes in the length of the unwinder string and changes of the balloon size may induce subtle effects in the temperature spike filter.

46.3.2 Pressure

Radiosonde-based pressure measurements use technologies similar to surface-based pressure measurements (Chap. 10). However, radiosondes require low cost sensors, which are capable of measuring absolute pressure over a range from 1000 hPa at the surface to $< 5 \text{ hPa}$ in the stratosphere. Piezoresistive strain gauges and capacitive sensors are currently the leading technologies for these sensors. Common to all technologies is that they need to be calibrated over the entire pressure range and that they need to operate over a large temperature range.

Operating procedures for Vaisala radiosondes include a one-point recalibration of the pressure sensor prior to launch; all other manufacturers offering pressure sensors rely on their factory calibration.

Geopotential height is calculated from the measurements of pressure, temperature, and humidity using the hypsometric equation (Chaps. 1 and 10)

$$\Delta z = \frac{R_d T_v}{g_0} \ln \left(\frac{P_0}{P_1} \right), \quad (46.3)$$

where Δz is the layer thickness in meters, $R_d = 287.058 \text{ J kg}^{-1} \text{ K}^{-1}$ is the specific gas constant for dry air, T_v is the mean virtual temperature of the layer in kelvin, P_0 and P_1 are the pressure at the base and the top of the layer, and $g_0 = 9.80665 \text{ m s}^{-2}$ is the standard gravitational acceleration. The integration of this equation over the profile of pressure, temperature, and humidity gives the profile of geopotential height. Offset errors in pressure or temperature add to increasing biases in geopotential height. Small pressure offsets are inconsequential for most applications in the troposphere but may lead to significant errors in the calculations of height and mixing ratio of trace gas species

in the stratosphere [46.64–66]. Accurate integration of (46.3) requires small integration steps and, thus, data with high vertical resolution. Large data gaps may cause significant biases for all geopotential heights calculated beyond any data gap.

Recently, many radiosonde manufacturers have been replacing a direct pressure measurement with pressure derived from GNSS height measurements. The basis of this technology is again the hypsometric equation, which can be inverted to

$$P_0 = P_1 \exp \left[-\frac{\Delta z g(z, \varphi)}{R_d T_v} \right]. \quad (46.4)$$

In contrast to (46.3), here, the measured height z is geometric height measured by GNSS, and $g(z, \varphi)$ is the height and latitude dependent gravitational acceleration. Using this equation, the pressure profile can be integrated from a profile of geometric height, temperature, and humidity. However, (46.4) requires that the surface pressure at the launch site is well known, which requires a pressure measurement from an independent surface reference, which must be fed into the sounding system. Errors in the surface pressure mostly affect the tropospheric pressure profile and become small in the stratosphere.

Height errors from GNSS are considered random and may add noise to the calculated pressure profile but do not contribute to any systematic bias. In the lower to middle troposphere, the GNSS-induced pressure noise is typically larger than that from a measured pressure profile, and a possible bias depends on the quality of the reference pressure. In the stratosphere, bias and random noise induced by the GNSS height measurements are less than those from true pressure measurements.

Equation (46.4) makes the implicit assumption of hydrostatic stability. In storms and in strong gravity wave activity, vertical up and downdrafts speeds may reach up to several tens of meters per second. Under these conditions, hydrostatic stability is no longer valid and using (46.4) leads to significant pressure errors.

Currently, the best pressure profile observations rely on a combination of measured pressure in the lower to middle troposphere and GPS derived pressure in the upper troposphere and stratosphere. This combined observation scheme has been employed by GRUAN [46.62].

Uncertainty requirements for pressure provided by the WMO [46.56] range from 2.0 hPa at 1 km (≈ 900 hPa) to 0.1 hPa at 32 km (≈ 10 hPa) at a confidence level of two standard deviations. In the lower troposphere, directly measured pressure by the best radiosondes may achieve these requirements. In the stratosphere, GNSS derived pressures achieve these requirements, if the surface-based reference pressure sensor used in the

initialization of the pressure profile has been properly maintained.

Pressure observations, whether from a pressure sensor or derived from GNSS altitude, are considered fast and in equilibrium with the ambient pressure. No lag correction is applied to pressure measurements; however, smoothing of noise, either from GNSS or pressure sensor noise, may be applied, slightly degrading the effective vertical resolution.

46.3.3 Relative Humidity

All humidity measurements on modern radiosondes use thin-film capacitance sensors [46.53]. Other technologies for humidity measurements that may be found in surface-based measurements (Chap. 8) are not practical or are too expensive for almost all radiosonde applications. The thin-film technology is based on work by *Suntola* [46.67], who first described thin-film capacitive elements with sufficient stability for radiosonde applications. It was first introduced by *Vaisala* in the radiosonde model RS-80 in the 1980s. These sensors make use of the ability of polymer or other materials to absorb water vapor, thereby changing their dielectric constant (Sect. 9.4.3). Polymer materials, such as polyimides or cellulose acetate, are easily manufactured as thin films between permeable electrodes that allow ambient water molecules to move into and out of the material (Fig. 9.9). Thin-film capacitive sensors for radiosondes need to be sufficiently fast to provide good vertical resolution on a rising balloon. They also need to be able to operate over a large temperature range, must be able to operate at saturated conditions as well as very low humidity conditions, and must show minimal hysteresis.

The capacitance of the polymer material changes nearly linearly with ambient relative humidity. However, calibration of the sensor over the entire humidity and temperature range is required for high-accuracy measurements on radiosondes.

While the basic principle is the same for all manufacturers, sensors differ by a number of characteristics. Thinner polymer films allow faster measurements but also allow stronger calibration drifts and require better electronics to measure lower capacitance values. Some materials are less susceptible to contamination by other gases, in particular volatile organic compounds, but are also less sensitive to water vapor. Production processes in the manufacturing of the devices play an important role in maintaining stable and consistent response. The choice of polymer material influences the hysteresis that a sensor exhibits. The best humidity sensors currently in use on radiosondes show a hysteresis of significantly less than $\pm 1\%$ RH.



Fig. 46.4 Humidity sensor of the Chang Feng CF-06-A radiosonde underneath its protective cap

Older technologies, such as carbon hygriators, may still be found in some national radiosonde networks and are mentioned here just for completeness. These technologies are inferior to thin-film capacitance sensors and are not discussed further.

Historically, icing of humidity sensors has been a significant issue. Icing may occur in supercooled liquid clouds and even in colder ice clouds. If significant amounts of ice accumulate around the humidity sensor, it may lose exposure to the atmosphere and no longer report accurate humidities. This condition may last until most of the accumulated ice on the sensor has evaporated above the cloud layer and may lead to considerable parts of the profile, where artificially high humidity readings are reported.

For accurate measurements, most humidity sensors require that the sensor be in thermal equilibrium with the atmosphere or that the temperature of the sensor is measured. Sensors that are warmer than their surroundings report low biased relative humidity readings, if their temperature is assumed to be ambient. In typical radiosonde applications, most humidity sensors are protected by a highly reflective cap to minimize solar heating of the sensor (Fig. 46.4).

Furthermore, this cap reduces the risk of icing of the sensing element but also reduces ventilation around the sensor, which may not be desired.

Some manufacturers have included heating elements in the humidity sensors that prevent or at least minimize icing of the sensor. The older Vaisala RS92 radiosonde employed a pair of humidity sensing elements, in which one element was set to measurement mode, while the other was in heating mode. At regular intervals, the elements were switched, which provided one continuous humidity profile and minimized the risk for icing and contamination. Since both sensing elements were exposed to solar radiation, this sensor design suffered a significant dry bias [46.68], which required an empirical correction.

Several newer humidity sensors also include a temperature sensor in the humidity-sensing element

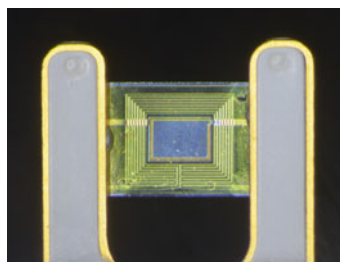


Fig. 46.5 Heated humidity sensor of the Internet iMet-54 radiosonde showing the polymer film and electrodes in the center, surrounded by a heater coil/temperature sensor

(Fig. 46.5). This allows simultaneous active heating and measurement of the humidity sensor temperature. Raw humidity readings are reported at sensor temperature and are corrected for the difference between sensor temperature and air temperature in signal processing using

$$R_{\text{ambient}} = R_{\text{Sensor}} \frac{E_w(t_{\text{sensor}})}{E_w(t_{\text{ambient}})}, \quad (46.5)$$

where R_{ambient} is the ambient relative humidity of the surrounding air at the ambient temperature t_{ambient} , and R_{sensor} is the relative humidity measured by the sensor at the elevated sensor temperature t_{sensor} ; E_w is the saturation vapor pressure equation over liquid water (46.6).

Measurement errors in heated sensors are amplified by the ratio of the vapor pressures in (46.5). This requires a compromise between the benefits of sensor heating and limiting additional measurement errors. For well-calibrated temperature sensors, this can be done without significantly compromising the overall measurement uncertainty. The inclusion of a temperature measurement in the humidity element, furthermore, eliminates the need for a protective cap, since solar heating no longer represents a problem for the actively heated sensor.

The response time of thin-film humidity sensors is highly temperature dependent. Sensors for radiosondes may have response times $\ll 1$ s at 20°C but > 60 s at -60°C . Some manufacturers correct the slow sensor response using specialized time-lag algorithms (e.g., [46.53, 62]). Especially at low temperatures, this correction improves the representation of the atmospheric humidity profile. Unfortunately, the time-lag correction also amplifies noise in the raw signal, which must be filtered before correction. This reduces the effective vertical resolution of humidity measurements especially at cold temperatures.

Contamination by other gases, in particular volatile organic compounds, may interfere with the absorption of water vapor into the polymer material and permanently change the calibration of the sensor. Therefore, exposure of the sensor to contaminants should be min-

imized during storage. Sensors with integrated heating elements may be capable of driving off contaminants by applying high amounts of heat for some time and thereby restoring the original calibration.

Operational uncertainty requirements for humidity range from 6% RH above -50°C to 10% RH below that. Uncertainty requirements for climate are more stringent with 5% of a reading (not 5% RH) and a stability of $0.3\% \text{ decade}^{-1}$ [46.57]. The operational uncertainties may be met by some manufacturers using modern thin-film sensors; however, the more demanding uncertainty requirement for climate may require improvements in sensor technology and operational procedures.

Some of the best performing sensors report reliable humidity values well below -60°C . By convention, relative humidity is reported as relative humidity over liquid water at all temperatures, extending to very cold temperatures, where liquid water no longer exists. This may cause confusion for the conversion of relative humidity to other measures of water vapor (e.g., mixing ratio), which make use of the saturation vapor pressure equation. Different formulas for saturation vapor pressure over liquid water are in use, which may lead to significantly different results at cold temperatures. At -60°C , different vapor pressure equations may differ by as much as 10% and at -80°C by more than 20%, which exceeds the stated uncertainty of some of these sensors (see [46.69] and [46.53] for more details).

The proper solution to this challenge would be to use the same saturation vapor pressure equation that the manufacturer used in the calibration of their sensors. However, this information is usually not available, and some manufacturers may not share calibration details. Nash et al. [46.53] recommended three formulations: Wexler [46.70], Hyland and Wexler [46.71], and Sonntag [46.72]. These three formulations agree with each other to within less than 0.5% over the entire atmospheric temperature range. Preference may be given to the formulation by Sonntag [46.72], which is based on the ITS90 temperature scale and given in (46.6),

$$\begin{aligned} \ln(E_w(T)) = & -6096.9385T^{-1} + 16.635794 \\ & - 2.711193 \times 10^{-2}T \\ & + 1.673952 \times 10^{-5}T^2 \\ & + 2.433502 \ln(T), \end{aligned} \quad (46.6)$$

where T is in K and E_w is the water vapor pressure over liquid water in hPa. The range of validity for this formula is given as $173.15 \leq T \leq 373.15 \text{ K}$.

The Magnus formula [46.56, Annex 4.B, Eq. 4.B.1], which is also referenced in Chap. 8, should not be used for radiosonde applications at temperatures colder than -45°C , since the difference to the equations used by

most manufacturers increases rapidly below that temperature.

46.3.4 Winds

The horizontal motion of a rising balloon is a direct indication of horizontal wind speed and direction. The balloon ascent rate is considered slow enough so that the inertia of the balloon train in wind shear can be neglected. Most current radiosonde systems track the payload motion using GNSS. Tracking through radio theodolites and active radar tracking is currently done only in Russia and China.

The implementation of GNSS winds may differ between different manufacturers. Modern GNSS receivers are capable of calculating and reporting winds independent of position. Some systems may simply report position and calculate winds as its derivative.

The use of differential GNSS, where GNSS signals are received both by the ground station and by the radiosonde, allows reducing some errors related to GNSS positioning and thereby improving wind and position estimates. This technology is implemented by some systems.

Since position and wind are measured by the radiosonde itself, these measurements include the pendulum motion of the radiosonde underneath the balloon. This pendulum motion needs to be filtered from the data using appropriate filters in processing on the ground. Manufacturers need to take great care to filter only the pendulum motion and not to smooth the wind profile excessively. A typical unwinder length is 30 m, which would allow a pendulum period of $\approx 11 \text{ s}$. Immediately after launch, however, the pendulum period is much shorter and changes quickly as the unwinder releases the string, forcing swinging of the sonde underneath the balloon. These launch-induced sonde oscillations may take 1 min or more to dampen. At a typical ascent rate of 5 m s^{-1} , the balloon reaches an altitude of 300 m. This implies that wind measurements with an unwinder in the lowest few hundred m of the profile may have only poor vertical resolution and may not represent the wind gradients near the surface well.

Almost all GNSS wind-finding radiosondes specify uncertainties of $< 0.5 \text{ m s}^{-1}$ for wind speed and 2° for wind direction, which meets the requirements for GCOS essential climate variables and for WMO operational observations [46.56, 57]. Aside from GNSS for measurements of wind, two older systems are still in use to measure the track of the balloon: radio-theodolites and radar.

Radio theodolites or radio direction finders (RDF) only track the azimuth and elevation angle from which the transmitter signal is received. With height from

a pressure measurement onboard the radiosonde, the horizontal position can be derived. Uncertainties and biases in the pressure measurements may lead to errors in position, especially at low elevation angles, and may cause significant errors in the determination of winds.

Radar as a wind finding method uses a ground-based radar to track the radar reflection off a dedicated radar reflector, which may be part of the parachute. Radar measurements provide the azimuth and elevation angles, as well as the distance of a balloon, from which horizontal position and height can be derived. In radar and radio-theodolite tracking, wind speed and direction are simply calculated as the change in position.

Russian and Chinese radiosondes utilize a radar-transponder combination (secondary radar), in which the radar signal is received by the sonde, which, in turn, sends out its own data in reply. Radio direction finding provides azimuth and angle, while the radar return provides the distance and meteorological parameters. Russian radiosondes do not carry pressure sensors but calculate the pressure from the hypsometric equation using radar heights as input.

Early radiosondes including GNSS were significantly more expensive than those without, providing a significant cost advantage for these secondary wind-finding systems. In modern radiosondes, the cost of GNSS receivers has decreased dramatically, and only some national manufacturers produce sondes without GNSS receivers. Both Russia and China have started a transition to GNSS-based radiosondes, but GNSS-based radiosondes were not yet operational in either country in 2018.

Radar tracking and radio theodolites require a high level of maintenance of the ground equipment and regular calibration of the direction finding. Poor main-

tenance and calibration errors may lead to significant errors in wind and height measurements. Furthermore, the temporal resolution of wind measurements is limited. Uncertainties in wind speed and direction are considered significantly larger compared to those from GNSS measured winds.

Profiles of wind speed and direction may also be observed by tracking pilot balloons (pibals), which carry only a transmitter or no instrumentation at all. These balloons may be followed by a radio theodolite or an optical theodolite, where azimuth and elevation angle are recorded at regular intervals. Although height is not measured, it may be estimated by assuming a suitable ascent rate of the balloon [46.73] and recording the time of the measurements. Uncertainties in the height of the measurement and in calculated wind increase with altitude as the height errors compound. However, the simplicity and low cost of this method makes it attractive for some applications.

Since the southernmost sounding station is at the South Pole, reporting wind directions at that site and, in fact close to both poles, requires a special convention. At both poles the conventional wind directions are not defined, which would cause problems in the reports of wind direction. By historical agreement, wind directions within 1° of the poles are reported with respect to *grid north*, which is an artificial convention that defines the direction *north* on the azimuth ring as the direction of the 0° Greenwich meridian, *south* as the opposite direction, i.e., of the 180° meridian, *east* as the 90° meridian, and *west* as the 270° meridian. Upper-air wind directions measured by soundings should be reported using this convention, as long as the launch site is within 1° of the poles, even if the balloon travels outside of this circle [46.56].

46.4 Devices and Systems

Aerological sensors are not only installed in radiosondes but also in dropsondes, which are deployed from aircraft, in tethered systems, and more recently, in unmanned aircraft systems (UAS). A reliable balloon technology is an essential component in aerological measurements up to the middle stratosphere. Standardized data formats underpin the widespread exchange of aerological observations and are often overlooked.

46.4.1 Radiosondes

Currently, there are more than 20 radiosonde manufacturers worldwide, some with many decades of experience, and some that were established relatively

recently. Table 46.3 lists manufacturers, countries of origin, the current radiosonde model(s), and the technology to measure temperature, humidity, pressure, and wind. There may be more radiosonde manufacturers producing radiosondes, and Table 46.3 may not be complete, since information from some countries is difficult to collect or may not be shared with the WMO. Some manufacturers offer variants of their radiosondes with different transmission frequencies, optional sensors, and other modifications, which are too numerous to list here. Previous models, which are no longer produced, or which are currently being phased out, are also omitted. As example, three modern radiosondes are shown in Fig. 46.6. The last formal WMO

Table 46.3 Radiosonde manufacturers and their current models with some sensor specifications. Older models are not listed. A * in the pressure column indicates that the radiosonde may be optionally equipped with a pressure sensor

Manufacturer	Country	Model	Temperature	Humidity	Pressure	Wind
Vaisala	Finland	RS41	Platinum	Polymer	GNSS *	GNSS
Vaisala	Finland	RS92	Platinum	Polymer	Sensor	GNSS
Modem	France	M20	Thermistor	Polymer	GNSS *	GNSS
Modem	France	M10	Thermistor	Polymer	GNSS	GNSS
Graw	Germany	DFM-17	Thermistor	Polymer	GNSS *	GNSS
Graw	Germany	DFM-09	Thermistor	Polymer	GNSS	GNSS
Meisei	Japan	RS-11G	Thermistor	Polymer	GNSS	GNSS
Meisei	Japan	iMS-100	Thermistor	Polymer	GNSS	GNSS
Intermet Africa	South Africa	Imet-54	Bead thermistor	Polymer	GNSS	GNSS
Jinyang	South Korea	RSG-20A	Disk thermistor	Polymer	GNSS *	GNSS
Meteorlabor	Switzerland	SRS-C34	Thermocouple	Polymer	GNSS	GNSS
Intermet	USA	Imet-4	Bead thermistor	Polymer	Sensor	GNSS
LMS	USA	LMS-17	Thermistor	Polymer	GNSS *	GNSS
LMS	USA	LMS-6	Thermistor	Polymer	GNSS	GNSS
Taiyuan	China	GTS1	Rod thermistor	Hygristor	Sensor	Radar
Shanghai	China	GTS1	Rod thermistor	Hygristor	Sensor	Radar
Nanjing	China	GTS1	Rod thermistor	Hygristor	Sensor	Radar
Beijing Changfeng	China	CF-06	Bead thermistor	Polymer	GNSS	Radar
Nanjing Daqiao	China	XGP-3G	Bead thermistor	Polymer	Sensor	Radar
TianJin Huayun	China	GTS(U)1	Bead thermistor	Polymer	GNSS	Radar
UPP Vector	Russia	RZM-2	Rod thermistor	Polymer	Radar	Radar
NPF Multiobrabotka	Russia	I-2012	Rod thermistor	Polymer	Radar	Radar
Radiy	Russia	MRZ-3AK1	Rod thermistor	Polymer	Radar	Radar
Radiy	Russia	MRZ-3MK	Bead thermistor	Polymer	Radar	Radar
Aeropribor	Russia	AK2-02	Rod thermistor	Polymer	Radar	Radar
Aeropribor	Russia	AK2m	Rod thermistor	Polymer	Radar	Radar

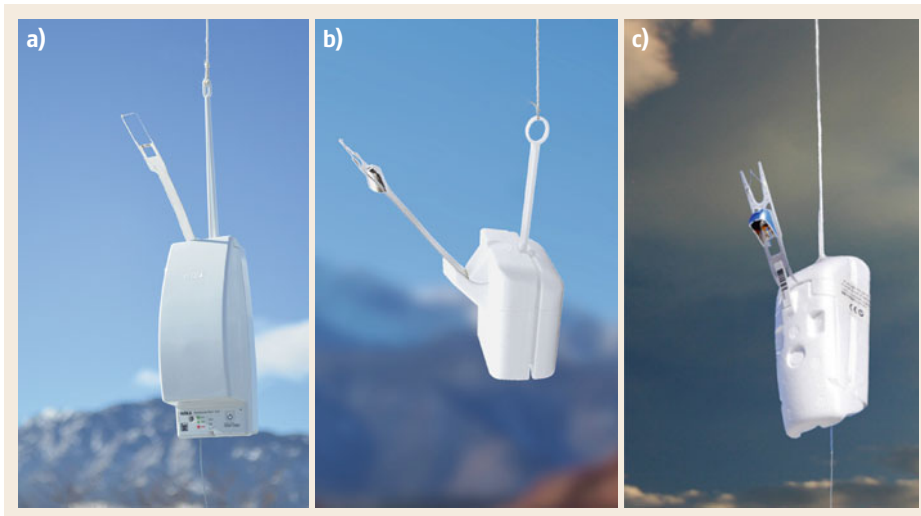


Fig. 46.6a–c Examples of modern radiosondes: (a) Vaisala RS41-SGP, (b) Graw DFM-17, and (c) Meisei iMS-100 radiosonde (from left to right)

radiosonde intercomparison took place at Yangjiang, China [46.53]. Most radiosonde models that participated in that campaign are no longer produced and have been replaced by newer models using more recent technology. This level of movement in the radiosonde

market highlights the need for regular intercomparisons as well as standardized procedures of observation. The report by [46.52] and the references therein provide an overview of formal intercomparisons preceding the Yangjiang campaign. Comparisons of different sonde

types are being conducted by a number of research groups for different purposes ([46.74–77]).

In both China and Russia, radiosondes are produced for the specific needs of the respective National Hydro-Meteorological Service (NHMS) and used only there. In each country, very similar radiosondes are produced under the same product code by different manufacturers. In Russia, radiosondes use secondary radar tracking for winds and pressure. In China, radiosondes use secondary radar only for winds, while the pressure is measured with a dedicated pressure sensor. In both countries, sensors may change without notice, hindering traceability and making identification of sondes by the numerical forecast centers difficult.

The recent trend is not to equip the radiosonde with a dedicated pressure sensor but to use GNSS geometric height measurements to calculate pressure and geopotential height data. Due to the large pressure range, small solid-state sensors may have significant biases in the stratosphere, while the GNSS method gives much better pressure and geopotential height data in this altitude region. However, in the lower troposphere, in-situ measured pressure may have lower uncertainties compared to the GNSS calculated pressure. For that reason, a number of manufacturers offer radiosondes with optional pressure sensors for customers who require the higher accuracy levels. In addition, using radiosondes with pressure sensor relaxes the need for an independent surface pressure measurement needed to initialize the GNSS pressure calculation and, thereby, relaxes operational requirements. For the most accurate measurements, the pressure sensor is typically recalibrated prior to launch using an external reference pressure sensor.

Radiosondes operate in two frequency bands allocated for meteorological applications: 400.15–406.0 MHz and 1675–1695 MHz. The majority of, but not all, GNSS tracking radiosondes operate in the 400 MHz band; almost all secondary radar systems operate in the 1680 MHz band. These frequencies are among the essential wavelength bands reserved for meteorological applications.

Currently, three different temperature sensor types can be found in operational radiosondes. Most radiosonde manufacturers use small bead or disk thermistors. These may differ slightly in size, but are all considered reasonably fast for atmospheric soundings. Most Chinese and some Russian sondes still use a rod thermistor (see [46.78] for details on this sensor), which is considerably slower and may require a time-lag correction in processing. Vaisala uses a platinum resistance wire with a response time comparable to that of bead and disk thermistors. Since radiosonde temperature sensors are completely exposed, the level of solar

shortwave heating and atmospheric long-wave heating/cooling of the sensor is determined by sensor size and by the reflective coating that the manufacturers apply to the sensors. Smaller sensors and highly reflective coatings minimize radiative heating biases but cannot eliminate them. The WMO [46.56] recommends that the coating be a metallic coating that is reflective also in the infrared range. Some manufacturers still use white-painted sensors, which have a significant radiative cold bias at night due to their high infrared emissivity. The coating of the temperature sensor and sensor boom should also be hydrophobic to minimize evaporative cooling errors after passage through wet clouds. Little information is available from the manufacturers regarding their coatings, often due to its proprietary nature. The effectiveness of these coatings is evaluated during formal intercomparisons. Some efforts have been undertaken to quantify the influence of radiation on radiosonde temperature measurements using multiple thermistors with different coatings [46.79]; however, these efforts have not found widespread use.

Almost all humidity sensors are based on the thin-film technology. However, there are significant differences between the different sensors. Vaisala and Meisei manufacture their own sensors, while all other companies use various third-party sensors. Currently, only Vaisala and Internet Africa use humidity sensors that are heated. The temperature range over which humidity sensors operate varies significantly between the different radiosonde manufacturers. Some manufacturers have implemented a time-lag correction algorithm into the processing software to correct for the slow response time of polymer thin-film sensors at cold temperatures.

Russia and China have started evaluating GNSS-based radiosondes, but as of 2018, secondary-radar tracking remains the dominant wind-finding method for these countries.

Most modern radiosondes require communication with the ground system during sounding preparation to exchange calibration information, to set the transmitter frequency, and to perform some instrument checks and calibrations prior to launch. This communication may be done through serial cable and increasingly wirelessly through near field communication.

46.4.2 Dropsondes

Targeted in-situ observations for specific meteorological conditions, especially in remote locations such as in tropical storms over oceans, are taken using small instruments that are dropped from research aircraft. Dropsondes (historically also called dropwindsonde or dropwinsonde) measure the same parameters as radiosondes using very similar technology. An overview

Table 46.4 List of dropsonde manufacturers

Manufacturer	Dropsonde model(s) (sounding system)	Country
Vaisala/NCAR	RD41, NRD41 (AVAPS)	USA
KIT	KIT-Sonde	Germany
Meisei	iMDS-17	Japan
Modem	Dropsonde	France
Yankee	XDD (HDSS)	USA

of dropsonde manufacturers is shown in Table 46.4. Dropsonde systems are installed on aircraft of more than 12 research organizations worldwide, including aircraft such as the US Air Force WC-130J and NOAA WP-3D hurricane hunters, the NASA RQ-4 Global Hawk high-altitude UAS, or the NCAR G-V research aircraft, among others.

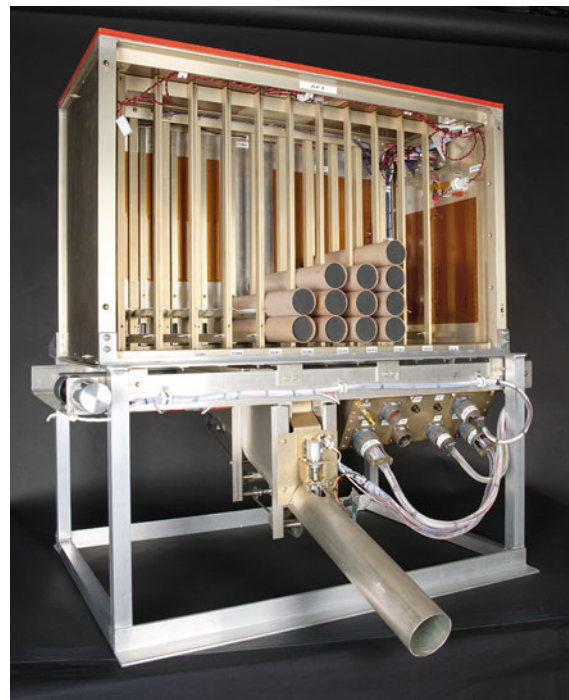
Airborne Vertical Atmospheric Profiling System (AVAPS[®]) dropsondes have been developed by NCAR, based on their work dating back to the 1960s [46.32]. These sondes have been licensed to Vaisala, who market these to the meteorological community. These sondes are the most widely used dropsondes and are deployed operationally for hurricane and severe weather forecast,

**Fig. 46.7** Image of the NCAR NRD41 dropsonde

in US university and government supported research and internationally for typhoon research and meteorological research. Currently, two versions of this sonde exist, which differ largely only in their geometry to fit two different launch systems. Both sondes use the Vaisala RS41 sensor module but a special GPS module for high-resolution wind measurements. The RD41 uses a launch system dating back to the 1980s, while the newer NRD41 (Fig. 46.7) is about half the weight and about half the diameter. This sonde had been developed for remote controlled release onboard the NASA Global Hawk but may be used also on the NCAR G-V, NCAR C-130, NOAA G-IV, and NOAA WP-3 aircraft. The automated launch system for the NASA Global Hawk is shown in Fig. 46.8.

The KIT-sonde was developed by the Karlsruhe Institute of Technology (KIT), Germany, based on the Graw DFM-09 radiosonde [46.80]. This dropsonde consists of four sondes, which separate after release to provide higher spatial coverage than regular dropsondes. KIT-sondes have been tested on the German DLR HALO G-V aircraft and the Dornier Do 128 of the Technical University Braunschweig, Germany.

Meisei developed the iMDS-17, which is currently deployed from a Diamond Air Service (DAS) Gulfstream-II aircraft for typhoon research [46.81].

**Fig. 46.8** NCAR-AVAPS automated dropsonde launch system for the Global Hawk UAS (NASA photo/Tony Landis)

Modem [46.82] has developed a dropsonde based on their M10 radiosonde model, which has not yet seen wider use.

Yankee [46.83] has developed the Expendable Digital Dropsonde (XDD) for their High-Definition Sounding System (HDSS). These dropsondes have been deployed from the Center for Interdisciplinary Remotely Piloted Aircraft Studies (CIRPAS) Twin Otter, the NASA DC-8, and the NASA WB-57 high-altitude aircraft.

Despite their similarity, there are some significant differences to radiosondes. Dropsondes need to be mechanically robust, since they experience a strong mechanical shock when they are deployed out of aircraft at speeds of up to 200 m s^{-1} . This represents a significant challenge for small lightweight sensors. Their descent is typically slowed using small parachutes or special geometries that increase their drag. Fall rates typically range between 25 m s^{-1} at 14 km altitude and 10 m s^{-1} near the surface. Although dropsondes may report at data rates of 2 Hz or higher, the lag of the sensors at the higher vertical speeds compared to radiosondes is significant. Some algorithms dedicated to dropsondes have been implemented in the processing of these data to remove response lag artifacts in temperature, humidity, and winds (e.g., [46.84]). In particular, humidity measurements are subject to significant response lag due to the considerable time constants at cold temperatures and faster vertical speed of dropsondes compared to radiosondes.

Many dropsonde applications require a higher spatial and temporal coverage of observations. This requires that dropsonde systems be capable of receiving multiple sondes simultaneously. AVAPS systems allow up to 8 simultaneous sondes and HDSS allows up to 40 simultaneous sondes.

The geopotential height for dropsondes using (46.3) may be calculated downward using aircraft observations to initialize the integration. The geopotential height may also be calculated upward using the last dropsonde observations before landing for initialization. Downward integration is less desirable, because uncertainties in aircraft pressure, temperature, and altitude, and less reliable dropsonde data immediately after deployment may lead to significant height uncertainties in the profile. Upward integration may be preferable, as long as telemetry data have been received up to the landing of the sonde. In severe weather such as hurricanes, this may not always be the case.

Unlike radiosondes, dropsondes do not suffer much from sensor icing. This is largely due to the fact that dropsondes fall from colder into warmer regions and into temperatures above freezing, where any accumulated ice will melt and be blown off by the airflow.

Furthermore, dropsondes fall through critical regions faster, exposing them to icing conditions for less time. Properly coated temperature sensors are unlikely to be subject to evaporative cooling after exiting clouds.

Dropsondes, which mostly use temperature sensors based on operational radiosonde models, are less likely to be subject to radiative heating temperature biases. The downward pointing of the sensors with the main sonde body above and shading by parts of the dropsonde lead to a smaller actinic flux compared to radiosondes where the sensor is fully exposed. The two to four times faster vertical speed provides much stronger ventilation of the sensor, and the highly reflective coating reduces the heat absorption of the temperature sensor. When these factors are combined, radiative heating of the temperature sensor is considered negligible for dropsondes.

Air-traffic control regulations may lead to some operational limitations for the deployment of dropsondes. While observations within hurricanes encounter few conflicts with other aircraft, observations of winter storms over the Atlantic generally require close air-traffic coordination due to the proximity of the North Atlantic flight corridors between Europe and North America. Dropsonde releases over land may be possible but are more restricted than releases over remote oceans.

46.4.3 Tethered Sondes

Observations on tethered balloons and kites were made at the very beginning of upper-air observations. This technology is still in use today, although almost exclusively for focused research projects and no longer for routine observations. The most significant limitation for tethered platforms lies in their inherent danger for aviation, which limits these platforms generally to low altitudes within the boundary layer and to restricted or closely controlled airspaces.

Tethered systems consist of a winch, a tether, and a balloon. The winch has to be strong enough to be able to reel in the balloon or kite even under significant wind load. The winch has to coil the tether in a safe fashion, such that the tension on the tether due to buoyancy and wind load does not damage the tether on the spool. The tether has to have a high tensile strength and must not break even under excess load. The load on the tether needs to be monitored during operation to avoid breakage of the tether. Unlike sounding balloons, tether balloons are typically not made out of natural rubber but out of a number of different materials and fabrics, which are coated for gas tightness, weather resistance, and other purposes. Many tether systems are equipped with an automatic rapid deflation device, which activates if the balloon escapes its tether. Tether balloon operations are generally not allowed close to cloud base

or inside clouds and are usually restricted in height. Flying in special-use airspaces may allow operation of tether systems outside of these limitations. Balloons for tethered operations may have special shapes (blimp, helikite, and others) to maintain their orientation into the wind and possibly to provide additional lift. Operators are required to monitor the atmospheric conditions constantly to be able to bring a tethered balloon back to the ground if atmospheric conditions change such that the operation is no longer safe for the balloon or the operators on the ground. Different types of balloons have different surface wind limits under which they can be launched.

The most common use of tethered systems is for observations in the lower troposphere and boundary layer, rarely exceeding 1 km above the surface. These systems allow placing sensors at relatively fixed heights for extended periods and allow observing changes in atmospheric conditions over hours to days. Sensors may include typical radiosondes, turbulence probes, particle instruments, radiation sensors, icing sensors, chemical sensors for air pollution, and others. Wind measurements require lightweight anemometers, typical cup anemometers and wind vanes for direction, or sonic anemometers (Chap. 9), which have to be corrected for the movement of the balloon. Tethered balloons may also be used to lift one end of optical fibers as part of the distributed temperature sensing (DTS; Chap. 20; [46.85]) to measure continuous vertical profiles of air temperature.

Raising and lowering tethered balloons at regular intervals provides vertical profiles of the measured parameters. Winch speeds are typically less than $0.5\text{--}1.0\text{ m s}^{-1}$, allowing high-resolution profiles of the parameters measured.

Sensor ventilation may vary significantly over the range of operating conditions. Therefore, the influence of solar heating and of nearby heat sources needs to be carefully analyzed and corrected. Since the sensors may remain at a constant altitude and, therefore, at near constant conditions for an extended amount of time, icing, rain, and the accumulation of pollutants may interfere with the measurements. Data need to be carefully screened for these artifacts.

Kite observations ended largely with the introduction of radiosondes into the operational network. Some research on kite technology has taken place since then [46.86]; however, few if any research projects currently use kites for atmospheric science.

46.4.4 Balloons

Modern meteorological balloons are made of thin rubber, and their size is conventionally expressed by their



Fig. 46.9 Balloon inflation building (*right*) and hydrogen room (*left*) at the sounding station at Yangjiang China

mass in grams. For single radiosonde soundings, balloons between 100 and 600 g are typically used, depending on the desired ceiling height of the profile (e.g., 18 or 32 km, respectively). For soundings with slightly larger payloads, such as ozonesondes, frostpoint hygrometers, and other scientific instrumentations (Sect. 46.8.2), 1000, 1200 g, or larger balloons may be used to reach altitudes ≈ 32 km. Larger balloons can lift heavier payloads and may reach higher altitudes but use larger amounts of fill gas. The volume of the balloon expands during its ascent into lower pressures, up to points where the rubber envelope is stretched to its maximum, and where the balloon finally bursts (see [46.87] for an image of a bursting balloon at the DWD Observatory Lindenberg and GRUAN Lead Center). After bursting the remains of the balloon and the payload fall back into the lower atmosphere and the surface. Equipping the payload with a parachute, which is usually attached below the balloon but in some cases may already be provided inside the balloon by the balloon manufacturer, substantially reduces the fall speed and risk of damage on the ground and may be required by national code to achieve fall rates near the surface of 6 m s^{-1} or less [46.56].

Meteorological balloons are filled with either hydrogen or helium. Most operational stations use a special building with one or several large doors (Fig. 46.9) for inflation; some operations inflate balloons in an open space outside. Although pure methane produces some lift as well, it is not sufficient to reach higher altitudes. Handling these gases requires diligent safety precautions, and improper handling may result in injury or even death. The WMO [46.56] provides a more detailed discussion of gas handling and balloon inflation-related safety topics than can be provided here.

Helium and hydrogen gas can be provided to most stations in high-pressure gas cylinders. A pressure regulator gauge should be used when a balloon is inflated.

Table 46.5 Typical balloon performance

Balloon weight (g)	100	200	350	600	1000	1500
Payload weight (g)	100	250	250	250	250	1000
Free lift (g)	500	500	600	900	1100	1300
Gas volume (m ³)	0.67	0.91	1.15	1.68	2.26	3.65
Rate of ascent (m min ⁻¹)	250	300	300	300	300	300
Maximum height (km)	18	21	26	31	34	34

Helium is inherently safer than hydrogen, since it is an inert gas and will not combust. However, pure helium gas should not be breathed in because of the risk of suffocation due to the lack of oxygen, which requires some safety measures for inflation in closed shelters.

Hydrogen gas is significantly cheaper but forms explosive mixtures with air. Static electricity and any open flame must strictly be avoided during balloon inflation and handling of the inflated balloon. Some stations, where delivery of gas cylinder is not feasible, generate hydrogen on site using dedicated hydrogen-generation systems usually based either on the electrolysis of water or using a number of chemical systems.

The appropriate amount of gas depends on the mass of balloon and payload and on the target ascent rate (typically ≈ 300 m min⁻¹ or 5 m s⁻¹). The gross lift L_g expressed in grams is

$$L_g = m_b + m_p + L_f, \quad (46.7)$$

where m_b is the mass of the balloon, m_p is the mass of the payload (including instrument(s), unwinder, and parachute), and L_f is the free lift.

A number of studies exist to estimate the balloon ascent rate based on balloon size, payload weight, and other parameters [46.88, 89]. The ascent rate also depends on the balloon manufacturer, the balloon shape, the drag coefficient, and in parts also on the atmospheric temperature profile. Therefore, it is difficult to provide exact equations for the relationship between the free lift and the desired ascent rate. An approximate empirical relationship [46.56] between the ascent rate v in m min⁻¹, free lift L_f , and gross lift L_g (both in g) can be given as

$$v = k \frac{\sqrt{L_f}}{\sqrt[3]{L_g}}. \quad (46.8)$$

Here, k is a factor depending on the balloon manufacturer and on balloon types (size and color) and may be approximately in the range between 130 and 150. In practice, the actual set of L_f , L_g , and v is obtained empirically by test launches for a specific set of balloon type and payload weight at a particular station.

Some stations measure the amount of fill gas not by the nozzle lift but by the volume of gas used to fill the

balloon. Assuming that the gross lift is due to hydrogen or helium in a pressure-dependent volume V throughout the sounding ascent, we obtain the following relationship between the gas volume V and the gross lift L_g

$$V = \beta L_g, \quad (46.9)$$

and

$$\beta = \frac{1}{M_{\text{air}} - M_{\text{gas}}} \frac{RT}{P}, \quad (46.10)$$

where M_{air} is the molar mass of air (29×10^{-3} kg mol⁻¹), M_{gas} is the molar mass of the fill gas (2.0×10^{-3} kg mol⁻¹ for hydrogen and 4.0×10^{-3} kg mol⁻¹ for helium), R is the molar gas constant (8.3 J K⁻¹ mol⁻¹), T is the temperature in K, and P is the pressure in Pa. With $T = 288$ K and $P = 1000$ hPa, the factor β becomes 0.89 m³ kg⁻¹ for hydrogen and 0.96 m³ kg⁻¹ for helium. Since industrial gases are typically not pure gases and contain small amounts of air, this factor is typically slightly larger than the values given here.

Typical balloon performance values for different balloon sizes and payloads are given in Table 46.5. Larger balloons for the same payload size will reach higher ceiling altitudes. Increasing the free lift and gas volume for the same balloon and payload will increase the ascent rate and decrease the ceiling height. These parameters may be adjusted for specific performance and operational requirements. Larger balloons for radiosondes are used to observe higher into the stratosphere. GUAN typically uses 600 or 1000 g balloons to reach well > 30 km.

In very cold environments, especially in the dark polar winter stratosphere and the nighttime tropical tropopause region, the balloon rubber may change to a glassy state through a glass transition (e.g., [46.90]), resulting in a much higher risk of early balloon burst. During normal soundings, the generally warmer balloon gas and solar heating during daytime flights keep the rubber above this transition point. Some balloon manufacturers offer special models with a different mixture of rubber materials for extremely cold temperatures, likely using a material with a lower glass-transition temperature.

Some polar stations use regular soundings balloons during winter that are treated with kerosene prior to launch. This method has also been used in tropical soundings at night by the Sounding of Ozone and Water in the Equatorial Region (SOWER; e.g., [46.91]). In this treatment, the balloon is dipped into a bucket of kerosene, which is absorbed into the rubber, and then hung on a laundry pole to dry before inflating the balloon. It is speculated that the chemical bonds between rubber molecules are modified such that the glass transition is delayed. However, the treatment may also start to break down the balloon material, such that many hours after the kerosene treatment, balloons are considered degraded and may not be useful for any sounding. Diesel or gasoline fuel, instead of kerosene, may also work. For example, during some SOWER tropical campaigns and at Syowa, Antarctica, kerosene has been used, while at the AWIPEV Arctic Research Base at Ny Ålesund, Svalbard, a mixture of 40% diesel, 40% kerosene, and 20% motor oil has been used.

In addition to the kerosene treatment, stations such as Ny Ålesund and Lindenberg, Germany, store balloons in a warm storage (55–60°C) for hours to days, which makes the balloons softer and more flexible. After being taken out of storage, the balloons are inflated and flown immediately.

Plastic balloons (Fig. 46.10) are a completely different type of balloon, and are generally used for much larger payloads than radiosondes. However, these shall be mentioned here as well, since at the South Pole, plastic balloons are also used for meteorological soundings, in particular for ozone soundings. Plastic balloons are made of thin inelastic polyethylene film. Unlike rubber balloons, whose size is given as the weight of the balloon, plastic balloon sizes are given by their volume at complete inflation, which they reach at their target al-



Fig. 46.10 Plastic balloon launch at McMurdo, Antarctica

titude. At inflation, the fill gas takes up only a small fraction of the available volume, leading to the typical teardrop shape at launch. The material does not stretch and withstands all atmospheric temperatures. Plastic balloons are used for reliable stratospheric observations, for long duration flights lasting from many hours to many months (Sect. 46.9), and for lifting heavy payloads up to a few tons.

Small plastic sounding balloons are typically over-inflated, such that the balloon breaks due to overpressure when reaching the ceiling altitude. Larger balloons are equipped with pressure control and pressure relief devices, which actively control the balloon behavior. Due to their high cost, plastic sounding balloons are only used in special situations, such as the investigation of the Antarctic ozone hole.

46.4.5 Autolaunching Systems

In recent years, some stations have deployed autolaunching systems for radiosondes to reduce personnel expenses. Different manufacturers are providing different models, but in general, the systems are similar. A small compartment inside a container is used to load radiosondes, balloons, and unwinders into a moving system of trays. These trays contain the communication hardware between sonde and main computer, as well as the inflation hardware. Once the balloons, radiosondes, and filling gas are situated within the system, all procedures (ground check, gas filling, launch, data acquisition, and data transmission) happen automatically at a preprogrammed schedule or may be initiated through remote control. At the scheduled launch time, the trays transport radiosonde and balloon to the filling section of the autolaunching system, which may be inside the main container or outside. Balloons are inflated using a prescribed amount of gas. When the balloon is ready, a retractable roof or cover is opened to release the balloon. Depending on the model, between 12 and 60 sets of radiosondes and balloons can be loaded at once. At stations with twice-daily soundings, these systems require service visits to refill sondes and balloons at schedules between once per week and once every four weeks. Automation may be an important step for the future of aerological measurements, but some questions need to be investigated carefully. The data quality for radiosondes from autolauncher systems, including balloon burst height statistics, should be comparable to that for manual launches. If not, further system improvements need to be considered. For example, if autolaunches under strong surface wind conditions tend to be unsuccessful, the obtained data records may have biases compared to the manual-launch data records. Maintenance costs need to be carefully monitored be-

cause the system is much more complicated than that for manual launches, and additional maintenance costs may be required. A number of issues may be aggravated in autolaunching systems, such as corrosion in coastal and small-island stations, insects in stations near forests and wetlands, or prolonged open storage of the balloon inside the launcher, which may lead to early balloon burst. Other site-specific issues may negatively affect the overall performance of a site and require changes in setup or additional maintenance. Furthermore, if an autolaunch system stops functioning, no sonde releases are possible at a site, until a service technician addresses the problem, which lowers the availability of upper-air data, in particular under bad weather conditions, when issues are more likely to occur.

46.4.6 Data Transmission and Formats

Radiosonde and dropsonde observations are heavily used in near real-time weather forecasting and weather advisories. Observations are distributed to the national meteorological centers (NMC) through the WMO Global Telecommunication System (GTS). Data sent through this network are highly regulated and require adherence to strict formatting requirements.

In-situ sounding profile data are mainly sent in two different format conventions [46.92]. The WMO [46.93] defines coded messages for meteorological data and other geophysical data relating to meteorology, which are transmitted through the GTS. For radiosondes and dropsondes, alphanumeric code forms have been defined: FM-35 TEMP (fixed land-based station), FM-36 TEMP SHIP (ship-based station), FM-37 TEMP DROP (dropsonde released from carrier balloon or aircraft), and FM-38 TEMP MOBIL (mobile land-based station). The origin of these messages dates back to the late 1940s, when compact data formats were a necessity and, therefore, they contain highly compressed data with limited vertical resolution and a minimal set of metadata. Modern computer and communication systems are capable of handling much larger data files, and alphanumeric code messages are currently being phased out.

46.5 Specifications

Accuracy specifications by the manufacturers cover a large range of observed conditions and do not necessarily meet the requirements by all user communities.

Uncertainties of upper-air measurements are influenced not just by the performance of the sensor but also by how well environmental influences, foremost solar radiation, are minimized through appropriate coatings and correction in postprocessing algorithms. Most

To meet the need for more comprehensive representation of observations, in 2005 the WMO decided to migrate from the traditional alphanumeric code (TAC) forms to table-driven code forms (TDCF) using the binary universal form for the representation of meteorological data (BUFR) format, a process which has not yet been completed. For radiosonde and dropsonde observations, the BUFR format allows storing observations up to 1 s resolution, including location and time information with each data point, and adding significantly more metadata, which may be used in the interpretation of the observations. At present, both formats, TAC and TDCF, are still in widespread use. Templates have been defined for both radiosonde data [46.94] and dropsonde data [46.95]. These templates describe the exact content that radiosonde and dropsonde data files in BUFR format should contain. Both formats were defined by the meteorological community, but only few software tools exist in the general research community to work with the BUFR format. This is likely to change as more software tools become available, such as those developed by the European Centre for Medium-Range Weather Forecasts (ECMWF, [46.96]), and as the benefits of the higher information-content BUFR data are becoming obvious.

In addition to these WMO standard formats, a large zoo of formats for radiosonde and dropsonde data exists. Most manufacturers provide their own ASCII output, which has been tailored to the needs of their customers. Some data centers, such as GRUAN, the Earth Observing Laboratory (EOL) of NCAR, and the Atmospheric Radiation Measurements (ARM) program of the US Department of Energy have started using netCDF (network common data form) formatted data files for radiosondes, some of these implementing the Climate and Forecasting (CF) metadata conventions to improve interoperability of these data. The netCDF format has the advantage that libraries for many software packages are freely available and that this format is in use well beyond the meteorological community. Properly coded netCDF files are self-describing and may contain extensive metadata to support the use of these data.

manufacturers provide uncertainty estimates for the instruments; however, the methods by which these estimates have been determined are not standardized, and large differences may exist in the methods by which manufacturers determine their uncertainties.

Independent intercomparisons provide a real-world snapshot of the instrument performance and uncertainties of measurements at the time of the intercompari-

Table 46.6 Uncertainty and requirements matrix. See text for more explanations; *n/d* stands for *not defined*

Variable	Manufacturer specifications	WMO optimum radiosonde	WMO optimum parameter	GCOS climate	GCOS stability
Temperature at 0–16 km (K)	0.2–0.5	0.4	0.6–1.0	0.5	0.05 K decade ⁻¹
Temperature > 16 km (K)	0.3–1.0	0.8	1.0	0.5	0.05 K decade ⁻¹
Humidity troposphere at 40 to –50 °C	3–5%	6%	2–4%	5%	0.3 % decade ⁻¹
Humidity troposphere at –50 to –90 °C	3–7%	10%	4%	5%	0.3 % decade ⁻¹
Pressure near the surface (hPa)	0.3–1.2	2	n/d	n/d	n/d
Pressure near 32 km (hPa)	0.04–2.0	0.1	n/d	n/d	n/d
Wind speed (m s ⁻¹)	0.15–2.0	1	1–2	2	0.5 m s ⁻¹ decade ⁻¹
Wind direction (°)	1–5	2	n/d	20	5° decade ⁻¹
Geopotential height (m)	8–15	20–60	24–100	n/d	n/d

son. The WMO has organized intercomparisons since 1950, with the last happening in 2010 at Yangjiang, China [46.53].

The WMO has compiled different sets of requirements for upper-air measurement uncertainties, depending on the target of the observations [46.56, Annexes 12.A and 12.B]; [46.57]. Different requirement levels have been specified, depending on the intended use of the measurements. The most lenient requirement is the uncertainty at which measurements become useful. Measurements with uncertainties larger than this threshold may be considered not meaningful for numerical weather prediction or for climate monitoring. The most stringent requirement is the uncertainty below which no further improvement in scientific result is expected. The WMO also specified a breakthrough requirement, which is an intermediate level at which significant improvement in scientific usefulness over the threshold requirement is expected. In addition, GCOS [46.57] has specified a stability requirement, which describes the required stability of the measurement system over decades, so that possible drifts in the measurement system are less than the expected climate change signals over long periods. Some level of random uncertainty is allowed over long periods, but, on average, any change in systematic bias must be below this stability requirement. Other requirements for process studies and campaign-based observations may exist but are not discussed here.

Table 46.6 lists the range of uncertainties specified by most manufacturers and the WMO and GCOS uncertainty requirements. Column *WMO optimum radiosonde* lists the optimum requirements for measurements by radiosondes based on the technological capability assessed after the 2010 international radiosonde intercomparison at Yangjiang [46.56, Annex 12.A]. Column *WMO optimum parameter* lists the optimum requirements for measurements by any system based on the WMO rolling review of requirements of upper-air observations [46.56, Annex 12.B]. These two columns are targeted for numerical weather prediction. Column

GCOS climate lists the requirements for measurements by any system targeted for climate observations [46.57]. Column *GCOS stability* lists the stability requirements for climate observations.

All uncertainties and requirements combine estimates of repeatability and of systematic bias. It is assumed that the distribution of measurements under identical conditions is Gaussian and all specifications and requirements are expressed as two standard deviations of this distribution (95% confidence level).

Russian and Chinese manufacturers have been excluded from the range of manufacturer specifications in Table 46.6 and from the discussions below, due to the sparseness of publicly available information. The few available specifications for temperature for these manufacturers range between 0.6 and 1.8 K and for humidity between 5 and 10%. No specification for pressure, wind, and height are available, as these depend largely on the performance of the secondary radar system, not on the radiosonde itself.

The manufacturer specifications need to be treated with caution, since not all manufacturers have the ability to rigorously evaluate the performance under all conditions, and some may overstate their specifications. Independent formal intercomparisons, such as those by the WMO or characterizations in independent laboratories, are vital for proper evaluations of the performance of radiosondes.

The geopotential height and stratospheric pressure derived from GNSS measurements may satisfy all requirements. In most cases, GNSS altitude uncertainties are in the range of 10–20 m, which is consistent with the manufacturer's specifications. Near the poles, GNSS height uncertainties on radiosondes may be larger due to the unfavorable geometry of GNSS satellite orbits [46.97]; however, this has not been evaluated yet.

GNSS derived pressure profiles near the surface critically depend on the reference pressure sensor used to initialize the profile. Proper placement and calibration of the reference pressure sensor are additional

influences on the uncertainty estimate at a given station. Operational procedures must take proper maintenance and calibration of the reference sensor into account.

GNSS-derived wind measurements meet all requirements, including stability requirements for long-term climate observations. The lower uncertainty range provided by manufacturers may be overestimating the GNSS performance, in particular considering that filtering of the balloon pendulum motion is an important step in the derivation of winds. Changes in the processing of GNSS winds, such as GNSS filter modes, balloon pendulum filters, or reception of additional GNSS systems, may lead to small changes in the reported values; however, these changes are likely to be within the most restrictive requirements.

Temperature measurements at nighttime do not suffer from solar radiation but depending on coating may be subject to long wave cooling, which is considered a small to negligible effect for most modern sensors. The uncertainties at nighttime should largely reflect the uncertainties of the calibration and measurement electronics. Daytime observations need to be corrected for solar radiation error and have larger uncertainties due to variations in the effectiveness of the reflective coating, due to the quality of the correction algorithm, and due to variations of the actinic flux due to varying albedo.

Humidity measurements by a number of modern polymer thin-film sensors meet the uncertainty requirements in the lower and warmer troposphere. However, calibration and a slow response time at cold temperatures in the upper troposphere still presents a significant

challenge for accurate humidity measurements for most sensors. Stratospheric humidity is outside the capabilities of almost all radiosonde humidity sensors.

The stability requirements for upper-air observations for climate are very stringent and are probably not met by most instruments (except for GNSS upper-air winds). Stability requirements affect all aspects of radiosondes, from sensor hardware to radiosonde production, to sensor calibration, to operational procedures. Small changes in any of these areas may not significantly change the overall combined uncertainty and, therefore, not degrade the usefulness for numerical weather prediction, but may degrade the usefulness of some systems for climate research, because many climate signals are small. Technological advances and improvements in operating procedures may bring more radiosondes within range for observations of small climate signals.

Almost all sondes rely on the factory calibration for their sensors, and no manufacturer, except Vaisala with the RS41 pressure sensor, currently performs a one-point calibration check or one-point recalibration to capture the extent of possible calibration drifts. To support climate observations, GRUAN is implementing independent ground-check measurements for pressure, temperature, and humidity in a controlled environment prior to launch [46.62]. Understanding the changes in calibration between production and use of the sondes, and possible changes in manufacturing itself, is an essential component in reducing uncertainties of long-term trend estimates using radiosondes.

46.6 Quality Control

Upper-air observations from radiosondes are usually processed automatically and sent to the numerical weather prediction (NWP) centers with only little human oversight. Therefore, the first level of quality control is performed automatically within the software provided by the radiosonde manufacturers. The details differ greatly between manufacturers, and only some general descriptions can be provided, without assumptions that these procedures are actually implemented in the software.

On all parameters, a physical range check assures that reported measurements are within physically possible limits. Bad values failing this test are more likely due to telemetry errors but may also be caused by failures of electronic components. Outlier filters make sure that changes over short time periods (neighboring data points) are within physical limits. Outliers may be caused by telemetry errors but may also be caused by temperature spikes in the stratosphere as the instru-

ments swings through the balloon wake and do not represent the state of the atmosphere. Outliers and physically impossible readings may simply be ignored, and neighboring readings may be interpolated to fill in gaps. Some sounding systems can specify the extent of the gap over which the software may interpolate data.

Some sounding systems may require that pressure be monotonically decreasing, i.e., that the balloon constantly rises to produce a uniform vertical profile. This may eliminate data during some periods of a sounding, when a balloon is descending, either due to strong icing on the balloon and payload inside a storm cloud, or possibly due to strong gravity wave activity in the stratosphere. Such a temporary descent may introduce a small temperature discontinuity at the transition from rising to temporary sinking of the balloon.

The temperature profile within the atmosphere is largely limited by the adiabatic lapse rate. Vertical gradients in temperature exceeding the adiabatic lapse rate

in the middle and upper troposphere are suspicious and may be flagged as invalid. One cause for a reported superadiabatic lapse rate may be evaporative cooling of the temperature sensor after exiting a cloud. A superadiabatic lapse rate near the surface may be possible under some conditions and may or may not be removed.

For sondes using GNSS to determine pressure, large vertical updrafts inside storms due to hydrostatic instability may lead to large pressure biases. The vertical rise rate of the balloon may be used to remove or flag pressure values that have been calculated during and above instability conditions.

Relative humidity measurements are poorly constrained and range between 0% and about 100%. Most manufacturers truncate relative humidity values to 100%, although small amounts of supersaturation above liquid water may be possible in updrafts. However, the typical uncertainty of most relative humidity sensors is larger than the range of possible supersaturation in the lower to middle troposphere. Unheated humidity sensors may accumulate sufficient amounts of ice such that they are no longer exposed to the atmosphere. These sensors may incorrectly report high relative humidity values well beyond the extent of a cloud. Complementary observations or expert knowledge may be required to identify observations impacted by icing that may not be filtered out operationally.

Wind measurements using GNSS may be invalid, if the GNSS receiver does not receive a sufficient number of satellites to calculate position and winds properly. These data may be interpolated, if the period of loss of satellite reception is short.

National meteorological services may have additional quality control procedures implemented to detect suspicious observations before transmitting data through the GTS. These additional quality control procedures have the ability to make use of other nearby observations to check the consistency of observations. The details of these additional quality control procedures depend on the capabilities of the meteorological service.

Some meteorological services perform essential corrections, such as solar radiation correction, calculation of the geopotential height, and others, not as part of the radiosonde sounding system but as part of the data processing chain within the service.

Numerical weather prediction (NWP) centers have additional quality control procedures after receiving data through the GTS. During data assimilation into the NWP model, all observations, including radiosonde observations, are compared with the atmospheric state calculated by the NWP model (called *background*). If the difference between observation and background is too large, then the observation may be flagged and ignored. If, over a period of time, a substantial fraction

of observations coming from a station or from a particular radiosonde model is flagged by the NWP center, then these data may be flagged permanently, and all observations from this station or this radiosonde model may be ignored. Large NWP centers may also evaluate the performance of each radiosonde type in comparison to their model background based on the information provided with the observations. This model comparison needs to be cognizant of the model errors itself and cannot replace a direct evaluation of the radiosonde types, but it does provide information about the limitations of different radiosonde types [46.98].

Meteorologists issuing weather forecasts or radiosonde data for other research purposes may analyze individual radiosonde profiles and use their expert knowledge about the radiosonde system and the atmospheric conditions to flag, correct, or ignore profiles or parts of profiles. In particular, for significant weather events, a detailed understanding of the radiosonde system and the atmospheric situation is essential to avoid misinterpretation of either the observation or the output of the NWP model.

GRUAN implemented additional manufacturer-independent ground checks into the operational procedures. In this network, radiosondes prior to launch are compared against well-characterized references under controlled conditions. These tests may identify small but significant calibration problems that cannot be identified any other way. Since this step may be labor intensive, it will be limited to small, dedicated networks. For long-term climate monitoring, this quality check is considered essential.

In addition to the actual measurements by the radiosonde, the metadata accompanying these observations also require quality control. Metadata include the information about the site, such as location, latitude, longitude, altitude, and station identifier, and about the instrumentation, such as manufacturer, sonde type, system configuration, etc. For regular observations, this quality control may need to be done only during configuration of the site; however, regular reviews of this information avoid errors in the description of the observation.

At well performing stations, the quality-control information is collected and analyzed to help improve the collection of observations. Most quality problems are most likely due to either specific atmospheric conditions or other rare circumstances. However, recurring quality concerns may point to deeper problems that need to be rectified. Frequent quality problems may be due to operational procedures, weaknesses in the instrumentation, or problems in the manufacturing of the radiosondes. Addressing these root causes should improve the overall data collection process.

46.7 Maintenance

Most radiosondes are single-use instruments. These instruments should be stored in a dry environment and kept in the manufacturer-sealed bag until they are used. The sensor calibration may drift slightly over the course of storage. Manufacturer-recommended procedures to restore the original factory calibration should be followed, where they are available.

Modern electronic ground systems require little maintenance. Operational sites may need to keep spares of key components in case of failure. Electrical connections that are exposed to severe weather conditions, especially corroding environments with high humidity and high concentrations of sea-salt spray, may need to be inspected regularly.

Updates of the sounding software need to be carefully evaluated before installing them in the sounding system. In particular, changes in any of the calculations need to be carefully evaluated, since they may negatively affect the ability for long-term trend detection.

Systems that track radiosondes by mechanically moving antennas may require regular inspection of all moving parts of the system. Stations using these systems should follow the maintenance protocol provided by the manufacturer.

The gas handling equipment needs to be inspected regularly. High-pressure gas cylinders holding either helium or hydrogen are normally connected to a pressure regulator and a fill valve. All components must be in good working order and not create any safety hazard. The maintenance protocol of the manufacturer should be followed for these systems. Gas systems handling hydrogen must also be electrically grounded to minimize the buildup of static electricity. The grounding connections need to be inspected to assure that all components are properly grounded. Proper safety gear should be worn by the operators and should be available at the launch site.

Inflation buildings should be properly ventilated, and shelters used for hydrogen inflation should be built following the appropriate safety codes. Regular inspection may be required to assure that the inflation shelter and the gas handling system are still operating within safety regulations.

Balloons typically have a short shelf life and should not be stored much beyond 1 year. They should be stored in a dark, cool place, since ultraviolet light quickly deteriorates the natural rubber material.

46.8 Application

Operational sounding data are shared in near real time by national and international meteorological services through the GTS of the WMO, together with meteorological data taken at surface stations and obtained onboard aircrafts and by satellites [46.99]. These data are used for meteorological analyses, in which they are compiled to generate a best estimate of the global meteorological fields during the analysis period as initial conditions for NWP at all participating national and international NWP centers. Since operational radiosonde data provide simultaneous information about vertical profiles of pressure, temperature, humidity, and winds, they are one of the key components of the global weather forecasting systems.

The historical record of radiosonde observations collected through the GTS since the 1950s may be an important basis to analyze upper air climate change. However, these real-time radiosonde data are generally not sufficiently homogeneous to be used for the detection of temperature trends of the order of $0.1 \text{ K decade}^{-1}$ [46.100]. Changes in instrumentation (radiosonde types and manufacturers), in operational procedures, and even in station location (e.g., a move

within a city with a significant station altitude change) in a timescale of decades may easily have caused larger changes than the possible atmospheric trend. To remove these possible artifacts in radiosonde temperature data, researchers have created different *homogenized* radiosonde temperature products for climate research using different methodologies [46.54, 101]. Global atmospheric reanalyses compile all available observations to generate a best estimate evolution of the atmospheric state over the period covered by the reanalysis. Instead of using the original real-time radiosonde data, most of these reanalysis projects use homogenized radiosonde temperature data sets [46.55].

Radiosondes are also used for studies of specific atmospheric processes and for the validation of ground-based and satellite remote-sensing instruments. For these purposes, radiosondes may be launched in intervals as short as 30 min to capture short-period variabilities; their launch may be timed with satellite overpasses, or radiosondes may be coordinated with observations from other platforms, such as aircraft, for simultaneous measurements. Radiosondes are also flown with specialized atmospheric sensors to measure parameters that

are not measured by radiosondes. Recent technological advances have allowed a significant expansion of the use of radiosondes for many upper-air applications that were previously out of reach.

46.8.1 Sounding Networks

Coordinated aerological observations provide a snapshot of the atmospheric state over large regions using similar technology and standardized practices. These networks are part of the overall coordinating efforts of the WMO and are described in greater detail in Chap. 63.

The global operational radiosonde network as part of the WMO Global Observing System (GOS) contains approximately 900 stations, which are operated by national meteorological services and research institutions. The WMO coordinates these observations through the infrastructure commission, which oversees the implementation and operation of the observing systems and data communication and management. The infrastructure commission also provides technical guidance on the instrumentation, as well as on operational procedures. More than two-thirds of these stations launch radiosondes twice daily at 00:00 UTC and at 12:00 UTC.

GUAN [46.50] is a subset of the larger operational radiosonde network, which was defined in the mid-1990s. GUAN includes stations with long-term, high-quality radiosonde observations that follow the GCOS climate monitoring principles to establish an upper-air climate monitoring network. To resolve synoptic-scale weather disturbances, stations on land are spaced approximately at 5°–10° latitude. By 2014, GUAN had grown to 170 stations worldwide.

In recognition of the need for stronger technical leadership within the network, GRUAN was started in 2008 [46.87, 102]. This network included a dedicated lead center, hosted at the German Meteorological Service, which coordinates research activities on various aspects of the upper-air climate measurements within the network. One of the essential characteristics of all GRUAN data products is vertically resolved uncertainty estimates attached to every data point. This effort has stimulated numerous research activities both within GRUAN, as well as within different suppliers of upper-air instrumentation. GRUAN currently consists of 26 high-quality, long-term, upper-air observing stations that are built on, but not confined to, the GUAN. Of these stations, 10 have been certified, and 16 are awaiting certification (as of 2018).

Radiosondes for operational weather forecast are also launched from commercial ships as part of the Automated Shipboard Aerological Program (ASAP), which is coordinated by the Joint WMO-IOC (Inter-

governmental Oceanographic Commission) Technical Commission for Oceanography and Marine Meteorology (JCOMM). Radiosoundings from commercial ships partially fill the large gap of missing in-situ observations over the oceans. These soundings may be done through autolaunching systems or through manual launches by a ship's crew [46.103]. The operations are supported by several national meteorological services in Europe, Asia, and South Africa.

46.8.2 Scientific Soundings

Radiosondes provide an ideal platform for additional scientific sounding instruments to measure the vertical distribution of atmospheric parameters for thermodynamics, composition, and radiation, up to 30–35 km. Over the last decade, a new de-facto interface standard (XDATA, [46.104]) has been implemented by several radiosonde manufacturers, which allows the transmission of additional channels for external instruments through the telemetry stream of operational radiosondes. This technology allows simultaneous measurements of parameters such as ozone, stratospheric water vapor, cloud backscatter, aerosol size distribution, supercooled liquid-water content, long-wave and short-wave radiation, SO₂, and others, in addition to the basic meteorological parameters. Special care is needed in developing external instruments for radiosondes, because environmental parameters may change relatively quickly (e.g., temperature from +30 to –80 °C in 45 min and pressure from 1000 to 10 hPa in 90 min), and because radiosondes may cause significant radio-frequency interference due to their proximity to the scientific instrument.

Most external instruments are used in short research campaigns, but ozonesondes are a notable exception. These instruments are flown operationally by many national meteorological services stations to monitor the ozone layer and tropospheric pollution and to validate satellite-based ozone measurements. The WMO Global Atmosphere Watch (GAW) coordinates the operational ozonesonde network, and its data are archived at the World Ozone and Ultraviolet Radiation Data Centre (WOUDC) hosted at Environment and Climate Change Canada. Worldwide, there are about 70 operational ozonesonde stations with weekly soundings in many cases. The Southern Hemispheric Additional Ozonesondes (SHADOZ) network is a subset of the global ozone sonde network, which focuses on ozone observations in the Southern Hemisphere and, most importantly, the tropics [46.105].

Two types of ozone sondes are currently in use: the electrochemical concentration cell (ECC) ozonesonde [46.38], which is produced by two man-

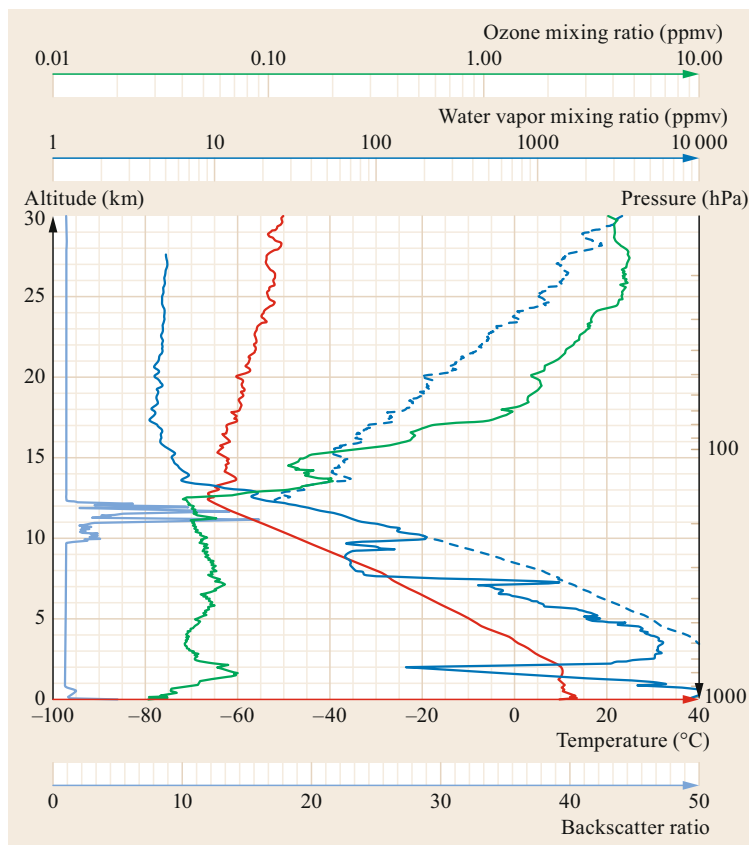


Fig. 46.11 Scientific sounding launched at the DWD Meteorological Observatory Lindenberg, Germany, on 08.10.2018. The instruments launched as part of this payload are the Vaisala RS41 radiosonde, the ECC ozone sonde, the CFH water vapor sonde, and the COBALD backscatter sonde. The temperature is shown in red, the backscatter ratio at a wavelength of 455 nm in light blue, the measured water vapor mixing ratio as a solid line in dark blue, the calculated saturation mixing ratio as a dashed line in dark blue, and the ozone mixing ratio in green

ufacturers, and the Brewer–Mast sonde, which is produced on a small scale by only one manufacturer. ECC ozonesondes are supported by several radiosonde types, where the ground-system software processes the data coming from the ozone sonde. These instruments consist of a small pump and a cell, in which ozone pumped through a solution of potassium iodide converts iodide to iodine. This reaction generates an electrical current within the cell that can be measured [46.38]. See [46.105] and the references therein for more information on the ozonesonde.

All radiosonde relative humidity sensors measure tropospheric water vapor concentration, with decreasing capability in the cold upper troposphere, but currently none of them have the capability to measure stratospheric humidity. However, the concentration of stratospheric water vapor can be measured by small frostpoint hygrometers, such as the cryogenic frostpoint hygrometer (CFH, [46.106]) or the NOAA frostpoint hygrometer (FPH [46.107]), or by optical hygrometers based on the Lyman- α fluorescence method [46.108]. Currently, there are fewer than ten stations worldwide that measure stratospheric water vapor routinely using cryogenic frostpoint hygrometers [46.107, 109]; most

of these are coordinated within the Network for the Detection of Atmospheric Composition Change (NDACC; Chap. 63). These instruments operate on the chilled mirror principle, where the temperature of a mirror is controlled such that condensation forms on the surface of the mirror and remains constant. The condensation on the mirror may be dew or ice, which determines whether the instrument measures the dewpoint or frostpoint temperature. The condensate on the mirror is measured by an optical detector and used in a feedback controller to regulate the mirror's temperature. The use of cryogenic liquids in these instruments allows them to measure the very cold frostpoint temperatures corresponding to stratospheric water vapor concentrations.

Scientific instruments exist to measure aerosol and cloud particles onboard small radiosonde balloons ([46.110, 111] and references therein). These instruments focus on upper tropospheric cirrus clouds and aerosols in the upper troposphere and lower stratosphere. These instruments may be combined with newly developed sensors for sulfur dioxide [46.112] to measure, for example, volcanic emissions.

A profile of tropospheric and stratospheric water vapor, ozone, and the cloud backscatter ratio using the

balloon-borne backscatter sonde COBALD (Compact Optical Backscatter and Aerosol Detector, [46.113]) measured at the DWD Meteorological Observatory Lindenberg, Germany, is shown in Fig. 46.11. These profiles are measured regularly as part of the monitoring activities of GRUAN and NDACC and to better understand the details of upper tropospheric and stratospheric chemistry and dynamics.

The content of supercooled liquid water in clouds can be measured using vibrating wire sensors [46.114] onboard small radiosonde payloads. In-situ measurements of this kind are notoriously difficult due to the risk of icing for aircraft.

46.9 Further Development

Although remote-sensing observations from space and from the ground have dramatically expanded our ability to observe the global atmosphere, in-situ observations on small balloons continue to play a very important role. Radiosondes remain the only technology to observe all atmospheric state variables at the same time and at the same location and thereby help reducing observational errors due to poor spatial and temporal correlation between remote sensing observations. Radiosondes are one of the most important observing systems contributing to forecast skill of global NWP models, and their degradation has immediate impacts on weather forecast [46.117].

The improvement of radiosonde sensors is driven by the need for better traceability of observations and for standardizations of procedures. A significant amount of research is invested in better characterizing sensor performance in their atmospheric environment, not just under laboratory conditions. The close cooperation with national standards laboratories is currently leading to a better quantification of measurement uncertainties and the recognition of their importance in atmospheric observations.

Technological progress has significantly improved the observations of upper tropospheric humidity and it is expected that observations of lower stratospheric humidity may be significantly expanded through developments of new sensors and improvements of existing sensors. The adoption of the XDATA protocol by many commercial radiosonde manufacturers allows adding new sensors, thereby significantly expanding their capabilities. This de-facto interface standard has laid the foundation for a strong upper air research community.

For measurements of carbon dioxide and other long-lived greenhouse gases in the stratosphere, the cryogenic whole-air sampling method with large plastic balloons has been used ([46.91, 115] and references therein). Over the last decade, a new approach called *AirCore* has been developed to measure the vertical distribution of carbon dioxide and methane and other constituents [46.116]. For both air-sampling methods, the air samples are recovered, and the composition is analyzed in the laboratory using the nondispersive infrared gas analyzers, gas chromatographs, and mass spectrometers. *AirCore* is the first whole air sampler small enough to fly on small radiosonde balloons.

In-situ observations from UAS (Chap. 49) and commercial aircraft (Chap. 43) provide great spatial coverage. These systems complement radiosondes, which are capable of reaching much greater altitudes than these systems and are not biased by the need to avoid aviation hazards. UAS platforms require small, lightweight, and highly accurate sensors. Many synergies exist between UAS technology and radiosonde technology for mutual benefit. Most UAS lack the capabilities to reach much above the boundary layer, for technical and logistical reasons. Some projects have combined small balloons and UAS to achieve the altitudes of balloons and to maintain the ability for control of UAS. For example, *Kräuchi* and *Philipona* [46.118] launched a dedicated glider, equipped with pressure, temperature, humidity, GPS, and radiation sensors on a small sounding balloon. At 24 km, the glider was released from the balloon and returned autonomously back to the launch site. Winds were measured only on ascent, while the other parameters were measured throughout the flight. This development has the potential to reduce costs for soundings, which are more complex than normal radiosondes. However, coordination with civilian air traffic is a significant hurdle in the development of these systems and adds significant logistical overhead. As regulations and UAS technology further develops, it is expected that UAS will be better integrated into regulated airspace.

Long-duration plastic balloons such as those during the *Concordiasi* project [46.119], which have been launched since the 1960s, have the ability to stay afloat for several months in the lowermost stratosphere. These projects provide a unique Lagrangian view of the atmosphere, as they drift with the prevailing winds.

46.10 Further Readings

A reference for aerological technologies and observations is the Guide to Meteorological Instruments and Methods of Observation of the WMO Commission for Instruments and Methods of Observations [46.56]. This guide is regularly updated by a panel of experts from the operational and research community. Part I, Chap. 12 of this guide deals with measurements of upper air pressure, temperature, and humidity; Part I, Chap. 13 deals with measurements of upper air wind.

The formal intercomparisons organized by the WMO present a review of the current state of radiosonde technology at that time. The most recent inter-

comparison took place at Yangjiang, China [46.53] with next intercomparison planned in 2022 at the GRUAN Lead Center, Lindenberg, Germany.

The GRUAN documents (<https://www.gruan.org/documentation/>, Accessed 20 July 2021) provide detailed information on a number of specific topics relating to upper air observations. This network manages upper air observations for climate and relies on a detailed understanding of the observing technology.

Other important works for upper air observations have been published, many of which are listed in the references below.

References

- 46.1 J.L. DuBois, R.P. Multhaupt, C.A. Ziegler: *The Invention and Development of the Radiosonde, with a Catalog of Upper-Atmospheric Telemetering Probes in the National Museum of American History* (Smithsonian Institution Press, Washington 2002)
- 46.2 R. Assmann: Brockhaus' Konversations-Lexikon, *Das Wetter*, Monatsschr. Witterungskd. **26**(10), 240 (1908)
- 46.3 D. Fisk: *Exploring the upper atmosphere* (Faber & Faber, London 1933)
- 46.4 S.P. Fergusson: The exploration of upper air by means of balloons sondes, *Sci. Am.* **100**, 169–170 (1909)
- 46.5 L. Teisserenc de Bort: Variations de la température de l'air libre dans la zone comprise entre 8 km et 13 km d'altitude, *Compt. Rend. Séances Acad. Sci. Paris* **134**, 987–989 (1902)
- 46.6 R. Assmann: Über die Existenz eines wärmeren Luftstromes in der Höhe von 10 bis 15 km, *Sitzber. Königl. Preuss. Akad. Wiss. Berlin* **24**, 495–504 (1902)
- 46.7 K.P. Hoinka: The tropopause: Discovery, definition and demarcation, *Meteorol. Z.* **6**, 281–303 (1997)
- 46.8 K.-H. Bernhardt: Remarks to the paper "The tropopause discovery, definition and demarcation" by K. P. Hoinka, *Meteorol. Z.* **8**, 43–46 (1999)
- 46.9 J.M. Lewis: Ooishi's observation viewed in the context of jet stream discovery, *Bull. Am. Meteorol. Soc.* **84**, 357–369 (2003)
- 46.10 W. Ooishi: *Raporto de la Aerologia Observatorio de Tateno*, Aerological Observatory Rep., Vol. 1 (Central Meteorological Observatory, Tokyo 1926), in Esperanto
- 46.11 H. Seilkopf: Maritime Meteorologie. In: *Handbuch der Fliegerwetterkunde*, Vol. 2, ed. by R. Habermehl (Radetzke, Berlin 1939), in German
- 46.12 J. Bjerknes, E. Palmén: Investigations of selected European cyclones by means of serial ascents, *Geofys. Publik.* **12**(2), 5–62 (1937)
- 46.13 University of Chicago, Department of Meteorology: On the general circulation of the atmosphere in middle latitudes, *Bull. Am. Meteorol. Soc.* **28**, 255–280 (1947)
- 46.14 C.G. Rossby: On the distribution of angular velocity in gaseous envelopes under the influence of large-scale horizontal mixing processes, *Bull. Am. Meteorol. Soc.* **28**, 53–68 (1947)
- 46.15 H. Riehl: Jet stream in upper troposphere and cyclone formation, *Trans. Am. Geophys. Union* **29**, 175–186 (1948)
- 46.16 C.-G. Rossby and Collaborators: Relation between variations in the intensity of the zonal circulation of the atmosphere and the displacements of the semi-permanent centers of action, *J. Mar. Res.* **2**, 38–55 (1939)
- 46.17 R. Grund: Drachen oder Drachenballon mit selbsttätiger Schrägstellvorrichtung, Patent 302569, Reichspatentamt, Germany (1919), in German
- 46.18 W. Adam, H. Dier, U. Leiterer: 100 years aerology in Lindenberg and first long-time observations in the free atmosphere, *Meteorol. Z.* **14**, 597–607 (2005)
- 46.19 K.-E. Michelsen: How it all started. The 1st Vaisala radiosonde, *Vaisala News* **171**, 11–13 (2006)
- 46.20 C.E. Palmer: The general circulation between 20 mb and 10 mb over the equatorial Pacific, *Weather* **9**, 341–349 (1954)
- 46.21 F.E. McCreary: Stratospheric winds over the tropical Pacific Ocean. In: *Minneapolis Meet. Am. Meteorol. Soc.* (1959)
- 46.22 R.J. Reed, W.J. Campbell, L.A. Rasmussen, D.G. Rogers: Evidence of a downward-propagating, annual wind reversal in the equatorial stratosphere, *J. Geophys. Res.* **66**, 813–818 (1961)
- 46.23 R.A. Ebdon, R.G. Veryard: Fluctuations in equatorial stratospheric winds, *Nature* **189**, 791–793 (1961)
- 46.24 M.P. Baldwin, L.J. Gray, T.J. Dunkerton, K. Hamilton, P.H. Haynes, W.J. Randel, J.R. Holton,

- M.J. Alexander, I. Hirota, T. Horinouchi, D.B.A. Jones, J.S. Kinnersley, C. Marquardt, K. Sato, M. Takahashi: The quasi-biennial oscillation, *Rev. Geophys.* **39**(2), 179–229 (2001)
- 46.25 K. Hamilton, T. Kazazaki: Exploring the “prehistory” of the equatorial stratosphere with observations following major volcanic eruptions, *Weather* **73**, 154–159 (2018)
- 46.26 R.S. Lindzen, J.R. Holton: A theory of the quasi-biennial oscillation, *J. Atmos. Sci.* **25**, 1095–1107 (1968)
- 46.27 M.R. Schoeberl: Stratospheric warmings: Observations and theory, *Rev. Geophys.* **16**, 521 (1978)
- 46.28 A.H. Butler, J.P. Sjöberg, D.J. Seidel, K.H. Rosenlof: A sudden stratospheric warming compendium, *Earth Syst. Sci. Data* **9**, 63–76 (2017)
- 46.29 M.J. Brettle, J.F.P. Galvin: Back to basics: Radiosondes: Part 1—The instrument, *Weather* **58**, 336–341 (2003)
- 46.30 R.H. Bushnell, V.M. Glover, R.D. Chu: *Engineering Report on a Dropsonde for Measuring Vertical Wind Velocity in Thunderstorms*, NCAR Technical Note, Vol. NCAR/TN–83+EDD, 1973)
- 46.31 P.K. Govind: Dropwindsonde instrumentation for weather reconnaissance aircraft, *J. Appl. Meteorol.* **14**, 1512–1520 (1975)
- 46.32 T.F. Hock, J.L. Franklin: The NCAR GPS dropwindsonde, *Bull. Am. Meteorol. Soc.* **80**, 407–420 (1999)
- 46.33 R.W. Burpee, S.D. Aberson, J.L. Franklin, S.J. Lord, R.E. Tuleya: The impact of omega dropwindsondes on operational hurricane track forecast models, *Bull. Am. Meteorol. Soc.* **77**, 925–933 (1996)
- 46.34 V.F. Hess: Über Beobachtungen der durchdringenden Strahlung bei sieben Freiballonfahrten, *Phys. Z.* **13**, 1084–1091 (1912)
- 46.35 J. Winker: Scientific ballooning, past and present. In: *9th Aerodyn. Decelerator Balloon Technol. Conf., Albuquerque, NM, U.S.A.* (1986)
- 46.36 V.E. Lally, E.W. Lichfield: Summary of status and plans for the GHOST Balloon Project, *Bull. Am. Meteorol. Soc.* **50**, 867–875 (1969)
- 46.37 NCAR: *μ -Ghost* (National Center for Atmospheric Research, Boulder 1980), http://www.eol.ucar.edu/system/files/files/field_project/GHOST%20Balloon/u-GHOST_0.pdf, Accessed 20 July 2021
- 46.38 W.D. Komhyr: Electrochemical concentration cells for gas analysis, *Ann. Geophys.* **25**, 203–210 (1969)
- 46.39 G.M.B. Dobson, A.W. Brewer, B.M. Cwilong: Meteorology of the lower stratosphere, *Proc. R. Soc. London* **A185**, 144–175 (1946)
- 46.40 A.W. Brewer: Evidence for a world circulation provided by measurements of helium and water vapour distribution in the stratosphere, *Q.J.R. Meteorol. Soc.* **75**, 351–363 (1949)
- 46.41 H.J. Mastenbrook, J.E. Dinger: Distribution of water vapor in the stratosphere, *J. Geophys. Res.* **66**, 1437–1444 (1961)
- 46.42 H.J. Mastenbrook: *The Vertical Distribution of Water Vapor over Kwajalein Atoll, Marshall Islands*, Tech. Rep. NRL, Vol. 6367 (Naval Research Laboratory, Washington 1965)
- 46.43 H.J. Mastenbrook: *Water Vapor Observations at Low, Middle and High Latitudes During 1964 and 1965*, Tech. Rep. NRL, Vol. 6447 (Naval Research Laboratory, Washington 1966)
- 46.44 D.F. Hurst, S.J. Oltmans, H. Vömel, K.H. Rosenlof, S.M. Davis, E.A. Ray, E.G. Hall, A.F. Jordan: Stratospheric water vapor trends over Boulder, Colorado: Analysis of the 30 year Boulder record, *J. Geophys. Res.* **116**, D02306 (2011)
- 46.45 S. Solomon, K.H. Rosenlof, R.W. Portmann, J.S. Daniel, S.M. Davis, T.J. Sanford, G.–K. Plattner: Contributions of stratospheric water vapor to decadal changes in the rate of global warming, *Science* **327**, 1219–1223 (2010)
- 46.46 H. Vömel, S.J. Oltmans, F. Hasebe, M. Shiotani, M. Fujiwara, N. Nishi, M. Agama, J. Cornejo, F. Paredes, H. Enriquez: Balloon-borne observations of water vapor and ozone in the tropical upper troposphere and lower stratosphere, *J. Geophys. Res.* (2002)
- 46.47 H. Vömel, S.J. Oltmans, D.J. Hofmann, T. Deshler, J.M. Rosen: The evolution of the dehydration in the Antarctic stratospheric vortex, *J. Geophys. Res.* **100**, 13919–13926 (1995)
- 46.48 B. Ballot: *Suggestions on a Uniform System of Meteorological Observations* (Royal Dutch Meteorological Institute, Utrecht 1872)
- 46.49 A.L. Rotch: The international aeronautical congress at Berlin, *Mon. Weather Rev.* **30**, 356–362 (1902)
- 46.50 P.N. Edwards: *A Vast Machine. Computer Models, Climate Data, and the Politics of Global Warming* (MIT Press, Cambridge 2010)
- 46.51 GCOS (Global Climate Observing System): *Guide to the GCOS Surface Network (GSN) and GCOS Upper-Air Network (GUAN), Update of GCOS-73, GCOS-144 (WMO/TD No. 1558)* (World Meteorological Organization, Geneva 2010), https://library.wmo.int/doc_num.php?explnum_id=3855, Accessed 20 July 2021
- 46.52 P. Jeannot, C. Bower, B. Calpini: *Global Criteria for Tracing the Improvements of Radiosondes over the last Decades, WMO/TD–No. 1433, Instruments And Observing Methods Report No. 95* (World Meteorological Organization, Geneva 2008), https://library.wmo.int/doc_num.php?explnum_id=9383, Accessed 20 July 2021
- 46.53 J. Nash, T. Oakley, H. Vömel, L. Wei: *WMO Inter-comparison of High Quality Radiosonde Systems Yangjiang, China, 12 July–3 August 2010, Technical report, WMO/TD–No. 1580, Instruments and Observing Methods Report No. 107* (World Meteorological Organization, Geneva 2011), https://library.wmo.int/doc_num.php?explnum_id=9467, Accessed 20 July 2021
- 46.54 R. Philipona, C. Mears, M. Fujiwara, P. Jeannot, P. Thorne, G. Bodeker, L. Haimberger, M. Hervo, C. Popp, G. Romanens, W. Steinbrecht, R. Stübi, R. Van Malderen: Radiosondes show that after decades of cooling the lower stratosphere is now

- warming, *J. Geophys. Res. Atmos.* **123**, 12509–12522 (2018)
- 46.55 M. Fujiwara, J.S. Wright, G.L. Manney, L.J. Gray, J. Anstey, T. Birner, S. Davis, E.P. Gerber, V.L. Harvey, M.I. Hegglin, C.R. Homeyer, J.A. Knox, K. Krüger, A. Lambert, C.S. Long, P. Martineau, A. Molod, B.M. Monge-Sanz, M.L. Santee, S. Tegtmeier, S. Chabrilat, D.G.H. Tan, D.R. Jackson, S. Polavarapu, G.P. Compo, R. Dragani, W. Ebisuzaki, Y. Harada, C. Kobayashi, W. McCarty, K. Onogi, S. Pawson, A. Simmons, K. Wargan, J.S. Whitaker, C.-Z. Zou: Introduction to the SPARC Reanalysis Intercomparison Project (S-RIP) and overview of the reanalysis systems, *Atmos. Chem. Phys.* **17**, 1417–1452 (2017)
- 46.56 WMO: *Guide to Instruments and Methods of Observation, WMO-No.8, Volume I – Measurement of Meteorological Variables* (World Meteorological Organization, Geneva 2018)
- 46.57 GCOS (Global Climate Observing System): *The Global Observing System for Climate: Implementation Needs, GCOS-200* (Global Climate Observing System, Geneva 2016), https://library.wmo.int/doc_num.php?explnum_id=3417, Accessed 20 July 2021
- 46.58 I.S. Steinhart, R. Hart: Calibration curves for thermistors, *Deep-Sea Res. Oceanogr. Abstr.* **15**, 497–503 (1968)
- 46.59 K. Shimizu, F. Hasebe: Fast-response high-resolution temperature sonde aimed at contamination-free profile observations, *Atmos. Meas. Tech.* **3**, 1673–1681 (2010)
- 46.60 Vaisala: *Vaisala Radiosonde RS41 Measurement Performance, White paper* (Vaisala, Helsinki 2013), <https://www.vaisala.com/sites/default/files/documents/White%20paper%20RS41%20Performance%20B211356EN-A.pdf>, Accessed 20 July 2021
- 46.61 M.S. Van Dusen: Platinum-resistance thermometry at low temperatures, *J. Am. Chem. Soc.* **47**, 326–332 (1925)
- 46.62 R.J. Dirksen, M. Sommer, F.J. Immler, D.F. Hurst, R. Kivi, H. Vömel: Reference quality upper-air measurements: GRUAN data processing for the Vaisala RS92 radiosonde, *Atmos. Meas. Tech.* **7**, 4463–4490 (2014)
- 46.63 M.W. Hodge: Superadiabatic lapse rates of temperature in radiosonde observations, *Mon. Weather Rev.* **84**, 103–106 (1956)
- 46.64 W. Steinbrecht, H. Claude, F. Schönenborn, U. Leiterer, H. Dier, E. Lanzinger: Pressure and temperature differences between Vaisala RS80 and RS92 radiosonde systems, *J. Atmos. Ocean. Technol.* **25**, 909–927 (2008)
- 46.65 Y. Inai, M. Shiotani, M. Fujiwara, F. Hasebe, H. Vömel: Altitude misestimation caused by the Vaisala RS80 pressure bias and its impact on meteorological profiles, *Atmos. Meas. Technol.* **8**, 4043–4054 (2015)
- 46.66 R.M. Stauffer, G.A. Morris, A.M. Thompson, E. Joseph, G.J.R. Coetzee, N.R. Nalli: Propagation of radiosonde pressure sensor errors to ozonesonde measurements, *Atmos. Meas. Tech.* **7**, 65–79 (2014)
- 46.67 T. S. Suntola: Capacitive humidity transducer, US patent file 4164868 (1979)
- 46.68 H. Vömel, H. Selkirk, L. Miloshevich, J. Valverde, J. Valdés, E. Kyrö, R. Kivi, W. Stolz, G. Peng, J.A. Diaz: Radiation dry bias of the Vaisala RS92 humidity sensor, *J. Atmos. Ocean. Technol.* **24**, 953–963 (2007)
- 46.69 H. Vömel: Saturation vapor pressure formulations, <http://cires.colorado.edu/~voemel/vp.html> (2016), Accessed 20 July 2021
- 46.70 A. Wexler: Vapor pressure formulation for water in range 0 to 100 °C. A revision, *J. Res. Natl. Bur. Stand.* **80A**, 775–785 (1976)
- 46.71 R.W. Hyland, A. Wexler: Formulations for the thermodynamic properties of the saturated phases of H₂O from 173.15 K to 473.15 K, *ASHRAE Trans.* **89**(2A), 500–519 (1983)
- 46.72 D. Sonntag: Advancements in the field of hygrometry, *Meteorol. Z.* **3**, 51–66 (1994)
- 46.73 B.J. Sherry: The rate of ascent of pilot balloons, *Mon. Weather Rev.* **48**, 692–694 (1920)
- 46.74 J. Bian, H. Chen, H. Vömel, Y. Duan, Y. Xuan, D. Lu: Intercomparison of humidity and temperature sensors: GTS1, Vaisala RS80 and CFH, *Adv. Atmos. Sci.* **28**(1), 139–146 (2011)
- 46.75 M.P. Jensen, D.J. Holdridge, P. Survo, R. Lehtinen, S. Baxter, T. Toto, K.L. Johnson: Comparison of Vaisala radiosondes RS41 and RS92 at the ARM Southern Great Plains site, *Atmos. Meas. Tech.* **9**, 3115–3129 (2016)
- 46.76 Y. Kawai, M. Katsumata, K. Oshima, M.E. Hori, J. Inoue: Comparison of Vaisala radiosondes RS41 and RS92 launched over the oceans from the Arctic to the tropics, *Atmos. Meas. Tech.* **10**, 2485–2498 (2017)
- 46.77 V. V. Petrov: On the work of the aerological network of the Russian Federation 2017, <http://caoncr.mipt.ru/monitor/stuff/upperair/upperair-rf2017.pdf> (2018), Accessed 20 July 2021, in Russian
- 46.78 M.E. Tschudin, S.R. Schroeder: Time constant estimates for radiosonde temperature sensors, *J. Atmos. Ocean. Technol.* **30**, 40–56 (2013)
- 46.79 J.K. Luers, R.E. Eskridge: Temperature corrections for the VIZ and Vaisala radiosondes, *J. Appl. Meteorol.* **34**, 1241–1253 (1995)
- 46.80 A. Wieser: KITsonde – A new modular multi-sensor dropsonde system for high-resolution measurements, <https://www.imk-tro.kit.edu/english/5370.php> (2014), Accessed 20 July 2021
- 46.81 Meisei: MDSS: Dropsonde Receiving System, <https://www.meisei.co.jp/english/products/meteorology/upper-air/p849> (2018), Accessed 20 July 2021
- 46.82 Modem: Dropsonde, <http://www.meteomodem.com/dropsonde.html> (2018), Accessed 20 July 2021
- 46.83 P. Black, L. Harrison, M. Beaubien, R. Bluth, R. Woods, A. Penny, R.W. Smith, J.D. Doyle: High-Definition Sounding System (HDSS) for atmospheric profiling, *J. Atmos. Ocean. Technol.* **34**, 777–796 (2017)

- 46.84 V.E. Lally, R. Leviton: Accuracy of wind determination from the track of a falling object, *Airf. Surv. Geophys. Rep.* **93**, AFRC-TN-58-213 (1958)
- 46.85 S.A.P. de Jong, J.D. Slingerland, N.C. van de Giesen: Fiber optic distributed temperature sensing for the determination of air temperature, *Atmos. Meas. Tech.* **8**, 335–339 (2015)
- 46.86 B.B. Balsley, M.L. Jensen, R.G. Frehlich: The use of state-of-the-Art kites for profiling the lower atmosphere, *Bound.-Layer Meteorol.* **87**, 1 (1998)
- 46.87 G.E. Bodeker, S. Bojinski, D. Cimini, R.J. Dirksen, M. Haefelin, J.W. Hannigan, D.F. Hurst, T. Leblanc, F. Madonna, M. Maturilli, A.C. Mikalsen, R. Philipona, T. Reale, D.J. Seidel, D.G.H. Tan, P.W. Thorne, H. Vömel, J. Wang: Reference upper-air observations for climate: From concept to reality, *Bull. Am. Meteorol. Soc.* **97**, 123–135 (2016)
- 46.88 J. Wang, J. Bian, W.O. Brown, H. Cole, V. Grubišić, K. Young: Vertical air motion from T-REX radiosonde and dropsonde data, *J. Atmos. Ocean. Technol.* **26**, 928–942 (2009)
- 46.89 A. Gallice, F.G. Wienhold, C.R. Hoyle, F. Immeler, T. Peter: Modeling the ascent of sounding balloons: derivation of the vertical air motion, *Atmos. Meas. Tech.* **4**, 2235–2253 (2011)
- 46.90 M.J.R. Loadman: The glass transition temperature of natural rubber, *J. Therm. Anal.* **30**, 929–941 (1985)
- 46.91 F. Hasebe, S. Aoki, S. Morimoto, Y. Inai, T. Nakazawa, S. Sugawara, C. Ikeda, H. Honda, H. Yamazaki, Halimurrahman, N. Komala, F.A. Putri, A. Budiyo, M. Soedjarwo, S. Ishidoya, S. Toyoda, T. Shibata, M. Hayashi, N. Eguchi, N. Nishi, M. Fujiwara, S.-Y. Ogino, M. Shiotani, T. Sugidachi: Coordinated upper-troposphere-to-stratosphere balloon experiment in Biak, *Bull. Am. Meteorol. Soc.* **99**, 1213–1230 (2018)
- 46.92 B. Ingleby, P. Pauley, A. Kats, J. Ator, D. Keyser, A. Doerenbecher, E. Fucile, J. Hasegawa, E. Toyoda, T. Kleinert, W. Qu, J. St. James, W. Tennant, R. Weedon: Progress toward high-resolution, real-time radiosonde reports, *Bull. Am. Meteorol. Soc.* **97**, 2149–2161 (2016)
- 46.93 WMO: *Manual on Codes – International Codes, Volume I.1, Annex II to the WMO Technical Regulations: Part A – Alphanumeric Codes, WMO-No.306, 2011 Edition updated in 2019* (World Meteorological Organization, Geneva 2019)
- 46.94 WMO: *B/C25 – Regulations for reporting TEMP, TEMP SHIP and TEMP MOBIL data in TDCF; in Manual on Codes, International Codes, Volume I.2, Annex II to the WMO Technical Regulations, Part B – Binary Codes, Part C – Common Features to Binary and Alphanumeric Codes* (World Meteorological Organization, Geneva 2021)
- 46.95 WMO: *B/C26 – Regulations for reporting TEMP DROP data in TDCF; in Manual on Codes, International Codes, Volume I.2, Annex II to the WMO Technical Regulations, Part B – Binary Codes, Part C – Common Features to Binary and Alphanumeric Codes* (World Meteorological Organization, Geneva, 2021)
- 46.96 ECMWF: *ecCodes Home*, <https://confluence.ecmwf.int/display/ECC/ecCodes%2bHome> (2018), Accessed 22 July 2021
- 46.97 A.B.O. Jensen and L. Ruotsalainen: Challenges for positioning and navigation in the Arctic, United Nations/Russian Federation Workshop on the Applications of Global Navigation Satellite Systems, Krasnoyarsk, Russian Federation, 18–22 May 2015, <http://www.unoosa.org/documents/pdf/psa/activities/2015/RussiaGNSS/Presentations/52.pdf>, Accessed 20 July 2021
- 46.98 B. Ingleby: *An Assessment of Different Radiosonde types 2015/2016*, ECMWF Technical Memorandum, Vol. 807 (European Centre for Medium Range Weather Forecasts, Reading 2017)
- 46.99 WMO: *General Meteorological Standards and Recommended Practices, Basic Documents No. 2, WMO – No. 49*, Technical Regulations, Vol. I, 1988th edn. (World Meteorological Organization, Geneva 1988), https://library.wmo.int/?lvl=notice_display&id=14073#.YPaMcExCS70, Accessed 20 July 2021
- 46.100 D.J. Gaffen: Temporal inhomogeneities in radiosonde temperature records, *J. Geophys. Res.* **99**, 3667–3676 (1994)
- 46.101 B.D. Santer, P.W. Thorne, L. Haimberger, K.E. Taylor, T.M.L. Wigley, J.R. Lanzante, S. Solomon, M. Free, P.J. Gleckler, P.D. Jones, T.R. Karl, S.A. Klein, C. Mears, D. Nychka, G.A. Schmidt, S.C. Sherwood, F.J. Wentz: Consistency of modeled and observed temperature trends in the tropical troposphere, *Int. J. Climatol.* **28**, 1703–1722 (2008)
- 46.102 D.J. Seidel, F.H. Berger, H.J. Diamond, J. Dykema, D. Goodrich, F. Immeler, W. Murray, T. Peterson, D. Sisterson, M. Sommer, P. Thorne, H. Vömel, J. Wang: Reference upper-air observations for climate: rationale, progress, and plans, *Bull. Am. Meteorol. Soc.* **90**, 361–369 (2009)
- 46.103 R. Krockauer: Weather observations, *Seaways*, December 2009, 22–23 (2009)
- 46.104 J. Wendell and A. Jordan: *iMet-1-RSB Radiosonde XDATA Protocol & Daisy Chaining*, <https://gml.noaa.gov/aftp/user/jordan/iMet-1-RSB%20Radiosonde%20XDATA%20Daisy%20Chaining.pdf> (2016), Accessed 22 July 2021
- 46.105 A. Thompson, H. Smit, J. Witte, R. Stauffer, B. Johnson, G. Morris, P. von der Gathen, R. Van Malderen, J. Davies, A. PETERS, M. Allaart, F. Posny, R. Kivi, P. Cullis, N. Hoang Anh, E. Corrales, T. Machinini, F. da Silva, G. Paiman, K. Thiong'o, Z. Zainal, G. Brothers, K. Wolff, T. Nakano, R. Stübi, G. Romanens, G. Coetzee, J. Diaz, S. Mitro, M. Mohamad, S. Ogino: Ozone-sonde quality assurance: The JOSIE-SHADOZ (2017) experience, *Bull. Am. Meteorol. Soc.* **100**, 155–171 (2018)
- 46.106 H. Vömel, D.E. David, K. Smith: Accuracy of tropospheric and stratospheric water vapor measurements by the cryogenic frost point hygrometer: Instrumental details and observations, *J. Geophys. Res.* **112**, D08305 (2007)

- 46.107 E.G. Hall, A.F. Jordan, D.F. Hurst, S.J. Oltmans, H. Vömel, B. Küuehneich, V. Ebert: Advancements, measurement uncertainties, and recent comparisons of the NOAA frostpoint hygrometer, *Atmos. Meas. Tech.* **9**, 4295–4310 (2016)
- 46.108 H. Vömel, V. Yushkov, S. Khaykin, L. Korshunov, E. Kyrö, R. Kivi: Intercomparisons of stratospheric water vapor sensors: FLASH-B and NOAA/CMDL frost-point hygrometer, *J. Atmos. Ocean. Technol.* **24**, 941–952 (2007)
- 46.109 H. Vömel, T. Naebert, R. Dirksen, M. Sommer: An update on the uncertainties of water vapor measurements using cryogenic frost point hygrometers, *Atmos. Meas. Tech.* **9**, 3755–3768 (2016)
- 46.110 J.-B. Renard, F. Dulac, G. Berthet, G. Lurton, D. Vignelles, F. Jégou, T. Tonnelier, M. Jeannot, B. Couté, R. Akiki, N. Verdier, M. Mallet, F. Gensdarmes, P. Charpentier, S. Mesmin, V. Duverger, J.-C. Dupont, T. Elias, V. Crenn, J. Sciare, P. Zieger, M. Salter, M. Roberts, J. Giacomoni, M. Gobbi, E. Hamonou, H. Olafsson, P. Dagsson-Waldhauserova, C. Camy-Peyret, C. Mazel, T. Décamps, M. Piringer, J. Surcin, D. Daugeron: LOAC: a small aerosol optical counter/sizer for ground-based and balloon measurements of the size distribution and nature of atmospheric particles – Part 1: Principle of measurements and instrument evaluation, *Atmos. Meas. Tech.* **9**, 1721–1742 (2016)
- 46.111 M. Fujiwara, T. Sugidachi, T. Arai, K. Shimizu, M. Hayashi, Y. Noma, H. Kawagita, K. Sagara, T. Nakagawa, S. Okumura, Y. Inai, T. Shibata, S. Iwasaki, A. Shimizu: Development of a cloud particle sensor for radiosonde sounding, *Atmos. Meas. Tech.* **9**, 5911–5931 (2016)
- 46.112 G.A. Morris, W.D. Komhyr, J. Hirokawa, J. Flynn, B. Lefer, N. Krotkov, F. Ngan: A balloon sounding technique for measuring SO₂ plumes, *J. Atmos. Ocean. Technol.* **27**, 1318–1330 (2010)
- 46.113 M. Brabec, F.G. Wienhold, B.P. Luo, H. Vömel, F. Immler, P. Steiner, E. Hausammann, U. Weers, T. Peter: Particle backscatter and relative humidity measured across cirrus clouds and comparison with microphysical cirrus modelling, *Atmos. Chem. Phys.* **12**, 9135–9148 (2012)
- 46.114 D. Serke, E. Hall, J. Bognar, A. Jordan, S. Abdo, K. Baker, T. Seitel, M. Nelson, R. Ware, F. McDonough, P. Marcia: Supercooled liquid water content profiling case studies with a new vibrating wire sonde compared to a ground-based microwave radiometer, *Atmos. Res.* **149**, 77–87 (2014)
- 46.115 A. Engel, T. Mobius, H. Bonisch, U. Schmidt, R. Heinz, I. Levin, E. Atlas, S. Aoki, T. Nakazawa, S. Sugawara, F. Moore, D. Hurst, J. Elkins, S. Schaufli, A. Andrews, K. Boering: Age of stratospheric air unchanged within uncertainties over the past 30 years, *Nat. Geosci.* **2**, 28–31 (2009)
- 46.116 A. Karion, C. Sweeney, P. Tans, T. Newberger: AirCore: An innovative atmospheric sampling system, *J. Atmos. Ocean. Technol.* **27**, 1839–1853 (2010)
- 46.117 Y. Sato and L. P. Riishojgaard (eds.): Sixth WMO Workshop on the Impact of Various Observing Systems on Numerical Weather Prediction, Shanghai, China, 10–13 May 2016, <https://www.cgms-info.org/Agendas/GetWpFile.ashx?wid=f4f2a3bc-aa1f-4d72-a16b-7a2e7ec97b28&aid=35b3024d-2a25-43d9-bd83-318b4c7a6a6e> (2016), Accessed 21 July 2021
- 46.118 A. Kräuchi, R. Philipona: Return glider radiosonde for in situ upper-air research measurements, *Atmos. Meas. Tech.* **9**, 2535–2544 (2016)
- 46.119 F. Rabier, A. Bouchard, E. Brun, A. Doerenbecher, S. Guedj, V. Guidard, F. Karbou, V. Peuch, L. El Amraoui, D. Puech, C. Genthon, G. Picard, M. Town, A. Hertzog, F. Vial, P. Cocquerez, S.A. Cohn, T. Hock, J. Fox, H. Cole, D. Parsons, J. Powers, K. Romberg, J. VanAndel, T. Deshler, J. Mercer, J.S. Haase, L. Avallone, L. Kalnajs, C.R. Mechoso, A. Tangborn, A. Pellegrini, Y. Frenot, J. Thépaut, A. McNally, G. Balsamo, P. Steinle: The Cordias Project in Antarctica, *Bull. Am. Meteorol. Soc.* **91**, 69–86 (2010)

Holger Vömel

Earth Observing Laboratory
National Center for Atmospheric Research
Boulder, USA
voemel@ucar.edu



Holger Vömel is a scientist at the National Center for Atmospheric Research at Boulder, CO, USA. He graduated in Physics from the University Heidelberg, Germany in 1990 and received a PhD in Chemical Physics from the University of Colorado at Boulder in 1996. His research interests focus around high-quality observations of atmospheric parameters such as water vapor, ozone, temperature, pressure, and winds, to provide reliable data for studies of climate change and atmospheric processes.

Masatomo Fujiwara

Faculty of Environmental Earth Science
Hokkaido University
Sapporo, Japan
fuji@ees.hokudai.ac.jp



Masatomo Fujiwara is Associate Professor of the Faculty of Environmental Earth Science at Hokkaido University in Japan. He received a PhD in Science in 1999. His research interests include atmospheric dynamical and chemical processes in the upper troposphere and lower stratosphere and upper-air climate observations, based on balloon measurements, development of balloon-borne instruments, and data analysis and evaluation of global atmospheric reanalysis data sets.

47. Composite Atmospheric Profiling

Christoph Kottmeier , Bianca Adler , Norbert Kalthoff , Ulrich Löhnert , Ulrich Górsdorf

Each observation system that vertically profiles one or several atmospheric parameters by performing in-situ or remote-sensing measurements has its own distinct characteristics in terms of vertical range and resolution, temporal resolution, and height-dependent error. Combining several profiling instruments of the same type or different types—known as composite atmospheric profiling—bypasses the limitations of using those instruments separately, allowing additional information on the state of the atmosphere to be retrieved, thus enhancing the retrieval accuracy and the temporal and/or spatial resolution of atmospheric parameters. New quantities with added value can also be obtained using this approach. In this chapter, the state of the art in composite vertical atmospheric profiling is discussed. It is described how multiple systems that measure different parameters and have different height ranges as well as vertical, temporal, and spatial resolutions can be optimally combined. Some examples from recent research are presented to demonstrate the successful implementation of composite profiling techniques.

47.1	The Relevance of Composite Atmospheric Measurements	1282
47.2	History	1285
47.3	Theory	1287
47.3.1	Example of the Application of Composite Atmospheric Profiling to Extend the Measurement Range and Increase Spatial Resolution: The Dual-Doppler Technique	1287
47.3.2	Example of the Derivation of Compound Quantities: Sensible and Latent Heat Fluxes	1288
47.3.3	Example of the Application of Composite Atmospheric Profiling to Increase Spatial and Temporal Resolution: Humidity Profiles	1289
47.3.4	Example of the Derivation of Compound Quantities: Cloud Properties and Hydrometeor Classification	1290
47.4	Observation Platforms	1291
47.4.1	Mobile Platforms	1291
47.4.2	Permanent Platforms	1293
47.5	Specifications	1294
47.6	Quality Control	1294
47.7	Maintenance	1295
47.8	Applications	1295
47.8.1	Dual-Doppler Lidar Measurements: The Virtual Tower Technique	1295
47.8.2	Dual-Doppler Lidar Measurements: Coplanar Scans	1295
47.8.3	Latent Heat Flux Profiles	1296
47.8.4	Increasing the Vertical and Temporal Resolution of Humidity Profiles	1297
47.8.5	Humidity Profiles from Active and Passive Remote Sensing	1297
47.8.6	Target Classification with Cloudnet	1299
47.9	Future Developments	1299
47.10	Further Reading	1299
	References	1300

Composite atmospheric profiling is the practice of combining instruments and techniques in a manner that yields enhanced vertical and temporal resolution, vertical range, accuracy, and information content compared to those provided by any of the instruments individually. It can be considered an offshoot of three-dimensional composite observation that focuses on mea-

surements in the vertical direction, where changes are typically largest. Such composite information is needed to:

- Understand vertically coupled atmospheric processes at scales ranging from the microscale to the mesoscale

- Drive and validate numerical models of such processes
- Validate data from satellites
- Assimilate data into weather prediction models at high resolution
- Retrieve statistical information (e.g., relating to renewable energies)
- Monitor the climate.

The instruments that are combined in composite atmospheric profiling can be of the same type or different types. Some lidar and radar systems have scanning capabilities, meaning that they can retrieve data from various directions, not just the vertical, potentially providing quasi-hemispherical coverage. Such coverage is provided by a variety of integrated observation platforms and networks around the world, including the KITcube [47.1] and atmospheric radiation measurement (ARM) mobile facilities [47.2] as well as LACROS [47.3]. Fixed platforms or networks that possess this ability include the Richard Aßmann Observatory (MOL-RAO) in Lindenberg, Germany [47.4], the CESAR observatory in Cabauw, Netherlands [47.5], the JOYCE observatory in Jülich, Germany [47.6], and the CNR-IMAA observatory in Potenza, Italy [47.7]. Fixed stations are often operated by national weather services, and different systems are often combined in order to improve weather forecasts and enhance climatological studies [47.8]. The mobile systems mentioned above have been utilized in various international field campaigns to provide comprehensive high-resolution data for limited time periods, facilitating process studies and model evaluation; for instance, the ARM mobile facility was used in African Monsoon Multidisciplinary Analysis (AMMA) [47.9] and Convective and Orographically-induced Precipitation Study (COPS) [47.10, 11], the KITcube was used during the Hydrological Cycle of the Mediterranean (HYMEX) campaign [47.12], and the KITcube and LACROS were

operated in the HD(CP)² Observational Prototype Experiment (HOPE) [47.13].

The objectives of composite atmospheric profiling are to:

- Extend the measurement range and/or temporal resolution compared to those achieved with individual instruments
- Enhance temporal and/or spatial resolution in the horizontal and vertical directions
- Obtain parameters that cannot be accessed with a single instrument.

For the first objective, the profiles provided by different instruments are either simply concatenated and analyzed in parallel without performing any calculations [47.14], or they are merged via interpolation/extrapolation or variational analysis in overlapping regions, taking into account error characteristics (e.g., by integrating microwave radiometer (MWR) measurements with water-vapor lidar data [47.7, 15] or combining in-situ and remote sensing systems to retrieve wind and temperature profiles [47.16]). The second objective can be achieved by combining systems of the same type (e.g., by applying the virtual tower method [47.17, 18] or the coplanar scan technique [47.19] to Doppler lidars), combining instruments that perform measurements under different atmospheric conditions (e.g., a Doppler lidar that provides wind information in cloud-free regions and a cloud radar that yields data on wind in clouds [47.20]), or combining different types of systems that have different resolutions or spatial coverages (e.g., water vapor data from radiosondes and information from a global navigation satellite system, GNSS [47.21]). The third objective involves the use of complementary variables to retrieve added-value quantities such as convection indices, turbulent fluxes, or micro- and macrophysical cloud properties (as performed by Cloudnet [47.22], for example).

47.1 The Relevance of Composite Atmospheric Measurements

Composite atmospheric profiling is required when no single instrument or observation system can probe all of the parameters needed to fully characterize the state of the atmosphere. This is important when attempting to study complex process interactions or to initialize models. Any physical measurement principle (whether based on mechanical, acoustic, or thermodynamic variations, changes in electrical conductivity or capacity, or on radiation emission, absorption, or scattering; see Chap. 1) can only be used to investigate particular properties, and those properties can only be studied under specific at-

mospheric conditions or in certain regions in which the physical measurement process is effective. For example, an aerosol Doppler lidar requires backscatter caused by the presence of small particles (e.g., aerosols and ice crystals), so it is only rarely able to provide any information on the free atmosphere where the aerosol content is low. Depending on the purpose for which measurements are made, quite different instruments can be applied. For example, the wind measurements that are needed to assess the wind energy potential at a particular site differ considerably from the wind measurements that are

required to calculate turbulent fluxes in micrometeorology. Instruments are therefore designed by the manufacturer to achieve a specific sensitivity, resolution, and range, and to be used in particular operating conditions. In addition, the platform on which the instrument is installed (e.g., the ground, a mast, a tower, a balloon, an aircraft, or a satellite) imposes certain geometric constraints on the height range that can be accessed, and operational issues (e.g., frequency of radiosoundings, orbital period, and the observation geometry of the satellite) limit the temporal resolution.

In this chapter, we discuss composite atmospheric profiling by in-situ sensing and ground-based remote sensing. Ground-based remote sensing offers many possibilities for combining data from different instruments to obtain more accurate or additional information, and overviews of this topic are also provided in [47.8, 23]. Composite vertical profiling from satellites is not treated in this chapter, although height-resolved satellite data may usefully complement in-situ- and ground based vertical profiling. The spatial and temporal resolution, the satellite orbit characteristics and the instrument viewing angles strongly differ between satellite sensors, and optimum merging of data normally needs data assimilation within a full four-dimensional model.

This section gives an overview of common instrument combinations. In one type of combination, the measurement range is extended and/or the temporal resolution of temperature, humidity, and wind measurements is increased (Fig. 47.1a–c). Table 47.1 summarizes the strengths and weaknesses of important instrument types in terms of vertical resolution, temporal resolution, coverage of the free atmosphere, spatial coverage, and performance in the presence of clouds. The limited vertical range of tower-based instruments (Chap. 6) can, for example, be extended by combining them with remote-sensing instruments such as lidars (Chaps. 26, 27) or radar wind profilers (Chap. 31). Research aircraft (Chap. 48), radiosondes (Chap. 46), and certain unmanned aircraft systems (UASs; Chap. 49) can provide

temperature, humidity, and wind profiles throughout the troposphere. However, these profiles are not continuous; they are snapshots of the state of the atmosphere. All of the instrument types considered in the table have particular advantages and disadvantages (see the relevant chapters in Parts C–E of this Handbook for details). For example, while lidars cannot obtain measurements from optically thick clouds, while aerosol lidars cannot obtain measurements inside clouds, cloud radars provide information on the vertical cloud structure inside optically thick clouds. Using Doppler lidar and cloud radar, also combined wind profiling below and inside clouds is possible, the vertical resolution of a profile retrieved using a microwave radiometer (Chap. 29) or an infrared spectrometer (Chap. 28) is rather coarse and not suitable for resolving sharp gradients, but the temporal resolution of the profile data is quite high. Raman lidars (Chap. 25) generally perform better at night than during the day. Even high towers (up to 300 m high) can only measure the wind vector, temperature, and humidity in the lowest few hundred meters of the atmospheric boundary layer (ABL). To cover the whole ABL (which is typically ≈ 1 km thick), it is necessary to use a Doppler lidar (Chap. 27), Raman lidar, or differential absorption lidar (DIAL, Chap. 26). Sodar (Chap. 23) and radar wind profilers (Chap. 31) can probe winds at heights of up to about several hundred meters and several kilometers, respectively. Adding a radio acoustic sounding system (RASS) to a sodar or radar wind profiler allows temperature variances to be obtained along with wind variances.

It has been demonstrated that combining passive with active remote sensing [47.15] and in-situ with remote sensing [47.16] leads to improved profiling. For instance, integrating GNSS with radiosonde measurements increased the spatial resolution of the retrieved humidity information compared to the corresponding information obtained from a single instrument [47.21]. Combining microwave radiometer data with radiosonde data yields temperature and humidity data with increased vertical and temporal resolution [47.24, 25].

Table 47.1 Strengths and weaknesses of selected instruments in terms of vertical resolution, temporal availability (i.e., the temporal resolution for remote-sensing instruments and towers, and the time interval between individual soundings or profile flights for radiosondes, UAS, and aircraft), free atmosphere coverage, spatial coverage, and performance in the presence of clouds

Parameter	Tower	Lidar/ DIAL	Microwave radiometer	Infrared spectrometer	Radar wind profiler/RASS	Sodar/ RASS	Cloud radar	Radio- sonde	UAS	Aircraft
Vertical resolution	–	+	–	–	+	+	+	+	+	+
Temporal availability	+	+	+	+	+	+	+	–	–	–
Free atmosphere coverage	–	–	+	+	+	–	+	+	–	+
Spatial coverage	–	–	–	–	–	–	–	–	+	+
Clouds	+	–	+	–	+	+	+	+	–	+

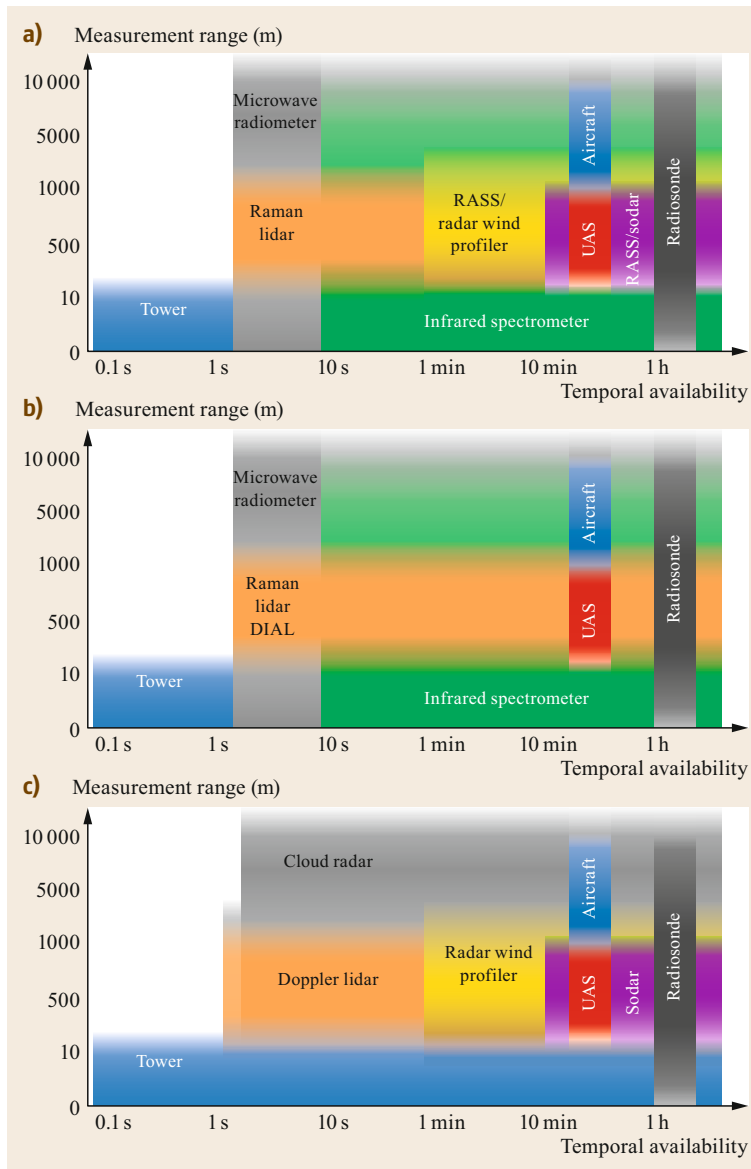


Fig. 47.1a–c Typical temporal availabilities and height ranges of common instruments that are used to measure temperature (a), humidity (b), and wind (c). For remote-sensing instruments and towers, the left margin of the colored section indicates the minimum time interval between profiles (i.e., minimum integration time) under very good measurement conditions, although the sampling rate may be considerably higher than the temporal resolution. For UAS, aircraft, and radiosondes, the temporal availability indicates the typical time interval between soundings or profile flights (diagrams © B. Adler)

Another type of instrument combination permits the retrieval of quantities that cannot be measured with a single instrument. Examples of these *added-value* or *compound* quantities and the instrument combinations that can access them are given in Table 47.2. For instance, flux profiles can be derived by combining Doppler lidar with Raman lidar or DIAL [47.26]. The ABL height is often obtained from a lidar or radiosonde profile, but the applicability of each method strongly depends on the atmospheric conditions present [47.27]. As radiosondes measure temperature, humidity, and wind at the same time, convection indices can be estimated from radiosonde profiles [47.28]. Micro- and

macrophysical cloud properties can be determined by combining active and passive remote-sensing data with in-situ information [47.22, 29].

The site requirements for composite measurements are similar to those for the individual instruments themselves. To achieve a spatial overlap or to perform dual observations (such as dual-Doppler lidar or dual-Doppler radar), the scanned volumes must be free of obstacles. It has been shown, however, that adequate site conditions can be found even in urban environments (Sect. 47.8.1) and large valleys [47.25].

Methods that can merge datasets from different instruments in order to derive the best estimate for the

Table 47.2 Selected added-value quantities and instrument combinations that are used to probe them

Added-value quantity	Instrument combination
Sensible and latent heat flux profiles	Doppler lidar and Raman lidar or DIAL [47.26]
ABL height	Doppler lidar and radiosondes [47.27]
Convection indices (e.g., convectively available potential energy (CAPE), konvektiv-index (KO), lifted index (LI), bulk Richardson number	Radiosondes with temperature, humidity, and wind measurements [47.28]
Vertical cloud structure characteristics (microphysics, turbulence, precipitation fluxes)	Cloud radar, ceilometer, microwave radiometer, Doppler lidar, radiosondes [47.22, 29]
Humidity profile	Raman lidar and microwave radiometer [47.30, 31] Microwave radiometer and radar wind profiler [47.32]
Bulk cloud properties	liquid water path (LWP) from microwave radiometer and infrared (IR) measurements [47.33, 34] Cloud radar and microwave radiometer for cloud liquid water content (LWC) profile retrieval [47.35]
Temperature profile, humidity profile, and bulk cloud properties	Microwave radiometer, infrared spectrometer, and ceilometer [47.36, 37] Microwave radiometer, cloud radar, and ceilometer [47.38]

state of the atmosphere at a site (the site atmospheric state best estimate, SASBE) are available. Such methods allow the spatial and temporal resolution of the measurements to be enhanced [47.14, 39, 40] or can be used to generate a data product that best meets the research needs of specific data users [47.41].

Water-vapor profile retrievals can be improved by combining wind profiler and microwave radiometer measurements [47.32] or by combining Raman lidar with microwave radiometer measurements. A physically consistent method of enhancing the retrieval of low-LWP clouds by combining an infrared spectrometer with a microwave radiometer was introduced in [47.33], whereas a similar method that utilized a robust neural network approach, a two-channel broadband IR radiometer, and a microwave radiometer is reported in [47.34]. Radiative closure studies highlight the advantages of com-

posite measurements. Also, active remote-sensing measurements of liquid clouds obtained with a cloud radar can be constrained by the column-integrated liquid water path retrieval from a microwave radiometer to achieve improved estimates of the cloud liquid water content (LWC) in non-drizzling clouds [47.35]. A microwave radiometer, an infrared spectrometer atmospheric emitted radiance interferometer (AERI instrument [47.42]), and a ceilometer [47.36] represent a very powerful combination for simultaneously retrieving temperature, humidity, and bulk cloud properties (optical depth, effective radius) in a physically consistent manner. Finally, the spatial coverage and temporal resolution of wind information can be enhanced by combining multiple Doppler lidars (e.g., by applying the virtual tower technique [47.17, 18] or performing coplanar scans [47.19]) or by combining Doppler winds from a lidar and a cloud radar [47.20].

47.2 History

The history of composite atmospheric profiling can be traced back to the early Age of Enlightenment at the end of the eighteenth century, when much innovative research on natural phenomena and processes was initiated. New measurement techniques were invented and applied in research during subsequent decades.

The desire to perform observations from altitudes above buildings or mountains expressed by scientists in the eighteenth century. Although a kite experiment was carried out in 1749 to study lightning and electricity [47.43], measurements of the atmosphere at high altitudes necessitated a form of transportation that could carry instruments up to the altitude of interest and return those instruments safely back to earth for data recovery. The first air transportation of this kind to be invented

was the tethered balloon. The same year, 1783, saw the invention of both the manned gas-filled balloon, by *Jacques Alexandre César Charles* (1746–1823), and the manned hot-air balloon, by two brothers: *Joseph-Michel Montgolfier* (1740–1810) and *Jacques-Étienne Montgolfier* (1745–1799) [47.44]. Thus, starting in the late eighteenth century, instruments that had already been used to perform measurements on the ground were taken aloft by balloons to obtain measurements and the first vertical profiles up to high altitudes.

By the end of the nineteenth century, there was a need for greater knowledge of the ABL, given the increasing popularity of aviation. Driven by this need, *Hugo Emil Hergesell* (1859–1938), *Richard Aßmann* (1845–1918), and *Wladimir Köppen* (1846–1940) performed

various observations in the ABL as well as the free atmosphere above the ABL, and are therefore regarded as the founders of aerology. Aerological measurements (Chap. 46) of more than one variable can be considered an early example of composite vertical profiling.

The advent of gliders [47.45] and motorized aircraft [47.46] in the early twentieth century allowed heavier instrumentation to be carried, including sensors of properties other than the classical parameters of temperature, humidity, and pressure. A multitude of other instruments that measured, for instance, the electric field strength, radiation flux, cloud liquid water, aerosols, ice particles, turbulence, and icing conditions at high altitudes or that performed visual photography were tested and applied for research purposes [47.47, 48].

Over the last 70 years there has been—and there continues to be—rapid development in the instrumentation used for ground-based remote sensing in the visible, infrared, and microwave bands. The physical base of interaction of electromagnetic waves with atmospheric matter (gases and particles), such as the Rayleigh and Mie scattering theories developed in the late 19th and early 20th century, or the description of the dielectric properties of liquid phase water molecules in 1929 [47.49] has been laid already decades before. But only the development of detectors for very low level amplitude signals, e.g., the microwave radiometer invented and described in 1947 [47.50], and various theoretical improvements regarding absorption spectra, in particular line shape models, temperature and humidity weighting functions at different frequencies, as well as calibration methods, allowed for this progress.

Recent decades have seen major progress, particularly in radar and lidar technology for atmospheric remote sensing. The remote sensing of macro- and microphysical cloud properties and associated processes has been possible since the mid-1990s [47.51]. The first combination of a microwave radiometer with wind profiler auxiliary sensors for humidity profiling was also reported [47.52].

Early examples of composite techniques included sodar/RASS and radar wind profiler/RASS techniques for coincident measurements of horizontal wind and temperature. An overview of the wealth of sensors available for combination is given in Parts B and C of this Handbook, while a comprehensive account of the synergetic use of sensors is provided in [47.8].

A new era in vertical composite atmospheric profiling began in the mid-twentieth century with the arrival of satellite-based remote sensing (see Chap. 37). While it has some similarities to surface-based remote sensing in terms of its physical basis (radiative transfer calculations, absorption and scattering by gases and aerosols, and detector and calibration requirements), satellites represent a completely new source of regular global



Fig. 47.2 Obtaining integrated vertical profiles with a 45 m high mast and a kite-mounted tethered sonde at the German Antarctic Neumayer Station in 1983 (after [47.55] photo © Ch. Kottmeier)

observations of the atmosphere. The system of geostationary satellites and polar orbiters has become the backbone of data acquisition for weather prediction. Cloud coverage and surface conditions as well as the gas-phase composition of the upper atmosphere can be observed at unprecedented detail from satellites. However, the horizontal and vertical resolution of measurements by satellites remains quite limited, meaning that such data will tend to be used in conjunction with complementary data from other systems, although the latest generation of Meteosat satellites provide rapid-scan information every 15 min. Some satellite series such as the afternoon train (A-Train) constellation [47.53] are designed to acquire synergetic information to improve cloud surveys, for example. Specifically, there have been many studies of clouds and their radiative effects based on composite atmospheric profiling using data from the A-Train satellites CloudSat (cloud radar) and CALIPSO (backscatter lidar) [47.54].

Several historical developments are still relevant to operational weather services and climate monitoring, as well as for specific research purposes.

High instrumented masts have been operated for decades. The Boulder Atmospheric Observatory (BAO) [47.56] was the first research facility to study the plan-

etary boundary layer and to test and calibrate atmospheric sensors. This facility includes a 300 m tower instrumented with fast- and slow-response sensors, a variety of remote-sensing systems, and a real-time processing and display capability that greatly reduces the time required for scientists to analyze current or archived data. In the past four years of operation, the BAO has been involved in several large cooperative experiments and numerous smaller ones. The 200 m mast of the KITcube has been operated since 1986 and is equipped with extensive instrumentation at 7 heights. Mean and turbulence data are continuously collected and are used for environmental monitoring and climate studies.

High instrumented masts have been also equipped with movable sondes for profiling [47.56, 57], and have been used in combination with tethered balloons and kites in boundary-layer research in Antarctica (Fig. 47.2).

The international network of about 800 radiosonde stations provide the foundations for numerical weather prediction (see Chap. 46). Aircraft-based measurements have steadily improved, and reconnaissance flights are conducted by a fleet of aircraft with quite different purposes, instrumentation, ranges, and durations (Chap. 37). High-altitude jet aircraft such as the National Center for

Atmospheric Research (NCAR) high performance instrumented airborne platform for environmental research (HIAPER) and the German high altitude and long range research aircraft (HALO) can carry a variety of in-situ and remote-sensing instruments simultaneously around the world and up to the lower stratosphere.

Information from surface-based remote-sensing stations is acquired by and distributed across large national and international networks of instruments. Operational use is already being made of C-band precipitation radars, ceilometers, and aerosol robotic network (AERONET) stations. Regional networks that include, for example, radar wind profilers, radiosondes, and ceilometers have also been established and successfully operated.

Data provided by surface and upper air (radiosonde) networks as well as by surface-based remote-sensing stations (e.g., precipitation radars) and various remote-sensing satellites are funneled into the data assimilation cycles of numerical weather prediction models. The results of numerical analyses performed after each data assimilation step can be considered the best estimate of the global state of the atmosphere and—in a sense—the most advanced example of vertical composite atmospheric profiling.

47.3 Theory

In this section, we introduce methods and algorithms that can be used to:

- Enhance the spatial (vertical or horizontal) and/or temporal resolution of data
- Provide added-value parameters.

Higher spatial and temporal resolution is targeted for parameters such as temperature, humidity, and wind. An example of an added-value quantity are turbulent flux profiles in the ABL.

47.3.1 Example of the Application of Composite Atmospheric Profiling to Extend the Measurement Range and Increase Spatial Resolution: The Dual-Doppler Technique

Combining several lidar systems allows us to simultaneously derive spatial information on the three-dimensional wind with high temporal resolution. The dual- and triple-Doppler lidar techniques utilize two or three lidars located at different physical locations. The technique follows simple geometrical arguments, which are demonstrated below by considering two Doppler lidars labeled 1 and 2, respectively. To apply

the technique, the radial velocity must be measured simultaneously by the two lidars at a particular point in space. This allows the two-dimensional wind vector at the crossing point in the plane spanned by both beams to be retrieved provided that the beams are not parallel. First, the data for the region in which both lidar beams overlap are mapped onto a Cartesian grid and aggregated at each grid point. The vector $\mathbf{rv} = (rv_1, rv_2)^T$ contains the radial velocities measured by both lidars in the range gate around the point where the beams intersect. If $\mathbf{u} = (u, v, w)^T$ is the Cartesian wind vector at this point and \mathbf{A} is the lidar projection matrix containing the directional unit vectors describing the plane spanned by the lidar beams, we can write

$$\mathbf{rv} = \mathbf{A} \cdot \mathbf{u} . \quad (47.1)$$

For example, if we consider a plane parallel to the ground in which az_1 and az_2 are azimuth angles, the equations for the u and v components in that plane are, respectively,

$$u = \frac{rv_1 \cos(az_2) - rv_2 \cos(az_1)}{\sin(az_1 - az_2)} , \quad (47.2)$$

$$v = \frac{rv_2 \sin(az_1) - rv_1 \sin(az_2)}{\sin(az_1 - az_2)} . \quad (47.3)$$

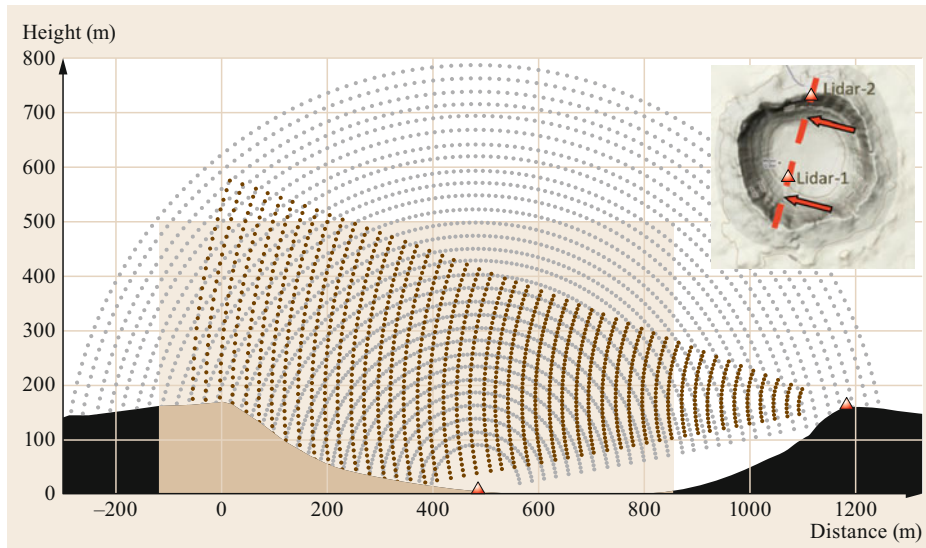


Fig. 47.3 Application of the dual-Doppler technique. The locations of the lidars are indicated by *triangles* and the scan sectors are shown as viewed perpendicular to the plane. The *vertical axis* of the plot shows the height from the crater floor, and the *horizontal axis* shows the distance from the highest point on the rim in the scan plane. The *rectangular grid* represents the plane in which the two-dimensional wind vector is retrieved. The *inset* provides a view of the crater from above, showing the location of the plane for coplanar scans and the relative positions of the two lidars (after [47.19])

More detailed information on this technique is given in [47.58].

A proven way to combine measurements from two lidars is to perform a fixed beam scan in which both lidar systems stare at the same point in space [47.59]. In [47.17, 18, 60], the virtual tower method was applied to two lidars that retrieved horizontal wind and turbulence profiles at selected locations in space, while three lidars were used in [47.61, 62] to retrieve virtual towers of the three-dimensional wind and turbulence. The dual-Doppler technique also yields information on the spatial two-dimensional wind field. Two scan types are often used to achieve this: low-elevation plan position indicator (PPI) scans are performed to obtain the horizontal wind components and range height indicator (RHI) scans are implemented to retrieve the vertical velocity and the horizontal wind component in the vertical plane spanned by both lidars. An application of this method is illustrated in Fig. 47.3 [47.19]. In this application, RHI scans were performed to retrieve the wind field in a meteor crater [47.63]. Other applications can be found in [47.64]. Those authors assembled radial velocity measurements from independent Doppler lidars into velocity vectors in the vertical plane using a least squares retrieval method. In [47.60], the coplanar scan technique was employed to investigate coherent structures in a horizontal plane over homogeneous terrain. The great advantage of applying the dual-Doppler technique is that information on the spatial distribution of wind in layers that can

only otherwise be probed with aircraft or radiosondes can be obtained with high temporal resolution (on the order of minutes or less) and spatial resolution (on the order of a few tens of meters). When selecting the lidar sites for dual-Doppler scans, it is important to ensure that the angle Δaz between the laser beams of the lidars in the targeted atmospheric volume is not too large or too small to avoid too large propagation errors (it should be approximately $30^\circ < \Delta\text{az} < 150^\circ$). Also, when performing coplanar horizontal PPI scans to investigate the horizontal wind field, the lidars must be installed at the same height above sea level.

47.3.2 Example of the Derivation of Compound Quantities: Sensible and Latent Heat Fluxes

The sensible and latent turbulent heat fluxes are parameters that characterize the conditions in the convective boundary layer. To obtain their profiles, it is necessary to perform simultaneous turbulence-resolving measurements of vertical velocity and temperature or humidity in approximately the same atmospheric volume and with roughly the same temporal resolution (see also Chap. 55). For example, the kinematic latent heat flux is calculated as

$$\overline{w'q'} = \frac{1}{N} \sum_{i=1}^N (w - \bar{w})(q - \bar{q}), \quad (47.4)$$

where N is the number of samples, q is the specific humidity, and w is the vertical wind speed. Alternatively, the flux can be computed using the covariance spectrum Co_{wq} via

$$\overline{w'q'} = \int_{f=\frac{1}{T}}^{\frac{n}{2T}} \text{Co}_{wq}(f) df. \quad (47.5)$$

The volume should be no larger than a few tens of meters cubed, and the temporal resolution should be on the order of seconds. So far, most flux measurements have been derived from aircraft-based in-situ observations [47.65], meaning that data are only available from extensive field experiments. Airborne vapor and Doppler lidar systems have been used in combination to derive latent heat flux profiles based on the covariance spectrum [47.26]. Much progress has been made in obtaining variance and higher order measurements of water vapor, temperature, and wind [47.66, 67]. However, the extraction of reliable vertical flux profiles from synergetic, turbulence-scale-resolving remote-sensing measurements of vertical wind, temperature, and humidity is still a major challenge in boundary-layer research.

47.3.3 Example of the Application of Composite Atmospheric Profiling to Increase Spatial and Temporal Resolution: Humidity Profiles

Humidity often shows high spatiotemporal variability at the mesoscale. This high variability is known to be a crucial influence on the timing and location of moist convection development [47.21]. However, most observation systems have either high temporal resolution but low or no vertical resolution (e.g., a microwave radiometer or GNSS) or high vertical resolution but low temporal resolution (e.g., radiosondes). Other systems, such as water-vapor lidars or DIALs, are not yet incorporated into networks with sufficient horizontal density. Since single systems are not able to resolve this high spatiotemporal variability, different methods have been introduced to increase the spatiotemporal resolution of humidity.

For example, in [47.21], high vertically resolved water-vapor profiles from radiosoundings were combined with integrated water-vapor (IWV) data from GNSS stations [47.68, 69], which are continuously measured and available with high horizontal resolution. In a first step, the GNSS-driven IWV data $\text{IWV}^g(x_g, y_g)$ were combined with the radiosonde-derived IWV data $\text{IWV}^r(x_r, y_r)$ to generate an IWV

field on a high-resolution grid, $\text{IWV}^{g,r}(x, y)$. In the second step, the water-vapor profiles from radiosondes, $q^r(x_r, y_r, z)$, were interpolated to the same high-resolution grid, yielding the profiles $q^r(x, y, z)$. A new IWV field $\text{IWV}^r(x, y)$ on the high-resolution grid was then estimated from these interpolated $q^r(x, y, z)$ profiles. Except for radiosonde sites, the $\text{IWV}^r(x, y)$ and $\text{IWV}^{g,r}(x, y)$ data did not necessarily agree. The difference between them was used to adjust the interpolated $q^r(x, y, z)$ profiles to get new water-vapor profiles

$$q(x, y, z) = q^r(x, y, z) + \text{AF}(x, y)q^r(x, y, z), \quad (47.6)$$

where $\text{AF}(x, y)$ is an adjustment function that is calculated via [47.21]

$$\text{AF}(x, y) = \frac{\text{IWV}^{g,r}(x, y) - \text{IWV}^r(x, y)}{\text{IWV}^r(x, y)}. \quad (47.7)$$

The resulting highly resolved water-vapor profiles and accompanying convection-related indices highlighted the areas in which deep convection occurred.

Radiosonde and microwave radiometer data have also been successfully combined to enhance the vertical and temporal resolution of humidity profiles [47.25]. In this scheme, a ground-based scanning microwave radiometer that provided IWV^m was used to determine the vertical distribution of water vapor between radiosonde ascents, $q(z, t)$. Multiplying the linearly temporally interpolated water-vapor field detected by radiosondes, $q^r(z, t)$, by the ratio of $\text{IWV}^m(t)$ to the linearly interpolated $\text{IWV}^r(t)$ yielded

$$q(z, t) = q^r(z, t) \frac{\text{IWV}^m(t)}{\text{IWV}^r(t)}. \quad (47.8)$$

The integrated profiling technique (IPT [47.24, 38]) is a variational technique for deriving temperature and humidity profiles at high temporal and vertical resolution based on microwave radiometry and radiosonde ascents. The advantage of microwave radiometers is that they provide low-resolution water vapor profiles at high temporal resolution (≈ 1 s). Although the accuracy of IWV^m is very good ($\approx 0.5 \text{ kg m}^{-2}$), the signal only has approximately two degrees of freedom [47.37], which means that only two independent height intervals of water vapor can be distinguished. This is due to the fact that microwave radiometer radiance observations (also expressed as *brightness temperatures*) are purely passive (i.e., they only receive radiation emitted by the gases—mostly water vapor and oxygen—themselves). The temperature profile can be retrieved with ≈ 4 degrees of freedom, and the best vertical resolution is obtained in the lowest 1 km of the atmosphere.

By combining radiosonde and microwave radiometer data, IPT can add significant profile information to the time period between two subsequent operational radiosonde ascents, regardless of whether both sets of measurements are performed at the same site or different sites. Depending on the density of the radiosonde network, a ground-based profiling station has the potential to significantly improve the quality of the network or even to substitute specific radiosonde stations.

Ground-based Raman lidar water-vapor profiles and microwave radiometer brightness temperatures can be used synergetically to enhance the vertical resolution of humidity. Due to the fact that a water-vapor Raman lidar measures atmospheric backscatter at a slightly different frequency than the emitted laser pulse, these observations deliver a water vapor extinction profile that can be directly related to a high vertical resolution atmospheric humidity profile. However, strong extinction due to hydrometeors hinders water vapor profiling of Raman lidars within or above clouds. In addition, incomplete overlap of the transmitter and the receiver telescope near the surface as well as the decrease in the signal-to-noise ratio with height limit height coverage.

A retrieval algorithm that combines the advantages of both instruments in an optimal estimation approach, which allows the uncertainty in the estimated humidity profile to be determined directly, has been reported [47.30]. The analysis showed that accurate lidar retrieval dominated the accuracy within the range of the lidar, but information gain was achieved through composite atmospheric profiling beyond this range, especially during the daytime, when the vertical range of the lidar was limited by a low signal-to-noise ratio. A similar variational retrieval based on a Kalman filtering approach showed that water-vapor profile retrieval is also possible in cloudy conditions [47.31]. As mentioned above, other composite profiling studies that combine radiometer and radar wind profiler data have also been reported [47.32].

47.3.4 Example of the Derivation of Compound Quantities: Cloud Properties and Hydrometeor Classification

Besides the thermodynamic and dynamic properties of the ABL, it is very important to probe the micro- and macrophysical cloud properties. One reason why this is important is that clouds and their associated microphysical properties actively regulate the radiation budget and the hydrological cycle. However, nearly

all remote-sensing systems have limitations regarding measurements in clouds. For example, lidar signals normally only penetrate thin cloud layers. Cloud radars are not able to detect the cloud base due to the *large droplet issue* (i.e., a few small droplets from drizzle dominate the radar signal and obscure backscatter from smaller cloud droplets). Microwave radiometers have poor vertical resolution and only provide estimates for the liquid water path (LWP) of clouds. Therefore, different algorithms have been developed to determine cloud properties by applying a combination of different sensors. One of these algorithms, Cloudnet [47.22], determines cloud properties from ground-based observations. The core instruments used in the cloud retrievals are a Doppler cloud radar, a ceilometer, a microwave radiometer, a rain gauge, and the output of a numerical weather prediction (NWP) model. Cloudnet algorithms can provide various meteorological products: the cloud base height and target classification (e.g., aerosol, insects, ice, melting ice, cloud droplets, drizzle, rain, and clear sky), the liquid water content (LWC), and the ice water content (IWC). Furthermore, in principle, the turbulent kinetic energy (TKE) and the eddy dissipation rate can be derived. Within the framework of the European aerosols, clouds and trace gases research infrastructure (ACTRIS) research initiative, Cloudnet algorithms are applied to a number of permanent cloud observatories such as Chilbolton (UK), CE-SAR (Netherlands), Palaiseau (France), CNR-IMAA atmospheric observatory (C-IAO, Italy), and JOYCE & MOL-RAO (Germany). Combining the various remote-sensing systems was found to considerably enhance operational observations of liquid water clouds. The Cloudnet software is for example implemented at the KITcube, where additional remote-sensing systems are available (Sect. 47.4.1).

Another method of obtaining cloud properties is to extend the integrated profiling technique to retrieve not only temperature and humidity profiles from microwave radiometers and radiosondes but also profiles of cloud liquid water content and cloud droplet effective radius [47.29]. This can be achieved by adding reflectivity profiles from cloud radar data as well as the cloud boundaries derived through the Cloudnet target classification. Microphysical properties of warm clouds have also been derived by applying the SYRSOC (synergistic remote sensing of cloud) technique, as described in [47.70]. This technique involves combining cloud radar, microwave radiometer, and lidar/ceilometer data to derive profiles of liquid water content and cloud droplet number concentration.

47.4 Observation Platforms

Various integrated observation platforms are deployed around the world. While many of the instruments used in these integrated platforms are similar (e.g., ceilometers, Doppler lidars, microwave radiometers, cloud radars, radiosonde stations; see Tables 47.1 and 47.2), the platforms do differ in the purpose and main scientific objectives of the site. It is possible to distinguish between mobile platforms, which are mainly deployed for limited periods during field campaigns, and fixed platforms, which are operated for long periods at the same location. Without any claim to be complete, a selection of mobile and fixed observation platforms are introduced in the following (see also Table 47.3).

47.4.1 Mobile Platforms

Some prominent examples of mobile platforms currently operated by certain institutions worldwide are described below. These platforms are evolving due to technological progress, and are partly already operated in an information environment comprising a high-resolution model with assimilation of data (Table 47.3).

The ARM Mobile Facilities (AMFs)

The ARM Mobile Facilities are primarily used to investigate the phenomena that control radiative transfer in the atmosphere. In order to explore research questions that are not addressed by ARM's fixed atmospheric observatories [47.2], scientists can propose a field campaign that utilizes one of the three AMFs to collect atmospheric and climate data from undersampled regions around the world. Each AMF is designed to operate in any environment—ranging from the cold of the Arctic to the heat of the tropics—during cam-

paigns that typically last about a year. The ARM Mobile Facilities consist of several portable shelters, a baseline suite of instruments, and communication and data systems. When deployed for a field campaign, an experienced project management and engineering team travels with the AMF to set up and modify the shelters and instruments and to train and manage the staff who will continuously operate the facilities. Scientific and infrastructure staff are also available for collaborative planning activities, as is local on-site or virtual support for scientists who are using an AMF for their research. An overview of AMF deployments is given in [47.2].

The AMFs have instrumentation and data systems that are similar to those in fixed atmospheric observatories. About 50 instruments are deployed with each facility, enabling continuous measurements of clouds, aerosols, precipitation, energy, and other meteorological variables. Measurement capabilities of the AMFs include standard meteorological instrumentation, a broadband and spectral radiometer suite, and remote-sensing systems, including lidars and cloud radars.

The instrumentation available with AMF2 is, with a few notable exceptions, the same as that available with AMF1 and AMF3. Because AMF2 was designed to support shipboard deployments, its baseline suite of instruments is marine-focused. The AMFs are also designed to host guest instruments or collaborate with experiments from other agencies, making them ideal platforms for conducting joint research anywhere in the world. Data from these facilities undergo quality checks and are made freely available to the international research community in near real-time through the ARM Data Center via Data Discovery.

Table 47.3 Examples of mobile and permanent observation platforms and their key instruments (bolded entries indicate core instruments that are relevant to Cloudnet retrievals)

System	Platform						
	KITcube	LACROS	ARM	C-IAO	CESAR	JOYCE	MOL-RAO
Energy balance	+	+	+	–	+	+	+
Meteo station	+	+	+	+	+	+	+
Radiosonde station	+	+	+	+	–	–	+
Wind profiler	–	–	+	–	+	–	+
Doppler lidar	+	+	+	–	–	+	+
Raman lidar	–	+	+	+	+	–	+
Microwave radiometer	+	+	+	+	+	+	+
Ceilometer	+	+	+	+	+	+	+
Cloud radar	+	+	+	+	+	+	+
Rain radar	+	–	+		+	+	+
Sun photometer	+	+	+	+	+	+	+
Enhanced aerosol properties	–	+	+	+	+	–	–



Fig. 47.4 A composite photo of KITcube in operation. *From left to right:* X-band radar, cloud radar, ceilometer, micro rain radar, disdrometers, two Doppler radars, 30 m tower, energy-balance station, and office container (photo © Markus Breig/KIT, used with permission)

The Karlsruhe Observatory for Convection Studies (KITcube)

KITcube (Fig. 47.4) is an advanced integrated atmospheric observation system operated by the Karlsruhe Institute of Technology (KIT). It is designed to be deployed and operated in international measurement campaigns involving boundary-layer, convection, and atmospheric transport studies over heterogeneous terrain defined by e.g. changes in surface properties and orography [47.1]. The mobile KITcube includes various remote-sensing and in-situ systems that permit the observation of process (chain) of convection including the energy exchange at the Earth's surface, the evolution of the ABL, exchanges of heat, moisture, and aerosols between the ABL and free troposphere, and the development of moist shallow and deep convection. The spectrum of interest ranges from the micro- to the mesoscale, and KITcube is designed to effectively probe cross-scale interactions in particular. One specific highlight is the deployment of several powerful scanning Doppler lidars that have been successfully used in dual-Doppler [47.58, 60] and multi-Doppler [47.71, 72] lidar studies of the spatial distribution of wind. Examples are given in Sect. 47.8.1. Other highlights of the studies performed with KITcube include the

application of a Doppler lidar and cloud radar in combination to measure the vertical wind below and within clouds [47.1, 20] and the synergetic utilization of a Doppler lidar and scanning microwave radiometer to analyze moisture transport [47.25].

The Leipzig Aerosol and Cloud Remote Observations System (LACROS)

LACROS [47.3] (Table 47.3) is designed to investigate unresolved questions concerning the interaction between aerosol particles and clouds and the corresponding indirect effects on precipitation and radiative transfer. Synergetically extracting information about cloud and aerosol properties from multi-instrument and hence multi-sensor observations is key to overcoming our current lack of knowledge in this area. LACROS comprises a set of active and passive remote-sensing instruments that are partially available for use in field campaigns. The active remote-sensing instruments span the wavelength range from the UV to microwave radiation. Passive instrumentation is included to help interpret the active remote-sensing measurements. The system also includes meteorological surface, radiation-balance, and radiosonde stations that enable it to fulfill the criteria of the Baseline Surface Radiation Network (BSRN).

47.4.2 Permanent Platforms

Permanently operated platforms at fixed locations are used to monitor processes and various atmospheric changes. They also provide data for comparison with satellite data. Some of the main facilities are described below.

The CNR-IMAA Advanced Observatory for Atmospheric Research (C-IAO)

The Istituto di Metodologie per l'Analisi Ambientale of the Italian National Research Council (CNR-IMAA) operates the C-IAO (the CNR-IMAA Atmospheric Observatory) [47.7]. This advanced atmospheric observatory is located in Tito Scalo, close to Potenza in southern Italy. Its main scientific objective is to perform long-term measurements of water vapor, aerosols, and cloud properties. The observatory's equipment consists of ground-based remote-sensing instruments for aerosols, water vapor, and clouds, including active and passive sensors (Table 47.2). The observation strategy is to provide quality-assured measurements for satellite validation and model evaluation. The measurements obtained with the active and passive instruments are also used synergetically to improve atmospheric profiling and integration algorithms (e.g., water-vapor profiling using Raman lidar and microwave radiometer data). The C-IAO database is utilized in satellite data validation programs. The station additionally hosts two European aerosol research lidar network (EARLINET) multiwavelength Raman lidars, one of which acts as the mobile reference for the network [47.73]. A detailed description of the C-IAO infrastructure, its scientific activities, and its observation strategy is given in [47.7].

The CESAR Observatory in Cabauw

The Cabauw Experimental Site for Atmospheric Research (CESAR [47.5]) is located in the southwest region of the Netherlands. At CESAR, a large set of instruments are employed to study the atmosphere and its interaction with the land surface. CESAR focuses on monitoring long-term trends in atmospheric changes, studying atmospheric and land-surface processes for climate modeling, validating spaceborne observations, and developing and implementing new measurement techniques. The observatory collaborates with several Dutch universities and major research institutes and is involved in intense international cooperation. Besides the instruments listed in Table 47.3, a 213 m high tower is used to investigate the links between land-surface conditions, the state of the ABL, and general weather conditions. A scanning X-band radar operated by Delft University of Technology is located on top of the tower. The remote-sensing systems are located ≈ 300 m from the tower.

The Richard Aßmann Observatory

The Lindenberg Meteorological Observatory—Richard Aßmann Observatory (MOL-RAO) of the German Meteorological Service (DWD) was founded in 1905 [47.74]. It is situated in Lindenberg, eastern Germany. For over 100 years, the main focus of the work carried out at this observatory has been vertical atmospheric profiling. This was originally done using captive balloons and kites, which were replaced in the 1930s with radiosondes (from 1947 on, the observatory released radiosondes four times a day). With the beginning of the 1990s, the observatory has increasingly used ground-based remote sensing methods such as radar, lidar, and microwave radiometer to enhance the profiling [47.75].

Currently, its research activities also encompass measuring programs to study solar and terrestrial radiation as well as interaction processes between the Earth's surface and the atmosphere [47.76, 77]. The data derived from the measurement systems operated at the observatory are used to produce a reference dataset, the *Lindenberg Column*, which characterizes the vertical structure of the atmosphere from the ground up to the stratosphere [47.4, 78]. Additionally, the MOL-RAO is the lead center of the Global Climate Observing System (GCOS) Reference Upper-Air Network (GRUAN), and it also acts as a testbed for other networks such as BSRN.

The data from the observatory, which are also obtained through sensor synergy [47.16, 79], contribute significantly to efforts to monitor the Earth's climate. They are also used to validate satellite sensors and to verify weather prediction and climate models. In addition, the observatory is testing new sensors and observing systems that will potentially be incorporated into the DWD's measuring network.

The JOYCE Observatory

The Jülich Observatory for Cloud Evolution (JOYCE [47.6]) in Jülich, Germany was established to probe boundary-layer cloud development, including the impacts of factors such as dynamics, thermodynamics, and aerosols, as well as interactions with vegetation and the Earth's surface. Another focus of the observatory is precipitation generation, including the ice phase [47.80] and drizzle production during the warm rain process [47.81]. In 2016, JOYCE was funded to become a DFG (Deutsche Forschungsgemeinschaft) core facility, with the goal being to provide users from the scientific community with regulated access to the observation facility and the continuous datastream. JOYCE is part of the European ACTRIS observatory network for monitoring the atmospheric column, and is evolving into the ACTRIS topical center for microwave radiometers. This topical center shall define ACTRIS-

wide harmonized procedures for measurement configuration, calibration, quality control and retrieval development and application. To achieve these aims, JOYCE is equipped with a variety of in-situ and remote-sensing instruments (Table 47.3). Composite profiling at JOYCE is complemented by measurements of two scanning X-Band radars, one located on a close-by pit-mining hill (Sophienhöhe), the other located at the University of Bonn. JOYCE was also selected for the HOPE field campaign [47.13], which focuses on ABL clouds.

47.5 Specifications

In this section, we discuss the specifications of instruments that are used for integrated profiling. The instruments considered are those described in the rel-

This campaign served as the observational basis for the critical evaluation of high-resolution models (< 1 km). JOYCE exploits instrument synergy to implement integrated profiling techniques [47.29], which are used to retrieve physically consistent profiles of temperature, humidity, LWC, and the effective radius of the water cloud droplets, along with the corresponding uncertainties. Finally, long-term observational data from JOYCE are used to improve the parameterization schemes of numerical weather and climate prediction models.

evant instrument-focused chapters of this Handbook (in Parts B, C, and D); we do not consider any other instruments here.

47.6 Quality Control

Composite atmospheric profiling is a field that is generally characterized by rapid development in terms of both the underlying measurement systems used and the fusion techniques applied. A general methodology for quality control or international standardization in this field appears to be missing from the literature, although some subcommunities that focus on specific instrumentation (e.g., for cloud parameters) have recently started to address this issue. Therefore, we now present some quality-control considerations for basic types of composite profiling.

When composite atmospheric profiling is applied to extend the measurement range and to increase spatial and temporal resolution (Sect. 47.3.1), quality control can be achieved by comparing the various parameters (e.g., temperature, humidity, and wind speed) in layers of overlapping redundant measurements. For example, profile measurements from towers can be used to check profiles from scanning wind lidars by collocating measurements and comparing data for the lidar range gate next to a tower instrument. Furthermore, integrated information can be exploited to assess the quality of observations (e.g., IWV data from GNSS, radiosondes, and microwave radiometers) (Sect. 47.3.3). When composite atmospheric profiling is employed to derive compound quantities such as turbulent heat and moisture flux profiles (Sect. 47.3.2), the quality of the resulting data can be assessed by comparing them with values obtained from in-situ measurements that have known uncertainties, such as data from high towers with instruments to measure the turbulence-resolving temperature, humidity, and wind, or data from aircraft equipped with turbulence-probing systems [47.82].

The variational retrieval frameworks used when performing composite atmospheric profiling are frequently based on Gaussian statistics, i.e., the random uncertainties in atmospheric parameters and observables are assumed to follow a normal distribution. Variational retrievals require prior knowledge of the random uncertainties (not only the uncertainties in the signal observables but also their covariances). If a forward model is applied (i.e., there is a conversion from atmospheric state space to measurement space), the random uncertainty in this model must also be considered. While observational uncertainty can be determined largely through the application of calibration standards, model uncertainty is difficult to quantify, as the true state of the atmosphere is seldom known.

Aside from prior knowledge of random errors, quality-controlled, bias-free observations are crucial when performing composite atmospheric profiling in variational retrieval approaches (such as optimal estimation). If the observations include errors due to unidentified systematic bias, the retrieval results will most probably be affected in a nonlinear way. Thus, bias error must be identified and removed beforehand if possible. While it may be possible to compare the observations to independent data sources, remote-sensing approaches often also offer inherent quality checks. For instance, a microwave radiometer spectral consistency check that can be applied directly to brightness temperature measurements and can reveal channels strongly affected by bias has been developed [47.29]. Obviously, in such an approach, spectral consistency statistics must be known a priori. In addition, the results of the variational retrieval itself can serve as

a further quality check of the observations, particularly in clear-sky cases; nonconvergence or physically

inconsistent solutions may hint at measurement offset errors.

47.7 Maintenance

The maintenance that must be performed on the observation systems used in composite atmospheric profiling is the same as that described in the relevant instrument-focused chapters of Parts B, C, and D of this Handbook.

There is little information in the literature about additional maintenance requirements or common standards, such as maintenance intervals, when instruments are used for composite profiling.

47.8 Applications

A wide range of applications of composite atmospheric profiling have been proposed in the last few decades. We focus on a few prototypical examples below.

region of Stuttgart. Note the spatial variability of the horizontal wind field over hilly terrain.

47.8.1 Dual-Doppler Lidar Measurements: The Virtual Tower Technique

An example of the application of the so-called virtual tower technique is displayed in Fig. 47.5. One way to use this technique is to have two Doppler lidars perform coordinated stop-and-stare scans [47.83]. In this configuration, both lidars measure simultaneously at discrete points in space for approx. 10 s. By varying the azimuth and elevation angles, virtual towers can be placed at different locations over otherwise inaccessible terrain. Figure 47.5b shows the horizontal distribution of wind profiles obtained with the virtual tower technique in the

47.8.2 Dual-Doppler Lidar Measurements: Coplanar Scans

An example of the retrieval of a wind field in a vertical plane from dual-Doppler lidar measurements is given in Fig. 47.6. The data were measured during an experiment in a meteor crater in Arizona [47.63], where two scanning Doppler lidars were located on the crater's north rim and the floor of the crater, respectively. The dual-Doppler retrievals were calculated from continuous coplanar RHI scans. The lidar on the rim scanned at elevation angles ranging from -10° to 20° . The scan resolution of this lidar was 0.75° , and the range gate length was 15 m. The lidar on the crater floor scanned at eleva-

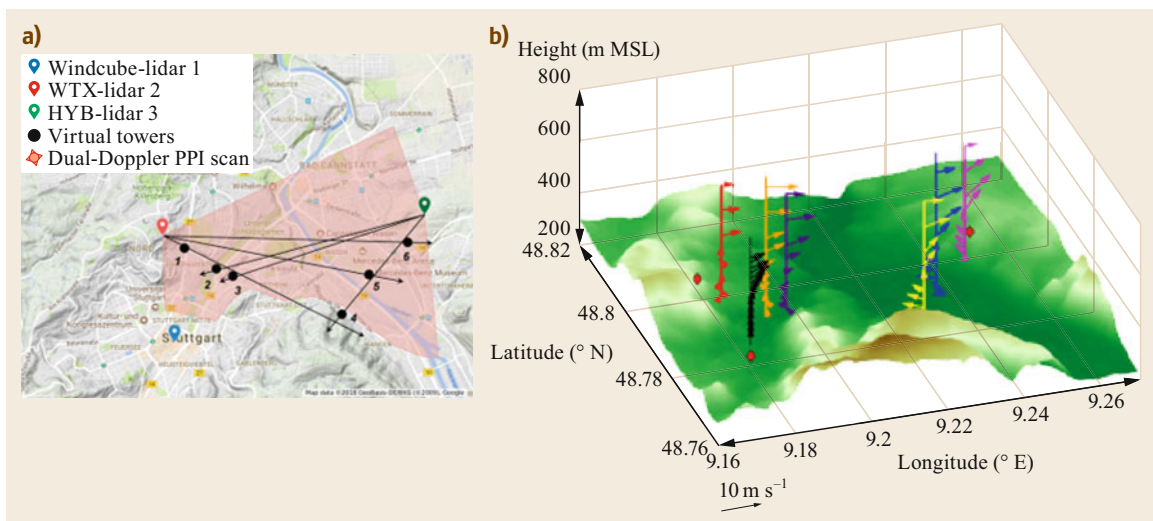


Fig. 47.5 (a) Schematic of the intersecting lidar beams used in an application of the virtual tower technique, and (b) some vertical profiles of horizontal wind measured at different virtual tower sites (measurements were performed at 06:00–07:00 on 19.07.2017; schematics from current project work at KIT © B. Adler)

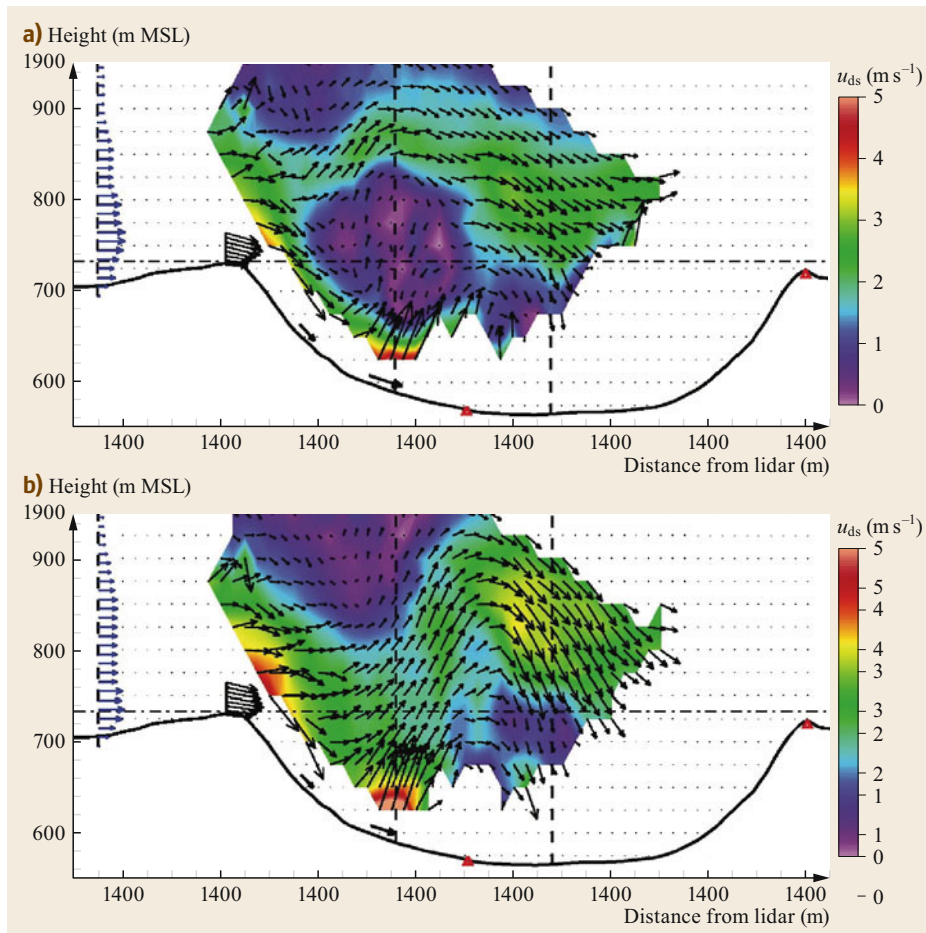


Fig. 47.6a,b Two-dimensional wind field in a vertical plane above the Meteor Crater in Arizona, USA, based on dual-Doppler lidar measurements. An abrupt change in flow structure between the bifurcation and warm air intrusion phases can be seen from the 2.5-min-mean dual-Doppler wind retrievals obtained at 22:40 MST (**a**) and 22:52 MST (**b**). The positions of the two Doppler lidars (crater floor and on the rim) used for the dual-Doppler lidar measurements are indicated by *red triangles* (after [47.84] with permission from the American Meteorological Society)

tion angles ranging from 10° to 150° . The scan resolution of the lidar on the crater floor was 1.4° and the range gate length was 24 m. The data were interpolated onto a $25\text{ m} \times 25\text{ m}$ grid [47.84]. The dual-Doppler lidar wind field retrievals allowed the development of a hydraulic jump in the atmosphere above the crater to be studied in detail. At 22:40 MST (Mountain Standard Time) (Fig. 47.6a) there was a bifurcation of the wind flow, with a cavity separating the warmer upper and colder lower currents and a hydraulic jump on the lower slope. However, an unsteady lee wave was present in the statically stable upper current. By 22:52 MST (Fig. 47.6b), the cold and warm air currents had merged, eliminating the cavity between the two currents and bringing warm residual-layer air down into the basin. The merging of the two currents and the stable layers increased the downslope wind speeds as well as the layer depth.

The hydraulic jump strengthened (Fig. 47.6b) as the flow became more negatively buoyant relative to the adjacent warm air and as momentum was transported downward into the stable layer from the warm air intrusion. The warm descending air over the upwind sidewall was actually the descending branch of the first wave of a two-wave train that extended across the basin with a wavelength approximately equal to the basin radius and an amplitude of approximately twice the basin depth.

47.8.3 Latent Heat Flux Profiles

As described in Sect. 47.3.2, extracting reliable vertical sensible and latent heat flux profiles for the ABL is still a major challenge due to the need for simultaneous measurements of wind and temperature or humidity with high vertical and temporal resolution. One of the

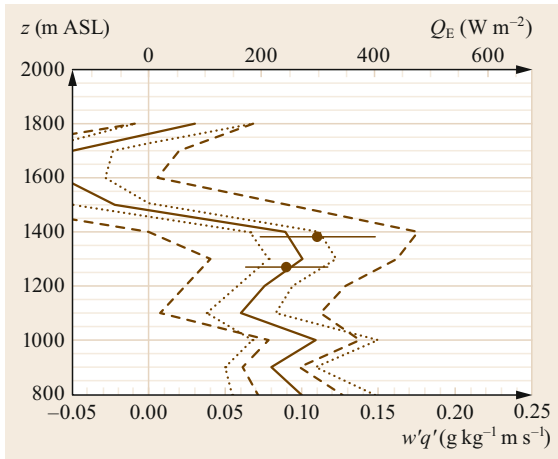


Fig. 47.7 Latent heat flux profile, Q_E from airborne lidar data and in-situ results for the same leg. The measurements were taken at about 11:00 UTC. The average top of the convective boundary layer (CBL) was at ≈ 1500 m ASL. Included are sampling (*thin dashed*) and noise (*thin dotted*) uncertainty ranges, plus an in situ results (*black dot with sampling uncertainty bar*) (after [47.26] with permission from Wiley and Sons)

few studies that successfully obtained latent heat flux profiles [47.26] used an airborne nadir-pointing differential absorption lidar (DIAL) and a $2 \mu\text{m}$ Doppler lidar to derive profiles of latent heat flux and then compared them to the latent heat flux profiles calculated from in-situ measurements performed with the Do 128 research aircraft [47.82, 85]. The measurements were performed over hilly terrain. On average, the latent heat fluxes obtained with remote-sensing instruments agreed with the in-situ values (Fig. 47.7). The latent heat flux values in the ABL (i.e., $\lesssim 1500$ m ASL) varied between 100 and 500 W m^{-2} . This example illustrates the considerable

potential of remote-sensing instruments to study turbulent exchange processes in the ABL, which requires knowledge of the sensible and latent heat flux profiles.

47.8.4 Increasing the Vertical and Temporal Resolution of Humidity Profiles

By combining high temporal resolution IWV measurements from a microwave radiometer with high vertical resolution humidity profiles from radiosoundings, it is possible to explore the evolution of the humidity profile between individual radiosoundings [47.25]. Figure 47.8 shows humidity profiles for a valley on the mountainous island of Corsica that were retrieved with this method. The arrival of a sea breeze at the measurement site at around 12:30 LT (local time)—as indicated by an increase in humidity in the region up to 1000 m—was detected due to the high temporal resolution of the profiles. It would not have been possible to detect the exact arrival time of the sea breeze using only the radiosonde profiles (obtained every 3 h) or by simply interpolating linearly between the radiosonde profiles.

47.8.5 Humidity Profiles from Active and Passive Remote Sensing

A water-vapor Raman lidar and a microwave radiometer were used during HOPE to retrieve atmospheric humidity profiles in the lowest 3 km of the atmosphere. A variational retrieval (as defined in [47.30]) was applied to the lidar-only, microwave radiometer-only, and composite microwave radiometer and lidar observations, with both instruments located within a few meters of each other. As expected from the physics underpinning these measurements, the derived lidar-only retrieval uncertainty during cloud-free conditions ($< 0.2 \text{ g m}^{-3}$) with a sufficient signal-to-noise ratio was significantly bet-

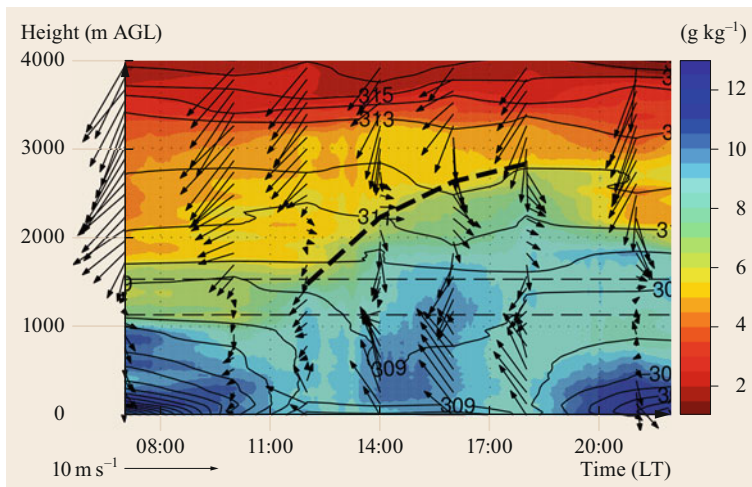


Fig. 47.8 Specific humidity (*color-coded*), potential temperature (*black isolines*), and horizontal wind vector (*arrows*) measured by radiosondes at Corte on the island of Corsica on 19 August 2012. The specific humidity was interpolated from microwave radiometer and radiosonde data, and the potential temperature was linearly interpolated from the radiosoundings (after [47.25])

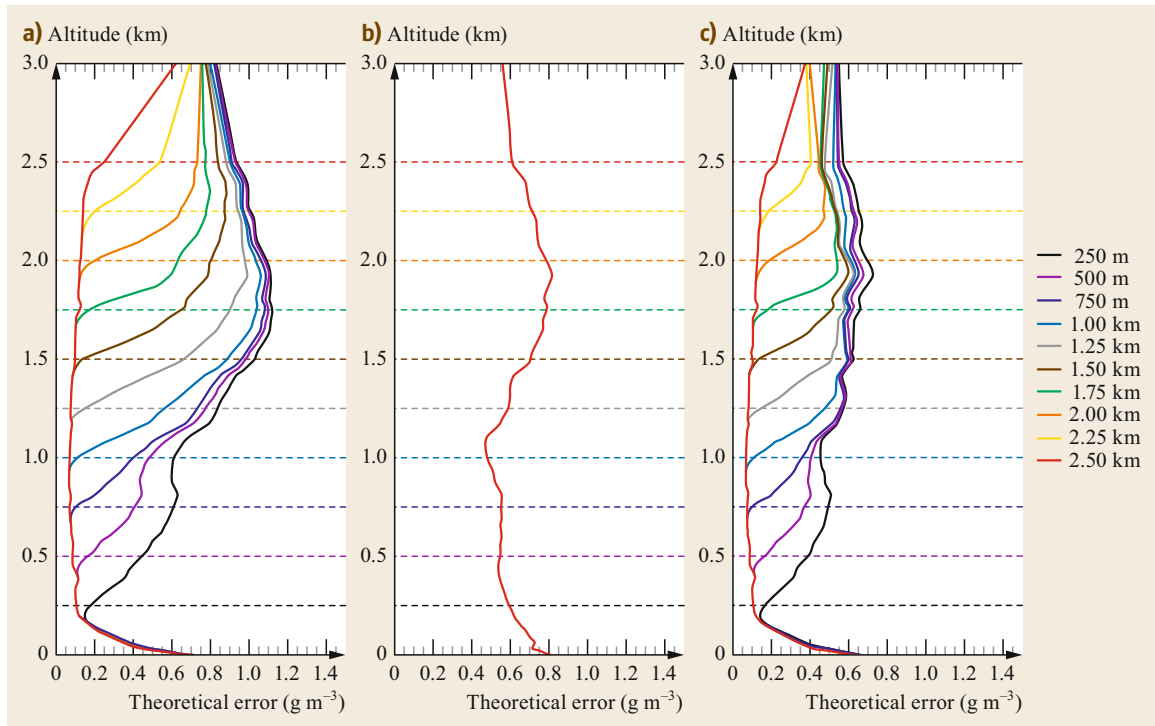


Fig. 47.9a–c Vertical profiles of the random uncertainty (theoretical error) in the absolute humidity retrieved from water vapor lidar and/or microwave radiometer measurements for 100 clear-sky cases during HOPE. **(a)** Water vapor lidar only, **(b)** microwave radiometer only, and **(c)** combination of both lidar and microwave radiometer (composite profiling). The dashed horizontal lines indicate levels of full hypothetical lidar attenuation due to the presence of cloud or a signal-to-noise ratio that is too low. The corresponding colored lines (bold) show the uncertainty when there is no lidar signal above the dashed line (after [47.86])

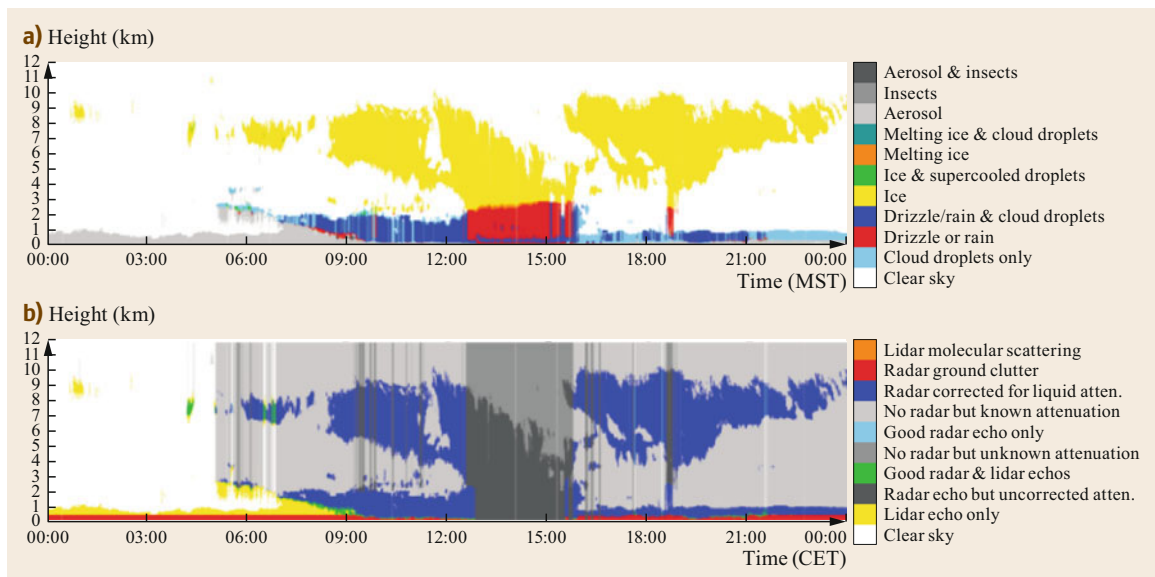


Fig. 47.10a,b Examples of **(a)** target classification and **(b)** radar and lidar detection status for measurements from Chilbolton Observatory using Cloudnet on 17 November 2003 (after [47.22] with permission from the American Meteorological Society)

ter than the microwave radiometer-only retrieval uncertainty ($0.6\text{--}0.8\text{ g m}^{-3}$; compare Fig. 47.9a,b, red lines). However, above the height where the Raman lidar signal dropped off because the maximum range of the lidar had been exceeded or due to the presence of a liquid cloud, the lidar-only retrieval uncertainty increased with height towards the background humidity profile assumed (the so-called a priori profile). Due to the vertical correlation of humidity at the different height levels considered in the optimal estimation retrieval, the uncertainty increases gradually and not in an ad-hoc manner. The benefit of composite atmospheric profiling is shown in Fig. 47.9c. At heights above the detection threshold of the lidar signal, the retrieval uncertainty stays well below the lidar-only and microwave radiometer-only values (up

to 0.3 g m^{-3}). The degrees of freedom (DOF) for the signal in the microwave radiometer measurements are used to improve the profile above the height of the lidar detection threshold, whereas these DOF are used to retrieve the full profile in the microwave radiometer-only case. This underlines the added value of composite profiling.

47.8.6 Target Classification with Cloudnet

One of Cloudnet's products is a target classification. Utilizing the fact that a radar and a lidar are sensitive to different particle sizes and concentrations, the atmospheric targets of each radar/lidar pixel are categorized into classes. One example of the target classification provided by Cloudnet is given in Fig. 47.10.

47.9 Future Developments

Currently, most composite atmospheric profiling methods combine only two or a few different sensors or sensor systems. However, given that this is a rather new and rapidly growing research field, we can expect considerable advances in such methods in the near future. These advances will likely involve enhancing the temporal and spatial resolution of variables and retrieving new variables. [47.87] outlines how higher order moments and fluxes can be derived from high-resolution lidar measurements as well as future directions in this field. Differential absorption lidars (DIALs, Chap. 26) for retrieving water-vapor profiles with temporal resolutions of approximately 20 s to 20 min are being developed which are not sufficient for fluxes but allow to obtain high vertical resolution profiles in the boundary layer [47.88], and will probably become commercially available soon.

A more comprehensive approach to combining many observed variables can be realized by extending the site atmospheric state best estimate (SASBE) method [47.39, 40]. Variational approaches for optimal merging, as in Sect. 47.8.5, with known systematic and stochastic errors have a big potential for synergistic use of multiple sensors.

This is actually what we have shown above applying the optimal estimation approaches for optimal merging with known systematic and stochastic errors characteristics of different have a big potential for synergistic use of multiple sensors.

In addition to ground-based observations, satellite sensors will also bring a wealth of additional information into tropospheric research. Composite profiling of ground-based and satellite-based remote sensing for atmospheric stability retrieval, e.g., has been successfully carried out [47.89]. The EarthCare mission [47.47, 90] provides an excellent example of a future spaceborne mission to measure aerosols, clouds, rain, and radiation.

Beyond composite atmospheric profiling, it is easy to predict that there will be rapid progress in the assimilation of observed data from many different kinds of instruments into numerical models. Future networks of lidar, radar, and passive remote-sensing systems will allow much more detailed analysis and predictions of the state of the atmosphere, particularly at the mesoscale and in relation to convection modeling, for both urban and mountainous areas.

47.10 Further Reading

A summary of combinations of different ground-based remote-sensing stations is given in COST (European Cooperation in Science and Technology) Report 720:

- A.M. Engelbart, W.A. Monna, J. Nash, C. Mätzler: *The Integrated Ground-Based Remote Sensing Stations for Atmospheric Profiling* (COST, Brussels 2009)

A very good overview of how boundary-layer measurements were obtained thirty years ago can be found in:

- D.H. Lenschow (Ed.): *Probing the Atmospheric Boundary Layer* (AMS, Boston 1986)

More recent treatises on the same subject are provided by:

- S. Emeis: *Measurement Methods in Atmospheric Sciences – In Situ and Remote*, Quantifying the Environment, Vol. 1 (Borntraeger, Stuttgart 2010)
- S. Emeis: *Surface-Based Remote Sensing of the Atmospheric Boundary Layer* (Springer, Heidelberg 2011)
- M. Banta, C.M. Shun, D.C. Law, W. Brown, R.F. Reinking, R.M. Hardesty, C.J. Senff, W.A. Brewer, M.J. Post, L.S. Darby: *Observational Techniques: Sampling the Mountain Atmosphere*. In: *Mountain Weather Research and Forecasting: Recent Progress and Current Challenges*, ed. by F.K. Chow, S.F. De Wekker, B.J. Snyder (Springer, Dordrecht 2013) pp. 409–530

A thorough overview of measurements performed over complex terrain is presented in:

References

- 47.1 N. Kalthoff, K. Träumner, B. Adler, S. Späth, A. Behrendt, A. Wieser, J. Handwerker, F. Madonna, V. Wulfmeyer: Dry and moist convection in the boundary layer over the Black Forest – A combined analysis of in situ and remote sensing data, *Meteorol. Z.* **22**, 445–461 (2013)
- 47.2 M.A. Miller, K. Nitschke, T.P. Ackerman, W.R. Ferrell, N. Hickmon, M. Ivey: The ARM mobile facilities, *Meteorol. Monogr.* **57**, 9.1–9.15 (2016)
- 47.3 J. Bühl, P. Seifert, U. Wandinger, H. Baars, T. Kanitz, J. Schmidt, A. Myagkov, R. Engelmann, A. Skupin, B. Heese, A. Klepel, D. Althausen, A. Ansmann: LACROS: The Leipzig aerosol and cloud remote observations system, *Proc. SPIE* (2013), <https://doi.org/10.1117/12.2030911>, Event: SPIE Remote Sensing, Dresden 2013
- 47.4 F. Beyrich, D.A.M. Engelbart: Ten years of operational boundary-layer measurements at the Aßmann Observatory Lindenberg: The role of remote sensing, *IOP Conf. Ser. Earth Environ. Sci.* **1**, 012026 (2008)
- 47.5 A. Apituley, H. Russchenberg, H. van der Marel, F. Bosveld, R. Boers, H. ten Brink, G. de Leeuw, R. Uijlenhoet, B. Arbresser-Rastburg, T. Röckmann: Overview of research and networking with ground based remote sensing for atmospheric profiling at the Cabauw Experimental Site for Atmospheric Research (CESAR) – The Netherlands. In: *IGARSS 2008 – Geoscience and Remote Sensing Symposium* (2008), <https://doi.org/10.1109/IGARSS.2008.4779496>
- 47.6 U. Löhnert, J.H. Schween, C. Acquistapace, K. Ebell, M. Maahn, M. Barrera-Verdejo, A. Hirsikko, B. Bohn, A. Knaps, E. O'Connor, C. Simmer, A. Wahner, S. Crewell: JOYCE Jülich Observatory for Cloud Evolution, *Bull. Am. Meteorol. Soc.* **96**, 1157–1174 (2015)
- 47.7 F. Madonna, A. Amodeo, A. Boselli, C. Cornacchia, V. Cuomo, G. D'Amico, A. Giunta, L. Mona, P. Pappalardo: CIAO: The CNR-IMAA Advanced Observatory for Atmospheric Research, *Atmos. Meas. Tech.* **4**, 1191–1208 (2011)
- 47.8 D.A.M. Engelbart, W.A. Monna, J. Nash, C. Mätzler: *The Integrated Ground-Based Remote Sensing Stations for Atmospheric Profiling* (COST, Brussels 2009)
- 47.9 J.-L. Redelsperger, C.D. Thorncroft, A. Diedhiou, T. Lebel, D.J. Parker, J. Polcher: African Monsoon Multidisciplinary Analysis: An international research project and field campaign, *Bull. Am. Meteorol. Soc.* **87**, 1739–1746 (2006)
- 47.10 C. Kottmeier, N. Kalthoff, U. Corsmeier, C. Barthlott, J. Van Baelen, A. Behrendt, R. Behrendt, A. Blyth, R. Coulter, S. Crewell, M. Dorninger, C. Flamant, T. Foken, M. Hagen, C. Hauck, H. Höller, H. Konow, M. Kunz, H. Mahlke, S. Mobbs, E. Richard, R. Steinacker, T. Weckwerth, A. Wieser, V. Wulfmeyer: Mechanisms initiating deep convection over complex terrain during COPS, *Meteorol. Z.* **17**, 931–948 (2008)
- 47.11 V. Wulfmeyer, A. Behrendt, C. Kottmeier, U. Corsmeier, C. Barthlott, G.C. Craig, M. Hagen, D. Althausen, F. Aoshima, M. Arpagaus, H.-S. Bauer, L. Bennett, A. Blyth, C. Brandau, C. Champollion, S. Crewell, G. Dick, P. Di Girolamo, M. Dorninger, Y. Dufournet, R. Eigenmann, R. Engelmann, C. Flamant, T. Foken, T. Gorgas, M. Grzeschik, J. Handwerker, C. Hauck, H. Höller, W. Junkermann, N. Kalthoff, C. Kiemle, S. Klink, M. König, L. Krauss, C.N. Long, F. Madonna, S. Mobbs, B. Neininger, S. Pal, G. Peters, G. Pigeon, E. Richard, M.W. Rotach, H. Russchenberg, T. Schwitalla, V. Smith, R. Steinacker, J. Trentmann, D.D. Turner, J. van Baelen, S. Vogt, H. Volkert, T. Weckwerth, H. Wernli, A. Wieser, M. Wirth: The Convective and Orographically-Induced Precipitation Study (COPS): The scientific strategy, the field phase, and research highlights, *Q. J. R. Meteorol. Soc.* **137**, 3–30 (2011)
- 47.12 V. Ducrocq, I. Braud, S. Davolio, R. Ferretti, C. Flamant, A. Jansa, N. Kalthoff, E. Richard, I. Taupier-Letage, P.-A. Ayrat, S. Belamari, A. Berne, M. Borga, B. Boudevillain, O. Bock, J.-L. Boichard, M.-N. Bouin, O. Bousquet, C. Bouvier, J. Chiggiano, D. Cimini, U. Corsmeier, L. Coppola, P. Cocquerez, E. Defer, J. Delanoë, P. Di Girolamo, A. Dorenbacher, P. Drobinski, Y. Dufournet, N. Fourrié, J.J. Gourley, L. Labatut, D. Lambert, J. Le Coz, F.S. Marzano, G. Molinié, A. Montani, G. Nord, M. Nuret, K. Ramage, B. Rison, O. Roussot, F. Saïd, A. Schwarzenboeck, P. Testor, J. van Baelen, B. Vincendon, M. Aran, J. Tamayo: HyMeX-SOP1: The field campaign dedicated to heavy precipitation and flash flooding in the northwestern Mediterranean, *Bull. Am. Meteorol. Soc.* **95**, 1083–1100 (2013)

- 47.13 A. Macke, P. Seifert, H. Baars, C. Barthlott, C. Beekmans, A. Behrendt, B. Bohn, M. Brueck, J. Bühl, S. Crewell, T. Damian, H. Deneke, S. Düsing, A. Foth, P. Di Girolamo, E. Hammann, R. Heinze, A. Hirsikko, J. Kalisch, N. Kalthoff, S. Kinne, M. Kohler, U. Löhnert, B.L. Madhavan, V. Maurer, S.K. Muppa, J. Schween, I. Serikov, H. Siebert, C. Simmer, F. Späth, S. Steinke, K. Träumner, S. Trömel, B. Wehner, A. Wieser, V. Wulfmeyer, X. Xie: The HD(CP)² Observational Prototype Experiment (HOPE) – An overview, *Atmos. Chem. Phys.* **17**, 4887–4914 (2017)
- 47.14 P. Groenemeijer, C. Barthlott, U. Corsmeier, J. Handwerker, M. Kohler, C. Kottmeier, H. Mahlke, A. Wieser, A. Behrendt, S. Pal, M. Radlach, V. Wulfmeyer, J. Trentmann: Observations of kinematics and thermodynamic structure surrounding a convective storm cluster over a low mountain range, *Mon. Weather Rev.* **137**, 585–602 (2009)
- 47.15 A. Foth, H. Baars, P. Di Girolamo, B. Pospichal: Water vapour profiles from Raman lidar automatically calibrated by microwave radiometer data during HOPE, *Atmos. Chem. Phys.* **15**, 7753–7763 (2015)
- 47.16 U. Górsdorf, F. Beyrich, H. Dier, U. Leiterer: Composite wind and temperature profiles obtained from a complex of in-situ and remote sensing measurements systems for the forcing of boundary layer model, *Theor. Appl. Climatol.* **73**, 97–105 (2002)
- 47.17 R. Calhoun, R. Heap, M. Princevac, R. Newsom, H. Fernando, D. Ligon: Virtual towers using coherent Doppler lidar during the Joint Urban 2003 Dispersion Experiment, *J. Appl. Meteorol. Climatol.* **46**, 1116–1126 (2006)
- 47.18 L. Röhner, K. Träumner: Aspects of convective boundary layer turbulence measured by a dual-Doppler lidar system, *J. Atmos. Ocean. Technol.* **30**, 2132–2142 (2013)
- 47.19 N.W. Cherukuru, R. Calhoun, M. Lehner, S.W. Hoch, C.D. Whiteman: Instrument configuration for dual-Doppler lidar coplanar scans: METCRAX II, *J. Appl. Remote Sens.* **9**, 096090 (2015)
- 47.20 N. Kalthoff, B. Adler, A. Wieser, M. Kohler, K. Träumner, J. Handwerker, U. Corsmeier, S. Khodayar, D. Lambert, A. Kopmann, N. Kunke, G. Dick, M. Ramatschi, J. Wickert, C. Kottmeier: KITcube – A mobile observation platform for convection studies deployed during HyMeX, *Meteorol. Z.* **22**, 633–647 (2013)
- 47.21 S. Khodayar, N. Kalthoff, J. Wickert, U. Corsmeier, C.J. Morcrette, C. Kottmeier: The increase of spatial data resolution for the detection of the initiation of convection. A case study from CSIP, *Meteorol. Z.* **19**, 179–198 (2010)
- 47.22 A.J. Illingworth, R.J. Hogan, E.J. O'Connor, D. Bouniol, M.E. Brooks, J. Delanoë, D.P. Donovan: Cloudnet: Continuous evaluation of cloud profiles in seven operational models using ground-based observations, *Bull. Am. Meteorol. Soc.* **88**, 883–898 (2007)
- 47.23 E.N. Kadyrov: *Operational Aspects of Different Ground-Based Remote Sensing Observing Techniques for Vertical Profiling of Temperature, Wind, Humidity and Cloud Structure: A Review* (WMO, Geneva 2006), Instruments and Observing Methods Report 89, CIMO/OPAG-UPPER-AIR/ET-RSUAT&T-1/Doc.6.2(1)
- 47.24 U. Löhnert, E. van Meijgaard, H.K. Baltink, S. Groß, R. Boers: Accuracy assessment of an integrated profiling technique for operationally deriving profiles of temperature, humidity and cloud liquid water, *J. Geophys. Res. Atmos.* **112**, D04205 (2007)
- 47.25 B. Adler, N. Kalthoff: Multiple-scale transport processes observed in the boundary layer over a mountainous island, *Bound.-Layer Meteorol.* **153**, 515–537 (2014)
- 47.26 C. Kiemle, M. Wirth, A. Fix, S. Rahm, U. Corsmeier, P. Di Girolamo: Latent heat flux measurements over complex terrain by airborne water vapour and wind lidars, *Q. J. R. Meteorol. Soc.* **137**, 190–203 (2011)
- 47.27 K. Träumner, C. Kottmeier, U. Corsmeier, A. Wieser: Convective boundary-layer entrainment: Short review and progress using Doppler lidar, *Bound.-Layer Meteorol.* **141**, 369–391 (2011)
- 47.28 B. Adler, N. Kalthoff, M. Kohler, J. Handwerker, A. Wieser, U. Corsmeier, C. Kottmeier, D. Lambert, O. Bock: The variability of water vapour and pre-convective conditions over the mountainous island of Corsica, *Q. J. R. Meteorol. Soc.* **142**, 335–346 (2016)
- 47.29 K. Ebell, U. Löhnert, E. Päschke, E. Orlandi, J.H. Schween, S. Crewell: A 1-D variational retrieval of temperature, humidity and liquid cloud properties: Performance under idealized and real conditions, *J. Geophys. Res. Atmos.* **122**, 1746–1766 (2017)
- 47.30 M. Barrera-Verdejo, S. Crewell, U. Löhnert, E. Orlandi, P. Di Girolamo: Ground-based lidar and microwave radiometry synergy for high vertical absolute humidity profiling, *Atmos. Meas. Tech.* **9**, 4013–4028 (2016)
- 47.31 A. Foth, B. Pospichal: Optimal estimation of water vapour profiles using a combination of raman lidar and microwave radiometer, *Atmos. Meas. Tech.* **10**, 3325–3344 (2017)
- 47.32 L. Bianco, D. Cimmini, F.S. Marzano, R. Ware: Combining microwave radiometer and wind profiler radar measurements for high-resolution atmospheric humidity profiling, *J. Atmos. Ocean. Technol.* **22**, 949–965 (2005)
- 47.33 D.D. Turner: Improved ground-based liquid water path retrievals using a combined infrared and microwave approach, *J. Geophys. Res. Atmos.* **112**, D15204 (2007)
- 47.34 T. Marke, K. Ebell, U. Löhnert, D.D. Turner: Statistical retrieval of thin liquid cloud microphysical properties using ground-based infrared and microwave observations, *J. Geophys. Res. Atmos.* **121**, 14558–14573 (2016)
- 47.35 A.S. Frisch, G. Feingold, C.W. Fairall, T. Uttal, J.B. Snider: On cloud radar and microwave radiometer measurements of stratus cloud liquid water profiles, *J. Geophys. Res. Atmos.* **103**, 23195–23197 (1998)

- 47.36 W.G. Blumberg, D.D. Turner, U. Löhnert, S. Castleberry: Ground-based temperature and humidity profiling using spectral infrared and microwave observations. Part II: Actual retrieval performance in clear sky and cloudy conditions, *J. Appl. Meteorol. Climatol.* **54**, 2305–2319 (2016)
- 47.37 U. Löhnert, D. Turner, S. Crewell: Ground-based temperature and humidity profiling using spectral infrared and microwave observations: Part I: Simulated retrieval performance in clear sky conditions, *J. Appl. Meteorol. Climatol.* **48**, 1017–1032 (2009)
- 47.38 U. Löhnert, S. Crewell, O. Krasnov, E. O'Connor, H. Russchenberg: Advances in continuously profiling the thermodynamic state of the boundary layer: Integration of measurements and methods, *J. Atmos. Ocean. Technol.* **25**, 1251–1266 (2008)
- 47.39 D.C. Tobin, H.E. Revercomb, R.O. Knuteson, B.M. Lesht, L.L. Strow, S.E. Hannon, W.F. Feltz, L.A. Moy, E.J. Fetzer, T.S. Cress: Atmospheric radiation measurement site atmospheric state best estimates for atmospheric infrared sounder temperature and water vapour retrieval, *J. Geophys. Res. Atmos.* **111**, D09S01 (2006)
- 47.40 J.S. Tradowsky, G.E. Bodeker, R.R. Querel, P.J.H. Builtjes, J. Fischer: Combining data from the distributed GRUAN site Lauder-Invercargill, New Zealand, to provide a site atmospheric state best estimate of temperature, *Earth Syst. Sci. Data* **10**, 2195–2211 (2018)
- 47.41 S. Xie, R.B. McCoy, S.A. Klein, R.T. Cederwall, W.J. Wiscombe, E.E. Clothiaux, K.L. Gaustad, J.C. Golaz, S.D. Hall, M.P. Jensen, K.L. Johnson, Y. Lin, C.N. Long, J.H. Mather, R.A. McCord, S.A. McFarlane, G. Palanisamy, Y. Shi, D.D. Turner: ARM climate modeling best estimate data: A new data product for climate studies, *Bull. Am. Meteorol. Soc.* **91**, 13–20 (2010)
- 47.42 R.O. Knuteson, H.E. Revercomb, F.A. Best, N.C. Ciganovich, R.G. Dedecker, T.P. Dirkx, S.C. Ellington, W.F. Feltz, R.K. Garcia, H.B. Howell, W.L. Smith, J.F. Short, D.C. Tobin: Atmospheric Emitted Radiance Interferometer. Part I: Instrument design, *J. Atmos. Ocean. Technol.* **21**, 1763–1776 (2004)
- 47.43 W. Hesse: *Handbuch der Aerologie* (Akademische Verlagsgesellschaft Geest & Portig, Leipzig 1961)
- 47.44 R. Aßmann, A. Berson, H. Gross: *Wissenschaftliche Luftfahrten, I. Band: Geschichte und Beobachtungsmaterial* (Friedrich Vieweg und Sohn, Braunschweig 1899)
- 47.45 W. Georgi: Das Segelflugzeug als Meßträger aerologischer Forschung. In: *Handbuch der Aerologie*, ed. by W. Hesse (Akademische Verlagsgesellschaft Geest & Portig, Leipzig 1961) pp. 250–282
- 47.46 H. Berg: Aerologische Flugzeugaufstiege. In: *Handbuch der Aerologie*, ed. by W. Hesse (Akademische Verlagsgesellschaft Geest & Portig, Leipzig 1961) pp. 282–380
- 47.47 M. Diem: Messungen der Größe von Wolkenelementen, *Meteorol. Rundsch.* **1**, 261–273 (1948)
- 47.48 J.P. Küttner, P.A. Hildebrand, T.L. Clark: Convection waves: Observations of gravity wave systems over convectively active boundary layers, *Q. J. R. Meteorol. Soc.* **113**, 445–467 (1987)
- 47.49 P. Debye: *Polar Molecules* (Chemical Catalog Company, New York, Dover 1929)
- 47.50 R.H. Dicke: The measurement of thermal radiation at microwave frequencies. In: *Classics in Radio Astronomy*, Studies in the History of Modern Science, Vol. 10, ed. by R.S. Cohen, E.N. Hiebert, E.I. Mendelsohn (Springer, Dordrecht 1946) pp. 106–113
- 47.51 E.E. Clothiaux, M.A. Miller, B.A. Albrecht, T.P. Ackerman, J. Verlinde, D.M. Babb, R.M. Peters, W.J. Syrett: An evaluation of a 94-GHz radar for remote sensing of cloud properties, *J. Atmos. Ocean. Technol.* **12**, 201–229 (1995)
- 47.52 B.B. Stankov: Multisensor retrieval of atmospheric properties, *Bull. Am. Meteorol. Soc.* **79**, 1835–1854 (1998)
- 47.53 G.L. Stephens, D.G. Vane, R.J. Boain, G.G. Mace, K. Sassen, Z. Wang, A.J. Illingworth, E.J. O'Connor, W.B. Rossow, S.L. Durden, S.D. Miller, R.T. Austin, A. Benedetti, C. Mitrescu: The CloudSat mission and the A-Train, *Bull. Am. Meteorol. Soc.* **83**, 1771–1790 (2002)
- 47.54 G. Mace, Q. Zhang, M. Vaughan, R. Marchand, G. Stephens, C. Trepte, D. Winker: A description of hydrometeor layer occurrence statistics derived from the first year of merged Cloudsat and CALIPSO data, *J. Geophys. Res. Atmos.* **114**, D00A26 (2009)
- 47.55 C. Kottmeier, H.-J. Belitz: Meteorological research using a high mast on the Antarctic ice shelf, *Mar. Technol.* **1**, 5–10 (1987)
- 47.56 J.C. Kaimal, J.E. Gaynor: The Boulder Atmospheric Observatory, *J. Appl. Meteorol. Climatol.* **22**, 863–880 (1983)
- 47.57 C. Kottmeier, D. Lege, R. Roth: Ein Meßsystem zur Sondierung der planetarischen Grenzschicht, *Meteorol. Rundsch.* **33**, 9–13 (1980)
- 47.58 C. Stawiarski, K. Träumner, C. Knigge, R. Calhoun: Scopes and challenges of dual-Doppler lidar wind measurements – An error analysis, *J. Atmos. Ocean. Technol.* **30**, 2044–2062 (2013)
- 47.59 P. Brugger, K. Träumner, C. Jung: Evaluation of a procedure to correct spatial averaging in turbulence statistics from a Doppler lidar by comparing time series with an ultrasonic anemometer, *J. Atmos. Ocean. Technol.* **33**, 2135–2144 (2016)
- 47.60 T. Damian, A. Wieser, K. Träumner, U. Corsmeier, C. Kottmeier: Nocturnal low-level jet evolution in a broad valley observed by dual Doppler lidar, *Meteorol. Z.* **23**, 305–313 (2014)
- 47.61 J.F. Newman, T.A. Bonin, P.M. Klein, S. Wharton, R.K. Newsom: Testing and validation of multi-lidar strategies for wind energy applications, *Wind Energy* **19**, 2239–2254 (2016)
- 47.62 L. Pauscher, N. Vasiljevic, D. Callies, L. Guillaume, J. Mann, T. Klaas, J. Hieronimus, J. Gottschall, A. Schwesig, M. Kühn, M. Courtney: An inter-comparison study of multi- and DBS lidar measurements in complex terrain, *Remote Sens.* **8**, 782 (2016)
- 47.63 M. Lehner, D. Whiteman, S.W. Hoch, E. Crossman, M. Jeglum, N. Cherukuru, R. Calhoun,

- B. Adler, N. Kalthoff, R. Rotunno, T. Horst, S. Semmer, W.O.J. Brown, S.P. Oncley, R. Vogt, A.M. Grudzielanek, J. Cermak, N.J. Fonteyne, C. Bernhofer, A. Pitacco, P. Klein: The METCRAX II field experiment – A study of downslope wind-storm-type flows in Arizona’s Meteor Crater, *Bull. Am. Meteorol. Soc.* **97**, 217–235 (2016)
- 47.64 M. Hill, R. Calhoun, H.J.S. Fernando, A. Wieser, A. Dörnbrack, M. Weissmann, G. Mayr, R. Newsom: Coplanar Doppler lidar retrieval of rotors from T-REX, *J. Atmos. Sci.* **67**, 713–729 (2010)
- 47.65 J. Grunwald, N. Kalthoff, U. Corsmeier, F. Fiedler: Comparison of areally averaged turbulent fluxes over non-homogeneous terrain: Results from the EFEDA-field experiment, *Bound.-Layer Meteorol.* **77**, 105–134 (1996)
- 47.66 D.D. Turner, R.A. Ferrare, V. Wulfmeyer, A.J. Scarino: Aircraft evaluation of ground-based raman lidar water vapor turbulence profiles in convective mixed layers, *J. Atmos. Ocean. Technol.* **31**, 1078–1088 (2014)
- 47.67 S.K. Muppa, A. Behrendt, F. Späth, V. Wulfmeyer, S. Metzendorf, A. Riede: Turbulent humidity fluctuations in the convective boundary layer: Case studies using water vapour differential absorption lidar measurements, *Bound.-Layer Meteorol.* **158**, 43–66 (2016)
- 47.68 M. Bevis, S. Businger, T.A. Herring, C. Roken, R.A. Anthes, R.H. Ware: GPS meteorology: Remote sensing of atmospheric water vapour using the global positioning system, *J. Geophys. Res.* **97**, 15787–15801 (1992)
- 47.69 J. Wickert, G. Gendt: Fernerkundung der Erdatmosphäre mit GPS, *Promet Meteorol. Fortbild.* **32**, 176–184 (2006)
- 47.70 G. Martucci, C.D. O’Dowd: Ground-based retrieval of continental and marine warm cloud microphysics, *Atmos. Meas. Tech.* **4**, 2749–2765 (2011)
- 47.71 B. Adler, N. Kalthoff, O. Kiseleva: Detection of structures in the horizontal wind field over complex terrain using coplanar Doppler lidar scans, *Meteorol. Z.* **29**(6), 467 (2020)
- 47.72 B. Adler, A. Gohm, N. Kalthoff, N. Babić, U. Corsmeier, M. Lehner, M.W. Rotach, M. Haid, P. Markmann, E. Gast, G. Tsaknakis: CROSSINN: A field experiment to study the three-dimensional flow structure in the Inn Valley, Austria, *Bull. Am. Meteorol. Soc.* **102**(1), E38–E60 (2021)
- 47.73 G. Pappalardo, A. Amodeo, A. Apituley, A. Comeron, V. Freudenthaler, H. Linné, A. Ansmann, J. Bösenberg, G. D’Amico, I. Mattis, L. Mona, U. Wandinger, V. Amiridis, L. Alados-Arboledas, D. Nicolae, M. Wiegner: EARLINET: Towards an advanced sustainable European aerosol lidar network, *Atmos. Meas. Tech.* **7**, 2389–2409 (2014)
- 47.74 P. Dubois: *Das Observatorium Lindenberg in seinen ersten 50 Jahren 1905–1955*, Geschichte der Meteorologie in Deutschland (DWD, Offenbach 1993)
- 47.75 J. Neisser, W. Adam, F. Beyrich, U. Leiterer, H. Steinhagen: Atmospheric boundary layer monitoring at the meteorological observatory Lindenberg as a part of the ‘Lindenberg Column’: Facilities and selected results, *Meteorol. Z.* **11**, 241–253 (2002)
- 47.76 F. Beyrich, H.-J. Herzog, J. Neisser: The LITFASS Project of DWD and the LITFASS-98 Experiment: The project strategy and the experimental setup, *Theor. Appl. Climatol.* **73**, 3–18 (2002)
- 47.77 F. Beyrich, H.-T. Mengelkamp: Evaporation over a heterogeneous land surface: EVA_GRIPS and the LITFASS-2003 Experiment – An overview, *Bound.-Layer Meteorol.* **121**, 5–32 (2006)
- 47.78 J. Neisser: 100 Jahre Atmosphärensondierung am Meteorologischen Observatorium Lindenberg, *Promet Meteorol. Fortbild.* **31**, 81–207 (2005)
- 47.79 J. Bühl, R. Leinweber, U. Górsdorf, M. Radenz, A. Ansmann, V. Lehmann: Combined vertical-velocity observations with Doppler lidar, cloud radar and wind profiler, *Atmos. Meas. Tech.* **8**, 3527–3536 (2015)
- 47.80 S. Trömel, A.V. Ryzhkov, T. Bick, C. Simmer: Now-casting winter precipitation: The Black Ice Event in Berlin 2014, *Meteorol. Z.* **26**, 147–160 (2017)
- 47.81 C. Acquistapace, S. Kneifel, U. Löhnert, P. Kollias, M. Maahn, M. Bauer-Pfundstein: Optimizing observations of drizzle onset with millimeter-wavelength radars, *Atmos. Meas. Tech.* **10**, 1783–1802 (2017)
- 47.82 D.H. Lenschow, J. Mann, L. Kristensen: How long is long enough when measuring fluxes and other turbulence statistics?, *J. Atmos. Ocean. Technol.* **11**, 661–673 (1994)
- 47.83 N. Wittkamp, B. Adler, N. Kalthoff, O. Kiseleva: Mesoscale wind patterns over the complex urban terrain around Stuttgart investigated with dual-Doppler lidar profiles, *Meteorol. Z.* **30**(2), 185–200 (2021)
- 47.84 C.D. Whiteman, M. Lehner, S.W. Hoch, B. Adler, N. Kalthoff, R. Vogt, I. Feigenwinter, T. Haiden, M.O. Hills: The evolution of atmospheric structure as a nocturnal katabatic flow is lifted over the rim of a basin, *J. Appl. Meteorol. Climatol.* **57**, 969–989 (2018)
- 47.85 U. Corsmeier, R. Hankers, A. Wieser: Airborne turbulence measurements in the lower troposphere onboard the research aircraft Dornier 736 128–6, *D-IBUF, Meteorol. Z.* **10**, 315–329 (2001)
- 47.86 A.R. Nehrir, C. Kiemle, M.D. Lebsock, G. Kirchengast, S.A. Buehler, U. Löhnert, Cong-Liang Liu, P.C. Hargrave, M. Barrera-Verdejo, D.M. Winker: Emerging Technologies and Synergies for Airborne and Space-Based Measurements of Water Vapor Profiles, *Surveys in Geophysics* **38**(6), 1445–1482 (2017)
- 47.87 V. Wulfmeyer, S.K. Muppa, A. Behrendt, E. Hammann, F. Späth, Z. Sorbjan, D.D. Turner, R.M. Hardesty: Determination of convective boundary layer entrainment fluxes, dissipation rates, and the molecular destruction of variances: Theoretical description and a strategy for its confirmation with a novel lidar system synergy, *J. Atmos. Sci.* **73**, 667–692 (2016)
- 47.88 T.M. Weckwerth, K.J. Weber, D.D. Turner, S.M. Spuler: Validation of a water vapor mi-

- cropulse differential absorption lidar (DIAL), *J. Atmos. Ocean. Technol.* **33**, 2353–2372 (2016)
- 47.89 M. Toporov, U. Löhnert: Synergy of satellite- and ground-based observations for continuous monitoring of atmospheric stability, liquid water path and integrated water vapor, *J. Appl. Meteorol. Climatol.* **59**(7), 1153–1170 (2020)
- 47.90 A.J. Illingworth, H.W. Barker, A. Beljaars, M. Ceccaldi, H. Chepfer, N. Clerbaux, J. Cole, J. Delanoë, C. Domenech, D.P. Donovan, S. Fukuda, M. Hirakata, R.J. Hogan, A. Huenerbein, P. Kollias, T. Kubota, T. Nakajima, T.Y. Nakajima, T. Nishizawa, Y. Ohno, H. Okamoto, R. Oki, K. Sato, M. Satoh, M.W. Shephard, A. Velázquez-Blázquez, U. Wandinger, T. Wehr, G.-J. van Zadelhoff: The EarthCARE Satellite: The next step forward in global measurements of clouds, aerosols, precipitation, and radiation, *Bull. Am. Meteorol. Soc.* **96**, 1311–1332 (2015)

Christoph Kottmeier

Institute of Meteorology and Climate Research, Department Troposphere
Karlsruhe Institute of Technology (KIT)
Karlsruhe, Germany
christoph.kottmeier@kit.edu



Christoph Kottmeier is professor of meteorology and headed the Institute of Meteorology and Climate Research (Department Troposphere) at the KIT until 2020. His conducts tropospheric research by applying advanced observation techniques (aircraft, automatic buoys, lidar, and radar) as well as numerical modelling with COSMO and ICON model systems. He initiated the construction of the KITcube facility for integrated observation.

Bianca Adler

CIRES, University of Colorado Boulder
Boulder, CO, USA

NOAA/Physical Sciences Laboratory
Boulder, CO, USA
bianca.adler@noaa.gov



Bianca Adler was an atmospheric scientist in the Land Surface and Boundary Layer research group at the Institute of Meteorology and Climate Research (Karlsruhe Institute of Technology, Germany). Since 2020, Bianca Adler is a research scientist at CIRES in Boulder working at the NOAA Physical Science Laboratory (PSL). Her research focuses on multiscale processes in the boundary layer over complex terrain and the synergistic use of remote sensing, in-situ measurements, and high-resolution numerical simulations to gain the best possible insights into atmospheric conditions and processes.

Norbert Kalthoff



Institute of Meteorology and Climate Research, Department Troposphere
Karlsruhe Institute of Technology (KIT)
Karlsruhe, Germany
no.kalthoff@web.de

Norbert Kalthoff is group leader of the Land Surface and Boundary Layer research group at the Institute of Meteorology (Department Troposphere) and Climate Research at the Karlsruhe Institute of Technology in Germany. He received his PhD in meteorology in 1986 from the University of Bonn, Germany. His research team contributes to several national and international field campaigns worldwide, investigating land–surface processes and its impact on the atmospheric boundary layer as well as on the initiation of moist convection. His main scientific focus is on processes over complex terrain.

Ulrich Löhnert



Institute for Geophysics and Meteorology
University of Cologne
Köln, Germany
ulrich.loehnert@uni-koeln.de

Ulrich Löhnert is a Professor at the University of Cologne (Germany). His research focuses on the use of ground-based atmospheric remote sensing for a better understanding of the physical processes within the atmospheric boundary layer as well as for improving weather forecast models. For this, he leads JOYCE – the Jülich Observatory for Cloud Evolution (www.joyce.cloud).

Ulrich Görzdorf

Meteorologisches Observatorium
Lindenberg – Richard Altmann
Observatorium
German Meteorological Service (DWD)
Lindenberg, Germany
ulrich.goersdorf@dwd.de



Ulrich Görzdorf is a research associate in the Remote Sensing Group of the Lindenberg Meteorological Observatory, operated by the DWD. He studied meteorology at the Humboldt University in Berlin, and obtained his PhD in radar wind profiling in 1999. His current research focuses on the assessment and evaluation of cloud radar and ceilometer measurements.

48. Aircraft-Based Flux Density Measurements

Raymond L. Desjardins , Devon E. Worth, Ian MacPherson, Matthias Mauder , Jens Bange 

This chapter presents aircraft-based methods of measuring the flux densities of sensible and latent heat, carbon dioxide, ozone, nitrous oxide, methane, and other trace gases. The main techniques and sensors that are used to measure flux densities with an aircraft are briefly described. Factors that affect the accuracy of those flux density measurements are discussed, including analysis techniques, run lengths, sampling heights, surface and environmental conditions, and data quality assessment. The use of aircraft-based flux density measurements to evaluate the representativeness of tower-based flux measurements is examined. The versatility of aircraft to act as sensor platforms under a wide range of conditions is demonstrated using several interesting examples. Future potential research directions are mentioned.

48.1	Measurement Principles and Parameters	1306	48.4	Devices and Systems	1310
48.1.1	Flux Measurement Techniques	1306	48.4.1	Flux Aircraft	1310
48.1.2	Measured Variables and Parameters Calculated	1306	48.4.2	Aircraft Position and Altitude	1311
48.2	History	1307	48.4.3	Wind Measurements	1311
48.2.1	Initial Flux Density Measurements	1307	48.4.4	Scalar Sensors	1312
48.2.2	Importance of Large-Scale Field Experiments	1307	48.4.5	Solar Radiation Sensors and Satellite Simulators	1312
48.2.3	Flux Density Measurements from Smaller-Scale Experiments	1308	48.4.6	REA System	1313
48.3	Theory	1308	48.4.7	Data Acquisition	1313
48.3.1	Eddy Covariance (EC) Technique	1308	48.5	Specifications of Sensors for Flux Density Measurements	1313
48.3.2	Relaxed Eddy Accumulation (REA) Technique	1309	48.6	Quality Control	1314
48.3.3	Wavelet Covariance	1309	48.6.1	Quality Assessment	1314
48.3.4	Mass Balance	1310	48.6.2	Spectral Response	1315
			48.7	Maintenance	1315
			48.8	Applications	1315
			48.8.1	Comparison of Aircraft-Based and Ground-Based Flux Density Measurements	1316
			48.8.2	Quantifying Flux Density Over Complex Ecosystems	1318
			48.8.3	Evaluation of GHG Emission Inventories	1318
			48.9	Future Developments	1320
			48.10	Further Reading	1321
			48.A	Appendix	1321
			48.A.1	True Airspeed by the Flight Mechanical Angles α and β	1321
			48.A.2	True Airspeed, Temperature, and Pressure	1322
			48.A.3	Flow Angles	1324
			References		1325

Aircraft are versatile sensor platforms that have the ability to measure surface-atmosphere exchange throughout the planetary boundary layer and can be rapidly deployed to areas of interest. Such flux measurements complement tower-based flux measurements (Chap. 55)

that provide data for long periods of time at one location. This combination of flux measurements has been widely used for ecosystem studies and for developing and validating atmosphere-biosphere models.

48.1 Measurement Principles and Parameters

This section briefly presents the main techniques for obtaining flux density measurements using aircraft-based systems as well as the variables measured and parameters calculated.

48.1.1 Flux Measurement Techniques

Several techniques have been used to measure the vertical fluxes of momentum, sensible heat, water vapor, and other scalars using aircraft-based systems. The eddy covariance (EC) technique provides the most direct measurements of mass and energy exchange at the land–atmosphere interface. Wavelet analysis, which yields wavelet cross-scalograms between vertical wind and various scalars, provides spatial information that makes it easier to relate flux density measurements to surface characteristics along a flight track. Both of these techniques require fast-response (10–20 Hz) sensors. For gases such as nitrous oxide (N₂O), volatile

organic compounds (VOCs), and agrochemicals, for which fast-response analyzers are unavailable on an aircraft, the relaxed eddy accumulation (REA) technique has proven to be extremely useful (Chap. 56). Mass balance, inverse modeling, and tracer gas techniques have also facilitated the quantification of gas emissions from large sources such as urban centers, landfill sites, and leakages from natural gas infrastructure. All these flux-measuring techniques complement each other, and the best choice depends on the types of gas and source involved.

48.1.2 Measured Variables and Parameters Calculated

Summaries of the variables measured and the parameters calculated for aircraft-based flux-density measurements are presented in Tables 48.1 and 48.2, respectively.

Table 48.1 Variables measured for aircraft-based flux density calculations and chapters in which they are discussed in this Handbook

Parameter	Description (sensor)	Symbol	Unit	Relevant chapter
Horizontal wind components	Scalar components of horizontal wind speed (multiport pressure transducer)	u, v	m s^{-1}	Chap. 9
Vertical wind velocity	Vertical component of wind speed (multiport pressure transducer)	w	m s^{-1}	Chap. 9
Air temperature	Air temperature (heated or unheated total air temperature probe)	T	K	Chap. 1
	Potential air temperature (total air temperature, pitot static systems)	θ	K	
Mass density	Mass of constituent per volume air (various gas analyzers: infrared differential absorption, cavity ring-down spectroscopy, off-axis cavity output spectroscopy)	ρ_s	kg m^{-3}	Chaps. 16–18
Air density	Mass air per volume air (wet: thermometer, air pressure; dry: thermometer, hygrometer, air pressure)	ρ_a, ρ_d	kg m^{-3}	Chaps. 7, 8, 10, 16
Pressure	Atmospheric pressure (pitot static systems)	p	hPa	Chap. 10

Table 48.2 Other variables and parameters calculated for aircraft-based flux density measurements and chapters in which they are discussed in this Handbook

Parameter	Description	Symbol	Unit	Relevant chapter
Shear stress	$\tau = \rho \sqrt{(\overline{w'u'})^2 + (\overline{w'v'})^2}$	τ	$\text{kg m}^{-1} \text{s}^{-2}$	Chaps. 1, 55
Friction velocity	$u_* = \sqrt{(\overline{w'u'})^2 + (\overline{w'v'})^2}$	u_*	m s^{-1}	Chaps. 1, 55
Sensible heat flux	$Q_H = c_p \rho \overline{w'T'}$ or $Q_H = c_p \rho \overline{w'\theta'}$, where c_p is the specific heat at constant p and $\theta = T \left(\frac{1000}{p} \right)^{\frac{2}{7}}$ to correct for changes in flight altitude	Q_H	W m^{-2}	Chaps. 1, 55
Latent heat flux	$Q_E = \lambda \rho \overline{w'q'}$, where λ is the specific heat of vaporization	Q_E	W m^{-2}	Chaps. 1, 55
Trace gas flux	$Q_{\chi_{sm}} = \rho_d \overline{w'\chi'_{sm}}$, where χ_{sm} is the dry mixing ratio (kg kg^{-1} dry air) of the gas being measured	$Q_{\chi_{sm}}$	$\text{g m}^{-2} \text{s}^{-1}$	

48.2 History

Since the dawn of aviation, aircraft have been used for both civilian and military purposes. Environmental and meteorological observations have been made by aircraft since World War I [48.1]. The speed, payload flexibility, and ability of aircraft to provide an aerial perspective has consistently provided value to a variety of industries. These same capabilities have proven to be extremely useful for atmospheric flux measurements.

48.2.1 Initial Flux Density Measurements

Aircraft-based EC measurements have been carried out in the planetary boundary layer for almost five decades. Early aircraft-based measurements quantified the fluxes of momentum and heat [48.2]. This was shortly followed by measurements of water vapor (H_2O) flux during the Barbados Oceanographic and Meteorological Experiment (BOMEX) [48.3], a study of the structure of turbulence in the lower atmosphere [48.4], and measurements of the variations in the turbulent fluxes of momentum, heat, and moisture over Lake Ontario at several altitudes [48.5]. Later, the average vertical flux of ozone (O_3) over a distance of 100 km was evaluated [48.6] (measurements over such a large distance were required because of the small correlation coefficient between ozone and vertical wind velocity). Aircraft-based flux measurements of CO_2 collected for a wide range of ecosystems showed that repeatable flux measurements could be obtained by making several passes 4–5 km in length over a given site, and that the frequency response of the sensors was adequate to perform EC flux measurements at altitudes as low as 25 m [48.7, 8].

48.2.2 Importance of Large-Scale Field Experiments

Soon after these initial flux studies, aircraft became essential flux-measuring platforms for many large-scale field experiments. The Amazon/Arctic Boundary Layer Experiments (ABLE), which took place from 1985 to 1990, used a combination of tower-based and aircraft-based flux measurements to study ecosystems that were considered to strongly influence atmospheric chemistry globally [48.9, 10]. Two major ecosystems studied were the rain forest of Brazil during the dry and wet seasons and the northern wetlands of the Hudson Bay lowland. The focus was on quantifying the rate of exchange of mass between the Earth's surface and the atmospheric boundary layer. In 1986, the Hydrologic Atmospheric Pilot Experiment (HAPEX)-MOBILHY

experiment in France attempted to characterize the hydrological budget of an area 100 km by 100 km [48.11]. In this experiment, instrumented aircraft were used to obtain simultaneous measurements of atmospheric fluxes and remotely sensed properties of the Earth's surface. In 1987 and 1989, the First ISLSCP (International Satellite Land Surface Climatology Project) Field Experiment (FIFE), carried out in Kansas (USA), set out to develop methodologies to study a grassland ecosystem at a scale of 15 km by 15 km using a variety of measuring systems [48.12]. It was designed to obtain satellite and ground observations for the development and validation of models relating surface fluxes to spectral data [48.13]. Aircraft flights over the FIFE research area provided the data required to evaluate the various terms in the conservation equation and to elucidate that the underestimation seen in aircraft-based flux measurements was mainly due to the undersampling of long-wavelength contributions and the divergence of flux with height [48.14, 15].

Between 1994 and 1996, the Boreal Ecosystem–Atmosphere Study (BOREAS) was undertaken to examine the role of the boreal forest in global environmental changes [48.16]. The region selected covered an area of 1000 km by 1000 km. In order to characterize the heterogeneity of the boreal landscape, a flux-unmixing method based on aircraft-based flux measurements was developed, along with a land-cover map derived from the Landsat thematic mapper and tower-based flux measurements from eight cover types [48.17]. Using this information, they were able to derive flux data for cover types for which there were no tower-based measurements. Several additional large-scale studies soon followed, such as the Southern Great Plains (SGP) hydrology experiment, which was motivated by the scientific interest in estimating soil moisture conditions at the continental scale using remotely sensed data [48.18], whereas the Large-Scale Biosphere–Atmosphere (LBA) experiment in Amazonia focused on how tropical forest conversion affects carbon and nitrogen dynamics as well as trace gas fluxes [48.19]. These large-scale experiments were an excellent opportunity to develop more sophisticated technology and data analysis techniques for aircraft-based flux measurements. It soon became clear that it was easier to get comparable flux measurements between aircraft [48.20] than between aircraft and tower-based systems [48.21] because of different averaging periods, different footprints, and the divergence of flux with height.

Table 48.3 Important milestones in aircraft-based flux measurements and chapters in which they are discussed in this Handbook

Year	Milestone	Reference(s)	Relevant chapter
Early 1970s	First reported aircraft-based EC measurements of sensible and latent heat fluxes	[48.2, 3]	Chap. 55
1980s	First reported aircraft-based EC CO ₂ flux measurements	[48.8]	Chap. 16
1990s	First reported aircraft-based flux measurements of agrochemicals and VOCs with REA	[48.22, 23]	
2000s	Wavelet transform used for obtaining aircraft-based flux measurements over short distances	[48.24, 25]	Chap. 56
2010s	Aircraft-based EC and REA (CH ₄ , N ₂ O) flux measurements	[48.26–29]	

48.2.3 Flux Density Measurements from Smaller-Scale Experiments

Aircraft-based flux density measurements were also obtained during many smaller-scale experiments. The prime focus of the California Ozone Deposition Experiment (CODE) was to improve estimates of the absorption of ozone by crops [48.30]. The Mackenzie GEWEX Study (MAGS) focused on the hydrological cycle and energy fluxes of the Mackenzie River Basin [48.31]. This was an area for which there were few measurements, so it was important to develop land-surface algorithms based on satellite data. Another part of the global energy and water exchange (GEWEX) project, the GAME-Siberia (GEWEX Asian Monsoon Experiment), conducted aircraft-based flux measurements in the Yakutsk region that highlighted the spatial variability in flux estimates for a forest-grass landscape in spring [48.24], and completed pioneering work to apply wavelet transforms to aircraft-measured turbulence and turbulent fluxes [48.32]. Also, aircraft measurements obtained during the GAME-Siberia project helped to identify the conditions in which local circulation patterns [48.33] exacerbate the common problem of flux underestimation observed by tower-based measurement systems [48.34]. The Soil Moisture Atmosphere

Coupling Experiment (SMACEX) was designed to use a combination of aircraft-based and tower-based flux measurements, satellite data, and models to help understand the impact of spatial and temporal variability in vegetation cover, soil moisture, and other land-surface states on atmosphere–surface interactions across a wide range of scales [48.35]. Many other small-scale experiments were carried out. For example, methane (CH₄) and VOC emissions over shale gas production regions were measured [48.36]. In that study, the EC technique was applied to measure the fluxes of CH₄ and benzene. Results indicated that in the two regions studied, 10% of the facilities contributed 40% of the CH₄ emissions. Aircraft-based measurements have been used to quantify CH₄ and ammonia emissions from a beef feedlot [48.37] and to apportion the emissions to appropriate sources (cattle, effluent ponds, and manure piles) within the feedlot. Recently, a suite of commercial and custom instrumentation was employed to acquire the fluxes of CO₂, CH₄, sensible heat, and latent heat at high spatial resolution in order to gain new insights into biophysical and biogeochemical processes [48.26].

Some milestones in the development of aircraft-based flux methods are given in Table 48.3. A common theme is that techniques developed for tower-based systems were adapted for use on aircraft-based systems.

48.3 Theory

Several techniques have been successfully used to obtain aircraft-based flux measurements. The EC technique (Chap. 55) is the most frequently used of these techniques, but others such as wavelet analysis, relaxed eddy accumulation, and mass balance have all provided useful information.

48.3.1 Eddy Covariance (EC) Technique

The EC technique (Chap. 55) is widely used for the measurement of mass and energy exchange at the land–atmosphere interface [48.38]. In this technique, the flux density is integrated over time for a tower-based system and over space for an aircraft-based system. The aircraft is flown at a constant velocity and altitude and

the covariance between the vertical wind and the scalar of interest is calculated, i.e.,

$$F_c = \frac{1}{N} \sum_{i=1}^N (c_i - \bar{c})(w_i - \bar{w}) = \frac{1}{N} \sum_{i=1}^N (c'_i w'_i), \quad (48.1)$$

where the mixing ratio of the scalar c_i is the sum of the mean mixing ratio \bar{c} and the deviation from the mean c'_i ; similarly, the vertical air velocity w_i is the sum of the mean vertical wind \bar{w} and the fluctuations from the mean w'_i . These values are measured at constant time intervals over a certain time period or a certain distance. Reasonably stationary conditions, negligible horizontal advection, and an absence of chemical reac-

tions involving the gas of interest within the air column below the measuring system are required for accurate flux measurements. Ignoring these conditions leads to flux divergence with height, causing the surface flux to be underestimated.

In a tower-based EC system, wind and scalar measurements are closely collocated in space to ensure that the same eddies are being sampled. This is often not possible in aircraft-based EC systems: there is substantial physical separation (on the order of one to several meters) between the vertical wind and scalar measurements. Therefore, to compute aircraft-based fluxes, the data must be adjusted for the time taken for a parcel of air to pass from the nose boom, where the air velocity is measured, to the other sensors [48.39]. This adjustment is particularly important for measurements performed at low altitude, where the spacing of the sensors can become a significant fraction of the typical eddy size [48.40]. The mean must be calculated to determine the flux using the EC technique. This can be done by either block averaging, linear detrending, or high-pass filtering the time series. The practice of comparing the flux estimates obtained from raw, linearly detrended, and high-pass-filtered time series has proven to be a useful screening technique for identifying non-stationary conditions [48.21, 39].

48.3.2 Relaxed Eddy Accumulation (REA) Technique

For many years, only the fluxes of heat, momentum, and a limited number of gases (e.g., CO₂, H₂O, and O₃) were measured using the EC technique on aircraft. This was the case because there were no fast-response analyzers for most of the other gases. The eddy accumulation (EA) technique was suggested by [48.41] as a potential solution to this problem (Chap. 56). In this technique, air is collected in one of two reservoirs using fast-response valves [48.42]. The reservoir used for collection is selected based on whether a vertical wind anemometer detects ascending or descending air, and the rate at which air is collected depends on the vertical wind speed. The air collected over a half-hour period was subsequently analyzed using a slow-response gas analyzer such as a mass spectrometer [48.41]. Several years later, the REA technique was proposed [48.43]. This technique is simpler to implement than the EA technique and gives similar results [48.44]. With the REA technique, the flux density (FC_{REA}) is equal to the product of the difference between the mean concentrations of the gas of interest in the ascending (\bar{C}^+) and descending (\bar{C}^-) air, the standard deviation of the vertical wind σ_w (m s⁻¹), the air density ρ_d , the ratio of the molar mass of the scalar $M(C)$ to the molar mass of air

$M(\text{Air})$, and an empirical parameter A [48.45]; in other words,

$$\text{FC}_{\text{REA}} = A\sigma_w\rho_d \left(\bar{C}^+ - \bar{C}^- \right) \frac{M(C)}{M(\text{Air})}. \quad (48.2)$$

This technique has been used successfully on aircraft to measure the fluxes of agrochemicals, VOCs, N₂O, and CH₄ [48.22, 23, 27, 29]. Similar to the discussion in Sect. 48.3.1, there can be significant physical separation between the vertical wind measurements and the pump, tubing, and valve assembly needed to partition the gas samples in the REA technique. Thus, the time lag between the wind measurements and the gas partitioning must be precisely determined, otherwise the flux can be significantly underestimated [48.46].

48.3.3 Wavelet Covariance

Wavelet analysis [48.47], which is a powerful tool for signal analysis in the frequency and time domains, has been increasingly used to estimate turbulent fluxes obtained using aircraft-based sensors [48.25, 32, 48–50]. The wavelet method provides estimates of the spectra and cospectra over a larger scale interval than the Fourier transform. It also provides both frequency and spatial localization. This information is important in studies connecting flux measurements to surface characteristics. The Morlet wavelet has been used to show the various scales that contribute to the fluxes of mass and energy exchange along a nonhomogeneous transect over a boreal forest [48.25]. In general, a continuous wavelet transform of a discrete sequence $x(n)$ is defined as the convolution of $x(n)$ with a wavelet function,

$$W_x(a, b) = \sum_{n=0}^N x(n)\psi_{p,a,b}^*(n), \quad (48.3)$$

where $W_x(a, b)$ are the wavelet coefficients as functions of the scale or dilatation parameter a and the shift or translation parameter b , and $\psi_{p,a,b}^*$ is the complex conjugate of a wavelet function. Averaging the cross-scalogram matrix $W_x(a, b)W_y^*(a, b)$ yields the wavelet cross-spectrum [48.51]

$$E_{xy} = \frac{\delta t}{C_\delta} \frac{1}{N} \sum_{n=0}^{N-1} W_x(a, b)W_y^*(a, b), \quad (48.4)$$

where δt is the time step of the time series. The factor C_δ originates from a delta (δ) function that was used to reconstruct the band-pass filtered original time series from the wavelet transform, and is a constant for each wavelet function [48.47].

Table 48.4 Advantages and disadvantages of the main aircraft-based flux measurement techniques

Measuring technique	Advantages	Disadvantages
Eddy covariance	Provides the most direct measurement of turbulent flux	Requires measurements over long distances, fast-response sensors, complex instrumentation, and synchronization of the data collected
Wavelet covariance	Provides spatially resolved flux estimates, including long-wave components	Requires EC instrumentation
Relaxed eddy accumulation	Enables flux measurements of gases for which there are no aircraft-compatible fast-response analyzers	Cone of influence: edge effects reduce confidence in flux estimates Precise determination of the time lag between a wind gust and gas sampling is essential Due to the nature of the sample collection, it is not possible to perform corrections ex post facto
Mass balance	Simpler instrumentation and calculations; provides flux density estimates for sources of various sizes	Requires nontrivial assumptions regarding the wind direction, boundary layer height, background concentration, and even mixing

The covariance of two signals x and y can be calculated from the real part of the cross-spectrum,

$$\text{cov}_{xy} = \delta j \sum_{j=0}^J \frac{\text{Re}(E_{xy}(j))}{a(j)}, \quad (48.5)$$

where δj , a nondimensional factor, determines the spacing between discrete scales of the wavelet transform [48.47].

48.3.4 Mass Balance

The mass balance computation of the flux of trace gases depends on the assumptions that winds are steady in the horizontal direction, that the atmospheric boundary layer is well developed, that there is complete and even mixing, and the measurements are taken upwind and downwind of the source. The difference between what goes into and out of an area is the magnitude of the emission. In general, the flux (mols s^{-1}) of a scalar (FC_{MB}) is calculated as

$$\text{FC}_{\text{MB}} = U \int_{-p}^p \Delta C \left(\int_{z_{\text{ground}}}^{z_{\text{pbl}}} n_{\text{air}} dz \right) \cos \gamma dx, \quad (48.6)$$

where U is the mean horizontal wind speed, the increase in the concentration of the scalar above the background (ΔC) is integrated over the total measured plume width ($-p$ to p), n_{air} is the average molar density of air between the ground surface (z_{ground}) and the planetary boundary layer (z_{pbl}), and γ is the angle between the mean horizontal wind direction and a line normal to the aircraft flight direction. Therefore, along a flight track of length x , $\cos \gamma dx$ is the distance that is perpendicular to the mean horizontal wind.

This technique has been used to quantify urban emissions for a wide range of gases [48.52, 53]. Constant wind conditions are very important, and while accurate mean emissions can be obtained, emission estimates from individual flights have a high uncertainty [48.54]. Convective boundary layer budgeting has also been carried out to estimate fluxes using concentration profiles. Regional-scale CH_4 emissions from a predominantly agricultural area were estimated using aircraft-measured concentration profiles [48.55]. Methane fluxes calculated under strong wind conditions were shown to be consistent with bottom-up estimates.

A brief overview of the advantages and disadvantages of these techniques for measuring the flux density is presented in Table 48.4.

48.4 Devices and Systems

A variety of aircraft ranging from a small single-engine ultralight [48.56] to larger multiengine aircraft [48.8, 24, 28] have been used to conduct flux measurements. These aircraft can carry a wide array of instrumentation to measure positions, air motions, temperatures, trace-gas concentrations, and radiative exchange.

48.4.1 Flux Aircraft

Aircraft have become elaborate measuring platforms for obtaining flux density measurements of mass and

energy over a wide range of ecosystems [48.24, 28, 40, 56]. Many different types of flux aircraft have been used [48.20, 26, 32, 56]. It has been found to be easier to get agreement between aircraft than between aircraft and tower-based systems. It is possible to have relatively similar footprints for two aircraft, but this is not possible in aircraft-to-tower comparisons [48.20, 21, 56]. In a comparison of the measurements from four aircraft, some differences were noted, but generally the fluxes and variances did not differ by more than expected given the separation of the aircraft [48.20].

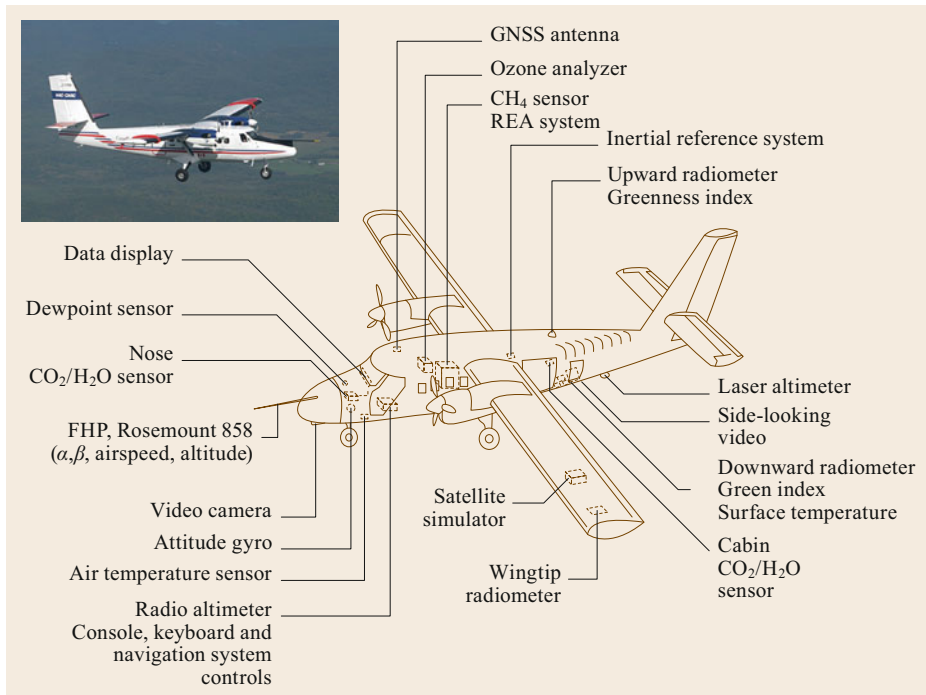


Fig. 48.1 The NRC Twin Otter Aircraft as configured for flux measurements (after [48.57] photo is presented courtesy of the Flight Research Laboratory of the NRC Canada)

However, since each flux aircraft is unique, generalizations regarding aircraft type, the instrumentation used, and the positioning of that instrumentation are not possible. A typical setup features nose-mounted wind-speed and temperature sensors complemented by cabin-mounted gas-sampling and radiation equipment. Alternatively, wind and temperature measurements can be performed in a wing-mounted pod, as described in [48.58]. Figure 48.1 provides an example of instrumentation onboard the National Research Council (NRC) Canada Twin Otter flux aircraft for measuring the position and altitude of the aircraft, three wind components, the air pressure, the air and dewpoint temperatures, and the concentrations of H_2O , CO_2 , O_3 , and CH_4 . Data acquisition and computer systems for real-time data analysis and a video camera are also shown, as well as a wide range of multispectral sensors for measuring the incoming and reflected solar radiation, net radiation, surface temperature, and the greenness of vegetation using various satellite simulators. Unmanned aircraft systems (UASs)—another type of aircraft—are also used to obtain flux density measurements (see Chap. 49).

48.4.2 Aircraft Position and Altitude

Many different systems have been used on aircraft to measure location. The Twin Otter used sensors such as the Litton LTN-90-100 IRS, Trimble GNSS TNL-8100,

and Novatel GNSS RT-20 [48.57]. Global navigation satellite systems (GNSSs) represent the current standard for location measurements. When operated in nondifferential mode, the accuracy of a GNSS is about 5 m, although centimeter accuracies can be achieved if the system is operated in the differential mode, where signals recorded by an accompanying ground station are incorporated. In this mode, GNSS also provides accurate measurements of the height of the aircraft above mean sea level.

The absolute altitude can also be measured with many different instruments. Radio and laser altimeters can be used to measure the absolute height above the terrain (Fig. 48.1). Altimeter measurements can be combined with pressure–altitude or GNSS altitude data to produce records of the height and roughness of the terrain over which the flux measurements are being made.

48.4.3 Wind Measurements

Flux aircraft are instrumented to measure the three-dimensional meteorological wind vector \mathbf{v} at a frequency range of more than 10 Hz. The wind vector can be calculated from navigation, flow, and attitude measurements in the Meteorological Orthonormal Coordinate System (MONS, index m) using the relation [48.59]

$$\mathbf{v} = \mathbf{v}_{\text{gs}} + \mathbf{M}_{\text{mf}} (\mathbf{v}_{\text{tas}} - \boldsymbol{\Omega} \times \mathbf{s}_{\text{L}}). \quad (48.7)$$

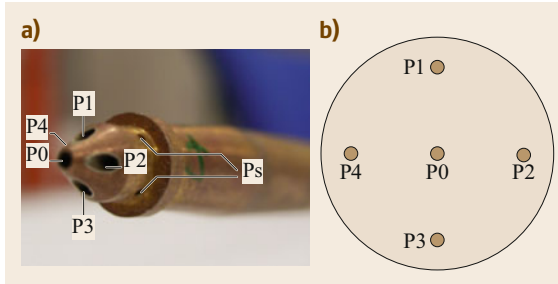


Fig. 48.2 (a) Five-hole probe manufactured by the Institute for Fluid Dynamics, TU Braunschweig (after [48.60]); (b) schematic of a FHP showing pressure ports P0 through P4 (in a head-on perspective, i.e., starboard is on the left side from this point of view)

Here, the ground-speed vector \mathbf{v}_{gs} describes the movement of the origin of an aircraft-fixed coordinate system known as the Aircraft-Fixed Orthonormal System (ACONS; index f) with respect to the Earth's surface, and is determined using the onboard inertial navigation system (INS), which is usually an inertial measurement unit (IMU) combined with a GNSS via a Kálmán filter.

The true airspeed vector \mathbf{v}_{tas} is the flow vector measured by the in-situ flow probe (e.g., a five-hole probe, FHP; see Fig. 48.2) on a nose boom, and is therefore defined with respect to the FHP. Thus, for a fast-flying aircraft with $|\mathbf{v}| \ll |\mathbf{v}_{tas}|$, the true airspeed is oriented more or less towards the ground speed.

The location of the FHP in relation to the origin of the ACONS is described by the lever-arm vector $\mathbf{s}_L = (x_p, y_p, z_p)$. The vector of angular body rates $\boldsymbol{\Omega} = \Omega_p, \Omega_q, \Omega_r$ contains the angular velocities (roll, pitch, yaw) of the ACONS in relation to the MONS, and is among the primary output data of the IMU.

The vector sum $(\mathbf{v}_{tas} - \boldsymbol{\Omega} \times \mathbf{s}_L)$ describes the measured airflow vector with respect to the ACONS, and is transformed into the MONS via the operator \mathbf{M}_{mf} in (48.7). Since the (relatively small) meteorological wind vector is obtained by combining two large vectors in (48.7), the challenge is to determine \mathbf{v}_{tas} and \mathbf{v}_{gs} with very high precision. While the ground speed \mathbf{v}_{gs} is measured by the INS in an Earth-fixed coordinate system, the second term in (48.7) requires more attention. Please see the Appendix for further details regarding the calculation of the meteorological wind vector, as well as [48.61, 62].

48.4.4 Scalar Sensors

A wide range of fast-response sensors (Table 48.1) have been fitted to flux aircraft to measure the air temperature, the dewpoint, and the H_2O , CO_2 , O_3 ,

and CH_4 concentrations [48.63, 64]. Rosemount fast-response heated (or unheated) probes mounted on the nose of the aircraft are frequently used to determine air-temperature fluctuations. Humidity is usually measured using a dewpoint sensor (Chap. 8). Several kinds of infrared gas analyzers have been used to measure carbon dioxide and water vapor fluctuations (Chap. 16). Ozone fluctuations have been measured using chemiluminescence-based sensors and UV absorption sensors have frequently been used to determine absolute ozone concentrations [48.65]. Cavity ring-down spectrometers and integrated off-axis cavity output spectrometers are now available for accurate measurements of CH_4 fluctuations [48.63, 66].

48.4.5 Solar Radiation Sensors and Satellite Simulators

A variety of sensors have been used to measure solar radiation (Chap. 11). Thermopile-type pyranometers with a typical spectral range of 300–2800 nm have been used to measure downwelling ($S \downarrow$) and reflected ($S \uparrow$) solar radiation. Software routines have been developed that can continuously correct the $S \downarrow$ measurements on an aircraft for the mounting alignment and for variations in the pitch and roll attitude, heading, latitude and longitude, and time of day throughout each flight [48.57, 58]. The net radiation (Q_s^*) on the Twin Otter has been calculated at intervals of 1/32 s using downwelling and reflected solar radiation and long-wave radiation derived from the surface temperature (T_0 in K, measured with an infrared thermometer) and the air temperature (T in K) using the equation

$$Q_s^* = S \downarrow - S \uparrow + [1.20 \sigma T^4 - 17] - [0.98 \sigma T_0^4], \quad (48.8)$$

where the last two terms represent the incident and reflected long-wave components estimated using the Stefan–Boltzmann constant $\sigma = 5.6924 \times 10^{-8}$ and a surface emissivity of 0.98. The net radiation has also been measured with a Kipp and Zonen CNR-1 net radiometer housed in a specially modified port wingtip (Fig. 48.1). The CNR-1 consists of two CM3 pyranometers with a spectral range of 305–2800 nm and two CG3 pyrgeometers with a spectral range of 5000–50 000 nm.

Spectrometers with spectral ranges that are similar to those of specific satellites have also been used on aircraft during flux campaigns to attempt to collect data that can be used to adjust satellite data to correspond to the time that flux density measurements were made. The Twin Otter aircraft carried several upward- and downward-looking spectrometers. The Skye Indus-

tries greenness indicator, which is based on the ratio of near-IR (730 nm) to red (660 nm) radiation, indicates the amount of green vegetation beneath the aircraft. Another instrument used on the Twin Otter to measure vegetation characteristics is the downward-looking Exotech 100BX satellite simulator. This simultaneously measures the reflected radiation in four wavelength bands, and can be configured to simulate two modes of Landsat operation—the Thematic Mapper (TM) and the Multispectral Scanner (MSS)—as well as the Satellite Pour l’Observation de la Terre (SPOT). Hyperspectral reflectance measurements offer increased flexibility, allowing the selection of custom spectral ranges that are matched to corresponding satellite measurements [48.67]. When mounted on a low-flying flux aircraft, these spectral sensors provide information on only a narrow strip directly under the aircraft, but the data can be compared and integrated with wider scenes provided by various satellites. In most large-scale experiments, many kinds of spectral data have been collected. For example, in the Southern Great Plains (SGP) 1997 Hydrology Experiment, wide-angle sensing spectrometers such as the ESTAR (Electronically Scanned Thinned Array Radiometer) on the National Aeronautics and Space Administration (NASA) P-3 measured surface characteristics that could be directly superimposed on the footprint sensed by the flux aircraft [48.18].

48.4.6 REA System

Fast-response sensors are not available for some trace gases such as agrochemicals, VOCs, N_2O , and CH_4 ; gas chromatographs and slow-response gas analyzers have been used to measure the fluxes of these gases using REA systems. A variety of gas-collection devices have been used: polyurethane foam plugs for agrochemicals [48.22], stainless steel canisters for CO_2 and isoprene [48.23, 68], and polytetrafluoroethylene (PTFE) bags for N_2O and CH_4 [48.29, 69]. Basically, air is drawn by two diaphragm pumps and is then split between up and down channels. The air flow is maintained constant by two mass flow controllers. Two

fast-response switching three-way valves allow the flow to be directed to either sample bags or the vent line. The vertical wind signal controlling the switching of the valves is high-pass filtered in real time to remove any potential bias in the vertical wind measurement. The signal is also adjusted to correct for any time delay in the sampling assembly. The use of a dead band helps to increase the valve lifetime and also enhances the concentration difference between the upward-moving and downward-moving air samples. The parameter A in (48.2) has been shown to be dependent on the magnitude of the dead band, and has been determined by simultaneous in-situ EC measurements for water vapor [48.44, 45].

48.4.7 Data Acquisition

Much progress has been achieved in the area of data acquisition. Great strides in computer speed, storage capacity, and ruggedness have made data collection much more reliable in the demanding environment of an aircraft, and have allowed the computation and display of an ever-increasing list of variables, including real-time flux estimates [48.70]. Signals that must be recorded in flight originate in a host of analog and digital devices. In the Twin Otter, for example, the input/output (I/O) boards that interface to the input and output devices include RS232 serial boards, analog to digital, digital to analog, and digital I/O boards, small computer systems interfaces, along with a video graphics array. The analog signals are conditioned with a two-phase filtering process. The signals first pass through hardware and signal conditioning, where each signal is low-pass filtered at 100 Hz, amplified, and biased. These signals are then digitally sampled at a rate of 256 Hz. A digital 47-point 10-Hz low-pass filter is applied and the data are then recorded at 32 Hz on various types of recording media. It is important that all data sets for calculating the various fluxes are treated the same way in order to avoid phase shifts in the various signals, as these would lead to errors in the flux density calculations. The use of a 10 Hz low-pass filter implies that, at a true airspeed of 60 m s^{-1} , a full data record is collected every 6 m traveled.

48.5 Specifications of Sensors for Flux Density Measurements

Many different sensors have been used for aircraft-based flux measurements. A list of the variables measured on the NRC Twin Otter aircraft is given in Table 48.5, as are details regarding accuracy and frequency response. For flux density measurements realized using the EC and wavelet covariance tech-

niques, sensors with a fast frequency response are required, especially for measurements at low altitudes. High-resolution measurements are essential, while the reliability of the absolute values is not as critical. A flight evaluation of two vertical wind-measuring systems [48.71] showed that the sensible heat flux

Table 48.5 Specifications of the sensors used on the Canadian Twin Otter flux aircraft

Variable	Reliability of absolute value	Resolution	Frequency response	Instrument type
Vertical wind velocity	0.1 m s ⁻¹	0.01 m s ⁻¹	16 Hz	Gust probe; IMU ¹ /GNSS ²
Horizontal wind velocity components	0.5 m s ⁻¹	0.01 m s ⁻¹	16 Hz	Gust probe; IMU/GNNS
Humidity	0.5 × 10 ⁻³ kg m ⁻³	10 ⁻⁴ kg m ⁻³	2 K s ⁻¹	Dewpoint hygrometer
Humidity fluctuations	10 ⁻³ kg m ⁻³	0.005 × 10 ⁻³ kg m ⁻³	10 Hz	Infrared gas analyzer
Air temperature	0.5 K	0.05 K	10 Hz	Platinum resistance
Carbon dioxide	0.5 ppmv	0.05 ppmv	10 Hz	Infrared gas analyzer
Pressure	40 Pa	5 Pa	10 Hz	Quartz crystal transducer
Absolute altitude	2–3 m	0.2 m	16 Hz	Radar altimeter
Heading	1°	0.001°	100 Hz	IMU/GNSS
Attitude	0.25°	0.0001°	100 Hz	IMU/GNSS
Position	2 m	0.01 m	10 Hz	IMU/GNSS
Surface temperature	1.0 K	0.02 K	10 Hz	Infrared radiometer
Solar radiation (upward and downward)	20 W m ⁻²	2 W m ⁻²	0.2 Hz	Thermopile
Ozone	1 ppbv	0.1 ppbv	10 Hz	Chemiluminescence-based
Methane	50 ppbv	3 ppbv	5 Hz	Cavity ring-down spectroscopy

¹ Inertial Measurement Unit, the hardware that typically provides input to the Inertial Navigation System (INS)

² Global Navigation Satellite System

agreed within 1 W m⁻². For trace gases that lack fast-response analyzers, slow-response gas analyzers have been used with the REA and mass balance techniques. In these cases, the resolution requirements are greater than those with EC. For example, with the available slow-response gas analyzers, the resolutions for N₂O

(10 pptv) and CH₄ (90 pptv) are adequate to measure agricultural emissions using aircraft-based technology [48.27, 29]. Slow-response sensors are sufficient for determining parameters such as the location and the atmospheric and surface conditions during the measurements.

48.6 Quality Control

Aircraft-based flux measurements involve the collection of large quantities of data. Many factors can affect the accuracy of flux measurements. It is therefore important to minimize the collection of poor data by assessing data quality during and after data collection. For further information, refer to Chap. 3.

48.6.1 Quality Assessment

Assessing the quality of the data helps to minimize the amount of poor data collected. This can best be done by performing preliminary flux calculations in real time during the flight and displaying the resulting estimated flux values to the flight engineer. During a typical month-long field campaign during BOREAS, approximately 100 variables were recorded by the Twin Otter data acquisition system 32 times per second for about 100 h. This represents about a billion data points. Quality control of the data should also be carried out after each flight prior to calculating the flux; for instance, the data should

be despiked to remove outliers [48.72] and it should be synchronized to maximize the correlation between the vertical wind and the scalar of interest [48.73]. This corrects for the spacing between various sensors. Several software packages such as EddyPro and TK3 have been developed to standardize and automate EC data preparation, flux computation, and quality assessment [48.74], and these can be applied to aircraft-based data. An open-source and extensible EC data processing software package that can be applied to aircraft-based data is also available [48.75]. Errors can also occur because the flux sampling criteria are not met due to a poor sample size resulting from either a run that was too short or an insufficient number of repeated passes. For trace gas flux measurements such as CH₄, it has been found to be extremely useful to perform a flight with a constant gas concentration flowing through the analyzer in order to evaluate the accuracy of the flux measurements and develop techniques for minimizing errors caused by the sensitivity of the analyzer to pressure fluctuations [48.29].

48.6.2 Spectral Response

An inappropriate frequency response of a sensor can be detected by inspecting the shape of the spectra. All variables used for flux density calculations should show a well-behaved spectral shape with a $-5/3$ slope down to a wavelength of 10 m (5 Hz). Examining the

cospectra can also help identify potential problems. For example, as reported in [48.40], plots of the normalized cospectra for various heights indicated that the $\text{CO}_2/\text{H}_2\text{O}$ analyzer response was not adequate to measure the high-frequency contribution to the flux density for runs at a height of 10 m, but it was adequate for runs at 25 and 50 m.

48.7 Maintenance

Sensor calibration is important for ensuring the quality of the measurements. However, a wide range of sensors are used on flux aircraft, and calibration requirements tend to vary among sensors (Table 48.6). Several procedures are used to routinely check the accuracy of measured variables. After each flight, the data from each sensor are examined; if anomalies are detected in one of the measurements, a partial calibration check of the sensor is carried out. The three-dimensional wind measurements that are integral to flux measurements, pressure sensors, and radiation sensors are calibrated before each measuring campaign. Atmospheric variables such as pressure, temperature, humidity, and wind are compared with measurements from towers during low-level passes and with data from other aircraft during formation flights [48.20]. Gas sensors such as

those for O_3 , CO_2 , and CH_4 all have different calibration requirements depending on the type of sensor used at the time. The original fast-response $\text{CO}_2/\text{H}_2\text{O}$ analyzer used on the Twin Otter had to be cleaned after each flight, as it tended to drift due to dirt on the mirrors. It was eventually replaced with a LiCor $\text{CO}_2/\text{H}_2\text{O}$ analyzer, which is much more stable. Ozone analyzers are probably the sensors that require the most frequent calibration. Some of the calibration details for the NRC Twin Otter aircraft are given in [48.76], while [48.77] describes the performance and calibration information for a newer instrument. An infrared surface temperature sensor needs to be calibrated on occasion using a black metal cone immersed in a well-mixed water bath mounted under the temperature sensor.

Table 48.6 Maintenance of aircraft-based sensors for flux measurement campaigns

Maximum interval	Pressure sensors	Gas sensors	Air-temperature sensors	Radiation sensors	Dewpoint sensors	Surface temperature
Weekly		×			×	
Monthly						×
Beginning of campaign	×		×	×		

48.8 Applications

Over time, aircraft have consistently demonstrated their relevance to the study of mass and energy exchange over a wide range of ecosystems. Their versatility and their ability to be deployed in remote locations and to sample large surface areas make them an excellent complement to tower-based measurement systems. Examples of aircraft-based flux density measurements for several applications will now be presented. Although aircraft-based flux density measurements are available from many research groups, as a matter of convenience, the examples presented in this review are mainly taken from the authors' research. Many patterns have been flown to attempt to evaluate the accuracy of aircraft-based flux measurements and improve our

understanding of biosphere-atmosphere exchange. Flying by a tower has been a common flight pattern to perform in order to check the representativeness of tower-based flux measurements. Flight patterns consisting of L and T shapes (i.e., with an intersection at the endpoint or midpoint of perpendicular flight passes) at multiple altitudes provided the data required to calculate the flux divergence with height as well as to compare aircraft-based and tower-based flux measurements. A *reciprocal grid* pattern at a constant altitude provided spatial coverage of fluxes at a particular instant in time; these fluxes could then be compared to surface features [48.78]. Over hilly terrain such as the FIFE site, data from long transects, double stacks, and

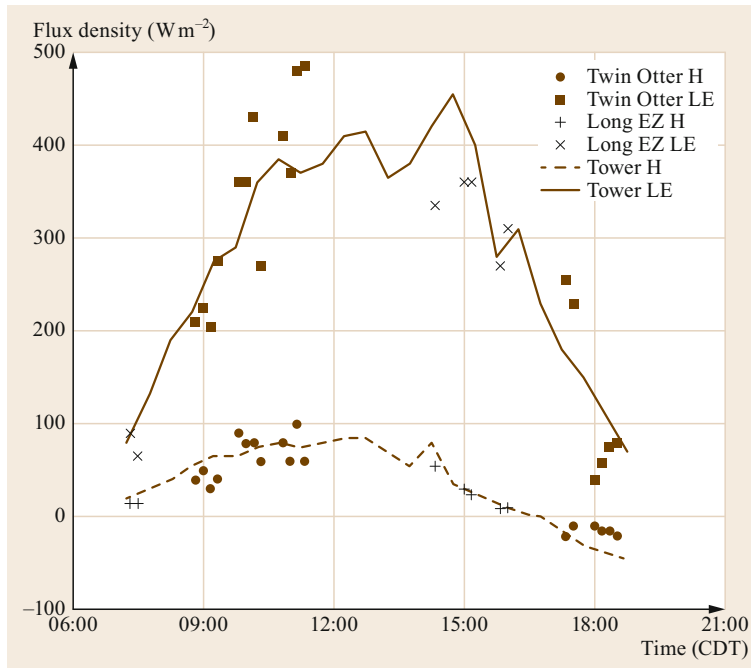


Fig. 48.3 Comparison of sensible (H) and latent heat (LE) fluxes measured using aircraft and tower-based systems over grassland on 2 July 1997 (CDT: central daylight time). Flux measurements are presented for two aircraft platforms (the Twin Otter and Long EZ) and one tower-based platform (after [48.79])

grid flights were used to show that flux measurements over a 15 km distance were sometimes substantially underestimated [48.80]. A double-stack pattern of sixteen 15 km runs along two tracks 11 km apart—which consisted of four runs at approximately 75, 220, 500, and 740 m AGL followed by eight runs on the other track at 740, 500, 220, 75, 75, 220, 500, and 740 m and then four more runs on the first track at 740, 500, 220, and 75 m—provided the data needed to estimate all the terms in the budget equation for a conserved scalar [48.14, 15]. Data obtained over different types of surfaces were used [48.81] to examine the vertical depth of the influence of surface heterogeneity on blending height theory, convective boundary layer scaling, and internal boundary layer theory.

48.8.1 Comparison of Aircraft-Based and Ground-Based Flux Density Measurements

Many studies have focused on comparing aircraft-based and tower-based flux measurements [48.82]. However, several studies [48.78, 83] have shown that large differences in footprint size (Chap. 1) between those two platforms make it impossible to sample the same area. Even when flying a circle around a tower, it is highly unlikely that the flux measurements will be the same unless the area is homogeneous [48.21]. Nevertheless, comparable flux measurements are frequently obtained for relatively homogeneous areas. Figure 48.3 shows

the half-hourly sensible (H) and latent heat (LE) fluxes measured over grassland using a 1.5 m tower-based system. The corresponding fluxes measured using the NRC Twin Otter and the Long EZ aircraft funded by NOAA are also shown for individual runs of 3.7 km measured at an altitude of 30 m [48.79]. The time series for the flux calculations for the Twin Otter were linearly detrended, whereas the Long EZ data were high-pass filtered with a 3 km cutoff. In this case, the detrending and high-pass filtering of the data had little impact, and the agreement between tower-based and aircraft-based flux measurements was quite good. This meant that the surface conditions along the flight track were similar to those within the tower-based flux footprint, and the long-wavelength contribution to the flux measurements was small.

Aircraft-based flux density measurements have aided the interpretation of surface flux measurements. A comparison of midday and nighttime flux measurements obtained over the FIFE site using the Twin Otter aircraft and two tower-based systems is presented in Table 48.7. The aircraft-based fluxes at night are the average of five passes over a distance of 15 km and the tower-based flux values are the half-hourly averages obtained during the period the aircraft made the measurements. The tower-based fluxes of CO_2 were about -0.2 to $-0.6 \text{ mg m}^{-2} \text{ s}^{-1}$ at midday and 0.1 – $0.2 \text{ mg m}^{-2} \text{ s}^{-1}$ at night, while the aircraft flux measurements made at an altitude of about 100 m along the 15 km tracks were about -0.4 to $-0.6 \text{ mg m}^{-2} \text{ s}^{-1}$ around midday and

Table 48.7 Daytime and nighttime fluxes measured over the Konza Prairie on 10 August 1989

	Time of day ^a (CDT)	Distance ^b (km)	Altitude (m)	Radiation (W m ⁻²)	Latent heat (W m ⁻²)	Sensible heat (W m ⁻²)	CO ₂ flux (mg m ⁻² s ⁻¹)
Aircraft	11:52–11:58	15.5	106	764	131	157	−0.44
Tower 1	11:38–12:07	–	2.5	775	248	174	−0.57
Aircraft	12:06–12:11	16.1	101	666	125	205	−0.62
Tower 2	12:01–12:30	–	12.5	–	107	256	−0.22
Aircraft	21:18–22:15	16.0	98	0	−1	3	0.0
Tower 1	21:00–22:30	–	2.5	2	8	−19	0.16
Aircraft	21:39–22:39	16	107	0	−1	2	0.0
Tower 2	21:31–22:30	–	12.5	–	6	−26	0.12

^a Duration of flight measurement for the aircraft or the average of half-hourly measurements for the tower

^b Distance refers to the average length of the aircraft flight track

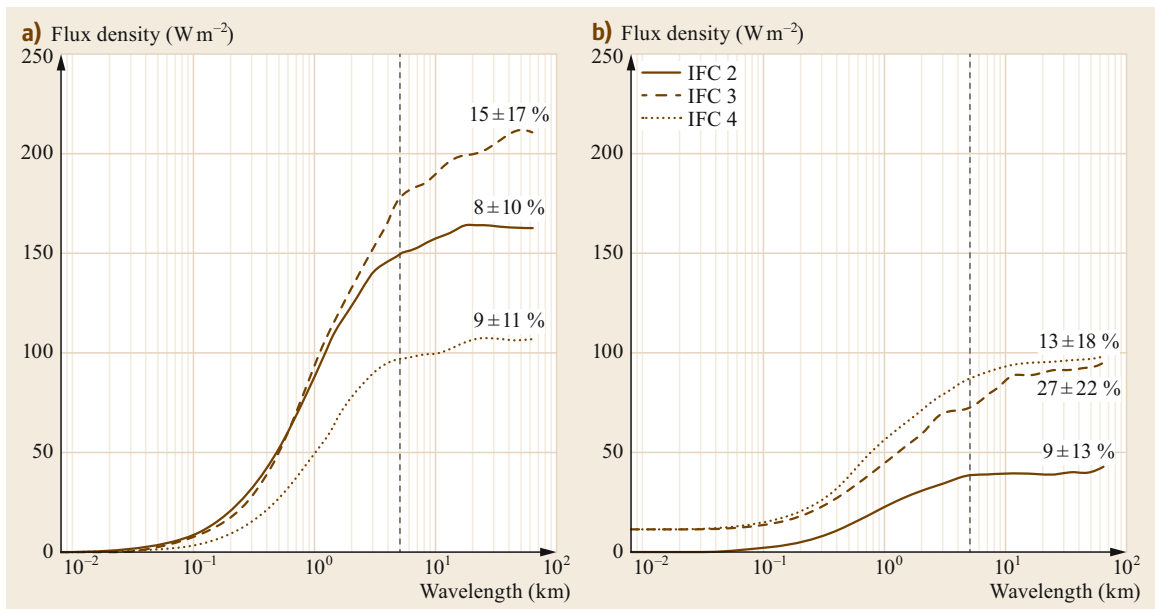


Fig. 48.4a,b Cumulative contributions to the latent (a) and sensible (b) heat fluxes for a 75 km flight track at an altitude of 150 m during three intensive field campaigns (IFCs). The vertical lines show a turbulent wavelength cutoff threshold of 5 km. The percent contributions above this cutoff are also given, along with the percent standard deviations

zero at night. The measured flux magnitudes at the top of the nocturnal boundary layer (100 m) were all found to be negligible at night, which is what is what would be expected from estimating the flux at night by measuring the change in concentration in the nocturnal boundary layer [48.84].

A second example is provided by measurements of the change in the CO₂ concentration over Candle Lake during BOREAS [48.85, 86], which showed that the large temperature differences between the forest and the lake surface during the night resulted in a nocturnal land/lake breeze. This led to substantial transport of CO₂ from the forest to the lake, which was vented over the lake in the morning. Under these conditions, some

of the CO₂ respired by the forest would go undetected by a tower-based flux system located over a forest close to a lake.

Figure 48.4 shows the contributions of various scales to the sensible and latent heat fluxes at an altitude of 150 m along a 75 km transect. These data were collected as part of three intensive field campaigns (IFCs) during FIFE. The flight track passed over part of the Konza Prairie at one end and flatter terrain with mixed agriculture at the other end. The percent contributions (and their standard deviations) to the sensible and latent heat fluxes for wavelengths longer than 5 km are shown for about ten runs per IFC. The 5 km cutoff was chosen based on the height of the measurements.

These results show that the flux density contributions at wavelengths greater than 5 km were substantial and that they were slightly larger during the late growing season (IFC 3). For latent and sensible heat, the mean long-wavelength flux contributions during IFC 3 were 15 and 27%, respectively. The long-wavelength contributions were also very variable from day to day, as can be seen by the standard deviations.

48.8.2 Quantifying Flux Density Over Complex Ecosystems

The versatility of an aircraft-based flux system for different situations is now demonstrated with a couple of examples. During the CODE project [48.30], there was concern that nitric oxide emissions from vehicle exhausts might impact O₃ fluxes at sites near to a major interstate highway. The hypothesis was that nitric oxide emitted by vehicles would destructively react with and thereby increase the downward flux of O₃. Aircraft-based flux measurements proved to be a suitable way to address this concern. By conducting flux measurements upwind and downwind of the interstate, it was shown that regions downwind to a distance of 1 km were impoverished in O₃ and featured larger downward O₃ fluxes [48.65]. However, at a flight altitude of 60 m, measurements conducted 1.5 km downwind of the interstate showed O₃ concentrations and fluxes that were comparable to those observed upwind of the interstate.

Flux measurements over the city of Fresno in California provide another example of the versatility of aircraft-based flux systems. Figure 48.5 shows the average fluxes of sensible and latent heat as well as CO₂ and O₃ measured along a 45 km transect that crossed over the city of Fresno during a clear sunny day on the afternoon of 29 July, based on one pass flown at an altitude of 150 m. The track extended from about 10 km northwest of the city to approximately 15 km southeast of the city. The wind was from the west at 4 m s⁻¹. The flux density estimates were calculated using wavelet analysis. The large contribution from wavelengths greater than 5 km for latent heat as compared to the other fluxes implies that long-wave transfer of water vapor was much greater than for the other scalars. This means that if these fluxes had been measured at the same level using a tower-based system, there would have been considerably more underestimation of the latent heat flux than the other scalars. It also means that, in this case, if the fluxes had been adjusted for energy budget closure using the Bowen ratio technique, there would have been considerable errors in the flux estimates of CO₂ and O₃.

48.8.3 Evaluation of GHG Emission Inventories

Aircraft-based flux-measuring techniques have frequently been used to obtain the regional flux of CO₂ over a wide range of ecosystems [48.9, 13, 21, 30–32, 35, 67]. However, until the last decade, there had not been any independent estimates of agricultural GHG emission inventories of N₂O and CH₄. Such independent estimates are important considering that bottom-up inventories of N₂O and CH₄ fluxes from agricultural sources have been reported to be highly uncertain [48.87, 88] and account for 52% and 84% of the global anthropogenic CH₄ and N₂O emissions, respectively [48.89]. Aircraft-based flux measurements of N₂O were compared with model estimates for an agricultural region [48.27]. Since process-based models only estimate direct emissions whereas an aircraft-based system measures the total N₂O emissions, it was then possible to estimate the contribution from indirect emissions and to show that the 20% value associated with the Intergovernmental Panel on Climate Change (IPCC) methodology was a reasonable estimate for the region studied.

Methane emissions from flux measurements and inventory estimates are compared in [48.66] for the agriculturally dominated Reuss Valley. The measured flux densities were found to be larger than the expected CH₄ emissions. This implied that the Swiss agricultural CH₄ inventory estimates were likely to be too low. Similarly, data from the Scanning Imaging Absorption Spectrometer for Atmospheric Cartography (SCIAMACHY) satellite [48.90] indicated that there was a 40% underestimation of the CH₄ emissions from US livestock. In contrast, it was concluded that the Canadian agricultural CH₄ emission inventory for a region that was 90% agriculture agreed reasonably well with aircraft flux measurements [48.29]. However, the authors of that work emphasized that validating agricultural CH₄ emissions inventories using top-down measurements is challenging because of the presence of other CH₄ sources such as wetlands as well as anthropogenic sources such as waste treatment plants, biodigesters, etc. Figure 48.6 shows the bottom-up agricultural CH₄ emissions and the top-down CH₄ emissions obtained by flying at an altitude of 150 m along two 20 km transects [48.29]. For the flight track dominated by agricultural land use (Fig. 48.6a), the agreement is good but not perfect (Fig. 48.6c). The most likely reasons for the small disagreement are that it was impossible to replicate the mixing that takes place in the boundary layer in the calculation of the bottom-up es-

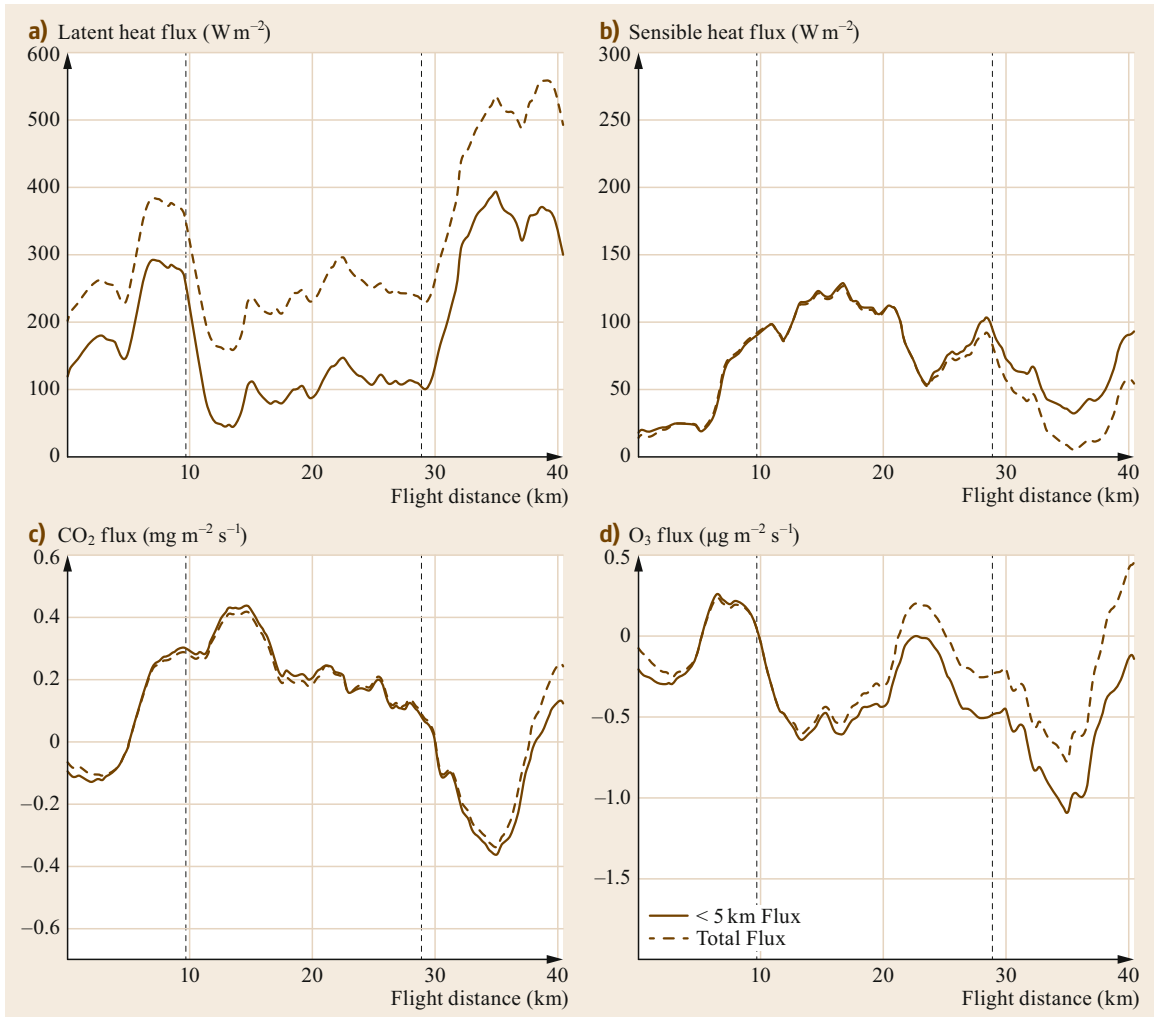


Fig. 48.5 Spatially resolved fluxes of sensible and latent heat and of CO_2 and O_3 measured at 150 m over the city of Fresno in California between 13:56 and 14:10 PDT (Pacific Daylight Time) on 29 July 1991. The city limits along the flight track are indicated by vertical lines

timates based on the data available, and that there were also small patches of wetlands that were emitting CH_4 . In contrast, when much of the aircraft footprint corresponded to wetlands (Fig. 48.6b), the substantial CH_4 emissions from the wetlands in relatively warm conditions led to very poor agreement between the top-down and bottom-up agricultural CH_4 emissions estimates (Fig. 48.6d).

Aircraft-based measurement platforms have also demonstrated their value for monitoring emissions from the oil and gas sector, enabling comparisons with inventory estimates. For example, the CH_4 emissions from an oil- and gas-producing region in Utah (USA) were

estimated from aircraft-based measurements using the mass balance approach [48.91], and top-down emissions were found to be a factor of 1.8 greater than bottom-up inventory estimates. Similarly, a recent study of aircraft estimates of CH_4 emissions from the oil and gas infrastructure in two regions of Alberta (Canada) reported that CH_4 emissions were four times greater than the region-specific bottom-up inventory-based estimate [48.92]. The authors of that study hypothesized that underreporting of the venting gas associated with cold heavy oil production in this region was the most likely source of the discrepancy between bottom-up and top-down estimates.

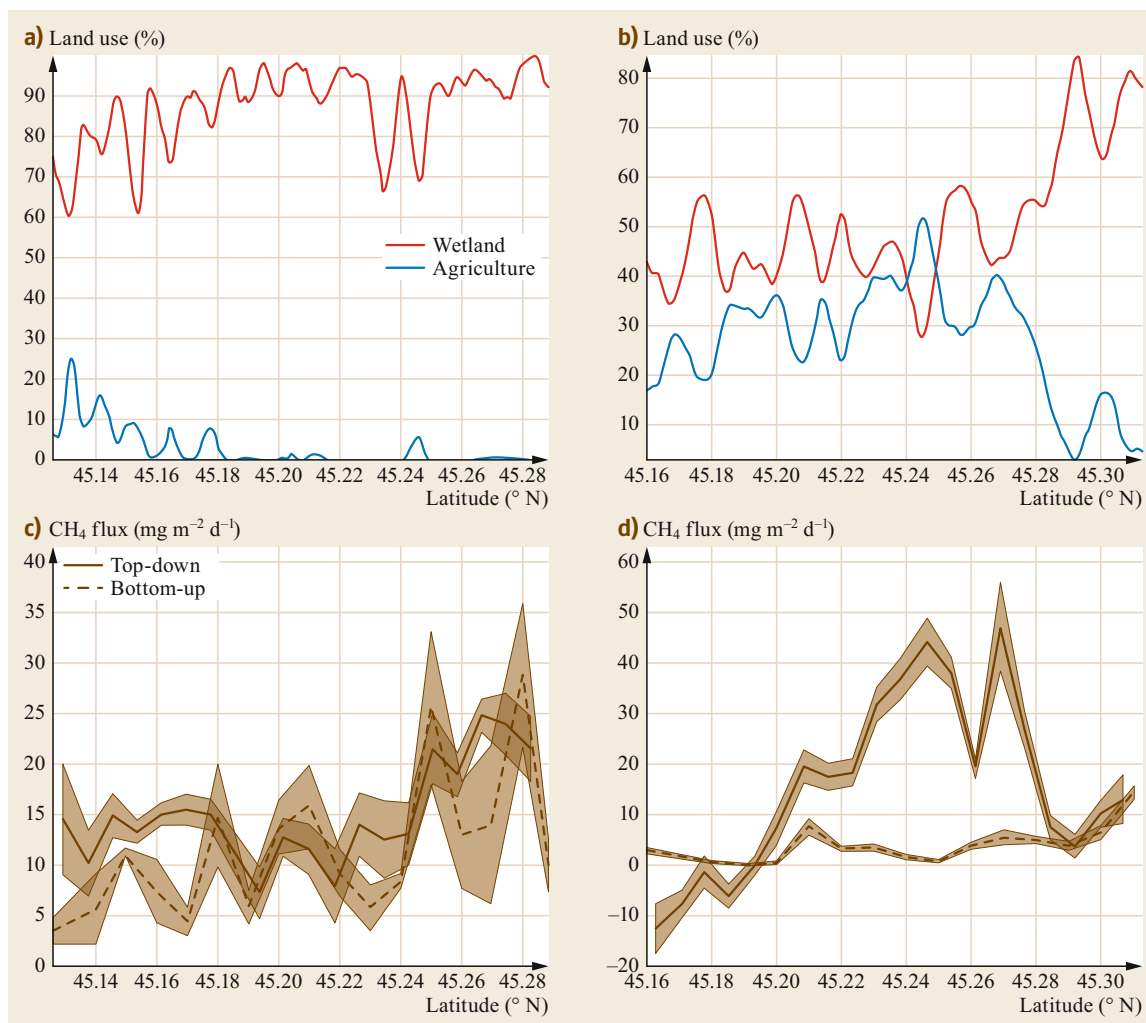


Fig. 48.6a–d Major land-use types and their distribution within the aircraft flux footprint (**a,b**) and 1 km spatially resolved CH_4 fluxes based on bottom-up agricultural CH_4 inventory estimates and top-down aircraft flux measurements (**c,d**). The plots highlight the difference between a flight track dominated by agricultural land use (**a,c**) and a flight track with substantial wetland areas (**b,d**). The shaded gray area represents ± 1 SE

48.9 Future Developments

Many aircraft-based flux density measurements have already been collected during large field campaigns such as HAPEX, ABLE, FIFE, BOREAS, SGP, and LBA. These measurements have the potential to provide valuable information on biosphere–atmosphere exchange. To facilitate the development of new applications, the data collected between 1987 and 2011 using the NRC Twin Otter atmospheric research aircraft are available for anyone interested [48.93]. These are high-quality data from over 4000 flux runs flown over a variety of

ecosystems. A wide range of spectral data using various types of satellite simulators have been collected simultaneously with flux measurements of $\text{CO}_2/\text{H}_2\text{O}$, and only very limited use has been made of these data. The development of environmental response functions to increase the value of satellite information is a very promising area of research [48.50]. More efforts should be made to identify the various ecosystems over which flux measurements have been taken, as this may yield flux data for ecosystems that are currently short of such

data [48.17]. Aircraft flux measurements also have the potential to help quantify mesoscale transfer, which is the cause of the lack of energy budget closure with many tower-based flux measurements [48.94]. The data already collected from the many aircraft flux campaigns probably include the information needed to improve our understanding of mesoscale transfer.

New developments such as small aircraft [48.56], the miniaturization of gas sensors, and the potential to deploy gas sensor packages on UASs (Chap. 49) all point to the increased use of aircraft-based flux density measurements in the coming years. Further, given the ongoing development of gas-detecting satellites [48.95], combining the data from them with aircraft-based flux density measurements [48.29] is an

area of research that has the potential for a major research breakthrough in the coming years. These technologies have the potential to greatly reduce the cost of flux measurements and help improve and validate GHG emission inventories, which is essential if the changes are to be included in the inventories [48.96, 97]. Data from satellites that are now being proposed should provide better geographical coverage coupled with higher temporal resolution [48.97]. However, before this information can be effectively used to estimate GHG emissions and verify the impacts of mitigation practices, it will be essential to calibrate the satellites. This will probably be best achieved using aircraft-based flux measurements owing to the comparable spatial and temporal scales of the measurements.

48.10 Further Reading

- Desjardins, R.L., MacPherson, J.I. and Schuepp, P.H., 2000. Aircraft-based flux sampling strategies. In: R.A. Meyers (Editor), *Encyclopedia of Analytical Chemistry*. John Wiley and Sons Ltd., Chichester, pp. 3573–3588.
- Garratt, J.R., 1992. *The Atmospheric Boundary Layer*. University Press, Cambridge, 316 pp.
- Kumar, P. and Foufoula-Georgiou, E., 1994. Wavelet analysis in geophysics: an introduction. In: E. Foufoula-Georgiou and P. Kumar (Edi-

tors), *Wavelet in Geophysics*. Academic Press, San Diego, pp. 1–43.

- Stull, R.B., 1988. *An Introduction to Boundary Layer Meteorology*. Springer Netherlands, Dordrecht, 670 pp.
- M.A. Strunin: Investigation of methods of the thermodynamic condition of the atmosphere using aircraft-observatory (in Russian). (Central Aerological Observatory, Moscow, 2020)

48.A Appendix

48.A.1 True Airspeed by the Flight Mechanical Angles α and β

To obtain a proper solution of (48.7), we start in the aerodynamic coordinate system ADONS (index a) of the flight. The ADONS is defined as the system in which the airspeed vector has the components

$$\mathbf{v}_{\text{tas},a} = (-|\mathbf{v}_{\text{tas}}|, 0, 0),$$

and is therefore called the airspeed-fixed coordinate system. A rotation of the ADONS about the vertical (lift) axis z_a by the angle $-\beta$

$$\mathbf{T}_{\text{ea}}(-\beta) = \begin{pmatrix} \cos \beta & -\sin \beta & 0 \\ \sin \beta & \cos \beta & 0 \\ 0 & 0 & 1 \end{pmatrix} \quad (48.9)$$

and then about the transverse axis (cross-force) axis y_a by the angle α

$$\mathbf{T}_{\text{fe}}(\alpha) = \begin{pmatrix} \cos \alpha & 0 & -\sin \alpha \\ 0 & 1 & 0 \\ \sin \alpha & 0 & \cos \alpha \end{pmatrix} \quad (48.10)$$

yields the description of the airspeed vector in the ACONS [48.98],

$$\begin{aligned} \mathbf{v}_{\text{tas}} &= \begin{pmatrix} u_{\text{tas}} \\ v_{\text{tas}} \\ w_{\text{tas}} \end{pmatrix} = \mathbf{T}_{\text{fe}}(\alpha) \mathbf{T}_{\text{ea}}(-\beta) \mathbf{v}_{\text{tas},a} \\ &= -|\mathbf{v}_{\text{tas}}| \begin{pmatrix} \cos \alpha \cos \beta \\ \sin \beta \\ \sin \alpha \cos \beta \end{pmatrix}. \end{aligned} \quad (48.11)$$

The angle α is positive for nose-lifting rotations, while β is positive for rotations to the port side. Both

the angles and the order of rotation have their origins in wind-tunnel experiments. The first rotation \mathbf{T}_{ea} leads to the experimental coordinate system (index e) that is cross-axis fixed. The components of the true airspeed vector \mathbf{v}_{tas} in the ACONS are:

- u_{tas} , which is oriented along the roll axis of the aircraft and positive in the flight direction
- v_{tas} , which is oriented along the pitch axis of the aircraft and positive in the starboard direction
- w_{tas} , which is oriented along the normal (or yaw) axis and positive downwards.

True Airspeed by the FHP Angles $\tilde{\alpha}$ and $\tilde{\beta}$

The outputs of the FHP (Fig. 48.2) are pressure differences that are used to calculate \mathbf{v}_{tas} in spherical coordinates in the ACONS:

- $\tilde{\alpha}$ (air flow from below gives a positive $\tilde{\alpha}$)
- $\tilde{\beta}$ (air flow from starboard gives a positive $\tilde{\beta}$)
- $|\mathbf{v}_{tas}|$ (the norm of the true airspeed vector).

The flow angles $\tilde{\alpha}$ and $\tilde{\beta}$ should not be confused with the rotation angles α and β that are commonly used in flight mechanics and wind-tunnel experiments [48.98].

There is a well-defined relationship between the two sets of angles,

$$\cos \tilde{\alpha} = \frac{u_{tas}}{\sqrt{u_{tas}^2 + w_{tas}^2}} = \cos \alpha \quad (48.12)$$

and [48.61]

$$\tan \tilde{\beta} = \frac{v_{tas}}{u_{tas}} = \frac{\tan \beta}{\cos \alpha}. \quad (48.13)$$

Using only the measurable angles $\tilde{\alpha}$ and $\tilde{\beta}$ (where $\tilde{\alpha} \equiv \alpha$), the expression for the true airspeed vector equals the well-known definition in [48.99],

$$\mathbf{v}_{tas} = -\frac{|\mathbf{v}_{tas}|}{D} \begin{pmatrix} 1 \\ \tan \tilde{\beta} \\ \tan \alpha \end{pmatrix}, \quad (48.14)$$

where the normalization factor

$$D = \sqrt{1 + \tan^2 \alpha + \tan^2 \tilde{\beta}} \quad (48.15)$$

(see also [48.59, 61, 100]).

Rotation into the MONS

The attitude of the aircraft can be described by the Eulerian angles Θ (pitch), Φ (bank or roll), and Ψ (yaw,

heading, or azimuth; see Fig. 48.7). Transformation from the ACONS to the MONS is performed via three sequential rotations [48.98, 100],

$$\mathbf{T}_1(\Phi) = \begin{pmatrix} 1 & 0 & 0 \\ 0 & \cos \Phi & -\sin \Phi \\ 0 & \sin \Phi & \cos \Phi \end{pmatrix} \quad (48.16)$$

(i.e., about the x_f axis),

$$\mathbf{T}_2(\Theta) = \begin{pmatrix} \cos \Theta & 0 & \sin \Theta \\ 0 & 1 & 0 \\ -\sin \Theta & 0 & \cos \Theta \end{pmatrix} \quad (48.17)$$

(pitching about the y_f axis), and

$$\mathbf{T}_3(\Psi) = \begin{pmatrix} \cos \Psi & -\sin \Psi & 0 \\ \sin \Psi & \cos \Psi & 0 \\ 0 & 0 & 1 \end{pmatrix} \quad (48.18)$$

(yawing about the z_f axis). The permutation

$$\mathbf{T}_4 = \begin{pmatrix} 0 & 1 & 0 \\ 1 & 0 & 0 \\ 0 & 0 & -1 \end{pmatrix} \quad (48.19)$$

is necessary to transform into the MONS, which is defined by the following meteorological wind vector components:

- u , which is positive eastwards
- v , which is positive northwards
- w , which is positive upwards.

Finally, $\mathbf{M}_{mf} = \mathbf{T}_4 \cdot \mathbf{T}_3 \cdot \mathbf{T}_2 \cdot \mathbf{T}_1$ is inserted into (48.7), and the components of the meteorological wind \mathbf{v} can then be calculated.

48.A.2 True Airspeed, Temperature, and Pressure

The true airspeed $|\mathbf{v}_{tas}|$ of the aircraft in relation to the stagnant air causes a significant discrepancy between the total temperature T_{tot} and the total air pressure p_{tot} (both located at the tip of the FHP) on the one hand and the intrinsic properties T and p (the static temperature and pressure) of the undisturbed atmosphere on the other. The total pressure at the tip of the FHP is

$$p_{tot} = p + \Delta p_q, \quad (48.20)$$

where Δp_q is the dynamic pressure increment due to the airspeed. This can be determined from (48.20) by measuring p in a hole in the aircraft fuselage at a location

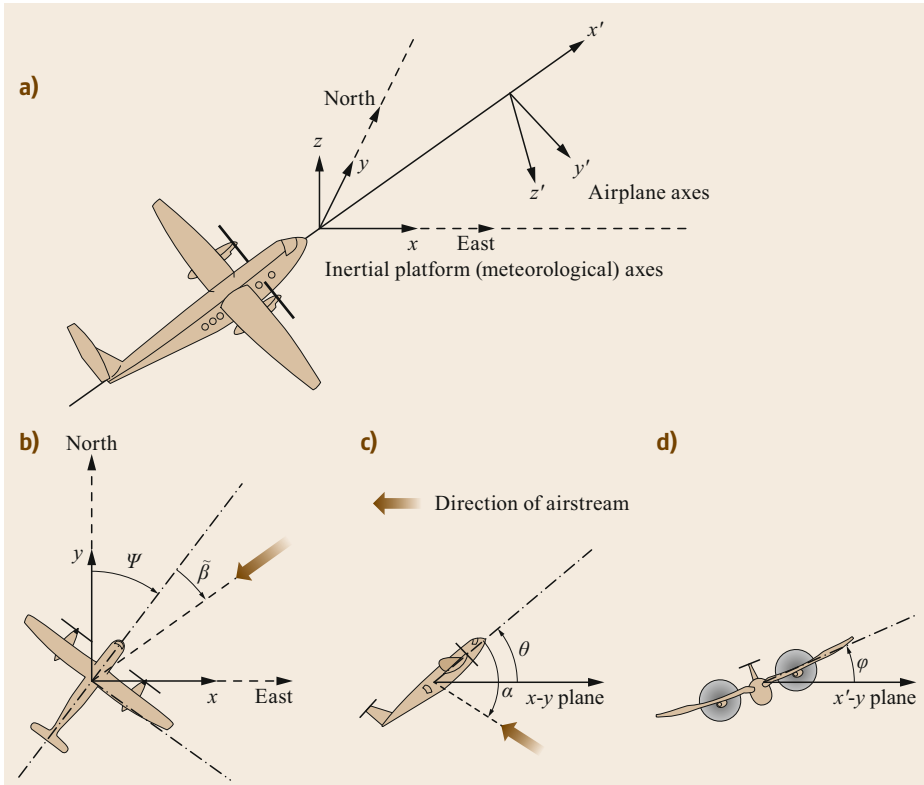


Fig. 48.7 (a) Aircraft attitude angles Θ and Ψ in the MONS and air-flow angles α , β in the ACONS: (b) top view, (c) side view, (d) front view (after [48.99] © American Meteorological Society, used with permission)

where the flow is parallel to the aircraft skin, similar to a Prandtl (Pitot static) tube.

Energy conservation in a compressible flow,

$$\frac{u_1^2}{2} + c_p T_1 = \frac{u_2^2}{2} + c_p T_2 \quad (48.21)$$

(where c_p is the specific heat capacity of air, $u_1 = |\mathbf{v}_{\text{tas}}|$, $u_2 = 0$, $T_1 = T$, and $T_2 = T_{\text{tot}}$), leads to the true airspeed as a function of the temperature difference,

$$|\mathbf{v}_{\text{tas}}|^2 = 2c_p (T_{\text{tot}} - T) \quad (48.22)$$

(see also [48.100]). Since the intrinsic air temperature T is not measured, T is replaced using the equation for an ideal fluid undergoing an adiabatic process,

$$\frac{T}{T_{\text{tot}}} = \left(\frac{p}{p_{\text{tot}}} \right)^\kappa, \quad (48.23)$$

where the Poisson number

$$\kappa = \frac{R_L}{c_p} = \frac{\gamma - 1}{\gamma}. \quad (48.24)$$

Here, $R_L = c_p - c_V = 287 \text{ J (kg K)}^{-1}$ and $\gamma = c_p/c_V$, where $c_V = 718 \text{ J (kg K)}^{-1}$ is the specific heat at constant volume. Finally, the true airspeed can be obtained

without the intrinsic temperature via

$$|\mathbf{v}_{\text{tas}}|^2 = 2c_p T_{\text{tot}} \left[1 - \left(\frac{p}{p_{\text{tot}}} \right)^\kappa \right]. \quad (48.25)$$

Remaining measurement uncertainties are treated by including calibration and installation coefficients that can only be determined through comparison with a pressure sensor that is not influenced by the flow field around the aircraft, for instance with a trailing cone on a calibration flight [48.101].

Using the Mach Number

Applying the definition of the Mach number (the ratio of the true airspeed to the speed of sound) [48.102, 103],

$$\text{Ma}^2 = \frac{2}{\gamma - 1} \left[\left(\frac{p_{\text{tot}}}{p} \right)^\kappa - 1 \right], \quad (48.26)$$

to (48.25) transforms it into

$$|\mathbf{v}_{\text{tas}}|^2 = \gamma R_L T \text{Ma}^2, \quad (48.27)$$

and applying (48.26) to (48.23) transforms it into

$$\frac{T_{\text{tot}}}{T} = 1 + \frac{\gamma - 1}{2} \text{Ma}^2. \quad (48.28)$$

Recovery Factor

In practice, the temperature cannot be measured at the same location as the true airspeed vector v_{tas} (located at the stagnation point at the tip of the FHP). Also, the heat produced by the dynamic pressure increment immediately starts to diffuse into the surrounding air. The temperature T_m measured somewhere in the vicinity of the FHP is smaller than T_{tot} but still larger than the intrinsic temperature T . The ratio [48.99, 103, 104]

$$r_c = \frac{T_m - T}{T_{\text{tot}} - T} \leq 1 \quad (48.29)$$

is referred to as the recovery factor. It depends on the sensor and is usually a function of the true airspeed (but not the air moisture). Inserting (48.29) into (48.23) gives the static (intrinsic) temperature of the air,

$$T = \frac{T_m}{r_c \left[\left(\frac{p_{\text{tot}}}{p_s} \right)^\kappa - 1 \right] + 1} \quad (48.30)$$

(in contrast to [48.99, equation 15]). It is also advisable to apply the recovery factor to the true airspeed calculation in (48.27), yielding

$$|v_{\text{tas}}|^2 = \frac{2c_p T_m}{r_c + \frac{2}{\text{Ma}^2(\gamma-1)}} \quad (48.31)$$

(unlike [48.99, equation 16]).

If the recovery factor r_c is not known (i.e., not provided by the manufacturer of the sensor), the pressure p_T at the location of the temperature probe has to be measured using an additional pressure probe. The static temperature is then calculated using (48.23)

$$T = T_m \left(\frac{p_s}{p_T} \right)^\kappa. \quad (48.32)$$

This method was applied in the fast temperature probe of the Helipod [48.105]. The true airspeed is then calculated by inserting (48.32) into (48.27).

48.A.3 Flow Angles

The following description addresses the application of typical FHPs, which (in addition to the static pressure) only measure differential pressures [48.106]. Air flow systems involving more or less than five holes [48.104, 107, 108] or a single turning sensor [48.109] for differential pressure measurement are treated in a very similar way. In larger probes (e.g., pressure holes in the aircraft fuselage, as used in the Space Shuttle and the F-18 High Angle of Attack Research Vehicle), it is possible to measure individual absolute pressures and determine flow angles even more accurately [48.110]. The

description of outdated systems such as vanes [48.2, 102, 103, 111] exceeds the limits of this analysis.

The local wind vector in the ACONS is determined from the dynamic pressure increment Δp_q and the pressure differences between opposite pressure holes in the FHP (i.e., the pressure differences in the horizontal plane $\Delta p_\beta = P2 - P4$ and the vertical plane $\Delta p_\alpha = P1 - P3$, where p_j denotes the individual holes of the FHP and the central hole is denoted P0; see Fig. 48.2). The pressure differences Δp_α and Δp_β increase as the flow angles α and β increase, but they also depend on the airspeed (and therefore on the dynamic pressure increment Δp_q and the Mach number) and the air density ρ (and therefore the altitude z). In general, this can be expressed via

$$\varphi = F(\Delta p_\varphi, \Delta p_q, z) \quad \text{where } \varphi = \alpha, \beta. \quad (48.33)$$

Here, F denotes a functional relationship.

Usually, the influences of the airspeed and the altitude can be considered by weighting the pressure difference by the dynamic pressure increment. The simplest assumption is therefore

$$\varphi = \frac{1}{K_{\text{FHP}}} \frac{\Delta p_\varphi}{\Delta p_q}, \quad (48.34)$$

where the calibration coefficient K_{FHP} considers any disturbance of the airstream by the FHP (and also by the entire aircraft fuselage) and local stream effects directly at the pressure hole.

It is difficult to determine the dynamic pressure increment Δp_φ and the total pressure p_{tot} (48.20) since the stagnation point is usually located somewhere between the holes of the FHP, so it cannot be measured directly. Approximating the total pressure by the pressure p_5 measured at the central hole of the FHP would lead to a wind vector measurement that is very sensitive to the aircraft attitude, wind speed, and wind direction (see also [48.109]).

It is understood that any offset angles α_0 or β_0 due to either bias in the pressure transducers or asymmetry of the FHP must be quantified in a laboratory, a wind tunnel, or in flight tests beforehand. Calibration routines for both wind-tunnel experiments and flight maneuvers can be found in the literature [48.59, 60, 101–103, 110, 112–114].

The well-known FHP made by Goodrich Sensor Systems (formerly Rosemount) provides an additional pressure difference

$$\Delta p_{\text{ref}} = P0 - P2 \quad (48.35)$$

between one of the horizontal holes and the central hole. The dynamic pressure increment is then estimated using

$$\Delta p_q \approx \Delta p_{\text{ref}} + \frac{1}{2} \Delta p_\beta, \quad (48.36)$$

and the flow angles are determined via (48.34) with K_{FHP} set to 0.088 for airspeeds below 0.6 Ma [48.115].

It should be noted that Δp_{ref} refers only to the horizontal plane (i.e., the stagnation point is assumed to be located somewhere along the line connecting the two opposite holes #2 and #4).

An improvement on the Rosemount method requires an additional differential pressure measurement between the central hole and one of the holes in the vertical plane (#1 or #3), resulting in two disjunct equa-

tions of the same type as (48.34),

$$\alpha = \frac{1}{K_{\text{FHP},\alpha}} \frac{\Delta p_\alpha}{\Delta p_{\text{ref},\alpha} + \frac{1}{2} \Delta p_\alpha} \quad (48.37)$$

$$\tilde{\beta} = \frac{1}{K_{\text{FHP},\beta}} \frac{\Delta p_\beta}{\Delta p_{\text{ref},\beta} + \frac{1}{2} \Delta p_\beta}. \quad (48.38)$$

It is obvious that this method represents only a slight rather than a fundamental improvement on the usual Rosemount method, since no consistent dynamic pressure increment can be determined. This is mainly due to the general strategy of using a Cartesian approach to solve a rotationally symmetric problem. More sophisticated and complex methods have also been published [48.60–62].

References

- 48.1 W.R. Moninger, R.D. Mamrosch, P.M. Pauley: Automated meteorological reports from commercial aircraft, *Bull. Am. Meteorol. Soc.* **84**, 203–216 (2003)
- 48.2 D.H. Lenschow: Airplane measurements of planetary boundary layer structure, *J. Appl. Meteorol.* **9**, 874–884 (1970)
- 48.3 B.R. Bean, R. Gilmer, R.L. Grossman, R. McGavin: An analysis of airborne measurements of vertical water vapor flux during BOMEX, *J. Atmos. Sci.* **29**, 860–869 (1972)
- 48.4 R.L. Grossman, B.R. Bean: An aircraft investigation of turbulence in the lower layers of a marine boundary layer. In: *Tech. Rep. NOAA*, Vol. TR ERP 291 NOAA (1973)
- 48.5 G.A. McBean, R.D. Paterson: Variations of turbulence fluxes of momentum, heat and moisture above Lake Ontario, *J. Phys. Oceanogr.* **5**, 523–531 (1975)
- 48.6 D.H. Lenschow, A.C. Delany, B.B. Stankov, D.H. Stedman: Airborne measurements of the vertical flux of ozone in the boundary layer, *Bound.-Layer Meteorol.* **19**, 249–265 (1980)
- 48.7 P. Alvo, R.L. Desjardins, P.H. Schuepp, J.I. MacPherson: Aircraft measurements of CO₂ exchange over various ecosystems, *Bound.-Layer Meteorol.* **29**, 167–183 (1984)
- 48.8 R.L. Desjardins, E.J. Brach, P. Alvo, P.H. Schuepp: Aircraft monitoring of surface carbon dioxide exchange, *Science* **216**, 733–735 (1982)
- 48.9 R.C. Harriss, S.C. Wofsy, D.S. Bartlett, M.C. Shipham, D.J. Jacob, J.M. Hoell Jr., R.J. Bendura, J.W. Drewry, R.J. McNeal, R.L. Navarro, R.N. Gidge, V.E. Rabine: The Arctic Boundary Layer Expedition (ABLE 3a): July–August 1988, *J. Geophys. Res. Atmos.* **97**, 16383–16394 (1992)
- 48.10 W.A. Glooschenko, N.T. Roulet, L.A. Barrie, H.I. Schiff, H.G. McAdie: The Northern Wetlands Study (NOWES): An overview, *J. Geophys. Res.* **99**, 1423–1428 (1994)
- 48.11 J.-C. André, J.-P. Goutorbe, A. Perrier: HAPEX-MO-BILHY: a hydrologic atmospheric experiment for the study of water budget and evaporation at the climatic scale, *Bull. Am. Meteorol. Soc.* **67**, 138–144 (1986)
- 48.12 P.J. Sellers, F.G. Hall, G. Asrar, D.E. Strebil, R.E. Murphy: The first ISLSCP field experiment, *Bull. Am. Meteorol. Soc.* **69**, 22–27 (1988)
- 48.13 P.J. Sellers, F.G. Hall, G. Asrar, D.E. Strebil, R.E. Murphy: An overview of the first International Satellite Land Surface Climatology Project (ISLSCP) Field Experiment (FIFE), *J. Geophys. Res.* **97**, 18345–18371 (1992)
- 48.14 A.K. Betts, R.L. Desjardins, J.I. MacPherson: Budget analysis of the boundary layer grid flights during FIFE 1987, *J. Geophys. Res.* **97**(D17), 18533–18546 (1992)
- 48.15 A.K. Betts, R.L. Desjardins, J.I. MacPherson, R.D. Kelly: Boundary-layer heat and moisture budgets from FIFE, *Bound.-Layer Meteorol.* **50**, 109–138 (1990)
- 48.16 P.J. Sellers, F.G. Hall, R.D. Kelly, A. Black, D.D. Baldocchi, J. Berry, M. Ryan, K.J. Ranson, P.M. Crill, D.P. Lettenmaier, H. Margolis, J. Cihlar, J. Newcomer, D.R. Fitzjarrald, P.G. Jarvis, S.T. Gower, D. Halliwell, D. Williams, B. Goodison, D.E. Wickland, F.E. Guertin: BOREAS in 1997: Experiment overview, scientific results, and future directions, *J. Geophys. Res.* **102**, 28731–28769 (1997)
- 48.17 J.M. Chen, S.G. Leblanc, J. Cihlar, R.L. Desjardins, J.I. MacPherson: Extending aircraft- and tower-based CO₂ flux measurements to a boreal region using a landsat thematic mapper land cover map, *J. Geophys. Res.* **104**, 16859–16877 (1999)
- 48.18 T.J. Jackson, D.M. Le Vine, A.Y. Hsu, A. Oldak, P.J. Starks, C.T. Swift, J.D. Isham, M. Haken: Soil moisture mapping at regional scales using mi-

- crowwave radiometry: the southern great plains hydrology experiment, *IEEE Trans. Geosci. Remote Sens.* **37**, 2136–2151 (1999)
- 48.19 M. Keller, A. Alencar, G.P. Asner, B. Braswell, M. Bustamante, E. Davidson, T. Feldapusch, E. Fernandes, M. Goulden, P. Kabat, B. Kruijt, F. Luizao, S. Miller, D. Markewitz, A.D. Nobre, C.A. Nobre, N.P. Filho, H. da Rocha, P.S. Dias, C. von Randow, G.L. Vourlitis: Ecological research in the large-scale biosphere-atmosphere experiment in Amazonia: Early results, *Ecol. Appl.* **14**, 3–16 (2004)
- 48.20 R.J. Dobosy, T.L. Crawford, J.I. MacPherson, R.L. Desjardins, R.D. Kelly, S.P. Oncley, D.H. Lenschow: Intercomparison among four flux aircraft at BOREAS in 1994, *J. Geophys. Res.* **102**, 29101–29111 (1997)
- 48.21 R.L. Desjardins, J.I. MacPherson, L. Mahrt, P.H. Schuepp, E. Pattey, H. Neumann, D. Baldocchi, S. Wofsy, D.R. Fitzjarrald, H. McCaughey, D.W. Joiner: Scaling up flux measurements for the boreal forest using aircraft-tower combinations, *J. Geophys. Res.* **102**, 29125–29133 (1997)
- 48.22 T. Zhu, R.L. Desjardins, J.I. MacPherson, E. Pattey, G. St. Amour: Aircraft measurements of the concentration and flux of agrochemicals, *Environ. Sci. Technol.* **32**, 1032–1038 (1998)
- 48.23 T. Zhu, D. Wang, R.L. Desjardins, J.I. MacPherson: Aircraft-based volatile organic compounds flux measurements with relaxed Eddy accumulation, *Atmos. Environ.* **33**, 1969–1979 (1999)
- 48.24 T. Hiyama, M.A. Strunin, R. Suzuki, J. Asanuma, M.Y. Mezrin, N.A. Bezrukova, T. Ohata: Aircraft observations of the atmospheric boundary layer over a heterogeneous surface in Eastern Siberia, *Hydrol. Process.* **17**, 2885–2911 (2003)
- 48.25 M. Mauder, R.L. Desjardins, J.I. MacPherson: Scale analysis of airborne flux measurements over heterogeneous terrain in a boreal ecosystem, *J. Geophys. Res.* **112**, D13112 (2007)
- 48.26 G.M. Wolfe, S.R. Kawa, T.F. Hanisco, R.A. Hannun, P.A. Newman, A. Swanson, S. Bailey, J. Barrick, K.L. Thornhill, G. Diskin, J. DiGangi, J.B. Nowak, C. Sorenson, G. Bland, J.K. Yungel, C.A. Swenson: The NASA carbon airborne flux experiment (CARAFE): instrumentation and methodology, *Atmos. Meas. Tech.* **11**, 1757–1776 (2018)
- 48.27 R.L. Desjardins, E. Pattey, W.N. Smith, D. Worth, B.B. Grant, R. Srinivasan, J.I. MacPherson, M. Mauder: Multiscale estimates of N₂O emissions from agricultural lands, *Agric. For. Meteorol.* **150**, 817–824 (2010)
- 48.28 K. Kohnert, A. Serafimovich, S. Metzger, J. Hartmann, T. Sachs: Strong geologic methane emissions from discontinuous terrestrial permafrost in the Mackenzie delta, Canada, *Sci. Rep.* **7**, 5828 (2017)
- 48.29 R.L. Desjardins, D.E. Worth, R. Srinivasan, E. Pattey, A.C. VanderZaag, M. Mauder, S. Metzger, D. Worthy, C. Sweeney: The challenge of reconciling bottom-up agricultural methane emissions inventories with top-down measurements, *Agric. For. Meteorol.* **248**, 48–59 (2018)
- 48.30 J.R. Pederson, W.J. Massman, L. Mahrt, A. Delany, S. Oncley, G.D. Hartog, H.H. Neumann, R.E. Mickle, R.H. Shaw, K.T. Paw U, D.A. Grantz, J.I. MacPherson, R. Desjardins: California ozone deposition experiment: Methods, results, and opportunities, *Atmos. Environ.* **29**, 3115–3132 (1995)
- 48.31 R.E. Stewart, H.G. Leighton, P. Marsh, G.W.K. Moore, H. Ritchie, W.R. Rouse, E.D. Soulis, G.S. Strong, R.W. Crawford, B. Kochtubajda: The Mackenzie GEWEX study: The water and energy cycles of a major north American river basin, *Bull. Am. Meteorol. Soc.* **79**, 2665–2683 (1998)
- 48.32 M.A. Strunin, T. Hiyama: Applying wavelet transforms to analyse aircraft-measured turbulence and turbulent fluxes in the atmospheric boundary layer over Eastern Siberia, *Hydrol. Process.* **18**, 3081–3098 (2004)
- 48.33 T. Hiyama, M.A. Strunin, H. Tanaka, T. Ohta: The development of local circulations around the Lena river and their effect on tower-observed energy imbalance, *Hydrol. Process.* **21**, 2038–2048 (2007)
- 48.34 K. Wilson, A. Goldstein, E. Falge, M. Aubinet, D. Baldocchi, P. Berbigier, C. Bernhofer, R. Ceulemans, H. Dolman, C. Field: Energy balance closure at fluxnet sites, *Agric. For. Meteorol.* **113**, 223–243 (2002)
- 48.35 W.P. Kustas, J.L. Hatfield, J.H. Prueger: The Soil Moisture-Atmosphere Coupling Experiment (SMACEX): background, hydrometeorological conditions, and preliminary findings, *J. Hydrometeorol.* **6**, 791–804 (2005)
- 48.36 B. Yuan, L. Kaser, T. Karl, M. Graus, J. Peischl, T.L. Campos, S. Shertz, E.C. Apel, R.S. Hornbrook, A. Hills, J.B. Gilman, B.M. Lerner, C. Warneke, F.M. Flocke, T.B. Ryerson, A.B. Guenther, J.A. de Gouw: Airborne flux measurements of methane and volatile organic compounds over the Haynesville and Marcellus shale gas production regions, *J. Geophys. Res. Atmos.* **120**, 6271–6289 (2015)
- 48.37 J.A. Hacker, D. Chen, M. Bai, C. Ewenz, W. Junkermann, W. Lieff, B. McManus, B. Neininger, J. Sun, T. Coates, T. Denmead, T.K. Flesch, S.M. McGinn, J. Hill: Using airborne technology to quantify and apportion emissions of CH₄ and NH₃ from feedlots, *Anim. Prod. Sci.* **56**, 190–203 (2016)
- 48.38 J.C. Kaimal, J.J. Finnigan: *Atmospheric Boundary Layer Flows: Their Structure and Measurement* (Oxford Univ. Press, New York 1994)
- 48.39 R.L. Desjardins, P. Rochette, E. Pattey, J.I. MacPherson: Measurements of greenhouse gas fluxes using aircraft- and tower-based techniques. In: *Agricultural Ecosystem Effects on Trace Gases and Global Climate Change*, ASA Special Publication, Vol. 55, ed. by L. Harper, J. Duxbury, A. Mosier (1993) pp. 45–62
- 48.40 R.L. Desjardins, J.I. MacPherson, P.H. Schuepp, F. Karanja: An evaluation of aircraft flux mea-

- surements of CO₂, water vapor and sensible heat, Bound.-Layer Meteorol. **47**, 55–69 (1989)
- 48.41 R.L. Desjardins: *A Study of Carbon Dioxide and Sensible Heat Fluxes Using the Eddy Correlation Technique*, Ph.D. Thesis (Cornell University, Ithaca 1972)
- 48.42 D.J. Buckley, R.L. Desjardins, J.L.M. Lalonde, R. Brunke: A Linearized, fast response gas sampling apparatus for Eddy accumulation studies, Comput. Electron. Agric. **2**, 243–250 (1988)
- 48.43 J.A. Businger, S.P. Oncley: Flux measurement with conditional sampling, J. Atmos. Ocean. Technol. **7**, 349–352 (1990)
- 48.44 J.I. MacPherson, R.L. Desjardins: Airborne tests of flux measurement by the relaxed Eddy accumulation technique. In: *Proc. 7th Symposium on Meteorological Observation and Instrumentation* (American Meteorological Society, Boston 1991) pp. 6–11
- 48.45 E. Pattey, R.L. Desjardins, P. Rochette: Accuracy of the relaxed Eddy-accumulation technique, evaluated using CO₂ flux measurements, Bound.-Layer Meteorol. **66**, 341–355 (1993)
- 48.46 A. Moravek, I. Trebs, T. Foken: Effect of imprecise lag time and high frequency attenuation on surface-atmosphere exchange determined with the relaxed Eddy accumulation method, J. Geophys. Res. Atmos. **118**, 10,210–10,224 (2013)
- 48.47 C. Torrence, G.P. Compo: A practical guide to wavelet analysis, Bull. Am. Meteorol. Soc. **79**, 61–78 (1998)
- 48.48 L. Mahrt, J.F. Howell: The influence of coherent structures and microfronts on scaling laws using global and local transforms, J. Fluid Mech. **260**, 247–270 (1994)
- 48.49 J.-L. Attié, P. Durand: Conditional wavelet technique applied to aircraft data measured in the thermal internal boundary layer during sea-breeze events, Bound.-Layer Meteorol. **106**, 359–382 (2003)
- 48.50 S. Metzger, W. Junkermann, M. Mauder, K. Butterbach-Bahl, B. Trancón y Widemann, F. Neidl, K. Schäfer, S. Wieneke, X.H. Zheng, H.P. Schmid, T. Foken: Spatially explicit regionalization of airborne flux measurements using environmental response functions, Biogeosciences **10**, 2193–2217 (2013)
- 48.51 L.E. Hudgins, M.E. Mayer, C.A. Friehe: Fourier and wavelet analysis of atmospheric turbulence. In: *Progress in Wavelet Analysis and Applications*, Editions Frontiers, ed. by E. Meyers, S. Roques (1993) pp. 491–498
- 48.52 K.L. Mays, P.B. Shepson, B.H. Stirm, A. Karion, C. Sweeney, K. Gurney: Aircraft-based measurements of the carbon footprint of Indianapolis, Environ. Sci. Technol. **43**, 7816–7823 (2009)
- 48.53 J. Turnbull, A. Karion, M.L. Fischer, I. Faloona, T. Guilderson, S.J. Lehman, B.R. Miller, J.B. Miller, S.A. Montzka, T. Sherwood, S. Saripalli, C. Sweeney, P. Tans: Assessment of fossil fuel carbon dioxide and other anthropogenic trace gas emissions from airborne measurements over Sacramento, California in spring 2009, Atmos. Chem. Phys. **11**, 705–721 (2011)
- 48.54 M.O. Cambaliza, P.B. Shepson, D. Caulton, B. Stirm, D. Samarov, K.R. Gurney, J. Turnbull, K.J. Davis, A. Possolo, A. Karion, C. Sweeney, B. Moser, A. Hendricks, T. Lauvaux, K. Mays, J. Whetstone, J. Huang, L. Razlivanov, N.L. Miles, S.J. Richardson: Assessment of uncertainties of an aircraft-based mass-balance approach for quantifying Urban greenhouse gas emissions, Environ. Sci. Technol. **49**, 7904–7913 (2013)
- 48.55 D.S. Wratt, N.R. Gimson, G.W. Brailsford, K.R. Lassey, A.M. Bromley, M.J. Bell: Estimating regional methane emissions from agriculture using aircraft measurements of concentration profiles, Atmos. Environ. **35**, 497–508 (2001)
- 48.56 S. Metzger, W. Junkermann, M. Mauder, F. Beyrich, K. Butterbach-Bahl, H.P. Schmid, T. Foken: Eddy-covariance flux measurements with a weight-shift microlight aircraft, Atmos. Meas. Tech. **5**, 1699–1717 (2012)
- 48.57 J.I. MacPherson, M. Wolde: *NRC Twin Otter Operations in the Soil Moisture-Atmospheric Coupling Experiment*, Tech. Rep., Vol. 46-7373-2 (National Research Council Canada, Ottawa 2002)
- 48.58 P.R. Isaac, J. McAneney, R. Leuning, J.M. Hacker: Comparison of aircraft and ground-based flux measurements during OASIS95, Bound.-Layer Meteorol. **110**, 39–67 (2004)
- 48.59 A. Williams, D. Marcotte: Wind measurements on a maneuvering twin-engine turbo-prop aircraft accounting for flow distortion, J. Atmos. Ocean. Technol. **17**, 795–810 (2000)
- 48.60 A.C. van den Kroonenberg, T. Martin, M. Buschmann, J. Bange, P. Vörsmann: Measuring the wind vector using the autonomous mini aerial vehicle M²AV, J. Atmos. Ocean. Technol. **25**, 1969–1982 (2008)
- 48.61 J. Bange: *Airborne Measurement of Turbulent Energy Exchange between the Earth Surface and the Atmosphere* (Sierke, Göttingen 2009)
- 48.62 J. Bange, M. Esposito, D.H. Lenschow: Measurement of aircraft state, thermodynamic and dynamic variables. In: *Airborne Measurements for Environmental Research – Methods and Instruments* (Wiley-VCH, Weinheim 2013) p. 641
- 48.63 E.R. Crosson: A cavity ring-down analyzer for measuring atmospheric levels of methane, carbon dioxide, and water vapor, Appl. Phys. B **92**, 403–408 (2008)
- 48.64 D.K. McDermitt, J.M. Welles, R.D. Eckles: *Effects of Temperature, Pressure and Water Vapor on Gas Phase Infrared Absorption by CO₂*, Tech. Rep. (LICOR Inc., Lincoln 1993)
- 48.65 J.I. MacPherson, R.L. Desjardins, P.H. Schuepp, R. Pearson: Aircraft-measured ozone deposition in the San Joaquin valley of California, Atmos. Environ. **29**, 3133–3145 (1995)
- 48.66 R.V. Hiller, B. Neininger, D. Brunner, C. Gerbig, D. Bretscher, T. Künzle, N. Buchmann, W. Eugster: Aircraft-based CH₄ flux estimates for validation of emissions from an agriculturally dominated area

- in Switzerland, *J. Geophys. Res. Atmos.* **119**, 4874–4887 (2014)
- 48.67 R.C. Zulueta, W.C. Orchel, J.G. Vergaillie, S.J. Hastings: Aircraft regional-scale flux measurements over complex landscapes of mangroves, desert, and marine ecosystems of Magdalena Bay, Mexico, *J. Atmos. Ocean. Technol.* **30**, 1266–1294 (2013)
- 48.68 E. Pattey, R.L. Desjardins, H. Westberg, B. Lamb, T. Zhu: Measurement of isoprene emissions over a black spruce stand using a tower-based relaxed Eddy-accumulation system, *J. Appl. Meteorol.* **38**, 870–877 (1999)
- 48.69 E. Pattey, G.C. Edwards, R.L. Desjardins, D.J. Pennock, W. Smith, B. Grant, J.I. MacPherson: Tools for quantifying N₂O emissions from agroecosystems, *Agric. For. Meteorol.* **142**, 103–119 (2007)
- 48.70 J.I. MacPherson, M. Bastian: *Archive of NRC Twin Otter Data from the 1991–2003 Flux Projects*, Tech. Rep., Vol. LTR-FR-204 (National Research Council Canada Institute for Aerospace Research, Ottawa 2003)
- 48.71 R. Srinivasan: *Flight Evaluation of the FRL-Integrated Honeywell HG1700 Strapdown Inertial/Novatel GPS Navigation System in the NRC Twin Otter*, Tech. Rep. (National Research Council Canada, Ottawa 2005)
- 48.72 D. Vickers, L. Mahrt: Quality control and flux sampling problems for tower and aircraft data, *J. Atmos. Ocean. Technol.* **14**, 512–526 (1997)
- 48.73 F. Chahuneau, R.L. Desjardins, E. Brach, R. Verdon: A micrometeorological facility for Eddy flux measurements of CO₂ and H₂O, *J. Atmos. Ocean. Technol.* **6**, 193–200 (1989)
- 48.74 G. Fratini, M. Mauder: Towards a consistent Eddy-covariance processing: an Intercomparison of Eddypro and TK3, *Atmos. Meas. Tech.* **7**, 2273–2281 (2014)
- 48.75 S. Metzger, D. Durden, C. Sturtevant, H. Luo, N. Pingintha-Durden, T. Sachs, A. Serafimovich, J. Hartmann, J. Li, K. Xu, A.R. Desai: Eddy4r 0.2.0: a DevOps model for community-extensible processing and analysis of Eddy-covariance data based on R, Git, Docker, and HDF5, *Geosci. Model Dev.* **10**, 3189–3206 (2017)
- 48.76 J.I. MacPherson: *NRC Twin Otter Operations in the 1991 California Ozone Deposition Experiment*, Tech. Rep., Vol. LTR-FR-118 (National Research Council Canada Institute for Aerospace Research, Ottawa 1992)
- 48.77 A. Zahn, J. Weppner, H. Widmann, K. Schlote-Holubek, B. Burger, T. Kuhner, H. Franke: A fast and precise chemiluminescence ozone detector for Eddy flux and airborne application, *Atmos. Meas. Tech.* **5**, 363–375 (2012)
- 48.78 R.L. Desjardins, R.L. Hart, J.I. MacPherson, P.H. Schuepp, S.B. Verma: Aircraft- and tower-based fluxes of carbon dioxide, latent, and sensible heat, *J. Geophys. Res.* **97**, 18477–18485 (1992)
- 48.79 J.I. MacPherson, R. Dobosy, S. Verma, W.P. Kustas, J.H. Prueger, A.G. Williams: Intercomparisons between flux aircraft and towers in SGP97. In: *Proc. 14th Conference on Hydrology* (American Meteorological Society, Boston 1999) pp. 125–128
- 48.80 R.L. Desjardins, P.H. Schuepp, J.I. MacPherson, D.J. Buckley: Spatial and temporal variations of the fluxes of carbon dioxide and sensible and latent heat over the FIFE site, *J. Geophys. Res.* **97**(D17), 18467–18475 (1992)
- 48.81 L. Mahrt: Surface heterogeneity and vertical structure of the boundary layer, *Bound.-Layer Meteorol.* **96**, 33–62 (2000)
- 48.82 L. Mahrt: Flux sampling errors for aircraft and towers, *J. Atmos. Ocean. Technol.* **15**, 416–429 (1998)
- 48.83 R.L. Desjardins, J.I. MacPherson, P.H. Schuepp, N.H. Hayhoe: Airborne flux measurements of CO₂, sensible and latent heat over the Hudson Bay lowland, *J. Geophys. Res. Atmos.* **99**, 1551–1561 (1994)
- 48.84 E. Pattey, I.B. Strachan, R.L. Desjardins, J. Massheder: Measuring nighttime CO₂ flux over terrestrial ecosystems using Eddy covariance and nocturnal boundary layer methods, *Agric. For. Meteorol.* **113**, 145–158 (2002)
- 48.85 J. Sun, R.L. Desjardins, L. Mahrt, J.I. MacPherson: Transport of carbon dioxide, water vapor, and ozone by turbulence and local circulations, *J. Geophys. Res.* **103**, 25873–25885 (1998)
- 48.86 J. Sun, D.H. Lenschow, L. Mahrt, T.L. Crawford, K.J. Davis, S.P. Oncley, J.I. MacPherson, Q. Wang, R.J. Dobosy, R.L. Desjardins: Lake-induced atmospheric circulations during BOREAS, *J. Geophys. Res.* **102**, 29155–29166 (1997)
- 48.87 J.J. Hutchinson, B.B. Grant, W.N. Smith, R.L. Desjardins, C.A. Campbell, D. Worth, X.P.C. Vergé: Estimates of direct nitrous emissions from Canadian agroecosystems and their uncertainties, *Can. J. Soil Sci.* **87**, 141–152 (2007)
- 48.88 Y. Karimi-Zindashty, J.D. Macdonald, R.L. Desjardins, D.E. Worth, J.J. Hutchinson, X.P.C. Vergé: Sources of uncertainty in the IPCC tier 2 Canadian livestock model, *J. Agric. Sci.* **150**, 556–569 (2012)
- 48.89 P. Smith, D. Martino, C. Zucong, D. Gwary, H.H. Janzen, P. Kumar, B. McCarl, S. Ogle, F. O'Mara, C. Rice, B. Scholes, O. Sirotenko, M. Howden, T. McAllister, G. Pan, V. Romanenkov, U. Schneider, S. Towprayoon, M. Wattenbach, J. Smith: Greenhouse gas mitigation in agriculture, *Philos. Trans. R. Soc.* **363**, 789–813 (2008)
- 48.90 K.J. Wecht, D.J. Jacob, C. Frankenberg, Z. Jiang, D.R. Blake: Mapping of North American methane emissions with high spatial resolution by inversion of SCIAMACHY satellite data, *J. Geophys. Res. Atmos.* **119**, 7741–7756 (2014)
- 48.91 A. Karion, C. Sweeney, G. Pétron, G. Frost, M. Hardesty, J. Kofler, B.R. Miller, T. Newberger, S. Wolter, R. Banta, A. Brewer, E.J. Dlugokencky, P. Lang, S.A. Montzka, R. Schnell, P. Tans, M. Trainer, R. Zamora, S. Conley: Methane emissions estimate from airborne measurements over a western United States natural gas field, *Geophys. Res. Lett.* **40**, 1–5 (2013)

- 48.92 M.R. Johnson, D.R. Tyner, S. Conley, S. Schwietzke, D. Zavala-Araiza: Comparison of airborne measurements and inventory estimates of methane emissions in the Alberta upstream oil and gas sector, *Environ. Sci. Technol.* **51**, 13008–13017 (2017)
- 48.93 R.L. Desjardins, D.E. Worth, J.I. MacPherson, M. Bastian, R. Srinivasan: Flux measurements by the NRC Twin Otter atmospheric research aircraft: 1987–2011, *Adv. Sci. Res.* **13**, 43–49 (2016)
- 48.94 F. Eder, M. Schmidt, T. Damian, K. Träumner, M. Mauder: Mesoscale Eddies affect near-surface turbulent exchange: Evidence from lidar and tower measurements, *J. Appl. Meteorol. Climatol.* **54**, 189–206 (2015)
- 48.95 A.J. Turner, D.J. Jacob, K.J. Wecht, J.D. Maasakkers, E. Lundgren, A.E. Andrews, S.C. Biraud, H. Boesch, K.W. Bowman, N.M. Deutscher, M.K. Dubey, D.W.T. Griffith, F. Hase, A. Kuze, J. Notholt, H. Ohyama, R. Parker, V.H. Payne, R. Sussmann, C. Sweeney, V.A. Velasco, T. Warneke, P.O. Wennberg, D. Wunch: Estimating global and north American methane emissions with high spatial resolution using GOSAT satellite data, *Atmos. Chem. Phys.* **15**, 7049–7069 (2015)
- 48.96 A.C. VanderZaag, J.D. MacDonald, L. Evans, X.P.C. Vergé, R.L. Desjardins: Towards an inventory of methane emissions from manure management that is responsive to changes on Canadian farms, *Environ. Res. Lett.* **8**, 035008 (2013)
- 48.97 J.P. Veefkind, I. Aben, K. McMullan, H. Forster, J. de Vries, G. Otter, J. Claas, H.J. Eskes, J.F. de Haan, Q. Kleipool, M. Van Weele, O. Hasekamp, R. Hoogeveen, J. Landgraf, R. Snel, P. Tol, P. Ingmann, R. Voors, B. Bruizinga, R. Vink, H. Visser, P.F. Levelt: TROPOMI on the ESA sentinel-5 precursor: a GME mission for global observations of the atmospheric composition for climate, air quality and ozone layer applications, *Remote Sens. Environ.* **120**, 70–83 (2012)
- 48.98 J.-L. Boiffier: *The Dynamics of Flight – the Equations* (John Wiley & Sons, Chichester 1998)
- 48.99 D.H. Lenschow: Aircraft measurements in the boundary layer. In: *Probing the Atmospheric Boundary Layer*, ed. by D.H. Lenschow (American Meteorological Society, Boston 1986) pp. 39–53
- 48.100 J.A. Leise, J.M. Masters: *Wind Measurements from Aircraft*, Tech. Rep. (US Department of Commerce, National Oceanic and Atmospheric Administration, Aircraft Operation Centre, Miami 1993)
- 48.101 E.A. Haering: *Airdata Measurement and Calibration*, Tech. Mem., Vol. 104316 (National Aeronautics and Space Administration (NASA), Washington 1995)
- 48.102 E.A. Haering: *Airdata Calibration of a High-Performance Aircraft for Measuring Atmospheric Wind Profiles*, Tech. Mem., Vol. 101714 (National Aeronautics and Space Administration (NASA), Washington 1990)
- 48.103 J.D.W. Barrick, J.A. Ritter, C.E. Watson, M.W. Wynkoop, J.K. Quinn, D.R. Norfolk: *Calibration of NASA Turbulent Air Motion Measurement System*, Technical Paper, Vol. 3610 (National Aeronautics and Space Administration (NASA), Washington 1996)
- 48.104 T.L. Crawford, R.J. Dobosy: A sensitive fast-response probe to measure turbulence and heat flux from any airplane, *Bound.-Layer Meteorol.* **59**, 257–278 (1992)
- 48.105 A. Muschinski, R. Frehlich, M. Jensen, R. Hugo, A. Hoff, F. Eaton, B. Balsley: Fine-scale measurements of turbulence in the lower troposphere: An intercomparison between a kite- and balloon-borne, and a helicopter-borne measurement system, *Bound.-Layer Meteorol.* **98**, 219–250 (2001)
- 48.106 G. Lemonis, M. Schmücker, H. Struck: A fast response probe system for in-flight measurements of atmospheric turbulence, *Aerosp. Sci. Technol.* **6**, 233–243 (2002)
- 48.107 D. Sumner: Calibration methods for a seven-hole pressure probe. In: *Proc. Sixth Triennial International Symposium on Flow Control, Measurement and Visualization (FLUCOME 2000)*, ed. by A. Laneville (2000) p. 6
- 48.108 A. Pfau, J. Schlienger, A.I. Kalfas, R.S. Abhari: Virtual four sensor Fast Response Aerodynamic Probe (FRAP). In: *Proc. 16th Symposium on Measuring Techniques in Transonic and Supersonic Flow in Cascades and Turbomachines* (2002)
- 48.109 J. Schlienger, A. Pfau, A.I. Kalfas, R.S. Abhari: Single pressure transducer probe for 3D flow measurements. In: *Proc. 16th Symposium on Measuring Techniques in Transonic and Supersonic Flow in Cascades and Turbomachines* (2002)
- 48.110 S. Weiß: Comparing three algorithms for modeling flush air data systems. In: *Proc. AIAA Aerospace Sciences Meeting and Exhibition, 40th* (2002) p. AIAA-2002-2535
- 48.111 D.H. Lenschow: Vanes for sensing incidence angles of the air from an aircraft, *J. Appl. Meteorol.* **10**, 1339–1343 (1971)
- 48.112 C.A. Friehe, S.P. Burns, D. Khelif, X. Song: Meteorological and flux measurements from the NOAA WP3D aircraft in toga coare. In: *Proc. 8th Conference on Air-Sea Interaction, AMS* (1996) pp. J42–J45
- 48.113 D. Khelif, S.P. Burns, C.A. Friehe: Improved wind measurements on research aircraft, *J. Atmos. Ocean. Technol.* **16**, 860–875 (1999)
- 48.114 N. Wildmann, S. Ravi, J. Bange: Towards higher accuracy and better frequency response with standard multi-hole probes in turbulence measurement with remotely piloted aircraft (RPA), *Atmos. Meas. Tech.* **7**, 1027–1041 (2014)
- 48.115 Rosemount: *Model 858 Flow Angle Sensors*, Bulletin, Vol. 1014 (Rosemount Inc., Shakopee 1982), Tech. Rep.

Raymond Desjardins

Science and Technology Branch
Agriculture and Agri-Food Canada
Ottawa, Canada
ray.desjardins@canada.ca



Raymond Desjardins is an Emeritus Scientist at the Ottawa Research and Development Centre, Central Experimental Farm, Science and Technology Branch, Agriculture and Agri-Food Canada. He received a PhD in Micrometeorology from Cornell University in 1972. He is a Member of the Order of Canada, Member of the Order of Ontario, and a Fellow of the Royal Society of Canada. He develops techniques to quantify mass and energy exchange over a wide range of ecosystems using tower and aircraft-based systems. Some of his recent research is focused on improving estimates of the carbon footprint of agricultural products and helping Canadian farmers compete on the international markets.

Devon Worth

Science and Technology Branch
Agriculture and Agri-Food Canada
Ottawa, Canada
devon.worth@canada.ca



Devon Worth is a physical scientist at the Science and Technology Branch of Agriculture and Agri-Food Canada at the Ottawa Research and Development Centre in Canada. He obtained an MSc from McMaster University in micrometeorology in 2002. His work focusses on mass and energy exchange using aircraft-based measurement techniques.

John Ian MacPherson

National Research Council of Canada
Ottawa, Canada
ian.macpherson@rogers.com



John Ian MacPherson is a retired Principal Research Officer from the Flight Research Laboratory, Institute of Aerospace Research, National Research Council of Canada. He received a Master of Applied Science in Aerospace Engineering from the University of Toronto in 1966. He was the principal scientist in charge of the NRC Twin Otter Atmospheric Research Aircraft and conducted national and international experiments in cloud physics, remote sensing, atmospheric turbulence, and the airborne measure of trace gas fluxes.

Matthias Mauder

Institute of Hydrology and Meteorology
Technische Universität Dresden
Dresden, Germany
matthias.mauder@tu-dresden.de



Matthias Mauder is a Professor in meteorology at the Technical University Dresden, Germany. Up to September 2021 he was the head of the group "Transport Processes in the Atmospheric Boundary Layer" at Karlsruhe Institute of Technology. He received his Doctorate in Micrometeorology from the University of Bayreuth (2006). As a postdoc, he developed new methods for the analysis of airborne eddy-covariance measurements and multitower measurements. His research aims to combine different observational techniques with numerical modeling to improve our understanding of turbulent transport processes and boundary-layer dynamics.

Jens Bange

Centre for Applied Geo-Science
University of Tübingen
Tübingen, Germany
jens.bange@uni-tuebingen.de



Jens Bange is a Professor for Environmental Physics at the University of Tübingen since 2010. He received a PhD in meteorology in 1998 and a diploma in physics in 1992 at the University of Hannover. His research interests include atmospheric turbulence, boundary-layer meteorology, wind-energy research, airborne meteorology, and environmental measurement technology. He is a founding member of the research networks ISARRA and WindForS.

Unmanned Aircraft

49. Unmanned Aircraft Systems

Jens Bange , Joachim Reuder , Andreas Platis 

UAS (unmanned aircraft systems) for atmospheric research are able to fulfill scientific tasks comparable to manned research aircraft and carry similar instruments. On the one hand, the payload aboard small UAS is much smaller and lighter and the endurance is shorter. On the other hand, the logistic efforts are more manageable, and disturbance of the turbulent atmospheric flow by UAS is also much weaker. In this chapter, we focus on the measurement of temperature, water vapor, aerosol, and the three-dimensional (3-D) wind vector measured aboard UAS, also considering the statistical uncertainty of turbulence measurements. We also discuss rotary-wing and fixed-wing UAS, weight classes, engines, autopilots, legal limits, and flight strategies. Finally, some exemplary field campaigns of the past are introduced.

49.1	Measurement Principles and Parameters	1332	49.3.1	Terminology	1333
49.2	History	1332	49.3.2	UAS for Atmospheric Research	1334
49.3	Theory	1333	49.4	Devices and Systems	1334
			49.4.1	Airborne Carrier	1334
			49.4.2	Temperature Sensors for UAS	1337
			49.4.3	Humidity Sensors for UAS	1337
			49.4.4	Wind Sensors for UAS	1337
			49.4.5	Aerosol and Particle Sensors for UAS	1338
			49.5	Specifications	1339
			49.6	Quality Control	1339
			49.6.1	Statistical Tools	1339
			49.6.2	Statistical Uncertainty of Turbulence Quantities	1340
			49.7	Maintenance	1340
			49.8	Applications	1341
			49.8.1	Civil Aviation Authority Rules and Regulations	1341
			49.8.2	Flight Strategies	1342
			49.8.3	Important UAS Campaigns	1343
			49.9	Future Developments	1344
			49.10	Further Readings	1344
			References		1344

Research aircraft, in general, close the spatial gap between ground stations (including meteorological masts and towers) and ground-based or satellite-based remote sensing. Like micrometeorological stations, aircraft can be equipped with fast and accurate sensors in order to measure atmospheric turbulence. Modern unmanned research aircraft (UAS) can be equipped with similar measurement systems to manned aircraft, limited of course by the size of the UAS (Sect. 49.8.1). There are many other names in use for UAS, like drones, UAV (unmanned aerial vehicle) or RPA (remotely piloted aircraft). However, in this text, UAS is used for unmanned instrumented aircraft.

Since UAS are commonly controlled by autopilot systems, flight path and altitude can be maintained with a higher accuracy compared to many manned systems. This can be very helpful for various meteorological missions. Small UAS can carry less scientific payload

and have less endurance compared to large and manned aircraft, on the one hand. On the other hand, their disturbance to the atmospheric flow is much smaller, as are the logistic efforts necessary to operate small UAS (smaller crew, very mobile, almost no ground facilities required). Moreover, if they are propelled by an electric engine, also the environmental impact is minimized (e.g., less noise in bird protection areas, no exhaust fumes during air chemistry and aerosol experiments). UAS can be operated in areas that are too dangerous for manned flight (e.g., active volcanoes) or too remote (e.g., polar regions). Last but not least, the purchase and especially the operation and maintenance of UAS is much less costly compared to manned research aircraft.

In this chapter, we can give only examples and an incomplete overview on the meteorological UAS applications, since a vast number of research groups are working with these new instruments, and every month

new publications occur in various journals. In addition, we will focus on smaller and medium-sized airframes, because the really big ones (e.g., the Global Hawk or

the Ikhana), are both under the aspects of instrumentation and operation very similar to manned research aircraft.

49.1 Measurement Principles and Parameters

Essentially, UAS are sensor carriers. That is, the user of UAS can mount any sensor described in this book that is light and small enough to be carried by the chosen aircraft. In order to inform on measurement principles and parameters, we refer to the corresponding chapters in this handbook, but especially to the chapter on research aircraft. In Tables 49.1 and 49.2, the most common parameters measured by UAS are listed. Further variables used there are:

- Air density ρ
- Specific heat at constant pressure c_p
- Heat of evaporation for water λ
- Turbulent fluctuations of wind vector components (u' , v' , w')
- Turbulent fluctuations of potential temperature θ'
- Turbulent fluctuations of specific humidity q' .

49.2 History

Atmospheric research can claim the privilege of having been the main driver for the adaptation and application of UAS technology in the field of nonmilitary science. Other research fields with extended spatial and temporal sampling requirements, e.g., forestry [49.1], biology [49.2], or archeology [49.3], have followed during the past years and profited from those developments. A comprehensive overview on small UAS for atmospheric research is given by [49.4].

The first documented application of unmanned, remotely controlled aircraft for atmospheric research dates back to 1970 [49.5]. The authors of that work used a commercially available hobby model airplane with a wingspan of ≈ 2.5 m and a combustion engine to measure profiles of temperature and humidity up to 3 km above ground. Systematic attempts to use UAS on a larger scale for meteorological research started in the 1990s, mainly based on rather large airframes of military origin that had been modified and adapted for scientific use [49.6, 7].

A first step towards smaller and more cost-effective systems was the development of the Aerosonde [49.8], with a wingspan of 2.9 m, an overall takeoff weight of 15 kg, and a scientific payload of around 5 kg [49.8]. The Aerosonde was developed as medium to long en-

Table 49.1 The most common meteorological parameters measured by UAS

Parameter	Description	Unit	Symbol
Height above ground	Altitude with respect to the underlying surface	m	z_{agl}
Height above sea level	Altitude with respect to the sea level	m	z_{asl}
Pressure	Air pressure	hPa	p
Wind vector	(Turbulent) meteorological wind speed and direction	m s^{-1}	$\mathbf{v} = (u, v, w)$
Temperature	(Turbulent) air temperature	K	T
Humidity	(Turbulent) water vapor mixing ratio	g kg^{-1}	m

duration UAS with a range exceeding 4000 km and was the first small UAS to cross the Atlantic and penetrate into the eye of tropical cyclones [49.9].

The rapid progress in microelectronics and component miniaturization made in the beginning of the millennium paved the way for a soaring development of airframes, autopilots, and meteorological sensors for meteorological research. One of the first low-cost attempts was the remotely controlled, but not autopiloted, system

Table 49.2 Other relevant parameters measured by UAS

Parameter	Description	Unit	Symbol
Vertical sensible heat flux	$Q_H = \rho c_p \overline{w'\theta'}$	W m^{-2}	Q_H
Vertical latent heat flux	$Q_E = \rho \lambda \overline{w'q'}$	W m^{-2}	Q_E
Vertical flux of horizontal momentum in direction of x	$\tau_{zx} = \rho \overline{w'u'}$	N m^{-2}	τ_{zx}
Vertical flux of horizontal momentum in direction of y	$\tau_{zy} = \rho \overline{w'v'}$	N m^{-2}	τ_{zy}
Turbulent kinetic energy	$\text{TKE} = \rho/2(u'^2 + v'^2 + w'^2)$	J m^{-3}	TKE

Kali, which performed more than 150 flights in Nepal and Bolivia to investigate thermally driven flows modified by orography in high alpine regions [49.10, 11]. The following years saw rapidly increasing activities by various research groups making their sensors and instrumentation airborne within a reasonable budget. Most of those early systems were based on fixed-wing airframes, such as e.g., SUMO (Small Unmanned Meteorological Observer) [49.12], M2AV (Meteorological Mini Aerial Vehicle) [49.13], MASC (Multi-purpose Airborne Sensor Carrier) [49.14], Smartsonde [49.15, 16], ALADINA (Application of Light-Weight Aircraft for Detecting In Situ Aerosol) [49.17], and Pilatus [49.18], to name a few. From around 2010, the use of rotary-wing multicopter systems (Fig. 49.1) for atmospheric research began to increase [49.19–21]. With their ability to hover and to slowly ascend and descend vertically, they are now the preferred choice for many measurement tasks related to boundary and surface layer profiling.

During the past decade, a series of community activities were initiated to foster the international col-

laboration in development and application of UAS in atmospheric research. These started in Europe with the successful Cooperation in Science and Technology (COST) Action ES0802 *Unmanned Aerial Systems for Atmospheric Research* [49.22] that resulted after its finalization in 2013 in the Foundation of ISARRA (International Society for Atmospheric Research with Remotely Piloted Aircraft Systems, www.isarra.org). ISARRA aims to provide a discussion and knowledge exchange platform for all aspects of the development and application of UAS in atmospheric research, including relevant airframe and sensor development, and also in the field of regulatory issues for UAS operations. Another recent activity to be mentioned was the *National Center for Atmospheric Research/Earth Observing Laboratory (NCAR/EOL) Community Workshop on Unmanned Aircraft Systems for Atmospheric Research* in February 2017, which resulted in an interesting overview report of all aspects related to UAS in atmospheric research [49.23].

49.3 Theory

UAS technology is a very fast-growing market with numerous daily new inventions and developments, therefore several names are currently used to designate these unmanned aircraft systems.

49.3.1 Terminology

The term *unmanned aircraft system* (UAS) refers to the unmanned aircraft and all of its components, including ground control stations and software, remote control transmitters, telemetry and payloads. This term has prevailed in international authorities such as American and British organizations. The United Kingdom's Civil Aviation Authority (CAA) provides a complete definition and explanation of this choice:

The terms Unmanned Aircraft (UA) or Remotely Piloted Aircraft (RPA) are used to describe the aircraft itself, whereas the term Unmanned Aircraft System (UAS) is generally used to describe the entire operating equipment including the aircraft, the control station from where the aircraft is operated and the wireless data link.

This UAS terminology is also exploited by the Federal Aviation Administration (FAA—United States), the European Aviation Safety Agency (EASA), and the Unmanned Aerial Vehicle Systems Association (UAVSA).

Formerly, the EASA (European Union Aviation Safety Agency), EUROCONTROL (European Organisation for the Safety of Air Navigation), and other civil aviation authorities used the term RPAS (remotely piloted aircraft), its associated remote pilot station(s), the required command and control links, and any other components as specified in the type design. However, this term was recently replaced by UAS. The catch-all term *drone* is the broadest terminology and is very common on the Internet but is not officially used by authorities.

A general weight-naming classification also exists for UAS. According to their mass, different names are used:

- MAV (micro air vehicle): for unmanned aircraft with a mass of < 1 kg
- sUAS (small unmanned aircraft system): for unmanned aircraft < 25 kg
- UAS: for unmanned aircraft with a weight of > 25 kg.

In this text, we use the term UAS to describe the unmanned airborne platform for meteorological measurements regardless of their takeoff weight.

Currently, UAS cannot perform all of their functions without the supervision or intervention of an operator, e.g., sense and avoid other aircraft or unexpected envi-

ronmental obstacles. These UAS still require a human action, such as preprogramming of their flight paths with Global Navigation Satellite System (GNSS) waypoints. Therefore, UAS are not fully autonomous but automated as in automated systems, an operator decides the course of its action. Describing a system as *autonomous* entails the absence of an operator that is responsible for that system.

49.3.2 UAS for Atmospheric Research

One of the most interesting applications of UAS in meteorology is the in-situ measurement of atmospheric turbulence. Small UAS cause little disturbance to the atmospheric flow due to their small size, especially when the propulsion is mounted on the rear of the aircraft (pusher configuration), while the measurement instrumentation is mounted at the nose, in sufficient distance to the front of the fuselage and the wings, see e.g., Figs. 49.2 and 49.3. Thus, small UAS are possibly the most suited (and less costly) instrument filling the gap between micrometeorological ground stations and remote sensing. Applications extend from fundamental science in remote areas [49.24–26] to wind-energy research [49.27], also in complex terrain [49.28].

Turbulent datasets should be sampled on straight and level flight sections (legs) in order to avoid any disturbing aerodynamic effects while turning. During measurement flight, track and altitude should be kept as constant as possible. This gives a distinguished orientation in space, e.g., x (which later helps with the data analysis). Also, most turbulent quantities are scaled with altitude z , especially in the atmospheric boundary layer (ABL).

49.4 Devices and Systems

In the following, UAS types are classified e.g., by weight, and the measurement systems most common aboard UAS are presented.

49.4.1 Airborne Carrier

There are several different types of UAS with specific limitations, benefits, and drawbacks. The main classification by the legal authorities is primarily by the takeoff weight of the UAS. The weight category is the crucial factor for the CAA rules in many countries and the handling abilities, see Table 49.3. Further, depending on the flight mission, a variety of different aircraft designs are available. The main airframe types are the fixed-wing aircraft and the multicopter (also often called multirotor, copter, quadcopter, etc.).

Since turbulent motion causes air parcels to change altitude z within a flow, only adiabatically invariant quantities should be used in turbulence analyses, e.g., the potential temperature θ and the water-vapor mixing ratio m , or their specific humidity q .

A very important criteria to fulfill for any research aircraft is the Taylor hypothesis of frozen turbulence in order to transform measured time series based on time t to spatial series based on coordinate

$$x = tU_x, \tag{49.1}$$

with airspeed U_x of the aircraft along x with respect to resting (stationary) air. Unfortunately, there is no absolute quantitative criteria that states when Taylor’s hypothesis is fulfilled, i.e., when (49.1) is applicable. Willis and Deardorff suggest that Taylor’s hypothesis is valid for moderately turbulent conditions and gives the empirical threshold of $\sigma_U/U < 0.5$ [49.29, 30]. In order to sample a significant number of large turbulent eddies (to keep the statistical error of a turbulent dataset small) the integral length scale I_θ of a turbulent quantity θ (potential temperature in this example) should be covered many times by one leg (ideally 100 times, which is often not achievable on one leg due to the changing characteristics of the Earth’s surface, for instance). The integral length scale is defined via the integral time scale [49.31]

$$I_\theta = U_x \int_0^{\tau_1} \text{Cor}_\theta(\tau) d\tau, \tag{49.2}$$

with autocorrelation function $\text{Cor}_\theta(\tau)$, time lag τ , and the first zero of $\text{Cor}_\theta(\tau)$ at τ_1 [49.32].

Multicopter

Multicopters (Fig. 49.1) are the most common used UAS on the global market. They consist of a central body and multiple rotors that power rotor blades to maneuver the UAS. These usually have four rotors (quadcopter) but can have as many six or eight (hexacopter and octocopter) and are always powered by electrical engines. Once in the air, a multicopter

Table 49.3 Weight classes of UAS

Type	Class	Weight (kg)	Example
sUAS	Very light	< 5	SUMO [49.12]
sUAS	Light	< 10	MASC [49.14]
sUAS	Medium	< 25	ALADINA [49.17]
UAS	Heavy	> 25	Aerosonde



Fig. 49.1 Example of a multicopter research UAS. This system is equipped with a particle and pollen trap (photo © Jens Bange, University of Tübingen)

controls its attitude and vehicle motion by varying the revolution speed of each rotor to change the thrust and torque produced, allowing movement in each direction and hovering on a fixed position.

The *advantages* of a multicopter are the following.

- Unlike fixed-wings aircraft, multicopters can perform vertical takeoffs and landings. They also require less space to take flight, can hover mid-flight, and maneuver in any required direction, see also Sect. 49.8.2.
- Multicopters do not require the surface area or wingspan that fixed-wing aircraft need.
- Multicopters are easier to fly for both humans and autopilots.

The *disadvantages* of a multicopter are the following.

- The main limitation is the flight range on a single battery, as they have a high demand for power consumption during flight. Most multicopters can fly for about 10–30 min before returning home for battery replacement; thus the flight range is limited.
- They have a high impact on the atmospheric small-scale flow due to the strong production of swirls by the rotor blades during flight. Therefore, accurate turbulence measurements with a multicopter are not possible.

Fixed-Wing Aircraft

Fixed-wing UAS are designed like traditional model aircraft, which look similar to an aeroplane. They are made of a central fuselage that has two attached wings



Fig. 49.2 Example of a very light class UAS: the SUMO, designed and operated by the University of Bergen Norway (after [49.12] photo is not included in [49.12])



Fig. 49.3 Example of a light class UAS: the Multipurpose Airborne Sensor Carrier MASC-3, designed and operated by the University of Tübingen, Germany (photo © B. Altstädter)

and usually a single engine. Once in the air, the two wings generate lift that compensates for its weight, allowing the aircraft to remain in flight. Nowadays, most fixed-wing aircraft come with an electrical impulsion, as it makes the aircraft easier to handle and simplifies maintenance. However, for long-distance UAS flights, aircraft with combustion engines are in use, as they have a better fuel-weight to range ratio compared to a battery-powered aircraft. Depending on the weight and the design of the aircraft, different take-off strategies are available. The most common in use are catapult, hand start, bungee start, takeoff on a winch or self launch.

The *advantages* of a fixed-wing aircraft are.

- Fixed-wing aircraft have a significant range as they can fly longer than multicopters on a single battery cycle.



Fig. 49.4 Example of a medium class UAS: ALADINA, designed and operated by the TU Braunschweig, Germany (photo after [49.17], © B.Altstädter et al. 2015, Creative Commons Attribution 3.0 License)

- The air-frame design of fixed-wing aircraft gives most designs greater stability in high winds over multicopters. This is important for flying in environments where higher winds are expected or frequent. Further, turbulence measurements are very accurate, as the flow sensor can be attached in a nose boom in front of the fuselage, where the influence by the aircraft on the flow during the flight is marginal.
- Safer recovery from motor power loss: if a fixed-wing aircraft loses motor power, it is able to glide down. A multicopter will always crash.

The *disadvantages* of a fixed-wing aircraft are.

- Fixed-wing aircraft require a larger takeoff and landing zone, which can make them unsuitable for special missions.
- They are less compact, meaning that they are harder to pack away and often require assembly before flights.
- For most types of fixed-wing aircraft the requirements on the operators are higher, especially the flying skills of the pilot.

A very new category is vertical takeoff and landing (VTOL) UAS. These systems combine the benefits of vertical takeoff and landing with a fixed-wing cruising flight mode.

Autopilots

UAS are controlled by an airborne autopilot as well as by a ground station encompassing a mission planning and monitoring software utilizing a bidirectional data

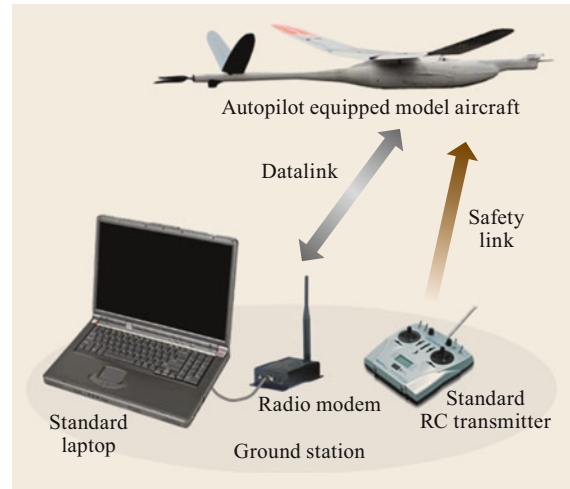


Fig. 49.5 Sketch of all the relevant components of a UAS (image © Andreas Platis, University of Tübingen)

link for telemetry and control as displayed in Fig. 49.5. There are several commercial and noncommercial systems on the market. Two very commonly used systems for research UAS are the Paparazzi [49.33] and the Pixhawk autopilot and ground-station software.

The key components of flight control on airframe systems are:

- Main autopilot board
- Autopilot sensors including:
 - attitude sensors, such as an inertial measurement unit (IMU) or IR sensors
 - GPS receiver
 - Pressure sensors
- Datalink radio modem
- Actuators (servos)
- Propulsion system, usually with an electric motor(s) with motor-controller and speed-controller
- Radio control receiver (safety link)
- Batteries.

The ground-control station is where an operator interacts with an unmanned aircraft. It generally consists of several parts, usually providing feedback about UAS activity, allowing command and control of the aircraft, and providing a method of override control for the system. The key components of the flight control on the airframe systems are:

- Ground computer
- Ground software
- Groundside datalink
- Radio control transmitter (safety link).

The ground station provides the interface between the UAS and the human for configuration, monitoring, and control of the UAS.

The basic component of the flight-control system on the airframe is the inertial navigation system (INS), which estimates the exact position, speed, and attitude. The INS consists of the GPS and an inertial measurement unit (IMU). Theoretically, an IMU alone is sufficient to obtain the position and attitude of an aircraft, by integrating linear accelerations caused by the motion and the rotation of the aircraft, with the gravity as a reference. However, due to the mathematical integration, small errors cumulate over time to an increasing position error. Therefore, a correction must be applied by using a long-term accurate system (like a satellite measurement) as a reference and a mathematical algorithm. This algorithm, a Kalman filter, merges the IMU and GPS signal to estimate the state the UAS, which is more accurate than an estimate based on the individual measurements alone.

49.4.2 Temperature Sensors for UAS

Principles for temperature measurements aboard UAS are very similar or identical to those on manned research aircraft (Chap. 48). Since at least fixed-wing UAS are move quickly through the air volume, the sensors must have a short response time (small sensor inertia), especially if turbulence has to be resolved. For operation on small UAS (Table 49.3: medium weight and lighter), the sensor has to be small, light, and robust with low power consumption (heavy UAS can use the same technology as manned aircraft; Chap. 48). For thermometer principles, see Chapt. 7. Two principles became common on UAS with respect to turbulence measurements [49.34]: the thermocouple and the thin-wire resistance thermometer (Fig. 49.6). Aboard a slow-moving multicopter (which is not well suited for turbulence measurements anyway), simple resistance thermometers (e.g., Pt-100) are sufficient (Chap. 7).

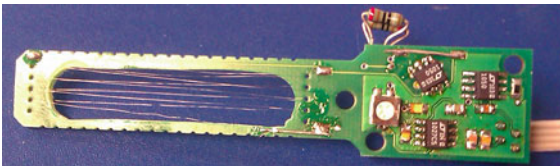


Fig. 49.6 Fine-wire fast-response thermometer aboard MASC. The entire instrument is about 4 cm in length and is attached to a measuring bridge (after [49.34] © N. Wildmann et al. 2013, Creative Commons Attribution 3.0 License)

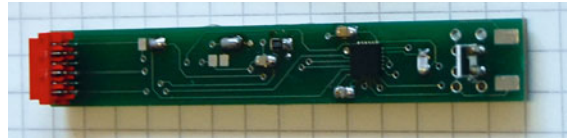


Fig. 49.7 Capacitive hygrometer of about 10 mm × 70 mm in size (adapted from © Norman Wildmann, University of Tübingen, Creative Commons Attribution 3.0 License)

49.4.3 Humidity Sensors for UAS

Similar to temperature measurements, hygrometers aboard small UAS (Table 49.3: medium weight and lighter) should be small, light, and robust with low power consumption. Among those hygrometers mentioned in (Chap. 8, only capacitive and resistance hygrometers (Fig. 49.7) fulfill these requirements today. However, aboard small UAS such hygrometers are usually too slow to resolve atmospheric turbulence, especially aboard fast moving UAS. Coupled with a numerical sensor model, temporal resolution up to 3 Hz has been achieved [49.35]. Dewpoint mirrors, similar to those attached to radiosondes, might be an alternative in future developments. Medium-sized and heavy UAS might use infrared absorption hygrometers (IRGA) like the well-known LiCor 7500 or similar [49.36].

49.4.4 Wind Sensors for UAS

Any precise 3-D wind-vector measurement aboard research aircraft of any size, manned or unmanned, is based on a multihole flow probe (MFP) that measures the angle of attack α , side slip β , and the dynamic pressure enhancement p_{stag} in the coordinate system of the aircraft. These flow variables are then combined with the Eulerian angles of the aircraft attitude (pitch, roll and yaw, or heading), the ground speed of the aircraft, and its position; all of these variables are measured in Earth's coordinates. Fast attitude changes are usually measured using an inertia measurement platform (IMU), while the slow changes are very precisely measured using a Global Navigation Satellite System (GNSS, e.g., GPS, GLONASS, Galileo). Both slow and fast navigation data are usually combined using a Kalman filter. Together they form an INS (inertial navigation system). For details, see Chap. 36.

The approach above applies to small UAS as well. Due to its size, the MFP aboard a small UAS can even be calibrated in a wind tunnel while attached to the carrying aircraft. This is a big advantage compared to larger UAS or manned aircraft, since systematic measurement errors due to mounting imprecision can be minimized [49.37]. Besides the proper measurement

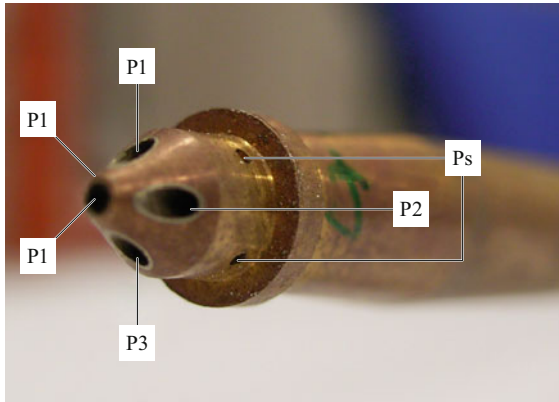


Fig. 49.8 Five-hole flow probe used aboard MASC. This probe is somewhat thinner than a pencil. Five pressure ports (P0 to P4) are used to measure the pressure differences caused by the angle of attack α , side slip β , and dynamic pressure enhancement p_{stag} . The holes denoted by Ps give the static pressure (photo after [49.37] © American Meteorological Society, used with permission)

and calculation of all the above quantities, a significant challenge is to achieve high (several 10 Hz) temporal resolution and an optimum in the signal-to-noise ratio (SNR). In addition to suitable pressure transducers based on MEMS (microelectromechanical systems) technology, the tubing strategy for connecting the MFP to the pressure transducers is of crucial importance [49.14]. In the end, the wind measurement unit aboard a UAS must also be calibrated in flight. However, this can be carried out much more easily compared to a manned research aircraft [49.37].

If turbulence is not of main concern, mean wind velocity components can be measured using simple Prandtl tubes or even no flow sensor at all [49.38]. In the latter approach, the wind shift of the aircraft is measured in order to calculate the mean horizontal wind [49.39]. Aboard multicopters, the wind measurement is even more difficult, since the downwash of the rotor blades distorts any flow measurement. An interesting approach, using the airframe itself as wind sensor, was published recently, e.g., [49.21, 40].

49.4.5 Aerosol and Particle Sensors for UAS

Atmospheric aerosols play an important role in our climate system [49.41] and in human health [49.42, 43]. Nowadays, UAS are a helpful tool to investigate small-scale vertical and horizontal variability of aerosol particles in the atmosphere by airborne in-situ measurements, mainly due to the improvement and the miniaturization of electronic components [49.17, 44, 45].

Two common instruments are used for in-situ particle investigation on UAS. For particles in the accumulation mode (diameter 0.1–1 μm) and the coarse mode (diameter > 1 μm), an optical particle counter (OPC) is used. A condensation particle counter (CPC) is used for *ultrafine particles* in the lower Aitken mode (diameter 10–30 nm), Aitken mode (diameter 30–100 nm) and nucleation mode (diameter 5–10 nm).

In the ALADINA UAS (Fig. 49.4), the OPC (model GT-526, Met One Instruments Inc., Washington, USA) and two CPCs (model 3007, TSI Inc., St Paul, USA) were miniaturized and implemented as displayed in Fig. 49.9 [49.17]. By using two airborne CPCs systems

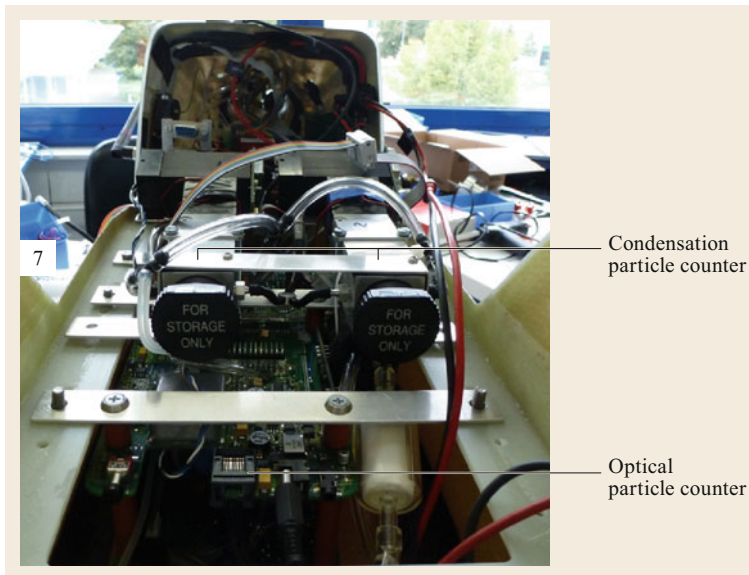


Fig. 49.9 The aerosol payload installed in the UAS ALADINA in the front compartment of the air plane. The payload consists of two condensation particle counters and one optical particle counter that is mounted underneath (view from the rear). The first CPC (left) detects particle number concentrations in a particle diameter range of 5 nm to 2 μm . The second CPC (right) measures the particle number concentrations between 10 nm and 2 μm [49.25] (photo after [49.17] © B.Altstädter et al. 2015, Creative Commons Attribution 3.0 License)

simultaneously with different lower threshold diameters e.g., 10 nm and 5 nm, the difference between the number concentrations of the two CPCs can be used as an indicator of freshly formed particles (nucleation mode) [49.25]. When performing measurements with an OPC, special attention has to be paid to the

aerosol inlet, which should be isokinetic. If the sampling is nonisokinetic, the air measured will not be representative of the actual air, leading to particles of certain diameters being undersampled or oversampled, ultimately causing errors in the calculated concentrations.

49.5 Specifications

Table 49.4 give an overview on the technical properties of UAS sensors.

Table 49.4 Technical properties of sensors suited for small UAS, including relative (rel.) and absolute (abs.) accuracy, temporal resolution (maximum response frequency freq.), and references (ref.)

Quantity	Sensor	Range	Abs.	Rel.	Freq.	Ref.
Temperature	Fine-wire thermometer	−10 to 50 °C	0.2 K	0.01 K	10 Hz	[49.34]
Temperature	Thermocouple	−10 to 50 °C	0.2 K	0.01 K	10 Hz	[49.34]
Humidity	Capacitive hygrometer	15–85%	1%	0.1%	3 Hz	[49.27]
Wind speed	MFP incl. INS	$\alpha < 20^\circ$	0.5 m s^{-1}	0.05 m s^{-1}	20 Hz	[49.27, 37]
Wind direction	MFP incl. INS	$\alpha < 20^\circ$	1°	0.1°	20 Hz	[49.27, 37]

49.6 Quality Control

Since UAS are able to carry all kinds of sensors, the quality control of certain measurands is discussed in the corresponding chapters. However, some quality-control tools that are especially important in airborne turbulence measurements are discussed in the following. Also see Chap. 48.

49.6.1 Statistical Tools

The most important statistical tools for airborne in-situ turbulence measurements are the power spectrum $PS_\theta(f)$ and the structure function

$$D_\theta(\tau) = \frac{1}{t_{\text{tot}} - \tau} \int_0^{t_{\text{tot}} - \tau} [\theta(t + \tau) - \theta(t)]^2 dt \quad (49.3)$$

of measured quantity θ (the potential temperature in this example) during measurement period t_{tot} . The structure function (49.3) (Fig. 49.10) is well suited to assess the overall quality of the turbulence measurement. Due to less variation compared to the power spectrum, the identification of the Kolmogorov subscale of quasi isotropic turbulence (the famous $\tau^{2/3}$ -law) is easy and straightforward. A sudden deviation from this law at small time lags τ usually marks the inertia timescale of the sensor regarded.

The power spectrum

$$PS_\theta(f) = \frac{1}{t_{\text{tot}}} |\tilde{\theta}(f)|^2 \quad (49.4)$$

(with Fourier-transformed data series $\tilde{\theta}$) is very suited to identify systematic errors in the data, like noise, vibrancy, hum, crosstalk, and interspersions (Fig. 49.11).

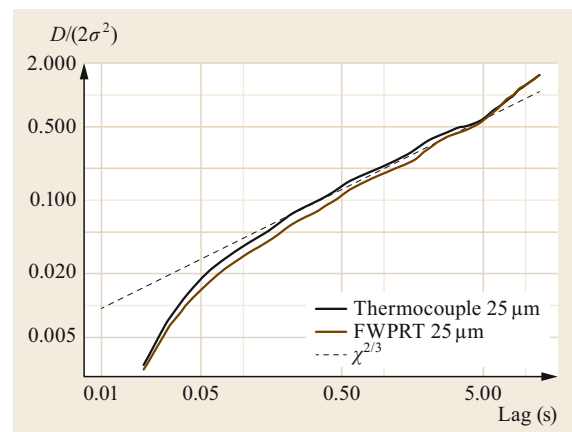


Fig. 49.10 Structure functions of two thermometers aboard a MASC UAS: a thermocouple and a fine-wire sensor (after [49.34]). The Kolmogorov distribution is marked by a dashed line

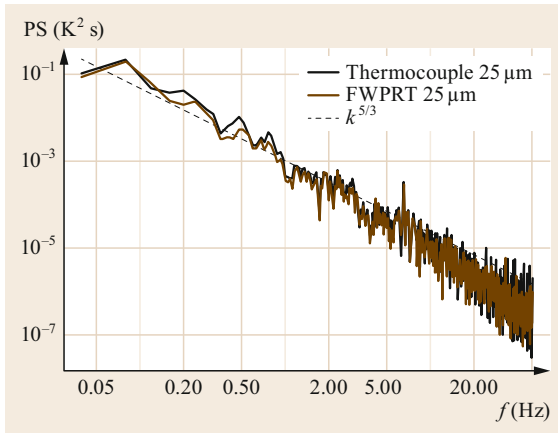


Fig. 49.11 Power spectra of two thermometers aboard a MASC UAS: a thermocouple and a fine-wire sensor (after [49.34]). The Kolomogorov distribution is marked by a dashed line

Noise usually marks the physical limit of the measuring amplifier and the resolution of the sensor. On small UAS, this is an important issue, since electronics and sensor have to be small and light and are, thus, less perfectly built compared to heavy instruments for ground stations, for instance. Vibrancy can be caused by engine vibration. Hum can be an issue due to missing electrical grounding and shielding (many UAS are built of glass fiber). Crosstalk can happen within small and light ADC (analog digital converters). Moreover, interspersion is often caused by the remote-control systems and data telemetry to a ground station. Thin-wire thermometers are often prone to electro-magnetic fields in the environment, for instance.

49.6.2 Statistical Uncertainty of Turbulence Quantities

Flight legs of a UAS measurement flight are usually limited in space. If legs do not exceed the largest

eddies in size, the corresponding turbulent quantities will be sampled insufficiently. This causes a systematic statistical error by systematically underestimating or overestimating the turbulent quantity and its statistical properties. For more details, see [49.32, 46–48].

For the example, the vertical turbulent flux of sensible heat

$$H = \rho c_p \langle w' \theta' \rangle \tag{49.5}$$

(with leg average $\langle \dots \rangle$, air density ρ , specific heat at constant pressure c_p , and the turbulent fluctuations of the vertical wind w') is afflicted by a systematic statistical error

$$\Delta H \leq 2 \rho c_p \sigma_w \sigma_\theta \frac{\sqrt{I_w I_\theta}}{x_{\text{leg}}}, \tag{49.6}$$

with leg length x_{leg} and integral length scales I (49.2). The standard deviations σ also have a systematic statistical error given by

$$\Delta \sigma_\theta = 2 \frac{I_\theta}{x_{\text{leg}}} \sigma_\theta. \tag{49.7}$$

Even when $x_{\text{leg}} > I_\theta, I_w$ (the leg length exceeds the integral scales), different measurements under identical boundary conditions lead to different fluxes H due to its random statistical error σ_H , which can be calculated by [49.48]

$$\sigma_H = \rho c_p \sqrt{2 \frac{I_H}{x_{\text{leg}}} (\langle w'^2 \theta'^2 \rangle - \langle w' \theta' \rangle^2)}. \tag{49.8}$$

Of course, the ratio of systematic to random statistical error decreases with increasing leg length

$$\frac{\Delta H}{\sigma_H} \propto \frac{1}{\sqrt{x_{\text{leg}}}}. \tag{49.9}$$

49.7 Maintenance

In aviation, be it manned or unmanned, *safety is paramount*. Therefore, according to CAA rules in most countries unmanned aircraft systems (similar to manned aircraft) must be subjected to regular maintenance intervals. These intervals depend on the aircraft type and are usually documented in the operating man-

ual of the manufacturer. Scheduled inspections and maintenance that follow the manufacturer’s recommendations form the foundation on which a good safety record is built. An exemplary section of a maintenance table for a fixed wing UAS is shown in Table 49.5.

Table 49.5 Exemplary section of a maintenance table for a fixed wing UAS. All time intervals are usually subject to the manufactures maintenance and operating manual and only exemplified here

Time interval	Fuselage	Control surface	Engine	Batteries	Telemetry	Sensors
Before each flight	Visible check	Operational check	Test run	Capacity check	Status	Status
Before each flight day	Visible outside and inside check	Operational check	Test run visible rotor blade check	Capacity check voltage check of each battery cell	Status and range test	Calibration status check
Flight time 10 h	Visible outside and inside check	Operational check servo check	Grease rotor blade replacement	Complete charge and discharge capacity check	Status and range test	Calibration status check
Flight time 100 h	Overhauling visible outside and inside check	Servo replacement	Grease visible rotor blade check	Replacement	Overhauling	Calibration status check according to sensor type

49.8 Applications

Overall, UAS have become a well-established tool and sensor carrier for a wide range of measurement applications in atmospheric sciences and are used for a wide range of applications, and in particular in boundary-layer meteorology. This includes, among other fields, the investigations of the convective boundary layer (CBL) [49.49–51] and boundary-layer transitions [49.16, 52, 53], fine scale in-situ measurements of turbulence parameters [49.16, 24, 54–58], wind-power meteorology [49.27, 28, 59–61], hurricane [49.9, 62] and severe-storm research [49.63], aerosol and air-pollution measurements [49.25, 64, 65], data assimilation for the improvement of model simulations for weather forecast [49.66, 67], or the validation of atmospheric models [49.68–71] and remote sensing [49.15, 72–74]. One favored area of applications is stably stratified boundary layer (SBL) research in polar regions, where smaller to medium sized UAS can operate with limited infrastructural support [49.26, 56, 69, 75–77].

49.8.1 Civil Aviation Authority Rules and Regulations

Currently, there are no international agreements on UAS flight rules and classifications, since UAS lighter than 150 kg fall under the jurisdiction of national authorities and, therefore, manufacturers and operators are subject to different safety requirements and legal restrictions. National legislation and case laws differ in

each country. In some countries, legislation even only exists in the development process.

A useful practical guide based on hands-on experience is given by [49.78], who explains general airspace regulations and how UAS operations fit into the legal structure.

National and international aviation authorities started to collaborate in the framework of the *Joint Authorities for Rulemaking on Unmanned Systems* (JARUS) in recent years. JARUS is a group of experts from the national aviation authorities and regional aviation safety organizations including over 50 countries, as well as the EASA and EUROCONTROL. They give recommendation to national authorities and regional safety organizations to introduce a risk assessment methodology. This risk assessment allows for the establishment of a sufficient level of confidence that specific UAS operation can be conducted safely and how UAS can be integrated into airspace and at aerodromes.

On 31 July 2017, JARUS announced the publication of the *Specific Operations Risk Assessment* (SORA) of UAS. It allows the evaluation of the intended concept of operation and a categorization into six different specific assurance and integrity levels and is now being applied in many countries, e.g., in Germany and Norway as a basic tool for their legislation. Therefore, some basic regulations can be found in most of JARUS countries. Some of the most important regulations will be briefly listed using Germany, as an example.

The necessity and scope of a permit for UAS operation depends primarily on the weight, the kinetic energy of the UAS (speed and weight), the flight altitude, and the flight area (urban or rural, sight conditions, etc.). As an example according to the EU drone regulation, UAS below 25 kg do not need any specific approval by the authorities for the operation, if the UAS is not operated over uninformed persons, crowds of people and buildings. For the operation of UAS above 250 g, the pilot must always hold a drone license. For UAS heavier than 25 kg, an airworthiness certification of the aircraft has to be applied. The flight altitude for UAS is limited to a maximum of 120 m above ground level, and the flight always has to be in the visual line of sight (VLOS) of a safety pilot. In Germany, VLOS is 500 m. If the operation requires higher flight altitudes or is outside the line of sight, the drone license and the approval by national aviation authorities are again mandatory. Further, the operation of UAS is not permitted over sensitive areas, such as residential areas, aerodromes and their vicinity, controlled airspace, public facility, crowds, nature reserves, industrial plants, federal roads, etc.; exceptions can also be approved here.

Approval assessment and evaluation of the authorities is regulated mainly by SORA (Specific Operations Risk Assessment). Depending on the potential risks of a flight mission, UAS users may have to establish operational concepts for their mission and an assessment by expert inspectors.

For example, if you plan the operation with a 1 kg-light UAS over uninhabited area the risk category is very low. If the operation, however, is over a densely populated area or a crowd of people, and the UAS also weighs more than 25 kg, a complex approval process is to be expected, as this kind of mission is a very high risk class. For such a special permission, among other things, proof is required that certain flight procedures are applied, which are generally classified as safe and that safety-relevant systems on board the UAS system are redundant.

The ICAO works on a fundamental international regulatory framework for UAS operation [49.79]. However, at the time of writing, there were no international agreements on UAS flight rules and classifications. According to the UK Civil Aviation Authority [49.80], for instance, UAS can be classified by weight (Table 49.3).

49.8.2 Flight Strategies

Flight strategies for UAS have to take into account several boundary conditions. In addition to CAA rules (Sect. 49.8.1) and minimized statistical errors (Sect. 49.6.2), a limited flight endurance usually has to be considered. However, in comparison to most manned research aircraft, UAS autopilots are able to maintain



Fig. 49.12 Repeated legs for maximum significance or temporal development (after [49.38] © A. Rautenberg et al. 2018, Creative Common Attribution 4.0 License)

track and altitude with very high precision with only a few meters of deviation.

Repeated legs at identical height and location increase the statistical significance of turbulent statistics or describe, in highly non-stationary conditions, the temporal development in a fixed air volume (Fig. 49.12).

Vertical profiles of atmospheric quantities can be achieved by slant ascending and descending flights or by following a helical flight pattern. Typical vertical velocities are in the order of several meters per second, and UAS are able to perform such profiles up to several 1000 m.

A combination of horizontal straight and level sections (legs) with slant flights gives a spatial dataset of atmospheric quantities, and when repeated within the same volume, even its temporal development (Fig. 49.13).



Fig. 49.13 A combination of legs with slant flights gives a spatial data set of atmospheric quantities (after [49.38] © A. Rautenberg et al. 2018, Creative Common Attribution 4.0 License)



Fig. 49.14 Stacked race-track patterns are well suited for wind-energy research (after [49.38] © A. Rautenberg et al. 2018, Creative Common Attribution 4.0 License)

Stacked race-track patterns (Fig. 49.14) consist of pairs of legs at various altitudes with only slight height difference. This flight strategy gives a maximum spatial resolution of a relatively small air volume and is well suited for wind-energy research upstream or downstream of wind turbines, both for the initialization and validation of numerical flow simulations.

With multicopter UAS, vertical profiles and fixed-position measurements are feasible. The advantages of a fixed-point measurements is a longer sampling time at a certain location. This enables better statistics if the time resolution of the sensor is low, which is often the case for airborne aerosol particle and gas instruments onboard small UAS. The drawback is the limited spatial resolution of the fixed-point observation.

Many other flight strategies have been described and published, for instance with respect to ABL transitions [49.52], entrainment on top of the convec-

tive ABL [49.24], or for monitoring surface temperatures [49.51].

49.8.3 Important UAS Campaigns

A selection of important and ground-breaking campaigns with the participation of small to medium-sized UAS is presented in Table 49.6. This overview does not—by far—cover all UAS activities in atmospheric science during the most recent years, as the development and application of UAS systems seems to increase exponentially. In addition, some interesting and successful activities and campaigns (e.g., the *Characterization of Arctic Sea Ice Experiment* (CASIE)) are often not adequately covered by peer-review scientific publications.

It is worth to present one very recent and ground-breaking activity in more detail. In August 2018, the University of Colorado, Boulder, initiated and led the international LAPSE-RATE (Lower Atmospheric Process Studies at Elevation—a Remotely Piloted Team Experiment) field campaign. This field experiment [49.90], held in connection with the 6th ISARRA Conference, took place in the San Luis Valley, a large valley in the Colorado Rocky Mountains. More than 100 scientists from 18 universities, research institutions, and companies gathered for 1 week to investigate various relevant BL phenomena. Specifically, this included the role of BL structure and development for the convective initialization of thunderstorms, the importance of thermally driven circulations for the valley wind climate, the morning boundary layer transition in complex terrain, and the aerosol properties of a high-altitude valley. With more than 50 different UAS systems performing nearly 1300 scientific flight missions over 6 days, this campaign marks the beginning of a new era in the application of UAS in BL research.

Table 49.6 Selection of important UAS campaigns

Campaign	Location	# UAS flights	Reference
LHOMAR II 2001	Nepal, Kali Gandaki valley	108	[49.10]
JUIPIT'AYA 2003	Bolivian Altiplano	85	[49.11]
Typhoon eye-wall penetration 2005	Taiwan	1	[49.9]
MAC 2006	Maldives	45	[49.81–83]
FLOHOF 2007	Hofsjokull, Central Iceland	112	[49.68, 84]
CoCoNUE 2009	Pawnee, Colorado	5	[49.85]
LITFASS 2009	Lindenberg, Germany	ca. 50	[49.24, 54, 86]
BLLAST 2011	Lannemezan, France	ca. 350	[49.49, 51]
MISOPEX 2013	Oliktok Point, Alaska	24	[49.87]
CLOUD-MAP (since 2015)	Oklahoma, US	ca. 750	[49.88]
ISOBAR I 2017	Hailuoto, Finland	127	[49.26, 89]
ISOBAR II 2018	Hailuoto, Finland	387	[49.26, 89]
WINSSENT (since 2017)	Swabian Alp, Germany	ca. 50	[49.70, 71]
NPF (DFG) 2014, 2018	Germany and Svalbard	ca. 100	[49.25]
LAPSE-RATE 2018	San Luis Valley, Colorado	ca. 1200	[49.90]

49.9 Future Developments

There is no reason to assume that the rapid development in a number of relevant fields, such as material science (for lighter and more robust airframes), battery technology (for increased endurance and payload capacities), or microelectronics (for even smaller, lighter, faster, and less energy-consuming sensors and instruments) will slow down in the future. Experience from the past has shown that relevant innovations will be adapted and utilized on a rather short time horizon. The capabilities and level of application of UAS for scientific purposes will be increased in general and atmospheric research in particular.

With respect to sensors and instrumentation, there is an increasing demand for a fast, stable, and accurate humidity sensor that can be used on UAS of all sizes. Additional active development areas of high scientific interest are the further miniaturization of sensor systems for air chemistry and aerosols and the reliable measurement of wind and turbulence from multicopter systems, e.g., by a sonic anemometer mounted on a horizontal boom outside the flow distortion and downwash area of the rotors. The atmospheric measurement community would also highly benefit from the development of a standardized and exchangeable sensor suite for the basic meteorological parameters, at least temperature, humidity, and pressure (Chaps. 7, 8, 10) and a corresponding affordable and mobile calibration unit.

New airframe design and production methods (such as 3-D-printing) will be able to produce very specific and targeted UAS systems, with an increasing tendency to fuse airframe and sensors, in particular for the most lightweight classes. The ongoing development of hybrid systems, enabling vertical takeoff and landing, and normal fixed-wing operation during the scientific mission, will further ease and increase the applicability of UAS systems, e.g., for ship-based operation.

The development of new flight strategies, based on progress in communication and machine learning, will in the near future allow for the operation of multiple UAS in swarms and flocks [49.91–93]. Guided by artificial intelligence, such systems will be able to optimize flight strategies and data coverage for a given measurement task, without or only with very limited interaction by the UAS pilot and, thus, further paving the road from automated to autonomous operations.

The big open question remains of how these scenarios can be realized within the existing regulatory framework. The application of UAS in atmospheric science, both for increased experimental activities and envisaged operational application, will strongly depend on a transparent, reliable and, it is hoped, an internationally homogenized set of rules and regulations provided by the aviation authorities.

49.10 Further Readings

- J. Elston, B. Argrow, M. Stachura, D. Weibel, D. Lawrence, D. Pope: Overview of Small Fixed-Wing Unmanned Aircraft for Meteorological Sampling, *J. Atmos. Ocean. Technol.* **32**(1), 97–115 (2015)
- M. Lange, J. Reuder: UAS Report, COST Action ES0802 Unmanned Aerial Systems in Atmospheric Research, 24 pp. (2013)
- H. Vömel, B.M. Argrow, D. Axisa, P. Chilson, S. Ellis, M. Fladeland, E.W. Frew, J. Jacob, M. Lord, J. Moore, S. Oncley, G. Roberts, S. Schoenung, C. Wolff: Final Report on the NCAR/EOL Community Workshop on Unmanned Aircraft Systems for Atmospheric Research, 21–24 February, 2017 Boulder, Colorado, 80 pp., <https://www.eol.ucar.edu/system/files/UAS.Workshop.20180206.pdf> (2018), Accessed 20 July 2021

References

- | | | | |
|------|--|------|---|
| 49.1 | C. Torresan, A. Berton, F. Carotenuto, S.F. Di Genaro, B. Gioli, A. Matese, F. Miglietta, C. Vagnoli, A. Zaldei, L. Wallace: Forestry applications of UAVs in Europe: A review, <i>Int. J. Remote Sens.</i> 38 (8–10), 2427–2447 (2017) | 49.3 | M. Sauerbier, H. Eisenbeiss: UAVs for the documentation of archaeological excavations. In: <i>Part 5, Proc. ISPRS Comm. V Mid-Term Symp. "Close Range Image Measurement Techniques"</i> , ISPRS Archives, Vol. XXXVIII (2010) pp. 526–531 |
| 49.2 | K. Anderson, K.J. Gaston: Lightweight unmanned aerial vehicles will revolutionize spatial ecology, <i>Front. Ecol. Environ.</i> 11 (3), 138–146 (2013) | 49.4 | J. Elston, B. Argrow, M. Stachura, D. Weibel, D. Lawrence, D. Pope: Overview of small fixed- |

- wing unmanned aircraft for meteorological sampling, *J. Atmos. Ocean. Technol.* **32**(1), 97–115 (2015)
- 49.5 T.G. Konrad, M.L. Hill, J.R. Rowland, J.H. Meyer: A small, radio-controlled aircraft as a platform for meteorological sensor, *APL Tech, Dig* **10**, 11–19 (1970)
- 49.6 J.S. Langford, K.A. Emanuel: An unmanned aircraft for Dropwindsonde deployment and hurricane reconnaissance, *Bull. Am. Meteorol. Soc.* **74**(3), 367–375 (1993)
- 49.7 G.L. Stephens, S.D. Miller, A. Benedetti, R.B. McCoy, R.F. McCoy, R.G. Ellingson, J. Vitko, W. Bolton, T.P. Tooman, F.P.J. Valero, P. Minnis, P. Pilewskie, G.S. Phipps, S. Sekelsky, J.R. Carswell, A. Lederbuhr, R. Bambha: The Department of Energy's Atmospheric Radiation Measurement (ARM) Unmanned Aerospace Vehicle (UAV) Program, *Bull. Am. Meteorol. Soc.* **81**(12), 2915–2938 (2000)
- 49.8 G.J. Holland, P.J. Webster, J.A. Curry, G. Tyrell, D. Gauntlett, G. Brett, J. Becker, R. Hoag, W. Vaglianti: The Aerosonde robotic aircraft: A new paradigm for environmental observations, *Bull. Am. Meteorol. Soc.* **82**(5), 889–901 (2001)
- 49.9 P.-H. Lin, C.-S. Lee: The eyewall-penetration reconnaissance observation of typhoon Longwang (2005) with unmanned aerial vehicle, *Aerosonde, J. Atmos. Ocean. Technol.* **25**(1), 15–25 (2008)
- 49.10 J. Egger, S. Bajrachaya, R. Heinrich, P. Kolb, S. Lämmlein, M. Mech, J. Reuder, W. Schäper, P. Shakya, J. Schween, H. Wendt: Diurnal winds in the himalayan Kali Gandaki valley. Part III: Remotely piloted aircraft soundings, *Mon. Weather Rev.* **130**(8), 2042–2058 (2002)
- 49.11 J. Egger, L. Blacutt, F. Ghezzi, R. Heinrich, P. Kolb, S. Lämmlein, M. Leeb, S. Mayer, E. Palenque, J. Reuder, W. Schäper, J. Schween, R. Torrez, F. Zaratti: Diurnal circulation of the Bolivian Altiplano. Part I: Observations, *Mon. Weather Rev.* **133**(4), 911–924 (2005)
- 49.12 J. Reuder, P. Brisset, M. Jonassen, M. Müller, S. Mayer: The Small Unmanned Meteorological Observer SUMO: A new tool for atmospheric boundary layer research, *Meteorol. Z.* **18**(2), 141–147 (2009)
- 49.13 T. Spiess, J. Bange, M. Buschmann, P. Vörsmann: First application of the meteorological Mini-UAV "M²AV", *Meteorol. Z.* **16**(2), 159–169 (2007)
- 49.14 N. Wildmann, S. Ravi, J. Bange: Towards higher accuracy and better frequency response with standard multi-hole probes in turbulence measurement with remotely piloted aircraft (RPA), *Atmos. Meas. Tech.* **7**(4), 1027–1041 (2014)
- 49.15 P.B. Chilson, A. Gleason, B. Zielke, F. Nai, M. Yeary, P. Klein, W. Shalamunenc, T. Bonin, W. Bocangel: SMARTsonde: A small UAS platform to support radar research. In: *Proc. 34th Conf. Radar Meteorol* (2009) p. 12B.6
- 49.16 T. Bonin, P. Chilson, B. Zielke, E. Fedorovich: Observations of the early evening boundary-layer transition using a small unmanned aerial system, *Bound.-Layer Meteorol.* **146**(1), 119–132 (2012)
- 49.17 B. Altstädter, A. Platis, B. Wehner, A. Scholtz, N. Wildmann, M. Hermann, R. Käthner, H. Baars, J. Bange, A. Lampert: ALADINA – An unmanned research aircraft for observing vertical and horizontal distributions of ultrafine particles within the atmospheric boundary layer, *Atmos. Meas. Tech.* **8**, 1627–1639 (2015)
- 49.18 G. de Boer, S. Palo, B. Argrow, G. LoDolce, J. Mack, R.-S. Gao, H. Telg, C. Trussel, J. Fromm, C.N. Long, G. Bland, J. Maslanik, B. Schmid, T. Hock: The Pilatus unmanned aircraft system for lower atmospheric research, *Atmos. Meas. Tech.* **9**, 1845–1857 (2016)
- 49.19 P.P. Neumann, M. Bartholmai: Real-time wind estimation on a micro unmanned aerial vehicle using its inertial measurement unit, *Sens. Actuators A* **235**, 300–310 (2015)
- 49.20 R.L. Brouwer, M.A. de Schipper, P.F. Rynne, F.J. Graham, A.J.H.M. Reniers, J.H. MacMahan: Surfzone monitoring using rotary wing unmanned aerial vehicles, *J. Atmos. Ocean. Technol.* **32**(4), 855–863 (2014)
- 49.21 R.T. Palomaki, N.T. Rose, M. van den Bossche, T.J. Sherman, S.F.J. De Wekker: Wind estimation in the lower atmosphere using multicopter aircraft, *J. Atmos. Ocean. Technol.* **34**(5), 1183–1191 (2017)
- 49.22 M. Lange, J. Reuder: UAS Report, COST Action ES0802 Unmanned Aerial Systems in Atmospheric Research, 24 pp, (2013)
- 49.23 H. Vömel, B.M. Argrow, D. Axisa, P. Chilson, S. Ellis, M. Fladeland, E.W. Frew, J. Jacob, M. Lord, J. Moore, S. Oncley, G. Roberts, S. Schoenung, C. Wolff: *Final Report on the NCAR/EOL Community Workshop on Unmanned Aircraft Systems for Atmospheric Research, 21–24 February, 2017* (Boulder, Colorado 2018) p. 80
- 49.24 S. Martin, F. Beyrich, J. Bange: Observing entrainment processes using a small remotely piloted aircraft system: A feasibility study, *Bound.-Layer Meteorol.* **150**, 449–467 (2014)
- 49.25 A. Platis, B. Altstädter, B. Wehner, N. Wildmann, A. Lampert, M. Hermann, W. Birmilli, J. Bange: An observational case study on the influence of atmospheric boundary-layer dynamics on new particle formation, *Bound.-Layer Meteorol.* **158**(1), 67–92 (2016)
- 49.26 S.T. Kral, J. Reuder, T. Vihma, I. Suomi, E. O'Connor, R. Kouznetsov, B. Wrenger, A. Rautenberg, G. Urbancic, M.O. Jonassen, L. Baserud, B. Maronga, S. Mayer, T. Lorenz, A.A.M. Holtslag, G.-J. Steeneveld, A. Seidl, M. Müller, C. Lindenberg, C. Langohr, H. Voss, J. Bange, M. Hundhausen, P. Hilsheimer, M. Schygulla: Innovative strategies for observations in the arctic atmospheric boundary layer (ISOBAR) – The Hailuoto 2017 campaign, *Atmosphere* **9**(268), 1–29 (2018)
- 49.27 N. Wildmann, M. Hofsäß, F. Weimer, A. Joos, J. Bange: MASC – A small Remotely Piloted Aircraft (RPA) for Wind Energy Research, *Adv. Sci. Res.* **11**, 55–61 (2014)
- 49.28 N. Wildmann, S. Bernard, J. Bange: Measuring the local wind field at an escarpment using small remotely-piloted aircraft, *Renew. Energy* **103**, 613–619 (2017)

- 49.29 G.E. Willis, J.W. Deardorff: On the use of Taylor's translation hypothesis for diffusion in the mixed layer, *Q. J. R. Meteorol. Soc.* **102**(434), 817–822 (1976)
- 49.30 R.B. Stull: *An Introduction to Boundary Layer Meteorology* (Springer, Dordrecht 1988)
- 49.31 J.C. Rotta: *Turbulente Strömungen. Eine Einführung in die Theorie und ihre Anwendung* (Teubner, Stuttgart 1972)
- 49.32 J. Bange, F. Beyrich, D.A.M. Engelbart: Airborne measurements of turbulent fluxes during LITFASS-98: A case study about method and significance, *Theor. Appl. Climatol.* **73**, 35–51 (2002)
- 49.33 P. Brisset, A. Drouin, M. Gorraz, P.-S. Huard, J. Tyler: The Paparazzi Solution. In: *Proc. MAV 2006, 2nd US-Eur. Competition Workshop Micro Air Veh., Oct 2006, Sandestin, United States* (2006) p. 15
- 49.34 N. Wildmann, M. Mauz, J. Bange: Two fast temperature sensors for probing of the atmospheric boundary layer using small remotely piloted aircraft (RPA), *Atmos. Meas. Tech.* **6**, 2101–2113 (2013)
- 49.35 N. Wildmann, F. Kaufmann, J. Bange: An inverse-modelling approach for frequency response correction of capacitive humidity sensors in ABL research with small remotely piloted aircraft (RPA), *Atmos. Meas. Tech.* **7**(9), 3059–3069 (2014)
- 49.36 A. Lampert, J. Hartmann, F. Pätzold, L. Lobitz, P. Hecker, K. Kohnert, E. Larmanou, A. Serafimovich, T. Sachs: Comparison of Lyman-alpha and Li-COR infrared hygrometers for airborne measurement of turbulent fluctuations of water vapour, *Atmos. Meas. Tech.* **11**(4), 2523–2536 (2018)
- 49.37 A.C. van den Kroonenberg, T. Martin, M. Buschmann, J. Bange, P. Vörsmann: Measuring the wind vector using the autonomous mini aerial vehicle M²AV, *J. Atmos. Ocean. Technol.* **25**, 1969–1982 (2008)
- 49.38 A. Rautenberg, M. Graf, N. Wildmann, A. Platis, J. Bange: Reviewing wind measurement approaches for fixed-wing unmanned aircraft, *Atmosphere* **9**(11), 422 (2018)
- 49.39 S. Mayer, G. Hattenberger: A 'no-flow-sensor' wind estimation algorithm for unmanned aerial systems, *J. Micro Air Veh.* **4**(1), 15–29 (2012)
- 49.40 M. Marino, A. Fisher, R. Clothier, S. Watkins, S. Prudden, C.S. Leung: An evaluation of multi-rotor unmanned aircraft as flying wind sensors, *Int. J. Micro Air Veh.* **7**(3), 285–299 (2015)
- 49.41 V. Ramanathan, P.J. Crutzen, J. Lelieveld, A.P. Mitra, D. Althausen, J. Anderson, M.O. Andreae, W. Cantrell, G.R. Cass, C.E. Chung, A.D. Clarke, J.A. Coakley, W.D. Collins, W.C. Conant, F. Dulac, J. Heintzenberg, A.J. Heymsfield, B. Holben, S. Howell, J. Hudson, A. Jayaraman, J.T. Kiehl, T.N. Krishnamurti, D. Lubin, G. McFarquhar, T. Novakov, J.A. Ogren, I.A. Podgorny, K. Prather, K. Priestly, J.M. Prospero, P.K. Quinn, K. Rajeev, P. Rasch, S. Rupert, R. Sadournym, S.K. Satheesh, G.E. Shaw, P. Sheridan, F.P.J. Valero: Indian ocean experiment: An integrated analysis of the climate forcing and effects of the great Indo-Asian haze, *J. Geophys. Res.* **106**(D22), 28371–28398 (2001)
- 49.42 D.M. Stieb, S. Judek, R.T. Burnett: Meta-analysis of time-series studies of air pollution and mortality: effects of gases and particles and the influence of cause of death, age, and season, *J. Air Waste Manag. Assoc.* **52**(4), 470–484 (2002)
- 49.43 C.I. Davidson, R.F. Phalen, P.A. Solomon: Airborne particulate matter and human health: A review, *Aerosol Sci. Technol.* **39**(8), 737–749 (2005)
- 49.44 T.S. Bates, P.K. Quinn, J.E. Johnson, A. Corless, F.J. Brechtel, S.E. Stalin, C. Meinig, J.F. Burkhardt: Measurements of atmospheric aerosol vertical distributions above Svalbard, Norway using unmanned aerial systems (UAS), *Atmos. Meas. Tech. Discuss.* **6**(2), 2483–2499 (2013)
- 49.45 C.E. Corrigan, G.C. Roberts, M.V. Ramana, D. Kim, V. Ramanathan: Capturing vertical profiles of aerosols and black carbon over the Indian Ocean using autonomous unmanned aerial vehicles, *Atmos. Chem. Phys.* **8**(3), 737–747 (2008)
- 49.46 J. Mann, D.H. Lenschow: Errors in airborne flux measurements, *J. Geophys. Res. D* **99**, 14519–14526 (1994)
- 49.47 D.H. Lenschow, J. Mann, L. Kristensen: How long is long enough when measuring fluxes and other turbulence statistics?, *J. Atmos. Ocean. Technol.* **11**, 661–673 (1994)
- 49.48 J. Bange, M. Esposito, D.H. Lenschow, P. Brown, V. Dreiling, A. Giez, L. Mahrt, S. Malinowski, A.R. Rodi, R.A. Shaw, H. Siebert, H. Smit, M. Zöger: Measurement of aircraft state, thermodynamic and dynamic variables. In: *Airborne Measurements for Environmental Research – Methods and Instruments*, ed. by M. Wendisch, J.-L. Brenguier (Wiley, Weinheim 2013)
- 49.49 M. Lohthon, F. Lohou, D. Pino, F. Couvreur, E.R. Pardyjak, J. Reuder, J. Vilá-Guerau de Arellano, P. Durand, O. Hartogensis, D. Legain, P. Augustin, B. Gioli, D.H. Lenschow, I. Faloua, C. Yagüe, D.C. Alexander, W.M. Angevine, E. Bargain, J. Barrié, E. Bazile, Y. Bezombes, E. Blay-Carreras, A. van de Boer, J.L. Boichard, A. Bourdon, A. Butet, B. Campistron, O. de Coster, J. Cuxart, A. Dabas, C. Darbieu, K. Deboudt, H. Delbarre, S. Derrien, P. Flament, M. Fourmentin, A. Garai, F. Gibert, A. Graf, J. Groebner, F. Guichard, M.A. Jiménez, M. Jonassen, A. van den Kroonenberg, V. Magliulo, S. Martin, D. Martinez, L. Mastorillo, A.F. Moene, F. Molinos, E. Moulin, H.P. Pietersen, B. Pignatelli, E. Pique, C. Román-Cascón, C. Rufin-Soler, F. Said, M. Sastre-Marugán, Y. Seity, G.J. Steeneveld, P. Toscano, O. Traullé, D. Tzanos, S. Wacker, N. Wildmann, A. Zaldei: The BLLAST field experiment: Boundary-layer late afternoon and sunset turbulence, *Atmos. Chem. Phys.* **14**(20), 10931–10960 (2014)
- 49.50 N.L. Dias, J.E. Gonçalves, L.S. Freire, T. Hasegawa, A.L. Malheiros: Obtaining potential virtual temperature profiles, Entrainment fluxes, and spectra from mini unmanned aerial vehicle data, *Bound.-Layer Meteorol.* **145**(1), 93–111 (2012)
- 49.51 J. Reuder, L. Båserud, M.O. Jonassen, S.T. Kral, M. Müller: Exploring the potential of the RPA system SUMO for multipurpose boundary-layer missions

- during the BLLAST campaign, *Atmos. Meas. Tech.* **9**(6), 2675–2688 (2016)
- 49.52 N. Wildmann, G.A. Rau, J. Bange: Observations in the early morning boundary layer transition with small RPA, *Bound.-Layer Meteorol.* **157**(3), 345–373 (2015)
- 49.53 A. Lampert, F. Pätzold, M.A. Jiménez, L. Lobitz, S. Martin, G. Lohmann, G. Canut, D. Legain, J. Bange, D. Martínez-Villagrasa, J. Cuxart: A study of local turbulence and anisotropy during the afternoon and evening transition with an unmanned aerial system and mesoscale simulation, *Atmos. Chem. Phys.* **16**, 8009–8021 (2016)
- 49.54 A.C. van den Kroonenberg, S. Martin, F. Beyrich, J. Bange: Spatially-averaged temperature structure parameter over a heterogeneous surface measured by an unmanned aerial vehicle, *Bound.-Layer Meteorol.* **142**, 55–77 (2012)
- 49.55 B.B. Balsley, D.A. Lawrence, R.F. Woodman, D.C. Fritts: Fine-scale characteristics of temperature, wind, and turbulence in the lower atmosphere (0–1,300 m) over the south Peruvian coast, *Bound.-Layer Meteorol.* **147**(1), 165–178 (2013)
- 49.56 S.L. Knuth, J.J. Cassano: Estimating sensible and latent heat fluxes using the integral method from in situ aircraft measurements, *J. Atmos. Ocean. Technol.* **31**(9), 1964–1981 (2014)
- 49.57 L. Bäserud, J. Reuder, M.O. Jonassen, S.T. Kral, M.B. Paskyabi, M. Lothon: Proof of concept for turbulence measurements with the RPAS SUMO during the BLLAST campaign, *Atmos. Meas. Tech.* **9**(10), 4901–4913 (2016)
- 49.58 R. Calmer, G.C. Roberts, J. Preissler, K.J. Sanchez, S. Derrien, C. O'Dowd: Vertical wind velocity measurements using a five-hole probe with remotely piloted aircraft to study aerosol–cloud interactions, *Atmos. Meas. Tech.* **11**(5), 2583–2599 (2018)
- 49.59 G. Kocer, M. Mansour, N. Chokani, R.S. Abhari, M. Müller: Full-Scale Wind Turbine Near-Wake Measurements Using an Instrumented Uninhabited Aerial Vehicle, *J. Sol. Energy Eng.* **133**(4), 041011 (2011)
- 49.60 B. Subramanian, N. Chokani, R.S. Abhari: Drone-based experimental investigation of three-dimensional flow structure of a multi-megawatt wind turbine in complex terrain, *J. Sol. Energy Eng.* **137**(5), 051007 (2015)
- 49.61 J. Reuder, L. Bäserud, S. Kral, V. Kumer, J.W. Wageenaar, A. Knauer: Proof of concept for wind turbine wake investigations with the RPAS SUMO, *Energy Procedia* **94**(1876), 452–461 (2016)
- 49.62 J.J. Cione, E.A. Kalina, E.W. Uhlhorn, A.M. Farber, B. Damiano: Coyote unmanned aircraft system observations in hurricane Edouard, *Earth Space Sci.* **3**(9), 370–380 (2014), 2016
- 49.63 J.S. Elston, J. Roadman, M. Stachura, B. Argrow, A. Houston, E. Frew: The tempest unmanned aircraft system for in situ observations of tornadic supercells: Design and VORTEX2 flight results, *J. Field Robot.* **28**(4), 461–483 (2011)
- 49.64 B. Altstädter, A. Platis, M. Jähn, H. Baars, J. Lücknerath, A. Held, A. Lampert, J. Bange, M. Hermann, B. Wehner: Airborne investigations of newly formed boundary layer aerosol particles under cloudy conditions, *Atmos. Chem. Phys.* **18**, 8249–8264 (2018)
- 49.65 T. Villa, F. Gonzalez, B. Miljevic, Z. Ristovski, L. Morawska: An overview of small unmanned aerial vehicles for air quality measurements: present applications and future Prospectives, *Sensors* **16**(7), 1072 (2016)
- 49.66 M.O. Jonassen, H. Ólafsson, H. Ágústsson, Ó. Rögnvaldsson, J. Reuder: Improving high-resolution numerical weather simulations by assimilating data from an unmanned aerial system, *Mon. Weather Rev.* **140**(11), 3734–3756 (2012)
- 49.67 D.D. Flagg, J.D. Doyle, T.R. Holt, D.P. Tyndall, C.M. Amerault, D. Geiszler, T. Haack, J.R. Moskaitis, J. Nachamkin, D.P. Eleuterio: On the impact of unmanned aerial system observations on numerical weather prediction in the coastal zone, *Mon. Weather Rev.* **146**(2), 599–622 (2018)
- 49.68 S. Mayer, A. Sandvik, M.O. Jonassen, J. Reuder: Atmospheric profiling with the UAS SUMO: A new perspective for the evaluation of fine-scale atmospheric models, *Meteorol. Atmos. Phys.* **116**(1–2), 15–26 (2010)
- 49.69 S. Mayer, M.O. Jonassen, A. Sandvik, J. Reuder: Profiling the arctic stable boundary layer in advent valley, Svalbard: measurements and simulations, *Bound.-Layer Meteorol.* **143**(3), 507–526 (2012)
- 49.70 H. Knaus, A. Rautenberg, J. Bange: Model comparison of two different non-hydrostatic formulations for the Navier–Stokes equations simulating wind flow in complex terrain, *J. Wind. Eng. Ind. Aerodyn.* **169**, 290–307 (2017)
- 49.71 H. Knaus, M. Hofsäb, A. Rautenberg, J. Bange: Application of different turbulence models simulating wind flow in complex terrain: A case study for the WindForS test site, *Computation* **6**(43), 1–25 (2018)
- 49.72 J.R. Taylor, N.J. Segal, M.R. Bradshaw, D.J. Low: Verification of RASS-measured temperature profiles using a radio-controlled model glider, *Meteorol. Atmos. Phys.* **119**(3–4), 197–206 (2013)
- 49.73 F. Beyrich, J. Bange, O.K. Hartogensis, S. Raasch, M. Braam, D. van Dinther, D. Gräf, S. Martin, A. van den Kroonenberg, A. Moene, B. van Kesteren, B. Maronga: Towards a validation of scintillometer measurements: The LITFASS-2009 experiment, *Bound.-Layer Meteorol.* **144**(1), 83–112 (2012)
- 49.74 M. Braam, F. Beyrich, J. Bange, A. Platis, S. Martin, B. Maronga, A.F. Moene: On the discrepancy in simultaneous observations of the structure parameter of temperature by scintillometers and unmanned aircraft, *Bound.-Layer Meteorol.* **158**(2), 257–283 (2016)
- 49.75 J.A. Curry, J. Maslanik, G. Holland, J. Pinto: Applications of Aerosondes in the Arctic, *Bull. Am. Meteorol. Soc.* **85**(12), 1855–1861 (2004)
- 49.76 J.J. Cassano: Observations of atmospheric boundary layer temperature profiles with a small unmanned aerial vehicle, *Antarc. Sci.* **26**(02), 205–213 (2014)
- 49.77 M.O. Jonassen, P. Tisler, B. Altstädter, A. Scholtz, T. Vihma, A. Lampert, G. König-Langlo, C. Lüpkes: Application of remotely piloted aircraft systems

- in observing the atmospheric boundary layer over Antarctic sea ice in winter, *Polar Res.* **34**(1), 25651 (2015)
- 49.78 A. Platis: *Drohnenführerschein kompakt: Das Grundwissen zum Kenntnissnachweis und Drohnenflug* (Motorbuch, Stuttgart 2018) p. 128
- 49.79 ICAO: *Unmanned Aircraft Systems (UAS)*, Vol. Cir 328 AN/190 (International Civil Aviation Organization, Montreal 2011)
- 49.80 UK CAA: *Unmanned Aircraft System Operations in UK Airspace – Guidance*, Vol. 722 (UK Civil Aviation Authority, Safety and Airspace Regulation Group, West Sussex 2015)
- 49.81 V. Ramanathan, M.V. Ramana, G. Roberts, D. Kim, C. Corrigan, C. Chung, D. Winker: Warming trends in Asia amplified by brown cloud solar absorption, *Nature* **448**(7153), 575–578 (2007)
- 49.82 M.V. Ramana, V. Ramanathan, D. Kim, G.C. Roberts, C.E. Corrigan: Albedo, atmospheric solar absorption and heating rate measurements with stacked UAVs, *Q. J. R. Meteorol. Soc.* **133**(629), 1913–1931 (2007)
- 49.83 C.E. Corrigan, G.C. Roberts, M.V. Ramana, D. Kim, V. Ramanathan: Capturing vertical profiles of aerosols and black carbon over the Indian Ocean using autonomous unmanned aerial vehicles, *Atmos. Chem. Phys.* **8**(3), 737–747 (2008)
- 49.84 J. Reuder, M. Ablinger, H. Ágústsson, P. Brisset, S. Brynjólfsson, M. Garhammer, T. Jóhannesson, M.O. Jonassen, R. Kühnel, S. Lämmlein, T. Lange, C. Lindenberg, S. Malardel, S. Mayer, M. Müller, H. Ólafsson, Ó. Rögnvaldsson, W. Schäper, T. Spengler, G. Zängl, J. Egger: FLOHOF 2007: An overview of the mesoscale meteorological field campaign at Hofsjökull, Central Iceland, *Meteorol. Atmos. Phys.* **116**(1–2), 1–13 (2011)
- 49.85 A.L. Houston, B. Argrow, J. Elston, J. Lahowetz, E.W. Frew, P.C. Kennedy: The Collaborative Colorado–Nebraska Unmanned Aircraft System Experiment, *Bull. Am. Meteorol. Soc.* **93**(1), 39–54 (2011)
- 49.86 S. Martin, J. Bange, F. Beyrich: Meteorological profiling of the lower troposphere using the research UAV “M²AV Carolo”, *Atmos. Meas. Tech.* **4**, 705–716 (2011)
- 49.87 J.A. Maslanik: Investigations of Spatial and Temporal Variability of Ocean and Ice Conditions in and Near the Marginal Ice Zone. The “Marginal Ice Zone Observations and Processes Experiment” (MIZOPEX) Final Campaign Summary, (February) (2016) 55 pp.
- 49.88 J. Jacob, P. Chilson, A. Houston, S. Smith: Considerations for atmospheric measurements with small unmanned aircraft systems, *Atmosphere* **9**(7), 252 (2018)
- 49.89 S.T. Kral, J. Reuder, T. Vihma, I. Suomi, K.F. Haualand, G.H. Urbancic, B.R. Greene, G. Steeneveld, T. Lorenz, B. Maronga, M.O. Jonassen, H. Ajosenpää, L. Båserud, P.B. Chilson, A.A.M. Holtslag, A.D. Jenkins, R. Kouznetsov, S. Mayer, E.A. Pillar-Little, A. Rautenberg, J. Schwenkel, A.W. Seidl, B. Wrenger: The innovative strategies for observations in the Arctic Atmospheric Boundary Layer Project (ISOBAR): Unique finescale observations under stable and very stable conditions, *Bull. Am. Meteorol. Soc.* **102**(2), E218–E243 (2021)
- 49.90 G. de Boer, B. Argrow, J.J. Cassano, J. Cione, E. Frew, D. Lawrence, G. Wick, C. Wolff: Advancing unmanned aerial capabilities for atmospheric research, *Bull. Am. Meteorol. Soc.* **100**(3), E5105–E5108 (2019)
- 49.91 C. Fuchs, C. Borst, G.C.H.E. de Croon, M.M.R. van Paassen, M. Mulder: An ecological approach to the supervisory control of UAV swarms, *Int. J. Micro Air Veh.* **6**(4), 211–229 (2014)
- 49.92 A. Ismail, B. Bagula, E. Tuyishimire: Internet-of-things in motion: A UAV coalition model for remote sensing in smart cities, *Sensors* **18**(7), 2184 (2018)
- 49.93 J. Schwarzrock, I. Zacarias, A.L.C. Bazzan, R. Queiroz de Araujo Fernandes, L.H. Moreira, E.P. de Freitas: Solving task allocation problem in multi unmanned aerial vehicles systems using swarm intelligence, *Eng. Appl. Artif. Intell.* **72**(April 2017), 10–20 (2018)

Jens Bange

Centre for Applied Geo-Science
University of Tübingen
Tübingen, Germany
jens.bange@uni-tuebingen.de



Jens Bange is a Professor for Environmental Physics at the University of Tübingen since 2010. He received a PhD in meteorology in 1998 and a diploma in physics in 1992 at the University of Hannover. His research interests include atmospheric turbulence, boundary-layer meteorology, wind-energy research, airborne meteorology, and environmental measurement technology. He is a founding member of the research networks ISARRA and WindForS.

Joachim Reuder

Geophysical Institute, and Bjerknes
Centre for Climate Research
University of Bergen
Bergen, Norway
joachim.reuder@gfi.uib.no



Joachim Reuder is Professor in Experimental Meteorology at the Geophysical Institute at the University of Bergen, Norway. He has more than 25 years of experience in boundary layer meteorology and has been involved in the development and application of small unmanned aircraft systems for boundary layer research for nearly 20 years. He is a founding member of the International Society Atmospheric Research using Remotely piloted Aircraft (ISARRA).

Andreas Platis

Centre for Applied Geo-Science
University of Tübingen
Tübingen, Germany
andreas.platis@uni-tuebingen.de



Andreas Platis studied Meteorology in Munich and did his PhD at the Environmental Physics Group at the University of Tübingen in the field of aerosol particles and turbulence measurements with unmanned research aircraft. Currently, he is working as a post-doc in the group. His research interests are atmospheric turbulence, boundary-layer meteorology, wind-energy research, airborne meteorology, and environmental measurement technology.

50. Ground-based Mobile Measurement Systems

Eberhard Parlow , Thomas Foken 

While stationary measurements can be performed relatively frequently, they do not permit detailed spatial analyses of meteorological variables, particularly air temperature. This problem can be resolved by making the sensor mobile and then taking measurements at a variety of locations within the area of interest. Mobile measurements have therefore been used in climatological research since the early twentieth century. Due to improvements in and the miniaturization of the relevant measurement technologies, mobile measurements have undergone a renaissance since the 1970s. Urban climatology has become an important field of great scientific interest. The realization that the measurements of just one urban weather station—generally located (in line with the recommendations of the World Meteorological Organization) on short-cut lawn—is not sufficient to represent all of the climates present in an urban area has led to the acceptance of and even the need for mobile measurements taken on cars, bikes, or buses. New methodologies have been implemented, and advances in digital measurement and storage on data loggers have made mobile measurements an important tool for spatially distributed studies of air temperature, air humidity, and air pollution.

Three important aspects must be considered when mobile measurements are analyzed:

- (1) A complete mobile measurement covers a time interval for the measurement, within which the meteorological variable changes its value. This change has to be corrected for to obtain quasi-synchronous data.
- (2) Since the instrumentation changes location, accurate geolocation of the measured data must be guaranteed. This can be achieved by operating a global navigation satellite system (GNSS) in parallel with the measurements.
- (3) Due to the spatial dimension of the measured data, it is convenient to perform some of the data analysis and visualization using modern geographic information system (GIS) technologies.

50.1	Measurement Principles and Parameters	1352
50.2	History	1353
50.2.1	The First Systems in the Early Twentieth Century	1353
50.2.2	The Renaissance in Mobile Measurements Since the 1970s	1353
50.2.3	Systems with Horizontal Mobility over Short Distances	1353
50.2.4	Vertical Mobile Systems	1354
50.3	Theory	1354
50.3.1	Technical Requirements	1354
50.3.2	Response Time and Dynamic Error	1355
50.3.3	Measurement Strategies: Designing Itineraries Involving Large Distances ..	1356
50.4	Devices and Systems	1358
50.4.1	Large-Scale Horizontal Measurement Systems	1358
50.4.2	Small-Scale Horizontal Measurement Systems	1360
50.4.3	Vertical Measurement Systems	1361
50.4.4	Comparison of Different Methods	1361
50.5	Specifications	1361
50.6	Quality Control	1361
50.7	Maintenance	1362
50.8	Application	1362
50.8.1	Urban Climate and the Urban Heat Island Effect	1362
50.8.2	Ventilation and Mountain Breezes	1363
50.8.3	Forest Climate at an Edge	1363
50.9	Future Developments	1365
50.10	Further Readings	1365
	References	1366

Mobile measurements are performed to circumvent a major problem with fixed stations. While these stations can provide data with high temporal resolution, the spatial aspects of meteorological fields are difficult to investigate in detail using fixed stations. Even when several fixed stations are maintained and the measurements from those stations are interpolated, the resulting data are often not sufficient to be able to probe the high spatial variability of meteorological fields in an urban, rural, or agricultural environment, such as frost risk for a hilly terrain. This issue can be resolved by making the sensor

mobile, meaning that measurements can be performed at a variety of locations within the area of interest. When the methodology of mobile measurements was devised approximately a century ago, automatic data recording was not possible, so measurements were carried out manually at given points in an effort to obtain a dense two-dimensional field of meteorological variables.

It should also be noted that there is a disadvantage of the mobile measurement method: it often does not yield a time series of measurements for a particular location.

50.1 Measurement Principles and Parameters

Mobile measurement methods can be classified into horizontal and vertical mobile measurement systems. The range of heights available with a vertical system is limited to just a few meters or decameters above the ground. Measurements at greater heights can be achieved with either aerological measurements (see Chap. 46) or by combining different systems (see Chap. 47). Horizontal mobile systems can be classified according to the horizontal distance covered by the measurements.

Mobile systems of both types can perform measurements along a traverse using either *continuous data sampling* or by implementing a *stop-and-go strategy* (e.g., moving the platform and sampling the data at the new location, and then relocating the platform and re-sampling). The strategy employed depends very much

on the meteorological element to be sampled. Because unmanned aircraft systems (UASs, see Chap. 49) fly at low altitudes, they can complement ground-based mobile systems or can be used instead of them.

An overview of mobile measurement systems is given in Table 50.1. The synchronization of measurement data with geographical coordinates to enable subsequent analysis of the two-dimensional data field is crucial for mobile measurement techniques.

Most meteorological variables are scalars, but a few variables (e.g., wind speed and direction) are vectors. It is quite tricky to separate wind speed and direction during data sampling when the measuring instrument is moved. Table 50.2 lists the most important parameters measured by mobile systems, together with possible sampling strategies for each.

Table 50.1 Classification of mobile measurement systems

Direction of sampling	Scale (m)	Typical systems	Remarks
Vertical mobile systems	1–100	Lifts on towers, balloons, unmanned aircraft systems (UASs)	See also Chaps. 46 and 49
Horizontal mobile systems	10–100	Fixed systems on rails or cables	See also Chap. 49
	100–10 000 (or larger)	Cars, trams, bicycles, etc. UASs	

Table 50.2 Parameters measured by mobile systems

Parameter	Sampling strategy		Remark
	Continuously	Stop and go	
Air temperature	×	×	Requires a radiation-shielded and ventilated detector, see Chaps. 7 and 8
Relative humidity	×	×	
Absolute humidity	×	×	
Wind speed		×	See Chap. 10
Wind direction		×	
Radiation (mainly global radiation)	×	×	See Chap. 11
Trace gas concentration (with a fast-response analyzer)	×	×	See Chaps. 8, 16, and 18
Trace gas concentration (with a slow-response analyzer)		×	

50.2 History

It had become apparent by the beginning of the twentieth century that the true spatial variability of the air temperature could not be determined with just a few fixed stations. To overcome this issue with fixed-point measurements, continuous mobile measurements were implemented. The first mobile systems performed long horizontal traverses. Fixed horizontal and vertical measurement systems that are capable of moving short distances have been available since the 1930s. Most meteorological variables can generally be sampled by mobile units. The main driving force for developing these systems was the desire to measure the air temperature fields in urban and rural environments in order to study heat stress in cities or frost risk in agricultural areas.

50.2.1 The First Systems in the Early Twentieth Century

The first publication on mobile measurements in climatology was written by *Wilhelm Schmidt* (1883–1936) [50.1]. He mounted a mercury thermometer on a car such that it was 20 cm away from the exterior and 1.2 m above the ground, and then performed temperature measurements within the city of Vienna (Austria) during three frosty nights in May 1927. Since automatic data recording systems were yet to be invented, he mounted a magnifying glass on the thermometer and noted the measurement time and location (e.g., house numbers) in order to make it easier to take accurate readings during his car trips. Soon after, and probably stimulated by Schmidt's work, *Albert Peppler* (1882–1942) also used this new mobile measurement method to determine the air temperature on the move [50.2]. In 1929, he measured air temperatures along several profiles across the city of Karlsruhe (Germany) using a car equipped with ventilated Assmann psychrometers (see Chap. 8). Since cars were not readily available in the 1920s, the car and driver used by each author were provided by local public services. The first measurements made using a bicycle-mounted instrument were conducted in 1933 [50.3] in the city of Munich. The unique advantage of this technique over other measurement techniques—that it can sample large areas in a very short time—was mentioned in [50.1, 2].

50.2.2 The Renaissance in Mobile Measurements Since the 1970s

While important urban climatology studies were carried out during the 1950s and 1960s, they were mostly based on data from fixed stations [50.4, 5]. Only a few papers that utilized data from mobile platforms were

published during this period [50.6, 7]. However, in the 1970s, mobile meteorological measurements underwent a renaissance. Micrometeorological research developed rapidly. One of the first mobile measurement systems developed in the 1970s was used to analyze the urban heat island of Freiburg (Germany) [50.8], the urban climate of Uppsala (Sweden) [50.9], and minimum temperatures and the frost risk in the wine-growing area of the Kaiserstuhl (SW Germany) [50.10]. Field measurements from mobile units that used special computer programs to study not only the air temperature distribution but also the humidity of the air, the vertical gradients of these parameters, and bioclimatological fields of equivalent temperature were published in [50.11]. Urban climatology became an increasingly important driver of climatological research. More and more urban climate studies were conducted, very often using a combination of mobile field measurements and up-and-coming remote-sensing technologies that used thermal infrared sensors aboard aircraft, which offered the ability to measure relevant meteorological variables to a resolution that was previously unobtainable. The spatial distributions of urban air and surface temperatures became important information for urban planning agencies. During that time, the methodologies used steadily improved. Initially, Pt100 resistance thermometers and thermocouples (see Chap. 7) were connected to a heavy registration unit driven by 220 V; this unit printed the recordings on a paper spool. In the 1980s, the first computer-based data-recording units and data loggers entered service, improving data analysis. During this period, measurement geolocation remained a major problem, as modern global navigation satellite systems (GNSS) were not yet available. In recent years, many works in which the spatial distribution of temperature within an urban area was measured using bicycles or public buses have been published [50.12]. Horizontal mobile system technology has become an important tool in local climatological studies and urban planning issues and has therefore been partly standardized [50.13]. It has also been used in combination with imaging techniques such as infrared imaging from aircraft (see Chaps. 42 and [50.14]).

50.2.3 Systems with Horizontal Mobility over Short Distances

Measuring systems with mobility over short horizontal distances have mainly been applied to study the heterogeneity of ecosystems. Investigations of this type started in the middle of the last century (see the review in [50.15]). These mobile systems were used when the heterogeneity was too large to be adequately captured

by fixed sensors, e.g., in woodlands. In the first studies, the mobile measuring systems mostly carried radiometers above and below forest canopies to measure the areal distribution of upwelling and/or downwelling radiation within forests [50.16–22] and grasslands [50.23, 24].

The *Asa Shuttle*, described in [50.25, 26], was a mobile system that measured the radiation and the air temperature along a horizontal transect of decreasing shelterwood density of Norway spruce. The TRAM (Transect Measurement) system [50.27] travels a loop through a forest ecosystem and over a creek (the Ameri-Flux site at Niwot Ridge, see Sect. 50.4.2). A similar system, but based on a small train [50.15], was built to measure radiation components, the air temperature and humidity, and the CO₂ and O₃ concentrations on both sides of a forest edge (see Sects. 50.4.2 and 50.8.3).

50.2.4 Vertical Mobile Systems

The first vertical temperature profile measurements achieved with lifts were obtained in the 1930s–1940s

over water bodies, such as off the island of Greifswalder Oie in the Baltic Sea [50.28] and above a freshwater pond [50.29, 30]. In the 1960s, an initiative by *Hans Hinzpeter* (1921–1999) led to the construction of highly sensitive temperature lifts [50.31, 32] that utilized 1–2 μm thick platinum wire. These had a lifting speed of $\approx 1 \text{ m s}^{-1}$, a vertical resolution of $< 1 \text{ mm}$, and were used to study the molecular layer above the surface of the water in the Baltic Sea and Caspian Sea.

A lift was also installed in the 80 m high tower of the Aerological Observatory Lindenberg (Germany) in the 1950s to study the air temperature and air humidity structure in the lowest part of the atmospheric boundary layer [50.33].

Vertical mobile systems are still of interest for air chemistry studies. They allow profiles to be measured using only one gas analyzer providing the response time is sufficiently fast that the transport and reaction timescales are larger than the duration of a measurement performed with the lift [50.34, 35].

50.3 Theory

Mobile measuring systems are highly dynamic systems, and most can be assumed to be first-order dynamic systems (see Chap. 2). Therefore, the response time of the sensor and the velocity of the system determine the dynamic error and the time shift (related to the change in the distance) of the signal. Furthermore, the sampling theorem together with the horizontal or vertical structures of the distributions of the meteorological parameters in the field (see Chap. 1) determine the time constant and sampling rate.

50.3.1 Technical Requirements

The itinerary for mobile measurements is dictated by the technical requirements of the measurements. The measurements should ideally follow the rules given below (which are valid for all types of mobile systems), otherwise the quality of the data may be affected [50.13]:

- Cover all relevant regions in which the meteorological variable of interest is expected to vary over space and time.
- For nonfixed systems, the itinerary must ensure that the system has the right of way at traffic crossings in order to avoid excessively long stops and any influence of heat or exhaust emissions from the mobile unit on the measurements.

- The movement of the mobile unit should be relatively slow compared to the instrument response time to circumvent issues due to a relatively long response time. However, the time needed to carry out the whole itinerary should not be too long, and a reasonable area should be sampled. Chemical sensors may require special attention.
- Measurements for the area investigated should be available from at least one fixed station as a means to validate and potentially calibrate the mobile measurements.
- The longer the time taken to cover the itinerary, the more that the variable(s) of interest (e.g., the air temperature) will change over that period, and these changes will need to be corrected for.
- In the presence of low wind speeds and the nocturnal cooling effect, warm exhaust gases must not be allowed to contaminate the temperature probes during measurements.
- In any case, a proper radiation shield is needed. The speed of the mobile unit normally results in enough ventilation of the sensor when the speed is $> 3 \text{ m s}^{-1}$; below this, separate ventilation is required.
- It is recommended that a modern GNSS system should be used during the itinerary to synchronize the measurements with spatial information. Data can also be stored for further analysis in an attribute

Table 50.3 Typical moving speeds and response times of various mobile systems. Note that smaller-scale rather than larger-scale systems are used to investigate smaller structures (see Table 50.3)

Direction of sampling	Typical systems	Moving speed (m s ⁻¹)	Time constant (s)	Duration of one measurement cycle (min)
Vertical mobile systems	Lifts on towers or balloons	0.1–1	0.5–30	2–15
Horizontal mobile systems	Fixed systems on trails or cables	0.1–1	0.5–30	2–15
	Cars, trams, bicycles, etc.	3–5	10–60	60–90
	Unmanned aircraft systems (UASs)	10–30	0.05–1	10–60

databank linked to the appropriate geographic coordinates within a geographic information system (GIS).

Table 50.3 lists typical characteristics of the mobile systems classified in Table 50.1. Sensors must be chosen according to the time constant and stability required during the measurements.

50.3.2 Response Time and Dynamic Error

It is very important to consider the sensor response time in mobile systems. The output signal from a sensor with a substantial response time will suffer from two distortions: a delay (a lag time) before a change in the measured variable is registered by the system, and signal damping caused by the finite response time of the sensor to the registered change in the variable. The damping will depend on not only the sensor response time but also the frequencies of the temporal and spatial variations in the measured quantity (i.e., the dynamics), and can cause substantial spatial errors in the measurements obtained from the sensor [50.15, 34, 36], as illustrated in Fig. 50.1.

One special type of transfer function (i.e., the relationship between the input and output of a sensor) is that in which the signal changes sharply from $X = X_0$ when $t \leq t_0$ to $X = X_\infty$ when $t > t_0$. A first-order measurement system such as a system for evaluating the temperature can be described by the differential equation

[50.37] (see also Fig. 50.1b and Chap. 2)

$$X_s(t) = X_i(t) + \tau \frac{dX_i}{dt}. \quad (50.1)$$

Thus, the relationship between the input X_i and output X_s signals depends on the time constant τ . The time constant describes the dynamic error of a measurement system. In meteorology, a dynamic error typically arises due to a near-linear change in the value of the meteorological parameter over a given time span. However, for mobile measurement systems, a change in location is also possible. The solution of the above equation for the time-dependent variable after the value of the variable has changed markedly is

$$X(t) = a t - a \tau \left(1 - e^{-\frac{t}{\tau}}\right), \quad (50.2)$$

where the second term on the right-hand side in (50.2),

$$\Delta X_d(t) = a \tau \left(1 - e^{-\frac{t}{\tau}}\right), \quad (50.3)$$

is responsible for the time lag in the measured signal relative to the input signal, and is called the dynamic error.

If the input signal varies linearly over time, the output signal is shifted in relation to the input signal by the time difference $\Delta t = \tau$. Dynamic errors often lead to hysteresis. When the input signal function is known, the

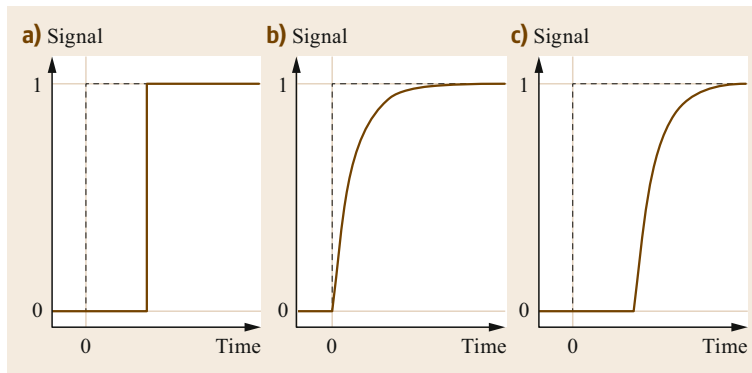


Fig. 50.1a–c Schematic showing the response of a measurement system (black line) to a prescribed step change in the measured variable at time $t = 0$ (gray line) under the influence of (a) the sensor lag time only, (b) the sensor response time only (i.e., dynamic error), and (c) both the lag time and the response time (after [50.34] with permission from Borntraeger, Stuttgart, Germany)



Fig. 50.2 Itinerary and locations of fixed weather screens (A–F) used in an urban climate study performed in the city of Freiburg. Measurements were initially taken at point A; all measurements were corrected for the base temperature at point E (after [50.8] with the permission of the Department of Physical Geography, University of Freiburg, Germany)

dynamic error can easily be corrected for either mathematically or using a correction network. This may be important when precisely determining the temperature gradient of a vertically thin inversion layer. For measurements near the Earth’s surface, the dynamic error correction was also demonstrated for vertically and horizontally mobile measurement systems [50.15, 34].

50.3.3 Measurement Strategies: Designing Itineraries Involving Large Distances

Generally, a zigzag pattern is the best itinerary design if it is necessary to perform detailed mobile measurements across a large area. This design offers several options for data correction and is therefore useful when the itinerary will overlap at several points. If the itinerary and the time needed for one course is short, we can assume, as a first guess, that the meteorological variables change linearly over time in the area of interest. The gradient of the variable over time can then easily be computed from the measurements taken at the overlapping points along the itinerary. On

the other hand, if the itinerary is long, and the measurements take some time, nonlinear behavior of the variable over time can be assumed during data correction [50.13]. When the start and end points of the itinerary coincide, a further control is available. The difference between the temperatures measured at the start and the end of the itinerary tends to reflect the general trend in the measured variable during the sampling time. Finally, data from a fixed station within the study area can be studied to determine whether the variable has decreased or increased, and to what extent. This makes data correction much easier. Since the intervals between mobile measurements tend to be longer than those between fixed-position measurements, and mobile measurements are normally not performed continuously, a fixed station can be used to link the mobile measurements to a longer time series, which makes the mobile measurements more representative. Figure 50.2 shows the itinerary from an urban climate study performed in the city of Freiburg, which used a microbus with sensors for dry and web bulb temperature, both at 2 and 0.6 m AGL.

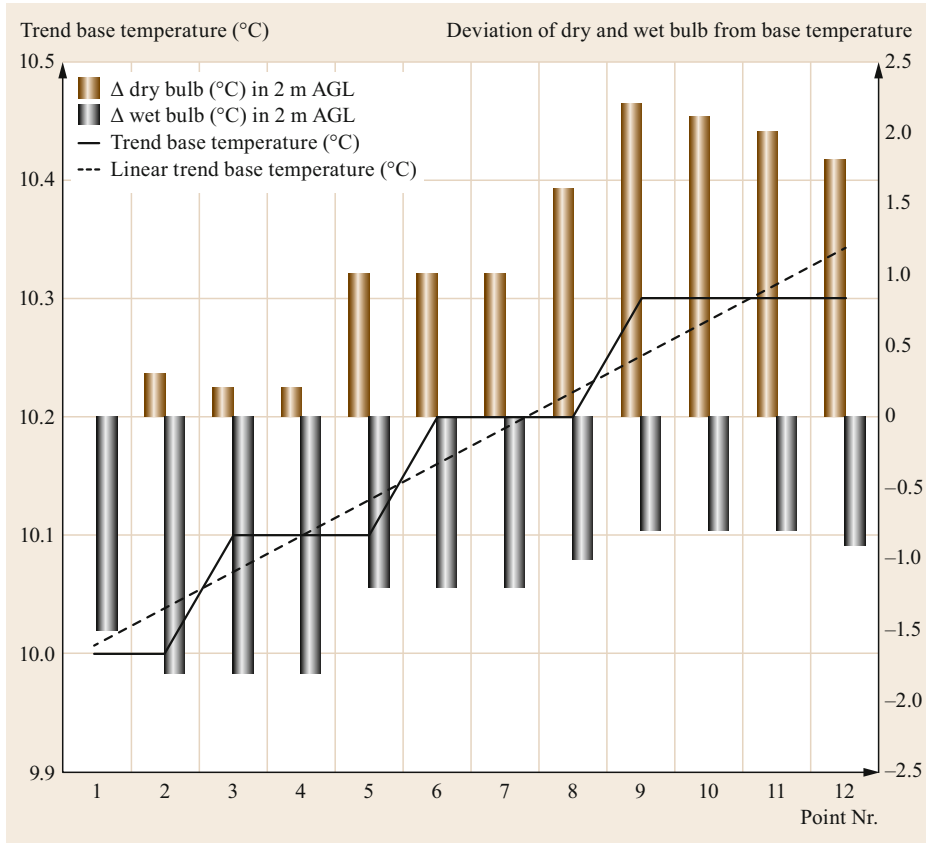


Fig. 50.3 Variation of air temperature and deviation of dry and wet bulb temperature from linear temperature trend during mobile measurements taken at 12 points (locations) in Basel before sunrise (cloud coverage 1/8, cloud type As)

A further aspect to consider is that the absolute value of the meteorological variable studied tends to be of much less interest than the variation in the variable along the itinerary (it is not much of a scientific challenge to investigate whether it is warmer in summer than in winter!). Therefore, measurement data should be stored as the deviations from the mean trend in the variable. The linear trend during the time of the measurement can be computed as

$$\text{Trend } (T) = \frac{T(\text{end}) - T(\text{start})}{\Delta t}, \quad (50.4)$$

where T is the air temperature and Δt is the duration of the itinerary.

Since the deviation of the variable is quite often similar at various multiple measurements along the same itinerary, a more representative mean deviation accounting for all itineraries can be calculated and mapped with a GIS system. The technique of splitting the measurements into a basic temperature trend and the deviation from the trend at each point along the itinerary allows the measured temperature (dry and wet bulb)

and all relevant air variables like mixing ratio and dew-point to be calculated in an appropriate manner. An example is shown in Fig. 50.3.

Ideally, mobile data sampling would be performed across a large area in a very short time, resulting in quasi-simultaneously measured data. However, in reality, it takes a significant amount of time to carry out the itinerary, and most of the meteorological variables change in value to some extent during that time. Depending on the time of day that the itinerary is traveled, these changes may be very large (e.g., during the warming phase of the day) or very small (e.g., shortly before sunrise in the early morning). In any case, the temperature changes must be accounted for to obtain accurate data. Therefore, mobile data sampling requires weather patterns with low pressure gradients (very low wind speeds).

As already mentioned, if the itinerary is relatively short and does not take much time, the measured quantity can generally be assumed to present a linear trend over time, which can easily be computed. For longer itineraries, the trend can be estimated from measurements obtained at intersections in the itinerary. In any

case, it is advisable to run a permanent station or to utilize the data from an official station in the area to correct for meteorological peculiarities (changes in air mass, passages of fronts, etc.). A permanent station is also useful when attempting to determine how representative the mobile measurements are of the local environment [50.13]. Other influencing factors on mobile measurements are:

- The tail wind, as this can transport gases from the exhaust pipe to the sensors. The itinerary should therefore be selected so as to prevent sensor contamination from exhaust gases. Note that this problem is negligible with electric cars.
- Traffic jams or stop-and-go traffic, because there is no or very little sensor ventilation when the vehicle is not moving.

50.4 Devices and Systems

Since they were first performed in the early twentieth century, mobile measurements have been synchronized with geographical coordinate data to enable analysis of the two-dimensional data field for the variable of interest. With the advent of technology that allowed the automated recording of mobile measurements at predefined intervals on an electric or electronic device, it became important to be able to determine the position of a mobile unit at a particular time during a field campaign, as this makes it much easier to subsequently associate each measurement with the location at which it was performed. Today, modern GNSS systems that automatically coregister geolocation and measurement data very precisely have become standard. Also, the size of the instrument setup used to take mobile measurements has decreased in recent decades to such an extent that it can be installed on bicycles or even on UASs (see Chap. 49).

50.4.1 Large-Scale Horizontal Measurement Systems

Most recent studies that have utilized mobile measurements have investigated spatial variations in air temperature and humidity. There are now many ways

for mobile units to investigate two-dimensional variations in air temperature and humidity as well as bioclimatological variables. Mobile measurements have been performed for a variety of meteorological elements due to the development of more sophisticated electronic measurement and data storage methods, instrument miniaturization, and easier access to mobile platforms [50.38]. Besides mobile air temperature and humidity sampling, mobile measurements have also been used to study air pollution [50.40], nitrogen dioxide (NO_2) and ozone levels (O_3) [50.41], ultrafine particles ($\text{PM}_{0.1}$) [50.42, 43], carbon dioxide levels [50.44, 45], particulate matter ($\text{PM}_{2.5}$, i.e., particles $< 2.5 \mu\text{m}$



Fig. 50.4 Mobile measurement system used by the German Meteorological Service (DWD) (photo © DWD)



Fig. 50.5 Combined temperature sensor and GNSS logger mounted on a public bus (after [50.39] © the authors, CC Attribution 3.0 License)



Fig. 50.6 (a) Bicycle unit with a thermistor (red frame) on the handlebar and (b) data storage box on the luggage rack (photo © E. Parlow)

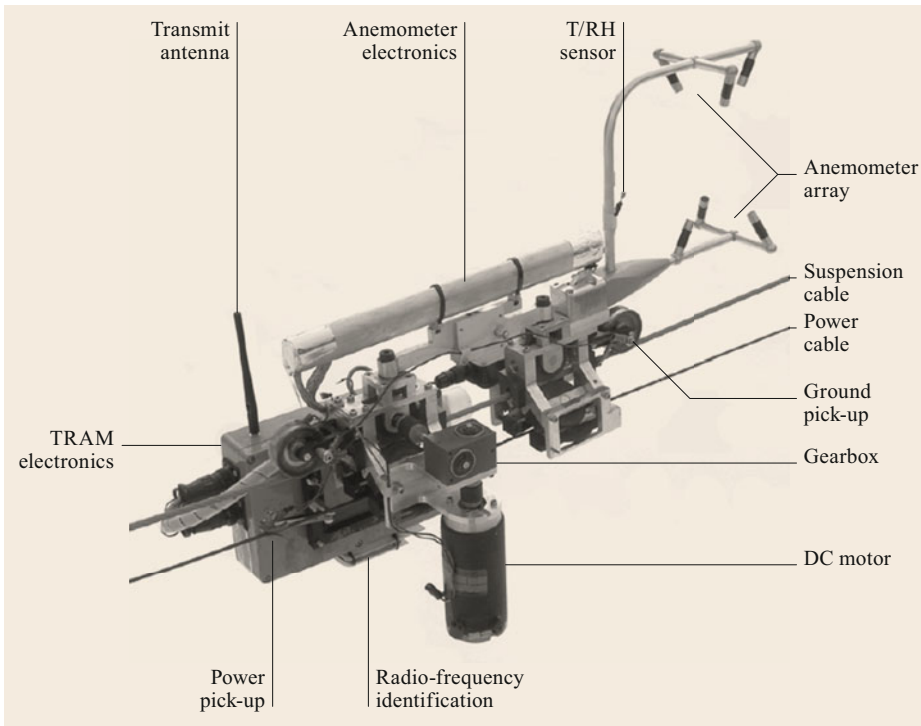


Fig. 50.7 The Transect Measurement (TRAM) system trolley, with key components labeled (after [50.27] © American Meteorological Society, used with permission)

in diameter) and black carbon concentrations [50.46, 47], and radiation in urban street canyons [50.48], for example.

Using a car makes it possible to investigate a large area within a reasonably short time frame. This method has the advantage that a construction can be attached to the front of the car which can measure vertical temperature or humidity profiles of the atmospheric boundary layer up to a height of 2 m (Fig. 50.4).

Another useful and comfortable way to measure these variables is to attach the sensor to a public bus

or tram [50.12], Fig. 50.5). The advantage of this approach is that it is easy to obtain a large number of meteorological profiles (normally more than could be measured in an individual campaign) of a sizable area in a relatively short space of time. A disadvantage of it is that the route is fixed and does not necessarily represent the optimal itinerary for a micrometeorological study. A further disadvantage is that these vehicles stop frequently, potentially leading to the sensor ventilation and contamination issues mentioned earlier, which can significantly affect the quality of the mea-

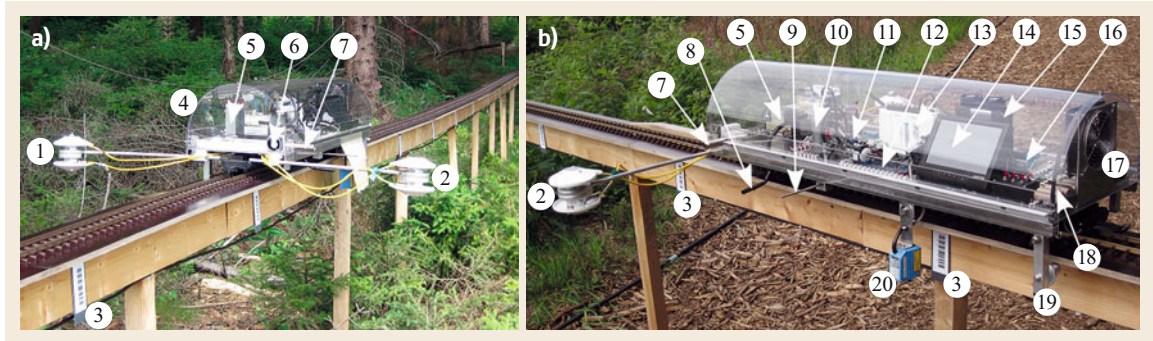


Fig. 50.8 (a) Front and (b) lateral views of the Horizontal Mobile Measuring System (HMMS). 1 Shortwave radiation sensors on a 0.4 m long boom, 2 longwave radiation sensors on a 0.4 m long boom, 3 barcode, 4 Makrolon® cover to protect the HMMS from rain and dirt, 5 Enviroscope O₃ analyzer, 6 fan to ventilate the HMP 155 temperature and humidity sensor, 7 double-shielded inlet for the HMP 155, 8 PTFE (polytetrafluoroethylene) inlet for the O₃ analyzer, 9 aluminum inlet for the CO₂ analyzer, 10 pump for the O₃ analyzer, 11 pump for the CO₂ analyzer, 12 Edinburgh Instruments Ltd. Gascard® NG CO₂ analyzer, 13 National Instruments data acquisition device, 14 7" TFT (thin-film transistor) monitor, 15 micro PC, 16 LGB (Lehmann-Groß-Bahn – Lehmann-big-train) analog throttle with potentiometer, 17 fan to cool the entire system, 18 onboard storage battery, 19 lateral holder to protect the HMMS against falls, 20 Sick CLV412-1010 barcode scanner (after [50.15]) © the authors, CC Attribution 3.0 License)

Fig. 50.9 External sampling unit of the LOPAP (gray box) and inlet for NO_x on the lift system on the forest floor. The three heights (1.6, 0.4, and 0.1 m) at which the profile measurements were performed are indicated in red (after [50.35]) © the authors, CC Attribution 3.0 License) ►

measurements. It is then necessary to correct or remove the corresponding problematic data from the overall dataset.

In recent years, some studies have used bicycles to transport the instrumentation employed for mobile measurements. An advantage of this is that it is possible to traverse areas in which cars are prohibited, such as urban green areas and parks. Figure 50.6 shows a bicycle with a thermistor mounted on the handlebar and appropriate data logger infrastructure on the luggage rack.

50.4.2 Small-Scale Horizontal Measurement Systems

The mobile systems that are used for short itineraries tend to be miniaturized systems with many integrated sensors. Such systems are applied to study small-scale heterogeneities at the micro- β and micro- γ meteorological scales (10–100 m, see Chap. 1). These heterogeneities are caused by vegetation (forest) and urban areas. In the following, two systems that were recently developed for mobile studies in heterogeneous forests are discussed.

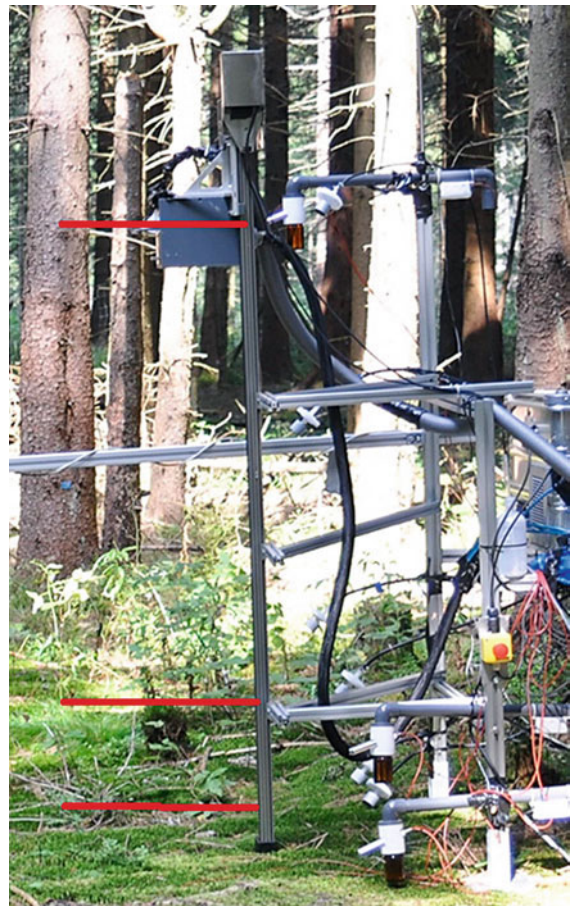


Table 50.4 Comparison of various mobile systems with various fixed multisensor systems

	Mobile systems	Fixed multisensor systems
General remarks	Can only be used for short measurement periods Often use simple or miniaturized sensors, a high level of quality control is required Possibility of time shifts between measurement points and dynamic error	Useful for short- and long-term measurements Application of recommended sensors [50.49] is possible
Large-scale horizontal measurement systems	Larger areas are covered, high flexibility in terms of area studied (dependent on weather conditions)	Only a few measuring points, no flexibility in terms of area studied
Small-scale horizontal measurement systems	High spatial resolution, dynamic error is possible	Only a few points can be observed
Vertical measurement systems	Use expensive instruments with a small offset and time shift	Highly accurate systems are necessary

The TRAM (Transect Measurement) system [50.27] runs in a loop while measuring the wind speed (using an ultrasonic anemometer), CO₂ concentration, air temperature, and humidity. Its developers were able to create a measurement track through a forest ecosystem and over a creek through the use of steel cables and masts, allowing mobile measurements to be obtained across long horizontal distances and at different heights (Fig. 50.7).

The HMMS (Horizontal Mobile Measurement System) is a small train on rails [50.15] that measures short- and longwave radiation components, the air temperature, the air humidity, and the CO₂ and O₃ concentrations 150 m from both sides of the edge of a forest at a height of ≈ 1 m above the forest floor (see Fig. 50.8; for results, see Sect. 50.8.3).

50.4.3 Vertical Measurement Systems

The system presented in this section was constructed to measure the vertical mixing ratio profile of nitrous acid

(HONO) near a forest floor [50.35] using a long-path absorption photometer (LOPAP; QUMA, Wuppertal, Germany) with a time resolution of 3 min. Because this photometer has low time resolution, the vertical lift (Fig. 50.9) was used in a stop-and-go mode, remaining at each of the three levels for 7–9 min. Therefore, it was possible to measure a vertical profile every 30 min. A benefit of this construction was that it required only one expensive analyzer. The need for just one analyzer was also advantageous because there were small gradients of the mixing ratio in the region studied, meaning that small offsets between multiple instruments would have caused problems with the measurements.

50.4.4 Comparison of Different Methods

Table 50.4 provides a comparison of various mobile systems with various fixed multisensor systems to aid the selection of the most appropriate type of measuring system for a particular application.

50.5 Specifications

The sensor specifications largely depend on the sensor quality. Table 43.10 lists the specifications of highly accurate single sensors [50.49], compact or multiparameter

sensors (see Chap. 43), and simple sensors (crowdsourcing, see Chap. 44). The relevant variables should be measured with a mobile system of the same quality class.

50.6 Quality Control

Quality control is a very important issue for mobile systems due to the high mechanical stress of such systems and the often low accuracy in relation to effects such as delay time and dynamic error. It is therefore very important to obtain reference measurements for two main reasons:

- To correct for changes in the values of the measured meteorological variables during the time taken to perform the itinerary. The system should pass the reference measurement station as often as possible.
- To recalibrate simple sensors or sensors where there is time drift. Therefore, the frequency with which

Table 50.5 Recommended maintenance activities for mobile systems

Maintenance interval	Sensors without drift	Sensors with drift
Before each measurement cycle or daily	Visual check	Comparison with the reference instrument
Before each batch of measurement cycles or weekly	Comparison with a reference instrument	Sensor recalibration
Before using the system after a long period of disuse, or annually	Recalibration or comparison with the reference instrument for very stable sensors	Sensor recalibration

the mobile system should stop at the reference station depends on the response time of the sensor.

Reference measurements should be made with high-quality sensors, and the siting conditions should be of the highest class [50.49] (for more details, see the relevant parameter-specific chapters).

Mobile systems encounter windy and calm areas, sunny and shaded areas, and so on during their itineraries. Therefore, the effects of environmental parameters such as the wind speed, wind direction, solar radiation, and humidity on the measurement system should be investigated before the measurements are first performed. If necessary, temperature screens, ventilation, inlets that are not wind-direction sensitive, etc. should be applied. The influence of the vehicle (e.g., the car) used to transport the measurement system on

the measurements should also be investigated. Uncorrectable influences on the measured data should be at least one order of magnitude lower than the effects that are being investigated.

Quality control should also be carried out in accordance with the meteorological situation. Because vertical gradients may be very large during stable stratification (see Chap. 1), small changes in the sensor height or the surrounding canopy height may generate changes in the measured variables.

All relevant sensor-specific quality control procedures (e.g., those for temperature, see Chap. 7; humidity, see Chap. 8; wind, see Chap. 9; or radiation, see Chap. 11) should be applied. Because the quality control process may differ markedly between mobile systems, the procedure performed should be carefully documented and all relevant metadata should be recorded.

50.7 Maintenance

Maintenance should be carried out as recommended for the applied sensors or described in the relevant chapters of this Handbook. Because of the high mechanical stress on mobile systems, maintenance should not only

be performed at predefined time intervals (just as for fixed sensors), but should also be adjusted according to the frequency of use of the mobile system. Table 50.5 gives some maintenance recommendations.

50.8 Application

Applications of the three types of mobile systems defined above are richly diverse. The following examples show how powerful such systems can be at yielding information on meteorological field distributions that cannot be extracted using only fixed sensors or satellite images that have no dynamic component.

50.8.1 Urban Climate and the Urban Heat Island Effect

One of the major applications of mobile measurements has been to investigate the climate and air quality in urban regions. Initially, nearly all of the studies in this area investigated nocturnal air temperature fields—mainly frost risk and minimum temperature fields. In

recent decades, however, the urban heat island effect has become a major driver for these investigations, although the development of appropriate instruments has also led to studies of air chemistry and fine particles in urban areas.

Figure 50.10 shows the air temperature variations in the city of Basel (Switzerland) and the effect of urban parks on afternoon and nocturnal air temperatures measured during three bicycle campaigns during summer 2005 (on 5 August 2005 at 18:50 CET (Central European Time), 11 August 2005 at 00:05 CET, and 30 August 2005 at 01:15 CET). Note that the nocturnal air temperature is significantly lower (by several degrees) in the two urban parks with different quantities of vegetation than in other areas traversed during the bicycle campaigns.

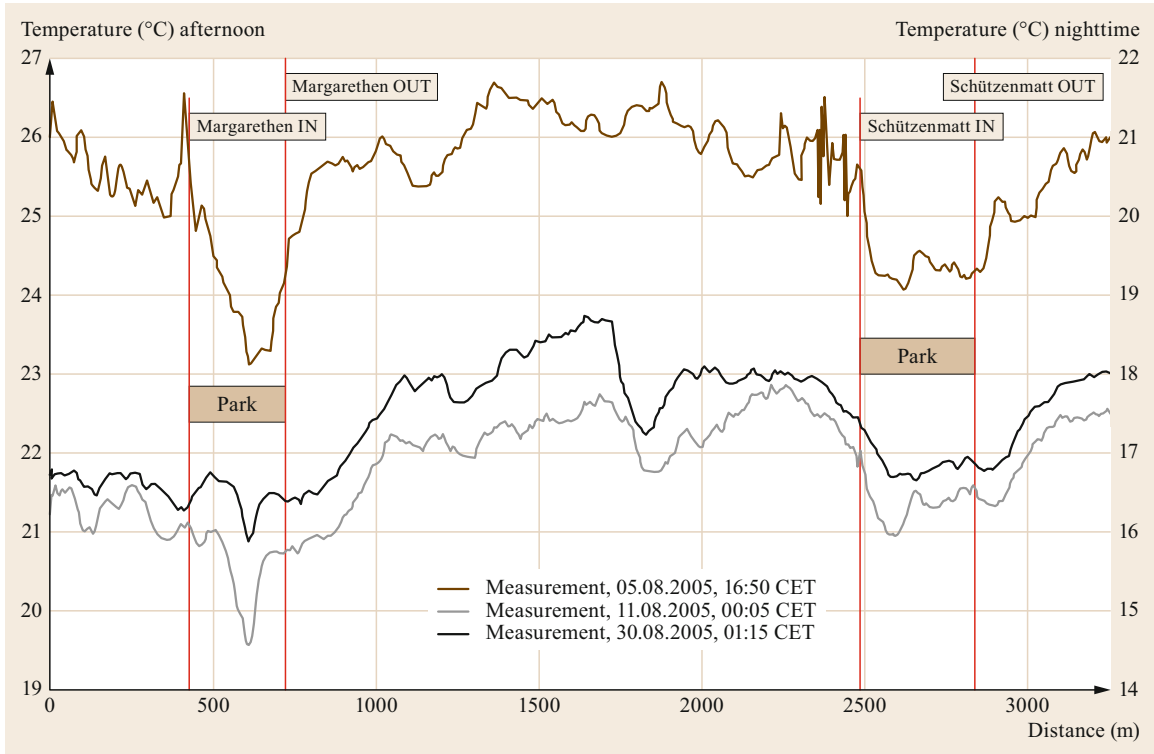


Fig. 50.10 Nocturnal bicycle-based measurements taken in urban parkland in the city of Basel (Switzerland). The red lines indicate the entry and exit points for two urban parks (Margarethen Park and Schützenmatt Park). The temperature from measurement at 05.08.2005 is shown on the left axis and the temperatures from measurements at 11.08.2005 and at 30.08.2005 are shown on the right axis

50.8.2 Ventilation and Mountain Breezes

An important issue in urban planning is the existence and distribution of cold air drainage systems or mountain breezes. One of the most well-known mountain breeze systems, and one of the first to be reported, is the *Höllentäler* wind system in the city of Freiburg (Black Forest, Germany). The effects of this wind system on the urban climate of Freiburg were first published in 1840 [50.50]; since then, numerous studies have investigated the wind system in more detail [50.51]. Figure 50.11 shows the variation in the air temperature during mobile measurements in Freiburg.

50.8.3 Forest Climate at an Edge

Various meteorological parameters were observed at the edge of a 25 m high spruce forest next to a clearing by the Horizontal Mobile Measurement System (HMMS) described in Sect. 50.4.2 [50.15]. Because the response

time of the sensors was relatively slow compared to the speed of travel of the system, the resulting dynamic error was accounted for using (50.2). Figure 50.12 shows the shortwave downwelling radiation before and after the correction. It is easy to discern when the system was moving from the forest to the clearing or in the opposite direction in the uncorrected data, but not in the corrected data. A linear radiation gradient at the edge was assumed for the purposes of correction as a first approximation.

Figure 50.13 presents the daily cycles of the four radiation components based on corrected data obtained at a height of ≈ 1 m above the forest floor. The shortwave radiation plot shows sunny spots in the forest and, in the morning, a shadow effect at the forest edge. The downwelling longwave radiation is strongest in the forest during daytime due to the warm crown area of the trees, while the upwelling longwave radiation is strongest above the clearing during daytime. Similar plots were generated for temperature, humidity, and carbon dioxide, and ozone.

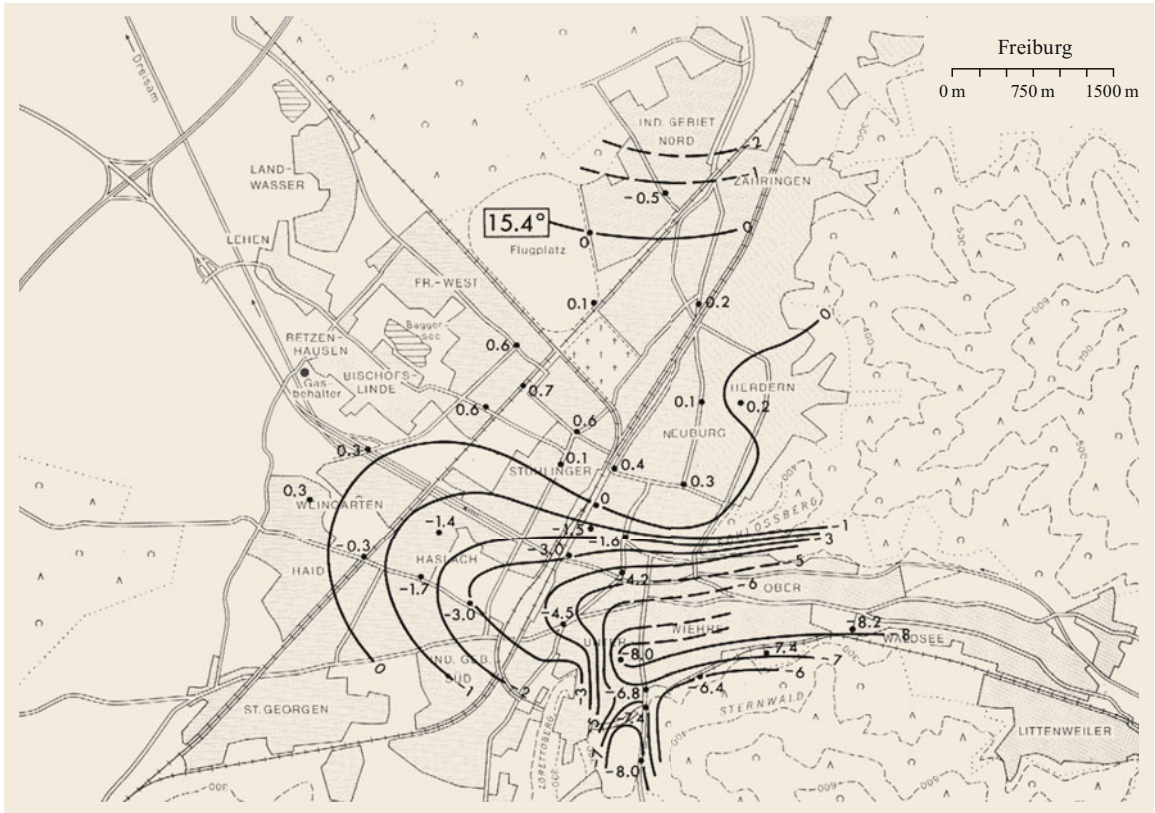


Fig. 50.11 The nocturnal mountain breeze in Freiburg at 19:00 CET on 5 October 1972 decreased the air temperature by up to 8 K in the valley outlet as compared with the base temperature of 15.4 °C measured at a fixed station in the western part of the city (after [50.8] with the permission of the Department of Physical Geography, University of Freiburg, Germany)

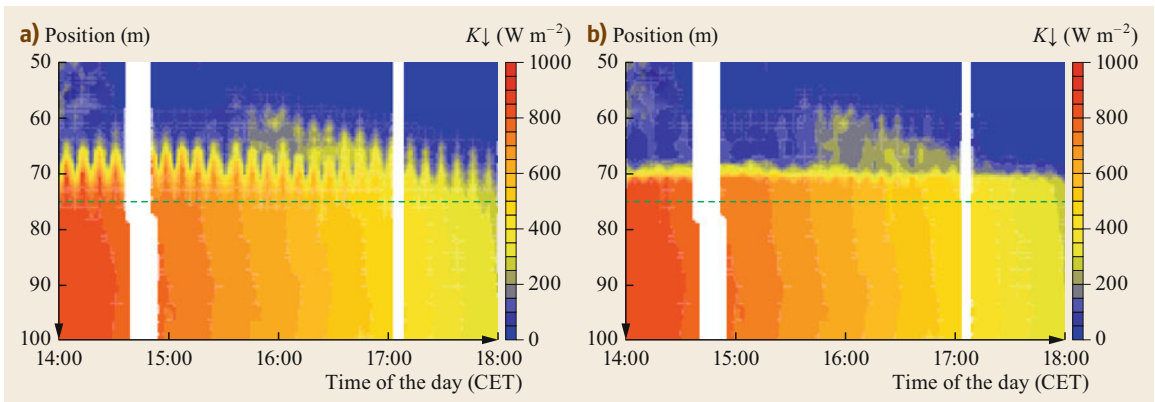


Fig. 50.12a,b Horizontal profile of the downwelling shortwave radiation ($K \downarrow$) 1 m above the forest floor at the forest edge (dashed line) on 28 June 2011, 14:00–18:00 CET (a) without and (b) with dynamic error correction. Position corresponds to the distance from the starting point in the forest; the forest edge was 75 m from the starting point (horizontal green dotted line) and the far side of the clearing was 150 m from the starting point (after [50.15] © the authors 2014. CC Attribution 3.0 License)

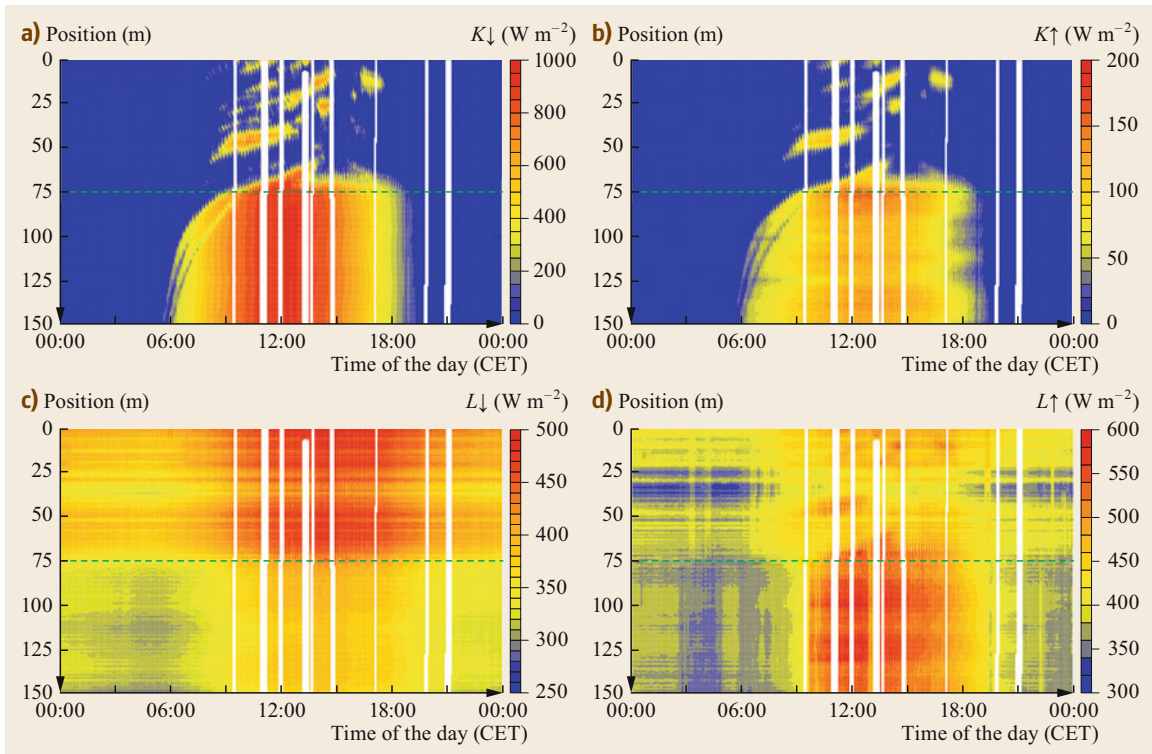


Fig. 50.13a–d Horizontal profiles of the four radiation components 1 m above the forest floor at a forest edge (*dashed line*) on 28 June 2011 (Waldstein-Weidenbrunnen site, Fichtelgebirge mountains, Germany): (a) downwelling shortwave radiation ($K \downarrow$), (b) upwelling shortwave radiation ($K \uparrow$), (c) downwelling longwave radiation ($L \downarrow$), and (d) upwelling longwave radiation ($L \uparrow$). Note that the four plots have different irradiance scales. *Position* corresponds to the distance from the starting point in the forest; the forest edge was 75 m from the starting point (*horizontal green dotted line*) and the far side of the clearing was 150 m from the starting point (after [50.15] © the authors 2014. CC Attribution 3.0 License)

50.9 Future Developments

Mobile systems that cover short distances are currently used mainly for specific research questions, and horizontal mobile systems that travel large distances are mainly used for urban measurements (see Chap. 52). However, other systems have become increasingly popular in recent years, such as UASs (see Chap. 49), crowdsourcing (see Chap. 44), and satellite imaging (see Chap. 42), all of which are used in combination

with GNSS and geoinformation systems [50.14]. It is a major methodological challenge to combine all of these systems in order to obtain comprehensive three-dimensional pictures at various time steps in areas of interest. Thus, in the near future, mobile systems will generally be used in conjunction with other systems rather than on their own. This approach will influence measuring strategies and sensor selection.

50.10 Further Readings

- Landsberg, H. (1981): The urban climate. International Geophysics Series, Vol 28, Academic Press, New York.
- VDI 3785 Pt. 2 (2011, update 2023): Umweltmeteorologie – Methoden bodengebundener Stadt- und Standortklimamessungen mit mobilen Messsystemen (Environmental Meteorology – Methods of Ur-

ban and Site-Related Ground-Based Climate Measurements with Mobile Measurement Systems). Beuth, Berlin.

- Oke, T., G. Mills, A. Christen, J. Voogt (2017): *Urban Climates*. Cambridge University Press.

References

- 50.1 W. Schmidt: Die Verteilung der Minimumtemperaturen in der Frostnacht des 12. Mai 1927 im Gemeindegebiet von Wien, *Fortschr. Landwirtsch.* **21**, 1–11 (1927)
- 50.2 A. Peppler: *Die Temperaturverhältnisse von Karlsruhe an heißen Sommertagen, Deutsches Meteorologisches Jahrbuch für 1929*, Veröffentlichungen der Badischen Landeswetterwarte, Vol. 16, (1930)
- 50.3 A. Büdel, J. Wolf: Münchner stadtklimatische Studien, *Wetter* **50**, 4–10 (1933)
- 50.4 T.J. Chandler: *The Climate of London* (Hutchinson, London 1965)
- 50.5 A. Kratzer: *The Climate of Cities* (Air Force Cambridge Research Laboratories, Cambridge 1956)
- 50.6 H. Aichele: Frostgefährdete Gebiete in der Baar, eine kleinklimatische Geländekartierung, *Erdkunde* **5**, 70–73 (1951)
- 50.7 H. Aichele: Über die Verwendung fahrbarer Temperaturschreiber bei geländeklimatischen Untersuchungen, *Angew. Meteorol.* **5**, 267–276 (1968)
- 50.8 W. Nübler: Konfiguration und Genese der Wärmeinsel der Stadt Freiburg, *Freibg. Geogr. Hefte* **16**, 113 (1979)
- 50.9 R. Taesler: *Studies of the Development and Thermal Structure of the Urban Boundary Layer in Uppsala, Part I (57 p), Experimental Program, and Part II (177 p), Data Analysis and Results*, Report No. 61, Tech. Rep. (Meteorological Institute, Uppsala University, Uppsala 1980)
- 50.10 W. Endlicher: Geländeklimatologische Untersuchungen im Weinbaugebiet des Kaiserstuhls, *Ber. Dtsch. Wetterd.* **150**, 1–124 (1980)
- 50.11 E. Parlow: Geländeklimatologische Untersuchungen im Bereich der Staufferen Bucht unter Besonderer Berücksichtigung lokaler Ausgleichsströmungen, *Freibg. Geogr. Hefte* **21**, 1–175 (1983)
- 50.12 J. Seidel, G. Ketzler, B. Bechtel, B. Thies, A. Philipp, J. Böhner, S. Egli, M. Eisele, F. Herma, T. Langkamp, E. Petersen, T. Sachsen, D. Schlabling, C. Schneider: Mobile measurement techniques for local and micro-scale studies in urban and topoclimatology, *Erde* **147**, 15–39 (2016)
- 50.13 VDI: *Umweltmeteorologie – Methoden bodengebundener Stadt- und Standortklimamessungen mit mobilen Messsystemen (Environmental Meteorology – Methods of Urban and Site-Related Ground-Based Climate Measurements with Mobile Measurement Systems)*, VDI 3785 Part 2 (Beuth, Berlin 2011), update 2023
- 50.14 W. Kresse, D.M. Danko (Eds.): *Springer Handbook of Geographic Information*, 2nd edn. (Springer, Dordrecht 2021)
- 50.15 J. Hübner, J. Olesch, H. Falke, F.X. Meixner, T. Foken: A horizontal mobile measuring system for atmospheric quantities, *Atmos. Meas. Tech.* **7**, 2967–2980 (2014)
- 50.16 R.E. Leonard, A.R. Eschner: *A Treetop Tramway System for Meteorological Studies*, Tech. Rep. Northeastern Forest Experiment Station (Forest Service, US Dept. of Agriculture, US Forest Service Research, Upper Darby 1968), Paper, NE-92
- 50.17 E.I. Mukammal: Some aspects of radiant energy in a pine forest, *Arch. Meteorol. Geophys. Bioklim. Ser. B* **19**, 29–52 (1971)
- 50.18 G.W. Brown: Measuring transmitted global radiation with fixed and moving sensors, *Agric. Meteorol.* **11**, 115–121 (1973)
- 50.19 D. Baldocchi, B. Hutchison, D. Matt, R. McMillen: Seasonal variations in the radiation regime within an oak-hickory forest, *Agric. For. Meteorol.* **33**, 177–191 (1984)
- 50.20 D.D. Baldocchi, D.R. Matt, B.A. Hutchison, R.T. McMillen: Solar radiation within an oak-hickory forest: an evaluation of the extinction coefficients for several radiation components during fully-leaved and leafless periods, *Agric. For. Meteorol.* **32**, 307–322 (1984)
- 50.21 G. Péch: Mobile sampling of solar radiation under conifers, *Agric. For. Meteorol.* **37**, 15–28 (1986)
- 50.22 X. Lee, T.A. Black: Atmospheric turbulence within and above a douglas-fir stand, part ii: eddy fluxes of sensible heat and water vapour, *Bound.-Layer Meteorol.* **64**, 369–389 (1993)
- 50.23 N. Rodskjer, A. Kornher: Eine Methode zur Registrierung der räumlichen Verteilung der Globalstrahlung in einem Pflanzenbestand, *Arch. Meteorol. Geophys. Bioklim. Ser. B* **15**, 186–190 (1967)
- 50.24 N. Rodskjer, A. Kornher: Über die Bestimmung der Strahlungsenergie im Wellenlängenbereich von 0,3–0,7 μ in Pflanzenbeständen, *Agric. Meteorol.* **8**, 139–150 (1971)
- 50.25 O. Langvall, M. Ottosson Löfvenius: Effect of shelterwood density on nocturnal near-ground temperature, frost injury risk and budburst date of Norway spruce, *For. Ecol. Manag.* **168**, 149–161 (2002)
- 50.26 G. Örländer, O. Langvall: The Asa shuttle – a system for mobile sampling of air temperature and radiation, *Scand. J. For. Res.* **8**, 359–372 (1993)
- 50.27 S.P. Oncley, K. Schwenz, S.P. Burns, J. Sun, R.K. Monson: A cable-borne tram for atmospheric measurements along transects, *J. Atm. Ocean. Tech.* **26**, 462–473 (2009)
- 50.28 H. Bruch: *Die vertikale Verteilung der Windgeschwindigkeit und der Temperatur in den untersten Metern über der Wasseroberfläche*, Veröffentlichungen des Instituts für Meereskunde der Univ. Berlin, Reihe A, Vol. 38, (1940)

- 50.29 A.H. Woodcock, H. Stommel: Temperature observed near the surface of a fresh-water pond at night, *J. Meteorol.* **4**, 102–103 (1947)
- 50.30 H.U. Roll: Temperaturmessungen nahe der Wasseroberfläche, *Dtsch. Hydrogr. Z.* **5**, 141–143 (1952)
- 50.31 T. Foken: Die Messung der Mikrostruktur der vertikalen Lufttemperaturverteilung in unmittelbarer Nähe der Grenze zwischen Wasser und Atmosphäre, *Z. Meteorol.* **25**, 292–295 (1975)
- 50.32 H. Hinzpeter, P. Lobmeyer: Versuche zum Nachweis laminarer Grenzschichten über dem Meer, *Ann. Meteorol.* **4**, 19–20 (1969)
- 50.33 J. Rink: Fernregistrierung des Temperatur- und Feuchtegefälles in der bodennahen Luftschicht (80 m), *Z. Meteorol.* **14**, 113–120 (1960)
- 50.34 J.-C. Mayer, K. Hens, U. Rummel, F.X. Meixner, T. Foken: Moving measurement platforms – specific challenges and corrections, *Meteorol. Z.* **18**, 477–488 (2009)
- 50.35 M. Sörgel, I. Trebs, D. Wu, A. Held: A comparison of measured HONO uptake and release with calculated source strengths in a heterogeneous forest environment, *Atmos. Chem. Phys.* **15**, 9237–9251 (2015)
- 50.36 T. Foken: *Micrometeorology*, 2nd edn. (Springer, Berlin 2017)
- 50.37 F.V. Brock, S.J. Richardson: *Meteorological Measurement Systems* (Oxford Univ. Press, New York 2001)
- 50.38 W. Kuttler, D. Dütemeyer: Umweltmeteorologische Untersuchungsmethoden, *Promet* **30**, 15–27 (2003)
- 50.39 M. Buttstädt, T. Sachsen, G. Ketzler, H. Merbitz, C. Schneider: A new approach for highly resolved air temperature measurements in urban areas, *Atmos. Meas. Tech. Discuss.* **4**, 1001–1019 (2011)
- 50.40 S. Weimar, C. Mohr, R. Richter, J. Keller, M. Mohr, A.S.H. Prévôt, U. Baltensperger: Mobile measurements of aerosol number and volume size distributions in an alpine valley: influence of traffic versus wood burning, *Atmos. Environ.* **43**, 624–630 (2009)
- 50.41 L.D. Cavellin, S. Weichenthal, R. Tack, M. Ragetti, A. Smargiassi, M. Hatzopoulou: Investigating the use of portable air pollution sensors to capture the spatial variability of traffic-related air pollution, *Environ. Sci. Tech.* **50**, 313–320 (2016)
- 50.42 D. Westerdahl, S. Fruin, T. Sax, P.M. Fine, C. Sioutas: Mobile platform measurements of ultrafine particles and associated pollutant concentrations on freeways and residential streets in Los Angeles, *Atmos. Environ.* **39**, 3597–3610 (2005)
- 50.43 M.S. Ragetti, E. Corradi, C. Braun-Fahrländer, C. Schindler, A. de Nazelle, M. Jerrett, R.E. Ducret-Stich, N. Künzli, H.C. Phuleria: Commuter exposure to ultrafine particles in different urban locations, transportation modes and routes, *Atmos. Environ.* **77**, 376–384 (2013)
- 50.44 W. Kuttler, A. Strassburger: Air quality measurements in urban green areas – a case study, *Atmos. Environ.* **33**, 4101–4108 (1999)
- 50.45 S. Henninger, W. Kuttler: Methodology for mobile measurements of carbon dioxide within the urban canopy layer, *Clim. Res.* **34**, 161–164 (2007)
- 50.46 B. Elen, J. Peters, V.M. Poppel, N. Bleux, J. Theunis, M. Reggente, A. Standaert: The Aeroflex: a bicycle for mobile air quality measurements, *Sensors* **13**, 221–240 (2013)
- 50.47 M. Van Poppel, J. Peters, N. Bleux: Methodology for setup and data processing of mobile air quality measurements to assess the spatial variability of concentrations in urban environments, *Environ. Pollut.* **183**, 224–233 (2013)
- 50.48 J. Holst, H. Mayer: Urban human-biometeorology: Investigations in Freiburg (Germany) on human thermal comfort, *Urban Clim.* **News **38**, 5–10 (2010)**
- 50.49 WMO: *Guide to Instruments and Methods of Observation*, WMO-No. 8, Volume I – Measurement of Meteorological Variables (World Meteorological Organization, Geneva 2018)
- 50.50 Baumgärtner: Der Gesundheitszustand Freiburgs. In: *Freiburg im Breisgau und seine Umgebung*, 3rd edn., ed. by H. Schreiber (Herder, Freiburg 1840) pp. 218–230
- 50.51 S.A. Ernst: Tagesperiodische Windsysteme und Belüftungsverhältnisse in Freiburg i. Brsg. – planungsrelevante Aspekte eines Bergwindsystems, *Freibg. Geogr. Hefte* **49**, 103 (1995)

Eberhard Parlow

Department of Environmental Sciences
Atmospheric Sciences
University Basel
Basel, Switzerland
eberhard.parlow@unibas.ch



Eberhard Parlow is Professor Emeritus at the Department of Environmental Sciences and was previously Full Professor and Director of the Meteorology, Climatology, and Remote Sensing Lab at the University of Basel. He was President of the Commission for Remote Sensing at the Swiss Academy of Natural Sciences and President of the European Association of Remote Sensing Laboratories. His research combines micrometeorological flux measurements with remote-sensing techniques, especially in urban climatology.

Thomas Foken

University of Bayreuth
Bayreuth, Germany
thomas.foken@uni-bayreuth.de



Thomas Foken is a retired Professor of Micrometeorology at the University of Bayreuth. He was the head of Laboratories at the meteorological observatories at Potsdam (1981–1994) and Lindenberg (1994–1997). His research interests include the interaction between the Earth's surface and the atmosphere and the measurement and modeling of energy and matter fluxes, with a strong focus on experimental meteorology. His scientific contributions have been recognized through various international awards.

51. Measurement Systems for Wind, Solar and Hydro Power Applications

Stefan Emeis , Stefan Wilbert 

Wind, solar, and hydropower are major forms of the so-called renewable energies. Effective application of renewable energies to supply heat and electricity is weather dependent and needs short-term weather forecasts, as well as historical and climatological information. All relevant measurement sensors were introduced in previous chapters. Here, the special requirements of wind, radiation, and precipitation measurements for planning and operating renewable energy power plants are addressed. The cooling of conventional thermal power plants, the transmission of electricity in cables above ground, and the overall energy demand are weather dependent as well, and thus need atmospheric measurements.

51.1	Measured Parameters	1370	51.3.2	Dependence of Solar Energy on Meteorological Parameters	1374
51.2	History	1371	51.3.3	Dependence of Hydropower on Meteorological Parameters	1376
51.2.1	History of Measurements for Wind Energy	1371	51.3.4	Dependence of Thermal (Conventional) Power Plants on Meteorological Parameters	1376
51.2.2	History of Measurements for Solar Energy	1372	51.3.5	Dependence of Energy Transmission on Meteorological Parameters	1376
51.2.3	History of Measurements for Hydropower	1372	51.3.6	Dependence of Energy Demand on Meteorological Parameters	1377
51.2.4	History of Measurements for Conventional Power Plants, Grid Operation, and Electricity Transmission	1372	51.4	Devices and Systems	1377
51.3	Theory	1373	51.4.1	Cup and Sonic Anemometers	1377
51.3.1	Dependence of Wind Energy on Meteorological Parameters	1373	51.4.2	Surface-Based Remote Sensing of Wind and Temperature	1377
			51.4.3	Satellite Wind Observations	1378
			51.4.4	Measurement Stations for Solar Energy	1378
			51.4.5	Satellite-Based Radiation Measurements	1382
			51.4.6	Comparison of Methods	1382
			51.5	Specifications	1382
			51.6	Quality Control	1383
			51.7	Maintenance	1383
			51.8	Application	1384
			51.8.1	Wind Energy Applications	1385
			51.8.2	Solar Energy Applications	1385
			51.9	Future Developments	1386
			51.10	Further Readings	1386
			References		1387

Meteorological competence directed to a meaningful and smooth application of devices that supply electricity and heat from fossil and renewable energy sources is summarized in the subdiscipline “energy meteorology” today. Energy meteorology comprises theoretical considerations, data capture, data analysis, and weather forecasts relevant to power generation, distribution, and consumption. Energy meteorology for wind energy is covered in [51.1]. For solar energy applications, more detailed information is provided, e.g., in [51.2]. For hy-

dropower applications, the reader can refer to [51.3] for more details. A short review on the present status of the whole subject is found in [51.4].

Although fossil and renewable energy supply devices have been operated for a long time, energy meteorology mainly developed during the last three decades due to the growth of the renewable energy capacity and its much larger need for meteorological information compared to fossil power plants. With a few exceptions the main difference in the required meteorological

knowledge for power generation purposes is that for fully fossil power plants, meteorological information is mainly needed in order to assess the load (e.g., high

loads during cold spells). For renewable energy, meteorological information is also needed to estimate the energy production.

51.1 Measured Parameters

Table 51.1 gives an overview on the meteorological parameters needed for the planning and operation of renewable energy sources and an electricity grid with fossil and renewable energy sources. The parameters are listed next to the form in which the parameter is required, its application, unit, and symbol.

The deployment of measurement instruments for site assessment or performance monitoring of renewable energy power plants will be very much determined

by the intended use of the generated power (e.g., the instantaneous generation of electricity or the accumulative storage of heat). The main requirement is that the measurements are representative for an area or an air volume covered by the foreseen devices for power generation. For instance, wind measurements often have to be performed at exposed sites, such as hilltops. In this case, attention has to be paid to the problem of curved streamlines, as described in Sect. 23.6.3 of this

Table 51.1 Measured parameters used in renewable energy applications

Parameter	Form	Relevance	Unit	Symbol
Wind speed	Time series, statistics, extreme values, vertical profiles	Wind energy, power lines, solar energy	m s^{-1}	u
Wind direction	Time series, statistics, vertical profiles	Wind energy, solar energy	$^{\circ}$	
Air temperature	Instantaneous values (wind energy, power lines, cooling towers), weekly or monthly average (cooling water for hydropower)	Wind energy (air density, risk of icing), power lines, solar energy, hydropower (evaporation, warming of cooling water), operation of cooling towers, load estimations	K	T
Pressure	Time series, statistics	Wind energy (air density), power lines, cooling towers	hPa	p
Humidity	Instantaneous values, weekly or monthly averages	Wind energy (air density, risk of icing), hydropower (evaporation), operation of cooling towers, power lines	% (relative humidity), $10^{-3} \text{ kg kg}^{-1}$ (absolute humidity)	RH, q
Global horizontal irradiance	Time series, statistics, extreme values	Solar energy, hydropower (evaporation), power lines	W m^{-2}	G (according to [51.5]), often GHI, atmospheric sciences use K_{\downarrow}
Direct normal irradiance	Time series, statistics, extreme values	Concentrating solar technologies	W m^{-2}	G_b , according to [51.5], also DNI
Global tilted irradiance	Time series, statistics, extreme values	Non or low concentrating photovoltaic plants, flat plate collectors	W m^{-2}	G_t , also GTI
Beam attenuation	Time series, statistics	Solar tower plants	–	A
Solar and circum-solar radiance profile	Time series, statistics	Concentrating solar technologies	$\text{W m}^{-2} \text{ sr}^{-1}$	S
Circumsolar contribution	Time series, statistics	Concentrating solar technologies	–	CSC
Soiling rate	Time series, statistics, extreme values	Solar energy	s^{-1}	$\hat{\xi}$
Solar spectral irradiance	Time series, statistics	Photovoltaic plants	$\text{W m}^{-2} \mu\text{m}^{-1}$	E_{λ}
Precipitation	Amount and intensity (spatial averages), time series, statistics, extreme values, form (snow, hail)	Hydropower, solar energy	L, mm	P
Snow cover	Amount	Solar energy	cm	

book, which is relevant for remote sensing of wind profiles in complex terrain. Normal representativeness considerations, which are relevant for climatological and meteorological studies, and which have been listed

in the respective sections of this handbook, cannot be fulfilled in every case. Therefore, further hints and details for power-related measurements can be found in Sect. 51.4.

51.2 History

The usage of renewable energies and the operation of classical fossil energy infrastructures (power plants and power lines) are based on existing meteorological expertise and data and site-specific measurements (see the sections below). By around the turn of the millennium the paramount importance of meteorological data for the operation of renewable energies became clearer, and the subdiscipline energy meteorology started to emerge. The first German specialty conference on energy meteorology took place 2009. The inaugural International Conference on Energy & Meteorology was convened in Australia in 2011. The development of renewable energies is very much driven by private companies. Thus, additional site-specific measurements up to now have very often been planned and executed by these private companies. This data is usually not publicly available.

51.2.1 History of Measurements for Wind Energy

Wind measurements have accompanied the usage of the kinetic energy contained in winds through all times. Traditional windmills have been built for centuries in Europe, and the growing political and economic importance of sailing ships in the eighteenth and nineteenth centuries led, e.g., to the development of the Beaufort wind scale. Compared to this the construction and deployment of wind turbines for the generation of electricity was a rather new development that emerged in the twentieth century. In the beginning until the 1980s, 10 m wind data were extrapolated to the then hub heights of the first wind turbines of less than 50 m. Later, the erection of meteorological masts became the most accepted wind assessment technology, when hub heights were about 50 m and above. In the 1990s, the interest in surface-based acoustic remote sensing (Chap. 23) grew, since the deployment of taller masts in the order of 100 m height became more expensive than ground-based acoustic remote sensing, although the trust in remote-sensing data remained less than the trust in in-situ cup anemometer measurements. A major reason for the persisting trust in cup anemometer data was that these instruments could be easily calibrated in wind tunnels.

In the 2000s, optical remote sensing (Chap. 27 on wind lidars) took over from sodars, because wind lidars

became commercially available, and the data availability of wind lidars is considerably better than that from sodars. After 2015, wind energy guidelines [51.6] started to accept optical remote sensing as an independent source for reliable wind data.

Specific data capture for the development of offshore wind farms started with large masts as well. Near-coastal masts were, e.g., erected close to the Danish west coast at a wind turbine test site at Høvsøre in 2002 [51.7]. In the German part of the North Sea, the first real offshore meteorological mast about 45 km off the coast was erected (the 100 m-high mast FINO 1 [51.8]) in 2003. Two more similarly instrumented masts (FINO 2 in the Baltic Sea and FINO 3 in the northern part of the North Sea) followed a few years later. Remote sensing was no option for these offshore measurement platforms, because acoustic remote sensing due to unavoidable fixed echoes (Chap. 23 on sodars and RASS) was not possible close to the mandatory masts on these platforms, and optical remote sensing was not commercially available at the time of planning the first of these measurement platforms. Even today, wind lidars are not part of the standard instrumentation on these three platforms. Such devices were only brought to the platforms during limited measurement campaigns.

Specific data for winds in complex terrain are available from a 200 m-mast erected on the Rödeser Berg near Kassel, Germany, at the end of 2011 [51.9]. A test site for wind turbines in complex terrain exists south of Boulder, Colorado, close to the foothills of the Rocky Mountains [51.10]. A further wind turbine test site with meteorological masts close to an about 200 m-high escarpment is presently being designed and erected east of Stuttgart, Germany.

Temperature profile measurements to assess the thermal stratification of the atmospheric boundary layer for the purpose of generating energy from the wind are rarely executed. For a long time, the impact of thermal stratification on wind energy generation was considered to be negligible with higher wind speeds. Today, for issues such as low-level jets and wake propagation, these measurements appear to be more and more necessary for a proper assessment of wind energy.

51.2.2 History of Measurements for Solar Energy

Solar energy applications have a long history, starting centuries before the first solar radiation measurements became possible (Chap. 11 for the history of radiation measurements). The first simple solar heating and lighting applications did not require the measurement of solar radiation or other meteorological parameters. By the end of the nineteenth century *Augustin Mouchot* (1825–1911) developed the first solar powered engine [51.11], which was demonstrated at the Universal Exhibition in Paris in 1878. At the latest then atmospheric data were required for solar energy in order to decide whether or not this new technology was a competitive alternative to other power sources, such as coal. Apparently, decision-makers estimated that this was not the case, as more intense research on solar energy started only after World War II. By then, pyrheliometers and pyranometers were already available, as well as measurement systems for most of the other relevant atmospheric parameters. These instruments could be used for performance testing and system characterization, two main applications of meteorological measurements for solar energy. With the growing interest in solar energy in the 1970s due to the oil crisis, it became increasingly clear that the already available meteorological data were not enough to provide a good estimate of the solar resource available at a given site and, hence, the corresponding expected power plant yield. Due to the spatial variability of meteorological conditions and, in particular, solar irradiance it was found that the resource data must be collected for a site close to the envisioned power plant site. Even today data from ground-based measurements are not available close to most potential power plant sites. Therefore, existing measurement networks were enhanced and model approaches were investigated.

As interesting power plant sites are often remote, it is often not feasible to maintain pyranometers and pyrheliometers good enough to achieve the desired accuracy. Therefore, and to reduce the costs of the instrumentation, less maintenance intense instruments, such as the rotating shadowband irradiometer (RSI) were developed [51.12]. Such instruments were continuously improved and are widely used for solar energy applications, especially for the planning of solar power plants.

Even if a measurement station is deployed for the resource assessment at a site, the dataset is typically too short to analyze the interannual variability of the irradiance well enough for the determination of the expected solar plant yield. Therefore, methods to derive long-term datasets were developed. Long-term datasets are mostly derived from related measurements. His-

torically, modeling efforts included the determination of global horizontal and direct normal irradiance from sunshine duration measurements [51.13], as these were much more frequent than pyranometric or pyrheliometric measurements. Today, irradiance models based on sunshine duration are only of historic interest and are no longer recommended according to best practices [51.2]. Modeling efforts also included the creation of irradiance maps, for example based on interpolation techniques between the stations. Such spatial interpolations are still used today in some cases, but the application of satellite derived long-term datasets is much more common. Satellite-based measurements of the radiation reflected from the ground or clouds to the satellite have been used to derive irradiance since the 1980s (Chap. 40) and have become a standard data source for the planning of solar power plants.

Today, combinations of satellite and ground-based measurements are used for the planning of large solar power plants with several MW output power, as will be explained in more detail in Sect. 51.4.5. Due to the growing grid penetration of solar energy irradiance forecasting systems were developed in the last two decades. These systems also rely on ground measurements of irradiance, ground-based all-sky imagers and/or satellite data.

51.2.3 History of Measurements for Hydropower

Since there has not been much development in the usage of hydropower in the last decades, the means of measurements have not changed either. Hydropower relied and still relies on monitoring the discharge of rivers for hydropower plants at rivers and the water level in natural and artificial reservoirs for hydropower plants operating below such reservoirs.

51.2.4 History of Measurements for Conventional Power Plants, Grid Operation, and Electricity Transmission

Engineering sciences have dealt with the weather impact on conventional power plants, electricity transmission structures, and grid operations. Meteorological data was required for these assessments, but no special measurement techniques have been developed for this purpose.

Measures such as heating degree days (HDD) [51.14] and cooling degree days (CDD) [51.15] have been developed for the assessment of the energy demand. However, these measures were computed from the available classical weather and climate data.

51.3 Theory

This section summarizes the relevance of the different atmospheric parameters for the different forms of power generation (see the respective column in Table 51.1). A proper operation of power grids (and less strictly, also heating/cooling systems) requires a nearly perfect balance of generation and consumption at any moment. Therefore, atmospheric parameters are necessary to assess the production potential, as well as the expected consumption. These estimates have to be supplied at least 1 day ahead and then have to be refined in several steps until 15 min before the very moment. For example, the regulation of the electricity grid in Germany is performed by trade at the energy stock exchange in Leipzig. Expectations computed from atmospheric data are the basis for this trade. The generation of electrical energy from wind power depends on meteorological parameters in several respects, which are addressed in the following.

51.3.1 Dependence of Wind Energy on Meteorological Parameters

The harvest of electrical energy from the wind principally depends on the third power of the wind speed [51.1], as long as the rated power of the used wind turbines is not reached. Between the rated power of the turbines and the cut-off wind speed (see below) the harvested electrical energy is maximum and independent on wind speed. Additionally, the energy harvest below the rated power of the turbines depends on air density. Cooler and dryer air is denser than warmer and more humid air. The energy harvest is linearly proportional to the density of the air.

The power available from the wind energy, P_{wind} in atmospheric flow, i.e., the kinetic energy of the air, $0.5\rho u^2$ advected with the wind, u is quantified by the following relation

$$P_{\text{wind}} = 0.5\rho A_r u^2 u = 0.5\rho A_r u^3, \quad (51.1)$$

where ρ is the air density, A_r is the rotor area of the turbine, and u is the average wind speed over the rotor area. Equation (51.1) gives the available wind power over the rotor disk in Watt when the air density is given in kg m^{-3} , the rotor area in m^2 , and the wind speed in m s^{-1} . Theoretically, turbines can extract up to 16/27 of this power [51.16, 17]. This limit is known as Betz limit today.

Assessments of annual energy harvest potentials not only depend on the mean annual wind speed but also on the distribution of the wind speed due to the non-linear dependence of the energy harvest on the wind

speed. Weibull (Swedish engineer, scientist, and mathematician *Ernst Hjalmar Waloddi Weibull*, 1887–1979) statistics [51.18] are usually computed for the annual distribution of 10 min mean wind speeds. Additionally, Gumbel (German mathematician *Emil Julius Gumbel*, 1891–1966) statistics [51.19] are used to estimate extreme 10 min mean wind and gust speeds that are load relevant. The probability $F(u)$ of the occurrence of a wind speed smaller or equal to a given speed u is expressed in terms of the Weibull distribution by

$$F(u) = 1 - \exp\left(-\left(\frac{u}{A}\right)^k\right), \quad (51.2)$$

where A is the scale factor of this distribution in m/s, and k is the shape factor. Once the two factors A and k are known, the available annual wind power resource can be computed by replacing u^3 in (51.1) by the third central moment of the Weibull distribution

$$E_{\text{wind}} = 0.5\rho A_r A^3 \Gamma\left(1 + \frac{3}{k}\right), \quad (51.3)$$

where Γ is the Gamma function.

The Gumbel distribution gives the probability $F(u)$ of the occurrence of a wind speed smaller than or equal to a given speed u by

$$F(u) = e^{-e^{-(u-a)/b}}, \quad (51.4)$$

with the scale factor a and the shape factor b (both in m/s). An extreme value is then computed from known factors a and b by

$$u_{\text{max}} = a(-\ln(-\ln(p))) + b, \quad (51.5)$$

where the probability p depends on the number of available data within the addressed return period. The probability of a, e.g., 50-year extreme from such a time series with 10 min-intervals (52 560 data points a year) is given by $p = 1 - 1/(50 \times 52 560)$, giving $-\ln(-\ln(p)) = 14.78$. For a time series with hourly values, the threshold value would be 12.99.

Wind turbines only run when the 10 min mean wind speed is in a certain range of wind speeds. They start to operate at the cut-in wind speed of 4–5 m/s. They usually stop operating at the cut-off wind speed of 25 m/s. The cut-off at higher wind speeds is necessary in order to avoid too large loads on the wind turbines.

The vertical profile of wind speed is of paramount importance for wind energy. For the assessment of energy yields and mean loads on today's large rotors

with diameters of much more than 100 m, the rotor-equivalent wind speed (REWS) is computed from an (rough) integration of the wind speed distribution across the rotor plane. The provision of wind speed profiles with a vertical resolution of about 20–30 m is necessary for the computation of rotor-equivalent wind speeds. The 2017 version of the IEC standard 61400-12-1 [51.6] now refers to the REWS, which is defined by a weighted sum of the cubes of simultaneous wind speed measurements at a number of heights spanning the complete rotor diameter between lower tip and upper tip [51.20]

$$v_{\text{eq}} = \left(\sum_{i=1}^n v_i^3 \frac{A_i}{A} \right)^{1/3} \quad \text{with} \quad \sum_{i=1}^n A_i = A, \quad (51.6)$$

where n is the number of measurements across the rotor area, v_i is the 10 min mean wind speed at height $z = z_i$, A_i is the area of the i -th rotor segment, and A is the total rotor area. The segment areas are computed between two lines z_j and z_{j+1} , which are positioned exactly halfway between two measurements

$$A_i = \int_{z_j}^{z_{j+1}} c(z) dz, \quad (51.7)$$

where $c(z)$ is the area of a segment of a circle

$$c(z) = 2\sqrt{R^2 - (z - H)^2}, \quad (51.8)$$

where R is the rotor radius, and H is the hub height.

Loads on wind turbines increase with increasing vertical shear and increasing turbulence intensity. The turbulence intensity is given by

$$I_u(z) = \left(\ln\left(\frac{z}{z_0}\right) - \Psi_m\left(\frac{z}{L_*}\right) \right)^{-1}. \quad (51.9)$$

This means that turbulence intensity increases with shear (the left-hand term of (51.9)) and with decreasing stability (the right-hand term of (51.9)); Ψ is the integral correction function for atmospheric thermal stability [51.21–25]. See Chap. 1 for a basic treatment of this parameter. Several extreme atmospheric phenomena such as gusts, thunderstorms, lightning, and icing have an impact on the operation of wind turbines.

51.3.2 Dependence of Solar Energy on Meteorological Parameters

Here, we have to differentiate between different available solar energy technologies (Fig. 51.1). Common photovoltaic (PV) plants and nonconcentrating solar heating and cooling collectors use the global tilted irradiance (G_{tilt}) incident on the collector plane. Bifacial

PV modules also use the in-plane rear-side irradiance. PV modules can also be tracked in one or two axes to increase G_{tilt} ; PV cells can also be mounted behind a focusing lens or in the focal point of mirrors that are tracked to the sun. In this case, direct normal irradiance (G_b) is used. This is also the case for concentrating solar power (CSP) plants that use mirrors to focus the direct radiation on an absorber to create heat. This heat can be used for industrial processes, heating, cooling, or to generate electricity using a thermodynamic cycle. Depending on the plant type, actually not G_b , but its projection on the collectors' aperture is used. This projection is calculated in plant models, and G_b is provided as a result of the meteorological measurements. Low concentrating PV collectors are tracked to the sun and only have a small ratio of the aperture to the PV cell surface. In this case, G_b and another diffuse fraction of G_{tilt} is used. The fact that different technologies use different components of solar radiation greatly affects their production. Clouds and fog diminish the yield of all solar collectors, but concentrating collectors are much more sensitive to clouds and fog than flat-plate collectors and nonconcentrating PV, as they only use direct radiation.

The specification of direct normal irradiance (G_b) is actually not a complete description of the resource used for concentrating collectors. Depending on the concentrator and the receiving surface, radiation from a different angular region around the sun is used by solar collectors. While pyrheliometers measure the irradiance coming from an approximately 2.5°-wide circular region around the sun (half-angle), most concentrating solar plants for solar thermal electricity generation and high concentrating PV systems accept only a narrower region (e.g., 1.5°). For concentrating PV systems and process heat collectors, also wider acceptance angles can be found. This effect is accounted for in state-of-the-art plant models, but this requires another input parameter – the sunshape. The sunshape is the radiance of the sun and the circumsolar region closely around the sun as a function of the angular distance from the center of the sun, normalized to 1 in the center of the sun. The description of the radiance distribution with a sunshape corresponds to the assumption that it is radially symmetric. The sunshape can be characterized by the circumsolar contribution: the ratio of the circumsolar normal irradiance coming from a given angular region between an inner and an outer boundary angle close to the sun and the direct normal irradiance including radiation from the solar disk and the circumsolar radiation up to the outer boundary angle.

For flat plate collectors and nonconcentrating PV, also the angular distribution of the irradiance is of interest, as the efficiency of the collectors depends on the incidence angle. The specification of the contribution



Fig. 51.1a–d Solar collectors at CIEMAT’s Plataforma Solar de Almería. **(a)** Tower plant CESA-1, **(b)** parabolic trough collector, **(c)** solar thermal collector, and **(d)** photovoltaic plant **(a)** photo © Christoph Prah, DLR, **(b–d)** photos © Stefan Wilbert, DLR

of direct and diffuse irradiance to G_{tilt} is nearly always sufficient for such models.

In the case of PV, also the spectral distribution of the irradiance is of importance, as PV cells only use

a certain part of the solar spectrum. Furthermore, the efficiency of PV cells varies strongly on the incoming wavelength, even within the accepted wavelength interval.

Besides radiation several other parameters affect the solar plant yield. PV cells operate most efficiently at low module temperatures. Thus, air temperature and wind speed are relevant as well. Thermal collectors operate more efficiently in warm conditions with low wind speeds, as heat losses are lower in such cases. However, the cooling for the thermodynamic cycle of CSP plants is less efficient for high temperatures and low wind speed. Also the pressure and humidity affect cooling.

Wind speed, direction, and wind gust also pay another important role in solar power generation, as wind can damage the plant components. This is of high importance for tracking collectors that do not withstand strong winds in operation, but only in a security position (stow position). This leads to production losses, as the collectors might not be able to collect energy (CSP, high concentrating PV), or as they will only collect significantly less radiation (tracked PV systems, low concentrating PV).

The effects of precipitation are descriptive. Snow cover on the collectors stops their operation while snow in front of a snow free PV module or flat plate collector increases the ground reflected radiation on the collector. Very large hail stones are a threat to the integrity of solar collectors. Rain accumulating on the collector surface reduces its transmittance or reflectance, but it can also have positive effects. One positive effect is the cooling of the PV module. Another positive and more relevant effect is the potential cleaning of the collectors. Atmospheric dust can settle on the collectors and greatly reduce the transmittance or reflectance. This effect is described by the cleanliness, which is the ratio of the efficiency in the current potentially soiled status of the device and the efficiency of a clean device under otherwise unchanged conditions. Soiling is described by the soiling rate, the change of the cleanliness with time. Note that at times, rain actually does not clean the collectors but on the contrary decreases the cleanliness by wet deposition of particles.

For solar tower plants, another parameter is of high relevance: the atmospheric extinction between the mirrors (heliostats) and the receiver. The path between the heliostats and the receiver can be greater than 1 km. Even for a clean, dry atmosphere with a high visibility of about 75 km, about 5% of the reflected radiation is lost on a 1 km light path to the receiver. For hazy conditions, this loss can be 100%, and high losses of about 50% can occur even at high direct irradiance levels.

51.3.3 Dependence of Hydropower on Meteorological Parameters

Assessment of hydropower potentials requires the capture of areal instantaneous and seasonal averaged precipitation amounts in the catchment areas of rivers and

reservoirs. Evaporation processes are only relevant, if the water is to be stored over several months or even years. See Chap. 57 for evaporation measurements and calculations.

Peak river discharges depend on the precipitation amounts of the last hours and days in the catchment area of rivers. Soils saturated with moisture from preceding precipitation events enhance the river discharge, because most of the new rain water cannot infiltrate the wetted soil and runs off immediately. Thus, the soil's water content in the catchment area is to be monitored as well. In springtime, melting snow covers in the catchment area can contribute considerably to river discharges. Long frost periods, dry spells, and droughts can cause very low river discharges. The water levels in reservoirs depend on longer-term precipitation amounts over a few days to months. Again, melting snow and ice from the last winter can contribute considerably to the water level.

51.3.4 Dependence of Thermal (Conventional) Power Plants on Meteorological Parameters

Temperature and humidity influence the conditions for wet cooling towers and water cooling of thermal power plants. In a wet cooling tower (or open-circuit cooling tower), warm water can be cooled to a temperature lower than the ambient temperature. As ambient air is drawn past a flow of water, a small portion of the water evaporates, and the energy required to evaporate that portion of the water is taken from the remaining mass of water, thus reducing its temperature. This type of cooling is most effective when the saturation deficit of the air is large.

If sufficient water is available (at the banks of larger rivers) direct cooling using water from the river (once-through cooling) can be used. Here, the efficiency depends on the temperature of the water from the river. Often, the warming-up of the water from the river downstream of the power plant is limited by regulations to a given threshold temperature for ecological reasons. If the temperature of the water upstream of the power plant already exceeds this threshold temperature, once-through cooling is no longer permitted.

In longer drought situations, low water levels in rivers can cause problems in transporting the necessary coal to the power plants. In hard winters, the coal could also be frozen in goods waggons, which hampers the supply of power plants as well.

51.3.5 Dependence of Energy Transmission on Meteorological Parameters

Cables in overhead transmission lines warm up in operation proportionally to the electrical resistance of the

cable and the strength of the electrical current flowing through them. Warmer cables expand, and, thus, transmission cables hanging from masts sag more and come closer to the ground. In order to prevent excessive sagging, the temperature of these cables must be limited. Normal high-voltage transmission cables with steel cores are not allowed to warm up to more than 80 °C during normal operation and 100 °C at peak operation. Special ACCC (aluminum conductor composite core) cables have a smaller thermal expansion coefficient and can be operated up to a temperature of 175 °C.

On the other hand, the temperature of transmission cables is influenced by the environmental atmospheric conditions [51.26]. The cables are cooled by heat conduction to the air flowing past them, and they are warmed up by absorbing incoming short-wave radiation. The cooling depends on wind speed, air density, and the heat conductivity of the air. Air density and heat conductivity depend on air pressure, temperature, and humidity. Without any temperature monitoring transmission cables must be operated according to the worst-case scenarios given in standards and guidelines (e.g., [51.27]) assuming 35 °C air temperature, 0.6 m s⁻¹ wind speed, and 900 W/m² global radiation. Monitoring the cable temperature and/or near-cable atmospheric data can help with a much more efficient use of the transmission cables.

The accretion of ice at transmission cables could become a problem in wintry weather situations, when rain falls from warmer layers above into colder near-surface

air layers with temperatures below the freezing point. This may sometimes happen in the case of approaching warm fronts. The weight of the accreted ice can lead to extreme sagging of cables. In some cases, even the breaking of cables and entire electricity pylons has been observed. Excessive ricing in the case of advection of very humid air masses and fog to power cables at temperatures below the freezing point can lead to similar effects.

Extreme winds may be a hazard for above-surface power lines and electric pylons as well. This could be the direct impact of the wind on the power lines, as well as the impact of falling trees and other structures on these lines.

51.3.6 Dependence of Energy Demand on Meteorological Parameters

Electric energy demand for heating and cooling, as well as lighting of living places and work spaces depends on the ambient air temperature, wind speed, incoming daytime short-wave radiation (especially direct normal irradiation), and nocturnal long-wave radiation. Very often, heating-degree days [51.14] and cooling-degree days [51.15] are used as an approximate measure to assess the demand for heating and cooling. It is anticipated that the future energy demand for individual electric mobility is temperature-dependent as well, because the performance of batteries is strongly temperature dependent.

51.4 Devices and Systems

Many of the devices and systems described in detail earlier in this handbook and briefly in [51.28] are used to capture the necessary data for running energy systems. This section summarizes specific comments on some of these devices. Precipitation gauges are described in Chap. 12.

51.4.1 Cup and Sonic Anemometers

Near-surface wind speed is very often measured by cup anemometers (Chap. 9) that have been calibrated in wind tunnels. Site-specific wind speed measurements up to heights in the order of 50–100 m are quite often made from masts erected for this purpose. See Chap. 9 on anemometry and [51.29] for details. Measurements of turbulence are described in [51.30]. Cup and sonic anemometers deliver scalar means of wind speed representative for small measurement volumes (in-situ measurements). Sonic anemometers are also

able to deliver turbulence measurements. Because they are much more expensive than cup anemometers, sonic anemometers have not found widespread usage in wind energy so far, but their usage is increasing. For instance, they have now found a role in wind turbine nacelles for wind speed and yaw control purposes. Appropriate calibration standards comparable to those for cup anemometers have not yet been developed [51.31].

51.4.2 Surface-Based Remote Sensing of Wind and Temperature

Today's wind energy applications require knowledge of vertical wind distributions above those heights that can meaningfully be reached by mast measurements. Surface-based remote sensing has been used for this purpose for about 20 years [51.32]. The first sodars were deployed at potential wind energy sites, and now Doppler wind lidars are operated, because they promise

better data availability, a higher vertical range, and less environmental interference. See Chap. 23 and [51.33] for details on sodars and Chap. 27 and [51.34] for details on wind lidars. Wind profile measurements together with temperature profile measurements are available from radio-acoustic sounding systems (RASS) as well. RASS are described in Chap. 23 and [51.35]. Remote sensing of wind profiles would also be feasible with wind profilers (Chap. 31 and [51.36, 37]), but these instruments are not movable, and they do not have sufficient vertical resolution in the height range of wind turbines. Remote sensing delivers vector means of wind speed for larger measurement volumes determined by the pulse length and the opening angle between the beams originating from the instrument.

Passive radiometers (Chap. 29) are also designed to measure vertical temperature (and humidity) profiles. However, their vertical resolution is in the order of 50 and 100 m, which is not sufficient for wind energy purposes. Scanning at very low elevation angles in order to obtain a better vertical resolution would result, in turn, in more extended horizontal averaging, which in most cases is unwanted in energy site assessments.

51.4.3 Satellite Wind Observations

A meaningful option to capture areal distributions of offshore near-surface winds is the analysis of synthetic aperture radar (SAR) images from satellites. SAR data allow for a determination of the near surface wind speed and the detection of spatial gradients in these near-surface wind fields from the observation of capillary waves on the ocean's surface [51.38]. Capillary waves are supposed to change nearly immediately with the near-surface wind speed. These small-scale waves cause scattering of the radar waves emitted from the satellite, and less radiation is scattered directly backwards towards the satellite during the presence of these waves.

Principally, the evaluation of these images gives near-surface winds only. It is only the application of vertical extrapolations based on wind profile laws (i.e., the logarithmic law with possible corrections for atmospheric thermal stability or the power law with a suitable exponent) that allows the estimation and assessment of the hub height wind speed for wind energy applications. However, these extrapolations need additional input data, especially the vertical temperature profile. Nevertheless, the usability of SAR images to detect offshore wind-farm wakes was proven for the first time in [51.39]. First comparisons between SAR images and mesoscale wind simulations using the weather research and forecasting WRF model have been shown in [51.40]. The results from model simula-

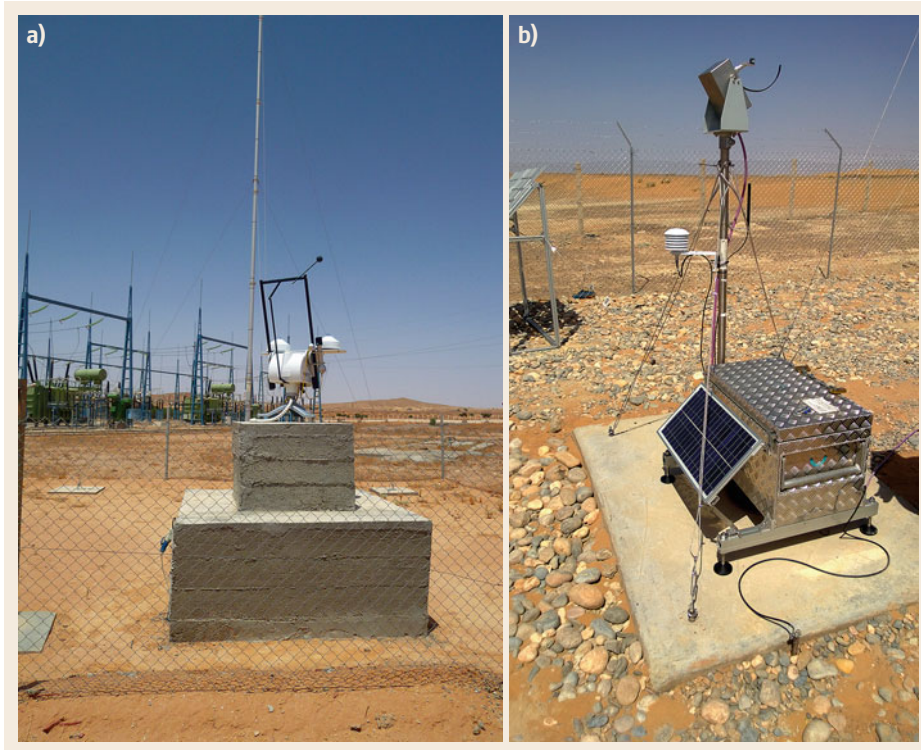
tions and SAR images were proved for the first time by aircraft measurements behind North Sea wind farms in 2016 [51.41]. See Chap. 41 on microwave radiometers as well.

51.4.4 Measurement Stations for Solar Energy

During the planning, commissioning, and operation of large solar power plants with a capacity of about 1 MW or more on-site measured meteorological data are required. Meteorological measurements are also necessary for the testing of solar plant technologies.

Radiometers are the core of measurement stations for solar energy. Radiation measurements are described in Chap. 11. Also the other relevant and typically measured parameters have been discussed in previous chapters (wind speed and direction in Chap. 9, air temperature in Chap. 7, humidity in Chap. 8, pressure in Chap. 10, and precipitation in Chap. 12).

The instruments, their application and maintenance for solar energy applications are basically the same as for other atmospheric measurements. However, there are some differences. Specific recommendations for solar energy related measurements can be found in [51.2, 42]. The mentioned differences are caused basically by two reasons. First of all the measurements must characterize the conditions at the power plant site or in the plant. Therefore, stations must at times be positioned such that they do not fulfil fundamental requirements of measurements carried out for other purposes. For example, in the case of climate research, a free horizon is recommended for the site with no obstructions above 5° elevation [51.43]. For climate research, the baseline surface radiation network (BSRN) recommends that stations should not be close to major roadways or airports [51.44]. For the maintenance of the station during the solar resource assessment and for the costs of the power plant construction such infrastructure can be of great advantage, so that such recommendations do not apply to solar energy-specific measurements. Obviously, such differences also exist for other meteorological applications, such as transport meteorology, where measurements must be carried out close to airports and roads. The second reason why solar energy specific measurements might deviate from other atmospheric measurement stations is that different applications also bring along different optimal cost/benefit ratios. The most important example for this is that it is often not feasible to set up a high accuracy measurement station with a solar tracker and thermopile sensors (Fig. 51.2a) at the envisioned plant site for the resource assessment if this site is remote. For such sites, it is often impossible or at least too costly to assure

**Fig. 51.2**

(a) Measurement station for solar resource assessment in Tataouine, Tunisia, equipped with thermopile radiometers, cup anemometer, wind vane, pressure, temperature, and relative humidity sensors. (b) Rotating shadowband irradiometer as part of a solar resource assessment station close to Erfoud, Morocco (photos © Birk Kraas, CSP-Services)

the required daily maintenance by sufficiently qualified personnel. Reduced cleaning frequency and the corresponding soiling of the entrance windows is especially relevant for pyrheliometers, but also pyranometers with clear entrance windows suffer from soiling. Therefore, less maintenance intense sensors, such as rotating shadowband irradiometers (RSI, at times also called RSP or RSR, with P for pyranometer and R for radiometer) are often used at remote sites (Fig. 51.2b). They achieve lower accuracy in well-maintained stations with daily cleaning of the instruments' entrance windows, but if specific correction functions are applied, a better accuracy is reached for less frequent maintenance [51.45], for example only once every week or every 2 weeks. Correction functions are needed, as simple silicon pyranometers with higher incidence angle, temperature, and spectral errors are used in most cases. The lower maintenance requirement is due to the fact that RSIs apply pyranometers with diffusors in front of the detector, without an additional clear entrance window. Furthermore, RSIs are cheaper than thermopile sensors with solar trackers and are more robust and simpler, which leads to less frequent malfunctions, user mistakes, and data loss [51.46]. Another option to reduce the cost and maintenance requirements compared to pyrheliometers are instruments with sensor arrays and specific shading structures that avoid the requirement

of any moving part for direct irradiance measurements. However, unlike RSIs, such instruments still require the same cleaning frequency as thermopile pyranometers. An example of such a sensor is the SPN1 radiometer [51.47].

A significant cost reduction of a meteorological station can be achieved if direct normal irradiance (G_b) is not measured. For concentrating solar power plants (CSP and concentrating PV), G_b is required, and for tracked PV plants and large power plants it is desirable. For concentrating technologies, this is obvious. For the other plants mentioned, in principle, only global tilted irradiance G_{tilt} must be known. However, for more accurate plant yield calculations, the direct component in G_{tilt} is of interest, as mentioned in Sect. 51.3.2. In the case of tracked PV collectors, G_{tilt} measurements would also require a tracker for the pyranometer, so that no significant cost advantage remains. Furthermore, measuring the three radiation components (direct, global, and diffuse) allows for a better quality control of the data, which is of high value. For fixed collectors, G_{tilt} can be measured with an adequately mounted pyranometer without a solar tracker. Typically, for solar resource assessments for fixed PV and flat plate collectors, common global horizontal irradiance measurements are used combined with conversion models to derive G_{tilt} .

The sunshape and circumsolar contribution can be measured with special cameras [51.48, 49]: pyrheliometers with different fields of view [51.50] or RSIs [51.51]. For remote sites, RSI is the only commercially available measurement option. Camera-based instruments for circumsolar radiation measurements are only used at research stations, as they are highly maintenance intense and expensive.

Solar spectral irradiance measurements have so far been limited mainly to research sites. To change this, radiative transfer calculations can be used based on simpler measurements, such as the multifilter rotating shadowband radiometer [51.52], sun photometers, or multifilter radiometers [51.53].

In recent years, measurement stations for solar tower plants have also started including meteorological optical-range (MOR) measurements to obtain information on the beam attenuation between the mirrors and the receiver on the tower. Chapter 13 introduced visibility sensors. It is important to mention that the conversion from the MOR [51.54] to the required broadband beam attenuation is not a simple task (broadband refers to the wavelength range from about 280 to 4000 nm), as the instruments and the definition of MOR do not refer to broadband radiation. Therefore, correction functions are required [51.55].

Also, soiling rate measurements have been included in meteorological stations for solar energy applications in the last decade. For PV, such measurements can be obtained by comparing the short-circuit current or power output of cleaned and uncleaned PV reference cells or modules [51.56]. For concentrating collectors with mirrors, the reflected direct normal irradiance is compared to G_b [51.57], or reflectance measurements are carried out on exposed mirror samples.

Solar radiation measurements are important input for the accurate forecasting of solar radiation. Additional ground measurements are provided in the form of all-sky images mainly relating to forecasting for the next 15 min. Such images of the complete upper hemi-

sphere are taken with fisheye lenses or curved mirrors. The images can be used to detect clouds and to track and forecast their position. Finally, with additional assumptions on the clear-sky atmosphere, this allows the prediction of the solar irradiance in a power plant or in an area with several power plants (e.g., a city with many PV rooftop systems). For these irradiance forecasts, the cloud height is required if spatially resolved irradiance maps are to be forecasted. Cloud height measurements can come from different sources, such as ceilometers or multiple all-sky imagers. Current research indicates that all-sky imagers are the preferable option [51.58]. All-sky imagers have also been used to measure the current downwelling shortwave irradiance (G , G_b). However, such methods do not reach the accuracy required for solar energy applications so far.

At times, PV reference cells are also applied in solar resource assessment to obtain data that are more comparable to the expected production of PV collectors. While thermopile pyranometers are designed to measure broadband irradiance with low errors introduced by the incidence angle, temperature, and spectral effects, such effects occur in PV modules and reference cells. If the applied reference cells are similar to the PV module of interest, the data collected with the reference cell can be used more easily to calculate the expected PV production, as the mentioned errors do not have to be modeled in the PV plant yield model. However, most PV models include the modeling of these errors, so that PV reference cell data must be used with great care. Furthermore, PV reference cell measurements are difficult to compare with other existing datasets from pyranometers and satellites, which further complicate their application. Therefore, measurements with reference cells are rather carried out as additional measurements next to other radiometers. A dataset that only contains PV reference cell data must currently be considered of lower quality. Advantages and disadvantages of the measurement options mentioned for solar energy applications are included in Table 51.2.

Table 51.2 Advantages and disadvantages of selected measurement devices with respect to energy meteorology

Device	Advantages	Disadvantages
Cup anemometer	Can be calibrated in wind tunnel, calibration standards exist	Needs masts for locating at height of rotor plane, extrapolation to greater heights necessary, limited turbulence measurements, horizontal wind speed only
Sonic anemometer	High-frequency wind measurements, turbulence measurements, all three wind components available	Rain droplets or ice at the sound transducers can disturb the measurements, appropriate calibration standards have not been developed
Wind lidar	Does not need calibration, direct profile measurements	Measurement obstructed by fog, clouds, and precipitation
SAR on satellites	Not obstructed by clouds, operates day and night, large areas are covered simultaneously	Several days between satellite overpasses, offshore application only, near-surface winds only

Table 51.2 (Continued)

Device	Advantages	Disadvantages
Thermopile pyranometer	Achieves the highest available accuracy for tilted irradiance measurements under well-maintained conditions in high frequency	Require frequent cleaning and other maintenance (daily). Available stations are rare, especially for long-term data sets (> 10 years). Costs
Thermopile pyrheliometer	Achieves the highest available accuracy for direct irradiance measurements under well-maintained conditions in high frequency	Requires frequent cleaning and other maintenance (daily) and expensive and error-prone solar trackers. Available stations are rare, especially for long-term datasets (> 10 years). Costs
Rotating shadowband irradiometer	Simple, robust, frequent, and cheap option for determination of global horizontal, direct normal and global tilted irradiance. Only less frequent cleaning required compared to instruments with clear optics (e.g., every week)	Achieves a lower accuracy compared to thermopile sensors even if correction functions for systematic errors are applied. Available stations are rare, especially for long-term datasets (> 10 years)
PV reference cell	Measures an output signal close to that of specific corresponding PV modules in high frequency	Difficult to compare with more frequently available broadband irradiance data and incompatible with many PV plant models. Available stations are rare, especially for long-term datasets (> 10 years)
Ground-based spectroradiometer	Accurate and frequent measurements of solar spectra can be obtained	Difficult to maintain, too expensive for most stations
Satellite-based imager for irradiance measurements	Long-term datasets (> 10 years) available for the whole planet, even spectrally resolved. No data gaps, maintenance issues. Relatively low costs, as satellites are paid by somebody else	Lower accuracy compared to ground-based methods, lower temporal frequency (15 min compared to 1 min or higher)
Camera-based circumsolar radiation measurement	Some systems can reach high accuracy. Complete information for plant models measured, including sunshape	High costs and maintenance requirements
Pyrheliometer pairs with different field of views for circumsolar radiation measurements	High accuracy for the circumsolar contribution and integrated irradiance for one angular interval	No angular resolved radiance, only integrated irradiance for one angular interval. Modeling needed for determination of sunshapes. Daily maintenance required, error-prone to soiling
Rotating shadowband irradiometers for circumsolar radiation measurements	Low maintenance effort, simple data evaluation	No angular resolved radiance, only integrated irradiance for one angular interval. Modeling needed for determination of sunshapes. Lower accuracy compared to camera and pyrheliometer-based methods
Beam attenuation measurement based on MOR measurements	Simple measurement method	Requires correction for spectral and broadband effect
Satellite-based imager for circumsolar irradiance measurements and beam attenuation measurements	Long-term datasets (> 10 years) can be determined for the whole planet. No data gaps, maintenance issues. Relatively low costs, as satellites are paid by somebody else	Still in development phase, low accuracy compared to ground measurements
Soiling-rate measurement with test mirrors or test PV cells/modules	Frequent measurements of cleanliness and soiling rate	Maintenance intense
Ground-based all-sky imager for forecasting	Highly temporally and spatially resolved irradiance data can be determined	Costs, maintenance. Forecasts confined to the next approximately 15 min
Satellite-based imager for forecasting of irradiance	Forecasts can be determined for the whole planet. No data gaps, maintenance issues. Relatively low costs, as satellites are paid by somebody else. Forecast horizon up to approximately 6 h	Lower accuracy, temporal and spatial resolution than all-sky imagers

51.4.5 Satellite-Based Radiation Measurements

As explained in Sect. 51.3.2, satellite-based surface radiation measurements are a standard data source for solar energy applications to create the required long-term datasets (≈ 10 years or more). The applied methods and technology are explained in Chap. 40 on airborne radiation sensors and in Sect. 22.4.3 on cloud observations that are an important intermediate result. For solar energy applications the postprocessing of these data is of high importance.

As the accuracy of satellite-derived data is significantly lower than that of well-maintained ground measurements, the latter are frequently merged with the satellite data to create bankable solar resource data during the planning phase of the power plant. This is especially relevant for the planning of solar plants with several MW power output, as financing costs depend on the risk of the project and, hence, on the uncertainty of the resource data. The final long-term dataset is created by merging the at least 1 year-long dataset from ground measurements and the satellite-derived data [51.59]. Plant yield calculations for the feasibility study and plant layout are carried out with these long-term datasets. For the detailed design of the plant, also measurement data are used due to the higher temporal resolution and accuracy.

51.5 Specifications

Users of wind speed measurement data for the assessment of available wind energy often request a rather high accuracy in the order of 1%, because wind energy depends on the third power of the wind speed (51.1). A 1%-error in wind speed thus means up to 3% error in wind energy. Therefore, most guidelines [51.6] favor cup anemometers as in-situ devices for wind energy purposes, because they can be carefully calibrated in wind tunnels to achieve the requested accuracy. Remote-sensing instruments cannot be calibrated in the same way as cup anemometers in wind tunnels. Actually, they do not even need to be calibrated, because they are based on fundamental physical principles. Please note, that wind

Satellite-derived irradiance data are also applied at times for the power plant monitoring of some medium-sized facilities. Furthermore, the data are key for radiation forecasts with a horizon of up to 6 h. Cloud-motion vectors are determined from series of satellite images, and the detected cloud positions are then extrapolated to the future. These predicted cloud positions are then used to calculate the solar irradiance.

Apart from broadband direct normal, global horizontal, and global tilted irradiance, satellite data may also be used to derive further parameters, such as circumsolar radiation, beam attenuation in tower plants, and spectral irradiance. For circumsolar radiation, such efforts [51.60] are still in the development phase and are not used commercially. The same holds for beam attenuation studies. Spectral irradiance can be derived from satellite data [51.61], and such datasets have already been integrated in selected PV yield analysis tools [51.62].

51.4.6 Comparison of Methods

The advantages and disadvantages of some of the mentioned measurement methods for wind (first four lines) and solar (rest of the table) energy applications are compared in Table 51.2.

data from remote sensing and in-situ measurements are not fully comparable due to the different measurement principles (cup anemometers are in-situ instruments; sodars and wind lidars are volume-averaging instruments).

Specifications of solar energy related instruments are also included in Table 51.3.

While cup anemometer data is nearly always available, wind lidar data is not available during fog and precipitation events. The vertical range of optical remote sensing can also be limited by the aerosol content of the atmosphere. Very low aerosol concentrations may lead to insufficient signal-to-noise ratios of the backscattered signal.

Table 51.3 Specifications of selected measurement methods for the application in the field of generation of renewable energies

Method	Typical total uncertainty	Temperature range (°C)	Humidity range (%)
Cup anemometer	±1% [51.6]	−10 to 50	0–100
Wind lidar	±0.1 m s ^{−1} (Class A), ±0.5 m s ^{−1} (Class B), ±1.0 m s ^{−1} (Class C) [51.34]	−20 to 40	0–100
Thermopile pyrheliometer	0.7% (1 min resolution)	−40 to 80	0–100
Thermopile pyranometer	1.2% (1 min resolution)	−40 to 80	0–100
Silicon pyranometer with correction functions for global horizontal measurements	3.5% (1 min resolution)	−40 to 65	0–100
Twin RSI	3.5% (global horizontal and direct normal irradiance in 10 min resolution)	−40 to 65	0–100
Satellite-derived irradiance data after site adaptation with ground measurements	Annual average: 4% for global horizontal irradiance, (for complex areas higher) Hourly: 7% to 35% for global irradiance (depending on cloud, aerosol and ground conditions) Direct irradiances errors are typically about twice the errors for global horizontal irradiance [51.2]	Does not apply	Does not apply
Beam attenuation measurements with MOR sensors	≈ 5% in terms of broad band transmittance over a path of 1 km [51.55]	−55 to 65	0–100
Camera-based circumsolar radiation measurements [51.49]	15% for circumsolar contribution, minimum 0.01	−10 to 45	0–100
Pyrheliometer-based circumsolar radiation measurements [51.50]	15% for circumsolar contribution, minimum 0.01	−40 to 65	0–100
RSI-based circumsolar radiation measurements	20% to 30% for circumsolar contribution, minimum 0.02 [51.51]	−40 to 65	0–100
Soiling rate measurement systems	≈ 0.2%/day [51.57]	−40 to 65	0–100
Ground-based spectroradiometers (350–1600 nm)	0.2 nm wavelength uncertainty below ≈ 1000 nm, 5% spectral irradiance	−10 to 40	0–100
Tipping bucket (Cs700) precipitation measurement	2%	0 to 70	0–100
Optical weather sensor (FD12P) with precipitation measurement	30%	−40 to 55	0–100

51.6 Quality Control

Planning, siting, and operation of renewable energy facilities need data of high accuracy and quality, because the financial success of these facilities often crucially depends on data quality. While companies and organizations working in planning and siting of energy converters have to fulfil the usual data quality demands for their measurement devices (mostly according to the instructions given by the manufacturers of these instruments),

instruments mounted at or near to operating energy facilities should be included in the data quality procedures of these installations. Please refer to the respective chapters on specific quality control procedures for the different instruments. For cup anemometers, see also [51.63], for sonic anemometers [51.64], and for wind lidars [51.34]. For solar energy applications, specific minor adaptations of the common quality checks exist; see, e.g., [51.65].

51.7 Maintenance

The demands and strategies for the maintenance of instruments delivering meteorological parameters for planning, siting, and operation of energy conversion facilities are very much similar to those given for data quality in Sect. 51.6 above. For the required maintenance procedures please refer to the respective chapters

on the specific instruments. It should be mentioned again that the feasible maintenance intensity for solar resource assessment stations might be more limited than recommendations for solar radiation measurements as already discussed in Sect. 51.4.4.

51.8 Application

This section gives two application examples of measurements. The first example refers to the wind and thermal stability conditions for the operation of offshore wind parks; the second example displays radiation measurements relevant for solar power plants.

Fig. 51.3 Stability wind rose indicating the frequency (number of 10-min intervals per 12° wind direction sector) of atmospheric stability. Lines are labeled in terms of the stability measure z/L , where z is the height above ground, and L is the Obukhov length. Blue and red shading indicate stable and unstable stratification, respectively. The higher the value of z/L , the stronger the stability. Data are from the FINO 1 offshore platform in the North Sea for the whole year of 2005 at a height of 60 m above the sea surface. Data is available from <http://fino.bsh.de/>. Only data with wind speeds between the cut-in (5 m s^{-1}) and cut-off (25 m s^{-1}) wind speed were considered (after [51.41]) ▶

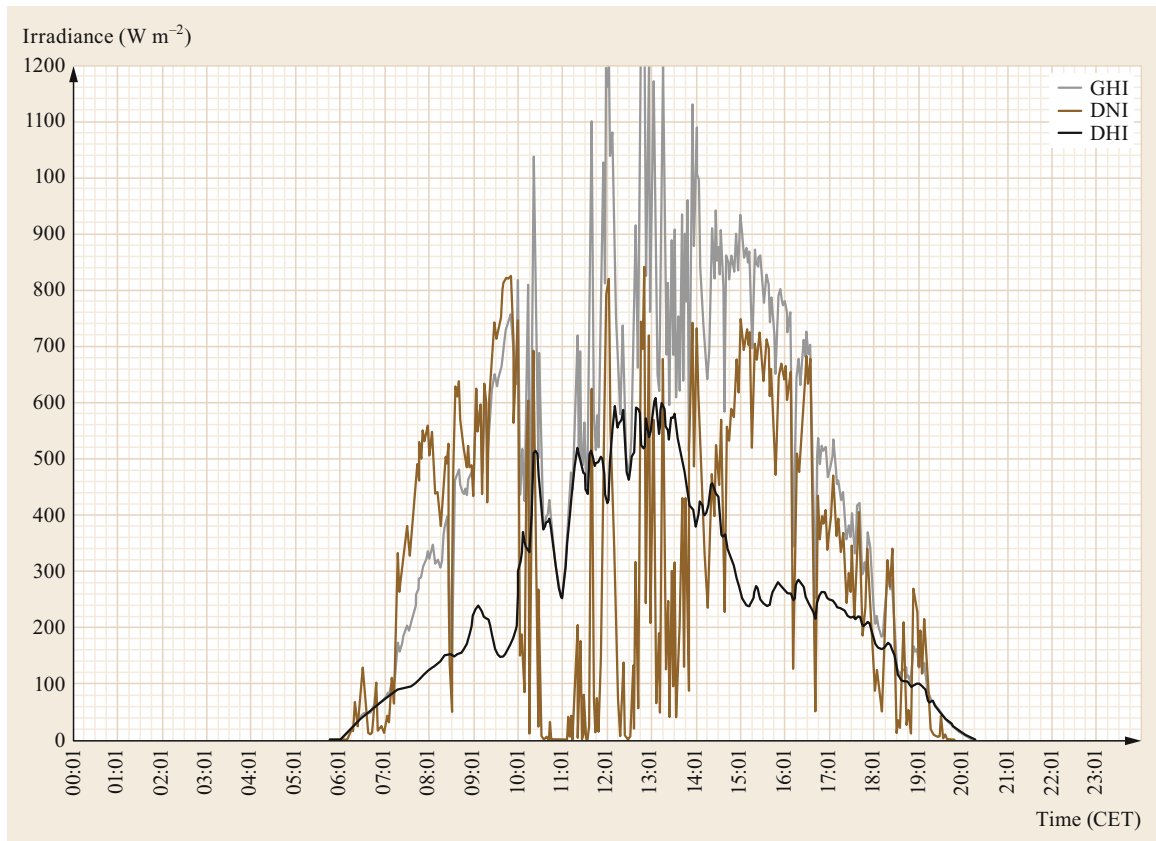
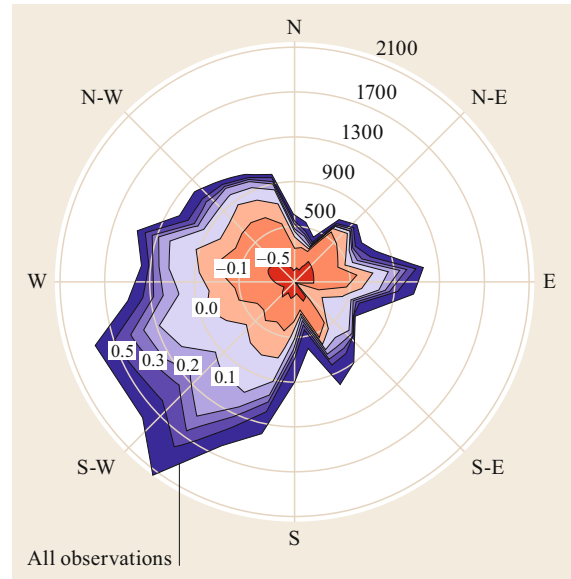


Fig. 51.4 Irradiance measurements in 1 min-resolution from a meteorological station equipped with thermopile sensors close to Tabernas, Spain on 23.05.2018 (GHI: global horizontal irradiance, DNI: direct normal irradiance, DHI: diffuse horizontal irradiance)

51.8.1 Wind Energy Applications

It has been stated in this chapter that atmospheric turbulence (at the end of Sect. 51.3.1) and wakes behind wind turbines (at the end of Sect. 51.2.1) not only depend on wind speed but also on the atmospheric thermal stability. Therefore, for the assessment of wake interactions and fatigue issues of wind turbines, both parameters have to be assessed together. Figure 51.3 gives an example of an evaluation of 10 min-mean data obtained at 60 m above sea level at the FINO1 platform in the German Bight from a cup anemometer for wind speed and from a sonic anemometer for atmospheric stability. The FINO1 platform was erected for the investigation of the wind conditions in the marine atmospheric boundary layer in the German Bight. These data serve for the planning of the large offshore wind farms, which are presently being erected there. Figure 51.3 demonstrates that wind direction and thermal stability are correlated with each other offshore [51.41]. Stable atmospheric stability mainly occurs with southwesterly wind directions. Southwest is the prevailing wind direction in warm sectors of cy-

clones on the Northern Hemisphere, where warmer air is advected over colder waters. Likewise, we observe unstable conditions mainly occurring with northwesterly winds. This is the prevailing wind direction in the cold air masses behind the cold front of cyclones in the Northern Hemisphere. Such a correlation is not observed for onshore conditions, because here the diurnal day–night variation of the thermal stability dominates.

51.8.2 Solar Energy Applications

As was already briefly mentioned in Sects. 51.3.2, 51.4.3, and 51.4.4, different measurement techniques have different applications. As an example the results of typical measurement stations with thermopile pyranometers and pyrhemometers for 1 day are shown in Fig. 51.4. Such graphs are used for the daily quality control of the collected measurements. Figure 51.5 shows a histogram of the three irradiance components for a measurement station in India in April 2018. Such histograms are used as a tool to evaluate the variability of the solar irradiance.

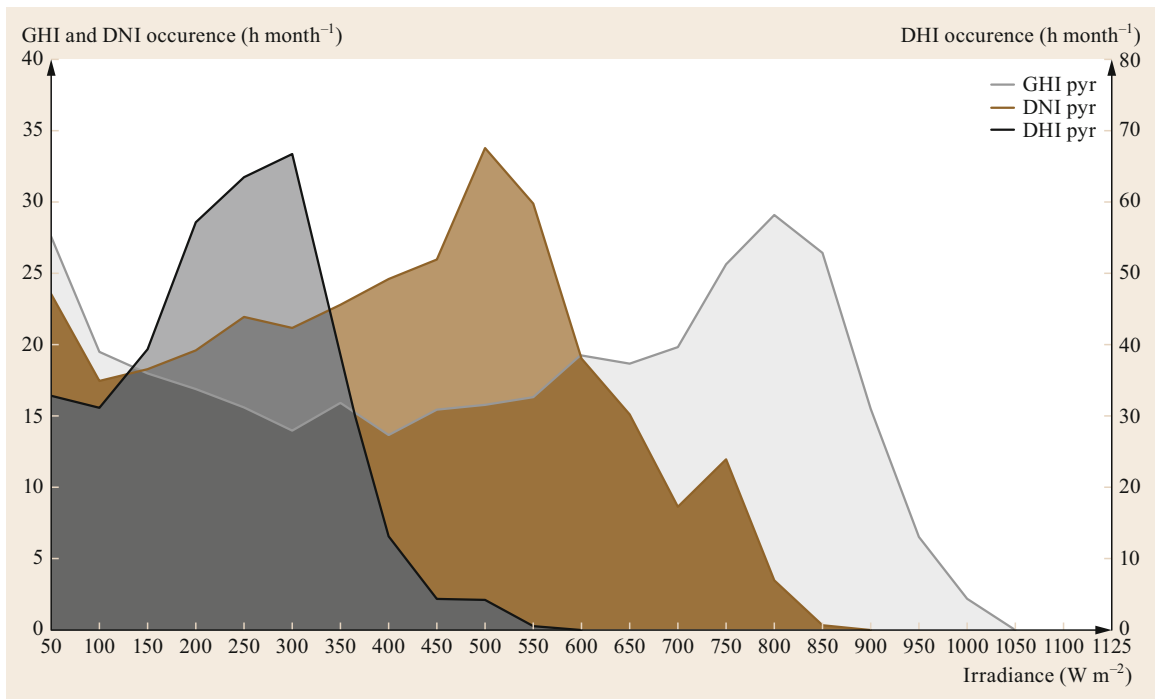


Fig. 51.5 Histogram of irradiance measurements with thermopile sensors from a meteorological station close to Greater Noida India in April 2018 derived based on data in hourly resolution (GHI pyr: global horizontal irradiance measured by a pyranometer, DNI pyr: direct normal irradiance by a pyrhemometer, DHI pyr: diffuse horizontal irradiance by a shaded pyranometer). Irradiance is given in units of $W m^{-2}$ within a $\pm 25 W m^{-2}$ interval. Courtesy of Birk Kraas, CSPS Services, Stefan Wilbert, DLR

51.9 Future Developments

Measurement techniques for atmospheric parameters at hub height of wind turbines and over the area swept by their rotors have changed. In-situ measurements by cup and sonic anemometers are no longer fully sufficient. The growing hub heights and upper tip heights of the turbine rotors make it more and more impossible to perform in-situ measurements from masts specially erected for this purpose. Therefore, in many cases, ground-based remote sensing has replaced mast measurements in the last few years. Overviews of the basic abilities to probe the atmospheric boundary layer by ground-based remote sensing are given in [51.28, 32]; however, the development of some of the techniques has proceeded in the last 7 to 8 years since their publication. The substitution process from in-situ to remote-sensing measurements is to be accompanied by scientific investigations that compare the wind and turbulence data obtained from masts and remote-sensing techniques. Such investigations are continuing and have already led to rewritten standards for measurement procedures [51.6]. Given the present state of instrument development, optical techniques such as wind lidars will be the main measurement tools of the future [51.66]. SAR satellite image evaluation techniques are presently evaluated by data from in-situ aircraft data and may become an increasingly important tool for marine wind assessment [51.41].

However, not only wind conditions must be captured by ground-based remote sensing. It has become increasingly clear that atmospheric thermal stability is a really important parameter for the assessment of wind energy. Increasing stability (potential temperature increases with height above ground) reduces turbulence

intensity, increases vertical wind shear, and prolongs wakes of wind turbines and entire wind farms. Devices for ground-based remote sensing of temperature are still limited in their capabilities. Passive radiometers (Chap. 41) have a very coarse vertical resolution (50–100 m); active devices such as Raman lidars (Chap. 25) still require large technical efforts and have a low signal-to-noise ratio in the daytime due to disturbing sunlight. RASS (Chap. 23) is not a perfect alternative, as it cannot be operated in the vicinity of settlements because of its audible acoustic signals.

With respect to solar energy, future developments will surely be related to increase the accuracy of ground and satellite-based measurements of all relevant parameters. The respective guidelines are under revision or have been revised recently [51.67]. For ground-based sensors, this will, on the one hand, be achieved by increasing their accuracy under well-maintained conditions. However, improving their robustness and simplicity and their maintenance requirements – especially including the need for frequent cleaning – is another way to improve the accuracy. Future developments will also include alternatives to thermopile sensors and the required corrections for systematic errors. For satellite-derived irradiance, accuracy improvement will be developed by applying higher temporal, spectral, and spatial resolutions. The speed of this enhancement will depend on the deployment of the next generations of satellites. Some of the mentioned parameters related to solar energy are still in early development stages (e.g., satellite-derived attenuation and circum-solar radiation measurements). Such methods should be elaborated further in the future.

51.10 Further Readings

A thorough introduction into wind energy meteorology can presently be obtained from two books:

- S. Emeis: *Wind Energy Meteorology – Atmospheric Physics for Wind Power Generation*, 2nd edn. (Springer, Heidelberg 2018) XXVI + 255 pp.
- L. Landberg: *Meteorology for Wind Energy*. Wiley, XIX+204 pp. (2016)

Related to solar energy meteorology:

- M. Sengupta, A. Habte, C. Gueymard, S. Wilbert, D. Renné, P. Blanc, A. Dobos, E. Lorenz, R. Meyer, D. Myers, L. Ramírez, K.P. Nielsen, A. Lopez,

J. Kleissl, J. Remund, J.A. Ruiz-Arias, R. Perez, J. Polo, L.M. Pomares, M. Suri, T. Stoffel, F. Vignola, S. Wilcox, J. Wood, Y. Xie, L. Zarzalejo. *Best Practices Handbook for the Collection and Use of Solar Resource Data for Solar Energy Applications*. Second Edition, NREL Technical Report NREL/TP-5D00-68886, 238 pp. (2017)

A broad overview on all renewable energy techniques can be found in:

- M. Kaltschmitt, W. Streicher, A. Wiese: *Renewable Energy* (Springer, Heidelberg 2007), XXXII+564 pp. A revised 5th German edition of this book appeared in 2013.

References

- 51.1 S. Emeis: *Wind Energy Meteorology – Atmospheric Physics for Wind Power Generation*, Green Energy and Technology, 2nd edn. (Springer, Cham 2018)
- 51.2 M. Sengupta, A. Habte, C. Gueymard, S. Wilbert, D. Renné, T. Stoffel: *Best Practices Handbook for the Collection and Use of Solar Resource Data for Solar Energy Applications*, 2nd edn. (NREL, Golden 2017), NREL/TP-5D00-68886
- 51.3 C.S. Kaunda, C.Z. Kimambo, T.K. Nielsen: Hydropower in the context of sustainable energy supply: A review of technologies and challenges, *ISRN Renew. Energy* (2012), <https://doi.org/10.5402/2012/730631>
- 51.4 L. Dubus, S. Muralidharan, A. Troccoli: What does the energy industry require from meteorology? In: *Weather & Climate Services for the Energy Industry*, ed. by A. Troccoli (Palgrave Macmillan, Cham 2018)
- 51.5 ISO 9488: *Solar Energy Vocabulary* (ISO, Geneva 1999)
- 51.6 IEC 61400-12-1: *Wind Energy Generation Systems – Part 12-1: Power Performance Measurements of Electricity Producing Wind Turbines* (VDE, Berlin 2017)
- 51.7 A. Peña, R. Floors, A. Sathe, S.E. Gryning, R. Wagner, M.S. Courtney, X.G. Larsén, A.N. Hahmann, C.B. Hasager: Ten years of boundary-layer and wind-power meteorology at Høvsøre, Denmark, *Bound.-Layer Meteorol.* **158**(1), 1–26 (2016)
- 51.8 M. Türk, K. Grigutsch, S. Emeis: The wind profile above the sea—Investigations basing on four years of FINO 1 data, *DEWI Magazin* **33**, 12–16 (2008)
- 51.9 J. Mann, N. Angelou, J. Arqvist, D. Callies, E. Cantero, R. Chávez Arroyo, M. Courtney, J. Cuxart, E. Dellwik, J. Gottschall, S. Ivanell, P. Kühn, G. Lea, J.C. Matos, J.M.L.M. Palma, L. Pauscher, A. Peña, J. Sanz Rodrigo, S. Söderberg, N. Vasiljevic, C. Veiga Rodrigues: Complex terrain experiments in the new European wind atlas, *Philos. Trans. R. Soc.* **375**(2091), 20160101 (2017)
- 51.10 A. Clifton, S. Schreck, G. Scott, N. Kelley, J.K. Lundquist: Turbine inflow characterization at the National Wind Technology Center, *J. Sol. Energy Eng.* **135**, 031017 (2013)
- 51.11 A.B. Mouchot: *La Chaleur Solaire et ses Applications Industrielles* (Gauthier-Villars, Paris 1869)
- 51.12 M.L. Wesely: Simplified techniques to study components of solar radiation under haze and clouds, *J. Appl. Meteorol.* **21**, 373–383 (1982)
- 51.13 G.O.G. Löf, J.A. Duffie, C.O. Smith: World distribution of solar radiation, *Sol. Energy* **10**, 27–37 (1966)
- 51.14 H.C.S. Thom: The rational relationship between heating degree days and temperature, *Mon. Weather Rev.* **82**, 1–6 (1954)
- 51.15 H. Landsberg: Bioclimatology of housing. In: *Recent Studies in Bioclimatology*, Meteorological Monographs, Vol. 2 (AMS, Boston 1954) pp. 81–98
- 51.16 A. Betz: Das Maximum der theoretisch möglichen Ausnützung des Windes durch Windmotoren, *Z. Gesamte Turbinenwes.* **26**, 307–309 (1920)
- 51.17 A. Betz: *Wind-Energie und ihre Ausnutzung durch Windmühlen* (Vandenhoeck & Ruprecht, Göttingen 1926)
- 51.18 W. Weibull: A statistical distribution function of wide applicability, *J. Appl. Mech.* **73**, 293–297 (1951)
- 51.19 E.J. Gumbel: *Statistics of Extremes* (Columbia Univ. Press, New York, London 1958)
- 51.20 R. Wagner, B. Cañadillas, A. Clifton, S. Feeney, N. Nygaard, M. Poodt, C. St. Martin, E. Tüxen, J.W. Wagenaar: Rotor equivalent wind speed for power curve measurement – Comparative exercise for IEA Wind Annex 32, *J. Phys. Conf. Ser.* **524**(1), 012108 (2014)
- 51.21 C.A. Paulson: The mathematical representation of wind speed and temperature profiles in the unstable atmospheric surface layer, *J. Appl. Meteorol.* **9**, 857–861 (1970)
- 51.22 U. Högström: Non-dimensional wind and temperature profiles in the atmospheric surface layer: A re-evaluation, *Bound.-Layer Meteorol.* **42**, 55–78 (1988)
- 51.23 J.A. Businger, J.C. Wyngaard, Y. Izumi, E.F. Bradley: Flux profile relationships in the atmospheric surface layer, *J. Atmos. Sci.* **28**, 181–189 (1971)
- 51.24 A.J. Dyer: A review of flux-profile relations, *Bound.-Layer Meteorol.* **7**, 363–372 (1974)
- 51.25 A.A.M. Holtslag, H.A.R. de Bruin: Applied modeling of the nighttime surface energy balance over land, *J. Appl. Meteorol.* **27**, 689–704 (1988)
- 51.26 M. Bartos, M. Chester, N. Johnson, B. Gorman, D. Eisenberg, I. Linkov, M. Bates: Impacts of rising air temperatures on electric transmission ampacity and peak electricity load in the United States, *Environ. Res. Lett.* **11**(11), 114008 (2016)
- 51.27 EN 50341-1:2012: *Overhead Electrical Lines Exceeding AC 1 kV. General Requirements – Common Specifications* (CENELEC, Brussels 2012)
- 51.28 S. Emeis: *Measurement Methods in Atmospheric Sciences – In Situ and Remote*, Quantifying the Environment, Vol. 1 (Borntraeger, Stuttgart 2010)
- 51.29 VDI 3786-2: *Environmental Meteorology – Meteorological Measurements – Wind* (Beuth, Berlin 2018)
- 51.30 VDI 3786-12: *Environmental Meteorology – Meteorological Measurements – Turbulence Measurements with Sonic Anemometers* (Beuth, Berlin 2019)
- 51.31 T.F. Pedersen, J.-Å. Dahlberg, A. Cuerva, F. Mouzakis, P. Busche, P. Eecen, A. Sanz-Andres, S. Franchini, S.M. Petersen: *ACCUWIND – Accurate Wind Speed Measurements in Wind Energy (Summary Report)* (Risø National Laboratory, Roskilde 2006), Risø Report Risø-R-1563(EN), <http://www.windspeed.co.uk/ws/public/ACCUWIND-ris-r-1563.pdf>, Accessed 21 July 2021
- 51.32 S. Emeis: *Surface-Based Remote Sensing of the Atmospheric Boundary Layer*, Atmospheric and Oceanographic Sciences Library, Vol. 40 (Springer, Dordrecht, Heidelberg, London, New York 2011)
- 51.33 VDI 3786-11: *Environmental Meteorology – Ground-Based Remote Sensing of the Wind Vector and the*

- Vertical Structure of the Boundary Layer – Doppler Sodar (Beuth, Berlin 2015)
- 51.34 ISO 28902-2: *Air Quality – Environmental Meteorology – Part 2: Ground-Based Remote Sensing of Wind by Heterodyne Pulsed Doppler Lidar* (ISO, Geneva 2017)
- 51.35 VDI 3786-18: *Environmental Meteorology – Ground-Based Remote Sensing of Temperature – Radio-Acoustic Sounding Systems (RASS)* (Beuth, Berlin 2010)
- 51.36 J. Röttger, M.-F. Larsen: UHF/VHF radar techniques for atmospheric research and wind profiler applications. In: *Radar in Meteorology*, ed. by D. Atlas (AMS, Boston 1990) pp. 235–281
- 51.37 VDI 3786-17: *Environmental Meteorology – Ground-Based Remote Sensing of the Wind Vector – Wind Profiler Radar* (Beuth, Berlin 2007)
- 51.38 W. Koch, F. Feser: Relationship between SAR-derived wind vectors and wind at 10-m height represented by a mesoscale model, *Mon. Weather Rev.* **134**, 1505–1517 (2006)
- 51.39 M.B. Christiansen, C.B. Hasager: Wake effects of large offshore wind farms identified from satellite SAR, *Remote Sens. Environ.* **98**, 251–268 (2005)
- 51.40 C.B. Hasager, P. Vincent, R. Husson, A. Mouche, M. Badger, A. Peña, P. Volker, J. Badger, A. Di Bella, A. Palomares, E. Cantero, P.M.F. Correia: Comparing satellite SAR and wind farm wake models, *J. Phys. Conf. Ser.* **625**, 012035 (2015)
- 51.41 A. Platis, S.K. Siedersleben, J. Bange, A. Lampert, K. Bärfuss, R. Hankers, B. Canadillas, R. Foreman, J. Schulz-Stellenfleh, B. Djath, T. Neumann, S. Emeis: First in situ evidence of wakes in the far field behind offshore wind farms, *Sci. Rep.* **8**, 2163 (2018)
- 51.42 ISO 9901: *Solar Energy – Field Pyranometers – Recommended Practice for Use* (ISO, Geneva 1990)
- 51.43 WMO: *Guide to Instruments and Methods of Observation*, WMO-No. 8, Volume I – Measurement of Meteorological Variables (World Meteorological Organization, Geneva 2018)
- 51.44 L.J.B. McArthur: *Baseline Surface Radiation Network (BSRN). Operations Manual (Version 2.1)* (WMO, Geneva 2005), WCRP-121, WMO/TD-No. 1274
- 51.45 S. Wilbert, S. Kleindiek, B. Nouri, N. Geuder, A. Habte, M. Schwandt, F. Vignola: Uncertainty of rotating shadowband irradiometers and Si-pyranometers including the spectral irradiance error, *AIP Conf. Proc.* **1734**, 150009 (2016)
- 51.46 D. Schüler, S. Wilbert, N. Geuder, R. Affolter, F. Wolfertstetter, C. Prah, M. Röger, M. Schroedter-Homscheidt, G. Abdellatif, A. Allah Guizani, M. Balghouthi, A. Khalil, A. Mezrhab, A. Al-Salaymeh, N. Yassaa, F. Chellali, D. Draou, P. Blanc, J. Dubranna, O.M.K. Sabry: The enerMENA meteorological network – Solar radiation measurements in the MENA region, *AIP Conf. Proc.* **1734**, 150008 (2016)
- 51.47 J. Badosa, J. Wood, P. Blanc, C.N. Long, L. Vuilleumier, D. Demengel, M. Haeffelin: Solar irradiances measured using SPN1 radiometers: Uncertainties and clues for development, *Atmos. Meas. Tech.* **7**(12), 4267–4283 (2014)
- 51.48 S. Schrott, T. Schmidt, T. Hornung, P. Nitz: Scientific system for high-resolution measurement of the circumsolar radiation, *AIP Conf. Proc.* **1616**, 88–91 (2014)
- 51.49 S. Wilbert, B. Reinhardt, J. DeVore, M. Röger, R. Pitz-Paal, C. Gueymard, R. Buras: Measurement of solar radiance profiles with the Sun and aureole measurement system, *J. Sol. Energy Eng.* **135**, 041002 (2013)
- 51.50 S. Wilbert, R. Pitz-Paal, J. Jaus: Comparison of measurement techniques for the determination of circumsolar irradiance, *AIP Conf. Proc.* **1556**, 162–167 (2013)
- 51.51 S. Wilbert, M. Röger, J. Csambor, M. Breitbach, F. Klinger, B. Nouri, N. Hanrieder, F. Wolfertstetter, D. Schüler, S. Shaswattam, N. Goswami, S. Kumar, A. Ghennioui, R. Affolter, N. Geuder, B. Kraas: Sun-shape measurements with conventional rotating shadowband irradiometers, *AIP Conf. Proc.* **2033**, 190016 (2018)
- 51.52 L. Harrison, J. Michalsky, J. Berndt: Automated multifilter rotating shadow-band radiometer: An instrument for optical depth and radiation measurements, *Appl. Opt.* **33**, 5118–5125 (1994)
- 51.53 V. Tatsiankou, K. Hinzer, H. Schriemer, S. Kazadzis, N. Kouremeti, J. Gröbner, R. Beal: Extensive validation of solar spectral irradiance meters at the World Radiation Center, *Sol. Energy* **166**, 80–89 (2018)
- 51.54 ISO 28902-1:2012: *Air Quality – Environmental Meteorology – Part 1: Ground-Based Remote Sensing of Visual Range by Lidar* (ISO, Geneva 2012)
- 51.55 N. Hanrieder, S. Wilbert, R. Pitz-Paal, C. Emde, J. Gasteiger, B. Mayer, J. Polo: Atmospheric extinction in solar tower plants: Absorption and broadband correction for MOR measurements, *Atmos. Meas. Tech.* **8**, 3467–3480 (2015)
- 51.56 T. Sarver, A. Al-Qaraghuli, L.L. Kazmerski: A comprehensive review of the impact of dust on the use of solar energy: History, investigations, results, literature, and mitigation approaches, *Renew. Sustain. Energy Rev.* **22**, 698–733 (2013)
- 51.57 F. Wolfertstetter, K. Pottler, N. Geuder, R. Affolter, A.A. Merrouni, A. Mezrhab, R. Pitz-Paal: Monitoring of mirror and sensor soiling with TraCS for improved quality of ground based irradiance measurements, *Energy Procedia* **49**, 2422–2432 (2014)
- 51.58 P. Kuhn, M. Wirtz, N. Killius, S. Wilbert, J.L. Bosch, N. Hanrieder, B. Nouri, J. Kleissl, L. Ramirez, M. Schroedter-Homscheidt, D. Heinemann, A. Kazantzidis, P. Blanc, R. Pitz-Paal: Benchmarking three low-cost, low-maintenance cloud height measurement systems and ECMWF cloud heights against a ceilometer, *Sol. Energy* **168**, 140–152 (2018)
- 51.59 J. Polo, S. Wilbert, J.A. Ruiz-Arias, R. Meyer, C. Gueymard, M. Suri, L. Martin, T. Mieslinger, P. Blanc, I. Grant, J. Boland, P. Ineichen, J. Remund, R. Escobar, A. Troccoli, M. Sengupta, K.P. Nielsen, D. Renne, N. Geuder, T. Cebecauer: Preliminary survey on site-adaption techniques for satellite-derived and reanalysis solar radiation datasets, *Sol. Energy* **132**, 25–37 (2016)

- 51.60 B. Reinhardt, R. Buras, L. Bugliaro, S. Wilbert, B. Mayer: Determination of circumsolar radiation from Meteosat Second Generation, *Atmos. Meas. Tech.* **7**, 823–838 (2014)
- 51.61 R. Mueller, T. Behrendt, A. Hammer, A. Kemper: A new algorithm for the satellite-based retrieval of solar surface irradiance in spectral bands, *Remote Sens. Environ.* **4**, 622–647 (2012)
- 51.62 T. Huld, A.G. Amillo: Estimating PV module performance over large geographical regions: The role of irradiance, air temperature, wind speed and solar spectrum, *Energies* **8**, 5159–5181 (2015)
- 51.63 ISO 17713-1: *Meteorology – Wind Measurements – Part 1: Wind Tunnel Test Methods for Rotating Anemometer Performance* (ISO, Geneva 2007)
- 51.64 ISO 16622: *Meteorology – Sonic Anemometers/Thermometers – Acceptance Test Methods for Mean Wind Measurements* (ISO, Geneva 2003)
- 51.65 N. Geuder, F. Wolfertstetter, S. Wilbert, D. Schüler, R. Affolter, B. Kraas, E. Lüpfer, B. Espinar: Screening and flagging of solar irradiation and ancillary meteorological data, *Energy Procedia* **69**, 1989–1998 (2015)
- 51.66 J.-J. Trujillo, F. Bingöl, G.C. Larsen, J. Mann, M. Kühn: Light detection and ranging measurements of wake dynamics. Part II: Two-dimensional scanning, *Wind Energy* **14**, 61–75 (2011)
- 51.67 ISO 9060:2018: *Solar Energy – Specification and Classification of Instruments for Measuring Hemispherical Solar and Direct Solar Radiation* (ISO, Geneva 2018)

Stefan Emeis

Institute of Meteorology and Climate Research
Karlsruhe Institute of Technology (KIT)
Garmisch-Partenkirchen, Germany
stefan.emeis@kit.edu



Stefan Emeis is an unsalaried Professor of Meteorology at the University of Cologne, group leader at KIT, and editor-in-chief of *Meteorologische Zeitschrift*. His research mainly involves ground-based remote sensing of the atmospheric boundary layer. He has written books on measurement techniques and wind energy, organized conferences (e.g., ISARS 13, METTOOLS VI), and was awarded the Honorary Medal of the VDI and the Reinhard Süring Medal from the German Meteorological Society.

Stefan Wilbert

Institut für Solarforschung
Deutsches Zentrum für Luft- und
Raumfahrt e. V. (DLR)
Almeria, Spain
stefan.wilbert@dlr.de



Stefan Wilbert works in the Institute of Solar Research at DLR in the permanent delegation at the Plataforma Solar de Almería, Spain since 2006. He is leader of the research group “Solar Energy Meteorology”. Both his Diploma thesis in physics at the University of Bonn and his PhD thesis at the University of Aachen were related to meteorological effects on solar power plants. His research interests are meteorological measurements for solar energy applications, radiative transfer modelling, nowcasting of solar radiation and solar power plant simulation.

52. Urban Measurements and Their Interpretation

Sue Grimmond , Helen C. Ward 

Urban environments create distinct challenges for successful atmospheric measurements primarily due to their complex surface structure (i.e., presence of buildings, a wide variety of construction materials, and heterogeneous land cover). In addition, human-generated emissions of heat, water, or pollutants may be considerable and can often vary dramatically in both space and time. Observational techniques have been adapted and theoretical frameworks developed to address some of these challenges of the urban environment. This chapter provides an overview of commonly used approaches to measure the urban atmosphere (including observations of temperature, humidity, wind, precipitation, radiation, the surface energy balance, and boundary layer height and dynamics), plus the key parameters used to quantify the urban environment (e.g., roughness length, surface cover fraction). Additional considerations that need to be made when measuring or interpreting urban measurements are discussed, alongside open issues that are the subject of ongoing research. Examples of various applications are given.

52.1 Measurement Principles and Variables	1392
52.1.1 Challenges of the Urban Environment to Standard Measurement Techniques	1392
52.1.2 Measured Variables	1393
52.2 History	1394
52.3 Theory	1396
52.3.1 Idealized Layers of the Atmosphere....	1396
52.3.2 Scales of Measurement	1397
52.3.3 Characterizing the Urban Environment	1398
52.4 Devices and Systems	1400
52.4.1 Temperature	1400
52.4.2 Humidity	1401
52.4.3 Wind	1401
52.4.4 Precipitation	1402
52.4.5 Radiation	1404
52.4.6 Surface Energy Fluxes	1404
52.4.7 Boundary Layer Height	1406
52.5 Specifications	1407
52.6 Quality Control	1408
52.7 Maintenance	1409
52.8 Applications	1409
52.8.1 Human Comfort and Health.....	1410
52.8.2 Building Design, Construction, Management, and Planning.....	1411
52.8.3 Data Assimilation	1412
52.9 Future Developments	1412
52.10 Further Reading	1413
References	1413

With the majority of the world's population now living in cities [52.1] understanding the urban atmosphere is critical for the short and long-term well-being of citizens. Accurate and reliable meteorological measurements are fundamental to improving our knowledge of this extremely complex environment. As urban areas are the major source of greenhouse gases and aerosols that impact the global atmosphere [52.2, 3], cities are also highly relevant to many global problems. For examples of needs and applications, see Sect. 52.8.

Compared to their rural surroundings, cities are known to modify the surface-atmosphere exchange of energy, water, and pollutants. Exactly how this exchange is modified depends on the surface properties, such as the density of buildings or the amount and type of vegetation present [52.4], as well as the human activities. Hence, surface-atmosphere exchanges typically have considerable variation both within and between urban areas [52.5]. Furthermore, urban areas affect the climate not only within the city itself but also at regional scales [52.6].

Urban observations are undergoing a massive transition because of a combination of factors occurring almost simultaneously. These include: technological changes (e.g., miniaturization of measurement devices, developments in ground and satellite-based remote sensing), communication improvements (e.g., WiFi networks via mobile phone), smart data (e.g., combining data from multiple sources), citizen science (e.g., using mobile phones or local citizens [52.7] to gather meteorological data), enhanced computer power (e.g., allowing higher-resolution weather forecasts), development of climate services (e.g., Global Framework for Climate

Services [52.8], integrated urban services [52.9]) that expect meteorological services to go the *last mile* to deliver the information actually needed, and urbanization itself causing numerous agencies to recognize that urban residents' needs have to be addressed because of their density of exposure (e.g., UN Habitat [52.10, 11], World Bank [52.12–14], and WMO [52.15]). This creates both opportunities and some potential pitfalls. In this chapter, we focus on identifying what needs to be considered in undertaking measurements in urban areas and provide examples of applications to help facilitate the design of appropriate systems.

52.1 Measurement Principles and Variables

Given the complexity of the urban environment and its rapid rate of change, undertaking measurements in urban areas requires a careful four-dimensional (4-D) characterization of the site and its surroundings throughout the period of interest.

52.1.1 Challenges of the Urban Environment to Standard Measurement Techniques

With respect to measurements, what makes urban areas distinct from most other landscapes is the large size of the roughness elements (e.g., buildings and trees) and the wide range of land cover types that are typically found in varying proportions across a city. A critical characteristic of almost all cities is that they vary horizontally and vertically, and, with buildings in cities becoming ever taller, the influence of the surface extends to ever greater heights.

One of the main challenges of undertaking measurements in urban environments is to ensure that the observations are representative of the area of interest. Great care needs to be taken in siting instruments to consider their measurement principles. For example, a downward-facing pyranometer will respond to the surface below the sensor that is within its field of view. When installed on a rooftop, the field of view (which depends on the height and location of the pyranometer) may encompass a single rooftop of uniform material or multiple roofs of varying materials, slopes, and aspects, plus perhaps some vegetation or road surface. In most neighborhoods there will be many different roof types with a wide range of properties. For a micro-scale study, it may be important that the radiometer measures only the rooftop of interest; for a local- or neighborhood-scale

study, the radiometer should provide a representative measurement for the neighborhood (Sect. 52.3.2). To ensure that this is the case requires careful siting of the sensors such that the area sampled is sufficiently large, which usually means measuring at greater height. If this is not possible, multiple sensors installed at different locations may be needed to provide a more accurate estimate of the neighborhood-scale value and its spatial variability [52.16].

Due to the heterogeneity of urban areas many instruments need to be installed at considerable height in order to obtain representative measurements for the area of interest. Moreover, the effective height of the surface is typically raised to a height of several meters above ground level because of the presence of buildings (and trees). These large bluff bodies present an obstacle to the flow and deflect the flow both around them and over the top, similar to flow over forests. This increase in the height of the effective surface is described by the displacement height. Locating measurements sufficiently above the displacement height can be challenging given the financial and safety considerations associated with installing a tall (e.g., 10–50 m) tower on a rooftop or within a street canyon (more on ground-based platforms can be found in Chap. 6). Moreover, for all urban measurements (not only those at height), obtaining site permissions can be problematic, and theft or vandalism may occur, as in nonurban locations. The practicalities of installing and maintaining the equipment in a populated area must be considered. Cranes and road closures may be required, which must cause minimal disruption to the daily life of the city. Non-eye-safe lasers or sodars, which emit audible sounds, are generally better suited to less populated areas.

52.1.2 Measured Variables

Almost all variables that are measured in other environments are also of interest in urban environments, along with some additional variables. The most commonly considered variable in urban areas is temperature. This is because of the well-known urban heat island (UHI) effect [52.17]. Different types of urban heat islands are defined, depending on what type of temperature is measured (e.g., air, surface, or soil temperature) and where it is measured (e.g., between the roughness elements or above the surface layer within the boundary layer).

In urban areas, air temperature measurements at standard screen height (Chap. 7) will lie within the urban canopy layer (Fig. 52.1), where the flow is highly heterogeneous and is affected by nearby roughness elements. The air in this layer may be separated from the inertial sublayer (or constant flux layer) above, particularly if buildings are close together, such that air skims across the top of the buildings rather than flowing into the urban canyon. As buildings become taller, the level of standard screen height may lie deep within a street canyon and be separated from the overlying air by several tens of meters. Careful interpretation is therefore required.

Other types of urban heat islands are based on the surface, soil or ground temperature, or the temperature measured higher in the boundary layer. These UHIs generally have different magnitudes and different diurnal patterns to each other. A critical aspect of the UHI intensity is the *rural* measurement, which also needs careful consideration with respect to sensor placement and fetch to ensure it provides a suitable and representative baseline with which to compare the urban temperature.

Beyond enhanced temperatures, urban areas have distinct humidity patterns, complex interactions with precipitation, a strong influence on wind due to the roughness introduced by buildings and trees, and impacts on boundary layer height, surface energy fluxes, and air quality [52.5]. As with temperature, any comparison with nonurban sites or other urban sites must also carefully consider the characteristics of the surroundings. As an illustration, whilst urban areas are typically associated with lower evaporation rates than outside the city because of reduced vegetation and increased impervious cover, the opposite result has been observed for some urban environments (e.g., in Sacramento [52.18], Phoenix [52.19], and Salt Lake City [52.20]), with higher evaporation rates observed in the city as many residents have irrigated gardens and the surroundings are semiarid.

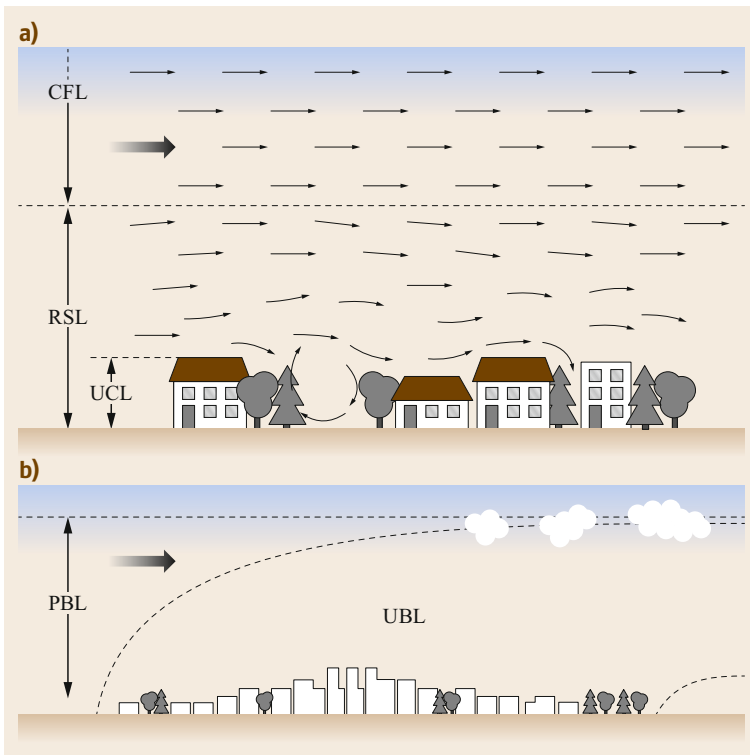


Fig. 52.1a,b Layers of the atmosphere including (a) the urban canopy layer (UCL), roughness sublayer (RSL), and constant flux layer (CFL) or inertial sublayer (ISL), and (b) the planetary boundary layer (PBL) and urban boundary layer (UBL). Winds are indicated by arrows with the prevailing wind from the left (*large arrow*)

To assist interpretation and analysis it is often essential to collect additional data about the study area. Such data fall into two categories: approximately static or slowly changing site characteristics (such as building height, building materials, or land cover type) and temporally varying information about processes that rarely need to be considered in nonurban environments but can have a significant impact in urban environments. Examples of the latter include vehicle counts (used to relate carbon dioxide emissions to traffic load [52.21] or to quantify sources of anthropogenic heat) and building energy use statistics (used to calculate the anthropogenic heat release [52.22, 23]). Ideally, high-resolution spatiotemporal datasets would be collected for the study site and study period to accompany the observed meteorological datasets, but this is rarely achievable in practice. Instead, models may be used to estimate the anthropogenic heat emissions or traffic load based on more readily available (often coarser resolution) data [52.24]. Such additional information can be extremely useful in quantitatively relating observed trends to human activities.

The urban surface energy balance is more complicated than that over many nonbuilt surfaces. Firstly, there is the additional anthropogenic heat flux term describing the additional energy supplied as a result of

human activities (including building heating, combustion associated with transport and human metabolism). Secondly, the storage heat flux is much greater than for many vegetated environments and often constitutes a large proportion of the available energy. This is because buildings receive intense radiation loads, and the building materials have large thermal capacity. The storage heat flux includes the energy stored and released in the urban fabric (e.g., buildings' roofs and walls, roads, pavements, vegetation, and the air) and, thus, varies considerably in space and time. There is no known way to measure the storage heat flux directly given the complexity of the urban surface [52.25, 26]; the most common approach is to approximate it from the residual of the energy balance, but this means all the errors associated with the other energy balance terms are combined in this term. As the observed surface energy balance rarely closes even in simple environments, there are always uncertainties with this approach. Thirdly, the advection term in the surface energy balance is usually assumed to be negligible, although this may not always be an appropriate assumption in the urban environment. Thus, in addition to the *measured variables*, there are also *nonmeasured variables* or *nonmeasurable variables* that may have to be estimated.

52.2 History

As cities or towns are places where people have lived for thousands of years, the earliest measurements (e.g., concerning air pollution [52.27]) were associated with urban locations. Similarly, the development of more formal instrumentation (e.g., European development of the temperature sensor, Chap. 7) also involved urban measurements. In neither case was the original intent to observe the urban environment per se but rather to measure the locale or region. However, once multiple sensors were installed across the region, urban–rural differences became evident.

The first to take measurements and to recognize through analysis of the data that there was an urban effect was *Luke Howard* (1772–1864) [52.28]. Through temperature observations sited in various places in London in the early part of the nineteenth century, he identified regions of the city with warmer temperatures and related these to a higher density of buildings and greater release of anthropogenic heat (Sect. 52.1.2) which, at the time, was predominately associated with

fires [52.29, 30]. As more sensors became available other urban areas and additional variables were measured.

Key historical measurement innovations in the urban environment have involved trying to measure the spatial variability. The first spatial measurements using a vehicle mounted sensor, by *Wilhelm Schmidt* (1883–1936) in Vienna, observed thermal minima [52.31]. Other notable developments included mobile traverses by car, bike, or on foot; identifying the effects of the urban environment by concurrent measurements at multiple sites within and around a city, and investigating vertical profiles of various quantities both in between and above the buildings. See Chap. 50 for an overview of mobile measuring systems.

The influence of urban areas on precipitation has been the subject of much debate and research over an extended period [52.32–36]. Much of the early debate comes about because of the difficulties of undertaking measurements in an urban environment and the

range of factors that may be influenced by the presence of a city. These include the urban heat island, larger roughness elements, and added aerosols. The METROMEX (Metropolitan Meteorological Experiment) studies were prompted by the so-called *La Porte anomaly* [52.32, 37], which was suggested to indicate a precipitation enhancement downwind of Chicago (and Gary, Indiana). Although METROMEX and companion studies did not answer the precipitation debate, they resulted in a number of important firsts in urban meteorological observations [52.38, 39]. Surface energy balance fluxes were measured using eddy-covariance techniques, and the challenges of storage heat flux and advection were addressed [52.40–43]. In addition, measurements that crossed a wide range of spatial scales (Sect. 52.3) were combined to give a 4-D view of the urban atmosphere, using (at the time) state-of-the-art instrumentation.

The use of eddy covariance to study the surface energy balance and turbulent exchange in urban areas has grown considerably in the last few decades. Urban flux towers are now found all over the world [52.5, 44], although there remain more in the northern mid-latitudes. Observations of turbulent fluxes from these towers have revealed a huge amount of information about energy partitioning and flow patterns in cities, in particular how surface cover and human activities strongly influence flux partitioning and turbulent exchange. As one example, the Institute of Atmospheric Physics' (IAP) 320-m-tall tower in Beijing has, since 1979, provided one of the tallest vertical profiles of meteorological variables in a city, but because of the immense changes in the city, these observations are also an amazing record of urbanization. Notably, the change in the wind regime as the city became taller, and the aerodynamic parameters became larger [52.45]. Scintillometry has also been used to determine sensible heat fluxes in cities [52.46–54]. Small-aperture scintillometers operating over paths of 50–250 m have been used to study the different fluxes from rooftops and canyons in Basel [52.55], whereas large aperture scintillometers provide fluxes representative of much larger areas ([52.56], Fig. 52.3).

Notable urban meteorological campaigns in the last two decades have combined physical and chemical measurements. Examples include dispersion-related studies in Hamburg [52.57], Salt Lake City (URBAN 2000 [52.58]), Oklahoma City (Joint Urban 2003 [52.59]), New York City (Madison Square Garden [52.60]), and London (DAPPLE: dispersion of air

pollution and its penetration into the local environment [52.61]), REPARTEE (Regents Park and Tower Environmental Experiment) [52.62], ClearfLo (Clean air for London) [52.63]), which consider the indoor and outdoor environments, from street canyon to neighborhood scale. Large campaigns, such as ECSOMPTE (French acronym for a field experiment to constrain the models of pollution emission transport) in Marseille [52.64, 65], crossed from the regional scale to the city scale, where poor air quality (from refineries) was an issue. Network designs for different purposes in cities have been a key focus [52.66, 67], for example air temperatures in Birmingham [52.68, 69], canopy layer variables in Oklahoma city [52.70], precipitation in Dallas-Fort Worth [52.71], and multivariable, multi-scale, and multipurpose studies in Shanghai [52.72] and Seoul [52.73].

With air quality, a critical public health issue in urban areas globally, the measurement of boundary layer depth has been an important and ongoing observational concern. COST (European Cooperation in Science and Technology) 710 [52.74, 75] provided a significant review of measurement approaches and a detailed comparison of the techniques and their relative strengths and weaknesses.

The AMDAR (Aircraft Meteorological Data Relay) data from onboard sensors mounted on commercial aircraft (Chap. 63) has provided cities with a new source of boundary layer data as planes take off and land [52.76, 77]. Cities with dense networks of airports have close to realtime data, which are delivered via the WMO Integrated Global Observing System and the Global Observing System (Chap. 63). These data are obviously limited to times when planes are flying (many cities have late night curfews because of noise, e.g., Sydney and London) and flight path locations. Although the three-dimensional (3-D) position of the data sample is provided, the time the plane spends within the boundary layer is very short. Also, as many airports may be some distance from the city, these data may not be directly relevant to the urban environment.

There have been reviews of the state of urban measurements that address full-scale [52.78–81] and physical (or hardware) models [52.82] plus numerous recommendations [52.83–86]. Consideration has also been given to network design in urban areas [52.66] and what metadata should be provided [52.67]. Other reviews have been more focused to include such topics as thermal remote sensing [52.87, 88] or the urban heat island [52.89].

52.3 Theory

An important consideration before undertaking measurements in the urban environment is the basic measurement principle. Although new technology is constantly being developed, even the *latest* sensor poorly sited will not overcome fundamental issues in understanding. Related to this, a critical requirement prior to undertaking observations is a clear understanding of what is of interest. For example, observational needs will be different if the interest is in the urban effect on a process relative to the surrounding area or the variability of a process within a city. This section provides an overview of some of the key concepts in urban micrometeorology that are used to understand and interpret measurements.

52.3.1 Idealized Layers of the Atmosphere

The urban atmosphere is normally characterized by a series of vertical layers (Fig. 52.1). Understanding their characteristics and where they are likely to be located is fundamental to correct instrument deployment and interpretation of measurements.

The four layers extending from ground level into the atmosphere are (Chap. 1):

- *Urban canopy layer.* The urban canopy layer is the region between the buildings, trees, and vehicles from the ground up to the top of the roughness elements. In nonurban areas, this is equivalent to the air between the grass blades in the prairie environment, between the crops and the soil in farmland, between vines in a vineyard, or between the trees in an orchard. The urban canopy layer is where humans spend their day-to-day life, and thus, for the provision of many climate services, this is the layer of interest. The vertical extent of the urban canopy layer is becoming ever larger as buildings become taller. Across a city there may be neighborhoods where trees are the tallest elements and other areas where trees are dwarfed by buildings. In this layer, conditions are very variable. For example, the sunlit or shaded side of the street; building density, shape, and orientation to the prevailing wind; vents of buildings; and traffic and people moving through the area all combine to mean that sensors located anywhere in this 3-D space can be measuring different microclimates. Moving the sensors from one area to another means that different radiation, temperature, wind, and humidity environments are to be expected. Thus, to sample appropriately at this scale to get some sort of representative measurement, or to document the spatial variability, usually requires extensive sampling. Challenges may also arise because access to many areas is restricted (e.g., walkways, traffic routes), although the use of sensors mounted on vehicles or people means that some variables can be measured in otherwise inaccessible areas (Chap. 50, Sect. 52.2).
- *Roughness sublayer (RSL).* The roughness sublayer extends from the surface to above the roughness elements. The vertical extent depends on the packing of the roughness elements and the variability of their height. Generally, more dense areas with consistent heights (low standard deviation) will have a shallower RSL (in proportion to the mean height of the roughness elements) than areas where their packing density is lower or the variability in building (and tree) height is larger. A rule of thumb to estimate the height of the RSL is about two to five times the mean height of the roughness elements [52.90, 91]. The roughness sublayer defines the region within which the flow is affected by individual objects. The flow patterns are, therefore, highly complex and spatially heterogeneous. Thus, measurements in this region are still considered to be at the micro-scale and moving sensors a small distance will result in potentially large variations, as in the urban canopy layer.
- *Inertial sublayer or constant flux layer.* Above the roughness sublayer lies the inertial sublayer or constant flux layer. Here, the effects of individual roughness elements are no longer evident; the individual disturbances are averaged out. In the constant flux layer, the fluxes are approximately constant with height and do not vary dramatically in space. Thus, observations conducted within this layer are representative of larger areas, referred to as a local or neighborhood scale. If instruments at these heights are moved small distances, only small differences in the measurements should result. This is referred to as having one-dimensional (1-D) scaling. In nonurban areas, the equivalent measurements would be a few meters above an extensive grass surface or cropland. In the urban environment, a key challenge is to ensure that the sensors are high enough and there is sufficient fetch; i.e., an upwind area with consistent characteristics. The constant flux layer is typically the lowest 10% of the boundary layer.
- *Boundary layer.* Between the surface and the free atmosphere there is the dynamic boundary that grows and collapses daily in response to surface heating and regional and synoptic scale conditions. The urban boundary layer (UBL), as with boundary layers over other surfaces, tends to have convective growth during the daytime. Stable boundary layers may be less common in urban areas because of the large storage heat flux

release at night, enhanced sensible heat and anthropogenic heat fluxes. This may result in deeper nocturnal and daytime boundary layers than for surrounding land surfaces. Moreover, this urban effect may extend downwind for some distance aloft (Fig. 52.1b).

As urban areas have extensive emissions of pollutants, air quality is of significant concern for public health. Therefore, the dynamic nature of the UBL is important. Often, major air quality episodes are related to changes in UBL depth rather than changes in emissions, which have regular weekly and annual cycles. Thus, understanding how synoptic conditions modify city scale UBL depth, and hence air quality, is very important for citizens' wellbeing. Concern for urban air quality has led to behavioral changes (e.g., reducing vehicle use to lower emissions – in Paris [52.92] and Beijing [52.93]).

52.3.2 Scales of Measurement

It is critical that the scale of interest for an application is understood and is appropriate before deciding upon a suitable measurement technique and sensor siting. The distinct microclimates found within a city may exhibit larger differences than those between neighborhoods of similar types in different cities. For example, the central business districts (CBDs) of two European cities may be more similar to each other than, say, the CBD compared to an adjacent neighborhood with large mature trees in one city. The scale of interest influences the measurement technique, sensor location, number of sensors, sample rate, and measurement time, and depends on the physical processes involved (Fig. 52.2, Chap. 1).

In urban areas, there are three general scales that may be of interest:

- *Microscale.* At the microscale (< 10 m), urban areas are made up of different facets (e.g., walls, roofs, ground). Examples of microscale observations include the temperature differences between the sunlit and shaded sides of the same street or the flow distortion around a building. Thus, sensors installed within a street canyon will measure very different microscale environments if moved even a short distance horizontally and/or vertically. In order to characterize the microscale environment, the radiative properties, flow patterns, and thermal behavior need to be considered. There are various strategies that can be used to achieve this:
 - Locate the sensors at one point and carefully describe the site including potential factors that could influence the measurement.
 - Deploy many sensors to capture the spatial variability.
 - Use numerical modeling (e.g., computational fluid dynamics (CFDs), such as Reynolds-averaged Navier–Stokes (RANS), large eddy simulation (LES), or direct numerical simulation (DNS)) to inform where sensors should be located to investigate the process of interest. Numerical models can also be used to indicate how measurements might vary across the microscale [52.94] and to understand potential bias due to the location of sensors.
 - Use hardware modeling (e.g., wind tunnels, water tanks) to understand microscale variability [52.82, 95, 96].
- *Local or neighborhood scale.* Cities consist of areas with similar *repeated* characteristics, which, typically, were built at about the same time, with similar form (driven by architectural design or planning regulations) and materials. These neighborhoods (10^2 – 10^4 m), if sufficiently large, can create their own local-scale climates. Several distinct neighborhood types can be found within a city (e.g., old residential, new residential, low-rise commercial, large parks, etc.). Within each neighborhood, the urban form and characteristics should be similar. That is, building height, height-to-width ratio of the street canyons, land-cover fractions, age of vegetation, etc., should not vary much across the neighborhood. Local-scale measurements aim to provide representative measurements for the neighborhood (i.e., to capture the influence of this composite surface). It is, thus, critical to mount instruments high enough above the roughness elements to get an integrated response: measurements should be within the constant flux layer (Sect. 52.3.1). Flux measurements using eddy covariance are usually local-scale observations.
- *City scale.* At the city scale (0.5×10^4 – 10^5 m), measurements need to describe the integrated effect of the city as a whole.

In both hardware and numerical modeling there are some critical challenges and benefits. Challenges come from models assuming neutral atmospheric stability, but in urban areas this is less frequent than in other environments. In addition, models are by definition simplifications of reality and influential details may be missed or too expensive to include. However, both hardware and numerical models provide the capability to assess observations already made and/or inform measurement strategies for future campaigns.

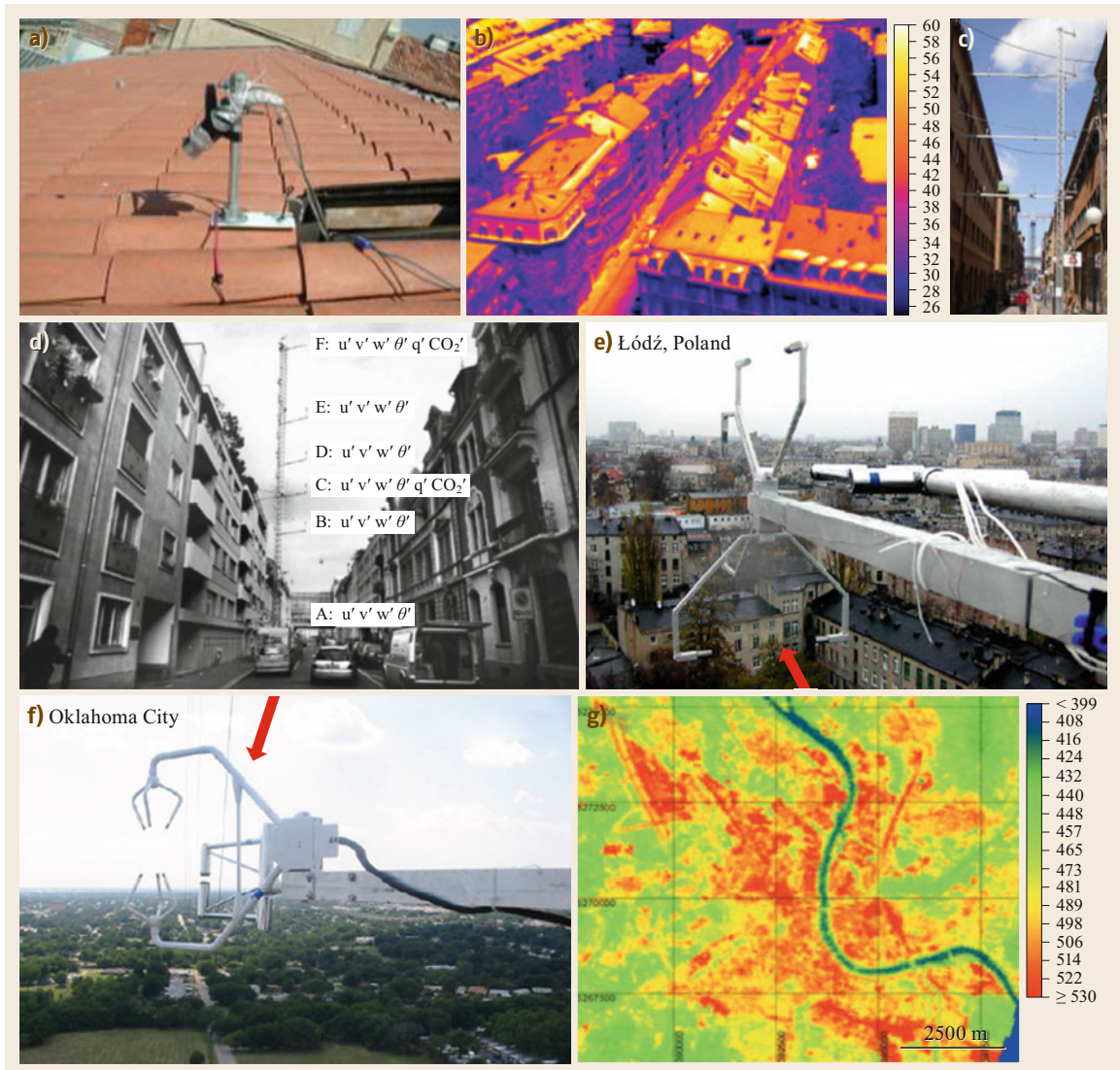


Fig. 52.2a–g Examples of urban measurements at various scales. (a) Microscale measurements of the temperature of a tiled roof surface in Marseilles. (b) Thermal image showing substantial microscale differences in surface temperature in an urban canyon and nearby courtyards in Basel (after [52.55] © American Meteorological Society, used with permission). The temperature variability reflects the variation in building materials, roof angle, and receipt of solar radiation. Eddy-covariance towers equipped with multiple measurement levels in (c) Gothenburg (after [52.97] with permission from Elsevier) and (d) Basel (after [52.98]) to study microscale flow patterns in street canyons and local-scale turbulence (top levels). Local-scale eddy-covariance measurements in (e) Łódź and (f) Oklahoma. (g) City-scale, longwave emissions from Basel (after [52.98]) derived from satellite data with calibration against surface measurements

52.3.3 Characterizing the Urban Environment

There are several parameters used to describe important characteristics of the urban environment (Table 52.1). There have been a number of efforts to provide basic parameters (e.g., [52.99]), to map areas with common

characteristics (e.g., [52.100]) and to provide tools to determine parameters (e.g., [52.24]).

- *Height*. The height of the roughness elements (i.e., buildings and trees) is a key parameter.
 - It is often used to estimate the depth of the roughness sublayer and, hence, to identify a suit-

- able height for neighborhood-scale measurements [52.90, 91], Sects. 52.3.1 and 52.3.2).
- It is one of the main controls on the aerodynamic roughness parameters.
- It is used to derive the *height-to-width* ratio of street canyons. This is related to the sky view factor and affects the radiation balance. In canyons with a large height-to-width ratio (H:W), radiation trapping can occur, reducing the outgoing longwave radiation and nocturnal cooling [52.101, 102]. The ratio is also used to classify flow at the microscale between skimming, wake, and isolated flow [52.90, 103]. These distinguish flow that skims across the tops of the buildings, penetrates the canyons generating turbulent wakes, or is affected by isolated buildings.
- *Aerodynamic roughness parameters.* There are many different methods to estimate roughness length (z_0) and zero plane displacement height (z_d) from information about the surface roughness elements [52.90, 104]; the simplest require only the mean height of the roughness elements, whilst others also take into account the height variability through the standard deviation of building height and maximum building height or consider the density of buildings through the plan area index or the frontal area index [52.104]. As well as these morphometric methods to estimate z_d and z_0 , there are anemometric methods that use wind speed data to

calculate z_d and z_0 from in-situ measurements. Unfortunately, there is considerable variation between the methods and no clear way to identify the *true* values [52.104]. Recent research appears to suggest that accounting for the variability in building height is important, with the consequence that the displacement height could be much higher than traditionally thought [52.104–106]. An accurate displacement height is important for applications that employ similarity scaling (e.g., comparison of results between sites, calculation of heat fluxes from scintillometry).

- *Plan area index.* The plan area index is the ground area of buildings relative to the total ground area of interest. This two-dimensional (2-D) description, along with other *surface cover fractions*, provides a way to broadly classify the surface composition. The fraction of vegetated area is an important control on energy partitioning and carbon dioxide fluxes and, therefore, can often explain differences in observed fluxes between neighborhoods [52.48, 107–109]. Surface cover fractions are a helpful metric for assessing how similar or different neighborhoods are, and, therefore, are useful for planning network sampling density across a city. Furthermore, surface cover fractions are extremely useful for making comparisons between studies and can even be used to predict typical fluxes for areas where measurements are not available [52.107, 110].

Table 52.1 Parameters used to describe the urban environment

Parameter	Description	Applications
Mean height of roughness elements	Mean building height Mean tree height	Wind profile Radiation modeling
Variability in height of roughness elements	Standard deviation of building/tree height	Wind profile
Maximum height of roughness elements	Maximum building/tree height	Wind profile
Aerodynamic roughness length	The height above the zero-plane displacement height that the mean wind speed becomes 0 m s^{-1} . This is based on extrapolation of the logarithmic wind speed profile towards the surface into the roughness sublayer	Wind profile Similarity scaling Dispersion Scintillometry Model input
Zero-plane displacement height	With tall roughness elements, the logarithmic wind profile is displaced vertically upwards. The displacement height is the mean height of the momentum sink	Wind profile Model input
H:W	Height to width ratio of street canyon	Sky view factor Flow regime
Surface cover fraction	Proportion of buildings, paved surfaces, grass, trees, water, and soil in the study area	Bowen ratio estimation Energy balance studies
LCZ	Local climate zones – neighborhoods with particular characteristics	Thermal regime UHI (urban heat island) studies Provides typical values for parameters, e.g., for model input

- *Frontal area index.* The frontal area index is the total surface area presented to the oncoming flow (i.e., walls) relative to the total ground area. The frontal area index varies with wind direction.

To describe, compare, and parameterize urban areas, the features of an urban canyon are often used. The urban canyon space can be complex, as it comprises a range of urban forms, from widely-spaced single-storey buildings, to row houses with long canyons and intersections, to tall building clusters. However,

the parameters in Table 52.1 provide a way to classify the urban environment in terms of a few key quantities. The benefits of such a classification are illustrated by the widespread usage of the local climate zones (LCZ); these describe typical regions of an urban area (e.g., compact mid-rise, sparsely built, heavy industry) and suggest reasonable ranges for these parameters [52.111]. The intent of the LCZ are to allow international comparison of observational sites so that a city and the rural area are better understood and measurements can be put into context.

52.4 Devices and Systems

There is nothing particularly distinct about measurement systems in urban areas per se. Rather, the critical needs are related to siting. Sampling frequencies used during deployments are dependent on sensor design and spatial scales of interest (Chap. 2). In general, new sensors are capable of increasingly rapid sampling, allowing, for example, vertical lidar (light detection and ranging, Chaps. 25 and 27) profiles with shorter gates and more rapid profile repetition. Data acquisition systems will determine how much raw data can be saved or realtime processing can occur (Chap. 2).

52.4.1 Temperature

Whilst it is relatively easy to measure air temperature (Chap. 7), obtaining a representative measurement for an urban area is much more challenging. Numerous studies have investigated the spatial variability in air temperature across a city using a variety of techniques; for example, installing a temperature sensor on a bike or car and traversing (Chap. 50) selected routes through the city [52.112]. The disadvantages of this approach are that it is noncontinuous and labor intensive (data are only generated when and where the traverses are made), and the measurements are not synchronized in time, so the traverses have to be short enough that any change in atmospheric conditions during the traverse is small compared to changes due to spatial variation. For such studies, it is important that the response time of the sensor is fast enough that the measurements correspond to the vehicle location at the specified time and not to the region through which the vehicle was passing several minutes previously.

Recently, crowdsourced data from amateur weather stations [52.7, 113] or mobile telephones [52.114] have been used to demonstrate spatial patterns in temperature. These sources offer a large amount of data but with many quality control issues, such as improper siting

or incorrect metadata. Nevertheless, efforts are being made to make this growing pool of data more useful to atmospheric scientists, for example the development of algorithms to exclude data from amateur weather stations that have likely been installed inside rather than outside buildings [52.115].

In some studies, however, it is the temperature of an internal building that is of interest. An example could be how the temperature inside a building (which is important for the thermal comfort of residents) responds to factors such as height above ground or window aspect in an apartment block [52.116]. Radiation shielding may be necessary, but otherwise small sensors strategically located allow spatial variations to be assessed. With increasing numbers of smart sensors, the sensor itself may play a key role in regulating the thermal environment (e.g., heating on/off, opening windows for natural ventilation).

Vertical profiles of temperature can provide very important data across a range of spatial scales, if there is sufficient resolution. The release of radiosondes is often restricted because of air traffic. Arranging permission for specified flight lines over a city for observations can be extremely difficult and subject to last minute changes. Sensors that are audible at frequencies that humans can hear (e.g., RASS: radio acoustic sounding system, sodar: sonic detection and ranging; Chap. 23) are not usable (i.e., there are too many complaints). Drones or unmanned aircraft systems (UAS) (Chap. 49) provide a platform to mount sensors that allows the 3-D characteristics of the air to be sampled. However, in many urban areas there are very stringent height restrictions because of aviation and privacy concerns. The limitations posed from other mobile traverse systems also apply. Sensors mounted on towers or other infrastructure provide a way to obtain vertical information but are obviously constrained by the height of the structure, and mounting possibilities for towers may be very lim-

ited. Furthermore, the structure itself will modify the flow, which may mean that booms need to be used to minimize the effect on the measurements. Microwave radiometer (Chap. 41) techniques have the potential to provide useful information at greater heights but may be of quite coarse resolution close to the surface. Thus, combining techniques for long-term sampling may be essential. Mobile platforms may provide a useful way to get detailed information close to the surface for short-term studies or intensive observations periods, providing that security permissions allow their use.

Surface temperatures of the urban facets (e.g., walls, roofs, roads) may be measured using noncontact thermal infrared (IRT) sensors (e.g., cameras, pyrgeometers, etc. [52.117–120]) or with fine wire thermocouples attached to a surface with a thin veneer on the surface material covering the sensors ([52.121], Chap. 11). The challenge with IRT sensors or longwave radiometers is that an emissivity is needed to convert the brightness temperature. Measuring emissivity is challenging, and there are only a few spectral libraries with values for urban materials [52.122]. Given the increasing potential of using satellite thermal remote sensing or earth observation [52.123, 124] the need to properly understand the surface heterogeneity (materials and morphology) and the thermal anisotropy requires more detailed observations [52.87, 120, 125, 126].

52.4.2 Humidity

Many studies of temperature also include humidity, and, therefore, the previous comments are also applicable. As errors in humidity measurements are larger at the extremes (Chap. 8), it is important to consider which conditions are of interest and what are acceptable measurement errors.

As the surface-based emissions of water vapor can be immense and variable, the variations in humidity in urban areas can be large. Natural controls include the amount of vegetation, which may be very spatially variable (e.g., very little in the central business district compared to highly vegetated parks), and the density of people and animals [52.127, 128]. In addition, urban infrastructure releases large amounts of moisture, including transport (from fuel combustion), building ventilation (e.g., mechanical vents, windows) and industry (from chimneys releasing water vapor as a byproduct). The implications are that there may be some locations where there are very high humidities for long periods of time. These locations need to be considered when siting instruments. These sources of humidity may be of interest, as they may be the cause of ice fog in high-latitude winters, where the air is regionally extremely dry because of the cold temper-

atures (Chap. 8) and, therefore, be important for road safety. Or they may represent microscale anomalies in a local-scale measurement (e.g., building vents on roofs or mechanical floors in high-rise buildings, Fig. 52.3), which, ideally, would be avoided [52.129].

In hot, humid environments under heat-wave conditions, life-threatening humidity levels may be reached (e.g., Chicago 1995 [52.131–133] and Indian cities [52.134]; Sect. 52.8.1), which require that sensors perform very well under challenging observational conditions (Chap. 8). As airports are highly impacted by fog, and small changes in topography and moisture sources can influence the location and density of fog, a dense network of sensors that perform well at high humidity may be warranted in addition to visibility sensors.

52.4.3 Wind

The type and location of wind sensors depends on the application (Chap. 9). Is it the mean wind speed and direction that are of interest, or rather the variability of the flow and intensity of turbulence? For microscale studies, such as the flow around a building, measurements are made close to the building and within the roughness sublayer. For local-scale studies, the measurements should be above the roughness sublayer, such that the wind field is not distorted by individual roughness elements but rather responds to the properties of the neighborhood. For measurements much higher than the roof level or over long distances, wind profiles can be derived from lidar measurements [52.135] (Chap. 27); a variety of outputs are available depending on the scan strategy and number of lidars available.

Extreme spatial variability and the impact of individual buildings and streets on the flow have been demonstrated in the few studies which deployed a vertical profile of sonic anemometers from within the street canyon to above the roughness sublayer (Fig. 52.4). For the lowest measurement levels, the observations suggest vortices within the street canyon; near the rooftops turbulence is greatest, and wakes may be induced by the edges of buildings; at a greater height above the rooftops the flow is less turbulent and less spatially variable. Given the financial and logistical challenges of making such observations, models have been used to extend such analyses, for example to analyze the role of height-to-width ratio, roof shape, or canyon orientation on the flow patterns [52.136]. Wind tunnel studies, either using idealized arrays [52.137] or replicas of real cities [52.138] have also proven to be very useful in probing spatial variability [52.82]. It has also been shown that vehicles can influence the flow, both due to their presence (i.e., their roughness) and motion (i.e.,

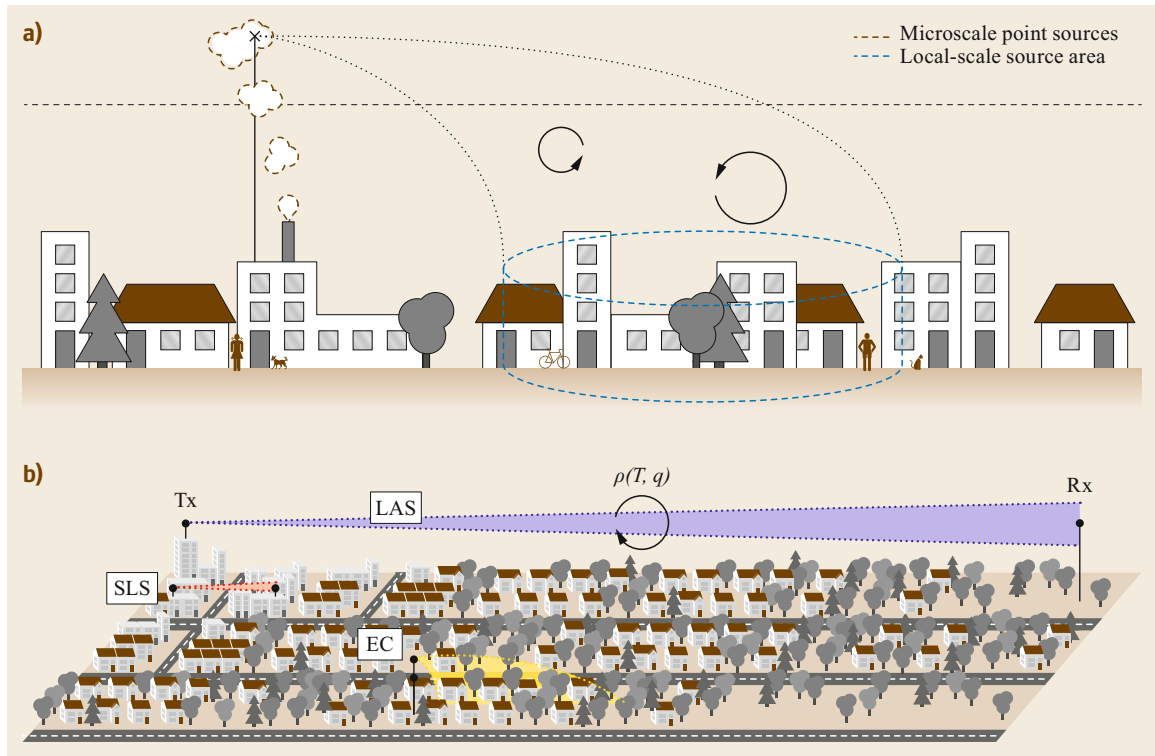


Fig. 52.3 (a) Eddy-covariance measurements (cross) of the local-scale source area influenced by a microscale point source. The *black dashed line* indicates the blending height or top of the roughness sublayer or the bottom of the constant flux (or inertial sub)layer (Chap. 1) (after [52.129] with permission from Elsevier). (b) Difference of source area extent (not to scale) between a large-aperture scintillometer (LAS, *blue violet*), a surface-layer scintillometer (SLS, *red*), and an eddy-covariance station (EC, *yellow*). For the scintillometer a beam is sent from the transmitter (Tx) to a receiver (Rx). The beam is scattered by turbulent eddies that have a density ρ at temperature T and humidity q (after [52.130] © IOP Publishing, reproduced with permission)

generation of wakes [52.57], which affects the transport and dispersion of pollutants in the street canyon.

52.4.4 Precipitation

Intense precipitation can have rapid and severe consequences for areas of cities or across the whole city. Intense rainstorms combined with large fractions of impervious surfaces (e.g., buildings, pavement) enhance runoff rates (in terms of both volume and timing) potentially causing flooding. Snow, hail, and freezing rain can make transport networks unusable or dangerous. Intense hailstorms can cause a lot of damage to infrastructure and vehicles. Intense convective precipitation, if associated with thunderstorms, also has the potential of electrical activity creating another hazard to both citizens and infrastructure.

As noted (Sect. 52.2), the measurement of precipitation processes in urban areas is notoriously difficult. The measurement of rain even in the most ideal setting (i.e.,

without large rough elements) is challenging (Chap. 12), and the problem is further complicated in the city. The sheltering effects of buildings, the impact of enhanced wind speed at roof level, and drip effects from vegetation all need to be considered. For example, driving rain causes the windward wall of buildings to be much wetter than the leeward wall. This may be of significant interest at the building scale but prevents meaningful measurements when detecting city-wide movement of a storm. Often, an extensive roof top (i.e., to minimize edge effects) with appropriate surroundings may be the best site for precipitation measurements in dense urban areas.

Radar data with increasing spatial resolution and the ability to dynamically change scan patterns with meteorological conditions (Chap. 32) likely provide the best neighborhood-scale information on precipitation events. The calibration in urban areas may be challenging, and the noise from tall buildings may require additional processing of data. However, with these systems, storm paths can be tracked across cities, allowing

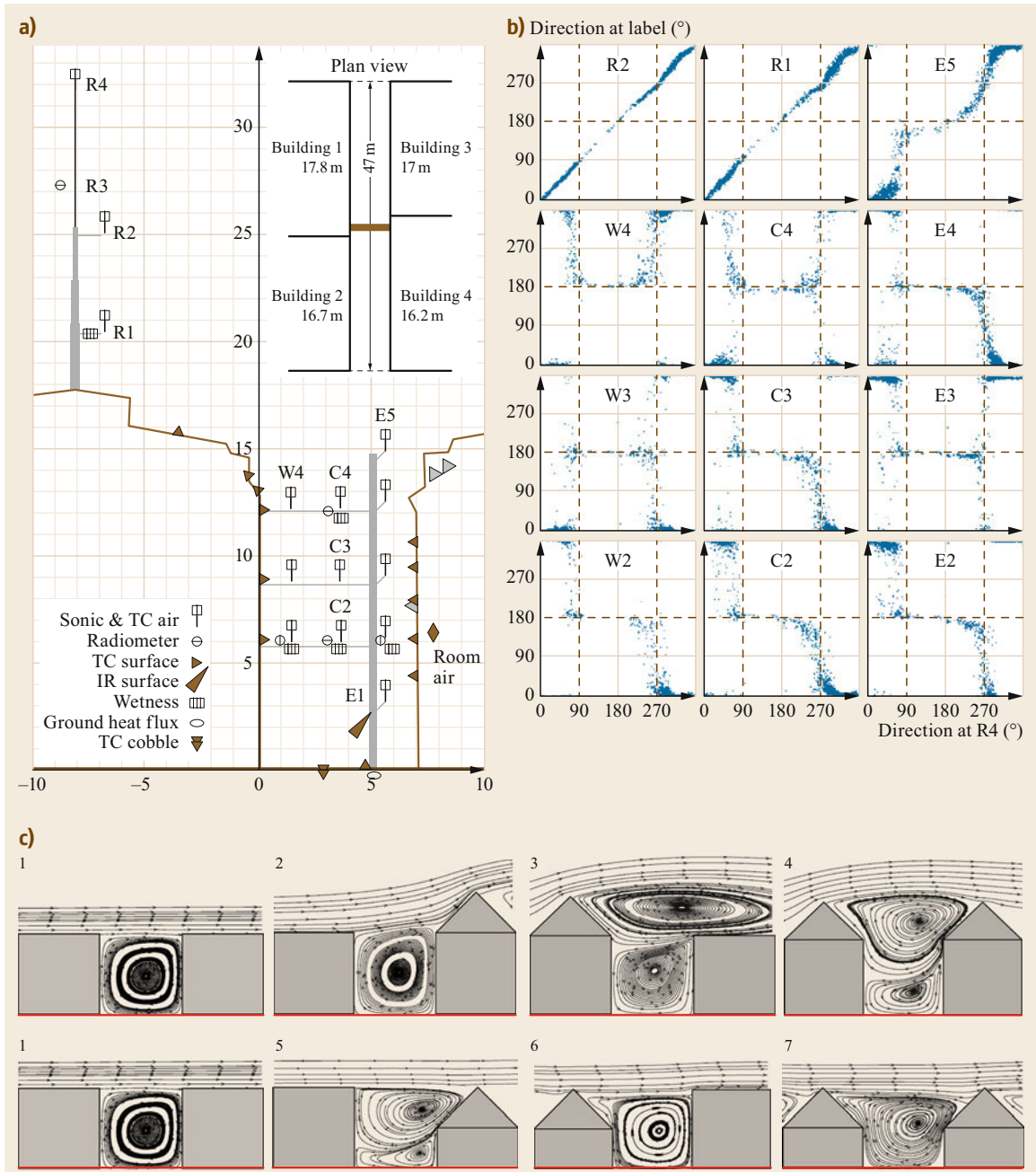


Fig. 52.4a-c Observations of wind direction with sonic anemometers (number and letter) in and above an urban canyon at 13 positions **(a)** shown relative to the highest sensor (R4). Conditions are when R4 has wind speeds $> 2 \text{ m s}^{-1}$ **(b)** (after [52.97] with permission from Elsevier). The influence of the surroundings becomes greater as the sensors move away from the highest sensor. Numerical simulations **(c)** show how roof shape and building height influence flow in the street canyon and the formation of vortices (after [52.136] with permission from Elsevier)

forecasts to be made of where the highest intensity precipitation is expected (Sect. 52.8.3).

There are various attributes of hydrometeors beyond ground-based rainfall that may be of interest. The drop-size distribution can be measured using a disdrom-

eter; a present weather detector (PWD) allows type and visibility to be observed, and automatic lidar and ceilometers (ALC) can detect the presence of raindrop size aerosols from large attenuated backscatter. The performance of different sensors has been compared generally (e.g., [52.139]). As the impact of hydrometers may be significant to transport operations and safety (e.g., fog to airports, intense precipitation to roads) these sensors are often located in the vicinity of this infrastructure.

52.4.5 Radiation

All four components of radiation (i.e., incoming and outgoing shortwave and longwave radiation) are affected by the urban environment. Incoming shortwave radiation can be reduced by polluted urban areas [52.140]. Outgoing shortwave radiation depends on the albedo of the surface, which is usually lower in urban areas than over vegetated surfaces (Chap. 11), but it of course depends on the urban materials used and thus varies between regions [52.122, 141, 142]. Incoming longwave radiation is affected by cloud cover and atmospheric transmissivity. Outgoing longwave radiation is generally larger in urban areas, because the surface temperatures tend to be higher than for vegetated areas, although radiation trapping can occur in street canyons, which restricts the outgoing flux. As always, the application determines the variables of interest and, hence, the type of sensor (pyranometer, pyrgeometer, four-component radiometer, or net radiometer), and how it should be deployed.

There are numerous applications related to radiation. These include determining the optimum position for solar panels to maximize solar energy receipt [52.143–145] or estimating the radiation load on pedestrians [52.146–148]. For the latter, a specialized setup may be used that involves mounting three four-component radiometers perpendicular to each other at 1.1 m above ground level to determine the 3-D radiation field [52.149].

Scale models (e.g., [52.82, 150–152]) have been built to allow for facet-scale radiative exchange processes to be measured. The models can be large (e.g., 1 : 4) if realistic variability of the facets is to be captured. For local-scale energy balance studies, the source area needs to be large enough to include a representative range of surfaces. The simple radiative footprint can be approximated using the height above the surface as 50% of the radius of the field of view [52.153], although large roughness elements and the presence of vertical surfaces make the calculation of the probable area more challenging.

A typical urban canyon will have multiple materials that are part of the walls (e.g., glass windows, painted wooden doors, brick and mortar walls), the road (e.g., concrete side walk, asphalt road with painted lines, vegetated median), and the roof (e.g., pitched with terracotta tiles). These facets are at a range of pitch angles and orientations, and their detailed arrangements all modify the radiative exchange. The impact of microscale variability on local-scale radiation measurements can be large in some situations [52.154]. By plotting outgoing shortwave radiation as a function of the azimuth angle, it is also possible to identify reflections from roof windows (Fig. 52.5).

To get a detailed understanding of which surfaces are being measured or to calculate representative surface temperatures, models such as DART (discrete anisotropic radiative transfer) [52.156] or TUF3-D (temperatures of facets in 3-D) [52.157] are very useful. Given the complexity of urban surfaces and the coarseness of thermal remote sensing these models provide a way to interpret the details of ground-based observations [52.126, 158] and consider how satellite-based sensors are biased (e.g., towards the surfaces seen, [52.87, 125]).

Spectral measurements of radiation (Chap. 11) are extremely useful for architects and others in construction industries interested in material characteristics and their interaction with both shortwave and longwave radiation at the microscale. Measurements in the shortwave region are reasonably straightforward and can be easily be conducted outdoors, as the sample sizes are large and, therefore, easily representative of the material (although measurements of glass and highly reflective coatings are more difficult). Measurements in the longwave region are more challenging, because it is necessary to account for longwave emission from all objects (Chap. 11; [52.122]).

52.4.6 Surface Energy Fluxes

The most widely used and most direct method to study the surface energy balance in urban (and nonurban) areas is eddy covariance (Chap. 55). Particular challenges in the urban environment are mostly related to siting (i.e., achieving sufficient measurement height in the constant flux layer and a reasonably homogeneous source area), although the size of fluxes (very low water vapor fluxes in city centers have large uncertainties) and appropriate quality control measures (Sect. 52.6) are also important considerations.

A sonic anemometer provides the momentum flux and the turbulent sensible heat flux. With a gas analyzer, latent heat fluxes and carbon dioxide fluxes can

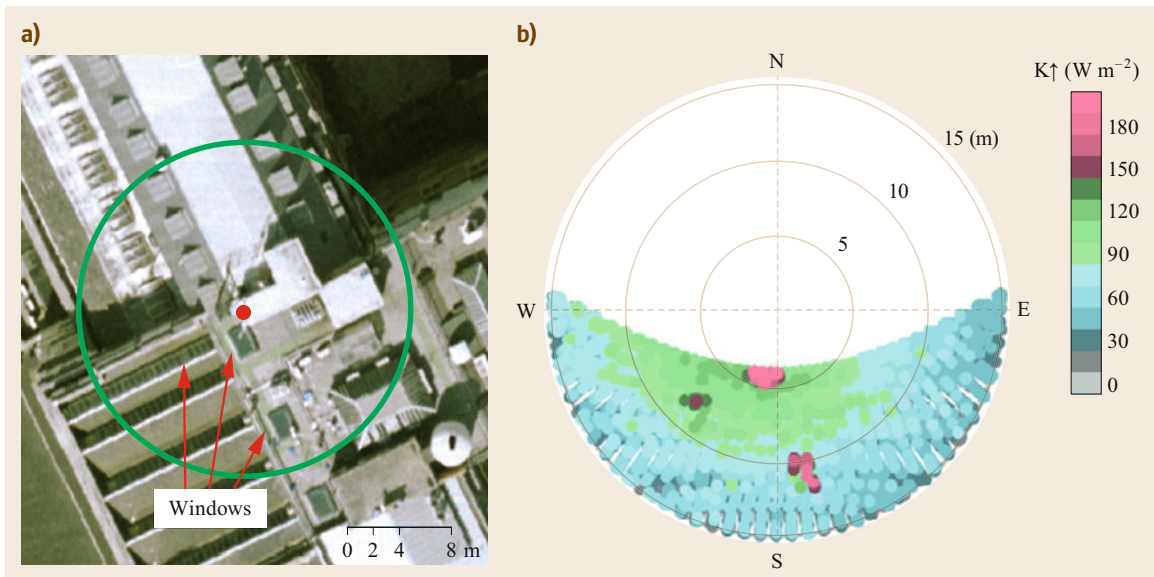


Fig. 52.5 (a) Aerial photo (NERC ARSF 2008) of the field of view of a downwards facing radiometer installed at King's College London (the *green line* indicates 80% of the source area) and (b) the observed median reflected shortwave radiation arranged by solar azimuth angle and distance of maximum specular reflection. Three windows clearly show up as peaks in the outgoing shortwave radiation (after [52.155])

be obtained (and more exotic species with more expensive equipment). For energy balance studies, a key issue is the compatibility of the turbulent flux footprint, which influences the sensible and latent heat flux measurements, and the radiometer footprint, which influences the net radiation measurements. Due to the very different measurement principles, these two footprints are not the same. Whilst the radiometer footprint is fixed in time (although influenced by diurnal and seasonal shadow patterns), the turbulent flux footprint varies with atmospheric conditions including wind direction, friction velocity, and stability (Chaps. 1 and 55). Differences in footprint (Chap. 1) composition can be estimated using footprint models [52.159–164] and minimized by siting the instruments such that the composition of their source areas is similar. Note, however, that footprint models were developed for much simpler environments, although they are widely used in urban areas to provide an indication of the region influencing the measurements.

Scintillometry (Chap. 34) can provide observations of sensible and latent heat flux [52.48, 49, 56, 130]. Scintillometry offers several advantages: a much larger source area than eddy covariance, meaning that the fluxes are representative of a larger area and, thus, often vary less with atmospheric conditions; robust statistics at shorter timescales allowing for shorter averaging times than are recommended for eddy covari-

ance; and minimal influence of turbulence distortion around the mounting structures at the ends of the path, which means that it can be easier to find suitable sites. However, there are also disadvantages: fluxes must be derived from structure parameters via similarity theory and so have large uncertainties due to the potentially questionable applicability of similarity theory and uncertainties in the input data (particularly z_0 and z_d) [52.52]; and sites must be obtained for both the transmitter and receiver with clear line-of-sight between.

It is worth considering what is expected from the observations given the site characteristics (e.g., land cover, climate), so that resources can be directed to where they are most useful. For example, a city-center site with very little vegetation or available water would be expected to partition very little energy into evaporation, and it may not be worth the effort to try to measure such small water vapor fluxes. On the other hand, if the study is specifically interested in the water balance, additional steps may need to be taken to try to improve the reliability of the water-vapor flux measurements.

In addition to net radiation, the sensible heat flux, and latent heat flux, the energy balance can include considerable contributions from the anthropogenic heat flux and storage heat flux, which cannot be directly measured (Sect. 52.1.2). Storage heat flux has been estimated by surface energy balance residuals or by

combining numerous sensors (e.g., surface infrared thermometers (Chap. 11), internal air temperature sensors, and soil heat flux plates (Chap. 49) etc. [52.25, 165]), but there are large uncertainties associated with these approaches. The anthropogenic heat flux has been estimated by the energy balance residual [52.166, 167] or by using eddy-covariance sensors to estimate releases from individual buildings [52.129]. Since the anthropogenic heat flux is associated with human activities, it is extremely variable in space and time. It is always an extra source of energy and impacts heat fluxes and the surface temperature [52.22, 23]. As well as an anthropogenic heat flux, there is also an anthropogenic moisture flux [52.168]. The importance of the anthropogenic heat flux, relative to other fluxes, varies by season and location. For example, in cold (high-latitude) climates, the flux can be much larger than the wintertime net all-wave radiation contributing to both the sensible heat flux but also to the latent heat flux. The anthropogenic heat flux is typically much larger in the central business district than in residential areas (e.g., almost three orders of magnitude [52.169]) because of the much higher population density, larger building volume, and associated energy demand. In hot climates, air conditioning becomes a more important source but constitutes a smaller percentage of the net all-wave radiation, as the shortwave radiation receipt is higher [52.23].

These considerations mainly concern the local-scale energy balance. At the microscale, the transport of air into and out of buildings is of interest, as processes within buildings influence the external environment. Concerning the construction industry, a critical issue in building design is ventilation. This can be natural (e.g., opening windows, cracks around doors) or mechanical (e.g., air conditioning, forced ventilation systems). The chosen location of ventilation inlets needs to consider air quality (e.g., proximity to vehicles or other building exhausts [52.170, 171]) and meteorological conditions (pressure, wind speed, and wind direction). Forced ventilation systems modify microscale conditions significantly (e.g., [52.129]) and can impact temperature, humidity, and air quality in the street canyon.

52.4.7 Boundary Layer Height

As noted (Sects. 52.1 and 52.3), the boundary layer height is of critical interest in urban areas because of air quality concerns. The air plume that extends downwind

of a city is also potentially of ecological interest or concern, as it is likely to carry warmer polluted air, which influences the surroundings (e.g., [52.172]), is entrained into the developing boundary layer associated with the new nonurban area, or is transported regionally or globally. Downwind urban effects are starting to be detected by satellite remote sensing, which needs to be calibrated by aircraft mounted and other sensors [52.173] (Chaps. 16–18, 25, 26, and 55).

A variety of different types of lidars (Chaps. 25–27, and 38) and aircraft sensors (e.g., AMDAR data; Sect. 52.1) can be used to infer properties of the urban boundary layer (e.g., mixing height (MH), mixed layer height (MLH)). However, the measurement technique is critical, depending on the boundary layer variable obtained (e.g., the height of the temperature inversion, MH with a threshold in vertical velocity variance measured with doppler lidar [52.79, 174], or MLH from aerosol concentrations from attenuated aerosol backscatter as measured by a lidar or ceilometer [52.75, 175]). Lidars allow continuous measurements with high temporal resolution, but few cities have this as an ongoing capability. Comparisons between lidar techniques also highlight the critical need to stratify conditions by cloud cover, as averaging across all conditions can apparently give contradictory results biased by synoptic frequency relative to sensor behavior [52.175]. Additional uncertainty between lidar sensor types arises from differences in gate size and range (Chaps. 25–27, and 38), where the first measurement is usable above ground level. For all techniques, analysis of the raw sensor data needs to be done with care. There is still minimal knowledge about the horizontal variability of MLH (or MH) with land cover beyond short-term campaigns, and appreciable measurement uncertainties require involved data processing.

Automatic lidar and ceilometer (ALC) measurement of cloud height and cover, and more recently, volcanic ash [52.176], can also be used to determine MLH characteristics [52.177–182]. A range of software is available for analysis of ALC data [52.183–188]. The ceilometer attenuated backscatter signal can provide high resolution (5 or 10 m vertically, 15 or 30 s samples) information on aerosols [52.189, 189, 190], and their use is being explored for data assimilation (Sect. 52.8.3). Doppler lidars [52.175, 191–193] and other research lidars and profilers have provided an extensive amount of knowledge from short campaigns (e.g., [52.194–199]).

52.5 Specifications

For sensors and their expected specifications, see the appropriate chapters throughout this volume (Chap. 1). Decisions about the appropriate or required instrument specifications are dependent on having a good understanding of the objective of the measurements, the acceptable measurement errors, and the expected spatial and temporal variability of processes or phenomena to be measured at the scale of interest. Other issues that must be factored in are the likelihood of theft or vandalism (i.e., cost versus benefit), and where the sensors can practically be installed. With current technologies, there is often a tradeoff between quality and quantity of instruments. Again, the appropriate choice is obviously dependent on the goal of the measurements. If quantity seems helpful, then it is always essential to incorporate some higher specification instruments to provide ongoing interinstrument performance assessments on a routine basis (e.g., by bringing sensors into a lab for

calibration, locating sensors near each other in the field, or using mobile transects).

When designing a network, it is important to consider which factors to keep constant between sites and which factors to vary. For example, a network of temperature sensors spread over a city with the aim of measuring the spatial variability between neighborhoods requires individual sensors to be installed in as similar a location as possible. If some sensors are in sunlit locations, and others in shaded ones, it is likely that direct insolation will largely determine the measurements, probably concealing any spatial variation due to neighborhood characteristics. It is useful to build in some redundancy to network design so that initial hypotheses based on a few sensors can be supported or rejected by additional measurements.

In almost all applications, there is an essential need for those designing meteorological sensor networks to



Fig. 52.6 Location of a weather station in St James' Park (red circle) London, which has much lower sky-view factor (SVF) (white) than the surrounding built-up areas. The streets are black (lower SVF) and the roofs white (higher SVF). SVF at 4 m-resolution modified (after [52.146])

work closely with the end users of the data to ensure that the most appropriate instrumentation and network design (e.g., spacing, configuration) are selected. For almost all urban measurements, standard WMO surface station design [52.200] is very likely to result in a station being located in an anomalous location rather than a typical urban setting (e.g., in London, St James’

Park location versus the surrounding urban landscape – Fig. 52.6). Therefore, careful consideration of the process and the scales of interest (Sect. 52.3) should guide the network or instrument deployment. Guidelines exist for urban surface stations [52.201] (Chap. 63), but these should be used as guidance and not as regulations in light of the need for the measurements.

52.6 Quality Control

When quality controlling data from urban environments, it is important to remember that methods designed for rural environments may not be applicable in urban areas. The simplest example is threshold checking, whereby data exceeding a specified threshold value are excluded on the basis that they are not physically reasonable. For vegetated mid-latitude environments, an upper threshold for the sensible heat flux of, say, 400 W m^{-2} may be appropriate, whereas this value may often be exceeded in an urban area subject to the same synoptic conditions. Thus, threshold values may need adjusting so that they are better suited to the urban area, in the same way as adjustments may be required for a site in a different climate zone. Given the strong influence of surface cover within a city and the resulting variability in meteorological conditions (Sect. 52.3.3), general values for a city are likely to be inappropriate and need to be developed with an understanding of the local and microscale conditions and the goal of measurements themselves.

For eddy covariance, several of the quality-control tests given in the literature are not particularly useful in urban areas. The low friction velocity screening to reject nighttime periods with low turbulence is not always applicable, since the rough urban surface tends to generate high friction velocities, and the urban atmosphere often remains unstable through the night [52.202]. Integral turbulence tests may also not be appropriate, since urban measurements may not follow ideal surface-layer scaling [52.203, 204]; even for nonurban locations, there is variation between the similarity relations identified at different sites. Energy balance closure is often used as an indicator of the reliability of the measurements (Chaps. 11 and 55). However, this cannot really be used in the urban environment, since the storage heat flux and the anthropogenic heat flux can be significant yet cannot be accurately directly determined. In most cases, the storage flux must be estimated as the residual of the energy balance (Sect. 52.1.2) and a degree of closure assumed.

Due to the heterogeneity of urban areas, measurements generally have greater variability (i.e., from one

measurement to the next) compared to more micro-meteorologically *ideal* sites. Some urban studies use longer averaging periods to produce more stable results, but there is always a compromise to be made with stationarity.

Depending on the site, additional quality control measures may be necessary. These can include removing spikes or troughs in radiation data caused by an isolated reflection or shadow, excluding data from certain wind sectors that may be unduly influenced by nearby structures, or minimizing the impact of microscale anthropogenic heat emissions on local-scale flux measurements. Procedures are available to filter out nearby microscale sources of waste heat, water, and carbon dioxide emissions from eddy-covariance measurements; when applied to the roof of a university building in London, this approach made it possible to simultaneously provide an estimate of the building-scale anthropogenic heat flux, as well as the local-scale fluxes [52.129].

Other methods to quantify the anthropogenic contribution to the observed dataset include comparing different time periods. Comparison of weekdays and weekends frequently reveals differences that can be related to patterns of human behavior (e.g., in the diurnal pattern of carbon dioxide fluxes related to traffic patterns and commuting to and from work [52.52, 205]). Similarly, the larger anthropogenic heat flux in winter resulting from increased building heating demand is often identifiable in comparisons of summer and winter data. For these methods to work successfully, it is important that datasets are long enough that there are no significant differences in weather patterns between weekdays and weekends that could explain the observed differences.

More focused studies have investigated the impact of a particular event, such as an irrigation ban [52.18, 206], driving restrictions [52.207], the Olympic Games [52.208], or the Burning-Man ephemeral city [52.209]. For these comparisons, it is crucial to consider any changes in background conditions (e.g., synoptic meteorology), as well as the change in human behavior.

Data collated from citizen weather stations require additional quality control, since there is limited knowledge of the station available (compared to stations installed and maintained by research groups), and

some stations may be inappropriately sited for the research question. These issues were briefly discussed in Sect. 52.4, and further details can be found elsewhere (e.g., [52.115])

52.7 Maintenance

Maintenance details for any specific instrument will be found in the relevant chapters elsewhere in this volume. Urban specific maintenance issues are most likely related to air pollution, which means that sensors become covered in aerosols (large and small) more rapidly than in more pristine environments and may require more frequent cleaning. Given the wide range of vegetation normally present in cities, biological contamination (e.g., leaves in rain gauges, pollen on radiation shields) may extend over longer time periods than in areas with less diversity in species where phenology changes occur over a short period.

In urban areas, sensors must often be mounted higher, either to make it difficult for the public to interfere with them or to be at sufficient height to make representative measurements. Hence, the equipment may be difficult to access, which complicates maintenance. For example, if cherry pickers are needed to access towers, this usually results in additional cost and/or the restriction of limited periods when such vehicles can park on roadways, therefore requiring out-of-hours maintenance. Maintenance of sensors mounted high above the ground may require people qualified to climb towers or access rooftops. Health, safety, and liability issues may mean the owners (or managers) of the infrastructure specify who can work on the infrastructure. This can necessitate both payment (or negotiated in-kind support) to access the installation and also the training of those who have access (e.g., riggers) to undertake the work that needs to be done.

Having instruments accessible over the internet, which is normally achievable in urban areas (due to

good mobile network coverage), allows for a large amount of diagnosis and repair to be undertaken without necessarily needing direct access to the instruments. Through careful setup, data can be delivered for routine systematic processing and errors that require attention flagged (e.g., automatic email messages sent to appropriate groups) and responded to rapidly. Preliminarily, data analysis can also be undertaken (e.g., fluxes calculated) for review on a regular basis.

During maintenance visits it is extremely helpful to always take photographs of sites. As urban areas change rapidly, knowing the time window when changes occur that might impact measurements is extremely helpful. Given that such changes occur at many times scales (e.g., reroofing, roadworks, new buildings), it is almost impossible to capture all of these. If understanding the chronology of such changes is important, then webcams can provide valuable data that also include information on other relevant human activities (e.g., traffic patterns, snow clearing).

Regularly noting relevant activities (e.g., outdoor irrigation, outdoor lighting) in a digitally searchable record can also help with data interpretation. Such records can help determine if a *real* phenomenon is being measured and the data should be kept, or if there is some sort of interference or contamination that justifies data removal, instrument maintenance, or resiting. With mobile phones it is possible for these data to be captured and emailed to team members or uploaded to a database in realtime to allow feedback or suggested remedies to be made while people are in the field.

52.8 Applications

As integrated urban weather, water, environment, and climate services are developed [52.9,210], the need for observations will become increasingly more clearly specified (Fig. 52.7). Today there is a wide range of reasons for needing observations in urban areas. This section provides examples of applications that require meteorological measurements in urban environments.

It is critical that the meteorological observation networks are designed in conjunction with an interdisciplinary team so that the meteorologist is aware of the critical thresholds that need to be measured well (e.g., absolute humidity thresholds), and so that those using the data are aware of how they may differ from previously used data (e.g., Sect. 52.8.2) for design and decision-making. For example, air-quality related ob-

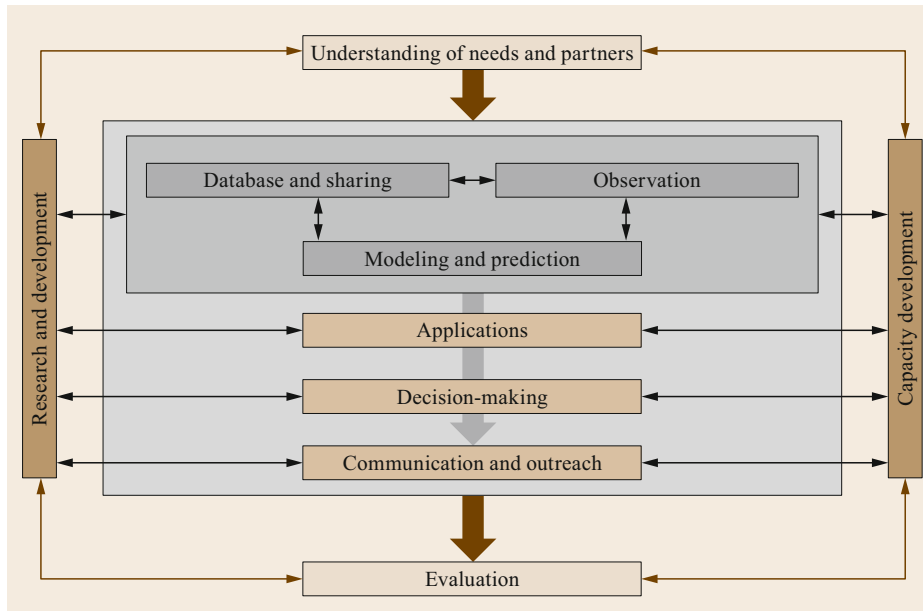


Fig. 52.7 Components of an urban integrated Hydro-Meteorological, Climate, and Environmental Service. Central to this are observations, closely linked to modeling and the communication in an appropriate manner to a wide range of end users who need information in an appropriate form for their decision-making processes (after [52.9, 210])

servations need collaboration between practitioners in a range of fields (e.g., transport planning, environmental meteorologists (i.e., measuring air-quality concentrations and fluxes), atmospheric chemistry researchers (e.g., trying to understand new chemical species and their reactions within the urban environments), public health planners, and physical meteorologists).

52.8.1 Human Comfort and Health

As extreme heat and cold cause premature deaths and hospital admissions of vulnerable people [52.148, 211], increasing efforts are being directed to the development of models to predict the areas within cities most at risk and to identify preventative measures. The evaluation of these models requires observations at ever higher spatial resolution. The conditions (e.g., temperature, humidity, radiation) in the areas where people are exposed (e.g., bedroom, workspace, metro, parks, courtyards) need to be known. As people adapt over time to their regional climate, it is insufficient to have an absolute value of, say, temperature. Rather, knowledge of the temperature distribution is needed so that a percentile-related metric [52.143] can be used. This requires long-term measurements to provide the city context.

Outdoors, people are exposed to a wide range of conditions that need to be forecast (with well-verified models) throughout the year: heat, humidity, ultraviolet radiation, wind chill, pollutants, etc. That is, the need for information about microscale variations in conditions is extensive. Critical limits vary with the

people exposed: school children, outdoor workers, elderly walkers, marathon runners, etc. In addition to forecasting the expected conditions, it is also critical for agencies to recommend mitigation strategies. These also need to be evaluated through a combination of careful measurements and modeling to ensure that interventions have the intended consequences. It should be remembered that resources may be limited for those at risk. Through careful design of observation campaigns to look at the local-scale and microscale variability of the pertinent meteorological variables *in conjunction with* socioeconomic data, public health experts and building designers can ensure that the available resources are most appropriately used, and support is directed to the most appropriate areas when an extreme condition is forecast.

Under conditions of high humidity combined with high temperatures [52.148, 212, 213], the body becomes unable to cool itself, which can be fatal. Thus, cities located in hot, humid climates need to ensure that the human comfort metrics also take humidity into account.

However, in many cities winter conditions can put increased stress on health services [52.214] with reduction in absolute humidity thought to be critical to allowing the influenza virus to spread more easily [52.215, 216]. Thus, awareness of spatial variability of hygrothermal conditions provides useful data for public health planning. With COVID-19, the importance of observations of ventilation patterns both indoors and outdoors, has become very apparent to help understand aerosol transport in urban areas.

As modeling becomes more sophisticated, identifying where people may be exposed to critical thresholds (both indoors and outdoors) allows for mitigation strategies to be developed. A comprehensive view of this hygrothermal environment is needed, which covers indoors (e.g., schools, hospitals, theaters), microscale (e.g., streets), local scale (e.g., across city neighborhood variability), and public transport (e.g., vehicles, stations). This requires standardized instrument siting, instrument calibration, sensor sampling and postprocessing, and rapid data transmission. These data also have important value for postevent evaluation of whole-system services.

In many cities, the residents are exposed to harmful air-quality concentrations [52.217]. With changing vehicle fleet characteristics, building materials and interiors fabrics, travel to work patterns (e.g., increasing number of cars in China [52.218], increasing number of bicycles in London [52.219]), the chemical nature of emissions is always changing. The need to measure these well for high spatial resolution emissions inventories (< 1 km) is critical for chemical transport modeling (CTM). With numerous new low-cost atmospheric chemistry sensors being developed ensuring that the data are appropriate still requires significant efforts [52.220, 221] and consideration of deployment strategies [52.222].

Chemical emissions tend to have regular patterns based on human activities (e.g., weekday, weekend travel patterns, daily cooking patterns [52.223]). However, with changing meteorology, the chemical reactions change (e.g., temperature, ultraviolet (UV), humidity) [52.224, 225], and with changing boundary layer depth the volume of air that they are being mixed in, and, therefore, the concentrations, change. Air-quality measurements are often microscale measurements (e.g., curb side) and, therefore, should be expected to vary significantly if sensors are moved (Sect. 52.3). As the emissions vary with socioeconomic context (e.g., where cooking occurs, what fuels are used [52.226, 227]), governance or regulatory environments (e.g., permitted concentrations, enforcement policies), and climatic settings, the critical meteorological thresholds may vary. With time, acceptable air-quality limits also change (e.g., London in the 1950s compared to now).

52.8.2 Building Design, Construction, Management, and Planning

The time scales that need to be considered for buildings and planning are long (from decades to centuries), which means structures and cities will experience meteorological extremes and should be built

to withstand these. On the other hand, the presence of new buildings or a development will impact its surroundings (e.g., wind flow, shadows, thermal environment), and this must be considered at the planning stage.

Although datasets exist to provide likely climate conditions (e.g., building design, typical meteorological year (TMY), design summer year (DSY), test reference year (TRY)), these are often regional (e.g., 14 for the UK CISBE (Chartered Institution of Building Services Engineers) [52.228]; ASHRAE (American Society of Heating, Refrigerating, and Air-Conditioning Engineers) for 8118 places globally [52.229]) and, therefore, extremely coarse relative to any building or subdivision development. During building design, decisions are made about lighting, ventilation, heating, cooling, etc. using these data. A growing awareness of building energy use and its consequences (e.g., greenhouse gas emissions) has encouraged low-energy alternative design-rating systems (e.g., BREEAM (building research establishment environmental assessment method) [52.230], LEED (leadership in energy and environmental design) [52.231]). Many local planning authorities use these as part of their decision process. As natural heating, ventilation, and cooling are encouraged, the local climatological conditions become increasingly important to ensure that these buildings work as intended.

The canopy layer (2 m air temperature) urban heat island under extreme conditions can be > 10°C warmer in the center of a city [52.5], but parks of varying size can significantly modify these temperatures. Thus, the design of buildings needs to consider the neighborhood and the microscale siting effects, otherwise the building (e.g., ventilation) will not operate as intended once built. This can lead to costly renovations (e.g., [52.232, 233]) and/or operating costs [52.234]. For example, if the buildings are too hot in summer, then the need for air conditioning in the future may result in additional energy use and have feedback on outdoor temperatures, making it necessary for others to also install air conditioning. Not taking the wind environment into account can be deadly and/or require expensive retrofitting [52.235]. If the building surroundings are not pleasant (e.g., too little or too much shading) then it may not be a desirable location (e.g., in terms of office rentals).

Thus, a good understanding of the microclimate setting is critical for design. Clearly, the constraint in real-world measurements is that the new structure does not exist, and once it does, it will modify the microscale climate (or a larger region). Models to *urbanize* meteorological data are being developed [52.143]. It is important that these be well evaluated with a wide range

of meteorological observations (including mean variables and their extremes).

Monitoring of postoccupancy buildings (both indoors and outdoors) provides more robust data for model verification. Understanding critical thresholds in building operations (e.g., what should trigger ventilation changes), how people are using the building (e.g., is this as designers intended or not), and how the building managers maintain and operate the building systems is important. There is an increasing tendency for building designers to be required to operate the building for some time after completion to ensure the stated efficiencies are achieved. With careful network design, indoor and outdoor building operations can be automated and allow for dynamic response to people's behavior and meteorological conditions. This can improve the efficiency of buildings from assuming fixed seasonal heating (e.g., on and off by date in a year) independent of users' needs (e.g., unseasonably hot or cold), which may also save money.

Green and blue infrastructure (e.g., trees, green roofs, water features) are generally encouraged [52.236, 237], but their success is dependent on having enough water for them to provide the intended benefits (e.g., cooling, water retention, flood prevention). Careful monitoring of the soil moisture status can help ensure that the irrigation (if needed) is sufficient to maintain vegetation without excess use (or wastage) of this resource. Irrigation (or hosepipe) bans are a common local policy to save water (e.g., [52.238–240]), which have other local climate impacts. To prevent peri-urban wildfires, there are occasions where intense irrigation is being considered (e.g., Melbourne). Thus, there is an increasing need to have a good network of soil moisture,

temperature, and wind sensors to assess how to provide benefits at the microscale and manage city-scale threats (e.g., water shortages, wildfires, heat waves, flooding).

52.8.3 Data Assimilation

Data assimilation to improve forecasting in urban areas is starting to be explored. Increasing locally generated energy (e.g., from solar (PV, photovoltaic) panels, wind turbines) requires high-resolution meteorological data (e.g., 1 min cloud cover or solar radiation data) for real-time energy forecasting and power grid management. Dense networks of solar panels can provide useful data as clouds pass over a large city (e.g., 50 km wide) – the early observations from the direction of the synoptic flow provides information that can be used to improve nowcasting (< 6 h) [52.145, 190].

Similarly, rain gauge networks and radar data can be important for providing improved realtime forecasting of flood hazards [52.241]. As the city topography and drainage network are constant over the lifetime of a storm (except in the most damaging of events), once the rainstorm track and intensity are known precalculated flood forecasts can be used to improve the spatial resolution of warnings and reduce the emergency response needs. Sensitivity testing with hydrological models can inform rain gauge network design and radar scanning patterns [52.242].

Ceilometer networks are also being explored to provide a source of data for data assimilation into numerical weather prediction [52.225, 226]. Vertical profiles of attenuated backscatter (Sect. 52.4.7) or other variables are likely to be useful, as they provide an integration across spatial scales (Sect. 52.3; [52.243]).

52.9 Future Developments

Urban areas are extremely complex and, despite progress made in recent years, major challenges remain. There is huge uncertainty in roughness length and displacement height values; the storage heat flux is a significant term in the energy balance but remains extremely difficult to quantify; and models and observations reveal that the flow below the constant flux layer is extremely difficult to characterize. Progress in other areas may be more easily achievable, such as better estimates of anthropogenic heat flux via more detailed information on building energy use and traffic volume. In this respect, greater availability of high-resolution data from energy companies and city authorities would be extremely beneficial. The issues of privacy and commercial sensitivities remain, but as smart cities bring

more and more data together, these difficulties may be overcome more effectively.

Use of big data is likely to develop further as an affordable method to capture spatial variability, particularly if data quality can be improved and uncertainties reduced. The demand for mapped data of various quantities (e.g., temperature, rainfall, air quality) over large areas suggests a greater focus on combining ground-based sensors with satellite-based remote-sensing instruments with numerical models. Unfortunately, satellite-retrieved datasets have been largely developed for nonurban regions and often struggle to give reasonable values in cities [52.87, 125]. Nevertheless, recent efforts to improve understanding [52.119] and accuracy in urban areas could lead to substantial

Table 52.2 Examples of applications of urban measurements

Application	Of interest to	Relevant scale	Relevant variables
Impact assessment for new buildings/roads/parks	Architects, construction industry, town planners	Micro – local	Wind, radiation
Wind load on buildings	Architects, construction industry	Micro	Wind
Optimal location for wind-energy generation	Energy companies, homeowners	Micro	Wind, turbulence
Optimal location for solar panel installation	Energy companies, homeowners	Micro	Radiation
Pedestrian thermal comfort	Town planners	Micro	Temperature, humidity, radiation, wind
Air quality alerts	Health agencies	Local – city	Wind, energy fluxes, boundary layer height

advances in the future [52.123]. Ground-based remote-sensing instrumentation, such as lidars, offer a wealth of information about the flow and turbulence above the city [52.135, 244–246]. Newly developed scan strategies or configurations with multiple lidars [52.247] are also promising in terms of increasing measurement capability.

With taller and taller buildings, established theory breaks down [52.248]. What happens when the roughness sublayer becomes so deep that there is no constant flux layer? Understanding the impacts of tall buildings (i.e., considering vertical as well as horizontal homo-

geneity) is logistically challenging but necessary for understanding the cities of today and correctly representing their effects in mesoscale models.

Over the last 30–40 years, the field of urban meteorology has grown considerably [52.249]. Today, we have a vast amount of data available to us and increasingly closer links with numerous applications (Table 52.2), which means science is being used more and more to influence planning and policy decisions. It is crucial, now more than ever, that urban measurements are conducted and interpreted correctly.

52.10 Further Reading

- Barlow J.F. 2014: Progress in observing and modelling the urban boundary layer, *Urban Climate*, 10, 216–240.
- Feigenwinter C., Vogt, R., Christen, A. Eddy covariance measurements over urban areas in *Eddy Covariance*, M. Aubinet, T. Vesala, and D. Papale, Eds. 2012, pp. 377–397.
- Oke T.R., Mills, G., Christen, A, Voogt, J.A. 2017: *Urban Climates*. Cambridge: Cambridge University Press.
- Pardyjak, E.R., Stoll, R. 2017: Improving measurement technology for the design of sustainable cities *Meas. Sci. Technol.* 28 092001
- World Meteorological Organization (WMO), “Urban Observations,” in *Guide to Meteorological Instruments and Methods of Observation WMO – No 8*, Volume III – Observing Systems, 2018, Chap. 9.

References

- 52.1 UN Department of Economic and Social Affairs: *2018 Revision of world urbanization prospects – Multimedia library – United Nations Department of Economic and Social Affairs* (2018). <https://www.un.org/development/desa/publications/2018-revision-of-world-urbanization-prospects.html>, Accessed 21 July 2021
- 52.2 L. Parshall, K. Gurney, S.A. Hammer, D. Mendoza, Y. Zhou, S. Geethakumar: Modeling energy consumption and CO₂ emissions at the urban scale: Methodological challenges and insights from the United States, *Energy Policy* **38**(9), 4765–4782 (2010)
- 52.3 M. Fragkias, J. Lobo, D. Strumsky, K.C. Seto: Does size matter? Scaling of CO₂ emissions and US urban areas, *PLoS One* **8**(6), e64727 (2013)
- 52.4 D.E. Pataki, H.R. McCarthy, E. Litvak, S. Pincetl: Transpiration of urban forests in the Los Angeles metropolitan area, *Ecol. Appl.* **21**(3), 661–677 (2011)
- 52.5 T.R. Oke, G. Mills, A. Christen, J.A. Voogt: *Urban Climates* (Cambridge Univ. Press, Cambridge 2017)

- 52.6 C.G. Collier: The impact of urban areas on weather, *Q. J. R. Meteorol. Soc.* **132**(614), 1–25 (2006)
- 52.7 Met Office: *Met Office WOW – Home page* (2019). <http://wow.metoffice.gov.uk/>, Accessed 21 July 2021
- 52.8 World Meteorological Organisation: *GFCS – Global framework for climate services* (2019). <http://www.wmo.int/gfcs/>, Accessed 21 July 2021
- 52.9 A. Baklanov, C.S.B. Grimmond, D. Carlson, D. Terblanche, X. Tang, V. Bouchet, B. Lee, G. Langendijk, R.K. Kolli, A. Hovenspyan: From urban meteorology, climate and environment research to integrated city services, *Urban Clim.* **23**, 330–341 (2018)
- 52.10 UN Habitat: *Planning for climate change* (2014). <https://unhabitat.org/books/planning-for-climate-change-a-strategic-values-based-approach-for-urban-planners-cities-and-climate-change-initiative/>, Accessed 21 July 2021
- 52.11 UN Habitat: *Goal 11: Sustainable development knowledge platform* (2019). <https://sustainabledevelopment.un.org/sdg11>, Accessed 21 July 2021
- 52.12 P. Pillai, B. Philips, P. Shyamsundar, K. Ahmed, L. Wang: *Climate Risks and Adaptation in Asian Coastal Megacities* (World Bank, Washington, D.C. 2010)
- 52.13 E. Dickson, J.L. Baker, D. Hoornweg, T. Asmita: *Urban Risk Assessments* (World Bank, Washington, D.C. 2012)
- 52.14 World Bank: *Urban development overview* (2018). <http://www.worldbank.org/en/topic/urbandevelopment/overview#2>, Accessed 21 July 2021
- 52.15 S. Grimmond, W. Secretariat: Towards integrated urban weather, environment and climate services, *World Meteorol. Organ. Bull.* **63**(1), 10–14 (2014)
- 52.16 H.-P. Schmid, C.S.B. Grimmond, H.A. Cleugh, T.R. Oke: Spatial variability of energy fluxes in urban terrain, *Boundary-Layer Meteorol.* **54**, 249–276 (1991)
- 52.17 T.R. Oke: The energetic basis of the urban heat island, *Q. J. R. Meteorol. Soc.* **108**(455), 1–24 (1982)
- 52.18 C.S.B. Grimmond, T.R. Oke, H.A. Cleugh: The role of 'rural' in comparisons of observed suburban-rural flux differences, *Int. Assoc. Hydrol. Sci. Publ.* **212**, 165–174 (1993)
- 52.19 P. Gober, B. Brazel, R. Quay, W. Myint, S. Grossman-Clarke, A. Miller, S. Rossi: Using watered landscapes to manipulate urban heat island effects: How much water will it take to cool Phoenix?, *J. Am. Plan. Assoc.* **76**(1), 109–121 (2009)
- 52.20 P. Ramamurthy, E.R. Pardyjak: Toward understanding the behavior of carbon dioxide and surface energy fluxes in the urbanized semi-arid Salt Lake Valley, Utah, USA, *Atmos. Environ.* **45**(1), 73–84 (2011)
- 52.21 L. Järvi, A. Nordbo, H. Junninen, A. Riikonen, J. Moilanen, E. Nikinmaa, T. Vesala: Seasonal and annual variation of carbon dioxide surface fluxes in Helsinki, Finland, in 2006–2010, *Atmos. Chem. Phys.* **12**(18), 8475–8489 (2012)
- 52.22 C.S.B. Grimmond: The suburban energy balance: Methodological considerations and results for a mid-latitude west coast city under winter and spring conditions, *Int. J. Climatol.* **12**(5), 481–497 (1992)
- 52.23 D.J. Sailor: A review of methods for estimating anthropogenic heat and moisture emissions in the urban environment, *Int. J. Climatol.* **31**, 189–199 (2011)
- 52.24 F. Lindberg, C.S.B. Grimmond, A. Gabey, B. Huang, C.W. Kent, T. Sun, N.E. Theeuwes, L. Järvi, H.C. Ward, I. Capel-Timms, Y. Chang, P. Jonsson, N. Krave, D. Liu, D. Meyer, K.F.G. Olofson, J. Tan, D. Wästberg, L. Xue, Z. Zhang: Urban Multi-scale Environmental Predictor (UMEP): An integrated tool for city-based climate services, *Environ. Model. Softw.* **99**, 70–87 (2018)
- 52.25 S.M. Roberts, T.R. Oke, C.S.B. Grimmond, J.A. Voogt: Comparison of four methods to estimate urban heat storage, *J. Appl. Meteorol. Climatol.* **45**(12), 1766–1781 (2006)
- 52.26 B. Offerle, C.S.B. Grimmond, K. Fortuniak: Heat storage and anthropogenic heat flux in relation to the energy balance of a Central European city centre, *Int. J. Climatol.* **25**(10), 1405–1419 (2005)
- 52.27 H.E. Landsberg: *The Urban Climate* (Academic Press, Cambridge 1981)
- 52.28 G. Mills: Luke Howard and The Climate of London, *Weather* **63**(6), 153–157 (2008)
- 52.29 L. Howard: *The Climate of London, Deduced from Meteorological Observations Made in the Metropolis*, Vol. I (W. Phillips, London 1818)
- 52.30 L. Howard: *The Climate of London. Deduced from Meteorological Observations, Made at Different Places in the Neighbourhood of the Metropolis*, Vol. II (W. Phillips, London 1820)
- 52.31 W. Schmidt: Die Verteilung der Minimumtemperaturen in der Frostnacht des 12.5.1927 im Gemeindegebiet von Wien, *Fortschr. Landwirtsch.* **2**(21), 681–686 (1927)
- 52.32 W.P. Lowry: Urban effects on precipitation amount, *Prog. Phys. Geogr.* **22**(4), 477–520 (1998)
- 52.33 J.M. Shepherd: A review of current investigations of urban-induced rainfall and recommendations for the future, *Earth Interact.* **9**(12), 1–27 (2005)
- 52.34 R. Bornstein, Q. Lin: Urban heat islands and summertime convective thunderstorms in Atlanta: Three case studies, *Atmos. Environ.* **34**(3), 507–516 (2000)
- 52.35 D. Rosenfeld: Suppression of rain and snow by urban and industrial air pollution, *Science* **287**(5459), 1793–1796 (2000)
- 52.36 S.A. Changnon, F.A. Huff, R.G. Semonin: METROMEX: An investigation of inadvertent weather modification, *Bull. Am. Meteorol. Soc.* **52**(10), 958–968 (1971)
- 52.37 S.A. Changnon: The La Porte weather anomaly – Fact or fiction?, *Bull. Am. Meteorol. Soc.* **49**(1), 4–11 (1968)

- 52.38 E.X. Berry, R.W. Beadle: Project METROMEX, *Bull. Am. Meteorol. Soc.* **55**(2), 86–121 (1974)
- 52.39 Principal Investigators of METROMEX: METROMEX update, *Bull. Am. Meteorol. Soc.* **57**(3), 304–308 (2018)
- 52.40 D. Doll, J.K.S. Ching, J. Kaneshiro: Parameterization of subsurface heating for soil and concrete using net radiation data, *Boundary-Layer Meteorol.* **32**(4), 351–372 (1985)
- 52.41 J.K.S. Ching, J.F. Clarke, J.M. Godowitch: Modulation of heat flux by different scales of advection in an urban environment, *Boundary-Layer Meteorol.* **25**(2), 171–191 (1983)
- 52.42 J.M. Godowitch, J.K.S. Ching, J.F. Clarke: Evolution of the nocturnal inversion layer at an urban and nonurban location, *J. Appl. Meteorol.* **24**(8), 791–805 (1985)
- 52.43 J.M. Godowitch, J.K.S. Ching, J.F. Clarke: Spatial variation of the evolution and structure of the urban boundary layer, *Boundary-Layer Meteorol.* **38**(3), 249–272 (1987)
- 52.44 S. Grimmond, A. Christen: Flux measurements in urban ecosystems, *FluxLetter Newsl. FLUXNET* **5**(1), 1–8 (2012)
- 52.45 Y. Liu, H.Z. Liu, L. Wang: The vertical distribution characteristics of integral turbulence statistics in the atmospheric boundary layer over an urban area in Beijing, *Sci. China Earth Sci.* **60**(8), 1533–1545 (2017)
- 52.46 M. Kanda, R. Moriwaki, M. Roth, T. Oke: Area-averaged sensible heat flux and a new method to determine zero-plane displacement length over an urban surface using scintillometry, *Boundary-Layer Meteorol.* **105**(1), 177–193 (2002)
- 52.47 J.-P. Lagouarde, M. Irvine, J.-M. Bonnefond, C.S.B. Grimmond, N. Long, T.R. Oke, J.A. Salmond, B. Offerle: Monitoring the sensible heat flux over urban areas using large aperture scintillometry: Case study of Marseille city during the ESCOMPTE experiment, *Boundary-Layer Meteorol.* **118**(3), 449–476 (2006)
- 52.48 H.C. Ward, J.G. Evans, C.S.B. Grimmond: Multi-scale sensible heat fluxes in the suburban environment from large-aperture scintillometry and eddy covariance, *Boundary-Layer Meteorol.* **152**(1), 65–89 (2014)
- 52.49 H.C. Ward, J.G. Evans, C.S.B. Grimmond, J. Bradford: Infrared and millimetre-wave scintillometry in the suburban environment – Part 1: Structure parameters, *Atmos. Meas. Tech.* **8**(3), 1385–1405 (2015)
- 52.50 M. Zieliński, K. Fortuniak, W. Pawlak, M. Siedlecki: Influence of mean rooftop-level estimation method on sensible heat flux retrieved from a large-aperture scintillometer over a city centre, *Boundary-Layer Meteorol.* **164**(2), 281–301 (2017)
- 52.51 M. Zieliński, K. Fortuniak, W. Pawlak, M. Siedlecki: Long-term turbulent sensible-heat-flux measurements with a large-aperture scintillometer in the centre of Łódź, Central Poland, *Boundary-Layer Meteorol.* **167**, 469–492 (2018)
- 52.52 B. Crawford, C.S.B. Grimmond, H.C. Ward, W. Morrison, S. Kotthaus: Spatial and temporal patterns of surface-atmosphere energy exchange in a dense urban environment using scintillometry, *Q. J. R. Meteorol. Soc.* **143**(703), 817–833 (2017)
- 52.53 H. Sugawara, A. Inagaki, M. Roth, M. Kanda: Evaluation of scintillometry measurements of fluxes of momentum and sensible heat in the roughness sublayer, *Theor. Appl. Climatol.* **126**(3–4), 673–681 (2016)
- 52.54 S.-H. Lee, J.-H. Lee, B.-Y. Kim: Estimation of turbulent sensible heat and momentum fluxes over a heterogeneous urban area using a large aperture scintillometer, *Adv. Atmos. Sci.* **32**(8), 1092–1105 (2015)
- 52.55 J.A. Salmond, M. Roth, T.R. Oke, A. Christen, J.A. Voogt: Can surface-cover tiles be summed to give neighborhood fluxes in cities?, *J. Appl. Meteorol. Climatol.* **51**(1), 133–149 (2012)
- 52.56 H.C. Ward, J.G. Evans, C.S.B. Grimmond: Infrared and millimetre-wave scintillometry in the suburban environment – Part 2: Large-area sensible and latent heat fluxes, *Atmos. Meas. Tech.* **8**(3), 1407–1424 (2015)
- 52.57 S. Di Sabatino, P. Kastner-Klein, R. Berkowicz, R.E. Britter, E. Fedorovich: The modelling of turbulence from traffic in urban dispersion models – Part I: Theoretical considerations, *Environ. Fluid Mech.* **3**(2), 129–143 (2003)
- 52.58 K.J. Allwine, J. Shinn, G. Streit, K. Clawson, M. Brown: Overview of URBAN 2000: A multiscale field study of dispersion through an urban environment, *Bull. Am. Meteorol. Soc.* **83**(4), 521–536 (2002)
- 52.59 K.J. Allwine, M.J. Leach, J.C.L.W. Stockham, J.S. Shinn, R.P. Hosker, J.F. Bowers, J.C. Pace: Overview of Joint Urban 2003: An atmospheric dispersion study in Oklahoma City. In: *Symp. Plan. Nowcast. Forecast. Urban Zone Eighth Symp. Integr. Obs. Assim. Syst. Atmos. Oceans Land Surf.* (2004) p. J7.1
- 52.60 S.R. Hanna, J. White, Y. Zhou, A. Kosheleva: Analysis of Joint Urban 2003 (JU2003) and Madison Square Garden 2005 (MSG05) meteorological and tracer data (2006 – Annual2006_6urban). In: *86th AMS Ann. Meet, Atlanta* (2006) p. j7.1
- 52.61 S.J. Arnold, H. ApSimon, J. Barlow, S. Belcher, M. Bell, J.W. Boddy, R. Britter, H. Cheng, R. Clark, R.N. Colville, S. Dimitroulopoulou, A. Dobre, B. Grealley, S. Kaur, A. Knights, T. Lawton, A. Makepeace, D. Martin, M. Neophytou, S. Neville, M. Nieuwenhuijsen, G. Nickless, C. Price, A. Robins, D. Shallcross, P. Simmonds, R.J. Smalley, J. Tate, A.S. Tomlin, H. Wang, P. Walsh: Introduction to the DAPPLE air pollution project, *Sci. Total Environ.* **332**(1–3), 139–153 (2004)
- 52.62 R.M. Harrison, M. Dall'Osto, D.C.S. Beddows, A.J. Thorpe, W.J. Bloss, J.D. Allan, H. Coe, J.R. Dorsey, M. Gallagher, C. Martin, J. Whitehead, P.I. Williams, R.L. Jones, J.M. Langridge, A.K. Benton, S.M. Ball, B. Langford, C.N. Hewitt, B. Davison, D. Martin, K.F. Petersson, S.J. Henshaw,

- I.R. White, D.E. Shallcross, J.F. Barlow, T. Dunbar, F. Davies, E. Nemitz, G.J. Phillips, C. Helfter, C.F. Di Marco, S. Smith: Atmospheric chemistry and physics in the atmosphere of a developed megacity (London): An overview of the REPAR-TEE experiment and its conclusions, *Atmos. Chem. Phys.* **12**(6), 3065–3114 (2012)
- 52.63 S.I. Bohnenstengel, S.E. Belcher: Meteorology, air quality, and health in London: The ClearLo project, *Bull. Am. Meteorol. Soc.* **96**(5), 779–804 (2015)
- 52.64 B. Cros, P. Durand, H. Cachier, P. Drobinski, E. Fréjafon, C. Kottmeier, P.E. Perros, V.-H. Peuch, J.-L. Ponche, D. Robin, F. Said, G. Toupance, H. Wortham: The ESCOMPTE program: An overview, *Atmos. Res.* **69**(3–4), 241–279 (2004)
- 52.65 P.G. Mestayer, P. Durand, P. Augustin, S. Bastin, J.-M. Bonnefond, B. Bénech, B. Campistron, A. Coppalle, H. Delbarre, B. Dousset, P. Drobinski, A. Druilhet, E. Fréjafon, C.S.B. Grimmond, D. Groleau, M. Irvine, C. Kergomard, S. Kermadi, J.-P. Lagouarde, A. Lemonsu, F. Lohou, N. Long, V. Masson, C. Moppert, J. Noilhan, B. Offerle, T.R. Oke, G. Pigeon, V. Puygrenier, S. Roberts, J.-M. Rosant, F. San'id, J. Salmond, M. Talbaut, J. Voogt: The urban boundary-layer field campaign in Marseille (UBL/CLU-ESCOMPTE): Set-up and first results, *Boundary-Layer Meteorol.* **114**, 315–365 (2005)
- 52.66 C.L. Muller, L. Chapman, C.S.B. Grimmond, D.T. Young, X. Cai: Sensors and the city: A review of urban meteorological networks, *Int. J. Climatol.* **33**(7), 1585–1600 (2013)
- 52.67 C.L. Muller, L. Chapman, C.S.B. Grimmond, D.T. Young, X.-M. Cai: Toward a standardized metadata protocol for urban meteorological networks, *Bull. Am. Meteorol. Soc.* **94**(8), 1161–1185 (2013)
- 52.68 L. Chapman, C.L. Muller: The Birmingham Urban Climate Laboratory: An open meteorological test bed and challenges of the smart city, *Bull. Am. Meteorol. Soc.* **96**(9), 1545–1560 (2015)
- 52.69 E.L. Warren, D.T. Young, L. Chapman, C. Muller, C.S.B. Grimmond, X.-M. Cai: The Birmingham Urban Climate Laboratory – A high density, urban meteorological dataset, from 2012–2014, *Sci. Data* **3**, 160038 (2016)
- 52.70 J.B. Basara, B.G. Illston, C.A. Fiebrich, P.D. Browder, C.R. Morgan, A. McCombs, J.P. Bostic, R.A. McPherson, A.J. Schroeder, K.C. Crawford: The Oklahoma City microne, *Meteorol. Appl.* **18**(3), 252–261 (2011)
- 52.71 S. Pulkkinen, V. Chandrasekar, A.-M. Harri: Nowcasting of precipitation in the high-resolution Dallas–Fort Worth (DFW) urban radar remote sensing network, *IEEE J. Sel. Top. Appl. Earth Obs. Remote Sens.* **11**(8), 2773–2787 (2018)
- 52.72 J. Tan, L. Yang, C.S.B. Grimmond, J. Shi, W. Gu, Y. Chang, P. Hu, J. Sun, X. Ao, Z. Han: Urban integrated meteorological observations: Practice and experience in Shanghai, China, *Bull. Am. Meteorol. Soc.* **96**(1), 85–102 (2015)
- 52.73 M.-S. Park, S.-H. Park, J.-H. Chae, M.-H. Choi, Y. Song, M. Kang, J.-W. Roh: High-resolution urban observation network for user-specific meteorological information service in the Seoul Metropolitan Area, South Korea, *Atmos. Meas. Tech.* **10**(4), 1575–1594 (2017)
- 52.74 B.E.A. Fisher, J.J. Erbrink, S. Finardi, P. Jeannot, S. Joffre, M.G. Morselli, U. Pechinger, P. Seibert, D.J. Thomson: *Cost Action 710 – Final Report: Harmonisation of the Pre-processing of Meteorological Data for Atmospheric Dispersion Models* (Office for Official Publications of the European Communities, Luxembourg 1998)
- 52.75 P. Seibert, F. Beyrich, S.E. Gryning, S. Joffre, A. Rasmussen, P. Tercier: Review and intercomparison of operational methods for the determination of the mixing height, *Atmos. Environ.* **34**(7), 1001–1027 (2000)
- 52.76 W.R. Moninger, R.D. Mamrosh, P.M. Pauley: Automated meteorological reports from commercial aircraft, *Bull. Am. Meteorol. Soc.* **84**(2), 203–216 (2003)
- 52.77 C. Drüe, W. Frey, A. Hoff, T. Hauf: Aircraft type-specific errors in AMDAR weather reports from commercial aircraft, *Q. J. R. Meteorol. Soc.* **134**(630), 229–239 (2008)
- 52.78 C.S.B. Grimmond: Progress in measuring and observing the urban atmosphere, *Theor. Appl. Climatol.* **84**(1–3), 3–22 (2006)
- 52.79 J.F. Barlow: Progress in observing and modelling the urban boundary layer, *Urban Clim.* **10**, 216–240 (2014)
- 52.80 W.F. Dabberdt: Urban meteorological measurements. In: *Urban Meteorology: Forecasting, Monitoring, and Meeting Users' Needs*, ed. by Committee on Meteorology (National Academies Press, Washington, D.C. 2012) pp. 137–148
- 52.81 E.R. Pardyjak, R. Stoll: Improving measurement technology for the design of sustainable cities, *Meas. Sci. Technol.* **28**(9), 092001 (2017)
- 52.82 M. Kanda: Progress in the scale modeling of urban climate: Review, *Theor. Appl. Climatol.* **84**(1–3), 23–33 (2006)
- 52.83 C.S.B. Grimmond: *Observing London: Weather Data Needed for London to Thrive* (London Climate Change Partnership, London 2013)
- 52.84 C.S.B. Grimmond, M. Roth, T.R. Oke, Y.C. Au, M. Best, R. Betts, G. Carmichael, H. Cleugh, W. Dabberdt, R. Emmanuel, E. Freitas, K. Fortuniak, S. Hanna, P. Klein, L.S. Kalkstein, C.H. Liu, A. Nickson, D. Pearlmutter, D. Sailor, J. Voogt: Climate and more sustainable cities: Climate information for improved planning and management of cities (producers/capabilities perspective), *Procedia Environ. Sci.* **1**(1), 247–274 (2010)
- 52.85 National Research Council: *Urban Meteorology: Forecasting, Monitoring, and Meeting Users' Needs* (National Academies Press, Washington, D.C. 2012)
- 52.86 W.F. Dabberdt, M.A. Carroll, D. Baumgardner, G. Carmichael, R. Cohen, T. Dye, J. Ellis, G. Grell, S. Grimmond, S. Hanna, J. Irwin, B. Lamb,

- S. Madronich, J. McQueen, J. Meagher, T. Odman, J. Pleim, H.P. Schmid, D.L. Westphal: Meteorological research needs for improved air quality forecasting, *Bull. Am. Meteorol. Soc.* **85**(4), 563–586 (2004)
- 52.87 J.A. Voogt, T.R. Oke: Thermal remote sensing of urban climates, *Remote Sens. Environ.* **86**(3), 370–384 (2003)
- 52.88 Q. Weng: Thermal infrared remote sensing for urban climate and environmental studies: Methods, applications, and trends, *ISPRS J. Photogramm. Remote Sens.* **64**(4), 335–344 (2009)
- 52.89 I.D. Stewart: A systematic review and scientific critique of methodology in modern urban heat island literature, *Int. J. Climatol.* **31**(2), 200–217 (2011)
- 52.90 C.S.B. Grimmond, T.R. Oke: Aerodynamic properties of urban areas derived from analysis of surface form, *J. Appl. Meteorol.* **38**(9), 1262–1292 (1999)
- 52.91 M. Roth: Review of atmospheric turbulence over cities, *Q. J. R. Meteorol. Soc.* **126**(564), 941–990 (2000)
- 52.92 The Local: *Smog Monday: Paris air pollution levels to hit dangerous high* (2018). <https://www.thelocal.fr/20180219/smog-monday-paris-air-pollution-levels-to-hit-dangerous-high>, Accessed 21 July 2021
- 52.93 P. Chandola: *Beijing imposes traffic measures to curb air pollution* (2015). <https://www.downtoearth.org.in/news/air/beijing-imposes-traffic-measures-to-curb-air-pollution-50659>, Accessed 21 July 2021
- 52.94 M.-F. King, H.L. Gough, C. Halios, J.F. Barlow, A. Robertson, R. Hoxey, C.J. Noakes: Investigating the influence of neighbouring structures on natural ventilation potential of a full-scale cubical building using time-dependent CFD, *J. Wind Eng. Ind. Aerodyn.* **169**, 265–279 (2017)
- 52.95 J.F. Barlow, J. Harrison, A.G. Robins, C.R. Wood: A wind-tunnel study of flow distortion at a meteorological sensor on top of the BT Tower, London, UK, *J. Wind Eng. Ind. Aerodyn.* **99**(9), 899–907 (2011)
- 52.96 H.L. Gough, Z. Luo, C.H. Halios, M.-F. King, C.J. Noakes, C.S.B. Grimmond, J.F. Barlow, R. Hoxey, A.D. Quinn: Field measurement of natural ventilation rate in an idealised full-scale building located in a staggered urban array: Comparison between tracer gas and pressure-based methods, *Build. Environ.* **137**, 246–256 (2018)
- 52.97 I. Eliasson, B. Offerle, C.S.B. Grimmond, S. Lindqvist: Wind fields and turbulence statistics in an urban street canyon, *Atmos. Environ.* **40**(1), 1–16 (2006)
- 52.98 M.W. Rotach, R. Vogt, C. Bernhofer, E. Batchvarova, A. Christen, A. Clappier, B. Feddersen, S.-E. Gryning, G. Martucci, H. Mayer, V. Mitev, T.R. Oke, E. Parlow, H. Richner, M. Roth, Y.-A. Roulet, D. Ruffieux, J.A. Salmond, M. Schatzmann, J.A. Voogt: BUBBLE – An urban boundary layer meteorology project, *Theor. Appl. Climatol.* **81**(3–4), 231–261 (2005)
- 52.99 J. Ching, M. Brown, S. Burian, F. Chen, R. Cionco, A. Hanna, T. Hultgren, T. McPherson, D. Sailor, H. Taha, D. Williams: National urban database and access portal tool, *Bull. Am. Meteorol. Soc.* **90**(8), 1157–1168 (2009)
- 52.100 J. Ching, G. Mills, B. Bechtel, L. See, J. Feddema, X. Wang, C. Ren, O. Brousse, A. Martilli, M. Neophytou, P. Mouzourides, I. Stewart, A. Hanna, E. Ng, M. Foley, P. Alexander, D. Aliaga, D. Niyogi, A. Shreevastava, P. Bhalachandran, V. Masson, J. Hidalgo, J. Fung, M. Andrade, A. Baklanov, W. Dai, G. Milcinski, M. Demuzere, N. Brunzell, M. Pesaresi, S. Miao, Q. Mu, F. Chen, N. Theeuwes: WUDAPT: An urban weather, climate, and environmental modeling infrastructure for the anthropocene, *Bull. Am. Meteorol. Soc.* **99**(9), 1907–1924 (2018)
- 52.101 R.A. Spronken-Smith, T.R. Oke: Scale modelling of nocturnal cooling in urban parks, *Boundary-Layer Meteorol.* **93**(2), 287–312 (1999)
- 52.102 F. Lindberg, C.S.B. Grimmond: Continuous sky view factor maps from high resolution urban digital elevation models, *Clim. Res.* **42**(3), 177–183 (2010)
- 52.103 M. Hussain, B.E. Lee: A wind tunnel study of the mean pressure forces acting on large groups of low-rise buildings, *J. Wind Eng. Ind. Aerodyn.* **6**(3–4), 207–225 (1980)
- 52.104 C.W. Kent, S. Grimmon, J. Barlow, D. Gatey, S. Kotthaus, F. Lindberg, C.H. Halios: Evaluation of urban local-scale aerodynamic parameters: Implications for the vertical profile of wind speed and for source areas, *Boundary-Layer Meteorol.* **164**(2), 183–213 (2017)
- 52.105 M. Kanda, A. Inagaki, T. Miyamoto, M. Gryschka, S. Raasch: A new aerodynamic parameterization for real urban surfaces, *Boundary-Layer Meteorol.* **148**(2), 357–377 (2013)
- 52.106 J.T. Millward-Hopkins, A.S. Tomlin, L. Ma, D. Ingham, M. Pourkashanian: Estimating aerodynamic parameters of urban-like surfaces with heterogeneous building heights, *Boundary-Layer Meteorol.* **141**(3), 443–465 (2011)
- 52.107 C.S.B. Grimmond, T.R. Oke: Turbulent heat fluxes in urban areas: Observations and a local-scale urban meteorological parameterization scheme (LUMPS), *J. Appl. Meteorol.* **41**(7), 792–810 (2002)
- 52.108 A. Christen, R. Vogt: Energy and radiation balance of a central European city, *Int. J. Climatol.* **24**(11), 1395–1421 (2004)
- 52.109 B. Offerle, C.S.B. Grimmond, K. Fortuniak, K. Klysik, T.R. Oke: Temporal variations in heat fluxes over a central European city centre, *Theor. Appl. Climatol.* **84**(1–3), 103–115 (2005)
- 52.110 L. Järvi, C.S.B. Grimmond, A. Christen: The Surface Urban Energy and Water Balance Scheme (SUEWS): Evaluation in Los Angeles and Vancouver, *J. Hydrol.* **411**(3–4), 219–237 (2011)

- 52.111 I.D. Stewart, T.R. Oke: Local climate zones for urban temperature studies, *Bull. Am. Meteorol. Soc.* **93**(12), 1879–1900 (2012)
- 52.112 B.G. Heusinkveld, G.J. Steeneveld, L.W.A. van Hove, C.M.J. Jacobs, A.A.M. Holtslag: Spatial variability of the Rotterdam urban heat island as influenced by urban land use, *J. Geophys. Res. Atmos.* **119**(2), 677–692 (2014)
- 52.113 L. Chapman, C. Bell, S. Bell: Can the crowdsourcing data paradigm take atmospheric science to a new level? A case study of the urban heat island of London quantified using Netatmo weather stations, *Int. J. Climatol.* **37**(9), 3597–3605 (2017)
- 52.114 A. Overeem, J.C.R. Robinson, H. Leijnse, G.J. Steeneveld, B.K.P. Horn, R. Uijlenhoet: Crowdsourcing urban air temperatures from smartphone battery temperatures, *Geophys. Res. Lett.* **40**(15), 4081–4085 (2013)
- 52.115 F. Meier, D. Fenner, T. Grassmann, M. Otto, D. Scherer: Crowdsourcing air temperature from citizen weather stations for urban climate research, *Urban Clim.* **19**, 170–191 (2017)
- 52.116 M. Shahrestani, R. Yao, Z. Luo, E. Turkbeyler, H. Davies: A field study of urban microclimates in London, *Renew. Energy* **73**, 3–9 (2015)
- 52.117 A. Christen, F. Meier, D. Scherer: High-frequency fluctuations of surface temperatures in an urban environment, *Theor. Appl. Climatol.* **108**(1–2), 301–324 (2012)
- 52.118 W. Morrison, S. Kotthaus, C.S.B. Grimmond, A. Inagaki, T. Yin, J.-P. Gastellu-Etchegorry, M. Kanda, C.J. Merchant: A novel method to obtain three-dimensional urban surface temperature from ground-based thermography, *Remote Sens. Environ.* **215**, 268–283 (2018)
- 52.119 B. Crawford, S.B. Grimmond, A. Gabey, M. Marconcini, H.C. Ward, C.W. Kent: Variability of urban surface temperatures and implications for aerodynamic energy exchange in unstable conditions, *Q. J. R. Meteorol. Soc.* **144**(715), 1719–1741 (2018)
- 52.120 C. Adderley, A. Christen, J.A. Voogt: The effect of radiometer placement and view on inferred directional and hemispheric radiometric temperatures of an urban canopy, *Atmos. Meas. Tech.* **8**, 2699–2714 (2015)
- 52.121 J.A. Voogt, T.R. Oke: Complete urban surface temperatures, *J. Appl. Meteorol.* **36**(9), 1117–1132 (1997)
- 52.122 S. Kotthaus, T.E.L. Smith, M.J. Wooster, C.S.B. Grimmond: Derivation of an urban materials spectral library through emittance and reflectance spectroscopy, *ISPRS J. Photogramm. Remote Sens.* **94**, 194–212 (2014)
- 52.123 N. Chrysoulakis, C. Grimmond, C. Feigenwinter, F. Lindberg, J.-P. Gastellu-Etchegorry, M. Marconcini, Z. Mitraka, S. Stagakis, B. Crawford, F. Olofson, L. Landier, W. Morrison, E. Parlow: Urban energy exchanges monitoring from space, *Sci. Rep.* **8**(1), 11498 (2018)
- 52.124 C. Small, D. Sousa, G. Yetman, C. Elvidge, K. MacManus: Decades of urban growth and development on the Asian megadeltas, *Glob. Planet. Change* **165**, 62–89 (2018)
- 52.125 M. Roth, T.R. Oke, W.J. Emery: Satellite-derived urban heat islands from three coastal cities and the utilization of such data in urban climatology, *Int. J. Remote Sens.* **10**(11), 1699–1720 (1989)
- 52.126 W. Morrison, S. Kotthaus, C.S.B. Grimmond, A. Inagaki, T. Yin, J.-P. Gastellu-Etchegorry, M. Kanda, C.J. Merchant: A novel method to obtain three-dimensional urban surface temperature from ground-based thermography, *Remote Sens. Environ.* **215**, 268–283 (2018)
- 52.127 C.A. Kennedy, I. Stewart, A. Facchini, I. Cersosimo, R. Mele, B. Chen, M. Uda, A. Kansal, A. Chiu, K. Kim, C. Dubeux, E. Lebre La Rovere, B. Cunha, S. Pincetl, J. Keirstead, S. Barles, S. Pusaka, J. Gunawan, M. Adegbile, M. Nazariha, S. Hoque, P.J. Marcotullio, F. González Otharán, T. Genena, N. Ibrahim, R. Farooqui, G. Cervantes, A. Duran Sahin: Energy and material flows of megacities, *Proc. Natl. Acad. Sci. U.S.A.* **112**(19), 5985–5990 (2015)
- 52.128 I.D. Stewart, C.A. Kennedy: Metabolic heat production by human and animal populations in cities, *Int. J. Biometeorol.* **61**(7), 1159–1171 (2017)
- 52.129 S. Kotthaus, C.S.B. Grimmond: Identification of micro-scale anthropogenic CO₂, heat and moisture sources – Processing eddy covariance fluxes for a dense urban environment, *Atmos. Environ.* **57**, 301–316 (2012)
- 52.130 H.C. Ward: Scintillometry in urban and complex environments: A review, *Meas. Sci. Technol.* **28**(6), 064005 (2017)
- 52.131 D.P. Johnson, A. Stanforth, V. Lulla, G. Luber: Developing an applied extreme heat vulnerability index utilizing socioeconomic and environmental data, *Appl. Geogr.* **35**(1–2), 23–31 (2012)
- 52.132 K.E. Kunkel, S.A. Changnon, B.C. Reinke, R.W. Arritt: The July 1995 heat wave in the Midwest: A climatic perspective and critical weather factors, *Bull. Am. Meteorol. Soc.* **77**(7), 1507–1518 (1996)
- 52.133 S.A. Changnon, K.E. Kunkel, B.C. Reinke: Impacts and responses to the 1995 heat wave: A call to action, *Bull. Am. Meteorol. Soc.* **77**(7), 1497–1506 (1996)
- 52.134 M. Safi: *India slashes heatwave death toll with series of low-cost measures* (2018). <https://www.theguardian.com/world/2018/jun/02/india-heat-wave-deaths-public-health-measures>, Accessed 21 July 2021
- 52.135 S.E. Lane, J.F. Barlow, C.R. Wood: An assessment of a three-beam Doppler lidar wind profiling method for use in urban areas, *J. Wind Eng. Ind. Aerodyn.* **119**, 53–59 (2013)
- 52.136 X. Xie, Z. Huang, J. Wang: Impact of building configuration on air quality in street canyon, *Atmos. Environ.* **39**(25), 4519–4530 (2005)
- 52.137 R.W. Macdonald, R.F. Griffiths, D.J. Hall: A comparison of results from scaled field and wind tunnel modelling of dispersion in arrays of obstacles, *Atmos. Environ.* **32**(22), 3845–3862 (1998)
- 52.138 J. Song, S. Fan, W. Lin, L. Mottet, H. Woodward, M. Davies Wykes, R. Arcucci, D. Xiao, J.-E. Debay, H. ApSimon, E. Aristodemou, D. Birch, M. Carpen-

- tieri, F. Fang, M. Herzog, G.R. Hunt, R.L. Jones, C. Pain, D. Pavlidis, A.G. Robins, C.A. Short, P.F. Linden: Natural ventilation in cities: The implications of fluid mechanics, *Build. Res. Inf.* **46**(8), 809–828 (2018)
- 52.139 X.C. Liu, T.C. Gao, L. Liu: A comparison of rainfall measurements from multiple instruments, *Atmos. Meas. Tech.* **6**(7), 1585–1595 (2013)
- 52.140 C.L. Ryder, R. Toumi: An urban solar flux island: Measurements from London, *Atmos. Environ.* **45**(20), 3414–3423 (2011)
- 52.141 M. Aida: Urban albedo as a function of the urban structure? A model experiment, *Boundary-Layer Meteorol.* **23**(4), 405–413 (1982)
- 52.142 M. Santamouris, A. Synnefa, T. Karlessi: Using advanced cool materials in the urban built environment to mitigate heat islands and improve thermal comfort conditions, *Sol. Energy* **85**(12), 3085–3102 (2011)
- 52.143 F. Lindberg, C.S.B. Grimmond, A. Gabey, B. Huang, C.W. Kent, T. Sun, N.E. Theeuwes, L. Järvi, H.C. Ward, I. Capel-Timms, Y. Chang, P. Jons-son, N. Krave, D. Liu, D. Meyer, K.F.G. Olofson, J. Tan, D. Wästberg, L. Xue, Z. Zhang: Urban Multi-scale Environmental Predictor (UMEP): An integrated tool for city-based climate services, *Environ. Model. Softw.* **99**, 70–87 (2018)
- 52.144 G. Desthieux, C. Carneiro, R. Camponovo, P. Ineichen, E. Morello, A. Boulmier, N. Abdennadher, S. Dervey, C. Ellert: Solar energy potential assessment on rooftops and facades in large built environments based on LiDAR data, image processing, and cloud computing. Methodological background, application, and validation in Geneva (Solar Cadaster), *Front. Built Environ.* **4**, 14 (2018)
- 52.145 J. Zhang, R. Verschae, S. Nobuhara, J.-F. Lalonde: Deep photovoltaic nowcasting, *Sol. Energy* **176**, 267–276 (2018)
- 52.146 F. Lindberg, C.S.B. Grimmond: Nature of vegetation and building morphology characteristics across a city: Influence on shadow patterns and mean radiant temperatures in London, *Urban Ecosyst.* **14**(4), 617–634 (2011)
- 52.147 F. Lindberg, B. Holmer, S. Thorsson: SOLWEIG 1.0 – Modelling spatial variations of 3D radiant fluxes and mean radiant temperature in complex urban settings, *Int. J. Biometeorol.* **52**(7), 697–713 (2008)
- 52.148 E. Johansson, S. Thorsson, R. Emmanuel, E. Krüger: Instruments and methods in outdoor thermal comfort studies – The need for standardization, *Urban Clim.* **10**(2), 346–366 (2014)
- 52.149 S. Thorsson, F. Lindberg, I. Eliasson, B. Holmer: Different methods for estimating the mean radiant temperature in an outdoor urban setting, *Int. J. Climatol.* **27**, 1983–1993 (2007)
- 52.150 K. Richards: Hardware scale modelling of summertime patterns of urban dew and surface moisture in Vancouver, BC, Canada, *Atmos. Res.* **64**(1–4), 313–321 (2002)
- 52.151 K. Richards: Observation and simulation of dew in rural and urban environments, *Prog. Phys. Geogr.* **28**, 76–94 (2004)
- 52.152 J.R. Simpson, E.G. McPherson: The effects of roof albedo modification on cooling loads of scale model residences in Tucson, Arizona, *Energy Build.* **25**(2), 127–137 (1997)
- 52.153 W.E. Reifsnyder: Radiation geometry in the measurement and interpretation of radiation balance, *Agric. Meteorol.* **4**(4), 255–265 (1967)
- 52.154 S. Kotthaus, C.S.B. Grimmond: Energy exchange in a dense urban environment – Part II: Impact of spatial heterogeneity of the surface, *Urban Clim.* **10**(2), 281–307 (2013)
- 52.155 S. Kotthaus, C.S.B. Grimmond: Energy exchange in a dense urban environment – Part II: Impact of spatial heterogeneity of the surface, *Urban Clim.* **10**(P2), 281–307 (2014)
- 52.156 J.-P. Gastellu-Etchegorry, T. Yin, N. Lauret, T. Cajglinger, T. Gregoire, E. Grau, J.-B. Feret, M. Lopes, J. Guilleux, G. Dedieu, Z. Malenovsky, B.D. Cook, D. Morton, J. Rubio, S. Durrieu, G. Cazanave, E. Martin, T. Ristorcelli: Discrete anisotropic radiative transfer (DART 5) for modeling airborne and satellite spectroradiometer and LIDAR acquisitions of natural and urban landscapes, *Remote Sens* **7**(2), 1667–1701 (2015)
- 52.157 E.S. Krayenhoff, J.A. Voogt: A microscale three-dimensional urban energy balance model for studying surface temperatures, *Boundary-Layer Meteorol.* **123**(3), 433–461 (2007)
- 52.158 A. Soux, J.A. Voogt, T.R. Oke: A model to calculate what a remote sensor ‘sees’ of an urban surface, *Boundary-Layer Meteorol.* **111**(1), 109–132 (2004)
- 52.159 R. Kormann, F.X. Meixner: An analytical footprint model for non-neutral stratification, *Boundary-Layer Meteorol.* **99**(2), 207–224 (2001)
- 52.160 M.Y. Leclerc, T. Foken: *Footprints in Micrometeorology and Ecology* (Springer, Berlin, Heidelberg 2014)
- 52.161 C.-I. Hsieh, G. Katul, T.W. Chi: An approximate analytical model for footprint estimation of scalar fluxes in thermally stratified atmospheric flows, *Adv. Water Resour.* **23**(7), 765–772 (2000)
- 52.162 C.-I. Hsieh, G.G. Katul, J. Schieldge, J.T. Sigmon, K.K. Knoerr: The Lagrangian stochastic model for fetch and latent heat flux estimation above uniform and nonuniform terrain, *Water Resour. Res.* **33**(3), 427–438 (1997)
- 52.163 N. Kljun, P. Calanca, M.W. Rotach, H.P. Schmid: A simple two-dimensional parameterisation for Flux Footprint Prediction (FFP), *Geosci. Model Dev.* **8**, 3695–3713 (2015)
- 52.164 H.P. Schmid: Footprint modeling for vegetation atmosphere exchange studies: A review and perspective, *Agric. For. Meteorol.* **113**(1–4), 159–183 (2002)
- 52.165 B. Offerle, C.S.B. Grimmond, K. Fortuniak: Heat storage and anthropogenic heat flux in relation to the energy balance of a central European city centre, *Int. J. Climatol.* **25**(10), 1405–1419 (2005)

- 52.166 B. Offerle, C.S.B. Grimmond, K. Fortuniak: Heat storage and anthropogenic heat flux in relation to the energy balance of a central European city centre, *Int. J. Climatol.* **25**(10), 1405–1419 (2005)
- 52.167 G. Pigeon, D. Legain, V. Durand, V. Masson: Anthropogenic heat release in an old European agglomeration (Toulouse, France), *Int. J. Climatol.* **27**(14), 1969–1981 (2007)
- 52.168 R. Moriwaki, M. Kanda, H. Senoo, A. Hagishima, T. Kinouchi: Anthropogenic water vapor emissions in Tokyo, *Water Resour. Res.* **44**(11), W11424 (2008)
- 52.169 M. Iamarino, S. Beevers, C.S.B. Grimmond: High-resolution (space, time) anthropogenic heat emissions: London 1970–2025, *Int. J. Climatol.* **32**(11), 1754–1767 (2012)
- 52.170 M. Rigby, R. Toumi, R. Fisher, D. Lowry, E.G. Nisbet: First continuous measurements of CO₂ mixing ratio in central London using a compact diffusion probe, *Atmos. Environ.* **42**(39), 8943–8953 (2008)
- 52.171 N. Sparks, R. Toumi: Remote sampling of a CO₂ point source in an urban setting, *Atmos. Environ.* **44**(39), 5287–5294 (2010)
- 52.172 B.W. Lafranchi, A.H. Goldstein, R.C. Cohen: Observations of the temperature dependent response of ozone to NO_x reductions in the Sacramento, CA urban plume, *Atmos. Chem. Phys.* **11**(14), 6945–6960 (2011)
- 52.173 D. Ionov, A. Poberovskii: Observations of urban NO_x plume dispersion using mobile and satellite DOAS measurements around the megacity of St. Petersburg (Russia), *Int. J. Remote Sens.* **40**(2), 719–733 (2019)
- 52.174 J.F. Barlow, T.M. Dunbar, E.G. Nemitz, C.R. Wood, M.W. Gallagher, F. Davies, E. O'Connor, R.M. Harrison: Boundary layer dynamics over London, UK, as observed using Doppler lidar during REPARTEE-II, *Atmos. Chem. Phys.* **11**(5), 2111–2125 (2011)
- 52.175 S. Kotthaus, C.H. Halios, J.F. Barlow, C.S.B. Grimmond: Volume for pollution dispersion: London's atmospheric boundary layer during ClearFlo observed with two ground-based lidar types, *Atmos. Environ.* **190**, 401–414 (2018)
- 52.176 A.J. Illingworth, D. Cimini, A. Haeefe, M. Haefefelin, M. Hervo, S. Kotthaus, U. Löhnert, P. Martinet, I. Mattis, E.J. O'Connor, R. Potthast: How can existing ground-based profiling instruments improve European weather forecasts?, *Bull. Am. Meteorol. Soc.* **100**(4), 605–619 (2019)
- 52.177 D. van der Kamp, I. McKendry: Diurnal and seasonal trends in convective mixed-layer heights estimated from two years of continuous ceilometer observations in Vancouver, BC, *Boundary-Layer Meteorol.* **137**(3), 459–475 (2010)
- 52.178 C. Münkel: Mixing height determination with lidar ceilometers – Results from Helsinki testbed, *Meteorol. Z.* **16**(4), 451–459 (2007)
- 52.179 K. Schäfer, P. Wagner, S. Emeis, C. Jahn, C. Muenkel, P. Suppan: Mixing layer height and air pollution levels in urban area, *Proc. SPIE* **8534**, 853409 (2012)
- 52.180 N. Eresmaa, J. Härkönen, S.M. Joffre, D.M. Schultz, A. Karppinen, J. Kukkonen: A three-step method for estimating the mixing height using ceilometer data from the Helsinki testbed, *J. Appl. Meteorol. Climatol.* **51**(12), 2172–2187 (2012)
- 52.181 D.G. Steyn, M. Baldi, R.M. Hoff: The detection of mixed layer depth and entrainment zone thickness from lidar backscatter profiles, *J. Atmos. Ocean. Technol.* **16**(7), 953–959 (1999)
- 52.182 S. Kotthaus, C.S.B. Grimmond: Atmospheric boundary-layer characteristics from ceilometer measurements. Part 2: Application to London's urban boundary layer, *Q. J. R. Meteorol. Soc.* **144**(714), 1511–1524 (2018)
- 52.183 Y. Morille, M. Haefefelin, P. Drobinski, J. Pelon: STRAT: An automated algorithm to retrieve the vertical structure of the atmosphere from single-channel lidar data, *J. Atmos. Ocean. Technol.* **24**(5), 761–775 (2007)
- 52.184 M. Haefefelin, F. Angelini, Y. Morille, G. Martucci, S. Frey, G.P. Gobbi, S. Lolli, C.D. O'Dowd, L. Sauvage, I. Xueref-Rémy, B. Wastine, D.G. Feist: Evaluation of mixing-height retrievals from automatic profiling lidars and ceilometers in view of future integrated networks in Europe, *Boundary-Layer Meteorol.* **143**(1), 49–75 (2012)
- 52.185 Y. Poltera, G. Martucci, M. Collaud Coen, M. Hervo, L. Emmenegger, S. Henne, D. Brunner, A. Haefeler: PathfinderTURB: An automatic boundary layer algorithm. Development, validation and application to study the impact on in situ measurements at the Jungfrauoch, *Atmos. Chem. Phys.* **17**(16), 10051–10070 (2017)
- 52.186 A. Geiß, M. Wiegner, B. Bonn, K. Schäfer, R. Forkel, E. von Schneidmesser, C. Münkel, K.L. Chan, R. Nothard: Mixing layer height as an indicator for urban air quality?, *Atmos. Meas. Tech.* **10**(8), 2969–2988 (2017)
- 52.187 J. Peng, C.S.B. Grimmond, X. Fu, Y. Chang, G. Zhang, J. Guo, C. Tang, J. Gao, X. Xu, J. Tan: Ceilometer-based analysis of Shanghai's boundary layer height (under rain- and fog-free conditions), *J. Atmos. Ocean. Technol.* **34**(4), 749–764 (2017)
- 52.188 S. Kotthaus, C.S.B. Grimmond: Atmospheric boundary-layer characteristics from ceilometer measurements. Part 1: A new method to track mixed layer height and classify clouds, *Q. J. R. Meteorol. Soc.* **144**(714), 1525–1538 (2018)
- 52.189 M. Wiegner, I. Mattis, M. Pattantyús-Ábrahám, J.A. Bravo-Aranda, Y. Poltera, A. Haeefe, M. Hervo, U. Górsdorf, R. Leinweber, J. Gasteiger, M. Haefefelin, F. Wagner, J. Cermak, K. Komínková, M. Brettle, C. Münkel, K. Pönitz: Aerosol backscatter profiles from ceilometers: validation of water vapor correction in the framework of CeilInEx2015, *Atmos. Meas. Tech.* **12**(1), 471–490 (2019)
- 52.190 C. Münkel, N. Eresmaa, J. Räsänen, A. Karppinen: Retrieval of mixing height and dust concentration with lidar ceilometer, *Boundary-Layer Meteorol.* **124**(1), 117–128 (2007)

- 52.191 J.F. Barlow, C.H. Halios, S.E. Lane, C.R. Wood: Observations of urban boundary layer structure during a strong urban heat island event, *Environ. Fluid Mech.* **15**(2), 373–398 (2015)
- 52.192 X. Liang, S. Miao, J. Li, R. Bornstein, X. Zhang, Y. Gao, F. Chen, X. Cao, Z. Cheng, C. Clements, W. Dabberdt, A. Ding, D. Ding, J.J. Dou, J.X. Dou, Y. Dou, C.S.B. Grimmond, J.E. González-Cruz, J. He, M. Huang, X. Huang, S. Ju, Q. Li, D. Niyogi, J. Quan, J. Sun, J.Z. Sun, M. Yu, J. Zhang, Y. Zhang, X. Zhao, Z. Zheng, M. Zhou: SURF: Understanding and predicting urban convection and haze, *Bull. Am. Meteorol. Soc.* **99**(7), 1391–1413 (2018)
- 52.193 M. Huang, Z. Gao, S. Miao, F. Chen, M.A. LeMone, J. Li, F. Hu, L. Wang: Estimate of boundary-layer depth over Beijing, China, using Doppler lidar data during SURF-2015, *Boundary-Layer Meteorol.* **162**(3), 503–522 (2017)
- 52.194 R.F. Banks, J. Tiana-Alsina, F. Rocadenbosch, J.M. Baldasano: Performance evaluation of the boundary-layer height from lidar and the weather research and forecasting model at an urban coastal site in the north-east Iberian peninsula, *Boundary-Layer Meteorol.* **157**, 265–292 (2015)
- 52.195 C.J. Senff, M. Trainer, W.M. Angevine, M.A. Ayoub, A.B. White, R.M. Banta: Urban-rural contrasts in mixing height and cloudiness over Nashville in 1999, *J. Geophys. Res.* **108**(D3), 4092 (2003)
- 52.196 R.M. Banta: Mixing-height differences between land use types: Dependence on wind speed, *J. Geophys. Res.* **108**(D10), 4321 (2003)
- 52.197 F. Davies, D.R. Middleton, K.E. Bozier: Urban air pollution modelling and measurements of boundary layer height, *Atmos. Environ.* **41**(19), 4040–4049 (2007)
- 52.198 S. Pal, I. Xueref-Remy, L. Ammoura, P. Chazette, F. Gibert, P. Royer, E. Dieudonné, J.-C. Dupont, M. Haeffelin, C. Lac, M. Lopez, Y. Morille, F. Ravetta: Spatio-temporal variability of the atmospheric boundary layer depth over the Paris agglomeration: An assessment of the impact of the urban heat island intensity, *Atmos. Environ.* **63**, 261–275 (2012)
- 52.199 D.R. Drew, J.F. Barlow, S.E. Lane: Observations of wind speed profiles over Greater London, UK, using a Doppler lidar, *J. Wind Eng. Ind. Aerodyn.* **121**, 98–105 (2013)
- 52.200 World Meteorological Organization: *Guide to Meteorological Instruments and Methods of Observation*, Vol. 8 (WMO, Geneva 2017)
- 52.201 World Meteorological Organization: Urban observations. In: *Guide to Meteorological Instruments and Methods of Observation*, Vol. 8 (WMO, Geneva 2017), Chapter 9
- 52.202 B. Crawford, C.S.B. Grimmond, A. Christen: Five years of carbon dioxide fluxes measurements in a highly vegetated suburban area, *Atmos. Environ.* **45**(4), 896–905 (2011)
- 52.203 K. Fortuniak, W. Pawlak, M. Siedlecki: Integral turbulence statistics over a Central European city centre, *Boundary-Layer Meteorol.* **146**(2), 257–276 (2013)
- 52.204 H.C. Ward, J.G. Evans, C.S.B. Grimmond: Multi-season eddy covariance observations of energy, water and carbon fluxes over a suburban area in Swindon, UK, *Atmos. Chem. Phys.* **13**(9), 4645–4666 (2013)
- 52.205 H.C. Ward, S. Kotthaus, C.S.B. Grimmond, A. Björkegren, M. Wilkinson, W.T.J. Morrison, J.G. Evans, J.I.L. Morison, M. Iamarino: Effects of urban density on carbon dioxide exchanges: Observations of dense urban, suburban and woodland areas of southern England, *Environ. Pollut.* **198**, 186–200 (2015)
- 52.206 A.M. Coutts, E. Daly, J. Beringer, N.J. Tapper: Assessing practical measures to reduce urban heat: Green and cool roofs, *Build. Environ.* **70**, 266–276 (2013)
- 52.207 A.B. Björkegren, C.S.B. Grimmond, S. Kotthaus, B.D. Malamud: CO₂ emission estimation in the urban environment: Measurement of the CO₂ storage term, *Atmos. Environ.* **122**, 775–790 (2015)
- 52.208 T. Song, Y. Wang: Carbon dioxide fluxes from an urban area in Beijing, *Atmos. Res.* **106**, 139–149 (2012)
- 52.209 A.J. Oliphant, S. Stein, G. Bradford: Micrometeorology of an ephemeral desert city, the Burning Man experiment, *Urban Clim.* **23**, 53–70 (2018)
- 52.210 World Meteorological Organization: *Guide for Urban Integrated Hydro-Meteorological, Climate and Environmental Services Part 1a: Concept and Methodology* (WMO, Geneva 2018)
- 52.211 A.M. Vicedo-Cabrera, B. Forsberg, A. Tobias, A. Zanobetti, J. Schwartz, B. Armstrong, A. Gasparri: Associations of inter- and intraday temperature change with mortality, *Am. J. Epidemiol.* **183**(4), 286–293 (2016)
- 52.212 A. Matzarakis, D. Fröhlich, M. Gangwisch, C. Ketterer, A. Peer: Developments and applications of thermal indices in urban structures by RayMan and SkyHelios model. In: *9th Int. Conf. Urban Clim.* (2015)
- 52.213 K.E. Taylor, R.J. Stouffer, G.A. Meehl: An overview of CMIP5 and the experiment design, *Bull. Am. Meteorol. Soc.* **93**(4), 485–498 (2012)
- 52.214 P.G. Dixon, D.M. Brommer, B.C. Hedquist, A.J. Kalkstein, G.B. Goodrich, J.C. Walter, C.C. Dickerson IV, S.J. Penny, R.S. Cervený: Heat mortality versus cold mortality: A study of conflicting databases in the United States, *Bull. Am. Meteorol. Soc.* **86**(7), 937–943 (2005)
- 52.215 J. Shaman, V.E. Pitzer, C. Viboud, B.T. Grenfell, M. Lipsitch: Absolute humidity and the seasonal onset of influenza in the continental United States, *PLoS Biol.* **8**(2), e1000316 (2010)
- 52.216 J. Shaman, M. Kohn: Absolute humidity modulates influenza survival, transmission, and seasonality, *Proc. Natl. Acad. Sci. U.S.A.* **106**(9), 3243–3248 (2009)
- 52.217 World Health Organization: *Exposure to ambient air pollution* 2018). <https://www.who.int/>

- gho/phe/outdoor_air_pollution/exposure/en/, Accessed 21 July 2021
- 52.218 Statista: *China: Car production 2018* 2018). <https://www.statista.com/statistics/281133/car-production-in-china/>, Accessed 21 July 2021
- 52.219 United Kingdom Department of Transport: *Walking and Cycling Statistics, England: 2017* (DfT, London 2018)
- 52.220 A. Lewis, P. Edwards: Validate personal air-pollution sensors, *Nature* **535**(7610), 29–31 (2016)
- 52.221 A.C. Lewis, J. Lee, P.M. Edwards, M.D. Shaw, M.J. Evans, S.J. Moller, K. Smith, M. Ellis, J.W. Buckley, S. Gillott, A. White: Evaluating the performance of low cost chemical sensors for air pollution research, *Faraday Discuss.* **189**, 85–103 (2016)
- 52.222 K.R. Smith, P.M. Edwards, M.J. Evans, J.D. Lee, M.D. Shaw, F. Squires, S. Wilde, A.C. Lewis: Clustering approaches to improve the performance of low cost air pollution sensors, *Faraday Discuss.* **200**, 621–637 (2017)
- 52.223 J.D. Allan, P.I. Williams, W.T. Morgan, C.L. Martin, M.J. Flynn, J. Lee, E. Nemitz, G.J. Phillips, M.W. Gallagher, H. Coe: Contributions from transport, solid fuel burning and cooking to primary organic aerosols in two UK cities, *Atmos. Chem. Phys.* **10**(2), 647–668 (2010)
- 52.224 A. Geisinger, A. Behrendt, V. Wulfmeyer, J. Strohbach, J. Förstner, R. Potthast: Development and application of a backscatter lidar forward operator for quantitative validation of aerosol dispersion models and future data assimilation, *Atmos. Meas. Tech.* **10**(12), 4705–4726 (2017)
- 52.225 E. Warren, C. Charlton-Perez, S. Kotthaus, H. Lean, S. Ballard, E. Hopkin, S. Grimmond: Evaluation of forward-modelled attenuated backscatter using an urban ceilometer network in London under clear-sky conditions, *Atmos. Environ.* **191**, 532–547 (2018)
- 52.226 M.R. Alfarra, A.S.H. Prevot, S. Szidat, J. Sandradewi, S. Weimer, V.A. Lanz, D. Schreiber, M. Mohr, U. Baltensperger: Identification of the mass spectral signature of organic aerosols from wood burning emissions, *Environ. Sci. Technol.* **41**(16), 5770–5777 (2007)
- 52.227 S. Naz, A. Page, K.E. Agho: Household air pollution from use of cooking fuel and under-five mortality: The role of breastfeeding status and kitchen location in Pakistan, *PLoS One* **12**(3), e0173256 (2017)
- 52.228 CIBSE: *Weather data 2016* 2016). <https://www.cibse.org/weatherdata>, Accessed 21 July 2021
- 52.229 ASHRAE: *ASHRAE climate data center* 2019). <https://www.ashrae.org/technical-resources/bookstore/ashrae-climate-data-center>, Accessed 21 July 2021
- 52.230 BREEAM: *The world's leading sustainability assessment method for masterplanning projects, infrastructure and buildings* 2019). <https://www.breeam.com/>, Accessed 21 July 2021
- 52.231 USGBC: *LEED* 2019). <https://new.usgbc.org/leed>, Accessed 21 July 2021
- 52.232 C.A. Short, K.J. Lomas, A. Woods: Design strategy for low-energy ventilation and cooling within an urban heat island, *Build. Res. Inf.* **32**(3), 187–206 (2004)
- 52.233 Construction Manager: *Roofing: A walkie-talkie on the wildside* 2015). <http://www.constructionmanagermagazine.com/onsite/roofing-w4alkie-talk6ie-wildside/>, Accessed 21 July 2021
- 52.234 C. Thoua, J. Hines: *Post-occupancy evaluation of five schools by Architype* 2016). <https://www.architectsjournal.co.uk/buildings/post-occupancy-evaluation-of-five-schools-by-architype/10004526>.article, Accessed 21 July 2021
- 52.235 BBC News: *Leeds' Bridgewater Place owners to foot £900,000 wind bill* 2016). <https://www.bbc.co.uk/news/uk-england-leeds-38174624>, Accessed 21 July 2021
- 52.236 C.R. Thorne, E.C. Lawson, C. Ozawa, S.L. Hamlin, L.A. Smith: Overcoming uncertainty and barriers to adoption of Blue-Green Infrastructure for urban flood risk management, *J. Flood Risk Manag.* **11**, S960–S972 (2018)
- 52.237 T. Sun, C.S.B. Grimmond, G.–H. Ni: How do green roofs mitigate urban thermal stress under heat waves?, *J. Geophys. Res.* **121**(10), 5320–5335 (2016)
- 52.238 S. Barr: *Hosepipe ban: Where in UK is it being imposed and what will happen if you break it?* 2018). <https://www.independent.co.uk/life-style/hosepipe-ban-2018-north-west-uk-explained-united-utilities-water-shortage-rules-a8450621.html>, Accessed 21 July 2021
- 52.239 B. Cooper, M. Burton, L. Crase: Urban water restrictions: Attitudes and avoidance, *Water Resour. Res.* **47**(12), W12527 (2011)
- 52.240 S. Guhathakurta, P. Gober: The impact of the Phoenix urban heat island on residential water use, *J. Am. Plan. Assoc.* **73**(3), 317–329 (2007)
- 52.241 S. Pulkkinen, V. Chandrasekar, A.M. Harri: Now-casting of precipitation in the high-resolution Dallas-Fort Worth (DFW) urban radar remote sensing network, *IEEE J. Sel. Top. Appl. Earth Obs. Remote Sens.* **11**(8), 2773–2787 (2018)
- 52.242 S. Thorndahl, T. Einfalt, P. Willems, J.E. Nielsen, M.–C. ten Veldhuis, K. Arnbjerg-Nielsen, M.R. Rasmussen, P. Molnar: Weather radar rainfall data in urban hydrology, *Hydrol. Earth Syst. Sci.* **21**, 1359–1380 (2017)
- 52.243 H. Lean, J. Barlow, C.H. Halios: The impact of spin up and resolution on the representation of a clear convective boundary layer over London in order 100 m grid-length versions of the Met Office Unified Mode, *Q. J. R. Meteorol. Soc.* **145**, 1674–1689 (2019)
- 52.244 C.R. Wood, L. Pauscher, H.C. Ward, S. Kotthaus, J.F. Barlow, M. Gouvea, S.E. Lane, C.S.B. Grimmond: Wind observations above an urban river using a new lidar technique, scintillometry and anemometry, *Sci. Total Environ.* **442**, 527–533 (2013)
- 52.245 J.F. Barlow, M. Dunbar, E.G. Nemitz, C.R. Wood, M.W. Gallagher, F. Davies, E. O'Connor, R.M. Har-

- 52.246 rison: Boundary layer dynamics over London, UK, as observed using Doppler lidar during REPARTEE-II, *Atmos. Chem. Phys.* **11**, 2111–2125 (2011)
- 52.247 C.R. Wood, A. Lacser, J.F. Barlow, A. Padhra, S.E. Belcher, E. Nemitz, C. Helfter, D. Famulari, C.S.B. Grimmond: Turbulent flow at 190 m height above London during 2006–2008: A climatology and the applicability of similarity theory, *Boundary–Layer Meteorol.* **137**(1), 77–96 (2010)
- 52.248 R. Calhoun, R. Heap, M. Princevac, R. Newsom, H. Fernando, D. Ligon: Virtual towers using coherent Doppler lidar during the Joint Urban 2003 dispersion experiment, *J. Appl. Meteorol. Climatol.* **45**(8), 1116–1126 (2006)
- 52.249 J. Barlow, M. Best, S.I. Bohnenstengel, P. Clark, S. Grimmond, H. Lean, A. Christen, S. Emeis, M. Haeffelin, I.N. Harman, A. Lemonsu, A. Martilli, E. Paradyjak, M.W. Rotach, S. Ballard, I. Boutle, A. Brown, X. Cai, M. Carpentieri, O. Coceal, B. Crawford, S. Di Sabatino, J. Dou, D.R. Drew, J.M. Edwards, J. Fallmann, K. Fortuniak, J. Gornall, T. Gronemeier, C.H. Halios, D. Hertwig, K. Hirano, A.A.M. Holtslag, Z. Luo, G. Mills, M. Nakayoshi, K. Pain, K.H. Schlünzen, S. Smith, L. Soulhac, G. Steeneveld, T. Sun, N.E. Theeuwes, D. Thomson, J.A. Voogt, H.C. Ward, Z. Xie, J. Zhong: Developing a research strategy to better understand, observe, and simulate urban atmospheric processes at kilometer to subkilometer scales, *Bull. Am. Meteorol. Soc.* **98**(10), ES261–ES264 (2017)
- 52.249 A.J. Arnfield: Two decades of urban climate research: A review of turbulence, exchanges of energy and water, and the urban heat island, *Int. J. Climatol.* **23**(1), 1–26 (2003)

Sue Grimmond

Department of Meteorology
University of Reading
Reading, UK
c.s.grimmond@reading.ac.uk



Sue Grimmond, Professor of Urban Meteorology and Met Office Joint Chair, Department of Meteorology, University of Reading, UK, received her BSc(Hons) from the University of Otago (NZ), her MSc and PhD from the University of British Columbia (Canada). She was Assistant/Associate/Full Professor at Indiana University and Chair of Physical Geography at King's College London. Her research group undertakes measurement and modeling of urban–atmosphere exchanges across a wide range of scales.

Helen Ward

Department of Atmospheric and
Cryospheric Sciences
University of Innsbruck
Innsbruck, Austria
helen.ward@uibk.ac.at



Helen Ward studied physics at Oxford University and received her PhD in urban micrometeorology from King's College London (2013). She carried out postdoctoral research at the Centre for Ecology and Hydrology, Reading University and Yonsei University and is currently based at Innsbruck University, Austria. Her research focuses on improving understanding of turbulent exchange, particularly in complex environments (e.g., urban areas and mountainous terrain), through measurements (eddy covariance, scintillometry) and modeling.

Fog Deposition

53. Fog Deposition

Shih-Chieh Chang , Robert S. Schemenauer

Atmospheric water, in its liquid form, is deposited on surfaces mainly through wet deposition processes driven by gravity (rain, snow, or hail). However, at some locations, or during specific time periods, the dominant wet deposition process is the deposition of fog droplets.

Unlike the relatively simple methodology for quantifying precipitation deposition, the deposition rate of fog droplets depends on the properties of the surface as well as the micrometeorological conditions present, such as the wind speed, fog liquid–water content, and droplet size distribution. Therefore, there is no standard method or simple equipment that is universally applicable for measuring fog deposition rates under all conditions. The methodology for quantifying fog deposition in diverse ecosystems has been developed over many decades. One straightforward method is the direct quantification of the water mass that is captured by plant surfaces under foggy conditions. When rainfall, canopy interception, throughfall, and stemflow are measured simultaneously, the amount of fog water deposited can be quantified by simple algebraic calculations. The downward flux of fog water from the atmosphere to the canopy can be determined via the eddy–covariance method using 3–D sonic anemometers and fog droplet spectrometers. Under some atmospheric conditions, the deposition of fog droplets is predominantly driven by gravitation, so the deposition of fog water can be calculated using droplet size classes and the respective deposition velocities. In this chapter, these methods are reviewed and the operational processes are summarized.

Fog droplet diameters range from 1 to 40 μm , with the droplet size distribution varying considerably depending on the type of fog and meteorological conditions present. A typical mean volume diameter would be 10 μm . A droplet of this size has a terminal velocity of $\approx 0.3 \text{ cm s}^{-1}$. This is much smaller than typical windspeeds near the

surface, so the resulting fog flux is nearly horizontal and parallel to the surface. For this reason, fog flux measurements and fog water collectors are often made with specially constructed vertical surfaces. These and additional measurement techniques and instrumentation will be discussed in this chapter.

53.1	Measurement Principles and Parameters	1426
53.1.1	Basic Physical and Chemical Properties of Fog	1426
53.1.2	Measured Parameters	1427
53.1.3	Measurement Principles	1428
53.2	History	1430
53.3	Theory	1432
53.3.1	Direct Quantification of the Deposited Water Mass	1432
53.3.2	Estimation Using Surrogates	1433
53.3.3	Inference from a Canopy Water Budget	1434
53.3.4	Eddy–Covariance Method	1435
53.4	Devices and Systems	1436
53.4.1	Canopy Water Balance Monitoring System	1436
53.4.2	Eddy–Covariance Method	1436
53.4.3	Fog Collectors for Chemical Analysis ...	1437
53.4.4	Visibility Sensor	1438
53.4.5	Comparison of the Methods	1438
53.5	Specifications	1438
53.6	Quality Control	1439
53.7	Maintenance	1440
53.8	Applications	1441
53.9	Further Developments	1441
53.10	Further Reading	1442
	References	1442

The atmosphere is a source of important nutrients (e.g., nitrogen) as well as fresh water for terrestrial ecosystems. Therefore, atmospheric deposition processes determine the form and viability of life on land. For most of the land area on Earth, a good understanding of the atmospheric water input can be gained by determining the level of precipitation (rain and snow) deposition. However, fog deposition plays an important or even a key

role in the atmospheric water input at some locations on Earth. Atmospheric water deposition also includes the condensation of water vapor on surfaces (i.e., the formation of dew, and the conversion of water vapor into frost when the temperature is below freezing). Although all of these deposition pathways can contribute significantly to the total atmospheric water deposition, we only consider fog deposition in this chapter.

53.1 Measurement Principles and Parameters

Fog droplets are much smaller than raindrops. This makes the fog deposition process different from rainfall. In this section, the properties of fog droplets will be highlighted, and the major principles and parameters for quantifying fog deposition will be introduced.

53.1.1 Basic Physical and Chemical Properties of Fog

Fog is composed of liquid water droplets (although fog also exists as ice particles in some extremely cold environments) with diameters ranging from 1 to 40 μm . The fog droplet size range varies with the type of fog considered. Radiation fog typically has droplets that are < 10 μm in diameter. Many advection fogs have droplets that are up to 25 μm in diameter and have a mean volume diameter of $\approx 10 \mu\text{m}$. The largest droplet sizes are obtained when convective clouds move over the terrain or when the terrain is immersed in deep stratus clouds. Except for the larger particles in the droplet size spectrum, most droplets are too light to have significant settling velocities. Fog droplets therefore move with horizontal, vertical, and turbulent air movements. When the windblown fog droplets collide with an obstacle, they are removed from the air. Unlike the precipitation deposition process, which is driven by gravity, the rate of fog deposition is dependent on droplet size, the characteristics of the collecting surface, and the wind speed. The fog deposition rate is significantly affected by the arrangement and surface properties of obstacles. About 200 years ago, during hydrologic studies performed in Britain, it was observed that more water came from hilly areas than could be accounted for by precipitation alone. This led to speculation that there was another water deposition process in play, which was sometimes called *occult* deposition [53.1]. Also, because fog droplets generally move horizontally with the wind and may, for example, be collected by the line of trees at the edge of a forest, fog deposition is sometimes called *horizontal deposition*.

Depending on its relative contribution to the total atmospheric water deposition, fog deposition can be negligible for ecosystems that receive ample precipitation or can be the most important water source for entire ecosystems in dry regions. A famous example of a fog-water-fed ecosystem is Fray Jorge, a coastal forest ecosystem in north-central Chile, where the annual precipitation is only $\approx 150 \text{ mm}$. The windward edges of the forest patches receive extra water from fog, which is sufficient to support the growth of trees in this semi-arid region [53.2, 3]. In general, it is not just the fog deposition itself that increases the water available to ecosystems in foggy conditions. Fog-induced reductions in solar radiation, air temperature, and vapor pressure deficit all weaken the driving force for evapotranspiration and thus indirectly increase the available water in the soil. A comprehensive review of the contribution of fog deposition to ecosystem water budgets has been written by *Bruijnzeel et al.* [53.4].

As with precipitation, fog deposits chemical components onto the recipient surfaces. The relative importance of precipitation compared to fog deposition at a particular site depends on the amount of water received by each mechanism, the chemical compositions of the rain, snow, and fog, and the vulnerabilities of the recipient surfaces to vertical and horizontal water inputs. Using size-fractionating fog water collectors, it has been shown that the chemical concentrations in smaller fog droplets are higher than those in larger ones, which are also higher than those in rainwater [53.5]. While the nutrients in fog water may have a positive effect on the recipient ecosystems, the H^+ ions and other pollutants in the fog water may be harmful [53.6]. Acidic fog has received considerable attention since the 1960s as air pollution has become increasingly problematic in heavily industrialized regions. In the 1980s, forest dieback on hills and mountains in Europe and in eastern North America that are frequently covered in fog generated considerable concern [53.7, 8].

Table 53.1 Measured and calculated fog deposition parameters

Parameter	Unit	Description
Fog deposition rate	mm yr ⁻¹	Annual fog water input from the atmosphere to the ground surface Any other unit of time may also be employed
Nutrient/pollutant deposition due to fog	kg ha ⁻¹ yr ⁻¹	Atmospheric deposition of nutrients, pollutants, or other materials in fog water Any other units of time and area may also be employed
Fog interception rate	g H ₂ O m ⁻² h ⁻¹ or L m ⁻² d ⁻¹	Amount of fog intercepted per unit surface area of the intercepting objects and unit time

Table 53.2 Other relevant parameters for fog deposition measurements

Parameter	Unit	Description
Surface area	m ²	The cross-sectional surface area of the fog-intercepting object
Surface area index (SAI)	m ² m ⁻²	The total surface area per unit ground surface
Visibility	m	Horizontal visibility measured by optical sensors
Liquid water content	g m ⁻³	Mass of fog liquid water in a specified volume of air
Fog droplet distribution	–	Size spectrum of fog droplets
Wind speed	m s ⁻¹	Horizontal wind speed measured on top of the canopy and where the fog flux (interception) measurements are made
Wind direction	°	Horizontal wind direction measured on top of the canopy

53.1.2 Measured Parameters

Fog deposition is a form of atmospheric water deposition, so it is generally expressed as a water depth (in mm) on the ground surface per unit time—the same unit used for precipitation measurements (Table 53.1). Fog deposition expressed in this way allows direct assessment of the contribution of fog deposition to the total atmospheric water deposition. The contribution of fog deposition can be ignored for most lowland areas, where fog occurrence is a rare event or the fog occurs as radiation fog with little or no wind present. However, substantial fog deposition rates are observed in elevated areas covered with orographic fog or fog produced by the advection of clouds over the terrain. It can also be substantial in coastal regions, where the advection of low stratus cloud forms fog when it touches the ground on coastal hills and mountains. For example, the annual fog deposition measured in a high-elevation *Erica arborea* forest in Portugal [53.9] was stated to be 4170 mm yr⁻¹, or ≈ 160% of the annual precipitation.

Airborne fog droplets must first be intercepted by obstacles, such as vegetation components (leaves and twigs), before they have the chance to reach the ground surface. Therefore, the fog interception rate, often expressed as the amount of fog water captured by a unit surface area of the obstacle during a certain period of time (e.g., g H₂O m⁻² h⁻¹), is the parameter that can be experimentally quantified. This parameter is also used for some artificial materials of interest, for example to understand the fog collection efficiency of mesh (Sect. 53.8; [53.10]). The determination of the fog de-

position rate requires knowledge of three parameters: the free stream fog flux, the fog droplet collection efficiency of the vegetation or material, and the surface area index (SAI), which is the total surface area of a fog-capturing obstacle that will produce water for one square meter of ground surface (Table 53.2). Although large uncertainties arise from the heterogeneous distribution pattern of the canopy components and the variations in wind speed and fog droplet distribution in the 3-D canopy space, an approximate value for the fog deposition rate can be obtained via

$$\begin{aligned} \text{Fog deposition rate} \\ &= \text{free stream fog flux} \\ &\quad \times \text{efficiency of collecting surface} \times \text{SAI}, \quad (53.1) \end{aligned}$$

where the fog deposition rate is the fog water input on the ground (g H₂O m⁻² h⁻¹) under specific atmospheric conditions, as calculated from the fog interception rate (g H₂O m⁻² h⁻¹) of the obstacle, which is the product of the measured free-stream fog flux and the measured or estimated efficiency of the collecting surface under the specific atmospheric conditions present. This is multiplied in turn by the SAI, which is the surface area index (m² m⁻²) of a collecting object such as a tree. Here, the relevant atmospheric conditions are mainly the wind speed, the fog liquid-water content, and the fog droplet size distribution. However, it is important to note that there are considerable uncertainties associated with translating the collection of a horizontal flux of fog water on a vertical 3-D surface into a depth of water on a horizontal 2-D ground surface.

When the chemical composition of fog water has been determined, the atmospheric deposition of the chemical compounds in fog can be calculated by simply multiplying the fog deposition rate by the concentration of the specific chemical compound.

53.1.3 Measurement Principles

Unlike most atmospheric parameters for which measurement principles and techniques have been studied extensively and equipment has been developed and commercialized, there is currently no standard method for the quantification of fog deposition. For the fog droplets in the airstream to be effectively intercepted, the surface of the ground requires some vertical components such as aboveground stems, twigs, and leaves. These parts are referred to below as the *intercepting surfaces*. Table 53.3 provides a summary of the measurement principles of fog deposition for different types of ground cover.

- *Direct measurement of the deposited water mass or volume.* The direct quantification of water deposited on an intercepting surface is the most straightforward method of ascertaining the amount of fog water that has been deposited. A report of measurements of the fog water collected by a bundle of reeds placed over the top of a rain gauge on Table Mountain in Cape Town, South Africa was published as far back as 1905 [53.17]. The uncomplicated theoretical basis for this method means that the fog deposition rate is determined by simply measuring the volume of water collected or the weight gain of the object during a certain time interval under foggy conditions. The calculated intercepting-surface-based deposition rate must then be converted to the ground-surface-based deposition rate using a carefully derived scaling factor, such as that derived from measurements of dew on vegetation [53.18]. The cross-sectional area of the tree or other natural obstacle is important when determining the amount of fog water that will be collected. *Schemenauer* and *Cereceda* [53.19] reviewed the literature and found that the vertical cross-section of a tree collects fog water at a rate of $\approx 10 \text{ L m}^{-2} \text{ d}^{-1}$ during fog events. This led to a depth of water on the ground under the trees of $1\text{--}5 \text{ cm d}^{-1}$. If the weight changes of the ground surface and the intercepting surface or the volumes of water received by those surfaces can both be measured, additional information on the fog deposition rate for a specific time interval can be extracted. Complicating factors include the retention of water in the structure of the vegetation and the possibility of fog deposition from both wind-driven impaction on the surface and the sedimentation of fog droplets directly on the surface of the ground. Care must also be taken to account for any wind-driven drizzle or raindrops that may form part of the collected water [53.20].
- *Surrogate method.* To understand the potential for fog deposition at a certain location, an artificial object mimicking the surface properties of vegetation can be placed in the field. The volume of water collected or the weight gain of the object under foggy conditions can be recorded, and a deposition rate can then be calculated. This method allows a comparison of the fog deposition potentials at different locations. However, it is not realistic to build different fog collectors for every type of vegetation to be investigated, for fogs with different droplet sizes, or for different wind speed ranges. To overcome this problem, the Standard Fog Collector (SFC) was developed [53.13]. This is an easy-to-replicate 1 m^2 fog collector made of an inexpensive Raschel mesh that is effective at collecting wind-blown fog droplets [53.21]. It collects 50–60% of the free-stream fog water arriving at the surface of the mesh, and has been used in over 40 countries to date. However, the construction and utilization of many different types of fog collectors by different investigators led to an inability to quantitatively compare different sets of measurements. This issue remains a challenge to this day. A range of different types of fog-collecting materials and structures are reviewed in [53.13]. Any fog collector will collect only a fraction of the fog water arriving at its surface. This is because the wind that brings the fog droplets must pass through the collector, taking some of the fog droplets with it. Field measurements of the collection efficiency at the surface of the Raschel mesh have been performed [53.21]. A cylindrical fog collector that uses teflon strings was developed [53.22] and has been used in various slightly modified forms to sample fog water for chemical analysis. Its collection efficiency has been directly compared to the SFC under limited conditions [53.13]. In the 1950s and 1960s, a fog collector consisting of a small vertical cylinder made of metal mesh was in use [53.23]. Another cylindrical fog collector utilized a louvered metal screen [53.24]. It was developed in Hawaii and is still used in some locations today. These are all examples of *passive fog collectors*, where the wind provides the energy to impact the fog droplets on the collection surface. A variety of *active fog collectors* (e.g., that of *Daube* et al. [53.25]) that utilize a fan powered by electricity to draw in outside air

Table 53.3 Summary of fog deposition measurement principles for different land cover types and different site conditions

Method	Land cover type	Intercepting surface	Parameters	Conversion factor	Device	Procedure in brief	Limitations	References
Direct measurement of collected water mass or volume	Short vegetation	Whole vegetation including soil surface	Fog deposition, both wind-driven and through sedimentation	–	Precision balance, instruments to measure meteorological and soil conditions	Monitoring the mass and seepage of water from an isolated soil pit, including vegetation	Weight loss due to evaporation and transpiration may bias the estimation; formation of dew needs to be monitored	[53.11]
Direct measurement of collected water mass or volume	Forest	Canopy components, e.g., needles, leaves	Fog interception rate, fog droplet sizes, fog flux	SAI (m ² m ⁻²)	Precision balance/lysimeter, rain gauges for fog drip, material for stemflow, device to determine SAI	Measure the weight increase of samples when fog is present, measure all water removed and stored by vegetation	Large uncertainty in upscaling, representativeness of canopy components sampled	[53.12]
Surrogate method	Open area	Artificial fog-collecting material, e.g., mesh, 3-D rigid mesh, filaments	Fog collection efficiency; horizontal fog flux	SAI (m ² m ⁻²)	Rain gauge at ground level; fog collector with recording device	Record fog flux in L m ⁻² d ⁻¹ ; verify the presence or absence of rain and drizzle using the rain gauge	The measurement represents only the potential deposition rate depending on the similarity of the artificial material and the vegetation	[53.13, 14]
Water budget method	Forest	Whole canopy or canopy top	Throughfall (fog drip), stemflow, fog flux at canopy top, precipitation	Cross-sectional area of exposed trees at canopy top	Gauges for rain, throughfall (fog drip), and stemflow; fog collectors at canopy top	Monitoring the components of the canopy water budget allows the fog water input to be calculated	Water storage in canopy is subject to estimation errors; forest may be nonuniform in nature; complex terrain affects wind flow	[53.15]
Eddy-covariance method	Any homogeneous and low-slope surface	–	Vertical flux of fog droplets	–	3-D sonic anemometer, fog droplet spectrometer	Instruments installed on a flux tower continuously measure the vertical transport of fog droplets due to turbulence in the air above the canopy top	Generally limited by the terrain conditions for the eddy-covariance method; demanding in terms of power and maintenance; not well suited to radiation fog due to low turbulence	[53.16]

and move it past the collection fibers or mesh have also been developed. These designs typically have a downward-facing opening and minimize the entry of drizzle or raindrops. The amount of sample collected is normally fairly small but sufficient for chemical analysis. When designing the collector, it is important to consider whether the fog droplets collected will be representative of those present under free-stream conditions.

- **Water budget method.** If the surface of interest is tall vegetation, the principle of water balance can be applied to derive the fog deposition component. The vegetation canopy exposed to the wind flow (canopy top) is the main area of fog deposition. The atmospheric water deposition—the sum of the precipitation and fog deposition—will equal the liquid water outflow due to throughfall and stemflow and the temporary storage in the canopy (53.4) [53.4]. Therefore, to calculate the input fog deposition, it is necessary to quantify the other four water budget terms in the equation. *Schemenauer* and *Cereceda* [53.26] gave an example of two intertwined olive trees in southern Oman that dripped an average of 860 L d⁻¹ into a 5 m diameter cement reservoir during one 79 d fog season and 580 L d⁻¹ in a second 83 d fog season. In this case, all of the throughfall derived from the fog deposition, which represented an average of 4 and 3 cm H₂O d⁻¹ on the reservoir base during the fog seasons at that location.
- **Eddy-covariance method.** The turbulent transport of fog droplets can be quantified by applying the eddy-

covariance method, which has been widely used to measure CO₂/H₂O fluxes between ecosystems and the atmosphere. The instruments needed for this purpose are a fast-response fog droplet spectrometer and a 3-D sonic anemometer mounted on a measurement tower downwind of the targeted surface. A detailed description of the theory and application of the eddy-covariance method can be found in Chap. 55. For more on the specific application of the eddy-covariance method to fog deposition estimation, readers may refer to [53.16, 27, 28].

- **Isotope method.** Stable isotopes of H and O have been used to infer the contributions of fog water to soil water, stream water, and plant water use. The analytic techniques employed are beyond the scope of this chapter. The basic concept is that fog has been found to have higher concentrations of the heavier isotopes ²H and ¹⁸O than rain due to differences in formation temperature and air mass history. Isotopic signatures in soil and surface water, as well as in tree sap, can be compared to standard values, and the differences can be used to estimate the relative proportions of fog water and rainwater sources. Readers interested in this method can refer to [53.16, 29–31]. This methodology has been used for decades [53.32] but is not in widespread use. Sampling protocols need to be well defined and carefully followed. This method is especially useful in locations where other information indicates that fog may contribute substantially to the groundwater.

53.2 History

A number of extensive reviews of the collection and use of fog have been written [53.1, 33, 34]. Comments on fog go back to biblical and Roman times. *Gilbert White* (1720–1793), a naturalist in England, observed that vegetation collected substantial amounts of fog water [53.35]. Records of fog deposition in the early literature were mostly limited to qualitative descriptions, rather than quantitative measurements. For example, in 1917, *William S. Cooper* (1884–1978) published his observations regarding the distribution of redwood (*Sequoia sempervirens*) in a coastal area of California (USA), and noted that there was a higher soil water content under the redwood canopy, possibly due to the contribution of fog water that had dripped from the canopy to the soil [53.36]. He also noticed that the redwood only occurred in locations where fog was a frequent occurrence. The shape of redwood needles may help them to intercept fog droplets in the airstream [53.37]. In

1905, *Rudolf Marloth* (1855–1931) published possibly one of the first scientific articles on fog deposition rate estimation [53.17]. During some dry summer months (December 1902 to February 1903) in South Africa, he installed two rain gauges on top of Table Mountain, where the vegetation is much more abundant than the short bushes seen in the lowland and hill areas. As noted earlier, the top of one of the gauges was fitted with a bunch of reeds to intercept fog water. The difference in deposition between the modified and unmodified gauges was very large—it corresponded to the deposition of an extra 190 mm of water within 56 days. However, this difference is not an accurate reflection of the additional contribution of fog water, since the reeds would also have collected wind-blown drizzle and rain, so there would have been a far higher input of drizzle and rain into the gauge with the reeds than into the unmodified rain gauge [53.20]. This is a common mea-

surement error in many measurements of fog collection rates.

Ever since it was first applied at the beginning of the twentieth century, this two rain-gauge system has been widely used to evaluate the amount of fog deposition. Therefore, in locations where fog, drizzle, and rain are all present during the measurement period, the utilization of this gauge system has resulted in significant errors in reported values of the ratio of fog deposition to precipitation deposition due to factors such as ignoring the contribution of wind-blown precipitation and the placement of the unmodified rain gauge above ground level, where the catch may be influenced (reduced) by strong winds. In addition, the conversion of the amount of fog water collected by the modified rain gauge to a depth of water on the ground is often problematic; indeed, the process used to perform this conversion is frequently not explained. These factors make it difficult to draw quantitative conclusions from many of the studies that have used this two rain-gauge system. That said, the importance of fog deposition, especially in upland areas, has been clearly demonstrated. In 1968, *Hubert W. Vogelmann* (1928–2013) and coworkers installed this system along an elevation gradient that increased from 540 to 1080 m ASL in Vermont (USA), and demonstrated a clear corresponding elevation gradient in fog deposition rate [53.38]. The same measurement technique was used on the Hoher Sonnblick, a mountain in Austria, and the fog deposition rate was found to decrease with distance from the ocean [53.39]. Similar observations of the variation in fog deposition along a slope were made along an elevation gradient from 16 to 2425 m in Mexico [53.40] and another gradient from 300 to 900 m in Chile (where measurements were also taken at several points along the crest of a ridge line) [53.41]. Both the altitude and the characteristics of the terrain were found to be important influences on the fog deposition rate. As the altitude increased, the soil became more acidic due to increasing fog interception by the forest canopy [53.42].

Fog may be seen on hills in arid coastal locations due to the onshore advection of marine cloud decks that are too thin to form precipitation. Such conditions occur on the coasts of Chile, Peru, California, the Sultanate of Oman, and Namibia, for example. In these arid regions, or during a dry season when rainfall is minimal, normal rain gauges positioned below vegetation have been used to estimate the deposition of fog water on the ground. For example, a study of normal rain gauges installed beneath different tree species in coastal Californian hills during dry summer months showed that the water collected was only fog water that dripped from the tree crown [53.43]. The tree species, the exposure of the individual tree, as well as the topography of the

site determined the amount of fog intercepted and thus the fog deposition rate.

Starting in the 1960s, when it became apparent that the atmospheric deposition of pollutants/nutrients was a serious problem in industrialized countries, ecosystem nutrient cycling has been monitored using the vegetation canopy as the domain for budget calculations. The nutrient input to the canopy via wet (precipitation and fog) and dry (particulates and gases) deposition is balanced by the output: throughfall, stemflow, and the canopy interaction. The term *occult deposition*—a deposition process other than precipitation and dry deposition—has been used to denote water and chemical deposition by fog/cloud droplets onto canopy surfaces. The fog deposition can be estimated when other terms of the budget equation are known or negligible [53.15]. The water budget principle has proven useful at the watershed scale. During a period without rainfall, the streamflow may peak sometime after the occurrence of fog. The water depth on the ground contributed by fog can be inferred [53.44].

Instead of placing fog-collecting materials on top of rain gauges, an artificial tree has been used to intercept fog water, and the collection efficiency of this artificial tree has been compared with those of a real tree and a passive string fog collector [53.14]. The collection efficiencies of these three collectors, while different, were highly correlated. This confirmed the applicability of artificial fog collectors to the estimation of fog deposition; however, the coefficient for the conversion from the collector to the fog deposition rate on vegetation needs to be carefully deduced.

In a recent study, a water budget method for determining fog deposition in a blanket bog ecosystem was developed [53.45]. An undisturbed peat monolith was isolated, and its change in weight due to the difference between the precipitation and fog deposition (input) and the evaporation (output) was measured regularly. The precipitation was recorded using a normal rain gauge, and the evaporation was calculated using the Bowen ratio/energy balance method. Unlike the other methods mentioned previously, this calculated fog deposition rate represented the *real* net fog deposition rate, especially when there was no rain during the measurement period (≈ 12 h in this case).

In remote mountainous regions where conventional water resources are limited, techniques for the collection of fog water for domestic use have been developed [53.26, 33, 34]. Evaluating the horizontal fog flux using small portable instruments permits the selection of appropriate locations for large fog collectors and allows the amount of water that might be collected to be predicted [53.13]. The largest fog collection project ever undertaken was on a coastal mountain in Chile, El



Fig. 53.1 A portion of the array of large fog collectors used in the El Tofo project in Chile during the late 1980s and 1990s (photo © Robert S. Schemenauer 2020; all rights reserved)

Tofo, where water from 100 large fog collectors, each with a surface area of 48 m^2 , was taken through a 7 km pipeline to the coastal village of Chungungo [53.26] (Fig. 53.1). The average daily water production was $3 \text{ L m}^{-2} \text{ d}^{-1}$, giving a total average production of almost 15000 L d^{-1} when the water generated by the project was at its maximum. The project ran for 10 years. The peak daily production from fog water collection exceeded 100000 L on some days. Websites main-

tained by nonprofit organizations provide descriptions of many past fog collection projects as well as access to proceedings from a series of eight conferences on Fog, Fog Collection, and Dew that began in 1998 [53.46, 47].

With the development of fog deposition models, a new gateway for studying fog deposition has been opened [53.48]. The application of simulation models has become popular, and the on-site measurement of dripping fog water by gauges can be used to verify these models, enabling them to be improved so that they are more accurate when applied at larger spatial and temporal scales [53.49]. At the watershed scale, where fog frequently occurs, the incorporation of fog deposition into a hydrological model has greatly improved the simulation of streamflow [53.50]. For sites where direct measurements are not feasible, models can be a useful alternative way to estimate fog deposition, although some basic meteorological parameter values and surface measurements are still needed before the models can be applied and verified.

The application of fog deposition models to areas beyond small forest plots remains a major challenge, particularly when moving away from flat domains to complex mountainous terrain [53.51]. A detailed discussion of the methodology and limitations of fog deposition models is beyond the scope of this chapter but can be found in the literature [53.52].

53.3 Theory

In this section, the theories behind the fog deposition measurement methods discussed in Sect. 53.1.3 are explained in detail. Except for the eddy-covariance method and the isotope method, the methods of quantifying fog deposition are based simply on the law of mass conservation.

53.3.1 Direct Quantification of the Deposited Water Mass

The most straightforward way of determining how much fog water is deposited onto a specific surface may be to directly measure the weight change of the object. There are two kinds of natural intercepting surfaces for which different direct measurement approaches can be used. The first kind of intercepting surface is the forest canopy. A direct measurement taken on the canopy must then be converted to the ground-surface-based fog water flux. The second kind of intercepting surface is short vegetation, for which there are fewer technical difficulties when performing a *real* direct measurement of the fog deposition rate. A measurable subset of the

ground surface (soil and vegetation) can be separated from its surroundings, and its change in total weight due to fog deposition can be measured.

In both cases, a precision balance is needed to weigh the intercepting surface plus the deposited fog water. The maximal load of the balance and the required balance precision (usually 0.1 g) should be determined in advance according to the object to be measured. If continuous recording is preferred, the balance should have a serial output port that allows values to be sent to a storage device (either a datalogger or a computer).

To mimic the real fog deposition process, the measurement system should be placed at the location within the original vegetation from which the leaves/small vegetation were taken.

For forested ecosystems, the canopy is the main place to receive atmospheric deposition, including wet, dry, and fog deposition. The leaves/needles in the forest canopy have a much larger total surface area overall than the twigs and branches, which partly explains why they are the main intercepting surface for fog droplets. Another reason is that the leaves or needles make up the

outer layer of a tree, and it is this layer that is primarily exposed to the wind carrying the fog droplets. The air that penetrates beyond the outer structure of the tree will have been stripped of many of the fog droplets, and the wind speed will have been reduced. Both of these factors will result in lower fog deposition in the internal structure of a tree or other vegetation.

To conduct the measurement, sample leaves are taken from the canopy and placed at the same position to intercept fog droplets under foggy conditions. The weight of the leaves, including any water dripping from the leaves, can be repeatedly determined by a precision balance. The fog interception rate (FIR) of the intercepting surface, in units of $\text{g H}_2\text{O m}^{-2} \text{h}^{-1}$, can be calculated when the surface area of the sample leaves is determined afterwards. The FIR applies to the leaves at that specific location. Factors such as wind speed and fog liquid water content that determine the FIR normally decrease downwards from the canopy top. The FIR might need to be determined at different depths from the top of the canopy.

Subsequently, the FIR is converted to the fog water deposition rate at the ground surface using the leaf area index (LAI) via

$$\begin{aligned} \text{Fog deposition rate (mm h}^{-1}\text{)} \\ &= \text{FIR (g m}^{-2} \text{h}^{-1}\text{)} \times \text{LAI (m}^2 \text{m}^{-2}\text{)} \\ &\quad \times 10^{-3} \text{ (mm m}^2 \text{g}^{-1}\text{)}, \end{aligned} \quad (53.2)$$

where $10^{-3} \text{ (mm m}^2 \text{g}^{-1}\text{)}$ is the factor needed to convert the water flux from mass units to length units. If the vertical gradient of the FIR is considered, the vertical distribution of the leaf area index must be determined accordingly. From a practical perspective, the canopy can be divided into n layers, and the overall fog deposition rate can then be determined using

$$\text{Fog deposition rate} = \sum_{i=1}^n \text{FIR}_i \times \text{LAI}_i \times 10^{-3}. \quad (53.3)$$

Chang et al. [53.12] estimated the fog deposited in a *Chamaecyparis obtusa* var. *formosana* forest by this method. The fog deposition rate calculated from a single measurement event indicated that the FIR was higher at higher positions in the canopy, indicating that a multilayer approach is necessary for forest canopies. However, this one-time in situ exposure experiment only provided the fog deposition rate under the specific micrometeorological conditions of the experiment. Chang et al. also performed the experiments under a range of visibility conditions and used the results to

build an empirical model of fog deposition in which the fog deposition rate was a function of visibility. Using that model and the visibility monitoring data obtained at that site, the annual fog deposition rate was estimated to be 328 mm yr^{-1} .

53.3.2 Estimation Using Surrogates

Microscale, mesoscale, and macroscale factors influence real-world fog deposition rates. The fog deposition rate is greatly influenced by the arrangement, density, and surface characteristics of the intercepting surface. Short of bringing the actual vegetation into a wind tunnel, a surrogate fog-collecting material will never be identical to real vegetation. Whether a wind tunnel is employed with droplet spray devices or computer models are used to simulate the wind flow around surrogate structures, there will always be compromises that have to be made. Despite these difficulties, artificial intercepting surfaces have been shown to have comparable collecting efficiencies to real vegetation in some conditions [53.13]. For instance, Joslin, Mueller, and Wolfe [53.14] used a passive fog collector, an artificial tree, and a live spruce tree to collect fog and observed good correlations between the collection efficiencies of these intercepting surfaces.

An alternative approach is to directly measure the free-stream flux of fog water and then use this flux as an input to estimate fog water deposition on various surfaces, including natural vegetation and artificial fog collectors. The fog water flux can be determined from measurements of wind speed and fog liquid-water content (LWC) in open terrain or at the canopy top. In practice, this is only viable for experiments where personnel are available at the site and the research has considerable funding. An alternative is to use a passive (no energy required) fog collector made of a material that is effective at collecting fog droplets. This provides a direct measurement of the fog flux at the location of the collector.

In recent years, there have been claims in the literature that the *collection efficiency* can be improved by changing the surface characteristics of the fibers in fog collectors; in some cases, the claims are that the efficiency can be greatly enhanced. The collection efficiency of a fiber increases with decreasing fiber width, increasing droplet velocity, and increasing droplet size. It is the aerodynamics that determines whether a fog droplet with a typical diameter of $1\text{--}20 \mu\text{m}$ will be collected by a fiber $\approx 1 \text{ mm}$ wide. The droplet has no knowledge of what the surface characteristics of the fiber are until after it is collected. This means that nanoscale changes to the hydrophobic or hydrophilic characteristics of the fiber or other minute modifica-

tions to the fiber surface will not change the collection efficiency. The collection efficiency is the fraction of the fog droplets that approach the surface that actually strike it. The second important consideration is whether they stay attached to the surface. This factor is termed the coalescence efficiency (coalescence is discussed in cloud physics textbooks [53.53]). It is effectively 1 (100%) for these conditions, i.e., 10 μm diameter fog droplets that strike a 1 mm wide fiber will remain attached. This means that changing the surface characteristics can at best change the drainage of water in a fog collector; however, in practical terms, this is not an issue, as was shown in field studies that used artificial fog collectors in Chile [53.54]. A large fog collector with a mesh panel that is 4 m high and 10 m long will begin to drain water within $\approx 30\text{--}45$ min and then continue to drain water from the mesh as long as fog and wind are present.

53.3.3 Inference from a Canopy Water Budget

The fog deposition rate on the surface of the ground is most often inferred from the canopy water budget of a forest ecosystem [53.55]. The spatial scale at which this method is applied is a forest stand. Assuming that the forest canopy is the system of interest, precipitation (P) is the main input flux of water for most forest ecosystems. For forests with frequent fog immersion, fog deposition (FG) is another input pathway for water into the canopy. Water leaves the canopy by dripping to the forest floor as throughfall (TF), by flowing downwards along the surfaces of branches and stems as stemflow (SF) (Fig. 53.2), or by interception and subsequent evaporation. The water budget of the canopy is a simple mass balance equation,

$$P + FG = TF + SF + IL, \quad (53.4)$$

where IL is the interception loss, representing the amount of water that has been stored on the surfaces of leaves and twigs that later evaporates and exits the system (i.e., the canopy). Absorption of water by plant tissue may also occur in some plant species, but this is typically a small component of the IL. Due to the time lags associated with the movements of deposited water in the canopy space, a practical temporal scale for mass balance measurements would be no shorter than a whole day. Thus, the deposition rates for these water balance terms can be given in mm d^{-1} or mm yr^{-1} .

A detailed description of precipitation measurement can be found in Chap. 12. Here, we present the general principles of precipitation measurement. Precipitation can be measured using a simple funnel and bottle system for manual measurement (Fig. 53.2), or automatic rain gauges that record the rain intensity with high temporal resolution. A typical automatic instrument is the tipping bucket rain gauge, with a resolution of 0.1–0.5 mm, depending on the collecting area and the capacity of the tipping bucket. To estimate the precipitation input to the forest canopy, the rain gauges are usually installed in a nearby clearing. The installation of the gauges must follow defined guidelines, mainly to prevent the distortion of air flow by obstacles near the gauges.

In mountainous regions, it is very difficult to determine the amount of rainfall that would reach the ground surface using only standard rain gauges mounted 1 or 1.5 m AGL. This has long been recognized [53.56], and specialized conferences on hydrology in mountainous regions have addressed this problem. The terrain plays a large role in influencing the amount of rainfall reaching the ground surface, and there are significant differences between windward and leeward slopes. One modification to rainfall measurements is to place the rain gauge below ground level, with the opening of the rain gauge angled to be parallel to the surface of the

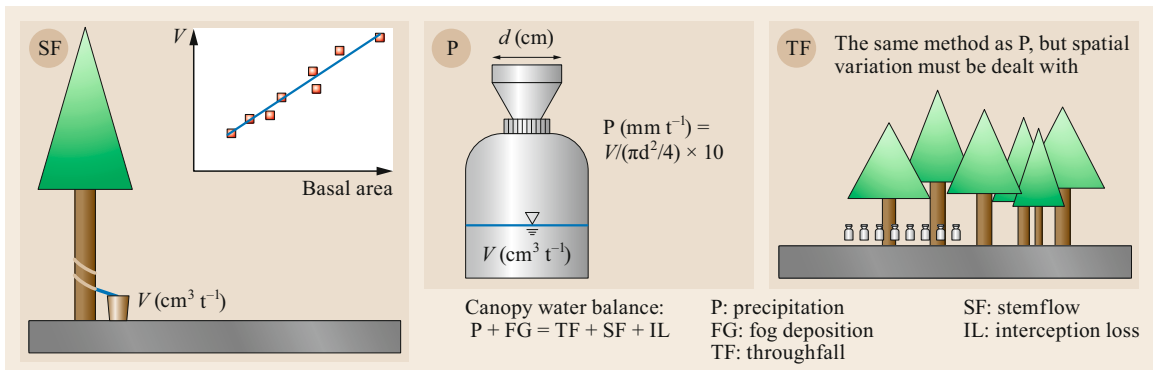


Fig. 53.2 Fog deposition rate quantification via the canopy water balance; note that FG can be calculated once IL has been estimated

ground [53.57]. There is also the possibility of using remote-sensing technologies such as radar to measure precipitation above the forest canopy and then use this as an input to large sites or regions.

Throughfall (water dripping from the vegetation to the forest floor) in forest ecosystems can be monitored with the same type of rain gauge as used to monitor precipitation. These throughfall gauges are placed beneath the canopy on the forest floor (Fig. 53.2). The distribution of leaves and twigs (and thus the gaps) in a forest canopy will influence the throughfall distribution at a small scale. The distribution pattern at a larger scale depends on the spatial distribution of individual trees and the wind both above and within the canopy. Therefore, the amount of throughfall may have large spatial variations. To get a reliable mean value for the throughfall beneath a heterogeneous canopy structure, throughfall gauges with a sufficient number of replicates are needed. An alternative way of collecting throughfall is to increase the collecting surface area of the gauge [53.58]. Trough-type gauges with long troughs and large-capacity tipping bucket gauges are flexible in terms of construction and setup, making them ideal for use in cloud forests [53.59]. In all cases, a protocol must be established to assess whether there are enough throughfall gauges to be able to estimate the errors and uncertainties in the measurements [53.60].

The estimation of stemflow (water flowing down the trunk of a tree) demands more effort than measurements of precipitation and throughfall. A detailed review of stemflow has been given by *Levia and Germer* [53.61]. The stem of a tree is referred to as a trunk. The water flowing down the trunk needs to be conducted to a large gauge. A spiral conduit fixed around the trunk can serve this function [53.62] (Fig. 53.2). To convert the water volumes collected by single trees to the stand-scale water flux, a certain number of sample trees must be selected for stemflow collection. For a natural forest composed of many different tree species, a quadrat of certain size will be selected and all trees within that quadrat will be used for stemflow collection. The total water volume (in L) divided by the ground area of the quadrat (in m²) will give the stemflow as a depth of water expressed in mm. On the contrary, if a plantation with a single dominant tree species is studied, a couple of sample trees with different diameters at breast height (DBHs) can be selected from the stand and used to collect the stemflow. A correlation equation predicting the stemflow volume as a function of DBH can then be created, which in turn allows the stemflow volumes generated by all of the trees within the stand to be calculated from the DBH values of the trees. Finally, the stand-scale stemflow can be calculated using the same

procedure as that used for the natural forest. There are, however, complicating factors. For instance, the relationship may well vary depending on the precipitation rate, fog deposition rate, and ratio of the rainfall input to the fog input. A range of input intensities must be examined. Light precipitation or fog events, which can reduce incoming radiation, evaporation, and evapotranspiration, may result in little or no stemflow.

When the three components P, TF, and SF have been quantified, an estimate for IL is needed to solve for FG using (53.4). To get this, the general form of canopy water balance (53.4) is modified such that the interception loss IL is replaced by the interception capacity (IC), yielding

$$P + FG = TF + SF + IC \quad (53.5)$$

Here, IC represents the maximum amount of water stored on the surface of the canopy; i.e., IC is a constant that is specific to each forest canopy. It is assumed that TF and SF only occur when the canopy storage is saturated and any further input of water from the atmosphere starts to produce detectable TF and SF. The constant IC can be derived from (53.5) by selecting some sampling periods during which there is no fog but sufficient P, TF, and SF. Finally, the FG can then be calculated for any sampling period with fog.

It will be apparent that there are large uncertainties in the measurements and in the models used to apply the measurements to the entire forest plot under consideration. The resulting expected error in the final results will also be large and should always be kept in mind. This means that if the goal is to use the water fluxes P, TF, and SF to calculate FG by (53.5), then the calculated FG value will necessarily have considerable uncertainty. When the values are reported, the number of significant figures should reflect the expected error in the measurements.

53.3.4 Eddy-Covariance Method

A detailed description of the eddy-covariance methodology is given in Chap. 55. The part of this method that is specific to the measurement of fog deposition is given in this section.

The eddy-covariance method can be used to determine the vertical turbulent transport of any scalar (e.g., momentum, gases, particles) that can be measured very frequently, typically at a rate of 10 Hz. To measure the vertical turbulent fog droplet flux, a 3-D sonic anemometer and a fog droplet spectrometer are needed to measure the vertical wind speed (w) and the fog droplet concentrations (C) for various droplet size

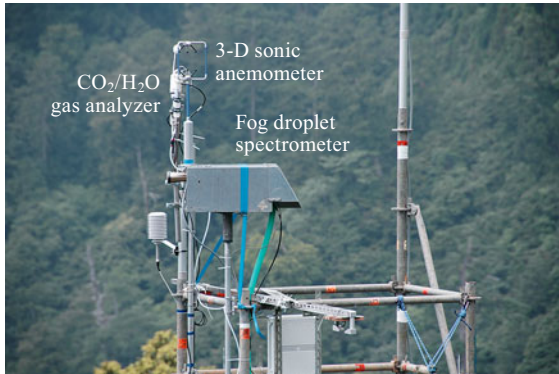


Fig. 53.3 Eddy-covariance system for measuring the fog deposition rate at the Chi-Lan Mountain site in northern Taiwan (photo © Shih-Chieh Chang 2020; all rights reserved)

classes [53.28] (Fig. 53.3). Due to the cubic relationship between droplet diameter and droplet volume, smaller size classes are better for quantifying the LWCs of the respective size classes. The flux of droplets within a specific size class can be calculated as

$$F_{\text{drop}} = \overline{w' C'}$$

Here, w' and C' are the turbulent fluctuations of the vertical wind speed and the fog droplet concentration for a specific size class, respectively. The turbulent fluctuations are calculated by subtracting the mean w and C during the averaging period (typically 30 min) from the time series of w and C . The overbar denotes the mean of the averaging period for which the turbulent flux is calculated. The droplet flux in each size class is converted to the LWC flux and then integrated across all droplet sizes to yield the total water volume flux.

53.4 Devices and Systems

Table 53.3 gives a summary of the devices and systems that are used for the different methods of quantifying fog deposition. In this section, common laboratory devices such as the balance used in weighing procedures are not discussed. Some sensors that are needed to derive the parameters in Table 53.2 (e.g., the anemometer for measuring the wind and the droplet spectrometer for determining the fog droplet size distribution and liquid water content) are discussed in the relevant chapters of this Handbook.

53.4.1 Canopy Water Balance Monitoring System

To employ the water budget method (Sect. 53.1.3) of deriving the fog deposition rate, a monitoring system for the canopy water budget is needed. Such a system includes collectors for precipitation, throughfall, and stemflow (along with suitable replicates) installed in the forest/shrub land. Since the 1980s, long-term ecosystem research sites around the world have used this monitoring system to study the atmospheric deposition of water, nutrients, and pollutants. Collectors for evaluating nutrient/pollutant deposition must be made of an inert material such as high-density polyethylene (HDPE) or even HDPE with teflon coatings. The sampling frequency has to be high enough to enable temporal changes in the chemical composition of the collected water samples to be discerned. Figure 53.2 shows the most commonly used system. When fog occurs frequently, FG contributes to the canopy water balance and must be calculated (Sect. 53.3.3).

53.4.2 Eddy-Covariance Method

A flux tower must be erected at a location sufficiently downwind of the fog-intercepting surfaces. This area surrounding the tower that influences the flux measurements is called the flux footprint. The eddy-covariance method provides an opportunity for continuous observations of vertical droplet fluxes to study the characteristics and temporal variability of processes. On the other hand, the actual fog deposition values obtained using this method are not very comparable with other methods of estimating fog deposition.

The constraints of the eddy-covariance method, which commonly arise during gas flux measurements (e.g., the less-developed turbulence during the night), must also be dealt with. This is especially important when quantifying fog deposition in radiation fog, which only develops under stable boundary layer conditions with nearly no turbulence. Moreover, the application of the eddy-covariance method under foggy conditions is problematic as fog droplets interfere with the operation of sonic anemometers. The accuracy of the measurements are strongly influenced by droplets deposited on transducer surfaces and those that are floating in the air [53.63]. The data acquisition rate and/or data quality are therefore not always satisfactory.

In addition, the eddy-covariance method demands a continuous supply of alternating current (AC) power to drive the air pump for the droplet spectrometer. This, as well as the considerable expense of the instruments used, has prevented the wide application of the eddy-covariance method in the measurement of fog deposition.

53.4.3 Fog Collectors for Chemical Analysis

Wet deposition [53.64] and dry deposition from the atmosphere are important pathways into vegetation and the ground surface for both pollutants and nutrients. In locations where fog is frequent, it has the potential to dominate the wet deposition process. This has been shown to be the case in mountain locations. While the amount of water deposited as rain and snow at higher elevations may be greater than the amount of water deposited from fog, the concentrations of major ions, heavy metals, and some organic compounds may be 3–5 times higher in fog water than in rainwater or snow [53.5, 65].

Although the additional input of plant nutrients provided by fog water can be beneficial to plant growth, any harmful chemicals present in the fog water could damage the ecosystem. In some cases, such as nitrate deposition, it can be both the amount and the timing of the deposition during the year that determines whether the nitrate input is beneficial or harmful to the forest. The chemical fluxes can be calculated by multiplying the concentrations of the chemicals in fog water by the fog deposition rate. To sample fog water for chemical analysis, specialized fog collectors are needed.

There are two main categories of fog collectors: passive collectors and active collectors. The most widely used passive fog collector uses vertically strung teflon strings as the intercepting surface (Fig. 53.4). It was designed by *Falconer and Falconer* in 1980 [53.22] and subsequently modified by *Mohnen and Kadlec* in 1989 [53.66] and termed the Atmospheric Sciences Research Center (ASRC) collector. This collector has been widely used in projects such as those noted above. The strings are normally arranged cylindrically to reduce the influence of the wind direction. It is not possible to avoid drizzle, rain, and snow collection when sampling under windy conditions. Additionally, dry deposition in the form of both gases and particulates will impact on the collecting strings. Therefore, the chemical concentrations obtained from passive fog collectors have to be interpreted with care. Baseline values can be obtained by exposure under no-fog conditions and through comparison with the concentrations in samples obtained from bulk collectors installed in parallel.

The usual approach is to have parallel measurements of rainfall and snowfall intensity to define periods when precipitation is known to have occurred. This can help to identify periods when there is only fog deposition. It is not possible to eliminate the dry deposition component, but it is typically much smaller than the wet deposition component. The dry deposition component can be estimated by exposing the passive fog collector under conditions when there is no fog or precipitation to determine the possible contamination from



Fig. 53.4 The 1 m² SFC (*on the left*) and the Environment Canada version of the ASRC collector (after [53.66]) (*on the right*). The photo was taken during the Chemistry of High Elevation Fog project in southern Québec, Canada (photo © Robert S. Schemenauer 2020; all rights reserved)

this source [53.5]. A further possibility is to break up the periods when water is collected by the passive fog collector into three parts: fog only, precipitation only, and a mixture of both fog and precipitation [53.5]. This effectively defines the range of wet deposition events to which forests and mountain vegetation are regularly exposed. Sampling and analytical protocols relating to the use of the ASRC collector have been discussed in the literature [53.5, 54].

When sufficient power is available, active fog collectors can be used to address some of the problems mentioned above. An active fog collector has its intercepting surface inside the equipment. The air containing fog droplets is sucked into the equipment by fans located downstream of the intercepting surface. Many active fog collectors are based on the designs of *Daube et al.* [53.25]. The fans can be activated by a relay system triggered by a datalogger that receives signals from a visibility sensor. The active fog collectors can be set to work only when the visibility is < 1000 m (the standard meteorological definition of fog), meaning that particulates and gases in the air will not contaminate the intercepting surface when there is no fog. Problems may occur when visibility is reduced by smoke or heavy precipitation if the sensor cannot distinguish the source of the visibility reduction. The main difficulty with active collectors is attempting to suck in an air sample that contains a free stream concentration of fog droplets. The sampling process in which droplets are brought into the collector can be size selective, which in turn can bias the chemistry of the bulk fog water sample obtained. This needs to be considered during the design of the active collector.

The fog droplet collection efficiency depends on the wind speed, the fog droplet size, and the size and arrangement of the collecting strings in the active fog collector [53.67]. When the chemical concentrations in

Table 53.4 Advantages and disadvantages of the different methods of calculating fog water deposition in a forest

Method	Advantages	Disadvantages
Direct measurement of collected water mass or volume	Relatively simple	Weight loss due to evaporation and transpiration may bias the estimation A conversion factor is needed to convert to ground-based deposition rate Difficult to sample all representative vegetation and locations
Surrogate method	Useful for understanding the potential fog deposition rate	Weight loss due to evaporation and transpiration may bias the estimation A conversion factor is needed to convert to ground-based deposition rate It is difficult to create surrogates of all exposed vegetation types
Water budget method	Low maintenance costs Applicable to diverse forest/shrub land-cover types	Cannot detect small/short fog events Large errors when calculating the parameters in the water budget equation
Eddy-covariance method	Provides undisturbed, continuous (usually 30 min) vertical fog water flux data	Only feasible under suitable micrometeorological conditions Instruments and maintenance are expensive AC power is required Does not directly measure fog deposition
Free-stream fog flux	Fog water flux above or approaching the forest is measured using passive fog collectors	Measured fog fluxes are used as input for a computer model of the forest that calculates the deposition parameters Complex terrain and complex forest canopies are difficult to model

droplets belonging to different size classes are of interest, the active fog collector can be designed accordingly.

Another factor to keep in mind is sample volume. Different analytical procedures may require different fog water sample sizes. A longer sampling time will clearly lead to a larger sample with less time resolution. A 1 m² SFC that is used to measure fog fluxes will typically collect about five times as much water as the ASRC teflon string fog collector [53.13]. The ASRC collector will in turn normally collect more water per unit time than an active fog collector, but this depends on a variety of factors, including wind speed and the design of the active fog collector.

When the goal is to understand the chemistry of fog water collected for human consumption, there are several different issues. First, the collection surfaces on large fog collectors or the interiors of the water storage tanks are typically not cleaned prior to sampling. Second, the chemistry of the fog water is compared to the World Health Organization drinking water standards, and so certain levels of major ions or heavy metals are deemed acceptable [53.68]. Third, careful storage and transport protocols need to be put in place when moving samples from remote locations to laboratories.

In all chemical analyses of fog water, the instrumentation used for analysis must have suitable detection

limits. These should be in the range of 0.01 ppm for major ions and 0.5–10 ppb for trace elements, depending on the element.

53.4.4 Visibility Sensor

According to the World Meteorological Organization, fog is present when the horizontal visibility is < 1000 m [53.69]. Having a visibility sensor installed on site leads to a better understanding of fog climatology. It provides information about the pattern of fog occurrence and thus a presumption of the significance of FG at the site. Visibility is expressed in meters, and its magnitude is a nonlinear function of the size spectrum of water droplets in the air. The sensor typically uses infrared forward-scatter technology to detect the optical properties of the suspended particles between the light source and the detector arms, which are usually less than a meter apart.

53.4.5 Comparison of the Methods

An outline of the different methods for quantifying fog deposition is given in Table 53.3. A brief description of the advantages and disadvantages of each method is given in Table 53.4.

53.5 Specifications

As described in Sect. 53.1, there is no standard method of fog deposition quantification. Researchers design the measurement system according to their site characteristics. The uncertainty in the final fog deposition rate comes from the instruments employed, the system de-

sign, the operation of the system, and the difficulty involved in calculating fog deposition in a complex natural ecosystem that may be hectares or square kilometers in extent. Table 53.5 lists the uncertainties, measurement ranges, and resolutions of the basic instru-

Table 53.5 Typical characteristics of instruments used for fog deposition measurements

Instrument	Typical total uncertainty	Range	Resolution
Balance	Variable	0.01 g–5 kg	0.01 g
Rain gauges or other collecting systems for fog water	–15% to +20%	Minimum: 0.1 mm–0.2 mm	Typically 0.1 mm, can be lower or higher depending on instrument
Visibility sensor	±10%	10 m–20 km	1 m
Fog droplet spectrometer	< ±10% (small droplets) to ±90% (larger droplets)	Droplet diameter 2–50 μm	Individual droplet in each size bin
Standard fog collector (SFC)	±5% to 10%	All droplet sizes	Depends on rain gauge used to measure the collected fog water

ments. The uncertainty and specifications associated with a general instrument such as a datalogger are given in Chap. 2. An eddy-covariance system used for fog deposition measurement contains a 3-D sonic anemometer and a fog droplet spectrometer. The uncertainty and specifications associated with the former are given in Chap. 55 on eddy covariance.

Because most fog deposition processes result in whole or in part from the horizontal movement of wind-driven fog, the conversion of the interception of fog by vertical surfaces, such as the cross-sectional area of a tree, to a depth on the ground is not straightforward, and calculations are often problematic. The uncertainties introduced by these extrapolations are typically greater than the expected errors in the instrument measurements.

The accuracy and precision of an electrical balance are important when it is employed to weigh the deposited fog water. Windy conditions in the field may cause continuous and irregular changes in balance readings [53.11]. Nevertheless, this is one of the more precise measurements used to estimate fog deposition rates.

Strictly speaking, the method used to quantify the canopy water balance shown in Fig. 53.2 is only applicable in situations where there is no wind, when the input is from rainfall, and when the fog deposition component is zero. When there is no wind above the canopy, the raindrops will fall vertically. When wind is present, the raindrops will fall at an angle determined by the wind speed and the droplet fall velocity, which is in turn directly related to the droplet diameter [53.20]. When wind is present, exposed treetops play the primary role in collecting both raindrops and

fog droplets [53.51]. Emergent treetops will collect proportionally more windblown rain, and the amount collected will be related to the rain shadow area downwind of the treetop. Emergent treetops will also be prime collectors of fog droplets. The uniformity, or lack thereof, of the canopy top will significantly impact the uniformity of water delivered to the surface of the ground. The cross-sectional area of the emergent treetops is an important factor in calculations of water input from windblown precipitation and fog. In the case of precipitation in the form of snowfall, the interception loss component can be much higher than for an equivalent water input in the form of rainfall.

One can assume that the precipitation input to a forest plot is, to a first approximation, independent of the leaf or needle shape and the density of foliage coverage. This is not the case for the fog water input component. The shape and dimension of a leaf or needle are critical influences on its efficiency at collecting microscopic fog droplets. The collection efficiency of a pine needle, for example, will increase as the wind speed increases, the droplet size increases, and the needle diameter decreases. These issues are discussed in the literature [53.21] and are important factors when choosing or designing materials for artificial fog collectors. The porosity of the treetop when viewed from the side is another important determinant of the fog collection/deposition rate. If the tree is very dense, the streamlines of the wind flow will pass around the tree and carry most of the fog droplets past the object. A treetop with an open structure composed of fine pine needles will be a much better collector of fog droplets than a treetop with large leaves and a dense structure.

53.6 Quality Control

To ensure the precision and accuracy of the estimated fog deposition rate, the instruments must be regularly calibrated and the measurement procedures standardized. Table 53.6 lists the general guidelines for quality control. If fog water is to be collected for chemical analysis, all of the steps—from cleaning the collectors

to collecting, storing, and shipping the sample as well as analysis in the laboratory—are critical. These procedures have been discussed in detail in works cited earlier [53.5]. Eddy-covariance instruments must be calibrated according to the instructions of the company prior to the field trip and repeated in the field as required.

Table 53.6 Quality control for various methods of estimating the fog deposition rate

Method	Instrument/procedure	Quality control
Direct measurement of collected water mass or volume	Balance	Use on level base and prevent vibration caused by wind Calibration with standard weights
Water budget method	Water collectors	Precipitation collectors must be located where the wind is not disturbed by surrounding obstacles Sufficient throughfall and stemflow collectors are required to determine the spatial heterogeneity
Eddy-covariance method	Instruments	The guidelines for the installation of the eddy-covariance instruments must be strictly followed since any deviations from the correct installation can strongly influence the data acquisition and the interpretation of the flux data Flagging systems must be used for data quality control
Fog flux	SFC	Check that the mesh is undamaged and that there are no leaks from the trough or pipe Calibrate rain gauges with a measured amount of water

53.7 Maintenance

Table 53.7 gives an overview of the maintenance requirements of the systems used for fog deposition measurements. General rules for maintenance apply; e.g., the cleanliness of the equipment must be routinely checked. When rain gauges are used to record water fluxes in the water budget method, the gauges should be inspected and detritus from the forest and soil must be removed from them. The dataloggers that are used to record sensor readings must also be checked, especially for power supply outages at remote sites.

Eddy-covariance systems and visibility sensors can produce erroneous readings if the sensor heads are contaminated (e.g., by bird droppings or spider webs). Also, optical surfaces must be regularly cleaned to remove dust and chemicals deposited by rain and fog droplets. Infrared gas analyzers must

be calibrated regularly using zero and span gases. Both infrared gas analyzers and fog droplet spectrometers have to be factory calibrated at least every 2 years.

Specialized protocols must be implemented when the instrumentation is operated in difficult weather conditions. Many mountain locations at temperate latitudes experience severe winter weather, including temperatures that can drop to -30°C , which will affect many instruments, power supplies, etc. Snow will need to be regularly cleared from instrumentation. Hoar frost may form on instruments; if present on optical surfaces, this frost will prevent proper operation. Fog droplets are present in the liquid form down to perhaps -20°C , or sometimes even lower temperatures under certain conditions when there is no wind. When these fog droplets strike a cold surface they freeze, forming rime ice. This

Table 53.7 Maintenance of instruments used for fog deposition measurements

Maximum interval	Balance	Rain gauges	Water collectors for chemical analysis	Standard fog collector	Visibility sensor	Eddy-covariance system	Data logging system
Each time before use	Calibration		Spray with deionized water and save sample	Check for any visible evidence of damage	Check for obstructions and dirt		
2 weeks		Clean, check for mechanical function	Thoroughly wash and clean with deionized water	Clean tipping bucket and trough	Clean sensor heads	Clean sensor heads	Inspect data collected for possible instrument malfunctions
3 months				Calibrate tipping bucket; check all water seals; check that frame is vertical		Calibration of gas analyzer	
2 years		Calibration	Re-string the collectors with new teflon fibers	Retighten the mesh on the SFC frame	Factory calibration	Factory calibration of fog droplet spectrometer	Factory calibration

is an opaque white build-up that is familiar to skiers and can result in large ice deposits on surfaces. Freezing rain occurs when liquid raindrops fall onto surfaces with temperatures $< 0^{\circ}\text{C}$. The raindrops spread over the surface, forming a hard layer of clear ice. All of these conditions must be effectively dealt with when measuring fog water in winter conditions. Some instruments have heated inlets or optics, and they should be checked daily or at least during every visit by the site operator.

53.8 Applications

There are two practical applications of fog deposition. They both involve the collection of microscopic fog droplets in enormous numbers. It takes about 10 million fog droplets to make a water drop the size of a match head. Fortunately, wind-blown fluxes of fog contain huge numbers of droplets, typically $\approx 300\text{ cm}^{-3}$ or 300 million m^{-3} . The first practical application involves planting tree species in open areas where fog is frequent in order to reforest clearcut areas or introduce native species into areas that have long been free of trees. The second application involves installing man-made fog collectors to collect fog water for human consumption or for use in agriculture. A blended application is to use fog collectors to generate water that irrigates tree seedlings until they are large enough to collect sufficient irrigation water themselves. A major project to investigate the utilization of fog deposition in this manner took place along the southern coast of Peru for 5 years in the late 1990s [53.33].

Fog collection has been shown to be a useful option for providing domestic water in some remote regions

where normal water resources such as rain, surface water, and groundwater are scarce. The history of this work was discussed above [53.26]. To collect the tiny fog droplets from the air in a cost-efficient way, an enlarged version of the passive SFC with a collection surface of up to 40 m^2 is constructed. In a typical construction process, the fog collectors utilize commercial shade nets to ensure that construction costs are low enough for sustainable operation. There are also projects or experiments that use mesh with a plastic backing, rigid fabrics, and 3-D rigid fabrics. Worldwide, there are numerous systems that successfully collect fog water for use by villages and remote farms. Such systems, which collect fog water at an annual average rate of $3\text{--}10\text{ L m}^{-2}\text{ d}^{-1}$, have greatly improved the quality of life in many areas by supporting small-scale agriculture and providing drinking water for people and animals [53.34]. A detailed manual that describes the scientific background for fog collection and provides the technical construction information needed to select sites and build large fog collectors is available [53.70].

53.9 Further Developments

Quantifying the interception of fog water in situ at different locations in the canopy may lead to a greater understanding of the fog deposition process in forest ecosystems. A useful methodology to achieve this could be to install strain gauges on branches, although the sensitivity of the gauges would need to be increased and it would be necessary to filter out wind-induced vibrations. Additionally, the application of low-cost open-source electronics platforms (e.g., Arduino, <https://www.arduino.cc/>, Accessed 21 July 2021) to data acquisition could increase the spatial sampling framework.

A number of research efforts are underway to determine if adjusting the fiber dimensions or weave of

the collecting material can improve fog collection rates, and whether changing the physical structure could be advantageous for fog collection. There is also considerable interest in using nanotech coatings on plastic or metal meshes in fog collectors. All of these developments require rigorous field testing in a variety of actual fog conditions before they may be adopted. The increased cost of these materials and structures must be balanced against the potential for a significant increase in water production compared to the inexpensive double layer of Raschel mesh that has been used effectively for 40 years.

53.10 Further Reading

Tropical montane cloud forests are research hotspots for fog, fog deposition, and the influences of fog on ecosystems. A collection of synthesized findings and individual research at diverse tropical locations can be found in:

- L.A. Bruijnzeel, F.N. Scatena, L.S. Hamilton (Eds.): Tropical Montane Cloud Forests: Science for Conservation and Management, International Hydrology Series (Cambridge University Press, 2010)

In 1998, an international conference series was initiated that aimed to provide a forum where scientists working in the many areas relating to fog and dew could interact with scientists and development specialists working in applications of fog collection. Its goals were to improve fog and dew science and to directly benefit people in need of alternative water supplies. To date, there have been eight conferences in the series, with the most recent taking place in 2019 in Taipei, Taiwan. Information on this conference series and proceedings from it can be found at www.fogquest.org, Accessed 21 July 2021 and www.fogdew.org, Accessed 21 July 2021.

References

- 53.1 O. Kerfoot: Mist precipitation on vegetation, For. Abstr. **29**, 8–20 (1968)
- 53.2 E. del-Val, J.J. Armesto, O. Barbosa, D.A. Christie, A.G. Gutiérrez, C.G. Jones, P.A. Marquet, K.C. Weathers: Rain forest islands in the Chilean semiarid region: Fog-dependency, ecosystem persistence and tree regeneration, *Ecosystems* **9**, 598–608 (2006)
- 53.3 J. Kummerow: Quantitative Messungen des Nebelniederschlags im Walde von Fray-Jorge an der nordchilenischen Küste, *Naturwissenschaften* **49**, 203–204 (1962)
- 53.4 L.A. Bruijnzeel, W. Eugster, R. Burkard: Fog as a hydrologic input. In: *Encyclopedia of Hydrological Sciences*, ed. by M.G. Anderson (John Wiley & Sons, Ltd., Hoboken 2006) pp. 1–24
- 53.5 R.S. Schemenauer, C.M. Banic, N. Urquizo: High elevation fog and precipitation chemistry in southern Quebec, Canada, *Atmos. Environ.* **29**, 2235–2252 (1995)
- 53.6 M. Igawa, T. Kase, K. Satake, H. Okochi: Severe leaching of calcium ions from fir needles caused by acid fog, *Environ. Pollut.* **119**, 375–382 (2002)
- 53.7 C.T. Driscoll, G.B. Lawrence, A.J. Bulger, T.J. Butler, C.S. Cronan, C. Eagar, K.F. Lambert, G.E. Likens, J.L. Stoddard, K.C. Weathers: Acidic deposition in the northeastern United States: Sources and inputs, ecosystem effects, and management strategies, *Bioscience* **51**, 180–198 (2001)
- 53.8 J.B. Anderson, R.E. Baumgardner, V.A. Mohnen, J.J. Bowser: Cloud chemistry in the eastern United States, as sampled from three high-elevation sites along the Appalachian mountains, *Atmos. Environ.* **33**, 5105–5114 (1999)
- 53.9 S. Prada, M.M. de Sequeira, C. Figueira, R. Vasconcelos: Cloud water interception in the high altitude tree heath forest (*Erica arborea* L.) of Paul Da Serra Massif (Madeira, Portugal), *Hydrol. Process.* **26**, 202–212 (2012)
- 53.10 C. Schunk, P. Trautwein, H. Hruschka, E. Frost, L. Dodson, A. Derhem, J. Bargach, A. Menzel: Testing water yield, efficiency of different meshes and water quality with a novel fog collector for high wind speeds, *Aerosol Air Qual. Res.* **18**, 240–253 (2018)
- 53.11 J. Tav, O. Masson, F. Burnet, P. Paulat, T. Bourriane, S. Conil, L. Pourcelot: Determination of fog-droplet deposition velocity from a simple weighing method, *Aerosol Air Qual. Res.* **18**, 103–113 (2018)
- 53.12 S.C. Chang, C.F. Yeh, M.J. Wu, Y.J. Hsia, J.T. Wu: Quantifying fog water deposition by in situ exposure experiments in a mountainous coniferous forest in Taiwan, *For. Ecol. Manag.* **224**, 11–18 (2006)
- 53.13 R.S. Schemenauer, P. Cereceda: A proposed standard fog collector for use in high-elevation regions, *J. Appl. Meteorol.* **33**, 1313–1322 (1994)
- 53.14 J.D. Joslin, S.F. Mueller, M.H. Wolfe: Tests of models of cloudwater deposition to forest canopies using artificial and living collectors, *Atmos. Environ. A* **24**, 3007–3019 (1990)
- 53.15 G.M. Lovett, W.A. Reiners, R.K. Olson: Cloud droplet deposition in subalpine balsam fir forests: Hydrological and chemical inputs, *Science* **218**, 1303–1304 (1982)
- 53.16 S. Schmid, R. Burkard, K.F.A. Frumau, C. Tobón, L.A. Bruijnzeel, R. Siegwolf, W. Eugster: Using eddy covariance and stable isotope mass balance techniques to estimate fog water contributions to a Costa Rican cloud forest during the dry season, *Hydrol. Process.* **25**, 429–437 (2011)
- 53.17 R. Marloth: Results of experiments on table mountain for ascertaining the amount of moisture deposited from the south-east clouds, *Trans. S. Afr. Philos. Soc.* **14**, 403–408 (1903)
- 53.18 J.D. Price, R. Clark: On the measurement of dewfall and fog-droplet deposition, *Bound.-Layer Meteorol.* **152**, 367 (2014)
- 53.19 R.S. Schemenauer, P. Cereceda: The use of fog for groundwater recharge in arid regions. In: *Proc. Int. Semin. Groundw. Environ. Arid Semiarid Areas* (Chinese Academy of Geological Sciences, Beijing 1992) pp. 84–91

- 53.20 R.S. Schemenauer, P. Cereceda: The role of wind in rainwater catchment and fog collection, *Water Int.* **19**, 70–76 (1994)
- 53.21 R.S. Schemenauer, P.I. Joe: The collection efficiency of a massive fog collector, *Atmos. Res.* **24**, 53–69 (1989)
- 53.22 R.E. Falconer, P.D. Falconer: Determination of cloud water acidity at a mountain observatory in the Adirondack mountains of New York State, *J. Geophys. Res.* **85**, 7465–7470 (1980)
- 53.23 J. Grunow: The productiveness of fog precipitation in relation to the cloud droplet spectrum. In: *Physics of Precipitation: Proc. Cloud Phys. Conf., Woods Hole*, Geophysical Monograph Series, Vol. 5 (AGU, Washington 1960) pp. 110–117
- 53.24 J.O. Juvik, P.C. Ekern: *A Climatology of Mountain Fog on Mauna Loa, Hawaii Island* (Univ. Hawaii at Manoa, Honolulu 1978), Tech. Rep. 118
- 53.25 B. Daube, K.D. Kimball, P.A. Lamar, K.C. Weathers: Two new ground-level cloud water sampler designs which reduce rain contamination, *Atmos. Environ.* **21**, 893–900 (1987)
- 53.26 R.S. Schemenauer, P. Cereceda: Fog collection's role in water planning for developing countries, *Nat. Resour. Forum* **18**, 91–100 (1994)
- 53.27 W. Eugster, R. Burkard, F. Holwerda, F.N. Scatena, L.A.S. Bruijnzeel: Characteristics of fog and fogwater fluxes in a Puerto Rican elfin cloud forest, *Agric. For. Meteorol.* **139**, 288–306 (2006)
- 53.28 T.S. El-Madany, J.B. Walk, M.J. Deventer, D.T. Degeffie, S.C. Chang, J.Y. Juang, F. Griessbaum, O. Klemm: Canopy-atmosphere interactions under foggy condition – Size-resolved fog droplet fluxes and their implications, *J. Geophys. Res. Biogeosci.* **121**, 796–808 (2016)
- 53.29 M. Scholl, W. Eugster, R. Burkard: Understanding the role of fog in forest hydrology: Stable isotopes as tools for determining input and partitioning of cloud water in montane forests, *Hydrol. Process.* **25**, 353–366 (2011)
- 53.30 M.A. Scholl, T.W. Giambelluca, S.B. Gingerich, M.A. Nullet, L.L. Loope: Cloud water in windward and leeward mountain forests: The stable isotope signature of orographic cloud water, *Water Resour. Res.* **43**, W12411 (2007)
- 53.31 S.S.O. Burgess, T.E. Dawson: The contribution of fog to the water relations of *Sequoia sempervirens* (D. Don): Foliar uptake and prevention of dehydration, *Plant Cell Environ.* **27**, 1023–1034 (2004)
- 53.32 R. Aravena, O. Suzuki, A. Pollastri: Coastal fog and its relation to groundwater in the IV region of northern Chile, *Chem. Geol. Isot. Geosci. Sect.* **79**, 83–91 (1989)
- 53.33 R.S. Schemenauer, P. Cereceda: Fog-water collection in arid coastal locations, *Ambio* **20**, 303–308 (1991)
- 53.34 O. Klemm, R.S. Schemenauer, A. Lummerich, P. Cereceda, V. Marzol, D. Corell, J. van Heerden, D. Reinhard, T. Gherezghiher, J. Olivier, P. Osses, J. Sarsour, E. Frost, M.J. Estrela, J.A. Valiente, G.M. Fessehaye: Fog as a fresh-water resource: Overview and perspectives, *Ambio* **41**, 221–234 (2012)
- 53.35 G. White: Letter to the honourable Daines Barrington, *J. Meteorol.* **1978**, 115–117 (1776)
- 53.36 W.S. Cooper: Redwoods, rainfall and fog, *Plant World* **20**, 179–189 (1917)
- 53.37 W.A. Cannon: On the relation of redwoods and fog to the general precipitation in the redwood belt of California, *Torreya* **1**, 137–139 (1901)
- 53.38 H.W. Vogelmann, T. Siccama, D. Leedy, D.C. Ovitt: Precipitation from fog moisture in the Green Mountains of Vermont, *Ecology* **49**, 1205–1207 (1968)
- 53.39 J. Grunow, H. Tollner: Nebelniederschlag Im Hochgebirge, *Arch. Meteorol. Geophys. Bioklimatol. B* **17**, 201–228 (1969)
- 53.40 H.W. Vogelmann: Fog precipitation in the cloud forests of eastern Mexico, *Bioscience* **23**, 96–100 (1973)
- 53.41 R.S. Schemenauer, P. Cereceda, N. Carvajal: Measurements of fog water deposition and their relationships to terrain features, *J. Clim. Appl. Meteorol.* **26**, 1285–1291 (1987)
- 53.42 W.H. Hendershot, F. Courchesne, R.S. Schemenauer: Soil acidification along a topographic gradient on Roundtop Mountain, Quebec, Canada, *Water Air Soil Pollut.* **61**, 235–242 (1992)
- 53.43 G.T. Oberlander: Summer fog precipitation on the San Francisco peninsula, *Ecology* **37**, 851–852 (1956)
- 53.44 A.M. Gurnell: A note on the contribution of fog drip to streamflow, *Weather* **31**, 121–126 (1976)
- 53.45 J.S. Price: Blanket bog in Newfoundland. Part 1. The occurrence and accumulation of fog-water deposits, *J. Hydrol.* **135**, 87–101 (1992)
- 53.46 International Fog and Dew Association (IFDA): <http://www.fogdew.org>, Accessed 21 July 2021
- 53.47 FogQuest – Sustainable Water Solutions (Charity and Nonprofit Organization): <http://www.fogquest.org>, Accessed 21 July 2021
- 53.48 G.M. Lovett: Rates and mechanisms of cloud water deposition to a subalpine balsam fir forest, *Atmos. Environ.* **18**, 361–371 (1984)
- 53.49 S. Pahl, P. Winkler, T. Schneider, B. Arends, D. Schell, R. Maser, W. Wobrock: Deposition of trace substances via cloud interception on a coniferous forest at Kleiner Feldberg, *J. Atmos. Chem.* **19**, 231–252 (1994)
- 53.50 X.W. Yin, P.A. Arp: Fog contributions to the water budget of forested watersheds in the Canadian maritime provinces: A generalized algorithm for low elevations, *Atmosphere-Ocean* **32**, 553–566 (1994)
- 53.51 J.L. Walmsley, R.S. Schemenauer, H.A. Bridgman: A method for estimating the hydrologic input from fog in mountainous terrain, *J. Appl. Meteorol.* **35**, 2237–2249 (1996)
- 53.52 G. Katata: Fogwater deposition modeling for terrestrial ecosystems: A review of developments and measurements, *J. Geophys. Res. Atmos.* **119**, 8137–8159 (2014)
- 53.53 H.R. Pruppacher, J.D. Klett: *Microphysics of Clouds and Precipitation*, Atmospheric and Oceanographic Sciences Library, Vol. 18 (Springer, Dordrecht 2010)

- 53.54 R.S. Schemenauer, P. Cereceda: The quality of fog water collected for domestic and agricultural use in Chile, *J. Appl. Meteorol.* **31**, 275–290 (1992)
- 53.55 L. Köhler, C. Leuschner, M. Hauck, D. Hertel: Cloud water interception and element deposition differ largely between Norway spruce stands along an elevation transect in Harz Mountains, Germany, *Ecohydrology* **8**, 1048–1064 (2015)
- 53.56 G.D.T. De Villiers: Rainfall variations in mountainous regions. In: *Proc. Two Lausanne Symposia* (IAHS, Wallingford 1990) pp. 33–41, http://hydrologie.org/redbooks/a193/iahs_193_0033.pdf, Access 11 Oct. 2021
- 53.57 B. Sevruk: The use of stereo, horizontal, and ground level orifice gages to determine a rainfall–elevation relationship, *Water Resour. Res.* **10**, 1138–1141 (1974)
- 53.58 G. García-Santos, L.A. Bruijnzeel: Rainfall, fog and throughfall dynamics in a subtropical ridge top cloud forest, National Park of Garajonay (La Gomera, Canary Islands, Spain), *Hydrol. Process.* **25**, 411–417 (2011)
- 53.59 A.D. Ziegler, T.W. Giambelluca, M.A. Nullet, R.A. Sutherland, C. Tantasarin, J.B. Vogler, J.N. Negishi: Throughfall in an evergreen-dominated forest stand in northern Thailand: Comparison of mobile and stationary methods, *Agric. For. Meteorol.* **149**, 373–384 (2009)
- 53.60 J. Fan, K.T. Oestergaard, A. Guyot, D.G. Jensen, D.A. Lockington: Spatial variability of throughfall and stemflow in an exotic pine plantation of subtropical coastal Australia, *Hydrol. Process.* **29**, 793–804 (2015)
- 53.61 D.F. Levia, S. Germer: A review of stemflow generation dynamics and stemflow–environment interactions in forests and shrublands, *Rev. Geophys.* **53**, 673–714 (2015)
- 53.62 S.C. Chang, E. Matzner: The effect of beech stemflow on spatial patterns of soil solution chemistry and seepage fluxes in a mixed beech/oak stand, *Hydrol. Process.* **14**, 135–144 (2000)
- 53.63 T.S. El-Madany, F. Griessbaum, G. Fratini, J.-Y. Juang, S.-C. Chang, O. Klemm: Comparison of sonic anemometer performance under foggy conditions, *Agric. For. Meteorol.* **173**, 63–73 (2013)
- 53.64 E. Beiderwieden, A. Schmidt, Y.J. Hsia, S.C. Chang, T. Wrzesinsky, O. Klemm: Nutrient input through occult and wet deposition into a subtropical montane cloud forest, *Water Air Soil Pollut.* **186**, 273–288 (2007)
- 53.65 V.A. Mohnen, R.J. Vong: A climatology of cloud chemistry for the eastern United States derived from the Mountain Cloud Chemistry Project, *Environ. Rev.* **1**, 38–54 (1993)
- 53.66 V.A. Mohnen, J.A. Kadlec: Cloud chemistry research at Whiteface Mountain, *Tellus B* **41**, 79–91 (1989)
- 53.67 B.B. Demoz, J.L. Collett, B.C. Daube: On the Caltech active strand cloudwater collectors, *Atmos. Res.* **41**, 47–62 (1996)
- 53.68 WHO: *Guidelines for Drinking-Water Quality: Fourth Edition Incorporating the First Addendum* (World Health Organization, Geneva 2017)
- 53.69 WMO: *Guide to Meteorological Instruments and Methods of Observation (2008 Edition, Updated in 2010)* (World Meteorological Organisation, Geneva 2012), WMO-No. 8
- 53.70 R.S. Schemenauer, P. Cereceda, P. Osses: *FogQuest: Fog Water Collection Manual* (FogQuest, Toronto 2017)

Shih-Chieh Chang

Department of Natural Resources and Environmental Studies, Center for Interdisciplinary Research on Ecology and Sustainability
National Dong Hwa University
Hualien, Taiwan
scchang@gms.ndhu.edu.tw



Shih-Chieh Chang is Professor of Ecosystem Ecology at National Dong Hwa University in Taiwan. He received a MS from National Taiwan University in 1991 and a PhD in Soil Ecology from the Bayreuth Institute for Terrestrial Ecosystem Research (BITÖK), University of Bayreuth, Germany in 1999. His research has focused on the influences of fog on ecosystem processes, including nutrient cycling and carbon fluxes at montane cloud forests.

Robert S. Schemenauer

FogQuest: sustainable water solutions
Kamloops, Canada
fogquest@shaw.ca



Robert S. Schemenauer is a retired research scientist living in Canada. He had a lengthy career with Environment Canada and was the first emeritus research scientist in the Atmospheric Environment Service. He also held an adjunct professorship, founded the charity FogQuest: sustainable water solutions, and initiated the international conference series on Fog, Fog Collection and Dew. He has published extensively on fog and cloud microphysics and fog collection.

Immission and Dry Deposition

Ivonne Trebs , Christof Ammann , Jürgen Junk 

The Earth's surface is both an important source and sink for atmospheric trace compounds (gases and aerosols). This chapter provides a detailed overview of methods to determine immission, dry deposition fluxes, and deposition velocities of trace substances to the biosphere. In particular, relevant measurement techniques are described, and their requirements and limitations for determining accurate fluxes are analyzed. Furthermore, several quality control procedures are outlined. Typical applications are explained in detail, taking into account current and future challenges and developments.

54.1	Measurement Principles and Parameters	1446
54.2	History	1448
54.2.1	History of Immission and Dry Deposition Measurements	1448
54.2.2	Historically Relevant Measurement Methods	1448
54.3	Theory	1449
54.3.1	Influence of Turbulence and Surface Structure on Dry Deposition	1449
54.3.2	Influence of the Chemical Properties of Trace Substances	1450
54.3.3	Dry Deposition Inferential Method (DDIM): Application of the Resistance Analogy	1450
54.3.4	Aerodynamic Gradient Method (AGM) ..	1452
54.3.5	Modified Bowen Ratio Method (MBR) ..	1453
54.3.6	Vertical Flux Divergence Due to Chemical Reactions	1453
54.4	Devices and Systems	1454
54.4.1	Sampling and Detection Systems	1454
54.4.2	The Design of Flux-Gradient Systems ..	1456
54.4.3	Design of Immission and Deposition Measurement Networks	1457
54.5	Specifications	1458
54.6	Quality Control	1459
54.7	Maintenance	1460
54.8	Application	1460
54.8.1	Annual Cycles and Nitrogen Budgets of Ecosystems	1460
54.8.2	Daily Cycles and Process Studies	1461
54.9	Future Developments	1462
54.10	Further Reading	1463
	References	1463

The dry deposition of trace compounds to terrestrial ecosystems plays key roles in atmospheric chemistry, air quality, and the climate, as it constitutes a major sink for trace gases and aerosols in the troposphere. Furthermore, it influences the biogeochemical cycles of carbon and nitrogen and is a direct source of pollutants and/or nutrients for the biosphere, potentially causing eutrophication and acidification of ecosystems. Dry deposition occurs through passive turbulent transport (mixing) of the air constituents towards the surface, where they are absorbed due to various biological and physicochemical processes. Hence, the rate of dry deposition of an atmospheric compound is closely related to the concentration of the compound near the surface (i.e., the respective *immission*). The accurate quantification of dry deposition fluxes is crucial for our understanding

of and ability to predict the atmospheric composition, the chemical processes in the atmosphere (e.g., ozone production or the formation of aerosol particles), the atmospheric inputs to ecosystems, and the effects on the ecosystem. Dry deposition represents only part (on average about half) of the total deposition of many trace compounds to the surface. Locally, the contribution of dry deposition depends mainly on the frequency of rain events (climate zone) and the characteristics of the underlying surface [54.1–4]. Further deposition pathways are wet deposition, sedimentation, and fog deposition (Chap. 53). Moreover, some compounds may be both deposited to and emitted from surfaces, depending on their physiological/chemical production and consumption at the surface as well as the prevailing ambient concentration [54.5, 6].

54.1 Measurement Principles and Parameters

The measurement of dry deposition generally includes concentration measurements of the atmospheric trace compounds of interest near the surface (immission measurements). This approach is most relevant for the following inorganic trace gases and related aerosol compounds: sulfur dioxide (SO_2)/aerosol sulfate (SO_4^{2-}), ammonia (NH_3)/aerosol ammonium (NH_4^+), nitric acid (HNO_3)/aerosol nitrate (NO_3^-), nitrous acid (HNO_2), nitrogen dioxide (NO_2), peroxyacetyl nitrate (PAN), and ozone (O_3). Moreover, the deposition of metal ions in aerosols and of elemental mercury is of importance for terrestrial ecosystems. Since the transport of gases and particles from the surface layer to the Earth's surface is controlled by turbulent diffusion, dry deposition methods usually combine concentration measurements with a quantification of the vertical turbulent transport (micrometeorological methods). Generally, the eddy-covariance (EC) technique (Chap. 55) is considered to be the most direct and sophisticated micrometeorological flux method. It is often used as a reference for the measurement of surface–atmosphere exchange fluxes. The

relaxed eddy accumulation (REA) method can be a suitable alternative (Chap. 56). However, due to administrative, logistical, or financial restrictions, fast-response analyzers are not always available for some trace gases and aerosol compounds. Under these circumstances, other (indirect) methods based on vertical concentration gradients and similarity principles in the surface layer allow for the determination of dry deposition fluxes. Table 54.1 provides an overview of all available methods to determine dry deposition. Only indirect methods that are not covered in other chapters of this Handbook are described in detail here. These include the aerodynamic gradient method (AGM) and the modified Bowen ratio method (MBR). Aside from these, the so-called *inferential method* [54.7, 8] is a composite measurement-model approach that is often used in deposition monitoring networks. It requires knowledge of the surface uptake potential for the trace compound of interest, which has to be derived (*inferred*) from measurements obtained by the other methods mentioned above or by chamber methods (CHAM; see Chaps. 59 and 60).

Table 54.1 Measurement principles for dry deposition

Method	Description	Reference
Eddy covariance (EC)	Direct measurement of the turbulent trace gas flux by measuring the fluctuations in the vertical wind velocity and the trace gas concentration with high frequency	Chap. 55
Relaxed eddy accumulation (REA)	Concentrations are sampled by separating the sampled air into updraft and downdraft reservoirs based on the sign of the vertical wind speed	Chap. 56
Aerodynamic gradient method (AGM)	Measurements of wind velocity, air temperature, and the trace gas concentration at two or more levels (or turbulence characteristics are determined by the EC method)	Sect. 54.3.4
Modified Bowen ratio (MBR) method	Measurements of air temperature and the trace gas concentration at two levels, and the sensible heat flux is measured using the EC method	Sect. 54.3.5
Chamber methods (CHAM)	The trace gas concentration is measured at the inlet and outlet of a dynamic chamber or the trend over time inside a static chamber is monitored, and the surface resistance is subsequently calculated	Chaps. 59 and 60
Dry deposition inferential method (DDIM)	The concentration is measured at one level and then the <i>big leaf multiple resistance approach</i> is applied to estimate the deposition velocity	Sect. 54.3.3

Table 54.2 Parameters that are typically measured when determining dry deposition fluxes. The first three parameters are measured using the EC method at a sampling rate of 10–20 Hz (Chaps. 1 and 55)

Parameter	Description and sensor	Symbol	Unit
3-D wind components	Sonic anemometer (Chap. 55)	u, v, w	m s^{-1}
Sonic temperature	Sonic anemometer (Chap. 55)	T_s	K
Horizontal wind speed	Cup or sonic anemometer (Chap. 9)	u	m s^{-1}
Wind direction	Wind vane or sonic anemometer (Chap. 9)	\circ	
Air temperature	Pt-100 thermometer (Chap. 7)	T	K
Relative humidity	Capacitive hygrometer (Chap. 8)	RH	%
Global radiation	Pyranometer (Chap. 11)	$K \downarrow$	W m^{-2}
Concentration: mass concentration or density	Gas or aerosol analyzer (Chaps. 8 and 16)	ρ_s	$\mu\text{g m}^{-3}$
Concentration: molar concentration or density	Gas analyzer (Chaps. 8 and 16)	c_s	$\mu\text{mol m}^{-3}$

Table 54.3 Required measurements and input parameters for different methods of quantifying dry deposition

Required measurements or input parameters	EC	REA	AGM	MBR	CHAM	DDIM
Concentration: no. of sampling positions/levels	1	2 ^a	≥ 2	2	2	1
Concentration: typical time resolution	0.1 s	30 min	30 min	30 min	30 min	1 h to 1 month
Wind and air temperature: no. of measurement heights	1 ^b	1 ^b	1 ^b /2	2 ^c	–	1 ^d
Wind and air temperature: time resolution	0.1 s	0.1 s	0.1 s/30 min	0.1 s	–	1 h ^d
Displacement height d	–	–	×	–	–	×
Roughness length z_0	–	–	–	–	–	Estimated ^d
Surface resistance r_c	–	–	–	–	–	Estimated ^d

^a Conditionally sampled updraft and downdraft air at the same position
^b Three-dimensional wind measurement
^c Only the air temperature (proxy scalar profile)
^d The multiresistance-based deposition velocity v_D must be calculated (alternatively: use the estimated monthly/annual average value of v_D)

Table 54.4 Output parameters (quantities) of dry deposition measurements

Output	Description and calculation	Symbol	Unit
Deposition flux	Vertical turbulent (mass or molar) flux of trace gases or aerosols	F_c	$\mu\text{mol m}^{-2} \text{s}^{-1}$ $\mu\text{g m}^{-2} \text{s}^{-1}$
Concentration	Mass or molar concentration (density) of the trace compound in the air near the surface	c	$\mu\text{g m}^{-3}$ $\mu\text{mol m}^{-3}$
Deposition velocity	Deposition velocity determined as the ratio of the deposition flux to the measured concentration	v_D	m s^{-1}
Aerodynamic resistance	Turbulent transport bulk resistance between a reference height z_{ref} and the roughness length height z_0	r_a	s m^{-1}
Boundary layer resistance	Molecular–turbulent boundary layer bulk resistance (between z_0 and the solid (plant/soil) surface)	r_b	s m^{-1}
Surface resistance	Bulk residual surface resistance	r_c	s m^{-1}

In all dry deposition methods, the turbulent transport intensity (due to shear stress and buoyancy) is measured or estimated. This is achieved in various ways, depending on the dry deposition method adopted, and usually requires ground-based wind and air temperature measurements. These micrometeorological quantities and the concentration of the compound of interest must be measured at one or several measurement levels (vertical profile) (Tables 54.2 and 54.3). Furthermore, specific time resolutions are needed for these methods, and it may also be necessary to retrieve other input parameters (Table 54.3).

Table 54.4 shows the output parameters derived from the measurements listed in Tables 54.2 and 54.3. The retrieval of these quantities is discussed in Sects. 54.3 and 54.4.

The concepts and methods to quantify dry deposition fluxes presented here are only valid for condi-

tions of approximate stationarity and horizontal homogeneity of the wind, temperature, humidity and concentration fields within the measurement footprint (Chap. 1) [54.9]. Therefore, micrometeorological dry deposition measurements should be made over flat terrain with uniform surface cover. Because of the resulting violation of basic methodological assumptions, none of the methods presented here (except for chambers) should be applied within (or just above) plant canopies [54.1, 10].

It should be noted that chamber methods are not able to measure a representative deposition flux or velocity because the aerodynamic conditions inside the enclosed volume deviate markedly from undisturbed ambient conditions. However, they are suitable for investigating and quantifying the specific surface resistance r_c of the enclosed surface (or canopy) [54.11–13], which can be used in the DDIM.

54.2 History

Dry deposition measurements were initially made using various rather simple methods [54.14]. Historically, scientific progress in quantifying dry deposition fluxes has been closely coupled to advances in chemical measurement techniques [54.15]. Although more sophisticated techniques are now available, advanced versions of some historical methods are still in use today due to logistical or financial limitations. In the following, the most important historical methods are explained, including some of their advantages and disadvantages.

54.2.1 History of Immission and Dry Deposition Measurements

The first records of pollutant concentrations in ambient air, particularly those of O_3 , were produced in the last quarter of the nineteenth century [54.16] (Chaps. 16 and 24). During the era of atmospheric nuclear testing (starting in the late 1940s), the need to assess the risks of radioactive products to humans and the environment led to the use of deposit gauges as measurement devices [54.17] (Chap. 15). The problematic consequences of the acidification of soils and surface waters were discovered in 1967, and were subsequently recognized to be indicative of a large-scale problem with air pollution that required international action [54.18–20]. Later on, interest in immission and dry deposition measurements grew substantially [54.21–24], motivated by growing acid deposition rates of sulfur and nitrogen compounds in Europe and North America, which caused eutrophication and acidification of ecosystems. Although the first pioneering studies that used experimental and theoretical approaches to derive dry deposition fluxes of trace compounds occurred during the 1970s and 1980s [54.7, 8, 25–30], knowledge of the magnitudes of these fluxes for individual compounds, deposition velocities, and the processes that govern surface uptake was still quite limited at that time. Moreover, the time resolutions and precisions of most devices for measuring trace gases were not sufficient to facilitate direct flux measurement methods such as EC and REA (Chaps. 55 and 56). Accurate concentration measurements of some trace compounds were found to be particularly challenging due to their chemical and thermodynamic properties. This was especially the case for the sampling of water-soluble compounds and related semivolatile aerosol species—most prominently HNO_3 and aerosol NO_3^- , but also NH_3 and aerosol NH_4^+ [54.31, 32]. As HNO_3 can adsorb to and desorb from surfaces of inlets and sampling substrates (e.g., filter materials), it is very difficult to perform measurements without encountering some

form of interference [54.33]. Furthermore, the collection of aerosol species on filter packs without upstream (and downstream) scrubbing of related gases may cause significant artifacts (due to evaporation of semivolatile aerosol species from or collection of gaseous compounds such as NH_3 , HNO_3 , and SO_2 on the filters). In the last four decades, these problems have been a persistent impediment to the accurate determination of dry deposition fluxes of water-soluble trace gases and related chemical aerosol compounds.

54.2.2 Historically Relevant Measurement Methods

The first dry deposition measurements of HNO_3 and aerosol chemical compounds were made using surrogate surfaces [54.34–36]. However, this method was found to have substantial drawbacks, as the surface characteristics of the sampling vessel were different from those of natural surfaces, which modulated the surface uptake. Measurements based on foliar extraction (surface washing) were applied for NH_3 and HNO_3 as well as for their aerosol counterparts NH_4^+ and NO_3^- , but such measurements cannot distinguish between gas and aerosol phases [54.14]. In addition, throughfall estimates based on the difference between wet deposition and the washoff of deposited gases and particles were used to estimate dry deposition fluxes to forests [54.37, 38]. However, this method is hampered by the continuous uptake and release of chemical compounds by plant canopies, which results in low accuracy. The filter-pack method—in which a series of teflon and nylon or impregnated filters are typically employed to separate the particulate phase (e.g., NO_3^-) from the gas phase (e.g., HNO_3) and then offline analysis is performed using ion chromatography—is characterized by compactness, simplicity, and low power consumption but also relatively low accuracy [54.39, 40]. The development of this method permitted the measurement of vertical concentration profiles together with micrometeorological quantities over long sampling periods. Fluxes were subsequently derived using the MBR method (Sect. 54.3.5) [54.41, 42], or the DDIM when the concentration was only measured at one level (Sect. 54.3.3) [54.43]. The application of the denuder technique was a major step forward in the sampling of water-soluble trace gases. Dry-coated diffusion denuders were found to be reliable, but they also typically required long integration periods [54.44, 45]. Figure 54.1 shows an early version of a so-called total inorganic nitrate sampler that was capable of differentiating between gas and particulate phases and allowed performing measurements at several levels.

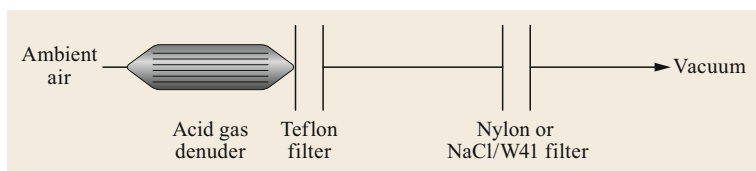


Fig. 54.1 Simplified scheme of an early total inorganic nitrate ($\text{HNO}_3 + \text{aerosol NO}_3^-$) sampler. Particulate nitrate is sampled on a Teflon filter following the passage of the ambient air sample through a vertically aligned coated diffusion denuder that removes HNO_3 . A downstream filter (made of nylon for example) collects nitrate lost from the Teflon filter by volatilization and/or reactions that release HNO_3 (NaCl/W41 filter – NaCl-impregnated Whatman 41 cellulose filter) (after [54.44] with permission from Elsevier)

The techniques mentioned above are only applicable over long sampling periods and require substantial quality control to maintain samples in good condition before offline analysis. More advanced denuder-filter pack setups are currently used for the long-term monitoring of dry deposition fluxes using the DDIM (Sects. 54.3.3 and 54.4.3). Selective and continuous measurements of water-soluble trace gases separated from the particulate phase can be achieved with diffusion scrubber and mist chamber techniques [54.46–48]. Moreover, various drawbacks were overcome by the development of various designs for wet diffusion denuders coupled to on-line ion chromatography systems with continuously renewed collection surfaces [54.32, 49–56].

54.3 Theory

In the following sections, the main processes that control dry deposition as well as the underlying theoretical principles are described. Various measurement methods are outlined, including important equations. The discussion below focuses on deposition to vegetated surfaces, which are the most complex and frequently investigated surfaces, but the methods presented are also used to examine deposition to other surfaces (bare soil, water, snow, and ice).

54.3.1 Influence of Turbulence and Surface Structure on Dry Deposition

The roughness (structure) of the surface strongly influences the efficiency of the dry deposition process. The turbulence induced by smooth surfaces (bare soil, snow, or ice) or short, dense, and homogeneous vegetation is less intense than that induced by a tall and heterogeneous forest environment, including trees of different lengths and open patches. The uptake of trace compounds by a vegetated ecosystem is determined by the structure, density, type, and age of the vegetation. This can be described by the leaf area index and surface

For other compounds, such as SO_2 , O_3 , NO_2 , and PAN, measurements of air concentrations and vertical profiles have been less challenging (Chaps. 16 and 18). For instance, vertical profiles of SO_2 were measured based on the fluorescence principle [54.57], and vertical profiles of O_3 were measured in 1971 using the electrochemical Ehmert technique [54.21, 58]. Since the 1980s, dry deposition fluxes of O_3 have often been determined with the EC method (Chap. 55) using fast-response sensors based on chemiluminescence [54.59–62]; and UV absorption measurements have been performed to provide reference concentrations. In the 1990s, the Luminox technique was used to measure vertical concentration profiles and EC fluxes in order to derive deposition velocities for NO_2 [54.63, 64].

roughness length for example. Uptake pathways can be categorized into [54.65]:

- Uptake controlled by plant physiological processes (stomatal uptake)
- Uptake by epicuticular waxes and water films (non-stomatal uptake)
- Soil uptake.

The efficiency of each uptake process depends on environmental conditions such as the solar radiation, air humidity, and temperature. Uptake through plant stomata is also controlled by the concentration of carbon dioxide (CO_2) and soil water availability.

The dry deposition of aerosol particles is mainly controlled by Brownian diffusion, interception, impaction, and gravitational settling, all of which are dependent on particle size. Additionally, particle deposition is a function of the particle density [54.26]. Dry removal of particles larger than a few micrometers is typically enhanced by the influence of gravitational settling [54.17], while Brownian diffusion influences the deposition rates of particles with diameters $< 0.1 \mu\text{m}$.

As a consequence of particle interception by surface elements and due to inertial impaction processes, any accurate calculation of aerosol fluxes must account for the leaf orientation and morphology, as well as the distribution and movements of in-canopy obstacles, which strongly influence the surrounding aerodynamics [54.17, 66].

54.3.2 Influence of the Chemical Properties of Trace Substances

The dry deposition process is also influenced by chemical interactions at the air–surface interface. Chemical reactions on leaf surfaces or in the leaf interior [54.5, 67–69] can substantially alter the magnitude of the deposition flux. These processes depend on the physicochemical and thermodynamic properties of the substance (its chemical reactivity and solubility in the aqueous phase) as well as on the surface properties (e.g., leaf microstructure, surface reactivity, the presence of epicuticular water films). For instance, very polar gases such as HCl, HNO₃, and NH₃ are strongly adsorbed by nearly all surfaces. In general, dry deposition is enhanced on wet surfaces, and the pH of the wetted surface influences the uptake process [54.70]. In addition, the deposition fluxes of NH₃ and SO₂ can be increased by codeposition processes, where the dissolution of one compound in surface water films enhances the uptake of the other compound [54.71]. The deposited compounds are either chemically decomposed in epicuticular water films or assimilated by the leaf as molecules react with the moist cells in the substomatal cavity and mesophyll [54.70]. The efficiency of each of these processes depends on the chemical properties of the compound and the biological activity of the leaf.

Some trace compounds (e.g., NH₃ or NO₂) are not only deposited and taken up by surfaces; they can also be emitted by vegetation and/or soils. In this case, the exchange between the surface and the atmosphere is bidirectional [54.72]. Whether (net) emission or deposition of these species occurs is controlled by the rates of production and consumption at the surface, for example in plant leaves or epicuticular waxes/water films and/or soils, as well as by the ambient concentration [54.3].

54.3.3 Dry Deposition Inferential Method (DDIM): Application of the Resistance Analogy

Deposition fluxes can be derived using a simplified theoretical framework. Determination of the flux of a chemically conservative trace compound within the

soil–vegetation–atmosphere continuum is based on the so-called *resistance analogy*, which is in accordance to Ohm's law [54.73, 74]. This method is also called the *big leaf multiple resistance approach* [54.7, 8], and can be expressed as

$$F_c = -\frac{1}{r_{\text{tot}}(z_R)} (c(z_R) - c_0), \quad (54.1)$$

where F_c is the flux density, r_{tot} is the total resistance to the exchange of the compound, $c(z_R)$ is the mean concentration at reference height z_R , and c_0 is the so-called compensation point concentration (the virtual equilibrium concentration of the trace compound at the liquid or solid surface). According to the micrometeorological sign convention, positive fluxes are directed upwards (aligned with the z -axis). Thus, deposition (negative flux) occurs if $c_0 < c(z_R)$, whereas the compound is emitted from the surface if $c_0 > c(z_R)$.

If we consider trace compounds for which the surface is a sink under all ambient conditions ($c_0 = 0$), the so-called deposition velocity (v_D) is defined as [54.23, 75]

$$\begin{aligned} v_D(z_R) &= \frac{1}{r_{\text{tot}}(z_R)} = \frac{1}{r_a(z_R) + r_b + r_c} \\ &= -\frac{F_c}{c(z_R)}, \end{aligned} \quad (54.2)$$

where r_a denotes the turbulent atmospheric resistance (due to turbulent exchange processes), r_b is the molecular turbulent resistance (which accounts for the exchange of trace compounds by molecular-turbulent diffusion across the viscous laminar sublayer in the vicinity of the vegetation), and r_c is the canopy resistance (which combines the influence of all uptake processes by the canopy on the deposition flux) [54.8] (Fig. 54.2). The values of v_D , r_{tot} , and c vary with measurement height and over time. Equation (54.2) assumes that the concentration at the soil and/or vegetation is near to zero (or always much lower than the ambient concentration); in other words, there is no emission (e.g., of O₃ and SO₂) from the surface.

The application typically requires the simultaneous operation of an EC station to determine the friction velocity, which is needed to calculate r_a and r_b . Alternatively, near-surface meteorological conditions can be monitored (e.g., the standard deviation of the wind direction, air temperature, solar radiation, etc.; see Tables 54.2 and 54.3). The resistances (54.2) are a function of wind speed and surface roughness, and can be derived as [54.77]

$$r_a(z_R) = \frac{1}{\kappa u_*} \left[\ln \left(\frac{z-d}{z_0} \right) - \Psi_H \left(\frac{z-d}{L} \right) \right]. \quad (54.3)$$

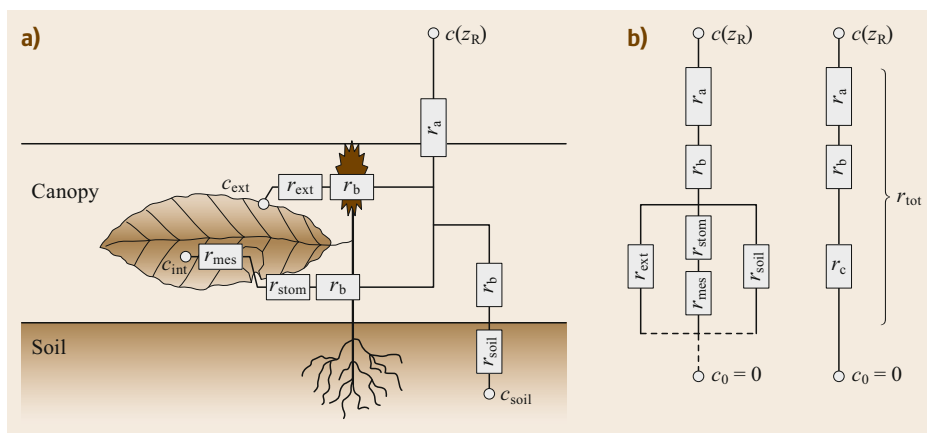


Fig. 54.2 (a) The big leaf multiple resistance scheme analogous to Ohm's law (after [54.76] © C. Ammann). r_{tot} total resistance, r_a turbulent atmospheric resistance, r_b molecular turbulent resistance, r_c canopy resistance (consisting of the stomata resistance r_{stom} , the external leaf surface (or cuticular) resistance r_{ext} , the mesophyll resistance r_{mes} , and the soil resistance r_{soil}). (b) Simplified resistance scheme

The roughness length z_0 and the displacement height d are typically retrieved from wind profile and turbulence measurements as a function of the canopy height (Chap. 1). Also,

$$r_b = \frac{2}{\kappa u_*} \left(\frac{Sc}{Pr} \right)^{\frac{2}{3}}. \quad (54.4)$$

Here, Sc and Pr are the molecular Schmidt and Prandtl numbers, respectively. Sc is a function of the molecular diffusivity of the trace gas [54.8].

As shown in Fig. 54.2, the value of r_c , the effective surface resistance of the whole plant–soil system [54.76], can be expressed as a combination of several resistances in parallel and in series that describe the various pathways for surface uptake, i.e.,

$$r_c = \left[\frac{1}{r_{stom} + r_{mes}} + \frac{1}{r_{soil}} + \frac{1}{r_{ext}} \right]^{-1}. \quad (54.5)$$

The value of r_c is specific to each trace compound and measurement site. As none of the resistances can be measured directly, the accurate retrieval of these individual values is the main challenge when using the DDIM. The value of r_{stom} can be estimated using latent heat fluxes measured with the EC method by inverting the Penman–Monteith equation (Chap. 57) and accounting for the ratio of molecular diffusivities between the compound of interest and water vapor. To correct for the influence of evaporation from soil pores and water films, it was proposed [54.78] that only data for dry conditions with $RH < 60\%$ should be used, as this

is the threshold at which liquid water on surfaces can be assumed to be fully evaporated. Additionally, a correction can be made for soil evaporation by plotting the inverse of r_{stom} against the gross primary production (for further details, see [54.78]). Due to insufficient knowledge of r_{mes} , it is typically set to zero, although recent evidence indicates that r_{mes} is non-negligible for some trace gases such as NO_2 [54.79]. The influence of r_{soil} depends on the soil moisture present, and parameterizations are based on experimental studies [54.80]. However, for sufficiently dense vegetation, the value of r_{soil} can be neglected. The uptake of compounds by external leaf surfaces is expressed as r_{ext} , and is controlled by the presence of epicuticular water films, their chemical composition, and the meteorological conditions [54.70]. Hence, the parameterization of this resistance is very complex [54.69, 81, 82].

For highly water-soluble and sticky gases (e.g., HNO_3) that are readily adsorbed by surfaces, the value of r_c is close to zero, which implies that the deposition velocity reaches the maximum value given by [54.83]

$$v_{Dmax}(z_R) = \frac{1}{r_a(z_R) + r_b}. \quad (54.6)$$

This may generally serve as an upper limit to test the plausibility of measured deposition fluxes. If the resulting v_D is larger than v_{Dmax} , additional sinks may be present between the measurement height and the surface. The inferential method delivers reliable results under daytime conditions over flat terrain, provided that the surface properties and the behavior of the vegetation are well characterized [54.84].

Table 54.5 Examples of typical deposition velocity ranges (values shown are in 10^{-2} m s^{-1}) for various compounds and particles to tall and low vegetation

Compound	Tall vegetation (forest)	Low vegetation (grassland/crops)	References
NO ₂	0.1–1.0	0.1–0.8	[54.3, 63, 64, 79, 85, 86]
HNO ₃	2.0–8.0	0.5–4.0	[54.3, 41, 87–92]
NH ₃	0.5–4.0	0.2–2.5	[54.87, 93–95]
SO ₂	0.2–2.0	0.2–1.5	[54.57, 87, 96–98]
O ₃	0.2–2.0	0.1–1.0	[54.65, 79, 96, 97, 99–102]
PAN	0.1–1.0	0.1–0.8	[54.103–106]
Particles (0.01–0.1 μm) ^a	0.05–1.5	0.02–0.06	[54.17, 107]
Particles (0.1–1 μm) ^a	0.1–2.0	0.01–0.3	[54.17, 107]
Particles (1–10 μm) ^a	0.6–5.0	0.1–4.0	[54.17, 107]
Particles (> 10 μm) ^a	1.0–20.0	2.0–10	[54.17, 107]

^a Mass-related deposition velocities of chemical aerosol compounds (e.g., NO₃⁻, NH₄⁺, and SO₄²⁻) are not given here (for more information on this topic, see [54.108, 109]).

Deposition velocities of aerosols are lower than those for trace gases, such that they are often within the experimental error [54.108]. It was shown that v_D is a function of particle size and can be parameterized with u_* for different size classes, but that there are large discrepancies between various experimental and modeling studies, especially for accumulation-mode particles [54.17]. In general, the deposition velocity for particles can be expressed as follows [54.108, 110]

$$v_D(z_R) = \frac{1}{r_a(z_R) + r_{cp}} + v_{ts}, \quad (54.7)$$

where v_{ts} is the terminal settling velocity (which is most relevant for large particles) and r_{cp} is the surface resistance, which combines the influences of turbulent transport and the collection of the particles by the vegetation within the canopy [54.110]. A detailed expression can be found in [54.111]. Aerosol fluxes are typically differentiated into *number fluxes* and *mass fluxes*, with the latter often used when considering certain chemical aerosol components. The concept expressed in (54.7) can be applied for both flux types, although direct measurements are generally obtained for aerosol number fluxes.

Deposition velocities are generally larger for tall canopies such as forests than for grassland and crops (Table 54.5), which is mainly due to the increased canopy roughness of tall canopies and its effect on turbulence. The highest values are typically observed for HNO₃, NH₃, and particles with diameters > 1 μm .

For trace gases that feature bidirectional fluxes, such as NH₃, the concentration at the soil and vegetation is not zero, so more complex approaches involving the compensation point concentration c_0 (54.1)—a concentration analog of r_c —must be applied [54.6, 112, 113].

54.3.4 Aerodynamic Gradient Method (AGM)

The aerodynamic gradient method (also called the profile method) is based on the flux-gradient theory and requires measured vertical profiles of wind, air temperature, humidity, and the concentration of the compound of interest (Tables 54.2 and 54.3 and Sect. 54.4.2). The turbulent vertical transport of a trace substance within the constant flux layer can be described analogously to Fick's first law, and is expressed as the product of the turbulent diffusion (transfer) coefficient and the vertical air concentration gradient $\partial c / \partial z$ [54.28], i.e.,

$$F_c = -K_H(u_*, z - d, L) \frac{\partial c}{\partial z}, \quad (54.8)$$

where F_c is the flux and K_H is the turbulent diffusion coefficient for sensible heat (Chap. 1) [54.74], which is a function of the friction velocity u_* , the height above the zero plane displacement ($z - d$), and the atmospheric stability parameterized by the Monin–Obukhov length L (Chap. 1). In the classical profile method that was mainly used in the past, the turbulence parameters u_* and L were determined from measurements of horizontal wind speed, air temperature, and moisture, ideally performed at 4–6 levels, using numerical iteration or regression calculations [54.114–116]. Nowadays, the turbulence parameters are typically retrieved from EC measurements of momentum and sensible heat flux using a sonic anemometer-thermometer (Chap. 55 and Tables 54.2 and 54.3). In the simpler case in which concentration measurements are obtained at only two levels z_1 and z_2 , the integration of (54.8) between the two measurement heights yields the integral form of the flux profile relationship that relates the flux directly to the measured concentration difference $\Delta c = c(z_2) - c(z_1)$ between the upper and lower mea-

surement heights [54.28, 117],

$$F_c = - \frac{u_* \kappa}{\underbrace{\ln\left(\frac{z_2-d}{z_1-d}\right) - \Psi_H\left(\frac{z_2-d}{L}\right) + \Psi_H\left(\frac{z_1-d}{L}\right)}_{v_{tr}}} \times [c(z_2) - c(z_1)], \quad (54.9)$$

where κ is the von Kármán constant (0.4) and Ψ_H is the integrated stability correction function for sensible heat. The first term of the product on the right hand side is often referred to as the transfer velocity v_{tr} (m s^{-1}), which represents the inverse resistance of the turbulent transport between the two heights z_1 and z_2 [54.76]. In contrast to the deposition velocity ((54.1) and (54.2)), it only includes turbulent transfer within an air layer and not the entire deposition to the surface. The AGM method assumes that the transfer of heat is similar to the transfer of the compound of interest within the surface layer, although this assumption is not always justified [54.77]. If the concentration profile is measured at more than two heights, a generalized form of the flux-profile relationship (54.9) can be used to evaluate a linear regression of the concentration against the stability-corrected logarithmic height [54.118].

54.3.5 Modified Bowen Ratio Method (MBR)

Another method based on the flux-gradient theory is the MBR. Assuming that the eddy diffusivity (v_{tr} , see (54.9)) for the compound of interest is equal to that for a so-called proxy scalar, the deposition flux is derived from the ratio of the difference between the upper and lower measurement heights for the trace compound of interest (Δc) to the difference in measurement heights for the proxy scalar (Δs) multiplied by the EC flux of the proxy scalar ($F_{s,EC}$) [54.28, 119], i.e.,

$$F_c = F_{s,EC} \frac{\Delta c}{\Delta s}. \quad (54.10)$$

In most cases, the air temperature is used as the proxy scalar, as measurements of vertical temperature profiles and sensible heat fluxes (Table 54.2) are relatively straightforward. However, under certain circumstances it may be advisable to choose a different proxy scalar (e.g., another trace gas such as CO_2 or O_3) that has a similar sink and source distribution to the compound of interest [54.103]. The MBR method is so named because the principle expressed by (54.10) was originally used to derive the Bowen ratio (the ratio of the sensible to the latent heat flux) from the corresponding temperature and water vapor profiles. Although measurements of wind speed or turbulence intensity are not explicitly

used in this method (54.10), it is recommended to check that fully turbulent conditions are prevailing [54.77].

54.3.6 Vertical Flux Divergence Due to Chemical Reactions

The measured or inferred flux may not represent the true surface exchange if there are additional sources or sinks in the air layer below the measurement height(s). This is particularly applicable to chemically reactive compounds. In taller canopies, the emission of nitric oxide (NO) by the soil may create an additional O_3 sink and NO_2 source due to the rapid reaction of these two trace gases [54.120–122]. Moreover, particulate NH_4NO_3 can be formed or can evaporate to the air during the deposition process [54.108] because NH_4NO_3 forms a reversible thermodynamic equilibrium with gaseous NH_3 and HNO_3 that is strongly dependent on the ambient relative humidity and temperature [54.123]. This modulates the vertical distributions of NH_3 and HNO_3 , as the timescale for equilibration between gaseous NH_3 , HNO_3 , and particulate NH_4NO_3 is within the timescale of turbulent transport (a few seconds for submicron particles) [54.124]. However, the methods presented here are based on the assumption that there are no chemical sources and sinks between the measurement height and the surface, which implies that the trace compounds are considered chemically inert tracers with constant fluxes within the atmospheric surface layer [54.73, 77, 125]. If this assumption is violated (i.e., gas-phase chemical sources and/or sinks are encountered between and below the measurement heights), sufficiently accurate fluxes of compounds can be estimated as long as any chemical reactions are much slower than the turbulent transport [54.124, 126]. This can be assessed quantitatively via the Damköhler number [54.127]

$$\text{Da} = \frac{\tau_{\text{turb}}}{\tau_{\text{chem}}}. \quad (54.11)$$

The characteristic turbulent and chemical timescales (τ_{turb} and τ_{chem} , respectively) can be determined according to [54.77, 79, 126, 128] and references therein. More details regarding the chemistry of the NH_4NO_3 - NH_3 - HNO_3 system are given in [54.108]. $\text{Da} > 1$ indicates that chemical reactions are significantly faster than turbulent transport (flux divergence). In this case, a correction for the chemical reactions is required to derive accurate turbulent fluxes of the reactive trace gas [54.129, 130]. The range $0.1 < \text{Da} < 1$ is commonly considered to be a critical range where an impact of chemistry cannot be excluded but should be of minor importance [54.79]. When $\text{Da} < 0.1$, the influence of chemistry can be neglected and the deposition fluxes can be determined as described above.

54.4 Devices and Systems

Table 54.6 summarizes the compounds for which dry deposition fluxes are typically measured and provides a selection of the most commonly used methods. It also specifies the measurement principles of analyzers that are used to determine the composition of the atmosphere [54.131]. More details on the characteristics of the sampling and detection systems employed to measure dry deposition fluxes are given in Sect. 54.4.1. Details on the quantification of particle fluxes are given in [54.17, 109, 110].

54.4.1 Sampling and Detection Systems

This section introduces the various analytical systems utilized with the indirect methods described above (AGM, MBR, DDIM). All of the systems listed below can also be applied to perform immission measurements at a single level or to infer fluxes with the DDIM.

Online Detection Systems (Time Resolution < 1 min)

For trace compounds that are not strongly water soluble, permitting longer inlet tubes, vertical concentration

profiles can be measured with high time resolution for the AGM or MBR method using one analyzer connected to a system of valves and pumps that allow sequential sampling at several levels (Fig. 54.3). In order to obtain a sufficient number of samples for a 30 min averaging interval (Table 54.3), the number of measurement levels should be limited (at least two), and an analyzer with a short response time, high time resolution, and high precision must be used. Examples of analyzers that fulfill these criteria include optical O₃ or NO_x analyzers based on UV absorption and chemiluminescence, respectively (Table 54.6, Chap. 16) [54.134, 144], as well as SO₂ fluorescence analyzers (Table 54.6, Chap. 16), which are applied for sequential measurements of vertical profiles [54.57]. To account for potential nonstationarities during the sampling period, a continuous concentration measurement can be performed with a second analyzer at a reference level. The integration time of the analyzers must be long enough to reduce the background noise of the signal. Furthermore, the tubes and analyzers have to be flushed for a certain time period after switching to another level, as the system needs to adjust to the new concentration.

Table 54.6 Overview of methods and typical measurement principles for the determination of dry deposition fluxes of various air constituents (Chaps. 16 and 18)

Compound	Method	Measurement principles
NO ₂	EC, CHAM+DDIM	Photolytic conversion to NO and subsequent chemiluminescence, Luminox technique, tunable diode laser absorption spectroscopy, laser-induced fluorescence, diffusion tubes (e.g., [54.79, 86, 132–135])
HNO ₃	EC, MBR, AGM, DDIM	Wet annular denuder, denuder-filter packs, diffusion-based samplers, chemical ionization mass spectrometry, thermal dissociation–laser-induced fluorescence (e.g., [54.3, 54, 136–138])
NH ₃	EC, MBR, AGM	Wet annular denuder, denuder-filter packs, diffusion-based samplers (AiR-Rmonia), chemical ionization and proton transfer reaction mass spectrometry, quantum cascade laser absorption spectrometry, differential optical absorption spectroscopy (DOAS), diffusion tubes (e.g., [54.139–141])
SO ₂	EC, MBR, AGM	UV fluorescence, chemical ionization mass spectrometry, diffusion tubes (e.g., [54.57, 98, 142, 143])
O ₃	EC, CHAM+DDIM	Chemiluminescence, UV absorption, diffusion tubes (e.g., [54.13, 62, 134, 144])
PAN	EC, REA, MBR, AGM	Gas chromatography with electron capture detection, thermal dissociation–chemical ionization mass spectrometry (e.g., [54.103, 106])
Chemical aerosol compounds (e.g., NO ₃ ⁻ , NH ₄ ⁺ , SO ₄ ²⁻)	EC, MBR, AGM	Steam-jet aerosol collector, particle-into-liquid sampler, aerosol mass spectrometry (e.g., [54.109, 145–148])
Particle number (0.01–1 μm)	EC, REA	Laser-based optical particle spectrometers, aerodynamic and electromobility spectrometers, condensation particle counter (combined with scanning mobility particle sizer) (e.g., [54.109, 149])
Particle number (1–10 μm)	EC, REA, MBR, AGM	Optical particle detectors (e.g., [54.109])
Dust deposition (2.5–80 μm)	Bulk samplers	Bergerhoff method using a passive sampler (Sigma-2) or other bulk bottle/funnel methods, subsequent offline analysis of heavy metals (measurement period 14–28 days) (e.g., [54.150, 151])
Mercury	REA, AGM, MBR, bulk samplers	Cartridge mercury vapor analyzer, bulk samplers made of glass (e.g., [54.150, 152, 153])

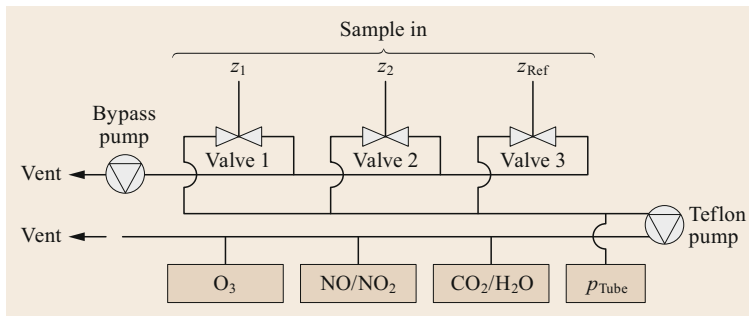


Fig. 54.3 Simplified scheme of the gas flow of a switched vertical trace gas profile (after [54.134] with permission from Elsevier)

To avoid condensation, the inlet tubing should be heated to slightly above ambient temperature.

Semicontinuous Systems with Automated Onsite Analysis (Time Resolution < 1 h)

A device that has become increasingly popular is the so-called wet annular denuder [54.50], which is capable of achieving high collection efficiencies at a relatively high time resolution (15–30 min) [54.54]. This denuder can be combined with continuous aerosol sampling devices such as the steam-jet aerosol collector (SJAC) (Table 54.6) [54.145]. These setups were integrated into transportable measurement devices that include an in-situ analytical unit to selectively and simultaneously measure water-soluble trace gases and corresponding chemical aerosol compounds with high precision ($\leq 10\%$) and high time resolution (15–60 min) (Fig. 54.4) [54.147, 154–157]. The major advantage of these systems is that two levels can be sampled simultaneously, thereby avoiding the potential influence of nonstationarities in the ambient concentrations on the flux determination.

A comparable setup was developed for PAN by modifying a commercially available gas chromatograph

with electron capture detection (GC-ECD). PAN was trapped on two preconcentration capillary columns over the sampling period, and analysis was then performed using the GC-ECD system [54.103, 158]. To ensure the accurate calculation of air concentrations, these systems typically utilize mass flow meters to monitor the flows of liquid solutions and air samples.

Accumulation Systems with Manual Offsite Analysis (Time Resolution 1 week – 1 month)

The DDIM, in particular, allows the determination of the dry deposition over longer time periods using so-called *low-cost methods* that are based on impregnated filter packs and dry-coated denuders. One prominent example is the Denuder for Long-Term Atmospheric Sampling (DELTA) (Fig. 54.5), which was successfully employed within the NitroEurope project to estimate the nitrogen deposition to several ecosystems in Europe [54.159, 160]. The samples are analyzed offsite in the laboratory and air concentrations are calculated using the sampled air volume.

The simplest method of determining dry deposition fluxes and immission concentrations is to use passive sampling techniques with diffusion tubes (Ta-

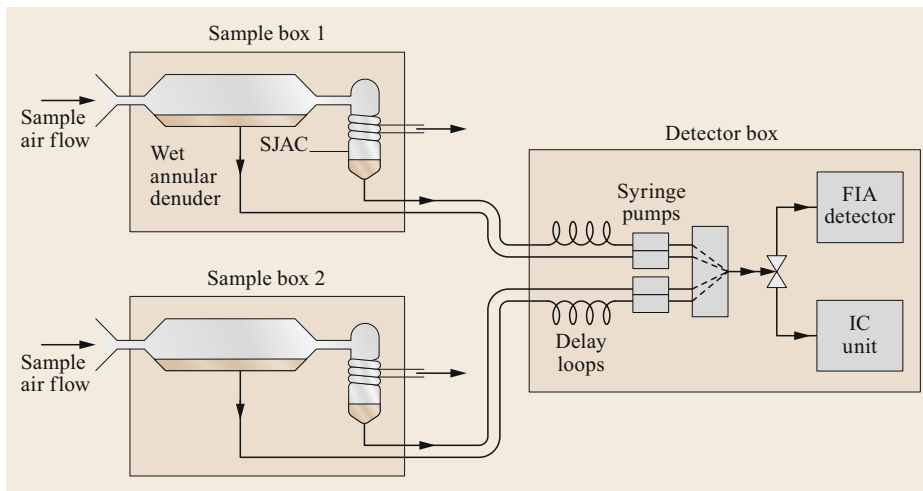


Fig. 54.4 Simplified scheme of the gradient analyzer for aerosols and gases (SJAC steam-jet aerosol collector, FIA flow injection analysis, IC ion chromatograph (after [54.157]))

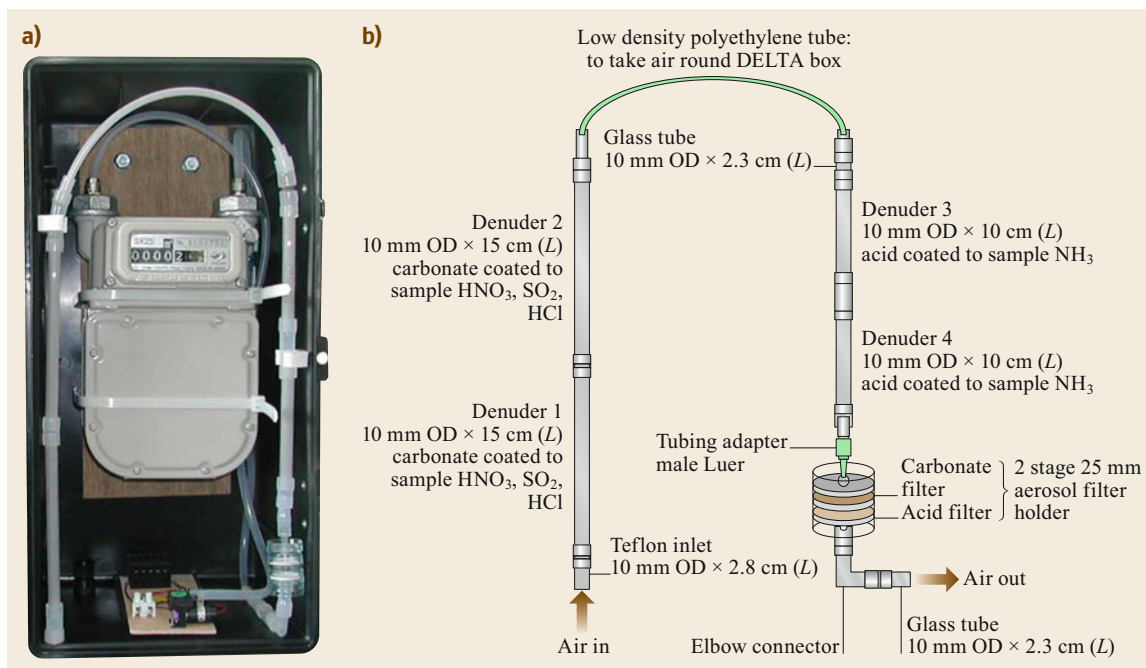


Fig. 54.5 (a) The Denuder for Long-Term Atmospheric Sampling (DELTA), which can be used for monthly measurements of trace gases and aerosols. (b) The sampling train consisting of coated denuders (OD outer diameter, L length) for determining HNO_3 , NH_3 , etc. and coated filters (for determining aerosol species) (after [54.160] with permission from Elsevier)

ble 54.6) [54.161, 162]. The absorbent material is analyzed in the laboratory, and the air concentration can be calculated based on the known diffusion rate and the exposure duration. Diffusion tubes are used for long-term monitoring with integration intervals of 2–4 weeks because sufficient quantities of the respective compounds must be absorbed.

A prerequisite for the application of accumulation systems to retrieve deposition fluxes is that the turbulent exchange conditions should remain reasonably constant throughout the measurement period. For instance, it is difficult to interpret results if the trace gas concentrations sampled during strongly labile conditions are mixed with those sampled during stable stratification.

54.4.2 The Design of Flux-Gradient Systems

While for the DDIM it is only necessary to measure the trace compound concentration at one level, the AGM and MBR require profile measurements at two or more levels. Although the AGM and MBR differ slightly in their approaches to flux determination, they employ very similar experimental setups. Analyzer accuracy and precision are typically not sufficient to permit the use of two different devices for verti-

cal profile measurements [54.1, 157, 158]. Therefore, various setups are applied to measure vertical profiles with one analyzer or using the same analytical unit/procedure (Sect. 54.4.1). Figure 54.6 shows a typical setup of a flux-gradient system with online detection (Fig. 54.3), allowing for the application of AGM and MBR. The height difference between the levels should be maximized to increase the measured concentration gradient and therefore reduce measurement errors, although this must be balanced against the length of the fetch (Sect. 54.5).

The design and setup of a flux-gradient system should generally be optimized to minimize any disturbance of the air flow and turbulence conditions by the mast/tower and the analyzer units as much as possible. This is challenging and may require a compromise if bulky instruments (or shelters for them) are used and short inlet lines are required (e.g., for HNO_3 , NH_3). In all cases, bulky units that could disturb the incoming air flow should be placed at a sufficient distance from the meteorological sensors and sample inlets, preferably away from the main wind direction sectors. In addition, to reduce inlet losses to a minimum, the inlet tube material should be selected according to the trace compound sampled (e.g., teflon for HNO_3 [54.33]).

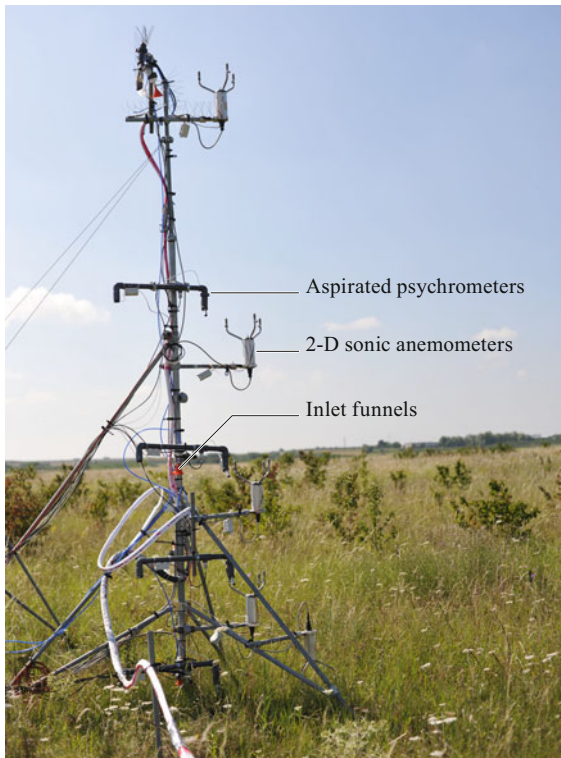


Fig. 54.6 Typical setup of a flux-gradient system with four measurement heights at a natural grassland site in southwestern Germany. In this example, air temperature and humidity profiles (aspirated psychrometers) as well as the horizontal wind speed profile (2-D sonic anemometers) were measured with individual sensors at each level, while online detection employing a valve switching system for sequential measurements was used to obtain trace gas concentration profiles (inlet funnels); see Sect. 54.4.1 (photo © J.-C. Mayer)

Above rough surfaces such as tall crops or forest canopies, deviations from the ideal flux-gradient relationship occur within the so-called roughness sublayer, which may extend up to twice the canopy height [54.77]. The application of flux-gradient relationships in this layer may lead to an underestimation of scalar fluxes by 10% or more [54.163, 164]. Hence, if possible, profile measurement levels should be positioned above the roughness sublayer.

54.4.3 Design of Immission and Deposition Measurement Networks

The simplest way to estimate a dry deposition flux is to measure the concentration of the trace compound at one level (immission) and subsequently multiply this

by a representative deposition velocity (Table 54.5) for long-term averages of the concentration ((54.1) and (54.2)), e.g., on a monthly or annual basis [54.135]. However, this method is prone to uncertainty, as diurnal fluctuations of turbulence and surface uptake, which strongly depend on environmental variables, are not taken into account. When micrometeorological quantities (or at least standard meteorological parameters) can be measured and requirements are met, it is recommended that the DDIM should be applied in combination with a multiresistance scheme (Sect. 54.3.3) that allows the aerodynamic resistances (r_a and r_b) to be quantified hourly.

National immission monitoring networks are operated by many governmental environment agencies. Additionally, dry deposition measurement networks that are less dense than governmental networks are also operational in, for example, Africa, Australia, Canada, Japan, Europe, and the United States (which contributes to the Global Atmosphere Watch or GAW) program; see Chap. 63). In most of these networks, measurements are limited to particulate and gaseous sulfur and nitrogen species as well as a few aerosol cations. The World Meteorological Organization (WMO) and the GAW program intend to establish laboratory intercomparison methods and specific data quality procedures for immission measurements that are analogous to those that already exist for wet deposition. A list of networks and programs dealing with dry deposition is given in Table 54.7.

A monitoring network to quantify the input of nutrients to agricultural sites was established in Europe in 1947, and data from this network highlighted the importance of transboundary fluxes of acidifying pollutants. This led to the establishment of the Convention on Long-Range Transboundary Air Pollutants (CLRTAP) in 1979. This convention currently includes the European Monitoring and Evaluation Programme (EMEP), a scientifically based and policy-driven program that aims to provide information on the concentrations and deposition of air pollutants by combining measurement and modeling approaches [54.180, 181].

In the US, a network dedicated to measuring dry deposition was established in 1986 by the US Environmental Protection Agency (EPA) to assess the magnitude of and the spatial variability and trends in dry deposition [54.175]. The National Dry Deposition Network (NDDN) consisted of 50 monitoring sites spread across the US. CASTNET was created from NDDN, and started operating in 1991. Aside from obtaining concentration measurements of O_3 at several rural locations, this network mainly focuses on the dry deposition of sulfate, nitrate, ammonium, sulfur dioxide, nitric acid, and base cations. It makes use of the filter pack

Table 54.7 Overview of selected measurement networks and communities that focus on dry deposition, Accessed 21 July 2021

Name	Region	Abbreviation	URL
Acid Deposition Monitoring Network	East Asia	EANET	http://www.eanet.asia/ (e.g., [54.165, 166])
International Network to Study Deposition and Atmospheric Chemistry in Africa	Africa	INDAAF (previously DEBITS)	https://indaaf.obs-mip.fr/ (e.g., [54.167, 168])
Atmospheric Mercury Network	US, CA, TW	AMNet	http://nadp.slh.wisc.edu/AMNet/ (e.g., [54.169, 170])
Canadian Air and Precipitation Monitoring Network	CA	CAPMoN	http://data.ec.gc.ca/data/air/monitor/networks-and-studies/canadian-air-and-precipitation-monitoring-network-capmon/ (e.g., [54.171–173])
Partnership with Clean Air Status and Trends Network	US	CASTNET	https://www.epa.gov/castnet (e.g., [54.173–177])
Ammonia Monitoring Network	US, CA	AMoN	http://nadp.slh.wisc.edu/amon/ (e.g., [54.161])
European Monitoring and Evaluation Programme	Europe	EMEP	http://www.emep.int (e.g., [54.178–180])

method to subsequently estimate dry deposition using a multilayer model representing an advanced version of the DDIM (Sect. 54.8.1) [54.176, 182].

WMO and GAW currently utilize a measurement–model fusion approach to derive global maps of wet,

dry, and total atmospheric deposition for different chemicals, but this requires high-quality global-scale measurements of atmospheric trace gases, particles, and precipitation as well as the output from chemical transport models for the same parameters [54.183].

54.5 Specifications

The accurate measurement of concentration differences for the substance of interest is the main challenge when applying the AGM and MBR methods. This is especially true for remote environments, where concentrations are very low [54.84] and vertical concentration differences are on the order of 1% to 20% of the mean concentration [54.28]. In order to determine dry deposition fluxes with an accuracy of at least 20% using vertical profile measurements, the precision error of the sensor and/or analyzer should be less than a tenth of the expected concentration difference between the two measurement heights (Table 54.8) [54.77]. The procedure used to determine precision requirements and flux uncertainties can be found in [54.77, 157, 158].

It should be noted that for some trace gases and a low ratio of measurement heights, the minimum detectable fluxes can be larger than the actual fluxes. It is recommended that the ratio of measurement heights z_2/z_1 should be between 4 and 8 for the AGM and MBR methods [54.77]. However, this is only possible above low vegetation. Above forests, this ratio is often ≤ 2 . On the other hand, over very smooth surfaces such as ice and water, the vertical concentration difference for a given measurement height ratio is generally smaller

than that over rough surfaces, and the largest gradients are typically found very close to the surface. In this case, the precision of the instrument must be even better to achieve the same flux accuracy as attained for rough surfaces. Consequently, the AGM and MBR methods require analyzers that are able to resolve very small concentration differences (high precision) over the typical integration time of 30 min (Table 54.3).

Table 54.9 compares all of the methods used to determine dry deposition fluxes (including EC, REA, and CHAM) in terms of their major advantages and disadvantages.

Table 54.8 Typical instrument precision (c_{\min}) and resulting minimum detectable concentration difference and flux (20% error) of different compounds for low ($z_2/z_1 = 8$) and tall ($z_2/z_1 = 1.25$) vegetation under neutral stratification and $u_* = 0.2 \text{ m s}^{-1}$ (the concentration values are in $\mu\text{g m}^{-3}$ and the flux values are in $\mu\text{g s}^{-1} \text{ m}^{-2}$) [54.77]

Compound	c_{\min}	Δc_{\min}	Flux (low veg.)	Flux (tall veg.)
NO ₂	0.1	1.0	0.05	0.1
O ₃	1.0	10.0	0.5	1.0
NH ₃	0.014	0.14	0.007	0.014
HNO ₃	0.2	2.0	0.1	0.2

Table 54.9 Advantages and disadvantages of the different methods of measuring immission/dry deposition (Chap. 1)

Method	Advantages	Disadvantages	Restrictions
EC	Direct method, no relevance of Da , ^a retrieval of r_c and v_D	High analyzer precision and fast response time	Sufficient footprint area, turbulent conditions
REA	Applicable for water-soluble/sticky compounds, ^b retrieval of r_c and v_D	Selection of the proxy scalar, high analyzer precision	Sufficient footprint area, scalar similarity, no local influence on integral turbulence characteristics [54.72]
AGM	Applicable for water-soluble/sticky compounds, retrieval of r_c and v_D	Scalar similarity, ^c high analyzer precision	Da , sufficient footprint area, turbulent conditions, stationarity
MBR	Applicable for water-soluble/sticky compounds, retrieval of r_c and v_D	Scalar similarity, ^c high analyzer precision	Da , sufficient footprint area, turbulent conditions, stationarity
CHAM	Direct retrieval of r_c	Corrections for chemical reactions ^d	Plot/leaf scale
DDIM	Inexpensive, simple installation and maintenance	Estimation or parameterization of r_c or v_D	Existence of a compensation point concentration

^a See Chap. 55 for details
^b See Chap. 56 for details
^c Assumption that heat or proxy scalar transfer is similar to the transfer of the compound of interest is not always justified
^d See Chaps. 59 and 60 for details

54.6 Quality Control

Several quality control procedures must be performed in-situ and after the field measurements (Table 54.10; Chap. 3). Besides regular calibrations (Sect. 54.7), periodic *side-by-side* measurements (SbS) are required to validate profile-based flux measurements. In these measurements, the inlets that are usually installed at different measurement levels are brought to the same height (side-by-side) and operated for a number of hours in this configuration. This is the most reliable method of identifying potential systematic errors between the different measurement levels and quantifying the precision (detection limit) of the measured concen-

tration difference for the AGM and MBR methods (cf. Table 54.8). It is mandatory to use this test to check whether an analyzer can be used for vertical profile measurements at a specific location.

Online vertical trace gas profiles that are obtained using a switching procedure with just one analyzer may be exposed to rapid concentration changes between the different measurement levels. Hence, in-situ tests should be performed to characterize the response of the system. For reactive trace gases such as the NO-NO₂-O₃ triad, the conditions within the inlet tubes are of particular relevance because chemical conversions might occur.

Table 54.10 Typical quality control (QC) procedures for analyzers used for immission and dry deposition measurements (see also Chap. 3)

Analyzer	Procedure/test	Reason
Online detection systems	Quantification of various error sources SbS measurements Significance of Δc (<i>t</i> -test, signal-to-noise ratio [54.144]) Characterization of system response time Consideration of chemical reactions in inlet tubing Da Stationarity test Outlier test	Errors in $c(z_R)$ and micrometeorological quantities Check for potential effects of different inlet lines and filters Sufficient instrument precision Sufficient instrument response Chemical reactions in inlet tubing bias measurements Chemical divergence Insufficient turbulent conditions Potential instrument failure, contaminated or clogged inlets
Semicontinuous systems with automated onsite analysis	Quantification of various error sources SbS measurements	Errors in $c(z_R)$ and micrometeorological quantities Sufficient instrument precision
Accumulation systems with manual offsite analysis	Complete denuder coating QC of analytical system in laboratory Intercomparison with online systems Outlier test	Incomplete trace gas capture Accuracy of $c(z_R)$

These depend on:

- The residence time of the sampled air in the inlet tubes
- The tubing material
- The trace gas concentrations.

Consequently, corrections for chemical reactions in the inlet tube may be necessary [54.184]. Moreover, stationarity tests should be performed if sequentially measured data points are combined into averages for half-hourly intervals (Chap. 55).

54.7 Maintenance

Fast online detection and semicontinuous systems with automated onsite analysis are typically deployed during intensive observation periods because maintenance requirements are relatively high. Consequently, the measurement systems must be maintained at least weekly and sometimes also daily by qualified personnel. The analyzers should be calibrated regularly with certified concentration standards. Additionally, the limit of detection should be determined periodically, for instance by sampling field blanks or zero air.

When operating accumulation systems with manual offsite analysis, regular calibrations of the analytical equipment in the laboratory must be performed. Coated filters and denuders should be prepared under extremely clean conditions. Field blanks of these measurement systems should be taken on a monthly basis (or between subsequent samples). As listed in Table 54.11, maintenance intervals for these systems are much larger than those for online detection and semicontinuous systems with automated onsite analysis.

Table 54.11 Maintenance of analyzers used for immission and dry deposition measurements (see also Chap. 3)

Maximum interval	Online detection	Semicontinuous with automated onsite analysis	Accumulation with manual offsite analysis
1 week	Check sampling flow rates (or line pressure) Check drying agents, chemicals, and other consumables Download raw data and check its plausibility visually	Check liquid and air flow rates Check chemical solutions and other consumables Download raw data and check its plausibility visually	
1 month	Check for tubing leaks Calibration Exchange inlet filters System response tests SbS measurements	Check for tubing leaks Field blanks Calibration Clean inlet material SbS measurements	Check sampling flow rates Field/transport blanks Check for tubing leaks Calibration and blanks of analytical equipment in the laboratory
1 year	Full service of analyzer	Full service of analyzer	

54.8 Application

The following section outlines some typical applications and related objectives of dry deposition measurements.

54.8.1 Annual Cycles and Nitrogen Budgets of Ecosystems

Investigations of annual cycles and seasonal variations are generally performed within the framework of long-term studies (or measurement networks) using accumulation systems with manual offsite analysis, long integration times, and subsequent application of the DDIM (or more advanced versions that are used as modules within atmospheric chemistry and transport models or multilayer models) (Sect. 54.4.3) [54.159, 175, 185].

However, in some studies, semicontinuous systems with automated onsite analysis have also been deployed for long-term measurements [54.186]. Advanced versions of these systems are currently employed for the long-term characterization of atmospheric chemistry and to monitor the deposition of nitrogen and sulfur with high time resolution [54.155, 187, 188].

The importance of dry deposition measurements is revealed when analyzing nitrogen storage and its evolution in ecosystems over time as a result of global change. Although the nitrogen input to ecosystems from dry deposition is small compared to the amounts of nitrogen cycled between soil and vegetation, it can substantially affect ecosystem functioning and biodiversity given that it is the limiting nutrient for plant growth in

many natural and seminatural ecosystems. Increasing N inputs to terrestrial ecosystems may cause:

- Ecosystem eutrophication and acidification
- A reduction in biodiversity
- Increased carbon storage
- Enhanced leaching of nitrate and soil nutrients
- Intensified trace gas exchange [54.189, 190].

Likewise, deposition of O_3 may cause biodiversity losses in natural ecosystems and crop yield losses in agricultural areas [54.191, 192]. Purely ecologically oriented studies often overlook the availability of methods for determining dry deposition, even though it is an important component of the overall nitrogen budget [54.193]. This may be due to the complexity of the various dry deposition measurement techniques that are used for individual compounds. There are barely any long-term studies that have applied state-of-the-art techniques such as EC, AGM, or MBR in combination with the determination of, e.g., nitrogen fixation, retention, and export processes to establish the overall nitrogen budget of an ecosystem. Within the framework of the NitroEurope project, nitrogen inputs and outputs together with nitrogen turnover in plants and soils as well as net greenhouse gas exchanges were measured for different European ecosystems [54.194, 195]. Long-term studies using the DDIM provide important information on the atmospheric nitrogen input into ecosystems and may help to identify when critical loads are exceeded.

54.8.2 Daily Cycles and Process Studies

When online or semicontinuous systems with automated onsite analysis are used (Sect. 54.4.1), it is possible to analyze diurnal cycles, as shown for HNO_3 and NH_3 in Fig. 54.7. The application of the AGM or MBR method for intensive observation periods that typically last for a few days to several weeks enables process-level studies, in particular investigations of surface uptake and chemical interactions. When there is substantial chemical divergence, fluxes of total nitrate/ammonium are sometimes determined to derive the total nitrogen input [54.196], or the influences of chemical reactions on the derived fluxes are assessed through modeling approaches [54.124, 129, 130, 197].

Such process studies potentially provide the basis for developing new parameterizations for r_c and its components for different surface types and meteorological conditions [54.70, 80, 87, 144]. An important step in the detailed analysis of r_c (or its inverse, the canopy conductance g_c) is the partitioning into stom-

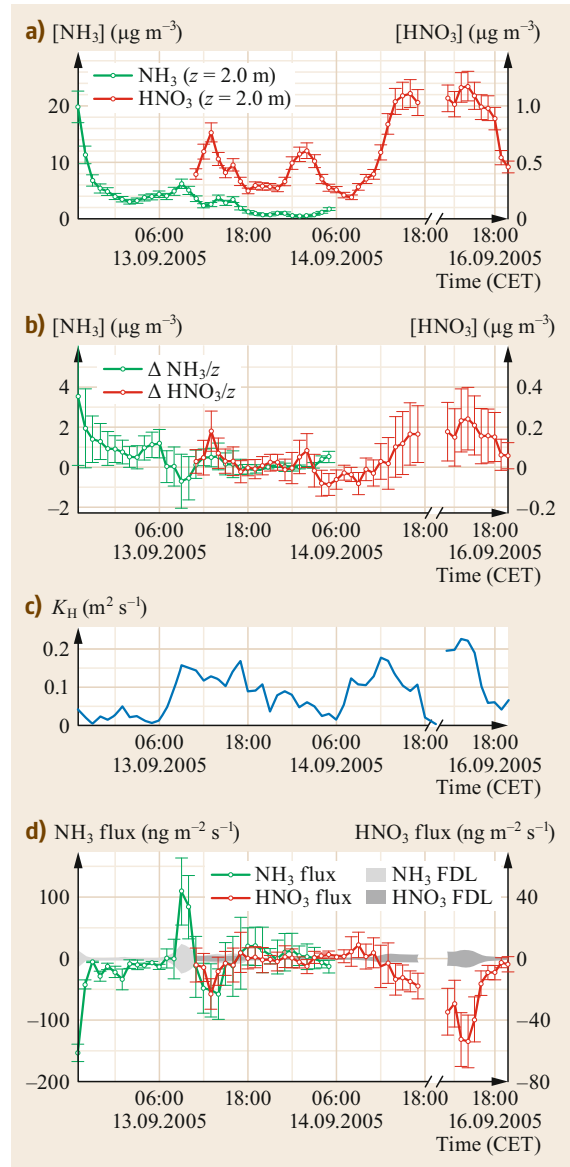


Fig. 54.7 (a) Measured concentrations, (b) vertical concentration differences, (c) turbulent exchange coefficient, and (d) fluxes determined with the AGM method for NH_3 and HNO_3 at a managed grassland site in southern Germany. Calculated flux detection limits (FDL) are shaded gray and correspond to the minimum detectable fluxes retrieved from side-by-side measurements (Sect. 54.6) (after [54.147] © 2009, reprinted with permission)

atal and nonstomatal deposition pathways (Fig. 54.8). These new insights can be used to apply the DDIM at comparable sites or to facilitate the improvement of inferential models, or they can be applied in atmospheric chemistry and transport models [54.198, 199].

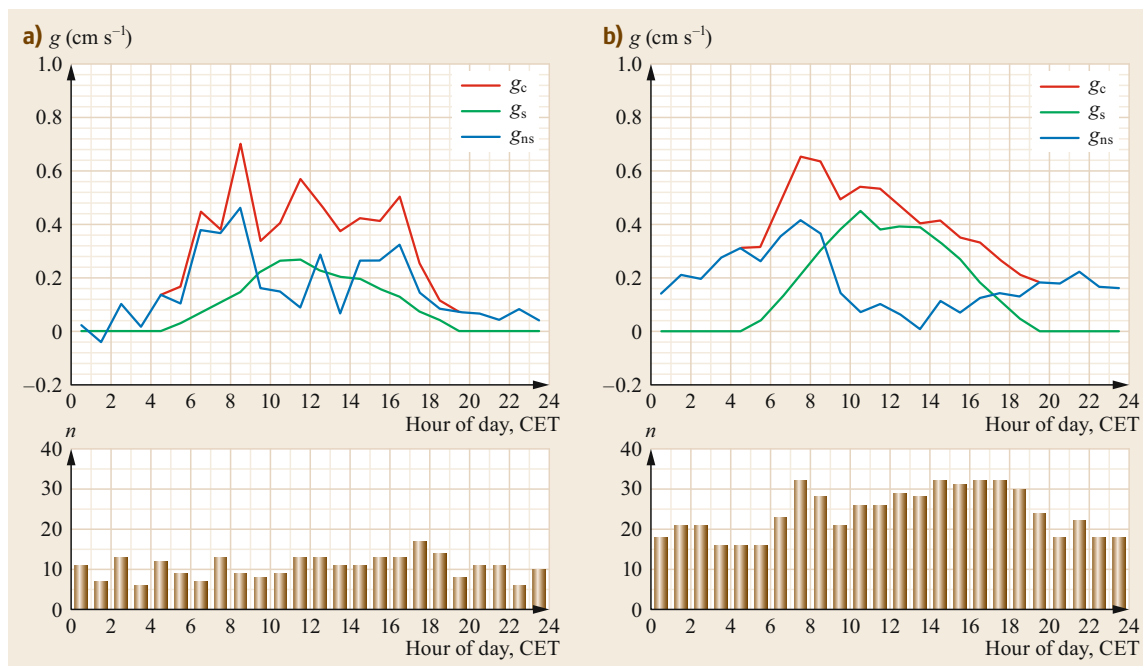


Fig. 54.8a,b Canopy conductance (g_c) and partitioning into stomatal (g_s) and nonstomatal (g_{ns}) conductances (inverses of the resistances in Fig. 54.2) for (a) PAN and (b) O₃, as derived from MBR and EC measurements of the respective deposition fluxes at a natural grassland site in southwestern Germany (after [54.103] © A. Moravek et al. 2015, Creative Commons Attribution 3.0 License)

54.9 Future Developments

The major challenge in the forthcoming years will be to spatially intensify immission and dry deposition measurements, particularly in hot-spot regions where considerable emissions of air pollutants cause high deposition rates in nearby natural ecosystems. This is crucial to obtaining spatial and temporal information on patterns and trends as well as to monitoring the magnitudes of critical loads and level exceedances, thus forming the basis for decisions by policy makers. In order to achieve this goal, inexpensive low-power online systems (e.g., semiconductor-based ozone sensors and electrochemical NO₂ sensors [54.200]) with high time resolutions must be developed. The main requirements are sufficient accuracy and a need for only minimal maintenance, permitting standalone application over long time periods. For water-soluble and sticky compounds, the use of open-path instruments without inlet lines and pumps would be a major step

forward as it would improve accuracy at high time resolution [54.141, 201, 202].

Another challenge that must be addressed is the quantification of dry deposition in urban areas to complement current standard immission measurements [54.203, 204]. Additionally, remote-sensing methods to determine spatially resolved regional immission fields should be developed. New techniques such as satellite observations of the Earth and other remote-sensing instruments (e.g., drones) can be used to augment ground-based measurements (Chap. 28) [54.205–207].

The development of methods to quantify the nonstomatal surface resistances (e.g., leaf surface chemistry) in a mechanistic way would lead to a great improvement in the accuracy of dry deposition fluxes estimated using the DDIM. Furthermore, corrections for chemical flux divergence must be investigated in more detail.

54.10 Further Reading

- B.B. Hicks, R.D. Saylor, B.D. Baker: Dry Deposition of Particles to Canopies – A Look Back and the Road Forward, *Journal of Geophysical Research-Atmospheres* 121, 14691–14707 (2016)
- E. Nemitz: Surface/Atmosphere Exchange of Atmospheric Acids and Aerosols, Including the Effect and Model Treatment of Chemical Interactions. In: Review and Integration of Biosphere-Atmosphere Modelling of Reactive Trace Gases and Volatile Aerosols, ed. by R.-S. Massad, B. Loubet (Springer, Dordrecht, Heidelberg, New York, London 2015)
- M.A. Sutton, E. Nemitz, J.W. Erisman, C. Beier, K.B. Bahl, P. Cellier, W. de Vries, F. Cotrufo, U. Skiba, C. Di Marco, S. Jones, P. Laville, J.F. Sousana, B. Loubet, M. Twigg, D. Famulari, J. Whitehead, M.W. Gallagher, A. Neftel, C.R. Flechard, B. Herrmann, P.L. Calanca, J.K. Schjoerring, U. Daemmgen, L. Horvath, Y.S. Tang, B.A. Emmett, A. Tietema, J. Penuelas, M. Kesik, N. Brueggemann, K. Pilegaard, T. Vesala, C.L. Campbell, J.E. Olesen, U. Dragosits, M.R. Theobald, P. Levy, D.C. Mobbs, R. Milne, N. Viovy, N. Vuichard, J.U. Smith, P. Smith, P. Bergamaschi, D. Fowler, S. Reis: Challenges in Quantifying Biosphere-Atmosphere Exchange of Nitrogen Species, *Environmental Pollution* 150, 125–139 (2007)
- J. Vilà-Guerau de Arellano, C.C. Van Heerwaarden, B.J.H. Van Stratum, K. Van den Dries: Atmospheric Boundary Layer, (Cambridge University Press, Cambridge 2015)
- M.L. Wesely, B.B. Hicks: A Review of the Current Status of Knowledge on Dry Deposition, *Atmospheric Environment* 34, 2261–2282 (2000)

References

- 54.1 T. Foken, R. Dlugi, G. Kramm: On the determination of dry deposition and emission of gaseous compounds at the biosphere-atmosphere interface, *Meteorol. Z.* **4**, 91–118 (1995)
- 54.2 H. Sievering, D. Rusch, L. Marquez: Nitric acid, particulate nitrate and ammonium in the continental free troposphere: Nitrogen deposition to an Alpine tundra ecosystem, *Atmos. Environ.* **30**, 2527–2537 (1996)
- 54.3 I. Trebs, L.S. Lara, L.M. Zeri, L.V. Gatti, P. Artaxo, R. Dlugi, J. Slanina, M.O. Andreae, F.X. Meixner: Dry and wet deposition of atmospheric inorganic nitrogen in a tropical environment (Rondônia, Brazil), *Atmos. Chem. Phys.* **6**, 447–469 (2006)
- 54.4 N. Poor, R. Pribble, H. Greening: Direct wet and dry deposition of ammonia, nitric acid, ammonium and nitrate to the Tampa Bay estuary, FL, USA, *Atmos. Environ.* **35**, 3947–3955 (2001)
- 54.5 G.D. Farquhar, P.M. Firth, R. Wetselaar, B. Weir: On the gaseous exchange of ammonia between leaves and the environment – Determination of the ammonia compensation point, *Plant Physiol.* **66**, 710–714 (1980)
- 54.6 M.A. Sutton, J.K. Burkhardt, D. Guerin, E. Nemitz, D. Fowler: Development of resistance models to describe measurements of bi-directional ammonia surface-atmosphere exchange, *Atmos. Environ.* **32**, 473–480 (1998)
- 54.7 D.D. Baldocchi, B.B. Hicks, P. Camara: A canopy stomatal-resistance model for gaseous deposition to vegetated surfaces, *Atmos. Environ.* **21**, 91–101 (1987)
- 54.8 B.B. Hicks, D.D. Baldocchi, T.P. Meyers, R.P. Hosker, D.R. Matt: A preliminary multiple resistance routine for deriving dry deposition velocities from measured quantities, *Water Air Soil Pollut.* **36**, 311–330 (1987)
- 54.9 M.Y. Leclerc, T. Foken: *Footprints in Micrometeorology and Ecology* (Springer, Berlin, Heidelberg 2014)
- 54.10 D.D. Baldocchi, B.B. Hicks, T.P. Meyers: Measuring biosphere-atmosphere exchanges of biologically related gases with micrometeorological methods, *Ecology* **69**, 1331–1340 (1988)
- 54.11 C. Breuninger, F.X. Meixner, J. Kesselmeier: Field investigations of nitrogen dioxide (NO₂) exchange between plants and the atmosphere, *Atmos. Chem. Phys.* **13**, 773–790 (2013)
- 54.12 L. Pape, C. Ammann, A. Nyfeler-Brunner, C. Spirig, K. Hens, F.X. Meixner: An automated dynamic chamber system for surface exchange measurement of non-reactive and reactive trace gases of grassland ecosystems, *Biogeosciences* **6**, 405–429 (2009)
- 54.13 D. Plake, P. Stella, A. Moravek, J.C. Mayer, C. Ammann, A. Held, I. Trebs: Comparison of ozone deposition measured with the dynamic chamber and the eddy covariance method, *Agric. For. Meteorol.* **206**, 97–112 (2015)
- 54.14 P.J. Hanson, S.E. Lindberg: Dry deposition of reactive nitrogen-compounds – A review of leaf, canopy and non-foliar measurements, *Atmos. Environ. A* **25**, 1615–1634 (1991)
- 54.15 M.A. Sutton, E. Nemitz, J.W. Erisman, C. Beier, K.B. Bahl, P. Cellier, W. de Vries, F. Cotrufo, U. Skiba, C. Di Marco, S. Jones, P. Laville, J.F. Sousana, B. Loubet, M. Twigg, D. Famulari, J. Whitehead, M.W. Gallagher, A. Neftel, C.R. Flechard, B. Herrmann, P.L. Calanca, J.K. Schjoerring, U. Daemmgen, L. Horvath, Y.S. Tang, B.A. Emmett,

- A. Tietema, J. Penuelas, M. Kesik, N. Brueggemann, K. Pilegaard, T. Vesala, C.L. Campbell, J.E. Olesen, U. Dragosits, M.R. Theobald, P. Levy, D.C. Mobbs, R. Milne, N. Viovy, N. Vuichard, J.U. Smith, P. Smith, P. Bergamaschi, D. Fowler, S. Reis: Challenges in quantifying biosphere-atmosphere exchange of nitrogen species, *Environ. Pollut.* **150**, 125–139 (2007)
- 54.16 A. Volz, D. Kley: Evaluation of the Montsouris Series of ozone measurements made in the 19th century, *Nature* **332**, 240–242 (1988)
- 54.17 B.B. Hicks, R.D. Saylor, B.D. Baker: Dry deposition of particles to canopies – A look back and the road forward, *J. Geophys. Res. Atmos.* **121**, 14691–14707 (2016)
- 54.18 S. Odén: *The Acidification of Air Precipitation and Its Consequences in the Natural Environment*, *Bulletins from the Ecological Research Committee*, Vol. 1 (Oikos Editorial Office, Lund 1968)
- 54.19 Ø. Hov, E. Hesstvedt, I.S.A. Isaksen: Long-range transport of tropospheric ozone, *Nature* **273**, 341–344 (1978)
- 54.20 P. Borrell, P.J.H. Builtjes, P. Grennfelt, Ø. Hov: *Photo-Oxidants, Acidification and Tools: Policy Applications of Eurotrac Results* (Springer, Berlin, Heidelberg 1997)
- 54.21 I.E. Galbally: Ozone profiles and ozone fluxes in the atmospheric surface layer, *Q. J. R. Meteorol. Soc.* **97**, 18–29 (1971)
- 54.22 J.A. Garland: On the size dependence of particle deposition, *Water Air Soil Pollut. Focus* **1**, 323–332 (2001)
- 54.23 R. Roth: Der vertikale Transport von Luftbeimengungen in der Prandtl-Schicht und die Depositionsgeschwindigkeit, *Meteorol. Rundsch.* **28**, 65–71 (1975)
- 54.24 M.L. Wesely, B.B. Hicks: Some Factors that affect deposition rates of sulfur-dioxide and similar gases on vegetation, *J. Air Pollut. Control Assoc.* **27**, 1110–1116 (1977)
- 54.25 U. Platt: Dry deposition of SO₂, *Atmos. Environ.* **12**, 363–367 (1978)
- 54.26 G.A. Sehmel: Particle and gas dry deposition – A review, *Atmos. Environ.* **14**, 983–1011 (1980)
- 54.27 M.L. Wesely, D.R. Cook, R.L. Hart, R.E. Speer: Measurements and parameterization of particulate sulfur dry deposition over grass, *J. Geophys. Res. Atmos.* **90**, 2131–2143 (1985)
- 54.28 J.A. Businger: Evaluation of the accuracy with which dry deposition can be measured with current micrometeorological techniques, *J. Clim. Appl. Meteorol.* **25**, 1100–1124 (1986)
- 54.29 B.B. Hicks: Measuring dry deposition – A reassessment of the state-of-the-art, *Water Air Soil Pollut.* **30**, 75–90 (1986)
- 54.30 D.H. Lenschow, A.C. Delany: An analytic formulation for NO and NO₂ flux profiles in the atmospheric surface layer, *J. Atmos. Chem.* **5**, 301–309 (1987)
- 54.31 B.R. Appel, Y. Tokiwa, M. Haik, E.L. Kothny: Artifact particulate sulfate and nitrate formation on filter media, *Atmos. Environ.* **18**, 409–416 (1984)
- 54.32 J. Slanina, P.J. de Wild, G.P. Wyers: The application of denuder systems to the analysis of atmospheric components, *Adv. Environ. Sci. Technol.* **24**, 129–154 (1992)
- 54.33 J.A. Neuman, L.G. Huey, T.B. Ryerson, D.W. Fahey: Study of inlet materials for sampling atmospheric nitric acid, *Environ. Sci. Technol.* **33**, 1133–1136 (1999)
- 54.34 C.I. Davidson, S.E. Lindberg, J.A. Schmidt, L.G. Cartwright, L.R. Landis: Dry deposition of sulfate onto surrogate surfaces, *J. Geophys. Res. Atmos.* **90**, 2123–2130 (1985)
- 54.35 N.F. Islitzer, R.K. Dumbauld: Atmospheric diffusion-deposition studies over flat terrain, *Int. J. Air Water Pollut.* **7**, 999–1022 (1963)
- 54.36 A. Bytnerowicz, P.R. Miller, D.M. Olszyk: Dry deposition of nitrate, ammonium and sulfate to a *Ceanothus crassifolius* canopy and surrogate surfaces, *Atmos. Environ.* **21**, 1749–1757 (1987)
- 54.37 G.M. Lovett, S.E. Lindberg: Dry deposition and canopy exchange in a mixed oak forest as determined by analysis of throughfall, *J. Appl. Ecol.* **21**, 1013–1027 (1984)
- 54.38 H. Sievering: Dynamics of sulfur exchange at the air/forest canopy interface: A review of throughfall inferred deposition rates, *Glob. Biogeochem. Cycles* **1**, 233–249 (1987)
- 54.39 B.R. Appel: Sampling of selected labile atmospheric pollutants. In: *Measurement Challenges in Atmospheric Chemistry*, *Advances in Chemistry*, Vol. 232, ed. by L. Newman (ACS, Washington 1993) pp. 1–40, Chap. 1
- 54.40 B.B. Hicks, R.P. Hosker, T.P. Meyers, J.D. Womack: Dry deposition inferential measurement techniques – I. Design and tests of a prototype meteorological and chemical-system for determining dry deposition, *Atmos. Environ. A* **25**, 2345–2359 (1991)
- 54.41 B.J. Huebert, C.H. Robert: The dry deposition of nitric acid to grass, *J. Geophys. Res. Atmos.* **90**, 2085–2090 (1985)
- 54.42 G.W. Lee, L.Z. Zhuang, B.J. Huebert, T.P. Meyers: Concentration gradients and dry deposition of nitric acid vapor at the Mauna Loa Observatory, Hawaii, *J. Geophys. Res. Atmos.* **98**, 12661–12671 (1993)
- 54.43 T.P. Meyers, B.B. Hicks, R.P. Hosker, J.D. Womack, L.C. Satterfield: Dry deposition inferential measurement techniques – II. Seasonal and annual deposition rates of sulfur and nitrate, *Atmos. Environ. A* **25**, 2361–2370 (1991)
- 54.44 B.R. Appel, Y. Tokiwa, M. Haik: Sampling of nitrates in ambient air, *Atmos. Environ.* **15**, 283–289 (1981)
- 54.45 M. Ferm: A Na₂CO₃-coated denuder and filter for determination of gaseous HNO₃ and particulate NO₃⁻ in the atmosphere, *Atmos. Environ.* **20**, 1193–1201 (1986)
- 54.46 D.A. Phillips, P.K. Dasgupta: A diffusion scrubber for the collection of gaseous nitric acid, *Sep. Sci. Technol.* **22**, 1255–1267 (1987)

- 54.47 R.W. Talbot, A.S. Vijgen, R.C. Harriss: Measuring tropospheric HNO_3 – Problems and prospects for nylon filter and mist chamber techniques, *J. Geophys. Res. Atmos.* **95**, 7553–7561 (1990)
- 54.48 P.K. Simon, P.K. Dasgupta: Continuous automated measurement of gaseous nitrous and nitric acids and particulate nitrite and nitrate, *Environ. Sci. Technol.* **29**, 1534–1541 (1995)
- 54.49 P.K. Dasgupta: Automated measurement of atmospheric trace gases – Diffusion-based collection and analysis. In: *Measurement Challenges in Atmospheric Chemistry*, Advances in Chemistry, Vol. 232, ed. by L. Newman (ACS, Washington 1993) pp. 41–90, Chap. 2
- 54.50 M.P. Keuken, C.A.M. Schoonebeek, A. Wensveen-Louter, J. Slanina: Simultaneous sampling of NH_3 , HNO_3 , HCl , SO_2 and H_2O_2 in ambient air by a wet annular denuder system, *Atmos. Environ.* **22**, 2541–2548 (1988)
- 54.51 M.P. Keuken, A. Waijers-Ijpelaar, J.J. Mols, R.P. Otjes, J. Slanina: The determination of ammonia in ambient air by an automated thermodenuder system, *Atmos. Environ.* **23**, 2177–2185 (1989)
- 54.52 M.T. Oms, P.A.C. Jongejan, A.C. Veltkamp, G.P. Wyers, J. Slanina: Continuous monitoring of atmospheric HCl , HNO_2 , HNO_3 , and SO_2 , by wet-annular denuder air sampling with on-line chromatographic analysis, *Int. J. Environ. Anal. Chem.* **62**, 207–218 (1996)
- 54.53 J. Slanina, G.P. Wyers: Monitoring of atmospheric components by automatic denuder systems, *Fresenius J. Anal. Chem.* **350**, 467–473 (1994)
- 54.54 G.P. Wyers, R.P. Otjes, J. Slanina: A continuous-flow denuder for the measurement of ambient concentrations and surface-exchange fluxes of ammonia, *Atmos. Environ. A* **27**, 2085–2090 (1993)
- 54.55 A. Neftel, A. Blatter, R. Hesterberg, T. Staffelbach: Measurements of concentration gradients of HNO_2 and HNO_3 over a semi-natural ecosystem, *Atmos. Environ.* **30**, 3017–3025 (1996)
- 54.56 Z. Vecera, P.K. Dasgupta: Measurement of atmospheric nitric and nitrous acids with a wet effluent diffusion denuder and low-pressure ion chromatography-postcolumn reaction detection, *Anal. Chem.* **63**, 2210–2216 (1991)
- 54.57 J.W. Erisman, A.H. Versluis, T. Verplanke, D. Dehaan, D. Anink, B.G. Vanelzakker, M.G. Mennen, R.M. Vanaalst: Monitoring the dry deposition of SO_2 in the Netherlands – Results for grassland and heather vegetation, *Atmos. Environ. A* **27**, 1153–1161 (1993)
- 54.58 I. Galbally: An evaluation of the Ehmert technique for measuring ozone profiles in the atmospheric surface layer, *J. Geophys. Res.* **74**, 6869–6872 (1969)
- 54.59 A.C. Delany, D.R. Fitzjarrald, D.H. Lenschow, R. Pearson, G.J. Wendel, B. Woodruff: Direct measurements of nitrogen oxides and ozone fluxes over grassland, *J. Atmos. Chem.* **4**, 429–444 (1986)
- 54.60 J.G. Droppo: Concurrent measurements of ozone dry deposition using eddy-correlation and profile flux-methods, *J. Geophys. Res. Atmos.* **90**, 2111–2118 (1985)
- 54.61 J.A. Eastman, D.H. Stedman: A fast response sensor for ozone eddy-correlation flux measurements, *Atmos. Environ.* **11**, 1209–1211 (1977)
- 54.62 J.B.A. Muller, C.J. Percival, M.W. Gallagher, D. Fowler, M. Coyle, E. Nemitz: Sources of uncertainty in eddy covariance ozone flux measurements made by dry chemiluminescence fast response analysers, *Atmos. Meas. Tech.* **3**, 163–176 (2010)
- 54.63 U. Joss, W.K. Graber: Profiles and simulated exchange of H_2O , O_3 , NO_2 between the atmosphere and the HartX Scots pine plantation, *Theor. Appl. Climatol.* **53**, 157–172 (1996)
- 54.64 W. Eugster, R. Hesterberg: Transfer resistances of NO_2 determined from eddy correlation flux measurements over a litter meadow at a rural site on the Swiss plateau, *Atmos. Environ.* **30**, 1247–1254 (1996)
- 54.65 D. Fowler, K. Pilegaard, M.A. Sutton, P. Ambus, M. Raivonen, J. Duyzer, D. Simpson, H. Fagerli, S. Fuzzi, J.K. Schjoerring, C. Granier, A. Neftel, I.S.A. Isaksen, P. Laj, M. Maione, P.S. Monks, J. Burkhardt, U. Daemmgen, J. Neiryneck, E. Personne, R. Wichink-Kruit, K. Butterbach-Bahl, C. Flechard, J.P. Tuovinen, M. Coyle, G. Gerosa, B. Loubet, N. Altimir, L. Gruenhage, C. Ammann, S. Cieslik, E. Paoletti, T.N. Mikkelsen, H. Røpoulsen, P. Cellier, J.N. Cape, L. Horvath, F. Loreto, U. Niinemets, P.I. Palmer, J. Rinne, P. Misztal, E. Nemitz, D. Nilsson, S. Pryor, M.W. Gallagher, T. Vesala, U. Skiba, N. Brüeggemann, S. Zechmeister-Boltenstern, J. Williams, C. O’Dowd, M.C. Facchini, G. de Leeuw, A. Flossman, N. Chaumerliac, J.W. Erisman: Atmospheric composition change: Ecosystems-atmosphere interactions, *Atmos. Environ.* **43**, 5193–5267 (2009)
- 54.66 A. Petroff, L.M. Zhang, S.C. Pryor, Y. Belot: An extended dry deposition model for aerosols onto broadleaf canopies, *J. Aerosol Sci.* **40**, 218–240 (2009)
- 54.67 J. Burkhardt, C.R. Flechard, F. Gressens, M. Mattsson, P.A.C. Jongejan, J.W. Erisman, T. Weidinger, R. Meszaros, E. Nemitz, M.A. Sutton: Modelling the dynamic chemical interactions of atmospheric ammonia with leaf surface wetness in a managed grassland canopy, *Biogeosciences* **6**, 67–84 (2009)
- 54.68 E. Nemitz, M.A. Sutton, J.K. Schjoerring, S. Husted, G.P. Wyers: Resistance modelling of ammonia exchange over oilseed rape, *Agric. For. Meteorol.* **105**, 405–425 (2000)
- 54.69 S. Sun, A. Moravek, I. Trebs, J. Kesselmeier, M. Sorgel: Investigation of the influence of liquid surface films on O_3 and PAN deposition to plant leaves coated with organic/inorganic solution, *J. Geophys. Res. Atmos.* **121**, 14239–14256 (2016)
- 54.70 J.W. Erisman, A. Vanpul, P. Wyers: Parametrization of surface-resistance for the quantification of atmospheric deposition of acidifying pollu-

- tants and ozone, *Atmos. Environ.* **28**, 2595–2607 (1994)
- 54.71 J.W. Erisman, G.P. Wyers: Continuous measurements of surface exchange of SO₂ and NH₃ – Implications for their possible interaction in the deposition process, *Atmos. Environ. A* **27**, 1937–1949 (1993)
- 54.72 M.A. Sutton, J.K. Schjoerring, G.P. Wyers: Plant-atmosphere exchange of ammonia, *Philos. Trans. R. Soc.* **351**, 261–278 (1995)
- 54.73 X. Lee: *Fundamentals of Boundary-Layer Meteorology* (Springer, Cham 2018)
- 54.74 J. Vilà-Guerau de Arellano, C.C. Van Heerwaarden, B.J.H. Van Stratum, K. Van den Dries: *Atmospheric Boundary Layer: Integrating Air Chemistry and Land Interactions* (Cambridge Univ. Press, New York 2015)
- 54.75 A.C. Chamberlain: *Aspects of Travel and Deposition of Aerosol and Vapour Clouds* (AERE, Harwell, Berkshire 1961) p. 38, Report HPIR 1261 (RP/14)
- 54.76 C. Ammann: *On the Applicability of Relaxed Eddy Accumulation and Common Methods for Measuring Trace Gas Fluxes*, Ph.D. Thesis (ETH, Zürich 1999)
- 54.77 T. Foken: *Micrometeorology*, 2nd edn. (Springer, Berlin, Heidelberg 2017)
- 54.78 E. Lamaud, B. Loubet, M. Irvine, P. Stella, E. Personne, P. Cellier: Partitioning of ozone deposition over a developed maize crop between stomatal and non-stomatal uptakes, using eddy-covariance flux measurements and modelling, *Agric. For. Meteorol.* **149**, 1385–1396 (2009)
- 54.79 P. Stella, M. Kortner, C. Ammann, T. Foken, F.X. Meixner, I. Trebs: Measurements of nitrogen oxides and ozone fluxes by eddy covariance at a meadow: Evidence for an internal leaf resistance to NO₂, *Biogeosciences* **10**, 5997–6017 (2013)
- 54.80 P. Stella, B. Loubet, E. Lamaud, P. Laville, P. Cellier: Ozone deposition onto bare soil: A new parameterisation, *Agric. For. Meteorol.* **151**, 669–681 (2011)
- 54.81 G. Kerstiens, R. Federholzner, K.J. Lenzian: Dry deposition and cuticular uptake of pollutant gases, *Agric. Ecosyst. Environ.* **42**, 239–253 (1992)
- 54.82 F. Schrader, C. Brummer, C.R. Flechard, R.J.W. Kruit, M.C. van Zanten, U. Zoll, A. Hensen, J.W. Erisman: Non-stomatal exchange in ammonia dry deposition models: Comparison of two state-of-the-art approaches, *Atmos. Chem. Phys.* **16**, 13417–13430 (2016)
- 54.83 G.J. Dollard, D.H.F. Atkins, T.J. Davies, C. Healy: Concentrations and dry deposition velocities of nitric acid, *Nature* **326**, 481–483 (1987)
- 54.84 M.L. Wesely, B.B. Hicks: A review of the current status of knowledge on dry deposition, *Atmos. Environ.* **34**, 2261–2282 (2000)
- 54.85 S.A. Watt, C. Wagner-Riddle, G. Edwards, R.J. Vet: Evaluating a flux-gradient approach for flux and deposition velocity of nitrogen dioxide over short-grass surfaces, *Atmos. Environ.* **38**, 2619–2626 (2004)
- 54.86 C.V. Horii, J.W. Munger, S.C. Wofsy, M. Zahniser, D. Nelson, J.B. McManus: Fluxes of nitrogen oxides over a temperate deciduous forest, *J. Geophys. Res. Atmos.* **109**, D08305 (2004)
- 54.87 E. Nemitz, M.A. Sutton, G.P. Wyers, P.A.C. Jongejan: Gas-particle interactions above a Dutch heathland: I. Surface exchange fluxes of NH₃, SO₂, HNO₃ and HCl, *Atmos. Chem. Phys.* **4**, 989–1005 (2004)
- 54.88 F.X. Meixner, F. Böswald, C. Buck, K. Eiblmeier, H. Müller: Measurement of HNO₃ dry deposition by gradient techniques. In: *Field measurements and interpretation of species derived from NO_x, NH₃, and VOC emissions in Europe* (CEC, Brussels 1990), Air Pollution Research Report 25
- 54.89 J.W. Erisman, A.W.M. Vermetten, W.A.H. Asman, A. Waijers-Ijpelaar, J. Slanina: Vertical distribution of gases and aerosols: The behaviour of ammonia and related components in the lower atmosphere, *Atmos. Environ.* **22**, 1153–1160 (1988)
- 54.90 T.P. Meyers, B.J. Huebert, B.B. Hicks: HNO₃ deposition to a deciduous forest, *Bound.-Layer Meteorol.* **49**, 395–410 (1989)
- 54.91 S.C. Pryor, R.J. Barthelmie, B. Jensen, N.O. Jensen, L.L. Sorensen: HNO₃ fluxes to a deciduous forest derived using gradient and REA methods, *Atmos. Environ.* **36**, 5993–5999 (2002)
- 54.92 H. Sievering, T. Kelly, G. McConville, C. Seibold, A. Turnipseed: Nitric acid dry deposition to conifer forests: Niwot Ridge Spruce-Fir-Pine Study, *Atmos. Environ.* **35**, 3851–3859 (2001)
- 54.93 F. Schrader, C. Brümmer: *Genfer Luftreinhaltkonvention der UNECE: Literaturstudie zu Messungen der Ammoniak-Depositionsgeschwindigkeit* (UBA, Dessau-Roßlau 2014), Tech. Rep. 67/2014
- 54.94 J. Duyzer: Dry deposition of ammonia and ammonium aerosols over heathland, *J. Geophys. Res. Atmos.* **99**, 18757–18763 (1994)
- 54.95 J.H. Duyzer, H.L.M. Verhagen, J.H. Weststrate, F.C. Bosveld: Measurement of the dry deposition flux of NH₃ on to coniferous forest, *Environ. Pollut.* **75**, 3–13 (1992)
- 54.96 P.L. Finkelstein, T.G. Ellestad, J.F. Clarke, T.P. Meyers, D.B. Schwede, E.O. Hebert, J.A. Neal: Ozone and sulfur dioxide dry deposition to forests: Observations and model evaluation, *J. Geophys. Res. Atmos.* **105**, 15365–15377 (2000)
- 54.97 Z.Y. Wu, R. Staebler, R. Vet, L.M. Zhang: Dry deposition of O₃ and SO₂ estimated from gradient measurements above a temperate mixed forest, *Environ. Pollut.* **210**, 202–210 (2016)
- 54.98 J.L. Tsai, C.L. Chen, B.J. Tsuang, P.H. Kuo, K.H. Tseng, T.F. Hsu, B.H. Sheu, C.P. Liu, M.T. Hsueh: Observation of SO₂ dry deposition velocity at a high elevation flux tower over an evergreen broadleaf forest in central Taiwan, *Atmos. Environ.* **44**, 1011–1019 (2010)
- 54.99 U. Rummel, C. Ammann, G.A. Kirkman, M.A.L. Moura, T. Foken, M.O. Andreae, F.X. Meixner: Seasonal variation of ozone deposition to a tropical rain forest in southwest Amazonia, *Atmos. Chem. Phys.* **7**, 5415–5435 (2007)

- 54.100 G. Wohlfahrt, L. Hortnagl, A. Hammerle, M. Graus, A. Hansel: Measuring eddy covariance fluxes of ozone with a slow-response analyser, *Atmos. Environ.* **43**, 4570–4576 (2009)
- 54.101 P. Keronen, A. Reissell, U. Rannik, T. Pohja, E. Siivola, V. Hiltunen, P. Hari, M. Kulmala, T. Vesala: Ozone flux measurements over a Scots pine forest using eddy covariance method: Performance evaluation and comparison with flux-profile method, *Boreal Environ. Res.* **8**, 425–443 (2003)
- 54.102 B. Loubet, P. Cellier, C. Flechard, O. Zurfluh, M. Irvine, E. Lamaud, P. Stella, R. Roche, B. Durand, D. Flura, S. Masson, P. Laville, D. Garrigou, E. Personne, M. Chelle, J.F. Castell: Investigating discrepancies in heat, CO₂ fluxes and O₃ deposition velocity over maize as measured by the eddy-covariance and the aerodynamic gradient methods, *Agric. For. Meteorol.* **169**, 35–50 (2013)
- 54.103 A. Moravek, P. Stella, T. Foken, I. Trebs: Influence of local air pollution on the deposition of peroxyacetyl nitrate to a nutrient-poor natural grassland ecosystem, *Atmos. Chem. Phys.* **15**, 899–911 (2015)
- 54.104 P.V. Doskey, V.R. Kotamarthi, Y. Fukui, D.R. Cook, F.W. Breitbeil, M.L. Wesely: Air-surface exchange of peroxyacetyl nitrate at a grassland site, *J. Geophys. Res. Atmos.* **109**, D10310 (2004)
- 54.105 A.A. Turnipseed, L.G. Huey, E. Nemitz, R. Stickel, J. Higgs, D.J. Tanner, D.L. Slusher, J.P. Sparks, F. Flocke, A. Guenther: Eddy covariance fluxes of peroxyacetyl nitrates PANs and NO_y to a coniferous forest, *J. Geophys. Res. Atmos.* **111**, D09304 (2006)
- 54.106 G.M. Wolfe, J.A. Thornton, R.L.N. Yataavelli, M. McKay, A.H. Goldstein, B. LaFranchi, K.E. Min, R.C. Cohen: Eddy covariance fluxes of acyl peroxy nitrates (PAN, PPN and MPAN) above a ponderosa pine forest, *Atmos. Chem. Phys.* **9**, 615–634 (2009)
- 54.107 A. Petroff, A. Mailliat, M. Amielh, F. Anselmet: Aerosol dry deposition on vegetative canopies. Part II: A new modelling approach and applications, *Atmos. Environ.* **42**, 3654–3683 (2008)
- 54.108 E. Nemitz: Surface/atmosphere exchange of atmospheric acids and aerosols, including the effect and model treatment of chemical interactions. In: *Review and Integration of Biosphere-Atmosphere Modelling of Reactive Trace Gases and Volatile Aerosols*, ed. by R.-S. Massad, B. Loubet (Springer, Dordrecht 2015)
- 54.109 S.C. Pryor, M. Gallagher, H. Sievering, S.E. Larsen, R.J. Barthelmie, F. Birsan, E. Nemitz, J. Rinne, M. Kulmala, T. Groenholm, R. Taipale, T. Vesala: A review of measurement and modelling results of particle atmosphere-surface exchange, *Tellus B* **60**, 42–75 (2008)
- 54.110 A. Petroff, A. Mailliat, M. Amielh, F. Anselmet: Aerosol dry deposition on vegetative canopies. Part I: Review of present knowledge, *Atmos. Environ.* **42**, 3625–3653 (2008)
- 54.111 W.G.N. Slinn: Predictions for particle deposition to vegetative canopies, *Atmos. Environ.* **16**, 1785–1794 (1982)
- 54.112 R.J.W. Kruit, W.A.J. van Pul, F.J. Sauter, M. van den Broek, E. Nemitz, M.A. Sutton, M. Krol, A.A.M. Holtslag: Modeling the surface-atmosphere exchange of ammonia, *Atmos. Environ.* **44**, 945–957 (2010)
- 54.113 M.A. Sutton, D. Fowler: A model for inferring bi-directional fluxes of ammonia over plant canopies. In: *WMO Conf. Meas. Model. Atmos. Compos. Changes Incl. Pollut. Transp.* (World Meteorological Organization, Geneva 1993) pp. 179–182
- 54.114 T. Foken, G. Skeib: The accuracy and evaluation of profile measurements serving the calculation of the energy exchange, *Z. Meteorol.* **30**, 346–360 (1980)
- 54.115 L. Horvath, Z. Nagy, T. Weidinger: Estimation of dry deposition velocities of nitric oxide, sulfur dioxide, and ozone by the gradient method above short vegetation during the TRACT campaign, *Atmos. Environ.* **32**, 1317–1322 (1998)
- 54.116 F. Nieuwstadt: The computation of the friction velocity u^* and the temperature scale T^* from temperature and wind velocity profiles by least-square methods, *Bound.-Layer Meteorol.* **14**, 235–246 (1978)
- 54.117 H. Müller, G. Kramm, F. Meixner, G.J. Dollard, D. Fowler, M. Possanzini: Determination of HNO₃ dry deposition by modified Bowen-ratio and aerodynamic profile techniques, *Tellus B* **45**, 346–367 (1993)
- 54.118 C.R. Flechard, D. Fowler: Atmospheric ammonia at a moorland site. II: Long-term surface-atmosphere micrometeorological flux measurements, *Q. J. R. Meteorol. Soc.* **124**, 759–791 (1998)
- 54.119 T.P. Meyers, M.E. Hall, S.E. Lindberg, K. Kim: Use of the Modified Bowen-ratio technique to measure fluxes of trace gases, *Atmos. Environ.* **30**, 3321–3329 (1996)
- 54.120 J.R. Dorsey, J.H. Duyzer, M.W. Gallagher, H. Coe, K. Pilegaard, J.H. Weststrate, N.O. Jensen, S. Walton: Oxidized nitrogen and ozone interaction with forests. I: Experimental observations and analysis of exchange with Douglas fir, *Q. J. R. Meteorol. Soc.* **130**, 1941–1955 (2004)
- 54.121 J.H. Duyzer, J.R. Dorsey, M.W. Gallagher, K. Pilegaard, S. Walton: Oxidized nitrogen and ozone interaction with forests. II: Multi-layer process-oriented modelling results and a sensitivity study for Douglas fir, *Q. J. R. Meteorol. Soc.* **130**, 1957–1971 (2004)
- 54.122 U. Rummel, C. Ammann, A. Gut, F.X. Meixner, M.O. Andreae: Eddy covariance measurements of nitric oxide flux within an Amazonian rain forest, *J. Geophys. Res. Atmos.* **107**, LBA 17-11–LBA 17-19 (2002)
- 54.123 A.W. Stelson, J.H. Seinfeld: Relative-humidity and temperature dependence of the ammonium nitrate dissociation constant, *Atmos. Environ.* **16**, 983–992 (1982)
- 54.124 G. Kramm, R. Dlugi: Modeling of the vertical fluxes of nitric acid, ammonia, and ammonium nitrate, *J. Atmos. Chem.* **18**, 319–357 (1994)

- 54.125 N. Mölders, G. Kramm: *Lectures in Meteorology* (Springer, Cham 2014)
- 54.126 J. Vilà-Guerau De Arellano, P.G. Duynkerke: Influence of chemistry on the flux-gradient relationships for the NO–O₃–NO₂ system, *Bound.-Layer Meteorol.* **61**, 375–387 (1992)
- 54.127 G. Damköhler: Der Einfluss der Turbulenz auf die Flammgeschwindigkeit in Gasgemischen, *Z. Elektrochem. Angew. Phys. Chem.* **46**, 601–652 (1940)
- 54.128 A.S. Wexler, J.H. Seinfeld: Analysis of aerosol ammonium nitrate – Departures from equilibrium during SCAQS, *Atmos. Environ. A* **26**, 579–591 (1992)
- 54.129 J.H. Duyzer, G. Deinum, J. Baak: The interpretation of measurements of surface exchange of nitrogen oxides – Correction for chemical reactions, *Philos. Trans. R. Soc. A* **351**, 231–248 (1995)
- 54.130 G. Kramm, R. Dlugi, G.J. Dollard, T. Foken, N. Mölders, H. Müller, W. Seiler, H. Sievering: On the dry deposition of ozone and reactive nitrogen species, *Atmos. Environ.* **29**, 3209–3231 (1995)
- 54.131 WMO: *Guide to Instruments and Methods of Observation, WMO-No. 8, Volume I*, Measurement of Meteorological Variables (World Meteorological Organization, Geneva 2018)
- 54.132 C. Breuninger, R. Oswald, J. Kesselmeier, F.X. Meixner: The dynamic chamber method: Trace gas exchange fluxes (NO, NO₂, O₃) between plants and the atmosphere in the laboratory and in the field, *Atmos. Meas. Tech.* **5**, 955–989 (2012)
- 54.133 W. Eugster, W. Senn: A cospectral correction model for measurement of turbulent NO₂ flux, *Bound.-Layer Meteorol.* **74**, 321–340 (1995)
- 54.134 J.C. Mayer, A. Bargsten, U. Rummel, F.X. Meixner, T. Foken: Distributed modified Bowen ratio method for surface layer fluxes of reactive and non-reactive trace gases, *Agric. For. Meteorol.* **151**, 655–668 (2011)
- 54.135 M. Schmitt, L. Thoni, P. Waldner, A. Thimonier: Total deposition of nitrogen on Swiss long-term forest ecosystem research (LWF) plots: Comparison of the throughfall and the inferential method, *Atmos. Environ.* **39**, 1079–1091 (2005)
- 54.136 K. Matsuda, N. Fukuzaki, M. Maeda: A case study on estimation of dry deposition of sulfur and nitrogen compounds by inferential method, *Water Air Soil Pollut.* **130**, 553–558 (2001)
- 54.137 L.G. Huey, E.J. Dunlea, E.R. Lovejoy, D.R. Hanson, R.B. Norton, F.C. Fehsenfeld, C.J. Howard: Fast time response measurements of HNO₃ in air with a chemical ionization mass spectrometer, *J. Geophys. Res. Atmos.* **103**, 3355–3360 (1998)
- 54.138 D.K. Farmer, P.J. Wooldridge, R.C. Cohen: Application of thermal-dissociation laser induced fluorescence (TD-LIF) to measurement of NO₃, ∑alkyl nitrates, ∑peroxy nitrates, and NO₂ fluxes using eddy covariance, *Atmos. Chem. Phys.* **6**, 3471–3486 (2006)
- 54.139 K. von Bobruzki, C.F. Braban, D. Famulari, S.K. Jones, T. Blackall, T.E.L. Smith, M. Blom, H. Coe, M. Gallagher, M. Ghalaieny, M.R. McGillen, C.J. Percival, J.D. Whitehead, R. Ellis, J. Murphy, A. Mohacsi, A. Pogany, H. Junninen, S. Rantanen, M.A. Sutton, E. Nemitz: Field inter-comparison of eleven atmospheric ammonia measurement techniques, *Atmos. Meas. Tech.* **3**, 91–112 (2010)
- 54.140 M. Norman, C. Spirig, V. Wolff, I. Trebs, C. Flechard, A. Wisthaler, R. Schnitzhofer, A. Hansel, A. Neftel: Intercomparison of ammonia measurement techniques at an intensively managed grassland site (Oensingen, Switzerland), *Atmos. Chem. Phys.* **9**, 2635–2645 (2009)
- 54.141 J. Sintermann, K. Dietrich, C. Hani, M. Bell, M. Jocher, A. Neftel: A miniDOAS instrument optimised for ammonia field measurements, *Atmos. Meas. Tech.* **9**, 2721–2734 (2016)
- 54.142 M. Hanke, B. Umann, J. Uecker, F. Arnold, H. Bunz: Atmospheric measurements of gas-phase HNO₃ and SO₂ using chemical ionization mass spectrometry during the MINATROC field campaign 2000 on Monte Cimone, *Atmos. Chem. Phys.* **3**, 417–436 (2003)
- 54.143 J.G. Porter, W. De Bruyn, E.S. Saltzman: Eddy flux measurements of sulfur dioxide deposition to the sea surface, *Atmos. Chem. Phys.* **18**, 15291–15305 (2018)
- 54.144 P. Stella, B. Loubet, P. Laville, E. Lamaud, M. Cazaunau, S. Laufs, F. Bernard, B. Grosselin, N. Mascher, R. Kurtenbach, A. Mellouki, J. Kleffmann, P. Cellier: Comparison of methods for the determination of NO–O₃–NO₂ fluxes and chemical interactions over a bare soil, *Atmos. Meas. Tech.* **5**, 1241–1257 (2012)
- 54.145 A. Khlystov, G.P. Wyers, J. Slanina: The steam-jet aerosol collector, *Atmos. Environ.* **29**, 2229–2234 (1995)
- 54.146 D.A. Orsini, Y.L. Ma, A. Sullivan, B. Sierau, K. Baumann, R.J. Weber: Refinements to the particle-into-liquid sampler (PILS) for ground and airborne measurements of water soluble aerosol composition, *Atmos. Environ.* **37**, 1243–1259 (2003)
- 54.147 R. Thomas, I. Trebs, R.P. Otjes, P.A.C. Jongejan, H. ten Brink, G. Phillips, M. Kortner, F.X. Meixner, E. Nemitz: An automated analyzer to measure surface-atmosphere exchange fluxes of water soluble inorganic aerosol compounds and reactive trace gases, *Environ. Sci. Technol.* **43**, 1412–1418 (2009)
- 54.148 D.K. Farmer, J.R. Kimmel, G. Phillips, K.S. Docherty, D.R. Worsnop, D. Sueper, E. Nemitz, J.L. Jimenez: Eddy covariance measurements with high-resolution time-of-flight aerosol mass spectrometry: A new approach to chemically resolved aerosol fluxes, *Atmos. Meas. Tech.* **4**, 1275–1289 (2011)
- 54.149 M.J. Deventer, A. Held, T.S. El-Madany, O. Klemm: Size-resolved eddy covariance fluxes of nucleation to accumulation mode aerosol particles over a coniferous forest, *Agric. For. Meteorol.* **214**, 328–340 (2015)
- 54.150 M. Amodio, S. Catino, P.R. Dambruoso, G. de Gennaro, A. Di Gilio, P. Giungato, E. Laiola, A. Marzocca, A. Mazzone, A. Sardaro, M. Tutino: Atmospheric deposition: Sampling procedures, analyt-

- ical methods, and main recent findings from the scientific literature, *Adv. Meteorol.* **2014**, Article ID 161730 (2014)
- 54.151 VDI 2119:2013-06: *Ambient Air Measurements – Sampling of Atmospheric Particles > 2.5 μm on an Acceptor Surface Using the Sigma-2 Passive Sampler* (Beuth, Berlin 2013)
- 54.152 J. Fritsche, G. Wohlfahrt, C. Ammann, M. Zeeman, A. Hammerle, D. Obrist, C. Alewell: Summertime elemental mercury exchange of temperate grasslands on an ecosystem-scale, *Atmos. Chem. Phys.* **8**, 7709–7722 (2008)
- 54.153 S. Osterwalder, J. Fritsche, C. Alewell, M. Schmutz, M.B. Nilsson, G. Jocher, J. Sommar, J. Rinne, K. Bishop: A dual-inlet, single detector relaxed eddy accumulation system for long-term measurement of mercury flux, *Atmos. Meas. Tech.* **9**, 509–524 (2016)
- 54.154 I. Trebs, F.X. Meixner, J. Slanina, R.P. Otjes, P. Jongejan, M.O. Andreae: Real-time measurements of ammonia, acidic trace gases and water-soluble inorganic aerosol species at a rural site in the Amazon basin, *Atmos. Chem. Phys.* **4**, 967–987 (2004)
- 54.155 I.C. Rumsey, J.T. Walker: Application of an online ion-chromatography-based instrument for gradient flux measurements of speciated nitrogen and sulfur, *Atmos. Meas. Tech.* **9**, 2581–2592 (2016)
- 54.156 M.M. Twigg, E. House, R. Thomas, J. Whitehead, G.J. Phillips, D. Famulari, D. Fowler, M.W. Gallagher, J.N. Cape, M.A. Sutton, E. Nemitz: Surface/atmosphere exchange and chemical interactions of reactive nitrogen compounds above a manured grassland, *Agric. For. Meteorol.* **151**, 1488–1503 (2011)
- 54.157 V. Wolff, I. Trebs, C. Ammann, F.X. Meixner: Aerodynamic gradient measurements of the NH_3 - HNO_3 - NH_4NO_3 triad using a wet chemical instrument: An analysis of precision requirements and flux errors, *Atmos. Meas. Tech.* **3**, 187–208 (2010)
- 54.158 A. Moravec, T. Foken, I. Trebs: Application of a GC-ECD for measurements of biosphere-atmosphere exchange fluxes of peroxyacetyl nitrate using the relaxed eddy accumulation and gradient method, *Atmos. Meas. Tech.* **7**, 2097–2119 (2014)
- 54.159 C.R. Flechard, E. Nemitz, R.I. Smith, D. Fowler, A.T. Vermeulen, A. Bleeker, J.W. Erisman, D. Simpson, L. Zhang, Y.S. Tang, M.A. Sutton: Dry deposition of reactive nitrogen to European ecosystems: A comparison of inferential models across the NitroEurope network, *Atmos. Chem. Phys.* **11**, 2703–2728 (2011)
- 54.160 Y.S. Tang, I. Simmons, N. van Dijk, C. Di Marco, E. Nemitz, U. Dammggen, K. Gilke, V. Djuricic, S. Vidic, Z. Gliha, D. Borovecki, M. Mitosinkova, J.E. Hanssen, T.H. Uggerud, M.J. Sanz, P. Sanz, J.V. Chorda, C.R. Flechard, Y. Fauvel, M. Ferm, C. Perrino, M.A. Sutton: European scale application of atmospheric reactive nitrogen measurements in a low-cost approach to infer dry deposition fluxes, *Agric. Ecosyst. Environ.* **133**, 183–195 (2009)
- 54.161 T. Butler, F. Vermeylen, C.M. Lehmann, G.E. Likens, M. Puchalski: Increasing ammonia concentration trends in large regions of the USA derived from the NADP/AMoN network, *Atmos. Environ.* **146**, 132–140 (2016)
- 54.162 J.N. Cape: The use of passive diffusion tubes for measuring concentrations of nitrogen dioxide in air, *Crit. Rev. Anal. Chem.* **39**, 289–310 (2009)
- 54.163 I.J. Simpson, G.W. Thurtell, H.H. Neumann, G. Den Hartog, G.C. Edwards: The validity of similarity theory in the roughness sublayer above forests, *Bound.-Layer Meteorol.* **87**, 69–99 (1998)
- 54.164 A.S. Thom: Vegetation and the atmosphere. In: *Momentum, Mass and Heat Exchange*, ed. by J.L. Moneith (Academic Press, Chichester 1975) pp. 57–109
- 54.165 S. Ban, K. Matsuda, K. Sato, T. Ohizumi: Long-term assessment of nitrogen deposition at remote EANET sites in Japan, *Atmos. Environ.* **146**, 70–78 (2016)
- 54.166 T. Totsuka, H. Sase, H. Shimizu: Major activities of acid deposition monitoring network in East Asia (EANET) and related studies. In: *Plant Responses to Air Pollution and Global Change*, ed. by K. Omasa, I. Nouchi, L.J. De Kok (Springer, Tokyo 2005) pp. 251–259
- 54.167 M. Adon, C. Galy-Lacaux, C. Delon, V. Yoboue, F. Solmon, A.T.K. Tchuente: Dry deposition of nitrogen compounds (NO_2 , HNO_3 , NH_3), sulfur dioxide and ozone in West and Central African ecosystems using the inferential method, *Atmos. Chem. Phys.* **13**, 11351–11374 (2013)
- 54.168 C. Galy-Lacaux, C. Delon: Nitrogen emission and deposition budget in West and Central Africa, *Environ. Res. Lett.* **9**, 125002 (2014)
- 54.169 D.A. Gay, D. Schmeltz, E. Prestbo, M. Olson, T. Sharac, R. Tordon: The atmospheric mercury network: Measurement and initial examination of an ongoing atmospheric mercury record across North America, *Atmos. Chem. Phys.* **13**, 11339–11349 (2013)
- 54.170 X. Lan, R. Talbot, M. Castro, K. Perry, W. Luke: Seasonal and diurnal variations of atmospheric mercury across the US determined from AMNet monitoring data, *Atmos. Chem. Phys.* **12**, 10569–10582 (2012)
- 54.171 A.L. Zbieranowski, J. Aherne: Long-term trends in atmospheric reactive nitrogen across Canada: 1988–2007, *Atmos. Environ.* **45**, 5853–5862 (2011)
- 54.172 L. Zhang, R. Vet, J.M. O'Brien, C. Mihele, Z. Liang, A. Wiebe: Dry deposition of individual nitrogen species at eight Canadian rural sites, *J. Geophys. Res. Atmos.* **114**, D02301 (2009)
- 54.173 D. Schwede, L.M. Zhang, R. Vet, G. Lear: An inter-comparison of the deposition models used in the CASTNET and CAPMoN networks, *Atmos. Environ.* **45**, 1337–1346 (2011)
- 54.174 R.E. Baumgardner, T.F. Lavery, C.M. Rogers, S.S. Isil: Estimates of the atmospheric deposition of sulfur and nitrogen species: Clean air status and trends network, 1990–2000, *Environ. Sci. Technol.* **36**, 2614–2629 (2002)

- 54.175 J.F. Clarke, E.S. Edgerton, B.E. Martin: Dry deposition calculations for the clean air status and trends network, *Atmos. Environ.* **31**, 3667–3678 (1997)
- 54.176 C.M. Rogers, T.F. Lavery, M.O. Stewart, W.R. Barnard, H.K. Howell: CASTNET methodology for modeling dry and total deposition. In: *Air Pollution Modeling and Its Application XXIII*, Springer Proceedings in Complexity, (Springer, Cham 2014) pp. 49–53
- 54.177 D.B. Schwede, G.G. Lear: A novel hybrid approach for estimating total deposition in the United States, *Atmos. Environ.* **92**, 207–220 (2014)
- 54.178 M. Engardt, D. Simpson, M. Schwikowski, L. Granat: Deposition of sulphur and nitrogen in Europe 1900–2050. Model calculations and comparison to historical observations, *Tellus B* **69**, 1328945 (2017)
- 54.179 A.G. Hjellbrekke, L. Tarrason: Mapping of concentrations in Europe combining measurements and acid deposition models, *Water Air Soil Pollut.* **130**, 1529–1534 (2001)
- 54.180 K. Tørseth, W. Aas, K. Breivik, A.M. Fjæraa, M. Fiebig, A.G. Hjellbrekke, C. Lund Myhre, S. Solberg, K.E. Yttri: Introduction to the European monitoring and evaluation programme (EMEP) and observed atmospheric composition change during 1972–2009, *Atmos. Chem. Phys.* **12**, 5447–5481 (2012)
- 54.181 A. Ryaboshapko, I. Ilyin, A. Gusev, O. Afinogenova: *Mercury in the Atmosphere of Europe: Concentrations, Deposition Patterns, Transboundary Fluxes* (Meteorological Synthesizing Centre-East, Moscow 1998), EMEP/MSC-E Report 7/98
- 54.182 T.P. Meyers, P. Finkelstein, J. Clarke, T.G. Ellestad, P.F. Sims: A multilayer model for inferring dry deposition using standard meteorological measurements, *J. Geophys. Res. Atmos.* **103**, 22645–22661 (1998)
- 54.183 WMO: *Global Atmosphere Watch (GAW) Implementation Plan: 2016–2023* (World Meteorological Organization, Geneva 2017), GAW Report No. 228
- 54.184 N. Beier, R. Schneewind: Chemical reactions of gases in tubes of probing systems and their influence on measured concentrations, *Ann. Geophys.* **9**, 703–707 (1991)
- 54.185 R.D. Saylor, G.M. Wolfe, T.P. Meyers, B.B. Hicks: A corrected formulation of the multi layer model (MLM) for inferring gaseous dry deposition to vegetated surfaces, *Atmos. Environ.* **92**, 141–145 (2014)
- 54.186 G.P. Wyers, J.W. Erisman: Ammonia exchange over coniferous forest, *Atmos. Environ.* **32**, 441–451 (1998)
- 54.187 I.C. Rumsey, K.A. Cowen, J.T. Walker, T.J. Kelly, E.A. Hanft, K. Mishoe, C. Rogers, R. Proost, G.M. Beachley, G. Lear, T. Frelink, R.P. Otjes: An assessment of the performance of the monitor for aerosols and gases in ambient air (Marga): A semi-continuous method for soluble compounds, *Atmos. Chem. Phys.* **14**, 5639–5658 (2014)
- 54.188 B. Stieger, G. Spindler, B. Fahlbusch, K. Müller, A. Gruner, L. Poulain, L. Thoni, E. Seitler, M. Wal-
lasch, H. Herrmann: Measurements of PM₁₀ ions and trace gases with the online system MARGA at the research station Melpitz in Germany – A five-year study, *J. Atmos. Chem.* **75**, 33–70 (2018)
- 54.189 P.M. Vitousek, J.D. Aber, R.W. Howarth, G.E. Likens, P.A. Matson, D.W. Schindler, W.H. Schlesinger, D. Tilman: Human alteration of the global nitrogen cycle: Sources and consequences, *Ecol. Appl.* **7**, 737–750 (1997)
- 54.190 J.W. Erisman, J.N. Galloway, S. Seitzinger, A. Bleeker, N.B. Dise, A.M.R. Petrescu, A.M. Leach, W. de Vries: Consequences of human modification of the global nitrogen cycle, *Philos. Trans. R. Soc. B* **368**, 20130116 (2013)
- 54.191 S. Avnery, D.L. Mauzerall, J.F. Liu, L.W. Horowitz: Global crop yield reductions due to surface ozone exposure: 2. Year 2030 potential crop production losses and economic damage under two scenarios of O₃ pollution, *Atmos. Environ.* **45**, 2297–2309 (2011)
- 54.192 M.L. Hillstrom, R.L. Lindroth: Elevated atmospheric carbon dioxide and ozone alter forest insect abundance and community composition, *Insect Conserv. Divers.* **1**, 233–241 (2008)
- 54.193 D.W. Johnson, J. Turner: Nitrogen budgets of forest ecosystems: A review, *For. Ecol. Manag.* **318**, 370–379 (2014)
- 54.194 U. Skiba, J. Drewer, Y.S. Tang, N. van Dijk, C. Helfter, E. Nemitz, D. Famulari, J.N. Cape, S.K. Jones, M. Twigg, M. Pihlatie, T. Vesala, K.S. Larsen, M.S. Carter, P. Ambus, A. Ibrom, C. Beier, A. Hensen, A. Frumau, J.W. Erisman, N. Brüggemann, R. Gasche, K. Butterbach-Bahl, A. Neftel, C. Spirig, L. Horvath, A. Freibauer, P. Cellier, P. Laville, B. Loubet, E. Magliulo, T. Bertolini, G. Seufert, M. Andersson, G. Manca, T. Laurila, M. Aurela, A. Lohila, S. Zechmeister-Boltenstern, B. Kitzler, G. Schaufler, J. Siemens, R. Kindler, C. Flechard, M.A. Sutton: Biosphere-atmosphere exchange of reactive nitrogen and greenhouse gases at the NitroEurope core flux measurement sites: Measurement strategy and first data sets, *Agric. Ecosyst. Environ.* **133**, 139–149 (2009)
- 54.195 C. Ammann, C. Spirig, J. Leifeld, A. Neftel: Assessment of the nitrogen and carbon budget of two managed temperate grassland fields, *Agric. Ecosyst. Environ.* **133**, 150–162 (2009)
- 54.196 V. Wolff, I. Trebs, T. Foken, F.X. Meixner: Exchange of reactive nitrogen compounds: Concentrations and fluxes of total ammonium and total nitrate above a spruce canopy, *Biogeosciences* **7**, 1729–1744 (2010)
- 54.197 E. Nemitz, M.A. Sutton: Gas-particle interactions above a Dutch heathland: III. Modelling the influence of the NH₃-HNO₃-NH₄NO₃ equilibrium on size-segregated particle fluxes, *Atmos. Chem. Phys.* **4**, 1025–1045 (2004)
- 54.198 E. Nemitz, C. Milford, M.A. Sutton: A two-layer canopy compensation point model for describing bi-directional biosphere-atmosphere exchange of ammonia, *Q. J. R. Meteorol. Soc.* **127**, 815–833 (2001)

- 54.199 G. Spindler, U. Teichmann, M.A. Sutton: Ammonia dry deposition over grassland – Micrometeorological flux–gradient measurements and bidirectional flux calculations using an inferential model, *Q. J. R. Meteorol. Soc.* **127**, 795–814 (2001)
- 54.200 M. Mueller, J. Meyer, C. Hueglin: Design of an ozone and nitrogen dioxide sensor unit and its long-term operation within a sensor network in the city of Zurich, *Atmos. Meas. Tech.* **10**, 3783–3799 (2017)
- 54.201 D.J. Miller, K. Sun, L. Tao, M.A. Khan, M.A. Zondlo: Open-path, quantum cascade-laser-based sensor for high-resolution atmospheric ammonia measurements, *Atmos. Meas. Tech.* **7**, 81–93 (2014)
- 54.202 E. Dammers, M. Schaap, M. Haaime, M. Palm, R.J.W. Kruit, H. Volten, A. Hensen, D. Swart, J.W. Erisman: Measuring atmospheric ammonia with remote sensing campaign: Part 1 – Characterisation of vertical ammonia concentration profile in the centre of the Netherlands, *Atmos. Environ.* **169**, 97–112 (2017)
- 54.203 M. Aikawa, T. Hiraki, M. Tamaki: Estimation of the amount of dry deposition in an urban area (Kobe City, Japan) by the inferential method, *Environ. Chem. Lett.* **3**, 62–65 (2005)
- 54.204 H.B. Wang, F.M. Yang, G.M. Shi, M. Tian, L.M. Zhang, L.Y. Zhang, C.A. Fu: Ambient concentration and dry deposition of major inorganic nitrogen species at two urban sites in Sichuan Basin, China, *Environ. Pollut.* **219**, 235–244 (2016)
- 54.205 M.M. Cheng, H. Jiang, Z. Guo, X.Y. Zhang, X.H. Lu: Estimating NO₂ dry deposition using satellite data in Eastern China, *Int. J. Remote Sens.* **34**, 2548–2565 (2013)
- 54.206 J.A. Geddes, R.V. Martin: Global deposition of total reactive nitrogen oxides from 1996 to 2014 constrained with satellite observations of NO₂ columns, *Atmos. Chem. Phys.* **17**, 10071–10091 (2017)
- 54.207 Y.L. Jia, G.R. Yu, Y.N. Gao, N.P. He, Q.F. Wang, C.C. Jiao, Y. Zuo: Global inorganic nitrogen dry deposition inferred from ground- and space-based measurements, *Sci. Rep.* **6**, 19810 (2016)

Ivonne Trebs

Environmental Research and Innovation (ERIN)
Luxembourg Institute of Science and Technology (LIST)
Belvaux, Luxembourg
ivonne.trebs@list.lu



Working as a lead engineer in the Environmental Research and Innovation Department of the Luxembourg Institute of Science and Technology (LIST), Ivonne Trebs measures and models evapotranspiration from the biosphere. She is a recipient of the Otto Hahn Medal of the Max Planck Society, and was a MINERVA Junior Research Group Leader at the Max Planck Institute for Chemistry, where she studied the surface–atmosphere exchange of reactive nitrogen compounds.

Christof Ammann

Climate and Agriculture
Agroscope Research Institute
Zürich, Switzerland
christof.ammann@agroscope.admin.ch



Christof Ammann is Senior Scientist at the Swiss Federal Research Institute Agroscope, and leads a research team on agricultural greenhouse gas emissions. His interdisciplinary research focuses on field measurements of the exchange of reactive/nonreactive trace gases between the biosphere and the atmosphere using various measurement techniques. Since 2011, he has been a member of the Swiss Federal Commission on Air Hygiene—the clean air advisory board of the Swiss Government.



Jürgen Junk

Environmental Research and Innovation (ERIN)
Luxembourg Institute of Science and Technology (LIST)
Belvaux, Luxembourg
juergen.junk@list.lu

Jürgen Junk is a climatologist who has been working at the Luxembourg Institute of Science and Technology (LIST) since 2007. He received his PhD from the University of Trier (Germany) in 2010 and is now responsible for LIST's air quality projects. He has a special interest in biometeorology, in particular the behavior of nanoparticles in the near-surface atmosphere, their chemical compositions, and their impact on human health.

Eddy-Covariance

55. Eddy-Covariance Measurements

Matthias Mauder , Thomas Foken , Marc Aubinet , Andreas Ibrom 

The eddy-covariance method represents the only direct way to measure the turbulent fluxes of momentum, temperature, trace gases, and particles between the land surface and the atmosphere. It is a direct measurement of the net carbon-dioxide budget and dry deposition. For that purpose, it is widely used in networks of long-term ecosystem observatories around the world and is the centerpiece of intensive field campaigns investigating biosphere-atmosphere exchange processes. The instrumentation typically consists of a 3-D sonic anemometer/thermometer and one or more additional gas analyzers that are able to measure the high-frequency fluctuations of the scalar to be transported. These instruments are mounted on a meteorological mast to sample the turbulent field under the assumption that eddies are carried along with the mean wind. Further prerequisites of the method are horizontal homogeneity, steady-state conditions and well-developed turbulence. For successful application of the method, a series of quality tests and flux corrections is required, which will be presented together with commonly used instrumentation and postprocessing software. Moreover, we will provide a historical overview and provide guidelines for site selection and setup and the necessary maintenance procedures.

55.1	Measurement Principles and Variables	1474
55.1.1	Principles of Flux Measurements.....	1474
55.1.2	Measurement Variables.....	1474
55.1.3	Site Considerations.....	1476
55.2	History	1477
55.3	Theory	1478
55.3.1	Conservation Equations and General Definitions.....	1478
55.3.2	Flux Calculation, Corrections, and Conversions.....	1479
55.3.3	Overall Data Corrections and Data Handling.....	1485
55.4	Devices and Systems	1486
55.4.1	Sonic Anemometers.....	1486
55.4.2	Measurement of the Sensible Heat Flux.....	1486
55.4.3	Measurement of the Latent Heat Flux.....	1486
55.4.4	Measurement of the CO ₂ Flux and Fluxes of Other Air Constituents ..	1487
55.4.5	Guidelines for Designing an Eddy-Covariance System	1487
55.4.6	Advantages and Disadvantages of the Different Trace Gas Sensors and Installations.....	1488
55.5	Specifications	1489
55.6	Quality Control	1489
55.6.1	Calibration of Turbulence Sensors	1489
55.6.2	Specific Quality Control Methods.....	1489
55.6.3	Uncertainty Assessment	1492
55.7	Maintenance	1494
55.8	Application	1494
55.8.1	Intensive Measurement Campaigns and Process Studies.....	1494
55.8.2	Long-Term Measurements of Greenhouse-Gas Exchange Between Terrestrial Ecosystems and the Atmosphere.....	1494
55.9	Future Developments	1495
55.9.1	Energy Balance Closure Problem	1495
55.9.2	Correction and of Probe-Induced Flow Distortion Effects and Sensor Optimizations	1495
55.9.3	Spatial Eddy Covariance, Eddy Covariance from Lidar Measurements ..	1495
55.10	Further Readings	1496
	References	1496

Turbulent energy and matter fluxes between the land surface and the atmosphere are of increasing interest for climate and ecological studies. The components of the energy balance are important forcing parameters for both areas of research. Particularly, direct measurement of the latent heat flux is one of the most important quantities (Chap. 57). In the context of climate change research, also the fluxes of other greenhouse gases, mainly carbon dioxide and methane, and the dynamics of ecosystems have become highly important ([55.1]; Chap. 64). Therefore, the eddy-covariance technique has become widely used as the only direct method for measuring biosphere-

atmosphere exchange on the ecosystem scale. It is typically applied in the surface layer, which is approximately 20–50 m high in the case of unstable stratification and a few meters in stable stratification [55.2, 3]. In this layer, fluxes are approximately constant with height, and atmospheric turbulence is the dominant transport mechanism; hence, measurements taken on different ground-based platforms (Chap. 6) are assumed to be representative of underlying surface fluxes. Besides these ground-based systems, the eddy-covariance method can also be used on tall towers and airborne platforms for measuring fluxes over larger areas (Chap. 48).

55.1 Measurement Principles and Variables

This section describes the basics of the eddy-covariance method and the dimensions and transformations of different units, mainly for scalar fluxes.

55.1.1 Principles of Flux Measurements

The description of turbulent fluxes in the following theory Sect. 55.3 requires the decomposition of the time series of each variable x into a mean part, \bar{x} , and a fluctuating part, x' , the so-called Reynolds decomposition (Fig. 55.1). This can be written as

$$x = \bar{x} + x', \quad (55.1)$$

where

$$\bar{x} = \frac{1}{T} \int_t^{t+T} x(t') dt', \quad (55.2)$$

where t is the time and T the averaging interval.

Under several assumptions, notably ergodicity and steady-state conditions (Sect. 55.3.1), the vertical flux within an averaging interval of approximately 10–30 min may be given by

$$F_x = \overline{wx} = \overline{w\bar{x}} + \overline{w'x'}, \quad (55.3)$$

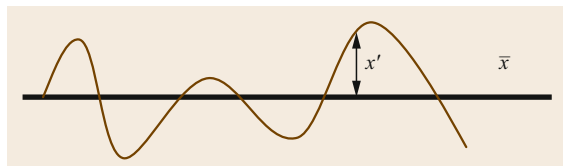


Fig. 55.1 Reynolds decomposition of the value x into its mean part \bar{x} and its fluctuation, x' (after [55.2])

where w is the vertical wind velocity component, and x is either the horizontal wind velocity u in the direction of the mean flow in the case of a momentum flux or a scalar in the case of scalar fluxes, such as the sensible heat flux, the latent heat flux, or trace gas fluxes. Typically, sampling frequencies of about 10–20 Hz are used in order to capture the smallest relevant turbulent fluctuations. This flux is identical to the covariance

$$\overline{w'x'} = \frac{1}{N-1} \left[\sum_i (w_i - \bar{w})(x_i - \bar{x}) \right], \quad (55.4)$$

when the product of the mean values in (55.3) is zero, e.g., for the vertical flux in the horizontally homogeneous case, where $\bar{w} = 0$ (for simplicity, some known effects that challenge this condition were neglected).

55.1.2 Measurement Variables

An overview of the variables measured with the eddy-covariance technique is provided in Table 55.1. Scalars are measured in different units by the different types of devices. These quantities are related by the ideal gas and the Dalton laws.

Only the dry molar mixing ratio and the dry mass mixing ratio are conserved quantities in the presence of changes in temperature, pressure, and water vapor content [55.6]. The dry mass mixing ratio can be transformed into the dry molar mixing ratio through a multiplication by the molar mass ratio of dry air to component s . Unfortunately, out of the above mentioned variables, only the mass density and molar density are directly measured in the field by gas analyzers (Table 55.3). Since these quantities are not conserved during heat conduction, air compression/expansion or evaporation/condensation and water vapor diffusion,

Table 55.1 Measured variables with turbulence sensors with 10–20 Hz sampling frequency, including alternative names for the same quantities, which are sometimes used in ecological applications, in round brackets [55.4]

Variable	Description and sensor	Symbol	Unit
Vertical wind velocity	Sonic anemometer (Chap. 9)	w	m s^{-1}
Horizontal wind components	Sonic anemometer (Chap. 9)	u, v	m s^{-1}
Temperature	Cold wire thermometer (Chap. 7)	T	K
Sonic temperature	Temperature calculated from the speed of sound; sonic anemometer (Chap. 9)	T_s	K
Scalar: mass density (mass concentration)	Gas analyser (Chaps. 8 and 16)	ρ_s	kg m^{-3}
Dry air mass density	Thermometer, hygrometer, pressure sensor (Chaps. 7, 8 and 10)	ρ_d	kg m^{-3}
Scalar: molar density (molar concentration)	Gas analyzer (Chaps. 8 and 16)	c_s	mol m^{-3}
Scalar: molar mixing ratio	The ratio of the constituent mole number to the total number in the mixture; gas analyser (Chaps. 8 and 16)	χ	mol mol^{-1}
Scalar: dry molar mixing ratio (molar dry fraction)	The ratio of the constituent mole number to those of dry air; gas analyzer (Chaps. 8 and 16)	χ_s	mol mol^{-1}
Scalar: dry mass mixing ratio (mass dry fraction)	The ratio of the mass of the constituent to the mass of dry air; gas analyzer (Chaps. 8 and 16)	χ_{sm}	kg kg^{-1}

Table 55.2 Typical fluxes measured with the eddy-covariance method

Flux	Description and calculation	Symbol	Dimension
Shear stress	Component of the stress tensor in the direction of the mean wind velocity $\tau = \rho \sqrt{(\overline{w'u'})^2 + (\overline{w'v'})^2} \approx -\rho \overline{w'u'_h}$ with u'_h : wind velocity fluctuation in direction of the mean horizontal wind velocity	τ	$\text{kg m}^{-1} \text{s}^{-2}$
Friction velocity	Shear stress in the dimension of a velocity $u_* = \sqrt[4]{(\overline{w'u'})^2 + (\overline{w'v'})^2} = \sqrt{-\overline{w'u'_h}}$	u_*	m s^{-1}
Buoyancy flux ^a	The flux includes the buoyancy effect by temperature and humidity, ignoring the small difference between the sonic temperature and virtual temperature (Chap. 7)	$\overline{w'T'_s}$	m K s^{-1}
Sensible heat flux ^a	For calculation from buoyancy flux, see Sect. 55.3.2	$\overline{w'T'}$	m K s^{-1}
Latent heat flux ^b	Water vapor flux with water vapor partial pressure e or specific humidity q (Chap. 8)	$\overline{w'e'}$ $\overline{w'q'}$	hPa m s^{-1} $\text{kg kg}^{-1} \text{m s}^{-1}$
Trace gas fluxes	Trace gas flux in different units dependent on the sensor (Chaps. 8 and 16), see Tables 55.1 and 55.3	$\overline{w'c'_s}$ $\overline{w'\rho'_s}$ $\overline{w'\chi'_s}$ $\overline{w'\chi'_{sm}}$	$\text{mol m}^{-2} \text{s}^{-1}$ $\text{kg m}^{-2} \text{s}^{-1}$ $\text{m mol mol}^{-1} \text{s}^{-1}$ $\text{m mol mol}^{-1} \text{s}^{-1}$

^a Transformation in energetic units for sensible heat flux (buoyancy flux), for details, see Chap. 5

$$Q_H = c_p \rho \overline{w'T'} = c_p \frac{p}{R_d T_v} \overline{w'T'} = 1004.832 \frac{p}{287.0586 T_v} \overline{w'T'} \quad [\text{W m}^{-2}],$$

c_p : specific heat at constant pressure, ρ : air density, R_d : gas constant for dry air, T_v : virtual temperature (can be replaced by T with an error < 1% on the resulting flux)

^b Transformation in energetic units for latent heat flux; for details, see Chap. 5

$$Q_E = \lambda \rho \overline{w'q'} = \lambda \frac{p}{287.0586 T} \overline{w'q'} = \lambda \frac{p}{287.0586 T} \frac{0.62198}{p} \overline{w'e'} \quad [\text{W m}^{-2}].$$

Table 55.3 Conversion factors between different variables characterizing scalar intensity (use p in hPa in the following equations) [55.5], alternative names for the same quantities, which are sometimes used in ecological applications, are provided in round brackets [55.4]

	Dry molar mixing ratio (molar dry fraction, dry air mole fraction) χ_s (mol mol ⁻¹)	Dry mass mixing ratio (mass dry fraction) χ_{sm} (kg kg ⁻¹)	Molar density (molar concentration) c_s (mol m ⁻³)	Mass density (mass concentration) ρ_s (kg m ⁻³)
χ_s	1	$\frac{m_s}{m_d} = \frac{m_s}{0.0289645}$	$\frac{p_d}{R^*T} \approx \frac{p \times 100}{8.3145T}$	$\frac{m_s p_d}{R^*T} \approx \frac{m_s p \times 100}{8.3145T}$
χ_{sm}	$\frac{m_d}{m_s} = \frac{0.0289645}{m_s}$	1	$\frac{m_d p_d}{m_s R^*T} \approx \frac{p \times 100}{287.0586 m_s T}$	$\frac{m_d p_d}{R^*T} \approx \frac{p \times 100}{287.0586T}$
c_s	$\frac{R^*T}{p_d} \approx \frac{8.3145T}{p \times 100}$	$\frac{m_s R^*T}{m_d p_d} \approx \frac{287.0586 m_s T}{p \times 100}$	1	m_s
ρ_s	$\frac{R^*T}{m_s p_d} \approx \frac{8.3145T}{m_s p \times 100}$	$\frac{R^*T}{m_d p_d} \approx \frac{287.0586T}{p \times 100}$	$\frac{1}{m_s}$	1

variations may appear even in the absence of production, absorption, or transport of the respective measured component in the atmosphere. The necessary corrections [55.7–9] will be discussed in Sect. 55.3.2.

The typical fluxes measured with the eddy-covariance technique are shown in Table 55.2, and the calculation of different units for scalars is given in Table 55.3. Thereby the transformation from the dry molar mixing ratio or dry mass mixing ratio into molar density or mass density is only an approximation, shown for the example of the calculation of the mass density from the dry mass mixing ratio

$$\rho_s = \frac{m_s p_d}{R^*T} = \chi_{sm} \frac{m_d p_d}{R^*T}, \tag{55.5}$$

where R^* is the universal gas constant, m_s is the molar mass of the scalar, p_d is the partial pressure of dry air, and m_d is the molar mass of dry air.

The pressure of dry air is not available and must be replaced by the difference of the air pressure and the partial pressure of water vapor ($p - e$) for which an approximation with the virtual temperature (T_v) (Chaps. 7 and 8) is possible

$$\begin{aligned} T_v &= T \left(1 + q \frac{R_w - R_d}{R_d} \right) = T(1 + 0.608q) \\ &\approx T \left(1 + 0.38 \frac{e}{p} \right), \end{aligned} \tag{55.6}$$

with the specific humidity q , and R_w and R_d the gas constants for water and dry air, respectively. The error of the above approximation is negligible in comparison to the error of using p instead of p_d , since

$$p_d = (p - e) = p - p \frac{T_v - T}{0.38T} = p \left(1 - \frac{T_v - T}{0.38T} \right). \tag{55.7}$$

According to Table 5.18 the virtual temperature excess $T_v - T$ of saturated humid air is in the order of about 1–5 K. Therefore, the second summand of (55.7) is in the order of about 0.01–0.05, following the error of this approximation is maximal 5% but in most of the cases < 2%. The calculations according to Table 55.3 are only possible for mean quantities. For fluctuations of the scalars, the fluctuations of temperature and water vapor must be taken into account ([55.6, 9], Sect. 55.3.2).

55.1.3 Site Considerations

The assumptions of horizontally homogeneous surfaces and steady-state conditions are the most limiting factors with respect to site considerations. Surface representative eddy-covariance flux measurements require a certain extension of the homogeneous area (*fetch*) in the wind direction and the footprint (source weight distribution function, see Chap. 1) area, which should be over a uniform underlying surface to match the requirements for all stability conditions. Both effects from internal boundary layers and influences by obstacles should be avoided (Chap. 1). The fetch requirement is most critical for the selection of the measurement site and the measurement height above the surface. This is especially relevant for forest sites, where additional characteristics of tall vegetation must be taken into account. Here, it is primarily important to place the eddy-covariance system either above the roughness sublayer (Chap. 1) or within the upper part of the roughness sublayer, because otherwise, the measured flux may be disturbed by effects from single roughness elements and no longer represents the flux from the entire ecosystem under study. Additionally, in the lower parts of the roughness sublayer, Monin–Obukhov similarity is no longer applicable, which is prerequisite for some of the necessary flux corrections.

55.2 History

The eddy-covariance method was proposed by *Raymond B. Montgomery* (1910–1988) [55.10], *William Christopher Swinbank* (1913–1973) [55.11], and *Alexander Mikhailovich Obukhov* (1918–1989) [55.12] for measuring exchanges of heat, mass, and momentum between a flat, horizontally homogeneous surface and the overlying atmosphere. For such an ideal surface, the net transport between the surface and atmosphere can be treated as 1-D, and the vertical flux density represents the total flux, which can be calculated by the covariance between turbulent fluctuations of the vertical wind speed and the quantity of interest.

Instrumentation limitations hampered the early implementation of this approach. In 1949, *Konstantinonov* [55.12] developed a wind vane with two hot-wire anemometers to measure the shear stress (Fig. 55.2). A similar instrument – but already for the sensible and latent heat flux – was constructed by *W.C. Swinbank* [55.11] in 1951 (Fig. 55.3). First, time series of the fluctuations of wind direction, wind velocity, temperature, and humidity were shown, and even the sensible heat flux was calculated from this data. Significant problems were the different response times of the sensors and the problem of the fast registration. At the time, and in the following 10–15 years, the time series were recorded with a galvanometer with a mirror on photographic paper. This system was updated in Australia by the middle of the 1960s, e.g., with a propeller anemometer for the measurement of the vertical wind fluctuation with a similar response time to the thermocouples [55.13, 14].

The full potential of the eddy-covariance method only emerged after the development of sonic anemometers, for which the basic equations were given by *Richard M. Schotland* (1927–2006) [55.16]. After the development of the first sonic thermometer [55.17], a vertical

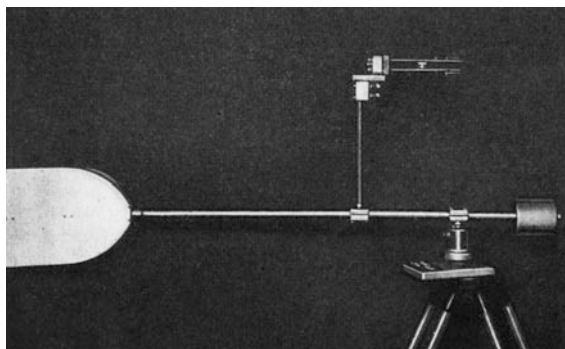


Fig. 55.2 Wind vane with two hot wire anemometers (90° angle) for the measurement of the friction velocity based on *Konstantinonov's* work in 1949 (after [55.12, 15])

sonic anemometer with a 1 m path length [55.18] was used during the O'Neill experiment in 1953 [55.19]. The design of today's anemometers was developed by *Viktor Markovich Bovscheverov* (1905–1995) [55.20], and later by *Jagadish Chandran Kaimal* (1930–2021) and *Jost A. Businger* [55.21] and *Yasushi Mitsuta* [55.22]. These phase-shift anemometers have now been replaced by running time anemometers with delay time measurements [55.23]. For more details of the development of sonic anemometer technique see Chap. 9.

Early micrometeorological experiments in the 1950s to 1970s were designed to study fundamental aspects of atmospheric turbulence over homogeneous surfaces [55.24–26], whereas studies in the 1980s investigated the turbulent fluxes of momentum, and sensible and latent heat over heterogeneous surfaces. Similar experiments were conducted in the USA (FIFE, [55.27]), France (HAPEX, [55.28]), and in Russia (KUREX, [55.29]). These experiments became the basis of many further micrometeorological experiments [55.2] that needed researchers who were highly experienced in micrometeorology and sensor handling. During this period also most of the necessary theory, corrections, and quality tests were developed; see Sect. 55.3.

At the beginning of the 1990s, the first closed and open-path gas analyzers were commercially available mainly for water vapor and carbon dioxide and replaced custom-made sensors (for the history of fast response humidity sensors: Chap. 8; for all other trace gases: Chap. 16).

The technical feasibility of continuous eddy-flux measurements arose in the 1990s with the development of new generation sonic anemometers [55.55, 62]

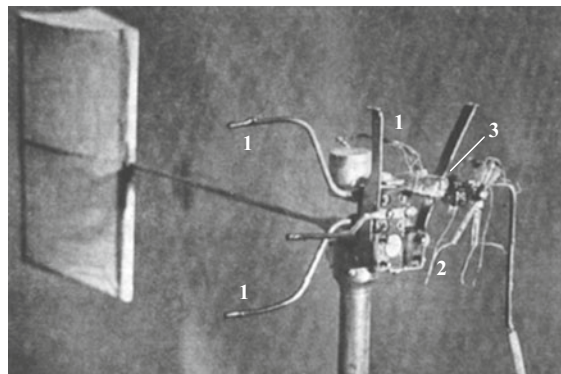


Fig. 55.3 Wind vane with 1 μm hot-wire anemometer (1) together with a wet bulb thermocouple (2) and a thermocouple for air temperature measurements (3) according to *W.C. Swinbank* in 1951 (after [55.11]) © American Meteorological Society, used with permission

Table 55.4 Historical milestones in the development of the eddy-covariance method [55.5]

Year	Historical milestone	References	Chapter
1950s	Theoretical basis of the eddy-covariance method	Montgomery [55.10], Swinbank [55.11], Obukhov [55.12]	
1960s	3-D sonic anemometer	Bovscheverov and Voronov [55.20], Kaimal and Businger [55.21], Mitsuta [55.22]	Chap. 9
1970s	Instrumental requirements Gas analyzer for water vapor (ultraviolet, UV)	McBean [55.30] Buck [55.31], Kretschmer and Karpovitsch [55.32], Martini et al. [55.33]	Chap. 8
1980s	Gas analyzer for water vapor (infrared, IR), based on <i>Elagina</i> [55.34] Corrections: effect of the air density, sonic temperature, high-frequency spectral loss Gas analyzer for carbon dioxide (IR) Real-time data processing software	Hyson and Hicks [55.35], Raupach [55.36] Webb et al. [55.9], Schotanus et al. [55.37], Moore [55.38] Ohtaki and Matsui [55.39], Elagina and Lazarev [55.40] McMillen [55.41]	Chap. 8 Chaps. 8 and 16
1990s	1 and 2-D source areas for flux measurements (footprint), based on <i>Gash</i> [55.42] Correction: low-frequency spectral loss Relaxed eddy-accumulation method, based on <i>Desjardins</i> [55.47] Coordinate rotation, based on <i>Kaimal and Haugen</i> [55.49] Influence of tubing of closed path sensors Theoretical basis for flux footprints and sampling strategies Addressing the problem of the unclosed energy balance at the surface Quality tests for eddy-covariance data, based on <i>Zubkovskij</i> [55.56] Addressing the problem of vertical advection Methodology for FLUXNET network (EuroFlux) Organization of an international network (FLUXNET)	Schmid and Oke [55.43], Schuepp et al. [55.44] Desjardins et al. [55.45], Oncley et al. [55.46] Businger and Oncley [55.48] Kaimal and Finnigan [55.50], Wilczak et al. [55.51] Leuning and Moncrieff [55.52] Horst and Weil [55.53], Lenschow et al. [55.54] Foken and Oncley [55.55] Foken and Wichura [55.57], Vickers and Mahrt [55.58] Lee [55.59] Aubinet et al. [55.60] Baldochi et al. [55.61]	Chap. 1 Chap. 56 Chap. 64

and infrared gas analyzers for water vapor and carbon dioxide, reliable and sufficiently fast data acquisition systems, together with the first comprehensive software packages for the eddy-covariance method [55.41]. In the early 1990s, the eddy-covariance method became more and more widely used by the ecological community for the measurement of the energy, carbon dioxide, and water vapor exchange between ecosystems and the atmosphere. The first long-term measuring towers

were installed, which formed the seed for the international FLUXNET network [55.61], and introductions into the eddy-covariance method for nonmicrometeorologists were written [55.60, 63, 64]. In parallel, the development of new analyzer types allowed an extension of the investigated trace gas spectrum and even atmospheric particles (Chaps. 8, 16, 17, and 18).

Some milestones in the development of the eddy-covariance method are given in Table 55.4.

55.3 Theory

The theory of the eddy-covariance technique is the subject of several textbooks [55.2, 3, 65, 66], which also contain many references to further papers. Therefore, only the most important topics are briefly discussed in this section.

55.3.1 Conservation Equations and General Definitions

Conservation equations for dry air mass, momentum, temperature, and air constituents are given in the lit-

erature [55.3, 65, 67]. Since the method is not applied directly at the surface, which exchanges scalars with the atmosphere, but at a certain height above the surface and partially also above heterogeneous terrain, further assumptions must be made. In the simplest case, these terms balance each other or become negligibly small. For flat terrain, the net flux of a scalar exchanged by the surface is

$$F_\chi = \underbrace{\overline{\rho_d w' \chi'_{sm}}}_{\text{I}} \Big|_{z_m} + \underbrace{\int_0^{z_m} \overline{\rho_d \frac{\partial \chi_{sm}}{\partial t}} dz}_{\text{II}}, \quad (55.8)$$

with χ_{sm} as the dry mass mixing ratio and $\overline{\rho_d}$ as the density of dry air. Term I is the flux at the upper boundary of the volume element measured with the eddy-covariance method. Term II is the storage change between the surface and the measurement height, which can be ignored for the momentum flux. However, for sensible heat, water vapor, and other gases, such as carbon dioxide, its contribution can be significant. In particular, in the morning hours, when the accumulated gasses in the air column underneath the sensor is dispersed into the boundary layer, the storage change term (calculated from the change in time of the partial density of the investigated matter integrated over the whole profile underneath the eddy-covariance system) may become important.

In heterogeneous or sloped terrain, the net flux is equal to the flux at the upper boundary of the control volume (term I), the storage term II, and also a horizontal (term III) and vertical (term IV) advection term, plus the horizontal flux divergence (term V)

$$\begin{aligned} F_\chi = & \underbrace{\overline{\rho_d w' \chi'_{sm}}}_{\text{I}} \Big|_{z_m} + \underbrace{\int_0^{z_m} \overline{\rho_d \frac{\partial \chi_{sm}}{\partial t}} dz}_{\text{II}} \\ & + \underbrace{\int_0^{z_m} \left[\overline{\rho_d u' \frac{\partial \chi_{sm}}{\partial x}} + \overline{\rho_d v' \frac{\partial \chi_{sm}}{\partial y}} \right]}_{\text{III}} + \underbrace{\int_0^{z_m} \left[\overline{\rho_d w' \frac{\partial \chi_{sm}}{\partial z}} \right]}_{\text{IV}} \\ & + \underbrace{\int_0^{z_m} \left[\overline{\rho_d \frac{\partial u' \chi'_{sm}}{\partial x}} + \overline{\rho_d \frac{\partial v' \chi'_{sm}}{\partial y}} \right]}_{\text{V}}. \end{aligned} \quad (55.9)$$

In this form, the method is called the *generalized eddy-covariance method* [55.2, 65].

Especially in complex terrain, the quantification of the advection terms is still the subject of ongoing research and extensive experiments [55.68, 69]. Due to

the large errors in the determination of the advection terms, there is a large risk that applying these terms will introduce large errors to the flux estimates [55.70]. To avoid this risk, data that is considerably affected by advection, e.g., such data collected at night under low-turbulence conditions, can be discarded and gap filled [55.71]. The challenge remains to define quantitative criteria that safely identify low-turbulence conditions and also apply adequate gap filling. Due to the lack of better practical knowledge on when exactly advection becomes a dominating influence, empirical methods have been developed [55.60]. In the case of CO₂ flux measurements, such objective criteria were defined based on u_* threshold values. Beyond a site-specific u_* threshold value, it is usually observed that the normalized flux becomes independent of u_* [55.72]. Measurements taken at conditions with u_* smaller than this threshold value are excluded and parameterized with empirical gap-filling algorithms in order to calculate monthly or annual fluxes [55.73, 74].

55.3.2 Flux Calculation, Corrections, and Conversions

The eddy-covariance method is a direct measurement method solely based on first principles [55.2, 3, 65]. However, the derivation of the mathematical algorithm is based on a number of simplifications so that the method can only be applied if certain assumptions are fulfilled. The quality of the measurements primarily depends more on the site conditions and the application of necessary corrections, rather than on the presently available highly sophisticated measurement systems [55.75]. The most limiting conditions are the assumptions of horizontally homogeneous surfaces and steady-state conditions. The latter restrictions cannot be corrected; they are subject of the quality control (Sect. 55.6) to identify data that need to be discarded.

Preparation of Raw Data

The preparation of the input data starts with the exclusion of missing values and outliers, which can be found by plausibility tests, checking whether a measurement value is within predefined limits given by the expected meteorological conditions and the range of the instrument or the data acquisition system (Chap. 2). Further tests should detect unfavorable meteorological conditions or technical problems of the instruments, whereby separating these two factors is often difficult [55.58]. Spikes, i.e., values that are significantly above the normal variation of the measured value but still within the possible range, are often electronically caused. The usual *despiking* test is based on the determination of the standard deviation of the variable (σ).

All individual values $> 3.5\sigma$ [55.76] are considered as spikes. If single spikes are large, it is recommended that the test be repeated two to three times, because otherwise the estimated σ is overestimated if they are included. To make this test even more effective, running standard deviations are used for flux calculations. Measurement series with $> 1\%$ of spikes should not be used. More robust is the application of the absolute deviation from the median (MAD) [55.77], $\text{MAD} = \text{median}_i (|x_i - \text{median}_j (x_j)|)$, where all values that are larger or lower than a multiple of the MAD-value, are identified as spikes

$$\text{median}(x) - \frac{q\text{MAD}}{0.6745} \leq x_i \leq \frac{q\text{MAD}}{0.6745} + \text{median}(x), \quad (55.10)$$

where 0.6745 is the corresponding value of the normal distribution by Gauss. It is recommended to use $q = 7$ for this application [55.75].

Even if measurement signals are recorded on the same data logger records, it may occur that the data sampled at the same point of time are not stored at the same point in time. This can be partially corrected in the software of the data logger, but such time delays can vary over time. A typical example is a measurement system where air is drawn in through a tube from close to the measurement volume of the sonic anemometer down to a displaced analyzer. Then, depending on the travel time of the air sample in the tube, the concentration measurements are recorded significantly later than the wind speed component. The time lag can be determined with a *cross-correlation* analysis, and the concentration time series are shifted relative to the vertical wind measurements by the time difference of the maximum cross correlation. If the signal is too small, correlation maxima may appear at unlikely time differences. In this context, it is important to note that intake tubes should not be longer than necessary. This would lead to systematically overestimated flux values, which may be particularly critical for N_2O or CH_4 budgets. The synchronization of the wind speed and the scalar measurement must be done before any further calculations are made. From the synchronized data, initial covariances can be calculated.

High-Pass Filtering after Block Averaging or Detrending

Data from sensors in an eddy-covariance system are routinely processed to calculate fluctuations from the mean; see (55.3). Historically, different averaging and detrending operators have been applied to this end. Several methods are available to separate the active, turbulent transport that we treat as eddy flux from the slower,

deterministic atmospheric motions, flux instationarity due to changing weather conditions, and instrumental drift. Amongst others ways, linear detrending, a spectral high-pass filter, or a recursive running mean are often used by practitioners in order to extract the turbulent part from a time series [55.41]. The choice of detrending method depends, thus, on the understanding of the nature of low-frequency contributions to the covariance by the practitioner. Sometimes, a clear spectral gap is found between the time scales of atmospheric variability ([55.78] and Chap. 1), which, however, often appears not to be as evident, especially above rough surfaces and at unstable stratification. This circumstance normally makes it difficult to draw a clear line between turbulence and variability due to weather. On top of this problem, sensor drift might add an artificial bias to the low-frequency parts of the time series, which should also be removed before the calculation of covariances.

Fortunately, in many cases, spectral turbulence models can be easily defined with some certainty from measured 30 min turbulence spectra, often aggregated for classes of atmospheric stratifications [55.79]. If the model of the peak frequency is well parameterized, it is safe to apply modest detrending algorithms, because the low-frequency loss of turbulence that is caused by such high-pass filters can easily be calculated and restored from the known high-pass filter transfer functions of these operations [55.80]. Examples for the beneficial, i.e., noise-reducing, effects from using detrending methods compared to simple block averaging have been provided by [55.81].

Some scientists prefer using only block averaging by calculating the arithmetic mean over a certain time period [55.81, 82] because of potential conflicts with the Reynold's decomposition and the uncertainties of applying spectral models to low-frequency domains, where the data is noisy. Block averaging is, like linear detrending and recursive filtering, a high-pass filter, with the spectral cutoff depending on the nonoverlapping averaging time. For a rough estimation, its average length can be estimated by, e.g., the ogive method for any site [55.45, 46, 83, 84]. However, by selecting a fixed length of the averaging interval, this method implicitly puts an assumption on the low-frequency turbulent contributions, i.e., that turbulent time scales are constant at a site and that the signal in lower frequencies than captured by block averaging can be neglected. This assumption is challenged by the observed dependency of the wind speed normalized peak frequency on atmospheric stratification, with lower values at unstable conditions. As the eddy-covariance system samples the turbulent signal in natural frequencies, the low-frequency loss is inversely related to the wind speed. Not considering this dependency with the length of

the averaging time means that the coverage of low-frequency signals measured by the eddy-covariance system depends on atmospheric conditions. This bias is only considered when correcting for the high-pass filtering effects.

From this it follows that whatever the high-pass filter method is being used, i.e., detrending, recursive filtering, or block averaging, effects need to be corrected with the appropriate high-pass filter correction method based on a site and measurement height-specific spectral model that covers the relevant spectral domains.

Low-Pass Filtering and Other Corrections

This section describes corrections that must be applied to measurements because practical instrumentation cannot fully meet the requirements of the underlying micrometeorological theory. Typically, measurements are conducted in a finite sampling volume rather than at a single point, and the maximum frequency response of the sensors may be smaller than the highest frequencies of the turbulent eddies responsible for the heat and mass transport. Both of these instrument limitations cause a loss of the high-frequency signal. Errors also arise in calculating fluxes of trace gas quantities using open-path analyzers because of spurious density fluctuations arising from the fluxes of heat and water vapor. This chapter gives an overview of how these sources of error can be eliminated or reduced using some model assumptions and additional measurements.

Here, we assume that an initial preprocessing of the raw velocity and scalar time series has been completed, including despiking and an adjustment of possible time delays. The acoustic temperature measured by sonic anemometers must be corrected for an increased sonic travel time due to winds blowing orthogonally to the measurement path (cross wind) [55.37, 85]. Current sonic anemometers include this *crosswind correction* in their firmware, but this is not the case for some older anemometers. It is also assumed that the coordinate system has been rotated to ensure zero vertical wind velocity over a certain averaging time (Sect. 55.1.1). This rotation is called a tilt correction [55.86, 87] or coordinate rotation [55.50] and can be applied to two or three axes, where the three-axis rotation is not recommended. The *double-rotation* method may be suitable for flat sites with a low vegetation canopy [55.81]. Currently, the *planar-fit method* [55.51] is often used, which overcomes some deficiencies of the double-rotation method above tall vegetation or at low-wind speed conditions, and it also accounts for a possible instrument caused offset of the w -component.

Furthermore, a correction for density fluctuations is applied (*WPL correction* according to Webb, Pearman, and Leuning, formerly also called Webb correc-

tion) [55.9]. Technically, this is rather a unit conversion for the measurement of gas concentration per unit volume instead of per unit mass, and it compensates for rapid changes of temperature and air composition caused by the turbulent fluxes. After the first publication, several authors discussed this problem, often controversially. A clarification of the problem was given by Leuning [55.7, 8]. The correction is necessary because fluctuations in temperature and humidity cause fluctuations in trace gas concentrations that are not associated with the flux of the trace gas that we wish to measure (correlated dilution/expansion/condensation of the gas sample due to spectral similarity with water vapor and heat). The correction to the measured flux can be large, i.e., the additive correction may significantly change the CO₂ flux calculated using the covariance of vertical velocity and partial density. A very careful application of this correction is essential for all trace gas fluxes as discussed below, unless these are measured in units of mass or molar mixing ratio.

For open-path sensors, the corrected flux of a scalar quantity, e.g., CO₂ or CH₄, is calculated after

$$F_s = \overline{w'\rho'_c} + \mu \frac{\overline{\rho_s}}{\overline{\rho_d}} \overline{w'\rho'_w} + (1 + \mu\sigma) \overline{\rho_s} \frac{\overline{w'T'}}{\overline{T}}, \quad (55.11)$$

with the correct flux of scalar quantity F_s , the mass density of a scalar quantity ρ_s , the mass density of dry air ρ_d , the density of water vapor ρ_w , and

$$\mu = \frac{m_d}{m_w} = 1.6; \quad \sigma = \frac{\overline{\rho_w}}{\overline{\rho_d}}. \quad (55.12)$$

For practical purposes, the general formula (55.8) can be simplified for the correction of H₂O-fluxes/latent heat fluxes

$$F_w = (1 + \mu\sigma) \left(\overline{w'\rho'_w} + \overline{\rho_w} \frac{\overline{w'T'}}{\overline{T}} \right). \quad (55.13)$$

In (55.11) and (55.13), ρ'_w and T' represent fluctuations of water vapor and temperature inside the measurement volume. For low trace gas fluxes this additive correction can be in the order of magnitude of the actual flux [55.88].

For closed-path sensors, only the water vapor dilution component is necessary, because temperature fluctuations are effectively dampened in the tubes [55.89]. Here, the dampened water vapor flux rather than the actual water vapor flux in the atmosphere needs to be used in the modified (55.11) [55.90, 91].

Conversion of buoyancy flux into sensible heat flux is known as *SND correction* after the three authors

Schotanus, Nieuwstadt, and DeBruin [55.37], formerly also called the Schotanus correction. It is based on the transformation of sonic or acoustic temperature (T_s) to actual air temperature. The sonic temperature is given as (Chaps. 7 and 9) [55.21, 92]

$$T_s = T(1 + 0.531q) \approx T \left(1 + 0.33 \frac{e}{p} \right), \quad (55.14)$$

where q is the specific humidity, p is atmospheric pressure, and e is the partial pressure of water vapor; the numerical values differ slightly because of the application of the International Temperature Scale of 1990 (ITS-90). For the SND correction of the sensible heat flux in kinematic units without the crosswind correction, which is often included in this equation, it follows

$$\overline{w'T'} = \frac{\overline{w'T'_s}}{1 + \frac{0.51c_p\bar{T}}{\lambda Bo}}, \quad (55.15)$$

with the *Bowen* ratio Bo , being the ratio of the sensible over the latent heat flux. Therefore, measurements of humidity and the water vapor flux are needed to calculate the sensible heat flux [55.92].

An important correction to the actual available turbulence spectra is the adjustment of the spectral losses of the measurement system. Hence, effects due to time resolution (time constant) of the sensor, the path-length averaging, and the separation between different sensors must be corrected. This *low-path filter correction* is typically applied using transfer functions (Chap. 2). For each eddy-covariance sensor configuration, there are separate filters for the time constant, the measurement path length, and the sensor separation, which must be determined. The convolution of these single spectral filter functions is the total filter transfer function [55.38, 93]. The method can also be applied using different transfer functions accordingly [55.64, 79]. For a chosen measurement system, it is also possible to use a simple analytical correction for a site that takes into account the observed spectra [55.94, 95]. However, such simplified corrections should only be applied with care, because they need to be adapted to the specific site conditions. Past experience showed that this approach often ignores essential causes of frequency loss, e.g., the impact of a rain cap [55.96, 97] and the tube length [55.98], and leads to systematic biases. In these conditions, an alternative is to base the correction on empirical transfer functions obtained by computing the ratio of the measured (co)spectra with an ideal (co)spectrum. Considering that high-frequency losses on vertical velocity and temperature are small, the measured sensible heat cospectra may be used as a reference [55.60, 99].

Often, a sampling time of 30 min is not long enough to measure the low-frequency part of the fluxes, particularly in the presence of heterogeneity-induced secondary circulations. Given the reservations mentioned above when addressing the high-pass filter effects of an eddy-covariance system, it can be tested whether the flux has its maximum value within the usual averaging time. This is done using the so-called *ogive test* [55.45, 46, 83]. It is calculated using the cumulative integral of the cospectrum of the turbulent flux beginning with the highest frequencies. If the value of the integral approaches a constant value (flux) for low frequencies, and if an enhancement of the averaging interval gives no significant changes, then no additional correction is necessary. Otherwise, the choice of a different averaging interval may be considered for the covariance calculation. The ogive test is only meaningful if the fluxes are not too small and steady-state conditions can be assumed [55.100].

There is often considerable loss of flux data when open-path gas analyzers are used at sites where rain, fog, mist, and snow impair measurements of trace gas concentrations. Closed-path gas analyzers provide an attractive alternative because of lower rates of data loss, but such measurement systems require significantly different corrections for time delays, low-pass filtering, and density effects compared to those needed for open-path systems. Temperature fluctuations in tubings with high thermal conductivity are reduced to 1% of their initial value when the ratio of tubing length to radius $L_t/r_t > 1200$ for laminar flow in the tube and when $L_t/r_t > 500$ for turbulent flow [55.89]. When temperature fluctuations at all frequencies are eliminated by the air sampling system, there is no need for the respective part of the WPL correction, but still effects from water vapor fluctuations in the sample on the scalar concentration need to be taken into account, if such a correction is not already included in the instruments firmware. Complete elimination of temperature fluctuations may not be achievable for practical lengths of tubing with walls of low thermal conductivity, in which case some unknown fraction of the $\overline{w'T'}$ density correction must be applied. The solution is to measure the temperature and pressure fluctuations within the gas analyzer at the same 10 or 20 Hz normally used for flux determination.

Corrections that Should be Used with Care

An overview of all corrections, conversions, and tests is given in Table 55.5. This table also includes a number of corrections that should not or only be used with care. These corrections are partly related to single instruments. Some very specific corrections are discussed in Sect. 55.4. The *angle of attack correction* assumes that turbulence elements move through

Table 55.5 Data handling and corrections

Method	Description	References
Preparation of the raw data		
Despiking	Deleting and replacing of outliers in the raw data with standard deviation or MAD, the latter is more effective	[55.75, 76]
Synchronization	Correction of possible time delays between different sensors	[55.99, 101]
Averaging operator	Either block averaging or another appropriate high-pass filtering method needs to be selected, and the corresponding high-pass filter correction applied	[55.81]
Necessary and recommended corrections		
Crosswind correction	Correction of the influence of the wind perpendicular to the sonic path on the sonic temperature measurement, usually part of the sonic anemometer firmware	[55.37, 85]
Double rotation	Rotation into the mean wind direction and to achieve $\overline{w} = 0$, applied for each averaging interval, recommended for flat terrain and continuously running measurement programs	[55.50, 102]
Planar-fit rotation	Rotation into the mean wind direction and parallel to a plane following the streamlines to achieve $\overline{w} = 0$, applied for longer averaging periods, recommended for complex terrain and research programs	[55.51, 102]
SND correction	Transformation of the buoyancy flux into the sensible heat flux (compulsory)	[55.37]
WPL correction	Correction of the moisture influence on density fluctuations, compulsory for open, enclosed and closed path; correction for temperature influence only compulsory for open and enclosed path gas analyzers	[55.7–9]
Low-pass filter correction	Correction of the spectral losses of fluxes at high frequencies, different methods possible, strongly recommended	[55.38, 64, 99]
High-pass filter correction (ogive test)	Correction of the loss of fluxes of periods larger than the averaging time, strongly recommended, but only under steady-state conditions	[55.45, 46, 80, 83, 84]
Enclosed/Closed-path gas analyzer correction	Correction of frequency loss and still existing density fluctuations, strongly recommended	[55.89–91]
Cross sensitivity correction	Oxygen cross sensitivity of the krypton hygrometer	[55.103, 104]
Iterative correction	Repeating of the correction in an iterative cycle, $\approx 1\%$ correction of fluxes	[55.105]
Corrections that should be used with care and not recommended corrections		
Specific heat correction	Wrong assumption that fluctuations of the specific heat have an effect on fluxes	[55.99, 106]
Modification of the WPL correction due to the unclosed energy balance	Should not be used as long as no correction procedure for the unclosed energy balance is available	[55.99, 107]
Aliasing correction	The aliasing correction of the spectral correction [55.38] is wrong	[55.99]
Transducer-shadow effect	Probe-induced flow distortion of the sonic anemometer transducer	[55.108–110]
Angle of attack correction	Flow distortion correction for each single measurement according to a wind tunnel flow distortion analysis, probably not directly transferable to the turbulent atmosphere	[55.99, 111, 112]
Burba correction	Correction of sensor self-heating of the LiCor 7500 gas analyzer, use only with care in cold environments	[55.99, 113]
Sonic anemometer heating corrections	The heating of the sonic anemometer has probably an influence on fluxes, the problem is under investigation	[55.113, 114]
Digitalization error	Limited digitalization (relevant for historical measurements)	[55.58, 115]

the sonic anemometer on waveform patterns and, thus, reach the anemometer at a specific angle. The correction approach is based on wind-tunnel measurements under quasi-laminar conditions [55.111]. These measurements were repeated in a turbulent field with inclined sonic anemometers [55.112], but the measurement setup was questionable [55.116, 117]. These corrections should, therefore, only be applied with care.

Flow distortion by the sonic anemometer probe has been a well-known problem since the beginnings of sonic anemometry [55.118]. The reasons are the

installations of the sensors and the size of the transmitters/receivers. In general, a large ratio of the path length, d , to the transmitter/receiver diameter, a , of at least $d/a = 20$ is required to minimize the influence of flow distortion. Furthermore, the angle, θ , between the wind vector and the transmitter–receiver path should be large [55.50, 108, 119]. These results are based on wind tunnel investigations for a sonic anemometer with orthogonal measurement paths [55.109]. Recently, some papers explained a reduction of the vertical wind velocity by *transducer-shadow effects* [55.110, 120, 121]

and proposed to apply the correction. This correction is currently only available for the CSAT3 anemometer and an orthogonal configuration with 25 cm path length [55.119]. It is also still under validation, and we do not recommend it generally for standard applications.

The sensor head of the LiCor 7500 open-path gas analyzer is heated and, therefore, generates expansion of the air sample within the sampling volume, which has an influence on the application of the WPL correction [55.122, 123]. Apart from a correction using additional fine-wire thermometers within the measurement volume [55.124] or the comparison with a closed path sensor [55.113, 125], no general consensus has been reached yet as to which method is the most effective and efficient. In general, these corrections depend on wind speed and the inclination of the sensor. Therefore, such *self-heating correction* should only be applied with great care.

Corrections for CH₄ and N₂O Analyzers

In recent years, fast response sensors for trace gases other than CO₂ have become commercially available. Particularly, analyzers for the non-CO₂ greenhouse gases (GHG) CH₄ and N₂O are gaining more and more attention in climate-change research. As for the CO₂/H₂O analyzers, these sensors are also based on molecular absorption spectra. However, since atmospheric concentrations of these gas species are much smaller than, e.g., for CO₂, a more specific radiation source is necessary to minimize cross sensitivity with other gasses, and this is why these sensors generally use lasers instead of noncoherent radiation sources. In this context, two basic measurement principles can be distinguished [55.126]:

- Tunable diode laser (TDL) spectroscopy, where the output wavelength of the laser is tunable over a certain spectral range, so that the laser can scan across a specific absorption band of a molecule. For many of those analyzers, the actual measurement is carried out in an optical cell at a very low pressure. This has the disadvantage of requiring high-power pumps but leads to a wanted narrowing of the absorption bands and, therefore, better separation between different gas species. Examples for this type of analyzer are the Campbell TGA-100/200 or the Aerodyne Quantum Cascade Laser (QCL). The Licor LI-7700 also uses a tunable laser source but in an open-path measurement setup, similar to the LI-7500 but with a longer path length and at ambient pressure.
- Cavity ring-down spectroscopy (CRDS) or off-axis integrated cavity output spectroscopy (ICOS), allow

for considerably larger path lengths per unit volume of the optical cavity and, thus, lower gas concentration detection limits. The devices operate at low pressures (1/10 of ambient), which requires powerful vacuum pumps. The intensity decay rate of radiation trapped in an optical cavity is measured, which is a function of the concentration of a gas species that absorbs radiation at that specific wavelength. The CRDS principle is applied, for example, by the PICARRO analyzers, whereas ICOS is used by the Los Gatos Fast Greenhouse Gas Analyzer.

The corrections required for CH₄ and N₂O analyzers are the same as for the commonly used H₂O or CO₂ analyzers, depending whether they have an open or closed measurement path. Analyzers that do not measure H₂O in the cells are problematic, not only because of the WPL correction but also because of water-vapor line broadening effects that, if unconsidered, would contaminate the signal with effects from turbulent water-vapor concentration fluctuations. In order to reduce uncertainty regarding these effects, sometimes a scrubber is deployed between the tube inlet and the measurement cell to remove water vapor from the sampling air. However, only if all temperature and pressure fluctuations are eliminated and humidity is completely removed, do the application of the WPL and line broadening correction become redundant.

The laser spectroscopic gas analyzers need to keep the physical conditions in the measurement cell or cavity constant with very high precision. To reach the highest precision of the gas concentration analysis, physical fluctuations of the sensor environment should be avoided, and, thus, this sensitive equipment is best kept in air-conditioned enclosures. However, for real applications, this often means that the distance between the gas analysis and the air sampling itself and, consequently, the lengths of the tubes, are large compared to other closed-path eddy-covariance applications. The appropriate characterization of the low-pass filter effects and the time lag between the gas analysis and the wind speed measurement is of comparably larger importance for such systems.

In principle, the methods to characterize the low-pass filtering effects do not differ between non-CO₂ GHG and CO₂. In all cases, the tube effects are mainly related to the velocity profiles in the tube and the mixing in the cells/cavities, rather than to surface effects. The effects can largely be kept within acceptable and rather constant limits by applying large air-sampling flow rates. However compared to CO₂ and H₂O, the non-CO₂ GHG flux levels are very often very low, making it necessary to carefully select the time series to be used for the spectral analysis. A usually lower

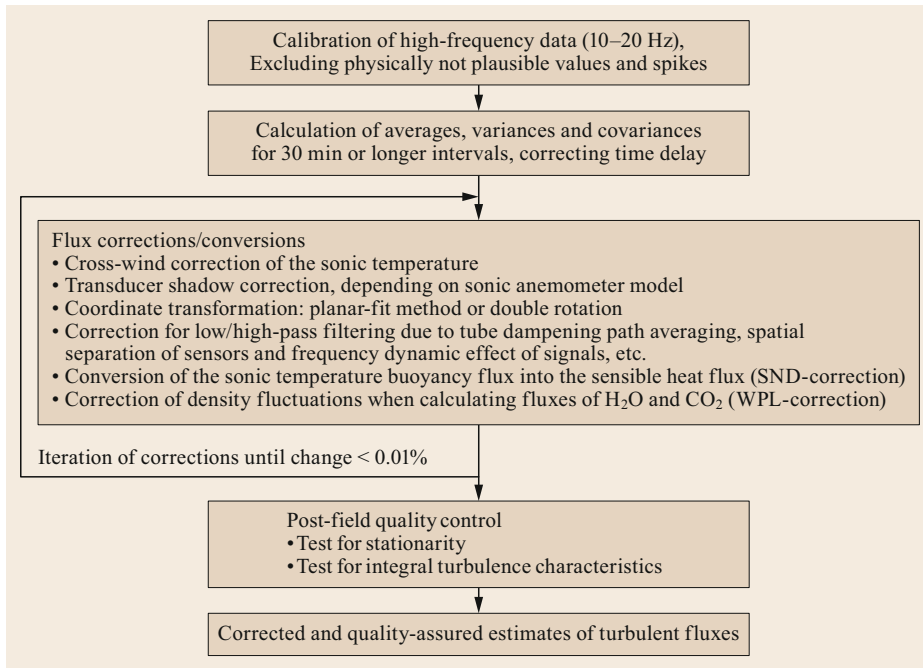


Fig. 55.4 Postfield data processing (after [55.105] with permission from Schweizerbart'sche Verlagsbuchhandlung)

signal-to-noise ratio in non-CO₂ GHG turbulent flux measurements leads to higher contributions of noise to power spectra, which has to be considered when deriving spectral transfer functions from power spectra. Generally, a smaller data basis of usable spectra makes the estimation of spectral transfer functions more difficult and uncertain.

For closed-path instruments, a correct determination of the time delay between the analyzer signal and the sonic signal is crucial to obtain accurate flux estimates. This turns out to be difficult in situations where the fluxes are episodic on a low background flux level, such as often observed with non-CO₂ GHGs. At low fluxes, covariance maximization results in erratic time lags and flux calculation. Therefore, as with spectral analysis, careful selection of time series for empirical time lag estimation is needed. To experimentally estimate a feasible window size for the lag-time search, step-change experiments are useful. In these experiments, a well measurable gas concentration is sporadically and abruptly diluted with a constant fraction of synthetic air, leading to a fast and constant drop in concentration. The time constant of the eddy-covariance system can then be derived from the deviance between the true signal at the tube intake and the measured signal in the analyzer.

The results from empirical time-lag determination indicated that some non-CO₂ GHG analyzers are affected by large drifts of their internal computer clocks. This can be easily derived from steadily increasing em-

pirical lag times, which, suddenly, fall back to zero at a date shift or at times the computer clock is externally adjusted. Some analyzers even eventually stop fast response data transmission, while performing computationally intensive operations, such as storing spectra on their internal hard disks. The challenges of data synchronization are more severe with sensors that sample large amounts of raw data (molecule spectra) and fit this data to spectral models to form a single trace gas concentration value. Future increased computing capacity should solve these kinds of problems very soon. However, for the time being, a user should be aware of the risk of such analyzer imperfections and carefully study time stamps that are mostly available with fast response data.

55.3.3 Overall Data Corrections and Data Handling

Many corrections depend on atmospheric stability or need the turbulent fluxes as input parameters. Therefore, the corrections often are performed iteratively. Although the math is tedious, it was shown [55.127] that the above corrections can be solved without iteration (Table 55.5) as a set of simultaneous equations. Figure 55.4 shows a schematic for how to organize the system of raw data correction, covariance correction as discussed in this section, and data quality tests (Sect. 55.6). This *iteration* typically has an effect of $\leq 1\%$ on the fluxes.

This exemplary flowchart (Fig. 55.4) of eddy-covariance calculation is realized in many software tools. Overviews of the available tools together with all possible sensors and calculations are available in the literature [55.2, 65, 128]. Software intercomparison studies show that the selection of the available alternative options is more important for obtaining com-

parable flux estimates than the software itself, as long as a well-tested and widely used software package is used [55.129]. Some level of expertise is required to choose the appropriate settings for a specific site and a specific sensor setup, so that using the default settings is not generally recommended. Furthermore, only well-documented software packages should be used.

55.4 Devices and Systems

The main instrument for all flux measurements is a 3-D sonic anemometer (Chap. 9) that can be combined with different sensors for scalars. In this section, only a brief description is given; for more details, see Chaps. 7–9 and 16. Figure 55.5 shows as an example the combination of a sonic anemometer with an open-path gas analyzer. An overview of recently available sensors is given in Table 55.6, and recommended additional measurements are listed in Table 55.7. In the following section, the typical configurations are briefly discussed.

55.4.1 Sonic Anemometers

In basic research, sonic anemometers with a selected inflow sector to exclude flow distortion are often used (Chap. 9). For most applications, wind direction-

independent omnidirectional sonic anemometers are sufficient, but these are generally more affected by flow distortions of the vertical velocity component due to mountings and sensor heads. For flux measurements, it is important that interfering parts of devices are kept at a minimum, in particular below the measurement path for the vertical component of the wind, because the vertical oscillations of relatively small turbulence elements are much faster than the horizontal movements of larger turbulence elements. This difference can be noted in the frequency shift of the spectral maximum for vertical and horizontal wind fluctuations by more than one order of magnitude.

55.4.2 Measurement of the Sensible Heat Flux

Most sonic anemometers also measure the fluctuations of the speed of sound, and therefore allow a computation of the so-called sonic temperature (which is nearly identical with the virtual temperature; Chap. 7). The flux calculated with this temperature is the buoyancy flux, typically about 10–20% greater than the sensible heat flux. The sensible heat flux can be determined by applying additional corrections, which need additional moisture measurements. Direct temperature measurements made with thin thermocouples or freely spanned resistance wires (diameter < 15 μm to reduce the radiation error, see Chap. 7) are more expensive.

55.4.3 Measurement of the Latent Heat Flux

Additional hygrometers are used for the determination of the latent heat flux (evapotranspiration). Such devices are currently mostly optical devices (Chap. 8).

Fig. 55.5 Typical installation of a sonic anemometer and an open-path gas analyzer (here CSAT3 with LiCor 7500). The probe to the left of the sonic anemometer volume is a fast-response fine-wire temperature sensor (photo © T. Foken) ◀



Table 55.6 Typical instruments for scalar flux measurements (open-path instruments, if not specified otherwise)

Scalar flux	Instrument type	Commercially available type
Sensible heat flux	Cold-wire thermometer (Chap. 7)	Not available
Buoyancy flux	Sonic anemometer (sonic temperature; Chap. 7)	All types of sonic anemometers
Latent heat flux	UV-hygrometer, Lyman-alpha source (Chap. 8)	Not available
Latent heat flux	UV-hygrometer, krypton source (Chap. 8)	KH20 (Campbell Sci. Inc.)
Latent heat flux and CO ₂ flux	IR-spectrometer (Chap. 8)	LI-7500 (LI-COR), EC-150, IRGASON (Campbell Sci. Inc.)
Latent heat flux and CO ₂ flux (closed-path instrument)	Closed-path IR-spectrometer (Chaps. 8 and 16)	LI-7000, LI-7200 (LI-COR), EC-155 (Campbell Sci. Inc.)
CH ₄ flux	IR spectrometer (Chap. 16)	LI-7700 (LI-COR)
CH ₄ flux (closed-path instrument)	Closed-path laser spectrometer (Chap. 16)	QCL (Aerodyne) Model 911-0010 (Los Gatos) G2311-f (PICARRO)
N ₂ O flux (closed path instrument)	Closed-path laser spectrometer (Chap. 16)	QCL (Aerodyne) Model 913-1054 (Los Gatos)

Table 55.7 Additionally required measurements

Sensor type	Reason/Usage	Remark
Inclinometer	Control of the leveling of the instruments, for application of planar-fit rotation [55.51], recommended	Included in some sonic anemometers
Pressure sensor (low-frequency)	Necessary for concentration calculation	Chap. 10
Temperature sensor (low-frequency)	Reference temperature, sonic temperature often not accurate enough, for corrections	Chap. 7
Humidity sensor (low-frequency)	Reference humidity, humidity of some analyzers is not accurate enough, for corrections and control	Chap. 8

These have either an open measurement path or are a closed path contained in an optical measurement cell. The open-path hygrometer is mounted near the sonic anemometer, and the closed-path instrument is usually placed some meters away, while the air is sucked in from below the sonic anemometer. Open-path instruments operate in the UV or the IR range, and closed-path instruments work only in the IR range. UV devices should be used for low-humidity conditions (water vapor pressure 0–20 hPa) and IR devices for more moist air (5–40 hPa). The effort for maintenance and calibration for all devices is considerable.

55.4.4 Measurement of the CO₂ Flux and Fluxes of Other Air Constituents

The CO₂ gas analyzers generally operate in the IR range and always measure water vapor as well, which is necessary due to overlapping absorption bands between CO₂ and water vapor molecules and line broadening effects from water vapor on the CO₂ spectra. Similar to pure hygrometers, open and closed-path instruments are available. Recently, there has been a trend to combine the advantages of both principles by using a very short intake tube (< 1 m), which is often called an enclosed-path system. However, even for such a short tube length, the dampening of high-frequency fluctuations can be

considerable [55.130]. The dampening can be strongly reduced by minimizing the rain cap volume [55.96, 97]. Another trend is the integration of the gas analyzer into the sonic anemometer in so-called compact systems. Fast response optical devices for other gaseous components (e.g., ozone, methane, nitrous oxide, sulfur dioxide) are also available, and the deposition flux can be measured in a similar way. Tunable diode lasers, which are commercially available for carbon isotopes 12 and 13, methane, nitrous oxide, and other gases, are being increasingly applied [55.131, 132].

55.4.5 Guidelines for Designing an Eddy-Covariance System

The turbulent fluctuations of the components of the wind vector and of scalar parameters must be measured at a high sampling frequency, so that the turbulence spectra (Chap. 1) can be extended to 10–20 Hz. The measurement or sampling time depends on the atmospheric stratification, the wind velocity, and the measurement height. For measurement heights of 2–5 m, at least 10–20 min would be required for daytime unstable stratification (summer) and about 30–60 and sometimes as high as 120 min for nighttime stable stratification due to intermittency. Although the peak of the cospectral density is shifted towards high frequencies

Table 55.8 Advantages and disadvantages of the different setups

Devices	Advantages	Disadvantages
Sonic anemometer with separated open-path gas analyzer	Very few high-frequency dampening effects (only due to path averaging and sensor separation) Only cleaning of sensor required for maintenance Low power consumption	Disturbed by water droplets, ice, and dirt on the optical windows or within the measurement path Heating of the window
Sonic anemometer with integrated open-path gas analyzer (compact system)	Minimal sensor separation Only cleaning of sensor required for maintenance Low power consumption	Disturbed by water droplets, ice, and dirt on the optical windows or within the measurement path Increased flow distortion
Sonic anemometer with enclosed-path gas analyzer (tube ≤ 1 m)	Reduced tube dampening compared to closed-path systems with longer tubes Can be used during times of precipitation or fog Less calibration drift due to dirt Considerably smaller number of technical data gaps in humid climates	Large tube and rain cap dampening compared to open-path sensors Requires regular checks of flow rate and exchange of filters for maintenance High power consumption due to the use of a pump Need to measure chamber temperature at high frequency
Sonic anemometer with closed-path gas analyzer (long tube)	Can be used during times of precipitation or fog Less calibration drift due to dirt No need for high-frequency temperature correction Considerably smaller number of technical data gaps in humid climates	Larger tube dampening compared to open-path and enclosed-path systems Requires regular checks of flow rate and exchange of filters for maintenance High power consumption due to the use of a pump

with increasing stability, the intermittent character of turbulence under stable conditions often requires an increased averaging time. Nevertheless, for practicality reasons and to facilitate an efficient data handling, a sampling time of 30 min is used over the entire day. This choice is always a tradeoff. For short sampling times, the low-frequency contributions to the fluxes are missed, and for long sampling times, the steady-state condition may not be fulfilled. Moreover, the high-pass filter correction can only compensate for a too-short sampling time under the assumption that heterogeneity-induced low-frequency contributions are negligible.

The choice of the measurement height depends on the vegetation height, the path length, and the separation between a sonic anemometer and an additional device to measure the scalars of interest (e.g., hygrometer). Devices with a path length of > 12 cm should not be used below 2 m, and devices with a path length of > 20 cm should be not used below 4 m [55.22, 50]. The minimum distance between a sonic anemometer and an additional device depends on the flow distortions caused by the devices and should be determined in a wind tunnel. Typically, for fine-wire temperature sensors, the minimum distance is 5 cm, and for hygrometers it is 20–30 cm. These additional instruments should be mounted downwind of the sonic

anemometers and 5–10 cm below the wind measurement path [55.133]. Therefore, to reduce the corrections of the whole system, the measurement height must be estimated, dependent on the path length of the sonic anemometer and on the separation of the measurement devices. Also, the measurement height should be twice the canopy height in order to exclude effects of the roughness sublayer. This is, however, often not feasible when measuring over tall vegetation. Flow distortion due to the measurement system can hardly be avoided [55.118]. Nevertheless, care must be taken that instrument mounts, tower elements, or other sensors are installed at a sufficient distance from the turbulence measurements (a distance that is five to tenfold of the dimension of the disturbing structure [55.134–137]).

55.4.6 Advantages and Disadvantages of the Different Trace Gas Sensors and Installations

The specific challenges and advantages of different types of gas analyzers used in eddy-covariance measurements have been investigated in several studies [55.138–140]. An overview is presented in Table 55.8.

55.5 Specifications

A general specification of flux measuring systems is difficult because the accuracy of the measurement depends not only on the sensor configuration but also on the turbulent conditions and, therefore, e.g., if the turbulence is fully developed and steady state [55.55,

141]. In Sect. 55.6.3 and Table 55.12, this connection of sonic anemometer type and data quality concerning the accuracy is shown. In Table 55.9, only some general specifications are given, see also the relevant chapters for the sensors: Chaps. 7–9 and 16.

Table 55.9 Specification of the sensors of eddy-covariance systems

Sensor	Range of measurements	Typical accuracy	Temperature range for application (°C)
Sonic anemometer, wind velocity, scientific instruments	0 to 60 m s ⁻¹	0.1 m s ⁻¹ for ≤ 5 m s ⁻¹ 2% for > 5 m s ⁻¹	–40 to 60 ^a
Sonic anemometer, sonic temperature	–40 to 60 °C	1 K	–40 to 60 ^a
Open-path gas analyzer, water vapor	0 to 60 ppt	1% of reading	–25 to 50 ^a
Open-path gas analyzer, carbon dioxide	0 to 3000 ppm	2% of reading	–25 to 50 ^a
Open-path gas analyzer, methane	0 to 30 ppm	1% of reading	–25 to 50 ^a
Closed-path gas analyzer, water vapor	0 to 60 ppt	1% of reading	–25 to 50 ^a
Closed-path gas analyzer, carbon dioxide	0 to 3000 ppm	1% of reading	0 to 50
Closed-path gas analyzer, methane	0 to 100 ppm	1% of reading	15 to 35
Closed-path gas analyzer, nitrous oxide	300 to 1500 ppb	1% of reading	15 to 35

^a Temperatures below 0 °C only in dry air or if the sensor is heated

55.6 Quality Control

A careful quality assurance (QA) and quality control (QC) process (Chap. 3) for eddy-covariance measurements is particularly recommended because of the very complex calculation procedure [55.57, 58, 75, 99, 142]. Such a procedure should include not only tests for instrument errors and problems with the sensors but also evaluate how closely the actual conditions agree with the underlying theoretical assumptions. Due to the variability of meteorological conditions, eddy-covariance quality control tools must comprise a combination of a typical test for high-resolution time series and an examination of the turbulent conditions. A second problem is connected with the representativeness of the measurements depending on the footprint of the measurement. The fraction of the footprint that is in the area of interest must be calculated (Chap. 1). A concise overview of quality control methods for eddy-covariance is summarized in Table 55.10.

55.6.1 Calibration of Turbulence Sensors

For the calibration of turbulence sensors, see the respective instrument chapters, such as Chaps. 7–9 and 16. However, it should be examined whether the calibration also holds under the measurement conditions in the field, with respect to e.g., temperature, pressure, and humidity.

55.6.2 Specific Quality Control Methods

Comprehensive and systematic procedures for quality control of eddy-covariance measurements were first developed in the 1990s [55.57, 58]. The corresponding tests are also summarized in several textbook chapters [55.99, 142]. An extension of these methods is presented in [55.75], with a special focus on long-term eddy-covariance measurements and their particular requirements with respect to automation and uncertainty assessment. Several instruments generate a specific error code or measure control parameters that can be used for data quality issues. Examples are shown in Table 55.11.

Steady-State Test

For the eddy-covariance method, steady-state conditions are required. Meteorological measurements fulfil this underlying assumption for short-time periods up to ≈ 1 h only roughly. There are several tests, which can be used directly or indirectly. For example, stationarity can be determined by examining the fluxes for different averaging times [55.56, 57]. In this way, the flux is determined over short intervals each of only ≈ 5 min duration, and then the average over the short time intervals is calculated. Steady-state conditions can be assumed, if this value does not differ by more than 30% from the

Table 55.10 Overview of quality control methods for eddy-covariance measurements

Method	Description	References
Sensor-specific quality control, see Sect. 55.6.1		
Calibration of gas analyzers	Typical calibration procedures according to manufacturers recommendations	Chap. 8
Zero-wind chamber	Zero-wind chamber test for sonic test for possible offsets	[55.143], Chap. 9
Test of the fulfilment of basic assumptions for eddy covariance, see Sect. 55.6.2		
Steady-state test	Trend of a time series	[55.58]
	Non-steady state periods in the time series	[55.57, 99]
Skewness and kurtosis test	Statistical distribution of turbulence	[55.58]
Integral turbulence characteristics	Test on developed turbulence	[55.57, 99]
Footprint	Test of the target area of the flux	[55.144–146]
Vertical advection	Test on mean vertical velocity (on nonrotated raw data or after planar fit correction)	[55.75, 141]
Test on the accuracy of flux measurements, see Sect. 55.6.3		
Sensor comparison	Accuracy on the basis of sensor comparisons	[55.99, 141, 147]
Energy balance closure	Systematic error due the unclosed energy balance caused by unaccounted mesoscale transport	[55.99, 148, 149]

Table 55.11 Additionally necessary signals of the instruments

Sensor	Signal	Reason
Sonic anemometer	Error code	E.g., wet transducer
Gas analyzer	Error code	E.g., wet or dirty windows
	Internal temperature	Data correction
	Internal pressure	Data correction
	Flow rate	Determine Reynolds number to ensure turbulent flow, quality control, delay correction
	Heating voltage/amperage	Quality control of the intake system

30 min-covariance. A gradation of the differences can be used as a classification of the data quality

$$\text{Stat} = \left| \frac{[\overline{x'y'}]_{5\text{min}} - [\overline{x'y'}]_{30\text{min}}}{[\overline{x'y'}]_{30\text{min}}} \right| \times 100\% , \quad (55.16)$$

where $[\overline{x'y'}]_{5\text{min}}$ is calculated as the average of six 5 min covariances within this 30 min-interval, see [55.57] for details.

Development of Turbulence

The development of turbulent conditions can be investigated with the flux-variance similarity [55.57]. In this case, the measured integral turbulence characteristics (ITC) are compared with the modeled characteristics given in the literature, e.g., [55.2]. Good data quality is suggested for differences < 30%.

$$\text{ITC} = \left| \frac{\left(\frac{\sigma_x}{X_*}\right)_{\text{Model}} - \left(\frac{\sigma_x}{X_*}\right)_{\text{Meas}}}{\left(\frac{\sigma_x}{X_*}\right)_{\text{Model}}} \right| \times 100\% , \quad (55.17)$$

where σ_x is the standard deviation of a quantity x , and X_* is its respective scaling parameter (Chap. 1).

Overall Data Flagging

An evaluation system for turbulent fluxes consists of two steps. The single tests should be evaluated according to the threshold values and corresponding data quality classes, and the overall quality of a measurement is expressed as an appropriate combination of the single tests [55.99, 142]. The highest priority should be given to the steady-state test. Note that for the test on integral turbulence characteristics for neutral stratification, the errors in the determination of the characteristics for scalars can be very high. This test should, therefore, not be overly interpreted, and the test on the characteristics of the wind parameters should dominate. In any case, the classification results of the single tests should be stored to have them available later in cases of doubt. For fundamental research, only data with highest quality should be used. Medium quality can still be used for long-term measurements of fluxes without limitations. Measurements with poor quality should only be used for ballpark estimates and should be discarded [55.75, 150, 151].

Footprint Climatology

The footprint analysis is a tool to estimate the source areas of the flux measurement [55.152–155] that is

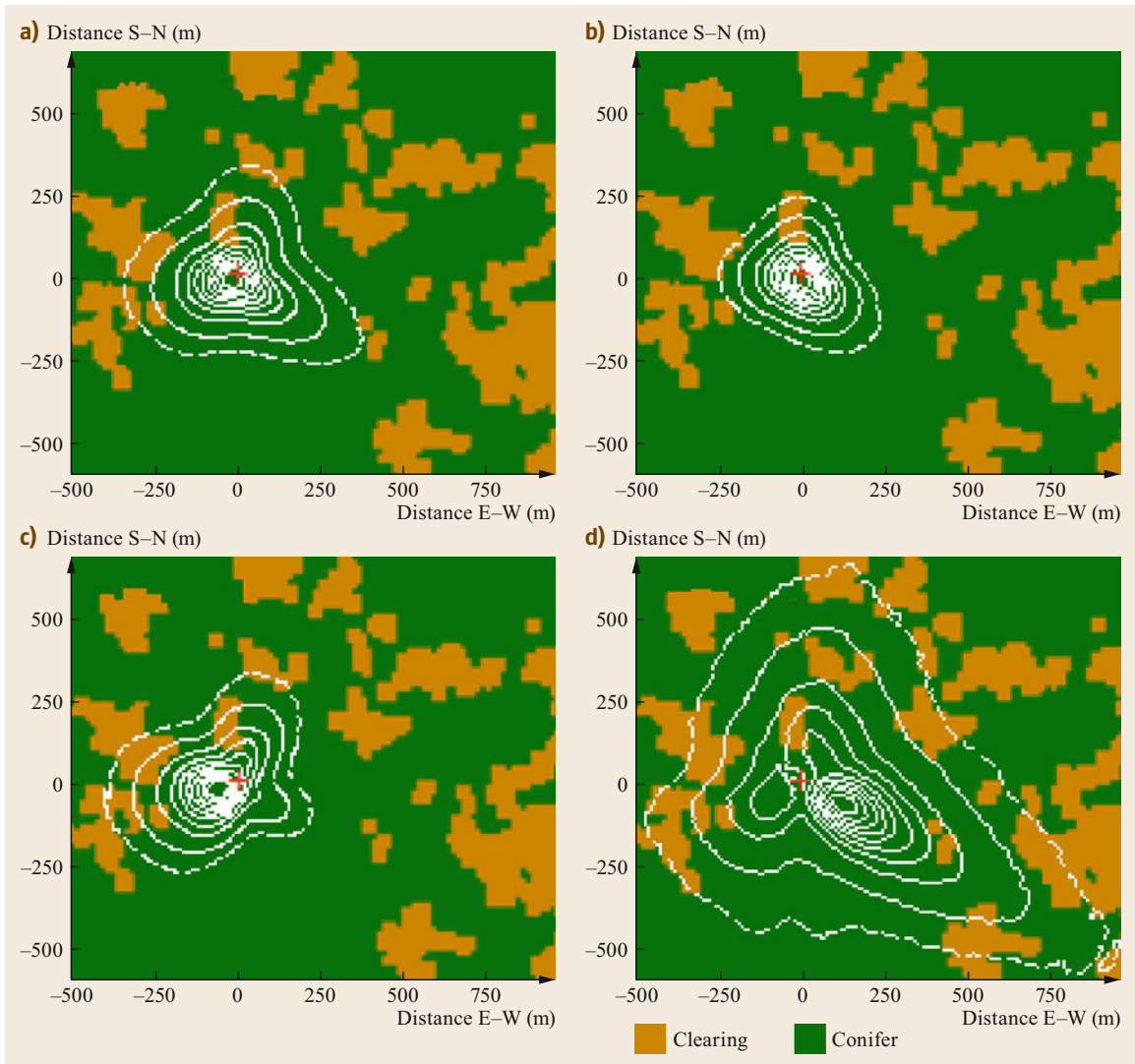


Fig. 55.6a–d Top-down view on footprint climatologies (*white lines*), accumulated for different regimes of atmospheric stability and obtained for the FLUXNET DE-Bay Waldstein–Weidenbrunnen site. Panels give footprint climatologies for all cases (**a**), unstable (**b**), neutral, (**c**) and stable (**d**) stratification. Values are in percentages of the integrated contribution around the peak of the function, with *solid lines* ranging from 90 to 10%, and the *dashed line* as 5% of the maximum. High values indicate a high relative contribution of the specific area to the fluxes measured in the given observation period. Colors in the background indicate land-cover classes. Distances to the tower position (*red cross*) are given in m. The analysis based on a nearly 3-month dataset in summer 2003 (after [55.152])

described in Chap. 1. An integral part of the footprint-based quality assessment approach is the average source weight function created over a longer measurement period, i.e., the footprint climatology [55.152, 156]. By means of 2-D footprint models [55.157, 158], it is possible to calculate footprint climatologies for individual grid cells rather than integrated over a wind direction sector [55.144, 145]. For such a more detailed analysis, each 30-min-source-weight function is projected onto

a gridded land-cover map, assigning a weighting factor to each grid cell that represents its relative contribution to actual measurements. The distribution of flux contributions from the different land-cover types can then be obtained by accumulating these weights arranged in different land-cover types. The application of footprint analysis to a larger dataset reveals patterns in the composition of the footprint that depend on wind sector and stability regime (Fig. 55.6).

Footprint-Dependent Data Quality Control

For data-quality assessment maps, any measured parameter (scalars and fluxes) can be linked to footprint analyses and data-quality flags. To ensure representative findings, footprint analyses for data-quality assessment should use a database of several months (at least 2–3) of meteorological measurements, so that several thousand half-hourly averaged observations are available. The correct interpretation of the findings relies on a good sample of the local wind climatology and sufficient coverage of different atmospheric stability conditions for all wind sectors. The analysis will be strengthened by choosing a database that covers a period of the year with high absolute values of exchange fluxes between surface and atmosphere.

A classic example of this application would be the visualization of spatial structures in the mean vertical wind component. Other examples include visualizing the flux fields for sensible or latent heat, which may indicate spatially variable sources for these parameters.

An additional, powerful way to apply footprints to eddy-covariance quality assessment is to link data quality to terrain features. In this scenario, the footprint results are then coupled to other approaches used to evaluate flux data quality. The choice of the method to assign flux data quality, as well as the definition and resolution of quality classes, can be chosen by the user and customized for each study, as long as the quality ratings are numeric to allow aggregation [55.145, 153].

55.6.3 Uncertainty Assessment

Besides qualitative information characterizing a flux measurement, i.e., quality flags, it is important to also provide quantitative information about the error or uncertainty associated with a specific flux estimate for proper interpretation and further use of the data. However, the discussion of the uncertainty of eddy-covariance measurements is not trivial because of the stochastic character of the input parameters. Therefore, different approaches are applied [55.159].

Results of Comparison Experiments

On the basis of long-term experience in sensor comparisons [55.141, 160, 161] as well as software comparisons [55.160, 162], some numbers for the possible accuracy of eddy-covariance measurements may be obtained according to the present state of knowledge. A significant dependency was found on the type of sonic anemometer with respect to their suitability for fundamental turbulence research and on the data quality (Sect. 55.6.2). The results are summarized in Table 55.12. To transfer these data to the carbon-dioxide

Table 55.12 Evaluation of the accuracy of the eddy-covariance method on the basis of the experimental results [55.141], data quality, and type of sonic anemometer

Sonic anemometer	Data quality class	Sensible heat flux	Latent heat flux
Selected open sector e.g., CSAT3	High quality	5% or 10 W m ⁻²	10% or 20 W m ⁻²
	Moderate quality	10% or 20 W m ⁻²	15% or 30 W m ⁻²
Omnidirectional e.g., uSonic-3	High quality	10% or 20 W m ⁻²	15% or 30 W m ⁻²
	Moderate quality	15% or 30 W m ⁻²	20% or 40 W m ⁻²

flux the results for the latent heat flux should be used with a threshold of $\approx 0.2 \text{ mg m}^{-2} \text{ s}^{-1}$.

Systematic Errors

After wide application of the eddy-covariance method including all corrections and storage terms, and after the availability of highly accurate net radiometers it became obvious that the energy balance at the Earth's surface could not be closed with experimental data [55.55], indicating a general systematic error (Sect. 55.9.1). The available energy, i.e., the sum of the net radiation and the ground heat flux, was in most cases found to be larger than the sum of the turbulent fluxes of sensible and latent heat. For many field experiments and also for the carbon-dioxide flux networks [55.60, 163], a closure of the energy balance of $\approx 80\%$ was found [55.164, 165]. The residual is defined as

$$\text{Res} = Q_S^* - Q_G - Q_H - Q_E, \tag{55.18}$$

with Q_S^* the net radiation, Q_G the soil heat flux at the surface, Q_H the sensible heat flux, and Q_E the latent heat flux. Over tall canopies, additional storage terms in the biomass and the air volume below the sensor should also be accounted for.

The problem cannot be described as only an effect of statistically distributed measurement errors because of the systematic underestimation of turbulent fluxes or overestimation of the available energy. In the literature, several reasons for this incongruity have been discussed [55.148]. The reason most often discussed is the heterogeneity of the land surface [55.166], which is not considered in the 1-D eddy covariance theory. The authors assumed that the heterogeneity in the vicinity of a flux-measurement site generates coherent structures, but such turbulent features generated by heterogeneities close to the measurement tower can be captured by the eddy-covariance method as long as their temporal extent is shorter than the sampling interval [55.167, 168].

As a first step, the energy exchange between the atmosphere and the underlying surface on scales larger than 1 km can be corrected with the Bowen ratio [55.148, 169–171]. With this approach, the residual will be distributed to the sensible and latent heat flux by preserving the Bowen ratio. However, this method is only valid if a similarity of both scalar fluxes is given even at larger scales, which is obviously not always realized. Some studies [55.105, 172] propose that a large part of the unclosed energy balance is related to the sensible heat flux and propose a correction with the buoyancy flux [55.2, 100].

Noise and Statistical Errors

Due to the very complicated algorithms of the eddy-covariance method, errors cannot easily be estimated according to the error propagation law [55.173]. Quite promising are statistical methods. Hereby, it must be noted that the time series used for eddy covariance are autocorrelated, and the usual statistical criteria for random numbers cannot be applied [55.54, 174, 175]. It is distinguished between:

Noise: error due to instrumental noise [55.75], see Chap. 2

Random error: statistical sampling error of a covariance measurement [55.75, 159, 175, 176], see Chap. 2.

The noise error is determined from the autocorrelation of the measurement signal, using the property of white noise being uncorrelated: a quantity x can be decomposed in its mean \bar{x} , deviations from that mean, x' , with a mean of $\bar{x'} = 0$, and a noise error term εx [55.177]

$$x = \bar{x} + x' + \varepsilon x. \quad (55.19)$$

The second-order autocovariance is then

$$C_{11}(p) = \overline{(x' + \varepsilon x)(x'_p + \varepsilon x_p)}, \quad (55.20)$$

where the subscript p denotes the same quantity as without the subscript but shifted in time by the amount p . If the noise εx is uncorrelated with the signal, then the noise term only appears at zero lag in the autocovariance. The variance of the noise error can, thus, be estimated as

$$\overline{\varepsilon x^2} = C_{11}(0) - C_{11}(p \rightarrow 0), \quad (55.21)$$

where $C_{11}(p \rightarrow 0)$ is $C_{11}(p)$, without $C_{11}(0)$, extrapolated to zero lag.

Thus, the noise of the errors of two time series εx and εy lead to an error of the covariance [55.75],

$$\sigma_{\text{covariance}}^{\text{noise}} = \sqrt{\frac{1}{N} \sqrt{\varepsilon x^2 y^2 + \varepsilon y^2 x^2}}. \quad (55.22)$$

Several authors determined the stochastic error of eddy-covariance fluxes based on raw data [55.175], while others determined an error estimate from final fluxes [55.176]. In general, the random flux error depends on the number of independent observations, which is not identical with the absolute number of observations n when time series are auto and cross correlated. The integral time scale is a measure for how long the variables are correlated and, therefore, not independent. The integral time scale is, therefore, often used to determine the number of independent observations. However, this metric is not always estimated reliably [55.54]. This problem is overcome by an algorithm [55.175] to determine the statistical variance of the covariance, which is a statistically profound and mathematically rigorous approach

$$\sigma_{\text{cov}(x,y)}^{\text{stoch}} = \sqrt{\frac{1}{n} \sum_{p=-m}^m (\overline{x'x'_p} \cdot \overline{y'y'_p} + \overline{x'y'_p} \cdot \overline{y'x'_p})}, \quad (55.23)$$

where $\overline{x'x'_p}$ and $\overline{y'y'_p}$ are the autocovariances with lag p , $\overline{x'y'_p}$ is the cross covariance with lag p on y , while for $\overline{y'x'_p}$, the lag p is on x . The summation bound m should be $n/2$.

55.7 Maintenance

Regular maintenance of eddy-covariance systems is critical for producing reliable flux data. In addition to site visits, online raw data surveillance is very useful to detect instrumental malfunctions as early as possible and to react swiftly to problems that may compro-

mise the data quality and continuous data acquisition. For specific maintenance issues of single sensors, see Chaps. 7–9 and 16. Some maintenance activities of the whole system are listed in Table 55.13.

Table 55.13 Maintenance of eddy-covariance measuring systems (site-specific intervals may be adjusted)

Maximum interval	Single sonic anemometer	Compact system	Sonic anemometer with open-path analyzer	Sonic anemometer with closed-path analyzer, short tubes	Sonic anemometer with closed-path analyzer, long tubes
1 day	Quick look on data or automatic data quality analysis				
1 week	–	Clean optical windows	Clean optical windows	Replace intake tube filter, clean rain-cap mesh	Check/replace intake tube filter, clean rain-cap mesh
1 month	Clean sonic transducers	Clean sonic transducers	Clean sonic transducers	Clean sonic transducers	Clean sonic transducers
1 year	Chamber test of the sonic anemometer [55.143], Chap. 9				
1 year			Replace scrubber chemicals and lab calibration	Replace scrubber chemicals and lab calibration	Replace scrubber chemicals and lab calibration

55.8 Application

The eddy-covariance method has been successfully applied to quantify the turbulent exchange of heat, water, CO₂, and other trace gases for numerous ecosystems in all climate zones of the Earth.

55.8.1 Intensive Measurement Campaigns and Process Studies

One of the earliest large-scale projects using eddy-covariance measurements was the Boreal Ecosystem–Atmosphere Study (BOREAS). Eleven flux towers were deployed during the intensive field campaigns of 1994 and 1996, representing the particularly climate-sensitive boreal ecosystem [55.178]. The primary objective of BOREAS was to collect the data needed to improve numerical climate models with a specific focus on biosphere-atmosphere exchange processes. Another important large-scale intensive measurement campaign using 13 eddy-covariance towers was the LITFASS-2003 experiment (Lindenberg Inhomogeneous Terrain—Fluxes Between Atmosphere and Surface: a Long-Term Study), which was part of the Evaporation at Grid-Pixel Scale (EVA-GRIPS) project [55.179]. Here, the study region was located in central Europe, and the objective was to provide data for investigating the effect of surface heterogeneity on the atmospheric water fluxes, leading to improved parameterization schemes for area-averaged evaporation. While the above-mentioned field campaigns aimed at

providing data for the development of weather and climate models, the Energy Balance Experiment (EBEX-2000) was conducted to work on methodological issues of the eddy-covariance technique. To this end, micrometeorologists from esteemed institutions around the world deployed 14 eddy-covariance towers at a carefully selected site in the Central Valley of California, where almost ideal conditions, such as surface homogeneity, high net radiation, and uniform weather conditions, were expected [55.127]. One of the most recent large-scale measurement campaigns using eddy-covariance measurements was Scale-X (Scale-Crossing Land Surface and Boundary Layer Processes in the TERENO-preAlpine Observatory), which took place in 2015 and 2016. This campaign went beyond the goals of the previously mentioned experiments, since it had a special focus on the transport processes above the eddy-covariance towers throughout the entire boundary layer, at the same time investigating methodological aspects such as advection in complex terrain and the energy balance closure problem [55.180].

55.8.2 Long-Term Measurements of Greenhouse-Gas Exchange Between Terrestrial Ecosystems and the Atmosphere

Long-term eddy-covariance measurements are usually conducted as part of ecological observatories aim-

ing to quantify the biosphere-atmosphere exchange of energy, water, and greenhouse gases, particularly CO₂. The main motivation for these measurements was the large uncertainty in the CO₂ sink strength of the terrestrial biosphere at the global scale and the ground-breaking opportunity for fundamental ecosystems research through observing ecosystems' responses to environmental conditions without any disturbance at the ecosystem scale. Two pioneering networks developed in parallel in Europe (EUROFLUX) and in northern America (AMERIFLUX). From these networks, a global initiative, FLUXNET, was founded and hundreds of long-term eddy-covariance stations have been established across most of the world's climate space and representative biomes [55.61]. These sites are not directly operated by FLUXNET, but it links across

a confederation of regional networks. FLUXNET provides a common infrastructure to archive and share flux and driver data from across the entire globe, it supports calibration, standardization, and intercomparison activities, and it enables global-scale synthesis studies on the terrestrial carbon, water, and energy cycle. Thereby, ensuring and improving intercomparability between sites is one of the main objectives. Since missing or poor-quality data are inevitable in a long-term time series of 30 min fluxes, a variety of gap-filling algorithms were elaborated in order to compute the desired annual estimates of CO₂ net ecosystem exchange and evapotranspiration [55.73, 74, 181]. A review of the scientific outcome of the first 20 years of FLUXNET, including future perspectives, is provided by [55.182] (Chap. 64).

55.9 Future Developments

Over the past 70 years, eddy covariance has become a mature method for measuring turbulent fluxes on the ecosystem scale. Nevertheless, there are still some unresolved issues related to certain details of the methodology, which need to be addressed in the future in order to further improve the accuracy of flux estimates.

55.9.1 Energy Balance Closure Problem

During the late 1980s it became obvious that the energy balance at the Earth's surface could not be closed with experimental data (e.g., [55.183]). In most cases, the available energy, i.e., the sum of the net radiation, the ground heat flux, and the rate of change of the sensible and latent heat storage within the air column underneath the sensor was found to be larger than the sum of the turbulent fluxes of sensible and latent heat. This was a main topic of a workshop held in 1994 in Grenoble [55.55], which resulted in the EBEX-2000 [55.127]. For various sites around the world, an average closure of the energy balance of $\approx 80\%$ was found [55.164]. This indicates a systematic underestimation of the turbulent fluxes, which has been mainly attributed to advection by the mean flow and horizontal flux divergence associated with secondary circulations impacting near-surface tower measurements [55.184, 185]. Current research on this topic investigates the partitioning of the energy balance residual between the sensible and the latent heat flux (e.g., [55.100, 171]) and the predictability of the magnitude of the missing flux [55.186]. It is still debated, whether the closure problem indicates a possible general underestimation also of other scalars, such as, e.g., CO₂.

55.9.2 Correction and of Probe-Induced Flow Distortion Effects and Sensor Optimizations

Probe-induced flow distortion, which is sometimes reduced to transducer shadowing effects, has been a topic of increasing interest over the past years, in part also related with investigations of the energy balance closure problem. Several studies suggesting that most of today's commercially available sonic anemometers are prone to a nonnegligible systematic underestimation of vertical velocity fluctuations and, consequently, velocity variances, covariances and, thus, flux estimates [55.110, 120]. The findings are, however, mostly based on field intercomparison studies, which are afflicted with the general problem that they do not have a clear reference measurement. This is only available in a wind tunnel, however it is questionable whether the flow-distortion effects can be transferred from these quasi laminar conditions to real-world boundary layer flows with very high Reynolds numbers [55.187]. To overcome these difficulties, the use of numerical simulations of the turbulent air flow around an anemometer was proposed [55.121]. Further development of this approach will probably allow us to obtain more accurate correction algorithms in the future and help to optimize the instruments' geometry.

55.9.3 Spatial Eddy Covariance, Eddy Covariance from Lidar Measurements

Another reason for the nonclosure of the energy balance can be the inherent high-pass filtering of any eddy-

covariance measurement on a single tower [55.81]. Even corrections to account for the missing low-frequency flux contribution cannot fully compensate for these losses, because all currently available methods are based on cospectra measured over homogeneous and flat terrain, so that any heterogeneity-induced circulations are not considered. In addition, secondary circulations often do not propagate with the mean wind and, therefore, cannot be captured by a temporal covariance [55.188]. A solution for this problem could be the calculation of a spatial covariance from multiple tow-

ers as proposed in the Large Eddy Simulation study of [55.189]. This principle has been partially tested under field conditions by means of airborne measurements [55.190] and multitower experiments [55.191, 192]. However, further field campaigns with a larger number of eddy-covariance towers are needed in order to fully explore the potential of a spatial eddy-covariance approach. Perhaps this will even be implemented by using a combination of wind, temperature, and water vapor lidars (light detection and ranging) in the future [55.193].

55.10 Further Readings

- M. Aubinet, T. Vesala, D. Papale (Eds.): *Eddy Covariance: A Practical Guide to Measurement and Data Analysis* (Springer, Dordrecht, Heidelberg, London, New York 2012)
 - T. Foken: *Micrometeorology*, 2nd edn. (Springer, Berlin, Heidelberg 2017)
 - X. Lee: *Fundamentals of Boundary-Layer Meteorology* (Springer, Cham 2018)
 - X. Lee, W.J. Massman, B. Law (Eds.): *Handbook of Micrometeorology: A Guide for Surface Flux Measurement and Analysis* (Springer, Dordrecht 2004)
- A comprehensive review of the diverse sensors, applications and maintenance of eddy-covariance systems is given by:
- G. Burba (2013) Eddy Covariance Method—for Scientific, Industrial, Agricultural, and Regulatory Applications, available at: https://www.licor.com/env/products/eddy_covariance/resources, Accessed 22 July 2021

References

- | | | | |
|------|---|-------|--|
| 55.1 | D. Baldocchi: Measuring fluxes of trace gases and energy between ecosystems and the atmosphere – The state and future of the eddy covariance method, <i>Glob. Chang. Biol.</i> 20 , 3600–3609 (2014) | 55.8 | R. Leuning: The correct form of the Webb, Pearman and Leuning Equation for eddy fluxes of trace gases in steady and non-steady state, horizontally homogeneous flows, <i>Bound.-Layer Meteorol.</i> 123 , 263–267 (2007) |
| 55.2 | T. Foken: <i>Micrometeorology</i> , 2nd edn. (Springer, Berlin, Heidelberg 2017) | 55.9 | E.K. Webb, G.I. Pearman, R. Leuning: Correction of the flux measurements for density effects due to heat and water vapour transfer, <i>Q. J. R. Meteorol. Soc.</i> 106 , 85–100 (1980) |
| 55.3 | X. Lee: <i>Fundamentals of Boundary-Layer Meteorology</i> (Springer, Cham 2018) | 55.10 | R.B. Montgomery: Vertical eddy flux of heat in the atmosphere, <i>J. Atmos. Sci.</i> 5 , 265–274 (1948) |
| 55.4 | ISO 80000-9:2009: <i>Quantities and Units – Part 9: Physical Chemistry and Molecular Physics</i> (Beuth, Berlin 2009) | 55.11 | W.C. Swinbank: The measurement of vertical transfer of heat and water vapor by eddies in the lower atmosphere, <i>J. Atmos. Sci.</i> 8 , 135–145 (1951) |
| 55.5 | T. Foken, M. Aubinet, R. Leuning: The eddy-covarianced method. In: <i>Eddy Covariance: A Practical Guide to Measurement and Data Analysis</i> , ed. by M. Aubinet, T. Vesala, D. Papale (Springer, Dordrecht, Heidelberg, London, New York 2012) pp. 1–19 | 55.12 | A.M. Obukhov: Charakteristiki mikrostruktury vetra v prizemnom sloje atmosfery (Characteristics of the micro-structure of the wind in the surface layer of the atmosphere), <i>Izv. AN SSSR Ser. Geofiz.</i> 3 , 49–68 (1951) |
| 55.6 | A.S. Kowalski, P. Serrano-Ortiz: On the relationship between the eddy covariance, the turbulent flux, and surface exchange for a trace gas such as CO ₂ , <i>Bound.-Layer Meteorol.</i> 124 , 129–141 (2007) | 55.13 | A.J. Dyer, F.J. Maher: Automatic eddy-flux measurement with the evapotron, <i>J. Appl. Meteorol.</i> 4 , 622–625 (1965) |
| 55.7 | R. Leuning: Measurements of trace gas fluxes in the atmosphere using eddy covariance: WPL corrections revisited. In: <i>Handbook of Micrometeorology: A Guide for Surface Flux Measurements and Analysis</i> , ed. by X. Lee, W.J. Massman, B. Law (Kluwer, Dordrecht 2004) pp. 119–132 | 55.14 | A.J. Dyer, B.B. Hicks, K.M. King: The Fluxatron – A revised approach to the measurement of eddy fluxes in the lower atmosphere, <i>J. Appl. Meteorol. Climatol.</i> 6 , 408–413 (1967) |

- 55.15 T. Foken: 50 years of the Monin–Obukhov similarity theory, *Bound.-Layer Meteorol.* **119**, 431–447 (2006)
- 55.16 R.M. Schotland: The measurement of wind velocity by sonic waves, *J. Meteorol.* **12**, 386–390 (1955)
- 55.17 E.W. Barrett, V.E. Suomi: Preliminary report on temperature measurement by sonic means, *J. Meteorol.* **6**, 273–276 (1949)
- 55.18 V.E. Suomi: Sonic anemometer – University of Wisconsin. In: *Exploring the Atmosphere's First Mile*, Vol. 1, ed. by H.H. Lettau, B. Davidson (Pergamon Press, London, New York 1957) pp. 256–266
- 55.19 H.H. Lettau, B. Davidson (Eds.): *Exploring the Atmosphere's First Mile*, Vol. 1 (Pergamon Press, London, New York 1957)
- 55.20 V.M. Bovscheverov, V.P. Voronov: Akusticheskii fljuzer (Acoustic rotor), *Izv. AN SSSR Ser. Geofiz.* **6**, 882–885 (1960)
- 55.21 J.C. Kaimal, J.A. Businger: A continuous wave sonic anemometer–thermometer, *J. Appl. Meteorol.* **2**, 156–164 (1963)
- 55.22 Y. Mitsuta: Sonic anemometer–thermometer for general use, *J. Meteorol. Soc. Japan* **44**, 12–24 (1966)
- 55.23 T. Hanafusa, T. Fujitana, Y. Kobori, Y. Mitsuta: A new type sonic anemometer–thermometer for field operation, *Pap. Meteorol. Geophys.* **33**, 1–19 (1982)
- 55.24 A.J. Dyer, J.R. Garratt, R.J. Francey, I.C. McIlroy, N.E. Bacon, P. Hyson, E.F. Bradley, D.T. Denmead, L.R. Tsvang, J.A. Volkov, B.M. Kaprov, L.G. Elagina, K. Sahashi, N. Monji, T. Hanafusa, O. Tsukamoto, P. Frenzen, B.B. Hicks, M. Wesely, M. Miyake, W.J. Shaw: An international turbulence comparison experiment (ITCE 1976), *Bound.-Layer Meteorol.* **24**, 181–209 (1982)
- 55.25 M. Miyake, R.W. Stewart, R.W. Burling, L.R. Tsvang, B.M. Kaprov, O.A. Kuznecov: Comparison of acoustic instruments in an atmospheric flow over water, *Bound.-Layer Meteorol.* **2**, 228–245 (1971)
- 55.26 L.R. Tsvang, B.M. Kaprov, S.L. Zubkovskij, A.J. Dyer, B.B. Hicks, M. Miyake, R.W. Stewart, J.W. McDonald: Comparison of turbulence measurements by different instruments; Tsimlyansk Field Experiment 1970, *Bound.-Layer Meteorol.* **3**, 499–521 (1973)
- 55.27 P.J. Sellers, F.G. Hall, G. Asrar, D.E. Strebel, R.E. Murphy: The first ISLSCP field experiment (FIFE), *Bull. Am. Meteorol. Soc.* **69**, 22–27 (1988)
- 55.28 J.-C. André, P. Bougeault, J.-P. Goutorbe: Regional estimates of heat and evaporation fluxes over non-homogeneous terrain, examples from the HAPEX-MOBILHY programme, *Bound.-Layer Meteorol.* **50**, 77–108 (1990)
- 55.29 L.R. Tsvang, M.M. Fedorov, B.A. Kader, S.L. Zubkovskii, T. Foken, S.H. Richter, J. Zelený: Turbulent exchange over a surface with chessboard-type inhomogeneities, *Bound.-Layer Meteorol.* **55**, 141–160 (1991)
- 55.30 G.A. McBean: Instrument requirements for eddy correlation measurements, *J. Appl. Meteorol.* **11**, 1078–1084 (1972)
- 55.31 A.L. Buck: Development of an improved Lyman-alpha hygrometer, *Atmos. Technol.* **2**, 213–240 (1973)
- 55.32 S.I. Kretschmer, J.V. Karpovitsch: Maloinercionnyj ultrafioletovyy vlagometer (Sensitive ultraviolet hygrometer), *Izv. AN SSSR Fiz. Atmos. Okeana* **9**, 642–645 (1973)
- 55.33 L. Martini, B. Stark, G. Hunsalz: Elektronisches Lyman-Alpha-Feuchtigkeitsmessgerät, *Z. Meteorol.* **23**, 313–322 (1973)
- 55.34 L.G. Elagina: Opticheskij pribor dlja izmerenija turbulentnykh pulsacii vlaschnosti (Optical sensor for the measurement of turbulent humidity fluctuations), *Izv. AN SSSR Ser. Geofiz.* **12**, 1100–1107 (1962)
- 55.35 P. Hyson, B.B. Hicks: A single-beam infrared hygrometer for evaporation measurement, *J. Appl. Meteorol.* **14**, 301–307 (1975)
- 55.36 M.R. Raupach: Infrared fluctuation hygrometer in the atmospheric surface layer, *Q. J. R. Meteorol. Soc.* **104**, 309–322 (1978)
- 55.37 P. Schotanus, F.T.M. Nieuwstadt, H.A.R. DeBruin: Temperature measurement with a sonic anemometer and its application to heat and moisture fluctuations, *Bound.-Layer Meteorol.* **26**, 81–93 (1983)
- 55.38 C.J. Moore: Frequency response corrections for eddy correlation systems, *Bound.-Layer Meteorol.* **37**, 17–35 (1986)
- 55.39 E. Ohtaki, T. Matsui: Infrared device for simultaneous measurement of fluctuations of atmospheric carbon dioxide and water vapor, *Bound.-Layer Meteorol.* **24**, 109–119 (1982)
- 55.40 L.G. Elagina, A.I. Lazarev: Izmerenija tschasotnykh spektrov turbulentnykh pulsacij CO₂ v prizemnom sloje atmosfery (Measurement of the turbulence spectra of CO₂ in the atmospheric surface layer), *Izv. AN SSSR Fiz. Atmos. Okeana* **20**, 536–540 (1984)
- 55.41 R.T. McMillen: An eddy correlation technique with extended applicability to non-simple terrain, *Bound.-Layer Meteorol.* **43**, 231–245 (1988)
- 55.42 J.H.C. Gash: A note on estimating the effect of a limited fetch on micrometeorological evaporation measurements, *Bound.-Layer Meteorol.* **35**, 409–414 (1986)
- 55.43 H.P. Schmid, T.R. Oke: A model to estimate the source area contributing to turbulent exchange in the surface layer over patchy terrain, *Q. J. R. Meteorol. Soc.* **116**, 965–988 (1990)
- 55.44 P.H. Schuepp, M.Y. Leclerc, J.I. MacPherson, R.L. Desjardins: Footprint prediction of scalar fluxes from analytical solutions of the diffusion equation, *Bound.-Layer Meteorol.* **50**, 355–373 (1990)
- 55.45 R.L. Desjardins, J.I. MacPherson, P.H. Schuepp, F. Karanja: An evaluation of aircraft flux measurements of CO₂, water vapor and sensible heat, *Bound.-Layer Meteorol.* **47**, 55–69 (1989)

- 55.46 S.P. Oncley, J.A. Businger, E.C. Itsweire, C.A. Friehe, J.C. LaRue, S.S. Chang: Surface layer profiles and turbulence measurements over uniform land under near-neutral conditions. In: *9th Symp. Bound. Layer Turbul.* (AMS, Washington 1990) pp. 237–240
- 55.47 R.L. Desjardins: Description and evaluation of a sensible heat flux detector, *Bound.-Layer Meteorol.* **11**, 147–154 (1977)
- 55.48 J.A. Businger, S.P. Oncley: Flux measurement with conditional sampling, *J. Atmos. Ocean. Technol.* **7**, 349–352 (1990)
- 55.49 J.C. Kaimal, D.A. Haugen: Some errors in the measurement of Reynolds stress, *J. Appl. Meteorol.* **8**, 460–462 (1969)
- 55.50 J.C. Kaimal, J.J. Finnigan: *Atmospheric Boundary Layer Flows: Their Structure and Measurement* (Oxford Univ. Press, New York 1994)
- 55.51 J.M. Wilczak, S.P. Oncley, S.A. Stage: Sonic anemometer tilt correction algorithms, *Bound.-Layer Meteorol.* **99**, 127–150 (2001)
- 55.52 R.L. Leuning, J.B. Moncrieff: Eddy covariance CO₂ flux measurements using open and closed path CO₂ analysers: Correction for analyser water vapour sensitivity and damping of fluctuations in air sampling tubes, *Bound.-Layer Meteorol.* **53**, 63–76 (1990)
- 55.53 T.W. Horst, J.C. Weil: How far is far enough?: The fetch requirements for micrometeorological measurement of surface fluxes, *J. Atmos. Ocean. Technol.* **11**, 1018–1025 (1994)
- 55.54 D.H. Lenschow, J. Mann, L. Kristensen: How long is long enough when measuring fluxes and other turbulence statistics?, *J. Atmos. Ocean. Technol.* **11**, 661–673 (1994)
- 55.55 T. Foken, S.P. Oncley: Workshop on instrumental and methodical problems of land surface flux measurements, *Bull. Am. Meteorol. Soc.* **76**, 1191–1193 (1995)
- 55.56 A.E. Gurjanov, S.L. Zubkovskij, M.M. Fedorov: Mnogokanalnaja avtomatizirovannaja sistema obrabotki signalov na baze EVM (Automatic multi-channel system for signal analysis with electronic data processing), *Geod. Geophys. Veröff. Reihe II* **26**, 17–20 (1984)
- 55.57 T. Foken, B. Wichura: Tools for quality assessment of surface-based flux measurements, *Agric. For. Meteorol.* **78**, 83–105 (1996)
- 55.58 D. Vickers, L. Mahrt: Quality control and flux sampling problems for tower and aircraft data, *J. Atmos. Ocean. Technol.* **14**, 512–526 (1997)
- 55.59 X. Lee: On micrometeorological observations of surface-air exchange over tall vegetation, *Agric. For. Meteorol.* **91**, 39–49 (1998)
- 55.60 M. Aubinet, A. Grelle, A. Ibrom, Ü. Rannik, J. Moncrieff, T. Foken, A.S. Kowalski, P.H. Martin, P. Berbigier, C. Bernhofer, R. Clement, J. Elbers, A. Granier, T. Grünwald, K. Morgenstern, K. Pilegaard, C. Rebmann, W. Snijders, R. Valentini, T. Vesala: Estimates of the annual net carbon and water exchange of forests: The Euroflux methodology, *Adv. Ecol. Res.* **30**, 113–175 (1999)
- 55.61 D. Baldocchi, E. Falge, L. Gu, R. Olson, D. Hollinger, S. Running, P. Anthoni, C. Bernhofer, K. Davis, R. Evans, J. Fuentes, A. Goldstein, G. Katul, B. Law, X.H. Lee, Y. Malhi, T. Meyers, W. Munger, W. Oechel, K.T. Paw U, K. Pilegaard, H.P. Schmid, R. Valentini, S. Verma, T. Vesala: Fluxnet: A new tool to study the temporal and spatial variability of ecosystem-scale carbon dioxide, water vapor, and energy flux densities, *Bull. Am. Meteorol. Soc.* **82**, 2415–2434 (2001)
- 55.62 S.F. Zhang, J.C. Wyngaard, J.A. Businger, S.P. Oncley: Response characteristics of the U.W. sonic anemometer, *J. Atmos. Ocean. Technol.* **2**, 548–558 (1986)
- 55.63 J.B. Moncrieff, R. Valentini, S. Greco, G. Seufert, P. Ciccioli: Trace gas exchange over terrestrial ecosystems: Methods and perspectives in micrometeorology, *J. Exp. Bot.* **48**, 1133–1142 (1997)
- 55.64 J.B. Moncrieff, J.M. Massheder, H. DeBruin, J. Elbers, T. Friborg, B. Heusinkveld, P. Kabat, S. Scott, H. Sjøgaard, A. Verhoef: A system to measure surface fluxes of momentum, sensible heat, water vapor and carbon dioxide, *J. Hydrol.* **188/189**, 589–611 (1997)
- 55.65 M. Aubinet, T. Vesala, D. Papale (Eds.): *Eddy Covariance: A Practical Guide to Measurement and Data Analysis* (Springer, Dordrecht, Heidelberg, London, New York 2012)
- 55.66 X. Lee, W.J. Massman, B. Law (Eds.): *Handbook of Micrometeorology: A Guide for Surface Flux Measurement and Analysis* (Kluwer, Dordrecht 2004)
- 55.67 N. Mölders, G. Kramm: *Lectures in Meteorology* (Springer, Cham, Heidelberg, New York, Dordrecht, London 2014)
- 55.68 M. Aubinet, B. Heinesch, M. Yernaux: Horizontal and vertical CO₂ advection in a sloping forest, *Bound.-Layer Meteorol.* **108**, 397–417 (2003)
- 55.69 M. Aubinet, P. Berbigier, C. Bernhofer, A. Cescatti, C. Feigenwinter, A. Granier, T. Grünwald, K. Havrankova, B. Heinesch, B. Longdoz, B. Marcolla, L. Montagnani, P. Sedlak: Comparing CO₂ storage and advection conditions at night at different carboeuroflux sites, *Bound.-Layer Meteorol.* **116**, 63–94 (2005)
- 55.70 M. Aubinet, C. Feigenwinter, B. Heinesch, C. Bernhofer, E. Canepa, A. Lindroth, L. Montagnani, C. Rebmann, P. Sedlak, E. Van Gorsel: Direct advection measurements do not help to solve the night-time CO₂ closure problem: Evidence from three different forests, *Agric. For. Meteorol.* **150**, 655–664 (2010)
- 55.71 M. Aubinet, C. Feigenwinter, B. Heinesch, Q. Laffineur, D. Papale, M. Reichstein, J. Rinne, E. Van Gorsel: Nighttime flux correction. In: *Eddy Covariance: A Practical Guide to Measurement and Data Analysis*, ed. by M. Aubinet, T. Vesala, D. Papale (Springer, Berlin, Heidelberg 2012) pp. 133–157
- 55.72 L. Gu, E.M. Falge, T. Boden, D.D. Baldocchi, T. Black, S.R. Saleska, T. Sumi, S.B. Verma, T. Vesala, S.C. Wofsy, L. Xu: Objective threshold

- determination for nighttime eddy flux filtering, *Agric. For. Meteorol.* **128**, 179–197 (2005)
- 55.73 M. Reichstein, E. Falge, D. Baldocchi, D. Papale, M. Aubinet, P. Berbigier, C. Bernhofer, N. Buchmann, T. Gilmanov, A. Granier, T. Grünwald, K. Havránková, H. Ilvesniemi, D. Janous, A. Knohl, T. Laurila, A. Lohila, D. Loustau, G. Matteucci, T. Meyers, F. Miglietta, J.-M. Ourcival, J. Pumpanen, S. Rambal, E. Rotenberg, M. Sanz, J. Tenhunen, G. Seufert, F. Vaccari, T. Vesala, D. Yakir, R. Valentini: On the separation of net ecosystem exchange into assimilation and ecosystem respiration: Review and improved algorithm, *Glob. Chang. Biol.* **11**, 1424–1439 (2005)
- 55.74 E. Falge, D. Baldocchi, R. Olson, P. Anthoni, M. Aubinet, C. Bernhofer, G. Burba, R. Ceulemans, R. Clement, H. Dolman, A. Granier, P. Gross, T. Grunwald, D. Hollinger, N.O. Jensen, G. Katul, P. Keronen, A. Kowalski, C.T. Lai, B.E. Law, T. Meyers, H. Moncrieff, E. Moors, J.W. Munger, K. Pilegaard, Ü. Rannik, C. Rebmann, A. Suyker, J. Tenhunen, K. Tu, S. Verma, T. Vesala, K. Wilson, S. Wofsy: Gap filling strategies for defensible annual sums of net ecosystem exchange, *Agric. For. Meteorol.* **107**, 43–69 (2001)
- 55.75 M. Mauder, M. Cuntz, C. Drüe, A. Graf, C. Rebmann, H.P. Schmid, M. Schmidt, R. Steinbrecher: A strategy for quality and uncertainty assessment of long-term eddy-covariance measurements, *Agric. For. Meteorol.* **169**, 122–135 (2013)
- 55.76 J. Højstrup: A statistical data screening procedure, *Meas. Sci. Technol.* **4**, 153–157 (1993)
- 55.77 D.C. Hoaglin, F. Mosteller, J.W. Tukey: *Understanding Robust and Exploratory Data Analysis* (John Wiley & Sons, New York 2000)
- 55.78 I. Van der Hoven: Power spectrum of horizontal wind speed in the frequency range from 0.0007 to 900 cycles per hour, *J. Meteorol.* **14**, 160–164 (1957)
- 55.79 T.W. Horst: A simple formula for attenuation of eddy fluxes measured with first-order-response scalar sensors, *Bound.-Layer Meteorol.* **82**, 219–233 (1997)
- 55.80 Ü. Rannik, T. Vesala: Autoregressive filtering versus linear detrending in estimation of fluxes by the eddy covariance method, *Bound.-Layer Meteorol.* **91**, 259–280 (1999)
- 55.81 J.J. Finnigan, R. Clement, Y. Malhi, R. Leuning, H.A. Cleugh: A re-evaluation of long-term flux measurement techniques, Part I: Averaging and coordinate rotation, *Bound.-Layer Meteorol.* **107**, 1–48 (2003)
- 55.82 J. Moncrieff, R. Clement, J. Finnigan, T. Meyers: Averaging, detrending, and filtering of eddy covariance time series. In: *Handbook of Micrometeorology. A Guide for Surface Flux Measurement and Analysis*, ed. by X. Lee, W. Massman, B. Law (Kluwer, Dordrecht 2004) pp. 7–31
- 55.83 T. Foken, R. Dlugi, G. Kramm: On the determination of dry deposition and emission of gaseous compounds at the biosphere-atmosphere interface, *Meteorol. Z.* **4**, 91–118 (1995)
- 55.84 T. Foken, F. Wimmer, M. Mauder, C. Thomas, C. Liebenthal: Some aspects of the energy balance closure problem, *Atmos. Chem. Phys.* **6**, 4395–4402 (2006)
- 55.85 H. Liu, G. Peters, T. Foken: New equations for sonic temperature variance and buoyancy heat flux with an omnidirectional sonic anemometer, *Bound.-Layer Meteorol.* **100**, 459–468 (2001)
- 55.86 P. Hyson, J.R. Garratt, R.J. Francey: Algebraic and electronic corrections of measured *uw* covariance in the lower atmosphere, *Bound.-Layer Meteorol.* **16**, 43–47 (1977)
- 55.87 C.B. Tanner, G.W. Thurtell: *Anemoclinometer Measurements of Reynolds Stress and Heat Transport in the Atmospheric Surface Layer* (ECOM, Atmospheric Sciences Laboratory, Fort Huachuca 1969), Tech. Rep. ECOM 66–G22–F
- 55.88 K. Jentsch, A. Schulz, N. Pirk, T. Foken, S. Crewell, J. Boike: High levels of CO₂ exchange during synoptic-scale events introduce large uncertainty into the Arctic carbon budget. *Geophys Res Letters*. **48**, e2020GL092256 (2021)
- 55.89 R. Leuning, M.J. Judd: The relative merits of open- and closed path analysers for measurements of eddy fluxes, *Glob. Chang. Biol.* **2**, 241–254 (1996)
- 55.90 A. Ibrom, E. Dellwik, H. Flyvbjerg, N.O. Jensen, K. Pilegaard: Strong low-pass filtering effects on water vapour flux measurements with closed-path eddy correlation systems, *Agric. For. Meteorol.* **147**, 140–156 (2007)
- 55.91 A. Ibrom, E. Dellwik, S.E. Larsen, K. Pilegaard: On the use of the Webb–Pearman–Leuning theory for closed-path eddy correlation measurements, *Tellus B* **59**, 937–946 (2007)
- 55.92 J.C. Kaimal, J.E. Gaynor: Another look to sonic thermometry, *Bound.-Layer Meteorol.* **56**, 401–410 (1991)
- 55.93 T.W. Horst: On frequency response corrections for eddy covariance flux measurements, *Bound.-Layer Meteorol.* **94**, 517–520 (2000)
- 55.94 W.J. Massman: A simple method for estimating frequency response corrections for eddy covariance systems, *Agric. For. Meteorol.* **104**, 185–198 (2000)
- 55.95 W. Eugster, W. Senn: A cospectral correction for measurement of turbulent NO₂ flux, *Bound.-Layer Meteorol.* **74**, 321–340 (1995)
- 55.96 M. Aubinet, L. Joly, D. Loustau, A. De Ligne, H. Chopin, J. Cousin, N. Chauvin, T. Decarpenterie, P. Gross: Dimensioning IRGA gas sampling systems: Laboratory and field experiments, *Atmos. Meas. Tech.* **9**, 1361–1367 (2016)
- 55.97 S. Metzger, G. Burba, S.P. Burns, P.D. Blanken, J. Li, H. Luo, R.C. Zulueta: Optimization of an enclosed gas analyzer sampling system for measuring eddy covariance fluxes of H₂O and CO₂, *Atmos. Meas. Tech.* **9**, 1341–1359 (2016)
- 55.98 A. Moravek, I. Trebs, T. Foken: Effect of imprecise lag time and high-frequency attenuation on surface-atmosphere exchange fluxes determined

- with the relaxed eddy accumulation method, *J. Geophys. Res. Atmos.* **118**, 10210–10224 (2013)
- 55.99 T. Foken, R. Leuning, S.P. Oncley, M. Mauder, M. Aubinet: Corrections and data quality. In: *Eddy Covariance: A Practical Guide to Measurement and Data Analysis*, ed. by M. Aubinet, T. Vesala, D. Papale (Springer, Dordrecht, Heidelberg, London, New York 2012) pp. 85–131
- 55.100 D. Charuchittipan, W. Babel, M. Mauder, J.-P. Leps, T. Foken: Extension of the averaging time of the eddy-covariance measurement and its effect on the energy balance closure, *Bound.-Layer Meteorol.* **152**, 303–327 (2014)
- 55.101 O. Peltola, I. Mammarella, S. Haapanala, G. Burba, T. Vesala: Field intercomparison of four methane gas analyzers suitable for eddy covariance flux measurements, *Biogeosciences* **10**, 3749–3765 (2013)
- 55.102 C. Rebmann, O. Kolle, B. Heinesch, R. Queck, A. Ibrom, M. Aubinet: Data acquisition and flux calculations. In: *Eddy Covariance: A Practical Guide to Measurement and Data Analysis*, ed. by M. Aubinet, T. Vesala, D. Papale (Springer, Dordrecht, Heidelberg, London, New York 2012) pp. 59–83
- 55.103 B.D. Tanner, E. Swiatek, J.P. Greene: Density fluctuations and use of the krypton hygrometer in surface flux measurements. In: *Management of Irrigation and Drainage Systems: Integrated Perspectives*, ed. by R.G. Allen (ASCE, New York 1993) pp. 945–952
- 55.104 A. van Dijk, W. Kohsiek, H.A.R. DeBruin: Oxygen sensitivity of krypton and Lyman-alpha hygrometers, *J. Atmos. Ocean. Technol.* **20**, 143–151 (2003)
- 55.105 M. Mauder, T. Foken: Impact of post-field data processing on eddy covariance flux estimates and energy balance closure, *Meteorol. Z.* **15**, 597–609 (2006)
- 55.106 R.R. Brook: The influence of water vapor fluctuations on turbulent fluxes, *Bound.-Layer Meteorol.* **15**, 481–487 (1978)
- 55.107 H. Liu, J.T. Randerson, J. Lindfors, W.J. Massman, T. Foken: Consequences of incomplete surface energy balance closure for CO₂ fluxes from open-path CO₂/H₂O infrared gas analyzers, *Bound.-Layer Meteorol.* **120**, 65–85 (2006)
- 55.108 J.C. Kaimal, J.E. Gaynor, H.A. Zimmerman, G.A. Zimmerman: Minimizing flow distortion errors in a sonic anemometer, *Bound.-Layer Meteorol.* **53**, 103–115 (1990)
- 55.109 J.C. Wyngaard, S.-F. Zhang: Transducer-shadow effects on turbulence spectra measured by sonic anemometers, *J. Atmos. Ocean. Technol.* **2**, 548–558 (1985)
- 55.110 T.W. Horst, S.R. Semmer, G. Maclean: Correction of a non-orthogonal, three-component sonic anemometer for flow distortion by transducer shadowing, *Bound.-Layer Meteorol.* **155**, 371–395 (2015)
- 55.111 T. Nakai, M.K. van der Molen, J.H.C. Gash, Y. Kodama: Correction of sonic anemometer angle of attack errors, *Agric. For. Meteorol.* **136**, 19–30 (2006)
- 55.112 T. Nakai, K. Shimoyama: Ultrasonic anemometer angle of attack errors under turbulent conditions, *Agric. For. Meteorol.* **162/163**, 14–26 (2012)
- 55.113 F. Kittler, W. Eugster, T. Foken, M. Heimann, O. Kolle, M. Göckede: High-quality eddy-covariance CO₂ budgets under cold climate conditions, *J. Geophys. Res. Biogeosci.* **122**, 2064–2084 (2017)
- 55.114 J.P. Goodrich, W.C. Oechel, B. Gioli, V. Moreaux, P.C. Murphy, G. Burba, D. Zona: Impact of different eddy covariance sensors, site set-up, and maintenance on the annual balance of CO₂ and CH₄ in the harsh Arctic environment, *Agric. For. Meteorol.* **228/229**, 239–251 (2016)
- 55.115 T. Foken, W. Babel, C. Thomas: Possible errors in flux measurements due to limited digitalization, *Atmos. Meas. Tech.* **12**, 971–976 (2019)
- 55.116 J. Kochendorfer, T. Meyers, J. Frank, W. Massman, M. Heuer: How well can we measure the vertical wind speed? Implications for fluxes of energy and mass, *Bound.-Layer Meteorol.* **145**, 383–398 (2012)
- 55.117 M. Mauder: A comment on “How well can we measure the vertical wind speed? Implications for fluxes of energy and mass” by J. Kochendorfer, T. Meyers, J. Frank, W. Massman, M. Heuer, *Bound.-Layer Meteorol.* **147**, 329–335 (2013)
- 55.118 A.J. Dyer: Flow distortion by supporting structures, *Bound.-Layer Meteorol.* **20**, 363–372 (1981)
- 55.119 J.C. Kaimal: Sonic anemometer measurement of atmospheric turbulence. In: *Proceedings of the Dynamic Flow Conference 1978 on Dynamic Measurements in Unsteady Flows*, ed. by B.W. Hansen (Springer, Dordrecht 1978) pp. 551–565
- 55.120 J.M. Frank, W.J. Massman, B.E. Ewers: Underestimates of sensible heat flux due to vertical velocity measurement errors in non-orthogonal sonic anemometers, *Agric. For. Meteorol.* **171/172**, 72–81 (2013)
- 55.121 S. Huq, F. De Roo, T. Foken, M. Mauder: Evaluation of probe-induced flow distortion of Campbell CSAT3 sonic anemometers by numerical simulation, *Bound.-Layer Meteorol.* **165**, 9–28 (2017)
- 55.122 G. Burba, D.K. McDermitt, A. Grelle, D.J. Anderson, L. Xu: Addressing the influence of instrument surface heat exchange on the measurements of CO₂ flux from open-path gas analyzers, *Glob. Chang. Biol.* **14**, 1854–1876 (2008)
- 55.123 G. Burba, D. Anderson: *A Brief Practical Guide to Eddy Covariance Flux Measurements* (Li-COR Inc., Lincoln 2010)
- 55.124 A. Grelle, G. Burba: Fine-wire thermometer to correct CO₂ fluxes by open-path analyzers for artificial density fluctuations, *Agric. For. Meteorol.* **147**, 48–57 (2007)
- 55.125 L. Järvi, I. Mammarella, W. Eugster, A. Ibrom, E. Siivola, E. Dellwik, P. Keronen, G. Burba, T. Vesala: Comparison of net CO₂ fluxes measured with open- and closed-path infrared gas analyzers in urban complex environment, *Boreal Environ. Res.* **14**, 499–514 (2009)

- 55.126 P. Werle, F. D'Amato, S. Viciani: Tunable diode-laser spectroscopy: Principles, performance, perspectives. In: *Lasers in Chemistry – Probing Matter*, ed. by M. Lackner (Wiley-VCH, Weinheim 2008) pp. 255–275
- 55.127 S.P. Oncley, T. Foken, R. Vogt, W. Kohsiek, H.A.R. DeBruin, C. Bernhofer, A. Christen, E. van Gorsel, D. Grantz, C. Feigenwinter, I. Lehner, C. Liebenthal, H. Liu, M. Mauder, A. Pitacco, L. Ribeiro, T. Weidinger: The energy balance experiment EBEX-2000. Part I: Overview and energy balance, *Bound.-Layer Meteorol.* **123**, 1–28 (2007)
- 55.128 VDI 3786, Part 12:2019-06: *Environmental Meteorology – Meteorological Measurements – Turbulence Measurements with Sonic Anemometers* (Beuth, Berlin 2019)
- 55.129 G. Fratini, M. Mauder: Towards a consistent eddy-covariance processing: An intercomparison of EddyPro and TK3, *Atmos. Meas. Tech.* **7**, 2273–2281 (2014)
- 55.130 G. Fratini, A. Ibrom, N. Arriga, G. Burba, D. Papale: Relative humidity effects on water vapour fluxes measured with closed-path eddy-covariance systems with short sampling lines, *Agric. For. Meteorol.* **165**, 53–63 (2012)
- 55.131 D.R. Bowling, D.E. Pataki, J.R. Ehleringer: Critical evaluation of micrometeorological methods for measuring ecosystem-atmosphere isotopic exchange of CO₂, *Agric. For. Meteorol.* **116**, 159–179 (2003)
- 55.132 E. Pattey, I.B. Strachan, R.L. Desjardins, G.C. Edwards, D. Dow, I.J. MacPherson: Application of a tunable diode laser to the measurement of CH₄ and N₂O fluxes from field to landscape scale using several micrometeorological techniques, *Agric. For. Meteorol.* **136**, 222–236 (2006)
- 55.133 L. Kristensen, J. Mann, S.P. Oncley, J.C. Wyngaard: How close is close enough when measuring scalar fluxes with displaced sensors?, *J. Atmos. Ocean. Technol.* **14**, 814–821 (1997)
- 55.134 C. Barthlott, F. Fiedler: Turbulence structure in the wake region of a meteorological tower, *Bound.-Layer Meteorol.* **108**, 175–190 (2003)
- 55.135 J. Wieringa: A revaluation of the Kansas mast influence on measurements of stress and cup anemometer overspeeding, *Bound.-Layer Meteorol.* **18**, 411–430 (1980)
- 55.136 J.C. Wyngaard: The effects of probe-induced flow distortion on atmospheric turbulence measurements, *J. Appl. Meteorol.* **20**, 784–794 (1981)
- 55.137 J.C. Wyngaard, J.A. Businger, J.C. Kaimal, S.E. Larsen: Comments on 'A revaluation of the Kansas mast influence on measurements of stress and cup anemometer overspeeding', *Bound.-Layer Meteorol.* **22**, 245–250 (1982)
- 55.138 A. Haslwanter, A. Hammerle, G. Wohlfahrt: Open-path vs. closed-path eddy covariance measurements of the net ecosystem carbon dioxide and water vapour exchange: A long-term perspective, *Agric. For. Meteorol.* **149**, 291–302 (2009)
- 55.139 M. Helbig, K. Wischniewski, G.H. Gosselin, S.C. Biraud, I. Bogojev, W.S. Chan, E.S. Euskirchen, A.J. Glenn, P.M. Marsh, W.L. Quinton, O. Sonnentag: Addressing a systematic bias in carbon dioxide flux measurements with the EC150 and the IRGASON open-path gas analyzers, *Agric. For. Meteorol.* **228/229**, 349–359 (2016)
- 55.140 M. Detto, J. Verfaillie, F. Anderson, L. Xu, D. Baldocchi: Comparing laser-based open- and closed-path gas analyzers to measure methane fluxes using the eddy covariance method, *Agric. For. Meteorol.* **151**, 1312–1324 (2011)
- 55.141 M. Mauder, C. Liebenthal, M. Göckede, J.-P. Leps, F. Beyrich, T. Foken: Processing and quality control of flux data during LITFASS-2003, *Bound.-Layer Meteorol.* **121**, 67–88 (2006)
- 55.142 T. Foken, M. Göckede, M. Mauder, L. Mahrt, B.D. Amiro, J.W. Munger: Post-field data quality control. In: *Handbook of Micrometeorology: A Guide for Surface Flux Measurement and Analysis*, ed. by X. Lee, W.J. Massman, B. Law (Kluwer, Dordrecht 2004) pp. 181–208
- 55.143 ISO 16622: *Meteorology – Sonic Anemometer/Thermometer – Acceptance Test Method for Mean Wind Measurements* (ISO, Geneva 2002)
- 55.144 M. Göckede, C. Rebmann, T. Foken: A combination of quality assessment tools for eddy covariance measurements with footprint modelling for the characterisation of complex sites, *Agric. For. Meteorol.* **127**, 175–188 (2004)
- 55.145 M. Göckede, T. Markkanen, C.B. Hasager, T. Foken: Update of a footprint-based approach for the characterisation of complex measuring sites, *Bound.-Layer Meteorol.* **118**, 635–655 (2006)
- 55.146 Ü. Rannik, A. Sogachev, T. Foken, M. Göckede, N. Kljun, M.Y. Leclerc, T. Vesala: Footprint analysis. In: *Eddy Covariance: A Practical Guide to Measurement and Data Analysis*, ed. by M. Aubinet, T. Vesala, D. Papale (Springer, Berlin, Heidelberg 2012) pp. 211–261
- 55.147 M. Mauder, M.J. Zeeman: Field intercomparison of prevailing sonic anemometers, *Atmos. Meas. Tech.* **11**, 249–263 (2018)
- 55.148 T. Foken: The energy balance closure problem – An overview, *Ecol. Appl.* **18**, 1351–1367 (2008)
- 55.149 M. Mauder, T. Foken, J. Cuxart: Surface energy balance closure over land: A review, *Bound.-Layer Meteorol.* **177**, 395–426 (2020)
- 55.150 C. Rebmann, M. Göckede, T. Foken, M. Aubinet, M. Aurela, P. Berbigier, C. Bernhofer, N. Buchmann, A. Carrara, A. Cescatti, R. Ceulemans, R. Clement, J. Elbers, A. Granier, T. Grünwald, D. Guyon, K. Havránková, B. Heinesch, A. Knohl, T. Laurila, B. Longdoz, B. Marcolla, T. Markkanen, F. Miglietta, H. Moncrieff, L. Montagnani, E. Moors, M. Nardino, J.-M. Ourcival, S. Rambal, Ü. Rannik, E. Rotenberg, P. Sedlak, G. Unterhuber, T. Vesala, D. Yakir: Quality analysis applied on eddy covariance measurements at complex forest sites using footprint modelling, *Theor. Appl. Climatol.* **80**, 121–141 (2005)
- 55.151 B.R.F. Oliveira, C. Schaller, J.J. Keizer, T. Foken: Estimating immediate post-fire carbon fluxes

- using the eddy-covariance technique. *Biogeosci.* **18**, 285–302 (2021)
- 55.152 M.Y. Leclerc, T. Foken: *Footprints in Micrometeorology and Ecology* (Springer, Heidelberg, New York, Dordrecht, London 2014)
- 55.153 M. Göckede, T. Foken, M. Aubinet, M. Aurela, J. Banza, C. Bernhofer, J.-M. Bonnefond, Y. Brunet, A. Carrara, R. Clement, E. Dellwik, J.A. Elbers, W. Eugster, J. Fuhrer, A. Granier, T. Grünwald, B. Heinesch, I.A. Janssens, A. Knohl, R. Koeble, T. Laurila, B. Longdoz, G. Manca, M. Marek, T. Markkanen, J. Mateus, G. Matteucci, M. Mauder, M. Migliavacca, S. Minerbi, J.B. Moncrieff, L. Montagnani, E. Moors, J.-M. Ourcival, D. Papale, J. Pereira, K. Pilegaard, G. Pita, S. Rambal, C. Rebmann, A. Rodrigues, E. Rotenberg, M.J. Sanz, P. Sedlak, G. Seufert, L. Siebicke, J.F. Soussana, R. Valentini, T. Vesala, H. Verbeeck, D. Yakir: Quality control of CarboEurope flux data – Part 1: Coupling footprint analyses with flux data quality assessment to evaluate sites in forest ecosystems, *Biogeosciences* **5**, 433–450 (2008)
- 55.154 H.P. Schmid, C.R. Lloyd: Spatial representativeness and the location bias of flux footprints over inhomogeneous areas, *Agric. For. Meteorol.* **93**, 195–209 (1999)
- 55.155 T. Vesala, N. Kljun, Ü. Rannik, J. Rinne, A. Sogachev, T. Markkanen, K. Sabelfeld, T. Foken, M.Y. Leclerc: Flux and concentration footprint modelling: State of the art, *Environ. Pollut.* **152**, 653–666 (2008)
- 55.156 B.D. Amiro: Footprint climatologies for evapotranspiration in a boreal catchment, *Agric. For. Meteorol.* **90**, 195–201 (1998)
- 55.157 H.P. Schmid: Experimental design for flux measurements: Matching scales of observations and fluxes, *Agric. For. Meteorol.* **87**, 179–200 (1997)
- 55.158 Ü. Rannik, T. Markkanen, T. Raittila, P. Hari, T. Vesala: Turbulence statistics inside and above forest: Influence on footprint prediction, *Bound.-Layer Meteorol.* **109**, 163–189 (2003)
- 55.159 A.D. Richardson, M. Aubinet, A.G. Barr, D.Y. Hollinger, A. Ibrom, G. Lasslop, M. Reichstein: Uncertainty quantification. In: *Eddy Covariance: A Practical Guide to Measurement and Data Analysis*, ed. by M. Aubinet, T. Vesala, D. Papale (Springer, Berlin, Heidelberg 2012) pp. 173–209
- 55.160 M. Mauder, S.P. Oncley, R. Vogt, T. Weidinger, L. Ribeiro, C. Bernhofer, T. Foken, W. Kohsiek, H.A.R. DeBruin, H. Liu: The energy balance experiment EBEX-2000. Part II: Intercomparison of eddy covariance sensors and post-field data processing methods, *Bound.-Layer Meteorol.* **123**, 29–54 (2007)
- 55.161 H.W. Loescher, T. Ocheltree, B. Tanner, E. Swiatek, B. Dano, J. Wong, G. Zimmerman, J. Campbell, C. Stock, L. Jacobsen, Y. Shiga, J. Kollas, J. Liburdy, B.E. Law: Comparison of temperature and wind statistics in contrasting environments among different sonic anemometer-thermometers, *Agric. For. Meteorol.* **133**, 119–139 (2005)
- 55.162 M. Mauder, T. Foken, R. Clement, J. Elbers, W. Eugster, T. Grünwald, B. Heusinkveld, O. Kolle: Quality control of CarboEurope flux data – Part 2: Intercomparison of eddy-covariance software, *Biogeosciences* **5**, 451–462 (2008)
- 55.163 K.B. Wilson, A.H. Goldstein, E. Falge, M. Aubinet, D. Baldocchi, P. Berbigier, C. Bernhofer, R. Ceulemans, H. Dolman, C. Field, A. Grelle, B. Law, T. Meyers, J. Moncrieff, R. Monson, W. Oechel, J. Tenhunen, R. Valentini, S. Verma: Energy balance closure at fluxnet sites, *Agric. For. Meteorol.* **113**, 223–234 (2002)
- 55.164 P.C. Stoy, M. Mauder, T. Foken, B. Marcolla, E. Boegh, A. Ibrom, M.A. Arain, A. Arneth, M. Aurela, C. Bernhofer, A. Cescatti, E. Dellwik, P. Duce, D. Gianelle, E. van Gorsel, G. Kiely, A. Knohl, H. Margolis, H. McCaughey, L. Merbold, L. Montagnani, D. Papale, M. Reichstein, P. Serrano-Ortiz, M. Sottocornola, M. Saunders, D. Spano, F. Vaccari, A. Varlagin: A data-driven analysis of energy balance closure across fluxnet research sites: The role of landscape-scale heterogeneity, *Agric. For. Meteorol.* **171/172**, 137–152 (2013)
- 55.165 F. Eder, F. De Roo, K. Kohnert, R. Desjardins, H. Schmid, M. Mauder: Evaluation of two energy balance closure parametrizations, *Bound.-Layer Meteorol.* **151**, 195–219 (2014)
- 55.166 G.N. Panin, G. Tetzlaff, A. Raabe: Inhomogeneity of the land surface and problems in the parameterization of surface fluxes in natural conditions, *Theor. Appl. Climatol.* **60**, 163–178 (1998)
- 55.167 C. Thomas, T. Foken: Flux contribution of coherent structures and its implications for the exchange of energy and matter in a tall spruce canopy, *Bound.-Layer Meteorol.* **123**, 317–337 (2007)
- 55.168 G. Zhang, C. Thomas, M.Y. Leclerc, A. Karipot, H.L. Gholz, T. Foken: On the effect of clearcuts on turbulence structure above a forest canopy, *Theor. Appl. Climatol.* **88**, 133–137 (2007)
- 55.169 T.E. Twine, W.P. Kustas, J.M. Norman, D.R. Cook, P.R. Houser, T.P. Meyers, J.H. Prueger, P.J. Starks, M.L. Wesely: Correcting eddy-covariance flux underestimates over a grassland, *Agric. For. Meteorol.* **103**, 279–300 (2000)
- 55.170 F. Eder, F. De Roo, E. Rotenberg, D. Yakir, H.P. Schmid, M. Mauder: Secondary circulations at a solitary forest surrounded by semi-arid shrubland and their impact on eddy-covariance measurements, *Agric. For. Meteorol.* **211/212**, 115–127 (2015)
- 55.171 M. Mauder, S. Genzel, J. Fu, R. Kiese, M. Soltani, R. Steinbrecher, M. Zeeman, T. Banerjee, F. De Roo, H. Kunstmann: Evaluation of energy balance closure adjustment methods by independent evapotranspiration estimates from lysimeters and hydrological simulations, *Hydrol. Process.* **32**, 39–50 (2018)
- 55.172 J. Ingwersen, K. Steffens, P. Högy, K. Warrach-Sagi, D. Zhunusbayeva, M. Poltoradnev, R. Gäbler, H.-D. Witzmann, A. Fangmeier, V. Wulfmeyer, T. Streck: Comparison of Noah simulations with eddy covariance and soil water measurements at

- a winter wheat stand, *Agric. For. Meteorol.* **151**, 345–355 (2011)
- 55.173 I.G. Huges, T.P.A. Hase: *Measurements and Their Uncertainties* (Oxford Univ. Press, Oxford 2010)
- 55.174 J. Bartels: Zur Morphologie geophysikalischer Zeitfunktionen, *Sitzungsber. Preuss. Akad. Wiss. Phys. Math. Kl.* **30**, 504–522 (1935)
- 55.175 P.L. Finkelstein, P.F. Sims: Sampling error in eddy correlation flux measurements, *J. Geophys. Res. Atmos.* **106**, 3503–3509 (2001)
- 55.176 A.D. Richardson, D.Y. Hollinger, G.G. Burba, K.J. Davis, L.B. Flanagan, G.G. Katul, J.W. Munger, D.M. Ricciuto, P.C. Stoy, A.E. Suyker, S.B. Verma, S.C. Wofsy: A multi-site analysis of random error in tower-based measurements of carbon and energy fluxes, *Agric. For. Meteorol.* **136**, 1–18 (2006)
- 55.177 D.H. Lenschow, V. Wulfmeyer, C. Senff: Measuring second-through fourth-order moments in noisy data, *J. Atmos. Ocean. Technol.* **17**, 1330–1347 (2000)
- 55.178 P.J. Sellers, F.G. Hall, R.D. Kelly, A. Black, D. Baldocchi, J. Berry, M. Ryan, K.J. Ranson, P.M. Crill, D.P. Lettenmaier, H. Margolis, J. Cihlar, J. Newcomer, D. Fitzjarrald, P.G. Jarvis, S.T. Gower, D. Halliwell, D. Williams, B. Goodison, D.E. Wickland, F.E. Guertin: BOREAS in 1997: Experiment overview, scientific results, and future directions, *J. Geophys. Res. Atmos.* **102**, 28731–28769 (1997)
- 55.179 H.-T. Mengelkamp, F. Beyrich, G. Heinemann, F. Ament, J. Bange, F.H. Berger, J. Bösenberg, T. Foken, B. Hennemuth, C. Heret, S. Huneke, K.-P. Johnsen, M. Kerschgens, W. Kohsiek, J.-P. Leps, C. Liebethal, H. Lohse, M. Mauder, W.M.L. Meijninger, S. Raasch, C. Simmer, T. Spieß, A. Tittebrand, S. Uhlenbrook, P. Zittel: Evaporation over a heterogeneous land surface, *Bull. Am. Meteorol. Soc.* **87**, 775–786 (2006)
- 55.180 B. Wolf, C. Chwala, B. Fersch, J. Garvelmann, W. Junkermann, M.J. Zeeman, A. Angerer, B. Adler, C. Beck, C. Brosy, P. Brugger, S. Emeis, M. Dannenmann, F. De Roo, E. Diaz-Pines, E. Haas, M. Hagen, I. Hajnsek, J. Jacobeit, T. Jagdhuber, N. Kalthoff, R. Kiese, H. Kunstmann, O. Kosak, R. Krieg, C. Malchow, M. Mauder, R. Merz, C. Notarnicola, A. Philipp, W. Reif, S. Reineke, T. Rödi-ger, N. Ruehr, K. Schäfer, M. Schrön, A. Senatore, H. Shupe, I. Völksch, C. Wanninger, S. Zacharias, H.P. Schmid: The SCALEX campaign: Scale-crossing land surface and boundary layer processes in the TERENO-prealpine observatory, *Bull. Am. Meteorol. Soc.* **98**, 1217–1234 (2017)
- 55.181 D.D. Baldocchi: Assessing the eddy covariance technique for evaluating carbon dioxide ex-
change rates of ecosystems: Past, present and future, *Glob. Chang. Biol.* **9**, 479–492 (2003)
- 55.182 D. Baldocchi, H. Chu, M. Reichstein: Inter-annual variability of net and gross ecosystem carbon fluxes: A review, *Agric. For. Meteorol.* **249**, 520–533 (2018)
- 55.183 R.L. Desjardins: Carbon dioxide budget of maize, *Agric. For. Meteorol.* **36**, 29–41 (1985)
- 55.184 T. Foken, M. Aubinet, J. Finnigan, M.Y. Leclerc, M. Mauder, K.T. Paw U: Results of a panel discussion about the energy balance closure correction for trace gases, *Bull. Am. Meteorol. Soc.* **92**, ES13–ES18 (2011)
- 55.185 M. Kanda, A. Inagaki, M.O. Letzel, S. Raasch, T. Watanabe: LES study of the energy imbalance problem with eddy covariance fluxes, *Bound.-Layer Meteorol.* **110**, 381–404 (2004)
- 55.186 F. De Roo, M. Mauder: The influence of idealized surface heterogeneity on virtual turbulent flux measurements, *Atmos. Chem. Phys.* **18**, 5059–5074 (2018)
- 55.187 U. Höglström, A. Smedman: Accuracy of sonic anemometers: Laminar wind-tunnel calibrations compared to atmospheric in situ calibrations against a reference instrument, *Bound.-Layer Meteorol.* **111**, 33–54 (2004)
- 55.188 L. Mahrt: Computing turbulent fluxes near the surface: Needed improvements, *Agric. For. Meteorol.* **150**, 501–509 (2010)
- 55.189 G. Steinfeld, M.O. Letzel, S. Raasch, M. Kanda, A. Inagaki: Spatial representativeness of single tower measurements and the imbalance problem with eddy-covariance fluxes: Results of a large-eddy simulation study, *Bound.-Layer Meteorol.* **123**, 77–98 (2007)
- 55.190 M. Mauder, R.L. Desjardins, I. MacPherson: Scale analysis of airborne flux measurements over heterogeneous terrain in a boreal ecosystem, *J. Geophys. Res. Atmos.* **112**, D13112 (2007)
- 55.191 M. Mauder, R.L. Desjardins, E. Pattey, Z. Gao, R. van Haarlem: Measurement of the sensible eddy heat flux based on spatial averaging of continuous ground-based observations, *Bound.-Layer Meteorol.* **128**, 151–172 (2008)
- 55.192 C. Engelmann, C. Bernhofer: Exploring eddy-covariance measurements using a spatial approach: The eddy matrix, *Bound.-Layer Meteorol.* **161**, 1–17 (2016)
- 55.193 C.W. Higgins, M. Froidevaux, V. Simeonov, N. Vercauteren, C. Barry, M.B. Parlange: The effect of scale on the applicability of Taylor's frozen turbulence hypothesis in the atmospheric boundary layer, *Bound.-Layer Meteorol.* **143**, 379–391 (2012)

Matthias Mauder

Institute of Hydrology and Meteorology
Technische Universität Dresden
Dresden, Germany
matthias.mauder@tu-dresden.de



Matthias Mauder is a Professor in meteorology at the Technical University Dresden, Germany. Up to September 2021 he was the head of the group “Transport Processes in the Atmospheric Boundary Layer” at Karlsruhe Institute of Technology. He received his Doctorate in Micrometeorology from the University of Bayreuth (2006). As a postdoc, he developed new methods for the analysis of airborne eddy-covariance measurements and multitower measurements. His research aims to combine different observational techniques with numerical modeling to improve our understanding of turbulent transport processes and boundary-layer dynamics.

Thomas Foken

University of Bayreuth
Bayreuth, Germany
thomas.foken@uni-bayreuth.de



Thomas Foken is a retired Professor of Micrometeorology at the University of Bayreuth. He was the head of Laboratories at the meteorological observatories at Potsdam (1981–1994) and Lindenberg (1994–1997). His research interests include the interaction between the Earth’s surface and the atmosphere and the measurement and modeling of energy and matter fluxes, with a strong focus on experimental meteorology. His scientific contributions have been recognized through various international awards.

Marc Aubinet

TERRA Teaching and Research Centre
University of Liege
Gembloux, Belgium
marc.aubinet@uliege.be



Marc Aubinet is Honorary Professor in general and environmental physics at the University of Liege. He received a PhD in Agricultural Sciences in 1991. He is a specialist in micrometeorology, eddy covariance, and ecosystem-atmosphere exchanges. He was recognized as a Highly Cited Researcher by the Web of Science in 2014 and in 2017 received the Award For Outstanding Achievement in Biometeorology from the American Meteorological Society.

Andreas Ibrom

Environmental Engineering
Technical University of Denmark (DTU)
Lyngby, Denmark
anib@env.dtu.dk



Andreas Ibrom is Senior Scientist at the DTU and Apl. Prof. at the Georg August University of Gottingen, Germany. Trained as Biologist in ecosystems research, he focuses on land–atmosphere exchange processes. His main scientific contributions are the development of the eddy-covariance technique and more than 30 site years of flux data that are available in international flux networks (FLUXNET, ICOS).

56. Alternative Turbulent Trace Gas Flux Measurement Methods

Janne Rinne , Christof Ammann , Elizabeth Pattey , Kyaw Tha Paw U ,
Raymond L. Desjardins 

The eddy-covariance (EC) method is the most direct micrometeorological approach to measure the surface-atmosphere trace gases under turbulent conditions. The measurement of trace gas fluxes by eddy covariance requires fast-response instruments (higher than 1 Hz) to measure the turbulent fluctuations of vertical wind velocity and trace gas mixing ratio. For many trace gas species, such fast-response analyzers are either not available or do not meet the required precision, long-term stability, and ease of operation under field conditions. Thus, a range of alternative flux measurement techniques have been developed to relax the requirement for fast response time and precision of analysis of the targeted trace gases. These alternative trace gas flux measurement methods are based on surface layer gradients, eddy accumulation, and disjunct eddy-covariance approaches. Of these, the two latter are presented in this chapter. In addition, the surface layer renewal approach, which can be used to understand turbulent exchange processes, and the nocturnal boundary layer Keeling plot approach for determination of the isotopic composition of emitted gases under stable conditions are also described.

56.1	Measurement Principles and Parameters	1506
56.2	History	1507
56.2.1	Disjunct Eddy Covariance	1507
56.2.2	Eddy Accumulation	1507
56.2.3	Surface Renewal	1508
56.3	Theory	1509
56.3.1	Disjunct Eddy Covariance (DEC)	1509
56.3.2	Conditional Sampling Methods	1510
56.3.3	Surface Renewal Methods (SR)	1513
56.3.4	Nocturnal Boundary-Layer Keeling Plot Method (NBL-K)	1515
56.4	Devices and Measuring Systems	1516
56.4.1	Disjunct Eddy Covariance	1516
56.4.2	Conditional Sampling	1518
56.4.3	Surface Renewal	1521
56.4.4	Nocturnal Boundary-Layer Keeling Plot Method	1521
56.4.5	Comparison of the Methods	1521
56.5	Specifications	1522
56.6	Quality Control	1523
56.6.1	Sample Volumes in Conditional Sampling Systems	1523
56.6.2	Disjunct Eddy Covariance	1523
56.6.3	Linearity and Statistics of the Keeling Plot	1523
56.7	Maintenance	1523
56.8	Application	1524
56.9	Future Developments	1525
56.10	Further Readings	1525
	References	1525

The Earth's atmosphere is mostly composed of nitrogen (N_2), oxygen (O_2) and argon (Ar). However, several gases present in trace amounts have considerable effect on the functioning of the atmosphere, either via their radiative effects or due to their chemical reactions. For many of these gases, the terrestrial biosphere is either an important source or sink. Thus, the measurement of the surface exchange is crucial for our understanding

of atmospheric and ecosystem functioning. Turbulent fluxes of some trace gases, such as carbon dioxide and methane, can be measured by the standard eddy-covariance method (Chap. 55). However, for many trace gases, this is either not possible or is very expensive. Thus, this chapter gives an overview on alternative flux measurement methods.

56.1 Measurement Principles and Parameters

The trace gases for which no operational eddy-covariance system is available are a large group with varying characteristics and concentrations. Unlike the common greenhouse gases (H₂O, CO₂, CH₄, N₂O) some of these compounds interact heavily with surfaces, while others rapidly react in the atmosphere. Thus, the design of any flux measurement system needs to be adapted to the properties of the targeted compounds. The primary measurements of these flux measurement methods are typically trace gas concentrations and vertical wind velocity (Table 56.1).

The alternative flux measurement methods share the same basic assumptions as the eddy-covariance method:

- i) The measurement site must be horizontally homogenous for horizontal flux divergence to be negligible.
- ii) The flux is assumed to be constant between surface and measurement height, i.e., there is no vertical flux divergence.
- iii) Stationarity is assumed so that Reynolds decomposition is valid, and the time-dependent term in the average concentration is negligible.

While in the eddy-covariance, disjunct eddy-covariance, and eddy-accumulation methods, the turbulent fluxes are measured directly, the gradient and (hyperbolic) relaxed eddy-accumulation methods use more or less empirical parameterizations.

The most important assumption is the requirement of horizontal homogeneity, as it usually restricts the use of these methods, as well as the eddy-covariance method (Chap. 55), to locations with a relatively large flat and homogenous surface.

The alternatives for eddy-covariance flux measurements used nowadays can be classified either as gradient techniques, eddy-accumulation (or conditional-sampling) techniques, or disjunct eddy-covariance measurements. The gradient technique was already presented in Chap. 54, and thus is omitted from this chapter. In addition to the above-mentioned flux measurement methods, we will describe the surface-layer renewal technique, which can shed light on turbulent transport dynamics. Although the nocturnal boundary-layer Keeling plot method for determining the isotopic composition of emitted gas is not strictly a turbulent method, it will be presented here as an alternative flux measurement approach.

Table 56.1 Primary measurements (w is the vertical wind velocity (i.e., a vector)), with the usual convention of ascend being positive and descend being negative, and output of alternative flux measurement methods (EA: eddy accumulation; DEA: disjunct eddy accumulation; REA: relaxed eddy accumulation; HREA: hyperbolic relaxed eddy accumulation; DEC: disjunct eddy covariance; SR: surface renewal (H : sensible heat flux; LE: latent heat flux); NBL-K: nocturnal boundary-layer Keeling plot)

Method	Primary measurements (response time)	Output	Symbol	Dimension
DEC	Vertical wind velocity (0.1 s) Concentration of trace gas with 1–30 s intervals (0.1 s)	Mass flux	F_s	$\mu\text{g m}^{-2} \text{s}^{-1}$ $\mu\text{mol m}^{-2} \text{s}^{-1}$
EA	Vertical wind velocity (0.1 s) Average concentration of trace gas in updrafts and downdrafts (30 min)	Mass flux	F_s	$\mu\text{g m}^{-2} \text{s}^{-1}$ $\mu\text{mol m}^{-2} \text{s}^{-1}$
DEA	Vertical wind velocity (0.1 s) Average concentration of trace gas in updrafts and downdrafts (30 min)	Mass flux	F_s	$\mu\text{g m}^{-2} \text{s}^{-1}$ $\mu\text{mol m}^{-2} \text{s}^{-1}$
REA	Vertical wind velocity (0.1 s) Average concentration of trace gas in updrafts and downdrafts (30 min)	Mass flux	F_s	$\mu\text{g m}^{-2} \text{s}^{-1}$ $\mu\text{mol m}^{-2} \text{s}^{-1}$
HREA	Vertical wind velocity (0.1 s) Scalar, e.g., CO ₂ H ₂ O or temperature (0.1 s) Average concentration of trace gas in updrafts and downdrafts (30 min)	Mass flux	F_s	$\mu\text{g m}^{-2} \text{s}^{-1}$ $\mu\text{mol m}^{-2} \text{s}^{-1}$
SR for H and LE	Temperature (0.1 s) Net radiation (30 min) Soil heat flux (30 s)	Heat flux	H, LE	W m^{-2}
SR for trace gas	Concentration of trace gas with 1–30 s intervals (0.1 s)	Mass flux	F_s	$\mu\text{g m}^{-2} \text{s}^{-1}$ $\mu\text{mol m}^{-2} \text{s}^{-1}$
NBL-K	Isotopic composition of trace gas (1–30 min) Concentration of trace gas (1–30 min)	Isotopic signature of emitted gas	$\delta^{13}\text{C}$ $\delta^{14}\text{C}$ $\delta^{15}\text{N}$	‰

56.2 History

Before the advent of turbulent flux measurement methods, such as eddy covariance, most surface–atmosphere flux measurements were made by observation of the vertical gradients of the gas of interest, as well as the gradient of the horizontal wind with some assumptions made to derive turbulent mixing coefficients [56.1]. While this approach is still useful in a number of cases [56.2], new methods based on eddy covariance (Chap. 55), disjunct eddy covariance, and conditional sampling have supplemented our flux measurement toolbox.

Today, the most commonly used alternative flux measurement techniques are relaxed eddy accumulation, disjunct eddy covariance by mass scanning, and gradient techniques. However, there have also been other interesting methodological developments in the



Fig. 56.1 DEC system with two grab sampling inlets and intermediate storage reservoirs (white cylindrical containers) in operation at an alfalfa field near Fort Morgan, Colorado, August 2000 (after [56.3, 4]). The DEC sampling unit is positioned 0.6 m below the sonic anemometer at 3.2 m (photo © Janne Rinne)

past decades that may be of interest. The development of various techniques has been parallel in time. Thus, the order of the methods below is not chronological but reflects the ordering of the theories in the Methods section (Sect. 56.3).

56.2.1 Disjunct Eddy Covariance

The concept of deriving fluxes and other turbulence statistics from disjunct time series was first proposed by *D. Haugen* in 1978 [56.5], with early practical applications to overcome limitations of data storage and transfer at the Boulder Atmospheric Observatory in the early 1980s [56.6]. The first application of the disjunct eddy-covariance (DEC) method to measure trace gas fluxes was presented by *J. Rinne* et al. with a system using physical grab samplers (Fig. 56.1; [56.3]). In this application type, which was used mainly until about 2010, finite air volumes were sampled during typically 0.2 s into a reservoir at repetition intervals of 10–60 s [56.3, 4, 7, 8]. The grab air sample could then be analyzed during that interval with a trace gas analyzer having a slower response compared to conventional EC measurements. For the covariance flux calculation, the trace gas concentration of each grab sample analysis was combined with the vertical wind velocity measured at the respective air sampling time (Sect. 56.3.1).

A more feasible method of disjunct eddy covariance by mass scanning was introduced by *T. Karl* et al. [56.9]. This variant of the disjunct eddy-covariance method was commonly used for volatile organic compound (VOC) fluxes in the 2000s and 2010s.

56.2.2 Eddy Accumulation

In the early 1970s *R. Desjardins* [56.10, 11] developed the concept of accumulating air from up and down moving air parcels, or turbulent eddies, and then measuring the mean concentrations, with slow response gas analyzers, of the various trace gases in the air samples collected. This method was based on the same principle as the eddy-covariance (EC) technique, which was mainly being used for measuring the flux of water vapor and sensible heat. At the time, a technique that reduced the requirement for fast-response gas analyzers of EC was very welcome. The eddy-accumulation (EA) method, which involved the continuous separation of the sampled gas in two streams, depending on whether the vertical wind moved upwards or downwards, and with sample flow proportional to the vertical wind speed, solved the problem of the need for a faster response sensor than the state-of-the-art afforded.

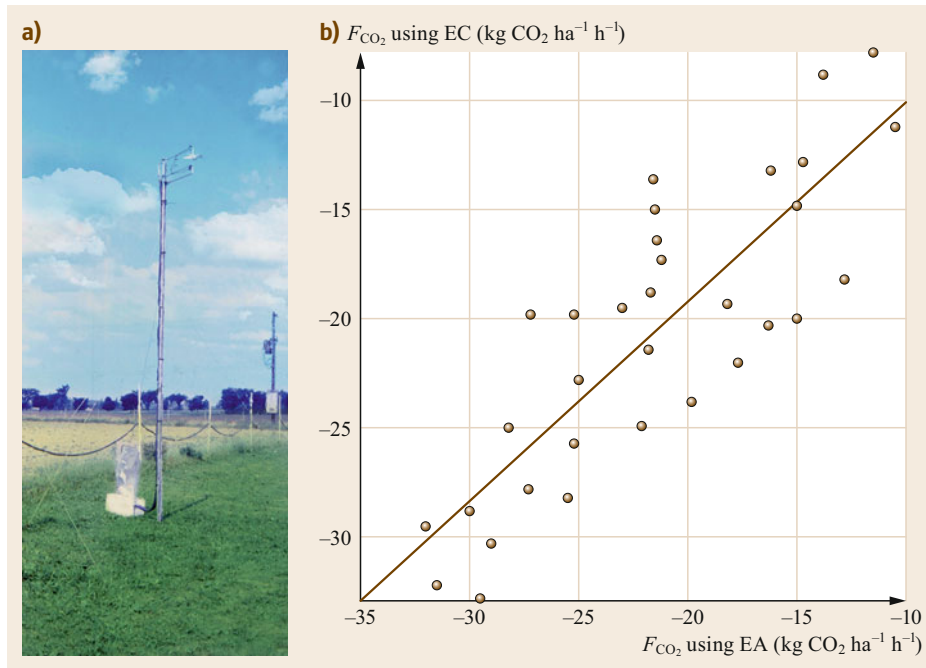


Fig. 56.2 (a) Eddy-accumulation system with bags as a sample storage system. Central Experimental Farm, Ottawa Canada, 1971 (photo © Ray Desjardins). (b) 10-minute mean CO₂ flux densities simultaneously obtained using eddy-covariance (EC) and eddy-accumulation (EA) measuring systems (after [56.12] with permission from Elsevier)

Fast sensing, followed by multiplication and averaging, was replaced by fast valve-controlled sampling and storage and measurement of the average concentration with a slow-response gas analyzer. For example, by measuring the difference of the mean concentrations of the up and downdraft air samples with a mass spectrometer, Desjardins demonstrated that one could measure the flux of many gas species simultaneously [56.10]. Figure 56.2a shows one of the first EA systems, which used fast-response solenoid valves situated in close proximity to a vertical axis propeller anemometer. Figure 56.2b shows 10-min mean CO₂ flux densities measured with a fast-response CO₂ analyzer and the EA bag sampling system. The 1 : 1 relationship between the results from the two sampling systems indicated that there were no systematic errors due to the different sampling techniques [56.12].

At the time, the fast-response valves were opened for about 25 ms for a preselected each 10 cm of vertical air travel. A decade later, proportional sampling valves with a frequency response of about 10 Hz were developed [56.13, 14]. Flow rates of up to 150 cm³ s⁻¹ were possible for a vertical wind of 1.5 m s⁻¹. These valves were ideal for the eddy-accumulation method because they could even correct for flow restrictions in the sampling line. However, soon after their development, J. Businger and S. Oncley suggested the use of constant sample flow [56.15]. This relaxation of the proportionality between the vertical wind velocity and sample flow rate led to the relaxed eddy-

accumulation (REA) method. Since this method gave fairly similar results to the EA and EC methods, the EA measurements using the proportional sampling valves was discontinued (see, however, the latest development [56.16]).

E. Pattey et al. developed an implementation of the density fluctuation correction WPL (Webb–Pearman–Leuning) specific to the REA method [56.17] according to the trapping media (i.e., using bags or traps as reservoirs). An independent verification of the REA method based on CO₂ fluxes by comparing them with EC shows that REA can be successfully implemented [56.18]. The same REA measuring system was used to determine isoprene fluxes over black spruce in the Boreal forest in 1994 during the BOREAS (Boreal Ecosystem–Atmosphere Study) campaign [56.19].

56.2.3 Surface Renewal

The origin of the surface renewal paradigm originates from chemical engineering and was developed to connect reactions occurring during molecular diffusion into turbulent parcels of fluid near a surface [56.20, 21].

From a micrometeorological perspective, K.T. Paw U et al. suggested that the turbulent coherent structures in plant canopies could be thought of as air parcels descending into a plant canopy and moving along horizontally through the canopy, while the scalar sources in the canopy increase scalar concentrations in the parcel (or sinks decrease the concentrations in a par-

cel) [56.22–24]. This process creates ramp structures in the high frequency time series of the scalar. The original micrometeorological surface renewal method involves

high-frequency measurement of scalar values to obtain fluxes and does not involve explicit transfer coefficients or mean scalar gradients.

56.3 Theory

In this chapter, we will briefly introduce the theory of the different alternative flux measurement methods to help the reader understand the technical requirements of measurement systems. These presentations are very brief, and the interested reader is encouraged to read the references given.

In the conventional eddy-covariance method (Chap. 55), the flux of a trace gas (or scalar quantity s) is determined as the covariance of the discretely recorded time series of the vertical wind velocity w_i and trace gas mixing ratio $\chi_{s,i}$ (equivalent to (55.4))

$$\begin{aligned} F_s &= \overline{\bar{\rho} w' \chi'_s} = \frac{\bar{\rho}}{N-1} \sum_{i=1}^N [(w_i - \bar{w})(\chi_{s,i} - \bar{\chi}_s)] \\ &= \frac{\bar{\rho}}{N-1} \sum_{i=1}^N (w'_i \chi'_{s,i}), \end{aligned} \quad (56.1)$$

where $\bar{\rho}$ is the average molar density of the air. It is assumed here that the time series w_i and $\chi_{s,i}$ are effectively synchronized in time (i.e., corrected for an eventual time lag; Sect. 55.3.2). Using a typical EC data sampling frequency of 10 Hz and a flux averaging interval of $T = 30$ min results in a total of $N = 18000$ data points for the flux calculation. In the ideal case, the *sampling interval* $\Delta = 0.1$ s between individual measurement recordings also equals the effective response time (or signal averaging time) τ_R of the w and χ_s sensors, leading to continuous nonoverlapping measurement series.

56.3.1 Disjunct Eddy Covariance (DEC)

The basic idea of DEC is that the flux may be calculated using (56.1) from a random-like subsampling ($n \ll N$ data points) of the full w_j and $\chi_{s,i}$ data series. Since well-developed turbulence in the surface layer is not periodic, subsamples taken at regular intervals can be considered random-like. In this case, the sampling interval $\Delta = T/n$ is increased to typically between 1 and 30 s, while the measurement response time τ_R is kept short at about 0.1 s. Accordingly, in the DEC approach the number of samples n taken over 0.5 h is reduced to between 1800 and 60. The principle is illustrated in Fig. 56.3a. In practice, the DEC concept can be applied in two different ways (Sect. 56.4.1):

- Disjunct air sampling (*grab sampling*)
- Continuous air sampling flow with disjunct detection of a certain trace gas.

The second application type is sometimes called *virtual disjunct eddy covariance* vDEC. However, this expression can be misleading because the described DEC principle equally applies for both application types [56.25]. The DEC method has been evaluated against the conventional EC method by data simulations and field experiments [56.7, 26–29]. The results confirm the theoretical considerations [56.5, 28] that the reduced sample number of the DEC method does not cause systematic error to the measured flux values but increases its random uncertainty. These main characteristics are explained in the following.

For conventional EC, as well as for DEC systems, the ability to detect the flux contributions of all relevant frequencies is limited by the response time τ_R of the measurement system, not the sampling interval Δ . The contribution of frequencies above the respective cutoff frequency $f_c = 1/(2\pi\tau_R)$ is mostly lost [56.30]. For DEC systems with grab sampling, τ_R is determined by the time it takes to fill the intermediate reservoirs (Sect. 56.4.1). For EC and DEC measuring systems with a continuous sample air flow, τ_R typically depends on the dimensions of the analyzer detection cell and its inlet tube, internal signal integration, or averaging time, as well as on the sample tube geometry and flow rate. Similarly to conventional EC systems, it has to be assured also for DEC systems that either τ_R is kept short (at typically 0.1 s) or the spectral loss of covariance has to be quantified and corrected for (Chap. 55). While in conventional EC systems, the sampling interval Δ is typically close to $0.5\tau_R$ to avoid aliasing when performing spectral analysis, it is considerably longer in DEC systems. The correspondingly reduced sampling frequency $f_s = 1/\Delta$ of DEC systems does not imply that frequencies above f_s (and below f_c) are lost, but they are aliased (mirrored) to frequencies below $f_s/2$ [56.25]. The integral of this aliased spectrum equals the integral of the full spectrum obtained from the nondisjunct time series, and thus no bias is introduced to the flux [56.25]. One drawback of DEC cospectra, however, is that the aliased and nonaliased contributions cannot easily be separated.

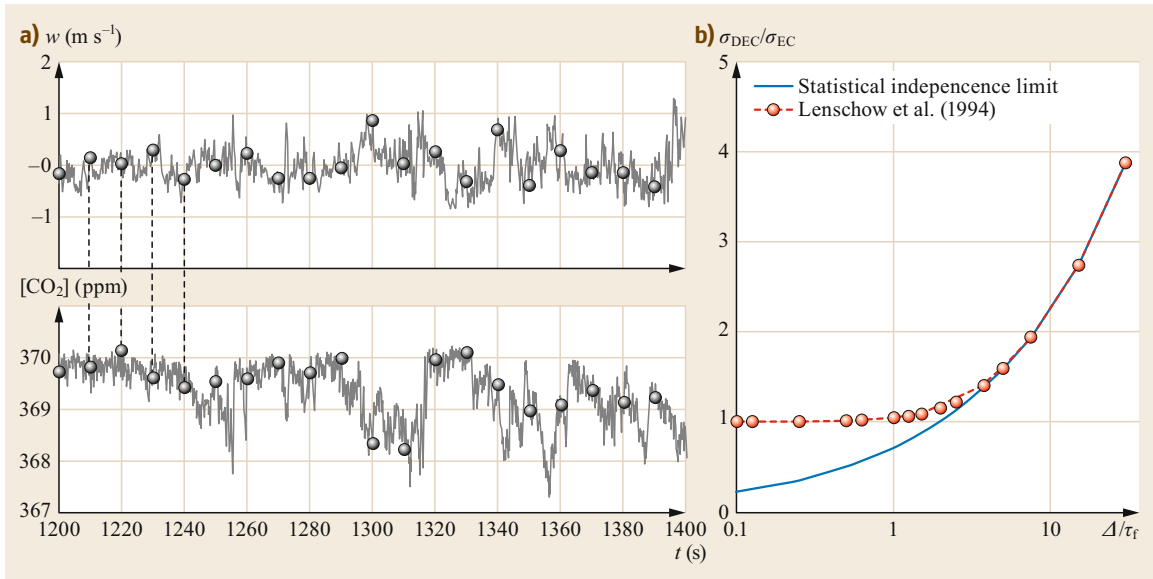


Fig. 56.3 (a) Disjunct subsampling of fast-response time series. The gray line represents the original continuous 10 Hz time series of the vertical wind speed w and the CO_2 mixing ratio χ_s , while the black dots are 0.1 s-long subsamples taken from these data at intervals $\Delta = 10$ s (after [56.25]). (b) Relative enhancement of DEC flux uncertainty compared to EC flux uncertainty ($\sigma_{\text{DEC}}/\sigma_{\text{EC}}$) as a function of the ratio between the sampling interval (Δ) and the integral covariance flux time scale (τ_f). For large x -axis values, the uncertainty increases like for statistically independent data points according to $1/\sqrt{n}$

The random uncertainty of fluxes measured by the EC and DEC methods was described as a function of T , Δ , and τ_f representing the integral timescale of the time series $w'c'$ [56.28]. This is illustrated in Fig. 56.3b. In the case when the sample interval is shorter than the integral timescale, the DEC flux uncertainty is very similar as for conventional EC. When the sample interval is longer than the integral timescale, the DEC flux uncertainty increases relative to EC approaching a simple $1/\sqrt{n}$ function that would be valid for full statistical independence of subsequent records of the $w'c'$ time series [56.7]. As the additional uncertainty of the DEC flux is random, it is decreased when fluxes are averaged over longer periods. The integral timescale is the $1/e$ -width of the covariance function peak and (besides wind speed and stability) mainly scales with the measurement height. As a rule of the thumb, one can assume τ_f (in units of s) similar to z (in units of m) [56.25]. Thus, especially for measurements over low vegetation, the sample interval is mostly longer than the integral timescale and the number of samples rather than the sample interval being the parameter controlling the uncertainty of the fluxes.

The DEC approach is generally used in combination with closed-path trace gas analyzers, which makes it necessary to account for the delay between the vertical wind velocity and mixing ratio measurements. The

time lag for synchronization is often identified empirically by the position of the peak (absolute maximum) in the cross-covariance function between w and the trace gas mixing ratio of interest [56.31]. In the case of DEC, the covariance function has to be calculated with the full w' time series (10 Hz) and the disjunct χ'_s time series that is gap-filled with zeros to the same time resolution. The time lag is best determined under conditions with well-developed turbulence and high fluxes.

56.3.2 Conditional Sampling Methods

Conditional sampling is the generic name covering the following methods:

- Eddy accumulation (EA)
- Disjunct eddy accumulation (DEA)
- Relaxed eddy accumulation (REA)
- Hyperbolic relaxed eddy accumulation (HREA).

The common requirements for conditional sampling approaches are as follows: 1) atmospheric turbulence is the dominant transfer mechanism in the surface layer, and 2) the vertical wind velocity is measured at high frequency in order to operate a conditional sampler that will separate air samples according to the vertical wind direction. Air needs to be sampled close to the

fast-response ultrasonic anemometer. The conditionally sampled air is then temporarily stored for further analysis on high-precision analyzers. Although conditional sampling methods are relatively easy to understand, and their theory is well-known, great care is required for their proper implementation. First, in order to sample the air conditionally, fast-response sampling valves are needed, which are under the control of unbiased high-frequency vertical velocity measurement. Second, conditionally sampled air needs to be kept in separate reservoirs, which can preserve the integrity of the trace gas samples of interest until their analysis. The analytical method requires high accuracy to measure precisely the difference between updraft and downdraft mixing ratios of the gas of interest. Third, several specifications need to be met. Turbulent flows need to be maintained in the intake, prior to conditionally separating the air samples. The lag between the wind velocity data and the air intake need to be accounted for. Any biases on the vertical wind velocity need to be removed in quasi realtime.

The theory of conditional sampling methods can be divided into two categories – eddy accumulation and relaxed eddy accumulation. In the former, the air is collected in up and downdraft reservoirs proportionally to the vertical wind velocity, whereas in the latter, the air is collected in the reservoirs at constant flow rate.

Eddy Accumulation (EA)

With the volume of air collected in the up and downdraft reservoirs proportionally to the vertical wind velocity (Fig. 56.4), the flux of the trace gas of interest can be calculated as

$$F_s = \overline{\rho \chi' w'} = \frac{\overline{\rho}}{T} \left[\chi^\uparrow \int_{t_1}^{t_2} w \delta^+ dt + \chi^\downarrow \int_{t_1}^{t_2} w \delta^- dt \right] - \overline{\rho} \overline{\chi} \overline{w}, \quad (56.2)$$

where χ^\uparrow and χ^\downarrow are trace gas mixing ratios in updraft and downdraft reservoirs, w is the vertical wind speed, δ^+ and δ^- are delta functions, and T is the length of the averaging period ($t_2 - t_1$). The values of delta functions are defined as

$$\begin{aligned} \delta^+ &= 1, & \delta^- &= 0 & \text{when } w > 0, \\ \delta^+ &= 0, & \delta^- &= 1 & \text{when } w < 0. \end{aligned}$$

Equation (56.2) can be mathematically derived from the eddy-covariance equation [56.10, 26, 32, 33].

If a sample representing the mean average mixing ratio, $\overline{\chi}$, is not collected separately, this can be estimated by the average of updraft and downdraft samples [56.10, 29]. If the vertical wind measurements are high-pass filtered at about 0.001 Hz, the last term in (56.2) can be neglected, as $\overline{w} = 0$, and w will correspond w' .

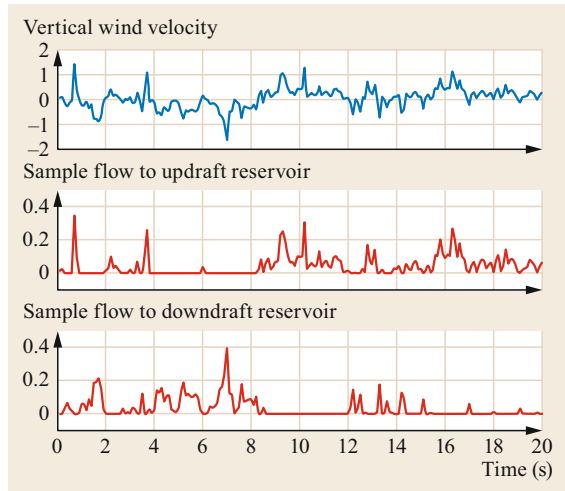


Fig. 56.4 Graph illustrating the sampling procedure of the eddy-accumulation method, in which the volume of air (10^{-3} m^3) collected in updraft and downdraft reservoirs is proportional to vertical wind velocity (m s^{-1}). Vertical wind velocity and sample flows are in arbitrary units

Disjunct Eddy Accumulation (DEA)

The fast and accurate control and adjustment of valve opening, which is required in the eddy-accumulation technique, has proven to be a challenging task. Thus, in disjunct eddy accumulation, sampling of air proportionally to vertical wind speed is realized using the disjunct eddy-sampling approach. This bypasses the challenge of fast flow control [56.26].

In disjunct eddy accumulation, sampling is conducted in two steps. First, the primary sampling is based on the same principle as in disjunct eddy covariance with grab sampling. The second step is the subsequent processing of air samples, which follows the principle in eddy accumulation. While in disjunct eddy covariance, the trace gas concentration in each air sample is measured separately, in DEA, air is accumulated in updraft and downdraft reservoirs from intermediate storage reservoirs (ISR, Sect. 56.4.2) for a duration proportional to the vertical wind velocity at the moment of the corresponding primary sampling, allowing the use of a constant flow rate. This leads to mathematical identity between disjunct eddy covariance and disjunct eddy accumulation.

While in the continuous sampling eddy-accumulation system, the sampling flow needs to be continuously adjusted to follow the variations in vertical wind velocity (Fig. 56.4), in DEA, the sample flow from ISR through an adsorbent cartridge can be kept constant while the sampling period is adjusted (Fig. 56.5). This is realized by adjusting the sampling time from the intermediate storage reservoir to the updraft or downdraft reservoir, as is shown in the two bottom panels in Fig. 56.5.

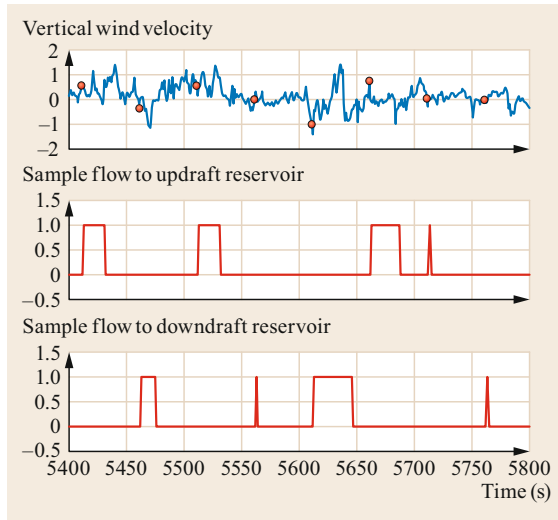


Fig. 56.5 Graph illustrating the sampling procedure of the disjunct eddy-accumulation technique. The air is sampled to intermediate storage reservoirs at times shown with *red dots* in vertical wind data (m s^{-1}). A volume (10^{-3} m^3) proportional to the vertical wind velocity at this moment is then transferred to either the updraft or downdraft reservoir. This is realized by integrating the quite constant sample flow from the ISR to the updraft or downdraft reservoir and terminating the sampling when the desired sample volume has been reached. Vertical wind velocity and sample flows are in arbitrary units

Relaxed Eddy Accumulation (REA)

The requirement of the EA method, which consisted of sampling air proportionally to the vertical velocity, was simplified by using a constant flow rate to collect the ascending and descending moving air samples separately ([56.15]; Fig. 56.6). The trace gas flux is proportional to the difference in the mean scalar mixing ratio (χ_s) of upward and downward moving air.

$$F_s = \bar{\rho} \overline{w' \chi'_s} = b \sigma_w \bar{\rho} (\overline{\chi_s^\uparrow} - \overline{\chi_s^\downarrow}) \quad (56.3)$$

Where b is an empirical constant, σ_w is the standard deviation of the vertical wind velocity, and $\bar{\rho}$ is the molar air density.

The value of the b coefficient in (56.3) is relatively constant when turbulence is well established, and fluxes are measurable [56.18]. Values are similar between different scalars at about 0.56 [56.18, 34, 35]. An analytical solution to account for the impact of the non-Gaussian nature of turbulence on the b coefficient by using the fourth-order Gram–Charlier functions has been derived [56.35]. The stability dependence of the b coefficient was also studied for various scalars [56.36]; for unstable conditions, no systematic dependence on

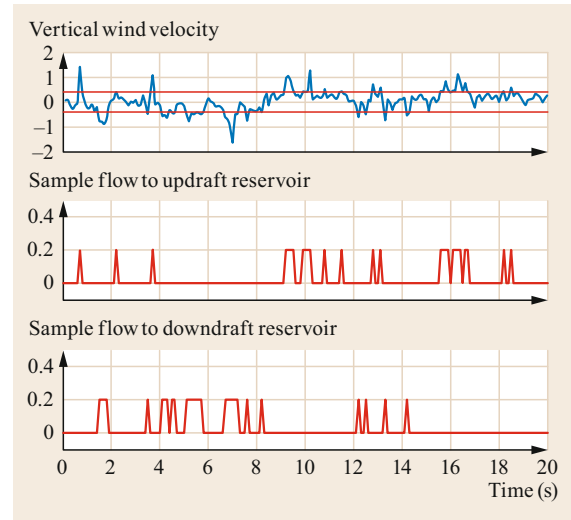


Fig. 56.6 Graph illustrating the sampling procedure of the relaxed eddy-accumulation method, in which the air is collected at a constant flow rate ($10^{-3} \text{ m}^3 \text{ min}^{-1}$) into updraft and downdraft reservoirs (*blue*), and when the absolute value of the wind velocity (m s^{-1}) is greater than the dead-band interval threshold (m s^{-1} , *red*). Vertical wind velocity and sample flows are in arbitrary units

stability is observed, and the value of 0.56 is confirmed, while for more stable conditions, a systematic increase of the b value is estimated using 10-min averaged fluxes. However, as for any measuring methods based on turbulence, the lack of turbulence at night limits the validity of the REA technique.

In order to enlarge the difference between the updraft and downdraft mean scalar mixing ratio, a deadband can be introduced into the REA measuring systems. A deadband is an interval of vertical wind velocities centered at zero, for which no air is collected in the updraft or downdraft reservoirs. The deadband also helps to extend the lifespan of the conditional sampling valves. The deadband could be a fixed interval or set to be proportional to the standard deviation of the vertical wind speed, σ_w . In the latter case, the actual deadband value could use σ_w calculated either from σ_w of the previous flux measurement period or from a running mean σ_w (dynamic deadband). By measuring the concentration of e.g., CO_2 in sample reservoirs together with eddy-covariance measurements of CO_2 fluxes, the b coefficient can be empirically calculated using (56.3). A robust model to predict the impact of the normalized deadband on the empirical coefficient b [56.18] shows that deadband intervals up to $0.2 \sigma_w$ could be used reliably because it is possible to predict their impact. To optimize the signal-to-noise ratio a larger deadband of $0.6 \sigma_w$ has been suggested [56.37]. Increasing the dead-

band is highly desirable for studying natural isotopes. By introducing a dynamic deadband of $0.5 \sigma_w$, it has been shown that the b coefficient has a relatively steady value equal to 0.42 [56.38].

The conditional sampling techniques require any bias on the vertical wind velocity to be removed in quasi realtime before activating the fast-response valves controlling the air collection. A relative bias of 20% on the vertical wind velocity will generate a 5% relative flux bias [56.18]. Several filtering approaches were successfully used to remove the bias on w , such as a digital high-pass filter [56.19] or a 5-min block averaging of the three wind velocity components [56.39]. At ideal sites (e.g., flat terrain, tall towers), when the bias on w is very limited, an unfiltered w signal provides good-quality REA fluxes [56.40].

The REA method had a high rate of adoption by the scientific community in cases when no fast-response gas analyzers were available or affordable.

Hyperbolic Relaxed Eddy Accumulation (HREA)

In order to maximize the difference between the updraft and downdraft sample mixing ratios of stable isotopes, the deadband was implemented differently [56.41]. Using the hyperbolic deadband, only the turbulent events contributing the most to the flux are sampled. The approach consists in excluding the values close to the mean using two hyperbolas, defined as follows

$$H = \left| \left(\frac{w'}{\sigma_w} \right) \left(\frac{\chi'_s}{\sigma_s} \right) \right|, \quad (56.4)$$

where H is the hyperbolic deadband defined as a function of the vertical wind velocity and mixing ratio of a scalar [56.41]. This requires knowing, at the time of sampling, the means and standard deviations of the vertical wind velocity and those of the relevant scalar for the stable isotope under consideration. These statistics can be obtained from digital recursive filters applied to the fast-response time series [56.42]. Poor scalar similarity can lead to considerably biased flux values by HREA [56.43]. This technique was marginally adopted by the scientific community.

56.3.3 Surface Renewal Methods (SR)

Surface renewal methods in micrometeorology [56.22–24] are conceptually based on a paradigm of turbulent coherent structures being the major flux-bearing eddies in surface roughness layers [56.44, 45], and that these turbulent coherent structures represent parcels of air interacting with surfaces (Figs. 56.7 and 56.8). The mass or energy balance of the surface renewal parcel can readily be written for this paradigm. As an example,

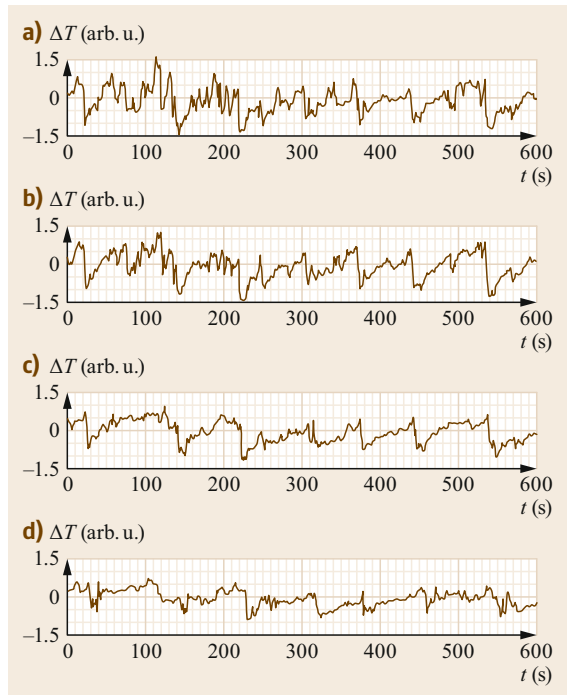


Fig. 56.7a–d Air temperature patterns at the canopy height z of 17.6 m (a) and below the canopy ($z = 15.4$ m (b), $z = 10.5$ m (c), and $z = 5.9$ m (d)), showing ramp shapes that are caused by turbulent coherent structure *sweeps* and *ejections* (after [56.44])

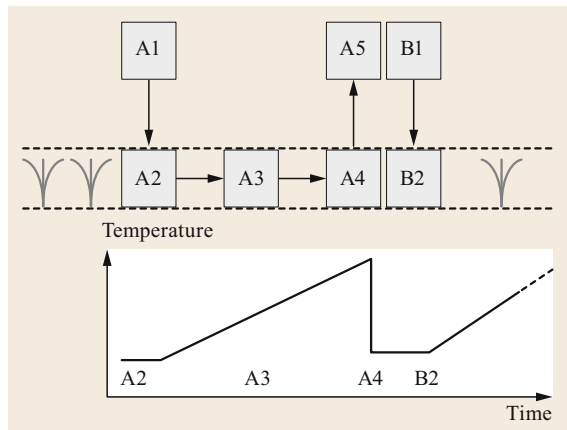


Fig. 56.8 Surface renewal paradigm of a turbulent coherent structure *sweep* entering a plant canopy (A2) from above the canopy (A1), accumulating a scalar (in this example temperature, phase A3), and then being ejected (A4) to above the canopy (A5), to be instantly replaced by another sweep from (B1) to inside the canopy (B2). The corresponding scalar pattern with time is shown in the *lower diagram* (after [56.23, 24])

the scalar heat energy balance (temperature), leading to measurements of sensible heat flux H can be written as

$$H = \alpha \rho c_p \frac{a}{d+s} h_c, \quad (56.5)$$

where ρ is the density of air (kg m^{-3}), c_p is the specific heat of air ($\text{J K}^{-1} \text{kg}^{-1}$), a is the amplitude of the ramp (K), d is the length of the ramp (s), s is quiescent time between ramps (s), and h_c is the height of the measurement (m), originally assumed to be the height of the plant canopy. Because one or more of the assumptions used in surface renewal, discussed later, may not always be valid, a calibration factor α is usually included in the equation.

For determination of the amplitude and duration for repetition of the ramps, Van Atta's structure function [56.46] has been used [56.23, 47]. The Van Atta method requires calculation of the second, third, and fifth-order structure functions, defined as

$$S^m(r) = \frac{1}{m} \sum_{i=1}^{i=m-j} [T(i+j) - T(i)]^m. \quad (56.6)$$

Using the assumptions of random turbulence contributions to structure functions, and with substitutions, one can derive these equations to solve for the ramp amplitude a and the ramp repetition interval ($d+s$) [56.46].

A cubic solution is used to obtain the ramp amplitude a for which Paw U and Su [56.23] used the standard analytical algebraic/polynomial-based cubic solution. Other researchers [56.47] used the trigonometric solution. For both methods, although there are up to three separate solutions to the cubic equation, typically one of them is the realistic solution that can be used.

The need for calibration of surface renewal against another independent measure of the scalar flux have been discussed because of several potential differences between the assumed idealized parcel exchange and reality [56.24, 48]:

- Equation (56.5) and its physical picture of turbulent coherent structures is based on a Lagrangian viewpoint, but measurements of the scalar change are made in a Eulerian framework. Therefore, the horizontal microadvection in turbulent coherent structures must be assumed to be zero for the Eulerian framework ramps to be used in place of the Lagrangian total derivative of the ramp structures.
- When the scalar change is measured at only one height, assumptions must be made about how the scalar change occurs at the other heights within the canopy.
- Like any vertical column-based model, mean horizontal and vertical advection divergence could

represent a significant portion of the canopy-atmosphere exchange process [56.49].

- Turbulent coherent structures may not represent 100% of the exchange.
- Multiple coherent structure sizes might be important in exchange processes, instead of a single size [56.50, 51].
- If the scalar is temperature and measured by thermocouples or other physical sensors, their response time, related to their size, may influence the characterization of the derivative dT/dt needed for surface renewal, and other possible issues [56.48].

Practical application of surface renewal depends on arriving at a value of alpha either by theoretical considerations or by direct calibration with other trace gas or scalar flux measurements, such as eddy covariance.

In the above theories, it is assumed that the ramps have an instantaneous change in the scalar at the termination of each ramp. Experimental data show that this is not strictly true, so equations accounting for this have been derived [56.52, 53], although with simplified paradigms such that there was no quiescent period.

It was hypothesized that modification of the original chemical engineering paradigms could be used, where the molecular diffusion from a surface into a parcel of fluid during the ramp phase of a coherent structure is replaced by a similarity-based turbulent diffusion paradigm [56.54]. It has been found that this method is relatively successful in arriving at the surface renewal calibration coefficient α [56.55–57]

$$\alpha = \begin{cases} \left[\frac{k(z-d)}{\pi z^2} \tau u_* \phi_h^{-1}(\zeta) \right]^{1/2} & (z-d) > z^* \\ \left[\frac{k z^*}{\pi z^2} \tau u_* \phi_h^{-1}(\zeta) \right]^{1/2} & h \leq (z-d) \leq z^* \end{cases}. \quad (56.7)$$

However, there are theoretical concerns about the application of similarity relationships, which are based on empirical results for idealized extensive horizontal surfaces and both large and small turbulent scales, to small-scale turbulence exchanging scalars within a coherent structure, and within the roughness elements of a plant canopy, during the relatively short ramp timescales.

One potential advantage of surface renewal, apart from its reliance on inexpensive sensors, is that it could require less fetch than eddy covariance. Its original theory envisions the sensor height at the canopy top, hence the fetch, if the processes are assumed analogous to conventional theoretical paradigms, would be something like 100 times the canopy height.

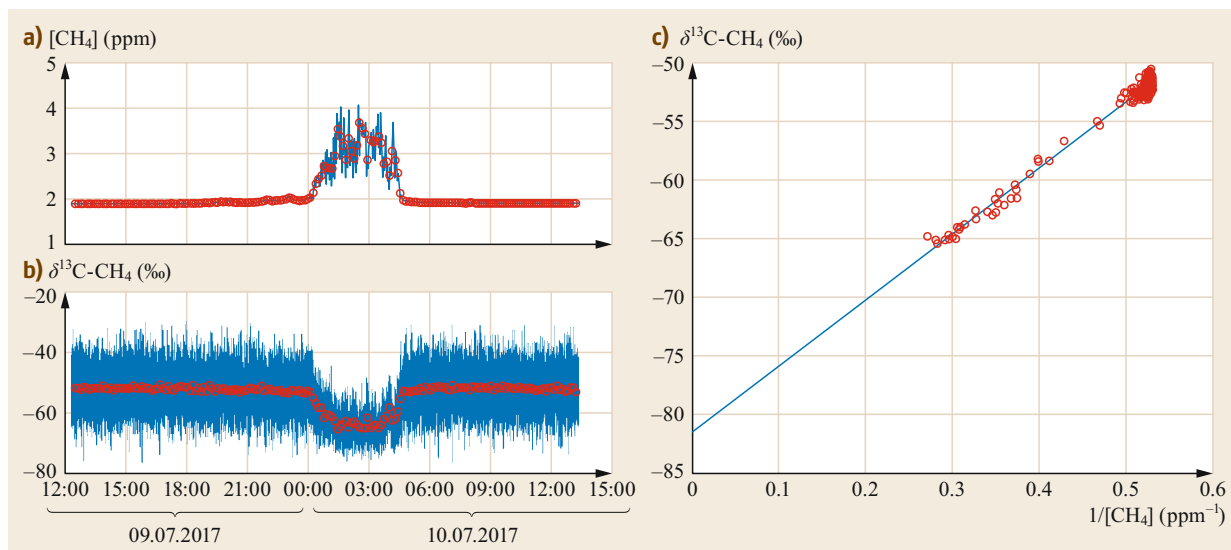


Fig. 56.9a–c Example of (a) one night of methane concentration and (b) $\delta^{13}\text{C-CH}_4$ data recorded at Mycklemossen peatland site, Sweden on 09.–10.07.2017, and (c) Keeling plot derived with the data. The blue line in (a) and (b) indicates the raw 1 Hz data and red circles the 10 min-averages. The intercept in (c) indicates a $\delta^{13}\text{C-CH}_4$ value of -81% . The online isotopic analyzer used here is Picarro G2201-i

Direct Surface Renewal of Trace Gases Such as Water Vapor and Carbon Dioxide

Several researchers have tested the ability to directly determine the fluxes of trace gases, such as water vapor and carbon dioxide, using surface renewal analysis of the ramp patterns seen in these trace gas scalars [56.55, 56.58, 59]. It should be noted that one of the main advantages of surface renewal is its relative simplicity and inexpensiveness compared to other methods, such as eddy covariance. This applies to derivation of water vapor flux, which can be calculated using the energy budget, for which SR requires only low-cost thermocouples and net radiation [56.60]. Direct surface renewal of trace gas scalars requires the usually expensive fast-response gaseous concentration sensors, such as infrared absorption gas analyzers (IRGAs), and, therefore, would not be as advantageous over eddy covariance.

56.3.4 Nocturnal Boundary-Layer Keeling Plot Method (NBL-K)

In the Keeling plot method for determining the isotopic signature of an emitted compound, e.g., $\delta^{13}\text{C}$ of respired carbon dioxide or emitted methane, we apply the so-called two-end-member mixing model [56.61–63]. This can be explained by considering a static chamber placed

at the surface to measure emission. At the beginning of the measurement, the mixing ratio (χ) and isotopic ratios inside the chamber equal those of the ambient atmosphere, considered as the first end member. During chamber closure the emission from soil increases the mixing ratio in the chamber, and the isotopic ratios approach those of the emitted gases, the second end member. Theoretically, the isotope ratios in the chamber reach the isotope ratio of the emitted gas as the mixing ratio approaches infinity. It can be shown that in such a case, the isotopic δ -value behaves linearly in relation to the inverse of the mixing ratio, following the equation

$$\delta = a_0 + a_1\chi^{-1}, \quad (56.8)$$

where δ is the isotopic composition, χ is the trace gas mixing ratio, and a_0 and a_1 are coefficients found by fitting the equation to the data (Fig. 56.9). Thus, the intercept, i.e., a_0 , gives us the isotopic signature of the emitted gas.

In the nocturnal boundary-layer Keeling plot method, the stable surface layer acts as the volume into which the two end members are mixed. Although the mixing is not as ideal as in a chamber with an internal fan, the use of the nocturnal surface layer data leads to similar Keeling plots to the chamber measurements. The footprint of the isotopic signature derived by the

nocturnal boundary layer is considerably larger than that of chamber measurement and depends on, e.g., stability and measurement height.

In order to derive a reliable δ value at the intercept, the measurements must cover the range on the

$1/\chi$ axis. The required range will depend on the variability of measured δ values around the linear $\delta-1/\chi$ line. Generally, the statistical uncertainty of the δ value at the intercept will decrease with the increasing range of mixing ratios.

56.4 Devices and Measuring Systems

The systems for measuring fluxes with the alternative methods presented here are mostly built in-house with very little standardization. Thus, each system is different. However, in the following, we describe typical measurement systems as references for readers aiming to design their own system.

56.4.1 Disjunct Eddy Covariance

Here, we describe the measurement systems for two variants of the disjunct eddy-covariance method. While the theory of these is largely similar, the practical approach is very different. In the first one, physically disjunct air samples are taken, while in the second one, disjunct measurement is a result of consecutive detection of different compounds with one analyzer. Disjunct eddy covariance can also be used to reduce the burden on data storage at remote sites [56.64]. In that case, the measurement system was a standard open-path eddy-covariance system (Chap. 55), which is not discussed here in detail.

Disjunct Eddy Covariance with Grab Sampling

A typical sampler design employs two intermittent storage reservoirs (ISRs), which can be evacuated by a vacuum pump and subsequently filled by opening a fast reacting high-flow conductance valve (S1, S2 in Fig. 56.10). The interval between the grab sampling is used to analyze the trace gas concentrations in the ISR and to evacuate it for the next sample. The alternating grab sampling in two reservoirs allows a parallel analysis of one ISR and the full evacuation of the other ISR. This way, the interval between consecutive grab samples can be halved, and the number of data points for covariance calculation can be doubled.

As inlet valves S1 and S2 (Fig. 56.10), direct-acting solenoid valves have to be used. They provide very short opening/closing times of only a few milliseconds in combination with a relatively large orifice to obtain a sufficient air sample volume (1.0–1.5 L) within the opening time of 0.1–0.2 s. The valves between the ISRs and analyzer need to be of suitable material to minimize surface losses. For example, for VOCs, Teflon-bodied valves have been used. Depending on the analyzer one can also direct the return gas from the analyzer back to

the ISR to prevent a pressure drop [56.7]. Also a system in which the ISRs are equipped with pistons to push all the air to the analyzer without pressure drop has been developed [56.65]. The typical sampling interval has been 20–40 s. In order to guarantee a fast sampling flow into the ISRs, no additional inlet tubing was used, and, thus, the somewhat bulky ISRs (with inlet valves) had to be positioned near the sonic anemometer to limit sensor separation effects (Chap. 55). However, this could lead to flow distortion effects around the sonic anemometer. The optimal position of the scalar sampler is below the sonic anemometer (Fig. 56.1), leading to minimal flux underestimation [56.66].

The flux underestimation due to vertical displacement of anemometer and sampler, when the sampler is below the anemometer, can be estimated by

$$\frac{F_m}{F} = \left[1 - 0.1 \left(\frac{z_w}{z_s} - 1 \right) \right], \quad (56.9)$$

where F_m is the flux measured by displaced sensors, F is the true flux, z_w is the height of the anemometer, and z_s is the height of the sampler [56.66]. Equation (56.9) shows that for a sonic anemometer at 3 m and a sampler at 2.5 m ($z_w/z_s = 1.2$), the flux underestimation is only 2%. For samplers 0.5–1 m below the anemometer on

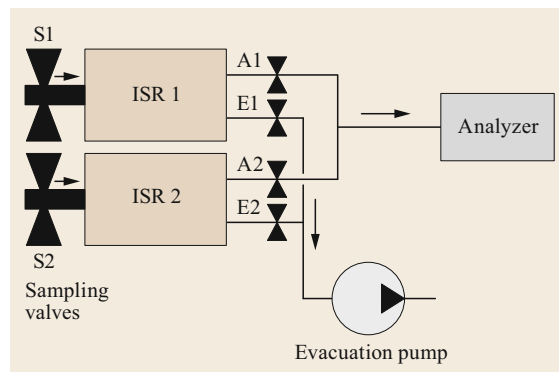


Fig. 56.10 A DEC system with two grab samplers. S1 and S2 are primary sampling valves, ISR 1 and ISR 2 are intermittent storage reservoirs, A1 and A2 are valves to the analyzer, and E1 and E2 are evacuation valves (after [56.3, 25])

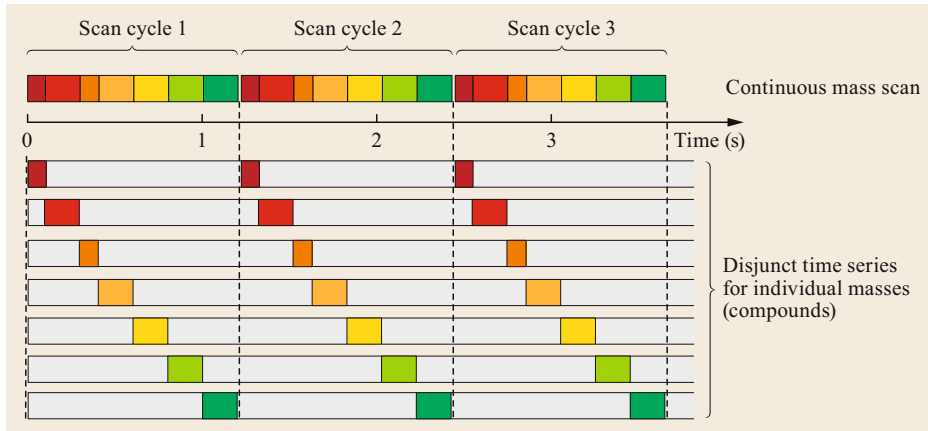


Fig. 56.11 Schematic example of a continuous mass scan covering 7 different masses/compounds (represented by different colors) with different dwell times on each mass (0.1 or 0.2 s) and the resulting disjunct time series for the individual masses. The cycle length corresponding to the DEC sampling interval Δ in this example is 1.2 s

tall towers, the resulting underestimation is, thus, negligible. The situation is not symmetrical with samplers above the sonic anemometer, which leads to a much larger flux underestimation. Other potential problems include a nonperfect evacuation of the ISRs prior to sampling leading to carry-over effects [56.67], and an alteration of reactive trace gases by the various inner-wall materials of the sampling system.

Disjunct Eddy Covariance by Mass Scanning

Up until now, the DEC approach has been applied predominantly for the measurement of volatile organic compounds (VOC) in combination with mass spectrometry detectors, like the PTR-QMS (proton transfer reaction quadrupole mass spectrometer) [56.68]. These instruments provide a relatively fast-response online measurement with a continuous sampling flow but can only detect one compound/charge-to-mass-ratio at a time. Thus, they can be used for conventional EC measurements of a single VOC species, like isoprene or methanol [56.69], but this way, their capability to measure a suite of different VOC species (with different molecular masses) is not exploited. Yet, with the DEC method, a simultaneous flux measurement for several compounds can be obtained by scanning through the respective masses [56.9], as illustrated in Fig. 56.11. This has been realized with typical mass scan cycle periods (representing the DEC sampling interval Δ , Sect. 56.2.1) between 1 and 10 s [56.70, 71]. These Δ values are commonly shorter than those used for grab sampling devices and are, thus, less prone to increased random uncertainty (Fig. 56.3b).

The measurement setup of a DEC system with mass scanning on a continuous air flow is simple (Fig. 56.12),

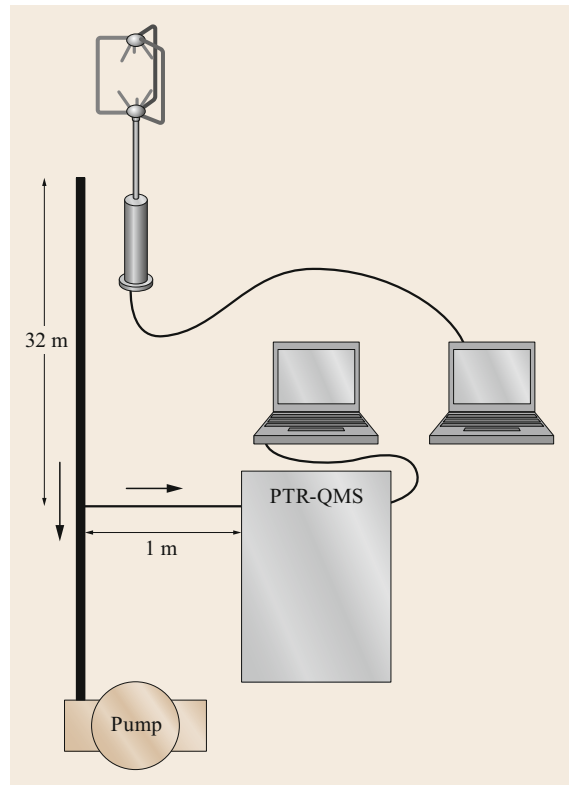


Fig. 56.12 Example schematic of a measurement system for disjunct eddy covariance with mass scanning [56.9]. The 32-meter long sample line (8 mm i.d.) had a flow rate of 10 L min^{-1} . The inlet was located near the sonic anemometer. The PTR-QMS sampled air (0.1 L min^{-1}) from the main sample line through a tube of 1.6 mm i.d. (after [56.71] © Authors)

as it does not require a complicated grab sampler. In many ways, the setup is similar to conventional EC systems with closed-path analyzers. Therefore, also many of the measurement issues are similar (Chap. 55). For example, the air flow in the sample line has to be fast enough to guarantee a high Reynolds number and, thus, a turbulent flow regime without strong streamwise mixing. In some cases, the response time of the PTR-QMS is slowed down either by the choice of longer dwell times for the signal to be above the detection limit or by physicochemical damping effects in longer inlet lines. If the effective response time is close to the DEC sampling rate Δ , also a conventional EC flux calculation can be applied by expanding (interpolating) the disjunct concentration time series to the 10 Hz resolution of the vertical wind measurements [56.70]. However, such procedures have to be applied with care, as they can lead to flux underestimation due to high-frequency loss [56.72].

For determination of the lag time due to the sample line of PTR-QMS (and potentially due to drifting computer clocks if sonic and mass scan data are recorded on separate logging devices), one can use the ion mass 37 (M37) water cluster signal. Since the water vapor flux is orders of magnitudes higher than the fluxes of VOC species, the peak in the covariance function between w and M37 signal is much clearer. Thus, one can first identify the peak position of the covariance function for the M37 signal and then apply it for the other masses, taking into account the scan sequence-dependent time shift illustrated in Fig. 56.11. However, wall sorption effects can cause the lag time to be different for compounds with different solubility or polarity [56.73].

56.4.2 Conditional Sampling

Many different EA and REA systems have been developed. In principle, these consist of sampling valves controlled by the vertical wind velocity measured by a sonic anemometer, mass flow controllers to ensure the proportionality between vertical wind speed and sampling flow, sample reservoirs for updraft and downdraft samples, and a slow analyzer or method to store the samples for subsequent laboratory analysis (Fig. 56.13).

The storage *bins* were initially aluminized polyethylene bags, but other types of storage techniques were also used. A sensible heat-flux detector made up of a fast-response thermocouple sensor for sensing temperature and two electronic bins for temperature measurements was also developed [56.74]. Electronic bins were also used to weigh the frequency of the concentration measurements from a fast-response CO₂ analyzer simultaneously with the air collected in bags.

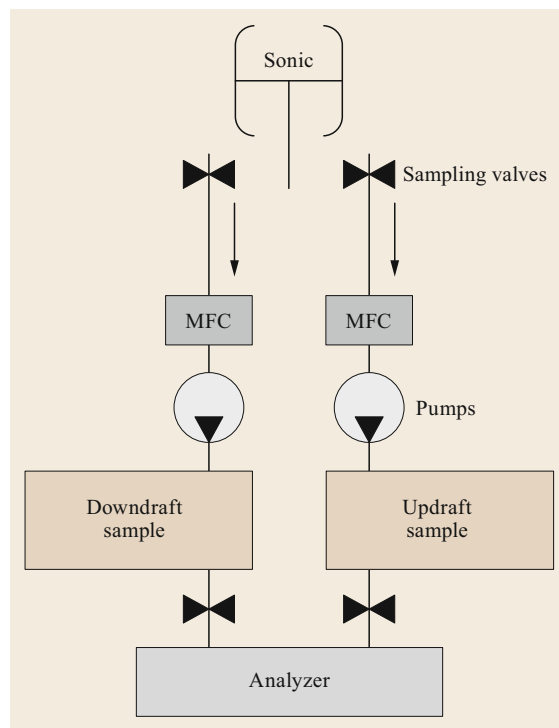


Fig. 56.13 Simplified schematic of an eddy-accumulation system. The analyzer can be replaced with a system to prepare samples for transportation and subsequent laboratory analysis

Recently, a new EA system development has taken place, utilizing digital mass flow controllers, leading to good correspondence with fluxes measured by EC [56.16]. Due to the difficulty of accurately controlling the fast variations in the sample flow, the eddy-accumulation method has not been extensively used.

Disjunct Eddy-Accumulation System with Adsorbent Sampling

A disjunct eddy-accumulation system [56.26, 75] consists of two intermediate storage reservoirs, each with its own primary sampling valve, a set of valves, pump, and flow meter for taking a known volume of air from the ISR to either the updraft or downdraft reservoir, and valves and a pump for evacuation of ISRs (Fig. 56.14). A sonic anemometer is used to obtain wind data that controls the sample accumulation. The updraft and downdraft reservoirs have been adsorbent cartridges used to collect volatile organic compounds. The disjunct sampling is realized by opening the high-conductance valve that lets the air rush into an evacuated intermittent storage reservoir. This is done at regular intervals and alternating the two ISRs. After air has been sampled in the ISR, a part of it is passed

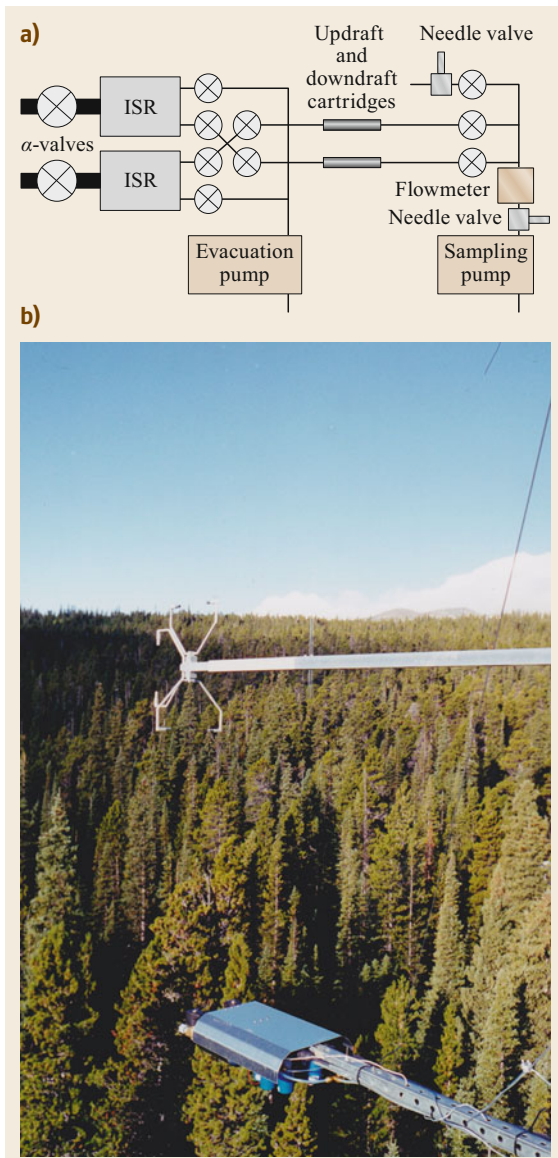


Fig. 56.14 (a) Disjunct eddy-accumulation system (after [56.26] with permission from John Wiley and Sons). The sampling valves (α -valves), intermediate storage reservoirs, and subsequent six valves were situated in a sampler unit below the sonic anemometer, while the sample cartridges, three of the valves, pumps, and controlling electronics were situated at the tower. (b) Disjunct eddy sampler in the Niwot Ridge tower in Colorado, summer 1999. Note the vertical separation between sampler and sonic anemometer, the sonic anemometer being at 20.3 m and the sampler at 19.3 m (photo © Janne Rinne)

through the updraft or downdraft reservoir, depending on the sign of the vertical wind speed at the moment of the primary sampling. The volume passed through the cartridge must be proportional to the vertical wind speed. This has been achieved by integrating the flow rate measured by a flow meter and closing the accumulation valves when the required volume has been sampled. After the sampling, the ISR is evacuated for the next disjunct sample.

Critical design features of a disjunct eddy-accumulation system are the primary and secondary sampling. For the system to be able to resolve the contribution of high-frequency turbulence (Sect. 56.3.1; disjunct eddy-covariance theory), the primary sampling time must be as short as possible to obtain the short effective response time τ_R . This can be achieved by fast, direct-acting high flow-conductance solenoid valves. There should be as little dead volume upstream of the valve, excluding the use of sample tubing. This together with substantial volume of ISRs makes the sampler aerodynamically bulky. The ideal location of the sampler is below the sonic anemometer, as for DEC systems (Sect. 56.4.1). The challenge of the secondary sampling is to determine the sampled volume accurately. Thus, a good flow meter with little dead volume should be used, and its output read and integrated at sufficient frequency.

Finally, the materials used in the samplers should be such as to cause as small artifacts for the measurements as possible. The ISR with a low surface to volume ratio has been constructed from electropolished stainless steel or Teflon. Primary valves have commonly been stainless steel bodied, as large enough Teflon bodied valves have not been available. The tubing and valves for secondary sampling have commonly been Teflon.

Relaxed Eddy Accumulation

Several configurations of REA systems exist, mainly depending of the volume of air to collect and the kind of storage/trapping media used to collect the conditional samples.

At tower-based REA systems filling a pair of 10–20 L flexible bags can be done with a very small diaphragm pump located close to the ultrasonic anemometer pushing the air through the conditional valves and bags [56.18, 19, 41]. Also, adsorbent traps have been used as updraft and downdraft reservoirs [56.40, 76]. To automate the selection of reservoirs, either indexation of traps kept in carousels or selections of arrays of valves have been successfully implemented [56.76, 77].

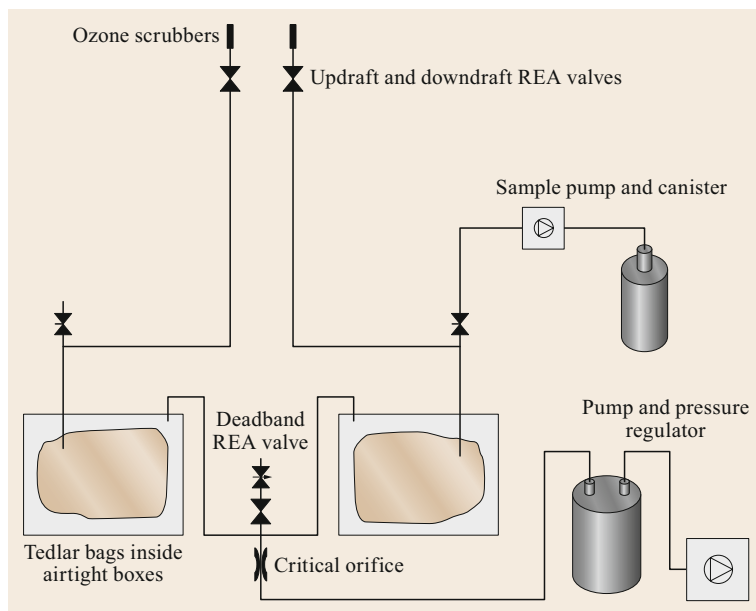


Fig. 56.15 REA system for measuring VOC fluxes (after [56.78])

Figures 56.15 and 56.16 show a schematic and a photo of a realization of another REA system [56.78]. This system is designed for measuring VOCs, thus the materials with which air is in contact are either Teflon or Tedlar. In this system, the two Teflon sampling valves on top are located next to the sonic anemometer used to control the sampling. In front of each valve, there is an ozone scrubber preventing ozone–VOC reactions inside the REA system and in subsequent air samples. Up and downdraft reservoirs are Tedlar bags, located inside rigid airtight boxes. The pump is located downstream and is used to create slight underpressure in these boxes. This design prevents the sample air from passing the pump, a potential source of contamination. The pressure regulator is a buffer volume that dampens the pressure fluctuations from the pump and reduces its effect on measured flow rates. There is an adjustable valve at the deadband line, creating flow resistance that is similar to sample lines. After a half-hour sampling period, a part of both the updraft and downdraft air is transferred to electropolished stainless steel canisters (Rasmussen canisters) by a dedicated valve and a sample pump. The analysis of these samples was subsequently conducted by gas chromatography. As the system required manual operations, it was suited only for short measurement campaigns.

Yet another REA realization does not collect samples for a set interval and then analyze them, but rather continuously samples through mixing reservoirs (Fig. 56.17; [56.39, 79]). In this system, which is de-

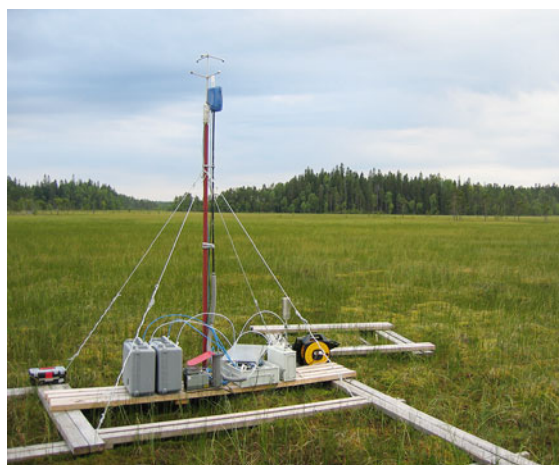


Fig. 56.16 Relaxed eddy-accumulation system as presented in Fig. 56.15 (after [56.78]) in the Siikaneva wetland in Finland, summer 2005. The conditional sampling valves are situated in the blue box next to sonic anemometer and the sample bags inside the gray boxes (photo © Janne Rinne)

signed to measure size-resolved aerosol fluxes or VOC fluxes, the aerosol or VOC concentrations in sample reservoirs are measured in an alternating pattern with a single analyzer. A CO_2 analyzer measuring the concentrations in the reservoirs, together with EC measurements of CO_2 fluxes, can be used to calculate the values of b coefficient. With this system, automated long-term measurements are feasible.

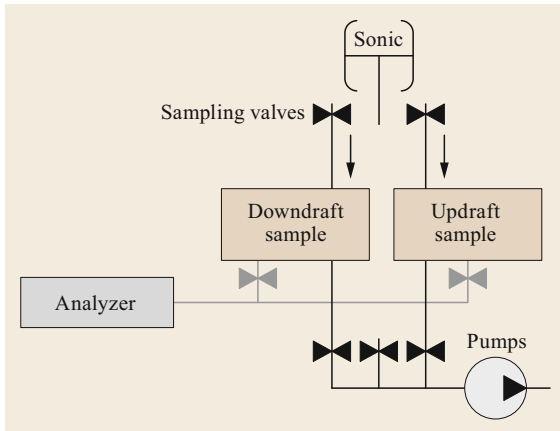


Fig. 56.17 An REA system with flow-through reservoirs, see also [56.39, 79]

Hyperbolic Relaxed Eddy Accumulation

The sampling system for HREA measurements is, in principle, very similar to that for REA measurements. The most significant difference is the need for a fast-response scalar sensor alongside the sonic anemometer to control the conditional sampling. Here, for example, temperature, CO₂, H₂O, or O₃ can be used [56.80, 81].

56.4.3 Surface Renewal

The major gas for which the surface renewal has been used is water vapor. The water vapor flux has been obtained by using surface renewal for the sensible heat flux density and then using the energy budget residual equation to obtain the latent heat flux and, thus, the water vapor flux.

The basic instrumentation needed is a fine wire thermocouple (to measure the surface renewal-based sensible heat flux density H), a net radiometer to measure R_n , ground heat flux plates and one or more soil temperature sensors to measure G , and a data-logging device that can not only record data but analyze the structure functions and calculate H on the fly. All of these can be obtained for relatively low cost compared to a direct eddy-covariance system for water vapor exchange (which requires at least an ultrasonic anemometer and a fast-response gas analyzer in addition to a data logger). If custom built, the system can be even less expensive.

The thermocouple size is an important issue because the accuracy of structure functions depends on the high frequency response of these sensors, linked to narrow wire diameters. Practically, the thermocouple size needs to be large enough to be physically sufficiently robust to withstand the stresses of field deployment, especially related to arachnids and insects. A related solution is to use two relatively fine wire thermocouples,

such that at least one of them will be operational even if the other is broken by the elements.

For measurement of trace gas fluxes with the surface renewal method, a fast response gas analyzer is needed, while a sonic anemometer is not. Thus, this method does not considerably ease the instrumental requirements for trace gas flux measurements, as the fast trace gas analyzer is commonly more expensive than the sonic anemometer.

56.4.4 Nocturnal Boundary-Layer Keeling Plot Method

The aim of the measurements is to cover a large mixing ratio range with corresponding isotopic ratios during an individual night. In principle, any system resolving isotopic ratios and mixing ratios from the same air mass can be used for the nocturnal boundary-layer Keeling plot method. These can be either methods in which air is sampled to be later analyzed in the laboratory, or online measurements. As the analytical techniques for stable isotopes are described in Chap. 17, here only the sampling systems are described.

A system for collecting air samples for subsequent laboratory analysis can consist of sample bags (e.g., Tedlar), a pump for filling up the bags, and tubing to reach the selected sampling height. For example, in an experiment in Finnish mires, air was sampled from heights of 42 and 280 cm above the peat layer. Samples were 4 L in volume and taken at 1 h intervals to 5 L Tedlar bags with 2 L min⁻¹ sample flow, flushing them before [56.82].

In an online measurement system, air is drawn from the selected measurement height to the analyzer. As analyzers need to be protected from elements, they are typically placed 10 to 30 m from sampling tower. As sample flow into the analyzer can be low (< 100 mL min⁻¹); one can use a pump to have a reasonable flow rate in the sample line and take a sample into the analyzer as side flow in an analogous way to that shown in Fig. 56.12.

56.4.5 Comparison of the Methods

While the eddy-covariance method is the preferable method for turbulent flux measurements, there is a need for the above-described alternative methods when fast-response analyzers for a certain trace species are not easily available. It may also be that the existing fast-response analyzers do not operate well in field conditions or are not suitable for field use due to, e.g., high power consumption. In this case, the methods in this chapter or the surface-layer gradient techniques introduced in Chap. 54 may be considered. Table 56.2 gives an overview of the pros and cons of these methods.

Table 56.2 Table summarizing pros and cons of different alternative turbulent flux measurement methods

Measurement method	Advantages	Disadvantages
Disjunct eddy covariance with grab sampling	Theoretically sound and direct method Enables direct flux measurements with slow analyzers (1–60 s)	Bulky and complicated inlet (compared to EC and DEC with mass scanning)
Disjunct eddy covariance with mass scanning	Theoretically sound and direct method No bulky and complicated sampler needed	Requires fast analyzer (< 1 s)
Eddy accumulation	Theoretically sound and direct method	Complexity of fast sample flow control
Disjunct eddy accumulation	Theoretically sound and direct method No need for fast sample flow control	Reduced number of samples lead to increased random uncertainty Bulky sampler Typically needs line power
Relaxed eddy accumulation	Feasible as sample flow is kept constant Low-power system possible	Theoretically less direct than EA but still proven robust
Hyperbolic relaxed eddy accumulation	Feasible as sample flow is kept constant Low-power system possible Higher concentration difference than in REA	Theoretically less direct than EA Needs high-frequency measurement of another scalar, with no time lag
Surface renewal	Based on theoretical turbulent transport mechanisms Simple, inexpensive and low power	May require field calibration Theoretically less direct than EC
Nocturnal boundary-layer Keeling plot	Feasible way for obtaining isotopic signatures of emitted gases	Poor time resolution

56.5 Specifications

The ability to measure fluxes of trace gases typically depends mostly on chemical analysis. We can estimate the accuracy of the chemical analysis needed for EA, REA and HREA measurements by inverting the equations used for calculating the fluxes (Table 56.3).

For DEC, we can estimate the magnitude of uncorrelated noise in the concentration signal that can be

allowed [56.25] for a certain flux level with a 95% confidence interval

$$\sigma_{n,\text{noise}} = \frac{\Delta F \sqrt{n}}{2\sigma_w}$$

This is presented in Table 56.4 for sample intervals of 10 and 30 s, within a measurement period of 0.5 h.

Table 56.3 Required precision of concentration measurement to achieve flux measurements of $1 \mu\text{mol m}^{-2} \text{s}^{-1}$ with conditional sampling systems at $\sigma_w = 0.6 \text{ m s}^{-1}$. Equations obtained by deriving the flux error using standard error propagation for the equation in the given reference and inverting this to solve for error in the concentration measurement

Measurement method	Equation to estimate the required accuracy/noise level	Required precision/noise level
Eddy accumulation	$\Delta c = \frac{\Delta F \sqrt{2}}{\sigma_w}$ [56.83]	2.4
Relaxed eddy accumulation, no deadband	$\Delta c = \frac{\Delta F}{b\sigma_w \sqrt{2}}$ [56.38]	2.1
Relaxed eddy accumulation, dynamic deadband of $0.5\sigma_w$	$\Delta c = \frac{\Delta F}{b\sigma_w \sqrt{2}}$ [56.38]	2.8
Hyperbolic relaxed eddy accumulation, with deadband of 1.0	$\Delta c = \frac{\Delta F}{b_{\text{HREA}} \sigma_w \sqrt{2}}$ [56.40]	5.4

Table 56.4 The level of uncorrelated noise in the concentration measurements allowed to achieve a flux measurement of 1 using the DEC method with different sample numbers

n	180	60
$\sigma_{c,\text{noise}}$	11	6.5

56.6 Quality Control

The quality of the measured fluxes depends on three parts:

- Turbulence statistics
- Trace gas concentration measurement
- Functioning of the flux measurement system.

In principle, for turbulence statistics, similar criteria apply as for the eddy-covariance method (Chap. 55). However, the alternative flux measurement methods provide no or only limited data on high-frequency variations of the trace gas. Thus, these tests can only be applied to vertical wind speed or by using e.g., CO₂ as a proxy.

Each trace gas analyzer has its own parameters for quality control of measured trace gas concentrations, and these should be referred to for the quality of the concentration measurement. Below, the quality control parameters typical for each flux measurement method are discussed.

56.6.1 Sample Volumes in Conditional Sampling Systems

In conditional sampling systems (EA, DEA, REA, HREA), the volume of air collected into updraft and downdraft reservoirs during an averaging period should be roughly equal. Any major deviation from this would indicate that either the average wind deviates considerably from horizontal wind, the sonic anemometer is badly misaligned, or there is some technical problem in the system. Therefore, the sample volumes provide a feasible check for proper functioning of the measurement system.

56.7 Maintenance

As there exists such a variety of different designs, general rules of maintenance cannot be readily given. Most of the flux measurement systems described above require either extensive maintenance or are designed for manual measurements, with an operator on site (Table 56.5). The conditional sampling systems can be automatized but then require maintenance of valves, pumps, and analyzers. In systems

56.6.2 Disjunct Eddy Covariance

In principle, similar quality control as for conventional eddy covariance is applicable for disjunct eddy covariance. However, some quality control tests, such as the stationarity test, can be challenging due to the reduced sample number leading to noisier statistics. Also, spectral analysis is affected by low sampling frequency and aliasing effects [56.25].

In a DEC system with grab samplers (Fig. 56.10), a systematic difference between the trace gas concentrations obtained from the two ISRs can indicate contamination in the sampler. In such systems, it is also advisable to record the ISR pressures, as anomalies may reveal malfunctions of the primary sampling valves or the evacuation system. Continuous-flow DEC systems work much the same way as conventional eddy-covariance systems.

56.6.3 Linearity and Statistics of the Keeling Plot

For the intercept of the Keeling plot to have low uncertainty, the concentration data should have a sufficiently large range. The assumption of two-end-member mixing leads to linearity of the δ -to- $1/\chi$ plot. Thus, the tests for linearity of the data, the correlation between δ and $1/\chi$ can be used to assess the quality of the data collected. Furthermore, statistical tools calculating the confidence intervals for a fitted line can be used to derive the confidence intervals for intercept values, i.e., the isotopic signature of emitted gas.

employing online analysis, the analyzer may require frequent attention. For example, in disjunct eddy-covariance systems, proton transfer reaction mass spectrometer (PTR-MS) analyzers typically need calibration several times per month. The systems for automated isotope measurements and the surface renewal method are at the lower end of maintenance requirements.

Table 56.5 Generic list for maintenance items for different measurement methods. As designs differ from each other, so does the actual maintenance procedure for each individual system design

System	Maintenance
Disjunct eddy covariance with grab sampler (DEC)	Check the valves Check the pump Monitor flow rates and ISR pressures
Disjunct eddy covariance with continuous sample flow (DEC)	Cleaning the tube at intervals Check pump Check the flow in the main tube
Conditional sampling systems (EA, DEA, REA, HREA)	Check the valves Check pumps Check sample reservoirs, especially in automated systems Monitor flow rates in system
Surface renewal	Follow the maintenance protocols of sensors
Nocturnal boundary layer Keeling plot	Check the flow in the main sample tube Check the pump

56.8 Application

As many trace gas flux measurement systems described in this section are experimental and mostly developed and built in-house for specific research questions, a comprehensive account for their applications is elusive. In Table 56.6, we give some examples of the applications of each measurement method discussed in

this chapter. Some techniques, such as eddy accumulation, have barely been used, while, for example, there have been many diverse applications of relaxed eddy accumulation. Unfortunately, the less successful developments, from which we could also learn, are rarely reported in the scientific literature.

Table 56.6 Compounds for which alternative flux measurement techniques are used. For details, see the text below

Method	Compound/Parameter	Analyzer	References
Disjunct eddy covariance, with grab samplers	VOCs	Proton transfer reaction mass spectrometer	[56.3, 4, 8]
Disjunct eddy covariance, with continuous flow	VOCs	Proton transfer reaction mass spectrometer	[56.2, 9, 70, 71, 84]
Eddy accumulation	Aerosol particles	Electric low pressure impactor	[56.85]
Disjunct eddy accumulation	C ₆ H ₆ , pesticides	Mass spectrometer	[56.76]
Relaxed eddy accumulation	VOCs	Gas chromatography	[56.26, 75, 86]
	NO _x	Chemoluminescence	[56.87]
	NH ₃	Ion chromatography	[56.88–90]
		Colorimetry	[56.89]
	VOC	Gas chromatography	[56.19, 40, 78, 79, 91]
	Mercury	Cold vapor atomic fluorescence spectrophotometry	[56.92–94]
	Herbicides	Gas chromatography	[56.76, 95, 96]
	Aerosol particles	Differential mobility particle sizer, Hygroscopicity tandem differential mobility analyzer	[56.39, 97, 98]
Hyperbolic relaxed eddy accumulation	$\delta^{13}\text{C}$ in CO ₂	Gas chromatography	[56.41, 99]
	Peroxyacetyl nitrate	Gas chromatography	[56.80]
Surface renewal	H, LE		[56.24, 60, 100]
	CO ₂		[56.58, 101]
Nocturnal boundary layer Keeling plot	$\delta^{13}\text{C}$ and $\delta^{18}\text{O}$ in CO ₂	Gas chromatography	[56.102–104]
	$\delta^{13}\text{C}$ in CH ₄	Gas chromatography	[56.82, 105, 106]

56.9 Future Developments

The eddy-covariance method is the most direct micrometeorological method for measuring turbulent fluxes and does not require complicated samplers. Thus, the development of novel fast-response analyzers usually leads to the use of the EC method over the more indirect methods described in this chapter, as it is the preference of most researchers [56.107]. This has been observed, for example, in the case of methane, for which the development of cavity ring-down laser spectroscopy has led to proliferation of eddy-covariance measurements [56.108].

However, there will always be compounds for which analyzers that are suitable for eddy-covariance measurements do not exist or can not be suitably operated in the field environment. For those compounds, the micrometeorologist's toolbox includes methods such as gradient methods, conditional sampling methods, and disjunct eddy-covariance methods. Due to the large variety of gases and aerosols of interest and their different chemical and physical properties, the method used has to be tailored separately for each application.

56.10 Further Readings

- D.R. Bowling, A.A. Turnipseed, A.C. Delany, D.D. Baldocchi, J.P. Greenberg, R.K. Monson: The use of relaxed eddy accumulation to measure biosphere-atmosphere exchange of isoprene and other biological trace gases, *Oecologia* **116**, 306–315 (1998)
- E. Pattey, R.L. Desjardins, P. Rochette: Accuracy of the relaxed eddy-accumulation technique, evaluated using CO₂ flux measurements, *Bound.-Layer Meteorol.* **66**, 341–355 (1993)
- J. Rinne, C. Ammann: Disjunct eddy covariance method. In: *Eddy Covariance – A Practical Guide to Measurement and Data Analysis*, ed. by M. Aubinet, T. Vesala, D. Papale. Springer Atmospheric Sciences (Springer, Dordrecht 2012), pp. 291–307

References

- 56.1 E.R. Lemon: Photosynthesis under field conditions. II. An aerodynamic method for determining the turbulent carbon dioxide exchange between the atmosphere and a corn field, *Agron. J.* **52**, 697–703 (1960)
- 56.2 P. Rantala, R. Taipale, J. Aalto, M.K. Kajos, J. Patakoski, T.M. Ruuskanen, J. Rinne: Continuous flux measurements of VOCs using PTR-MS – Reliability and feasibility of disjunct-eddy-covariance, surface-layer-gradient, and surface-layer-profile methods, *Boreal Environ. Res.* **19**, 87–107 (2014)
- 56.3 H.J.I. Rinne, A.B. Guenther, C. Warneke, J.A. de Gouw, S.L. Luxembourg: Disjunct eddy covariance technique for trace gas flux measurements, *Geophys. Res. Lett.* **28**, 3139–3142 (2001)
- 56.4 C. Warneke, S.L. Luxembourg, J.A. de Gouw, H.J.I. Rinne, A.B. Guenther, R. Fall: Disjunct eddy covariance measurements of oxygenated volatile organic compounds fluxes from an alfalfa field before and after cutting, *J. Geophys. Res. Atmos.* **107**, ACH 6-1–ACH 6-10 (2002)
- 56.5 D.A. Haugen: Effects of sampling rates and averaging periods on meteorological measurements. In: *4th Symp. Meteorol. Obs. Instrum.* (AMS, Boston 1978) pp. 15–18
- 56.6 J.C. Kaimal, J.E. Gaynor: The Boulder Atmospheric Observatory, *J. Clim. Appl. Meteorol.* **22**, 863–880 (1983)
- 56.7 J. Rinne, T. Douffet, Y. Prigent, P. Durand: Field comparison of disjunct and conventional eddy covariance techniques for trace gas flux measurements, *Environ. Pollut.* **152**, 630–635 (2008)
- 56.8 W. Grabmer, M. Graus, C. Lindinger, A. Wisthaler, B. Rappenglück, R. Steinbrecher, A. Hansel: Disjunct eddy covariance measurements of monoterpene fluxes from a Norway spruce forest using PTR-MS, *Int. J. Mass Spectrom.* **239**, 111–115 (2004)
- 56.9 T.G. Karl, C. Spirig, J. Rinne, C. Stroud, P. Prevost, J. Greenberg, R. Fall, A. Guenther: Virtual disjunct eddy covariance measurements of organic compound fluxes from a subalpine forest using proton transfer reaction mass spectrometry, *Atmos. Chem. Phys.* **2**, 279–291 (2002)
- 56.10 R.L. Desjardins: *A Study of Carbon Dioxide and Sensible Heat Fluxes Using the Eddy Correlation Technique*, Ph.D. Thesis (Cornell Univ, Ithaca 1972)
- 56.11 R.L. Desjardins: Technique to measure CO₂ exchange under field conditions, *Int. J. Biometeorol.* **18**, 76–83 (1974)
- 56.12 R.L. Desjardins, D.J. Buckley, G.S. Amour: Eddy flux measurements of CO₂ above corn using a microcomputer system, *Agric. For. Meteorol.* **32**, 257–265 (1984)
- 56.13 W.S. Reid, R.L. Desjardins, W. Fagan, A. Ginsburg: An open-loop fast response gas sampling valve with current control, *J. Phys. E* **17**, 323–327 (1984)

- 56.14 D.J. Buckley, R.L. Desjardins, J.L.M. Lalonde, R. Brunke: A linearized, fast response gas sampling apparatus for eddy accumulation studies, *Comput. Electron. Agric.* **2**, 243–250 (1988)
- 56.15 J.A. Businger, S.P. Oncley: Flux measurement with conditional sampling, *J. Atmos. Ocean. Technol.* **7**, 349–352 (1990)
- 56.16 L. Siebicke, A. Emad: True eddy accumulation trace gas flux measurements: Proof-of-concept, *Atmos. Meas. Tech.* **12**, 4393–4420 (2019)
- 56.17 E. Pattey, R.L. Desjardins, F. Boudreau, P. Rochette: Impact of density fluctuations on flux measurements of trace gases: Implications for the relaxed eddy accumulation technique, *Bound.-Layer Meteorol.* **59**, 195–203 (1992)
- 56.18 E. Pattey, R.L. Desjardins, P. Rochette: Accuracy of the relaxed eddy-accumulation technique, evaluated using CO₂ flux measurements, *Bound.-Layer Meteorol.* **66**, 341–355 (1993)
- 56.19 E. Pattey, R.L. Desjardins, H. Westberg, B. Lamb, T. Zhu: Measurement of isoprene emissions over a black spruce stand using a tower-based relaxed eddy-accumulation system, *J. Appl. Meteorol.* **38**, 870–877 (1999)
- 56.20 R. Higbie: The rate of absorption of a pure gas into a still liquid during short periods of exposure, *Transactions AIChE* **31**, 365–389 (1935)
- 56.21 P.V. Danckwerts: Significance of liquid-film coefficients in gas absorption, *Ind. Eng. Chem.* **43**, 1460–1467 (1951)
- 56.22 K.T. Paw U, Y. Brunet: A surface renewal measure of sensible heat flux density. In: *20th Conf. Agric. For. Meteorol.* (AMS, Boston 1991)
- 56.23 K.T. Paw U, H.-B. Su: The usage of structure functions in studying turbulent coherent structures and estimating sensible heat flux. In: *21st Conf. Agric. For. Meteorol.* (AMS, Boston 1994)
- 56.24 K.T. Paw U, J. Qiu, H.-B. Su, T. Watanabe, Y. Brunet: Surface renewal analysis: A new method to obtain scalar fluxes, *Agric. For. Meteorol.* **74**, 119–137 (1995)
- 56.25 J. Rinne, C. Ammann: Disjunct eddy covariance method. In: *Eddy Covariance – A Practical Guide to Measurement and Data Analysis*, Springer Atmospheric Sciences, ed. by M. Aubinet, T. Vesala, D. Papale (Springer, Dordrecht 2012) pp. 291–307
- 56.26 H.J.I. Rinne, A.C. Delany, J.P. Greenberg, A.B. Guenther: A true eddy accumulation system for trace gas fluxes using disjunct eddy sampling method, *J. Geophys. Res. Atmos.* **105**, 24791–24798 (2000)
- 56.27 F.C. Bosveld, A.C.M. Beljaars: The impact of sampling rate on eddy-covariance flux estimates, *Agric. For. Meteorol.* **109**, 39–45 (2001)
- 56.28 D.H. Lenschow, J. Mann, L. Kristensen: How long is long enough when measuring fluxes and other turbulence statistics?, *J. Atmos. Ocean. Technol.* **11**, 661–673 (1994)
- 56.29 A.A. Turnipseed, S.N. Pressley, T. Karl, B. Lamb, E. Nemitz, E. Allwine, W.A. Cooper, S. Shertz, A.B. Guenther: The use of disjunct eddy sampling methods for the determination of ecosystem level fluxes of trace gases, *Atmos. Chem. Phys.* **9**, 981–994 (2009)
- 56.30 J.C. Kaimal, J.J. Finnigan: *Atmospheric Boundary Layer Flows, Their Structure and Measurement* (Oxford Univ. Press, New York, Oxford 1994)
- 56.31 F. Chahuneau, R.L. Desjardins, E. Brach, R. Verdon: A Micrometeorological facility for eddy correlation measurements of CO₂ and H₂O, *J. Atmos. Ocean. Technol.* **6**, 193–200 (1989)
- 56.32 B.B. Hicks, R.T. McMillen: A simulation of the eddy accumulation method for measuring pollutant fluxes, *J. Clim. Appl. Meteorol.* **23**, 637–643 (1984)
- 56.33 J. Rinne: *Application and Development of Surface Layer Flux Techniques for Measurement of Volatile Organic Compound Emissions from Vegetation*, Ph.D. Thesis (Univ. Helsinki, Helsinki 2001), <http://urn.fi/URN:ISBN:952-10-0101-1>, Accessed 22 July 2021
- 56.34 J.M. Baker, J.M. Norman, W.L. Bland: Field-scale application of flux measurement by conditional sampling, *Agric. For. Meteorol.* **62**, 31–52 (1992)
- 56.35 R. Milne, A. Mennim, K. Hargreaves: The value of the β coefficient in the relaxed eddy accumulation method in terms of fourth-order moments, *Bound.-Layer Meteorol.* **101**, 359–373 (2001)
- 56.36 C. Ammann, F.X. Meixner: Stability dependence of the relaxed eddy accumulation coefficient for various scalar quantities, *J. Geophys. Res. Atmos.* **107**, ACL7-1–ACL7-9 (2002)
- 56.37 S.P. Oncley, A.C. Delany, T.W. Horst, P.P. Tans: Verification of flux measurement using relaxed eddy accumulation, *Atmos. Environ. A* **27**, 2417–2426 (1993)
- 56.38 T. Grönholm, S. Haapanala, S. Launiainen, J. Rinne, T. Vesala, Ü. Rannik: The dependence of the β coefficient of REA system with dynamic deadband on atmospheric conditions, *Environ. Pollut.* **152**, 597–603 (2008)
- 56.39 A. Gaman, Ü. Rannik, P. Aalto, T. Pohja, E. Siivola, M. Kulmala, T. Vesala: Relaxed eddy accumulation system for size-resolved aerosol particle flux measurements, *J. Atmos. Ocean. Technol.* **21**, 933–943 (2004)
- 56.40 D.R. Bowling, A.A. Turnipseed, A.C. Delany, D.D. Baldocchi, J.P. Greenberg, R.K. Monson: The use of relaxed eddy accumulation to measure biosphere-atmosphere exchange of isoprene and other biological trace gases, *Oecologia* **116**, 306–315 (1998)
- 56.41 D.R. Bowling, A.C. Delany, A.A. Turnipseed, D.D. Baldocchi, R.K. Monson: Modification of the relaxed eddy accumulation technique to maximize measured scalar mixing ratio differences in updrafts and downdrafts, *J. Geophys. Res. Atmos.* **104**, 9121–9133 (1999)
- 56.42 R.T. McMillen: An eddy correlation technique with extended applicability to non-simple terrain, *Bound.-Layer Meteorol.* **43**, 231–245 (1988)
- 56.43 J. Ruppert, C. Thomas, T. Foken: Scalar similarity for relaxed eddy accumulation methods, *Bound.-Layer Meteorol.* **120**, 39–63 (2006)

- 56.44 W. Gao, R.H. Shaw, K.T. Paw U: Observation of organized structure in turbulent-flow within and above a forest canopy, *Bound.-Layer Meteorol.* **47**, 349–377 (1989)
- 56.45 K.T. Paw U, Y. Brunet, S. Collineau, R.H. Shaw, T. Maitani, J. Qiu, L. Hipps: On coherent structures in turbulence above and within agricultural plant canopies, *Agric. For. Meteorol.* **61**, 55–68 (1992)
- 56.46 C.W. Vanatta: Effect of coherent structures on structure functions of temperature in atmospheric boundary-layer, *Arch. Mech.* **29**, 161–171 (1977)
- 56.47 R.L. Snyder, D. Spano, K.T. Paw U: Surface renewal analysis for sensible and latent heat flux density, *Bound.-Layer Meteorol.* **77**, 249–266 (1996)
- 56.48 K.T. Paw U, L. Snyder, D. Spano, H.-B. Su: Surface renewal estimates of scalar exchange. In: *Micrometeorology of Agricultural Systems*, ed. by J.L. Hatfield (ASA, Madison 2005) pp. 455–483
- 56.49 K.T. Paw U, D.D. Baldocchi, T.P. Meyers, K.B. Wilson: Correction of eddy-covariance measurements incorporating both advective effects and density fluxes, *Bound.-Layer Meteorol.* **97**, 487–511 (2000)
- 56.50 T.M. Shapland, A.J. McElrone, R.L. Snyder, K.T. Paw U: Structure function analysis of two-scale scalar ramps. Part I: Theory and modelling, *Bound.-Layer Meteorol.* **145**, 5–25 (2012)
- 56.51 T.M. Shapland, A.J. McElrone, R.L. Snyder, K.T. Paw U: Structure function analysis of two-scale scalar ramps. Part II: Ramp characteristics and surface renewal flux estimation, *Bound.-Layer Meteorol.* **145**, 27–44 (2012)
- 56.52 W.J. Chen, M.D. Novak, T.A. Black, X.H. Lee: Coherent eddies and temperature structure functions for three contrasting surfaces. Part I: Ramp model with finite microfront time, *Bound.-Layer Meteorol.* **84**, 99–123 (1997)
- 56.53 W.J. Chen, M.D. Novak, T.A. Black, X.H. Lee: Coherent eddies and temperature structure functions for three contrasting surfaces. Part II: Renewal model for sensible heat flux, *Bound.-Layer Meteorol.* **84**, 125–147 (1997)
- 56.54 F. Castellvi: Combining surface renewal analysis and similarity theory: A new approach for estimating sensible heat flux, *Water Resour. Res.* **40**, W05201 (2004)
- 56.55 F. Castellvi, R.L. Snyder, D.D. Baldocchi: Surface energy-balance closure over rangeland grass using the eddy covariance method and surface renewal analysis, *Agric. For. Meteorol.* **148**, 1147–1160 (2008)
- 56.56 K. Suvocarev, T.M. Shapland, R.L. Snyder, A. Martinez-Cob: Surface renewal performance to independently estimate sensible and latent heat fluxes in heterogeneous crop surfaces, *J. Hydrol.* **509**, 83–93 (2014)
- 56.57 F. Castellvi, R.L. Snyder: A comparison between latent heat fluxes over grass using a weighing lysimeter and surface renewal analysis, *J. Hydrol.* **381**, 213–220 (2010)
- 56.58 K.T. Paw U, H.-B. Su, D.A. Braaten: The usage of structure functions in estimating water vapor and carbon dioxide exchange between plant canopies and the atmosphere. In: *22nd Conf. Agric. For. Meteorol.* (AMS, Boston 1996)
- 56.59 D. Spano, R.L. Snyder, P. Duce, K.T. Paw U, M. Falk: Determining scalar fluxes over an old-growth forest using surface renewal. In: *24th Conf. Agric. For. Meteorol.* (AMS, Boston 2000)
- 56.60 R.L. Snyder, D. Spano, P. Duce, K.T. Paw U, M. Rivera: Surface renewal estimation of pasture evapotranspiration, *J. Irrig. Drain. Eng.* **134**, 716–721 (2008)
- 56.61 C.D. Keeling: The concentration and isotopic abundances of atmospheric carbon dioxide in rural areas, *Geochim. Cosmochim. Acta* **13**, 322–334 (1958)
- 56.62 D. Yakir, L.D.L. Sternberg: The use of stable isotopes to study ecosystem gas exchange, *Oecologia* **123**, 297–311 (2000)
- 56.63 D. E. Pataki, J.R. Ehleringer, L.B. Flanagan, D. Yakir, D.R. Bowling, C.J. Still, N. Buchmann, J.O. Kaplan, J.A. Berry: The application and interpretation of Keeling plots in terrestrial carbon cycle research, *Glob. Biogeochem. Cycles* **17**, 1022 (2003)
- 56.64 D. Holl, C. Wille, T. Sachs, P. Schreiber, B.R.K. Runkle, L. Beckebanze, M. Langer, J. Boike, E.M. Pfeiffer, I. Fedorova, D.Y. Bolshianov, M.N. Grigoriev, L. Kutzbach: A long-term (2002 to 2017) record of closed-path and open-path eddy covariance CO₂ net ecosystem exchange fluxes from the Siberian Arctic, *Earth Syst. Sci. Data* **11**, 221–240 (2019)
- 56.65 R. Baghi, P. Durand, C. Jambert, C. Jarnot, C. Delon, D. Serca, N. Striebig, M. Ferlicoq, P. Keravec: A new disjunct eddy-covariance system for BVOC flux measurements – Validation on CO₂ and H₂O fluxes, *Atmos. Meas. Tech.* **5**, 3119–3132 (2012)
- 56.66 L. Kristensen, J. Mann, S.P. Oncley, J.C. Wyngaard: How close is close enough when measuring scalar fluxes with displaced sensors?, *J. Atmos. Ocean. Technol.* **14**, 814–821 (1997)
- 56.67 B. Langford, B. Davison, E. Nemitz, C.N. Hewitt: Mixing ratios and eddy covariance flux measurements of volatile organic compounds from an urban canopy (Manchester, UK), *Atmos. Chem. Phys.* **9**, 1971–1987 (2009)
- 56.68 W. Lindinger, A. Jordan: Proton-transfer-reaction mass spectrometry (PTR-MS): On-line monitoring of volatile organic compounds at pptv levels, *Chem. Soc. Rev.* **27**, 347–354 (1998)
- 56.69 T. Karl, A. Guenther, C. Lindinger, A. Jordan, R. Fall, W. Lindinger: Eddy covariance measurements of oxygenated volatile organic compound fluxes from crop harvesting using a redesigned proton-transfer-reaction mass spectrometer, *J. Geophys. Res. Atmos.* **106**, 24157–24167 (2001)
- 56.70 C. Spirig, A. Neftel, C. Ammann, J. Domen, W. Grabmer, A. Thielmann, A. Schaub, J. Beauchamp, A. Wisthaler, A. Hansel: Eddy covariance flux measurements of biogenic VOCs during ECHO 2003 using proton transfer reaction mass spectrometry, *Atmos. Chem. Phys.* **5**, 465–481 (2005)

- 56.71 J. Rinne, R. Taipale, T. Markkanen, T.M. Ruuskanen, H. Hellen, M.K. Kajos, T. Vesala, M. Kulmala: Hydrocarbon fluxes above a scots pine forest canopy: Measurements and modeling, *Atmos. Chem. Phys.* **7**, 3361–3372 (2007)
- 56.72 L. Hörtnagl, R. Clement, M. Graus, A. Hammerle, A. Hansel, G. Wohlfahrt: Dealing with disjunct concentration measurements in eddy covariance applications: A comparison of available approaches, *Atmos. Environ.* **44**, 2024–2032 (2010)
- 56.73 C. Ammann, A. Brunner, C. Spirig, A. Neftel: Technical note: Water vapour concentration and flux measurements with PTR-MS, *Atmos. Chem. Phys.* **6**, 4643–4651 (2006)
- 56.74 R.L. Desjardins: Description and evaluation of a sensible heat flux detector, *Bound.-Layer Meteorol.* **11**, 147–154 (1977)
- 56.75 S. Haapanala, H. Hakola, H. Hellen, M. Vestenius, J. Levula, J. Rinne: Is forest management a significant source of monoterpenes into the boreal atmosphere?, *Biogeosciences* **9**, 1291–1300 (2012)
- 56.76 E. Pattey, A.J. Cessna, R.L. Desjardins, L.A. Ken, P. Rochette, G. St-Amour, T. Zhu, K. Headrick: Herbicides volatilization measured by the relaxed eddy-accumulation technique using two trapping media, *Agric. For. Meteorol.* **76**, 201–220 (1995)
- 56.77 E. Pattey, W.G. Royds, R.L. Desjardins, D.J. Buckley, P. Rochette: Software description of a data acquisition and control system for measuring trace gas and energy fluxes by eddy-accumulation and correlation techniques, *Comput. Electron. Agric.* **15**, 303–321 (1996)
- 56.78 S. Haapanala, J. Rinne, K.H. Pystynen, H. Hellen, H. Hakola, T. Riutta: Measurements of hydrocarbon emissions from a boreal fen using the REA technique, *Biogeosciences* **3**, 103–112 (2006)
- 56.79 M. Graus, A. Hansel, A. Wisthaler, C. Lindinger, R. Forkel, K. Hauff, M. Klauer, A. Pfichner, B. Rappenglück, D. Steigner, R. Steinbrecher: A relaxed-eddy-accumulation method for the measurement of isoprenoid canopy-fluxes using an online gas-chromatographic technique and PTR-MS simultaneously, *Atmos. Environ.* **40**, S43–S54 (2006)
- 56.80 A. Moravek, T. Foken, I. Trebs: Application of a GC-ECD for measurements of biosphere-atmosphere exchange fluxes of peroxyacetyl nitrate using the relaxed eddy accumulation and gradient method, *Atmos. Meas. Tech.* **7**, 2097–2119 (2014)
- 56.81 M. Riederer, J. Huebner, J. Ruppert, W.A. Brand, T. Foken: Prerequisites for application of hyperbolic relaxed eddy accumulation on managed grasslands and alternative net ecosystem exchange flux partitioning, *Atmos. Meas. Tech.* **7**, 4237–4250 (2014)
- 56.82 S. Srisikantharajah, R.E. Fisher, D. Lowry, T. Aalto, J. Hatakka, M. Aurela, T. Laurila, A. Lohila, E. Kuitunen, E.G. Nisbet: Stable carbon isotope signatures of methane from a Finnish subarctic wetland, *Tellus B* **64**, 18818 (2012)
- 56.83 B.B. Hicks, R.T. McMillen: On the measurement of dry deposition using imperfect sensors and in non-ideal terrain, *Bound.-Layer Meteorol.* **42**, 79–94 (1988)
- 56.84 A. Bachy, M. Aubinet, C. Amelynck, N. Schoon, B. Bodson, C. Moureaux, P. Delaplace, A. De Ligne, B. Heinesch: Methanol exchange dynamics between a temperate cropland soil and the atmosphere, *Atmos. Environ.* **176**, 229–239 (2018)
- 56.85 A. Held, K.P. Hinz, A. Trimborn, B. Spengler, O. Klemm: Towards direct measurement of turbulent vertical fluxes of compounds in atmospheric aerosol particles, *Geophys. Res. Lett.* **30**, ASC 8–1–ASC 8–4 (2003)
- 56.86 G.D. Edwards, D.K. Martins, T. Starn, K. Pratt, P.B. Shepson: A disjunct eddy accumulation system for the measurement of BVOC fluxes: Instrument characterizations and field deployment, *Atmos. Meas. Tech.* **5**, 2115–2132 (2012)
- 56.87 A. Brut, D. Legain, P. Durand, P. Laville: A relaxed eddy accumulator for surface flux measurements on ground-based platforms and aboard research vessels, *J. Atmos. Ocean. Technol.* **21**, 411–427 (2004)
- 56.88 T. Zhu, E. Pattey, R.L. Desjardins: Relaxed eddy-accumulation technique for measuring ammonia volatilization, *Environ. Sci. Technol.* **34**, 199–203 (2000)
- 56.89 A.J. Nelson, S. Koloutsou-Vakakis, M.J. Rood, L. Myles, C. Lehmann, C. Bernacchi, S. Balasubramanian, E. Joo, M. Heuer, M. Vieira-Filho, J. Lin: Season-long ammonia flux measurements above fertilized corn in central Illinois, USA, using relaxed eddy accumulation, *Agric. For. Meteorol.* **239**, 202–212 (2017)
- 56.90 L. Myles, T.P. Meyers, L. Robinson: Relaxed eddy accumulation measurements of ammonia, nitric acid, sulfur dioxide and particulate sulfate dry deposition near Tampa, FL, USA, *Environ. Res. Lett.* **2**, 034004 (2007)
- 56.91 T. Zhu, D. Wang, R.L. Desjardins, J.I. Macpherson: Aircraft-based volatile organic compounds flux measurements with relaxed eddy accumulation, *Atmos. Environ.* **33**, 1969–1979 (1999)
- 56.92 S. Osterwalder, J. Fritsche, C. Alewell, M. Schmutz, M.B. Nilsson, G. Jocher, J. Sommar, J. Rinne, K. Bishop: A dual-inlet, single detector relaxed eddy accumulation system for long-term measurement of mercury flux, *Atmos. Meas. Tech.* **9**, 509–524 (2016)
- 56.93 D.R. Cobos, J.M. Baker, E.A. Nater: Conditional sampling for measuring mercury vapor fluxes, *Atmos. Environ.* **36**, 4309–4321 (2002)
- 56.94 J. Sommar, W. Zhu, L. Shang, X. Feng, C.-J. Lin: A whole-air relaxed eddy accumulation measurement system for sampling vertical vapour exchange of elemental mercury, *Tellus B* **65**, 19940 (2013)
- 56.95 M. Leistra, J.H. Smelt, J.H. Weststrate, F. van den Berg, R. Aalderink: Volatilization of the pesticides chlorpyrifos and fenpropimorph from a potato crop, *Environ. Sci. Technol.* **40**, 96–102 (2006)

- 56.96 T. Zhu, R.L. Desjardins, J.I. Macpherson, E. Pattey, G. St. Amour: Aircraft measurements of the concentration and flux of agrochemicals, *Environ. Sci. Technol.* **32**, 1032–1038 (1998)
- 56.97 T. Grönholm, P.P. Aalto, V. Hiltunen, Ü. Ran-
nik, J. Rinne, L. Laakso, S. Hyvonen, T. Vesala,
M. Kulmala: Measurements of aerosol particle dry
deposition velocity using the relaxed eddy accumu-
lation technique, *Tellus B* **59**, 381–386 (2007)
- 56.98 N. Meskhidze, T.M. Royalty, B.N. Phillips,
K.W. Dawson, M.D. Petters, R. Reed, J.P. Wein-
stein, D.A. Hook, R.W. Wiener: Continuous flow
hygroscopicity-resolved relaxed eddy accumu-
lation (Hy-Res REA) method of measuring size-
resolved sodium chloride particle fluxes, *Aerosol
Sci. Technol.* **52**, 433–450 (2018)
- 56.99 D.R. Bowling, D.E. Pataki, J.R. Ehleringer: Critical
evaluation of micrometeorological methods for
measuring ecosystem-atmosphere isotopic ex-
change of CO₂, *Agric. For. Meteorol.* **116**, 159–179
(2003)
- 56.100 D. Spano, R.L. Snyder, P. Duce, K.T. Paw U: Es-
timating sensible and latent heat flux densities
from grapevine canopies using surface renewal,
Agric. For. Meteorol. **104**, 171–183 (2000)
- 56.101 D. Spano, C. Sirca, S. Marras, P. Duce, P. Zara,
A. Arca, R.L. Snyder: Mass and energy flux mea-
surements over grapevine using micrometeoro-
logical techniques. In: *5th Int. Symp. Irrig. Horti-
cult. Crops*, Acta Horticulturae, Vol. 792, ed. by
I. Goodwin, M.G. O’Connell (ISHS, Leuven 2008)
- 56.102 C.T. Lai, W. Riley, C. Owensby, J. Ham, A. Schauer,
J.R. Ehleringer: Seasonal and interannual varia-
tions of carbon and oxygen isotopes of respired
CO₂ in a tallgrass prairie: Measurements and mod-
eling results from 3 years with contrasting water
availability, *J. Geophys. Res. Atmos.* **111**, D08s06
(2006)
- 56.103 N. Buchmann, J.M. Guehl, T.S. Barigah,
J.R. Ehleringer: Interseasonal comparison of
CO₂ concentrations, isotopic composition, and
carbon dynamics in an Amazonian rainforest
(French Guiana), *Oecologia* **110**, 120–131 (1997)
- 56.104 D.R. Bowling, N.G. McDowell, B.J. Bond, B.E. Law,
J.R. Ehleringer: ¹³C content of ecosystem respira-
tion is linked to precipitation and vapor pressure
deficit, *Oecologia* **131**, 113–124 (2002)
- 56.105 R.E. Fisher, J.L. France, D. Lowry, M. Lanoiselle,
R. Brownlow, J.A. Pyle, M. Cain, N. Warwick,
U.M. Skiba, J. Drewer, K.J. Dinsmore, S.R. Leeson,
S.J.B. Bauguutte, A. Wellpott, S.J. O’Shea, G. Allen,
M.W. Gallagher, J. Pitt, C.J. Percival, K. Bower,
C. George, G.D. Hayman, T. Aalto, A. Lohila, M. Au-
rela, T. Laurila, P.M. Crill, C.K. McCalley, E.G. Nis-
bet: Measurement of the C-13 isotopic signature
of methane emissions from Northern European
wetlands, *Glob. Biogeochem. Cycles* **31**, 605–623
(2017)
- 56.106 D. Lowry, C.W. Holmes, N.D. Rata, P. O’Brien,
E.G. Nisbet: London methane emissions: Use of
diurnal changes in concentration and δ¹³C to
identify urban sources and verify inventories,
J. Geophys. Res. Atmos. **106**, 7427–7448 (2001)
- 56.107 J. Rinne, T. Karl, A. Guenther: Simple, stable, and
affordable: Towards long-term ecosystem scale
flux measurements of VOCs, *Atmos. Environ.* **131**,
225–227 (2016)
- 56.108 O. Peltola: *Towards More Consistent Estimates of
Methane Fluxes by the Eddy Covariance Tech-
nique*, Ph.D. Thesis (Univ. Helsinki, Helsinki
2016), <http://urn.fi/URN:ISBN:978-952-7091-45-6>,
Accessed 22 July 2021

Janne Rinne

Department of Physical Geography and
Ecosystem Science
Lund University
Lund, Sweden
janne.rinne@nateko.lu.se



Janne Rinne is Professor of Physical Geography at the Department of Physical Geography and Ecosystem Science at Lund University in Sweden. He received his PhD in Meteorology in 2001 from the University of Helsinki. His research interest is the effect of the biosphere on the atmospheric composition, which he has been studying especially using a variety of micrometeorological surface-layer flux measurement methods. He teaches courses in meteorology and physical geography.

Christof Ammann

Climate and Agriculture
Agroscope Research Institute
Zürich, Switzerland
christof.ammann@agroscope.admin.ch



Christof Ammann is Senior Scientist at the Swiss Federal Research Institute Agroscope, and leads a research team on agricultural greenhouse gas emissions. His interdisciplinary research focuses on field measurements of the exchange of reactive/nonreactive trace gases between the biosphere and the atmosphere using various measurement techniques. Since 2011, he has been a member of the Swiss Federal Commission on Air Hygiene—the clean air advisory board of the Swiss Government.

**Elizabeth Pattey**

Science and Technology Branch
Agriculture and Agri-Food Canada
Ottawa, Ontario, Canada
elizabeth.pattey@canada.ca

Elizabeth Pattey is Principal Research Scientist at the Ottawa Research and Development Centre, Science and Technology Branch, Agriculture and Agri-Food Canada. She received her PhD in Plant Science – Micrometeorology from Laval University, QC, Canada (1990). She quantifies trace gas fluxes using flux towers. She is Chair of an Expert Team for the Commission for Agricultural Meteorology of World Meteorological Organization (WMO) and Editor of Agricultural and Forest Meteorology.

**Kyaw Tha Paw U**

Land, Air and Water Resources
University of California
Davis, CA, USA
ktpawu@ucdavis.edu

Kyaw Tha Paw U is a Professor of Atmospheric Science and Biometeorologist in the Department of Land, Air, and Water Resources at the University of California, Davis(USA). He received his PhD in Biometeorology from Yale University. His areas of interest are biometeorology, turbulence theory, applications of turbulence analysis to measurements, such as evapotranspiration and carbon dioxide fluxes, and bioaerosol transport, from both a modeling and an experimental perspective.

Raymond Desjardins

Science and Technology Branch
Agriculture and Agri-Food Canada
Ottawa, Canada
ray.desjardins@canada.ca



Raymond Desjardins is an Emeritus Scientist at the Ottawa Research and Development Centre, Central Experimental Farm, Science and Technology Branch, Agriculture and Agri-Food Canada. He received a PhD in Micrometeorology from Cornell University in 1972. He is a Member of the Order of Canada, Member of the Order of Ontario, and a Fellow of the Royal Society of Canada. He develops techniques to quantify mass and energy exchange over a wide range of ecosystems using tower and aircraft-based systems. Some of his recent research is focused on improving estimates of the carbon footprint of Agricultural products and helping Canadian farmers compete on the international markets.

57. Evapotranspiration Measurements and Calculations

Richard Allen , Thomas Foken , Ayse Kilic , Ricardo Trezza , Samuel Ortega-Farias 

Actual and maximum rates of evaporation (E) and evapotranspiration (ET) are important to the operation of atmospheric process models and for hydrologic and agricultural modeling. Because rates of evapotranspiration are limited by both the available energy at the surface and the availability of water, a variety of techniques can be used for estimation. The near-maximum ET under nonlimiting water availability can be closely approximated by the reference ET concept using near-surface observations of air temperature, humidity, wind speed, and solar radiation via the Penman–Monteith or a similar method. The determination of actual rates of ET when water is limiting demands a more complex approach, and often requires daily (or even more frequent) water balance data for the upper soil layers. An alternative is to measure the actual ET using micrometeorological techniques such as the eddy-covariance and Bowen ratio methods. The application of standardized calculations for the reference ET is discussed, as are iterative surface energy balance–aerodynamic combinations, which are useful in conditions where water is limiting.

57.1	Principles of Evapotranspiration Determination	1532
57.2	History	1532
57.2.1	Measurement Devices	1532
57.2.2	Concept and Development of a Reference Evapotranspiration	1533
57.2.3	Concept and Development of Reference Evapotranspiration	1534
57.3	Theory	1535
57.3.1	Evaporation Pans for Potential Evaporation Measurements	1535
57.3.2	The Bowen Ratio Method for Determining the Actual Evapotranspiration	1536
57.3.3	Evapotranspiration by the Residual in the Energy Balance	1537
57.3.4	Soil Water Balance	1537
57.3.5	Bulk Approaches	1538
57.3.6	Priestley–Taylor Method	1539
57.3.7	Penman Method	1539
57.3.8	Penman–Monteith Method	1540
57.3.9	Cover, Crop, and Landscape Coefficients: Applications and Limitations	1544
57.3.10	Remote Sensing for Estimating Evapotranspiration	1553
57.3.11	Standardization	1555
57.4	Devices and Methods	1555
57.4.1	Measurement Devices	1555
57.4.2	Class A Pan	1555
57.4.3	Bowen Ratio System	1556
57.5	Specifications	1556
57.6	Quality Control	1556
57.6.1	Class A Pan	1558
57.6.2	Bowen Ratio System	1558
57.6.3	Collection of Data for Calculation Methods	1558
57.7	Maintenance	1559
57.8	Application	1560
57.8.1	Comparison of the Bowen Ratio Method with the Eddy-Covariance Method and the Penman–Monteith Approach	1560
57.8.2	Comparison of the Penman–Monteith Approach with Lysimeter Data	1560
57.9	Future Developments	1561
57.10	Further Reading	1561
	References	1562

Evapotranspiration is a highly relevant parameter in agriculture, hydrology, and weather and climate prediction and forecasting. Water vapor is not only the most important greenhouse gas; it is also responsible for weather phenomena, including cloud formation and

precipitation and atmospheric vapor transport. In contrast to estimating evapotranspiration, measuring evapotranspiration is not a simple task. It often requires the use of parameterizations, which are also discussed in this chapter.

57.1 Principles of Evapotranspiration Determination

Evaporation is one of the steps in the hydrological cycle. It is defined as the transport of water via various flow paths into the atmosphere [57.1]. If the path is through the stomata of vegetation, it is called *transpiration*. Because it is not easy to distinguish between transpiration and direct evaporation from water or soil, especially during measurement, the two processes are often considered together; this combined process of evaporation and transpiration is generally called *evapotranspiration (ET)*. The evaporation of ice is referred to as *sublimation*. *Interception evaporation* is the water vapor flux from, e.g., wet leaves and plant canopies after rain or dewfall. These terms are often prefixed with the word *actual* to indicate that the ET represents the true rate or depth of evaporation at a certain time and location. *Potential evaporation* is the maximum rate of evaporation (limited by surface energy availability) from a large area that is completely covered with a free-water surface or

by actively growing vegetation with adequate moisture at all times. Multiplying the evaporation rate—usually given in millimeters per time interval—by the heat of vaporization yields the *latent heat flux*. This latent heat is used to transform liquid water to vapor, and is expressed in units of W m^{-2} (i.e., it is an energy density flux). A daily average of 1 W m^{-2} is equal to a water column of 0.0347 mm d^{-1} at 0°C or 0.0353 mm d^{-1} at 20°C (the latter is recommended in [57.2]).

Evaporation is difficult to measure in the environment directly. Only a few methods are able to measure the loss of water from an evaporating water surface or soil volume, or the associated latent heat flux (Table 57.1). Most of these are indirect methods that use a parameterization approach. Many indirect methods only require classical measurements, such as those of temperature, humidity, wind speed, solar or net radiation, and soil parameters.

Table 57.1 Parameters measured by evaporation sensors

Parameter	Description	Unit	Symbol
Depth of evaporation over time	Change in the water level due to evaporation (e.g., Class A pan; see Sect. 57.4.2)	mm	h
Weight of evaporated water	Loss of mass of water from a volume (of soil with plants; see Chap. 58)	$\text{kg m}^{-2} = \text{mm}$	m
Fluctuations in vertical wind and humidity	Latent heat flux with the eddy-covariance method (Chap. 55)	W m^{-2}	Q_E
Near-surface gradients of air temperature and humidity	Latent heat flux with the Bowen ratio method (Sect. 57.3.2)	W m^{-2}	Q_E

57.2 History

Many of the instruments that were developed to measure evaporation directly, such as the atmometer and evaporation pan, are no longer widely used. Because of the difficulty involved in measuring evaporation directly, several indirect methods based on standard meteorological parameters have been developed. These conventional developments are covered in this section too.

57.2.1 Measurement Devices

There has been an awareness of evaporation, as a process through which wet surfaces dry, since ancient times. The first techniques for measuring humidity were proposed by *Leonardo da Vinci* (Chap. 8), and were based on determining the change in weight of a material as it dried. The first devices that were actually used to determine evaporation were constructed in the seventeenth century [57.3]. In 1687,

Edmond Halley (1656–1742) constructed a pan with a thermometer to investigate the evaporation from the ocean [57.4]. In St. Petersburg, *Georg Wilhelm Richmann* (1711–1753) built an evaporation gauge in which variations in the weight of a vessel were balanced by the buoyancy provided by supports located in lower tanks [57.5, 6]. He named this instrument an atmometer. This name was also used, along with the term *atmidometer*, for instruments developed by *John Leslie* (1766–1832) and *Horace Bénédicte de Saussure* (1740–1799) (Chap. 8). Several atmometers that were generally based on a vessel filled with water were subsequently constructed; these instruments used various construction techniques to weigh the mass of the evaporated water [57.3, 7].

Significant progress in atmometer or evaporimeter design was made by *Albert Piche* [57.8], who used absorbent paper as the evaporating area and surface (Fig. 57.1). A glass cylinder was filled with water and

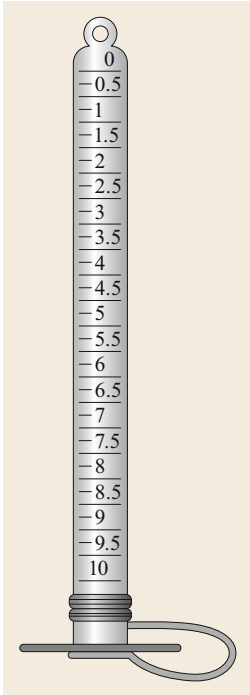


Fig. 57.1 Atmometer or evaporimeter developed by Piche [57.8] (after [57.9])

sealed with a disk of filter paper that had a pinhole in the middle. Piche found that the measured evaporation was nearly identical to the ventilation term E_a of the Penman equation [57.10] (see (57.18) in Sect. 57.3.7). Ceramic material has also been used for the evaporating surface instead of filter paper. A mechanical system for measuring evaporation depth was developed. In this system, the vessel from which the water evaporated is connected to another water tank containing a float that registers the



Fig. 57.2 Evaporimeter developed by Czeratzki (photo © Adolf Thies GmbH & Co. KG, Göttingen, Germany)

water loss from the system. This instrument was widely used in agrometeorology and is still available. A version of this sensor that employed a ceramic evaporating surface was modified by Czeratzki and used with a mechanical registration system [57.11], Fig. 57.2. Also, the ETgauge—which uses a canvas cover—was developed by Altenhofen [57.12, 13] in the US.

57.2.2 Concept and Development of a Reference Evapotranspiration

The terms *potential evaporation* (E_p) and *potential evapotranspiration* (ET_p) have taken on a number of meanings over the past century. E_p is defined here as the quantity of water that is evaporated per unit area and per unit time from an idealized extensive free-water surface under existing atmospheric conditions. Three primary methods of estimating E_p or ET_p have been used during the past century: pan evaporation measurement; estimation of the potential evapotranspiration based on weather data; and the reference evapotranspiration approach. Among these, reference evapotranspiration (ET_o) has been found to be the most practical. The term ET_p was widely used from the 1940s to the 1970s, when it was defined as the maximum evaporative index (from which estimates of the actual ET from vegetation were derived). However, there have also been several other important and contrasting definitions for ET_p . One of the primary definitions of ET_p is the rate of evaporation and transpiration from a saturated (free-water) vegetated surface such that the evaporation process occurs at the potential level. However, while this is a theoretically attractive definition of ET_p , the difficulty involved in sustaining a saturated surface and obtaining simultaneous weather data makes it rather impractical. Standardized parameterizations of the Penman–Monteith equation for calculating ET from nonsaturated grass and alfalfa surfaces are described later in this chapter. The reference evapotranspiration approach, despite some shortcomings, can be a consistent and reproducible method of assessing weather-based potential evaporation.

Although practically challenging, the potential evaporation from a large open water surface can be measured using relatively small evaporation pans, and the resulting measurement presents relatively consistent relationships to the available energy, aerodynamics, and surface temperature. In contrast, as well as the difficulties involved in maintaining a saturated soil or vegetation surface to sustain ET_p , another challenge when measuring ET_p is that its magnitude varies with surface characteristics such as the aerodynamic roughness of the vegetation (although the magnitude of ET_p

depends primarily on the atmospheric conditions and surface albedo). Thus, ET_p should actually be defined for a specific vegetation type (in terms of height, leaf area, and roughness). This can be done using a predictive equation such as the Penman–Monteith relation (introduced later; *Howard Latimer Penman* (1909–1984), *John Lennox Monteith* (1929–2012)), where the surface resistance is taken to be very small or zero and aerodynamic and radiative properties that fit the vegetation are employed. However, this dependence of ET_p on the vegetation type considered makes its application and measurement very challenging, and it is less relevant to hydrological and weather processes due to its assumption of a saturated surface.

A second definition of ET_p relaxes the free-water surface (i.e., a saturated vegetation surface) requirement and sets ET_p equal to the rate of ET expected from disease- and stress-free, relatively tall, dense, leafy vegetation in the presence of a relatively high soil-water content and dry leaf surfaces, implying that the vegetation is transpiring at a rate governed by near-maximum leaf and boundary layer conductances and energy availability. The advantage of this definition of ET_p is that it gives values that are closer to the upper bound on ET expected from vegetation on days without rain. This second definition was used in papers and equations developed by Penman [57.14], where ET_p was taken to be the measured ET from clipped cool-season grass. However, one issue with this definition for ET_p is the need to define the specific characteristics and aerodynamic structure of the vegetation represented by ET_p . Another problem is that, when determining the upper bound for ET_p for a specific type of vegetation, it is necessary to identify appropriate values of the surface (leaf and canopy) conductances, which vary with environmental factors such as the solar radiation, relative humidity at the leaf surface, leaf temperature, soil water potential, and carbon dioxide concentration. In some ways, the use of a reference ET_{ref} (as discussed later) is more consistent and convenient. Also, the feedback between the characteristics of the defined potential surface and the associated weather measurements should be considered. It is important not to *mix and match* the ET_p from tall forest vegetation, for example, with weather data collected over a surface covered with short grass.

A third definition of ET_p , and perhaps the best one for process modeling, is the potential ET expected from any specified type and condition of vegetation or other terrestrial surface when soil water is sufficient not to limit transpiration. This definition even applies to vegetation with a relatively low leaf area, such as very

young plants, and is therefore synonymous with what is often termed the potential *crop ET* in agricultural applications [57.2]. The value of ET_p is strongly governed by the relative leaf area over the surface and the leaf conductance. When this definition of ET_p is used, it is sometimes assumed that the soil surface between plants is relatively dry, meaning that the soil evaporation component is small. Other works [57.2] include a soil evaporation component that can change daily as the soil dries; the actual ET can then be modeled as being equal to ET_p unless the soil-water availability in the effective root zone falls to a level that can no longer supply water to the plant at the rate assumed for this definition of ET_p [57.2].

57.2.3 Concept and Development of Reference Evapotranspiration

The term *reference evapotranspiration* (ET_{ref}) was first defined and used in the 1970s [57.15, 16] to resolve ambiguities associated with the definition and interpretation of the potential evapotranspiration (as discussed in the previous section). The inclusion of the word *reference* implies the use of a specific type of vegetation or a specific definition of vegetation properties to define the evaporative index. *Wright* and *Jensen* suggested that the maximum ET in unsaturated conditions may be approximated by the ET from a well-watered reference crop of alfalfa (also called lucerne) at least 0.2 m high. *Doorenbos* and *Pruitt* defined their ET_{ref} (denoted ET_0) as

the rate of evapotranspiration from an extensive surface of 8–15 cm tall, green grass cover of uniform height, actively growing, completely shading the ground and not short of water.

Subsequently, this definition specified that the grass cover should be a cool-season grass with roughness, density, leaf area, and canopy resistance characteristics that are similar to those of perennial ryegrass (*Lolium perenne*) or alta fescue (*Festuca arundinacea* Schreb. Alta), since warm-season grass varieties such as Bermuda (*Cynodon dactylon*) exercise considerable control over transpiration and have relatively low ET_{ref} rates. The FAO [57.2] later narrowed the definition of ET_0 in terms of the Penman–Monteith equation (introduced in Sect. 57.3.8) as the rate of evapotranspiration from

a hypothetical reference crop with an assumed crop height of 0.12 m, a fixed surface resistance of 70 s m^{-1} and an albedo of 0.23,

and where the reference surface

closely resembles an extensive surface of green grass of uniform height, actively growing, completely shading the ground and with adequate water.

One benefit of using the reference concept is the ability to readily measure and validate the reference ET using living, standardized vegetation. In addition, because the stomatal control of the reference surface

is intended to approximate that of most agricultural vegetation, ET_{ref} is generally closer than E_p or ET_p to the actual ET. Another advantage of using ET_{ref} is that weather data are commonly or preferably measured above standardized weather surfaces such as grass or other short growing vegetation, so the predicted ET flux is synchronized with the temperature, humidity, and wind measurements taken over the weather station surface, and reflects the impact of feedback mechanisms between the vegetation and overlying boundary layer.

57.3 Theory

Several methods of measuring evapotranspiration are available. These methods are described in other chapters of this Handbook. The most direct methods are the eddy-covariance method (Chap. 55) for measuring evapotranspiration in the footprint of the sensor (Chap. 1) and lysimetry (Chap. 58) for measuring the evapotranspiration from a small sample (i.e., the size of the lysimeter). Chamber measurements can also be used (Chaps. 59 and 60). The aerodynamic and modified Bowen ratio methods, which are similar to the Bowen ratio method (Sect. 57.3.2), are used to determine dry deposition (Chap. 54). Measurement methods (Sects. 57.3.1–57.3.4) and calculation methods (Sects. 57.3.5–57.3.10) are described in the following sections.

57.3.1 Evaporation Pans for Potential Evaporation Measurements

Evaporation pans are still used, especially in hydrological networks. In the US, the main pan used is the Class A evaporation pan [57.17], which is round and has a water surface area of 1.14 m². The evaporation is calculated by measuring the water loss in the pan, and complicated corrections [57.18, 19] for the wind velocity, atmospheric moisture, and water temperature are needed. A reliable but much simpler method for determining the total daily evaporation [57.20] uses the change in the height (h) of the water in the evaporation pan corrected for the precipitation, i.e.,

$$ET_p = k_p (h_{\text{day before}} - h_{\text{measurement day}}) \tag{57.1}$$

(in mm d⁻¹), where the values of the pan factor (k_p) [57.15] listed in Table 57.2 are correction coefficients to include when estimating ET from a clipped grass reference surface or the evaporation from shallow water bodies. These coefficients take into account the effects of the upwind fetch on pan evaporation (both

dry and moist), the mean relative humidity, and the total daily wind [57.2, 15, 21–23].

There is no general theory for all evaporation pans, and all recommended methods of transforming pan evaporation data into estimates of ET_p or E_p are based on empirical methods. However, some rules must be applied. The evaporation from the pan depends on the wind velocity as well as the water vapor pressure deficit between the water surface (saturated vapor pressure of water) and the air. Both of these terms are strongly affected by the distance between the water surface and the edge of the pan, as this distance influences the wind velocity at the surface and because water vapor can accumulate in the small volume from the water surface to the edge of the pan. Therefore, standard calculation procedures are only valid when the range of possible

Table 57.2 Values of the coefficient k_p in (57.2) that are applied when using the Class A pan to determine the grass reference ET of meadows or cereals (or bare soil: *values in parentheses*) in the vicinity of the device (mean wind speed and minimum relative humidity on the day of measurement) [57.20, 24]

Mean wind speed	Extension of results to the area in the surrounding (m)	Coefficient k_p for the minimum of the relative humidity	
		> 40%	< 40%
≤ 2 m s ⁻¹ (low)	1	0.65 (0.80)	0.75 (0.85)
	10	0.75 (0.70)	0.85 (0.80)
	100	0.80 (0.65)	0.85 (0.75)
	1000	0.85 (0.60)	0.85 (0.70)
2.1–4.4 m s ⁻¹ (moderate)	1	0.60 (0.75)	0.65 (0.80)
	10	0.70 (0.65)	0.75 (0.70)
	100	0.75 (0.60)	0.80 (0.65)
	1000	0.80 (0.55)	0.80 (0.60)
≥ 4.5 m s ⁻¹ (strong)	1	0.50 (0.65)	0.60 (0.70)
	10	0.60 (0.55)	0.65 (0.65)
	100	0.65 (0.50)	0.70 (0.60)
	1000	0.70 (0.45)	0.75 (0.55)

distances from the water surface to the edge of the pan has been clearly defined. Furthermore, the water vapor pressure of the air above the pan depends on the ET flux and the conditions near the surface of the surrounding area. It is therefore necessary to use recommendations for the vegetation in the surroundings and the soil moisture. However, the latter is not generally measured or documented. Any calculation of evaporation pan data depends on these criteria and is only valid for these circumstances. Evaporation from a pan is also strongly influenced by the water surface temperature, which is in turn influenced by the absorption of solar radiation by the shallow water body as well as the absorption or reflection of radiation by the bottom and sides of the pan.

When pan evaporation data are used to estimate the evaporation from large water bodies, E_{pan} tends to overestimate the total amount of open water evaporation and distort the seasonal distribution due to differing thermal and aerodynamic characteristics between the pan and open water. Thus, E_{pan} can often peak several months before the peak evaporation from deep lakes. Early studies in semiarid to arid climates in the US revealed a very significant influence of pan size on E_{pan} , but it is now clear that this is primarily due to a decreasing effect of local advection as the water surface area increases [57.15]. A good discussion of the issue of accounting for the influence of the local pan environment on the estimated evaporation from a lake is presented in [57.25]. Subsequent studies in India [57.26] and in Prosser (WA, USA) and California [57.27–29] have clearly demonstrated that unless the local environment of the pan is taken into account, the estimated ET (or evaporation from a lake) can be subject to errors of up to 35%.

Whereas the US Class A pan is elevated above the ground surface, other pan designs, such as the Colorado sunken pan, the Russian GGI-3000 sunken pan, and the Russian 20 m² tank, have rims that are almost level with the ground or grassed surface [57.30]. These pans bypass some of the aerodynamic and solar radiation issues associated with the Class A pan but are more difficult to maintain.

57.3.2 The Bowen Ratio Method for Determining the Actual Evapotranspiration

The Bowen ratio method is one of the most popular methods of determining the sensible and latent heat fluxes from a land or water surface. The method is based on Bowen ratio similarity and the energy balance equation [57.31]

$$\text{Bo} = \gamma \frac{\Delta T}{\Delta e} \quad (57.2)$$

$$-Q_s^* = Q_H + Q_E + Q_G, \quad (57.3)$$

where the psychrometric constant $\gamma = 0.667 \text{ hPa K}^{-1}$ for $p = 1013.25 \text{ hPa}$ and $t = 20^\circ\text{C}$ (Chap. 8). ΔT is the temperature difference between two heights and Δe is the water-vapor pressure difference between two heights, with the value at the upper height subtracted from that at the lower height in each case. $-Q_s^*$ is the net radiation, Q_H is the sensible heat flux, Q_E is the latent heat flux, and Q_G is the ground heat flux. From both equations, the sensible and latent heat fluxes can be determined as

$$Q_H = (-Q_s^* - Q_G) \frac{\text{Bo}}{1 + \text{Bo}}, \quad (57.4)$$

$$Q_E = \frac{-Q_s^* - Q_G}{1 + \text{Bo}}. \quad (57.5)$$

In addition to the net radiation (Chap. 11), the ground heat flux (Chap. 61) must be determined along with the temperature and humidity at two levels (Chaps. 7 and 8) according to (57.2).

An advantage of the Bowen ratio method is that the equations do not require the wind speed and do not prescribe that the measurement heights must be separated by a certain distance. However, to ensure that a sufficiently turbulent regime is present, it is recommended that only measurements where the wind speed at the upper height is greater than 1 m s^{-1} and the difference of the wind speed at the two heights is greater than 0.3 m s^{-1} should be used [57.31]. This can require additional instrumentation with anemometers, which is typically ignored. Even though the height difference between the measurements (Δz) is not required in the equations, increasing Δz also increases the differences in temperature and humidity between the two heights. Consequently, the influence of measurement error decreases as Δz is increased, so it is recommended that the ratio of measurement heights should be greater than 4–8 [57.31]. In practice, these recommendations are rarely followed because the aerodynamic height ratio is limited for practical reasons to about 1.5 for measurements over high vegetation [57.32, 33]. Fetch size requirements, which increase with increasing Δz , also come into play.

Equations (57.4) and (57.5) are singular for $\text{Bo} = -1$. Consequently, the estimated energy fluxes for early morning and evening hours are often unrealistic. Therefore, the range $-1.25 < \text{Bo} < -0.75$ should be excluded from further analysis. To overcome this problem, an hourly Penman equation was used in [57.34] to derive the ET for periods when $\text{Bo} \rightarrow -1$. To obtain ET estimates for these problematic periods, the ET_{ref} from the Penman equation is multiplied by a reference ET fraction $\text{ET}_r F$ that is determined during daylight periods before or after the periods with unstable Bowen

ratio energy balance (BREB) estimates by dividing the measured ET by ET_{ref} . In 1967, Tanner suggested that simple combination equations could be substituted for BREB estimates during these problematic periods. This approach requires the use of instrumentation for measuring wind speed.

To determine the correct sign of the flux when $Bo < 0$, the decision criteria

$$\begin{aligned} \text{if } (-Q_s^* - Q_G) > 0 & \text{ then } (\lambda \Delta q + c_p \Delta T) > 0, \\ \text{if } (-Q_s^* - Q_G) < 0 & \text{ then } (\lambda \Delta q + c_p \Delta T) < 0, \end{aligned} \quad (57.6)$$

where c_p is the heat capacity at constant pressure, should be applied [57.35]. If these criteria are not fulfilled, the fluxes should be omitted from the analyses.

The crucial disadvantage of the Bowen ratio method is that, due to the unclosed energy balance [57.36, 37] (Chap. 55), any residual is either added to the net radiation or distributed according to the Bowen ratio to the sensible and latent heat fluxes. In general, the fluxes determined with the Bowen ratio method are larger than those determined with the eddy-covariance method. By definition, the Bowen ratio method fulfills the energy balance equation, but the quantitative accuracy of the fluxes may be limited by uncertainties or systematic error in the measurement of $-Q_s^*$ and Q_G .

The Bowen ratio method is often superior to the direct use of turbulent transfer equations to estimate the water vapor transport above a surface. This is primarily due to constraints on the estimates obtained using the Bowen ratio method, which arise from the inclusion of the radiation balance in the method. Errors in the estimates of temperature/humidity gradients are not directly related to the estimates of Q_E or Q_H , in contrast to strictly aerodynamic methods. In some situations, however, the net radiation or heat transfer below the surface is not easily measurable. For forests, brushlands, or orchards, it can be important to account for changes in the heat storage of the canopy over periods shorter than 24 h. For water bodies, it is difficult to accurately measure $-Q_s^*$ and Q_G . In these situations, one should consider using aerodynamic methods, as described in Chap. 54.

An overall evaluation of the method is given in Sect. 57.5. The error associated with this method is gauged under the assumption of accurate net radiometer measurements (Chap. 11). Furthermore, the heat storage in the soil should be calculated very accurately to reduce the influence of the residual of the energy balance closure (Chaps. 55 and 61).

57.3.3 Evapotranspiration by the Residual in the Energy Balance

Solving (57.3) makes it possible to determine the evapotranspiration as the residual when the sensible heat

flux, the net radiation, and the ground heat flux are known, i.e.,

$$Q_E = -Q_s^* - Q_G - Q_H. \quad (57.7)$$

The advantage of this approach is that there is no need for the expensive instrumentation required to measure the latent heat flux (evapotranspiration). Eddy-covariance systems may be used to measure Q_H and the low-cost surface renewal method may be employed to measure Q_H [57.38], see Chaps. 55 and 56. However, this method has two disadvantages. Measuring the sensible heat flux with the eddy-covariance method may not lead to sufficiently accurate values for Q_H , meaning that the energy balance equation may not be adequately closed due to methodical problems [57.36]. Assumptions must be made to correct for this (Chap. 55). Furthermore, sonic anemometers are used to measure the buoyancy flux, which must then be converted into the sensible heat flux using the latent heat flux [57.39, 40]. Therefore the equation should be solved iteratively. Surface renewal methods that require only a fine-wire thermocouple and estimates for the net radiation and Q_G can provide an empirical approximation for Q_H , and thus for Q_E , based on surface heat ramping and exchange theory, but they must be calibrated for the surface type and the vegetation conditions present and are generally less accurate than using eddy-covariance techniques. Furthermore, the results of the energy balance residual method can be affected by biases in the net radiation and ground heat flux measurements, including a lack of representativeness over nonuniform surfaces.

57.3.4 Soil Water Balance

All of the methods for estimating ET only provide estimates of the average actual ET from a field, watershed, or region under consideration. As might be expected, for point measurements, the larger and more diverse the area, the more uncertain the estimate. This issue becomes particularly problematic when the area under consideration encompasses a wide variety of vegetation species, vegetation heights, aerodynamic roughnesses, leaf development stages, rooting depths, soil types, and differing responses to soil water levels and weather conditions (e.g., watersheds or regions).

For watersheds, all components of the soil water balance are usually estimated, including water runoff, and the ET is estimated from the resulting equation. For small watersheds where interbasin groundwater flow is highly restricted and runoff can be measured, the ET can be determined from the hydrologic balance if the watershed precipitation is accurately measured or estimated.

The basic soil-water balance equation for a study volume (i.e., a defined area with a depth z_s) during a specific time period Δt can be written as

$$\Delta\theta z_s = P - Q_r + I - ET_a - DP + GW, \quad (57.8)$$

where $\Delta\theta$ is the change in the mean water content of the soil profile over the depth z_s of the soil profile monitored. The depth of the surface runoff Q_r that is leaving the study area is measured or estimated, and the gross irrigation depth I is the depth of water that infiltrates from irrigation over the study area. The most challenging measurements and estimates in (57.8) are the depth of percolation below z_s DP and the depth of the groundwater (GW) that moves upward or horizontally into the profile. Equation (57.8) is solved for ET_a as the actual evapotranspiration depth over the area. Generally, the soil profile depth of interest is the plant root zone, which is by definition the upper portion of the soil where water is extracted by plant roots. In this case, GW and DP are, respectively, the total flux densities into and out of the bottom or side of the root zone during the time period of interest.

Generally, when solving the soil-water balance equation for ET, θ should be sampled to depths well below the root zone. Even if there is no change in the soil water content at lower depths between sampling dates, we cannot assume that there is no drainage, because drainage can occur under a unit hydraulic gradient with no apparent change in the soil water content. Periods with little or no precipitation are generally selected for evaluation. Occasionally, sharp changes in soil texture such as a sand or gravel layer below the root zone or the presence of bedrock can reduce the rate of deep percolation and improve measurement accuracy.

Situations where there are saturated conditions (i.e., a water table) near the root zone should be avoided. In the absence of a shallow water table (GW = 0), and with an adequate sampling depth, a record of the soil water fluctuations over a period of 7–10 days or more can yield reliable measurements of ET at the measurement site [57.41].

57.3.5 Bulk Approaches

The simplest method of determining the evaporation is to use the bulk approach. In this approach, a uniform (linear) gradient is assumed for the given layer, and only values at the upper and lower boundaries are used [57.42]. If the lower boundary of this layer has properties that are identical to those of the surface, then, strictly speaking, the method is only applicable over water bodies because the gradient between surface values and the measurement data at a certain upper measurement height (generally 10 m) can only be ex-

PLICITLY determined over a water body. Therefore, the method can be used to determine the potential evaporation. That is not to say that there are no problems when applying the bulk method above water bodies, because it is often not the surface temperature that is measured but the temperature decimeters below the water surface, and this temperature may be about 0.5 K higher than the cold film temperature due to evaporative cooling at the surface. Also, the absorption of shortwave-infrared and infrared radiation at the surface can lead to a warmer film temperature at the surface than immediately below it. Remote-sensing methods such as infrared thermometers or satellite sensors can be used to determine the surface temperature with absolute accuracy, similar to that of the subsurface measurements [57.43].

Instead of turbulent diffusion coefficients, bulk coefficients are used in bulk approaches. The latent heat flux can be determined via the Dalton number C_E using

$$\frac{Q_E}{\rho\lambda} = C_E(z)u(z)[e(z) - e(0)]. \quad (57.9)$$

The bulk coefficients depend on the stability and wind speed. Over the ocean, with mostly neutral stratification, the first of these influences is generally not a problem. On average, the Dalton number $C_E \approx 10^{-3}$. The values over lakes are slightly higher [57.44]. Several approaches that utilize the bulk concept are available. A theoretical formulation for C_E under neutral conditions is

$$C_E = \frac{0.622}{\rho_w P} \frac{\kappa^2}{\ln\left(\frac{z}{z_o}\right) \ln\left(\frac{z}{z_{oq}}\right)}, \quad (57.10)$$

with appropriate units. The roughness height for water vapor z_{oq} is generally considered to be similar to or smaller than z_o for momentum, or it may even exceed z_{om} when applied to water [57.45], κ is the von Kármán constant (values of 0.40 and 0.41 are used by different authors). In saline water bodies, the salinity of the water will reduce the surface saturation vapor pressure.

Dalton Approach

The simplest way to determine the potential evaporation over open water is the Dalton approach. Instead of the Dalton number alone, simple correction functions are used to account for the wind-speed dependency, i.e.,

$$\frac{Q_E}{\rho\lambda} = f(u)[E(T_0) - e(z)] \quad \text{with } f(u) = a + bu^c, \quad (57.11)$$

where $a = 0.16 \text{ m s}^{-1}$, $b = 0.2 (\text{m s}^{-1})^{0.5}$, $c = 0.5$ for lakes in Northern Germany [57.46], and E the water-vapor pressure of saturation at a certain temperature. Possible areas of application for this method are given in Sect. 57.5.

57.3.6 Priestley–Taylor Method

The Bowen ratio is the starting point for the derivation of several methods that are used to determine sensible and latent heat fluxes. The Priestley–Taylor approach starts from (57.2), which can be written with the potential temperature and the dry adiabatic temperature gradient $\Gamma_d = 0.0098 \text{ K m}^{-1}$ as

$$\text{Bo} = \gamma \frac{\partial \bar{\theta} / \partial z}{\partial \bar{q} / \partial z} = \frac{\gamma [(\partial \bar{T} / \partial z) + \Gamma_d]}{\partial \bar{q} / \partial z}. \quad (57.12)$$

Using the temperature dependence of the saturation water vapor pressure given by the Clausius–Clapeyron equation (Chap. 5)

$$\frac{dq_s}{dT} = s_c(\bar{T}), \quad (57.13)$$

it follows that

$$\text{Bo} = \frac{\gamma [(\partial \bar{T} / \partial z) + \Gamma_d]}{s_c(\partial \bar{T} / \partial z)} = \frac{\gamma}{s_c} + \frac{\gamma \Gamma_d}{s_c(\partial \bar{T} / \partial z)} \quad (57.14)$$

if the dry adiabatic temperature gradient is significantly smaller than the temperature gradient in the surface layer; γ is the psychrometric constant in K^{-1} (Chap. 8).

For the further derivation, the second term on the right-hand side of (57.12) will be ignored. However, this is valid only if the gradient in the surface layer is significantly greater than the dry adiabatic gradient, which is not the case for neutral stability. Introducing the Priestley–Taylor coefficient $\alpha_{\text{PT}} \approx 1.26$ for region-scaled surfaces with an adequate water supply and applying energy balance equation (57.3) yields the Priestley–Taylor approach [57.47]

$$Q_H = \frac{[(1 - \alpha_{\text{PT}}) s_c + \gamma] (-Q_s^* - Q_G)}{s_c + \gamma}, \quad (57.15)$$

$$Q_E = \alpha_{\text{PT}} s_c \frac{-Q_s^* - Q_G}{s_c + \gamma}. \quad (57.16)$$

Typical values of the ratios $c_p/\lambda = \gamma$ and $de_s/dT = s_c$ in K^{-1} are given in Table 57.3. These can be calculated approximately with the relation [57.31, 48] (t : temperature in $^\circ\text{C}$)

$$\frac{s_c}{\gamma} = -0.40 + 1.042e^{0.0443t}. \quad (57.17)$$

This method can be used for vegetated surfaces at the regional scale if the Priestley–Taylor coefficient is adjusted for its dependence on the regional water availability (i.e., the soil water content) and therefore the stomatal resistance [57.49]. Possible areas of application for this method are given in Sect. 57.5.

Table 57.3 Values of the temperature-dependent parameters γ and s_c [57.48]

Temperature (K)	γ (K^{-1})	s_c (K^{-1})
270	0.00040	0.00022
280	0.00040	0.00042
290	0.00040	0.00078
300	0.00041	0.00132

57.3.7 Penman Method

A commonly used method for determining the potential evaporation or reference ET is the combination method that was proposed by Penman [57.14] to eliminate the need to measure the surface temperature. This method was developed for southern England and tends to underestimate the evaporation in arid regions when using the original wind function. The derivation involves combining the Dalton approach with the energy balance via the Bowen ratio. The evaporation in mm d^{-1} is

$$Q_E = \frac{s_c (-Q_s^* - Q_G) + \gamma E_a}{s_c + \gamma}, \quad (57.18)$$

where the available energy must be expressed in mm d^{-1} . The conversion factor from mm d^{-1} to W m^{-2} is 0.0353 at 20°C . The second term in the numerator of (57.18), E_a (also in mm d^{-1}), is called the ventilation term, and represents the influence of turbulence according to the Dalton approach. In humid regions, E_a is significantly smaller than the first term and is often ignored in the simplified Penman approach [57.50] to derive the Priestley–Taylor equation [57.51] when $\alpha_{\text{PT}} = 1.26$.

The ventilation term is a function of the wind speed and the saturation deficit,

$$E_a = (E - e) (f_1 + f_2 u) \quad [\text{mm d}^{-1}]. \quad (57.19)$$

While one can use daily averages in (57.18), the use of 10–60 min averages is considerably more meaningful, although the units must be converted in this case. Typical values for the wind factors f_1 and f_2 are given in Table 57.4. These values are valid for water surfaces, but they can also be used for well-saturated grass surfaces, where ET is to a large degree the potential evaporation for a grassed surface, largely equivalent to the grass reference ET. To include the effects of increased roughness, the ventilation term can be applied according to the approach devised by van Bavel [57.52],

$$E_a = \frac{314 \text{ K}}{T} \frac{u}{[\ln(z/z_0)]^2} (E - e) \quad [\text{hPa m s}^{-1}]. \quad (57.20)$$

Table 57.4 Values of the wind factors in the ventilation term of (57.19) [57.31]

Surface and reference	f_1 (mm d ⁻¹ hPa ⁻¹)	f_2 (mm d ⁻¹ hPa ⁻¹ m ⁻¹ s)
Original approach for water bodies [57.54]	0.131	0.141
Small water bodies [57.51]	0.136	0.105
Water bodies [57.55]	0.0	0.182
Grass surfaces [57.24, 56]	0.27	0.233

Possible values for different areas of application of this method are given in Table 57.4. With no surface resistance term, the Penman equation is not particularly accurate for many vegetated surfaces, especially those with insufficient soil water to supply the potential ET rate. When it is applied to open water, a shortcoming is the need to measure or estimate Q_G , which can be substantial for deep cold-water systems and thus cannot be ignored [57.53]. Possible areas of application of this method are given in Sect. 57.5.

Another, very simple, approach to calculating the evaporation from the available radiation energy is that employed by Turc,

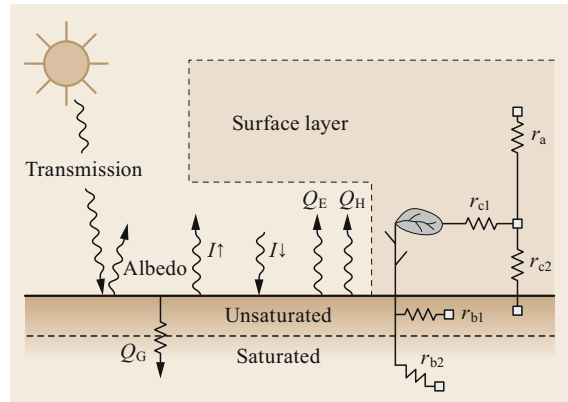
$$Q_{E-TURC} = k(K\downarrow + 209) \frac{0.0933t}{t + 15}, \quad (57.21)$$

where the only input parameters are the air temperature t (in °C) and global radiation (in W m⁻²) [57.57], and k is an empirical factor. The Turc method is empirical and was developed to approximate the potential ET in the Mediterranean region. To make it applicable in Germany, (57.12) requires a correction factor of about $k = 1.1$ [57.51]. The Turc method tends to yield an underestimate in dry convective conditions where evaporation can substantially exceed the available energy due to regional and local advection. Possible areas of application of this method are given in Sect. 57.5.

57.3.8 Penman–Monteith Method

The transition from the Penman to the Penman–Monteith approach [57.14, 48, 58, 59] includes considering unsaturated surfaces and cooling due to evaporation, which reduces the energy of the sensible heat flux. Including both of these aspects leads to the Penman–Monteith method for determining the actual evaporation (evapotranspiration),

$$Q_H = \frac{\gamma(-Q_s^* - Q_G) - F_w}{R_{Gs_c} + \gamma}, \quad (57.22)$$


Fig. 57.3 Schematic representation of the modeling of the atmospheric surface layer, including plants and soil (after [57.66])

$$Q_E = \frac{R_{Gs_c}(-Q_s^* - Q_G) + F_w}{R_{Gs_c} + \gamma}, \quad (57.23)$$

where the ventilation term

$$F_w = C_E \bar{u} (R_G - R_s) q_{sat}. \quad (57.24)$$

Here, R_G is the relative humidity of the surface, R_s is the relative humidity close to the surface, and q_{sat} is the specific humidity for saturation.

Equation (57.23) can also be formulated according to the resistance approach, where the near-surface domain is not separated into different layers. Instead, it is assumed that plants act like a big leaf over the soil (the *big leaf model*), and only the saturation vapor pressure and actual vapor pressure at a height of z are utilized, following Penman's original formulation. These models are mainly based on surface layer physics and are illustrated schematically in Fig. 57.3 [57.60–65].

The resistance concept is based on the assumption that the turbulent resistance counteracts the turbulent flux in the turbulent layer, a molecular turbulent resistance counteracts the flux in the viscous and molecular layer, and all resistances in the plant and soil can be combined into a resistance known as the canopy resistance. The canopy resistance is exerted along various transfer pathways, especially the stomata–mesophyll pathway, the cuticula pathway, and direct transfer to the soil, as schematically illustrated in Fig. 57.2 (right-hand side). The simplest generalization is the comparison with Ohm's law,

$$I = \frac{U}{R}. \quad (57.25)$$

Here, the flux is analogous to the current I , and the vertical difference in wind speed or temperature is analogous to the voltage U . The resistance R can be de-

scribed as a network of individual resistances with the simple form

$$r_g = r_a + r_{mt} + r_c + r_b. \quad (57.26)$$

This concept neglects the molecular turbulent resistance, and the soil resistance is included in the canopy resistance. The ventilation term

$$F_w = \frac{q_{sat} - q_a}{r_a + r_c}. \quad (57.27)$$

In the simplest case, the canopy resistance r_c is replaced by the bulk stomatal resistance r_s , and it is assumed that the stomatal cavities are at saturation and the surface temperature. The bulk stomatal resistance can be calculated from the stomatal resistance of a single leaf r_{si} and the active leaf-area index (LAI, the leaf surface of the upper side per elemental area of the underlying surface) via

$$r_s = \frac{r_{si}}{\text{LAI}_{\text{active}}}, \quad (57.28)$$

where $\text{LAI}_{\text{active}}$ is the leaf-area index of the active sunlit leaves. Generally, this is only the upper part of a dense canopy, so $\text{LAI}_{\text{active}} = 0.5\text{LAI}$ [57.2]. In the simplest case, the turbulent resistance is given by [57.48]

$$r_a = \frac{1}{C_E \bar{u}}. \quad (57.29)$$

Usually, however, r_a is calculated from the profile equation for the surface layer (Chap. 1),

$$r_a = \frac{\ln\left(\frac{z-d}{z_0}\right) \ln\left(\frac{z-d}{z_{0q}}\right)}{\kappa^2 u(z)}. \quad (57.30)$$

In the non-neutral case, universal functions can be used in (57.30), leading to

$$r_a = \frac{\left[\ln\left(\frac{z-d}{z_0}\right) - \Psi_m\right] \left[\ln\left(\frac{z-d}{z_{0q}}\right) - \Psi_{q,h}\right]}{\kappa^2 u(z)}, \quad (57.31)$$

and the resistance-style formulation of the Penman–Monteith equation is

$$Q_E = \frac{s_c (-Q_s^* - Q_G) + \frac{\rho c_p (E - e)}{r_a}}{s_c + \gamma \left(\frac{r_s + r_a}{r_a}\right)}. \quad (57.32)$$

Equation (57.32) is generally simpler to apply than (57.23) and (57.24) because it does not require the R of the surface, R_G , which is difficult or nearly impossible to measure. Typical values of the parameters are given in Table 57.5. Possible areas of application of this method are given in Sect. 57.5.

Table 57.5 Typical values of the LAI [57.67] and the stomatal resistance of single leaves [57.53, 68]

Surface	Height (m)	LAI ($\text{m}^2 \text{m}^{-2}$)	r_{si}^a (s m^{-1})
Seedlings (beginning to grow)	0.05	0.5	
Clipped grass	0.05–0.15	2–3	70–150
Grassland	0.3–1	2–3	100–500
Sagebrush	1	0.5	1000
Cereal	1	3.0	50–320
Maize	2–3	3–6	80–100
Lucerne	0.3–0.7	3–5	80–100
Forest	12–20	1–6	120–2700

^a The lower values in the range represent high-moisture conditions; the higher values in the range represent moderately dry moisture conditions

Implications of Boundary Layer Feedback in the Penman–Monteith Method

When it is applied in hydrology, a disadvantage of the Penman–Monteith (PM) equation is that it is challenging to quantify the bulk surface resistance for complex canopies, especially when the soil water is limiting [57.69]. In addition, significant errors may be introduced when weather data used in the PM equation are measured above surfaces that are significantly different from a complex canopy. For example, applications that use weather measurements taken over a clipped grass surface to estimate the ET from forest vegetation do not represent surface boundary layer profiles that exist in nature because the air temperature, vapor content, and wind speed conditions are different over a forest than over grass.

Other challenges when using the PM and other combination equations include the difficulty involved in characterizing the relationships between the leaf stomatal resistance and environmental variables for sparse or multilayered vegetation, such as forests in semiarid regions and immature crops [57.70, 71]. In these situations, the mean heights and locations of sinks for momentum and radiation are different from the mean heights and locations of sources for Q_E and Q_H . These variations can create differences in eddy diffusivities and aerodynamic resistances within and directly above canopies. In such situations, multisource and/or multilayer models may be more suitable.

In its simplest form (in which the outgoing radiation and ground heat flux are used, only the air temperature is employed to calculate s_c , and neutral stability is assumed), the PM works best only under well-watered conditions and for near-full vegetation cover, for example when it is used as a reference ET method [57.2, 72]. Under these conditions, the surface temperature is

closest to the air temperature and the surface resistance is relatively constant, so these simplifying assumptions are valid.

Necessary Allowances for Nonpotential Conditions

The single-layer PM model blends microclimate variations within the vegetation and soil surface and assumes that each surface contributes to energy exchange at similar temperatures and with the same saturation deficit at its surface. In the PM method, all surface resistance values for leaf and soil subareas must contribute to the value of the bulk r_s .

It is often assumed during the application of the combination equation that the surface temperature is sufficiently similar to the air temperature that s_c , as well as the longwave radiation emitted from the surface and the ground heat flux, can be calculated using the air temperature only, and the stability correction can be ignored. However, dry nonpotential surfaces tend to have substantially higher temperatures than the air temperature, and under these conditions s_c , the net radiation, the soil heat flux, and the boundary layer stability correction should be calculated using both the surface and air temperatures, where the surface temperature is derived iteratively based on Q_E , Q_H , Q_G , and Q_s^* and the energy balance. As illustrated by AFIB (aerodynamic fluxes using iterative energy balance) method described later in this section, the PM formulation is only completely accurate when T_s is a measured quantity or determined iteratively.

The Penman–Monteith Method as a Reference ET Method

The Food and Agriculture Organization of the United Nations (FAO) and the American Society of Civil Engineers (ASCE) have put much effort into developing a uniform standardized method of determining the reference evapotranspiration, and they recommend the use of a convenient equation with a limited input dataset [57.2, 53, 72–74]. To facilitate comparisons of evapotranspiration rates from around the world and to ensure that the input parameters are available every-

where, the FAO has formulated a (grass) reference ET equation [57.2] that is based on (57.16) but includes the estimated input parameters given in Table 57.10. A further standardization was made by the ASCE, which unified the calculation steps and applied the equation to both grass and alfalfa (lucerne) reference surfaces [57.75].

When applied to estimate the reference ET, three important simplifications to the PM method facilitated by the assumption of near-neutral conditions are generally practiced, as proposed by Penman [57.14]. These three simplifying assumptions are that s_c can be estimated using the air temperature only, that stability correction of r_a is not required, and that longwave radiation emitted from the surface can be estimated using T_a only.

When expressed using terms adopted for this Handbook, the standardized PM equation for reference ET becomes

$$Q_E = \frac{s_{cc} (-Q_s^* - Q_G) + \rho c_p \frac{E - e}{r_a}}{s_{cc} + \gamma_c \left(1 + \frac{r_s}{r_a}\right)}, \quad (57.33)$$

where r_s and r_a are given by (57.28) and (57.30), respectively (Table 57.6). The factors $s_{cc} = s_c p / 0.622$ and $\gamma_c = \gamma p / 0.622$ are both in units of hPa K⁻¹, just as in the original reference.

The Penman–Monteith-based reference ET approach is widely used in diverse applications, such as in hydrologic studies and irrigation water management. During the daytime, the accuracy of data computed hourly is satisfactory, and daily sums of the evaporation and sensible heat fluxes are generally acceptable. The available energy is the main forcing, but the atmospheric turbulence and humidity and the control by the plants – defined for the reference surfaces – influences the ventilation term.

When the supporting parameter equations for r_a , ρ_a , and λ are simplified and incorporated into (57.32), the PM equation simplifies to a standardized reference form presented by the FAO [57.2] and ASCE [57.74] and commonly found in the literature,

Table 57.6 Input parameters for the FAO (grass) reference evaporation [57.2]

Parameter	Value	Remark
r_a	$d = 2/3z_B$; $z_0 = 0.123z_B$; $z_{0q} = 0.1z_0$, with $z_B = 0.12$ m for the short grass reference (ET ₀) and $z_B = 0.50$ m for the tall alfalfa reference (ET _T), and $z = 2$ m produces $r_a = 208/u$ (2 m) for the short grass reference	$\kappa = 0.41$ is applied
r_s	For $LAI_{active} = 0.5LAI$; $LAI = 24z_B$ for the short grass reference with $r_{si} = 100$ s m ⁻¹ for 24 h timesteps, and for $z_B = 0.12$ m follows $r_s = 70$ s m ⁻¹ for 24 h timesteps, and $r_s = 50$ s m ⁻¹ for daytime hourly timesteps for the grass reference	
$-Q_s^* - Q_G$	Other simplifications are a recommended albedo of 0.23 and an assumption that $T_s \cong T_a$	[57.2]; see Chap. 11 for $-Q_s^*$ and Chap. 61 for Q_G

Table 57.7 Values of C_n and C_d in (57.25) and the ratio Q_G/Q_s^* that is used to estimate the soil heat flux density [57.74]

Calculation timestep	Short reference, ET _o			Tall reference, ET _r			Units for ET _o , ET _r	Units for Q _s [*] and Q _G
	C _n	C _d	Q _G /Q _s [*]	C _n	C _d	Q _G /Q _s [*]		
Daily	900	0.34	0.00	1600	0.38	0.00	mm d ⁻¹	MJ m ⁻² d ⁻¹
Hourly during daytime	37	0.24	0.10	66	0.25	0.04	mm h ⁻¹	MJ m ⁻² h ⁻¹
Hourly during nighttime	37	0.96	0.50	66	1.7	0.20	mm h ⁻¹	MJ m ⁻² h ⁻¹

$$ET_{\text{ref}} = \frac{0.408s_{\text{cc}}(-Q_s^* - Q_G) + \gamma \frac{C_n}{(t+273)} u_2 (e_s - e_a)}{\Delta + \gamma_c (1 + C_d u_2)}, \quad (57.34)$$

where ET_{ref} has units of mm d^{-1} for 24 h timesteps and mm h^{-1} for hourly timesteps, and applies to both clipped grass and alfalfa reference surfaces. Q_s^* and Q_G are in units of $\text{MJ m}^{-2} \text{d}^{-1}$ or $\text{MJ m}^{-2} \text{h}^{-1}$; t is the mean daily or hourly air temperature ($^{\circ}\text{C}$); u_2 (m s^{-1}) is the mean daily or hourly wind speed at a height of 2 m; e_s and e_a are the saturation and actual vapor pressures for the air in kPa; s_{cc} and γ are in units of $\text{kPa } ^{\circ}\text{C}^{-1}$; and C_n and C_d are coefficients that vary with the calculation timestep, reference type (grass ET_o or alfalfa ET_r), and, in some cases, with the time of day, as shown in Table 57.7. The values of the hourly C_d for ET_o are based on the use of $r_s = 50 \text{ s m}^{-1}$ during the daytime and $r_s = 200 \text{ s m}^{-1}$ during nighttime, and the 24 h timestep value for C_d is based on $r_s = 70 \text{ s m}^{-1}$. Additional background on r_s for ET_o is provided in [57.72, 74]. For ET_r, the values of the hourly C_d are based on the use of $r_s = 30 \text{ s m}^{-1}$ during the daytime and $r_s = 200 \text{ s m}^{-1}$ during nighttime, and the 24 h timestep value for C_d is based on $r_s = 45 \text{ s m}^{-1}$. The standardized definitions imply vegetation heights for the ET_o and ET_r surfaces of 0.12 and 0.5 m, respectively. Generally, ET_r is 20–30% stronger than ET_o (depending on the wind and aridity) due to the stronger aerodynamic features of the alfalfa reference and its lower stomatal resistance and larger leaf area. ET_r is often used as an upper limit on the ET for an extensive, well-watered surface.

The AFIB Alternative (Aerodynamic Fluxes Using Iterative Energy Balance)

For dry nonreference surfaces, with increasing T_s , the net radiation can decrease by as much as 100 W m^{-2} compared with the reference condition due to the increased thermal radiative emission from the warmer surface. In addition, buoyancy-driven mixing of the boundary layer with the increased T_s (as compared with T_a) caused by increasing Q_H can mean that stability correction is required to reduce r_{ah} (resistance for sensible heat). It is also necessary to provide an accurate estimation of Q_G . Therefore, when the vegetation cover is low or the water supply limits ET (i.e., there are nonreference crop conditions), T_s should be iteratively

determined using, for example, the AFIB procedure. Ironically, when T_s is iteratively solved for or measured, the reason for the existence of the PM and other combination equations essentially evaporates because the substitution of a T_s - and T_a -based computation of s_{cc} into the equation causes it to decompose back to the original component equations for Q_H and Q_E , making the formulation of the PM unnecessary.

The required suite of equations and the inversion of the sensible heat equation to replace the PM equation is termed the AFIB (aerodynamic fluxes via iterative solution of the energy balance) approach [57.53], and can be summarized as

$$Q_s^* = (1 - \alpha)R_s + R_{L\text{-in}}(1 - \varepsilon) - \varepsilon\sigma T_s^4, \quad (57.35)$$

$$Q_G = [0.05 + K_G \exp(-0.5\text{LAI})] (Q_s^* + Q_H), \quad (57.36)$$

$$Q_E = \frac{\rho_a c_p [e^0(T_s) - e^0(T_a)]}{\gamma_c \frac{r_a + r_s}{r_a + r_s}}, \quad (57.37)$$

$$T_s = \frac{(-Q_s^* - Q_G - Q_E) r_{\text{ah}}}{\rho_a c_p} + T_a, \quad (57.38)$$

$$Q_H = \rho_a c_p \frac{T_s - T_a}{r_{\text{ah}}} \quad (57.39)$$

$$r_{\text{ah}} = r_{\text{aq}} = \frac{\left\{ \ln\left(\frac{z_u - d}{z_o}\right) - \Psi_m\left[\frac{z_u}{L(Q_H)}\right] \right\} \left\{ \ln\left(\frac{z_T - d}{z_{0h}}\right) - \Psi_h\left[\frac{z_T}{L(Q_H)}\right] \right\}}{\kappa^2 u_z}, \quad (57.40)$$

where r_{ah} is the resistance of sensible heat, z_u is the height above the ground surface for the wind speed measurement, d is the zero plane displacement of the logarithmic wind profile, z_o is a roughness length governing the transfer of momentum from the surface, ψ_m is the correction factor for momentum transfer to account for the instability or stability of the boundary layer, z_T is the height of the air temperature measurement above the ground surface, z_{0h} is an assumed roughness length governing the transfer of sensible heat from the surface, ψ_h is a correction factor for sensible heat transfer to account for the instability or stability of the boundary layer, and u_z is the wind speed measured at a height of z_u . Equations for estimating ψ_m and ψ_h are given in [57.53, 76, 77]; see also Chap. 1. Equation (57.36) represents the likelihood that Q_G is influenced by Q_H due to their codependence on temper-

ature gradients that share a common T_s . K_G is a fitting coefficient that is affected by the relative thermal conductivity of the soil; $K_G = 0.2$ is recommended for tilled soils and $K_G = 0.10\text{--}0.15$ is recommended for soils in a natural state with less bulk particle-to-particle contact. When Q_H is low and most of the Q_s^* is converted into Q_E , Q_G becomes a function of Q_s^* , which is a traditional estimation method [57.78]. The $L(Q_H)$ in (57.40) indicates that the Obukhov length L is a function of Q_H and thus T_s . Equations (57.35)–(57.40) are iteratively solved until the estimate for T_s is obtained. At that point, Q_E can be evaluated via (57.37).

Once T_s is known from (57.38), Q_E can be calculated from the PM equation, if desired, using

$$s_{cc} = \frac{e^0(T_s) - e^0(T_a)}{(T_s - T_a)} \quad (57.41)$$

and Q_s^* , Q_G , and r_{ah} from (57.35)–(57.40). Estimates will be within a few percent of, or even identical to, the value of Q_E obtained using (57.37), provided that similar estimates are made for Q_s^* , Q_G , and r_{ah} , including the stability correction. Application areas for the AFIB method are listed in Sect. 57.5.

Solving (57.35)–(57.40) does not represent a computational challenge for modern computing systems, and, once coded, these equations tend to provide consistent estimates. The iteration can progress through the equations in any order, and can be initiated with the assumption that $Q_H = 0$. Numerical stability can be ensured for the solution by dampening the calculations, which is achieved by averaging the new values of T_s and—if needed—the correction parameters ψ_m and ψ_h with their values from the previous iteration step.

Upon observing the performance of the AFIB method, it becomes apparent that the PM equation—or any combination equation—is only really useful for *reference* conditions, based only on T_a , neglecting T_s (to adjust the estimates of s_c , Q_G , Q_s^*), and r_a , and where the reference conditions represent the near-maximum ET. Under all conditions other than the reference conditions, the AFIB method of (57.35)–(57.40) is recommended. It is best applied using data obtained hourly or even more frequently. This limitation is caused by the potentially strong nonlinearity in the buoyancy or stability corrections, which can vary hourly.

57.3.9 Cover, Crop, and Landscape Coefficients: Applications and Limitations

The Penman–Monteith equation is now widely used to estimate the ET in hydrology, meteorology, and agriculture, where the equation serves as the reference ET (ET_{ref}) (57.34) in a two-step crop (or cover) coefficient

$K_c ET_{ref}$ approach. The $K_c ET_{ref}$ procedure is not a measurement technique but rather a method of inferring the ET by considering the influence of boundary-layer and radiation effects on ET demand and including a scaling factor to account for specific vegetation effects. It is described here because it is a robust and consistent method of estimating ET that has physically imposed constraints. The first step in the two-step approach is to estimate the ET_{ref} that accounts for near-potential weather or climate effects on the ET process. The second step is to apply a crop or vegetation (cover) coefficient to estimate the actual ET (ET_c) according to growth stage, plant type, cover, and the wetness of the soil surface and soil profile. This section focuses on the use of the two-step approach to estimate the ET for farm crops, landscapes, and some natural vegetation. Applications of this approach to forests are described in the *ASCE Handbook of Hydrology* [57.79].

The crop (or cover) coefficient K_c was proposed as a modifier of ET_{ref} in [57.80], and its usage was popularized internationally by the FAO [57.24]. The two-step procedure for estimating the ET for well-watered agricultural crops can be applied to various types of natural vegetation, to crops under rainfed conditions, and to hydrologic studies in general. For these reasons, K_c is perhaps more appropriately referred to as a *vegetation cover coefficient* rather than a *crop coefficient*. The K_c approach is an empirical approach, but it has limits that are physically based, and the method tends to have good reproducibility and transferability. K_c is readily visualized and therefore relatively straightforward to parameterize.

Some K_c curves have been refined for dry surface soil or visually dry soil (i.e., visual inspection suggests that the soil is dry); the corresponding coefficients are called *basal crop coefficients* (K_{cb}) [57.81]. More accurate ET estimates can be obtained by adjusting K_{cb} for the wetness of the surface soil for several days following rain or irrigation using the dual K_c approach [57.2, 81].

Numerous publications over the past decades have focused on the measurement of ET and the calculation of associated crop coefficients. The primary factor that influences the crop coefficient is a change in plant cover or the evolution of leaf area per unit area (LAI) as a plant develops, which results in a decrease in bulk surface resistance. Most publications on crop coefficient curves have presented K_c as a function of some form of absolute or scaled time. Some studies provide the rate of increase in LAI and therefore K_c as a function of the daily weather, such as cumulative degree days, as discussed in the section on lengths of growth states.

When applying the standardized reference ET equation (57.34) under humid conditions (where most of the

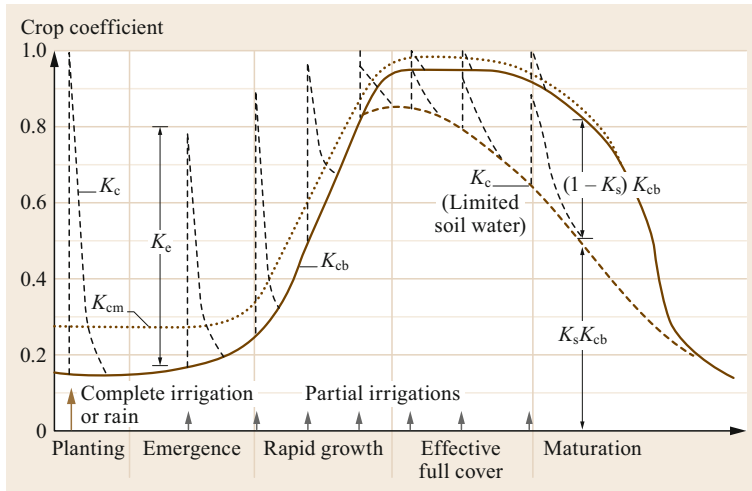


Fig. 57.4 Generalized K_c cover coefficient curves showing the effects of growth stage, wet surface soil, and limited available soil water (after [57.53] republished with the permission of the American Society of Civil Engineers)

energy for the ET process comes from the net radiation) for large expanses of similar vegetation, K_c does not exceed about 1.0 relative to the alfalfa reference and about 1.2 relative to the grass reference. In dry climates, where additional advection of warm, dry air can increase the ET from wet surfaces, K_c still does not exceed about 1.0–1.1 relative to the alfalfa reference, but it can reach about 1.3–1.4 relative to the grass reference. The reason for the near-constant crop coefficients of 1.0–1.1 for the alfalfa reference is that this reference crop has about the same albedo, LAI, stomatal resistance, and roughness as most agricultural crops at full cover. An expanse of a reference crop (especially alfalfa) will approach the maximum conversion of available energy into Q_E , so the ratio of Q_E for any other tall, leafy crop to the Q_E for alfalfa will be around 1.0. Higher values for K_c are likely to indicate problems with field measurements. Such measurement problems include:

- 1) Improper computation of the vegetated area in lysimeter studies [57.82, 83]
- 2) Violation of the fetch requirements in boundary-layer (energy-balance) measurements
- 3) Weather data collection difficulties and errors [57.83].

Two families of K_c curves for agricultural crops have been developed, based on the two commonly used reference crops (tall and short). These are the grass-based curves produced by William Pruitt [57.2, 21, 24] and the alfalfa-based K_c curves of James Wright [57.81, 84] and others [57.85–87]. It is clearly important to avoid mixing a grass-reference-based K_c with an alfalfa reference and vice versa.

Generalized crop coefficient curves for estimating the ET_c are shown in Fig. 57.4. The K_{cb} curve presents the *basal* crop coefficient for conditions where the soil surface is visually dry, so that evaporation from the soil is minimal, but where the availability of soil water does not limit plant growth or transpiration. This curve represents a minimum potential ET_c situation for adequate soil water. The spikes in Fig. 57.3 indicate precipitation or irrigation events that wet the soil surface and temporarily increase the total ET_c for 1–5 days. These spikes decay to the K_{cb} curve as the soil surface dries. The spikes generally approach a maximum value of 0.8–1.0 for an alfalfa ET_r base [57.81] and 1.0–1.2 for a grass ET_o base [57.2]. The K_{cm} curve in Fig. 57.3 presents the so-called *mean* crop coefficient, which includes the averaged effects of wet soil (spikes) under specific rainfall or irrigation frequencies. K_{cm} is sometimes referred to as the *single* K_c . The final *limited soil water* curve in the figure represents the decrease in ET_c when plant water uptake is limited by the available soil water.

The actual ET, denoted $ET_{c,act}$ or ET_a here, is the ET rate that occurs under actual field conditions. The value of $ET_{c,act}$ may be less than the value of the potential ET_c , sometimes denoted $ET_{c,pot}$, when water stress occurs in the vegetation. $ET_{c,act}$ or ET_c is calculated as

$$ET_{c,act} = ET_c = K_c ET_{ref} \quad (57.42)$$

Both $ET_{c,act}$ and ET_c (and $ET_{c,pot}$) can include varying degrees of direct evaporation from the soil, as represented by the evaporation coefficient K_e .

Basal Crop Coefficients

Basal crop coefficients mainly represent the transpiration component of ET, although they also incorporate

a small evaporation component from soil that is visually dry at the surface. It is necessary to adjust for wet soil effects after rain or irrigation when using these coefficients, as this leads to better daily estimates of ET_c for use in soil water modeling than achieved using mean coefficients, where the effects of local rainfall or irrigation frequencies are averaged. The total crop coefficient K_c is computed from K_{cb} as

$$K_c = K_s K_{cb} + K_e, \quad (57.43)$$

where K_s is a dimensionless coefficient that is dependent on the available soil water and K_e is a coefficient to account for the increased evaporation from wet soil immediately after rain or irrigation. The value of K_s is 1 unless the available soil water limits transpiration, in which case it is less than 1. The values of K_e represent the spikes shown in Fig. 57.3. The estimation of K_e for bare soil conditions is described later in this chapter; see (57.45)–(57.47).

Evaporation from Soil

Evaporation from bare soil is often divided temporally into two or three stages characterized by different limitations on the evaporation process and rate. Ritchie and others [57.88] defined stage 1 evaporation as the rate of evaporation following wetting, when the evaporation rate is limited by energy availability. During stage 1, the soil is sufficiently wet that water is transported to the surface at a rate that is at least equal to the evaporation potential. The duration of stage 1 and the amount of water evaporated are related to the hydraulic conductivity and water-holding capacity of the soil and the evaporative conditions. In stage 2, the surface soil water content has decreased to a level at which the hydraulic capacity of the soil is unable to supply the potential-energy-limited rate. The evaporation rate progressively decreases during stage 2, often in proportion to the square root of time [57.89, 90]. Occasionally, with deep-cracking soils, there is a third evaporation stage in which there is a low rate of evaporation of water exposed by deep cracks over a long period [57.75, 91–93].

The duration of stage 1 can range from one to several days after rainfall or irrigation, depending on the amount of water applied and the soil and evaporative conditions present. The total depth of cumulative evaporation during stage 1, referred to as the readily evaporable water (REW) in the FAO 56 procedure [57.2], varies with soil type. The REW can be estimated from Table 57.8 based on recommendations in [57.94], or using methods presented in [57.53, 88], where cumulative amounts of stage 1 evaporation for four soils are reported, ranging from 6 mm for sand to 12 mm for a clay loam. Stage 2 evaporation is often said to begin when

Table 57.8 Typical values of the evaporation parameter REW for different soil types (for more on the US soil texture classification, see Chap. 5) [57.2]

Soil type	REW (mm)
Sand	2–7
Loamy sand	4–8
Sandy loam	6–10
Loam	8–10
Silt loam	8–11
Silt	8–11
Silty clay loam	8–11
Silty clay	8–12
Clay	8–12

the soil surface becomes visibly dry for most of the day. Local observations of the REW are recommended.

E for stage 1 drying can be estimated using

$$E_1 = K_{e\max} ET_{\text{ref}}, \quad (57.44)$$

where the reference ET represents the potential evaporation energy. E_1 can change daily, depending on the value of ET_{ref} . $K_{e\max}$ generally ranges from 1.05 to 1.2 when used with ET_o and from 0.8 to 1.0 when used with ET_r , depending on the ambient temperature of the soil prior to wetting, as heat stored in hot, dry soil prior to wetting may contribute to the evaporation rate. When the total E_1 during stage 1 exceeds the REW, stage 1 ends and stage 2 begins.

The FAO 56 [57.2] evaporation procedure calculates the water balance for the effective evaporation layer of the soil (Z_e), which tends to be approximately 0.1–0.15 m in depth. This method represents a compromise between complexity and general application, as it assumes that the upward flux of water or vapor into this layer from below is small, or that its effects are incorporated into the effective depth of Z_e , which dries to a threshold dryness point. The threshold point is taken as the mean soil water content halfway between the air-dry and wilting points. This is an arbitrary dry point, but it is straightforward to utilize this point in the field, and it is reproducible. The maximum depletion depth for the layer provides a consistent stopping point for the evaporation cycle to ensure conservation of mass, and can be customized for each application to fit observations. Z_e is typically the upper 0.1–0.15 m during the first three or four weeks of a drying event, but potentially increases to depths of 0.2–0.25 m for longer time periods between wetting events.

The general FAO model for K_e in stage 2 is

$$K_e = K_r (K_{c\max} - K_s K_{cb}), \quad (57.45a)$$

such that

$$K_e \leq f_{ew} K_{c\max}, \quad (57.45b)$$

where $K_{c\max}$ is the maximum value of K_c for wet vegetated conditions following rain or irrigation and K_r is a dimensionless evaporation reduction coefficient (0–1). K_r is expressed as a function of the cumulative depth of water depleted by evaporation from the soil. f_{ew} is the fraction of the soil surface from which most of the evaporation occurs, which is generally taken to be the fraction of the soil surface that is both wetted during the wetting event and exposed to drying. The use of the cumulative depth of evaporation to estimate K_r stretches out drying periods when ET_{ref} is low and shortens them when ET_{ref} is high. The daily water balance of the effective surface evaporation layer is required. In (57.40), energy consumption through transpiration is preferred to energy consumption through evaporation from the soil. $K_s K_{cb}$ is set to 0 when (57.40) is applied to completely bare soil.

$K_{c\max}$ is the maximum value of K_c following rain or irrigation for both bare soil and soil with some degree of vegetation cover. The value of $K_{c\max}$ is governed by the amount of energy available to evaporate water, which is largely encapsulated by the reference ET_{ref} . Because K_c is the ratio of ET to ET_{ref} , the value of $K_{c\max}$ is not expected to exceed 1.0–1.3 for the grass reference or approximately 1.05 for the alfalfa reference. For the grass reference, the value varies with the general climate [57.2, 95]. When it is applied with ET_o , $K_{c\max}$ is adjusted for the effects of air dryness and wind speed via

$$K_{c\max o} = \max \left\{ 1.2 + [0.04(u_2 - 2) - 0.004(R_{\min} - 45)] \left(\frac{h}{3} \right)^{0.3}, (K_{cb o} + 0.05) \right\}, \quad (57.46)$$

where u_2 is the average wind speed at 2 m, R_{\min} is the average daily minimum relative humidity (%), and h is the mean plant height (m) during the growth stage or period (initial, development, midseason, or late season). $K_{c\max o}$ denotes the use of $K_{c\max}$ with ET_o , and K_{cbo} denotes the use of K_{cb} with ET_o .

$K_{c\max}$ for the tall reference ET_r , denoted $K_{c\max r}$, does not need to be adjusted for the climate due to the increased roughness of the alfalfa reference basis. Thus,

$$K_{c\max r} = \max[1.0, (K_{cb r} + 0.05)], \quad (57.47)$$

where K_{cbr} denotes a basal K_{cb} that is used with ET_r . Equations (57.46) and (57.47) require that $K_{c\max}$ is greater than or equal to the sum $K_{cb} + 0.05$, suggesting that K_c exceeds K_{cb} by at least 0.05 following complete wetting of the soil surface, even during periods of full ground cover.

Assuming that the soil is at field capacity (θ_{fc}) shortly after rainfall or irrigation, and that it can dry to halfway between 0 and the wilting point (θ_{wp}), the total amount of water that can be evaporated from the effective evaporation layer during a drying cycle can be estimated as

$$TEW = 1000(\theta_{fc} - 0.5\theta_{wp})z_e, \quad (57.48)$$

where TEW is the total evaporable water in mm, θ_{fc} and θ_{wp} are in $m^3 m^{-3}$, and z_e is the effective depth (in m) of the surface layer dried by evaporation. The value of θ_{fc} in (57.48) may be set a few percentage points above the normal values listed in Table 57.9 to compensate for the extra soil water retained in the evaporation layer above θ_{fc} for a few days after wetting.

The cumulative depth of evaporation D_e at the end of stage 1 is the readily evaporable water (REW), which normally ranges from 5 to 12 mm depending on the soil texture [57.88]. During the falling rate stage, where $D_e > REW$, the evaporation rate is estimated as a proportion of the amount of water remaining in the surface soil layer, and K_r in (57.45) from [57.53] is calculated via

$$K_r = F_{stage 1} + (1 - F_{stage 1}) \times \max \left[\min \left(\frac{TEW - D_{e(i-1)}}{TEW - REW}, 1.0 \right), 0.0 \right], \quad (57.49)$$

where $D_{e(i-1)}$ is the cumulative depth of evaporation at the end of timestep $i-1$ (the previous timestep), and $F_{stage 1}$ is the fraction of the timestep (day or hour) during which there is stage 1 evaporation (i.e., stage 2 evaporation occurs during $1 - F_{stage 1}$ of the timestep). The max and min functions limit the value of K_r to $0 \leq K_r \leq 1.0$.

According to [57.96], $F_{stage 1}$ can be approximated as

$$F_{stage 1} = \frac{REW - D_{REW, i-1}}{K_{e\max} ET_{ref}}, \quad 0 \leq F_{stage 1} \leq 1.0, \quad (57.50)$$

where the timestep can be a day, a tenth of a day, or one hour in length. $D_{REW, i-1}$ is the depletion (in mm) of the upper soil surface layer (the *skin* layer) that directly contributes to stage 1 drying at the end of timestep $i-1$, and $K_{e\max}$ is the expected value of K_e during stage 1 drying. $K_{e\max}$ can typically be set equal to $K_{c\max}$, as defined earlier. $F_{stage 1}$ is limited to the range $0 \leq F_{stage 1} \leq 1.0$. The water balance equation for determining D_{REW} is given later in this chapter; see (57.54). Figure 57.5 illustrates three distinct soil profile layers in the presence of plants: the skin layer, the total evaporation layer z_e ,

and the root zone depth z_r . Each layer is a subset of the next layer down in the FAO 56 model, which is different from most layered soil water models.

In the FAO 56 dual K_c model described in (57.2), f_w (the fraction of the surface wetted by irrigation and/or precipitation) is used to limit the potential spatial extent of evaporation. When the soil surface is completely wetted by precipitation or a sprinkler, the fraction of exposed wetted soil f_{ew} is set equal to $(1 - f_c)$, where f_c is the fraction of the soil surface that is effectively covered by vegetation. For irrigation systems where only a fraction of the ground surface is wetted (f_w), f_{ew} is limited to f_w and

$$f_{ew} = \min(1 - f_c, f_w). \quad (57.51)$$

For numerical stability, both $(1 - f_c)$ and f_w are limited to the range 0.01–1. f_c (and thus f_{ew}) can be estimated using a general relationship between f_c and K_{cb} given in FAO 56,

$$f_c = \left(\frac{K_{cb} - K_{c \min}}{K_{c \max} - K_{c \min}} \right)^{1+0.5h}, \quad (57.52)$$

where $K_{c \min}$ is the minimum (basal) K_c for dry bare soil with no ground cover and h is the height of the vegetation in m. The differences $K_{cb} - K_{c \min}$ and $K_{c \max} - K_{c \min}$ are limited to ≥ 0.01 for numerical stability. The value of f_c can change daily as K_{cb} fluctuates. $K_{c \min}$ ordinarily has the same value as K_{cb} during the initial growth period of vegetation, which has a dormant period and a leaf-off period when the soil is almost bare (i.e., $K_{c \min} \approx 0.10-0.15$). $K_{c \min}$ is set to zero or nearly zero in scenarios where there are long time periods between wetting events (e.g., in applications involving natural vegetation in deserts). The value of f_c decreases during the late season in proportion to K_{cb} to account for the local transport of sensible heat from senescing leaves to the soil surface. The FAO 56 dual K_c model can be applied using both references (ET_0 and ET_r) provided the K_{cb} values used in the procedure are associated with the specific reference.

The estimation of K_e requires daily (or even more frequent) water balance data for the fraction f_{ew} of the surface soil layer, i.e.,

$$D_{e,i} = D_{e,i-1} - \left[(1 - f_b) \left(P_i - RO_i + \frac{I_i}{f_w} \right) + f_b \left(P_{i+1} - RO_{i+1} + \frac{I_{i+1}}{f_w} \right) \right] + \frac{E_i}{f_{ew}} + T_{ei,i}, \quad (57.53)$$

where $D_{e,i-1}$ and $D_{e,i}$ are the cumulative depletion depths (in mm) at the end of day $i-1$ and the end of day i , respectively; P_i and RO_i are the precipitation and the precipitation runoff from the soil surface on day i

(both in mm); I_i is any irrigation depth on day i that infiltrates the soil (in mm); E_i is the evaporation on day i (i.e., $E_i = K_e ET_{ref}$) (in mm); $T_{ei,i}$ is the depth of transpiration from the exposed and wetted fraction of the soil surface layer on day i (in mm); and f_b is the fraction of the precipitation and irrigation that occurs during a calculation timestep (hour or day) which is assumed to contribute immediately to evaporation during the same timestep ($1 - f_b$ of the precipitation and irrigation does not contribute to the evaporation until the following timestep, on average). The value of f_b is limited to the range 0–1.0; if its value is not known, it can be set to 0.5. f_b effectively controls the immediacy of evaporation from a wetting event, which may occur at an unknown time within the calculation timestep (e.g., nighttime precipitation events during a daily timestep). Variables with subscripts of $i+1$ correspond to values for the timestep following the current timestep i . Assuming that the surface layer is at field capacity following heavy rain or irrigation, the minimum value for $D_{e,i}$ is zero. The values of $D_{e,i}$ and $D_{e,i-1}$ are constrained to $0 \leq D_{e,i} \leq TEW$. Any P or I additions in excess of $D_{e,i}$ and $D_{REW,i}$ in (57.54) are assumed to infiltrate to depths below z_e (or below the skin in the case of $D_{REW,i}$).

Dividing the irrigation depth I_i by f_w gives the approximate depth of infiltration into the wetted portion f_w of the soil surface. Similarly, E_i is divided by f_{ew} because all E_i other than the residual evaporation implicit to K_{cb} is assumed to be taken from the exposed fraction f_{ew} of the surface layer.

The parameter $D_{REW,i-1}$ in (57.50) is the depletion of water from the REW layer, also referred to as the skin layer, at the end of the previous timestep ($i-1$). Equation (57.50) estimates F_{stage1} in order to simulate any stage 1 evaporation that may occur from light or heavy wetting events. The calculation of $D_{REW,i}$ is designed to be forward-looking with regard to the wetting event, so that the soil surface wetting and corresponding evaporation from a wetting event occurring during the current timestep i are considered. Therefore,

$$D_{REW,i} = D_{REW,i-1} - \left[(1 - f_b) \left(P_i - RO_i + \frac{I_i}{f_w} \right) + f_b \left(P_{i+1} - RO_{i+1} + \frac{I_{i+1}}{f_w} \right) \right] + \frac{E_i}{f_{ew}}, \quad (57.54)$$

where $D_{REW,i-1}$ and $D_{REW,i}$ are the cumulative depletion depths (in mm) at the end of day $i-1$ and the end of day i , respectively; all other terms have the same definitions as in (57.53). The values of $D_{REW,i}$ and $D_{REW,i-1}$ are constrained to the range $0 \leq D_{REW,i} \leq REW$.

For shallow-rooted annual crops with rooting depths of less than about 0.5 m and in the absence of

deep cultivation, T_e , fed by lateral extraction by plant roots, may significantly affect the water balance of the surface layer and therefore the estimation of the evaporation component during the development period. An extension to FAO 56 proposed in [57.95] estimates T_e from the exposed fraction f_{ew} of the evaporation layer as a proportion of the water content of that layer. In this extension,

$$T_e = K_t K_s K_{cb} ET_{ref}, \quad (57.55)$$

where K_t (range: 0–1) is the proportion of the basal ET ($= K_{cb} ET_{ref}$) extracted as transpiration from the exposed fraction f_{ew} of the surface soil layer. K_s is the soil water stress factor computed for the root zone (range: 0–1). K_t is determined in proportion to the relative water availability in the layers z_e and z_r (the root zone; recall that z_e is a subset of z_r) along with the presumed rooting distribution. For f_{ew} ,

$$K_t = \frac{1 - D_e/TEW}{1 - D_r/TAW} \left(\frac{z_e}{z_r} \right)^{0.6}, \quad (57.56)$$

where TAW is the total depth of available water in the root zone that can be extracted by roots before any stress occurs. The numerator and denominator of the first expression are limited to values ≥ 0.001 , and the value of K_t is limited to ≤ 1.0 . z_e and z_r have the same units. D_r is the depletion of the total effective root zone, estimated as $D_r = (\theta_{fc} - \theta)z_r$, where θ is the mean volumetric soil water in the root zone (in $\text{m}^3 \text{m}^{-3}$). In the simple water balance procedure described in FAO 56, the soil water content of the surface layer is assumed to

be limited to $\leq \theta_{fc}$ on the day of a wetting event that is larger in depth than REW. This is a reasonable assumption considering the shallowness of the surface layer.

Adjustment for Water Stress

Several linear and curvilinear functions have been proposed to account for the influence of the available water on the ET or for the K_s used in (57.37) and (57.39). A commonly used simple linear model for estimating K_s is [57.97]

$$K_s = \frac{\theta - \theta_{wp}}{\theta_t - \theta_{wp}} \quad \text{for } \theta < \theta_t, \quad (57.57)$$

where θ is the mean volumetric soil water in the root zone (in $\text{m}^3 \text{m}^{-3}$) and θ_t is the threshold θ below which transpiration decreases linearly due to water stress. $K_s = 1.0$ for $\theta \geq \theta_t$. The wilting point θ_{wp} is the soil water at the lower limit of soil water extraction by plant roots (in $\text{m}^3 \text{m}^{-3}$). Typical values of θ_{wp} and θ_{fc} for various soil texture classes are listed in Table 57.9. The threshold soil water θ_t can be estimated from the relationship

$$\theta_t = (1 - p)(\theta_{fc} - \theta_{wp}) + \theta_{wp}, \quad (57.58)$$

where p is the average fraction of available soil water that can be depleted before water stress arises and ET decreases. All θ parameter values are averages over the effective root zone.

Parameter p normally ranges from 0.30 (i.e., 30% depletion of the available soil water, $\theta_{fc} - \theta_{wp}$) for shallow-rooted plants at high rates of ET_c ($> 8 \text{ mm d}^{-1}$)

Table 57.9 General soil water classes for agricultural soils (the water contents are given on a volume basis) [57.53]

Texture class	Field capacity		Permanent wilting point		Available water	
	Average range		Average range		Average range	
	(%)	(%)	(%)	(%)	(%)	(%)
Coarse						
Sand	12	7–17	4	2–7	8	5–11
Loamy sand	14	11–19	6	3–10	8	6–12
Moderately coarse						
Sandy loam	23	18–28	10	6–16	13	11–15
Medium						
Loam	26	20–30	12	7–16	15	11–18
Silt loam	30	22–36	15	9–21	15	11–19
Silt	32	29–35	15	12–18	17	12–20
Moderately fine						
Silty clay loam	34	30–37	19	17–24	15	12–18
Fine						
Silty clay	36	29–42	21	14–29	15	11–19
Clay	36	32–39	21	19–24	15	10–20

to 0.70 (i.e., 70% depletion of the available soil water) for deep-rooted plants at low rates of ET_c ($< 3 \text{ mm d}^{-1}$) [57.2, 53, 98]. A value of 0.50 is commonly used for many agricultural crops.

The mean soil water balance for the root zone can be computed on a daily basis in terms of θ using

$$\begin{aligned} \int_0^{z_r} \theta_{2z} dz &= \int_0^{z_r} \theta_{1z} dz + \Delta \theta_{z_r} \\ &= \int_0^{z_r} \theta_{1z} dz + P - Q_t - ET_a - DP + GW, \end{aligned} \quad (57.59)$$

where $\theta_{1(z)}$ is the volumetric water content to depth z ($\text{m}^3 \text{ m}^{-3}$) at time $t = 1$, $\theta_{2(z)}$ is the volumetric water content to depth z ($\text{m}^3 \text{ m}^{-3}$) at time $t = 2$, and z_s is the effective depth of the root zone (mm). Generally, the deep percolation flux density is estimated using the field capacity of the soil. θ_{fc} represents the water content that the soil will attain after draining under a unit hydraulic gradient (gravity) for 2–3 days after wetting, which represents the upper limit of the soil's ability to retain water after initial rapid drainage. The available water is calculated as $AW = \theta_{fc} - \theta_{wp}$. Where possible, specific values for θ_{fc} and θ_{wp} should be determined from field studies [57.99].

When the calculation timestep for (57.59) is 1 day, DP is often assumed to occur if the total θ of the root zone is greater than θ_{fc} on any particular day. In this case,

$$\begin{aligned} \text{if } & \int_0^{z_s} \theta_{2(z)} dz > \theta_{fc} z_s, \\ \text{then } & DP = \int_0^{z_s} \theta_{2(z)} dz - \theta_{fc} z_s \\ & \text{and } \theta_{2(z)} = \theta_{fc} \text{ from } 0 \text{ to } z_s; \\ \text{otherwise } & DP = 0. \end{aligned} \quad (57.60)$$

One may wish to delay applying (57.60) until two days after a major precipitation or irrigation event to account for the ET of water above θ_{fc} during the first two days while the soil profile is draining to field capacity. When it is applied to layered soils with different water-holding characteristics, the term $\theta_{fc} z_s$ can be replaced with an integral of θ_{fc} from 0 to z_s to account for the variation of θ_{fc} with z . Computations are performed for the complete root depth z_r , including the evaporation layer.

Capillary rise (CR). The amount of water transported upward by capillary rise (or GW) from the water

table to the root zone or soil surface depends on the soil type, the depth of the water table, and the wetness of the root zone. CR can normally be assumed to be zero when the water table is more than a few meters below the bottom of the root zone. Medium-textured soils tend to have higher upward fluxes than fine- and coarse-textured soils due to a favorable combination of capillarity and hydraulic conductivity. The equations that are used to estimate the CR for a range of soil textures are presented in [57.53].

Values for Basal Crop Coefficients

Extensive tables of K_{cb} for agricultural crops and for some forms of natural vegetation are available on the Internet; for example, those provided by FAO [57.2]. The FAO approach is to construct a simple linear curve of K_{cb} piecewise, as demonstrated in Fig. 57.5.

The procedure for constructing crop (cover) coefficients is presented in [57.2, 24]. In the FAO procedure, a K_{cb} curve such as that shown in Fig. 57.4 is constructed by:

- Dividing the growing season into four parts corresponding to distinct crop phenology or growth stages:
 - Initial period (1)
 - Crop development period (2)
 - Midseason period (3)
 - Late-season period (4)
- Selecting three K_{cb} values that represent:
 - The average K_{cb} during the initial period ($K_{cb\text{ini}}$)
 - The average K_{cb} during the midseason period ($K_{cb\text{mid}}$)
 - The average K_{cb} at the end of the late season (i.e., around harvest or leaf-fall) ($K_{cb\text{end}}$)
- Drawing a straight line through the points in each period (the lines through the initial and midseason periods are horizontal).

Only three tabularized values of K_{cb} are required to describe and construct an FAO-style K_{cb} curve. $K_{cb\text{mid}}$ represents the average value of K_{cb} expected during the midseason period, rather than the absolute peak daily K_{cb} presented by the crop or other vegetation.

The four vegetation growth stages generally correlate with benchmark growth stages. The initial period is from the planting or greening of vegetation to the attainment of 10% ground cover. The crop development period corresponds to the increase in ground cover from 10% to effective cover (i.e., 80% or more shading of the ground or the initiation of flowering for many vegetation types). The midseason period stretches from the attainment of effective cover to the start of senescence (browning of leaves), while the late-

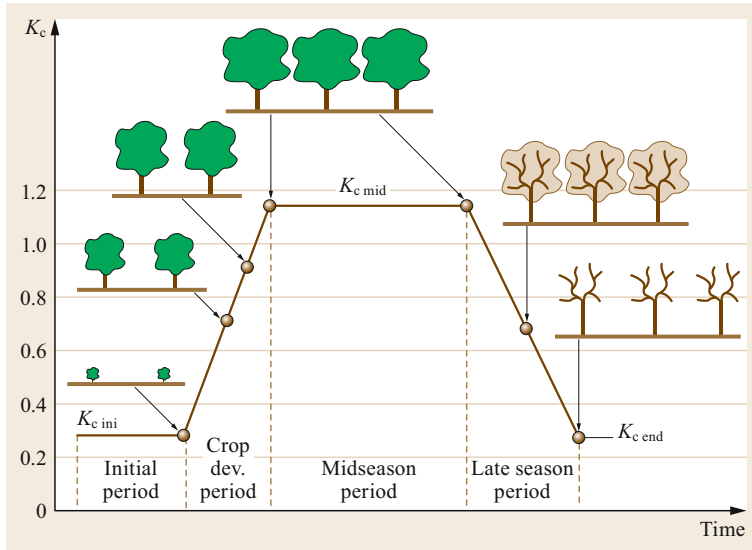


Fig. 57.5 FAO crop coefficient curve and stage definitions (after [57.75] republished with the permission of the American Society of Civil Engineers)

season period is from the start of maturity to harvest or complete leaf death. The length of the initial period is strongly dependent on the type of vegetation present and the time of year. Trees have a relatively short initial–development period of only a few days to a week, whereas broadleaved annuals may have an initial–development period of more than a month. The start of the late period is often indicated by the onset of leaf aging, yellowing, or senescence, or fruit browning.

This approach to identifying generalized values for K_{cb} is most successful for agricultural crops due to the height uniformity and consistent stand density of this vegetation, as well as the reproducibility of the canopy characteristics from region to region. Natural vegetation systems present more of a challenge when attempting to specify universal values for K_{cb} . Such K_{cb} values are more likely to be useful when canopy characteristics such as the fraction of ground cover and the height as well as the relative stomatal resistance are used to estimate an expected value [57.100], or when (57.52) is inverted and solved for K_{cb} .

Estimated K_c Curves for Natural and Agricultural Vegetation

The two-step $K_c ET_{ref}$ approach provides a simple and convenient way to estimate ET_c from natural vegetation, where, if necessary, K_c can be estimated from the fraction of the ground that is covered by vegetation. The resulting cover (crop) coefficient curves represent the ratio of ET_c to ET_{ref} during various growth stages. The previous section described the estimation of growth stage durations. Often, when the K_c curve is not available, the K_c during the peak growth period ($K_{c\ mid}$) can be estimated from the amount of ground shaded by veg-

etation, the plant density and height, and the amount of stomatal regulation under moist soil conditions. When soil water availability is low, the value of K_c is generally determined using (57.57) coupled with (57.43).

The K_c development process should adhere to the upper limit for K_c of 1.1 with an alfalfa reference and about 1.25 with a grass reference for stands of vegetation larger than 500–2000 m² in order to adhere to energy-exchange principles within established equilibrium boundary layers. When there are *clothesline effects* (i.e., the vegetation is higher than its surroundings) or *oasis effects* (the vegetation has higher soil water availability than its surroundings), the peak K_c may exceed these limits.

The value of $K_{c\ mid}$ for natural vegetation decreases when the plant density or leaf area is less than that required for full ground cover, which is often taken to be when $LAI < 3$. $K_{c\ mid}$ can be expressed as a function of the density coefficient K_d , [57.100], where

$$K_{cb\ mid} = K_{c\ min} + K_d (K_{cb\ full} - K_{c\ min}) . \quad (57.61)$$

Here, $K_{cb\ mid}$ is the approximation for K_{cb} during the midseason period, $K_{cb\ full}$ is the estimated basal K_c during peak plant growth when there is almost full ground cover (or $LAI > 3$), and $K_{c\ min}$ is the minimum basal K_c for bare soil ($K_{c\ min} \approx 0.15$ under typical agricultural conditions and ≈ 0.0 – 0.15 for native vegetation, depending on the rainfall frequency). The density coefficient K_d can be estimated as a function of the measured or estimated leaf-area index LAI or as a function of the fraction of the ground that is covered by vegetation. For trees or forest with grass or some other ground cover beneath the primary tree canopy, (57.61)

can take the form [57.53, 100]

$$K_{cb\,mid} = K_{cb\,cover} + K_d \left[\max \left(K_{cb\,full} - K_{cb\,cover}, \frac{K_{cb\,full} - K_{cb\,cover}}{2} \right) \right], \quad (57.62)$$

where $K_{cb\,cover}$ is the K_{cb} of the ground cover in the absence of tree foliage. The second term of the max function reduces the estimate for $K_{cb\,mid}$ by half of the difference between $K_{cb\,full}$ and $K_{cb\,cover}$ when this difference is negative. This accounts for the impact of surface shading by vegetation with a lower K_{cb} than that of the ground cover due to differences in stomatal conductance. Equation (57.61) can be applied to estimate K_{cb} during other periods besides the midseason by estimating K_d using (57.65) and (57.66) along with the LAI or $f_{c\,eff}$ for that period.

For large vegetation stands ($\approx 500\text{ m}^2$) where the crops are not listed in the literature, the $K_{c\,full}$ used with ET_o can be approximated as a function of the mean plant height and adjusted for climate similar to the $K_{c\,mid}$ parameter [57.2], as shown below.

For ET_o ,

$$K_{cb\,full} = \min(1.0 + 0.1h, 1.20) + [0.04(u_2 - 2) - 0.004(R_{min} - 45)] \left(\frac{h}{3} \right)^{0.3}, \quad (57.63)$$

and for ET_r ,

$$K_{cb\,full} = \min(0.8 + 0.1h, 1.0), \quad (57.64)$$

where the parameters are defined as in (57.46). The climatic correction is not required for $K_{cb\,full}$ when it is used to derive the K_{cb} for ET_r because of the aerodynamic and canopy characteristics of the alfalfa reference crop.

$K_{c\,full}$ represents a general upper limit on $K_{cb\,mid}$ for tall vegetation with full ground cover and $LAI > 3$ under a full water supply. Equations (57.65) and (57.66) yield general approximations for the increase in $K_{cb\,full}$ with plant height and climate.

When LAI can be measured or approximated, K_d can be approximated under normal conditions [57.2] as

$$K_d = 1 - e^{(-0.7LAI)}. \quad (57.65)$$

The LAI is defined as the area of leaves per area of ground surface averaged over a large area, in units of $\text{m}^2\text{ m}^{-2}$. Only one side of healthy green leaves that are active in vapor transfer is considered. The relationship in (57.65) is similar to that used in [57.101].

When estimates of the fraction of the ground surface covered by vegetation are available, K_d can be estimated as [57.100]

$$K_d = \min \left[1, M_L f_{c\,eff}, f_{c\,eff}^{\left(\frac{1}{1+h}\right)} \right], \quad (57.66)$$

where M_L is a multiplier (range: 1.5–2.0) of $f_{c\,eff}$ that encompasses the effects of canopy density and conductance on the maximum relative ET per fraction of the ground shaded, $f_{c\,eff}$ is the effective fraction of the ground that is covered or shaded by vegetation near solar noon (range: 0.01–1), and h is the mean height of the vegetation in m. For canopies such as trees or randomly planted (i.e., not in rows) vegetation, $f_{c\,eff}$ can be estimated according to [57.2] via

$$f_{c\,eff} = \frac{f_c}{\sin(\beta)} \leq 1, \quad (57.67)$$

where β is the mean angle of the sun above the horizon during the period of maximum ET (generally between 11.00 and 15.00). $f_{c\,eff}$ can generally be assigned to solar noon (12.00), so β can be calculated as

$$\beta = \arcsin [\sin(\phi) \sin(\delta) + \cos(\phi) \cos(\delta)], \quad (57.68)$$

where ϕ and δ are the latitude and solar declination, respectively (Chap. 5).

M_L , the multiplier of $f_{c\,eff}$ in (57.66), imposes an upper limit on the relative magnitude of transpiration per unit of ground area as represented by $f_{c\,eff}$ [57.2], and is expected to range from 1.5 to 2.0, depending on the canopy density, thickness, and maximum conductance. M_L is an attempt to simulate the physical limits imposed on the water flux through the plant root, stem, and leaf systems [57.100]. The value of M_L can be modified to fit the specific vegetation. K_d values for a range of $f_{c\,eff}$ and h values and for $M_L = 1.5$ and $M_L = 2$ when $h = 5\text{ m}$ are shown in [57.100].

When the mean stomatal control exerted by the vegetation is greater than that for agricultural vegetation, then FAO 56 [57.2] suggests that the estimate obtained using (57.65) and (57.66) should be reduced by about 10 or 20% for each doubling of r_1 above 100 s m^{-1} . The value of $K_{cb\,mid}$ estimated from (57.62) is applied as a basal coefficient using the dual $K_{cb} + K_c$ method, where the actual K_c may increase to 1.0 for ET_r or 1.2 for ET_o following precipitation (even if the estimated $K_{cb\,mid}$ is small) due to surface evaporation from sparse vegetation. In addition, K_c should be reduced using K_s from (57.57) when the soil water is low.

Equation (57.66) suggests that as h increases, the total leaf area and resulting net radiation capture will increase, thereby increasing K_c . In addition, as h increases, there is more opportunity for the microadvection of heat from the soil to the canopy, and turbulent exchange within the canopy increases for the same amount of ground coverage. Both of these conditions increase the relative magnitude of $K_{cb, mid}$. Values of $K_{cb, end}$ can be scaled from $K_{cb, mid}$ in proportion to the health and leaf condition of the vegetation at termination as well as the length of the late-season period (i.e., whether leaves senesce slowly or are killed by frost). f_c and h are probably the simplest indices to estimate in the field. In [57.102], it was suggested that C3 photosynthetic behavior should be distinguished from C4 photosynthetic behavior when performing LAI- and f_c -based estimation, because C4 vegetation can have limited stomatal control. Equations (57.54)–(57.57) and (57.59) were applied in [57.103] to savannah vegetation in Ethiopia, and good agreement between the estimated ET and the ET measured gravimetrically was observed. Vegetation types ranged from sparse grazed grasses to the full forest canopy.

The techniques of this section can also be applied to landscaped systems such as those found in urban and residential environments, including lawns, gardens, and shade trees. Specific equations for the application of these techniques are given in [57.53, 76, 83], as are examples and tables.

Lengths of Growth Stages

FAO 24 [57.24] and FAO 56 [57.2] provide guidance regarding the durations of the growth (development) stages for various types of climates and locations. The rate of vegetative development and attainment of effective full cover is affected by the weather conditions, especially the mean daily air temperature [57.104]. Therefore, the length of time between planting or plant emergence and effective full cover for various crops or other vegetation will vary with climate, latitude, elevation, and planting date (if cultivated), as well as with species and cultivar (variety). Generally, once effective full cover has been reached for a plant canopy, the rate of phenological development (flowering, seed development, ripening, and the senescence or death of leaf tissue) often proceeds at a rate that depends on plant genotype rather than weather [57.81]. In some situations, the emergence of vegetation, greenup, and the attainment of effective full cover can be estimated using cumulative degree-based regression equations or plant growth models [57.38, 104–112]. The use of cumulative growing degree days allows the K_c curves generated for years or growing seasons that run cooler or warmer than average to be quantitatively stretched or compressed. K_c

curves are provided in [57.53]; those curves are based on the cumulative number of growing degree days.

Local observations of plant stage development should be utilized where possible, with tabular values used as a guide and for comparison. Local information can be obtained from farmers, ranchers, agricultural extension agents, local researchers, or remote sensing. When determining stage dates from local observations, the following guidelines may be helpful.

Effective full cover for annual vegetation is generally considered to occur when the leaves of plants in adjacent rows intermingle such that near-complete soil shading occurs near solar noon, or when the plants reach nearly full size if there is no intermingling and the plant cover is $> 75\%$ [57.81]. Incomplete ground cover may occur due to reductions in plant growth caused by disease, grazing, pests, soil water stress, or cultural practices that call for vegetation-free strips between crop rows.

Because it is difficult to visually determine when dense vegetation such as grasses and cereals have reached effective full cover, the more easily detectable stage of heading has been used [57.81]. For dense grasses, effective full cover will occur at a height of about 0.10–0.15 m. For thin stands of grass (dry rangeland), the grass height may approach 0.3–0.5 m before effective full cover is reached. Densely planted forages reach effective full cover at a height of about 0.3–0.4 m. For many agricultural plants, effective full cover is considered to occur when the leaf area index (LAI) approaches 3.0 [57.81, 88, 104, 113, 114].

57.3.10 Remote Sensing for Estimating Evapotranspiration

Techniques for determining E and ET from both local and large areas using the energy balance and ground-based, aerial, and satellite imaging have been available since about 1990 [57.76, 115–125]. Remote-sensing techniques are inference techniques, rather than direct measurements of ET. The emerging field of energy balance determination using satellite imaging is showing substantial promise, and has already been used to quantify and demonstrate the variance in ET for the same vegetation type, and even to refine crop (or cover) coefficient curves [57.76, 125–127]. Remotely sensed energy-balance techniques are useful for identifying areas that are experiencing water stress and the corresponding reductions in ET. The use of thermal imaging by satellite systems to estimate [57.120, 123] the stress-limited ET and the ability of satellites to view the signatures of evaporation from wet soil are reviewed in [57.128, 129]. Those reviews discuss the constraints caused by the resolution of satellite images and derived

ET images. The Landsat system currently provides the highest-resolution images (pixel size: 30 m), repeat coverage, and thermal images. 16 day return coverage is needed to follow the evolution of vegetation development and increases or decreases in water stress. The Landsat thermal archive covers a period of more than 35 years, beginning in 1982.

Many satellite-based energy-balance models for determining ET solve (57.7) for Q_E or solve (57.39) for Q_H [57.76, 116, 119, 126, 129, 130]. For example, the remote-sensing-based models SEBAL (Surface Energy Balance Algorithms for Land) [57.116, 131] and METRIC (Mapping Evapotranspiration at High Resolution Using Internalized Calibration) [57.124, 125] apply (57.39), estimating the difference $T_s - T_a$ or $\theta_{T2} - \theta_{T1}$ by indexing to the surface temperature: $\theta_{T2} - \theta_{T1} = a + bT_s$, where a and b are empirical coefficients that depend on the satellite image date and T_s is the surface temperature for each pixel in the satellite image. The relationship between $\theta_{T2} - \theta_{T1}$ and T_s is established in SEBAL and METRIC by inverse calibration under extreme (wet and dry) conditions to reduce the impact of biases in the estimates for net radiation, soil heat flux, and other parameters [57.124, 132, 133].

Other remote-sensing models apply the PM equation (57.32), estimating resistance parameters from vegetation indices and obtaining the vapor pressure deficit terms from weather measurements and iteration [57.134–136]. The advantage of the PM equation and other models is that they can be applied using routine hourly or daily weather data. This has several notable benefits: it incorporates the effects of precipitation and changing weather conditions on the total aggregated ET, and such data can be coupled with soil water balances to provide feedback on the water available for the ET process. On the other hand, a disadvantage of soil- and weather-based process models is the need to parameterize these models for large areas with wide variations in vegetation and surface conductance, water availability, and boundary-layer characteristics (air temperature, humidity, and wind speed). Biases in estimates are commonplace. Generally, the remotely sensed information is provided by satellites, given their vast surface coverage.

Consistent satellite coverage at moderate resolution (< 50 m pixel sizes) is generally only available from polar-orbiting satellites such as Landsat, Sentinel 2 SPOT (Satellite Pour l'Observation de la Terre), and QuickBird, so each location is imaged rather infrequently. Generally, the greater the spatial resolution (i.e., the smaller the pixel size), the longer the revisit time. On its own, such infrequent coverage may be insufficient to estimate the time-integrated ET [57.124]. However, even infrequent satellite imaging can greatly

improve estimates of surface albedo, surface temperature, surface roughness, and the partitioning of surface energy between latent and sensible heat fluxes. Coupling such data with an hourly or daily ET process model that may be based on the reference ET can markedly enhance the accuracy of the estimates provided by the model. The use of airborne thermal data for surface energy balance computations is becoming more prevalent [57.137, 138].

Remotely sensed measurements of surface reflectance and temperature were used in [57.139] to improve estimates of percent vegetation cover and canopy resistance before applying the PM equation to partially vegetated fields. The PM equation was combined with the energy balance equation to estimate the T_s values of surfaces characterized by full-cover vegetation and bare soil under potential and zero-evaporation conditions. T_s values from satellite data were linearly interpolated between full-cover and bare-soil conditions to provide information for intermediate states. Maps of surface air temperature and wind speed were combined with maps of surface temperature and spectral vegetation index to produce regional estimates of evaporation rates for a grassland biome.

The development of the two-source patch model TSEB (Two Source Energy Balance), which utilizes radiometric surface temperature inputs from satellites, surface reflectance, and vegetation indices to estimate ET from sparse canopies, is described in [57.119–123, 140].

The Mapping Evapotranspiration at High Resolution Using Internalized Calibration (METRIC) model [57.124] and its counterpart based on the Google Earth Engine, EEFlux (Earth Engine Flux), apply a full-surface energy balance to image products from thermally equipped satellites such as Landsat, MODIS (Moderate Resolution Imaging Spectroradiometer), and VIIRS (Visible Infrared Imaging Radiometer Suite, Chap. 42) to develop images of the fraction of alfalfa-reference ET, which are interpolated between satellite image dates using a spline function and then multiplied by the daily ET_r to produce time series of daily and monthly ET. Satellite-based mapping of ET provides valuable spatial information on within-field and field-to-field variations in ET [57.126, 133, 137, 138, 140], which will be increasingly utilized in water rights management, water transfers, and streamflow depletion studies, as well as to inform other ET models.

Equations (57.7) and (57.39) are commonly used in ground-based research studies to estimate ET. The technique works best for surfaces with uniform vegetation, where measurements of Q_s^* and Q_G are representative of the source areas of Q_H and Q_E . Additional challenges are associated with the measurement of T_s , as there are directional effects due to the position of the sun and

shading that complicate bulk surface temperature determination.

Simpler, easy-to-apply approaches have been used to estimate the basal K_{cb} or a mean value for K_c based on vegetation indices such as the normalized difference vegetation index (NDVI). The resulting K_{cb} or K_c is then multiplied by a ground-based calculation of ET_{ref} . Examples include [57.141–144]. One challenge when using direct vegetation indices to estimate ET is to detect the effects of soil water shortages, as these tend to reduce ET but may not affect the NDVI.

57.4 Devices and Methods

This section describes devices and methods associated with the determination of evaporation and evapotranspiration. More detailed discussions of these devices and methods are provided in other chapters. For eddy-covariance system measurements, see Chap. 55; for lysimeter measurements, see Chap. 58; for chamber measurements, see Chaps. 59 and 60; and for aerodynamic and modified Bowen ratio systems, see Chap. 54.

57.4.1 Measurement Devices

Specifications for measuring air temperature and near-surface humidity are covered in Chaps. 7 and 8. For the localized determination of evapotranspiration (ET), temperature and humidity measurements must be performed in the near-surface layer, where gradients are in equilibrium with the fluxes from the surface (Chap. 1). In other words, fluxes in the near-surface equilibrium layer should be constant in the vertical and horizontal directions, which requires sufficient fetch of a relatively uniform surface. This also applies to temperature, humidity, and wind velocity (Chap. 9) measurements used in the Penman and PM equations, where the measurements should reflect the flux characteristics of the surface, as described earlier. Some of the station types described in Chap. 43—mainly agrometeorological stations—can be employed for ET calculations. Compact sensors can also be used if the requirements for the measurement height are fulfilled.

Specifications for measurements of net radiation and ground heat flux are discussed in Chaps. 11 and 61. For these measurements, there must be a sufficient number of sensors to develop weighted averages of measurements that can highlight any heterogeneities in the vegetation and surface. Heterogeneities are caused by variations in vegetation densities and types in natural

57.3.11 Standardization

The American Society of Civil Engineers (ASCE) has standardized the calculation of the reference ET via the ASCE Penman–Monteith equation [57.74], utilizing most of the parameterizations from the international standardizations outlined by the Food and Agriculture Organization in FAO 56 [57.2]. Similar standards have been adopted in Germany by the Association of German Engineers [57.145] and the German Water Association [57.146].

systems and canopy variations in agricultural systems such as row architectures. For forested systems, net radiometers should be elevated well above the canopies, and the use of multiple sensors is recommended to obtain averages and to facilitate intercomparisons for error checking (see Chaps. 2 and 3). Ground heat flux sensors should be used in even greater numbers in heterogeneous systems since they provide point measurements. Sensor measurements should be weighted according to vegetation type and cover and the level of shading. Any systematic biases in net radiation and ground heat flux measurements will translate into direct systematic errors in latent heat fluxes determined by the Bowen ratio method, the eddy-covariance method (with forced closure), the Penman and Penman–Monteith equations, and residual methods such as (57.7).

Generally, it is best to carry out the measurements performed using the methods described in this section on an hourly basis (or even more frequently), so that the hourly variations in radiation, air temperature and humidity, wind speed, and ground conduction remain synchronized. For example, the air temperature and vapor pressure deficit often increase in the afternoon, when wind speeds are also larger. These parameters are often multiplicative in the methods described here. That said, although many of the methods are nonlinear, the use of daily or daytime averages for weather data can often provide sufficiently accurate estimates for evapotranspiration [57.74].

57.4.2 Class A Pan

The US Class A pan [57.17] is a round pan with a water surface area of 1.14 m² (diameter 120.65 cm, height 25.4 cm) (Sect. 57.3.1). The water should be 15.2–17.8 m deep; if it is not, the water level must be corrected. The water depth is measured in a cylinder connected to the water body, so that the measurements



Fig. 57.6 Class A pan with a cylinder to measure the water level; temperature and wind sensors are also present (photo provided courtesy of the Hong Kong Observatory of HKSAR)

are not affected by an uneven water surface. The height of the water level in the connected cylinder is measured using a needle connected to a micrometer screw gauge. Electrical systems are also available. The US Class A pan is shown in Fig. 57.6. Instruments for performing the required accompanying wind and temperature measurements are also visible in the figure. Measurements from an accurate rain gauge are necessary to correct the gross pan measurements. Additional maintenance precautions and physical effects are described in Sect. 57.6.1.

57.4.3 Bowen Ratio System

The Bowen ratio system consists of ventilated temperature (Chap. 7) and humidity (Chap. 8) sensors at two levels. Additional wind measurements at both levels are also recommended as a means to monitor

57.5 Specifications

The characteristics of the three primary measurement methods other than eddy covariance (Chap. 55) are summarized in Tables 57.10–57.12. The errors associated with the Bowen ratio and residual methods are evaluated assuming that the net radiometer measure-

57.6 Quality Control

Generally, all of the quality control procedures for sensors that are used to determine evapotranspiration are applicable to the methods of this chapter.

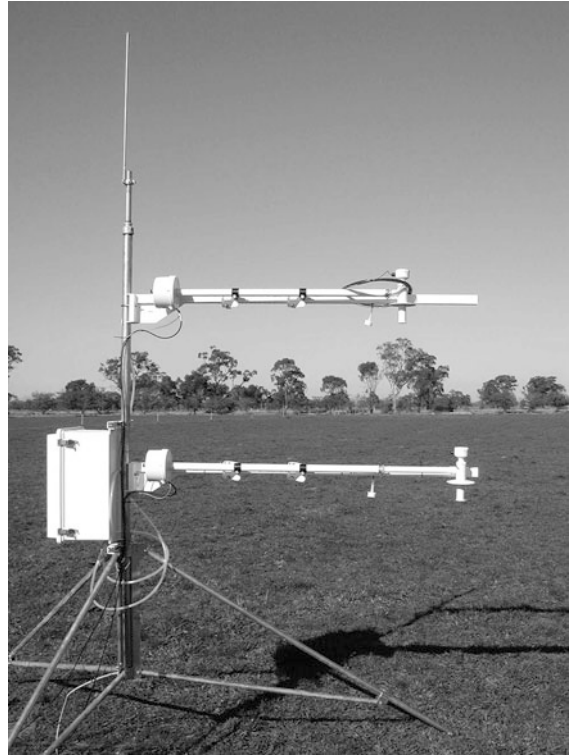


Fig. 57.7 Bowen ratio measurement system (photo © Campbell Scientific, Inc.)

the atmospheric turbulence [57.31]. A net radiometer (Chap. 11), soil temperature sensors, soil moisture sensors, and heat flux plates (Chap. 61) are also required. A commercially available instrument is shown in Fig. 57.7. The distance between the two levels should be as large as possible, but the lowest level should be at least 20 cm above the plant surface and the upper level should be below any possible internal boundary layers (Chap. 1 and Sect. 57.6.2).

ments are accurate (Chap. 11). Furthermore, the heat storage in the soil should be calculated very accurately (Chap. 61) to reduce the influence of the residual of the energy balance closure (Chap. 55).

Intercomparisons between instruments in terms of equation inputs and Q_E and Q_H are strongly encouraged. Intercomparisons can detect differences caused

Table 57.10 Characteristics of the three primary measurement methods other than eddy covariance according to Sects. 57.3.2–57.3.4

Criterion	Class A pan	Bowen ratio method [57.31]	Residual of the energy balance
Area of application	Applied research, short-time and continuously running programs		
Personnel required	Technical support	Partly continuous scientific and technical support	
User education required	Knowledge of measurement techniques	Knowledge of micrometeorology and measurement techniques	Knowledge of measurement techniques and radiation and convection physics
Error		10–30% (depending on the micrometeorological conditions, and assuming a closed energy balance)	
Sampling	Daily to weekly	1–10 s	
Time resolution of evapotranspiration	Daily to weekly	10–30 min	
Requirements for application	Grass in the surroundings	Sufficient footprint area, turbulent conditions	Surroundings with a homogeneous surface

Table 57.11 Potential areas of application of the simpler estimation approaches [57.31] according to Sects. 57.3.5–57.3.7

Criterion	Dalton approach	Turc approach	Penman approach	Priestley–Taylor approach
Defining quantity	Potential evaporation from free-water bodies	Potential evaporation from free-water bodies, possibly for well-watered meadows	Potential evaporation from free-water bodies and a reference ET representing well-watered conditions	Potential evaporation from free-water bodies or regional well-watered vegetation in the absence of advection
Area of application	According to the validity of the area-specific constants [57.51]	Mediterranean Sea, Germany (lowlands) with correction factor $k = 1.1$	Universally	Universally
Resolution of input parameters (min)	10–60 averages	10–60 averages	10–60 averages	10–60 averages
Representativeness of the results	(Daily), decadal, and monthly averages	Decadal and monthly averages	(Hourly, daily), decadal, and monthly averages	(Daily), decadal, and monthly averages
Error (%)	20–40	20–40	10–20	10–40

Table 57.12 Potential areas of application of the more complex estimation approaches according to Sects. 57.3.8–57.3.10

Criterion	Penman–Monteith approach [57.31]	AFIB approach	Remote-sensing approach
Defining quantity	Actual, potential, or reference evapotranspiration	Actual, potential, or reference evapotranspiration	Actual or potential evapotranspiration
Area of application	Universally	Universally	Universally
Resolution of input parameters (min)	3–60 averages and extremes	10–60 averages	10–60 averages combined with 24 h weather data
Representativeness of the results	Hourly and daily averages	Hourly and daily averages	Hourly and daily averages
Error (%)	10–30	10–25	10–30

by variations in manufacturer design, fabrication, and calibration, as well as differences between sensors of the same type caused by age, malfunction, or manufacturing variations. Care should be taken to stabilize the uniformity of the surfaces over which the intercomparisons are conducted. Error statistics for intercomparisons are provided in Chaps. 2 and 3.

In addition to intercomparisons, comparisons of measurements with independently derived estimates are encouraged. These include calculations of net radiation from individual shortwave and longwave components, comparisons of measured solar radiation with theoretical clear-sky solar radiation, and estimations of ground heat flux from a ground temperature balance. Remotely

sensed surface temperatures and reflectances can be useful for developing independent comparisons.

57.6.1 Class A Pan

Proper guidelines for the siting and maintenance of evaporation pans are not always followed closely. Care should be taken to locate pans in settings that are not obstructed by buildings, trees, fences, and tall vegetation. The pan should be surrounded by substantial evaporating surfaces such as well-watered grass out to a distance of ≥ 50 m. Some pans have screens placed on them to keep birds and animals from drinking the water. If used, the impact of such a screen on the evaporation rate should be quantified. The side and bottom surfaces of the pan must be kept clean so that they maintain their original reflection characteristics, and the water should be clear, with no turbidity due to dust or algae. Heating devices have been used to keep ice from forming on the pan in the spring and fall, thus facilitating observations during those seasons. When used, the energy input from the heating device should be quantified and used to adjust the calculated evaporation rate accordingly. Pans are sometimes moved to new locations that do not meet the criteria for a representative pan evaporation site. Differences in pan behavior should be monitored by performing the double mass balance or a similar technique [57.147].

57.6.2 Bowen Ratio System

Error analyses for the Bowen ratio method are widely available (see [57.31, 148–150] and references therein). However, many of these investigations have yielded unreasonable or faulty conclusions because they are based on either single measurements or false assumptions. Often, the electrical error of the sensor (about 0.01–0.001 K) is considered but the error associated with the adaptation of the sensor to the surrounding medium and atmosphere (which influence sensor readings through radiation, ventilation, and other effects) is ignored. It is possible to achieve differences of less than 0.05–0.1 K or hPa between sensors that are mounted close together and experience the same meteorological conditions, but this requires considerable effort and attention to measurement techniques and instrument placement. Therefore, errors in atmospheric temperature and humidity measurements are significantly higher than the electrical error alone [57.151].

The error plots given in Fig. 57.7, which are taken from [57.150], are based on an accepted measurement error of ± 0.05 K or hPa. From Fig. 57.7, we can see that an error of 20 or 40% in the Bowen ratio corresponds to an error of about 10 or 20% in the sensible and la-

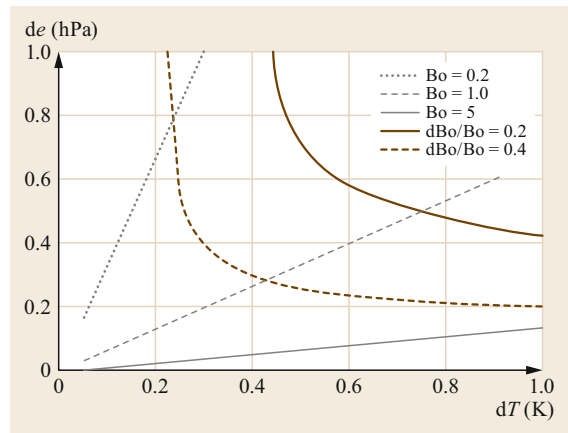


Fig. 57.8 Dependence of the error in the Bowen ratio (20 or 40%) on the measured temperature and water vapor differences (after [57.150] with permission from the Austrian Meteorological Society)

tent heat flux, respectively. Examination of the three Bowen ratio values in Fig. 57.8 shows that the error is smallest when $Bo = 0.667$. To keep the error in the Bowen ratio down to $< 20\%$ ($< 40\%$), temperature and humidity differences must be > 0.6 (> 0.4) K or hPa. This underlines the need for a large distance between the measurement heights. Limitations result from internal boundary layers and possible roughness sublayers, which should be avoided within the measurement range (Chap. 1). Note that in this error analysis, the potential error due to energy imbalances caused by measurement and the estimation error in Q_s^* and Q_G are not taken into account. Utilizing systems that periodically interchange their temperature and humidity sensors can help to remove sensor bias.

57.6.3 Collection of Data for Calculation Methods

As previously discussed, quality control of the measurements used in ET calculation methods must consider the accuracy of the measurement itself and how representative the measurement is of the surface for which ET is calculated. Measurement accuracy is affected by sensor design and functioning as well as by the local environment of the sensor, including the effects of radiation shielding on air temperature measurements and local obstacles that may affect anemometer measurements.

It is important to remember that most ET and energy balance methods assume that the near-surface layer and surface are in equilibrium, so T , q , u , and Q_s^* must be measured over the target surface and with appropriate fetch. In nearly all cases, except for the reference

ET, weather data should be collected under ambient conditions in the equilibrated boundary layer. In dry climates, surface and boundary-layer measurements may exhibit the effects of reduced ET from the surface due to a shortage of soil water. Consequently, the air temperature is elevated and humidity is reduced compared to that above a well-watered surface.

However, the weather measurements performed to calculate the reference ET are somewhat different from those performed to estimate the ET under ambient conditions. For both the grass and alfalfa reference estimates yielded by the standardized PM method, the weather measurements are *expected* to be performed over well-watered clipped grass surfaces. Thus, the calculated ET_{ref} represents the ET rate that is expected to occur from an extensive and well-watered vegetated surface with the near-surface boundary layer in equilibrium, such that the Penman–Monteith combination equation is applicable.

However, meteorological datasets collected from true *reference* settings in agricultural locations are generally difficult to come by. Often, weather stations are located over or adjacent to annual row crops that may undergo a distinct annual growth and cover cycle, or stations may be placed over pasture land that is subject to seasonal deficits in soil moisture or is within the vicinity of small buildings, roadways, or dry airports. Many urban weather stations fail to comply with both the underlying surface requirement and the recommended separation distance from obstacles for reference ET estimation. The failure of a weather station site to meet the defined reference conditions does not preclude the use of the data to estimate ET_{ref} . However, data from such a station should be examined carefully before use, and may in some cases require adjustment to make it more representative of reference

conditions. New weather stations installed for the express purpose of estimating ET_{ref} should be located in sites that closely approximate the reference conditions expected by the PM reference equation. In addition, operators of agricultural weather stations should not be lulled into assuming that T and q measurements collected over small patches of grass, rather than over an extensive fetch, will fulfill the requirements of a reference weather station and produce weather data that accurately reflect the characteristics of the reference surface. These requirements recognize that the ET_{ref} method has been calibrated to utilize reference weather data. Further discussion of weather data quality and the location requirements when calculating ET_{ref} are given in [57.53, 74].

Accurate estimation of the evapotranspiration (ET) requires accurate and representative weather data. Combination equations such as the Penman–Monteith equation are relatively sensitive to the error in the weather data. This sensitivity varies depending on the time of year and the climate. During summer, solar radiation can dominate the ET estimate. Therefore, especially in humid and subhumid climates where the vapor pressure deficit/wind term of the PM is relatively small compared to the radiation term, the error in solar radiation measurements can have the greatest impact on the accuracy of the ET estimate. During wintertime, when there is less solar radiation, the wind speed and vapor pressure deficit can be strong drivers of the accuracy of the ET calculation. Errors in the wind speed and vapor pressure deficit can also dominate in arid and semiarid climates.

Quality assessment and quality control (QA/QC) are discussed for various input measurements in Chaps. 7–9 and 11. In addition, simple and rapid visual assessments of weather data are described in [57.2, 23, 53, 75]. The utilization of these methods is encouraged.

57.7 Maintenance

This section addresses the maintenance of the various sensors that are used to measure and calculate evapotranspiration. Further information on this topic is available in the relevant chapters: Chap. 7 (temperature), Chap. 8 (humidity), Chap. 9 (wind speed and direction), Chap. 11 (radiation), and Chap. 12 (precipitation). For more on combinations of sensors, see Chap. 43. The Class A pan and Bowen ratio measurement systems require system-specific maintenance, as described in Table 57.13.

Table 57.13 Maintenance requirements for the Class A pan and Bowen ratio methods, including the requirements for specific sensors ►

Maximum interval	Class A pan	Bowen ratio system
Daily	Check the water level	
Weekly	Control/cut the vegetation in the surroundings	Check the distance between the vegetation and the lowest measurement level Clean the radiation sensors
Monthly	Clean the pan	
Annually		Calibrate or replace the sensors

57.8 Application

The methods described in this chapter are widely used, and examples of their application can be found in several publications, along with operating and maintenance instructions. The following provides a few examples, primarily of comparisons between methods.

57.8.1 Comparison of the Bowen Ratio Method with the Eddy-Covariance Method and the Penman–Monteith Approach

The Bowen ratio method is based on the energy balance equation (57.3), and it implicitly assumes that the energy balance is closed at the Earth's surface and that the net radiation and soil heat flux measurements are accurate representations. This may not be true in heterogeneous landscapes [57.36]. Furthermore, the Bowen ratio method fails if $Bo = -1$ and (57.4) and (57.5) cannot be solved. Often, such data are replaced with a zero flux or an estimate from a calibrated combination equation, because these cases only occur during transition times in the morning and evening. The variation in the latent heat flux over a grassland over the course of a day obtained with the Bowen ratio method is shown in Fig. 57.9, as are the corresponding latent heat flux measurements provided by the eddy-covariance method. It is obvious that the energy balance is not closed for the site, given that the flux values from the eddy-covariance method are lower than those from the Bowen ratio method.

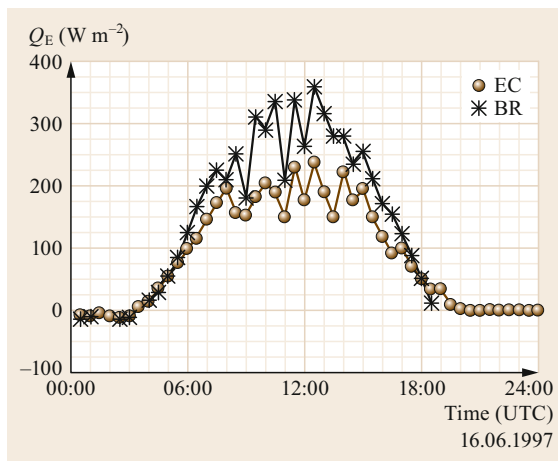


Fig. 57.9 Curves showing the variation in the latent heat flux over a grassland, obtained using the Bowen ratio (BR) and eddy-covariance (EC) methods (after [57.152] with permission from Schweizerbart'sche Verlagsbuchhandlung, Stuttgart, Germany)

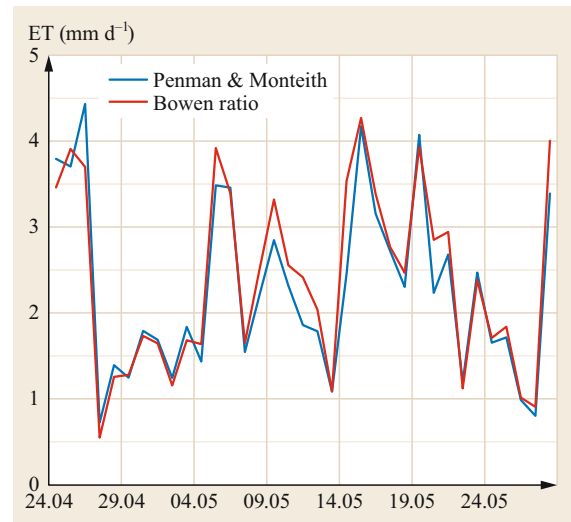


Fig. 57.10 Daily evapotranspiration measured with the Bowen ratio method and calculated with the Penman–Monteith method over a grassland in Bayreuth, Germany (measurements were taken during April to May 2013)

In another example shown in Fig. 57.10, values of the daily evapotranspiration over a grassland over the course of a month are plotted. The values were obtained using either the Bowen ratio method or the Penman–Monteith approach. Because both methods base their estimates on the available energy (the net radiation reduced by the ground heat flux), the fluxes provided by the two methods are clearly similar, and are not independent. Differences between the two methods are mainly caused by the influence of the wind speed on the temperature and the moisture field.

57.8.2 Comparison of the Penman–Monteith Approach with Lysimeter Data

Figure 57.11 shows the variation in the latent heat flux for alfalfa (lucerne) grown in Kimberly (ID, USA) over a number of months, as measured with a weighing lysimeter (Chap. 58) and estimated using the standardized Penman–Monteith method (57.34). Only periods in which the vegetation height was greater than 0.3 m are shown. The PM method was applied using a calculation timestep of 24 h. The correlation between the two datasets is relatively good; both show similar fluctuations over time as the weather varied.

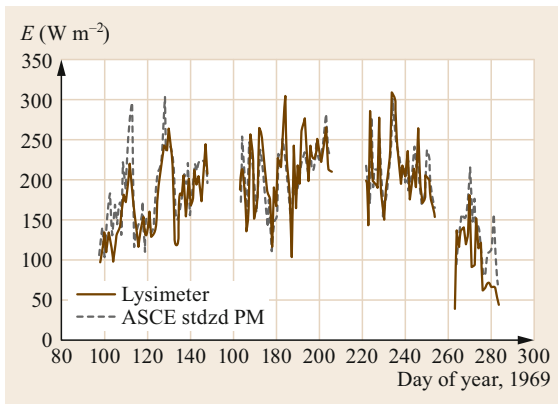


Fig. 57.11 Variation in the latent heat flux for alfalfa (lucerne) grown in Kimberly (ID, USA) over many months, as measured by a weighing lysimeter and estimated using the standardized Penman–Monteith method (57.34). Only periods in which the vegetation was taller than 0.3 m are shown. The PM method was applied using a calculation timestep of 24 h. Data from Dr. J.L. Wright, USDA-ARS ◀

57.9 Future Developments

The remote sensing of evapotranspiration using satellite, aerial (Chap. 42), and UAS (Unmanned Aircraft Systems, Chap. 49) imaging is advancing rapidly and will play a major role in future estimation programs. Satellite-based remote sensing provides high spatial coverage of the globe, and satellites such as Landsat—with its thermal imaging—allow ET to be estimated at the 30 m scale, which is generally sufficient to capture the impacts of human activity on vegetation and water consumption. It is, however, challenging to obtain accurate ET values using remote sensing on its own. Its main strength is its ability to provide the spatial distribution of ET. Ground-based ET and surface energy balance measurements will remain essential for calibrating and verifying remote-sensing procedures, and weather measurements or forecasting will be needed to interpolate ET values between satellite overpasses.

ET determinations using the eddy-covariance method have long been plagued by a lack of energy balance closure (Chap. 55) [57.36]. However, recent improvements in the correction of the transducer-shadow effect of sonic anemometers [57.153, 154] and correction methods [57.37] suggest that substantially improved closure is possible. It is anticipated that further advances will be made.

Evapotranspiration measurement techniques continue to evolve, and the costs of the corresponding systems continue to decrease. With the evolution of low-cost wireless communication systems and the reduced measurement system cost, the deployment of localized networks of ET measurement systems is expected to expand rapidly in the future (see Chap. 45).

57.10 Further Reading

- T. Foken: *Micrometeorology*, 2nd edn. (Springer, Berlin, Heidelberg 2017)
- M.E. Jensen, R.G. Allen (Eds.): *Evaporation, Evapotranspiration, and Irrigation Water Requirements* (ASCE, Reston 2016), <https://doi.org/10.1061/9780784414057>
- VDI3786, Blatt 21: *Umweltmeteorologie – Meteorologische Messungen – Verdunstung (Environmental Meteorology – Meteorological Measurements – Evaporation)* (Beuth, Berlin 2018)
- WMO: *Guide to Instruments and Methods of Observation*, WMO-No. 8, Volume I - Measurement of Meteorological Variables. (World Meteorological Organization, Geneva, 2018)

References

- 57.1 W. Brutsaert: *Hydrology* (Cambridge Univ. Press, Cambridge 2005)
- 57.2 R.G. Allen, L.S. Pereira, D. Raes, M. Smith: *Crop Evaporation – Guidelines for Computing Crop Water Requirements* (FAO, Rome 1998), FAO Irrigation Drainage Paper 56
- 57.3 W.E.K. Middleton: *Invention of the Meteorological Instruments* (The Johns Hopkins Press, Baltimore 1969)
- 57.4 E. Halley: An estimate of the quantity of vapour raised out of the sea by the warmth of the Sun; derived from an experiment shown before the Royal Society, at one of their late meetings, Philos. Trans. R. Soc. **16**, 366–370 (1687)
- 57.5 G.W. Richmann: Atmometri sive machinae hydrostaticae ad evaporationem aquae certae temperie mensurandam aptae constructio talis, ut ope illius decrementum paucorum granorum observari et lex evaporationis confirmari possit, Novi Comment. Acad. Sci. Imp. Petropol. **2**, 121–127 (1749)
- 57.6 G.W. Richmann: Inquisitio in rationem phaenomeni, cur aqua profunda in vasis homogeneae materiae plus evaporet, quam aqua minus profunda et confirmatio experimento nova ratione instituto, Novi Comment. Acad. Sci. Imp. Petropol. **2**, 134–144 (1749)
- 57.7 E. Kleinschmidt (Ed.): *Handbuch der Meteorologischen Instrumente und ihrer Auswertung* (Springer, Berlin 1935)
- 57.8 A. Piche: Note sur l'atmosphère instrument destiné a mesurer l'évaporation, Bull. Hebd. Assoc. Sci. Fr. **10**, 166–168 (1872)
- 57.9 R. Sauermost, D. Freudig (Eds.): *Lexikon der Biologie* (Spektrum Akademischer Verlag, Heidelberg 2006), Gesamtausgabe in 14 Bänden
- 57.10 G. Stanhill: The use of the Piche evaporimeter in the calculation of evaporation, Q. J. R. Meteorol. Soc. **88**, 80–82 (1962)
- 57.11 W. Czeratzki: Ein Verdunstungsmesser mit keramischer Scheibe, Landbauforsch. Völknerode FAL Agric. Res. **18**, 93–98 (1968)
- 57.12 J. Altenhofen: A modified atmometer for on-farm evapotranspiration determination. In: *Proc. Natl. Conf. Adv. Evapotranspiration* (ASAE, St. Joseph 1985) pp. 177–184
- 57.13 F. Chen, P.J. Robinson: Estimating reference crop evapotranspiration with ETgages, J. Irrig. Drain. Eng. **135**, 335–342 (2009)
- 57.14 H.L. Penman: Natural evaporation from open water, bare soil and grass, Proc. R. Soc. A **193**, 120–195 (1948)
- 57.15 W.O. Pruitt, J. Doorenbos: Empirical Calibration, a requisite for evapotranspiration formulae based on daily or longer mean climatic data? In: *Proc. Int. Round Table Conf. Evapotranspiration, Budapest* (1977)
- 57.16 J.L. Wright, M.E. Jensen: Peak water requirements of crops in southern Idaho, J. Irrig. Drain. Div. **96**, 193–201 (1972)
- 57.17 T.P. DeFelice: *An Introduction to Meteorological Instrumentation and Measurement* (Prentice Hall, Upper Saddle River 1998)
- 57.18 E.T. Linacre: Estimating U.S. Class A pan evaporation from climate data, Water Int. **19**, 5–14 (1994)
- 57.19 P.C. Sentelhas, M.V. Folegatti: Class-A pan coefficients (Kp) to estimate daily reference evapotranspiration (ET₀), Rev. Bras. Eng. Agric. Ambient. **7**, 111–115 (2003)
- 57.20 A.G. Smajstrla, F.S. Zazueta, G.A. Clark, D.J. Pitts: *Irrigation Scheduling with Evaporation Pans* (Univ. Florida, Gainesville 2000), IFAS Bulletin 254
- 57.21 M.E. Jensen, R.D. Burman, R.G. Allen: *Evapotranspiration and Irrigation Water Requirements* (ASCE, Reston 1990), ASCE Manuals and Reports on Engineering Practice No. 70
- 57.22 W.J. Shuttleworth: Evaporation. In: *Handbook of Hydrology*, ed. by D.R. Maidment (McGraw-Hill Inc., New York 1992)
- 57.23 R.G. Allen: Assessing the integrity of weather data for use in reference evapotranspiration, J. Irrig. Drain. Eng. **122**, 97–106 (1996)
- 57.24 J. Doorenbos, W.O. Pruitt: *Guidelines for Predicting Crop Water Requirements*, 2nd edn. (FAO, Rome 1977), FAO Irrigation Drainage Paper 24
- 57.25 A.A. Young: *Evaporation from Water Surfaces in California: A Summary of Pan Records and Coefficients 1881 to 1946* (California State Printing Office, Sacramento 1947), Bulletin No. 54
- 57.26 L.A. Ramdas: Evaporation and potential evapotranspiration over the Indian sub-continent, Indian J. Agric. Sci. **27**, 137–149 (1957)
- 57.27 W.O. Pruitt: Relation of consumptive use of water to climate, Transactions ASAE **3**, 9–13 (1960)
- 57.28 W.O. Pruitt: Empirical method of estimating evapotranspiration using primarily evaporation pans. In: *Proc. Conf. Evapotranspiration Its Role Water Resour. Manag.*, ed. by M.E. Jensen (ASAE, St. Joseph 1966) pp. 57–61
- 57.29 Department of Water Resources: *Vegetative Water Use in California, 1974* (CDWR, Sacramento 1975), DWR-Bulletin No. 113–3
- 57.30 G.P. Srivastava: *Surface Meteorological Instruments and Measurement Practices* (Atlantic Publishers & Dist, New Delhi 2009)
- 57.31 T. Foken: *Micrometeorology*, 2nd edn. (Springer, Berlin, Heidelberg 2017)
- 57.32 C. Bernhofer: Estimating forest evapotranspiration at a non-ideal site, Agric. For. Meteorol. **60**, 17–32 (1992)
- 57.33 A.G. Barr, K.M. King, T.J. Gillespie, G.D. Hartog, H.H. Neumann: A comparison of Bowen ratio and eddy correlation sensible and latent heat flux measurements above deciduous forest, Bound.-Layer Meteorol. **71**, 21–41 (1994)
- 57.34 W.O. Pruitt, E. Fereres, K. Kaita, R.L. Snyder: *Reference Evapotranspiration (ET₀) for California* 1987, Agriculture and Experiment Station Bulletin 1922

- 57.35 A. Ohmura: Objective criteria for rejecting data for Bowen ratio flux calculations, *J. Clim. Appl. Meteorol.* **21**, 595–598 (1982)
- 57.36 T. Foken: The energy balance closure problem – An overview, *Ecol. Appl.* **18**, 1351–1367 (2008)
- 57.37 M. Mauder, T. Foken, J. Cuxart: Surface energy balance closure over land: A review, *Bound.-Layer Meteorol.* **177**, 395–426 (2020)
- 57.38 R.L. Snyder, P.W. Brown, K.G. Hubbard, S.J. Meyer: A guide to automated weather station networks in North America. In: *Advances in Bioclimatology*, Vol. 4, ed. by G. Stanhill (Springer, Berlin 1996) pp. 1–61
- 57.39 H. Liu, G. Peters, T. Foken: New equations for sonic temperature variance and buoyancy heat flux with an omnidirectional sonic anemometer, *Bound.-Layer Meteorol.* **100**, 459–468 (2001)
- 57.40 P. Schotanus, F.T.M. Nieuwstadt, H.A.R. DeBruin: Temperature measurement with a sonic anemometer and its application to heat and moisture fluctuations, *Bound.-Layer Meteorol.* **26**, 81–93 (1983)
- 57.41 P.S. Eagleson: Climate, soil, and vegetation: 1. Introduction to water balance dynamics, *Water Resour. Res.* **14**, 705–712 (1978)
- 57.42 L. Mahrt: The bulk aerodynamic formulation over heterogeneous surfaces, *Bound.-Layer Meteorol.* **78**, 87–119 (1996)
- 57.43 J.R. Schott, S.J. Hook, J.A. Barsi, B.L. Markham, J. Miller, F.P. Padula, N.G. Raqueno: Thermal infrared radiometric calibration of the entire Landsat 4, 5, and 7 archive (1982–2010), *Remote Sens. Environ.* **122**, 41–49 (2012)
- 57.44 G.N. Panin, T. Foken: Air–sea interaction including a shallow and coastal zone, *J. Atmos. Ocean Sci.* **10**, 289–305 (2005)
- 57.45 W.H. Brutsaert: *Evaporation into the Atmosphere: Theory, History and Application* (D. Reidel, Dordrecht 1982)
- 57.46 D. Richter: *Zur einheitlichen Berechnung der Wassertemperatur und der Verdunstung von freien Wasserflächen auf statistischer Grundlage*, Abhandlungen des Meteorologischen Dienstes der Deutschen Demokratischen Republik, Vol. 119 (Akademie-Verlag, Berlin 1977)
- 57.47 C.H.B. Priestley, J.R. Taylor: On the assessment of surface heat flux and evaporation using large-scale parameters, *Mon. Weather Rev.* **100**, 81–92 (1972)
- 57.48 R.B. Stull: *An Introduction to Boundary Layer Meteorology* (Kluwer, Dordrecht 1988)
- 57.49 H.A.R. DeBruin: A model for the Priestley–Taylor parameter α , *J. Clim. Appl. Meteorol.* **22**, 572–578 (1983)
- 57.50 S.P. Arya: *Introduction to Micrometeorology* (Academic Press, San Diego 2001)
- 57.51 DVWK: *Ermittlung der Verdunstung von Land- und Wasserflächen* (DWA, Hennef 1996), DVWK-Merkblätter zur Wasserwirtschaft 238
- 57.52 C.H.M. van Bavel: Potential evapotranspiration: The combination concept and its experimental verification, *Water Resour. Res.* **2**, 455–467 (1986)
- 57.53 M.E. Jensen, R.G. Allen (Eds.): *Evaporation, Evapotranspiration, and Irrigation Water Requirements* (ASCE, Reston 2016), <https://doi.org/10.1061/9780784414057>
- 57.54 D. Hillel: *Environmental Soil Physics* (Academic Press, New York 1998)
- 57.55 H. Dommermuth, W. Trampf: *Die Verdunstung in der Bundesrepublik Deutschland, Zeitraum 1951–1980, Teil 1* (DWD, Offenbach 1990)
- 57.56 H. Schrödter: *Verdunstung, Anwendungsorientierte Meßverfahren und Bestimmungsmethoden* (Springer, Berlin, Heidelberg 1985)
- 57.57 L. Turc: Evaluation des besoins en eau d'irrigation évapotranspiration potentielle, *Ann. Agron.* **12**, 13–49 (1961)
- 57.58 H.A.R. DeBruin, A.A.M. Holtslag: A simple parametrization of the surface fluxes of sensible and latent heat during daytime compared with the Penman–Monteith concept, *J. Clim. Appl. Meteorol.* **21**, 1610–1621 (1982)
- 57.59 J.L. Monteith: Evaporation and environment, *Symp. Soc. Exp. Biol.* **19**, 205–234 (1965)
- 57.60 B.B. Hicks, D.D. Baldocchi, T.P. Meyers, R.P. Hosker Jr., D.R. Matt: A preliminary multiple resistance routine for deriving dry deposition velocities from measured quantities, *Water Air Soil Pollut.* **36**, 311–330 (1987)
- 57.61 G. Kramm, M. Beier, T. Foken, H. Müller, P. Schröder, W. Seiler: A SVAT scheme for NO, NO₂, and O₃ – Model description and test results, *Meteorol. Atmos. Phys.* **61**, 89–106 (1996)
- 57.62 G. Schädler, N. Kalthoff, F. Fiedler: Validation of a model for heat, mass and momentum exchange over vegetated surfaces using LOTREX-10E/HIBE88 data, *Contrib. Atmos. Phys.* **63**, 85–100 (1990)
- 57.63 P.J. Sellers, J.L. Dorman: Testing the simple biosphere model (SiB) for use in general circulation models, *J. Clim. Appl. Meteorol.* **26**, 622–651 (1987)
- 57.64 G. Groß: *Numerical Simulation of Canopy Flows* (Springer, Berlin, Heidelberg 1993)
- 57.65 E.M. Gusev, O.N. Nasonova: *Modelirovanie Teplo- i Vлагообмена Poverchnosti Sush' s Atmosferoj (Modelling of the Heat and Moisture Exchange of Land Surfaces with the Atmosphere)* (Nauka, Moskva 2010)
- 57.66 A.K. Blackadar: *Turbulence and Diffusion in the Atmosphere* (Springer, Berlin, Heidelberg 1997)
- 57.67 J.C. Kaimal, J.J. Finnigan: *Atmospheric Boundary Layer Flows: Their Structure and Measurement* (Oxford Univ. Press, New York 1994)
- 57.68 J.R. Garratt: *The Atmospheric Boundary Layer* (Cambridge Univ. Press, Cambridge 1992)
- 57.69 I. Alves, A. Perrier, L. Pereira: Aerodynamic and surface resistances of complete cover crops: How good is the 'Big Leaf'?, *Transactions ASAE* **41**, 345–351 (1998)
- 57.70 O.T. Denmead: Plant physiological methods for studying evapotranspiration: Problems of telling the forest from the trees, *Agric. Water Manag.* **8**, 167–189 (1984)

- 57.71 J.B. Stewart: A discussion of the relationships between the principal forms of the combination equation for estimating crop evaporation, *Agric. Meteorol.* **30**, 111–127 (1983)
- 57.72 R.G. Allen, W.O. Pruitt, J.L. Wright, T.A. Howell, F. Ventura, R. Snyder, D. Itenfisu, P. Steduto, J. Berengena, J.B. Yrisarry, M. Smith, L.S. Pereira, D. Raes, A. Perrier, I. Alves, I. Walter, R. Elliott: A recommendation on standardized surface resistance for hourly calculation of reference ET_0 by the FAO56 Penman–Monteith method, *Agric. Water Manag.* **81**, 1–22 (2006)
- 57.73 A.F. Moene, J.C. van Dam: *Transport in the Atmosphere–Vegetation–Soil Continuum* (Cambridge Univ. Press, Cambridge 2014)
- 57.74 ASCE: *The ASCE Standardized Reference Evapotranspiration Equation. Task Committee on Standardized Calculation of Reference Evapotranspiration Calculation* (EWRI, Reston 2005)
- 57.75 R.G. Allen, I.A. Walter, R. Elliott, T. Howell, D. Itenfisu, M. Jensen: *The ASCE Standardized Reference Evapotranspiration Equation* (EWRI, Reston 2005)
- 57.76 R.G. Allen, M. Tasumi, A. Morse, R. Trezza, J.L. Wright, W. Bastiaanssen, W. Kramber, I. Lorite, C.W. Robison: Satellite–based energy balance for mapping evapotranspiration with internalized calibration (METRIC)–Applications, *J. Irrig. Drain. Eng.* **133**, 395–406 (2007)
- 57.77 G.G. Katul, M.B. Parlange: A Penman–Brutsaert model for wet surface evaporation, *Water Resour. Res.* **28**, 121–126 (1992)
- 57.78 B.J. Choudhury, S.B. Idso, R.J. Reginato: Analysis of an empirical model for soil heat flux under a growing wheat crop for estimating evaporation by an infrared–temperature based energy balance equation, *Agric. For. Meteorol.* **39**, 283–297 (1987)
- 57.79 R.G. Allen, W.O. Pruitt, J.A. Businger, L.J. Fritschen, M.E. Jensen, F.H. Quinn (Eds.): Evaporation and transpiration. In: *ASCE Handbook of Hydrology*, 2nd edn. (ASCE, New York 1996), Chap. 4
- 57.80 M.E. Jensen: Water consumption by agricultural plants. In: *Water Deficits and Plant Growth* (Academic Press, New York 1968), Chap. 1
- 57.81 J.L. Wright: New evapotranspiration crop coefficients, *J. Irrig. Drain. Div.* **108**, 57–74 (1982)
- 57.82 R.G. Allen, T.A. Howell, W.O. Pruitt, I.A. Walter, M.E. Jensen (Eds.): Lysimeters for evapotranspiration and environmental measurements. In: *Proc. Int. Symp. Lysimetry* (ASCE, Reston 1991)
- 57.83 R.G. Allen, L.S. Pereira, T.A. Howell, M.E. Jensen: Evapotranspiration information reporting: I. Factors governing measurement accuracy, *Agric. Water Manag.* **98**, 899–920 (2011)
- 57.84 J.L. Wright: Crop coefficients for estimates of daily crop evapotranspiration. In: *Proc. Irrig. Sched. Conf* (ASAE, St. Joseph 1981) pp. 16–26
- 57.85 J.A. Tolck, T.A. Howell: Measured and simulated evapotranspiration of grain sorghum with full and limited irrigation in three high plains soils, *Transactions ASAE* **44**, 1553–1557 (2001)
- 57.86 T.A. Howell, S.R. Evett, J.A. Tolck, A.D. Schneider: Evapotranspiration of full–, deficit–irrigated, and dryland cotton on the Northern Texas High Plains, *J. Irrig. Drain. Eng.* **130**, 277–285 (2004)
- 57.87 T.A. Howell, D.A. Dusek, J.A. Tolck, K.S. Copeland, P.D. Colaizzi, S.R. Evett: Crop coefficients developed at bushland, Texas for corn, wheat, sorghum, soybean, cotton, and alfalfa. In: *Proc. World Environ. Water Resour. Congress 2006* (EWRI, Reston 2006)
- 57.88 J.T. Ritchie: Model for predicting evaporation from a row crop with incomplete cover, *Water Resour. Res.* **8**, 1204–1213 (1972)
- 57.89 J.R. Philip: Evaporation, and moisture and heat fields in the soil, *J. Meteorol.* **14**, 354–366 (1957)
- 57.90 T.A. Black, W.R. Gardner, G.W. Thurtell: The prediction of evaporation, drainage, and soil water storage for a bare soil, *Soil Sci. Soc. Am. J.* **33**, 655–660 (1969)
- 57.91 S.B. Idso, R.J. Reginato, R.D. Jackson, B.A. Kimball, F.S. Nakayama: The three stages of drying of a field soil, *Soil Sci. Soc. Am. J.* **38**, 831–837 (1974)
- 57.92 J.T. Ritchie, J.E. Adams: Field measurement of evaporation from soil shrinkage cracks, *Soil Sci. Soc. Am. J.* **38**, 131–134 (1974)
- 57.93 C.M. Burt, A. Mutziger, D.J. Howes, K.H. Solomon: *Evaporation from Irrigated Agricultural Land in California* (ITRC, San Luis Obispo 2002), ITRC Report No. 02–001
- 57.94 J.T. Ritchie, D.C. Godwin, U. Singh: Soil and weather inputs for the IBSNAT crop models. In: *Proc. IBNAT Symp. Decis. Support Syst. Agrotechnol. Transf. Part 1* (Univ. Hawaii, Honolulu 1989) pp. 31–45
- 57.95 R.G. Allen, L.S. Pereira, M. Smith, D. Raes, J.L. Wright: FAO–56 dual crop coefficient method for estimating evaporation from soil and application extensions, *J. Irrig. Drain. Eng.* **131**, 2–13 (2005)
- 57.96 R.G. Allen: Skin layer evaporation to account for small precipitation events—An enhancement to the FAO–56 evaporation model, *Agricultural Water Management* **99**(1), 8–18 (2011)
- 57.97 J. Doorenbos, A.H. Kassam: *Yield Response to Water*, 2nd edn. (FAO, Rome 1979), FAO Irrigation Drainage Paper 33
- 57.98 D. Raes, P. Steduto, T.C. Hsiao, E. Fereres: AquaCrop—The FAO crop model to simulate yield response to water: II. Main algorithms and software description, *Agron. J.* **101**, 438–447 (2009)
- 57.99 L.F. Ratliff, J.T. Ritchie, D.K. Cassel: Field–measured limits of soil water availability as related to laboratory–measured properties, *Soil Sci. Soc. Am. J.* **47**, 770–775 (1983)
- 57.100 R.G. Allen, L.S. Pereira: Estimating crop coefficients from fraction of ground cover and height, *Irrig. Sci.* **28**, 17–34 (2009)
- 57.101 J.T. Ritchie: Evaluating irrigation needs for southeastern U.S.A. In: *Spec. Conf. Contrib. Irrig. Drain. World Food Supply* (ASCE, New York 1975) pp. 262–279

- 57.102 J. Ringersma, A.F.S. Sikkink: Determining transpiration coefficients of Sahelian vegetation barriers, *Agrofor. Syst.* **51**, 1–9 (2001)
- 57.103 K. Descheemaeker, D. Raes, R. Allen, J. Nyssen, J. Poesen, B. Muys, M. Haile, J. Deckers: Two rapid appraisals of FAO–56 crop coefficients for semi-arid natural vegetation of the northern Ethiopian highlands, *J. Arid Environ.* **75**, 353–359 (2011)
- 57.104 J.T. Ritchie, D.S. Nesmith: Temperature and crop development. In: *Modeling Plant and Soil Systems*, Agronomy Monographs, Vol. 31, ed. by R.J. Hanks, J.T. Ritchie (ASA, Madison 1991) pp. 5–29
- 57.105 T.R. Sinclair: Leaf area development in field-grown soybeans, *Agron. J.* **76**, 141–146 (1984)
- 57.106 R.L. Snyder, D. Spano, C. Cesaraccio, P. Duce: Determining degree-day thresholds from field observations, *Int. J. Biometeorol.* **42**, 177–182 (1999)
- 57.107 C. Cesaraccio, D. Spano, P. Duce, R.L. Snyder: An improved model for determining degree-day values from daily temperature data, *Int. J. Biometeorol.* **45**, 161–169 (2001)
- 57.108 J.E. Ayars, R.B. Hutmacher, R.A. Schoneman, R.W.O. Soppe, S.S. Vail, F. Dale: Realizing the potential of integrated irrigation and drainage water management for meeting crop water requirements in semi-arid and arid areas, *Irrig. Drain. Syst.* **13**, 321–347 (1999)
- 57.109 K. Djaman, S. Irmak: Actual crop evapotranspiration and alfalfa- and grass-reference crop coefficients of maize under full and limited irrigation and rainfed conditions, *J. Irrig. Drain. Eng.* **139**, 433–446 (2013)
- 57.110 S. Irmak, I. Kabenge, D. Rudnick, S. Knezevic, D. Woodward, M. Moravek: Evapotranspiration crop coefficients for mixed riparian plant community and transpiration crop coefficients for common reed, cottonwood and peach-leaf willow in the Platte River Basin, Nebraska–USA, *J. Hydrol.* **481**, 177–190 (2013)
- 57.111 A. Martínez-Cob: Use of thermal units to estimate corn crop coefficients under semiarid climatic conditions, *Irrig. Sci.* **26**, 335–345 (2008)
- 57.112 G. Piccinni, J. Ko, T. Marek, T. Howell: Determination of growth-stage-specific crop coefficients (Kc) of maize and sorghum, *Agric. Water Manag.* **96**, 1698–1704 (2009)
- 57.113 S. Kang, B. Gu, T. Du, J. Zhang: Crop coefficient and ratio of transpiration to evapotranspiration of winter wheat and maize in a semi-humid region, *Agric. Water Manag.* **59**, 239–254 (2003)
- 57.114 B. Duchemin, R. Hadria, S. Erraki, G. Boulet, P. Maisongrande, A. Chehbouni, R. Escadafal, J. Ezzahar, J.C.B. Hoedjes, M.H. Kharrou, S. Khabba, B. Mougenot, A. Olioso, J.C. Rodriguez, V. Simonneaux: Monitoring wheat phenology and irrigation in central Morocco: On the use of relationships between evapotranspiration, crops coefficients, leaf area index and remotely-sensed vegetation indices, *Agric. Water Manag.* **79**, 1–27 (2006)
- 57.115 J.L. Hatfield: Wheat canopy resistance determined by energy balance techniques, *Agron. J.* **77**, 279–283 (1985)
- 57.116 W.G.M. Bastiaanssen, M. Menenti, R.A. Feddes, A.A.M. Holtlag: A remote sensing surface energy balance algorithm for land (SEBAL). 1. Formulation, *J. Hydrol.* **212/213**, 198–212 (1998)
- 57.117 W.G.M. Bastiaanssen, H. Pelgrum, J. Wang, Y. Ma, J.F. Moreno, G.J. Roerink, T. van der Wal: A remote sensing surface energy balance algorithm for land (SEBAL). 2. Validation, *J. Hydrol.* **212/213**, 213–229 (1998)
- 57.118 M.C. Anderson, J.M. Norman, G.R. Diak, W.P. Kustas, J.R. Mecikalski: A two-source time-integrated model for estimating surface fluxes using thermal infrared remote sensing, *Remote Sens. Environ.* **60**, 195–216 (1997)
- 57.119 M.C. Anderson, J.M. Norman, W.P. Kustas, F. Li, J.H. Prueger, J.R. Mecikalski: Effects of vegetation clumping on two-source model estimates of surface energy fluxes from an agricultural landscape during SMACEX, *J. Hydrometeorol.* **6**, 892–909 (2005)
- 57.120 W.P. Kustas, J.M. Norman: Evaluation of soil and vegetation heat flux predictions using a simple two-source model with radiometric temperatures for partial canopy cover, *Agric. For. Meteorol.* **94**, 13–29 (1999)
- 57.121 W.P. Kustas, J.M. Norman, M.C. Anderson, A.N. French: Estimating subpixel surface temperatures and energy fluxes from the vegetation index–radiometric temperature relationship, *Remote Sens. Environ.* **85**, 429–440 (2003)
- 57.122 F. Li, W.P. Kustas, J.H. Prueger, C.M.U. Neale, T.J. Jackson: Utility of remote sensing-based two-source energy balance model under low- and high-vegetation cover conditions, *J. Hydrometeorol.* **6**, 878–891 (2005)
- 57.123 J.M. Norman, M.C. Anderson, W.P. Kustas, A.N. French, J. Mecikalski, R. Torn, G.R. Diak, T.J. Schmugge, B.C.W. Tanner: Remote sensing of surface energy fluxes at 10¹-m pixel resolutions, *Water Resour. Res.* **39**, 1221 (2003)
- 57.124 R.G. Allen, M. Tasumi, R. Trezza: Satellite-based energy balance for mapping evapotranspiration with internalized calibration (METRIC)–Model, *J. Irrig. Drain. Eng.* **133**, 380–394 (2007)
- 57.125 A. Irmak, R.G. Allen, J. Kjaersgaard, J. Huntington, B. Kamble, R. Trezza, I. Ratcliffe: Operational remote sensing of ET and challenges. In: *Evapotranspiration, Remote Sensing and Modeling*, ed. by A. Irmak (IntechOpen, London 2012) pp. 467–492
- 57.126 M. Tasumi, R.G. Allen, R. Trezza, J.L. Wright: Satellite-based energy balance to assess within-population variance of crop coefficient curves, *J. Irrig. Drain. Eng.* **131**, 94–109 (2005)
- 57.127 R.K. Singh, A. Irmak: Estimation of crop coefficients using satellite remote sensing, *J. Irrig. Drain. Eng.* **135**, 597–608 (2009)
- 57.128 M.C. Anderson, C. Hain, B. Wardlow, A. Pimstein, J.R. Mecikalski, W.P. Kustas: Evaluation of

- drought indices based on thermal remote sensing of evapotranspiration over the continental United States, *J. Clim.* **24**, 2025–2044 (2010)
- 57.129 M.C. Anderson, R.G. Allen, A. Morse, W.P. Kustas: Use of Landsat thermal imagery in monitoring evapotranspiration and managing water resources, *Remote Sens. Environ.* **122**, 50–65 (2012)
- 57.130 M. Tasumi, R. Trezza, R.G. Allen, J.L. Wright: Operational aspects of satellite-based energy balance models for irrigated crops in the semi-arid U.S., *Irrig. Drain. Syst.* **19**, 355–376 (2005)
- 57.131 W.G.M. Bastiaanssen, E.J.M. Noordman, H. Pelgrum, G. Davids, B.P. Thoreson, R.G. Allen: SEBAL model with remotely sensed data to improve water-resources management under actual field conditions, *J. Irrig. Drain. Eng.* **131**, 85–93 (2005)
- 57.132 A. Kilic, R. Allen, R. Trezza, I. Ratcliffe, B. Kamble, C. Robison, D. Ozturk: Sensitivity of evapotranspiration retrievals from the METRIC processing algorithm to improved radiometric resolution of Landsat 8 thermal data and to calibration bias in Landsat 7 and 8 surface temperature, *Remote Sens. Environ.* **185**, 198–209 (2016)
- 57.133 D. de la Fuente-Sáiz, S. Ortega-Farías, D. Fonseca, S. Ortega-Salazar, A. Kilic, R. Allen: Calibration of METRIC model to estimate energy balance over a drip-irrigated apple orchard, *Remote Sens.* **9**, 670 (2017)
- 57.134 G. D’Urso, M. Menenti, A. Santini: Regional application of one-dimensional water flow models for irrigation management, *Agric. Water Manag.* **40**, 291–302 (1999)
- 57.135 S. Consoli, G. D’Urso, A. Toscano: Remote sensing to estimate ET-fluxes and the performance of an irrigation district in southern Italy, *Agric. Water Manag.* **81**, 295–314 (2006)
- 57.136 R. Leuning, Y.Q. Zhang, A. Rajaud, H. Cleugh, K. Tu: A simple surface conductance model to estimate regional evaporation using MODIS leaf area index and the Penman-Monteith equation, *Water Resour. Res.* **44**, W10419 (2008)
- 57.137 S. Ortega-Farías, S. Ortega-Salazar, T. Poblete, A. Kilic, R. Allen, C. Poblete-Echeverría, L. Ahumada-Orellana, M. Zuñiga, D. Sepúlveda: Estimation of energy balance components over a drip-irrigated olive orchard using thermal and multispectral cameras placed on a helicopter-based unmanned aerial vehicle (UAV), *Remote Sens.* **8**, 638 (2016)
- 57.138 J.M. Ramírez-Cuesta, A. Kilic, R. Allen, C. Santos, I.J. Lorite: Evaluating the impact of adjusting surface temperature derived from Landsat 7 ETM+ in crop evapotranspiration assessment using high-resolution airborne data, *Int. J. Remote Sens.* **38**, 4177–4205 (2017)
- 57.139 M.S. Moran, A.F. Rahman, J.C. Washburne, D.C. Goodrich, M.A. Weltz, W.P. Kustas: Combining the Penman-Monteith equation with measurements of surface temperature and reflectance to estimate evaporation rates of semiarid grassland, *Agric. For. Meteorol.* **80**, 87–109 (1996)
- 57.140 W. Kustas, M. Anderson: Advances in thermal infrared remote sensing for land surface modeling, *Agric. For. Meteorol.* **149**, 2071–2081 (2009)
- 57.141 C.M.U. Neale, W.C. Bausch, D.F. Heermann: Development of reflectance-based crop coefficients for corn, *Transactions ASAE* **32**, 1891–1900 (1990)
- 57.142 L.F. Johnson, T.J. Trout: Satellite NDVI assisted monitoring of vegetable crop evapotranspiration in California’s San Joaquin Valley, *Remote Sens.* **4**, 439–455 (2012)
- 57.143 M. Carrasco-Benavides, S. Ortega-Farías, L.O. Lagos, J. Kleissl, L. Morales, C. Poblete-Echeverría, R.G. Allen: Crop coefficients and actual evapotranspiration of a drip-irrigated Merlot vineyard using multispectral satellite images, *Irrig. Sci.* **30**, 485–497 (2012)
- 57.144 A. Calera, I. Campos, A. Osann, G. D’Urso, M. Menenti: Remote sensing for crop water management: From ET modelling to services for the end users, *Sensors* **17**, E1104 (2017)
- 57.145 VDI 3786, Blatt (Part) 21: *Umweltmeteorologie – Meteorologische Messungen – Verdunstung (Environmental Meteorology – Meteorological Measurements – Evaporation)* (Beuth, Berlin 2018)
- 57.146 DWA: *Ermittlung der Verdunstung von Land- und Wasserflächen, Teil 1: Grundlagen, Experimentelle Bestimmung, Gewässerverdunstung* (Beuth, Berlin 2018), Merkblatt DWA-M 504-1
- 57.147 T.C. Peterson, D.R. Easterling: Creation of homogeneous composite climatological reference series, *Int. J. Climatol.* **14**, 671–679 (1994)
- 57.148 M. Fuchs, C.B. Tanner: Error analysis of Bowen ratios measured by differential psychrometry, *Agric. Meteorol.* **7**, 329–334 (1970)
- 57.149 T.R. Sinclair, L.H. Allen Jr., E.R. Lemon: An analysis of errors in the calculation of energy flux densities above vegetation by Bowen-ratio profile method, *Bound.-Layer Meteorol.* **8**, 129–139 (1975)
- 57.150 T. Foken, S.H. Richter, H. Müller: Zur Genauigkeit der Bowen-Ratio-Methode, *Wetter Leben* **49**, 57–77 (1997)
- 57.151 W.A. Dugas, L.J. Fritschen, L.W. Gay, A.A. Held, A.D. Matthias, D.C. Reicosky, P. Steduto, J.L. Steiner: Bowen ratio, eddy correlation, and portable chamber measurements of sensible and latent heat flux over irrigated spring wheat, *Agric. For. Meteorol.* **56**, 12–20 (1991)
- 57.152 H. Liu, T. Foken: A modified Bowen ratio method to determine sensible and latent heat fluxes, *Meteorol. Z.* **10**, 71–80 (2001)
- 57.153 J.M. Frank, W.J. Massman, B.E. Ewers: Underestimates of sensible heat flux due to vertical velocity measurement errors in non-orthogonal sonic anemometers, *Agric. For. Meteorol.* **171/172**, 72–81 (2013)
- 57.154 T.W. Horst, S.R. Semmer, G. Maclean: Correction of a non-orthogonal, three-component sonic anemometer for flow distortion by transducer shadowing, *Bound.-Layer Meteorol.* **155**, 371–395 (2015)

Richard Allen

Soil and Water Systems
University of Idaho
Kimberly, USA
rallen@uidaho.edu



Richard Allen has degrees in agricultural engineering and civil engineering. An expert in engineering estimates of evapotranspiration, he developed the METRIC process for crop water consumption over large areas, and helped develop Google EEFlux for free global access to water consumption information. Allen was a member of the NASA/USGS Landsat Science Team from 2007 to 2017, and is a member of the NASA ECOSTRESS Science Team.

Thomas Foken

University of Bayreuth
Bayreuth, Germany
thomas.foken@uni-bayreuth.de



Thomas Foken is a retired Professor of Micrometeorology at the University of Bayreuth. He was the head of Laboratories at the meteorological observatories at Potsdam (1981–1994) and Lindenberg (1994–1997). His research interests include the interaction between the Earth's surface and the atmosphere and the measurement and modeling of energy and matter fluxes, with a strong focus on experimental meteorology. His scientific contributions have been recognized through various international awards.

Ayse Kilic

School of Natural Resources and Dept.
Civil Engineering
University of Nebraska–Lincoln
Lincoln, USA
akilic@unl.edu

Dr. Ayse Kilic is a Professor at the University of Nebraska–Lincoln and has degrees from the University of Florida in agricultural and biological engineering. She develops procedures for applying satellite imagery to determine evapotranspiration from agricultural and natural vegetation. Her Google Earth Engine EEFlux software supports satellite-based remote sensing of water consumption around the globe. Dr. Kilic was a member of the national Landsat Science Team from 2012 to 2017.

Ricardo Trezza

California Irrigation Management
Information System (CIMIS)
California Department of Water Resources
Sacramento, USA
ricardo.trezza@water.ca.gov

Ricardo Trezza is a Senior Environmental Scientist at the California Department of Water Resources and a former Associate Research Professor at the University of Idaho. He is the manager of the California Irrigation Management Information System (CIMIS), which handles a network of more than 150 agricultural weather stations in California. His research focuses on the application of remote sensing and micrometeorological weather data to estimate evapotranspiration using surface energy balance.

Samuel Ortega-Farías

Research and Extension Center for
Irrigation and Agroclimatology (CITRA)
Universidad de Talca
Talca, Chile
sortega@utalca.cl



Dr. Samuel Ortega-Farías obtained a bachelor's degree in agronomic science at the Catholic University in Chile. He obtained both a master's degree and a PhD in bioresource engineering from Oregon State University. His research has focused on regulated deficit irrigation, sustainable water management, and mapping evapotranspiration and plant water status using remote-sensing images obtained from unmanned aircraft systems (UASs) and remote-sensing satellites.

Lysimeter

58. Lysimeter

Sascha Reth , Oscar Perez–Priego , Heinz Coners , Reinhard Nolz 

It is challenging to study the mechanisms underlying the dynamics of water in the soil–plant–atmosphere continuum. Although micrometeorological techniques are widely used in hydrology, their applicability is typically restricted to certain environmental conditions (i.e., homogeneous and flat surfaces, sufficiently turbulent conditions). Weighing lysimeters allow the water fluxes in vegetated soil columns to be measured gravimetrically with high accuracy. They are complementary and provide valuable information on transport processes within and across the upper and lower boundaries of undisturbed monolith samples. Measurements include evapotranspiration and precipitation, seepage into groundwater, and additional supporting information—soil hydraulic properties such as soil water retention and hydraulic conductivity, which are key parameters for model parameterization. In addition to water fluxes, the transportation of matter into, within, and from soil can be probed.

58.1	Principles and Parameters	1570	58.3	Theory	1572
58.1.1	Principle and Relevance of Lysimeter Measurements	1570	58.3.1	Water Balance Components.....	1572
58.1.2	Measured Variables	1570	58.3.2	Weighing System.....	1572
58.2	History	1571	58.3.3	Soil Water.....	1572
			58.3.4	Tension Control at the Lower Boundary	1573
			58.3.5	Soil Temperature Control.....	1573
			58.3.6	Comparison of Evapotranspiration Measurements to Eddy–Covariance Measurements	1573
			58.3.7	Acoustic Tomography.....	1573
			58.4	Devices and Systems	1574
			58.4.1	Lysimeter Sizes.....	1574
			58.4.2	Lysimeter Filling Techniques.....	1576
			58.5	Specifications	1578
			58.6	Quality Control	1578
			58.7	Maintenance	1579
			58.8	Applications	1579
			58.8.1	Measurements Under Controlled Conditions.....	1579
			58.8.2	Application of Small Lysimeters In-Situ.....	1580
			58.8.3	Green Roof Lysimeters	1580
			58.8.4	Large Lysimeter Facilities.....	1580
			58.9	Future Developments	1581
			58.10	Further Reading	1581
			References		1582

A lysimeter is an instrument for investigating the water budget of a volume of bare or vegetated soil. There are a variety of distinctive lysimeter designs and sizes that are suitable for specific purposes and site characteristics. Depending on the object studied, lysimeters can range in size from just a few centimeters in diameter (which are used to study grass swards or herbaceous vegetation) to several meters in diam-

eter (which are used to study large trees). There are also various possible lysimeter configurations, including weighing lysimeters, controlled-temperature systems, and controlled-tension systems. In this chapter, we provide an overview of lysimetry, including the general concepts involved, the procedure used to calculate the flux, and quality control. We also present practical recommendations for the appropriate use of lysimeters.

58.1 Principles and Parameters

In general, a lysimeter consists of a soil-filled container that is inserted into the ground such that its top is level with the surrounding surface. The soil inside the container can be an excavated soil monolith, soil with near-natural horizons, or an artificial substrate, depending on the goal of the investigation. A weighing lysimeter is a well-established tool that monitors changes in the weight of the soil mass over time. These changes are then used to estimate the water budget of the confined soil. The main advantage of lysimetry is that it enables precise determination of evapotranspiration (ET).

Lysimeters are also utilized to investigate water and solute fluxes through soil and the chemical properties of percolating water. For instance, the rates at which plant nutrients are leached from soils are of broad interest in many ecological studies. In this regard, containers equipped with suction plates or suction cups for sampling soil water are sometimes referred to as lysimeters. Note that we do not cover hydrochemical aspects here, as this Handbook is focused on atmospheric measurements.

58.1.1 Principle and Relevance of Lysimeter Measurements

Lysimeter experiments are suitable methods for determining water-balance components at different scales (ranging from individual plants to ecosystems) or the crop water used by rainfed crops. When used in combination with precipitation measurements, a weighing lysimeter experiment can be carried out to directly calculate the ET rate from the recorded soil mass changes. A lysimeter equipped with a leachate collection system

allows seepage water to be investigated both quantitatively and qualitatively (in the laboratory).

Lysimeters can also be equipped with additional sensors such as tensiometers, soil moisture probes, thermometers, and suction probes, permitting the investigation of ecosystem functions and mechanisms. As they can be employed to perform long-term field investigations, lysimeter experiments can be used to explore differences in water balance between climate scenarios. A common research goal is a comparison of the results from several identical lysimeters located in areas with different weather conditions, or a comparison of different soil types or vegetation under the same weather conditions over a long period. Such investigations provide the foundations for many of the models that are used to estimate the effects of climate change, the spread of contamination in the soil, and the success of remediation measures.

58.1.2 Measured Variables

The main parameters measured by weighing lysimeters are the evapotranspiration ET (mm h^{-1}) and the drainage F (mm h^{-1}), which are the quantities of water exiting the soil mass per unit time through its upper and lower boundaries (i.e., the surface and bottom of the mass), respectively (Table 58.1). Changes in soil water content θ ($\text{m}^3 \text{m}^{-3}$ or % vol) can also be calculated from the water balance if the soil bulk density ρ (kg m^{-3}) is known (Table 58.2).

Other parameters that are relevant when calculating the water balance include the soil water storage over time ΔS (kg h^{-1}) and the water input in the form of precipitation P or irrigation I (mm). Finally, the soil

Table 58.1 Parameters measured using lysimeters

Parameter	Description	Unit	Symbol
Evapotranspiration	Sum of evaporation from all surfaces and plant transpiration	mm h^{-1}	ET
Drainage	Water leaving the soil mass at the bottom	mm h^{-1}	F
Soil water content	Total volume of water inside the lysimeter	$\text{m}^3 \text{m}^{-3}$ or % vol.	θ
Ground heat flux	Heat flux through the soil surface	W m^{-2}	G

Table 58.2 Other relevant parameters for lysimeter measurements

Parameter	Description	Unit	Symbol
Soil water storage	Change in soil water storage over time	kg h^{-1}	ΔS
Precipitation	Water entering the system by precipitation	mm	P
Irrigation	Water entering the system by irrigation	mm	I
Soil matric potential	Potential energy (expressed as a negative pressure) of soil water due to the capillary forces between water and the soil matrix	hPa	H
Soil bulk density	Dry mass density (depends on particle composition and compaction)	kg m^{-3}	ρ

matric potential H (hPa)—the potential energy of the soil water due to both the water content and the soil texture—is relevant for vegetated soil masses in lysime-

ters. For more detailed information on soil-related parameters, see Chap. 61 on soil chamber measurements.

58.2 History

The word *lysimeter* is derived from the Greek words *lysis* (dissolution or movement) and *metron* (to measure) [58.1]. Lysimeters have been used for over 300 years to investigate percolation processes and the utilization of water by vegetation [58.2]. *F.B. Salisbury and C.W. Ross* [58.3] were among the first to review the development of lysimeter technology chronologically. Detailed information on lysimeter installations from 1688 to 1939 and the chronology of lysimeter development is also provided by *H. Kohnke, F. R. Dreibelbis, and J. M. Davidson* (see Table 58.2 and Table 58.3 [58.4]). Lysimeters have mainly been used in two fields of research: plant physiology and hydrological expertise [58.5]. The techniques used in lysimetry have gradually been improved, and lysimetry has been applied to ever more complex research topics.

We now highlight the main achievements in lysimeter studies in chronological order (see also the reviews [58.5, 6]). Johan Baptista van Helmont (1580–1644) is credited with performing the first quantitative soil water budget investigation [58.5]. He grew a willow tree for 5 years in a pot filled with disturbed soil and then sealed the pot with a perforated lead lid to show that the willow removed water from the soil.

It is believed that the first actual lysimeter investigation was started in Paris in 1688 by Philippe de La Hire (1640–1718), who was interested in determining the origin of springs [58.4]. The first lysimeter designs were simple, consisting of vessels that isolated a volume of soil from the surface to a certain depth. However, such lysimeters can only be used for empirical experiments, not to explore processes occurring in the soil. It was not until 1724 that Stephen Hales (1677–1761) provided

the first evidence of processes that cause soil weight loss, thus demonstrating the roles of evaporation and transpiration. Following this study, John Dalton (1766–1844) and Maurice reported the first hydrological study that included water budgets [58.5]. In 1850, Way reported first results of soil chemistry using a laboratory lysimeter experiment.

A great advance in lysimeter design occurred in 1870, when John Bennet Lawes (1814–1900) and his colleagues built the first undisturbed *monolith* lysimeters, which preserved the natural structure and profile of the soil. Another advanced configuration utilized a perforated iron bottom that was placed under the soil and surrounding masonry walls. This system was used to investigate the quantity and chemical quality of the deep drainage component of the water balance. Further improvements to weighing lysimeters by Conrad von Seelhorst (1853–1930) in 1937 included the first self-recording weighing systems.

Due to technological advances in the field of recording systems, weighing lysimeters became widely established as reference measuring instruments for ET. Although they were initially used in hydrological studies, highly instrumented lysimeters have also found increasing application in ecology. One example of the use of lysimetry in hydrological studies is the large-scale field lysimeter installation established at a site in Oxfordshire, UK, in 1978 (for more details, see [58.6]). In Europe, more than 2500 lysimeters are operated by research institutes and industry [58.7] to study, for example, soil hydrology, biodiversity, ecosystem approaches, remediation, and the fate of pollutants.

Table 58.3 Principles and applications of lysimeter measurements

Type of lysimeter	Lower interface material	Pressure at lower soil interface	Application	
			Stationary	Mobile
Free drainage	Sand, gravel	Atmospheric	×	×
Wick drainage	Fleece, wicks	−100 hPa m ^{−1} wick length/soil pit depth → usually −10 to −100 hPa		×
Suction plate	Ceramics	0 to −1000 hPa, fixed or controlled by tensiometers	×	×
Groundwater	Impermeable, e.g., plastics, concrete	Sealed, no interface at bottom	×	
Non-rain water input NRWI microlysimeters	Impermeable, e.g., metal, plastics	Sealed, no interface at bottom	×	×

58.3 Theory

In this section, after describing the basic principles of lysimeter measurements, we discuss some of the considerations associated with lysimeter measurements and provide some examples of the applications of lysimeters.

58.3.1 Water Balance Components

The main purpose of a weighing lysimeter is to determine ET (mm h^{-1}) from changes in soil water storage over time (ΔS), excluding the water entering and leaving the system due to precipitation (P), irrigation (I), and infiltration (F) (58.1). Precipitation can enter the system in the form of rain or snow or as non-rain water input (NRWI) such as dew hoarfrost or water absorbed by soil particles. Note that, by convention, ET is expressed as a positive integer, and is calculated as

$$\text{ET} = \Delta S + P + I + F. \quad (58.1)$$

Drainage is usually assessed by collecting the amount of water that leaves the soil monolith at the bottom.

Lysimeter-based ET measurements provide independent estimates that are used when developing and validating ET models [58.8–10].

58.3.2 Weighing System

Some traditional weighing facilities still utilize a lever-arm system with a balancing mass to reduce a mass of several tons to a fractional amount. Such systems incorporate a single load cell.

Modern lysimeters typically employ three precision weighing cells of accuracy class C3/C6 (Table 58.5). A structure made of tubular stainless steel mounted on a concrete base provides a safe support for the weighing technology. The so-called load triangle guarantees stable and precise installation of the weighing cells, ensuring that measurements performed with the cells are sufficiently accurate. The weighing cells are installed with shock mounts that are torque-free and shear force-free. These shock mounts provide some mechanical flexibility when force is directed onto the scales. This prevents tension between the weighing cells due to temperature fluctuations, flexion, and vibrations, which could lead to considerable measurement errors.

58.3.3 Soil Water

While ET can be determined by simply measuring changes in soil water storage, studies may wish to ex-

plore other parameters too, such as the soil water status or the vertical water fluxes within the soil. Such investigations require measurements of soil water tension and soil water content at different depths in the soil profile. The relationship between soil water tension and soil water content measured in-situ, which is typically visualized as a retention function (or pF curve), is an important aspect of the hydraulic properties of a studied soil mass. These hydraulic properties depend on soil parameters such as particle size distribution and bulk density. The soil water tension encompasses all of the influences of the soil matrix on the water, and is also called the soil matric potential (or simply the pressure head H , in kPa). This tension is defined as a negative pressure, and is therefore positive if the applied pressure is negative. A pressure of -50 kPa in the pore water accords a tension of 50 kPa. The tension is closely linked to the water content of the soil. At the groundwater surface, H is zero, and a drier soil has a higher H value. H can be understood as the force that a plant must apply at its roots to extract water from the soil pores. The difference in tension between two points in the soil is the driving force for soil water transport. This process is expressed by the well-known Richards equation [58.11] (Chap. 61). Several numerical and analytical models are based on this equation that describes the transport of water and solutes through the soil [58.12–14].

The soil water tension is typically measured using a tensiometer. Determining a gradient with tensiometers enables the movement of water in the soil to be investigated (i.e., the flow direction and velocity). Most of the instruments used in this context are water-filled tensiometers, which typically cover the narrow range 0–90 kPa [58.15]. Using the latest tensiometer techniques and designs, including high-capacity tensiometers (filled with a polymer) and those based on electrical resistance, H values of up to 1.5 MPa (pF4.2) can be measured [58.16].

The soil water content θ ($\text{m}^3 \text{m}^{-3}$ or % vol.) relates the volume of water to the volume of soil. Changes in water content in a monitored volume are due to fluxes into and from this volume. There are well-established principles for measuring the soil water content in-situ that are based on correlations of the frequency-dependent electric and dielectric properties of the soil with its water content. Established sensor techniques include time-domain reflectometry and frequency-domain resonance (capacitance).

58.3.4 Tension Control at the Lower Boundary

Water movement in the soil is mainly driven by the matric potential present. However, in a typical lysimeter, the matric potential within the vessel can be very different from the actual matric potential in the field. Hence, without tension control, the processes observed in a lysimeter often do not accurately reflect the actual processes that occur in the field. To address this issue, porous ceramic bars can be installed at the bottom of the lysimeter to link the capillary system of the soil to a water reservoir with regulated pressure. The pressure in the reservoir can be adjusted to either the tension in the surrounding soil (as measured by a tensiometer) or an arbitrary value. This allows the tension in the surrounding soil to be transferred to the bottom of the lysimeter or the tension at the lysimeter bottom to be adjusted regardless of the natural conditions present.

Without any drainage system, the soil matric potential at the bottom of a lysimeter will equal the air pressure (i.e., the potential will be zero). This differs markedly from the conditions in the intact soil surrounding the lysimeter, and can lead to artificially high soil moisture levels in the lower compartment. In vegetated lysimeters, this may attract root growth, modifying allocation patterns.

58.3.5 Soil Temperature Control

Temperature control is needed to ensure a congruent temperature regime inside the lysimeter vessel and the surrounding soil, making it an important tool for ecosystem studies. When cutting the monolith from the surrounding soil, the soil temperature changes significantly, so it must be regulated. This is important because, for instance, microorganisms are affected by changes in soil temperature. An example of the N_2O efflux from soil as a function of the temperature is provided in [58.17]. The amount of N_2O emissions is to be mapped with an optimum curve with regard to the soil moisture content. Similar effects were found in several investigations of the CO_2 efflux (e.g., [58.18]). To control the soil temperature within the lysimeter vessel, the vessel is first insulated to prevent heat exchange between the surrounding air and the soil in the lysimeter. Furthermore, heat exchange between the surrounding soil and the lysimeter soil is facilitated by a closed water cycle system between the outside soil and the lysimeter soil installed at the same depth [58.19]. Temperature differences between the lysimeter and the surrounding

soil can be minimized to 0.5 K, in contrast to the differences of up to 1.6 K that occur without temperature control [58.20].

58.3.6 Comparison of Evapotranspiration Measurements to Eddy-Covariance Measurements

Lysimeters provide direct, independent measurements of the ET, and are thus recommended by the World Meteorological Organization for the evaluation and calibration of eddy-covariance measurements [58.21] (Chap. 55). It is, however, difficult to directly link these two methods, given their different temporal and spatial scales. For example, eddy-covariance measurements are typically performed every half-hour. However, the widely observed lack of energy balance closure introduces uncertainty into eddy-covariance ET measurements, which could lead to a less accurate description of the diurnal ET course as compared to that derived through lysimeter measurements [58.22]. The data obtained from a lysimeter are most reliable when measurements are taken at intervals of hours to days, depending on the size and resolution of the installed weighing technique. The spatial dimensions of the two methods also differ markedly. The footprint area of an eddy-covariance system has a radius of several dozen to several thousand meters, depending on the relief, installation height, and wind speed. This size cannot be addressed using a single lysimeter. Thus, the size, number, and distribution of the lysimeters that are used to investigate an eddy-covariance system must be considered carefully. Furthermore, surface properties may vary in the eddy footprint area; for example, there may be plant communities with various heights and densities or areas of bare soil [58.23]. Attempts to represent this variation in surface properties may necessitate even more lysimeters.

58.3.7 Acoustic Tomography

With the aid of runtime measurements involving the correlation analysis of acoustic sound paths, the air temperature, wind speed, and wind direction at different levels above the measuring surface of a lysimeter can be determined in a contactless manner. Based on these data, the energy and material flows, especially evapotranspiration, can be elucidated from the gas concentration changes along the flow lines determined with different gas analyzers and temperature sensors. This technique is described in more detail in Chap. 35.

58.4 Devices and Systems

Lysimeters can be categorized according to (i) size, (ii) the drainage control system employed, and (iii) the soil texture (defined by the filling technique used). In a given research facility, these three components can be varied according to the actual goal and physical and financial circumstances. A general classification of lysimeter types is still under discussion [58.24].

58.4.1 Lysimeter Sizes

Lysimeters can be classified according to size (or weight) into microlysimeters (< 1 kg), medium-sized lysimeters, and large lysimeters (> 1000 kg). Their dimensions can also be tailored to particular applications and scientific goals.

Small Lysimeters

Small lysimeters (those with internal diameters of between 70 and 200 mm) have been used for both seepage water collection and to measure ET and dewfall [58.25, 26]. Early studies with lysimeters indicated that the accuracy of ET estimates is strongly affected by the dimensions (width and depth) of the lysimeter [58.27]. Lysimeters with small surface areas and short lengths can suffer from an increased influence of boundary effects, inhomogeneities, and disturbances from installed sensors on measurements than encountered with large lysimeters. Therefore, small lysimeters should be installed in larger numbers to compensate for individual errors through repetition. Furthermore, obtaining and inserting several natural soil monoliths can be beneficial when investigating small-scale variations in soil properties.

Large Lysimeters

There are a range of materials that can be used to house large lysimeters. Firstly, it is possible to build the lysimeter basement from solid concrete, which is usually selected for large installations. Europe's largest lysimeter station, which has 72 lysimeters, is well described in [58.28, 29]; Asia's largest (which has 92 lysimeters) is discussed in [58.30]. Concrete shafts can also be constructed for individual lysimeters. These shafts are created from separate concrete rings. A good alternative is a hermetically sealed polyethylen high density (PE-HD) container station, which has many advantages compared to a concrete structure; for instance, it is waterproof and gas-tight. PE-HD is also considerably lighter and more stable than concrete, greatly simplifying transportation and installation.

Unlike concrete, a plastic station can also be used in contaminated and aggressive media. Finally, in contrast

to a lysimeter shaft constructed from concrete rings, the basement integrated into a PE-HD station permits simple access to the lysimeter, in turn allowing simple and comprehensive maintenance.

Drainage Control Systems

One major component of the lysimeter water balance (58.1) is the infiltration F . As the bottom of the monitored soil mass is disconnected from the natural soil water tension gradient, it is important to consider the drainage control system of the lysimeter.

Free Drainage

The simplest solution is a free-drainage system where the bottom of the lysimeter soil consists of a layer of gravel and coarse sand with a low water-holding capacity. Water percolating downwards through the lysimeter can run off freely and is captured by a drop collector. This low-cost solution requires almost no maintenance and needs no extra instrumentation.

The disadvantage of a free-drainage system is the risk of a relatively high soil water content, particularly in the lower horizons (due to missing water tension). This is especially important when there is a large fine particle fraction (i.e., a high water storage capacity) in the soil under investigation. A high subsoil water content can attract artificial root growth, which will influence the transpiration rate, leading to an underestimated percolation rate. Furthermore, if soil water propagates upwards, it can influence the measured ET rates through a small-scale oasis effect.

Regulated-Tension Lysimeters

In this design, porous ceramic cups are installed in the bottom of the lysimeter. These cups connect the capillary system of the soil to an adjustable-pressure water tank.

The pressure in the tank can be adjusted according to the tension in the surrounding soil as measured by a tensiometer, or to any preferred value. In this way, it is possible to transfer the soil water tension present outside to the lower boundary of the lysimeter or to check the soil water tension in the lysimeter soil regardless of the natural conditions. Tension control can occur in both directions. Separate feed and discharge lines enable the cups to be easily vented and rinsed.

Wick Drainage

When an active draining system (e.g., one that uses regulated-pressure ceramic plates) is unaffordable, a constant negative water potential can be achieved by applying a wick drainage system [58.31]. In this case,

a bundle of small wick fibers are spread across the bottom of the soil such that they merge and pass through the bottom plate via a small tube [58.23]. Inside this tube, a hanging water column in the wick pore space generates a negative pressure proportional to the length of the system, which is usually limited by the space available under the lysimeter.

Groundwater Lysimeters

A groundwater control system enables the groundwater level beneath the soil surface to be adjusted [58.33]. Disconnecting this control system leads to free drainage. The core part of a groundwater control system is a vertically aligned acrylic tube mounted to the ceiling next to each lysimeter. When the system is run in automatic mode, the equalizing tank and the lysimeter are connected. Therefore, the water level inside the lysimeter adjusts until it is the same as in the equalizing tank due to gravimetric equalization (Fig. 58.1). The water level in the equalizing tank is controlled by a pressure transducer at the bottom of the tank. If the water level is lower than the value set in the data logger, the pump is automatically switched on and

water is transferred from the reservoir into the equalizing tank until the designated water level is reached. The data logger saves the water level in the equalizing tank before refilling it. This means that the height difference at every control interval is known and can be used to work out the amount of water drawn into the lysimeter. When it rains, the water level inside the lysimeter will rise, and so will the water level in the equalizing tank. If the water level in the equalizing tank gets higher than the designated water level, water is discharged back into the reservoir.

Closed-Bottom Lysimeters

In some cases (e.g., in microlysimeters that measure dewfall in the desert), percolation is irrelevant and unlikely to occur. Thus, simple cup lysimeters with closed bottoms can be applied [58.34, 35].

Comparison of Drainage Systems

Each of the three main drainage categories—free drainage, wick drainage, and controlled tension—has its advantages and limitations (Table 58.4). Free drainage, the most affordable and simple technique,

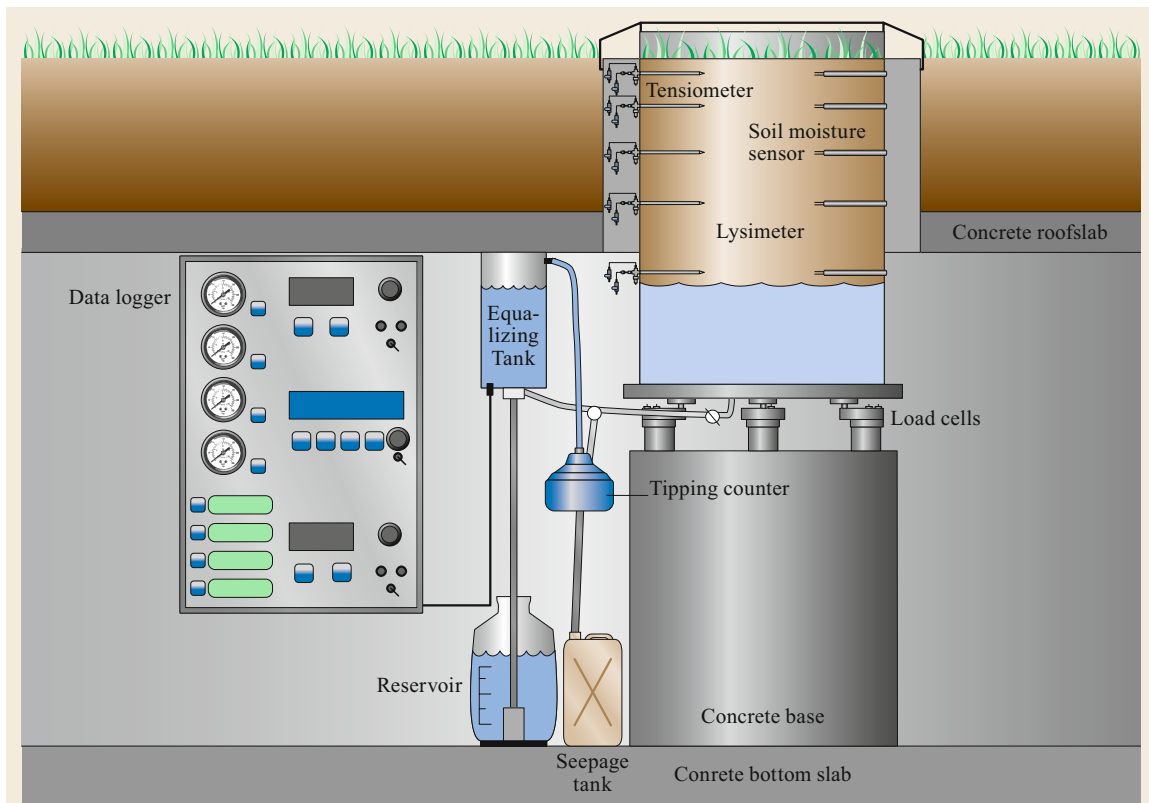


Fig. 58.1 Scheme of a lysimeter with a groundwater control system and a concrete basement (after [58.32] © UGT GmbH, reprinted with permission)

Table 58.4 Advantages and disadvantages of the different drainage methods

Device	Advantages	Disadvantages
Free drainage	Inexpensive, easy to set up	Incomplete drainage, artificially high water content inside lysimeter
Wick drainage	Inexpensive, prevents waterlogging at low horizons	Just one small, fixed tension is available, which depends on the available depth/length of the water column; drainage is still poorer than that of surrounding dry soil
Controlled tension		Expensive, laborious to set up and maintain, drainage is still limited compared to that of very dry soil ($H < 1000$ hPa)

can lead to an artificially high water content inside the lysimeter due to incomplete drainage. Depending on the soil and experimental conditions, waterlogging may even occur. This can be prevented using wick drainage, which is still comparatively inexpensive and easy to install. On the other hand, a wick drainage system can only apply one fixed tension, which depends on the space available below the lysimeter vessel. Finally, although they are laborious and expensive, controlled-tension drainage systems can highly accurately simulate the soil water conditions in surrounding moist to moderately dry soils ($H < 1000$ hPa).

58.4.2 Lysimeter Filling Techniques

Lysimeters can be filled with soil in different ways depending on, for example, the goals and funding of the research project, the type of soil and vegetation to be studied, and the planned period of lysimeter operation. The properties of the investigated soil substrate strongly influence the operation of the lysimeter. Sandy soils exhibit relatively constant density under dry and moist conditions, whereas loamy substrates tend to swell and shrink according to the soil moisture present. Gleyic horizons can hinder vertical water flow through the lysimeter and introduce errors into the calculated water balance. The quality of the water balance can also be impaired by the presence of artificially introduced preferential flow pathways. For instance, water can condense on and flow along the walls of the vessel. Stones sliding along the wall during monolith retrieval can form vertical water channels. Inhomogeneities caused by artificial vessel filling or soil cracks induced by movement during near-natural soil monolith retrieval can also influence water flow paths inside the lysimeter.

Soil monoliths can be classified as disturbed or undisturbed.

Disturbed Filling

The lysimeter vessel can be filled with a more or less homogeneous substrate, or an attempt can be made to

construct a more natural sequence of horizons with different soil materials. Compared to natural soil, the latter filling technique usually results in lower soil densities, and settling processes may occur over time. Disturbed soil monoliths can be filled with loose soil, or they can be excavated without accounting for the influence of excavation on the soil.

Monolith Excavation

A soil monolith with its natural horizons and soil density can be excavated and transferred into the lysimeter vessel. This can be done manually or using a machine. During the transfer process, the soil structure will likely be disturbed. Also, there may be irregular contact of the soil with the vessel wall, and the resulting gaps may lead to artificial preferential flow pathways.

Better soil–wall contact is achieved when the lysimeter vessel is forced into the soil using a hydraulic cylinder or an excavator. In order to stop the cylinder from tilting on stones or other obstacles, the area around the cylinder is excavated so that the lower rim can be monitored and stones can be removed as the vessel is forced into the soil. This means that quite a large area of soil is disturbed during monolith extraction.

More sophisticated techniques allow the excavation of undisturbed monoliths using cutting techniques. In general, the cutting tool gradually excavates the soil monolith, and the lysimeter vessel is then lowered onto it gravitationally or with the aid of a little external force (Fig. 58.2). A lot of experience is needed to use a cutting technique effectively, and it is offered as a commercial service. Different techniques have been developed and patented for the extraction of distinct soil horizons or soils with particular properties (e.g., mineral soil or organic and fen soil) [58.36–38].

A simple method for extracting small ready-to-measure monoliths with minimal destruction is shown in Figs. 58.3 and 58.4. Soil monoliths that include natural vegetation and are intended for small lysimeters ($d < 20$ cm) can be retrieved onsite and subsequently reinserted directly into the hole they were extracted from. This saves coring space and allows a sufficient

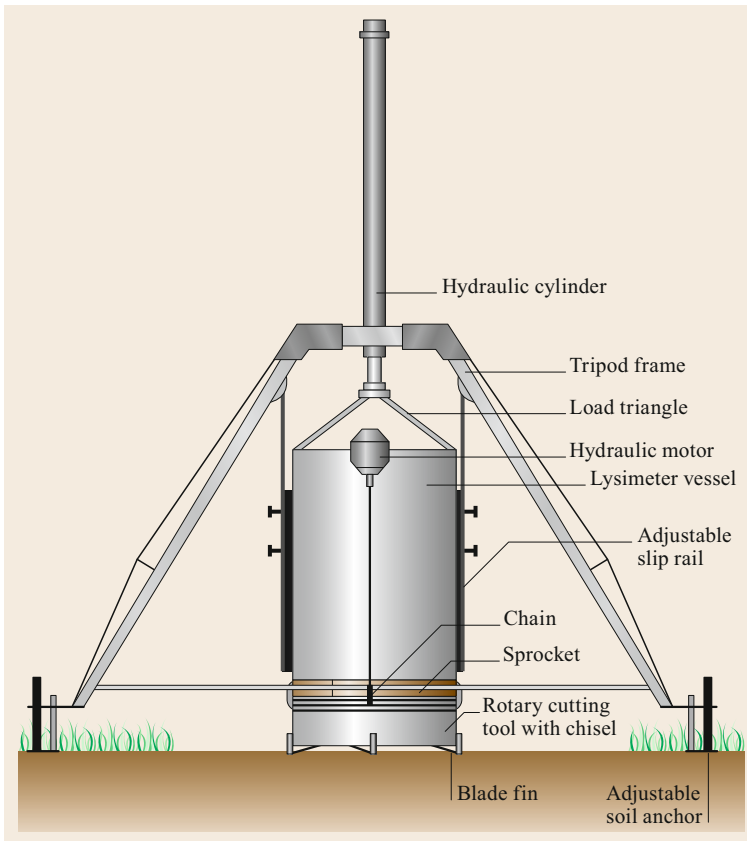


Fig. 58.2 Schematic of equipment employed for the vertical collection of large undisturbed soil monoliths (after [58.32] © UGT GmbH, reprinted with permission)



Fig. 58.3 Excavation of a monolith intended for a small lysimeter in three steps (photo © S. Reth)

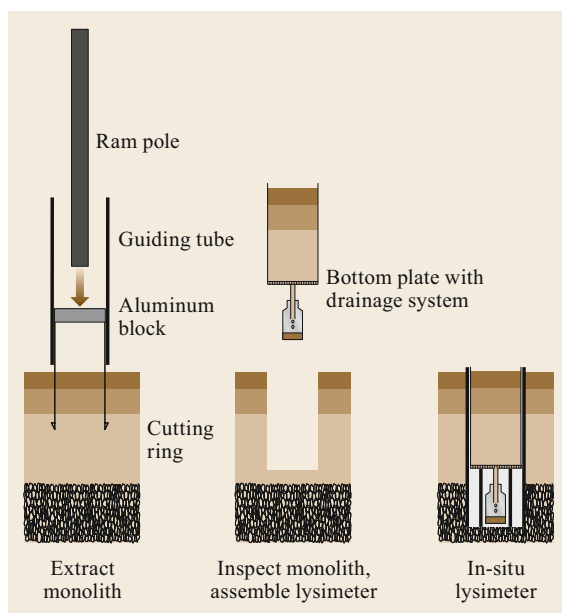


Fig. 58.4 Manual extraction of a near-natural monolith and conversion into a small in-situ lysimeter (schematic adapted from [58.23] with permission from Elsevier) ◀

number of replicate measurements to be performed relatively quickly. A Plexiglas tube segment fitted with a steel cutting ring at the bottom and an aluminum plate at the top is driven into the ground with a soil-filled ram pole. After it has been extracted, the monolith is inspected through the transparent wall for texture disturbance or artificial preferential drainage. Following this optical inspection, the monolith remains in the Plexiglas segment, and this system is converted into a lysimeter with a drainage plate glued to the bottom. The hole in the ground produced by monolith extraction is extended and then fitted with a supporting tube that is slightly larger in diameter than the monolith and about 20 cm deeper, which leaves enough room for the drainage system. When the lysimeter is finally reinserted into the hole the height is adjusted so that lysimeter surface and surrounding soil surface are at one level.

58.5 Specifications

The weighing module is the main measuring device of a weighing lysimeter. A variety of high-precision load cells such as compression load cells, tension load cells, and beam weighing cells with a wide range of maximum capacities are commercially available. Optimal selection of the load capacity is essential to maximize the signal. In practice, this will depend on the application; load capacities range from a few grams (suitable for a microlysimeter that measures tiny mass changes) up to several tons (when large lysimeters are used). Another specification to consider is their temperature dependency. Typically, high-precision load cells with high load capacities (> 3 tons) are operated in the temperature range between -20 and $+65^{\circ}\text{C}$ (effect of temperature on the sensitivity: $< 0.001\%$ of the rated load/ $^{\circ}\text{C}$), and can detect mass changes in the lysimeter of up to 10 gm^{-2} . It is worth noting that fluxes

Table 58.5 Comparison of weighing systems used in lysimetry

Type of lysimeter	Weighing system	Measurement range (kg)	Accuracy (g)
Lab lysimeter	Platform weighing	60	1
Small lysimeter	C3 weighing cells	3×2500	10
Large lysimeter	C6 weighing cells	3×4500	10

below the accuracy of the load cell, such as dewfall, can be measured with large lysimeters by optimizing the rate of change in mass. Other error sources can also influence the performance of the lysimeter. The main characteristics of various weighing systems for lysimeters are summarized in Table 58.5. The next section sheds some light on lysimeter data processing and quality control procedures.

58.6 Quality Control

The first step in the processing of lysimeter data is to convert the analog output signal from the load cell to digital data and store that data for further processing. Typical storage intervals are 1–10 min; each stored value represents the mean of several read-

ings. Using a calibration function, the measurements are converted into physical mass changes. The latter correspond to water fluxes into and from the lysimeter. The load cell resolution and the quality of the calibration function determine the data preci-

sion and accuracy. State-of-the-art systems enable mass changes of ± 0.1 kg to be measured. Frequent evaluation of the weighing system and the calibration function is recommended to assure high-quality lysimeter data.

Like any measurement system, a lysimeter weighing device is prone to measurement errors and inaccuracies. An important possible error source is wind-induced forces, which can cause the weighing system to oscillate, leading to unintended fluctuations in the weighing signal [58.39]. The key challenge is to separate such noise from real mass changes due to ET and rainfall. In this regard, filtering and smoothing routines can help to improve data quality by reducing noise and errors and excluding outliers [58.40]. Traditional approaches include well-adjusted averaging procedures such as moving average and Savitzky–Golay filters. In [58.41–43], a polynomial spline function was ap-

plied to a noisy lysimeter weighing dataset to improve data quality. In general, a critical measurement period is needed to achieve efficient routines, and the length of the filtering window crucially influences the result [58.43]. Recently developed routines utilize adaptive filter parameters that depend on the signal strength and noise [58.40].

The advantage of high-quality datasets (high quality in terms of accuracy, temporal resolution, integrity, and sophisticated data processing) is that they allow both the ET and P as well as sources such as dewfall to be determined directly from the weighing data [58.44]. This involves the use of a simple water balance equation for which changes in soil water and fluxes across the lower boundary of the lysimeter are known from measurements. Consequently, negative mass changes within a short measurement interval are assigned to ET and increases in mass are assigned to P .

58.7 Maintenance

Though a lysimeter is a self-measuring system, the quality of the results it provides depends on how well the installation is maintained (see Table 58.6). A visual

inspection of the installation, including the sensors, and a data plausibility check should normally be performed at least once a week.

Table 58.6 Maintenance of lysimeter systems

Maximum interval	Balance	Tensiometer	Full-range tensiometer	Soil moisture sensor	Suction system	Tension control
1 week		Refill water if needed			Change the collection bottles	Refill tank water if needed
	Visual check of the complete system, data plausibility check					
6 months	Check mechanical function and accuracy Check cable and connectors		Zero-point calibration			
1 year	Calibrate instruments If the check reveals a possible malfunction, the instrument should be replaced					

58.8 Applications

Lysimeter experiments can be conducted in the laboratory or the field. Typical areas in which lysimeters are used include agricultural sites, forest sites, landfill sites, postmining landscapes, and contaminated sites that require rehabilitation. In order to be able to draw statistically verifiable conclusions, it is recommended that several lysimeters should be used in combination.

58.8.1 Measurements Under Controlled Conditions

A laboratory lysimeter is a miniature lysimeter that is especially designed for use in labs (indoors). The design and functionality of a laboratory lysimeter are always defined by the aim of the experiment (Fig. 58.5).

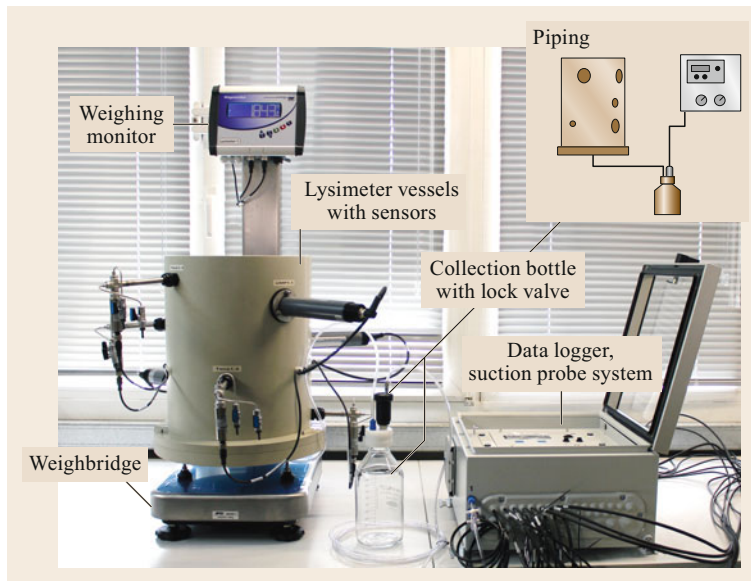


Fig. 58.5 Example of a laboratory lysimeter (photo © S. Reth)

Studying soil processes under laboratory conditions has several advantages: the controlled environment allows more precise experiments; the scale is suited to several processes and permits shorter test times than in field studies; and different materials can be integrated quickly.

Column experiments with laboratory lysimeters are used to examine physical soil parameters in multistep outflow or multistep flux experiments. They can also be used to measure conservative or reactive transport.

58.8.2 Application of Small Lysimeters In-Situ

Small lysimeters can be applied in large numbers to monitor ET and F in large field-research projects. In [58.45], 20 cm diameter lysimeters with intact soil monoliths and constant-tension ceramic bottom plates were used in a multidisciplinary onsite experiment with a randomized block design. Also, soil degradation on the Tibetan plateau was investigated at different scales using a combination of eddy-covariance and lysimeter measurements [58.46].

58.8.3 Green Roof Lysimeters

Among the most popular areas of research relating to ecological roofs and urban tracks are new technological vegetation systems to bind particulate matter (fine dust) and the development of new substrates, vegetation mats, and fertilizer products. Plants such as succulents and xerophytes are used in large green roofs and train tracks because they are slow-growing and require less

maintenance. Scientific measurement tasks and advantages of green roofs can be measured with the help of lysimeters [58.47, 48]. Parallel measurements of the climate at the lysimeter site (Fig. 58.6) can aid data interpretation:

- Reduced precipitation runoff from the roof, and relief of canalization and clarification plants
- Decreased rainwater (by 50–90%) and successive release of moisture into the atmosphere through evapotranspiration, thereby increasing air humidity and cooling the surrounding air
- Decreased heat irradiation of buildings during the summer period
- Decreased air pollution due to the deposition of particulate matter on the rough vegetation surface, where it can be adsorbed, bound, or taken up
- Reduced sound reflection

58.8.4 Large Lysimeter Facilities

When a high number of parameters must be examined, a large number of replicates are required. The largest lysimeter station in Europe was built by Agroscope Reckenholz Zürich in 2009. It contains 72 lysimeters each with a surface area of 1 m^2 and a depth of 1.5 m [58.29]. The three main soils of Switzerland are united in this large-scale lysimeter system. The work done at this lysimeter station relates to the need to minimize the ingress of fertilizers—particularly nitrate—into groundwater, as specified by agricultural policy guidelines. The effects of different farming approaches



Fig. 58.6 Green roof lysimeter and climate station at the Hochschule Weihenstephan campus (photo © S. Reth)



Fig. 58.7 Large lysimeter station of the RDA South Korea (photo © S. Reth)

and crop rotation on groundwater contamination with fertilizers are examined under the same climatic conditions.

Asia's largest lysimeter station was constructed at Jeonju by the National Institute of Agricultural Science (RDA) South Korea in 2012 (Fig. 58.7). The research

performed at this station has a similar focus to the Swiss station. Again, the three most typical soils of Korea are united in a total of three lysimeter systems on campus. Fifty-four lysimeters each with a surface area of 1 m² and a depth of 1.7 m as well as 38 small lysimeters each with a diameter of 0.3 m and a depth of 1 m are utilized in research into a healthy environment for agricultural production. The research also addresses the protection and preservation of the Korean environment through technological development, such as renewable bioenergy production.

A different approach is followed in a large lysimeter network known as TERENO (TERrestrial ENvironmental Observatories), which includes 132 lysimeters, each with a surface area of 1 m² and a depth of 1.5 m. These lysimeters obtain data on the hydrosphere, biosphere, pedosphere, lower atmosphere, and anthroposphere along multiple spatial and temporal gradients in climate-sensitive regions across Germany [58.49]. The long-term ecological, social, and economic impacts of global climate change are being explored by this lysimeter network.

58.9 Future Developments

Lysimeters will increasingly be used in complex controlled conditions to identify drivers of ecosystem changes. These *ecotrons* (lysimeter applications; not necessarily investigations of soil processes) are per-

formed to investigate processes occurring in the soil–plant–atmosphere system as well as interactions between the compartments. Good examples of *ecotrons* are given in [58.50–52].

58.10 Further Reading

For more information on lysimeters, the reader is referred to the following reference book:

- J.-C. Munch and S. Reth. Lysimeters for Global Change Research: Biological Processes and the Environmental Fate of Pollutants. *Water, Air & Soil Pollution: Focus*. Volume 8, No 2, 2008

References

- 58.1 A. Aboukhaled, A. Alfaro, M. Smith: *Lysimeters, Irrigation and Drainage*, Vol. 39 (FAO, Rome 1982)
- 58.2 T.A. Howell, A.D. Schneider, M.E. Jensen: History of lysimeter design and use for evapotranspiration measurements. In: *Proc. Lysimeters Evapotranspir. Environ. Meas.* (ASCE, New York 1991) pp. 1–9
- 58.3 F.B. Salisbury, C. Ross: *Plant Physiology* (Wadsworth, Belmont 1969)
- 58.4 H. Kohnke, F.R. Dreibelbis, J.M. Davidson: *A Survey and Discussion of Lysimeters and a Bibliography on Their Construction and Performance* (US Department of Agriculture, Washington DC 1940) p. 372
- 58.5 M.J. Goss, W. Ehlers: The role of lysimeters in the development of our understanding of soil water and nutrient dynamics in ecosystems, *Soil Use Manag.* **25**, 213–223 (2009)
- 58.6 M.J. Goss, W. Ehlers, A. Unc: The role of lysimeters in the development of our understanding of processes in the vadose zone relevant to contamination of groundwater aquifers, *Phys. Chem. Earth* **35**, 913–926 (2010)
- 58.7 C. Lanthaler, J. Fank: Lysimeter stations and soil hydrology measuring sites in Europe—results of a 2004 survey. In: *Proc. 11th Lysimeter Conf., Raumberg, Gumpenstein* (2005) pp. 19–24
- 58.8 S. Lovelli, M. Perniola, M. Arcieri, A.R. Rivelli, T. Di Tommaso: Water use assessment in muskmelon by the Penman–Monteith “one-step” approach, *Agric. Water Manag.* **95**, 1153–1160 (2008)
- 58.9 P.J. Vaughan, T.J. Trout, J.E. Ayars: A processing method for weighing lysimeter data and comparison to micrometeorological eto predictions, *Agric. Water Manag.* **88**, 141–146 (2007)
- 58.10 R. López-Urrea, F. Martín de Santa Olalla, C. Fabeiro, A. Moratalla: Testing evapotranspiration equations using lysimeter observations in a semiarid climate, *Agric. Water Manag.* **85**, 15–26 (2006)
- 58.11 H. Vereecken, A. Schnepf, J.W. Hopmans, M. Javaux, D. Or, T. Roose, J. Vanderborght, M.H. Young, W. Amelung, M. Aitkenhead, S.D. Allison, S. Assouline, P. Baveye, M. Berli, N. Brüggemann, P. Finke, M. Flury, T. Gaiser, G. Govers, T. Ghezzehei, P. Hallett, H.J.H. Franssen, J. Heppell, R. Horn, J.A. Huisman, D. Jacques, F. Jonard, S. Kollet, F. Lafolie, K. Lamorski, D. Leitner, A. McBratney, B. Minasny, C. Montzka, W. Nowak, Y. Pachepsky, J. Padarian, N. Romano, K. Roth, Y. Rothfuss, E.C. Rowe, A. Schwen, J. Šimůnek, A. Tiktak, J. Van Dam, S.E.A.T.M. van der Zee, H.J. Vogel, J.A. Vrugt, T. Wöhling, I.M. Young, A. Tiktak: Modeling soil processes: review, key challenges, and new perspectives, *Vadose Zone J.* **15**, 1–57 (2016)
- 58.12 J. Šimůnek, S.A. Bradford: Vadose zone modeling: introduction and importance, *Vadose Zone J.* **7**, 581–586 (2008)
- 58.13 C. Steenpass, J. Vanderborght, M. Herbst, J. Šimůnek, H. Vereecken: Estimating soil hydraulic properties from infrared measurements of soil surface temperatures and TDR data, *Vadose Zone J.* **9**, 910–924 (2010)
- 58.14 V. Phogat, M.A. Skewes, J.W. Cox, J. Alam, G. Grigson, J. Šimůnek: Evaluation of water movement and nitrate dynamics in a lysimeter planted with an orange tree, *Agric. Water Manag.* **127**, 74–84 (2013)
- 58.15 W.R. Whalley, E.S. Ober, M. Jenkins: Measurement of the matric potential of soil water in the rhizosphere, *J. Exp. Bot.* **64**, 3951–3963 (2013)
- 58.16 A. Degré, M.J. van der Ploeg, T. Caldwell, H.P.A. Gooren: Comparison of soil water potential sensors: a drying experiment, *Vadose Zone J.* **16**, 1–8 (2017)
- 58.17 S. Reth, K. Hentschel, M. Drösler, E. Falge: Denit – experimental analysis and modelling of soil N₂O efflux in response on changes of soil water content, soil temperature, soil pH, nutrient availability and the time after rain event, *Plant Soil* **272**, 349–363 (2005)
- 58.18 S. Reth, M. Göckede, E. Falge: CO₂ efflux from agricultural soils in Eastern Germany – comparison of a closed chamber system with eddy covariance measurements, *Theor. Appl. Climatol.* **80**, 105–120 (2005)
- 58.19 J. Punzel, M. Seyfarth: Lysimeter lower boundary condition controlling method, involves providing porous filter plate with high thermal conductivity at same voltage and temperature of water from water volume of soil column transferred to lysimeter, Patent No. De102010051333a1 (2011)
- 58.20 C. Podlasly, K. Schwarzel: Development of a continuous closed pipe system for controlling soil temperature at the lower boundary of weighing field lysimeters, *Soil Sci. Soc. Am. J.* **77**, 2157–2163 (2013)
- 58.21 WMO: Guide to Instruments and Methods of Observation, WMO–No. 8, Volume I – Measurement of Meteorological Variables. (World Meteorological Organization, Geneva, 2018)
- 58.22 O. Perez-Priego, T.S. El-Madany, M. Migliavacca, A.S. Kowalski, M. Jung, A. Carrara, O. Kolle, M.P. Martín, J. Pacheco-Labrador, G. Moreno, M. Reichstein: Evaluation of eddy covariance latent heat fluxes with independent lysimeter and sapflow estimates in a Mediterranean savannah ecosystem, *Agric. For. Meteorol.* **236**, 87–99 (2017)
- 58.23 H. Coners, W. Babel, S. Willinghofer, T. Biermann, L. Kohler, E. Seeber, T. Foken, Y.M. Ma, Y.P. Yang, G. Mieke, C. Leuschner: Evapotranspiration and water balance of high-elevation grassland on the Tibetan plateau, *J. Hydrol.* **533**, 557–566 (2016)
- 58.24 C. Lanthaler: *Lysimeter Stations and Soil Hydrology Measuring Sites in Europe: Purpose, Equipment, Research Results, Future Developments*, Diploma Thesis, University of Graz, 2004)
- 58.25 C.C. Daamen, L.P. Simmonds, J.S. Wallace, K.B. Laryea, M.V.K. Sivakumar: Use of microlysi-

- ters to measure evaporation from sandy soils, *Agric. For. Meteorol.* **65**, 159–173 (1993)
- 58.26 O. Uclés, L. Villagarcía, M.J. Moro, Y. Canton, F. Domingo: Role of dewfall in the water balance of a semiarid coastal steppe ecosystem, *Hydrol. Proc.* **28**, 2271–2280 (2014)
- 58.27 R.W. Shawcroft, H.R. Gardner: Direct evaporation from soil under a row crop canopy, *Agric. Meteorol.* **28**, 229–238 (1983)
- 58.28 V. Prasuhn, C. Humphrys, E. Spiess: Seventy-two lysimeters for measuring water flows and nitrate leaching under arable land. In: *Proc. NAS Int. Workshop Appl. Lysimeter Syst. Water Nutr. Dyn., Wanju, South Korea* (2016) pp. 124–146
- 58.29 S. Oberholzer, V. Prasuhn, A. Hund: Crop water use under Swiss pedoclimatic conditions – evaluation of lysimeter data covering a seven-year period, *Field Crops Res.* **211**, 48–65 (2017)
- 58.30 K.H.L. Han, Y. J., M.J. Seo, K.H. Jung, H.R. Cho: Current and future water management technology for upland crops using lysimeter. In: *NAS Int. Lysimeter Workshop* (2016)
- 58.31 G.W. Gee, B.D. Newman, S. Green, R. Meissner, H. Rupp, Z. Zhang, J.M. Keller, W. Waugh, M. Van der Velde, J. Salazar: Passive wick fluxmeters: design considerations and field applications, *Water Resour. Res.* **45**, W04420 (2009)
- 58.32 Umwelt-Geräte-Technik GmbH (UGT): Novel Lysimeter Techniques, https://www.ugt-online.de/fileadmin/Public/downloads/Produkte/Lysimetertechnik/Lysimeter2013_en_.pdf (2013), Accessed 27 July
- 58.33 O. Dietrich, M. Fahle, M. Seyfarth: Behavior of water balance components at sites with shallow groundwater tables: possibilities and limitations of their simulation using different ways to control weighable groundwater lysimeters, *Agric. Water Manag.* **163**, 75–89 (2016)
- 58.34 B.G. Heusinkveld, S.M. Berkowicz, A.F.G. Jacobs, A.A.M. Holtslag, W.C.A.M. Hillen: An automated microlysimeter to study dew formation and evaporation in arid and semiarid regions, *J. Hydrometeorol.* **7**, 825–832 (2006)
- 58.35 O. Ucles, L. Villagarcia, Y. Canton, F. Domingo: Microlysimeter station for long term non-rainfall water input and evaporation studies, *Agric. For. Meteorol.* **182**, 13–20 (2013)
- 58.36 R. Meißner, H. Rupp, M. Seyfarth, H. Friedrich: Lysimeter for extracting a monolithic column of soil comprises blades that pivot inwards under the action of springs to cut a narrow slit in the soil, where upon rotation is reversed and the blades cut deeper into the soil, Patent No. DE102005062896b3 (2007)
- 58.37 H. Friedrich, R. Meissner, M. Seyfarth: Apparatus and method for removing soil columns, Patent No. DE102011006374b4 (2011)
- 58.38 R. Meisner, M. Seyfarth, H. Friedrich, H. Rupp, M. Beuter, K. Kesler: A device for taking soil monolithic columns, Patent No DE10048089c2 (2003)
- 58.39 R. Nolz, G. Kammerer, P. Cepuder: Interpretation of lysimeter weighing data affected by wind, *J. Plant Nutr. Soil Sci.* **176**, 200–208 (2013)
- 58.40 A. Peters, T. Nehls, H. Schonsky, G. Wessolek: Separating precipitation and evapotranspiration from noise – a new filter routine for high-resolution lysimeter data, *Hydrol. Earth Syst. Sci.* **18**, 1189–1198 (2014)
- 58.41 W.M. Gary, R.E. Steven, H.G. Prasanna, A.H. Terry, S.C. Karen, R.L. Baumhardt: Post-processing techniques for reducing errors in weighing lysimeter evapotranspiration (ET) datasets, *Transactions ASABE* **57**, 499–515 (2014)
- 58.42 R.W. Malone, D.J. Stewardson, J.V. Bonta, T. Nelsen: Calibration and quality control of the Coshocton weighing lysimeters, *Transactions ASAE* **42**, 701–712 (1999)
- 58.43 P.J. Vaughan, J.E. Ayars: Noise reduction methods for weighing lysimeters, *J. Irrig. Drain. Eng.* **135**, 235–240 (2009)
- 58.44 M. Hannes, U. Wollschläger, F. Schrader, W. Durner, S. Gebler, T. Pütz, J. Fank, G. von Unold, H.J. Vogel: A comprehensive filtering scheme for high-resolution estimation of the water balance components from high-precision lysimeters, *Hydrol. Earth Syst. Sci.* **19**, 3405–3418 (2015)
- 58.45 L. Rose, H. Coners, C. Leuschner: Effects of fertilization and cutting frequency on the water balance of a temperate grassland, *Ecohydrology* **5**, 64–72 (2012)
- 58.46 W. Babel, T. Biermann, H. Coners, E. Falge, E. Seeber, J. Ingrisch, P.M. Schleuss, T. Gerken, J. Leonbacher, T. Leopold, S. Willinghofer, K. Schutzenmeister, O. Shibtova, L. Becker, S. Hafner, S. Spielvogel, X. Li, X. Xu, Y. Sun, L. Zhang, Y. Yang, Y. Ma, K. Wesche, H.F. Graf, C. Leuschner, G. Guggenberger, Y. Kuzyakov, G. Miede, T. Foken: Pasture degradation modifies the water and carbon cycles of the Tibetan highlands, *Biogeosciences* **11**, 6633–6656 (2014)
- 58.47 K. DiGiovanni, F. Montalto, S. Gaffin, C. Rosenzweig: Applicability of classical predictive equations for the estimation of evapotranspiration from urban green spaces: green roof results, *J. Hydrol. Eng.* **18**, 99–107 (2012)
- 58.48 K. DiGiovanni, S. Gaffin, F. Montalto: Green roof hydrology: results from a small-scale lysimeter setup (Bronx, NY). In: *Low Impact Development 2010: Redefining Water in the City* (ASCE, Reston 2010) pp. 1328–1341
- 58.49 T. Pütz, R. Kiese, U. Wollschläger, J. Groh, H. Rupp, S. Zacharias, E. Priesack, H.H. Gerke, R. Gasche, O. Bens, E. Borg, C. Baessler, K. Kaiser, M. Herbrich, J.C. Munch, M. Sommer, H.J. Vogel, J. Vanderborght, H. Vereecken: TERENO-SOILCan: a lysimeter-network in Germany observing soil processes and plant diversity influenced by climate change, *Environ. Earth Sci.* **75**, 1242 (2016)
- 58.50 J. Roy, C. Picon-Cochard, A. Augusti, M.L. Benot, L. Thiery, O. Darsonville, D. Landais, C. Piel, M. Defosse, S. Devidal, C. Escape, O. Ravel, N. Fromin, F. Volaire, A. Milcu, M. Bahn, J.F. Soussana: Ele-

- vated CO₂ maintains grassland net carbon uptake under a future heat and drought extreme, *Proc. Natl. Acad. Sci. USA* **113**, 6224–6229 (2016)
- 58.51 N. Eisenhauer, M. Türke: From climate chambers to biodiversity chambers, *Front. Ecol. Environ.* **16**, 136–137 (2018)
- 58.52 M. Türke, R. Feldmann, B. Fürst, H. Hartmann, M. Herrmann, S. Klotz, G. Mathias, S. Meldau, M. Ottenbreit, S. Reth: Multitrophische Biodiversitätsmanipulation unter kontrollierten Umweltbedingungen im Idiv Ecotron. In: *Proc. Lysimetertag*. (2017) pp. 107–114

Sascha Reth

UGT GmbH
Hallbergmoos, Germany
sascha.reth@ugt-online.de



Sascha Reth is Managing Director of and a partner in UGT GmbH. He previously coordinated scientific research at the lysimeter station of the Institute of Soil Ecology at the German Research Center for Environmental Health. His own research focused on observing trace gas emissions in lysimeters in the context of climate change. Since 2007, he has been a member of the steering committee of the International Lysimeter Research Group.

Oscar Perez-Priego

Biological Science
Macquarie University
Sydney, NSW, Australia
oscarperezpriego@gmail.com



Dr Oscar Perez-Priego is postdoctoral research fellow at Macquarie University, Australia. He received a PhD in Bioscience (2011), a postdoc at University of Granada (2011–2013, Spain) and the Max Planck Institute for Biogeochemistry (2014–2018, Germany). He studies soil–plant–atmosphere interactions by combining field experiments and models. He is interested in gas and energy exchange from single leaves to the whole plant and ecosystem scales, ecosystem modeling, and theory.

Heinz Coners

Plant Ecology and Ecosystems Research
University of Göttingen
Göttingen, Germany
hconers@uni-goettingen.de



Heinz Coners is Technical Director for Research at the Department of Plant Ecology, Albrecht von Haller Institute for Plant Sciences, University of Göttingen. His research focuses on plant–water relationships, and he has developed and applied many techniques at the plant and ecosystem levels in this context (e.g., sap flow gauges, lysimeters). He is involved in projects in central European lowlands, tropical rain forests, and alpine pastures on the Tibetan Plateau.

Reinhard Nolz

Institute for Soil Physics and Rural Water Management
University of Natural Resources and Life Sciences, Vienna
Wien, Austria
reinhard.nolz@boku.ac.at



Reinhard Nolz is Senior Scientist at the Institute for Soil Physics and Rural Water Management (SoPhy) at the University of Natural Resources and Life Sciences, Vienna (BOKU). He received a PhD in 2013, and a postdoctoral lecture qualification (*venia docendi*) in 2017. His research interests include agricultural water management, lysimetry, soil water monitoring, and environmental soil physics.

59. Plant Chamber Measurements

Oscar Perez-Priego 

Enclosure-based techniques are widely used in physiological studies and largely constitute the foundation of our current understanding of the processes controlling the plant–soil–atmosphere gas exchange, such as photosynthesis, respiration, and evaporation. Back in the 1970s, chamber systems became highly developed to overcome the difficulties in integrating gas-exchange measurements from single leaves to obtain whole canopy estimates (whole plant or plant parts). The main principle of chamber-based measurements involves enclosures of a relatively large volume of air, so that the changes in the gas properties by diffusive processes can be continuously monitored over time. Typically, the basic components of a chamber system consist of an infrared gas analyzer, an air sampling circuit, the transparent enclosure, and a software-logging module to store and process data. Although a variety of types of enclosures and operating systems can be found, chamber fluxes can be subject to considerable uncertainties, making it fundamental to adapt appropriate error treatment protocols and flux calculation methods to improve the flux estimates. Accuracy and precision of the fluxes are largely determined by the degree of chamber disturbance. In addition to the more stable compounds, such as CO₂, CH₄ and water vapor, canopy chambers have been adapted to measure reactive trace gases (e.g., NO₂, NO, O₃, VOCs, HONO, HNO₃, CH₂O, etc.) with short lifetimes. In this chapter, we will provide a practical guide to the use of plant chambers and an elaborated discussion on basic considerations, including error treatment protocols and flux calculation procedures.

59.1	Measurement Principles and Parameters	1586
59.2	History of Chamber Measurements ...	1587
59.3	Theory	1587
59.3.1	Steady-State Flowthrough (Open-Top Chambers)	1588
59.3.2	Non-Steady-State Flowthrough (Transient Chambers)	1588
59.3.3	Non-Steady-State Non-Flowthrough (Closed Static)	1589
59.3.4	Flux Calculation and Error Analysis	1589
59.4	Devices and Systems	1591
59.4.1	Gas Analysis.....	1591
59.4.2	Transparent Enclosures	1592
59.5	Specifications	1593
59.6	Quality Control	1593
59.7	Maintenance	1594
59.8	Application	1594
59.8.1	Effect of Water Supply on Water Use Efficiency of Single Trees	1594
59.8.2	Evaluating Functional Properties Across Scales	1594
59.8.3	Other Relevant Processes.....	1597
59.9	Future Developments	1597
59.10	Further Readings	1598
	References	1598

Canopy chambers are currently the only tool for measuring integrated fluxes directly, such as photosynthesis and transpiration rates on an intermediate scale between leaf-scale cuvette measurements and ecosystem-scale eddy-covariance measurements. This includes branch, stem (or even root) scales to the whole-plant

scale [59.1]. Such enclosure measurements are also able to observe the primary emissions of compounds that are not detected by atmospheric studies over forests due to their high reactivity. In the following section, we will describe the principles and relevance of chamber measurements.

59.1 Measurement Principles and Parameters

The operating principle of chambers is somewhat simple and offers flexibility at a comparatively low cost. Although canopy chambers are usually portable, and a suitable number of replicates can be performed (measurements can be made in < 3 min), their design can be adapted, and automatic measurements can be obtained over the course of a day and or a season [59.2]. This is particularly interesting for manipulation experiments that do not require extensive experimental areas, e.g., studies focusing on treatment effects such as irrigation and nutrient amendments [59.3–5], or those evaluating different soil management techniques [59.6, 7].

The configuration and design can be customized, so that environmental conditions of the chamber can be artificially controlled. This provides a unique tool to elucidate component fluxes under certain conditions. For instance, transparent and opaque enclosures can be combined quasi simultaneously to measure directly net CO_2 exchange rates and respiration during daytime conditions [59.4]. Isolated enclosures can be used to separate below and aboveground processes, so that

plant and soil components can be independently characterized [59.3, 8]. In addition, chambers have been proven to be a valid tool for separating the isotopic composition of the transpired water vapor [59.9]. Both provide the means to partition evapotranspiration into its constitutive components (plant transpiration and soil evaporation), which is necessary to link plant-water use strategies to environmental variability.

Canopy chambers allow measurements over a wide range of environmental conditions, which is particularly relevant for situations where other techniques are less appropriate. For instance, chamber data provides independent and complementarity information to eddy-covariance measurements in situations with stable conditions (i.e., calm nights) or in terrains with pronounced slopes [59.10]. Other benefits are, for instance, when the research objective is to cover spatial features within eddy-covariance footprints due to moisture gradients or coverage by different functional plant forms [59.11–13]. With air-controlled settings, such as free-air CO_2 enrichment experiments, open-top cham-

Table 59.1 Parameters measured parameters in a chamber system

Parameter	Description	Unit	Symbol
Trace gas	Molar fraction of the trace gases M_i	mol mol^{-1}	$[M_i]$
Air temperature	Air temperature inside the chamber	K	T_a
Atmospheric pressure	Atmospheric pressure inside the chamber	hPa	P_a
Partial pressure of water vapor	Derived from the molar water vapor fraction (C_w) as $e_a = P_a C_w$	kPa	E_w
Absolute humidity	Mass of water vapor in a given volume or mass of air	kg m^{-3}	AH
Light intensity	Photosynthetic active radiation	$\mu\text{mol m}^{-2} \text{s}^{-1}$	PAR

Table 59.2 Other relevant physiological parameters for chamber measurements

Parameter	Description	Unit	Symbol
Evaporation	Total or plant evaporation	$\text{mmol m}^{-2} \text{s}^{-1}$	ET
Photosynthesis	Gross photosynthetic flux	$\mu\text{mol m}^{-2} \text{s}^{-1}$	P_h
Respiration	Ecosystem or plant respiration	$\mu\text{mol m}^{-2} \text{s}^{-1}$	R_{eco}
Net ecosystem exchange	Net ecosystem CO_2 exchange	$\mu\text{mol m}^{-2} \text{s}^{-1}$	NEE
Water use efficiency	Ratio between P_h and transpiration	$\mu\text{mol mol}^{-1}$	WUE
Leaf area index	Surface of leaf per unit of ground surface area	$\text{m}^2 \text{m}^{-2}$	LAI
Radiometric temperature	Vegetation surface temperature	K	T_{sur}
Plant-to-air water vapor pressure deficit	Calculated as the difference between saturated E_w (considering plant/leaf surface temperature) and ambient (E_w)	hPa	VPD_{veg}
Absolute humidity	Mass of water vapor in a given volume or mass of air	g m^{-3}	AH
Volume	Effective chamber headspace volume	m^3	V_e
Air flow rate	Air flow velocity	m s^{-1}	F
Leakage error	Error due to leakage	%	ϵ_l
Leakage diffusion coefficient	Diffusion-based coefficient determining the leakage error	$\text{m}^2 \text{s}^{-1}$	θ
Starting time	Time after chamber enclosure that defines the initial slope of the nonlinear fit	s	δ

bers are typically used to evaluate how elevated CO₂ impacts vegetation processes [59.14–16] as well as air pollution [59.17, 18].

Other studies use chamber data as a valuable reference for comparing other techniques, such as sap flow [59.3, 19], micrometeorological methods [59.2,

12, 20–23], gravimetric methods [59.24], or even to facilitate interpretation of remotely sensed observations [59.4]. Chamber measurements have also provided a valuable tool for modeling proposes [59.25].

Tables 59.1 and 59.2 include the most relevant parameters measured in chamber systems.

59.2 History of Chamber Measurements

First canopy chamber measurements were conducted under field conditions over more than a century ago. In 1905, a pioneering study by W.A. Cannon [59.26] described the principles of a *transpiration apparatus* (Fig. 59.1) and developed an analytical method and the equations to calculate plant transpiration. The methodology was simple and effective: single plants were placed in a tight bell glass, and transpiration rates were computed as a function of the changes in the absolute humidity (AH) of the confined atmosphere. This measurement technique was formerly termed the polymeter method. The polymeter system consists of a hygrometer and a thermometer and was originally designed to be placed on the inside a translucent bell to observe changes in air moisture. This system preceded the fast-response psychrometer that allowed ET measures for shorter periods [59.27, 28].

The use of translucent chambers also became very popular in photosynthesis research, and pioneering studies with canopy CO₂ exchange measurements can be found elsewhere [59.28–32]. For instance, an early study by A.J. Heinicke and N.F. Childers [59.32] described the first prototype of an open system that maintained steady-state conditions by continuously drawing air into the chamber headspace of the chamber. Former chamber prototypes measured CO₂ in the samples with colorimetric detection methods, which relied on the electrical conductivity properties of a dry absorbent material (typically, alkali solution) to provide accurate CO₂ estimates [59.28]. The rapid interest in the use of canopy chambers occurred with the first developments of infrared gas analyzers, which made chamber mea-

surements more feasible, portable, and accurate [59.33]. With the advancement of gas analyzers, hybrid designs provided simultaneous measurements of both CO₂ and water vapor exchange, which was the start of a new era in ecophysiological measurements [59.18, 27, 28, 33–38]. Currently, canopy chambers are also used to measure reactive trace gaseous fluxes (e.g., NO₂, NO, O₃, VOCs, HONO, HNO₃, CH₂O, etc.), as well as their isotopic compositions. For these measurements, a twin-cuvette system with an empty reference enclosure can be of great advantage [59.39–42]. The empty reference enclosure will act as a *zero calibration* for all effects of the chamber and piping materials on the composition of the flushing air (Fig. 59.1).



Fig. 59.1 Twin-cuvette system that can be used for measuring reactive trace gaseous fluxes under field and laboratory conditions (photo © Jürgen Kesselmeier)

59.3 Theory

The basic principle of the canopy chamber technique is to confine a given volume of air around a plant so that the transient-state changes of the air properties (i.e., humidity, CO₂, temperature) can be monitored over time. Given that disturbances in the internal mi-

croclimate (e.g., humidification and overheating) are typically introduced by sporadic enclosures, new chamber configurations and techniques were developed to minimize measurement bias. Therefore, chambers can be designed to operate under two different condi-

tions: open (steady-state) and closed (transient-state) systems [59.38]. Regardless the differences associated with the operating conditions, a common aspect of the chambers is that they modify the microenvironment of the canopy to varying degrees. Here, we will discuss basic aspects with respect to each operating configuration, with particular focus on canopy enclosures; general descriptions of the chamber techniques can be found in Chap. 60 along with classical literature [59.33, 43].

59.3.1 Steady-State Flowthrough (Open-Top Chambers)

Canopy chambers operating under steady-state flowthrough conditions are typically referred to as open-top chambers [59.44]. As an open system, a constant air flow is maintained through the chamber head space and is controlled via an air control unit that regulates the atmosphere inside in a way that does not depart from the actual conditions outside (open-top chambers, Fig. 59.2a) or any other targeted conditions (i.e., climate-controlled chambers or glasshouses). When the volume of air enclosed by the chamber is proportionate to the capacity of a pump, unvarying environments can be held without the needing to be controlled (passive open-top chambers). In both cases, once the flow rate is known, and after a steady-state condition has been

reached inside the chamber, fluxes are computed from the differences in concentration of the air entering and exiting the chamber. Based on this equilibrium status, open-top chambers are suitable for prolonged measurements.

For large climate chambers they require heavy machinery and a strong power supply, which make them less portable and, hence, less suitable for field research. However, passive open-top chamber systems can be transported in the field, and their use has been extended to measure whole-plant gas exchange under natural conditions [59.45–49]. Among different designs, enclosure materials with a mylar balloon provide a practical solution for mid-size plants [59.48].

59.3.2 Non-Steady-State Flowthrough (Transient Chambers)

Closed dynamic chambers are typically designed to be light and more portable than open-top chambers. Transient chambers (also known as closed dynamic chambers) are usually restricted to mid-size plants (e.g., crops). A closed sampling circuit is used to derive a subsample of air from the chamber to the IRGA (Fig. 59.2b). Fluxes are calculated from the rate of change in the gas concentration during the enclosure period. Although measurements require an operator,

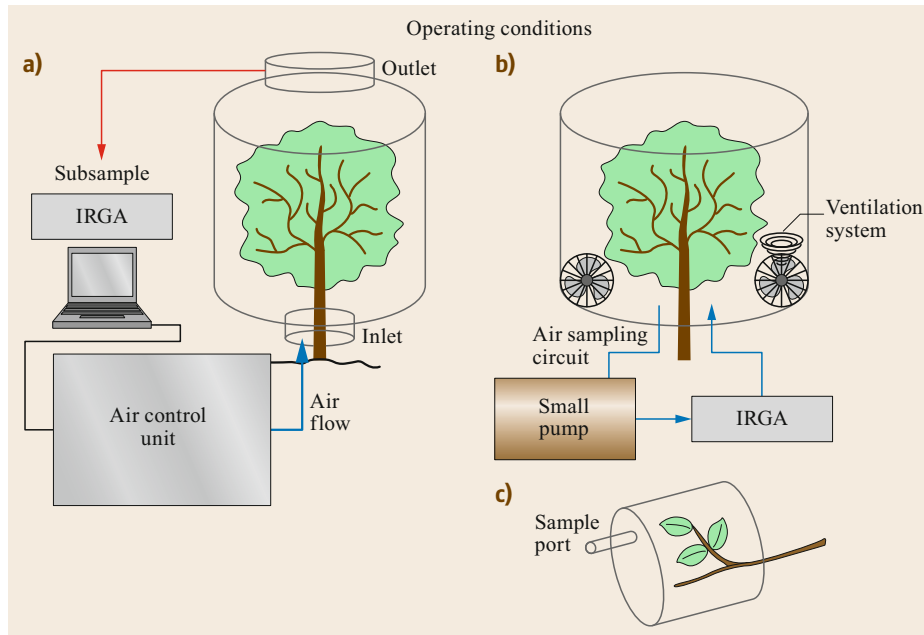


Fig. 59.2a–c Whole-plant gas-exchange systems of the (a) flow-through steady-state system, (b) flow-through non-steady-state system, and (c) non-flow-through non-steady state system. The basic components of a chamber system consist of an infrared gas analyzer (IRGA), an air sampling circuit connected to a pump, the transparent enclosure, the air control unit, and software and logging modules to store and process data

they can be automatized [59.2]. Given the difficulties of moving large chambers, Perez-Priego et al. [59.3] built a framed-type transient chamber of $\approx 40 \text{ m}^{-3}$ around a tree with a novel design that can be compatible with orchard use. Transitory closures were made with a revolving top and windows, which could be left open just after the measurements were taken. This minimizes disturbances to the tree environment and provides an alternative to open-top chambers.

59.3.3 Non-Steady-State Non-Flowthrough (Closed Static)

Measurements with a closed static system (also known as the cover-box method) require a series of manual samplings of the targeted gas at an appropriate frequency over short enclosure periods [59.50]. This is a fundamental aspect to better interpret the evolution of the gas concentration inside the chamber and its associated diffusive flux over time. Typically, a number of air samples are taken during the enclosure time with a gas syringe and through a sample port (Fig. 59.2c).

59.3.4 Flux Calculation and Error Analysis

Field measurements with chambers are subject to a number of pitfalls and disturbances. Regular calibration of the system and adapting adequate error treatment protocols in data processing and flux calculation methods are essential. Prior to field measurements it is crucial to understand the performance of the chamber system through a rigorous protocol, including a number of calibration methods together with the final flux calculation and error analysis.

Chamber Calibration

Depending on the enclosure/configuration type, a series of adjustments and tests are recommended. Typically, this consists of (i) calibration of the gas analyzer using reference gas samples and the chemical properties of the cover material (Sect. 59.7), and (ii) characterization of the main systematic source of errors, including leaks, determination of the effective chamber volume (V_e , particularly relevant for closed chamber), the effects of condensation of water vapor and alteration of the radiation by the chamber wall, and turbulence regimes by the ventilation system:

- **Leaks:** While leakages induce minor errors in open-top chambers [59.51], this artefact causes flux underestimation in closed systems and should be accounted for [59.3]. With a diffusion-based model, Perez-Priego et al. [59.3] predicted that the degree of these errors depends largely on the magnitude

of the fluxes, the time of enclosure (Δt), and the geometry of the chamber, which is defined by a dimensional factor (i.e., collar contact length (l_c) – the enclosure surface, typically the bottom of the chamber for closed systems – to V_e ratio)

$$\varepsilon_1 = \frac{\theta l_c}{2V_e} \Delta t, \quad (59.1)$$

where θ is the leakage diffusion coefficient that can be determined experimentally by inducing an artificial gradient in CO_2 between the confined atmosphere in the chamber and the outside one as

$$\theta = \frac{-V_e}{\Delta t l_c} \ln \left(\frac{[\text{CO}_2]_{t2} - [\text{CO}_2]_{\text{atm}}}{[\text{CO}_2]_{t1} - [\text{CO}_2]_{\text{atm}}} \right), \quad (59.2)$$

where $[\text{CO}_2]_{t1}$ and $[\text{CO}_2]_{t2}$ are the chamber CO_2 concentration at times 1 ($t1$) and 2 ($t2$), with Δt the period considered between $t1$ and $t2$; $[\text{CO}_2]_{\text{atm}}$ refers to the ambient CO_2 concentration outside the chamber. As an example, for typical θ values between 6.5×10^{-5} and $1 \times 10^{-4} \text{ m}^2 \text{ s}^{-1}$, 3 min of Δt , and a l_c (4 m) and V_e (1 m^3), ε_1 would result in 2% of the flux. However, it is worth remarking here that ε_1 would cause much larger errors, with V_e lower than 0.2 m^3 . Although tight enclosures can be obtained with foam gaskets, it should be kept in mind that nondiffusive leakage issues due to pressure differences from wind gusts can occur in the field. In particular, this might cause leakage in nonrigid enclosures, such as the mylar balloon. Avoiding pressure artefacts caused by chamber deployments is crucial for closed static chambers [59.52]. In addition, it has been demonstrated that a small differential pressure of 0.1 kPa between inside and outside the chamber might change the concurrent flux rate by a factor of 10 [59.53]. This suggests the benefits of small leaks when they might act as an air-vent system ensuring pressure equilibration.

- **Determination of V_e .** Flux biases can also be caused by inaccurate determination of V_e [59.54]. The V_e is usually considered as the nominal volume of the chamber but is dispersed by the volume occupied by the plant or when the chamber is placed on a soil collar with undetermined porosity. Similar to the leakage test, Drewitt et al. [59.55] proposed an injection technique to derive V_e values under field conditions.
- **Effects of the condensation of water vapor.** The injection technique can be also used to determine the water absorption properties of the wall chamber and the sampling circuit [59.3]. To this end, hydroponic systems or lysimeters have been used to calibrate transpiration [59.27, 36]. Dew formation inside the

chamber and saturation problems remain an important limitation of the use of chamber, particularly under wet conditions. Particular attention of the influence of water condensation should be paid for measuring soluble trace gases species (e.g., NH_3 , SO_2 , and NO_x among others), for which an empty chamber might be required as a reference to account for such effects [59.40].

- *Effects of light attenuation.* As it has already been discussed, the transmission properties of the wall chamber can disturb the light environment within the chamber, decreasing the intensity of incident radiation and changing light quality (i.e., the direct to diffuse radiation ratio). To account for such effects, a characterization of the optical properties of the translucent material is usually recommended. According to the typical photosynthetic light response curve, Perez-Priego et al., pointed out in 2010 that this effect is minor under light-saturation conditions ($< 10\%$ of the flux when $\text{PAR} > 50 \text{ mol m}^{-2} \text{ s}^{-1}$). However, caution should be taken under light-limitation conditions when small light disturbances would cause stronger impacts on photosynthesis. It is also important to consider edge effects, when self-shading of the chamber frames may affect radiation inside the chamber, particularly in small-size chambers [59.56].
- *Effects of ventilation.* Similar to leaf-cuvette measurements, a critical aspect of chambers lies in the fact that enclosures always modify the aerodynamic characteristics of the confined atmosphere. This is a common problem for closed and open chambers; while a good mixing is required in closed systems to ensure a representative sampling, the effect can be large in open systems when they require recirculating a large air stream through the chamber head space. In closed systems, a sampling circuit consisting of a number of hanging tubes with intake points spaced over the head space of the chamber provides an effective multisampling strategy without the need for a high-power pump or ventilation system [59.3].
- *Effects of flushing air composition.* The quality of the air flushing of the enclosures may be of great relevance in particular for reactive trace gases. Primary emissions of highly reactive compounds can only be detected when oxidizing processes are excluded. For example, it may be necessary to filter ozone before entering the enclosure under field conditions. Otherwise, sensitive compounds will not be observed. However, cleaning the flushing air may also lead to fundamental errors. Purified air may cause a release of compounds that are typically taken up under normal conditions.

- *Effects of wall materials.* All enclosures may affect trace gas compositions by physical and chemical interactions between trace gases and wall materials. These effects must be carefully checked before making final conclusions on exchange processes. A twin-cuvette system may help to overcome such problems.

This needs particular consideration in high-ventilated systems such as large open-top chambers, the strong airstream of which is needed to hold the steady-state conditions inside the chamber [59.57]. However, some authors have concluded that ventilated chambers have a very little impact on transpiration rates under certain environmental conditions, such as equilibrium evaporation [59.37] and those measurement conditions when the aerodynamic resistance (a measure of turbulence and defined by the wind speed inside the chamber) to stomatal resistance ratio is very low [59.3]. The latter can be suitable to sclerophyll plants with roughness surfaces, which are very well coupled to the environment, and transpiration rates are mostly controlled by stomata regulation. Under such conditions, disturbances that are potentially caused by the extent on which stomata respond to overheating and/or changes in humidity during chamber deployments. In closed or transient chambers, those impacts can be minimized by short enclosure times and the use of nonlinear models that allow regressing instantaneous fluxes at the initial time of measurements.

Flux Calculation

Given that the use of closed chambers is more widespread than that of open-top chambers [59.53], in this section, we will focus on the chamber configuration of the transient-state type. The general assumption of this technique is that short enclosure times have a minor impact on the calculated fluxes. However, measurements should last long enough to increase confidence in flux estimates. Therefore, optimizing, the time window of chamber enclosure is crucial to reduce uncertainties [59.11]. The determination of an optimal enclosure time involves the following:

- *The starting time (δ),* which is defined as the time required for stabilizing the atmospheric conditions inside the chamber (*stabilization time*) and for transporting a gas sample of it to the gas analyzer (*lag time*). While the stabilization time depends on the ventilation system and the dimensions of the chamber, the lag is determined by the pump power (typically 1 L min^{-1}) and the distance of the sampling circuit.
- *Number and frequency of gas samples.*

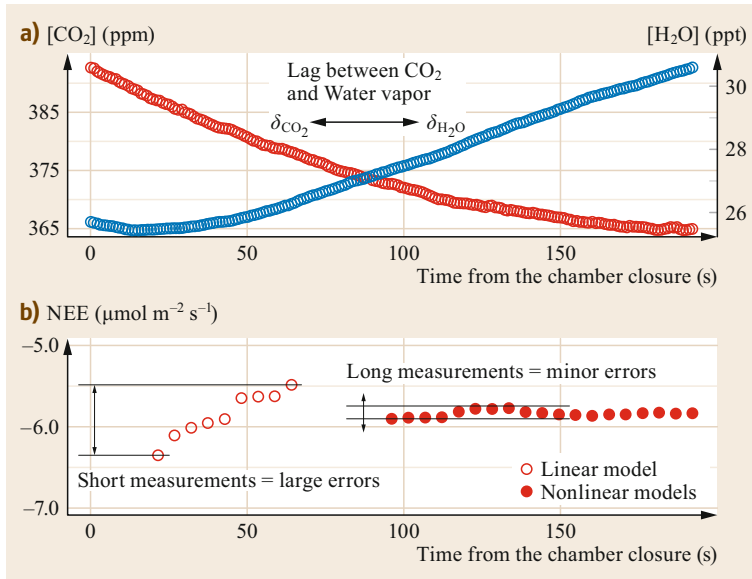


Fig. 59.3 (a) Dynamics of changes in CO₂ and water vapor molar fractions during a measurement on April 2014 in a grassland, and (b) calculated net CO₂ fluxes from different window lengths. According to the time from the chamber closure a rapid measurement is classified as those deployments < 1 min. It is shown that while short measurement periods cause large uncertainties, longest measurements (3 min) improve confidence in flux estimates. Net CO₂ fluxes were calculated using the RespChamber-Proc package (after [59.58])

As an example, Fig. 59.3a illustrates the progression of changes in the CO₂ and water vapor concentration inside a transient chamber. Although ongoing processes, such as photosynthesis and evapotranspiration drive changes in CO₂ and water vapor just after chamber closure, a different stabilization time is observed between trace gases. While a rapid decrease in CO₂ was detected after chamber closure, a longer δ for water vapor was identified with a change-point detection algorithm. These varying responses across scalars cause important uncertainties in the respective flux estimates, particularly in the absence of any criteria to optimize the duration of the chamber enclosure. This is a particular issue for rapid measurements (< 1 min), which flux uncertainties are largely subject to IRGA noise and a fixed calculation window [59.11]. On the other hand, the environmental and physiological conditions are modified, uncertainties are largely reduced with prolonged closure times (3 min), as long as undisturbed fluxes can be inferred with nonlinear models (Fig. 59.3b). Even though the shape of the curvature of the gas progression

might change upon physiological and meteorological conditions, the principles to select the appropriate fitting function remains a subject of debate. A number of alternative nonlinear regression models have been proposed [59.59–62]. To overcome fitting problems, a practical algorithm implemented in the RespChamberProc package and developed in R software [59.58] incorporates novel methods for accuracy and precision analysis of systematic and random errors. Based on statistical tests of residuals, different nonlinear and linear regressions are evaluated, and fluxes are then inferred from the best parameter fit of the regression (instead of fitting a specific regression model to a fixed calculation window). Parameters from the different regressions are sensitive and may fluctuate largely depending on enclosure time *duration* and *noise* inherent to the gas analyzer. While δ is determined using the change-point detection method, duration and noise are addressed using a bootstrapping resampling-based flux calculation method, which enable a better assessment of random errors and improve flux precision.

59.4 Devices and Systems

The elementary components of a canopy chamber consist of a cover material with a sample port or an air sampling circuit attached to an instrument for gas analysis. Other components include a software-logging module to store and process data. Here, we will focus on the most common principles of gas analysis and the enclosure material.

59.4.1 Gas Analysis

Flux calculations from observations of any trace gases inside the chamber involves density effects, which can bias flux estimates [59.63]. In practice, the addition of water molecules through transpiration depresses the mole fraction of any component of a gas mixture (e.g.,

Table 59.3 Advantages and disadvantages of the different chamber configurations

Operating conditions	Advantages	Limitations
Closed dynamic	Simple, portable and suitable for field conditions, adaptable (transparent and opaque for photosynthesis and respiration) Instantaneous during an optimal period of enclosure at low ventilation rates can be achieved	An operator is required but unattended systems is possible Disturbances and artefacts during the enclosure periods (e.g., physiology, non-steady-state conditions with increasing humidification and saturation problems, dew formation, leakages)
Open dynamic	Continuous and repeated measurements Allows flux measurements under controlled conditions Capacity to hold unvarying environmental conditions during the enclosure period	Requires heavy equipment Ventilation regimes can be highly altered Complex operation (particularly under intermittent environmental conditions)

CO₂). Another disturbance is, typically, overheating, and therefore, any trace gas quantity taken from inside a *control-volume* chamber is better expressed in terms of the mixing ratio (i.e., dry mole fraction; [59.64]). That being said, chamber measurements do not require fast-response or high-precision instrumentation to detect small fluxes – a standard gas analyzer can detect fluxes 100 times smaller in chambers than what it can detect in micrometeorological applications [59.53]. According to such requirements, we will proceed to describe the principles of the most relevant infrared gas analyzers and spectroscopy devices for chamber use. To simplify the discussion, here we will focus on CO₂ gas analyzers, while a wide range of devices for other trace gases species can be found elsewhere, e.g., [59.5, 39, 40, 42, 53, 65–70]

Trace gases are measured by determining the absorption of a released infrared light source through a particular sample gas. Two main instrumentations are available: open-path and closed-path IRGAs. Since most of the off-the-shelf IRGAs incorporate a water vapor channel with a temperature and pressure-controlled cell, the trace gas molar fraction is provided (e.g., Licor 7000, 7200, 6400). Although Li-840/840A measures water vapor pressure and cell temperature and pressure, it does not give dry mole fractions, and thus water dilution correction is required. By contrast, when using IRGAs with no water vapor channel (e.g., Li-820) the change in density due to fluctuations in relative humidity and temperature must be quantified with independent sensors.

Although IRGAs are the most common technique in use for chamber measurements, a range of spectrometric techniques are available for measuring trace gases. A detailed technical description of the methods is provided in Chaps. 16 and 28.

59.4.2 Transparent Enclosures

A common issue in the chamber technique regards the impact of the translucent material on the radiative properties. A wide range of materials are typically used to build canopy chambers including acrylic glass [59.71], transparent polycarbonate [59.2], transparent low-density polyethylene [59.45], fluorinated ethylene propylene [59.42] or biaxially oriented polypropylene [59.72], as well as polyester-like films [59.3]. Those studies reported that the attenuation might range between 3 and 20% of the incident light according to the optical properties of the enclosures.

Another property to consider is the gas permeability and adsorption characteristics, as well as the chemical properties of the cover material. This is particularly relevant to certain volatile sulfur compounds, such as carbonyl sulfide (COS), which require inert material (e.g., glass bells with a sample line of Teflon and a pump head covered by polytetrafluoroethylene; [59.73]).

As a conclusion, Table 59.3 summarizes the main advantages and limitations of the two main chamber configurations. Comparative studies evaluating the performance of the two enclosure types can be found elsewhere [59.35, 74, 75].

59.5 Specifications

Here, we will focus on the gas analyzer, the main measuring device in the chamber system. A wide range of gas analyzers with different specifications and characteristics are available commercially. As previously discussed in Sect. 59.4.1, chamber measurements do not require fast-response or high-precision instrumentation to detect small fluxes with high accuracy. Although most commonly used gas analyzers typically provide measurements of CO₂ and water vapor within a wide range (i.e., 0–20 000 ppm and 0–60 ppt, respectively), the output signal can be optimized to more appropriate measurement ranges upon instrument configu-

ration options; e.g., an analog voltage range 0–2.5 V and 1 Hz signal filtering are recommended for the LI-840A, which gives an accuracy of < 1.5% of reading (< 1 ppm close to ambient CO₂). Generally, gas analyzers with low power requirements (12–30 V DC) are light (1 kg), which allows portability and flexibility of operation within an acceptable temperature range (–20 to +45 °C). Finally, when measuring fluxes in evaporative surfaces, factors including spectral cross sensitivity and inherent instrument cross sensitivity, as well as the dilution effects of the gas samples by the addition of water vapor molecules should be accounted for.

59.6 Quality Control

As part of the quality control procedure, removing bad data by instrument malfunction or measurement artefacts is highly advisable to guarantee high-quality chamber data. In addition to adapting appropriate flux calculation and error analysis protocols (Sect. 59.3.4), flagging or rejecting data that are out of the established range of tolerance is suggested (Table 59.4). Another

common practice to identify problems and validate the plausibility of the data is simply the verification of the chamber measurements according to theoretical expectations (e.g., light-response curve) or the comparison with other measurement approaches (i.e., eddy covariance). A short overview of this application is given in the following sections.

Table 59.4 Typical test criteria for chamber measurements

Method	Error	Reason
IRGA	Initial CO ₂ out of the expected range (e.g., 380–450 ppm) Dewpoint temperature (e.g., > 40 °C)	New calibration necessary
Flux	Flux out of the accepted range according to the experimental conditions	Poor fitting caused by potential disturbances, which will depend on chamber configuration (e.g., air flushing system malfunctioning for open-top chambers or leakages by pressure gradients for closed systems). Visual inspection on the progression of the respective gas concentration over chamber deployment. Check IRGA values as new calibration might be required
Statistical analysis (e.g., median absolute deviation) of a group of observations	Residual analysis from the expected response (e.g., photosynthetic light response curve) or based on the distribution of a set of observations	Potential outlier
Ancillary data	Values of T_a , P_a , VPD, PAR within the expected ranges	Replacement of the sensor or new calibration necessary

Note: particular consideration should be paid to reactive gases species (Sect. 59.8.3)

Table 59.5 Basic maintenance tasks of chamber systems

Maximum interval	IRGA	Filters and sampling tubes	Chamber cover
Regular maintenance	Cleaning of the optical bench and/or calibration		Cleaning of the chamber material
> 1 year	Check the manufacture for estimated duration of life of the infrared source (e.g., LI-840 is rated for about 18 000 h of life)	Replacement (but depending on hours of chamber use and conditions it might require a regular maintenance)	

59.7 Maintenance

One practical aspect of the maintenance procedure regards the regular calibration of the gas analyzer and chamber checking. That said, careful attention should be paid to the choice of the chamber material and an appropriate setup according to the conditions. For instance, sorption/desorption of water vapor by chamber materials might compromise the suitability of the chamber method. This does not only apply to the transparent cover but any other material, such as the sampling tubes. For this reason, short gas lines that minimize this effect are recommended, mostly in humid environments where heating sampling tubes up to 30 °C have been proven to

prevent water vapor condensation [59.66]. When the enclosure components, air lines and/or filters get dirty, dust acts as water condenser particles, so frequent cleaning and exchange when appropriate is compulsory.

Other artefacts are associated with the chemical properties of the chamber components. For example, foam gaskets typically used to tighten up the enclosure might emit COS to a varying degree. In such a case, performing a reference or *zero-flux* measurement with the empty chamber is required [59.76]. Table 59.5 summarizes some basic maintenance tasks of chamber systems.

59.8 Application

Studies concerning leaf gaseous exchange have proven to be elusive when most of the observations have typically been reported under light-saturated conditions, which might fail in representing the whole plant behavior [59.77]. This can explain the observed mismatch between leaf gas exchange and landscape-scale eddy-covariance measurements [59.78]. The main appeal for measuring canopy-scale processes is to then integrate the whole canopy trait plasticity and microclimate of a plant into a single measurement.

A number of chamber applications have already been described in the introductory part of this chapter. Below is a brief summary with particular examples of canopy chamber measurements and applications.

59.8.1 Effect of Water Supply on Water Use Efficiency of Single Trees

The following example shows the novel design of a canopy chamber for measuring CO₂ and water vapor fluxes of individual trees of up to 30 m³ under different water supply conditions (Fig. 59.4). Note that one of the novelties is that the chamber excluded soil fluxes, and only aboveground fluxes were measured (i.e., net canopy photosynthesis (P_n) and transpiration, Fig. 59.4a).

The example in Fig. 59.4 shows the diurnal time courses of canopy P_n (Fig. 59.4b) and transpiration

rates (Fig. 59.4c) for two olive trees under varying water status. No differences in plant leaf area were found ($\approx 23 \text{ m}^2$), both P_n and transpiration rates were clearly reduced by the water stress effect compared to the well-irrigated tree. Overall, canopy P_n peaked early in the morning and decreased over the afternoon. On the contrary, transpiration rates were high in the afternoon (note that a less accentuated pattern was observed in the deficit-irrigated tree). As a result, high water-use efficiency (WUE, the amount of CO₂ assimilated by unit of water transpired, Fig. 59.5a) was found in the morning and low in the afternoon. Nevertheless, higher P_n rates per a given stomatal conductance during the morning led to divergent enhanced WUE for the deficit-irrigated tree compared to full irrigation (Fig. 59.5b). This reveals the importance of considering not only spatial but also temporal scales when optimal shifts in the transpiration pattern (e.g., maximum in the morning or in the growing period when P_n is higher) may cause a higher increased WUE at the daily and seasonal scales.

59.8.2 Evaluating Functional Properties Across Scales

The next example in Fig. 59.6 illustrates the varying responses of canopy P_n to variable light conditions, phenology, and degree of water stress. Following mi-

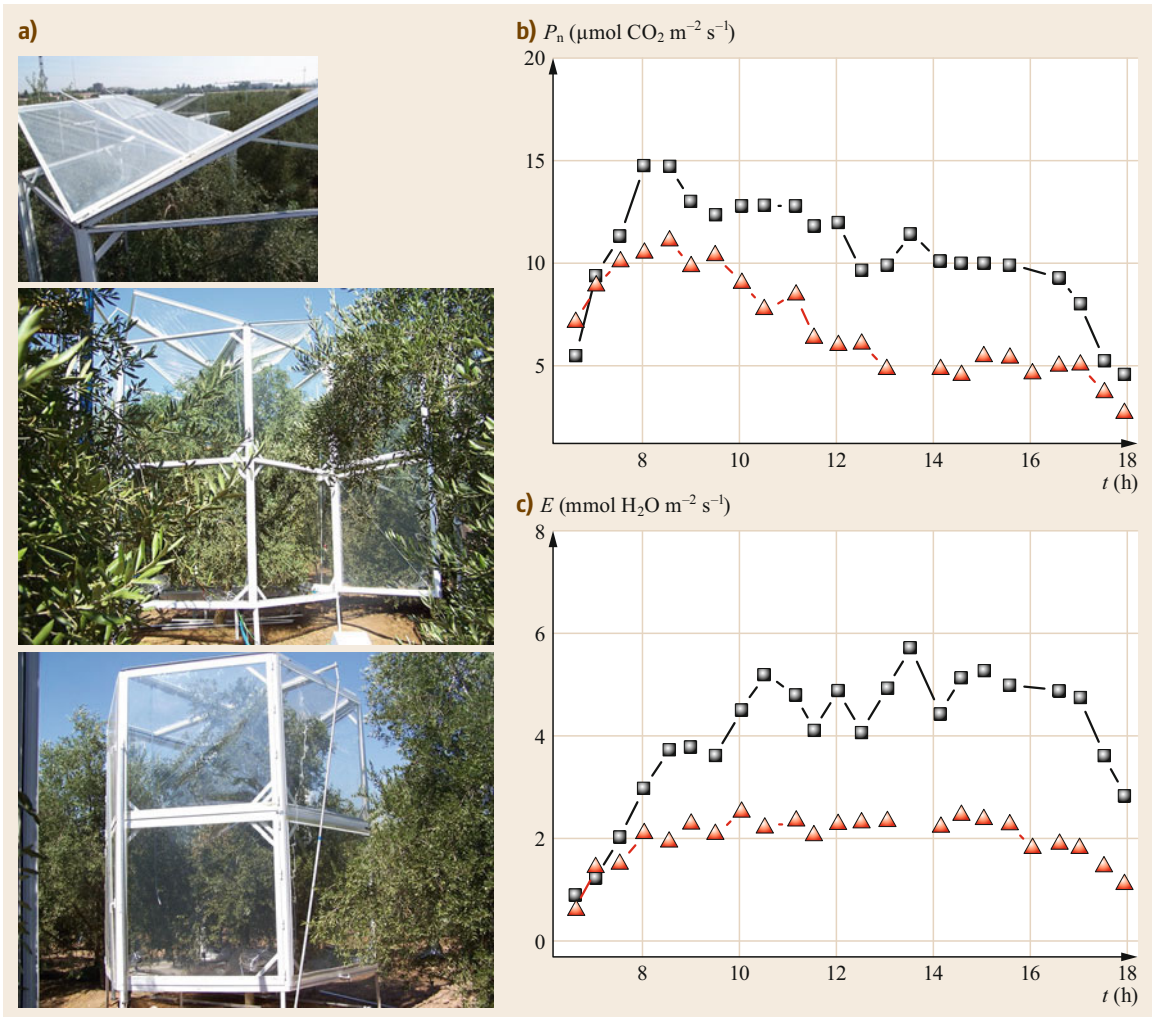


Fig. 59.4 (a) The photos show the performance of the chamber during a field campaign in an olive orchard measuring CO_2 and water vapor fluxes from single trees. (b,c) Example of a diurnal pattern of canopy photosynthesis (P_n) and transpiration rates from single trees under different water irrigation management. Squares represent the well-irrigated tree (absence of water stress), while red triangles represent the tree under moderate water stress by deficit irrigation treatment. The reduction in P_n and transpiration by water stress is observed (photos © Oscar Perez-Priego)

cometeorological convention, P_n rates are expressed as negative (net CO_2 uptake) and positive values (net CO_2 release). Measurements were conducted in two coexisting Mediterranean species from a shrubland for two different phenological periods (black squares indicating the growing period during spring, and red triangles the beginning of the dry period in summer). A divergent pattern in the response was found for the two contrasting periods, which reflects diverse functionalities. Although both species showed similar responses in spring (with similar leaf water potentials), the grasses (*Festuca* sp.) reduced P_n rates during the dry period when the shrubs (*Genista* sp.) showed moderate drought

effects. This opposing physiological behavior among coexisting species revealed a higher capacity of shrub canopies for carbon sequestration under water-limited conditions.

Aboveground fluxes along with soil respiration measurements with chambers were used to scale the net CO_2 flux up to the ecosystem level (NEE) and compared measurements of a nearby eddy-covariance tower (Fig. 59.7). Consistently, the comparison of eddy-covariance NEE and chambers showed that shrubs dominated NEE during the summer period. Chamber measurements shed lights onto our understanding of adaptive strategies for sclerophyll shrublands to im-

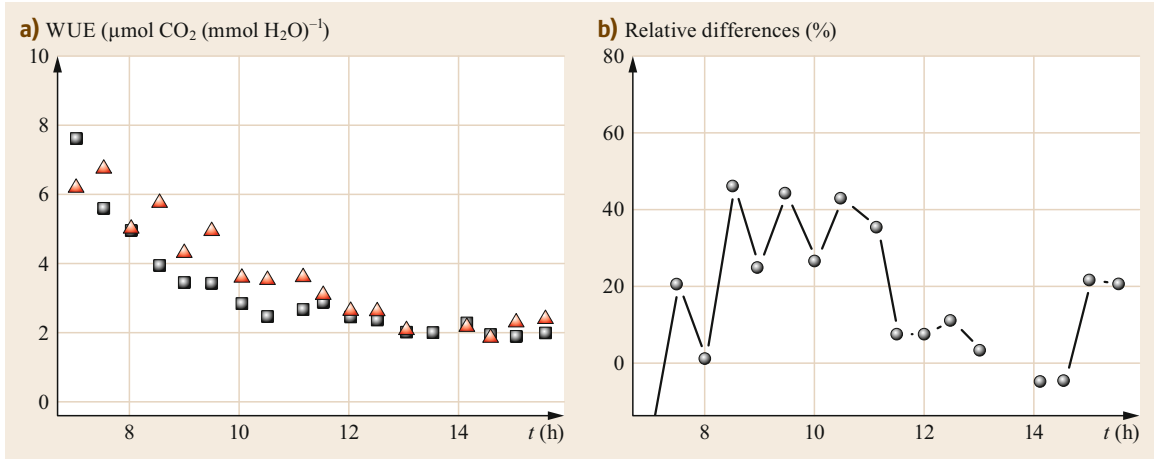


Fig. 59.5 (a) Diurnal time course of water use efficiency (WUE) for two trees under varying water supply (*squares* represent the well-irrigated tree (absence of water stress), while *red triangles* represent the tree under moderate water stress by deficit-irrigation treatment), and (b) relative differences of WUE calculated as $(\text{WUE}_{\text{deficit}} - \text{WUE}_{\text{irrigated}}) / \text{WUE}_{\text{irrigated}}$

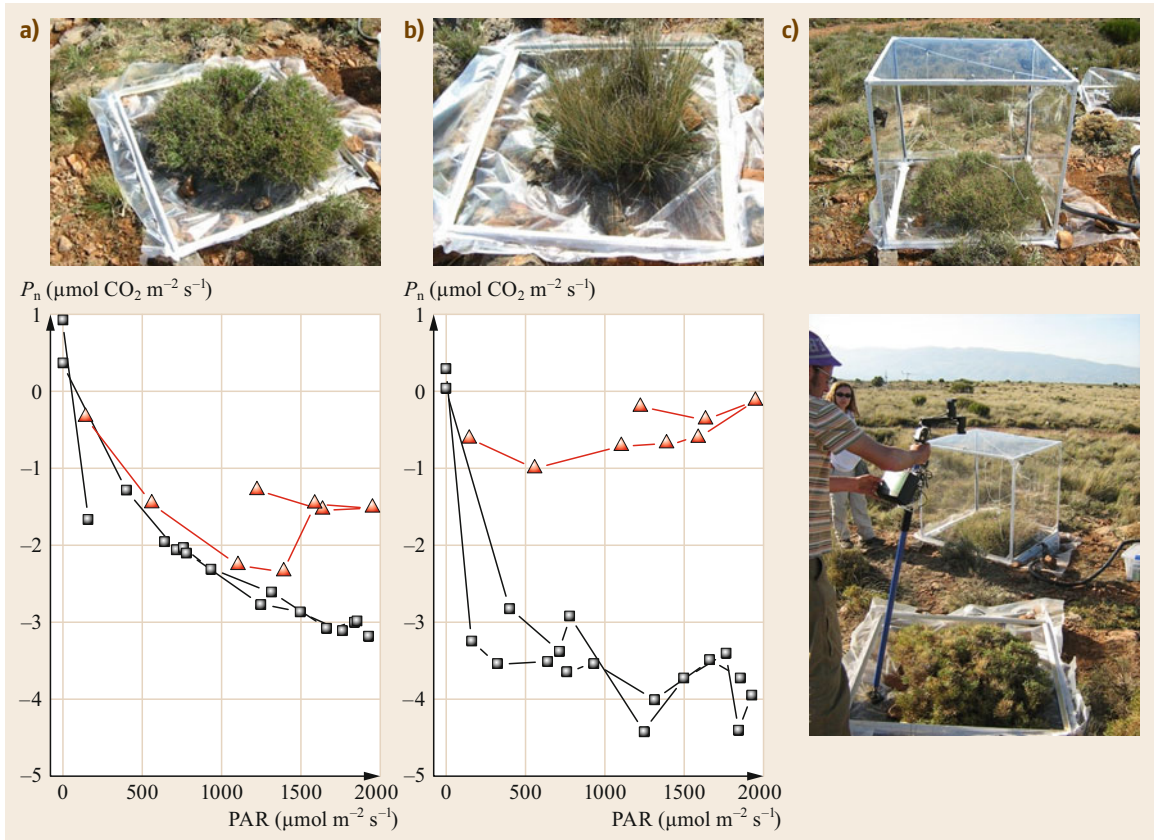


Fig. 59.6a–c Photosynthetic light response curves taken in two coexisting Mediterranean species: (a) *Genista* sp. and (b) *Festuca* sp. of a semiarid shrubland (Sierra de Gador, Spain). Midday leaf water potential was -2.8 and -2.1 MPa in the spring (*squares*) and -7.9 and -3.5 MPa in the summer (*triangles*) for *Festuca* sp. and *Genista* sp., respectively. (c) Radiometric measurements taken quasi simultaneously to determine the optical properties of the species under study (photos © Oscar Perez-Priego)

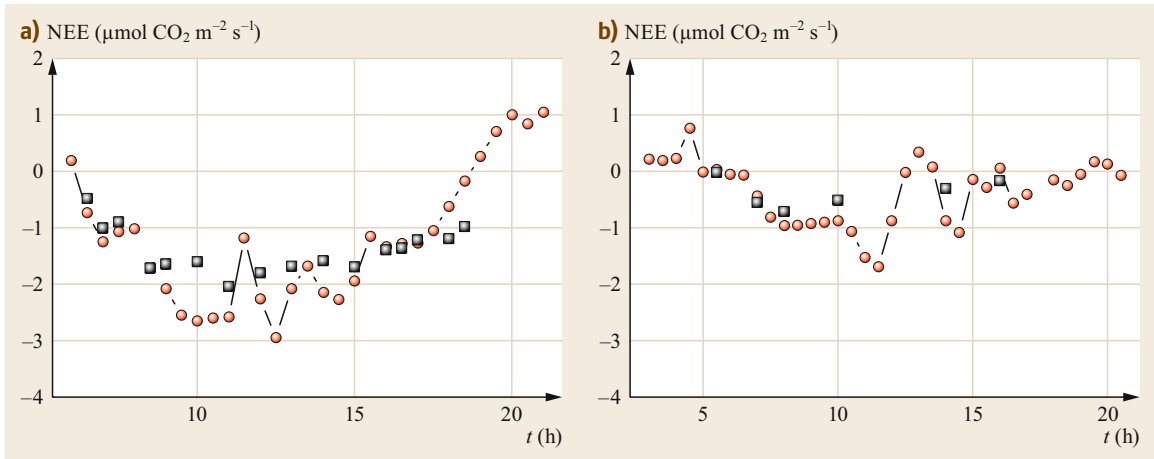


Fig. 59.7a,b Diurnal time courses of NEE rates derived from chamber-based (*circles*) and eddy-covariance methods (*squares*) during (a) spring and (b) summer periods in Sierra de Gador, Spain

prove carbon productivity and stress resistance in arid environments.

59.8.3 Other Relevant Processes

Exchange processes of other important trace gases, including COS, CO, CH₄, N₂O, as well as a variety of reactive trace gases (e.g., VOC, NO_x, O₃) by vegetation have been extensively studied with chamber enclosures [59.5, 39, 40, 42, 53, 65–70]. Gas-exchange rates of reactive trace gases are typically determined by using a carrier gas system either using a reference gas or atmospheric gas samples. To this end, ambient-air enclosures are widely used for measuring biogenic sulfur gases such as isoprene, monoterpenes, and sesquiter-

penes, among others, which are rapidly oxidized in the atmosphere [59.69, 70]. Advance setups not only allow measurements in the gaseous phase but also in the aerosol phases [59.79]. The load of atmospheric aerosol and its radiative properties represents an important research line due to their associated role in pollution and climate-related processes [59.69, 73]. In addition to enclosure systems, dedicated infrastructures to monitor atmospheric aerosol by combining multiwavelength lidar and ceilometer-radiometer instruments are in common use by global networks (e.g., AERONET). It is also worth remarking here that the use of chambers have been extended beyond terrestrial plants; for instance, in estimating CH₄ emissions from aquatic plants [59.80], or even from animals [59.81].

59.9 Future Developments

A common criticism of chamber-based measurements is that they may not reflect the real gas-exchange process due to the disturbances of enclosures. Although this remains the main pitfall of the technique, a number of methods have been described to quantify and reduce the impact of such disturbances. On making the best of it, understanding to what extent enclosures impact the process under study always helps us to better interpret how plants respond to varying environmental conditions (independently of the nature of those impacts, and whether they are artificially or naturally imposed). Therefore, chamber designs capable of regulating and mimicking atmospheric conditions are highly desirable.

In such a way, open-top chambers operate under the premise that a steady-state situation is achieved af-

ter establishing certain conditions. The time scale at which it is realistic to achieve steady-state conditions remains elusive, particularly when plants respond faster than in 1 min. It is also clear that the imposed steady air flow is often higher than the natural wind speed and does not reflect certain atmospheric conditions, i.e., low turbulence. In practice, internal ventilation is also used by transient-state configurations to facilitate air sampling. It has been proven that multisampling methods that assure a well-distributed air sampling over the whole head space of the chamber provide a solution for achieving optimal air mixing. This may provide certain advantages against open-top chambers when considering aerodynamic effects. Although a suitable ventilation rate is difficult to get, controlled transient-state enclo-

tures capable of automatizing the actual aerodynamic conditions within a canopy are required. This would definitely improve our current understanding of leaf gaseous exchange processes across layers and canopy structures. Finally, improvements in the technique and methods aiding the reduction of uncertainty errors are always encouraging, particularly those relevant to the associated water vapor condensation effects.

59.10 Further Readings

Classical literature with a more exhaustive description of the principles of chamber-based gas exchange measurements:

- Z. Sestak, J. Catský, P. G. Jarvis: Plant Photosynthetic Production. Manual of Methods, Plant photosynthetic production. Manual of methods. Dr. W. Junk N. V., The Hague (1971).
- O. T. Denmead: Plant Physiological Methods for Studying Evapotranspiration – Problems of Telling the Forest from the Trees, *Agricultural Water Management* 8, 167–189 (1984).
- G. Livingston, G. Hutchinson: Enclosure-Based Measurement of Trace Gas Exchange: Applications and Sources of Error, *Biogenic trace gases: measuring emissions from soil and water*, 14–51 (1995).

Acknowledgments. The author is grateful to Dr. Jürgen Kesselmeier for his thoughtful review of an earlier draft of this chapter and to Prof. Andrew S. Kowalski, Prof. Penélope Serrano-Ortíz, Dr. Enrique P. Sanchez-Cañete, Ana López-Ballesteros, and Dr. Arnaud Carrara for providing eddy-covariance and soil respiration data and field assistance at the Gador site.

- S. P. Long, P. K. Farage, R. L. Garcia: Measurement of Leaf and Canopy Photosynthetic CO₂ Exchange in the Field, *Journal of Experimental Botany* 47, 1629–1642 (1996).
- O. Perez-Priego, A. Lopez-Ballesteros, E. P. Sanchez-Canete, P. Serrano-Ortiz, L. Kutzbach, F. Domingo, W. Eugster, A. S. Kowalski: Analysing Uncertainties in the Calculation of Fluxes Using Whole-Plant Chambers: Random and Systematic Errors, *Plant and Soil* 393, 229–244 (2015).
- S. Sun, A. Moravek, I. Trebs, J. Kesselmeier, M. J. J. o. G. R. A. Sörgel: Investigation of the Influence of Liquid Surface Films on O₃ and Pan Deposition to Plant Leaves Coated with Organic/Inorganic Solution, *Geophys. Res. Atmos.* 121(23), 14239–14256 (2016).

References

- 59.1 O. Perez-Priego, L. Testi, A.S. Kowalski, F.J. Villalobos, F. Orgaz: Aboveground respiratory CO₂ effluxes from olive trees (*Olea europaea* L.), *Agrofor. Syst.* **88**, 245–255 (2014)
- 59.2 P. Steduto, O. Cetinkoku, R. Albrizio, R. Kanber: Automated closed-system canopy-chamber for continuous field-crop monitoring of CO₂ and H₂O fluxes, *Agric. For. Meteorol.* **111**, 171–186 (2002)
- 59.3 O. Perez-Priego, L. Testi, F. Orgaz, F.J. Villalobos: A large closed canopy chamber for measuring CO₂ and water vapour exchange of whole trees, *Environ. Exp. Bot.* **68**, 131–138 (2010)
- 59.4 O. Perez-Priego, J. Guan, M. Rossini, F. Fava, T. Wutzler, G. Moreno, N. Carvalhais, A. Carrara, O. Kolle, T. Julitta, M. Schrupf, M. Reichstein, M. Migliavacca: Sun-induced chlorophyll fluorescence and photochemical reflectance index improve remote-sensing gross primary production estimates under varying nutrient availability in a typical Mediterranean savanna ecosystem, *Biogeosciences* **12**, 6351–6367 (2015)
- 59.5 O. Denmead, B. Macdonald, G. Bryant, I. White, W. Wang, P. Moody, R. Dalal, W. Stainlay: Greenhouse gas emissions from sugarcane soils and nitrogen fertiliser management: II. In: *Proc. 2007 conference Aust. Soc. Sugar Cane Technol.* (Cairns, Queensland 2007) pp. 97–105
- 59.6 P. Cid, O. Perez-Priego, F. Orgaz, H. Gomez-Macpherson: Short- and mid-term tillage-induced soil CO₂ efflux on irrigated permanent- and conventional-bed planting systems with controlled traffic in southern Spain, *Soil Res.* **51**, 447–458 (2013)
- 59.7 O. Denmead, D. Reicosky: Tillage-induced gas fluxes: comparison of meteorological and large chamber techniques. In: *Proc. Int. Soil Tillage Res. Organ. 16th Trienn. Conf., Brisbane, Australia* (2003) pp. 357–363
- 59.8 A. Lopez-Ballesteros, P. Serrano-Ortiz, E.P. Sanchez-Canete, C. Oyonarte, A.S. Kowalski, O. Perez-Priego, F. Domingo: Enhancement of the net CO₂ release of a semiarid grassland in SE Spain by rain pulses, *J. Geophys. Res. Biogeosci.* **121**, 52–66 (2016)
- 59.9 M. Dubbert, M. Cuntz, A. Piayda, C. Werner: Oxygen isotope signatures of transpired water vapor: the role of isotopic non-steady-state transpiration under natural conditions, *New Phytol.* **203**, 1242–1252 (2014)

- 59.10 D.C. Reicosky: Canopy gas exchange in the field: closed chambers, *Remote Sens. Rev.* **5**, 163–177 (1990)
- 59.11 O. Perez-Priego, A. Lopez-Ballesteros, E.P. Sanchez-Canete, P. Serrano-Ortiz, L. Kutzbach, F. Domingo, W. Eugster, A.S. Kowalski: Analysing uncertainties in the calculation of fluxes using whole-plant chambers: random and systematic errors, *Plant Soil* **393**, 229–244 (2015)
- 59.12 P. Laville, C. Jambert, P. Cellier, R. Delmas: Nitrous oxide fluxes from a fertilised maize crop using micrometeorological and chamber methods, *Agric. For. Meteorol.* **96**, 19–38 (1999)
- 59.13 S. Christensen, P. Ambus, J.R.M. Arah, H. Clayton, B. Galle, D.W.T. Griffith, K.J. Hargreaves, L. Klemetsson, A.M. Lind, M. Maag, A. Scott, U. Skiba, K.A. Smith, M. Welling, F.G. Wienhold: Nitrous oxide emission from an agricultural field: comparison between measurements by flux chamber and micrometeorological techniques, *Atmos. Environ.* **30**, 4183–4190 (1996)
- 59.14 E.A. Ainsworth, S.P. Long: What have we learned from 15 years of free-air CO₂ enrichment (face)? A Meta-analytic review of the responses of photosynthesis, canopy properties and plant production to rising CO₂, *New Phytol.* **165**, 351–372 (2005)
- 59.15 P.W. Leadley, B.G. Drake: Open top chambers for exposing plant canopies to elevated CO₂ concentration and for measuring net gas exchange, *Vegetatio* **104**, 3–15 (1993)
- 59.16 B. Kimball, S. Idso: Increasing atmospheric CO₂: effects on crop yield, water use and climate, *Agric. Water Manag.* **7**(1–3), 55–72 (1993)
- 59.17 C.L. Mulchi, L. Slaughter, M. Saleem, E.H. Lee, R. Pausch, R. Rowland: Growth and physiological characteristics of soybean in open-top chambers in response to ozone and increased atmospheric CO₂, *Agric. Ecosyst. Environ.* **38**, 107–118 (1992)
- 59.18 A.S. Heagle, D.E. Body, W.W. Heck: An open-top field chamber to assess the impact of air pollution on plants, *J. Environ. Qual.* **2**, 365 (1973)
- 59.19 D. Dragoni, A.N. Lakso, R.M. Piccioni: Transpiration of apple trees in a humid climate using heat pulse sap flow gauges calibrated with whole-canopy gas exchange chambers, *Agric. For. Meteorol.* **130**, 85–94 (2005)
- 59.20 I.A. Janssens, A.S. Kowalski, R. Ceulemans: Forest floor CO₂ fluxes estimated by eddy covariance and chamber-based model, *Agric. For. Meteorol.* **106**, 61–69 (2001)
- 59.21 A.A. Held, P. Steduto, F. Orgaz, A. Matista, T.C. Hsiao: Bowen ratio/energy balance technique for estimating crop net CO₂ assimilation, and comparison with a canopy chamber, *Theor. Appl. Climatol.* **42**, 203–213 (1990)
- 59.22 W.A. Dugas, L.J. Fritschen, L.W. Gay, A.A. Held, A.D. Matthias, D.C. Reicosky, P. Steduto, J.L. Steiner: Bowen ratio, eddy correlation, and portable chamber measurements of sensible and latent heat flux over irrigated spring wheat, *Agric. For. Meteorol.* **56**, 1–20 (1991)
- 59.23 W.A. Dugas, D.C. Reicosky, J.R. Kiniry: Chamber and micrometeorological measurements of CO₂ and H₂O fluxes for three C₄ grasses, *Agric. For. Meteorol.* **83**, 113–133 (1997)
- 59.24 G. Ferrara, J.A. Flore: Comparison between different methods for measuring transpiration in potted apple trees, *Biol. Plant.* **46**, 41–47 (2003)
- 59.25 R.C. Dewar, O. Franklin, A. Makela, R.E. McMurtrie, H.T. Valentine: Optimal function explains forest responses to global change, *Bioscience* **59**, 127–139 (2009)
- 59.26 W.A. Cannon: A new method of measuring the transpiration of plants in place, *Bull. Torrey Bot. Club* **32**, 515 (1905)
- 59.27 D. Reicosky, D. Peters: A portable chamber for rapid evapotranspiration measurements on field plots, *Agron. J.* **69**, 729–732 (1977)
- 59.28 M.D. Thomas, G.R. Hill: The continuous measurement of photosynthesis, respiration, and transpiration of alfalfa and wheat growing under field conditions, *Plant Physiol.* **12**, 285 (1937)
- 59.29 P.B. Jensen: Studies on the production of matter in light- and shadow-plants, *Bot. Tidskr.* **36**, 219–262 (1918)
- 59.30 H. Lundegardh: Neue Apparate zur Analyse des Kohlensäuregehalts der Luft, *Biochem. Z.* **131**, 109 (1922)
- 59.31 F. Eckardt: Techniques De Mesure De La Photo-Synthèse Sur Le Terrain Basées Sur L'emploi D'enceintes Cli-Matisées, Functioning of terrestrial ecosystems at the primary production level. In: *Proc. UNESCO Cph. Symp., Belgium* (1968) pp. 289–319
- 59.32 A.J. Heinicke, N.F. Childers: *Daily Rate of Photosynthesis, During the Growing Season of 1935, of a Young Apple Tree of Bearing Age* 1937
- 59.33 Z. Sestak, J. Catský, P.G. Jarvis: *Plant Photosynthetic Production. Manual of Methods* (Junk, The Hague 1971)
- 59.34 R.B. Musgrave, D.N. Moss: Photosynthesis under field conditions. I. A portable, closed system for determining net assimilation and respiration of corn, *Crop Sci.* **1**, 37–41 (1961)
- 59.35 A.D. Matthias, D.N. Yarger, R.S. Weinbeck: A numerical evaluation of chamber methods for determining gas fluxes, *Geophys. Res. Lett.* **5**, 765–768 (1978)
- 59.36 D. Reicosky: Advances in evapotranspiration measured using portable field chambers. In: *Proc. Natl. Conf. Adv. Evapotranspir., Hyatt Regency Chicago, IL (USA), 16–17 Dec 1985* (ASAE, St. Joseph 1985)
- 59.37 F.X. Dunin, E.A.N. Greenwood: Evaluation of the ventilated chamber for measuring evaporation from a forest, *Hydrol. Proc.* **1**, 47–62 (1986)
- 59.38 O.T. Denmead: Plant physiological methods for studying evapotranspiration – problems of telling the forest from the trees, *Agric. Water Manag.* **8**, 167–189 (1984)
- 59.39 T. Dindorf, U. Kuhn, L. Ganzeveld, G. Schebeske, P. Ciccioli, C. Holzke, R. Koble, G. Seufert, J. Kesselmeier: Significant light and temperature dependent monoterpene emissions from European beech (*Fagus Sylvatica* L.) and their potential impact on the European volatile organic com-

- pound budget, *J. Geophys. Res. Atmos.* (2006), <https://doi.org/10.1029/2005JD006751>
- 59.40 S. Sun, A. Moravek, L. von der Heyden, A. Held, M. Sorgel, J. Kesselmeier: Twin-Cuvette measurement technique for investigation of dry deposition of O₃ and pan to plant leaves under controlled humidity conditions, *Atmos. Meas. Tech.* **9**(599), 599–617 (2016)
- 59.41 S. Sun, A. Moravek, I. Trebs, J. Kesselmeier, M. Sörgel: Investigation of the influence of liquid surface films on O₃ and pan deposition to plant leaves coated with organic/inorganic solution, *JGR Atmospheres* **121**, 14239–14256 (2016)
- 59.42 C. Breuninger, R. Oswald, J. Kesselmeier, F.X. Meixner: The dynamic chamber method: trace gas exchange fluxes (NO, NO₂, O₃) between plants and the atmosphere in the laboratory and in the field, *Atmos. Meas. Tech.* **5**, 955–989 (2012)
- 59.43 G. Livingston, G. Hutchinson: Enclosure-based measurement of trace gas exchange: applications and sources of error. In: *Biogenic Trace Gases: Measuring Emissions from Soil and Water*, ed. by P.A. Matson, R.C. Harris (Blackwell, Oxford 1995) pp. 14–51
- 59.44 J.P. Pena, J. Tarara: A portable whole canopy gas exchange system for several mature field-grown grapevines, *Vitis* **43**, 7–14 (2004)
- 59.45 L. Corelli-Grappadelli, E. Magnanini: A whole-tree system for gas-exchange studies, *Hort. Sci.* **28**, 41–45 (1993)
- 59.46 O.T. Denmead, F.X. Dunin, S.C. Wong, E.A.N. Greenwood: Measuring water-use efficiency of eucalypt trees with chambers and micrometeorological techniques, *J. Hydrol.* **150**, 649–664 (1993)
- 59.47 S. Poni, E. Magnanini, B. Rebucci: An automated chamber system for measurements of whole-vine gas exchange, *Hort. Sci.* **32**, 64–67 (1997)
- 59.48 D.P. Miller, G.S. Howell, J.A. Flore: A whole-plant, open, gas-exchange system for measuring net photosynthesis of potted woody plants, *Hort. Sci.* **31**, 944–946 (1996)
- 59.49 D. Intrigliolo, A. Lakso, R. Piccioni: Grapevine Cv. 'Riesling' water use in the northeastern United States, *Irrig. Sci.* **27**, 253–262 (2009)
- 59.50 A. Heinemeyer, N.P. McNamara: Comparing the closed static versus the closed dynamic chamber flux methodology: implications for soil respiration studies, *Plant Soil* **346**, 145–151 (2011)
- 59.51 R.L. Garcia, J.M. Norman, D.K. McDermitt: Measurements of canopy gas exchange using an open chamber system, *Remote Sens. Rev.* **5**, 141–162 (1990)
- 59.52 E.A. Davidson, K. Savage, L.V. Verchot, R. Navarro: Minimizing artifacts and biases in chamber-based measurements of soil respiration, *Agric. For. Meteorol.* **113**, 21–37 (2002)
- 59.53 O.T. Denmead: Approaches to measuring fluxes of methane and nitrous oxide between landscapes and the atmosphere, *Plant Soil* **309**, 5–24 (2008)
- 59.54 R.S. Jassal, T.A. Black, Z. Nestic, D. Gaumont-Guay: Using automated non-steady-state chamber systems for making continuous long-term measurements of soil CO₂ efflux in forest ecosystems, *Agric. For. Meteorol.* **161**, 57–65 (2012)
- 59.55 G.B. Drewitt, T.A. Black, Z. Nestic, E.R. Humphreys, E.M. Jork, R. Swanson, G.J. Ethier, T. Griffis, K. Morgenstern: Measuring forest floor CO₂ fluxes in a Douglas-fir forest, *Agric. For. Meteorol.* **110**, 299–317 (2002)
- 59.56 S. Long, C. Bernacchi: Gas exchange measurements, what can they tell us about the underlying limitations to photosynthesis? Procedures and sources of error, *J. Exp. Bot.* **54**, 2393–2401 (2003)
- 59.57 M.H. Unsworth: Evaporation from forests in cloud enhances the effects of acid deposition, *Nature* **312**, 262–264 (1984)
- 59.58 T. Wutzler, O. Perez-Priego: Respchamberproc: processing data from respiration chambers. R package version 0.6.2/R3, <https://R-Forge.R-project.org/projects/respchamberproc/> (2017)
- 59.59 S.W. Wagner, D.C. Reicosky, R.S. Alessi: Regression models for calculating gas fluxes measured with a closed chamber, *Agron. J.* **89**, 279–284 (1997)
- 59.60 P.E. Levy, A. Gray, S.R. Leeson, J. Gaiawyn, M.P.C. Kelly, M.D.A. Cooper, K.J. Dinsmore, S.K. Jones, L.J. Sheppard: Quantification of uncertainty in trace gas fluxes measured by the static chamber method, *Eur. J. Soil Sci.* **62**, 811–821 (2011)
- 59.61 L. Kutzbach, J. Schneider, T. Sachs, M. Giebels, H. Nykänen, N.J. Shurpali, P.J. Martikainen, J. Alm, M. Wilmking: CO₂ flux determination by closed-chamber methods can be seriously biased by inappropriate application of linear regression, *Biogeosciences* **4**, 1005–1025 (2007)
- 59.62 M.K. Pihlatie, J.R. Christiansen, H. Aaltonen, J.F.J. Korhonen, A. Nordbo, T. Rasilo, G. Benanti, M. Giebels, M. Helmy, J. Sheehy, S. Jones, R. Juszczak, R. Klefoth, R. Lobo-do-Vale, A.P. Rosa, P. Schreiber, D. Serça, S. Vicca, B. Wolf, J. Pumpaenen: Comparison of static chambers to measure CH₄ emissions from soils, *Agric. For. Meteorol.* **171/172**, 124–136 (2013)
- 59.63 E.K. Webb, G.I. Pearman, R. Leuning: Correction of flux measurements for density effects due to heat and water-vapor transfer, *Q. J. R. Meteorol. Soc.* **106**, 85–100 (1980)
- 59.64 A.S. Kowalski, P. Serrano-Ortiz: On the relationship between the eddy covariance, the turbulent flux, and surface exchange for a trace gas such as CO₂, *Bound.-Layer Meteorol.* **124**, 129–141 (2007)
- 59.65 J. Kesselmeier, F.X. Meixner, U. Hofmann, A.L. Ajavon, S. Leimbach, M.O. Andreae: Reduced sulfur compound exchange between the atmosphere and tropical tree species in southern Cameroon, *Biogeochemistry* **23**, 23–45 (1993)
- 59.66 J. Kesselmeier, N. Teusch, U. Kuhn: Controlling variables for the uptake of atmospheric carbonyl sulfide by soil, *J. Geophys. Res. Atmos.* **104**, 11577–11584 (1999)
- 59.67 J. Kesselmeier, L. Merk: Exchange of carbonyl sulfide (COS) between agricultural plants and the atmosphere – studies on the deposition of COS to

- peas, corn and rapeseed, *Biogeochemistry* **23**, 47–59 (1993)
- 59.68 J. Kesselmeier, P. Ciccioli, U. Kuhn, P. Stefani, T. Biesenthal, S. Rottenberger, A. Wolf, M. Vitullo, R. Valentini, A. Nobre, P. Kabat, M.O. Andreae: Volatile organic compound emissions in relation to plant carbon fixation and the terrestrial carbon budget, *Global Biogeochem. Cycles* (2002), <https://doi.org/10.1029/2001GB001813>
- 59.69 M.O. Andreae, O.C. Acevedo, A. Araujo, P. Artaxo, C.G.G. Barbosa, H.M.J. Barbosa, J. Brito, S. Carbone, X. Chi, B.B.L. Cintra, N.F. da Silva, N.L. Dias, C.Q. Dias, F. Ditas, R. Ditz, A.F.L. Godoi, R.H.M. Godoi, M. Heimann, T. Hoffmann, J. Kesselmeier, T. Konemann, M.L. Kruger, J.V. Lavric, A.O. Manzi, A.P. Lopes, D.L. Martins, E.F. Mikhailov, D. Moran-Zuloaga, B.W. Nelson, A.C. Nolscher, D.S. Nogueira, M.T.F. Piedade, C. Pohlker, U. Poschl, C.A. Quesada, L.V. Rizzo, C.U. Ro, N. Ruckteschler, L.D.A. Sa, M.D. Sa, C.B. Sales, R.M.N. dos Santos, J. Saturno, J. Schongart, M. Sorgel, C.M. de Souza, R.A.F. de Souza, H. Su, N. Targhetta, J. Tota, I. Trebs, S. Trumbore, A. van Eijck, D. Walter, Z. Wang, B. Weber, J. Williams, J. Winderlich, F. Wittmann, S. Wolff, A.M. Yanez-Serrano: The Amazon Tall Tower Observatory (Atto): overview of pilot measurements on ecosystem ecology, meteorology, trace gases, and aerosols, *Atmos. Chem. Phys.* **15**, 10723–10776 (2015)
- 59.70 A.M. Yanez-Serrano, A.C. Nolscher, J. Williams, S. Wolff, E. Alves, G.A. Martins, E. Bourtsoukidis, J. Brito, K. Jardine, P. Artaxo, J. Kesselmeier: Diel and seasonal changes of biogenic volatile organic compounds within and above an Amazonian rainforest, *Atmos. Chem. Phys.* **15**, 3359–3378 (2015)
- 59.71 M. Langensiepen, M. Kupisch, M.T. van Wijk, F. Ewert: Analyzing transient closed chamber effects on canopy gas exchange for optimizing flux calculation timing, *Agric. For. Meteorol.* **164**, 61–70 (2012)
- 59.72 J. Pérez-Peña, J. Tarara: A portable whole canopy gas exchange system for several mature field-grown grapevines, *Vitis* **43**, 7–14 (2015)
- 59.73 M.V. Hobe, U. Kuhn, H.V. Diest, L. Sandoval-Soto, T. Kenntner, F. Helleis, S. Yonemura, M.O. Andreae, J. Kesselmeier: Automated in situ analysis of volatile sulfur gases using a sulfur gas analyser (sugar) based on cryogenic trapping and gas-chromatographic separation, *Int. J. Environ. Anal. Chem.* **88**, 303–315 (2008)
- 59.74 O. Denmead: Chamber systems for measuring nitrous oxide emission from soils in the field, *Soil Sci. Soc. Am. J.* **43**, 89–95 (1979)
- 59.75 M.B. Rayment, P.G. Jarvis: An improved open chamber system for measuring soil CO₂ effluxes in the field, *J. Geophys. Res. Atmos.* **102**, 28779–28784 (1997)
- 59.76 F. Kitz, K. Gerdel, A. Hammerle, T. Laterza, F.M. Spielmann, G. Wohlfahrt: In situ soil CO₂ exchange of a temperate mountain grassland under simulated drought, *Oecologia* **183**, 851–860 (2017)
- 59.77 T.F. Keenan, Ü. Niinemets: Global leaf trait estimates biased due to plasticity in the shade, *Nat. Plants* **3**, 16201 (2016)
- 59.78 B.E. Medlyn, M.G. De Kauwe, Y.S. Lin, J. Knauer, R.A. Duursma, C.A. Williams, A. Arneeth, R. Clement, P. Isaac, J.M. Limousin, M.L. Linderson, P. Meir, N. Martin-StPaul, L. Wingate: How do leaf and ecosystem measures of water-use efficiency compare?, *New Phytol.* **216**, 758–770 (2017)
- 59.79 M.S. Castro, J.N. Galloway: A comparison of sulfur-free and ambient air enclosure techniques for measuring the exchange of reduced sulfur gases between soils and the atmosphere, *J. Geophys. Res. Atmos.* **96**, 15427–15437 (1991)
- 59.80 A. Knapp, J. Yavitt: Evaluation of a closed-chamber method for estimating methane emissions from aquatic plants, *Tellus B* **44**, 63–71 (1992)
- 59.81 R. Leuning, S.K. Baker, I.M. Jamie, C.H. Hsu, L. Klein, O.T. Denmead, D.W.T. Griffith: Methane emission from free-ranging sheep: a comparison of two measurement methods, *Atmos. Environ.* **33**, 1357–1365 (1999)

Oscar Perez-Priego

Biological Science
Macquarie University
Sydney, NSW, Australia
oscarperezpriego@gmail.com



Dr Oscar Perez-Priego is postdoctoral research fellow at Macquarie University, Australia. He received a PhD in Bioscience (2011), a postdoc at University of Granada (2011–2013, Spain) and the Max Planck Institute for Biogeochemistry (2014–2018, Germany). He studies soil–plant–atmosphere interactions by combining field experiments and models. He is interested in gas and energy exchange from single leaves to the whole plant and ecosystem scales, ecosystem modeling, and theory.

Soil Chamber

60. Soil Chamber Measurements

Jens-Arne Subke , Lars Kutzbach , David Risk 

Chamber measurements form a fundamental approach in quantifying the exchange of trace gases between soils and the atmosphere. A range of chamber approaches has been used, reflecting the progress in our understanding of soil gas flux dynamics and technical capabilities. Minimizing measuring artefacts that are associated with soil chamber measurements have mainly driven these advances, along with a need to obtain soil flux data of appropriate spatial replication and temporal resolution. We here present an overview of the main *classic* CO₂ flux chamber approaches, noting that general principles apply also to chamber measurements of other trace gases. The chapter introduces measuring principles, data evaluation, and key parameters, and covers recent advances in autonomous measurements in the field. We explicitly address the respective strengths and weaknesses of some automated measuring approaches, as these are likely to be critical for long-term assessments of gas flux across many biomes and linked to other atmospheric gas exchange approaches.

60.1	Measurement Approaches, Principles, and Parameters	1604	60.3	Theory	1608
60.2	History of Soil Chamber Measurements	1606	60.3.1	Mass Flow and Pressure Issues	1608
60.2.1	Offline Sampling and Chemical Absorption	1606	60.3.2	Concentration Corrections and Flux Calculations	1609
60.2.2	Steady-State Flowthrough Chamber Designs (<i>Open Chambers</i>)	1607	60.3.3	Non-Steady-State Chambers	1609
60.2.3	Field-Portable Chambers	1607	60.3.4	Steady-State Chambers	1610
			60.3.5	Forced Diffusion Chambers	1611
			60.3.6	Comparison of Measuring Principles	1612
			60.4	Devices and Systems	1612
			60.4.1	Manual Chambers	1612
			60.4.2	Automated Chambers	1614
			60.4.3	Overview	1616
			60.5	Specifications	1616
			60.6	Quality Control	1616
			60.6.1	Uncertainties in Instrumental Gas Concentration Analysis	1617
			60.6.2	Uncertainties Due to Artefacts by the Non-Steady-State (Closed) Chamber Method	1617
			60.6.3	Uncertainties Due to Spatial Variability	1618
			60.6.4	Uncertainties Due to Temporal Variability	1618
			60.7	Maintenance	1619
			60.8	Application	1619
			60.8.1	Ecosystem Flux Components	1619
			60.8.2	Long-Term Monitoring of Soil Gas Flux	1620
			60.8.3	Gas Exchange in Remote Locations	1620
			60.9	Future Developments	1621
			60.10	Further Readings	1621
			References		1621

Soil CO₂ efflux constitutes the most significant route for carbon assimilated by an ecosystem back into the atmosphere. It integrates a range of different sources of CO₂, such as heterotrophic decomposition of organic matter, metabolic processes by roots and associated mycorrhizas, respiration by soil-dwelling animals, and mineral CO₂ sources [60.1, 2]. Accurate measurement of this flux is fundamental for establishing C

exchange dynamics within ecosystems, and chamber methods are the most commonly employed methodology to do so. Knowledge of soil CO₂ efflux dynamics over diurnal, synoptic, seasonal, or annual scales provides important insights into the processes underlying it and allows a more detailed analysis of ecosystem-scale fluxes (such as total ecosystem CO₂ exchange) into aboveground and belowground fluxes. As well as

providing direct estimates of soil metabolic activity and its biotic and abiotic drivers, flux measurements are often coupled with experimental manipulations or complementary measurements that enable a more detailed investigation of flux sources (e.g., autotrophic versus heterotrophic C sources) and biological interactions (e.g., root and mycorrhizal dynamics, or soil faunal and plant phenological dynamics).

The exchange of other trace gases between soil and atmosphere is no less important and has similarly received considerable attention in the scientific literature. For example, the emission of methane (CH_4) in wetlands is an important component of the greenhouse-gas balance of these systems [60.3]. Uptake of methane through microbial oxidation in upland soils, on the other hand, also affects regional budgets, whilst emissions of nitrous oxide (N_2O) is of relevance in agricultural studies, particularly under high fertilizer use [60.4, 5].

The aim of this chapter is to give an updated appraisal of the main chamber designs in the scientific literature and to highlight current systems and recent advances. A number of overviews of chamber methods for soil trace gas exchange exist, and we acknowledge the range of information provided in these [60.6, 7]. We summarize information also given in earlier reviews, with our own critical appraisal of designs and data processing, and include recent approaches and instrumentation to measure soil–atmosphere gas exchange using chambers. Much of the overview focuses on soil CO_2 flux chambers, as the majority of published methods and applications are on CO_2 exchanges, but general principles apply to the measurement of other trace gas exchanges between soil and atmosphere, and we include some details on recent instrumentation and considerations for applications of chambers.

60.1 Measurement Approaches, Principles, and Parameters

The purpose of any chamber is to create an enclosed air volume in which changes in concentration of gases exchanged between soil and atmosphere can be monitored. As such, the placement of a chamber on the soil surface causes an alteration of the natural conditions in terms of abiotic parameters (e.g., temperature and humidity), as well as gas concen-

trations and exchange processes due to alterations of diffusive and turbulent transport across boundary layers [60.8, 9] or variations in static pressure [60.10–12]. The degree to which any artefacts resulting from chamber placement affect flux estimates depends on the type of chamber and measuring principle involved.

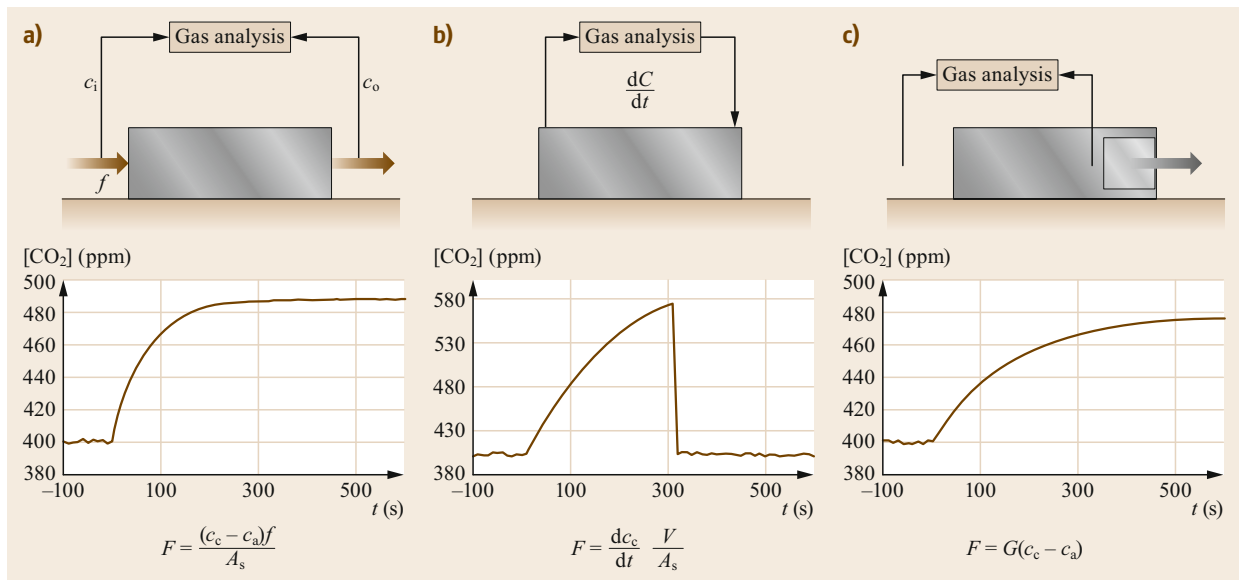


Fig. 60.1a–c Overview (principle, internal CO_2 concentration, flux calculation) of main chamber designs used to measure trace gas exchange between soil and atmosphere: (a) steady-state chamber, (b) non-steady-state chamber, and (c) forced diffusion chamber. See Table 60.1 for the meaning of measurement parameters of flux calculations

Soil chambers have been used to measure CO₂ flux for the past 100 years [60.13, 14], and different shapes, designs, and principles have evolved throughout this period. Chamber types have been categorized into *closed/open*, *dynamic/static*, *flowthrough/non-flowthrough*, or *steady-state/non-steady-state* designs [60.15]. Many of these descriptors are, in fact, synonymous, e.g., an *open* chamber is also necessarily *flowthrough* and *steady state*, and a *closed* chamber can be *flowthrough* or *non-flowthrough*, and measurements are derived from *non-steady-state* conditions. For simplicity, we here adhere to the classification of chambers based on whether fluxes are measured at *steady state* or *non-steady state* [60.16], but note the potentially confusing use of other categorizations used in the literature.

Non-steady-state chambers work on the principle that chambers are closed for a specific length of time, and fluxes are calculated from changes in chamber con-

centration during this period. *Steady-state* chambers monitor gas exchange based on the concentration differential between ambient air and chamber headspace volumes. The steady-state conditions are created by continuous exchange of CO₂ with the ambient atmosphere. *Open* chambers have a continuous flow of air through the headspace, maintaining a connection to the ambient atmosphere. Flux calculations are based on the concentration differential between air entering and leaving the chamber. A novel *steady-state* approach measures the rate of CO₂ diffusion across a permeable membrane to establish soil CO₂ efflux based on the CO₂ concentration within an otherwise closed chamber headspace (*forced diffusion*). Figure 60.1 gives an overview of the key features of these broad chamber categories, whilst a detailed description of theory of operation and implications for specific measurement tasks are given in Sect. 60.3.

Table 60.1 Measured parameters of soil chamber measurements

Parameter	Description	Unit	Symbol
All chamber approaches			
Gas concentration in chamber	Amount (mass) of gas species in chamber headspace	kg m ⁻³	c_c
Ambient gas concentration	Amount (mass) of gas species in ambient air	kg m ⁻³	c_a
Molar fraction	Fraction of a gas species in air	mol mol ⁻¹ or ppmv	χ
Pressure	Air pressure in chamber headspace	Pa	p
Temperature	Air temperature in chamber headspace	K	T
Water vapor concentration	Fraction of water vapor in air	mol mol ⁻¹ or ppmv	χ_{H_2O}
Chamber area	Area of soil covered by chamber	m ²	A_s
Chamber volume	Total volume of chamber (including external volume of tubing, analysis cell and pump)	m ³	V
Steady-state chamber			
Air flow rate	Volume flow of external air passing through chamber headspace	m ³ s ⁻¹	f
Non-steady-state chamber			
Duration of closure	Exact time of sampling from headspace since start of chamber closure	s	t
Forced diffusion chamber			
Diffusivity	Area-specific effective membrane diffusivity	m ² s ⁻¹	D
Path length	Effective diffusive path length	m	L
Scalar	Single term for conversion of chamber-specific membrane area, diffusivity and path length	m s ⁻¹	G

Table 60.2 Other measurements commonly performed alongside chamber flux measurements

Parameter	Description	Unit	Symbol
Soil temperature	Current temperature of soil, ideally covering a number of depth increments	°C	T_s
Soil moisture	Volumetric or gravimetric water content of soil; normally applied to surface soil layers, but ideally obtained across several depths	m ³ m ⁻³ or kg kg ⁻¹	SWC
Air temperature	Temperature of ambient air	°C	T_{ambient}
Water table depth	Depth of water table below soil surface	m	h

60.2 History of Soil Chamber Measurements

Soil CO₂ flux chambers have been used for about 100 years [60.13], and their design has changed with the variety of research and monitoring requirements, analytical capabilities, and the advancement of the understanding of the disturbance that may be created by chambers themselves. The main measurement principles of chambers used today have not changed over many decades, and the basic theory outlined in Sect. 60.3 and models presented in Sect. 60.4 represent refinements on what has been only a small number of successful measurement designs.

However, whilst the principal physical design of soil chambers has not changed fundamentally, methods of determining the flux rates measured with these chambers have, in fact, evolved. In this section, we outline a number of key methods to determine CO₂ concentrations that have been widely used in the past but are now only rarely used.

60.2.1 Offline Sampling and Chemical Absorption

Initial chamber designs follow the current *closed chamber* principle, where a headspace of known volume is created over a specific soil area to trap CO₂ emitted from the soil (Sect. 60.3.1). This *respiration bell* (Fig. 60.2) [60.13] was left in place over a defined period of time (e.g., 10–20 min [60.13] or 1 h [60.17]), and CO₂ concentrations were determined either by extracting a small volume of gas (e.g., 20 mL) from the headspace for determination of CO₂ concentration at the end of this period, or by allowing CO₂ to be absorbed onto a chemical trap throughout the period of chamber closure. The calculation of soil CO₂ flux rates was then simply based on the total amount of CO₂ observed in the headspace, following analogous calculations to those presented in Sect. 60.3.1.

These early measurements provided useful insights into the general dynamics of CO₂ flux and allowed comparative studies of flux rates from different soils and over different measurement periods. However, the static nature of these measurements creates a number of

problems associated with the buildup of the CO₂ concentration following chamber closure.

The offline sampling method assumes that the buildup of concentration in the headspace is linear or, in other words, that the rate of CO₂ flux from soil to chamber is constant throughout the period. However, the soil surface flux rate is highly sensitive to changes in the concentration differential between the chamber headspace and air in superficial soil pores. As the headspace volume progressively enriches in CO₂, this differential progressively decreases, leading to a lower rate of net flux of CO₂ from soil to chamber. Over time, also the soil profile beneath the chamber is enriched in CO₂ relative to the natural soil CO₂ profile, leading to lateral diffusion of CO₂ and, hence, an underestimation of CO₂ efflux. Figure 60.3a illustrates the reduction in the concentration gradient from the headspace into the soil profile. Note that the graph is not based on direct measurements but was produced using a 1-D diffusion model. It clearly shows the reduction in concentration difference between headspace and superficial soil pores, as well as within the soil profile (here illustrated for 3 and 5 cm soil depth), resulting in a diminishing diffusion gradient and hence decreasing measured CO₂ flux (Fig. 60.3c). The 1-D model does not account for lateral diffusion in soil pore spaces adjacent to the chamber footprint, which is likely to occur once a lateral gradient has been established. This would further reduce the CO₂ gradients beneath the chamber, as the observed increase in soil pore concentration would be less pronounced owing to the *loss* of CO₂ from soil pores beneath the chamber. Scenarios shown in Fig. 60.3 simulate an initial surface CO₂ flux of 1.5 μmol m⁻² s⁻¹. For a static chamber with continuous CO₂ enrichment, the flux reduces soon after chamber closure (0 min) and continues to drop up until the chamber is opened after 60 min. The spike in soil CO₂ efflux seen after 60 min is a result of the artificially increased CO₂ concentrations in the soil profile. Early measurements of soil CO₂ flux based on prolonged period of concentration enrichment are, therefore, likely to represent underestimates of soil CO₂ efflux.

Closed chamber methods using continuous chemical absorption of CO₂ have the opposite effect on the atmosphere–soil concentration gradient, as the efficient absorption of CO₂ in the headspace would artificially increase the CO₂ concentration differential to soil pore spaces. The impact on the soil CO₂ gradient is much lower compared to chambers with CO₂ enrichment, so that the overall bias from this effect alone is of smaller magnitude (Fig. 60.3b,d). However, there are

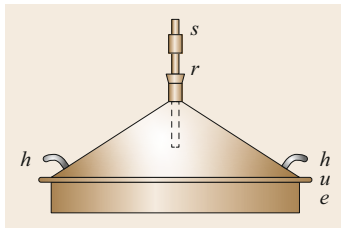


Fig. 60.2 Early model of a closed respiration chamber termed *respiration bell* by Lundegårdh in 1926 (after [60.13])

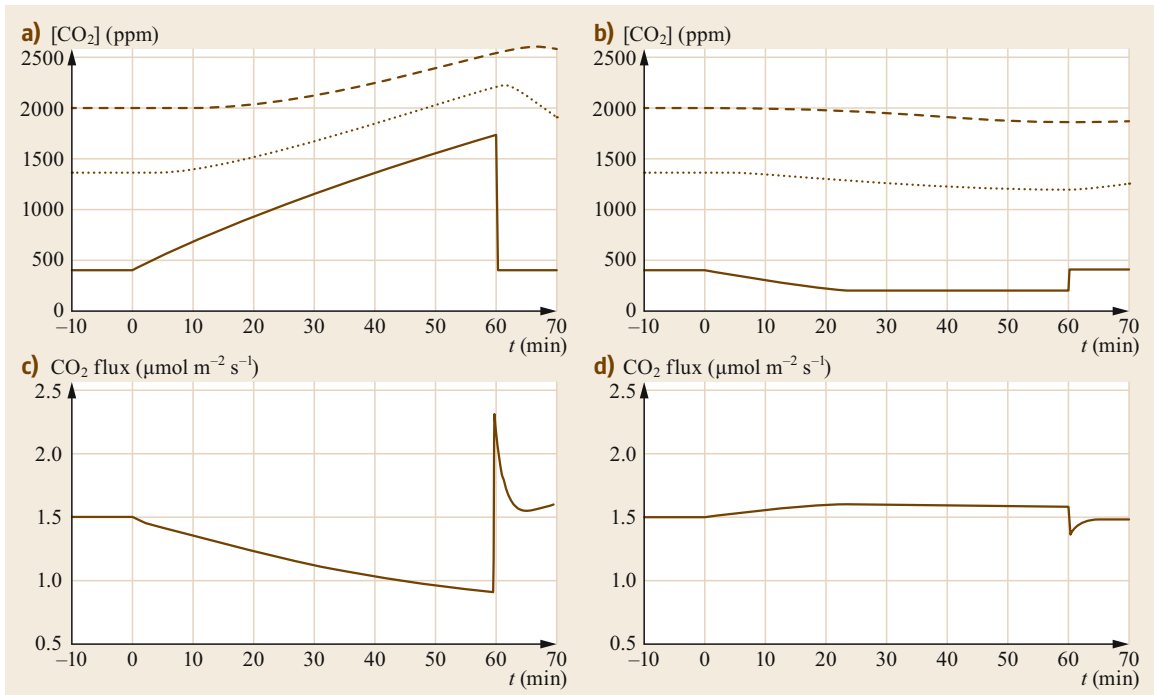


Fig. 60.3a–d Simulated CO₂ concentrations in the chamber headspace (*solid black line*) and soil pores beneath the chamber at 3 cm (*dotted line*) and 5 cm (*dashed line*) soil depth for a closure time of 1 h. **(a)** CO₂ enrichment scenario, **(b)** CO₂ absorption scenario, and **(c,d)** calculated surface CO₂ flux for both scenarios

further uncertainties associated with the efficiency of CO₂ absorption over the period of chamber closure, and additional efforts associated with handling of chemical reagents in the field combined with a more labor intensive analysis of CO₂ concentration determination mean that this method is used very rarely for flux measurements of CO₂ in the field.

60.2.2 Steady-State Flowthrough Chamber Designs (*Open Chambers*)

An early design for continuous soil respiration measurement from a single chamber was proposed in 1953 by drawing ambient air through the headspace of a soil cover to estimate soil CO₂ efflux from the enrichment in CO₂ [60.18]. These early chambers consisted of a frame firmly anchored in the soil, on which a lid was placed to create a chamber headspace. Single chambers of this design were then connected to an infrared gas analyzer (IRGA), with air flowing at a known rate through the chamber, and the difference between ambient air and chamber air recorded (Sect. 60.3). Further development of that technique with multiple chambers sampled sequentially were reported in the late 1960s [60.19–21] to improve spatial coverage and pro-

duce a first complete time series of soil CO₂ efflux in forest ecosystems. To avoid prolonged disturbance of the soil environment caused by the presence of chambers, early versions of these steady-state chambers already included *moving chamber* designs, where robotic drives opened and closed chambers between measurement cycles [60.22].

60.2.3 Field-Portable Chambers

Field-deployable IRGAs enabled direct monitoring of CO₂ increase in chamber headspace concentrations. Commercial availability of small IRGA units from the early 1990s facilitated shorter deployment periods and a more robust analysis of CO₂ concentration evolution in headspaces [60.23, 24]. In this chamber design, air is continuously exchanged between the chamber headspace and a portable infrared gas analyzer via tubing or by directly mounting the analyzer on the chamber (Fig. 60.4). This (quasi) continuous monitoring of concentration increments over the deployment period yields data with which assumptions regarding the linearity of the concentration increase can be tested, and potential errors resulting from a diminishing CO₂ diffusion gradient corrected (Sect. 60.3.1). The more

portable design of chamber and analyzer and significantly shorter deployment period when compared to the chemical absorption methodology meant that researchers could measure from a larger number of loca-

tions with significantly reduced effort. Several off-the-shelf measuring systems have since become available, incorporating much of the advancement provided by the early experimental setups (Sect. 60.4).

60.3 Theory

Gas exchange between soil and atmosphere is mainly driven by the gradient in concentration within the soil profile, where there may be a range of sources of sinks of trace gases. Random movements of molecules lead to a net flux across the soil surface due to concentration differentials between soil layers and across the soil–atmosphere interface. In the absence of turbulent exchange or mass movement of air due to pressure fluctuation caused by wind, the trace gas flux could theoretically be calculated using Fick's law if concentration profiles, effective soil porosity, and diffusion constants in air are known [60.25]. However, the typical heterogeneity in physical structure, as well as organic matter and moisture contents of especially the superficial soil horizons, renders it difficult to predict

the actual diffusivity across the soil–atmosphere interface. Furthermore, atmospheric turbulence induced by advection (wind) near the soil surface or pressure fluctuations due to wind gusts results in a *flushing* of superficial soil pores. Such mass movements of air produce a much faster transport of trace gases than diffusion processes and also impact the soils' internal concentration gradients.

Besides the fluxes into the chamber headspace, the design of flux chambers must account for the processes driving exchanges of CO₂ *within* chambers. Some chamber models use small fans to minimize the development of boundary layers that would cause the buildup of concentration gradients within chambers as an artefact of chamber placement. Especially in the case of the non-steady-state chambers, where fluxes are calculated based on the changes in concentration over time, an effective mixing of chamber headspace is important. Turbulence caused by fans partly compensates for the absence of the *natural* turbulence caused by wind but has the risk of increasing soil–surface exchanges by artificially *eroding* the soil surface boundary layer and enhancing the flushing of soil pore spaces, resulting in artificially large soil CO₂ efflux estimates [60.9]. Moderation of fan speeds and careful placement of fans to avoid directing airflow directly towards the soil surface can mitigate this risk. Many chamber designs, however, do not include forced air movement by fans and use airflow induced by the circulation of air between analyzers and chamber to create an effective mixing of the chamber headspace (Fig. 60.4).

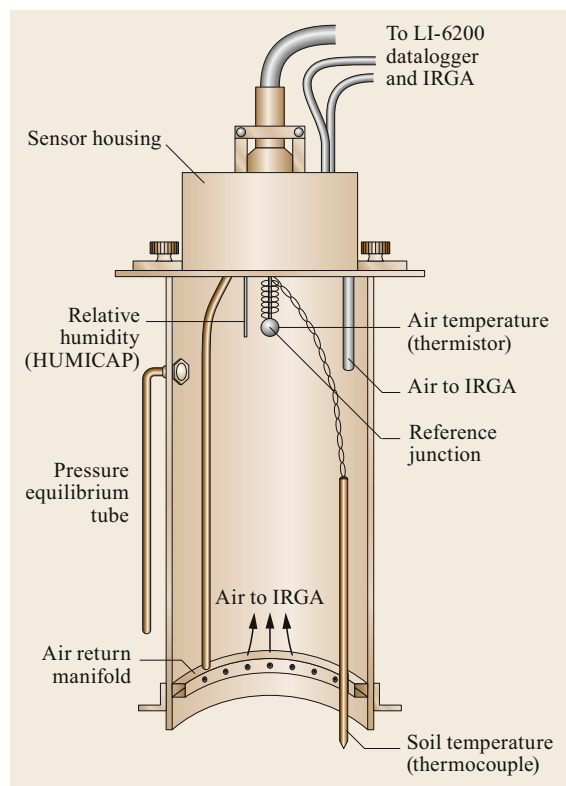


Fig. 60.4 Portable non-steady-state soil CO₂ flux chamber (after [60.23] © John Wiley and Sons)

60.3.1 Mass Flow and Pressure Issues

Pressure changes within the chamber headspace result in mass flow of air in and out of soils [60.26]. Where the chamber itself induces pressure changes, this represents a potentially significant artefact for flux rate measurements [60.27, 28]. Placement of a chamber on the soil, or closure of chamber covers onto a chamber base or collar, are potential situations where a positive pressure within the chamber may push atmospheric air into the soil profile. In situations where the presence of the chamber operator near the chamber causes compression of soil, displacement of air volumes under the measure-

ment area of a chamber would also influence observed chamber fluxes owing to artificial flushing of soil pores. This is likely to be a significant consideration in peatlands or other high-organic soils, where compaction of soil leads to lateral movement of either air or water, hence propagating mass movement and artificial soil–atmosphere gas exchange.

The act of pushing air volumes from the chamber headspace into the superficial soil layers alters the gas concentration profile and is likely to lead to an initially lower exchange of the trace gas, as an artificially low concentration gradient between the uppermost part of the soil column and atmosphere is created. Compaction of soil around chambers is likely to result in the opposite effect, where air is forced from pore spaces beneath the chamber, creating an apparently greater flux than what would occur naturally.

Prolonged chamber deployment (commonly used for the measurement of rarer gases than CO₂) may also lead to a heating of the chamber volume, resulting in an expansion of the air volume and resulting in pressurization of the headspace. Alongside the physical expansion of air following an increase in temperature (following the relationship between temperature and pressure described by the ideal gas law), evaporation of water from soil and plant surfaces can contribute to a slight increase in chamber pressure, whilst also diluting the concentration of trace gases (Sect. 60.3.2).

In contrast to such artificial pressures effects in soil chambers, naturally occurring atmospheric pressure fluctuations can be considered to form part of the inherent gas exchange between soil and atmosphere. However, closing off these fluctuations by the use of a chamber could underestimate flux values.

Most chamber models include small pressure vents that minimize air pressure differentials between ambient and chamber headspace atmospheres (Fig. 60.4). These vents mitigate both pressure artefacts from placement/closure of chambers and continuous wind-induced fluctuations. The design of the vents with small diameters aims to minimize ingress and egress of CO₂, whilst allowing equilibration of pressure differentials by a small volume flow of air.

60.3.2 Concentration Corrections and Flux Calculations

All chamber approaches have to account for changes in partial pressure of other gases that occur during the period of measurement. Evaporation from the soil surface, as well as transpiration by plants present within the chamber, can cause increases in water vapor in the chamber headspace. This addition of water molecules to the mixture of gases making up the chamber air means

that the rate of trace gas fluxes can be underestimated (in the case of a net efflux from soil) or overestimated (in the case of a net soil uptake).

It is, therefore, advised to include measurement of water vapor pressure ($\chi_{\text{H}_2\text{O}}$; Table 60.1) content in both air streams and correct measured CO₂ concentrations accordingly. Many commercial chamber systems can perform such a correction as a factory default, providing e.g., *dry* CO₂ readings.

60.3.3 Non-Steady-State Chambers

Non-steady-state chambers are the most commonly used in the scientific literature. The measuring principle relies on a chamber being placed on the ground to create an effective isolation of a defined airspace (*headspace*) in which gas exchange with the underlying soil surface leads to changes in headspace gas concentrations. These gas concentration changes are then monitored continuously by either having a sensor placed directly in the chamber or by pumping a small volume in a closed loop between chamber headspace and the measurement cell of an analyzer (e.g., nondispersive infrared gas analyzer, cavity ringdown spectrometer). The CO₂ mass flux rate at a given time point during the chamber closure ($F(t)$; in kg m⁻² s⁻¹) is calculated from the mass concentration change with time ($dc/dt(t)$; in kg m⁻³ s⁻¹), chamber volume (V ; in m³), and chamber area (A ; in m²)

$$F(t) = \frac{dc}{dt}(t) \frac{V}{A}. \quad (60.1)$$

The mass concentration of the gas of interest $c(t)$ is calculated from the measured fraction of CO₂ in air ($\chi(t)$; in mol mol⁻¹), pressure ($p(t)$; in Pa) and temperature ($T(t)$, in K) of the headspace air, molar mass of the gas of interest (M ; in kg mol⁻¹) and the universal gas constant ($R \approx 8.314 \text{ m}^3 \text{ Pa K}^{-1} \text{ mol}^{-1}$) [60.29]

$$c(t) = \chi(t) \frac{p(t)}{T(t)} \frac{M}{R}. \quad (60.2)$$

Commonly, water vapor evaporates from the soil surface or vegetation (if present) into the chamber headspace during chamber closure. This addition of molecules leads to expansion of the headspace air and dilution of the gas of interest [60.16, 30, 31]. The effect of this dilution on the molecular fraction of the gas of interest can be approximately corrected for if the amount fraction of water vapor $\chi_{\text{H}_2\text{O}}(t)$ is monitored in the chamber headspace

$$\chi_{\text{corr}}(t) = \chi_{\text{uncorr}}(t) \frac{1 - \chi_{\text{H}_2\text{O}}(t_0)}{1 - \chi_{\text{H}_2\text{O}}(t)}, \quad (60.3)$$

where $\chi_{\text{H}_2\text{O}}(t_0)$ is water vapor amount fraction at the start of chamber closure.

Unfortunately, there is no general agreement about the best time interval for determining dc/dt following chamber closure. Traditionally, a linear regression function was fitted to the complete concentration time series recorded during chamber closure, and the slope of that linear function was set equal to dc/dt . However, various studies demonstrated that the concentration time series often does not develop in a linear way, even over short closure periods [60.32–34]. Whilst linear regressions applied over short periods provide robust estimates, it should be noted that they can underestimate real fluxes by up to 40%, depending on the absolute flux rates [60.33, 35]. There is no consensus about how long exactly a measurement (chamber closure) should last, or which nonlinear regression method is the most appropriate. Software solutions are now available [60.36] that provide diagnostic statistics and initial recommendations for whether nonlinear or linear regression is the most appropriate. They allow users to define custom criteria for a given experimental setting.

Non-steady-state chambers need to open after completing measurement to allow the reequilibration of CO_2 concentrations between soil and atmosphere and to minimize the modification of abiotic conditions through e.g., rainfall exclusion or temperature increases. In order to obtain continuous time series of soil flux measurements, robotic systems that close and open chambers at predetermined intervals have been widely used. As, generally, multiple chambers are measured using a single gas analyzer, switching between different chamber locations is required to enable quasi continuous measurement of flux within a given area. The size of this area is determined mainly by the length of tubing (radius of 10 m, with additional pumps included, up to 20 m) between chambers and CO_2 analyzer, where an efficient exchange of air between headspace and analyzer has to be guaranteed in order to obtain meaningful estimates of concentration change over time. Power draw of robotic drives as well as pumps to circulate air over considerable distances are a major consideration for these systems, and there are usually higher maintenance costs due to the necessity of having moving parts within the chamber design compared to manually operated systems or passive methods (Sect. 60.3.3).

60.3.4 Steady-State Chambers

Steady-state chambers operate by having a continuous flow of air through the headspace. As air passes through the chamber, the CO_2 concentration within the headspace is enriched by soil CO_2 efflux, and air leaving the chamber will over time equilibrate at a con-

stant concentration (assuming constant soil CO_2 efflux) that is determined by the rate at which the headspace atmosphere is turned over by the air stream. Calculation of the soil CO_2 efflux rate, hence, relies on direct measurements of the CO_2 concentration drawn from the chamber headspace (out-flowing concentration, c_o ; ppm, or $\mu\text{mol mol}^{-1}$), the ambient air CO_2 concentration (incoming concentration, c_i ; ppm, or $\mu\text{mol mol}^{-1}$), the flow rate of air through the headspace (f ; mol s^{-1}), and the surface area of soil enclosed by the chamber (A_s ; m^2)

$$F = f \frac{c_o - c_i}{A_s} . \quad (60.4)$$

The flow of air through the chamber headspace is commonly achieved by continuously drawing air from within the headspace and allowing air to enter the headspace passively from the ambient atmosphere. Alternative modes of either pumping air into the chamber, with chamber air exiting the headspace passively [60.25, 37], or creating airflow by simultaneous drawing and pushing of air out of and into the chamber [60.26] have also been trialled but are less common.

As for all chamber methods, a complete seal between chamber headspace and ambient atmosphere is critical. An intentional opening integral to the chamber design to either allow ingress or egress of air (depending on whether air is actively drawn or pushed from/into the chamber), therefore, has to be designed carefully to achieve an effective air seal. This means that the rate at which air flows through the inlet/outlet has to exceed the diffusion speed of CO_2 in air for the range of temperatures under which the chamber operates. The cross-sectional area of the inlet/outlet must, therefore, be dimensioned in accordance with the volumetric air-flow rate (f). The critical speed of air flow (a_c) across the cross-sectional area of an inlet has been determined experimentally to be around 50 cm s^{-1} [60.10], and the appropriate inlet area (A_i ; cm^2) for a given volumetric flow rate of air through the headspace (f_V ; $\text{cm}^3 \text{ s}^{-1}$) can, hence, be calculated according to

$$A_i = \frac{f_V}{a_c} . \quad (60.5)$$

To ensure that no CO_2 is lost through the inlet, this critical speed should be maintained over some distance by the use of an inlet tube of the appropriate diameter. However, it should be noted that any airflow generated by drawing air from the chamber headspace necessarily results in a lower pressure inside the headspace compared to the ambient atmosphere (as this is the principle on which air is drawn into the chamber). The magnitude of this pressure differential is a function of the length

and diameter of the inlet tube, as well as the airflow velocity. An excessive length of the inlet tube should be avoided, as a longer inlet tube increases air friction and, hence, the pressure differential between atmosphere and chamber headspace.

In contrast to closed chambers, open chamber designs have the potential to measure continuously, without the need to open and reclose chambers, as steady-state conditions are created within the headspace. A change in F over time is detected through the continuous monitoring of $(c_o - c_i)$, meaning that a different soil CO₂ efflux rate will result in a new steady-state chamber concentration and, hence, a new concentration differential between soil surface and headspace.

60.3.5 Forced Diffusion Chambers

Forced diffusion (FD) chambers are a specific type of steady-state chamber, which were first described by Risk et al. [60.38]. Like for other steady-state chambers, the soil CO₂ efflux rate is calculated based on the difference between the outside atmospheric concentration and the concentration inside the chamber. The main difference is that the FD chamber uses a membrane instead of a pump. The membrane is responsible for maintaining proportionality between chamber air and outside air through molecular diffusion instead of active pumping. In the currently available commercial forced diffusion chambers, a single IRGA measures both atmosphere and chamber concentrations through a switching arrangement. Forced diffusion chambers, therefore, have reduced power demand and better long-term durability compared to robotic chambers.

The factors that control the exhaust rate of a FD chamber and the proportionality between flux and inside air concentration include the area-specific effective membrane diffusivity (D), the effective diffusive path length (L), and surface areas exposed to the soil and air (A_a , A_s). Changing any of these factors alters the proportionality between chamber and atmospheric air, or the concentration retained in the chamber per unit flux. These factors are represented by a single scalar (G), which is established for each FD chamber by calibration on a flux generator [60.39]

$$F = \frac{A_a}{A_s} \left(D \frac{c_c - c_a}{L} \right) = G (c_c - c_a). \quad (60.6)$$

The empirical calibration simplifies the design requirements and mathematical approach for flux calculations. It also validates that the FD chamber measures fluxes accurately. Most other chamber systems are calibrated only for concentration, which means that pump issues, air leaks, or other operational issues are more likely to go unnoticed in those systems.

Modern FD chambers incorporate two membrane-covered cavities within the same structure. The main cavity consists of a chamber that is exposed to the soil at the bottom and in contact with the atmosphere through a membrane. This membrane imposes the diffusional limitation or *forces* it to a specific rate. The secondary cavity is to measure the free atmospheric concentration of the gas, at the same height above ground as the primary chamber membrane. Both cavities should have identical membranes and the same volume-to-surface-area characteristics, so that they respond with identical time constants to changes in atmospheric concentration. Membranes are normally made of a synthetic material that is hydrophobic, impermeable, highly diffusive, and resistant to ultraviolet (UV) degradation.

Ideally, the FD chamber should be designed to retain a minimum level of soil gas (small $c_c - c_a$ per unit flux) in order to minimize lateral diffusion [60.40]. However, higher diffusivity is not necessarily better if the FD chamber analyzer or sensor cannot adequately resolve small concentration differences between the cavities. If concentration differences cannot be resolved at flux rates of interest, $c_c - c_a$ per unit, the concentration buildup must be increased by decreasing the membrane surface area or by using less diffusive membrane material.

Forced diffusion chambers use less power than other chamber variants, mainly because active pumping is not required. FD autochambers and their sensors can theoretically remain unpowered most of the time and only need to be activated to *grab* concentration values at preprogrammed intervals. FD chambers are also tolerant to long-term analyzer baseline drift, because a single analyzer is used to measure the difference in concentrations between the two cavities. Because FD chambers lack moving parts, maintenance intervals are reduced. However, annual recalibration of chambers is advised, but more frequent calibration may be necessary, for example in environments where biofouling is important. Because they lack moving parts, FD chambers can be used in snow, as long as the snowpack is fresh and highly diffusive, or where special-purpose manufacturer add-on accessories are used. Winter deployments often require a reduction in measurement frequency, to minimize heating and snowmelt, and to conserve battery power when solar charging is at a minimum. Owing to their low power consumption and good reliability, FD chamber systems have been used year-round even under harsh Arctic and Antarctic conditions [60.41, 42]. FD chambers can also be used without modification on floating platforms in studies that aim to contrast terrestrial and aquatic fluxes or on vertical surfaces including trees to quantify bole flux.

60.3.6 Comparison of Measuring Principles

All chamber measurements create some degree of disturbance to the physical environment, affecting the natural flux of gases between soil and atmosphere. The contrasting measuring principles of steady-state and non-steady-state chambers influence different aspects of the headspace environment, relating to e.g., duration of chamber closure or effects of pressure and airflow. Several studies have compared different chambers directly, indicating general biases between the different principles [60.15, 43–45]. For earlier non-steady-state chamber systems, consistent underestimates of known

flux rates have been reported. Subsequent changes to chamber designs, for example introducing controlled air vents and improving air flow within chamber headspaces, seem to have eliminated this bias. The most recent comparison study showed that both steady-state and non-steady-state chambers provided estimates close to known flux rates [60.15]. Forced diffusion chambers, however, have not been included in any comprehensive comparison study. Nonetheless, since individual FD chambers are calibrated against known flux rates before deployment, any biases resulting from instruments, chamber geometry, or materials are accounted for in the measured fluxes.

60.4 Devices and Systems

A variety of chamber systems have been built by researchers over the past decades, driving the development of the methodologies outlined above. The considerable volume of existing publications reflects this diversity of devices and measuring setups, in turn reflecting the variety of contexts and research questions being addressed. Here, we outline some of the most commonly used systems with examples of commercially available models. Further development of chamber systems is ongoing and is largely driven by modifications of existing setups or custom-built designs.

The objective of most soil gas flux studies is to better understand the sources and sinks of gases and drivers of flux dynamics across the soil–atmosphere interface. Analyses of the relation of flux rates from chamber measurements with abiotic conditions, such as air or soil temperature, precipitation volumes and frequencies, soil moisture content, or static pressure, are performed regularly, guided mainly by the specific objectives of a given investigation. Many commercially available chamber systems provide at least some of these ancillary measurements as part of the setup. However, as these ancillary measurements are not an integral part of the chamber approach, we do not cover them in any detail here.

60.4.1 Manual Chambers

Portability is an important requirement for soil chambers to enable surveys across wider areas, during which instruments often have to be carried between measurement locations. Infrared gas analyzers (IRGAs) have been used for soil CO₂ flux measurements for many decades now and continue to be widely used. The decrease in size of IRGA units over the years has

promoted the development of portable systems, with a number of models now commercially available.

Battery power is a further crucial factor for the use of portable systems in field surveys. Energy consumption, and hence the need to carry sufficient battery power into the field, is driven by the need to pump air between chamber and analyzer as well as auxiliary functions, such as internal fans or chamber closing mechanisms and the thermostatic requirements of the optical bench within the analyzer.

Operation of manual survey chambers is nowadays greatly facilitated by simple routines carried out by analytical units that facilitate flushing of chamber headspaces prior to chamber closure, automatic logging of chamber concentration changes over time, and direct computation of flux rates based on chamber geometry.

The small and relatively lightweight chambers by PP Systems (Amesbury, Massachusetts, USA) are placed directly on the soil surface or on previously installed soil collars to initiate a flux measurement. A choice exists between a smaller opaque chamber for respiration measurements and a larger chamber of transparent materials (enabling net CO₂ exchange) (Fig. 60.5, top). The console containing the infrared gas analyzer provides a numerical and graphical display of CO₂ concentration, and raw data as well as computed fluxes can be stored on an external USB (Universal Serial Bus) flash drive. The relatively simple operation with low power consumption means that battery power of the control unit is sufficient for more than 6 h of continuous flux measurements (assuming about 20 measurements per hour). The unit alone weighs only 1.5 kg (including batteries), with the two types of chambers weighing an additional 1 kg.

Li-Cor Biosciences (Lincoln, Nebraska USA) commercializes a very robust survey chamber setup, with

**Fig. 60.5a–c**

Portable soil respiration chambers used with infrared gas analyzers.

(a) PP Systems soil chamber (diameter: 10 cm, $V = 1180 \text{ cm}^3$).

(b) PP Systems canopy chamber (diameter: 14.6 cm, $V = 2430 \text{ cm}^3$).

(c) Li-Cor survey chamber (diameter: 20 cm, $V = 4840 \text{ cm}^3$).

Note that other sizes of chambers are available from these and other manufacturers (images **(a)** and **(b)** reprinted with permission from PP Systems; image reprint with permission of LI-COR Biosciences)

the infrared gas analyzer contained in a rugged hard case and without a physical user interface to protect electronics and gas handling parts (Fig. 60.5, bottom). Survey chambers with a diameter of 10 or 20 cm can be placed either directly on the soil surface or onto matching soil collars prior to flux measurements. An individual measurement is initiated by the system's on-board control, with which the user can either interact directly via wireless devices or an Ethernet/serial cable, or by preprogramming a sequence of measurements at user-specified intervals. To minimize disturbance from chamber placement, the Li-Cor survey chambers have

a bellows that operates the closing mechanism to initiate a measurement; CO_2 concentrations are then logged by the analyzer unit and stored along with any auxiliary measurements, and flux rates are computed at the end of measurements. Data are stored in a large internal memory and can be downloaded after field operation. The Li-Cor analyzer unit (Li8100A) in combination with the bellows-based closure mechanism in chambers has relatively high power demands. With a battery providing power for about 2 h of measurements (assuming about 20 measurements per hour), the analyzer unit weighs about 6.7 kg, with the 10 and



Fig. 60.6a–c Portable gas analyzers suitable for combined chamber-based measurements of CH_4 , H_2O and CO_2 . **(a)** GasScouter™ by Picarro, with attached soil chamber (diameter: 28 cm, $V = 9340 \text{ cm}^3$), which has the analytical unit contained in a backpack. (Reprinted with permission of Picarro Inc.) **(b)** Ultra-portable gas analyzer by Los Gatos Research ($29.5 \times 34 \times 12 \text{ cm}$) (reprinted with permission from ABB). **(c)** Li-7810 by Li-Cor ($51 \times 33 \times 18 \text{ cm}$) (image reprint with permission of LI-COR Biosciences)

20 cm chambers weighing a further 1.6 and 2.9 kg, respectively.

Recent advances in laser spectroscopy, and particularly the cavity-ringdown technique, have led to new, portable analyzers capable of measuring CH_4 and H_2O alongside CO_2 . The Picarro GasScouter (Picarro, Santa Clara, CA, USA) weighs just over 10 kg and is housed in a backpack case (Fig. 60.6). A soil chamber is available for this analyzer, and battery life enables measurement of up to 8.5 h (according to manufacturer specifications). Using a related technology (cavity-enhanced absorption), two further portable trace gas analyzers have recently become available. The Microportable Greenhouse Gas Analyzer (M-GGA) by Los Gatos Research (San Jose, CA, USA) weighs only around 5.4 kg, which includes a small internal battery that allows operation of up to 2 h. The Li-7810 by Li-Cor (Lincoln, NE, USA) weighs 11.4 kg and like the M-GGA comes in a hard case. All three trace gas analyzers provide on-board data storage and easy interfacing for external data storage or remote downloads. Combining these trace gas analyzers with existing custom-built chambers or commercially available CO_2 flux systems is relatively unproblematic.

60.4.2 Automated Chambers

Continuous soil flux measurements can be carried out using chamber systems from a number of manufacturers. As in the case of portable chambers, the automated chambers can be interfaced with either CO_2 analyzers or other trace gas analyzers. As these systems are typically employed in more permanent setups, portability and energy supply are of less relevance, and larger analyzers with potentially better analytical resolution and greater signal stability can be used. They do, however, require a weather-proof shelter.

Most automated chambers are equipped with moving components to ensure that soil conditions of the chamber footprint (usually contained within a soil collar) are disturbed as little as possible by the presence of the chamber. However, it should be noted that the chambers are likely to have indirect impacts, even when in their *open* position. The physical presence of chamber, support structures, and motor drives can affect the thermal regime through shading or reflectance of solar radiation. The same is true for the rainfall and soil wetting regime, through interception and displacement of nonvertical rain, which can result in artefacts from ad-

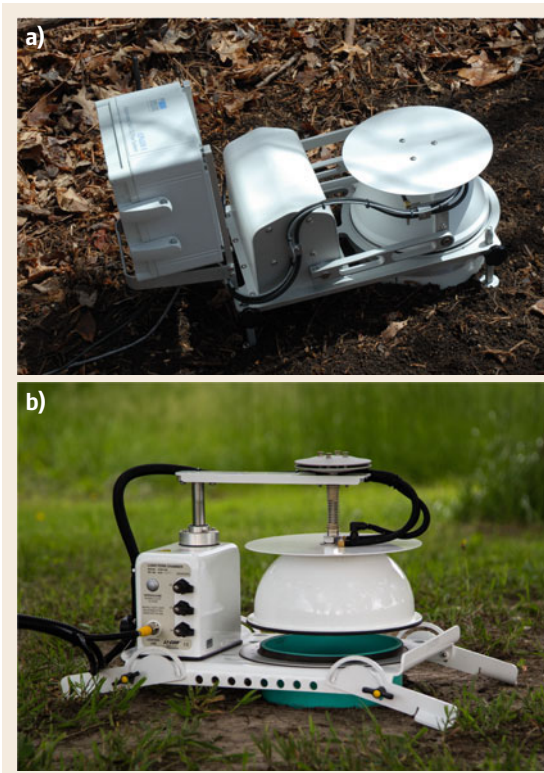


Fig. 60.7a,b Automated long-term chamber models. **(a)** PP Systems (diameter: 20 cm, $V = 2500 \text{ cm}^3$) (image reprinted with permission from PP Systems). **(b)** Li-Cor (diameter: 20 cm, $V = 4080 \text{ cm}^3$) (image reprint with permission of LI-COR Biosciences)

ditional or reduced rain splash and infiltration into the collar area.

Robotic non-steady-state chamber models are available from a number of suppliers; Fig. 60.7 shows two examples. The CFLux-1 model (PP Systems) opens and closes by lifting a dome-shaped chamber vertically and locking it in an open position adjacent to the chamber collar. The gas analyzer is located next to the chamber, so that gas analysis occurs locally with only electricity having to be provided externally. The eosAC model (Eosense, Dartmouth, NS, Canada) has a similar mechanical layout as the CFLux-1 but requires air from the chamber headspace to be pumped to and from a centrally located analyzer via a multiplexed switching unit. This is also the case for the Li-8100A system (Li-Cor). Its chambers open and close in a combined vertical and swing motion, so that the chamber covers in the open position rest at a greater distance from the soil collars than is the case for other systems.



Fig. 60.8 Forced diffusion chamber eosFD by Eosense (diameter: 10.2 cm, 20 cm high) (reprinted with permission from Eosense Inc.)

The maximum length of tubes and power/data cables limits the spatial reach of continuous chambers. Tube length is limited by the associated increase in flow resistance and, hence, by pressure considerations for pumping air between chambers and analyzers or multiplexers. Excessive tube length also increases the time required to flush tube volumes prior to measurements and leads to attenuation of concentrations that may affect the calculation of CO_2 evolution rates. The PP Systems approach of individual gas analyzers for each long-term chamber overcomes these constraints on spatial reach, but the costs per automated chamber are comparatively high because of these individual analyzers.

All automated chambers have moving parts, so their maintenance is an important consideration. Long-term measurements in environments with extreme conditions (high or low temperatures, precipitation, dust) have to be carefully considered because of the increased likelihood of mechanical failures. Appropriate housing particularly for analyzers and power supply are clearly critical for such systems.

Forced diffusion systems provide a recent alternative to the above-mentioned systems (Fig. 60.8).

Using steady-state chambers, FD systems operate well in continuous mode, and their relatively low power consumption means that long-term measurements are easily achieved. Chambers run on extremely low power (average below 1 W for longer deployment) and have onboard data storage. Having no moving parts, FD systems furthermore have a reduced risk of mechanical failure. However, continuous operation of FD chambers at the same location is likely to have substantial impacts on the abiotic environment inside the chamber, as the headspace is likely to heat to temperatures above those of the surroundings and as it excludes rainfall. This limitation can be (partially) overcome by relocating the chambers at regular intervals, so that roving FD chamber systems should have an elevated potential for continuous monitoring in locations with no continuous electricity supply [60.42].

60.4.3 Overview

This section aims to provide an overview of some of the most commonly used chamber-based measuring systems to give a representative sample for users. Table 60.3 summarizes the main advantages and disadvantages of the three main types of measuring systems and reflects a general summary of most common features of the systems available at the time of writing. The most appropriate measuring setup will depend strongly on the specific research question(s). Given a certain research budget, there will often be a clear tradeoff between the spatial and temporal resolution that can be achieved, using portable versus automated systems. In many cases, however, a combination of both systems will be ideal for a comprehensive assessment.

Table 60.3 Advantages and disadvantages of the three main types of systems

Devices	Advantages	Disadvantages
Manual chambers	Few spatial constraints due to low weight & small size Versatile for comparative analyses across ecosystems and treatments	Manual operation Limited by battery power Limited temporal replication
Automated chambers	Low demand on person time High temporal resolution Can be operated in response to specific environmental triggers/events	Significant maintenance demand for continuous operation Risk of mechanical failure Limited in spatial reach Requires secure power supply
Forced diffusion chambers	No spatial limitation Continuous data collection Very low power demand Reduced maintenance requirements due the absence of moving parts	Potential impacts on abiotic and biotic conditions in the case of prolonged placement at the same location

60.5 Specifications

Soil flux chambers are available over a range of sizes (Sect. 60.4), and there is a range of analytical equipment that can be interfaced with these. We here provide an overview of analyzers that are commonly used in soil flux studies and are included in the overview given in Sect. 60.4. Note that the specific information is provided by manufacturers, and variations from stated values may occur depending on, e.g., integration intervals of laser spectrometers or across concentration

and temperature ranges. Specification should, therefore, be regarded as indicative only. In this overview, we focus on portable chamber systems, which are of most immediate interest to many researchers. Permanently installed, continuous chamber systems may use these same analyzers, but a wide range of other analyzers is available, as permanent setups typically involve few restrictions on the size and weight of analyzers.

60.6 Quality Control

Estimates of soil–atmosphere gas fluxes based on soil chamber measurements are characterized by the following four major sources of uncertainty:

- Imperfections of the instrumental analysis of the gas concentration (e.g., due to noise, drift, and cross sensitivities).

Table 60.4 Error and temperature ranges for a selection of key instruments used in currently chamber systems to measure soil gas flux. (All specifications from manufacturers' information)

Instrument	Error (precision)	Temperature range (°C)	Manufacturer
Infrared gas Analyzers			
Li-8100	1.5% of reading	−20 to 45	Li-Cor, Lincoln, NE, USA
EGM-5	1% over calibrated range	0 to 50	PP Systems, Amesbury, MA, USA
Laser spectrometers			
GasScouter™	CO ₂ : 0.4 ppm CH ₄ : 3 ppb H ₂ O: 100 ppm	10 to 45	Picarro, Santa Clara, CA, USA
M-GGA	CO ₂ : 0.25 ppm CH ₄ : 1.2 ppb H ₂ O: 60 ppm	5 to 45	Los Gatos Research, San Jose, CA, USA
Li-7810	CO ₂ : 0.25 ppm CH ₄ : 1.5 ppb H ₂ O: 20 ppm	−25 to 45	Li-Cor, Lincoln, NE, USA
Solid-state sensor (FD chambers)			
Vaisala GMP343	±3 ppm + 1% of reading	−40 to 60	Vaisala, Helsinki, Finland

- Artefacts induced by the chamber method, such as pressure shocks during chamber setting; pressure differences between chamber headspace and ambient air; decreased or increased turbulence strength in the headspace compared to ambient conditions; reduced insolation levels due to the chamber walls; changed air, plant and soil temperatures; changes in the gas concentration gradients between soil and headspace air during chamber closure; leakages through the soil and chamber structure.
- Imperfect sampling of spatial variability in gas fluxes at the relevant scales (centimeters to kilometers).
- Imperfect sampling of temporal variability in gas fluxes at the relevant scales (seconds to years).

These different sources of uncertainty need to be estimated and specified when presenting and interpreting results. The uncertainty thresholds should be defined when planning a study, and the experimental setup should be designed considering the different sources of uncertainty.

60.6.1 Uncertainties in Instrumental Gas Concentration Analysis

The accuracy and precision of the measurements of the molar fraction of the gas of interest, as well as of the headspace air temperature and pressure, and of the gas transport rate in flow-through systems has to be regularly evaluated to assess and minimize uncertainty due to instrumental gas analysis. Systematic errors must be kept small through regular calibration of the instruments involved, and it is important to evaluate drift of gas analyzers in response to temperature and pres-

sure changes. The same is true for cross sensitivities of analyzers between different gases. The effects of water vapor on gas measurements based on absorption spectroscopy are particularly important, because water vapor has many absorption bands, and its concentration typically increases during chamber closure. This is especially true for non-steady-state chambers. The precision of the instruments should be checked regularly across the entire measurement range. A deterioration of precision indicates staining of sensors and/or electronic problems and implies the need for instrument maintenance or repair.

60.6.2 Uncertainties Due to Artefacts by the Non-Steady-State (Closed) Chamber Method

It is very important to minimize the various potential artefacts associated with the closed chamber method through careful chamber design and experiment planning. The functioning of non-steady-state chambers should be tested under controlled conditions at regular intervals. It is necessary that:

- Chambers walls are composed of gas-tight and non-reactive materials.
- The air-tightness of the seals between chamber bases and tops is tested for leakages.
- Chamber bases are sealed well against the soil surface, potentially inserted deep enough into the soil to prevent any mass flow of air between the chamber headspace and the ambient air (where experimental objectives allow).
- The chamber is equipped with a properly dimensioned vent that is open during chamber deployment

and allows propagation of ambient air pressure fluctuations into the chamber [60.32].

- The chamber is equipped with additional closable large-diameter vents that are opened during chamber placement to avoid short-time pressurization of the chamber headspace.
- Turbulent mixing of the headspace air is ensured by installation of appropriately dimensioned fans or, in the case of flowthrough systems, by a properly designed sample intake manifold.
- The change of temperature during chamber closure is recorded and – if necessary – controlled by a cooling system.

Some artefacts due to suboptimal chamber application can be identified by careful evaluation of the time series of gas concentrations during chamber closure. The measurement principle of the closed chamber method assumes that the gas concentration time series during a successful chamber closure experiment can be well described by either a strictly monotonically increasing (net gas release) or a strictly monotonically decreasing (net gas uptake) function. Based on diffusion theory, the monotonically increasing or decreasing functions are expectedly nonlinear and degressive. The relative quality of different regression functions can be compared with the Akaike information criterion [60.46] or tested using an F-test of the residual variances of two potential regression functions [60.47]. A best-fitting function that shows a nonlinear progressive form cannot be explained by diffusion theory, indicating a disturbed chamber experiment that should be flagged for quality control [60.48]. The most important quality control criterion is the standard deviation of the residuals of the best-fitting function, as it provides an estimate of the unexplained variance in the gas concentration time series during chamber closure. A standard deviation of the residuals for the best-fitting function higher than a critical threshold level indicates technical errors or other problematic artefacts, which should be flagged for quality control. By contrast, the coefficient of determination, R^2 , cannot be recommended as a quality control criterion, as it inherently discriminates against lower fluxes [60.33].

60.6.3 Uncertainties Due to Spatial Variability

Soils are characterized by a pronounced spatial heterogeneity on the scales of centimeters up to many kilometers [60.49]. The higher the spatial variability of soils within the investigated area of interest, the greater the uncertainty of the estimated mean of the fluxes due to sampling variability $u_{\text{mean,space}}$. Under the assumption

that the sampled population is normally distributed, $u_{\text{mean,space}}$ can be estimated as

$$u_{\text{mean,space}} = t_{\alpha/2, n-1} \frac{s}{\sqrt{n}}, \quad (60.7)$$

where s is the sample standard deviation, n is the sample size, and $t_{\alpha/2, n-1}$ is the upper $(1-\alpha/2)$ quantile of the Student's t -distribution, and α is the significance level. A pilot study should be performed for estimating s and assessing the distance between sample plots that is enough for spatial interdependence (e.g., by a semivariogram, e.g., [60.50]), which is needed for an unbiased estimation of the population variance by s .

The necessary sample size n_{min} to estimate a mean flux within a specified margin of uncertainty d at a confidence level α can be estimated by finding the lowest value of n for which the following inequality is true

$$\frac{\sqrt{n}}{t_{\alpha/2, n-1}} \geq \frac{s}{d}. \quad (60.8)$$

Since the number of spatial replicates in typical soil chamber measurement campaigns is severely limited by resources and logistical constraints, these are prone to considerable margins of error due to suboptimal sampling in space (e.g., [60.51, 52]). With large uncertainties due to small sample sizes, effect sizes (i.e., means or differences between means from different areas) must be large to be detected at usually accepted significance levels (e.g., $\alpha \leq 0.05$) [60.53].

60.6.4 Uncertainties Due to Temporal Variability

Soil gas fluxes are highly variable through time. Temporal variability occurs on scales of seconds to years. Chamber flux measurements are discrete samples in time with a specified temporal resolution. Chamber closure times can vary from 15 s [60.54] to about an hour [60.55]. Chamber closure intervals at a specific measurement spot can vary from hours for automatic chamber systems [60.55] to weeks for manual chamber campaigns [60.56]. Depending on the research question of the study, the sampling design must account for diurnal cycles, meteorological changes on the synoptic scale, seasonal cycles, and inter-annual variability. For unbiased gas balances, sampling must not be restricted to certain environmental conditions, e.g., only summer, only daytime, or only times without precipitation [60.57]. A low sampling frequency can lead to high uncertainty of seasonal or annual gas-exchange balances [60.58, 59].

Since chamber measurements cannot provide continuous time series of flux measurements, smaller and

larger gaps need to be filled by models. The uncertainty of seasonal or annual cumulative fluxes due to temporal variability is typically dominated by the ability of the models to simulate the true fluxes [60.60, 61]. Model performance is characterized by residuals between sim-

ulated and measured data. These should be evaluated in both the time and frequency domain [60.62]. Monte Carlo simulations are useful to assess the uncertainty of cumulative fluxes due to the uncertainty in the model predictions used for gap filling [60.63].

60.7 Maintenance

In order to obtain reliable flux estimates, chambers and associated analytical equipment require maintenance. Exact intervals for maintenance are strongly dependent

on the application, but Table 60.5 provides a general overview of typical maintenance schedules.

Table 60.5 Servicing schedule for contrasting chamber systems

	Manual chambers	Automated chambers	Forced diffusion
Weekly	<p> Tubes are free of dust, condensation or obstructions, all electrical and gas connections sound</p> <p> Fans (where present) working</p>	<p> Check physical condition, no obstruction in closing mechanisms</p>	N/A
Monthly	<p> Check zero and span of analyzers</p> <p> If used consistently in dusty environments, check filters</p>	<p> Check physical condition and if deployed over long periods, either relocate or check seal with soil is intact</p>	
Annually	<p> Send analyzer for service and calibration</p> <p> Pump replacement (potentially)</p>	<p> Full service of all moving parts</p>	<p> Send entire chamber setup to manufacturer for recalibration</p>

60.8 Application

Soil gas flux chambers have been used in a wide variety of settings, where they may measure a number of different trace gases and serve a range of purposes. Whilst it is beyond the scope of this chapter to cover the full range of chamber applications over the past decades, we use a small number of examples here to illustrate the applicability of soil flux chambers. The examples were selected to cover the key chamber types outlined in Sect. 60.3 and address aspects of continuous monitoring, experimental manipulation, and challenges of remote operation.

60.8.1 Ecosystem Flux Components

Chambers have been widely used in order to quantify constituent fluxes from different parts of ecosystems. Methods such as the eddy-covariance technique (Chap. 55) provide net fluxes between ecosystems and the atmosphere integrated over time (usually 30 min) and space. However, researchers generally require a more detailed understanding of the flux contributions from different areas within the *flux footprint* of

the eddy-covariance setup (Chap. 55). Knowledge of the relative contributions of, e.g., vegetation versus soil versus open water, contrasting vegetation types/covers, distinct (micro)topographic units are critical in order to understand the drivers of the fluxes from these contrasting areas and provide a way to independently validate net ecosystem fluxes. It also allows a more detailed understanding of contributing fluxes, such as the separation of CO₂ assimilation and respiration by canopy and understorey vegetation and respiration from soil, which is not possible by eddy covariance alone.

Analyses of fluxes from within the footprint area of eddy-covariance towers are typically conducted using manual chambers in distinct measurement campaigns [60.33, 64–66]. This enables the measurement of fluxes across the entire flux footprint area, which is typically larger than what an automated flux system with permanently installed chambers can accomplish. Such campaigns should aim to capture a wide range of flux situations, i.e., resolve diurnal as well as seasonal patterns. The exact number of measurement points required depends on the nature of the footprint area, i.e.,

the multitude of different surface covers, and spatial variability within these units. Ideally, all relevant surface cover types are sampled to allow an upscaling of contributing flux estimates at any given period using the weighted areal representation of the respective covers.

Whilst manual chamber measurements have the benefit of a wider spatial reach, they require the presence of an experimenter within the footprint of the eddy-covariance measurement, possibly affecting the flux estimate within that particular time interval. Depending on the magnitude of ecosystem fluxes and the size of the footprint, this disturbance may be significant for the net ecosystem flux estimates, and a direct comparison of fluxes obtained by the two techniques may not be possible. Most studies attempt an area-weighted average of fluxes within footprint areas that is then compared to representative flux averages that are not necessarily obtained simultaneously but based on comparable conditions (in terms of abiotic drivers of fluxes). Continuous measurements using automated chambers have also been used to develop a more detailed understanding of the contribution from soils or even subcomponents within the soil to ecosystem carbon exchange (Sect. 60.8.2) [60.67, 68].

60.8.2 Long-Term Monitoring of Soil Gas Flux

Continuous measurements of soil–atmosphere gas exchange enable powerful investigations into the drivers of gas fluxes as well as their temporal dynamics over short (intraday) to long intervals (interannual). Automated systems with multiple chambers (both steady-state and non-steady-state), can give up to (half-)hourly soil CO₂ efflux readings and have been powerful in disentangling influences of temperature and soil moisture, as well as diurnal and seasonal flux dynamics. The wealth of data generated by continuous measurements (subject to appropriate quality checks) allows detailed analysis of, e.g., temperature responses under contrasting moisture regimes or during different parts of the growing season [60.69].

In manipulative field experiments, continuous soil flux measurements can reveal further details, for example, on the interaction of biotic and abiotic drivers of gas fluxes. Studies in a boreal black spruce forest [60.68] and a temperate oak forest [60.67] illustrate compellingly how the allocation of carbon by plants to the soil via root and mycorrhizal networks differs between seasons. As both studies were carried out within the footprint of an above-canopy eddy-covariance tower, the continuous data further enabled a detailed analysis

of the relationship between soil flux and total ecosystem dynamics, revealing a link between C assimilation by the canopy and magnitude of soil fluxes.

Long-term chamber systems can be interfaced with a range of gas analyzers to provide continuous soil–atmosphere gas exchange for trace gases other than CO₂. For example, by integrating a methane analyzer into a measuring setup for soil CO₂ efflux, it was possible to resolve short-term dynamics of methane uptake by forest soil [60.70]. Apart from a known relationship with soil moisture, these measurements revealed novel insights into the diurnal fluctuation of methane oxidation flux in response to small changes in background methane concentration above the forest floor.

60.8.3 Gas Exchange in Remote Locations

Accessibility to field sites and availability of grid power have been key factors in the selection of long-term observation sites. This has created a strong bias towards areas easily accessed by road and well-equipped research sites. For Arctic areas, this bias is extreme, given the much sparser population and, hence, lower density of road and power infrastructure. As an illustration, about 31% of all Arctic studies focused on climate change (including many flux studies) originate from measurements within 50 km of just two Arctic research sites (Toolik Lake, Alaska, and Abisko, Sweden) [60.71]. There is, therefore, a real need to obtain more data from more remote and less accessible areas. The portability of analyzers and chamber systems has enabled researchers to obtain soil flux measurements from a wide range of locations, but this is limited to distinct, infrequent measuring campaigns.

Whilst this has so far been mostly limited to CO₂ flux systems, advances in analyzer design have led to more frequent measurements also of other trace gases (Sect. 60.4). For continuous measurements in remote locations, moving chamber designs associated with air pumps between chambers and analyzers are limited by power availability. Forced diffusion chambers offer a new opportunity to continuously monitor CO₂ flux in remote locations. This is illustrated by a 1-year record obtained by permanently installed FD chambers in the dry valleys of Antarctica [60.42]. Whilst the steady-state measurement in nonmoving chambers creates some problems in relation to precipitation and organic matter entering the soil environment, this study was able to identify specific abiotic conditions during which microbial activity led to soil CO₂ efflux. The dry and cold nature of the study system facilitated the use of FD chambers, which may be prone to greater artefacts when deployed continuously in other ecosystems.

60.9 Future Developments

Chamber measurements of all trace gases form an important part of gas exchange studies. They can resolve small spatial scales and are adaptable to specific settings with regards to, e.g., microtopography, vegetation cover, or landscape features that larger scale flux approaches, such as eddy covariance, cannot address. Therefore, chamber measurements will continue to play an important role in future investigations.

The scientific literature is rich in contrasting designs of flux chambers, and there are many applications besides soil respiration measurements that have driven their original development. Recent advances in the detection of important atmospheric trace gases have led to ever-smaller analyzers capable of resolving small concentration changes with good accuracy and precision. Gas flux measurements that were historically

severely limited by the requirement of using offline sample collection and a-posteriori analyses of samples in the laboratory can now be carried out using in-situ analyzers, enabling fast and more mobile measuring setups. We anticipate this trend to continue, and more gases, as well as isotopic ratios of trace gases, to become detectable by flux chambers operated on portable or automated devices. The development of chambers has led to a great level of sophistication, so that current models can operate at minimal disturbance of the soil environment. Further advances, e.g., in materials used or in chamber geometry for specific tasks, are likely to occur in the future, but the general measuring principles described in this chapter will most likely continue to be the basis of any chamber flux measurement.

60.10 Further Readings

- E.A. Davidson, K. Savage, L.V. Verchot, R. Navarro: Minimizing artefacts and biases in chamber-based measurements of soil respiration, *Agric. For. Meteorol.* **113**, 21–23 (2000)
- J. Pumpanen, P. Kolari, H. Ilvesniemi, K. Minkkinen, T. Vesala, S. Niinistö, A. Lohila, T. Larmola, M. Morero, M. Pihlatie, I. Janssens, J.C. Yuste, J.M. Grünzweig, S. Reth, J.-A. Subke, K. Savage, W. Kutsch, G. Østreng, W. Ziegler, P. Anthoni, A. Lindroth, P. Hari: Comparison of different chamber techniques for measuring soil CO₂ efflux, *Agric. For. Meteorol.* **123**(3/4) 159–176 (2004)
- W. Kutsch, M. Bahn, A. Heinemeyer (Eds.): *Soil Carbon Dynamics: An Integrated Methodology* (Cambridge Univ. Press, Cambridge (2009)
- A.R. Pedersen, S.O. Petersen, K. Schelde: A comprehensive approach to soil-atmosphere trace-gas flux estimation with static chambers, *Eur. J. Soil Sci.* **61**(6) 888–902 (2010)

References

- 60.1 J.A. Subke, I. Inglisma, M.F. Cotrufo: Trends and methodological impacts in soil CO₂ efflux partitioning: A metaanalytical review, *Glob. Change Biol.* **12**(6), 921–943 (2006)
- 60.2 B. Bond-Lamberty, A. Thomson: A global database of soil respiration data, *Biogeosciences* **7**(6), 1915–1926 (2010)
- 60.3 S.D. Bridgman, H. Cadillo-Quiroz, J.K. Keller, Q. Zhuang: Methane emissions from wetlands: Biogeochemical, microbial, and modeling perspectives from local to global scales, *Glob. Change Biol.* **19**(5), 1325–1346 (2013)
- 60.4 L. Liu, T.L. Greaver: A review of nitrogen enrichment effects on three biogenic GHGs: The CO₂ sink may be largely offset by stimulated N₂O and CH₄ emission, *Ecol. Lett.* **12**(10), 1103–1117 (2009)
- 60.5 A.J. Thomson, G. Giannopoulos, J. Pretty, E.M. Baggs, D.J. Richardson: Biological sources and sinks of nitrous oxide and strategies to mitigate emissions, *Philos. Trans. R. Soc. B* **367**(1593), 1157–1168 (2012)
- 60.6 J. Pumpanen, B. Longdoz, W.L. Kutsch: Field measurements of soil respiration: Principles and constraints, potentials and limitations of different methods. In: *Soil Carbon Dynamics: An Integrated Methodology*, ed. by W. Kutsch, M. Bahn, A. Heinemeyer (Cambridge Univ. Press, Cambridge 2009) pp. 16–33
- 60.7 G.P. Livingston, G.L. Hutchinson: Enclosure-based measurement of trace gas exchange: Applications and sources of error. In: *Biogenic Trace Gases: Measuring Emissions from Soil and Water*, ed. by P.A. Matson, R.C. Harriss (Blackwell Science Ltd., Oxford 1995) pp. 14–51
- 60.8 D. Hooper, Z. Cardon, F. Chapin, M. Durant: Corrected calculations for soil and ecosystem measurements of CO₂ flux using the LI-COR 6200

- portable photosynthesis system, *Oecologia* **132**(1), 1–11 (2002)
- 60.9 V. Le Dantec, D. Epron, E. Dufrêne: Soil CO₂ efflux in a beech forest: Comparison of two closed dynamic systems, *Plant Soil* **214**(1/2), 125–132 (1999)
- 60.10 M. Rayment, P. Jarvis: An improved open chamber system for measuring soil CO₂ effluxes in the field, *J. Geophys. Res. Atmos.* **102**(D24), 28779–28784 (1997)
- 60.11 B. Widen, A. Lindroth: A calibration system for soil carbon dioxide efflux measurement chambers: Description and application, *Soil Sci. Soc. Am. J.* **67**(1), 327–334 (2003)
- 60.12 E. Takle, W. Massman, J. Brandle, R. Schmidt, X. Zhou, I. Litvina, R. Garcia, G. Doyle, C. Rice: Influence of high-frequency ambient pressure pumping on carbon dioxide efflux from soil, *Agric. For. Meteorol.* **124**(3/4), 193–206 (2004)
- 60.13 H. Lundegårdh: Carbon dioxide evolution of soil and crop growth, *Soil Sci.* **23**(6), 417–453 (1927)
- 60.14 F. Bornemann: *Kohlensäure und Pflanzenwachstum*, 2nd edn. (P. Parey, Berlin 1923)
- 60.15 J. Pumpanen, P. Kolari, H. Ilvesniemi, K. Minkkinen, T. Vesala, S. Niinistö, A. Lohila, T. Larmola, M. Morero, M. Pihlatie, I. Janssens, J.C. Yuste, J.M. Grünzweig, S. Reth, J.-A. Subke, K. Savage, W. Kutsch, G. Østregren, W. Ziegler, P. Anthoni, A. Lindroth, P. Hari: Comparison of different chamber techniques for measuring soil CO₂ efflux, *Agric. For. Meteorol.* **123**(3/4), 159–176 (2004)
- 60.16 P. Rochette, G.L. Hutchinson: Measurement of soil respiration in situ: Chamber techniques. In: *Micrometeorology in Agricultural Systems*, Agronomy Monographs, Vol. 47, ed. by J.L. Hatfield, J.M. Baker (ASA, CSSA, SSSA, Madison 2005) pp. 247–286
- 60.17 M. Witkamp: Rates of carbon dioxide evolution from forest floor, *Ecology* **47**(3), 492–494 (1966)
- 60.18 H. Koepf: Die Verwendung des Ultrarotabsorptionsschreibers (URAS) für die kontinuierliche Registrierung der Bodenatmung im Freiland, *Landwirtsch. Forsch.* **5**, 54–62 (1953)
- 60.19 W. Reiners: Carbon dioxide evolution from floor of three Minnesota forests, *Ecology* **49**(3), 471–483 (1968)
- 60.20 M. Witkamp, M. Frank: Evolution of CO₂ from litter, humus, and subsoil of a pine stand, *Pedobiologia* **9**(5/6), 358–365 (1969)
- 60.21 N. Edwards, P. Sollins: Continuous measurement of carbon-dioxide evolution from partitioned forest floor components, *Ecology* **54**(2), 406–412 (1973)
- 60.22 N. Edwards: Moving chamber design for measuring soil respiration rates, *Oikos* **25**(1), 97–101 (1974)
- 60.23 J. Norman, R. Garcia, S. Verma: Soil surface CO₂ fluxes and the carbon budget of a grassland, *J. Geophys. Res. Atmos.* **97**(D17), 18845–18853 (1992)
- 60.24 M. Blanke: Soil respiration in an apple orchard, *Environ. Exp. Bot.* **36**(3), 339–348 (1996)
- 60.25 E. DeLong, R. Redmann, E. Ripley: Comparison of methods to measure soil respiration, *Soil Sci.* **127**(5), 300–306 (1979)
- 60.26 C. Fang, J. Moncrieff: An improved dynamic chamber technique for measuring CO₂ efflux from the surface of soil, *Funct. Ecol.* **10**(2), 297–305 (1996)
- 60.27 E.A. Davidson, K. Savage, L.V. Verchot, R. Navarro: Minimizing artifacts and biases in chamber-based measurements of soil respiration, *Agric. For. Meteorol.* **113**(1–4), 21–37 (2002)
- 60.28 C. Fang, J. Moncrieff: An open-top chamber for measuring soil respiration and the influence of pressure difference on CO₂ efflux measurement, *Funct. Ecol.* **12**(2), 319–325 (1998)
- 60.29 NIST: Fundamental Physical Constants, available via <https://physics.nist.gov/cgi-bin/cuu/Value?r>, Accessed 23 July 2021
- 60.30 J. Welles, T. Demetriades-Shah, D. McDermitt: Considerations for measuring ground CO₂ effluxes with chambers, *Chem. Geol.* **177**(1/2), 3–13 (2001)
- 60.31 O. Perez-Priego, A. Lopez-Ballesteros, E.P. Sanchez-Canete, P. Serrano-Ortiz, L. Kutzbach, F. Domingo, W. Eugster, A.S. Kowalski: Analysing uncertainties in the calculation of fluxes using whole-plant chambers: Random and systematic errors, *Plant Soil* **393**(1/2), 229–244 (2015)
- 60.32 G. Hutchinson, A. Mosier: Improved soil cover method for field measurement of nitrous-oxide fluxes, *Soil Sci. Soc. Am. J.* **45**(2), 311–316 (1981)
- 60.33 L. Kutzbach, J. Schneider, T. Sachs, M. Giebels, H. Nykanen, N.J. Shurpali, P.J. Martikainen, J. Alm, M. Wilking: CO₂ flux determination by closed-chamber methods can be seriously biased by inappropriate application of linear regression, *Biogeosciences* **4**(6), 1005–1025 (2007)
- 60.34 M.K. Pihlatie, J.R. Christiansen, H. Aaltonen, J.F.J. Korhonen, A. Nordbo, T. Rasilo, G. Benanti, M. Giebels, M. Helmy, J. Sheehy, S. Jones, R. Juszczak, R. Klefoth, R. Lobo-do-Vale, A.P. Rosa, P. Schreiber, D. Serça, S. Vicca, B. Wolf, J. Pumpanen: Comparison of static chambers to measure CH₄ emissions from soils, *Agric. For. Meteorol.* **171**, 124–136 (2013)
- 60.35 A.R. Pedersen, S.O. Petersen, K. Schelde: A comprehensive approach to soil-atmosphere trace-gas flux estimation with static chambers, *Eur. J. Soil Sci.* **61**(6), 888–902 (2010)
- 60.36 A.R. Pedersen: Package 'HMR' – Flux Estimation with Static Chamber Data, <https://cran.r-project.org/web/packages/HMR/HMR.pdf> (2017), Accessed 23 July 2021
- 60.37 E. Kanemasu, W. Powers, J. Sij: Field chamber measurements of CO₂ flux from soil surface, *Soil Sci.* **118**(4), 233–237 (1974)
- 60.38 D. Risk, N. Nickerson, C. Creelman, G. McArthur, J. Owens: Forced diffusion soil flux: A new technique for continuous monitoring of soil gas efflux, *Agric. For. Meteorol.* **151**(12), 1622–1631 (2011)
- 60.39 J. Martin, P. Bolstad, J. Norman: A carbon dioxide flux generator for testing infrared gas analyzer-based soil respiration systems, *Soil Sci. Soc. Am. J.* **68**(2), 514–518 (2004)
- 60.40 C. Creelman, N. Nickerson, D. Risk: Quantifying lateral diffusion error in soil carbon dioxide res-

- piration estimates using numerical modeling, *Soil Sci. Soc. Am. J.* **77**(3), 699–708 (2013)
- 60.41 Y. Kim, S. Park, B. Lee, D. Risk: Continuous measurement of soil carbon efflux with forced diffusion (FD) chambers in a tundra ecosystem of Alaska, *Sci. Total Environ.* **566**, 175–184 (2016)
- 60.42 D. Risk, C.K. Lee, C. MacIntyre, S.C. Cary: First year-round record of Antarctic dry valley soil CO₂ flux, *Soil Biol. Biochem.* **66**, 193–196 (2013)
- 60.43 I.A. Janssens, A.S. Kowalski, B. Longdoz, R. Ceulemans: Assessing forest soil CO₂ efflux: An in situ comparison of four techniques, *Tree Physiol.* **20**, 23–32 (2000)
- 60.44 J. Norman, C. Kucharik, S. Gower, D. Baldocchi, P. Crill, M. Rayment, K. Savage, R. Striegl: A comparison of six methods for measuring soil–surface carbon dioxide fluxes, *J. Geophys. Res. Atmos.* **102**(D24), 28771–28777 (1997)
- 60.45 F. Gao, S. Yates: Laboratory study of closed and dynamic flux chambers: Experimental results and implications for field application, *J. Geophys. Res. Atmos.* **103**(D20), 26115–26125 (1998)
- 60.46 H. Akaike: New look at statistical–model identification, *IEEE Trans. Autom. Control* **19**(6), 716–723 (1974)
- 60.47 R.A. Fisher: On a distribution yielding the error functions of several well known statistics. In: *Proc. Int. Congr. Math., Toronto*, Vol. 2 (Univ. Toronto Press, Toronto 1924) pp. 805–813
- 60.48 C.M. Görres, L. Kutzbach, L. Elsgaard: Comparative modeling of annual CO₂ flux of temperate peat soils under permanent grassland management, *Agric. Ecosyst. Environ.* **186**, 64–76 (2014)
- 60.49 M. Herbst, L. Bornemann, A. Graf, G. Welp, H. Vereecken, W. Amelung: A geostatistical approach to the field–scale pattern of heterotrophic soil CO₂ emission using covariates, *Biogeochemistry* **111**(1–3), 377–392 (2012)
- 60.50 E. Leon, R. Vargas, S. Bullock, E. Lopez, A.R. Panosso, N. La Scala Jr.: Hot spots, hot moments, and spatio–temporal controls on soil CO₂ efflux in a water–limited ecosystem, *Soil Biol. Biochem.* **77**, 12–21 (2014)
- 60.51 M. Herbst, N. Prolingheuer, A. Graf, J.A. Huisman, L. Weihermueller, J. Vanderborght: Characterization and understanding of bare soil respiration spatial variability at plot scale, *Vadose Zone J.* **8**(3), 762–771 (2009)
- 60.52 D.R. Chadwick, L. Cardenas, T.H. Misselbrook, K.A. Smith, R.M. Rees, C.J. Watson, K.L. Mcgeough, J.R. Williams, J.M. Cloy, R.E. Thorman, M.S. Dhanoa: Optimizing chamber methods for measuring nitrous oxide emissions from plot–based agricultural experiments, *Eur. J. Soil Sci.* **65**(2), 295–307 (2014)
- 60.53 J.C.F. de Winter: Using the student’s t–test with extremely small sample sizes, *Pract. Assess. Res. Eval.* **18**, Article 10 (2013)
- 60.54 R. Angell, T. Svejcar: A chamber design for measuring net CO₂ exchange on rangeland, *J. Range Manag.* **52**(1), 27–31 (1999)
- 60.55 S.G. Morris, S.W.L. Kimber, P. Grace, L. Van Zwieten: Improving the statistical preparation for measuring soil N₂O flux by closed chamber, *Sci. Total Environ.* **465**, 166–172 (2013)
- 60.56 M. Vanselow–Algan, S.R. Schmidt, M. Greven, C. Fiencke, L. Kutzbach, E.–M. Pfeiffer: High methane emissions dominated annual greenhouse gas balances 30 years after bog rewetting, *Biogeochemistry* **12**(14), 4361–4371 (2015)
- 60.57 M. Ryan, B. Law: Interpreting, measuring, and modeling soil respiration, *Biogeochemistry* **73**(1), 3–27 (2005)
- 60.58 T. Parkin, T. Kaspar: Temporal variability of soil carbon dioxide flux: Effect of sampling frequency on cumulative carbon loss estimation, *Soil Sci. Soc. Am. J.* **68**(4), 1234–1241 (2004)
- 60.59 K. Savage, E.A. Davidson, A.D. Richardson: A conceptual and practical approach to data quality and analysis procedures for high–frequency soil respiration measurements, *Funct. Ecol.* **22**(6), 1000–1007 (2008)
- 60.60 A.D. Richardson, B.H. Braswell, D.Y. Hollinger, P. Burman, E.A. Davidson, R.S. Evans, L.B. Flanagan, J.W. Munger, K. Savage, S.P. Urbanski, S.C. Wofsy: Comparing simple respiration models for eddy flux and dynamic chamber data, *Agric. For. Meteorol.* **141**(2–4), 219–234 (2006)
- 60.61 V. Huth, S. Vaidya, M. Hoffmann, N. Jurisch, A. Guenther, L. Gundlach, U. Hagemann, L. Elsgaard, J. Augustin: Divergent NEE balances from manual–chamber CO₂ fluxes linked to different measurement and gap–filling strategies: A source for uncertainty of estimated terrestrial C sources and sinks?, *J. Plant Nutr. Soil Sci.* **180**(3), 302–315 (2017)
- 60.62 R. Vargas, M.S. Carbone, M. Reichstein, D.D. Baldocchi: Frontiers and challenges in soil respiration research: From measurements to model–data integration, *Biogeochemistry* **102**(1–3), 1–13 (2011)
- 60.63 A. Knohl, A.R.B. Soe, W.L. Kutsch, M. Goeckede, N. Buchmann: Representative estimates of soil and ecosystem respiration in an old beech forest, *Plant Soil* **302**(1/2), 189–202 (2008)
- 60.64 J.A. Subke, J.D. Tenhunen: Direct measurements of CO₂ flux below a spruce forest canopy, *Agric. For. Meteorol.* **126**(1/2), 157–168 (2004)
- 60.65 M.C. Myklebust, L.E. Hipps, R.J. Ryel: Comparison of eddy covariance, chamber, and gradient methods of measuring soil CO₂ efflux in an annual semi–arid grass, *Bromus tectorum*, *Agric. For. Meteorol.* **148**(11), 1894–1907 (2008)
- 60.66 J.M. Wang, J.G. Murphy, J.A. Geddes, C.L. Winsborough, N. Basiliko, S.C. Thomas: Methane fluxes measured by eddy covariance and static chamber techniques at a temperate forest in central Ontario, Canada, *Biogeosciences* **10**(6), 4371–4382 (2013)
- 60.67 A. Heinemeyer, M. Wilkinson, R. Vargas, J.–A. Subke, E. Casella, J.I.L. Morison, P. Ineson: Exploring the “overflow tap” theory: Linking forest soil CO₂ fluxes and individual mycorrhizosphere components to photosynthesis, *Biogeosciences* **9**, 79–95 (2012)
- 60.68 D. Gaumont–Guay, T.A. Black, A.G. Barr, R.S. Jassal, Z. Nesic: Biophysical controls on rhizospheric

- and heterotrophic components of soil respiration in a boreal black spruce stand, *Tree Physiol.* **28**(2), 161–171 (2008)
- 60.69 J.A. Subke, M. Reichstein, J.D. Tenhunen: Explaining temporal variation in soil CO₂ efflux in a mature spruce forest in Southern Germany, *Soil Biol. Biochem.* **35**(11), 1467–1483 (2003)
- 60.70 J.A. Subke, C.S. Moody, T.C. Hill, N. Voke, S. Toet, P. Ineson, Y. Teh: Rhizosphere activity and atmospheric methane concentrations drive variations of methane fluxes in a temperate forest soil, *Soil Biol. Biochem.* **116**, 323–332 (2018)
- 60.71 D.B. Metcalfe, T.D.G. Hermans, J. Ahlstrand, M. Becker, M. Berggren, R.G. Bjork, M.P. Bjorkman, D. Blok, N. Chaudhary, C. Chisholm, A.T. Classen, N.J. Hasselquist, M. Jonsson, J.A. Kristensen, B.B. Kumordzi, H. Lee, J.R. Mayor, J. Prevey, K. Pantazatou, J. Rousk, R.A. Sponseller, M.K. Sundqvist, J. Tang, J. Uddling, G. Wallin, W. Zhang, A. Ahlstrom, D.E. Tenenbaum, A.M. Abdi: Patchy field sampling biases understanding of climate change impacts across the Arctic, *Nat. Ecol. Evol.* **2**(9), 1443–1448 (2018)

Jens-Arne Subke

Biological and Environmental Sciences
University of Stirling
Stirling, UK
jens-arne.subke@stir.ac.uk



Jens-Arne Subke is Professor at the University of Stirling, UK. He received his PhD in Ecosystem Ecology from the University of Bayreuth and has held research positions at the Second University of Naples (Italy) and York (UK). He leads a research team investigating the impacts of climate and land use on ecosystem carbon and nutrient fluxes, focusing on interactions between plants, microbes, and soil organic matter.

Lars Kutzbach

Institute of Soil Science
Universität Hamburg
Hamburg, Germany
lars.kutzbach@uni-hamburg.de



Lars Kutzbach is Professor at the Institute of Soil Science of Universität Hamburg (Germany), leading the working group “Soils in the Climate System”. He is a principal investigator of the cluster of excellence “Climate, Climate Change, and Society – CLICCS” funded by the German Research Foundation. He received his PhD in Earth Sciences from the University of Hamburg. He focuses his research on the interconnected soil and vegetation processes and their coupling to the atmosphere.

David Risk

Earth Sciences
St. Francis Xavier University
Antigonish, Canada
drisk@stfx.ca



David Risk is an Associate Professor of Earth Sciences at St. Francis Xavier University. His interests lie in gas measurement, isotope tracers, developing new sensor techniques, and in risk studies of soil gas emissions in natural ecosystems, and the energy industry.

Soil Measurement

61. Soil Measurements

Bernd Huwe , Christina Bogner , Thomas Foken 

Atmosphere and soil are intensively coupled and interlinked in manifold aspects. The most relevant interfaces are the very soil surface, where water is stored and water fluxes are split into evaporation, runoff and infiltration, and the soil–root system, which controls transpiration. Hence, important topics are surface properties like roughness, wettability, sealing and crusting, water storage, water availability for plant roots, water retention, and conductivity characteristics of the subsurface soil. In this chapter, we give an overview of soil hydraulic measurements and analyses with relevance for the soil–plant–atmosphere system that have been used in the past and are still of high relevance in the context of ecosystem research. More specifically, we focus on devices and procedures that are fundamental for soil systems and highlight recent developments. We close this chapter with an outline of promising future developments.

61.1	Measurement Principles and Parameters	1626	61.2	History	1630
61.1.1	Measured and/or Estimated Parameters.....	1626	61.3	Theory	1631
61.1.2	Principles of Measurements.....	1629	61.3.1	Potentials and Forces.....	1631
			61.3.2	Gradients, Fluxes, and Transport Equations.....	1632
			61.3.3	Ground Heat Flux.....	1633
			61.3.4	Soil Heat Flux Plates.....	1634
			61.4	Devices, Systems, and Analyses	1634
			61.4.1	Infiltration and Runoff.....	1634
			61.4.2	Water in the Soil Profile.....	1636
			61.4.3	Soil Heat.....	1643
			61.4.4	Specific Analyses.....	1644
			61.5	Specifications	1646
			61.6	Quality Control	1647
			61.7	Maintenance	1647
			61.8	Applications	1648
			61.8.1	Water Storage on the Soil Surface.....	1648
			61.8.2	Time Series of Soil Matric Potentials and Corresponding Weighted Permutation Entropies.....	1648
			61.8.3	Daily Cycle of Soil Temperature.....	1649
			61.9	Further Developments	1650
			61.10	Further Reading	1651
			References		1651

Soil and atmosphere are two compartments of ecosystems that are closely interlinked by direct fluxes of heat, water, gas, and matter, as well as by mutual coupling of system parameters. These coupling processes occur, on the one hand, at the interface between soil and atmosphere, the soil surface, and, on the other hand, through the activity of vegetation cover, mainly the plant–root system. The atmosphere constitutes the upper boundary for the soil system (e.g., infiltration, evaporation and heat fluxes) and the soil the lower boundary for the atmosphere (e.g., surface temperature, albedo, evaporation, and surface roughness). On the macroscopic scale (m^2), plant roots represent a sink or a source in the soil system by taking up water and nutrients or secreting root exudates, for example.

Another aspect in soils that is of uppermost importance for the atmospheric system is storage, storage change (water, energy, and solutes), and availability of water and solutes for plants. To understand these processes, we need to consider the distributions of particle and pore sizes, porosity (aggregate and interaggregate porosity), transport and storage characteristics for all species involved (water, gases, heat, and solutes), and their mutual interactions (process coupling). The result is a nonlinear system of interacting (transport) processes, described by a system of (fully-coupled) partial differential equations (PDEs). Their handling is still demanding and time as well as labor consuming. Crucial in this respect is the extreme spatial heterogeneity of almost all soil parameters, which challenges the

manageability and predictability and, thus, limits the practical use of PDEs to a high degree. However, parameters characterizing the hydrological and thermal behavior of the soil system, especially near the soil–atmosphere interface, can support the understanding of atmospheric systems and may even be used to improve the quality of atmospheric models.

The protection of soils from erosion by wind and water is another important ecological aspect that links soils and the atmosphere. Here, relevant soil parame-

ters are cohesion of soil particles at the soil surface, surface roughness, surface water storage potential, soil aggregate size, and aggregate stability. In this chapter, we focus on soil hydrological processes and parameters and on heat transport. We mainly give an overview of state variables and transport characteristics and present selected measurements and case studies exemplarily. For both water and heat flow, we present estimation functions for transport parameters that are increasingly used on the landscape scale.

61.1 Measurement Principles and Parameters

Multiple interactions between soil and the atmosphere exist, as described in the introduction to this chapter. On the very soil surface, snow cover, snow melt, runoff, infiltration, and water storage are important and need to be measured in an adequate way. In the soil profile, water availability, storage of available water, and hydraulic conductivities are directly linked to water uptake by plant roots. The upper (atmospheric) boundary has a pronounced impact on the coupled transport of water, vapor, and heat in soil. Soil temperature affects water properties relevant for heat storage, heat transport, water binding, and water transport. This influence is moderate for most parameters over a range of 0–55 °C, except for dynamic viscosity (which has a direct impact on soil water conductivity).

61.1.1 Measured and/or Estimated Parameters

Table 61.1 provides an overview of basic soil physical parameters that are regularly measured to characterize compaction, porosity, and aggregation. Particle density is almost exclusively used to calculate porosity. Note that for the calculation of the porosities n_A and n_I , the determination of the volume of individual aggregates n_i is required.

Loam soils have the highest compaction potential, while clay soils possess the highest porosity due to the *card-house* structure of the primary platy clay minerals. However, in clays, most of the water is strongly bound in very fine pores and is unavailable to plant roots.

Table 61.1 Basic soil physical parameters with m_t : mass of dry soil, v_{soil} : volume of bulk soil, v_{slid} : volume of solids, v_{por} : volume of pore space, v_A : volume of pores in soil aggregates, v_I : volume of pores between soil aggregates, v_{agg} : volume of aggregates. Index i indicates individual aggregates

Parameter	Definition	Unit	Significance	Comment
Bulk density	$\rho_b = \frac{m_t}{v_{\text{soil}}}$	kg m ⁻³	Soil compaction, calculation of porosity	Used in pedotransfer functions ^a
Particle density	$\rho_s = \frac{m_t}{v_{\text{slid}}}$	kg m ⁻³	Mean density of individual grains	Calculation of porosity
Bulk porosity	$n = \frac{v_{\text{por}}}{v_{\text{soil}}}$	m ³ m ⁻³	Maximum available pore space	$n = \frac{1 - \rho_b}{\rho_s}$
Individual aggregate ^b porosity	$n_i = \frac{v_A}{v_{\text{agg}}}$	m ³ m ⁻³	Aggregate pore content within soil aggregates	$n_i = \frac{1 - \rho_i}{\rho_s}$
Bulk aggregate porosity	$n_A = \frac{v_A}{v_{\text{soil}}}$	m ³ m ⁻³	Aggregate pore content of bulk soil	$n_A = n_i \frac{1 - n}{1 - n_i}$
Bulk interaggregate porosity	$n_I = \frac{v_I}{v_{\text{soil}}}$	m ³ m ⁻³	Interaggregate pore content of bulk soil	$n_I = n - n_A$
Void ratio	$e = \frac{v_{\text{por}}}{v_{\text{slid}}}$	m ³ m ⁻³	Soil compaction studies	$e = \frac{n}{1 - n}$

^aSee Sect. 61.4.4 for more details.

^bIndividual spatial units of organization of solids in soils as a result of swelling/shrinking and biological activity (e.g., earthworms, microorganisms) [61.1].

Table 61.2 Soil material functions for water and heat transport with ψ : matric potential, θ : volumetric water content (for quantities see Chap. 5)

	Definition	Unit	Significance	Comment
Particle size distribution	Equivalent particle diameters (spheres), Stoke's law	m	Used in pedotransfer functions ^a	Synonym for soil texture
Water retention curve (WRC)	$\theta = f(\psi, \text{soil structure})$	$\text{m}^3 \text{m}^{-3}$	Ecological functions of soil water transport modeling	Nonlinear function of matric potential
Pore size distribution	Equivalent pore diameters (tubes), equation for capillary rise	m	Same as WRC used in pedotransfer functions ^a	Classification of pore systems
Hydraulic conductivity function	Parameter in Darcy's law $k = f(\theta, \text{soil structure})$	m s^{-1}	Water transport in soil, water transport modeling	Nonlinear function of water content
Volumetric heat capacity function	$c_V = f(\theta, \text{soil composition})^a$	$\text{J m}^{-3} \text{K}^{-1}$	Heat storage in soil heat transport modeling	Linear function of water content
Thermal conductivity function	Parameter in Fourier's law $\lambda = f(\theta, \text{soil composition})$	$\text{J m}^{-1} \text{s}^{-1} \text{K}^{-1}$	Heat transport modeling	Nonlinear function of water content

^aSee Sect. 61.4.4 for more details.

^bHere, soil composition means volumetric contents of quartz, other minerals, organic matter, water, and air [61.2, 3].

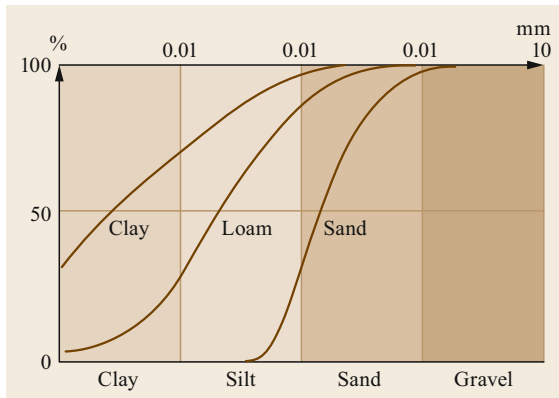


Fig. 61.1 Particle size distribution of typical soil textures. Please note that clay and sand have two meanings, namely particle size class (x -axis) and texture class (i.e., a particular distribution curve)

Soil is physically characterized by scalar parameters (porosity, bulk/particle density, mineral composition, wilting point, etc.), as well as by material functions like particle and pore size distribution, and parameter functions like conductivity characteristics (water, heat), water retention curve, and volumetric heat capacity (Table 61.2).

In principle, all these functions can be measured in the laboratory, some of them also under field conditions. However, measurements are time and labor consuming and are often not applicable at the catchment or landscape scale. Thus, for most of these characteristics, numerous estimation functions have been developed in the past. Some frequently used approaches will be presented in Sect. 61.4.4.

Particle size distribution is a fundamental material function for the characterization of soils. It is

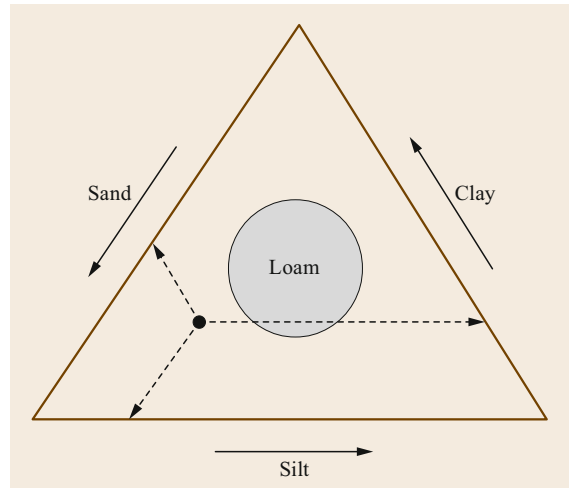


Fig. 61.2 Texture triangle with three main particle size classes: sand, silt, and clay; the soil texture class *loam* is a balanced mixture of sand, silt, and clay

required in soil genesis, as well as in soil fertility assessment. In soil hydraulic studies, it is often used for the estimation of soil hydraulic parameters and parameter functions. Basically, it is a cumulative distribution function of particle sizes (Fig. 61.1). For practical purposes, it is usually aggregated to soil texture classes and represented in triangle diagrams as a function of clay, silt, and sand contents (Fig. 61.2). Unfortunately, most nations have their own particle size classifications and triangle diagrams. Figure 5.1a–d (Chap. 5) exemplarily show the soil texture classes according to FAO/HYPRES (Hydraulic Properties of European Soils/Food and Agriculture Organization of the United Nations), USDA (United States Department of Agriculture), GEPPA (Groupe d'Étude pour les Problèmes de

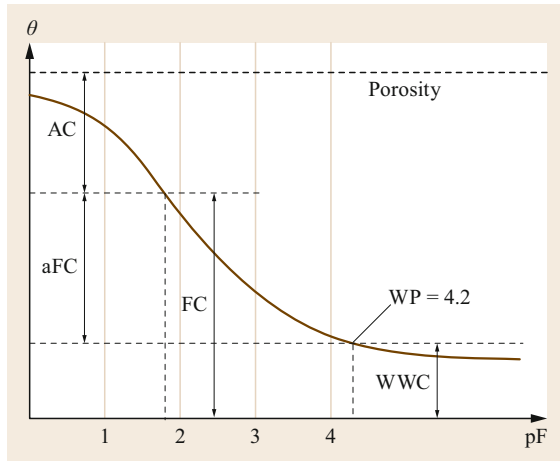


Fig. 61.3 Ecologically relevant points and ranges of a water retention curve, also called pF-curve (AC: air capacity; FC: field capacity; aFC: available field capacity; WP: wilting point; WWC: wilting point water capacity)

Pédologie Appliquée, France), and SSSG (Soil Science Society of Germany). Following the SSSG, particle size classes are defined as clay (T): < 2 μm, silt (U): 2–63 μm, sand (S): 63–2000 μm. This differs slightly

from the USDA system with clay (T): < 2 μm, silt (U): 2–50 μm, sand (S): 50–2000 μm [61.2, 4].

A second basic material function is the (equivalent) pore size distribution. It is typically derived from the water retention curve assuming cylindrical pores with a contact angle of 0°. A symbolic diagram is given in Fig. 61.3. As the pF-value (see the definition in Table 61.3) is a logarithm, soil saturation occurs at $pF \rightarrow -\infty$. Figure 61.3 also contains the ecological subdivision of the pore space. An important characteristic of almost all material functions is a pronounced *hysteresis*. For example, the water retention curve, the hydraulic conductivity–soil-water, and the thermal conductivity–soil-water relationships change shape depending on whether soil drying or wetting occurs. Thus, a whole family of (scanning) curves can be derived, restrained by upper and lower envelopes (Fig. 61.4). Hysteresis is hard to predict and introduces a considerable uncertainty in estimates of the target variables and the prediction of future changes, even when initial and boundary conditions are perfectly known.

Parameters and material functions characterize the relevant physical properties of soil regarding water and heat status and dynamics, and contribute to the understanding of complex hydraulic and thermal behavior

Table 61.3 Variables of soil moisture and water availability with v_w : water volume, v_s : soil volume, m_w : water mass, m_t : dry soil mass, n : porosity

Variable	Symbol	Definition	Units	Comments
Water content (volumetric)	θ_v	$\frac{v_w}{v_s}$	$m^3 m^{-3}$	Soil volume based water content $\max(\theta_v) = n^a$
Water content (gravimetric)	θ_g	$\frac{m_w}{m_s} = \theta_v \frac{\rho_w}{\rho_b}$	$kg kg^{-1}$	Soil dry mass based water content $\theta_g \gg 1$ is possible (organic soils)
Degree of saturation	s	$\frac{\theta_v}{n} \times 100\%$	–	$s_{\max} = 100\%$
Matric potential	h, ψ	Specific binding energy of pore water	m; Pa	Corresponds to soil water tension $t_{sw} = -\psi$
pF-Value	pF	$\log_{10}(-\psi)$	–	ψ in cm, defined only for unsaturated conditions
Air entry point	ψ_{aep}	$\max(\psi)$ with $\theta_v < n$	m; Pa	Defines capillary fringe in soil profiles Note that $\psi < 0$ in unsaturated soil Ecological indicator for soil aeration
Field capacity potential ^b	ψ_{fc}	$\psi_{fc} = -10^{1.8} \times 10^{-2}$	m	Matric potential at hydraulic equilibrium, i.e., water flux close to zero throughout the soil profile;
Wilting point potential	ψ_{wp}	$\psi_{wp} = -10^{4.2} \times 10^{-2}$	m	Matric potential at which typical crops start wilting
Field capacity ^b	θ_{fc}	$\theta(\psi_{fc})$	$m^3 m^{-3}$	Ecological indicator for water retention against gravity
Air capacity	θ_{ac}	$n - \theta_{fc}$	$m^3 m^{-3}$	Ecological indicator for soil aeration
Wilting point water capacity	θ_{wwc}	$\theta(\psi_{wp})$	$m^3 m^{-3}$	Ecological indicator for water stress
Plant available field capacity	θ_{pwc}	$\theta_{fc} - \theta_{wwc}$	$m^3 m^{-3}$	Ecological indicator for plant available water

^a For definition of n see Table 61.1

^b There are two approaches for the definition of field capacity: (a) the amount of water that is kept by the soil against the gravitational force at hydrological equilibrium (not a material characteristic); (b) the field capacity as a point of the water retention curve (θ_v at $pF = 1.8$); here we use approach (b), which is a property of the soil pore system.

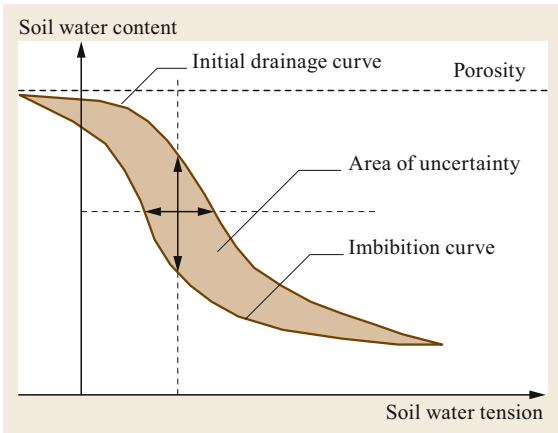


Fig. 61.4 Hysteretic behavior of the water retention curve. The shaded area is the area of scanning curves, i.e., curves of incomplete drainage and/or imbibition. The imbibition/drainage history of a soil is usually unknown and so is the position within the shaded area

of ecosystems. However, direct measurements of processes, dynamics, and fluxes are quite often likewise of great interest.

Most important for the hydrological and ecological behavior of soils and landscapes is the division of fluxes at the soil surface. For water, the relevant processes are given in the water balance equation

$$P + I = ET + D + \Delta W + R + \Delta S, \quad (61.1)$$

where P represents precipitation, I irrigation, ET evapotranspiration, D deep seepage, ΔW storage change in the soil profile (including surface storage), R surface runoff, and ΔS storage change in snow cover, respectively.

Parameters and fluxes related to surface processes comprise infiltration and infiltration capacity, surface runoff, surface storage, and surface roughness. The division of incoming water into infiltration and runoff is quite often controlled by the uppermost few mm of a sealing layer at the soil surface [61.5, 6].

Relevant variables to determine soil heat flux are soil temperature, thermal conductivity, volumetric heat capacity, ground heat flux at the soil surface, and heat fluxes in the soil profile. Undisturbed measurement of soil water and soil heat fluxes is occasionally attempted by direct use of Darcy’s and Fourier’s transport equations (gradient method). In soil hydrology, this approach is in most cases misleading due to the extreme spatial variability and other uncertainties. However, the variability is usually lower and accuracy of measurements is higher for heat flux measurements or rather estimates. Lysimeters and soil heat plates are alternative devices for water and heat flux measurements. However, these methods may disturb the soil to an unknown degree and, thus, change the fluxes. Table 61.4 gives an (incomplete) overview of water and heat fluxes in the soil.

61.1.2 Principles of Measurements

In general, measurements are to be justified by specific project goals (e.g., assessment of soil fertility, soil mapping, process-based modeling, hypothesis testing), and the validity of underlying model concepts. For example, measuring the hydraulic conductivity when Darcy’s law is invalid will yield meaningless results. Measurements are in many cases linked to models. However, intuitive measurement approaches justified by empirical concepts like soil fertility, soil health, or sustainability also exist. From a hydrological point of view, soil is a *hierarchical porous medium* with a pronounced spatial heterogeneity, nonlinear material functions, and associated hydrological processes like runoff, infiltration, and redistribution, especially under field conditions.

Spatial heterogeneity of soil needs to be reflected by adapted *sampling strategies*. One concept is the *representative elementary volume REV*, a sampling volume that covers all relevant structural elements of the site and reduces the fluctuations of a variable to its minimum. However, each variable has its own REV, and it

Table 61.4 Water and heat flux measurements near the soil surface

Flux	Unit	Measurement, determination	Comments
Throughfall	$\text{m}^3 \text{m}^{-2} \text{s}^{-1}$	Rain gauges	High spatial variability, direct interface soil–atmosphere
Stemflow	$\text{m}^3 \text{m}^{-2} \text{s}^{-1}$	Stemflow collectors	Point infiltration, generation of heterogeneity and preferential flow
Runoff	$\text{m}^3 \text{m}^{-2} \text{s}^{-1}$	Runoff plots, flow divider systems	Complementary to infiltration
Infiltration	$\text{m}^3 \text{m}^{-2} \text{s}^{-1}$	Infiltration rings, runoff plots, flow divider systems	Critical processes: sealing, crusting, surface storage
Evaporation	$\text{m}^3 \text{m}^{-2} \text{s}^{-1}$	Estimated from ET_p (potential evaporation) and LAI (Leaf Area Index)	Direct interface soil–atmosphere
Ground heat flux	W m^{-2}	Application of Fourier’s law, heat flux plates	Upper boundary for soil heat flux
Soil temperature profiles	K, °C	Soil temperature sensors, several principles	Installation along soil profile

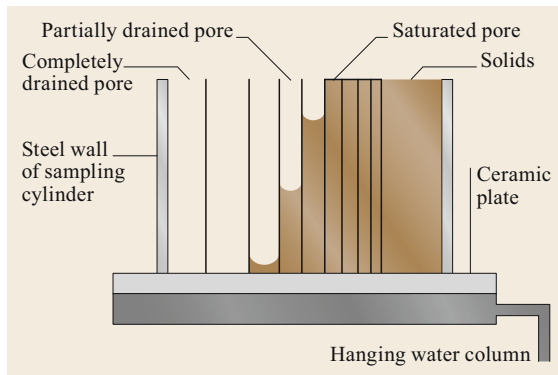


Fig. 61.5 Determination of the water retention curve in a sampling cylinder (principle)

may even not exist for specific site conditions. Mapping requires the set up of *sampling grids* and demands consideration of spatial autocorrelations in the field and in landscapes. Here again, each soil variable has its own spatial structure expressed in terms of autocorrelation length and variance. *Bulk samples*, usually taken with a soil auger (Sect. 61.4.1) are used for soil texture and for soil chemical analyses. Many soil hydrological parameters shown in Tables 61.1–61.3 require *volume samples* (Sect. 61.4.1). Bulk samples and volume samples are both destructive, i.e., it is not possible to repeat measurements at the same sampling location. Therefore, in order to measure temporal changes in form of *time series*, great effort has been devoted in the past to develop sensors for relevant state variables in the soil like water content, matric potential, or soil temperature. A major obstacle is quite often the limited number of sensors due to financial restrictions.

Because soil hydrological processes are nonlinear, their *averaging* requires special care. A physically meaningful averaging should always be preferred to standard statistical averaging. Averaging is a vast field and cannot be covered comprehensively in this chapter. In practical applications, effective parameters may often be obtained by calibrations at the study scale

61.2 History

A comprehensive history of measurements in soil physics and soil hydrology is outside of the scope of this chapter. However, the following overview gives a short impression of the milestones. Soil physics and soil physical measurements are as old as agricultural land use. Irrigation, drainage, and storage of soil water for plant use were the processes early farmers were particularly interested in, and this remains relevant today [61.2, 9]. Progress in measurements and in theory

based on distributed point measurements. Some measurements are *intuitive* in the sense that basic and intuitive understanding of soil processes and properties allows the development of measurement designs, e.g., for bulk/particle density, water content, infiltration tests, surface runoff, surface storage, or surface roughness. Intuitive does not imply simple (e.g., Fig. 61.5). Measurement design is often derived from basic physical properties and/or transport laws (Darcy's law, Fick's law, Fourier's law, Richards equation, etc.). Advanced measurements use field data or soil column experiments in the laboratory together with *inverse modeling* to identify soil hydrological parameters like conductivity, for example [61.7].

Measuring soil physical and hydrological parameters in the lab as well as in-situ faces many challenges that cannot be fully covered in this contribution. We emphasize the most important ones only like shrinking, swelling, heterogeneity of soil parameters, system disturbance by measurements, hysteresis of material functions, or violation of assumptions for field measurements (homogeneity, isotropy). Further, technical restrictions and problems like impermeable core walls in soil column experiments, smearing effects, or boundary fluxes along measurement devices (field sensors) can hamper measurements. For some sensors like thermocouples, tensiometers, and gypsum blocks, equilibrium between the soil and the sensors is a precondition that is not always met in dynamic situations (e.g., rapid infiltration of water).

Forces acting on the soil water cannot be measured directly. However, we can measure potentials and calculate the forces as their negative gradients. Water flux can be measured in lysimeters of different sizes and locations in the soil profile. The main limitation of lysimeters is the disturbance of the flow field in the soil. This can lead to completely wrong measurements. Devices to overcome this problem are expensive and need intensive maintenance. Soil heat fluxes are often measured using heat-flux plates assuming that disturbances by the plates can be neglected [61.8].

were interlinked. However, quite often improvements of measurements resulted from a general technological progress in mechanics, electronics, and computer technology and not from advances in theory.

Henry Darcy (1803–1858) was the first to study the movement of water experimentally and developed a simple empirical linear formula for the description of water fluxes in saturated soils with the saturated hydraulic conductivity k_s as a proportionality con-

stant [61.10]. Darcy's law was often criticized for its simplicity, and its validity is doubted to date. However, it is still used in even advanced theoretical approaches and models. *Edgar Buckingham* (1867–1940) [61.11] extended the applicability of Darcy's law to unsaturated soil conditions by replacing k_s by the nonlinear conductivity function $k(\theta)$ and the matric potential (61.8), which can be measured with tensiometers. This marked the birth of the potential theory in soil hydrology. *Lorenzo A. Richards* (1904–1993) [61.12] built upon this approach and combined it with the equation of continuity (61.9). The resulting Richards equation (61.10) is a nonlinear, second-order parabolic differential equation that cannot be solved with elementary methods. Thus, empirical formulas like the approach by *Green* and *Ampt* [61.13] for infiltration or the Ernst equation [61.9, 14] for the determination of k_s have survived to date. Simultaneously, mathematicians, physicists, and soil hydrologists developed the potential theory and quasi-analytical solutions of Richards equation at advanced levels [61.15–18] with useful applications in drainage and irrigation science [61.19–22]. As they claim to be mathematically exact, the solutions of these days are still useful at least for the testing of numerical models.

This theoretical progress was accompanied by a technological progress that brought about substantial improvements of sensors, data recording and transmission technologies, automating methods, tomographic methods for microscale structure analyses [61.23–26], and computer power. The latter considerably accelerated the application of numerical methods and the

development of numerical, process-based simulation models [61.27, 28]. Numerical and statistical models were increasingly used for the analysis of measurements, parameter and process identification by inverse modeling [61.7, 29], time series, risk, and error analyses [61.30–32]. The improvement of the sensors allowed the development of sophisticated measurement designs in soil profiles and in the laboratory [61.7, 29, 33].

Recent and still ongoing research focuses on non-Darcian flow in macropore systems (kinematic wave theory) [61.34–36], the analysis of preferential flow paths, e.g., with dye tracers [61.31, 32, 37, 38], tomographic methods for detailed structural analyses and modeling at the microscale [61.23, 25], time series methods for hydrological time series [61.30], spectral methods, and remote sensing [61.39, 40].

Measurements of surface temperatures have been part of the measurement program since the beginning of regular meteorological measurements in the second half of the nineteenth century. The soil temperature as a part of the heat balance of the Earth's surface was already discussed in textbooks of this time. With the beginning of comprehensive surface energy studies in the 1950s to 1970s (Chap. 55) and more accurate radiation measurements, the interest to measure the ground heat flux increased [61.41]. One of the first comprehensive studies was published in 1973 [61.42]. The available energy as the sum of net radiation and ground heat flux was necessary for the determination of evapotranspiration with the Bowen-ratio method or the Penman–Monteith method (Chap. 57). *Sauer* and co-workers [61.43] offer a review of different thermal sensors.

61.3 Theory

Soil water storage and dynamics are governed by forces and local balances (equation of continuity). Forces cannot be measured directly in soils. However, assuming that they are conservative, forces can be derived from potential fields. Therefore, potential theory together with transport laws and local balances constitute the theoretical backbone of water dynamics in porous media.

61.3.1 Potentials and Forces

Water in soil is moved by forces in force fields that are considered as conservative (force field without curls: $\nabla \times \mathbf{F} = 0$). Such forces can be formulated as negative gradients of associated potentials [61.44] (e.g., gravitational force can be derived from gravitational potential)

$$\mathbf{F} = -\text{grad } V = -\nabla V. \quad (61.2)$$

The symbol ∇ is called the nabla operator and is defined in Cartesian coordinates as

$$\nabla \equiv \begin{pmatrix} \frac{\partial}{\partial x} \\ \frac{\partial}{\partial y} \\ \frac{\partial}{\partial z} \end{pmatrix}. \quad (61.3)$$

In soil hydrology, ∇ is used as formal operator to express gradients of potential fields (∇V), divergence of flow fields ($\nabla \cdot \mathbf{v}$), and curl densities of force fields ($\nabla \times \mathbf{F}$).

The potential of soil water is defined as work to transfer a given amount of water (mass, weight, volume) from a chosen point (\mathbf{r}_1) in the soil to an (arbi-

trarily) defined reference point (level, r_0)

$$V(x, y, z) = - \int_{r_0}^{r_1} \mathbf{F} ds. \quad (61.4)$$

This integral is independent of the selected integration path, and the potential difference between two points (r_1, r_2) is given by the difference of their potentials.

$$\begin{aligned} W &= \int_{r_1}^{r_2} \mathbf{F}(\mathbf{r}) ds = - \int_{r_1}^{r_2} \nabla V ds \\ &= - \int_{r_1}^{r_2} dV = -(V(r_2) - V(r_1)). \end{aligned} \quad (61.5)$$

This is equivalent to

$$\oint \mathbf{F} ds = 0. \quad (61.6)$$

In each point in the soil, several forces are superimposed. Accordingly, the total hydraulic potential H is the sum of subpotentials h_i along any selected path

$$\begin{aligned} H &= \int_r^{r_0} \mathbf{F} ds = \int_r^{r_0} \left(\sum_i \mathbf{F}_i \right) ds \\ &= \sum_i \int_r^{r_0} \mathbf{F}_i ds = \sum_i h_i. \end{aligned} \quad (61.7)$$

Dimensions and units of potentials depend on the type of reference quantity, namely mass, volume, and weight of water. In soil hydrology, all three references are used and have their distinct advantages and disadvantages (Table 61.5). The hydrologically relevant subpotentials are given in Table 61.6.

61.3.2 Gradients, Fluxes, and Transport Equations

Transport of soil water is widely described by Darcy's law [61.10], which was extended by *Buckingham* [61.11] for unsaturated conditions. It states that flux densities are proportional to the driving force

$$\mathbf{q} = -\bar{\mathbf{k}} \cdot \nabla \psi_t, \quad (61.8)$$

where ψ_t is the total hydraulic potential and $\bar{\mathbf{k}}$ the hydraulic conductivity tensor, respectively. Under isotropic conditions $\bar{\mathbf{k}}$ simplifies to the scalar parame-

ter k . Please note that $\bar{\mathbf{k}}$ is a nonlinear function of the soil water content θ .

Storage change in soil is described by the equation of continuity

$$\frac{\partial \theta}{\partial t} = -\nabla \cdot \mathbf{q}, \quad (61.9)$$

in which \mathbf{q} denotes the vector of water flux density. Equation (61.9) describes the temporal change of water content by the spatial change of local flux densities and is also called a local balance of soil water.

Combining (61.8) and (61.9) and adding a source/sink term yields the transport equation for saturated/unsaturated transient conditions, the so-called extended Richards equation [61.12]

$$\frac{\partial \theta(\psi_m)}{\partial t} = \nabla \cdot [\bar{\mathbf{k}}(\theta(\psi_m)) \cdot \nabla \psi_t] + U. \quad (61.10)$$

Usually, transpiration is considered in the sink term U , whereas evaporation from the soil surface is taken into account by an appropriate formulation of the upper boundary condition of the flow region. Similarly, using Fourier's law of heat conduction $\mathbf{Q} = -\bar{\lambda} \cdot \nabla T$, a corresponding continuity equation and adding a convection term yields the equation for heat transport in soil

$$\frac{\partial (c_v(\theta)T)}{\partial t} = \nabla \cdot [\bar{\lambda}(\theta(\psi_m)) \nabla T] - c_w \nabla \cdot (T \cdot \mathbf{q}) + V. \quad (61.11)$$

For isotropic conditions, the thermal conductivity tensor $\bar{\lambda}$ simplifies to the scalar parameter λ . Parameter functions $\theta(\psi_m)$, $\bar{\mathbf{k}}(\theta(\psi_m))$, and $\bar{\lambda}(\theta(\psi_m))$ are nonlinear functions, whereas $c_v(\theta)$ is a linear function of water content.

If we further assume that water flow is negligible, water content is constant in a homogeneous soil, and no heat sources or sinks are present, (61.11) simplifies to

$$c_v \frac{\partial T}{\partial t} = \lambda \nabla^2 T, \quad (61.12)$$

and

$$\frac{\partial T}{\partial t} = \frac{\lambda}{c_v} \nabla^2 T = D_T \nabla^2 T, \quad (61.13)$$

which is the thermal diffusion equation with $D_T :=$ heat diffusivity. In one dimension this is

$$\frac{\partial T}{\partial t} = D_T \frac{\partial^2 T}{\partial z^2}. \quad (61.14)$$

This simplified version is quite often successfully used in micrometeorology to determine D_T with field data by a finite difference approximation of (61.14), for example.

Table 61.5 Dimensions and units of potentials in soil

Reference quantity	Dimensions	Unit	Comments
Mass	$L^2 T^{-2}$	$m^2 s^{-2}$	Reference quantity unchanged at pressure changes
Volume	$MT^{-2} L^{-1}$	Pa	Corresponds to measurement devices like tensiometers and piezometers
Weight	L	m	Intuitive for gravitational potential and experimental setups in laboratories (column experiments, pressure plates)

Table 61.6 Relevant sub-potentials of soil water; all sub-potentials add up to the total potential and contribute to the driving force of water movement in soil

Potential	Symbol	Corresponding forces	Comments
Matric potential	h_m, ψ_m	Capillary forces	Caused by surface tension at the water air interface in unsaturated soil pores
Piezometric potential	h_p, ψ_p	Water pressure forces in saturated soil	Corresponds to hydrostatic pressure only at hydraulic equilibrium (zero flux for all depths)
Gravitational potential	h_g, ψ_g	Gravitational force	Depends on the position of the reference level (which cancels out in transport equations)
Osmotic potential	h_o, ψ_o	Force to move water against a concentration gradient	In moist soils negligible (in dry soils are the extremely low conductivities the limiting factor), particularly important in the vicinity of semipermeable membranes
Gas potential	h_a, ψ_a	Pressure forces of soil air in unsaturated soil	Pressure changes caused by soil temperature variation, air pressure variation at the soil surface, nonequimolar chemical reactions in soil (CH ₄ and N ₂ O production, O ₂ consumption)
External load potential	h_l, ψ_l	Forces associated to mechanical stresses by grain–grain contacts	Not well defined in the sense of (61.4)

61.3.3 Ground Heat Flux

The ground heat flux is an important parameter in atmospheric science because it is part of the energy balance equation at the Earth's surface together with the net radiation and the sensible and latent heat fluxes. In contrast to the scales in the atmosphere, the scale of measurements in the soil is very small, and the heterogeneity of soil properties is ignored [61.45] (Chap. 1, Sect. 61.4.3). The ground heat flux, Q_G , is mainly based on molecular heat transfer and is proportional to the temperature gradient and the thermal molecular conductivity λ in the soil (Sect. 61.1.1).

$$Q_G = -\lambda \frac{\partial T}{\partial z}, \quad (61.15)$$

where T is the temperature and z the depth, respectively.

The heat flux directly at the surface is particularly interesting. Several methods are used [61.46–48], and two principles are common, namely the calculation according to (61.15), where the temperature gradient is extrapolated to the surface, or the determination of the heat flux at a certain depth and the calculation of the change of the heat storage in the layer above.

$$Q_G(0) = Q_G(-z) + \int_{-z}^0 \frac{\partial}{\partial t} c_v(z) T(z) dz, \quad (61.16)$$

with the time t and the volumetric heat capacity c_v . Based on (61.16) and a sensitivity analysis [61.8] two optimal designs for ground heat flux measurements are possible: (i) a soil heat-flux plate should be buried rather deeply (0.1–0.2 m) with several temperature measurements made above it to calculate the heat storage; (ii) a similar accuracy can be achieved if only one temperature profile is measured to calculate both the soil heat flux according to (61.15) over the depth of 0.1–0.2 m and the heat storage term above this layer and the surface.

The volumetric heat capacity $c_v = a_G/\nu_T$ (ν_T is the molecular thermal diffusivity; see Chap. 5) can be assumed constant with depth in the case of a uniform soil moisture and can be determined as [61.3]

$$c_v = c_{v,m}x_m + c_{v,o}x_o + c_{v,w}\theta, \quad (61.17)$$

with the heat capacity of the mineral and organic compounds

$$c_{v,m} = 1.9 \times 10^6 \text{ J m}^{-3} \text{ K}^{-1},$$

$$c_{v,o} = 2.479 \times 10^6 \text{ J m}^{-3} \text{ K}^{-1},$$

and for water

$$c_{v,w} = 4.12 \times 10^6 \text{ J m}^{-3} \text{ K}^{-1}.$$

The contribution of mineral components (assumed particle density of minerals: 2650 kg m^{-3}), x_m , in $\text{m}^3 \text{ m}^{-3}$

can be determined by measurements of bulk density and volumetric content of organic matter of the soil. For depths up to 20 cm, the volumetric content of organic matter x_o can often be neglected. The volumetric moisture content of the soil is θ and is given in $\text{m}^3 \text{m}^{-3}$. For the calculation of soil heat flux from the temperature gradient according to (61.15), the coefficient of heat conductance, λ , is necessary

$$\lambda = c_v D_T, \quad (61.18)$$

where D_T is the thermal diffusion coefficient that can be determined using a simple method [61.49], in which the temperature sensors are installed at three depths (0.10, 0.15, and 0.20 m), and the temperature difference between two time steps ($\Delta t = 1 \text{ min}$, $\Delta z = 0.1 \text{ m}$) is determined

$$\frac{T_{15 \text{ cm}}^{n+1} - T_{15 \text{ cm}}^n}{D_T \Delta t} = \frac{T_{20 \text{ cm}}^n - 2T_{15 \text{ cm}}^n + T_{10 \text{ cm}}^n}{(\Delta z)^2}. \quad (61.19)$$

The simplest method is the measurement with an integrating temperature sensor of the mean temperature of the soil layer between the surface and the heat-flux plate. For the ground heat flux near the surface, it then follows that

$$Q_G(0) = Q_G(-z) + \frac{c_v |\Delta z| \left[\overline{T(t_2)} - \overline{T(t_1)} \right]}{t_2 - t_1}. \quad (61.20)$$

For the modeling of the ground heat flux, multiple layers are used. The most appropriate and accurate model is the two-layer model (force-restore method) developed by *Blackadar* [61.50]. The ground heat flux can be calculated from two components, i.e., from the change of the temperature of the thin surface layer due to radiation and from the slow wave of the temperature difference between the surface layer and a deeper layer [61.51].

61.3.4 Soil Heat Flux Plates

Soil heat flux can be measured at a certain depth with soil heat flux plates. They consist of two metal-

lic plates separated by a layer of resin, with a heat conductance matching that of the soil. The temperature difference between the plates is measured with thermocouples; their output signal is proportional to the soil heat flux (61.15). The most important sources of measurement errors are the differences of the heat conductivities between the plates and the soil and at the edges of the plates (deflection error), which are insufficiently included in the temperature measurement [61.52]. The widely used correction factor f suggested by *Philip* [61.53] relates the measured soil heat flux, Q_G and the soil heat flux through the surrounding soil, Q_G

$$f = \frac{Q_G}{Q_G} = \frac{\epsilon}{1 + (\epsilon - 1)H}, \quad (61.21)$$

where ϵ is the ratio of the heat conductivities $\lambda_{\text{plate}}/\lambda_{\text{soil}}$. The factor H depends on the geometry of the heat flux plate and is given for square plates as

$$H = 1 - \frac{1.7d_{\text{plate}}}{L} \quad (61.22)$$

and for round plates as

$$H = 1 - \frac{1.92d_{\text{plate}}}{D}, \quad (61.23)$$

where d_{plate} is the thickness of the plate, L is the length of the square plate, and D is the diameter of the round plate. A similar correction is the one by *Morgensen* [61.54]

$$f = \frac{Q_G}{Q_G} = \frac{\epsilon}{\epsilon - 1.7(d_{\text{plate}}/\sqrt{A_{\text{plate}}})(\epsilon - 1)}. \quad (61.24)$$

Such a correction is recommended by some authors [61.55], however, it is doubted by others [61.51]. The problem is the knowledge of λ in the soil that is highly variable [61.56] (Sect. 61.1.1).

61.4 Devices, Systems, and Analyses

In this section, we describe selected hydrological and thermal measurements and associated evaluations. We start with surface processes, including surface runoff, infiltration, and surface storage. Then, we continue with soil moisture, hydraulic parameters, and hydraulic functions, and finally, we present thermal methods to characterize and quantify the heat transport in soil. For

more complete information, the reader is referred to Sect. 61.10.

61.4.1 Infiltration and Runoff

At the soil surface the incoming precipitation or irrigation water is divided into runoff and infiltration. Quite

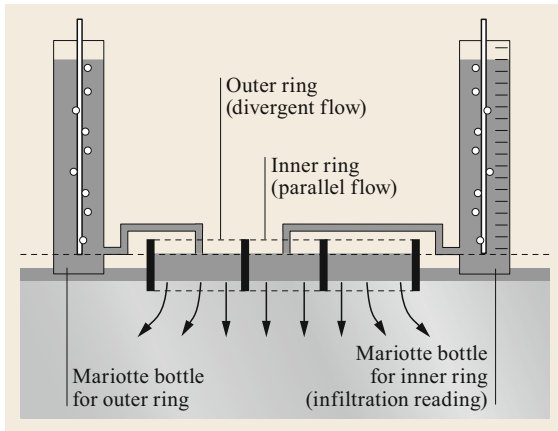


Fig. 61.6 Double-ring infiltrometer for quantifying actual infiltration capacity and/or field saturated conductivity. The water levels in the inner and outer rings are the same (and as low as possible) and are kept constant using two Mariotte bottles. The reading is performed only in the inner ring where parallel flow is assumed

often, e.g., in erosion studies, one is interested in the infiltration capacity, i.e., the maximum influx rate of water under the given boundary conditions. No runoff will be generated as long as infiltration capacity and surface storage capacity remain below their respective thresholds. In this section, we present standard methods to measure the saturated and unsaturated infiltration and a more demanding method for surface roughness and surface storage capacity.

Double-Ring Infiltrometer

Double-ring infiltrometers are simple devices for measuring actual infiltration capacities (Fig. 61.6). However, considering infiltration theory in a homogeneous soil they further allow us to interpret the infiltration rate as field saturated conductivity (or as effective saturated conductivity in the case of not perfectly homogeneous soils), as $\lim_{t \rightarrow \infty} d\psi/dz = 0$ and – according to Darcy’s law – we get $\lim_{t \rightarrow \infty} q = k_s$. In principle, this is a constant head infiltration experiment and different empirical, semiempirical, analytical, and numerical methods can be used to evaluate the measured data.

The *Green and Ampt* equation [61.13] is derived using a physically motivated approach with unrealistic assumptions. It is still used nowadays, even in comprehensive simulation packages like the Soil and Water Assessment Tool (SWAT) [61.57].

$$i = i_f + \frac{b}{I}, \quad (61.25)$$

where i is the infiltration rate, I the cumulative infiltration, and i_f and b are characteristic constants, respec-

tively. Please note that initially $I = 0$ and $\lim_{I \rightarrow 0} i = \infty$. On the other hand, $\lim_{I \rightarrow \infty} i = i_f$ and, thus, i_f may be interpreted as the saturated conductivity k_s .

The equation by *Kostiakov* [61.58] is simple and completely empirical

$$i = at^b. \quad (61.26)$$

The parameters a and b are completely empirical. For $b < 0$ the infiltration rate, i asymptotically approaches zero. Therefore, it is impossible to estimate k_s from this equation.

Horton [61.59] introduced an initial infiltration rate i_0 and a final infiltration rate i_f in an exponentially decreasing function, which intuitively makes sense

$$i = i_f + (i_0 - i_f)e^{-kt}. \quad (61.27)$$

For $t = 0$, this equation gives $i = i_0$, for $t \rightarrow \infty$ we find $i = i_f$, which again may be interpreted as the (effective) saturated conductivity.

The equation by *Philip* [61.15] is a simplification of a rigorous mathematical treatment (power series) of Richard’s equation (61.10).

$$i = \frac{1}{2}st^{-1/2} + i_f, \quad (61.28)$$

where the sorptivity s is given by $s = I/t^{1/2} = s(\theta_0, \theta_i)$. Again, for $t \rightarrow 0$ the infiltration rate is ∞ .

Surface Runoff

The second important water flux at the very soil surface is surface runoff. The splitting of the incoming rainfall or irrigation into infiltration and runoff is often controlled by a thin sealing layer with a thickness of only few millimetres [61.5, 60]. It makes no sense to take undisturbed soil cores for laboratory measurements. However, in a constant rate irrigation experiment microtensiometer arrays can be used to determine integrated hydraulic parameters for characterization of the sealing layer, the hydraulic impedance, defined by

$$I_h = \int_{z_s}^{z_0} \frac{1}{k} dz,$$

and the hydraulic conductance, which is just the reciprocal of I_h . Parameters z_s and z_0 are the sealing depth and the soil surface, and k is the hydraulic conductivity [61.61]).

Other important factors are slope and microtopography. The latter plays an important role for surface storage of soil water and can delay runoff and reduce



Fig. 61.7 Using stereo photography for quantifying surface storage of water

associated erosion losses considerably. An effective method for the assessment of the topographical surface structure is stereo photography with adequate analysis tools [61.62] (Fig. 61.7).

Runoff in the landscape can be measured using runoff collectors (Fig. 61.8) [61.63–67]. Under field conditions routing of soil water and soil suspension needs to be considered. Nowadays, this can be performed using geographic information systems (GIS). Runoff collectors need to be equipped with flux partitioning devices to measure short and intensive runoff events. A simple but effective flow diver system is shown in Fig. 61.9. A rather complex experimental design to study the interaction of precipitation, surface properties, runoff, and infiltration was used in [61.68] and is presented in Fig. 61.10. Results from a similar study at an agricultural study site in Avignon (France) are presented in Sect. 61.8.1 [61.62].

61.4.2 Water in the Soil Profile

Soil water is an essential and temporally variable constituent of soils that is fundamental for ecological func-

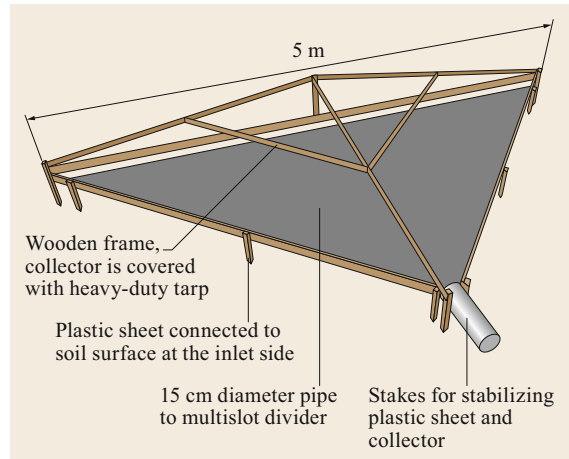


Fig. 61.8 Collector for surface runoff and sediment delivery measurements in the landscape (image courtesy of *Arnhold* [61.63]); runoff water and sediment is measured with flow divider systems (Fig. 61.9)

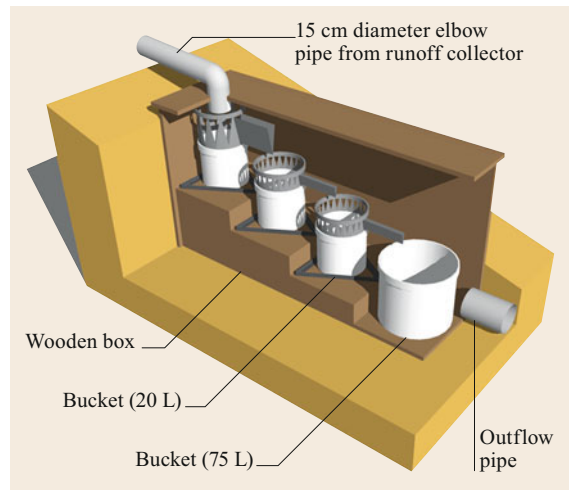


Fig. 61.9 Flow divider system for surface runoff and sediment delivery measurements in the landscape (image courtesy of *Arnhold* [61.63]); runoff water and sediment is collected with a runoff collector (Fig. 61.8)

tioning. The water content is a basic parameter that is highly variable in space and time. For the same soil matric potential the water content varies with the textural composition of sand, silt, and clay. Other sources of this pronounced spatiotemporal variability are the dynamics and spatial heterogeneity of precipitation and/or irrigation water caused by the canopy structure, and the heterogeneity of the subsurface root system.

However, the water content alone is often not very meaningful. It is crucial to distinguish between mass-based and volume-based water content. Further, the

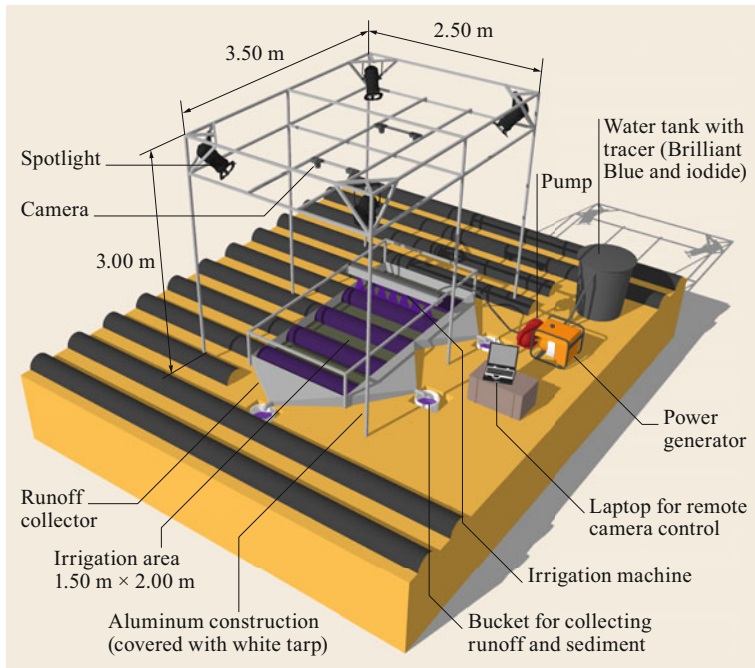


Fig. 61.10 Experiment design for assessment of surface storage, runoff, infiltration, and seepage (image courtesy of Arnhold [61.63])

availability of water to plants (see *Soil Water Potentials* in this subsection) and the mobility regarding seepage or evaporation (see *Conductivities* in this subsection) are important characteristics of water in soil porous media.

Gravimetric Measurement of Water Content

Gravimetric measurement of θ_g and θ_v is basic and straightforward (Figs. 61.11 and 61.12) [61.69]. Often, disturbed soil is used to determine mass-based gravimetric water content θ_g . However, to determine water storage in soil, volumetric water contents θ_v are required, which can be calculated by $\theta_g \rho_b / \rho_w$ (Table 61.3). Gravimetric measurements have the disadvantages to be labor-consuming and destructive. However, they are still the reference for calibrations of other methods, even though these methods face some problems themselves, like swelling and shrinking of the

samples. Indeed, it remains unclear how to define a reference volume in shrinking soil.

Indirect Methods for Water Content Measurements

The drawbacks of gravimetric water content measurements (time and labor-consuming, destructive) brought about the urgent need for nondestructive and fast methods to measure repeatedly at the same location with sufficient accuracy. Early attempts to use matric potential measurements and the water retention curve for water content estimations proved unsuccessful due to the limited measurement range of tensiometers (< -800 hPa) and the often pronounced hysteresis of the water retention curve (Fig 61.4). Successful indirect devices are based on radioactive radiation (neutron scattering, gamma-ray attenuation). Overviews can be found in [61.69, 70].

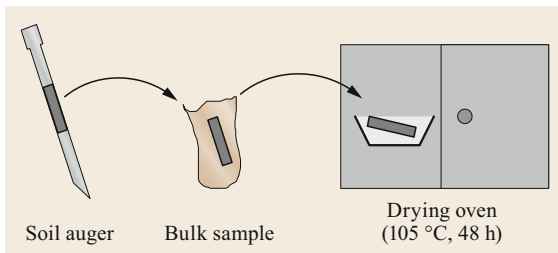


Fig. 61.11 Bulk sampling of soil. The sampling is destructive, and the internal pore structure is destroyed by sampling

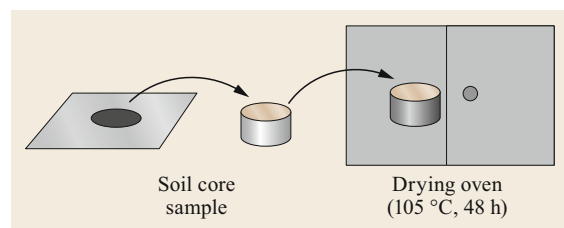


Fig. 61.12 Volume-based sampling of soil. The sampling is still destructive. The internal pore structure is ideally not destroyed by sampling

Neutron probes based on neutron thermalization were the first widely accepted indirect and reliable instruments for water content measurements [61.2, 71] and are probably still used today. The idea is to capture thermalized neutrons as a measure for protons in the soil. The probe consists of a source of fast neutrons (Ra-Be mixture) and a detector for thermalized neutrons. It is (manually) inserted via a cable through the protection shield into an access tube (consisting of Al, for example) to the desired depth. Thermalized neutrons are counted by battery powered external rate meter. As the ratio of protons to soil water varies with organic matter and clay content, the method needs site-specific calibration [61.72]. Thus, it is most suitable for long-lasting monitoring programs. The method faces difficulties in shallow (neutron emissions partly go into the atmosphere) and in stony soils, in which an accurate installation of the access tube may be impossible. The major drawback, however, is the radiation exposure hazard, the required protection measures, and safety rules (dosimeters, secured storage space, trained radiation protection officials).

The *γ-ray absorption method* is another radioactive approach for the measurement of soil water [61.2, 73, 74]. It typically needs two access tubes, one containing the radioactive source emitting gamma radiation (^{137}Cs) and the other for a detector, typically a scintillation counter. The method was first developed for laboratory studies. *Vomocil* [61.75] customized the design for field conditions. The method has a better depth resolution compared to neutron scattering that allows the identification of wetting fronts, measurements around sharp material layers, and measurements closer to the soil surface. However, the installation of two exact parallel tubes might pose serious problems, especially in stony soils. It also needs thorough calibration, which can be difficult for a higher resolution in the range of, e.g., 1 cm [61.76]. The *radioactivity* drawbacks are the same as for the neutron probe.

Customization of the *time-domain reflectometry* (TDR) method – which was initially and is still a technique to detect cable leakages – to soil conditions brought a great progress for water content measurements in the field [61.2, 70, 77, 78]. The method is nonradioactive and allows recording of high-resolution time series. It relies on the considerable difference of the relative dielectric constant of water ($\epsilon_r \approx 81$) and dry soil ($\epsilon_r \approx 4-8$). The principle of measurement is the analysis of the propagation velocity v of a high-frequency electromagnetic wave in soil and the calculation of ϵ_r from $v = c/\epsilon_r^{0.5}$, where c is the velocity of light in vacuum. The measurement design comprises a high-frequency generating and recording unit and, typically, two parallel antenna rods inserted

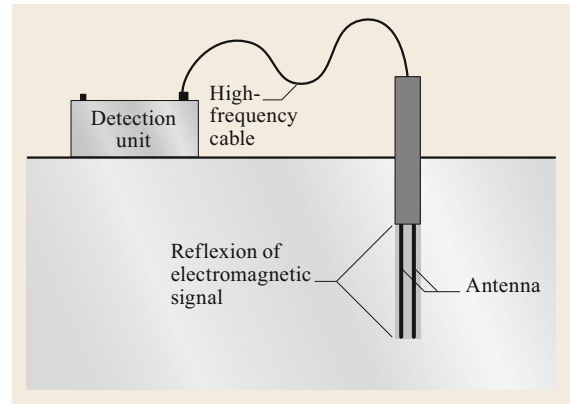


Fig. 61.13 Nondestructive measurement of volumetric water content using the TDR technique. The sensors can be installed in any depth, and the signal can easily be recorded by data loggers

into the soil (Fig 61.13). The electromagnetic wave is reflected on each discontinuity, and the reflected signal is recorded and analyzed in the TDR unit. With L being the length of the rods, ϵ_r can be calculated as $\epsilon_r = (ct/2L)^2$. An empirical functional relation between θ_v and ϵ_r was provided by [61.79]

$$\theta_v = -5.3 \times 10^{-2} + 2.9 \times 10^{-2} \epsilon_r - 5.5 \times 10^{-4} \epsilon_r^2 + 4.3 \times 10^{-6} \epsilon_r^3. \quad (61.29)$$

This equation was successfully used in an irrigation scheduling study in [61.77]. Other calibration curves were provided, e.g., by [61.80–82]. The measurements need a precise insertion of the waveguides into the soil to avoid air gaps around the rods. TDR measurements are sensitive to salinity, which can be measured simultaneously but may also disturb the water content measurements. For organic soils, a recalibration is recommended, as (61.29) only holds for mineral soils.

TDR measurements are known to have accuracy limitations in clayey soils and heavy soils with high salinity [61.83–85]. *Frequency domain reflectometry* (FDR) tries to overcome or mitigate these problems by analyzing the frequency domain instead of the time domain. Early attempts to transform time-domain waveforms into the frequency domain were later replaced by techniques that capture the signals directly in the frequency domain with significant improvements, like lower sensitivity to salinity. A sensor that has a bandwidth that allows us to measure salinity as well as water content with improved accuracy was developed in [61.83].

In recent years, capacity probes and impedance probes have been developed that are all based on the difference of ϵ_r between water and soil. Princi-

ples of measurements are the determination of capacitance or impedance (fixed frequency, shifting frequency, often using amplitude changes along a standing wave [61.86]), sometimes called *amplitude domain reflectometry* (ADR). The signal is often converted to a voltage to simplify the measurement and facilitate data recording [61.86, 87]. Twelve dielectric sensors of different types under saline conditions were compared in [61.88]. Results were reported by the authors to be comparable and acceptable.

Other Methods for Water Content Estimation

Other methods for water content estimation exist and are based on physical principals and stochastic correlations, like thermogravimetry, electrical conductivity, soil thermal properties, heat pulse sensors, ground penetrating radars, electromagnetic induction, direct current resistivity, passive and active remote sensing, acoustic wave propagation, or optical methods. Several of these methods have the potential of soil moisture mapping on different scales. These methods were described and discussed comprehensively in [61.70].

Soil Water Potentials

Soil water potentials were defined in Sect. 61.3. Relevance and measurements are described, e.g., in [61.2, 69]. For water movement in the soil matrix, the matric potential (unsaturated soil), piezometer potential (saturated soil), and gravitational potential are generally the most relevant potentials. The availability of soil water to plant roots is controlled by matric potentials (specific binding energy). However, unsaturated conductivities are another essential soil property when we look at water uptake by plant roots and transpiration rates.

The measurement of potentials is comparatively simple (Sect. 61.10). The *gravimetric potential* is the length difference between a point of measurement and the reference level in the gravity field (soil surface, groundwater, or elsewhere), provided that the reference quantity is weight (Table 61.5). The *piezometer potential* corresponds to the matric potential in the saturated zone. It can be measured as pressure at the bottom of piezometers (groundwater access tubes that are open at the bottom). In the case of hydraulic equilibrium (zero flux at all points), the measurements reflect the hydrostatic pressure. This is not the case under nonequilibrium conditions like drainage in agriculture or in confined aquifers.

Matric potentials are measured using tensiometers. A simple design is shown in Fig. 61.14. The range of measurements depends on the pore size distribution of the porous cell and is typically > -800 hPa. Tensiometers can also be operated under saturated conditions and may, thus, replace piezometers. The size of the

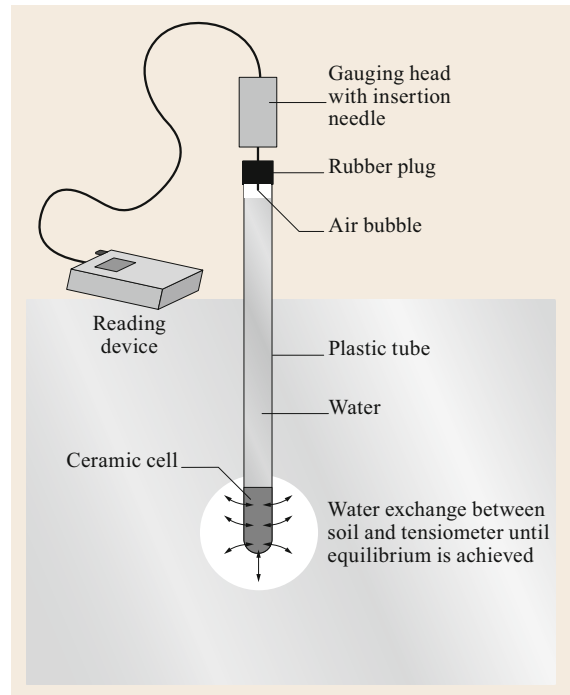


Fig. 61.14 A simple tensiometer for manual matric potential measurement in soils. The pressure caused by the water column must be subtracted from the pressure reading

porous cell must be chosen according to the research question (sample size, spatial resolution). Under field conditions, the pressure sensors are typically connected to data loggers. Measurement of matric potentials requires equilibrium between the soil and porous cell. This condition is violated under highly dynamic field conditions. The retardation of equilibrium depends on the amount of air in the system and the soil type. Most critical are sandy soils, because hydraulic conductivities are close to zero at high potentials of, e.g., -100 hPa already (which is a moist soil).

In the drier range down to $-15\,000$ hPa (wilting point), *electrical resistance blocks* (gypsum blocks, fiber) can be used [61.2, 89]. However, the precision is quite low [61.69]. These sensors need careful calibration in the laboratory and are prone to hysteresis (Fig 61.4) [61.90]. This also holds for newer approaches based on water content measurement in ceramic blocks. The so-called *pF-meter* [61.91], for example, is based on the volumetric heat capacity. However, c_v is a function of the volumetric water content and not of the matric potential. Hence, calibration and hysteresis are again issues to be addressed. Another sensor for dry conditions is the *thermocouple psychrometer* that determines the relative humidity in air-filled porous cells that are in hydraulic equilibrium with the soil [61.92].

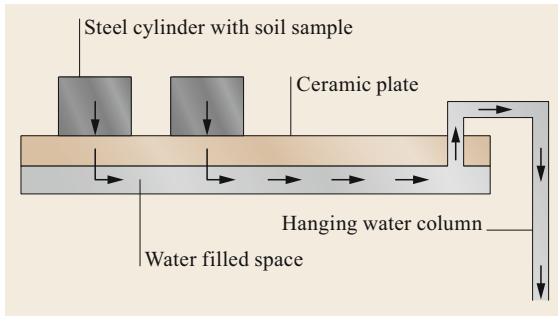


Fig. 61.15 Measurement of points of the water retention curve in the low-pressure range (wet to moist soil) with a ceramic plate equipment

The required moist and dry temperatures are obtained by utilizing the so-called Peltier effect. The measuring range is rather narrow, with a maximum pF value of 4.8 and a minimum one of 3.3 [61.93].

Matric potential measurements provide information about the momentary availability of soil water but tells us nothing about the available amounts. To get this information we need the *water-retention curve* (WRC), which was already defined in Fig. 61.3 and Table 61.3. WRC can be estimated from field data of θ_v and ψ_m using a suitable parametrization of WRC and nonlinear regression. However, the result is quite often unsatisfactory due to the small range of measurements and the tremendous spatial heterogeneity of data. Water retention curves are, therefore, in most cases measured in the laboratory. Typical devices are ceramic suction (Fig. 61.15, $-\infty < \text{pF} \leq 2.5$) and pressure plates (Fig. 61.16, $2.5 < \text{pF} < 4.2$). Values for the drier range can be obtained with high-concentration salt solutions equilibrated with soil samples [61.92]. WRC is mostly determined as the drainage curve starting from saturated samples. Hysteresis is usually not considered. Anyway, even if we had hysteresis information we would still face considerable unavoidable uncertainties under field conditions, as the *history* of measured water contents and associated matric potentials remains unknown [61.2].

Conductivities

Hydraulic conductivity is – in addition to the potential gradients – the crucial parameter function that controls water flow to groundwater (groundwater recharge) and/or soil surface (evaporation) and plant roots (transpiration). The function is strongly nonlinear and hysteretical. Nonlinearity is extreme for sandy soil which hydrologically behaves like a switch. Down to a matric potential of -10^4 Pa (pF = 1), the conductivity is close

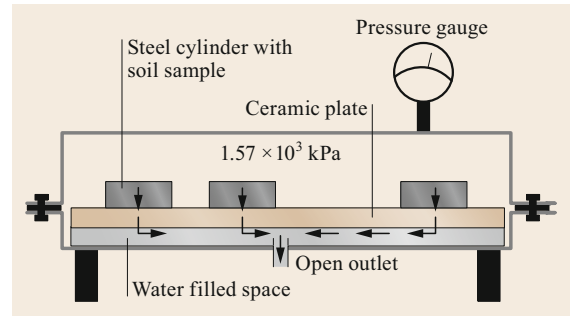


Fig. 61.16 Measurement of points of the water retention curve in the high-pressure range (dry soil) with ceramic plate equipment; the height of the samples is drastically reduced due to the extremely low hydraulic conductivity in the moist to dry range

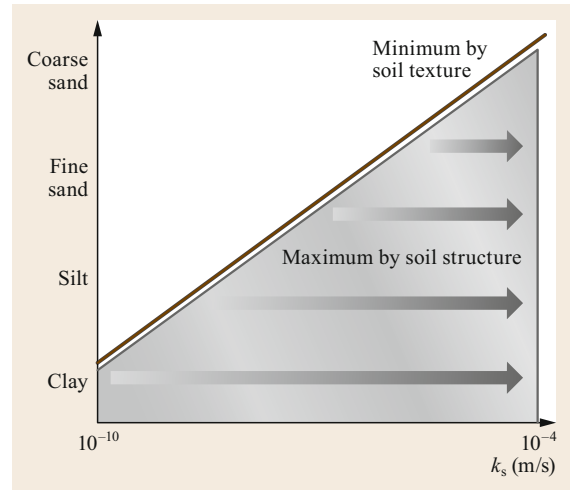


Fig. 61.17 Hydraulic conductivity in soils at saturation (k_s). The minimum values are determined by soil texture, the maxima by soil structure. The maximum values are independent of texture and more or less the same for all texture classes

to saturation and falls within a 1 pF step (pF = 2) to practically zero [61.2]. Typical for conductivities is the pronounced spatial heterogeneity. Figure 61.17 gives an impression of possible ranges of values. Measurements are done under controlled laboratory conditions, as well as in the field. For several practical and theoretical reasons, laboratory data cannot be easily used under field conditions (e.g., isolation of the sample from the continuous pore system of the soil). In this section, we focus on selected field methods for hydraulic conductivity in saturated and unsaturated soils. For other methods and more details, the reader is referred to [61.77, 94, 95].

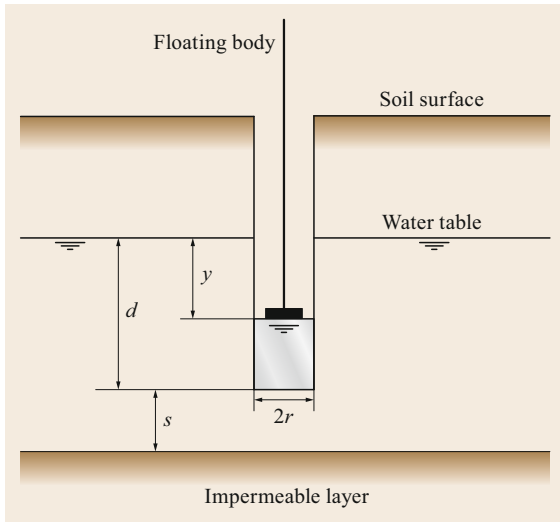


Fig. 61.18 Borehole method

In Sect. 61.4.1, we already discussed the use of double-ring infiltrometers *double-ring infiltrometer* for the measurement of k_s . The method assumes homogeneity over the extent of the infiltration front in which $d\psi_m/dz = 0$ and, thus, k_s is equal to the infiltration rate i . The double-ring infiltrometer is typically used in initially unsaturated soil. The required amount of water is comparably high.

The *borehole method* (Fig. 61.18) was developed to measure hydraulic conductivity in saturated soils in landscapes with high groundwater levels. It is a rising-head borehole measurement. The water level is lower to the desired depth. The initial velocity of the rising water level is measured and used for the calculation of the conductivity. Water flow is described by the Laplace differential equation. Boundary conditions are clearly defined by the experiment. However, there are two solutions to this boundary value problem, namely the equations of *Ernst* [61.14] and the solution of *Boast and Kirkham* [61.96]. Both solutions are based on the potential theory. Ernst proposed a set of two equations

$$k_s = \frac{4000r}{(d + 20r)(2 - y/d)} \frac{r \Delta y}{y \Delta t} \quad (61.30)$$

for $3 \text{ cm} < r < 7 \text{ cm}$, $20 \text{ cm} < d < 200 \text{ cm}$, $0.2 < y/d < 1$, and $s > d$, or

$$k_s = \frac{3600r}{(d + 10r)(2 - y/d)} \frac{r \Delta y}{y \Delta t} \quad \text{for } s = 0. \quad (61.31)$$

The restrictions of (61.30) and (61.31) were later lowered in [61.9, 97] for unknown reasons. In [61.96], an

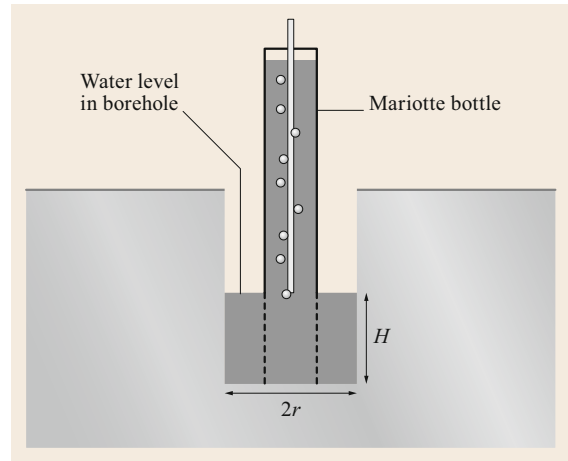


Fig. 61.19 Principal design of a Guelph permeameter

analytical solution to the boundary value problem was derived

$$k_s = c_{\text{bk}} \frac{\Delta y}{\Delta t}, \quad (61.32)$$

$$c_{\text{bk}} = \frac{864\pi r}{[Q/k_s y r] y}, \quad (61.33)$$

$$\frac{Q}{k_s y r} = 2\pi \left[\frac{r}{2s} - \sum_{m=1,2,\dots}^{\infty} A_m \frac{I_1(m\pi r/s)}{I_0(m\pi r/s)} + \sum_{n=1,2,\dots}^{\infty} B_n b_n \frac{1 - \cos(n\pi)}{n\pi} \right], \quad (61.34)$$

where Q is the amount of water per time that flows into the borehole. Constants A_m , B_n , and b_n are described in detail in [61.96]. Functions $I_0(x)$ and $I_1(x)$ are modified Bessel functions. A table with c_{bk} -values (Table 61.8) was prepared in [61.96]. A comparison of (61.30) and (61.31) with (61.34) was made in [61.98], where differences of up to 30% were found. These results were confirmed using a numerical approach in [61.99].

The *Guelph permeameter* [61.100] is a constant head borehole permeameter for measuring field-saturated hydraulic conductivity k_{fs} under unsaturated soil conditions. The possibility to measure in unsaturated field soils, the low water consumption per measurement, and the possibility to perform measurements in different depths are clear advantages of this method. A similar instrument following the same principles was developed by [61.101]. The so-called *Amoozometer* uses a more rigid operating scheme compared to the Guelph permeameter [61.101]. Assumptions of the method are homogeneity and isotropy of the soil under study. The principal geometry is given in Fig. 61.19. Technical details can be found, e.g., in [61.102]. Data

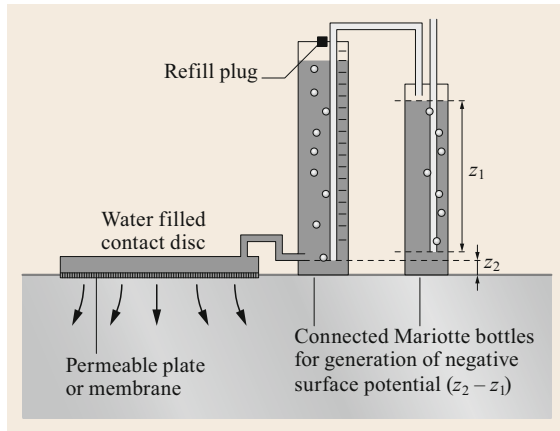


Fig. 61.20 Tension infiltrometer for quantifying unsaturated infiltration at prescribed negative matric potentials at the soil surface. The negative boundary matric potential is achieved by using two connected Mariotte bottles

evaluation is based on equations in [61.100]

$$Q = \left(\frac{2\pi H^2}{C} + r^2 \pi \right) k_s + \left(\frac{2\pi H}{C} \right) \Phi_m$$

$$= Ak_s + B\Phi_m, \quad (61.35)$$

where Q is the water uptake per time of the soil, k_s is the saturated conductivity, H the height of the water table in the borehole, r the radius of the borehole, $C = f(H/r)$ a dimensionless form factor [61.102], and Φ_m the matric flux potential (61.37), respectively. For a simplified model for $k(\psi)$, the parameter Φ_m is usually determined from $\alpha^* = K_s/\phi_m$, which depends on soil structure and texture. Values for α^* are provided in [61.100]: for coarse sand and strongly aggregated soils $\alpha^* = 0.36 \text{ cm}^{-1}$, for medium and fine sand or normal structured soils $\alpha^* = 0.12 \text{ cm}^{-1}$, for unstructured, fine textured soils $\alpha^* = 0.04 \text{ cm}^{-1}$, and for compact clay $\alpha^* = 0.01 \text{ cm}^{-1}$. These values are rough estimates, and an error analysis is strongly recommended.

Tension infiltrometers (Fig. 61.20) are used to determine infiltration rates in unsaturated soils with a known (prescribed) negative matric potentials at the soil surface. Like double-ring infiltration, it is also a constant head boundary experiment with a negative matric potential at the upper boundary, and we can derive unsaturated conductivities for the prescribed soil suction ψ_i for homogeneous and isotropic soils. In contrast to double-ring infiltration, only a single ring is used here. Thus, the analysis is less straightforward. The evaluation follows the approach of *Elrick* and *Reynolds* [61.100] to describe the (steady) end infiltration rate Q_{TI}

$$Q_{TI} = \pi r^2 K(\psi_t) + 4.2r\Phi_m. \quad (61.36)$$

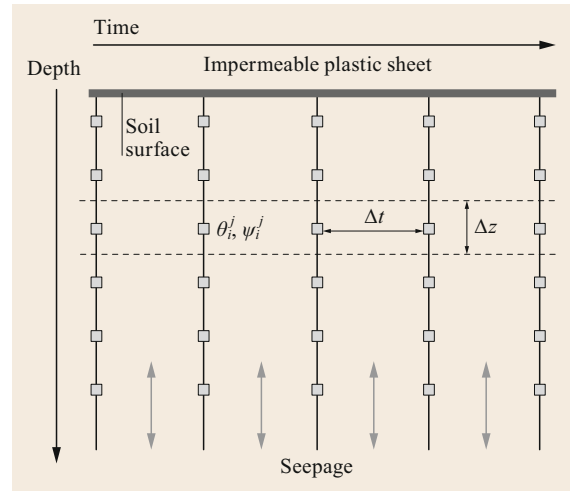


Fig. 61.21 Instantaneous profile method

Rearranging (61.36) and introducing $\alpha_{TI}^* = K(\psi_t)/\Phi_m$ we get

$$K(\psi_t) = \frac{Q_{TI}}{\pi r^2 + 4.2r/\alpha_{TI}^*}. \quad (61.37)$$

The parameter Φ_m is the matric flux potential, defined by

$$\Phi_m = \int_{\psi_i}^{\psi_t} k(\psi) d\psi.$$

ψ_i is the initial matric potential, and ψ_t the matric potential at the infiltration front (i.e., potential at the upper boundary). Values for α_{TI}^* are provided by [61.100] and can be found in Table 61.7.

The *instantaneous profile method* or *internal drainage method* is another concept for measuring unsaturated conductivities in the laboratory and directly in the field [61.2, 33, 103]. Measurements are based on a time–space grid of matric potential and water content measurements (Fig. 61.21). Initial conditions are known from the first measurement. The upper boundary is typically a zero flux condition, and the evaluation is done by a finite difference approximation of the continuity equation and Darcy–Buckingham’s law for unsaturated conditions (i.e., in fact, Richard’s equation). Starting from the top of the profile with a known upper boundary, the flux in the next compartment can be calculated and solved for the conductivity using Darcy–Buckingham’s law. To smooth out uncertainties in measurements the difference of integrated water contents to depth z and $z + \Delta z$ are used instead of local water content measurements alone. This step is repeated



Fig. 61.22 Measurement plot for soil temperatures according to World Meteorological Organization (WMO) regulations (after [61.104] photo © T. Foken)

sequentially for all compartments by using the just calculated flux from the upper compartment as the upper boundary condition.

61.4.3 Soil Heat

Soil temperature measurements in several depths near the soil surface are basic for the analysis of soil heat dynamics and provides valuable information about amplitudes and damping depths (the depth where $A_0/A_z = 1/e$). Soil heat fluxes may be calculated using the gradient method by applying (61.19) for determination of the thermal diffusivity D_T . Using heat flux plates is an alternative that is usually preferred due to its simplicity and robustness.

Temperature Sensors

Soil temperature measurements are part of a standard meteorological station ([61.104], Chap. 43). Within the station area, a bare patch of ground of about $2\text{ m} \times 2\text{ m}$ is used for observations of the state of the ground (Chap. 22) and of soil temperature measurements (Fig. 61.22). Typical depths for liquid-in-glass thermometers (Chap. 7) are -0.05 , -0.10 , and -0.20 m (seldom -0.02 m). Soil temperatures at depths greater than 20 cm can be installed outside this bare patch of

ground, and the liquid-in-glass thermometers for -0.5 and -1.0 m are mounted on wooden, glass, or plastic tubes. Recently, these thermometers have been replaced by tubes with platinum wire (Pt 100) temperature sensors (Chap. 7) in the relevant levels. Soil temperature measurements for the determination of the ground heat flux must be installed below natural surfaces. Usually, some more levels are necessary or temperature sensors integrating over a certain soil column, if (61.17) is to be applied. For the determination of the soil heat capacity, parallel measurements of the soil moisture are necessary.

Soil Heat Flux Plates

The principle construction of a heat flux plate is shown in Fig. 61.23. A number of thermocouples (Chap. 7) is connected with the upper and lower surfaces of the plate. The sensor body has an averaged heat conductivity of soil. Therefore, the heat flux can be calculated from the temperature difference between the upper and lower sides with (61.15). Self-calibrated plates have a heater at the upper surface. The heater generates a well-known heat flux for a short time period. From this flux, the deflection error can be calculated, and the data can be corrected. This type of plate has the advantage of a higher accuracy but a significant disadvantage in that the data cannot be used during the heating and immediately after the heating [61.105]. An important disadvantage of heat flux plates is the installation of the plates in the soil, because both sides should have an excellent contact with the soil, which should be free of stones. Rain or a water flow along the cables may also be a reason for contact problems. Therefore, the installation at a depth of about 0.2 m (Sect. 61.3.3) may reduce these effects, and the flux is lower, and possible errors have a less significant influence on the ground heat flux at the surface. The installation of three or more plates would help to identify possible misreadings.

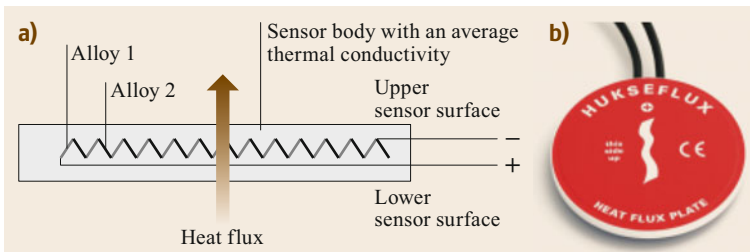


Fig. 61.23 (a) Principal schema of a heat flux plate with a number of thermocouples of two different alloys, where the connections of the alloys are connected to the upper and lower sides of the plate. In the case of a self-calibrating plate, a heater is connected with the upper surface of the plate, (b) heat flux plate (image used with permission from Hukseflux, Delft, The Netherlands)

61.4.4 Specific Analyses

Measured time series of state variables (temperatures, potentials, etc.) may contain information that is not intuitively detectable. Adequate analysis methods are, therefore, needed to elucidate their hidden complexity. Permutation entropy, a promising method in this context, is briefly introduced in this section. Measurement of hydraulic and thermal transport parameters is often time, labor, and cost-consuming. For many practical applications (e.g., studies on the landscape level), it is preferable to replace these measurements by estimation functions or algorithms that use parameters that are readily available from soil maps or can be measured easily. Some of these so-called pedotransfer functions, like capillary bundle models and neural networks for hydraulic parameter functions [61.106–108], or mixing models for thermal parameters [61.3, 109, 110], are presented below.

Complexity of Time Series

Time series capture the temporal dynamics or patterns in soils. Typical examples of time series are water content or water potential measurements. Time-series analysis is a vast field in statistics, and many different methods and models exist. Here, we want to highlight the *permutation entropy*, an ordinal method that allows us to describe the complexity of time series. The method is called ordinal because it operates on ranks values instead of actual values in a time series. It has the advantage of being simple, fast, robust, and of having only a few assumptions about the data [61.111]. Permutation entropy was proposed by *Bandt* and *Pompe* in 2002 [61.112] as a *natural measure of complexity* for real time series. Generally speaking, a complexity measure characterizes the dynamics in a time series. Low complexity means a regular time series (e.g., a sine wave), and a high complexity is typical for noise. The complexity in a time series of the water potential, for example, is a result of underlying processes, like infiltration and evapotranspiration, and is influenced by soil hydraulic properties and measurement noise.

Here, we show briefly how to calculate the permutation entropy. For more details the reader is referred to the original publication [61.112]. We take as an example the time series $x = (3.2, 4.2, 6.8, -3.5, 4.0, 12.3, 0.1)$ and compare the direct neighbors by counting pairs for which $x_t < x_{t+1}$ (we call this permutation 01) and pairs for which $x_t > x_{t+1}$ (we call this permutation 10), t being the time index. In this time series, we find four

pairs of permutation 01 and two pairs of permutation 10. This information is plugged into the famous formula for entropy introduced by *Shannon* [61.113]

$$H(n) = - \sum p(\pi) \log(p(\pi)), \quad (61.38)$$

where $p(\pi)$ are the probabilities of the permutations, and summation runs over all permutations of order n . Thus, in our case, using the relative frequencies of permutations 01 and 10 determined above, we get

$$\begin{aligned} H(2) &= - \left(\frac{4}{6}\right) \log\left(\frac{4}{6}\right) - \left(\frac{2}{6}\right) \log\left(\frac{2}{6}\right) \\ &\approx 0.92. \end{aligned} \quad (61.39)$$

There are $n!$ permutations of order n , and the permutation entropy will vary between 0 and $\log(n!)$. By dividing it by $\log(n!)$ we obtain a normalized measure in the range $[0, 1]$. Obviously, the number of samples (consecutive values) that we can use to determine the permutations decreases for increasing n . *Bandt* and *Pompe* [61.112] suggested that the length of the time series should be larger than $n!$ and recommend *for practical purposes* [...] $n = 3, \dots, 7$. The time series of the water content of the matric potential often show abrupt changes (e.g., when water infiltrates rapidly into the soil). To take this behavior into account, an extension of the permutation entropy, the so-called *weighted permutation entropy* (WPE) can be used [61.114]. It modifies the original permutation entropy (PE) by weighting the frequencies of permutations by the variance of the measured values.

Estimation of Soil Hydraulic Material Functions

Direct measurements of hydraulic and thermal parameters and functions in the laboratory and in-situ are cost, labor, and time intensive. For landscape studies, they can only be conducted at selected sites. For areal studies, geostatistical methods may be used if the measuring grid is sufficiently dense. In most cases, utilization of pedotransfer functions is required. The accuracy and reliability of these functions depend on underlying models and most often on site conditions. In principle, pedotransfer functions use easily measurable soil parameters like bulk density, porosity, soil texture, organic matter content, and – for thermal conductivities – quartz content. Direct estimations of soil physical material functions from geophysical methods and remote-sensing data are still a matter of ongoing research.

While water retention (desorption) curves and saturated hydraulic conductivity can be measured by standard procedures in the laboratory, the measurement of the hydraulic conductivity characteristics for unsaturated conditions is still time consuming and demanding. In an early approach [61.106], a capillary bundle approach was developed that calculates the relative conductivities k_r from the saturated conductivity k_s and M points of the water retention curve (θ_i, h_i) , assuming a pore size distribution of continuous cylindrical pores derived from the water retention curve using the Young–Laplace equation, a contact angle between pores and water of zero, and a uniform tortuosity for all pore size classes.

$$k(\theta_s - i\Delta\theta) = k_s k_r (\theta_s - i\Delta\theta) \\ = k_s \frac{\sum_{j=i+1}^M \frac{1}{h_j^2}}{\sum_{j=1}^M \frac{1}{h_j^2}} \quad (61.40)$$

This approach was improved by [61.108] by considering the tortuosity of the pore system

$$k(\theta_i) = k_s \left(\frac{\theta_i}{\theta_s} \right)^{4/3} \frac{\sum_{j=i+1}^M [2(j-i) + 1] \frac{1}{h_j^2}}{\sum_{j=1}^M [2j-1] \frac{1}{h_j^2}}. \quad (61.41)$$

Water content θ_i is again $\theta_s - \theta_i$. Please note that $\theta_0 = \theta_s$. In (61.40) and (61.41), the summation index is given by j . Index i denotes the i -th point of the discretized water retention curve. *Mualem* [61.107] came up with an integral approach to allow for continuous calculation of relative conductivities

$$k_r = \Theta^{1/2} \left[\frac{\int_{s=0}^{s=\Theta} \frac{1}{h(s)} ds}{\int_{s=0}^{s=1} \frac{1}{h(s)} ds} \right]^2, \quad (61.42)$$

where the reduced degree of saturation Θ is given by $\Theta = (\theta - \theta_r)/(\theta_s - \theta_r)$ with the porosity θ_s , and the residual water content θ_r (at which the continuity of the liquid phase is interrupted).

Later, *van Genuchten* [61.115] introduced a parameterization of the water retention curve, which can be analytically integrated in (61.42) under the assumption

$$m = 1 - 1/n$$

$$\theta(h) = \theta_r + \frac{\theta_s - \theta_r}{[1 + (\alpha h)^n]^m}, \quad (61.43)$$

$$k(h) = k_s \frac{\left\{ 1 - (\alpha h)^{n-1} [1 + (\alpha h)^n]^{(1-n)/n} \right\}^2}{[1 + (\alpha h)^n]^{(n-1)/(2n)}}. \quad (61.44)$$

This approach was extended by [61.116] to be able to consider multimodal pore size distributions. Methods for estimation of the *van Genuchten–Mualem* parameters can be found in [61.117–119].

Estimation of Soil Thermal Material Functions

De Vries [61.3] developed and tested functions for estimating volumetric heat capacity $c_v(\theta)$ and thermal conductivity $\lambda(\theta)$. The parameter c_v is a strictly linear equation of volumetric water content (X_0), quartz content (X_1), other minerals (X_2), organic matter (X_3), and soil air (X_4)

$$c_v = \sum_{i=0}^4 X_i c_{v,i}. \quad (61.45)$$

Values for $c_{v,i}$ can be found in Table 61.9. Values for quartz and other minerals are obviously identical (61.17).

Values for the thermal conductivity characteristics of a soil material $\lambda(\theta)$ can be estimated as weighted mean of the thermal conductivities λ_i of its components X_i (water, quartz, other minerals, organic matter, and soil air)

$$\lambda = \frac{\sum_{i=0}^4 k_i X_i \lambda_i}{\sum_{i=0}^4 k_i X_i}. \quad (61.46)$$

The weighting factors are calculated as

$$k_i = \frac{1}{3} \sum_{j=1}^3 \frac{1}{1 + ((\lambda_i/\lambda_0) - 1) g_j}. \quad (61.47)$$

Here, λ_0 is the embedding component (air or water) depending on water and air contents. Parameters g_i are shape factors, and $g_1 + g_2 + g_3 = 1$. Under the assumption of ellipsoids of rotation, a value of $g_1 = 0.125$ is often assumed [61.109] (values of $g_1 = g_2 = g_3 = 1/3$ hold for spherical particles). For k_4 (air) approximation formulas are provided in [61.3, 110].

61.5 Specifications

Below we give some specific information about coefficients in some formulas and specific data for some selected sensor types.

Values for α_{TI}^* in (61.37) are provided in Table 61.7, for c_{bk} in (61.32) in Table 61.8, and for thermal properties for (61.45) and (61.46) in Table 61.9.

Soil temperature measurements have a range from -50 to 50 °C, a resolution of 0.1 K, an uncertainty 0.2 K, a time constant 20 s, and an averaging time of 1 min [61.104]. Heat flux plates can be operated from -30 to $+70$ °C. They have a range of ± 2000 W m⁻² and an uncertainty $\pm 3\%$.

Table 61.7 Values for α_{TI}^* [(61.100), simplified]

Yolo clay		Structured soil		Structureless sand	
ψ_t/ψ_i	α_{TI}^* (m ⁻¹)	ψ_t/ψ_i	α_{TI}^* (m ⁻¹)	ψ_t/ψ_i	α_{TI}^* (m ⁻¹)
0.004	4.27	0.006	42.84	0.005	4.01
0.025	4.54	0.019	66.97	0.088	6.76
0.100	2.84	0.109	17.88	0.250	13.90
0.500	1.21	0.234	8.07	0.550	7.76
0.700	1.44	0.688	5.00	0.850	7.47

Table 61.8 Values for factor c_{bk} [61.96]

d/r	y/d	s/d								
		0	0.05	0.1	0.2	0.5	1	2	5	∞
1	1	447	423	404	375	323	286	264	255	254
	0.75	469	450	434	408	360	324	303	292	291
	0.5	555	537	522	497	449	411	386	380	379
2	1	186	176	167	154	134	123	118	116	115
	0.75	196	187	180	168	149	138	133	131	131
	0.5	234	225	218	207	188	175	169	167	167
5	1	51.9	48.6	46.2	42.8	38.7	36.9	36.1		35.8
	0.75	54.8	52.0	49.9	46.8	42.8	41.0	40.2		40.0
	0.5	66.1	63.4	61.3	58.1	53.9	51.9	51.0		50.7
10	1	18.1	16.9	16.1	15.1	14.1	13.6	13.4		13.4
	0.75	19.1	18.1	17.4	16.5	15.5	15.0	14.8		14.8
	0.5	23.3	22.3	21.5	20.6	19.5	19.0	18.8		18.7
20	1	5.91	5.53	5.30	5.06	4.81	4.70	4.66		4.64
	0.75	6.27	5.94	5.73	5.50	5.25	5.15	5.10		5.08
	0.5	7.67	7.34	7.12	6.88	6.60	6.48	6.43		6.41
50	1	1.25	1.18	1.14	1.11	1.07	1.05			1.04
	0.75	1.33	1.27	1.23	1.20	1.16	1.14			1.13
	0.5	1.64	1.57	1.54	1.50	1.46	1.44			1.43
100	1	0.37	0.35	0.34	0.34	0.33	0.32			0.32
	0.75	0.40	0.38	0.37	0.36	0.35	0.35			0.35
	0.5	0.49	0.47	0.46	0.45	0.44	0.44			0.44

Table 61.9 Densities (ρ_s), volumetric heat capacities (c_v), and thermal conductivities (λ) of soil constituents (10 °C) and of ice (0 °C) (after [61.2], modified)

Material	ρ_s (kg m ⁻³)	c_v (J m ⁻³ K ⁻¹)	λ (W m ⁻¹ K ⁻¹)
Quartz	2.66×10^3	2.0×10^6	8.8
Other minerals	2.55×10^3	2.0×10^6	2.9
Organic matter	1.3×10^3	2.5×10^6	0.25
Water	1.0×10^3	4.2×10^6	0.57
Ice	0.92×10^3	1.9×10^6	2.2
Air	1.25	1.25×10^3	0.025

Conventional tensiometers typically have a range from -800 hPa under unsaturated to values > 0 hPa under saturated conditions, and an accuracy of about 1 hPa. The maximum value under saturated conditions depends on the height of the water table above the sensor and the flow situation (e.g., around drain tubes). According to the data sheet of the manufacturer [61.91] pF-meters have a range from $pF = 0$ to $pF = 7$ and resolution of $pF = \pm 0.01$.

61.6 Quality Control

Experimental studies need to keep scientific standards in measurement design and data evaluation, like site selection, instrumentation schemes, and sampling designs in relation to project goals and hypothesis, statistical analyses, and data-based modeling studies. Furthermore, operational and technical aspects have to be considered to perform successful measurement campaigns. Some of these quality control measures are listed below. Disturbed and undisturbed soil sampling should consider spatial heterogeneity of soils either by taking enough replicates or by taking (weighted) pooled samples.

Soil cores should be big enough to cover most organizational soil structures (REVs). Further, they should be inserted perfectly in axial direction. Smearing at the upper and lower boundary planes should be strictly avoided. Samples should be checked for voids along the cylinder walls. Both would be detrimental for conductivity measurements and column experiments. Smearing is also a problem in borehole measurements in saturated (borehole method) and unsaturated soils (Guelph permeameter). For double-ring infiltrometers, voids between soil and steel cylinders must be avoided.

For tensiometers and tension infiltrometers, close contact between measuring surfaces and soil is of uppermost importance. For both instruments, air entrapments need to be controlled. This holds equally

for laboratory measurements of water retention curves with ceramic plate systems. Voids around the steel rods of TDR and FDR sensors are an important source of measurement errors. The installation of TDR and FDR probes should be carried out with care. Accompanying sampling for improving indirect measurements of soil water content is recommended to improve calibration and accuracy.

Volume-based water content has a range from 0% to 100%. Standard gravimetric methods with oven drying are reported to have an accuracy (given in % of volumetric water content) of $< 1\%$. Neutron probes were found to have a standard error of 2%. For TDR and FDR probes, similar values for root-mean-square error (RMSE) of 2% were determined. However, in the case of poor probe construction, dielectric dispersion (permittivity change with frequency), and/or salinity, the errors may increase up to 40% [61.70].

Outlier control should be carried out very cautiously. Extreme values are typical for soil parameters and are an intrinsic ecologically relevant property of the soil system. Therefore, extreme values are not automatically measurement errors.

For temperature sensors, all quality control actions according to Chap. 7 should be applied. Because of the problem of good contact of the sensor and the soil, gradients should additionally be controlled. This can be done by a nonlinear approximation of the temperature profile. If one sensor shows differences of > 0.2 K for longer times, this sensor should be replaced or newly installed.

The best quality control for heat flux plates is the installation of at least three identical plates. As long as all show nearly the same result, an averaged value should be the best measure. If one sensor fails, the installation of the sensor should be controlled.

61.7 Maintenance

Maintenance of measuring equipment should meet at least the following requirements:

- i) Regular (weekly, daily) check of devices (permeameters, tensiometers, suction plates) for air inclusions, obstruction of tubes, and soil–sensor contact. If necessary, sensors are to be replaced.
- ii) Regular technical control of data recording units. Regular read-out and check for data losses and malfunctioning.
- iii) Check for mechanical damages of equipment. If required add mechanical protection (against animals, humans, rain, heat, radiation) and/or replace the devices.
- iv) Weakly or after rainfall control of the temperature gradients and the heat flux plates.

61.8 Applications

To give an impression of hydrological and thermal measurements in the context of ecosystems, in this section, we briefly present selected results from different agricultural and forest sites. The first example describes a study on surface water storage and addresses the very interface between soil and atmosphere on a partly compacted agricultural field soil. In the second study, we highlight the moisture dynamics in a soil profile of a forest stand, and the third example illustrates daily temperature propagation in the soil of an open grassland.

61.8.1 Water Storage on the Soil Surface

The microtopography of the soil surface influences the partitioning of incoming precipitation into surface storage, surface runoff, and infiltration. Agricultural soils often have a dynamic microtopography because of tillage and compaction by agricultural machinery. A combination of an irrigation experiment and stereo photography allows us to study the dynamics of water storage and surface runoff. Here, we describe some results of such an irrigation experiment. For a complete report, the reader is referred to the original publication [61.62].

The irrigation experiment was done at the Institut National de Recherche pour l'Agriculture, l'Alimentation et l'Environnement (INRAE) research station in Avignon (France) on an agricultural soil previously tilled with a plough share followed by a circular spike harrow combined with a cultipacker. Subsequently, the middle part of the plot was compacted by repeated passage of a tractor wheel. A stereo system equipped with two Nikon D100 cameras installed at ≈ 3 m height (Fig. 61.7) was used to take pictures of the soil surface before and during the irrigation (64 mm h^{-1} for 1 h) to calculate a digital surface model (DSM), delineate puddles, and derive the stored volume of water. The stereo system produced paired images of the soil surface from different angles that were matched point-by-point to derive the DSM. This procedure is called photogrammetry, e.g., [61.120]. Figure 61.24 shows the microtopography before the start of irrigation, i.e., after tillage and compaction. The central depression created by compaction stored most of the water during the irrigation. Despite the compaction of the soil, puddles infiltrated quickly after the stop of irrigation (Fig. 61.25).

61.8.2 Time Series of Soil Matrix Potentials and Corresponding Weighted Permutation Entropies

Figure 61.26 shows the time series of precipitation and matric potentials in three depths measured in a forest

stand at the study site Coulissenhieb II in the Lehstenbach Catchment (Fichtelgebirge Mountains, Germany), together with calculated weighted permutation entropies (WPE). The WPE values are complexity measures that quantify the dynamics of the measured time series. The

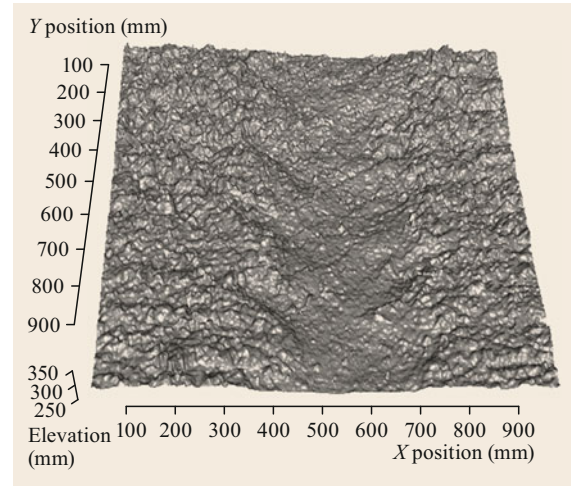


Fig. 61.24 Digital surface model of a bare soil with compaction by a tractor tire, obtained by stereo photography (Fig. 61.7) for assessment of surface storage, runoff, infiltration, and seepage (after [61.62] © John Wiley & Sons, Ltd). The image was generated in R (after [61.121])

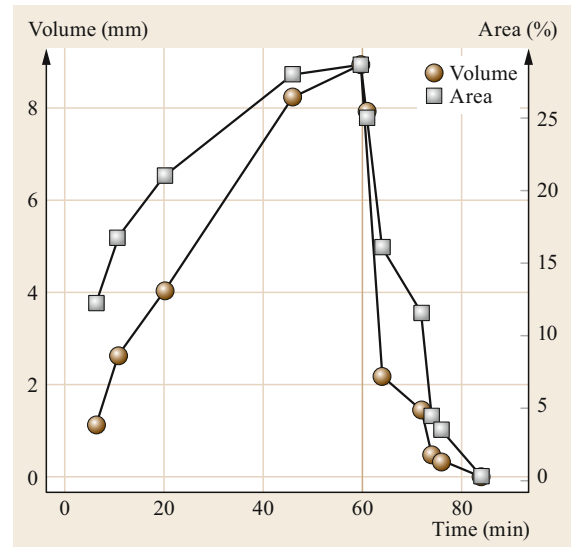


Fig. 61.25 Surface storage of water and puddle area ($> 20 \text{ cm}^2$) in an irrigation experiment with a dye tracer on the plot in Fig. 61.24. The irrigation was stopped after 60 min (after [61.62] © John Wiley & Sons, Ltd.)



Fig. 61.26 (a) Rainfall, matric potentials (Ψ_m , gray curves) in (b) 20 cm, (c) 40 cm and (d) 90 cm depth and associated weighted permutation entropies (WPE, blue curves) in a forest stand (after [61.30])

interested reader can find more information on this long-term research and monitoring site in [61.122]. In general, the drying of the soil and its subsequent rewetting (for example, during summer 2008) are characterized by a minimum of the matric potential and a drop of the WPE. Indeed, decreasing/increasing matric potentials contain mainly monotonically descending/ascending patterns and, therefore, have a low complexity. The overall level and variation of the WPE are comparable in different depths, indicating similar dynamics. Note that the measured matric potentials are different. This is, of course, the very definition of a rank-based statistical measure,

Fig. 61.27 Daily cycle of soil temperatures at different depths on 05.06.1998 at the field site of the Richard-Aßmann Observatory Lindenberg, Germany (high clouds for 11:00–15:00 UTC high clouds (after [61.45]) ►

i.e., it is sensitive to the relative order of the measured values not to their absolute value.

61.8.3 Daily Cycle of Soil Temperature

The soil temperature is an important parameter in agricultural meteorology. Furthermore, it is important for the energy balance at the Earth's surface and, therefore, for all fluxes between the atmosphere and the underlying surface. The upper levels up to a depth of -0.1 to -0.2 m are highly influenced by solar radiation, while the lower levels are phase shifted and give only information as to the temperature of the previous days (Fig. 61.27). The upper few centimeters are even affected by variations of the irradiation. At -10 m depth, the phase shift is about half a year.

61.9 Further Developments

Both new instruments and new algorithms are expected to contribute to further advances in soil physical measurements. A new development in recent years for indirect in-situ soil water content measurements along larger transects (up to a scale of kilometers) is based on carbon-fiber heated cable technology (CFHC). Volumetric water content is derived from temperature–time curves. A detailed description of technical details, procedures, and algorithms of this SM-DTS (soil moisture distributed temperature sensing) can be found in [61.123]. The method assumes that the surrounding soil is uniform and isotropic, and the thermal diffusivity is constant. The method requires calibration of soil water content against thermal response in the laboratory. The authors found absolute errors (in terms of volumetric water content) in the range of 0.01% to 6.6%. The use of the actively heated fiber optic method for mapping of water content in three depths along transects of 250 m length was impressively demonstrated in [61.124].

Another promising new method for water content measurements in topsoil is the application of cosmic-ray neutron sensors (CRNS) [61.125]. The sensors count neutrons from cosmic rays reflected from topsoil molecules with relatively heavy atoms (compared to hydrogen, which thermalizes neutrons due to the same atomic mass). A comparison with the incoming radiation gives a measure for water content. In contrast to neutron probes, which are inserted into the soil using access tubes, CRNS measures above ground and is nondestructive. Neutron probes count thermalized, actively emitted neutrons, whereas CRNS counts fast neutrons from cosmic radiation. CRNS is restricted to topsoil (10–40 cm), while the averaging area might be in the magnitude of hectares. A detailed intercomparison study in complex terrain on these sensors was performed by [61.126]. The authors developed strate-

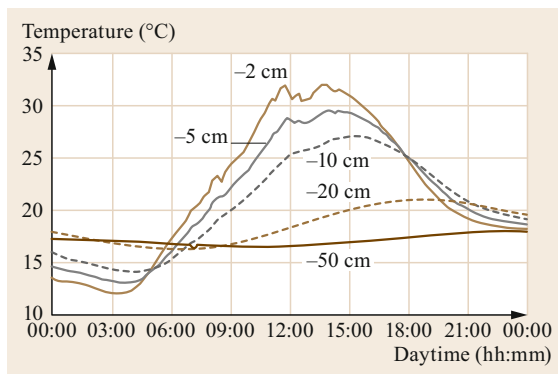
gies that improved the accuracy especially in drying periods.

In [61.127], the authors analyze and point out the potential and relevance of new technologies together with methodological progress for understanding and quantifying soil hydrological processes at several spatial scales. In their conclusion, they emphasize the need to better understand hydrological processes at the soil–plant–atmosphere interfaces at the local scale with high spatiotemporal resolution. They underline the potential of combining noninvasive techniques with online stable isotope analysis of gaseous and water fluxes. They further recommend the establishment of networks of hydrological observatories for hypothesis testing and reducing uncertainties in large-scale models.

In this context, we would like to highlight the development of spectroscopic proximal soil-sensing instruments and the increased use of machine learning algorithms in the field of pedometrics. Proximal soil sensing provides information on the observed target without changing it, i.e., without sample destruction. In contrast to remote sensing, the measurement is done from close by (e.g., within 2 m) [61.128]. Diffuse reflectance spectroscopy of soils in the visible to mid-infrared domains has been used to derive several soil properties from spectra of dry or even moist soils, e.g., [61.40, 129]. Combining visible, near-infrared, and X-ray sensors offers new opportunities to acquire soil data rapidly and cost efficiently [61.130, 131].

Soil spectra cannot be used directly to derive soil properties, and a calibration against classical laboratory measurements is required. Because of nonlinear relationships between spectra and soil properties like soil carbon or texture, for example, machine learning algorithms have proved to be very successful. The most prominent ones are random forests [61.132] and partial least-squares regression, e.g., [61.133]. However, with the increasing popularity of deep learning, in particular in remote sensing [61.134], we expect these algorithms from artificial intelligence to be incorporated in soil spectroscopy sooner or later. Indeed, because both remote sensing and soil spectroscopy deal with hyperspectral data, many data analysis steps are similar.

Calibration in soil spectroscopy is one prominent application of pedometrics that is defined as the use of statistical techniques in soil science. Digital soil mapping is another example that is particularly interesting for other disciplines of environmental sciences because it provides spatial soil data like texture, carbon content and even soil hydraulic properties [61.135, 136]. Although it is still challenging to



assess the precision of these data sets and sometimes their meaning (e.g., for soil hydraulic conductivities at 0.25° resolution), standardized and georeferenced

soil data are undoubtedly required in many applications [61.137].

61.10 Further Reading

For more information on soil processes, soil physics, physical soil protection and soil physical methods the reader is referred to following reference books:

- H.-P. Blume, G.W. Brümmer, H. Fleige, R. Horn, E. Kandeler, I. Kögel-Knabner, R. Kretzschmar, K. Stahr, B.-M. Wilke: *Scheffer/Schachtschabel – Soil Science* (Springer, Berlin Heidelberg 2016)
- D. Hillel: *Environmental Soil Physics: Fundamentals, Applications, and Environmental Considerations* (Academic Press, Waltham 1998)
- D. Kirkham, W.L. Powers: *Advanced Soil Physics* (Wiley, New York 1972)
- R.P.C. Morgan: *Soil Erosion and Conservation* (Wiley, Hoboken 2009)
- N. Lu, W.J. Likos: *Unsaturated Soil Mechanics* (Wiley, Hoboken 2004)
- W.G. Teixeira, M. Bacis Ceddia, M. Vasconceles Ottoni, G. Kangussu Donnagema: *Application of Soil Physics in Environmental Analyses* (Springer, Cham 2014)
- J.H. Dane, C.G. Topp (Eds.): *Methods of Soil Analysis: Part 4 Physical Methods*, SSSA Book Series 5.4. (SSSA, Madison 2002)
- M.R. Carter, E.G. Gregorich: *Soil Sampling and Methods of Analysis*, 2nd edn. (CRC Press, Boca Raton 2007)

Acknowledgments. Figures 61.8–61.10 were created by Sebastian Arnhold in the context of his PhD thesis [61.63] at the Department of Soil Physics, University of Bayreuth. They have not been published so far. Sebastian Arnhold died on 11 November 2017.

References

- 61.1 Soil Science Division Staff: *Soil Survey Manual* (USDA, Washington 2018)
- 61.2 D. Hillel: *Environmental Soil Physics: Fundamentals, Applications, and Environmental Considerations* (Academic Press, Waltham 1998)
- 61.3 D.A. De Vries: Thermal properties of soils. In: *Physics of Plant Environment*, ed. by W.R. Van Wijk (North-Holland Publishing Company, Amsterdam 1963) pp. 210–235
- 61.4 H.-P. Blume, G.W. Brümmer, H. Fleige, R. Horn, E. Kandeler, I. Kögel-Knabner, R. Kretzschmar, K. Stahr, B.-M. Wilke: *Scheffer/Schachtschabel – Soil Science* (Springer, Berlin, Heidelberg 2016)
- 61.5 A.R. Mermut, S.H. Luk, M.J.M. Römkens, J.W.A. Poesen: Micromorphological and mineralogical components of surface sealing in loess soils from different geographic regions, *Geoderma* **66**(1/2), 71–84 (1995)
- 61.6 S.H. Luk, Q.G. Cai: Laboratory experiments on crust development and rainsplash erosion of loess soils, China, *Catena* **17**(3), 261–276 (1990)
- 61.7 W. Durner, U. Jansen, S.C. Iden: Effective hydraulic properties of layered soils at the lysimeter scale determined by inverse modelling, *Eur. J. Soil Sci.* **59**(1), 114–124 (2008)
- 61.8 C. Liebethal, B. Huwe, T. Foken: Sensitivity analysis for two ground heat flux calculation approaches, *Agric. For. Meteorol.* **132**(3/4), 253–262 (2005)
- 61.9 R. Eggelsmann: *Dränanleitung für Landbau, Ingenieurbau und Landschaftsbau* (Paul Parey, Hamburg, Berlin 1981)
- 61.10 H. Darcy: *Les fontaines publiques de la ville de Dijon: Exposition et application* (Victor Dalmont, Paris 1856)
- 61.11 E. Buckingham: *Studies on the Movement of Soil Moisture* (USDA, Washington 1907), Bulletin No. 38
- 61.12 L.A. Richards: Capillary conduction of liquids through porous mediums, *Physics* **1**(5), 318–333 (1931)
- 61.13 W.H. Green, G.A. Ampt: Studies on Soil Physics, *J. Agric. Sci.* **4**(1), 1–24 (1911)
- 61.14 L.F. Ernst: *Een nieuwe formule voor de berekening van de doorlaatfactor met de boorgatenmethode* (En Bodemkundig Inst. TNO, Groningen 1950), Rap. Landbouwproefsta
- 61.15 J.R. Philip: Theory of infiltration, *Adv. Hydrosci.* **5**, 215–296 (1969)
- 61.16 J.-Y. Parlange, I. Lisle, R.D. Braddock, R.E. Smith: The three-parameter infiltration equation, *Soil Sci.* **133**(6), 337–341 (1982)
- 61.17 J.-Y. Parlange, R. Haverkamp, J. Touma: Infiltration under ponded conditions: 1. Optimal analytical solution and comparison with experimental observations, *Soil Sci.* **139**(4), 305–311 (1985)
- 61.18 D. Kirkham, W.L. Powers: *Advanced Soil Physics* (Wiley, New York 1972)

- 61.19 R.M. Hagan, H.R. Haise, T.W. Edminster (Eds.): *Irrigation of Agricultural Lands*, Agronomy Monograph, Vol. 11 (ASA, Madison 1967)
- 61.20 J. van Schilfgaarde (Ed.): *Drainage for Agriculture*, Agronomy Monograph, Vol. 17 (ASA, Madison 1974)
- 61.21 R.R. van der Ploeg, M. Marquardt, D. Kirkham: On the history of the ellipse equation for soil drainage, *Soil Sci. Soc. Am. J.* **61**(6), 1604–1606 (1997)
- 61.22 R.R. Van der Ploeg, M. Marquardt, M.B. Kirkham: The Colding equation for soil drainage: Its origin, evolution, and use, *Soil Sci. Soc. Am. J.* **63**(1), 33–39 (1999)
- 61.23 H.-J. Vogel, K. Roth: Quantitative morphology and network representation of soil pore structure, *Adv. Water Resour.* **24**(3/4), 233–242 (2001)
- 61.24 H.-J. Vogel, U. Weller, S. Schlüter: Quantification of soil structure based on Minkowski functions, *Comput. Geosci.* **36**(10), 1236–1245 (2010)
- 61.25 A. Carminati, A.B. Moradi, D. Vetterlein, P. Vontobel, E. Lehmann, U. Weller, H.-J. Vogel, S.E. Oswald: Dynamics of soil water content in the rhizosphere, *Plant Soil* **332**(1/2), 163–176 (2010)
- 61.26 A. Carminati, C.L. Schneider, A.B. Moradi, M. Zarebanadkouki, D. Vetterlein, H.-J. Vogel, A. Hildebrandt, U. Weller, L. Schüler, S.E. Oswald: How the rhizosphere may favor water availability to roots, *Vadose Zone J.* **10**(3), 988–998 (2011)
- 61.27 O. Ippisch: *Contributions to the Large-Scale Simulation of Flow and Transport in Heterogeneous Porous Media*, Habilitation Thesis (IWR, Clausthal-Zellerfeld 2014)
- 61.28 J. Winter, O. Ippisch, H.-J. Vogel: Dynamic processes in capillary fringes, *Vadose Zone J.* **14**(5), 1–2 (2015)
- 61.29 B. Schultze, O. Ippisch, B. Huwe, W. Durner: Dynamic nonequilibrium during unsaturated water flow. In: *Proc. Int. Workshop Charact. Meas. Hydraul. Prop. Unsatur. Porous Media*, ed. by M.T. van Genuchten, F.J. Leij, L. Wu (USDA, Riverside 1999) pp. 877–892
- 61.30 C. Bogner, B. Aufgebauer, O. Archner, B. Huwe: Dynamics of water flow in a forest soil: Visualization and modelling. In: *Energy and Matter Fluxes of a Spruce Forest Ecosystem*, Ecological Studies, Vol. 229, ed. by T. Foken (Springer, Cham 2017) pp. 137–156
- 61.31 M. Schlather, B. Huwe: A risk index for characterising flow pattern in soils using dye tracer distributions, *J. Contam. Hydrol.* **79**(1/2), 25–44 (2005)
- 61.32 C. Bogner, B. Wolf, M. Schlather, B. Huwe: Analysing flow patterns from dye tracer experiments in a forest soil using extreme value statistics, *Eur. J. Soil Sci.* **59**(1), 103–113 (2008)
- 61.33 R. Plagge, G. Scheffler, J. Grunewald, M. Funk: On the hysteresis in moisture storage and conductivity measured by the instantaneous profile method, *J. Build. Phys.* **29**(3), 247–259 (2006)
- 61.34 K. Beven, P. Germann: Macropores and water flow in soils, *Water Resour. Res.* **18**(5), 1311–1325 (1982)
- 61.35 P.F. Germann, K. Beven: Kinematic wave approximation to infiltration into soils with sorbing macropores, *Water Resour. Res.* **21**(7), 990–996 (1985)
- 61.36 P.F. Germann: *Preferential Flow. Stokes Approach to Infiltration and Drainage* (Geographica Bernensia, Bern 2014)
- 61.37 M. Flury, H. Flüher: Tracer characteristics of brilliant blue FCF, *Soil Sci. Soc. Am. J.* **59**(1), 22–27 (1995)
- 61.38 M. Weiler, H. Flüher: Inferring flow types from dye patterns in macroporous soils, *Geoderma* **120**(1/2), 137–153 (2004)
- 61.39 C. Bogner, A. Kühnel, B. Huwe: Predicting with limited data – Increasing the accuracy in vis-nir diffuse reflectance spectroscopy by smote. In: *6th Workshop Hyperspectr. Image Signal Process. Evol. Remote Sens. (WHISPERS), Lausanne* (2014) pp. 1–4, <https://doi.org/10.1109/WHISPERS.2014.8077584>
- 61.40 A. Kühnel, C. Bogner: *In-situ* prediction of soil organic carbon by vis–NIR spectroscopy: An efficient use of limited field data, *Eur. J. Soil Sci.* **68**(5), 689–702 (2017)
- 61.41 T.J. Sauer, R. Horton: Soil heat flux. In: *Micrometeorology in Agricultural Systems*, Agronomy Monograph, Vol. 47, ed. by J.L. Hatfield, J.M. Baker (ASA, CSSA, SSSA, Madison 2005) pp. 131–154
- 61.42 J.B. Stewart, A.S. Thom: Energy budgets in pine forest, *Q. J. R. Meteorol. Soc.* **99**(419), 154–170 (1973)
- 61.43 T.J. Sauer: Heat flux density. In: *Methods of Soil Analysis: Part 4 Physical Methods*, SSSA Book Series, (SSSA, Madison 2002) pp. 1233–1248
- 61.44 W. Greiner: *Theoretische Physik* (Harri Deutsch, Thun, Frankfurt a. M. 1981)
- 61.45 T. Foken: *Micrometeorology*, 2nd edn. (Springer, Berlin, Heidelberg 2017)
- 61.46 K. Yang, J. Wang: A temperature prediction-correction method for estimating surface soil heat flux from soil temperature and moisture data, *Sci. China Ser. D* **51**(5), 721–729 (2008)
- 61.47 C. Liebenthal, T. Foken: Evaluation of six parameterization approaches for the ground heat flux, *Theor. Appl. Climatol.* **88**(1/2), 43–56 (2007)
- 61.48 Z. Gao, E.S. Russell, J.E.C. Missik, M. Huang, X. Chen, C.E. Strickland, R. Clayton, E. Arntzen, Y. Ma, H. Liu: A novel approach to evaluate soil heat flux calculation: An analytical review of nine methods, *J. Geophys. Res. Atmos.* **122**(13), 6934–6949 (2017)
- 61.49 R. Horton, P.J. Wierenga, D.R. Nielsen: Evaluation of methods for determining the apparent thermal diffusivity of soil near the surface, *Soil Sci. Soc. Am. J.* **47**(1), 25–32 (1983)
- 61.50 A.K. Blackadar: Modeling the nocturnal boundary layer. In: *Third Symp. Atmos. Turbul. Diffus. Air Qual., Raleigh* (AMS, Boston 1976)
- 61.51 R.B. Stull: *An Introduction to Boundary Layer Meteorology* (Kluwer Academic, Dordrecht, Boston, London 1988)

- 61.52 W.K.P. Van Loon, H.M.H. Bastings, E.J. Moors: Calibration of soil heat flux sensors, *Agric. For. Meteorol.* **92**(1), 1–8 (1998)
- 61.53 J.R. Philip: The theory of heat flux meters, *J. Geophys. Res.* **66**(2), 571–579 (1961)
- 61.54 V.O. Morgensen: The calibration factor of heat flux meters in relation to the thermal conductivity of the surrounding medium, *Agric. Meteorol.* **7**, 401–410 (1970)
- 61.55 M. Fuchs: Heat flux. In: *Methods of Soil Analysis, Part 1. Physical and Mineralogical Methods*, SSSA Book Series, ed. by A. Klute (SSSA, ASA, Madison 1986) pp. 957–968
- 61.56 T.J. Sauer, D.W. Meek, T.E. Ochsner, A.R. Harris, R. Horton: Errors in heat flux measurement by flux plates of contrasting design and thermal conductivity, *Vadose Zone J.* **2**(4), 580–588 (2003)
- 61.57 K.R. Douglas-Mankin, R. Srinivasan, J.G. Arnold: Soil and water assessment tool (SWAT) model: Current developments and applications, *Transactions ASABE* **53**(5), 1423–1431 (2010)
- 61.58 A.N. Kostikov: On the dynamics of the coefficient of water percolation in soils and the necessity of studying it from the dynamic point of view for the purposes of amelioration, *Trans. Sixth Comm. Int. Soc. Soil Sci.* **1**, 17–21 (1932), in Russian
- 61.59 R.E. Horton: The infiltration-theory of surface-runoff, *Eos* **21**(2), 541 (1940)
- 61.60 M.J.M. Römkens, S.N. Prasad, J.Y. Parlange: Surface seal development in relation to rainstorm intensity. In: *Soil Erosion: Experiments and Models*, Catena Supplement, Vol. 17, ed. by R.B. Bryan (Catena Verlag, Cremlingen 1990) pp. 1–11
- 61.61 S.C. Chiang, D.E. Radcliffe, W.P. Miller: Comparison of seal hydraulic properties between Ultisols and Alfisols/Mollisols. In: *Soil Surface Sealing and Crusting*, Catena Supplement, Vol. 24, ed. by J.W.A. Poesen, M.A. Nearing (Catena Verlag, Cremlingen 1993) pp. 47–54
- 61.62 C. Bogner, M. Mirzaei, S. Ruy, B. Huwe: Microtopography, water storage and flow patterns in a fine-textured soil under agricultural use, *Hydrol. Process.* **27**(12), 1797–1806 (2013)
- 61.63 S. Arnhold: *Soil Erosion and Conservation – Potential of Row Crop Farming in Mountainous Landscapes of South Korea*, Ph.D. thesis (Univ. Bayreuth, Bayreuth 2013)
- 61.64 S. Arnhold, M. Ruidisch, S. Bartsch, C.L. Shope, B. Huwe: Simulation of runoff patterns and soil erosion on mountainous farmland with and without plastic-covered ridge-furrow cultivation in South Korea, *Transactions ASABE* **56**(2), 667–679 (2013)
- 61.65 W.T. Pinson, D.C. Yoder, J.R. Buchanan, W.C. Wright, J.B. Wilkerson: Design and evaluation of an improved flow divider for sampling runoff plots, *Appl. Eng. Agric.* **20**(4), 433 (2004)
- 61.66 C.A. Bonilla, D.G. Kroll, J.M. Norman, D.C. Yoder, C.C. Molling, P.S. Miller, J.C. Panuska, J.B. Topel, P.L. Wakeman, K.G. Karthikeyan: Instrumentation for measuring runoff, sediment, and chemical losses from agricultural fields, *J. Environ. Qual.* **35**(1), 216–223 (2006)
- 61.67 R.P.C. Morgan: *Soil Erosion and Conservation* (Wiley-Blackwell, Oxford, Malden 2005)
- 61.68 M. Ruidisch, S. Arnhold, B. Huwe, C. Bogner: Is ridge cultivation sustainable? A case study from the Haean catchment, South Korea, *Appl. Environ. Soil Sci.* **2013**, ID 679467 (2013)
- 61.69 W.G. Teixeira, F.L. Sinclair, B. Huwe, G. Schroth: Soil water. In: *Trees, Crops and Soil Fertility: Concepts and Research Methods*, ed. by G. Schroth, F.L. Sinclair (CABI Publishing, Cambridge, MA 2003) pp. 209–234
- 61.70 D.A. Robinson, C.S. Campbell, J.W. Hopmans, B.K. Hornbuckle, S.B. Jones, R. Knight, F. Ogden, J. Selker, O. Wendroth: Soil moisture measurement for ecological and hydrological watershed-scale observatories: A review, *Vadose Zone J.* **7**(1), 358–389 (2008)
- 61.71 C.H.M. Van Bavel: Neutron scattering measurement of soil moisture: Development and current status. In: *Humidity and Moisture*, Int. Symp. Humidity Moisture, Vol. 4, ed. by P.N. Winn Jr. (Reinhold, New York 1965) pp. 171–184
- 61.72 J.W. Holmes: Calibration and field use of the neutron scattering method of measuring soil water content, *Aust. J. Appl. Sci.* **7**(1), 45–58 (1956)
- 61.73 C.G. Gurr: Use of gamma rays in measuring water content and permeability in unsaturated columns of soil, *Soil Sci.* **94**(4), 224–229 (1962)
- 61.74 H. Ferguson, W.H. Gardner: Water content measurement in soil columns by gamma ray absorption, *Soil Sci. Soc. Am. J.* **26**(1), 11–14 (1962)
- 61.75 J.A. Vomocil: In situ measurement of bulk density of soil by gamma-ray absorption technique, *Soil Sci.* **77**(4), 341–342 (1954)
- 61.76 C.H.M. Van Bavel, R.J. Lascano, J.M. Baker: Calibrating two-probe, gamma-gauge densitometers, *Soil Sci.* **140**(5), 393–395 (1985)
- 61.77 G.C. Topp, J.L. Davis: Time-domain reflectometry (TDR) and its application to irrigation scheduling. In: *Advances in Irrigation*, Vol. 3, ed. by D. Hillel (Academic Press, Orlando 1985) pp. 107–127
- 61.78 L.W. Petersen, A. Thomsen, P. Moldrup, O.H. Jacobsen, D.E. Rolston: High-resolution time domain reflectometry: Sensitivity dependency on probe-design, *Soil Sci.* **159**(3), 149–154 (1995)
- 61.79 G.C. Topp, J.L. Davis, A.P. Annan: Electromagnetic determination of soil water content: Measurements in coaxial transmission lines, *Water Resour. Res.* **16**(3), 574–582 (1980)
- 61.80 M.A. Malicki, R. Plagge, C.H. Roth: Improving the calibration of dielectric TDR soil moisture determination taking into account the solid soil, *Eur. J. Soil Sci.* **47**(3), 357–366 (1996)
- 61.81 K. Roth, R. Schulin, H. Flüßler, W. Attinger: Calibration of time domain reflectometry for water content measurement using a composite dielectric approach, *Water Resour. Res.* **26**(10), 2267–2273 (1990)
- 61.82 A.M. Weitz, W.T. Grauel, M. Keller, E. Veldkamp: Calibration of time domain reflectometry tech-

- nique using undisturbed soil samples from humid tropical soils of volcanic origin, *Water Resour. Res.* **33**(6), 1241–1249 (1997)
- 61.83 M.G. Pelletier, R.C. Schwartz, G.A. Holt, J.D. Wanjura, T.R. Green: Frequency domain probe design for high frequency sensing of soil moisture, *Agriculture* **6**(4), 60–72 (2016)
- 61.84 S.D. Logsdon: Experimental limitations of time domain reflectometry hardware for dispersive soils, *Soil Sci. Soc. Am. J.* **70**(2), 537–540 (2006)
- 61.85 S.B. Jones, D. Or: Frequency domain analysis for extending time domain reflectometry water content measurement in highly saline soils, *Soil Sci. Soc. Am. J.* **68**(5), 1568–1577 (2004)
- 61.86 G.J. Gaskin, J.D. Miller: Measurement of soil water content using a simplified impedance measuring technique, *J. Agric. Eng. Res.* **63**(2), 153–159 (1996)
- 61.87 M.S. Borhan, L.R. Parsons: Monitoring of soil water content in a citrus grove using capacitance ECH20 probes. In: *ASAE Annu. Meet, Paper No. 042110* (ASABE, St. Joseph 2004), <https://doi.org/10.13031/2013.16383>
- 61.88 M. Inoue, B.A. Ould Ahmed, T. Saito, M. Irshad: Comparison of twelve dielectric moisture probes for soil water measurement under saline conditions, *Am. J. Environ. Sci.* **4**(4), 367–372 (2008)
- 61.89 G.S. Campbell, G.W. Gee: Water potential: Miscellaneous methods. In: *Methods of Soil Analysis, Part 1. Physical and Mineralogical Methods*, Agronomy Monograph, Vol. 9 (SSSA, ASA, Madison 1986) pp. 619–633
- 61.90 C.B. Tanner, R.J. Hanks: Moisture hysteresis in gypsum moisture blocks, *Soil Sci. Soc. Am. J.* **16**(1), 48–51 (1952)
- 61.91 UP Umweltanalytische Produkte GmbH: pF-Meter zur Bestimmung der Saugspannung bis > 14.000 hPa, https://www.upgmbh.com/fileadmin/produkte/pdf/10850_pF_Meter.pdf (2013), Accessed 24 July 2021
- 61.92 N. Lu, W.J. Likos: *Unsaturated Soil Mechanics* (Wiley, Hoboken 2004)
- 61.93 Ł. Guz, D. Majerek, H. Sobczuk, E. Guz, B. Połednik: Comparison of interpretation methods of thermocouple psychrometer readouts, *AIP Conf. Proc.* **1866**, 040013 (2017)
- 61.94 W.G. Teixeira, M. Bacis Ceddia, M. Vasconceles Ottoni, G. Kangussu Donnagema: *Application of Soil Physics in Environmental Analyses* (Springer, Cham 2014)
- 61.95 M.R. Carter, E.G. Gregorich: *Soil Sampling and Methods of Analysis*, 2nd edn. (CRC Press, Boca Raton 2007)
- 61.96 C.W. Boast, D. Kirkham: Auger hole seepage theory, *Soil Sci. Soc. Am. J.* **35**(3), 365–373 (1971)
- 61.97 DIN 19682, Blatt 8: *Soil Quality – Field Tests – Determination of the Hydraulic Conductivity by Auger Hole Method* (Beuth, Berlin 1972)
- 61.98 R.R. van der Ploeg, B. Huwe: Some remarks concerning the determination of the hydraulic conductivity with the auger hole method, *Z. Pflanzenernähr. Bodenkd.* **151**(4), 251–253 (1988), in German
- 61.99 R. Kretzschmar, B. Huwe, R.R. van der Ploeg: Entwicklung eines Computerverfahrens zur Berechnung der hydraulischen Leitfähigkeit von wassergesättigten Böden mit der Bohrlochmethode, *Z. Pflanzenernähr. Bodenkd.* **152**(1), 17–20 (1989), in German
- 61.100 D.E. Elrick, W.D. Reynolds: Infiltration from constant-head well permeameters and infiltrometers. In: *Advances in Measurement of Soil Physical Properties: Bringing Theory into Practice*, SSSA Special Publications, Vol. 30, ed. by G.C. Topp, W.D. Reynolds, R.E. Green (SSSA, Madison 1992) pp. 1–24
- 61.101 A. Amoozegar: A compact constant-head permeameter for measuring saturated hydraulic conductivity of the vadose zone, *Soil Sci. Soc. Am. J.* **53**(5), 1356–1361 (1989)
- 61.102 Eijkelkamp Agrisearch Equipment (EAE): *Operating Instructions 09.07 Guelph Permeameter 2012*, <https://de.eijkelkamp.com/produkte/feldmesser-te/guelph-in-situ-permeameter.html>, Accessed 24 July 2021
- 61.103 K.K. Watson: An instantaneous profile method for determining the hydraulic conductivity of unsaturated porous materials, *Water Resour. Res.* **2**(4), 709–715 (1966)
- 61.104 WMO: *Guide to Instruments and Methods of Observation, WMO-No. 8, Volume I – Measurement of Meteorological Variables*. (World Meteorological Organization, Geneva 2018)
- 61.105 C. Liebethal, T. Foken: On the significance of the Webb correction to fluxes, *Bound.-Layer Meteorol.* **109**(1), 99–106 (2003)
- 61.106 E.C. Childs, N. Collis-George: The permeability of porous materials, *Proc. R. Soc. A* **201**(1066), 392–405 (1950)
- 61.107 Y. Mualem: A new model for predicting the hydraulic conductivity of unsaturated porous media, *Water Resour. Res.* **12**(3), 513–522 (1976)
- 61.108 R.J. Millington, J.P. Quirk: Permeability of porous media, *Nature* **183**(4658), 387–388 (1959)
- 61.109 D.A. De Vries: Heat transfer in soils. In: *Heat and Mass Transfer in the Biosphere*, ed. by D.A. de Vries, N.H. Afgan (Scripta Book Co., Washington 1975) pp. 5–28
- 61.110 T.J.M. Blom, S.R. Troelstra: *Simulation Model of the Combined Transport of Water and Heat Produced by a Thermal Gradient in Porous Media*, M.S. thesis (Agricultural University, Wageningen 1972)
- 61.111 C. Bandt: Ordinal time series analysis, *Ecol. Model.* **182**(3/4), 229–238 (2005)
- 61.112 C. Bandt, B. Pompe: Permutation entropy: A natural complexity measure for time series, *Phys. Rev. Lett.* **88**(17), 174102 (2002)
- 61.113 C.E. Shannon: A mathematical theory of communication, *Bell Syst. Tech. J.* **27**(3), 379–423 (1948)
- 61.114 B. Fadlallah, B. Chen, A. Keil, J. Príncipe: Weighted-permutation entropy: A complexity measure for time series incorporating amplitude information, *Phys. Rev. E* **87**(2), 022911 (2013)

- 61.115 M.T. van Genuchten: A closed-form equation for predicting the hydraulic conductivity of unsaturated soils, *Soil Sci. Soc. Am. J.* **44**(5), 892–898 (1980)
- 61.116 W. Durner: Hydraulic conductivity estimation for soils with heterogeneous pore structure, *Water Resour. Res.* **30**(2), 211–223 (1994)
- 61.117 L.M. Arya, J.F. Paris: A physicoempirical model to predict the soil moisture characteristic from particle size distribution and bulk density data, *Soil Sci. Soc. Am. J.* **45**, 1023–1030 (1981)
- 61.118 H. Vereecken, M. Weynants, M. Javaux, Y. Pachepsky, M.G. Schaap, M.T. van Genuchten: Using pedotransfer functions to estimate the van Genuchten–Mualem soil hydraulic properties: A review, *Vadose Zone J.* **9**(4), 795–820 (2010)
- 61.119 M.G. Schaap, F.J. Leij, M.T. van Genuchten: Neural network analysis for hierarchical prediction of soil hydraulic properties, *Soil Sci. Soc. Am. J.* **62**(4), 847–855 (1998)
- 61.120 W. Jeschke: Digital close-range photogrammetry for surface measurement, *Proc. SPIE* **1395**, 13953R (1990)
- 61.121 R Core Team: *R: A Language and Environment for Statistical Computing* (R Foundation for Statistical Computing, Vienna 2016)
- 61.122 T. Foken (Ed.): *Energy and Matter Fluxes of a Spruce Forest Ecosystem*, Ecological Studies, Vol. 229 (Springer, Berlin, Heidelberg 2017)
- 61.123 D. Cao, B. Shi, H. Zhu, G. Wei, S.-E. Chen, J. Yan: A distributed measurement method for in-situ soil moisture content by using carbon-fiber heated cable, *J. Rock Mech. Geotech. Eng.* **7**, 700–707 (2015)
- 61.124 C. Sayde, J. Benitez Buelga, L. Rodriguez-Sinobas, L. El Khoury, M. English, N. van de Giesen, J.S. Selker: Mapping variability of soil water content and flux across 1–1000 m scales using the actively heated fiber optic method, *Water Resour. Res.* **50**, 7302–7317 (2014)
- 61.125 M. Schrön, M. Köhli, L. Scheffele, J. Iwema, H.R. Bogaen, L. Lv, E. Martini, G. Baroni, R. Rosolem, J. Weimar, J. Mai, M. Cuntz, C. Rebmann, S.E. Oswald, P. Dietrich, U. Schmidt, S. Zacharias: Improving calibration and validation of cosmic-ray neutron sensors in the light of spatial sensitivity, *Hydrol. Earth Syst. Sci.* **21**(10), 5009–5030 (2017)
- 61.126 M. Schrön, S. Zacharias, G. Womack, M. Köhli, D. Desilets, S.E. Oswald, J. Bumberger, H. Mollenhauer, S. Kögler, P. Remmler, M. Kasner, A. Denk, P. Dietrich: Intercomparison of cosmic-ray neutron sensors and water balance monitoring in an urban environment, *Geosci. Instrum. Method. Data Syst.* **7**(1), 83–99 (2018)
- 61.127 H. Vereecken, J.A. Huismans, H.J. Hendricks Franssen, N. Brüggemann, H.R. Bogaen, S. Kollet, M. Javaux, J. van der Krug, J. Vanderborght: Soil hydrology: Recent methodological advances, challenges, and perspectives, *Water Resour. Res.* **51**(4), 2616–2633 (2015)
- 61.128 R.A. Viscalla Rossel, A.B. McBratney, B. Minasny (Eds.): *Proximal Soil Sensing*, Progress in Soil Science (Springer, Dordrecht 2010)
- 61.129 J.M. Soriano-Disla, L.J. Janik, R.A. Viscarra Rossel, L.M. Macdonald, M.J. McLaughlin: The performance of visible, near-, and mid-infrared reflectance spectroscopy for prediction of soil physical, chemical, and biological properties, *Appl. Spectrosc. Rev.* **49**(2), 139–186 (2014)
- 61.130 B.M. Duda, D.C. Weindorf, S. Chakraborty, B. Li, T. Man, L. Paulette, S. Deb: Soil characterization across catenas via advanced proximal sensors, *Geoderma* **298**, 78–91 (2017)
- 61.131 S.M. O'Rourke, B. Minasny, N.M. Holden, A.B. McBratney: Synergistic use of Vis-NIR, MIR, and XRF spectroscopy for the determination of soil geochemistry, *Soil Sci. Soc. Am. J.* **80**(4), 888–899 (2016)
- 61.132 L. Breiman: Random forests, *Mach. Learn.* **45**(1), 5–32 (2001)
- 61.133 S. Wold: Personal memories of the early PLS development, *Chemom. Intell. Lab. Syst.* **58**(2), 83–84 (2001)
- 61.134 L. Zhang, L. Zhang, B. Du: Deep learning for remote sensing data: A technical tutorial on the state of the art, *IEEE Geosci. Remote Sens. Mag.* **4**(2), 22–40 (2016)
- 61.135 T. Hengl, J. Mendes de Jesus, G.B.M. Heuvelink, M. Ruiperez Gonzalez, M. Kilibarda, A. Blagotić, S. Wei, M.N. Wright, X. Geng, B. Bauer-Marschallinger, M.A. Guevara, R. Vargas, R.A. MacMillan, N.H. Batjes, J.G.B. Leenaars, E. Ribeiro, I. Wheeler, S. Mantel, B. Kempen: SoilGrids250m: Global gridded soil information based on machine learning, *PLOS ONE* **12**(2), e0169748 (2017)
- 61.136 C. Montzka, M. Herbst, L. Weihermüller, A. Verhoef, H. Vereecken: A global data set of soil hydraulic properties and sub-grid variability of soil water retention and hydraulic conductivity curves, *Earth Syst. Sci. Data* **9**(2), 529–543 (2017)
- 61.137 N.H. Batjes, E. Ribeiro, A. van Oostrum, J. Leenaars, T. Hengl, J. Mendes de Jesus: WoSIS: Providing standardised soil profile data for the world, *Earth Syst. Sci. Data* **9**(1), 1–14 (2017)

Bernd Huwe

Soil Physics
University of Bayreuth
Bayreuth, Germany
bernd.huwe@uni-bayreuth.de



Bernd Huwe received Habilitation degree in 1991 in Soil Physics. From 1992 to 2017, he was Professor of Soil Physics at the University of Bayreuth. His research addressed theoretical and practical questions of water, heat, and nutrient and pollutant transport in soils. In this context, soil landscape modeling, regionalization of soil processes, effective modeling, and risk and parameter uncertainty analysis were important tools of his research group.

Christina Bogner

Institute of Geography
University of Cologne
Cologne, Germany
christina.bogner@uni-koeln.de



Christina Bogner is Professor of Physical Geography at the Institute of Geography at the University of Cologne in Germany and Head of the Ecosystem Research Group there. She received her PhD in Soil Physics in 2009 and was awarded a Habilitation in Geoecology in 2017. In her multidisciplinary research, she uses experimental techniques and modeling to understand water flow in soils, land use change, and microplastic transport in soils.

Thomas Foken

University of Bayreuth
Bayreuth, Germany
thomas.foken@uni-bayreuth.de



Thomas Foken is a retired Professor of Micrometeorology at the University of Bayreuth. He was the head of Laboratories at the meteorological observatories at Potsdam (1981–1994) and Lindenberg (1994–1997). His research interests include the interaction between the Earth's surface and the atmosphere and the measurement and modeling of energy and matter fluxes, with a strong focus on experimental meteorology. His scientific contributions have been recognized through various international awards.

Water Measure

62. Water Measurements

Volker Mohrholz , Anita Flohr 

Physical properties and fluxes at the lower interface of the atmosphere set important boundary conditions for their dynamics and matter fluxes. Since 70% of this interface is governed by the world ocean, its surface water properties are of high importance. This chapter provides an overview on the measurement techniques of water temperature, salinity, waves, and currents, as well as fluxes of greenhouse and trace gases in surface water. Actual sensors use a wide spectrum of electronic, optical, and acoustic methods. The use of multi-sensor devices is very common in marine science. As example of such a device the conductivity-temperature-depth (CTD) probe is presented in more detail. The methods described are applied in seawater and fresh water environments.

62.1	Measurement Principles and Parameters	1658
62.2	History	1660
62.2.1	History of Water Measurements	1660
62.2.2	Historically Relevant Measurement Methods	1660
62.3	Theory	1662
62.3.1	Water Temperature	1662
62.3.2	Surface Salinity	1663
62.3.3	Surface Waves	1663
62.3.4	Currents	1663
62.3.5	Dissolved Greenhouse Gases	1664
62.4	Devices and Systems	1667
62.4.1	Temperature Sensors	1667
62.4.2	Conductivity Sensors	1667
62.4.3	The CTD Probe	1668
62.4.4	Wave-Rider Buoy	1669
62.4.5	Current Meters	1670
62.4.6	Dissolved Long-Lived Greenhouse Gases	1672
62.4.7	Comparison of Methods	1673
62.5	Specifications	1673
62.6	Quality Control	1674
62.6.1	Sensor Calibration	1674
62.6.2	Specific Quality Control Methods	1675
62.7	Maintenance	1675
62.8	Application	1676
62.8.1	Variability in the Surface Mixed Layer	1676
62.8.2	Spatial Variability of Greenhouse Gases off the Coast of Namibia	1676
62.9	Future Developments	1678
62.10	Further Reading	1678
	References	1678

Mainly four major processes at the ocean-atmosphere interface have a strong impact on the state and dynamics of the atmosphere: heat flux, evaporation of water, impulse flux into the ocean, and the exchange of thermal active trace gases. Heat fluxes at the ocean-atmosphere interface are important sources or sinks for thermal energy in the atmosphere. They have a high impact on the stratification and, thus, on the stability of the lower atmosphere. Heat fluxes are also strongly related to the evaporation at the ocean surface, which is the main source of water vapor in the atmosphere. Wind at the ocean surface causes an impulse flux into the ocean that acts like boundary friction and causes the formation of an Ekman layer in the lower atmosphere. In the ocean surface layer, the impulse flux forces currents and turbulent mixing, which, in turn, affect the sea surface

temperature (SST), sea surface salinity (SSS), and the heat and gas exchange with the atmosphere.

The fluxes at the ocean-atmosphere interface depend on the particular conditions in the lower atmosphere, as well as on the properties of the ocean surface mixed layer, which vary on a large range of space and time scales.

Usually, empirical formulas are applied to quantify the fluxes [62.1]. Beside atmospheric parameters information about the SST, SSS, current velocity, waves, and concentration of trace and greenhouse gases in surface water are required to calculate the fluxes. Measurements of these variables are conducted either in-situ or via remote sensing, with various methods and sensors [62.2]. This chapter cannot provide a comprehensive picture of ocean observation methods and focusses

mainly on an overview on in-situ measurement methods of some key parameters in the ocean surface layer.

Atmospheric greenhouse gases absorb and emit thermal energy and, thereby, contribute to warming the Earth's surface. Water vapor is the most abundant greenhouse gas in the Earth's atmosphere, varying strongly between < 1% and 5% and contributing between 60% and 71% to the natural greenhouse effect [62.3, 4] (Chap. 8). Many other long-lived greenhouse gases exist in the Earth's atmosphere, such as carbon dioxide (CO₂), methane (CH₄), nitrous oxide (N₂O), chlorofluorocarbons (CFCs), hydrofluorocarbons (HFCs), and others [62.5]. Among these gases, CO₂, CH₄ and N₂O are the only greenhouse gases with both anthropogenic but also natural sources and are, thus, focused on in this chapter. Carbon dioxide contributes ≈ 26% to the greenhouse effect, whereas CH₄

and N₂O jointly account for ≈ 6% of the greenhouse effect [62.3, 6]. Aquatic ecosystems play a major role among the natural sinks and sources of these gases. Regarding CO₂, some (sub)tropical coastal areas are net sources of CO₂ to the atmosphere, but overall the ocean is a net sink for CO₂ [62.7–9]. This is largely due to the fact that CO₂ not only dissolves, but it also reacts with seawater to form the carbonate system. It is the chemical basis for the mitigation of atmospheric CO₂ increase by the ocean [62.10, 11]. Regarding CH₄ and N₂O, aquatic systems are net sources to the atmosphere, accounting for ≈ 27% of natural CH₄ sources and for ≈ 50% of natural N₂O sources [62.8]. Current research largely evolves around identifying the main drivers of the spatial and temporal variability of these greenhouse gas fluxes, including the effect of human perturbations.

62.1 Measurement Principles and Parameters

The standard instrument for in-situ temperature and salinity observation and water sampling in the ocean is the CTD probe (this stands for conductivity-temperature-depth probe). CTD is a measuring platform that combines temperature, conductivity, and pressure sensors with a rosette water sampler for taking samples at selected depth. Nowadays, CTDs are equipped with additional sensors for, e.g., oxygen concentration, turbidity, fluorescence, and pH. CTD is usually deployed on a wire from a vessel. During lowering from the sea surface to the end depth of the profile, data of all sensors are recorded continuously. The classical CTD delivers a vertical 1-D profile at each sampled position. Today, CTDs are also mounted on undulating towed devices (e.g., ScanFish [62.12]) and autonomous operating gliders [62.13, 14], remotely operated vehicles [62.15], and profiling moorings [62.16]. In that case, mostly 2-D datasets are obtained.

The particular CTD sensors use different measurement methods. The temperature is usually obtained with a thermistor or platinum wire resistor. Conductivity is measured either with a multielectrode conductivity cell or with an inductive sensor, and the pressure is usually gathered by a quartz crystal resonator, whose oscillation frequency depends on the pressure-induced stress. Besides vertical profiling CTDs also vessel-mounted underway systems, called thermosalinographs (TSGs), are widely used. They obtain temperature and conductivity in surface water, which is continuously pumped through a temperature and conductivity sensor package.

Current observations in the marine environment are performed mainly with acoustic methods, since mechanical current meters are outdated for the most ap-

plications. The acoustic current meters use either the Doppler effect of a single ultrasound pulse or the phase shift of two subsequent transmitted ultrasound pulses. The transmitted sound pulses are scattered at particles (e.g., zooplankton, suspended matter). The travel time of the backscattered signal is used to determine the distance between the sensor and the measuring volume. Using temporal windowing current profiles can be obtained. For some specialized applications, also the travel time of sound between a fixed transmitter and receiver is used.

There are several methods to measure wave parameters [62.17]. Pressure sensors mounted at a certain depth are very common. Also acoustic methods that obtain the distance to the surface from the travel time of a sound pulse are widely applied. Modern acoustic current meters are also able to estimate wave parameters and directional wave spectra. Wave rider buoys that swim at the sea surface use accelerometers for wave measurements. Radar applications and optical methods are used less often.

The concentration of dissolved greenhouse gases in seawater can be measured from discrete water samples or from continuous sampling systems. Discrete water sampling is usually done to retrieve the vertical distribution of dissolved gases in the water column. Continuous underway measurements are being applied to determine the spatial and temporal distribution of dissolved trace gases in surface water, e.g., to calculate fluxes across the air–water interface. We will focus on this approach, as it is of more relevance from the meteorological perspective. Irrespective of the sampling method, the fundamental principle of analysis involves

Table 62.1 Measured parameters for the calculation of state and fluxes at the atmosphere–ocean interface

Parameter	Description	Unit	Symbol
Temperature	Temperature of the upper mixed layer	K	T
Conductivity	Conductivity of the upper mixed layer	mS cm^{-1} , S m^{-1}	C
Current velocity	Horizontal speed of surface layer	m s^{-1}	u
Significant wave height	Height of wind forced gravity waves at the surface	m	H_s
Mean wave period	Mean wave period of all surface waves in a certain time period	s	T_m
Peak wave period	Period of the most abundant surface waves in a certain period of time	s	T_{peak}
Mole fraction of trace gas	Mole fraction of gas	$\mu\text{mol mol}^{-1}$; ppm (CO_2), nmol mol^{-1} ; ppb (CH_4 , N_2O)	x_{gas}
Mole fraction of water vapor	Mole fraction of water vapor in air	ppm	$x_{\text{H}_2\text{O}}$
In-situ water temperature	Temperature of the water at the intake	K	T_{insitu}
Water temperature in equilibrator	Temperature of water in the equilibrator	K	T_{equ}
Air temperature	Temperature of air usually at 10 m above water surface	K	T_{air}

Table 62.2 Other relevant parameters for the calculation of state and fluxes at the atmosphere–ocean interface

Parameter	Description	Unit	Symbol
Sea pressure	Absolute pressure at depth of measurement reduced by the standard atmosphere pressure	dbar	p
Practical salinity	Salinity of seawater	(psu)	S_p
Reference salinity	Mass of dissolved salt according the reference composition of sea salt.	g kg^{-1}	S_R
Absolute salinity	Derived from sea pressure, temperature, and conductivity Mass of dissolved salt, derived from sea pressure, temperature, conductivity, and local anomaly of salt composition	g kg^{-1}	S_A
Partial pressure of gas	Partial pressure of gas in dry air	atm, ppm (CO_2), atm, ppb (CH_4 , N_2O)	p_{gas}
Atmospheric pressure	Absolute atmospheric pressure	atm	p_{atm}
Partial pressure of water vapour	Saturation vapor pressure of water in equilibrium with the atmosphere	atm	$p_{\text{H}_2\text{O}}$
Solubility	Solubility of a gas in water or seawater	$\text{mol kg}^{-1} \text{atm}^{-1}$	s_{gas}
Concentration	Concentration of a gas in water	$\mu\text{mol kg}^{-1}$ (CO_2) nmol kg^{-1} (CH_4 , NO_2)	c_{gas}
Wind speed	Wind speed at 10 m above the water surface	m s^{-1}	u

Table 62.3 Principles of water measurements and applications

Type of sensor	Measurement principle					Application	
	Mechanical	Electrical	Optical	Acoustic	Chemical	Mean	Turbulent
Temperature sensor		×				×	×
Conductivity		×				×	×
Pressure sensor		×				×	
Current meter	×			×		×	×
Accelerometer		×				×	
Absorption spectrometer			×			×	
GC-MS, GC-ECD		×			×	×	

the extraction of the dissolved gas from the aqueous phase and the analysis of the gas sample by means of absorption spectrometry or gas chromatography coupled to an electron capture detector (GC-ECD) or mass

spectrometer (GC-MS), e.g., [62.17–20] (Sect. 62.4.6). An overview of the most important parameters for the characterization of the sea surface properties is given in Tables 62.1 and 62.2.

62.2 History

Observations of water properties and sea state date back to the early seafarers in antiquity. At that time knowledge about tides, currents, and waves were used mainly for navigation purposes. The scientific interest in ocean dynamics started to grow in the nineteenth century.

62.2.1 History of Water Measurements

The expedition of the HMS Challenger Expedition from 1872 to 1876 marks the start of systematic marine observations on the ocean scale [62.18]. Although this expedition was focused on biological sampling, also physical observations were performed. Prior to this voyage oceanographic data were gathered occasionally by merchant and military ships and were collected by some national authorities, mainly for navigational purposes. Regular time series observations of temperature, salinity and currents have been performed on light ships since the late nineteenth century. At the beginning of the twentieth century the Scandinavian school of oceanographers made substantial progress in the theoretical description of ocean dynamics. Inspired by *Fridtjof Nansen's* (1861–1930) observations of the Arctic ice drift *Walfrid Ekman* (1874–1954) developed a theory of wind-driven currents [62.19]. First hydrographic tables of the state of seawater that define the relation between temperature, salinity, and density were provided by *Martin Knudsen* (1871–1949) [62.20]. The German Meteor expedition of 1925–1927 was the first expedition focused mainly on physical properties of the ocean [62.21]. After the Second World War the frequency and intensity of ocean observations increased considerably. International coordinated programs addressed the understanding of ocean processes on a basin-wide and global scale (e.g., the World Ocean Circulation Experiment WOCE). A dramatic increase in the frequency, coverage, and spatial and temporal resolution of ocean observations was achieved by the development of electronic sensors and the beginning of remote sensing of the Earth's surface using satellite-based sensors.

62.2.2 Historically Relevant Measurement Methods

This section provides a general overview of the most important historical measurement methods for the properties of the ocean surface layer. For more detailed information, please refer to the cited literature.

Temperature

The sea surface temperature is the parameter in the ocean that has been the easiest to measure since the

beginning of scientific ocean observations. The main principle of measuring temperature is the detection of the volume change of a liquid. Simple alcohol and mercury thermometers were widely used in oceanography from the 1700s to the 1980s. During the Challenger Expedition the minimum and maximum temperatures of the water column were recorded with the newly developed Miller–Casella thermometers [62.22]. However, the vertical temperature gradients altered readings from deeper layers, and, consequently, the temperatures from the depth of interest could not be accurately measured. In 1874, the invention of the reversing mercury thermometer [62.23] by Negretti and Zambra overcame this problem. When this thermometer is reversed at the depth of interest, mercury in the stem separates from the reservoir, and the temperature is captured. Reversing thermometers (Fig. 62.1) were used on water sample bottles until the mid-1980s. Comparison measurements using reversal thermometers for in-situ calibration of electronic temperature sensors were performed till the end of the twentieth century.

With the development of semiconductor electronics, mercury thermometers were replaced by platinum-resistance thermometers [62.24] and thermistor-based temperature sensors, which today are the standard sensors for accurately temperature observations in the oceans.

Salinity

The first chemical analysis of seawater composition was performed by *Antoine Lavoisier* (1743–1794). An early method to determine the mass of salt in seawater was boiling a seawater sample until all water vaporized and weighing the remaining salt. Later, the methods to measure salinity were based on the idea that the chemical composition, i.e., the relative abundance of solutes in seawater, is nearly constant in the world ocean. This



Fig. 62.1 Open and closed reversing mercury thermometers (*middle and bottom*) and the reading magnifier (*top*) (photo © V. Mohrholz)

principle dates back to *Alexander Marcet* (1770–1822). Consequently, if the fraction of one particular component on the total mass of salt is known, it is sufficient to measure this component to calculate the salinity. As it is the most abundant substance, chloride (Cl^-) is the best component to use for this purpose. Salinity was determined by titration of seawater with silver nitrate (AgNO_3) till 1978. The chlorinity, or more precisely the total abundance of halogens dissolved in water, is then converted to Knudsen salinity S_K by the empirical relationship [62.20]

$$S_K = 0.03 + 1.805 \cdot \text{chlorinity} . \quad (62.1)$$

In 1967, the formula was slightly modified to the Cox salinity S_C [62.25]

$$S_C = 1.80655 \cdot \text{chlorinity} . \quad (62.2)$$

In the 1970s, the titration method was replaced by measuring the conductivity of seawater to calculate the salinity. In 1978, the Practical Salinity Scale (PSS-78) was introduced [62.26]. It defines the salinity based on the conductivity ratio of a seawater sample to a potassium chloride (KCl) solution with a mass fraction of 0.0324356 [62.27]. This practical salinity S_P is a unitless quantity, since it is defined as a conductivity ratio. In 2010, the new International Thermodynamic Equation of Seawater – 2010 introduced the reference salinity S_R and the absolute salinity S_A , which define the mass of salt in seawater with reference composition and the true salt mass in a seawater sample, respectively [62.28].

Current Meter

Current and wave measurements are among the most difficult measurements to access in the ocean. However, due to their importance for shipping, simple methods for their observation were developed at a very early stage. First measurements of the surface current were carried out with the aid of drift bodies. The path and direction of a drift body is tracked over a certain period of time. Then the averaged velocity is calculated. This method, initially carried out with simple pieces of wood, was further developed over time. With the help of bottle-post experiments and drift cards [62.29], also large currents were investigated until the 1960s. A modern form of drift bodies are the WOCE drifter [62.30] and the Argo float [62.31, 32]. They drift for up to 3 years at the surface or at depths in the ocean and collect data along the pathway. From the drifter position, which is determined by satellites at intervals of some minutes to a few days, the average current velocity and direction is determined.

Point and time series measurements of currents required a different approach, which led to the develop-

ment of the first mechanical current meters at the end of the nineteenth century [62.33]. Initially, the devices were only used to determine the flow velocity. The flow direction was usually observed visually. The flow velocity was determined by means of an impeller or propeller. In the first devices, the number of revolutions of the propeller was counted by an observer. Later, numerous mechanical constructions were developed, which registered the number of revolutions with the help of a clockwork. Also the flow direction could be roughly determined with a drop-ball mechanism [62.34]. These flowmeters only revealed a single average value of the current speed and direction per deployment. In 1926, *Ekmann* developed the first mechanical current meter, which enabled up to 47 individual measurements in one deployment [62.35]. For the start/stop of a single measurement, drop weights, so-called messengers, were used on the wire. The mechanical registration of the flowmeters was further improved to allow continuous measurement of flow velocity and direction. This required a recorder mechanism in a pressure housing that registered on paper or blackened glass plates. At the beginning of the 1970s, mechanical recording was replaced by electronic storage of measured data. The decisive disadvantage of mechanical flowmeters is their susceptibility to contamination and biofouling. Besides the mechanical flow meters, electromagnetic methods for flow measurement were also developed since the 1950s [62.36]. These devices used induction in conductors moving in the Earth's magnetic field. However, due to their high uncertainty, these methods have not been widely disseminated.

The rapid development of microelectronics and electronic signal processing enabled the development and application of acoustic current meters in the late 1970s [62.37]. Acoustic current meters uses the travel time of sound between two points, the Doppler effect, or the phase shift between two subsequently submitted pulses of sound. The latter is the most accurate method, but it has some important limitations [62.38]. Today, acoustic Doppler current profilers (ADCPs) have become the standard instrument for current measurement in marine research. With the availability of accurate remote-sensing data of sea surface elevation large-scale currents in the upper ocean are also estimated using geostrophic equations [62.39].

Long-Lived Greenhouse Gases

The beginning of the study of the impact of greenhouse gases dates back to the early nineteenth century and was initiated by the theory that the Earth's climate had undergone glacial periods in the past [62.40], provoking the question as to what might have caused those climatic variations. *John Tyndall* (1820–1893) was the first to measure the heat absorption of atmospheric gases, emphasizing the importance of water vapor and

CO₂ in maintaining the Earth's current climate [62.41, 42]. In 1896, *Svante Arrhenius* (1859–1927) revived this theory by quantifying the sensitivity of the Earth's climate to changes in atmospheric CO₂ concentrations [62.43]. He further claimed that a substantial amount of the CO₂ emitted from fossil fuel combustion is absorbed by the ocean. This provoked studies aiming to understand the spatiotemporal variability of atmospheric CO₂ concentrations [62.44–46]. Analysis of atmospheric CO₂ concentrations were done mostly by manometric and microgasometric techniques. Using

62.3 Theory

In this section, the theory of basic measurement methods used in the marine environment is briefly described.

62.3.1 Water Temperature

For in-situ measurements of temperature, two basic groups of sensors are applied: platinum resistance thermometers (Chap. 7) and thermistors. Platinum resistance thermometers use the increasing resistance of a platinum wire with increasing temperature. Thermistors are semiconductor elements with a high dependency of their resistance on temperature. The thermistor resistance can be positively or negatively correlated with temperature, called PTC (positively correlated with temperature) and NTC (negatively correlated with temperature), respectively. For further types of temperature sensors the reader is also referred to Chap. 7.

Platinum resistance thermometers have a highly linear characteristic at a wide temperature range. Thus, in the range between 13.8 K (the triple point of hydrogen) and 961.78 °C (the freezing point of silver), the actual International Temperature Scale 90 (ITS-90, Chaps. 5 and 7) is defined by the resistance of a platinum wire [62.57]. The temperature according to this scale is referred to as T_{90} . Before 1990, the temperature scale IPTS-68 was used. In the range between –2 and 40 °C, temperatures measured in IPTS-68 can be converted to ITS-90 by multiplication with a constant factor according to

$$T_{68} [^{\circ}\text{C}] = 1.00024T_{90} [^{\circ}\text{C}]. \quad (62.3)$$

The temperature obtained from platinum resistance thermometers is calculated from the ratio W of the resistance R at the measured temperature T_{90} and the resistance at the temperature of the triple point of pure water (273.16 K).

$$W(T_{90}) = \frac{R(T_{90})}{R(273.16\text{ K})} \quad (62.4)$$

more precise infrared analysis, [62.47] were the first to show and quantify the continuous increase of atmospheric CO₂ concentrations due to the impact of fossil fuel combustion, known as the Keeling curve. This encouraged studies on the processes and timescales governing CO₂ exchange between the atmosphere and the sea [62.48–50]. Likewise, investigations of anthropogenic and natural sources of N₂O and CH₄, mainly based on gas chromatography [62.51–54], confirmed the importance of aquatic systems as sources and sinks of these gases, e.g., [62.54–56].

The temperature in degrees Celsius is derived from the resistance ratio by

$$T_{90} [^{\circ}\text{C}] = D_0 + \sum_{i=1}^9 D_i \left[\frac{W(T_{90}) - 2.64}{1.64} \right]^i. \quad (62.5)$$

The constants D_0 – D_9 are given in [62.57]. Platinum resistance thermometers depict minimal aging effects and a high accuracy. Further details of the properties of platinum resistance thermometers are also given in Chap. 7.

Compared to platinum resistance thermometers, thermistors have the advantage of higher sensitivity, usually about a magnitude higher. However, their characteristic is highly nonlinear and depends on the specific doping of the semiconductor material. Their characteristic can be approximated with

$$R(T) = ae^{b/T}, \quad (62.6)$$

where a and b are material specific constants for the particular thermistor, T is the absolute temperature, and R is the resistance of the thermistor. The temperature characteristic of NTC thermistors can be described by the Steinhart–Hart equation [62.58]. For the typical temperature range of environmental observations, the simplified form of the equation can be used

$$T^{-1} = a_0 + a_1 \ln(R(T)) + a_3 \ln^3(R(T)). \quad (62.7)$$

The Steinhart–Hart coefficients a_0 , a_1 , and a_3 are device specific and are obtained with calibration measurements. The resistance of the thermal active elements is measured with bridge circuits.

Besides the direct measurement with in-situ sensors, the surface temperature can be obtained with remote-sensing techniques from airplanes and satellites. These radiometric methods use a wide spectral range from infrared to microwave radiation. A general overview on temperature measurement methods is given in [62.59].

62.3.2 Surface Salinity

The current definition of salinity of seawater is given by the International Thermodynamic Equation of Seawater – 2010 (TEOS-10) [62.28] (Chap. 5). TEOS-10 defines the properties of seawater as partial derivations of a thermodynamic potential, the so-called Gibbs function. The specific Gibbs function for pure water and its extension for seawater were derived empirically from high precision measurements. TEOS-10 replaces the former Practical Salinity Scale PSS-78 [62.27]. The Practical Salinity (S_p) of seawater is derived from measurements of electrical conductivity. Since it depends also on temperature and pressure, the calculation of S_p also requires an accurate measurement of these parameters. The pressure is given as *sea pressure*, which is the absolute pressure reduced by the standard atmosphere pressure at the sea surface (1013.25 hPa).

PSS-78 defined the S_p as a ratio K_{15} of the conductivity of a seawater sample and the conductivity of a standard potassium chloride solution at temperature of 15 °C and pressure of 101.325 kPa. The mass fraction of the KCl standard solution is 32.4356×10^{-3} . By definition the S_p is 35 for a ratio $K_{15} = 1$. TEOS-10 defines a reference salinity S_R , which is the mass fraction of salt in a seawater sample with a standard composition of salt, given by [62.60]. In contrast to the unitless practical salinity, the reference salinity is given in g kg^{-1} . The conversion from S_p to S_R is given by

$$S_R [\text{g kg}^{-1}] = \left(\frac{35.165047}{35} \right) S_p. \quad (62.8)$$

However, the real sea-salt composition depicts local and regional deviations from the reference composition of standard seawater. Variations in the silicate concentration are the main contribution to this anomaly. In most practical cases, the deviations from the standard composition can be neglected but must be considered if accurate density is required. TEOS-10 provides a global dataset of the salinity anomaly δS_A , derived from available observations. The absolute salinity S_A can be calculated from the reference salinity S_R using the salinity anomaly

$$S_A = S_R + \delta S_A(\varphi, \lambda, p), \quad (62.9)$$

where φ , λ , and p are the latitude, longitude, and sea pressure, respectively. In TEOS-10, the density is defined as a function of sea pressure, temperature, and the absolute salinity. Since most observations use conductivity measurements and reveal the practical salinity, the calculation of density requires the conversion to absolute salinity.

62.3.3 Surface Waves

The wave field at a certain location consists of the swell, which are long waves generated far away, and the wind waves forced by local wind. The most important wave properties that have a significant impact on air sea fluxes are the significant wave height, the mean wave period, and the peak period. The significant wave height H_S is the mean vertical distance between the wave crest and the wave trough of the highest third of all waves. Today, it is also defined as four times the standard deviation of the surface elevation η . For a particular period (t_0 – t_1) H_S can be calculated as

$$H_S = 4 \sqrt{\frac{\int_{t_0}^{t_1} \eta(t)^2 dt}{t_1 - t_0}}. \quad (62.10)$$

The mean wave period T_m is derived from the nondirectional wave spectrum $S(f)$, where f is the wave frequency; T_m is the weighted average of the frequency spectrum

$$T_m = \frac{\int S(f) df}{\int f S(f) df}. \quad (62.11)$$

The peak wave period T_{peak} is the wave period at the energy maximum of the wave spectrum $S(f)$. Together with the significant wave height, the mean wave period and the peak wave period define the sea state. The larger the mean wave period for a given significant wave height, the more energy the wave field contains. A comprehensive theory on wind waves is given in [62.61].

62.3.4 Currents

Today, in-situ current measurements are carried out mainly with acoustic current meters, since they have important advantages for measurements in the marine environment (Table 62.4). Water is much more transparent for sound than for visible light, although the sound attenuation coefficient depends highly on the frequency used and the concentration of some constituents of sea salt, namely magnesium sulfate, borate, and magnesium carbonate [62.62, 63]. Generally, the sound attenuation coefficient is proportional to the square of the sound frequency. Thus, in sea water low-frequency sound has a higher range than high-frequency sound. In contrast to electromagnetic waves, sound waves are longitudinal waves that need a compressible medium for propagation. If the medium is moving, the sound waves are shifted with it. The most acoustic current meters use the frequency range between 38 kHz and 5 MHz.

The simplest method that uses sound for current measurements utilizes the change of travel time along

a defined pathway between a fixed transmitter and a receiver. The theoretical travel time is given by the distance divided through the speed of sound. Deviations from the theoretical travel time can be attributed to the movement of the water between the transmitter and the receiver. The current component along the acoustic beam v_b can be calculated from the distance L between transmitter and receiver, the measured travel time t , and the sound velocity of the water v_s

$$v_b = \frac{L}{t} - v_s. \quad (62.12)$$

The sound velocity depends on the density of sea water, which is not easy to measure. If the travel time along the measuring section is measured in both directions, the velocity v_b can be calculated without information about the sound velocity

$$v_b = \frac{L(t_1 - t_2)}{2t_1 t_2}. \quad (62.13)$$

Also the Doppler effect can be used for measuring current speed. If a sound transmitter and a receiver depict a relative velocity to each other, a frequency shift of the transmitted sound is observed. For nonrelativistic velocities, the frequency shift Δf is proportional to the velocity component v_b along the direction of sound propagation

$$\Delta f = f_s \frac{v_b}{v_s}, \quad (62.14)$$

where f_s is the frequency of the transmitted sound. By measuring the frequency shift and knowing the sound velocity (v_s) in water, the velocity component v_b can be calculated. To measure the current velocity either the transmitter or the receiver must be fixed, whereas the other device moves passively with the mean current. This is not appropriate for most applications.

For practical reasons, the sound transmitter and the receiver are combined in a single device. The sound transmitted as a focused beam is scattered in the water at small particles that move passively with the current. The backscattered sound is used to estimate the current velocity. In that case, the frequency shift is doubled, since the sound waves travel the same path twice. The current component v_b along the sound beam can be calculated from the frequency shift as

$$v_b = \frac{\Delta f v_s}{2f_s}. \quad (62.15)$$

The strength of the backscattered signal depends on the abundance and the acoustic properties of the scatter particles in the water, which are mainly zooplankton but also suspended matter.

A third method that is widely used is the detection of the phase shift of two subsequently transmitted pulses of sound that are backscattered at particles to the receiver. The travel time t_p of two pulses transmitted with a time delay of Δt_{trans} differs if the backscattering target is moving, since the distance between the transmitter and the backscatter target changes between the arrivals of the two pulses. The difference of the travel time Δt_p is proportional to the current component v_b .

$$t_{p1} - t_{p2} = \Delta t_p = \frac{2v_b \Delta t_{\text{trans}}}{v_s} \quad (62.16)$$

Δt_p is not detected directly. Instead, the phase shift between the transmitted pulses is determined. This can be done with high accuracy. However, if the phase shift exceeds 2π , the estimation of the current velocity becomes ambiguous. The maximum velocity v_{b_max} that can be distinctly measured with that method depends on the sound frequency f_s and the time delay Δt_{trans} between pulse transmission

$$v_{b_max} = \frac{v_s}{2f_s \Delta t_{\text{trans}}}. \quad (62.17)$$

To overcome the ambiguity problem the transmitted pulses are modulated to detect phase shifts larger than 2π [62.38].

Most acoustic methods require the knowledge of the actual sound velocity along the pathway of the signal. At oceanic conditions the sound speed of water varies in the upper layer approximately between 1450 and 1550 m s^{-1} . If the actual sound speed is unknown, a constant value of 1500 m s^{-1} can be applied. That results in an uncertainty of 3.5%, which is acceptable for most applications.

Measuring the current velocity along an acoustic beam will only reveal the current component along the beam. To obtain the three-dimensional current vector three and more acoustic beams that point in different space directions are used. From the current components obtained, the true current vector is calculated. If moving platforms, e.g., vessels, autonomous underwater vehicles (AUVs) or gliders, are used the motion of the platform has to be considered additionally.

62.3.5 Dissolved Greenhouse Gases

The solubility of a gas in water depends on the physical and chemical properties of the gas and the water, such as temperature, pressure, and the presence of other chemicals. *William Henry* (1774–1836) was an English chemist who studied the solubility of gases in the

early nineteenth century. He found that at constant temperature the amount of dissolved gas in a solvent is proportional to the partial pressure of the gas phase in equilibrium with the solvent [62.64]. The solubility of gases in liquids according to Henry's law reads as follows

$$c_{\text{gas}} = H p_{\text{atm}} x_{\text{gas}}, \quad (62.18)$$

where c_{gas} is the dissolved gas concentration, H is Henry's law constant, p_{atm} is the atmospheric pressure during equilibration, and x_{gas} is the dry mole fraction of the respective gas in the gas phase. Modifications have been applied, which mainly account for the impact of salinity and temperature on the solubility of the gas and the nonideal behavior of the gas [62.65–67] (Sect. 62.3.5). In addition, some gases like CH_4 and N_2O simply dissolve in water, whereas CO_2 also reacts with water and forms aqueous CO_2 ($\text{CO}_{2\text{aqu}}$) and carbonic acid (H_2CO_3), summarized as H_2CO_3^* , which dissociates to bicarbonate (HCO_3^-) and carbonate (CO_3^{2-}) ions. The sum of all these species is referred to as dissolved inorganic carbon (DIC). This reaction is the fundamental basis for the high inventory of DIC in the oceans. It is the reason why the oceans play an important role in modulating atmospheric CO_2 concentrations both on shorter time scales but also on glacial-interglacial time scales [62.68–73].

Extraction

The basic principle of dissolved gas analysis involves the extraction of the dissolved gas from the aqueous phase and the analysis of the gas sample by means of gas chromatography or laser absorption spectrometry. Extraction techniques include headspace equilibration, adsorbing the gas onto a sorbent, freeze and trap, or purge and trap methods. Headspace equilibration is widely used for continuous measurements used to derive trace gas fluxes between the surface water and the atmosphere. Since the focus of this book is on atmospheric processes, the emphasis of this chapter is on continuous measurements using headspace equilibration.

For continuous measurements, e.g., on board ships, equilibrators are used to convert a liquid phase sample into a gas phase sample. In general, a fixed volume (closed loop) of air passes through and equilibrates with a continuous stream of surface water, which is continuously renewed. The mole fraction of the respective gas (x_{gas}) in air equilibrated with the surface water is then measured. A variety of different equilibrator types have been developed, such as shower or spray-

type, e.g., [62.74–77], bubble-type, e.g., [62.78–80], marble-type [62.81], and Raschig rings-type [62.82]. The recently evolving membrane equilibration techniques, e.g., [62.83–85] allow in-situ extraction of dissolved gases and are, thus, mainly used for vertical profiling of dissolved gases in the water column. However, the aim of these diverse equilibrator designs is to achieve an optimal response time (τ). The response time τ is a measure of how fast the equilibrator setup responds to changes in gas concentrations of the water phase. The response time τ is usually defined as the time (t) it takes until an exponential drop of $1/e$ (36.78%) can be observed for Δp_{gas} , i.e., for the difference between the gas concentration in the gaseous and aqueous phase with respect to its initial value p_{gas}^0

$$\Delta p_{\text{gas}} = p_{\text{gas}}^0 e^{(-t/\tau)}. \quad (62.19)$$

τ has to be determined experimentally because it does not only depend on the gas species and equilibrator setup but also on flow rates in the system, e.g., [62.86, 87]. To determine τ experimentally two batches of water with known p_{gas} , usually one ambient (equilibrated with atmosphere) and one with a high p_{gas} , are prepared. The equilibrator is then flushed first with the ambient p_{gas} batch, followed by the high p_{gas} batch and then ambient p_{gas} batch again. Each time, the change in p_{gas} in the headspace versus time is measured until equilibrium is reached. For guidance on the derivation of τ from the experimental data, the reader is referred to, e.g., [62.80, 86, 87]. Reported τ ranges are ≈ 230 s for CO_2 [62.74, 78, 81, 87, 88], ≈ 680 s for CH_4 [62.87, 89], and ≈ 180 s for N_2O [62.77, 86] implying that *full* equilibration is usually observed after ≈ 6 – 12 min for CO_2 , after ≈ 35 min for CH_4 and after ≈ 9 min for N_2O . Different τ observed for same gases are mainly a result of differences in the equilibration chamber design and the water flow. Different τ between gas species can be explained by their differences in solubility and the extent of disequilibrium between the surface layer and the atmosphere [62.87]. In consequence, equilibrator-based underway measurements (e.g., on board a ship) in regions with a high variability of dissolved trace gas concentrations, will likely not reflect full equilibrium conditions but will represent integrated values. Additionally, they will lag in time, depending on the speed of the vessel. Thus, it is recommended to take discrete water samples on a regular basis from the same water supplying the equilibrator (e.g., from a bypass), to confirm the integrity of the underway results or to correct them if necessary. However, it needs to be noted that, depending on the overall dissolved greenhouse gas variability in surface water and

the speed of the vessel, discrete samples will be affected by a time lag as well. That means that, e.g., discrete triplicates will not be directly comparable to each other.

Calculations

Extraction of the dissolved gas by an equilibrator yields the mole fraction of the respective trace gas (x_{gas}) in the headspace, which is equilibrated with the surface water. The equilibrated headspace air within the equilibration chamber can be assumed to have a humidity of 100%. To reduce the interference of this water vapor in the spectroscopic measurements of a given gas (due to altered partial pressure and band-broadening effects), usually the sample gas stream is dried. Remaining traces of water vapor in the sample gas stream can be detected by most current analyzers and corrected for by the analyzer's internal software. In principle, to calculate the partial pressure of the given gas (p_{gas}) from its mole fraction in dry air (x_{gas}), a correction has to be applied that accounts for the water vapor pressure

$$p_{\text{gas}} = x_{\text{gas}} (p_{\text{atm}} - p_{\text{H}_2\text{O}}) , \quad (62.20)$$

where p_{atm} is the absolute atmospheric pressure, and the $p_{\text{H}_2\text{O}}$ is saturation vapor pressure of water in equilibrium with the atmosphere.

The $p_{\text{H}_2\text{O}}$ from seawater measurements is a function of temperature (T) and salinity (S) and is calculated from [62.66]

$$\ln(p_{\text{H}_2\text{O}}) = 24.4543 - \frac{67.4509 \cdot 100}{T} - 4.8489 \ln\left(\frac{T}{100}\right) - 0.000544S . \quad (62.21)$$

For $p_{\text{H}_2\text{O}}$ from freshwater measurements, the reader is referred to the calculation of E_w discussed in Chap. 8. The isochemical dependence of p_{CO_2} on temperature is about $15 \times 10^{-6} \text{ atm K}^{-1}$, and, thus, accurate measurements of temperature of the seawater in the equilibrator are vital. To account for temperature differences between the in-situ water temperature (T_{insitu}) and the equilibrator water temperature (T_{equ}) the following correction is applied for CO_2

$$p_{\text{CO}_2} = p_{\text{CO}_2 \text{ equ}} \exp[0.0423 (T_{\text{insitu}} - T_{\text{equ}})] , \quad (62.22)$$

using the temperature coefficient 0.0423 K^{-1} determined by [62.90]. The impact of temperature differ-

ences on p_{CH_4} and $p_{\text{N}_2\text{O}}$ is less pronounced. They are calculated as follows

$$p_{\text{CH}_4, \text{N}_2\text{O}} = \frac{s_{T_{\text{equ}}}}{s_{T_{\text{insitu}}}} p_{\text{CH}_4, \text{N}_2\text{O equ}} , \quad (62.23)$$

where $s_{T_{\text{equ}}}$ and $s_{T_{\text{insitu}}}$ are the solubility coefficients ($\text{mol L}^{-1} \text{ atm}^{-1}$) for CH_4 and for N_2O , which can be calculated following [62.66, 91] using T_{insitu} and T_{equ} (both in K). After having applied these corrections, the concentration of the respective trace gas in seawater, (c_{gas}) can then be calculated following Henry's law

$$c_{\text{gas}} = s_{\text{gas}} p_{\text{gas}} , \quad (62.24)$$

where s_{gas} ($\text{mol L}^{-1} \text{ atm}^{-1}$) is the solubility coefficient of the respective gas [62.65, 66, 91], and p_{gas} (atm) is the partial pressure of the respective gas in the headspace equilibrated with seawater.

The gas flux (F_{gas}) across the air–water interface ($\text{mol m}^{-2} \text{ s}^{-1}$) is calculated by

$$F_{\text{gas}} = k(C_{\text{gas}_w} - \lambda C_{\text{gas}_a}) , \quad (62.25)$$

where k is the gas transfer velocity (m s^{-1}), C_{gas_w} and C_{gas_a} are the concentrations of the gas in water and air, respectively (mol m^{-3}) and λ is the dimensionless Ostwald solubility coefficient. Among other factors, k depends strongly on wind speed, i.e., the hydrodynamics of turbulent and molecular processes within the surface layer. For the determination and calculation of k , the reader is referred to specialized literature, e.g., [62.92–95].

For precise calculations of CO_2 air-sea fluxes, the fugacity of CO_2 , f_{CO_2} should be used, which accounts for the nonideal behavior of CO_2

$$F_{\text{CO}_2} = k (f_{\text{CO}_2_w} - \lambda f_{\text{CO}_2_a}) , \quad (62.26)$$

where the term in brackets is the concentration gradient between the sea surface, $f_{\text{CO}_2_w}$, and the atmosphere, $f_{\text{CO}_2_a}$. The f_{CO_2} is derived according to

$$f_{\text{CO}_2} = p_{\text{CO}_2} e^{p(B+\delta)/(RT)} , \quad (62.27)$$

where B is the first virial coefficient, δ is the cross virial coefficient (both in $\text{m}^3 \text{ mol}^{-1}$), and R is the gas constant ($R = 8.314 \text{ J K}^{-1} \text{ mol}^{-1}$). For further details on the calculation of the virial constants, the reader is referred to [62.65].

62.4 Devices and Systems

There exist a large number of sensors and devices that have been developed for marine applications. One can distinguish two main groups. There are sensors and devices that need an external control and power supply, and devices that combine one or more sensors with an internal data logger and power supply for autonomous deployments. Most in-situ sensors and devices consist of a pressure housing that protects the electronics from the high sea pressure, which can amount up to 1100 bar in the case of deep-sea deployments. Different materials are used for pressure housings, depending on their intended depth range. For upper-ocean deployments with depths up to 500 m, plastic housings are common. For depths greater than 500 m, mainly stainless steel or titanium housings are used. Due to the large number of sensors and devices available this chapter cannot provide a comprehensive compilation. Instead, the most important sensors and devices for field observations of sea surface properties are described briefly. For more detailed information, the reader is referred to the cited literature.

62.4.1 Temperature Sensors

Today, mainly two types of temperature sensors are applied for observations of water temperature: platinum resistance thermometers and thermistors.

Platinum Thermometers

Platinum resistance thermometers are used in applications where a high accuracy and long-term stability of the measurement is required. There exist standard sensors PT25, PT100, and PT1000 with an electrical resistance at 0 °C of 25, 100, and 1000 Ω , respectively. The most common in commercial devices for marine applications is the PT100. To measure the resistance a known constant current flows through the sensor. It causes a moderate self-heating of the sensor due to the power loss in the resistor. This effect is minimized by using low measuring currents in the order of 100 μ A and the mechanical design of the particular sensor. Due to the high heat capacity and heat conductivity of water the effect of self-heating on the temperature measurement is lower than in other environments. Sensors that use platinum wires must be designed in such a way that the platinum wire is able to contract and expand with changing temperature without significant strain and deformation. This makes them susceptible to mechanical shocks and vibration. To overcome this problems film sensors have been developed in recent times. These sensors consist of a thin platinum film on a suitable

substrate. Their resistance is often trimmed with laser techniques to the desired value. Compared to sensors with platinum wires, film sensors are much more robust and depict a lower response time. Since film sensors require less effort in the production process, they are often cheaper than wire sensors.

Thermistors

The second important type of temperature sensors, thermistors, are also widely used in oceanographic applications. The higher sensitivity compared to platinum resistance sensors allows highly accurate temperature observations with low response times of the sensors. Thus, thermistors are applied in conditions with high temperature variability, e.g., for profiling measurements and turbulence measurements. However, the long-term stability of thermistors is significantly lower than that of platinum resistance sensors. To overcome this disadvantage many manufactures use only artificially aged thermistors, which depict a low temporal drift. The response times of thermistor temperature sensors depend on the particular type and range between 150 and 10 ms. The absolute precision of the sensor is reciprocal to its response time.

62.4.2 Conductivity Sensors

To calculate salinity in-situ measurements of seawater conductivity are performed. Concurrently, also temperature and pressure have to be measured, since the conductivity of an electrolyte like seawater also depends on these quantities. Today, two different types of sensors are used to measure conductivity: conductivity cells and inductive sensors.

Conductivity Cells

The standard method to measure conductivity is the direct measurement of the electrical resistance between two electrodes that are in direct contact with seawater. Usually, glass tubes with annular electrodes are used. Due to current flow, reactions with the electrolyte occur at the electrodes, resulting in a counter voltage. This effect is called polarization and produces a systematic bias. To minimize this effect, high-frequency alternating current is used to measure the conductivity. The measurement is performed by two additional electrodes located within the linear range of the voltage drop between the two outer electrodes (Fig. 62.2).

Conductivity cells are susceptible to impurities, air bubbles, and biofouling. Thus, for long-term deployment, the use of copper inlets or toxic coatings is

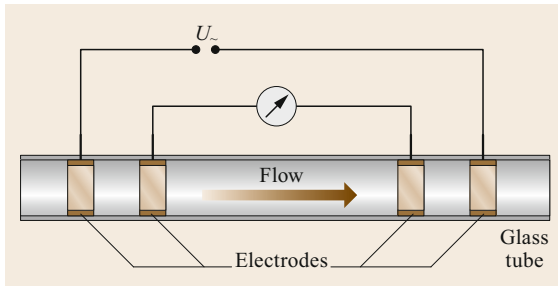


Fig. 62.2 A four-electrode conductivity cell

customary. The response time of a conductivity cell depends mainly on the flushing rate of the cell, which depends on the cell geometry and on the flow field around the sensor. For highly accurate measurements, the seawater is pumped actively with a constant flow rate through the cell. The response time can then be derived from the cell volume and the flow rate. However, sensors for autonomous long-term deployments operate without a pump to minimize power consumption.

Inductive Conductivity Sensors

Inductive conductivity sensors consist of two electrical coils arranged around a tube, which is filled with seawater (Fig. 62.3). An alternating current is applied in the primary coil which generates an alternating magnetic field. A current is induced in the tube and in the surrounding medium. In turn, the current generates a magnetic field, which induces a voltage in the secondary coil of the sensor. The measured current in the secondary coil is a measure for the conductivity of the seawater in the tube.

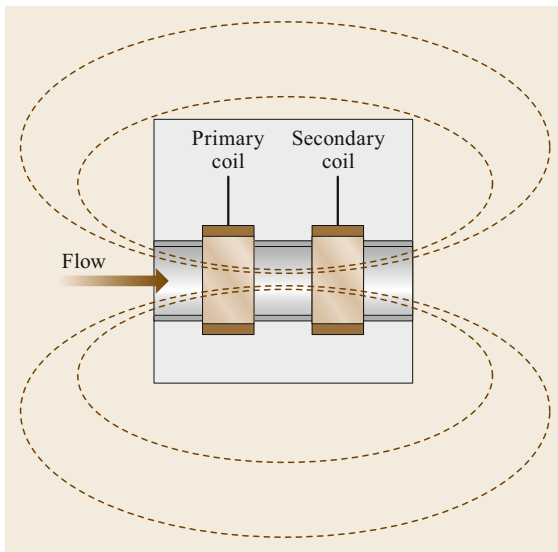


Fig. 62.3 Sketch of an inductive conductivity cell

The main advantage of inductive conductivity cells is their robustness against biofouling and high loads of suspended matter. They can be easily cleaned, since no electrodes are in direct contact with the seawater. However, a significant part of the measured signal is influenced by the external field of the sensor. The sensor output can be biased if the conductivity in the surrounding water differs significantly from the conductivity of the water inside the cell. This can occur due to small-scale fluctuations in temperature and salinity but also due to adjacent objects, e.g., other sensors, devices, or cables. Thus, the calibration of the sensor has to be done in the particular configuration of the intended deployment. The inductive sensors are not usable in pumped systems because of the high impact of the tube system and the pump on the external field. Inductive sensors are mainly used in autonomous long-term deployments where their robustness against biofouling is important.

62.4.3 The CTD Probe

The conductivity-temperature-depth (CTD) probe is the standard instrument for shipborne in-situ observations of hydrographic parameters. Usually, it combines several sensors with a water sampling system that enables the collection of water samples from selected depths (Fig. 62.4). However, also systems without water samplers are used. Depending on the particular application, a CTD probe can be operated with external or internal power supply and data acquisition. A CTD probe consists at least of temperature, conductivity, and pressure sensors, but today also oxygen concentration, fluorescence, and turbidity sensors are standard sensors on CTD probes. In recent decades, the US company SeaBird Electronics has set the standard regarding accuracy and reliability of CTD probes. Around 1990, SeaBird Electronics invented a pumped CTD system where sensors are arranged subsequently in a tube system to assure that all mounted sensors measure the same water parcel. The temporal delay due to the travel time of the water in the tube is corrected in the postprocessing of the data. This approach could suppress the effect of salinity spiking that occurs during profiling in stratified waters, due to the different response times and flushing rates of the temperature and conductivity sensors in open CTD systems.

CTD probes have been adapted to many different platforms and observation strategies. Besides the standard vertical profiling mode, CTDs are used in undulating towed systems, gliders, free-falling underway systems, moored platforms, and many more.

As an example, the special case of a microstructure profiler is briefly described. Mixing is a key parameter for the state of the ocean. Thus, advanced CTDs

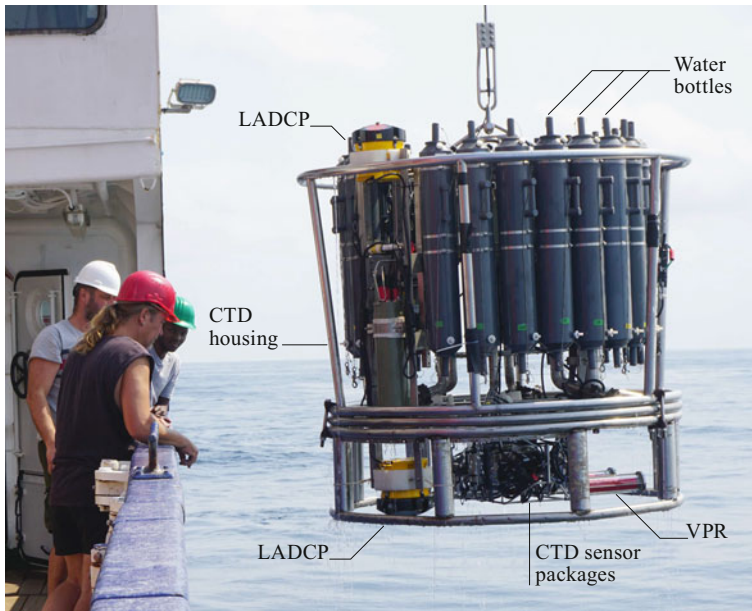


Fig. 62.4 Deployment of a CTD probe on board the research vessel (RV) Meteor. The instrument consisted of the CTD probe with a rosette water sampler, a current meter system (LADCP—lowered acoustic Doppler current profiler), and a video plankton recorder (VPR), mounted in a stainless steel frame (photo © V. Mohrholz)

have been developed that measure temperature, conductivity, and current shear on the scale of turbulence with a spatial resolution of 0.01 m. This requires fast response times of the sensors and a profiling mode that do not disturb the fine structure to be measured. The main difference of a microstructure probe from the standard CTD is the higher sampling rate of up to 1024 Hz and the special streamlined design, which should prevent a tilt and any vibrations during profiling (Fig. 62.5). Microstructure profilers are mainly used in free-falling mode, without tension in the measuring cable. The vertical profiling velocity is controlled by the buoyancy of the instrument, usually about 0.5 m s^{-1} . With a sampling rate of 1024 Hz, the nominal vertical resolution is 0.5 mm. However, the real resolution is determined by the particular sensor size and its specific response time.

62.4.4 Wave-Rider Buoy

Surface waves can be measured with a number of methods. The most common application to obtain information on the wavefield parameters is the wave-rider buoy. The instruments obtain a directional wave spectrum and all important wave parameters. Wave-rider buoys are buoyancy floats that are fixed with an anchor at the sea bottom. The buoyancy float sits at the sea surface and follows its wave-induced displacements. Inside the float, a set of sensors detect the movement of the buoy. The data are processed and stored in a data logger, and/or transmitted online via radio or satellite communication. The movement of the buoy can be detected by accelerometers, motion reference units (MRU) [62.96], and GPS Doppler shift sensors [62.97].

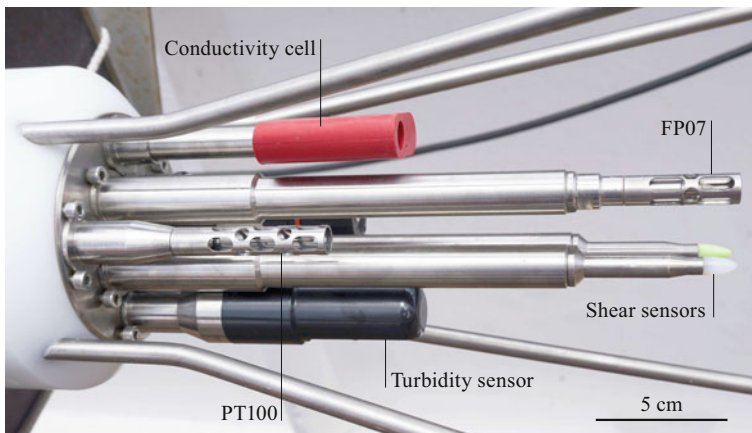


Fig. 62.5 Sensor head of a microstructure probe. The device is equipped with a full set of CTD sensors, pressure, conductivity cell, PT100 temperature sensor, oxygen sensor, and turbidity sensor. Additionally, to measure the microstructure, two shear sensors and a fast FP07 temperature sensor have been mounted (photo © V. Mohrholz)

A comparison between the latter two methods is given in [62.98].

62.4.5 Current Meters

Two major types of current meters for marine applications are available: single-point current meters that measure the 2-D or 3-D current vector as a time series at a single point, and current profilers that obtain time series of 1-D profiles of the 2-D or 3-D current vector from remote backscatter signals of transmitted sound pulses.

Single-Point Current Meters

Although current profilers are the standard instrument for current measurements, single-point current meters are still in use. There are mechanical and acoustic single-point current meters. Mechanical current meters consist of a propeller (or rotor) and, optionally, a wing that aligns the propeller in the current direction. The current speed is obtained by counting the rotations per time unit. The current direction is measured by a compass. This type of current meter gathers only 2-D horizontal current components. Today, mechanical current meters have been replaced almost completely by acoustic devices. Mechanical current meters are still used only in some special applications, e.g., for discharge measurements.

Acoustic single-point current meters split up into 2-D and 3-D devices. An example for a 2-D single point current meter is RCM Blue from Aanderaa Data Instruments AS [62.99]. The device uses four acoustic beams, two each in x and y directions, which radiate in opposite directions. The horizontal current components are derived from the beam velocities and the compass information. The use of two beams for each horizontal

axis increases the accuracy and minimizes the impact of the instrument's own current field on the measurement. 3-D single point current meters operate with at least three beams forming a 3-D vector space, e.g., the AQUADOPP current meter from Nortek [62.100]. Acoustic single-point current meters usually work with high sound frequencies of 1 MHz or more and high sampling rates. Their range is up to 5 m. The gathered velocity data are an average value over the measurement volume, defined by the instrument's specific range and beam geometry. Sound transducers are also used as receivers of backscattered signals. The main advantages of single-point current meters are high accuracy and low power consumption, which make them particularly suitable for long-term deployments.

A special type of single-point current meter is the acoustic Doppler velocimeter (ADV), which is mainly used for small-scale and turbulence measurements [62.101]. In contrast to the instruments described above, where the acoustic beams diverge from the sensor head and span a relatively large sampling volume, ADV measures all three velocity components in a small volume of about 1 cm^3 . An ADV consists of a single sound transmitter and two to four separate sound receivers that measure the scattered sound from different directions (Fig. 62.6).

Profile Current Meters

In recent decades, profiling acoustic current meters have become the standard instrument for current measurements in natural waters. They are available in many different designs and configurations, depending on the intended application and the particular manufacturer. The principal design consists of three or more sound transducers that are combined in a transducer head, similar to the sketch in Fig. 62.6a.

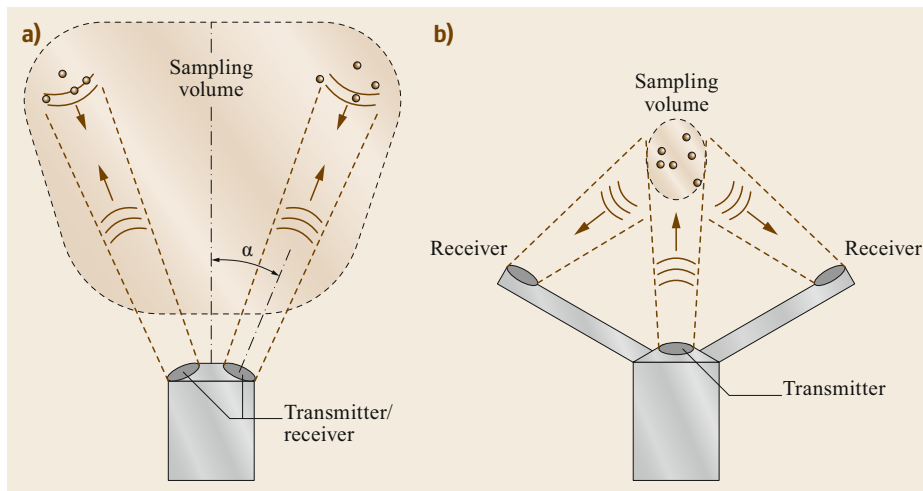


Fig. 62.6a,b

Acoustic beam geometry for an acoustic current meter with diverging beams (a), and an ADV (b). Only two beams are displayed. Usually the instruments consist of three or more acoustic beams, slanted from the vertical axis by the beam angle α

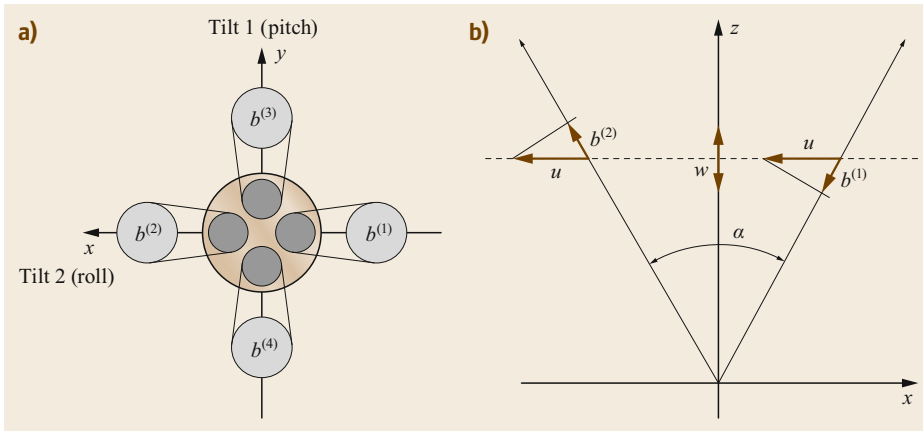


Fig. 62.7a,b Top view of a four-beam ADCP transducer head with acoustic beams (a). The horizontal velocity component u and the vertical velocity w can be calculated from the beam velocities $b^{(1)}$ and $b^{(2)}$ in the x - z plane (b) by simple trigonometric functions. A similar operation is applied to the y - z plane. The difference between the two estimates for the vertical velocity w is used as measure for the uncertainty of the measurement

For many years, the acoustic Doppler current profiler (ADCP) with a four-beam configuration (from Teledyne – RD Instruments) was the most used instrument. Other manufactures use different names for profiling acoustic current meters, like AD2CP (acoustic Doppler dual current profiler) or ADP (acoustic Doppler profiler). However, the main principle of operation is the same, and the acronym ADCP is used in this chapter as a synonym for all profiling acoustic current meters and not as a special brand.

ADCPs deliver a 1-D profile of the 3-D current vector. To measure a profile a sound pulse is transmitted into the water by each transducer. Then the transducer is switched into receive mode and records the backscattered signal for a certain period. The incoming signal is split into time windows of equal length, which are sorted to distances (depth cells) from the transducer head, according to the actual sound velocity and travel time of the sound pulse. From the velocities obtained along the particular beams, a 3-D current vector is calculated for each depth cell (Fig. 62.7). Since the four beams provide an overestimated system, also a measure for the uncertainty of the 3-D current vector can be derived. A detailed description of the principles of ADCP operation is given in [62.102].

The spatial resolution and the length of the current profile depend on the pulse length of the transmitted signal, the sound frequency used, and the abundance and properties of the backscattering particles in the water. There are some general rules. The lower the sound frequency, the larger the range of a profiler. An ADCP with a frequency of 38 kHz can reach ranges of about 1000 m and more. Its spatial resolution is between 16 and 32 m. This ADCP type is mainly used as a vessel-

mounted ADCP. Devices with very high frequencies of about 2 MHz have a range of only some meters and a spatial resolution of a few centimeters. These high-frequency devices are applied for turbulence measurements and observation of small-scale processes, e.g., in boundary layers. For a fixed frequency of sound, the accuracy of an ADCP depends on the selected size of the depth cells. The larger the depth cell, the higher the accuracy and, partly, the total range of the instrument. The accuracy increases also with the number of single-ping current estimates that are averaged. The uncertainty of the averaged velocity value decreases proportionally to the square root of the number of single pings. A precondition for reliable measurements is the availability of suitable scatter particles. Devices with lower sound frequency need larger particles, mainly zooplankton, for backscatter of the transmitted signal. However, the zooplankton distribution depends on the particular environmental conditions at the observation site. Thus, ADCP measurements sometimes fail due to the lack of scatter, e.g., in the winter season with low zooplankton abundance or in large oxygen minimum zones of tropical and subtropical oceans. Another important prerequisite for the calculation of an unbiased 3-D current vector from the beam velocities is the assumption of a homogeneous current field. Due to the diverging acoustic beams, the horizontal distance of the beams increases with increasing distance from the transducer. With a beam angle of 30° the horizontal distance between the beams is equal to the vertical distance from the transducer. For a depth cell that is 100 m off the transducer, the current field should be homogeneous over that distance. Turbulence and small-scale disturbances often violate this condition. However, this can

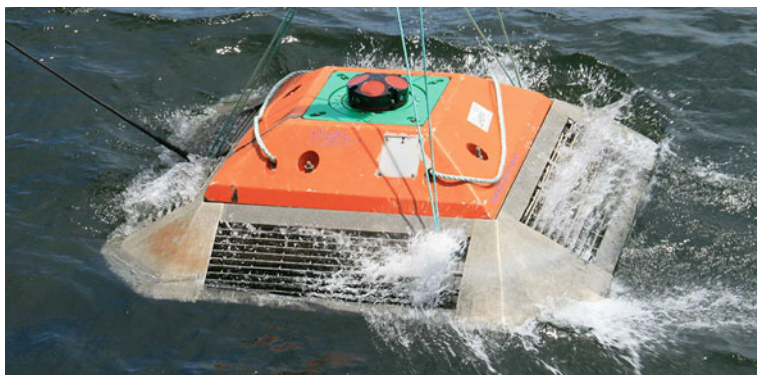


Fig. 62.8 A four-beam ADCP mounted in a trawl-resistant bottom frame during deployment for long-term observation (photo © V. Mohrholz)

be detected with the error estimate of a four-beam system.

Besides ADCPs with four-beam configuration, also instruments with three and five beams are available. Three-beam ADCPs provide a current profile but no uncertainty estimate for the current measurements. Five-beam devices are used to additionally detect the surface elevation for wave measurements. The fifth beam is also used to measure the vertical current component for turbulence measurements.

A special configuration is an ADCP with a phased array transducer head [62.103]. There the acoustic beam is sent out subsequently in four different directions from a single transducer head. The beam-forming and transmit direction is controlled by a large array of small transducers that are combined in a single sensor head. The advantage of these systems is the smaller size, which is important for devices with low sound frequencies. However, due to the subsequent transmission of the four beams, the sampling frequency is lower than that of devices with four fixed transducers.

Profiling current meters are mainly used to obtain vertical current profiles. They are mounted on a wide range of different platforms, which are moorings, vessels, drifters, AUVs, and many more. For measurements in shallow water, so-called horizontal ADCPs (HADCP) have been developed. They provide a 1-D horizontal profile of the 2-D horizontal current vector and are used to obtain current data in harbors and channels, as well as discharge measurements in rivers [62.104].

62.4.6 Dissolved Long-Lived Greenhouse Gases

Recommendations for the setup of underway $p\text{CO}_2$ measurements have been developed to assure uniform data quality and comparability [62.75, 105]. To the best of our knowledge, no specific recommendations are available for underway CH_4 or N_2O measurements to date, but the Scientific Committee on Oceanic Re-

search (SCOR) Working Group 143 is in the process of developing standard operation procedures for these gases [62.106].

Different setups for surface seawater underway measurements exist, but the fundamental principle is the same, i.e., an underway system usually consists of a *wet unit*, a *dry unit*, and a *deck unit* [62.75, Fig. 1]. The *wet unit* includes the water circulation system, i.e., the equilibrator, water flow meter, and valves controlling the water flow. The electronic parts, i.e., the analyzer, the valves, the power supplies, etc., are part of the dry unit. The deck unit holds the GPS receiver, the pressure transducer, and the iridium satellite modem allowing data transmission.

Seawater is pumped from the ship's bow pump, passing a water filter and then flowing into the equilibrator, which is commonly a shower, spray, or bubble-type equilibrator (Sect. 62.3.5). A bypass chamber fitted with a valve is used for discrete water sampling. The headspace gas equilibrated with the seawater is then dried by passing a condenser, and a Nafion® tube enters the analyzer and is redirected to the equilibrator, thereby forming a closed loop. The equilibrator, analyzer, the condenser, and the deck box are fitted with high-precision temperature sensors and pressure sensors (except for the condenser). A vent maintains ambient pressure inside the equilibrator. A secondary, smaller equilibrator is often used and connected to the main equilibrator by another vent to compensate for any gas loss from the main equilibrator headspace. Flow meters measure the combined flow through both equilibrators: the sample gas flow at the outlet of the analyzer and at the vent that connects the two equilibrators.

For CO_2 analysis, closed-path nondispersive infrared (IR) analyzers have been widely used (e.g., LI-7000; Chap. 8, Fig. 8.25). Conventional methods for the determination of N_2O and CH_4 are mainly based on gas chromatography (following headspace equilibration) coupled to an electron capture detector (GC-ECD) or mass spectrometer (GC-MS), e.g., [62.52, 107, 108]. The recent development and implementa-

Table 62.4 Advantages and disadvantages of the different methods

Devices	Advantages	Disadvantages
Platinum resistance temperature sensors	High accuracy High long-term stability Linear signal characteristic	Larger response time
Thermistor temperature sensors	High sensitivity High accuracy Fast response time	Larger temporal drift Aging effects Highly nonlinear signal characteristic
Conductivity cells	High accuracy Fast response time	Problems with biofouling at longer deployments Low mechanical robustness
Inductive conductivity sensors	High tolerance against bio fouling High mechanical robustness Fast response time	Limited accuracy Not applicable in pumped CTD systems
Wave-rider buoys	High accuracy Directional wave spectra	High maintenance effort
Mechanical single-point current meters	Easy to handle Low power consumption	Limited accuracy Measures only the horizontal velocity Susceptible to contamination
Acoustic single-point current meters	High accuracy Low power consumption	Only single-point measurements
Acoustic Doppler velocimeters	High accuracy High sampling rate	Only single-point measurements
Three-beam acoustic current profilers	Profile measurements	No error estimation possible
Four-beam acoustic current profilers	Profile measurements Error estimation possible	Higher power consumption
Five-beam acoustic current profilers	Profile measurements Error estimation possible Additional wave data	Higher power consumption Complex data processing
Absorption spectroscopy	Low maintenance effort, Cost effective	Analytes are limited
GC-MS and GC-ECD	Highly sensitive	High maintenance effort, labor intensive, costly

tion of near-infrared laser absorption spectroscopy, such as cavity ring-down spectroscopy (CRDS), enhanced integrated cavity output spectroscopy (ICOS), and off-axis integrated cavity output spectroscopy (OA-ICOS) (Chap. 28) provides sensitive, low-maintenance, and cost-effective methods for the measurement of a number of climate-relevant trace gases, including CO₂, N₂O, and CH₄ along with their isotopic signatures. Fourier-transform infrared (FTIR) trace gas analyzers are used for trace gas and isotope measurements as well. Crucially, these methods have enabled scientists to significantly enlarge the spatial and temporal coverage of dissolved greenhouse gas concentrations in surface wa-

ter and associated fluxes across the air–water interface and are increasingly being used for continuous measurements [62.77, 86, 87, 109–112].

62.4.7 Comparison of Methods

In this chapter, only a limited selection of the most important methods for surface water properties is presented. Thus, it is not intended to provide a comprehensive comparison of all available methods for water measurements. Instead, Table 62.4 summarizes the main advantages and disadvantages of the methods described in the previous sections.

62.5 Specifications

Typical values for the range, uncertainty, and response time of temperature, conductivity, and current velocity sensors are given in Table 62.5. The specifications are valid for the most common in-situ sensors. For calibration purposes, special reference instruments with a lower uncertainty are used. The velocity range of

acoustic current meters depends on the frequency of sound used and the principle of operation employed, but instruments for the entire range between 0 and 10 m s⁻¹ exist. However, this requires controlled laboratory conditions. The equilibrator specifications for trace gas measurements are given in Table 62.6.

Table 62.5 Specifications of typical sensors for in-situ measurements of temperature, conductivity wave parameters, and currents

Sensor/Device	Method/active element	Parameter	Range	Typical uncertainty	Response time
PT100	Platinum resistance	Temperature	−2 to 40 °C	≤ 0.003 K	0.15 s
NTC	Thermistor	Temperature	−5 to 40 °C	≤ 0.003 K	0.06 s
NTC FP07	Thermistor	Temperature microstructure	−2 to 40 °C	≤ 0.02 K	0.01 s
Conductivity cell	7-pole cell	Conductivity	0–65 mS cm ^{−1}	0.006 mS cm ^{−1}	0.1 s
Inductive conductivity sensor	Coupled inductive coils	Conductivity	0–65 mS cm ^{−1}	0.01 mS cm ^{−1}	> 0.2 s
Mechanical current meter		Current velocity and direction	0–10 m s ^{−1}	≤ 3%	–
Acoustic current meters	Acoustic Doppler effect and/of phase shift	3-D current vector	0–10 m s ^{−1}	≤ 1%	–

Gas species	Response time (min)	Error (%)	Equilibrator type	Reference
CO ₂	6.1	< 0.2	Shower head	[62.74]
CO ₂	3.8		Bubble	[62.87]
CO ₂	0.7		Column	[62.81]
CH ₄	158.3	≈ 2	Shower head	[62.74]
CH ₄	11.3		Bubble	[62.87]
N ₂ O	6.4	< 0.2	Shower head	[62.74]
N ₂ O	2.4		Shower head	[62.77]
N ₂ O	2.4	< 0.7	Bubble	[62.86]

Table 62.6 Response times and errors (if available) for different equilibrator types and gas species. Equilibrators are usually custom made, i.e., no off-the-shelf-products. Thus, please note that the response times are not directly comparable due to the different designs of the equilibration chamber, as well as background settings, such as the water flow rate. For further information, the reader is referred to the referenced publication ◀

62.6 Quality Control

The particular measurement systems used in water measurements require different strategies to ensure high data quality. Generally, two steps of quality control are performed. Before any sensor deployment most sensors have to be calibrated in the laboratory to correct the sensors for temporal drifts due to aging effects. The interval of calibration differs for the particular sensors. Secondly, during the deployment of the sensors comparison measurements are carried out with independent methods to ensure the data quality and to discover sensor failures.

62.6.1 Sensor Calibration

Temperature and conductivity sensors are usually calibrated in the laboratory at least once a year. Platinum resistance reference thermometers are used to calibrate the temperature sensors at some reference points distributed over the full range of the sensor, usually every 5 K between 0 and 35 °C. The calibration of conductivity is performed with high precision conductivity cells [62.113] and so-called standard seawater that has a reference composition of sea salt [62.60]. Since the conductivity is highly temperature dependent, also the temperature must be measured with high precision.

Current meters are calibrated by the manufacturer before delivery. They can be calibrated in flow chan-

nels, but this requires a high effort and causes high costs. Thus, current meters are usually not calibrated again during their lifetime. This can be accepted, since their principle of velocity measurement is highly robust for temporal drift and aging. However, most current meters consist of a magnetic compass that needs a proper compensation prior to each deployment. This is performed with built-in compass calibration procedures.

For daily calibration procedures of greenhouse gas measurements, secondary standard gases are used, which need to be calibrated against primary standard gases. Primary standard gases for CO₂, CH₄, and N₂O, which are traceable to the World Meteorological Organization Scale, are provided by the National Oceanic and Atmospheric Administration (NOAA) Central Calibration Laboratory (CCL). Calibration procedures to check for long-term drift and for postcorrection of the data differ between types of analyzers and between applications. For Li-COR-based CO₂ measurements, it is recommended to run a set of four reference gases every 3 h. The gases should closely bracket the range of expected gas concentrations [62.75, 105]. In contrast, the OA-ICOS analyzers only need a one-point calibration that is stable for 1–2 weeks, whereas CRDS analyzers need at least three standard gases to perform their calibration. However, standard operation proce-

dures for underway CO₂, CH₄, and N₂O measurements based on near infrared laser absorption spectroscopy are currently being developed by the Scientific Committee on Oceanic Research (SCOR) Working Group 143 [62.106].

62.6.2 Specific Quality Control Methods

During the field deployments of sensors mainly comparison measurements with independent instruments are performed to check the data quality. Temperature sensors can be checked with electronic reversal thermometers or with in-situ platinum resistance reference thermometers. Conductivity sensors are usually compared with independent conductivity measurements of collected water samples. During field expeditions comparison measurements are carried out usually at least once a day. In the case of long-term deployments, comparison measurements are performed immediately after the deployment and prior to the recovery. A new development is the usage of double-sensor packages on CTDs that allow the fast detection of sensor drift and failures by comparison of the data output of two identical sensors. This method has the advantage that the failure of a single sensor does not cause data loss.

Current meters can be compared to each other for a quality check. For example, a current meter that is deployed in a mooring will be checked with the

vessel-mounted ADCP of the ship that performs the maintenance of the mooring. Another opportunity is so-called bottom tracking. An ADCP that measures down to the seabed can estimate its relative movement to the bottom. This is compared to the movement of the measuring platform, derived from independent navigation data (e.g., GPS). With this method, velocity errors and also compass bias can be detected. Further checks are possible if a specific current component is well known. The main axis of a tidal current is very stable and can be used to correct compass bias.

The performance of the equilibrator for trace gas measurements should be checked to determine the gas-specific equilibration time in a set of tests at the home laboratory. In the field, the results of the continuous underway measurements should be checked by taking discrete samples from a bypass connected to the same water flow that supplies the continuous system to confirm the integrity of the underway results or to correct them if necessary. However, it needs to be noted that, depending on the overall variability in surface water and the speed of the vessel, discrete samples will be affected by a time lag as well, and triplicate discrete samples will not be directly comparable to each other. Additionally, regular calibration of the analyzer is needed to check for long-term drift and for postcorrection of the data (Sect. 62.6.1).

62.7 Maintenance

Sensors that are deployed in seawater are exposed to two major stresses: corrosion and biofouling. To prevent serious impacts on sound-sensor operation regular maintenance is required. Although seawater-resistant materials are used for water sensors, the combination of different metals or even plastics, like polyvinyl chloride (PVC), can cause corrosion of the metal parts of sensors. Usually, sacrificial anodes are used to preclude corrosion. Sacrificial anodes have to be checked carefully after each deployment and have to be exchanged if necessary. A particular problem is corrosion on electrical plugs and connectors, especially if they are under power. Any direct contact to seawater must be excluded. For this purpose, special silicon grease is applied to the electrical connections and plugs. Biofouling is another issue. It occurs at the surface as well as at depth. At the surface mainly mussels or barnacles can grow on the instruments and seal, e.g., inlets and tubes of conductivity sensors. They are also able to destroy the coating of acoustic transducers of modern current meters. Copper coatings or tubes are used to minimize biofouling. However, they never prevent it completely. At greater depths biofilms built up by bacteria are very common. Thus, regular

cleaning of instruments is necessary. For conductivity cells, special bleaching solutions are available, since mechanical cleaning would destroy the electrodes. The maintenance interval depends on the particular deployment conditions, but also on battery lifetime and memory capacity for self-contained instruments. Common maintenance intervals reach from 2 weeks in productive surface waters up to 2 years for deep-water deployment.

For maintenance of trace gas systems, care needs to be taken that flow rates of both water and headspace air are monitored and stay constant. Anomalies are indicative of blockage or leakage. Usually, a condenser and Nafion[®] drying tubes, which are low-maintenance parts, are used to dry the gas sample before it enters the analyzer. However, some systems contain additional drying agents, such as magnesium perchlorate (Mg(ClO₄)₂), which need to be replaced regularly. An increase of $x_{\text{H}_2\text{O}}$ readings of the analyzed gas is an indicator for reduced drying efficiency. It is also recommended to back-flush the system to reduce fouling during long measurements and to flush the water filter, tubing, etc., with freshwater after use and before storage to keep it clean and free from blockage.

62.8 Application

Applications of water sensors cover manifold fields, e.g., scientific field observations, environmental monitoring, and waste-water treatment. In this section, two examples for scientific applications are presented.

62.8.1 Variability in the Surface Mixed Layer

The interface between ocean and atmosphere is bounded at the ocean side by the surface mixed layer (SML). The properties of the SML have a high impact on the matter and energy fluxes through the ocean–atmosphere interface. To gather undisturbed data for a process study of the SML an autonomous drifter was deployed during an expedition of RV Meteor (M87/4) in the central Baltic Sea. The drifter consisted of a surface float and a 40-m-long sensor string mounted underneath, which covered the SML. On the sensor string 11 temperature sensors were mounted with a distance of 4 m between the single instruments. At 40 m depth an upward-looking ADCP was fixed to measure the current field in the SML. The deployment covered a period of 10 days. From the time series of the single-point temperature sensors, a Hovmöller plot of the temperature distribution was compiled (Fig. 62.9). It depicts a highly stratified upper layer with a warm surface layer of 10–20 m thickness. Solar radiation has heated the water to a temperature of about 16 °C. The layer below 30 m conserved the late winter temperatures of about 4 °C.

The increasing wind speed during the measuring period led to enhanced mixing in the SML. At the bottom of the mixed layer the thermocline was eroded by the transformation of turbulent kinetic energy into potential energy of stratification. The thickness of the SML increased from 10 m in the beginning to nearly 20 m depth at the end of the time series. This process also increased the vertical temperature gradient between the SML and the cold water layer below.

Wind pulses also generate inertial motions and waves in the SML and below. The current measurements gathered with the ADCP depict the current field of the inertial motions (Fig. 62.10). At the latitude of the observations of 57.3° N the inertial processes have a period of 14.2 h. The observed periodic changes of the surface current fit to this value.

The eastward and northward components of the surface current are phase-shifted by about 90°. This points to inertial motions rather than inertial waves. The strong vertical temperature gradient at the bottom of the SML caused a strong density gradient, which decouples the SML dynamically from the layer below. Thus, the deepening of the SML is also seen in the current field. The deflection of the internal motions at the edges of the basin causes a phase shift of 180° between the currents in the SML and the layer directly below it. At the surface the impact of wind waves on the current measurements is visible as enhanced noise. Since their wavelength is lower than the distance between the particular acoustic beams of the ADCP, which is ≈ 30 m near the surface, the precondition of a homogenous current field is not fulfilled (Sect. 62.4.5). This caused a higher bias in the current measurements gathered in the upper 5 m of the SML. However, this disturbance can be used as an indicator of wave intensity at the surface.

62.8.2 Spatial Variability of Greenhouse Gases off the Coast of Namibia

An example of how the subsurface hydrography links to biogeochemical processes in the surface is illustrated in Fig. 62.11, which shows a cross section through a filament offshore of the Namibian coast [62.115]. This area is part of the Benguela Current Upwelling System and is affected by coastal upwelling of cold, nutrient, and CO₂-enriched subsurface water [62.116, 117]. Fila-

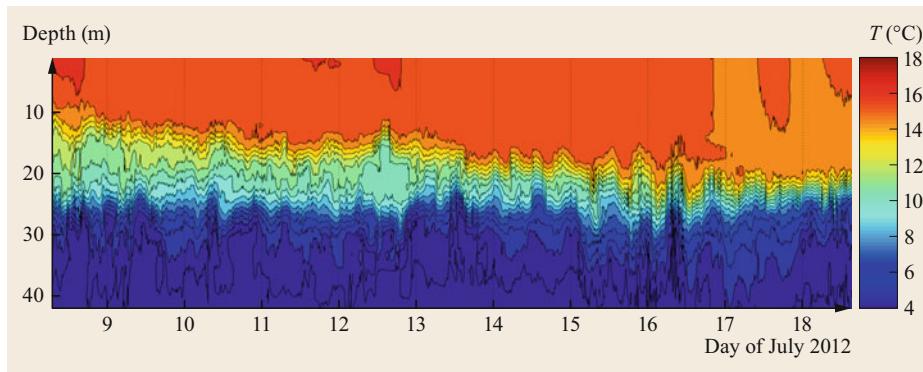


Fig. 62.9 High-resolution time series of SML temperature in the central Baltic Sea, gathered with an autonomous drifter during the RV Meteor expedition M87/4

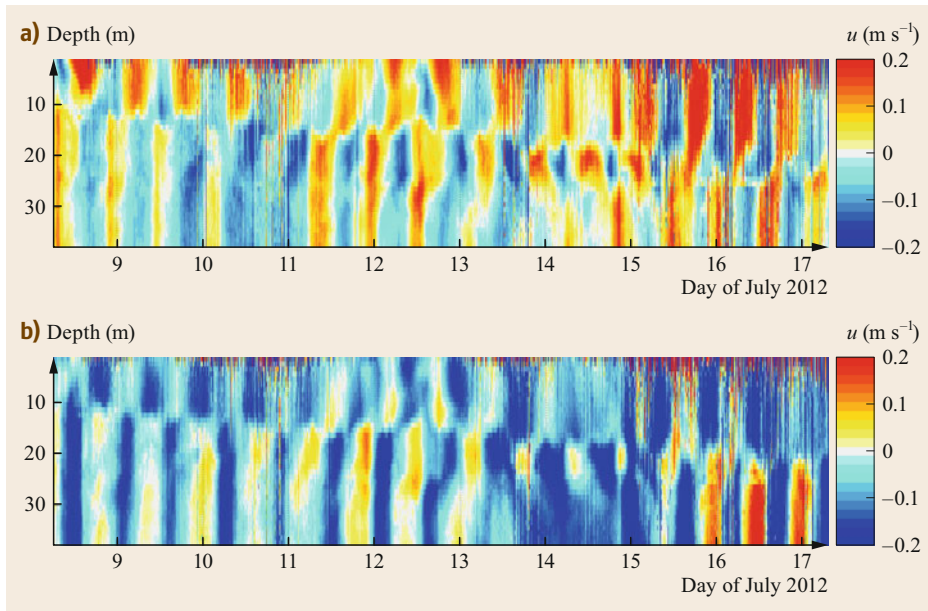


Fig. 62.10a,b
High-resolution time series of currents in the SML in the central Baltic Sea, gathered with an autonomous drifter during the RV Meteor expedition M87/4: (a) current east, (b) current north

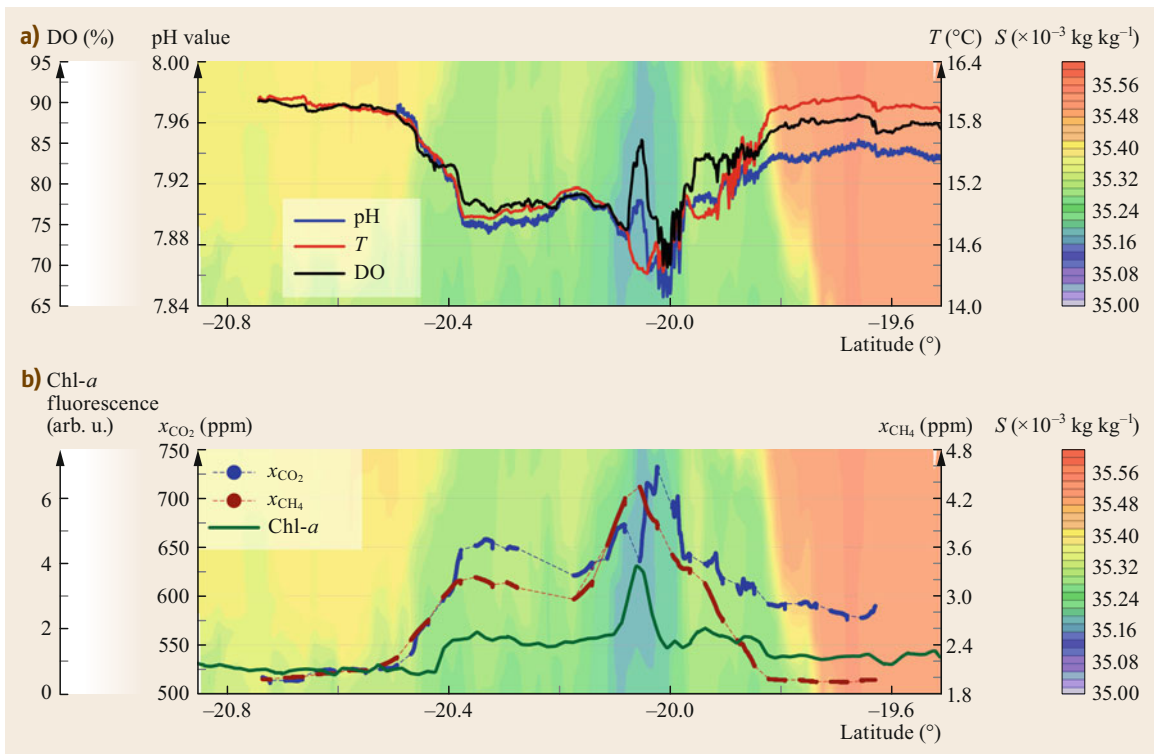


Fig. 62.11a,b North-south cross section through a filament offshore of the Namibian coast. (a) Vertical distribution of salinity (color coded, background) is overlain by pH, temperature, and DO saturation, which were measured in surface water along the transect. (b) Vertical distribution of salinity (color coded, background) is overlain by x_{CO_2} , x_{CH_4} , and Chl-*a* fluorescence, which were measured in surface water along the same transect. For reference, atmospheric dry mole fractions of CO_2 and CH_4 measured at the NOAA station in Namibia ranged between 394–397 ppm and 1.76–1.79 ppm at that time (after [62.114])

ments are tongues of cold, upwelled water that separate from the main upwelling front and spread offshore. The filament is indicated by a core of low salinity in the (sub)surface (green and blue colored shading) coinciding with a drop of surface temperature (red line, top panel). The uplift of subsurface water is associated with an increase in x_{CO_2} , as well as x_{CH_4} , but decreased pH and dissolved oxygen (DO) saturation in surface water, which is caused by aerobic decomposition and anaero-

bic methanogenesis of organic matter in sinking organic particles and in the sediments [62.118–120]. The nutrient input associated with the upwelling fuels primary production, which is indicated by a peak in Chl-*a* fluorescence coinciding with a rise in DO saturation and a drop in x_{CO_2} in the center of the filament. In contrast, CH_4 is mainly oxidized in the surface water and is not source for biological primary production and is, thus, not affected by primary production the way that CO_2 is.

62.9 Future Developments

Future in-situ sensors for water measurements will benefit from the rapid development of microelectronics. It will lead to higher integrated systems with lower power consumption, which will enable higher sampling rates and longer autonomous deployment times. The miniaturization of sensors will also allow the faster response times needed for turbulence observations. However, there are physical limits. Since most chemical poisons are banned for in-situ applications, new antifouling concepts have to be developed to ensure data quality during long-term deployments, e.g., on Argo floats. A rapid development of measuring platforms is also expected. The usage of autonomous operating devices, like gliders and AUV, will become a common tool in ocean ob-

servations, although they cannot replace the shipborne observations completely.

Sensors for in-situ trace gas measurements are being developed and are promising tools, e.g., as part of autonomous long-term deployments for monitoring the ocean surface. Sensors for in-situ trace gas measurements are being developed and are promising tools, e.g., as part of autonomous long-term deployments for monitoring the ocean surface. Sensors for in-situ N_2O measurements are not yet commercially available. However, given the strong demand and focus on the development of in-situ sensors to date, the range of available in-situ trace gas sensors, as well as their performance, is likely to improve in future.

62.10 Further Reading

- J.E. Corredor: *Coastal Ocean Observing – Platforms, Sensors and Systems* (Springer, Cham 2018)
- A. Joseph: *Measuring Ocean Currents: Tools, Technologies, and Data* (Elsevier, Amsterdam 2013)
- I.S. Robinson: *Measuring the Oceans from Space: The Principles and Methods of Satellite Oceanography* (Springer, Berlin, Heidelberg 2004)
- E. Delory, J. Pearlman: *Challenges and Innovations in Ocean in Situ Sensors: Measuring Inner Ocean Processes and Health in the Digital Age* (Elsevier, Amsterdam 2018)
- R. Kunzig, W.S. Broecker: *Fixing Climate: The Story of Climate Science – and How to Stop Global Warming* (Profile Books, London 2010)
- M. Denny: *How the Ocean Works: An Introduction to Oceanography* (Princeton Univ. Press, Princeton 2008)

References

- | | | | |
|------|---|------|--|
| 62.1 | W.T. Liu, K.B. Katsaros, J.A. Businger: Bulk parameterization of air–sea exchanges of heat and water vapor including the molecular constraints at the interface, <i>J. Atmos. Sci.</i> 36 , 1722–1735 (1979) | 62.3 | J.T. Kiehl, K.E. Trenberth: Earth’s annual global mean energy budget, <i>Bull. Am. Meteorol. Soc.</i> 78 , 197–208 (1997) |
| 62.2 | L.D. Talley, G.L. Pickard, W.J. Emery, J.H. Swift: <i>Descriptive Physical Oceanography: An Introduction</i> (Elsevier, Amsterdam 2011) | 62.4 | G. Myhre, D. Shindell, F.-M. Bréon, W. Collins, J. Fuglestedt, J. Huang, D. Koch, J.-F. Lamarque, B.M.D. Lee, T. Nakajima, A. Robock, G. Stephens, T. Takemura, H. Zhang: Anthropogenic and natural radiative forcing. In: <i>Climate Change 2013: The Physical Science Basis. Contribution of Work-</i> |

- ing Group I to the Fifth Assessment Report of the Intergovernmental Panel on Climate Change, ed. by T.F. Stocker, D. Qin, G.-K. Plattner, M. Tignor, S.K. Allen, J. Boschung, A. Nauels, Y. Xia, V. Bex, P.M. Midgley (Cambridge Univ. Press, Cambridge, New York 2013) pp. 659–740
- 62.5 P. Forster, V. Ramaswamy, P. Artaxo, T. Berntsen, R. Betts, D.W. Fahey, J. Haywood, J. Lean, D.C. Lowe, G. Myhre, J. Nganga, R.G. Prinn, G. Raga, M. Schulz, R. Van Dorland: Changes in atmospheric constituents and in radiative forcing. In: *Climate Change 2007: The Physical Science Basis. Contribution of Working Group I to the Fourth Assessment Report of the Intergovernmental Panel on Climate Change*, ed. by S. Solomon, D. Qin, M. Manning, Z. Chen, M. Marquis, K.B. Averyt, M. Tignor, H.L. Miller (Cambridge Univ. Press, Cambridge, New York 2007)
- 62.6 T.J. Blasing: *Recent Greenhouse Gas Concentrations* 2016), <https://doi.org/10.3334/CDIAC/atg.032>
- 62.7 C. Le Quéré, R.M. Andrew, P. Friedlingstein, S. Sitch, J. Pongratz, A.C. Manning, J.I. Korsbakken, G.P. Peters, J.G. Canadell, R.B. Jackson, T.A. Boden, P.P. Tans, O.D. Andrews, V.K. Arora, D.C.E. Bakker, L. Barbero, M. Becker, R.A. Betts, L. Bopp, F. Chevallier, L.P. Chini, P. Ciais, C.E. Cosca, J. Cross, K. Currie, T. Gasser, I. Harris, J. Hauck, V. Haverd, R.A. Houghton, C.W. Hunt, G. Hurtt, T. Ilyina, A.K. Jain, E. Kato, M. Kautz, R.F. Keeling, K. Klein Goldewijk, A. Körtzinger, P. Landschützer, N. Lefèvre, A. Lenton, S. Lienert, I. Lima, D. Lombardozzi, N. Metz, F. Millero, P.M.S. Monteiro, D.R. Munro, J.E.M.S. Nabel, S.-I. Nakaoka, Y. Nojiri, X.A. Padin, A. Peregon, B. Pfeil, D. Pierrot, B. Poulter, G. Rehder, J. Reimer, C. Rödenbeck, J. Schwinger, R. Séférian, I. Skjelvan, B.D. Stocker, H. Tian, B. Tilbrook, F.N. Tubiello, I.T. van der Laan-Luijckx, G.R. van der Werf, S. van Heuven, N. Viovy, N. Vuichard, A.P. Walker, A.J. Watson, A.J. Wiltshire, S. Zaehle, D. Zhu: Global carbon budget 2017, *Earth Syst. Sci. Data* **10**, 405–448 (2018)
- 62.8 P. Ciais, C. Sabine, G. Bala, L. Bopp, V. Brovkin, J. Canadell, A. Chhabra, R. DeFries, J. Galloway, M. Heimann, C. Jones, C.L. Quéré, R.B. Myneni, S. Piao, P. Thornton: Carbon and other biogeochemical cycles. In: *Climate Change 2013: The Physical Science Basis. Contribution of Working Group I to the Fifth Assessment Report of the Intergovernmental Panel on Climate Change*, ed. by T.F. Stocker, D. Qin, G.-K. Plattner, M. Tignor, S.K. Allen, J. Boschung, A. Nauels, Y. Xia, V. Bex, P.M. Midgley (Cambridge Univ. Press, Cambridge, New York 2013)
- 62.9 A.V. Borges, B. Delille, M. Frankignoulle: Budgeting sinks and sources of CO₂ in the coastal ocean: Diversity of ecosystems counts, *Geophys. Res. Lett.* **32**, 1–4 (2005)
- 62.10 C. Le Quéré, R.M. Andrew, J.G. Canadell, S. Sitch, J.I. Korsbakken, G.P. Peters: Global carbon budget 2016, *Earth Syst. Sci. Data* **8**, 605–649 (2016)
- 62.11 T. Volk, M.I. Hoffert: Ocean carbon pumps: Analysis on the relative strengths and efficiencies in ocean-driven atmospheric CO₂ changes. In: *The Carbon Cycle and Atmospheric CO₂: Natural Variations Archean to Present*, Geophysical Monograph Series, Vol. 32, ed. by E.T. Sandquist, W.S. Broecker (AGU, Washington 1985) pp. 99–110
- 62.12 J. Brown, K. Brander, L. Fernand, A.E. Hill: Scanfish: High performance towed undulator, *Sea Technol.* **37**, 23–27 (1996)
- 62.13 D.C. Webb, P.J. Simonetti, C.P. Jones: Slocum: An underwater glider propelled by environmental energy, *IEEE J. Ocean. Eng.* **26**, 447–452 (2001)
- 62.14 R. Bachmayer, N.E. Leonard, J. Graver, E. Fiorelli, P. Bhatta, D. Paley: Underwater gliders: Recent developments and future applications. In: *Proc. 2004 Int. Symp. Underwater Technol.* (2004) pp. 195–200, <https://doi.org/10.1109/UT.2004.1405540>
- 62.15 S. Cohan: Trends in ROV development, *Mar. Technol. Soc. J.* **42**, 38–43 (2008)
- 62.16 R.D. Prien, D.E. Schulz-Bull: Godess – A profiling mooring in the Gotland Basin, *Ocean Sci.* **12**, 899–907 (2016)
- 62.17 S.R. Massel: *Ocean Surface Waves: Their Physics and Prediction*, Advanced Series on Ocean Engineering, Vol. 36, 2nd edn. (World Scientific, Singapore 2013)
- 62.18 H.-G. Gierloff-Emden: *Geographie Des Meeres – Ozeane Und Küsten* (Walter de Gruyter, Berlin, New York 2011)
- 62.19 V.W. Ekman: *On the Influence of the Earth's Rotation on Ocean-Currents*, Arkiv för Matematik, Astronomi och Fysik, Vol. 2 (Almqvist & Wiksells, Uppsala 1905)
- 62.20 M. Knudsen (Ed.): *Hydrographische Tabellen* (G.E.C. Gad, L. Friedrichsen & Co., Copenhagen, Hamburg 1901)
- 62.21 G. Wüst, G. Böhnecke, H.H.F. Meyer: Ozeanographische Methoden und Instrumente. In: *Wissenschaftliche Ergebnisse der Deutschen Atlantischen Expedition auf dem Forschungs- und Vermessungsschiff "Meteor" 1925–1927, Bd. 4, Teil 1* (Walter de Gruyter, Berlin 1932)
- 62.22 T.H. Tizard, H.N. Moseley: *Narrative of the Cruise of HMS Challenger: With a General Account of the Scientific Results of the Expedition*, Vol. 2 (HM Stationery Office, London 1882)
- 62.23 Science Museum Group: Deep-Sea Reversing Mercury Thermometer, 1870–1875, <https://collection.sciencemuseum.org.uk/objects/co2849>, Accessed 24 July 2021. Science Museum Group Collection Online, Object-No. 1958–255
- 62.24 R. Price: The platinum resistance thermometer, *Platin. Met. Rev.* **3**, 78–87 (1959)
- 62.25 R.A. Cox, F. Culkin, J.P. Riley: The electrical conductivity/chlorinity relationship in natural sea water, *Deep Sea Res. Oceanogr. Abstr.* **14**, 203–220 (1967)
- 62.26 R. Pawlowicz, R. Feistel, T.J. McDougall, P. Ridout, S. Seitz, H. Wolf: Metrological challenges for

- 62.27 measurements of key climatological observables Part 2: Oceanic salinity, *Metrologia* **53**, R12 (2016)
- 62.28 UNESCO, ICES, SCOR, IAPSO: *Background Papers and Supporting Data on the Practical Salinity Scale 1978* (UNESCO, Paris 1981), UNESCO Technical Papers in Marine Science 37
- 62.28 IOC, SCOR, IAPSO: *The International Thermodynamic Equation of Seawater – 2010: Calculation and Use of Thermodynamic Properties* (UNESCO, Paris 2010), Manuals and Guides 56
- 62.29 L.V. Shannon, G.H. Stander, J.A. Campbell: *Oceanic Circulation Deduced from Plastic Drift Cards* (Sea Fisheries Branch, Department of Industries, Cape Town 1973), Investigational Report 108
- 62.30 D.V. Hansen, P.-M. Poulain: Quality control and interpolations of WOCE-TOGA drifter data, *J. Atmos. Ocean. Technol.* **13**, 900–909 (1996)
- 62.31 K.V. Lebedev, H. Yoshinari, N.A. Maximenko, P.W. Hacker: *YoMaHa'07: Velocity Data Assessed from Trajectories of Argo Floats at Parking Level and at the Sea Surface* (IPRC, Honolulu 2007), IPRC Technical Note 4(2)
- 62.32 S.C. Riser, H.J. Freeland, D. Roemmich, S. Wijffels, A. Troisi, M. Belbéoch, D. Gilbert, J. Xu, S. Pouliquen, A. Thresher: Fifteen years of ocean observations with the global Argo array, *Nat. Clim. Change* **6**, 145–153 (2016)
- 62.33 E. Bruns: *Ozeanometrie II*, *Ozeanologie*, Vol. 3 (B.G. Teubner, Leipzig 1968)
- 62.34 V.W. Ekman: Kurze Beschreibung eines Propell-Strommessers, *ICES J. Mar. Sci.* **1**, 3–4 (1905)
- 62.35 V.W. Ekman: On a new repeating current-meter, *ICES J. Mar. Sci.* **1**, 1–32 (1926)
- 62.36 W.S. Von Arx: *An Electromagnetic Method for Measuring the Velocities of Ocean Currents from a Ship under Way* (MIT, WHOI, Cambridge, Woods Hole 1950)
- 62.37 L.A. Stall-Worth: Acoustic method for determining current, *J. Acoust. Soc. Am.* **55**, 419–419 (1974)
- 62.38 B.H. Brumley, R.G. Cabrera, K.L. Deines, E.A. Terray: Performance of a broad-band acoustic Doppler current profiler, *IEEE J. Ocean. Eng.* **16**, 402–407 (1991)
- 62.39 P.Y. Le Traon, R. Morrow: Ocean currents and eddies. In: *Satellite Altimetry and Earth Sciences: A Handbook of Techniques and Applications*, International Geophysics, Vol. 69, ed. by L.-L. Fu, A. Cazenave (Academic Press, San Diego, London 2001) pp. 171–215, Chap. 3
- 62.40 L. Agassiz, A.V. Carozzi: *Studies on Glaciers, Preceded by the Discourse of Neuchâtel* (Hafner, New York 1967), *Etudes sur les Glaciers*: L. Agassiz (1840), translated into English and ed. by A.V. Carozzi
- 62.41 J. Tyndall: *Heat Considered as a Mode of Motion*, 2nd edn. (Green and Co., London 1865)
- 62.42 B. Bolin: *A History of the Science and Politics of Climate Change: The Role of the Intergovernmental Panel on Climate Change* (Cambridge Univ. Press, Cambridge 2007)
- 62.43 S.A. Arrhenius: On the influence of carbonic acid in the air upon the temperature of the ground, *Philos. Mag. J. Sci.* **41**, 237–276 (1896)
- 62.44 S. Fonselius, F. Koroleff, K.-E. Wärme: Carbon dioxide variations in the atmosphere, *Tellus* **8**, 176–183 (1956)
- 62.45 S. Fonselius, F. Koroleff, K. Buch: Microdetermination of CO₂ in the air, with current data for Scandinavia, *Tellus* **7**, 259–265 (1955)
- 62.46 C.D. Keeling: The concentration and isotopic abundances of atmospheric carbon dioxide in rural areas, *Geochim. Cosmochim. Acta* **13**, 322–355 (1958)
- 62.47 C.D. Keeling, R.B. Bacastow, A.E. Bainbridge, C.A. Ekdahl, P.R. Guenther, L.S. Waterman, J.F.S. Chin: Atmospheric carbon dioxide variations at Mauna Loa Observatory, Hawaii, *Tellus* **28**, 538–551 (1976)
- 62.48 R. Revelle, H.E. Suess: Carbon dioxide exchange between atmosphere and ocean and the question of an increase of atmospheric CO₂ during the past decades, *Tellus* **9**, 18–27 (1957)
- 62.49 B. Bolin: On the exchange of carbon dioxide between the atmosphere and the sea, *Tellus* **12**, 274–281 (1960)
- 62.50 K. Buch: Beobachtungen über das Kohlensäuregleichgewicht und über den Kohlensäureaustausch zwischen Atmosphäre und Meer im Nordatlantischen Ozean, *Acta Acad. Aboensis Math. Phys.* **11**, 3–32 (1939)
- 62.51 H. Craig, L.I. Gordon: Nitrous oxide in the ocean and the marine atmosphere, *Geochim. Cosmochim. Acta* **27**, 949–955 (1963)
- 62.52 J.H. Butler, J.W. Elkins: An automated technique for the measurement of dissolved N₂O in natural waters, *Mar. Chem.* **34**, 47–61 (1991)
- 62.53 J.W. Elkins: Determination of dissolved nitrous oxide in aquatic systems by gas chromatography using electron-capture detection and multiple phase equilibration, *Anal. Chem.* **52**, 263–267 (1980)
- 62.54 L.P. Atkinson, F.A. Richards: The occurrence and distribution of methane in the marine environment, *Deep Sea Res.* **14**, 673–684 (1967)
- 62.55 J.W. Elkins, S.C. Wofsy, M.B. McElroy, C.E. Kolb, W.A. Kaplan: Aquatic sources and sinks for nitrous oxide, *Nature* **275**, 602–606 (1978)
- 62.56 D. Pierotti, R.A. Rasmussen: The atmospheric distribution of nitrous oxide, *J. Geophys. Res.* **82**, 5823–5832 (1977)
- 62.57 H. Preston-Thomas: The International Temperature Scale of 1990 (ITS-90), *Metrologia* **27**, 3–10 (1990)
- 62.58 J.S. Steinhart, S.R. Hart: Calibration curves for thermistors, *Deep Sea Res. Oceanogr. Abstr.* **15**, 497–503 (1968)
- 62.59 P.R.N. Childs, J.R. Greenwood, C.A. Long: Review of temperature measurement, *Rev. Sci. Instrum.* **71**, 2959 (2000)
- 62.60 F.J. Millero, R. Feistel, D.G. Wright, T.J. McDougall: The composition of standard seawater and the definition of the reference-composition salinity

- scale, Deep Sea Res. Part I Oceanogr. Res. Pap. **55**, 50–72 (2008)
- 62.61 B. Kinsman: *Wind Waves: Their Generation and Propagation on the Ocean Surface* (Dover Publications, Mineola 1984)
- 62.62 R.H. Mellen, P.M. Scheifele, D.G. Browning: *Global Model for Sound Absorption in Sea Water* (NUSC, New London 1988), NUSC Tech. Rep.
- 62.63 P.G. Brewer, D.M. Glover, C. Goyet, D.K. Shafer: The pH of the North Atlantic Ocean: Improvements to the global model for sound absorption in seawater, *J. Geophys. Res. Oceans* **100**, 8761–8776 (1995)
- 62.64 W. Henry: Experiments on the quantity of gases absorbed by water, at different temperatures, and under different pressures, *Philos. Trans. R. Soc.* **93**, 29–274 (1803)
- 62.65 R.F. Weiss: Carbon dioxide in water and seawater: The solubility of a non-ideal gas, *Mar. Chem.* **2**, 203–215 (1974)
- 62.66 R.F. Weiss, B.A. Price: Nitrous oxide solubility in water and seawater, *Mar. Chem.* **8**, 347–359 (1980)
- 62.67 S. Yamamoto, J.B. Alcauskas, T.E. Crozier: Solubility of methane in distilled water and seawater, *J. Chem. Eng. Data* **21**, 78–80 (1976)
- 62.68 C.L. Sabine, R.A. Feely, N. Gruber, R.M. Key, K. Lee, J.L. Bullister, R. Wanninkhof, C.S. Wong, D.W.R. Wallace, B. Tilbrook, F.J. Millero, T.-H. Peng, A. Kozyr, T. Ono, A.F. Rios: The oceanic sink for anthropogenic CO₂, *Science* **305**, 367–371 (2004)
- 62.69 T. Takahashi: The fate of industrial carbon dioxide, *Science* **305**, 352–353 (2004)
- 62.70 C. Le Quéré, G.P. Peters, R.J. Andres, R.M. Andrew, T.A. Boden, P. Ciais, P. Friedlingstein, R.A. Houghton, G. Marland, R. Moriarty, S. Sitch, P.P. Tans, A. Anreth, A. Arvanitis, D.C.E. Bakker, L. Bopp, J.G. Canadell, L.P. Chini, S.C. Doney, A. Harper, I. Harris, J.I. House, A.K. Jain, S.D. Jones, E. Kato, R.F. Keeling, K. Klein Goldewijk, A. Körtzinger, C. Koven, N. Lefèvre, F. Maignan, A. Omar, T. Ono, G.-H. Park, B. Pfeil, B. Poulter, M.R. Raupach, P. Regnier, C. Rödenbeck, S. Saito, J. Schwinger, J. Segsneider, B.D. Stocker, T. Takahashi, B. Tilbrook, S. van Heuven, N. Viroy, R. Wanninkhof, A. Wiltshire, S. Zehle: Global carbon budget 2013, *Earth Syst. Sci. Data* **6**, 235–263 (2014)
- 62.71 D.M. Sigman, E.A. Boyle: Glacial/interglacial variations in atmospheric carbon dioxide, *Nature* **407**, 859–869 (2000)
- 62.72 D.M. Sigman, M.P. Hain, G.H. Haug: The polar ocean and glacial cycles in the atmospheric CO₂ concentration, *Nature* **466**, 47–55 (2010)
- 62.73 W.S. Broecker: Glacial to interglacial changes in ocean chemistry, *Prog. Oceanogr.* **2**, 151–197 (1982)
- 62.74 J.E. Johnson: Evaluation of a seawater equilibrator for shipboard analysis of dissolved oceanic trace gases, *Anal. Chim. Acta* **395**, 119–132 (1999)
- 62.75 D. Pierrot, C. Neill, K. Sullivan, R. Castle, R. Wanninkhof, H. Lüger, T. Johannessen, A. Olsen, R.A. Feely, C.E. Cosca: Recommendations for autonomous underway pCO₂ measuring systems and data-reduction routines, Deep Sea Res. Part II Top. Stud. Oceanogr. **56**, 512–522 (2009)
- 62.76 C.D. Keeling, N.W. Rakestraw, L.S. Waterman: Carbon dioxide in surface waters of the Pacific Ocean 1. Measurements of the distribution, *J. Geophys. Res.* **70**, 6087–6097 (1965)
- 62.77 D.L. Arévalo-Martínez, M. Beyer, M. Krumbholz, I. Piller, A. Kock, T. Steinhoff, A. Körtzinger, H.W. Bange: A new method for continuous measurements of oceanic and atmospheric N₂O, CO and CO₂: Performance of off-axis integrated cavity output spectroscopy (OA-ICOS) coupled to non-dispersive infrared detection (NDIR), *Ocean Sci.* **9**, 1071–1087 (2013)
- 62.78 B. Schneider, K. Kremling, J.C. Duinker: CO₂ partial pressure in northeast Atlantic and adjacent shelf waters: Processes and seasonal variability, *J. Mar. Syst.* **3**, 453–463 (1992)
- 62.79 T. Takahashi: Carbon dioxide in the atmosphere and in Atlantic ocean water, *J. Geophys. Res.* **66**, 474–494 (1961)
- 62.80 A. Körtzinger, H. Thomas, B. Schneider, N. Gronau, L. Mintrop, J.C. Duinker: At-sea intercomparison of two newly designed underway pCO₂ systems – Encouraging results, *Mar. Chem.* **52**, 133–145 (1996)
- 62.81 M. Frankignoulle, A. Borges, R. Biondo: New design of equilibrator to monitor carbon dioxide in highly dynamic and turbid environments, *Water Res.* **35**, 1344–1347 (2001)
- 62.82 L.E. Rafelski, B. Paplawsky, R. Keeling: An equilibrator system to measure dissolved oxygen and its isotopes, *J. Atmos. Ocean. Technol.* **30**, 361–377 (2013)
- 62.83 P. Fietzek, B. Fiedler, T. Steinhoff, A. Körtzinger: In situ quality assessment of a novel underwater pCO₂ sensor based on membrane equilibration and NDIR spectrometry, *J. Atmos. Ocean. Technol.* **31**, 181–196 (2014)
- 62.84 R. Grilli, J. Triest, J. Chappellaz, M. Calzas, T. Desbois, P. Jansson, C. Guillemin, B. Ferré, L. Lechevalier, V. Ledoux, D. Romanini: Sub-Ocean: Subsea dissolved methane measurements using an embedded laser spectrometer technology, *Environ. Sci. Technol.* **52**, 10543–10551 (2018)
- 62.85 M. Troncoso, G. Garcia, J. Verdugo, L. Farías: Toward high-resolution vertical measurements of dissolved greenhouse gases (nitrous oxide and methane) and nutrients in the eastern South Pacific, *Front. Mar. Sci.* **5**, 1–15 (2018)
- 62.86 I. Grefe, J. Kaiser: Equilibrator-based measurements of dissolved nitrous oxide in the surface ocean using an integrated cavity output laser absorption spectrometer, *Ocean Sci.* **10**, 501–512 (2014)
- 62.87 W. Gülzow, G. Rheder, B. Schneider, J. Schneider von Deimling, B. Sadkowiak: A new method for continuous measurement of methane and carbon dioxide in surface waters using off-axis integrated cavity output spectroscopy (ICOS): An example from the Baltic Sea, *Limnol. Oceanogr. Methods* **9**, 176–184 (2011)

- 62.88 B. Schneider, B. Sadkowiak, F. Wachholz: A new method for continuous measurements of O₂ in surface water in combination with pCO₂ measurements: Implications for gas phase equilibration, *Mar. Chem.* **103**, 163–171 (2007)
- 62.89 L. Yuhong, Z. Liyang, J. Zhang, L. Chen: Equilibrator-based measurements of dissolved methane in the surface ocean using an integrated cavity output laser absorption spectrometer, *Acta Oceanol. Sin.* **34**, 34–41 (2015)
- 62.90 T. Takahashi, J. Olafsson, J.G. Goddard, D.W. Chipman, S.C. Sutherland: Seasonal variation of CO₂ and nutrients in the high-latitude surface of oceans: A comparative study, *Glob. Biogeochem. Cycles* **7**, 843–878 (1993)
- 62.91 D.A. Wiesenburg, N.L. Guinasso: Equilibrium solubilities of methane, carbon monoxide, and hydrogen in water and sea water, *J. Chem. Eng. Data* **24**, 356–360 (1979)
- 62.92 R. Wanninkhof: Relationship between wind speed and gas exchange over the ocean, *J. Geophys. Res.* **97**, 7373–7382 (1992)
- 62.93 D.T. Ho, C.S. Law, M.J. Smith, P. Schlosser, M. Harvey, P. Hill: Measurements of air–sea gas exchange at high wind speeds in the Southern Ocean: Implications for global parameterizations, *Geophys. Res. Lett.* **33**, L16611 (2006)
- 62.94 R. Wanninkhof, W.E. Asher, D.T. Ho, C. Sweeney, W.R. McGillis: Advances in quantifying air–sea gas exchange and environmental forcing, *Annu. Rev. Mar. Sci.* **1**, 213–244 (2009)
- 62.95 P.D. Nightingale, M. Gill, C.S. Law, A.J. Watson, P.S. Liss, M.I. Liddicoat, J. Boutin, R.C. Upstill-Goddard: In situ evaluation of air–sea gas exchange parameterizations using novel conservative and volatile tracers, *Glob. Biogeochem. Cycles* **14**, 373–387 (2000)
- 62.96 H.E. Krogstad, S.F. Barstow, S.E. Aasen, I. Rodriguez: Some recent developments in wave buoy measurement technology, *Coast. Eng.* **37**, 309–329 (1999)
- 62.97 T.H.C. Herbers, P.F. Jessen, T.T. Janssen, D.B. Colbert, J.H. MacMahan: Observing ocean surface waves with GPS–tracked buoys, *J. Atmos. Ocean. Technol.* **29**, 944–959 (2012)
- 62.98 G. Jeans, I. Bellamy, J.J. de Vries, P. van Weert: Sea trial of the new Datavell GPS directional waverider. In: *Proc. IEEE/OES Seventh Work. Conf. Curr. Meas. Technol. San Diego* (2003) pp. 145–147, <https://doi.org/10.1109/CCM.2003.1194302>
- 62.99 Aanderaa Data Instruments AS: RCM Blue Current Meter, <https://www.aanderaa.com/productsdetail.php?RCM-Blue-37> (2019), Accessed 24 July 2021
- 62.100 Nortek: Ocean Currents, <https://www.nortekgroup.com/products/ocean-currents> (2019), Accessed 24 July 2021
- 62.101 G. Voulgaris, J.H. Trowbridge: Evaluation of the acoustic Doppler velocimeter (ADV) for turbulence measurements, *J. Atmos. Ocean. Technol.* **15**, 272–289 (1998)
- 62.102 R.L. Gordon: *Acoustic Doppler Current Profiler – Principles of Operation – A Practical Primer* (RD Instruments, San Diego 1996)
- 62.103 J.M. Hummon, E. Firing: A direct comparison of two RDI shipboard ADCPs: A 75–kHz ocean surveyor and a 150–kHz narrow band, *J. Atmos. Ocean. Technol.* **20**, 872–888 (2003)
- 62.104 Y. Nihei, A. Kimizu: A new monitoring system for river discharge with horizontal acoustic Doppler current profiler measurements and river flow simulation, *Water Resour. Res.* **44**, W00D20 (2008)
- 62.105 A.G. Dickson, C.L. Sabine, J.R. Christian: *Guide to Best Practices for Ocean CO₂ Measurements* (PICES, Sidney 2007), IOCCP Report 8
- 62.106 SCOR Working Group 143 – Dissolved N₂O and CH₄ measurements: Working towards a global network of ocean time series measurements of N₂O and CH₄, <https://scor-int.org/group/143/>, Accessed 24 July 2021
- 62.107 J. Charpentier, L. Fariás, O. Pizzaro: Nitrous oxide fluxes in the central and eastern South Pacific, *Glob. Biogeochem. Cycles* **24**, GB3011 (2010)
- 62.108 G. Rehder, R.W. Collier, K. Heeschen, P.M. Kosro, J. Barth, E. Suess: Enhanced marine CH₄ emissions to the atmosphere off Oregon caused by coastal upwelling, *Glob. Biogeochem. Cycles* **16**, 2–1–2–11 (2002)
- 62.109 C. O'Reilly, I.R. Santos, T. Cyronak, A. McMahon, D.T. Maher: Nitrous oxide and methane dynamics in a coral reef lagoon driven by pore water exchange: Insights from automated high-frequency observations, *Geophys. Res. Lett.* **42**, 2885–2892 (2015)
- 62.110 D.W.T. Griffith, N.M. Deutscher, C. Caldwell, G. Kettlewell, M. Riggenbach, S. Hammer: A Fourier transform infrared trace gas and isotope analyser for atmospheric applications, *Atmos. Meas. Tech.* **5**, 2481–2498 (2012)
- 62.111 D. Müller, H.W. Bange, T. Warneke, T. Rixen, M. Müller, A. Mujahid, J. Notholt: Nitrous oxide and methane in two tropical estuaries in a peat-dominated region of northwestern Borneo, *Biogeosciences* **13**, 2415–2428 (2016)
- 62.112 D. Müller, T. Warneke, T. Rixen, M. Müller, A. Mujahid, H.W. Bange, J. Notholt: Fate of terrestrial organic carbon and associated CO₂ and CO emissions from two southeast Asian estuaries, *Biogeosciences* **13**, 691–705 (2016)
- 62.113 T. Dauphinee, H. Klein, C. Kirby, J. Kathnelson: A portable salinometer based on direct measurement of the conductivity ratio R_t, *IEEE J. Ocean. Eng.* **8**, 288–292 (1983)
- 62.114 E.J. Dlugokencky, J.W. Mund, A.M. Croswell, M.J. Croswell, K.W. Thoning: *Atmospheric carbon dioxide dry air mole fractions from the NOAA GML carbon cycle cooperative global air sampling network 1968–2020*. <https://gml.noaa.gov/dv/data/index.php?site=NMB>, Accessed 24 July 2021
- 62.115 N. Lahajnar, V. Mohrholz, S. Angenendt, M. Ankele, M. Annighöfer, S. Beier, M. Birkicht, K. Bohata, J. Brust-Möbius, F. Bucholz, C. Chikwililwa, H.M. Cordts, K. Dähnke, A. Denda,

- A. Flohr, S. Geist, M. Gerth, A. Hansen, T. Heene, F. Höring, S. Janssen, R. Koppelman, A. Kunzmann, L. Kretzschmann, F. Langenberg, B. Martin, L. Mlambo, J. Möbius, A. Muyongo, G. Nickel, T. Ngutjinazo, O. Numwa, T. Ohde, C. Pavludi, N. Paul, T. Rixen, J. Rejoice, M. Schmidt, A. Schukat, H. Siegel, S. Simon, A. Stöber, L. Teichert, M.-E. Vorrath, N. Wasmund, T. Werner: *Geochemistry and Ecology of the Namibian Upwelling System Namufil: Namibian Upwelling Filament Study* (MARUM, Bremen 2015), https://doi.org/10.2312/Cr_M103, Cruise No. M103
- 62.116 L. Hutchings, C.D. van der Lingen, L.J. Shannon, R.J.M. Crawford, H.M.S. Verheye, C.H. Bartholomae, A.K. van der Plas, D. Louw, A. Kreiner, M. Ostrowski, Q. Fidel, R.G. Barlow, T. Lamont, J. Coetzee, F. Shillington, J. Veitch, J.C. Currie, P.M.S. Monteiro: The Benguela current: An ecosystem of four components, *Prog. Oceanogr.* **83**, 15–32 (2009)
- 62.117 P.M.S. Monteiro: The Benguela current system. In: *Carbon and Nutrient Fluxes in Continental Margins – A Global Synthesis*, Global Change – The IGBP Series, ed. by K.-K. Liu, L. Atkinson, R.A. Quiñones, L. Talae-McManus (Springer, Berlin, Heidelberg 2010) pp. 65–77
- 62.118 T.G. Ferdelman, H. Fossing, K. Neumann, H.D. Schulz: Sulfate reduction in surface sediments of the southeast Atlantic continental margin between 15°38' S and 27°57' S (Angola and Namibia), *Limnol. Oceanogr.* **44**, 650–661 (1999)
- 62.119 C. Niewöhner, C. Hensen, S. Kasten, M. Zabel, H.D. Schulz: Deep sulfate reduction completely mediated by anaerobic methane oxidation in sediments of the upwelling area off Namibia, *Geochim. Cosmochim. Acta* **62**, 455–464 (1998)
- 62.120 P.M.S. Monteiro, A. van der Plas, V. Mohrholz, E. Mabilie, A. Pascall, W. Joubert: Variability of natural hypoxia and methane in a coastal upwelling system: Oceanic physics or shelf biology?, *Geophys. Res. Lett.* **33**, L16614 (2006)

Volker Mohrholz

Physical Oceanography and Instrumentation
Leibniz-Institute for Baltic Sea Research
Warnemünde
Rostock, Germany
volker.mohrholz@io-warnemuende.de



Volker Mohrholz is Senior Scientist at the Leibniz-Institute for Baltic Sea Research in Warnemünde, Germany, heading the research group Physical-Biogeochemical Coupling of Marine Systems. He received his PhD in natural sciences in 1995 from the University of Rostock. His work covers the dynamics and variability of circulation in the Baltic Sea, as well as the dynamics of upwelling areas and oxygen minimum zones. His group focuses on high-resolution hydrographic observations and turbulence measurements in the marine environment.

Anita Flohr

Ocean and Earth Science
University of Southampton
Southampton, UK
a.flohr@southampton.ac.uk



Anita Flohr is Postdoctoral Research Fellow at the School of Ocean and Earth Science at the University of Southampton. She received her PhD in Marine Biogeochemistry from the University of Hamburg (2015) for her work on the strength and efficiency of the marine carbon pump of the northern Benguela upwelling system. She is working on a project that develops monitoring strategies for marine carbon capture and storage using tracer gases.

Measurement **Part F**

Part F Measurement Networks

63 Networks of Atmospheric Measuring Techniques
Rolf Philipona, Davos Dorf, Switzerland

64 Integration of Meteorological and Ecological Measurements
Hans Peter Schmid,
Garmisch-Partenkirchen, Germany
Corinna Rebmann, Leipzig, Germany

63. Networks of Atmospheric Measuring Techniques

Rolf Philipona 

Networks of atmospheric measuring techniques are fundamental to ensuring the scientific and climatic usefulness of atmospheric measurements. Because air masses can move hundreds of kilometers every day, weather, air pollution, and climate are international issues—they cannot be addressed at the national level alone. However, measurement stations and systems are usually operated and funded at the national level or at even more local levels. To ensure that results are comparable and to address global problems, it is therefore crucial to coordinate goals, operating procedures, stations, systems, standards, traceability, etc. at the international level. International networks allow the implementation of different atmospheric measuring techniques at specifically selected sites and are relevant to all stages of the generation of atmospheric data on physical properties and chemical compositions. The purpose of this chapter is to introduce and describe the history, structure, instruments, methods, and other aspects of these atmospheric observing networks. It chronologically describes the birth and formation of the various atmospheric measurement networks around the globe, which has mainly been driven by the need for atmospheric monitoring that provides long-term climate change observations. The relevance of networks, measurement principles, and the different parameters observed are presented. Quality control, maintenance, and future developments in this field to facilitate various applications are also discussed.

63.1	Relevance and Parameters of Networks	1688
63.1.1	Relevance of Atmospheric Measurement Networks.....	1688
63.1.2	Measurement Principles and Parameters.....	1689
63.2	History	1691
63.2.1	History of Atmospheric Measurement Networks.....	1691
63.3	Network Structure	1693
63.3.1	The WMO/GAW International Network and Stations.....	1693
63.3.2	The NDACC International Network.....	1695
63.3.3	The BSRN International Radiation Network.....	1697
63.3.4	The GRUAN International Upper-Air Network.....	1697
63.4	Other Important Networks	1699
63.4.1	Networks Contributing to the GAW Program.....	1699
63.4.2	NDACC Cooperating Networks.....	1701
63.4.3	BSRN Collaborating Networks.....	1705
63.4.4	Collaborations of GRUAN with Other Networks.....	1705
63.5	Quality Control	1708
63.5.1	Objectives of Quality Control.....	1708
63.5.2	Regulations for Quality Control.....	1708
63.6	Maintenance	1709
63.6.1	Regulations for Maintenance.....	1709
63.7	Application	1709
63.7.1	Modeling Applications of GAW Data.....	1709
63.7.2	Objectives and Membership of SAG-APPs.....	1710
63.8	Future Developments	1710
63.9	Further Reading	1710
	References	1710

Climate change and its links to various changes in the atmosphere have prompted several initiatives to build networks of atmospheric measuring techniques in recent decades. Global Atmosphere Watch (GAW) is a worldwide system that was established by the World Meteorological Organization (WMO) to monitor trends in the Earth's atmosphere. A forerunner to GAW was conceived as far back as the 1950s, when the WMO began a program that aimed to monitor the atmosphere for trace chemicals and research air pollution from a meteorological perspective. GAW was eventually created in 1989 by combining the Global Ozone Observing System (GO3OS) with the Background Air Pollution Monitoring Network (BAPMoN). In 1991, after five years of planning, the Network for the Detection of Atmospheric Composition Change (NDACC) officially began operating. Originally named the Network for the Detection of Stratospheric Change (NDSC), the goal of NDACC is to observe changes in chemical and physical state in the stratosphere and upper troposphere and to assess the impact of such changes on the lower troposphere and climate. In the early

1990s, the World Climate Research Program (WCRP) initiated a new radiometric network, the Baseline Surface Radiation Network (BSRN), to support climate research. This network provides validation material for satellite radiometry and climate models and detects long-term variations in irradiance at the Earth's surface, which are believed to play an important role in climate change. Around 2010, the Global Climate Observing System (GCOS) Reference Upper-Air Network (GRUAN) moved from concept to reality. The goal of GRUAN is to provide reference-quality in-situ and ground-based remote-sensing observations of important climate variables for the upper air.

The four networks (GAW, NDACC, BSRN, and GRUAN) described above are linked to each other to some extent, and are connected to a number of additional regional, national, and international networks and programs that are also briefly presented below. All of these networks support atmospheric climate monitoring and research as well as broader components of the WMO Global Observing System (GOS), its research, and applications.

63.1 Relevance and Parameters of Networks

Global or Regional GAW stations are operated by WMO members. A *contributing station* is a station that is operated by a WMO partner network or organization that contributes data of known quality to one of the GAW World Data Centres and is linked to the GAW Primary Standard for a particular variable relating to atmospheric physics or chemistry.

63.1.1 Relevance of Atmospheric Measurement Networks

When the origins of atmospheric measurement techniques and research into measuring and understanding changes in the chemical composition of the atmosphere are discussed, two phenomena are usually mentioned. The first is regional air quality and, in particular, the first observations of photochemical *smog*. Hazardous air quality was reported as far back as the nineteenth century, but studies of air pollution generally date back to the 1950s, when the chemical and physical processes that lead to unhealthy urban environments were first identified [63.1]. The second phenomenon is chemical threats to the atmosphere as a whole, which were observed and investigated by scientists during the 1960s and 1970s [63.2–8]. These investigations were inspired by views of our planet from space, and

were boosted by measurement projects initiated during 1957–58: the International Geophysical Year (IGY). During the IGY, background monitoring stations began to measure gases such as carbon dioxide, methane, and total column ozone along with related constituents, many of which were heavily concentrated in the stratosphere. Unlike many short-lived chemical pollutants, carbon dioxide and lower stratospheric ozone have long lifetimes and relatively uniform global distributions. Furthermore, they are related to the radiative properties of the atmosphere. Water vapor and carbon dioxide are primary greenhouse gases, and the thickness of the column abundance of ozone determines the amount of ultraviolet (UV) radiation that reaches the Earth's surface [63.9].

Air quality, photochemical smog, and chemical threats to the atmosphere as a whole were therefore the original drivers for the development of standard procedures for achieving uniform ozone observations and the creation of the Global Ozone Observing System (GO3OS). They also provided the impetus to establish the Background Air Pollution Monitoring Network (BAPMoN) in the late 1960s. These two programs, which were guided by the World Meteorological Organization (WMO) and its Global Atmosphere Watch (GAW) initiative, were ultimately combined into the

GAW program and network in 1989. This network consists of global and regional GAW measurement stations, with additional measurements provided by contributing stations. The global and regional GAW stations are operated by national meteorological services or other national scientific organizations in their host countries. More than 80 countries actively host GAW stations [63.10].

The Network for the Detection of Atmospheric Composition Change (NDACC) is an international global network composed of more than 70 high-quality remote-sensing research stations. NDACC was originally named the Network for the Detection of Stratospheric Change (NDSC), and its goal was to observe changes in the chemical and physical state of the stratosphere and upper troposphere as well as to assess the impact of those changes on the lower troposphere and global climate. While NDACC remains committed to monitoring changes in the stratosphere (with an emphasis on the long-term evolution of the ozone layer), its priorities have broadened considerably to include, for instance, the detection of trends in overall atmospheric composition, understanding the impacts of those trends on the stratosphere and troposphere, and establishing links between climate change and atmospheric composition. Following five years of planning, instrument design, and implementation, NDACC began network operations in January 1991. NDACC is structured around various categories: ground-based observational techniques, timely cross-cutting themes (ozone, water vapor, measurement strategies and emphases), satellite measurement systems, and theory and analysis. To widen its scope, NDACC has established formal collaborative agreements with eight other cooperating networks [63.9].

To support climate research, a new international global radiometric network—the Baseline Surface Radiation Network (BSRN)—was initiated in the early 1990s by the Global Energy and Water Exchanges (GEWEX) project of the World Climate Research Programme (WCRP). This network aims at providing validation material for satellite radiometry and climate models. It also detects long-term variations in irradiance at the Earth's surface, which play an important role in climate change. The network and its instrumentation are designed to (i) cover major climate zones, (ii) provide the accuracy required to meet the objectives, and (iii) ensure homogenized standards far into the future.

The limits on the accuracy of the network that is needed to reach these goals have been defined. Suitable instruments have been determined and the methods to be used for observations and data management have been agreed upon by all (currently 59) stations. The central archive of BSRN is the World Radiation

Monitoring Center (WRMC), which was initiated in 1992 [63.11].

The Global Climate Observing System (GCOS) was established during the Second World Climate Conference in 1992 to ensure that the observations and information needed to address climate-related issues are obtained and made available to all potential users. GCOS is co-sponsored by the World Meteorological Organization (WMO), the Intergovernmental Oceanographic Commission (IOC) of UNESCO, the United Nations Environment Programme (UNEP), and the International Council for Science (ICSU). GCOS is a system that comprises the climate-relevant components of many contributing observing systems and networks. The mission of the GCOS program is to help ensure that these contributing systems, taken as a whole, provide the comprehensive information on the global climate system that is required by users, including individuals, national and international organizations, and institutions and agencies [63.12].

The GCOS Reference Upper-Air Network (GRUAN) is an international reference observing network of sites that measure important climate variables above the Earth's surface in order to fill an important gap in the current global observing system. GRUAN measurements provide high-quality long-term climate data records on, for example, atmospheric water vapor, temperature, wind components, and pressure from the surface through the troposphere and into the stratosphere. These records are used to determine trends, to constrain and calibrate data from more spatially comprehensive observing systems (including satellites and current radiosonde networks), and to provide appropriate data for studying atmospheric processes. GRUAN started in 2008 with about 15 stations, and it is envisaged that it will eventually grow into a global network of 30–40 sites that, if and where possible, builds on existing observational networks and capabilities [63.13].

63.1.2 Measurement Principles and Parameters

The WMO's Global Atmosphere Watch (GAW) program integrates many monitoring and research activities involving the measurement of the chemical composition and physical properties of the atmosphere. The parameters measured by the four main atmospheric measurement networks are shown in Table 63.1.

GAW

GAW serves as an early warning system for further changes in atmospheric concentrations, including the acidity and toxicity of rain as well as the atmospheric burden of aerosols. GAW provides framework design,

standards, intercalibrations, and data collection systems for global monitoring and data evaluation. Its focal areas are aerosols, greenhouse gases, reactive gases, ozone, UV radiation, and precipitation chemistry, and it includes the GAW Urban Research Meteorology and Environment Project (GURME) [63.10].

NDACC

As noted above, NDACC was originally committed to monitoring changes in the stratosphere with an emphasis on the long-term evolution of the ozone layer, but its priorities have recently broadened considerably to encompass issues such as the detection of trends in overall atmospheric composition and understanding the impacts of these trends on the stratosphere and troposphere. Concerns about global ozone intensified with the realization that stratospheric ozone chemistry included catalytic cycles involving reactive halogens, nitrogen, and hydrogen. Early spectroscopic balloon measurements confirmed the presence of trace species such as NO₂, HNO₃, and HCl. Scientists were also beginning to investigate the effects of the growing use of chlorofluorocarbons (CFCs) in myriad applications. Hence, NDACC expanded rapidly, and today it measures total column and vertical profiles of major atmospheric variables (constituents and physical parameters) such as ozone, water vapor, trace species, chlorofluorocarbons, greenhouse gases, reactive gases, aerosols, UV radiation, and temperature up to the mesosphere [63.9].

BSRN

Observations made by BSRN are divided into three main categories: basic, expanded, and other measurements. Because the irradiances in the basic measurement program provide the foundations for the data requirements of BRSM, they have the highest priority in BSRN, and improving their derivation was the focus of development during the initial stages of implementing BSRN. The basic measurements required for these quantities are the direct solar irradiance, diffuse sky irradiance, and longwave downward irradiance. The measurement of global irradiance by a pyranometer is included as part of the basic measurement program to provide closure of the solar radiometer system. Stations with an expanded measurement program provide additional information that is mainly used to improve satellite algorithms and for data interpretation. This includes direct solar spectral irradiance at the specific wavelength, cloud amount and type, vertical distributions of temperature and water vapor, cloud-base height and aerosols, precipitable water, and ozone. During

the course of the project, it was found that measurements of this category are also extremely useful for data quality control. BSRN stations are also encouraged to undertake additional measurements mainly to advance atmospheric radiation research. These include short- and longwave upward irradiance from a tower and low-resolution shortwave and longwave hemispheric spectral irradiance such as UV measurements. These will provide detailed information on radiative effects on the climate system and help to improve parameterization in climate models [63.11].

GRUAN

The GRUAN measurement strategy aims to maintain measurements over several decades in order to accurately quantify trends. It provides data for validating and calibrating measurements from observing systems that are more spatially extensive, such as satellite systems and the global radiosonde network, leading to improved satellite data products. The measurements are performed to fully characterize the properties of the atmospheric column. Major essential climate variables such as atmospheric water vapor, temperature, and wind components are measured using a number of different but complementary techniques to validate derived measurement uncertainties. The final goals are to characterize observational biases and estimate measurement uncertainties, describe measurements using extended metadata, comprehensively document the observing technique, tie measurements to SI units or internationally accepted standards, and ensure the long-term stability of measurement series by managing instrument changes, thus improving the overall upper-air observing network [63.13].

Table 63.1 Important parameters measured by the four main atmospheric measurement networks

Network	Important parameters measured by network
GAW	Greenhouse gases, ozone, aerosols, selected reactive gases, atmospheric deposition, UV radiation
NDACC	Total column and vertical profiles of ozone, water vapor, trace species, chlorofluorocarbons, greenhouse gases, reactive gases, aerosols, UV radiation, and temperature up to the mesosphere
BSRN	Basic measurements include direct solar irradiance, diffuse sky irradiance, and longwave downward irradiance. Global irradiance is measured by a pyranometer to provide closure of the solar radiometer system
GRUAN	Vertical profiles of atmospheric water vapor, atmospheric temperature, and atmospheric wind components

63.2 History

The monitoring of trace atmospheric constituents was originally driven by scientific curiosity. However, it was not long before researchers began to question how closely the observed increases in certain trace chemicals were connected to human activities, and what the consequences would be for humanity if these trends continued unabated. For a discussion of the history of meteorological networks in general, see Chap. 1.

63.2.1 History of Atmospheric Measurement Networks

The WMO played an important role in converting scientifically driven events into regular monitoring by formally embarking on a monitoring program for atmospheric chemistry and meteorological aspects of air pollution during the 1950s. Adequate information on the chemical composition of the atmosphere is needed, and the global consequences of anthropogenic changes to the atmosphere can only be estimated if all measurements of the component of interest are expressed in the same units or on the same scale (i.e., if the measurements performed by different countries are comparable).

GAW

The first step towards the development of atmospheric measurement networks was taken by the WMO, which began to coordinate chemical measurements internationally during the International Geophysical Year in 1957. The WMO took responsibility for developing standard procedures for uniform ozone observations and established the Global Ozone Observing System (GO3OS). GO3OS organized a coordinated Dobson (and later Brewer) spectrophotometer network for measuring total atmospheric ozone, performed ozonesonde intercomparisons, prepared ozone bulletins and assessments, and supported the Ozone Data Centre in Canada.

In the late 1960s, the Background Air Pollution Monitoring Network (BAPMoN) was established. This network focused on precipitation chemistry and aerosol and carbon dioxide measurements. It included regional and background stations and established the WMO World Data Center in the USA.

During the 1970s, three atmospheric issues became increasingly prominent:

- (a) The threat of CFCs to the ozone layer
- (b) The acidification of lakes and forests in large parts of North America and Europe, caused principally by the conversion of sulfur dioxide to sulfuric acid through precipitation processes in the atmosphere

- (c) The global warming caused by the accumulation of greenhouse gases in the atmosphere.

Each of these issues is now the subject of international treaties or conventions. The initial development of these agreements and subsequent assessments of the mitigation measures they specify were heavily dependent on the information provided by the WMO's atmospheric composition monitoring program.

In 1989, the two observing networks BAPMoN and GO3OS were consolidated into the WMO's Global Atmosphere Watch (GAW) program [63.10, 14].

NDSC/NDACC

At a meeting in Geneva in 1989, NASA, NOAA, and the WMO convened a forum in which several international agencies and institutions participated. At that meeting, the organizational structure of the Network for the Detection of Stratospheric Change (NDSC) was formalized [63.15]. Annual Steering Committee (SC) meetings commenced in 1990, and these meetings led to the realization that this research and monitoring program needed to be global. In 1991, after five years of planning, NDSC began official operations. Thus, from its very beginnings, NDSC has been a consortium of countries and sponsoring organizations that is endorsed by the United Nations Environment Programme (UNEP), the WMO, and the International Ozone Commission (IO3C)—a body of the IUGG/IAMAS (International Union of Geodesy and Geophysics/International Association of Meteorology and Atmospheric Science).

NDSC has provided a unique and enduring framework for the international community to perform long-term ground-based measurements of atmospheric composition at the global scale. To celebrate the 10th anniversary of NDSC in 2001, a symposium highlighting its scientific achievements was held in Arachon, France, in conjunction with an international symposium. In 2005, during the 16th Annual SC Meeting in Tenerife, Spain, the name of the Network for the Detection of Stratospheric Change (NDSC) was changed to the Network for the Detection of Atmospheric Composition Change (NDACC) to better reflect the expanded focus of its measurements. For its 25th anniversary, an article on NDACC was featured in *The Earth Observer* [63.16], and a special issue on NDACC was jointly published in the journals *Atmospheric Chemistry and Physics*, *Atmospheric Measurement Techniques*, and *Earth System Science Data*. This special issue included an introductory paper written by the NDACC community [63.9].

BSRN

The radiation budget of the Earth–atmosphere system is a fundamental influence on the thermal conditions and circulation in both the atmosphere and the oceans, and thus shapes the main characteristics of the Earth’s climate. The irradiance at the Earth’s surface is an especially important factor in climate processes, as the Earth’s surface transforms about 60% of the solar radiation it absorbs. This irradiance also plays an important role in the energy budget of the ocean surface, which ultimately influences the major features of ocean currents. While a small change in irradiance at the Earth’s surface may cause a profound change in its climate, until a few decades ago, radiometric networks were not capable of achieving the accuracy required for climate research. Our understanding of the vertical and horizontal radiation distributions was not sufficient to understand the climate. The results of simulations of previous and future climate fluctuations induced by changes in solar radiation flux had high uncertainties. This was the background for the World Climate Research Programme (WCRP) to initiate a new radiometric network to support the research projects of the WCRP and other scientific programs.

In October 1988, the World Meteorological Organization/International Council of Scientific Unions (WMO/ICSU) Joint Scientific Committee for the WCRP proposed the international Baseline Surface Radiation Network (BSRN), with the following goals:

- (1) To perform irradiance measurements at the Earth’s surface that can be used to validate satellite-based estimates of the surface radiation budget and radiation transfer through the atmosphere
- (2) To provide the irradiance data needed to validate and improve radiation codes of climate models
- (3) To monitor long-term changes in the irradiance at the Earth’s surface.

To achieve these goals, it is necessary to ensure that the entire network adheres uniformly to the highest achievable standards of accuracy, observation procedures, and calibration methods. Consequently, sustained efforts to develop more accurate and stable instruments, more reliable weather protection, and more uniform calibration procedures are a necessary component of BSRN. It is also important to carry out radiometry concurrently with measurements of relevant atmospheric characteristics such as temperature, water vapor, ozone, aerosol, and clouds. The initial proposal for the network included about 20 strategically located stations. A working group for the implementation of the project

was formed in 1989. The group was charged with the following tasks:

- (1) To identify the optimal sites and the organizations to carry out the observations
- (2) To formulate the observational requirements and procedures, including instrument selection (or development if necessary), method deployment, and calibration processes
- (3) To develop the data administration scheme, including quality control, permanent archiving, and data retrieval [63.11].

BSRN began operating in 1992, utilizing nine sites and an archive at the WCRP World Radiation Monitoring Center (WRMC) in the Swiss Federal Institute of Technology (ETH) in Zurich. To facilitate attainment of the target accuracy and to ensure the standardization of observations and data handling, the working group published manuals for observational procedures [63.17] and for data management and quality control [63.18]. The fully automated data administration and data access system has been operational at ETH Zurich since June 1995. Since 2008, the WRMC has been operated by the Alfred Wegener Institute for Polar and Marine Research (AWI), Germany. The data this network provides are hugely important for the validation and confirmation of satellite and computer model estimates of surface radiation quantities. At an increasing number of stations (currently 59) in contrasting climatic zones that range in latitude from 80° N to 90° S, solar and atmospheric radiation is measured with instruments of the highest available accuracy and with high time resolution (1–3 min).

In 2004, BSRN was designated the global baseline network for surface radiation for the Global Climate Observing System (GCOS). BSRN stations also contribute to Global Atmospheric Watch (GAW). In 2011, BSRN and NDACC reached a formal agreement to become cooperative networks.

GRUAN

The GCOS Reference Upper-Air Network (GRUAN) is an international reference observing network that was specifically designed to meet the needs of climate monitoring and to fill a major void in the current global observing system. The key aspects of GRUAN were developed during three workshops. The first, held at NOAA in Boulder (CO, USA) in February 2005, identified the requirements of a reference upper-air network for climate observations. The second, held at the University of Washington in Seattle (WA, USA) in May 2006, explored potential technologies and net-

works that could meet the stated requirements. Details on these two workshops were reported by GCOS in 2007 [63.19]. The third workshop, held at the Lindenberg Meteorological Observatory in Germany in February 2008, reached decisions on issues relating to instrumentation, observation protocols, management, and the relationships between GRUAN and other programs and organizations [63.20], all of which were needed to initiate the program [63.21].

GRUAN was designed to:

- Comprise several dozen stations that would become operational in a phased process. This network serves primarily as a long-term reference for other networks. GRUAN is not intended to include stations in every region of the world; instead, it samples major climatic regimes, latitudes, altitudes, and surface types. Each station is associated with a host institution that has the necessary scientific and technical expertise and a commitment to the long-term operation of the site.
- Adhere to the climate monitoring principles of GCOS, such as ensuring the quality and the long-term continuity and homogeneity of observations (and the metadata needed to interpret them), the use of the data in research and assessments, establishing the requirements at the outset of system design and implementation, and incorporating data management systems that facilitate data access.
- Measure the *essential climate variables* identified by GCOS in 2003, with a particular focus on the highest priority upper-air variables. High-quality instruments are employed to provide the most accurate data possible.
- Perform ongoing real-time and retrospective cross-validation of different measurements of the same parameter and evaluate measurement accuracies and drifts.
- Include a strong lead center that provides scientific leadership and oversight, manages the network, trains operators, and ensures proper data archival

and free dissemination. The Meteorological Observatory Lindenberg (Richard Aßmann Observatory) serves as the GRUAN Lead Centre due to the German Meteorological Service (DWD) offer of substantial financial, scientific, and technical support in response to a call for interest issued by the GCOS Secretariat.

- Incorporate a strong commitment to coordinate with other existing networks and observing systems and to provide a scientifically robust service to the user community. Achieving coordination among networks is recognized to be a challenge, but it is seen as critical to the long-term success of GRUAN and other networks.

These concepts help to clarify what GRUAN is, but it is also important to clearly articulate what GRUAN is not. It is not a set of identical stations; some will be more comprehensive than others, although all will obtain a core set of first-priority observations. It is not a replacement for the existing radiosonde network, which has a higher spatial density (necessary for some weather observations), nor for the GCOS Upper-Air Network (GUAN). The 30- to 40-station GRUAN network aims to provide reference observations, i.e., the long-term anchor points that comprehensively characterize the atmospheric column based on the best measurements currently available. The basis of the system is the complete global upper-air observing system, which serves a wide variety of purposes (primarily weather prediction), includes the operational radiosonde network, aircraft and satellite observations, etc., and embraces model-assimilated upper-air datasets and reanalyses.

GRUAN is a key component of GCOS, and GCOS is, in turn, the formal climate component of the Global Earth Observing System of Systems (GEOSS) [63.22]. GRUAN contributes to GEOSS's goal to "understand, assess, predict, mitigate, and adapt to climate variability and change" [63.23]. GRUAN is also a crucial element of the Global Space-Based Inter-Calibration System [63.21, 24].

63.3 Network Structure

Research at GAW is focused on conducting observations to document changes in atmospheric composition, continuously improving the observational and data management infrastructure, analyzing the data to improve our understanding of the processes that lead to changes in atmospheric composition, and developing GAW products and services.

63.3.1 The WMO/GAW International Network and Stations

The backbone of the GAW program is its network of measurement stations. Three types of stations are identified in the GAW strategic plan for 2008–2015: global GAW stations, regional GAW stations, and contribut-



Fig. 63.1 Map showing the locations of global GAW stations (after [63.25])

ing stations operated by contributing networks. Both the global and the regional stations are operated by national meteorological services or other national scientific organizations in their host countries. More than 80 countries actively host GAW stations.

Currently, GAW coordinates activities and data from 31 global stations, more than 400 regional stations, and around 100 contributing stations operated by contributing networks (Fig. 63.1).

Any station that contributes to GAW must satisfy the following requirements:

- For the variables measured, the station location must be regionally representative and generally free of any influences from local sources of significant pollution.
- The station must have adequate power, air conditioning, communications, and building facilities to sustain long-term observations with greater than 90% data capture (i.e., <10% missing data).
- Technical support at the station must be trained in the operation of the equipment.
- The agency responsible must commit to carrying out long-term observations of at least one variable relating to one of the six focal areas of GAW (ozone, aerosols, greenhouse gases, reactive gases, UV radiation, and precipitation chemistry).
- GAW observations must be of known quality and linked to the GAW Primary Standard.
- The data (and associated metadata) should be submitted to one of the GAW World Data Centres no later than one year after the observation was made. Changes to the metadata (including instrumentation, traceability, observation procedures) should be reported to the responsible WDC in a timely manner.
- If required, data should be submitted to a designated data distribution system in near real time.
- Standard meteorological in-situ observations that are required for the accurate determination and interpretation of GAW variables should be made with known accuracy and precision.
- The station characteristics and observational program must be updated in the GAW Station Information System (GAWSIS) on a regular basis.
- A station logbook (i.e., a record of observations made and activities that may have affected the observations) should be maintained and used in the data validation process.

Additional characteristics are also required for a global GAW station:

- The station must measure variables in at least three of the six focal areas of GAW (see previous list)
- It must have a strong scientific support program with appropriate data analysis and interpretation within the host country as well as—if possible—the support of more than one agency.

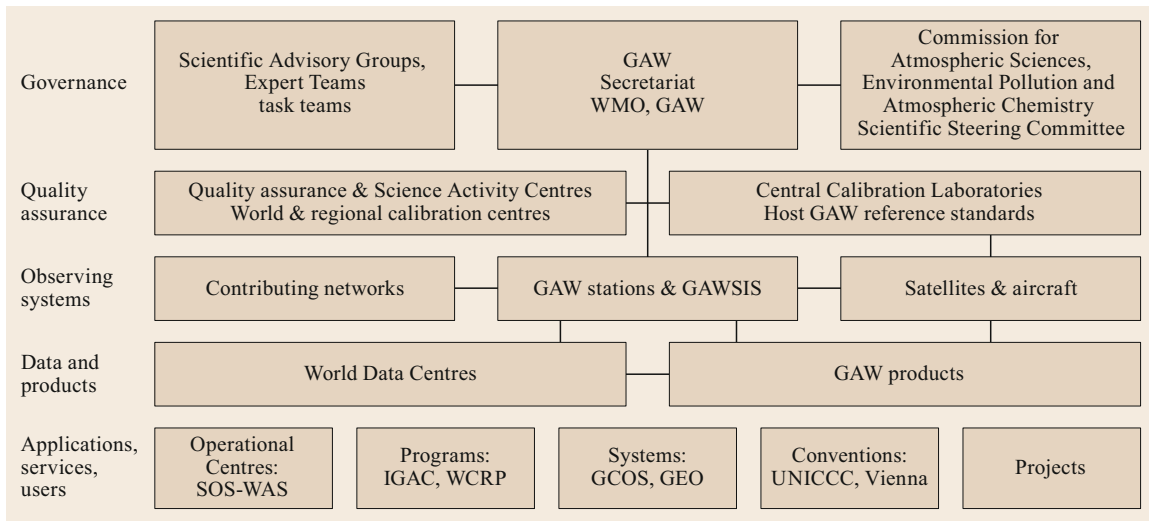


Fig. 63.2 The organizational structure of GAW (after [63.26] with the permission of the WMO)

- The station should measure other atmospheric variables that are relevant to weather and climate, including variables measured with upper-air radiosondes at the station site or in the same region.
- The station should provide a facility where intensive campaign research can be performed to augment long-term routine GAW observations, and where the testing and development of new GAW methods can be undertaken.
- 6 World Data Centres that archive the observational data and metadata, which are integrated by the GAW Station Information System (GAWSIS).

Several organizations operate a number of CCLs and WCCs at the same time (Fig. 63.2).

In recent years, satellite programs have yielded important measurements of atmospheric compounds and related parameters that complement GAW network measurements. When highly accurate local measurements from ground-based GAW stations are coupled with the near-global coverage of satellite measurements, a more complete picture of atmospheric composition and processes at the global scale can be achieved, and this approach also allows complementary checks of instrument calibrations. The Committee on Earth Observation Satellites (CEOS) has developed a strategy for achieving this cooperation within an integrated system for monitoring the atmosphere [63.27].

Since its inception in 1992, GAW has matured and developed into a program supported by a large number of WMO members. More than 100 countries have registered more than 800 stations with the GAW Station Information System (GAWSIS).

There are various GAW expert groups and central facilities that are overseen by the WMO Commission for Atmospheric Sciences (CAS) and its Environmental Pollution and Atmospheric Chemistry Scientific Steering Committee (EPAC SSC, as of CAS-16 Session). As of January 2014, these comprise:

- 7 Scientific Advisory Groups (SAGs) to organize and coordinate GAW activities by parameter and Expert Teams on World Data Centres (ET-WDC) and Near-Real Time Chemical Data Transfer (ET-NRT CDT).
- 4 Quality Assurance/Science Activity Centres (QA/SACs) that perform network-wide data quality and science-related functions.
- 35 Central Calibration Laboratories (CCLs) and World and Regional Calibration Centres (WCCs, RCCs) that maintain calibration standards and provide instrument calibration and training to the stations.

63.3.2 The NDACC International Network

The international Network for the Detection of Atmospheric Composition Change (NDACC) consists of more than 70 globally distributed, ground-based, remote-sensing research stations (Table 63.2) with over 160 currently active instruments. These instruments provide high-quality, consistent, standardized, long-term measurements of atmospheric temperatures and trace gases, particles, spectral UV radiation that reaches the Earth's surface, and physical parameters. The availability of such data allows trends in overall atmospheric composition to be detected, and the impacts of these trends on the stratosphere, troposphere, and mesosphere

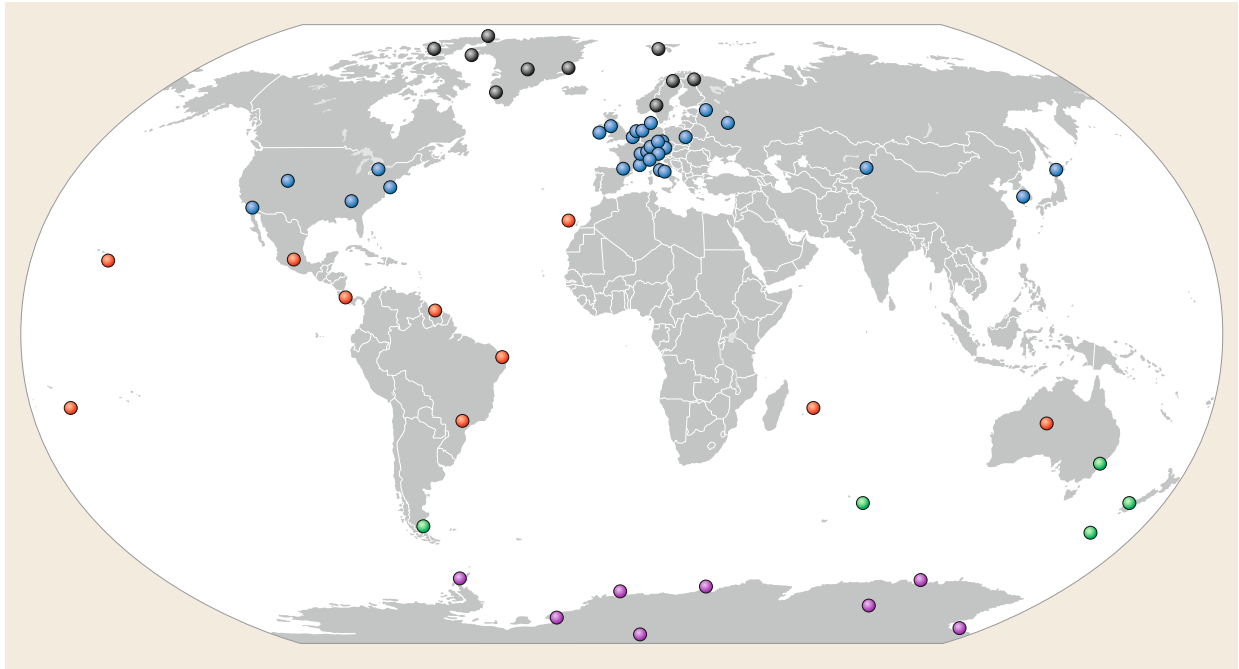


Fig. 63.3 Locations of currently active NDACC stations: *black dots* Northern Hemisphere (NH) high-latitude (> 60° N) stations, *blue dots* NH mid-latitude stations, *red dots* tropical & subtropical stations, *green* Southern Hemisphere (SH) mid-latitude stations, *purple* Antarctic stations (after [63.28])

Table 63.2 Currently active NDACC stations (stations are color-coded as defined for Fig. 63.3)

NH high-latitude stations	NH mid-latitude stations		Tropical & subtropical stations	SH mid-latitude stations	Antarctic stations
Alert	St. Petersburg	Bern	Izana	Wollongong	Palmer
Eureka	Onsala	Zimmerwald	Hilo	Lauder	Dumont dUrville
Ny Alesund	Zvenigorod	Payerne	Mauna Loa	Kerguelen	Neumayer
Thule	Bremen	Arosa	Altzomoni	Rio Gallegos	Concordia Dome-C
Summit	Legionowo	Jungfrauoch	San Jose	Macquarie	Arrival Heights
Scoresbysund	Aberystwyth	OHP (Observatoire de Haute Provence)	Paramaribo		Scott Base
Kiruna	Lindenberg	Toronto	Natal		Belgrano II Station
Sodankylä	DeBilt	Rikubetsu	Cape Matatula		South Pole
Sendre Stromfjord	Valentia	Midi-Pyrénées	La Réunion		
Harestua	Uccle	Issk-Kul	Bauru		
	Villeneuve dAscq	Rome	Alice Springs		
	Praha	Potenza			
	Gross-Enzerdorf	Boulder			
	Hohenpeissenberg	Wallops			
	Garmisch	Seoul			
	Zugspitze	Huntsville			
	Hoher Sonnblick	Table Mtn			

to be elucidated; it also makes it possible to identify links between climate change and atmospheric composition, to test and validate atmospheric measurements from satellites, to support process-focused scientific field campaigns, and to test and improve theoretical models of the atmosphere (Fig. 63.3).

The principal goal of NDACC is to allow the earliest possible identification of long-term changes to the stratospheric ozone layer and to establish the causes of such changes. This aim is achieved by performing high-quality measurements of a wide range of stratospheric chemical species and parameters using instru-

ments operated at a number of ground stations around the world.

More specifically, the network aims to:

- Study the temporal and spatial variability of atmospheric composition and structure in order to provide early detection and subsequent long-term monitoring of changes in the physical and chemical state of the stratosphere and upper troposphere; in particular, the aim is to provide the means to discern and understand the causes of such changes
- Establish the links between changes in stratospheric ozone, UV radiation at the ground, tropospheric chemistry, and climate
- Provide independent calibrations and validations of space-based sensors of the atmosphere, and supply complementary measurements
- Support field campaigns focusing on specific processes that occur at various latitudes and during various seasons
- Produce verified data sets for testing and improving multidimensional models of both the stratosphere and the troposphere.

NDACC has been endorsed by national and international scientific agencies, including the United Nations Environment Programme (UNEP) and the International Ozone Commission of the International Association of Meteorology and Atmospheric Sciences. NDACC is a major contributor to the GAW program of the WMO, and a key component of the Integrated Global Atmospheric Chemistry Observation (IGACO) initiative.

63.3.3 The BSRN International Radiation Network

The objective of BSRN is to provide observations of the best possible quality for short- and longwave surface radiation fluxes with a high sampling rate. These readings are taken from a small number of selected stations in contrasting climatic zones, together with collocated surface and upper-air meteorological data and other supporting observations.

The uniform and consistent measurements obtained throughout the BSRN network are used to:

- Monitor the background (least influenced by immediate human activities) shortwave and longwave radiative components and their variations using the best methods currently available
- Provide data that can be used to validate and evaluate satellite-based estimates of surface radiative fluxes

- Produce high-quality observational data that can be used for comparison with global climate model (GCM) calculations and for the development of regionally representative radiation climatologies.

At present, 48 BSRN stations are in operation and 11 stations are temporarily or permanently closed (Fig. 63.4). The stations measure different sets of radiation values. Some stations carry out only *basic measurements* [63.16]. Other stations carry out *other measurements* in addition to the basic measurements. Some stations also perform synoptic observations, upper-air soundings, ozone measurements and *expanded measurements*.

Additional stations are also being prepared; some of these stations should begin operating within the next few years.

63.3.4 The GRUAN International Upper-Air Network

GRUAN is envisaged as a network of 30–40 observing stations (Fig. 63.5). It builds on existing observational networks and operational capabilities and is expected to be complemented by ground-based state-of-the-art instrumentation. The task of GRUAN is to provide long-term, highly accurate measurements of the atmospheric profile, particularly the upper troposphere and lower stratosphere (upper air). The particular aim of this network is to define and assure reference quality for data and data products. The essential climate variables (ECVs) defined by GCOS—temperature, wind speed and direction, water vapor, cloud properties, and the Earth’s radiation budget (including solar irradiance)—are prioritized. High data reliability—which necessarily includes well-estimated uncertainties, thus enabling different techniques to be compared—is required to fully characterize the properties of the atmospheric column and quantitatively explore climate change and its underlying causes (e.g., to separate the long-term change signal from natural variability).

The definition of reference quality includes the full traceability of all measurements to SI units or internationally accepted standards in a consistent way, uncertainty analyses that distinguish the contributions from systematic and random errors, comprehensive documentation, data validation, and metadata collection and management. Due to the high quality of the data from GRUAN, results from more spatially comprehensive global observing systems, including satellites and current radiosonde networks, can be constrained and calibrated.

GRUAN is a heterogeneous network that includes sites supported by both research institutes and national

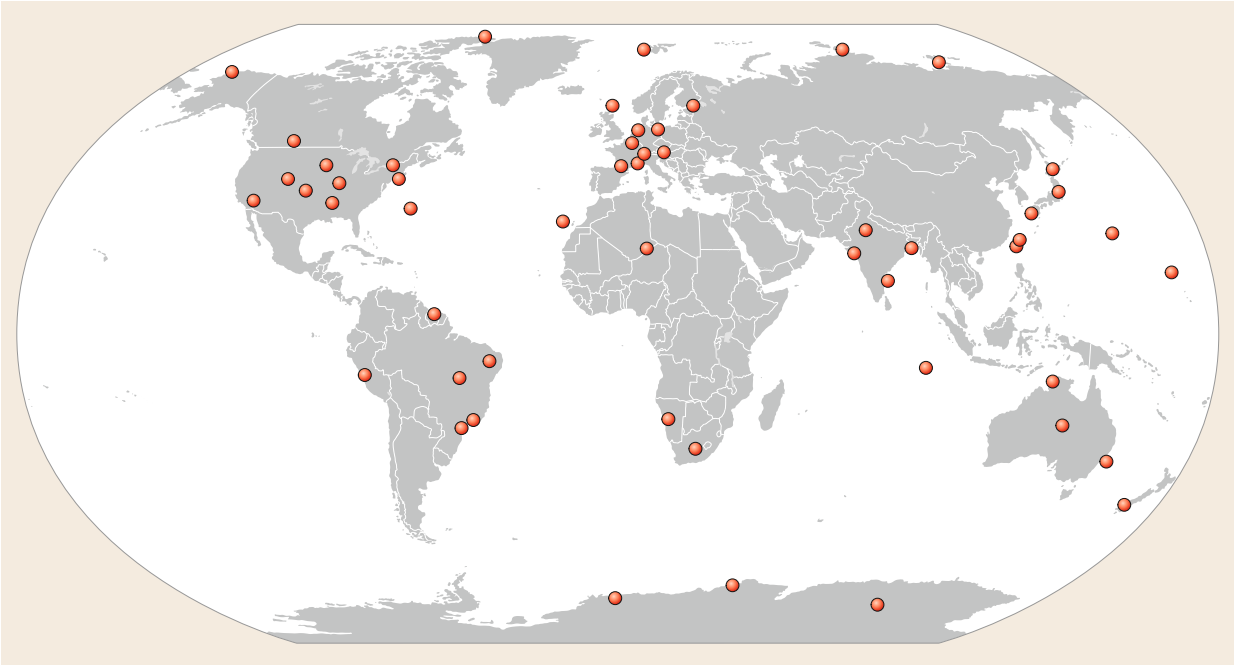


Fig. 63.4 Locations of BSRN global sites (stations that were active in 2019 (after [63.29]))

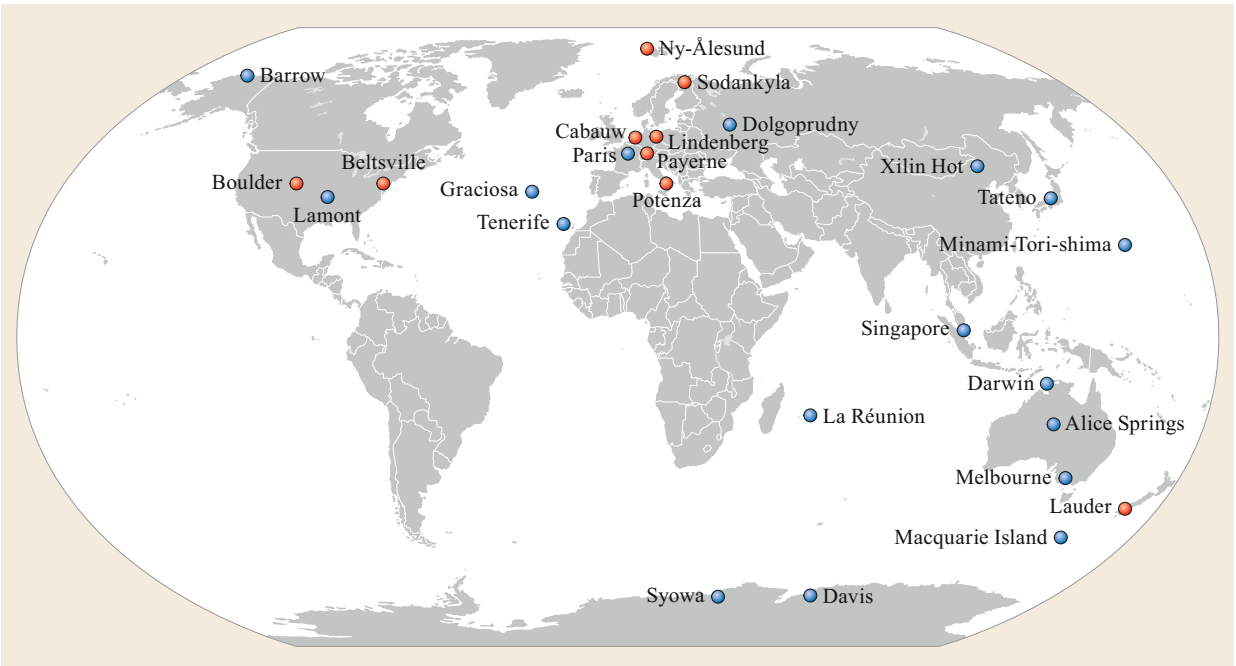


Fig. 63.5 Map of GRUAN global sites in 2017: *red* sites that are certified, *blue* sites that are yet to be certified (after [63.30])

weather services. With this in mind, the GRUAN governance structure (Fig. 63.6) was finalized in 2012 at a WMO Integrated Global Observing System (WIGOS) pilot project meeting. This structure enables the WMO,

through its technical commissions, to guide GRUAN on operational practices and procedures; to assist GRUAN in extending its operations to include a near-real-time operational mode of data delivery; and, in doing so, to

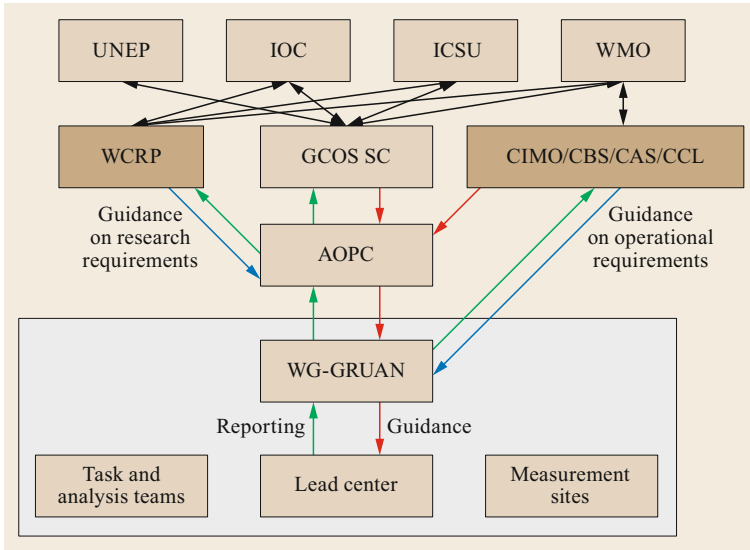


Fig. 63.6 The GRUAN heritage and governance structure. *Green arrows* show reporting responsibilities while *red arrows* show guidance responsibilities. *Blue arrows* show specific paths for guidance from the World Climate Research Programme (WCRP) and from the WMO’s technical commissions to GRUAN. *Gray arrows* show how GRUAN is linked to the highest governing bodies. The *gray box* encompasses what is referred to as GRUAN (after [63.13] © American Meteorological Society, used with permission)

help nurture additional participation of WMO members in the desired GRUAN expansion. The emergence of sites from both the research and operational measurement communities requires careful management and recognition of competing demands on different stations. Through the GRUAN Lead Centre (located in Lindenberg, Germany), the task team of site representatives, and the Working Group on GRUAN (WG-GRUAN),

efforts are being made to provide appropriate support and guidance to all sites. The WG-GRUAN and its task teams, including ex-officio members and invited experts, gather annually at GRUAN Implementation and Coordination Meetings (ICMs), which provide a forum for communication, coordination, WG-wide decision-making, community building, and the sharing of ideas and expertise.

63.4 Other Important Networks

The most important international networks of atmospheric measurements are likely the four programs discussed above, GAW, NDSC/NDACC, BSRN, and GRUAN. These four programs are strongly promoted and supported by the WMO and other international organizations. While these four programs collaborate with each other, each also collaborates with a number of additional regional, national, and international networks and programs, as described below.

63.4.1 Networks Contributing to the GAW Program

A GAW contributing network is one that has signed a letter of agreement (LoA) with the WMO. Any such agreement contains a list of the stations that are included in the GAW network as contributing stations as well as their characteristics. The list of stations that con-

tribute to the individual GAW contributing programs is available on the internet.

TCCON

The Total Carbon Column Observing Network (TCCON [63.31]) is a ground-based network of high-resolution Fourier-transform spectrometers (FTSs) that record the near-infrared solar absorption spectrum and retrieve column-average mixing ratios of CO₂, CH₄, N₂O, and several other gases with high precision and accuracy. TCCON data are a valuable complement to in-situ surface data and can be included in global inversions and other models of greenhouse gases, including studies of the carbon and nitrogen cycles. Furthermore, the column measurements serve to validate measurements from the currently active satellites GOSAT (Greenhouse Gases Observing Satellite) and SCIAMACHY (Scanning Imaging Absorption Spectrometer for Atmospheric

Chartography), and will serve the same role for data from future satellite missions such as OCO-2. TCCON also contributes to the NDACC program (see further information in Sect. 63.4.2).

EARLINET

The European Aerosol Research Lidar Network (EARLINET [63.32]), which was established in 2000, is the first aerosol lidar network. Its main goal is to provide a comprehensive quantitative database of the three-dimensional time-dependent distribution of aerosols over Europe. The network currently comprises 28 sites that are broadly distributed across Europe. Network-wide observations take place on a fixed schedule. Lidar surveillance adheres to a regular timetable of once per week at around noon, when the boundary layer is usually well developed, and twice weekly at night under low background light conditions in order to perform Raman extinction measurements. Other network activities include monitoring extraordinary events such as Saharan dust outbreaks, forest fires, photochemical smog, and volcanic eruptions. EARLINET is expected to contribute to defining and standardizing the aerosol-related products within GRUAN.

IMPROVE

The Interagency Monitoring of Protected Visual Environments (IMPROVE) program is a cooperative measurement effort governed by a steering committee composed of representatives from federal and regional-state organizations [63.33]. The IMPROVE optical monitoring network uses open-air nephelometers to measure particulate scattering hourly in primarily rural environments. In addition, the temperature and relative humidity are measured hourly at each site. These data are used in conjunction with IMPROVE aerosol data to assess light scattering status and trends and to better understand the optical properties of aerosols.

AD-Net

The Asian Dust and Aerosol Lidar Observation Network (AD-Net [63.34]) is an Asian coordinated lidar network that was established in 2001. It measures aerosol backscattering and depolarization for Asian dust and performs regional air pollution studies over East Asia.

LALINET

The Latin America Lidar Network (LALINET, a.k.a. ALINE [63.35]), is a Latin American coordinated lidar network that was established in 2001 to measure

aerosol backscatter coefficients and aerosol extinction profiles for climatological studies of the aerosol distribution over Latin America, as well as other atmospheric species such as ozone and water vapor. This federated lidar network aims to establish a consistent and statistically sound database that can enhance understanding of the aerosol distribution over the continent and its direct and indirect influences on the climate.

NADP

The US-based National Atmospheric Deposition Program (NADP) is a long-term measurement cooperative composed of representatives from federal, state, tribal, and national agencies, universities, private companies, and nongovernmental organizations. Most NADP stations are located in the United States, but several are located in Canada and in other nations. NADP operates three precipitation chemistry networks: the National Trends Network (NTN), the Atmospheric Integrated Research Monitoring Network (AIRMoN), and the Mercury Deposition Network (MDN). It also operates two gaseous atmospheric chemistry networks: the Atmospheric Mercury Network (AMNet) and the Ammonia Monitoring Network (AMoN). A central office coordinates program activity and oversees field and lab operations, data management, and quality assurance for each network. Each monitoring network follows well-defined protocols to measure acidic compounds, nutrients, base cations, and mercury in precipitation (NTN, AIRMoN, and MDN) as well as ambient concentrations of ammonia and mercury for estimating dry deposition (AMoN and AMNet). Program data are used to assess the geographic patterns and long-term temporal trends in the concentrations and deposition of major ions and mercury in precipitation, and to better understand the cycling of these chemicals in a variety of physical environments for a multitude of applications.

The IDAF (IGAC/DEBITS AFRICA) Project

The international Deposition of Biogeochemically Important Trace Species (DEBITS) program started in 1990 as part of the IGAC/IGBP (International Global Atmospheric Chemistry/International Geosphere–Biosphere Programme) core project. The aim of this project is to assess the wet and dry atmospheric deposition in tropical regions.

The IDAF (IGAC/DEBITS AFRICA) project for tropical Africa started in 1994 and is implemented in partnership with INSU (Institut National des Sciences de l'Univers, France) and the CNRS (Centre National de la Recherche Scientifique, France) as a part of the

Observatory Service (SO, France) networks. The aim of SO/IDAF is to establish a long-term measuring network to study the atmospheric composition and wet and dry atmospheric processes. As such, IDAF performs high-quality measurements of atmospheric chemical data (gaseous concentrations and the chemical composition of precipitation) in a multiyear monitoring scheme. This project has established ten monitoring sites in the major African ecosystems over West and Central Africa and South Africa: dry savanna (Niger, Mali, South Africa), wet savanna (Côte d'Ivoire and Benin), and equatorial forest (Cameroun, Congo). The sites in West and Central Africa are coordinated by the Laboratoire d'Aérodologie in Toulouse (France) and sustained by a French national proposal funded by INSU/CNRS. The South African sites are coordinated by the North West University in Potchefstroom (South Africa) and sustained by national and/or private South African projects.

The NASA Micro-Pulse Lidar Network (MPLNET)

The NASA Micro-Pulse Lidar Network (MPLNET) is a federated network of micro-pulse lidar (MPL) systems that measure aerosol and cloud vertical structure continuously, day and night, over long time periods. The resulting data are utilized in climate change studies, related aerosol and cloud research, and to provide ground validation of satellite sensors in the Earth Observing System (EOS). MPLNET also contributes to the NDACC program (see further information in Sect. 63.4.2).

The Clean Air Status and Trends Network (CASTNET)

The Clean Air Status and Trends Network (CASTNET) is a well-established national air quality monitoring network in the US that provides data which is used to assess trends in air quality, atmospheric deposition, and ecological effects due to changes in air pollutant emissions. CASTNET began collecting measurements in 1991, following the incorporation of 50 sites from the National Dry Deposition Network, which had been in operation since 1987. The National Park Service (NPS) operates more than 20 CASTNET sites within national parks and Class 1 areas. The Bureau of Land Management, Wyoming State Office joined CASTNET in 2012 when they converted five Wyoming Air Resource Monitoring System (WARMS) sites to CASTNET protocol sites. CASTNET provides long-term monitoring of air quality in rural areas so that trends in regional atmospheric nitrogen, sulfur, and ozone concentrations and deposition fluxes of sulfur and nitrogen pollutants can be discerned, thus allowing the effectiveness of national and regional air pollution control programs to be evaluated. CASTNET operates more than 85 regional sites throughout the contiguous United States, Alaska, and

Canada. Sites are located in areas where urban influences are minimal. Data from these stations therefore ideally complement the measurements of regional and global GAW stations in North America.

In-service Aircraft for a Global Observing System (IAGOS)

The European Research Infrastructure IAGOS (In-service Aircraft for a Global Observing System [63.36]) operates a global-scale monitoring system for atmospheric trace gases, aerosols, and clouds that utilizes existing global civil aircraft. This new monitoring infrastructure builds on the heritage of the research projects MOZAIC (Measurement of Ozone and Water Vapour on Airbus In-service Aircraft) and CARIBIC (Civil Aircraft for the Regular Investigation of the Atmosphere Based on an Instrument Container). The CARIBIC project is still active within IAGOS, and acts as an important airborne measurement reference standard within the wider IAGOS fleet. IAGOS is a major contributor to the in-situ component of the Copernicus Atmosphere Monitoring Service (CAMS), and provides data for users in science, weather services, and international policy-making relating to atmospheric composition. IAGOS is unique in that it makes regular in-situ observations of reactive gas and greenhouse gas concentrations and aerosol properties in the upper troposphere and lowermost stratosphere (UTLS) at high spatial resolution. It also provides routine vertical profiles of these species in the troposphere over continental sites or regions, many of which are undersampled by other networks, particularly in Africa, Southeast Asia, and South America. These stations ideally complement the measurements of GAW regional and global stations. In combination with MOZAIC and CARIBIC, IAGOS has provided long-term observations of atmospheric chemical composition in the UTLS since 1994.

63.4.2 NDACC Cooperating Networks

The Network for the Detection of Atmospheric Composition Change (NDACC) recognizes the importance of new measurement capabilities and of existing capabilities that were developed externally to NDACC. In many cases, the NDACC Steering Committee has encouraged proposals that such measurements should be formally affiliated, and has often designated measurement locations as NDACC sites. To achieve NDACC measurement status, the proposing investigators must affiliate with a specific NDACC instrument working group and agree to comply with the various NDACC protocols (measurements, intercomparisons, validation, and data). Documentation of the measurement capability and operational scope, instrument validation, and

the data quality must appear in a proposal requesting designation as an NDACC measurement. The appropriate working group is responsible for evaluating the proposal and recommending a course of action to the Steering Committee.

However, in some cases where there are regional, hemispheric, or even global networks of instruments that operate independently of NDACC, strong measurement and scientific collaboration between these networks and NDACC is of mutual benefit. Such networks have often established their own quality assurance guidelines, operational requirements, and data archiving policies, and they have national or international recognition. In such cases, bringing the complete network under the NDACC umbrella is neither practical nor desirable.

To collaborate with such networks, NDACC established the concept of a *NDACC cooperating network* to formalize its mutually beneficial relationships with regional, hemispheric, or global networks. Each cooperating network may request ex-officio representation on the NDACC Steering Committee in order to provide information on collaborative activities at the Annual NDACC Steering Committee Meeting. Where appropriate, NDACC may request representation on the corresponding oversight group of the cooperating network. Aside from BSRN and GRUAN, the six independent networks discussed below have finalized agreements that will designate them as cooperating networks, allowing them to collaborate with NDACC.

AERONET

The AERONET (Aerosol Robotic Network) program [63.39] is a federation of ground-based, remote-sensing aerosol networks established by NASA and the University of Lille that has greatly expanded due to collaborators from national agencies, institutes, universities, individual scientists, and partners. The program provides a long-term, continuous, and readily accessible public domain database of aerosol optical, microphysical, and radiative properties for aerosol research and characterization, the validation of satellite retrievals, and synergism with other databases.

The AERONET collaboration provides globally distributed observations at over 500 sites of spectral aerosol optical depth (AOD), inversion products, and precipitable water in diverse aerosol regimes (Fig. 63.7 [63.37]).

AGAGE

The Advanced Global Atmospheric Gases Experiment (AGAGE) performs real-time, high-frequency measurements of approximately 50 trace gases at stations around the world (Fig. 63.8), and interprets these measurements using three-dimensional models and inverse theory to further understand ozone depletion and climate change and to address verification issues arising from the Montreal (ozone) and Kyoto (climate) protocols. AGAGE utilizes the Medusa gas chromatography with mass spectrometry (GC-MS) and

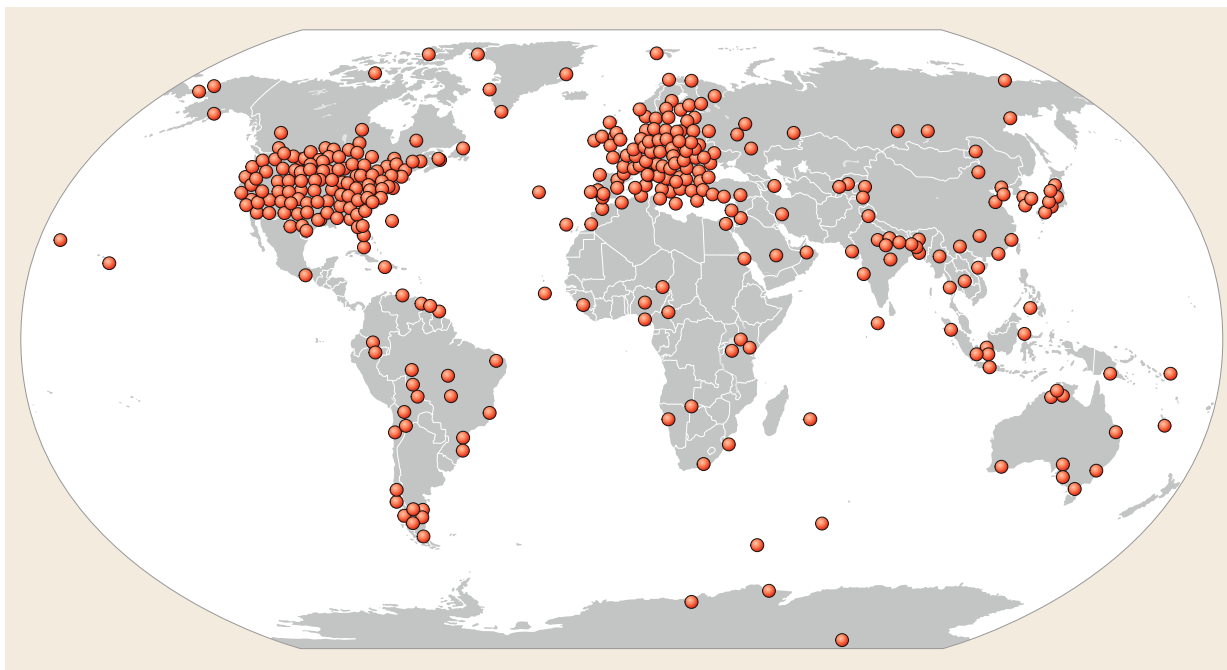


Fig. 63.7 AERONET site distribution in 2014 (after [63.37])



Fig. 63.8 AGAGE measurement sites (after [63.38])

GC-multidetector instruments, and is distinguished by its ability to measure all the important species in the Montreal Protocol and all non-CO₂ gases in the Kyoto Protocol with high frequency. The scientific objectives of AGAGE are important for furthering understanding of global chemical and climatic phenomena [63.38].

HATS

The Halocarbons and other Atmospheric Trace Species (HATS) program is a global in-situ and flask network for the measurement and analysis of halocarbons and other atmospheric trace gases that is maintained by the National Oceanic and Atmospheric Administration's Earth System Research Laboratory (NOAA/ESRL) (Fig. 63.9). The network began operating in 1977 with measurements of three trace gases (nitrous oxide, CFC-11, CFC-12) at five flask locations, and has grown to include observations of over 40 trace gases at over 30 locations as well as airborne campaigns that include both flask and in-situ monitoring. The purpose of this work is to study atmospheric trace gases that affect climate change, stratospheric ozone depletion, and air quality based on observations at NOAA and cooperating stations. Some atmospheric trace gases (e.g., SF₆) are used as atmospheric clocks to retrieve important information on atmospheric transport [63.40].

MPLNET

The NASA Micro-Pulse Lidar Network (MPLNET) [63.41] is a ground-based network of micro-pulse lidar

(MPL) [63.41] instruments collocated with sun photometers in AERONET [63.25]. These joint supersites provide both column and vertically resolved aerosol and cloud information such as optical depths, single-scatter albedos, size distributions, aerosol and cloud heights, planetary boundary layer (PBL) structure and evolution, and extinction and backscatter profiles. Principal investigators for individual sites may be from NASA, other US government agencies, universities, or foreign research groups. MPLNET is a federated network consisting of NASA sites and others run by, or run with the help of, partner research groups from around the world (Fig. 63.10 [63.42]).

SHADOZ

The Southern Hemisphere Additional Ozonesondes (SHADOZ) is a project that aims to augment balloon-borne ozonesonde launches and to archive data from tropical and subtropical operational sites (Fig. 63.11). This project was initiated in 1998 by the NASA/Goddard Space Flight Center along with NOAA and international coinvestigators in Europe, South America, Asia, and Africa. There are currently 13 operational stations in the network. The collective dataset provides the first profile climatology of tropical ozone in the equatorial region, enhances validation studies aimed at improving satellite remote-sensing techniques for tropical ozone estimation, and serves as an educational tool for students, especially in the participating countries. SHADOZ is a flexible archive that has grown and evolved as scientific

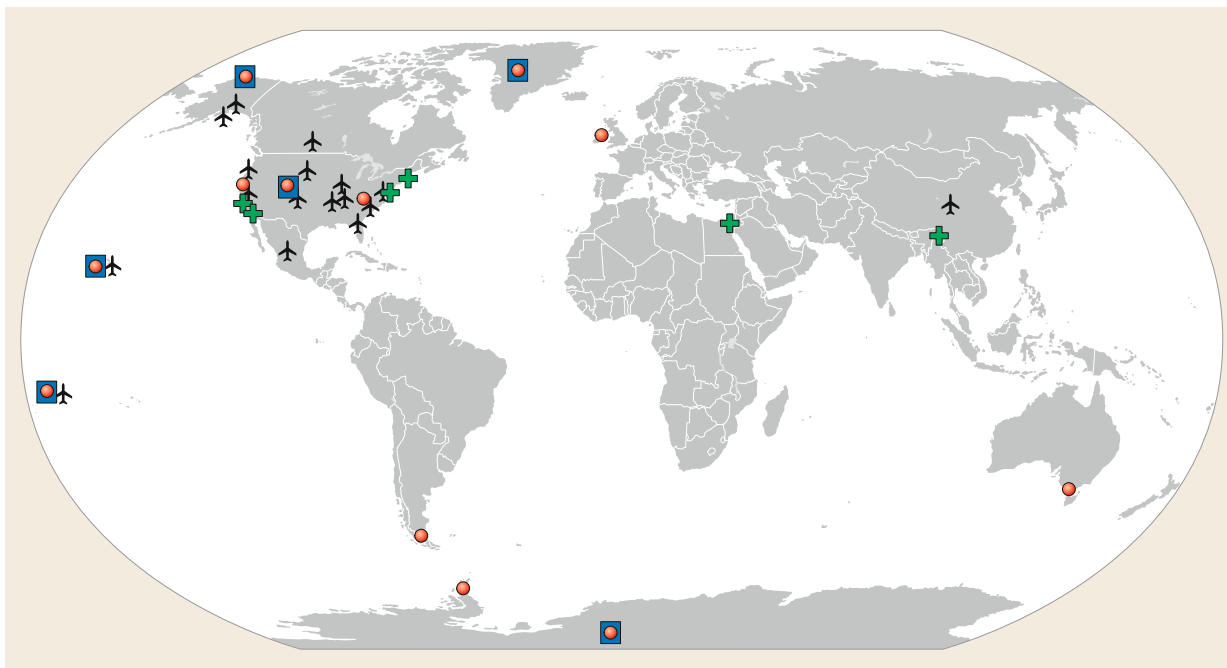


Fig. 63.9 HATS stations: *circles* flask sites, *boxes* in-situ sites, *planes* airborne sites, *crosses* flasks at airborne sites (after [63.40])

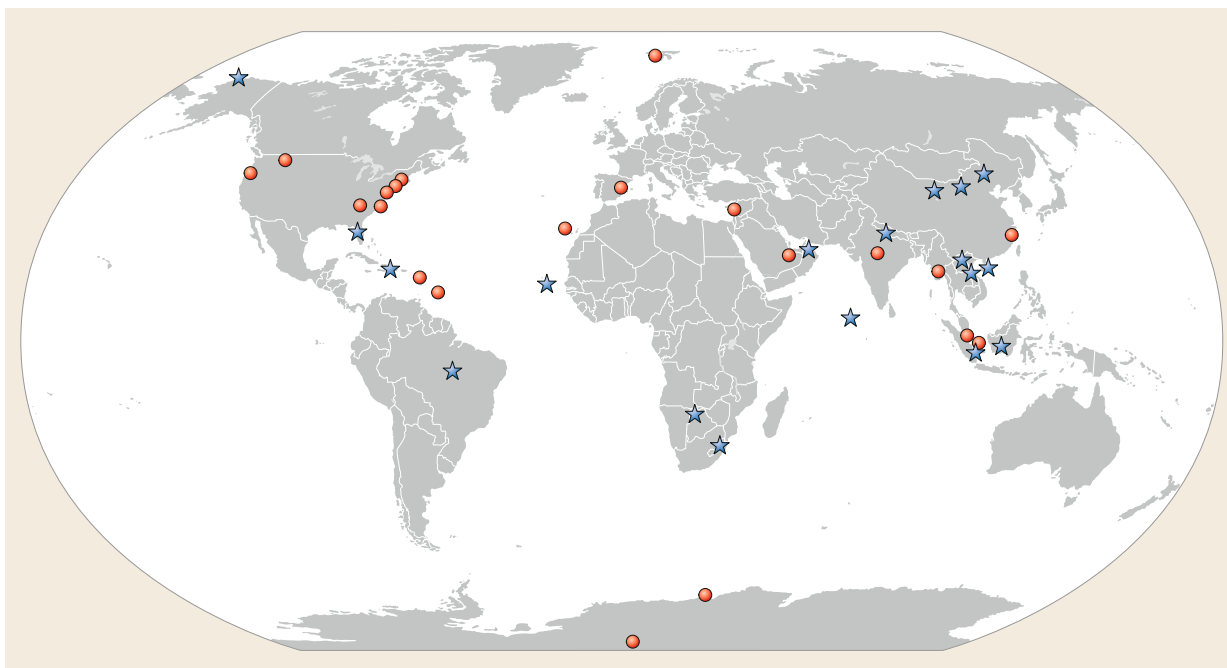


Fig. 63.10 Long-term MPLNET stations (*circles*) and field campaigns (*stars*) (after [63.43])

needs and research questions have changed. In addition to the NDACC link, SHADOZ data are transmitted regularly to the World Ozone and Ultraviolet Radiation

Data Centre (WOUDC) and archived in Hierarchical Data Format (HDF) for the satellite user community at the Aura Validation Data Center.

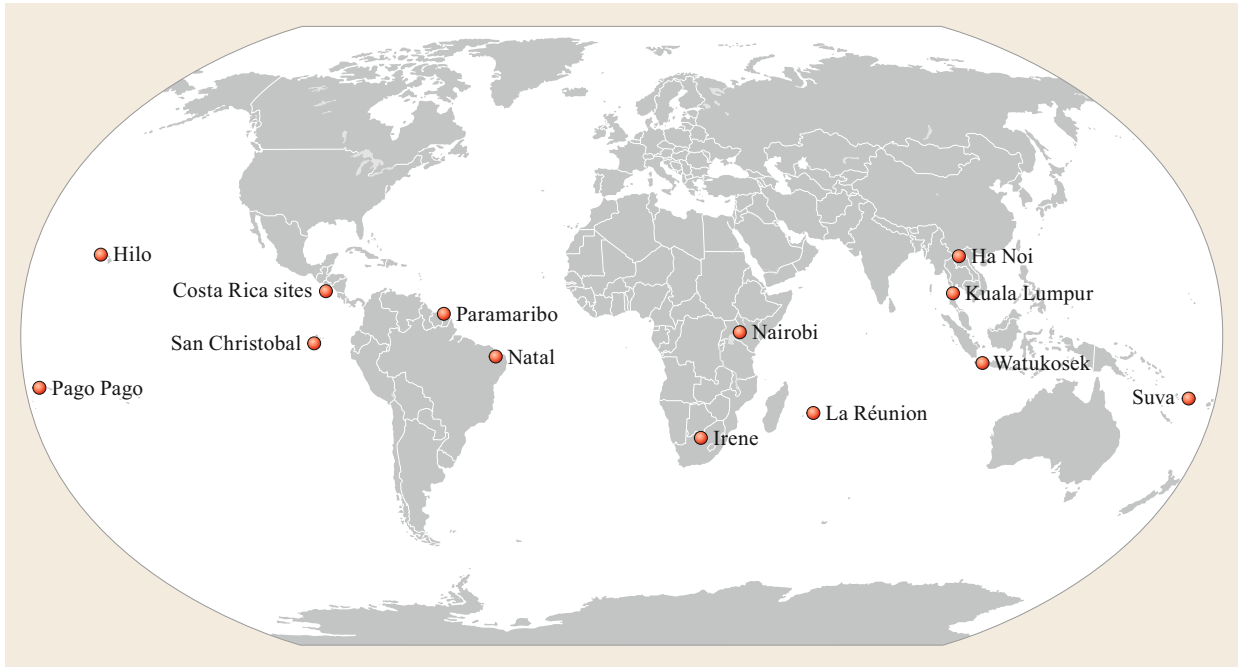


Fig. 63.11 SHADOZ stations (after [63.44])

TCCON

The Total Carbon Column Observing Network (TCCON) is a network of ground-based Fourier-transform spectrometers that record direct solar spectra in the near-infrared spectral region. The project was initiated in 2004 with support from National Institute of Water and Atmospheric Research (NIWA) (New Zealand) and NASA. It has expanded to include international coinvestigators around the world. The primary data products are high-precision total columns of CO_2 and CH_4 . Other gases, including HDO, CO, and N_2O , are also retrieved and archived. Sites for the network span the globe and thus provide diverse and targeted data to validate observations from the GOSAT and OCO-2 CO_2 -monitoring satellites as well as to probe the seasonal cycles and long-term trends in CO_2 and CH_4 (Fig. 63.12). The network shares common methodologies and technical issues with, and is a member of, the NDACC Fourier-transform infrared spectroscopy (FTIR) Working Group [63.31].

63.4.3 BSRN Collaborating Networks

BSRN is closely linked to NDACC in that atmospheric composition is a primary determinant of the nongeometric variability of the surface irradiances observed by BSRN. BSRN encourages, but does not require, simultaneous observations of aerosol optical depth, water vapor, and ozone close to its sites. Some sites belong to both networks, but most do not.

In the mid-1990s, BSRN was included in the WCRP program called The Global Energy and Water Cycle Experiment (GEWEX). By the late 1990s, BSRN had been designated a contributing network for the WMO Global Atmospheric Watch (GAW) program, and in the early 2000s it was designated the global baseline surface radiation network of the Global Climate Observing System (GCOS).

63.4.4 Collaborations of GRUAN with Other Networks

The GRUAN guide states that GRUAN shall not operate in isolation of existing networks and is not intended to replace existing networks in any way. Many GRUAN sites already belong to existing networks such as GUAN, GAW, NDACC, BSRN, and SHADOZ. For GRUAN to be successful, it must coordinate closely with the user community, and many of these networks are also likely to be users of GRUAN data. Similarly, complementary measurements from these other networks should be collated in a database to enable cross-comparisons and to quantitatively link GRUAN measurements to similar measurements made within other networks. As a result, close coordination between the governing bodies of these networks and WG-GRUAN is required on a continuous basis. This close coordination can be achieved by having members of WG-GRUAN attend steering group meetings of partner networks, and by inviting co-



Fig. 63.12 Operational TCCON stations (after [63.45])

chairs or steering group members from partner networks and projects to attend WG-GRUAN meetings.

Several currently active networks perform measurements that fall within the scope of GRUAN (e.g., sites that obtain upper-air measurements of parameters that are not the temperature, pressure, or water vapor content). Many of these networks, including the GCOS Upper-Air Network (GUAN), have developed systems for assuring the quality of their measurements. Where the systems that are currently in place are sufficient to meet the operational requirements of GRUAN, they should be used by GRUAN. Where networks are working towards QA/QC procedures, GRUAN should partner with these networks to develop systems that meet the operational requirements of both parties. In some cases, sites within these partner networks may also become GRUAN sites. This is encouraged since it promotes a traceable link between GRUAN measurements and measurements obtained at all other sites within the partner network (if the measurements within the partner network are traceable and can be quantitatively linked). Existing networks and potential resources from within those networks that are likely to be of value to GRUAN are discussed below.

GOS (Global Observing System)

The GOS provides a coordinated system of methods and facilities for making meteorological and other environmental observations at the global scale in support

of all WMO programs. The system comprises operationally reliable surface-based and space-based subsystems. The GOS includes observing facilities on land, at sea, in the air, and in space. These facilities are owned and operated by the member countries of the WMO, each of which undertakes to meet certain responsibilities in the agreed global scheme so that all countries can benefit from the consolidated efforts. Since GRUAN is intended to be an important component of the GOS, GRUAN operations must be cognizant of, and engage with, all related components of the GOS.

GUAN

As noted above, GRUAN will provide a reference backbone for GUAN. The greater the number of GUAN sites that become GRUAN sites, the more efficient the transfer of outcomes from GRUAN to GUAN. New measurement methodologies developed at GRUAN sites operating as NMHS (National Meteorological and Hydrometeorological Services) sites should efficiently propagate to other GUAN sites operated by the same NMHS.

WOUDC

The World Ozone and UV Data Centre (WOUDC) is part of the GAW program of the WMO. The WOUDC, which is operated by the Experimental Studies Section of Environment Canada in Toronto, is not so much a network as an international repository for ozone

and UV data. Many of the practices employed within the ozone measurement community are likely to be useful to GRUAN. For example, the management of the Dobson spectrophotometer and Brewer spectroradiometer networks, both of which provide data to the WOUDC, demonstrate many of the principles upon which GRUAN is founded.

SHADOZ

The Southern Hemisphere Additional Ozonesondes (SHADOZ) project was initiated to remedy the lack of consistent tropical ozonesonde observations. This was done by increasing the frequency and improving the quality of ozonesonde launches at selected tropical ozone observation sites. Rather than establishing an entirely new network, SHADOZ aims to enhance ozonesonde launches at existing facilities on a cost-share basis with international partners. The geographical coverage of the network was specifically designed to address targeted research questions.

AERONET

AERONET also contributes to the NDACC program (see Sect. 63.4.2).

EARLINET

EARLINET also contributes to the GAW program (see Sect. 63.4.1).

ARM

The goal of the US Department of Energy Atmospheric Radiation Measurement (ARM) program is to study alterations in climate, land productivity, oceans or other water resources, atmospheric chemistry, and ecological systems that may alter the capacity of the Earth to sustain life. This includes improving the atmospheric datasets used in regional and global climate models. A primary objective of the ARM user facility is improving scientific understanding of the fundamental physics of interactions between clouds and radiative feedback processes in the atmosphere. Five of the current GRUAN sites are also ARM sites, in part because the radiation measurements made at these sites satisfy many of the ECV measurement requirements within GRUAN.

Cloudnet

The Cloudnet project aims to provide systematic evaluations of clouds in forecast and climate models by comparing the model output with continuous ground-based observations of the vertical profiles of cloud properties. In the models, the properties of clouds are simplified and expressed in terms of the fraction of the model grid box filled with cloud together with the liq-

uid and ice water content of the clouds [63.46, 47]. The Cloudnet project produces vertical profiles of cloud and aerosol properties at high temporal and spatial resolution for the following reasons:

- To optimize the use of existing datasets in the development and validation of new cloud remote-sensing synergy algorithms
- To continuously evaluate the representation of clouds in climate and weather forecast models
- To demonstrate the potential of an operational network to improve the representation of clouds in models.

Partnership with Meteorological Agencies

Meteorological agencies that produce global real-time analyses (e.g., UK Met Office (UKMO), German Meteorological Service (DWD), European Centre for Medium-Range Weather Forecasts (ECMWF), National Centers for Environmental Prediction (NCEP), NOAA, and Japan Meteorological Agency (JMA)) or historical reanalyses (e.g., NCEP/NCAR (National Center for Atmospheric Research), NCEP/DOE (Department of Energy), NCEP-CFSR (Climate Forecast System Reanalysis), ECMWF, JMA, NOAA, and NASA) are likely to use the high-quality data produced by GRUAN. There are well-developed systems for monitoring the quality of operational observations, whether it is the performance of individual radiosonde sites or the bias corrections required by current satellite observations. Therefore, diagnostics obtained from the various assimilation schemes used in such activities provide valuable metadata on the consistency of the GRUAN measurements with other data used in the operational analyses (thereby facilitating comparisons of GRUAN measurements with, for example, satellite-based measurements) and on the representativeness of the estimated uncertainty in the GRUAN data. If GRUAN data are to be used in 4-D Var assimilation schemes for ingestion or validation purposes, the precise 4-D (latitude, longitude, altitude, and time) coordinates associated with any measurement must be available. Reference sites will be essential aids when characterizing observational biases and the impact of observing system changes and when attempting to understand model errors, all of which are important aspects of high-quality reanalysis. Studies which demonstrate the value that GRUAN measurements add to numerical weather prediction (NWP) and to meteorological reanalyses are currently lacking. Some GRUAN sites may also be National Meteorological Service (NMS) sites, or they may be paired with a NMS site to extend the variety of measurements performed, with the result that NMSs are likely to provide partial or full support for a site.

63.5 Quality Control

Quality control of atmospheric measurement techniques and the data measured at network stations was first addressed in the WMO GAW program. Other networks that overlap considerably with the GAW network follow the same quality assurance routines as used in GAW. See also Chap. 3, which specifically addresses quality control.

63.5.1 Objectives of Quality Control

The primary objectives of the GAW QA system are to ensure that the data in the World Data Centres (WDCs) are consistent and are of known and adequate quality, and that they meet GAW data-quality objectives and are supported by a comprehensive description of the methodology. They must be supported by comprehensive metadata and should be sufficiently complete to describe global atmospheric states with respect to spatial and temporal distributions. The QA system involves quality assurance and calibration centers that ensure the quality of observations through adherence to measurement guidelines established by the Scientific Advisory Groups and through calibrations that are traceable to World Calibration Standards.

The GAW quality assurance (QA) system impacts all aspects of atmospheric physics and chemistry observations, including:

- The training of station personnel
- The assessment of infrastructure, operations, and the quality of observations at the sites
- The documentation of data submitted to the WDCs
- Improvements in the quality and documentation of legacy data at the WDCs.

Five types of central facilities dedicated to six groups of measurement variables are operated by WMO members and form the basis for quality assurance and data archiving in the GAW global monitoring networks (Fig. 63.13). They include Central Calibration Laboratories (CCLs) that host Primary Standards (PS), Quality Assurance/Science Activity Centres (QA/SACs), World Calibration Centres (WCCs), Regional Calibration Centres (RCCs), and World Data Centres (WDCs) that are responsible for archiving and providing access to GAW data.

63.5.2 Regulations for Quality Control

The principles of the GAW QA system are to:

- Fully support the GCOS climate monitoring principles
- Use only one reference standard or scale (the Primary Standard) across the network, meaning that

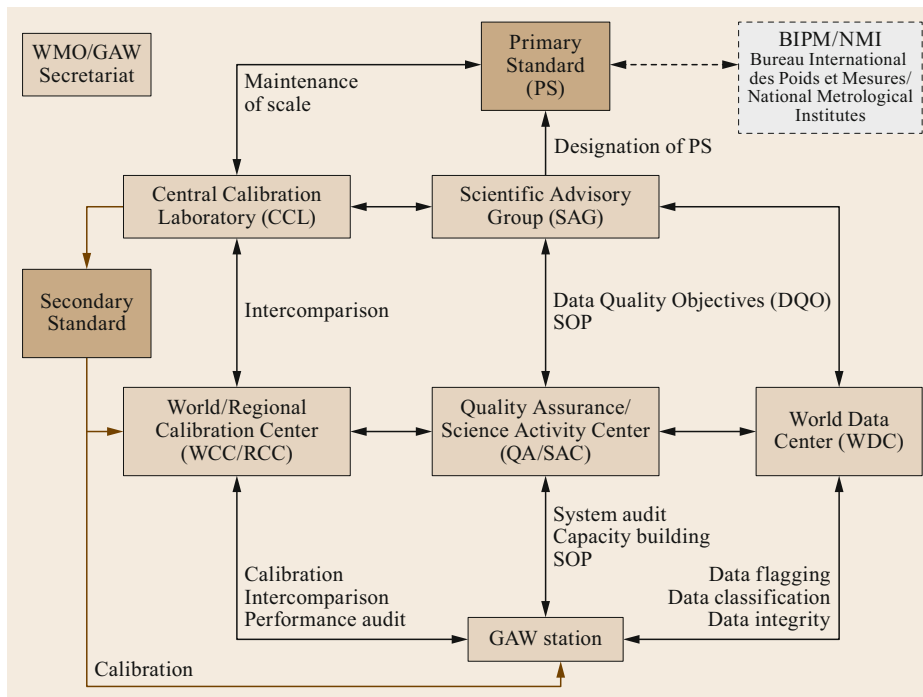


Fig. 63.13 Conceptual framework of the GAW quality system (after [63.48] with the permission of the WMO)

there is only one institution that is responsible for this standard

- Ensure full traceability of all measurements made by GAW global, regional, and contributing stations to the primary standard
- Define data quality objectives (DQOs)
- Provide established guidelines on how to meet these quality targets, i.e., harmonized measurement techniques based on measurement guidelines (MGs) and standard operating procedures (SOPs)

- Establish MGs or SOPs for these measurements
- Use detailed logbooks for each parameter that contain comprehensive metadata relating to the measurements, maintenance, and *internal* calibrations
- Perform regular independent assessments (system and performance audits)
- Submit data and associated metadata to the responsible World Data Centre in a timely manner in order to facilitate independent reviews of the data by the wider community.

63.6 Maintenance

Long-term education, training, workshops, calibration station audits/visits, and twinning are provided to build capacity in the atmospheric sciences in the GAW network. These capacity-building activities have become increasingly important as many GAW stations in developing countries have initiated operations.

63.6.1 Regulations for Maintenance

GAW procedures address the quality of an observation through the maintenance of components of the entire measurement process, ranging from operational procedures at stations to the submission of appropriately quality-controlled data to the World Data Centre. The recommended GAW principles are as follows [63.49]:

- Harmonize the measurement methodologies used at all stations using measurement guidelines and standard operating procedures
- Conduct regular intercomparison campaigns.

In addition, certain measurement principles are parameter specific:

- Use data-quality objectives that specify tolerable levels of uncertainty, as well as completeness, comparability, and representativeness
- Maintain full traceability to the World Reference Standard for all measurements performed by GAW global and regional stations
- Establish standard operating procedures for the measurements
- Maintain a detailed *logbook* of measurement methodologies and procedures for instruments, maintenance, and *internal* calibration.

63.7 Application

The main task of the WMO and other networks of atmospheric measuring techniques is to obtain continuous information on the physical state and chemical composition of the atmosphere at a detailed scientific level. The corresponding World Data Centres provide long-term records of a wide variety of atmospheric data for scientific research and climate change investigations, which help to improve our understanding of interactions between the atmosphere and the Earth's surface.

63.7.1 Modeling Applications of GAW Data

The GAW Scientific Advisory Group (SAG) on Modelling Applications (SAG-APPs) was established in 2016 by the WMO Congress to enhance exchange between the GAW observational community, the modelling communities, and other end users of atmospheric

composition data. Near-real-time data applications such as air quality forecasting require timely access to observations. Therefore, one of the main objectives of this group is *to demonstrate the usefulness of exchanging chemical observational and modeling data in near real time (NRT: hours to days) to support monitoring and forecasting applications.*

Members of SAG-APPs represent a broad range of disciplines and a variety of research and user communities. SAG-APPs promotes current and envision future applications that (will) make use of NRT data delivery at regional to global scales. It is a collaborative effort between GAW, the World Weather Research Programme (WWRP), and the World Climate Research Programme (WCRP). This SAG also works closely with WIS/WIGOS—the WMO's Integrated Global Observation System.

An important service that is already operational is the Copernicus Atmosphere Monitoring Service (CAMS; <https://atmosphere.copernicus.eu/about-cams>, Accessed 24 July 2021), which provides near-real-time data analyses of and forecasts for multiple atmospheric chemical constituents that are relevant to air quality and other environmental issues at global and regional scales. The Sand and Dust Storms Warning Advisory and Assessment System (SDS-WAS; <https://sds-was.aemet.es/>, Accessed 24 July 2021) provides health-relevant information relating to sand and dust storms. A schematic of potential GAW services is given in a figure under (WMO; <https://community.wmo.int/activity-areas/gaw/science/modelling-applications>, Accessed 24 July 2021).

63.7.2 Objectives and Membership of SAG-APPs

The main objective of SAG-APPs is to develop a portfolio of modeling products and services relating to atmospheric composition, and more specifically to

demonstrate the benefits of exchanging observational chemical data in near real time to support monitoring and forecasting applications. The rationale for creating SAG-APPs is the WMO's strategy of providing advice and support to meteorological institutions who wish to broaden their services and products from conventional weather forecasting to services that include aspects of the atmospheric environment. The idea is that developing a portfolio of demonstration projects (i.e., designing concepts, endorsing initiatives, and stimulating communities to develop these projects) will provide the necessary impetus to speed up the emergence and expansion of such services. These developments will not only benefit NRT applications but also provide a closer link to assessment activities such as those currently performed by the Task Force on Hemispheric Transport of Air Pollution (TF HTAP) and partner organizations in the health (e.g., World Health Organization (WHO)), agriculture/vegetation (e.g., Convention on Long-Range Transboundary Air Pollution (CLRTAP)), and climate (e.g., Chemistry Climate Model Initiative (CCMI)) communities.

63.8 Future Developments

The WMO Global Atmosphere Watch (WMO-GAW) program recognizes the need to develop up-to-date GAW products and services for a variety of user communities as well as the need to support cross-cutting research activities relating to the forecasting of atmo-

spheric composition changes and the environmental phenomena induced by them. In this context, ensuring that observations are made available to modeling activities in a timely manner is crucial [63.14].

63.9 Further Reading

Much of the content of this chapter is also available on the Internet. The WMO, GAW, and all the networks that were created after them have websites that can be consulted for further reading. Internet links for differ-

ent networks are provided in this chapter and in the following references: GAW [63.14], NDACC [63.45], BSRN [63.29], GRUAN [63.30].

References

- | | | | |
|------|---|------|---|
| 63.1 | D.R. Bates, M. Nicolet: The photochemistry of atmospheric water vapor, <i>J. Geophys. Res.</i> 55 , 301–327 (1950) | 63.4 | R.S. Stolarski, R.J. Cicerone: Stratospheric chlorine: a possible sink for ozone, <i>Can. J. Chem.</i> 52 , 1610–1615 (1974) |
| 63.2 | D.G. Murcray, T.G. Kyle, F.H. Murcray, W.J. Williams: Nitric acid and nitric oxide in the lower stratosphere, <i>Nature</i> 218 , 78–79 (1968) | 63.5 | M.J. Molina, F.S. Rowland: Stratospheric sink for chlorofluoromethanes: chlorine atom-catalysed destruction of ozone, <i>Nature</i> 249 , 810–812 (1974) |
| 63.3 | P.J. Crutzen: Estimates of possible future ozone reductions from continued use of fluorochloromethanes (CF ₂ Cl ₂ , CFCl ₃), <i>Geophys. Res. Lett.</i> 1 , 205–208 (1974) | 63.6 | M. Ackerman, D. Frimout, C. Muller, D. Nevejans, J.C. Fontanella, A. Girard, L. Gramont, N. Louisnard: Recent stratospheric spectra of NO and NO ₂ , <i>Can. J. Chem.</i> 52 , 1532–1535 (1974) |

- 63.7 R.J. Cicerone, R.S. Stolarski, S. Walters: Stratospheric ozone destruction by man-made chlorofluoromethanes, *Science* **186**, 1165–1167 (1974)
- 63.8 W.J. Williams, J.J. Kusters, A. Goldman, D.G. Murray: Measurement of the stratospheric mixing ratio of HCl using infrared absorption technique, *Geophys. Res. Lett.* **4**, 383–385 (1976)
- 63.9 M. De Mazière, A.M. Thompson, M.J. Kurylo, J.D. Wild, G. Bernhard, T. Blumenstock, G.O. Braathen, J.W. Hannigan, J.-C. Lambert, T. Leblanc, T.J. McGee, G. Nedoluha, I. Petropavlovskikh, G. Seckmeyer, P.C. Simon, W. Steinbrecht, S.E. Strahan: The Network for the Detection of Atmospheric Composition Change (NDACC): history, status and perspectives, *Atmos. Chem. Phys.* **18**, 4935–4964 (2018)
- 63.10 GAW Report No. 228: WMO Global Atmosphere Watch (GAW) implementation plan: 2016–2023, https://library.wmo.int/opac/doc_num.php?explnum_id=3395 (2017), Accessed 24 July 2021
- 63.11 A. Ohmura, E.G. Dutton, B. Forgan, C. Fröhlich, H. Gilgen, H. Hegner, A. Heimo, G. König-Langlo, B. McArthur, G. Müller, R. Philipona, R. Pinker, C.H. Whitlock, K. Dehne, M. Wild: Baseline Surface Radiation Network (BSRN/WCRP): new precision radiometry for climate research, *Bull. Am. Meteorol. Soc.* **79**, 2115–2136 (1998)
- 63.12 WMO Pub No. GCOS – 200: The Global Observing System for Climate: implementation needs, https://library.wmo.int/opac/doc_num.php?explnum_id=3417 (2016), Accessed 24 July 2021
- 63.13 G.E. Bodeker, S. Bojinski, D. Cimini, R.J. Dirksen, M. Haefelin, J.W. Hannigan, D.F. Hurst, T. Leblanc, F. Madonna, M. Maturilli, A.C. Mikalsen, R. Philipona, T. Reale, D.J. Seidel, D.G.H. Tan, P.W. Thorne, H. Vömel, J. Wang: Reference upper-air observations for climate: from concept to reality, *Bull. Am. Meteorol. Soc.* **97**, 123–135 (2016)
- 63.14 World Meteorological Organization: Global Atmosphere Watch Programme (GAW), <https://community.wmo.int/activity-areas/gaw>, Accessed 24 July 2021
- 63.15 M.J. Kurylo, S. Solomon: *Network for the Detection of Stratospheric Change: a Status and Implementation Report* (NASA, Washington, D. C 1990)
- 63.16 M.J. Kurylo, A.M. Thompson, M. De Mazière: The Network for the Detection of Atmospheric Composition Change: 25 Years Old and Going Strong, *Earth Obs.* **28**, 4–15 (2016)
- 63.17 L.B.J. McArthur: *Baseline Surface Radiation Network (BSRN) operation manual (version 1.0)*, WMO/TD–No. 879, World Climate Research Programme (World Meteorological Organization, Geneva 1998)
- 63.18 H. Gilgen, C. Whitlock, F. Koch, G. Müller, A. Ohmura, D. Steiger, R. Wheeler: *Technical Plan for BSRN (Baseline Surface Radiation Network) Data Management (version 2.1, final)*, *World Radiation Monitoring Center Tech. Rep. 1*, WMO/TDNo. 443, World Climate Research Programme (World Meteorological Organization, Geneva 1995)
- 63.19 GCOS: *Global Climate Observing System: Ensuring the Availability of Global Observations for Climate* (Secretariat of the World Meteorological Organization, Geneva 2007) p. 16
- 63.20 GCOS: *GCOS Cooperation Mechanism: Improving Climate Observations for Sustainable Development and Adaptation to Climate Change* (Secretariat of the World Meteorological Organization, Geneva 2008) p. 4
- 63.21 D.J. Seidel, F.H. Berger, H.J. Diamond, J. Dykema, D. Goodrich, F. Immler, W. Murray, T. Peterson, D. Sisterson, M. Sommer, P. Thorne, H. Vömel, J. Wang: Reference upper-air observations for climate: rationale, progress, and plans, *Bull. Am. Meteorol. Soc.* **90**, 361–369 (2009)
- 63.22 GEOSS: 10-year implementation plan, as adopted 14 February 2005, https://www.jodc.go.jp/info/ioc_doc/INF/139522e.pdf (2005), Accessed 24 July 2021
- 63.23 GEO: *The Full Picture* (Tudor Rose, Leicester 2007)
- 63.24 G. Ohring: Achieving satellite instrument calibration for climate change. Workshop report, <https://www.nist.gov/system/files/documents/2017/03/15/asic3.pdf> (2007), Accessed 24 July 2021
- 63.25 World Meteorological Organization: GAW station, networks and other measurements, <https://community.wmo.int/gaw-stations-network-and-other-measurements>, Accessed 24 July 2021
- 63.26 World Meteorological Organization: Structure of GAW, <https://community.wmo.int/activity-areas/gaw/structure-gaw>, Accessed 24 July 2021
- 63.27 WMO/CEOS: *GAW No. 140: Report on a Strategy for Integrating Satellite and Ground-Based Observations of Ozone*, WMO TD No. 1046 (World Meteorological Organization, Geneva 2001)
- 63.28 M. De Mazière, A.M. Thompson, M.J. Kurylo, J.D. Wild, G. Bernhard, T. Blumenstock, G.O. Braathen, J.W. Hannigan, J.C. Lambert, T. Leblanc, T.J. McGee, G. Nedoluha, I. Petropavlovskikh, G. Seckmeyer, P.C. Simon, W. Steinbrecht, S.E. Strahan: The Network for the Detection of Atmospheric Composition Change (NDACC): history, status and perspectives, *Atmos. Chem. Phys.* **18**, 4935–4964 (2018)
- 63.29 World Radiation Monitoring Center – Baseline Surface Radiation Network: <https://bsrn.awi.de/nc/stations/maps/>, Accessed 24 July 2021
- 63.30 GCOS Reference Upper-Air Network (GRUAN): The climate reference network, <http://www.gruan.org/>, Accessed 24 July 2021
- 63.31 Total Carbon Column Observing Network: <http://www.tccon.caltech.edu/>, Accessed 24 July 2021
- 63.32 EARLINET: A European aerosol research network to establish an aerosol climatology, <https://www.earlinet.org/>, Accessed 24 July 2021
- 63.33 IMPROVE: Interagency monitoring of protected visual environments, <http://vista.cira.colostate.edu/improve/>, Accessed 24 July 2021
- 63.34 AD-Net: The Asian dust and aerosol lidar observation network, <https://www-lidar.nies.go.jp/AD-Net/>, Accessed 24 July 2021
- 63.35 LALINET: Latin American lidar network, <http://www.lalinet.org/>, Accessed 24 July 2021

- 63.36 IAGOS: In-service aircraft for a global observing system, <https://www.iagos.org/>, Accessed 24 July 2021
- 63.37 Godard Space Flight Center: AERONET – aerosol robotic network, <https://aeronet.gsfc.nasa.gov/>, Accessed 24 July 2021
- 63.38 Advanced global atmospheric gases experiment, <http://agage.mit.edu/>, Accessed 24 July 2021
- 63.39 B.N. Holben, T.F. Eck, I. Slutsker, D. Tanre, J.P. Buis, K.A. Setzer, E. Vermote, J.A. Reagan, Y.J. Kaufman, T. Nakajima, F. Lavenue, I. Jankowiak, A. Smirnov: AERONET—A federated instrument network and data archive for aerosol characterization, *Remote Sens. Environ.* **66**, 1–16 (1998)
- 63.40 NOAA Earth System Research Laboratory: Global monitoring division, <https://gml.noaa.gov/>, Accessed 24 July 2021
- 63.41 E.J. Welton, K.J. Voss, P.K. Quinn, P.J. Flatau, K. Markowicz, J.R. Campbell, J.D. Spinhirne, H.R. Gordon, J.E. Johnson: Measurements of aerosol vertical profiles and optical properties during INDOEX 1999 using micropulse lidars, *J. Geophys. Res.* **107**, 8019 (2002)
- 63.42 J.D. Spinhirne, J.A.R. Rall, V.S. Scott: Compact eye safe lidar systems, *Rev. Laser Eng.* **23**, 112–118 (1995)
- 63.43 Network for the Detection of Atmospheric Composition Change: <http://www.ndaccdemo.org/about/cooperating-networks/nasa-micro-pulse-lidar-network>, Accessed 24 July 2021
- 63.44 NASA: SHADOZ – Southern Hemisphere Additional OZonesondes, <https://tropo.gsfc.nasa.gov/shadoz/>, Accessed 24 July 2021
- 63.45 Network for the Detection of Atmospheric Composition Change: Total carbon observing network, <http://www.ndaccdemo.org/about/cooperating-networks/total-carbon-column-observing-network>, Accessed 24 July 2021
- 63.46 A.J. Illingworth, R.J. Hogan, E.J. O'Connor, D. Bouniol, M.E. Brooks, J. Delanoé, D.P. Donovan, J.D. Eastment, N. Gaussiat, J.W.F. Goddard, M. Haeffelin, H. Klein Baltink, O.A. Krasnov, J. Pelon, J.-M. Piriou, A. Protat, H.W.J. Russchenberg, A. Seifert, A.M. Tompkins, G.-J. van Zadelhoff, F. Vinit, U. Willén, D.R. Wilson, C.L. Wrench: CLOUDNET – continuous evaluation of cloud profiles in seven operational models using ground-based observations, *BAMS* **88**, 883–898 (2007)
- 63.47 Cloudnet: A network of stations for the continuous evaluation of cloud and aerosol profiles in operational NWP models, <http://www.cloud-net.org/>, Accessed 24 July 2021
- 63.48 World Meteorological Organization: Quality assurance, <https://community.wmo.int/quality-assurance>, Accessed 24 July 2021
- 63.49 WMO: *GAW No. 142: Strategy for the Implementation of the Global Atmosphere Watch Programme (2001–2007)*, WMO TD No. 1077 (World Meteorological Organization, Geneva 2001)

Rolf Philipona

Federal Office of Meteorology and
Climatology MeteoSwiss
Davos Dorf, Switzerland
rolf.philipona@gmail.com



Rolf Philipona's research interests are radiation and upper-air measurements and related climate change. He was a senior scientist at the World Radiation Center at Davos and at the Federal Office of Meteorology and Climatology (MeteoSwiss). He lectured at the Institute for Atmospheric and Climate Sciences at ETH Zurich. He received the 2002 WMO Prof. Dr. Vilho Vaisala Award and 2007 WMO-Norbert Gerbier-Mumm International Award. He retired from MeteoSwiss in 2017.

Integration

64. Integration of Meteorological and Ecological Measurements

Hans Peter Schmid , Corinna Rebmann 

Recent developments in both environmental measurement technology and numerical modeling have cleared the way for integrative approaches to Earth system science. Modern Earth system models can now account for interactions and feedback between the atmosphere, oceans, the cryosphere, and ecosystems at global to regional scales and over timescales ranging from hours to decades or longer. In turn, such models call for integrated data fields from observations in each of these Earth system compartments as well as their interactions. The nature, spatial scale, and data structure of ecological measurements (soil and vegetation parameters, ecosystem–atmosphere exchange fluxes) are distinctly different from those of most meteorological measurements. This chapter summarizes the basic notions of ecological measurement networks and addresses the challenges of integrating data from ecological and meteorological networks.

64.1	Relevance and Parameters of Networks	1714
64.1.1	Ecological Measurement Networks.....	1715
64.1.2	Measured Parameters.....	1716
64.2	History	1716
64.2.1	History of Ecological Measurements.....	1716
64.3	Structures of Notable Networks	1717
64.4	Temporal and Spatial Scales	1720
64.5	Quality Control of Ecological Measurement Networks	1720
64.6	Maintenance	1721
64.7	Applications	1721
64.8	Further Developments	1721
64.9	Further Reading	1722
	References	1722

Ecology is the branch of biology that studies the interactions between organisms and their environment [64.1]. A community of living organisms that interact with each other and with the inanimate components of their environment is known as an *ecosystem* [64.2]. All organisms on Earth depend on the availability of water, energy, carbon, and nutrients, and ecosystems typically evolve to optimize the way these *life elixirs* are exchanged and cycled between their biotic and abiotic components. These interactions can involve biological, chemical, physical, and—depending on the timescale—geological processes. Thus, one speaks of biogeochemical or biogeophysical cycling. With these definitions in mind, it is quite obvious that the relationship between ecology and meteorology must be an intricate one. For most terrestrial organisms, the primary source of water is precipitation (directly or indirectly); for plants, the primary source of energy is solar radiation and the most important source of carbon is atmospheric CO₂. While the basic distribution of nutrients (mostly compounds containing N, P, or S) is governed over the long term by geological and hydrological processes, a significant amount of nutrients is

redistributed by the atmosphere (as cloud condensation nuclei, dissolved in precipitation water, as aerosols, or as trace-gas admixtures). The kinetics of biochemical reactions that both create and decompose organisms are directly dependent on temperature [64.3] and the stability of enzymes. The biological catalysts that make metabolic processes possible [64.4] are only functional within specific ranges of temperature. Clearly, plant growth and ecosystem development are largely governed by meteorological processes and the state of the atmosphere over timescales ranging from seconds to decades or longer.

On the other hand, the earliest regular meteorological observations (performed in India around 5000 years ago [64.5]) were likely motivated by agriculture and the need for crop yield optimization. So, interest in identifying the parameters that control ecosystem function drove the earliest development of meteorological instrumentation [64.6].

This chapter on the integration of meteorological and ecological measurements only addresses terrestrial ecosystems. Much of what is mentioned here is also relevant to aquatic (freshwater and marine) ecosys-

tems, but the spatial and temporal scales as well as the relevant parameters and measurement techniques for aquatic ecosystems can differ quite strongly from those of terrestrial ecosystems. Thus, the challenges involved in integrating meteorological and ecological measurements for terrestrial ecosystems are likely different from those involved in similar measurement integration for aquatic systems. The principal focus is

on regional or global networks of ecological measurements.

Historically, the first ecological measurements occurred at agricultural crop sites, and many of the most important measurement techniques (e.g., the eddy-covariance technique for CO₂ flux measurements and the eddy accumulation technique) were first developed for agricultural or agronomy applications [64.7, 8].

64.1 Relevance and Parameters of Networks

The establishment of meteorological and aerological measurement networks was driven by two primary motivations (see Chap. 63). One was to gain information on the temporal evolution of the weather or air quality in a given location or region. Measurements outside the region of interest (especially upstream) provided data on possible advection into the region. Networks, especially global networks, formalized and generalized this utilization of *upstream* information. One of the primary uses of modern meteorological and aerological measurement networks is thus to initialize and reanalyze global and regional prediction models.

The other motivation for creating meteorological and aerological networks derives from the increasing interest in global climate variability and climate change, which first gained public attention in the 1960s [64.9, 10]. Measurement networks have proven crucial to the detection of atmospheric variability (both spatial and temporal), short-term disturbances (e.g., due to volcanic eruptions, major industrial accidents, and wildfires), and long-term trends in the state of the atmosphere.

As outlined in Chap. 63, atmospheric networks are commonly not only networks of measurements but also networks of scientific exchange for the development and coordination of observational methods, techniques, quality control, and instrument calibration. Standardization of calibration routines and data quality control ensures that network datasets are internally consistent. In order to fulfill their purpose as meteorological and aerological networks that monitor a given region or the whole globe, the distance between neighboring measurement stations must be small enough to ensure that the variables sensed by different stations are correlated to some extent [64.11, 12]. Provided that condition is satisfied, continuous atmospheric fields can be estimated and reanalyzed to, for instance, generate regular grids using data assimilation techniques. Therefore, one requirement of such a measurement network is that it should represent the spatially explicit variability and temporal evolution of atmospheric fields [64.13].

In contrast, networks of ecological measurements do not, and probably cannot, represent the spatially ex-

PLICIT variability or temporal evolution of ecosystem characteristics or processes. To begin with, many ecological parameters (e.g., soil and vegetation properties such as soil texture, phenological data) are not physical field variables—they are neither continuous in space nor differentiable everywhere. Further, the spatial variability of terrestrial ecological variables typically manifests not as smooth gradients but as discrete boundaries over scales that are much smaller than those of the variations relevant to atmospheric networks (excluding turbulence scales, which become irrelevant after Reynolds averaging).

Thus, network design for ecological networks must serve objectives that are very different from those of atmospheric networks. Ecological measurement networks are usually collections of observation sites (often comprising extended areas with diameters of several tens of meters to several hundred meters) arranged over a given region (perhaps the entire globe) according to various network design approaches, with specific objectives in mind. Such network design approaches include:

- (i) Monitoring the most important ecosystem types in a given region [64.14, 15]
- (ii) Monitoring similar ecosystem types using stations arranged along gradients of climate, soil type/soil moisture, or elevation [64.16, 17]
- (iii) Monitoring similar ecosystem types with different ages or at different successional stages under similar climatic and substrate conditions [64.18, 19].

However, in contrast to atmospheric measurement networks, the behavior of ecological variables at one station cannot be expected to be spatially correlated to their behavior at a neighboring station. Long time series of data from individual stations are often used to develop and evaluate parametric or mechanistic process models, and it is only through such models that measurements from different sites in ecological networks can be objectively and systematically connected [64.20]. The latter two approaches to network design are often used in a quasi-experimental fashion

to simulate effects of, for example, climate change or stand age using a space-for-time analogy [64.21, 22]. In conjunction with models evaluated against station data, the first approach serves to integrate ecosystem processes over a region or for the entire globe [64.23].

Just as they are for atmospheric measurement networks, knowledge exchange among network scientists and technicians, coordination and standardization of observational methods, quality control, and calibration are key to the successful operation of ecological networks. Because of the larger number of variables that need to be measured at ecological sites (both meteorological and ecological variables), and because of the vast differences between ecosystem types (from Arctic tundra to tropical rainforest), standardization of ecological measurements is more difficult than it is for atmospheric measurements; indeed, it is a formidable challenge (see [64.24] and other papers in the same issue [64.25, 26]).

The increased knowledge of and interest in complex interactions and feedback loops between Earth system compartments in recent decades have led to considerable advances in observation and modeling techniques: higher resolution both spatially and temporally, improved precision and stability of measurement systems, and the inclusion of more detailed process interactions in models [64.27]. These developments have enabled models to track more complex interactions at increasingly fine scales in an integrated approach across Earth system compartments, and over larger spatial domains for longer time periods. The general tendency continues to be to move beyond offline compartment-specific atmospheric, oceanic, and dynamic ecosystem modeling to integrated Earth system modeling. The newest additions to Earth system modeling over the last two decades have been the inclusion of atmospheric chemistry, the carbon cycle, the nitrogen cycle, and dynamic vegetation [64.28, 29]. The results obtained using these new modeling capabilities have prompted a plethora of questions that need to be evaluated by independent observations. To serve this purpose, such observations also need to be integrated Earth system observations, with concerted measurement programs across all Earth system compartments. The integration required for regional assessments over the continents is essentially between long-term atmospheric and ecological measurement networks.

64.1.1 Ecological Measurement Networks

General environmental sensor networks are described and discussed in [64.30], where the authors differentiate between *large-scale single function* (LSSF) networks, *localized multifunction sensor* (LMS) networks,

biosensor (BS) networks, and *heterogeneous sensor* (HS) networks (hybrid forms that possess characteristics of all of the previously mentioned networks). The classic LSSF network is the network of thousands of standardized meteorological and climatological stations worldwide. Their primary purpose is to provide a data field for initializing or evaluating weather forecasts or for climatological statistics, and they commonly encompass a limited set of standardized sensors (see Chaps. 4 and 43). LMS networks cover smaller areas with greater density and serve multiple applications. Examples include the Oklahoma Mesonet (Chap. 45), which is designed to characterize the state of the environment over the domain and duration of mesoscale weather and hydrological events, and urban observation networks (Chap. 52), which observe the spatial and temporal variability of diverse parameters (including meteorological and hydrological parameters, the energy balance, air quality, and greenhouse gases) over an urbanized area. Biosensors are typically miniaturized devices with biochemical or biophysical detectors as well as data storage and transmission capabilities [64.31]. In ecological systems, biosensors are used to measure or derive physical or chemical properties of the soil, water, or organisms (e.g., the water, carbon, or nitrogen content in soils or sap flow in trees). Some BS networks employ a large number of biosensors of a similar type to cover an entire ecological unit (e.g., the soil and trees in a forest stand) or a small region; others include a variety of sensor types to monitor multiple aspects of the state of an ecosystem over time.

Ecological measurement networks that address biogeochemical cycling, biodiversity, and climate mitigation services by ecosystems are generally hybrid sensor networks (HS, see [64.32] for a review). As defined in [64.30], heterogeneous sensor networks integrate the characteristics of LSSF, LMS, and BS networks. Such integrated ecological measurement networks tend to cover large regions (countries, continents, or the entire globe). Their nodes are often arranged in clusters that can be considered LMS networks themselves, and sites within the clusters contain BS networks with specialized sensing or sampling structures. The variability of biogeochemical cycling processes covers a vast range of spatial scales, ranging from the size of intracellular organelles ($\approx 10^{-6}$ m) to the continental and global scales ($\approx 10^7$ m). For instance, when assessing the role of terrestrial ecosystems in the global carbon cycle, atmospheric transport by the global circulation is important, but the limiting processes to be captured are photosynthesis by chloroplasts inside the mesophyll cells of plant leaves, the diffusion of CO_2 molecules through their stomatal openings, and respiration by microbes in the soil. The range of timescales to be covered

is similar: the photosynthesis of leaves inside a forest canopy reacts to transient sunflecks within milliseconds, phenological changes (e.g., the springtime onset of plant growth, or leaf senescence in fall) respond to seasonal weather anomalies, and rising temperatures and atmospheric CO₂ levels affect plant physiology over climatic timescales. Thus, ecological measurement networks are commonly designed in a hierarchical way: principal nodes aim to represent the most important biomes and climatic zones [64.14], and some of these nodes are developed into supersites [64.33, 34] to collocate measurements for a variety of objectives. Supersites can be augmented by clusters of lower-grade sites to upscale observations from site to region [64.35] or to evaluate ecosystem function responses to gradients in elevation or climate [64.16].

64.1.2 Measured Parameters

Ecological networks commonly measure parameters and processes that characterize the thermal, physical, chemical, and biological conditions in soils, vegetation, the canopy airspace, and the atmospheric boundary layer, as well as exchanges between these Earth system compartments. Thus, all of the chapters in Part

B (focusing on in-situ measuring techniques) of this Handbook may be relevant, depending on the specific foci of individual networks or sites. Recently, many of the principal sites have also integrated ground-based remote-sensing techniques into their portfolio (see Part C), especially sensing systems for the thermal and dynamic structure of the atmospheric boundary layer (Chaps. 23–27) or to integrate across spatially heterogeneous landscapes (Chaps. 28, 34, 35, 48–50). Of primary importance from an ecological perspective are exchange fluxes of heat, trace gases, and aerosols over small, well-defined plots (Chaps. 53, 58, 59–61) or a turbulent flux footprint (Chaps. 1, 55, 56).

Of particular importance for all measurements in ecological networks is the detailed characterization of measurement sites by the BADM (Biological, Ancillary, Disturbance, and Metadata) protocol [64.25, 36–38]), as epitomized by the words of the late Australian micrometeorologist *Ray Leuning* (1948–2016): *know thy site!* (personal communication). Regularly updated BADM information is crucial for data interpretation across sites and for use as driving parameters in models.

An example of a well-established data management system for an ecological measurement network is described in [64.26, 39].

64.2 History

Since their inception in the mid-1970s, ecological measurements organized into networks have focused on long-term observations. In 1977, the US National Science Foundation (NSF) organized a workshop in Woods Hole (MA, USA) to discuss fundamental issues concerning long-term ecological measurements [64.40]. Discussions evolved around the recognition that all ecosystems are in a process of long-term change, including cyclic or irregular variability and long-term trends. Both trends and changes in variability can be due to natural processes or may have anthropogenic causes. The conclusion of the conference was a call to form a network of long-term ecological observations. As a result, the first Long-Term Ecological Research (LTER [64.41]) Network, with 28 sites across the United States, was established in 1980 by the National Science Foundation to support research on long-term ecological phenomena.

Over the last three decades, a growing need for observational data on ecosystem functions and biogeochemical cycling (primarily of water, carbon, nitrogen, and heat) in response to the so-called *missing carbon sink* problem [64.42, 43] has motivated the formation and expansion of large-scale and long-term ecological measurement networks that focus on carbon exchange and function in terrestrial ecosystems. Examples of

these (FLUXNET, AmeriFlux, NEON, and ICOS) will be briefly presented in the following.

64.2.1 History of Ecological Measurements

Likely the most important developments in the observational capabilities of ecological measurement networks are associated with the eddy-covariance technique (see Chap. 55) for the direct derivation of reliable ecosystem–atmosphere exchange fluxes of heat, water vapor, and CO₂, which can be operated continuously over long periods (up to decades).

There were four events that made this technique possible:

- The development of the infrared gas analyzer for the optical detection of CO₂ and water vapor concentrations. The first IRGA was patented in Germany in 1938 by two physicists working for a chemical company in Ludwigshafen [64.44] and was published in 1943 [64.45]. Soon after (in 1949), this principle was adopted for enclosure measurements of CO₂ exchange by plants at the University of Heidelberg [64.46]. In 1950, *Bruno Huber* (1899–1989) reported on the first use of an IRGA to estimate

- an ecosystem-scale CO₂ flux via a micrometeorological technique [64.47], albeit with a flux-profile approach based on a simple but unrealistic exchange coefficient.
- The principle of the eddy-covariance technique was pioneered by *William Christopher Swinbank* (1913–1973) [64.48] (see Chap. 55). The first successful CO₂ flux measurement by eddy-covariance (using an IRGA) was reported by *Ray Desjardins* (*1940) in 1974 [64.7].
- Arguably the first usable sonic anemometer for eddy covariance was developed by *J. Chandran Kaimal* (1930–2021) and *Joost Businger* (*1924) in the early 1960s [64.49].
- Stable continuous CO₂ flux measurements became available only after microprocessor technology and data storage capacity had advanced sufficiently in the 1980s and 1990s. See [64.50] for a personal anecdotal account of the history of eddy-covariance measurements by *Dennis Baldocchi* (*1955).

64.3 Structures of Notable Networks

FLUXNET is a global network of regional (CO₂) flux measurement networks [64.53] but does not operate measurement stations. Currently, its main function is to act as a global data portal for ecosystem-atmosphere exchange flux stations [64.54]. Over the years, more than 900 flux sites have been registered with FLUXNET, but many of those operated for relatively short periods and are now inactive. FLUXNET is thus mainly an organization that comprises scientists and experts, and as such it facilitates the discussion and formulation of measurement and data standards and the creation of quality-controlled synthesis datasets for flux stations around the globe. The latest synthesis data

release (FLUXNET2015, see Fig. 64.1) includes 212 sites. Over the years (up to 2016), the networks that participate in FLUXNET have included 914 sites, representing a total of 7479 site-years. In 2016, 459 of those sites were reported to be active. As is clearly evident in Figs. 64.1 and 64.2a, the geographical distribution of FLUXNET sites is very inhomogeneous and is highly correlated with the availability of funds to operate and maintain the flux stations. Among the major biomes represented in FLUXNET (Fig. 64.2b), sites in forests (of all kinds) are particularly well represented.

FLUXNET consists of a large number of regional networks [64.56], the largest of which is Ameri-

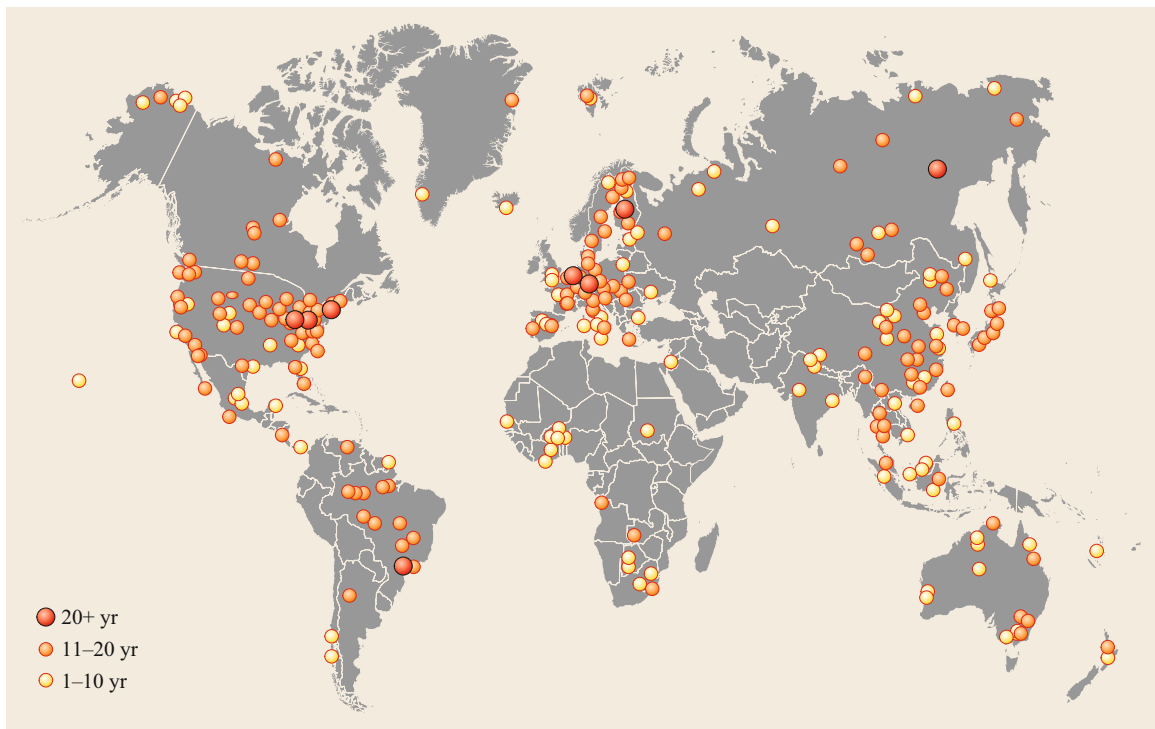
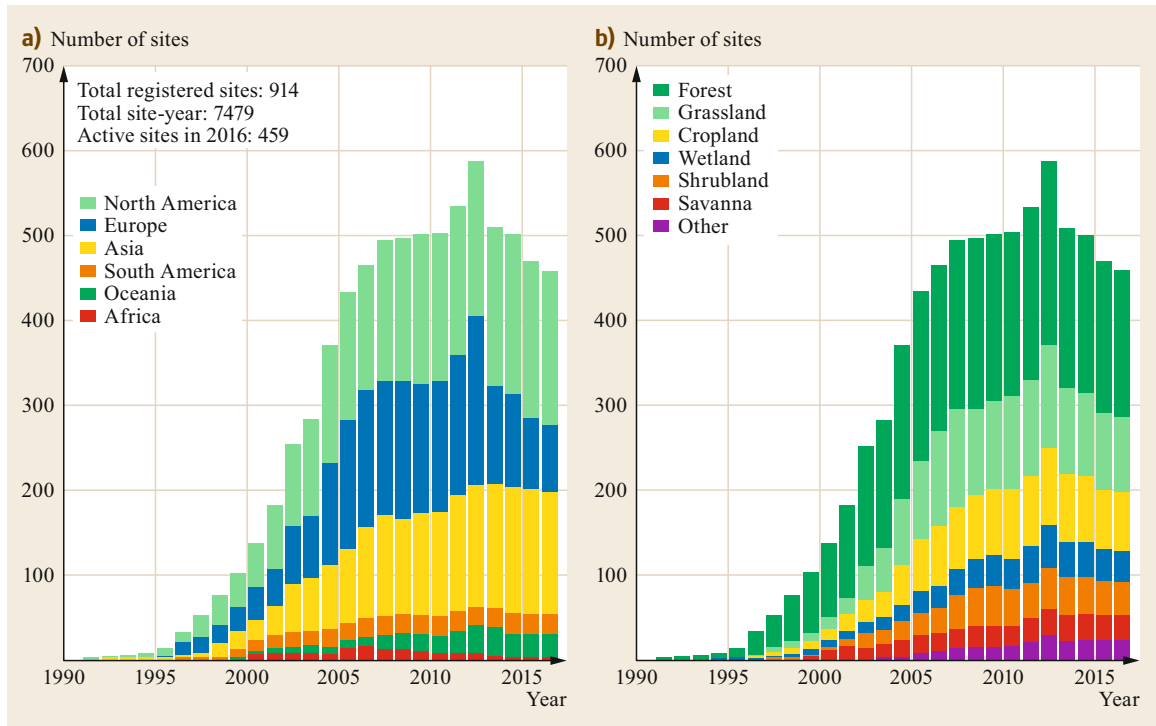


Fig. 64.1 Global distribution of the 212 eddy-covariance stations that contribute to the FLUXNET2015 synthesis dataset, including an indication of the years of data contributed (after [64.51])



Flux [64.57, 58]. Until recently, AmeriFlux sites had no central funding structure. For this reason, AmeriFlux evolved slowly; it consisted of only a handful of sites in 1996 when it was launched following a noted international workshop in La Thuile, Italy, in 1995 [64.59]. In part through necessity, AmeriFlux has adopted diversity of site design, instrumentation, and analysis methods as its *modus operandi*. However, this diversity developed during a period when the concept of long-term flux measurement campaigns was still in its infancy and standardization was based on arbitrary decisions. By establishing and deploying a mobile reference eddy-covariance system, the so-called *roving system*, it was possible to perform intranetwork field calibrations and comparisons between systems, which formed the basis for the emergence of standardized *best practices*, estimates of uncertainty, and cross-site compatibility of data [64.60]. Currently, AmeriFlux is coordinated by a long-term management project and consists of 276 sites across the Americas that are active or have provided data in the past (Fig. 64.3). About 80% of all registered sites are located in the United States, 16% are in Canada, and the remaining 4% are distributed among a number of countries throughout the Americas (see [64.57]).

Fig. 64.3 Site distribution of the AmeriFlux network (after [64.55]) ▶



Fig. 64.2a,b Temporal development of FLUXNET sites: (a) distribution among continents; (b) distribution among major biomes. In (b), *other* includes, for example, tundra and urban areas (after [64.52] with the permission of Housen Chu)

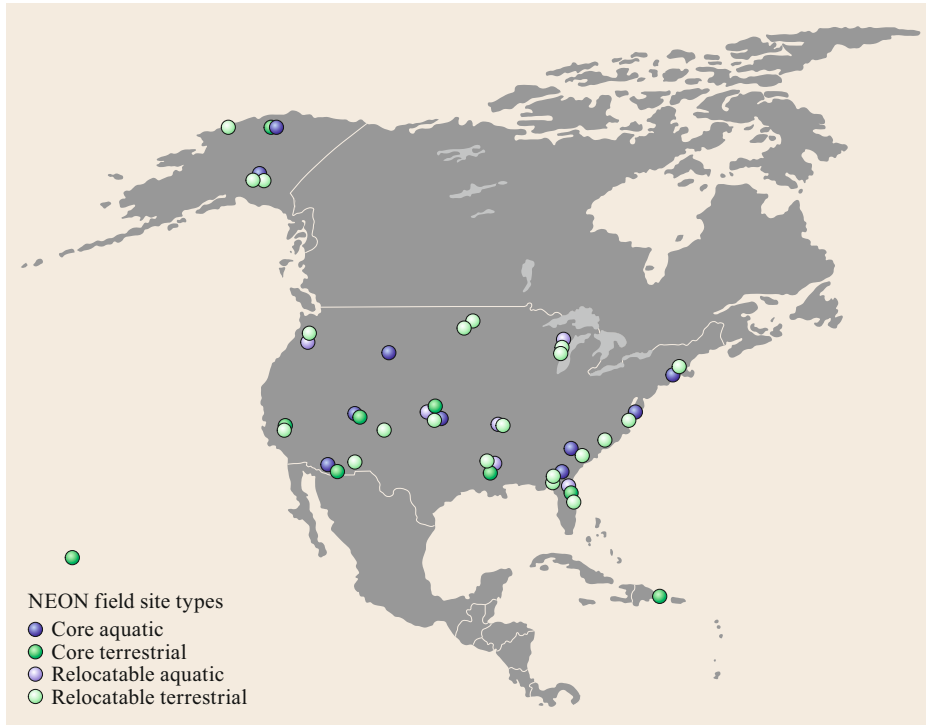


Fig. 64.4 NEON field site map; NEON core sites have a strong emphasis on aquatic environments (after [64.61])

Of the AmeriFlux sites within the United States, 44 (2018) have been selected as *core sites*, with assured long-term funding support for concerted operation and a more standardized maintenance schedule.

At the other end of the site design diversity spectrum is NEON (US National Ecological Observatory Network [64.62, 63], Fig. 64.4). The observational scope of NEON is broader than that of AmeriFlux, but it also has a strong focus on ecosystem-atmosphere exchange flux measurements. NEON is centrally funded and is highly standardized in terms of station design, instrumentation hardware, and methods of data analysis [64.26]. NEON is not currently contributing data to AmeriFlux or FLUXNET, but is moving towards that goal [64.26].

In terms of standardization and funding structure, ICOS (Integrated Carbon Observation System [64.64]) is somewhere between AmeriFlux and NEON. ICOS is a distributed European research infrastructure with independently funded national networks in 12 countries at present. ICOS consists of three parallel observation systems that concentrate on the atmosphere, the oceans, and (terrestrial) ecosystems. ICOS Ecosystems (see Fig. 64.5) is far along the road to establishing standardized instrumentation, data analysis, and quality



Fig. 64.5 The ICOS Ecosystem station network (after [64.64])

control protocols (see [64.24] and other contributions in the same issue).

All three of the ecological flux measurement networks featured here are intended to be operated over the

long term (> 20 years). They benefit from each other by frequently exchanging ideas and experience as well as collaborating in the preparation of synthesis projects and intercomparisons.

64.4 Temporal and Spatial Scales

For general questions about the temporal and spatial scales of environmental measurements, see Chap. 1. Ideally, the temporal and spatial scales that an ecological measurement network needs to cover correspond to the scales of the relevant processes that govern the development of the ecosystem of interest [64.65]. Spatial scales can be covered by positioning the nodes of the network strategically [64.15] and making use of satellite remote-sensing and ecosystem models [64.23, 66]. Temporal scales of ecological processes are limited only by the age of the ecosystem (including soils). At mid- and polar latitudes, this often corresponds to the time since the last glaciation, or about 10^4 years. Similarly, the spatial scales over which ecosystem processes can develop correspond to the size of the ecosystem (up to several 10^3 km), because an ecosystem is defined by similarity of processes and function. Of course, a timescale of 10^4 years cannot be covered directly by any ecological measurement network, but, as mentioned, long temporal scales can sometimes be spanned indirectly through a space-for-time analogy or chronosequence approach [64.21, 22].

An important aspect of the ecosystem–atmosphere interaction is that there are concurrent effects of a large number of interlinked processes that operate over vastly different timescales, ranging from, say, sunflecks that last for less than a second but affect the photosynthesis in a leaf to soil development processes that last for thousands of years. Therefore, it is clearly not practicable to include the entire spectrum of timescales for such a complex dynamic system when performing ecological observations. A more relevant approach is suggested by the concept of *ecological resilience* [64.67, 68], and by realizing that any natural ecosystem generally develops by experiencing successive disturbances and recovering from them, not under the influence of

equilibrium conditions. In its broadest sense, resilience describes [64.69]

the capacity of a system to absorb disturbance and reorganize while undergoing change so as to still retain essentially the same function, structure, identity, and feedbacks.

A more measurable concept of resilience is borrowed from engineering, where it is the timescale associated with the return of a system to equilibrium or a steady state after it has been disturbed [64.68]. A particular type of resilience timescale was proposed in [64.70] for a spruce forest ecosystem in the Bavarian Forest (Germany) after a stand-replacing disturbance by a windthrow as “the timescale over which all post-disturbance emitted carbon will have been fixed again by the ecosystem”. Based on observations of carbon exchange fluxes for several years after the windthrow and the projections of an ecosystem model, this resilience timescale was estimated to be about 20 years for that particular Norway spruce forest. A consequence for ecological measurements is that observation periods which are shorter than the resilience timescale may exhibit a systematic bias because they provide an incomplete representation of the dynamics of the ecosystem and its interaction with the atmosphere. Stand-replacing disturbances (e.g., caused by wind storms, fires, logging) are important but relatively rare occurrences; smaller disturbances are the norm in natural ecosystems. Thus, given the complex dynamic behavior of the system, identifying an observation timescale for ecological measurements that has the chance of capturing a full cycle of ecosystem development is a difficult problem, and is the subject of active research. The chronosequence (space-for-time) approach mentioned above may be of some help if a model is used to fill the gaps in the ecosystem stages captured by the chronosequence.

64.5 Quality Control of Ecological Measurement Networks

For general quality control issues associated with measured data, see Chap. 3. Similar to measurements in atmospheric networks (Chap. 63), the objectives of quality control in ecological measurement networks are

to make measured data within the network consistent and comparable.

Consistency refers to the aim that the quantities measured at different sites in a network should repre-

sent the same process or system state. For instance, if soil temperatures are measured at different depths in different locations, the ensuing dataset is not consistent. But if more than one depth is sampled at every location, the dataset may be made consistent by interpolating a given soil temperature profile at every location. Thus, the assessment of measurement consistency (and its assurance) in a network depends largely on the documentation of metadata detailing the circumstances of the measurements or observations [64.71]. As mentioned, a framework that is commonly used to report the biological, ancillary, disturbance, and metadata (BADM) is presented in [64.39].

Comparability is achieved by quantifying the random uncertainty in the measurements and by identifying and quantifying systematic biases. For some of the most important ecological observations (e.g., flux measurements obtained via chambers or eddy covariance; see Chaps. 55, 59, 60), there is no absolute standard instrument or measurement method. Moreover, for such instruments, their performance is highly dependent on the measurement setup, including the chamber or mast design, aerodynamic exposure, juxtaposition with other instruments, obstacles, etc. [64.72, 73]. Thus, the identification and avoidance of systematic biases are achieved

through checks of physical plausibility (e.g., no photosynthesis at night), internal consistency (e.g., balance closure requirements), and long-term integral requirements (e.g., negligible storage change integrated over daily or annual cycles).

In the absence of absolute standards, it is not possible to perform an absolute instrument calibration to estimate the error. For eddy flux measurements of CO₂, practical methods of estimating various types of random measurement uncertainties are presented in [64.74–76].

A useful, but costly, approach to ensuring network-wide consistency in field calibrations and enabling comparison against a reference standard (if not an absolute standard) is the use of a *roving system* [64.77]. In this approach, a mobile system of laboratory-calibrated component instruments is deployed and operated in close proximity to a comparable measurement system in the network. The two systems are operated in parallel over a duration of 10 days or 2 weeks, and the data are used to assess the random uncertainty and systematic deviations from the roving standard. Costs arise from maintaining the roving standard system and the personnel needed to operate and move the system. An example of using a roving-standard eddy-covariance flux system in the AmeriFlux network is described in [64.76].

64.6 Maintenance

For instrument maintenance strategies, see the individual chapters on instrumentation in this Handbook. To minimize data gaps during instrument maintenance in a network, it is advisable to perform minor routine maintenance in the field without removing instruments. If it is necessary to send instruments back to a lab-

oratory or the manufacturer, it is useful to deploy a temporary replacement system to bridge the gap. If several similar stations can be serviced in a rotation scheme, it is possible to implement a round-robin strategy with one redundant system.

64.7 Applications

The principal applications of integrated meteorological and ecological measurement networks involve the use of synthesis datasets, after standardized quality control and data analysis, to perform spatial and temporal integrations (e.g., of CO₂, water vapor, or

energy fluxes [64.53]) or to assess ecophysiological characteristics (e.g., water-use efficiency [64.78, 79]). See [64.80] for more examples of publications relating to applications of the FLUXNET synthesis datasets.

64.8 Further Developments

Developmental trends for meteorological and ecological measurement networks are primarily for further integration, data sharing, and standardization of instruments, analyses, and methods across various networks (including AmeriFlux, NEON, and ICOS [64.58]). Sites that serve multiple networks and objectives develop

into supersites [64.34] or meteorological–ecological observatories (e.g., the SMEAR I and II stations at the Hyytiälä site in Finland [64.33], the Niwot-Ridge AmeriFlux and LTER site in Colorado [64.81], the Harvard Forest site in Massachusetts [64.82], and the Fendt TERENO/ICOS/ScaleX site in Germany [64.16, 83]).

64.9 Further Reading

- D. Baldocchi, E. Falge, L. H. Gu, R. Olson, D. Hollinger, S. Running, (et al.): Fluxnet: A New Tool to Study the Temporal and Spatial Variability of Ecosystem-Scale Carbon Dioxide, Water Vapor, and Energy Flux Densities, *Bulletin of the American Meteorological Society* **82**, 2415–2434 (2001)
- D. Franz, M. Acosta, N. Altimir, N. Arriga, D. Arrouays, M. Aubinet, M. Aurela, E. Ayres, A. López-Ballesteros, M. Barbaste: Towards Long-Term Standardised Carbon and Greenhouse Gas Observations for Monitoring Europe's Terrestrial Ecosystems: A Review, *International Agrophysics* **32**, 439–455 (2018)
- R. Kiese, B. Fersch, C. Baessler, C. Brosy, K. Butterbach-Bahl, C. Chwala, M. Dannenmann, J. Fu, R. Gasche, R. Grote: The TERENO Pre-Alpine Observatory: Integrating Meteorological, Hydrological, and Biogeochemical Measurements and Modeling, *Vadose Zone J.* **17**, 180060 (2018)
- K. Novick, J. Biederman, A. Desai, M. Litvak, D. Moore, R. Scott, M. Torn: The Ameriflux Network: A Coalition of the Willing, *Agricultural and Forest Meteorology* **249**, 444–456 (2018)

References

- 64.1 Dictionary.com, search term 'ecology', <https://www.dictionary.com/browse/ecology>, Accessed 24 July 2021
- 64.2 F.S. Chapin III, P.A. Matson, P. Vitousek: *Principles of Terrestrial Ecosystem Ecology* (Springer, New York 2011)
- 64.3 S. Arrhenius: Über die Reaktionsgeschwindigkeit bei der Inversion von Rohrzucker durch Säuren, *Z. Phys. Chem.* **4**, 226–248 (1889)
- 64.4 L. Michaelis, M. Menten: Die Kinetik der Invertinwirkung, *Biochem. Z.* **49**, 333–369 (1913)
- 64.5 Wikipedia.org: Timeline of meteorology, https://en.wikipedia.org/wiki/Timeline_of_meteorology, Accessed 24 July 2021
- 64.6 I. Strangeways: *Precipitation: Theory, Measurement and Distribution* (Cambridge Univ. Press, Cambridge 2006)
- 64.7 R. Desjardins: A technique to measure CO₂ exchange under field conditions, *Int. J. Biometeorol.* **18**, 76–83 (1974)
- 64.8 R. Desjardins, E. Lemon: Limitations of an eddy-correlation technique for the determination of the carbon dioxide and sensible heat fluxes, *Bound.-Layer Meteorol.* **5**, 475–488 (1974)
- 64.9 S.H. Schneider: On the carbon dioxide–climate confusion, *J. Atmos. Sci.* **32**, 2060–2066 (1975)
- 64.10 T. Wigley, T. Barnett: Detection of the greenhouse effect in the observations. In: *Climate Change: The IPCC Scientific Assessment* (1990) pp. 239–256
- 64.11 L.S. Gandin: *Objective Analysis of Meteorological Fields* (Gidrometeorol. Lzd., Leningrad 1963)
- 64.12 M. Ghil, P. Malanotte-Rizzoli: Data assimilation in meteorology and oceanography, *Adv. Geophys.* **33**, 141–266 (1991)
- 64.13 I. Lopez-Coto, S. Ghosh, K. Prasad, J. Whetstone: Tower-based greenhouse gas measurement network design—the national institute of standards and technology north east corridor testbed, *Adv. Atmos. Sci.* **34**, 1095–1105 (2017)
- 64.14 F. Yang, A.X. Zhu, K. Ichii, M.A. White, H. Hashimoto, R.R. Nemani: Assessing the representativeness of the Ameriflux network using MODIS and GOES data, *J. Geophys. Res. Biogeosci.* **113**, G04036 (2008)
- 64.15 W.W. Hargrove, F.M. Hoffman, B.E. Law: New analysis reveals representativeness of the Ameriflux network, *Eos Trans. Am. Geophys. Union* **84**, 529–535 (2003)
- 64.16 R. Kiese, B. Fersch, C. Baessler, C. Brosy, K. Butterbach-Bahl, C. Chwala, M. Dannenmann, J. Fu, R. Gasche, R. Grote: The TERENO pre-alpine observatory: integrating meteorological, hydrological, and biogeochemical measurements and modeling, *Vadose Zone J.* **17**, 180060 (2018)
- 64.17 J. Fu, R. Gasche, N. Wang, H. Lu, K. Butterbach-Bahl, R. Kiese: Impacts of climate and management on water balance and nitrogen leaching from montane grassland soils of S-Germany, *Environ. Pollut.* **229**, 119–131 (2017)
- 64.18 B.E. Law, O. Sun, J. Campbell, S. Van Tuyl, P. Thornton: Changes in carbon storage and fluxes in a chronosequence of ponderosa pine, *Global Change Biol.* **9**, 510–524 (2003)
- 64.19 C. Coursolle, H. Margolis, M.-A. Giasson, P.-Y. Bernier, B. Amiro, M. Arain, A. Barr, T. Black, M. Goulden, J. McCaughey: Influence of stand age on the magnitude and seasonality of carbon fluxes in Canadian forests, *Agric. For. Meteorol.* **165**, 136–148 (2012)
- 64.20 M. Siqueira, G.G. Katul, D. Sampson, P.C. Stoy, J.Y. Juang, H.R. McCarthy, R. Oren: Multiscale model intercomparisons of CO₂ and H₂O exchange rates in a maturing southeastern US pine forest, *Global Change Biol.* **12**, 1189–1207 (2006)
- 64.21 S.T. Pickett: Space-for-time substitution as an alternative to long-term studies. In: *Long-Term Studies in Ecology*, ed. by G.E. Likens (Springer, New York 1989) pp. 110–135

- 64.22 C. Wang, Z. Chen, S. Unteregelsbacher, H. Lu, S. Gschwendtner, R. Gasche, A. Kolar, M. Schloter, R. Kiese, K. Butterbach-Bahl: Climate change amplifies gross nitrogen turnover in montane grasslands of Central Europe in both summer and winter seasons, *Global Change Biol.* **22**, 2963–2978 (2016)
- 64.23 F. Yang, M.A. White, A.R. Michaelis, K. Ichii, H. Hashimoto, P. Votava, A.-X. Zhu, R.R. Nemani: Prediction of continental-scale evapotranspiration by combining Modis and Ameriflux data through support vector machine, *IEEE Trans. Geosci. Remote Sens.* **44**, 3452–3461 (2006)
- 64.24 D. Franz, M. Acosta, N. Altimir, N. Arriga, D. Arrouays, M. Aubinet, M. Aurela, E. Ayres, A. López-Ballesteros, M. Barbaste: Towards long-term standardised carbon and greenhouse gas observations for monitoring Europe's terrestrial ecosystems: a review, *Int. Agrophys.* **32**, 439–455 (2018)
- 64.25 R.H. Kao, C.M. Gibson, R.E. Gallery, C.L. Meier, D.T. Barnett, K.M. Docherty, K.K. Blevins, P.D. Travers, E. Azuaje, Y.P. Springer: NEON terrestrial field observations: designing continental-scale, standardized sampling, *Ecosphere* **3**, 1–17 (2012)
- 64.26 S. Metzger, D. Durden, C. Florian, R. Lee, C. Lunch, H. Luo, N. Pingintha-Durden, J.A. Roberti, M. San-Clements, C. Sturtevant, K. Xu, R. Zulueta: From NEON field sites to data portal: a community resource for surface-atmosphere research comes online, *Bull. Am. Meteorol. Soc.* **100**, 2305–2325 (2019)
- 64.27 T.F. Stocker, D. Qin, G.-K. Plattner, M. Tignor, S.K. Allen, J. Boschung, A. Nauels, Y. Xia, B. Bex, B. Midgley: *IPCC, 2013: Climate Change 2013: The Physical Science Basis. Contribution of Working Group I to the Fifth Assessment Report of the Intergovernmental Panel on Climate Change* (Cambridge Univ. Press, Cambridge 2013)
- 64.28 J. Houghton, D. Albritton, L. Meira Filho, U. Cubasch, X. Dai, Y. Ding, D. Griggs, B. Hewitson, I. Isaksen, T. Karl: *Technical Summary of Working Group 1. In: Climate Change 2001: The Scientific Basis. Contributions of Working Group I to the Third Assessment Report of the Intergovernmental Panel on Climate Change* (Cambridge Univ. Press, Cambridge 2001)
- 64.29 U. Cubasch, D. Wuebbles, D. Chen, M. Facchini, D. Frame, N. Mahowald, J. Winther: Introduction. In: *Climate Change 2013: The Physical Science Basis. Contribution of Working Group I to the Fifth Assessment Report of the Intergovernmental Panel on Climate Change*, ed. by T.F. Stocker, D. Qin, G.-K. Plattner, M. Tignor, S.K. Allen, J. Boschung, A. Nauels, Y. Xia, V. Bex, P.M. Midgley (Cambridge Univ. Press, Cambridge 2013) pp. 119–158
- 64.30 J.K. Hart, K. Martinez: Environmental sensor networks: a revolution in the earth system science?, *Earth Sci. Rev.* **78**, 177–191 (2006)
- 64.31 A. Turner, I. Karube, G.S. Wilson: *Biosensors: Fundamentals and Applications* (Oxford Univ. Press, Oxford 1987)
- 64.32 P.W. Rundel, E.A. Graham, M.F. Allen, J.C. Fisher, T.C. Harmon: Environmental sensor networks in ecological research, *New Phytol.* **182**, 589–607 (2009)
- 64.33 P. Hari, E. Nikinmaa, T. Pohja, E. Siivola, J. Bäck, T. Vesala, M. Kulmala: Station for measuring ecosystem-atmosphere relations: SMEAR. In: *Physical and Physiological Forest Ecology*, ed. by P. Hari, K. Heliövaara, L. Kulmala (Springer, Dordrecht 2013) pp. 471–487
- 64.34 M. Karan, M. Liddell, S.M. Prober, S. Arndt, J. Beringer, M. Boer, J. Cleverly, D. Eamus, P. Grace, E. Van Gorsel: The Australian supersite network: a continental, long-term terrestrial ecosystem observatory, *Sci. Total Environ.* **568**, 1263–1274 (2016)
- 64.35 J. Xiao, K.J. Davis, N.M. Urban, K. Keller, N.Z. Saliendra: Upscaling carbon fluxes from towers to the regional scale: influence of parameter variability and land cover representation on regional flux estimates, *J. Geophys. Res. Biogeosci.* **116**, G00J06 (2011)
- 64.36 Y. Cheah, D. Christianson, H. Chu, G. Pastorello, F. O'Brien, Y. Ong, C. van Ingen, M. Torn, D. Agarwal: Ameriflux BADM: implementing lessons from 12 years of long-tail data management into next generation earth science systems. In: *Proc. AGU Fall Meet. Abstr.* (2018)
- 64.37 B.E. Law, T. Arkebauer, J.L. Campbell, J. Chen, O. Sun, M. Schwartz, C. van Ingen, S. Verma: *Terrestrial carbon observations: protocols for vegetation sampling and data submission* (FAO, Rome 2008)
- 64.38 B. Gielen, M. Acosta, N. Altimir, N. Buchmann, A. Cescatti, E. Ceschia, S. Fleck, L. Hörtnagl, K. Klumpp, P. Kolari: Ancillary vegetation measurements at ICOS ecosystem stations, *Int. Agrophys.* **32**, 645–664 (2018)
- 64.39 T.A. Boden, M. Krassovski, B. Yang: The Ameriflux data activity and data system: an evolving collection of data management techniques, tools, products and services, *Geosci. Instrum. Methods Data Syst.* **2**, 165–176 (2013)
- 64.40 National Technical Information Service (NTIS): Long term ecological measurements, Tech. Rep., <https://internet.edu/wp-content/uploads/2010/12/77workshop.pdf> (1977), Accessed 24 July 2021
- 64.41 National Science Foundation: Long Term Ecological Research (LTER) Network, <https://Internet.edu>, Accessed 24 July 2021
- 64.42 D.W. Schindler: Carbon cycling: the mysterious missing sink, *Nature* **398**, 105–107 (1999)
- 64.43 P.P. Tans, I.Y. Fung, T. Takahashi: Observational constraints on the global atmospheric CO₂ budget, *Science* **247**, 1431–1438 (1990)
- 64.44 E. Lehrer, K. Luft: Verfahren zur Bestimmung von Bestandteilen in Stoffgemischen mittels Strahlenabsorption, Patent DE730478C (1938)
- 64.45 K. Luft: Über eine neue Methode der registrierenden Gasanalyse mit Hilfe der Absorption ultraroter Strahlen ohne spektrale Zerlegung, *Z. Tech. Phys.* **24**, 97–104 (1943)
- 64.46 K. Egle, A. Ernst: Die Verwendung des Ultrarotabsorptionsschreibers für die vollautomatische und fortlaufende CO₂-Analyse bei Assimilations- und

- Atmungsmessungen an Pflanzen, *Z. Naturforsch. B* **4**, 351–360 (1949)
- 64.47 B. Huber: Registrierung Des CO₂-Gefälles und Berechnung des CO₂-Stromes über Pflanzen-Gesellschaften mittels Ultrarot-Absorptions-Schreiber, *Ber. Dtsch. Bot. Ges.* **63**, 52–63 (1950)
- 64.48 W. Swinbank: The measurement of vertical transfer of heat and water vapor by eddies in the lower atmosphere, *J. Meteorol.* **8**, 135–145 (1951)
- 64.49 J. Kaimal, J. Businger: A continuous wave sonic anemometer-thermometer, *J. Appl. Meteorol.* **2**, 156–164 (1963)
- 64.50 D. Baldocchi: A brief history on eddy covariance flux measurements: a personal perspective, *FluxLetter* **5**, 1–8 (2013)
- 64.51 Fluxdata: FLUXNET2015 dataset, <https://fluxnet.fluxdata.org//data/fluxnet2015-dataset/>, Accessed 24 July 2021
- 64.52 FLUXNET, History. <https://fluxnet.org/about/history/>, Accessed 24 July 2021
- 64.53 D. Baldocchi, E. Falge, L.H. Gu, R. Olson, D. Hollinger, S. Running, P. Anthoni, C. Bernhofer, K. Davis, R. Evans, J. Fuentes, A. Goldstein, G. Katul, B. Law, X.H. Lee, Y. Malhi, T. Meyers, W. Munger, W. Oechel, K.T.P. U, K. Pilegaard, H.P. Schmid, R. Valentini, S. Verma, T. Vesala, K. Wilson, S. Wofsy: FLUXNET: a new tool to study the temporal and spatial variability of ecosystem-scale carbon dioxide, water vapor, and energy flux densities, *Bull. Am. Meteorol. Soc.* **82**, 2415–2434 (2001)
- 64.54 FLUXNET: The data portal serving the FLUXNET community, <https://fluxnet.org/>, Accessed 24 July 2021
- 64.55 AmeriFlux: Network at a glance, <https://ameriflux.lbl.gov/about/network-at-a-glance/>, Accessed 24 July 2021
- 64.56 Fluxdata: Regional networks, <https://fluxnet.fluxdata.org/about/regional-networks/>, Accessed 24 July 2021
- 64.57 AmeriFlux: <https://ameriflux.lbl.gov/>, Accessed 24 July 2021
- 64.58 K. Novick, J. Biederman, A. Desai, M. Litvak, D. Moore, R. Scott, M. Torn: The Ameriflux network: a coalition of the willing, *Agric. For. Meteorol.* **249**, 444–456 (2018)
- 64.59 D. Baldocchi, R. Valentini, S. Running, W. Oechel, R. Dahlman: Strategies for measuring and modelling carbon dioxide and water vapour fluxes over terrestrial ecosystems, *Global Change Biol.* **2**, 159–168 (1996)
- 64.60 A. Schmidt, C. Hanson, W.S. Chan, B.E. Law: Empirical assessment of uncertainties of meteorological parameters and turbulent fluxes in the Ameriflux network, *J. Geophys. Res. Biogeosci.* **117**, G002100 (2012)
- 64.61 The National Ecological Observatory Network: NEON field sites, <https://www.neonscience.org/field-sites/field-sites-map>, Accessed 24 July 2021
- 64.62 The National Ecological Observatory Network (NEON): <https://www.neonscience.org/>, Accessed 24 July 2021
- 64.63 M. Keller, D.S. Schimel, W.W. Hargrove, F.M. Hoffman: A continental strategy for the National Ecological Observatory Network, *Front. Ecol. Environ.* **6**, 282–284 (2008)
- 64.64 Integrated Carbon Observation System (ICOS): <https://www.icos-ri.eu/>, Accessed 24 July 2021
- 64.65 H.R. Delcourt, P.A. Delcourt, T. Webb III: Dynamic plant ecology: the spectrum of vegetational change in space and time, *Quat. Sci. Rev.* **1**, 153–175 (1982)
- 64.66 F.A. Heinsch, M. Zhao, S.W. Running, J.S. Kimball, R.R. Nemani, K.J. Davis, P.V. Bolstad, B.D. Cook, A.R. Desai, D.M. Ricciuto: Evaluation of remote sensing based terrestrial productivity from MODIS using regional tower eddy flux network observations, *IEEE Trans. Geosci. Remote Sens.* **44**, 1908–1925 (2006)
- 64.67 C.S. Holling: Resilience and stability of ecological systems, *Annu. Rev. Ecol. Syst.* **4**, 1–23 (1973)
- 64.68 L.H. Gunderson: Ecological resilience—in theory and application, *Annu. Rev. Ecol. Syst.* **31**, 425–439 (2000)
- 64.69 B. Walker, C.S. Holling, S. Carpenter, A. Kinzig: Resilience, adaptability and transformability in social–ecological systems, *Ecol. Soc.* **9**, 5 (2004)
- 64.70 M. Lindauer: *Ecosystem–Atmosphere Exchange over a Wind-Throw-Disturbed Upland Spruce Forest in the Bavarian Forest National Park*, Thesis, Technische Universität München (2016)
- 64.71 M. Saunders, S. Dengel, P. Kolari, C. Moureaux, L. Montagnani, E. Ceschia, N. Altimir, A. López-Ballesteros, S. Marañón-Jimenez, M. Acosta: Importance of reporting ancillary site characteristics, and management and disturbance information at ICOS stations, *Int. Agrophys.* **32**, 457–469 (2018)
- 64.72 C. Reibmann, M. Aubinet, H. Schmid, N. Arriga, M. Aurela, G. Burba, R. Clement, A. De Ligne, G. Fratini, B. Gielen: ICOS eddy covariance flux-station site setup: a review, *Int. Agrophys.* **32**, 471–494 (2018)
- 64.73 M. Pavelka, M. Acosta, R. Kiese, N. Altimir, C. Brümmer, P. Crill, E. Darenova, R. Fuß, B. Gielen, A. Graf: Standardisation of chamber technique for CO₂, N₂O and CH₄ fluxes measurements from terrestrial ecosystems, *Int. Agrophys.* **32**, 569–587 (2018)
- 64.74 D.Y. Hollinger, A.D. Richardson: Uncertainty in eddy covariance measurements and its application to physiological models, *Tree Physiol.* **25**, 873–885 (2005)
- 64.75 A.D. Richardson, D.Y. Hollinger, G.G. Burba, K.J. Davis, L.B. Flanagan, G.G. Katul, J.W. Munger, D.M. Ricciuto, P.C. Stoy, A.E. Suyker, S.B. Verma, S.C. Wofsy: A multi-site analysis of random error in tower-based measurements of carbon and energy fluxes, *Agric. For. Meteorol.* **136**, 1–18 (2006)
- 64.76 D. Dragoni, H.P. Schmid, C.S.B. Grimmond, H.W. Loescher: Uncertainty of annual net ecosystem productivity estimated using eddy covariance flux measurements, *J. Geophys. Res. Atmos.* **112**, 9 (2007)
- 64.77 D. Billesbach, M. Fischer, M. Torn, J. Berry: A portable eddy covariance system for the measurement of ecosystem–atmosphere exchange of

- CO₂, water vapor, and energy, *J. Atmos. Ocean. Technol.* **21**, 639–650 (2004)
- 64.78 T.F. Keenan, D.Y. Hollinger, G. Bohrer, D. Dragoni, J.W. Munger, H.P. Schmid, A.D. Richardson: Increase in forest water-use efficiency as atmospheric carbon dioxide concentrations rise, *Nature* **499**, 324 (2013)
- 64.79 J. Knauer, S. Zaehle, B.E. Medlyn, M. Reichstein, C.A. Williams, M. Migliavacca, M.G. De Kauwe, C. Werner, C. Keitel, P. Kolari: Towards physiologically meaningful water-use efficiency estimates from eddy covariance data, *Global Change Biol.* **24**, 694–710 (2018)
- 64.80 Fluxdata: Publications, <https://fluxnet.fluxdata.org/community/publications/>, Accessed 24 July 2021
- 64.81 W.J. Sacks, D.S. Schimel, R.K. Monson, B.H. Braswell: Model-data synthesis of diurnal and seasonal CO₂ fluxes at Niwot Ridge, Colorado, *Global Change Biol.* **12**, 240–259 (2006)
- 64.82 S. Urbanski, C. Barford, S. Wofsy, C. Kucharik, E. Pyle, J. Budney, K. McKain, D. Fitzjarrald, M. Czikowsky, J. Munger: Factors controlling CO₂ exchange on timescales from hourly to decadal at Harvard Forest, *J. Geophys. Res.* **112**, G02020 (2007)
- 64.83 B. Wolf, C. Chwala, B. Fersch, J. Garvelmann, W. Junkermann, M.J. Zeeman, A. Angerer, B. Adler, C. Beck, C. Brosy, P. Brugger, S. Emeis, M. Dannenmann, F. De Roo, E. Diaz-Pines, E. Haas, M. Hagen, I. Hajsek, J. Jacobeit, T. Jagdhuber, N. Kalthoff, R. Kiese, H. Kunstmann, O. Kosak, R. Krieg, C. Malchow, M. Mauder, R. Merz, C. Notarnicola, A. Philipp, W. Reif, S. Reineke, T. Rodiger, N. Ruehr, K. Schafer, M. Schron, A. Senatore, H. Shupe, I. Volkoch, C. Wanninger, S. Zacharias, H.P. Schmid: The SCALEX campaign scale-crossing land surface and boundary layer processes in the Tereno-Prealpine observatory, *Bull. Am. Meteorol. Soc.* **98**, 1217–1234 (2017)

Hans Peter Schmid

Institute of Meteorology and Climate Research – Atmospheric Environmental Research
 Karlsruhe Institute of Technology (KIT)
 Garmisch-Partenkirchen, Germany
hape.schmid@kit.edu



Hans Peter (HaPe) Schmid (Ph.D., UBC Vancouver, Canada, 1988) is a Swiss micrometeorologist. He has headed the Institute of Meteorology and Climate Research (Department of Atmospheric Environmental Research) at the Karlsruhe Institute of Technology since 2007. He is also Professor of Atmospheric Environmental Research at the TU Munich. His research focuses on the atmosphere–land surface interaction. Before moving to Germany, he was full Professor at Indiana University, Bloomington (USA).

Corinna Rebmann

Department Computational Hydrosystems
 Helmholtz Centre for Environmental Research
 Leipzig, Germany
corinna.rebmann@ufz.de



Corinna Rebmann is a research scientist at the Helmholtz Centre for Environmental Research in Leipzig (Germany). Since finishing her PhD, she has worked on methodological development for the eddy-covariance method and procedures for quality assurance and control. Within TERENO and ICOS-RI, she is responsible for the coordination and scientific evaluation of ecosystem stations in central Germany. Corinna has chaired the ecosystem monitoring station assembly of ICOS-RI until June 2020.

Subject Index

- 3-D variational (3DVar) 732
 4-(Dicyanomethylene)-2-methyl-6-(4-dimethylaminostyryl)-4H-pyran (DCM) 488
 4-D variational (4DVar) 1164
- ### A
- Absolute
 – Cavity Pyrogeometer (ACP) 344
 – Sky-scanning Radiometer (ASR) 344
 absorption
 – coefficient 141
 – microwave 1157
 accreditation 76
 Acid Deposition Monitoring Network in East Asia (EANET) 1458
 acoustic
 – Doppler current profiler (ADCP) 1661
 – Doppler profiler (ADP) 1671
 – Doppler velocimeter (ADV) 1670
 – Horizontal ADCP (HADCP) 1672
 – received echo (ARE) 670
 – speed 664
 – tomography (AT) 1018
 – travel-time tomography (A-TOM) 1000
 Acoustic Doppler Dual Current Profiler (AD2CP) 1671
 acousto-optic modulator (AOM) 774
 acousto-optical spectrometers (AOS) 802
 Active
 – Sensing of CO₂ Emissions over Nights, Days, and Seasons (ASCENDS) 1086, 1181
 active electronically scanned array (AESA) 1123
 Advanced
 – Along Track Scanning Radiometer (AATSR) 1173
 – Baseline Imager (ABI) 1060, 1176
 – Global Atmospheric Gases Experiment (AGAGE) 1702
 – Himawari Imager (AHI) 1176
 – Microwave Scanning Radiometer (AMSR) 1154
 – Microwave Sounding Unit (AMSU) 1154
 – Scatterometer (ASCAT) 1061
 – Spaceborne Thermal Emission and Reflection Radiometer (ASTER) 1059
 – Technology Microwave Sounder (ATMS) 1060, 1154
 – TIROS Operational Vertical Sounder (TOVS) 1156
 – Very High Resolution Radiometer (AVHRR) 1061, 1173
 aerodynamic
 – coordinate system (ADONS) 1321
 – fluxes using iterative energy balance (AFIB) 1542
 – gradient method (AGM) 1446, 1452
 – particle sizer (APS) 535
 aerology 1248
 – history 1250
 – sounding 1254
 aerosol 5, 533, 567, 684
 – aqueous secondary organic (aqSOA) 579
 – formation, secondary 556
 – mass spectrometer (AMS) 557
 aerosol optical
 – depth (AOD) 333, 558, 697, 822, 1172, 1702
 – thickness (AOT) 1133, 1172, 1226
 Aerosol Robotic Network (AERONET) 77, 558, 822, 1179, 1287, 1702
 Aerosol–Cloud–Ecosystem (ACE) 1180
 Aerosols, Clouds and Trace Gases Research Infrastructure (ACTRIS) 837, 1290
 African Monsoon Multidisciplinary Analysis (AMMA) 1282
 afternoon train (A-Train) 1057, 1286
 air
 – capacity (AC) 1628
 – mass factor (AMF) 812
 – traffic control (ATC) 1189
 Air Ion Spectrometer (AIS) 547
 Airborne
 – FTIR (AFTIR) 486
 – phased array radar (APAR) 1123
 – Vertical Atmospheric Profiling System (AVAPS) 1263
 – Visible/Infrared Imaging Spectrometer (AVIRIS) 1062
 Aircraft
 – Communications Addressing and Reporting System (ACARS) 1189
 – Condition Monitoring System (ACMS) 1189
 – Meteorological Data Relay (AMDAR) 1189, 1395
 aircraft
 – flux measurement 1310
 – position 1311
 – true airspeed 1321
 aircraft-derived data (ADD) 1189
 Aircraft-Fixed Orthonormal System (ACONS) 1312
 Aladin Airborne Demonstrator (A2D) 1086
 albedo 300, 329, 1172
 – single-scattering 130, 138
 Algebraic Reconstruction Technique (ART) 1003, 1037
 aliasing effect 45
 Allgemeine Verwaltungsvorschrift (AVV) 425
 Aluminum Conductor Composite Core (ACCC) 1377
 Ambient Dose Equivalent Rate (ADER) 460

- America Lidar Network (ALINE) 1700
 - American Standard Code for Information Exchange (ASCII) 69
 - Ammonia Monitoring Network (AMoN) 1458, 1700
 - amplitude domain reflectometry (ADR) 1639
 - analog digital converter (ADC) 44
 - analyzer
 - calibration 495
 - anemometer
 - cup 249, 257, 1377
 - five-hole probe 1312
 - history 245
 - hot-wire 252, 261
 - laser doppler 252, 261
 - maintenance 266
 - multihole 1337
 - propeller 249, 257
 - rotation 257
 - sonic 1377
 - thermal 252, 261
 - transfer function 250
 - Ångström exponent 684
 - antenna-mounted receiver (AMR) 860
 - Apache Subversion (SVN) 70
 - Application of Light-weight Aircraft for Detecting In Situ Aerosol (ALADINA) 1333
 - Application programming interface (API) 70, 1219, 1236
 - Applications Technology
 - Satellite (ATS) 1055
 - System (ATS) 1174
 - Arctic
 - High-Spectral Resolution Lidar (AHSRL) 1179
 - Lidar Observatory (ALOMAR) 789
 - Radiation IceBridge Sea and Ice Experiment (ARISE) 1145
 - Study of Tropospheric Aerosol and Radiation (ASTAR) 1145
 - System Reanalysis (ASR) 1165
 - ARM mobile facility (AMF) 1291
 - arrival time difference (ATD) 437
 - artificial intelligence (AI) 1216
 - astronomical quantities 146
 - asymmetry parameter (ASY) 1145
 - Atlantic Stratocumulus Transition Experiment (ASTEX) 1179
 - atmosphere 4
 - structure 9
 - vertical structure 10
 - Atmospheric
 - Emitted Radiance Interferometer (AERI) 344, 753, 1285
 - Infrared Sounder (AIRS) 1059, 1164
 - Integrated Research Monitoring Network (AIRMoN) 1700
 - Laser Doppler Instrument (ALADIN) 780, 1057
 - Lidar (ATLID) 1057
 - Mercury Network (AMNet) 1458, 1700
 - Pressure Interface Time-of-flight (Api-TOF) 557
 - Radiation Measurement (ARM) 26, 77, 721, 837, 948, 1105, 1179, 1268, 1282, 1707
 - Radiative Transfer Simulator (ARTS) 1156
 - atmospheric
 - boundary layer (ABL) 11, 155, 670, 699, 977, 1334
 - surface layer (ASL) 1020
 - atmospheric boundary layer (ABL) 732
 - atmospheric measurement
 - history 1190
 - quality control 52
 - representativeness 20
 - audit 76
 - auto-correlation spectrometers (ACS) 802
 - Automated
 - Packet Reporting System (APRS) 1222
 - Shipboard Aerological Program (ASAP) 1273
 - Surface Observing System (ASOS) 1235
 - Automatic
 - Lidar and Ceilometers (ALC) 1404
 - Weather Station (AWS) 1190, 1235
 - automatic
 - dependent surveillance (ADS) 1189
 - frequency control (AFC) 863
 - gain control (AGC) 863
 - Autonomous Underwater Vehicle (AUV) 1664
 - available
 - field capacity (aFC) 1628
 - water (AW) 1550
 - avalanche photodiode (APD) 703, 1084
 - averaging
 - scalar 254
 - vector 254
- ## B
- Background Air Pollution Monitoring Network (BAPMoN) 1688
 - backpropagated local oscillator (BPLO) 772
 - backscatter 742
 - signal 720
 - spectrum 720, 766
 - backscatter coefficient 720
 - volumetric 684
 - balloon 1265
 - Barbados Oceanographic and Meteorological Experiment (BOMEX) 1132, 1307
 - barograph 285
 - barometer
 - aneroid 280, 285
 - capacitive 282, 287, 1256
 - electronic 281, 286
 - history 275
 - liquid 279, 283
 - maintenance 292
 - mercury 283
 - mercury-free liquid 285
 - piezoresistance 281
 - piezoresistive 287, 1256
 - principles of measurement 274
 - resonant 283, 288
 - wind correction 279
 - barometric equation 15
 - Baseline Surface Radiation Network (BSRN) 26, 52, 303, 1179, 1292, 1378, 1688
 - collaborating network 1705
 - international radiation network 1697
 - beam
 - dump (BD) 725
 - expander (BE) 725

- steering unit (BSU) 725
 - widening telescope (BWT) 687
 - Beaufort scale 650
 - BeiDou Navigation Satellite System (BDS) 1252
 - Bernoulli equation 278
 - bidirectional reflectance distribution function (BRDF) 1145, 1173
 - binary universal form for the representation of meteorological data (BUFR) 845, 1268
 - bioaerosol 568
 - Biological, Ancillary, Disturbance, and Metadata (BADM) 1716
 - biosensor (BS) 1715
 - Biosphere Effects on Aerosol and Photochemistry Experiment (BEARPEX) 491
 - black carbon (BC) 1209
 - blending height 15
 - Bluetooth (BT) 1209
 - low energy (BLE) 1209
 - body reference frame (BRF) 1076
 - bolychlorinated biphenyl (PCB) 590
 - Boreal Ecosystem–Atmosphere Study (BOREAS) 1307, 1494, 1508
 - Bouguer–Lambert–Beer law 405, 480, 826
 - boundary layer
 - atmospheric 11
 - convective (CBL) 13, 167, 669, 728, 1297, 1341
 - height 699, 1406
 - internal 15, 176
 - scintillometer (BLS) 972
 - urban 1393
 - Bowen ratio (BR) 1560
 - energy balance (BREB) 1537
 - Bowen ratio method 1536
 - modified (MBR) 1446, 1453
 - Bowen ratio system 1556
 - quality control 1558
 - Bragg condition 668
 - Brewer–Dobson circulation (BDC) 11
 - bridge circuit 192
 - Broad Band Radiometer (BBR) 1057
 - broadband (BB) 1139
 - Broadband Cavity-enhanced Spectrometer (BBCES) 483
 - brownian motion 573
 - building research establishment
 - environmental assessment method (BREEAM) 1411
 - built-in test equipment (BITE) 859, 867
 - bulletin board systems (BBS) 1201
 - buoy 168
 - buoyancy flux 1475
-
- C**
- Cabauw Experimental Site for Atmospheric Research (CESAR) 168, 1282
 - calibration 59
 - analytic function 59
 - and validation (CAL/VAL) 1152
 - catching-type gauge 379
 - factor (CAL) 412
 - non-catching-type gauge 380
 - pressure 291
 - radiation instruments 341
 - stable isotope 524
 - standard 62
 - temperature 203
 - California Ozone Deposition Experiment (CODE) 1308
 - Canadian Air and Precipitation Monitoring Network (CAPMoN) 1458
 - canopy chamber 1586
 - flux calculation 1589
 - history 1587
 - maintenance 1594
 - non-steady-state flowthrough 1588
 - non-steady-state non-flowthrough 1589
 - quality control 1593
 - steady-state flowthrough 1588
 - transparent enclosure 1592
 - capillary rise (CR) 1550
 - carbon-fiber heated cable technology (CFHC) 1650
 - carrier-to-noise ratio (CNR) 760
 - catch ratio (CR) 385
 - cathode ray tube (CRT) 883
 - Cavity Ring-down Spectroscopy (CRDS) 479, 510, 1484, 1673
 - Cavity-attenuated Phase-shift Spectroscopy (CAPS) 482, 546
 - cavity-enhanced
 - spectroscopy (CES) 487
 - spectroscopy (CES) 475
 - ceilometer 705
 - central business district (CBD) 1397
 - Central Processing Unit (CPU) 75, 619, 1238
 - certification 76
 - chamber method 1446
 - Characterization of Arctic Sea Ice Experiment (CASIE) 1343
 - charge-coupled device (CCD) 453, 486, 779, 808, 1089, 1138
 - chemical
 - ionization mass spectrometry (CIMS) 496
 - transport modeling (CTM) 1411
 - chemical conversion
 - device 491
 - method 485
 - chemiluminescence detector (CLD) 594
 - chirp transform spectrometers (CTS) 802
 - chlorofluorocarbon (CFC) 476, 1658, 1690
 - circular depolarization ratio (CDR) 843
 - citizen
 - science (CS) 1200, 1211, 1392
 - scientist 1210
 - Citizen Weather Observer Program (CWOP) 1189, 1219
 - Civil Aircraft for the Regular Investigation of the Atmosphere Based on an Instrument Container (CARIBIC) 1701
 - class A pan 1555
 - quality control 1558
 - Clean Air for London (ClearLo) 1395
 - Clean Air Status and Trends Network (CASTNET) 1458, 1701
 - clear-air turbulence (CAT) 761
 - Climate
 - Absolute Radiance and Refractivity Observatory (CLARREO) 1180
 - and Forecasting (CF) 1268
 - Forecast System Reanalysis (CFSR) 1707
 - climate
 - data record (CDR) 1163
 - diagram 205
 - climatology

- radiation 349
 - wind 267
 - Cloud
 - Physics Lidar (CPL) 1062, 1179
 - Profiling Radar (CPR) 1058
 - System Evolution in the Trades (CSET) 1120
 - cloud
 - cold 137
 - condensation nucleus (CCN) 558
 - cover 646, 653
 - droplet effective radius (DER) 1172
 - genera (type) 646, 651
 - height 646
 - ice 137
 - optical depth (COD) 836, 1172
 - optical thickness (COT) 1172
 - radar system (CRS) 1102
 - to cloud (CC) 436
 - to ground (CG) 436
 - top height (CTH) 1172
 - type 1172
 - warm 130
 - Cloud–Aerosol Lidar
 - and Infrared Pathfinder Satellite Observation (CALIPSO) 698, 1058, 1072, 1179
 - with Orthogonal Polarization (CALIOP) 1058, 1072
 - cloud–aerosol transport system (CATS) 1072
 - Clouds and the Earth’s Radiant Energy System (CERES) 1059
 - clutter ratio narrow (CRN) 878
 - Coastal Ocean Dynamics
 - Applications Radar (CODAR) 955
 - coherent on receive (COR) 863
 - color ratio (CR) 685
 - Community Radiative Transfer Model (CRTM) 1156
 - Compact Optical Backscatter and Aerosol Detector (COBALD) 1275
 - Complete Atmospheric Energetics Experiment (CAENEX) 1133
 - composite profiling
 - compound quantity 1288
 - Dual-Doppler technique 1287
 - history 1285
 - quality control 1294
 - resolution 1289
 - virtual tower technique 1295
 - Comprehensive Nuclear-Test-Ban Treaty (CTBT) 457
 - computational fluid dynamics (CFD) 385, 1397
 - computer-assisted tomography (CT) 1001
 - concentrating solar
 - power (CSP) 333, 1374
 - technologies (CSC) 1370
 - concentration 5, 476
 - activity 460
 - condensation nucleus counter (CNC) 543
 - condensation particle counter (CPC) 535, 1338
 - condensed water content (CWC) 937
 - conditional sampling 1518
 - method 1510
 - conductivity
 - air 443
 - hydraulic 143
 - relaxation 449
 - thermal 128, 143, 145
 - conductivity-temperature-depth (CTD) 1657, 1668
 - constant flux layer (CFL) 1393
 - constant-current anemometer (CCA) 252
 - constants 113
 - constant-temperature anemometer (CTA) 252
 - constant-voltage anemometer (CVA) 252
 - continuous high-precision tall tower observations of greenhouse gases (CHIOTTO) 18
 - continuous wave (CW) 688, 762, 783, 846, 1086
 - Convection Development in Operational Radar Products (CONRAD) 892
 - Convective
 - and Orographically-induced Precipitation Study (COPS) 732, 1282
 - Storms Initiation Project (CSIP) 732
 - convective
 - available potential energy (CAPE) 721, 1285
 - inhibition (CIN) 721
 - konvektiv-index (KO) 1285
 - Convention on Long-Range Transboundary Air Pollution (CLRTAP) 1457, 1710
 - cooling degree days (CDD) 1372
 - Cooperative Observer Program (COOP) 77
 - Coordinated Universal Time (UTC) 146
 - Copernicus
 - Atmosphere Monitoring Service (CAMS) 1701
 - Imaging Microwave Radiometer (CIMR) 1167
 - Coriolis parameter 269
 - cosmic-ray neutron sensor (CRNS) 1650
 - Cramer Rao lower bound (CRLB) 780
 - crowdsourcing 1200
 - calibration 1214
 - data quality 1206
 - data source 1200
 - dedicated system 1207
 - elements 1203
 - history 1201
 - mitigating human influence 1215
 - mobile (MCS) 1202
 - project 1219
 - quality control 1213
 - smartphone accessories 1208
 - uncertainty 1206
 - cryogenic
 - frostpoint hygrometer 1274
 - solar absolute radiometer (CSAR) 315
 - CubeSat Radiometer Radio Frequency Interference Technology Validation (CubeRRT) 1167
 - current 1663
 - meter 1670
-
- ## D
-
- Damköhler number 1453
 - damping 253
 - damping depth
 - diurnal 145
 - data
 - archival 71
 - assimilation (DA) 22, 732
 - problem 79

- processing 68
 - quality objective (DQO) 1709
 - requirements 54
 - shift 81
 - database 108
 - degrees of freedom (DOF) 1299
 - deionized water (DIW) 579
 - delta notation 510
 - density 145
 - current 443
 - humid (moist) air 115, 211
 - liquid water 129
 - seawater 129
 - soil 143
 - Denuder for Long-Term Atmospheric Sampling (DELTA) 1455
 - deposition
 - velocity 1450
 - wet 24
 - Deposition of Biogeochemically Important Trace Species (DEBITS) 1458, 1700
 - depth of percolation (DP) 1538
 - design summer year (DSY) 1411
 - detection
 - efficiency (DE) 450
 - of atmospheric composition change (NDACC) 1695
 - Deutsche Industrienorm (DIN) 469
 - device specification 23
 - diagram
 - Skew-T/Log-P 1249
 - diameter at breast height (DBH) 1435
 - Difference Frequency Generation laser spectroscopy (DFG) 510
 - differential
 - absorption of scattered energy (DASE) 743
 - frequency ratio (DFR) 853
 - optical absorption spectroscopy (DOAS) 475, 476, 486, 751, 799, 1454
 - differential mobility
 - analyzer (DMA) 546
 - particle sizer (DMPS) 546
 - differential-absorption lidar (DIAL) 5, 712, 741, 768, 1068, 1283
 - equation 744
 - history 743
 - quality control 751
 - system 749
 - diffuse horizontal irradiance (DHI) 299, 1384
 - diffusion
 - aerosol particle 573
 - diffusivity
 - particle 540
 - thermal 128, 145
 - digital
 - signal processor (DSP) 846
 - surface model (DSM) 1648
 - direct
 - aerosol radiative effect (DARE) 1143
 - digital waveform synthesis (DDS) 864
 - normal irradiance (DNI) 299, 425, 1370, 1384
 - numerical simulation (DNS) 1397
 - Direct Absorption Spectroscopy (DAS) 807
 - Directory Interchange Format (DIF) 70
 - discharge
 - corona and point 441
 - discrete
 - anisotropic radiative transfer (DART) 1404
 - dipole approximation (DDA) 1158
 - Fourier transform (DFT) 774, 853, 866, 910
 - Disjunct
 - Eddy Accumulation (DEA) 1506, 1511, 1518
 - Eddy Covariance (DEC) 1506
 - Dispersion of Air Pollution and its Penetration into the Local Environment (DAPPLE) 1395
 - dissolved inorganic carbon (DIC) 1665
 - distributed temperature sensing (DTS) 609, 1265
 - distribution
 - Gaussian 37
 - Student 38
 - domain
 - frequency 39, 852, 910
 - time 39, 852, 910
 - Doppler
 - beam swinging (DBS) 663, 767, 912
 - broadening 766
 - Orbitography and Radiopositioning Integrated by Satellite (DORIS) 1060
 - radar 851
 - shift 665, 668, 765, 851, 902, 940, 1099
 - Doppler Wind Lidar (DWL) 759, 1377
 - coherent-detection 768
 - coherent-detection system 773
 - direct-detection 772
 - direct-detection system 777
 - history 762
 - maintenance 784
 - principle of measurement 767
 - quality control 783
 - double
 - difference (DD) 1035
 - direction precision infrared radiometer (DDPIR) 330
 - fence intercomparison reference (DFIR) 382
 - double-beam laser scintillometer (DBLS) 971
 - drop-size distribution (DSD) 361, 848
 - dropsonde 1262
 - dry deposition 5, 24, 1445
 - chemical properties 1450
 - history 1448
 - inferential method (DDIM) 1446
 - maintenance 1460
 - quality control 1459
 - resistance analogy 1450
 - dual-frequency precipitation radar (DPR) 1105
 - dual-wavelength ratio (DWR) 942
 - dynamic
 - error 1355
 - frequency selection (DFS) 880
 - of measuring system 40
 - range (DYN) 408
 - dynamical system
 - first order 249
 - second-order 253
-
- ## E
-
- Earth
 - Engine Flux (EEFlux) 1554
 - Exploration Satellite Service (EESS) 1163
 - observation (EO) 1171
 - Observing Laboratory (EOL) 1268

- Observing System (EOS) 1058, 1155, 1701
- Parameter and Orbit System (EPOS) 1036
- rotation parameter (ERP) 1036
- Science and Applications from Space (ESAS) 1057
- eddy accumulation (EA) 1309, 1506, 1510
- eddy covariance (EC) 1306, 1308, 1446, 1474, 1505, 1560
- conservation equations 1478
- correction 1479
- disjunct 1509, 1516
- energy balance closure 1495
- flow distortion effect 1495
- generalized 1479
- history 1477
- maintenance 1494
- principle 1474
- quality control 1489
- site consideration 1476
- system design 1487
- uncertainty 1492
- Electra Doppler Radar (ELDORA) 1100
- electric field
 - machine 444
 - reduction factor 448
- electric supplementary material (ESM) 116
- electrical
 - aerosol analyzer (EAA) 546
 - low-pressure impactor (ELPI) 548
- electricity 5, 431
 - parameters 432
 - precipitation 440
- electricity measurement
 - disturbed weather 445
 - disturbed weather lightning 436
 - fair weather 434, 441
 - history 432
 - maintenance 450
 - quality control 448
- electrochemical concentration cell (ECC) 1273
- electromagnetic (EM) 1056
 - interference (EMI) 1089
- electromotive force (EMF) 317
- electron capture detector (ECD) 1659
- electronic pressure controller (EPC) 519
- Electronically Scanned Thinned Array Radiometer (ESTAR) 1313
- emission (fluorescence) spectroscopy 487
- emissivity
 - microwave 1153
 - surface 1156
- Energy Balance Experiment (EBEX) 1494
- energy spectrum 20
- Engine Exhaust Particle Sizer (EEPS) 547
- Enhanced
 - MODIS Airborne Simulator (eMAS) 1062
 - Thematic Mapper Plus (ETM+) 1059
 - Vegetation Index (EVI) 1172
- enhancement factor 218
 - water-vapor 125
- enthalpy 130
 - fusion 130
 - sublimation 130
 - vaporization 130
- Environmental
 - and Networking Technologies and Applications (ENTA) 1062
 - Response Function (ERF) 84
- ER-2
 - Doppler Radar (EDOP) 1102
 - X-Band Radar (EXRAD) 1102
- erbium-doped fiber amplifier (EDFA) 774
- error
 - in measurement 34
 - quantification 80
 - quantization 44
 - radiation 194
 - random 36
 - systematic 35
- error propagation 35
 - of random errors 37
- essential climate variable (ECV) 1180, 1255, 1697
- Euler equation 278
- EUMETSAT Polar System (EPS) 1061
 - Second Generation (EPS-SG) 1180
- European
 - Aerosol Research Lidar Network (EARLINET) 1293, 1700
 - Centre for Medium-Range Weather Forecasts (ECMWF) 1164, 1268, 1707
 - Cooperation in Science and Technology (COST) 837, 845, 1299, 1333
 - Field Experiment in a Desertification-Threatened Area (EFEDA) 971
 - Ground-Based Observations of Essential Variables for Climate and Operational Meteorology (EG-CLIMET) 837
 - Meteorological Network (EUMETNET) 845
 - Monitoring and Evaluation Programme (EMEP) 1458
 - Photoreactor (EUPHORE) 55
 - Radiological Data Exchange Platform (EURDEP) 460
 - standard (EN) 424
- European Committee for Standardization (CEN) 95
- evaporation 1532
 - bulk approach 1538
 - history 1532
 - pan 1535
- Evaporation at Grid-Pixel Scale (EVA-GRIPS) 1494
- evapotranspiration (ET) 5, 24, 982, 1531, 1532, 1570, 1629
- remote sensing 1553
- residual of the energy balance 1537
- Expendable Digital Dropsonde (XDD) 1263
- experiments 26
- extended boundary condition method (EBCM) 848
- Extended Ocean Vector Winds Mission (XOVWM) 1180
- extended-interaction amplifier (EIA) 1108
- extended-interaction klystron (EIK) 1105
 - amplifier (EIKA) 946, 1109
- extinction 405
 - coefficient (EXCO) 130, 137, 413, 684, 720, 823
- extreme ultraviolet (EUV) 1060
- extremely low frequency (ELF) 438
- extremely low-volatility organic compound (ELVOC) 557

F

fair, reasonable, nondiscriminatory (FRAND) 96

false alarm rate (FAR) 450

Fast

– Microwave Emissivity Model (FASTEM) 1153

– Mobility Particle Sizer (FMPS) 547

Fast Fourier Transform (FFT) 34, 802, 853, 956

– Spectrometer (FFTS) 802

fiber Bragg grating (FBG) 369

fiber-optic (FO) 611

– cable 621

field

– capacity (FC) 145, 1628

– of view (FOV) 687, 688, 748, 823, 1159

field-effect transistors (FET) 860

field-programmable gate array (FPGA) 774, 808, 1105

figure of merit (FOM) 946

file transfer protocol (FTP) 1236

filter dynamic measurement system (FDMS) 549

filtration 575

finite impulse response (FIR) 449, 910

fire radiative power (FRP) 1172

First

– GARP Global Experiment (FGGE) 169

– ISLSCP Field Experiment (FIFE) 1307

first null beam width (FNBW) 860

five-hole probe (FHP) 1312

float 171

flow

– distortion 158

– injection analysis (FIA) 1455

– meter (FM) 519

Fluorescence Assay by Gas

Expansion (FAGE) 475

FLuorescence EXplorer (FLEX) 1057, 1180

flux 5

– actinic 1135

– detection limit (FDL) 1461

– ocean–atmosphere 1657

– plant–atmosphere 5

– soil–atmosphere 5

– trace gas 5

flux measurement

– aircraft-based 1314

– aircraft-based quality control 1314

flux measurement method

– alternative 1506, 1507

– alternative, history 1507

– alternative, maintenance 1523

– alternative, quality control 1523

flux measurement technique

– aircraft-based 1306

– aircraft-based, history 1307

flux-gradient system 1456

fog collector 1437

fog deposition 5, 1425

– direct measurement 1428, 1432

– eddy-covariance method 1430, 1435, 1436

– history 1430

– isotope method 1430

– maintenance 1440

– quality control 1439

– rate 1427

– surrogate 1433

– surrogate method 1428

– water balance 1436

– water budget 1434

– water budget method 1430

fog interception

– rate (FIR) 1427, 1433

footprint 17, 1490

forced diffusion (FD) 1611

forecast sensitivity to observation index (FSOI) 73, 923

forward scatter signal (FSS) 412

Fourier-Transform

– Infrared Spectroscopy (FTIR) 475, 486, 511, 799, 1018, 1673, 1705

– Spectrometer (FTS) 1699

fraction of absorbed

photosynthetically active radiation (FAPAR) 1172

fractional

– absorption (FA) 1146

– cloud cover (CF) 1172

– vertical flux divergence (FVFD) 1144

free troposphere 698

free troposphere (FT) 761

frequency

– modulation (FMS) 807

– range 24

frequency-domain

– interferometry (FDI) 916

– reflectometry (FDR) 1638

frequency-modulated

– continuous wave (FMCW) 954, 1103

– continuous-wave radar (FMCW radar) 946

– interrupted continuous wave (FMICW) 954

friction velocity 978, 1475

frostpoint hygrometer (FPH) 1274

fugacity

– relative 218

full

– correlation analysis (FCA) 915

– width at half maximum (FWHM) 492, 700, 745, 766, 825, 1089, 1133

function

– density 36

– response 40

– transfer 40

– weighting 1157

fundamental climate data records (FCDR) 1163

G

Galileo thermometer 187

gallium arsenide phosphide (GaAsP) 335

gas

– chromatography (GC) 638, 1659

– dissolved 1664, 1672

– measurement 1672

gas analyzer 1454

– history 478

– intercomparison 496

– maintenance 496

– measurement principle 478

– parameter 477

gas flux

– trace 1475

Geiger–Müller (GM) tube 461

Geocentric Celestial Reference Frame (GCRF) 1076

Geographic Information System (GIS) 1217, 1351, 1636

geometric mean diameter (GMD) 541

Geometrical Displacement and Conduction Current Sensor (GDACCS) 444

- geopotential height 15, 279, 1256
 Geoscience Laser Altimeter System (GLAS) 1071, 1179
 Geostationary
 – Coastal and Air Pollution Event (GEO-CAPE) 1180
 – Earth Radiation Budget experiment (GERB) 1060
 – Meteorological Satellite (GMS) 1055
 – Operational Environmental Satellite (GOES) 1055, 1173, 1238
 – Operational Meteorological Satellite (GOMS) 1055
 geosynchronous orbit (GSO) 1174
 Gimballed Limb Observer for Radiance Imaging in the Atmosphere (GLORIA) 1062, 1064
 glass-fiber
 – filter coated with s.c. (GF (s.c.)) 580
 – reinforced plastic (GRP) 161
 Global
 – Drifter Program (GDP) 169
 – Earth Observing System of Systems (GEOSS) 1693
 – Energy and Water Exchanges (GEWEX) 1308, 1689
 – Horizontal Sounding Technique (GHOST) 1253
 – Observing System (GOS) 4, 7, 1273, 1688
 – Positioning System (GPS) 333, 752, 832, 981, 1026, 1073, 1109, 1136, 1180, 1210, 1252, 1336, 1669
 – Positioning System (GPS) Radio Occultation (GPSRO) 1180
 – Precipitation Measurement (GPM) 1101, 1154
 – Precipitation Measurement (GPM) Microwave Imager (GMI) 1154
 – Telecommunication System (GTS) 168, 1268
 global
 – horizontal irradiance (GHI) 299, 1370, 1384
 – tilted irradiance (GTI) 1370
 Global Atmosphere Watch (GAW) 523, 591, 1273, 1457, 1688
 – contributing network 1699
 – Precision Filter Radiometer (GAW-PFR) 822
 – Station Information System (GAWSIS) 1694
 – Urban Research Meteorology and Environment Project (GURME) 1690
 Global Atmosphere Watch(GAW) 1693
 Global Atmospheric
 – Aerosol and Radiation Study (GAARS) 1133
 – Composition Mission (GACM) 1180
 – Research Program (GARP) 169
 Global Climate Model (GCM) 1697
 Global Climate Observing System (GCOS) 26, 303, 836, 1180, 1254, 1293, 1688
 – Reference Upper-Air Network (GRUAN) 26, 836, 1254, 1293, 1688, 1697, 1705
 – Upper-Air Network (GUAN) 1254, 1273, 1693
 Global Navigation Satellite System (GLONASS) 1252, 1337
 Global Navigation Satellite System (GNSS) 5, 732, 1026, 1061, 1074, 1115, 1136, 1247, 1257, 1282, 1311, 1334, 1351
 – Receiver for Atmospheric Sounding (GRAS) 1061
 – system 1033
 – tomography system 1036
 Global Ozone
 – Monitoring Experiment (GOME) 812
 – Observing System (GO3OS) 1688
 gradient method (GM) 699
 gravitational field 574
 Gravity
 – Field and Steady-State Ocean Circulation Explorer (GOCE) 1057
 – Recovery and Climate Experiment II (GRACE-II) 1180
 greenhouse gas (GHG) 511, 1484
 – recommendation for compatibility 522
 Greenhouse Gases Observing Satellite (GOSAT) 1699
 ground
 – state of 646
 – water (GW) 1538
 ground-based radiative transfer for TIROS operational vertical sounder (RTTOV-gb) 837
 Guide to the Expression of Uncertainty in Measurement (GUM) 333
 Gulfstream V (GV) 1109
-
- ## H
-
- half-power beam width (HPBW) 860
 HALO Microwave Package (HAMP) 1105
 Halocarbons and other Atmospheric Trace Species (HATS) 1703
 hazard distance (HD) 704
 HD(CP)² Observational Prototype Experiment (HOPE) 732, 1282
 heat capacity 130
 – humid air 127
 – ice, isobaric 130
 – specific 145
 – volumetric 145
 – water, isobaric 130
 – water, isochoric 130
 heat flux
 – ground (soil) 5, 1633
 – latent 24, 978, 1288, 1404, 1475, 1486, 1532
 – sensible 5, 24, 977, 1288, 1404, 1475, 1486
 heating degree days (HDD) 1372
 Henry's constant 128, 1665
 Henry's law 115
 heterogeneous sensor (HS) 1715
 Hierarchical Data Format (HDF) 69, 1704
 – version 5 (HDF5) 845
 high
 – dose (HD) 463
 – frequency (HF) 953
 – spectral resolution (HSR) 1070
 High Frequency Radar 953
 – history 954
 – maintenance 961
 – quality control 961
 – systems 956

- High Spectral Resolution Lidar (HSRL) 697, 745, 1062, 1068, 1109
- High-Altitude
- and long range aircraft (HALO)microwave Package (HAMP) 1105
 - and Long Range Research Aircraft (HALO) 1110, 1287
 - Imaging Wind and Rain Airborne Profiler (HIWRAP) 1102
 - Radar (HAR) 1111
- High-Definition Sounding System (HDSS) 1263
- high-density polyethylene (HDPE) 1436
- high-efficiency particulate air (HEPA) 555
- highly
- coherent oscillator (COHO) 863
 - oxidized multifunctional molecule (HOM) 557
- High-Performance Instrumented Airborne Platform for Environmental Research (HIAPER) 1063, 1109, 1287
- Cloud Radar (HCR) 1109
- high-performance liquid chromatography (HPLC) 494
- High-Resolution
- Doppler Lidar (HRDL) 777, 1086
 - Dynamics Limb Sounder (HIRDLS) 1058
 - Infrared Radiation Sounder (HIRS/4) 1061
 - Transmission Molecular Absorption Database (HITRAN) 482, 511, 742, 1157
- Horizontal Mobile Measurement System (HMMS) 1361
- human-computer interaction (HCI) 1216
- Humidity
- and Temperature Profiler (HATPRO) 832
 - Sounder for Brazil (HSB) 1059
- humidity 5, 611, 1249, 1283, 1401
- absolute 211, 742
 - relative 23, 211, 217, 721
 - specific 185, 211
- hydrofluorocarbon (HFC) 1658
- Hydrologic Atmospheric Pilot Experiment (HAPEX) 1307
- Hydrological Cycle in the Mediterranean Experiment (HYMEX) 1282
- Hydrological Cycle in the Mediterranean Experiment (HyMeX) 1122
- hydropower 1376
- hygrometer
- capacitive 219, 224, 1257, 1337
 - dew cell 219
 - dewpoint 221, 229
 - frostpoint 221, 229
 - hair 219, 222
 - heated 1258
 - history 212
 - infrared (IR) 231
 - lithium chloride 219
 - maintenance 236
 - optical 221, 230
 - principles of measurements 211
 - reference standard 234
 - ultraviolet (UV) 230
- Hygroscopic Tandem Differential Mobility Analyzer (HTDMA) 550
- hypsometer 281, 286
-
- I**
- ice
- crystal size distribution (ISD) 137
 - nucleus (IN) 558
- Ice Cloud Imager (ICI) 1156
- ice water
- content (IWC) 137, 936, 1290
 - path (IWP) 1152
- Ice, Cloud, and Land Elevation Satellite II (ICESat-II) 1180
- Icosahedral Nonhydrostatic Large Eddy Model (ICON-LEM) 22
- image
- satellite system 1177
- imager
- limb sounder 1161
 - maintenance 1163
 - nadir sounder 1160
 - quality control 1163, 1180
 - wavelength 1175
- imaging 1171
- Imaging Infrared Radiometer (IIR) 1058
- immission 1445
- Impact of Melt Ponds on Energy and Momentum Fluxes between Atmosphere and Sea Ice (MELTEX) 1145
- Implementation and Coordination Meeting (ICM) 1699
- Improved TIROS Operational System (ITOS) 1174
- inconsistency
- internal/theoretical 82
- inertial
- measurement unit (IMU) 1115, 1312, 1336
 - navigation system (INS) 1109, 1136, 1312, 1337
 - sublayer (ISL) 1393
- Inertial Reference System (IRS) 1115
- infiltrometer 1635
- infinite impulse response (IIR) 877
- inflection point method (IPM) 699
- Infrared
- Atmospheric Sounding Interferometer (IASI) 732
 - Integrating Sphere Radiometer (IRIS) 344
- infrared (IR)
- gas analyzer (IRGA) 1588, 1607, 1716
 - radiation, downwelling 300
 - thermometer (IRT) 1401
- Infrared Absorption Gas Analyzer (IRGA) 1515
- Infrared Atmospheric Sounding Interferometer (IASI) 1061, 1164
- In-phase & Quadrature (I&Q) 1108
- In-service Aircraft for Global Observing System (IAGOS) 1701
- instantaneous automatic gain control (IAGC) 863
- instrument
- characteristics 55
 - intercomparison 63
 - odor measurement system (IOMS) 637
 - requirements 58
- instrumental line shape (ILS) 804
- insulated gate bipolar transistor (IGBT) 860
- integral turbulence characteristics (ITC) 1490
- Integrated

- Carbon Observation System (ICOS) 52, 165, 1179, 1716
- Cavity Output Spectroscopy (ICOS) 482, 1484, 1673
- Forecast System (IFS) 1078
- Global Atmospheric Chemistry Observation (IGACO) 1697
- Measuring and Information System for the Surveillance of Environmental Radioactivity (IMIS) 460
- Path Differential Absorption (IPDA) 1069
- Profiling Technique (IPT) 1289
- integrated water vapor 732
- intensive field campaign (IFC) 1317
- Interagency Monitoring of Protected Visual Environments (IMPROVE) 1700
- Interband Cascade Laser (ICL) 487, 807
- interception
 - capacity (IC) 1435
 - loss (IL) 1434
- intercomparison exercise (IE) 100
- interference
 - field 83
 - filter (IF) 687, 725
 - infrastructure 82
- interim reference sunshine recorder (IRSR) 335
- intermediate frequency (IF) 830, 863, 917
- digitizer (IFD) 863
- intermediate storage reservoir (ISR) 1511
- International
 - Arctic Buoy Program (IABP) 169
 - Geophysical Year (IGY) 303, 1688
 - Monitoring System (IMS) 470
 - Network to Study Deposition and Atmospheric Chemistry in Africa (INDAAF) 1458
 - Programme for Antarctic Buoys (IPAB) 169
 - Pyrgeometer comparison (IPgC) 343
 - Pyrhelimeter Comparison (IPC) 313
 - Pyrhelimetric Scale (IPS) 313
 - Satellite Land Surface Climatology Project (ISLSCP) 1307

- System of Units (Système international d'unités) (SI) 62, 108, 274, 300, 1690
- System of Units (Système international d'unités) (SI) unit 111
- Thermodynamic Equation of Seawater – 2010 (TEOS-10) 110, 1663
- Water Vapor Project (IHOP) 732
- International Civil Aviation Organization (ICAO)
 - standard atmosphere (ISA) 293
- International Civil Navigation Aviation (ICNA) 293
- International Organization for Standardization (ISO) 95
- International Temperature Scale (ITS) 62
 - 1968 (IPTS-68) 109, 1662
 - 1990 (ITS-90) 107, 184, 1662
- International Terrestrial Reference Frame (ITRF) 1036, 1076
- internet
 - of things (IoT) 293
 - protocol (IP) 1238
- intracloud (IC) 436
- ion
 - chromatograph (IC) 1455
 - chromatography (IC) 579
 - measurement 442
- ion-mobility spectroscopy (IMS) 638
- Isotope Ratio Mass Spectrometry (IRMS) 510
- isotope, stable 509
 - measurement system 522, 525

J

- Jena Reference Air Set (JRAS) 524
- Joint Polar Satellite System (JPSS) 1060

K

- Ka-Band Precipitation Radar (KPR) 1113
- Keeling plot 526, 1515, 1521
- kilometer-scale ensemble data assimilation (KENDA) 732
- kurtosis 936

L

- land surface
 - analysis (LSA) 1179
 - temperature (LST) 1152, 1172
- Land–Atmosphere Feedback Experiment (LAFE) 733
- Large Eddy Simulation (LES) 385, 1017, 1397
- Large-Scale Biosphere–Atmosphere (LBA) 1307
- large-scale single function (LSSF) 1715
- laser Doppler anemometer (LDA) 253
- laser mirror (LM) 725
- laser-induced
 - fluorescence (LIF) 475
 - phosphorescence (LIP) 475
 - phosphorescence of (methyl)glyoxal spectrometry (LIPGLOS) 491
- latent heat
 - evaporation 210
 - nudging (LHN) 893
 - sublimation 210
- latent heat (LE) 1316
- Latin America Lidar Network (LALINET) 1700
- launching system
 - auto 1267
- lead zirconate titanate (PZT) 283
- leadership in energy and environmental design (LEED) 1411
- Leaf-area Index (LAI) 1172, 1433, 1541, 1586, 1629
- least
 - expensive radar (LERA) 957
 - significant bit (LSB) 44, 863
- least squares (LSQ) 1036
 - estimation (LSE) 61
- lefthanded circular (LHC) 857
- Lehmann–Groß–Bahn (LGB) 1360
- Leipzig Aerosol and Cloud Remote Observations System (LACROS) 1282
- lens (L) 725
- letter of agreement (LoA) 1699
- Liaison Group on Radar Networking (GORN) 845
- Lidar
 - Atmospheric Sensing Experiment (LASE) 1084

- In-space Technology Experiment (LITE) 686, 1071
 - Surface Topography (LIST) 1180
 - lifted index (LI) 1285
 - light detection and ranging (lidar) 102, 168, 683, 959, 1496
 - aerosols nouvelle génération (LNG) 1084
 - backscatter 684
 - color ratio 698
 - data acquisition 727
 - depolarization 699
 - design consideration 704
 - elastic equation 690
 - equation 687
 - extension equation 695
 - history 686, 721
 - laser 700, 726
 - maintenance 709
 - optics 701
 - pour l'étude des interactions aérosols nuages dynamique rayonnement et du cycle de l'eau (LEANDRE) 1085
 - quality control 707, 729
 - Raman 719, 725
 - Raman equation 722
 - ratio (LR) 685, 690, 697, 720
 - receiver 726
 - signal 689
 - system 687, 728
 - telescope 701
 - temperature rotational Raman equation 722
 - transition method 697
 - visibility 427
 - water-vapor Raman equation 723
 - light-emitting diode (LED) 407, 483, 825, 972
 - limit of detection (LOD) 490
 - Lindenberg Inhomogeneous Terrain—Fluxes Between Atmosphere and Surface: a Long-Term Study (LITFASS) 971, 1494
 - line
 - of sight (LOS) 760, 1088
 - replaceable units (LRU) 869
 - linear
 - channel (LIN) 858
 - depolarization ratio (LDR) 843, 936, 1100
 - time-invariant (LTI) 39
 - Line-By-Line Radiative Transfer Model (LBLRTM) 344
 - liquid
 - nitrogen (LN₂) 834
 - scintillation spectroscopy (LSC) 461
 - water content (LWC) 131, 833, 936, 1285, 1433
 - water path (LWP) 825, 947, 1152, 1172, 1285
 - Local
 - Area Network (LAN) 987
 - Ensemble Transform Kalman Filter (LETKF) 732
 - local
 - climate zone (LCZ) 1399
 - data manager (LDM) 1236
 - oscillator (LO) 769, 830, 917
 - reference frame (LO) 1076
 - true solar time (LTST) 147
 - localized multifunction sensor (LMS) 1715
 - Location-aware Sensing System (LASS) 1223
 - logarithmic channel (LOG) 858
 - Long-path Absorption Photometer (LOPAP) 492, 1361
 - Long-Term Ecological Research (LTER) 1716
 - low
 - dose (LD) 463
 - Lower Atmospheric Process Studies at Elevation—a Remotely Piloted Team Experiment (LAPSE-RATE) 1343
 - Lowered Acoustic Doppler Current Profiler (LADCP) 1669
 - lower-upper (matrix decomposition) (LU) 1003
 - low-noise amplifier (LNA) 830, 862, 918
 - Low-power Wireless Integrated Microsensors (LWIM) 1202
 - low-pressure impactor (LPI) 548
 - L'Atmosphère Par Lidar Sur Saliout (ALISSA) 1071
 - lysimeter 1570
 - filling technique 1576
 - groundwater 1575
 - history 1571
 - large 1574
 - quality control 1578
 - small 1574
 - tension control 1573
 - weighing system 1572
-
- ## M
-
- machine learning 84
 - Mach–Zehnder Interferometer (MZI) 1084
 - Mackenzie GEWEX Study (MAGS) 1308
 - Magnetic Resonance Tomography (MRT) 1001
 - maintenance 64
 - Manipulation Nitrogen and Phosphorous (MaNiP) 176
 - Mapping Evapotranspiration at High Resolution Using Internalized Calibration (METRIC) 1554
 - mass
 - flow controller (MFC) 518
 - spectrometer (MS) 510, 1659
 - spectrometry, isotope ratio (IRMS) 513
 - master
 - chemical mechanism (MCM) 499
 - oscillator power amplifier (MOPA) 774
 - maximum
 - estimated size of hail (MESH) 891
 - length sequence (MLS) 1004
 - likelihood estimation (MLE) 61
 - mean
 - local time (MLT) 146
 - sea level (MSL) 1118
 - value of temperature 204
 - mean time between failures (MTBF) 924
 - measurement 1657
 - guideline (MG) 1709
 - historical 7
 - result (MR) 387
 - standardization 101, 102
 - strategy 1356
 - system, digital 46
 - uncertainty 38
 - measurement chain
 - analog 44
 - digital 44
 - Measurement of Ozone and Water Vapour on Airbus In-service Aircraft (MOZAIC) 1701

- Measurements of Pollution in the Troposphere (MOPITT) 1059
- median absolute deviation (MAD) 1480
- Mercury Deposition Network (MDN) 1700
- mesonet 1234
 - history 1235
 - maintenance 1240
 - Oklahoma 1242
 - quality control 1240
 - requirements 1235
 - sensor 1237
 - system 1237
- mesosphere (MS) 10, 761
- mesosphere-stratosphere-troposphere (MST) 903
- metadata 69
- Meteorological
 - Mini Aerial Vehicle (M2AV) 1333
 - Operation Satellite, Second Generation (MetOp-SG) 1156
 - Operational Satellite (MetOp) 1061, 1173
 - Orthonormal Coordinate System (MONS) 1311
- meteorological element 4
 - renewable energy 1370
 - variability 18
- meteorological measurement
 - representativeness 16
 - standardization 93
 - visualization 26
- meteorological optical range (MOR) 401, 403, 405, 653, 1380
- meteorological satellite (METEOSAT) 1055
 - Second Generation (MSG) 1055
 - Third Generation (MTG) 1055, 1180
 - Visible and Infrared Imager (MVI) 1173
- metrology 33
- Metropolitan Meteorological Experiment (METROMEX) 1395
- micro air vehicle (MAV) 1333
- microbalance
 - particle 540
- microchannel plate (MCP) 485
- microelectromechanical system (MEMS) 278, 1202, 1338
- Micro-orifice Uniform Deposit Impactor (MOUDI) 548, 582
- Microportable Greenhouse Gas Analyzer (M-GGA) 1614
- Micro-Pulse DIAL (MPD) 750
- Micro-Pulse Lidar (MPL) 1179, 1701
 - Network (MPLNET) 1701
- Microwave
 - and Millimeter-wave Integrated Circuit (MIMIC) 826
 - Humidity Sounder (MHS) 1061, 1154
 - Imager 1159
 - Imager (MWI) 1156
 - Limb Sounder (MLS) 802, 1058, 1154
 - Radiometer (MWR) 724, 822, 1152, 1282
 - Scintillometer (MWS) 971
 - Sounding Unit (MSU) 1155
 - Temperature Profiler (MTP) 832
- microwave
 - propagation model (MPM) 1157
 - radiometry (MWR) 799
 - sounder (MWS) 1156
- microwave (MW) 822
- mid-infrared (MIR) 515
- Mie spectrometer (MSP) 780
- minimum
 - chi square estimation (MCSE) 61
 - detectable signal (MDS) 842
- mixed layer (ML) 12
 - height (MLH) 669, 1406
- mixing height (MH) 1406
- mobile experience sampling (ESM) 1216
- mobile system 1352
 - history 1353
 - horizontal measurement system 1358
 - quality control 1361
 - requirement 1354
 - vertical measurement system 1361
- Mobility Particle Size Spectrometer (MPSS) 535
- mode
 - accumulation 568
 - Aiken 568
 - coarse 568, 591
 - nucleation 568
- MODerate resolution atmospheric TRANsmission (MODTRAN) 344
- Moderate Resolution Imaging Spectroradiometer (MODIS) 1059, 1173, 1554
- Mode-Selective Enhanced Surveillance Data (MODE-S EHS) 1189
- MODIS/ASTER Airborne Simulator (MASTER) 1062
- momentum flux 5, 1474
- Monin–Obukhov similarity theory (MOST) 970, 977
- monitor to measure the integral transmittance (MITRA) 315
- monitoring 74
- Monolithic Microwave-integrated Circuit (MMIC) 859
- Monte Carlo (MC) 1143
- Motion Reference Unit (MRU) 1669
- Mountain Standard Time (MST) 1296
- Moving Target Indicator (MTI) 844
- Multi-Angle
 - Absorption Photometer (MAAP) 546
 - Imaging SpectroRadiometer (MISR) 1059, 1176
- multifilter rotating shadowband radiometer (MFRSR) 333, 1133
- multihole flow probe (MFP) 1337
- multimode (MM) 613
- Multiple Signal Classification (MUSIC) 957
- Multiple-input Multiple-output (MIMO) 965
- multiplicative algebraic reconstruction technique (MART) 1003, 1037
- Multi-purpose Airborne Sensor Carrier (MASC) 1333
- Multispectral
 - Imager (MSI) 1057
 - Instrument (MSI) 1178
 - Scanner (MSS) 1313
- Mutual Recognition Arrangement (MRA) 315

N

National

- Airborne Sounder Testbed Interferometer (NAST-I) 1062
 - Atmospheric Deposition Program (NADP) 1700
 - Dry Deposition Network (NDDN) 1457
 - Ecological Observatory Network (NEON) 52, 1716
 - Meteorological Center (NMC) 1268
 - Polar-orbiting Operational Environmental Satellite System (NPOESS) 1062
 - Polar-orbiting Partnership (Suomi-NPP) 1060
 - Radiation Center (NRC) 341, 1311
 - Trends Network (NTN) 1700
 - near-infrared (NIR) 1173, 1313
 - negative temperature coefficient (NTC) 192, 1662
 - Net Ecosystem Exchange (NEE) 1586
 - net radiometer 329, 1312
 - solar 329
 - terrestrial 330
 - Network
 - for Environmental and Weather Application (NEWA) 1243
 - for the Detection of Atmospheric Composition Change (NDACC) 813, 1274, 1688, 1695
 - for the Detection of Stratospheric Change (NDSC) 1688
 - of FLUX Measurement Sites (FLUXNET) 1179, 1717
 - network
 - atmospheric measurement technique, history 26, 1691
 - atmospheric measuring technique 1688
 - common data form (netCDF) 1268
 - ecological measurement 1713, 1715, 1720
 - immission and deposition 1457
 - mesometeorological 1234
 - quality control 77, 1720
 - structure 1693
 - Neutral Cluster and Air Ion Spectrometer (NAIS) 547
 - Next-Generation
 - Airborne Visible/Infrared Imaging Spectrometer (AVIRIS-NG) 1062
 - Aircraft Remote Sensing for Validation (NARVAL) 1111
 - Radar (NEXRAD) 845
 - nocturnal
 - boundary-layer Keeling plot (NBL-K) 1506
 - stable boundary layer (NSBL) 164
 - noise
 - equivalent differential temperature (NEDT) 1164
 - figure (NF) 946
 - Nominal Ocular Hazard Distance (NOHD) 704
 - non-methane hydrocarbons (NMHC) 579
 - non-rain water input (NRWI) 1572
 - Normal Incidence Pyrheliometer (NIP) 307
 - normalized
 - radar cross-section (NRCs) 1115
 - Normalized Difference Vegetation Index (NDVI) 1172, 1555
 - North Atlantic Waveguide and Downstream Impact Experiment (NAWDEX) 1111
 - Nowcasting SAF (NWC SAF) 1179
 - Nuclear Instrumentation Module (NIM) 465
 - Numerical Weather
 - Model (NWM) 1078
 - Prediction (NWP) 22, 728, 782, 843, 892, 923, 970, 1041, 1152, 1172, 1270, 1290, 1707
 - Nyquist frequency 46
-
- O**
- observation
 - classification 646
 - Observations of Aerosols above Clouds and Their Interactions (ORACLES) 1144
 - observatory service (SO) 1701
 - Observing Systems Capability Analysis and Review Tool (OSCAR) 1039, 1057
 - obstacle 15, 256
 - Obukhov length 14
 - Ocean
 - and Land Colour Instrument (OLCI) 1061
 - and Sea Ice SAF (OSI SAF) 1179
 - Surface Current Radar (OSCR) 955
 - ocean
 - wind speed (OWS) 1152
 - odor 5, 633
 - olfactometry 636
 - parameter 634
 - principles of measurement 634
 - unit (OU) 634, 635
 - odor field inspection
 - grid mode 637
 - plume mode 637
 - odor measurement system (IOMS) 637, 638
 - quality control 640
 - off-axis integrated cavity output spectroscopy (OA-ICOS) 510, 1673
 - OPERA Data Information Model (ODIM) 845
 - Operational
 - Land Imager (OLI) 1059, 1178
 - Programme for the Exchange of Weather Radar Information (OPERA) 845
 - optical
 - density (OD) 480
 - depth (OD) 751, 823
 - parametric oscillator (OPO) 743, 1085
 - path difference (OPD) 780
 - thickness 130
 - optical particle
 - counter (OPC) 535, 1338
 - spectrometer (OPS) 543
 - Optical-Fiber Distributed Sensing (OFDS) 609
 - active heating system 620
 - active system 611
 - double-ended configuration 625
 - history 613
 - humidity measurement 617
 - maintenance 625
 - measurement principle 612
 - off-grid installation 622
 - passive system 611
 - quality control 624
 - Raman-backscatter device 619
 - single-ended configuration 624
 - soil moisture measurement 619
 - solar radiation 616

- temperature measurement 614
 - wind speed measurement 617
 - optical-microwave scintillometer (OMS) 971
 - orthomode transducer (OMT) 861
 - oxygenated VOC (OVOC) 492
 - Ozone
 - Mapping and Profiler Suite (OMPS) 1060
 - Monitoring Instrument (OMI) 812, 1058
- P**
-
- Pacific Northwest National Laboratory (PNNL) 1062
 - p.a.-coated paper filter (P(p.a.)) 580
 - participatory sensing (PS) 1200
 - particle
 - aerodynamic behavior 540, 548
 - atmospheric 534
 - diffusivity 547
 - electrical detection 539, 546
 - extinction 539, 545
 - flux 557
 - measurement principle 535
 - microbalance 549
 - mobility 539, 546
 - particle light
 - absorption 539, 545
 - scattering 538, 542
 - Particle Measuring Systems (PMS) 1113
 - particle migration
 - electric field 586
 - gravitational 586
 - particle migration and deposition
 - electric field 574
 - gravitational 574
 - particle sampling 567, 569, 571, 580
 - system 541
 - particle sensor
 - calibration 554
 - combination 549
 - for UAS 1338
 - maintenance 555
 - Particle Soot Absorption Photometer (PSAP) 545
 - particle-size
 - distribution (PSD) 131, 374, 541, 944
 - separation, inertia-based 571, 582
 - particulate matter (PM) 425, 570, 1209
 - path-integrated attenuation (PIA) 936
 - Pellin–Broca prism (PBP) 725
 - Penman method 1539
 - Penman–Monteith (PM) 1541
 - method 1540
 - reference method 1542
 - perfluoroalkoxy (PFA) 491
 - periodically poled lithium niobate (PPLN) 515
 - permutation entropy (PE) 1644
 - peroxy radical amplifier (PERCA) 488
 - peroxyacetyl nitrate (PAN) 490, 578, 1446
 - persistent organic pollutant (POP) 593
 - personal weather station (PWS) 1220
 - Photoacoustic
 - Extinctionmeter (PAX) 546
 - Soot Spectrometer (PASS) 546
 - photo-fragmentation (PF) 489
 - photomultiplier tube (PMT) 493, 687, 725, 1084
 - Photosynthetic Photon Flux Density (PPFD) 334
 - Photosynthetically Active Radiation (PAR) 83, 297, 1175, 1192, 1237, 1586
 - sensor 334
 - photovoltaic (PV) 1374, 1412
 - piston gauge 289
 - Pitot-static tube 253, 262
 - Plains Elevated Convection at Night (PECAN) 733, 919
 - plan position indicator (PPI) 767, 844, 1288
 - plan–do–check–act (PDCA) 76
 - planetary boundary layer (PBL) 11, 1393, 1703
 - plant chamber 1586
 - plastic scintillation counter 461
 - platform
 - aircraft 1053, 1098, 1305
 - impact on measured variables 159
 - infrastructure 171
 - mesometeorological 1237
 - satellite 1053
 - platform, airborne
 - aircraft 1057
 - history 1054
 - instrumental requirements 1056
 - satellite 1057
 - UAS 1332
 - platform, ground-based 155
 - composite profiling 1291
 - maintenance 175
 - mobile system 1352
 - relevant sensor 173
 - safety 175
 - Poisson's equation 14
 - Polarization
 - and Anisotropy of Reflectances for Atmospheric Science coupled with Observations from a Lidar (PARASOL) 1058, 1088
 - and Directionality of the Earth's Reflectances (POLDER) 1058, 1174
 - Polarizing Beam Splitter (PBS) 687
 - pollutants 99
 - polyaromatic hydrocarbon (PAH) 569
 - polybrominated diphenyl ether (PBDE) 593
 - polychlorinated
 - dibenzodioxin (PCDD) 593
 - dibenzofuran (PCDF) 593
 - polyethylene (PE) 620
 - high density (PE-HD) 1574
 - polyphase filter-bank (PFB) 808
 - polypropylene (PP) 577
 - polystyrene latex sphere (PLS) 553
 - polytetrafluoroethylene (PTFE) 325, 442, 491, 577, 636, 1313, 1360
 - polyurethane foam (PUF) 580
 - polyvinyl chloride (PVC) 1675
 - positive temperature coefficient (PTC) 192, 1662
 - potential
 - equalizer 442
 - gradient (PG) 432, 434
 - Prandtl number 128
 - turbulent 13
 - Prandtl tube 253, 262
 - precipitable water (PW) 1026
 - vapor (PWV) 823, 1152
 - precipitation 5, 23, 360, 646, 1402
 - Precipitation and All-Weather Temperature and Humidity (PATH) 1180
 - precipitation device
 - catching-type gauge 370

- drop counter 372
 - impact disdrometer 373
 - maintenance 392
 - microwave sensor 375
 - non-catching-type gauge 372
 - optical disdrometer 373
 - storage gauge 370
 - thermodynamic sensor 373
 - tipping-bucket gauge 371
 - tipping-bucket gauge (TBG) 368
 - weighing gauge 371
 - precipitation measurement
 - accuracy 367
 - bias 377
 - correction method 381
 - drop counting 369
 - environmental factors 378
 - gravimetric method 368
 - history 362
 - intercomparison result 389
 - measurement principle 360, 367
 - optical methods 369
 - other methods 370
 - precipitation 360
 - quality control 388
 - requirements 361
 - tilting siphon 368
 - tipping-bucket 368
 - uncertainty 387
 - weighing 369
 - precise point positioning (PPP) 1035
 - Precision Infrared Pyrgeometer (PIR) 327
 - Precision Spectral Pyranometer (PSP) 330
 - present weather detector (PWD) 1404
 - pressure 5, 23, 1249
 - adjusted to sea level (QNH) 274
 - dynamic 278
 - height corrected (HCP) 274
 - measurements for aircraft 293
 - reduction 279
 - static 278
 - unit 274
 - Priestley–Taylor method 1539
 - Primary Standard (PS) 1708
 - probability
 - matching method (PMM) 889
 - of false detection (POFD) 450
 - Probability of Severe Hail (POSH) 891
 - programmable ion mobility spectrometer (PIMS) 443
 - propagation of sound 1002
 - proportional counter 461, 462
 - proton transfer reaction (PTR) 1517
 - psychrometer 225
 - according to Assmann 227
 - according to August 227
 - coefficient 225
 - electrical 227
 - WMO reference 229
 - psychrometric method 220
 - Public Participatory Geographic Information Systems (PPGIS) 1200
 - public–private partnerships (PPP) 1200
 - pulse
 - forming network (PFN) 859
 - width (PW) 846
 - pulse repetition
 - frequency (PRF) 764, 842, 1103
 - time (PRT) 842
 - pulse-pair processing (PPP) 852
 - pyranometer
 - airborne 1137
 - calibration 342
 - classification 340, 341
 - photodiode-based 326
 - sunshine 333
 - with black thermopiles 324
 - with black-and-white thermopiles 326
 - with novel black thermopiles 325
 - pyrgeometer 327
 - calibration 343, 344
 - pyrheliometer 320
 - absolute 320
 - calibration 342
 - compensation 322
 - without self-calibration capability 322
 - pyrheliometric scale 313
 - pyrradiometer 328
-
- Q**
-
- quadratic phase coding (QPC) 1124
 - quadrupole mass spectrometer (QMS) 1517
 - quality 50
 - assessment 1559
 - management 50, 52
 - planning 53
 - quality assurance (QA) 50, 553, 809, 1489, 1695
 - quality control (QC) 50, 71, 388, 468, 525, 553, 784, 809, 1233, 1459, 1489, 1559
 - humidity measurements 235
 - radiation measurement 345
 - temperature measurement 203
 - wind measurement 265
 - quantum cascade laser (QCL) 487, 514, 807, 1484
 - absorption spectroscopy (QCLAS) 510
 - quantum efficiency (QE) 703
 - quasi-biennial oscillation (QBO) 11, 1252
-
- R**
-
- radar 1098
 - airborne 1098
 - airborne Doppler 1105
 - attenuation 939
 - calibration 1115
 - depolarization ratio 857
 - dual polarization 1108
 - equation 849
 - history 938
 - history (airborne) 1100
 - linear depolarization ratio 1100
 - maintenance 947
 - mm-range 935
 - polarization 852, 942
 - principles 935, 1102
 - quality control 947, 1116
 - reflectivity factor 849, 936, 938, 1099
 - speed 904
 - system (airborne) 1108
 - system (mm range) 946
 - wavelength 1103
 - Radar System Airborne (RASTA) 1105
 - Radar Wind Profiler (RWP) 901
 - accuracy 921
 - doppler system 912
 - history 903
 - maintenance 924
 - quality control 923
 - scattering 904
 - signal processing 908

- spaced antenna 913
- system 916
- radiance 823
- spectral 826
- radiation 5, 297, 1404
- classification of measurement sites 301
- daily and annual cycles 349
- diffuse solar 298
- global 23, 298
- photosynthetically active (PAR) 300, 1172
- separation of solar and terrestrial 319
- solar 298, 315, 611
- terrestrial 315
- thermal 300, 826
- tilted surface 350
- upward (reflected) 300
- upwelling infrared 300
- radiation measurement
- airborne 1131
- all-in-one solar monitoring system (RaZON+) 333
- history 303
- maintenance 348
- photodiode-based method 318
- principles 300
- thermoelectric method 317
- volumetric method 367
- radiative effect (RE) 1134
- radiative transfer (RT) 1164
- equation (RTE) 141, 827
- for ATOVS (RTTOV) 1156
- radio direction
- and ranging (radar) 664
- finder (RDF) 1259
- Radio-Acoustic Sounding System (RASS) 5, 661, 668, 673, 1283, 1378, 1400
- Doppler RASS 673
- maintenance 677
- quality control 675
- wind profiler RASS (Bragg RASS) 673
- radioactivity 5, 458
- monitoring 458
- parameters 458
- radioactivity measurement
- alpha/beta particulate monitor 464
- gamma dose rate 461
- gamma dose rate probe 463
- gamma-ray spectrometry 462
- gaseous iodine monitor 466
- high-purity germanium (HPGe) detectors 465
- history 459
- maintenance 469
- noble gas 463, 466
- principles 458
- quality control 468
- radio-frequency interference (RFI) 834, 910, 1163
- radiometer 822
- airborne 1134, 1136
- calibration 1139
- maintenance 835
- microwave (MWR) 822, 827, 830, 835
- microwave calibration 833
- multi 332
- rotating shadowband 332
- spaceborne and airborne microwave 1151
- radiometric quantities 299
- radiosonde 1040, 1260
- maintenance 1272
- quality control 1270
- rain gauge 387
- tipping-bucket (TBR) 371, 381
- range imaging (RIM) 916
- range-height indicator (RHI) 752, 767, 867, 1288
- rapid update cycle (RUC) 732
- Rayleigh
- limit 684
- spectrometer (RSP) 780
- Rayleigh–Doppler broadening 745
- readily evaporable water (REW) 1546
- Realtime Online Decision Support System (RODOS) 470
- receiver protectors (RP) 862
- receiver-over-elevation (gear) (ROE) 860
- recirculating ventilation and heating (RVH) 339
- recovery factor 1324
- reference standard
- barometer 291
- thermometer 202
- refractive index 973
- Regents Park and Tower Environmental Experiment (REPARTEE) 1395
- regional
- association (RA) 313
- network 1717
- radiation center (RRC) 341
- Regional Calibration Centre (RCC) 1695
- regression analysis 38
- Relaxed Eddy Accumulation (REA) 1306, 1446, 1506, 1512, 1519
- Hyperbolic (HREA) 1506, 1513
- technique, aircraft-based 1309
- remote
- automatic weather station (RAWS) 1242
- sensing (RS) 178
- remotely piloted aircraft (RPA) 1331
- system (RPAS) 1333
- remote-sensing techniques 23
- renewable energy 1370
- history 1371
- representative elementary volume (REV) 1629
- representativeness
- atmospheric measurement 20
- Research
- Aviation Facility (RAF) 1062
- Scanning Polarimeter (RSP) 1062
- research vessel (RV) 1669
- resistance scheme 1451
- resistor-capacitor (RC) 444
- resonant pressure transducer (RPT) 288
- response time 1355
- Reynolds decomposition 244
- Reynolds-averaged Navier–Stokes (RANS) 385, 1397
- Richardson number
- bulk 1285
- roadway weather information system (RWIS) 1242
- root mean square (RMS) 73, 702, 913, 1041, 1086
- error (RMSE) 382, 922, 1647
- rotating shadowband
- irradiometer (RSI) 332, 1372
- pyranometer (RSP) 332
- radiometer (RSR) 332
- rotational Raman (RR) 722
- rotor-equivalent wind speed (REWS) 1374
- roughness
- length 14, 255, 1399, 1451
- sublayer (RSL) 12, 1393, 1396
- runway visual range (RVR) 402

S

- Saharan Mineral Dust Experiment (SAMUM) 1145
- salinity 5, 129
 - water 1663
- salt solution
 - saturated 235
- sample 36
 - and hold (S&H) 44
- sampler
 - maintenance 592
- sampling
 - active 566, 570
 - diffusion-based 584
 - filter 587
 - inertia-based 571, 582
 - passive 566, 595
 - quality control 590
 - theorem 46
 - thermophoretic 584
 - trace gas 593
- Sand and Dust Storms Warning Advisory and Assessment System (SDS-WAS) 1710
- Satellite
 - Application Facility (SAF) 1163, 1179
 - Pour l’Observation de la Terre (SPOT) 1313, 1554
- scale 9, 12, 1397, 1720
- Scale-crossing Land-surface and Boundary Layer Processes (Scale-X) 1494
- Scanning
 - Imaging Absorption Spectrometer for Atmospheric Cartography (SCIAMACHY) 812, 1318, 1699
 - Mobility Particle Spectrometer (SMPS) 547
- Scanning Multichannel Microwave Radiometer (SMMR) 1155
- scatter meter calibration units (SCU) 421, 422
- Schotanus–Nieuwstadt–DeBruin (SND) correction 1481
- scintillometer 970
 - dual-beam 970
 - extra large-aperture (XLAS) 976
 - large-aperture (LAS) 971, 973, 980, 1402
 - maintenance 987
 - microwave (MWS) 970, 974, 982
 - quality control 985
 - single-beam 970
 - small-aperture 980
 - surface-layer (SLS) 980, 1019, 1402
- scintillometry 972
 - equation 975
 - history 971
 - principle 972
- screen radiation 195, 199
- Sea and Land Surface Temperature Radiometer (SLSTR) 1061, 1178
- sea ice concentration (SIC) 1152
- sea surface
 - salinity (SSS) 1152, 1657
 - temperature (SST) 1152, 1172, 1657
- sea-ice-air (SIA) 110
- secondary organic aerosol (SOA) 490, 557
- semiconductor 193
- semivolatile organic compound (SVOC) 569
- sensor
 - compact 1193
 - low-cost 1207
 - smart 47, 1207
 - smartphone 1210
- Service des Avions Francais Instrumentés pour la Recherche en Environnement (SAFIRE) 1062
- shadow band 337
- shortwave incoming surface radiation (SIS) 1172
- side by side (SbS) 1459
- signal processing
 - analog 44
 - digital 44
- signal-to-noise ratio (SNR) 667, 700, 720, 760, 905, 942, 1005, 1100, 1338
- Simulation of Atmospheric Photochemistry in a large Reaction Chamber (SAPHIR) 55, 496
- simultaneous
 - iterative reconstruction technique (SIRT) 1003, 1010
 - transmit and receive (STAR) 854
- single mode (SM) 613
- single scattering (SS) 696
 - albedo (SSA) 1145
- singular value decomposition (SVD) 912, 1029
- site
 - atmospheric state best estimate (SASBE) 1285
 - humidity 196
 - requirements 57
 - temperature 196
- site consideration
 - humidity 186, 212
 - microwave radiometer 825
 - precipitation 362
 - pressure 274
 - sodar and RASS 662
 - sun photometer 825
 - temperature 186
 - wind 245
- Six thermometer 189
- skewness 936
- skyvane 260
- sky-view factor (SVF) 1407
- slant
 - column density (SCD) 804
 - hydrostatic delay (SHD) 1027
 - total delay (STD) 1026
 - wet delay (SWD) 1027
- slant-integrated water vapor (SIWV) 1027
- Small
 - Cumulus Microphysics Study (SCMS) 1101
 - Unmanned Meteorological Observer (SUMO) 1333
- Snow and Cold Land Process (SCLP) 1180
- snow water equivalent (SWE) 1152
- social media analytic (SMA) 1211
- sodar 25, 661, 670
 - bistatic 672
 - maintenance 677
 - monostatic 672
 - phased-array 671
 - quality control 675
 - with antenna 671
- soil
 - chamber 1604
 - ecological characterization 145
 - gradient 1632
 - heat flux plate 1634, 1643
 - material function 1627
 - measurement 1626
 - measurement history 1630
 - moisture 5, 619
 - moisture distributed temperature sensing (SM-DTS) 1650
 - physical parameter 1626
 - pore size 1628

- potential and force 1631
- profile 1636
- texture 144, 1627
- Soil and Water Assessment Tool (SWAT) 1635
- soil chamber
 - automated 1614
 - flux calculation 1609
 - forced diffusion 1605, 1611
 - history 1606
 - maintenance 1619
 - manual 1612
 - mass flow 1608
 - non-steady-state 1605, 1609
 - quality control 1616
 - steady-state 1605, 1610
- soil measurement
 - gravimetric measurement 1637
 - Guelph permeameter 1641
 - neutron probe 1638
 - pF-meter 1639
 - quality control 1647
 - specific analysis 1644
 - temperature 1643
 - tension infiltrometer 1642
 - time-domain reflectometry 1638
 - water potential 1639
- Soil Moisture
 - Active–Passive (SMAP) 1154, 1180
 - and Ocean Salinity (SMOS) 1057, 1154
 - Atmosphere Coupling Experiment (SMACEX) 1308
- soil moisture
 - variables 1628
 - water retention curve 1629
- soil water 1631, 1632, 1636
 - balance 1537
- solar energy 1374, 1378
- Solar Ultraviolet Imager (SUI) 1060
- solar wavelength
 - phase function 140
- solar zenith angle (SZA) 315, 812
- solid-state
 - modulator (SSM) 860
 - power amplifier (SSPA) 858, 859, 1105
- sonic
 - detection and ranging (sodar) 168, 1400
 - temperature 194
- sonic anemometer 193, 251, 258, 1486
 - classification 264
 - zero-wind chamber calibration 265
- sorbent-impregnated PUF (SIP) 580
- sound
 - attenuation 666
 - backscatter 667
 - navigation and ranging (SONAR) 673
 - propagation 666
 - receiver 1012
 - source 1012
 - speed 126, 185, 193, 1003
- Sounding of Ozone and Water in the Equatorial Region (SOWER) 1267
- Southern
 - Great Plains (SGP) 721, 1307
 - Hemisphere Additional Ozonesondes (SHADOZ) 1273, 1703
- spaced antenna (SA) 913
- Special Sensor
 - Microwave Imager/Sounder (SSMIS) 1154
 - Microwave/Imager (SSM/I) 1154
- Specific Operations Risk Assessment (SORA) 1341
- spectrometer 799
 - airborne 1136
 - differential optical absorption(DOAS) 804, 805
 - Fourier-transform infrared (FTIR) 803, 805
 - laser 804, 807
 - maintenance 811
 - microwave 802, 805, 808
 - quality control 810
- spectroscopy
 - absorption 480
 - cascade laser absorption 520
 - cavity ring-down (CRDS) 514, 517
 - cavity-enhanced (CES) 482
 - difference frequency generation (DFG) laser 515
 - differential absorption 800
 - differential optical absorption (DOAS) 480
 - emission 483
- fluorescence assay by gas expansion (FAGE) 484
- Fourier-transform infrared (FTIR) 481, 511, 515, 518, 800
- history 801
- laser-induced fluorescence (LIF) 484
- off-axis integrated cavity output (OA-ICOS) 514
- photoacoustic 539, 546
- quantum cascade laser absorption (QCLAS) 514, 517
- tunable diode laser 481, 511
- tunable diode laser absorption (TDLAS) 514, 516
- spectrum
 - optical 315
- spike 81
- Spinning Enhanced Visible and Infrared Imager (SEVIRI) 1060, 1173
- sport utility vehicle (SUV) 674
- stable isotope 5
 - history of measurements 512
 - principle of measurement 510
- Stable Local Oscillator (STALO) 862
- stable stratified boundary layer (SBL) 1341
- standard
 - atmosphere 114, 279
 - operating procedure (SOP) 66, 1214, 1709
- Standard Fog Collector (SFC) 1428
- standardization 93
- Standards Developing Organization (SDO) 96
- standing wave ratio (SWR) 452
- statistical tools
 - turbulence 1339
- Steam-jet Aerosol Collector (SJAC) 1455
- stemflow (SF) 1434
- stimulated Brillouin scattering (SBS) 775
- stratosphere 10, 761
- Structure of Turbulent Processes Under Inhomogeneous Surface Conditions (STINHO) 1008
- structure parameter 973
- submillimeter radiometer (SMR) 1162
- sudden stratospheric warming (SSW) 1252

- sun photometer 822, 826, 830
 - calibration 833
 - maintenance 834
 - Sun/sky-radiometer Observation Network (SONET) 822
 - sunshine duration 5, 335
 - Campbell–Stokes recorder 336
 - instrument 335
 - sunshine pyranometer (SPN) 1134
 - Surface
 - Energy Balance Algorithms for Land (SEBAL) 1554
 - Layer Non-Doppler Acoustic Radar (SNODAR) 672
 - Synoptic Observations (SYNOP) 1179
 - Velocity Program (SVP) 169
 - Water and Ocean Topography (SWOT) 1180
 - surface
 - area index (SAI) 1427
 - layer (SL) 12, 13
 - mixed layer (SML) in the ocean 1676
 - velocity program barometer (SVPB) 169
 - surface renewal (SR) 1506, 1521
 - method 1513
 - synergistic remote sensing of cloud (SYRSOC) 1290
 - Synthetic Aperture Radar (SAR) 1055, 1378
 - Altimeter (SRAL) 1061
 - system
 - first-order 41, 42
 - on chip (SOC) 1202
 - second-order 42
-
- T**
- table-driven code form (TDCF) 1268
 - tapered element oscillating microbalance (TEOM) 549
 - technique
 - in-situ 5
 - remote sensing 5
 - Technology for Enabling Awareness (TEA) 1202
 - Teflon filter
 - for ion chromatographic analysis (T(IC)) 580
 - for x-ray fluorescence analysis (T(XRF)) 580
 - Television Infrared Observation Satellite (TIROS) 646, 1174
 - Operational System (TOS) 1174
 - temperature 5, 23, 611, 1249, 1283, 1400
 - acoustic virtual 1000
 - boiling 129
 - brightness 823, 1152, 1156
 - canopy 5
 - definition 184
 - dewpoint 123, 211
 - equivalent potential 185
 - frostpoint 124, 211
 - measurement, influence 196
 - platinum resistance 1255
 - potential 185
 - principle of measurement 40
 - radiation 352
 - Raman lidar (TRL) 719
 - rotational Raman lidar (TRL) 721
 - scale 189
 - soil 5
 - sonic 186
 - surface 1172
 - virtual 119, 185, 211, 279, 721, 1476
 - water 1662
 - wind-chill 186
 - tensiometer 1639
 - tension
 - soil water 143
 - Terrestrial Environmental Observatories (TERENO) 1581
 - test
 - reference year (TRY) 1411
 - signal generator (TSG) 867
 - tethered sonde 1264
 - Thematic Mapper (TM) 1313
 - thermal desorption laser-induced fluorescence (TDLIF) 490
 - thermal infrared (TIR) 1176
 - sensor (TIRS) 1059
 - thermistor 192, 1255, 1662, 1667
 - thermocouple 193
 - thermodynamic temperature scale (TTS) 109
 - thermograph 198
 - thermometer
 - bimetallic 190, 198
 - comparison 201
 - dry-bulb 225
 - history 187
 - liquid-in-glass 190, 196
 - maintenance 203
 - maximum 197
 - measuring principle 186
 - minimum 197
 - platinum resistance 191, 1662, 1667
 - resistance 190, 198
 - soil 197
 - specification 201
 - thin-wire 191, 1337
 - wet-bulb 225
 - thermosalinograph (TSG) 1658
 - thin-film transistor (TFT) 1360
 - thunderstorm 431
 - time
 - definition 146
 - equation 146
 - universal (UT) 146
 - time-dependent stochastic inversion (TDSI) 1010
 - time-domain reflectometry (TDR) 5, 1638
 - Time-Resolved Observations of Precipitation structure and storm Intensity with a Constellation of Smallsats (TROPICS) 1167
 - tomography 999
 - acoustic 1002
 - acoustic travel-time 1000
 - GNSS network 1034
 - GNSS processing 1035
 - inverse reconstruction 1010, 1028
 - quality control 1015, 1040
 - scalability 1014
 - water vapor 1025
 - Tool to Estimate
 - Sea Surface Emissivity from Microwave to Submillimeter Waves (TESSEM²) 1153
 - the Land Surface Emissivity from the Microwaves to the Millimeter Waves (TELSEM²) 1157
 - top of the atmosphere (TOA) 315, 823
 - tornado vortex signature (TVS) 843
 - Total
 - Carbon Column Observing Network (TCCON) 1699
 - Direct and Diffuse Radiometer (TDDR) 1133
 - total
 - amount of water that can be evaporated (TEW) 1547

- least squares estimation (TLSE) 61
- scattering (TS) 696
- solar irradiance (TSI) 299
- total suspended
 - matter (TSP) 591
 - particles (TSP) 1220
- Towards Operational Ground Based Profiling With Ceilometers, Doppler Lidars and Microwave Radiometers for Improving Weather Forecasts (TOPROF) 837
- tower
 - small 160
 - tall 164, 178
- trace gas 5
 - analyzer (TGA) 516
 - extractor (TREX) 521
 - flux 1487, 1506, 1587
 - sampling 570, 576
- trace substance 566
 - sampling 566
- traditional alphanumeric code (TAC) 1268
- Transect Measurement (TRAM) 1354
- transient luminous event (TLE) 453
- transmission electron microscope (TEM) 586
- transmissometer 407, 414
- transmittance 417
- transmitter 861
- transparency
 - atmospheric 1153
- transverse-excited, atmospheric pressure (TEA) 763
- travel time
 - acoustic 1004
 - recording 1012
 - signal from the GNSS satellite 1026
- traveling-wave tube (TWT) 858, 859, 1105
 - amplifier (TWTA) 946
- Triple-frequency and Polarimetric Radar Experiment (TRIPEx) 945
- Tropical
 - Composition, Cloud and Climate Coupling (TC⁴) 1141
 - Rainfall Measuring Mission (TRMM) 1102, 1154

- Rainfall Measuring Mission (TRMM) Microwave Imager (TMI) 1154
- troposphere 11
- Tropospheric Emission Spectrometer (TES) 1058
- TROPOspheric Monitoring Instrument (TROPOMI) 812, 1055
- true local time (TLT) 146
- TSI radiometer facility (TRF) 315
- Tunable
 - Diode Laser Absorption Spectroscopy (TDLAS) 510, 516, 802
 - Optical Profiler for Aerosol and Ozone (TOPAZ) 1085
- tunable diode laser (TDL) 1484
 - spectroscope (TDLS) 487
 - spectroscopy (TDLS) 475
- turbulence 9
 - spectrum 12, 974
 - statistical uncertainty 9, 1340
 - vehicle-induced 176
- turbulent kinetic energy (TKE) 6, 760, 1290, 1332
- two source energy balance (TSEB) 1554
- typical meteorological year (TMY) 1411

U

- ultra low frequency (ULF) 436
- ultrafine particle (UFP) 568
- ultra-high frequency (UHF) 664
- uniform resource locator (URL) 108, 1458
- uninterruptible power supply (UPS) 172, 867, 961
- United Nations Environment Programme (UNEP) 1689
- universal
 - thermal climate index (UTCI) 186
- Universal Serial Bus (USB) 47, 1612
- unmanned
 - aircraft (UA) 1333
 - autonomous (UA) 1400
- unmanned aerial vehicle (UAV) 1331

- unmanned aircraft system (UAS) 453, 730, 791, 1018, 1260, 1283, 1311, 1331, 1352, 1561
 - autopilot 1336
 - fixed-wing aircraft 1335
 - flight strategy 1342
 - history 1332
 - multicopter 1334
 - small (sUAS) 1333
 - terminology 1333
- Upper Atmospheric Research Satellite (UARS) 1155
- upper troposphere lower stratosphere (UTLS) 1090, 1701
- urban
 - boundary layer (UBL) 1393
 - canopy layer (UCL) 1393, 1396
 - heat island (UHI) 1393
- urban measurement 1392
 - history 1394
 - quality control 1408
- UV radiation sensor 334

V

- van Genuchten–Mualem model 146, 1645
- Variable Conditions Pyrhemometer Comparison (VCPC) 323
- vegetation index (VI) 5, 1172, 1179
- velocity azimuth display (VAD) 767
- vertical
 - cavity surface emitting laser (VCSEL) 807
 - columns density (VCD) 812
 - reflectivity profile (VRP) 881
 - takeoff and landing (VTOL) 1336
 - wind variance (VWV) 670
- vertically integrated ice (VII) 890
- vertically integrated liquid (VIL) 890
 - density (VILD) 890
- video plankton recorder (VPR) 1669
- Vienna
 - Pee Dee Belemnite (VPDB) 510
 - Standard Mean Ocean Water (VSMOW) 510
- viscosity
 - dynamic 128, 143
 - kinematic 128

- visibility 401, 646
 - parameter 402
 - standard (Normsichtweite) 403
 - visibility measurement
 - air, street, and sea traffic 423
 - determining the scatter coefficient 409
 - forward scatter meter 410
 - history 403
 - maintenance 421
 - quality control 418
 - scattered light sensor 415
 - setup rules 418
 - uncertainty 419
 - Visible Infrared Imaging Radiometer Suite (VIIRS) 1060, 1178, 1554
 - visual
 - line of sight (VLOS) 1342
 - observation 645
 - range (VIS) 539
 - visual observation
 - cloud 650
 - code 647
 - history 646
 - state of the ground 654
 - visibility 653
 - weather phenomena 647
 - wind direction 650
 - wind speed 650
 - volatile organic compound (VOC) 488, 569, 1211, 1306, 1507
 - volatility tandem differential mobility analyzer (VTDMA) 550
 - voltage standing wave ratio (VSWR) 860
 - volume coverage pattern (VCP) 873
 - volunteered geographic information (VGI) 1200
-
- W**
- water content of soil (SWC) 1605
 - water measurement
 - history 1660
 - water properties 1657
 - water properties measurement
 - maintenance 1675
 - quality control 1674
 - water retention curve (WRC) 143, 1627
 - water use efficiency (WUE) 1586
 - water vapor
 - and temperature Raman lidar (WVTRL) 720
 - differential absorption lidar (DIAL) 741
 - differential absorption lidar (WVDIAL) 723, 750
 - integrated 1031
 - integrated (IWV) 732, 1026, 1289
 - mass density 118
 - mole fraction 219
 - radiometer (WVR) 1040
 - Raman lidar (WVRL) 719
 - water vapor (GNSS) tomography 1029
 - water vapor pressure 185
 - deficit (VPD) 1593
 - saturation 116, 210
 - Water Vapour Lidar Experiment in Space (WALES) 1085, 1110
 - water-soluble organic
 - carbon (WSOC) 579
 - gas (WSOG) 579
 - wave height 5, 1663
 - wavelength modulation (WMS) 807
 - wavelet covariance 1309
 - wave-rider buoy 1669
 - weather
 - chart 293
 - condition 646
 - research and forecasting (WRF) 732, 1378
 - Weather Observation Website (WOW) 1189
 - weather radar 842
 - antenna 860
 - automated algorithm 888
 - beam propagation 847
 - calibration 871
 - correction 876
 - error 874
 - history 843
 - interpretation 886
 - maintenance 882
 - multiparameter approach 853
 - network 868
 - observables 854
 - phase measurement 851
 - presentation 883
 - product 883
 - pulse radar 846
 - quality control 871
 - receiver 862
 - reflectivity 847
 - regulation 867
 - scattering 847
 - signal processing 864
 - system 858
 - technical parameter 842
 - transmitter 859
- weather station 1187, 1207
 - compact system 1193
 - different types 1191, 1193
 - recommendation 1190
 - single-sensor 1192
- Webb–Pearman–Leuning (WPL) correction 1481, 1508
- weighing gauge (WG) 371
- weighted
 - least squares estimation (WLSE) 61
 - permutation entropy (WPE) 1644
- Wellen Radar (WERA) 955
- wet annular denuder (WAD) 579
- Wide Field Camera (WFC) 1058
- wilting point (WP) 145, 1628
 - water capacity (WWC) 1628
- wind 5, 23, 1249, 1283, 1401
 - classification of measurement sites 255
 - direction 244, 646, 662, 760, 902
 - energy 1373
 - geostrophic 267
 - gust 244, 269
 - speed 244, 611, 646, 662, 760, 902
 - tunnel 263
 - uniform 891
 - vane 253, 257
 - variance of the vertical component 662
 - vector 244, 902, 1000
 - velocity 244
- wind measurement
 - aircraft-based 1311
 - anemometer 259
 - signal generator 259
 - technique 245
- Wind Profiler Demonstration Network (WPDN) 904
- Window Probability Matching Method (WPMM) 889
- wind-temperature radar (WTR) 673
- windway 244
- wireless integrated network sensors (WINS) 1202

Wireless Local Area Network (WLAN) [47](#)
 wireless sensor networks (WSN) [1201](#)
 working group (WG) [110](#)
 World
 – Calibration Centre (WCC) [1695](#)
 – Climate Research Programme (WCRP) [169](#), [303](#), [1688](#)
 – Ocean Circulation Experiment (WOCE) [169](#), [1660](#)
 – Ozone and Ultraviolet Radiation Data Centre (WOUDC) [1273](#), [1704](#)

– Radiometric Reference (WRR) [314](#)
 – Weather Research Programme (WWRP) [1709](#)
 World Meteorological Organization (WMO) [9](#), [1236](#), [1688](#)
 – Integrated Global Observation System (WIS/WIGOS) [1709](#)
 – Integrated Global Observing System (WIGOS) [1698](#)
 – Solid Precipitation Intercomparison Experiment (WMO–SPICE) [366](#)
 Wyoming Air Resource Monitoring System (WARMS) [1701](#)

Y

yttrium aluminum garnet (YAG) [497](#)

Z

zenith
 – hydrostatic delay (ZHD) [1031](#)
 – total delay (ZTD) [1026](#)
 – wet delay (ZWD) [1031](#)
 zero-plane displacement [1399](#), [1451](#)